Interlayer grafting of glycidol (2,3-epoxy-1-propanol) on kaolinite

S. Letaief and C. Detellier

Abstract: An organic–inorganic nanohybrid material was prepared by grafting glycidol (2,3-epoxy-1-propanol) on the interlayer aluminol groups of kaolinite (K) using DMSO–K precursor as a starting material. The results of the physicochemical characterization of the synthesized materials (XRD, FTIR, DTA–TG, ^{13}C and ^{29}Si CP/MAS NMR) confirm that the grafting reaction of glycidol involved the opening of the oxirane ring. The resulting nanohybrid material is similar to the one obtained by the interlayer grafting of glycerol (M. Janek, K. Emmerich, S. Heissler, and R. Nüesch. Chem. Mater. **19**, 684, (2007)). Approximately, one glycidol moiety is grafted on each structural unit of kaolinite to afford a material with the chemical composition $Al_2Si_2O_5(OH)_4[C_3H_6O_2]_{0.9}$.

Key words: clays, clay minerals, kaolinite, intercalation, grafting, nanohybrid materials, DMSO, glycidol, glycerol, oxirane.

Résumé : Un matériau nanohybride organo–inorganique a été obtenu par greffage du glycidol (2,3-époxy-1-propanol) sur les groupements aluminol interfoliaires de la kaolinite (K), à partir des précurseurs DMSO–K. Les résultats de la caractérisation physico-chimique des matériaux synthétisés (DRX, IRTF, ATD–TG, RMN PC/RAM du ^{13}C et du ^{29}Si) confirment que la réaction de greffage du glycidol met en jeu l'ouverture de l'anneau oxirane. Le matériau nanohybride résultant est semblable à celui obtenu par le greffage interfoliaire du glycerol (M. Janek, K. Emmerich, S. Heissler, and R. Nüesch. Chem. Mater. **19**, 684, (2007)). Approximativement une unité de glycidol est greffée sur chaque unité structurale de la kaolinite pour donner un matériau de composition chimique $Al_2Si_2O_5(OH)_4[C_3H_6O_2]_{0.9}$.

Mots-clés : argiles, minéraux argileux, kaolinite, intercalation, greffage, matériaux nanohybrides, DMSO, glycidol, glycérol, oxirane.

Introduction

Recently, the preparation and the characterization of new organo–inorgano nanohybrid materials have received a lot of attention because of the combined benefits of the structural and textural properties of the inorganic matrix, joined to specific functionalities of the guest organic entities (1). These nanocomposite materials can be applied in several fields, such as catalysis, separation, isolation, biomaterials, and so forth. Due to their low price, large availability, and their environmental benefit, clay minerals are good candidates to be used as the inorganic component of nanohybrid materials (2).

Kaolinite (K) is one of the most common minerals on Earth. It is a 1:1 phyllosilicate, characterized by a dioctahedral structure composed of silicate sheets (Si_2O_5) bonded to aluminum oxide/hydroxide layers $Al_2(OH)_4$ with the global chemical composition $Al_2Si_2O_5(OH)_4$ (3). Kaolinite does not swell when exposed to water. It is mainly used in the ceramics industry for the production of bricks and pottery and also in the paper industry. Kaolinite can be directly intercalated by selected dipolar molecules, such as dimethylsulfoxide (DMSO), *N*-methylformamide (NMF) or urea, or by salts like potassium acetate. These intercalates were successfully used as precursors for further intercalation reactions of other organic molecules or polymers (4).

To achieve successfully the interlayer modification of kaolinite and to obtain a well-ordered nanohybrid material in which the guest organic entity is located between two adjacent individual aluminosilicate layers, several factors must be taken into account. The size and the physical properties of the organic molecules (melting point, boiling point, charge, and solubility) can give a good indication on the success of the interlayer structural modification. The nature of the starting intercalates, usually DMSO–K, Urea–K, NMF–K or K^+OAc^-–K can also be crucial for the success of the interlayer modification of kaolinite.

A variety of organic molecules have been grafted so far on the interlayer surfaces of kaolinite by making a covalent link with the aluminol groups of the internal surfaces (5). In view of future design of more sophisticated nanohybrid materials based on kaolinite, it is highly desirable to graft molecular entities with pending functionalities. The grafting of triethanolamine, with an available amino group for potential subsequent functionalizations was recently reported (5*m*).

In this work, the first grafting of an oxirane on the interlayer surfaces of kaolinite is reported, leading to available hydroxyl functions in the confined interlayer spaces (Scheme 1).

Received 28 August 2007. Accepted 25 October 2007. Published on the NRC Research Press Web site at canjchem.nrc.ca on 22 November 2007.

S. Letaief and C. Detellier.[1] Centre for Catalysis Research and Innovation and Department of Chemistry, University of Ottawa, 10 Marie Curie, Ottawa, ON K1N 6N5, Canada.

[1]Corresponding author (e-mail: dete@uottawa.ca).

 doi:10.1139/V07-130 © 2007 NRC Canada

Scheme 1. Process of intercalation and grafting of kaolinite by consecutive treatments with DMSO first, then glycidol.

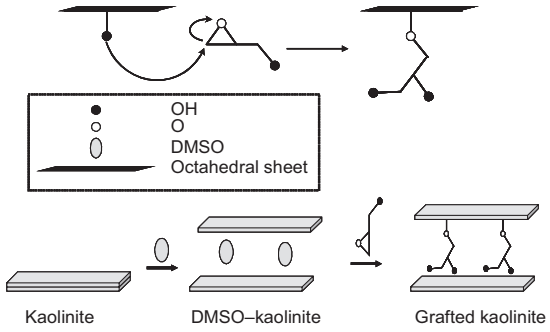

Experimental

Materials

Well-crystallized kaolinite (KGa-1b; Georgia) was obtained from the Source Clay Minerals Repository, University of Missouri. It was purified using standard sedimentation techniques and the <2 μm fraction was used in the experiments. DMSO and Glycidol (Aldrich; 96%) were used as received.

Sample preparation

DMSO–kaolinite intercalate (DMSO–K)

10 g of kaolinite were added to a mixture of 60 mL of DMSO and 5 mL of H_2O. The suspension was maintained under magnetic stirring for 10 d at 80 °C. The mixture was then allowed to stir for 5 d at room temperature. The resulting material was recuperated after two series of washing–centrifugation using dioxane (2 × 50 mL) first, then isopropanol (2 × 50 mL). The product was finally dried at 50 °C.

Glycidol–kaolinite grafting (Gly–K)

DMSO–K was used as starting material for the grafting of glycidol in the interlayer space of kaolinite. The reaction of Glycidol with DMSO–K was performed at 180 °C for 2 h under nitrogen. In a typical set of experiments, 0.5 g of DMSO–K was dispersed in 2 g of glycidol. The temperature of the mixture was then increased slowly from room temperature to 180 °C and maintained stable for 2 h. A few minutes after reaching 180 °C, a change in the color of solution (from white to sandy) is observed because of the removal and decomposition of DMSO. The resulting nanohybrid materials were recuperated after three series of centrifugation following washing with isopropanol (3 × 50 mL). They were dried at 60 °C overnight. Finally, to be sure that the compound was successfully grafted, the material was suspended in water and stirred for 72 h. It was washed, filtered, and ground for further characterization.

Characterization

XRD patterns were obtained using a Philips PW 3710 instrument equipped with Ni-filtered and Cu Kα radiation (λ = 0.15418 nm) operating at 45 kV and 40 mA, scanning from 2–70°.

Fourier transform infrared spectroscopy (FTIR) was carried out on the solid sample with a Mattson 3000 FTIR spectrometer by averaging 128 scans with a resolution of 4 cm^{-1}. The spectra were recorded using KBr pellets. Before recording the spectrum, a flow of hot air was circulated in the chamber containing the pellet during 30 min to remove water molecules adsorbed physically on the sample.

Differential thermal analysis (DTA) and thermogravimetric analysis (TGA) were recorded on a SDT 2960 Simultaneous DSC–TGA instrument under N_2 flow (100 mL min^{-1}) with a heating rate of 10 °C min^{-1}.

Solid-state ^{13}C CP/MAS NMR and ^{29}Si spectra were collected on a Bruker AVANCE 500 NMR spectrometer operating at 125.7 and at 99.35 MHz, respectively. The ^{13}C chemical shifts were referenced to TMS at 0 ppm using the high-frequency signal of adamantane at 38.4 ppm as a secondary standard. The ^{29}Si chemical shifts were referenced to TMS at 0 ppm using the high-frequency signal of tetrakis(trimethylsilyl) silane at 29.9 ppm as a secondary standard.

The ^{1}H and ^{13}C NMR spectra in solution were recorded on a Bruker 400 MHz spectrometer.

Elemental analysis (CHN) was performed at Guelph Chemical Laboratories Ltd.

Results and discussion

XRD patterns of kaolinite, DMSO–K intercalate, and Gly–K grafted nanohybrid are shown in Fig. 1. The basal spacings of kaolinite and DMSO–K are 0.71 nm and 1.10 nm, respectively. The intercalation ratio of DMSO–K is close to 98%. It is obtained as an approximation, by the ratio of the intensities of the 001 diffraction peaks of kaolinite and DMSO–K. After the treatment with glycidol, the XRD patterns present well-ordered reflections indicating that the structure of kaolinite was not affected or altered during the intercalation process. The intercalate resists hydrolysis, since it was recuperated without modification after treatment with water during 72 h. This confirms that glycidol is grafted to the interlayer aluminol groups (5*m*). The d_{001} spacing is 1.14 nm, very close to the one reported by Janek et al. (5*l*) (1.10 nm) when glycerol was grafted on the interlayer surfaces of kaolinite, using KOAc–kao as starting material (5*l*). The similarity of the d_{001} spacings results from the formation of very similar nanohybrid materials in the two cases. The ^{13}C CP/MAS NMR spectra show that glycidol reacts through opening the oxirane ring, resulting in the grafting of glycerol moieties (see later).

^{13}C CP/MAS NMR spectra of DMSO–K, Gly–K, glycidol, and glycerol are shown in Fig. 2. ^{13}C CP/MAS NMR constitutes a powerful technique to determine the structure of the organic host grafted into kaolinite. In the case of DMSO–K, the two signals at 43.9 and 42.8 ppm correspond to a dissymmetrical structuration of DMSO in the interlayer space of kaolinite. These two peaks disappear completely after treatment with glycidol, indicating a complete displacement of DMSO from the interlayer spaces of kaolinite. The NMR spectrum of Gly–K is characterized by two broad peaks at 72.0 and 65.1 ppm, which is quite different from the spectrum of glycidol. The NMR spectrum of glycidol is composed of three peaks at 62.3, 52.6, and 44.4 ppm. They correspond to the carbon bearing the hydroxyl group and to the carbons of the oxirane ring, re-

© 2007 NRC Canada

Fig. 1. XRD patterns of pure kaolinite, DMSO–K intercalate, and Gly–K grafted nanohybrid obtained from DMSO–K.

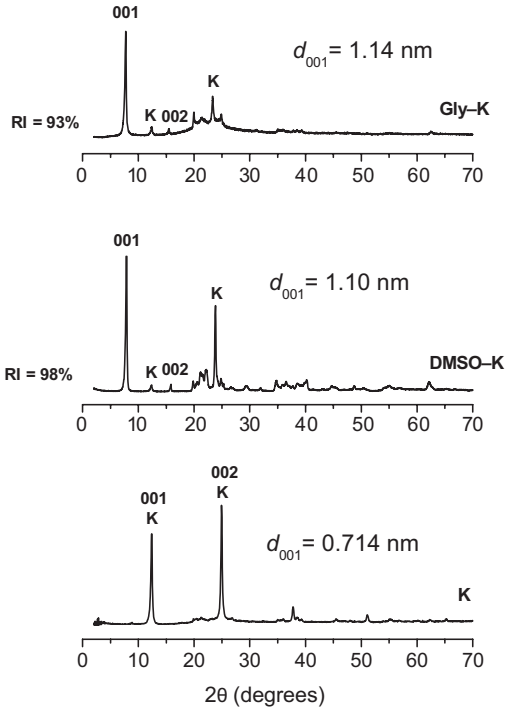

Fig. 2. ^{13}C NMR spectra DMSO–K intercalate (solid state), Glycidol (solution), Gly–K grafted nanohybrid obtained from DMSO–K (solid state), and Glycerol (solution).

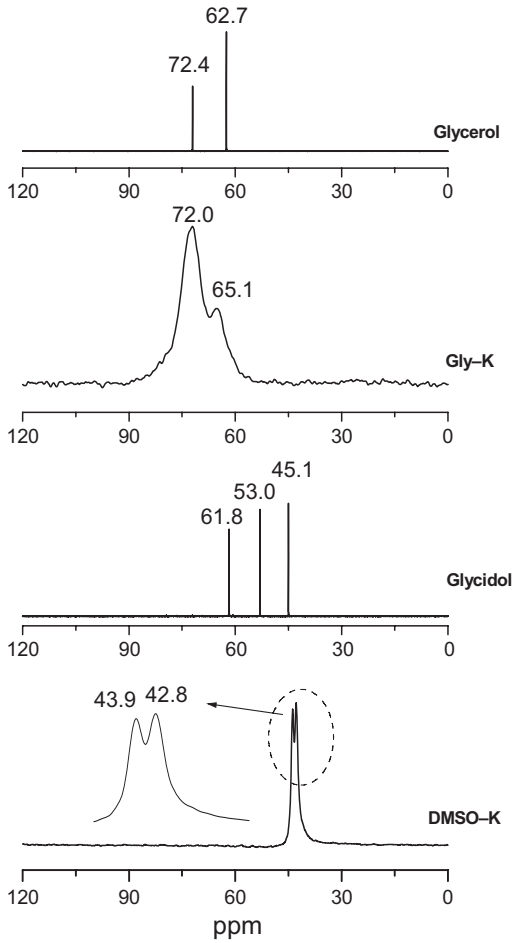

spectively. The ^{13}C CP/MAS NMR spectrum of Gly–K (two broad peaks at 65.1 and 72.0 ppm) is very similar to the one of glycerol, characterized by two peaks at 62.7 and 72.4 ppm (Fig. 2). Since the chemical shift of the Al–O–^{13}C group is close to the chemical shift of the H–O–^{13}C group (4*m*), and given the chemical shift dispersion expected in this kind of material, the observed ^{13}C CP/MAS NMR spectrum of Gly–K can be attributed to a grafted glycerol moiety. During the grafting process, glycidol undergoes a ring-opening reaction. Consequently, the grafting of glycidol or of glycerol (5*l*) leads to the same nanohybrid material.

Thermogravimetric traces (TG–DTG) of kaolinite, DMSO–K, and Gly–K are presented in Fig. 3. In the case of kaolinite, only one weight loss at 510 °C is observed, corresponding to the dehydroxylation. The experimental weight loss is 14%, very close to the theoretical value corresponding to the amount of removed water during the structural transformation of kaolinite $Al_2Si_2O_5(OH)_4$ to metakaolinite $Al_2Si_2O_7$. Upon intercalation of DMSO, three weight losses are observed. The first one, at a low temperature (59 °C), corresponds to the removal of water physically adsorbed on the external surfaces. The second one, around 180 °C, corresponds to the de-intercalation and decomposition of DMSO. Finally, the third one, which occurs at a temperature close to the case of kaolinite, corresponds to the dehydroxylation of the layers.

The dehydroxylation takes place in the same range of temperatures because the internal layer structure of the clay is not modified. After displacement of DMSO, the decomposition must be similar to the one observed for the pristine clay. In the case of the grafted nanohybrid, three weight losses are observed. The first one, at low temperature, corresponds also to the removal of water physically adsorbed. The second one, at 372 °C, corresponds to the decomposition of the organic entities, and the last one, which takes place at 480 °C, is due to the removal of the remaining organic molecules and to the dehydroxylation of the layer. The removal of the organic material, with a maximum at 372 °C, is also indicative of the grafting of the organic units (5*m*, 5*l*). Obviously, the TG behavior is quite different from the one observed in cases of intercalates, such as DMSO–K, since it happens at much higher temperatures. It is generally observed that, in the case of grafting on the interlayer surfaces, the dehydroxylation of kaolinite occurs at temperatures lower than what is observed in the case of intercalation (5*m*).

The TGA data give a direct measure of the amount of organic moieties into Gly–K; it is 31.5%. On the basis of this percentage, and of the weight loss of water to form metakaolinite $Al_2O_3{\cdot}2SiO_2$, the TGA data allow the calculation of the formula unit of Gly–K as $Al_2Si_2O_5(OH)_4[C_3H_6O_2]_{0.89}$. This stoichiometry is in fair agreement with the one obtained independently from elemental analysis (C: 9.29%; H: 2.76%), where a slightly lower stoichiometry was obtained: $Al_2Si_2O_5(OH)_4[C_3H_6O_2]_{0.82}$. The difference can be attributed mainly to the difficulty in combusting all the carbonaceous material during the elemental analysis, as was observed be-

© 2007 NRC Canada

Fig. 3. TG–DTG patterns of kaolinite (K), kaolinite intercalated with DMSO (DMSO–K), and kaolinite grafted with glycidol (Gly–K).

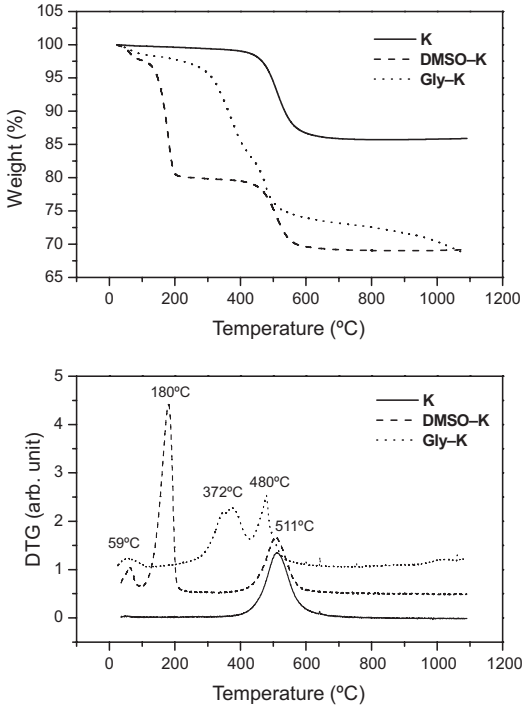

fore for other thermally robust organokaolinite derivatives (5*c*). Carbon–mineral nanocomposites are formed during the thermolysis process, by the trapping of carbonaceous materials in the interlayer spaces of kaolinite. This is indicated by a continuous slight decrease of weight up to 1100 °C, above the transition temperature from metakaolinite to mullite, normally observed near 1000°.

The ^{29}Si CP/MAS NMR spectra of kaolinite, DMSO–K, and Gly–K are shown in Fig. 4. In the case of kaolinite, two well-separated signals of equal intensities are observed, as expected, at –91.5 and –90.9 ppm (6). In the case of DMSO–K, the signal is shifted to lower frequencies, at –92.7 ppm, accounting for the keying of one of the DMSO methyl groups in the siloxane rings of the tetrahedral sheets (6). In contrast, the ^{29}Si CP/MAS NMR spectrum of the Gly–K material displays a relatively broad envelope around –91.6 ppm, with a dispersion of chemical shifts in the range of the kaolinite chemical shifts. This is an indication that the silicate layer is less affected by the presence of the glycerol moiety than it is by the strong interactions with DMSO. The local environments of the ^{29}Si nuclei are relatively similar in Gly–K and in kaolinite, since the structural stress imposed by the DMSO methyl group keyed into the siloxane ring, disappears when DMSO is replaced by the glycerol group grafted on the opposing aluminol surface.

FTIR spectra corresponding to the OH-stretching region of kaolinite, DMSO–K, and Gly–K are presented in Fig. 5. The band observed in the IR spectrum of kaolinite at 3621 cm^{-1} corresponds to the stretching vibrations of the internal hydroxyl group, while those at 3695, 3670, and 3653 cm^{-1} correspond to interlayer hydroxyl stretching modes (7). The intensity as well as the position of these

Fig. 4. ^{29}Si MAS NMR spectra of untreated kaolinite (K), kaolinite intercalated with DMSO (DMSO–K), and kaolinite grafted with glycidol (Gly–K).

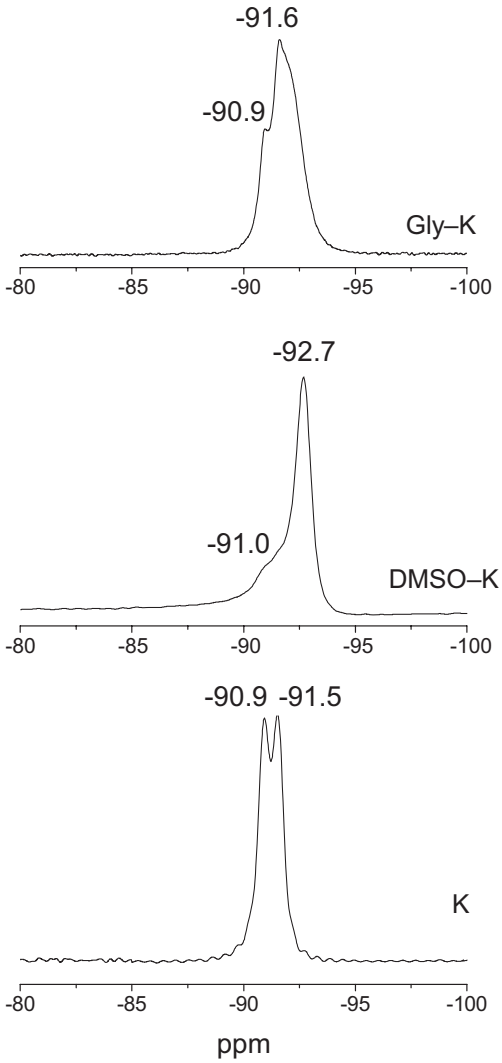

bands is usually sensitive to intercalation of organic molecules. Upon treatment with DMSO, the 3670 and 3653 cm^{-1} peaks disappear completely, and new peaks appear at 3664, 3538, and 3503 cm^{-1}. The band at 3620 cm^{-1} remains unperturbed, which confirms its attribution to the stretching of the inner hydroxyls. The two bands at 3538 and 3503 cm^{-1} can be attributed to the perturbed inner-surface hydroxyl groups, hydrogen bonded to the DMSO (8). After displacement of DMSO, we note the disappearance of the bands at 3664, 3538, and 3503 cm^{-1} and the appearance of new broad bands between 3660 and 3630 cm^{-1}. The broadness of this band could be plausibly due to the different positions of the hydroxyl groups. The IR spectrum of Gly–K shows also the bands at 2928 cm^{-1} ($\nu_{as}CH_2$) and 2881 cm^{-1} (ν_sCH_2), confirming the presence of the organic entity in the grafted material.

In conclusion, a functionalized nanohybrid material was prepared by the ring-opening reaction of an oxirane, glycidol, with the aluminol groups covering the interlayer surfaces of kaolinite. The resulting nanohybrid material,

© 2007 NRC Canada

Fig. 5. FTIR spectra (4000–2600 cm^{-1}) of untreated kaolinite (K), kaolinite intercalated with DMSO (DMSO–K), and kaolinite grafted with glycidol (Gly–K).

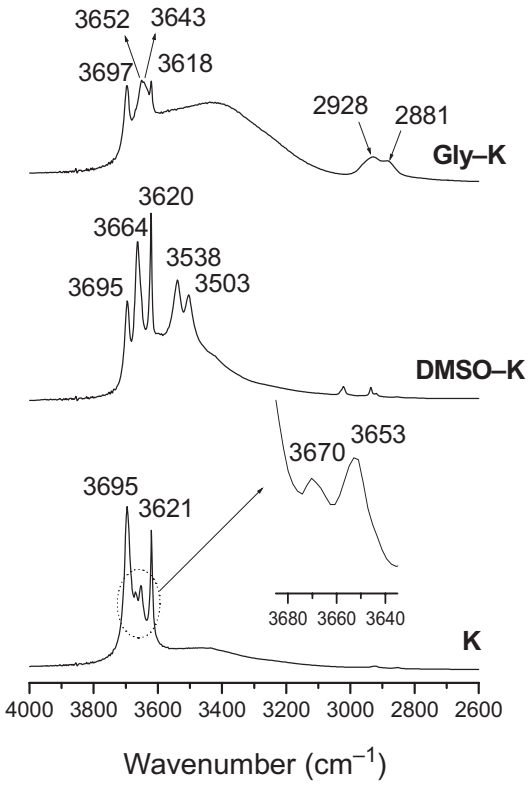

similar to the material obtained by direct grafting of glycerol, is well-structured, with two hydroxyl groups available for further reactions in the confined, dissymetric, interlayer space of kaolinite.

Acknowledgements

This work was financially supported by a Discovery Grant of the Natural Sciences and Engineering Research Council of Canada (NSERC). Dr Glenn A. Facey is thanked for recording the NMR spectra.

References

1. (*a*) T.J. Pinnavaia and G.W. Beall. *Editors*. Polymer–clay nanocomposites. John Wiley and Sons, West Sussex, UK. 2000; (*b*) M. Alexandre and P. Dubois. Mater. Sci. Eng. R. **28**, 1 (2000); (*c*) S.S. Ray and M. Okamoto. Prog. Polym. Sci. **28**, 1539 (2003); (*d*) W. Kuang, G.A. Facey, C. Detellier, B. Casal, J.M. Serratosa, and E. Ruiz-Hitzky. Chem. Mater. **26**, 4956 (2003); (*e*) P. Gómez-Romero and C. Sanchez. *Editors*. Functional hybrid materials. Wiley-VCH, Weinheim, Germany. 2004; (*f*) B.H. Tan and H. Tagaya. Chem. Lett. **34**, 1402, (2005); (*g*) G. Vilaca, B. Jousseaume, C. Mahieux, C. Belin, H. Cachet, M.C. Bernard, V. Vivier, and T. Toupance. Adv. Mater. **18**, 1073 (2006); (*h*) J. Minet, S. Abramson, B. Bresson, A. Franceschini, H. Van Damme, and N. Lequeux. J. Mater. Chem. **16**, 1379 (2006); (*i*) E. Ruiz-Hitzky and A. Van Meerbeeck. *In* Handbook of clay science. *Edited by* F. Bergaya, B.K.G. Theng, and G. Lagaly. Elsevier, Amsterdam, The Netherlands. 2006. Chap. 10.3, p. 583; (*j*) J. Li, S. Tang, L. Lu, and H.C. Zeng. J. Am. Chem. Soc. **129**, 9401 (2007).
2. (*a*) H. Lao, S. Latieule, and C. Detellier. Chem. Mater. **3**, 1009 (1991); (*b*) P. Aranda and E. Ruiz-Hitzky. Chem. Mater. **4**, 1395 (1992); (*c*) L. Mercier, G.A. Facey, and C. Detellier. J. Chem. Soc. Chem. Commun. **18**, 2111 (1994); (*d*) J.J. Tunney and C. Detellier. J. Mater. Chem. **6**, 1679 (1996); (*e*) M.-J. Binette and C. Detellier. Can. J. Chem. **80**, 1708 (2002); (*f*) S. Letaief, B. Casal, P. Aranda, M.A. Martin-Luengo, and E. Ruiz-Hitzky. Appl. Clay Sci. **22**, 263 (2003); (*g*) J.H. Chang, Y.U. An, S.C. Ryul, and E.P. Giannelis. Polym. Bull. **51**, 69 (2003); (*h*) E. Ruiz-Hitzky, P. Aranda, and J.M. Serratosa. Clay-organic interactions: Organoclay complexes and polymer-clay nanocomposites. *In* Handbook of layered materials. *Edited by* S.M. Auerbach, K.A. Carrado, and P.K. Dutta. Marcel Dekker, Inc., New York. 2004; (*i*) S. Letaief, P. Aranda, and E. Ruiz-Hitzky. Appl. Clay Sci. **28**, 183 (2005); (*j*) M. Darder, A.I. Ruiz, P. Aranda, H. Van Damme, and E. Ruiz-Hitzky. Curr. Nanosci. **2**, 23 (2006); (*k*) F. Bergaya and G. Lagaly. *In* Clay-based polymer nanocomposites. *Edited by* K. Carrado and F. Bergaya. CMS Workshop Lectures. Vol. 15. The Clay Minerals Society, Chantilly. 2007. Chap. 3, pp. 61–96.
3. (*a*) A.C.D. Newman and G. Brown. Chemistry of clays and clay minerals. *Edited by* A.C.D. Newman. Longman Scientific and Technical, Mineralogical Society, London. Monograph No. 6. 1987. p. 1; (*b*) S.W. Bailey. *Editor.* Hydrous phyllosilicates. American Mineralogical Society, Washington, DC. 1988; (*c*) F. Bergaya, B.K.G. Theng, and G. Lagaly. *Editors.* Handbook of clay science. Elsevier. Vol. 1. 2006.
4. (*a*) D.M.C. McEwan. Nature (London), **157**, 159 (1946); (*b*) K. Wada. Amer. Min. **46**, 78 (1961); (*c*) B.K.G. Theng. The chemistry of clay-organo reactions. Adam Hilger, London. 1974; (*d*) D.L. Bish. Clays Clay Miner. **41**, 738 (1993); (*e*) J.J. Tunney and C. Detellier. Chem. Mater. **8**, 927 (1996); (*f*) J.J. Tunney and C. Detellier. Can. J. Chem. **75**, 1766 (1997); (*g*) J.E. Gardolinski, P. Peralta-Zamora, and F. Wypych. J. Colloid Interface Sci. **211**, 137 (1999); (*h*) Y. Komori, Y. Sugahara, and K. Kuroda. Chem. Mater. **11**, 3 (1999); (*i*) J.E. Gardolinski, L.C.M. Carrera, M.P. Cantao, and F. Wypych. J. Mater. Sci., **35**, 3113 (2000); (*j*) R. Takenawa, Y. Komori, S. Hayashi, J. Kawamata, and K. Kuroda. Chem. Mater. **13**, 3741 (2001); (*k*) T. Itagaki, Y. Komori, Y. Sugahara, and K. Kuroda. J. Mater. Chem. **11**, 3291 (2001); (*l*) S. Letaief and C. Detellier. J. Mater. Chem. **15**, 4734 (2005); (*m*) T.A. Elbokl and C. Detellier. J. Phys. Chem. Solids. **67**, 950 (2006); (*n*) G. Lagaly, M. Ogawa, and I. Dekany. *In* Handbook of clay science. *Edited by* F. Bergaya, B.K.G. Theng, and G. Lagaly. Elsevier. 2006. Chap. 7.3, p. 309; (*o*) S. Letaief and C. Detellier. J. Mater. Chem. **17**, 1476, (2007).
5. (*a*) J.J. Tunney and C. Detellier. Chem. Mater. **5**, 747 (1993); (*b*) J.J. Tunney and C. Detellier. Clays Clay Miner. **42**, 552 (1994); (*c*) J.J. Tunney and C. Detellier. J. Mater. Chem. **10**, 1679 (1996); (*d*) J.L. Guimaraes, P. Peralta-Zamora, and F. Wypych. J. Colloid Interface Sci. **206**, 281 (1998); (*e*) Y. Komori, H. Enoto, R. J. Takenawa, S. Hayashi,Y.S. Sugahara, and K. Kuroda. Langmuir, **16**, 5506 (2000); (*f*) T. Itagaki and K. Kuroda. J. Mater. Chem. **13**, 1064 (2003); (*g*) K.B. Brandt, T.A. Elbokl, and C. Detellier. J. Mater. Chem. **13**, 2566 (2003); (*h*) J. Murakami, T. Itagaki, and K. Kuroda. Solid State Ionics, **172**, 279 (2004); (*i*) J.E.F.C. Gardolinski and G. Lagaly. Clay Miner. **40**, 537 (2005); (*j*) J.E.F.C. Gardolinski and G. Lagaly. Clay Miner. **40**, 547 (2005); (*k*) T.A. Elbokl and C. Detellier. Clay Sci. **12** (Suppl. 1), 38 (2005); (*l*) M.

© 2007 NRC Canada

Janek, K. Emmerich, S. Heissler, and R. Nüesch. Chem. Mater. **19**, 684, (2007); (*m*) S. Letaief and C. Detellier. Chem. Commun. 2613 (2007).
6. (*a*) P.F. Barron, R.L. Frost, J.O. Skjemstad, and A.J. Koppi. Nature (London), **302**, 49 (1983); (*b*) J.G. Thompson and P.F. Barron. Clays Clay Miner. **35**, 38 (1987).
7. (*a*) C.T. Johnston, G. Sposito, D. Bocian, and R.R. Birge. J. Phys. Chem. **88**, 5959 (1984); (*b*) M. Lipsicas, R. Raythatha, R.F.J. Giese, and P.M. Costanzo. Clays Clay Miner. **34**, 635 (1986); (*c*) M. Raupach,. P.F. Barron, and J.G. Thompson. Clays Clay Miner. **35**, 208 (1987).
8. (*a*) S. Olejnik, L.A.G. Aylmore, A.M. Posner, and J.P. Quirk. J. Phys. Chem. **72**, 241 (1968); (*b*) R.L. Ledoux and J.L. White. J. Colloid Interface Sci. **21**, 127 (1966).

© 2007 NRC Canada

Effect of chain ends on the structure of aramid oligomers

Hakim Mehenni, Hélène Guillou, Christian Tessier, and Josée Brisson

Abstract: Synthesis, X-ray diffraction, and Fourier transform infrared spectroscopy of aliphatic–aromatic aramid oligomers are reported with the aim of shedding light on the effect of end-chain substituent on the morphology and structure of poly(*para*-phenylene terephthalamide) or PPTA. Three types of X-ray powder diffraction patterns were observed: one similar to that of PPTA form I, one similar to that of PPTA form II, and an additional form never reported. Some compounds, differing by their internal distribution of amide–aromatic rings, adopt two different crystal structures, whereas compounds having the same internal amide–aromatic arrangements, but differing by the nature of the end-groups, can adopt the same crystal structure. This clearly shows that both factors influence the packing adopted by the chains. Single-crystal structures of two polymorphs of a nitro-terminated model compound were resolved; both forms incorporate dimethyl formamide, and both show completely different packing. Infrared amide I and II band positions of most studied compounds match those observed for PPTA forms I or II, indicating that they exhibit planar hydrogen bonded sheets of molecules.

Key words: aramid, crystal structure, poly(*para*-phenylene terephtalamide).

Résumé : La synthèse et des études de diffraction des rayons X, et de spectroscopie infrarouge à transformée de Fourier ont été effectués sur des oligomères aramides, dans le but de fournir des informations sur l'effet de substituants en bout de chaîne sur la morphologie et la structure du poly(*para*-phénylene téréphthalamide), ou PPTA. Trois types de clichés de diffraction de poudre ont été observés: un similaire à celui de la forme I du PPTA, un similaire à celui de la forme II, et une forme additionnelle jamais rapportée auparavant. Certains composés modèles qui diffèrent de par leur distribution interne de cycles aromatiques et de groupements amides adoptent des structures cristallines différentes, alors que certains composes modèles ayant le même arrangement interne de cycles aromatiques, adoptent la même structure cristalline. Ceci démontre clairement que ces deux facteurs influencent l'arrangement moléculaire adopté par les chaînes. Les structures cristallines de monocristaux de deux polymorphes d'un composé modèle ayant un substituant nitro en bout de chaîne ont été résolues, les deux incluent des molécules de diméthylformamide, et les deux adoptent des types d'empilement moléculaire complètement différents. En spectroscopie infrarouge, les positions des bandes amide I et II de la plupart des composes étudiés correspondent à celles observées pour les formes I et II du PPTA, indiquant que ces composés possèdent probablement des feuillets de molécules assemblées par liaison hydrogène.

Mots-clés : aramide, structure cristalline, poly(*para*-phénylène téréphtalamide).

Introduction

The variety of ways in which molecules can organize in a crystal phase has long fascinated scientists. Crystal structures obey symmetry and packing requirements, which are still largely unpredictable. Polymer structures offer even greater challenges as, more often than not, they are polymorphic, and diffraction data are too few for statistical direct structure resolution methods to apply. Polymer crystal-structure determination therefore still relies heavily on modelling techniques and on insights gained by model-compound studies.

The crystal structure has profound implications on most polymer properties. The knowledge of crystal structure can therefore be used in various ways, for example, to better understand the structure–property relationship, to help fine-tune the processing conditions, or to design polymers for specific applications.

Our group has been studying a specific subclass of rigid–flexible copolymers, referred to as hinged copolymers, with rigid crystallizable blocks linked via short flexible spacers to control chain folding. We have recently shown that, although poly(*para*-phenylene terephthalamide) (abbreviated PPTA) does not crystallize via chain folds, monosingle crystals of PPTA-based hinged copolymers can (1). This polymer, under highly oriented form, is commercialized as Kevlar™, and thus has received considerable attention. Two crystal structures have been proposed for PPTA: form I, obtained by pre-

Received 11 July 2007. Accepted 29 October 2007. Published on the NRC Research Press Web site at canjchem.nrc.ca on 1 December 2007.

H. Mehenni, H. Guillou, C. Tessier, and J. Brisson.[1] Centre de recherche en sciences et ingénierie des macromolécules (CERSIM), Département de chimie, Faculté des sciences et de génie, Université Laval, Québec, QC G1K 7P4, Canada.

[1]Corresponding author (email: josee.brisson@chm.ulaval.ca).

 doi:10.1139/V07-132 © 2007 NRC Canada

cipitation in methanol (2–4), and form II, obtained by precipitation in water (5–7). The crystal structure of both forms is the object of considerable debate (8–10). Various studies indicate that additional PPTA crystalline forms may exist, although experimental data are even further limited (11–12). New data is clearly needed to gain a better insight on the polymorphism of this polymer.

Inclusion of spacers in regular polymers has previously been shown to allow retention of crystallinity in polyethylene-based copolymers, although in the case of flexible–flexible copolymers, length and regularity in the size of the crystallizable block is critical (13). For PPTA-based hinged copolymers, length of the crystallizable block seems less of an issue, i.e., a block as small as one and a half repeat units (therefore containing three aromatic groups) crystallized in the same crystal structure as the parent PPTA polymer (1), whereas for polyethylene, 22 repeat unit blocks were necessary for crystallization to occur (13).

These observations prompted many questions. In particular, would such three aromatic-ring molecules crystallize alone in the same crystal structure when no flexible spacer was placed between them, or could flexible end-groups favor a different crystal phase? What is the influence of the substitution of the middle para-aromatic ring (NH-linked vs. C=O linked)?

Therefore, a series of aramids, comprising three aromatic rings, were synthesized in the aim of providing model compounds for PPTA polymporphism. These model compounds are also possible candidates for organic gelators (14), as their aspect ratio should favor the existence of fibrils, leading to sol–gel formation. Only one model structure of this type has been reported (15–16), the *N,N′-p*-phenylene dibenzamide, in which no substitution is present on the terminal aromatic rings. This compound has been shown to exist in two main forms, one crystal structure exhibiting hydrogen-bonded sheets of molecules placed in a parallel fashion, as in PPTA forms I and II, whereas the second exhibited a packing in which molecules overlap in a staggered arrangement. An infrared and Raman spectroscopy study has also been reported for this model compound, but in this study, the focus was put on normal vibrational analysis and estimation of tensile modulus using diagonal force constants derived from the spectroscopic data (17). No study has been reported on three-ring PPTA model compounds bearing para end-groups at each molecule extremity, and therefore, the effect of substituents of the crystal structure and chain packing of such rigid molecules remains to be investigated.

The present article will therefore report the synthesis of various three-ring aramid PPTA model compounds bearing para-substituents, and a preliminary investigation to determine to what extent these substituents and the internal arrangement of the amide–aromatic ring linkages affect crystal structures.

Experimental

All chemicals used were ACS reaction-grade and were purchased from Aldrich, unless otherwise specified. 1-Methyl-2-pyrrolidinone was purified by fractional distillation at 10 Torr (1 Torr = 101 325/760 Pa) to remove water as benzene azeotrope. Terephthaloyl chloride was crystallized from dry hexane. Tetrahydrofuran was distilled over sodium metal before use. *para*-Phenylenediamine was sublimed under vacuum to remove degradation products. Poly(methaphenylene isophtalamide) (mpI) was synthesized as described by Morgan (18).

Synthesis of *para*-diphenylene terephthalamide model compounds

A series of model compounds in which the central aromatic ring is C=O substituted have been synthesized according to the reaction scheme in Fig. 1. These are abbreviated 3ARA-X, where 3 stands for the number of aromatic rings, A corresponds to the CO substitution of the central aromatic ring, and X is the terminal substitution (or salient group thereof). In all cases, abbreviations are given in the figure.

Synthesis of undecanoyl chloride

Undecanoic acid (1 g) was inserted in a flask containing 10 mL oxalyl chloride under nitrogen atmosphere. The reactive medium was brought to reflux under nitrogen, and the reaction proceeded for 45 min. Residual oxalyl chloride was removed by evaporation under vacuum. Final product was liquid at room temperature. Yield: 100%. FTIR (cm^{-1}): 2922 (ν_a aliphatic (C–H)), 2851 (ν_s aliphatic (C–H)), 1775 (acid chloride ν(C=O)). ^{1}H NMR (δ, from TMS in DMSO-d_6): 2.23 (t, $2H_e$), 1.22 (q, $2H_f$), 1.15–1.25 (m, $18H_g$), 0.80 (t, $3H_h$).

Synthesis of 3ARA-NO_2 and 3ARA-NH_2

Synthesis of 3ARA-NO_2 was performed as described by Nakata and Brisson (19).

Synthesis of 3ARA-C10

To a solution of 0.42 (1.22 mmoles) 3ARA-NH_2 in 70 mL NMP were added 500 mg (2.44 mmol) undecanoyl chloride under nitrogen atmosphere. Reaction medium was mechanically stirred 3 h, during which time the desired product reprecipitated out. The resulting suspension was poured in water, the yellow precipitate filtered, washed with water, and dried under vacuum at 120 °C. Yield: 96%; decomposes above 350 °C before melting. FTIR (cm^{-1}): 2922 (δ_a aliphatic (C–H)), 2851 (δ_s aliphatic (C–H)), 1656 + 1640 (amide I), 1553 (amide II). ^{1}H NMR (δ, from TMS in DMSO-d_6): 10.10 (s, $2H_b$), 9.6 (s, $4H_e$), 8.03 (t, $4H_a$), 7.65 (d, $2H_c$), 7.51 (d, $2H_d$), 2.52 (t, $4H_f$), 1.57 (t, $4H_g$), 1.15–1.25 (m, $24H_h$), 0.80 (t, $6H_i$)

Synthesis of 3ARA-C12

Synthesis was performed as described for 3ARA-C10, using 1.8 mg (2.44 mmol) dodecanoyl chloride. Reaction medium was diluted by a factor of two (140 mL NMP instead of 70). Yield: 84%; decomposes above 350 °C before melting. FTIR (cm^{-1}): 2922 (ν_a aliphatic (C–H)), 2849 (ν_s aliphatic (C–H)), 1657 + 1641 (amide I), 1553 (amide I). ^{1}H NMR (δ, from TMS in DMSO-d_6): 10.30 (s, $2H_b$), 9.80 (s, $4H_e$), 8.05 (t, $4H_a$), 7.65 (d, $2H_c$), 7.52 (d, $2H_d$), 2.25 (t, $4H_f$), 1.50 (t, $4H_g$), 1.20–1.25 (m, $32H_h$), 0.81 (t, $6H_i$).

Synthesis of the *N,N′-para*-phenylene dibenzamide model compounds

A second series of model compounds has been synthesized, as depicted in Fig. 2. In this case, the central aromatic

© 2007 NRC Canada

Fig. 1. Reaction scheme for *para*-phenylene terephthalamide-based model compounds (the 3ARA-X series).

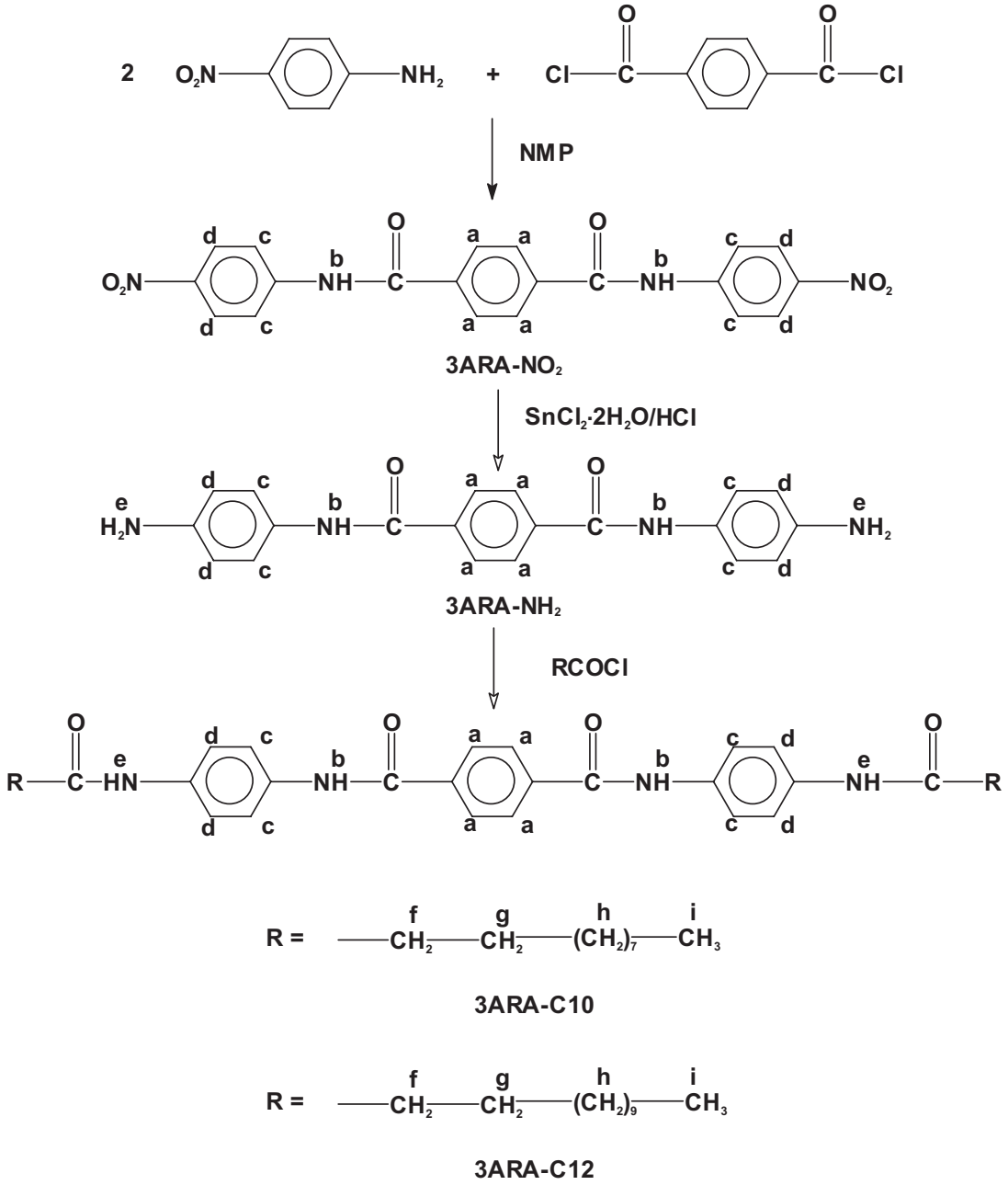

ring is NH-substituted. These are abbreviated 3ARB-X, B corresponding to the central NH aromatic ring substitution.

Synthesis of *para*-methoxycarbonyl benzoyl chloride

Synthesis for this product was already reported by Boivin and Brisson (20).

Synthesis of 3ARB-COOMe

A solution of 0.92 g (8.5 mmoles) *para*-phenylene diamine and 0.68 g (17 mmoles) NaOH in 35 mL distilled water was introduced in a flask. A solution of 3.4 g (17 mmoles) *para*-methoxycarbonyl benzoyl chloride in 15 mL tetrahydrofuran (THF) was added under vigorous mechanical stirring. Stirring was maintained for 30 min, after which the solution was poured in water and the resulting white precipitate filtered, washed thoroughly with water, dried under vacuum for 12 h, and recrystallized with DMF. Yield: 70%; mp (T_f): 310 °C. FTIR (cm^{-1}): 1725 [ester ν (C=O)], 1650 (amide I), 1556 (amide II). ^{1}H NMR (δ, from TMS in DMSO-d_6): 3.86 (s, $6H_e$), 7.73 (s, $4H_a$), 8.05 (t, $4H_c + 4H_d$), 10.42 (s, $2H_b$).

Synthesis of 3ARB-COOH

A solution was prepared using 1 g (2.5 mmoles) 3ARB-COOMe, 0.3 g (5.4 mmoles) KOH, 18 mL 95% ethanol, and 8.5 mL water. The solution was brought to reflux for 10 h. Then, the solution was poured in water and hydrochloric acid added until neutral pH was reached. Water was removed by evaporation under a rotating evaporator, and the resulting white solid was recrystallized using dimethylformamide and

© 2007 NRC Canada

Fig. 2. Reaction scheme for the *N*,*N*′-*para*-phenylene dibenzamide model compounds (the 3ARB-X series).

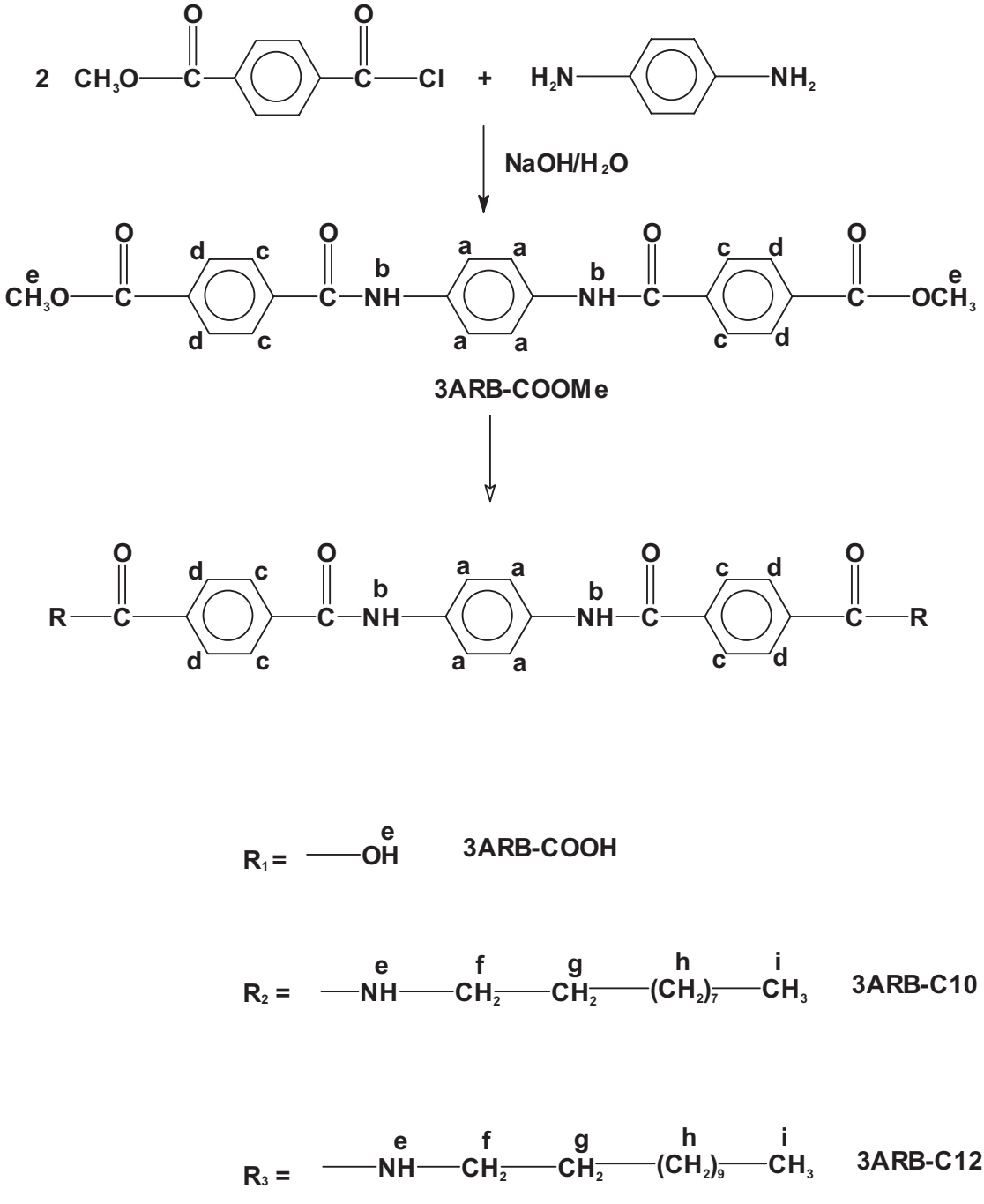

dried 12 h under vacuum. Yield: 94%; mp (T_f): 339 °C. FTIR (cm^{-1}): 1724 (ν carboxylic acid (C=O)), 1654 (amide I), 1556 (amide II). ^1H NMR (δ, from TMS in DMSO-d_6): 7.73 (s, $4H_d$), 7.90 (s, $4H_c$), 10.2 (s, $4H_b$), 10.40 (s, $2H_e$).

Synthesis of 3ARB-COCl

3ARB-COOH (1.15 g, 2.8 mmoles) was introduced in a flask containing 12 mL oxalyl chloride. The reactive medium was brought to reflux under nitrogen atmosphere for 45 min. Residual oxalyl chloride and solvent were removed by vacuum distillation. Yield: 100%; white solid. FTIR (cm^{-1}): 1782 and 1738 (ν acid chloride (C=O)), 1655 (amide I), 1527 (amide II). ^1H NMR (δ, from TMS in DMSO-d_6): 7.75 (s, $4H_a$), 1.86 (d, $4H_d$), 7.92 (d, $4H_c$), 10.20 (s, $4H_b$).

Synthesis of 3ARB-C10

To a solution of 0.6 g (1.4 mmole) 3ARB-COCl in 70 mL THF were added 0.56 mL (2.8 mmoles) undecaneamine under nitrogen atmosphere. Reaction and purification were performed as in the synthesis of 3ARA-C10. Yield: 42%; mp (T_f): 395 °C. FTIR (cm^{-1}): 2915 (ν_a aliphatic (C–H)), 2849 (ν_s aliphatic (C–H)), 1654 (amide I), 1554 and 1527 (amide

© 2007 NRC Canada

Table 1. Crystallographic data pertaining to data acquisition and structure resolution of 3ARA-NO_2 forms I and II.

	Form I	Form II
Empirical formula	$C_{26}H_{28}N_6O_8$	$C_{26}H_{28}N_6O_8$
Moiety formula	$C_{20}H_{14}N_4O_6$, $2(C_3H_7NO)$	$C_{20}H_{14}N_4O_6$, $2(C_3H_7NO)$
Formula mass	552.54	552.54
Color, habit	Colorless, needle	Colorless, needle
Crystal dimensions (mm)	0.2 × 0.2 × 0.1	0.05 × 0.2 × 0.1
Crystal system	Triclinic	Monoclinic
Space group	*P*-1 (no. 2)	$P2_1/n$ (no. 14)
Z	2	2
a [Å]	10.949(5)	3.8706(9)
b [Å]	11.918(5)	33.189(7)
c [Å]	11.976(5)	10.451(2)
α [°]	92.395(5)	90
β [°]	114.713(5)	97.819(3)
γ [°]	110.838(5)	90
Collection ranges	$-13 \le h \le 13$;	$4 \le h \le 4$;
	$-14 \le k \le 14$;	$-39 \le k \le 39$;
	$-14 \le l \le 14$	$-12 \le l \le 12$
Temperature (K)	200(2)	294(2)
Volume [$Å^3$]	1292.9(10)	1330.0(5)
$D_{calcd.}$ (Mg m^{-3})	1.419	1.380
Radiation	Mo Kα (λ = 0.71073 Å)	Mo Kα (λ = 0.71073 Å)
Absorption coeff. (μ) (mm^{-1})	0.107	0.104
Absorption correction	Semi-empirical from equivalents	Semi-empirical from equivalents
$F_{(000)}$	580	580
θ range for data collection (°)	1.88–25.00	2.06–25.00
Observed reflections collected	2940	1950
Independent reflections	4547 (R_{int} = 0.0412)	2358 (R_{int} = 0.0689)
Data/restraints/parameters	4547/0/365	2358/24/206
Maximum shift/error	0.00	0.00
Goodness-of-fit on *F*2	1.022	0.973
Final *R* indices [$I > 2\sigma(I)$]	R_1 = 0.0471, wR_2 = 0.1099	R_1 = 0.0406, wR_2 = 0.0916
R indices (all data)	R_1 = 0.0827, wR_2 = 0.1306	R_1 = 0.0671, wR_2 = 0.1011
Absolute structure parameter	N/A	N/A
Extinction coefficient	N/A	N/A
Largest diff. peak and hole	0.206 and –0.238 e $Å^{-3}$	0.188 and –0.159 e $Å^{-3}$

II). ^{1}H NMR (δ, from TMS in DMSO-d_6): 0.80 (t, $6H_i$), 1.15–1.30 (m, $24H_h$), 1.49 (q, $4H_g$), 2.71 (t, $4H_f$), 7.75 (s, $4H_a$), 7.86 (d, $4H_d$), 7.92 (d, $4H_c$), 10.20 (s, $4H_b$).

Synthesis of 3ARB-C12

The reaction was performed as for 3ARA-C10, using a solution of 0.6 g (1.4 mmol) 3ARB-COCl in 70 mL THF, to which was added a solution of 0.52 g dodecylamine in 20 mL THF containing 0.12 g NaOH. Yield: 74%; white solid; mp (T_f): 400 °C. FTIR (cm^{-1}): 2922 (ν_a aliphatic (C–H)), 2849 (ν_s aliphatic (C–H)), 1653 (amide I), 1554 (amide II). ^{1}H NMR (δ, from TMS in DMSO-d_6): 0.80 (t, $6H_i$), 1.15–1.30 (m, $32H_h$), 1.49 (q, $4H_g$), 2.45 (s, $4H_f$), 7.75 (s, $4H_a$), 7.85 (d, $4H_d$), 7.92 (d, $4H_c$), 10.20 (s, $4H_b$).

X-ray diffraction

X-ray powder diffraction was performed using a Bruker diffractometer, equipped with Kristalloflex 760 generator, a 3-circle goniometer, and a Hi-Star area detector. The generator produced a graphite monochromatized copper radiation (Cu Kα, λ = 1.5418 Å) at 40 kV and 40 mA.

Single crystals of 3ARA-NO_2 were obtained by slow cooling of a saturated dimethyl formamide solution. Two different crystal morphologies were observed, needles with square sections, which rapidly lost their birefringence upon being taken out of the solvent (form I), and needles with rectangular section, which kept longer their birefringence upon drying (form II). Details on the crystal structure data acquisition appear in Table 1. Crystals were mounted on a glass fiber using Paratone N hydrocarbon oil. Measurements were made on a Bruker APEX II area detector diffractometer with graphite monochromated Mo Kα radiation. Frames corresponding to an arbitrary hemisphere of data were collected using ω scans of 0.5° counted for a total of 30 s per frame. Orientation matrices corresponding to cell constants listed in Table 1 were obtained from a least-

© 2007 NRC Canada

squares refinement using the measured positions of 2546 centered reflections for form I 3ARA-NO_2 and 3455 centered reflections for form II. The program used for retrieving cell parameters and data collection was APEX version 2.0.2. from Bruker AXS Inc. Data were integrated using the program SAINT version 7.07a. from Bruker AXS Inc. The data were corrected for Lorentz and polarization effects. Multiscan absorption corrections were performed using the SADABS program for form I (21) and the TWINABS program for form II (22). The form II crystal was twinned. Data for this compound were integrated using two domains that are related by the transformation matrix 1 0 0, 0 –1 0, –0.75 0 –1 and a BASF factor of 0.248.

Structures were solved and full-matrix least-squares refinements performed on F^2 using SHELXS-97 and SHELXL-97 (23). All non-H atoms were refined anisotropically. Hydrogen atoms were placed at idealized positions, with the exception of the amide H atom for form II. For form II, NO_2 were found to be disordered, and the two positions were fixed during refinement at a 1:1 ratio. Neutral atom scattering factors were taken from the International Tables for X-Ray Crytallography (24). All calculations and drawings were performed using the SHELXTL version 6.12 supplied by Bruker AXS. The final model was checked either for missed symmetry or voids in the crystal structure using the approach proposed by Speck (25), as implemented in the PLATON software (26). None was found, these structures give a satisfactory chekcif report. Weighting schemes used were $w = 1/[s^2(F_o^2) + (0.0685P)^2]$, for 3ARA-$NO_2$ form I, and $w = 1/[s^2(F_o^2) + (0.0536P)^2]$for form II, where $P = (F_o^2 + 2F_c^2)/3$.[2]

Fourier transform infrared spectroscopy

Fourier transform infrared (FTIR) transmission spectra of the molecules blended and pressed into KBr disks were taken at a resolution of 4 cm^{-1} using a Nicolet Magna-IR 560 spectrometer equipped with a liquid nitrogen MCT detector, in the 4000–650 cm^{-1} spectral domain. FTIR attenuated total reflectance spectra (ATR) spectra of molecules and of mpI were also taken, using a resolution of 4 cm^{-1}, using the same spectrometer, using a Golden Gate sample holder and a DTGS detector in the 4000–530 cm^{-1} spectral domain.

^{1}H NMR spectra were recorded on a Bruker AC-300 apparatus functioning at 300 MHz, using tetramethylsilane (TMS) as an internal reference. The spectra consisted of 16 acquisitions and were analyzed using the SpinWorks version 1.3B software.

Results and discussion

Choice and synthesis of oligomer model compounds

To investigate the effect of end-groups on the crystallization of PPTA, it was essential to select oligomers for which the rigid block was of the same size, thus eliminating one variable from the system. It was further essential to select oligomers which could be obtained as pure and as monodisperse as possible. For this purpose, the three-ring oligomers were ideal: Short enough to be synthesized by usual organic-chemistry methods, which allowed perfect monodispersity to be obtained, relatively soluble as compared with their polymeric counterpart, allowing easier purification. Two series were selected, based on symmetry of the inner aromatic group: the 3ARA series, in which the inner aromatic group is –C=O substituted, and which corresponds to the previously studied copolymers (1), and the 3ARB series, in which the inner aromatic ring substitution is –NH based, as can be seen in Figs. 1 and 2, respectively. In both cases, these blocks correspond to AABB type polymers, as in poly(*para*-phenylene terephthalamide). A variety of end-groups to be added: –COOH, $–NH_2$, $–NO_2$, –COOMe, or longer aliphatic chains ($–COOC_{10}H_{21}$, $–COOC_{12}H_{25}$, $–NHCOC_{10}H_{21}$, and $–NHCO\text{-}C_{10}H_{25}$). In all cases, oligomers are abbreviated 3ARA-X or 3ARB-X, X corresponding to the chain-end substitution, as defined in Figs. 1 and 2.

Oligomer synthesis was performed using classical routes, and was fairly straightforward. In many cases, reaction conditions were taken from previous work in our group (19–20). The main problem encountered was the limited solubility of these oligomers, attributed to the formation of strong hydrogen bonds. Therefore, in many cases, dimethyl acetamide, dimethyl formamide, or 1-methyl-2-pyrrolidinone were used as solvents, based on PPTA synthesis conditions.

Effect of end-groups on X-ray powder diffraction

The two series of model compounds, 3ARA-X and 3ARB-X, differ by the presence of a carbonyl-bonded middle aromatic ring in the 3ARA-X series, whereas the middle aromatic group is amide NH bonded in the ARB-X series. Both molecules nevertheless exhibit the same two-dimensional symmetry. Symmetry in the crystalline form may differ because of the non-planarity of the aromatic ring and the amide group, a torsion angle of approximately 30° representing the equilibrium position between two opposing effects: electron delocalization, which favors planarity, and non-bonded interatomic repulsion between the aromatic ring hydrogens and the hydrogen atom of the amide group (27–28). Two main conformations can be adopted. In the first, torsion angles of +30° and –30° exist on each side of the aromatic ring, which is proposed to be the case for PPTA forms I and II (2–4), and leads to quasi-planar molecules, which form hydrogen bonded ribbons, the proposed forms I and II differing by the lateral packing of the hydrogen-bonded ribbons. In the second, +30° torsions occur on each side of the aromatic ring, a 60° dihedral angle is observed between the two amide groups, and hydrogen bonds are formed in two roughly perpendicular directions. This is the case of the crystal structure of poly(*meta*-phenylene isophtalamide), or mpI, an aramid from which the Nomex™ commercial fibers are made (29).

[2] Supplementary data for this article are available on the journal Web site (canjchem.nrc.ca) or may be purchased from the Depository of Unpublished Data, Document Delivery, CISTI, National Research Council Canada, Ottawa, ON K1A 0R6, Canada. DUD 5244. For more information on obtaining material, refer to cisti-icist.nrc-cnrc.gc.ca/irm/unpub_e.shtml. CCDC 653514 and 653515 contain the crystallographic data for this manuscript. These data can be obtained, free of charge, via www.ccdc.cam.ac.uk/conts/retrieving.html (or from the Cambridge Crystallographic Data Centre, 12 Union Road, Cambridge CB2 1EZ, UK; fax +44 1223 336033; or deposit@ccdc.cam.ac.uk).

© 2007 NRC Canada

Fig. 3. Effect of end-group length on structure, as observed by X-ray powder diffraction.

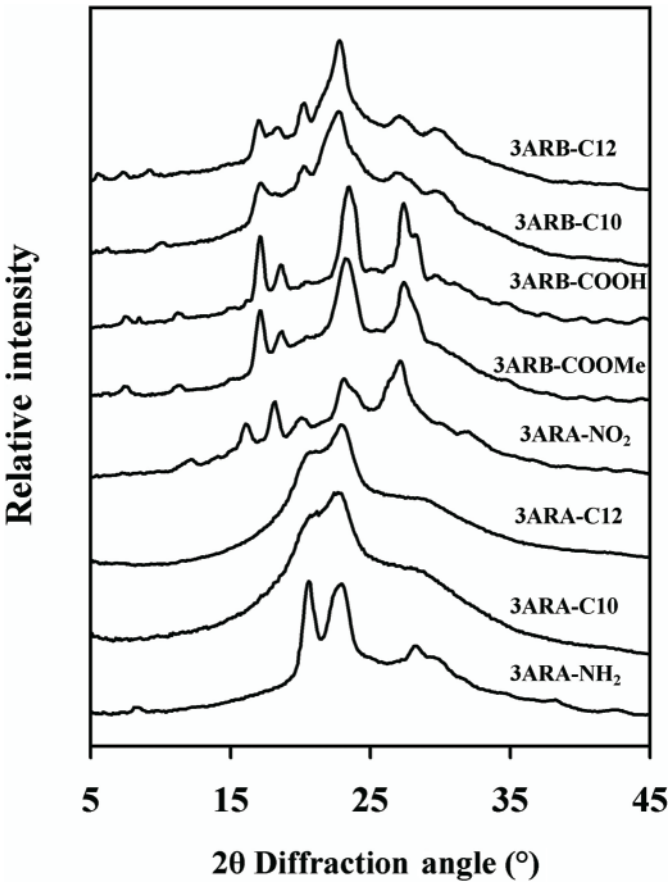

X-ray powder diffraction spectra of the two model compound series appear in Fig. 3. Three of the four powder spectra in the 3ARA series, appearing at the bottom of the figure, are similar. 3ARA-NH_2, 3ARA-C10, and 3ARA-C12 spectra all present, with various diffraction peak widths and therefore crystalline order, three main intense peaks: one at 20.6° (4.31 Å), a second at 22.9° (3.88 Å), and a wide peak (which is composed of at least two distinct diffraction peaks) between 28° and 30° (3.0–3.2 Å). These powder spectra correspond well to the observed diffraction diagram of PPTA form I, where these three main diffraction peaks are also observed. 3ARA-C10 and 3ARA-C12 show wider diffraction peaks, suggesting a less ordered crystalline form.

On top of the figure appear 3ARB-C10 and 3ARB-C12 spectra, which exhibit one main intense diffraction peak at 22.9° (3.88 Å) and medium-intensity peaks at 17.3° (5.13 Å), 20.3° (4.37 Å), 26.9° (3.31 Å), and 29.8° (3.40 Å). Powder diagram is similar to that of form II, obtained normally by water precipitation, as reported by Shen and coworkers (37).

Finally, 3ARA-NO_2, 3ARB-COOMe, and 3ARB-COOH show similar powder diffraction spectra, which differ from the ones discussed earlier, with main peaks located at 17.2° (5.15 Å), 18.7° (4.74 Å), 23.3° (3.82 Å), and 27.5° (3.24 Å). Peak positions are similar to those of PPTA form II, although relative intensities of the 23.3° and 27.5° peaks differ significantly from those of PPTA form II.

Surprisingly, in the 3ARB series, no compound seems to adopt a structure similar to that of PPTA form I. This is unexpected, as the rigidity of both series is comparable. The fact that 3ARA-C10 and 3ARA-C12 compounds show a completely different diffraction spectrum from that of the 3ARB-C10 and 3ARB-C12 compounds demonstrates the importance of internal group arrangements. The 3ARA-NO_2 powder diffraction spectrum is similar to that of 3ARB-COOH and 3ARB-COOMe, on the other hand, demonstrating that these internal differences can be counterbalanced by end-group interactions. It is noteworthy that the internal amide groups and aromatic ring arrangement appears to be as important, structure-wise, as the nature of end-groups.

X-ray diffraction on single crystals[2]

Although all model compounds were subjected to crystallization experiments, only one, 3ARA-NO_2, gave crystals large enough for single-crystal structure determination to be performed as of yet. Two distinct forms were observed, both incorporating DMF solvent molecules, hydrogen-bonded to the amide groups. Atomic coordinates and isotropic temperature factors are given for 3ARA-NO_2 form I in Table 2, and 3ARA-NO_2 form II in Table 3. For form I, two crystallographically independent molecules were located, each presenting an inversion center at the middle of the central aromatic ring. Interatomic bond distances, angles, and torsion angles (not shown) are very similar, and therefore packing requirements are probably responsible for this specific arrangement. For form II, a single molecule was located, again with an inversion center at the middle of the central aromatic ring. In this specific case, however, oxygen atoms of the NO_2 groups were found to be disordered with a ratio of 1:1. Both structures incorporate dimethyl formamide solvent molecules hydrogen-bonded to the 3ARA-NO_2 molecules in a very similar fashion, as seen in Fig. 4, where the hydrogen-bonding scheme of each independent molecule is seen. Hydrogen-bond geometry is in agreement with previous structures, i.e., for 3ARA-NO_2 form I, the N···O distance is 2.944(2) and 2.946(2) Å, whereas for form II, it is 2.971(2) Å. These values are well within those obtained for structures containing a benzamide group, such as the *N*,*N*′-oligomethylene dibenzamide series, for which the N···O distances varied from 2.790(2) Å (30) to 3.027(2) Å (31), which indicates that the strength of hydrogen bonds is typical to that found for similar compounds.

In both structures, the amide groups and aromatic cycles are planar. However, and in spite of their appearance, they are not perfectly coplanar with one another, i.e., the middle aromatic group deviates from the rest of the molecular plane, the C–C–C–O torsion angle, linking the central aromatic ring to the amide groups, have values of 168.3(2)° and 8.5(3)° for form I, whereas as value of –33.0(2)° is found in form II. The latter value is in good agreement with previous studies (27–28), whereas the values for the first structure are atypically low, indicating a better planarity. On the other hand, in all cases, the values for the C–C–C–N torsion angle between the aromatic cycles at the molecular extremities and the amide groups, which varies from +3.6(4) to –3.6(4) for form I, and to 0.4(3) for form II, indicate almost perfect planarity, as expected for this torsion angle.

© 2007 NRC Canada

Table 2. Atomic coordinates (× 10^4) and equivalent isotropic displacement parameters (Å^2 × 10^3) for 3ARA-NO_2 form I. $U_{(eq)}$ is defined as one third of the trace of the orthogonalized U_{ij} tensor.

	x	*y*	*z*	$U_{(eq)}$
O(11)	4893(2)	5045(1)	7995(1)	51(1)
O(12)	2547(2)	1289(2)	11501(2)	59(1)
O(13)	1397(2)	–443(2)	10140(2)	61(1)
N(11)	3640(2)	3035(2)	6967(2)	34(1)
N(12)	2145(2)	674(2)	10467(2)	44(1)
C(1)	4419(2)	4253(2)	7064(2)	34(1)
C(11)	3306(2)	2501(2)	7888(2)	31(1)
C(12)	3668(2)	3169(2)	9047(2)	36(1)
C(13)	3298(2)	2564(2)	9892(2)	36(1)
C(14)	2558(2)	1300(2)	9580(2)	34(1)
C(15)	2194(3)	618(2)	8434(2)	39(1)
C(16)	2567(3)	1219(2)	7600(2)	37(1)
C(17)	4675(2)	4591(2)	5963(2)	31(1)
C(18)	4414(2)	3753(2)	4961(2)	34(1)
C(19)	4737(2)	4156(2)	4014(2)	34(1)
O(21)	4893(2)	10052(1)	1927(2)	52(1)
O(22)	2488(2)	6306(2)	–3702(2)	59(1)
O(23)	1401(2)	4570(2)	–3340(2)	63(1)
N(21)	3633(2)	8045(2)	1823(2)	34(1)
N(22)	2119(2)	5688(2)	–3014(2)	44(1)
C(2)	4414(2)	9262(2)	2429(2)	35(1)
C(21)	3293(2)	7512(2)	602(2)	32(1)
C(22)	3650(3)	8180(2)	–222(2)	37(1)
C(23)	3275(2)	7571(2)	–1398(2)	37(1)
C(24)	2546(2)	6314(2)	–1753(2)	35(1)
C(25)	2181(3)	5632(2)	–946(2)	42(1)
C(26)	2560(3)	6232(2)	223(2)	40(1)
C(27)	4683(2)	9600(2)	3756(2)	32(1)
C(28)	4376(2)	8754(2)	4474(2)	33(1)
C(29)	4689(2)	9152(2)	5698(2)	35(1)
O(3)	2050(2)	946(1)	4775(2)	47(1)
N(3)	1074(2)	–1008(2)	3662(2)	36(1)
C(3)	1685(3)	200(2)	3826(2)	37(1)
C(31)	776(3)	–1557(2)	4635(2)	53(1)
C(32)	641(3)	–1831(2)	2508(2)	45(1)
O(4)	2134(2)	5916(1)	2640(2)	48(1)
N(4)	1121(2)	3966(2)	2837(2)	40(1)
C(4)	1709(3)	5177(2)	3224(2)	38(1)
C(41)	941(3)	3401(2)	1650(2)	60(1)
C(42)	656(3)	3165(2)	3591(2)	53(1)

Table 3. Atomic coordinates (× 10^4) and equivalent isotropic displacement parameters (Å^2 × 10^3) for 3ARA-NO_2 form II. $U_{(eq)}$ is defined as one third of the trace of the orthogonalized U_{ij} tensor.

	Occ.	*x*	*y*	*z*	$U_{(eq)}$
O(1)	1	2879(4)	832(1)	7041(1)	59(1)
O(2′)	0.50	–2500(20)	2828(4)	6263(13)	61(2)
O(3′)	0.50	–280(30)	2934(5)	4446(16)	68(2)
O(2″)	0.50	–1200(20)	2849(4)	6422(13)	67(2)
O(3″)	0.50	–1480(30)	2902(5)	4384(14)	68(2)
N(1)	1	3212(4)	1097(1)	5051(2)	45(1)
N(2)	1	–939(5)	2709(1)	5359(2)	55(1)
C(1)	1	2185(4)	1496(1)	5195(2)	38(1)
C(2)	1	2180(5)	1750(1)	4134(2)	45(1)
C(3)	1	1164(5)	2144(1)	4184(2)	47(1)
C(4)	1	154(4)	2290(1)	5308(2)	42(1)
C(5)	1	135(5)	2048(1)	6374(2)	50(1)
C(6)	1	1148(5)	1650(1)	6325(2)	49(1)
C(7)	1	4253(4)	385(1)	5415(2)	38(1)
C(8)	1	3071(4)	265(1)	4162(2)	42(1)
C(9)	1	3831(4)	–118(1)	3751(2)	44(1)
C(10)	1	3393(4)	789(1)	5919(2)	41(1)
N(3)	1	7837(4)	957(1)	608(1)	52(1)
O(4)	1	6105(4)	977(1)	2587(1)	78(1)
C(11)	1	7751(7)	526(1)	525(2)	97(1)
C(12)	1	8849(6)	1182(1)	–471(2)	81(1)
C(13)	1	7004(5)	1140(1)	1637(2)	60(1)

Packingwise, both structures are however completely different from one another. In form I, molecules are staggered, but in such a way that aromatic cycles form stacks perpendicular to the hydrogen bonding direction. Such a packing is reminiscent of the staggered packing previously observed for *N*,*N*′-*p*-phenylene dibenzamide (16), in that the axis of staggered molecules form approximately a 60° angle with one another. However, the packing differs in many respects. First, the molecules are hydrogen-bonded only to solvent molecules in the present case, contrary to the *N*,*N*′-*p*-phenylene dibenzamide structure in which aramid molecules were hydrogen-bonded to one another. Second, as can be seen on Fig. 5, the aromatic cycles on each end are stacked perpendicular to the hydrogen-bond plane in 3ARA-NO_2, and only the central aromatic ring is not found to π-stack. No such π-stacking was reported in the staggered *N*,*N*′-*p*-phenylene dibenzamide structure. Both staggered packings are unlikely to be present in crystal structures of PPTA derived from the liquid–crystalline form, as are forms I and II of PPTA, but variations thereof could exist in unknown polymorphs obtained by direct crystallization.

In form II, shown in Fig. 5*b*, sheets of molecules are observed, as in the case of PPTA forms I and II, and one of the observed polymorphs of *N*,*N*′-*p*-phenylene dibenzamide (15). As solvent molecules are intercalated between 3ARA-NO_2 molecules, this packing does not provide information on the way hydrogen-bonded sheets of PPTA can form. In this case, π-stacking results in a perfect alignment of the molecules perpendicular to the hydrogen-bonded sheets, which point to this feature as possible stabilizing effect for PPTA structures as well.

The amide I and II infrared spectral region

It is well-known that polyamide vibrations found in the infrared spectral region are sensitive to the strength of hydrogen bonds (32–35), to local conformations (36), and to the type of packing that the chains adopt (37). Comparison with infrared spectra reported in the literature should therefore give information on these specific aspects of model compounds. Figure 6 reports the amide I and II spectral region of the model compounds, whereas Table 4 reports assignments in this spectral region, based on the work by Shen, and co-workers (37). This region also features weak- or medium-intensity aromatic deformation vibrations. For 3ARB-COOMe, 3ARB-COOH, and 3ARA-NO_2, an additional intense vibration occurs, that of the carbonyl stretch-

© 2007 NRC Canada

Fig. 4. Hydrogen-bonding pattern in 3ARA-NO_2 crystal structures. Anisotropic atomic displacement ellipsoids for the non-hydrogen atoms are shown at the 50% probability level. (*a*) Form I, (*b*) Form II.

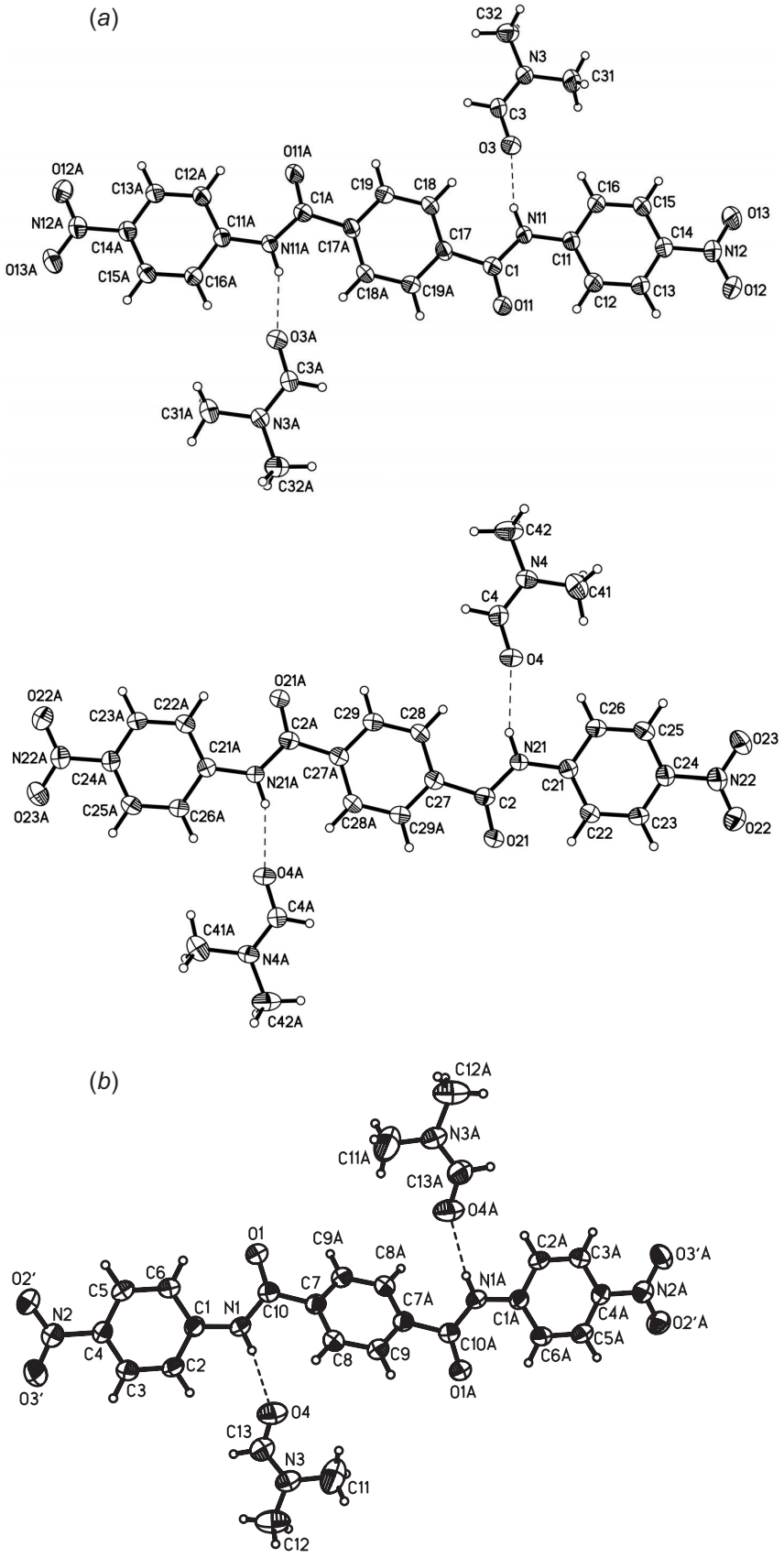

© 2007 NRC Canada

Fig. 5. Molecular packing of the 3ARA-NO_2 model compound. (*a*) Form I, (*b*) Form II**.**

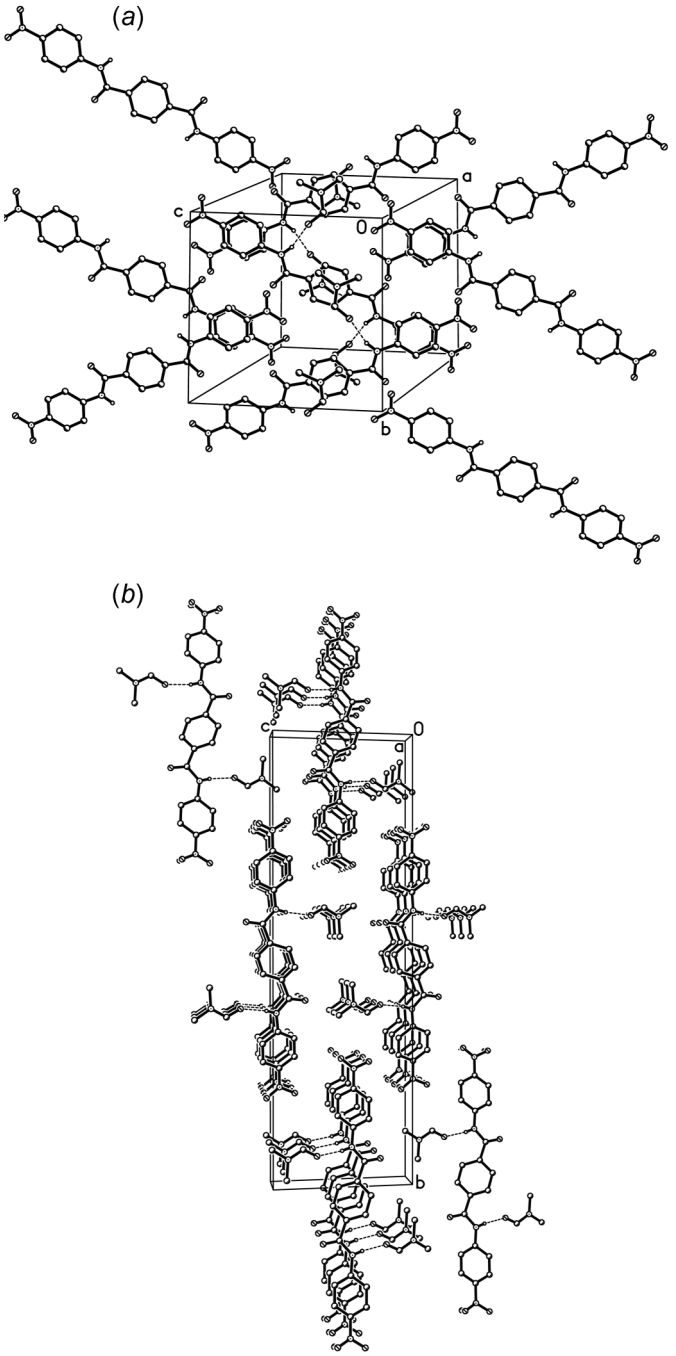

Fig. 6. The amide I and II spectral region (dotted lines indicate the peak positions of PPTA forms I and II at the same position for both forms).

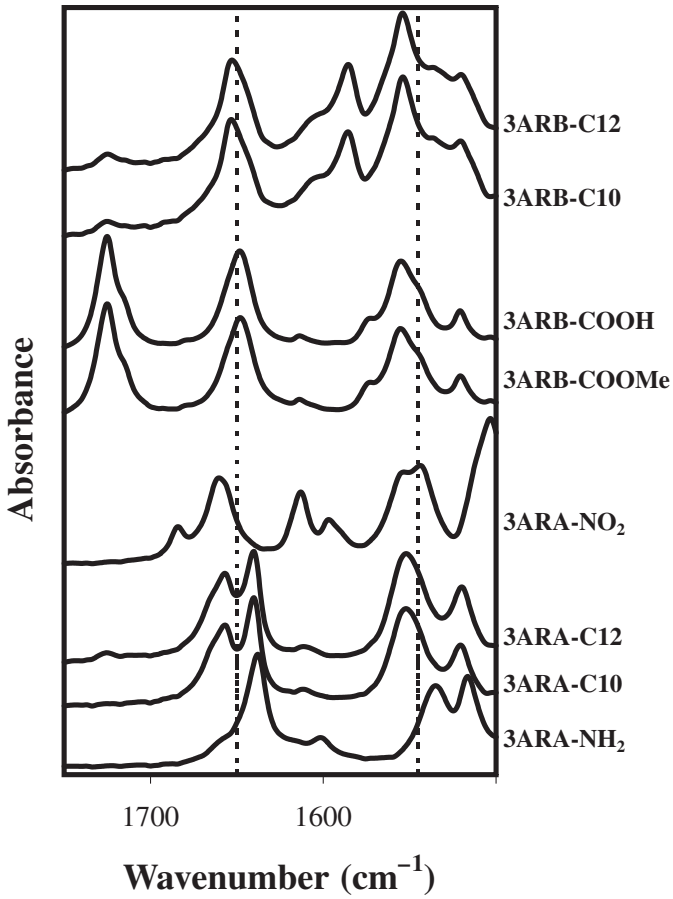

ing vibration around 1725 cm^{-1} for 3ARB-COOMe and 3ARB-COOH, and that of N=O asymmetrical stretching for 3ARA-NO_2 at 1504 cm^{-1}.

The position and intensity of ν(NH) and amide I bands are sensitive to the strength of hydrogen bonds and have been used to quantify the proportion of free and hydrogen-bonded amide groups in polyamides (32–35). The amide I band is attributed mostly to C=O stretching, but C–N stretching and C–C–N deformation also contributes to this band (38). For PPTA forms I and II, which only differ by the packing of the hydrogen-bonded sheets, this vibration does not show any shift in position (37).

Positions of the amide I and II bands of PPTA are indicated by dotted lines in Fig. 6. These positions are the same for forms I and II, hence a single dotted line is made for each band. For amide I, this position matches that observed for 3ARB model compounds. In the 3ARA series, however, variations occur. For 3ARA-C10 and 3ARA-C12, this vibration is split in two, with a difference in frequency of 20–25 cm^{-1}. This splitting may be due to transition dipole coupling, as the average position matches that observed for PPTA. In polypeptides and proteins, transition dipole coupling has been shown to cause splittings of the order of 5 cm^{-1} to 20 cm^{-1}, depending on the conformation of the polypeptides (39, 40). For 3ARA-NO_2, a shift is observed towards higher frequencies, which, in view of the known crystal structures, could be attributed to hydrogen bonds with solvent molecules, or alternatively to the formation of weaker hydrogen bonds after solvent removal from the structure. A small peak also occurs at a higher frequency of 1681 cm^{-1} for this compound, which is attributed to the presence of free amide carbonyl groups, and also indicates some disorder compatible with solvent removal. For 3ARA-NH_2, on the other hand, this band shifts to lower frequencies, indicative of stronger hydrogen bonding, possibly due to the presence of NH_2 groups.

© 2007 NRC Canada

Table 4. Assignment in the 1750–1500 cm^{-1} infrared spectral region.

	ν(C=O) Ester or acid (cm^{-1})	Amide I (cm^{-1})	$\delta_{in\text{-}plane}$ (C=C) Aromatic (cm^{-1})	Amide II (cm^{-1})	$\delta_{in\ plane}$ (C=C) Aromatic (cm^{-1})	ν(N–O) Nitro (cm^{-1})
PPTA form I (35)	–	1650 s	1610 w	1544 vs	1518 vs	–
PPTA form II (35)	–	1652 s	1606 w	1545 vs	1514 vs	–
3ARA-NH_2	–	1639 s	1602 w	1535 s	1516 s	–
3ARA-C10	–	1640 s + 1657 s	1611 w	1553 s	1521 m	–
3ARA-C12	–	1641 s + 1657 s	1610 w	1553 s	1520 m	–
3ARA-NO_2	–	1681 w + 1660 s	1613 m + 1596 w	1550 s + 1544 s	–	1504 s
3ARB-COOMe	1725 s	1650 s	1614 w	1574 w + 1556 m	1521 m	–
3ARB-COOH	1724 s	1654 s	1614 w	1573 w + 1556 m	1521 m	–
3ARB-C10	–		1607 sh + 1586 m	1554 s	1521 w	–
3ARB-C12	–	1653 s	1607 sh + 1586 m	1554 s	1536 w + 1521 w	–

Note: vs = very strong, s = strong,m = medium, w = weak, and vw = very weak.

Table 5. Assignment in the 850–600 cm^{-1} infrared spectral region.

	δ_{oop} (C–H) Aromatic (cm^{-1})	Amide IV (cm^{-1})	Amide V (cm^{-1})
PPTA form I (35)	789 w	730 m	668 m
PPTA form II (35)	789 w	717 m	660 m
mpI	779 w	711 m	683 m
3ARA-NH_2	769 w	730 m	660 m
3ARA-C10	731 w	728 m	676 m
3ARA-C12	731 w	728 m	676 m
3ARA-NO_2	748 m	720 m + 709m	685 m
3ARB-COOMe	787 m	700 m + 724 m	681 w + 645 m
3ARB-COOH	787 m	700 m + 724 m	681 w + 645 m
3ARB-C10	791 vw	730 m + 718 sh	647 m
3ARB-C12	791 vw	730 m + 718 sh	647 m

Note: vs = very strong, s = strong, m = medium, w = weak, vw = very weak, and sh = shoulder.

The amide II band is a mixed band comprising contributions from N–H in-plane bending, C–N stretching, and C–C stretching. Its position has been shown not to vary with relative strength of hydrogen bonds, and is correlated to pleated sheets or helicoidal structures in proteins (41). In poly(*n*-methylene terephthalamides) or nylons nT, the position of the amide II vibration has been correlated to two-dimensional versus three-dimensional hydrogen-bond network formation (36).

In the case of model compounds studies here, the amide II band is at a slightly higher frequency than in the case of PPTA for most model compounds. As this band position is sensitive to the hydrogen-bonded network, this shift may be attributed to the limited length of the molecules, and hence to the smaller size of hydrogen-bonded ribbons or sheets. Two compounds are at variance with this general behavior, and these are the same as in the case of the amide I band. First, for the 3ARA-NO_2, two peaks are observed in this region, in agreement with the observation of two different chemical structures. Second, for the 3ARA-NH_2 compound, a shift towards lower frequencies is observed, as in the case of three-dimensional networks found for nylon nT model compounds (28), in spite of the strong resemblance between the powder spectra of 3ARA-NH_2 and that of PPTA form I. It is therefore proposed that the network is different in this case, due to the presence of NH_2 end-groups, which can form additional hydrogen bonds. Hydrogen-bonded molecular ribbons or sheets may exist in arrangements similar to that of PPTA form I, whereas additional hydrogen bonds could link, in this particular case, various ribbons or sheets together, thus explaining the observed frequency shift.

The amide IV and V infrared spectral region

The second vibration region of interest, structurewise, for polyamides, is that of the amide IV and V bands. Both bands stem from highly mixed modes: the amide IV has been attributed mainly to O=C–N bending, whereas the amide V band is dominated by N–H out-of-plane deformation. For these medium-intensity bands, differences between PPTA forms I and II have been reported by Shen and co-workers (37) (as indicated in Table 5), showing that these are packing-sensitive. This may be linked in part to deformations in the hydrogen-bond geometry, as it has been proposed that frequency changes in this vibration are due to non-linearity of the proton donor (42). Further, in the case of aliphatic–aromatic nylons, the position of the amide V vibration was indicative of the torsion angle present between the terephthalamide moeity and the aliphatic chains (36). In poly(*meta*-phenylene isophtalamide), in which a three-dimensional network of hydrogen-bonded molecules exist,

© 2007 NRC Canada

Fig. 7. The amide IV and V spectral region (dotted lines indicate peak positions of PPTA form I, and full lines of PPTA form II).

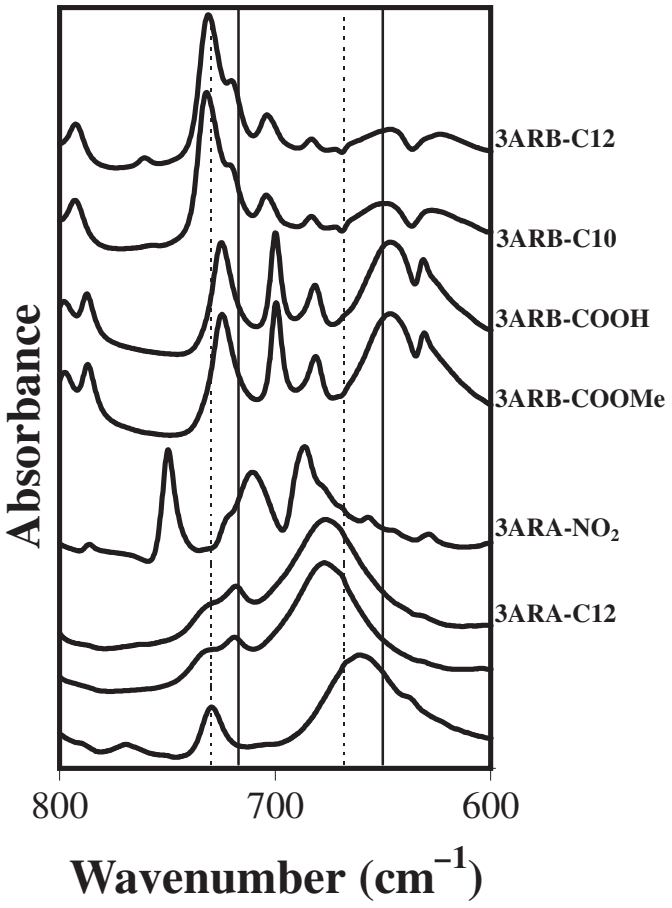

the position of these two vibrations is different from that of PPTA forms I and II, as seen in Table 5, thus showing that these vibrations are also hydrogen-bond-network-sensitive.

This spectral region for the ARA and ARB model compounds is reported in Fig. 7, and spectral assignments in Table 5. In this figure, positions of the amide IV and V bands for PPTA form I are depicted in dotted lines, and for form II in full lines.

In the case of the amide V vibration, which occurs in the 640–680 cm^{-1} range, model-compound peak positions correlate well to the form expected from X-ray diffraction diagrams, i.e., two main peak positions are found, one at 676 cm^{-1}, slightly above that for PPTA form I, which is at 668 cm^{-1}, and it can therefore be assigned to compounds exhibiting a structure similar to form I (3ARA-C10 and 3ARA-C12), and 645–647 cm^{-1}, at a position close to that of the PPTA form II at 660 cm^{-1}, observed for the 3ARB-C10, 3ARB-C12, 3ARB-COOH, and 3ARB-COOMe, indicative of a structure similar to PPTA form II for all these models compounds, in spite of the differences observed in the X-ray diffraction spectra. For 3ARB-C10 and 3ARB-C12, this was expected from X-ray diffraction data, whereas for 3ARB-COOH and 3ARB-COOMe, it indicates that the crystal form observed, although exhibiting different relative intensities in X-ray spectra, nevertheless presents packing similarities to PPTA form II. Again, two compounds differ from this basic behavior: for 3AR-NH_2, the peak is large and intermediate in position between that of forms I and II, which may be due to the disruptive effect of additional hydrogen bonds due to the NH_2 end-groups, as seen on the amide I and II vibration regions. Finally, for the 3ARA-NO_2, only weak peaks are observed in the amide V band region, which is attributed to the presence of the terminal nitro groups, which may affect specifically this vibration mode.

For the amide IV band, on the other hand, only 3ARA-NH_2 exhibits solely a medium-intensity band at the same position as form I of PPTA. In all other cases, variations occur. Two peaks of varying relative intensity are observed for 3ARA-C10, 3ARA-C12, 3ARB-C10, and 3ARB-C12, a peak at an intermediate position for 3ARB-COOH and 3ARB-COOMe, and a medium-intensity peak at a lower frequency for 3ARA-NO_2. It is concluded that the amide IV vibration, due to its complex nature, is sensitive to substituent effects as well as packing interactions, and cannot be used to compare packings of molecules having different end-groups.

Conclusion

X-ray and FTIR spectroscopy have been used to investigate the types of chain packing and hydrogen bonding occurring in rigid oligomers. These serve as model compounds to better understand structural changes in para-substituted aramids and are possible candidates as organogelators. The present work shows important structural variations occurring in these compounds. Molecules having a flexible aliphatic chain as an end-group present structures similar to PPTA form I (3ARA-C10 and 3ARA-C12) and II (3ARB-C10 and 3ARB-C12), indicating that the alternance of amide groups plays a role in the preferred chain packing. 3ARA-NH_2 also exhibits a structure similar to that of PPTA form I, but appears more complex in terms of hydrogen bonds, and it would be of particular interest to obtain its crystal structure. 3ARB-COOH and 3ARB-COOMe appear to present a chain packing close to PPTA form II, although the relative X-ray diffraction intensities are different, which is also of interest. Finally, 3ARA-NO_2, the model compound for which FTIR spectroscopy showed the largest differences as compared with PPTA, was the only compound for which single-crystal structure determination could be performed. It was found to adopt two different crystal structures, both incorporating solvent molecules hydrogen-bonded to the aramid oligomer, in one case a staggered structure and in the other, a pleated sheet structure (form II). Both forms showed, to a varying degree, π-stacking, which indicates that this feature should not be overlooked in proposed PPTA crystal structures.

Acknowledgement

The authors would like to acknowledge the financial support of NSERC (Natural Science and Engineering Research Council of Canada). The help of François Lapointe, of the CERSIM and Pierre Audet, of the Department of chemistry, is also gratefully acknowledged.

© 2007 NRC Canada

References

1. S. Manet, C. Tibirna, J. Boivin, C. Delabroye, and J. Brisson. Macromolecules, **39**, 1093 (2006).
2. M.G. Northholt. Eur. Polym. J. **10**, 799 (1974).
3. M.G. Northholt and J.J. van Aartsen. J. Polym. Sci. **B11**, 333 (1973).
4. R. Hasegawa, J. Jimoto, Y. Chatani, and H. Todokoro. Meet. Soc. Cryst. Japan, Abstr., Osaka, Japan, 21 (1973).
5. L. Penn and F. Larson. J. Appl. Polym. Sci. **23**, 59 (1979).
6. K. Haraguchi, T. Kajiyama, and M.Tagayanaki. J. Appl. Polym. Sci. **23**, 903 (1979).
7. K. Haraguchi, T. Kajiyama, and M.Tagayanaki. J. Appl. Polym. Sci. **23**, 915 (1979).
8. J. Liu, S.Z.D. Cheng, and P.H. Geil. Polymer, **37**, 1413 (1996).
9. K.H. Gardner, A.D. English, and V.T. Forsyth. Macromolecules, **37**, 9654 (2004).
10. M. Plazanet, F. Fontaine-Vive, K.H. Gardner, V.T. Forsyth, A Ivanov, A.J. Ramirez-Cuesta, and M.R. Johnson, J. Am. Chem. Soc. **127**, 6672 (2004).
11. G.C. Rutledge, D. Snetivy, and G.J. Vancso. Proc. U.S. Army Natick Research, 251 (1993).
12. G.C. Rutledge, U.W. Suter, and C.D. Papaspyrides. Macromolecules, **2**, 1934 (1991).
13. C. Le Fevere de Ten Hove, J. Penelle, D.A. Ivanov, and A.M. Jonas. Nature Mater. **3**, 33 (2004).
14. P. Terech and R.G. Weiss. Chem. Rev. **97**, 3133 (1997).
15. S. Harkema and R. J. Gaymans. Acta Cryst. **B33**, 3609 (1977).
16. W.W. Adams, A.V. Fratini, and D.R. Wiff. Acta Cryst. **B34**, 954 (1978).
17. P.K, Kim, C. Chang, and S.L. Hsu. Polymer, **27**, 34 (1986).
18. P.W. Morgan. Macromolecules, **10**, 1381 (1977).
19. S. Nakata and J. Brisson. J. Polym. Sci. A. **A35**, 2379 (1997).
20. J. Boivin and J. Brisson. J. Polym. Sci. A. **42**, 5098 (2004).
21. G.M Sheldrick. SADABS [computer program], Version 2004/1. Bruker AXS Inc., Madison, Wisconsin. 2004.
22. G.M Sheldrick. TWINABS [computer program], Version 1.05. Bruker AXS Inc., Madison, Wisconsin. 2002.
23. G.M. Sheldrick. SHELXS-97 and SHELXL-97 [computer programs]. Programs for the refinement of crystal structures. University of Gottingen, Germany. 1997.
24. A.J.C. Wilson. (*Editor*). International tables for crystallography. Vol. C. Tables 4.2.6.8 (pp. 219–222) and 6.1.1.4 (pp. 500–502). Kluwer Academic Publishers, Dordrecht, the Netherlands. 1992.
25. A.L. Spek. Acta Cryst. **A46**, C-34 (1990).
26. A.L. Spek. PLATON [computer program], A multipurpose crystallographic tool. University of Utrecht, Utrecht, the Netherlands. 2005.
27. K. Tashiro, M. Kobayashi, and H. Tadokoro. Macromolecules, **10**, 413 (1977).
28. J. Brisson and F. Brisse. Can. J. Chem. **63**, 3390 (1985).
29. H. Kakida, Y. Chatani, and H. Tadokoro. J. Polym. Sci., Polym. Phys. Ed. **14**, 427 (1976).
30. J. Brisson and F. Brisse. Macromolecules, **19**, 2632 (1986).
31. M.O. Awaleh, A. Nadia, and F. Brisse. Acta Cryst. **E62**, 01996 (2006).
32. L.R. Schroeder and S.L. Cooper. J. Appl. Phys. **47**, 4310 (1976).
33. M.M. Coleman, D.J. Skrovanek, W.E. Howe, and P.C. Painter. Macromolecules, **18**, 299 (1985).
34. D.J. Skrovanek, S.E. Howe, P.C. Painter, and M.M. Coleman. Macromolecules, **18**, 1676 (1985).
35. M.M. Coleman, D. Skrovanek, and P.C. Painter. Makromol. Chem. Macromol. Symp. **5**, 21 (1986).
36. F. Brisse and J. Brisson. Macromolecules, **19**, 2632 (1986).
37. D.Y. Shen, S.E. Molis, and S.L.Hsu. Polym. Eng. Sci. **23**, 543 (1983).
38. W.H. Moore and S. Krimm. Biopolymers, **15**, 2439 (1976).
39. Y. Abe and S. Krimm. Biopolymers, **17**, 2475 (1978).
40. P.C. Painter and M.M. Coleman. Biopolymers **17**, 2475 (1978).
41. S. Krimm. Biopolymers, **22**, 217 (1983).
42. D. Hadzi and S. Bratos. *In* The hydrogen bond. Vol. II. *Edited by* P. Shuster, G. Zundel, and C. Sandorfy. North-Holland Pub. Co., Amsterdam. 1976. p. 565.

© 2007 NRC Canada

Synthesis of the bulky *m*-terphenyl phenol Ar*OH (Ar* = C_6H_3-2,6-Mes_2, Mes = 2,4,6-trimethylphenyl) and the preparation and structural characterization of several of its metal complexes

Diane A. Dickie, Ian S. MacIntosh, Daisuke D. Ino, Qi He, Ojisamola A. Labeodan, Michael C. Jennings, Gabriele Schatte, Charles J. Walsby, and Jason A.C. Clyburne

Abstract: The bulky *m*-terphenyl phenol Ar*OH **1** (Ar* = C_6H_3-2,6-Mes_2, Mes = 2,4,6-trimethylphenyl) was synthesized via the treatment of Ar*Li with nitrobenzene. The phenol **1** is prepared in modest to good yield using this method. Attempts were also made to prepare **1** through oxidation of the bulky boronic acid Ar*$B(OH)_2$ with Oxone®, but this reaction was not suitable for preparative-scale reactions. Side products of the reaction between Ar*Li and nitrobenzene were identified as Ar*[N(O)Ph] and $[C_6H_5N(O)]_2$ and were characterized by X-ray crystallography and EPR spectroscopy. A variety of main-group and transition-metal complexes of Ar*OH were prepared, namely $Sn(OAr^*)_2$, $Ge(OAr^*)_2$, $[N(SiMe_3)_2]Ge(OAr^*)$, $[Me_2Al(OAr^*)]_2$, and $Ti(NMe_2)(OAr^*)_2$. All compounds were characterized spectroscopically and most were studied by single-crystal X-ray diffraction as well.

Key words: *m*-terphenyl, main-group compounds, X-ray crystallography, multinuclear NMR spectroscopy, EPR spectroscopy.

Résumé : On a réalisé la synthèse du *m*-terphénylphénol encombré, Ar*OH, **1**, (Ar* = C_6H_3-2,3-Mes_2; Mes = 2,4,6-triméthylphényle) en faisant réagir du Ar*Li avec du nitrobenzène. Avec cette méthode, on obtient le phénol **1** avec des rendements allant de modestes à bon. On a aussi tenté de préparer le phénol **1** en procédant à l'oxydation de l'acide boronique encombré Ar*$B(OH)_2$ avec de l'Oxone®, mais cette réaction n'est pas appropriée pour des réactions à l'échelle préparative. On a identifié des sous-produits de la réaction entre le Ar*Li et le nitrobenzène, dont le Ar*[N(O)Ph] et le $[C_6H_5N(O)]$ et on a procédé à leur identification par diffraction des rayons X et par spectroscopie RPE. On a préparé une variété de complexes du Ar*OH avec des métaux de transition et du groupe principal, dont $Sn(OAr^*)_2$, $Ge(OAr^*)_2$, $[N(SiMe_3)_2]Ge(OAr^*)$, $[Me_2Al(OAr^*)]_2$ et $Ti(NMe_2)(OAr^*)_2$. On a caractérisé tous les composés par spectroscopie et la plupart de ces composés ont été étudiés par diffraction des rayons X de cristaux uniques.

Mots-clés : *m*-terphényle, composés du groupe principal, diffraction des rayons X, spectroscopie RMN multinucléaire, spectroscopie RPE.

[Traduit par la Rédaction]

Introduction

The ability to control the coordination environment around a metal is perhaps the most important factor in controlling its reactivity. This is often achieved with the use of sterically demanding ligands. Perhaps the most common class of bulky substituents currently in use are *m*-terphenyls (1), molecules with two aryl substituents arranged *meta* to one another on a central phenyl ring. As shown in Fig. 1, the aryl groups twist out of the plane of the central ring to form a bowl-shaped pocket with a diameter of approximately 12 Å. This pocket acts as a steric shield for reactive species found within it. The steric protection provided by the *m*-terphenyl can be tuned by varying the nature of the aryl

Received 5 July 2007. Accepted 19 October 2007. Published on the NRC Research Press Web site at canjchem.nrc.ca on 7 December 2008.

D.A. Dickie, D.D. Ino, Q. He, O.A. Labeodan, and C.J. Walsby. Department of Chemistry, Simon Fraser University, Burnaby, BC V5A 1S6, Canada.
I.S. MacIntosh, and J.A.C. Clyburne.[1] Department of Chemistry, Saint Mary's University, Halifax, NS B3H 3C3, Canada.
M.C. Jennings. Department of Chemistry, The University of Western Ontario, London, ON N6A 5B7, Canada.
G. Schatte. Saskatchewan Structural Sciences Centre, University of Saskatchewan, Saskatoon, SK S7N 5C9, Canada.

[1]Corresponding author: (email: jason.clyburne@smu.ca).

 doi:10.1139/V07-131 © 2007 NRC Canada

Fig. 1. The pocket formed by the *m*-terphenyl 2,6-bis(2,4,6-trimethylphenyl)benzene is shown in the space-filling diagram.

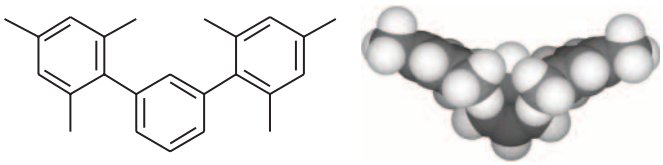

Fig. 2. Selected *m*-terphenyl phenols, from least to most bulky.

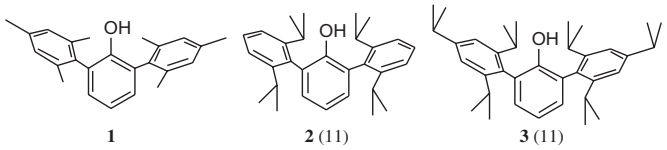

1 **2** (11) **3** (11)

substituents. Common groups include phenyl, 2,4,6-trimethylphenyl (mesityl, Mes), 2,6-diisopropylphenyl (Dipp), and 2,4,6-triisopropylphenyl (Trip).

During the past several years, we have been interested in the coordination chemistry of "substituted" *m*-terphenyl ligands. These studies have resulted in the isolation of unusual coordination geometries for amidinates (2) and carboxylates (3), and here we continue with an examination of phenoxide chemistry. Alkoxides and aryloxides are among the most versatile ligands known and have been placed on virtually every element of the periodic table (4). It is not surprising, therefore, that one of the very first substituted *m*-terphenyls to be used as a ligand was 2,6-diphenylphenol, in a tungsten complex that was subsequently used as an olefin metathesis catalyst (5). Rothwell (6) and others (7) have since explored the structure and reactivity, including catalytic behavior, of many other early transition-metal complexes of this ligand.

The search for new and improved catalysts has also motivated much of the research into main-group *m*-terphenyl phenol complexes (8), based largely on the pioneering work by Yamamoto and co-workers on aluminium tris(2,6-diphenylphenoxide) (9). This molecule and related complexes have served as useful catalysts for stereoselective Claisen rearrangements as well as conjugate addition to α,β-unsaturated carbonyl compounds, and *exo*-selective Diels–Alder additions (opposite to the typical *endo* preference) (10).

Key to the successful use of these bulky complexes is a simple preparation of the ligands. Whereas some bulky phenols, such as 2,6-diphenylphenol, are commercially available, most others are not. Since steric bulk often dominates or governs the chemistry observed for the complexes, a convenient route into these molecules is desirable. We note here that recent reports by the research group of Power and co-workers described the preparation of bulky phenols **2** and **3** (11) (Fig. 2). Our work aims to complement these studies.

Results and discussion

Ligand synthesis

The targeted *m*-terphenyl phenol for this study was 2,6-bis(2,4,6-trimethylphenyl)phenol, Ar*OH **1**, which had previously only been synthesized as a by-product in the reaction of the corresponding *m*-terphenyl copper complex with

Scheme 1. Synthesis of boronic acids **4** and **5**.

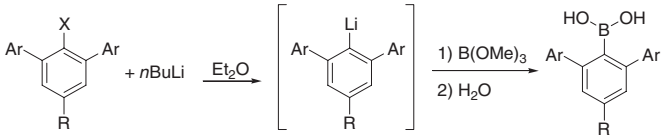

X = Br, Ar = Ph, R = Ph **4**
X = I, Ar = Mes, R = Ph **5**

oxygen (12), or through the palladium-catalyzed cross coupling of phenol with 2,4,6-trimethylbromobenzene (13). Neither of these routes involved the *m*-terphenyl precursors that were readily available, namely Ar*I or a convenient metallated derivative, so two alternative routes were developed.

One proposed route involved the oxidation of *m*-terphenyl boronic acids with Oxone® (14). Lithiation of either 2,4,6-triphenylbromobenzene or 2,6-bis(2,4,6-trimethylphenyl)iodobenzene (Ar*I) in diethyl ether, followed by addition of trimethylborate and aqueous work-up gave the *m*-terphenyl boronic acids **4** and **5**, respectively (Scheme 1). NMR spectroscopy was used to characterize the boronic acids **4** and **5**. The most definitive signal was the two-proton singlet at 4.11 or 4.06 ppm in the spectra of **4** and **5**, respectively, assigned to the $-B(OH)_2$ protons. The upfield shift of these protons relative to phenylboronic acid (4.61 ppm) (15) may be due to shielding by the aryl substituents. The ^{11}B NMR spectra of **4** and **5** each showed a single sharp peak, at 31.4 ppm for **4** and 29.3 ppm for **5**. These values are comparable to other phenylboronic acids (16).

Although these compounds were initially prepared as starting materials for the *m*-terphenyl phenol synthesis, somewhat surprising differences in the O–H absorption region in the IR spectra of **4** and **5** prompted us to more closely examine their intrinsic properties before proceeding further. In the triphenyl-substituted derivative **4**, there was a very strong O–H stretch at 3586 cm^{-1} and a broad absorption at 3280 cm^{-1}, while **5** showed instead four weak absorptions between 3668 and 3417 cm^{-1}. Since this region is primarily affected by hydrogen bonding interactions, attempts were made to grow crystals of both new *m*-terphenyl boronic acids to see if they exhibited different intermolecular interactions. Unfortunately, only **5** yielded crystals suitable for single crystal X-ray diffraction (Fig. 3).

The X-ray crystallographic analysis revealed that, as expected, there is intermolecular [O–H···O] hydrogen bonding in **5**, with O(2) as the donor and O(1) as the acceptor, forming a zigzag chain (Fig. 4). In the absence of other hydrogen bond donor/acceptor groups, all other structurally characterized (17) phenylboronic acid derivatives form homodimers with eight-membered $B_2O_4H_2$ rings rather than infinite chains like **5**. Similar head-to-head homo-dimerization was also observed in two related *m*-terphenyl substituted carboxylic acids (18). Since the carboxylic acids both feature smaller aryl substituents than **5** (phenyl vs. 2,4,6-trimethylphenyl), **4**, which also has the smaller phenyl substituents, may also form a homo-dimer, and that would explain the differences in the IR spectra of **4** and **5**.

Once the boronic acids **4** and **5** were in hand, reactions to oxidize them to the respective *m*-terphenyl phenols were performed using Oxone® in basic solution (14). This reac-

© 2007 NRC Canada

Fig. 3. Molecular structure of 2,6-bis(2,4,6-trimethylphenyl)phenylboronic acid **5**. Thermal ellipsoids are shown at 50% probability, and hydrogen atoms, except OH protons, have been removed for clarity. Selected bond lengths (Å) and angles (°): B(1)—O(1A) 1.603(18); B(1)— O(2A) 1.212(12); B(1)—C(1) 1.552(8); O(1A)–B(1)–O(2A) 112.9(9).

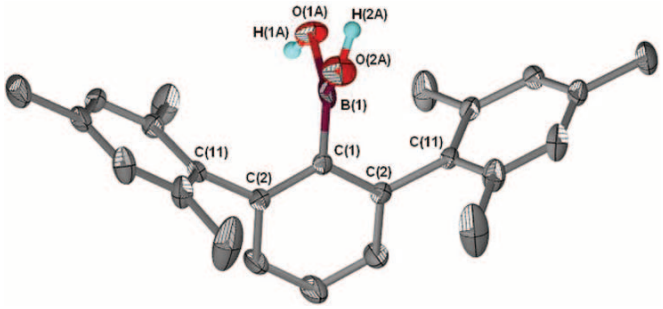

Scheme 2. Synthesis of *m*-terphenyl phenol **1** and nitrosobenzene complex **6**.

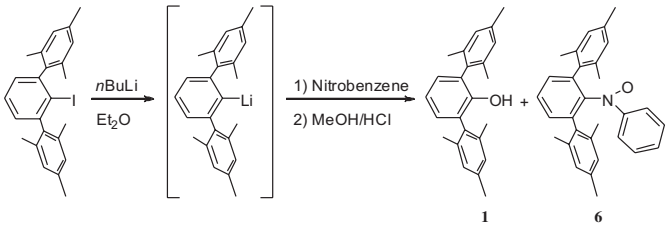

tion produces very low yield (trace) of the desired bulky phenols, and hence work in this area was stopped and a new route was sought.

Generation of bulky phenols from Ar*Li and nitrobenzene

During the course of our boronic acid experiments, Power and co-workers (11) developed a synthesis of bulkier *m*-terphenyl phenols, namely **2** and **3**, directly from the lithiated intermediate Ar*Li, so this more direct and higher yielding route was pursued. Lithiation of Ar*I with *n*-butyllithium in ethereal solution followed by addition of excess nitrobenzene at –78 °C results in the immediate formation of a dark red solution that is quenched with methanol to give **1** (Scheme 2).

In the ^{1}H NMR spectrum of the *m*-terphenyl phenol **1**, the O*H* appears as a singlet at 4.53 ppm. The methyl groups are found at 2.33 (*para*) and 2.06 (*ortho*) ppm. Additional evidence for the presence of the OH was provided by strong IR absorptions at 3486 and 3451 cm^{-1}. These stretches are comparable to those reported by Lüning and co-workers (19) for 2,6-bis(2,6-dimethylphenyl)phenol, at 3482 and 3431 cm^{-1}. Four other previously published *m*-terphenyl phenols, namely 2,6-diphenylphenol (20), 2,6-bis(3,5-dimethylphenyl)phenol (19), 2,6-bis(2,6-diisopropylphenyl)phenol **2** (11), and 2,6-bis(2,4,6-triisopropylphenyl)phenol **3** (11), each reported only a single OH stretch between 3520–3533 cm^{-1} in the IR spectrum. Since three of these five compounds had been crystallographically characterized, single-crystal X-ray diffraction studies were performed on **1** to see if there was a difference in hydrogen bonding that could explain the differences in the IR spectra.

Fig. 4. [O–H···O] hydrogen bonds in **5**, viewed along the crystallographic *a* axis.

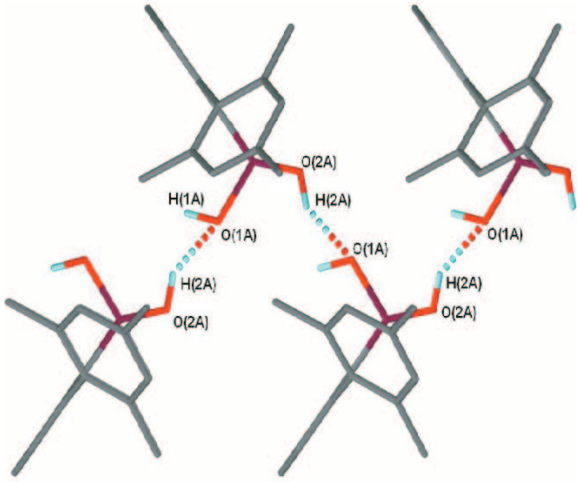

Fig. 5. Molecular structure of 2,6-bis(2,4,6-trimethylphenyl)phenol **1**. Thermal ellipsoids are shown at 50% probability, and all hydrogens, except phenolic protons, have been removed for clarity. Selected bond lengths (Å) and angles (°): O(1)—C(2) 1.356(3); O(31)—C(32) 1.375(3); O(1)–C(2)–C(7) 116.7(2); O(1)–C(2)–C(3) 121.7(2); O(31)–C(32)–C(37) 116.3(2); O(31)–C(32)–C(33) 121.0(2). Hydrogen-bond lengths (Å) and angles (°): O(1)···O(31) 2.823(3); O(1)–H(1A)···O(31) 152.9.

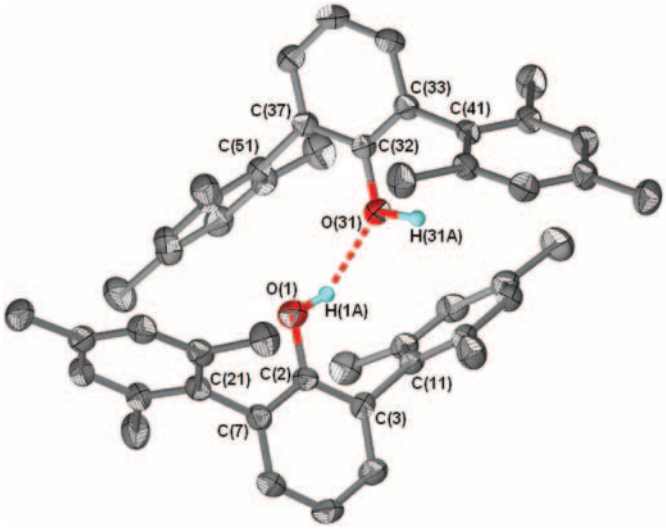

The crystallographic studies revealed that in the solid state, **1** exists as two crystallographically distinct molecules (Fig. 5). These molecules are connected by a weak [O–H···O] hydrogen bond to form a dimer. This is in contrast to the unsubstituted phenol (C_6H_5OH), which forms infinite hydrogen-bonded chains (21) with an average [O···O] distance of 2.67 Å, compared with 2.823(3) Å in **1**. It is also in contrast to all three previously structurally characterized *m*-terphenyl phenols, none of which exhibits [O–H···O] hydrogen bonds. Based on the IR evidence, it would appear that Lüning's 2,6-bis(2,6-dimethylphenyl)phenol follows the

© 2007 NRC Canada

Fig. 6. Molecular structure of nitrosobenzene complex **6** that was isolated as a co-crystal with $[C_6H_5N(O)]_2$, the dimer of nitrosobenzene. Thermal ellipsoids are shown at 50% probability, and hydrogen atoms have been removed for clarity. Selected bond lengths (Å) and angles (°):N(1)—O(1) 1.290(2); N(1)—C(1) 1.443(3); N(1)—C(31) 1.406(3); N(2)—N(2)* 1.128(6); N(2)—O(2) 1.301(5); N(2)—C(41) 1.564(5); O(1)–N(1)–C(1) 116.86(18); O(1)–N(1)–C(31) 119.32(17); C(1)–N(1)–C(31) 123.82(18).

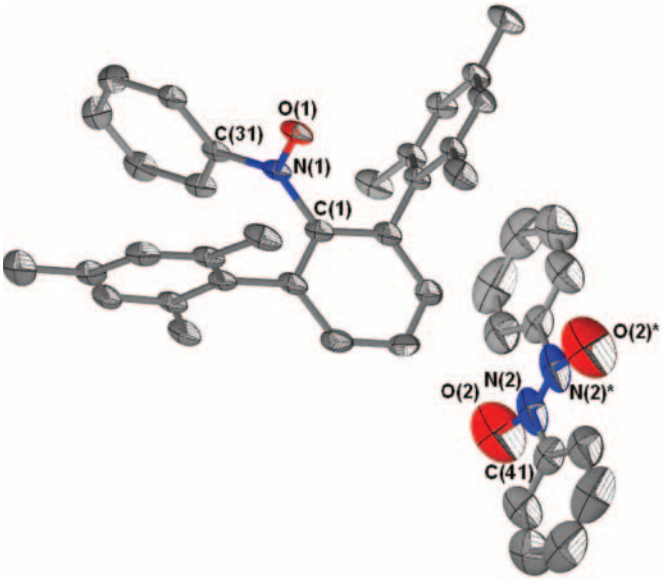

Fig. 7. Main panel: Experimental (top) and simulated (bottom) EPR spectra of nitrosobenzene complex **6** dissolved in CH_2Cl_2. Experimental parameters: ν = 9.86 GHz, microwave attenuation = 20 dB, scan time = 21 s, time constant = 10.24 ms, modulation amplitude = 0.0125 mT, receiver gain = 2.5×10^3, average of 17 scans. Simulation parameters: $a(^{14}N)$ = 1.024 mT; $a(^1H \times 3)$ = 0.247 mT; $a(^1H \times 2)$ = 0.088 mT, $a(^1H \times 3)$ = 0.054 mT, linewidth = 0.047 mT. Inset: EPR spectrum of single co-crystal of nitrosobenzene complex **6** with $[C_6H_5N(O)]_2$. Experimental parameters: ν = 9.86 GHz, microwave attenuation = 25 dB, scan time = 21 s, time constant = 10.24 ms, modulation amplitude = 0.01 mT, receiver gain = 6.3×10^3, 1 scan.

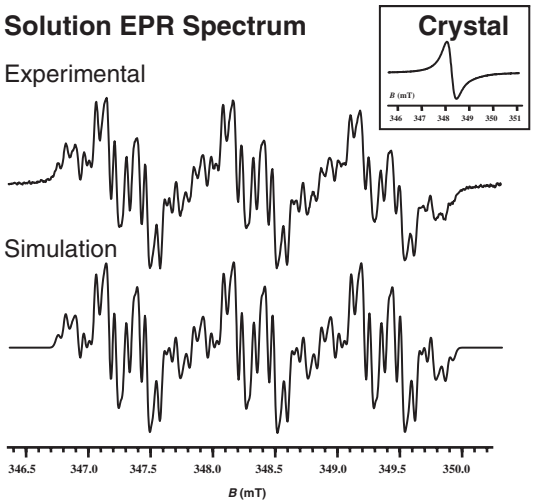

same pattern as **1**, while his 3,5-derivative is more similar to the others (11, 20).

Another feature that was found in each of the crystallographically characterized *m*-terphenyl phenols, including **1**, is an intramolecular [O–H···π] interaction. In the case of the extremely bulky 2,6-bis(2,4,6-triisopropylphenyl)phenol and 2,6-bis(2,6-diisopropylphenyl)phenol, steric hindrance hampers intermolecular [O–H···O] interactions, but does not prevent intramolecular [O–H···π] interactions with a flanking aryl. This interaction occurs primarily through the *ipso* carbon atoms (H···C_{ipso} = 2.64 and 2.39 Å, respectively) (11). In fact, the restricted rotation caused by the presence of such bulky groups may even enhance the interaction by locking the aryls into place.

Restricted rotation is clearly not necessary though, since the crystal structure of the least hindered *m*-terphenyl, 2,6-diphenylphenol, also showed an [O–H···π] interaction of 2.43 Å (20). The corresponding H···C_{ipso} distances in **1** are 2.41 and 2.47 Å [H(1A)···C(11) and H(31A)···C(41), respectively]. It is not immediately clear why 2,6-diphenylphenol does not also engage in [O–H···O] hydrogen bonds like **1**, but it may be that [C–H···π] interactions through the *para* hydrogen of the central phenyl provide more favorable packing interactions. Taken together, these examples illustrate how subtle changes in steric demands can have a large effect on intermolecular interactions.

During the work-up and recrystallization of **1**, a small amount of a highly colored red by-product was also isolated. We performed spectroscopic studies on the red material, and found that NMR studies were not informative because of extensive line broadening, and the IR studies indicated the presence of both aromatic C–H and alkyl C–H fragments, as well as peaks that were tentatively assigned to N–O bonds.

To unambiguously assign the structure, a crystallographic study was performed on the block-shaped crystals (Fig. 6). The results of these studies indicate that the *m*-terphenyl nitrosobenzene addition complex **6** was formed and co-crystallized with homodimerized nitrosobenzene, the other by-product of the phenol synthesis. The formation of the *m*-terphenyl by-product **6** was proposed by Power and co-workers during the preparation of the bulkier *m*-terphenyl phenols **2** and **3**, but was not observed because of the higher steric demands of his *m*-terphenyl backbone (11).

The structure of the nitrosobenzene compound **6** is interesting for two reasons. First of all, it confirms that the bulky Ar*Li can react with nitrobenzene either via oxygen atom abstraction or it can react via addition to nitrogen. Furthermore, the co-crystallized PhNO dimer was isolated in a rare *trans* configuration. Typically, PhNO does not dimerize, and when it does, it crystallizes in the *cis* form (22). Other structural parameters for both components of the red co-crystal are unremarkable, and no other unusual contacts were observed in the packing diagrams.

EPR of nitrobenzene complex 6

The EPR spectrum of a single co-crystal of complex **6** with homodimerized nitrosobenzene shows a single Lorentzian line with a relatively large peak-to-peak linewidth of 0.42 mT (Fig. 7, inset). This result is consistent with the presence of the paramagnetic nitroxide species,

© 2007 NRC Canada

Scheme 3. Synthesis of $[Me_2Al(\mu\text{-}OC_6H_3Mes_2)]_2$ **7**.

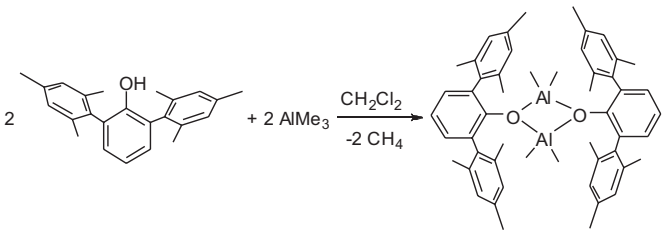

1 **7**

complex **6**; the broad, unresolved line is due to cross-relaxation between the spins of the radical species.

The crystal was dissolved in CH_2Cl_2 and a complex spectrum resulted, which was simulated accurately (Fig. 7, main panel). The magnitude and multiplicity of the hyperfine couplings are consistent with the structure of complex **6**. The large ^{14}N coupling (I = 1, $a(^{14}N)$ = 1.024 mT) indicates that the majority of the spin density lies on the nitroxide moiety; couplings from a total of eight ^1H nuclei (I = ½, $a(^1H \times 3)$ = 0.247 mT; $a(^1H \times 2)$ = 0.088 mT, $a(^1H \times 3)$ = 0.054 mT) demonstrate interactions with the eight protons of the phenyl groups directly attached to the nitroxide and indicate delocalization of spin density across both rings. The ^{14}N and ^1H hyperfine coupling constants measured for compound **6** are comparable to those observed for the symmetrical nitrosyl radical $C_6H_5N(O)C_6H_5$ (23).

Metal complexes derived from Ar*OH

The reaction of the *m*-terphenyl phenol **1** with an equimolar amount of $AlMe_3$ in dichloromethane gives the dialkylaluminium monophenoxide **7** (Scheme 3). Evidence for this product is found in the ^1H NMR spectrum, which showed peaks at –1.26, 2.15, and 2.19 ppm with relative intensities of 6:12:6, due to the aluminium methyls and *m*-terphenyl *ortho* and *para* methyl groups, respectively.

X-ray crystallographic studies (Fig. 8) confirmed the formula suggested by the ^1H NMR data, and showed that despite the bulk of the *m*-terphenyl ligand, **7** exists in the solid state as an oxygen-bridged dimer with a planar Al_2O_4 core. An identical motif was described by Rothwell for his less hindered 2,6-diphenylphenol aluminium complex (24). In contrast, Power's bulkier 2,6-bis(2,4,6-triisopropylphenyl)phenol aluminium complex was isolated as a base-stabilized monomeric ether solvate (25). As was the case in the free ligands, the effects of subtle steric differences around the *m*-terphenyl pocket have a remarkable effect on coordination within that pocket (Fig. 9).

To see if it was possible to establish a trend in the coordination behavior of the *m*-terphenyl phenols, group 14 derivatives were also prepared. Despite the fact that the first Sn(II) and Ge(II) compounds found to exist as dicoordinate monomers in the solid state were based upon bulky phenol ligands (26), structural data on divalent group 14 alkoxy or aryloxy compounds remains relatively rare. This makes the preparation of such compounds interesting simply from a fundamental perspective, but the fact that they are also being studied as catalysts (27) and as molecular precursors to superconductors and (or) ceramic materials for applications,

Fig. 8. Structure of $[Me_2Al(\mu\text{-}OC_6H_3Mes_2)]_2$ **7**. Thermal ellipsoids are shown at 50% probability, and hydrogen atoms and CH_2Cl_2 solvent have been removed for clarity. Selected bond lengths (Å): Al(1)—O(21) 1.8871(16); Al(1)—O(11) 1.8979(17); Al(2)—O(11) 1.8943(16); Al(2)—O(21) 1.9027(17); Al(1)—C(41) 1.942(3); Al(1)—C(42) 1.939(3); Al(2)—C(81) 1.942(3); Al(2)—C(82) 1.949(3); O(11)—C(11) 1.401(3); O(21)—C(51) 1.410(3). Selected bond angles (°): O(11)–Al(1)–O(21) 80.35(7); O(11)–Al(2)–O(21) 80.04(7); Al(1)–O(11)–Al(2) 99.54(7); Al(1)–O(21)–Al(2) 99.62(7).

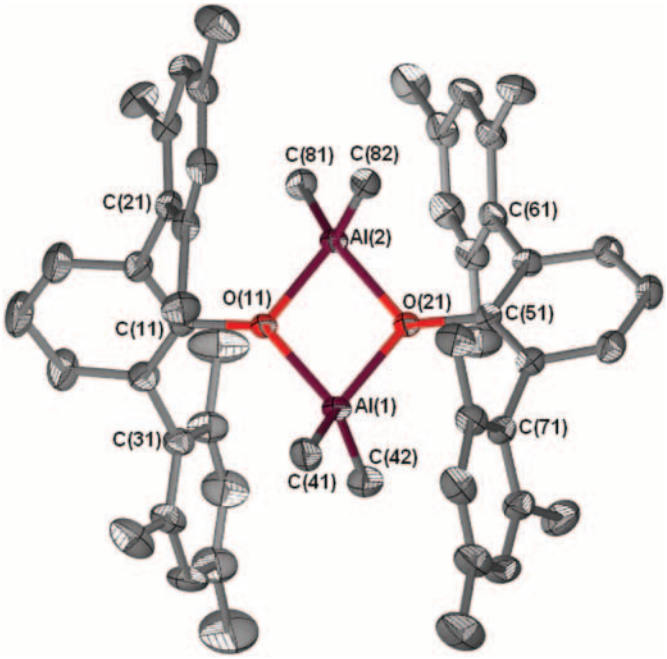

Fig. 9. Changes in the steric demands of the *m*-terphenyl backbone alter the coordination in the ligand binding pocket.

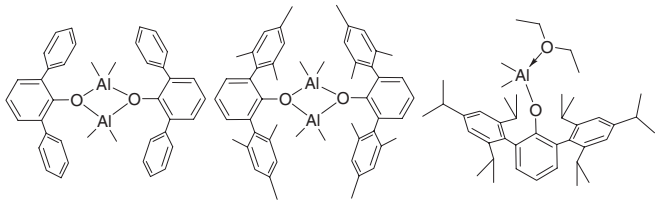

Ref. 24 **7** Ref. 25

Scheme 4. Synthesis of $[Sn(OC_6H_3Mes_2)_2]$ **8**.

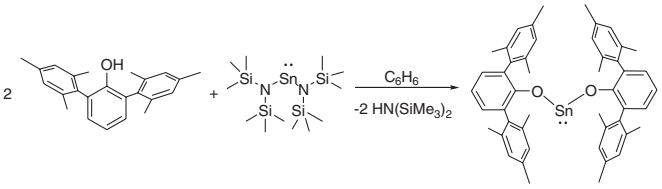

1 **8**

© 2007 NRC Canada

Fig. 10. Structure of $[Sn(OC_6H_3Mes_2)_2]$ **8**, showing Sn–π interactions. Thermal ellipsoids are shown at 50% probability, and hydrogen atoms have been removed for clarity. Selected bond lengths (Å) and angles (°): Sn(1)—O(1) 2.039(3); Sn(1)—O(2) 2.043(3); O(1)—C(101) 1.343(5); O(2)—C(201) 1.342(5); O(1)–Sn(1)–O(2) 87.32(11); Sn(1)–O(1)–C(101) 127.7(2); Sn(1)–O(2)–C(201) 125.7(2).

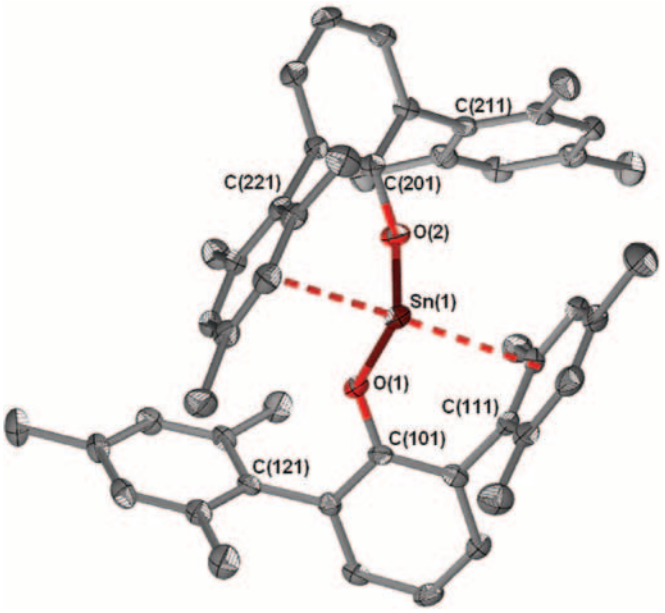

including flat panel displays, gas sensors, solar cells, and lithium battery anodes (28), makes structural data all the more important.

The protonolysis reaction (Scheme 4) of $Sn[N(SiMe_3)_2]_2$ with **1** in benzene gives the tin(II) complex **8** in good yield. No signal from the C*H*$_3$ groups of the trimethylsilylamide ligand was observed ^{1}H NMR spectrum of **8**, indicating that both amido groups had been lost to give the tin(II) bis(phenoxide) complex. The disappearance of the O*H* signal in both the ^{1}H NMR and IR spectra also indicated the formation of **8**, as did the peak at –344 ppm in the ^{119}Sn NMR spectrum. This value is upfield of the signal at –289 ppm for the most closely related $Sn(OAr)_2$ compound in the literature, namely Power's recently reported tin(II) bis(phenoxide) based on the *m*-terphenyl 2,6-bis(2,6-diisopropylphenyl)phenol **2** (25).

Final confirmation of the structure of **8** was provided by single-crystal X-ray diffraction. The crystallographic studies revealed that it does indeed exist as a monomer in the solid state (Fig. 10). The geometry at tin is v-shaped, due to the stereochemically active lone pair. As in the few other known monomeric Sn(II) bis(aryloxides) (25, 29), the O–Sn–O angle is quite acute, measuring only 87.32(11)°. The tin atom in **8** is not truly dicoordinate, however, as it has extensive Sn–π interactions resulting from being sandwiched between two flanking aryls of the *m*-terphenyl ligand. The Sn···centroid distances measure 2.942 and 2.980 Å for the C(111) and C(221) rings, respectively. Such interactions are also present in $Sn(OAr)_2$, where Ar = 2,6-bis(2,6-diisopropylphenyl) although they are somewhat longer [3.064 (C49 ring) and 3.262 (C7 ring)]. The observed upfield ^{119}Sn NMR shift for compound **8** may be due to the stronger Sn–arene interaction, but overall the interaction appears to be weak as shown by the appearance of only one set of signals for the *o*-Me protons in the ^{1}H NMR spectra of **8**.

Scheme 5. Synthesis of $[(Me_3Si)_2NGe(OC_6H_3Mes_2)]$ **9** and $Ge(OC_6H_3Mes_2)_2$ **10**.

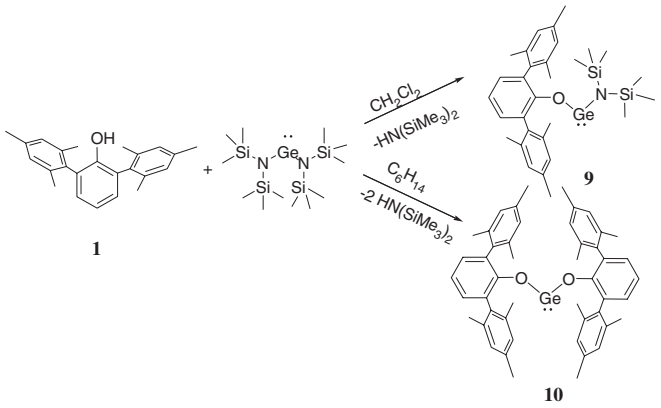

The reaction in dichloromethane of $Ge[N(SiMe_3)_2]_2$ with the *m*-terphenyl phenol **1** gave a mixture of compounds, one of which was the mixed aryloxy-amido germanium complex **9** (Scheme 5). This complex could be identified in the ^{1}H NMR spectrum of the crude reaction mixture as a singlet of 18 hydrogens at 0.00 ppm [–Si(C*H*$_3$)$_3$], and singlets at 2.18 and 2.42 ppm for the *ortho* and *para* methyls of the *m*-terphenyl ligand. Since $Sn[N(SiMe_3)_2]_2$ is known to react with dichloromethane solvent (3c, 30), it seemed possible that this could also be happening during the synthesis of **9**, so an attempt was made to repeat the synthesis in hexanes. Unfortunately, only traces of the mixed complex **9** were observed in the ^{1}H NMR spectrum. The major product was the germanium bis(aryloxide) **10**. As with the tin bis(aryloxide) **8**, the ^{1}H NMR spectrum of **10** showed a pronounced upfield shift of the *ortho* methyl protons to 1.79 ppm (1.82 ppm in **8**). Similarities were also seen in the elevated melting point of **10** at 318 °C, compared with 321 °C in **8**. Elemental analysis was consistent with the proposed composition of **10**.

Several attempts were made to grow crystals of **9** and **10**, but only **9** yielded single crystals suitable for X-ray diffraction studies (Fig. 11). Compound **9** is, to the best of our knowledge, the first structurally characterized monomeric, dicoordinate mixed aryloxy-amido germanium(II) complex (31). The Ge—O bond length of 1.8414(16) Å is longer than those found in other dicoordinate non-calixarene Ge(II) compounds [1.814(2) to 1.8296(14) Å] (25, 32). The opposite is true of the Ge—N bond, which, at 1.851(2) Å is shorter than in comparable compounds [1.855(2) to 1.939(6) Å] (33). The germanium atom does not engage in any significant inter- or intra-molecular interactions.

Given the interesting coordination patterns observed in the main-group complexes of **1**, we also wanted to probe its transition-metal coordination. For the related ligand 2,6-diphenylphenol, titanium complexes are by far the most common. Virtually, all of these complexes feature two *m*-terphenyl phenol ligands on the titanium centre, and a few even accommodate three (34). Only one complex is known with a single 2,6-diphenylphenol ligand, and it uses cyclo-

© 2007 NRC Canada

Fig. 11. Structure of $[(Me_3Si)_2NGe(OC_6H_3Mes_2)]$ **9**. Thermal ellipsoids are shown at 50% probability, and hydrogen atoms have been removed for clarity. Selected bond lengths (Å): Ge(1)—N(1) 1.851(2); Ge(1)—O(1) 1.8414(16); Si(1)—N(1) 1.753(2); Si(2)—N(1) 1.750(2); C(1)—O(1) 1.366(3). Selected bond angles (°): O(1)–Ge(1)–N(1) 97.59(8); Ge(1)–N(1)–Si(1) 122.83(11); Ge(1)–N(1)–Si(2) 114.71(11); Si(1)–N(1)–Si(2) 122.42(12).

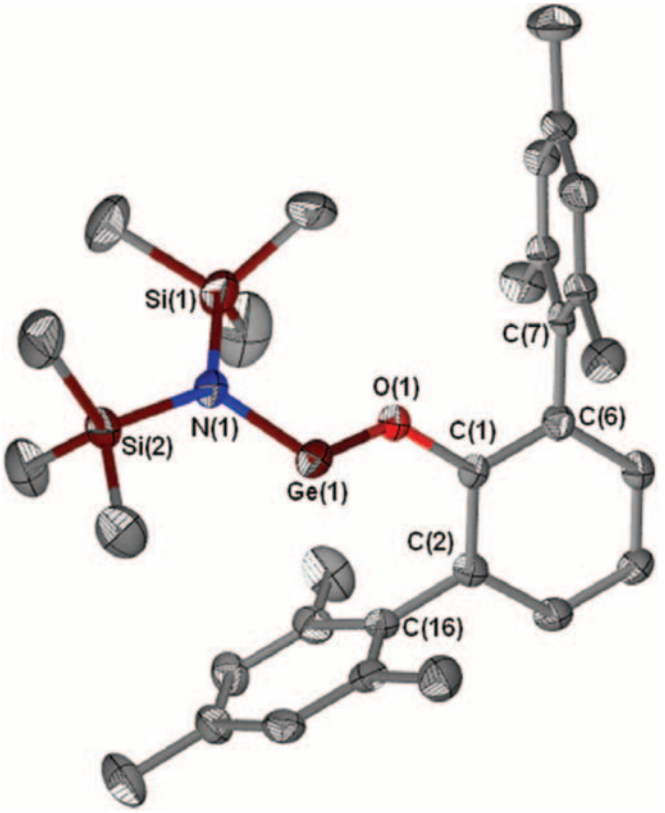

pentadienyl as an ancillary ligand (35). Would the increased bulk of **1** make it possible to isolate a titanium monophenoxide complex?

Addition of tetrakis(dimethylamino)titanium to a solution of **1** in dichloromethane resulted in the formation of an orange solid **11** (Scheme 6). The ^{1}H NMR spectrum showed a 1:1 ratio between the N*Me*$_2$ ligand at 2.30 ppm and the *m*-terphenyl at 2.24 (*para*) and 2.11 (*ortho*) ppm. Given that titanium is tetravalent, these data suggested the formation of a bis(phenoxide) complex with a formula of $(Me_2N)_2Ti(OC_6H_3Mes_2)_2$. This product was formed even when substoichiometric amounts of the *m*-terphenyl phenol ligand were added.

X-ray crystallographic studies of **11** confirmed the proposed structure (Fig. 12). The geometry at titanium is tetrahedral, with the greatest deviation in the O(11)–Ti(1)–O(21) angle [119.25.(5)°] and N(31)–Ti(1)–N(41) angle [102.88(6)°]. The Ti—O bonds are the same within experimental error, and are within the range of similar titanium complexes [1.786(2)–1.862(5) Å] (36). The same is true for the two Ti—N bond lengths, for which literature values of similar compounds range from 1.854(7) to 1.897(5) Å (36). The nature of the oxygen ligand appears to be the most-important factor governing the coordination at titanium. All but one of the structurally characterized examples of tetra-

Scheme 6. Synthesis of $[(Me_2N)_2Ti(OC_6H_3Mes_2)_2]$ **11**.

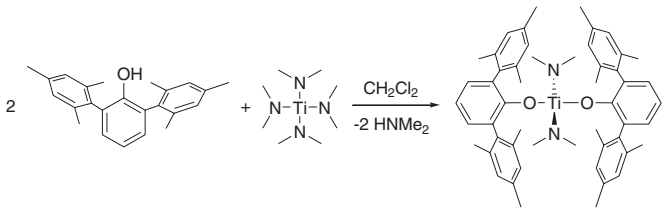

1 **11**

Fig. 12. Structure of $[(Me_2N)_2Ti(OC_6H_3Mes_2)_2]$ **11**. Thermal ellipsoids are shown at 50% probability, and hydrogen atoms have been removed for clarity. Selected bond lengths (Å): Ti(1)—N(31) 1.8822(13); Ti(1)—N(41) 1.8763(13); Ti(1)—O(11) 1.8460(10); Ti(1)—O(21) 1.8495(10). Selected bond angles (°): O(11)–Ti(1)–O(21) 119.25(5); O(11)–Ti(1)–N(41) 106.63(5); O(21)–Ti(1)–N(31) 107.72(5); O(21)–Ti(1)–N(41) 109.98(5); O(11)–Ti(1)–N(31) 109.17(5); N(31)–Ti(1)–N(41) 102.88(6).

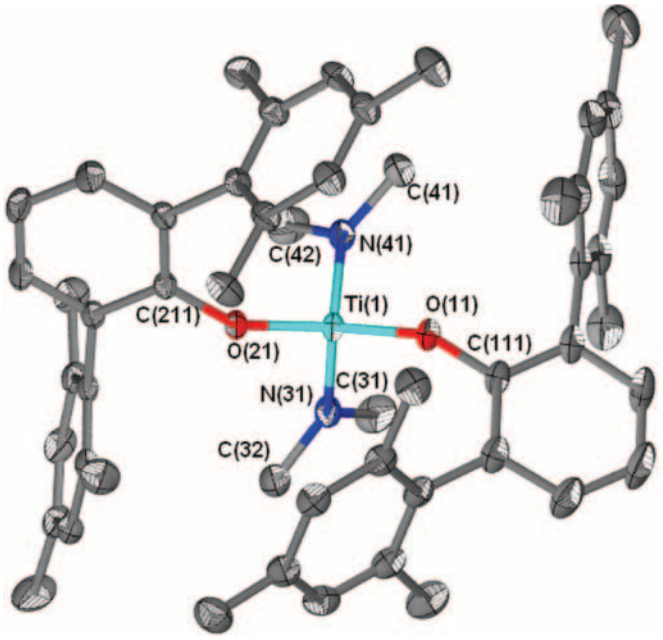

coordinate titanium complexes with two oxygen donors and two nitrogen donors of any type, i.e., $[(R_2N)_2Ti(OR)_2]$, were based on 2,6-disubstituted phenol ligands. The one exception featured a 2,6-disubstituted aniline instead (37). It is not immediately clear if this is merely a coincidence or if the steric shielding of the *meta* substituents is chemically required.

Summary and conclusions

The X-ray crystal structures of a *m*-terphenyl phenol and a *m*-terphenyl boronic acid were described. The hydrogen bonding pattern observed in phenol **1**, intermolecular [O–H···O] dimerization, is very different from that observed in related *m*-terphenyl phenols. The steric demands of **1** are intermediate between those of previously characterized derivatives. This balance appears to be the key to the supramo-

© 2007 NRC Canada

lecular interactions, as the same 2,4,6-trimethylphenyl substituent was used in the boronic acid **5** that also exhibited unprecedented [O–H···O] hydrogen bonds.

Given the differences in the structures of the free ligands, it seemed possible that the main-group and transition-metal complexes of **1** would also have features not found in more and (or) less bulky analogues. This was not the case for the titanium complex **11** and aluminium complex **7**. Both molecules were essentially isostructural to known 2,6-diphenylphenol derivatives. The tin complex **8**, on the other hand, did exhibit a spectroscopic difference. The secondary metal–π interaction between the tin atom and flanking aryls of the *m*-terphenyl ligand in **8** result in an up-field shift of the ^{119}Sn NMR resonance relative to that observed for $Sn(OAr)_2$, where Ar = 2,6-bis(2,6-diisopropylphenyl).

Experimental

General experimental

A nitrogen-atmosphere MBraun UL-99-245 dry box and standard Schlenk techniques on a double manifold vacuum line were used in the manipulation of air and moisture sensitive compounds. Solution-state NMR spectra were recorded in five millimetre tubes at Simon Fraser University on a Bruker AMX 400 or 600 MHz spectrometers or Varian AS 400 or 500 MHz spectrometers. Chemical shifts are reported in parts per million (ppm) downfield from $SiMe_4$ (^{1}H and ^{13}C), $BF_3{\cdot}Et_2O$ (^{11}B), or $SnMe_4$ (^{119}Sn). ^{1}H and ^{13}C spectra are calibrated to the residual signal of the solvent. ^{11}B and ^{119}Sn spectra are calibrated to the external $BF_3{\cdot}Et_2O$ or $SnMe_4$ standard. Infrared spectra were obtained using a Bomem MB spectrometer with the % transmittance values reported in cm^{-1}. EPR spectra were collected on a Bruker ECS-106 EPR spectrometer. The CH_2Cl_2 solution was deoxygenated by bubbling with nitrogen gas, to increase spectral resolution. Spectral simulation used the Bruker WinEPR SimFonia software. Melting points were measured using a Mel-Temp apparatus and are uncorrected. Elemental analyses were obtained at Simon Fraser University by Mr. M.K. Yang on a Carlo Erba Model 1106 CHN analyzer.

Anhydrous solvents were obtained from an MBraun Solvent Purification system, or were purchased from Aldrich and used without further purification. All other reagents and solvents were purchased from commercial sources, including Aldrich, Strem, and Gelest, and used without further purification, except deuterated solvents for NMR experiments on air- and (or) moisture-sensitive compounds, which were dried over P_2O_5 and distilled prior to use. The halogenated *m*-terphenyl precursors 2,4,6-triphenylbromobenzene (38) and 2,6-dimesityliodobenzene (39) were prepared according to literature procedures.

Synthesis of ligands and precursors

2,6-bis(2,4,6-Trimethylphenyl)phenol (1)

Under an inert atmosphere, *n*-BuLi (2.8 mL, 4.5 mmol, 1.6 mol/L in hexanes) was added dropwise to a suspension of 2,6-bis(2,4,6-trimethylphenyl)iodobenzene (1.32 g, 3.0 mmol) in 20 mL anhyd. Et_2O. After 2 h, the solution was cooled to –78 °C, and freshly distilled nitrobenzene (1.5 mL, 15 mmol) was added dropwise. The bright red solution was allowed to stir for 5 min, and then 20 mL of methanol was added slowly. After warming to RT, 30 mL of H_2O was added, and the organic layer was separated. The aq. layer was acidified with 1 mL concd. HCl and then extracted with Et_2O. The combined organic fractions were washed with water and saturated $NaCl_{(aq)}$ and then dried over $MgSO_4$. The solution was concentrated to ~10 mL and then passed through a plug of silica. After addition of ~10 mL pentane, the solution was left to evaporate slowly at room temperature overnight. The resultant pale brown solid was recrystallized to give colorless to pale blue crystals. Yield = 0.39 g (40%); mp = 145 °C. ^{1}H NMR ($CDCl_3$, 499.767 MHz,) δ: 7.03 (m, 3H), 6.98 (s, 4H), 4.53 (s, 1H), 2.33 (s, 6H), 2.06 (s, 12H). ^{13}C{^{1}H} NMR ($CDCl_3$, 100.624 MHz) δ: 137.5, 137.2, 135.9, 133.4, 129.6, 128.5, 128.1, 120.7, 21.2, 20.4. IR (nujol mull) ν: 3486 (s), 3451 (s), 1611 (w), 1584 (w), 1573 (w), 1490 (m), 1320 (s), 1260 (m), 1221 (vs), 1170 (s), 1089 (m), 1071 (m), 1030 (w), 1008 (w), 848 (vs), 829 (s), 797 (s), 780 (w), 752 (vs), 740 (w), 715 (w). Anal. calcd. for $C_{24}H_{26}O$: C, 87.23; H, 7.93. Found: C, 87.50; H, 8.04. HR-MS (*m/z*): [M$^+$] calculated for $C_{24}H_{26}O$, 330.198. Found: 330.198. During recrystallization small red single crystals of **6** can be isolated, a material that was identified as a co-crystal of $[C_6H_5N(O)]_2$ with $C_6H_5N(O)C_6H_3Mes_2$. The crystals can be isolated reproducibly in low yield (mg) per reaction. Mp = 120–123 °C. HR-MS $C_{30}H_{30}NO$ calcd.: 420.2327; found, 420.2315. IR (KBr pellet) ν: 2914 (s), 2857 (m), 1607 (m), 1573 (m), 1446 (vs), 1360 (m), 1307 (m), 1265 (m), 1221 (m), 1074 (m), 1024 (m), 846 (s), 753 (vs), 683 (s), 563 (m).

2,4,6-Triphenylphenylboronic acid (4)

Under an inert atmosphere, *n*-BuLi (9.7 mL, 1.6 mol/L in hexanes) was added to a suspension of 2,4,6-triphenylbromobenzene (5.00 g, 12.98 mmol) in 50 mL anhyd. Et_2O. After 2 h, the solution was cooled to –30 °C in a methanol/ice bath, and $B(OMe)_3$ (1.62 g, 15.57 mmol) was added dropwise. The reaction was warmed to RT and stirred overnight. The reaction was quenched with H_2O and allowed to stir 4 h before being extracted with Et_2O. The combined organic fractions were dried over $MgSO_4$, and then the solvent was removed under vacuum to give a pale yellow solid. Yield = 1.29 g (27%); mp = 356–357 °C. ^{1}H NMR ($CDCl_3$, 400.137 MHz) δ: 7.67 (d, 2H, *J* = 7.1 Hz), 7.63 (s, 2H), 7.53 (d, *J* = 6.8 Hz, 4H), 7.45 (t, *J* = 6.8 Hz, 6H), 7.40 (t, *J* = 7.1 Hz, 3H), 4.11 (s, 2H, B(O*H*)$_2$). ^{13}C{^{1}H} ($CDCl_3$, 125.679 MHz) δ: 146.8, 143.2, 142.1, 129.1, 128.8, 127.8, 127.5, 127.1, 126.9. ^{11}B ($CDCl_3$, 128.370 MHz) δ: 31.37. IR (nujol mull) ν: 3586 (vs), 3280 (br), 3056 (w), 3057 (w), 1595 (s), 1575 (w), 1538 (w), 1492 (s), 1445 (s), 1396 (s), 1335 (vs), 1208 (w), 1193 (w), 1083 (m), 1041 (m), 1030 (m), 983 (w), 917 (w), 888 (s), 821 (m), 782 (m), 761 (s), 751 (s), 699 (vs). Anal. calcd. for $C_{24}H_{19}BO_2$: C, 82.31; H, 5.47. Found: C, 82.62; H, 5.40.

2,6-bis(2,4,6-Trimethylphenyl)phenyl boronic acid (5)

Prepared according to the same procedure as **4**, beginning with 2,6-bis(2,4,6-trimethylphenyl)iodobenzene (5.0 g, 14.1 mmol). Yield = 3.67 g (73%); mp = 268–270 °C. ^{1}H NMR ($CDCl_3$, 400.137 MHz) δ: 7.53 (t, *J* = 7.5 Hz, 1H), 7.06 (d, *J* = 7.5 Hz, 2H), 6.99 (s, 4H), 4.06 (s, 2H), 2.33 (s,

© 2007 NRC Canada

6H), 2.02 (s, 12H). ^{13}C ($CDCl_3$, 125.679 MHz) δ: 146.9, 139.4, 137.8, 135.9, 130.9 (d), 129.1 (d), 128.6 (d), 21.4 (q), 20.8 (q). ^{11}B ($CDCl_3$, 128.370 MHz) δ: 29.30. IR (nujol mull) ν: 3668 (w), 3652 (w), 3646 (w), 3539 (br), 3417 (w), 1729 (w), 1613 (m), 1584 (m), 1561 (m), 1360 (s), 1309 (vs), 1261 (m), 1150 (w), 1112 (m), 1094 (m), 1087 (m), 1048 (m), 1038 (m), 848 (s), 811 (m), 759 (s), 742 (m), 666 (w), 656 (w). Anal. calcd. for $C_{24}H_{27}BO_2$: C, 80.46; H, 7.60. Found: C, 80.37; H, 7.49.

Synthesis of metal complexes

[$Me_2Al(\mu$-$OC_6H_3Mes_2)]_2$ (7)

Under an inert atmosphere, $AlMe_3$ (1.01 mL, 2.0 mol/L in hexanes) was added dropwise to a solution of 2,6-bis(2,4,6-trimethylphenyl)phenol **1** (0.56 g, 1.69 mmol) in 10 mL anhyd. CH_2Cl_2. After stirring for 5 min at RT, the solution was concentrated under vacuum and then cooled to –30 °C. The next day, the solution was decanted from colorless crystals. Yield = 0.25 g (38%); mp = 238–240 °C. ^{1}H NMR (C_6D_6, 499.767 MHz) δ: 6.85 (s, 4H), 6.69 (t, J = 7 Hz, 1H), 6.59 (d, J = 7 Hz, 2H), 2.19 (s, 6H), 2.15 (s, 12H), –1.26 (s, 6H). ^{13}C NMR (C_6D_6, 125.680 MHz) δ: 138.3, 137.9, 135.9, 133.1, 129.5, 129.3, 128.3, 21.9, 21.7. IR (nujol mull) ν: 1610 (w), 1405 (m), 1261 (w), 1190 (m), 1182 (m), 1091 (m), 1032 (w), 848 (m), 825 (m), 803 (w), 774 (w), 758 (w), 701 (s), 635 (m). Anal. calcd. for$C_{52}H_{62}Al_2O_2$, C, 80.80; H, 8.08. Found: C, 81.14; H, 8.18.

[$Sn(OC_6H_3Mes_2)_2$] (8)

Under an inert atmosphere, a solution of $Sn[N(SiMe_3)_2]_2$ (0.33 g, 0.76 mmol) in 2 mL anhyd. benzene was added dropwise to a solution of 2,6-bis(2,4,6-trimethylphenyl)phenol **1** (0.50 g, 1.51 mmol) in 10 mL anhyd. benzene. The mixture was allowed to stir for 3 h at RT and then filtered. Slow evaporation of the solvent gave a yellow solid that was recrystallized from warm hexanes to give colorless crystals: Yield = 0.48 g (81%); mp = 321–322 °C. ^{1}H NMR (CD_2Cl_2, 499.767 MHz) δ: 6.84 (d, J = 6.9 Hz, 2H), 6.79 (s, 4H), 6.73 (t, J = 6.9 Hz, 1H), 2.29 (s, 6H), 1.82 (s, 12H). ^{13}C NMR (100.624 MHz, C_6D_6) δ: 157.8, 138.5, 137.8, 137.4, 129.7, 129.5, 129.2, 117.9, 21.1, 20.5. ^{119}Sn{^{1}H} (CD_2Cl_2, 223.867 MHz) δ: -344.23. IR (nujol mull) ν: 1610 (m), 1584 (m), 1412 (s), 1262 (m), 1246 (s), 1088 (w), 1072 (m), 1031 (br), 844 (vs), 798 (w), 787 (w), 752 (m), 739 (w), 649 (m). Anal. calcd. for $C_{48}H_{50}O_2Sn$: C, 74.14; H, 6.48. Found: C, 74.03; H, 6.39.

[$(Me_3Si)_2NGe(OC_6H_3Mes_2)$] (9)

Under an inert atmosphere, a solution of $Ge[N(SiMe_3)_2]_2$ (0.57 g, 1.45 mmol) in 2 mL CH_2Cl_2 was added dropwise to a solution of 2,6-bis(2,4,6-trimethylphenyl)phenol **1** (0.48 g, 1.45 mmol) in 5 mL anhyd. CH_2Cl_2. After 5 min, the solvent was removed under vacuum, and the crude product was recrystallized from benzene. Mp = 84–86 °C. ^{1}H NMR (C_6D_6, 499.768 MHz) δ: 7.62 (t, J = 7.5 Hz, 1H), 7.22 (d, J = 7.5 Hz, 2H), 7.03 (s, 4H), 2.42 (s, 6H), 2.18 (s, 12H), 0.00 (s, 18H). (This molecule was not isolated as an analytically pure compound).

[$Ge(OC_6H_3Mes_2)_2$] (10)

Under an inert atmosphere, a solution of $Ge[N(SiMe_3)_2]_2$ (0.24 g, 0.61 mmol) in 2 mL hexanes was added dropwise to a suspension of 2,6-bis(2,4,6-trimethylphenyl)phenol **1** (0.20 g, 0.61 mmol) in 5 mL anhyd. hexanes. After 45 min, the solvent was decanted from a white precipitate. Yield = 0.16 g (72%); mp = 318–319 °C. ^{1}H NMR (CD_2Cl_2, 499.767 MHz) δ: 6.81–6.88 (m, 3H), 6.75 (s, 4H), 2.29 (s, 6H), 1.79 (s, 12H). ^{13}C NMR (CD_2Cl_2, 125.678 MHz) δ: 138.1, 136.2, 129.5, 129.2, 128.8, 128.5, 119.2, 21.0, 20.1. IR (nujol mull) ν: 1610 (w), 1585 (w), 1484 (m), 1414 (s), 1260 (s), 1230 (vs), 1091 (m), 1071 (s), 1016 (m), 948 (w), 845 (vs), 799 (m), 754 (s), 739 (w), 728 (w), 670 (m), 659 (s), 609 (m). Anal. calcd. for $C_{48}H_{50}GeO_2$: C, 78.81; H, 6.89. Found: C, 79.14; H, 7.08.

[$(Me_2N)_2Ti(OC_6H_3Mes_2)_2$] (11)

Under an inert atmosphere, a solution of $Ti(NMe_2)_4$ (0.26 g, 1.15 mmol) in 5 mL anhyd. CH_2Cl_2 was added dropwise to a solution of 2,6-bis(2,4,6-trimethylphenyl)phenol **1** (0.76 g, 2.30 mmol) in 10 mL anhyd. CH_2Cl_2. The solution was allowed to stir for 10 min at RT and then cooled to –30 °C. After 3 h, the solution was decanted from orange crystals. Yield = 0.59 g (64%); mp 180 °C (dec.). ^{1}H NMR (C_6D_6, 400.137 MHz) δ: 6.82–6.87 (m, 7H), 2.30 (s, 6H), 2.24 (s, 6H), 2.11 (s, 12H). ^{13}C NMR (C_6D_6, 100.624 MHz) δ: 160.2, 137.3, 136.7, 135.6, 131.1, 130.5, 128.3, 120.2, 43.8, 21.0, 20.9. IR (nujol mull) ν: 3279 (m), 1611 (m), 1580 (m), 1484 (m), 1413 (vs), 1345 (m), 1251 (vs), 1229 (vs), 1146 (m), 1083 (s), 1054 (m), 1029 (m), 1008 (m), 950 (s), 904 (m), 876 (vs), 849 (vs), 799 (m), 778 (m), 757 (vs), 741 (w), 691 (vs), 679 (s), 597 (s). Anal. calcd. for $C_{52}H_{62}N_2O_2Ti$: C, 78.57; H, 7.86; N, 3.52. Found: C, 78.20; H, 7.83; N, 3.37.

Crystallographic studies[2]

The crystal was mounted on a glass fibre (**1**, **10**) or on the top of the nylon fibre of a CryoLoop™ (diameter of the nylon fibre: 10 microns (1 micron = 1 μm); loop diameter = 0.2–0.3 mm; Hampton Research, USA) (**5**–**8**, **11**). Data were collected at the temperature indicated in Table 1 on a Nonius Kappa-CCD diffractometer using monochromated Mo Kα radiation (λ = 0.71073 Å) with COLLECT (40). The unit-cell parameters were calculated and refined from the full data set. Crystal cell refinement and data reduction were carried out using DENZO (41). The data were scaled using SCALEPACK (41). The structures were solved by direct methods using SHELXTL-NT V6.1 suite of programs (42) (**1**, **6**, **8**, **10**) or SIR-97 (43) (**5**, **7**, **11**). All of the non-

[2] Supplementary data for this article are available on the journal Web site (canjchem.nrc.ca) or may be purchased from the Depository of Unpublished Data, Document Delivery, CISTI, National Research Council Canada, Ottawa, ON K1A 0R6, Canada. DUD 5242. For more information on obtaining material, refer to cisti-icist.nrc-cnrc.gc.ca/irm/unpub_e.shtml. CCDC 618683, 618675, 652069, 618680, 618685, 618681, and 618686 contain the crystallographic data for this manuscript. These data can be obtained, free of charge, via www.ccdc.cam.ac.uk/conts/retrieving.html (Or from the Cambridge Crystallographic Data Centre, 12 Union Road, Cambridge CB2 1EZ, UK; fax +44 1223 336033; or deposit@ccdc.cam.ac.uk).

© 2007 NRC Canada

Table 1. Crystallographic data for all crystallographically characterized compounds.

Crystal	**1**	**5**	**6**	**7**	**8**	**9**	**11**
Formula	$C_{24}H_{26}O$	$C_{24}H_{27}BO_2$	$C_{36}H_{35}N_2O_2$	$C_{52}H_{62}Al_2O_2$	$C_{48}H_{50}O_2Sn$	$C_{30}H_{43}GeNOSi_2$	$C_{52}H_{62}N_2O_2Ti$
FW	330.45	358.27	527.66	772.98	777.59	562.42	794.94
T [K]	173(2)	173(2)	173(2)	173(2)	173(2)	223(2)	173(2)
Color	Colorless	Colorless	Red	Colorless	Colorless	Pale yellow	Orange
Size	0.20 × 0.15 × 0.15	Not recorded	0.25 × 0.15 × 0.15	0.30 × 0.25 × 0.25	0.10 × 0.08 × 0.08	0.35 × 0.42 × 0.5	0.30 × 0.25 × 0.25
Cryst. syst.	Triclinic	Orthorhombic	Monoclinic	Monoclinic	Triclinic	Orthorhombic	Triclinic
Space group	*P*-1	*Cmc*2(1)	$P2_1/c$	$P2_1/c$	*P*-1	*P*2(1)2(1)2(1)	*P*-1
a [Å]	9.9380(2)	23.1780(3)	16.209(3)	17.5020(3)	9.7264(2)	11.6223(8)	10.96300(10)
b [Å]	11.5740(3)	12.9813(4)	11.417(2)	13.1600(3)	11.6250(3)	11.8066(8)	13.1040(2)
c [Å]	17.7140(6)	6.7470(6)	19.225(6)	22.3220(4)	18.1089(3)	23.2495(15)	16.5680(2)
a [°]	105.4600(13)	90	90	90	107.0250(10)	90	101.2510(5)
β [°]	100.3660(15)	90	125.3861(17)	109.5440(11)	90.2950(10)	90	98.8800(5)
γ [°]	94.5700(18)	90	90	90	90.8970(10)	90	99.5070(7)
V [Å^3]	1914.14(9)	2030.0(2)	2900.51(16)	4845.12(16)	1957.49(7)	3190.3(4)	2259.10(5)
Z	4	4	4	4	2	4	2
$D_{calcd.}$ [Mg m^{-3}]	1.147	1.172	1.208	1.060	1.319	1.171	1.169
μ [mm^{-1}]	0.068	0.072	0.074	0.096	0.690	1.056	0.230
R_1[a]	0.0752	0.0464	0.0691	0.0581	0.0402	0.0280	0.0444
wR_2[a]	0.2019	0.1141	0.1971	0.1713	0.1206	0.0698	0.1051
CCDC no.	618683	618675	652069	618680	618685	618681	618686

[a] $R_1 = [\Sigma||F_o| - |F_c||]/[\Sigma|F_o|]$ for $[F_o^2 > 2\sigma(F_o^2)]$; $wR_2 = \{[\Sigma w(F_o^2 - F_c^2)^2]/[\Sigma w(F_o^2)^2]\}^{1/2}$.

© 2007 NRC Canada

hydrogen atoms were refined with anisotropic thermal parameters. The hydrogen-atom positions were calculated geometrically and were included as riding on their respective heavy atoms. All figures were generated using X-SEED (44).

Due to the poor quality of the crystals for compound **5**, the quality of the data is rather low (parameter-to-reflection ratio is 1:6), and the bond distances and angles for the disordered BO_2 part and for the hydrogen bonding are not precise (rotational disorder of the oxygen atoms around the C–B bond). However, we believe that the molecular structure of **5** is correct. The Friedel pairs were averaged during the refinement, since this structure does not contain elements heavier than Si.

The crystal structure of compound **7** contains a severely disordered CH_2Cl_2 solvent molecule per asymmetric unit. Attempts to refine, applying a split-atom model, were unsuccessful. The data were corrected for the disordered electron density using the SQUEEZE (45) procedure as implemented in PLATON (46). A total solvent-accessible void volume of 539.5 $Å^3$ (11% of the unit-cell volume). Its contribution to the structure factors was ascertained using PLATON/SQUEEZE (35 e/unit cell). Derived values (formula weight, density, absorption coefficient) do not contain the contribution of the disordered solvent molecule

Acknowledgement

The authors thank Dr. Andrew Lewis (SFU) for collection of ^{11}B and ^{119}Sn NMR data, and Dr. Hilary Jenkins (SMU) for collection of X-ray crystallographic data. Funding was provided by the Canada Research Chairs Program, the Canadian Foundation for Innovation (CFI), the Natural Sciences and Engineering Research Council of Canada (NSERC), Simon Fraser University, and Saint Mary's University.

References

1. (*a*) B. Twamley, S.T. Haubrich, and P.P. Power. Adv. Organomet. Chem. **44**, 1 (1999); (*b*) J.A.C. Clyburne and N. McMullen. Coord. Chem. Rev. **210**, 73 (2000).
2. (*a*) D. Abeysekera, K.N. Robertson, T.S. Cameron, and J.A.C. Clyburne. Organometallics, **20**, 5532 (2001); (*b*) H.A. Jenkins, D. Abeysekera, D.A. Dickie, and J.A.C. Clyburne. J. Chem. Soc. Dalton Trans. 3919 (2002).
3. (*a*) D.A. Dickie, D.D. Choytun, M.C. Jennings, H.A. Jenkins, and J.A.C. Clyburne. Organomet. Chem. **689**, 2186 (2004); (*b*) D.A. Dickie, M.C. Jennings, H.A. Jenkins, and J.A.C. Clyburne. Inorg. Chem. **44**, 828 (2005); (*c*) D.A. Dickie, P.T.K. Lee, O.A. Labeodan, G. Schatte, N. Weinberg, A.R. Lewis, G.M. Bernard, R.E. Wasylishen, and J.A.C. Clyburne. Dalton Trans. 2862 (2007).
4. G.A. Horley, M.F. Mahon, K.C. Molloy, M.M. Venter, and P.W. Haycock, C.P. Myers. Inorg. Chem. **41**, 1652 (2002).
5. F. Quignard, M. Leconte, and J.-M. Basset. J. Chem. Soc., Chem. Commun. 1816 (1985).
6. (*a*) A.E. Fenwick, K. Phomphrai, M.G. Thorn, J.S. Vilardo, C.A. Trefun, B. Hanna, P.E. Fanwick, and I.P. Rothwell. Organometallics, **23**, 2146 (2004); (*b*) S.W. Schweiger, M.M. Salberg, A.L. Pulvirenti, E.E. Freeman, P.E. Fanwick, and I.P. Rothwell. J. Chem. Soc., Dalton Trans. 2020 (2004); (*c*) M.R. Lentz, J.S. Vilardo, M.A. Lockwood, P.E. Fanwick, and I.P. Rothwell. Organometallics, **23**, 329 (2004).
7. (*a*) J.R. Dilworth, J. Hanich, M. Krestel, J. Beck, and J. Strähle. Organomet. Chem. **315**, C9, (1986); (*b*) F. Quignard, M. Leconte, J.-M. Basset, L.-Y. Hsu, J.J. Alexander, and S.G. Shore. Inorg. Chem. **26**, 4272 (1987); (*c*) D.J. Darensbourg, B.L. Mueller, C.K. Bischoff, S.S. Chojnacki, and J.H. Reibenspies. Inorg. Chem. **30**, 2418 (1991); (*d*) R.K. Minhas, J.J.H. Edema, S. Gambarotta, and A. Meetsma. J. Am. Chem. Soc. **115**, 6710 (1993); (*e*) M.B. O'Donoghue, R.R. Schrock, A.M. LaPointe, and W.M. Davis. Organometallics, **1**5 1334 (1996); (*f*) T. Hascall, M.-H. Baik, B.M. Bridgewater, J.H. Shin, D.G. Churchill, R.A. Friesner, and G. Parkin. Chem. Commun. 2644 (2002).
8. (*a*) A. Johansson and M. Håkansson. Chem. Eur. J. **11**, 5238 (2005); (*b*) T. Ooi, Y. Kondo, and K. Maruoka. Angew. Chem., Int. Ed. **37**, 3039 (1998).
9. (*a*) H. Ito, T. Nagahara, K. Ishihara, S. Saito, and H. Yamamoto. Angew. Chem., Int. Ed. **43**, 994 (2004); (*b*) S. Saito, T. Nagahara, M. Shiozawa, M. Nakadai, and H. Yamamoto. J. Am. Chem. Soc. **125**, 6200 (2003); (*c*) K. Maruoka, H. Imoto, S. Saito, and H. Yamamoto. J. Am. Chem. Soc. **116**, 4131 (1994).
10. (*a*) S. Saito and H. Yamamoto. Chem. Commun. 1585 (1997); (*b*) S. Saito, M. Shiozawa, T. Nagahara, M. Nakadai, and H. Yamamoto. J. Am. Chem. Soc. **122**, 7847 (2000).
11. C. Stanciu, M.M. Olmstead, A.D. Phillips, M. Stender, and P.P. Power. Eur. J. Inorg. Chem. 3495 (2003).
12. M. Niemeyer. Organometallics, **17**, 4649 (1998).
13. R.B. Bedford and M.E. Limmert. J. Org. Chem. **68**, 8669 (2003).
14. K.S. Webb and D. Levy. Tetrahedron Lett. **36**, 5117 (1995).
15. Y. Tokunaga, H. Ueno, Y. Shimomura, and T. Seo. Heterocycles, **5**7 787 (2002).
16. H. Nöth and B. Wrackmeyer. Nuclear magnetic resonance spectroscopy of Boron compounds. *In* NMR principles and progress. Vol. 14. *Edited by* P. Diehl, E. Fluck, and R. Kosfeld. Springer-Verlag, New York. 1978.
17. Cambridge Structural Database. Version 5.27. See: F.H. Allen. Acta Crystallogr. **B58**, 380 (2002).
18. (*a*) D.A. Dickie, A.Y.C. Chan, H. Jalali, H.A. Jenkins, H.-Z. Yu, and J.A.C. Clyburne. Chem. Commun. 2432 (2004); (*b*) D.A. Dickie, G. Schatte, M.C. Jennings, H.A. Jenkins, S.Y.L. Khoo, and J.A.C. Clyburne. Inorg. Chem. **45**, 1646 (2006).
19. M. Abbass, C. Kühl, C. Manthey, A. Müller, and U. Lüning. Collect. Czech. Chem. Commun. **69**, 1325 (2004).
20. K. Nakatsu, H. Yoshioka, K. Kunimoto, T. Kinugasa, and S. Ueji. Acta. Crystallogr., Sect. B. **34**, 2357 (1978).
21. V.E. Zavodnik, V.K. Belskii, and P.M. Zorkii. J. Struct. Chem. **28**, 793 (1987).
22. D.A. Dieterich, I.C. Paul, and D.Y. Curtin. J. Am. Chem. Soc. **96**, 6372 (1974).
23. P.H.H. Fisher and F.A Neugebauer. Z. Naturforsch, **19a**, 1514 (1964).
24. A.J.R. Son, M.G. Thorn, P.E. Fanwick, and I.P. Rothwell. Organometallics, **22**, 2318 (2003).
25. C. Stanciu, A.F. Richards, M. Stender, M.M. Olmstead, and P.P. Power. Polyhedron, **25**, 477 (2006).
26. B. Çetinkaya, I. Gümrükçü, M.F. Lappert, J.L. Atwood, R.D. Rogers, and M.J. Zaworotko. J. Am. Chem. Soc. **102**, 2088 (1980).
27. A. Kowalski, A. Duda, and S. Penczek. Macromolecules, **33**, 689 (2000).

© 2007 NRC Canada

28. (*a*) T.J. Boyle, J.M. Segall, T.M. Alam, M.A. Rodriguez, and J.M. Santana. J. Am. Chem. Soc. **124**, 6904 (2002); (*b*) T.J. Boyle, T.L. Ward, S.M. De'Angeli, H. Xu, and W.F. Hammetter. Chem. Mater. **15**, 765 (2003); (*c*) C.S. Weinert, P.E. Fanwick, and I.P. Rothwell. J. Chem. Soc., Dalton Trans. 1795 (2003).
29. D.M. Barnhart, D.L. Clark, and J.G. Watkin. Acta. Crystallogr., Sect. C **50**, 702 (1994).
30. M.F. Lappert, M.C. Misra, M. Onyszchuk, R.S. Rowe, and P.P. Power. J. Organomet. Chem. **330**, 31 (1987).
31. V.N. Khrustalev, I.A. Portnyagin, N.N. Zemlyansky, I.V. Borisova, M.S. Nechaev, Y.A. Ustynyuk, M.Y. Antipin, and V. Lunin. J. Organomet. Chem. **690**, 1172 (2005).
32. (*a*) C.S. Weinert, P.E. Fanwick, and I.P. Rothwell. J. Chem. Soc., Dalton Trans. 2948 (2002); (*b*) C.S. Weinert, A.E. Fenwick, P.E. Fenwick, and I.P. Rothwell. J. Chem. Soc., Dalton Trans. 532 (2003).
33. (*a*) R.W. Chorley, P.B. Hitchcock, M.F. Lappert, W.-P. Leung, P.P. Power, and M.M. Olmstead. Inorg. Chim. Acta, **198**, 203 (1992); (*b*) H. Braunschweig, P.B. Hitchcock, M.F. Lappert, and L.J.-M. Pierssens. Angew. Chem., Int. Ed. Engl. **33**, 1156 (1994); (*c*) M. Veith and A.Z. Rammo. Anorg. Allg. Chem. **627**, 662 (2001); (*d*) A. Meller, G. Ossig, W. Maringgele, M. Noltemeyer, D. Stalke, R. Herbst-Irmer, S. Freitag, and G.M. Sheldrick. Z. Naturforsch., Sect. B: Chem. Sci. **47**, 162 (1992). (*e*) C. Cui, M.M. Olmstead, J.C. Fettinger, G.H. Spikes, and P.P. Power. J. Am. Chem. Soc. **127**, 17530 (2005).
34. (*a*) R.W. Chesnut, L.D. Durfee, P.E. Fanwick, I.P. Rothwell, K. Folting, and J.C. Huffman. Polyhedron, **6**, 2019 (1987); (*b*) M.G. Thorn, Z.C. Etheridge, P.E. Fanwick, and I.P. Rothwell. J. Organomet. Chem. **591**, 148 (1999); (*c*) A. Sato, A. Hattori, K. Ishihara, S. Saito, and H. Yamamoto. Chem. Lett. **32**, 1006 (2003).
35. S.J. Sturla and S.L. Buchwald. Organometallics, **21**, 739 (2002).
36. (*a*) R.A. Jones, J.G. Hefner, and T.C. Wright. Polyhedron, **3**, 1121 (1984); (*b*) V.M. Visciglio, P.E. Fanwick, and I.P. Rothwell. Inorg. Chim. Acta, **211**, 203 (1993); (*c*) V.M. Visciglio. P.E. Fanwick, and I.P. Rothwell. Acta Crystallogr., Sect. C: Cryst. Struct. Commun. **50**, 896 (1994); (*d*) C.H. Zambrano, R.D. Profilet, J.E. Hill, P.E. Fanwick, and I.P. Rothwell. Polyhedron, **12**, 689 (1993).
37. J. Scholz, S. Kahlert, and H. Görls. Organometallics, **23**, 1594 (2004).
38. E.P. Kohler and L.W. Blanchard. J. Am. Chem. Soc. **57**, 367 (1935).
39. C.-J.F. Du, H. Hart, and K.K.D. Ng. J. Org. Chem. **51**, 3162 (1986).
40. B.V. Nonius. Kappa CCD Software [computer program]. Nonius BV, Delft, The Netherlands. 1999.
41. Z. Otwinowski and W. Minor. Processing of X-ray diffraction data collected in oscillation mode, methods in enzymology. *In* Macromolecular crystallography, Part A. *Edited by* C.W. Carter and R.M. Sweet. Academic Press. London. 1997. Vol. 276, pp. 307–326.
42. G.M. Sheldrick. SHELXTL NT V6.12, Program Library for Structure Solution and Molecular Graphics [computer program]. Bruker AXS, Inc. Madison, WI. 2000.
43. A. Altomare, G. Cascarano, C. Giacovazzo, A. Guagliardi, A.G.G. Moliterni, M.C. Burla, G. Polidori, M. Camalli, and R. Spagna. J. Appl. Crystallogr. **32**, 115 (1999).
44. (*a*) L.J. Barbour. J. Supramol. Chem. **1**, 189 (2001); (*b*) J.L. Atwood and L.J. Barbour. Cryst. Growth Des. **3**, 3 (2003).
45. P. van der Sluis and A.L. Spek. Acta Crystallogr. **46A**, 194 (1990).
46. A.L. Spek. PLATON: A multipurpose crystallographic tool [computer program]. Utrecht University, Utrecht, the Netherlands. 1998.

© 2007 NRC Canada

A convenient and efficient protocol for the synthesis of symmetrical *N,N′*-alkylidine bisamides by sulfamic acid under solvent-free conditions

Nagarajan Panneer Selvam, Sundar Saranya, and Paramasivan T. Perumal

Abstract: A simple and convenient approach to the synthesis of symmetrical *N,N′*-alkylidine bisamides is described. Aromatic and aliphatic nitriles react with aromatic aldehydes in the presence of sulfamic acid to give the corresponding bisamides in moderate yields.

Key words: alkylidine bisamides, nitrile, sulfamic acid.

Résumé : On a mis au point une méthode simple et pratique de réaliser la synthèse de *N,N′*-alkylidinebisamides symétriques. Les nitriles aliphatiques et aromatiques réagissent avec les aldéhydes aromatiques, en présence d'acide sulfamique, pour conduire à la formation des bisamides correspondants avec des rendements modérés.

Mots-clés : alkylidinebisamides, nitrile, acide sulfamique.

[Traduit par la Rédaction]

Introduction

The amidation of organic compounds using nitriles is a very useful tool in organic chemistry, as amide moieties are important constituents of many biologically significant compounds. In the last years, retro-amide links have successfully been incorporated in the synthesis of retro-inverso peptide analogues, such as enkephalinamide (1), substance P (2), somatosatin (3), or gastrin (4). Residues with retro-amide links are also the basic units of some aliphatic polyamides (nylons) (5), which are closely related to fibrous proteins. Specifically, bisamides are key fragments for the introduction of gem-iminoalkyl residues in retro-inverso pseudo peptide derivatives (6) by treating the corresponding amide with iodobenzene bistrifluoroacetate (7). In this regard, bisamides are of considerable interest in the synthesis of peptidomimetic compounds (5).

Result and discussion

Magat et al. (8) reported the synthesis of bisamides using sulfuric acid in good yields. However, this method suffers from few disadvantages, such as the use of 85% sulphuric acid (solvent) and the scope of the reaction was limited to few aldehydes only. Hence, the development of highly expedient protocol with wide applicability is necessary for their syntheses.

Received 18 October 2007. Accepted 7 November 2007. Published on the NRC Research Press Web site at canjchem.nrc.ca on 5 December 2008.

N.P. Selvam, S. Saranya, and P.T. Perumal.[1] Organic Chemistry Division, Central Leather Research Institute, Chennai 600020, India.

[1]Corresponding author (e-mail: ptperumal@gmail.com).

The increasing demands of environmental legislation have been prompting the chemical industry to minimize or preferably eliminate waste production in chemical manufacture (9). During the last few years, sulfamic acid has emerged as a substitute for conventional acidic catalysts. Sulfamic acid has been used as an efficient heterogeneous catalyst for acid-catalyzed reactions (10), Biginelli condensation (11), Beckmann rearrangement (12), inter- and intra-molecular imino Diels–Alder reactions (13), and Pechmann condensations (14). The distinctive catalytic features and intrinsic Zwitter ionic property of sulfamic acid are very different from conventional acidic catalysts. This has encouraged us to investigate further the application of sulfamic acid in carbon–carbon and carbon–hetero atom bond-forming reactions.

Recently, we reported the synthesis of acetamidophenols (15) from aldehydes, β-naphthols and acetonitrile via modified Ritter-type protocol catalyzed by anhyd. ceric sulphate. Encouraged by these results, we also extented the protocol by replacing β-naphthols with activated substituted benzenes, like anisole, toluene, and so forth. Interestingly, we observed that anisole or toluene was not involved in the reaction, while the aldehyde reacted with acetonitrile in the presence of anhyd. ceric sulfate, yielding symmetrical bisacetamides as the major product (Scheme 1).

However, this methodology suffers from few limitations; the reaction was not complete even after refluxing for 24 h, and it requires stoichiometric amount of catalyst. Hence, to overcome these limitations, we focused on an efficient and eco-benign protocol for the synthesis of bisamides.

In the present study, we report a highly efficient method for the synthesis of biologically valuable bisamides from aromatic aldehydes with a series of nitriles using sulfamic acid in moderate yields (Scheme 2).

Initially, we carried out the reaction of 4-nitrobenzaldehyde in acetonitrile using various catalysts for the synthesis of bisacetamides (Scheme 3). After systematic screening

 doi:10.1139/V07-134 © 2007 NRC Canada

Scheme 1.

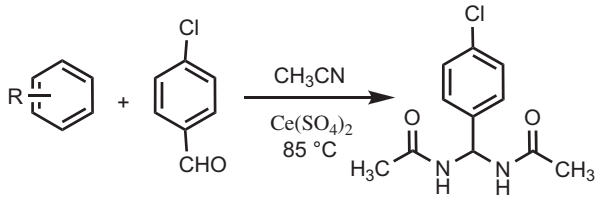

Scheme 2.

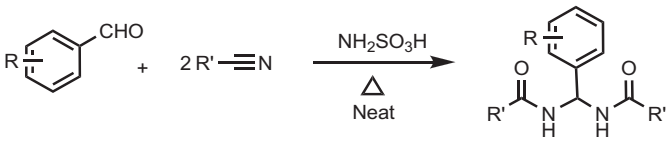

Scheme 3.

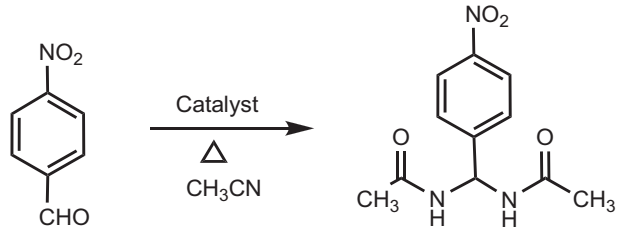

(Table 1), sulfamic acid was found to be the catalyst of choice. Similarly, the mole ratio of sulfamic acid was studied and found 50 mol% of sulfamic acid to be optimum.

We extended our protocol with various substituted aromatic nitriles. In the course of our study, we investigated the reaction of 3-nitrobenzaldehyde and 2-chlorobenzonitrile with sulfamic acid using various solvents for the synthesis of bisamides (Scheme 4), and found that solvent-free condition was the best for the conversion. The results are listed in Table 2.

The reaction was carried out with aldehyde (10 mmol) and nitrile (22 mmol) in the presence of sulfamic acid (50 mol%) and heated at 125 °C under solvent-free condition. This protocol is remarkably simple and requires non-hazardous reagents or inert atmosphere.

A mechanistic rationale portraying the probable sequence of events is given in Scheme 5. The substrate scope of the reaction under the optimized condition was investigated, and the results are summarized in Table 3. The reaction was amenable to wide variations in nitriles. The reaction went smoothly with aromatic aldehydes containing electron-withdrawing groups, while no product formation was seen with electron-rich aldehydes and aliphatic aldehydes. However, in the case of terephthalaldehyde, mono bis-amide was formed, wherein only one aldehydic group was involved in the reaction with nitrile (Table 3, entry 5).

Conclusion

Clearly, the results show that the sulfamic-acid-catalyzed protocol provides an efficient tool for the synthesis of *N*,*N*′-alkylidine symmetrical bisamides under relatively mild conditions. In conclusion, we have developed a green approach to the synthesis of symmetrical bisamides that requires neither harsh conditions nor hazardous acids. The present protocol offers several advantages, including clean and simple reaction procedure, isolation of products by crystallization without employing purification methods like column chromatography, use of an eco-friendly catalyst, and solvent-free conditions, which make it an attractive method for the synthesis of *N*,*N*′-alkylidine symmetrical bisamides.

Table 1. Screening of catalysts.

Entry	Catalyst (1 equiv.)	Time (h)	Yield[a] (%)
1	Anhyd. $Ce(SO_4)_2$	24	48
2	$InCl_3$	48	0
3	$BiCl_3$	48	0
4	$SnCl_2{\cdot}2H_2O$	48	0
5	Sulfamic acid	20	65
6	K10 montmorillonite	48	0
7	$H_3PW_{12}O_{40}$	48	5

[a]Isolated yield.

Experimental

General

Glassware was dried in a hot-air oven prior to use. 2-(Trifluoromethyl)benzonitrile and benzonitrile were purchased from Lancaster Research Chemicals. All other reagents were purchased from S. D. Fine. Chem. Limited and used as received. Acetonitrile was distilled from CaH_2 under nitrogen and stored over 4 Å molecular sieves. DMSO-d_6 was purchased from Aldrich. IR measurements were done as KBr pellets for solids using PerkinElmer Spectrum RXI FTIR. The ^{1}H and ^{13}C NMR spectra were recorded in DMSO-d_6 with JEOL 500 MHz high-resolution NMR spectrometer. DMSO-d_6 was used as the solvent for the NMR spectral measurements, and the spectra were recorded in ppm with TMS as internal standards. Multiplicities are abbreviated as follows: singlet (s), doublet (d), triplet (t), multiplet (m), and broad (br). Mass spectra were recorded by using an Electrospray Ionization Method with Thermo Fennigan Mass spectrometer. Melting points were determined in capillary tubes and are uncorrected. Analytical TLC was performed on precoated plastic sheets of silica gel G/UV-254 of 0.2 mm thickness (Macherey–Nagel, Germany). Elemental analysis data were recorded using Thermo Finnigan FLASH EA 1112 CHN analyzer. Column Chromatography was carried out using 100–200 mesh silica gel.

Representative procedure for the synthesis of *N*,*N*′-alkylidine bisamides

A mixture of aldehyde (10 mmol), nitrile (22 mmol), and sulfamic acid (5 mmol) was stirred at 125 °C for the appropriate time as mentioned in Table 3. When acetonitrile (taken in excess, 10 mL) was used, the reaction was carried out at 85 °C. After the completion of the reaction (as monitored by TLC), ethanol:water (8:2 mL) was added, and the reaction mixture was refluxed for 20 min and allowed to stay overnight. The solid obtained was filtered and dried.

© 2007 NRC Canada

Scheme 4.

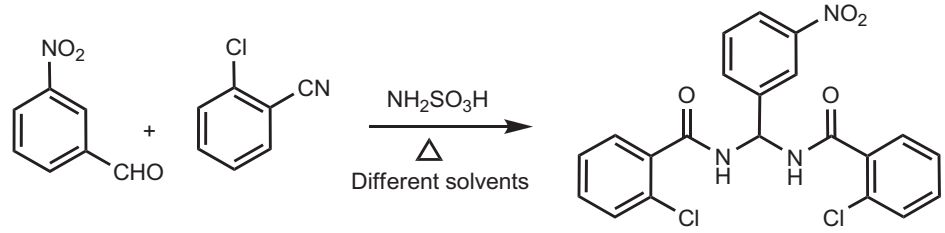

Scheme 5.

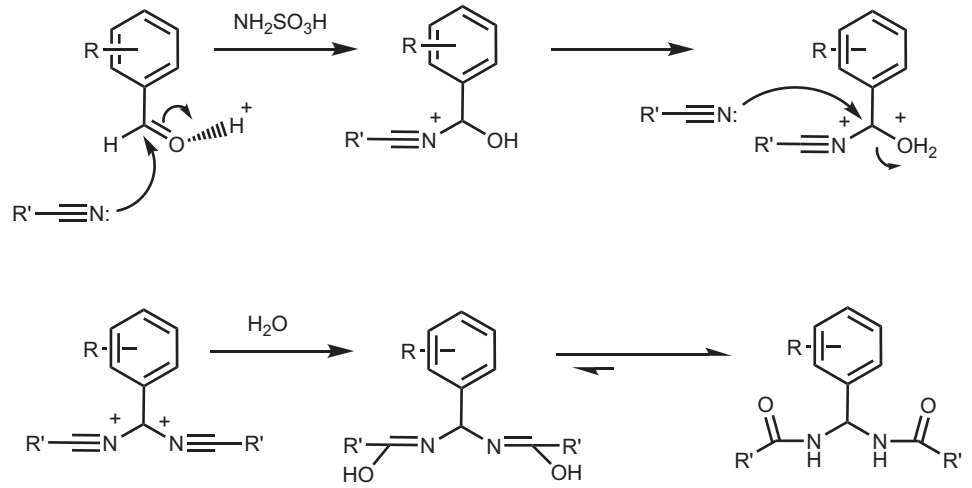

Table 2. Solvent-effect study.

Entry	Solvent	Temperature	Yield[a] (%)
1	1,2-Dichloroethane	Reflux	34
2	1,2-Dichlorobenzene	Reflux	Trace
3	PhMe	Reflux	22
4	Xylene	Reflux	48
5	Neat	125 °C	68

[a]Isolated yield.

N-[acetylamino-(4-nitrophenyl)methyl]-acetamide (Table 3, entry 1)

Pale brownish yellow solid. Yield: 65%, mp: 270–272 °C (Lit. 272 °C) (16). IR ν_{max}: 3270, 3107, 1672, 1518, 1352, 1194, 1094, 824 cm^{-1}. ^1H NMR (500 MHz, DMSO-d_6) δ: 1.85 (s, 6H), 6.53 (t, 1H, J = 7.65 Hz), 7.54 (d, 2H, J = 8.4 Hz), 8.17 (d, 2H, J = 9.15 Hz), 8.70 (d, 2H, J = 7.5 Hz, D_2O exchangeable). ^{13}C NMR (125 MHz, DMSO-d_6) δ: 22.94, 57.45, 123.99, 128.28, 147.41, 148.36, 169.53. MS (ESI): 251 (M^+). Anal. calcd. for $C_{11}H_{13}N_3O_4$: C 52.59, H 5.22, N 16.73. Found: C 52.68, H 5.15, N 16.67%.

N-[acetylamino-(4-chlorophenyl)methyl]-acetamide (Table 3, entry 2)

White solid. Yield: 60%, mp: 258–260 °C (Lit. 260–261 °C) (17). IR ν_{max} KBr: 3271, 3123, 1670, 1093, 1529, 1370 cm^{-1}. ^1H NMR (500 MHz, DMSO-d_6) δ: 1.83 (s, 6H), 6.42 (t, 1H, J = 8.05 Hz), 7.28 (d, 2H, J = 8.6 Hz), 7.37 (d, 2H, J = 8.6 Hz), 8.52 (d, 2H, J = 8.05 Hz, D_2O exchangeable). ^{13}C NMR (125 MHz, DMSO-d_6) δ: 22.96, 57.33, 128.73, 128.80, 132.66, 139.87, 169.35. LR-MS (EI^+): 240 (M^+). Anal. calcd. for $C_{11}H_{13}N_2O_2Cl$: C 54.89, H 5.44, N 11.64. Found: C 54.86; H 5.42; N,11.62%.

N-[acetylamino-(3-nitrophenyl)methyl]-acetamide (Table 3, entry 3)

White solid. Yield: 68%, mp: 256–257 °C (Lit 256–257 °C) (18). IR ν_{max}: 3275, 3118, 2369, 1665, 1561, 1529, 1350, 1272, 1095, 764 cm^{-1}. ^1H NMR (500 MHz, DMSO-d_6) δ: 1.86 (s, 6H), 6.53 (t, 1H, J = 7.45Hz), 7.62 (t, 1H, J = 8.05Hz), 7.74 (d, 1H, J = 7.45Hz), 8.14 (s, 2H, br), 8.71 (d, 2H, J = 7.45Hz, D_2O exchangeable). ^{13}C NMR (125 MHz, DMSO-d_6) δ: 98, 57.45, 121.47, 123.16, 130.50, 133.99, 143.22, 148.31, 169.49. MS (ESI): 251(M^+). Anal. calcd. for $C_{11}H_{13}N_3O_4$: C 52.59, H 5.22, N 16.73. Found: C 52.65, H 5.18, N 16.68%.

N-[acetylamino-(2-nitrophenyl)methyl]-acetamide (Table 3, entry 4)

Reddish brown solid. Yield: 60%, mp: 231–232 °C (Lit. 231–232 °C) (19). IR ν_{max}: 3273, 1668, 1526, 1359, 1097, 776 cm^{-1}. ^1H NMR (500 MHz, DMSO-d_6) δ: 1.79 (s, 6H), 6.82 (t, 1H, J = 7.65 Hz), 7.69 (t, 3H, J = 6.9 Hz), 7.88 (d, 1H, J = 8.4 Hz), 8.62 (d, 2H, J = 7.65 Hz, D_2O exchangeable).^{13}C NMR (125 MHz, DMSO-d_6) δ: 22.74, 54.83, 124.80, 128.92, 129.69, 133.60, 134.61, 148.81, 169.29. MS (ESI): 251 (M^+). Anal. calcd. for $C_{11}H_{13}N_3O_4$: C 52.59, H 5.22, N 16.73. Found: C 52.40, H 5.26, N 16.70%.

N-[(acetylamino)(4-formylphenyl)methyl]acetamide (Table 3, entry 5)

Off white solid. Yield: 40%, mp: 258–260 °C. IR ν_{max}: 3261, 3116, 1665, 1560, 1373, 1094, 802 cm^{-1}. ^1H NMR

© 2007 NRC Canada

Table 3. Results of the reactions under the optimized conditions.

Entry	Aldehyde	Nitrile	Product[a]	Time (h)	Mp (Ref.)	Yield (%)[b]
1	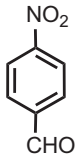	CH_3CN	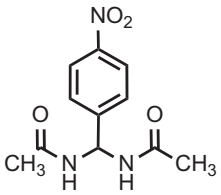	20	270–272 °C (Lit. 272 °C)[16]	65
2	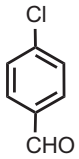	CH_3CN	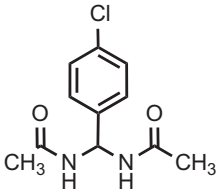	20	258–260 °C (Lit. 260–261 °C)[17]	60
3	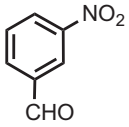	CH_3CN	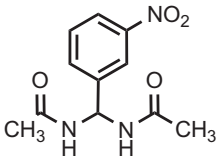	18	256–257 °C (Lit. 256–257 °C)[18]	68
4	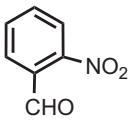	CH_3CN	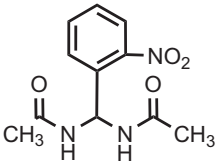	18	231–232 °C (Lit. 231–232 °C)[19]	60
5	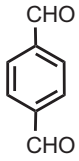	CH_3CN	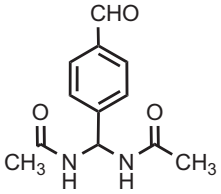	24	258–260 °C	40
6	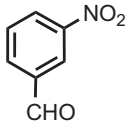	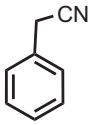	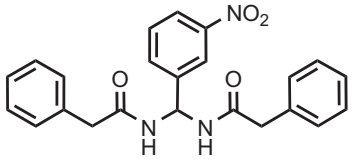	5	214–215 °C (Lit. 216 °C)[20]	65
7	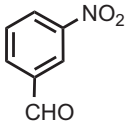	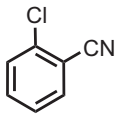	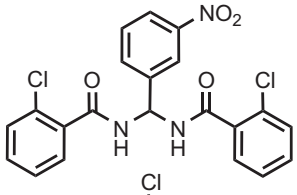	6	212–214 °C	68
8	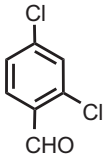	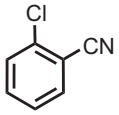	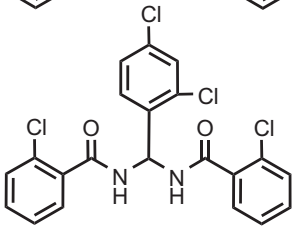	4	202–204 °C	65

© 2007 NRC Canada

Table 3 (*concluded*).

Entry	Aldehyde	Nitrile	Product[a]	Time (h)	Mp (Ref.)	Yield (%)[b]
9	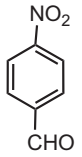	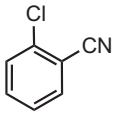	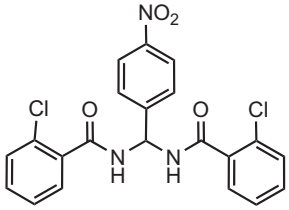	8	244–246 °C	60
10	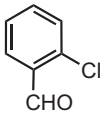	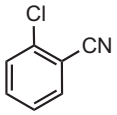	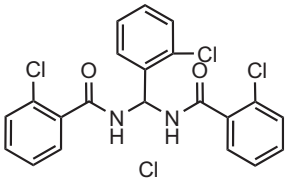	6	223–226 °C	63
11	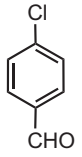	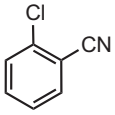	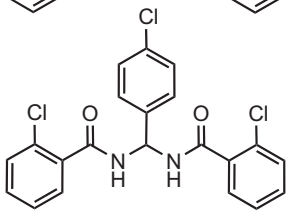	6	225–226 °C	68
12	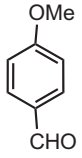	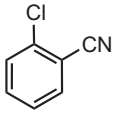	No product	24	–	–
13	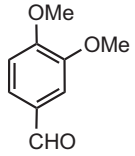	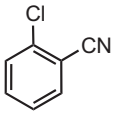	No product	24	–	–
14	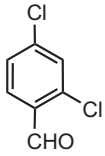	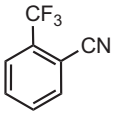	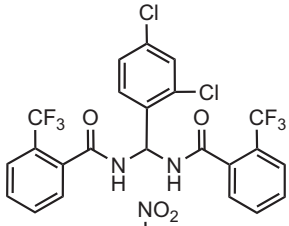	6	244–246 °C	45
15	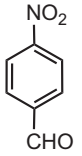	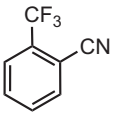	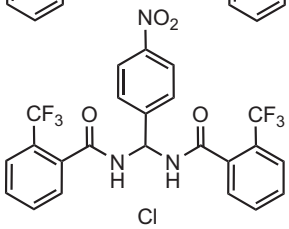	6	233–234 °C	60
16	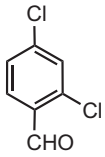	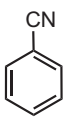	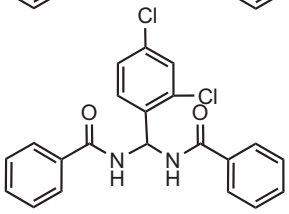	8	190–192 °C	42
17	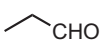	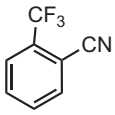	no product	24	–	-

[a]The products were characterized by IR, NMR, mass spectroscopy, and combustion analyses and compared with authentic samples.
[b]Isolated yields

© 2007 NRC Canada

(500 MHz, DMSO-d_6) δ: 1.84 (s, 6H), 6.51 (t, 1H, J = 7.65 Hz), 7.49 (d, 2H, J = 8.4Hz), 7.86 (d, 2H, J = 8.4 Hz), 8.71 (d, 2H, J = 7.65 Hz, D_2O exchangeable), 9.96 (s, 1H).^{13}C NMR (125 MHz, DMSO-d_6) δ: 22.98, 57.69, 127.67, 130.12, 136.07, 147.56, 169.36, 193.33. MS (ESI): 234 (M^+). Anal. calcd. for $C_{12}H_{14}N_2O_3$: C 61.53, H 6.02, N 11.96. Found: C 61.42, H 5.96, N 11.85%.

2-Phenyl-N-{(3-nitrophenyl)[(phenylacetyl)amino]methyl}acetamide (Table 3, entry 6)

Pale yellow solid. Yield: 65%, mp: 214–215 °C (Lit 216 °C) (16). IR ν_{max}: 3285, 3026, 1668, 1555, 1514, 1348, 704 cm^{-1}. ^{1}H NMR (500 MHz, DMSO-d_6) δ: 3.49 (s, 4H), 6.54 (t, 1H, J = 7.8 Hz), 7.21 (m, 10H), 7.52 (d, 2H, J = 8.4 Hz), 8.17 (d, 2H, J = 8.4Hz), 8.97 (d, 2H, J = 7.95 Hz, D_2O exchangeable).^{13}C NMR (125 MHz, DMSO-d_6) δ: 42.39, 57.66, 124.02, 126.97, 128.16, 128.77, 129.60, 136.45, 147.46, 148.15, 170.35. MS (ESI): 403 (M^+). Anal. calcd. for $C_{23}H_{21}N_3O_4$: C 68.47, H 5.25, N 10.42. Found: C 68.30, H 5.20, N 10.38%.

2-Chloro-N-[[(2-chlorobenzoyl)amino](3-nitrophenyl)methyl]benzamide (Table 3, entry 7)

Off white solid. Yield: 68%, mp: 212–214 °C. IR ν_{max}: 3276, 1667, 1594, 1529, 1346, 1068, 738 cm^{-1}. ^{1}H NMR (500 MHz, DMSO-d_6 + acetone-d_6) δ: 7.54 (t, 1H, J = 8.4 Hz), 7.84 (m, 6H), 8.00 (d, 2H, J = 7.6 Hz), 8.16 (t, 1H, J = 8.4Hz), 8.48 (d, 1H, J = 7.6 Hz), 8.65 (d, 1H, J = 8.65 Hz), 8.99 (s, 1H), 9.75 (d, 2H, J = 7.65 Hz, D_2O exchangeable).^{13}C NMR (125 MHz, DMSO-d_6) δ: 58.76, 122.30, 123.43, 127.69, 130.02, 130.43, 130.55, 131.16, 131.73, 134.24, 137.06, 142.83, 148.87, 166.83. MS (ESI): 466 (M + 23) – Na adduct. Anal. calcd. for $C_{21}H_{15}N_3O_4Cl_2$: C 56.77, H 3.40, N 9.46. Found: C 56.59, H 3.46, N 9.40%.

2-Chloro-N-[[(2-chlorobenzoyl)amino](2,4-dichlorophenyl)methyl]benzamide (Table 3, entry 8)

White solid. Yield: 65%, mp: 202–204 °C. IR ν_{max}: 3287, 3084, 2959, 1665, 1546, 745 cm^{-1}. ^{1}H NMR (500 MHz, DMSO-d_6) δ: 6.99 (t, 1H, J = 6.85 Hz), 7.35 (m, 11H), 9.33 (d, 2H, J = 7.65 Hz, D_2O exchangeable proton). ^{13}C NMR (125 MHz, DMSO-d_6) δ: 56.62, 127.48, 127.76, 128.68, 129.39, 129.74, 130.15, 130.27, 130.60, 131.11, 131.58, 133.95, 136.57, 166.22. MS (ESI): 489 (M + 23) – Na adduct. Anal. calcd. for $C_{21}H_{14}N_2O_2Cl_4$: C 53.88, H 3.01, N 5.98. Found: C 53.78, H 3.07, N 5.89%.

2-Chloro-N-[[(2-chlorobenzoyl)amino](4-nitrophenyl)methyl]-benzamide (Table 3, entry 9)

Yellow solid. Yield: 60%, mp: 244–246 °C. IR ν_{max}: 3239, 1671, 1523, 1348, 1069, 743 cm^{-1}. ^{1}H NMR (500 MHz, DMSO-d_6) δ: 6.95 (t, 1H, J = 7.65 Hz), 7.38 (t, 2H, J = 7.65 Hz), 7.43 (t, 2H, J = 7.65 Hz), 7.48 (t, 4H, J = 7.6Hz), 7.77 (d, 2H, J = 9.2 Hz), 8.26 (d, 2H, J = 8.4 Hz), 9.47 (d, 2H, J = 8.45 Hz, D_2O exchangeable). ^{13}C NMR (125 MHz, DMSO-d_6) δ: 58.30, 124.09, 127.58, 128.58, 129.73, 130.16, 130.59, 131.67, 136.50, 147.12, 147.68, 166.53. MS (ESI): 466 (M + 23) – Na adduct. Anal. calcd. for $C_{21}H_{15}N_3O_4Cl_2$: C 56.77, H 3.40, N 9.46. Found: C 56.70, H 3.42, N 9.50%.

2-Chloro-N-[[(2-chlorobenzoyl)amino](2-chlorophenyl)methyl]benzamide (Table 3, entry 10)

White solid. Yield: 63%, mp: 223–226 °C. IR ν_{max}: 3264, 1667, 1507, 1548, 1074, 749 cm^{-1}. ^{1}H NMR (500 MHz, DMSO-d_6) δ: 7.06 (t, 1H, J = 7.65 Hz), 7.35 (m, 4H), 7.41 (t, 2H, J = 7.65 Hz), 7.45 (t, 5H, J = 7.65 Hz), 7.71 (d, 1H, J = 6.9 Hz), 9.32 (d, 2H, J = 6.9 Hz, D_2O exchangeable). ^{13}C NMR (125 MHz, DMSO-d_6) δ: 56.94, 127.44, 127.56, 128.91, 129.79, 129.94, 130.12, 130.24, 130.63, 131.49, 133.02, 136.77, 137.28, 166.14. MS (ESI): 455 (M + 23) – Na adduct. Anal. calcd. for $C_{21}H_{15}N_2O_3Cl_3$: C 58.16, H 3.49, N 6.46. Found: C 58.32, H 3.54, N 6.38%.

2-Chloro-N-[[(2-chlorobenzoyl)amino](4-chlorophenyl)methyl]benzamide (Table 3, entry 11)

White solid. Yield: 68%, mp: 225–226 °C. IR ν_{max}: 3247, 1672, 1493, 1069, 742 cm^{-1}. ^{1}H NMR (500 MHz, DMSO-d_6) δ: 6.86 (t, 1H, J = 7.65Hz), 7.38 (t, 2H, J = 7.65Hz), 7.43 (m, 8H), 7.51 (d, 2H, J = 8.4Hz), 9.29 (d, 2H, J = 7.65Hz, D_2O exchangeable). ^{13}C NMR (125 MHz, DMSO-d_6) δ: 58.17, 127.53, 128.81, 129.09, 129.73, 130.13, 130.57, 131.55, 132.97, 136.74, 138.84, 166.31. MS (ESI): 455 (M + 23) – Na adduct. Anal. calcd. for $C_{21}H_{15}N_2O_3Cl_3$: C 58.16, H 3.49, N 6.46. Found: C 58.30, H 3.44, N 6.38%.

N-((2,4-dichlorophenyl){[2-(trifluoromethyl)benzoyl]-amino}methyl)-2-(trifluoromethyl)benzamide (Table 3, entry 14)

Off white solid. Yield: 45%, mp: 244–246 °C. IR ν_{max}: 3259, 1672, 1548, 1318, 1125, 766 cm^{-1}. ^{1}H NMR (500 MHz, DMSO-d_6) δ: 7.00 (t, 1H, J = 6.9 Hz), 7.49 (d, 1H, J = 8.4 Hz), 7.56 (d, 2H, J = 7.65 Hz),7.63 (m, 4H), 7.70 (t, 2H, J = 7.65 Hz), 7.76 (d, 2H, J = 7.65 Hz), 9.43 (d, 2H, J = 6.85 Hz, D_2O exchangeable). ^{13}C NMR (125 MHz, DMSO-d_6) δ: 56.56, 123.10, 125.27, 126.55, 126.79, 127.75, 129.45, 130.13, 130.57, 132.79, 133.97, 134.03, 136.08, 136.24, 166.94. MS (ESI): 557 (M + 23) – Na adduct. Anal. calcd. for $C_{23}H_{14}N_2O_2Cl_2F_6$: C 51.61, H 2.62, N 5.23. Found: C 51.75, H 2.56, N 5.17%.

N-((4-nitrophenyl){[2-(trifluoromethyl)benzoyl]-amino}methyl)-2-(trifluoromethyl)benzamide (Table 3, entry 15)

Pale yellow solid. Yield: 60%, mp: 233–234 °C. IR ν_{max}: 3259, 1669, 1530, 1349, 1315, 1126, 731 cm^{-1}. ^{1}H NMR (500 MHz, DMSO-d_6) δ: 6.95 (t, 1H, J = 7.6 Hz), 7.59 (d, 2H, J = 7.65 Hz), 7.64 (t, 2H, J = 7.65 Hz), 7.69 (t, 1H, J = 7.6 Hz), 7.73 (t, 2H, J = 7.6 Hz), 7.78 (d, 2H, = 7.65 Hz), 7.91 (d, 1H, J = 7.6 Hz) 8.19 (d, 1H, J = 8.4 Hz), 8.34 (s, 1H), 9.59 (d, 2H, J = 7.65 Hz, D_2O exchangeable). ^{13}C NMR (125 MHz, DMSO-d_6) δ: 58.18, 121.81, 123.47, 126.78, 129.33, 130.55, 130.62, 132.91, 134.06, 136.05, 141.83, 148.33, 167.25. MS (ESI): 534 (M + 23) – Na adduct. Anal. calcd. for $C_{23}H_{15}N_3O_4F_6$: C 59.23, H 3.46, N 6.01. Found: C 59.14, H 3.42, N 5.98%.

N-[(benzoylamino)(2,4-dichlorophenyl)methyl]benzamide (Table 3, entry 16)

Off white solid. Yield: 42%, mp: 190–192 °C. IR ν_{max}: 3286, 1640, 1542, 1514, 1145, 696 cm^{-1}. ^{1}H NMR

© 2007 NRC Canada

(500 MHz, DMSO-d_6) δ: 7.00 (t, 1H, J = 7.6 Hz), 7.43 (m, 5H), 7.50 (m, 2H), 7.61 (m, 2H), 7.88 (d, 4H, J = 7.6 Hz), 9.09 (d, 2H, J = 6.8Hz, D_2O exchangeable).^{13}C NMR (125 MHz, DMSO-d_6) δ: 57.47, 127.73, 128.20, 128.77, 129.33, 130.36, 132.14, 133.74, 134.00, 134.16, 137.08, 166.34. MS (ESI): 399 (M^+). Anal. calcd. for $C_{21}H_{16}N_2O_2Cl_2$: C 63.17, H 4.04, N 7.02. Found: C 63.42, H 3.95, N 6.94%.[2]

Acknowledgement

N.P. thanks the Council of Scientific and Industrial Research, New Delhi, India for the research fellowship.

References

1. M. Chorev, R. Shavitz, M. Goodman, S. Minick, and R. Guillemin. Science (Washington, DC), 204, 1210 (1979).
2. M. Chorev, M. Yacon, U. Wormser, D. Levian-Teitelbaum, C. Gilon, and Z. Selinger. Eur. J. Med. Chem. **21**, 96 (1986).
3. P. Pallai, S. Struthers, M. Goodman, J. Rivier, and W. Vale. Biopolymers, **22**, 2523 (1983).
4. M. Rodriguez, P. Dubreuil, J.P. Bail, and J. Martinez. J. Med. Chem. **30**, 758 (1987).
5. C. Aleman and J. Ruiggali. J. Org. Chem. **60**, 910 (1995); and references cited therein.
6. (*a*) P.V. Pallai, R.S. Struthers, M. Goodman, L. Moroder, E. Wunsch, and W. Vale. Biochemistry, **24**, 1933 (1985); (*b*) K.I. Nunami, T. Yamazaki, and M. Goodman. Biopolymers, **31**, 1503 (1991).
7. J. Pernak, B. Mrowczynski, and J. Weglewski. Synthesis, 1415 (1994).
8. (*a*) E.E. Magat, B.F. Faris, J.E. Reith, and L.F. Salibury. J. Am. Chem. Soc. **73**, 1028 (1951); (*b*) E.E. Magat, L.B. Chandler, B.F. Faris, J.E. Reith, and L.F. Salisbury J. Am. Chem. Soc. **73**, 1031 (1951); (*c*) E.E. Magat and L.F. Salisbury. J. Am. Chem. Soc. **73**, 1035 (1951).
9. F. Bigi, L. Chesini, R. Maggi, and G. Sartori. J. Org. Chem. **64**, 1033 (1999).
10. (*a*) T.S. Jin, G. Sun, Y.W. Li, and T.S. Li. Green Chem. **4**, 255 (2002); (*b*) W. Bo, Y.L. Ming, and S.J. Shuan. Tetrahedron Lett. **44**, 5037 (2003); (*c*) J. Tong-Shou. Synth. Commun. **28**, 3173 (1998); (*c*) B. Wang, L. Yang, and J. Suo. Synth. Commun. **33**, 3929 (2003).
11. J.T. Li, J.F. Han, J.H. Yang, and T.S. Li. Ultrason. Sonochem. **10**, 119 (2003).
12. B. Wang, Y.L. Gu, G.Y. Luo, T. Yang, L.M. Yang, and J.S. Suo. Tetrahedron Lett. **45**, 3369 (2004).
13. R. Nagarajan, C.J. Magesh, and P.T. Perumal. Synthesis, **69**, 16 (2004).
14. P.R. Singh, D.U. Singh, and S.D. Samant. Synlett, 1909 (2004).
15. N. Panneer Selvam and P.T. Perumal. Tetrahedron Lett. **47**, 7481 (2006).
16. (*a*) P.I. Ittegerah and K.C. Pandya. Proc. Indian Acad. Sci. **15A**, 2725 (1942); (*b*) P.I. Ittegerah and K.C. Pandya. Chem. Abstr. **37**, 2725 (1943).
17. S.W. Breuer, T. Bernarth, and D. Ben-Ishai. Tetrahedron, **23**, 2869(1947).
18. Y. Le Floc'h. Bulletin de la Societe Chimique de France, **7–8** (2), 409 (1979).
19. E. Glaser and S. Frisch. Arch. Pharm. **266**, 103 (1928).
20. Z. Csuros, G. Deak, M. Haraszthy-Papp, and I. Hoffmann, I. Acta Chim. Acad. Sci. Hung. **59** (1), 119 (1969).

[2] Supplementary data for this article are available on the journal Web site (canjchem.nrc.ca) or may be purchased from the Depository of Unpublished Data, Document Delivery, CISTI, National Research Council Canada, Ottawa, ON K1A 0R6, Canada. DUD 5248. For more information on obtaining material, refer to cisti-icist.nrc-cnrc.gc.ca/irm/unpub_e.shtml.

© 2007 NRC Canada

Interactions among $^{18}O_2$, C_2H_4, and NO on the surface of stepped Pt(332)

Yuhai Hu and Keith Griffiths

Abstract: The influence of co-adsorbed $^{18}O_2$ (^{18}O) on NO/C_2H_4 reactions on the surface of stepped Pt(332) has been investigated using Fourier transform infrared reflection–absorption spectroscopy (FTIR-RAS) and thermal desorption spectroscopy (TDS). The presence of $^{18}O_2$ (^{18}O) results in changes in C_2H_4 dissociation behavior, with formation of ethylidyne taking place at surface temperature much higher than that in the absence of $^{18}O_2$ (^{18}O). Pre-annealing $^{18}O_2/C_2H_4$ co-adlayers to 250 and 300 K does not lead to significantly different IR spectra, but a variety of spectra are observed when the 250 K and 300 K $^{18}O/C_2H_4$ co-adlayers are further exposed to 0.8 L NO at 90 K, depending on the $^{18}O_2$ pre-exposure. NO adsorption in bridge sites, both on steps and on terraces is more significantly suppressed for the co-adlayers in which $^{18}O_2/C_2H_4$ is pre-annealed to 250 K. This site-blocking effect is enhanced with increasing $^{18}O_2$ exposure. However, no new surface species, which are intermediates for N_2 production, are detected. Thermal desorption spectra indicate that various species are produced, but only N_2 and H_2 desorption have intensities that can be reliably analyzed (that is to be able to quantitatively elucidate how the yields of these two species vary with change in the ratios of NO to C_2H_4 and $^{18}O_2$). Desorption of both N_2 and H_2 is more strongly dependent on $^{18}O_2$ exposure than on the temperature to which $^{18}O_2/C_2H_4$ adlayers are pre-annealed. The presence of $^{18}O_2$, irrespective of the dosing sequence, suppresses N_2 desorption, but this effect is much weaker when $^{18}O_2$ is post-dosed. For the case with $^{18}O_2$ pre-dosed, irrespective of the annealing temperature (250 K or 300 K), N_2 desorption is greatly suppressed at an $^{18}O_2$ exposure of 0.2 L, but thereafter remains almost unchanged with increasing $^{18}O_2$ exposure from 0.4 to 1.6 L. This feature of N_2 desorption is explained by the restoration of the adsorption of NO onto steps and the subsequent NO dissociation on these sites. In contrast, H_2 desorption decreases continuously and disappears at 0.8 L $^{18}O_2$ and higher. It is concluded that the presence of $^{18}O_2$ in the reaction of NO with C_2H_4 on the surface of Pt(332) does not play any role of activating the surface reactants.

Key words: NO, platinum, C_2H_4, deNO*x*, hydrocarbon, selective catalytic reduction.

Résumé : Faisant appel à la spectroscopie de réflexion–absorption infrarouge en transformée de Fourier et à la spectroscopie de désorption thermique, on a étudié l'influence des entités coadsorbées $^{18}O_2$ (^{18}O) sur les réactions du NO et du C_2H_4 sur la surface de Pt(332) en escalier. La présence de $^{18}O_2$ (^{18}O) provoque des changements dans le comportement dissociatif du C_2H_4 avec une formation d'éthylidyne qui se fait sur la surface à une température beaucoup plus élevée qu'en l'absence de $^{18}O_2$ (^{18}O). À des températures allant de 250 et 300 K, la préannellation de couches coadsorbées de $^{18}O/C_2H_4$ ne conduit pas à des spectres IR qui présenteraient des différences significatives, mais dépendant de la nature de la préexposition au $^{18}O_2$, on observe une variété de spectres lorsque les couches de $^{18}O/C_2H_4$ qui ont été coadsorbées à des températures allant de 250 et 300 K sont exposées à 0,8 L de NO à 90 K. L'adsorption du NO sur les sites pontés, tant sur les marches que sur les terrasses est beaucoup plus supprimé pour les couches coadsorbées dans lesquelles la préannellation du $^{18}O/C_2H_4$ a été faite à 250 K. Cet effet de blocage de site est rehaussé avec une augmentation de l'exposition au $^{18}O_2$. Toutefois, on n'a pas détecté de nouvelles espèces à la surface qui pourraient conduire à la production de N_2. Les spectres de désorption thermiques indiquent qu'il y a production de diverses espèces, mais que seules les désorptions du N_2 et du H_2 présentent des intensités qui peuvent être analysées avec une exactitude suffisante pour être capable d'élucider comment les rendements de ces deux espèces varie avec un changement dans les rapports de NO / C_2H_4 et $^{18}O_2$. Les désorptions du N_2 et du H_2 dépendent toutes les deux beaucoup plus sur l'exposition au $^{18}O_2$ que sur la température à laquelle la préannellation des couches coadsorbées du $^{18}O/C_2H_4$ a été faite. Quelle que soit la séquence de dosage, la présence de $^{18}O_2$ supprime la désorption du N_2, mais cet effet est beaucoup faible lorsque le ^{18}O est post-dosé. Dans le cas du $^{18}O_2$ prédosé, quelle que soit la température d'annellation (250 K ou 300 K), la désorption du N_2 est fortement supprimée à une exposition de 0,2 L de $^{18}O_2$, mais par la suite elle demeure pratiquement constante avec un changement d'exposition au $^{18}O_2$ allant de 0,4 à 1,6 L. Cette caractéristique de la désorption du N_2 s'explique par une restauration de l'adsorption du NO sur les marches et une subséquente dissociation du NO sur ces sites. Par opposition, la désorption du H_2 augmente continuellement et elle

Received 9 August 2007. Accepted 6 November 2007. Published on the NRC Research Press Web site at canjchem.nrc.ca on 5 December 2007.

Y. Hu and K. Griffiths.[1] Department of Chemistry, The University of Western Ontario, London, ON N6A 5B7, Canada.

[1]Corresponding author (e-mail: griff@uwo.ca).

 doi:10.1139/V07-133 © 2007 NRC Canada

disparaît à partir 0,8 L. On en conclut que la présence de $^{18}O_2$ dans la réaction du NO avec le C_2H_4 sur la surface du Pt(332) ne joue aucun rôle dans l'activation des réactifs en surface.

Mots-clés : NO, platine, C_2H_4, deNO*x*, hydrocarbure, réduction catalytique sélective.

[Traduit par la Rédaction]

Introduction

The contribution of oxygen to the selective catalytic reduction (SCR) of NO in the presence of organic compounds is widely acknowledged. Oxygen is indispensable for the reaction to proceed effectively (1–4). Several mechanisms have been proposed to explain the role of oxygen in this kind of reactions (1). So far, more and more data from studies under ambient conditions support a mechanism of activation of one of the reactants (NO or organic compound) followed by scavenging polymeric carbonaceous deposits on the surface of working catalysts (1, 5, 6). Nonetheless, a consensus has not yet been reached.

Investigation of NO reduction in the presence of CO, NH_3, and H_2 has been extensively performed under ultra high vacuum (UHV) conditions (7, 8), providing insightful information on these reactions. However, few studies have dealt with the reactions with organic compounds in the same way (9–12). Therefore, we have attempted to address this problem by studying NO reactions with a series of organic compounds including C_2H_4, CH_3OH, and C_6H_6 on the surface of stepped Pt(332) (13–15). Very recently, we have extended our study to exploring the role of oxygen in the SCR of NO in the presence of C_2H_4, with special attention paid to understanding whether NO is activated (e.g., oxidized to higher-valence NO*x*) (16). In this paper, our effort concentrates on defining whether C_2H_4 reacts with O_2 (O) to produce new surface species that promote NO reduction; in other words, whether C_2H_4 is activated.

For this purpose, we annealed Pt(332), exposed at 90 K to various amounts of $^{18}O_2$ (pre-dosed) and a fixed amount of C_2H_4, to 250 and 300 K, producing a variety of co-adlayers with different carbon-containing species depending on the annealing temperatures and $^{18}O_2$ exposure. The resultant co-adlayers were then exposed to a fixed amount of NO at 90 K, and were interrogated using IR and TDS. It is found that the presence of oxygen does not apparently activate C_2H_4 to new surface species that promotes NO reduction.

Experimental

All the experiments were carried out in a standard UHV system described elsewhere (17, 18). Briefly, a stainless steel UHV chamber is pumped by a turbo-molecular pump, which is in turn backed by an oil diffusion pump. A base pressure of 1×10^{-10} Torr (1 Torr = 133 Pa) is routinely attained. The chamber is fitted with potassium chloride windows for grazing incidence surface IR spectroscopy.

The Pt(332) crystal was cleaned by repeated cycles of Ar^+ ion bombardment and oxidation. The final cleanliness was judged by the CO infrared spectrum, which is sensitive to the cleanliness and the state of perfection of the surface (19, 20). IR spectra were obtained in a single-reflection geometry at 7° grazing incidence using a Digilab FTS 7000 spectrometer. 1000 scans, which takes less than 2 min, were co-added at a resolution of 8 cm^{-1}. A narrow band mercury cadmium telluride (MCT) detector was used throughout, with a cut-off around 1000 cm^{-1}. Although some IR data is shown extending down to 800 cm^{-1}, the steep spectral function (cut-off) in the frequency region 800–950 cm^{-1} makes the data unreliable below about 950 cm^{-1}.

C_2H_4, $^{18}O_2$, and NO were introduced into the chamber by backfilling. The highly efficient pumping system can restore the background to workable levels quickly. Thermal desorption spectra were recorded by resistively heating the crystal at a rate of 4 K/s.

Results

IR spectra

C_2H_4 dissociation

The Pt(332) surface, exposed to only 0.8 L C_2H_4 at 90 K, was annealed to various target temperatures. IR spectra were recorded after cooling the annealed adlayer down to 90 K and are shown in Fig. 1. No peaks are observed in the spectra at this coverage (exposure) for annealing temperatures ≤200 K because C_2H_4 is adsorbed molecularly with its axis parallel to the surface. When the annealing temperature is increased to 300 K and higher, two peaks appear at ~1124 and ~1341 cm^{-1}, assigned to C–C stretching and CH_3 bend of ethylidyne, respectively, resulting from C_2H_4 dissociation (21). Both peaks disappear at 450 K, indicating that ethylidyne is dissociated completely.

$^{18}O/C_2H_4$ interaction

On Pt surfaces exposed to oxygen only, upon heating these adlayers, desorption competes with dissociation. Desorption becomes the predominant process at higher (close to saturation) oxygen exposure (22, 23). As a result, oxygen (as atoms) might be limiting in the $^{18}O_2/C_2H_4$ co-adlayers even when the surface is saturated with $^{18}O_2$. This could lead to a misinterpretation of the interaction between $^{18}O_2/C_2H_4$ in the adlayer. Bearing this in mind, we recorded IR spectra of $^{18}O_2$(saturation)/C_2H_4 and 18O(saturation)/C_2H_4 co-adlayers following the same annealing-temperature program. The spectral changes do not differ significantly between the two protocols. Therefore, only the interactions in the ^{18}O(saturation)/C_2H_4 co-adlayers are discussed in this paper.

The saturated layer of ^{18}O is prepared through three cycles of exposing Pt(332) at 90 K to 3 L $^{18}O_2$ and subsequent annealing to 200 K. The final ^{18}O adlayer was exposed at 90 K to 0.8 L C_2H_4 and was annealed to various target temperatures. IR spectra were recorded after cooling the annealed co-adlayers down to 90 K and are shown in Fig. 2. No peaks are detected in the spectra when the annealing temperatures are ≤250 K. At 300 K and higher, four peaks at

© 2007 NRC Canada

Fig. 1. IR spectra of 0.8 L of C_2H_4 adsorbed on Pt(332) following an anneal to various temperatures. C_2H_4 was exposed at 90 K. Spectra were recorded after cooling the annealed adlayer down to 90 K.

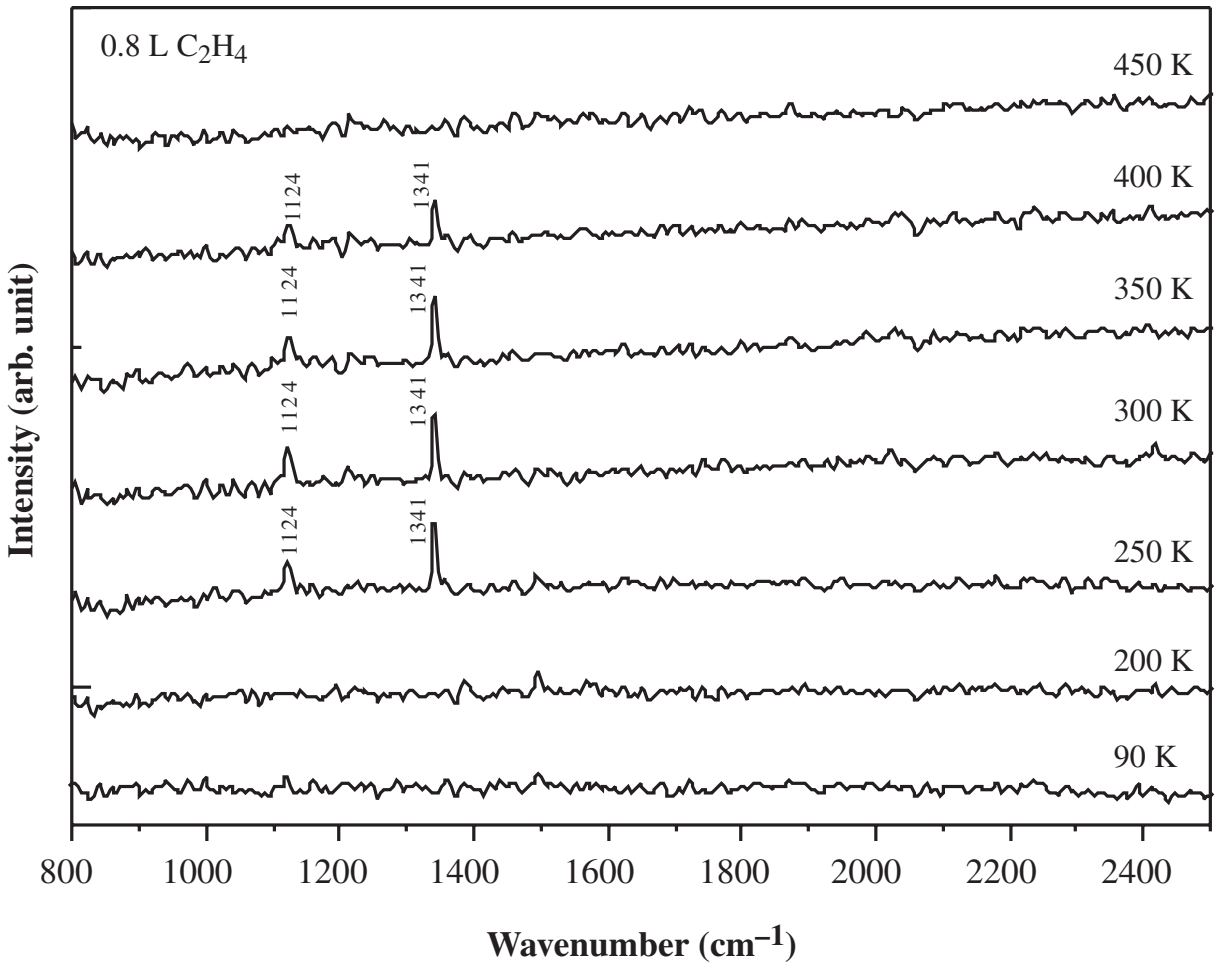

~1124, ~1342, 2000–2003, and ~2048 cm^{-1} are clearly observed. The first two peaks increased slightly with increasing the annealing temperature; the latter two gaining intensity steadily. Considering the fact that both ethylidyne from C_2H_4 dissociation and formate (formic acid) from C_2H_4 oxidation give rise to a vibrational peak at about 1340 cm^{-1}(21, 24), we repeated the experimental procedure by using $^{16}O_2$. The vibrational frequency of this peak (1340 cm^{-1}) does not vary from that in the presence of $^{18}O_2$, excluding the contribution of formate (formic acid). As such, this peak and the one at ~1124 cm^{-1} can both be attributed to the vibrations of ethylidyne, as assigned earlier. However, by comparing these results with those in Fig. 1, it is interesting that the temperature at which ethylidyne is formed in the presence of ^{18}O (300 K) is evidently higher than that in the absence of ^{18}O (250 K). This means that the process of C_2H_4 dissociation is changed in the presence of ^{18}O. Interaction of C_2H_4 with O on the surface of Pt(111) has been investigated in detail previously (25–28). It is generally agreed that C_2H_4 decomposes first via H_2 and H_2O desorption, followed by complete combustion of the remnants to CO_2 and more H_2O. However, so far, debate on the formation of ethylidyne and its contribution to the oxidation mechanism still exists. Our current results support suggestions of the formation of ethylidyne and will be discussed in more detail in another paper.

The peaks at 2000–2003 and ~2048 cm^{-1} most likely correspond to characteristic vibrations of $C^{18}O$ and $C^{16}O$ either from background exposure or from surface reaction. The experimental approach for distinguishing these two possibilities has been described in detail in another paper (29). In brief, when annealing ^{18}O(saturation)/C_2H_4 co-adlayer prepared at 90 K *directly* to 350 K (or 400 K), the peak at ~2048 cm^{-1} was not detected. This procedure vastly decreases the time that the crystal spends in ambient vacuum. The peak at 2000–2003 cm^{-1} is much less intense than that shown in Fig. 2. Consequently, we conclude that $C^{16}O$ and most of the $C^{18}O$ are from background exposure during long experiments, and only a very small amount of $C^{18}O$ is produced from the reaction. We estimate the total CO coverage to be 5% of saturation coverage of CO on the same surface (this amount of $C^{18}O$ can not be detected by TDS).

$^{18}O_2$/C_2H_4/NO interaction

The Pt(332), exposed at 90 K to various amounts of $^{18}O_2$ (pre-dosed) and 0.4 L C_2H_4, was annealed to, and held for 10 s at 250 K. The resultant co-adlayers were further exposed to 0.8 L NO at 90 K. IR spectra were recorded at

© 2007 NRC Canada

Fig. 2. IR spectra of $^{18}O/C_2H_4$ co-adlayer following an anneal to various temperatures. The Pt(332) surface was exposed at 90 K to a saturation of ^{18}O atoms and 0.8 L C_2H_4. Spectra were recorded after cooling the annealed co-adlayer down to 90 K.

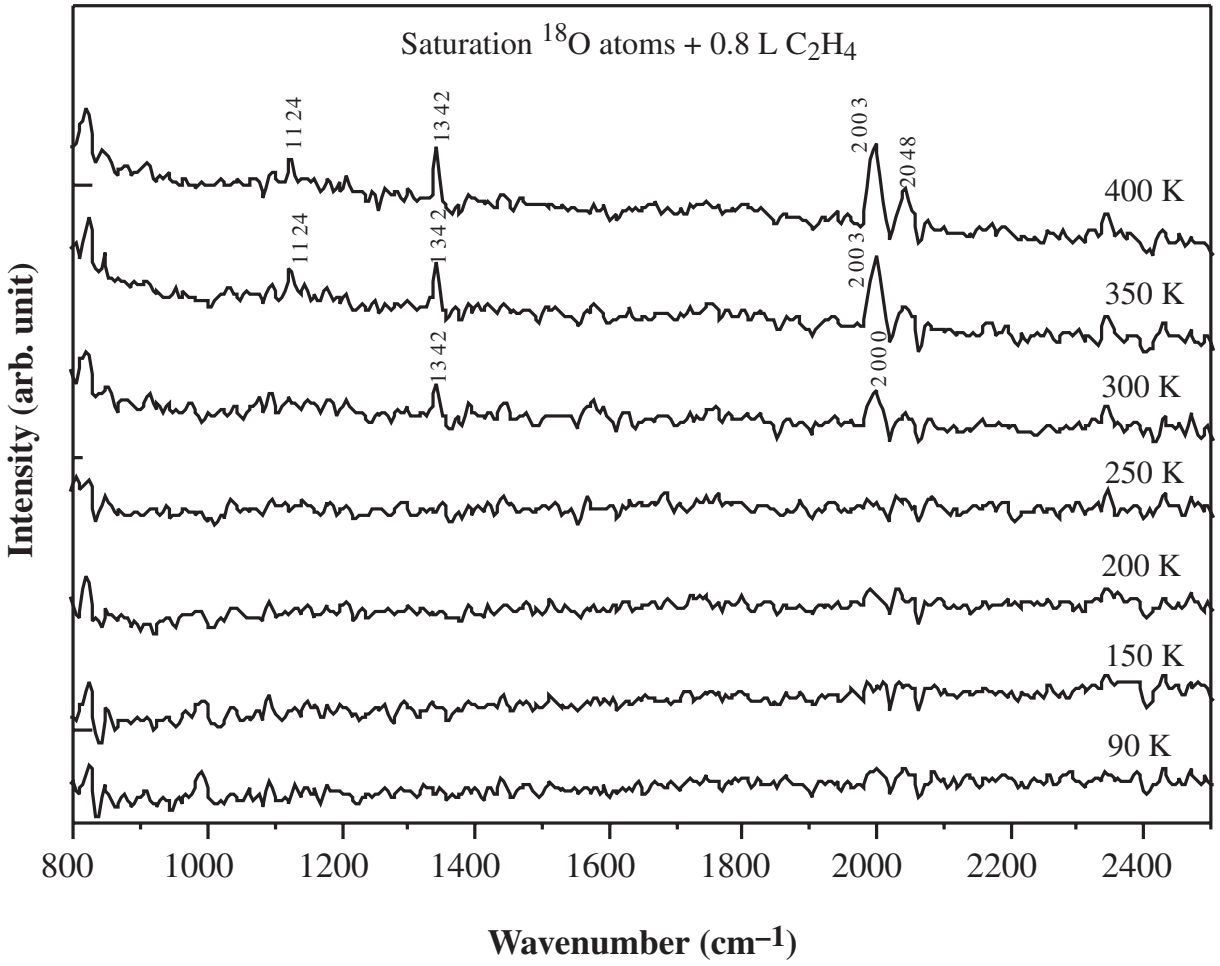

Table 1. Assignments for the infrared peaks observed in $^{18}O_2/C_2H_4/NO$ co-adlayers.

Vibrational frequency (cm^{-1})	Assignments
~1124	C–C stretching of ethylidine
~1340	CH_3 bend
1473–1487	Stretch of NO in bridge site on terrace
~1582	Stretch of NO in bridge site on steps that directly interacting with C_2H_4
1598–1600	Bent NO on steps
1620–1631	Stretch of NO in bridge sites on steps
1686–1723	Stretch of NO in atop sites
1819–1828	Stretch of NO in atop sites on step edge

90 K and are shown in Fig. 3. For the C_2H_4/NO coadlayer, i.e., without $^{18}O_2$, several peaks associated with characteristic vibrations of NO molecules adsorbed in different sites are observed, including that in bridge sites on terraces (~1478 cm^{-1}), in bridge sites on steps (~1611 cm^{-1}), and in atop sites (1682 cm^{-1}) (13–15). These assignments are collected in Table 1. The peak at ~1532 cm^{-1} has been attributed to the vibration of NO molecules adsorbed in other defect sites in our previous study (13). The validity of this assignment is to be discussed later.

The presence of pre-dosed $^{18}O_2$ results in significant changes in the spectra. The peaks associated with NO molecules adsorbed in bridge sites both on steps and on terraces are steadily attenuated with increasing $^{18}O_2$ pre-exposure. The peak at 1473–1483 cm^{-1} and 1532–1537 cm^{-1} disappear completely at an $^{18}O_2$ exposure of 0.8 L, the one at 1611–1634 cm^{-1} disappearing completely at 1.6 L $^{18}O_2$. In contrast, the peak associated with NO molecules adsorbed in atop sites (1688–1711 cm^{-1}) increases rapidly with increasing $^{18}O_2$ exposure, dominating in the spectra following $^{18}O_2$ exposures of 0.8 and 1.6 L.

Moreover, increasing the $^{18}O_2$ pre-exposure also leads to noticeable changes in the peak at ~1342 cm^{-1}. This peak is retained for $^{18}O_2$ exposures below 0.8 L, but disappears

© 2007 NRC Canada

Fig. 3. IR spectra of $^{18}O/C_2H_4/NO$ co-adlayers prepared as follows: the Pt(332), exposed at 90 K to various amounts of $^{18}O_2$ (prior to C_2H_4) and 0.4 L C_2H_4, was annealed to 250 K. The resultant co-adlayers were further exposed to 0.8 L NO at 90 K. Spectra were taken at 90 K.

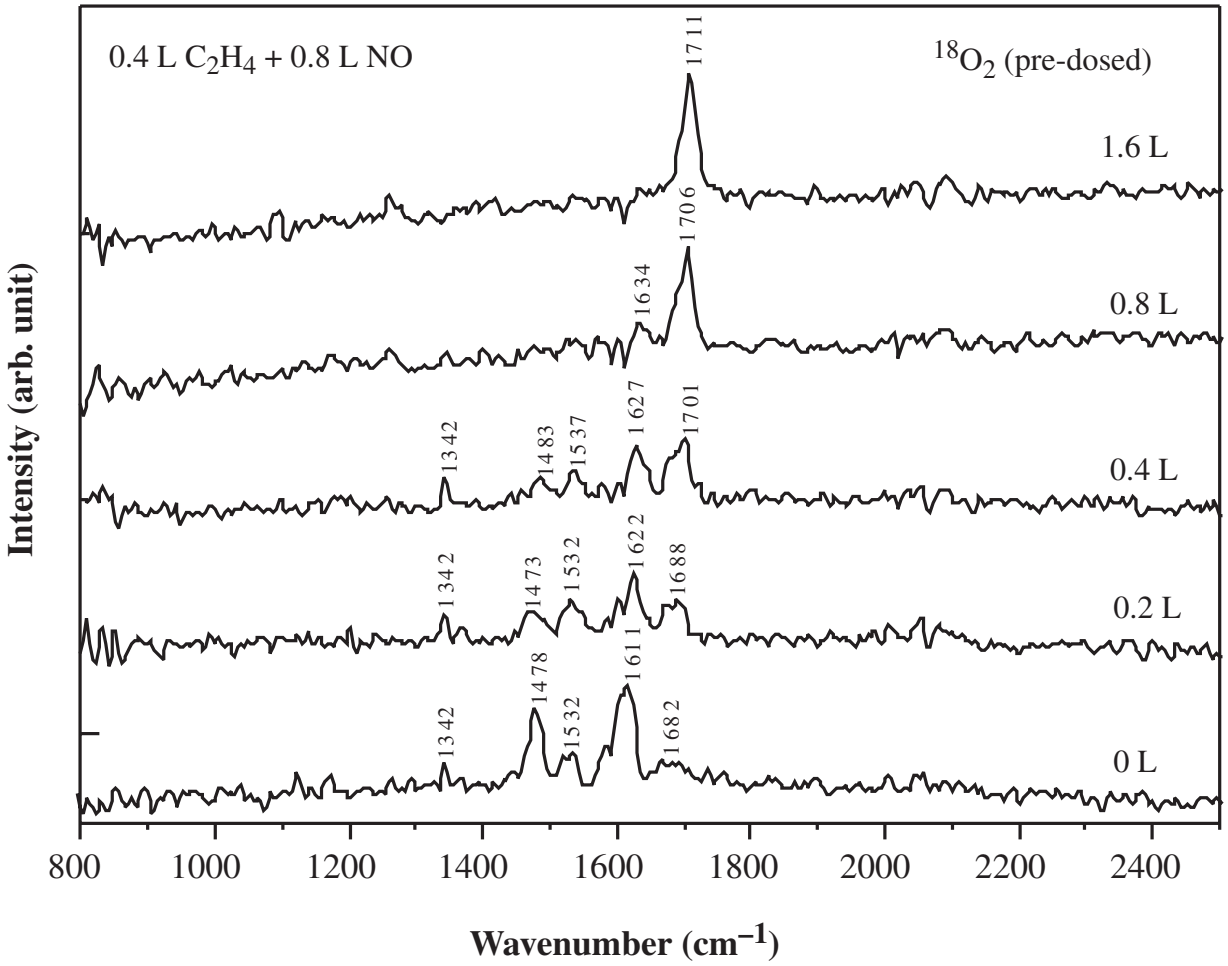

completely for $^{18}O_2$ exposures of 0.8 L and higher. The same change is observed in the IR spectra of co-adladyers with 0.4 L C_2H_4 following the same train of $^{18}O_2$ pre-exposure (spectra not shown here), confirming that the loss of this peak mainly results from interactions of C_2H_4 with $^{18}O_2$ rather than with NO and that the ratios of C_2H_4 to $^{18}O_2$ plays a key role.

Figure 4 shows IR spectra of co-adlayers prepared following the same procedure as that for the co-adlayers in Fig. 3, with the exception that $^{18}O_2/C_2H_4$ co-aldayers are pre-annealed to 300 K before being exposed to NO at 90 K. This temperature program results in spectra that are markedly different from those in Fig. 3. All the peaks associated with adsorbed NO molecules that appear in the $^{18}O_2$-free spectrum (the bottom one in Fig. 4, following exposures of only 0.4 L C_2H_4 and 0.8 L NO) are also observed in the spectra with $^{18}O_2$ exposures from 0.2 to 1.6 L, except that the peak intensities change slightly. This indicates that pre-annealing $^{18}O_2/C_2H_4$ co-adlayers to 300 K only slightly suppresses the adsorption of NO molecules in bridge sites both on steps and on terraces even when $^{18}O_2$ exposure is increased to 1.6 L. As a consequence, it can be deduced that the surface condition of $^{18}O_2/C_2H_4/NO$ co-adlayers in which $^{18}O_2/C_2H_4$ is pre-annealed to 300 K is very different from that following an anneal to 250 K (to be discussed later).

It is also evident that for these co-adlayers, the peak at 1527–1540 cm^{-1} persists throughout $^{18}O_2$ exposures, giving rise to intensities that are comparable to those at 1481–1486 cm^{-1}. This significant intensity has never been observed in the spectra of just NO adlayers (without co-adsorbents) or C_2H_4/NO co-adlayers when the C_2H_4 pre-exposures are less than about 0.16 L (13). Noticing that changes in this peak correspond to changes in the peak at 1473–1483 cm^{-1}, i.e., disappearing completely at 0.8 L O_2 (in Fig. 3), and that this peak is *not* detected in the absence of NO, we also tentatively assign this peak to vibrations of NO molecules adsorbed in bridge sites on terraces that are influenced in some way by C_2H_4-related surface species.

Thermal desorption spectra of N_2 and H_2

A general picture

Thermal desorption spectra indicate that a variety of desorbing species are detected from the surface reactions involving C_2H_4, NO, and $^{18}O_2$, but only desorption of N_2 and H_2 gives rise to intensities that can be reliably analyzed, en-

© 2007 NRC Canada

Fig. 4. IR spectra of $^{18}O/C_2H_4/NO$ co-adlayers prepared as follows: the Pt(332), exposed at 90 K to various amounts of $^{18}O_2$ (prior to C_2H_4) and 0.4 L C_2H_4, was annealed to 300 K. The resultant co-adlayers were further exposed to 0.8 L NO at 90 K. Spectra were taken at 90 K.

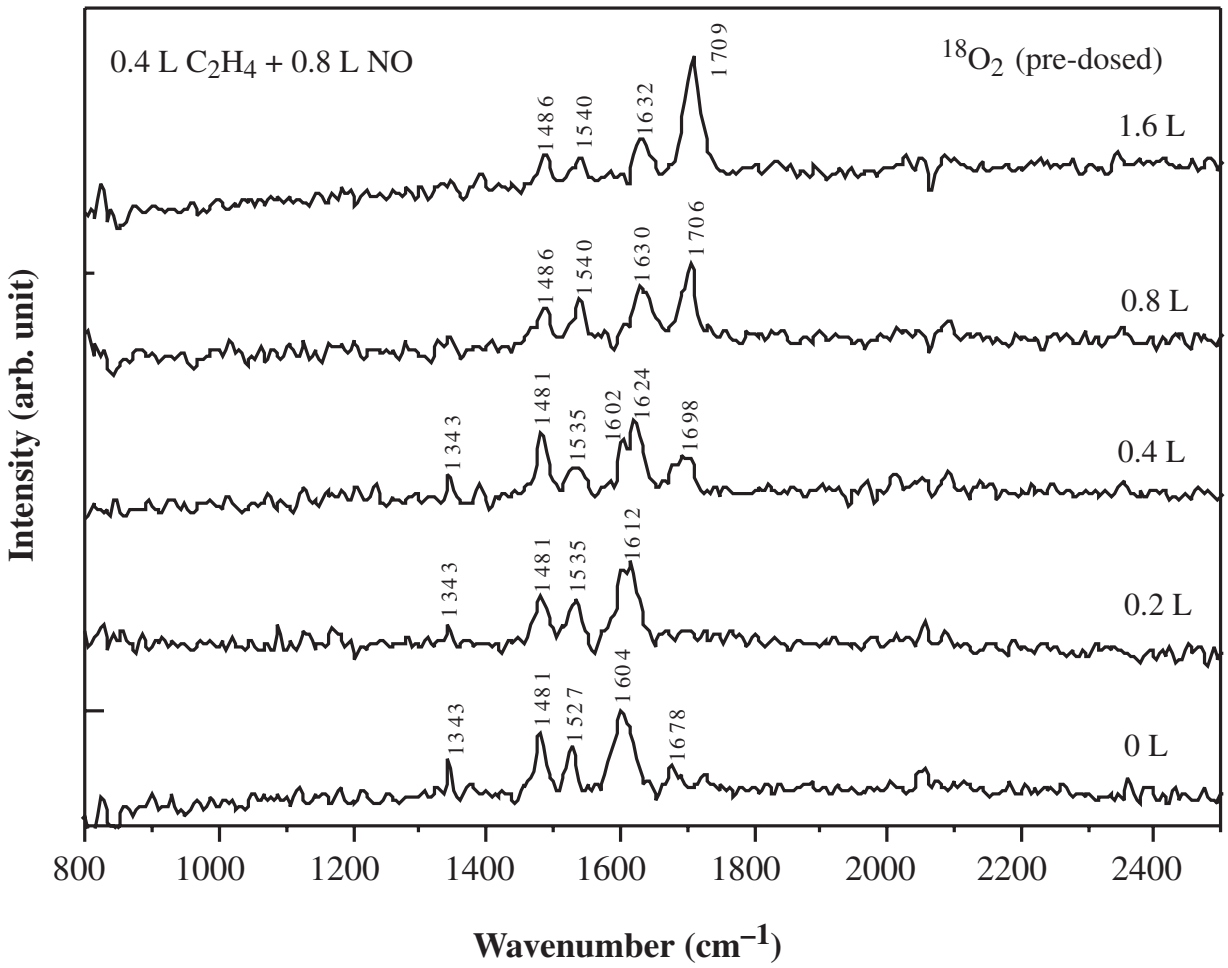

abling us to quantitatively elucidate how the yields of these two species vary with change in the ratios of NO to $^{18}O_2$ and C_2H_4. As such, this paper only addresses the desorption of these two species. Moreover, to provide a more detailed profile of the influence of oxygen on C_2H_4/NO interactions, such as coverage and the state (^{18}O and $^{18}O_2$) of oxygen, N_2 and H_2 desorption from co-adlayers in which $^{18}O_2$ is dosed after C_2H_4 and NO are also presented.

Co-adlayer in which $^{18}O_2$ is post-dosed

Thermal desorption spectra of N_2 and H_2 from co-adlayers in which $^{18}O_2$ is dosed "after" C_2H_4 and NO are shown in Fig. 5. The Pt(332) was exposed to 0.4 L C_2H_4 at 250 K. The higher adsorption temperature is used to prevent ethylene multi-layers from forming and so effectively reducing the contribution of C_2H_4 (also mass 28) to the N_2 desorption signal. The resultant C_2H_4 adlayer was further exposed to 0.8 L NO at 90 K (prior to $^{18}O_2$) and various amounts of $^{18}O_2$.

Compared to the N_2 desorption yield following *just* an exposure of 0.8 L NO, N_2 desorption is significantly enhanced in the presence of 0.4 L C_2H_4 (and no oxygen) which is predosed at 250 K. Two peaks appear at ~376 and ~455 K. This feature of N_2 desorption has been discussed previously (13) in detail, being attributed to facile NO dissociation arising from an electron-donation effect exerted by co-adsorbed C_2H_4 molecules. Both desorptions, i.e., at 376–380 K and at 455–460 K, are retained following $^{18}O_2$ exposures of up to at least 1.6 L, though the intensity of the desorption at ~380 K decreases somewhat at higher $^{18}O_2$ exposures.

H_2 desorption also undergoes some changes with varying post-exposures of $^{18}O_2$. For the co-adlayer without $^{18}O_2$, three peaks are observed at ~303, ~410, and ~530 K, corresponding to stepwise dehydrogenation of C_2H_4 (13). At an $^{18}O_2$ exposure of 0.4 L, the peak at ~303 K disappears completely. Simultaneously, the peak at 405–412 K is significantly enhanced, but the peak at 530–538 K remains almost unchanged. At higher $^{18}O_2$ exposures, i.e., 0.8 and 1.6 L, the peaks at 405–412 K and at 530–538 K do not appear to be changed. If we consider both N_2 and H_2 desorption, it is reasonable to suggest that increasing $^{18}O_2$ post-exposure *higher than* 0.4 L does not significantly affect the surface reaction, and the adsorbed $^{18}O_2$ molecules mostly desorb rather than decompose and react with C_2H_4. $^{18}O_2$ desorption from these co-adlayers was monitored. The higher-temperature recombinative desorption beyond 600 K was not

© 2007 NRC Canada

Fig. 5. Thermal desorption spectra of N_2 and H_2 from C_2H_4/NO/$^{18}O_2$ co-adlayers prepared as follows: the Pt(332) was exposed to 0.4 L C_2H_4 at 250 K. The resultant adlayer was further exposed to 0.8 L NO at 90 K (prior to $^{18}O_2$) and various amounts of $^{18}O_2$.

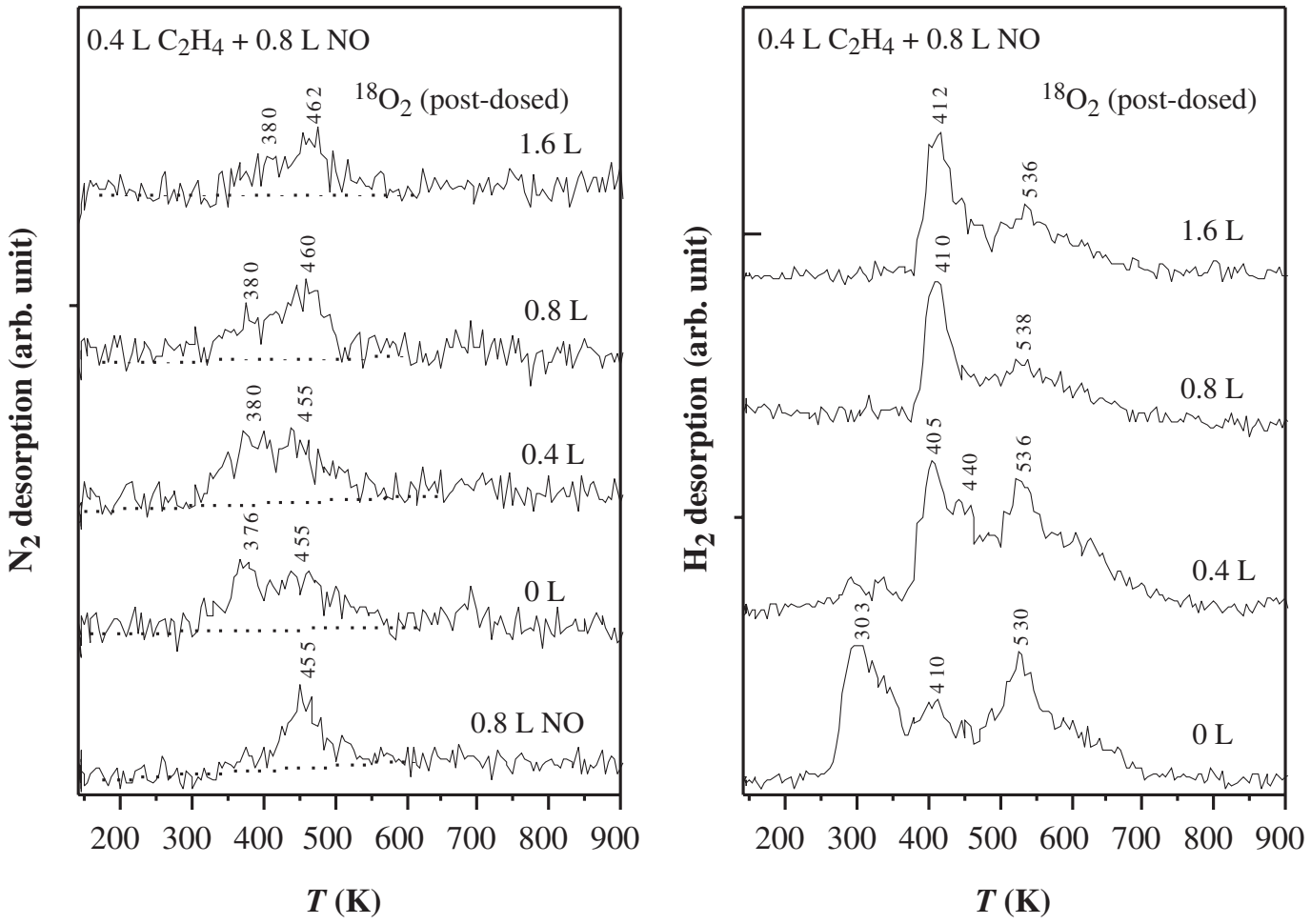

detected in these co-adlayers, but the lower-temperature molecular desoprtion, below 200 K, increases significantly with increasing the exposure from 0.4 to 1.6 L. (These spectra are not shown here for brevity).

Co-adlayers in which $^{18}O_2/C_2H_4$ is pre-annealed to 250 and 300 K

Figure 6 shows thermal desorption spectra of N_2 and H_2 from the surface in which $^{18}O_2/C_2H_4$ adlayers are pre-annealed to, and held for 10 s at 250 K before being exposed to NO at 90 K. In the absence of $^{18}O_2$, N_2 desorption gives rise to a primary peak at ~386 K, on the high-temperature side of which, a shoulder appears at ~455 K, as shown in the bottom spectrum in Fig. 6A. The lower-temperature desorption feature at ~386 K decreases rapidly following $^{18}O_2$ exposure and disappears completely at $^{18}O_2$ exposures of 0.4 L and higher. In contrast, the higher-temperature desorption at 455–462 K does not appear to change much.

Compared with N_2 desorption, H_2 desorption from the same co-adlayers is much more strongly related to $^{18}O_2$ exposure, undergoing dramatic changes both in peak shape and in peak intensity with increasing ^{18}O exposure, as shown in Fig. 6B. The peak at ~308 K, observed in the spectrum without $^{18}O_2$, disappears completely at an $^{18}O_2$ exposure of 0.2 L, at which the peak at ~412 K is significantly enhanced. H_2 desorption is further suppressed at an $^{18}O_2$ exposure of 0.4 L and disappears completely at 0.8 L and higher, suggesting that H_2 has been fully consumed by reaction with oxygen. However, it should be noted that almost no water was detected from these co-adlayers. This is a disappointing but explicable experimental artifact of our vacuum system (13). The vacuum system contains many surfaces, which are held at liquid-nitrogen temperature, providing an almost infinite pumping speed for water. Unfortunately, the geometry of the chamber cannot be reconfigured at this time for several reasons. It is worth noting that Friend et al. also reported difficulty in detecting water from methanol/NO_2 reaction (30).

Thermal desorption spectra of N_2 and H_2 from the co-adlayers in which $^{18}O_2/C_2H_4$ is pre-annealed to, and held for 10 s at 300 K are shown in Fig. 7. The development of N_2 desorption with varying $^{18}O_2$ pre-exposure is consistent with that for the co-adlayers in which $^{18}O_2/C_2H_4$ is pre-annealed to 250 K, as shown in Fig. 7A. To get further insight into the mechanism for N_2 production from the $^{18}O_2/C_2H_4$/NO co-adlayers, we quantified the relative N_2 desorption from the co-adlayers shown in Figs. 5, 6, and 7. The peak areas are collected in Table 2. It is evident that more N_2 is produced

© 2007 NRC Canada

Fig. 6. Thermal desorption spectra of N_2 and H_2 from $^{18}O/C_2H_4/NO$ co-adlayers prepared as follows: the Pt(332) was exposed to various amounts of $^{18}O_2$ (prior to C_2H_4) and 0.4 L C_2H_4 at 90 K. The surface was then annealed to 250 K. The resultant co-adlayers were further exposed to 0.8 L NO at 90 K.

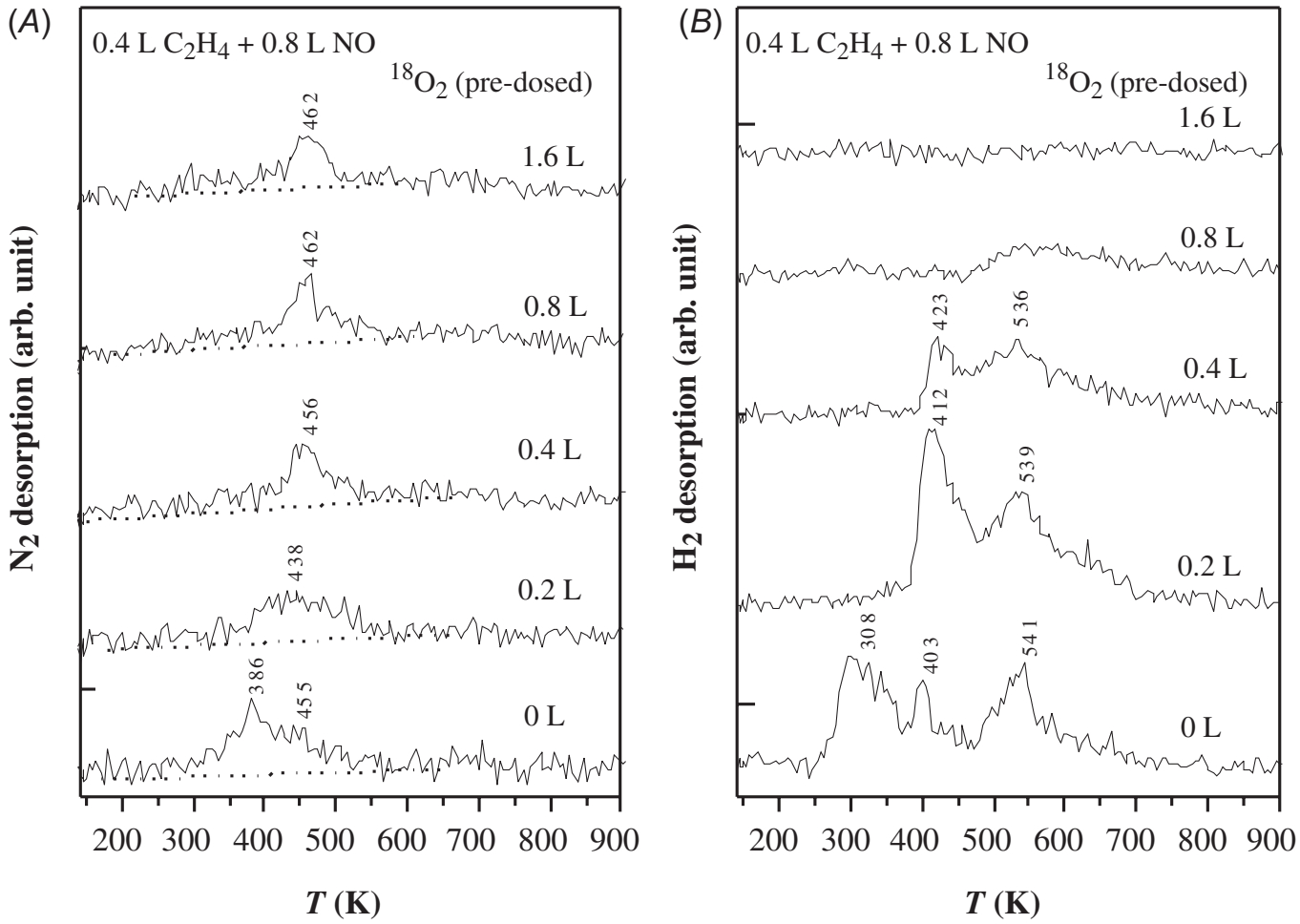

Table 2. N_2 yields from various $^{18}O_2/C_2H_4/NO$ co-adlayers.

	N_2 yield ($\times 10^{-8}$) (a.u.)		
$^{18}O_2$ exposure (L)	250 K[a]	250 K	350 K
0.8 L NO[b]	1.4[d]	–	–
0[c]	2.4	2.8	2.6
0.2	–	2.2	2.6
0.4	2.4	1.4	1.5
0.8	1.8	1.5	1.4
1.6	1.7	1.4	1.5

[a]Pt(332) was exposed to 0.4 L C_2H_4 at 250 K. The resultant adlayer was exposed to 0.8 L NO (prior to $^{18}O_2$) and various amounts of $^{18}O_2$ at 90 K.
[b]An adlayer following just an exposure of 0.8 L NO at 90 K.
[c]Without $^{18}O_2$ exposure, C_2H_4 is pre-treated following different-temperature program before being exposed to 0.8 L NO at 90 K.
[d]Uncertainty = $\pm 0.2 \times 10^{-8}$.

from the co-adlayers with $^{18}O_2$ post-dosed. For the case with O_2 *pre-dosed*, the desorption is almost equal at both annealing temperatures for $^{18}O_2$ exposures greater than 0.2 L. The slight difference at lower $^{18}O_2$ exposures is mainly due to the change in the amount of active C_2H_4-related species resulting from the change in surface temperature, as discussed previously (13). Consequently, it seems reasonable to suggest that even though the surface condition changes with varying the annealing temperature for $^{18}O_2/C_2H_4$ co-adlayers, N_2 production does not appear to be greatly affected.

Unlike N_2 desorption, changes in H_2 desorption induced by increasing the annealing temperature from 250 to 300 K are more evident, as shown by a comparison of the bottom spectrum in each of Figs. 6B and 7B. For these spectra (without $^{18}O_2$), the peak at ~338 K is significantly suppressed, and the spectrum is dominated by two peaks at ~414 and ~526 K. Increasing $^{18}O_2$ exposure quickly reduces H_2 desorption, which completely disappears at $^{18}O_2$ exposure of 0.8 L. This result indicates that increasing the annealing temperature leads to more H reacting with ^{18}O.

Discussion

N_2 and H_2 desorption arising from the reaction of NO with $^{18}O_2/C_2H_4$ co-adlayers that are pre-annealed to 250 and 300 K, combined with IR data, provides very insightful information on the role of oxygen in SCR of NO with hydrocarbons. Figures 1–4 unambiguously confirm that the

© 2007 NRC Canada

Fig. 7. Thermal desorption spectra of N_2 and H_2 from $^{18}O/C_2H_4$/NO co-adlayers prepared as follows: the Pt(332) was exposed to various amounts of $^{18}O_2$ (prior to C_2H_4) and 0.4 L C_2H_4 at 90 K. The surface was then annealed to 300 K. The resultant co-adlayers were further exposed to 0.8 L NO at 90 K.

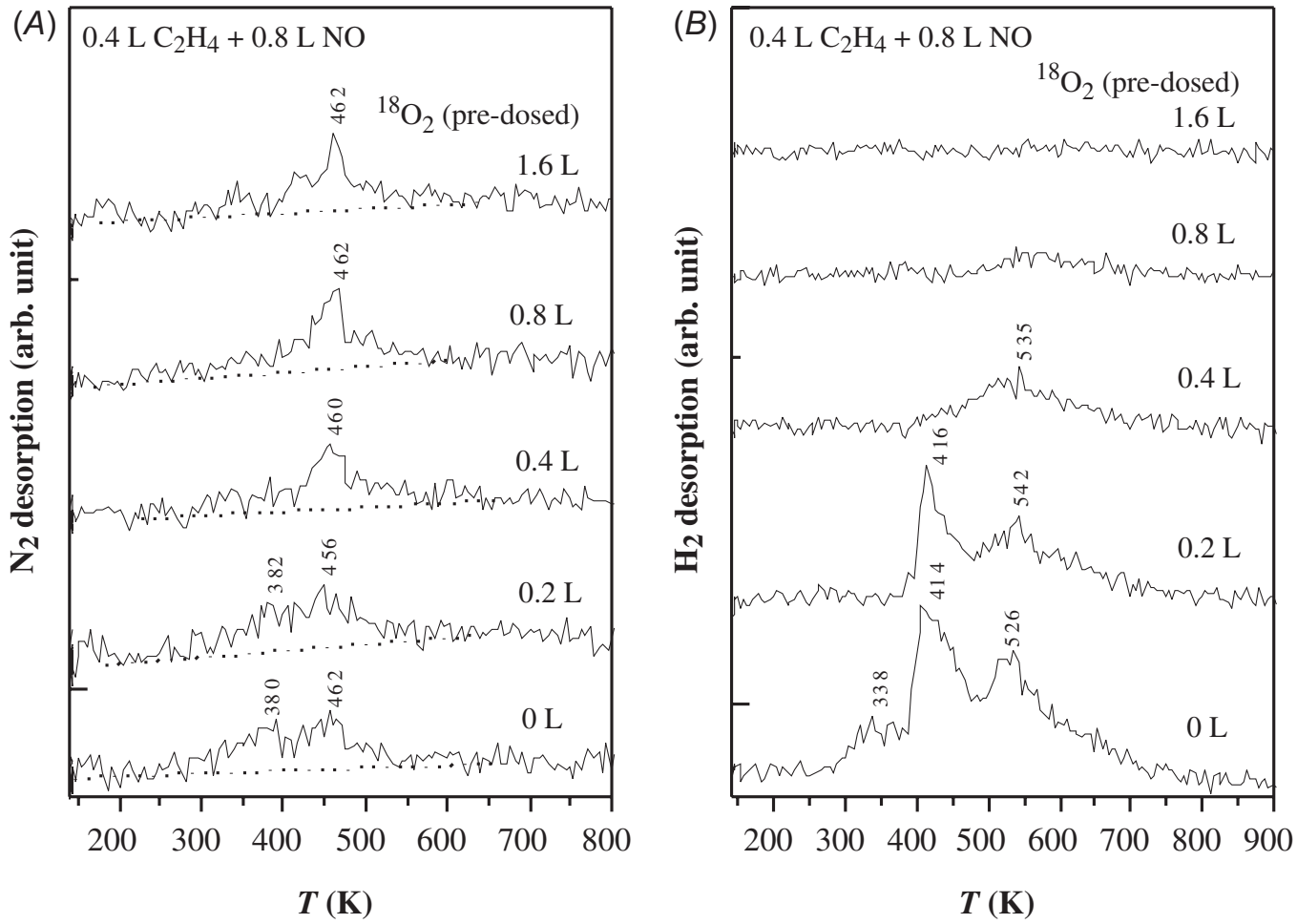

presence of $^{18}O_2$ (^{18}O) leads to evident changes in C_2H_4 dissociation. Specifically, formation of ethylidyne takes place at surface temperature higher than that in the absence of $^{18}O_2$ (^{18}O). The oxygen-induced changes for C_2H_4 dissociation also intimately depend on pre-exposure of $^{18}O_2$ in the co-adlayers (i.e., the ratio of $^{18}O_2$ to C_2H_4). For 0.4 L C_2H_4, formation of ethylidyne cannot be detected at a pre-exposure of 1.6 L $^{18}O_2$ at the annealing temperatures of 250 K and 300 K adopted in this study. These figures also indicate that no oxygen-containing surface species other than ^{18}CO (also a very small amount) are detectable under present experiment conditions, such as acetaldehyde, formate, acetate, and C_2H_4 oxide.

The adsorption of NO molecules on the surface of Pt(332) pre-exposed to $^{18}O_2$ and C_2H_4, is also strongly dependent on $^{18}O_2$ exposure and the temperatures to which $^{18}O_2/C_2H_4$ adlayers are pre-annealed. The presence of pre-dosed $^{18}O_2$ obviously suppresses the adsorption of NO molecules in bridge sites both on steps and on terraces, leading the post-dosed NO molecules to be mainly adsorbed in atop sites in the co-adlayers following higher $^{18}O_2$ pre-exposures. Moreover, a comparison between the IR spectra in Figs. 3 and 4 indicates that, unlike that at 250 K, the site-blocking effect induced by pre-dosed $^{18}O_2$ molecules is somewhat diminished when the annealing temperature is increased to 300 K, at which the adsorption of NO in bridge sites and in atop sites on both steps and terraces is retained. Figures 3 and 4 also indicate that there are no new surface species detectable that are supposed to be intermediates for N_2 production.

The site-blocking effect on NO adsorption exerted by $^{18}O_2/C_2H_4$ adlayers and its dependence on the annealing temperature and $^{18}O_2$ pre-exposure can be explained by the surface chemistry of C_2H_4 and ^{18}O atoms ($^{18}O_2$ has decomposed into ^{18}O at 250 and 300 K). A previous study has shown that the adsorption of C_2H_4 at a surface temperature of ~200 K on stepped Pt surfaces proceeds with C=C π-bound to the step corner and with the molecular axis perpendicular to the step edge (31). This configuration will inevitably shield (or block) the step sites that are preferred by NO adsorption. When the surface temperature reaches 250 K and higher, C_2H_4 dissociation begins, giving rise to ethylidyne initially. Unlike adsorbed C_2H_4, ethylidyne is preferentially adsorbed in terrace sites with its molecular axis parallel to the terrace normal (31), and as such, the step sites that were shielded (or blocked) are released and become available for NO adsorption.

This surface process for C_2H_4 does not apply to the situa-

© 2007 NRC Canada

tion in the presence of ^{18}O because the reaction of C_2H_4 with ^{18}O dominates. Like NO molecules, the adsorption of ^{18}O atoms on stepped Pt surfaces also prefers step sites, being mainly located in three-hollow sites. The adsorbed ^{18}O atoms recombinatively desorb only when the surface temperature is increased beyond 600 K. As a consequence, the adsorption of NO on steps is blocked when ^{18}O atoms are present on the surface of Pt(332). Besides the site-blocking effect, the presence of adsorbed ^{18}O atoms also weakens the NO/Pt interaction due to the much higher electronic affinity of ^{18}O (more d-electron density of Pt overlaps with O atoms rather than with anti-bond orbital of NO), leading NO dissociation to be suppressed. This situation can be reversed when a reducing species, e.g., C_2H_4, is added to the ^{18}O layer. Due to the reaction between these two species, which gives rise to H_2O (which is not detectable in our system) and $C^{18}O_2$, the site-blocking effect exerted by ^{18}O atoms and C_2H_4 lessens when the $^{18}O_2/C_2H_4$ co-adlayers are pre-annealed, as indicated by a comparison of the spectra at 250 and 300 K.

In conjunction with the analysis mentioned, the mechanism for N_2 production can be elucidated in detail by analysis of the thermal desorption spectra in Figs. 5, 6, and 7. It is shown that N_2 desorption is promoted in the presence of C_2H_4, but is significantly suppressed when ^{18}O is added into C_2H_4 adlayers. This effect occurs to a much larger extent when $^{18}O_2$ is "pre-dosed" to the surface. The positive contribution of C_2H_4 to NO reduction has been addressed in detail previously (13). The oxygen-induced suppression in N_2 desorption in this study can be explained by the facile reaction of ^{18}O with C_2H_x species that are supposed to be the key component that facilitates NO dissociation and N_2 desorption at ~380 K (13).

Another feature worth noting is that in the case in which $^{18}O_2$ is "pre-dosed", the amount of N_2 desorption does not appear to change significantly once the $^{18}O_2$ exposure exceeds 0.4 L, at which only one peak at ~460 K is detected irrespective of the annealing temperature as shown in Table 2. Since our IR results do not support a mechanism in which intermediates are needed for N_2 production, N_2 production from $^{18}O_2/C_2H_4$/NO co-adlayers most likely proceeds through a mechanism of NO dissociation and subsequent ^{18}O removal. Generally, it is well-known that the dissociation of the adsorbed NO molecules on stepped Pt surfaces mainly proceeds on the steps as the surface temperature is increased beyond 300 K (32–34). In another paper (16), we will confirm that although the adsorption of NO on steps is blocked by ^{18}O and C_2H_4; the restoration of NO to step sites is very rapid, enabling adsorbed NO molecules to be dissociated. This process accounts for N_2 production in the co-adlayers with annealing temperature of 250 K, at which the adsorption of NO on step sites would otherwise be fully suppressed.

On the other hand, though not quantified in detail, we also confirmed that only a limited amount of NO molecules are decomposed on the surface of Pt(332). This is because the (111)-oriented steps of the FCC (332) surface are less reactive than (100)-type steps to NO dissociation (35–37). A maximum N_2 desorption follows NO exposures of ~0.3 L and higher (15). This maximum value has been shown in Table 2, in which an NO exposure of 0.8 L is adopted. Accordingly, it is reasonable to suggest that N_2 production is to some extent, less dependent on how many NO molecules are present on the surface of Pt(332) to begin with. This reasoning accounts for the present observation that at both annealing temperatures, N_2 desorption does not appear to change much with increasing $^{18}O_2$ pre-exposure higher than 0.4 L, holding an intensity close to the same maximum one as observed for the NO/Pt(332) system (e.g., no other adsorbate present). In other word, providing that the adsorption of NO molecules on steps is restored (through an appropriate anneal step), a N_2 desorption, with an intensity at least comparable to the maximum one following only NO exposure, can be expected.

Conclusion

The role of oxygen in the SCR of NO with C_2H_4 was investigated by interrogating surface interactions in and measuring N_2 desorption from $^{18}O/C_2H_4$/NO co-adlayers, in which $^{18}O_2/C_2H_4$ is pre-annealed to 250 and 300 K before being exposed to 0.8 L NO at 90 K. The IR spectra of $^{18}O_2/C_2H_4$ co-adlayers are identical at annealing temperatures of 250 and 300 K, following the same amount of $^{18}O_2$ exposure. However, the adsorption of NO molecules on these co-adlayers and the resultant IR spectra are quite different with varying the annealing temperature and $^{18}O_2$ pre-exposure. The adsorption of NO molecules in bridge sites on steps is more significantly suppressed for the co-adlayers in which $^{18}O_2/C_2H_4$ is pre-annealed to 250 K. This site-blocking effect proceeds to a larger extent with increasing $^{18}O_2$ exposure. Nonetheless, no new surface species arising from the interaction among ^{18}O, C_2H_4, and NO, which are intermediates for N_2 production, are detected.

N_2 and H_2 are the primary desorbing species from the surface reaction, and their desorption is strongly dependent on $^{18}O_2$ exposure and the temperature to which $^{18}O_2/C_2H_4$ is pre-annealed. The presence of $^{18}O_2$, irrespective of the dosing sequence, suppresses N_2 desorption, but the suppression effect is much slighter when $^{18}O_2$ is "post-dosed". For the case with $^{18}O_2$ pre-dosed, despite the annealing temperature (250 or 300 K), N_2 desorption is greatly suppressed at an $^{18}O_2$ exposure of 0.2 L, but remains almost unchanged with increasing $^{18}O_2$ exposure from 0.4 to 1.6 L. In contrast, H_2 desorption is continuously decreased and disappears at 0.8 L $^{18}O_2$ and higher. This feature of N_2 desorption is explained by the restoration of the adsorption of NO molecules onto steps and the subsequent NO dissociation on these sites. It is concluded that the presence of $^{18}O_2$ in SCR of NO with C_2H_4 on the surface of Pt(332) does not play an role of activating reactants.

Acknowledgement

The financial assistance of the Natural Sciences and Engineering Research Council of Canada (NSERC) is gratefully acknowledged.

References

1. Z. Liu and S.I. Woo. Catal. Rev.-Sci. Eng. **48**, 43 (2006).
2. T. Horiuchi, T. Fujiwara, L. Chen, K. Suzuki, and T. Mori. Catal. Lett. **78**, 319 (2002).
3. H.Y. Chen and W.M.H. Sachtler. Catal. Today, **42**, 73 (1998).

© 2007 NRC Canada

4. K. Shimizu, A. Satsuma, and T. Hattori. Appl. Catal. B: Environ. **16**, 319 (1998).
5. V.I. Parvulescu, P. Grange, and B. Delmon. Catal. Today, **46**, 233 (1998).
6. A. Fritz and V. Pitchon. Appl. Catal. B: Environ. **13**, 1 (1997).
7. V.P. Zhdanov and B. Kasemo. Surf. Sci. Rep. **29**, 35 (1997).
8. F. Zaera. Prog. Surf. Sci. **69**, 1 (2001).
9. R.M. van Hardeveld, A.J.G.W. Schmidt, R.A. van Santen, and J.W. Niemantsverdriet. J. Vac. Sci. Technol. A, **15**, 1642 (1997).
10. D.R. Mullins and K. Zhang. J. Phys. Chem. B, **105**, 1374 (2001).
11. P. Zebisch, W. Huber, and H.P. Steinruck. Surf. Sci. **258**, 1 (1991).
12. S.M. Vesecky J. Paul J, and D.W. Goodman. J. Phys. Chem. **100**, 15242 (1996).
13. Y.H. Hu and K. Griffiths. J. Phys. Chem. C, **111**, 9919 (2007).
14. Y.H. Hu and K. Griffiths. Surf. Sci. **601**, 2467 (2007).
15. Y.H. Hu and K. Griffiths. Appl. Surf. Sci. 2007. In press.
16. Y.H. Hu and K. Griffiths. Appl. Surf. Sci. Submitted Oct. 2007.
17. B.W. Callen, K. Griffiths, and P.R. Norton. Phys. Rev. Lett. **66**, 1634 (1991).
18. B.W. Callen, K. Griffiths, P.R. Norton, and D.A. Harrington. J. Phys. Chem. **96**, 10905 (1992).
19. V.K. Agrawal and M. Trenary. Surf. Sci. **259**, 116 (1991).
20. H. Hopster and H. Ibach. Surf. Sci. **77**, 109 (1978).
21. J.N. Ohtani, T. Kubota, J. Kondo, C. Hirose, and K. Domen, J. Phys. Chem. B, **103**, 4562 (1999).
22. M. Sano, Y. Seimiya, Y. Ohno, T. Matsushima, S. Tanaka, and M. Kamada. Surf. Sci. **421**, 386 (1999).
23. C.E. Tripa and J.T. Yates. J. Chem. Phys. **115**, 8552 (2001).
24. T. Sawada, Z. Liu, N. Takagi, K. Watanabe, and Y. Matsumoto. Chem. Phys. Lett. **392**, 334 (2004).
25. H. Steininger, H. Ibach, and S. Lehwald. Surf. Sci. **117**, 685 (1982).
26. D.J. Burnett, A.M. Gabelnick, D.A. Fischer, A.L. Marsh, and J.L. Gland. J. Phys. Chem. B, **109**, 5659 (2005).
27. P. Berlowitz, C. Megiris, J.B. Butt, and H.H. Kung. Langmuir, **1**, 206 (1985).
28. R.L. Palmer. J. Vac. Sci. Technol. **12**, 1403 (1975).
29. Y.H. Hu and K. Griffiths. Surf. Sci. **601**, 5002 (2007).
30. L.J. Deiner, D.H. Kang, and C.M. Friend. J. Phys. Chem. B, **109**, 8085 (2005).
31. A.L. Backman and R.I. Masel. J. Phys. Chem. **94,** 5300 (1990).
32. G. Pirug, H.P. Bonzel, H. Hopster, and H. Ibach. J. Chem. Phys. **71**, 593 (1979).
33. J.M. Gohndrone and R.I Masel. Surf. Sci. **209**, 44 (1989).
34. Y.O. Park, W.F. Banholzer, and R.I. Masel. Surf. Sci. **155**, 341 (1985).
35. R.J. Mukerji, A.S. Bolina, and W.A. Brown. Surf. Sci. **547**, 27 (2003).
36. R.J. Mukerji, A.S. Bolina, and W.A. Brown. J. Chem. Phys. **119**, 10844 (2003).
37. W.A. Brown and D.A. King. J. Phys. Chem. B, **104**, 2578 (2000); and references cited therein.

© 2007 NRC Canada

New diformyldihydroxyaromatic precursors for luminescent Schiff base macrocycles: Synthesis, characterization, and condensation studies

Britta N. Boden, Amir Abdolmaleki, Cecily T.-Z. Ma, and Mark J. MacLachlan

Abstract: With the goal of preparing luminescent, fully conjugated Schiff base macrocycles, a series of precursors based on benzene, phenanthrene, and triphenylene with formylhydroxy functionalization have been prepared and characterized. The condensation of these compounds with substituted phenylenediamines to afford conjugated [2+2] or [3+3] Schiff base macrocycle has been investigated. Although the [3+3] Schiff base macrocycles could not be isolated, two new soluble and luminescent [2+2] Schiff base macrocycles with N_2O_2 binding pockets have been prepared and characterized.

Key words: Schiff base, macrocycle, condensation, salicylaldehyde, conjugated.

Résumé : Afin de pouvoir obtenir des bases de Schiff macrocycliques complètement conjuguées et luminescentes, on a préparé et caractérisé une série de précurseurs à base de benzène, de phénanthrène et de triphénylène portant des groupes hydroxyle et formyle. On a ensuite étudié la condensation de ces composés avec des phénylènediamines substituées qui peuvent conduire à des bases de Schiff macrocycliques avec conjugaison [2+2] ou [3+3]. Même si on n'a pas pu isoler les bases de Schiff macrocycliques [3+3], on a pu préparer et caractériser deux nouvelles bases de Schiff macrocycliques [2+2], solubles et luminescentes, comportant des poches de fixation du N_2O_2.

Mots-clés : base de Schiff, macrocycle, condensation, salicylaldéhyde, conjugué.

[Traduit par la Rédaction]

Introduction

Schiff base macrocycles formed from the condensation of diamines and dialdehydes are attractive ligands for multimetallic complexes (1–20). 2,6-Diformylphenol **1** and its analogues condense with diamine compounds in a 2:2 ratio to form compartmental ligands (Robson macrocycles **2**) (21–25) (Chart 1). Bimetallic complexes formed in the interior of this macrocycle are of interest for studying magnetic and electronic interactions between metal centres, and may serve as models for the active sites of enzymes (26, 27).

The hydroxyl group adjacent to the formyl moiety in the precursor is important for producing an N_2O_2 chelate and for stabilizing the imine in the metal-free macrocycle. While a vast assortment of diamines is available for incorporation into Schiff base macrocycles, much less attention has been placed on the bis(formylhydroxy) precursor development. By varying the geometry and structure of this component, one may access novel macrocycles with different sizes, shapes, and number of metal-binding sites (28–30). For example, condensation of compounds **3** (31–33) and **4** (34) with *o*-phenylenediamines gives triangular [3+3] and hexagonal [6+6] Schiff base macrocycles, respectively, and **5** (35) is expected to form [2+2] Schiff base macrocycles. Only a few other bis(formylhydroxy) compounds have been explored as precursors for Schiff base macrocycles (36–40). Expanding the number of bis(formylhydroxy) compounds available will open up avenues to explore macrocycles with new electronic, optical, and coordinating properties.

In this paper, we significantly expand the library of dihydroxydiformyl compounds predisposed for [2+2] and [3+3] Schiff base macrocycles. In an effort to obtain fully conjugated, luminescent macrocycles, we have prepared the first phenanthrene and triphenylene precursors with bis(formylhydroxy) functionality. Phenanthrene and triphenylene have received very little attention for incorporation into macrocycles (41, 42), yet they may have a large effect on the ring size and electronic or optical properties of the products. In addition, we have prepared new conjugated *m*-diethynylbenzene precursors for the preparation of [2+2] Schiff base macrocycles. We report on the optical properties of the novel diamond-shaped macrocycles.

Received 4 July 2007. Accepted 5 November 2007. Published on the NRC Research Press Web site at canjchem.nrc.ca on 13 December 2008.

B.N. Boden, A. Abdolmaleki, C.T.L. Ma, and M.J. MacLachlan.[1] Department of Chemistry, University of British Columbia, 2036 Main Mall, Vancouver, BC V6T 1Z1, Canada.

[1]Corresponding author (email: mmaclach@chem.ubc.ca).

Experimental

General

Tetrahydrofuran (THF) was distilled over Na and benzophenone under N_2. Triethylamine was distilled over NaOH under N_2. Stilbene **6** (43), 3,6-dimethoxyphenanthrene **7** (44), 3,6-dimethoxyphenanthrene-9,10-quinone **10** (45), 1,2-dibromo-4,5-dihexylbenzene **15** (46), 4-methoxyphenylboronic acid **16** (47), 1,3-diethynylbenzene **24** (48), 2,6-diethynylpyridine **25** (49), 1,2-diamino-4,5-dialkoxy-

 doi:10.1139/V07-136 © 2007 NRC Canada

Chart 1.

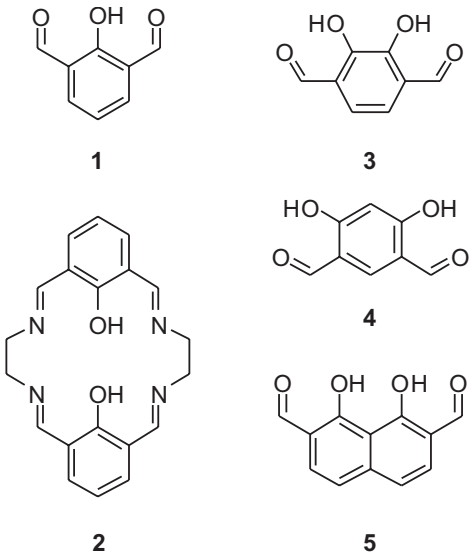

benzenes **28** (50), and BOC-protected phenylenediamine **32** (51) were prepared according to literature procedures. $Pd(PPh_3)_4$ was obtained from Strem Chemicals, Inc. Deuterated solvents were obtained from Cambridge Isotope Laboratories, Inc. All other chemicals were purchased from Aldrich, TCI, or Fisher and used as received. All reactions were carried out under nitrogen unless otherwise noted. ^{1}H NMR (300 or 400 MHz) and ^{13}C NMR (75.5 or 100.7 MHz) spectra were recorded on Bruker Avance 300 or Bruker Avance 400 spectrometers and were referenced internally to residual protonated solvent. Infrared spectra were obtained as KBr discs or on NaCl plates with a Bomem MB-100 spectrometer or a Nicolet 4700 FTIR spectrometer. UV–vis spectra were obtained on a Varian Cary 5000 UV–vis/near IR spectrometer using a 1 cm cuvette. Fluorescence spectra were obtained on a Photon Technology Intl. QuantaMaster fluorimeter. Matrix assisted laser desorption/ionization(MALDI) mass spectra were obtained on a Bruker Biflex IV time-of-flight (TOF) mass spectrometer equipped with a MALDI ion source. Electrospray ionization (ESI) mass spectra were obtained on a Micromass LCT time-of-flight (TOF) mass spectrometer equipped with an electrospray ion source. Samples were analyzed in methanol:dichloromethane at 1 μmol/L. EI spectra were obtained with a double focusing mass spectrometer (Kratos MS-50) coupled with a MASPEC data system with EI operating conditions of: source temperatures 120–220 °C and ionization energy 70 eV. Elemental analyses were obtained at the UBC Microanalytical facility. Melting points were recorded on a Fisher John's melting point apparatus.

Synthesis of 2,7-diformyl-3,6-dimethoxyphenanthrene (8)

3,6-Dimethoxyphenanthrene **7** (0.718 g, 3.01 mmol) was dissolved in 20 mL THF. BuLi (6.1 mL, 1.6 mol/L) was added, and the solution was stirred for 30 min, after which anhyd. DMF (0.77 mL, 9.98 mmol) was added. The reaction solution was poured into aq. HCl and extracted with dichloromethane (DCM). After drying over $MgSO_4$, the solvent was removed by rotary evaporation to reveal an orange solid. The product was chromatographed over silica with DCM and recrystallized from DCM to obtain 0.150 g of yellow solid (17% yield).

Data for 8

Mp 280 °C dec. UV–vis (CH_2Cl_2): λ_{max} (ϵ) = 281 (5.6×10^4), 338 (2.5×10^4), 440 (2.2×10^3) nm (L mol^{-1}cm^{-1}). IR (KBr): ν = 2947, 2862, 1681, 1615, 1502, 1457, 1406, 1369, 1265, 1220, 1181, 1136, 1109, 1017, 970, 842, 655 cm^{-1}. ^{1}H NMR (300 MHz, $CDCl_3$, 25 °C) δ: 10.63 (s, 2H, C*H*O), 8.36 (s, 2H, aromatic C*H*), 7.92 (s, 2H, aromatic C*H*), 7.65 (s, 2H, aromatic C*H*), 4.17 (s, 6H, OCH_3) ppm. ^{13}C NMR (75.5 MHz, $CDCl_3$, 25 °C) δ: 189.7, 159.0, 134.3, 130.6, 127.3, 126.1, 126.0, 103.8, 55.9 ppm. ESI-MS: *m*/*z* = 295 ([M + H]$^+$). Anal. calcd. for $C_{18}H_{14}O_4 \cdot 0.5\ H_2O$: C, 71.28; H, 4.98. Found: C, 71.35; H, 4.80.

Synthesis of 2,7-diformyl-3,6-dihydroxyphenanthrene (9)

To an ice-cooled solution of compound **8** (0.413 g, 1.40 mmol) in DCM was added BBr_3 (1 mL, 10.6 mmol). After stirring overnight, the solution was poured into 200 mL of ice water to obtain an orange solid. The solid was filtered, and the remaining aq. solution was extracted with DCM. The organic layer was dried and combined with the solid. After flashing the product through silica with DCM, 0.268 g (1.01 mmol) of orange crystals were obtained (72% yield).

Data for 9

Mp > 300 °C. UV–vis (CH_2Cl_2): λ_{max} (ϵ) = 284, 304, 326, 465 nm. IR (KBr): ν = 3449, 3253, 3017, 2884, 1652, 1530, 1338, 1205, 1157, 1106, 899 cm^{-1}. ^{1}H NMR (300 MHz, DMSO-d_6, 25 °C) δ: 10.96 (s, 2H, O*H*), 10.46 (s, 2H, C*H*O), 8.29 (s, 2H, aromatic C*H*), 7.99 (s, 2H, aromatic C*H*), 7.67 (s, 2H, aromatic C*H*) ppm. ^{13}C NMR (75.5 MHz, DMSO-d_6, 25 °C) δ: 191.3, 157.6, 134.0, 133.0, 130.6, 128.2, 125.9, 125.1, 124.2, 109.2 ppm. EI-MS: *m*/*z* = 266 (M$^+$). Anal. calcd. for $C_{16}H_{10}O_4$: C, 72.18; H, 3.79. Found: C, 72.05; H, 4.00.

Synthesis of 2,7-dibromo-3,6-dimethoxyphenanthrene-9,10-quinone (11)

To a solution of 3,6-dimethoxy-9,10-phenanthrenequinone **10** (1.090 g, 4.06 mmol) in 25 mL each DCM and MeCN was added Br_2 (1 mL, 19.5 mmol) and $FeCl_3$ (1.317 g, 8.12 mmol). The solution was heated to reflux until an orange solid precipitated. After filtration of the solid, the filtrate was poured in H_2O and extracted with DCM. The solvent was removed under vacuum until further precipitation. Both solids were combined and recrystallized from DCM to yield 1.298 g (3.05 mmol, 75%). The product was sometimes chromatographed on silica with DCM.

Data for 11

Mp > 300 °C. UV–vis (CH_2Cl_2): λ_{max} (ϵ) = 247 (1.6×10^4), 297 (5.8×10^4), 344 (1.3×10^4) nm (L mol^{-1}cm^{-1}). IR (KBr): ν = 3448, 2946, 1670, 1578, 1545, 1436, 1333, 1312, 1274, 1262, 1203, 1040, 854, 696, 678 cm^{-1}. ^{1}H NMR (300 MHz, $CDCl_3$, 25 °C) δ: 8.33 (s, 2H, aromatic C*H*), 7.22 (s, 2H, aromatic C*H*), 4.11 (s, 6H, OCH_3) ppm; ^{13}C NMR (100.7 MHz, $CDCl_3$, 25 °C) δ: 177.7, 162.0, 136.5, 136.1, 125.9, 114.7, 105.9, 57.0 ppm. EI-MS: *m*/*z* = 426

© 2007 NRC Canada

(M^+). Anal. calcd. for $C_{16}H_{10}O_4Br_2$: C, 45.10; H, 2.37. Found: C, 44.95; H, 2.66.

Synthesis of 2,7-dibromo-3,6,9,10-tetramethoxyphenanthrene (12)

Compound **11** (0.567 g, 1.33 mmol), Bu_4NBr (0.113 g, 0.351 mmol), $Na_2S_2O_4$ (0.610 g, 3.50 mmol), THF (50 mL) and H_2O (50 mL) were combined in a round-bottomed flask and stirred for 10 min, after which dimethyl sulfate (3 mL, 31.7 mmol) was added, followed by aq. sodium hydroxide (2 mL, 14 mol/L). After stirring 1 h, the aq. layer was separated and extracted with EtOAc (3 × 50 mL). The combined organic layers were washed with water (3 × 50 mL), NH_4OH solution (2 × 50 mL), and brine (1 × 50 mL). The organic layer was dried with $MgSO_4$, filtered, and the solvents were removed under vacuum, resulting in a brown solid. Washing the product with MeOH gave an orange solid. Additional impurities were removed by flashing the product through silica with a 1:1 mixture of hexanes and DCM, followed by recrystallization from DCM. Yield: 0.473 g, 1.0 mmol, 78%.

Data for 12

Mp 217–218 °C. UV–vis (CH_2Cl_2): λ_{max} (ϵ) = 264 (5.3 × 10^4), 225 (3.8 × 10^4), 384 (1.0 × 10^3) nm (L $mol^{-1}cm^{-1}$). IR (KBr): ν = 3448, 2933, 1597, 1491, 1451, 1432, 1364, 1245, 1074, 1056, 993, 676 cm^{-1}. ^1H NMR (400 MHz, $CDCl_3$, 25 °C) δ: 8.38 (s, 2H, aromatic C*H*), 7.77 (s, 2H, aromatic C*H*), 4.09 (s, 6H, OCH_3), 4.02 (s, 6H, OCH_3) ppm. ^{13}C NMR (100.7 MHz, $CDCl_3$, 25 °C) δ: 154.2, 142.1, 128.0, 127.5, 125.2, 114.1, 103.9, 61.3, 56.8 ppm. EI-MS: *m*/*z* = 456 (M^+). Anal. calcd. for $C_{18}H_{16}O_4Br_2$: C, 47.40; H, 3.54. Found: C, 47.2; H, 3.66.

Synthesis of 2,7-diformyl-3,6,9,10-tetramethoxyphenanthrene (13)

Compound **12** (0.373 g, 0.818 mmol) was dissolved in 18 mL THF and cooled to 0 °C. To the solution was added BuLi (1.2 mL, 1.6 mol/L). After 10 min stirring, DMF (0.3 mL, 3.87 mmol) was added. The solution was poured into acidified H_2O and extracted with DCM. Evaporation of the solvent gave a yellow solid (0.188 g, 0.531 mmol, 65% yield).

Data for 13

Mp 294 °C dec. UV–vis (CH_2Cl_2): λ_{max} (ϵ) = 287 (5.2 × 10^4), 342 (2.0 × 10^4), 448 (2.0 × 10^3) nm (L $mol^{-1}cm^{-1}$). IR (KBr): ν = 3448, 2935, 2858, 1686, 1610, 1491, 1452, 1429, 1358, 1278, 1249, 1205, 1145, 1128, 1014, 976, 570 cm^{-1}. ^1H NMR (300 MHz, $CDCl_3$, 25 °C) δ: 10.62 (s, 2H, C*H*O), 8.68 (s, 2H, aromatic C*H*), 7.68 (s, 2H, aromatic C*H*), 4.15 (s, 6H, OCH_3), 4.05 (s, 6H, OCH_3) ppm. ^{13}C NMR (75.5 MHz, $CDCl_3$, 25 °C) δ: 190.0, 158.8, 143.3, 132.6, 126.3, 125.3, 104.3, 61.4, 56.2 ppm. EI-MS: *m*/*z* = 354 (M^+). HR-MS calcd. for $C_{20}H1_8O_6$: 354.11034. Found: 354.11005.

Synthesis of 2,7-diformyl-3,6-dihydroxyphenanthrene-9,10-quinone (14)

Compound **13** was dissolved in 10 mL dry DCM and cooled to 0 °C. To the solution was added BBr_3. After stirring overnight, the dark solution was poured into H_2O to precipitate a purple solid. After filtration, some of the solid was dissolved in THF to make an initially purple solution, which slowly became yellow upon standing. The solvent was removed to give a brown solid (**14**). We believe the initially obtained solid is a tautomer or partially reduced form of **14**, but it was not possible to obtain a pure sample of the purple intermediate.

Data for 14

Mp > 300 °C. UV–vis (DMSO): λ_{max} (ϵ) = 314 nm. IR (KBr): ν = 3422, 2925, 2856, 1692, 1665, 1613, 1551, 1361, 1320, 1252, 1197, 1154, 947, 789, 652 cm^{-1}. ^1H NMR (300 MHz, DMSO-d_6, 25 °C) δ: 12.12 (s, 2H, O*H*), 10.33 (s, 2H C*H*O), 8.34 (s, 2H, aromatic C*H*), 7.59 (s, 2H, aromatic C*H*) ppm. EI-MS: *m*/*z* = 296 (M^+). HR-MS calcd. for $C_{16}H_8O_6$: 296.03209. Found: 296.03142.

Synthesis of 4′,5′-dihexyl-4,4″-dimethoxy-1,1′:2′,1″-terphenyl (17)

A mixture of 1,2-dibromo-4,5-dihexylbenzene **15** (1.049 g, 2.59 mmol), 4-methoxyphenylboronic acid **16** (0.971 g, 6.39 mmol), sodium carbonate (0.971 g, 9.16 mmol), and tetrakis(triphenylphosphine)palladium(0) (0.050 g, 0.043 mmol) was stirred under reflux in a mixture of toluene (18 mL), EtOH (18 mL), and water (6 mL) for 4 h. The solution was poured into water and extracted with DCM (3 × 100 mL). After drying with $MgSO_4$ and evaporating the solvent, a brown oil was obtained and purified by chromatography in 3:1 hexanes/DCM. Additional impurities were crystallized out from EtOH. The product was a colorless oil. Yield: 0.732 g, 1.60 mmol, 62%.

Data for 17

UV–vis (CH_2Cl_2): λ_{max} (ϵ) = 251 (4.7 × 10^4) nm (L $mol^{-1}cm^{-1}$). IR (KBr): ν = 2955, 2928, 2855, 1608, 1512, 1490, 1467, 1290, 1245, 1107, 1033, 831 cm^{-1}. ^1H NMR (400 MHz, $CDCl_3$, 25 °C) δ: 7.14 (s, 2H, aromatic C*H*), 7.06 (d, 4H, aromatic C*H*), 7.74 (d, 4H, aromatic C*H*), 3.76 (s, 6H, OCH_3), 2.64 (m, 4H, CH_2), 1.62 (m, 4H, hexyl chain), 1.41 (m, 4H, hexyl chain), 1.33 (m, 8H, hexyl chain), 0.89 (t, 6H, hexyl CH_3) ppm. ^{13}C NMR (100.7 MHz, $CDCl_3$, 25 °C) δ: 158.3, 139.8, 137.5, 134.5, 131.5, 131.1, 113.5, 55.4, 32.7, 32.0, 31.6, 29.8, 22.9, 14.3 ppm. EI-MS: *m*/*z* = 458 (M^+). HR-MS calcd. for $C_{32}H_{42}O_2$: 458.31848. Found: 458.31810.

Synthesis of 2,3-dihexyl-7,10-dimethoxytriphenylene (18)

Compound **17** (0.778 g, 1.69 mmol) and iodine (0.667 g, 2.6 mmol) were dissolved in 250 mL dry toluene. The solution was exposed to UV light for 72 h. Excess iodine was removed by washing the solution with aq. $NaSO_3$, and the resulting organic layer was dried with $MgSO_4$, and the solvent was removed under vacuum. Recrystallization of the product from EtOH afforded off-white crystals of **18**, while 0.629 g of terphenyl **17** was recovered and reused in subsequent reactions. Yield: 0.098 g (0.215 mmol, 66% yield based on recovered **17**).

Data for 18

Mp 73–75 °C. UV–vis (CH_2Cl_2): λ_{max} (ϵ) = 262 (9.3 × 10^4), 271 (1.2 × 10^5) nm (L $mol^{-1}cm^{-1}$). IR (KBr): ν = 2953, 2926, 2852, 1619, 1508, 1464, 1416, 1367, 1231, 1203,

© 2007 NRC Canada

1178, 1050, 1027, 835, 812 cm^{-1}. ^1H NMR (400 MHz, $CDCl_3$, 25 °C) δ: 8.52 (d, 2H, aromatic C*H*), 8.24 (s, 2H, aromatic C*H*), 7.92 (d, 2H, aromatic C*H*), 7.23 (dd, 2H, aromatic C*H*), 4.00 (s, 6H, OCH_3), 2.80 (m, 4H, CH_2), 1.71 (m, 4H, hexyl chain), 1.50 (m, 4H, hexyl chain), 1.24 (m, 8H, hexyl chain), 0.92 (t, 6H, hexyl CH_3) ppm. ^{13}C NMR (100.7 MHz, $CDCl_3$, 25 °C) δ: 158.6, 139.6, 130.8, 127.1, 125.0, 124.5, 123.1, 115.6, 106.3, 55.7, 33.4, 32.1, 31.8, 29.8, 22.9, 14.4 ppm. EI-MS: *m*/*z* = 456 (M^+). Anal. calcd. for $C_{32}H_{40}O_2$: C, 84.16; H, 8.83. Found: C, 84.32; H, 8.61.

Synthesis of 6,11-dibromo-2,3-dihexyl-7,10-dimethoxytriphenylene (19)

To an ice-cooled solution of **18** (0.532 g, 1.16 mmol) in DCM (20 mL), bromine (0.1 mL, 1.9 mmol) was added dropwise. The solution was allowed to stir for 2 h. After washing with aq. $Na_2S_2O_4$, the organic layer was dried with $MgSO_4$, and the solvent was removed under vacuum. Recrystallization from EtOH and DCM afforded white fibrous crystals. Yield: 0.563 g, 0.916 mmol, 79%.

Data for 19

Mp 166–168 °C. UV–vis (CH_2Cl_2): λ_{max} (ε) = 274 (1.6×10^5) nm (L $mol^{-1}cm^{-1}$). IR (KBr): ν = 2956, 2926, 2853, 1600, 1494, 1464, 1401, 1252, 1201, 1059, 866, 830, 701 cm^{-1}. ^1H NMR (400 MHz, $CDCl_3$, 25 °C) δ: 8.71 (s, 2H, aromatic C*H*), 8.13 (s, 2H, aromatic C*H*), 7.76 (s, 2H, aromatic C*H*), 4.11 (s, 6H, OCH_3), 2.81 (m, 4H, CH_2), 1.70 (m, 4H, hexyl chain), 1.47 (m, 4H, hexyl chain), 1.34 (m, 8H, hexyl chain), 0.91 (t, 6H, hexyl CH_3) ppm. ^{13}C NMR (100.7 MHz, $CDCl_3$, 25 °C) δ: 154.7, 140.7, 129.4, 128.6, 126.2, 125.7, 123.2, 114.0, 104.9, 56.7, 33.4, 32.0, 31.9, 29.8, 22.9, 14.4 ppm. EI-MS: *m*/*z* = 614 (M^+). Anal. calcd. for $C_{32}H_{38}O_2Br_2$: C, 62.55; H 6.23. Found: C, 62.70; H, 6.54.

Synthesis of 6,11-diformyl-2,3-dihexyl-7,10-dimethoxytriphenylene (20)

To a solution of **19** (0.795 g, 1.29 mmol) in dry THF (40 mL) cooled to –78 °C, 1.6 mol/L *n*-BuLi (4 mL, 6.4 mmol) was added to produce a milky white solution. After 10 min, anhyd. DMF (0.8 mL, 10.3 mmol) was added to form a pale yellow solution. The solution was warmed to room temperature, then poured into aq. HCl (1 mol/L). Extraction with DCM, drying with $MgSO_4$, and evaporation of the solvent afforded a brown oil. Yellow solid precipitated out upon addition of EtOH. Yield: 0.534 g, 1.04 mmol, 81%.

Data for 20

Mp 165–167 °C. UV–vis (CH_2Cl_2): λ_{max} (ε) = 264 (7.0×10^4), 279 (6.2×10^4), 384 (1.2×10^4) nm (L $mol^{-1}cm^{-1}$). IR (KBr): ν = 2960, 2927, 2860, 1687, 1614, 1472, 1421, 1412, 1255, 1207, 1165, 1047, 869, 830 cm^{-1}. ^1H NMR (400 MHz, $CDCl_3$, 25 °C) δ: 10.60 (s, 2H, C*H*=O), 8.94 (s, 2H, aromatic C*H*), 8.22 (s, 2H, aromatic C*H*), 7.67 (s, 2H, aromatic C*H*), 4.07 (s, 6H, OCH_3), 2.79 (m, 4H, CH_2), 1.68 (m, 4H, hexyl chain), 1.48 (m, 4H, hexyl chain), 1.36 (m, 8H, hexyl chain), 0.92 (t, 6H, hexyl CH_3) ppm. ^{13}C NMR (100.7 MHz, $CDCl_3$, 25 °C) δ: 190.0, 159.4, 141.2, 134.3, 126.9, 125.4, 125.2, 124.8, 123.5, 105.0, 55.9, 33.5, 32.1, 32.0, 29.9, 22.9, 14.4 ppm. EI-MS: *m*/*z* = 512 (M^+). Anal. calcd. for $C_{34}H_{40}O_4$: C, 79.65; H, 7.86. Found: C, 79.52; H, 7.93.

Synthesis of 6,11-diformyl-2,3-dihexyl-7,10-dihydroxytriphenylene (21)

To an ice-cooled solution of **20** (0.495 g, 0.965 mmol) in dry DCM (50 mL), boron tribromide (2.2 mL, 23.3 mmol) was added to produce a dark brown solution, which subsequently faded to orange. The solution was allowed to warm to room temperature overnight, then was poured into ice water (200 mL). After the mixture had warmed, it was filtered, and the filtrate was extracted with $CHCl_3$ (3 × 50 mL). The filtered solid and organic layer from extraction were combined, and the solvent was removed under vacuum. The residue was passed through a plug of silica in $CHCl_3$. After removal of the solvent, the product was recrystallized from $CHCl_3$ to obtain 0.357 g (0.736 mmol, 76% yield) of a yellow solid.

Data for 21

Mp 260–262 °C. UV–vis (CH_2Cl_2): λ_{max} (ε) = 248 (3.5×10^4), 274 (6.1×10^4), 393 (8.0×10^3) nm (L $mol^{-1}cm^{-1}$). IR (KBr): ν = 3444, 2952, 2926, 2855, 1659, 1584, 1543, 1467, 1341, 1230, 1184, 880, 826, 790, 725, 600 cm^{-1}. ^1H NMR (400 MHz, $CDCl_3$, 25 °C) δ: 10.68 (s, 2H, O*H*), 10.19 (s, 2H, C*H*=O), 8.71 (s, 2H, aromatic C*H*), 8.18 (s, 2H, aromatic C*H*), 7.96 (s, 2H, aromatic C*H*), 2.82 (m, 4H, CH_2), 1.72 (m, 4H, hexyl chain), 1.49 (m, 4H, hexyl chain), 1.36 (m, 8H, hexyl chain), 0.91 (t, 6H, hexyl CH_3) ppm. ^{13}C NMR (75.5 MHz, $CDCl_3$, 25 °C) δ: 196.8, 158.7, 141.1, 135.4, 130.4, 126.4, 124.8, 123.1, 121.9, 112.1, 33.4, 33.0, 31.9, 29.8, 22.9, 14.4 ppm. EI-MS: *m*/*z* = 484 (M^+). Anal. calcd. for $C_{32}H_{36}O_4$: C, 79.31; H, 7.49. Found: C, 79.06; H, 7.52.

Synthesis of 4-Iodosalicylaldehyde (23)

Under a nitrogen atmosphere, dry paraformaldehyde (4.05 g, 135 mmol) was added to a mixture of the 3-iodophenol **22** (4.40 g, 20 mmol), anhyd. $MgCl_2$ (2.86 g, 30 mmol), and anhyd. Et_3N (10.5 mL) in dry MeCN (100 mL). After heating the mixture to reflux for 2 h, the mixture was cooled to RT, and 100 mL of 2 mol/L aq. HCl was added. The product was extracted with 3 × 100 mL of Et_2O, dried over $MgSO_4$, filtered, and dried by rotary evaporation. The residue was dissolved in a mixture of 1:1 CH_2Cl_2/hexanes and was filtered through a short pad (~5 cm) of SiO_2 using the same solvent mixture as eluent. Rotary evaporation of the filtered solution gave an off-white solid. Recrystallization from hexanes gave white crystals of **23** (2.22 g, 9.0 mmol, 45%).

Data for 23

Mp 91–92 °C (lit. 87 °C) (52). UV–vis (CH_2Cl_2): λ_{max} (ε) = 327 (5.32×10^3) nm (L $mol^{-1}cm^{-1}$). IR (KBr): ν = 3431, 2927, 2856, 1665, 1609, 1458, 1260, 1169, 891, 796, 752, 704 cm^{-1}. ^1H NMR (300 MHz, $CDCl_3$) δ: 11.00 (s, 1H, O*H*), 9.83 (s, 1H, C*H*=O), 7.41 (s, 1H, C*H*), 7.37 (dd, $^3J_{HH}$ = 9.48 Hz, 1H, C*H*), 7.23 (d, $^3J_{HH}$ = 8.07 Hz, 1H, C*H*) ppm. ^{13}C NMR (75.5 MHz, $CDCl_3$) δ: 221.0, 196.0, 134.2, 129.4, 127.2, 105.1, 97.7 ppm. EI-MS: *m*/*z* = 247 (M^+, 100%).

© 2007 NRC Canada

Anal. calcd. for $C_7H_5IO_2$: C, 33.90; H, 2.03. Found: C, 34.11; H, 2.10.

Synthesis of Compound 26

Under a nitrogen atmosphere, 1,3-diethynylbenzene **24** (0.254 g, 2.0 mmol), 4-iodosalicylaldehyde **23** (0.992 g, 4.0 mmol), Ph_3P (0.015 g, 0.06 mmol), and *trans*-$[PdCl_2(Ph_3P)_2]$ (0.06 g, 0.08 mmol) were dissolved in 25 mL of anhyd. THF. Dry Et_3N (2.3 mL) was added, turning the solution from yellow to orange. After stirring for 20 min, CuI (0.02 g, 0.10 mmol) was added, and the solution then turned to dark brown. The solution was stirred overnight at RT, then the yellow precipitate was isolated on a Büchner funnel and washed with CH_2Cl_2/hexane (1:2). Yield: 0.549 g (1.5 mmol, 75%) of yellow powder.

Data for 26

Mp > 250 °C dec. UV–vis (CH_2Cl_2): λ_{max} (ϵ) = 297 (3.24×10^4), 331 (3.29×10^4) nm (L $mol^{-1}cm^{-1}$). IR (KBr): ν = 3430, 2958, 2926, 2855, 1664, 1609, 1224, 1168, 799, 704 cm^{-1}. ^1H NMR (300 MHz, DMSO-d_6) δ: 10.98 (s, 2H, O*H*), 10.28 (s, 2H, C*H*=O), 7.82 (s, 1H, *C*H), 7.68 (m, 4H, C*H*), 7.53 (t, $^3J_{HH}$ = 10.6 Hz, 1H, C*H*) 7.12–7.15 (m, 4H, *C*H) ppm. ^{13}C NMR (75.5 MHz, DMSO-d_6) δ: 190.3, 160.4, 134.4, 132.3, 129.5, 129.1, 122.5, 122.3, 119.6, 91.3, 89.3 ppm. EI-MS: *m*/*z* = 366 (M^+, 100%), 338 (85%). Anal. calcd. for $C_{24}H_{14}O_4 \cdot H_2O$: C, 74.99; H, 4.20. Found: C, 75.28; H, 4.20.

Synthesis of compound 27

Compound **27** was prepared using the same procedure as for **26**. Light yellow powder; yield: 0.514 g (1.4 mmol, 70%).

Data for 27

Mp > 250 °C dec. UV–vis (CH_2Cl_2): λ_{max} (ϵ) = 310 (3.52×10^4) nm (L $mol^{-1}cm^{-1}$). IR (KBr): ν = 3430, 2926, 2855, 1660, 1609, 1553, 1434, 1260, 1180, 795, 752, 704 cm^{-1}. ^1H NMR (400 MHz, DMSO-d_6): δ: 11.00 (s, 2H, O*H*), 10.29 (s, 2H, C*H*=O), 7.96 (t, $^3J_{HH}$ = 7.8 Hz, 1H, *C*H), 7.74 (d, $^3J_{HH}$ = 7.7 Hz, 2H, C*H*), 7.70 (d, $^3J_{HH}$ = 7.8 Hz, 2H, C*H*) 7.18 (m, 4H, *C*H) ppm. ^{13}C NMR (75.5 MHz, DMSO-d_6): δ: 190.2, 160.5, 142.3, 137.9, 129.1, 128.1, 127.7, 123.1, 122.7, 120.1, 90.7, 87.9 ppm. EI-MS: *m*/*z* = 367 (M^+, 100%), 339 (80%). Anal. calcd. for $C_{23}H_{13}O_4N \cdot 0.5H_2O$: C, 73.40; H, 3.75; N, 3.72. Found: C, 73.51; H, 3.75; N, 4.36.

Attempted synthesis of macrocycle 29

Equimolar amounts of compound **9** and 1,2-diamino-4,5-dialkoxybenzenes **28** were combined in a Schlenk flask. Degassed $CHCl_3$ was added, and the resulting solution was heated to reflux for 24 h. After cooling, any precipitate was filtered, or MeCN was added until precipitate formed. The products are unstable to chromatographic separation on silica or alumina.

Data for the insoluble product obtained when R = $^nC_6H_{13}$ (29b)

IR (KBr): ν = 3051, 2952, 2928, 2857, 1636, 1611, 1506, 1465, 1370, 1256, 1190, 1165, 1120, 1017, 959 cm^{-1}.

Data obtained for filtrate when R = $^nC_8H_{17}$ (29c)

^1H NMR (400 MHz, $CDCl_3$, 25 °C) δ: 12.97, 10.61, 10.07, 10.05, 8.66, 8.01, 7.99, 7.82, 7.49, 6.80, 6.34, 3.95, 1.82–0.86 (hexyloxy chain) ppm. ESI-MS: *m*/*z* = 614 (M^+, 1+1 fragment).

Data for solid obtained from reaction with R = $^nC_8H_{17}$ (29c)

^1H NMR (400 MHz, $CDCl_3$, 25 °C) δ: 13.00, 12.93, 10.63, 10.11, 10.09, 8.72, 8.52, 8.06, 8.03, 7.87, 7.51, 7.49, 6.83, 6.36, 3.95, 1.83–0.86 (hexyloxy chain) ppm. MALDI-TOF: *m*/*z* = 1785 ([**29c** + H]$^+$).

Attempted synthesis of macrocycle 30

Equimolar amounts of compound **21** and 1,2-diamino-4,5-dialkoxybenzenes were combined in a Schlenk flask. Solvent was added, and the resulting solution was heated to reflux. For specific conditions, see later. In each case, nearly the same inseparable mixture was obtained as indicated by ^1H NMR spectroscopy.

Data for 30

^1H NMR (300 MHz, $CDCl_3$, 25 °C) δ: 14.84, 13.66, 13.21, 13.02, 12.35, 12.28, 12.06, 11.65, 9.2–6.3, 4.2–3.8, 2.9–2.7, 2.0–0.8 ppm. MALDI-TOF-MS: *m*/*z* = 1935 ([M + H]$^+$).

Synthesis of compound 33

Compound **21** (0.058 g, 0.120 mmol) and *p*-anisidine **31** (0.46 g, 0.373 mmol) were combined in a flask and dissolved in dry THF to form a yellow solution. After refluxing for 4 h, the solution was cooled, and the volume of solvent was reduced. Upon addition of MeOH, an orange solid precipitated, was filtered, and was washed with MeOH and petroleum ether to yield 0.071 g (0.102 mmol, 86%) of product.

Data for 33

Mp 212–213 °C. UV–vis (CH_2Cl_2): λ_{max} (ϵ) = 287 (5.8×10^4), 340 (2.8×10^4), 359 (3.2×10^4), 401 (5.2×10^4) nm (L $mol^{-1}cm^{-1}$). IR (KBr): ν = 3424, 3029, 2952, 2926, 2861, 1616, 1507, 1457, 1366, 1297, 1250, 1183, 1032, 832, 696 cm^{-1}. ^1H NMR (300 MHz, $CDCl_3$, 25 °C) δ: 13.21 (s, 2H, O*H*), 8.86 (s, 2H, C*H*=N), 8.50 (s, 2H, aromatic C*H*), 8.16 (s, 2H, aromatic C*H*), 8.01 (s, 2H, aromatic C*H*), 7.36 (d, 4H, aromatic C*H*), 6.96 (d, 4H, aromatic C*H*), 3.85 (s, 6H, OCH_3), 2.81 (m, 4H, CH_2), 1.73 (m, 4H, hexyl chain), 1.48 (m, 4H, hexyl chain), 1.36 (m, 8H, hexyl chain), 0.92 (t, 6H, hexyl CH_3) ppm. ^{13}C NMR (75.5 MHz, $CDCl_3$, 25 °C) δ: 160.1, 159.3, 158.9, 141.5, 140.0, 132.9, 127.8, 126.8, 123.7, 122.9, 122.7, 120.9, 114.9, 110.9, 55.8, 33.5, 32.1, 31.9, 29.9, 23.0, 14.4 ppm. EI-MS: *m*/*z* = 694 (M^+). Anal. calcd. for $C_{46}H_{50}N_2O_4$: C, 79.51; H, 7.25; N, 4.03. Found: C, 79.74; H, 7.41; N, 4.19.

Synthesis of compound 34

Compound **21** (0.062 g, 0.128 mmol) and *N*-(*tert*-butyloxycarbonyl)-1,2-diaminobenzene **32** (0.087 g, 0.418 mmol) were combined in a flask and dissolved in 10 mL of THF. After refluxing the solution overnight, the solvent was reduced and precipitated by MeOH. The product

© 2007 NRC Canada

was recrystallized in DCM and hexanes. Filtration of the yellow solid yielded 0.091 g (0.105 mmol, 83%) of product.

Data for 34

Mp 223–226 °C. UV–vis (CH_2Cl_2): λ_{max} (ϵ) = 263 (5.2×10^4), 289 (5.5×10^4), 410 (3.8×10^4) nm (L $mol^{-1}cm^{-1}$). IR (KBr): ν = 3436, 2955, 2925, 1736, 1639, 1609, 1595, 1510, 1447, 1366, 1216, 1159, 1048, 898, 751 cm^{-1}. ^{1}H NMR (400 MHz, $CDCl_3$, 25 °C) δ: 12.22 (s, 2H, O*H*), 8.90 (s, 2H, N=C*H*), 8.63 (s, 2H, aromatic C*H*), 8.21 (s, 2H, aromatic C*H*), 8.20 (d, 2H, N*H*), 8.12 (s, 2H, aromatic C*H*), 7.31 (m, 2H, aromatic C*H*), 7.17–7.07 (m, 6H, aromatic C*H*), 2.82 (m, 4H, CH_2), 1.73 (m, 4H, hexyl chain), 1.53 (s, 18H, *t*-butyl *H*), 1.48 (m, 4H, hexyl chain), 1.36 (m, 8H, hexyl chain), 0.90 (t, 6H, hexyl CH_3) ppm. ^{13}C NMR (100.7 MHz, $CDCl_3$, 25 °C) δ: 164.2, 158.5, 152.8, 140.4, 138.1, 133.4, 132.9, 128.8, 128.5, 126.7, 124.2, 123.5, 123.0, 120.9, 119.6, 118.6, 111.2, 81.2, 33.4, 32.0, 31.9, 29.8, 28.6, 22.9, 14.4 ppm. ESI-MS: *m*/*z* = 865 (M^+). Anal. calcd. for $C_{54}H_{64}N_4O_6 \cdot 2\ H_2O$: C, 71.97; H, 7.61; N, 6.22. Found: C, 71.88; H, 7.29; N, 6.40.

Synthesis of macrocycle 35

Under a nitrogen atmosphere, compound **26** (0.366 g, 1.0 mmol) and 1,2-diethylhexyloxy-4,5-diaminobenzene **28d** (0.364 g, 1.0 mmol) were dissolved in 20 mL of degassed $CHCl_3$ and 10 mL of degassed MeCN. The solution was heated to reflux (90 °C) for 24 h, giving a clear, red solution. Upon cooling and adding MeCN, a red powder precipitated, which was isolated on a Büchner funnel and washed with MeCN. Yield: 1.22 g (0.88 mmol, 88%).

Data for 35

Mp > 300 °C. UV–vis (THF): λ_{max} (ϵ) = 325 (2.53×10^4), 362 (2.23×10^4) nm (L $mol^{-1}cm^{-1}$). Fluorescence: λ_{ex} = 370 nm, Φ = 3.0%. IR (KBr): ν = 3430, 2926, 2855, 2130, 1609, 1506, 1260, 1188, 752, 704 cm^{-1}. ^{1}H NMR (400 MHz, $CDCl_3$): δ 13.34 (s, 4H, O*H*), 8.62 (s, 4H, C*H*=N), 7.75 (s, 2H, C*H*), 7.48 (d, $^3J_{HH}$ = 7.8 Hz, 4H, C*H*), 7.38–7.30 (m, 4H, C*H*), 7.26 (s, 4H, C*H*), 7.07 (d, $^3J_{HH}$ = 7.9 Hz, 4H, C*H*), 6.82 (s, 4H, C*H*), 3.94 (d, $^3J_{HH}$ = 5.3 Hz, 8H, OCH_2), 1.85–0.90 (m, 60H, $OCH_2C_7H_{15}$) ppm. ^{13}C NMR (75.5 MHz, DMSO-d_6): δ 160.9, 160.5, 149.7, 135.7, 135.0, 131.9, 131.4, 128.5, 127.2, 123.4, 122.1, 120.7, 119.5, 104.2, 90.7, 89.9, 72.0, 39.6, 30.6, 29.1, 23.9, 23.1, 14.1, 11.2 ppm. MALDI-TOF-MS: *m*/*z* = 1390 ([M + H]$^+$, 100%), 1445 ([M + K + H_2O]$^+$, 10%). Anal. calcd. for $C_{92}H_{100}N_4O_8 \cdot 0.5H_2O$: C, 78.99; H, 7.28; N, 4.01. Found: C, 78.95; H, 7.22; N, 4.09.

Synthesis of macrocycle 36

Macrocycle **36** was prepared using the same procedure as for **35**, starting from compound **27**. Red solid; yield: 1.11 g (0.80 mmol, 80%).

Data for 36

Mp > 300 °C. UV–vis (THF): λ_{max} = 352 nm. Fluorescence (THF): λ_{ex} = 370 nm, Φ = 4.9%. IR (KBr): ν = 3430, 2926, 2855, 2130, 1609, 1506, 1446, 1260, 1180, 799, 752, 704 cm^{-1}. ^{1}H NMR (300 MHz, $CDCl_3$) δ: 13.31 (s, 4H, O*H*), 8.62 (s, 4H, C*H*=N), 7.65 (t, $^3J_{HH}$ = 8.3 Hz, 2H, C*H*), 7.47 (d, $^3J_{HH}$ = 7.83 Hz, 4H, C*H*), 7.0 – 7.4 (m, 12H, C*H*), 6.81 (s, 4H, C*H*), 3.93 (d, $^3J_{HH}$ = 5.0 Hz, 8H, OCH_2), 1.98–0.90 (m, 60H, $OCH_2C_7H_{15}$) ppm. ^{13}C NMR (75.5 MHz, DMSO-d_6): δ 160.9, 160.7, 149.7, 143.7, 136.4, 135.0, 131.8, 126.3, 123.0, 122.5, 121.3, 120.0, 104.5, 90.1, 89.3, 72.0, 39.6, 30.6, 29.2, 23.9, 23.1, 14.1, 11.2 ppm. MALDI-TOF-MS: *m*/*z* = 1392 ([M + H]$^+$, 100%), 1453 (35%), 1495 (15%). Anal. calcd. for $C_{90}H_{98}N_6O_8 \cdot 5H_2O$: C, 72.95; H, 7.35; N, 5.67. Found: C, 72.22; H, 7.32; N, 6.00.

X-ray crystallography[2]

A crystal of **14**·2DMSO was mounted on a glass fiber, and data were collected on a Bruker X8 APEX II diffractometer with graphite monochromated Mo Kα radiation. The data were collected to a maximum 2θ value of 55° in a series of ϕ and ω scans in 0.5° oscillations with 20 s exposures. The crystal-to-detector distance was 36 mm. Compound **14** crystallizes as a two-component twin with the two components related by a 180° rotation about the (010) reciprocal axis. Data were integrated for both twin components, including both overlapped and non-overlapped reflections. In total, 25882 reflections were integrated (10175 from component one only, 9903 from component two only, 5804 overlapped). Data were collected and integrated using the Bruker SAINT software packages (53). Data were corrected for absorption effects using the multi-scan technique (54), and were corrected for Lorentz and polarization effects.

The structure was solved by direct methods using non-overlapped data from the major twin component (55). Subsequent refinements were carried out using an HKLF 5 format data set containing complete data from both twin components. The material crystallizes with two molecules of DMSO in the asymmetric unit. All non-hydrogen atoms were refined anisotropically, and all hydrogen atoms were included in calculated positions but were not refined. The batch scale refinement showed a roughly 3:1 ratio between the major and minor twin components. The final cycle of full-matrix least-squares refinement (56) on F^2 was based on 5845 reflections from component one (including overlaps with component two) and 278 variable parameters. The data converged (largest parameter shift was 0.0 times its esd) with unweighted and weighted agreement factors of R_1 = 0.111 and wR_2 = 0.191. The standard deviation of an observation of unit weight (57) was 0.96. The weighting scheme was based on counting statistics. Neutral atom scattering factors were taken from Cromer and Waber (58). Anomalous dispersion effects were included in F_{calcd} (59); the values for $\Delta f'$ and $\Delta f''$ were those of Creagh and McAuley (60). The values for the mass attenuation coefficients are those of Creagh and Hubbell (61). All refinements were performed

[2] Supplementary data for this article are available on the journal Web site (canjchem.nrc.ca) or may be purchased from the Depository of Unpublished Data, Document Delivery, CISTI, National Research Council Canada, Ottawa, ON K1A 0R6, Canada. DUD 5249. For more information on obtaining material, refer to cisti-icist.nrc-cnrc.gc.ca/irm/unpub_e.shtml. CCDC 639250 contains the crystallographic data for this manuscript. These data can be obtained, free of charge, via www.ccdc.cam.ac.uk/conts/retrieving.html (or from the Cambridge Crystallographic Data Centre, 12 Union Road, Cambridge CB2 1EZ, UK; fax +44 1223 336033; or deposit@ccdc.cam.ac.uk).

© 2007 NRC Canada

Table 1. Crystallographic Data for **14**·2DMSO.

Crystal	**14**·2DMSO
Empirical formula	$C_{20}H_{20}O_8S_2$
Formula Mass	452.48
Color, habit	Yellow, tablet
Crystal dimensions (mm)	0.05 × 0.12 × 0.35
Crystal system	Triclinic
Space group	*P-1* (no. 2)
Z	2
a (Å)	6.5283(14)
b (Å)	12.203(3)
c (Å)	13.460(3)
α (°)	106.691(12)
β (°)	99.401(12)
γ (°)	95.689(12)
Collection ranges	$-8 \le h \le 8$; $-15 \le k \le 15$; $0 \le l \le 17$
Temperature	173(2)
Volume (Å^3)	1001.1(4)
D_{calcd} (Mg m^{-3})	1.501
Radiation	Mo Kα (λ = 0.71073 Å)
Absorption coeff. (μ) (mm^{-1})	0.313
Absorption correction	Multi-scan
F(000)	472
θ range for data collection (°)	1.6–27.5
Observed reflections	25882
Independent reflections	5845 (R_{int} = 0.060)
Data/restraints/parameters	5845/0/278
Maximum shift/error	0.00
Goodness-of-fit on F^2	0.96
Final *R* indices ($I > 2\sigma(I)$)	R_1 = 0.069, wR_2 = 0.171
R indices (all data)	R_1 = 0.111, wR_2 = 0.191
Largest diff. peak and hole (e Å^{-3})	0.80 and –0.60

using the SHELXTL crystallographic software package of Bruker-AXS (62). Additional details of the data collection and refinement are in Table 1.

Results and discussion

Diformyldihydroxy precursors

Phenanthrene derivatives

Scheme 1 shows the sequence of reactions used to obtain the parent diformyldihydroxyphenanthrene **9**. Photocyclization of 4,4′-dimethoxystilbene **6** gave 3,6-dimethoxyphenanthrene **7**. Dilithiation of **7** followed by quenching with DMF gave (after work-up) compound **8** with formyl groups in the 2,7 positions. Deprotection of the phenol groups with BBr_3 afforded target compound **9** in moderate yield. ^{1}H NMR spectroscopy of **9** confirms the structure of the diol, with a single hydroxyl resonance observed at 10.96 ppm (DMSO-d_6), shifted downfield due to hydrogen-bonding with the formyl groups.

The low solubility of compound **9** is a potential limitation to its further utility. To make soluble diformyldihydroxyphenanthrenes, we attempted to incorporate alkoxy groups

Scheme 1. Synthesis of diformyldihydroxyphenanthrene **9**.

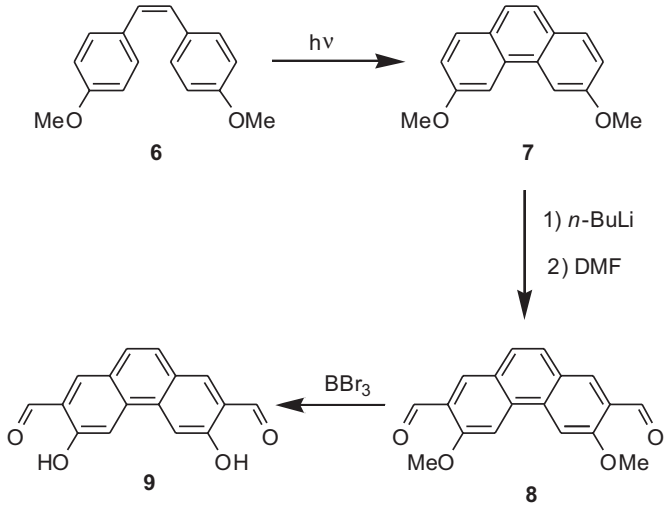

on the ring as shown in Scheme 2. We have previously reported the preparation of 3,6-dimethoxyphenanthrene-9,10-quinone **10** (45). Bromination of this compound gave **11**, along with some other by-products, which can easily be separated by chromatography. Reduction and methylation of the quinone yielded **12**, which was subsequently lithiated and quenched with dimethylformamide to give compound **13**. Reaction of **13** with BBr_3 gave, after work-up, compound **14**. This compound showed the expected ^{1}H NMR resonances, but we undertook a single crystal X-ray diffraction study to verify the correct tautomer was present. The solid-state structure of crystals of **14** grown from DMSO is depicted in Fig. 1, with relevant crystallographic details summarized in Table 1. The compound exhibits a nearly planar structure, with the formyl groups directed slightly out of the plane. In structures of salicylates, the formyl groups are typically hydrogen-bonded to the hydroxyl groups. The structure for **14** shows the oxygen of the aldehydes pointing away from the alcohol and the hydroxyl moieties instead hydrogen-bonding with the oxygen in co-crystallized DMSO. The extended structure shows phenanthrene molecules stacked in a staggered arrangement, with intermolecular separations of 3.1–3.3 Å, characteristic of π–π interactions.

To incorporate alkoxy groups on phenanthrene **14**, it was necessary to protect the hydroxyl groups. Having confirmed that the 3,6-dihydroxy tautomer was in solution, we anticipated that these could be readily protected. Unfortunately, attempts to selectively protect the 3,6-dihydroxy groups of **14** failed. Upon adding base to **14**, the compound undergoes a dramatic color change to purple, and reaction with protecting groups (e.g., Me_2SO_4) gave mixtures of products. It seems that with deprotonation compound **14** tautomerizes changing the reactivity of the hydroxyl groups, though we cannot isolate this intermediate in pure form. This approach was abandoned.

Triphenylene derivatives

We prepared diformyldihydroxytriphenylene **21** with peripheral hexyl groups by the route shown in Scheme 3. The synthesis of triphenylene **18** was based on previous research into unsymmetrically hexasubstituted triphenylenes (63, 64).

© 2007 NRC Canada

Scheme 2. Synthesis of diformyldihydroxyphenanthrenequinone **14**.

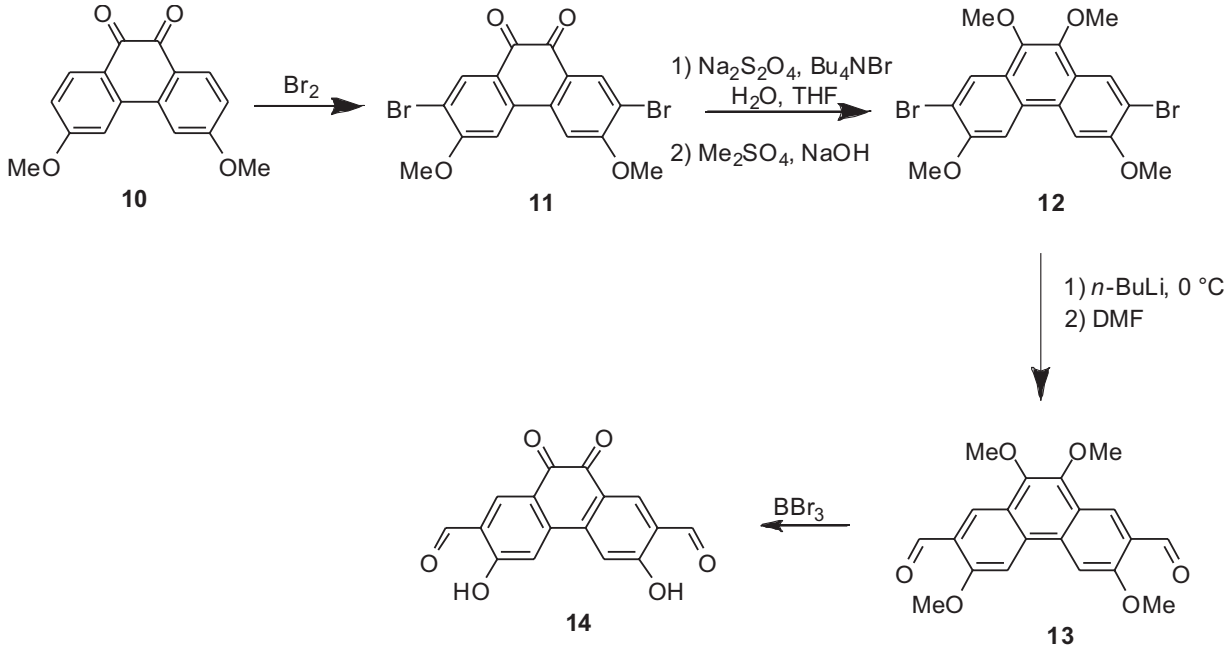

Fig. 1. Solid-state structure of **14**·2DMSO as determined by SCXRD. (*a*) The molecular structure, including two co-crystallized DMSO molecules, shows the planar structure with no intramolecular hydrogen-bonding. (*b*, *c*) The extended structure of **14**·2DMSO in the solid-state reveals strong intermolecular π–π interactions. Hydrogen atoms and DMSO molecules are omitted in the extended structure for clarity. Thermal ellipsoids are shown at 50% probability. Selected bond lengths: Aldehyde C=O: 1.202(4), 1.204(4) Å; hydroxyl C—O: 1.325(3), 1.334(4) Å; ketone C=O: 1.193(4), 1.201(4) Å.

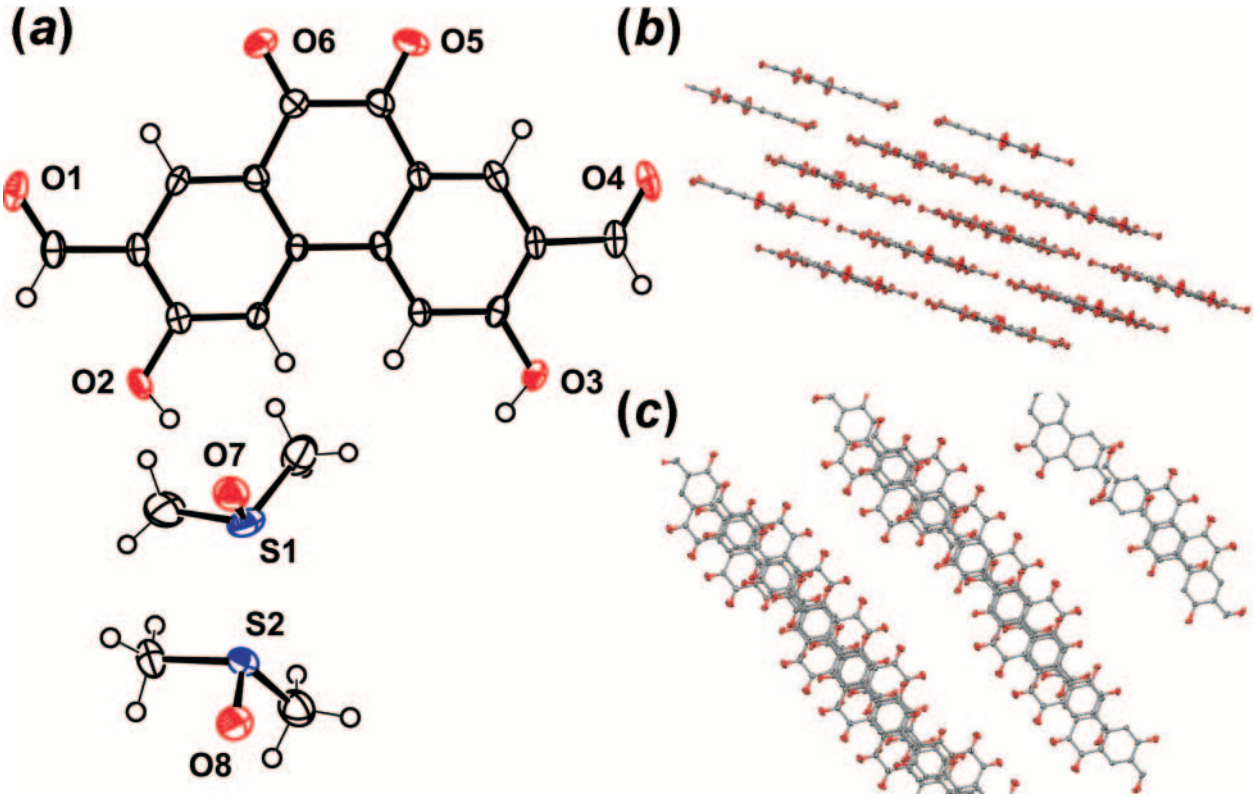

© 2007 NRC Canada

Scheme 3. Synthesis of diformyldihydroxytriphenylene **21**.

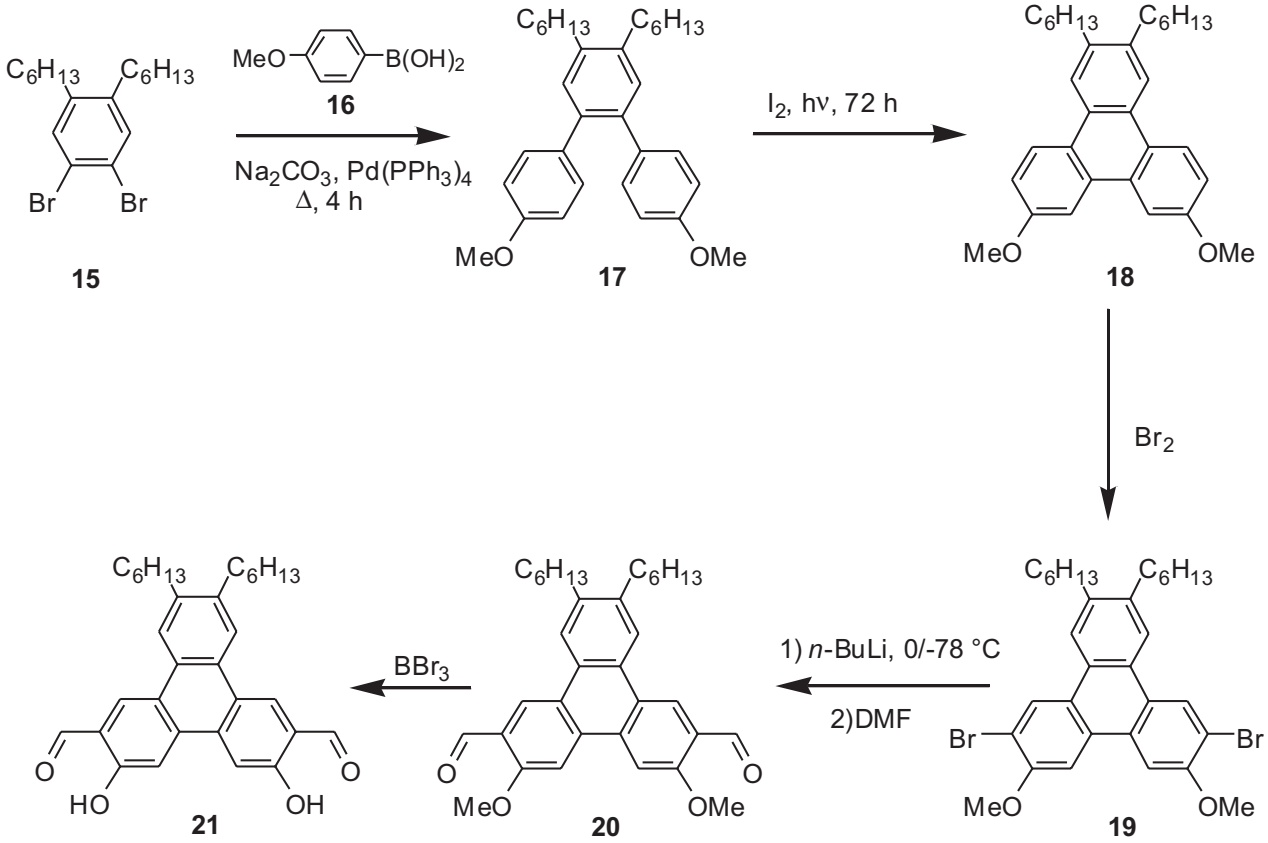

Scheme 4. Synthesis of 4-iodophenol **23**.

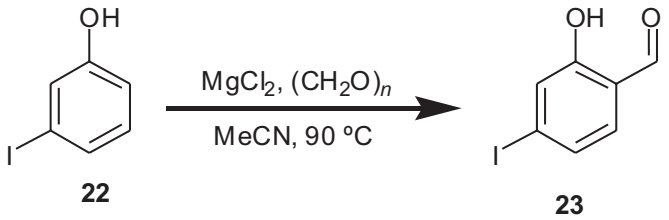

Scheme 5. Synthesis of bis(salicylaldehyde)s **26** and **27**.

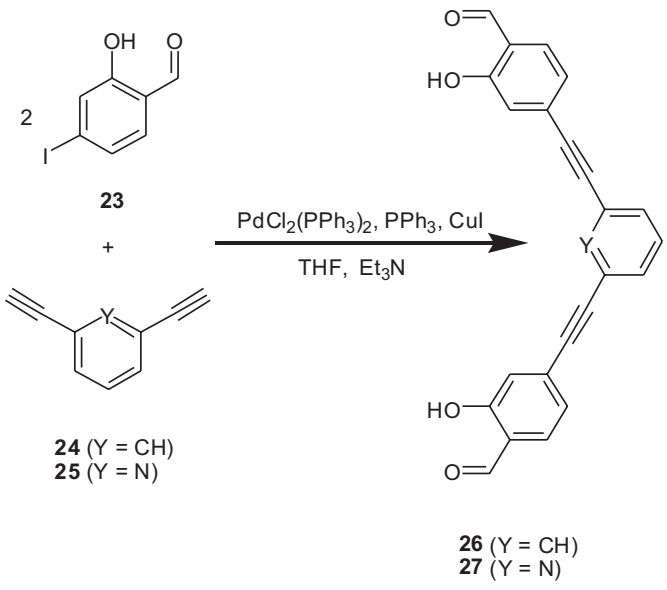

In the first step, terphenyl **17** was formed by Suzuki coupling of 1,2-dibromo-4,5-dihexylbenzene **15** and 4-methoxyphenylboronic acid **16**. Photocyclization in the presence of iodine gave triphenylene **18**. Selective double bromination of triphenylene **18** occurred at the 6,11 positions, yielding compound **19**. Subsequent metal–halogen exchange with ^{n}BuLi, and reaction with DMF gave the diformyldimethoxytriphenylene **20** after work-up. In the last step, the phenol was deprotected with BBr_3 to afford the diformyldihydroxytriphenylene **21** in 20% overall yield. All of the steps, with the exception of the photocyclization, are fast and high-yielding. Compounds **18**–**21** are easily purified through recrystallization, making **21** a convenient precursor for macrocycle studies.

m-*Bis(4-ethynylsalicylaldehyde)benzene and* m-*Bis(4-ethynylsalicylaldehyde)pyridine*

To synthesize conjugated bent bis(4-ethynylsalicylaldehyde) compounds, we required 4-iodosalicylaldehyde **23**. This compound has been made previously by the Reimer–Tiemann reaction starting with 3-iodophenol **22**, but this reaction generally proceeds in low yield and gives a mixture of products; the major products are 3-iodosalicylaldehyde and 2-iodo-4-hydroxybenzaldehyde (65–67). We found that using $MgCl_2$ and paraformaldehyde (68,69) reliably gave compound **23** in better (45%) yield, Scheme 4. This compound will likely prove useful for synthesizing other functionalized precursors to large macrocycles, such as [3+3] macrocycles we have previously studied (37).

© 2007 NRC Canada

Scheme 6. Proposed syntheses of target macrocycles **29** and **30**.

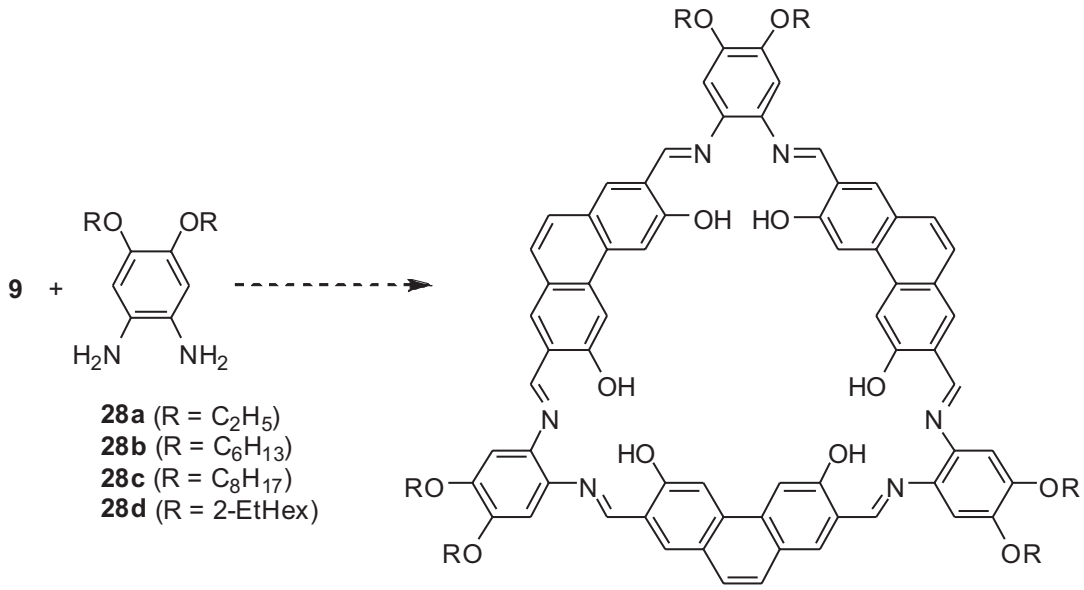

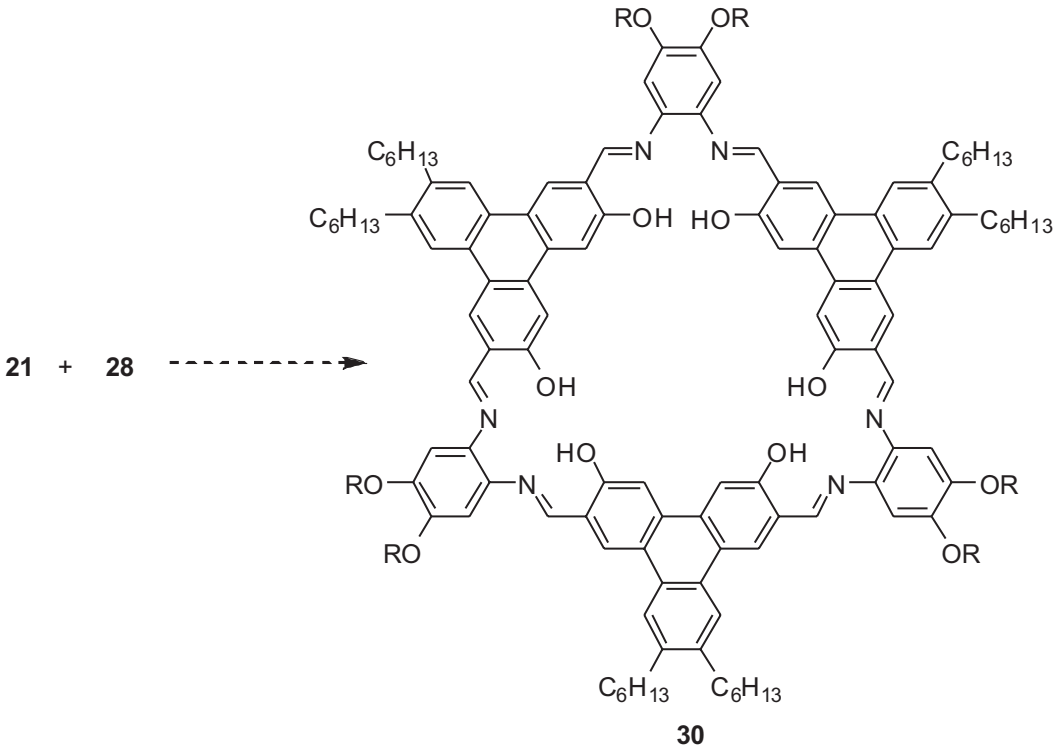

Pd(0)-catalyzed Sonogashira–Hagihara coupling of **24** with two equiv. of **23** yielded the bis(salicylaldehyde) **26** in 75% yield, Scheme 5. Pyridine analogue **27** was prepared by a similar procedure in 70% yield from **25**. The elbow-shaped bis(ethynylsalicylaldehyde) compounds were characterized by NMR spectroscopy and mass spectrometry.

Condensation studies

We investigated the condensation of the new diformyl-dihydroxy precursors with 4,5-diamino-1,2-dialkoxybenzenes in an effort to obtain conjugated Schiff base macrocycles. Reactions to form macrocycles are typically performed in mixtures of organic solvents selected to precipitate the macrocycle as it forms.

Phenanthrene derivatives

We expected that the reaction of **9** with diaminobenzene derivatives would afford [3+3] Schiff base macrocycle **29**, Scheme 6. Reaction of **9** was undertaken with several different *o*-phenylenediamines to control solubility. With 1,2-

© 2007 NRC Canada

Fig. 2. MALDI-TOF mass spectral evidence for the formation of macrocycle **29** (R = n-C_8H_{17}). The insets show a simulation of the isotope distribution for the [**29** + H]$^+$ ion (bottom) and the expanded experimental data for this peak (top). The peak at m/z = 1807 is the [**29** + Na]$^+$ ion.

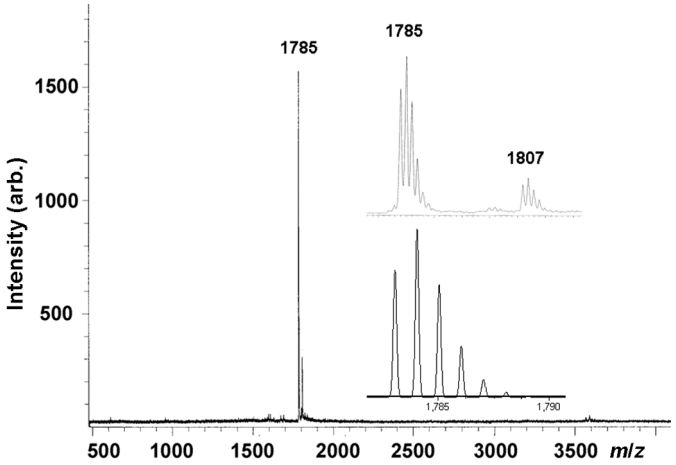

dioctyloxy-4,5-diaminobenzene **28c**, a solid was obtained. The ^{1}H NMR spectra of the product showed that multiple species were formed, and it appears that the major product is the 1:1 diol:diamine condensation species. Electrospray ionization mass spectrometry (ESI-MS) showed this fragment as the dominant species and also showed larger fragments of the expected macrocycle. Matrix-assisted laser desorption ionization time-of-flight (MALDI-TOF) mass spectrometry (Fig. 2) of the solid showed the presence of macrocycle **29** as the dominant high molecular mass component, along with traces of a larger [4+4] macrocycle. While there was evidence for the formation of the desired macrocycle in this reaction, we were unable to find conditions where the macrocycle selectively formed in the reaction mixture, an essential feature since the Schiff base macrocycles cannot be separated by column chromatography.

Triphenylene derivatives

Condensation of **21** with *o*-phenylenediamines was anticipated to form macrocycle **30**, Scheme 6. Unfortunately, the reaction of **21** with 4,5-dialkoxy-1,2-phenylenediamines **28** in an appropriate solvent, conditions that have worked well for other [3+3] Schiff base macrocycle reactions, afforded only inseparable mixtures of products. The ^{1}H NMR spectrum of the orange solid collected from the reaction showed several hydroxyl protons between 11.6 and 14.8 ppm. While the largest resonance at 13.2 ppm is characteristic of a hydroxyl group hydrogen-bonded to an imine, as in the intended Schiff base macrocycle, the positions of the other peaks are reminiscent of those observed for partially reduced Schiff base macrocycles, where imines are reduced in situ (this is a common problem in the formation of Schiff base macrocycles) (70–75). MALDI-TOF mass spectrometry of the orange product confirmed that the macrocycle was indeed present in the mixture. In fact, only the ring-closed [3+3] macrocycle **30** is observed in the MALDI-TOF mass spectrum. Further evidence for the formation of the [3+3] Schiff base macrocycle came from a metallation experiment, wherein the product was heated in THF in the presence of a metal salt. A color change indicated that reaction occurred, and, with vanadyl acetylacetonate, the MALDI-TOF mass spectrum clearly shows the incorporation of three metal centers into the macrocycle. The incorporation of three metals into the macrocycle supports the formation of macrocycle **30** in the reaction mixture.

Table 2. Conditions attempted for macrocycle **30** synthesis.

Solvent	R	Metal
$CHCl_3$/MeCN	C_6H_{13}	N/A
CH_2Cl_2/MeCN	C_2H_5	N/A
THF	C_2H_5	N/A
Toluene	C_2H_5	N/A
EtOH	C_2H_5	$Ni(OAc)_2$
EtOH	C_2H_5	$Zn(OAc)_2$

In an effort to selectively form macrocycle **30**, and to prevent possible side reactions (e.g., partial reduction of the macrocycle), a variety of conditions was used (Table 2). In all cases, the exact same series of resonances was reproduced in the ^{1}H NMR spectrum of the isolated solid, sometimes combined with fragments of the macrocycle. ESI-MS confirmed that fragments of the macrocycle were also present. Metal templation, which has proved to be critical in the synthesis of many Schiff base macrocycles, was also unsuccessful to obtain the fully conjugated macrocycle. Reaction of the diol and diamine in the presence of Ni^{2+} gave a black solid, which was revealed to be a 2:1 diol to diamine fragment coordinated to the metal through MALDI-TOF mass spectrometry. The same reaction in the presence of Zn^{2+} gave a mixture that included the starting material.

We were frustrated and surprised that compounds **9** and **21**, which appear ideal for forming [3+3] Schiff base macrocycles, were only yielding inseparable mixtures. In our experience, most diformyldihydroxyaromatics, such as **3**, yield the macrocycle in high yield. To understand whether or not the reactivity of the aldehydes on **9** and **21** were unusual, we made two model compounds by reaction of **21** with aniline derivatives **31** and **32**, Scheme 7. Compounds **33** and **34** were obtained as microcrystalline solids in high yield. The ^{1}H NMR spectra of these compounds show imine resonances

© 2007 NRC Canada

Scheme 7. Synthesis of model compounds **33** and **34**.

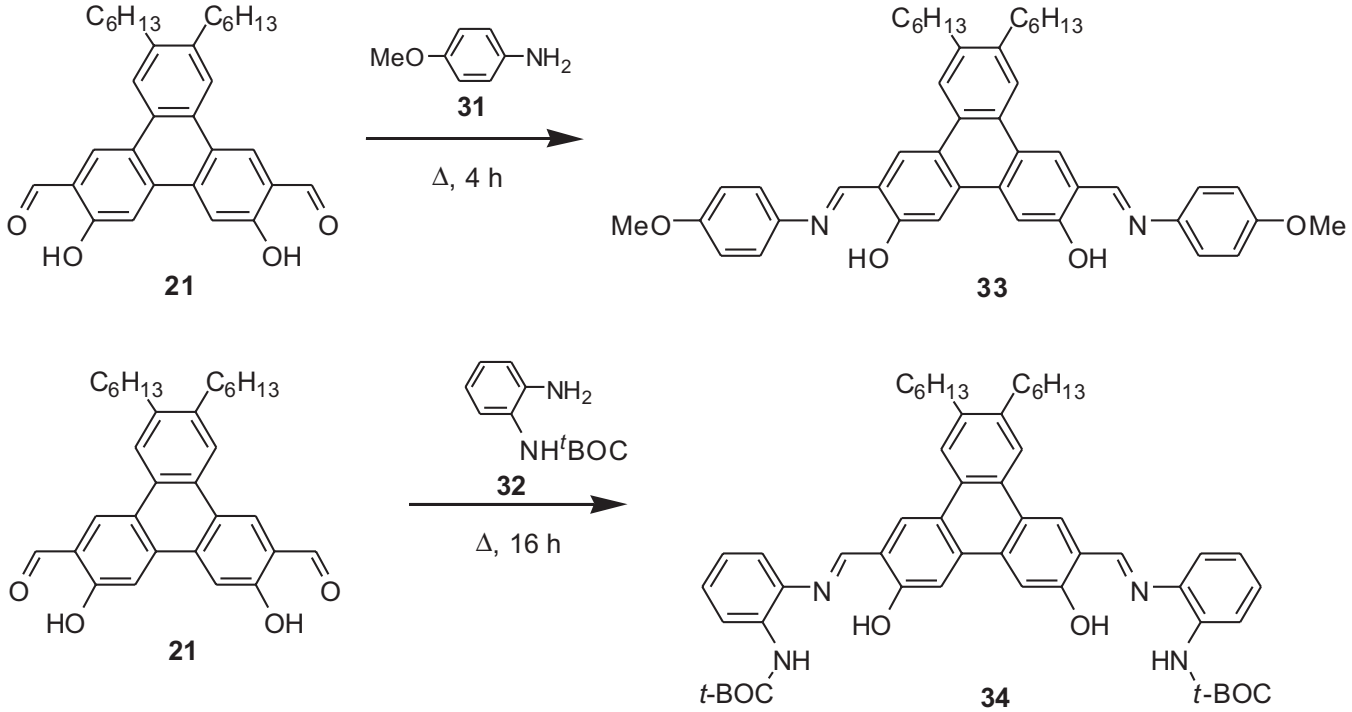

at 8.86 and 8.90 ppm, respectively. There is no indication of either reduction of the imine bond or isomerization to the keto–enamine tautomer, which was observed previously in a macrocycle prepared with a naphthalene diol (40). Isolation of these model compounds supports the use of **9** and **21** to build new multidentate Schiff base ligands.

m-*Bis(4-ethynylsalicylaldehyde)benzene and* m-*Bis(4-ethynylsalicylaldehyde)pyridine*

The geometry of compounds **26** and **27** are likely to favor [2+2] Schiff base macrocycles. Condensation of precursor **26** with 4,5-bis(2-ethylhexyloxy)-1,2-phenylenediamine **28d** gave the diamond-shaped macrocycle **35** in 88% yield, Scheme 8. Ethylhexyloxy substituents were required to render the macrocyclic product soluble. In this case, the branched substituents and the presence of a chiral center impart disorder to the macrocycles and ensure solubility. Macrocycles were initially prepared using phenylenediamines substituted with *n*-alkoxy chains (**28a**, **28b**), but these macrocycles were found to be insufficiently soluble in organic solvents to easily characterize or purify, though MALDI-TOF mass spectra indicated that the [2+2] macrocycles were the major, if not exclusive, products in each case.

The structure of red macrocycle **35** was verified by ^{1}H and ^{13}C NMR spectroscopies. Notably, the OH and imine groups are evident as singlets at 13.34 and 8.61 ppm, respectively, in $CDCl_3$, consistent with average D_{2h} symmetry for the macrocycle. The large downfield shift of the phenol resonance is characteristic of strong hydrogen-bonding to the imine group in the macrocycle. MALDI-TOF MS of **35** (Fig. 3) showed the molecular ion expected for the macrocycle ([**35** + H]$^+$) at *m*/*z* = 1390. The aldehyde C=O stretch observed at 1664 cm^{-1} in the IR spectrum of **26** was replaced by an intense C=N stretching mode at 1609 cm^{-1}.

With the goal of incorporating coordinating pyridine moieties into the macrocycles, we reacted **27** with diamine **28d** to yield macrocycle **36** in 80% yield, Scheme 8. The ^{1}H and ^{13}C NMR data were consistent with the proposed ring structure. MALDI-TOF MS showed the expected protonated molecular ion as the major peak for macrocycle **36**.

During the synthesis of macrocycles **35** and **36**, we found no evidence for formation of polymeric by-products. ^{1}H NMR analysis of the supernatant solution from the reaction showed mostly more macrocycle as well as putative oligomers that could not be separated. As with [3+3] Schiff base macrocycles we have previously investigated, these conjugated [2+2] macrocycles can be cleanly prepared in high yield. It was not necessary to use high dilution methods to favor macrocycle formation, or to remove water during the reaction to promote the condensation reaction. The macrocycles are stabilized from hydrolysis by the formation of strong hydrogen bonds between the imine and the phenol.

Optical properties

Our stated goal in expanding the conjugation of the dialdehyde precursors was to develop luminescent Schiff base macrocycles. These may be useful for chemical sensing applications or electronic devices. Figure 4 illustrates the absorption and emission spectra of macrocycle **35** in solution, which are similar to those of macrocycle **36**. An intense π–π* transition at 345 nm is accompanied by weaker transitions that extend the absorption edge to ~500 nm. Both macrocycles are weakly luminescent in solution, with maxima observed at 564 nm for both compounds, and quantum yields of 3%–5% in THF. This is almost identical to the fluorescence spectrum for **37**, a previously reported macrocycle (37) (Fig. 5), indicating that conjugation is essentially localized to the *N*,*N*′-bis(salicylidene)-1,2-phenylenediimine moi-

© 2007 NRC Canada

Scheme 8. Synthesis of conjugated diamond-shaped Schiff base macrocycles **35** and **36**.

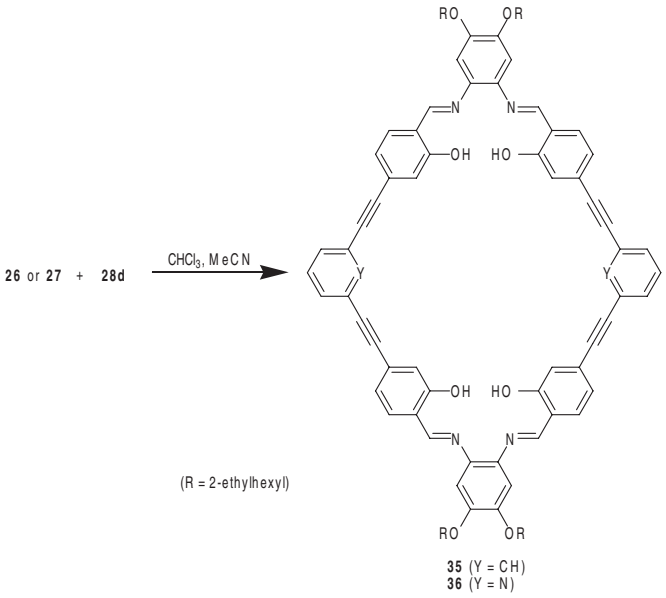

Fig. 3. MALDI-TOF MS of macrocycle **35**. Inset: Experimental (left) and simulated (right) isotope distribution patterns for the molecular ion.

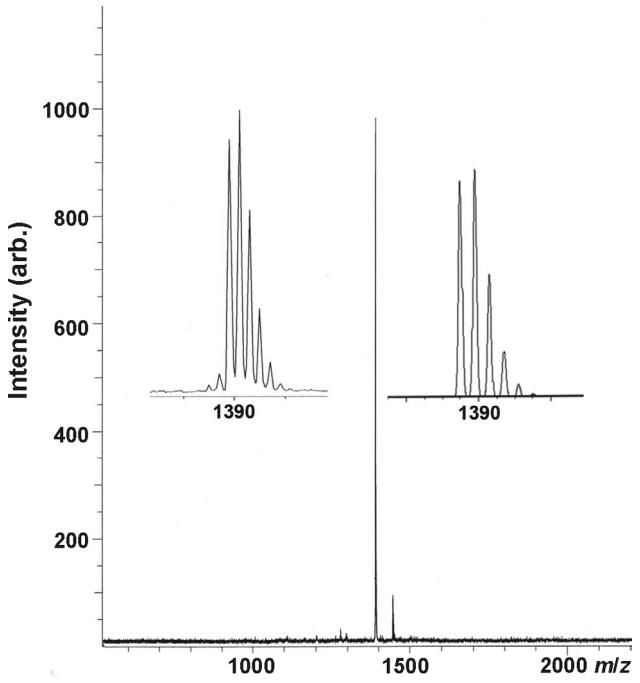

ety and is unaffected by the spacer. The meta linkage of the phenyl and pyridyl groups in **35** and **36**, respectively, should limit conjugation between the salicylaldehyde groups, and this is observed.

Conclusions

We have developed convenient routes to the first examples of diformyldihydroxy-functionalized phenanthrene (**9**, **14**) and triphenylene (**21**), as well as two new *m*-bis(4-ethynylsalicylaldehyde)aromatic compounds (**26**, **27**). Studies showed that **9** and **21** do not undergo clean cyclization reactions with *o*-phenylendiamines to selectively afford [3+3] Schiff base macrocycles, but these compounds are useful precursors for other Schiff base ligands, and perhaps even macrocycles with the appropriate choice of diamine. On the other hand, **26** and **27** underwent selective condensation to form fully conjugated [2+2] Schiff base macrocycles **35** and **36**. These luminescent macrocycles with two N_2O_2 binding pockets are anticipated to have interesting coordination chemistry and aggregation behavior, which we are studying.

Fig. 4. UV–vis (—) and fluorescence (---) spectra of macrocycle **35** (THF). Both spectra are normalized to unity intensity.

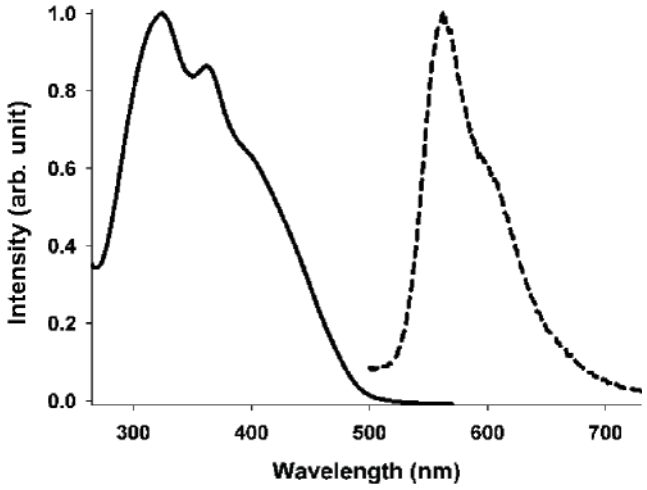

Fig. 5. Structure of macrocycle **37**.

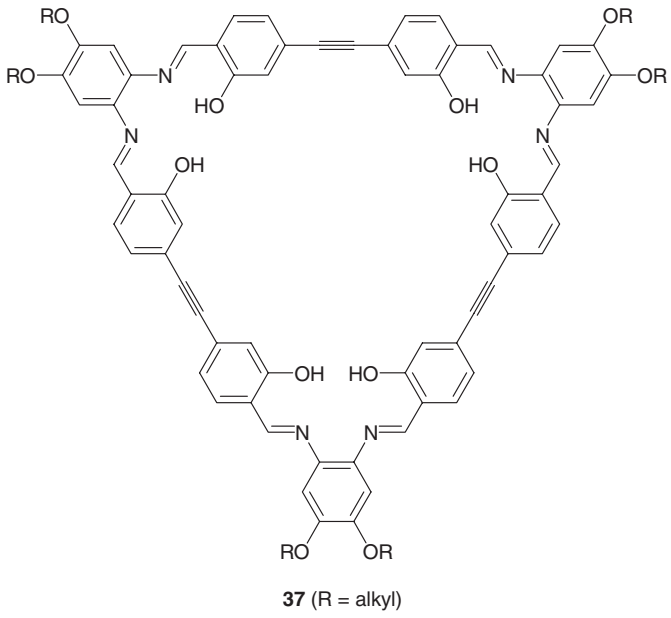

Acknowledgement

We thank the Natural Sciences and Engineering Research Council of Canada (NSERC) (Discovery Grant), UBC, and the Canadian Space Agency for funding. We are grateful to

© 2007 NRC Canada

Joseph Hui for MALDI-TOF data, and to Brian Patrick for solving the structure of **14**.

References

1. H. Shimakoshi, T. Takemoto, I. Aritome, and Y. Hisaeda. Inorg. Chem. **44**, 9134 (2005).
2. J. Gawronski, K. Gawronska, J. Grajewski, M. Kwit, A. Plutecka, and U. Rychlewska. Chem. Eur. J. **12**, 1807 (2006).
3. N. Kuhnert, A.M. Lopez-Periago, and G.M. Rossignolo. Org. Biomol. Chem. **3**, 524 (2005).
4. J. Gao, R.A. Zingaro, J.H. Reibenspies, and A.E. Martell. Org. Lett. **6**, 2453 (2004).
5. M. Weitzer and S. Brooker. Dalton Trans. 2448 (2005).
6. A.J. Atkins, D. Black, R.L. Finn, A. Marin-Becerra, A.J. Blake, L. Ruiz-Ramirez, W.-S. Li, and M. Schröder. Dalton Trans. 1730 (2003).
7. P. Arnold, A.J. Blake, C. Wilson, and J.B. Love. Inorg. Chem. **43**, 8206 (2004).
8. J.M. Veauthier, E. Tomat, V.M. Lynch, J.L. Sessler, U. Mirsaidov, and J.T. Markert. Inorg. Chem. **44**, 6736 (2005).
9. S.S. Tandon, S.D. Bunge, and L.K. Thompson. Chem. Commun. **28**, 798 (2007).
10. V.V. Pavlishchuck, S.V. Kolotilov, A.W. Addison, M.J. Prushan, R.J. Butcher, and L.K. Thompson. Chem. Commun. 468 (2002).
11. D.J. de Geest, A. Noble, B. Moubaraki, K.S. Murray, D.S. Larsen, and S. Brooker. Dalton Trans. 467 (2007).
12. L. Salmon, P. Thuéry, E. Rivière, S. Miyamoto, T. Yamato, and M. Ephritikhine. New J. Chem. **30**, 1220 (2006).
13. J.B. Fonteche, S. Goetz, and V. McKee. Angew. Chem., Int. Ed. **41**, 4553 (2002).
14. H. Houjou, A. Iwasaki, T. Ogihara, M. Kanesoto, S. Akabori, and K. Hiratani. New. J. Chem. **27**, 886 (2003).
15. J. Wang, B. Slater, A. Alberola, H. Stoekcli-Evans, F.S. Razavi, and M. Pilkington. Inorg. Chem. **46**, 4763 (2007).
16. H. Keypour, H. Goudarziafshar, A.K. Brisdon, and R.G. Pritchard. Inorg. Chim. Acta **360**, 2298, (2007).
17. J.L. Sessler, E. Tomat, and V.M. Lynch. Chem. Commun. 4486 (2006).
18. G. Givaja, M. Volpe, J.W. Leeland, M.A. Edwards, T.K. Young, S.B. Darby, S.D. Reid, A.J. Blake, C. Wilson, J. Wolowska, E.J.L. McInnes, M. Schröder, and J.B. Love. Chem. Eur. J. **13**, 3707 (2007).
19. S. Katsiaouni, S. Dechert, C. Brückner, and F. Meyer. Chem. Commun. 951 (2007).
20. M. Volpe, S.D. Reid, A.J. Blake, C. Wilson, and J.B. Love. Inorg. Chim. Acta **360**, 273 (2007).
21. N.H. Pilkington and R. Robson. Aust. J. Chem. **23**, 2225 (1970).
22. H. Furutachi and H. Okawa. Inorg. Chem. **36**, 3911 (1997).
23. H. Okawa, M. Tadokoro, Y. Aratake, M. Ohba, K. Shindo, M. Mitsumi, M. Koikawa, M. Tomono, and D.E. Fenton. J. Chem. Soc., Dalton Trans. 253 (1993).
24. R.R. Gagne, C.L. Spiro, T.J. Smith, C.A. Hamann, W.R. Thies, and A.D. Shiemke. J. Am. Chem. Soc. **103**, 4073 (1981).
25. W. Huang, Z. Chu, S. Gou, and T. Ogawa. Polyhedron, **26**, 1483 (2007).
26. K. Ikeda, K. Matsufuji, M. Ohba, M. Kodera, and H. Okawa. Bull. Chem. Soc. Jpn. **77**, 733 (2004).
27, B. Weber, I. Käpplinger, H. Görls, and E.-G. Jäger. Eur. J. Inorg. Chem. 2794 (2005).
28. P.A. Vigato and S. Tamburini. Coord. Chem. Rev., **248**, 1717 (2004).
29. P.A. Vigato, S. Tamburini, and L. Bertolo. Coord. Chem. Rev. **251**, 1311 (2007).
30. N.E. Borisova, M.D. Reshetova, and Y.A. Ustynyuk. Chem. Rev. **107**, 46 (2007).
31. S. Akine, T. Taniguchi, and T. Nabeshima. Tetrahedron Lett. **49**, 8861 (2001).
32. A.J. Gallant and M.J. MacLachlan. Angew. Chem., Int. Ed. **42**, 5307 (2003).
33. A.J. Gallant, J.K.-H. Hui, F.E. Zahariev, Y.A. Wang, and M.J. MacLachlan. J. Org. Chem. **70**, 7936 (2005).
34. J.K.-H. Hui and M.J. MacLachlan. Chem. Commun. 2480 (2006).
35. T. Glaser and I. Liratzis. Synlett, 735 (2004).
36. W. Moneta, P. Baret, and J.-L. Pierre. J. Chem. Soc., Chem. Commun. 899 (1985).
37. C. Ma, A. Lo, A. Abdolmaleki, and M.J. MacLachlan. Org. Lett. **6**, 3841 (2004).
38. H. Shimakoshi, H. Takemoto, I. Aritome, and Y. Hisaeda. Tetrahedron Lett. **43**, 4809 (2002).
39. W.T.S. Huck, F.C.J.M. van Veggel, and D.N. Reinhoudt. Recl. Trav. Chim. Pays-Bas **114**, 273 (1995).
40. A.J. Gallant, M. Yun, M. Sauer, C.S. Yeung, and M.J. MacLachlan. Org. Lett. **7**, 4827 (2005).
41. H. Meier, M. Fetten, and C. Schnorpfeil. Eur. J. Org. Chem. 779 (2001).
42. Y. Nakamura, T. Tsuihiji, T. Mita, T. Minowa, S. Tobita, H. Shizuka, and J. Nishimura. J. Am. Chem. Soc. **118**, 1006 (1996).
43. R.M. Letcher, L.R.M. Nhamo, and I.T. Gumiro. J. Chem. Soc., Perkin Trans. 1, 206 (1972).
44. A. Buquet, A. Couture, and A. Lablache-Combier. J. Org. Chem. **44**, 2300 (1979).
45. B.N. Boden, K.J. Jardine, A.C. W. Leung, and M.J. MacLachlan. Org. Lett. **8**, 1855 (2006).
46. M. Hanack, P. Haisch, H. Lehmann, and L.R. Subramanian. Synthesis, 387 (1993).
47. M. Schmid, R. Eberhardt, J. Kukral, and B. Rieger. Z. Naturforsch, **57b**, 1141 (2002).
48. K.A. Bunten and A.K. Kakkar. Macromolecules, **29**, 2885 (1996).
49. B.H. Dana, B.H. Robinson, and J. Simpson. J. Organomet. Chem. **648**, 251 (2002).
50. D.-J. Kim, M.J. Choi, and S.-K. Chang. Bull. Korean Chem. Soc. **21**, 145 (2000).
51. C.T. Seto, J.T. Mathias, and G.M. Whitesides. J. Am. Chem. Soc. **115**, 1321 (1993).
52. H.H. Hodgson and T.A. Jenkinson. J. Chem. Soc. 3041 (1927).
53. SAINT Version 7.03A [computer program]. Bruker AXS Inc., Madison, WI, USA. 1997–2003.
54. TWINABS [computer program]. Bruker Nonius scaling and absorption for twinned crystals– V1.05, Bruker AXS Inc., Madison, WI, USA. 2003.
55. A. Altomare, M.C. Burla, M. Camalli, G.L. Cascarano, C. Giacovazzo, A. Guagliardi, A.G.G. Moliterni, G. Polidori, and R. Spagna. J. Appl. Cryst. **32**, 115 (1999).
56. Least squares function minimized: $\Sigma w(F_o^2 - F_c^2)^2$ where $w = 1/(\sigma^2(F_o^2) + (0.1153P)^2 + 0.0000P)$, $P = (F_o^2 + 2F_c^2)/3$.
57. Standard deviation of an observation of unit weight: $[\Sigma w(F_o^2 - F_c^2)/(N_o - N_v)]^{1/2}$ where N_o = number of observations and N_v = number of variables.
58. D.T. Cromer and J.T. Waber. International tables for X-ray crystallography. Vol. IV. Kynoch Press, Birmingham, UK. Table 2.2 A. 1974.
59. J.A. Ibers and W.C. Hamilton. Acta Crystallogr. **17**, 781 (1964).
60. D.C. Creagh and W.J. McAuley. International tables for crystallography. Vol. C. *Edited by* A.J.C. Wilson. Kluwer Aca-

© 2007 NRC Canada

demic Publishers, Boston, MA, USA. Table 4.2.6.8, pp. 219–222. 1992.
61. D.C. Creagh and J.H. Hubbell. International tables for crystallography. Vol. C. *Edited by* A.J.C. Wilson. Kluwer Academic Publishers, Boston, MA, USA. Table 4.2.4.3, pp. 200–206. 1992.
62. SHELXTL Version 5.1 [computer program]. Bruker AXS Inc., Madision, WI, USA. 1997.
63. R.J. Bushby and C. Hardy. J. Chem. Soc., Perkin Trans. 1, 721 (1986).
64. A.N. Cammidge and H. Gopee. J. Mater. Chem. **11**, 2773 (2001).
65. C. Kuroda, A. Ochi, N. Nakane, T. Umeyama, N. Muto, N. Niimura, Y. Teramoto, H. Nogami, and G. N. Reddy. Bull. Chem. Soc. Jpn. **73**, 417 (2000).
66. S. Kobayashi, S. Tagawa, and S. Nakajima. Chem. Pharm. Bull. **11**, 123 (1963).
67. K.A. Thakar and D.D. Goswami. J. Indian Chem. Soc. **49**, 707 (1972).
68. R. Aldred, R. Johnston, D. Levin, and J. Neilan. J. Chem. Soc., Perkin Trans. 1, 1823 (1994).
69. H.F. Anwar, L. Skattebøl, J. Skramstad, and T. V. Hansen. Tetrahedron Lett. **46**, 5285 (2005).
70. A.J. Gallant, B.O. Patrick, and M.J. MacLachlan. J. Org. Chem. **69**, 8739 (2004).
71. A. Aguiari, E. Bullita, U. Casellato, P. Guerriero, S. Tamburini, and P.A. Vigato. Inorg. Chim. Acta **202**, 157 (1992).
72. K. Brychcy, K. Dräger, K.-J. Jens, M. Tilset, and U. Behrens. Chem. Ber. **127**, 1817 (1994).
73. D.S. Kumar and V. Alexander. Inorg. Chim. Acta **238**, 63 (1995).
74. F.L. Bowden and D. Ferguson. J. Chem. Soc., Dalton Trans. 460 (1974).
75. Y. Tian, J. Tong, G. Frenzen, and J.-Y. Sun. J. Org. Chem. **64**, 1442 (1999).

© 2007 NRC Canada

Synthesis of β-amino alcohols using MgO as a new catalyst under solvent-free conditions

Mona Hosseini-Sarvari

Abstract: MgO catalyzed efficiently the ring opening of epoxides with a range of aromatic and aliphatic amines to produce β-substituted alcohols in high yields under solvent-free conditions. Exclusive trans stereoselectivity is observed for cyclic epoxide.

Key words: MgO, β-amino alcohols, solvent-free, epoxide, amine.

Résumé : Dans des conditions n'impliquant aucun solvant, l'oxyde de magnésium, MgO, catalyse d'une façon efficace l'ouverture du cycle des époxydes avec une grande variété d'amines aliphatiques et aromatiques pour conduire avec des rendements élevés aux alcools β-substitués correspondants. On observe exclusivement l'ouverture stéréosélective *trans* avec les époxydes cycliques.

Mots-clés : MgO, β-aminoalcools, sans solvant, époxyde, amine.

[Traduit par la Rédaction]

Introduction

The formation of β-amino alcohols from epoxides and amines is an important reaction in medicinal and organic chemistry, as they are useful synthetic intermediates for the preparation of β-amino acids, natural products, and chiral auxiliaries (1). Opening of epoxides with amines developed in the past few years, and many catalysts (reagents) were used, such as metal triflates (2), metal halides (3), polymer supported (4), montmorillonite K10 (5), and metal salt (6). Different reaction media, such as ionic liquids (7), ultrasound (8), microwave irradiation (9), solvent-free conditions (SFC), and water (10) were also employed. These processes are useful; however, they suffer from disadvantages, such as the use of expensive or air-sensitive reagents, extended reaction times, and the requirement for protracted work-up procedures, or are limited in the range of amines specially aliphatic amines.

MgO is an environmentally safe, non-volatile, non hygroscopic, odourless, and white powder with outstanding physical properties and stability. It is commercially available and is a very cheap chemical. Recently, it was shown that MgO has the prospect to be used as a substitute for conventional basic catalytic materials. It has been used as an efficient heterogeneous catalyst in many important organic reactions (11).

In this pursuit, and during the course of the studies aimed at developing solvent-free procedures (12), for the first time, MgO-catalyzed ring opening of epoxides by amines in solvent-free conditions is reported in this paper (Scheme 1).

Received 27 September 2007. Accepted 2 November 2007. Published on the NRC Research Press Web site at canjchem.nrc.ca on 13 December 2008.

M. Hosseini-Sarvari.[1] Department of Chemistry, Shiraz University, Shiraz 71454, Islamic Republic of Iran.

[1](e-mail: hossaini@susc.ac.ir).

Scheme 1. Synthesis of β-amino alcohols catalyzed by MgO.

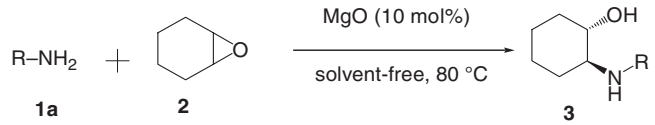

1a 2 3

R = alkyl and aryl

Results and discussion

The condensation between an amine and an epoxide leading to the formation of a β-amino alcohol should be a facile reaction due to the good electrophilic and nucleophilic properties of the epoxide and amine groups, respectively. This reaction may not require any catalytic assistance in the absence of electronic/steric factors that might decrease the electrophilicity/nucleophilicity of the epoxide/amine groups. Thus, the condensation of cyclohexene oxide with 4-methylaniline, 4-methoxyaniline, and 4-bromoaniline afforded 70%–90% yields, in 6–8 h, under neat conditions at 80 °C without the requirement of any additional reagent/catalyst. The treatment of cyclohexene oxide with aniline afforded the corresponding β–aminol alcohols in 60% yields in 12 h. However, no significant β-amino alcohol formation was observed (^{1}H NMR) when cyclohexene oxide was treated with 4-nitroaniline at 100 °C under neat conditions.

The presence of the strong electron-withdrawing property of the nitro group in 4-nitroaniline decreases the nucleophilicity of the amine group. Thus, the combination of this substrate with cyclohexene oxide constitutes a model reaction for evaluating the efficiency of a catalyst. Hence, cyclohexene oxide was treated with 4-nitroaniline under various conditions (Table 1). Clearly, the best results were reached with MgO under solvent-free conditions (Table 1, entry 1).

To evaluate the generality, reaction of various epoxides were carried out with various aromatic, aliphatic, primary,

 doi:10.1139/V07-135 © 2007 NRC Canada

Table 1. Reaction between cyclohexene oxide (**2d**) and 4-nitroaniline (**1l**) in the presence of various catalysts and conditions

Entry	Catalyst/conditions	Time (h)	Yield[a] (%)
1	MgO (10 mol%)/neat	12	65
2	MgO (10 mol%)/CH_2Cl_2	24	Trace
3	MgO (10 mol%)/PhMe	24	Trace
4	MgO (10 mol%)/THF	24	Trace
5	No catalyst/neat	No reaction	
6	Mesoporous aluminizilicate (13)	No reaction	
7	$H_3PW_{12}O_{40}$ (14)	24	35
8	Sulfamic acid (15)	No reaction	
9	CaO (10 mol%)/neat	24	Trace
10	K_2CO_3 (10 mol%)/neat	24	43
11	CuO (10 mol%)/neat	24	Trace

[a]Yields are for the isolated compounds.

and secondary amines under the catalytic influence of MgO, and excellent results were obtained (Table 2). The reaction protocol is simple and does not require dry glassware and reagents. This is very important for scaling-up the process. The final amino alcohol was isolated in >99% purity in 50%–98% yield.

The results summarized in Table 2 reveal that excellent yields were obtained with aromatic and aliphatic amines. In the case of cyclohexene oxide, in each occasion, the resultant racemic 2-aryl/alkylaminocyclohexanol was obtained with exclusive trans diastereoselectivity as detected by ^{1}H NMR spectroscopic analysis (Table2, entries 5–26). The reactions are remarkably clean, and no chromatographic separation is necessary to get the spectra-pure compounds except in a few cases (Table 2, entries 16–20) where some starting materials remained; the conversion being less than 100%. Primary and secondary amines react very rapidly. Aniline and its derivatives with electron-donating substitutes also react quite fast. However, anilines with electron-accepting substitutes, as well as satirically hindered anilines, react very slowly, and aminolysis required prolonged reaction times. The reaction of diamines showed good results without any significant influence of their structures on the product yields; these products can be used for preparation of macrocyclic compounds. The conversion of aniline into 2-aryl/alkylaminocyclohexanol on a 100 mmol scale proceeded just as well as the 1 mmol reaction.

The ratio of the two regioisomeric products was determined by GC–MS and ^{1}H NMR (based on the methane and methylene proton signals). In the MS the regioisomer of α-product exhibited a daughter ion at *m*/*z* ($M^+ - 31$) due to the CH_2OH, and the diagnostic feature in the mass spectra of the β-product (**3a**) was the ion peak at *m*/*z* ($M^+ - 106$) arising from the loss of PhCHO. The GC–MS revealed the product to be a mixture of β-product (**3a**) and α-product in a ratio of 95:5 on the basis of the daughter ions at *m*/*z* 228–106 and 228–31, corresponding to β-product (**3a**) and α-product, respectively. Also, a 95:5 ratio could be determined for β-product (**3a**): α-product, taking into consideration the integral values of the corresponding benzyl protons.

Excellent chemo selectivity was achieved with epichlorohydrin (Table 2, entry 4) resulting in 93% yield of the amino alcohol corresponding to nucleophilic attack at the terminal carbon of the epoxide moiety. No product arising from nucleophilic displacement of the chlorine could be detected through MS analysis of the reaction mixture.

The reuse ability and catalytic activity of MgO was studied in this system. The catalyst was recovered by centrifugation after diluting the reaction mixture with Et_2O and dried in an oven at 100 °C for 3 h and was reused repeatedly without any significant loss of catalytic activities. As shown in Table 3, the yields of 2-(2-picolylamine)cyclohexanol (**3d**) only decreases a little after the reuse of MgO for three times.

In conclusion, the results demonstrated that MgO efficiently catalyze the formation of β-amino alcohols from amines and epoxides in high yields under mild and solvent-free reaction conditions. The facile synthesis of these materials, their benign nature, the ease of handling, and the simplified reaction and isolation procedures make them a highly attractive alternative to current methodologies.

Experimental

Chemicals were purchased from Fluka, Merck, B. D. H., and Aldrich Chemical Companies. Progress of the reactions was followed by TLC using silica-gel polygrams SIL G/UV 254 plates. NMR spectra were recorded on a Bruker DPX 250 MHz instrument. Mass spectra were recorded on a Shimadzu GC MS-QP 1000 EX apparatus. Microanalyses were performed on a PerkinElmer 240-B microanalyzer.

General procedure

A mixture of MgO (10 mol%, 0.004 g), amine (1 mmol), and 1,2-epoxide (1 mmol) was heated in an oil bath at 80 °C and stirred with a magnetic stirrer. The progress of the reaction was monitored by TLC. After the reaction was complete, the obtained product was poured into water, stirred well to dissolve the MgO, and then extracted with ethyl acetate. The organic solvent was then evaporated, and the pure product was obtained. This was further purified by recrystallization with a suitable solvent (ether). The regioisomers were separated after silica-gel column chromatography (20% Hexane/EtOAc). The structures of the products were confirmed by GC–MS, ^{1}H NMR, ^{13}C NMR, and comparison with authentic samples obtained commercially or prepared by reported methods.

© 2007 NRC Canada

Table 2. Synthesis of β-amino alcohols.

Entry	Amine (**1**)		1,2-Epoxide (**2**)		Product (**3**)		Time (h)	Yields[a] %
1	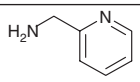	**1a**	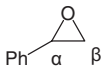	**2a**	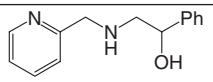	**3a**	2	90[b]
2	**1a**		**2a**		**3a**		12	33[c]
3	**1a**		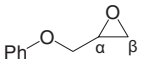	**2b**	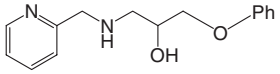	**3b**	3	95[b]
4	**1a**		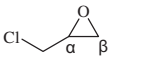	**2c**	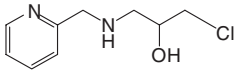	**3c**	1	93[b]
5	**1a**		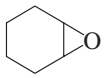	**2d**	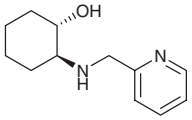	**3d**	1	98
6	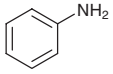	**1b**		**2d**	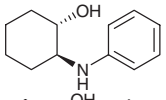	**3e**	3	95
7	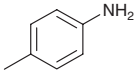	**1c**		**2d**	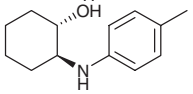	**3f**	2	98
8	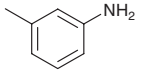	**1d**		**2d**	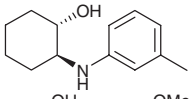	**3g**	1	98
9	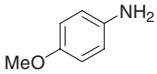	**1e**		**2d**	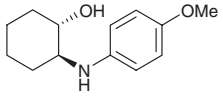	**3h**	1	97
10	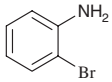	**1f**		**2d**	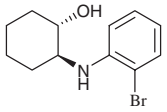	**3i**	3	90
11	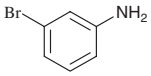	**1g**		**2d**	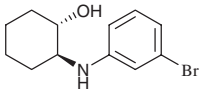	**3j**	3	95
12	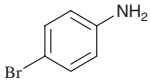	**1h**		**2d**	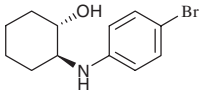	**3k**	0.5	90
13	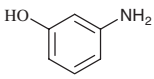	**1i**		**2d**	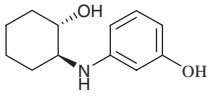	**3l**	1	95
14	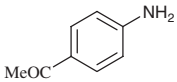	**1j**		**2d**	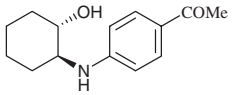	**3m**	2	98
15	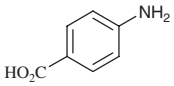	**1k**		**2d**	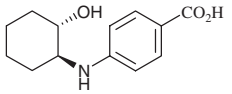	**3n**	3	94
16	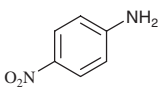	**1l**		**2d**	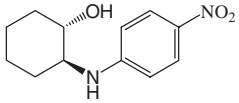	**3o**	12	65
17	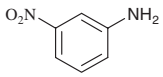	**1m**		**2d**	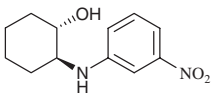	**3p**	18	63

© 2007 NRC Canada

Table 2 (*concluded*).

Entry	Amine (**1**)	1,2-Epoxide (**2**)	Product (**3**)	Time (h)	Yields[a] %
18	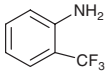	**1n** **2d**	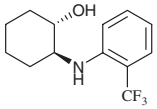	**3q** 4	78
19	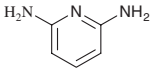	**1o** **2d**	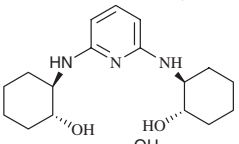	**3r** 3	73
20	PhNHPh	**1p** **2d**	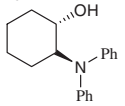	**3s** 24	50
21	$(CH_3)_2CHNHCH(CH_3)_2$	**1q** **2d**	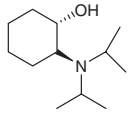	**3t** 2	86
22	$CH_3CH_2CH_2NH_2$	**1r** **2d**	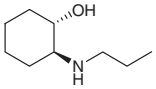	**3u** 3	94
23		**1s** **2d**	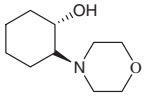	**3v** 1	95
24	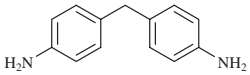	**1t** **2d**	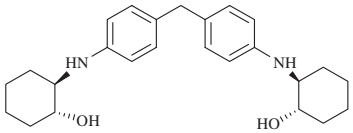	**3w** 2	93
25	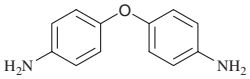	**1u** **2d**	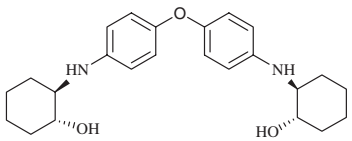	**3x** 2	90
26	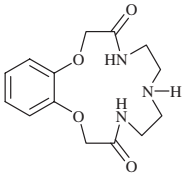	**1v** **2d**	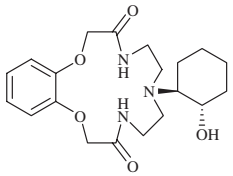	**3y** 3	82

[a] Yields of isolated pure product after silica-gel column chromatography (20% Hexane/EtOAc).
[b] Products isolated in a 95:5 ratio of regioisomers. The major product was shown.
[c] The reaction was carried out under catalyst-free conditions. Products isolated in 50:50 ratio of regioisomers.

Table 3. Reuse of MgO.

Number of use	Yield (%)	Recovery of MgO
1	98	96% (3.8×10^{-3} g)
2	94	95% (3.6×10^{-3} g)
3	92	95% (3.4×10^{-3} g)

1-Phenyl-2- ((pyridin-2-yl)methylamino)ethanol (3a)

Oily liquid. R_f = 0.13 (EtOAc/MeOH/Et_3N, 90/7/3). ^1H NMR ($CDCl_3$, ppm) δ: 8.34 (1H, d, J = 4.9), 7.49 (1H, m), 7.02–7.21 (7H, m), 4.72 (1H, d, J = 3.4), 4.62 (2H, dd, J = 2.8, 2.8), 3.90 (1H, –NH), 3.82 (1H, –OH), 2.64–2.76 (2H, m). ^{13}C NMR ($CDCl_3$) δ: 54.1, 56.8, 72.1, 122.5, 125.9, 127.3, 128.2, 136.6, 137.1, 149.0, 159.4. MS *m/z*: 228 [M+]. Anal. calcd. for $C_{14}H_{16}N_2O$: C, 73.66; H, 7.06; found: C, 73.34; H, 6.98.

1-Phenoxy-3-(pyridin-2-ylmethylamino)propan-2-ol (3b)

Oily liquid. R_f = 0.38 (EtOAc/MeOH/Et_3N, 90/7/3). ^1H NMR ($CDCl_3$, ppm) δ: 8.43 (1H, m), 7.50 (1H, m), 7.03–7.16 (4H, m), 6.71–6.84 (3H, m), 5.60 (2H, br s, –NH, –OH), 3.78–4.05 (5H, m). ^{13}C NMR ($CDCl_3$) δ: 53.2, 59.0, 114.5, 115.6, 121.0, 129.3, 137.0, 148.9, 158.4. MS *m/z:* 244 [M^+]. Anal. calcd. for $C_{14}H_{16}N_2O_2$: C, 68.83; H, 6.60; found: C, 68.65; H, 6.43.

1-Chloro-3-(pyridin-2-ylmethylamino)propan-2-ol (3c)

Oily liquid. R_f = 0.52 (EtOAc/MeOH/Et_3N, 90/7/3). ^1H NMR ($CDCl_3$, ppm) δ: 9.07 (1H, d, J = 5.1), 7.7 (1H, d, J = 5.9), 7.27 (2H, m), 5.61 (2H, br s, –NH, –OH), 3.97

© 2007 NRC Canada

(2H, m), 3.54 (2H, s), 2.76–3.01 (3H, m). ^{13}C NMR ($CDCl_3$) δ: 46.5, 54.2, 54.3, 122.7, 135.0, 148.6, 169.1. MS *m/z*: 200 [M^+]. Anal. calcd. for $C_9H_{13}ClN_2O$: C, 53.87; H, 6.53; found: C, 53.66; H, 6.22.

2-(Pyridin-2-ylmethylamino)cyclohexanol (3d)

Solid; mp 87 °C (lit. 87–88 °C) (2*d*). ^{1}H NMR ($CDCl_3$, ppm) δ: 8.55 (1H, d, *J* = 4.8), 7.76 (1H, t, *J* = 5.8), 7.40 (1H, d, *J* = 2.9), 7.26 (1H, m), 5.20 (2H, br s, –NH, –OH), 4.34 (1H, d, *J* = 14.5), 4.10 (1H, d, *J* = 14.5), 3.62 (1H, m), 2.57 (1H, m), 2.01–2.08 (2H, m), 1.67–1.74 (2H, m), 1.18–1.43 (4H, m). ^{13}C NMR ($CDCl_3$) δ: 24.0, 24.6, 28.8, 33.7, 50.0, 63.3, 72.0, 122.9, 137.1, 149.2, 156.0. MS *m/z*: 206 [M^+]. Anal. calcd. for $C_{12}H_{18}N_2O$: C, 69.87; H, 8.80; found: C, 69.76; H, 8.66.

2-(Phenylamino)cyclohexanol (3e)

Solid; mp 58 °C (lit. 58–59 °C) (3*c*). ^{1}H NMR ($CDCl_3$, ppm) δ: 7.13 (2H, t, *J* = 7.5), 6.65–6.89 (3H, m), 3.45 (2H, br s, NH, OH), 3.30–3.39 (1H, m), 3.10–3.14 (1H, m), 2.05–2.10 (2H, m), 1.66–1.76 (2H, m), 1.05–1.35 (4H, m). ^{13}C NMR ($CDCl_3$) δ: 23.9, 24.2, 31.3, 33.2, 60.3, 74.2, 115.2, 121.9, 129.3, 147.2. MS *m/z*: 191 [M^+]. Anal. calcd. for $C_{12}H_{17}NO$: C, 75.35; H, 8.96; Found: C, 75.00; H, 8.56.

2-(*p*-Toluidino)cyclohexanol (3f)

Oily liquid. ^{1}H NMR ($CDCl_3$, ppm) δ: 6.78 (2H, d, *J* = 2.27), 6.48 (2H, d, *J* = 2.50), 3.09–3.14 (1H, m), 3.98 (2H, br s, NH, OH), 2.87–2.93 (1H, m), 3.89 (3H, s), 1.89 (2H, m), 1.56 (2H, m), 1.06–1.18 (4H, m). ^{13}C NMR ($CDCl_3$) δ: 20.4, 24.5, 25.0, 31.5, 33.1, 60.5, 74.3, 115.3, 127.5, 129.3, 145.5. MS *m/z:* 205 [M^+]. Anal. calcd. for $C_{13}H_{19}NO$: C, 76.06; H, 9.33; found: C, 75.98; H, 9.02.

2-(*m*-Toluidino)cyclohexanol (3g)

Oily liquid. ^{1}H NMR ($CDCl_3$, ppm) δ: 7.02 (1H, s), 6.39–6.60 (3H, m), 3.46 (2H, br s, NH, OH), 3.23 (1H, m), 3.03 (1H, m), 2.21 (3H, s), 2.00 (2H, m), 1.61–1.69 (2H, m), 1.17–1.35(4H, m). ^{13}C NMR ($CDCl_3$) δ: 21.5, 23.7, 25.0, 31.0, 33.4, 59.9, 75.6, 111.5, 115.6, 118.5, 128.7, 139.0, 148.0. MS *m/z*: 205 [M^+]. Anal. calcd. for $C_{13}H_{19}NO$: C, 76.06; H, 9.33; found: C, 76.00; H, 9.30.

2-(4-Methoxyphenylamino)cyclohexanol (3h)

Solid; m.p. 53 °C. ^{1}H NMR ($CDCl_3$, ppm) δ: 7.01 (2H, d, *J* = 2.27), 6.84 (2H, d, *J* = 2.50), 3.29–3.21 (1H, m), 4.01 (2H, br s, NH, OH), 2.87–2.93 (1H, m), 3.91 (3H, s), 2.18 (2H, m), 1.86 (2H, m), 1.36–1.48 (4H, m). ^{13}C NMR ($CDCl_3$) δ: 21.4, 25.5, 25.8, 32.5, 34.1, 61.5, 75.7, 115.8, 127.1, 129.9, 145.1. MS *m/z*: 221 [M^+]. Anal. calcd. for $C_{13}H_{19}NO_2$: C, 70.56; H,8.65; found: C, 70.32; H, 8.62.

2-(2-Bromophenylamino)cyclohexanol (3i)

Oily liquid. ^{1}H NMR ($CDCl_3$, ppm) δ: 7.40–7.46 (1H, m), 7.16–7.18 (1H, m), 6.74–6.85 (1H, m), 6.56–6.60 (1H, m) 3.20 (2H, br s, NH, OH), 4.35 (1H, m), 3.38 (1H, m), 2.04–2.10 (2H, m), 1.67–1.74 (2H, m), 1.13–1.43 (4H, m). ^{13}C NMR ($CDCl_3$) δ: 24.0, 24.4, 31.5, 32.7, 59.7, 74.1, 112.9, 118.3, 128.3, 132.5, 144.9. MS *m/z*: 270 [M^+]. Anal. calcd. for $C_{12}H_{16}BrNO$: C, 53.35; H, 5.97; found: C, 53.01; H, 5.67.

2-(3-Bromophenylamino)cyclohexanol (3j)

Oily liquid. ^{1}H NMR ($CDCl_3$, ppm) δ: 6.93–6.99 (1H, m), 6.75–6.79 (2H, m), 6.53–6.58 (1H, m), 4.15 (2H, br s, NH, OH), 3.42 (1H, m), 3.10 (1H, m), 2.05 (2H, m), 1.64–1.73 (2H, m), 1.01–1.31 (4H, m). ^{13}C NMR ($CDCl_3$) δ: 24.4, 24.6, 31.6, 33.1, 56.9, 73.9, 115.7, 117.8, 120.4, 129.8, 148.4. MS *m/z*: 270 [M^+]. Anal. calcd. for $C_{12}H_{16}BrNO$: C, 53.35; H, 5.97; found: C, 53.01; H, 5.67.

2-(4-Bromophenylamino)cyclohexanol (3k)

Solid; mp 67 °C. ^{1}H NMR ($CDCl_3$, ppm) δ: 7.11 (2H, m), 6.45 (2H, m), 3.45 (2H, br s, NH, OH), 3.18–3.25 (1H, m), 2.93–2.99 (1H, m), 1.94 (2H, m), 1.58–1.67 (2H, m), 1.09–1.25 (4H, m). ^{13}C NMR ($CDCl_3$) δ: 24.4, 24.8, 31.4, 33.4, 59.9, 74.3, 115.7, 116.7, 131.8, 147.0. MS *m/z*: 269 [M^+]. Anal. calcd. for $C_{12}H_{16}BrNO$: C, 53.35; H, 5.97; found: C, 53.04; H, 5.86.

2-(3-Hydroxphenylamino)cyclohexanol (3l)

Oily liquid. ^{1}H NMR ($CDCl_3$, ppm) δ: 7.06 (1H, s), 6.18–6.27 (3H, m), 4.68 (2H, br s, NH, OH), 3.28 (1H, m), 3.03 (1H, m), 1.99–2.02 (2H, m), 1.61 (2H, m), 1.18–1.26 (4H, m). MS *m/z*: 206 [M^+]. Anal. calcd. for $C_{12}H_{18}NO_2$: C, 69.87; H, 8.79; found: C, 69.60; H, 8.70.

1-(4-(2-Hydroxycyclohexylamino)phenyl-ethenone (3m)

Solid; mp 79 °C. ^{1}H NMR ($CDCl_3$, ppm) δ: 7.76 (2H, d, *J* = 2.07), 6.56 (2H, d, *J* = 3.10), 4.30 (2H, br s, NH, OH), 3.43 (1H, m), 3.25 (1H, m), 2.48 (3H, s), 2.12 (2H, m), 1.69–1.79 (2H, m), 1.18–1.34 (4H, m). ^{13}C NMR ($CDCl_3$) δ: 23.9, 24.2, 24.6, 31.4, 33.5, 58.9, 74.2, 112.1, 113.6, 130.6, 130.8, 152.3, 196.6. MS *m/z*: 233 [M^+]. Anal. calcd. for $C_{14}H_{19}NO_2$: C, 72.07; H, 8.21; found: C, 71.89; H, 7.98.

4-(2-Hydroxycyclohexylamino)benzoic acid (3n)

Solid; mp 167 °C. ^{1}H NMR ($CDCl_3$, ppm) δ: 7.85 (2H, d, *J* = 2.32), 6.62 (2H, d, *J* = 2.12), 4.94 (2H, br s, NH, OH), 3.23–3.43 (2H, m), 2.10 (2H, m), 1.69 (2H, m), 1.02–1.47 (4H, m). ^{13}C NMR ($CDCl_3$) δ: 24.2, 24.4, 30.3, 32.9, 74.2, 113.7, 118.3, 132.2, 151.5, 171.1. MS *m/z*: 235 [M^+]. Anal. calcd. for $C_{13}H_{17}NO_3$: C, 66.36; H, 7.28; found: C, 66.02; H, 6.98.

2-(4-Nitrophenylamino)cyclohexanol (3o)

Solid; mp 143 °C. ^{1}H NMR ($CDCl_3$, ppm) δ: 7.21 (2H, m), 6.64 (2H, m), 3.54 (2H, br s, NH, OH), 3.28–3.35 (1H, m), 3.00–3.12 (1H, m), 2.02 (2H, m), 1.68–1.77 (2H, m), 1.10–1.35 (4H, m). ^{13}C NMR ($CDCl_3$) δ: 24.8, 24.3, 32.4, 33.8, 60.15, 75.3, 115.9, 116.1, 131.6, 147.9. MS *m/z*: 236 [M^+]. Anal. calcd. for $C_{12}H_{16}N_2O_3$: C, 61.00; H, 6.83; found: C, 61.04; H, 6.86.

2-(3-Nitrophenylamino)cyclohexanol (3p)

Solid; mp 157 °C. ^{1}H NMR ($CDCl_3$, ppm) δ: 7.48–7.54 (2H, m), 7.27 (1H, t, *J* = 8.04), 6.95 (1H, d, *J* = 5.04), 3.41 (2H, br s, NH, OH), 3.25 (1H, m), 3.20 (1H, m), 2.14 (2H, m), 1.73–1.82 (2H, m), 1.13–1.42 (4H, m). ^{13}C NMR ($CDCl_3$) δ: 24.1, 24.7, 31.4, 33.5, 59.7, 74.5, 107.5, 112.5, 119.7, 129.8, 148.8. MS *m/z*: 236 [M^+]. Anal. calcd. for $C_{12}H_{16}N_2O_3$: C, 61.00; H, 6.83; found: C, 60.97; H, 6.561.

© 2007 NRC Canada

2-(2-Trifluorophenylamino)cyclohexanol (3q)

Oily liquid. ^{1}H NMR ($CDCl_3$, ppm) δ: 7.16–7.35 (2H, m), 6.52–6.81 (2H, m) 4.27 (1H, m), 3.23–3.30 (1H, m), 3.19 (2H, br s, –NH, –OH), 1.92 (2H, m), 1.52 (2H, m), 1.07–1.15 (4H, m). ^{13}C NMR ($CDCl_3$) δ: 24.2, 24.5, 33.4, 55.9, 59.5, 112.4, 113.0, 113.6, 114.6, 115.7, 116.5, 116.8, 117.0, 117.2, 126.2, 126.4, 126.5, 132.9, 144.9, 145.8. MS *m/z*: 259 [M^+]. Anal. calcd. for $C_{13}H_{16}F_3NO$: C, 60.22; H, 6.22; found: C, 60.00; H, 6.02.

2-(6-(2-Hydroxycyclohexylamino)pyridin-2-ylamino) cyclohexanol (3r)

Oily liquid. ^{1}H NMR (DMSO, ppm) δ: 7.41 (2H, m), 6.97 (1H, t, *J* = 1.45), 5.50–5.70 (4H, m), 5.36 (4H, br s, NH, OH), 2.30 (4H, m), 1.55 (4H, m), 104–1.27 (8H, m). ^{13}C NMR (DMSO) δ: 23.7, 24.2, 31.1, 34.1, 56.0, 73.3, 95.1, 138.4, 158.3. MS *m/z*: 305 [M^+]. Anal. calcd. for $C_{17}H_{27}N_3O_2$: C, 66.85; H, 8.91; found: C, 66.78; H, 8.56.

2-(Diphenylamino)cyclohexanol (3s)

Oily liquid. ^{1}H NMR ($CDCl_3$, ppm) δ: 6.67–7.32 (10H, m), 4.13–4.54 (1H, m), 3.02–3.23 (1H, m), 3.01 (2H, br s, –NH, –OH), 2.34 (2H, m), 1.84 (2H, m), 1.12–1.34 (4H, m). ^{13}C NMR ($CDCl_3$) δ: 24.4, 25.9, 32.1, 33.4, 60.2, 74.1, 119.2, 120.6, 126.2, 146.4. MS *m/z*: 267 [M^+]. Anal. calcd. for $C_{18}H_{21}NO$: C, 80.86; H, 7.92; found: C, 80.45; H, 7.79.

2-(Diisopropylamino)cyclohexanol (3t)

Oily liquid. ^{1}H NMR ($CDCl_3$, ppm) δ: 3.73 (1H, m), 3.60 (2H, m), 3.39 (1H, m), 3.37 (2H, br s, –NH, –OH), 1.14–2.25 (20H, m). ^{13}C NMR ($CDCl_3$) δ: 19.3, 23.7, 23.8, 29.9, 32.9, 46.5, 67.5, 72.8. MS *m/z*: 199 [M^+]. Anal. calcd. for $C_{12}H_{25}NO$:, 72.31; H, 12.64; found: C, 72.01; H, 12.54.

2-(Propylamino)cyclohexanol (3u)

Oily liquid. ^{1}H NMR ($CDCl_3$, ppm) δ: 4.56 (2H, br s, –NH, –OH), 4.33 (1H, m), 4.13 (2H, dd, *J* = 7.15, 7.15), 3.61 (1H, m), 2.27 (2H, m), 2.08 (3H, s), 1.22–1.33 (6H, m). ^{13}C NMR ($CDCl_3$) δ: 14.1, 21.0, 24.1, 24.5, 30.9, 33.1, 60.4, 72.7, 87.0. MS *m/z*: 157 [M^+]. Anal. calcd. for $C_9H_{19}NO$: C, 68.74; H, 12.18; found: C, 68.65; H, 12.01.

2-Morpholinocyclohexanol (3v)

Oily liquid. ^{1}H NMR ($CDCl_3$, ppm) δ: 3.72 (4H, t, *J* = 4.9), 3.37 (1H, m), 2.72 (2H, t, *J* = 5.4), 2.41 (2H, t, *J* = 4.0), 2.15 (1H, m), 1.83 (2H, m), 1.71 (2H, m), 1.08–1.27 (4H, m). ^{13}C NMR ($CDCl_3$) δ: 22.2, 23.9, 25.4, 33.1, 48.7, 67.4, 68.3, 70.5. MS *m/z*: 185 [M^+]. Anal. calcd. for $C_{10}H_{19}NO_2$: C, 64.83; H, 10.34 ; found: C, 64.66; H, 10.02.

2-(4-(4-(2-Hydroxycyclohexylamino)benzyl)phenyl amino)cyclohexanol (3w)

Oily liquid. ^{1}H NMR ($CDCl_3$, ppm) δ: 6.80 (4H, d, *J* = 5.85), 6.43 (4H, d, *J* = 4.36), 3.90–3.98 (2H, m), 3.59 (2H, s), 3.44 (4H, br s, NH, OH), 2.88–3.15 (2H, m), 0.84–1.87 (16H, m). ^{13}C NMR ($CDCl_3$) δ: 20.8, 24.2, 30.8, 31.3, 40.0, 60.3, 73.8, 114.2, 129.4, 146.0. MS *m/z*: 392 [M^+]. Anal. calcd. for $C_{25}H_{32}N_2O_2$: C, 76.49; H, 8.22; found: C, 76.33; H, 8.12.

2-(4-(4-(2-Hydroxycyclohexylamino) phenoxy)phenylamino)cyclohexanol (3x)

Oily liquid. ^{1}H NMR ($CDCl_3$, ppm) δ: 6.78 (4H, d, *J* = 8.77), 6.59 (4H, d, *J* = 8.85), 3.44 (4H, brs, NH, OH), 3.29 (2H, ddd, *J*= 9.20, 3.57, 9.77), 2.99 (2H, ddd, 8.95, 3.60, 8.97), 2.01–2.03 (4H, m), 1.68–1.80 (4H, m), 1.00–1.36 (8H, m). ^{13}C NMR ($CDCl_3$, ppm) δ: 24.3, 24.8, 32.4, 33.3, 60.8, 74.0, 115.0, 119.0, 143.4, 150.2. MS *m/z*: 396 [M^+]. Anal. calcd. for $C_{25}H_{32}N_2O_2$: C, 72.70; H, 8.13; found: C, 72.63; H, 8.03.

7-(2-Hydroxycyclohexyl)-5,6,7,8,9,10-hexahydro-2-*H*-1,13,4,7,10-benzadioxatriazacyclopentadecine-3,11, (4*H*,12*H*)-dione (3y)

Oily liquid. ^{1}H NMR ($CDCl_3$, ppm) δ: 8.03 (1H, s, NH), 6.96–7.01 (2H, m), 6.85–6.91 (2H, m), 4.51 (4H, s), 3.49 (4H, t, *J* = 5.37), 3.36 (1H, m), 3.20 (1H, m), 2.94 (4H, t, *J* = 5.35), 2.0 (2H, m), 1.69 (2H, m), 1.26 (4H, m). ^{13}C NMR ($CDCl_3$) δ: 24.0, 24.8, 32.1, 32.7, 38.0, 47.3, 66.8, 73.2, 120.0, 122.0, 165.0, 168.1, 168.6. MS *m/z:* 391 [M^+]. Anal. calcd. for $C_{20}H_{29}N_3O_5$: C, 61.36; H, 7.47; found: C, 61.23; H, 7.43.

Acknowledgement

The support of this work by the Shiraz University Research Council is gratefully acknowledged.

References

1. (*a*) I. Cepanec, M. Litvic, H. Mikuldas, A. Bartolincic, and V. Vinkovic. Tetrahedron, **59**, 2435 (2003); (*b*) D.J. Ager, I. Prakash, and D.R. Schaad. Chem. Rev. **96**, 835 (1996); (*c*) P. O'Brien. Angew. Chem. Int. Ed. **38**, 326 (1999); (*d*) G. Li, H.T. Chang, and K.B. Sharpless. Angew. Chem. Int. Ed. **35**, 451 (1996); (*e*) J. Joossens, P. van der Veken, A.M. Lambeir, K. Augustyns, and A.J. Haemers. Med. Chem. **47**, 2411 (2004); (*f*) P.G. Williams, W.Y. Yoshida, R.E. Moore, and V.J. Paul. J. Nat. Prod. **65**, 29 (2002); (*g*) G.A. Rogers, S.M. Parsons, D.C. Anderson, L.M. Nilsson, B. Bahr, W.D. Kornreich, R. Kaufman, R.S. Jacobs, and B. Kirtman. J. Med. Chem. **32**, 1217 (1989).
2. (*a*) G. Sekar and V.K. Singh. J. Org. Chem, **64**, 287 (1999); (*b*) T. Ollevier and G. Lavie-Compin. Tetrahedron Lett. **45**, 49 (2004); (*c*) I. Cepanec, M. Litvic, H. Mikuldas, A. Bartolincic, and V. Vinkovie. Tetrahedron Lett. **44**, 2435 (2003); (*d*) F. Fringuelli, F. Pizzo, S. Tortoioli, and L. Vaccaro. J. Org. Chem. **69**, 7745 (2004).
3. (*a*) L.R. Reddy, M.A. Reddy, N. Bhanumathi, and K.R. Rao. New J. Chem. **25**, 221 (2001); (*b*) L. Duran Pachon, P. Gamez, J.J.M. Van Brussel, and J. Reedijk. Tetrahedron Lett. **44**, 6025 (2003); (*c*) A. Chakraborti and A. Kondaskar. Tetrahedron Lett. **44**, 8315 (2003); (*d*) J.R. Rodriguez and A. Navarro. Tetrahedron Lett. **45**, 7495 (2004); (*e*) S. Chandrasekhar, T. Ramachandar, and J.S. Prakash. Synthesis, 1817 (2000); (*f*) G. Sundarajan, K. Vijayakrishna, and B. Varghese. Tetrahedron Lett. **45**, 8253 (2004).
4. V.R. Yarapathy, S. Mekala, B.V. Rao, and S. Tammishetti. Catal. Commun. **7**, 466 (2006).
5. A.K. Chakraborti, A. Kondskar, and S. Rudrawar. Tetrahedron, **60**, 9085 (2004).

© 2007 NRC Canada

6. (*a*) P.-Q. Zhao, L.-W. Xu, and C.-G. Xia. Synlett, **5**, 846 (2004); (*b*) M. Curini, F. Epifano, M.C. Marcotullio, and O. Rosati. Eur. J. Org. Chem. **21**, 4149 (2001).
7. (*a*) U. Das, B. Crousse, V. Kesavan, D. Bonnet-Delpon, and J.-P. Begue. J. Org. Chem. **65**, 6749 (2000); (*b*) J.S. Yadav, B.V.S. Reddy, A.K. Basak, and A. Venkat Narsaiah. Tetrahedron Lett. **44**, 1047 (2003); (*c*) F.-S. Liang, A. Brik, Y.-C. Lin, J.H. Elder, and C.-H Wong. Bioorg. Med. Chem. **14**, 1058 (2006).
8. A. Kamal, S.F. Adil, and M. Arifuddin. Ultrason. Sonochem. **12**, 429 (2005).
9. R.I. Kureshy, S. Singh, N.H. Khan, S.H.R. Abdi, S. Agrawal, V.J. Mayani, and R.V. Jasra. Tetrahedron Lett. **47**, 5277 (2006).
10. (*a*) H. Eshghi, M. Rahimizadeh, and A. Shoryabi. J. Iran. Chem. Soc. **2**, 155 (2005); (*b*) N. Azizi and M.R. Saidi. Org. Lett. **7**, 3649 (2005).
11. (*a*) T. Seki, H. Kabashima, K. Akutsu, H. Tachikawa, and H. Hattori. J. Catal. **204**, 393 (2001); (*b*) B. Kaboudin and M. Karimi. Bioorg. Med. Chem. Lett. **16**, 5324 (2006); (*c*) A. Shockravi, H. Valizadeh, and M.M. Heravi. Phosphorus Sulfur Silicon Relat. Elem. 501 (2003).
12. (*a*) M. Hosseini Sarvari and H. Sharghi. J. Org. Chem. **69**, 6953 (2004); (*b*) H. Sharghi and M. Hosseini Sarvari. Synthesis, **8**, 1057 (2002); (*c*) M.Hosseini Sarvari. Synthesis, **5**, 787 (2005); (*d*) M. Hosseini Sarvari and H. Sharghi. Tetrahedron, **61**, 10903 (2005); (*e*) Y.J. Kim and R.S. Varma. Tetrahedron Lett. **45**, 7205 (2004); (*f*) M. Hosseini Sarvari and H. Sharghi. J. Org. Chem. **71**, 6652 (2006).
13. M.W.C. Robinson, D.A. Timms, S.M. Williams, and A.E. Graham. Tetrahedron Lett. **48**, 6249 (2007).
14. N. Azizi and M.R. Saidi. Tetrahedron, **63**, 888 (2006).
15. M. Hosseini-Sarvari and H. Sharghi. J. Iran. Chem. Soc. In press (2008).

© 2007 NRC Canada

Lewis acid catalyzed Claisen rearrangement: Regioselective synthesis of oxygen, nitrogen, and sulfur heterocycles

K.C. Majumdar and A.K. Pal

Abstract: Regioselective synthesis of pentacyclic heterocycles containing oxygen, nitrogen, and sulfur has been achieved in good to excellent yields by the sequential Claisen rearrangement of but-2-ynyl ethers and sulfides containing quinolone moiety. The substrates ethers and sulfides were prepared from 1-aryloxy-4-chlorobut-2-ynes with *N*-alkyl-4-hydroxyquinoline-2(1*H*)-ones.

Key words: regioselectivity, [3,3] sigmatropic rearrangement, nucleophilicity of sulfur, aluminium chloride, heterocycles.

Résumé : On a réalisé la synthèse régiosélective d'hétérocycles pentacycliques contenant des atomes d'oxygène, d'azote et de soufre avec des rendements allant de bons à excellents en procédant à un réarrangement de Claisen séquentiel d'éthers et de sulfures de but-2-ynyle comportant une portion quinoléinone. Les éthers et les sulfures utilisés comme substrats ont pour leur part été préparés à partir de 1-aryloxy-4-chlorobut-2-ynes avec des *N*-alkyl-4-hydroxyquinoléin-2-(1*H*)-ones.

Mots-clés: régiosélectivité, réarrangement sigmatropique [3.3], caractère nucléophile du soufre, chlorure d'aluminium, hétérocycles.

[Traduit par la Rédaction]

Introduction

Quinolone alkaloids are interesting owing to their antimicrobial activity and cytotoxicity against animal and plant tumors (1). Recently, a novel class of 4-hydroxy quinolin-2(1*H*)-one derivatives as selective glycine site NMDA antagonist, possessing potent centrally mediated in vivo activity on oral administration, has been reported (2). Quinolone derivatives exhibit different activities depending on their structural type (3). Flindersine, 2,2-dimethylpyrano[3,2-*c*]quinolin-5(2*H*)-one, various substituted flindersine, furo[3,2-*c*]quinolin-4(5*H*)-one, and 2*H*-pyrano[3,2-c]quinolin-5(6*H*)-one derivatives are widely distributed in nature (4). A good deal of work has been done on the synthesis (5) of these types of compounds with various substitutions in the aromatic ring. The familiar bioactivity of various quinolone derivatives has drawn our attention to this area, and we became interested in synthesizing [6,5] fused pentacyclic heterocycles in which the bioactive quinolone moiety is fused with benzofuran moiety.

Strategies involving Claisen rearrangement have emerged as important tools in the synthesis of various heterocyclic compounds. Since 1912, several classes of organic compounds have been synthesized by Claisen rearrangement, and many of them are biologically active (6). Claisen rearrangement can be performed catalytically (6, 7). Earlier studies in the synthesis of different oxygen, sulfur, and nitrogen heterocycles by the application of [3,3] sigmatropic rearrangement of suitably tailored 1,4-disubstitued but-2-ynes have led to the synthesis of new heterocyclic compounds derived from 4-hydroxy coumarin (8), 4-hydroxy dithiocoumarin (9). Both the first and second Claisen rearrangements were achieved thermally. This result has encouraged us to undertake a study on the sequential [3,3] sigmatropic rearrangement of *N*-alkyl-4-(4′-aryloxybut-2′-ynyloxy)quinolin-2(*1H*)-one and *N*-alkyl-(4-aryloxybut-2-ynyloxy)quinolin-2(*1H*)-thione to achieve our goal. Herein, we report the results.

Received 20 June 2007. Accepted 29 October 2007. Published on the NRC Research Press Web site at canjchem.nrc.ca on 18 December 2008.

K.C. Majumdar[1] and A.K. Pal. Department of Chemistry, University of Kalyani, Kalyani 741235, India.

[1]Corresponding author (e-mail: kcm_ku@yahoo.co.in).

Results and discussion

The requisite starting materials for this study, 1-alkyl-4-[(4′-aryloxybut-2′-ynyl)]quinoline-2(1*H*)-ones (**3a**–**3h**), were prepared by either classical alkylation of *N*-alkyl-4-hydroxyquine-2(1*H*)-ones (**1**) with a number of different 1-aryloxy-4-chlorobut-2-ynes (**2a**–**2e**) in acetone/K_2CO_3 or PTC alkylation using TBAB as a catalyst in aq. NaOH/chlorobenzene at 100 °C. The PTC alkylation was faster and gave higher yields (71%–85%), whereas classical alkylation needed longer reaction time, and yields of **3a**–**3h** were relatively lower (30%–40%). The formation of **3a**–**3h** was indicated in the IR spectra by the absence of –OH stretching and also from their ^{1}H NMR spectra (Scheme 1). When compound **3e** was refluxed with phosphrous pentasulfide in dry benzene for 3 h, a yellow solid was isolated from the reaction mixture. This was characterized as **4e** from its elemental analysis and spectroscopic data. Formation of a

 doi:10.1139/V07-139 © 2007 NRC Canada

Scheme 1. Reagents and conditions: (*i*) 1% aq. NaOH solution, chlorobenzene, TBAB, heating at 100 °C, stirring, 3 to 4 h, (*ii*) P_2S_5, dry benzene, reflux, 3 to 4h.

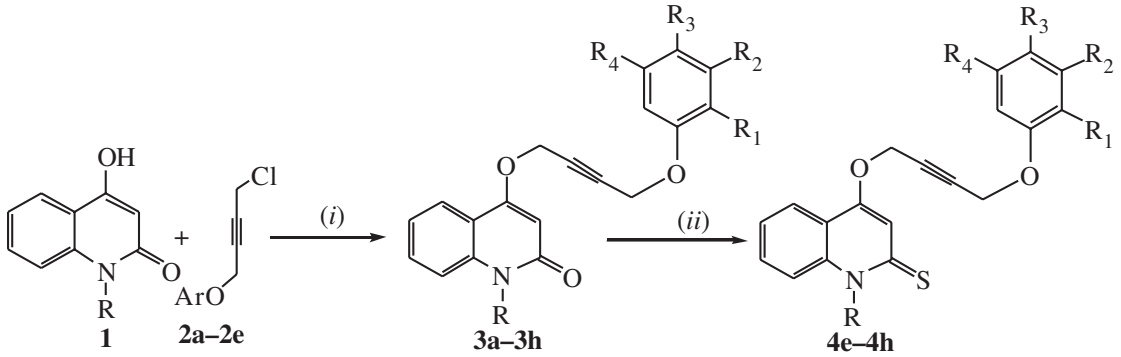

						Yield %	
	R	R_1	R_2	R_3	R_4	**3**	**4**
a	CH_3	CH_3	H	H	H	80	–
b	CH_3	CH_3	H	H	CH_3	76	–
c	CH_3	Cl	H	H	H	71	–
d	C_2H_5	CH_3	H	H	H	79	–
e	CH_3	CH_3	H	Cl	H	85	65
f	CH_3	H	CH_3	Cl	CH_3	82	63
g	C_2H_5	CH_3	H	Cl	H	74	69
h	C_2H_5	H	CH_3	Cl	CH_3	81	64

single product from the reaction encouraged us to synthesize other derivatives **4f**–**4h** from **3f**–**3h** in 63%–69% yields (Scheme 1).

Compounds **3a**–**3f** and **4e**–**4h** contain allyl-propargyl ether moiety and are prone to undergo [3,3] sigmatropic rearrangement. The substrate **3a** was refluxed in chlorobenzene (bp 132 °C) for 8 h to give angularly fused compound **5a** in 43% yield, whereas under the same reaction conditions, compound **4e** furnished linearly fused **6e** in 49% yield. When high boiling solvent like *o*-dichlorobenzene (bp 180 °C) was used, overall yields of the products were increased to 83% and 85%, respectively, and it also shortened the reaction time. On similar treatment, compounds **3b**–**3f** and **4f**–**4h** afforded **5b**–**5f** and **6f**–**6h** in 70%–81% and 81%–89% yields, respectively (Scheme 2).

The formation of products **5a**–**5f** and **6e**–**6h** from substrates **3a**–**3f** and **4e**–**4h** may easily be explained by the initial [3,3] sigmatropic rearrangement followed by rapid enolisation and [1,5] hydrogen shift to give intermediate **9** and 6π electrocyclic ring closure (ECR) to give final products **5a**–**5f** and **6e**–**6h**. The exclusive formation of **6e**–**6h** instead of **11** from **4e**–**4h** may be due to the presence of sulfur, which has larger nucleophilicity and greater polarisibility (10) (Scheme 3).

The products **5a**–**5f** and **6e**–**6h** contain allyl aryl ether moiety and therefore are suitable substrates for the occurrence of a second Claisen rearrangement. However, this would require higher temperature and longer time than the first [3,3] sigmatropic rearrangement of compounds **3a**–**3f** or **4e**–**4h**, as during this rearrangement, the aromaticity of the aryl moiety would be disturbed. The same transformation could also be carried out by using Lewis-acid-catalyzed Claisen rearrangement under mild conditions. The reaction of the substrates **5a** and **6e** were conducted with catalytic amount of anhyd. $AlCl_3$ in dry DCM and stirred at room temperature for 30–45 min. The rearranged products **12a** and **13e** were obtained in 79% and 75% yields, respectively (Scheme 4). Encouraged by the initial success, substrates **5b**–**5f** and **6f**–**6h** were similarly treated, and the corresponding products **12b**–**12f** and **13f**–**13h** were obtained in 72%–83% and 72%–79% yields, respectively. The stereochemistry of the furopyran ring junction, previously surmised from molecular model (Dreiding model) in similar situation to cis (10), was now established to be cis on the basis of molecular modeling and NOE correlation. In case of compound **12f**, NOE correlation was found between the ring junction methyl proton resonance at δ = 1.84 ppm and benzylic proton resonate at δ = 3.44 ppm, (Scheme 4).

The formation of products **12a**–**12f** may be mechanistically explained by the charge-accelerated [3,3] sigmatropic rearrangement of **5a**–**5f** to **15** via ether oxygen $AlCl_3$ complex **14** followed by rapid tautomerization and proton exchange to give intermediate **16**, which may then undergo 5-exo-cyclization leading to products **12a**–**12f**. Previously, [6,6] fused products were obtained (11). Intermediates, similar to **16**, were isolated (12) and converted to [6,6] fused products with pyridine hydrotribromide ($PyHBr_3$). However, we failed to isolate intermediate **16** or [6,6] fused products;

© 2007 NRC Canada

Scheme 2. Reagents and conditions: (*i*) o-dichlorobenzene, reflux, 1–4 h.

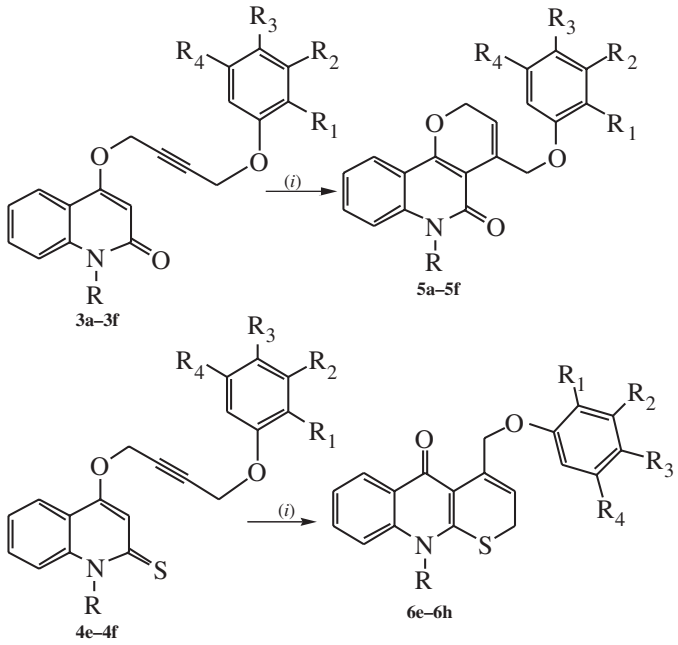

5	R	R_1	R_2	R_3	R_4	Yield %
a	CH_3	CH_3	H	H	H	83
b	CH_3	CH_3	H	H	CH_3	77
c	CH_3	Cl	H	H	H	70
d	C_2H_5	CH_3	H	H	H	81
e	CH_3	CH_3	H	Cl	H	79
f	CH_3	H	CH_3	Cl	CH_3	81

6	R	R_1	R_2	R_3	R_4	Yield %
e	CH_3	CH_3	H	Cl	H	85
f	CH_3	H	CH_3	Cl	CH_3	89
g	C_2H_5	CH_3	H	Cl	H	81
h	C_2H_5	H	CH_3	Cl	CH_3	79

Scheme 3.

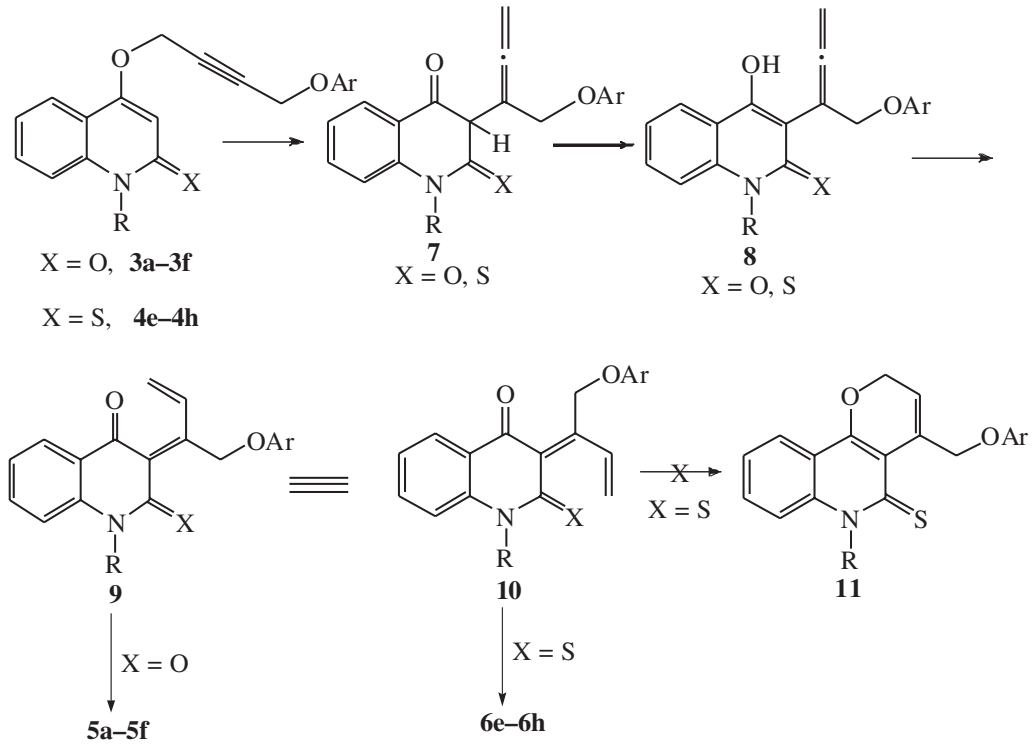

only [6,5] fused products **12a**–**12f** were obtained under catalytic condition. Formation of the products **13e**–**13h** from **6e**–**6h** can also be explained by the same mechanism as shown in Scheme 5.

In summary, we have successfully performed sequential Claisen rearrangement, a *oxy*-Claisen rearrangement of *N*-alkyl-4-(4′-aryloxybut-2′-ynyloxy)-quinoline-2(1*H*)-ones and *thio*-Claisen rearrangement of compound *N*-alkyl-4-(4′-aryloxybut-2′-ynyloxy)-quinoline-2(1*H*)-thione. This methodology is simple for the construction of furo pyran and furo thiopyran rings and displays appreciable regioselectivity.

Experimental

Melting points were determined in open capillaries and are uncorrected. IR spectra were recorded on a PerkinElmer L 120–000A spectrometer (ν_{max} in cm^{-1}) using samples as neat liquids, and solid samples were recorded in

© 2007 NRC Canada

Scheme 4. Reagents and conditions: (*i*) dry DCM, anhyd. $AlCl_3$, stirred, 30–40 min, RT.

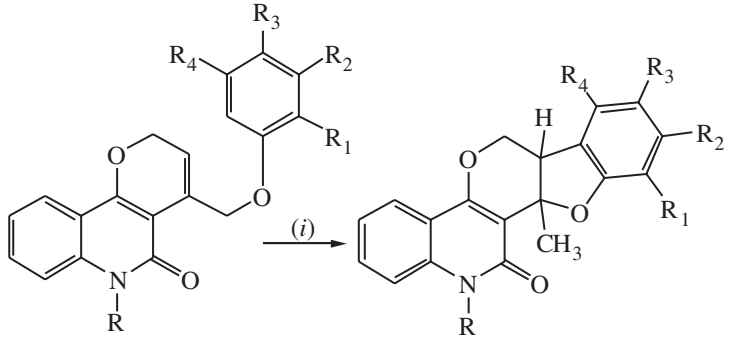

12	R	R_1	R_2	R_3	R_4	Yield %
a	CH_3	CH_3	H	H	H	79
b	CH_3	CH_3	H	H	CH_3	75
c	C_2H_5	Cl	H	H	H	72
d	C_2H_5	CH_3	H	H	H	76
e	CH_3	CH_3	H	Cl	H	82
f	CH_3	H	CH_3	Cl	CH_3	83

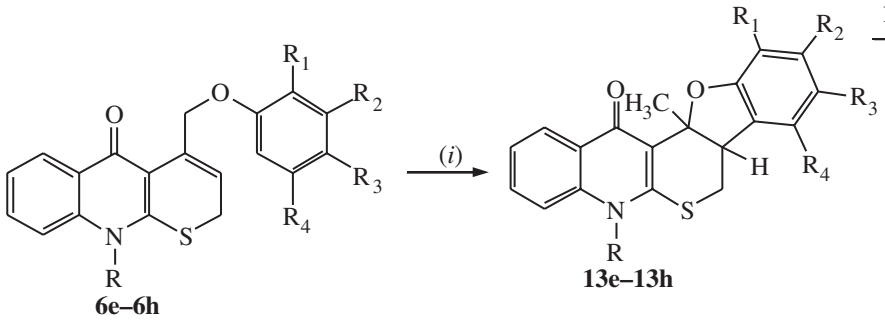

13	R	R_1	R_2	R_3	R_4	Yield %
e	CH_3	CH_3	H	Cl	H	75
f	CH_3	H	CH_3	Cl	CH_3	72
g	CH_3	CH_3	H	Cl	H	79
h	C_2H_5	H	CH_3	Cl	CH_3	73

Scheme 5.

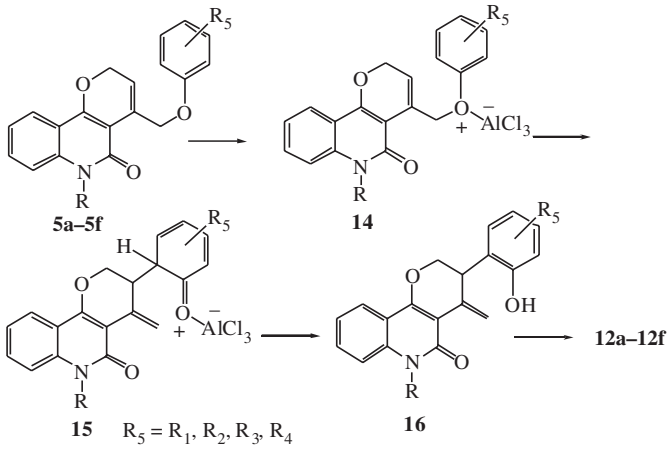

KBr disks. ^{1}H NMR (300 MHz, 400 MHz, 500 MHz) spectra were recorded on a Bruker DPX-300, Bruker DPX-400, and Bruker DRX-500 spectrometer in $CDCl_3$ (chemical shift in δ) with TMS as internal standard. Silica gel [(60–120 and 230–400 mesh), Spectrochem, India] was used for chromatographic separation. Silica gel G [E-Merck (India)] was used for TLC. Petroleum ether refers to the fraction boiling between 60 °C and 80 °C.

Preparation of *N*-alkyl-4-(4′-aryloxybut-2′-ynyloxy)quinoline-2(1H)-one derivatives 3a–3h

To a mixture of *N*-alkyl-4-hydroxy quinoline-2(1*H*)-one (**1**) (6 mmol) and 1-aryloxy-4-chloro-but-2-ynes (**2a**–**2e**) (7.2 mmol) in chlorobenzene (50 mL) was added a solution of TBAB (0.23 g, 0.72 mmol) in 1% aq. NaOH (50 mL), and the mixture was stirred for 3–4 h at 100 °C. The reaction mixture was diluted with water and extracted with CH_2Cl_2 (2 × 50 mL). The combined extract was washed successively with 2 N HCl (2 × 20 mL), water (3 × 30 mL), saturated brine solution (25 mL), and dried (Na_2SO_4). The solvent was removed in vacuo, and the crude products were purified by column chromatography over silica gel using petroleum ether/ethyl acetate (3:2) as eluant and recrystallized from dichloromethane/petroleum ether.

Compound 3a

Yield: 80%. Light yellow solid; mp 112–114 °C. IR (KBr) ν: 2978, 1641 cm^{-1}. ^{1}H NMR ($CDCl_3$, 400 MHz) δ_H: 2.18 (s, 3H), 3.67(s, 3H), 4.75 (s, 2H), 4.84 (s, 2H), 6.13 (s, 1H), 6.87–8.03 (m, 8H) ppm. MS *m*/*z*: 333 [M$^+$]. Anal. calcd. for $C_{21}H_{19}NO_3$: C, 75.66; H, 5.74; N, 4.20; found: C, 75.87; H, 5.86; N, 4.13.

Compound 3b

Yield: 76%. Light yellow solid; mp 101–103 °C. IR (KBr) ν: 2923, 1638 cm^{-1}. ^{1}H NMR ($CDCl_3$, 400 MHz) δ_H: 2.17 (s, 3H), 2.25 (s, 3H), 3.66 (s, 3H), 4.73 (s, 2H), 4.84 (s, 2H), 6.10 (s, 1H), 6.67–7.97 (m, 7H) ppm. MS *m*/*z*: 347 [M$^+$]. Anal. calcd. for $C_{22}H_{21}NO_3$: C, 76.06; H, 6.09; N, 4.03; found: C, 76.32; H, 6.23; N, 4.06.

Compound 3c

Yield: 71%. Light yellow solid; mp 120–122 °C. IR (KBr) ν: 2922, 1655 cm^{-1}. ^{1}H NMR ($CDCl_3$, 400 MHz) δ_H: 3.67 (s, 3H), 4.80 (s, 2H), 4.84 (s, 2H), 6.08 (s, 1H), 6.93–7.95 (m, 8H) ppm. MS *m*/*z*: 353, 355 [M$^+$]. Anal. calcd. for $C_{20}H_{16}ClNO_3$: C, 67.90; H, 4.56; N, 3.96; found: C, 67.87; H, 4.58; N, 3.89.

Compound 3d

Yield: 79%. Light yellow solid; mp 124–126 °C. IR (KBr) ν: 2937, 1642 cm^{-1}. ^{1}H NMR ($CDCl_3$, 400 MHz) δ_H: 1.34 (t,

© 2007 NRC Canada

J = 7.05 Hz, 3H), 2.23 (s, 3H), 4.29 (q, J = 7.02 Hz, 2H), 4.74 (s, 2H), 4.82 (s, 2H), 6.10 (s, 1H), 6.94–7.99 (m, 8H) ppm. MS *m/z*: 347 [M^+]. Anal. calcd. for $C_{22}H_{21}NO_3$: C, 76.06; H, 6.09; N, 4.03; found: C, 75.85; H, 6.08; N, 4.07.

Compound 3e

Yield: 85%. Light yellow solid; mp 119–121 °C. IR (KBr) ν: 2924, 1642 cm^{-1}. ^1H NMR ($CDCl_3$, 400 MHz) δ_H: 2.27 (s, 3H), 3.67 (s, 3H), 4.69 (s, 2H), 4.84 (s, 2H), 6.09 (s, 1H), 6.69–7.96 (m, 7H) ppm. MS *m/z*: 367, 369 [M^+]. Anal. calcd. for $C_{21}H_{18}ClNO_3$: C, 68.57; H, 4.93; N, 3.81; found: C, 68.40; H, 4.96; N, 3.84.

Compound 3f

Yield: 82%. Light yellow solid; mp 127–128 °C. IR (KBr) ν: 2912, 1644 cm^{-1}. ^1H NMR ($CDCl_3$, 400 MHz) δ_H: 2.28 (s, 6H), 3.66 (s, 3H), 4.68 (s, 2H), 4.84 (s, 2H), 6.09 (s, 1H), 6.65–7.96 (m, 6H) ppm. MS *m/z*: 381, 383 [M^+]. Anal. calcd. for $C_{22}H_{20}ClNO_3$: C, 69.20; H, 5.28; N, 3.67; found: C, 69.27; H, 5.24; N, 3.78.

Compound 3g

Yield: 74%. Light yellow solid; mp 145–147 °C. IR (KBr) ν: 2929, 1645cm^{-1}. ^1H NMR ($CDCl_3$, 400 MHz) δ_H: 1.31 (t, J = 7.12 Hz, 3H), 2.28 (s, 3H), 4.29 (q, J = 7.12 Hz, 2H), 4.69 (s, 2H), 4.83 (s, 2H), 6.08 (s, 1H), 6.69–7.97 (m, 7H) ppm. MS *m/z*: 381, 383 [M^+]. Anal. calcd. for $C_{22}H_{20}ClNO_3$: C, 69.20; H, 5.28, N, 3.67; found: C, 69.27; H, 5.22; N, 3.55.

Compound 3h

Yield: 81%. Light yellow solid; mp 132–134 °C. IR (neat) ν_{max}: 2927, 1629 cm^{-1}. ^1H NMR ($CDCl_3$, 400 MHz) δ: 1.30 (t, J = 7.05 Hz, 3H), 2.29 (s, 6H), 4.27 (q, J = 7.04 Hz, 2H), 4.68 (s, 2H), 4.84 (s, 2H), 6.09 (s, 1H), 6.66–7.97 (m, 6H) ppm. MS: *m/z* 395, 397 [M^+]. Anal. calcd. for $C_{23}H_{22}ClNO_3$: C, 69.78; H, 5.60; N, 3.54; found C, 69.52; H, 5.55; N, 3.75.

Thionation of compounds 3e–3h

P_2S_5 (3.35 g, 15 mmol) was added to a solution of **3e**–**3h** (6 mmol) in dry benzene (50 mL) and refluxed for 3–4 h. The reaction mixture was cooled and extracted with benzene (3 × 30 mL), and the benzene layer was washed with water (4 × 30 mL), brine solution (25 mL), and dried (Na_2SO_4). Evaporation of the solvent gave a crude mass, which was chromatographed over silica gel (60–120 mesh). Solid products **4e**–**4h** were isolated in 63%–69% yields when the column was eluted with petroleum ether/ethyl acetae (8.5:1.5). The products were recrystallized from dichloromethane/petroleum ether.

Compound 4e

Yield: 65%. Yellow solid; mp 147–148 °C. IR (neat) ν_{max}: 2952, 1591 cm^{-1}. ^1H NMR ($CDCl_3$, 400 MHz) δ: 2.29 (s, 3H), 4.28 (s, 3H), 4.68 (s, 2H), 4.88 (s, 2H), 6.71–8.04 (m, 7H) ppm. MS *m/z*: 383, 385 [M^+]. Anal. calcd. for $C_{21}H_{18}ClNO_2S$: C, 65.70; H, 4.73; N, 3.65; found C, 65.51; H, 4.63; N, 3.52%.

Compound 4f

Yield: 63%. Yellow solid; mp 136–138 °C. IR (neat) ν_{max}: 2948, 1600 cm^{-1}. ^1H NMR ($CDCl_3$, 400 MHz) δ: 2.28 (s, 6H), 4.29 (s, 3H), 4.67 (s, 2H), 4.88 (s, 2H), 6.65–8.02 (m, 6H) ppm. MS *m/z*: 397, 399 [M^+]. Anal. calcd. for $C_{22}H_{20}ClNO_2S$: C, 66.40; H, 5.07; N, 3.52; found C, 66.45; H, 5.16; N, 3.38.

Compound 4g

Yield: 69%. Yellow solid; mp 119–121 °C. IR (neat) ν_{max}: 2953, 1592 cm^{-1}. ^1H NMR ($CDCl_3$, 400 MHz) δ: 1.42 (t, J = 7.08 Hz, 3H), 2.28 (s, 3H), 4.70 (s, 2H), 4.87 (s, 2H), 5.01 (br s, 2H), 6.69–8.03 (m, 7H) ppm. MS *m/z*: 397, 399 [M^+]. Anal. calcd. for $C_{22}H_{20}ClNO_2S$: C, 66.40; H, 5.07; N, 3.52; found C, 66.64; H, 5.14; N, 3.37.

Compound 4h

Yield: 67%. Yellow solid; mp 155–157 °C. IR (neat) ν_{max}: 2948, 1610 cm^{-1}. ^1H NMR ($CDCl_3$, 300 MHz) δ: 1.42(t, J = 7.01 Hz, 3H), 2.30 (s, 6H), 4.70 (s, 2H), 4.88 (s, 2H), 4.95(br s, 2H), 6.67–8.04 (m, 6H) ppm. MS *m/z*: 411, 413 [M^+]. Anal. calcd. for $C_{23}H_{22}ClNO_2S$: C, 67.06; H, 5.38; N, 3.40; found C, 66.87; H, 5.39; N, 3.51.

Rearrangement of compounds 3a–3f and 4e–4h

Compound **3a**–**3f** and **4e**–**4h** (1.2 mmol) was dissolved in *o*-dichlorobenzene (5 mL) and refluxed for 1–4 h. The reaction mixture was chromatographed over silica gel (60–120 mesh). *o*-Dichlorobenzene was removed by washing the column with petroleum ether (60–80 °C), and pure products **5a**–**5f** and **6e**–**6h** were isolated by eluting the column with petroleum ether/ethyl acetate. These were recrystallized from dichloromethane/petroleum ether.

Compound 5a

Yield: 83%. Light yellow solid; mp 124–126 °C. IR (neat) ν_{max}: 2921, 1631 cm^{-1}. ^1H NMR ($CDCl_3$, 300 MHz) δ: 2.30 (s, 3H), 3.68 (s, 3H), 4.95 (d, J = 1.65 Hz, 2H), 5.27 (d, J = 1.53 Hz, 2H), 5.96 (t, J = 1.72 Hz, 1H), 6.82–7.97 (m, 8H) ppm. MS *m/z*: 333 [M^+]. Anal. calcd. for $C_{21}H_{19}NO_3$: C, 75.66; H, 5.74; N, 4.20; found C, 75.62; H, 5.97; N, 4.02.

Compound 5b

Yield: 77%. Light yellow solid; mp 139–142 °C. IR (neat) ν_{max}: 2923, 1654 cm^{-1}. ^1H NMR ($CDCl_3$, 400 MHz) δ: 2.25 (s, 3H), 2.30 (s, 3H), 3.68 (s, 3H), 4.96 (d, J = 1.88 Hz, 2H), 5.24 (d, J = 1.92 Hz, 2H), 5.99 (t, J = 1.88 Hz, 1H), 6.65–7.96 (m, 7H) ppm. MS *m/z*: 347 [M^+]. Anal. calcd. for $C_{22}H_{21}NO_3$: C, 76.06; H, 6.09; N, 4.03; found C, 76.32; H, 6.23; N, 4.05.

Compound 5c

Yield: 70%. Light yellow solid; mp 158–160 °C. IR (neat) ν_{max}: 2935, 1663 cm^{-1}. ^1H NMR ($CDCl_3$, 400 MHz) δ: 3.67 (s, 3H), 4.97 (d, J = 1.76 Hz, 2H), 5.33 (d, J = 1.84 Hz, 2H), 6.08 (t, J = 1.61 Hz, 1H), 6.86–7.96 (m, 8H) ppm. MS *m/z*: 353, 355 [M^+]. Anal. calcd. for $C_{20}H_{16}ClNO_3$: C, 67.90; H, 4.56; N, 3.96; found C, 67.83; H, 4.60; N, 3.85.

Compound 5d

Yield: 81%. Light yellow solid; mp 133–135 °C. IR (neat) ν_{max}: 2924, 1635 cm^{-1}. ^1H NMR ($CDCl_3$, 400 MHz) δ: 1.32 (t, J = 7.05, 3H), 2.29 (s, 3H), 4.29 (q, J = 7.01 Hz, 2H), 4.95 (d, J = 1.88 Hz, 2H), 5.27 (d, J = 1.99 Hz, 2H), 5.97 (t, J = 1.90 Hz, 1H), 6.79–7.98 (m, 8H) ppm. MS *m/z*: 347

© 2007 NRC Canada

[M+]. Anal. calcd. for $C_{22}H_{21}NO_3$: C, 76.06; H, 6.09; N, 4.03; found C, 75.84; H, 6.23; N, 3.97.

Compound 5e

Yield: 79%. Light yellow solid; mp 152–154 °C. IR (neat) ν_{max}: 2924, 1645 cm^{-1}. ^1H NMR ($CDCl_3$, 400 MHz) δ: 2.32 (s, 3H), 3.67 (s, 3H), 4.93(d, *J* = 1.89 Hz, 2H), 5.23 (d, *J* = 1.90 Hz, 2H), 5.88 (t, *J* = 1.89 Hz, 1H), 6.75–7.96 (m, 7H) ppm. MS *m/z*: 367, 369 [M+]. Anal. calcd. for $C_{21}H_{18}ClNO_3$: C, 68.57; H, 4.93; N, 3.81; found C, 68.59; H, 5.03; N, 3.95.

Compound 5f

Yield: 81%. Light yellow solid; mp 147–149 °C. IR (neat) ν_{max}: 2922, 1655 cm^{-1}. ^1H NMR ($CDCl_3$, 300 MHz) δ: 2.34 (s, 6H), 3.69(s, 3H), 4.95(d, *J* = 1.91 Hz, 2H), 5.23 (d, *J* = 1.84 Hz, 2H), 5.90 (t, *J* = 1.87 Hz, 1H), 6.75–7.97 (m, 6H) ppm. MS *m/z*: 381, 383 [M+]. Anal. calcd. for $C_{22}H_{20}ClNO_3$: C, 69.20; H, 5.28; N, 3.67; found C, 69.37; H, 5.22; N, 3.72.

Compound 6e

Yield: 85%. Yellow solid; mp 118–120 °C. IR (neat) ν_{max}: 2923, 1593 cm^{-1}. ^1H NMR ($CDCl_3$, 300 MHz) δ: 2.30 (s, 3H), 3.44 (d, *J* = 5.97 Hz, 2H), 4.00 (s, 3H), 5.25 (s, 2H, 6.08 (t, *J* = 5.91 Hz, 1H), 6.68–8.50 (m, 7H) ppm. MS *m/z*: 383, 385 [M+]. Anal. calcd. for $C_{21}H_{18}ClNO_2S$: C, 65.70; H, 4.73; N, 3.65; found C, 65.57; H, 4.79; N, 3.75.

Compound 6f

Yield: 89%. Yellow solid; mp 159–161 °C. IR (neat) ν_{max}: 2920, 1588 cm^{-1}. ^1H NMR ($CDCl_3$, 400 MHz) δ: 2.29(s, 6H), 3.41 (d, *J* = 5.86 Hz, 2H), 3.95 (s, 3H), 5.28 (s, 2H), 6.05(t, *J* = 5.89 Hz, 1H), 6.68–8.43 (m, 6H) ppm. MS *m/z*: 397, 399 [M+]. Anal. calcd. for $C_{22}H_{20}ClNO_2S$: C, 66.40; H, 5.07; N, 3.52; found C, 66.52; H, 5.11; N, 3.41.

Compound 6g

Yield: 81%. Yellow solid; mp 135–137 °C. IR (neat) ν_{max}: 2927, 1586 cm^{-1}. ^1H NMR ($CDCl_3$, 400 MHz) δ: 1.45 (t, *J* = 7.26 Hz, 3H), 2.25 (s, 3H), 3.40 (d, *J* = 5.96 Hz, 2H), 4.50 (q, *J* = 7.24 Hz, 2H), 5.24 (s, 2H), 6.07 (t, *J* = 5.94 Hz, 1H), 6.69–8.44 (m, 7H) ppm. MS *m/z*: 397, 399 [M+]. Anal. calcd. for $C_{22}H_{20}ClNO_2S$: C, 66.40; H, 5.07; N, 3.52; found C, 66.25; H, 5.11; N, 3.47.

Compound 6h

Yield: 79%. Yellow solid; mp 126–127 °C. IR (neat) ν_{max}: 2932, 1592 cm^{-1}. ^1H NMR ($CDCl_3$, 400 MHz) δ: 1.42 (t, *J* = 7.15 Hz, 3H), 2.35 (s, 6H), 3.44 (d, *J* = 5.97 Hz, 2H), 4.52 (q, *J* = 7.17 Hz, 2H), 5.26 (s, 2H), 6.04 (t, *J* = 5.88 Hz, 1H), 6.69–8.49 (m, 6H) ppm. MS *m/z*: 411, 413 [M+]. Anal. calcd. for $C_{23}H_{22}ClNO_2S$: C, 67.06; H, 5.38; N, 3.40; found C, 66.93; H, 5.39; N, 3.24.

Rearrangement of compounds 5a–5f and 6e–6h

Anhydrous $AlCl_3$ (0.025 mmol) was added to a solution of **5a** (0.25 mmol) in dry dichloromethane (10 mL) under nitrogen atmosphere and stirred at room temperature for 30–45 min. Dichloromethane (20 mL) and crushed ice were added to the reaction mixture. Dichloromethane layer was washed with water (2 × 10 mL), brine (10 mL), and dried over anhyd. Na_2SO_4. The solvent was distilled off and the residue was subjected to column chromatography over silica gel. Elution of the column with petroleum ether/ethyl acetate afforded compound **12a**. Products **12b**–**12f** and **13e**–**13h** were also similarly obtained. These products were recrystallized from dichloromethane/petroleum ether.

Compound 12a

Yield: 79%. Light yellow solid; mp 160–161 °C. IR (neat) ν_{max}: 2947, 1627 cm^{-1}. ^1H NMR ($CDCl_3$, 500 MHz) δ: 1.96 (s, 3H), 2.25 (s, 3H), 3.46 (dd, *J* = 4.64 and 8.97 Hz, 1H), 3.70 (s, 3H), 4.06 (t, *J* = 9.09 Hz, 1H), 4.45 (dd, *J* = 4.64 and 11.24 Hz, 1H), 6.78–7.95 (m, 7H) ppm. MS *m/z*: 333 [M+]. Anal. calcd. for $C_{21}H_{19}NO_3$: C, 75.66; H, 5.74; N, 4.20; found C, 75.69; H, 5.57; N, 4.03.

Compound 12b

Yield: 75%. Light yellow solid; mp 177–178 °C. IR (neat) ν_{max}: 2952, 1613 cm^{-1}. ^1HNMR ($CDCl_3$, 400 MHz) δ: 1.82 (s, 3H), 2.23 (s, 3H), 2.33 (s, 3H), 3.43 (dd, *J* = 4.52 and 8.02 Hz, 1H), 3.59 (t, *J* = 9.04 Hz, 1H), 3.71 (s, 3H),), 4.54 (dd, *J* = 4.65 and 11.18 Hz, 1H), 6.61–7.98 (m, 6H) ppm. ^{13}CNMR ($CDCl_3$, 125 MHz) δ: 15.6, 18.6, 23.6, 29.5, 48.4, 66.7, 82.5, 109.9, 114.2, 115.9, 118.8, 121.9, 122.0, 123.7, 124.3, 130.8, 131.8, 132.5, 139.8, 157.0, 159.0, 162.2. MS *m/z*: 347 [M+]. Anal. calcd. for $C_{22}H_{21}NO_3$: C, 76.06; H, 6.09; N, 4.03; found C, 75.94; H, 6.13; N, 4.14.

Compound 12c

Yield: 72%. Light yellow solid; mp 203–205 °C. IR (neat) ν_{max}: 2956, 1615 cm^{-1}. ^1H NMR ($CDCl_3$, 400 MHz) δ: 2.03 (s, 3H), 3.55 (dd, *J* = 4.49 and 8.56 Hz, 1H), 3.69 (s, 3H), 4.11 (t, *J* = 8.70 Hz, 1H), 4.45 (dd, *J* = 4.64 and 11.35 Hz, 1H), 6.80–7.93 (m, 7H) ppm. MS *m/z*: 353, 355 [M+]. Anal. calcd. for $C_{20}H_{16}ClNO_3$: C, 67.90; H, 4.56; N, 3.96; found C, 67.71; H, 4.46; N, 4.24.

Compound 12d

Yield: 76%. Light yellow solid; mp 184–186 °C. IR (neat) ν_{max}: 2955, 1631 cm^{-1}. ^1H NMR ($CDCl_3$, 400 MHz) δ: 1.32 (t, *J* = 7.09 Hz, 3H), 1.95 (s, 3H), 2.23(s, 3H), 3.44 (dd, *J* = 4.52 and 8.88 Hz, 1H), 4.04 (t, *J* = 9.07 Hz, 1H), 4.31 (q, *J* = 7.4 Hz, 2H), 4.43(dd, *J* = 4.60 and 11.22 Hz, 1H), 6.76–7.95 (m, 7H) ppm. MS *m/z*: 347 [M+]. Anal. calcd. for $C_{22}H_{21}NO_3$: C, 76.06; H, 6.09; N, 4.03; found C, 76.15; H, 6.22; N, 4.09.

Compound 12e

Yield: 82%. Light yellow solid; mp 168–170 °C. IR (neat) ν_{max}: 2967, 1624 cm^{-1}. ^1H NMR ($CDCl_3$, 500 MHz) δ: 1.98 (s, 3H), 2.29 (s, 3H), 3.46(dd, *J* = 4.33 and 8.03 Hz, 1H), 3.69(s, 3H),), 4.05 (t, *J* = 9.99 Hz, 1H), 4.43 (dd, *J* = 4.30 and 11.31 Hz, 1H), 6.79–7.95 (m, 6H) ppm. MS *m/z*: 367, 369 [M+]. Anal. calcd. for $C_{21}H_{18}ClNO_3$: C, 68.57; H, 4.93; N, 3.81; found C, 68.79; H, 5.07; N, 3.73.

Compound 12f

Yield: 83%. Light yellow solid; mp 163–164 °C. IR (neat) ν_{max}: 2926, 1617 cm^{-1}. ^1H NMR ($CDCl_3$, 500 MHz) δ: 1.84 (s, 3H), 2.33 (s, 3H), 2.40 (s, 3H), 3.44 (dd, *J* = 5.08 and 12.09 Hz, 1H), 3.62 (t, *J* = 11.05 Hz, 1H), 3.72 (s, 3H),), 4.53 (dd, *J* = 5.18 and 13.20 1H), 6.74–7.99 (m, 5H) ppm. MS *m/z*: 381; 383 [M+]. Anal. calcd. for $C_{22}H_{20}ClNO_3$: C, 69.20; H, 5.28; N, 3.67; found C, 69.17; H, 5.26; N, 3.89.

© 2007 NRC Canada

Compound 13e

Yield: 75%. Yellow solid; mp 186–188 °C. IR (neat) ν_{max}: 2943, 1599 cm^{-1}. ^1H NMR ($CDCl_3$) δ: 1.88 (s, 3H), 2.31 (s, 3H), 2.80 (t, *J* = 12.48 Hz, 1H), 3.00 (dd, *J* = 3.58 and 13.13 Hz, 1H), 3.33 (dd, *J* = 3.11 and 11.71 Hz, 1H), 3.87 (s, 3H), 6.79–8.52 (m, 6H) ppm. MS *m/z*: 383, 385 [M^+]. Anal. calcd. for $C_{21}H_{18}ClNO_2S$: C, 65.70; H, 4.73; N, 3.65; found C, 65.79; H, 4.67; N, 3.63.

Compound 13f

Yield: 72%. Yellow solid; mp 175–177 °C. IR (neat) ν_{max}: 2921, 1595 cm^{-1}. ^1H NMR ($CDCl_3$, 500 MHz) δ: 1.81 (s, 3H), 2.32 (s, 3H), 2.39 (s, 3H), 2.67 (t, *J* = 12.79 Hz, 1H), 2.95 (dd, *J* = 3.69 and 13.11 Hz, 1H), 3.28 (dd, *J* = 3.51 and 12.47 Hz, 1H), 3.88 (s, 3H), 6.74–8.52 (m, 5H) ppm. ^{13}C NMR ($CDCl_3$, 125 MHz) δ: 17.3, 21.8, 24.4, 29.7, 36.2, 51.9, 88.1, 111.5, 114.9, 117.8, 124.0, 126.0, 126.6, 126.8, 128.0, 132.5, 132.6, 137.6, 141.5, 152.7, 155.6, 175.2. MS *m/z*: 397, 399 [M^+]. Anal. calcd. for $C_{22}H_{20}ClNO_2S$: C, 66.40; H, 5.07; N, 3.52; found C, 66.33; H, 5.11; N, 3.41.

Compound 13g

Yield: 79%. Yellow solid; mp 210–212 °C. IR (neat) ν_{max}: 2951, 1586 cm^{-1}. ^1H NMR ($CDCl_3$, 400 MHz) δ: 1.42 (t, *J* = 6.77 Hz, 3H), 1.86 (s, 3H), 2.31(s, 3H), 2.71 (t, *J* = 12.81 Hz, 1H), 2.96 (dd, *J* = 3.05 and 12.95 Hz, 1H), 3.32 (dd, *J* = 2.89 and 11.25 Hz, 1H), 4.27–4.35 (m, 1H), 4.50–4.57 (m, 1H), 6.79–8.54 (m, 6H) ppm. MS *m/z*: 397, 399 [M^+]. Anal. calcd. for $C_{22}H_{20}ClNO_2S$: C, 66.40; H, 5.07; N, 3.52; found C, 66.54; H, 5.04; N, 3.57.

Compound 13h

Yield: 73%. Yellow solid; mp 195–197 °C. IR (neat) ν_{max}: 2943, 1591 cm^{-1}. ^1H NMR ($CDCl_3$, 500 MHz) δ: 1.46 (t, *J* = 6.79 Hz, 3H), 1.82 (s, 3H), 2.33 (s, 3H), 2.40 (s, 3H), 2.69 (t, *J* = 12.79 Hz, 1H), 2.94 (dd, *J* = 3.07 and 12.98 Hz, 1H), 3.29 (dd, *J* = 2.68 and 12.22 Hz, 1H), 4.29–4.37 (m, 1H), 4.51–4.59 (m, 1H), 6.77–8.55 (m, 5H) ppm. MS *m/z*: 411; 413 [M^+]. Anal. calcd. for $C_{23}H_{22}ClNO_2S$: C, 67.06; H, 5.38; N, 3.40; found C, 67.30; H, 5.57; N, 3.27.

Acknowledgements

We thank the Council of Scientific and Industrial Research (CSIR) (New Delhi) for financial assistance. A.K.P. is grateful to CSIR (New Delhi) for a senior research fellowship. We also thank the Department of Science and Technology (DST) (New Delhi) for providing IR spectrometer under the Financial Assistant for Infracstructural Development of Science and Technology (FIST) program.

References

1. C.F Neville, M.F. Grundon, V.N. Ramchandran, G. Reisch, and J. Reisch. J. Chem. Soc., Perkin Trans. 1, 2261 (1991).
2. (*a*) R.W. Carling, P.D. Lesson, K.W. Moore, J.D. Smith, C.R. Moyes, J.M. Mower, S. Thomas, T. Chan, R. Braker, A.C. Foster, S. Grimwood, J.A. Kemp, G.K. Marshall, M.T. Tricklebank, and K.L. Saywell. J. Med. Chem. **36**, 3386 (1993); (*b*) A.M. Mcleod, S. Grimwood, C. Barton, L. Bristow, K.L. Saywell, G.R. Marshall, and R.G. Ball. J. Med. Chem. **38**, 2239 (1995).
3. J.J. Kugalowski, R. Baker, N.R. Curtis, P.D. Lesson, I. Stansfield, A.C. Foster, S. Grimwood, R.G. Hill, J.A. Kemp, G.R. Marshall, K.L. Saywell, and M.D. Tricklebank. J. Med. Chem. **37**, 1402 (1994).
4. (*a*) R.F.C. Brown, J.J. Hobbs, G.K. Hughes, and E. Ritchie. Aust. J. Chem. **7**, 348 (1954); (*b*) R.F.C. Brown, G.K. Hughes, and E. Ritchie. Chem. Ind. (London) 1385 (1955); (*c*) D. Lavie, N. Danieli, R. Weitman, and E. Glotter. Tetrahedron, **4**, 3011 (1968); (*d*) D.L. Dreyer, and A. Lee. Phytochemistry, **11**, 763 (1972); (*e*) D.R. Taylor, and J.M. Warner. Phytochemistry, **12**, 1359 (1973); (*f*) L. Jurd and M. Benson. J. Chem. Soc., Chem. Commun. 92 (1983).
5. (*a*) J.W. Huffman, and T.M. Hsu. Tetrahedron Lett. 141 (1972); (*b*) A. Groot and B.J.M. Jansen. Tetrahedron Lett. 3407 (1975); (*c*) R.M. Bowman, M.F. Grundon, and K.J. James. J. Chem. Soc., Perkin Trans. 1, 1055 (1973).
6. (*a*) B.S. Thyagarajan. Adv. Heterocyclic Chem. **8**, 143 (1967); (*b*) J.E. Macor, O.D. Langer, J.Z. Gougoutas, M.F. Melley, and L.A.M. Cornelius. Tetrahedron Lett. **41**, 3541 (2000); (*c*) S.C. Ghosh and A. De. J. Chem. Soc., Perkin Trans. 1, **24**, 3705 (1999); (*d*) E.W. Baxter, D. Labaree, H.L. Ammon, and P.S. Mariano. J. Am. Chem. Soc. **112**, 7682 (1990); (*e*) Y. Tamaru, T. Harada, and Z. Yoshida. J. Am. Chem. Soc. **102**, 2392 (1980); (*f*) R.M. Lemieux and A.I. Meyers. J. Am. Chem. Soc. **120**, 5453 (1998).
7. (*a*) D.K. Bates and M.W. Janes. J. Org. Chem. **43**, 3856 (1978); (*b*) R.P. Lutz. Chem. Rev. **84**, 205 (1984); (*c*) K. Nonoshita, K., Banno, H., Maruoka, K., and Yamamoto, H. J. Am. Chem. Soc. **112**, 316 (1990); (*d*) F. Zulfiqur, and T. Kitazumi. Green Chem. **2**, 296 (2002).
8. (*a*) K.C. Majumdar, R.N. De, A.T. Khan, S.K. Chattopadhyay, and A. Patra. J. Chem. Soc., Chem. Commun. 777 (1988); (*b*) K.C. Majumdar and S.K. Ghosh. Tetrahedron Lett. **43**, 2115 (2002); (*c*) K.C. Majumdar and T. Bhattacharyya. Tetrahedron Lett. **42**, 4231 (2001).
9. (*a*) K.C. Majumdar, A. Bandyopadhyay, and A. Biswas. Tetrahedron, **59**, 5289 (2003); (*b*) K.C. Majumdar, A.T. Khan, and S. Saha. Synlett, 595 (1991).
10. K.C. Majumdar, and G.H. Jana. Synthesis, 924 (2001).
11. K.C. Majumdar, and U. Das. J. Org. Chem. **63**, 9997 (1998).
12. K.C. Majumdar, U.K. Kundu, and S.K. Ghosh. Org. Lett. **4**, 2629 (2002).

© 2007 NRC Canada

Erratum / Erratum

The use of β-cyclodextrins to enhance the aqueous solubility of trichloroethylene and perchloroethylene and their removal from soil organic matter — Effect of substituents

Salma Shirin, Erwin Buncel, and Gary W. vanLoon

Ref: Can. J. Chem. **81**(1): 45–52 (2003).

In the paper above, Table 3 was inadvertently omitted during the publication process. It is reproduced here in its entirety.

Table 3. Binding constants, K11 (M^{-1}), of TCE and PCE with different substituted CDs.

	K11 of TCE obtained from ^{1}H NMR experiment[a]	K11 of TCE obtained from solubility enhancement[b]	K_{11} of PCE obtained from solubility enhancement
HPβ-CD	60 ± 8	61 ± 4	400 ± 8
Mβ-CD	120 ± 1	114 ± 8	330 ± 14
Sβ-CD1	44 ± 3	57 ± 5	260 ± 17
Sβ-CD2	3.0	1.5 ± 0.2	2.0 ± 3.0
CMβ-CD1	31 ± 1	28 ± 4	270 ± 33
CMβ-CD2	20 ± 3	29 ± 0.6	56 ± 7

[a]Associated error is the deviation from the mean of duplicate experiments.
[b]Associated error is the standard error of the slope of linear regression analysis at the 95% confidence interval.

We apologize for any inconvenience.

Received 10 December 2007. Published on the NRC Research Press Web site at canjchem.nrc.ca on 8 January 2008.

S. Shirin, E. Buncel, and G.W. vanLoon.[1] Department of Chemistry, Queen's University, Kingston, ON K7L 3N6, Canada.

[1]Corresponding author (e-mail: vanloon@chem.queensu.ca).

 doi:10.1139/V07-144 © 2008 NRC Canada

Co-operative hydration of the carbonyl group — "Bifunctional catalysis" by 2-hydroxypyridine is achieved via a dihydrate of 2-pyridone

Yih-Huang Hsieh, Noham Weinberg, and Saul Wolfe

Abstract: Although 2-hydroxypyridine is one thousand times less acidic than its isomer 3-hydroxypyridine and ten million times less acidic than acetic acid, in the aqueous hydration of 1 mol/L acetone at 298 K the catalytic effect of added 2-hydroxypyridine is 600 000 times greater than that of 3-hydroxypyridine and 20 times greater than that of acetic acid. This experimental result is successfully reproduced by a theoretical treatment that assumes that solvent molecules participate in a cyclic cooperative mechanism that avoids the formation of charged intermediates. However, the theoretical treatment does not support the seemingly obvious conclusion that the origin of the enhanced catalytic activity of 2-hydroxypyridine lies in its bifunctional nature. Rather, this enhanced catalytic activity can be traced to the exceptional thermodynamic stability of the principal reactant complex, which contains a dihydrate of 2-pyridone.

Key words: hydration, isotope shift, bifunctional, cooperativity, cyclic mechanism, ab initio, SCRF

Résumé : Même si la 2-hydroxypyridine est mille fois moins acide que son isomère, la 3-hydroxypyridine, et dix millions de fois moins acide que l'acide acétique, l'effet catalytique provoqué par l'addition de 2-hydroxypyridine sur la réaction d'hydratation aqueuse d'une solution 1 mol/L d'acétone à 298 K est 600 000 fois plus grand que celui de la 3-hydroxypyridine et que 20 fois celui de l'acide acétique. On peut facilement reproduire ce résultat expérimental par un traitement théorique qui fait l'hypothèse que les molécules de solvant participent à un mécanisme coopératif cyclique qui évite la formation d'intermédiaires chargés. Toutefois, le traitement théorique n'apporte aucun support à la conclusion qui paraît évidente que l'origine de l'activité catalytique élevée de la 2-hydroxypyridine tient à sa nature bifonctionnelle. Cette activité catalytique élevée est plutôt attribuée à la stabilité thermodynamique exceptionnelle du complexe réactif principal qui contient un dihydrate de la 2-pyridone.

Mots-clés : hydratation, déplacement isotopique, bifonctionnel, coopération, mécanisme cyclique, ab initio, champ réactionnel autocohérent (CRAC).

[Traduit par la Rédaction]

Introduction

We have recently reported that the neutral hydration of a carbonyl group in water solvent *does not proceed via ionic intermediates* (1). Instead, as originally suggested by Eigen and by Long and co-workers (2), a cyclic *cooperative* process (e.g., eq. [1]) in which concurrent C–O bond formation and proton transfer to oxygen take place through a solvent bridge, comprises a neutral alternative that avoids the need to solvate and desolvate charged species continuously as these species appear and disappear.

The mechanism depicted in eq. [1] seems superficially to resemble eq. [2], "bifunctional" acid-base catalysis of the anomerization of tetramethylglucose (3), and other reactions (4) that are coupled to 2-hydroxypyridine/2-pyridone tautomerism within a cyclic neutral complex. However, unlike eq. [1], bifunctional catalysis by 2-hydroxypyridine requires a *nonaqueous* nonpolar environment that resembles the "water-repelling lipid-like" active site of an enzyme (5, cited in ref. 6), and this has led to the suggestion that "enzyme model studies in nonpolar solvents are … more relevant than similar studies in aqueous media" (5).

[1] 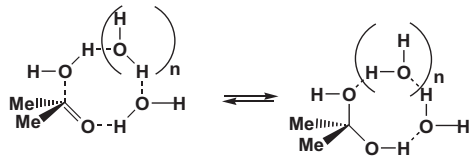

Received 17 April 2007. Accepted 7 June 2007. Published on the NRC Research Press Web site at canjchem.nrc.ca on 24 August 2007.

This paper is dedicated to the memory of Keith Yates, a good friend, wise editor, and father of modern physical organic chemistry in Canada.

Y.-H. Hsieh,[1] N. Weinberg,[2] and S. Wolfe.[3] Department of Chemistry, Simon Fraser University, Burnaby, BC V5A 1S6, Canada.

[1]Industrial Technology Research Institute, Hsin-Chu, Taiwan, 300 R.O.C.
[2]Department of Chemistry, University College of the Fraser Valley, Abbotsford, BC V2S 7MA, Canada.
[3]Corresponding author (email: swolfe@sfu.ca).

 doi:10.1139/V07-074 © 2007 NRC Canada

[2] 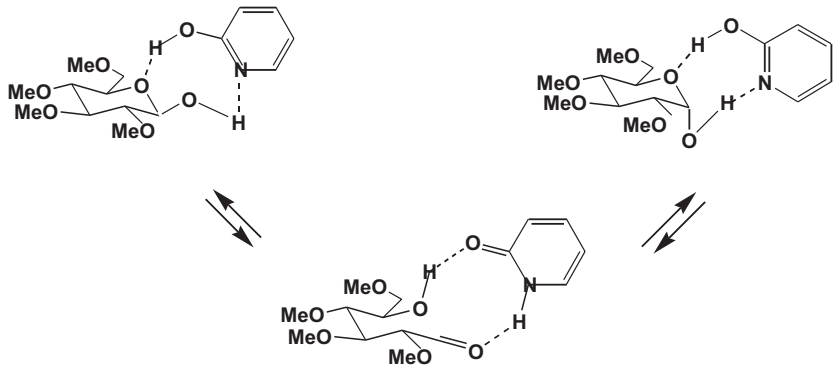

In the present paper we provide experimental evidence of substantial catalysis of the aqueous hydration of acetone by added 2-hydroxypyridine together with continued theoretical support for the notion of cooperativity in this reaction. However, the theoretical analysis also leads to the unexpected conclusion that the catalysis does not originate in the bifunctional nature of 2-hydroxypyridine, so that the aqueous and gas-phase (7) catalytic mechanisms are not the same.

Materials and methods

2-Hydroxypyridine (Sigma-Aldrich) and 3-hydroxypyridine (Sigma-Aldrich) were recrystallized from ethyl acetate-hexane. $H_2{}^{16}O$ was obtained from an Easypure UV/UF ultra pure water system. $H_2{}^{18}O$ (95% enriched) was purchased from Sigma-Aldrich. $D_2{}^{16}O$ (99.99% enriched) was obtained from CDN isotopes, Pointe Claire, Quebec. $H_2{}^{18}O$ (49.1% enriched), prepared by mixing $H_2{}^{18}O$ (2.2995 g, 95% enriched) with $H_2{}^{16}O$ (2.1714 g), was stored at –20 °C in a five-dram vial fitted with a Teflon pad. Acetone-2-^{13}C (1.0 g, 98% enriched, Sigma-Aldrich) was transferred by syringe into 50 microcapillary tubes which were sealed and stored at room temperature (22 °C).

Kinetic measurements

NMR spectra were recorded on a Bruker 600 AMX spectrometer operating at a frequency of 150.03 MHz. The probe temperature was maintained at 298.0 ± 0.1 K using a Euroterm VT temperature regulator. All runs were performed in the same 2.0 mm diameter micro NMR tube. Before every run, the tube was rinsed with acetone and water, oven dried at 110 °C for at least 15 min, and then cooled in vacuo for an additional 30 min.

Proton decoupled ^{13}C NMR spectra were recorded as a single scan at different times to obtain the peaks of $(CH_3)_2{}^{13}C={}^{16}O$ [^{16}O] and $(CH_3)_2{}^{13}C={}^{18}O$ [^{18}O], whose chemical shifts differ by 0.05 ppm (1*b*, 1*c*). These spectra were integrated to obtain the [^{18}O]/[^{16}O] ratio (ρ) as a function of time.

The pseudo first-order rate constant k_{obs} for 2-hydroxypyridine was obtained from the kinetic data by nonlinear least-squares fit to eq. [3*a*] (1*c*) using Version 3.07 of the computer programme GRAFIT (Erithacus Software Ltd., P. O. Box 274, Horley Surrey, UK, RH6 9YJ).

$$[3a] \quad \frac{1}{1+\rho} = Ae^{-k_{obs}t} + C$$

In the case of 3-hydroxypyridine, where the reaction was significantly slower and did not approach equilibrium, the rate constant k_{obs} was obtained from a linear least-squares fit to eq. [3*b*] (1*b*), which is derived from eq. [3*a*] when the equilibrium value of ρ is 1.

$$[3b] \quad \ln\left(\frac{1-\rho}{1+\rho}\right) - k_{obs}t + \ln\left(\frac{1-\rho_0}{1+\rho_0}\right)$$

Experiments with 2-hydroxypyridine (2-HP)

2-Hydroxypyridine (104.6 mg, 1.10 mmol), in $H_2{}^{16}O$, was diluted to 25.00 mL to give a 44.04 mmol/L solution, 2.50 mL of this solution were diluted to 25.00 mL with $H_2{}^{16}O$ to give a 4.40 mmol/L solution, 2.50 mL of the 4.40 mmol/L solution were diluted to 25.00 mL with $H_2{}^{16}O$ to give a 0.44 mmol/L solution, and 0.1596 g (8.9 mmol) of this solution was added to $H_2{}^{18}O$ (0.1800 g, 9.0 mmol, 95.0% enriched) to give 50.4% ^{18}O-enriched water. To begin a run, 8.0 µL of acetone-2-^{13}C (6.4 µg, 0.11 µmol, 98% enriched) were injected into 100.0 µL of the above solution to give a solution of 1.0 mol/L in acetone and 0.22 mmol/L in 2-hydroxypyridine. This solution was transferred immediately to the micro NMR tube and the spectra were recorded.

Experiments with 3-hydroxypyridine (3-HP)

3-Hydroxypyridine (26.0 mg, 0.27 mmol) was dissolved in 10.00 mL of $H_2{}^{16}O$ to give a 2.7×10^{-2} mol/L solution, and 47.0 µL of this solution were injected into $H_2{}^{18}O$ (53.0 µL, 95.0% enriched) to give a 1.3×10^{-2} mol/L 3-hydroxypyridine solution in 50.4% enriched $H_2{}^{18}O$. To begin a run, 8.0 µL of acetone-2-^{13}C (6.4 µg, 0.11 µmol, 98% enriched) were injected into 100.0 µL of the 3-hydroxypyridine solution to give a solution 1.0 mol/L in acetone and 1.3×10^{-2} mol/L in 3-hydroxypyridine. This solution was transferred immediately to the micro NMR tube and the spectra were recorded.

Computational details

Calculations were performed using Gaussian 98 (8) at the Hartree–Fock level with the 3–21G basis set (9). The nature of the fully optimized stationary points was verified using

© 2007 NRC Canada

frequency analysis. All transition structures exhibited one imaginary frequency.[4]

As in our previous work (1) the SCRF (Onsager) model (10, 11) was used to describe water solvent with a dielectric constant of 78.5. Free energies of bimolecular processes were corrected for the loss of translational and rotational degrees of freedom and were calculated using eq. [4] as described in refs. 1*a* and 1*b*.

$$[4]\qquad \Delta G = \Delta H - T\Delta S_{\text{vib}} - \\ -6RT\left\{\frac{\hbar\omega/kT}{\exp(\hbar\omega/kT)-1} - \ln\left[1-\exp\left(\frac{\hbar\omega}{kT}\right)\right]\right\}$$

The first term on the right is the enthalpy change calculated by the Gaussian programme corrected for the basis set superposition error (BSSE) (1, 12) associated with the use of the 3–21G basis set. The second term on the right accounts for the intramolecular vibration entropy change and is also calculated by the Gaussian programme. The third term on the right describes the entropy change because of the loss of six low-frequency vibration modes representing rotational and translational motions in solution. These vibrations are described by a mass-dependent effective frequency ω, scaled as a root of molecular mass (1*b*),

$$\omega = \omega_0\sqrt{m/m_0}$$

and defined in terms of a single adjustable parameter ω_0, that is estimated numerically for water monomer (m_0 = 18 au) to be ca 20 cm^{-1} (1*a*).

As a first step, the treatment of the cooperative *neutral* hydration of a carbonyl compound included the calculation of the free energies of each of the stationary structures and the equilibrium and rate constants shown in Scheme 1 in water solvent, wherein W_nC is a cyclic complex of a carbonyl compound C (RR′C=O) with n water molecules (n = 1–4), and $(TS)_n$ is a cyclic transition structure derived from W_nC.

The assumption that the water clusters W_n are in rapid equilibrium with each other and with the W_nC complexes allow the effective pseudo first-order rate constant k to be expressed as,

$$[5]\qquad k = \frac{\sum k_n[W_nC]}{[C]+[W_nC]} = \frac{\sum k_n K_n K_n^w [W_1]^n}{1+\sum K_n K_n^w [W_1]^n}$$

In eq. [5] the equilibrium constants K_n^w relate the concentrations of water clusters $[W_n]$ to the concentration of water monomer $[W_1]$, which can be expressed in terms of C_w, the overall concentration of water, by eq. [6],

$$[6]\qquad \sum K_n^w [W_1]^n = C_w$$

To extend this protocol to the hydration of acetone in the presence of 2-hydroxypyridine, Scheme 1 has to be expanded to Scheme 2, which includes monohydrates and dihydrates (13) of 2-hydroxypyridine (2-HP) and its 2-pyridone tautomer (2-PD) (14).

Scheme 1.

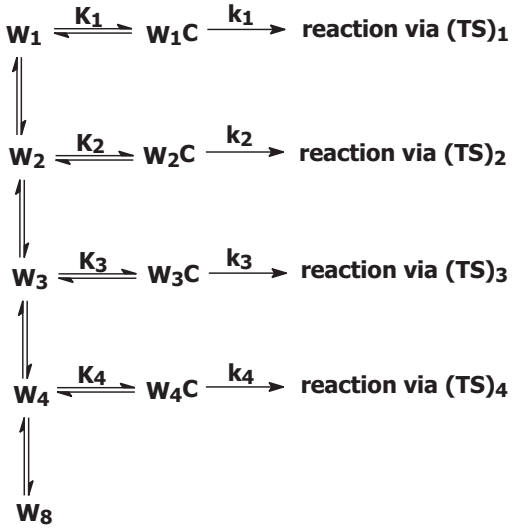

Here, as in Scheme 1, W_n, W_nC, and TS_n are water clusters, acetone–water complexes, and associated transition states, respectively. The unhydrated tautomers H (≡2-HP) and P (≡2-PD) are in equilibrium with each other and with their dimers H_nP_m ($n + m = 2$, structures **9a**–**9c**) (15), as well as with their monohydrates $W_1H\mu$ (μ = 1–4, structures **1a**–**1d**) and $W_1P\mu$ (μ = 1–3, structures **3a**–**3c**), and dihydrates $W_2H\mu$ (μ = 1–5, structures **2a**–**2e**), and $W_2P\mu$ (μ = 1, structure **4a**); $W_1HC\mu$ (μ = 1–2, structures **5a** and **5b**), $W_2HC\mu$ (μ = 1–4, structures **6a**–**6d**), $W_1PC\mu$ (μ = 1, structure **7**), and $W_2PC\mu$ (μ = 1–2, structures **8a** and **8b**) are acetone–water catalyst complexes, and TSH1μ, TSH2μ, TSP1μ, and TSP2μ are the transition structures of the catalyzed channels.

With K_n, K_τ, K_{nm}^{D}, K_n^{W}, $K_{n\mu}^{WH}$, $K_{n\mu}^{WP}$, $K_{n\mu}^{H}$, and $K_{n\mu}^{P}$ as the equilibrium constants, the following relationships exist among the equilibrium concentrations of the components of Scheme 2:

$$[P] = K_\tau[H]$$

$$[H_nP_m] = K_{nm}^{D}[H]^n[P]^m = (K_\tau)^m K_{nm}^{D}[H]^2$$

$$[W_nH\mu] = K_{n\mu}^{WH}[W_n][H] = K_{nm}^{WH}K_n^{W}[H][W_1]^n$$

$$[W_nP\mu] = K_{n\mu}^{WP}[W_n][P] = K_\tau K_{nm}^{WP}K_n^{W}[H][W_1]^n$$

$$[7]\qquad [W_nC] = K_n[W_n][C] = K_nK_n^{W}[C][W_1]^n$$

$$[8]\qquad [W_nHC\mu] = K_{n\mu}^{H}[W_nH\mu][C] \\ = K_{n\mu}^{H}K_{n\mu}^{WH}K_n^{W}[C][H][W_1]^n$$

[4] Supplementary data for this article are available on the journal Web site (canjchem.nrc.ca) or may be purchased from the Depository of Unpublished Data, Document Delivery, CISTI, National Research Council Canada, Ottawa, ON K1A 0R6, Canada. DUD 5198. For more information on obtaining material refer to cisti-icist.nrc-cnrc.gc.ca/irm/unpub_e.shtml.

© 2007 NRC Canada

Scheme 2.

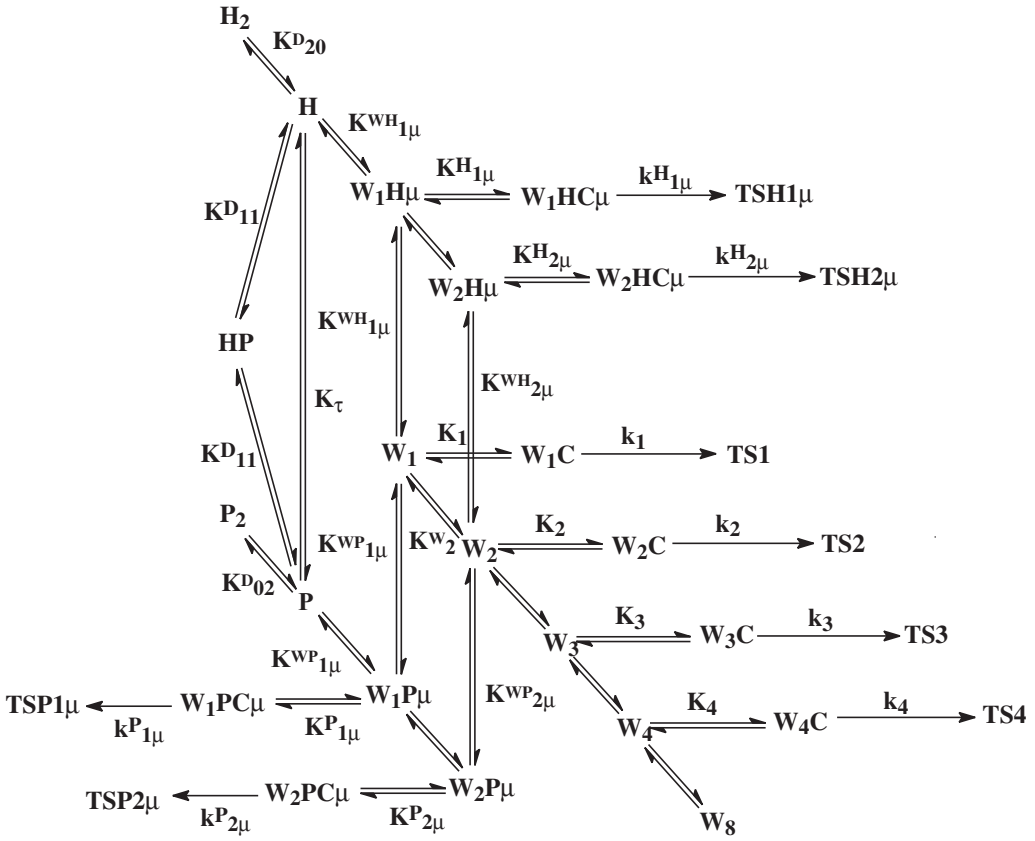

$$[9]\qquad [W_nPC\mu] = K^{P}_{n\mu}[W_nP\mu][C] = K_\tau K^{P}_{n\mu} K^{WP}_{n\mu} K^{W}_{n}[C][H][W_1]^n$$

Results

Hydration kinetics

Figures 1–4) show the kinetics of hydration of 1.0 mol/L aqueous solutions of acetone at 298 K in the presence of 2×10^{-4} mol/L 2-hydroxypyridine (Table 1) and 1.3×10^{-2} mol/L 3-hydroxypyridine (Table 2). The rate constants shown in these tables and figures contain contributions from k_o, the neutral reaction, and from $k_A C_A$, the catalyzed reaction (eq. [10]).[5] Table 3 collects the k_A determined in this work, together with those obtained in our previous work for HA = HOH and HOAc (1*b*, 1*c*).

$$[10]\qquad k_{obs} = k_o + k_A C_A$$

Although 2-HP is one thousand times less acidic than its isomer 3-HP and ten million times less acidic than acetic acid in the aqueous hydration of 1 mol/L acetone at 298 K, 2-HP is 600 000 times more reactive than 3-HP and 20 times more reactive than acetic acid. This would seem to constitute a priori evidence of bifunctional catalysis in water solvent.

The theoretical rate constant

The equilibrium and rate constants of Scheme 2 that are needed for the computation of the overall rate constant and the contributions to this rate constant from the different channels were obtained from the calculated thermodynamic data collected in Tables 4–8.

The overall reaction rate v is a sum of partial reaction rates arising from the reactant complexes $[W_nC]$, $[W_nHC\mu]$, and $[W_nPC\mu]$,

$$v = \sum_n k_n[W_nC] + \sum_{n,\mu} k^{H}_{n\mu}[W_nHC\mu] + \sum_{n,\mu} k^{P}_{n\mu}[W_nPC\mu]$$

Here k_n are partial rate constants for the neutral channels and $k^{H}_{n\mu}$ and $k^{P}_{n\mu}$ are partial rate constants for the catalyzed channels. Equations [7]–[9] allow the rate of the reaction to be expressed in terms of the concentrations of water monomer $[W_1]$, acetone [C], and 2-hydroxypyridine [H],

$$[11]\qquad v = \sum_n k_n K_n K^{W}_{n}[C][W_1]^n + \sum_{n,\mu} k^{H}_{n\mu} K^{H}_{n\mu} K^{WH}_{n\mu} K^{W}_{n}[C][H][W_1]^n + \sum_{n,\mu} k^{P}_{n\mu} k_\tau K^{P}_{n\mu} K^{WP}_{n\mu} K^{W}_{n}[C][H][W_1]^n$$

These concentrations were found as numerical solutions of a set of material balance equations for the overall concentrations of water (CW), acetone (CC), and 2-hydroxypyridine (CA),

$$C_C = [C] + \sum_n [W_nC] + \sum_{n,\mu} [W_nHC\mu] + \sum_{n,\mu} [W_nPC\mu]$$

[5] Under our experimental conditions $[H_3O^+]$ « [hydroxypyridine].

© 2007 NRC Canada

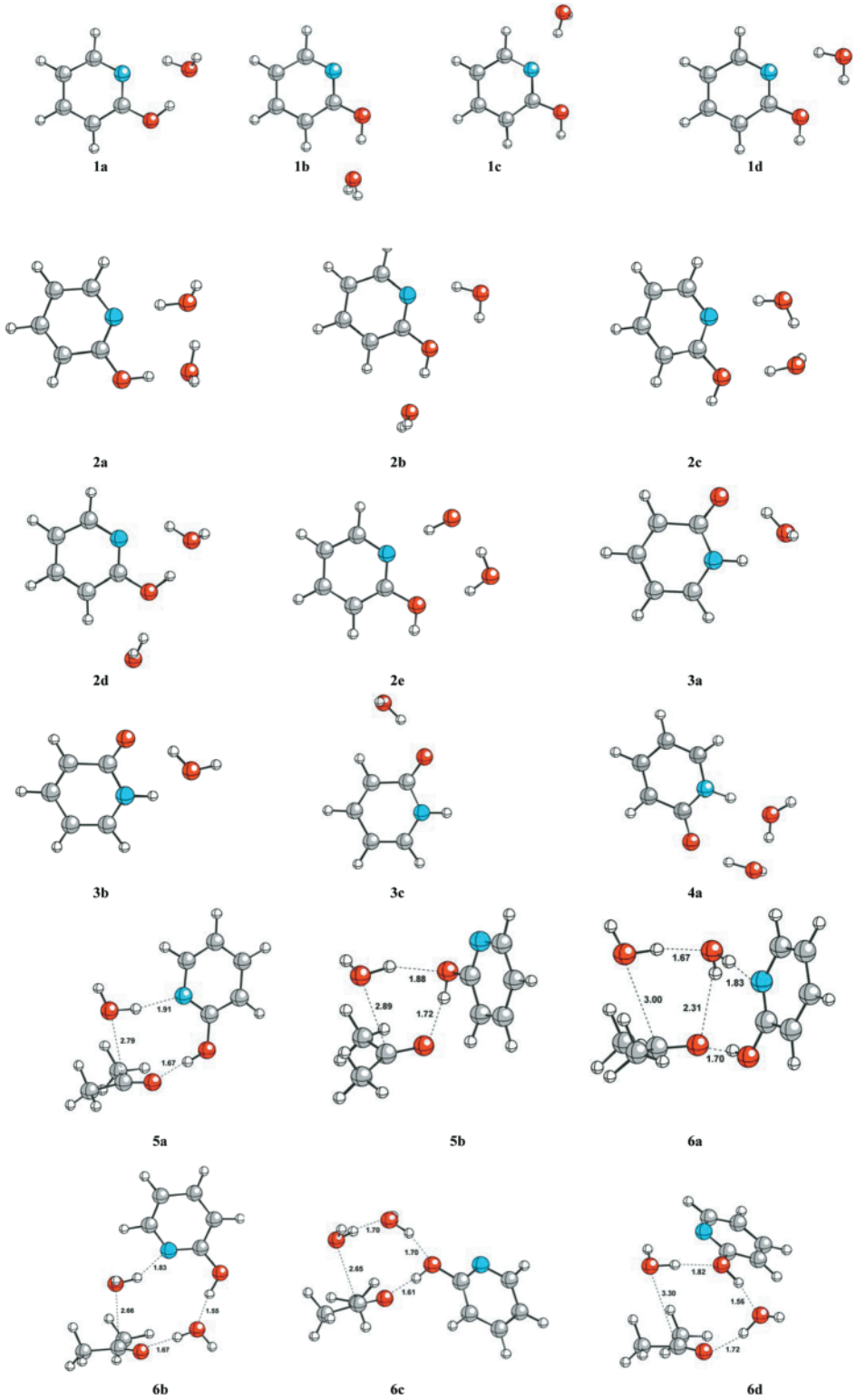

© 2007 NRC Canada

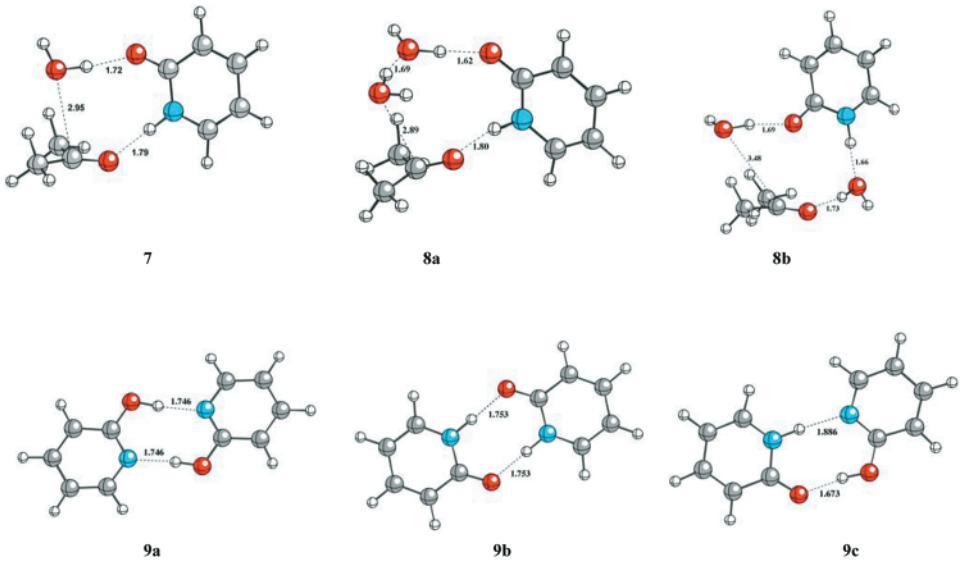

Figure 1. Hydration of acetone (1.0 mol/L) at 298 K in the presence of 2 x10^{-4} mol/L 2-hydroxypyridine (Run 1).

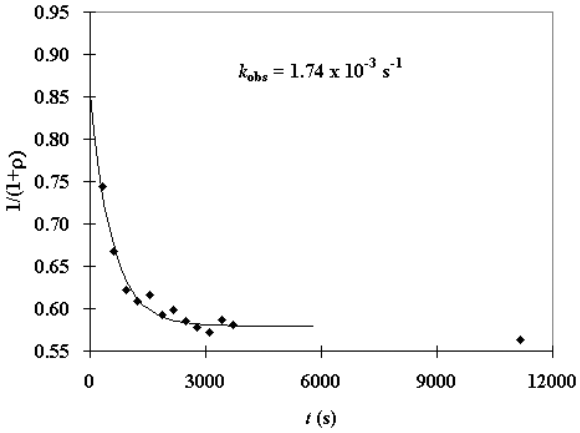

Figure 2. Hydration of acetone (1.0 mol/L) at 298 K in the presence of 2 x10^{-4} mol/L 2-hydroxypyridine (Run 2).

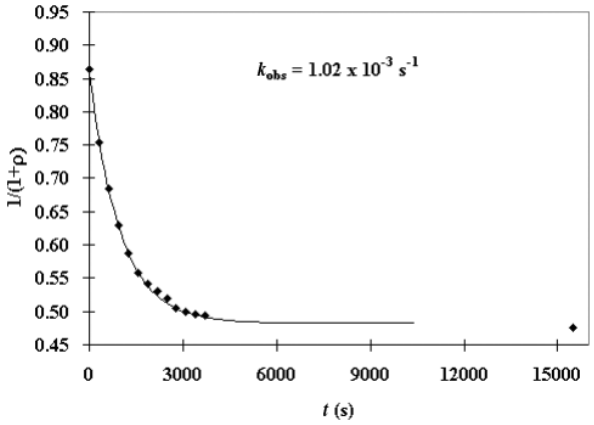

Figure 3. Hydration of acetone (1.0 mol/L) at 298 K in the presence of 2 x10^{-4} mol/L 2-hydroxypyridine (Run 3).

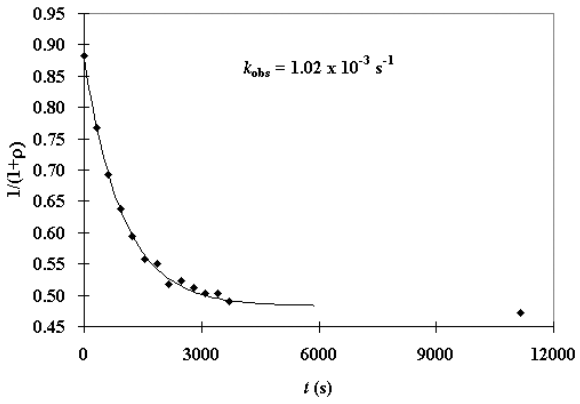

Figure 4. Hydration of acetone (1.0 mol/L) at 298 K in the presence of 1.3 x10^{-2} mol/L 2-hydroxypyridine.

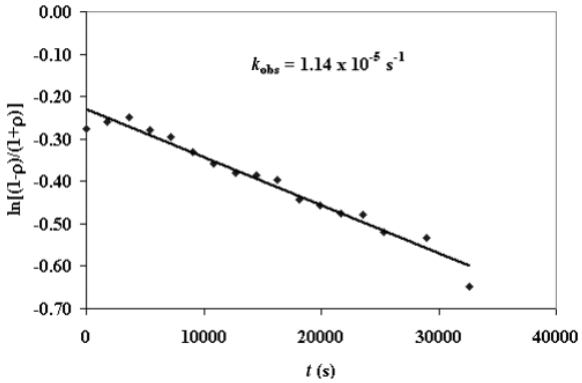

© 2007 NRC Canada

Table 1. Hydration of acetone (1.0 mol/L) at 298 K in the presence of 2×10^{-4} mol/L 2-hydroxypyridine.

Run 1		Run 2		Run 3	
Time (min)	ρ	Time (min)	ρ	Time (min)	ρ
5.2	0.3445	0.00	0.1577	0.00	0.1326
10.3	0.4978	5.17	0.3278	5.17	0.3037
15.5	0.6067	10.33	0.4630	10.33	0.4442
20.7	0.6428	15.50	0.5901	15.50	0.5675
25.8	0.6236	20.67	0.7035	20.67	0.6846
31.0	0.6886	25.83	0.7926	25.83	0.7910
36.2	0.6723	31.00	0.8470	31.00	0.8149
41.3	0.7085	36.17	0.8848	36.17	0.9335
46.5	0.7295	41.33	0.9236	41.33	0.9103
51.7	0.7464	46.50	0.9783	46.50	0.9514
56.8	0.7035	51.67	0.9997	51.67	0.9878
62.0	0.7234	56.83	1.0145	56.83	0.9920
186.0	0.7776	62.00	1.0267	62.00	1.0387
		186.00	1.0992	186.00	1.1225
k_{obs} (s^{-1})	1.74×10^{-3}		1.02×10^{-3}		1.02×10^{-3}
Average	$1.3 \pm 0.4 \times 10^{-3}$ s^{-1}				

Table 2. Hydration of acetone (1.0 mol/L) at 298 K in the presence of 1.3×10^{-2} mol/L 3-hydroxypyridine.

Time (min)	ρ
0.0	0.1282
30.2	0.1203
60.3	0.1160
90.5	0.1288
120.7	0.1369
150.8	0.1529
181.0	0.1651
211.2	0.1742
241.3	0.1775
271.5	0.1818
301.7	0.2026
331.8	0.2076
362.0	0.2167
392.2	0.2181
422.3	0.2358
482.7	0.2406
543.0	0.2889
k_{obs} (s^{-1})	1.14×10^{-5}

Table 3. Catalysis of acetone hydration by various acids at 298 K.

HA	pK_a	k_A ($(mol/L)^{-1}s^{-1}$)	k_{2HP}/k_A
HOH	15.72[a]	1.6×10^{-7} [b]	4×10^7
HOAc	4.76[c]	<0.3	>20
2-HP	11.62[d]	6.3	1
3-HP	8.78[d]	1.1×10^{-5}	6×10^{-5}

[a]Ref. 16
[b]$k_o/55$
[c]Ref. 17
[d]Ref. 18

Table 4. Gibbs free energies of 2-HP and 2-PD in water solvent.

Compound	G_{298} (a.u.)[a]	ΔG_{298} (kcal/mol)
2-HP	–319.696683	
2-PD	–319.702605	
2-HP $\rightleftharpoons$ 2-PD		–3.72

[a]1 a.u. = 627.5 kcal/mol

Table 5. Gibbs free energies of formation of 2-HP and 2-PD dimers in water solvent.

Dimer	ΔG (kcal/mol)
9a	–13.00
9b	–11.73
9c	–10.11

Table 6. Gibbs free energies of formation of 1:1 and 2:1 water–2-HP and water–2-PD complexes from individual components in water solvent.

Complex	ΔG (kcal/mol)	Complex	ΔG (kcal/mol)
1a	–2.21	**2c**	10.02
1b	–0.49	**2d**	15.25
1c	4.46	**2e**	8.26
1d	0.93	**3a**	3.34
2a	2.53	**3b**	2.48
2b	10.61	**3c**	3.37
		4a	–1.43

© 2007 NRC Canada

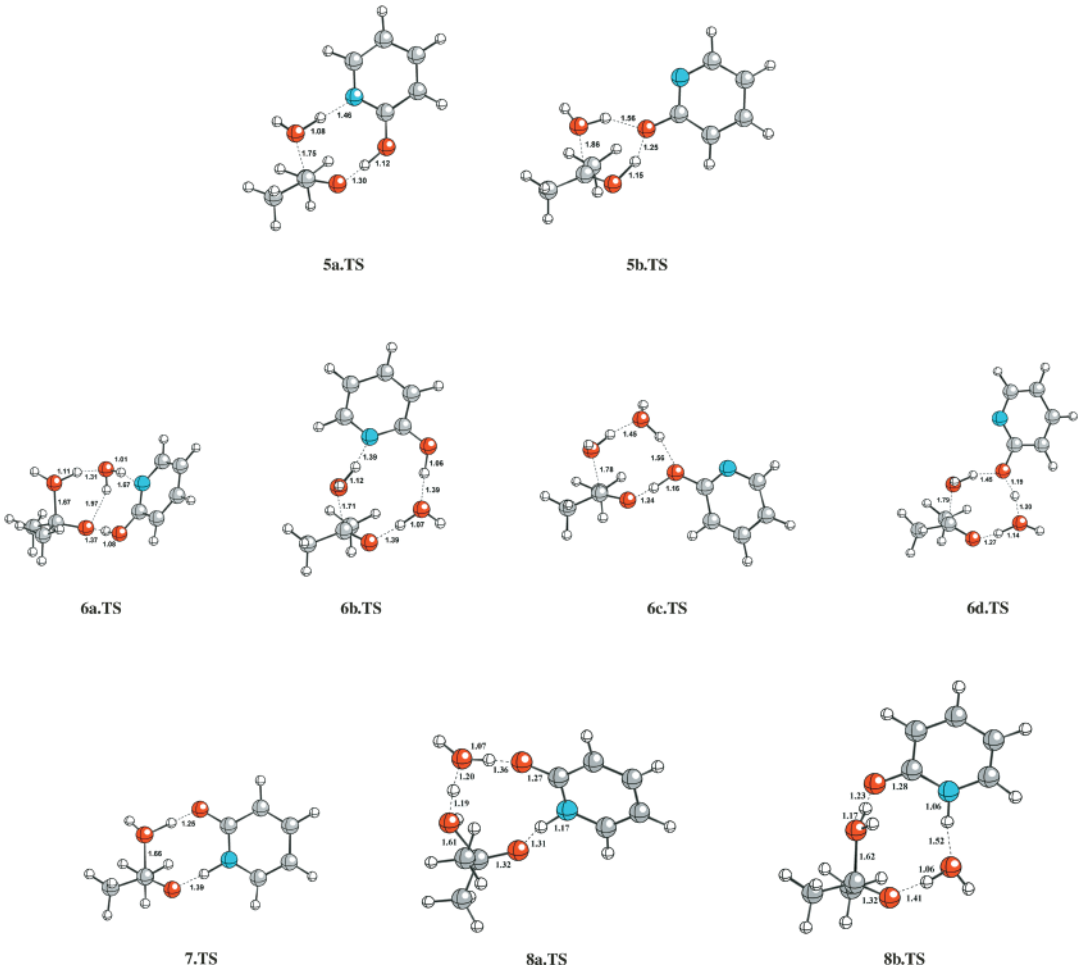

Table 7. Gibbs free energies of formation of the water–acetone catalyst complexes of Scheme 2 from individual components.

Complex	ΔG (kcal/mol)
5a	1.94
5b	6.08
6a	1.99
6b	6.73
6c	5.56
6d	7.50
7	–0.97
8a	0.17
8b	6.75

Table 8. Free energies of activation for the formation of the catalyzed transition structures of Scheme 2 from the respective reactant complexes.

Transition structure	$\Delta G^{\ddagger}$ (kcal/mol)
5a.TS	11.47
5b.TS	23.85
6a.TS	12.39
6b.TS	10.43
6c.TS	7.76
6d.TS	13.35
7.TS	15.21
8a.TS	11.97
8b.TS	12.94

$$C_{\mathrm{W}} = \sum_{n} n[\mathrm{W}_n] + \sum_{n} n[\mathrm{W}_n\mathrm{C}] + \sum_{n,\mu} n[\mathrm{W}_n\mathrm{H}\mu] + \sum_{n,\mu} n[\mathrm{W}_n\mathrm{P}\mu] + \sum_{n,\mu} n[\mathrm{W}_n\mathrm{HC}\mu] + \sum_{n,\mu} n[\mathrm{W}_n\mathrm{PC}\mu]$$

$$C_{\mathrm{A}} = [\mathrm{H}] + [\mathrm{P}] + 2\sum_{n,m} [\mathrm{H}_n\mathrm{P}_m] + \sum_{n,\mu} \mathrm{W}_n\mathrm{H}\mu] + \sum_{n,\mu} [\mathrm{W}_n\mathrm{P}\mu] + \sum_{n,\mu} [\mathrm{W}_n\mathrm{HC}\mu] + \sum_{n,\mu} [\mathrm{W}_n\mathrm{PC}\mu]$$

The final results are collected in Tables 9 and 10.

Discussion

It is known (18, 19) that at 20 °C an aqueous solution of 2-hydroxypyridine consists predominantly of the 2-pyridone tautomer. The tautomeric equilibrium constant K_{t} = [2PD]/[2HP] is over 900, corresponding to a free energy difference of 3.97 kcal/mol (1 cal = 4.184 J). It is also known (13) that 2-pyridone forms specific complexes to two water molecules, and that 2-hydroxypyridine complexes one water

© 2007 NRC Canada

Table 9. Calculated concentrations of acetone–water, acetone–water–2-hydroxypyridine, and acetone–water–2-pyridone complexes, calculated rate constants and partial rates for these complexes, and contributions of these complexes to the overall rate constant for the experimental conditions of Table 1.

Reactant complex	Concentration (mol/L)	Rate Constant (s^{-1})	Partial rate (mol/L s^{-1})	Contribution (%)
$\mathbf{W_1C}$	7.76×10^{-4}	6.01×10^{-21}	4.66×10^{-24}	0.00
$\mathbf{W_2C}$	5.24×10^{-6}	2.62×10^{-3}	1.37×10^{-8}	0.00
$\mathbf{W_3C}$	7.24×10^{-12}	1.14×10^{4}	8.29×10^{-8}	0.00
$\mathbf{W_4C}$	1.65×10^{-10}	1.21×10^{5}	2.00×10^{-5}	0.96
5a	4.59×10^{-12}	9.82×10^{4}	4.51×10^{-7}	0.03
5b	4.28×10^{-15}	8.27×10^{-5}	3.54×10^{-19}	0.00
6a	3.45×10^{-11}	2.08×10^{4}	7.16×10^{-7}	0.03
6b	1.16×10^{-14}	5.64×10^{5}	6.52×10^{-9}	0.00
6c	8.29×10^{-14}	5.10×10^{7}	4.23×10^{-6}	0.20
6d	3.16×10^{-15}	4.08×10^{3}	1.29×10^{-11}	0.00
7	3.29×10^{-7}	1.78×10^{2}	5.88×10^{-5}	2.81
8a	4.78×10^{-8}	4.20×10^{4}	2.01×10^{-3}	95.97
8b	7.29×10^{-13}	8.19×10^{3}	5.98×10^{-9}	0.00

Table 10. Rate constants of acetone hydration under the conditions of Table 1.

Calculated rate (s^{-1})	Experimental rate (s^{-1})	Calculated k_{HA} $((mol/L)^{-1}s^{-1})$	Experimental k_{HA} $((mol/L)^{-1}s^{-1})$
2.09×10^{-3}	1.30×10^{-3}	10.4	6.5

Table 11. The principal reaction channels of the hydration of acetone (1.00 mol/L) at 298 K under neutral conditions, in the presence of acetic acid (1.00 mmol/L) or 2-hydroxypyridine (1.00 mmol/L).

Reactant complex	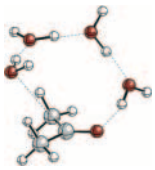	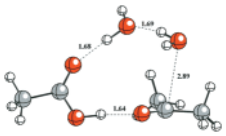	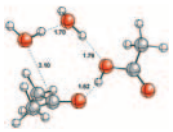	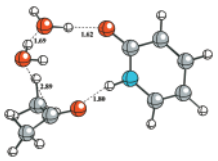
Conc. (Mol/L)	1.63×10^{-10} [a] (16.5)[b]	4.74×10^{-12} [b] (0.4)[b]	9.87×10^{-12} [c] (1.0)[b]	1.08×10^{-7} [d] (1.1×10^{4})[b]
$\Delta G^{\ddagger}$ (kcal/mol)	11.34[e]	7.44[f]	8.14[f]	11.97[d]
Rate (mol/L s^{-1})	1.99×10^{-5} (0.1)[b]	2.50×10^{-4} (1.0)[b]	2.65×10^{-4} (1.0)[b]	4.55×10^{-3} [d] (17.0)[b]

[a] From Table 5 of ref. 1*b*.
[b] Relative value.
[c] From Table 7 of ref. 1*c*.
[d] Present work.
[e] From Fig. 11 of ref. 1*b*.
[f] From Table 6 of ref. 1*c*.

molecule. The extent to which these complexes contribute to the tautomeric equilibrium constant has not previously been a topic of interest but has become known as a result of the present work (20). It is remarkable that a 3–21G/SCRF computational strategy does so well in reproducing kinetic (1*b*, 1*c*) and thermodynamic (20) experimental results in water solvent. A thermodynamic preference for the 2-pyridone tautomer is already evident in Table 4, which considers only the uncomplexed monomeric tautomers. From Table 6, the most stable complexes are the 2-HP monohydrate **1a** and the 2-PD dihydrate **4a**. In the presence of acetone, **1a** is the precursor of **5a**, and **4a** is the precursor of **8a**. From Table 7, **8a** is significantly more stable than **5a**, but the most stable acetone complex is **7**, derived from the 2-PD monohydrate **3b**. When the barriers are examined (Table 8), it is seen that **5a** and **8a** are comparable, but **7** is significantly higher. It is interesting that **6c**, which resembles a 3-water molecule neutral complex, has the lowest barrier, but **6c** is not stable (Table 7).

When the concentrations of the complexes are combined with the barriers (Table 9), the experimental rate constant is reproduced (Table 10) and **8a** is seen to be by far the dominant reaction channel, with minor contributions from **7**, **6c**, and $\mathbf{W_4C}$, the four-water molecule neutral channel.

The notion of cooperativity can, therefore, be extended from neutral (1*a*, 1*b*) and acetic acid-catalyzed (1*c*) to "2-hydroxypyridine"-catalyzed hydration of acetone. In each case the theoretical treatment reproduces experiment quite well. However, as seen in Table 11, it would be misleading to attribute 2-HP catalysis to its bifunctional character. Ta-

© 2007 NRC Canada

ble 11 compares the calculated barriers, the calculated concentrations of the principal reactive species, and the calculated rate constants of the hydration of acetone under neutral conditions and in the presence of acetic acid and 2-hydroxypyridine. *For the principal reaction channels*, *the neutral barrier and the 2-HP barrier are almost the same!* The acetic acid barrier is significantly lower. The predominance of 2-HP catalysis is seen to reside in a much higher concentration of the principal reactant complex. The relevance of this finding to the subject of bifunctional catalysis and the relationship of bifunctional catalysis to what takes place at an enzyme active site will be examined elsewhere (7).

Acknowledgements

This work was supported financially by Natural Sciences and Engineering Research Council of Canada (NSERC). We thank Drs. Chan-Kyung Kim, Kiyull Yang, and Zheng Shi for many discussions and for their interest and the reviewers for helpful comments.

References

1. (*a*) S. Wolfe, C.-K. Kim, K. Yang, N. Weinberg, and Z. Shi. J. Am. Chem. Soc. **117**, 4240 (1995); (*b*) S. Wolfe, Z. Shi, K. Yang, S. Ro, N. Weinberg, and C.-K. Kim. Can. J. Chem. **76**, 114 (1998); (*c*) Y.-H. Hsieh, N. Weinberg, K. Yang, C.-K. Kim, Z. Shi, and S. Wolfe. Can. J. Chem. **83**, 769 (2005).
2. M. Eigen. Discuss. Faraday Soc. **39**, 7 (1965); H.H. Huang, R.R. Robinson, and F.A. Long. J. Am. Chem. Soc. **88**, 1866 (1966).
3. C.G. Swain and J.F. Brown, Jr. J. Am. Chem. Soc. **74**, 2538 (1952); P.R. Rony, W.E. McCormack, and S.W. Wunderly. J. Am. Chem. Soc. **91**, 4244 (1969); P.R. Rony. J. Am. Chem. Soc. **91**, 6090 (1969); P.R. Rony and R.O. Neff. J. Am. Chem. Soc. **95**, 2896 (1973); K.-A. Engdahl, H. Bivehed, P. Ahlberg, and W.H. Saunders, Jr. J. Am. Chem. Soc. **105**, 4767 (1983); S. Morpurgo and M. Bossa. Phys. Chem. Chem. Phys. **5**, 1181 (2003).
4. Y.-N. Lee and G.L. Schmir. J. Am. Chem. Soc. **101**, 3026 (1979) and refs. cited therein.
5. N. Sharon. Sci. J. **2** (4), 81 (1966).
6. P.R. Rony. J. Am. Chem. Soc. **90**, 2824 (1968).
7. Y.-H. Hsieh, N. Weinberg, K. Yang, C.-K. Kim, and S. Wolfe. Manuscript in preparation.
8. M.J. Frisch, G.W. Trucks, H.B. Schlegel, G.E. Scuseria, M.A. Robb, J.R. Cheeseman, V.G. Zakrzewski, J.A. Montgomery, Jr., R.E. Stratmann, J.C. Burant, S. Dapprich, J.M. Millam, A.D. Daniels, K.N. Kudin, M.C. Strain, O. Farkas, J. Tomasi, V. Barone, M. Cossi, R. Cammi, B. Mennucci, C. Pomelli, C. Adamo, S. Clifford, J. Ochterski, G.A. Petersson, P.Y. Ayala, Q. Cui, K. Morokuma, D.K. Malick, A.D. Rabuck, K. Raghavachari, J.B. Foresman, J. Cioslowski, J.V. Ortiz, B.B. Stefanov, G. Liu, A. Liashenko, P. Piskorz, I. Komaromi, R. Gomperts, R.L. Martin, D.J. Fox, T. Keith, M.A. Al-Laham, C.Y. Peng, A. Nanayakkara, C. Gonzalez, M. Challacombe, P.M.W. Gill, B. Johnson, W. Chen, M.W. Wong, J.L. Andres, M. Head-Gordon, E.S. Replogle, J.A. Pople. Gaussian 98. Revision A.6 [computer program]. Gaussian, Inc., Pittsburgh, PA, USA. 1998.
9. W.J. Hehre, L. Radom, P.v.R. Schleyer, and J.A. Pople. Ab initio molecular orbital theory. Wiley, New York. 1986.
10. (*a*) O. Tapia and O. Goscinski. Mol. Phys. **29**, 1653 (1975); (*b*) S. Miertus, E. Scrocco, and J. Tomasi. Chem. Phys. **55**, 117 (1981); (*c*) J.L. Pascual-Ahuir, E. Silla, J. Tomasi, and R. Bonaccorsi. J. Comput. Chem. **8**, 778 (1987); (*d*) R. Bianco, G.W. A. Milne, M.C. Nicklaus, and M.J. Hodošček. J. Mol. Struct. **291**, 89 (1993); (*e*) F.J. Olivares del Valle, M.A. Aguilar, and J.C. Contador. Chem. Phys. **170**, 161 (1993); (*f*) M. Aguilar, R. Bianco, S. Miertus, M. Persico, and J. Tomasi. Chem. Phys. **174**, 397 (1993); (*g*) D.M.P. Mingos, A.L. Rohl and J. Burgess. J. Chem. Soc. Dalton Trans. 423 (1993); (*h*) B. Honig, K. Sharp, and A.-S. Yang. J. Phys. Chem. **97**, 1101 (1993); (*i*) H.J. Kim, R. Bianco, B.J. Gertner, and J.T. Hynes. J. Phys. Chem. **97**, 1723 (1993); (*j*) M. Bachs, F.J. Luque, and M. Orozco. J. Comput. Chem. **15**, 446 (1994).
11. (*a*) M.W. Wong, K.B. Wiberg, and M.J. Frisch. J. Chem. Phys. 95, 8991 (1991); (*b*) M.W. Wong, M.J. Frisch, and K.B. Wiberg. J. Am. Chem. Soc. **113**, 4776 (1991).
12. (*a*) S.F. Boys and F. Bernardi. Mol. Phys. **19**, 553 (1970); (*b*) O.N. Ventura, E.L. Coitiño, K. Irving, A. Iglesias, and A. LLedós. J. Mol. Struct. **210**, 427 (1990); (*c*) D.B. Cook, T.L. Sordo, and J.A. Sordo. J. Chem. Soc. Chem. Comm. 185 (1990); (*d*) P.O. Åstrand, A. Wallqvist, and G.J. Karlström. J. Phys. Chem. **95**, 6395 (1991); (*e*) R. Eggenberger, S. Gerber, H. Huber, and D. Searles. Phys. Lett. **183**, 223 (1991); (*f*) P. Valiron, A. Vibók, and I. Mayer. J. Comput. Chem. **14**, 401 (1993); (*g*) L. Turi and J.J. Dannenberg. J. Phys. Chem. **97**, 2488 (1993); (*h*) J.A. Dobado and J.M. Molina. J. Phys. Chem. **97**, 7499 (1993); (*i*) E.R. Davidson and S.J. Chakravorty. Chem. Phys. Lett. **217**, 48 (1993); (*j*) I. Mayer, A. Vibók and P. Valiron. Chem. Phys. Lett. **230**, 35 (1994); (*k*) T. Neuheuser, B.A. Hess, C. Reutel, and E. Weber. J. Phys. Chem. **98**, 6459 (1994); (*l*) M. Kieninger, S. Suhai, and I. Mayer. Chem. Phys. Lett. **230**, 485 (1994).
13. O. Bensaude, M. Chevrier, and J.-E. Dubois. J. Am. Chem. Soc. **101**, 2423 (1979); P. Beak, J.B. Covington, and J.M. White. J. Org. Chem. **45**, 1347 (1980); A. Held and D.W. Pratt. J. Am. Chem. Soc. **115**, 9708 (1993); Y. Matsuda, T. Ebata, and N. Mikami. J. Chem. Phys. **110**, 8397 (1999).
14. P. Beak, F.S. Fry, J. Lee, and F. Steele. J. Am. Chem. Soc. **98**, 171 (1976); P. Beak. Acc. Chem. Res. **10**, 186 (1977) and refs. cited therein; R.S. Brown, A. Tse, and J.C. Vederas. J. Am. Chem. Soc. **102**, 1174 (1980); Y. Matsuda, T. Ebata, and N. Mikami. J. Chem. Phys. **113**, 573 (2000); Y. Matsuda, T. Ebata, and N. Mikami. J. Phys. Chem. A, **105**, 3475 (2001).
15. P. Beak, J.B. Covington, S.G. Smith, J.M. White, and J.M. Zeigler. J. Org. Chem. **45**, 1354 (1980); M.G. Gallant, M.T.P. Viet, and J.D. Wuest. J. Am. Chem. Soc. **113**, 721 (1990); O. Bensaude, M. Chevrier, and J.E. Dubois. J. Am. Chem. Soc. **100**, 7055 (1978).
16. P. Ballinger and F.A. Long. J. Am. Chem. Soc. **82**, 795 (1960).
17. J.F.J. Dippy and F.R. Williams. J. Chem. Soc. 1888 (1934).
18. A. Albert and J.N. Phillips. J. Chem. Soc. 1294 (1956).
19. S.F. Mason. J. Chem. Soc. 674 (1958); P. Beak and J.T. Lee, Jr. J. Org. Chem. **34**, 2125 (1969).
20. S. Wolfe, N. Weinberg, and Y. Hsieh. Theor. Chem. Acc. **118**, 265 (2007).

© 2007 NRC Canada

Methanolysis of organophosphorus esters promoted by an M^{2+} catalyst supported on polystyrene-based copolymers

Benoit Didier, Mark F. Mohamed, Elizabeth Csaszar, Kate G. Colizza, Alexei A. Neverov and R. Stan Brown

Abstract: The methanolysis of three neutral organophosphorus esters (a phosphonate, a phosphonothioate, and a phosphorothionate) promoted by several polymer-supported Zn(II) or Cu(II) containing catalysts was studied. The catalysts consist of a Zn(II) or Cu(II) complex with 1,5,9-triazacyclododecane or phenanthroline attached to a porous polystyrene resin. In each case, the polymer supported catalyst showed activity at near neutral $^{s}_{s}$pH in methanol (8.38) and ambient temperature and provided accelerations of up to a factor of 2.9×10^6 relative to the background reaction at $^{s}_{s}$pH 9.05. The solid materials could be reused several times and could be reactivated when the activity diminished. Various polymers of different porosity and extent of cross-linking were studied, with the net result being that larger porosities offer the best reactivity for catalyzed methanolysis of these OP species in methanol. This is explained by different parameters including the accessibility to reactive sites, the increase of concentration of catalytic sites on the surface of the polymer, and some cooperative effects between neighboring catalytic groups.

Key words: functionalized polymer, metal containing, methanolysis, organophosphorus pesticides and CW agents, catalyst.

Résumé : La méthanolyse de trois esters organophosphorés neutres (un phosphate, un phosphonothioate et un phosphorothionate) ont été étudié en présence de plusieurs catalyseurs contenant du Zn(II) et du Cu(II) compléxés avec du 1,5,9-triazacyclododécane ou de la phénantroline supportés par des matrices polymères poreuses. Dans chacun des cas, le catalyseur supporté par le polymère est actif à température ambiante et à $^{s}_{s}$pH proche de la neutralité dans le méthanol (8,38) en fournissant des accélérations allant jusqu'à 2,9 x 10^6 par rapport aux vitesses de réaction obtenues en l'absence de catalyseur métallique à un $^{s}_{s}$pH de 9,05. Les matériaux utilisés peuvent être réutilisés plusieurs fois ou réactivés lorsque leur activité diminue. Divers matrices polymères de porosité et de degrés de réticulation différents ont été étudiés et il a été observé que les catalyseurs fixés sur les matrices ayant la porosité la plus large ont la plus forte activité catalytique pour la méthanolyse de ces esters phosphoriques dans le méthanol. Ce résultat s'explique par divers paramètres, incluant l'accessibilité des sites réactifs, l'augmentation de la concentration des sites catalytiques à la surface du polymère et de quelques effets de synergie entre des espèces catalytiques voisines.

Mots-clés : polymère fonctionnalisé contenant un métal, méthanolyse, pesticides organophosphorés, gaz de combat, catalyse.

[Traduit par la Rédaction

Introduction

Neutral organophosphorus (OP) compounds with leaving groups having pK_a values less than 8 comprise a very toxic family of compounds that inhibit acetylcholinesterase (1, 2) and thus have uses as chemical warfare (CW) agents, pesticides, and acaricides (3). Among the most nefarious of the CW agents are the phosphonothioate esters that are V-agents, such as VX (**1**) and Russian VX (**2**) and the phosphonoflouridate G-agents such as soman (**3**) and sarin (**4**). Other kinds of OP esters, such as the phosphate triesters and phosphorothionate esters (**5**, **6**), are used as pesticides.

Due to the noxious nature of these materials and the fact that some of them linger in the environment, methods for the decomposition and decontamination of these are continually sought (4). Only a few methods employ metal ions, but generally these are not very effective in water for hydrolysis because of substrate and metal ion solubility problems and also the inherent low activity of the metal ions in promoting solvolysis, which has yet to be overcome in aqueous media. In practice, a decomposition method should be inexpensive, have a high reaction rate, occur at neutral pH and ambient temperature, and convert the toxic starting material into far less toxic or nontoxic products.

Received 15 June 2007. Accepted 30 July 2007. Published on the NRC Research Press Web site at canjchem.nrc.ca on 20 September 2007.

This article is dedicated to the memory of Professor Keith Yates.

B. Didier, M.F. Mohamed, E. Csaszar, K.G. Colizza, A.A. Neverov, and R.S. Brown.[1] Department of Chemistry, Queen's University, Kingston, ON K7L 3N6, Canada.

[1]Corresponding author (e-mail: rsbrown@chem.queensu.ca).

 doi:10.1139/V07-099 © 2007 NRC Canada

Recent work in our laboratories indicates that neutral (uncharged) esters of phosphates and phosphorothioates (5*a*, 5*b*), phosphonates (5*c*), and phosphonothioates (5*d*) are rapidly solvolyzed in methanol solution in the presence of La^{3+} or a Zn(II)-complex of 1,5,9-triazacyclododecane (**7*a***), forming nontoxic methyl esters. In addition, we have found that the corresponding Cu(II)($^{-}OCH_3$) or Zn(II)($^{-}OCH_3$) complexes of **7a** (6, 7) and **8** (7) catalyze the methanolysis of phosphate triesters and phosphorothionate triesters with a particular propensity for the latter. Routinely we find that a 1 mmol/L solution of the metal species gives accelerations of the methanolysis of these materials by factors of 10^8–10^9 over the background reactions at neutral $^{s}_{s}$pH and ambient temperature (8). All these exhibit true catalytic turnover, and all seem to function according to the simple kinetic scheme given in eq. [1]. The disadvantage of complex with **8** is the formation of dimers that are inactive, so it seemed reasonable that fixing the ligands on a solid support could form exclusively monomeric catalysts and prevent the formation of inactive species.

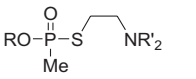

1; R=Et, R'=CH(CH$_3$)$_2$

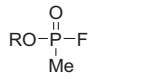

3; R=CH(CH$_3$)(C(CH$_3$)$_3$)

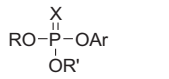

5; X=O, R, R'=alkyl, aryl

2; R=CH$_2$CH(CH$_3$)$_2$, R'=Et

4; R=CH(CH$_3$)$_2$

6; X=S, R, R' = alkyl, aryl

[1] $$\text{Substrate} + \text{Mx}^{+}(\text{-OR}) \overset{K_b}{\rightleftharpoons} \text{Substrate:Mx}^{+}(\text{-OR})$$

$$\text{Substrate} + \text{Mx}^{+}(\text{-OR}) \xrightarrow{\text{kcat}} \text{Substrate:Mx}^{+}(\text{-OR})$$

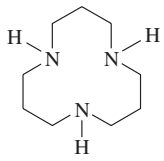

7a

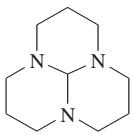

7b

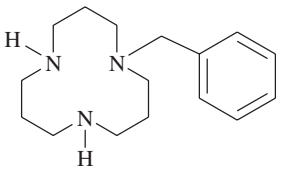

7c

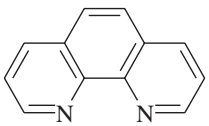

8

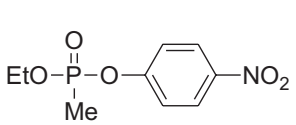

9

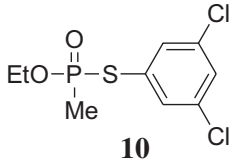

10

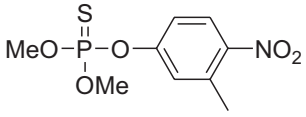

11

In some cases, affixing the catalytic group to a solid support can be expected to confer particular advantages of efficiency and cost effectiveness that come from being able to recover and reuse the catalyst. There are several reported studies of the hydrolytic decomposition of organophosphorus compounds promoted by solid supported M(II)-containing catalysts (9–12). In several cases the reactivity of the polymer supported catalyst decreases considerably compared with the activity in solution because of surface and diffusion effects, but in other cases the activity was still acceptable, particularly when the polarity of polymeric matrix was changed (10*b*, 10*c*), the coordination sphere of catalytic complex was modified (10*c*), or a linker was introduced between matrix and catalytic system (9). Nevertheless, all the prior reported studies concentrated on hydrolytic systems where the expected OP products would be acids that may present problems, such as inhibiting the activity of the M(II) through binding of the ionized anionic phosphate or phosphonate. In some cases, such as with the hydrolysis of V-agents, some of the hydrolytic products arise through cleavage of the P-OEt linkage, giving a product that is just as toxic as the starting materials but far more resistant to hydrolysis (1, 2).

Herein we report on the synthesis and analysis of some divinylbenzene (DVB) cross-linked meso- and macro-porous polystyrene resins functionalized with **7a**, **7b**, or 5-amino-1,10-phenanthroline (5-NH_2-**8**). After loading the resins with an M^{2+} ion (Cu^{2+} or Zn^{2+}), the catalytic activity was determined for the methanolysis of three different OP compounds proposed as simulants for the G-agents (*O*-ethyl-*O*-4-nitrophenyl methylphosphonate (**9**)), the V-agents, (3,5-*O*-ethyl-*S*-3,5-dichlorophenyl methylphosphonothioate (**10**)), and for phosphorothionate pesticides (fenitrothion® (**11**)).

Experimental

Materials

Methanol (99.8% anhydr.), DMF (99.8%), sodium methoxide (0.5 mol/L solution in methanol), $Cu(CF_3SO_3)_2$, $Zn(CF_3SO_3)_2$, 1,5,9-triazacyclododecane, styrene, 4-(chloromethyl)styrene, divinylbenzene, benzoyl peroxide, boric acid, and sodium hydroxide were purchased from Sigma-Aldrich and used as supplied. THF (extra dry, with molecular sieves, water < 50 ppm) and $HClO_4$ (70% aq. solution) was purchased from Acros Organics and used without further purification. Cellosize, xantham gum, and 5% Pd/C catalyst were purchased from Fluka and *n*-pentanol was purchased from BDH Chemical; these were used as supplied. Merrifield's polymer resin mesoporous (Meso-Ald) (2% crosslinked with DVB, 0.6–0.8 mmol Cl/g, 200–400 mesh) and macroporous (Macro-Ald) (1.2 mmol Cl/g, 100–200 mesh) were purchased from Sigma-Aldrich. PL-CMS MP resin (Macro-PL) (>12% of cross-linking with DVB, 2.8 mmol Cl/g, porosity size 100 Å, particle size 150–300 μm) was purchased from Polymer Laboratories. Fenitrothion (**11**, *O*,*O*-dimethyl *O*-(3-methyl-4-nitrophenyl) phosphorothioate), was a gift from Professors Erwin Buncel and Gary van Loon of this department. *O*-Ethyl-*S*-3,5-dichlorophenylmethylphosphonothioate (**10**) and *O*-ethyl-*O*-4-nitrophenylmethylphosphonate (**9**) were synthesized as reported previously (5*e*, 5*d*).

© 2007 NRC Canada

Suspension polymerization syntheses of macroporous resins (DVB20, DVB50, and DVB50-hl).

The following procedure was based on the work of Durie et al. (13). An aqueous phase was prepared by dissolving 0.087 g of xantham gum, 0.012 g of Cellosize, and 1.73 g of boric acid in 100 mL of water. This mixture was vigorously stirred to obtain a cloudy solution. Using 20% divinylbenzene cross-linker as an example to make DVB20, the monomer mixture comprised DVB (~80% grade) (1.50 mL, ~20 wt% actual DVB as compared with the other monomers), styrene (4.33 mL), and 4-(chloromethyl)styrene (0.59 mL, ~10% molar ratio with styrene), to which was added benzoyl peroxide (0.080 g) and *n*-pentanol (4.22 mL, ~40 vol% of the entire organic phase). The combined organic phase was added dropwise into the aqueous phase with vigorous stirring. The suspension was then stirred at 80 °C for six hours, cooled, and the polymeric beads were collected by filtration and washed with water (50 mL). The material was washed with methanol (50 mL) and then acetone (50 mL). The yield of polymeric beads was 60% after drying in an oven at 60 °C for 24 h.

Characterization of porosity

To characterize the porosity of the beads, we followed a procedure reported by Chemin et al. (14) where the volume of porosity and the accessible porous volume for methanol were characterized by a measurement of the apparent density of the polymeric beads in different solvents. Around 2 g of dry polymeric beads were weighed in a tared 50 mL volumetric flask, after which 40 mL of solvent were introduced. For the measurement with hexane, the flask was placed in an ultrasonic bath for 10 min, after which the mixture was allowed to stand for 2 h at room temperature. The volume was adjusted with hexane and the flask was weighed again. This procedure gives an apparent volumetric weight of beads in the given solvent (e.g., hexane, water, and methanol) by using the following formula:

$$[2] \qquad \rho^{s}{}_{a} = \frac{W_p}{100 - (W_2 - W_1) \times 1/\rho_s}$$

where W_p is the weight of polymer in g, W_1 is weight of the flask with beads, W_2 is the weight of the flask with the beads filled with the solvent, ρ_s is the density of the solvent, and $\rho^{s}{}_{a}$ is the apparent density of the beads in the solvent (in g/mL). The pore volume ($P\%$) or the accessible porous volume in methanol was calculated with the following equation:

$$[3] \qquad P(\%) = \left(1 - \frac{\rho^{w}{}_{a}}{\rho^{s}{}_{a}}\right) \times 100$$

where $\rho^{w}{}_{a}$ is the apparent density of the beads in water in g/mL, and $\rho^{s}{}_{a}$ is the apparent density of the beads in hexane for total pore volume or in methanol for accessible porous volume in methanol.

5-Amino-1,10-phenanthroline

5-Amino-1,10-phenanthroline was prepared via a modification of a previously published route (15).

***N*-benzyl-1,5,9-triazacyclododecane**

The title compound was made as described in ref. 16.

Modification of polymeric resins with 7a or 7b

Commercial Macro-Ald resin (0.50 g, 0.6 mmol of Cl, 1 equiv.) was swelled in 10 mL of THF for 1 h. 1,5,9-Triazacyclododecane (**7a**) (0.12 g, 0.7 mmol, 1.15 equiv.) was added and the mixture was heated at reflux and stirred carefully overnight. The polymer was recovered by filtration and washed with THF (3 × 10 mL) and dried in oven at 60 °C for 24 h.

The modification with the immediate precursor of **7a**, triazatricyclo[7.3.1.0]tridecane (**7b**), was done by the same procedure using the same molar ratios, after which the recovered polymer was subjected to hydrolysis using a solution of 10 mL each of ethanol and water containing 1.07 g of sodium hydroxide heated at reflux overnight to liberate the 1,5,9-triazacyclododecane-functionalized resin. In all cases the final polymer functionalized with **7a** was subsequently treated with a solution of THF–methanol (50:50 *v*/*v*, 20 mL) containing 200 µL of sodium methoxide (0.5 mol/L) for 15 h to remove all traces of acid and residual exposed chloromethyl functionality.

Modification of polymeric resins with 5-amino-1,10-phenanthroline

Polymer-bound phenanthroline was prepared via a modification of a published route (15). Commercial PL-CMS MP resin (0.824 g, 2.31 mmol of Cl, 1 equiv.) and solid 5-amino-1,10-phenanthroline (0.724 g, 3.71 mmol, 1.6 equiv.) were added to a 100 mL round-bottomed flask equipped with a reflux condenser and a small magnetic stirbar. To the flask was added 50 mL of anhydrous DMF and the mixture was gently stirred, to avoid crushing of the polymer, and heated to reflux. After 1 h of heating, triethylamine (520 µL, 3.7 mmol) was added to the reaction mixture and the mixture was allowed to continue refluxing. An additional 230 µL (1.65 mmol) of triethylamine was added after 24 h of heating and the two phase mixture was left to reflux for another 48 h. After cooling, the polymer was filtered and washed with 20 mL of DMF and 100 mL of methanol. The resin was left to stir gently in boiling DMF for three hours followed by filtration and rinsing with methanol. To remove residual DMF, the polymer was boiled in acetone at 60 °C overnight, collected, filtered, and washed with acetone and then methanol. The functionalized polymer was treated with a 20 mL solution of sodium methoxide (5 mmol/L) in methanol for 15 h to remove any traces of acid and residual exposed chloromethyl functionality.

Metal complexation of polymer bound ligand

A 0.1 mol/L solution of $M(OTf)_2$ was prepared in methanol and the polymer was immersed in this solution for 4 h after which it was separated by filtration, washed with methanol, and dried in oven at 60 °C for 24 h. A final step placed the material into a basic methanol solution (20 mL of methanol with 200 µL of 0.5 mol/L sodium methoxide) to obtain the active catalytic species of complexed M(II):($^{-}OCH_3$).

Analysis of the M(II) loading

The metal-loaded polymer (around 0.01 g) was immersed

© 2007 NRC Canada

Table 1. Characteristics of functionalized polystyrene resins synthesized and complexed with Copper (II).

Name	Triaza-precursor	Cl[a]	$M^{(II)}$[b]	Total pore volume (mL/g)[c]	Pore volume access CH_3OH (mL/g)[c]
DVB20	**7b**	0.7	0.009 (Cu)	0.4 (0.1)	0.27 (0.02)
DVB50	**7b**	0.7	0.033 (Cu)	0.6 (0.1)	0.49 (0.03)
DVB50-hl	**7a**	3.9	0.09 (Cu), 0.11 (Zn)	NA[d]	NA[d]
Macro-PL	**7b**	2.8	0.13 (Cu)	0.8 (0.1)	0.48 (0.05)
Macro-PL-(II)	**7a**	2.8	0.23 (Cu), 0.14 (Zn)	0.8 (0.1)	0.48 (0.05)
Macro-Ald	**7a**	1.2	0.15 (Cu), 0.02 (Zn)	0.8 (0.1)	0.31 (0.05)
Meso-Ald	**7b**	0.7	0.014 (Cu)	NA[d]	NA[d]

[a]Chlorine loading in mmol/g.
[b]Metal ion loading in mmol/g.
[c]Error limits given in brackets.
[d]NA = not available.

in 2 mL of nitric acid solution in methanol (5% *v*/*v*) for 30 min. The methanol solution was carefully decanted away from the polymer, reserved, and the acid wash was repeated with this material four times. The combined methanol washes were stripped of solvent to produce ~0.2 mL of a residue, which was diluted with water in a volumetric flask (25 or 50 mL). The concentration of M^{2+} in this solution was obtained by atomic absorption spectrometry using a Varian Spectra AA-20 Plus spectrometer. The spectrometer was calibrated with known [M^{2+}] solutions (0.5–5 ppm for copper, and 0.1–0.5 ppm for zinc).

Kinetics

All kinetics experiments with the polymers were conducted in 2.5 mL of a methanol solution buffered with *N*-*iso*-propylmorpholine (6.8×10^{-3} mol/L) at $^{s}_{s}$pH = 9.0 ± 0.4. The rates of methanolysis of **9** and **11** (0.03 mmol/L) catalyzed by heterogeneous M(II)-**7** complex (0.08 g to 0.75 g; 1×10^{-3} mol/L < [M(II)-**7**] < 30×10^{-3} mol/L suspended in the buffered methanol) were followed by monitoring the appearance of *p*-nitrophenol (or 3-methyl-4-nitrophenol) at 312 nm or the disappearance of starting material at 264 nm, using a Cary 100 UV–vis spectrophotometer with the cell compartment thermostatted at 25.0 ± 0.1 °C. The rates of methanolysis of **10** (0.3 mmol/L) were followed by monitoring its disappearance at 253 nm.

Kinetic experiments with the Zn(II) complex of *N*-benzyl-1,5,9-triazacyclododecane (**7c**/Zn(II)) were conducted in methanol under self-buffered conditions where the ligand, $Zn(OTf)_2$, and $NaOCH_3$ were formulated in stock solutions in a 1:1:0.5 molar ratio ($^{s}_{s}$pH = 10). The kinetics of the methanolysis of phenyl acetate (1.0×10^{-4} mol/L) and **9** (3.6×10^{-5} mol/L) were monitored at 280 and 320 nm, respectively, as a function of [**7c**/Zn(II)]$_{total}$. The k_2 value for the catalyzed methanolysis was determined as twice the gradient of the k_{obs} vs. [**7c**/Zn(II)]$_{total}$ plot, the factor of two being introduced because the active form is [**7c**/Zn(II):$^{-}$OCH$_3$], which is present at 1/2 the concentration of the total Zn(II) complex.

Results and discussion

Functionalized polymer preparation

The chloromethylated polystyrene support matrix was chosen for its desirable (17) physical and chemical properties, which include chemical inertness, structural stability that enables a controllable porosity that ensures accessibility of reagents to the internal catalytic domains, and the $ClCH_2$-functionalities that can be modified to attach various catalytic systems to the matrix. Three different commercial polymers were used in this study, one mesoporous (Meso-Ald) and two macroporous (Macro-Ald and Macro-PL). Macro-PL is defined by its manufacturer as macroporous but has an average size porosity of 10 nm and does not correspond to the IUPAC definition (18) that distinguishes three porous domains: microporosity (<2 nm), mesoporosity (2–50 nm), and macroporosity >50 nm).

Three other polystyrene resins were synthesized in this work by radical suspension polymerization wherein a mixture of monomer and a radical precursor (benzoyl peroxide) was dissolved in a solvent and was finely dispersed in an aqueous phase. Three different monomers in varying proportions were used, styrene and 4-(chloromethyl)styrene to ensure the reactive function of polymer and divinylbenzene to obtain cross-linking of the polymeric matrix. The solvent (pentanol) containing the monomeric phase was used as the porogen (17, 19) because it is known to permit a large porosity (19, 20). During the polymerization process, a phase separation occurs between the growing polymeric chain and the porogenic agent, and the matrix forms around the space where the solvent is occluded creating the porous structure. Two polymers were synthesized, one (DVB20) with 20 wt% of divinylbenzene and another (DVB50) with 50 wt%. In all cases the porogen was introduced to make up 40% of the volume of the organic phase. A third matrix was prepared with the same amount of DVB as for DVB50 but with only 4-(chloromethyl)styrene as the other monomer, to obtain a polymer with high loading (designated as DVB50-hl).

The porosities of the resins were characterized by measuring their apparent densities in different solvents (hexane, water, and methanol). From those values one calculates, from eqs. [2] and [3], the volume of total porosity and porous volume accessible to methanol (14). Data are reported in Table 1. The results show slightly higher pore volumes for the commercial polymers than for the synthesized polymers. However, the ratio of this volume to that accessible to methanol is 70%–80% for prepared polymers and somewhat less for the commercial polymers, ~60% for Macro-PL and ~40% for Macro-Ald. This result shows that a majority of pores are not accessible to methanol in Macro-Ald. For

© 2007 NRC Canada

Table 2. Apparent second-order rate constants of the complex **8**/Zn^{2+} in solution and of different polymer resins functionalized with **8**/Zn^{2+}, determined at $^{s}_{s}$pH = 9 in methanol, buffered with *N*-*iso*-propylmorpholine, T = 25 °C, [**10**] = 3 × 10^{-4} mol/L, and [**9**] = [**11**] = 3 × 10^{-5} mol/L.

Polymer	$M^{(II)-}$ loading (mmol/g)	k_2 (**10**) $((mol/L)^{-1}s^{-1})$	k_2 (**9**) $((mol/L)^{-1}s^{-1})$
DVB50-hl **8**/Zn^{2+}	0.065	0.49	0.31
Macro-PL **8**/Zn^{2+}	0.035	1.17	0.80
Macro-PL-(II) **8**/Zn^{2+}	0.098	11.75	0.61

Note: Error limits considered to be ±20%, based on the errors in the determination of metal loading and uncertainties in the duplicate rate measurements.

Fig. 1. Scheme of the modification of polystyrene resins.

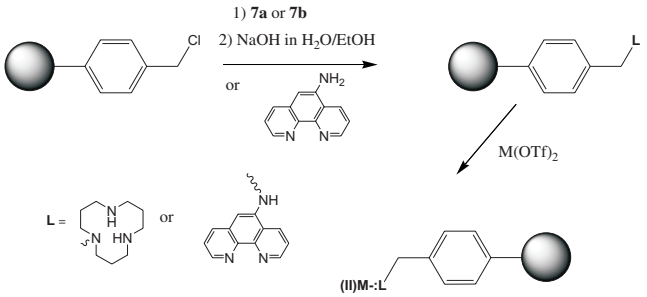

Macro-PL, the advertised pore size is 10 nm but the porosity for Macro-Ald, although not specified, seems to be smaller according to the criteria here.

All the polymeric matrices were functionalized by nucleophilic substitution of the benzylic chloride by 1,5,9-triazacyclododecane (**7a**) or its immediate precursor triazatricyclo[7.3.1.0]tridecane (**7b**) as shown in Fig. 1.

Using **7b**, the polymer must then be subjected to base catalyzed hydrolysis with sodium hydroxide in water–ethanol, to obtain the 1,5,9-triazacyclododecane functionalized polymer. Once functionalized, all the polymers are treated with a sodium methoxide THF–methanol solution to deprotonate the highly basic triazacyclododecane and to react with any residual benzylic chloride that might affect the future characteristics of the material. The subsequent steps involve the M^{2+} loading (Cu^{2+} or Zn^{2+}), wherein the polymeric matrix was immersed in an 0.1 mol/L $M(OTf)_2$ solution in methanol. In the case of copper, the loading is visually characterized for the **7a** functionalized polymer by an immediate green-blue colouring of the solid, which remained so after a final washing with methanol.

The M^{2+} loading was quantified by immersing a known quantity of the resin in a known volume of a 5% solution of nitric acid in methanol, which protonates the ligand and releases metal ion into the solution, as judged by the loss of colour of the solid in the case of copper. The solution was then analyzed by atomic absorption spectroscopy and the results are presented in Table 1. The data show that, in all cases, there is an incomplete conversion of chloride into metal complex. The best result was obtained with Macro-Ald with a conversion of 13% of the available chloride. The low conversion likely stems from the fact that some of the Cl is buried inside the polymer in sites inaccessible to the triaza ligand although the functionalization was done in THF, which is known to swell polystyrene appreciably. Since the metallation step was done in the nonswelling solvent methanol, it is possible that some of the ligand sites could not be accessed, which could also contribute to the relatively low amount of Cu^{2+} on the polymer. In fact, we have chosen to do the metallation under nonswelling conditions as this is the medium where all the subsequent catalytic reactions are performed, and the metal ion loading was determined under non-swelling conditions in aqueous acid. Another possibility for some materials is a difference in reactivity of **7a** and its precursor **7b**, since it is generally observed that materials prepared with the latter always have a slightly lower Cu^{2+} loading. Indeed, the only difference between Macro-PL and Macro-PL-(II), where the polymeric matrix is the same for each, is the triazacyclododecane precursor, which is **7b** for Macro-PL and **7a** for Macro-PL-(II). It could be that there is a higher reactivity with the more flexible **7a** relative to **7b** or that the hydrolysis step required for the latter in ethanol–water is not very efficient because of the low affinity between polystyrene resin and this solvent mixture. As a final note, we observed that the polymers prepared for this study have much lower conversion of chloride into the Cu^{2+}-loaded resin (<3%) relative to the commercial resins. This is possibly due to the high level of cross-linking, since it is known (21) that a higher level decreases the reactivity of functional groups on a rigid polymeric backbone.

The modification of polymeric resins with 5-amino-1,10-phenanthroline was done following a published procedure (15). The loading of zinc after this modification was low (see Table 2) with 0.035 mmol/g compared with 0.14 mmol/g for zinc loading to Macro-PL-(II) functionalized with **7a**. Subsequently we changed the functionalizing solvent to DMF, in which the 5-amino-1,10-phenanthroline is more soluble than in dioxane. The solvent change increased the loading about three-fold, giving a loading of ~0.1 mmol/g, which is close to that found with **7a**.

Catalytic studies

Study of the catalytic activity of the materials was conducted by determining the rate of change in the UV–vis absorbance for loss of substrate and formation of product in methanol solutions containing known amounts of the solid resins. Polymer (0.05 g to 0.75 g) was put into 2.5 mL of methanol solution buffered by *N*-*iso*-propylmorpholine (6.8 × 10^{-3} mol/L) at $^{s}_{s}$pH ~ 9 (the range of $^{s}_{s}$pH values is between 8.6 and 9.8) (22), which is slightly above neutrality ($^{s}_{s}$pH = 8.4 (22)). For practical reasons owing to the high absorptivities of the turbid media, the heterogeneous mixtures were not stirred continuously; rather, the cell was shaken every 2 to 5 min and the particles were allowed to settle prior to measurement of

© 2007 NRC Canada

Table 3. Apparent second-order rate constants of the complex **7a**/M^{2+} in solution and of different polymer resins functionalized with **7a**/M^{2+}, determined at $^{s}_{s}$pH = 9 in methanol, buffered with *N-iso*-propylmorpholine, T = 25 °C, [**10**] = 3 × 10^{-4} mol/L, and [**9**] = [**11**] = 3 × 10^{-5} mol/L.

Catalyst	k_2 (**10**) ((mol/L)$^{-1}$s^{-1})	k_2 (**9**) ((mol/L)$^{-1}$s^{-1})	k_2 (**11**) ((mol/L)$^{-1}$s^{-1})
$^{-}OCH_3$	2.17[a]	2.7[b]	(7.2±0.2)x10^{-4} [b]
7a/Cu^{2+} [c]	—	243[b]	12.2 [b]
DVB2**0** **7a**/Cu^{2+}	3	0.18	0.05
DVB5**0** **7a**/Cu^{2+}	3.1	0.07	0.02
DVB50-hl **7a**/Cu^{2+}	—	0.17	0.04
Macro-PL **7a**/Cu^{2+}	0.47	0.02	0.005
Macro-PL-(II) **7a**/Cu^{2+}	—	0.14	0.05
Macro-Ald **7a**/Cu^{2+}	0.21	0.017	0.006
Meso-Ald **7a**/Cu^{2+}	0.17	0.005	0.0003
7a/Zn^{2+} [d]	95.2	46.8	—
DVB50-hl **7a**/Zn^{2+}	0.95	0.33	—
Macro-PL-(II) **7a**/Zn^{2+}	0.38	0.09	—
Macro-Ald **7a**/Zn^{2+}	0.2	0.015	—

Note: Error limits considered to be ±20%, based on the errors in the determination of metal loading and uncertainties in the duplicate rate measurements.
[a]Ref. 7.
[b]Ref. 5*c*.
[c]M^{2+} complex of 1,5,9-triazacyclododecane in methanol.
[d]Ref. 5*d*.

the absorbance. In an attempt to quantify the amount of M^{2+} in the solution, the known amount of the heterogeneous resin was converted to concentrations as if it were completely dissolved (this is termed [bound M^{2+}]). Under this assumption, the metal concentration varied between 1 and 30 mmol/L, while those of the substrates were 0.3 mmol/L for **10** and 0.03 mmol/L for **9** and **11**. Under these conditions, the change in absorbance followed good first-order behaviour, and the pseudo first-order rate constants, k_{obs}, were evaluated by fitting the Abs. vs. time curves to a standard exponential model. The apparent second-order rate constants were evaluated as k_{obs}/[bound M^{2+}] and are given in Table 3 for material with **7a**/M^{2+} and in Table 2 for **8**/Zn^{2+}. Control experiments showed that in all but one case the rate constant obtained did not depend upon the frequency of shaking the mixture. This suggests that for these cases the overall catalytic process is not limited by transport through solution, although it might be limited by transport through the polymer or across the phase boundaries. On the other hand, we do have one case where there is a dependence of the reaction rate on the frequency of shaking for methanolysis of **9** in the presence of a relatively large amount (0.32 g) of Macro-PL-(II) **8**/Zn^{2+}. The kinetic results for the rate of disappearance of **9** and appearance of *p*-nitrophenol at $^{s}_{s}$pH = 8.52 (6.5 mmol/L *N-iso*propyl morpholine) shown in Table 4 indicate that the rate constants for each process increase with the frequency of shaking, although in all cases the rate for liberation of product is slower by roughly a factor of two than the rate of disappearance of **9**. This is consistent with a process where the reaction rate is partially limited by the diffusion of the substrate into the polymer and more so by the chemical step of methanolysis to form *p*-nitrophenol and (or) its diffusion out of the polymer.

To demonstrate that the polymers are truly catalytically active, an experiment with an excess of substrate was done

Table 4. Dependence of the pseudo first-order rate constants for the disappearance of **9** (0.03 mmol/L) and appearance of *p*-nitrophenol mediated by 0.32 g of Macro-PL-(II) **8**/Zn^{2+} on the frequency of

Frequency of shaking	k_{obs} for the loss of **9** (s^{-1})	k_{obs} for the appearance of *p*-nitrophenol (s^{-1})
30 s	0.011	0.0045
60 s	0.009	0.0038
120 s	0.007	0.0032

with 5.2 mg of Macro-PL-(II) **7a**/Cu^{2+} in 2.5 mL of methanol solution buffered by *N-iso*-propylmorpholine (6.8 mmol/L) at $^{s}_{s}$pH = 8.8 in presence of **9** at 1 mmol/L. In that case, the pseudo concentration of copper was 0.48 mmol/L and the Abs vs. time curve showed a complete loss of starting material with a k_{obs} value of 0.0083 min^{-1}, which corresponds to a second order rate constant of 0.28 (mol/L)$^{-1}$s^{-1}.

In the cases of the commercial macroporous polymers, and most prominently with Macro-Ald functionalized with **7a**/Cu^{2+} and **7a**/Zn^{2+}, a less than expected amount of product phenol was observed during the reaction of **9** and **11**, along with a complete disappearance of starting material, although analysis of the Abs vs. time curves for each gave the same value of k_{obs}. This suggests that the starting material is at equilibrium with respect to partitioning into the polymer and the rate-limiting step is the chemical one of cleavage, but the product partitions between the solution and the polymer phase.

Where comparisons can be made, and using the pseudo M^{2+} concentrations for the catalysts as described earlier, none of the functionalized polymers have second-order rate constants approaching those of the free **7a**/M^{2+} catalysts in

© 2007 NRC Canada

solution. This is a commonly observed phenomenon with polymeric catalysts and probably stems from a diminution of mobility in the solid catalytic systems, which impedes diffusion of substrate to the reactive sites. It is also possible that since the polymer supports described here require N-benzylated 1,5,9-triazacyclododecanes, that these are far more sterically hindered than **7a**/M^{2+}. Indeed, a recent report (23) indicates that the methanolysis of the carboxylate ester phenyl acetate promoted by **7c**/Zn(II):$^{-}OCH_3$ proceeds with a second-order rate constant of 0.046 $(mol/L)^{-1}s^{-1}$, which is fully 300 times slower than what is reported for the methanolysis of phenyl acetate by **7a**/Zn(II):$^{-}OCH_3$ (13.9 $(mol/L)^{-1}s^{-1}$ (24)). Our own repetition of the catalysis of methanolysis of phenyl acetate promoted by **7c**/Zn(II):$^{-}OCH_3$ indicates that the second-order rate constant is 4.0 ± 0.2 $(mol/L)^{-1}s^{-1}$, which is only a factor of three less than that reported for **7a**/Zn(II):$^{-}OCH_3$, which suggests that there is some anomalous error in the recently reported value (23). A similarly small steric effect of 2.5 fold is also evident in the second-order rate constant for the methanolysis of **9** exhibited by **7c**/Zn(II):$^{-}OCH_3$ (18.2 ± 0.2 $(mol/L)^{-1}s^{-1}$) relative to that of **7a**/Zn(II):$^{-}OCH_3$ (46.8 ± 0.5 $(mol/L)^{-1}s^{-1}$ (5*c*).

It therefore seems reasonable to ascribe the reduced activity of these functionalized polymers relative to the solution catalysts to surface effects with the polymers that impeded the mobility of the substrate in reaching the active sites. Nevertheless, the catalysts supported on these resins do accelerate appreciably the methanolysis of all the substrates compared with the background $^{-}OCH_3$-promoted reaction at the $^{s}_{s}$pH where the catalyzed reactions are conducted. For example, the acceleration of the methanolysis of fenitrothion (**11**), mediated by the catalyst at an apparent concentration of 1 mmol/L (0.028 g of DVB50-(II) **7a**/Cu^{2+} suspended in 2.5 mL of solution) is a factor of 2.9×10^6 greater at $^{s}_{s}$pH = 9.

In the case of the polymers containing **8**/Zn^{2+}, the k_2 values are higher than those obtained with **7a**/M^{2+} (see Tables 2 and 3). Previously we have found that the solution reactions of phenanthroline/M^{2+} complexes are slower than with the triazamacrocycle/M^{2+} complexes because of the fact that the former are inactivated by dimerization and must dissociate to the active monomeric forms (7, 25). However, the dimerization is minimized or precluded on the polymers so the phenanthroline grafted resins now become more active than their triazamacrocyle grafted comparisons (see Macro-PL-(II) **8**/Zn^{2+} and Macro-PL-(II) **7a**/Zn^{2+} entries in Tables 2 and 3).

As shown in Fig. 2, a plot of the pseudo first-order rate constant for the methanolysis of **9** at $^{s}_{s}$pH = 8.7 as a function of weight of added Macro-PL-(II)**7a**/Cu^{2+} or **7a**/Zn^{2+} polymer is linear, indicating there is no saturation phenomenon such as was observed with a previously reported (9) catalyst and the substrate diphenyl *p*-nitrophenyl phosphate in aqueous solution. The same linear dependence was observed with the **8**/Zn^{2+}-functionalized polymer except at high weight, where the reaction rate depends on the frequency of shaking.

There are other subtle differences observed between the phenanthroline and triazamacrocyle grafted complexes. In the case of **8**/Zn^{2+} grafts on the Macro-PL polymer, stronger absorption of the phenol products is initially observed relative to the **7a**/M^{2+} material. However, after several reactions

Fig. 2. Pseudo first-order rate constant, k_{obs}, for the methanolysis of **9** mediated by **7a**/Cu^{2+} (□) and **7a**/Zn^{2+} (●) functionalized Macro-PL-(II) vs. weight of the polymer at $^{s}_{s}$pH = 8.7, T = 25 °C.

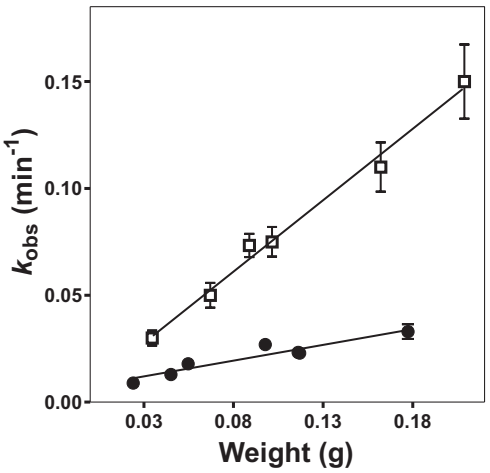

with the same **8**/Zn^{2+}-grafted polymer, the appearance of phenol in the solution is more pronounced. Control experiments establish that the absorbance of a solution of *p*-nitrophenol decreases in the presence of fresh polymer functionalized with **8**/Zn^{2+}. These observations confirm that phenol does partition between the polymer and solution, but that after several reactions the polymer eventually becomes saturated with the product.

Reuse of polymer catalysts

Except in the case of the methanolysis of substrate **10**, the activity of most of the polymeric catalysts showed good stability over several catalytic cycles. With substrate **9**, the second-order rate constant of 0.1 g of Macro-PL-(II) **7a**-Cu^{2+} ($[Cu^{2+}]$ = 9.20 mmol/L) is stable 0.14 ± 0.02 $(mol/L)^{-1}s^{-1}$ over 10 consecutive experiments. Similar experiments conducted with Macro-PL(II) Zn^{2+}/**7a** polymers showed a large inconsistency in reactivity between cycles (a complete cycle comprises the reaction to completion, followed by filtration, washing of the recovered polymer with 50 mL of methanol, and drying in air overnight). However, it was observed that the Macro-PL(II) Zn^{2+}-loaded polymers do recover complete reactivity when they are allowed to stand in the *N-iso*-propylmorpholine buffer solution for more than 12 h after a cycle. This phenomenon is tentatively attributed to an interaction between CO_2 and Zn^{2+}/**7a** complex in the air, which reversibly inhibits the catalyst. This decrease of reactivity is not observed with material functionalized with **8**/Zn^{2+}.

As a further check to see that any loss in acitivty was not due to the loss of metal ion through subsequent reactions, we have reanalyzed the polymers for metal ion content following at least three cycles. For example, Macro-Ald **7**a/Cu^{2+} and Macro-Ald **7**a/Zn^{2+}, after at least three cycles reacting with **9**, showed an analytical Cu^{2+} loading of 0.17 and 0.15 mmol/g before and after use, while the Zn^{2+} loading was 0.023 and 0.020 mmol/g before and after use. While the absolute numbers seem to show some decrease after use, the fact that the catalytic activity is unchanged with **9** over prolonged reuse suggests that the analytical numbers are the same within experimental uncertainty.

© 2007 NRC Canada

Table 5. Apparent second-order rate constants for different polymer resins functionalized with **7a**/M^{2+} or **8**/Zn^{2+}, determined at $^{s}_{s}$pH = 8.9 in methanol buffered with *N-iso*-propylmorpholine, T = 25 °C, [**10**] = 3×10^{-4} mol/L.

Polymer	k_2 (**10**), 1st exp. $((mol/L)^{-1}s^{-1})$	k_2 (**10**), 2nd exp. $((mol/L)^{-1}s^{-1})$
DVB50 **7a**/Cu^{2+}	3.1	0.36
Macro-Ald **7a**/Cu^{2+}	0.22	No reaction
Meso-Ald **7a**/Cu^{2+}	0.17	0.011
Macro-Ald **7a**/Zn^{2+}	0.20	0.18
DVB50-hl **8**/Zn^{2+}	0.49	0.49

However, in the case of *O*-ethyl-*S*-3,5-dichlorophenyl methylphosphonothioate (**10**) the results given in Table 5 with DVB20 and DVB50 show that the reactivity of the supported Cu((II) catalysts decreases with each cycle. For example, with [**10**] = 0.3 mmol/L, DVB50 **7a**/Cu^{2+} exhibits a k_2 = 3.1 $(mol/L)^{-1}s^{-1}$ for its first cycle and 0.36 $(mol/L)^{-1}s^{-1}$ for the second cycle. This drop of reactivity is also accompanied by a change of the blue-green color of the solid to yellow, suggesting that the active Cu(II) form of the metal ion was reduced to Cu(I). Monitoring the reaction of 0.3 mmol/L **10** at 253 nm shows that the starting material disappears, but none of the thiolate product, which should absorb strongly at 270 nm, is observed to appear, Fig. 3). This observation, coupled with the loss of activity of the catalyst suggests that the thiolate product is absorbed by the catalyst and oxidized to the disulfide with concomitant reduction of the Cu(II) to Cu(I) and loss of activity. Although it seems counterintuitive that the small amount of S-containing substrate could inactivate all the Cu(II) through reduction, it is possible that there exists a variety of Cu-containing sites that have variable accessibility, with the most available and reactive ones being inactivated first.

For the Zn^{2+} catalysts, a redox reaction between metal and thiolate cannot happen, and as shown in Table 5 there is no loss of reactivity observed for complex with **7a** and **8**.

Influence of water

Experiments to determine the effect of 2% of added water on the reactivity of the polymers in methanol were conducted in the presence of *N-iso*-propylmorpholine buffer (6.8 mmol/L) at $^{s}_{s}$pH = 8.9. The results over 10 cycles (defined earlier) for the reaction of **9** mediated by 50 mg of Macro-PL-(II) **8**/Zn^{2+} ([Zn^{2+}] = 1.96 mmol/L) are reported graphically in Fig. 4.

The first reaction is a reference one for the reaction using substrate **9** without water, after which the 2% water was added to the UV cell for all the subsequent reactions. As can be judged from the appearance of Fig. 4, water continually degrades the activity until it reaches a stable value of 0.03 min^{-1} after the **9** runs, corresponding to a loss of 85% of the initial reactivity.

General comments on activities

Comparison of the kinetic reactivities given in Table 3 suggests a general order of reactivity of Meso-Ald < Macro-Ald < Macro-PL < Macr-PL-hl ≈ synthesized polymers. The difference in reactivity between mesoporous and macroporous commercial polymers shows the importance of

Fig. 3. UV spectra for the disappearance of **10** (at 0.3 mmol/L) catalyzed by DVB50-(II) **7a**/Cu^{2+} ([Cu^{2+}] = 6.8 mmol/L) at $^{s}_{s}$pH = 9.1.

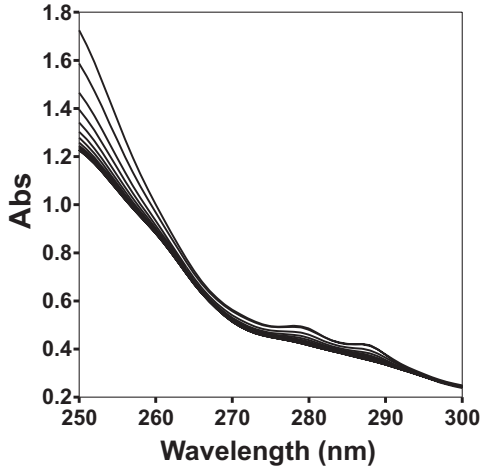

Fig. 4. Pseudo first-order rate constant, k_{obs}, for the methanolysis of **9** (10 cycles each with 0.03 mmol/L) with functionalized Macro-PL-(II) **8**/Zn^{2+} (50 mg) at $^{s}_{s}$pH = 8.9 in presence of 2% *v*:*v* of water.

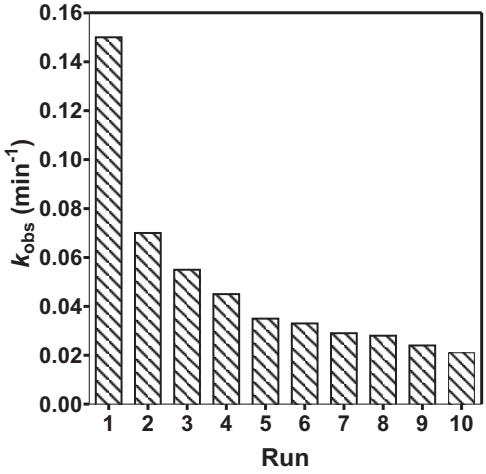

porosity in the activity of these supported catalysts. Since the polystyrene matrices used here as support materials do not swell in methanol solvent during the M^{2+}-complexation steps, the mesoporous polymers have the accessible catalytic sites present only on the surface of beads. It is known (21) that catalytically active polymers having an increased pore size allow an increased permeation of reagent and substrate into the beads, effectively increasing the local concentration of accessible catalyst. The activities of the synthetic resins made here are around 10 times better than the commercial polystyrenes, which is probably due, at least in part, to an increase in their pore size relative to the commercial macroporous polymers. However, the accessibility is not the only parameter that explains the difference of reactivity. The concentration of catalytic sites relative to the surface area is also important. The rather small bead size of the synthesized polymers and their higher loading gives a higher concentration of catalytic species on the surface. This is demonstrated by the difference in reactivity observed between Macro-PL

© 2007 NRC Canada

Fig. 5. Continuous flow system of total volume 1.5 mL, with polymer in the column represented as the shaded rectangle, a flow through UV cell, and a peristaltic pump to drive the solution at a flow rate of 1.17 mL/min.

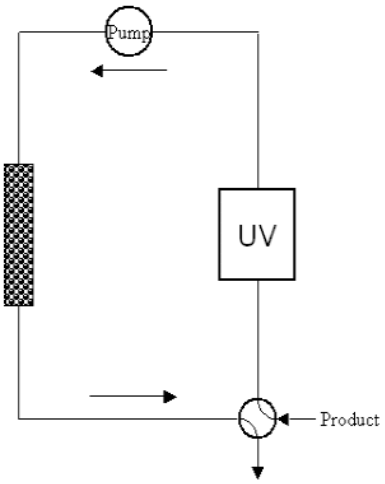

Fig. 6. Absorbance vs. time curves for the disappearance of **9** (0.03 mmol/L) (▲, absorbance at 275 nm) catalyzed by 0.113 g of functionalized Macro-PL **7a**/Cu^{2+} and for the appearance of *p*-nitrophenol (■, absorbance at 310 nm) at $^{s}_{s}$pH = 8.8.

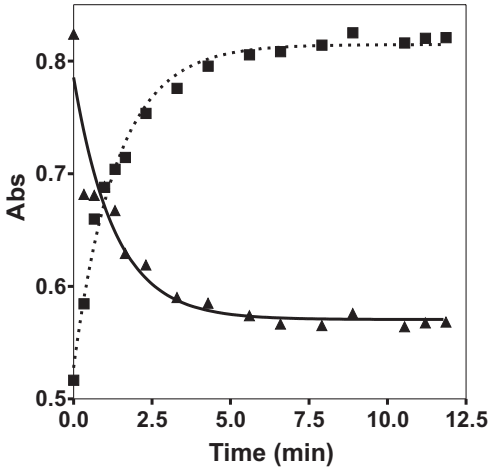

7/Cu^{2+} and Macro-PL-(II) **7**/Cu^{2+} for which the matrices are the same, but the loading of Macro-PL-(II) is higher by a factor 2 (see Table 1). The main difference between those materials is the surface concentration of Cu^{2+}, but the rate constant for the reaction with **9** and **11** vary by factors of 7 and 10 respectively. The increase of reactivity in the case of higher Cu^{2+} concentration on the surface is consistent with a cooperative effect between two neighboring metal ions.

Column system

The most efficient materials made with polystyrene resin purchased from Polymer Laboratories (PL-CMS MP resin) were used in an improvised column system. This system, as illustrated in Fig. 5, consists of a variable-flow low-flow peristaltic pump connected to a column (i.d. 3.0 mm, length 50 mm, from Chrom Tech), which was filled with about ~0.1 g of the polymer support, and an injection valve (Chrom Tech, OM-1114) permitting the injection of a known volume of methanol containing the OP substrate.

Also included in the system is a UV–vis flow cell that allows monitoring of the absorbance vs. time profile of the circulating solution. The total volume of the circulating system is around 1.5 mL. A solution containing the OP substrate was introduced through the system and the valve was closed to permit continuous circulation. Shown in Fig. 6 is the kinetic curve of disappearance of **9** catalyzed by functionalized Macro-PL **7**/Cu^{2+} (0.1130 g) with a rate flow of 1.17 mL min^{-1}.

Both absorbance vs. time curves can be fitted by NLLSQ fitting to a first-order kinetics model giving a pseudo first-order rate constant of 0.72 ± 0.05 min^{-1}. In general for this circulating system, the data do not exactly follow a first-order profile because of the fact that they have stairlike profile, where each step corresponds to one cycle of the system. In the case of the data in Fig. 6, the reaction appears to be done after three cycles through the polymeric support.

As shown in Fig. 7, the reaction of phosphonate **9** with Macro-PL-(II) **7a**/Cu^{2+} has the same rate constant over 10 different injections of 0.03 mmol/L OP solution. The same

Fig. 7. Pseudo first-order rate constant, k_{obs}, for the methanolysis of **9** (at 0.03 mmol/L) with Macro-PL-(II) Cu^{2+}/**7a** (0.1130g) in a column at a flow rate of 1.17 mL/min at $^{s}_{s}$pH = 8.8.

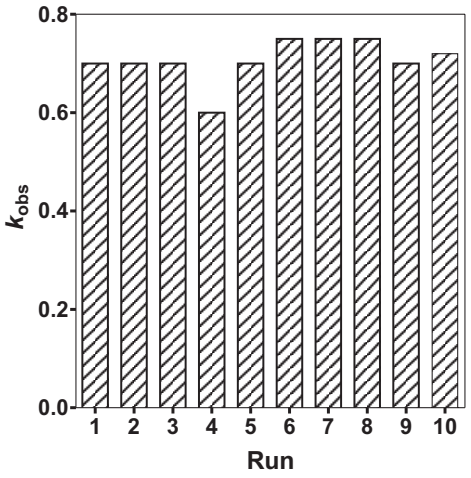

stability was observed for **11** with Macro-PL-(II) **7a**/Cu^{2+}, and **9** and **10** with Macro-PL-(II) **7a**/Zn^{2+}.

To demonstrate turnover of the catalyst on the polymer, an experiment monitoring the decomposition of an excess of substrate was conducted wherein 25 mL of methanol solution containing 1.2×10^{-2} mmol of **9** was circulated through a column (i.d. 3.0 mm, length 25 mm) containing 46.6 mg of Macro-PL-(II) **8**-Zn^{2+} (total amount of Zn^{2+} was 4.6×10^{-3} mmol). The observed rate constant for the disappearance of the substrate was 0.002 ± 0.0007 min^{-1}, corresponding to a rather large half-time of 5.75 h. However, under these conditions the volume of the column containing the active polymer was only 0.175 mL, and since the flow rate was 0.29 mL/min, the great bulk of the substrate was not in contact with the polymer. These data indicate that the polymer is capable of destroying an excess of substrate, surviving prolonged contact with the reacting system and suggest that far greater efficacy would be possible with large columns in

© 2007 NRC Canada

circulating systems, where the ratio of the column volume to total circulating volume is maximized.

Conclusion

In this work we have shown that polymer-supported metal and (or) complex catalysts can be prepared by grafting a ligand (**7a** or **8**) onto a suitable chloromethylated polystyrene resin, which can then be loaded with M^{2+} (Cu^{2+} or Zn^{2+}). This catalytic matrix shows good activity for mediating the methanolysis of different kinds of OP esters like *O*-ethyl-*S*-3,5-dichlorophenyl methylphosphonothioate (**10**), *O*-ethyl-*O*-4-nitrophenyl methylphosphonate (**9**), and fenitrothion (**11**), which are simulants for V-agents, G-agents, and P=S pesticides. In the most favourable case, 28 mg of DVB50-(II) **7a**/Cu^{2+} suspended in 2.5 mL of solution provides a factor of 2.9×10^6 in acceleration of the methanolysis of fenitrothion over the background reaction at ${}^{s}_{s}$pH = 9. The methanolysis reactivity is shown to be enhanced by a large porosity of the solids, which allows access of the OP ester substrates to the catalytic centers. This material can be used in column systems with a continuous flow and may show some promise for larger scale applications to cleanups of OP esters, where the contaminants can be dissolved in methanol that is passed through a column for decontamination.

Acknowledgements

The authors gratefully acknowledge the financial assistance of the Natural Science and Engineering Research Council of Canada (NSERC), Queen's University, the Canada Foundation for Innovation, and the Canada Council for the Arts. MFM thanks NSERC for the award of a CGS-M postgraduate scholarship EC thanks NSERC for the award of a Summer Undergraduate Research Award, and KGC thanks Queen's University for a Summer Work Experience Award.

References

1. Y.-C. Yang, J.A. Baker, and J.R. Ward. Chem. Rev. **92**, 1729 (1992).
2. (*a*) Y.-C. Yang. Acc. Chem. Res. **32**, 109 (1999); (*b*) Y.-C. Yang. Chem. Ind. (London), 334, (1995).
3. (*a*) A. Toy and E.N. Walsh. Phosphorus chemistry in everyday living. 2nd ed. American Chemical Society, Washington, DC. 1987. Chap. 18–20; (*b*) L.D. Quin. A guide to organophosphorus chemistry. Wiley, NY. 2000; (*c*) M.A. Gallo and N.J. Lawryk. Organic phosphorus pesticides. The handbook of pesticide toxicology. Academic Press, San Diego, CA. 1991; (*d*) P.J. Chernier. Survey of industrial chemistry. 2nd ed. VCH, NY. 1992. pp 389–417; (*e*) K.A. Hassall. The biochemistry and uses of pesticides. 2nd ed. VSH, Weiheim, Germany. 1990. pp 269–275.
4. H. Morales-Rojas and R.S. Moss. Chem Rev. **102**, 2497 (2002) and refs. cited therein.
5. (*a*) J.S. Tsang, A.A. Neverov, and R.S. Brown. J. Am. Chem. Soc. **125**, 7602 (2003); (*b*) T. Liu, A.A. Neverov, J.S.W. Tsang, and R.S. Brown. Org. Biomol. Chem. **3**, 1525 (2005); (*c*) R.E. Lewis, A.A. Neverov, and R.S. Brown. Org. Biomol. Chem. **3**, 4082 (2005); (*d*) S.A. Melnychuk, A.A. Neverov, and R.S. Brown. Angew. Chem. Int. Edit. **45**, 1767 (2006).
6. J.A.W. Tsang, A.A. Neverov, and R.S. Brown. Org. Biomol. Chem. **2**, 3457 (2004).
7. A.A. Neverov and R.S. Brown. Org. Biomol. Chem. **2**, 2245 (2004).
8. These comparisons are made under the reasonable assumption that the background reaction is attributable to $^{-}OCH_3$ at near neutral ${}^{s}_{s}$pH values, and that the autoprotolysis constant of methanol is $10^{-16.77}$. E. Bosch, F. Rived, M. Rosés, and J. Sales. J. Chem. Soc., Perkin Trans. 1, 2, 1953 (1999).
9. F.M. Menger and T. Tsuno. J. Am. Chem. Soc. **111**, 4903 (1989).
10. (*a*) Q. Lu, A. Singh, J.R. Deschamps, and E.L. Chang. Inorg. Chim. Acta, **309**, 82 (2000); (*b*) C.M. Hartshorn, A. Singh, and E.L. Chang. J. Mater. Chem. **12**, 602 (2002); (*c*) C.M. Hartshorn, J.R. Deschamps, A. Singh, and E.L. Chang. React. Funct. Polym. **55**, 219 (2003).
11. (*a*) S.G. Srivatsan and S. Verma. Chem. Eur. J. **7**, 828 (2001); (*b*) S.G. Srivatsan, M. Parvez, and S. Verma. Chem. Eur. J. **8**, 5184 (2002); (*c*) V. Chandraskhar, A. Athmoolan, S.G. Srivatsan, P. Shanmuga Sundaram, S. Verma, A. Steiner, S. Zacchini, and R. Butcher. Inorg. Chem. **41**, 5162 (2002); (*d*) S.G. Srivatsan and S. Verma. Chem. Commun. (Cambridge), 515 (2000).
12. A.I. Hanafy, V. Lykourinou-Tibbs, K.S. Bisht, and L.-J. Ming. Inorg. Chim. Acta, **358**, 1247 (2005).
13. S. Durie, K. Jerabek, C. Mason, and D.C. Sherrington. Macromolecules, **35**, 9665 (2002).
14. A. Chemin, H. Deleuze, and B. Maillard. Eur. Polym. J. **34**, 1395 (1998).
15. (*a*) K. Binnemans, P. Lenaerts, K. Driesen, and C. Görller-Warland. J. Mater. Chem. **14**, 191 (2004); (*b*) P. Lenaerts, K. Driesen, R. Van Deun, and K. Binnemans. Chem. Mater. **17**, 2148 (2004).
16. P. Brunet and J.D. Wuest. J. Org. Chem. **61**, 1847 (1996).
17. Y. Chauvin, D. Commereuc, and F. Dawans. Prog. Polym. Sci. **5**, 95 (1977).
18. K.S.W. Sing, D.H. Everett, R.A.W. Haul, L. Moscou, R.A. Pierotti, J. Rouquerol, and T. Siemieniewska. Pure Appl. Chem. **57**, 603 (1985).
19. A. Guyot and M. Bartholin. Prog. Polym. Sci. **8**, 277 (1982).
20. H. Jacobelli, M. Bartholin, and A. Guyot. Angew. Makromol. Chem. **80**, 31 (1979).
21. A. Guyot. Pure Appl. Chem. **60**, 365 (1988).
22. For the measurement of ${}^{s}_{s}$pH in methanol see: G. Gibson, A.A. Neverov, and R.S. Brown. Can. J. Chem. **81**, 495 (2003).
23. R. Cacciapaglia, A. Casnati, L. Mandolini, D.N. Reinhoudt, R. Salvio, A. Sartori, and R. Ungaro. Inorg. Chim. Acta, **360**, 981 (2007).
24. A.A. Neverov, N.E. Sunderland, and R.S. Brown. Org. Biomol. Chem. **3**, 65 (2005).
25. W. Desloges, A.A Neverov, and R.S. Brown. Inorg Chem. **43**(21), 6752 (2004).

© 2007 NRC Canada

Ketonization of the unusually acidic elongated enol generated by flash photolytic decarboxylation of *p*-formylphenylacetic acid in aqueous solution

Yvonne Chiang, Kirill Kolmakov, and A. Jerry Kresge

Abstract: Rates of photolysis of *p*-formylphenylacetic acid were measured flash photoytically in perchloric acid and sodium hydroxide solutions, and also in acetic acid, biphosphate ion, and tris-(hydroxymethyl)methaneammonium ion buffers, using H_2O and D_2O as solvents. The results provide rate profiles and solvent isotope effects, which indicate that photolysis occurs through an elongated enol intermediate. This enol is unusually strongly acidic, by some two to three pQ_a units, when compared with simple non-elongated enols.

Key words: flash photolysis, elongated enols, rate profiles, solvent isotope effects.

Résumé : Faisant appel à la photolyse éclair, on a mesuré les vitesses de photolyse de l'acide *p*-formylphénylacétique dans des solutions aqueuses ou dans le l'eau lourde d'acide perchlorique et d'hydroxyde de sodium ainsi que dans l'acide acétique en présence d'ion biphosphate et de tris(hydroxyméthyl)méthaneammonium comme tampons. Les résultats permettent d'obtenir des profils de vitesse et des effets isotopiques de solvant qui indiquent que la photolyse se produit par le biais d'un intermédiaire énolique allongé. Cet énol est particulièrement acide, par des valeurs de pQ_a de deux à trois unités supérieures à celles d'énols simples non allongés.

Mots-clés : photolyse éclair, énols allongés, profils de vitesse, effets isotopiques de solvant.

[Traduit par la Rédaction]

Introduction

Photodecarboxylation of *p*-benzoylphenylacetic acid (**1**) when carried out in aqueous solution, gives *p*-methylbenzophenone (**2**) as its reaction product (eq. [1]) (1).

[1] 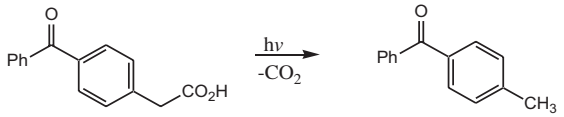

1 **2**

This substance is formed through a carbanion intermediate, whose negative charge is delocalized from methylene carbon (**3**) onto carbonyl oxygen (**4**) (eq. [2]).

[2] 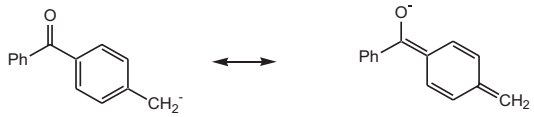

3 **4**

Received 16 May 2007. Accepted 18 July 2007. Published on the NRC Research Press Web site at canjchem.nrc.ca on 17 October 2007.

This article is dedicated to the memory of Keith Yates.

Y. Chiang, K. Kolmakov and A.J. Kresge.[1] Department of Chemistry, University of Toronto, Toronto, ON M5S 3H6, Canada.

[1]Corresponding author (e-mail: akresge@chem.utoronto.ca).

Product formation could therefore occur either by direct protonation of methylene carbon (eq. [3]) or by protonation of carbonyl oxygen to give an elongated enol intermediate, **5**, whose ketonization would afford the observed product (eq. [4]). In previously reported work (2), we carried out this decarboxylation flash photolytically and detected a short-lived transient species that we identified as elongated enol **5**. This enol has proved to be an unusually strong acid, several orders of magnitude more acidic than other simple enol analogs without the elongating cyclohexadienyl spacer.

[3] 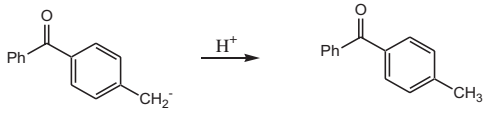

3 **2**

[4] 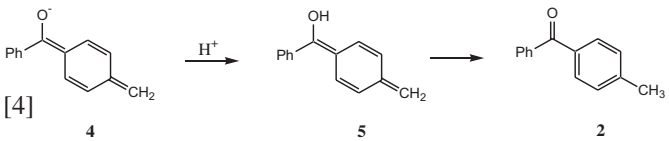

4 **5** **2**

We have now added to that previous study a companion investigation of the photodecarboxylation of *p*-formylphenylacetic acid (**6**) (eq. [5]). We found that this reaction

[5] 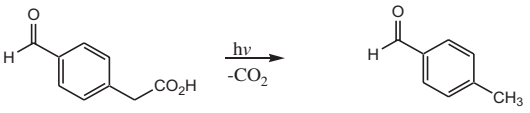

6 **7**

 doi:10.1139/V07-095 © 2007 NRC Canada

also occurs through an elongated enol intermediate, which is also unusually strongly acidic.

Experimental Section

Materials

p-Formylphenylacetic acid was prepared by a Sommelet reaction (3) on 4-chloromethylphenylacetic acid, itself synthesized by chloromethylation of phenylacetic acid (4).

4-Chloromethylphenylacetic acid

A 10 mL capacity vial, equipped with septa and stirring bar, was purged with argon, and 0.8 mL (1.78 g, 0.0068 mol) of $SnCl_4$ was introduced through a syringe. Dry phenylacetic acid (1.36 g, 0.010 mol) was dissolved in 2 mL (2.12 g, 0.026 mol) of monochloromethyl ether ($ClCH_2OCH_3$) at room temperature and the solution was slowly added into the vial within 20 min upon vigorous stirring at 0 °C. The reaction mixture was left at room temperature for 1 h under argon and then quenched with 30 mL of ice-cold water upon vigorous stirring. An amorphous white precipitate was separated. This was washed with water and dissolved in 20 mL of $CHCl_3$, and the solution was dried over $MgSO_4$. The solvent was evaporated to dryness, and the residue was recrystallized from a mixture of CH_2Cl_2 (10 mL) and hexane (20 mL) to afford 0.82 g (44%) of a product whose melting point (149–151 °C) was consistent with the literature (4). Its ^{1}H NMR ($CDCl_3$, 300 MHz) had the following signals: δ: 3.65 (s, 2H, CH_2), 4.57 (s, 2H, CH_2Cl), 7.26 (d, 2H, J = 9 Hz, *p*-C_6H_4), 7.35 (d, 2H, J = 9 Hz, *p*-C_6H_4).

4-Formylphenylacetic acid

Hexamethylenetetramine (840 mg, 0.0060 mol) and 4-chloromethylphenylacetic acid (740 mg, 0.0044 mol) were heated under reflux for 1 h in 20 mL of chloroform. The solvent was then evaporated to one half of its initial volume, and 990 mg (75%) of a colorless quaternary ammonium salt separated. This was dried and then heated under reflux in 10 mL of 50 vol% aqueous acetic acid for 1.5 h under an argon atmosphere. Upon cooling to ambient temperature, the mixture was quenched with a solution of 10 g of NH_4Cl in 40 mL of H_2O and was then extracted with CH_2Cl_2 (3 × 15 mL). The extract was washed with a solution of NH_4Cl (1.0 g) and 0.5 mL of concd. HCl in 10 mL of H_2O and was dried over $MgSO_4$. The solvent was removed under vacuum to afford 460 mg (70%) of crude product, which was chromatographed on a column containing 8 g of silica gel with mobile phase MeCN–CH_2Cl_2 (1:1 *v*/*v*). The main fraction furnished 330 mg (44%) of a relatively pure (>90%, NMR) compound. The course of the separation was monitored by TLC on SIL-G/UV 254 plates with acetone–acetonitrile (3:1) as the mobile phase. Further, an analytical sample (80 mg) with no detectable impurities (HPLC, TLC) and mp 128 to 129 °C was obtained, starting from 150 mg of the material, by recrystallization (2 times) from CH_2Cl_2–hexane (1:3 *v*/*v*) under an argon atmosphere. (Baker et al. (5), who originally obtained 4-formylphenylacetic acid with a very poor yield, reported mp 131 °C). The spectroscopic data (NMR, MS) listed here confirm the structure.

^{1}H NMR ($CDCl_3$, 300 MHz) δ: 3.75 (s, 2H, CH_2), 7.46 (d, 2H, J = 8 Hz, p-C_6H_4), 7.86 (d, 2H, J = 8 Hz, *p*-C_6H_4), 10.01 (s, 1H, CHO). ^{13}C NMR ($CDCl_3$, 75 MHz) δ: 41.05 (CH_2), 130.09, 130.19, 135.56 and 140.30 (C_{Ar}), 176.51 (CO_2H), 191.90 (C=O). MS (EI) *m*/*z*: 164 M^+ (85), 119 M^+ – CO_2-H (55), 91 M^+ –CO_2–OH (100). HRMS (EI) calcd. for (M^+) $C_9H_8O_3$: 164.0473; found 164.0476.

All other materials were best available commercial grades.

Kinetics

Rate measurements were made using either a conventional flash lamp (microsecond) flash photolysis system (6), or an eximer laser (nanosecond) system (7) operating at λ_{exc} = 248 nm, which have already been described (6, 7). This revealed a short-lived transient species, subsequently identified as an elongated enol intermediate (vide infra) with broad UV absorbance centered at λ = 330 nm. Decay of this absorbance, for the most part, followed the first-order rate law well, and rate constants were obtained by least-squares fitting of a single exponential function. In some cases, however, the data fit a double exponential function better than a single exponential function, and a double exponential was therefore used. In this situation, one of the two rate constants obtained changed its value when the reacting solution was degassed, and the other unchanging rate constant was then taken to be that for ketonization of the elongated enol intermediate.

Product identification

The reaction investigated was shown to be the decarboxylation of eq. 5 by HPLC analysis using an authentic sample of the expected product *p*-methylbenzaldehyde (**7**).

Results

Rates of decay of the broad UV absorption band centered at λ_{max} = 330 nm, generated by flashing 4-formylphenylacetic acid, were determined in aqueous perchloric acid and sodium hydroxide solutions, and also in acetic acid, biphosphate ion, and tris-(hydroxymethyl)methaneammonium ion buffer solutions, using H_2O as solvent; some rate measurements were made as well in perchloric acid and sodium hydroxide solutions and biphosphate ion buffers, using D_2O as solvent. The ionic strength of all reacting solutions was kept constant at 0.10 mol/L with sodium perchlorate as the inert electrolyte. The results are summarized in Tables S1–S3.[2,3]

[2] Supplementary data for this article are available on the journal Web site (canjchem.nrc.ca) or may be purchased from the Depository of Unpublished Data, Document Delivery, CISTI, National Research Council Canada, Ottawa, ON K1A 0R6, Canada. DUD 5207. For more information on obtaining material refer to cisti-icist.nrc-cnrc.gc.ca/irm/unpub_e.shtml.

[3] In perchloric acid solutions the absorbance from the transient species of interest here diminished as the acid concentration increased, consistent with decarboxylation occurring through the carboxylate form of the substrate, and HPLC analysis showed the formation of other (uninvestigated) products. These interferences could be diminished somewhat by using deoxygenated solutions and accumulating data from several replicate flash photolysis shots.

© 2007 NRC Canada

The measurements in buffers were made in a series of solutions of constant buffer ratio, and therefore constant hydronium ion concentration, but varying total buffer concentration. Buffer catalysis was strong, and observed rate constants within a given buffer solution series were accurately proportional to buffer concentration. The data were therefore analyzed by least-squares fitting of the linear buffer dilution expression shown in eq. [6]. The zero buffer concentration intercepts, k_{int}, obtained in this way, plus the rate constants determined in perchloric acid and sodium hydroxide solution, are displayed as the rate profiles shown in Fig. 1.

[6] $$k_{obs} = k_{int} + k_{buff}[buffer]$$

The shape of these rate profiles is characteristic of enol ketonization reactions, which are known to occur by rate-determining β-carbon hydronation of either the enol or its enolate ion by any available acid (8). Because these profiles refer to solvent-related species, the available acids will be either the hydronium ion, written here as L^+, or a solvent water molecule, L_2O, as shown in the reaction scheme of eq. [7].[4] The acid-catalyzed descending diagonal portions at the high acidity ends of these profiles then represent β-carbon hydronation of the enol by hydronium ion. These sections are followed by short "uncatalyzed" horizontal portions, which could be due either to β-carbon hydronation of enol by solvent water or to the ionization of enol to enolate and hydronium ions followed by β-carbon hydronation of the enolate ion by hydronium ion. This latter process generates hydronium ions in its rapid pre-equilibrium ionization step and then uses them up in its rate-determining step, to give an overall reaction independent of hydronium ion concentration.

[7]

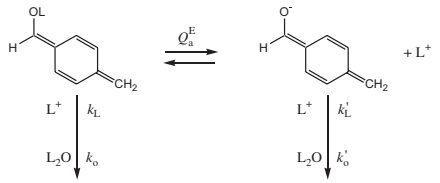

These short horizontal sections are followed by base-catalyzed ascending diagonal portions that can be assigned to the ionization of enol to enolate ion followed by hydronation of enolate by solvent water. This process produces hydronium ions in its rapid pre-equilibrium step but does not use then up in its rate-determining step, to give an overall reaction whose rate is inversely proportional to hydronium ion concentration and has the appearance of hydroxide ion catalysis. Finally at sufficiently low acidity, the position of the enol–enolate equilibrium shifts over to the side of the enolate ion, and the process reduces to simple hydronation of enolate β-carbon by solvent water. This gives the final horizontal rate profile plateau.

The rate law that applies to this reaction scheme is shown in eq. [8], where k_{uc} is used to designate the process of an uncertain mechanism represented by the central short horizontal sections of the rate profiles, and the other rate and equilibrium constants are defined by eq. [7].

Fig. 1. Rate profiles for the ketonization of elongated enol **8** in H_2O (○) and D (△) solutions.

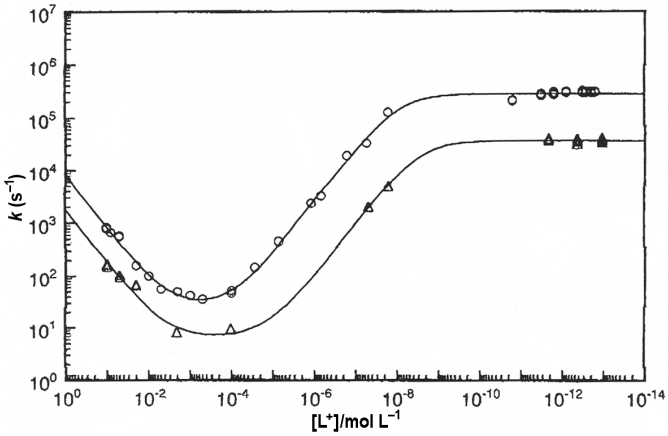

[8] $$k_{obs} = k_L[L^+] + k_{uc} + k_o'Q_a^E/(Q_a^E + [L^+])$$

Least-squares fitting using this expression gave for H_2O solutions: $k_H = (8.11 \pm 0.48) \times 10^3$ $(mol/L)^{-1}s^{-1}$, $k_{uc} = (2.62 \pm 0.28) \times 10^1$ s^{-1}, $Q_a^E = (9.20 \pm 0.58) \times 10^{-9}$ mol/L, $pQ_a^E = 8.04$, and $k_o' = (2.82 \pm 0.05) \times 10^5$ s^{-1}, and results for D_2O solutions that, when combined with their H_2O counterparts, gave the isotope effects: $k_H/k_D = 4.49 \pm 0.09$, $(k_o')_H/(k_o')_D = 7.74 \pm 0.36$, and $(Q_a^E)_H/(Q_a^E)_D = 3.41 \pm 0.14$.[5] The lines through the data points shown in Fig. 1 were drawn using these results. It may be seen that the data fit the reaction scheme of eq. [7] well and thus provide strong evidence that the process under observation is an enol ketonization reaction.

Further support for the assignment of the rate profiles of Fig. 1 to enol ketonization comes from the isotope effects obtained by comparing results determined in H_2O solution with those obtained in D_2O. The rate constants k_L and k_o' refer to rate-determining substrate hydronation, and isotope effects on these quantities can therefore be expected to contain primary isotope effect components in the normal direction ($k_H/k_D > 1$) of appreciable magnitude. These isotope effects, however, will also contain secondary components, with that on k_L in the inverse direction ($k_H/k_D < 1$) and that on k_o' in the normal direction ($k_H/k_D > 1$) (9). This will make the isotope effect on k_o' considerably stronger than that on k_H', which is nicely consistent with our observation, i.e., $(k_o')_H/(k_o')_D = 7.7$ whereas $k_H/k_D = 4.5$. The isotope effect on Q_a^E is also consistent with this quantity being the acidity constant of an enol ionizing as an oxygen acid. Such equilibrium isotope effects lie in the normal direction and generally fall in the range 3–5 (8); that of course agrees well with the observed value $(Q_a^E)_H/(Q_a^E)_D = 3.4$.

Thus, both solvent isotope effects and rate profiles agree that decarboxylation of *p*-formylphenylacetic acid occurs through an elongated enol intermediate, **8**, as shown in eq. [9].

[4] The symbol "L" is used to denote either protium or deuterium, "H" is used specifically for protium, and "D" specifically for deuterium.
[5] This is a concentration equilibrium constant applicable at the ionic strength (0.10 mol/L) of the solutions in which it was determined.

© 2007 NRC Canada

[9]

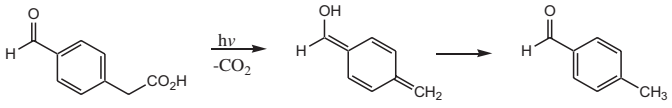

6 8 7

[10]

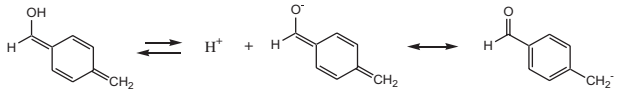

8 10 11

Discussion

The present results show the elongated enol **8** with pQ_a^E = 8.04, to have an unusually strongly acidic hydroxyl group; simple enols ionizing as oxygen acids ordinarily have acidity constants in the range pQ_a^E = 10–11 (8). An especially apt comparison of the present system can be made with the enol of acetaldehyde **9**, which lacks the elongating cyclo-

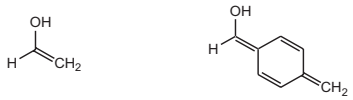

9 8

hexadienyl spacer
of enol **8**; acetaldehyde enol has pQ_a^E = 10.50 (6), some two and a half p*Q* units weaker than the acidity constant of elongated enol **8**. This striking difference is a result of the fact that ionization of enol **8** (eq. [10]) creates an anion whose negative charge can be delocalized from enolate oxygen **10** onto methylene carbon **11** (eq. [10]); this converts a cyclohexadienyl moiety into a benzene ring and thus benefits from a gain in benzene resonance energy. A similar shift of negative charge density is of course possible in the unionized enol, but that involves generation of charge and is consequently not as energetically advantageous. The anion is consequently stabilized more than the unionized enol, and that reduces the energy gap between the enol and enolate ion, making the enol a stronger acid than it would otherwise be.

Acknowledgement

We are grateful to the Natural Sciences and Engineering Research Council of Canada for its generous financial support of our work.

References

1. M. Xu and P. Wan. Chem. Commun. (Cambridge), 2147 (2000); L.A. Huck, M. Xu, K. Forest, and P. Wan. Can. J. Chem. **82**, 1760 (2004).
2. Y. Chiang, A.J. Kresge, I. Onyido, J.P. Richard, P. Wan, and M. Xu. Chem. Commun. (Cambridge, U.K.), 4231 (2005).
3. S.J. Angyal. *In* Organic reactions. Vol. 8. Wiley, NY. 1954. Chap. 4.
4. A.R. Mitchell, B.W. Erickson, M.N. Ryabtsev, R.S. Hodges and R.B. Merrifield. J. Am. Chem. Soc. **98**, 7357 (1976).
5. J.W. Baker, J.A.L. Brieux, and D.G. Saunders. J. Chem. Soc. 404 (1956).
6. Y. Chiang, M. Hojatti, J.R. Keeffe, A.J. Kresge, N.P. Schepp, and J. Wirz. J. Am. Chem. Soc. **109**, 4000 (1987).
7. J. Andraos, Y. Chiang, G.C. Huang, A.J. Kresge, and J.C. Scaiano. J. Am. Chem. Soc. **115**, 10605 (1993).
8. J.R. Keeffe and A.J. Kresge. *In* The chemistry of enols. *Edited by* Z. Rappoport. Wiley, NY. 1990. Chap. 7.
9. A.J. Kresge, R.A. More O'Ferrall, and M.F. Powell. *In* Isotopes in organic chemistry. Vol. 7. *Edited by* E. Buncel and C. C. Lee. Elsevier, Amsterdam, The Netherlands. 1987. Chap. 4.

© 2007 NRC Canada

Chemistry of photogenerated α-phenyl-substituted *o*-, *m*-, and *p*-quinone methides from phenol derivatives in aqueous solution

Li Diao and Peter Wan

Abstract: The enhanced photochemical reactivity of o-substituted phenols in its propensity to give *o*-quinone methide (*o*-QM) intermediates via excited state intramolecular proton transfer (ESIPT) was uncovered by Keith Yates as part of his now classic studies of photohydration of aromatic alkenes, alkynes, and related compounds. Photogeneration of QMs and the study of their chemistry along with potential biological applications are the focus of many groups. In this work, photochemical precursors to *o*-, *m*-, and *p*-QMs based on substituted phenols (hydroxybenzyl alcohols) and related compounds have been studied in aqueous solution as a function of pH and water content. The focus will be on QMs that are stabilized by an α-phenyl substituent, which enhances quantum yields for their formation, with the resulting QMs having longer lifetimes and easier to detect. Noteworthy is that all QM isomers can be photogenerated with the o and m isomers being the most efficient, consistent with the Zimmerman "ortho–meta" effect. *m*-QMs have formal non-Kekulé structures, and although they can be routinely photogenerated, are found to be most reactive. One *m*-QM was found to undergo a photocondensation reaction at high pH giving rise to m-substituted oligomers. The mechanism of QM formation in aqueous solution is believed to involve singlet excited phenols that undergo adiabatic deprotonation to give the corresponding photoexcited phenolate ion, which subsequently expels the hydroxide ion (photodehydroxylation). A pathway involving direct loss of water for the o-isomers is also possible in organic solvents.

Key words: quinone methides, phenols, excited state acidity, solvolysis, carbocations, meta effect, photopolymerization, non-Kekulé intermediates.

Résumé : La réactivité photochimique accrue des phénols *o*-substitués dans sa tendance à donner des intermédiaires *o*-quinométhides (*o*-QM) par le biais d'un transfert de proton intramoléculaire dans l'état excité (TPIEE) a été découverte par Keith Yates dans le cadre de ses études maintenant classiques sur la photohydratation des alcènes et des alcynes aromatiques et des composés apparentés. La photogénération de QM et l'étude de leur chimie en relation avec leurs applications biologiques potentielles sont les objets principaux de recherches de plusieurs groupes. Dans ce travail, opérant en solution aqueuse, on a examiné les précurseurs photochimiques de *o*-, *m*- et *p*-QM issus de phénols substitués (alcools hydroxybenzyliques) et de composés apparentés en fonction du pH et de la quantité d'eau présente. On s'est orienté vers les QM qui sont stabilisés par un substituant ἀ-phényle, ce qui augmente les rendements quantiques de leurs formations et qui conduit à des QM de temps de vie plus longs et une plus grande facilité de détection. Il est important de noter que tous les isomères de QM peuvent être photogénérés, mais que les isomères *o*- et *m*- sont les plus efficaces; ce qui est en accord avec l'effet "ortho-méta" de Zimmerman. Les *m*-QM comportent des structures formelles qui ne correspondent pas à celles de Kekulé et qui, même si elles peuvent facilement être photogénérées, sont les plus réactives. On a trouvé qu'un QM subit une réaction de photocondensation à un pH élevé conduisant à la formation d'oligomères *m*-substitués. On croit que le mécanisme de formation des QM en solution aqueuse implique l'état singulet de phénols excités qui subissent une déprotonation adiabatique conduisant à la formation de l'ion phénolate excité correspondant qui expulse subséquemment l'ion hydroxyde (photodéshydroxylation). Une voie réactionnelle impliquant une perte directe d'eau à partir des isomères ortho est aussi possible dans les solvants organiques.

Mots-clés: quinométhides, phénols, acidité de l'état excité, solvolyse, carbocations, effet méta, photopolymérisation, intermédiaires qui ne correspondent pas à ceux de Kekulé.

[Traduit par la Rédaction]

Received 17 July 2007. Accepted 15 October 2007. Published on the NRC Research Press Web site at canjchem.nrc.ca on 9 November 2007.

This article is dedicated to the memory of Professor Keith Yates.

L. Diao and P. Wan.[1] Department of Chemistry, Box 3065, University of Victoria, Victoria, BC V8W 3V6, Canada.

[1]Corresponding author (e-mail: pwan@uvic.ca).

 doi:10.1139/V07-125 © 2007 NRC Canada

Introduction

The study of photochemical generation and structure-reactivity of polar intermediates derived from substituted aromatic compounds gained a new practitioner in Keith Yates, starting in the early 1980s. After a distinguished career studying classic organic reaction mechanisms (e.g., hydrolysis of esters and amides) and the behaviour of strong acids on organic compounds (acidity functions and their applications), Keith Yates decided to investigate how organic photochemistry could serve the study of organic reaction mechanisms, with initial work on the photohydration of aromatic alkenes and alkynes (1). The idea he had at the time was that the well-known phenomenon of enhanced acidity or basicity of many aromatic compounds (2) could manifest itself in enhanced reactivity such as hydrolysis or electrophilic attack, under the right conditions. Yates and coworkers successfully demonstrated the utility of their ideas in a series of papers that span over 15 years. In particular, in one their studies of photohydration Yates and Kalanderopoulos (3) proposed that the photohydration mechanism of *o*-hydroxystyrene (**1**) involved initial irreversible excited state intramolecular proton transfer (ESIPT) from phenol OH to the β-carbon of the alkene moiety, to give *o*-quinone methides (*o*-QM) **2a** and **2b**, which on trapping by water, would give the expected hydration product **3** (eq. [1]). This mechanism offers a reasonable explanation for the much lower photohydration efficiency observed for *o*-methoxystyrene. Yates and Kalanderopoulos (3) initially wrote only species **2a** as the proposed intermediate in the initial ESIPT step. However, one would expect that the dominant resonance contributor is **2b**, which has the well-known *o*-QM structure. Although Yates ultimately did not pursue a study of QMs, this initial paper (3) indicated that he was already at its doorstep. QM intermediates have a long history, but more recently it has become a topic of renewed interest in both thermal chemistry and photochemistry (4, 5). In particular, recent studies concerning biological applications of QMs as electrophiles for DNA cross-linking and general reactivity and (or) stability with deoxynucleosides as nucleophiles have appeared (5*j*–5*m*) that improve the current understanding along with demonstrated potential applications of these intermediates in biology. With respect to photochemical generation of QMs, initial systematic studies could be traced back to Seiler and Wirz (5*a*) who studied the photohydrolysis of a variety of trifluoromethylphenols and naphthols (e.g., eq. [2]) and demonstrated the viability of photogenerating a variety of difluoro-substituted QMs.

[1]

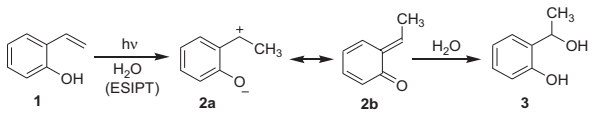

[2]

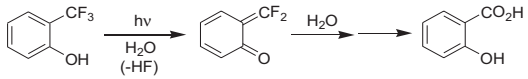

Continuing in the spirit of research direction laid out by Keith Yates, we reported a general method for photogenerating all of the parent QM isomers from hydroxyl-substituted benzyl alcohols (5*c*, 5*d*). This method offered an efficient and general method for making a variety of simple QMs in aqueous solution — including all three parent systems — from simple phenol derivatives and takes direct advantage of the enhanced acidity of phenols in the excited singlet state. Moreover, hydroxybenzyl alcohols are readily available and have a high tendency to give polar intermediates in aqueous solution even though the hydroxide ion is considered to be a very poor leaving group. Although the method and proposed mechanism(s) of reaction are now well known amongst practitioners, many of the original details have not been published. It is the purpose of this paper to address this deficiency and to provide additional new reactivity data for compounds that have been studied before and also for new substrates. The results that will be reported are for hydroxybenzyl alcohols and related derivatives that have at least one α-phenyl substituent (**4**–**11** and **15**–**17**), the latter having the desirable effect of making these systems much easier to handle and study.

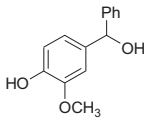

10

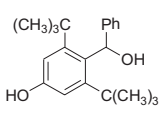

11

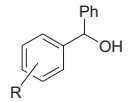

15 R = *o*-OCH_3
16 R = *m*-OCH_3
17 R = *p*-OCH_3

Results and discussion

Materials

The compounds studied (**4**–**11** and **15**–**17**) were readily synthesized using standard procedures, most involving the use of Grignard reagents (see Experimental section).

Product studies

Photolysis of *o*-, *m*-, and *p*-hydroxybenzhydrols (**4**–**6**) in 1:1 (*v*/*v*) H_2O/CH_3OH (Rayonet photochemical reactor, 254 nm lamps, argon purged, 3 min) gave the corresponding methyl ethers **12** (17%), **13** (15%), and **14** (7%), respectively, as the only products in low conversion runs (<20%) (eq. [3]). The ^1H NMR spectrum of the reaction mixture showed the characteristic methoxy singlet for the methyl ether product at δ 3.3–3.4. Similar photolysis of their methoxy-substituted analogs (**15**, **16**, and **17**) gave no reaction except for **15**, which gave about 4% of the corresponding methyl ether. Control experiments performed in the absence of light indicated that only the o and p isomers were reactive (yield up to 5%) if a small amount of $NaHCO_3$ was not added to the solution prior to photolysis. Therefore, all runs (photochemical and thermal) using CH_3OH were carried out in the presence of a pinch of $NaHCO_3$. It is postulated that the residual thermal reaction (solvolysis) in the absence of added $NaHCO_3$ is due to traces of acid present in CH_3OH.

[3]

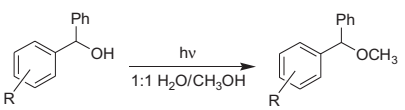

4 R = *o*-OH
5 R = *m*-OH
6 R = *p*-OH

12 R = *o*-OH
13 R = *m*-OH
14 R = *p*-OH

© 2007 NRC Canada

Prolonged photolysis (>20 min) of **4**–**6** gave increasing yields of the methyl ether and also formation of a secondary benzylphenol product (e.g., eq. [4]), which has a characteristic singlet at δ 4.0. As shown in Fig. 1 for **4**, the yield of methyl ether **12** rises rapidly within the first 20 min of irradiation after which its formation slows down and levels off at about 60% yield, while benzylphenol **18** builds up in the product mixture although never becoming a major product. It is reasonable to propose that **18** is the secondary product from photolysis of **12**. The mechanism probably involves initial homolytic cleavage of the C–OMe bond, followed by a disproportionation of the radical pair to form **18** and formaldehyde. We have shown (6) that related benzyl methyl ethers react this way on photolysis.

[4] 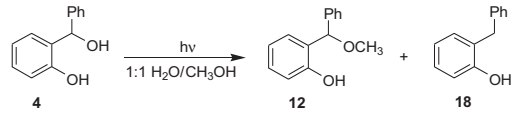

4 **12** **18**

Irradiation of coumaranone **7**, a known photoprogenitor (7) of *o*-QM **19**, gave **12** as the only product (~3% yield) under identical conditions as used for **4**. Extended photolysis (254 nm, 8 min), however, resulted in both methyl ether **12** (~13%) and benzhydrol **4** (~9%) as products (eq. [5]). These results are consistent with a mechanism of reaction via *o*-QM **19** from the photolysis of **7** via a standard photodecarbonylation mechanism. Since the photolysis of **4** resulted in similar chemistry, it is reasonable to suggest that *o*-QM **19** is also the essential intermediate in the photolysis of **4**. Following this rationale, the photomethanolysis of **5** and **6** are proposed to proceed via *m*- and *p*-QMs **20** and **21**, respectively. These proposals are confirmed in UV–vis and laser flash photolysis (LFP) studies (vide infra).

[5] 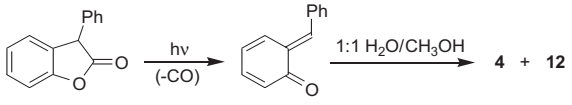

7 **19**

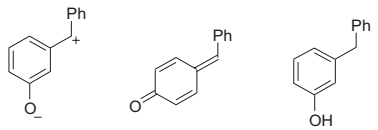

20 **21** **24**

Photolysis of α,α-diphenyl-substituted systems **8** and **9** in 1:1 H_2O/CH_3OH under identical conditions as for **4** and **5** resulted in significantly higher conversions to the corresponding methyl ethers (28% and 60%, respectively). Secondary photochemistry to give the reduced disproportionation products (vide supra) were not observed under the conditions employed. One possible reason for the lack of secondary photochemistry for these compounds is that the increased steric hindrance at the benzylic position (two phenyl groups) retards biradical disproportionation.

The effect of solution pH (aqueous portion) was examined. Acidic pH (pH < 4) could not be employed in product studies for the o and p isomers because of significant residual thermal reaction. Therefore, only the pH 7–14 range was examined for all substrates, although acidic pH levels were used for selected m isomers. In all cases, higher conversions to the methyl ethers were observed at higher pH values. For example, a plot of yield of **12** vs. pH (from 7–14) from photolysis of **4** in 1:1 H_2O/CH_3OH showed a sigmoid curve in the pH 11–13 range with an apparent inflection point at around 12. Since phenols have $pK_a(S_o)$ in the 9–12 range (in neat water), the increase in reaction efficiency at high pH is consistent with higher reactivity observed on directly exciting the phenolate ion. Indeed, the apparent pK_a of **4** in 1:1 H_2O/CH_3OH, as determined by UV–vis spectrometry, was estimated to be about 12.

Fig. 1. Plot of the photochemical conversion of **4** to **12** and **18** in 1:1 H_2O/MeOH as a function of photolysis time (λ_{ex} 254 nm).

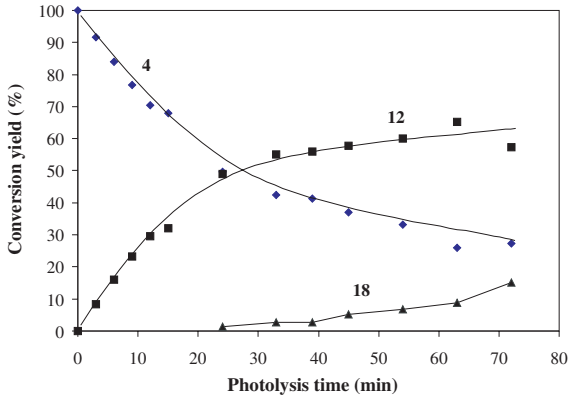

Photolysis of m isomers **5** and **9** in basic solution resulted in the formation of a cloudy solution. It was more pronounced for the α,α-diphenyl derivative **9** and not observed for all o and p isomers. Initial MS analysis of the precipitate showed formation of dimers and trimers, suggesting that a photoinitiated self-condensation pathway may be operative for the m isomers. To enhance the yield of these condensation products, photolysis of **9** was carried out in neat water at pH 12 to avoid the presence of CH_3OH acting as a nuclephile. Photolysis (10 min) gave a cloudy solution that was subsequently neutralized and extracted with CH_2Cl_2. The ^1H NMR spectrum of the product mixture showed a group of new peaks including two exchangeable protons (hydroxy singlets at δ 5.1 and 8.2) and a triplet near the aromatic region (δ 6.4), in addition to those expected for **9**. Prolonged irradiation (30 min) caused the formation of pale yellow flakes that precipitated out of solution and aggregated upon the addition of salt. This yellow substance gave a much cleaner ^1H NMR spectrum in which there are twice as many aromatic protons as hydroxyl protons than in the starting material and a $M^+ - 1$ of 533 (negative FAB), indicative of a dimeric structure. There are two pathways in which a dimer can arise. A "head-to-tail" dimerization pathway to give dimer **22** or electrophilic aromatic substitution of the diphenylmethyl moiety (as the cation) onto the phenolate (more activated) ring, which would give a tetraphenylmethane-type structure. We believe a head-to-tail pathway has occurred to give **22** (Scheme 1), since treatment of this dimer (and longer oligomers, vide infra) in mild acid (pH 1) in 1:1 $H_2O/(CH_3)_2CO$ gave back starting material **9**. Such a reversible reaction in mild acid would be anticipated for a highly activated benzylic ether linkage but not for the alter-

© 2007 NRC Canada

Fig. 2. Mass spectrum (negative ion FAB) of photoproduct **23** obtained on photolysis of **9** in 1:1 H_2O (pH 12)/CH_3CN. The highest mass observed at 2856 (n = 9; see Scheme 1) is not shown. All others from n = 8 to n = 0 match the expected masses reasonably well.

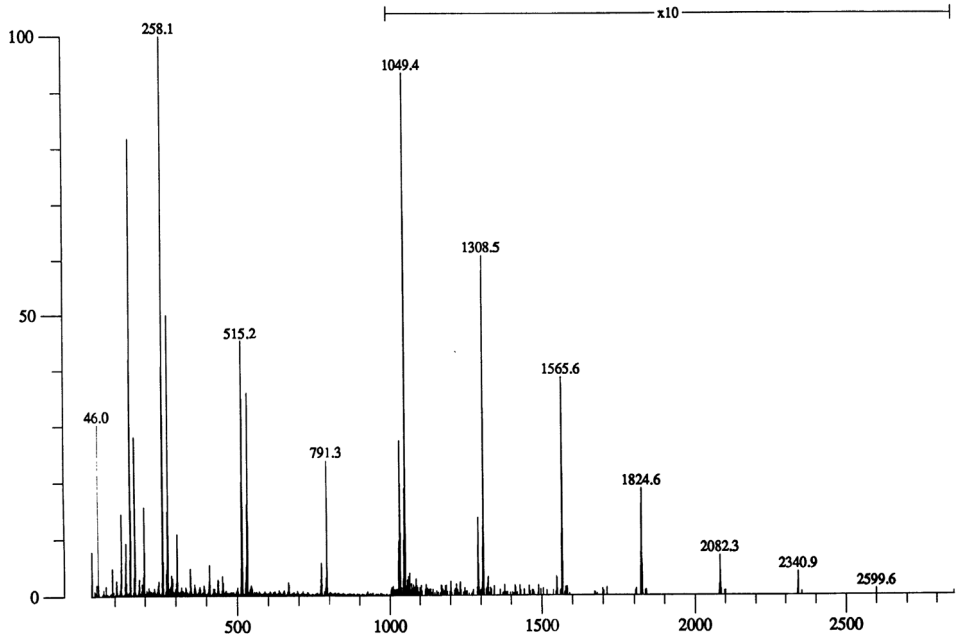

Scheme 1.

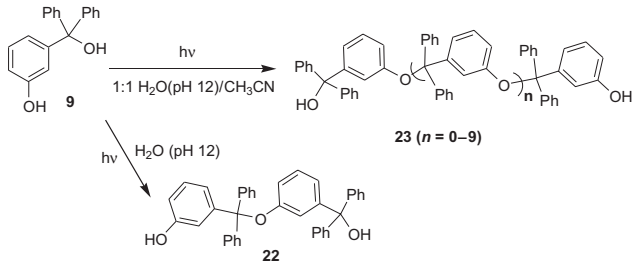

native tetraphenylmethane structure. Interestingly, similar photolysis of **9** in basic 1:1 H_2O/CH_3CN gave a yellow homogeneous solution after 30 min photolysis, which upon work-up was found to contain oligomers **23** of up to 11 units by negative ion FAB MS (Scheme 1, Fig. 2). The chemistry observed here for m isomer **9** is consistent with an *m*-QM intermediate that has a zwitterionic structure (**20** from **5** or **32** from **9**). In basic pH, the starting material **9** is in the (nucleophilic) phenolate form and shows great propensity to attack the positive charge of the *m*-QM structure, hence dimerization and oligomerization. Moreover, *m*-QM from **9** is longer lived than the corresponding QM from **5** (vide infra) and hence more prone to attack by the phenolate ion. The *o*- and *p*-QMs **19** and **21** are less reactive (they have a neutral quinoid structure) in this respect and dimerization and oligomerization is not as prominent, although it has also been reported for an o isomer under extended photolysis (8) and also in the photolysis of (2-hydroxybenzyl)trimethylammonium iodide precursor (5*j*), both in basic solution.

Quantum yields

Quantum yields for methyl ether formation for selected substrates were measured in 1:1 H_2O/CH_3OH using the photomethanolysis of **4** (Φ_p = 0.46) (5*c*) as a secondary actinometer (λ_{ex} 254 nm). Although in general, product quantum yields cannot be used as a direct measure of reactivity, comparisons of Φ_p values in Table 1 reveal that the hydroxyl-substituted alcohols have much higher quantum yields that their methoxy-substituted counterparts. The addition of an extra α-phenyl group also enhances quantum yield. Furthermore, o and m isomers have higher quantum yields than p isomers, which is consistent with Zimmerman's "ortho–meta" effect (9) for photoreactivity of substituted benzenes that undergo reaction via polar intermediates.

Table 1. Quantum yields (Φ_p) for methyl ether formation

Compound	Φ_p
4	0.46 ± 0.03
15	0.11
7	0.08
8	0.76
5	0.23
6	0.19
17	0.0

Note: In 1:1 (*v*/*v*) H_2O/CH_3OH. Measured using **4** as the secondary actinometer. Photolyses were carried out in a Rayonet RPR reactor (λ_{ex} 254 nm). Estimated errors are 10%–15% of quoted value. Conversions were kept <30%.

UV–vis studies

Selected o and p substituted isomers were studied using UV–vis spectrophotometry in aqueous CH_3CN (to avoid complications from methyl ether formation if MeOH was used) to gain insight into whether the corresponding pro-

© 2007 NRC Canada

Fig. 3. Absorption spectra of **4** in pure CH_3CN. (a) (full line) before photolysis, (b) immediately after 4 min photolysis (8 × 254 nm lamps) at –15 °C, (c) on standing for 3 h at RT, (d) (dashed line) standing overnight at RT.

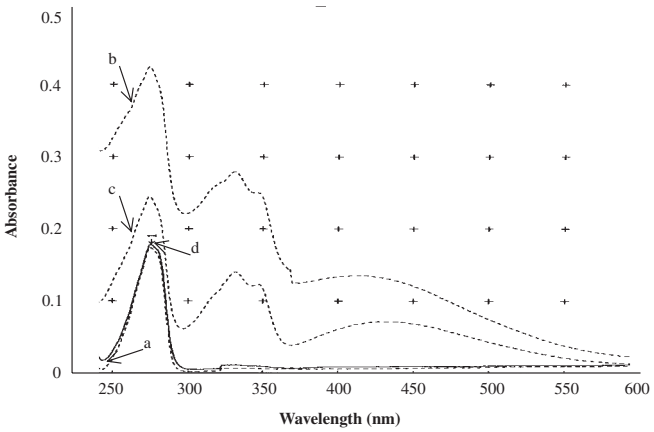

Table 2. Solvent effect on absorption maxima (λ_{max}) for *o*-QM **19** photogenerated from **4**.

Temperature (°C)	Solvent	λ_{max} (nm)	
<0 [a]	cyclohexane	333	410
	THF	333	427
	CH_3CN	332	434
ca. 5	1:9 H_2O/CH_3CN	333	438
ca. 20	1:1 H_2O/CH_3CN[b]	345	455

[a]Irradiated (254 nm) in an ethylene glycol/dry ice slurry (ca. –15 °C).
[b]Results from LFP studies.

posed QMs are observable without the need for LFP. None of the m isomers gave observable transients using standard UV–vis techniques and *m*-QM intermediates could only be observed using LFP (vide infra).

Photolysis of **4** in neat CH_3CN (~10^{-2} mol/L, 254 nm for ~1–5 min) in a quartz cuvette resulted in the formation of a initially yellow, then orange-red, and eventually a deep red-brown solution. UV–vis spectra were recorded before and after photolysis and are shown in Fig. 3 where the starting material absorbs only below 300 nm, with λ_{max} at 276 nm. On photolysis, the appearance of new absorption bands at 333 and 423 nm indicated the formation of a new species. This transient decayed slowly in neat CH_3CN; the yellow color remained even on sitting overnight. A similar transient was observed in THF and cyclohexane (at ca. –15 °C) (Table 2). The red shift of λ_{max} on going to more polar solvents indicate that these transitions of π,π^* in character, consistent with a highly conjugated *o*-QM **19**.

Photolysis of **4** in 1:9 H_2O/CH_3CN at ~5 °C produced an orange-red solution, which was formed more efficiently than in neat CH_3CN but with similar λ_{max} (Table 2). Upon removal from the UV source, the color gradually faded ($\tau \approx$ 40 s; shorter at 20 °C) with complete recovery of the UV spectrum prior to irradiation. When photolyzed in essentially neat H_2O (<5% CH_3CN as co-solvent), the same orange-red transient was generated but disappeared quickly (τ < 5 s), preventing the recording of a UV–vis spectrum.

Table 3. Absorption maxima (λ_{max}) and estimated lifetimes (τ) of photogenerated transient QMs from hydroxybenzhydrols.

Compound	Solvent[a]	λ_{max} (nm)[b]	τ[c]
4	100% H_2O	333, 438	<5 s
	1:9 H_2O/CH_3CN	333, 438	27 s
	1:9 H_2O/CH_3CN (~5 °C)	333, 438	40 s
6	H_2O	372	10 s
	1:1 H_2O/CH_3CN	360	216 s
	1:9 H_2O/CH_3CN	354	>60 min
10	pH 7 buffer	377	130 s
	1:1 H_2O/CH_3CN	377	>60 min
11	pH 7 buffer	356	>60 min
	1:1 H_2O/CH_3CN	356	>60 min

[a]At ~20 °C unless otherwise specified.
[b]Error is ca. 2 nm.
[c]Estimated lifetime from a fit to a single exponential decay.

Similar photolysis of *p*-hydroxybenzhydrols **6**, **10**, and **11** in aqueous CH_3CN also gave red colored transients, but none was capable of giving such a colored transient when photolyzed in neat CH_3CN. The transient from **6** absorbed strongly at 372 nm in H_2O (<5% CH_3CN) with a 10 s lifetime. It was 20 times longer-lived in 1:1 H_2O/CH_3CN (τ = 216 s.). Similar transient absorptions were observed for **10** (at 377 nm) and for **11** (at 356 nm) in either neat water or in 1:1 H_2O/CH_3CN. Table 3 summarizes the λ_{max} and τ for the transients observed. All of the observed transients return to starting materials eventually. The transient from **6** (*p*-QM **21**) has a longer lifetime than that from **4** (*o*-QM **19**). Electron-donating groups on the benzene ring (in **10** and **11**) produce transients that are even longer-lived and hence may be thought of as stabilizing substituents. This result is consistent with recent results of Rokita and co-workers (5*m*) in their study of *o*-QM adducts of deoxynucleotides. All of these observations are consistent with the transients being assignable to the corresponding *p*-QMs.

Fluorescence measurements

There is now considerable evidence supporting singlet state reactivity for substituted benzenes (without carbonyl substituents) undergoing photochemical reactions that gives rise to ionic (polar) intermediates (1–3, 5, 6). Earlier studies (5*c*, 5*d*, 6*c*) have shown that it is the singlet excited state of the precursor phenols that give rise to QMs. Nevertheless, fluorescence studies can give much additional ancillary data regarding mechanism and reactivity that cannot be easily obtained by other means.

o-Hydroxybenzyl alcohols **4** and **8** gave similar fluorescence emissions centered at ~300 nm in neat CH_3CN. The fluorescence quantum yields (Φ_f) measured using anisole (Φ_f = 0.29 in cyclohexane) as secondary standard (10) were drastically reduced by H_2O addition, accompanied by the red-shifted emission maxima (Table 4). Of the two alcohols, the fluorescence intensity of **4** was affected the most, where only a weak emission band was observed beside a clearly visible Raman band in 100% H_2O. The fluorescence lifetimes (τ) were essentially the same in 100% CH_3CN but were drastically decreased with increased water concentration. Similar fluorescence emissions were observed for two related derivatives of **4** (**15**, **18**) in the above mentioned sol-

© 2007 NRC Canada

Table 4. Effect of H_2O content in CH_3CN on emission maximum (λ_{max}), fluorescence quantum yields (Φ_f, excited at 270 nm), and lifetimes (τ, excited at 275 nm) of *ortho*-substituted compounds.

	Solvent	**4**	**8**	**15**	**18**
λ_{max}	100% CH_3CN	298	299	299	297
	1:1 CH_3CN/H_2O	302	304	—	299
	100% H_2O	—	—	300	—
Φ_f [a]	100% CH_3CN	1 (0.13)	1 (0.092)	1 (0.28)	1 (0.25)
	1:1 CH_3CN/H_2O	0.21	0.48	—	0.47
	100% H_2O	0.04	0.12	0.62	0.10
τ[b] (ns)	100% CH_3CN	4.5	4.6	5.3	5.1
	1:1 CH_3CN/H_2O	1.3	<2	4.6	3.0
	100% H_2O	—	—	1.9	<1

[a]Measured using anisole (Φ_f = 0.29 in cyclohexane) as secondary standard (10). Absolute quantum yield quoted in brackets. All other numbers are relative yields.
[b]Measured using PTI LS-1 time-correlated single photon counting system.

Table 5. Effect of H_2O content (in CH_3CN) on emission maximum (λ_{max}), fluorescence quantum yields (Φ_f, excited at 270 nm), and lifetimes (τ, excited at 275 nm) of *meta*-substituted compounds.

	Solvent	**5**	**16**	**24**	**9**
λ_{max}	CH_3CN	296	295	293	299
	1:1 H_2O/CH_3CN	299	295	297	302
	H_2O	—	296	297	—
Φ_f [a]	CH_3CN	1 (0.22)	1 (0.21)	1 (0.25)	1 (0.21)
	1:1 H_2O/CH_3CN	0.38	0.95	0.79	0.46
	H_2O	0.08	0.67	0.24	0.13
τ[b] (ns)	CH_3CN	5.4	—	5.0	4.9
	1:1 H_2O/CH_3CN	1.9	—	4.5	—
	H_2O	<1	—	1.3	<1

[a]Measured using anisole (Φ_f = 0.29 in cyclohexane) as secondary standard (10). Absolute quantum yield quoted in brackets. All other numbers are relative yields.
[b]Measured using PTI LS-1 time-correlated single photon counting system.

vent systems. Measurement of Φ_f revealed that the fluorescence of **18** was quenched by 90% in 100% H_2O, while the fluorescence of **15** was much less sensitive to the presence of water than that of **4** and **18**. The fluorescence lifetimes (τ) of **18** has an initial decrease to 3 ns in 1:1 H_2O/CH_3CN and then to <2 ns in 100% H_2O, while the τ of **15** was almost unchanged by the addition of 50% water and then dropped to 1.9 ns in 100% H_2O. Thus, the overall magnitude of water effect on these three compounds followed the order **4** > **18** > **15**. The lack of a fluorescence quenching effect for **15** can be attributed to its lack of a phenol moiety. Similar trends in fluorescence behaviour were observed for a series of m-substituted compounds (Table 5).

Fluorescence emissions of **4** and **8** were also observed in aqueous solutions of different pH values. However, their fluorescence emissions were in general so weak that it was not feasible to accurately measure the fluorescence quantum yield. Therefore, relative fluorescence intensity measurements (Φ_f^o/Φ_f; Φ_f^o = fluorescence quantum yield at pH 7) at ~290 nm were employed. No emission was observed in basic solution (0.1 N NaOH) for either ortho compound. Since their UV–vis spectra showed growth of the absorption of the corresponding phenolate ion (~290 nm) in basic media, excitation at 290 nm gave weak emissions at ~350 nm, which presumably are the fluorescence emissions of the corresponding phenolate. Similar experiments with phenol itself gave a weak emission at 335 nm, while *o*-cresol gave a weak emission at 346 nm. These weak signals indicate that excited phenolate ions are photochemically reactive, i.e., they decay through other routes competitive with fluorescence emission.

Stern–Volmer type plots of fluorescence quenching by added water (in CH_3CN solution) were carried out for a number of substrates. All the phenols displayed increasing fluorescence emission on the addition of small amounts of water (up to about 2 mol/L water) after which the fluorescence was quenched. The addition of initial water results in hydrogen bonding to the phenol OH (and to benzylic alcohol OH) resulting in a water–substrate complex that is more fluorescent than the substrate alone in CH_3CN. Addition of more water causes quenching of fluorescence due to water-mediated proton transfer from phenol OH to solvent. For those alcohols that can give rise to QMs, the addition of water also promotes the photodehydroxylation pathway. Indeed,

© 2007 NRC Canada

Fig. 4. Stern–Volmer plot of relative fluorescence intensity (Φ_f^o/Φ_f) vs. water concentration in CH_3CN for **4** (λ_{ex} 270 nm).

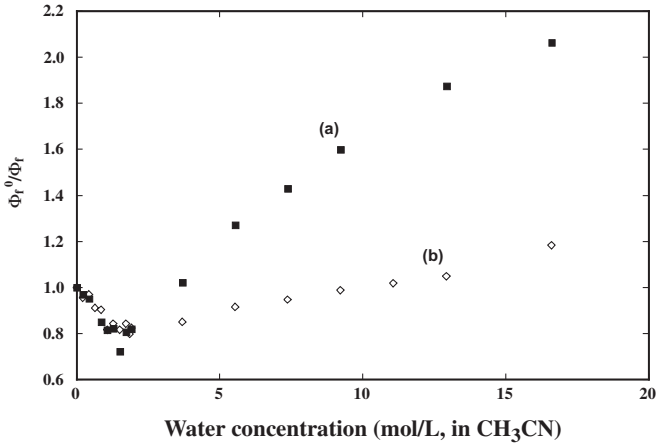

these substrates (e.g., **4**–**6**) are quenched more efficiently by water. A particularly informative Stern–Volmer type plot is shown in Fig. 4 in which H_2O and D_2O were employed as quenchers (in CH_3CN) for **4**. There was no observable solvent isotope effect in the enhanced fluorescence observed at low water content. However at higher water content, H_2O quenched significantly more efficiently (up to twofold) than D_2O at the same concentration. This is consistent with a mechanism of reaction in which **4** undergoes a concerted loss of H_2O (D_2O) assisted by solvent water to form *o*-QM **19**. A mechanism involving initial simple phenol ionization to solvent water such as that only available in **18** would not give rise to such a large solvent isotope effect.

Nanosecond laser flash photolysis (LFP)

The UV–vis studies described earlier have already shown that *o*- and *p*-QMs are observable under certain conditions. However, *m*-QMs are presumably too short-lived for this technique. Use of LFP should provide a better picture for whether transients can be assigned to all QM isomers and their relative efficiency for formation under various conditions and hence provide additional insights into reaction mechanism.

LFP of **4** in 1:1 H_2O/CH_3CN under either N_2 or O_2 gave the same strong signals as reported in the already mentioned UV–vis studies, with no observable decay within the millisecond range, the limit of the nanosecond LFP system. A significant amount of transient was also formed on photolysis in neat CH_3CN (under either N_2 or O_2), although the absorption bands were significantly blue-shifted (the 455 and 345 nm bands were shifted to 410 and 330 nm, respectively). Relative quantum yields for the formation of the transients as a function of water content in CH_3CN were measured by monitoring the ΔA at both 350 and 450 nm (Fig. 5). Interestingly, the yield of the transient decreased initially (at low water content), followed by a dramatic increase with the increase in water concentration. This observation corroborates the enhanced fluorescence emission observed at low water content and suggests that when the substrates is hydrogen-bonded to small amounts of water, it is *less* reactive than without water. When the water content reaches above 2 mol/L the compound becomes more reactive, consistent with a water-mediated mechanism. The maximum yield was reached in ca. 75% H_2O/CH_3CN, which was followed by a slight drop on approaching 100% H_2O.

Fig. 5. Relative quantum yields for the formation of *o*-QM **19** from **4** as a function of water content (in CH_3CN) as monitored at 350 and 450 nm using LFP (λ_{ex} 266 nm).

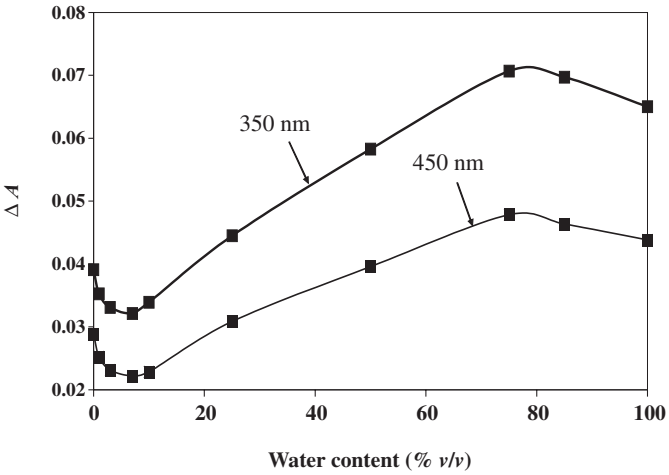

Fig. 6. Relative quantum yields (ΔA) for the formation of *o*-QM **19** from **4** vs. pH, monitored at 350 and 450 nm using LFP in neat H_2O (λ_{ex} 266 nm).

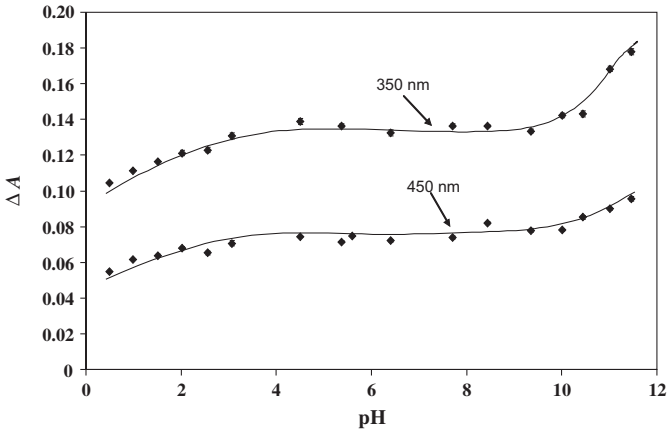

Transient spectra from **4** were also taken in neat H_2O at different pH values with the same transient being observed in the whole pH range. A plot of ΔA (relative quantum yield) vs. pH (Fig. 6) showed two "titration" regions, at pH ~1 to 2, and at pH 11 to 12. The first of these is shallow and not prominent but approximately corresponds to the $pK_a(S_1)$ of phenols, whereas the second corresponds to $pK_a(S_0)$. Although we were not able measure yields for methanolysis in acid for **4** because of competing thermal reactions, the LFP method is not encumbered by this problem since it monitors for transient QM formation on excitation. The "shallow" titration curve at low pH suggests that excited state proton dissociation prior to reaction is important but that there may also be an independent acid-catalyzed pathway operating at these values of pH that involves an acid-mediated loss of water followed by deprotonation of the phenol OH to give the QM. The lifetimes of this transient (pseudo first-order

© 2007 NRC Canada

decays) were measured between pH 0 and 5 (above pH 5 the lifetimes were too long for the detection system employed). A plot of log k_{obs} vs. pH gave a slope of –1 indicating that the transient has an acid-catalyzed pathway for reaction (with $k_{H+} = 1.0 \times 10^6$ (mol/L)$^{-1}$ s^{-1}), in general agreement with results of Kresge and co-workers (5*f*–5*h*) and McClelland et al. (5*i*).

LFP of **7** in 1:1 H_2O/CH_3CN afforded a transient spectrum essentially identical to that observed for **4** but with much weaker signal intensity, consistent with the lower reactivity of photomethanolysis and photohydration observed for **7**. Since **7** is known to give *o*-QM **19** upon photolysis (7), it is reasonable to infer that the transient from **4** is indeed *o*-QM **19**.

LFP of the *o*-methoxy derivative **15** 1:1 H_2O/CH_3CN gave a weak absorption at 420 nm, with a short-lived (13 ns) and a longer-lived species (~0.5 μs) (fitted to the sum of two single exponential decays). These transients are very different from those observed for **4**. Chateauneuf (11) found that the diphenylmethyl cation (**25**) has λ_{max} at 435 nm with ~1 ns lifetime by using picosecond LFP, while McClelland and co-workers (12) reported that (*p*-methoxyphenyl)phenyl methyl cation (**26**) absorbs at 455 nm with a 0.5 μs lifetime in 2:1 H_2O/CH_3CN. Since the LFP system used by the McClelland group has a pulse of ~20 ns, they were unable to observe the short-lived species. Considering that substituents on the benzene ring have similar electron donating and withdrawing abilities at the ortho and para positions, it is reasonable to propose that the ortho-substituted diphenylmethyl cations also absorb in the 400–500 nm region and have microsecond lifetimes. Therefore, the long-lived (~0.5 μs) species observed from **15** is assigned to carbocation **27**. Since Peters and Li (13) showed that the contact ion pair from diphenyl chloride had a lifetime of 150 ps, the short-lived (13 ns) species that we observed may be a radical cation.

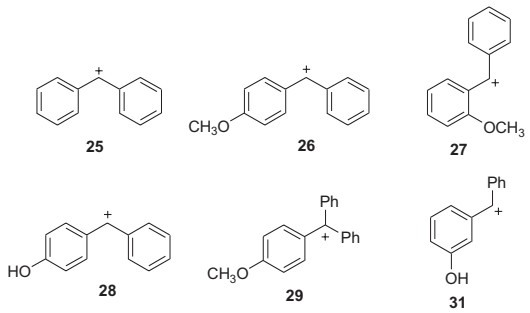

LFP of *p*-hydroxybenzhydrol (**6**) gave one strong absorption band at 360 nm with no observable decay within ms range in 1:1 H_2O/CH_3CN, under either N_2 or O_2. The signal was also observed in 5% H_2O/CH_3CN but not in neat CH_3CN. The yield of the transient (as measured by ΔA) increased with the increase in the water content to a maximum at 75% H_2O/CH_3CN. The transient absorption spectrum observed for the *p*-methoxy analog **17** had a weak band at 455 nm with small shoulders at 340 and 360 nm. Monitored at 455 nm, the decay consisted of two components, one with ~45 ns lifetime and another with a ~1 μs lifetime. The lifetime of the longer-lived species decreased significantly with increasing water content. In 0.5 mol/L NaOH, essentially no signal was observable in 400–500 nm region. These facts

Fig. 7. Transient absorption spectra observed from **8** by LFP under O_2 in (a) pH 7 and (b) pH 12 in 1:1 H_2O/CH_3CN (λ_{ex} 266 nm).

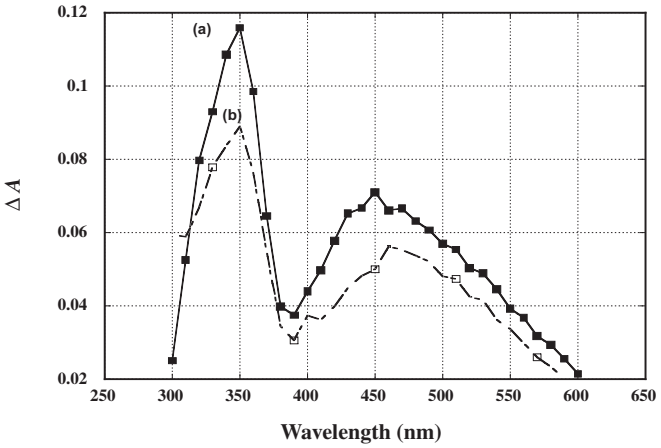

imply that the transient has cationic character. According to McClelland and co-workers (12) (*p*-methoxyphenyl)phenyl methyl cation (**26**) has λ_{max} = 455 nm in CH_3CN (diarylmethyl chloride as precursor), which is also accompanied by the (*p*-methoxyphenyl)phenylmethyl radical at 340 nm. The cation has a lifetime of 0.5 μs in 2:1 H_2O/CH_3CN. The long-lived species generated from **17** has absorption characteristics and lifetime that matches those of **26**. Although the transient generated from **6** (τ = 216 s in 1:1 H_2O/CH_3CN, vide supra) has similar absorption characteristics as cation **26**, it is too long-lived to be **28**. It seems reasonable that the transient is that of *p*-QM **21** consistent with it being much less reactive. Similarly, the transients observed for **10** and **11** (vide supra), which were quenchable by water and had even longer lifetimes than *p*-QM **21** are also the respective *p*-QMs.

[6] 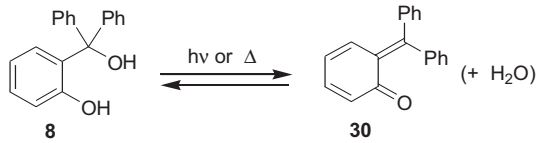

LFP of triphenyl alcohol **8** produced a strongly absorbing transient in either neat acetonitrile or in 1:1 H_2O/CH_3CN (Fig. 7), with no observable decay within 2 ms. The transient spectrum is almost identical to those obtained from **4** and **7**, indicating that a similar transient was being generated by all of these compounds and the additional phenyl substitution on benzylic carbon had little effect on absorption characteristics. McClelland et al. (12*b*) have reported that the (*p*-methoxyphenyl)diphenylmethyl cation **29** has a lifetime of 0.71 ms in 2:1 H_2O/CH_3CN, which is much shorter than the transient observed from **8**. Using the same rationale as for the benzhydrols, the transient observed for **8** is most likely *o*-QM **30**. Moreover, it is known that **8** and related compounds are thermo and photochromic and their coloured forms are believed to be due to their corresponding *o*-QM structures, with absorptions bands at 340 and 440 nm (14) (eq. [6]).

LFP of **5** in 1:1 H_2O/CH_3CN (O_2 purged) generated a strongly absorbing but short-lived transient with λ_{max} = 440 nm and a 30.1 ns lifetime (Fig. 8). This species was in-

© 2007 NRC Canada

Fig. 8. Transient absorption spectra observed for **5** (assigned to **20**) in 1:1 H_2O/CH_3CN (O_2) (λ_{ex} 266 nm). Top to bottom: recorded 10, 40, 80, and 200 ns after the laser pulse (Inset: top without ethanolamine and bottom with 0.24 mol/L ethanolamine, monitored at 450 nm).

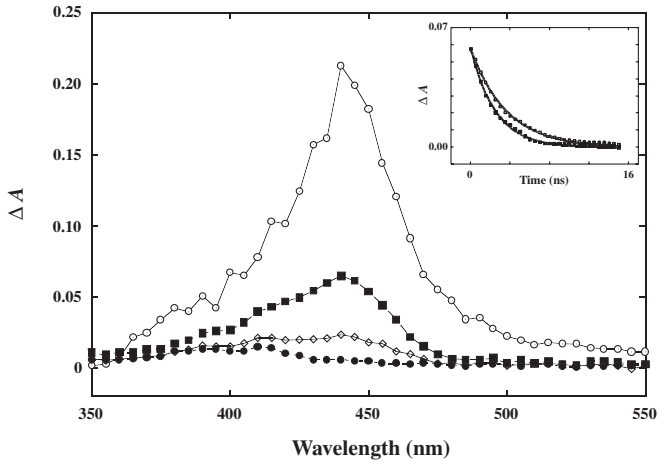

sensitive to oxygen and quenchable by water, added $NaBH_4$, and ethanolamine. A weak residual signal (390 and 410 nm) was observable after the 440 nm transient had decayed (Fig. 8, bottom trace), which is more predominant with decreased water content. LFP of **5** in neat CH_3CN under N_2 gave two strong signals at 330 and 410 nm, respectively, both of which disappeared with O_2 purging. No 440 nm transient was observed. LFP of *m*-methoxybenzhydrol (**16**) generated a short-lived transient with a lifetime of 75.5 ns and a long-lived one of 6.3 μs (λ_{max} = 428 nm) in 1:1 H_2O/CH_3CN (O_2). A similar LFP study of *m*-benzylphenol (**24**) gave a weak but long-lived transient at around 400 nm and a short-lived one at 750 nm. Both long-lived species from **16** and **24** might be the radical cation formed from an electron ejection, which is not the same as either transient from **5**. The relative quantum yield of formation of the 440 nm (ΔA_{440}) transient increased with increasing pH (in 1:1 H_2O/CH_3CN, lifetimes and ΔA_{440} could not be accurately measured at all pH values in 100% water because of acid quenching). The resulting plot of ΔA_{440} vs. pH showed a titration curve in basic pH at an apparent $pK_a(S_0)$ value of 12 and a $pK_a(S_1)$ of 2. A plot log k_{obs} vs. pH in 1:1 H_2O/CH_3CN showed that the lifetimes were unchanged between pH 4 and 11 and were shortened in either acidic or basic media.

The λ_{max} and band shape of the 440 nm transient observed on LFP of **5** is essentially identical to that of the corresponding diarylmethyl cations reported by McClelland et al. (12*b*). Although they did not photogenerate the exact *m*-hydroxy-substituted cations, the lifetimes of those that were reported are informative. For example, diarylmethyl cations without strongly electron donating substituents have lifetimes of less than 10 ns in aqueous solution and are not detectable by standard nanosecond LFP; τ was estimated to be 1 and 5 ns for the **25** and the (*p*-methylphenyl)phenylmethyl cations, respectively. Clearly, the transient observed from **5** is similar to an arylmethyl carbocation, but its lifetime is too long to be simply the (*m*-hydroxyphenyl)phenylmethyl cation (**31**). Additional evidence available is that the methoxy derivative of **16** did not produce any cationic transient by LFP. Moreover, **5** gave a significantly higher yield of the methyl ether product on photolysis in 1:1 $MeOH/H_2O$ compared with **16**, with a quantum yield (Φ_p = 0.40) only fractionally lower than that measured for the corresponding ortho isomer **4**. More important is the fact that the transient is quenchable both electrophilically and nucleophilically since its lifetime decreased in both acidic and basic media. The deprotonated hydroxy group (σ^-) is electron-donating on the benzene ring at a meta position (σ_m = –0.47) unlike the hydroxy group itself, which is electron-withdrawing at the meta position (σ_m = + 0.12). If the transients from **5** were simply the cation **31**, its expected lifetime in aqueous solution, using data from McClelland et al. (12*b*), would be less than 1 ns and hence not observable using our LFP system. Its much longer observed lifetime (30 ns) is consistent with the hydroxyl group having been deprotonated. We thus assign this transient as *m*-QM **20**. Therefore, the present method offers a simple and efficient way for photogeneration of *m*-QMs in their zwitterionic form.

Mechanisms of reaction

There are four aspects of the reaction mechanism that can be addressed for the QMs studied in this work: (*i*) their photochemical mechanism(s) of formation, (*ii*) their thermal mechanism(s) for subsequent hydration, methanolysis, or nucleophilic attack, depending on the solvent system and nucleophiles used, (*iii*) [4+2] cycloaddition with added dienophiles such as ethyl vinyl ether, and (*iv*) self-condensation (polymerization). Thermal hydration and nucleophilic attack of photochemically generated QMs (*o* and *p*) have been studied by several other groups (5*e*–5*k*). Some initial studies of [4+2] cycloaddition have been reported (5*c*, 5*d*), but more studies are required in this area before a more complete picture is available. Therefore, only the first and last aspects will be addressed in this section.

Formation of *o*-QMs **19** and **30** from **4** and **8**, respectively, in neat CH_3CN probably involves a unimolecular dehydration pathway as shown in eq. [7]. This mechanism takes advantage of the enhanced acidity of phenols in S_1 and the presence of the nearby benzylic alcohol (hydrogen bonded as shown), which in this mechanism formally acts as hydroxide ion. When these moieties are too far from each other, the mechanism does not operate. Indeed, none of the m and p isomers give QMs on photolysis in neat CH_3CN (they all require the presence of water). The addition of small amounts of water to CH_3CN (up to 2 mol/L) resulted in reduction of yield of *o*-QM and an enhancement of fluorescence yield and lifetime. Water is expected to hydrogen bond to the phenol and alcohol OH groups and break up the internal hydrogen bond already in place. This retards the simple dehydration mechanism and hence results in a drop in yield. Addition of more water opens up a new pathway for *o*-QM formation, viz., the water-assisted mechanism shown in eq. [8]. In this mechanism, the details of the water–hydrogen bonding is not known and only one water

[7]

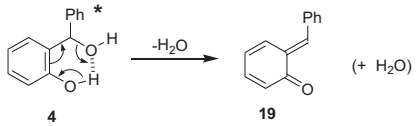

© 2007 NRC Canada

molecule is shown for hydrogen bonding to each of the substrate OH groups. Interestingly, Freccero and co-workers (5*k*) have carried out DFT calculations on the alkylation of the parent unsubstituted *o*-QM with water (in the gas phase) and found that the presence of two water molecules (one acting as a catalyst) accelerates the addition.

[8] 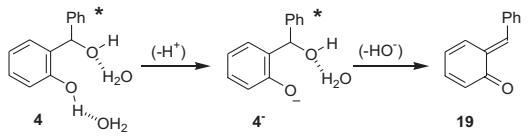

The observation that direct photolysis of the phenoate form of **4** (that is, **4**$^-$) resulted in a higher quantum yield of **19** supports the notion that the reaction probably involves two steps: the ionization step (-H^+) and the dehydroxylation step (-HO^-), although a concerted mechanism cannot be ruled out. Another pathway in which loss of hydroxide ion takes place first (photodehydroxylation) to give a cation followed by deprotonation of the phenol to give the *o*-QM can be ruled out, since this would not explain the enhanced quantum yield for the formation of QMs derived from these hydroxybenzyl alcohols (**4**–**6**) compared with the corresponding methoxy-substituted analogs **15**–**17**. Indeed, for **15**–**17** and related compounds, a simple photodehydroxylation pathway is operative for the formation of the corresponding benzylic cations (15).

A similar mechanism for the formation of *m*-QM **20** that requires the presence of water is shown in eq. [9]. The difference here is that the excited state of **5**$^-$ is expected to have a substantial portion of the negative charge localized at the m position (Zimmerman ortho–meta effect (9)), hence allowing the subsequent dehydroxylation step. Deactivation back to the ground state gives rise to a zwitterionic *m*-QM **20**, which has a non-Kekulé structure. Although no polymeric material was isolated from photolysis of **5** in base, photolysis of **8** gave substantial amounts of oligomers (Scheme 1). This is because the corresponding zwitterionic *m*-QM **32** is about 1000-fold longer-lived (30 ns for **20** compared with 10 μs for **32**). Thus, bimolecular attack by **8**$^-$ (eq. [10]) competes with attack by water and hydroxide ion. It is interesting to comment that *m*-QM condensation is due to attack of oxygen on the benzylic carbon, giving rise to oligomers held together with benzylic ether bonds. For comparison, the photocondenation of *o*-hydroxybenzyl alcohol (eq. [11]) results in attack via the benzene ring carbon (enolate-like attack), giving rise to phenol-formaldehyde condenation polymers (8). The key difference may be the increased steric

[9] 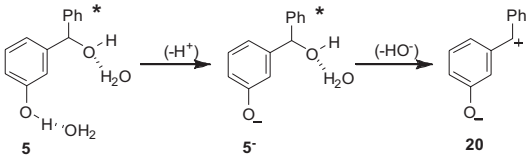

[10] 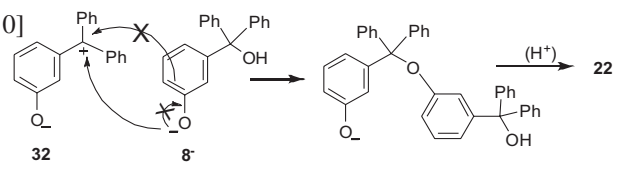

bulk of the two benzylic phenyl groups of **32**, which would hinder attack via the o position on the benzene ring.

In summary, QMs are the key intermediates in the

[11]

photochemistry of hydroxyl-substituted benzyl alcohols. These compounds are suitably designed to take advantage of the enhanced acidity of the phenol in S_1 and the propensity of benzylic alcohol to depart as hydroxide ion or water and its reluctance to leave as hydroxyl radical. This is unlike the situation if other leaving groups such as halides and acetate are used. Thus, hydroxyl-substituted benzyl alcohols react almost exclusively via polar or ionic intermediates. An added bonus is that they are generally fluorescent making them ideal for fluorescence studies. Other added features and uses await further discovery.

Experimental section

General

^{1}H NMR spectra were recorded on either a PerkinElmer R32 (90 MHz), a Bruker AC 300 (300 MHz), or a Bruker AM 360 (360 MHz) instrument using $CHCl_3$-*d*, CH_3CN-d_3 or acetone-d_6 as solvents. Mass spectra were taken on either a Finnigan 3300 (CI) or a Kratos Concept H (EI and FAB) instruments. Melting points were determined on a Koefler hot stage microscope (uncorrected). UV–vis spectra were recorded either on a Phillips PU 8740, Varian Cary 5, or Pye Unicam SP8–400 spectrophotometer. Analytical thin layer chromatogaphy (TLC) was performed on precoated silica gel plates (Macherey-Nagel, Sil/UV–vis_{254}), using solvent systems as indicated in each experiment. Preparative TLC was carried out on 20 cm × 20 cm silica gel GF 1000 micrometer Uniplates (Analtech).

Common laboratory reagents

Methylene Chloride (A.C.S., reagent grade) was distilled before use. Anhydrous THF was obtained by distillation over potassium. Acetonitrile was either HPLC grade for photolysis, UV and LFP studies or freshly distilled over CaH_2 under N_2 for steady state fluorescence measurements. HPLC grade MeOH was stirred with $NaHCO_3$ for at least one hour to remove any trace of acid prior to photolysis. Cyclohexane (HPLC) were used as received. Deuterated solvents, including D_2O, $CDCl_3$, $(CD_3)_2CO$, and CD_3CN were purchased from Cambridge Isotopes (99.9% D). Standard buffers were purchased from Fisher. Aqueous solutions of the appropriate pH were used directly or diluted from standardized stock of NaOH or H_2SO_4 with known concentration. Prior to photolysis, pH values of the water portion were checked by a pH meter. *o*-Benzylphenol (**18**) was purchased from Sigma-Aldrich Reagents and used as received. ^{1}H NMR and GC analysis showed that it was >98% pure. Ethanolamine (Sigma-Aldrich) was distilled before use. *o*-Methoxybenzhydrol (**15**) was available in the laboratory. ^{1}H NMR (300 MHz, acetone-d_6) δ: 3.8 (s, 3H), 4.6 (d, 1H, D_2O

© 2007 NRC Canada

exchangeable), 6.1 (d, 1H), 6.8–7.6 (m, 9H). MS (CI) *m/z*: 197 (M^+ – 17, base peak), 215 (M^+ + 1). (EI) 214 (M^+).

Materials

All readily available organic and inorganic reagents required in the synthesis reported below were purchased from Sigma-Aldrich and used as received.

Grignard reaction

Magnesium was washed with dilute HCl to remove magnesium oxide and thoroughly dried. Pre-dried PhBr was dissolved in freshly distilled THF and added dropwise (under N_2) to magnesium/THF (a pinch of I_2 added) in an ice bath, which was then vigorously stirred. After the addition, the reaction mixture was refluxed for 1 h and cooled to room temperature (RT). The reacting PhMgBr was transferred to a dropping funnel and added dropwise to a THF solution of the appropriate carbonyl compound. After addition, the solution was refluxed and reaction progress monitored by NMR. Work-up consisted of the addition of saturated aq. NH_4OAc to a cooled solution to quench excess PhMgBr. Diluted HCl was also used to further acidify the solution, if required. The solution was then extracted with CH_2Cl_2.

$NaBH_4$ reduction

The ketone was dissolved in 50–100 mL of MeOH and cooled in an ice bath. To this stirred solution, a suspension of $NaBH_4$ in ice water was added dropwise. The solution was then heated to 40–50 °C for 1–2 h. After cooling by ice, the solution was neutralized with aq. NH_4Cl and extracted with 3 × 50 mL of CH_2Cl_2. The organic solvent was removed using a rotary evaporator and residue was dried on a vacuum pump.

o-Hydroxybenzhydrol (4)

Method A

To a stirred solution of salicyaldehyde (Sigma-Aldrich, 2.0 g, 17.9 mmole) in 50 mL of dry THF, 30 mL of 1.8 mol/L phenyllithium solution (54 mmole) was added under nitrogen in a dry ice–acetone bath. After reflux (4 h), the reaction mixture was cooled to RT and 50 mL of wet THF was added carefully followed by a further 10 min reflux to decompose the excess phenyllithium. The reaction mixture was then transferred to a 500 mL erlenmeyer flask, and 100 mL of ice water was added and the solution acidified with saturated NH_4Cl. The solution was extracted with diethyl ether (3 × 70 mL). Removal of the ether afforded an oil (3.2 g, 90%), which solidified overnight.

Method B

Following the general procedure described above for making PhMgBr, 10 g salicyaldehyde (0.08 mol) was reacted with PhMgBr (0.24 mol). The crude yellow solid was recrystallized from 1:1 toluene/hexane to afford pure **112** as white crystals, mp 86 to 87 °C. ^{1}H NMR (300 MHz, acetone-d_6) δ: 4.3 (b, 1H, D_2O exchangeable), 6.1 (s, 1H), 6.7–7.3 (m, 9H), 8.6 (b, 1H, D_2O exchangeable). MS (CI) *m/z*: 183 (base peak, (M^+ – 17).

3-Phenylisocoumaranone (7)

The compound was made according to the procedure of Padwa et al. (7). To an ice-cooled mixture of finely pulverized phenol (26.5 g) and mandelic acid (30.45 g) was added 80 mL of a 70% sulfuric acid solution. The mixture was stirred at 0 °C until dissolution was nearly obtained and then heated at 115 °C for 45 min. The mixture was cooled to RT, poured into 400 mL of ice water slurry, and extracted with three 100 mL portions of methylene chloride. The combined organic layers were washed with 100 mL of a saturated aqueous sodium bicarbonate solution and dried over magnesium sulfate. The evaporation of the solvent under reduced pressure gave a red liquid as the crude product. When placed under vacuum, crystals slowly formed. White crystals were obtained after recrystallization from 95% ethanol, mp 111–114 °C (lit. value (7) 113 to 114 °C. ^{1}H NMR (300 MHz, acetone-d_6) δ: 5.2 (s, 1H), 7.1–7.5 (m, 9H). MS (CI) *m/z*: 211 (M^+ + 1, base peak), 183 (M^+ – 28).

m-Hydroxybenzhydrol (5)

Method A

Crude **5** was obtained by reducing *m*-hydroxybenzophenone (2.6 g, 0.013 mol) with $NaBH_4$ (0.75 g, 0.019 mol) following the general procedure.

Method B

Following the general procedure using PhMgBr, 4.3 g Mg (0.18 mol), and 27.4 g PhBr (0.18 mol) were used to make the Grignard reagent, which was reacted with 7 g of *m*-hydroxybenzaldehyde (0.057 mol) to give a brownish solid. The crude product was recrystallized from 8:1 toluene/ligroin to afford white fine needlelike crystals, mp 115 °C. ^{1}H NMR (300 MHz, acetone-d_6) δ: 4.7 (d, 1H, D_2O exchangeable), 5.7 (d, 1H), 6.4–7.5 (m, 9H), 8.2 (s, 1H, D_2O exchangeable). MS (CI) *m/z*: 183 (M^+ – 17, base peak), 201 (M^+ + 1).

m-Methoxybenzhydrol (16)

Using the general procedure for PhMgBr, 10 g of *m*-anisaldehyde (0.074 mol) was reacted with PhMgBr (0.24 mol). The crude product (yellow oil) was distilled under reduce pressure to afford pure **16** (clear oil). ^{1}H NMR (300 MHz, acetone-d_6) δ: 3.7 (s, 3H), 4.8 (d, 1H, D_2O exchangeable), 5.8 (d, 1H), 6.7–7.5 (m, 9H). MS (CI) *m/z*: 197 (M^+ – 17, base peak), 215 (M^+ + 1).

p-Hydroxybenzhydrol (6)

Following the general procedure for $NaBH_4$ reduction, *p*-hydroxy-benzophenone (1.98 g, 0.01 mol) was reduced by $NaBH_4$ (0.75 g, 0.02 mol). The crude product was recrystallized from toluene to afford **6**, mp 159–162 °C. ^{1}H NMR (300 MHz, acetone-d_6) δ: 4.6 (d, 1H, D_2O exchangeable), 5.7 (d, 1H), 6.4–7.5 (m, 9H), 8.2 (s, 1H, D_2O exchangeable). MS (CI) *m/z*: 183 (M^+ – 17, base peak), 201 (M^+ + 1).

3-Methoxy-4-hydroxybenzhydrol (10)

Following the general procedure for PhMgBr, 1 g of Mg (0.042 mol) and 6.54 g (0.042 mol) of PhBr were used to produce PhMgBr, which was subsequently reacted with

© 2007 NRC Canada

1.27 g (0.008 mol) of 3-methoxy-4-hydroxybenzaldehyde. On work-up, the resulting yellow oil was twice eluted through a silica gel column (CH_2Cl_2), which afforded **10** as a pure clear oil. ^{1}H NMR (300 MHz, acetone-d_6) δ: 3.4 (s, 3H), 4.6 (d, 1H, D_2O exchangeable), 5.7 (d, 1H), 5.9 (d, 1H, D_2O exchangeable), 7.0–7.5 (m, 8H). MS (CI) *m*/*z*: 213 (M^+ – 17), 231 (M^+).

3,5-Dibutyl-4-hydroxybenzhydrol (11)

Following the general procedure for PhMgBr, 1 g of Mg (0.042 mol) and 6.54 g (0.042 mol) of PhBr were used to produce PhMgBr, which was subsequently reacted with 3.36 g (0.014 mol) of 3,5-di-*t*-butyl-4-hydroxybenzaldehyde. The crude product was obtained as an orange solid which was recrystallized in ligroin to give white crystals, mp 123 to 124 °C. ^{1}H NMR (300 MHz, acetone-d_6) δ: 1.4 (s, 18H), 4.6 (d, 1H, D_2O exchangeable), 5.7 (d, 1H), 5.9 (d, 1H, D_2O exchangeable), 7.0–7.5 (m, 7H). MS (CI) *m*/*z*: 295 (M^+ – 17, base peak), 313 (M^+ + 1).

***p*-Methoxybenzhydrol (17)**

p-Methoxybenzophenone (2 g, 0.01 mol) was reduced using $NaBH_4$ (4.29 g, 0.13 mol) according to the general procedure. The crude product was recrystallized from petroleum ether to give a white crystalline solid, mp 59–62 °C. ^{1}H NMR (300 MHz, acetone-d_6) δ: 3.7 (s, 1H), 4.7 (d, 1H, D_2O exchangeable), 5.8(d, 1H), 6.7–7.5 (m, 9H), 8.2 (s, 1H, D_2O exchangeable). MS (CI) *m*/*z*: 197 (M^+ – 17, base peak), 215 (M^+ + 1). (EI) 214 (M^+).

α,α-Diphenyl-*o*-hydroxybenzyl alcohol (8)

Following the general procedure for PhMgBr, Mg (4.2 g, 0.17 mol) and PhBr (27 g, 0.17 mol) were used to make the PhMgBr, which then reacted with *o*-hydroxybenzoic acid methyl ester (4.5 g, 0.03 mol). The crude product was recrystallized from toluene to afford a white crystalline solid, mp 148–150 °C. ^{1}H NMR (360 MHz, acetone-d_6) δ: 6.4 (s/b, 1H, D_2O exchangeable), 6.4–7.5 (m, 14H), 9.1 (s/b, 1H, D_2O exchangeable); (300 MHz, $CDCl_3$) δ: 3.7 (s, 1H, D_2O exchangeable), 6.4–7.4 (m, 14H), 8.1 (s, 1H, D_2O exchangeable). MS (CI) *m*/*z*: 259 (M^+ – 17, base peak).

α,α-Diphenyl-*m*-hydroxybenzy alcohol (9)

The methyl ester of *m*-hydroxybenzoic acid was prepared by refluxing 20 g of *m*-hydroxybenzoic acid in 400 mL of MeOH with 1 mL of concd. H_2SO_4 for 10 h. After cooling to RT, 2–4 g of $NaHCO_3$ was added with stirring and most of the MeOH evaporated. To this was added 200 mL of CH_2Cl_2 and the solution backwashed with water and saturated aq. $NaHCO_3$. Crude *m*-hydroxybenzoic methyl ester was obtained after removal of the solvent and used without further purification.

Using the Grignard reaction procedure, 2 g of *m*-hydroxybenzoic methyl ester (0.013 mol) was reacted with PhMgBr produced from 2 g of Mg (0.083 mol) and 13 g of PhBr (0.084 mol) to generate a yellow gel as the crude product. The product was recrystallized from CH_3CN to give white crystals, mp 151 to 152 °C. ^{1}H NMR (300 MHz, acetone-d_6) δ: 5.2 (s, 1H, D_2O exchangeable), 6.6–7.4 (m, 14H), 8.2 (s, 1H, D_2O exchangeable). MS (CI) *m*/*z*: 199 (M^+ – 77, base peak), 277 (M^+ + 1).

***m*-Benzylphenol (24)**

A THF solution of 2.0 g of **5** was shaken under H_2 (2 atm, 1 atm = 101.325 kPa) for 30 h. The product mixture was eluted by CH_2Cl_2 in a silica column, which gave the initial crude product. Colorless **24** was obtained by distillation under reduced pressure. ^{1}H NMR (300 MHz, acetone-d_6) δ: 3.9 (d, 2H), 6.6–6.8 (m, 3H), 7.0–7.4 (m, 6H), 8.2 (s, 1H, D_2O exchangeable). MS (CI) *m*/*z*: 185 (M^+ + 1).

General photolysis procedure

All preparative photolysis were carried out in a Rayonet RPR 100 photochemical reactor equipped with 254 lamps, using quartz tubes (100–200 mL), which were cooled with an internal cold finger (tap water, <15 °C). Solutions were continuously purged with a stream of argon via a stainless steel syringe needle for 10 min before and during the irradiation to effect stirring and deoxygenation. The length of photolysis varied from 3–60 min depending on the conversion desired. After photolysis, work-up involved adding a saturated aqueous solution of NaCl and extracting with 5 × 75 mL portions of CH_2Cl_2. The organic extracts were then combined and dried over $MgSO_4$. Filtration of the $MgSO_4$ and evaporation of CH_2Cl_2 under reduced pressure provided crude photochemical products, which were then separated by preparative TLC, if necessary, and characterized by ^{1}H NMR and mass spectroscopy. Control experiments were repeated in the absence of light at RT (~22 °C). Possible thermal reactions in photomethanolysis were eliminated by the addition of a pinch of $NaHCO_3$.

Photolysis o-hydroxybenzhydrol (4)

A solution of 40 mg **4** in 100 mL 1:1 H_2O/MeOH ($NaHCO_3$ treated) was photolyzed at 254 nm. ^{1}H NMR analysis showed that ether **12** was the only product in low conversion runs and *o*-benzylphenol **18** was formed only in high conversion runs. Preparative TLC separation afforded pure **12**. ^{1}H NMR (300 MHz, acetone-d_6) δ: 3.3 (s, 3H), 5.7 (s, 1H), 6.7–7.4 (m, 9H), 8.5 (s, 1H, D_2O exchangeable). MS (CI) *m*/*z*: 183 (M^+ – 31, base peak). The identity of **18** was confirmed by comparison with an authentic sample.

Photolysis p-hydroxybenzhydrol (6)

A solution of 40 mg of **6** in 100 mL 1:1 H_2O/MeOH ($NaHCO_3$ treated) was photolyzed at 254 nm for 3 min. Methyl ether **14** was the only product purified by preparative TLC. ^{1}H NMR (300 MHz, acetone-d_6) δ: 2.9 (s, 3H), 5.2 (s, 1H), 6.6–7.4 (m, 9H), 8.3 (b, 1H, D_2O exchangeable). MS (CI) *m*/*z*: 121 (M^+ – 93, base peak), 183 (M^+ – 31), 215 (M^+ + 1).

Photolysis of 3-phenylisocoumaranone (7)

A solution of 40 mg of **7** in 100 mL 1:1 H_2O/MeOH was photolyzed at 254 nm for 3 min. The ^{1}H NMR of the product mixture showed that ~3% of **12** was formed, as indicated by the characteristic methoxy singlet at δ 3.3 (s, 3H) and methine singlet at δ 5.7 (s, 1H).

Photolysis of α,α-diphenyl-o-hydroxybenzyl alcohol (8)

A solution of 55 mg of **8** in 100 mL 1:1 H_2O/MeOH ($NaHCO_3$ treated) was photolyzed at 254 nm for 3 min. The product was its corresponding methyl ether (28%), purified

© 2007 NRC Canada

by preparative TLC. ^{1}H NMR (300 MHz, acetone-d_6) δ: 3.2 (s, 3H), 5.6 (s, 1H), 6.4–7.8 (m, 14H), 8.7 (s, 1H, D_2O exchangeable). MS (CI) *m*/*z*: 259 (M^+ – 31, base peak).

Photolysis m-hydroxybenzhydrol (5)

A solution of 100 mg of **5** was dissolved in 100 mL 1:1 H_2O/MeOH and photolyzed at 254 nm for 5, 30, and 60 min, respectively. The product mixture contained **13** (methoxy singlet δ 3.3 (s, 3H)) and **24** (methylene δ 3.9 (d, 2H) both of which were purified by preparative TLC. Compound **13**: ^{1}H NMR (300 MHz, acetone-d_6) δ: 3.2 (s, 3H), 5.2 (s, 1H), 6.3 (s, 1H), 6.8–7.8 (m, 18H), 8.3 (s, 1H, D_2O exchangeable); MS (FAB/LSIMS, *m*-NBA as Matrix) *m*/*z*: 395 (M^+ – 1, base peak). Product **24**: ^{1}H NMR (300 MHz, acetone-d_6) δ: 3.9 (s, 2H), 6.6–6.8 (m, 3H), 7.0–7.4 (m, 6H), 8.3 (s, 1H, D_2O exchangeable).

Photolysis of α-phenyl-m-hydroxybenzhydrol (9)

A solution of 55 mg of **9** in 100 mL 1:1 H_2O/MeOH ($NaHCO_3$ treated) was photolyzed at 254 nm for 3 min. The product was the corresponding methyl ether (10%), which was purified by preparative TLC. ^{1}H NMR (300 MHz, acetone-d_6) δ: 3.0 (s, 3H), 6.6–7.4 (m, 14H), 8.2 (s, 1H, D_2O exchangeable). MS (CI) *m*/*z*: 259 (M^+ – 31, base peak), 291 (M^+ + 1).

A solution of 200 mg of **9** was dissolved in 200 mL of neat water (pH 12) and photolyzed at 254 for 30 min (vigorous Ar purge), which resulted in very cloudy (milky) solution. The product mixture was worked up by adding large amounts of aq. NH_4Cl to aggregate the fine pale yellowish precipitate, which was then filtered out of the solution and allow to dry on the filter paper. ^{1}H NMR (300 MHz, acetone-d_6) showed that a new product was formed (>80%) which was identified as condensation product **22**, δ: 5.1 (s, 1H, D_2O exchangeable), 6.4 (t, 1H), 6.6–7.4 (m, 27H), 8.2 (s, 1H, D_2O exchangeable). Negative FAB/LSIMS (*m*-NBA as matrix) *m*/*z*: 533 (M^+ – 1, base peak).

A solution of 100 mg of **9** in 100 mL 1:1:2 1 mol/L of NaOH solution/H_2O/CH_3CN was photolyzed at 254 nm for 30 min. A clear and pale yellow solution was obtained. To this solution, 300 mL of water was added to give milky solution, which aggregated upon the addition of aq. NH_4Cl. The yellow precipitate thus obtained was filtered out and allowed to dry on filter paper. Negative FAB/LSIMS (*m*-NBA as Matrix) 258 (M^+ – 18, base peak), $n \times 258 + 275$ (*n* from 1 to 10, see Fig. 2). Therefore, the product was identified as a mixture of oligomers **23**.

Steady-state fluorescence and lifetime measurements

Steady-state fluorescence spectra (uncorrected) were recorded on a PerkinElmer MPF-66 or Photon Technology International (PTI) A-1010 fluorimeter. Fluorescence lifetimes were obtained by a PTI LS-1 time-correlated single photon counting system using a hydrogen flash lamp as the excitation source (λ_{ex} = 270 nm), with data fit using the iterative deconvolution program. Each sample (~10^{-5} mol/L, OD < 0.02) was prepared in 3.0 mL four-sided suprasil quartz cuvettes with flat transparent bottoms and saturated with a stream of Ar (10 min) prior to the measurement. Absolute fluorescence quantum yields (Φ_f) were measured in CH_3CN, using anisole (Φ_f = 0.29 in cyclohexane) (10) as external standard. Excitation wavelength was 275 nm. OD_{275} was measured for individual sample and kept at ~0.1.

Laser Flash Photolysis (LFP)

Nanosecond laser flash photolysis (LFP) experiments were carried out at the University of Victoria LFP Facility at 20 ± 2 °C. A Spectra Physics YAG laser Model GCR-12 (266 nm, ≤70 mJ/pulse) was used as excitation source. The laser pulse energies were typically attenuated to less than 20mJ/pulse by adjusting the high voltage for the flash lamp to avoid multiple photon process. The analyzing beam employed consists of a pulsed 150 W xenon lamp (Oriel housing Model 66057, PTI power supply Model LPS-220). Generally, a solution of $OD_{266} \leq 0.3$ was prepared by dilution from a stock solution, followed by 10 min prepurge of oxygen or nitrogen. Experiments were carried out in a flow system (7 mm × 7 mm quartz cell) with continuous purge of oxygen or nitrogen.

Acknowledgments

This research was supported by the Natural Sciences and Engineering Research Council (NSERC) of Canada and the University of Victoria. We thank Cheng Yang for initial contributions in this study.

References

1. (*a*) P. Wan, S. Culshaw, and K. Yates. J. Am. Chem. Soc. **104**, 2509 (1982); (*b*) P. Wan and K. Yates. Rev. Chem. Intermed. **5**, 157 (1984).
2. (*a*) J.F. Ireland and P.A.H. Wyatt. Adv. Phys. Org. Chem. **12**, 131 (1976); (*b*) P. Wan and D. Shukla. Chem. Rev. **93**, 571 (1993).
3. K. Yates and P. Kalanderopoulos. J. Am. Chem. Soc. **108**, 6290 (1986).
4. R.W. Van De Water and T.R.R. Pettus. Tetrahedron, **58**, 5367 (2002).
5. Representative papers: (*a*) P. Seiler and J. Wirz. Helv. Chim. Acta, **55**, 2693 (1972); (*b*) T.W. Lewis, D.Y. Curtin, and I.C. Paul. J. Am. Chem. Soc. **101**, 5717 (1979); (*c*) L. Diao, C. Yang, and P. Wan. J. Am. Chem. Soc. **117**, 5369 (1995); (*d*) P. Wan, B. Barker, L. Diao, M. Fischer, Y. Shi, and C. Yang. Can. J. Chem. **74**, 465 (1996); (*e*) K. Nakatani, N. Higashida, and I. Saito. Tetrahedron Lett. **38**, 5005 (1997); (*f*) Y. Chiang, A.J. Kresge, and Y. Zhu. J. Am. Chem. Soc. **122**, 9854 (2000); (*g*) Y. Chiang, A.J. Kresge, and Y. Zhu. Pure Appl. Chem. **72**, 2299 (2000); (*h*) Y. Chiang and A.J. Kresge. Org. Biomol. Chem. **2**, 1090 (2004); (*i*) R.A. McClelland, M.M. Moriarty, and J.M. Chevalier. J. Chem. Soc. Perkin Trans. 2, 2235 (2001); (*j*) E. Modica, R. Zanaletti, M. Freccero, and M. Mella. J. Org. Chem. **66**, 41 (2001); (*k*) C.D. Valentin, M. Freccero, R. Zanaletti, and M. Sarzi-Amade. J. Am. Chem. Soc. **123**, 8366 (2001); (*l*) S.N. Richter, S. Maggi, S. Colloredo-Mels, M. Palumbo, and M. Freccero. J. Am. Chem. Soc. **126**, 13973 (2004); (*m*) E.E. Weinert, R. Dondi, S. Colloredo-Mels, K.N. Frankenfield, C.H. Mitchell, M. Freccero, and S. Rokita. J. Am. Chem. Soc. **128**, 11940 (2006); (*n*) S. Colloredo-Mels, F. Doria, D. Verga, and M. Freccero. J. Org. Chem. **71**, 3889 (2006).
6. (*a*) P. Wan and E. Krogh. J. Am. Chem. Soc. **111**, 4887 (1989); (*b*) A. Blazek, M. Pungente, E. Krogh, and P. Wan. J.

© 2007 NRC Canada

Photochem. Photobiol. A, **64**, 315 (1992); (*c*) C. Yang and P. Wan. J. Photochem. Photobiol. A, **80**, 227 (1994).
7. A. Padwa, D. Dehm, T. Oine, and G. Lee. J. Am. Chem. Soc. **97**, 1837 (1975).
8. P. Wan and D. Hennig. J. Chem. Soc. Chem. Commun. 939 (1987).
9. (*a*) H.E. Zimmerman. J. Am. Chem. Soc. **117**, 8988 (1995); (*b*) H.E. Zimmerman. J. Phys. Chem. A, **102**, 5616 (1998).
10. I.B. Berlman. Handbook of fluorescence spectra of aromatic molecules. 2nd ed. Academic Press, NY. 1971.
11. J. Chateauneuf. J. Chem. Soc. Chem. Commun. 1437 (1991).
12. (*a*) J. Bartl, S. Steenken, H. Mayr, and R.A. McClelland. J. Am. Chem. Soc. **112**, 6918 (1990); (*b*) R.A. McClelland, V.M. Kanagasabapathy, N.S. Banait, and S. Steenken. J. Am. Chem. Soc. **111**, 3966 (1989).
13. K.S. Peters and B. Li. J. Phys. Chem. **98**, 401 (1994).
14. S. Hamai and H. Kokubun. Bull. Chem. Soc. Jpn. **47**, 2085 (1974).
15. P. Wan and B. Chak. J. Chem. Soc. Perkin Trans. 2, 1751 (1986).

© 2007 NRC Canada

Synthesis of possible *o*-thioquinone methide precursors

Kirill A. Kolmakov and A. Jerry Kresge

Abstract: Investigating the synthetic accessibility of *o*-thioquinone methide precursors containing electron donating groups, we prepared four methyl- and methoxy-substituted 2*H*-benzo[b]thiete derivatives by means of flash vacuum pyrolysis of the corresponding benzooxathiinone species. Methyl- and methoxy-substituted substrates proved to be compatible with the pyrolysis protocol. The pyrolysis can be performed at considerably lower temperatures and with higher yields than in previously reported syntheses of nonsubstituted 2*H*-benzo[b]thiete. Under proper conditions the reaction products can be isolated in excellent yields and with 100% purity, so the troublesome purification of temperature sensitive and volatile 2*H*-benzo[b]thiete derivatives becomes unnecessary. The sulfur-containing compounds so obtained are efficient *o*-thioquinone methide precursors and possible synthones for heterocyclic chemistry.

Key words: 2*H*-benzo[b]thietes, flash vacuum pyrolysis, methyl-substituted, methoxy-substituted, *o*-thioquinone methide precursors.

Résumé : Dans le cadre de nos travaux sur l'accessibilité synthétique de précurseurs de méthides de *o*-thioquinone contenant des groupes électrodonneurs, on a préparé quatre dérivés du 2*H*-benzo[b]thiète substitués par des groupes méthyles et méthoxy en faisant appel à la pyrolyse éclair sous vide des espèces benzooxathiinones correspondantes. Il est possible d'effectuer les pyrolyses à des températures beaucoup plus basses et avec de meilleurs rendements que ceux rapportés antérieurement pour les 2*H*-benzo[b]thiètes non substitués. Dans les bonnes conditions, les produits de la réaction peuvent être isolés avec d'excellents rendements et une pureté de 100, ce qui rend inutile la purification des dérivés 2*H*-benzo[b]thiètes volatils et sensibles à la température. Les composés contenant du soufrant ainsi obtenus sont des précurseurs efficaces de méthides de *o*-thioquinone et pourraient servir de synthons en chimie hétérocyclique.

Mots-clés : 2*H*-benzo[b]thiètes, pyrolyse éclair sous vide, substitué par un méthyle, substitué par un méthoxy, précurseurs de méthides de *o*-thioquinone

[Traduit par la Rédaction]

Introduction

Quinone methides and their far less studied sulfur analogs are interesting molecules with wide application in organic synthesis (1). Extending our investigation of quinone methides generated by flash photolysis to sulfur-containing species, we synthesized some substituted 2*H*-benzo[b]thiete derivatives (Scheme 1, structure **1**) as possible precursors of *o*-thioquinone methides (Scheme 1, structure **2**). In our previous research (2), we had established that 2*H*-benzo[b]thiete (**1a**, R = H), containing a strained four-membered ring, is a good precursor for clean and high-yielding photo-generation of **2a** (R = H), needed for accurate kinetic measurements of its hydration in aqueous solution by means of flash photolytic methods. *o*-Thioquinone methide (**2a**, R = H) proved to be quite short-lived in aqueous solutions (2). Expecting to obtain transients **2** with considerably longer lifetimes, we were particularly interested in the preparation of compounds **1** containing electron donating groups at 3- or 5- positions, which would correspond to ortho and para positions, respectively, in the "thioquinone" ring of **2**, relative to the methylene group.

Scheme 1.

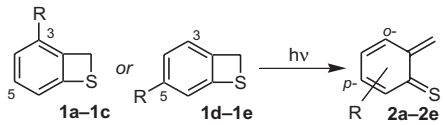

R = H, 3- *or* 5-Me, 3- *or* 5-MeO

Despite the merits of the 2*H*-benzo[b]thiete molecule, no compounds of type **1** *substituted in the benzene ring* have been described previously. The few known syntheses of **1a** made use of flash vacuum pyrolysis (FVP) at very high temperatures (700–1200 °C (3*a*–3*c*)), and no mention was made of substituted precursors (R = Me, MeO) that could be used in the synthetic procedures.

One could get the impression that because of the drastic reaction conditions of FVP, the synthesis of substituted 2*H*-benzo[b]thietes was unfeasible. Also, it is known that methyl- and methoxy-substituted aromatic hydrocarbons, including such simple derivatives as toluene and anisole,

Received 27 September 2007. Accepted 26 November 2007. Published on the NRC Research Press Web site at canjchem.nrc.ca on 21 December 2008.

This paper is dedicated to the memory of Keith Yates, a good friend, wise editor, and father of modern physical organic chemistry in Canada.

K.A. Kolmakov[1] and A.J. Kresge. Department of Chemistry, University of Toronto, Toronto, ON M5S 3H6, Canada.

[1]Corresponding author (e-mail: kkolmako@chem.utoronto.ca).

 doi:10.1139/V07-142 © 2008 NRC Canada

Scheme 2. (1 torr = 133.322 4 Pa)

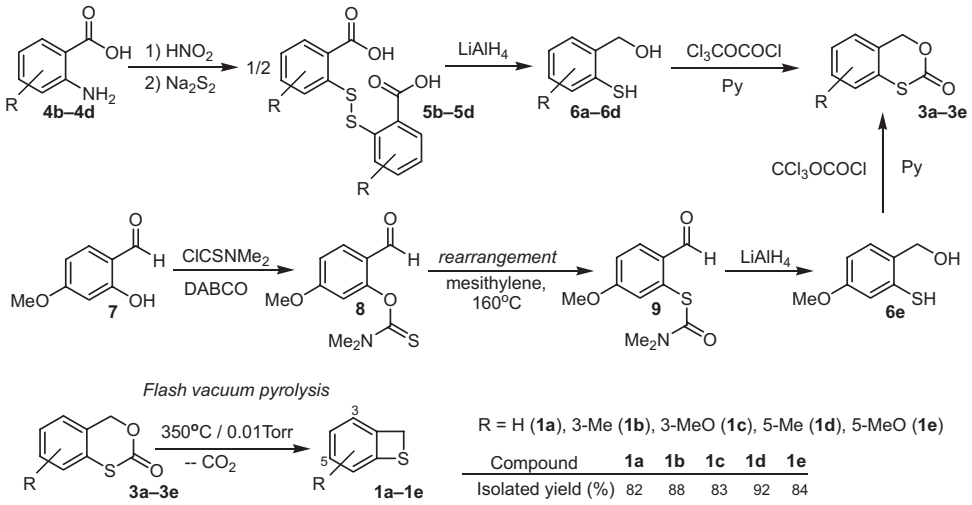

undergo demethylation when exposed to high temperatures (typically above 700 °C); soot and many other products are formed depending on conditions of the gas-phase pyrolysis (4). Finally, the existing syntheses of **1a** leave much to be improved.

According to H. Meier and A. Mayer (3*d*), 4*H*-benzo[d][1,3]oxathiin-2-one (Scheme 2, compound **3a**, R = H) undergoes decarboxylation at 140 °C already and therefore can be used as a synthetic equivalent of 2*H*-benzo[b]thiete (**1a**, R = H) in some reactions. Nonetheless, in the course of the preparative synthesis of **1a** via pyrolysis of **3a**, the authors maintained a rather high (550 °C) temperature (3*d*). We decided to check if the pyrolysis temperature could be considerably decreased. The lower the temperature, the better the chances are to obtain the derivatives of **1** in greater diversity, and, also importantly, utilize a pyrex apparatus instead of the traditionally used quartz. We explored the synthetic accessibility of *o*-thioquinone methide precursors of structure **1** containing methyl and methoxy groups. Now that the synthetic part of our research is complete, we wish to report the properties of the novel 2*H*-benzo[b]thiete derivatives and details of the syntheses.

Results and discussion

In our syntheses of compounds **1b**–**1e**, we decided to follow the route described by H. Meier and A. Mayer (5) for **1a**, which involved the preparation of the 4*H*-benzo[d][1,3]oxathiin-2-one (Scheme 2, **3a**, R = H) followed by decarboxylation performed under FVP conditions. As seen in Scheme 2, compounds **3b**–**3e** were obtained from the corresponding 2-mercaptobenzyl alcohols (**6a**–**6e**) by the reaction with trichloromethyl chloroformate (diphosgene). The alcohols **6**, of which all except **6a** are new compounds, were prepared from the commercially available substituted 2-aminobenzoic acids (**4a**–**4d**). The first stage of the syntheses involved a simplified Leukart reaction, which is known to provide good yields for 2,2′-dithiosalicylic acid **5a** and its methyl and methoxy derivatives **5b**–**5d** (5). The diazotization of the amino groups in **4a**–**4d** was followed by decomposition in aqueous solutions of sodium disulfide, and the disulfides **5a**–**5d** were reduced with a large excess of $LiAlH_4$, as described (6) for **5a** (R = H). On the other hand, the synthesis of 4-methoxy derivative (**6e**, R = 4-MeO) involved a Newman–Kwart reaction (7) on the commercially available 2-hydroxy-4-methoxybenzaldehyde (Scheme 2, **7**) followed by reduction (see the Experimental section for details).

Flash vacuum pyrolysis (FVP) generally involves controlled vaporization of neat compounds in vacuo and vapor passage through tube type reactors maintained at high temperatures (3–6). The initial experiments on the compound **3a** as a substrate gave promising results. First, we established that the flash vacuum pyrolysis does occur at considerably lower temperatures (i.e., 250–300 °C) than H. Meier and A. Mayer suggest (550 °C). Further, we found that the decarboxylation in this temperature range is selective. Apart from **1a**, the unreacted starting material **3a** was detected as the only impurity in some experiments (at low pyrolysis temperatures and with high substrate sublimation rates). This means that, under the right conditions, the reaction product can be collected pure, which is a great advantage considering the instability and volatility of 2*H*-benzo[b]thiete. The latter usually poses difficulties when solvents are being evaporated from dilute compound solutions — for example, after chromatographic separation in the final purification stage.

Besides the reaction temperature, another important parameter of the process is the so-called "contact time", which indicates how long the compound vapor is exposed to high temperature in the reactor. This depends on the length of the reaction tube and (or) substrate sublimation rate. Despite 100% selectivity achieved for the gas phase pyrolysis itself, all the compounds **3**, including the nonsubstituted **3a**, proved temperature sensitive and underwent polymerization to a noticeable extent even at 30–40 °C. Therefore, there is a limit to the sublimation temperature and consequently the process output. When we switched to methyl and methoxy derivatives **3b**–**3e** as substrates, we found that their volatility was 3–5 times lower than that of **3a**. As expected, the introduction of substituents into the small molecule **3a** drastically decreased the volatility. With the apparatus we had at our disposal and under high vacuum (0.005–0.010 torr, 1 torr = 133.322 4 Pa), the process output was some 1–1.5 mg/h.

© 2008 NRC Canada

With lower substrate sublimation rates and consequently longer contact times, temperature variations in the 300–450 °C range did not affect either yield or purity of the products. All the compounds were isolated in the pure state (~99%, HPLC, NMR) and in excellent yields (82–92%, see Scheme 2). The general procedure for flash vacuum pyrolysis is described in the Experimental section. The four derivatives **1b**–**1e** were characterized by ^{1}H and ^{13}C NMR, high- and low-resolution mass spectrometry, and by melting points.

In the NMR spectra of **1b**–**1e** at 4.30–4.40 ppm (^{1}H) and at 35.10–36.55 ppm (^{13}C), signals were observed that could be unmistakeably attributed to methylene groups (CH_2) in the four-membered ring. As expected, those signals were markedly shifted upfield, compared with that of oxymethylene groups (OCH_2) in oxathiinone precursors **3b**–**3e** (5.10–4.50 ppm (^{1}H) and 66.60–72.60 ppm (^{13}C), respectively). The latter compounds also develop "carbonyl" signals resonating in the low-field area at 166–168 ppm (^{13}C). Also, in proton NMR spectra of compounds **1b** and **1c**, one could observe the typical picture of meta-substituted benzene rings with well-resolved singlets and doublets (see Experimental section for NMR spectroscopic data).

It should be noted that compounds **1b**–**1e** proved much more temperature sensitive, especially in solutions, than the nonsubstituted compound **1a**. Polymerization of **1a** has been described in the literature (4c), and polymerization of the derivatives **1b**–**1e** was evidenced in our research by the formation of insoluble precipitates upon storage (even at –10 °C). In addition, chromatographic analyses showed a decrease in compound concentration, while no other products were detected (polymers could not pass through the column we have used for the analysis of compounds **2** and **3**; see Experimental section for details).

Conclusions

Four methyl- and methoxy-substituted 2*H*-benzo[b]thietes **1b**–**1e** were synthesized in excellent yields from the corresponding 4*H*-benzo[d][1,3]oxathiin-2-ones **3b**–**3e** via flash vacuum pyrolysis. The process was a substantial improvement on the previously reported syntheses of **3a**. Particularly, we showed that the pyrolysis can be performed at considerably lower temperatures (300 °C), which allows the use of pyrex instead of quartz in the apparatus. Our experiments demonstrated that methyl- and methoxy-substituted substrates are compatible with the pyrolysis protocol. Under proper conditions, the reaction products can be isolated in excellent yields and with a very high purity. The final purification step is thus avoided, which is very important in dealing with the temperature sensitive and volatile 2*H*-benzo[b]thiete derivatives.

Experimental section

General

Substituted 2-aminobenzoic acids (**4b**–**4d**) were purchased from Peakdale Molecular (UK), and the rest of the chemicals from Aldrich. Progress of the reactions was monitored either by HPLC using a 5500 Varian Vista chromatograph equipped with Waters Symmetry C-18 reverse-phase column (4.6/150 mm, 5 μ particle size, methanol/water (50:50 vol.) as mobile phase) or by or TLC on silica gel SIL G/UV 254 plates developed in hexane. Mass spectra were recorded on a Micromass 70S-250 sector mass spectrometer and NMR spectra on a Varian spectrometer at 300 MHz (^{1}H) and 75 MHz (^{13}C). All the solvents, including THF and pyridine, were freshly distilled and dried by conventional methods.

Flash vacuum pyrolysis — General procedure for the preparation of 2*H*-benzo[b]thiete derivatives (1a–1e).

The apparatus for flash vacuum pyrolysis consisted of a test tube for sublimation connected to a pyrex reactor (2.5 cm × 35 cm) placed inside a tube furnace. The oxathiinone precursors (30–50 mg) were dissolved in ~2 mL of methylene chloride and the solutions were evaporated inside the test tube under an argon purge to achieve better coverage of its inner surface by the solids, which assisted sublimation. The test tube was mainained at 30–35 °C by means of external heating. The vacuum was maintained at 0.005–0.010 torr by means of a rotary pump. The products were condensed in a trap, cooled with liquid nitrogen, and handled uner inert atmosphere. In a typical experiment, about 20 mg of a compound **1a**–**1e** was isolated.

General procedure for the preparation of 4*H*-benzo[d][1,3]oxathiin-2-one derivatives (3a–3e)

To a stirred solution of the thiol substrates (2 mmol) and pyridine (470 mg, 6 mmol) in 40 mL of THF, trichloromethylchlorocarbonate (260 mg, 1.30 mmol) in 5 mL of THF was added at –5 °C in 20 min under an argon atmosphere. Further, 0.5 mL of concd. HCl in 50 mL of water, 50 mL of saturated brine, 25 mL of hexane, and 5 mL of methylene chloride was added successively upon stirring at RT. The organic layer was separated, and the aqueous layer was extracted with a mixture of hexane (25 mL) and methylene chloride (5 mL). Combined extracts were washed with 15 mL of water and then with a solution of 28 mg (0.5 mmol) KOH in 10 mL of water. The extracts were dried over $MgSO_4$, and the solvents were evaporated under reduced pressure. Crude products were purified by column chromatography over a short column containing ~8 g of silica gel with methylene chloride/hexane (1:2 vol.) as liquid phase.

2-Mercaptobenzyl alcohols (6b–6d)

The compounds **6b**–**6d**were obtained by reduction of the corresponding dithiosalicylic acids **5b**–**5d** (Scheme 2), themselves prepared via a simplified Leukart reaction on 2-aminobenzoic acids (**4b**–**4d**) in good yields, according to known procedures (5*b* and 5*c*). The identity of the products identity was confirmed by melting point determination and by ^{1}H NMR spectroscopy. The most recent report on the preparation of 2-mercaptobenzyl alcohol **6a** (R = H) belongs to A. Arnoldi and M. Carughi (6), who used it as an intermediate without purification. Our recipe for the preparation of **6b**–**6d** is very simple and, more importantly, provides very high purities (~99%, HPLC) for all the produts. In a typical experiment, the reduction was carried out as follows: To an ice-cooled solution of the dithiosalicylic acid substrate **5b**–**5d** (0.004 mol) in THF (60 mL), $LiAlH_4$ powder

© 2008 NRC Canada

(0.800 g, 0.021 mol) was added in a few portions upon stirring under an argon purge. The solution was slowly (~30 min) warmed up to RT, stirred for 1 h at 55–60 °C, cooled again, and carefully poured onto a mixture of ice (100 g) and 30 mL of 10 wt% H_2SO_4 upon vigorous stirring. Benzene (20 mL) was added immediately afterwards, and the organic layer separated. Water phase was extracted with benzene (20 mL × 2) and the combined organic extract was washed with water (15 mL) and a saturated $NaHCO_3$ solution (10 mL). From the benzene solution, the compounds **6b**–**6d** were extracted with NaOH (0.400 g, 0.010 mol) in 15 mL of water. The alkaline extract was acidified with concd. HCl (1.5 mL) and treated with CH_2Cl_2 (20 mL × 2). The organic phase was washed with brine (10 mL), dried and evaporated in vacuo. For the final purification, the alcohols were decolorized with silica gel (0.10 g) in methylene chloride/pentane (~1:10 vol.) solutions at RT, and crystallized upon cooling to (–20)–(+30) °C (because of their low melting points; properties and yields are reported later). All the compounds **6** are air-sensitive, and therefore all the manipulations were carried out under an argon atmosphere. The identity and purity of the alcohols **6b**–**6d** (all four are new compounds) was confirmed by ^1H and ^{13}C NMR spectroscopic data and mass spectrometry (see following).

2-Mercapto-6-methylbenzyl alcohol (6b)

Yield 67%. Colorless needles, mp 74–76 °C (methylene chloride/pentane). ^1H NMR ($CDCl_3$, ppm) δ: 1.84 (br s, 1H, OH) 2.41 (s, 3H, CH_3), 3.64 (s, 1H, SH), 4.88 (s, 2H, CH_2) 6.99–7.25 (m, $3H_{Ar}$). ^{13}C NMR ($CDCl_3$, ppm) δ: 19.72 (CH_3), 60.57 (CH_2OH), 128.52, 128.73, 129.39, 131.90, 136.72, 138.40. MS EI (70 eV) *m/z* (%): 154 (10, M^+), 136 (100, $M^+ - H_2O$), 121 (12, $M^+ - H_2O - CH_3$). HRMS (EI) calcd. for (M^+) $C_8H_{10}O_2S$: 154.0452; found: 154.0456.

2-Mercapto-6-methoxybenzyl alcohol (6c)

Yield 62%. Colorless needles, mp 68 to 69 °C (methylene chloride/pentane). ^1H NMR ($CDCl_3$, ppm) δ: 2.22 (br s, 1H, OH), 3.64 (s, 1H, SH), 3.83 (s, 3H, OCH_3), 4.66 (s, 2*H*, CH_2), 6.71–7.49 (m, $3H_{Ar}$). ^{13}C NMR ($CDCl_3$, ppm) δ: 55.70 (OCH_3), 58.26 (CH_2OH), 108.52, 123.62, 127.20, 129.16, 132.77, 158.40. MS EI (70 eV) *m/z* (%): 170 (15, M^+), 152 (100, $M^+ - H_2O$), 121 (20, $M^+ - H_2O - OCH_3$). HRMS (EI) calcd. for (M^+) $C_8H_{10}O_2S$: 170.0402; found: 170.0407.

2-Mercapto-4-methylbenzyl alcohol (6d)

Yield 73%. Colorless needles, mp 42 to 43 °C (methylene chloride/pentane). ^1H NMR ($CDCl_3$ ppm) δ: 1.85 (br s, 1H, OH) 2.30 (s, 3H, CH_3), 3.66 (s, 1H, SH), 4.69 (s, 2H, CH_2) 6.98 (d, *J* = 7Hz, $1H_{Ar}$), 7.19 (s, $1H_{Ar}$), 7.24 (d, *J* = 7Hz, $1H_{Ar}$). ^{13}C NMR ($CDCl_3$, ppm) δ: 20.91 (CH_3), 64.29 (CH_2OH), 127.19, 128.94, 130.13, 131.99, 135.89, 138.48. MS EI (70 eV) *m/z* (%): 154 (12, M^+), 136 (100, $M^+ - H_2O$), 121 (15, $M^+ - H_2O - CH_3$). HRMS (EI) calcd. for (M^+) $C_8H_{10}O_2S$: 154.0452; found: 154.0451.

2-Mercapto-4-methoxybenzyl

The alcohol (**6e**) was obtained via a Newman–Kwart reaction (see Scheme 2) on the commercially available 2-hydroxy-4-methoxybenzaldehyde (**7**) by the following steps.

Dimethylthiocarbamic acid *O*-(2-formyl-5-methoxyphenyl) ester (8)

A solution of *N*,*N*-dimethylthiocarbamoyl chloride (3.10 g, 0.025 mol), 2-hydrohy-4-methoxybenzaldehyde (3.04 g, 0.02 mol), and DABCO (3.02g, 0.027 mol) in 20 mL of anhyd. DMF was stirred overnight at RT for 2 h at 35–40 °C, and then poured into 200 mL of ice cold water. The yellow powder was collected, dried, and recrystallized from a benzene/hexane mixture (1:3 vol.) to afford 3.32 g (70%) of a colorless product whose melting point was 88 to 89 °C. ^1H NMR and mass spectra agreed with the structure **8**. ^1H NMR ($CDCl_3$, ppm) δ: 3.41, 3.47 (2s, 6H, NCH_3), 3.88 (s, 3H, OCH_3), 6.63 (s, $1H_{Ar}$), 6.90 (d, *J* = 6Hz, $1H_{Ar}$), 7.85 (d, *J* = 6Hz, $1H_{Ar}$), 9.92 (s, 1H, CHO). MS (ESI) *m/z* (%): 262 (100, M + Na^+), 239 (15, M + H^+), 212 (10, M^+ – CO). HRMS (ESI) calcd. for (M + Na^+) $C_{11}H_{13}O_3NaS$: 262.0508; found: 262.0501.

Dimethylcarbamic acid *S*-(2-formyl-5-methoxyphenyl) ester (9)

The rearrangement of the *O*-ester **8** to the corresponding *S*-ester **9** (see Scheme 2) was performed at 165 °C using mesithylene as solvent instead of the commonly used biphenyl ether (7b). Mesithylene proved much easier to remove and, more importantly, higher reaction temperatures (190–200 °C) are unsuitable for **8** because of its thermal sensitivity. Compound **8** (2.00 g, 0.008 mol) was refluxed in 20 mL of mesithylene for 25 h under an argon atmosphere. The rearrangement was monitored by TLC on silica plates using methylene chloride/acetone (10:1) as mobile phase. The solution was evaporated in a Petrie plate at atmospheric pressure, the residue dissolved in a methylene chloride/hexane (1:2 vol.) mixture (180 mL), decolorized with 0.40 g of silica gel, and crystallized to afford 1.65 g (80%) of pale yellow needles with mp 78 °C. ^1H NMR ($CDCl_3$, ppm) δ: 3.04, 3.16 (2s, 6H, NCH_3), 3.88 (s, 3H, OCH_3), 7.02 (s, $1H_{Ar}$), 7.05 (d, *J* = 6Hz, $1H_{Ar}$), 8.01 (d, *J* = 6Hz, $1H_{Ar}$), 10.27 (s, 1H, CHO). MS (ESI) *m/z* (%): 262 (100, M + Na^+), 239 (30, M + H^+), 212 (10, M^+ – CO), 167 (20, $M^+ - CON(CH_3)_2$). HRMS (ESI) calcd. for (M + Na^+) $C_{11}H_{13}O_3NaS$: 262.0508; found: 262.0504.

Compound **9** (0.956 g, 0.004 mol) in 5 mL of THF was added to a stirred suspension of LiAlH4 (0.800 g, 0.021 mol) in 30 mL of THF at 0 °C during 10 min under an argon purge, the reaction mixture was stirred for 4 h at 50°, and then treated exactly as described for the alcohols **6b**–**6d** (see earlier) to furnish **6e** (0.456 g, 67%) as colorless needles with mp 26–28 °C (methylene chloride/pentane). ^1H NMR ($CDCl_3$, ppm) δ: 1.84 (br s, 1H, OH) 3.78 (s, 3H, OCH_3), 3.90 (s, 1H, SH), 4.66 (s, 2H, CH_2) 6.64 (d, *J* = 7Hz, $1H_{Ar}$), 6.87 (s, $1H_{Ar}$), 7.22 (d, *J* = 7Hz, $1H_{Ar}$). ^{13}C NMR ($CDCl_3$, ppm) δ: 55.52 (OCH_3), 64.09 (CH_2OH), 111.81, 116.69, 130.45, 131.20, 132.14, 159.45. MS EI (70 eV) *m/z* (%): 170 (25, M^+), 152 (100, $M^+ - H_2O$), 121 (15, $M^+ - H_2O - OCH_3$). HRMS (EI) calcd. for (M^+) $C_8H_{10}O_2S$: 170.0402; found: 170.0401.

3-Methyl-2*H*-benzo[b]thiete (1b)

Yield 88%. Colorless liquid, fp (–10)–(+)9 °C. ^1H NMR (CD_3CN, ppm) δ: 2.27 (s, 3H, CH_3), 4,33 (s, 2H, CH_2), 6.91–6.98 (m, $2H_{Ar}$), 7,18–7.24 (m, $1H_{Ar}$). ^{13}C NMR

© 2008 NRC Canada

(CD_3CN, ppm) δ: 15.08 (CH_3), 35.88 (CH_2), 118.52, 125.42, 129.51, 133.12, 138.88, 142.46. MS EI (70 eV) *m/z* (%): 136 (100, M^+), 121 (20, $M^+ - CH_3$), 91 (45, $M^+ - S - CH_3$). HRMS (EI) calcd. for (M^+) C_8H_8S: 136.0347; found: 136.0348.

5-Methyl-4*H*-benzo[d][1,3]oxathiin-2-one (3b)

Yield 55%. Colorless needles, mp 64–66 °C. ^1H NMR (CD_3CN, ppm) δ: 2.44 (s, 3H, CH_3), 5.47 (s, 2H, CH_2), 7.23–7.27 (m, $2H_{Ar}$), 7.33–7.38 (m, $1H_{Ar}$). ^{13}C NMR (CD_3CN, ppm) δ: 18.31 (CH_3), 69.39 (CH_2), 124.44, 128.18, 129.73, 130.09, 131.18, 136.47, 167.20 (C=O). MS EI (70 eV) *m/z* (%): 180 (20, M^+), 136 (100, $M^+ - CO_2$), 121 (45, $M^+ - CO_2 - CH_3$). HRMS (EI) calcd. for (M^+) $C_9H_8O_2S$: 180.0245; found: 180.0248.

3-Methoxy-2*H*-benzo[b]thiete (1c)

Yield 83%. Colorless liquid, fp 11–13 °C. ^1H NMR (CD_3CN, ppm) δ: 3.95 (s, 3H, OCH_3), 4.41 (s, 2H, CH_2), 6.64–6.66 (m, $2H_{Ar}$), 7.21–7.26 (m, $1H_{Ar}$). ^{13}C NMR (CD_3CN, ppm) δ: 35.10 (CH_2), 56.05 (OCH_3), 109.76, 114.41, 124.12, 130.67, 143.96, 153.01 (C3). MS EI (70 eV) *m/z* (%): 152 (100, M^+), 137 (10, $M^+ - CH_3$), 121 (40, $M^+ - OCH_3$), 107 (15, $M^+ - CH_2 - OCH_3$). HRMS (EI) calcd. for (M^+) C_8H_8OS: 152.0296; found: 152.0299.

5-Methoxy-4*H*-benzo[d][1,3]oxathiin-2-one (3c)

Yield 63%. Colorless needles, mp 68 to 69 °C. ^1H NMR (CD_3CN, ppm) δ: 3.93 (s, 3H, CH_3), 5.49 (s, 2H, CH_2), 7.95–7.10 (m, $2H_{Ar}$), 7.41–7.49 (m, $1H_{Ar}$). ^{13}C NMR (CD_3CN, ppm) δ: 56.25 (OCH_3), 66.63 (CH_2), 110.82, 117.42, 118.56, 131.17, 132.34, 156.61 (C3), 166.88 (C=O). MS EI (70 eV) *m/z* (%): 196 (15, M^+), 152 (100, $M^+ - CO_2$), 121 (40, $M^+ - CO_2 - OCH_3$). HRMS (EI) calcd. for (M^+) $C_9H_8O_3S$: 196.0194; found: 196.0193.

5-Methyl-2*H*-benzo[b]thiete (1d)

Yield 92%. Colorless prisms, mp 54 to 55 °C. ^1H NMR (CD_3CN, ppm) δ: 2.35(s, 3H, CH_3), 4.32 (s, 2H, CH_2), 6.81 (d, J = 8Hz, $1H_{Ar}$), 6.95 (s, $1H_{Ar}$), 6.97 (d, J = 8Hz, $1H_{Ar}$). ^{13}C NMR (CD_3CN, ppm) δ: 21.65 (CH_3), 36.55 (CH_2), 121.96, 123.13, 125.30, 137.23, 139.24, 142.53. MS EI (70 eV) *m/z* (%): 136 (100, M^+), 121 (15, $M^+ - CH_3$), 91 (25, $M^+ - S - CH_3$). HRMS (EI) calcd. for (M^+) C_8H_8S: 136.0347; found: 136.0346.

7-Methyl-4*H*-benzo[d][1,3]oxathiin-2-one (3d)

Yield 60%. Colorless needles, mp 71 to 72 °C. ^1H NMR (CD_3CN, ppm) δ: 2.40 (s, 3H, CH_3), 5.37 (s, 2H, CH_2), 7.24 (d, J = 8Hz, $1H_{Ar}$), 7.25 (s, $1H_{Ar}$), 7.36 (d, J = 8Hz, $1H_{Ar}$). ^{13}C NMR (CD_3CN, ppm) δ: 20.69 (CH_3), 72.19 (CH_2), 126.59, 126.87, 127.20, 128.81, 130.95, 140.57, 166.89 (C=O). MS EI (70 eV) *m/z* (%): 180 (25, M^+), 136 (100, $M^+ - CO_2$), 121 (8, $M^+ - CO_2 - CH_3$). HRMS (EI) calcd. for (M^+) $C_9H_8O_2S$: 180.0245; found: 180.0246.

5-Methoxy-2*H*-benzo[b]thiete (1e)

Yield 84%. Colorless prisms, mp 27 to 28 °C. ^1H NMR (CD_3CN, ppm) δ: 3.79 (s, 3H, OCH_3), 4,41 (s, 2H, CH_2), 6.55 (d, J = 7Hz, $1H_{Ar}$), 6.61 (s, $1H_{Ar}$), 6.69 (d, J = 7Hz, $1H_{Ar}$). ^{13}C NMR (CD_3CN, ppm) δ: 37.07 (CH_2), 56.11 (OCH_3), 108.18, 111.68, 118.80, 132.35, 143.91, 161.70 (C5). MS EI (70 eV) *m/z* (%): 152 (100, M^+), 137 (5, $M^+ - CH_3$), 121 (10, $M^+ - OCH_3$), 107 (25, $M^+ - CH_2 - OCH_3$). HRMS (EI) calcd. for (M^+) C_8H_8OS: 152.0296; found: 152.0297.

7-Methoxy-4*H*-benzo[d][1,3]oxathiin-2-one (3e)

Yield 62%. Colorless needles, mp 76 to 77 °C. ^1H NMR (CD_3CN, ppm) δ: 3.74 (s, 3H, CH_3), 5.16 (s, 2H, CH_2), 6.73 (d, J = 7.5Hz, $1H_{Ar}$), 6.76 (s, $1H_{Ar}$), 7.18 (d, J = 7.5 Hz, $1H_{Ar}$). ^{13}C NMR (CD_3CN, ppm) δ: 56.43 (OCH_3), 72.57 (CH_2), 112.46, 114.26, 121.92, 128.99, 133.10, 161.44 (C5), 167.23 (C=O). MS EI (70 eV) *m/z* (%): 196 (25, M^+), 152 (100, $M^+ - CO_2$), 121 (10, $M^+ - CO_2 - OCH_3$). HRMS (EI) calcd. for (M^+) $C_9H_8O_3S$: 196.0194; found: 196.0197.

Acknowledgement

We are grateful to the Natural Sciences and Engineering Research Council of Canada for its generous financial support of our work.

References

1. For a recent review see: P. Wan, B. Barker, L. Dio, M. Fischer, Y. Shi, and C. Yang. Can. J. Chem. **74**, 465 (1996).
2. Y. Chiang, A.J. Kresge, O. Sadovski, and H.Q. Hao-Qiang Zhan. J. Org. Chem. **70**, 1643 (2005).
3. For the preparation and properties of 2*H*-benzo[b]thiete see: (*a*) K. Kanakarajan and H. Meier. J. Org. Chem. **48**, 881 (1983); (*b*) R. Schulz and A. Schweig, Tetrahedron Lett. **21**, 343 (1980); (*c*) Y.-L. Mao and V. Boekelheide. Proc. Nat. Acad. Sci. USA, **77**, 1732 (1980); (*d*) H. Meier and A. Mayer. Synthesis, 327 (1996).
4. For a review see: (*a*) G.M. Badger. Progress in physical organic chemistry. Vol. 3. Wiley & Sons Inc., NY. 1965. pp. 1–40; for the pyrolysis of toluene see: (*b*) C.T. Brooks, C.P.R. Cummins, and S.J. Peacock. Trans. Faraday Soc. **67**, 3265, (1971); (*c*) S.J. Price. Can. J. Chem. **40**, 1310 (1962); for the pyrolysis of anisole see: (*d*) V.V. Platonov, V.A. Proskuryakov, S.V. Ryl'tsova, and Y.N. Popova. Russ. J. Appl. Chem. **74**, 1047 (2001); (*e*) Y. Tsujino, C. Wakai, N. Matubayasi, and M. Nakahara. Chem. Lett. **35**, 1334 (2006).
5. For the preparation of dithiosalicylic acid, its 6-methoxy-, 6- and 4-methyl derivatives, respectively, see: (*a*) Organic synthesis, coll. Vol. 2. NY-L. p. 580. 1943; (*b*) K.C. Roberts, L.A. Wiles, and B.A.S. Kent. J. Chem. Soc. **54**, 1792 (1932); (*c*) R. Ponci, V. Tullo, L. Amoretti, and F. Mossini. Farmaco, **22**, 935 (1967).
6. A. Arnoldi and M. Carughi. Synthesis, 155 (1988).
7. For Newman–Kwart rearrangement see; (*a*) M.S. Newman and H.A. Karnes. J. Org. Chem. **31**, 3980 (1966); (*b*) A. Mayer, N. Rumpf, and H. Meier. Liebigs Ann. 2221 (1995).

© 2008 NRC Canada

Bismuth(III)-catalyzed rapid and highly efficient synthesis of 2-aryl-1-arylmethyl-1*H*-benzimidazoles in water

J.S. Yadav, B.V. Subba Reddy, K. Premalatha, and K. Shiva Shankar

Abstract: 2-Aryl-1-arylmethyl-1*H*-benzimidazoles are prepared in high yields under extremely mild conditions via the condensation of aryl-1,2-diamines with aromatic aldehydes using 10 mol% of bismuth triflate in water. The use of water and readily available bismuth triflate makes this process quite simple, more convenient, and environment-friendly.

Key words: aryl-1,2-diamines, aromatic aldehydes, bismuth catalysis, benzimidazoles.

Résumé : On a préparé des 2-aryl-1-arylméthyl-1*H*-benzimidazoles avec des rendements élevés, sous des conditions extrêmement douces, en faisant appel à une condensation d'aryl-1,2-diamines avec des aldéhydes aromatiques en utilisant 10 moles pour cent de triflate de bismuth dans l'eau. L'utilisation de l'eau et la grande accessibilité du triflate de bismuth font que ce procédé est simple, très commode et environnementalement acceptable.

Mots-clés: aryl-1,2-diamines, aldéhydes aromatiques, catalyse par le bismuth, benzimidazoles.

[Traduit par la Rédaction]

Introduction

Benzimidazoles are important biologically active heterocycles possessing selective neuropeptide YY1 receptor antagonists (1) and as 5-lipoxygenase inhibitors for use as novel antiallergic agents (2), 5-HT3 antagonists in isolated guinea pig ileum (3), poly(ADP-ribose) polymerase (PARP) inhibitors (4), and factor Xa (Fxa) inhibitors (5). In addition, they exhibit significant activity against several viruses, such as HIV, herpes (HSV-1), RNA influenza, and human cytomegalovirus (HCMV) (6). Benzimidazole derivatives have found commercial applications in veterinarian medicine as anti-helmintic agents and in diverse human therapeutic areas, such as treatment of ulcers and as anti-histamines (7). Medicinal chemists would certainly classify benzimidazoles as privileged sub-structures for drug design, as they display affinity towards a variety of enzymes and protein receptors (8). Consequently, a variety of methods have been developed for the preparation of substituted benzimidazoles (9). Of these, one of the most traditional methods involves the condensation of an *o*-phenylenediamine with carboxylic acid or its derivatives (10). Subsequently, several improved protocols have been developed for the synthesis of benzimidazoles via the condensation of *o*-phenylenediamines with aldehydes in the presence of acid catalysts under various reaction conditions (11). However, many of these methods suffer from certain drawbacks, including longer reaction times, unsatisfactory yields, harsh reaction conditions, expensive reagents, tedious work-up procedures, co-occurrence of several side reactions, and poor selectivity. Since benzimidazole derivatives are useful and important in the field of drugs and pharmaceuticals, the development of simple, convenient, high yielding, and environmentally benign protocols is desirable. Therefore, the search continues for a better catalyst for the synthesis of benzimidazoles, in terms of operational simplicity, economic viability, and selectivity.

Recently, great attention has been focused on the use of water as green solvent for various organic transformations (12). In addition to its abundance and for economical and safety reasons, water has naturally become a substitute and an alternative environmentally benign solvent in organic synthesis. This becomes further sophisticated if these reactions can be performed using inexpensive and readily available reagents. Lanthanide triflates are unique Lewis acids that are currently of great interest (13). The high catalytic activity, low toxicity, moisture and air tolerance, and their recyclability make lanthanide triflates attractive alternatives to conventional Lewis acids (14). However, lanthanide triflates are rather expensive, and their use in large-scale synthesis is limited. Therefore, cheaper and more efficient catalysts are desirable. In this direction, bismuth triflate has evolved as remarkable Lewis acid catalyst for effecting various organic transformations (15). Compared with lanthanide triflates, bismuth triflate is cheap and is easy to prepare, even on a multi-gram scale, from commercially available bismuth oxide and triflic acid (16). The use of bismuth triflate for the synthesis of benzimidazoles has recently been reported under solvent-free conditions (17).

Results and discussion

Inspired by recent reports on the use of $Bi(OTf)_3$ in aqueous conditions (18) and our interest on the catalytic use of

Received 23 September 2007. Accepted 20 November 2007. Published on the NRC Research Press Web site at canjchem.nrc.ca on 4 January 2008.

J.S. Yadav,[1] B.V. Subba Reddy, K. Premalatha, and K.S. Shankar. Division of Organic Chemistry, Indian Institute of Chemical Technology, Hyderabad 500 007, India.

[1]Corresponding author (e-mail: yadav@iict.res.in).

 doi:10.1139/V07-140 © 2008 NRC Canada

Scheme 1.

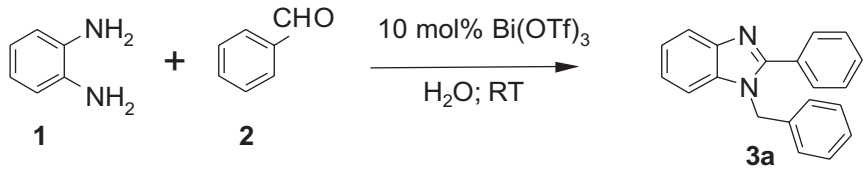

$Bi(OTf)_3$ (19), we herein report a mild and rapid synthesis of 2-aryl-1-arylmethyl-1*H*-benzimidazoles using a catalytic amount of $Bi(OTf)_3$ in water. Accordingly, treatment of *o*-phenylenediamine (**1**) with benzaldehyde (**2**) in the presence of 10 mol% of $Bi(OTf)_3$ in water resulted in the formation of benzimidazole (**3a**) in 97% yield (Scheme 1).

This result provided the incentive for further study of reactions with various substituted aryl 1,2-diamines and aryl aldehydes. Interestingly, several mono- and di-substituted aryl 1,2-diamines reacted efficiently with aldehydes to give the corresponding benzimidazoles (Table 1). The present protocol is effective for aromatic aldehydes bearing either electron-rich or electron-deficient substituents on the aromatic ring (Table 1, entries **b**–**h**). Similarly, α-naphthaldehyde (Table 1, entry **j**) and heteroaromatic aldehydes (Table 1, entries **k**–**m**) also reacted well with *o*-phenylenediamine to furnish the corresponding benzimidazoles in good yields. In all cases, the reactions proceeded rapidly at room temperature with high efficiency and were complete within a short time. The products were characterized by ^1H, ^{13}C NMR, IR, and mass spectroscopy and also by comparison with authentic samples (11). Unlike reported methods, the present protocol does not require harsh or drastic conditions to produce benzimidazoles. The effects of various metal triflates, such as $Cu(OTf)_2$, $In(OTf)_3$, and $Ce(OTf)_3$ were screened. Of these catalysts, bismuth(III) triflate was found to be the most effective in terms of conversion and reaction rates. Interestingly, 10 mol% of $Sc(OTf)_3$ was found to be an equally effective for this conversion. In the absence of catalyst, the reaction did not proceed in water even after long reaction times (12–24 h). Compared with conventional Lewis acids, $Bi(OTf)_3$ is particularly attractive because it can be used in water (18). Since a water solution of $Bi(OTf)_3$ is acidic (16), it may be possible that the true catalyst is TfOH produced from the hydrolysis of $Bi(OTf)_3$. However, TfOH is not as effective as $Bi(OTf)_3$ to catalyze the condensation of *o*-phenylenediamine with benzaldehyde (10% TfOH at 25 °C, 3 h, 65%), thus suggesting that a Lewis acid is likely involved in activating the aldehyde. Furthermore, the recovered aqueous solution of $Bi(OTf)_3$ could be reused in further reactions with gradual decrease in activity. For instance, treatment of *o*-phenylenediamine with benzaldehyde over 10 min gave 97%, 85%, and 71% yield, respectively, over three cycles. This observation clearly shows the reusability of the catalyst. The scope and generality of this process is illustrated with respect to various aryl 1,2-diamines and aldehydes, and the results are summarized in Table 1.

In conclusion, we have described a mild, convenient, and efficient protocol for the synthesis of highly substituted benzimidazoles using bismuth(III) triflate as the novel catalyst. This method not only offers substantial improvements in reaction rates and yields but also avoids the use of hazardous acids, environmentally unfavorable organic solvents, and harsh reaction conditions, which makes it useful and environment-friendly for the synthesis of biologically relevant benzimidazole scaffolds.

Experimental

Melting points were recorded on Buchi R-535 apparatus and are uncorrected. IR spectra were recorded on a PerkinElmer FTIR 240-c spectrophotometer using KBr optics. ^1H NMR spectra were recorded on Gemini 200 and Varian Bruker 300 spectrometers in $CDCl_3$ using TMS as internal standard. Mass spectra were recorded on a Finnigan MAT 1020 mass spectrometer operating at 70 eV. TLC was monitored on 0.25 mm pre-coated silica-gel plates (60F-254).

General procedure

A mixture of the 1,2-diamine (1.0 mmol), aldehyde (2 mmol), and $Bi(OTf)_3$ (10 mol%) in water (2 mL) was stirred at room temperature for the specified time (see Table 1). After completion of the reaction as indicated by TLC, the reaction mixture was extracted with ethyl acetate (2 × 10 mL). Evaporation of the solvent, followed by purification on silica gel (Merck, 100–200 mesh, ethyl acetate/hexane (1:5)), afforded pure benzimidazole.

1-Benzyl-2- phenyl-1*H*-benzo[*d*]imidazole (3a)

Solid; mp 139–141 °C. IR (KBr) ν_{max}: 3031, 2947, 1452, 1348, 1162, 967, 697 cm^{-1}. ^1H NMR (200 MHz, $CDCl_3$) δ: 5.45 (s, 2H), 7.08–7.12 (m, 3H), 7.21–7.30 (m, 5H), 7.35–7.44 (m, 3H), 7.62 (dd, J = 8.0 and 2.0 Hz, 2H), 7.84 (d, J = 8.0 Hz, 1H). EI-MS *m*/*z* (%): 284 (M^+, 45), 156 (10), 142 (30), 92 (100).

1-(4-Methylbenzyl)-2-(4-methylphenyl)-1*H*-benzo[*d*]imidazole (3b)

Solid; mp 128–130 °C. IR (KBr) ν_{max}: 3024, 2917, 2861, 1411, 1249 cm^{-1}. ^1H NMR (200 MHz, $CDCl_3$) δ: 2.34 (s, 3H), 2.40 (s, 3H), 5.37 (s, 2H), 6.96 (d, J = 8.1 Hz, 2H), 7.11–7.26 (m, 6H), 7.55 (d, J = 8.3 Hz, 2H), 7.79 (d, J = 7.9 Hz, 2H), EI-MS *m*/*z* (%): 312 (M^+, 92), 208 (26), 105 (100), 77 (10).

1-(4-Methoxybenzyl)-2-(4-methoxyphenyl)-1*H*-benzo[*d*]imidazole (3c)

Solid; mp 121–123 °C. IR (KBr) ν_{max}: 3064, 3043, 2959, 2943, 1604, 1452, 1243, 750 cm^{-1}. ^1H NMR (200 MHz, $CDCl_3$) δ: 3.65 (s, 3H), 3.85 (s, 3H), 5.38 (s, 2H), 6.78–6.85 (m, 3H), 6.95–7.05 (m, 3H), 7.08–7.35 (m, 4H), 7.62 (d, J = 8.0 Hz, 2H). EI-MS *m*/*z* (%): 344 (M^+, 64), 329 (6), 299 (30), 223 (100), 91 (64).

© 2008 NRC Canada

Table 1. $Bi(OTf)_3$-catalyzed synthesis of *N*-substituted benzimidazoles in water.

Entry	1, 2- Diamines	Aldehydes	Product[a]	Time (min)	Yield (%)[b]
a			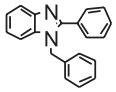	03	97
b		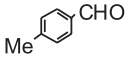	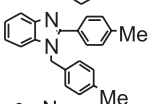	05	95
c		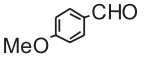	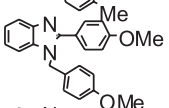	05	90
d		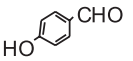	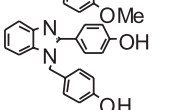	05	90
e		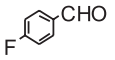	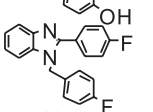	05	92
f		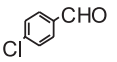	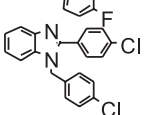	05	87
g		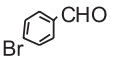	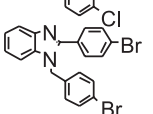	05	92
h		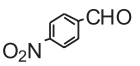	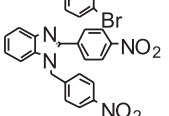	05	92
i			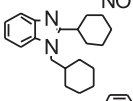	07	89
j		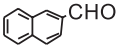	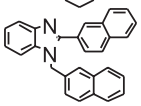	10	98
k			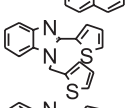	10	95
l			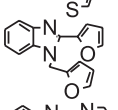	03	92
m			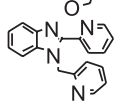	10	75
n	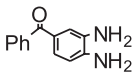		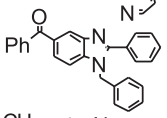	10	70
o	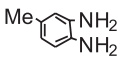		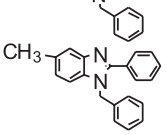	05	85
p	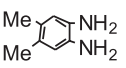		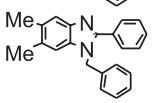	05	80
q		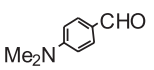	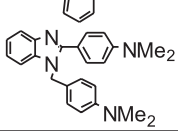	10	75

[a] All products were characterised by ^1H NMR, IR, and mass spectrometry.

[b] Yields refer to pure products after chromotography.

© 2008 NRC Canada

1-(4-Hydroxybenzyl)-2-(4-hydroxyphenyl)-1*H*-benzo[*d*]imidazole (3d)

Solid; mp 111–113 °C. IR (KBr) ν_{max}: 3420, 3089, 3045, 2955, 1605, 1455, 1245, 750 cm^{-1}. ^1H NMR (200 MHz, $CDCl_3$) δ: 5.28 (s, 2H), 6.87–6.90 (m, 3H), 7.02–7.08 (m, 3H), 7.18–7.25 (m, 4H), 7.78 (d, *J* = 8.0 Hz, 2H). ESI-MS *m/z* (%): 317 (M + 1).

1-(4-Fluorobenzyl)-2-(4-fluorophenyl)-1*H*-benzo[*d*]imidazole (3e)

Solid; mp 110–112 °C. IR (KBr) ν_{max}: 3032, 2935, 2835, 1465, 1423, 1078, 750 cm^{-1}. ^1H NMR (200 MHz, $CDCl_3$) δ: 5.45 (s, 2H), 6.92–7.18 (m, 4H), 7.21–7.32 (m, 5H), 7.62–7.78 (m, 3H). ESI-MS *m/z* (%): 321 (M + 1).

1-(4-Chlorobenzyl)-2-(4-chlorophenyl)-1*H*-benzo[*d*]imidazole (3f)

Solid; mp 137–139 °C. IR (KBr) ν_{max}: 3038, 2923, 2853, 1473, 1439, 1091 cm^{-1}. ^1H NMR (200 MHz, $CDCl_3$) δ: 5.39 (s, 2H), 7.03 (d, *J* = 9.0 Hz, 2H), 7.11–7.34 (m, 4H), 7.42 (d, *J* = 8.3 Hz, 2H), 7.58 (d, *J* = 8.3 Hz, 2H), 7.82 (d, *J* = 7.5 Hz, 2H). EI-MS *m/z* (%): 352 (M^+, 52), 227 (4), 192 (30), 125 (100), 90 (13).

1-(4-Bromobenzyl)-2-(4-bromophenyl)-1*H*-benzo[*d*]imidazole (3g)

Solid; mp 160–162 °C. IR (KBr) ν_{max}: 3045, 2928, 1569, 1468, 1091 cm^{-1}. ^1H NMR (200 MHz, $CDCl_3$) δ: 5.42 (s, 2H), 7.01 (d, *J* = 7.8 Hz, 2H), 7.15–7.35 (m, 3H), 7.42–7.59 (m, 6H), 7.78 (d, *J* = 7.8 Hz, 1H). ESI-MS *m/z* (%): 441 (M + 1).

1-(4-Nitrobenzyl)-2-(4-nitrophenyl)-1*H*-benzo[*d*]imidazole (3h)

Solid; mp 175–177 °C. IR (KBr) ν_{max}: 3043, 2978, 2240, 1470, 1352, 1188 cm^{-1}. ^1H NMR (200 MHz, $CDCl_3$) δ: 5.45 (s, 2H), 7.26–7.32 (m, 4H), 7.70–7.74 (m, 4H), 8.07–8.25 (m, 4H). ESI-MS *m/z* (%): 375 (M + 1).

2-Cyclohexyl-1-(cyclohexyl methyl)-1*H*-benzo[*d*]imidazole (3i)

Solid; mp 82–84 °C. IR (KBr) ν_{max}: 3743, 3042, 2926, 1581, 1454, 1344, 742 cm^{-1}. ^1H NMR (200 MHz, $CDCl_3$) δ: 0.995–2.0 (m, 22H), 3.88 (d, *J* = 7.8 Hz, 2H), 7.05–7.20 (m, 2H), 7.68–7.75 (m, 2H). EI-MS *m/z* (%): 296 (M^+, 15), 241 (10), 213 (20), 141 (40), 83 (15), 41 (100).

2-(Napthalene-3yl)-1-(napthlen-3-yl)methyl)-1*H*-benzo[*d*]imidazole(3j)

Solid; mp 122–124 °C. IR (KBr) ν_{max}: 3075, 2955, 1443, 1348, 1242, 1178, 968 cm^{-1}. ^1H NMR (200 MHz, $CDCl_3$): 5.65 (s, 2H), 7.21–7.35 (m, 4H), 7.42–7.52 (m, 5H), 7.69–7.75 (m, 2H), 7.81–7.98 (m, 6H), 8.18–8.22 (m, 1H). ESI-MS *m/z* (%): 385 (M + 1).

2-(Thiophen-2yl)-1-(thiophen-2yl)methyl)-1*H*-benzo[*d*]imidazole (3k)

Solid; mp 150–152 °C. IR (KBr) ν_{max}: 3095, 3072, 2929, 1449, 1421, 1219 cm^{-1}. ^1H NMR (200 MHz, $CDCl_3$): 5.71 (s, 2H), 6.86–6.70 (m, 2H), 7.12–7.16 (m, 1H), 7.23–7.40 (m, 4H), 7.46–7.53 (m, 2H), 7.82–7.85 (m, 1H). EI-MS *m/z* (%): 296 (M^+, 78), 172 (6), 109 (2), 97 (100), 77 (6).

2-(Furan-2-yl)-1-((furan-2-yl)methyl)-1*H*-benzo[*d*]imidazole (3l)

Solid; mp 88–89 °C. IR (KBr) ν_{max}: 3378, 3150, 1605, 1332, 1007, 735 cm^{-1}. ^1H NMR (200 MHz, $CDCl_3$) δ: 5.65 (s, 2H), 6.18 (d, *J* = 7.7 Hz, 1H), 6.24–6.26 (m, 1H), 6.59–6.61 (m, 1H), 7.17–7.32 (m, 4H), 7.40–7.44 (m, 1H), 7.61–7.62 (m, 1H), 7.71–7.74 (m, 1H). EI-MS *m/z* (%): 264 (M^+, 80), 141 (20), 81 (100), 53 (30).

2-(Pyridine-2-yl)-1-(pyridine-2-yl)methyl)-1*H*-benzo[*d*]imidazole (3m)

Solid; mp 128–123 °C. IR (KBr) ν_{max}: 3055, 2993 1675, 1442, 1350, 1256, 1135 cm^{-1}. ^1H NMR (200 MHz, $CDCl_3$) δ: 5.32 (s, 2H), 7.03–7.10 (m, 2H), 7.25–7.35 (m, 5H), 7.45–7.53 (m, 3H), 7.82–7.85 (m, 2H). ESI-MS *m/z* (%): 287 (M + 1).

1-Benzyl-2-phenyl-1*H*-benzo[*d*]imidazole-5-yl)(phenyl)methanone (3n)

Solid; mp 195–197 °C. IR (KBr) ν_{max}: 3053, 2995, 1673, 1453, 1350, 1236, 1145 cm^{-1}. ^1H NMR (200 MHz, $CDCl_3$) δ: 5.50 (s, 2H), 7.05–7.12 (m, 2H), 7.21–7.39 (m, 5H), 7.41–7.52 (m, 5H), 7.62–7.75 (m, 3H), 7.81–7.90 (m, 2H), 8.25 (d, *J* = 7.8 Hz, 1H). ESI-MS *m/z* (%): 389 (M + 1).

1-Benzyl-5-methyl-2-phenyl-1*H*-benzo[*d*]imidazole (3o)

Solid; mp 170–172 °C. IR (KBr) ν_{max}: 3062, 2954, 1670, 1441, 1355, 1265, 1150, 750 cm^{-1}. ^1H NMR (200 MHz, $CDCl_3$) δ: 3.0 (s, 3H), 5.45 (s, 2H), 7.05–7.12 (m, 3H), 7.28–7.33 (m, 4H), 7.43–7.51 (m, 4H), 7.59–7.61 (m, 2H). ESI-MS *m/z* (%): 299 (M + 1).

1-Benzyl-5,6-dimethyl-2-phenyl-1*H*-benzo[*d*]imidazole (3p)

Solid; mp 187–189 °C. IR (KBr) ν_{max}: 3422, 2919, 1448, 1314, 697 cm^{-1}. ^1H NMR (200 MHz, $CDCl_3$) δ: 2.35 (s, 6H), 5.41 (s, 2H), 7.28–7.49 (m, 10H), 7.65 (d, *J* = 7.7 Hz, 1H), 8.12 (d, *J* = 7.7 Hz, 1H). EI-MS *m/z* (%): 312 (M^+, 90), 222 (15), 141 (30), 119 (35), 91 (100).

4-(2-(4-(Dimethylamino)phenyl)-1*H*-benzo[*d*]imidazole-1-yl)methyl-*N*,*N*-dimethylbenzamine (3q)

Solid; mp165–167 °C. IR (KBr) ν_{max}: 3062, 2954, 1670, 1441, 1355, 1265, 1150, 750 cm^{-1}. ^1H NMR (200 MHz, $CDCl_3$) δ: 2.93 (s, 6H), 3.00 (s, 6H), 5.37 (s, 2H), 6.66–6.75 (m, 4H), 7.14–7.29 (m, 3H), 7.63–7.65 (m, 4H), 7.78 (d, *J* = 7.9 Hz, 1H). ESI-MS *m/z* (%): 371 (M + 1).

Acknowledgements

KPL and KSS thank CSIR, New Delhi for the fellowship awards.

References

1. H. Zarrinmayeh, A.M. Nunes, P.L. Ornstein, D.A. Zimmerman, S.L. Gackenheimer, R.F. Bruns, P.A. Hipskind,

© 2008 NRC Canada

T.C. Britton, B.E. Catrell, and D.R. Gehlert. J. Med. Chem. **41**, 2709 (1998).
2. H. Nakano, T. Inoue, N. Kawasaki, H. Miyataka, H. Matsumoto, T. Taguchi, N. Inagaki, H. Nagai, and T. Satoh. Bioorg. Med. Chem. **8**, 373 (2000).
3. Y. Kohara, K. Kubo, E. Imamiya, T. Wada, Y. Inada, and T. Naka. J. Med. Chem. **39**, 5228 (1996).
4. A.W. White, R. Almassy, A.H. Calvert, N.J. Curtin, R.J. Griffin, Z. Hostomsky, K. Maegley, D.R. Newell, S. Srinivasan, and B.T. Golding. J. Med. Chem. **43**, 4084 (2000).
5. Z.S. Zhao, D.O. Arainz, B. Greidel, S. Sakata, J.L. Dallas, M. Whitelow, L. Trinh, J. Post, A. Liang, M.M. Morrissey, and K.J. Shaw. Bioorg. Med. Chem. Lett. **10**, 963 (2000).
6. (*a*) M.J. Tebbe, W.A. Spitzer, F. Victor, S.C. Miller, C.C. Lee, T.R. Sattelberg, E. Mckinney, and C.J. Tang. J. Med. Chem. **40**, 3937 (1997); (*b*) A.R. Porcari, R.V. Devivar, L.S. Kucera, J.C. Drach, and L.B. Townsend. J. Med. Chem. **41**, 1252 (1998); (*c*) M. Roth, M.L. Morningstar, P.L. Boyer, S.H. Hughes, R.W. Bukheit, and C.J. Michejda. J. Med. Chem. **40**, 4199 (1997); (*d*) M.T. Migawa, J.L. Giradet, J.A. Walker, G.W. Koszalka, S.D. Chamberlain, J.C. Drach, and L.B. Townsend. J. Med. Chem. **41**, 1242 (1998); (*e*) M.T. Migawa, J.L. Giradet, J.A. Walker, G.W. Koszalka, S.D. Chamberlain, J.C. Drach, and L.B. Townsend. J. Med. Chem. **41**, 1242 (1998); (*f*) I. Tamm. Science (Washington DC), **126**, 1235 (1957).
7. A.A. Spasov, I.N. Yozhitsa, L.I. Bugaeva, and V.A. Anisimova. Pharm. Chem. J. **33**, 232 (1999).
8. (*a*) B.E. Evans, K.E. Rittle, M.G. Bock, R.M Dipardo, R.M. Freidinger, W.L. Whitter, G.F. Lundell, D.F. Veber, P.S. Anderson, R.S. Chang, R.S.L. Chang, V.J. Lotti, D.J. Gerino, T.B. Chen, P.J. Kling, K.A. Kunkel, J.P. Springer, and J. Hirshfield. J. Med. Chem. **31**, 2235 (1988); (*b*) J.S. Mason, I. Morize, P.R. Menard, D.L. Cheney, C. Hume, and R.F. Labaudiniere. J. Med. Chem. **42**, 3251 (1999).
9. (*a*) Z. Wu, P. Rea, and G. Wickam. Tetrahedron Lett. **41**, 9871 (2000) and refs. cited therein; (*b*) A. Mazurov. Bioorg. Med. Chem. Lett. **10**, 67 (2000).
10. (*a*) P.N. Preston. *In* Chemistry of heterocyclic compounds. *Edited by* A. Weissberger, E.C. Taylor. John Wiley and Sons, NY. 1981. Vol. 40; (*b*) Y.C. Chi and C.M. Sun. Synlett, 591 (2000); (*c*) W. Huang, and R.M. Scarborough. Tetrahedron Lett. **40**, 2665(1999); (*d*) L.M. Dudd, E. Venardou, E. Garcia-Verdugo, P. Licence, A.J. Blake, C. Wilson, and M. Poliakoff. Green Chem. **5**, 187(2003).
11. (*a*) B.H. Kim, R. Han, J.S. Kim, Y.M. Jun, W. Baik, and B.M. Lee. Heterocycles, **63**, 41 (2004); (*b*) T. Itoh, K. Nagata, H. Ishikawa, and A. Ohsawa. Heterocycles, **63**, 2769 (2004).
12. (*a*) P.A. Grieco. Organic synthesis in water. Blackie Academic and Professional, London. 1998; (*b*) C.J. Li and T.H. Chan. Organic reactions in aqueous media. John Wiley and Sons, NY. 1997.
13. W. Xie, Y. Jin, and P.G. Wang. CHEMTECH, **29**, 23 (1999).
14. (*a*) S. Kobayashi, M. Sugiura, H. Kitagawa, and W.W.L. Lam. Chem. Rev. **102**, 2227 (2002); (*b*) S. Kobayashi. Eur. J. Org. Chem. 15 (1999); (*c*) S. Kobayashi. Synlett, 689 (1994).
15. (*a*) H. Gaspard-Iloughmane and C. Le Roux. Eur. J. Org. Chem. 2517 (2004); (*b*) M.N. Leonard, L.C. Wieland, and R.S. Mohan. Tetrahedron, **58**, 8373 (2002).
16. S. Répichet, A. Zwick, L. Vendier, C. Le Roux, and J. Dubac. Tetrahedron Lett. **43**, 993 (2002).
17. I. Mohammadpoor-Baltork, A.R. Khosropour, and S.F. Hojati. Monatsh. Chem. **138**, 663 (2007).
18. (*a*) T. Ollevier and G. Lavie-Compin. Tetrahedron Lett. **45**, 49 (2004); (*b*) T. Ollevier, E. Nadeau, and A.A. Guay-Bégin. Tetrahedron Lett. **47**, 8351 (2006); (*c*) W. Frank, G.J. Reiss, and J. Schneider. Angew. Chem., Int. Ed. Engl. **34**, 2416 (1995).
19. (*a*) J.S. Yadav, B.V.S. Reddy, L. Chandraiah, and V. Sunitha. Synthesis, 2523, (2004); (*b*) J.S. Yadav, B.V.S. Reddy, T. Swamy, and K.R. Rao. Tetrahedron Lett. **45**, 6037 (2004); (*c*) J.S. Yadav, B.V.S. Reddy, B. Eeshwaraiah, and M.K. Gupta. Tetrahedron Lett. **45**, 5873 (2004); (*d*) J.S. Yadav, B.V.S. Reddy, and K. Premalatha. Synlett. 963, (2004).

© 2008 NRC Canada

Theoretical study on NO_3-initiated oxidation of acenaphthene in the atmosphere

Xiaohui Qu, Qingzhu Zhang, and Wenxing Wang

Abstract: Acenaphthene is widespread and toxic, and thus of substantial environmental concern. The reaction with NO_3 radicals is an important atmospheric loss process of acenaphthene at night time. In this work, the mechanism for the NO_3-initiated atmospheric oxidation reaction of acenaphthene has been studied using high level molecular orbital theory. Geometries of all the related species have been optimized at the MPWB1K level with the 6–31G(d,p) basis set. The single-point energy calculations have been carried out at the MPWB1K/6–311+G(3df,2p) level. The possible secondary reactions were also studied. Several energetically favorable reaction pathways were revealed for the first time.

Key words: acenaphthene, NO_3 radicals, reaction mechanism, product information, oxidation degradation.

Résumé : L'acénaphtène est toxique et très répandu et, d'un point de vue environnemental, il soulève donc beaucoup d'inquiétudes. La réaction des radicaux NO_3 est un processus atmosphérique important de perte de l'acénaphtène durant la nuit. Dans ce travail, faisant appel à la théorie des orbitales molécules à un niveau élevé, on a étudié le mécanisme de la réaction d'oxydation atmosphérique de l'acénaphtène initiée par le NO_3. Les géométries de toutes les espèces reliées ont été optimisées au niveau MPWBIK avec un ensemble de base 6-31G(d,p). Les calculs d'énergie ponctuelle ont été réalisés au niveau MPWB1K/6-311+G(3df,2p). On a aussi étudié les réactions secondaires potentielles. On a mis en évidence pour la première fois plusieurs voies réactionnelles énergétiquement favorables.

Mots-clés : acénaphtène, radicaux NO_3, mécanisme réactionnel, information sur le produit, dégradation par oxydation.

[Traduit par la Rédaction]

Introduction

Polycyclic aromatic hydrocarbons (PAHs) have attracted substantial environmental attention because of the widespread occurrences of these compounds and their adverse impacts on ecosystems and human health (1–6). PAHs are released into the atmosphere during incomplete combustion of fossil fuels and biomass from natural and agricultural fires (7–9). Vehicle emission also represents an important source of PAHs in urban areas (10–12).

Acenaphthene belongs to the family of PAHs. It is found both in outdoor and indoor air and is observed in high concentration in certain areas (13–16). Under typical atmospheric conditions, acenaphthene is predominately found in the gas phase and thus can be removed from the troposphere by gas-phase reactions with hydroxyl (OH) radicals, nitrate (NO_3) radicals, ozone (O_3), and by photolysis (16–19). These reactions are important sinks of acenaphthene in the atmosphere. Because of the presence of a cyclopenta-fused ring, the reactivity of acenaphthene may be significantly different from those PAHs only containing six-membered aromatic rings. Another reason why the atmospheric reactions of acenaphthene have drawn considerable environmental concern is because the reactions of acenaphthene in the atmosphere often yield degradation products that may be more carcinogenic and more mutagenic than the parent PAH. Thus, it is important to understand the transformation and fate of acenaphthene in the atmosphere.

Since OH radicals are ubiquitous in the atmosphere, the most important removal reactions of PAHs are initiated by OH radicals. However for acenaphthene, which contains a cyclopenta-fused ring, the reaction with NO_3 radicals is also expected to be an important atmospheric loss process (18). Moreover, as the formation of OH radicals only takes place under illumination, OH concentration rapidly decreases after sunset. As a consequence, OH-initiated reactions only occur during the day and strongly depend on the photon flux. NO_3 radicals undergo rapid photolysis upon absorption of radiation. The daytime NO_3 chemistry is expected to be unimportant for PAHs. However, NO_3 radicals have been identified and measured by long-path spectroscopic techniques in the nighttime atmosphere. The reaction with NO_3 radicals will dominate the loss pathway of acenaphthene during nighttime. Environmental chamber studies show generally high nitro-PAH yields from the NO_3-initiated reactions compared with OH-initiated reactions (2, 17–18). However, the current knowledge of the NO_3-initiated atmospheric oxidation of acenaphthene is very limited. Only two studies on the experimental rate constants are on record (17, 18). The reaction rate constant was measured to be $(4.6 \pm 2.6)\ 10^{-13}$ cm^3

Received 29 June 2007. Accepted 13 November 2007. Published on the NRC Research Press Web site at canjchem.nrc.ca on 8 January 2008.

X. Qu, Q. Zhang,[1] and W. Wang. Environment Research Institute, Shandong University, Jinan 250100, P.R. China.

[1]Corresponding author (e-mail: zqz@sdu.edu.cn).

 © 2008 NRC Canada

Fig. 1. MPWB1K/6–31G(d,p) optimized geometries for the reactant, products, and intermediates involved in the reaction of acenaphthene with NO_3 radicals. Distances are in ångströms and angles are in degrees (1 ångström = 0.1 nm). The values in parentheses are the experimental data (23).

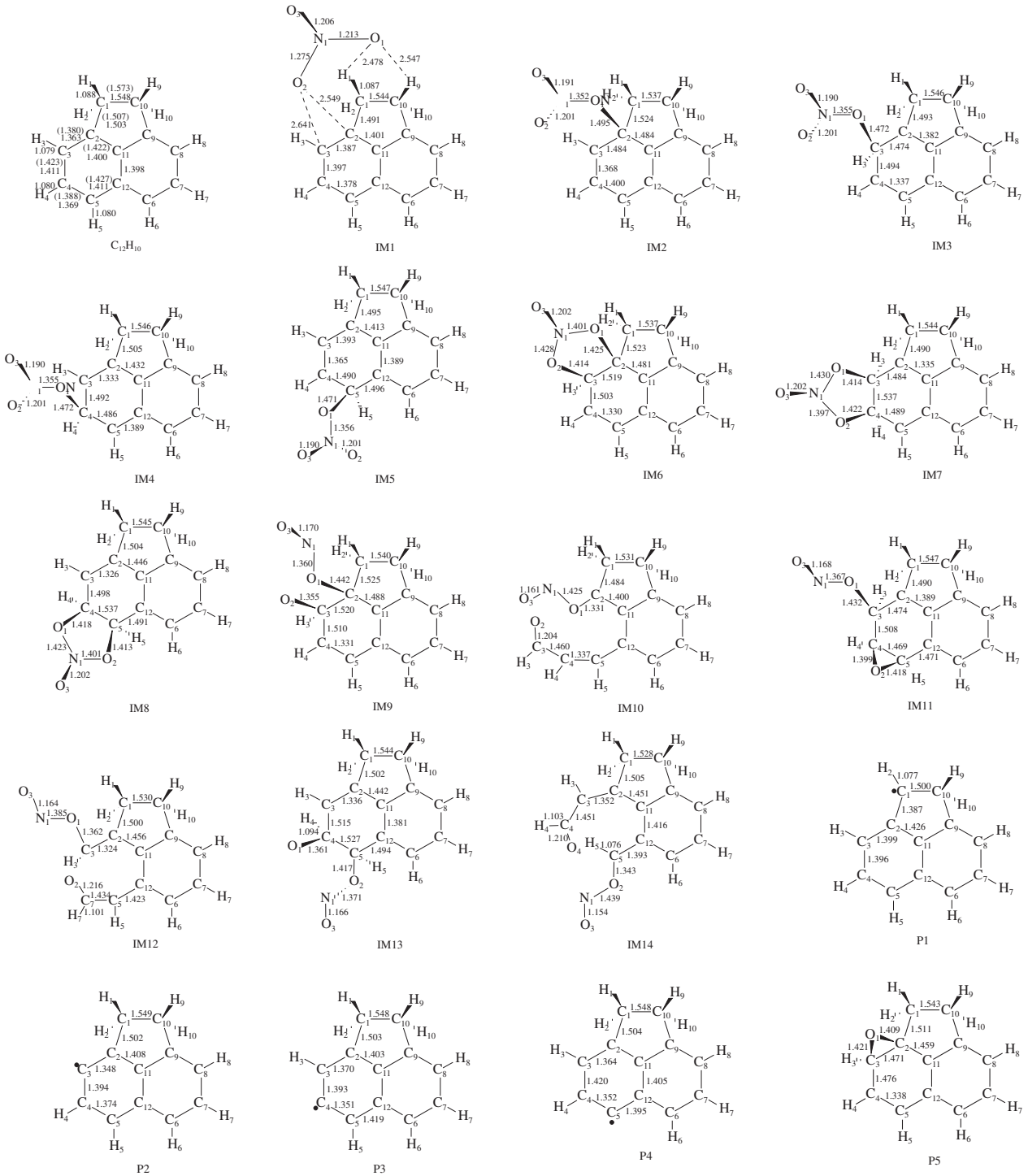

molecule^{-1} s^{-1} at room temperature. The mechanism has not been elucidated. In this work, we have initiated a theoretical study on the NO_3-initiated atmospheric oxidation reaction of acenaphthene. Fundamental knowledge of specific pathways, stable end products, and energy profile surface are vital in understanding the removal process of acenaphthene and the formation of secondary pollutants.

Computational methods

Using the Gaussian 03 program suite (19), high-level molecular orbital theory calculations have been carried out. The geometries have been optimized at the MPWB1K level (20) with the 6–31G(d,p) basis set. The vibrational frequencies have been calculated at the same level to determine the na-

© 2008 NRC Canada

Fig. 1 (*concluded*).

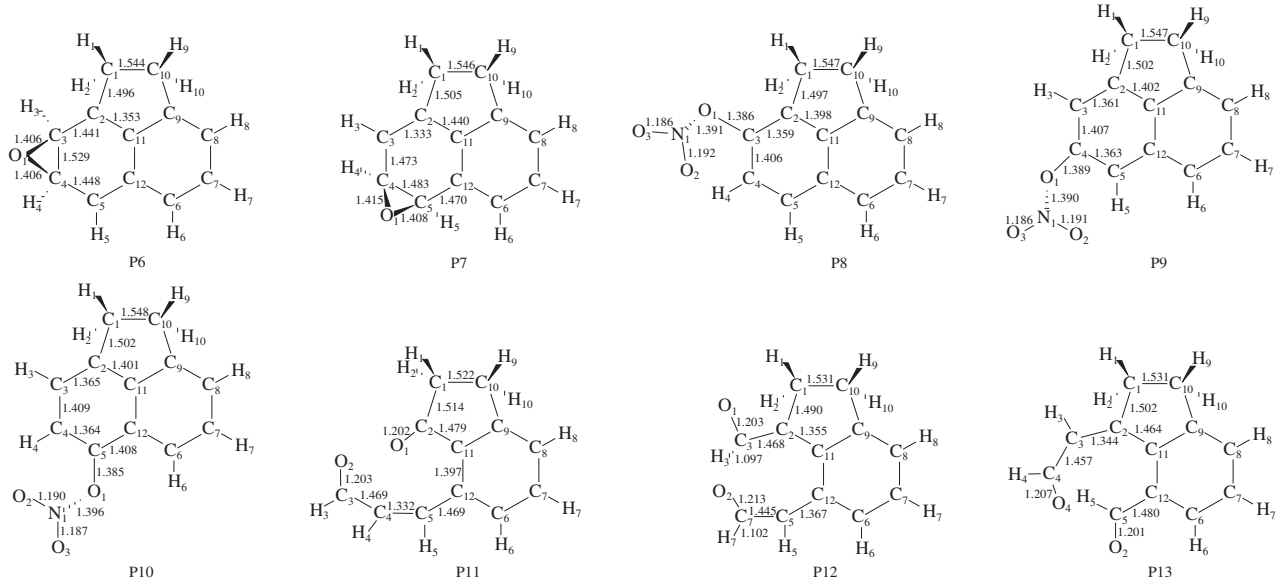

ture of the stationary points. Each transition state was verified to connect the designated reactants and products by performing an intrinsic reaction coordinate (IRC) (21) analysis. In the paper of Truhlar (22), the MPWB1K level was tested to be a good method for weak interaction and barrier height calculations. In this work, the MPWB1K level with a more flexible basis set, 6–311+G(3df,2p), was employed to calculate the single-point energies of various species.

To clarify the general reliability of theoretical calculations, it is useful to compare the predicated chemical properties of the present particular systems of interest with experimental data (23). The theoretical and geometry experimental parameters are shown in Figs. 1 and 2. The maximum relative errors are less than 1.6%. These good agreements give us confidence that MPWB1K/6–31G(d,p) theory is adequate to optimize the geometries.

Results and discussion

The reaction of acenaphthene with NO_3 radicals

H-abstraction channels

Hydrogen atoms in acenaphthene can be divided into two kinds: hydrogen atoms in the cyclopenta-fused ring (H_1, H_2, H_9, H_{10}) and the ones in the aromatic ring (H_3, H_8, H_4, H_7, H_5, H_6). Four hydrogen atoms in the cyclopenta-fused ring are equivalent. Thus, a primary process has been identified for H-abstraction from the cyclopenta-fused ring. First, a hydrogen bonding intermediate, IM1, is formed. Then, a H atom is abstracted via the transition state TS1. The unpaired electron is delocalized in the whole transition state. The atomic spin densities obtained by Mulliken population analysis are O_1 (0.307), C_1 (0.108), H_1 (0.002), C_5 (0.270), C_3 (0.196), C_6 (0.134), C_4 (–0.115), C_8 (0.104). It is interesting to note that spin densities on the C atoms of the aromatic ring are higher than on the C_1 atom from which the H atom is abstracted by NO_3 radicals. The electron delocalization stabilizes this H-abstraction transition state. Figure 3 shows that H-abstraction from the cyclopenta-fused ring has a rather low barrier height, only 3.06 kcal/mol (1 cal = 4.184 J). This process is strongly exothermic. Thus, H-abstraction from the cyclopenta-fused ring can occur readily and is expected to play an important role for the degradation of acenaphthene in the atmosphere. Atkinson (17) postulated that the reaction of NO_3 radical with acenaphthene proceeds mainly by H atom abstraction from the -CH_2- group of the cyclopenta-fused ring. The quantum calculation result is consistent with the postulation of Atkinson. It is interesting to compare the H-abstraction reactions by OH radical to H-abstraction reactions by NO_3 radical. The energy for the transition state of H-abstraction from the -CH_2- group of cyclopenta-fused ring by NO_3 radicals is 4.56 kcal/mol lower than the total energy of reactants. The energy for the transition state of H-abstraction from the -CH_2- group of cyclopenta-fused ring by OH radicals is only 0.79 kcal/mol lower than the total energy of reactants.

Six hydrogen atoms in the aromatic ring are unequivalent. Three transition states, denoted as TS2, TS3, and TS4, were located for H-abstraction from the aromatic ring. In contrast to the H-abstraction process from the cyclopenta-fused ring, H-abstraction reactions from the aromatic ring have high potential barriers, 8.06, 8.04, and 8.94 kcal/mol. Furthermore, all of these H-abstraction channels are endothermic. Therefore, the most important H-abstraction channel is H-abstraction from the cyclopenta-fused ring.

Association–elimination pathways

There exist C–C double bonds in the structure of acenaphthene. Thus, association–elimination is a possible reaction pathway for the reaction of acenaphthene with NO_3 radicals. Four different reaction sites are revealed; C2, C3, C4, and C5 atoms in acenaphthene are attacked by an O atom in NO_3 to form NO_3-acenaphthene adducts, IM2, IM3, IM4, and IM5, respectively. The energies of IM2, IM3, IM4, and IM5 are lower than the total energy of the original reactants by 16.04, 14.14, 13.12, and 17.80 kcal/mol, respectively. The energy-rich adducts can further react via unimolecular decomposition. The decomposition pathways

© 2008 NRC Canada

Fig. 2. MPWB1K/6–31G(d,p) optimized geometries for the transition states involved in the reaction of acenaphthene with NO_3 radicals. Distances are in ångströms and angles are in degrees.

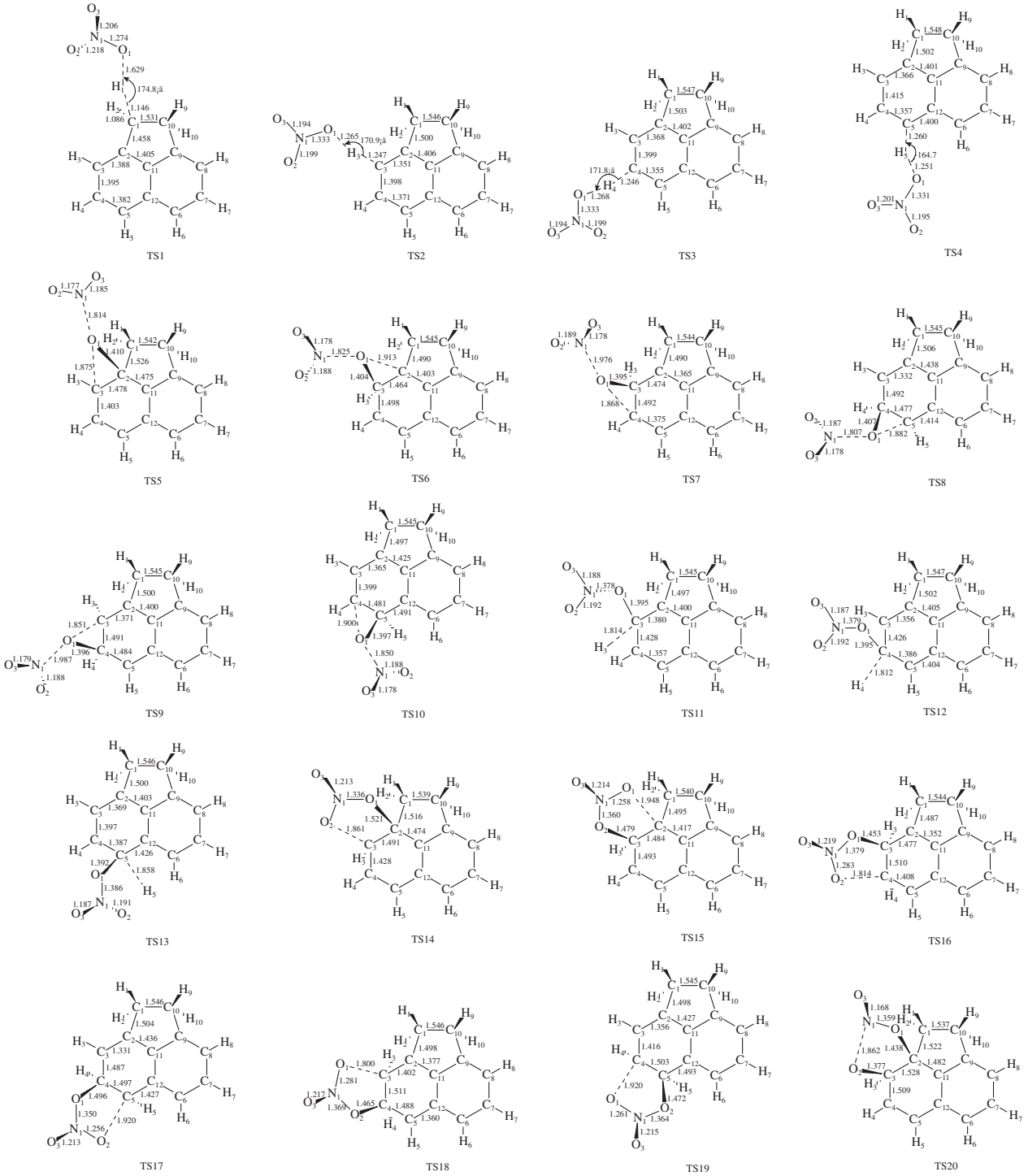

are too complicated. To clarify, we show the potential energy profiles in two different figures. The direct decomposition channels are shown in Fig. 4. The multi-step isomerization–decomposition pathways are depicted in Fig. 5. In the following discussion, the decomposition channels of the NO3-acenaphthene adducts, IM2, IM3, IM4, and IM5, were divided into three kinds.

The first decomposition channel is the loss of NO_2 to form epoxyacenaphthene. There are three different epoxyacenaphthene products, denoted as P5, P6, and P7 in Fig. 1. Both the formations of 2,3-epoxyacenaphthene (denoted as P5) and 4,5-expoxyacenapthene (denoted as P7) are exothermic by 5~10 kcal/mol, and the corresponding barrier heights are about 25 kcal/mol; whereas the formation of 3,4-expoxyacenaphtene (denoted as P6) is endothermic by about 11 kcal/mol, and the corresponding barrier height is more than 35 kcal/mol. Thus, the formations of P5 and P7 are relatively energetically favorable. Therefore, the main

© 2008 NRC Canada

Fig. 2 (*concluded*).

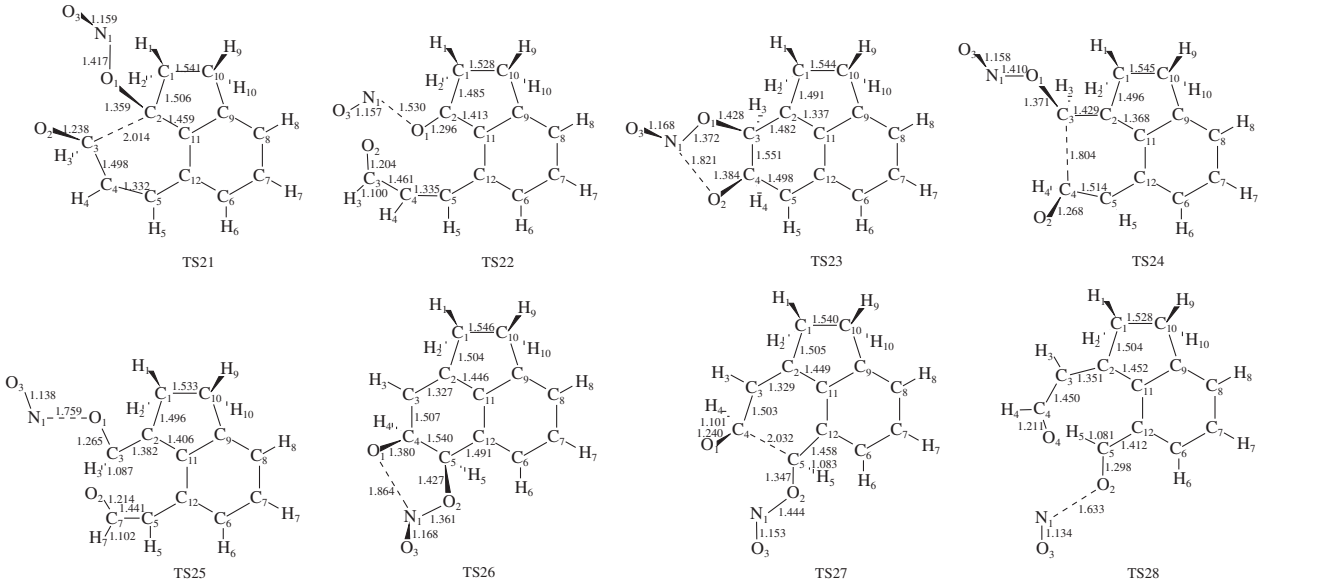

Fig. 3. Profile of the potential energy surface for H-abstraction channels at the MPWB1K /6–311+G(3df,2p) level (1 cal = 4.184 J).

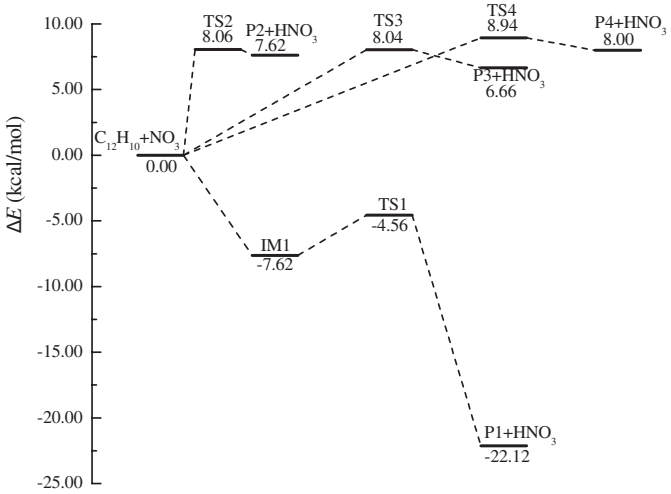

Fig. 4. Profile of the potential energy surface for the direct decomposition channels of NO_3-acenaphthene adducts at the MPWB1K /6–311+G(3df,2p) level.

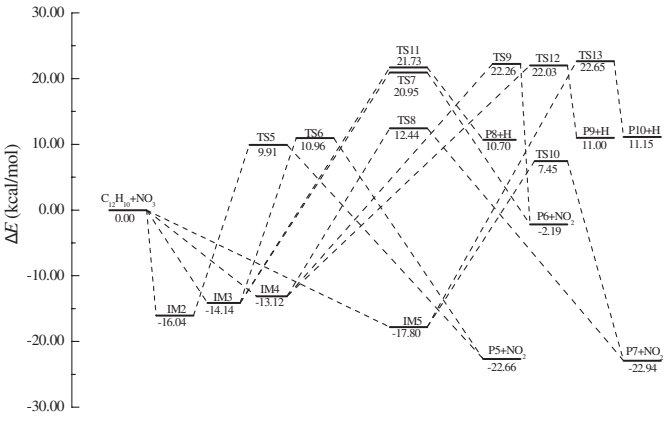

epoxyacenaphthene products will be 2,3-epoxyacenaphthene and 4,5-expoxyacenapthene. The detailed barrier heights and reaction enthalpies can be clarified as follows:

$$IM2 \rightarrow TS5 \rightarrow P5 + NO_2$$
$$\Delta E = 25.95 \text{ kcal/mol}, \Delta H = -6.62 \text{ kcal/mol}$$

$$IM3 \rightarrow TS6 \rightarrow P5 + NO_2$$
$$\Delta E = 25.10 \text{ kcal/mol}, \Delta H = -8.52 \text{ kcal/mol}$$

$$IM3 \rightarrow TS7 \rightarrow P6 + NO_2$$
$$\Delta E = 35.09 \text{ kcal/mol}, \Delta H = 11.95 \text{ kcal/mol}$$

$$IM4 \rightarrow TS8 \rightarrow P7 + NO_2$$
$$\Delta E = 25.56 \text{ kcal/mol}, \Delta H = -9.82 \text{ kcal/mol}$$

$$IM4 \rightarrow TS9 \rightarrow P6 + NO_2$$
$$\Delta E = 35.38 \text{ kcal/mol}, \Delta H = 10.93 \text{ kcal/mol}$$

$$IM5 \rightarrow TS10 \rightarrow P7 + NO_2$$
$$\Delta E = 25.25 \text{ kcal/mol}, \Delta H = -5.14 \text{ kcal/mol}$$

Another possible decomposition channel of the NO_3-acenaphthene adducts (IM3, IM4, or IM5) is the loss of an H atom bonded with the carbon atom (C_3, C_4, or C_5) to form nitrate species P8, P9, or P10. Figure 4 shows that all of these decomposition processes have high barrier heights, 35.87, 35.15, 40.45 kcal/mol, respectively. Furthermore, these channels are highly endothermic by 24.84, 24.12, or 28.95 kcal/mol, respectively. Therefore, these processes are the energetically unfavorable channels for the decomposition of NO_3-acenaphene adducts.

The third possible pathway involves multi-step isomerization and decomposition. The potential energy profile is shown in Fig. 5. First, the pathways initiate from the isomerization of NO_3-acenaphthene adducts to three intermediates containing a five-membered heterocyclic ring, IM6, IM7, and IM8. The formation of IM6 and IM8 are weakly endothermic, whereas the formation of IM7 is strongly en-

© 2008 NRC Canada

Fig. 5. Profile of the potential energy surface for the multi-step isomerization–decomposition pathways of NO_3-acenaphthene adducts at the MPWB1K /6–311+G(3df,2p) level.

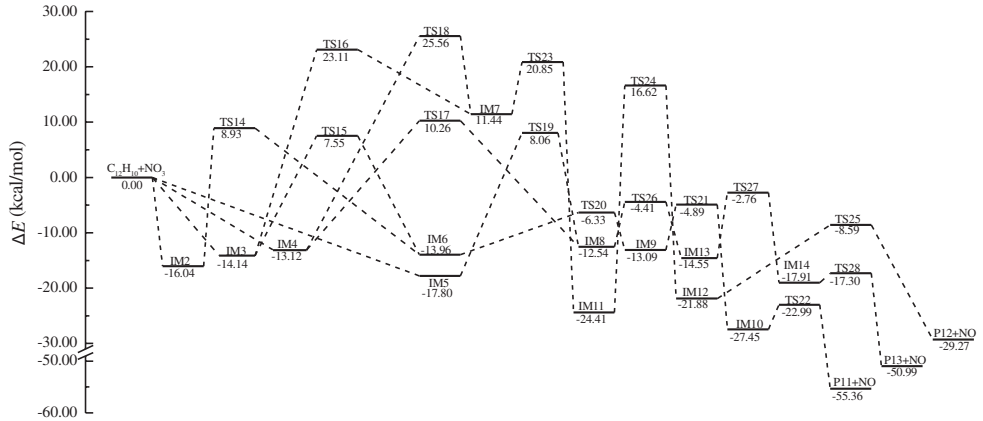

dothermic by about 25 kcal/mol, and the corresponding barrier height is about 38 kcal/mol. Thus, the formation of IM7 is energetically unfavorable. The most energetically favorable channel is the isomerization of IM3 to IM6. These pathways can be clarified as follows:

$$\text{IM2} \rightarrow \text{TS14} \rightarrow \text{IM6}$$
$$\Delta E = 24.97 \text{ kcal/mol}, \Delta H = 2.08 \text{ kcal/mol}$$

$$\text{IM3} \rightarrow \text{TS15} \rightarrow \text{IM6}$$
$$\Delta E = 21.69 \text{ kcal/mol}, \Delta H = 0.18 \text{ kcal/mol}$$

$$\text{IM3} \rightarrow \text{TS16} \rightarrow \text{IM7}$$
$$\Delta E = 37.25 \text{ kcal/mol}, \Delta H = 25.58 \text{ kcal/mol}$$

$$\text{IM4} \rightarrow \text{TS17} \rightarrow \text{IM8}$$
$$\Delta E = 23.38 \text{ kcal/mol}, \Delta H = 0.58 \text{ kcal/mol}$$

$$\text{IM4} \rightarrow \text{TS18} \rightarrow \text{IM7}$$
$$\Delta E = 38.68 \text{ kcal/mol}, \Delta H = 24.56 \text{ kcal/mol}$$

$$\text{IM5} \rightarrow \text{TS19} \rightarrow \text{IM8}$$
$$\Delta E = 29.20 \text{ kcal/mol}, \Delta H = 5.26 \text{ kcal/mol}$$

IM6 will isomerize to IM9. The potential barrier of this process is 7.63 kcal/mol. Then, IM9 will further isomerize to IM10. IM10 is more stable by 14.36 kcal/mol than IM9. The potential barrier of this process is 8.20 kcal/mol. The subsequent unimolecular decomposition of IM10 will produce a dicarbonyl product (denoted as P11) and NO. This process has a very low potential barrier, only 4.46 kcal/mol. The process is exothermic by 27.91 kcal/mol. The isomerization and decomposition of IM7 and IM8 is similar to that of IM6, except that the formation and isomerization of IM7 is not energetically favorable. Figure 5 shows that the dominant dicarbonyl products of the third possible pathway will be P11 and P13, which have been detected in Arey's environmental chamber experimental study for OH radical-initiated reactions of alkylnaphthalenes (24). The detailed mechanisms can be clarified as follows:

$$\text{IM6} \rightarrow \text{TS20} \rightarrow \text{IM9} \rightarrow \text{TS21} \rightarrow \text{IM10} \rightarrow \text{TS22} \rightarrow \text{P11} + \text{NO}$$

$$\text{IM7} \rightarrow \text{TS23} \rightarrow \text{IM11} \rightarrow \text{TS24} \rightarrow \text{IM12} \rightarrow \text{TS25} \rightarrow \text{P12} + \text{NO}$$

$$\text{IM8} \rightarrow \text{TS26} \rightarrow \text{IM13} \rightarrow \text{TS27} \rightarrow \text{IM14} \rightarrow \text{TS28} \rightarrow \text{P13} + \text{NO}$$

The study shows that H-abstraction from the cyclopenta-fused ring is the most energetically favorable reaction channel for the reaction of acenaphthene with NO_3 radicals. Because of the high potential barriers, other pathways cannot occur to any significant extent under atmospheric conditions. Thus, acenaphthenyl (P1) will be the dominant product. Figures 4 and 5 show that all of the decomposition channels of NO_3-acenaphthene adducts need high potential barriers, more than 20 kcal/mol. Therefore, their removal reactions with NO_x or O_2 may be competitive with their decompositions.

Secondary reactions

The NO_3-acenaphthene adducts (IM2, IM3, IM4, IM5) and acenaphthenyl (P1) are open-shell radicals and can react with NO_x or O_2 their removal from the troposphere (Fig. 6).

The reactions of acenaphthenyl (P1) with NO/O$_2$

Acenaphthenyl (P1) radicals can react with O_2 via barrierless association to form an intermediate, IM15. The energy of IM15 is 15.35 kcal/mol lower than the total energy of P1 and O_2. The energy-rich adduct IM15 has two forward reaction pathways. The first is the association with NO to form IM16. This process is also barrierless. Then, IM16 will decompose via transition state TS29 to produce acenaphthylen-1(2*H*)-one (denoted as P14) and HNO_2. Another reaction pathway of IM15 is to decompose via transition state TS30. The barrier height is 28.80 kcal/mol. This process is endothermic by 15.63 kcal/mol. The decomposition products are acenaphthylene (denoted as P15) and HO_2 radical. The mechanism can be clarified as follows:

$$\text{P1} + \text{O}_2 \rightarrow \text{IM15}$$
$$\Delta H = -15.35 \text{ kcal/mol}$$

$$\text{IM15} + \text{NO} \rightarrow \text{IM16}$$
$$\Delta H = -15.72 \text{ kcal/mol}$$

© 2008 NRC Canada

Fig. 6. MPWB1K/6–31G(d,p) optimized geometries for the products, transition states, and intermediates involved in the NO_3 radical-initiated secondary reactions. Distances are in ångströms and angles are in degrees.

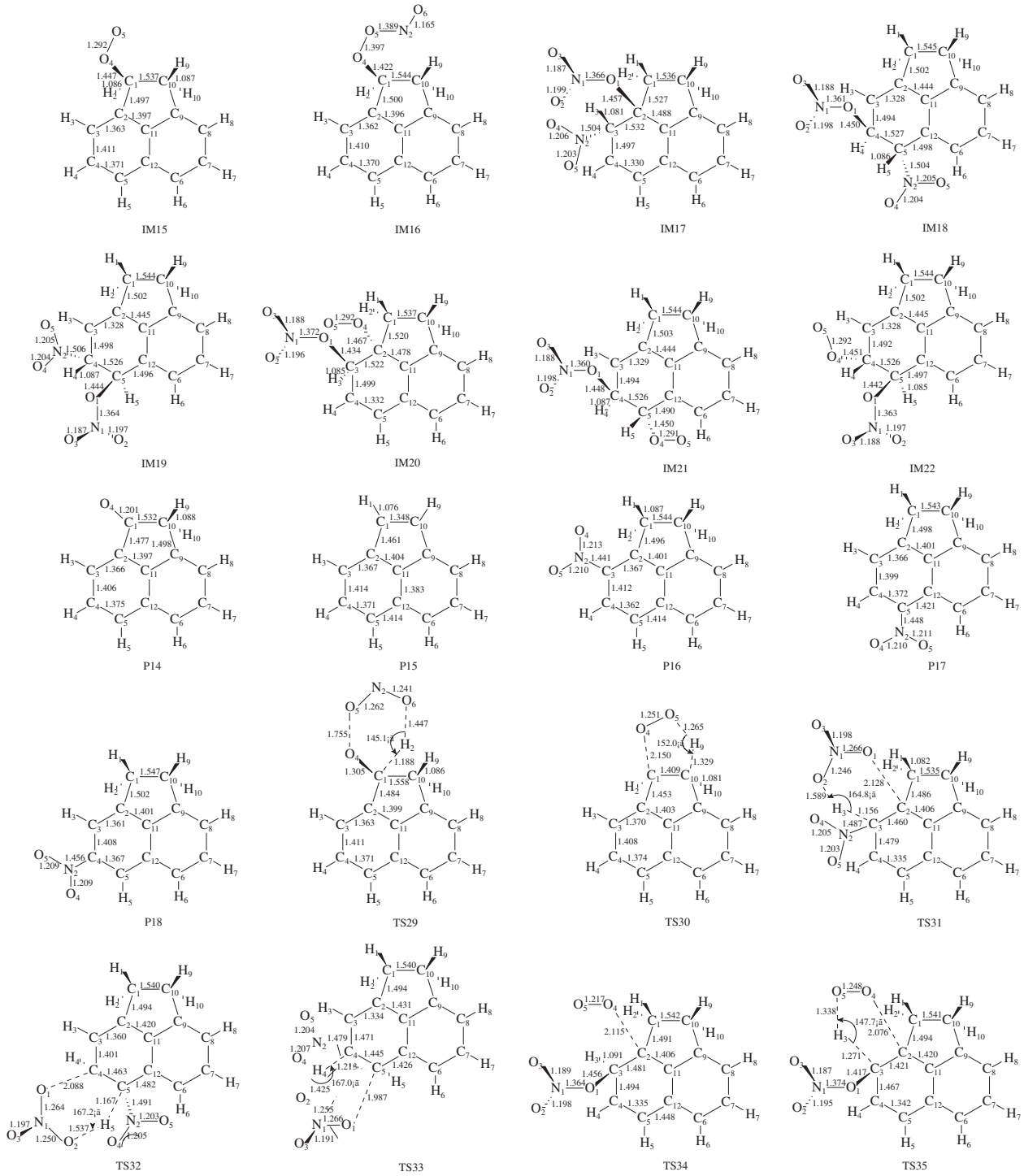

$$IM16 \rightarrow TS29 \rightarrow P14 + HNO_2$$

$$\Delta E = 42.44 \text{ kcal/mol}, \Delta H = -61.93 \text{ kcal/mol}$$

$$IM15 \rightarrow TS30 \rightarrow P15 + HO_2$$

$$\Delta E = 28.80 \text{ kcal/mol}, \Delta H = 15.63 \text{ kcal/mol}$$

The reactions of NO_3-acenaphthene adducts with NO_2

IM2 can react with NO_2 radicals via a barrierless association to form an intermediate, IM17. The energy of IM17 is 33.60 kcal/mol lower than the total energy of IM2 and NO_2. Then, the energy-rich adduct IM17 will further decompose. A transition state, denoted as TS31, corresponding to the decomposition of IM17 was located. This decomposition involves H-migration and cleavage of the C_2–O_1 bond.

© 2008 NRC Canada

Fig. 6 (*concluded*).

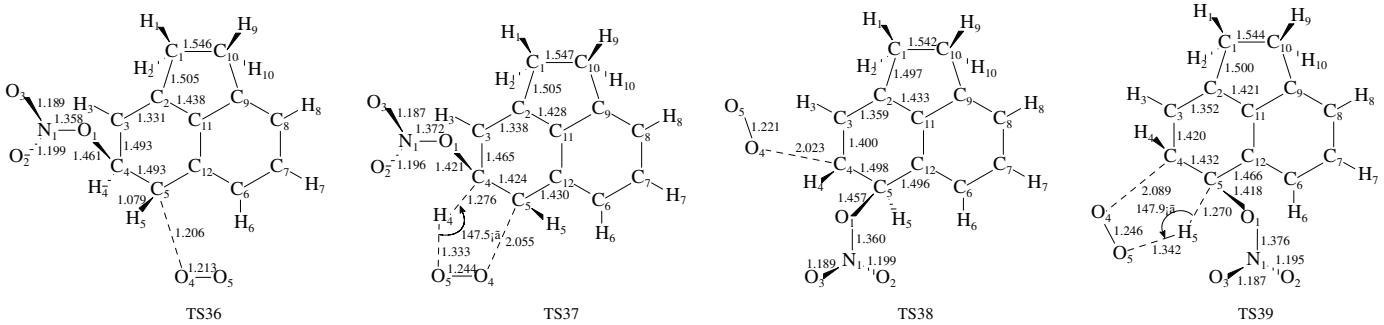

H-migration leads to a six-membered cycle in the structure of TS31. The decomposition products are 3-nitroacenaphthene (denoted as P16) and HNO_3. The potential barrier of this decomposition is 22.02 kcal/mol. The process is exothermic by 18.27 kcal/mol.

The reactions of IM4 and IM5 with NO_2 radicals are similar to the reactions of IM2, both reactions produce nitroacenaphthene. Atkinson (17) found that the NO_3 radical-initiated acenaphthene oxidation reaction rate depend on the NO_2 concentration. This is consistent with our calculation. The mechanism can be clarified as follows:

$$IM2 + NO_2 \rightarrow IM17$$
$$\Delta H = -33.60 \text{ kcal/mol}$$

$$IM17 \rightarrow TS31 \rightarrow P16 + HNO_3$$
$$\Delta E = 22.02 \text{ kcal/mol}, \Delta H = -18.27 \text{ kcal/mol}$$

$$IM4 + NO_2 \rightarrow IM18$$
$$\Delta H = -39.23 \text{ kcal/mol}$$

$$IM18 \rightarrow TS32 \rightarrow P17 + HNO_3$$
$$\Delta E = 26.80 \text{ kcal/mol}, \Delta H = -12.42 \text{ kcal/mol}$$

$$IM5 + NO_2 \rightarrow IM19$$
$$\Delta H = -34.75 \text{ kcal/mol}$$

$$IM19 \rightarrow TS33 \rightarrow P18 + HNO_3$$
$$\Delta E = 29.59 \text{ kcal/mol}, \Delta H = -14.14 \text{ kcal/mol}$$

The reactions of NO_3-acenaphthene adducts with O_2

For the reaction with IM3, O_2 attacks the aromatic ring to form an intermediate, IM20, via the transition state TS34. The barrier height for this process is only 4.56 kcal/mol. The reaction enthalpy is –12.68 kcal/mol. A possible decomposition channel will open for IM20. This decomposition will proceed via the transition state TS26. The products of this decomposition are a nitrate species (denoted as P8) and HO_2. The potential barrier is 19.56 kcal/mol. The process is exothermic by 6.89 kcal/mol.

The reactions of IM4 and IM5 with O_2 will also produce nitrate species (denoted as P9 and P10, respectively) and HO_2. The mechanism can be clarified as follows:

$$IM13 + O_2 \rightarrow TS34 \rightarrow IM20$$
$$\Delta E = 4.56 \text{ kcal/mol}, \Delta H = -12.68 \text{ kcal/mol}$$

$$IM20 \rightarrow TS35 \rightarrow P8 + HO_2$$
$$\Delta E = 19.56 \text{ kcal/mol}, \Delta H = -6.89 \text{ kcal/mol}$$

$$IM4 + O_2 \rightarrow TS36 \rightarrow IM21$$
$$\Delta E = 5.38 \text{ kcal/mol}, \Delta H = -12.81 \text{ kcal/mol}$$

$$IM21 \rightarrow TS37 \rightarrow P9 + HO_2$$
$$\Delta E = 21.31 \text{ kcal/mol}, \Delta H = -7.48 \text{ kcal/mol}$$

$$IM5 + O_2 \rightarrow TS38 \rightarrow IM22$$
$$\Delta E = 6.69 \text{ kcal/mol}, \Delta H = -7.53 \text{ kcal/mol}$$

$$IM22 \rightarrow TS39 \rightarrow P10 + HO_2$$
$$\Delta E = 18.78 \text{ kcal/mol}, \Delta H = -7.93 \text{ kcal/mol}$$

Conclusion

In this work, we present an exhaustive and theoretical study on the NO_3-initiated atmospheric oxidation reaction of acenaphthene. The comprehensive mechanism study has led to the following specific conclusions. (*i*) The reaction of acenaphthene with NO_3 radicals occurs primarily by H-abstraction from the cyclopenta-fused ring and NO_3 addition to the aromatic ring. Acenaphthenyl, acenaphthylen-1(2*H*)-one, acenaphthylene, epoxyacenaphthene, and dicarbonyl species are the possible products. (*ii*) The removal reactions of open-shell NO_3-acenaphthene adducts with NO_x, or O_2 are strongly competitive with their decompositions.

Acknowledgment

This work is supported by National Natural Science Foundation of China (NSFC, project No. 20507013).

References

1. M.P. Hannigan, G.R. Cass, B.W. Penman, L.L. Crespi, A.L. Lafleur, W.F. Busby, Jr., W.G. Thilly, and B.R.T. Simoneit. Environ. Sci. Technol. **32**, 3502 (1998).
2. R. Atkinson and J. Arey. Environ. Health Perspect. **102**, 117 (1994).
3. R.A. Hites. Acc. Chem. Res. **23**, 196 (1990).
4. H. Tokiwa and Y. Ohnishi. CRC Crit. Rev. Toxicol. **17**, 23 (1986).
5. P.D. Josephy, B. Mannervik, and P.O. de Montellano. Molecular toxicology. Oxford University Press, Oxford, UK. 1997.
6. A.P. Loibner, O.H.J. Szolar, R. Braun, and D. Hirmann. Environ. Toxicol. Chem. **23**, 557 (2004).

© 2008 NRC Canada

7. S.O. Baek, R.A. Field, M.E. Goldstone, P.W. Kirk, J.N. Lester, and R. Perry. Water Air Soil Pollut. **60**, 279 (1991).
8. C.E. Bostrom, P. Gerde, A. Hanberg, B. Jernstrom, C. Johansson, T. Kyrklund, A. Rannug, M. Tornqvist, K. Victorin, and R. Westerholm. Environ. Health Perspect. **110**, 451 (2002).
9. S. Xu, W. Liu, S. Tao, Environ. Sci. Technol. **40**, 702 (2006).
10. M. Howsam and K.C. Jones. Sources of PAHs in the environment; PAHs and related compounds. *In* The handbook of environmental chemistry. Vol. 31. Springer-Verlag, Berlin, Germany. 1998. pp. 137–174.
11. L.H. Lim, R.M. Harrison, and S. Harrad. Environ. Sci. Technol. **33**, 3538 (1999).
12. T. Nielsen. Atmos. Environ. **30**, 3481 (1996).
13. Y. Liu, L. Zhu, X. Shen. Environ. Sci. Technol. **35**, 840 (2001).
14. L. Zhu and J. Wang. Chemosphere, **50**, 611 (2003).
15. K.F. Chang, G.C. Fang, J.C. Chen, and Y.S. Wu. Environ. Pollut. **142**, 388 (2006).
16. S.S. Park, Y.J. Kim, and C.H. Kang. Atmos. Environ. **36**, 2917 (2002).
17. R. Atkinson and S.M. Aschmann. Int. J. Chem. Kinet. **20**, 513 (1988).
18. J. Arey, B. Zielinska, R. Atkinson, and S.M. Aschmann. Int. J. Chem. Kinet. **21**, 775 (1989).
19. F. Reisen and J. Arey. Environ. Sci. Technol. **36**, 4302 (2002).
20. Y. Zhao and D.G. Truhlar. J. Phys. Chem. A, **108**, 6908 (2004).
21. K. Fukui. Acc. Chem. Res. **14**, 363 (1981).
22. Y. Zhao, N. Gonzalez-Garcia, and D.G. Truhlar. J. Phys. Chem. A, **109**, 2012 (2005).
23. A.C. Hazell, R.G. Hazell, L. Norskov-Lauritsen, C.E. Briant, and D.W. Jones. Acta Crystallogr. C, **42**, 690 (1986).
24. L. Wang, R. Atkinson, and J. Arey. Environ. Sci. Technol. **41**, 2803 (2007).

© 2008 NRC Canada

Synthesis of isoxazole conjugates of sugars via 1,3-dipolar cycloaddition

Vipraja V. Vaidya, Karuna S. Wankhede, Manikrao M. Salunkhe, and Girish K. Trivedi

Abstract: Isoxazole conjugates of sugar have been synthesized by the aid of 1,3-dipolar cycloaddition in a click chemistry approach. The sugar-derived propargyl ethers underwent 1,3-dipolar cycloadditions smoothly with in situ generated nitrile oxides from aromatic oximes in good yields. The reaction exhibited a high degree of regioselectivity.

Key words: isoxazole conjugates, 1,3-dipolar cycloadditions, nitrile oxides.

Résumé : Faisant appel à une cycloaddition 1,3-dipolaire et une approche chimique qui marche très bien, on a réalisé la synthèse d'isoxazoles conjugués à un sucre. Les éthers propargyliques dérivés du sucre donnent lieu en douceur et avec de bons rendements à des réactions de cycloaddition 1,3-dipolaire avec les oxydes de nitrile générés in situ à partir d'oximes aromatiques. La réaction présente un degré élevé de régiosélectivité.

Mots–clés : produits conjugués de l'isoxazole, cycloadditions 1,3-dipolaires, oxydes de nitrile.

[Traduit par la Rédaction]

Introduction

Several compounds of natural and non-natural origin comprised of the isoxazole moiety possess a broad spectrum of biological properties viz., fungicidal, antibacterial, anti-inflammatory, anti-allergic, anti-tumor, herbicidal, etc. The isoxazole class of compounds are also synthetically important as 1,3-dicarbonyl equivalents (1). Among the plethora of protocols reported for the synthesis of the isoxazole skeleton, two major routes are the 1,3-dipolar cycloadditon of alkenes and alkynes with nitrile oxides and the reaction of hydroxylamine with a three-carbon atom component, such as 1,3-diketone or an α,β-unsaturated ketone. 1,3-Dipolar cycloaddition has proven particularly valuable for the construction of complex five-membered conformationally rigid heterocycles (2). Isoxazoles, also among the five-membered heterocycles, can be accessed by 1,3-dipolar cycloaddition reaction. In particular, nitrile oxides undergo cycloaddition with alkynes resulting in good yields of isoxazoles (3). A similar class of compounds, i.e., triazoles, have been synthesized via 1,3-dipolar cycloaddition of azides and alkynes. This reaction has been considered as the prototype of click chemistry (4). There are several excellent contributions from various groups in the domain of click chemistry, wherein 1,3–dipolar cycloadditions are employed as a tool to conjugate molecules of structural diversity (5). Such linkage may result in altogether new attributes and (or) an ensemble of attributes. The continuing interest in this field and the importance of the isoxazole moiety has encouraged us to report our results.

Received 22 October 2007. Accepted 23 November 2007. Published on the NRC Research Press Web site at canjchem.nrc.ca on 17 January 2008.

V.V. Vaidya, K.S. Wankhede, M.M. Salunkhe,[1] and G.K. Trivedi. Department of Chemistry, The Institute of Science, 15-Madam Cama Road, Mumbai 400 032, India.

[1]Corresponding author (e-mail: mmsalunkhe@hotmail.com).

Results and discussion

We herein report regioselective syntheses of sugar conjugates of isoxazoles (**1**–**10**) via 1,3-dipolar cycloaddition of carbohydrate derived alkynes and in situ generated nitrile oxides from oximes (Scheme 1). D-Glucose was utilized as a precursor to prepare all dipolarophiles i.e., sugar alkynes. The dipolarophiles (**1a**–**5a**) were synthesized following standard procedures. The dipoles, i.e., nitrile oxides, were generated in situ from the biphasic oxidation of the oximes with NaOCl in dichloromethane-triethyl amine (6). These dipoles underwent cycloaddition with dipolarophiles to afford cycloadducts, i.e., new isoxazole conjugates of sugars in good yields.

D-Glucose was utilized to synthesize 1,2:5,6 diisopropylidene-α-D-glucofuranose, which was subsequently subjected to etherification using propargyl bromide to yield the dipolarophile **1a**. The dipolarophile **1a** upon treatment with benzonitrile oxide, 4-methoxy benzonitrile oxide, and 3,4-dimethoxy benzonitrile oxide afforded cycloadducts (**1**–**3**) in 75%–80% yields.

The dipolarophile **2a** was also treated with the three previously mentioned nitrile oxides separately to generate corresponding cycloadducts (**4**–**6**) in 69%–75% yields. The dipolarophile **3a** was treated with benzonitrile oxide to yield cycloadduct **7** in 74% yield. The dipolarophile **4a** was accessed by Ferrier *O*-glycosylation of 3,4,6-tri-*O*-acetyl-D-glucal with propargyl alcohol. It was further subjected to 1,3-dipolar cycloaddition with benzonitrile oxide to yield cycloadduct **8** in 67% yield.

Our next objective was to synthesize bis-isoxazole derivatives, and in that direction we carried out the propargylation of the cycloadduct **7** to have one more site for cycloaddition

 doi:10.1139/V07-145 © 2008 NRC Canada

Scheme 1. Synthesis of isoxazole conjugates of sugars.

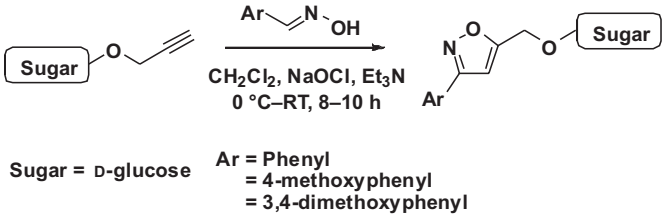

to yield the dipolarophile **5a**. The compound **5a** was subjected to cycloaddition with benzonitrile oxide and 4-methoxy benzonitrile oxide to afford bisisoxazole **9** and mixed bis-isoxazole **10**, in 65% and 67% yields, respectively. All gummy products (Table 1) were purified by silica gel column chromatography. The reaction exhibited a high degree of regioselectivity, which was confirmed from ^{1}H NMR spectra of the products. The signals in the range of δ 6.5–6.7, as singlet for vinylic proton, indicated only 5-substituted products were formed. Furthermore, all these isoxazole conjugates possess a protected furanoside ring that is accessible for elaboration after deprotection. The isoxazole moiety present can be cleaved to yield 1,3-functionalized compounds that can serve as handles for further manipulation.

In conclusion, we successfully employed a 1,3-dipolar cycloaddition strategy to conjugate sugar molecules with isoxazoles, which resulted in compounds bearing an appendage of aromatic moieties on sugar molecules. Thus, the biological profile of isoxazole coupled with sugar through C-O linkage was diversified. In the near future, we will continue our efforts to synthesize novel hybrid entities using the 1,3-dipolar cycloaddition reaction of nitrile oxides as a key step.

Experimental

General procedure for the preparation of isoxazole conjugates

A solution of the aldoxime (dipole precursor) (1 mmol), sugar alkyne (dipolarophile) (1 mmol), and triethylamine (2 to 3 drops) in dichloromethane (10 mL) was cooled to 0 °C. To this solution, sodium hypochlorite (4%, 10 mL) was added dropwise with stirring at 0 °C. The reaction mixture was warmed to RT and stirred for 8–10 h. On the disappearance of the starting material (TLC), the reaction phases were separated and the aqueous phase was extracted with dichloromethane. The combined layers were washed with brine, dried with sodium sulphate, and the solvent evaporated under reduced pressure to yield the crude cycloadduct. The crude product was chromatographed on a silica gel column. The purified products were characterized.

Characterization data

Cycloadduct 1

$[\alpha]_D^{27}$ –34.62 (*c* 2.0, $CHCl_3$). IR (cm^{-1}): 3037, 1525, 1383, 1232, 1082. ^{1}H NMR (300 MHz, $CDCl_3$, ppm) δ: 7.80 (dd, 2H, *J* = 2.8, 6.4 Hz), 7.47–7.45 (m, 3H), 6.69 (s, 1H), 5.91 (d, 1H, *J* = 3.6 Hz), 4.82 (s, 2H), 4.60 (d, 1H, *J* = 3.6 Hz), 4.36 (dd, 1H, *J* = 5.5, 12.7 Hz), 4.16–4.10 (m, 3H), 4.02 (dd, 1H, *J* = 5.2, 8.5 Hz), 1.49 (s, 3H), 1.43 (s, 3H), 1.37 (s, 3H), 1.32 (s, 3H). ^{13}C NMR (75 MHz, $CDCl_3$, ppm) δ: 169.09, 162.35, 130.04, 128.87, 128.80, 126.72, 111.96, 109.18, 105.18, 101.10, 82.66, 82.26, 81.06, 72.14, 67.47, 63.37, 26.84, 26.72, 26.15, 25.33.

Cycloadduct 2

$[\alpha]_D^{27}$ –19.84 (*c* 2.5, $CHCl_3$). IR (cm^{-1}): 3037, 1520, 1379, 1227, 1082. ^{1}H NMR (300 MHz, $CDCl_3$, ppm) δ: 7.74 (d, 2H, *J* = 8.7 Hz), 6.97 (d, 2H, *J* = 8.7 Hz), 6.63 (s, 1H), 5.90 (d, 1H, *J* = 3.6 Hz), 4.80 (s, 2H), 4.59 (d, 1H, *J* = 3.6 Hz), 4.35 (dd, 1H, *J* = 5.8, 13.3 Hz), 4.16–4.10 (m, 3H), 4.02 (dd, 1H, *J* = 5.2, 8.5 Hz), 3.85 (s, 3H), 1.49 (s, 3H), 1.43 (s, 3H), 1.37 (s, 3H), 1.32 (s, 3H). ^{13}C NMR (75 MHz, $CDCl_3$, ppm) δ: 168.87, 162.02, 161.07, 128.22, 121.38, 114.33, 112.03, 110.81, 109.24, 105.26, 100.94, 82.77, 82.34, 81.15, 72.24, 67.54, 63.46, 55.36, 26.91, 26.82, 26.22, 25.41.

Cycloadduct 3

$[\alpha]_D^{27}$ –15.05 (*c* 2.0, $CHCl_3$). IR (cm^{-1}): 3121, 1528, 1376, 1082, 853. ^{1}H NMR (300 MHz, $CDCl_3$, ppm) δ: 7.42 (d, 1H, *J* = 1.8 Hz), 7.28 (dd, 1H, *J* = 1.8, 8.1 Hz), 6.93 (d, 1H, *J* = 8.1 Hz), 6.63 (s, 1H), 5.91 (d, 1H, *J* = 3.9 Hz), 4.80 (s, 2H), 4.59 (d, 1H, *J* = 3.6 Hz), 4.35 (dd, 1H, *J* = 6.4, 13.3 Hz), 4.16–4.10 (m, 3H), 4.04–3.93 (overlapping peaks, 7H). ^{13}C NMR (75 MHz, $CDCl_3$, ppm) δ: 168.99, 162.17, 150.78, 149.44, 121.67, 119.99, 112.06, 111.13, 109.41, 105.30, 101.00, 82.82, 82.46, 81.20, 72.30, 67.58, 63.53, 56.08, 55.99, 26.92, 28.82, 26.26, 25.45. HRMS calcd. for $C_{24}H_{32}NO_9$ (M+H): 478.2077; found 478.2081.

Cycloadduct 4

$[\alpha]_D^{27}$ –30.8 (*c* 2.0, $CHCl_3$). IR (cm^{-1}): 3038, 2946, 1384, 1228, 1081, 1024. ^{1}H NMR (300 MHz, $CDCl_3$, ppm) δ: 7.77 (d, 2H, *J* = 3.9 Hz), 7.44 (m, 3H), 7.30 (m, 5H), 6.56 (s,1H), 5.95 (d, 1H, *J* = 3.6 Hz), 4.76–4.61 (m, 4H), 4.49 (d, 1H, *J* = 12 Hz), 4.43–4.38 (m, 1H), 3.97 (d, 1H, *J* = 2.7 Hz), 3.83 (d, 2H, *J* = 6.0 Hz), 1.48 (s, 3H), 1.31 (s, 3H). ^{13}C NMR (75 MHz, $CDCl_3$, ppm) δ: 169.58, 162.36, 137.31, 130.00, 128.90, 128.51, 127.99, 127.66, 126.81, 111.78, 105.17, 101.17, 82.16, 81.69, 79.12, 71.94, 68.79, 64.28, 26.80, 26.28.

Cycloadduct 5

$[\alpha]_D^{27}$ –28.89 (*c* 2.0, $CHCl_3$). IR (cm^{-1}): 3038, 2956, 1384, 1261, 1086. ^{1}H NMR (300 MHz, $CDCl_3$, ppm) δ: 7.72 (d, 2H, *J* = 8.7 Hz), 7.36–7.21 (m, 5H), 6.96 (d, 2H, *J* = 8.7 Hz), 6.50 (s, 1H), 5.95 (d, 1H, *J* = 3.9 Hz), 4.73–4.59 (m, 4H), 4.49 (d, *J* = 12 Hz, 1H), 4.43–4.38 (m, 1H), 3.97 (d, 1H, *J* = 3.3 Hz), 3.83 (overlapping peaks, 5H), 1.48 (s, 3H), 1.32 (s, 3H). ^{13}C NMR (75 MHz, $CDCl_3$, ppm) δ: 169.30, 161.96, 160.99, 137.33, 129.46, 128.51, 128.21, 128.10, 127.98, 127.69, 127.66, 121.44, 114.28, 111.78, 105.13, 100.94, 82.19, 81.71, 79.13, 71.96, 68.75, 64.25, 55.33, 26.80, 26.29.

Cycloadduct 6

$[\alpha]_D^{27}$ –22.7 (*c* 1.0, $CHCl_3$). IR (cm^{-1}): 3037, 2922, 1258, 1023. ^{1}H NMR (300 MHz, $CDCl_3$, ppm) δ: 7.41 (d, 1H, *J* = 1.8 Hz), 7.31 (overlapping peaks, 6H), 6.93 (d, 1H, *J* = 8.4 Hz), 6.53 (s, 1H), 5.95 (d, 1H, *J* = 3.6 Hz), 4.75–4.61 (m, 4H), 4.49 (d, 1H, *J* = 12 Hz), 4.43–4.38 (m, 1H), 3.97–3.93 (overlapping peaks, 7H), 3.83 (d, 2H, *J* = 6 Hz), 1.49

© 2008 NRC Canada

Table 1. Synthesis of isoxazole conjugates of sugars.

Entry	Dipolarophile	Dipole precursor	Cycloadduct
1.	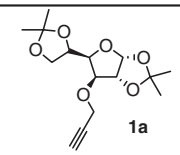 **1a**	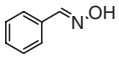	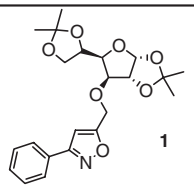 **1**
2.	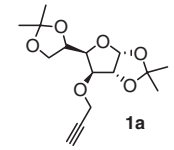 **1a**	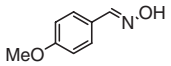	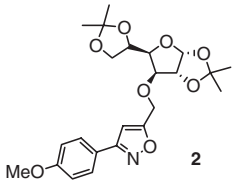 **2**
3.	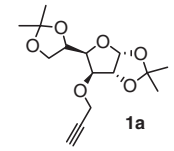 **1a**	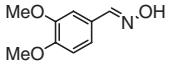	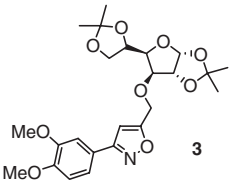 **3**
4.	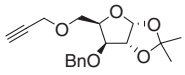 **2a**	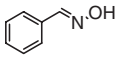	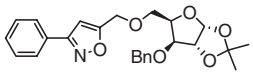 **4**
5.	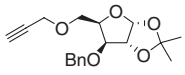 **2a**	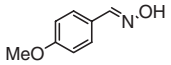	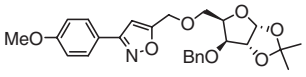 **5**
6.	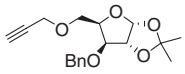 **2a**	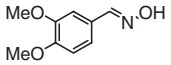	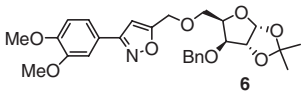 **6**
7.	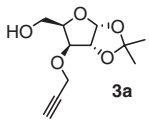 **3a**	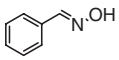	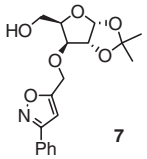 **7**
8.	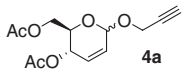 **4a**	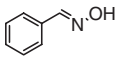	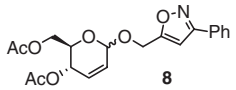 **8**
9.	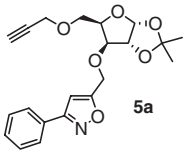 **5a**	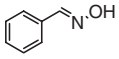	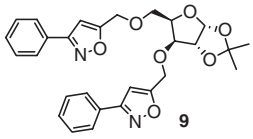 **9**
10.	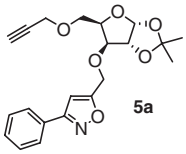 **5a**	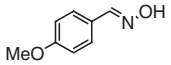	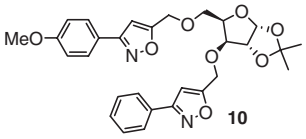 **10**

© 2008 NRC Canada

(s, 3H), 1.32 (s, 3H). ^{13}C NMR (75 MHz, $CDCl_3$, ppm) δ: 169.45, 162.06, 150.33, 149.22, 137.27, 128.49, 127.96, 127.64, 121.60, 119.91, 110.96, 109.21, 105.13, 100.97, 82.11, 81.65, 79.10, 71.91, 68.75, 64.29, 55.97, 55.91, 26.76, 26.25. HRMS calcd. for $C_{27}H_{32}NO_8$ (M+H): 498.2128; found 498.2140.

Cycloadduct 7

$[\alpha]_D^{27}$ –39.1 (*c* 2.0, $CHCl_3$). IR (cm^{-1}): 3431, 2929, 1612, 1373, 1214, 1078, 1019, 853. ^{1}H NMR (300 MHz, $CDCl_3$, ppm) δ: 7.80 (d, 2H, *J* = 6.6 Hz), 7.6–7.36 (m, 3H), 6.61 (s, 1H), 5.97 (d, 1H, *J* = 3.6 Hz), 4.83–4.65 (m, 3H), 4.40–4.21 (m, 1H), 4.10 (d, 1H, *J* = 2.7 Hz), 3.98–3.85 (m, 2H), 2.26 (bs, 1H), 1.50 (s, 3H), 1.32 (s, 3H). ^{13}C NMR (75 MHz, $CDCl_3$, ppm) δ: 168.54, 162.42, 130.13, 128.90, 128.52, 126.74, 111.91, 104.90, 101.42, 83.15, 82.32, 80.11, 62.79, 60.21, 26.66, 26.20.

Cycloadduct 8

$[\alpha]_D^{27}$ +44.9 (*c* 2.0, $CHCl_3$). IR (cm^{-1}): 3038, 2951, 1754, 1369, 1232, 1043. ^{1}H NMR (300 MHz, $CDCl_3$, ppm) δ: 7.80 (d, 2H, *J* = 3.6 Hz), 7.46–7.44 (m, 3H), 6.60 (s, 1H), 6.04–5.88 (m, 2H), 5.35 (d, 1H, *J* = 9 Hz), 5.19 (s, 1H), 4.96–4.75 (m, 2H), 4.29–4.13 (m, 3H), 2.094 (s, 3H), 2.09 (s, 3H). ^{13}C NMR (75 MHz, $CDCl_3$) δ: 170.74, 170.23, 169.12, 162.46, 130.11, 130.05, 129.51, 129.09, 128.96, 128.84, 128.39, 126.93, 126.82, 126.28, 101.39, 94.11, 67.39, 65.14, 63.93, 62.75, 60.65, 20.94, 20.77. HRMS calcd. for $C_{20}H_{21}NO_7$ Na (M+Na): 410.1216; found 410.1213.

Cycloadduct 9

$[\alpha]_D^{27}$ –27.10 (*c* 2.0, $CHCl_3$). IR (cm^{-1}): 3042, 2954, 1609, 1234, 1099, 1028. ^{1}H NMR (300 MHz, $CDCl_3$, ppm) δ: 7.8–7.76 (m, 4H), 7.51–7.37 (m, 6H), 6.59 (s, 1H), 6.58 (s, 1H), 5.95 (d, 1H, *J* = 3.6 Hz), 4.79–4.62 (m, 5H), 4.46–4.41 (m, 1H), 4.06 (d, 1H, *J* = 2.7 Hz), 3.90–3.79 (m, 2H), 1.49 (s, 3H), 1.32 (s, 3H). ^{13}C NMR (75 MHz, $CDCl_3$, ppm) δ: 169.29, 168.57, 162.41, 130.13, 130.01, 129.09, 128.93, 128.89, 128.62, 128.38, 126.78, 126.25, 112.00, 105.07, 101.57, 101.41, 82.45, 82.71, 78.64, 68.03, 64.20, 62.85, 26.75, 26.26. HRMS calcd. for $C_{28}H_{29}N_2O_7$ Na (M+H): 505.1975; found 505.1988.

Cycloadduct 10

$[\alpha]_D^{27}$ –20.74 (*c* 1.0, $CHCl_3$). IR (cm^{-1}): 3042, 2956, 1609, 1251, 1074, 1023. ^{1}H NMR (300 MHz, $CDCl_3$, ppm) δ: 7.75–7.68 (m, 4H); 7.42 (s, 3H), 6.92 (d, 2H, *J* = 8.7 Hz), 6.57 (s, 1H), 6.53 (s, 1H), 5.95 (d, 1H, *J* = 3.3 Hz), 4.79–4.61 (m, 5H), 4.46–4.41 (m, 1H), 4.06 (d, 1H, *J* = 3.3 Hz), 3.83 (overlapping peaks, 5H), 1.49 (s, 3H), 1.32 (s, 3H). ^{13}C NMR (75 MHz, $CDCl_3$, ppm) δ: 168.99, 168.60, 162.41, 161.97, 160.98, 130.11, 128.93, 128.65, 128.19, 126.78, 121.33, 114.28, 113.63, 112.00, 105.06, 101.53, 101.20, 82.46, 82.21, 78.63, 67.94, 64.20, 62.90, 55.32, 26.75, 26.27.

Acknowledgments

We wish to thank University Grants Commission (UGC), New Delhi, for the award of a fellowship and financial support [F-12–25/(2003)] and the Director, The Institute of Science, Mumbai.

References

1. P.G. Baraldi, A. Barco, S. Benetti, G.P. Pollini, and D. Simoni. Synthesis, 857 (1987).
2. (*a*) R. Huisgen. 1,3-Dipolar cycloaddition chemistry. Vols. 1 and 2. *Edited by* A. Padwa. John Wiley & Sons, NY. 1984; (*b*) K.V. Gothelf and K. A. Jørgensen. Chem. Rev. **98**, 863 (1998).
3. (*a*) D.P. Curran. *In* Advances in cycloaddition. Vol. 1. *Edited by* D.P. Curran. JAI Press, Greenwich, UK. 1988. pp. 129–189; (*b*) K.B.G. Torssell. *In* Nitrile oxides, nitrones, and nitronates in organic synthesis. VCH, NY. 1988; (*c*) S. Kanemasa and O. Tsuge. Heterocycles, **30**, 719 (1990).
4. (*a*) H.C. Kolb, M.G. Finn, and K. B. Sharpless. Angew. Chem. Int. Ed. **40**, 2004, (2001); (*b*) M. Gil, M. Arevalo, and O. Lopez. Synthesis, 1589 (2007).
5. (*a*) S.G. Gouin, L Bultel, C. Falentin, and J. Kovensky. Eur. J. Org. Chem. 1160 (2007); (*b*) J. Jung, Y.G. Lim, K.H. Lee, and B. Koo. Tetrahedron Lett. **48**, 6442 (2007); (*c*) D. Arosio, M. Bertoli, L. Manzoni, and C. Scolastico. Tetrahedron Lett. **47**, 369 (2006); (*d*) S. Hotha, R. Anegundi, and A. Natu. Tetrahedron Lett. **46**, 4585 (2005); (*e*) S. Chittaboina, F. Xie, Q. Wang. Tetrahedron Lett. **46**, 2331 (2005); (*f*) Q. Wang, T. Chan, R. Hilgraf, V. Fokin, K. Sharpless, and M. Finn. J. Am. Chem. Soc. **125**, 3192 (2003).
6. G. Lee. Synthesis, 508 (1982).

© 2008 NRC Canada

Ring opening of α,β-epoxy phenyl ketones with ceric ammonium nitrate (CAN) and potassium bromide

Zhou Lu, Wentao Wu, Lijun Peng, and Longmin Wu

Abstract: Ring-opening reaction of α,β-epoxy phenyl ketones was achieved cooperatively using cerium ammonium nitrate (CAN) and potassium bromide. The reaction occurred regioselectively at the β-C to afford *syn*-β-bromo-α-hydroxyl ketones as main outcomes.

Key words: ring-opening, epoxide, ceric ammonium nitrate, potassium bromide.

Résumé : Utilisant l'effet combiné du nitrate d'ammonium cérique (NAC) et du bromure de potassium comme catalyseurs, on a réalisé la réaction d'ouverture de cycle de α,β-époxy phénylcétones. La réaction se fait d'une façon stéréosélective au niveau du carbone β et elle conduit aux β-bromo-α-hydroxycétones *syn* comme produits principaux.

Mots-clés : ouverture de cycle, époxyde, nitrate d'ammonium cérique, bromure de potassium.

[Traduit par la Rédaction]

Introduction

Epoxides are important starting materials and intermediates in organic synthesis (1) because of their easy preparations and ready reactivities toward nucleophiles. Among the reports on epoxides, many were involved in ring-opening reactions (2). Most of the nucleophilic ring-opening reactions proceeded via an S_N2-like mechanism and afforded the corresponding *trans*-β-Nu alcohols (3). Our recent studies found that nitric oxide (NO) caused ring opening of 2,3-epoxides in either syn- or anti-selective fashion, which is strongly dependent on the α-C substituent (4). It was found that cerium ammonium nitrate (CAN, $(NH_4)_2Ce(NO_3)_6$), a single electron oxidant in organic oxidation reactions (5–11), efficiently catalyzed most ring-opening reactions of epoxides (12). These reactions occurred in distinct regioselectivity, β- or α-attack (12*e*–12*f*), and in anti and (or) syn manners, strongly depending upon the molecular structure, the stoichiometry of CAN used, and the solvent (12). CAN brought about the conversion of epoxides into β-nitrato alcohols in the presence of an excess of nitrate ion (12*a*–12*b*). Recently, it was reported that CAN mediated ring opening of cyclopropyl alcohols and specifically gave β-functionalized ketones in the presence of selected anions (13). The substitutent-dependent fashion in the NO-mediated ring-opening reaction of epoxides (4) stimulated us to explore whether a similar effect also exists in the ring-opening reaction of epoxides with CAN. In addition, the resulting vicinal alcohols from the ring-opening reaction of epoxides will be important intermediates in organic synthesis (14).

Received 24 September 2007. Accepted 4 December 2007. Published on the NRC Research Press Web site at canjchem.nrc.ca on 17 January 2008.

Z. Lu, W.T. Wu, L.J. Peng and L.M. Wu.[1] Sate Key Laboratory of Applied Organic Chemistry, Lanzhou University, Lanzhou 730000, China.

[1]Corresponding author (email: nlaoc@lzu.edu.cn).

Result and discussion

In the present work, *trans* chalcone epoxides were employed as substrates. We started with α,β-epoxy phenyl ketones **1**, which were easily prepared by the reaction of chalcone with H_2O_2. Upon treatment of 1 equiv. of **1** with 2.2 equiv. of CAN and 5 equiv. of KBr in acetone at room temperature (RT), ring-opening reactions occurred regioselectively at the β-C and brominations specifically at the β-C, giving β-bromo-α-hydroxyl ketones **2** in moderate yields (Scheme 1 and Table 1). All products were characterized by IR, MS, HRMS, ^1H, and ^{13}C NMR. Weber first synthesized chalcone bromohydrins using $SnBr_4$ in 1992. He determined his products to be syn configurations mainly by NMR parameters (15). As such, the configuration of products **2** was confirmed to be dominantly syn (4*a*, 15, 16).

It was also found that CAN and KBr acted cooperatively to cause the ring-opening reactions. No ring-opening reaction occurred in the absence of either CAN or KBr. Furthermore, the reaction proceeded very slowly when a catalytic amount of CAN was applied. One reason for this may be partially attributed to polar substituted epoxides having less activity toward the ring-opening reaction (12*d*). Although the reaction mechanism is far from clear, a possible pathway for the present ring-opening reaction and bromination may be rationalized in terms of bromine radical, which is formed by the oxidation of bromide ion with an excess amount of CAN (13, 17) and the subsequent addition of bromine radical to three-membered epoxide ring (10a, 18), leading to the ring opening. On reviewing previous works on similar topics (4, 19), it is found that the carbonyl group plays a key role in ring-opening regioselectivity. The carbonyl group causes

 doi:10.1139/V07-148 © 2008 NRC Canada

Scheme 1.

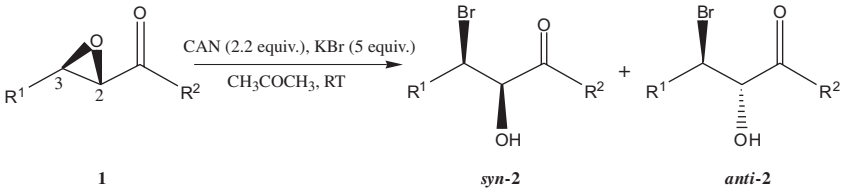

1 ***syn*-2** ***anti*-2**

dr of *syn* to *anti* up to 99:1

Table 1. Ring opening of 2,3-epoxy phenyl ketones with CAN and KBr in acetone.

Substrate	R^1	R^2	Time (h)	Yield (%)[a]	dr syn:anti (%)[b]
1a	Ph	Ph	10	77	> 99:1
1b	Ph	(p)-Br-Ph	18	73	88:12
1c	Ph	(p)-F-Ph	18	70	87:13
1d	(p)-MeO-Ph	Ph	0.1	0[c]	—
1e	(p)-Me-Ph	Ph	3	76[d]	90:10
1f	(p)-Cl-Ph	Ph	16	80	> 99:1
1g	(p)-Cl-Ph	(p)-Br-Ph	16	76	87:13
1h	(p)-Cl-Ph	(p)-MeO-Ph	14	85	96:4
1i	(p)-O_2N-Ph	Ph	24	51	70:30
1j	(p)-O_2N-Ph	(p)-MeO-Ph	20	71	77:23
1k	(m)-O_2N-Ph	Ph	24	58	73:27

[a]Yields refer to isolated products.
[b]The ratio of *syn*-**2** to *anti*-**2** was evaluated using the characteristic ^{1}H NMR peaks both of α- and β-H, such as in **2j**, 5.56 (*syn*-α-H) to 5.41 ppm (*anti*-α-H) as well as 5.33 (*syn*-β-H) to 5.10 (*anti*-β-H).
[c]Material decomposed in 5 min, giving 91% of 4-methoxybenzaldehyde.
[d]Along with 55% of 4-methylbenzaldehyde.

the ring opening uniquely at β-C, yet the stereochemistry strongly depends on reaction conditions. The assumption of a one-electron transfer reaction between epoxide and Ce(IV), with a catalytic amount leading to the formation of an expoxonium radical cation (12*b*–12*e*), will be ruled out in the present case.

The effect of solvents on this reaction was examined using **1a** as a substrate (Table 2). From Table 2 we can find that some aprotic solvents such as acetone and THF were the most favorable solvents, whereas CH_2Cl_2 disfavored the ring-opening reaction. In general, CAN is insoluble in organic solvents. If a small amount of water is contained in solvents, then the solvent polarity somewhat affects the solubility of CAN in reaction media. Otherwise, protic solvents would join the reaction (12*c*, 19*a*), as in the case of methanol (Table 2).

In summary, we have developed an efficient method for the regioselective and syn-selective conversion of *trans* chalcone epoxides to *syn* chalcone bromohydrins by CAN and potassium bromide.

Table 2. Effect of solvents on the yield of **2a**.

Solvent	Yield of **2a** (%)
CH_3COCH_3	77
CH_3CN	60
THF	66
Et_2O	64
CH_3COOEt	33
CH_2Cl_2	0
CH_3OH	19[a]

Note: The ratio of syn to anti in all solvents was ca. 99:1.
[a]Along with 75% of 2-hydroxy-3-methoxy-1,3-diphenylpropan-1-one (19*a*).

Experimental

General

Flash chromatography was carried out using silica gel 60 (200–300 mesh, particle size 0.040–0.062 mm) supplied by Qingdao Ocean Chemical Plant. Melting points were measured with a digital Koffer apparatus and were uncorrected. IR (KBr) analysis of solid compounds was performed on a Nicolet NEXUS 670 FT-IR spectrophotometer and reported in cm^{-1}. ^{1}H and ^{13}C NMR spectra were recorded on a Varian Mercury Plus 300 MHz NMR spectrometer. Chemical shifts (δ) for ^{1}H and ^{13}C NMR spectra are reported in parts per million (ppm) from solvent $CDCl_3$ (7.26 ppm) and (77.0 ppm), respectively, as internal standards relative to tetramethylsilane. MS data were obtained with EI (70 eV) on an HP-5988 spectrometer by direct inlet at 70 eV. HRMS data was obtained on a Bruker Daltonics APEX FT-ICR spectrometer. Chemicals were of highest grade commercially available and used as received, unless otherwise stated. All reagents were weighed and handled in air at RT.

Typical procedure for the preparation of 1a

To a solution of 1.040 g of chalcone (5 mmol) in 25 mL of methanol were added 1.035 g of K_2CO_3 (7 mmol) and

© 2008 NRC Canada

2 mL of H_2O_2 (30%). The mixture was stirred at ambient temperature until a white precipitate appeared, then isolated by filtration with the aid of Celite, and washed with water, affording **1a**. Other substrates were prepared by similar procedures.

Typical procedure for the ring-opening reaction of 1a with CAN and KBr

To a solution of 0.112 g (0.5 mmol) of **1a** in 15 mL of acetone were added 0.300 g of KBr (2.5 mmol) and 0.600 g of CAN (1.1 mmol). The mixture was stirred at ambient temperature until the reaction completed, water then added to dissolve the salts, and extracted with 3 × 10 mL Et_2O. The organic layer was dried over anhyd. Na_2SO_4, filtered, concentrated under vacuum, and purified by flash column chromatography on silica gel (petroleum ether/acetic ether 10:1), giving pure **2a**. All compounds were recrystalized from petroleum ether (60–80 °C)-acetic ether. Other ring-opening reactions were performed accordingly.

Characterization data for products

Syn-2a (15)

Yellow solid, yield 77%, mp 90–92. IR (KBr, cm^{-1}) ν: 3472, 1673, 1271, 977. ^{1}H NMR (300 MHz, $CDCl_3$, ppm) δ: 7.85 (d, *J* = 7.2 Hz, 2H), 7.64 (t, *J* = 7.5 Hz, *J* = 7.8 Hz, 1H), 7.50 (m, *J* = 7.5 Hz, *J* = 7.8 Hz, 2H), 7.18–7.23 (m, 5H), 5.59 (dd, *J* = 3.9 Hz, *J* = 7.2 Hz, 1H), 5.34 (d, *J* = 3.9 Hz, 1H), 3.73 (d, *J* = 7.5 Hz, 1H). ^{13}C NMR (75 MHz, $CDCl_3$, ppm) δ: 197.2, 135.8, 134.4, 134.2, 129.0, 128.9, 128.7, 128.6, 128.2, 76.9, 53.4. EI-MS *m/z*: 306 [M + 2], 304 [M^+], 224, 135. HRMS *m/z* calcd. for $C_{15}H_{13}O_2Br$ [M + Na]$^+$: 326.9991; found: 326.9995.

2b (15) (Obtained as a mixture 7:1 syn/anti isomers)

Yellow solid, yield 73%, mp 128–130. IR (KBr, cm^{-1}) ν: 3489, 1677, 1300, 860. ^{1}H NMR (300 MHz, $CDCl_3$, ppm) δ: 7.87 (d, *J* = 9.0 Hz, 0.4H), 7.72 (d, *J* = 9.0 Hz, 2H), 7.63 (d, *J* = 9.0 Hz, 2H), 7.46 (d, *J* = 9.0 Hz, 0.4H), 7.38 (d, *J* = 9.0 Hz, 0.4H), 7.33 (m, 2H), 7.23 (m, 3H), 5.72 (d, *J* = 8.1 Hz, 0.16H), 5.53 (d, *J* = 3.6 Hz, 1.1H), 5.31 (d, *J* = 3.6 Hz, 0.98H), 5.15 (d, *J* = 8.1 Hz, 0.14H), 3.73 (s, 1H). ^{13}C NMR (75 MHz, $CDCl_3$, ppm) δ: 196.5, 135.8, 133.0, 132.2, 131.3, 130.1, 129.3, 128.4, 127.2, 77.6, 53.2. MS-EI *m/z*: 304 [M – HBr], 303 [M – Br], 305, 302, 215, 213.

2c (15) (Obtained as a mixture 6.7:1 syn/anti isomers)

Yellow solid, yield 70%, mp 98–101. IR (KBr, cm^{-1}) ν: 3510, 1680, 1270, 863. ^{1}H NMR (300 MHz, $CDCl_3$, ppm) δ: 8.05 (t, *J* = 8.1 Hz, 0.17H), 7.89 (t, *J* = 8.1 Hz, 1.4H), 7.48 (t, *J* = 8.1 Hz, 0.6H), 7.46–7.15 (m, 7.7H), 6.87 (t, *J* = 8.1 Hz, 0.35H), 5.75 (d, *J* = 8.1 Hz, 0.15H), 5.53 (d, *J* = 4.2 Hz, 1H), 5.29 (d, *J* = 4.2 Hz, 1H), 5.20 (d, *J* = 8.1 Hz, 0.16H), 3.91 (s, 1H). ^{13}C NMR (75 MHz, $CDCl_3$, ppm) δ: 195.8, 167.9, 135.9, 131.4, 130.5, 128.7, 128.4, 127.2, 116.3, 76.3, 53.3. MS-EI *m/z*: 322 [M^+], 324 [M + 2], 306, 304, 169, 171, 153.

2e (15) (Obtained as a mixture 9.5:1 of syn/anti isomers)

Yellow solid, yield 76%, mp 88–91. IR (KBr, cm^{-1}) ν: 3480, 1658, 1266, 810. ^{1}H NMR (300 MHz, $CDCl_3$, ppm) δ: 7.92 (d, *J* = 8.1 Hz, 0.2H), 7.87 (d, *J* = 8.1 Hz, 2H), 7.70 (d, *J* = 8.1 Hz, 0.12H), 7.61 (d, *J* = 8.1 Hz, 1H), 7.53 (d, *J* = 8.1 Hz, 0.2H), 7.50 (d, *J* = 8.1 Hz, 2H), 7.28 (d, *J* = 8.1 Hz, 2H), 7.20 (d, *J* = 8.1 Hz, 0.2), 7.13 (d, *J* = 8.1 Hz, 2H), 7.07 (d, *J* = 8.1 Hz, 0.2H), 6.08 (d, *J* = 4.2 Hz, 1H), 5.81 (d, *J* = 8.1 Hz, 0.11H), 5.54 (d, *J* = 8.1 Hz, 0.11H), 5.37 (d, *J* = 4.2 Hz, 1H), 4.11 (s, 1H), 2.35 (s, 3H). ^{13}C NMR (75 MHz, $CDCl_3$, ppm) δ: 197.5, 139.3, 133.7, 130.8, 129.2, 128.6, 128.3, 127.8, 127.0, 84.3, 74.2, 21.1. MS-EI *m/z*: 318 [M^+], 320 [M + 2], 239 [M – Br], 238 [M – HBr].

Syn-2f (15)

Yellow solid, yield 80%, mp 93–95. IR (KBr, cm^{-1}) ν: 3512, 1692, 1280, 836. ^{1}H NMR (300 MHz, $CDCl_3$, ppm) δ: 7.84 (d, *J* = 7.5 Hz, 2H), 7.64 (t, *J* = 7.5 Hz, 1H), 7.45 (d, *J* = 7.5 Hz, 2H), 7.17 (m, 4H), 5.57 (d, *J* = 3.0 Hz, 1H), 5.30 (d, *J* = 3.0 Hz, 1H), 3.84 (s, 1H). ^{13}C NMR (75 MHz, $CDCl_3$, ppm) δ: 196.9, 134.7, 134.5, 134.4, 133.8, 129.9, 129.2, 128. 6, 128.4, 76.8, 52.1. MS-EI *m/z*: 338 [M^+], 340 [M + 2], 259 [M – Br], 258 [M – HBr], 261, 260.

2g (New compound obtained as a mixture 6.7:1 of syn/anti isomers)

Yellow solid, yield 76%, mp 140–142. IR (KBr, cm^{-1}) ν: 3510, 1688, 1276, 830. ^{1}H NMR (300 MHz, $CDCl_3$, ppm) δ: 7.86 (d, *J* = 8.4 Hz, 0.6 H), 7.70 (dd, *J* = 8.4 Hz, *J* = 8.4 Hz, 4H), 7.37 (d, *J* = 8.4 Hz, 0.6H), 7.21 (dd, *J* = 8.4 Hz, *J* = 8.4 Hz, 4H), 5.49 (d, *J* = 3.9 Hz, 1H), 5.30 (d, *J* = 9.0 Hz, 0.16H), 5.22 (d, *J* = 3.9 Hz, 1H), 5.06 (d, *J* = 8.7 Hz, 0.15H), 3.70 (s, 1H). ^{13}C NMR (75 MHz, $CDCl_3$, ppm) δ: 196.3, 134.9, 134.4, 132.7, 132.5, 132.2, 130.4, 130.1, 128.5, 76.7, 51.9. MS-EI *m/z*: 337 [M – Br], 336 [M – HBr], 338, 339. HRMS *m/z* calcd. for $C_{15}H_{11}O_2ClBr_2$ [M + Na]$^+$: 440.8398; found: 440.8392.

2h (New compound obtained as a mixture 25:1 of syn/anti isomers)

Yellow solid, yield 85%, mp 88–90. IR (KBr, cm^{-1}) ν: 3515, 1684, 1286, 836. ^{1}H NMR (300 MHz, $CDCl_3$, ppm) δ: 7.83 (d, *J* = 8.7 Hz, 2H), 7.17 (m, 3H), 6.98 (t, *J* = 8.7 Hz, 3H), 5.73 (d, *J* = 8.1 Hz, 0.06H), 5.50 (d, *J* = 3.6 Hz, 1H), 5.27 (d, *J* = 3.6 Hz, 1H), 5.11 (d, *J* = 8.1 Hz, 0.04H), 3.91 (s, 3H), 3.82 (s, 1H). ^{13}C NMR (75 MHz, $CDCl_3$, ppm) δ: 194.9, 164.6, 134.5, 131.0, 129.9, 128.8, 128.2, 126.5, 114.3, 76.2, 55.5, 52.5. MS-EI *m/z*: 289 [M – Br], 288 [M – HBr], 291, 290, 135. HRMS *m/z* calcd. for $C_{16}H_{15}O_3ClBr$ [M + Na]$^+$: 392.9868; found: 392.9862

2i (New compound obtained as a mixture 2.3:1 of syn/anti isomers)

Yellow solid, yield 51%, mp 112–115. IR (KBr, cm^{-1}) ν: 3530, 1705, 1355, 844. ^{1}H NMR (300 MHz, $CDCl_3$, ppm) δ: 8.22 (d, *J* = 8.1 Hz, 1H), 8.04 (m, 2H), 7.86 (d, *J* = 7.8 Hz, 1H), 7.49 (m, 3H), 7.36 (d, *J* = 8.1 Hz, 1H), 5.61 (d, *J* = 4.2 Hz, 0.7H), 5.41 (d, *J* = 8.4 Hz, 0.3H), 5.26 (d, *J* = 4.2 Hz, 0.7H), 5.14 (d, *J* = 8.4 Hz, 0.3H), 3.89 (s, 1.38H). ^{13}C NMR (75 MHz, $CDCl_3$, ppm) δ: 197.2, 193.5, 148.2, 146.3, 144.7, 142.3, 134.5, 133.3, 133.1, 132.7, 128.4, 128.1, 127.5, 127.1, 119.4, 119.1, 76.3, 74.5, 55.2, 52.8. MS-EI *m/z*: 270 [M – Br], 269 [M – HBr], 165, 105. HRMS *m/z* calcd. for $C_{15}H_{12}O_4NBr$ [M + H]$^+$: 351.0111; found: 351.0115.

© 2008 NRC Canada

2j (New compound obtained as a mixture 3.3:1 of syn/anti isomers)

Yellow solid, yield 71%, mp 103–105. IR (KBr, cm^{-1}) ν: 3518, 1695, 1338, 835. ^1H NMR (300 MHz, $CDCl_3$, ppm) δ: 8.22 (d, *J* = 8.7 Hz, 0.6H), 8.06 (d, *J* = 8.7 Hz, 2H), 7.97 (d, *J* = 8.7 Hz, 0.7H), 7.86 (d, *J* = 8.7 Hz, 2H), 7.66 (d, *J* = 8.7 Hz, 0.6H), 7.37 (d, *J* = 8.7 Hz, 2H), 7.00 (d, *J* = 8.7 Hz, 2H), 6.94 (d, *J* = 8.7 Hz, 0.6H), 5.56 (d, *J* = 3.6 Hz, 1H), 5.41 (d, *J* = 8.1 Hz, 0.3H), 5.33 (d, *J* = 3.3 Hz, 1H), 5.10 (d, *J* = 8.1 Hz, 0.3H), 3.91 (s, 4H), 3.87 (s, 1.2H). ^{13}C NMR (75 MHz, $CDCl_3$, ppm) δ: 194.7, 191.1, 164.9, 147.8, 142.9, 131.5, 131.2, 129.7, 128.4, 126.2, 123.5, 123.2, 114.6, 114.2, 109.7, 76.1, 55.7, 51.4. MS-EI *m/z*: 301 [M – Br], 299 [M – HBr], 165, 135. HRMS *m/z* calcd. for $C_{16}H_{14}O_5NBr$ $[M + H]^+$: 381.0214; found: 381.0219.

2k (New compound obtained as a mixture 2.8:1 of syn/anti isomers)

Yellow solid, yield 58%, mp 86–88. IR (KBr, cm^{-1}) ν: 3528, 1712, 1357, 720. ^1H NMR (300 MHz, $CDCl_3$, ppm) δ: 8.12 (m, 4H), 7.88 (m, 2H), 7.68 (m, 1H), 7.53 (m, 6H), 5.61 (d, *J* = 4.2 Hz, 1H), 5.42 (d, *J* = 8.4 Hz, 0.38H), 5.38 (d, *J* = 4.2 Hz, 1H), 5.19 (d, *J* = 8.4 Hz, 0.36H), 3.97 (s, 1.4H). ^{13}C NMR (75 MHz, $CDCl_3$, ppm) δ: 197.0, 193.8, 148.0, 147.8, 138.0, 134.5, 134.3, 134.0, 129.8, 129.6, 128.4, 128.1, 127.8, 123.7, 123.4, 122.0, 76.4, 73.8, 51.0, 47.5. MS-EI *m/z*: 270 [M – Br], 269 [M – HBr], 165, 105. HRMS *m/z* calcd. for $C_{15}H_{12}O_4NBr$ $[M + H]^+$: 351.0111; found: 351.0108.

Acknowledgement

Project 20572040 was supported by National Natural Science Foundation of China.

References

1. (*a*) R.M. Hanson. Chem. Rev. **91**, 437 (1991); (*b*) R.D. Fabio, T. Rossi, and R.J. Thomas. Tetrahedron Lett. **38**, 3587 (1997).
2. (*a*) A. Delgado, G. Leclerc, M.C. Lobato, and D. Mauleon. Tetrahedron Lett. **29**, 3671 (1988); (*b*) M. Mitani, H. Matsumato, N. Gouda, and K. Koyama. J. Am. Chem. Soc. **112**, 1286 (1990); (*c*) A.G. Myers, and K.L. Widdowson. Tetrahedron Lett. **29**, 6389 (1988); (*d*) W. Chamchaang and A.R. Pinhas. J. Org. Chem. **55**, 2531 (1990); (*e*) T. Ibyka, K. Nakai, H. Habashita, Y. Hotta, A. Otaka, H. Tamamura, N. Fujii, N. Mimura, Y. Miwa, T. Taga, Y. Chounan, and Y. Yamamoto. J. Org. Chem. **60**, 2044 (1995); (*f*) C.H. Behrens, S.Y. Ko, K.B. Sharpless, and F.J. Walker. J. Org. Chem. **50**, 5687 (1985); (*g*) S.Y. Ko, H. Masamune, and K.B. Sharpless. J. Org. Chem. **52**, 667 (1987).
3. M. Vijender, P. Kishore, P. Narender, and B. Satyanarayana. J. Mol. Catal. A Chem. **266**, 290 (2007).
4. (*a*) Z.Q. Liu, R. Li, D.S. Yang, and L.M. Wu. Tetrahedron Lett. **45**, 1565 (2004); (*b*) W.T. Wu, Q. Liu, Y.L. Shen, R. Li, and L.M. Wu. Tetrahedron Lett. **48**, 1653 (2007); (*c*) Y. Fan, X.J. Shang, Z.Q. Liu, and L.M. Wu. Synth. Commun. **36**, 3149 (2006).
5. (*a*) V. Nair, S.B. Panicker, L.G. Nair, T.G. George, and A. Augustine. Synlett, 156 (2003); (*b*) T. Sommermann. Synlett, 834 (1999); (*c*) V. Nair, L. Balagopal, R. Rajan, and J. Mathew. Acc. Chem. Res. **37**, 21 (2004).
6. (*a*) Y.R. Lee, B.S. Kim, and D.H. Kim. Tetrahedron, **56**, 8845 (2000); (*b*) V. Nair, V. Sheeba, S.B. Panicker, T.G. George, R. Rajan, L. Balagopal, M. Vairamani, and S. Prabhakar. Tetrahedron, **56**, 2461 (2000); (*c*) B.B. Snider and T. Kwon. J. Org. Chem. **55**, 4786 (1990).
7. (*a*) C.C. Smith, J.M. Jacyno, K.K. Zeiter, P.D. Parkanzky, C.E. Paxson, P. Pekelnicky, J.S. Harwood, A.D. Hunter, V.G. Lucarelli, M.W. Lufaso, and H.G. Cutler. Tetrahedron Lett. **39**, 6617 (1998); (*b*) Z. Duan, X. Xuan, T. Li, C. Yang, and Y. Wu. Tetrahedron Lett. **47**, 5433 (2006).
8. (*a*) V. Nair and L.G. Nair. Tetrahedron Lett. **39**, 4585 (1998); (*b*) V. Nair, T.G. George, L.G. Nair, and S.B. Panicker. Tetrahedron Lett. **40**, 1195 (1999); (*c*) V. Nair, L.G. Nair, T.G. George, and A. Augustine. Tetrahedron **56**, 7607 (2000).
9. C. Bosman, A.D. Annibale, S. Resta, and C. Trogolo. Tetrahedron Lett. **35**, 6525 (1994).
10. (*a*) V. Nair, S.B. Panicker, A. Augustine, T.G. George, S. Thomas, and M. Vairamani. Tetrahedron, **57**, 7417 (2001); (*b*) W.R. Roush, S. Narayan, C.E. Bennett, and K. Briner. Org. Lett. **1**, 895 (1999).
11. K. Itoh, S. Takahashi, T. Ueki, T. Sugiyama, T.T. Takahashi, and C.A. Horiuchi. Tetrahedron Lett. **43**, 7035 (2002).
12. (*a*) R.D. Fabio, T. Russi, and R.J. Thomas. Tetrahedron Lett. **38**, 3587 (1997); (*b*) N. Iranpoor and P. Salehi. Tetrahedron, **51**, 909 (1995); (*c*) V. Nair, L. Balagopal, R. Rajan, A. Deepthi, K. Mohanan, and N.P. Rath. Tetrahedron Lett. **45**, 2413 (2004); (*d*) N. Iranpoor, M.I. Baltork, and F.S. Zardaloo. Tetrahedron, **47**, 9861 (1991); (*e*) N. Iranpoor, F. Kazemi, and P. Salehi. Synth. Commun. 1247 (1997); (*f*) N. Iranpoor and F. Kazemi. Synth. Commun. 561 (1999); (*g*) N. Iranpoor and F. Kazemi. Synthesis, 821 (1996).
13. J.L. Jiao, L.X. Nguyen, D.R. Patterson, and R.A. Flowers II. Org. Lett. **9**, 1323 (2007).
14. (*a*) J.M. Mélot, F. Texier-Boullet, and A. Foucaud. Tetrahedron, **44**, 2215 (1988); (*b*) J.A. Ciller, C. Seoane, and J.L. Soto. J. Hetreocycl. Chem. **22**, 1663 (1985); (*c*) D.L. Boger, R.A. Lerner, and B.F. Cravatt. J. Org. Chem. **59**, 5078 (1994).
15. F.G. Weber, C. Kaatz, R. Radeglia, and H. Koeppel. Monatsh. Chem. **123**, 81 (1992).
16. J.M. Concellón and M. Huerta. Tetrahedron, **58**, 7775 (2002).
17. (*a*) E. Baciocci, C. Rol, G. V. Sebastiani, and B. Serena. J. Chem. Res. (S), 24 (1984); (*b*) C. M. Langkammerer, E.L. Jenner, D.D. Coffman, and B.W. Howk. J. Am. Chem. Soc. **82**, 1395 (1960).
18. V. Nair, S.B. Panicker, and S. Mathai. Res. Chem. Intermed. **29**, 227 (2003).
19. (*a*) C.S. Marques, N. Moura, and A.J. Burke, Tetrahedron Lett. **47**, 6049 (2006); (*b*) L.W. Xu, L. Li, C.G. Xia, and P.Q. Zhao. Tetrahedron Lett. **45**, 2435 (2004); (*c*) B. Das, M. Krishnaiah, and K. Venkateswarlu. Chem. Lett. **36**, 82 (2007).

© 2008 NRC Canada

Evaluating and understanding the hydrothermal stability of alumina aerogel doped with yttrium oxide and used as a catalyst support for the thermo-catalytic cracking (TCC) process

Nabil Al-Yassir and Raymond Le Van Mao

Abstract: The current work presents results concerning the hydrothermal stability of yttria-doped alumina aerogel, which was prepared by the sol–gel method using a supercritical drying technique. The influence of atmospheric steam at 750 and 1000 °C on the rate of sintering of yttria-doped alumina aerogel with various yttria contents was investigated. BET N_2 adsorption measurements, X-ray diffraction, thermogravimetric analysis, FTIR of adsorbed pyridine, and ^{1}H and ^{27}Al MAS NMR were used for characterization of solid samples. It was found that the hydrothermal stability of yttria-doped alumina aerogel was greatly improved compared with alumina aerogel and conventional alumina. This was evident from the decrease in the loss of surface area and pore volume, and the minimization of structural transformations. These significant improvements were attributed to the combined effect of sol–gel method and the presence of yttrium ions. Yttria-doped alumina aerogel with various yttria loadings, when compared with undoped alumina aerogel, exhibited lower concentrations of surface –OH groups, higher amounts of bridged –OH groups, and lower degrees of crystallinity with smaller particle sizes. It was also observed that the thermal and hydrothermal stabilities of both yttria-impregnated alumina aerogel and conventional alumina were improved but to a much lower extent. These improvements were attributed to the presence of yttria, and subsequently the formation of surface yttrium aluminate. This structure was found to be more thermally stable than bare alumina owing to the presence of less surface defects and –OH groups. Therefore, it was concluded that to observe the most effective role of yttria, it is quite essential to incorporate it into the alumina structure via the sol–gel technique.

Key words: thermo-catalytic cracking (TCC), yttria-doped alumina aerogel, yttria-impregnated alumina, hydrothermal stability, surface –OH groups, Lewis sites.

Résumé : Dans ce travail, on présente les résultats qui ont été obtenus relativement à la stabilité hydrothermique d'un aérogel d'alumine dopé à l'yttria qui a été préparé par la méthode sol-gel combinée à la technique de séchage supercritique. On a étudié l'influence d'une atmosphère de vapeur à 750 et 1000 °C sur la vitesse d'effritement de l'aérogel d'alumine dopé avec des quantités variable d'yttria. On a fait appel à des mesures d'adsorption de l'azote, de diffraction des rayons X, d'analyse thermogravimétrique, d'infrarouge à transformée de Fourier de la pyridine adsorbée et des spectres RMN du ^{1}H et du ^{27}Al à l'angle magique de spin pour faire la caractérisation des échantillons solides. On a trouvé que la stabilité hydrothermique de l'aérogel d'alumine dopé à l'yttria est de beaucoup améliorée par rapport à un aérogel d'alumine ou à de l'alumine conventionnelle. Ce fait était évident sur la base de la diminution de la perte de l'aire de superficie et du volume des pores ainsi que sur la minimisation des transformations structurales. Ces améliorations significatives sont attribuées à l'effet combiné de la méthode sol-gel et de la présence d'ions yttrium. Lorsqu'on a comparé l'aérogel d'alumine non dopé avec l'aérogel d'alumine dopé avec des quantités variable d'yttria, on a constaté que ce dernier comporte des concentrations plus faibles de groupes hydroxyles en surface, des quantités plus élevées de groupements hydroxyles pontés et des degrés plus faibles de cristallinité avec des grosseurs de particules plus faibles. On a aussi observé que les stabilités thermiques et hydrothermiques de l'aérogel d'alumine imprégné d'yttrie et l'alumine conventionnelle sont aussi améliorées, mais à un degré beaucoup moindre. Ces améliorations sont attribuées à la présence d'yttrie et, par la suite, à la formation en surface d'aluminate d'yttrium. On a trouvé que cette structure est thermiquement plus stable que l'alumine nue en raison de la présence, en surface, de moins de défauts et de moins de groupes hydroxyles. On en conclut donc que si on veut observer le rôle le plus efficace de l'yttrie, il est essentiel de l'incorporer dans la structure de l'alumine par le biais de la technique sol-gel.

Received 30 August 2007. Accepted 20 October 2007. Published on the NRC Research Press Web site at canjchem.nrc.ca on 17 January 2008.

N. Al-Yassir and R. Le Van Mao.[1] Industrial Catalysis Research Laboratory and Laboratories for Inorganic Materials, Department of Chemistry and Biochemistry, Concordia University, 7141 Sherbrooke West, Montreal, QC H4B 1R6, Canada.

[1]Corresponding author (e-mail: lvmao@alcor.concordia.ca).

 doi:10.1139/V07-138 © 2007 NRC Canada

Mots-clés : craquage thermocatalytique (CTC), aérogel d'alumine dopé à l'yttrie, alumine imprégnée d'yttrie, stabilité hydrothermique, groupes hydroxyles en surface et sites de Lewis.

[Traduit par la Rédaction]

Introduction

Recently, there has been much interest in the production of light olefins (i.e., ethylene and propylene) from petroleum feedstocks. The market demand for ethylene and propylene in year 2000 was 89 and 51 million tons, respectively, and will increase (projection) by year 2010 to about 140 and 90 million tons, respectively (1). The increase is driven largely by the escalating demand for the production of polyethylene and polypropylene, which was estimated to be approximately 110 million tons of polyolefins in 2005 (70 million tons of polyethylene and 40 million tons of polypropylene) (2, 3). Several light olefin technologies have been developed and are currently used for the production of ethylene and propylene, including steam cracking (SC), conventional fluid catalytic cracking (FCC), ZSM-5 modified FCC, and deep catalytic cracking (DCC) (4–6). However, these current technologies cannot respond sufficiently to the rapidly growing demand for propylene, which is growing at much faster rate than ethylene, since propylene is only produced as a co-product of ethylene production (2, 3). In addition, the high-energy consumption and the increasingly stringent environmental regulations that require low green-house gas emissions are also putting a pressure on the main light olefin technology (SC) (3).

Thermo-catalytic cracking (TCC) of petroleum feedstocks for the production of light olefins has been developed in an attempt to overcome some of these challenges (7–15). This emerging technology is considered more advantageous than others, since it produces higher combined yields of ethylene and propylene, it requires lower energy consumption, and is a more environment-friendly process. In one of its several versions, the TCC process employs supported metal oxides catalysts (i.e., bi-oxide MoO_3/CeO_2), which operates at mild temperature (725–750 °C) and in the presence of steam. Therefore, it is important to evaluate the thermal and hydrothermal stability of the catalyst support, as well as its ability to promote a homogenous dispersion and distribution of active species and promoters at high temperature.

Conventional γ-alumina was found to have poor thermal and hydrothermal stability, and also to show a weak ability to homogenously disperse active species at high temperature (16–23). Thus, to overcome these setbacks, alumina doped with Y_2O_3 was prepared via solution sol–gel using supercritical drying technique (14, 15). The resulting yttria-doped alumina aerogel exhibited outstanding physico-chemical properties, when compared with conventional γ-alumina. It displayed high surface area and enhanced thermal stability (14). Furthermore, it was characterized by superior ability to homogenously disperse the active species and the promoters at quite high calcination temperature (15). The overall improvements were attributed to the sol–gel method and more significantly to the incorporation of Y_2O_3 into alumina aerogel structure (14, 15). In addition to these enhanced properties, the hydrothermal stability remains a significant property to examine. Steam is co-fed in the TCC process along with hydrocarbons to lower the partial pressure of hydrocarbons (i.e., minimize the condensation-side reaction rate), and partially removed carbonaceous (coke) deposits ($C + H_2O \rightarrow CO + H_2$) (4). However, steam could have a negative impact on the catalyst, particularly the alumina-based support. This is attributed to the fact that surface area loss and phase transition of alumina are greatly facilitated by the presence of steam (19–25). Johnson (19) has investigated the effect of steam on the rate of sintering of alumina and concluded, "The main role of steam is to maintain the surface concentration of hydroxyl groups leading to an increase in the rate of sintering." Therefore, in this present work, we attempt to analyze and evaluate in details the hydrothermal stability of yttria-doped alumina aerogel under the TCC and harsher conditions. In addition to that objective, we would like to examine another interesting feature. It was noted (14, 26, 27) that Y_2O_3 played a major role in improving the thermal stability of alumina aerogel. This was observed when yttria precursor was incorporated into the alumina aerogel structure via the sol–gel preparation (one-pot synthesis) (14, 26, 27). We would like to investigate whether yttria will exert a similar effect on the thermal and hydrothermal stability if it is added onto the alumina via the impregnation method. It is worth mentioning that the outcome of this work will be of great significance to other industrial applications that require the presence of steam at high temperature, such as methane steam reforming for hydrogen production (28).

To the best of our knowledge, no work has been reported yet on hydrothermal stability of yttria-doped alumina aerogel, and only scarce reports (29) are available on the role of yttria on the thermal stability of alumina, via impregnation. Therefore, to fulfill our objectives, conventional alumina (conv.alumina), undoped alumina aerogel, and a series of yttria-doped alumina aerogel and yttria-impregnated alumina (conventional alumina and alumina aerogel) with variable amounts of Y_2O_3 were prepared. They were thoroughly characterized by diverse techniques such as Brunauer–Emmett–Teller (BET) surface area, X-ray diffraction (XRD), thermo gravimetric analysis (TGA), Fourier transform infrared spectroscopy (FTIR) of adsorbed pyridine, and ^1H and ^{27}Al solid-state nuclear magnetic resonance (^1H and ^{27}Al MAS NMR).

Experimental

Materials

Yttria-doped alumina aerogel

The yttria-doped alumina aerogel was prepared by previously reported synthetic technique (14, 26, 27), using aluminum tri-*sec*-butoxide (Strem chemicals, 98%) and yttrium (III) nitrate hexahydrate (Strem chemicals, 99.9%) as precursors. Yttrium concentration was varied to have 5, 10, and 20 wt%. Y_2O_3/Al_2O_3 with different Y_2O_3 contents is noted as

© 2007 NRC Canada

xY_2O_3/Al_2O_3, where x is the Y_2O_3 content in wt%. The preparation procedures for undoped alumina aerogel noted in this text as alumina aerogel were similar to that of yttria-doped alumina aerogel, except no dopant was used.

Yttria-impregnated alumina (i.e., conventional alumina and undoped alumina aerogel)

The required amount of yttrium (III) nitrate hexahydrate was dissolved in distilled water and then impregnated onto alumina. After impregnation, samples were first left at 60 °C for 10 h for slow evaporation of water, dried overnight at 120 °C, and finally calcined in air at either 750, 1000, 1100, or 1200 °C for 6 h. Two different aluminas were used: conventional alumina and alumina aerogel. The conventional alumina (γ-form, fine powder) was available commercially from Strem Chemicals and noted as conv.alumina. Y_2O_3/alumina with different Y_2O_3 loadings are noted as xY_2O_3/alumina, where x is the Y_2O_3 content in wt%. Prior to impregnation, the supports were calcined at 750 °C for 6 h.

Extrudates

The extrudates of all prepared supports were obtained by extrusion with bentonite clay (Aldrich), (Spectrum products, 20 wt%). They were dried overnight at 120 °C and then activated in air at 750 or 1000 °C for 3 h, depending on the test conditions. These extrudates were prepared and used solely in the hydrothermal stability tests.

Characterization

The specific surface areas and pore volume of samples were determined by the BET method using nitrogen physisorption at 77 K. The measurements were carried out using Micromeretics ASAP 2000 apparatus. Samples were outgassed in a vacuum for 3 h at 220 °C before N_2 physisorption. Specific surface areas were calculated by a multipoint point according to the Brunauer–Emmett–Teller (BET) method. The S_{BET} surface area results were reproducible within ±3 m^2/g. Pore volume results were obtained according to the Barret–Joyner–Halenda (BJH) method from the adsorption data, and were reproducible within ±0.003 cm^3/g.

X-ray powder diffraction (XRD) was carried out on a Philips diffractometer equipped with a PW 1050/25 focusing goniometer, which has been automated with the VisX122D system from diffraction technologies. The Ni filtered Kα radiation of Cu was used ($\lambda_{K\alpha 1}$ = 1.54051 Å) and diffractometer was operated at 40 kV and 20 mA. The patterns were recorded in the step scanning mode from 5°–60° (2θ) at a detector angular speed of 0.3°/min with a step size of 0.05°. The XRD phases were identified with the help of JCPDS (Joint Committee on Powder Diffraction Standards) powder files (30).

Thermogravimetric and differential thermal analysis (TGA/DTA) was carried out using the Stanton Redcroft STA 1500 simultaneous thermal analyzer (PL Thermal Sciences). The samples were heated from ambient temperature to 750 °C under dry air flow (20 mL min^{-1}). The sample weights were ~10 mg, and the heating rate was 10 °C min^{-1}. The average uncertainty in the TGA results was determined to be ±0.9 wt% for the weight loss.

Fourier transform infrared spectra of adsorbed pyridine were recorded to elucidate the presence of Lewis acid sites. The transmission spectra were recorded in Nicolet FTIR spectrometer (Magna 500 model) in the region of 1400–1700 cm^{-1}, with resolution of 4 cm^{-1}. The samples in the form of a self-supporting thin wafer were obtained by compressing a uniform layer of powder (sample/KBr mixture ≈ 0.020 g). The thin wafer was then placed in a pyrex cell and outgassed under vacuum (10^{-2} mbar; 1 bar = 100 kPa) at 300 °C for 4 h. Then, pyridine adsorption was carried out at 100 °C for 2 h under vacuum. After the evacuation at 100 °C for 1 h, the spectra of adsorbed pyridine were recorded at ambient temperature. Pyridine (Aldrich) was stored on activated molecular sieves. The area under each Lewis IR band was calculated using the Omnic software after correcting the baseline.

^{27}Al magic-angle spinning nuclear magnetic resonance (MAS NMR) measurements were carried out in a Bruker NMR spectrometer model DSX-300 (magnetic field 7.04 T). ^{27}Al MAS NMR spectra were obtained at frequency of 78.23 MHz with a 20° pulse length of 2 μs and 1 s delay between pulses and a spectral range of 40–75 kHz. The samples were spun at 14 KHz in N_2 using 4 mm ZrO_2 rotors, and typically 540 FID were collected for each sample. The chemical shifts were measured relative to external Al $(OH_2)_6^{3+}$ standard with an accuracy of ±0.5 ppm.

^1H MAS NMR measurements were carried out in a Bruker NMR spectrometer model AV-600 (magnetic field 14.1 T). ^1H MAS NMR spectra were obtained at frequency of 600.14 MHz with a 90° pulse length of 1.7 μs and 5 s delay between pulses and a spectral range of 100 kHz. The samples were spun at 25 KHz in air using 2.5 mm ZrO_2 rotors, and typically 32 FIDs were collected for each sample. The chemical shifts were referenced TMS (0 ppm). Prior to analysis, samples were dehydrated by evacuation to a pressure below 5 μm Hg (1 mm Hg = 133.322 Pa) in a Micromeritics ASAP-2000 instrument (BET apparatus) at 300 °C overnight. The samples were then transferred in helium atmosphere to a moisture-free N_2 atmosphere glovebox and packed in sealed tubes. Then, they were transferred from sealed tubes and packed into ZrO_2 rotors.

Hydrothermal stability tests

Hydrothermal stability experiments were performed using a Lindbergh one-zone tubular furnace. About 1 g of sample extrudate was placed in a quartz tube (55 cm in length and 1.5 cm in diameter). They were heated at 750 and 1000 °C, respectively, for n h (n = 1–24 h) in the presence of steam (H_2O flow = 1.1 mL/h) at atmospheric pressure.

Results and discussion

Short review of pertaining information to the thermal and hydrothermal stability of alumina

A great number of studies have shown that the thermal and hydrothermal stability of transition alumina, currently used as catalyst supports for many reactions, is influenced by several factors (16–24). These factors include the presence of intrinsic cationic and anionic vacancies, and more significantly the surface –OH groups. Burtin et al. (17) stated that the mechanism by which alumina loses its surface

© 2007 NRC Canada

Table 1. Changes in the BET specific surface area (S_{BET}) of different catalyst supports (in extrudate form) as a function of exposure time to steam, at T = 750 °C and H_2O flow rate = 1.1 mL/h.

	BET specific surface area (m^2/g)								
Duration of exposure to steam (h)	0	1	2	3	4	5	7	10	24
Bentonite	14.0	13.0	n.a.	13.0	n.a.	12.0	n.a.	10.0	9.0
		(0.93)		(0.93)		(0.86)		(0.71)	(0.64)
Conv.alumina	107	83.0	82.0	79.0	78.0	75.0	74.0	72.0	70.0
		(0.78)[a]	(0.77)	(0.74)	(0.73)	(0.70)	(0.69)	(0.67)	(0.65)
Alumina aerogel	203	167	165	165	160	157	154	154	149
		(0.82)	(0.82)	(0.82)	(0.79)	(0.77)	(0.76)	(0.76)	(0.73)
5 wt% Y_2O_3/Al_2O_3	198	188	187	184	182	179	177	172	168
		(0.95)	(0.95)	(0.93)	(0.92)	(0.91)	(0.89)	(0.87)	(0.85)
10 wt% Y_2O_3/Al_2O_3	188	185	182	176	176	174	170	170	169
		(1.02)	(0.97)	(0.94)	(0.94)	(0.93)	(0.91)	(0.91)	(0.90)
20 wt% Y_2O_3/Al_2O_3	143	135	127	126	126	126	124	125	123
		(0.94)	(0.89)	(0.88)	(0.88)	(0.88)	(0.87)	(0.87)	(0.86)

Note: No significant area loss was observed as a result of calcination in dry air.
[a]Number in parenthesis is the ratio of S_{BET} of sample exposed to wet air (in the presence of steam) to S_{BET} in dry air, at the same temperature.

area at high temperature is a direct result of an interaction between the intrinsic cationic vacancies and anionic vacancies. The latter is also formed by the dehydroxylation of surface –OH groups. The outcome of that reaction is the annihilation of these vacancies and subsequently the destruction of the spinel lattice and structural rearrangement of constituent ions. Johnson (19) suggested that the surface hydroxyl groups play a major role in alumina stability. In his proposed model, he stated that particle growth (sintering) occurs by successive elimination of water from two –OH groups residing on adjacent particles, close to an area of contact (19–22). These groups interact through lateral hydrogen bonding (19–22, 31). Subsequently, this will generate an Al–O–Al bond, which will bring more –OH groups into adjacency (condensation). A diffusive process is expected to follow condensations to form "necks" between particles. Finally, small particles will grow to larges ones accompanied by significant surface area loss (19). Whatever the case may be, it is quite evident that –OH groups play the foremost role in alumina sintering, and subsequently in the thermal and hydrothermal stability.

The presence of steam is expected to significantly participate in increasing the rate of sintering (19–25). This can be attributed to the main function of steam, which is to maintain the concentration of surface –OH groups that are mainly responsible for the nucleation and particle growth of transition alumina as described earlier. The ability of steam to rehydroxylate (rehydrate) the surface of alumina is enhanced by the presence of Lewis acid sites (coordinative unsaturated (cus) cations), which are formed as a result of the dehydroxylation (32–34). In the dehydroxylation process, oxygen ion is lost, and hence, oxygen vacancy should be created to maintain the electrical neutrality of the structure ($2{<}OH^-{>}^{+}_{2-} \rightarrow H_2O + {<}O^{2-}{>}^{0}_{2-} + {<}\ {>}^{2+}_{2-}$) (17). This will give rise to the coordinative unsaturated sites (Lewis sites). These sites will allow the interaction with water vapor via a two-step mechanism, which can be summarized as follow ($\square M^{n+1}O^{2-} + H_2O \rightarrow HO^-M^{n+-}OH$) ($\square$ indicates the vacancy or a coordinative unsaturation) (33–35). It involves a non-dissociative adsorption of water vapor on a Lewis acid sites that will essentially involve a transfer of electron density to a Lewis acid site (cus Al), followed by a dissociative chemisorption of water (33, 34). Therefore, to improve the hydrothermal stability, it is essential to have, to some extent, a low concentration of Lewis sites, which are mainly responsible for the rehydroxylation process. This can be achieved by reducing the degree of dehydroxylation process (removal of –OH groups) from the surface, which can be accomplished by reducing the number of hydroxyl groups that are responsible for the sintering process. It is worth mentioning that such reduction should not considerably diminish the acid–base properties or more significantly the ion-exchange properties of alumina. Moreover, the degree of dehydroxylation can be minimized by having higher number of bridged –OH groups (i.e., held by more than one bond) compared with the terminal ones (i.e., held by one bond) (31). The latter has been shown to be quite susceptible to sintering process (31). Furthermore, the contact between alumina particles should be minimized, since dehydroxylation is enhanced by close proximity of condensing particles (36). In addition, the utilization of strong and stable binder (i.e., bentonite) can also play a role in enhancing the hydrothermal stability. It is also vital to mention that the factors that influence the thermal stability should be also taken into consideration to improve the hydrothermal stability. This is due to the fact that hydrothermal stability is measured at high temperature. These factors include the presence of surface defects, degree of crystallinity (i.e., amorphous, crystalline, and so forth), and the crystallite sizes of crystalline materials (14). The presence of high number of surface defects and larger crystallites have shown to greatly enhance the sintering process (14).

Hydrothermal stability of yttria-doped alumina aerogel

BET surface area, pore volume, and XRD patterns

The changes in BET specific surface area and pore volume of different catalyst supports, which were subjected to

© 2007 NRC Canada

Fig. 1. Loss of total pore volume of various samples as a function of different exposure times to steam at (A) 750 °C and (B) 1000 °C.

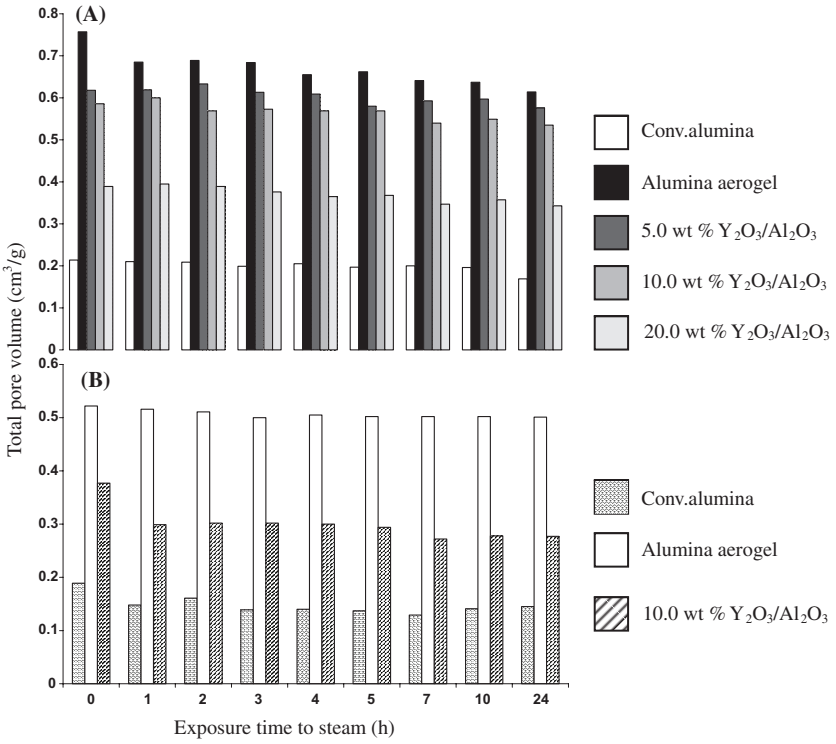

steam at 750 °C with different exposure time are shown in Table 1 and Fig. 1A, respectively. It can be seen that the rate of hydrothermal sintering of conv.alumina was greatly facilitated in the presence of steam at 750 °C, which has resulted in ~22% and 35% surface area loss when exposed for 1 h and 24 h, respectively (Table 1). Undoped alumina aerogel showed an improvement in the hydrothermal stability. The area loss of undoped alumina aerogel was ~18% and 26%, when exposed to steam for 1 h and 24 h, respectively (Table 1). On the contrary, the influence of steam becomes significantly less pronounced in yttria-doped alumina aerogel, and in fact it decreases as the amount of yttria increases from 5 to 10 wt%. For example, the area loss for 5 wt% yttria-doped alumina aerogel was ~5% and 15%, when exposed to steam for 1 h and 24 h, respectively (Table 1). Alumina aerogel doped with 10 wt% yttria showed more outstanding improvements in the hydrothermal stability. This was supported by the small loss in the surface area when compared with the other investigated supports (i.e., only ~1.6% and 10% area loss when subjected to steam for 1 h and 24 h, respectively (Table 1)). Although, alumina aerogel doped with 20 wt% yttria displayed a slightly higher surface area loss than 10 wt% yttria-doped alumina aerogel, it is still more hydrothermally stable than conv.alumina and alumina aerogel (Table 1). In addition, it was found that Bentonite (extrudate) is hydrothermally stable, as suggested by the low reduction of S_{BET} as function of exposure time to atmospheric steam (Table 1). It is worth mentioning that the changes in the total pore volume also followed the same pattern as the surface area loss (Fig. 1A). Furthermore, the XRD patterns of various investigated supports (extrudates) subjected to steam at 750 °C show that the diffraction peaks appeared to be quite the same when compared with the calcined extrudates (dry air only). The comparison between the XRD patterns of 10 wt% yttria-doped alumina aerogel extrudates that was subjected to dry air with those of the same treated with wet air leads to the same conclusion of unchanged structure. These results clearly suggest that the observed loss of surface area was due only to surface and textural transformations (i.e., condensation between hydroxyls on adjacent particles) and did not involve any structural transformation (i.e., formation of new phases such as δ, θ, or α).

It is worthwhile to note that the same pattern of improvements in the hydrothermal stability of yttria-doped alumina aerogel compared with alumina aerogel and conv.alumina was observed at 1000 °C (Table 2 and Fig. 1B). For example, the area loss of conv.alumina was ~28% and 37%, when exposed to steam for 1 h and 24 h, respectively (Table 2). Undoped alumina aerogel showed a significant improvement, as evidenced by the lower area loss, which was 22% and 32%, when exposed to steam for 1 h and 24 h, respectively (Table 2). As expected, alumina aerogel doped with 10 wt% yttria displayed much better hydrothermal stability compared with the other supports. The area loss, which was significantly lower than those observed with other studied supports, was ~9% and 14%, when exposed to steam for 1 h and 24 h, respectively (Table 2). Careful assessment of Fig. 1B, which displays the total pore volume loss of different supports as function of exposure time to steam at 1000 °C, displayed similar conclusion as surface area loss. It was also noted from the XRD patterns of different supports exposed to steam at 1000 °C (Figs. 2A–2C) that steam has provoked structural rearrangements to very small extent. On the other hand, it was quite clear that the structural rear-

© 2007 NRC Canada

Table 2. Changes in the BET specific surface area (S_{BET}) of different catalyst supports (in extrudate form) as a function of exposure time to steam, at T = 1000 °C, and H_2O flow rate = 1.1 mL/h.

	BET specific surface area (m^2/g)								
Duration of exposure to steam (h)	0	1	2	3	4	5	7	10	24
Conv.alumina	52.0	37.0 (0.71)	37.0 (0.71)	37.0 (0.71)	36.0 (0.70)	34.0 (0.70)	34.0 (0.65)	34.0 (0.65)	32.0 (0.62)
Alumina aerogel	111	86.0 (0.78)	85.0 (0.77)	85.0 (0.77)	85.0 (0.77)	84.0 (0.76)	78.0 (0.70)	76.0 (0.68)	75.0 (0.68)
10 wt% Y_2O_3/Al_2O_3	116	105 (0.91)	105 (0.91)	104 (0.90)	103 (0.89)	103 (0.89)	100 (0.86)	101 (0.87)	100 (0.86)

Note: For symbols, refer to Table 1.

Fig. 2. (*a*) XRD patterns of conv.alumina extrudates after exposure to steam at high temperature. A and B are sample powder (15) and extrudate, respectively, and C–F are sample extrudates exposed to steam for 1, 5, 10, and 24 h, respectively. (*b*) Patterns of the undoped alumina aerogel extrudate. (*c*) Patterns the 10 wt% yttria-doped alumina aerogel extrudate. (*): γ-Al_2O_3, (+): θ-Al_2O_3, (-): α-Al_2O_3, and (#): Bentonite.

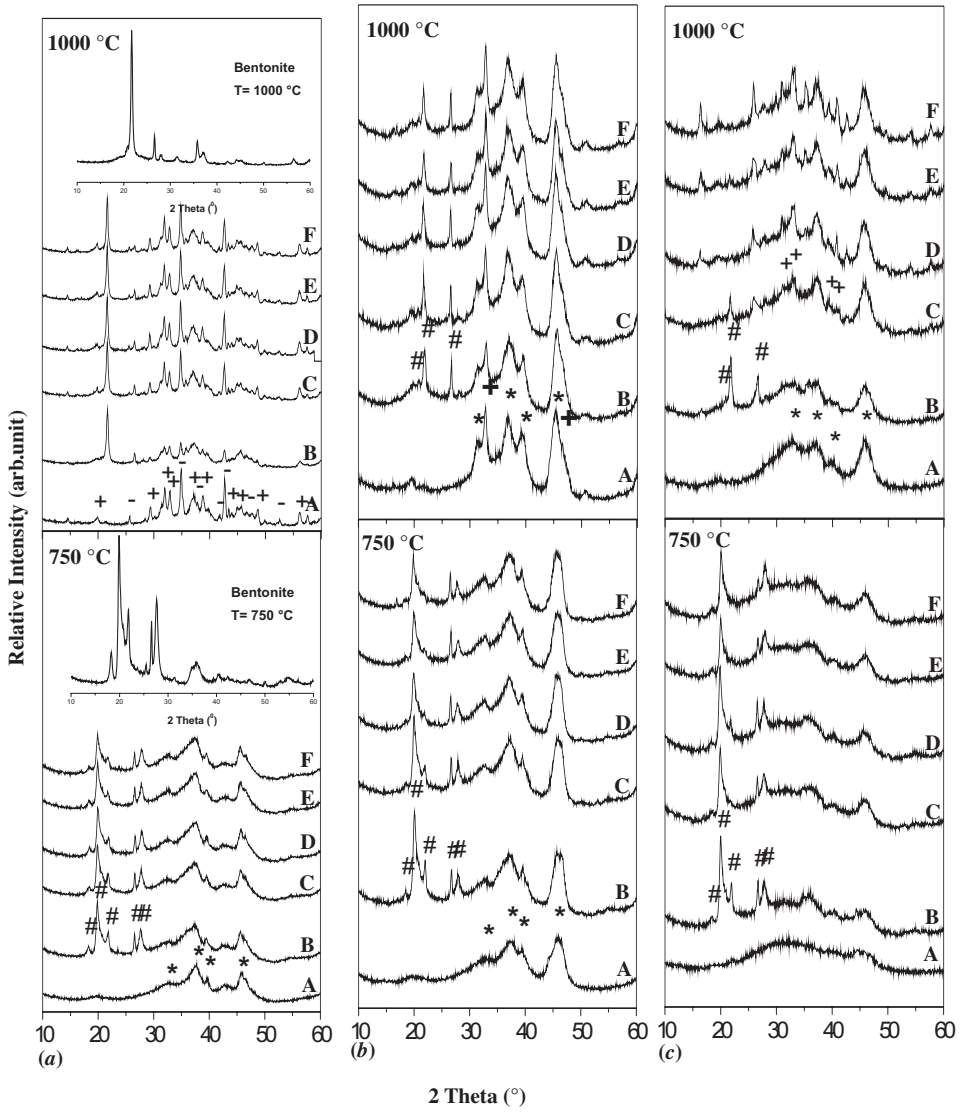

rangements caused by steam were less prominent in yttria-doped alumina aerogel samples compared with other studied supports. For instance, the XRD patterns of conv.alumina extrudates that were subjected to steam at 1000 °C showed that the intensity of the reflections that are assigned to α–phase increases when subjected to steam. In addition, the XRD patterns of undoped alumina aerogel extrudates displayed that the intensity of the reflections that are assigned

© 2007 NRC Canada

Table 3. Approximate amount of –OH groups lost and distribution of (subsequently formed) Lewis sites upon calcinations in dry air.

	Amount of –OH lost		Coordinative unsaturated Lewis acid sites (Al_{cus}) Estimated area of Lewis sites observed at 750 °C (arbitrary unit)[a]			
Sample	N (OH) (10^{-2} mol/g)[b]	N (OH) (10^{-2} mol/g)[c]	[py–L] (1440–1450 cm^{-1})	$_{VI}Al_{cus}$–py $[py–L]_o$ (1595 cm^{-1})	$_{IV}Al_{cus}$–O–□–O–$_{VI}Al_{cus}$–py $[py–L]_{o,t}$ (1610–1620 cm^{-1}): □: Vacancy	$_{IV}Al_{cus}$–py $[py–L]_t$ (1625 cm^{-1})
Conv.alumina	0.39	0.28	3.28	0.84	0.25	0.0
Alumina aerogel	1.33	0.98	7.31	1.28	0.47	0.0
5 wt% Y_2O_3/Al_2O_3	1.11	0.85	5.52	1.09	0.32	0.0
10 wt% Y_2O_3/Al_2O_3	0.92	0.44	4.87	1.17	0.12	0.0
20 wt% Y_2O_3/Al_2O_3	0.78	0.14	3.45	1.13	0.0	0.0
10 wt% Y_2O_3/conv.alumina	0.22	0.05	0.55	0.0	0.0	0.0
10 wt% Y_2O_3/Al_2O_3 aerogel	0.95	0.42	0.78	0.0	0.0	0.0

[a]The area under the Lewis IR band was calculated using the Omnic software after correcting the baseline.
[b]Amount (or Number (*N*)) of –OH lost in the region 25–250 °C (physisorbed water).
[c]Amount of –OH lost in the region between 300–750 °C.

to θ-phase increases when subjected to steam. Although, the reflections that are assigned to the θ-phase start to appear in the 10 wt% yttria-doped alumina aerogel extrudates, they were enormously weak and broad when compared with those observed with undoped alumina aerogel extrudates. The broadness of these reflections clearly indicates that the θ–phase is not well-crystalline.

Therefore, BET specific surface area, total pore volume, and XRD patterns results have shown that the hydrothermal stability of yttria-doped alumina aerogel was by far greatly improved compared with alumina aerogel and conv.alumina. The results of all investigated supports, which were exposed to steam at either 750 or 1000 °C, have unambiguously revealed that the loss of surface area and pore volume and structural transformation were greatly minimized according to the following order: yttria-doped alumina aerogel, followed by undoped alumina aerogel, followed by conv.alumina.

Sintering effects of high temperature and steam

It becomes evident that both the sol–gel preparation method and the incorporation of yttrium ions into the alumina aerogel structure play an important role in these improvements. Subsequently, these factors should have a direct effect on the number of Lewis acid sites (the main interaction sites of steam with the alumina surface at high temperature), which are influenced by the surface –OH groups (i.e., concentration and structure). Thus, evaluating the dehydroxylation pattern of surface hydroxyl groups and the Lewis acid sites are of paramount importance to elucidate the exact mechanism of hydrothermal stability.

Thermal gravimetric and differential analysis (TGA/DTA) and FTIR of adsorbed pyridine techniques were employed in this investigation to examine the dehydroxylation pattern and the Lewis sites of different supports, respectively. ^1H MAS NMR measurements were used to investigate the structure of surface –OH groups. It is worth mentioning that the TGA/DTA analysis was performed on samples calcined at 400 °C to be able to observe the dehydroxylation pattern, whereas the FTIR of adsorbed pyridine was carried out on samples that were calcined at 750 °C, which is the same temperature used to evaluate the hydrothermal stability. The TGA results obtained with conv.alumina, alumina aerogel, and yttria-doped alumina aerogel with different yttria loadings are shown in Table 3 (The TGA/DTA graphs are not shown here). The first weight loss in the range 25–250 °C, which was accompanied by an endothermic peak is primarily due to the removal of physisorbed water held on the surface by hydrogen bonding. This weight loss could be also due to the removal of water held in the small pores (Table 3). The second weight loss in the range of 300–750 °C (very broad endothermic peak) corresponded to the loss of water due to dehydroxylation of the surface. Thus, the approximate amounts of surface OH removed upon dehydroxylation by heating between 300–750 °C (N (OH) in mol/g of alumina) were determined by counting 2 mol of OH groups for 1 mol of water evolved. It is quite apparent from data of Table 3 that the dehydroxylation pattern was significantly influenced by the structure of the support. Conv.alumina displayed OH loss of about 0.28×10^{-2} mol/g, while the number for undoped alumina aerogel was much higher (0.98×10^{-2} mol/g). However, the OH loss for yttria-doped alumina aerogel was continuously decreasing as the amount of yttria-doped into alumina aerogel increased (Table 3). Therefore, it can be inferred from these results that undoped alumina aerogel had higher concentration of –OH groups, whereas the concentration of these removed groups decreased as the content of yttria-doped into alumina aerogel increased. It is worth mentioning that the noted weight loss in the region of 300–750 °C was a continuous mass loss. Thus, it could be suggested that the loss was not related to a multiple discrete –OH sites. In addition, the observed weight loss should be entirely due to the dehydroxylation, since the DTA curves did not show any exothermic peaks that can suggest a decomposition process for instance. The FTIR of pyridine adsorption technique was also employed to reveal the presence of Lewis acid sites. Figure 3 shows the presence of several IR bands, which are characteristics of different types of Lewis acid sites (35, 37, 38). The observed bands, which are more sensitive to aluminum coordination

© 2007 NRC Canada

Fig. 3. FTIR spectra of adsorbed pyridine on (*a*) conv.alumina, (*b*) undoped alumina aerogel, (*c*) – (*e*) yttria-doped alumina aerogel with 5, 10, and 20 wt% yttria, respectively, and (*f*) – (*g*) 10 wt% yttria-impregnated alumina and alumina aerogel, respectively. (*: Lewis acid sites).

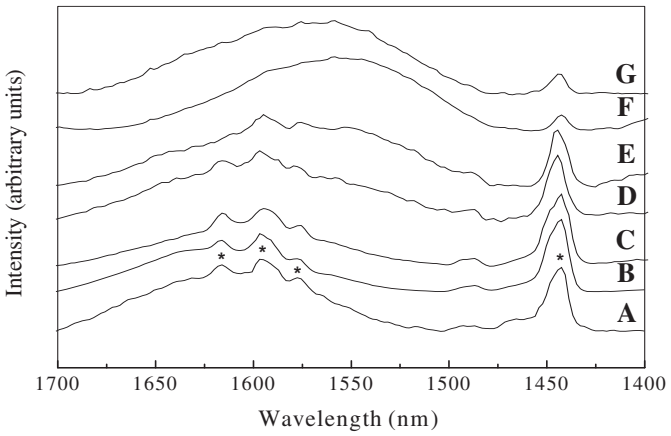

and structural vacancies were 1595, 1610–1620, and 1625 cm^{-1} (37). The band observed at 1595 cm^{-1} is ascribed to Lewis coordinated to $_{VI}Al_{cus}$ ions ($[py–L]_o$) (37). The band observed at 1610–1620 cm^{-1} can be ascribed to pyridine Lewis coordinated by an $_{VI}Al–Al_{IV}$ cation pair ($[py–L]_{o,t}$) (37), or to vacancies hared by two Al^{3+} ions according to Busca's model [35]. The band observed at 1625 cm^{-1} is ascribed to pyridine Lewis coordinated to $_{IV}Al_{cus}$ ions ($[py–L]_t$) (37). The band observed at 1440–1450 cm^{-1} is also ascribed to Lewis sites (37). Figure 3 shows the FTIR spectra of pyridine adsorbed on conv.alumina, alumina aerogel, and yttria-doped alumina aerogel with different yttria loadings (all being calcined at 750 °C), and the approximate concentrations of different Lewis acid sites are reported in Table 3 (the extinction coefficients of these adsorbed pyridine peaks being assumed to be equal). It is clear from Fig. 3 and Table 3 that alumina aerogel has a higher number of Lewis sites when compared with conv.alumina, as suggested by the higher Lewis site band area. Furthermore, the number of these sites decreases as the amount of yttria-doped into alumina aerogel increases, when compared with undoped alumina aerogel. It is worth mentioning that the observed Lewis sites are not entirely due to the dehydroxylation of the surface. Some of these sites are believed to exist in the structure as intrinsic (17).

Although the alumina aerogel, when compared with the conv.alumina, showed a higher dehydroxylation rate, and consequently a higher number of Lewis sites, it did not (surprisingly at first) experience a higher rate of hydrothermal sintering. The main reason behind the slightly lower rate of sintering of the undoped alumina aerogel can be ascribed to the sol–gel method, which strongly influenced the degree of crystallinity of the resulting material, and the structure and concentration of surface –OH groups. In fact, this aerogel was characterized by a low degree of crystallinity with small particle sizes compared with conv.alumina, as suggested by XRD and TEM measurements carried out in our previous communication concerning the thermal stability of alumina (14). Therefore, it can be inferred from these results that the degree of crystallinity and particle size by minimizing the extent of hydrothermal sintering played a larger role than expected. The observed significant improvements in the hydrothermal stability of alumina aerogel upon the incorporation of yttria are ascribed to the combined effect of sol–gel method and the presence of yttrium ions. The utilization of such procedures has resulted in minimizing the effect of several factors that are believed to favor the hydrothermal sintering. First, the number of –OH groups, which are well-known to play the foremost role in the sintering, has been reduced upon the incorporation of yttrium ions into the lattice gel. The reduction can probably be ascribed to an exchange interaction mechanism (cross-condensation) between yttrium and hydroxyl groups of alumina aerogel (19). Data of Table 3 showed that the dehydroxylation rate, and subsequently the number of Lewis sites were reduced as the amount of yttria loadings increased. Second, yttria-doped alumina aerogel is expected to contain higher number of bridged –OH groups with respect to terminal ones. This can be attributed to the sol–gel method, which allows in general the formation of different types of –OH groups. These groups are the bridging groups between metal (M) centres (M–OH–M) and the terminal ones (M–OH). The structure of these groups depends to a large extent on the degree of hydrolysis reaction, which is in turn dependable on the ratio of water to alkoxide. In our current synthesis, the ratio of water to aluminium tri-*sec*-butoxide (aluminium precursor) was 2.5, which is very close to the required stoichiometric ratio of 3 (14). This has allowed an increase in the extent of hydrolysis reaction (close to completion), and consequently the formation of highly branched polymeric alumina aerogel instead of linear structure that would have been observed at lower ratio (i.e., 1:1 water/alkoxide) (39). The highly branched structure would certainly be characterized with higher number of bridged hydroxyl groups over terminal ones. The presence of bridged –OH groups plays a major role in minimizing the extent of sintering. For instance, hydroxyl groups that are held by more than one bond (i.e., bridged, such as $Al_o–OH–Al_o$, $Al_t–OH–Al_o$, $3Al_o–OH$, and $Al_t–OH–Y$ where Al_o and Al_t are octahedral and tetrahedral alumina, respectively) are thus in fixed positions, and therefore, their relative orientation of their O–H bonds and free orbitals is very unfavorable for H-bonding between two adjacent hydroxyl groups (31). On the other hand, hydroxyl groups that are held by only one bond (i.e., terminal, such as $Al_o–OH$ and $Al_t–OH$) can provide more favorable orientation for H-bonding, since they will have more degree of freedom (31). It is worth mentioning that ^1H MAS NMR measurements were in complete agreement with these expectations. FTIR spectroscopy can be also used for that purpose; however, poor resolution of the hydroxyl stretching bands in the region of 3200–4000 cm^{-1} often makes it quite difficult to determine whether any changes have actually occurred (i.e., appearance of new bands or modification of existing bands) (40, 41). The ^1H MAS NMR spectra of conv.alumina, undoped alumina aerogel, and yttria-doped alumina aerogel with different yttria loadings, all calcined at 750 °C are presented in Fig. 4. The ^{1} H MAS NMR spectra of all samples clearly suggest a wide distribution of surface hydroxyl groups of variable basic and acidic strength of different structures (i.e., terminal and bridged –OH groups). ^1H MAS NMR spectrum of conv.alumina (Fig. 4A) exhibits

© 2007 NRC Canada

Fig. 4. ^{1}H MAS NMR of samples calcined at 750 °C for 3 h: (A) conv.alumina, (B) undoped alumina aerogel, (C) 10 Y_2O_3/Al_2O_3, and (D) 20 Y_2O_3/Al_2O_3.

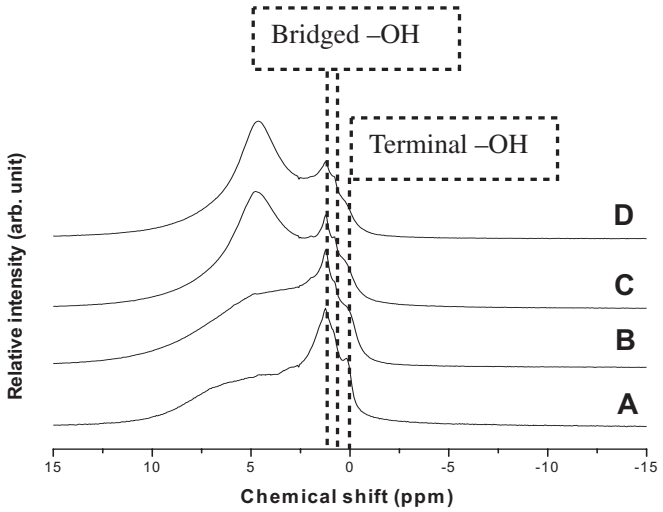

several resonance lines at approximately –0.3 (shoulder), 0.2, 0.7, 1.3, and 1.9 (shoulder) ppm, which shows that there are five different OH groups present on the surface of alumina. This is in complete agreement with the Knözinger and Ratnasamy model that was developed for alumina surface (31). The peak at –0.3 ppm was previously attributed to the terminal basic OH groups attached to one aluminum atom in octahedral coordination (Al_o–OH) (31, 40–43). The peak at 0.2 ppm can be also attributed to (Al_o–OH) but with an intermediate basic character (31). The remaining peaks at 0.7, 1.3, and 1.9 ppm, with the peak at 1.3 ppm being the most intense line of these lines, are attributed to an overlap of more than one type of bridged –OH groups (i.e., Al_o–OH–Al_o, Al_t–OH–Al_o and $3Al_o$–OH, where Al_o and Al_t are octahedral and tetrahedral coordination, respectively) (31, 40–43). The low-field shift of these peaks indicates their acidic character. In addition, a very broad signal was found at 4.7 ppm and assigned to small amount of physisorbed and chemisorbed water on the alumina surface that probably occurred during transferring samples into the NMR holder (ZrO_2 rotor) (43). Figure 4B also indicates that undoped alumina aerogel has the same types of hydroxyl groups as conv.alumina. However, Fig. 4B showed that the peak that is normally assigned to terminal –OH groups (~–0.3 and 0.2 ppm) was less-resolved and broader when compared with the one observed with conv.alumina. This could suggest that undoped alumina aerogel contained lower number of terminal –OH groups than conv.alumina. Yttria-doped alumina aerogel with 10–20 wt% Y_2O_3 loadings (Figs. 4C–4D), when compared with undoped alumina aerogel, showed that the intensity of the peak that is attributed to bridged –OH groups decreased with increasing the amount of yttria-doped into the alumina aerogel. No significant changes were observed with respect to the terminal –OH peak. The reduction in the intensity, which may reflect that the population of alumina surface bridged –OH groups were decreased, can be attributed to an interaction mechanism between alumina aerogel hydroxyl groups and yttrium ions, as stated previously. It is very important to mention that the appearance of the very broad ~4.7 ppm peak (due to physisorbed water) could have serious implications on our ^{1}H MAS NMR results. For instance, it will be tricky to distinguish between the real –OH groups and those formed as a result of H-bonding. Therefore, our observed results should be analyzed with extra caution. Detailed and thorough investigation of the chemistry of surface –OH groups on alumina aerogel and yttria-doped alumina aerogel with various contents using ^{1}H MAS NMR, which should take into consideration the complete elimination of the ~5.5 ppm peak, will be carried out, and the results will be the subject of future publication. Third, yttria-doped alumina aerogel with various yttria loadings displayed a lower degree of crystallinity with smaller particle sizes, when compared with undoped alumina aerogel and conv.alumina, as suggested by XRD and TEM measurements (14). Fourth, it is worthwhile mentioning that the improvements in the hydrothermal stability of alumina aerogel upon the incorporation of yttria into the alumina structure can be also attributed in part to the fact that yttria forms fairly stable $Y(OH)_3$ on contact with water. This can be ascribed to the highly alkaline character of yttrium oxide. Fifth, the utilization of stable and strong binder (Bentonite (Table 1)) also played a small role in the improvements of the hydrothermal stability. This effect appeared to exist on all investigated supports.

Thermal and hydrothermal stability of yttria-impregnated alumina

The thermal stability of both conv.alumina and alumina aerogel was improved upon the addition of yttria via impregnation method, as suggested by XRD and BET specific-surface-area results. Clearly, there was a delay or retardation of sintering and phase transformation of γ-phase into θ-phase and α-phase upon the addition of yttria via impregnation method. Furthermore, it was observed that the extent of stabilization was higher for alumina aerogel than conv.alumina.

The X-ray diffraction patterns of yttria-impregnated conventional alumina, which was calcined for 6 h at 750, 1000, 1100, and 1200 °C, are shown in Fig. 5. Their XRD patterns results are summarized in Table 4. Conv.alumina being metastable is transformed into several phases with increasing temperature. The observed phase transformation of conv.alumina in the present investigation was $\gamma \rightarrow \theta \rightarrow \alpha$, which was in complete agreement with previous investigations (14). Conventional alumina that was calcined at 750 °C showed the presence of γ-phase, and at 1000 °C, this phase was transformed to both θ- and α-phase. Calcination at 1200 °C resulted solely in the formation of the α-phase (corundum). Y_2O_3/conv.alumina with different yttria loadings (5–20 wt%), which were calcined at 750 °C, showed the presence of γ-phase in samples containing 5–10 wt% Y_2O_3. However, yttria-impregnated alumina with 20 wt% Y_2O_3 showed clearly the presence of segregated bulk Y_2O_3 crystallites. Further calcination of yttria-impregnated alumina with yttria loadings of 5–10 wt% to 1000 °C did not result in any changes when compared with the same samples calcined at 750 °C. In particular, the XRD pattern of sample containing 20 wt% yttria showed the presence of bulk Y_2O_3 crystallites, along with traces of $YAlO_3$. The latter was probably formed as a result of solid-state reaction between yttria and alumina. It is quite clear that yttria-impregnated conv.alumina with yt-

© 2007 NRC Canada

Table 4. X-ray diffraction pattern results of the conventional alumina, undoped alumina aeroge,l and yttria-doped alumina with various yttria loadings.

	Calcination temperature (°C)/6 h			
Sample	750 °C	1000 °C	1100 °C	1200 °C
Conventional alumina (15)	γ-Al_2O_3	θ-, and α-Al_2O_3	α-Al_2O_3 + traces of θ-phase	α-Al_2O_3
5 wt% Y_2O_3/conv.alumina	γ-Al_2O_3	γ-Al_2O_3	θ-Al_2O_3 + $YAlO_3$	α-Al_2O_3 + traces of $YAlO_3$
10 wt% Y_2O_3/conv.alumina	γ-Al_2O_3	γ-Al_2O_3	θ-Al_2O_3 + $YAlO_3$	α-Al_2O_3 + $YAlO_3$
20 wt% Y_2O_3/conv.alumina	Y_2O_3	Y_2O_3 + $YAlO_3$	Y_2O_3 + $YAlO_3$ + traces of θ-Al_2O_3	$YAlO_3$ + Y_2O_3 + traces of α-Al_2O_3
Alumina aerogel (15)	γ-Al_2O_3	γ-Al_2O_3 + traces of θ-phase	θ-Al_2O_3 + traces of α-phase	α-Al_2O_3
5 wt% Y_2O_3/alumina aerogel	γ-Al_2O_3	γ-Al_2O_3	θ-Al_2O_3 +$YAlO_3$	α-Al_2O_3 + traces of $YAlO_3$
10 wt% Y_2O_3/alumina aerogel	γ-Al_2O_3	γ-Al_2O_3	θ-Al_2O_3 +$YAlO_3$	$YAlO_3$ + traces of α-Al_2O_3
20 wt% Y_2O_3/alumina aerogel	Y_2O_3	Y_2O_3 + $YAlO_3$	$YAlO_3$	$YAlO_3$ + traces of α-Al_2O_3

Note: γ-Al_2O_3 (JCPDS No. 10-425), θ- Al_2O_3 (JCPDS No. 35-0121), α-Al_2O_3 (JCPDS No. 10-173), $YAlO_3$ (JCPDS No. 16-219 or 38–222), and Y_2O_3 (JCPDS No. 25-1200).

tria loadings up to 10 wt% did not show any diffraction peaks that could be attributed to either θ- or α-phase. This can be viewed as a clear indication of the improved thermal stability. However, further calcination of yttria-impregnated alumina (with yttria loadings up to 10 wt%) to 1100 °C showed, in addition to θ-phase, the presence of yttrium aluminate ($YAlO_3$) phase. The diffraction peaks of the latter were increased with increasing amount of yttria. It was also noted that yttria-impregnated alumina samples that were calcined at 1200 °C displayed clearly the presence of α-phase, along with $YAlO_3$, whose peaks were more pronounced with higher yttria loadings (10 wt%). The XRD pattern of 20 wt% yttria-impregnated alumina showed the presence of several reflections, which were attributed to bulk yttria and $YAlO_3$ crystallites, along with traces of α-phase. The X-ray diffraction patterns of Y_2O_3/alumina aerogel, which was calcined for 6 h at 750, 1000, 1100, and 1200 °C, are shown in Fig. 6 (also Table 4). Comparison between the XRD patterns of Y_2O_3/conv.alumina and Y_2O_3/alumina aerogel reveals that the thermal stability of alumina aerogel (which was already higher than that of conv.alumina (14)) was further improved upon incorporating yttria via impregnation. This was evident from the retardation of sintering and phase transformation of γ-alumina into θ-phase and α-phase. Furthermore, the formation of segregated yttria crystallites in yttria-impregnated alumina aerogel with 20 wt% yttria loading was significantly hindered when compared with conv.alumina. This can be attributed to the large surface area (14) and high number of –OH groups observed with undoped alumina aerogel. It is quite important to mention that the stabilization of conv.alumina and alumina aerogel upon incorporating yttria (5–10 wt%) via impregnation was noted to be no longer effective at temperatures higher than 1000 °C. This is due to nucleation of $YAlO_3$ structure at 1100 °C and due to the presence of $YAlO_3$ and α-phase at 1200 °C. Another important point to emphasize on is that the addition of 20 wt% yttria was not so effective in promoting thermal stabilization of alumina. This is due to the formation of segregated bulk yttria and yttrium aluminate crystallites. Table 5 also reports the changes in the BET specific surface area and total pore volume of yttria-impregnated alumina and alumina aerogel with various yttria loadings (5–20 wt% yttria) calcined at different temperatures for 6 h. It can be seen that yttria-impregnated alumina aerogel showed higher specific surface area when compared with its conv.alumina counterpart, irrespective of the calcination temperature (750 to 1100 °C) and the yttria loading (5–20 wt%). This can be mainly attributed to the higher specific surface area of alumina aerogel, which was ascribed to the supercritical (or hypercritical) drying of liquids contained in the gel (14). In addition, the N_2 adsorption results displayed in Table 5 are in complete agreement with the XRD measurements. First, the addition of yttria via impregnation onto either conv.alumina or alumina aerogel has resulted in significantly improved thermal stability, as suggested by the decrease in the sintering rate (smaller area loss). Second, the extent of the decrease was observed to be higher for yttria-doped alumina aerogel. It was also noted from Table 5 that 5 wt% yttria-impregnated conv.alumina or alumina aerogel that was calcined at 750–1100 °C displayed the higher S_{BET} area, when compared with the bare support or other yttria-loadings samples. The losses of specific surface area of yttria-impregnated conv.alumina and of alumina aerogel after 50 h of calcination at 750 and 1000 °C are presented in Fig. 7. Clearly, yttria-impregnated conv.alumina and alumina aerogel displayed higher thermal stability compared with the bare supports. This was observed irrespective of yttria loadings. In addition to that, it was demonstrated that the extent of thermal stability improvement upon the addition of yttria via impregnation was higher for alumina aerogel than for conv.alumina. For instance, yttria-impregnated conv.alumina with 5 wt% Y_2O_3 that was calcined at 1000 °C for 50 h suffered a loss of ~35% of its surface area, while alumina aerogel counterpart lost only ~18% of its surface area. The observed loss for undoped alumina aerogel was ~44%, whereas conv.alumina suffered ~69% loss upon calcination for 50 h at 1000 °C.

The change in BET specific surface area of 10 wt% yttria-impregnated conv.alumina or alumina aerogel, which were subjected to steaming at different temperatures with different exposure times are shown in Fig. 8 (the correlation factor (R^2) was obtained to evaluate the linearity of the noted changes, which in turns may reflect the extent of surface area loss). It was noted that the hydrothermal stability of conv.alumina and alumina aerogel were also improved as a result of adding yttria via impregnation. This was suggested

© 2007 NRC Canada

Fig. 5. XRD patterns of calcined samples at different temperature: (A) Conv.alumina, (B) 5 wt% Y_2O_3/Al_2O_3, (C) 10 wt% Y_2O_3/Al_2O_3, and (D) 20 wt% Y_2O_3/Al_2O_3. (*): γ-Al_2O_3, (+): θ-Al_2O_3, (-): α-Al_2O_3, (^): $YAlO_3$, and (<): Y_2O_3.

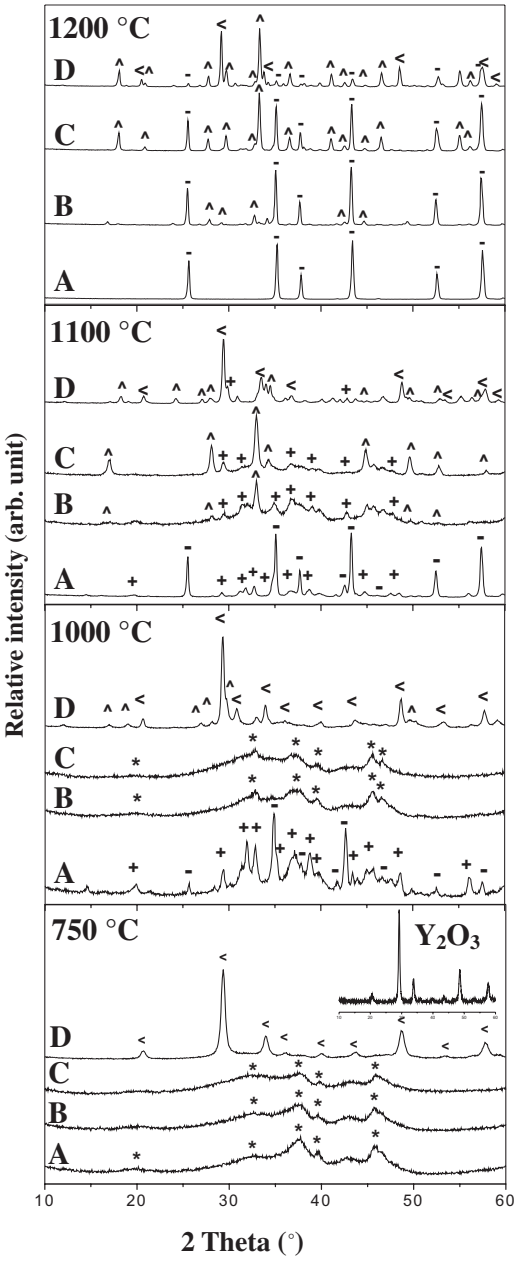

Fig. 6. XRD patterns of calcined samples at at different temperature: (A) alumina aerogel, (B) 5 wt% Y_2O_3/aerogel, (C) 10 wt% Y_2O_3/aerogel, and (D) 20 wt% Y_2O_3/aerogel. (Note: for symbols refer to Fig. 5).

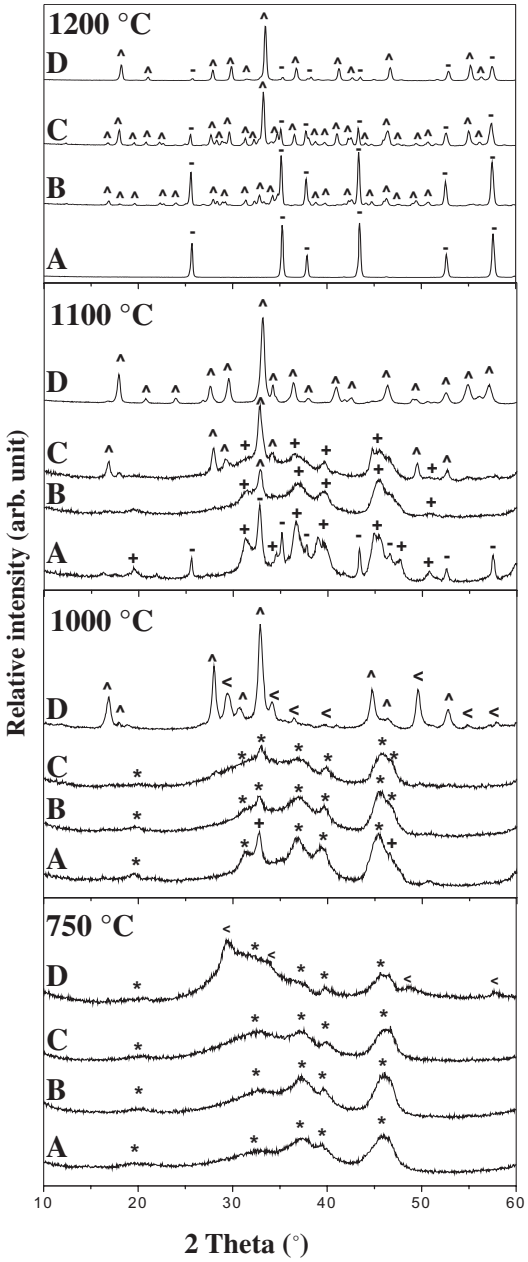

by the small loss in the surface area (Fig. 8A) and the minimization of structural transformations (XRD patterns not shown here), when compared with the bare support. For instance, the area loss for 10 wt% Y_2O_3/conv.alumina was ~6.5% and 14% when exposed to steam at 750 °C for 1 h and 24 h, respectively (Fig. 8A), while the corresponding area losses for conv.alumina were ~22% and 35%, respectively (Table1). On the other hand, the area loss for 10 wt% Y_2O_3/alumina aerogel was ~6.2% and 11% when exposed to steam at 750 °C for 1 h and 24 h, respectively (Fig. 8B), while these numbers for alumina aerogel were ~18% and 26%, respectively (Table 1). These results also suggested that the extent of hydrothermal stability was slightly higher for alumina aerogel than for conv.alumina upon yttria impregnation. It is worth mentioning that similar results were observed for 10 wt% yttria-impregnated conventional alumina or alumina aerogel, which were subjected to atmospheric steam at 1000 °C with different exposure times (Fig. 8B).

The improved thermal and hydrothermal stability of yttria-impregnated conventional alumina and alumina aerogel with yttria loadings of 5–10 wt% up to 1000 °C, when compared with the bare supports, can be attributed to the yttria. The loading of yttria via impregnation onto the

© 2007 NRC Canada

Table 5. Changes in the specific surface area (S_{BET}) and total pore volume of yttria-impregnated alumina (i.e., conv.alumina and alumina aerogel) as a function of calcination temperature for 6 h.

Sample	Calcination temperature (°C)							
	750 °C		1000 °C		1100 °C		1200 °C	
	S_{BET} (m^2/g)	PV[a] (cc/g)	S_{BET} (m^2/g)	PV (cc/g)	S_{BET} (m^2/g)	PV (cc/g)	S_{BET} (m^2/g)	PV (cc/g)
Conventional alumina (15)	116	0.253	51.0 (0.44)[b]	0.230	20.0 (0.17)	0.076	7.00 (0.06)	0.0
5 wt% Y_2O_3/conv.alumina	105	0.210	70.0 (0.67)	0.192	32.0 (0.30)	0.126	8.0 (0.08)	0.021
10 wt% Y_2O_3/conv.alumina	83.0	0.159	61.0 (0.73)	0.171	25.0 (0.30)	0.120	8.0 (0.08)	0.014
20 wt% Y_2O_3/conv.alumina	63.0	0.123	31.0 (0.50)	0.105	17.0 (0.27)	0.066	7.0 (0.11)	0.011
Alumina aerogel (15)	277	1.15	126 (0.46)	0.599	62.0 (0.22)	0.281	11.0 (0.04)	0.003
5 wt% Y_2O_3/alumina aerogel	192	0.503	137 (0.71)	0.465	102.0 (0.53)	0.351	11.0 (0.06)	0.062
10 wt% Y_2O_3/alumina aerogel	158	0.369	110.0 (0.70)	0.349	65.0 (0.41)	0.240	6.0 (0.04)	0.014
20 wt% Y_2O_3/alumina aerogel	110	0.279	57.0 (0.52)	0.204	31.0 (0.28)	0.140	5.0 (0.05)	0.011

[a]PV is total pore volume.
[b]ratio of S_{BET} of sample calcined at xT (°C) to S_{BET} of sample calcined at 750 °C, where x = 1000, 1100, or 1200 °C.

Fig. 7. Loss of BET specific surface area (S_{BET}) as a function of different calcination temperatures at different durations: (A) yttria-impregnated conv.alumina and (B) alumina aerogel with various yttria loadings.

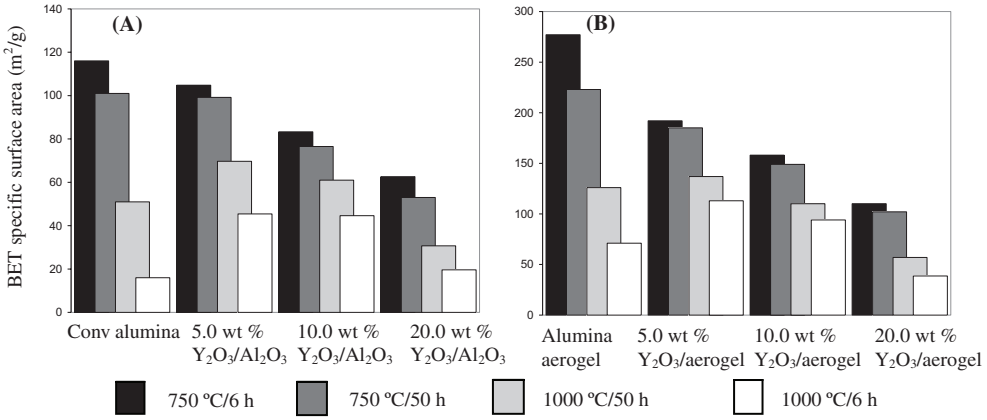

surface of alumina has resulted in decreasing or neutralizing the effect of cationic and anionic surface defects, and more importantly in reducing the number of –OH groups. The TGA and FTIR spectra of adsorbed pyridine clearly showed that the number of removed –OH groups (Table 3) and subsequently the number of Lewis sites (cus (surface defects)) (Fig. 3 and Table 3) were drastically reduced. The noted effect of yttria occurred most probably through the formation of dispersed yttrium aluminate structure, which is more thermally stable than alumina and whose presence has been confirmed indirectly by XRD patterns (i.e., bulk $YAlO_3$ crystallites were clearly detectable at $T > 1000$ °C). The higher extent of thermal and hydrothermal stability of alumina aerogel compared with conv.alumina, upon yttria impregnation, can be mainly attributed to alumina aerogel itself and in turn to the sol–gel method.

Comparison between yttria-doped alumina aerogel and yttria-impregnated alumina (conventional alumina and alumina aerogel)

Careful comparison between the properties of yttria-doped alumina aerogel and that of yttria-impregnated conv.alumina and alumina aerogel can lead to one explicit conclusion. The textural properties (i.e., surface area and dispersion) (14, 15) and thermal (14) and hydrothermal stability of alumina aerogel (current work) were significantly improved when yttria was incorporated via the sol–gel rather than the impregnation method. First, the surface area was noted to be much higher for alumina aerogel, even after incorporating the yttria. For instance, the S_{BET} of 10 wt% yttria-doped alumina aerogel was 319 m^2/g (14), which is 161 m^2/g higher than its impregnated alumina aerogel counterpart (158 m^2/g) (Table 5). Second, yttria-doped alumina aerogel was more ther-

© 2007 NRC Canada

Fig. 8. Loss of BET specific surface area (S_{BET}) as a function of different exposure times to steam at different temperatures: (A) 10 wt% yttria-impregnated conventional alumina and (B) alumina aerogel, respectively.

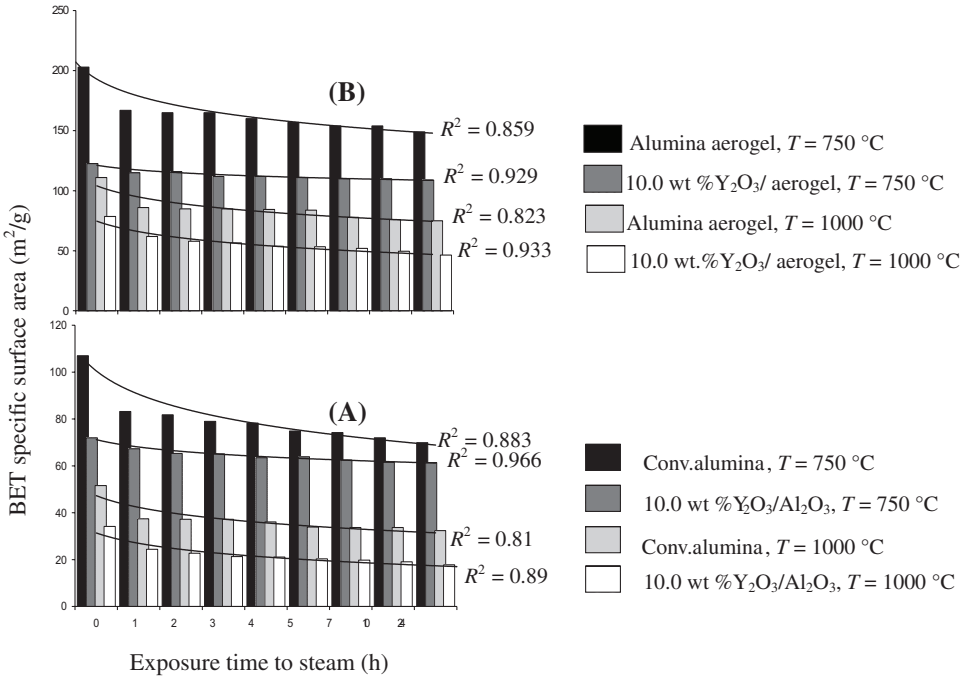

mally stable (14) compared with yttria-impregnated alumina (conv.alumina and aerogel). This was suggested by the lower area loss and further delay in the phase transitions upon calcination at high temperature (Figs. 5 and 6; Tables 4 and 5) (14). In addition, it was concluded that yttria-doped alumina aerogel, impregnated aerogel, and impregnated conv.alumina are only thermally stable up to temperatures below 1100 °C. The instability at higher temperature is due to nucleation of bulk $YAlO_3$ crystallites. Third, the influence of steam at high temperature was less pronounced in yttria-doped alumina aerogel (Figs. 1 and 2; Tables 1 and 2), compared with yttria-impregnated alumina (Fig. 8). Fourth, it was possible to incorporate a high loading of yttria (20 wt%) into alumina aerogel without observing the oxide segregation phenomenon (14), which on the contrary occurred easily with the impregnated samples (Figs. 5 and 6). Fifth, although the incorporation of yttria into alumina aerogel via sol–gel or impregnation has led to a reduction in the number of –OH groups, it was apparent that the extent of such reduction was smaller for yttria-doped alumina aerogel (Table 3). All this has a practical consequence: the important properties of alumina such as the acid–base characteristics and the ability to disperse active species and promoters are significantly preserved. In fact, we have unambiguously found that the dispersion of mono-oxide MoO_3 and bi-oxide MoO_3/CeO_2 were significantly improved when impregnated onto alumina aerogel (15). We do anticipate that such dispersion will be enormously weakened if yttria-impregnated alumina was used as a catalyst support. The main reason behind these outstanding properties of yttria-doped alumina aerogel when compared with yttria-impregnated alumina can be attributed to the fact that yttria was allowed to be efficiently inserted into the alumina aerogel lattice (or network). On the contrary, the solubility of yttria in alumina lattice

Fig. 9. ^{27}Al MAS NMR of samples calcined at 750 °C for 6 h: (A) conv.alumina (15), (B) alumina aerogel (15), (C) and (D) 10 and 20 wt% yttria-doped alumina aerogel, respectively (15), (E) and (F) 10 and 20 wt% yttria-impregnated conv.alumina, respectively, and (G) and (H) 10 and 20 wt% yttria-impregnated alumina aerogel, respectively. *: Spinning side bands (SSB).

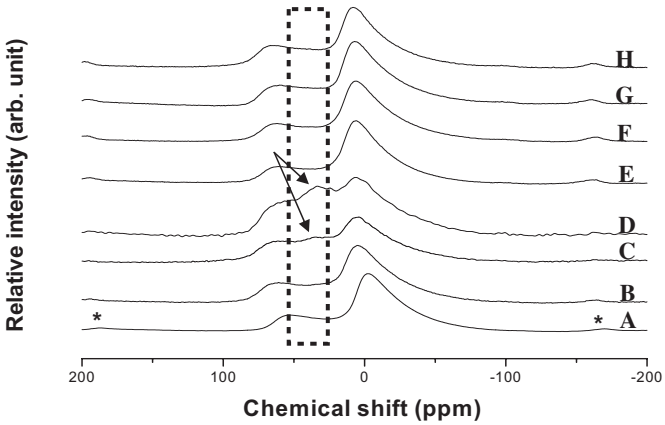

was quite limited in the case of impregnation method. This was clearly supported by the ^{27}Al MAS NMR study. The ^{27}Al MAS NMR of conv.alumina (14), alumina aerogel (14), 10 and 20 wt% yttria-doped alumina aerogel (14), and yttria-impregnated conv.alumina and alumina aerogel with various yttria loadings (current work) are shown in Figs. 9A–9H. The ^{27}Al MAS NMR spectra of yttria-impregnated conv.alumina or alumina aerogel with various yttria loadings (Fig. 9E–9H) reveal the presence of two peaks, at ~–3.0–7.0 ppm and another one at ~57–65 ppm. These peaks are assigned unambiguously to octahedral and tetrahedral coordinated aluminium, respectively (44, 45). No change can be

© 2007 NRC Canada

observed when comparing these spectra to those of the bare supports, which were performed during our previous study (Fig. 9A–9B) (14). On the contrary, these spectra are noticeably different from those of yttria-doped alumina aerogel, which were also carried out during our previous study (Fig. 9C–9D) (14). The peak at ~33.0 ppm, which was clearly observed in yttria-doped alumina aerogel and assigned to surface distorted Al_{tetra}–O–Y bond) (14), was absent in yttria-impregnated conv.alumina or alumina aerogel. Therefore, it can be inferred from these results that the incorporation of yttria via the sol–gel method provoked structural rearrangement of the aluminum coordination that played a major role in preventing the formation of segregated bulk Y_2O_3 crystallites, and hence decreasing the tendency of forming large $YAlO_3$ crystallites.

Conclusions

The results presented in this work reinforce our conclusion that yttria-doped alumina aerogel is an effective support for TCC process. It was found that the incorporation of Y_2O_3 into alumina aerogel structure via the sol–gel method has another significant beneficial role, besides improving the thermal stability (14) and the ability to homogenously disperse the active species and promoters at high calcination temperature (15). Yttria-doped alumina aerogel with various yttria loadings (5–20 wt%) was highly hydrothermally stable when compared with alumina aerogel and conv.alumina, as suggested by N_2 adsorption measurements, XRD, TGA, FTIR of adsorbed pyridine, and ^{1}H MAS NMR. We have also observed that the thermal and hydrothermal stability of both yttria-impregnated alumina aerogel and conv.alumina were improved but to a lower extent. These improved stabilities were attributed to the presence of yttria and subsequently the formation of surface yttrium aluminate. Therefore, it can be concluded that to observe the most efficient stabilizing effect of yttria, it is quite essential to incorporate it into the alumina structure via the sol–gel preparation technique.

Acknowledgment

Financial supports from NSERC (Natural Sciences and Engineering Research Council of Canada) and Valeo Management are acknowledged. The authors also thank Dr. Cedric Malveau (University of Montreal), and Dr. G. Denes (Concordia University) for technical assistance (^{1}H and ^{27}Al MAS NMR and XRD, respectively).

References

1. P. Pujado, D. Greer, J. Andersen, T. Foley, and V. Bhirud. Preprint archive-American Institute of chemical engineering [Spring National Meeting], New Orleans, LA, USA. March 11–14, 2000, 2471.
2. A. Corma, F.V. Melo, L. Sauvanaud, and F. Ortega. Catal. Today **107**, 699 (2005).
3. J.S. Plotkin. Catal. Today. **106**, 10 (2005).
4. A. Chauvel and G. Lefebvre. Petrochemical processes. Vol. 1. Technip. Paris, France. 1989. p. 117.
5. S. Matar and L.F. Hatch. *In* Chemistry of petrochemical processes. 2nd ed. Gulf Professional Publishing. Woburn, MA. 2001.
6. D.A. Hunt. *In* Handbook of petroleum refining processes. 2nd ed. *Edited by* R.A. Meyers. McGraw Hill. Boston, MA. 1997.
7. R. Le Van Mao. US Patent 4 732 881. Concordia University, Montreal, QC. 1988.
8. R. Le Van Mao, S. Melancon, C. Gauthier-Campbell, and P. Kletnieks. Catal. Lett. **73**, 181 (2001).
9. S. Melancon, R. Le Van Mao, P. Kletnieks, D. Ohayon, S. Intem, M.A. Saberi, and D. McCann. Catal. Lett. **80**, 103 (2002).
10. R. Le Van Mao, N. Al-Yassir, and D.T.T. Nguyen. Micropor. Mesopor. Mater. **85**, 176 (2005).
11. N. Al-Yassir, R. Le Van Mao, and F. Heng. Catal. Lett. **100**, 1 (2005).
12. N. Al-Yassir and R. Le Van Mao. Appl. Catal. A, **305**, 130 (2006).
13. R. Le Van Mao, N.-T. Vu, N. Al-Yassir, N. Francois, and J. Monnier. Top. Catal. **37**, 107 (2006).
14. N. Al-Yassir and R. Le Van Mao. Appl. Catal. A, **317**, 275 (2007) and refs. cited therein.
15. N. Al-Yassir and R. Le Van Mao. Appl. Catal. A, **332**, 273 (2007).
16. H. Schaper, E.B.M. Doesburg, and L.L. Van Reijen. Appl. Catal. **7**, 211 (1983).
17. P. Burtin, J.P. Brunelle, M. Pijolat, and M. Soustelle. Appl. Catal. **34**, 239 (1987).
18. F. Oudet, P. Courtine, and A. Vejux. J. Catal. **114**, 112 (1988).
19. M.F.L. Johnson. J. Catal. **123**, 245 (1990).
20. M. Ozawa, M. Kimura, and A. Isogai. J. Less-Common Met. **162**, 297 (1990).
21. B. Beguin, E. Garbowski, and M. Primet. J. Catal. **127**, 595 (1991).
22. H. Aria and M. Machida. Appl. Catal. A, **138**, 161 (1996).
23. H. Topsoe, B.S. Clausen, and F.E. Massoth. *In* Catalysis science and technology. *Edited by* J.R. Anderson, M. Boudart. Vol. 11. Springer. New York, NY. 1996.
24. M. Pijolat, M. Dauzat, and M. Soustelle. Solid State Ionics, **50**, 31 (1992).
25. J. Barbier Jr. and D. Duprez. Appl. Catal. B, **4**, 105 (1994).
26. E. Ponthieu, J. Grimblot, E. Elaloui, and G. Pajonk. J. Mater. Chem. **3**, 287 (1993).
27. E. Elaloui, R. Begag, B. Pommier, and G.M. Pajonk. Stud. Surf. Sci. Catal. **143**, 331 (2002).
28. R. Rostrup-Nielsen. *In* Catalysis science and technology. *Edited by* J.R. Anderson and M. Boudart. Vol. 5. Springer-Verlag. New York, NY. 1984.
29. V.I. Vereshchagin, V.Yu. Zelinski, T.A. Khabas, and N.N. Kolova. Zh. Prikl. Khim. **5**5 1046 (1982).
30. JCPDS. X-ray powder data file. International center for diffraction data, Swathmore, PA. 1989.
31. H. Knözinger and P. Ratnasamy. Catal. Rev. Sci. Eng. **71**, 31 (1978).
32. J.A. Wang, X. Bokhimi, O. Novaro, T. Lopez, F. Tzompantzi, R. Gomez, J. Navarrete, M.E. Llanos, and E. Lopez-Salinas. J. Mol. Catal. A, **137**, 239 (1999).
33. D.J. Coster, J.J. Fripiat, M. Muscas, and A. Auroux. Langmuir, **11**, 2615 (1995).
34. M. Trueba and S.P. Trasatti. Eur. J. Inorg. Chem. **1**7 3393 (2005).
35. G. Busca. Catal. Today, **4**1 191 (1998).
36. V. Baran. Coord. Chem. Rev. 6 65 (1971).
37. C. Morterra and G. Magnacca. Catal. Today, **27**, 497 (1996); and references cited therein.
38. S. Rajagopal, J.A. Marzari, and R. Miranda. J. Catal. **151**, 192 (1995).

© 2007 NRC Canada

39. R.D. Gonzalez, T. Lopez, and R. Gomez. Catal. Today, **35**, 293 (1997).
40. H. Kraus and R. Prines. J. Catal. **164**, 260 (1996).
41. E.C. Decanio, J.C. Edwards, and J.W. Bruno. J. Catal. **14**8 76 (1994).
42. V.M. Mastikhin, V.V. Terskikh, O.B. Lapina, S.V. Filimonova, M. Seidl, and H. Knozinger. J. Catal. **156**, 1 (1995).
43. L. Qu, W. Zhang, P.J. Kooyman, and R. Prins. J. Catal. **215**, 7 (2003).
44. G.A. Pozarnsky and A.V. McCormicks. J. Non-Cryst. Solid, **190**, 212 (1995).
45. T.E. Wood, A.R. Siedle, J.R. ill, R.P. Skarjune, and C.J. Goodbrake. J. Mater. Res. Soc. Symp. Proc. **180**, 97 (1997).

© 2007 NRC Canada

Photochemistry of 1,1′-bi-2-naphthol (BINOL) — ESIPT is responsible for photoracemization and photocyclization

Mitchel Flegel, Matthew Lukeman, and Peter Wan

Abstract: The photochemistry of 1,1′-bi-2-naphthol (BINOL, **5**) has been studied in aqueous solution and found to undergo rapid deuterium incorporation at the 4 and 5 positions (in D_2O-CH_3CN). All data is consistent with exchange arising via a formal excited state intramolecular proton transfer (ESIPT) from the naphtholic OH to the 4 and 5 positions of the other ring to give quinine methides (QMs) **8** and **9**, respectively, both of which subsequently revert to starting material. Photolysis of enantiomerically pure (+)-**5** in D_2O-CH_3CN resulted in racemization concurrent with deuterium incorporation. This is strong evidence to indicate that photoracemization of BINOL is a direct result of ESIPT, in keeping with the invocation of planar QM intermediates. Prolonged irradiation also gave a ring-closed product that is assigned as dihydrobenzoxanthene **7**, based on NMR and UV–vis data, and in analogy to known reactions of similar biaryl systems initiated by ESIPT. The formation of **7** is believed to arise via initial ESIPT from the naphtholic OH to the 7 position of the other naphthol ring generating an *o*-quinone methide intermediate that subsequently undergoes exclusive electrocyclic ring closure to give **7**. The deuterium exchange and photocyclization reach maximum quantum efficiency at ~8 mol/L water (in CH_3CN). A "water relay" mechanism for ESIPT is proposed that is consistent with the need for water in the photochemical deuterium exchange, racemization, and formation of **7**. The photostability and photoracemization of other related BINOL asymmetric catalysts in water should be a concern based on the reported results herein.

Key words: BINOL, ESIPT, photoprotonation, photoracemization, photocyclization, quinone methide.

Résumé : On a étudié la photochimie du 1,1′-bi-2-naphtol (BINOL, **5**) en solution aqueuse et on a trouvé que, dans un mélange D_2O/CH_3CN, il se produit une incorporation rapide de deutérium dans les positions 4 et 5. Toutes les données sont en accord avec un mécanisme d'échange qui se produirait formellement par le biais d'un transfert de proton intramoléculaire dans l'état excité (TPIEE) des groupes OH du naphtol vers les positions 4 et 5 de l'autre noyau avec les formations respectivement des quinines de méthides (QM) **8** et **9** qui se retransforment subséquemment en produit de départ. La photolyse du (+)-**5** énantiomériquement pur dans un mélange de D_2O/CH_3CN conduit à une racémisation qui accompagne l'incorporation du deutérium. Il y a beaucoup d'indications qui suggèrent que la photoracémisation du BINOL résulte directement du TPIEE en raison du fait qu'on invoque la présence d'intermédiaires QM plans. Une irradiation prolongée conduit aussi à la formation d'un produit à cycle auquel on a attribué la structure dihydrobenzoxanthène **7** en se basant sur les données de RMN et de spectroscopie UV–vis et en faisant une analogie avec des réactions connues de systèmes biaryles semblables initiées par de TPIEE. On croit que la formation du produit **7** se fait par le biais d'un TPIEE initial du groupe OH du naphtol avec la position 7 de l'autre noyau de naphtol qui conduit à la formation d'un intermédiaire méthide de *o*-quinone qui subit ensuite une fermeture de cycle électrocyclique exclusive conduisant au produit **7**. L'échange de deutérium et la photocyclisation atteignent une efficacité quantique maximale à environ 8 M d'eau dans le CH_3CN. On propose l'intervention d'un relais aqueux pour le TPIEE qui est en accord avec la nécessité de la présence d'eau dans l'échange photochimique de deutérium, la racémisation et la formation du produit **7**. Sur la base des résultats rapportés ici, on devrait s'inquiéter de la photostabilité et de la photoracémisation d'autres catalyseurs asymétriques apparentés au BINOL dans l'eau.

Mots-clés : BINOL, transfert de proton intramoléculaire dans l'état excité (TPIEE), photoprotonation, photoracémisation, photocyclisation, méthide de quinone.

[Traduit par la Rédaction]

Received 25 June 2007. Accepted 28 November 2007. Published on the NRC Research Press Web site at canjchem.nrc.ca on 18 January 2008.

M. Flegel, M. Lukeman, and P. Wan.[1] Department of Chemistry, Box 3065, University of Victoria, Victoria, BC V8W 3V6, Canada.

[1]Corresponding author (e-mail: pwan@uvic.ca).

Introduction

Excited state intramolecular proton transfer (ESIPT) is a fundamentally important reaction that has been studied in considerable detail (1, 2). ESIPT arises when a molecule contains both acidic and basic functionalities, which upon electronic excitation experience simultaneous enhancement of both their acidity and basicity allowing for the transfer of a proton from the acidic group to the basic group. Almost all

 doi:10.1139/V07-143 © 2008 NRC Canada

the known examples of ESIPT involve heteroatoms serving as the basic site with an OH or NH moiety serving as the acidic site, either as a substituent on or part of an aromatic ring system. ESIPT in these systems may be intrinsic or solvent-assisted, and are in general wholly reversible and in most cases are extremely fast, occurring on the subpicosecond time scale.

We recently reported the first examples of ESIPT from a phenol OH (or naphthol OH) to the carbons of an adjacent aromatic ring system, giving rise to *ortho* quinine methide (QM) intermediates (3). For example, photolysis of 1-(1′-naphthyl)-2-naphthol (**1**) in aqueous solution resulted in two modes of this new type of ESIPT (Scheme 1): (*i*) proton transfer from the phenol OH to the 2′ position, giving rise to the proposed *o*-QM **2**, which results in only deuterium incorporation at the 2′-position (observed when photolysis was carried out in D_2O-CH_3CN), and (*ii*) transfer to the more distal 7′ position, giving rise to the proposed *o*-QM **3**, which on (exclusive) electrocyclic ring closure gives the observed dihydropyran derivative **4**. Interestingly, these ESIPT reactions of **1** are observed only in the presence of water (maximal quantum efficiency in ~5 mol/L water), and no reaction was observed in dry CH_3CN. These observations suggest that these ESIPT processes for **1** are water-mediated.

Our current interest in the photochemistry of the title compound **5** (BINOL) stems naturally from our current investigations of the generality of the new type of ESIPT. BINOL and its derivatives have received considerable attention for their extensive use as ligands in stoichiometric and catalytic asymmetric reactions and in chiral recognition (4). Moreover, we note that an initial report by Cavazza et al. (5) on the photochemistry of **5** (in MeOH and aqueous CH_3CN) appeared some time ago in which compound **6** was reported to be isolated as the exclusive product using 334 nm argon ion laser excitation (Φ = 0.038) and as the most relevant product using traditional Hg lamp excitation (eq. [1]). In this same study, the authors also noted the photoracemization of **5**, although the mechanism for this process and its connection to formation of **6** was not made clear.

[1]

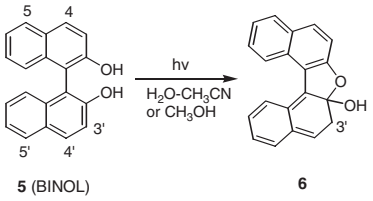

5 (BINOL) **6**

It was anticipated that a formal ESIPT process for **5**, from the naphthol OH to one or more aromatic carbon positions of the second naphthol moiety might lead to similar reactivity as observed for **1**, namely deuterium incorporation and (or) photocyclization. In this work, we show that the exclusive reaction pathways on photolysis of **5** in aqueous solution is water-mediated ESIPT from the 2-naphthol to the 4′, 5′, and 7′ positions of the other 2-naphthol ring. The QM arising from protonation at the 7 position undergoes exclusive cyclization to give a ring-closed product **7**. In addition, we show that the water-mediated ESIPT is directly correlated to the photoracemization of BINOL (**5**), an issue of some importance in the use of these types of materials in asymmetric catalysis and as fluorescent sensors in enantioselective recognition (6, 7), especially in aqueous systems. To our knowledge this is the first report of a photoracemization being the direct result of ESIPT.

Scheme 1.

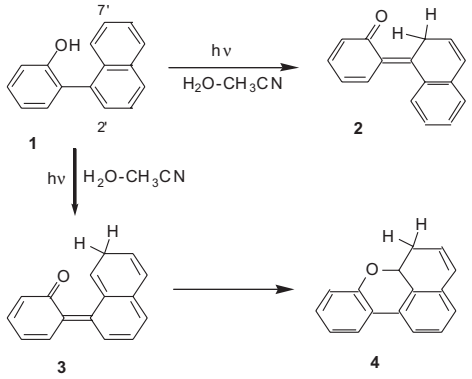

Fig. 1. UV–visible spectra showing the conversion of **5** to **7** with photolysis time. Traces were recorded every 10 s for a total of 140 s in a RPR 100 photoreactor fitted with 16 lamps (300 nm) (1:2 H_2O/CH_3CN, argon saturated). Spectral data for wavelengths longer than 250 nm are expanded in the inset. UV–vis changes are characterized by loss of absorbance at 225 nm and growth at 325 and 352 nm on photolysis.

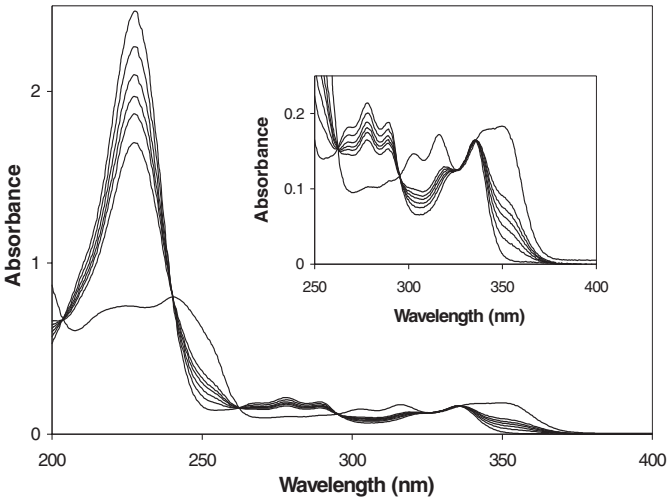

Results and discussion

Product studies and deuterium incorporation.

We first examined the photoreactivity of **5** by monitoring for changes in the UV–vis absorption spectra upon photolysis. Initial studies were carried out in 1:2 (*v*/*v*) H_2O/CH_3CN (~10^{-5} mol/L; argon saturated) in a Rayonet RPR 100 photochemical reactor (300 nm lamps). Traces were recorded at regular time intervals throughout the course of the irradiation and led to dramatic changes in the UV–vis spectrum (Fig. 1), indicating the photoreactivity of **5** under these conditions. The absorption maxima at 225, 276, and 334 nm, characteristic of **5**, were converted to new bands with maxima at 314 and 352 nm on photolysis. The spectra in Fig. 1 exhibit distinct isosbestic points, suggesting that

© 2008 NRC Canada

the photochemical reaction gives only one major photoproduct. The UV–vis spectra show a substantial decrease of the 225 nm naphthol absorption band intensity, suggesting loss of a naphthol ring system. The disappearance of the 225 nm band is accompanied by growth of a longer wavelength 352 nm band, indicating an increase of the conjugation in the molecule that would arise from rotation of the two naphthol rings towards planarity. Irradiation of **5** in anhyd. CH_3CN did not lead to any observable changes in the absorption spectrum, whereas photolysis in neat CH_3OH led to similar changes as observed for aq. CH_3CN, but much less efficiently, indicating that the reaction requires the mediation of a hydroxylic solvent. The photoproduct absorption bands reverted back to those of **5** when the temperature of the cuvette was raised to ~80 °C (<10 min). Photolysis of matched solutions of **5** in 1:2 H_2O/CH_3CN and 1:2 D_2O/CH_3CN (in UV cuvettes) gave a solvent deuterium isotope effect (Φ_H/Φ_D) of 1.3 ± 0.1 for formation of the 352 nm band assigned to the photoproduct. This is consistent with the requirement of a proton transfer step to form the more conjugated planar photoproduct. Although these initial observations are similar to those already reported (5), our results (vide infra) are entirely consistent with the operation of a new type (3) of water-mediated ESIPT reaction for **5**, a pathway that was not recognized by Cavazza et al. (5).

ESIPT pathways for **1** that did not give associated isolable products were implicated by irradiating in D_2O and analyzing the recovered starting material for deuterium exchange. To probe whether such processes can occur for **5**, irradiations were carried out as described above but with the H_2O portion replaced with D_2O. Irradiation of **5** in 1:3 D_2O/CH_3CN (~10^{-3} mol/L, λ_{ex} 300 nm, 1 h) yielded **5** (after H_2O wash) deuterated at the 4(4′) and 5(5′) positions (eq. [2], 96% and 56% exchange, respectively, by ^{1}H NMR). This method of analysis cannot differentiate between the extent of monodeuteration and dideuteration of the two positions. The reduction in the area of the NMR signal assigned to the 4(4′) and 5(5′) positions (δ 7.97 (d) and δ 7.88 (d), respectively) on photolysis is accompanied by formation of a singlet assigned to the neighbouring 3 position proton (δ 7.37 (d) and a broad doublet of the peak assigned to the 6 position proton (δ 7.36 (td)), as shown in Fig. 2. Analysis by ^{1}H NMR and ^{13}C NMR showed only deuterated **5** and no detectable side products upon photolysis. MS data confirmed the overall deuterium incorporation in **5** and significant amounts of M + 1 to M + 4 peaks were observed. No deuterium incorporation took place in the dark at ambient or at elevated temperatures up to 80 °C. This suggests that the deuterated photoproducts from the formal ESIPT in **5** most likely arise from the proposed *o*-QM intermediates **8** and **9** (eq. [2]). Therefore, formation of **5**–4(4′)D and **5**–5(5′)D most likely occur via tautomerization of **8** and **9**, respectively.

The dimethyl ether analogue **10** was studied in a similar manner as **5**. This derivative lacks an acidic proton and thus cannot undergo excited state proton transfer (ESPT) or ESIPT processes. Irradiation of **10** under the same conditions as **5** did not yield any photoproducts, and the recovered substrate did not show deuterium incorporation when D_2O was used as the co-solvent. Its lack of photoexchange is consistent with reaction in **5** resulting from a formal ESIPT pro-

Fig. 2. ^{1}H (500 MHz) NMR showing the spectrum (expanded aromatic region) of **5** before (top) and after (bottom) photolysis (300 nm, 1:3 D_2O/CH_3CN). NMR integration indicates 96% and 56% deuteration at the 4 and 5 positions, respectively.

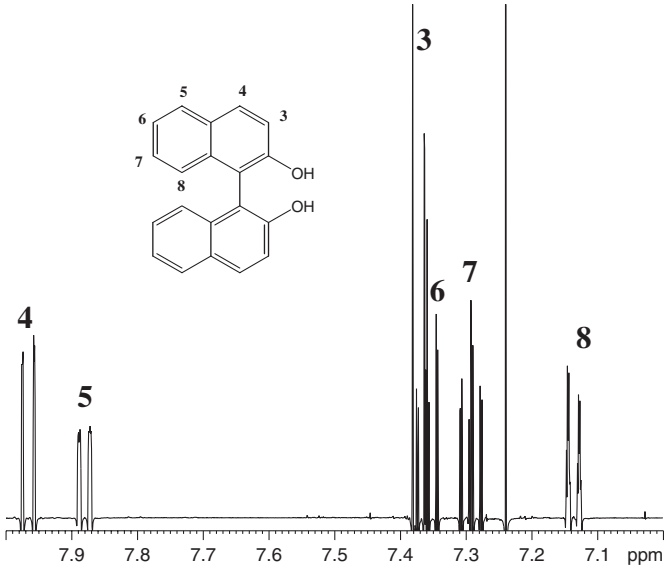

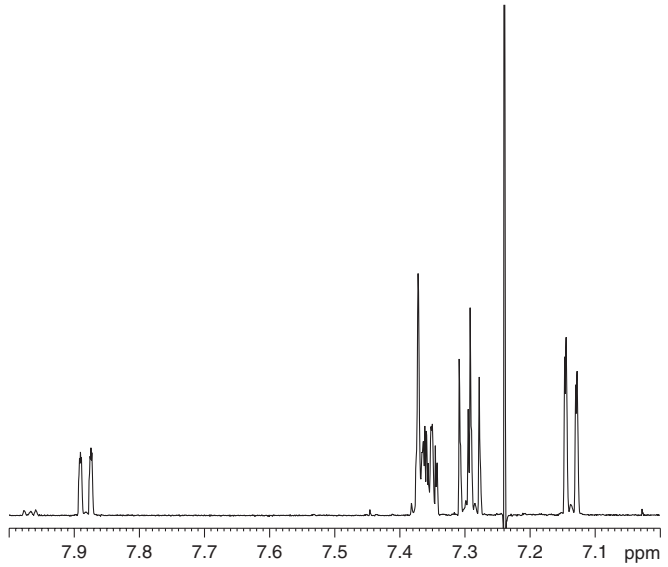

[2]

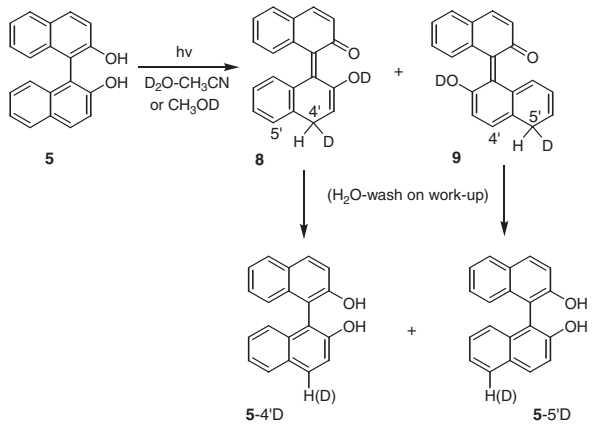

© 2008 NRC Canada

cess that requires an *o*-aryl-substituted naphthol (phenol) capable of undergoing ESIPT to the adjacent ring (3).

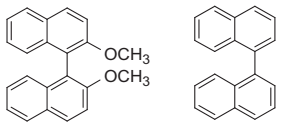

10 14

It is well known (8) that high water content is generally required for the efficient excited state proton transfer (ESPT) of phenols and other hydroxyarenes to water, while water-assisted ESIPT requires much less water for high quantum efficiency (2*g*, 3*b*). To explore the effect of water content on the proposed ESIPT of **5**, solutions containing varying amount of D_2O (in CH_3CN) were irradiated. The extent of exchange at the 4(4′) and 5(5′) positions was determined by ^1H NMR, and results are presented in Fig. 3. The efficiency of exchange (and hence formation of **8** and **9**) shows a strong dependence on water content with minimal reaction observed at low water concentrations. The yields of both 5–4(4′)D and 5–5(5′)D increased sharply as more D_2O was added to the solvent mixture, reaching a maximum at approximately 8 mol/L D_2O. Above 8 mol/L D_2O, the exchange efficiency becomes independent of water concentration as shown by the plateau in Fig. 3. No measurable deuterium incorporation occurred below 1 mol/L D_2O, and at all water concentrations the efficiency of exchange at the 5(5′)position was lower than that of the 4(4′) position.

Quantum yields of deuterium incorporation (Φ_{ex}) for **5** were measured using the deuterium exchange reaction of dibenzosuberene as a secondary reference standard. Dibenzosuberene is known to undergo deuterium exchange of the benzylic C-H hydrogens when irradiated in 1:4 D_2O/CH_3CN (Φ_{ex} = 0.021) (9). Φ_{ex} at the 4(4′) and 5(5′) positions of **5** (measured in 1:4 D_2O/CH_3CN) were 0.11 ± 0.01 and 0.040 ± 0.006, respectively. These values are similar to quantum efficiencies for deuterium exchange reported for **1** (3). The quantum yield for the actual protonation step should be higher than the measured quantum yield of exchange because the intermediate obtained from ESIPT can also lose deuterium to regenerate non-deuterated starting material.

Since the UV–vis traces (Fig. 1) give clear evidence of a reasonably stable photoproduct, attempts at its isolation were carried out. Prolonged irradiation of **5** in 1:3 H_2O/CH_3CN or MeOH (~10^{-3} mol/L, λ_{ex} = 300 nm, 15 h) resulted in the formation of a photoproduct that could be chromatographically isolated (30% ether in hexane, silica gel) in low quantum yield (Φ <0.01) as a mixture contaminated by about 20%–25% of starting material **5**. Indeed, heating this mixture or further treatment on silica gel gave higher proportions of **5**, indicating that this compound is thermally reverting back to **5**. Recent work from our group (3*b*) has shown that related naphthol biaryls such as **11** undergo an electrocyclic ring closure to yield the stable dihydroaromatic compound **12** in high quantum yield,

Fig. 3. Plot showing percent yield of **5**–4(4′)D (squares) and **5**–5(5′)D (circles) present in photolysate following irradiation of **5** in solvents of varying D_2O concentration (~10^{-3} mol/L, argon saturated, 300 nm lamps, 30 min) as measured by ^1H NMR.

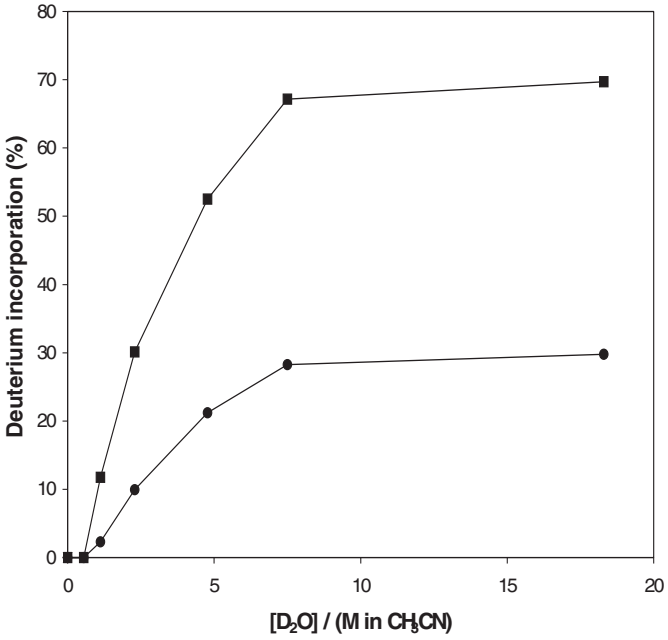

initiated by an ESIPT process to the 7′ position of the naphthalene ring (eq. [3]). Thus, we anticipated an analogous ring-closed product on photolysis of **5** in water. In the present case, the extra OH group on the adjacent naphthalene ring might make an analogous photoproduct much less stable because of increasingly crowded steric interactions. Moreover, the initial report of the photochemistry **5** in aqueous solution by Cavazza et al. (5) claimed that the only significant (ring-closed) product that is formed is **6**, which has a hemi-acetal functionality and has lost the aromaticity of both rings in one naphthalene system. Compound **6** would also not be expected to be stable and should readily revert back to **5**. More importantly, formation of compound **6** (on photolysis in D_2O) would be expected to eventually lead to deuterium incorporation at position 3(3′) of **5** when **6** decomposes thermally. Under our experimental conditions, no deuterium incorporation at the 3 position of **5** could be detected, a finding which is at odds with the photoproduct claimed by Cavazza. Therefore, if compound **6** is formed at all under our conditions, it must be formed at an exceedingly low yield to not perturb the observed deuterium incorporations observed.

Since we were able to isolate a sample of the photoproduct generated in our studies (albeit not with 100% purity), we used NMR to determine its structure (see Supplementary Data).[2] Our NMR data (^1H, ^1H-^1H COSY, and NOESY) are wholly consistent with the assignment of the photoproduct to dihydrobenzoxanthene **7** (eq. [4]), which is completely analogous to the photoproducts observed for both **1** and **11**. This product, in analogy to **1** and **11**, is most

[2] Supplementary data for this article are available on the journal Web site (canjchem.nrc.ca) or may be purchased from the Depository of Unpublished Data, Document Delivery, CISTI, National Research Council Canada, Ottawa, ON K1A 0R6, Canada. DUD 3700. For more information on obtaining material refer to cisti-icist.nrc-cnrc.gc.ca/irm/unpub_e.shtml.

© 2008 NRC Canada

readily visualized as arising from a third QM **13**. The UV–vis spectrum of this compound is shown by the "final" trace in Fig. 1. The significant loss of naphthalene absorption at 225 nm and growth of the 352 nm absorption are consistent with structure **7**, since one naphthalene ring has lost aromaticity in one ring (loss of 225 nm absorption), and there is now better conjugation in the biaryl system (phenyl and naphthalene rings) because of the more planar structure (growth of the 352 nm absorption). We note that structure **6** would be expected to have an absorption band in the visible (which was not observed) since the structure has a naphthalene (base peak at about 315 nm) conjugated to four double bond units (each contributing about 30 nm in red-shift).

[3]

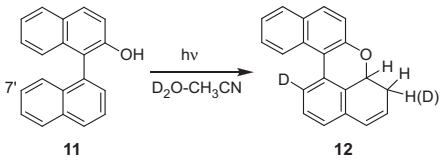

11 12

[4]

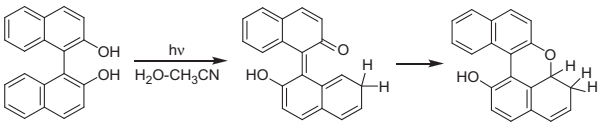

5 13 7

Photodeuteration and photoracemization

The photoracemization of a number of biaryl compounds, including BINOL derivatives, have been reported in the literature (5, 6, 10). The photoracemization of (–)-**5**, which has a rotational barrier of 158.3 kJ/mol in the ground state (11), was reported to occur upon irradiation at 334 nm in MeOH through a similar process that has been observed for other atropisomeric biaryl compounds (simple excited state planarization), although no direct evidence of this mechanism was reported (5, 10). In view of the extensive photodeuteration of **5** described earlier, we decided to examine the possible connection between ESIPT and photoracemization. A sample of (+)-**5** was irradiated in 2.8 mol/L D_2O/CH_3CN (~10^{-3} mol/L, λ_{ex} = 300 nm, 30–120 min), and aliquots were periodically removed. The optical rotation of each aliquot was measured, followed by evaporation of each sample and analysis by ^1H NMR. Since the racemization of **5** is expected to arise from the formation of the more planar *o*-QM intermediates **8**, **9**, and **13**, the total deuterium incorporation can be taken as a measure of the formation efficiency of these intermediates. Photolysis of (+)-**5** showed a significant decrease in the optical rotation and an increase in total deuterium incorporation with approximately the same time dependence (Fig. 4). Racemization was not observed in the dark (in aq. CH_3CN) or on photolysis in neat CH_3CN. The strong correlation between racemization and deuterium incorporation at the 4′ and 5′ positions strongly indicate that the racemization is a direct result of the ESIPT process.

Fluorescence measurements

In many of the systems (2*g*, 3) studied in our laboratory water is essential for reaction, acting as a bridge for the formal transfer of a phenol proton to a carbon site further away. The results obtained in the product studies for **5** indicate that

Fig. 4. Plot of optical rotation (circles) showing the racemization of **5** and total% deuterium incorporation at the 4 and 5 positions of **5** (squares) with photolysis time (~10^{-3} mol/L, argon saturated, 1:19 D_2O/ CH_3CN, 300 nm lamps). Points were recorded every 30 min.

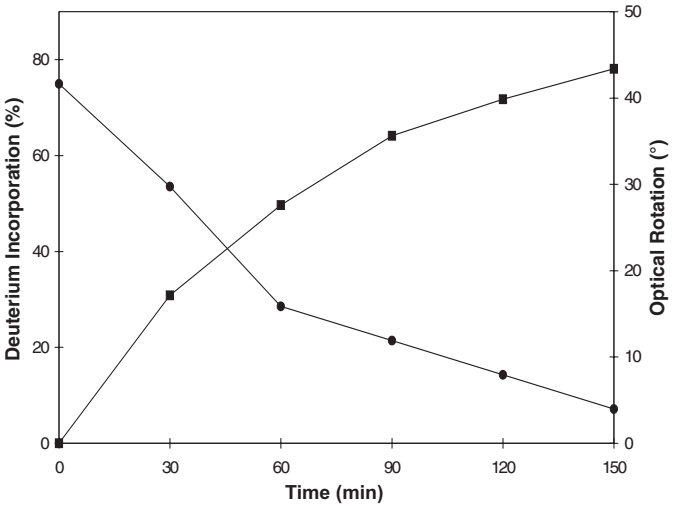

Fig. 5. Representative traces for **5** showing quenching of fluorescence emission (in CH_3CN) with added water (λ_{ex} = 300 nm). Concentrations are given in the figure.

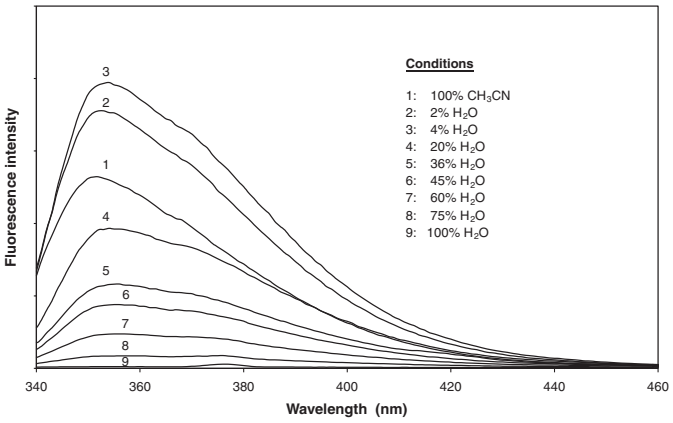

water is essential for formation of all QM intermediates. Fluorescence measurements should provide additional insights into the requirement of water on reactivity. Strong broad fluorescence emission was observed for **5** in neat CH_3CN (Fig. 5). The Stokes shift observed was much smaller than that observed for the parent 1,1′-binaphthyl (**14**). It has been shown for **14**, through Raman spectroscopy (12), that the equilibrium biaryl twist angle changes from 90° in the ground state to 69° in S_1. It is this twisting on excitation that is largely responsible for its sizable Stokes shift. The minimal Stokes shift observed for **5** suggests that little or no twisting takes place on excitation, presumably because of the additional steric crowding imparted by the two hydroxyl substituents (of the naphthols).

The addition of water (to CH_3CN) led to efficient quenching of the fluorescence emission above 2 mol/L H_2O (Fig. 5). A slight red shift in the λ_{max} is observed on addition of water

© 2008 NRC Canada

Fig. 6. Stern–Volmer plot of fluorescence emission quenching vs. water concentration (in CH_3CN) for **5**.

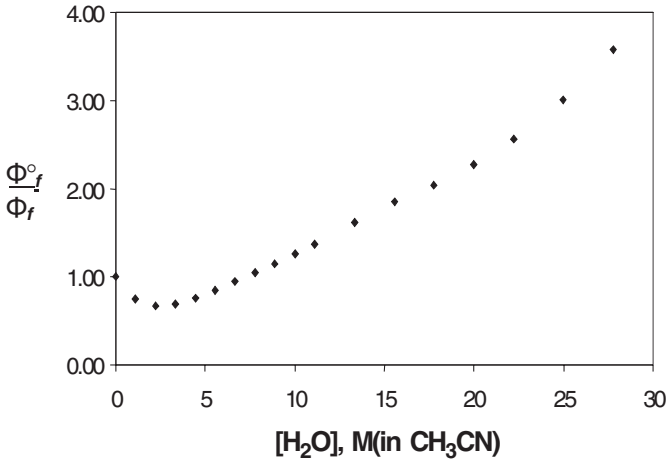

and is likely due to hydrogen bonding of the added water with the naphthol OH groups. The addition of up to ~2 mol/L water caused an increase in the emission, probably because of highly ordered solvent orientation. This is supported by the deuterium incorporation studies, where exchange was not observed below 1 mol/L H_2O content. Above 2 mol/L H_2O, the intensity of this band was progressively reduced because of the emergence of the ESIPT process. A Stern–Volmer plot of the quenching of the steady-state fluorescence by water is shown in Fig. 6. Addition of water led to the efficient quenching of the fluorescence emission above 2 mol/L H_2O content in a nonlinear fashion. Nonlinear fluorescence quenching by water has been previously shown for related phenols that can undergo water-mediated ESIPT processes and has been associated with the involvement of water clusters in the ESIPT process (2*g* and *h*). At water concentrations above 8 mol/L, there is significant deviation from linear behaviour. This deviation is indicative of a change in the mechanism of fluorescence quenching. It is important to note that the water concentration at which the deviation becomes pronounced (8 mol/L) coincides with the concentration of water at which the formation of **8** and **9** reached maximum efficiency, as described by product studies. On the basis of this correlation, we can assign the fluorescence quenching at concentrations between 1 mol/L and 8 mol/L H_2O as due to the increasing efficiency of the formal ESIPT reaction to give *o*-QMs **8**, **9**, and **13**, suggesting that the formation of QMs from **5** occurs from the S_1 state. The quenching of fluorescence at higher water concentrations is probably due to competitive formation of naphtholate $\mathbf{5}^-$ via ESPT to solvent (a known process for phenols at high water content). No new emission band was observed at high water content, indicating that $\mathbf{5}^-$, if formed, is not emissive.

Mechanism of deuterium incorporation, cyclization, and racemization

Our data and previous studies within our group (3, 13) are fully consistent with formation of *o*-QM intermediates **8**, **9**, and **13** on photolysis of **5** in aqueous CH_3CN or alcohol solutions. Singlet state reactivity is inferred from the fluorescence studies and is in accord with previous results of related systems (3, 13). It is informative to consider the changes in geometry that are required for these transformations. Chem 3D (MOPAC) minimized ground state structures are shown in Fig. 7 for **5**, **8**, and **9**. The two naphthol rings of the starting compound **5** are essentially orthogonal to each other, being able to rotate between 70° and 110° with an experimental ground state dihedral angle of 88° and an energy minimized dihedral angle of 95° (14). The distance between the naphtholic OH and carbon 4′ and 5′ positions on the other naphthol ring (positions of protonation) are 4.198 and 4.399 Å, respectively, which are too distant for simple direct proton transfer from the naphthol. Thus, similar to other previously reported systems, compound **5** does not react without the mediation of water (3*b*, 13). Moreover, reaction of **5** involves significant molecular distortions: (*i*) the original twisted biaryl rings must twist by about 90° such that it becomes coplanar and (*ii*) the naphthol ring puckers out of planarity as the 4′ and 5′ positions are protonated. The timing of these events is probably very fast (picosecond or faster time scale), and indeed our initial nanosecond laser flash photolysis (LFP) studies (~20 nanosecond time resolution) were only able to discern the "instantaneous" formations of three long-lived transients assignable to QMs **8** and **9** and the triplet state of **5**. QM **13** is not expected to be detectable owing to its low quantum yield of formation. These results agree with a number of other photoreactions of phenols in aqueous solutions reported by our group (2*h*, 2*g*, 3, 13, 15).

A provisional mechanism that is consistent with all experimental data for the observed photochemistry of **5** is presented in Scheme 2. On irradiation, a water-mediated ESIPT occurs from the S_1 state to give quinone methides **8**, **9**, and **13**. Both **8** and **9** return to **5** via enolization, while QM **13** is transformed to **7** via an electrocyclic ring closure. It is the formation of these more planar QM intermediates that is responsible for racemization.

For **5** to proceed to *o*-QMs **8** and **9**, the following must occur: (*i*) a formal proton transfer from the naphthol OH to the carbon atom at the 4′ and 5′ positions of the other naphthol ring, the latter resulting in the puckering of the naphthol ring and (*ii*) twisting about the biaryl bond to (or toward) planarity. These two events may be coupled (i.e., concerted) or stepwise. Fluorescence results indicate that in neat CH_3CN (a solvent that is unable to mediate the proton transfer and where there is no photochemistry), the excited state geometry remains highly twisted with essentially no Stokes shift. Charge transfer from one naphthol ring to the other in the excited state is thought to be the driving force for the ESIPT, but this cannot occur if the two rings remain in a perpendicular arrangement. The situation is altered when water (or alcohol) is present in the solvent mixture. Then, the formal ESIPT reaction proceeds readily, as determined by the product studies and fluorescence quenching results.

A simple pathway for the overall conversion is as follows. The added water mediates the ionization of the naphthol to give rise to the electronically excited naphtholate, which twists to a more planar form $\mathbf{5}^{-*}$. The planarization of these compounds has been shown to be possible in a stepwise fashion, where dissociation of the OH proton proceeds twisting (16). The more planar form can then protonate at either

© 2008 NRC Canada

Fig. 7. Chem 3D (MOPAC) minimized ground state structures of substrate **5** and proposed QM intermediates **8** and **9**. The dihedral angle between the naphthol rings of **5** is about 95°. The distance between the naphthol OH and the naphthol 4 and 5 positions (sites of protonation) of **5** are 4.198 and 4.399 Å, respectively, which is too far for a simple direct proton transfer.

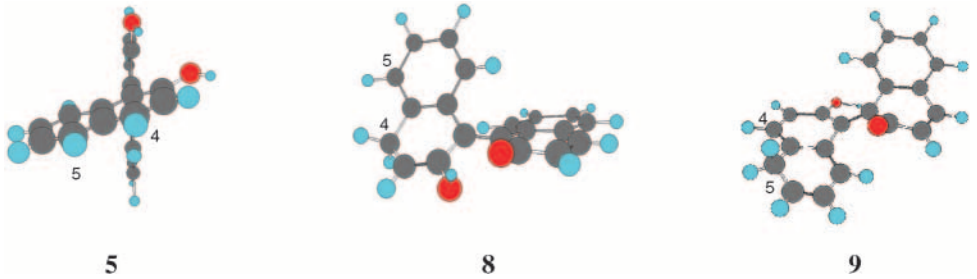

Scheme 2.

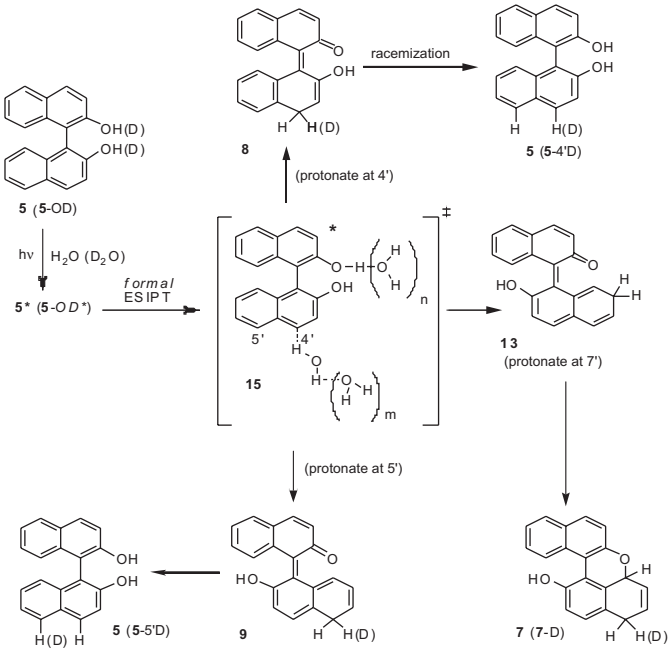

at either 4′, 5′, or 7′ position to give the *o*-QMs **8**, **9**, or **13**, respectively, depending on the direction that the biaryl system twists.

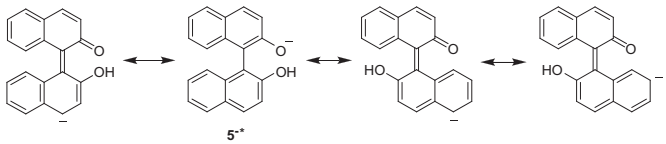

A more speculative mechanism for the efficient formation of **8** and **9** involves the concerted deprotonation of the naphthol with twisting motion of the naphthol ring coupled with proton transfer to either the carbon 4′ or 5′ position, mediated by water in a "water relay" mechanism as indicated in structure **15** (Scheme 2) (13). These intermediates can then undergo reverse proton transfer to generate **5**–4′D and **5**–5′D if the reaction is carried out in D_2O. No evidence of naphtholate formation was shown by fluorescence data (Fig. 5), which leads us to believe that the ESIPT mechanism is a concerted process. The racemization of (+)-**5** is also a direct result of proton exchange of the 4(4′) and 5(5′) positions. The high reactivity of biaryl naphthols is due to the tendency of the excited states of these species both to planarize and to become highly polarized.

The proposed mechanism for the formation of **7** is also outlined in Scheme 2. Much less efficient ESIPT to the 7′ position will generate QM **13**. This QM can then undergo electrocyclic ring closure to directly give **7** in a reaction that is entirely analogous to that already reported by us (3). We believe the electrocyclization to be strongly driven by the restoration of two aromatic rings. The photoproduct **7** is also thermally unstable to elevated temperatures due to the steric interaction between the alcohol and the naphthol ring and can decompose back to **5**. Similar instability was not seen in compound **12**, previously reported by our group (3*b*). No structures assignable to photoproduct **6** previously reported by Cavazza et al. (5) were observed under steady-state lamp photolysis.

The identification of a *formal* ESIPT process for **5** shows that the generality of ESIPT from phenol to aromatic ring carbons can be extended to 2-naphthols. The observation that only the derivative with the acidic naphthol OH group (**5** but not **10**) is reactive demonstrates the unique ability of naphthols to bring about the phototransformation of attached aromatic rings (via ESIPT). Of additional interest in this system is the apparently unique role of water in mediating the ESIPT reaction. While the ESIPT was also observed in CH_3OH, the highest efficiencies were observed when water was present in solution, presumably because of its superior ability to mediate the proton transfer. The use of chiral BINOL-type ligands is widespread in asymmetric chemistry, but the photoracemization reported herein should be a concern when these reactions are carried out in the presence of UV light (e.g., sunlight) in hydroxylic solvents.

Experimental section

General

^{1}H NMR spectra were recorded on Bruker AC300 (300 MHz) and Bruker 500 UltraShield (500 MHz) instruments. MS were recorded on a Kratos Concept H spectrometer using the LSIMS ionization method, using *m*-nitrobenzyl alcohol. UV–vis spectra were run on the Varian Cary 50 Bio instrument. Preparatory photolyses were carried out using a Rayonet RPR 100 photochemical reactor using 300 nm lamps.

© 2008 NRC Canada

Materials

Compounds (±)- and (+)-1,1′-bi-2-naphthol (**5**) (99%) were purchased from Sigma-Aldrich. 2,2′-Dimethoxy-1,1′-binaphthyl (**10**) (98%) was purchased from Acros. CH_3CN was dried over CaH_2 and distilled prior to use. Other solvents were spectral grade from Sigma-Aldrich and used as received.

UV–vis studies

Solutions (10^{-6}–10^{-5} mol/L) of **5** in the appropriate solvent system were prepared in 1.0 cm quartz cuvettes (3.0 mL) and deoxygenated by bubbling with a stream of argon gas (syringe needle) for 5 min and irradiated in a RPR 100 photochemical reactor containing 16 lamps (300 nm). A merry-go-round apparatus was employed if needed. Cooling was achieved with a fan. The irradiation was stopped at regular time intervals and UV–vis traces were recorded. Transfer time between the photoreactor and the spectrometer was approximately 5 s.

Product studies

Solutions (~10^{-3} mol/L) were prepared in a 100 mL quartz tube and purged with argon gas for 10 min prior to and continuously during irradiation in a RPR 100 photochemical reactor containing 16 lamps (300 nm). Cooling was achieved with an internal cold finger (~15 °C). To the photolysate was added 100 mL of H_2O, and the resulting mixture was extracted with CH_2Cl_2 and dried over $MgSO_4$; the solvent was removed under reduced pressure.

Photolysis of 5 in 1:3 D_2O/CH_3CN

A solution of 28 mg of **5** in 50 mL of 1:3 D_2O/CH_3CN was irradiated for 30 min (300 nm), and the photoproducts were analyzed by ^1H NMR, which showed deuterated starting material. The area of the peak corresponding to the 4 position of **5** (δ 7.97) was reduced by 70% and the area of the peak corresponding to the 5 position of **5** (δ 7.88) was reduced by 30%. This method of analysis cannot differentiate between the extent of mono- vs. di-deuteration of the above 4(4′) and 5(5′) positions. MS indicates extensive deuteration with noticeable M + 1 to M + 4 peaks. Runs at different D_2O concentrations were performed in the same way. Results from these runs appear in Fig. 3.

Prolonged irradiation of 5 in 1:9 H_2O/CH_3CN

A solution of 50 mg of **5** in 80 mL of 1:9 H_2O/CH_3CN was irradiated for 15 h (300 nm), and the photoproducts were analyzed by ^1H NMR, which showed a mixture of **5** and **7** in a 9:1 ratio. Attempts were made to isolated **7** in pure form but the best that could be achieved (silica, 3:7 ether/hexanes) was as a 4:1 ratio of **7/5** (see Supplementary Data).[2] The peaks assigned to **7** are listed as follows: ^1H NMR (500 MHz, $CDCl_3$) δ: 3.45–3.48 (m, 2H, H-3), 4.99 (broad s, exchangeable in D_2O, OH), 5.08–5.11 (m, 1H, H-6), 6.25–6.33 (m, 2H, H-4 and H-5), 7.04 (d, 1H, J = 8.5 Hz, H-1), 7.22 (d, 1H, J = 8.5 Hz, H-2), 7.36 (d, 1H, J = 8.5 Hz, H-7), 7.44 (ddd, 1H, J = 7.5 Hz, 7.0 Hz, 1.0 Hz, H-10), 7.60 (ddd, 1H, J = 7.7 Hz, 7.0 Hz, 1.5 Hz, H-11), 7.81 (d, 1H, J = 9.0 Hz, H-8), 7.84 (d, 1H, J = 8.5 Hz, H-12), 7.90 (d, 1H, J = 8.0 Hz, H-9). MS (m/z), 286 (M^+).

Racemization of (+)-5 in 1:19 D_2O/CH_3CN.

A solution of 200 mg of (+)-**5** in 1:19 D_2O/CH_3CN was irradiated in 30 min intervals (300 nm). In each interval, 10 mL of solution was removed from the photolysis and diluted with 10 mL of CH_3CN. The diluted solution was then placed in a 1 dm polarimetry cell, and the optical rotation was recorded. Following the measurement, the solution was evaporated to dryness and the ^1H NMR was recorded in $CDCl_3$ to follow the deuterium incorporation. A second experiment was done without the presence of D_2O. Racemization was not apparent in 100% CH_3CN.

Quantum yield of deuterium incorporation

A solution of 20 mg of suberene in 1:4 D_2O/CH_3CN was irradiated for 30 min (254 nm), and the photoproduct was analyzed by ^1H NMR, which showed 19% deuterium incorporation. A solution of 20 mg of **5** in 1:4 D_2O/CH_3CN was irradiated for 5 min (254 nm), and the photoproduct was analyzed by ^1H NMR, which showed 22% deuterium incorporation at the 4 position and 9% at the 5 position. This method was repeated twice to give a quantum yield (Φ_{ex}) of 0.11 ± 0.01 and 0.040 ± 0.006 at the 4 and 5 positions, respectively.

Steady-state and time-resolved fluorescence measurements

All solutions (OD ≈ 0.1 at excitation wavelength) were purged with argon for 5 min before analysis. Steady-state fluorescence spectra were obtained using a Photon Technology International A-1010 (PTI) Quanta-Master luminescence spectrometer.

Ground State geometry optimizations

The MOPAC module from the CambridgeSoft Chem 3D (pro version 5.0) was used for all geometry optimizations. Structures were drawn in ChemDraw 5.0 and imported into MOPAC before optimization. The AM1 method (closed shell, restricted) was used throughout.

Acknowledgments

Support of this work was provided by the Natural Sciences and Engineering Research Council (NSERC) of Canada. We thank NSERC for a summer research award (MF) and post-graduate scholarships (ML).

References

1. (*a*) S.M. Ormson and R.G. Brown. Prog. React. Kinet. **19**, 45 (1994); (*b*) D. Le Gourrierec, S. M. Ormson, and R.G. Brown. Prog. React. Kinet. **19**, 211 (1994); (*c*) S.J. Formosinho and L.G. Arnaut. J. Photochem. Photobiol. A, **75**, 21 (1993).
2. Representative papers: (*a*) P.-T. Chou, J.-H. Liao, C.-Y. Wei, C-Y. Yang, W.-S. Yu, and Y.-H. Chou. J. Am. Chem. Soc. **112**, 986 (2000); (*b*) A. Kyrychenko, J. Herbich, M. Izydorzak, F. Wu, R. P. Thummel, and J. Waluk. J. Am. Chem. Soc. **112**, 11179 (1999); (*c*) W.-H. Fang. J. Am. Chem. Soc. **120**, 7568 (1998); (*d*) M.C. Rios Rodriguez, J.C. Penedo, R.J. Willemse, M. Mosquera, and F. Rodriguez-Prieto. J. Phys. Chem. A, **103**, 7236 (1999); (*e*) S. Ameer-Beg, S. M. Ormson, R.G. Brown, P. Matousek, M. Towrie, E.T. Nibbering, P. Foggi, and F.V.R. Neuwahl. J. Phys. Chem. A, **105**, 3709 (2001); (*f*) P.-T. Chou,

© 2008 NRC Canada

Y.-C. Chen, W.-S. Yu, Y.-H. Chou, C.-Y. Wei, and Y.-M. Cheng. J. Phys. Chem. A, **105**, 1731 (2001); (*g*) M. Fischer and P. Wan. J. Am. Chem. Soc. **121**, 4555 (1999); (*h*) M. Fischer and P. Wan. J. Am. Chem. Soc. **120**, 2680 (1998).
3. (*a*) M. Lukeman and P. Wan. J. Am. Chem. Soc. **124**, 9458 (2002); (*b*) M. Lukeman and P. Wan. J. Am. Chem. Soc. **125**, 1164 (2003).
4. (*a*) J. M. Brunel. Chem. Rev. **105**, 857 (2005); (*b*) L. Pu. Chem. Rev. **104**, 1687 (2004).
5. M. Cavazza, M. Zandomeneghi, A. Ouchi, and Y. Koga. J. Am. Chem. Soc. **118**, 9990 (1996).
6. T. Hattori, Y. Shimazumi, O. Yamabe, E. Koshiishi, and S. Miyano. Chem. Commun. (Cambridge), 2234 (2002).
7. Representative papers: (*a*) N. B. Barhate and C.-T. Chen. Org. Lett. **4**, 2529 (2002); (*b*) S. Herres, P. Hesemann, and J.J.E. Moreau. Eur. J. Org. Chem. 99 (2003); (*c*) M.-H. Xu, J. Lin, Q.-S. Hu, and L. Pu. J. Am. Chem. Soc. **124**, 14239 (2002).
8. (*a*) R.A. Moore, J. Lee, and G. W. Robinson. J. Phys. Chem. **89**, 3648 (1985); (*b*) J. Lee, G.W. Robinson, S.P. Webb, L.A. Philips, and J.H. Clark. J. Am. Chem. Soc. **108**, 6538 (1986); (*c*) G.W. Robinson. J. Phys. Chem. **95**, 10386 (1991); (*d*) L.M. Tolbert and J.E. Haubrich. J. Am. Chem. Soc. **116**, 10593 (1994).
9. D. Budac and P. Wan. J. Org. Chem. **57**, 887 (1992).
10. (*a*) K.S. Burnham and G.B. Schuster. J. Am. Chem. Soc. **120**, 12619 (1998); (*b*) M. Irie, K. Yoshida, and K. Hayashi. J. Phys. Chem. **81**, 969 (1977); (*c*) H.E. Zimmerman and D.S. Crumrine. J. Am. Chem. Soc. **94**, 498 (1972).
11. L. Meca, D. Reha, and Z. Havlas. J. Org. Chem. **68**, 5677 (2003).
12. S. Fujiyoshi, S. Takeuchi, and T. Tahara. J. Phys. Chem. A, **108**, 5938 (2004).
13. M. Flegel, M. Lukeman, L.A. Huck, and P. Wan. J. Am. Chem. Soc. **126**, 7890 (2004).
14. F. Toda, K. Tanaka, H. Miyamoto, H. Koshima, I. Miyahara, and K. Hirotsu. J. Chem. Soc. Perkin Trans. 2, 1877 (1997).
15. L. Diao, C. Yang, and P. Wan. J. Am. Chem. Soc. **117**, 5369 (1995).
16. Y. Shi and P. Wan. Can. J. Chem. **83**, 1306 (2005).

© 2008 NRC Canada

Novel chiral fluorescent chemosensors for malate and acidic amino acids based on two-arm thiourea and amide

Xiao-Huan Huang, Yong-Bing He, Zhi-Hong Chen, Chen-Guang Hu, and Guang-Yan Qing

Abstract: The charge neutral anthracene based chiral fluorescent receptors **4a** and **4b** containing thiourea and amide groups were synthesized by simple steps in good yields, and their enantioselective recognition for chiral dicarboxylic anions (L/D-malate, L/D-aspartate, and L/D-glutamate) were examined by UV–vis, fluorescence, and ^{1}H NMR spectroscopy. The sensor **4a** exhibited an excellent enantioselective recognition ability towards malate (K_{ass} (L)/K_{ass} (D) = 9.65).

Key words: enantioselective recognition, chiral chemosensor, fluorescence, malate.

Résumé : Faisant appel à une méthode n'impliquant que des étapes simples, on a effectué avec de bons rendements la synthèse des récepteurs fluorescents chiraux liés à des anthracènes électriquement neutres, **4a** et **4b**, qui contiennent des groupes amide et thiourée; faisant appel à la spectroscopie UV-visible, à la spectroscopie de fluorescence et à la spectroscopie RMN du ^{1}H, on a aussi évalué leur habilité à reconnaître d'une façon énantiosélective les anions dicarboxyliques chiraux (L/D-malate; L/D-aspartate et L/D-glutamate). Le senseur **4a** possède une excellente habilité à reconnaître d'une façon énantiosélective le malate (K_{ass} (L)/K_{ass} (D) = 9,65).

Mots–clés : reconnaissance énantiosélective, senseur chimique chiral, fluorescence, malate.

[Traduit par la Rédaction]

Introduction

The development of molecule-based enantioselective fluorescence receptors is receiving growing research attention because such receptors can potentially provide a real time technique to determine the enantiomeric composition of chiral molecules and contribute to the understanding of biochemical systems, offering new perspectives for the development of pharmaceuticals, enantioselective sensors, and other molecular devices (1). The molecular recognition of biologically important anions by simple synthetic receptors is a hot topic in the field of supramolecular chemistry. Despite the fact that several elegant examples of chiral anion receptors have been reported over the years, these often involve the synthesis of complex and challenging organic hosts from scaffolds such as cholic acid (2*a*, 2*b*), calixarenes (2*c*), binaphthyls (2*d*), cyclodextrins (2*e*), but the use of anthracene based electroneutral chiral anion receptors has been less investigated (3).

The sensing and monitoring of dicarboxylates is of great interest in areas of bioanalytical and biomedical research (4). Thiourea and amide moieties have become the focus of the development of neutral anion receptors, because the hydrogen binding of these functional groups is directional in character, resulting in relatively strong complexes with various dicarboxylate anions (5). Gunnlaugsson et al. (6) have developed a series of anthracene based receptors for dicarboxylic acids and pyrophosphate, but the sensors for the enantioselective recognition of chiral dicarboxylates are still rare.

To our best knowledge, some receptors have been reported to bind and recognize the malate enantiomers. In our previous work, two sensors based on calix[4]arenes have been reported (7*a*), which showed good enantioselectivity for malate, but the structure is complex. Gonzalez-Alvarez et al. (7*b*) synthesized a water-soluble receptor for malate, but it does not exhibit a fluorescence response. Herein, we report two chiral fluorescent receptors **4a** and **4b** bearing anthracene, amino acid, and thiourea units, which were synthesized by simple steps and in good yields. Their enantioselective recognition of malate and acidic amino acids were studied by fluorescence emission, UV–vis, and ^{1}H NMR spectra.

Received 13 August 2007. Accepted 4 December 2007. Published on the NRC Research Press Web site at canjchem.nrc.ca on 18 January 2008.

X.-H. Huang, Y.-B. He,[1] Z.-H. Chen, C.-G. Hu, and G.-Y. Qing. Department of Chemistry, Wuhan University, Wuhan, Hubei 430072, P.R. China.

[1]Corresponding author (e-mail: ybhe@whu.edu.cn).

Results and discussion

The synthesis of chiral fluorescent receptors **4a** and **4b** is outlined in Scheme 1. 9,10-Bis (aminomethyl)anthracene was prepared following the published procedure in ref. 6*a*. The intermediate **2** was obtained by the reaction of **1** and *N*-Boc-L-alanine in the presence of CDI, which was treated with trifluoroacetic acid to obtain compound **3**. Receptors **4a** and **4b** were synthesized by the reaction of *p*-nitrophenylisothiocyanate or *p*-tolylisothiocyanate and **3** in

 doi:10.1139/V07-147 © 2008 NRC Canada

Scheme 1.

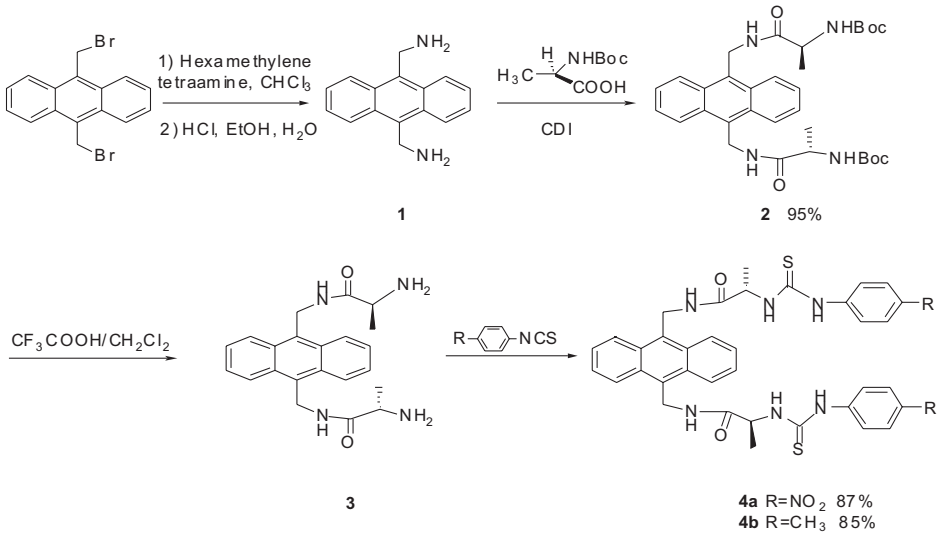

Fig. 1. (*a*) Fluorescence spectra of receptor **4a** (5×10^{-5} mol/L) with L-malate anion in DMSO. Anion equiv. 0→8.7. λ_{ex} = 372 nm. Inset: changes of fluorescence intensity of **4a** at 429 nm upon addition of L-malate anion. The line is a fitted curve. The correlation coefficient (*R*) of nonlinear curve fitting is 0.9986. (*b*) UV–vis absorption spectra of **4a** (5×10^{-5} mol/L) upon the addition of various amounts of L-malate in DMSO. Anion equiv. 0→9.2.

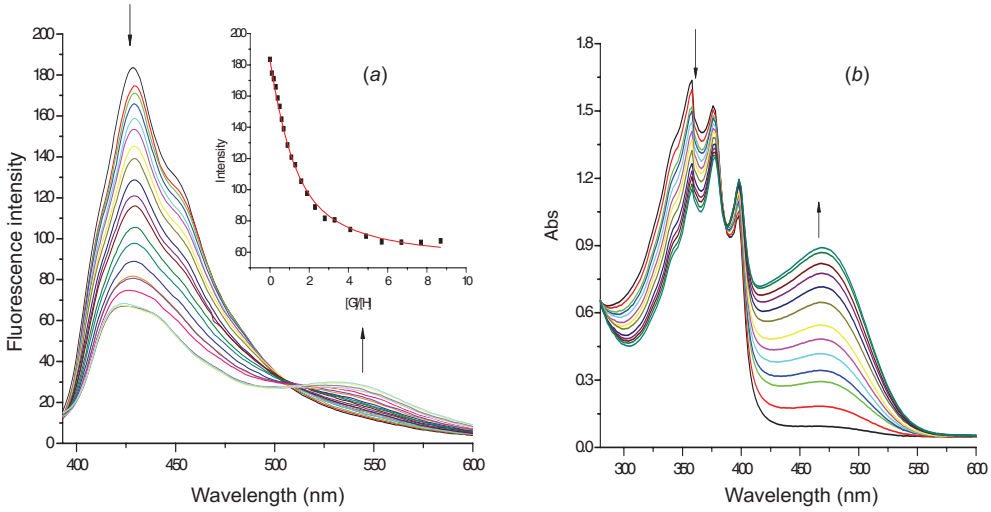

high yields. All of these compounds were characterized by IR, ^{1}H NMR, ^{13}C NMR, MS, and elemental analysis.

Fluorescence and UV–vis spectra study

The chiral recognition properties of receptors **4a** and **4b** were investigated for the enantiomers of malate, aspartate, and glutamate (Scheme 2). The fluorescence and UV–vis spectra were recorded from a solution of receptors **4a** and **4b** (5.0×10^{-5} mol/L) in DMSO in the absence or presence of various anions, and in each case the counter cations were tetrabutylammonium.

Figures 1*a* and 1*b* show the fluorescence emission and UV–vis spectra of **4a** with different concentrations of L-malate in DMSO. When gradually increasing the concentration of the anions, the fluorescence emission intensities of **4a** (5.0×10^{-5} mol/L) at 429 nm (λ_{ex} = 372 nm) decreased, while it gradually enhanced at 538 nm. A discernible isoemissive point was observed at 510 nm (8). It was particularly noteworthy that adding a small amount of L-malate (0.5 equiv.) made the color of solution of receptor **4a** change from light yellow to orange-red, which could be easily observed by the naked eye. When the receptor bound anions, hydrogen bonds were constructed to form stable complexes, and the electron density in the supramolecular system was increased to enhance the charge-transfer interactions between the electron-rich donor nitrogen of the thiourea units and electron-deficient *p*-nitrophenyl moieties, which resulted in a visible color change (9). As shown in Fig. 1*a*, the introduction of L-malate to the solution of receptor **4a** resulted in

Scheme 2. Structures of the chiral dicarboxylates.

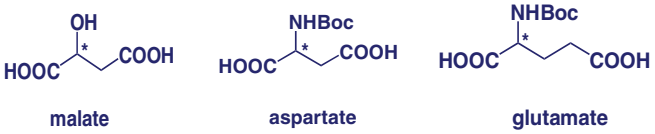

© 2008 NRC Canada

Fig. 2. (*a*) Fluorescence spectra of receptor **4a** (5×10^{-5} mol/L) with D-malate anion in DMSO. Anion equiv. 0→8.3. λ_{ex} = 372 nm. Inset: changes of fluorescence intensity of **4a** at 429 nm upon addition of L-malate anion. The line is a fitted curve. The correlation coefficient (*R*) of nonlinear curve fitting is 0.9941. (*b*) UV–vis absorption spectra of **4a** (5×10^{-5} mol/L) upon the addition of various amounts of D-malate in DMSO. Anion equiv. 0→9.5.

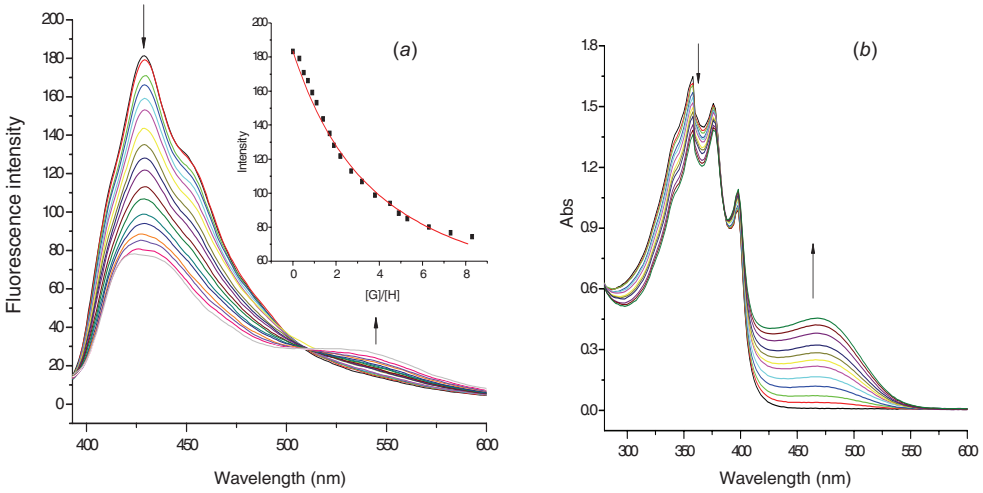

quenching of the locally excited emission at 429 nm, while enhancing the emission at 538 nm; the dual fluorescence peaks at 429 and 538 nm may be due to the locally excited (LE) state and charge transfer (CT) state in equilibrium, respectively (10). As shown in the inset of Fig. 1*a*, the satisfactory nonlinear fitting curve verified the formation of a 1:1 complex between **4a** and L-malate.

Figure 1*b* shows the UV–vis spectra of **4a** with different concentrations of L-malate in DMSO. On gradual increase of the concentration of L-malate, the intensity of the absorption band at 375 nm decreased gradually, and a new absorption band appeared with a maximum absorption at 470 nm. The obvious color change can be observed from light yellow to orange-red. The color change can be attributed to the appearance of a new long wavelength peak (9). When a protic solvent such as methanol was added to the orange-red solution of **4a** and L-malate in DMSO, the color of the solution returned to colorless, which illustrates that the interaction between **4a** and the anions was in essence a hydrogen-binding interaction.

Figures 2*a* and 2*b* show the fluorescence emission and UV–vis spectra of **4a** with different concentrations of D-malate in DMSO. When gradually increasing the concentration of the D-malate, the changes in fluorescence emission and UV–vis spectra were similar but smaller than when adding the equivalent L-malate into the solution of **4a**. The color change from light yellow to orange-red can also be observed. The quenching efficiency was about 50% with the addition of 2.0 equiv. of L-malate (Fig. 1*a*), while it was 30% with 2.0 equiv. of D-malate (Fig. 2*a*). The different quenching efficiencies ($\Delta I_L/\Delta I_D = 1.67$) indicated that receptor **4a** has a good enantioselective recognition ability for L- and D-malate. In addition, the association constants (K_{ass}) are different; the association constant of **4a** with L-malate is $(3.62 \pm 0.25) \times 10^4$ $(mol/L)^{-1}$, while that of **4a** with D-malate is $(3.75 \pm 0.33) \times 10^3$ $(mol/L)^{-1}$, and the enantioselectivity ($K_{ass}(L)/K_{ass}(D)$) is 9.65 for malate. These obvious changes in fluorescence and UV–vis spectra show that **4a** has an excellent chiral recognition ability towards the enantiomers of malate. Similar but smaller variations in the fluorescence and absorption spectra were obtained when adding L- or D-aspartate and L- or D-glutamate into the solution of **4a** in DMSO, respectively (see Supplementary Data, parts 1 and 3).[2] The corresponding association constants (K_{ass}) and correlation coefficients (*R*) of interaction between host and guest are listed in Table 1.

Figure 3 exhibits the fluorescence change of receptor **4a** with L- or D-malate. Different fluorescent responses indicate that **4a** has good enantioselective recognition ability for malate.

Figures 4*a* and 4*b* show the fluorescence emission spectra of **4b** with different concentrations of L- or D-malate in DMSO. When gradually increasing the concentration of the anions, the fluorescence emission intensities of **4b** (5.0×10^{-5} mol/L^{-1}) at 429 nm (λ_{ex} = 372 nm) decreased. The fluorescence quenching of receptor **4b** most likely arose from the change in free energy (ΔG_{PET}) of electron transfer between the excited fluorophore and the receptor (11*a*). When L- or D-malate interacted with receptor **4b**, the reductive potential of the amide group increased along with the ratio of the electron transfer from the HOMO orbit of the receptors to the excited anthracene group, which in turn leads to the intramolecular PET (photo-induced electron transfer) process being facilitated (11*b*), and therefore fluorescence quenching was observed. The changes in the absorption spectra of the anthracene moiety were only minor for **4b** in the presence of L- or D-malate (see Supplementary Data, part 4), which implies that a PET process occurred with anion binding.[2] Similar variations in the fluorescence and absorption spectra were observed when **4b** interacted with L- or D-aspartate and L- or D-glutamate (see Supplementary Data, part 2), respectively.[2] It was proposed that upon anion recog-

[2] Supplementary data for this article are available on the journal Web site (canjchem.nrc.ca) or may be purchased from the Depository of Unpublished Data, Document Delivery, CISTI, National Research Council Canada, Ottawa, ON K1A 0R6, Canada. DUD 3704.

© 2008 NRC Canada

Table 1. Association constants (K_{ass}) and correlation coefficients (R) of **4a** and **4b** with the chiral dicarboxylate anions in DMSO.

	Receptor **4a**			Receptor **4b**		
Anion[a]	K_{ass} ((mol/L)$^{-1}$)[b]	R	K_L/K_D	K_{ass} ((mol/L)$^{-1}$)[b]	R	K_L/K_D
L-malate	(3.62±0.25[c]) × 10^4	0.9986	9.65	(5.18±0.26[c]) × 10^3	0.9927	2.18
D-malate	(3.75±0.33[c]) × 10^3	0.9941		(2.38±0.32[c]) × 10^3	0.9945	
L-aspartate	(2.90±0.17[c]) × 10^4	0.9985	5.68	(9.91±0.17[c]) × 10^3	0.9939	4.04
D-aspartate	(5.11±0.24[c]) × 10^3	0.9970		(2.45±0.23[c]) × 10^3	0.9975	
L-glutamate	(1.78±0.48[c]) × 10^4	0.9907	2.16	(6.13±0.15[c]) × 10^3	0.9901	2.45
D-glutamate	(8.24±0.37[c]) × 10^3	0.9949		(2.50±0.34[c]) × 10^3	0.9911	

[a]The anions were used as their tetrabutylammonium salts.
[b]The data were calculated from results of fluorescence titrations in DMSO.
[c]All error values were obtained by the results of nonlinear curve fitting.

Fig. 3. Fluorescence intensity change of receptor **4a** (5×10^{-5} mol/L) with L- or D- malate in DMSO; the line is a fitted curve

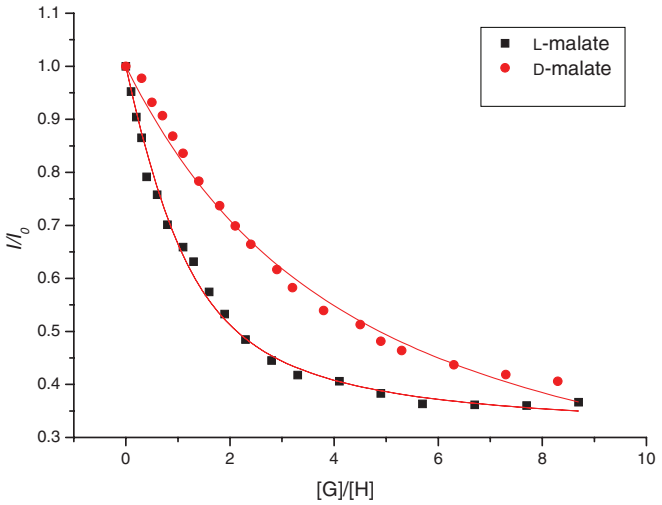

nition, the rate of the electron transfer from the HOMO orbit of the anion-receptor complex to the anthracene excited state enhanced, which caused the fluorescence emission to be quenched, with a little change of UV–vis spectra in the complexation.

The association constant of **4b** with L-malate is (5.18 ± 0.26) × 10^3 (mol/L)$^{-1}$, while that of **4b** with D-malate is (2.38 ± 0.32) × 10^3 (mol/L)$^{-1}$, which corresponds to the L/D-selectivity (K_{ass}(L)/K_{ass}(D)) of 2.18 for malate. Figure 5 shows the fluorescence change of receptor **4b** with L- or D-malate. K_{ass} and R of interaction between **4b** and aspartate and glutamate are listed in Table 1.

Continuous variation methods were employed to determine the stoichiometric ratio of the receptor **4a** with L/D-malate and **4b** with L/D-aspartate. The total concentration of host and guest was constant (1.0×10^{-4} mol/L^{-1}) in DMSO, with a continuously variable molar fraction of host ([H] / ([H] + [G])). Figure 6 shows the Job plots of receptors **4a** and **4b** with chiral anions (at 429 nm). When the molar fraction of the host was 0.50 the fluorescence intensity reached a maximum, which demonstrated that receptors **4a** and **4b** formed a 1:1 complex with L/D-malate and L/D-aspartate, respectively (12).

Assuming that the complex stoichiometry was 1:1, the association constant (K_{ass}) can be calculated by the following equation in Origin 7.0 (13),

$$X = X_0 + (X_{lim} - X_0)/2c_0 \{c_H + c_G + 1/K_{ass} - [(c_H + c_G + 1/K_{ass})^2 - 4c_H c_G]^{1/2}\}$$

where X represents the fluorescence intensity, c_H and c_G represent the corresponding concentrations of host and guest. The nonlinear curve fitting results of the fluorescence intensity (at 429 nm) of the interaction between **4a** or **4b** with L/D-malate, L/D-aspartate, and L/D-glutamate are shown in Table 1. The satisfactory result (the correlation coefficient is over 0.99) of the nonlinear curve fitting confirmed that the 1:1 complex between **4a** or **4b** and the chiral dicarboxylate anions has been formed.

The data in Table 1 illustrates that the association constants of **4a** with the anions are much higher than for **4b**. The results demonstrated that the introduction of a *p*-nitrophenyl group into the thiourea moiety provided an effective intromolecular charge transfer, conjugated with anion binding and enhanced the hydrogen bond ability, resulting in a strong anion binding. Receptor **4a** revealed an excellent enantioselective recognition to the enantiomers of the malate anion (K_{ass} (L)/K_{ass} (*d*) = 9.65). Receptors **4a** and **4b** exhibited good enantioselective recognition towards the L-enantiomer of the chiral guests, which is probably due to the L-enantiomer having a more complementary structure with receptors **4a** and **4b**.

^{1}H NMR study

^{1}H NMR experiments were undertaken to assess the enantioselective recognition properties between host and guest, because they can provide direct structural and dynamic information (14). Studies on the enantioselective recognition were carried out on a 300 MHz NMR spectrometer, using the receptor **4a** as a chiral solvating agent in DMSO at room temperature (RT).

Figure 7 shows the spectra of receptor **4a** and its complex with equimolar amounts of L-, D-, or racemic malate in DMSO-d_6. When treated with L-malate, the characteristic peaks of thiourea (N*H* b and N*H* c) of **4a** disappeared, while the amide (N*H* a) had a downfield shift from 8.36 to 8.52 ppm; the singlet peak of the CH_2 protons at 5.35 ppm linking with anthracene cleaved into multiple peaks when L-malate was added to the solution; when treated with D-malate, the peak of the amide (N*H* a) shifted from 8.36 to 8.68 ppm, while thiourea (N*H* c) became broadened and shifted from 10.41 to 10.65. When adding equimolar amounts of the racemic malate, thiourea (N*H* b and N*H* c) also disappeared, and the peak of the amide (N*H* a) shifted

© 2008 NRC Canada

Fig. 4. (*a*) Fluorescence spectra of receptor **4b** (5×10^{-5} mol/L) with L-malate anion in DMSO. Anion equiv. 0→82.0. λ_{ex} = 372 nm. Inset: changes of fluorescence intensity of **4b** at 429 nm upon addition of L-malate anion. The line is a fitted curve. The correlation coefficient (*R*) of nonlinear curve fitting is 0.9927. (*b*) Fluorescence spectra of receptor **4b** (5×10^{-5} mol/L) with D-malate anion in DMSO. Anion equiv. 0→90.2. λ_{ex} = 372 nm. Inset: changes of fluorescence intensity of **4b** at 429 nm upon addition of D-malate anion. The line is a fitted curve. The correlation coefficient (*R*) of nonlinear curve fitting is 0.9945.

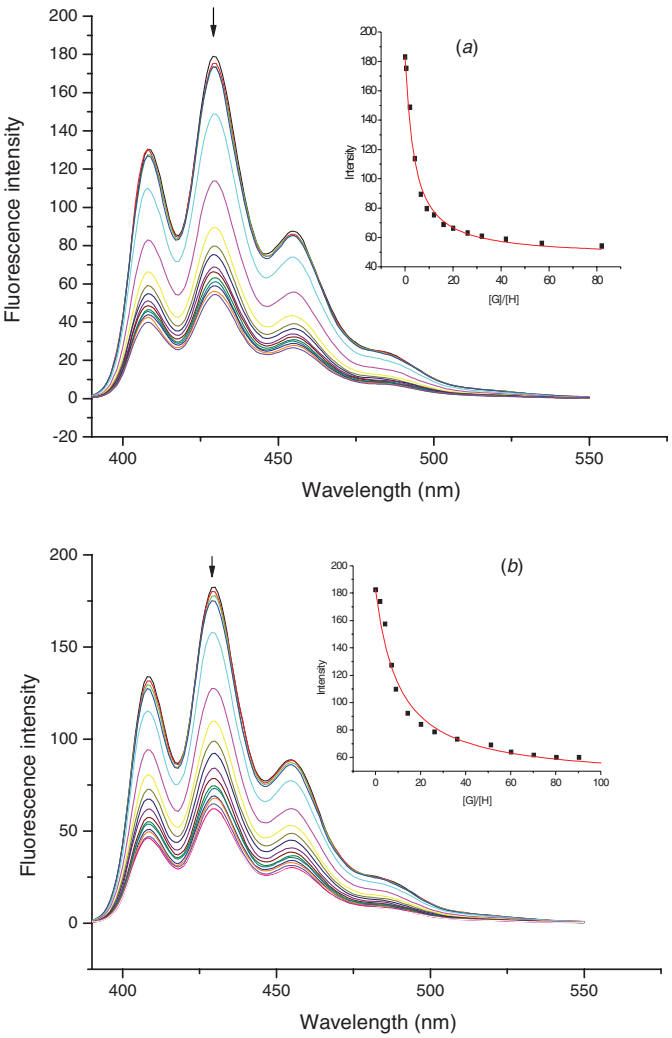

to 8.62 ppm. These results indicate that **4a** has a stronger interaction with L-malate than with D-malate. Notably, the signal change of the CH_2 protons of **4a** from singlet to multiple peaks when adding L-malate, means that there was strong interaction between **4a** and L-malate.

Conclusion

The anthracene based chiral fluorescent receptors **4a** and **4b** containing thiourea and amide groups were synthesized. The enantioselective recognition ability of **4a** and **4b** towards a series of chiral dicarboxylates were evaluated by fluorescence and ^{1}H NMR spectra. Receptor **4a** exhibits excellent chiral recognition ability towards the enantiomers of

Fig. 5. Fluorescence intensity change of receptor **4b** (5×10^{-5} mol/L) with L- or D-malate in DMSO; the line is a fitted curve.

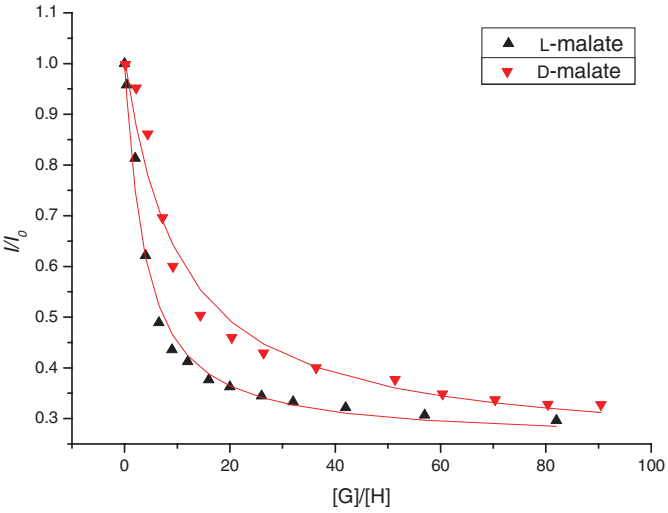

Fig. 6. Job plots of **4a** with L- or D-malate and **4b** with L- or D-aspartate (at 429 nm). The total concentration of the host and guest is 1.0×10^{-4} mol/L in DMSO. I_0 is the fluorescence intensity of **4a** or **4b**; *I* is the fluorescence intensity of **4a** or **4b** in the presence of the guest.

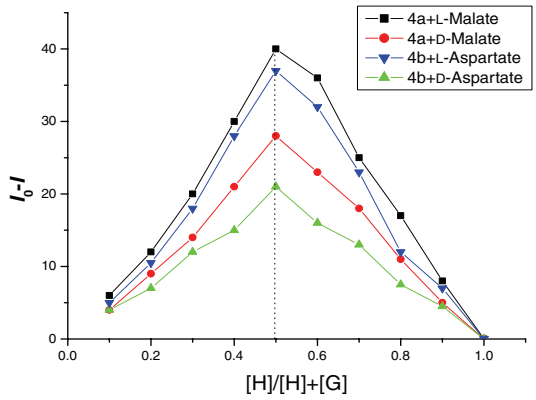

malate, while both **4a** and **4b** also shown good chiral recognition abilities towards L/D-aspartate. The steric effect of the receptors, structure-complementary with guest, and multiple hydrogen binding may be responsible for the enantioselective recognition. Sensitive fluorescent response and good enantioselective recognition ability reveal that **4a** can be used as fluorescent chemosensor for malate.

Experimental section

General methods

CH_2Cl_2 and Et_3N were dried and distilled from CaH_2. All other commercially available reagents were used without further purification. Melting points were determined with a Reichert 7905 melting-point apparatus and are uncorrected. Optical rotations were taken on a PerkinElmer Model 341 polarimeter. IR spectra were obtained on a Nicolet 670 FT-IR spectrophotometer. ^{1}H NMR spectra were performed on a Varian Mercury VX 300 MHz spectrometer in DMSO-d_6. ^{13}C NMR spectra were recorded on a Varian Inova Unity

© 2008 NRC Canada

Fig. 7. The ^{1}H NMR spectra of **4a** and its guest complex at 25 °C ([**4a**] = [guest] = 2.0×10^{-3} mol/L) in DMSO-d_6 at 300 MHz. (A) racemic malate, (B) receptor **4a**, (C) receptor **4a** + L-malate, (D) receptor **4a** + D-malate, (E) receptor **4a** + racemic malate.

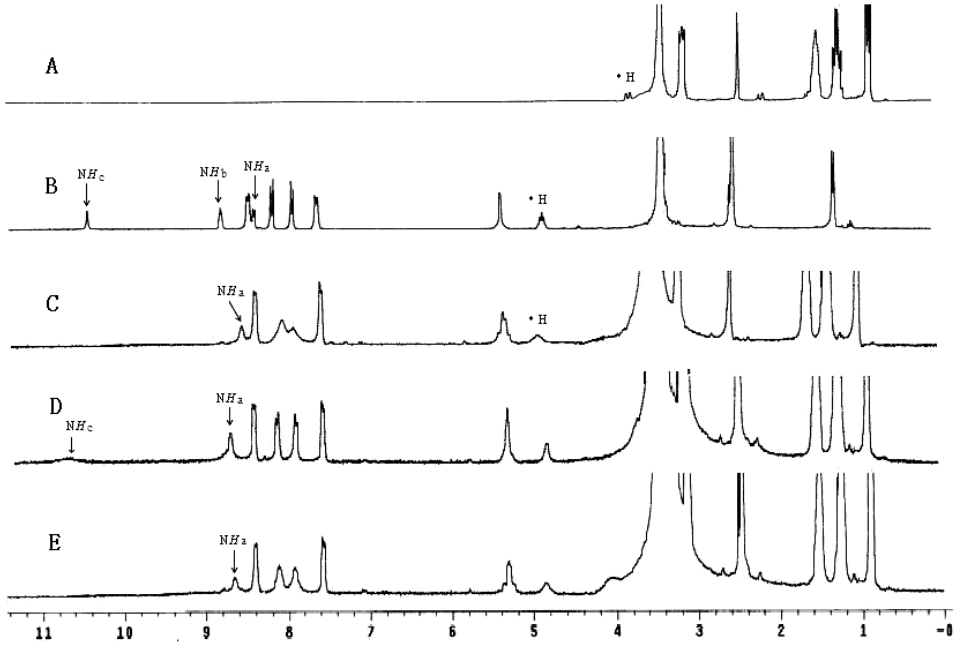

600 MHz spectrometer. Mass spectra were recorded on a Finnigan LCQ advantage mass spectrometer. Elemental analysis was determined with a Carlo-Erba 1106 instrument. Fluorescence spectra were obtained on a Shimadzu RF-5301 spectrometer. The UV–vis spectra were performed with a TU-1901 spectrophotomer.

Synthesis

Compounds 2

To a stirred and ice-cooled solution of *N*-Boc-L-alanine (0.38 g, 2.0 mmol) in dry CH_2Cl_2 (10 mL) was added 1,1′-carbonyldiimidazole (CDI) (0.39 g, 2.4 mmol), and the mixture was stirred for 2 h. Then a solution of 9,10-biaminomethylanthracene (0.24 g, 1.0 mmol) was added dropwise to the stirred mixture. The mixture was stirred under N_2 protection at RT for 18 h, and the yellow solid produced was filtered off, washed with $CHCl_3$ three times, and dried under vacuum. Pure compound **2** (0.55g) was obtained as a yellow solid in 95% yield, mp 175 to 177 °C. [α] = –7.5° (*c* 0.02, DMSO). IR (KBr, cm^{-1}) 3320, 2978, 2931, 1693, 1644, 1525, 1448, 1367, 1250, 1166, 1051, 754, 654. ^{1}H NMR (DMSO-d_6, ppm) δ: 8.38–8.41 (m, 4H, AnH), 8.21 (bs, 2H, CH_2NH), 7.56–7.59 (m, 4H, AnH), 6.84 (bs, 2H, NHBoc), 5.28 (bs, 4H, $AnCH_2$), 3.94–3.95 (m, 2H, *CH), 1.30 (s, 18H, CH_3), 1.08 (d, *J* = 7.5Hz, 6H, $^*CHCH_3$). ^{13}C NMR (DMSO-d_6, ppm) δ: 173.2, 155.6, 131.3, 130.4, 126.5, 125.8, 78.6, 50.3, 35.9, 19.1. ESI-MS *m/z* (%): 578 (M^+, 100). Anal. calcd. for $C_{32}H_{42}N_4O_6$: C 66.40, H 7.33, N 9.68; found: C 66.35, H 7.38, N 9.65.

Compounds 4a and 4b

TFA (0.5 mL) was added to the solution of compound **2** (0.29 g, 0.5 mmol) in dry CH_2Cl_2 (10 mL). The mixture was stirred at RT for 30 min to remove the Boc protecting groups. Then the solvent and excess acid was removed in vacuo, giving the TFA salt of **3** as a green solid, which was used directly without further purification. The green solid and triethylamine (0.5 mL) were dissolved in dry CH_2Cl_2 (10 mL), and a solution of *p*-nitrophenylisothiocyanate (0.18 g, 1.0 mmol) or *p*-tolylisothiocyanate (0.15 g, 1.0 mmol) was added slowly. The mixture was stirred vigorously overnight under N_2 protection at RT. The resulting precipitate was filtrated off and purified by crystallization from $CHCl_3$, obtaining pure products **4a** and **4b**, respectively.

Compound 4a

Yield 87%, mp 198 to 201 °C. [α] = +37.3° (*c* 0.02, DMSO). IR (KBr, cm^{-1}) 3323, 3056, 1655, 1597, 1509, 1329, 1302, 1253, 1180, 1112, 849, 732, 602, 567. ^{1}H NMR (DMSO-d_6, ppm) δ: 10.42 (s, 2H, NHAr), 8.78 (br, 2H, NHCS), 8.39–8.47 (m, 4H, AnH), 8.38 (d, *J* = 8.6Hz, 2H, NHCO), 8.16 (d, *J* = 8.7Hz, 4H, ArH), 7.92 (d, *J* = 8.7Hz, 4H, ArH), 7.59–7.62 (m, 4H, AnH), 5.35 (s, 4H, $AnCH_2$), 4.81–4.85 (m, 2H, *CH), 1.26 (d, *J* = 6.6Hz, 6H, CH_3). ^{13}C NMR (DMSO-d_6, ppm) δ: 179.5, 172.1, 147.0, 142.6, 131.2, 130.6, 126.6, 125.8, 125.1, 121.0, 79.9, 53.1, 36.1, 19.7. ESI-MS *m/z* (%): 739 (M^+ + 1,100). Anal. calcd. for $C_{36}H_{34}N_8O_6S_2$: C 58.52, H 4.64, N 15.17; found: C 58.45, H 4.71, N 15.13.

Compound 4b

Yield 85%, mp 189 to 191 °C. [α] = +96.5° (*c* 0.02, DMSO). IR (KBr, cm^{-1}) 3284, 2924, 1645, 1514, 1448, 1338, 1242, 1206, 818, 756, 721, 657, 600, 505. ^{1}H NMR (DMSO-d_6, ppm) δ: 9.68 (s, 2H, NHAr), 8.70 (br, 2H, NHCS), 8.41–8.44 (m, 4H, AnH), 7.70 (d, *J* = 8.1Hz, 2H, NHCO), 7.58–7.61(m, 4H, AnH), 7.29 (d, *J* = 8.1Hz, 4H, ArH), 7.10 (d, *J* = 8.1Hz, 4H, ArH), 5.31 (br, 4H, $AnCH_2$), 4.82–4.85 (m, 2H, *CH), 2.24 (s, 6H, $ArCH_3$), 1.21 (d, *J* = 6.6Hz, 6H, $^*CHCH_3$). ^{13}C NMR (DMSO-d_6, ppm) δ: 179.9,

© 2008 NRC Canada

172.5, 137.2, 134.1, 131.2, 130.5, 129.7, 126.5, 125.8, 123.8, 53.1, 46.4, 36.0, 21.1, 20.1. ESI-MS *m/z* (%): 676.5 (M^+, 100). Anal. calcd. for $C_{38}H_{40}N_6O_2S_2$: C 67.43, H 5.96, N 12.42; found: C 67.42, H 6.03, N 12.38.

Tetrabutylammonium salts

All tetrabutylammonium salts were prepared by adding 2 equiv. of tetrabutylammonium hydroxide in methanol to a solution of the corresponding malic acid (1 equiv.) or N-protected (by Boc) aspartic acid and glutamic acid (1 equiv.) in methanol. The mixture was stirred at RT for 4 h and evaporated to dryness under reduced pressure. The resulting syrup was dried at high vacuum for 24 h, checked by NMR, and stored in a desiccator.

Binding studies

The studies on the binding properties of **4a** and **4b** were carried out in DMSO. The fluorescence titration was performed with a series of 5×10^{-5} mol/L solutions of receptors **4a** and **4b** containing different amounts of chiral anions. The excited wavelengths were both 372 nm, ^{1}H NMR studies were recorded after adding equivalent anions into receptors (4×10^{-2} mol/L). Association constants were calculated by means of a nonlinear least-square curve fitting method with Origin 7.0 (Origin-Lab Corporation).

Acknowledgments

We thank the National Natural Science Foundation for financial support (Grant No. 20572080).

References

1. (*a*) Y. Kubo, S. Maeda, S. Tokita, and M. Kubo. Nature, **382**, 522 (1996); (*b*) C.P. McCoy, J.T. Rademacher, and T.E. Rice. Chem. Rev. **97**, 1515 (1997); (*c*) P.D. Beer and P.A. Gale. Angew. Chem. Int. Ed. **40**, 486 (2001); (*d*) M.R. Martinez and F. Sancenon. Chem. Rev. **103**, 4419 (2003); (*e*) L. Pu. Chem. Rev. **104**, 1687 (2004).
2. (*a*) A.P. Davis and R.S. Wareham. Angew. Chem. Int. Ed. **38**, 2978 (1999); (*b*) S.Y. Liu, L. Fang, Y.B. He, W.H. Chan, K.T. Yeung, Y.K. Cheng, and R.H. Yang. Org. Lett. **7**, 5825 (2005); (*c*) Y.S. Zheng and C. Zhang. Org. Lett. **6**, 1189 (2004); (*d*) T.J. Liu, Y.J. Chen, K.S. Zhang, D. Wang, D.W. Guo, and X.Z. Yang. Chirality, **13**, 595 (2001); (*e*) R. Corradini, A. Dossena, R. Marchelli, A. Panagia, G. Sartor, M. Saviano, A. Lombardi, and V. Pavone. Chem. Eur. J. **2**, 373 (1996).
3. (*a*) A. Ojida, Y. Mito-oka, M. Inoue, and I. Hamachi. J. Am. Chem. Soc. **124**, 6256 (2002); (*b*) J.Y. Kwon, Y.J. Jang, S.K. Kim, K.H. Lee, J.S. Kim, and J. Yoon. J. Org. Chem. **69**, 5155 (2004).
4. (*a*) M.S. Goodman, A.D. Hamilton, and J. Weiss. J. Am. Chem. Soc. **117**, 8447 (1995); (*b*) B.R. Linton, M.S. Goodman, E. Fan, S.A. van Arman, and A.D. Hamilton. J. Org. Chem. **66**, 7313 (2001); (*c*) K. Kacprzak and J. Gawronski. Chem. Commun. (Cambridge), 1532 (2003); (*d*) J.L. Wu, Y.B. He, Z.Y. Zeng, L.H. Wei, L.Z. Meng, and T.X. Yang. Tetrahedron, **60**, 4309 (2004).
5. (*a*) D.H. Lee, K.H. Lee, and J.I. Hong. Org. Lett. **3**, 5 (2001); (*b*) P. Piatek and J. Jurczak. Chem. Commun. (Cambridge), 2450 (2002).
6. (*a*) T. Gunnlaugsson, A.P. Davis, E.J. O'Brient, and M. Glynn. Org. Lett. **4**, 2449 (2002); (*b*) T. Gunnlaugsson, A.P. Davis, J.E. O'Brien, and M. Glynn. Org. Biomol. Chem. **3**, 48 (2005).
7. (*a*) G.Y. Qing, Y.B. He, Z.H. Chen, X.J. Wu, and L.Z. Meng. Tetrahedron: Asymmetry, **17**, 3144 (2006); (*b*) A. Gonzalez-Alvarez, I. Alfonso, P. Diaz, E. Garcia-Espana, and V. Gotor. Chem. Commun. (Cambridge, U.K.), 1227 (2006).
8. (*a*) J. Bourson, J. Pouget, and B. Valeur. J. Phys. Chem. **97**, 4552 (1993); (*b*) D.H. Lee, H.Y. Lee, K.H. Lee, and J.I. Hong. Chem. Commum. (Cambridge), 1188 (2001).
9. S. Nishizawa, R. Kato, T. Hayashita, and N. Teramae. Anal. Sci. **14**, 595 (1998).
10. (*a*) D. Braun, W. Retting, S. Delmond, J.F. Letard, and R. Lapouyade. J. Phys. Chem. A, **101**, 6836 (1997); (*b*) J.P. Malval and R. Lapouyade. Helv. Chim. Acta. **84**, 2439 (2001); (*c*) F.Y. Wu and Y.B. Jiang. Chem. Phys. Lett. **355**, 438 (2002).
11. (*a*) A.P. deSilva, H.Q.N. Gunaratne, T. Gunnlaugsson, A.J.M. Huxley, C.P. McCoy, J.T. Rademacher, and T.E. Rice. Chem. Rev. **97**, 1515 (1997); (*b*) R. Martinez and F. Sancen. Chem. Rev. **103**, 4419 (2003).
12. H.J. Schneider and A.K. Yatsimirsky. Principles and methods in supramolecular chemistry. John Wiley & Sons, NY. 2000.
13. B. Valeur, J. Pouget, and J. Bourson. J. Phys. Chem. **96**, 6545 (1992).
14. (*a*) W.H. Pirkle and T.C. Pochapsky. Chem. Rev. **89**, 347 (1989); (*b*) T. Grady, S.J. Harris, M.R. Smyth, D. Diamond, and P. Hailey. Anal. Chem. **68**, 3775 (1996).

© 2008 NRC Canada

AWARD LECTURE / CONFÉRENCE D'HONNEUR

Gaseous ions and chemical mass spectrometry[1]

Diethard K. Böhme

Abstract: The intrinsic chemical reactivities of ions can be monitored in the gas phase using mass spectrometers that are coupled to appropriate ion sources and reaction cells. Here the author surveys his own experiences over the past 40 years as an ion chemist. He used flow-tube techniques for room temperature measurements of the intrinsic chemical reactivities of a large variety of positive and negative ions, including bare atomic ions, ions found in solution, biological ions, carbonaceous ions, and interstellar, cometary, and ionospheric ions. Progress in the measurement of chemical reactions of these ions with flow-tube mass spectrometry in the author's laboratory was been driven largely by developments in techniques of ion injection into the flow tube and of ion production (e.g., by electron impact, plasma ionization, and electrospray ionization). Chemical topics that are covered include: acid-base and nucleophilic displacement reactions that have bridged the gap between the gas phase and solution; interstellar ions and their role in molecular synthesis such as the synthesis of amino acids; the chemistry of fullerene cations as a function of charge state; fundamentals and applications of the chemistry of atomic cations with an emphasis on transition metal and lanthanide cations; atomic metal-ion catalysis; and chemical reactions of singly and multiply charged biological anions and cations in the gas phase.

Key words: ions, mass spectrometry, kinetics, ion chemistry.

Résumé : Faisant appel à des spectromètres de masse couplés à des sources ioniques et des cellules réactionnelles appropriées, on a déterminé les réactivités chimiques intrinsèques d'ions en phase gazeuse. Voici une revue de mes propres expériences sur la période des quarante dernières années, en tant que chimiste des ions, que j'ai utilisées à mesurer les réactivités chimiques intrinsèques à la température ambiante d'une grande variété d'ions positifs et négatifs, y compris des ions atomiques nus, des ions en solution, des ions biologiques, des ions à base de carbone et des ions interstellaires, des ions associés à des comètes et des ions de l'ionosphère. Les progrès réalisés dans le laboratoire de l'auteur dans la mesure des réactions chimiques de ces ions à l'aide de la spectrométrie de masse à tube d'écoulement ont été régis principalement par les développements dans les techniques de l'injection des ions dans le tube à écoulement et de la production de l'ion (par exemple, par impact électronique, ionisation au plasma ou ionisation par électronébulisation). Les sujets chimiques qui sont couverts comprennent les réactions de déplacement acide-base ou nucléophile qui forment un pont entre la phase gazeuse et la solution; les ions interstellaires et leur rôle dans la synthèse moléculaire, telle la synthèse des acides aminés; la chimie des cations fullurènes comme fonction de l'état de charge; les fondements et les applications de la chimie des cations atomiques avec une emphase sur les cations des métaux de transition et des lanthanides; la catalyse atomique ion-métal et les réactions chimiques en phase gazeuse d'anions ou de cations biologiques à charge unique ou multiple.

Mots-clés : ions, spectrométrie de masse, cinétique, chimie des ions.

[Traduit par la Rédaction]

Introduction

Ernest Rutherford once remarked that "ions are jolly little beggars, you can almost see them !" (1). I can very much relate to that remark as I've been pleasantly teased by ions during my entire research career, ever since my training as a physical chemist at McGill University in the early 1960s. Not only have I been fascinated by the structures and energies of ions and their many chemical reactions in a wide range of natural environments, but I also have searched for better ways of seeing these ions, of producing and detecting them, and of measuring their stabilities and reactivities using

Received 25 September 2007. Accepted 18 November 2007. Published on the NRC Research Press Web site at canjchem.nrc.ca on 20 February 2008.

D.K. Böhme.[2] Department of Chemistry, Centre for Research in Mass Spectrometry and Centre for Research in Earth and Space Science, York University, Toronto, ON M3J 1P3, Canada.

[1]Text is based on the CIC medal address in Winnipeg, MB, on 27 May 2007.
[2]Contact (e-mail: dkbohme@yorku.ca).

 doi:10.1139/V07-146 © 2008 NRC Canada

evolving techniques of mass spectrometry. The happy result has been a journey of excitement and discovery and I will attempt here to share some of this with you.

Gaseous ions

Gaseous ions that have captured my attention over the years include small and large, positive and negative, singly and multiply charged, inorganic and organic, as well as biological ions.

Bubble 1 shows some smaller ions that are found or postulated to move freely in interstellar (2) and cometary (3) environments where they can be involved in collisions with molecules or particles and so promote molecular synthesis, including even the synthesis of biological molecules. In planetary ionospheres, the reactions of some of these ions play a role in determining the relative abundance of atomic and molecular ions (4) and, because there are huge differences in the rates of electron–ion recombination between atomic and molecular ions, in determining the densities of free electrons that are important in radio communication here on Earth.

Carbonaceous ions and metallated carbonaceous ions of the kind shown in Bubble 2 have intrigued physical chemists and astrochemists in their attempts to understand the molecular composition and chemistry of interstellar clouds and the atmospheres of carbon stars. These ions include carbon-chain and especially "bucky-ball" ions, which burst upon the chemical scene in 1990 when buckminsterfullerene powder first became available,

Here on earth, ions are often found in solution. The generation in the gas phase of ions that are found solvated in solution, such as those included in Bubble 3, allows studies of intrinsic reactivities in the absence of solvent and even as a function of added solvent molecules. So classic solution reactions, such as acid-base and nucleophilic displacement reactions and other reactions of organic and organometallic ions, can be investigated in the gas phase in the complete absence of solvent. Even biological ions, such as oligonucleotide anions (see Bubble 4), now can be transferred into the gas phase and exposed to chemistry that promises new insights into molecular biology.

Atomic ions, the smallest of all ions, become favoured in high-temperature environments where they carry information about the elemental composition of the environment. So atomic ions and their chemistry are important in elemental

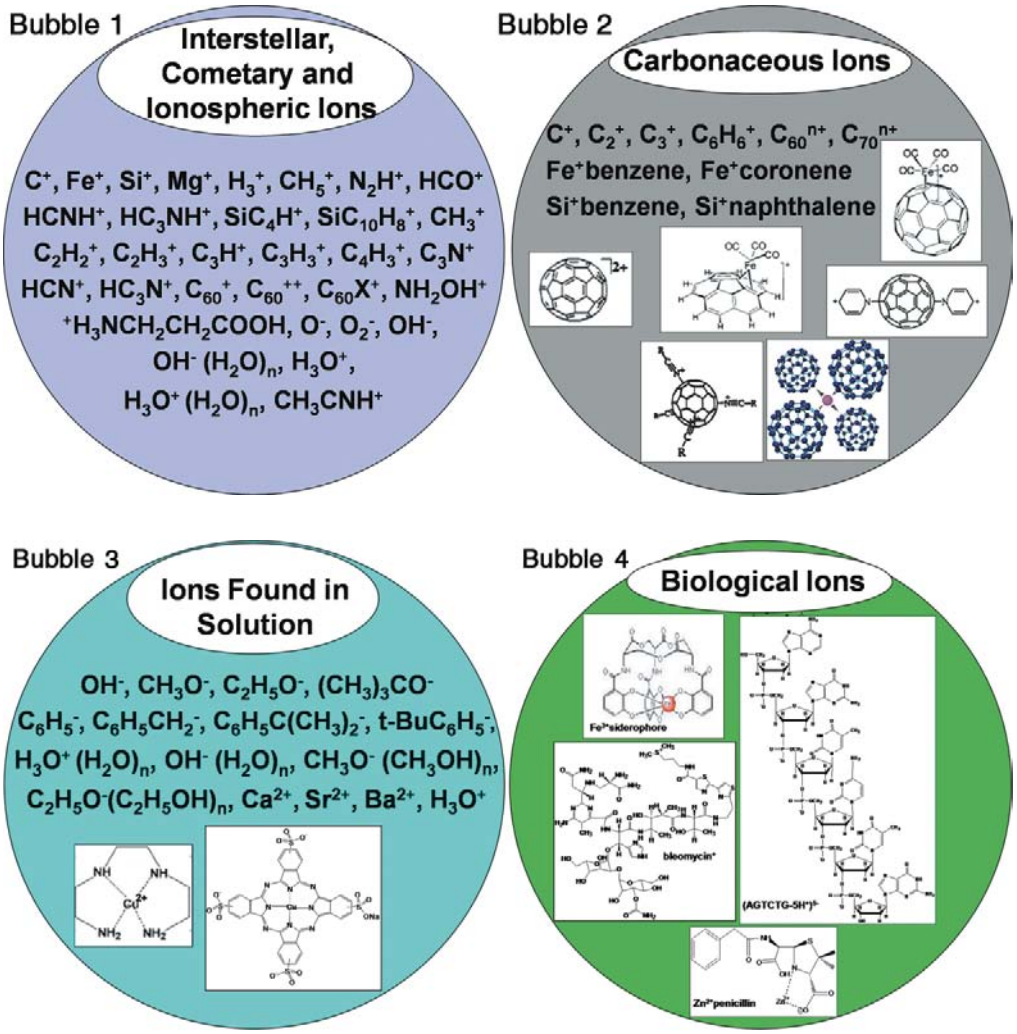

© 2008 NRC Canada

Fig. 1. Schematic view of sampling probe designed for sampling ions from a flowing nitrogen plasma excited with a microwave discharge (6).

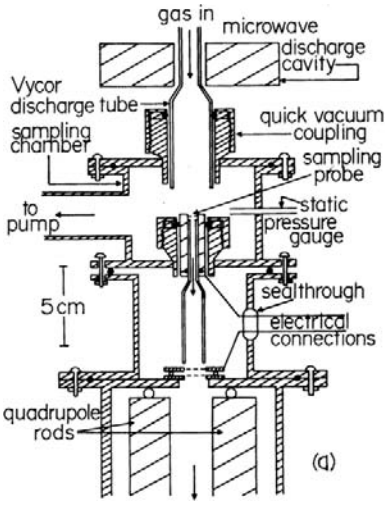

analysis. But atomic cations of alkali, alkali-earth, transition, main-group, and lanthanide metals, both singly and multiply charged, also have a wider function in physics, chemistry, and biology generally. For example, the catalytic activity of atomic ions can be explored, both as free or ligated atomic ions, and such studies promise new fundamental insights into the efficiency and mechanism of catalysis.

Looking for ions in a flowing nitrogen discharge plasma

I first saw ions slightly more than 43 years ago in Montreal as a graduate student at McGill University. My project was to build a quadrupole mass spectrometer and to look for ions in flowing nitrogen gas activated by a microwave discharge. This was before quadrupole mass spectrometers were commercially available and less than 10 years after Paul and Steinwedel (1953) published their paper in *Zeitschrift für Naturforschung* on the theory and operation of quadrupoles (5) (for which Paul would later win a Nobel Prize).

So my first task as a new graduate student was to design and construct a quadrupole mass spectrometer. This included building a high-voltage radio-frequency power supply from scratch, with the help of a *Radio Amateur's Handbook,* under the close and necessary guidance of my doctoral supervisor, John Goodings. The construction was a success and we did see ions in a microwave discharge of flowing nitrogen, with the help of the discharge-sampling probe that we invented and that is shown in Fig. 1 (6, 7). The first quadrupole mass spectra that we recorded on March 2, 1964, and probably the first such spectra recorded in Canada, are shown in Fig. 2. The main ions found to be present in the activated nitrogen included atomic and molecular nitrogen ions and there was a hint of the occurrence of ionic or molecular reactions with these ions, if not within the discharge itself, then at least in the sampling region.

Fig. 2. First mass spectra recorded with the quadrupole mass spectrometer fitted to the plasma sampling probe shown in Fig. 1. The spectrum on the right shows some resolved m/z OH_n^+ (n = 0–3) ion peaks (mis-assigned in the original scan).

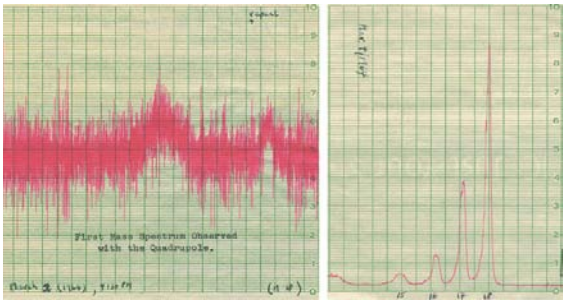

Fig. 3. Artistic view of the early flowing afterglow apparatus in Boulder, Colorado (8).

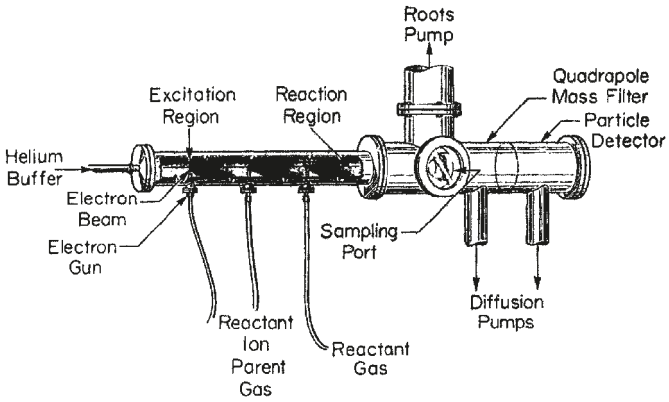

Ion chemistry in a flowing helium plasma

Meanwhile, quite independently, three physicists from Texas working at Environmental Science Services Administration (ESSA, now NOAA), a government research laboratory in Boulder, Colorado, showed that you could employ a flowing discharge plasma to study chemical reactions between ions and molecules, and to do so quantitatively! Eldon Ferguson, Fred Fehsenfeld, and Art Schmeltekopf set up the flowing He (instead of nitrogen) plasma that was activated with an electron gun (rather than microwaves) as shown in Fig. 3 (8). They demonstrated that, knowing the speed v of the flow (about 200 mph, 1 mile = 1.609 344 km), the length z of the reaction region, and the flow of the reagent, you could measure the rate coefficient k for a bimolecular reaction, say A^+ reacting with B, by monitoring the ions A^+ as a function of addition of neutral reagent B (at a fixed reaction time $t = z/v$) under pseudo first-order operating conditions, $[B] \gg [A^+]$! The rate eq. [1] can be cast in the form of eq. [2] and integrated. Equation [3] indicates that a semi-logarithmic plot of $[A^+]$ against the flow of B with a slope of $-k\ z/v$ can provide the rate coefficient k. The basic kinetic experiment then involves simply following the reactant (and product) ion signal as a function of added reagent and plotting the results appropriately.

$$[1] \qquad -d[A^+]/dt = k\ [A^+][B]$$

$$[2] \qquad -v\ d[A^+]/dz = k\ [A^+][B]$$

© 2008 NRC Canada

[3] $[A^+]_z = [A^+]_{z=0}\ e^{-k[B]z/v}$

In the example of experimental results shown in Fig. 4, electron ionization of oxygen upstream in the flow tube leads to formation of O^+ and O_2^+ ions that were exposed to hydrogen downstream in the flow tube. O_2^+ is seen to be unreactive, but O^+ reacts with a rate coefficient of 2.0×10^{-9} cm^3 molecule^{-1} s^{-1} that can be derived from the measured semi-logarithmic decay of O^+ as more and more hydrogen is added to the flow tube (9). Through a sequence of three H-atom transfer reactions, reactions 4a–4c, O^+ is rapidly converted to the hydronium ion, H_3O^+.

[4*a*] $O^+ + H_2 \rightarrow OH^+ + H$

[4*b*] $OH^+ + H_2 \rightarrow H_2O^+ + H$

[4*c*] $H_2O^+ + H_2 \rightarrow H_3O^+ + H$

Using this experimental approach in the 1960s and early 1970s, the three physicists from Texas were able to solve all of the important ion chemistry that occurs naturally in the earth's upper atmosphere (10, 11)!

Getting at the heart of chemistry: Bridging the gap between the gas phase and solution

By good fortune, I joined the Boulder group of physicists in 1967 along with Brewster Young, a graduate student at the University of Colorado at the time. With a freshman chemistry text book in our hands, we realized that chemical reactions predominant in solution could be investigated in a flowing He plasma in the gas phase, for the first time *in the complete absence of solvent*. We realized that appropriate neutral molecules, when ionized with an electron gun, could be deprotonated (reaction [5*a*]) or protonated (reactions [6*a*, 6*b*]) to produce negative or positive ions in the gas phase of the type found solvated in solution. These ions could then be exposed to chemical reaction downstream in the flow tube for measurements of reaction rates and products. Furthermore, they could even be solvated upstream first (reactions [5*b*] and [6*c*]), before reaction downstream so that the chemistry actually could be followed as a function of stepwise solvation.

[5*a*] $e + H_2O \rightarrow OH^- + H$

[5*b*] $OH^-(H_2O)_n + H_2O + He \rightarrow OH^-(H_2O)_{n+1} + He$

[6*a*] $e + H_2O \rightarrow H_2O^+ + 2e$

[6*b*] $H_2O^+ + H_2O \rightarrow H_3O^+ + OH$

[6*c*] $H_3O^+(H_2O)_n + H_2O + He \rightarrow H_3O^+(H_2O)_{n+1} + He$

With such ions in hand, I spent several intense years in the laboratory exploring the kinetics of textbook ion–molecule reactions such as acid base (e.g., reactions [7] and [8]) and nucleophilic substitution reactions (e.g., reaction [9]), in the absence and presence of solvent molecules.

[7] $OH^-(H_2O)_n + CH_3OH \rightarrow CH_3O^-(H_2O)_n + H_2O$

[8] $H_3O^+(H_2O)_n + CH_3OH \rightarrow CH_3OH_2^+(H_2O)_n + H_2O$

Fig. 4. Raw data recorded for the addition of H into a flowing He plasma in which O^+ and O_2^+ have been established upstream as predominant ions (9).

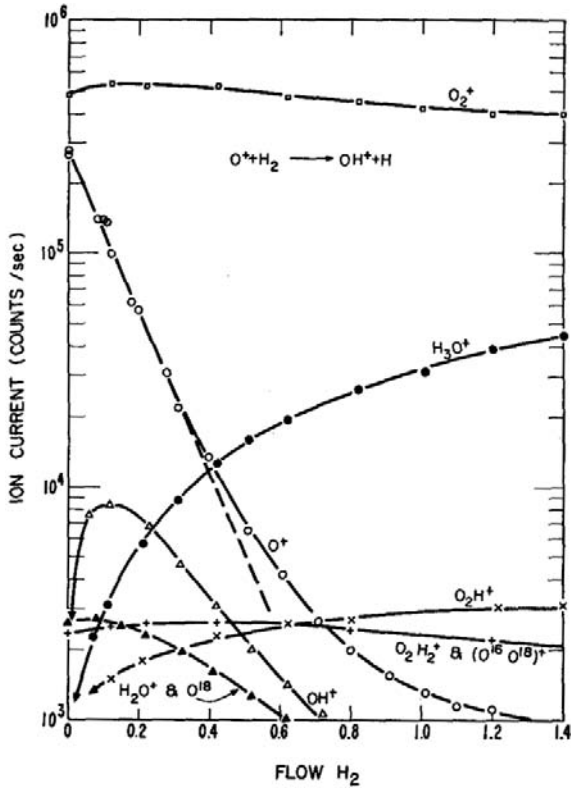

[9] $OH^-(H_2O)_n + CH_3Cl \rightarrow Cl^-(H_2O)_n + CH_3OH$

I continued these studies later at York University as an Assistant Professor with my first graduate student, Gervase Mackay, in the laboratory of Harold Schiff, who also had set up a flowing afterglow mass spectrometer. Here are some of our major findings.

Intrinsic acidities and the influence of solvation

Figure 5 shows data that illustrate the kinetics of proton transfer from methanol to the hydroxide anion and the influence of sequential hydration of the hydroxide anion on its ability to abstract a proton from methanol. The bare hydroxide ion was found to react at essentially every collision with $k = 1.5 \times 10^{-9}$ cm^3 molecule^{-1} s^{-1} at 296 ± 2 K (12–14).

[10] $OH^- + CH_3OH \rightarrow CH_3O^- + H_2O$

Equilibrium-constant measurements provided the means to track the shifting equilibrium and the reversal of the relative acidity of water and methanol from what it is in solution. The bare reaction was found to have a measured equilibrium constant at 296 K of 2.2×10^7, $\Delta G^\circ = -9.9$ kcal mol^{-1} (14). Also, the equilibrium constant is seen in Fig. 5 to decrease in magnitude with increasing hydration, as water becomes increasingly more acidic than methanol, and approach a value of 1 and even less than 1, at which point the standard free energy of reaction [10] has changed in sign and the relative acidity of water and methanol has reversed to that in solution. This appears to require hydration with

© 2008 NRC Canada

Fig. 5. (Top) Raw data for the room-temperature reaction between OH^- and methanol and for the step-wise hydration with up to three water molecules (14). (Bottom) Measured variation in the room-temperature equilibrium constant for proton transfer from methanol to OH^- with hydration and methanol solvation with up to three molecules of solvent (14).

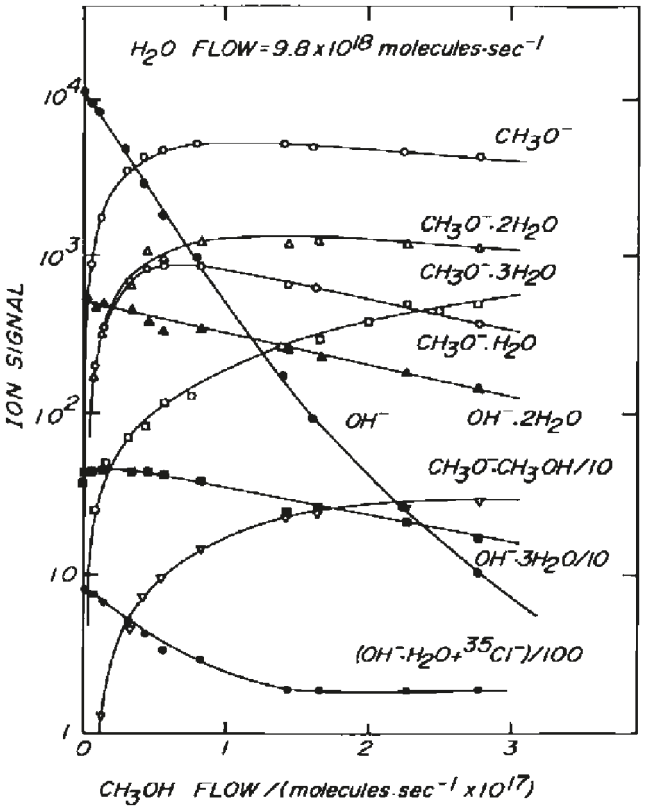

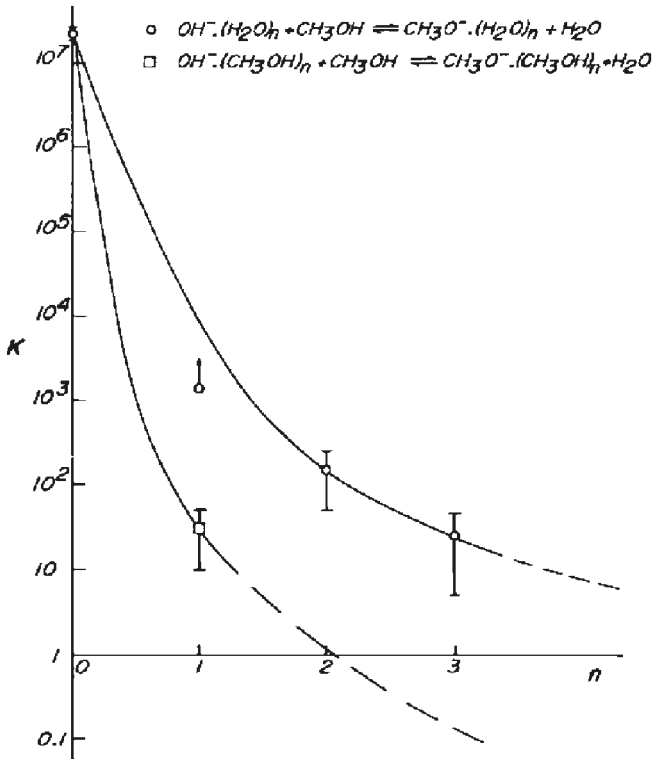

Fig. 6. Observed trends in the rate coefficient with extent of hydration for proton transfer reactions of hydrated hydroxide anions with several acids at 298 K. The values in parentheses indicate the relative intrinsic acidity of the acids AH and H_2O, $-\Delta G^o$ (in kcal mol^{-1}), for the unhydrated reactants (15).

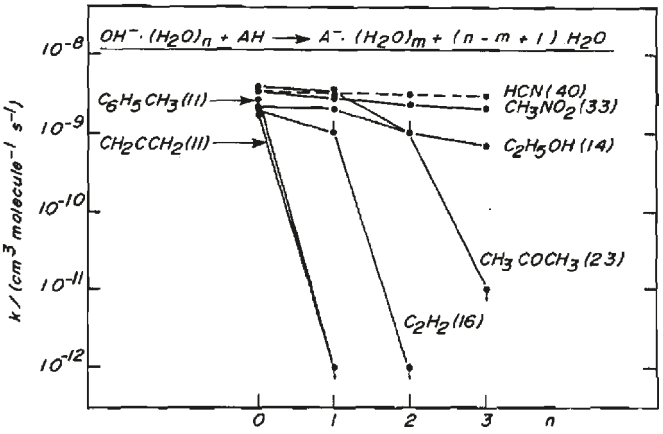

about 6 or 7 molecules of water and methanol solvation by only 2 molecules.

The influence of stepwise hydration on the kinetics of acid–base reactions with $OH^-(H_2O)_n$ also was explored (15).

[11] $OH^-(H_2O)_n + AH \rightarrow A^-(H_2O)_m + (n–m+1)\ H_2O$

The overview in Fig. 6 illustrates a reversal in acidity with hydration as signaled by a sharp drop in the rate of proton transfer with the addition of another water molecule. One water molecule appears sufficient with toluene and allene, two are required with acetylene, and three with acetone; no reversal is observed with hydrogen cyanide, nitromethane, or ethanol with up to four molecules of water.

Similar measurements became possible for reactions with protonated molecules. For example, reactions of H_3O^+ could be investigated in the gas phase as a function of molecular hydration, as shown in reaction [12]. Figure 7 shows results for the protonation of formaldehyde by "dry and wet" hydronium ions (16, 17) and the shifting equilibrium upon hydration.

[12] $H_3O^+(H_2O)_n + B \rightarrow BH^+(H_2O)_n + H_2O$

Reaction [12] was investigated with 11 different bases: 9 oxygen bases, NH_3, and H_2S. Figure 8 shows the measured variation in the rate coefficient for proton transfer with extent of hydration.

Transition between the gas phase and solution in the kinetics of nucleophilic displacement reactions

Another major finding, and this is perhaps an understatement, was that the hydroxide anion reacts with methyl chloride in the gas phase to yield Cl^- according to reaction [13] with a rate coefficient at room temperature of 1.9×10^{-9} cm^3 $molecule^{-1}$ s^{-1} (18), a stunning 17 orders of magnitude larger than in water where $k = 10^{-26}$ cm^3 $molecule^{-1}$ s^{-1}! The reaction occurs at essentially every collision in the gas phase without any kinetic barrier (19), an astounding illustration of the solvent effect.

[13] $OH^- + CH_3Cl \rightarrow Cl^- + CH_3OH$

© 2008 NRC Canada

Fig. 7. (Left) Raw data for the room-temperature reaction between H_3O^+ and formaldehyde and for the step-wise hydration with up to three water molecules. (Right) Measured variation in the room-temperature equilibrium constant for proton transfer from H_3O^+ to formaldehyde with hydration (16).

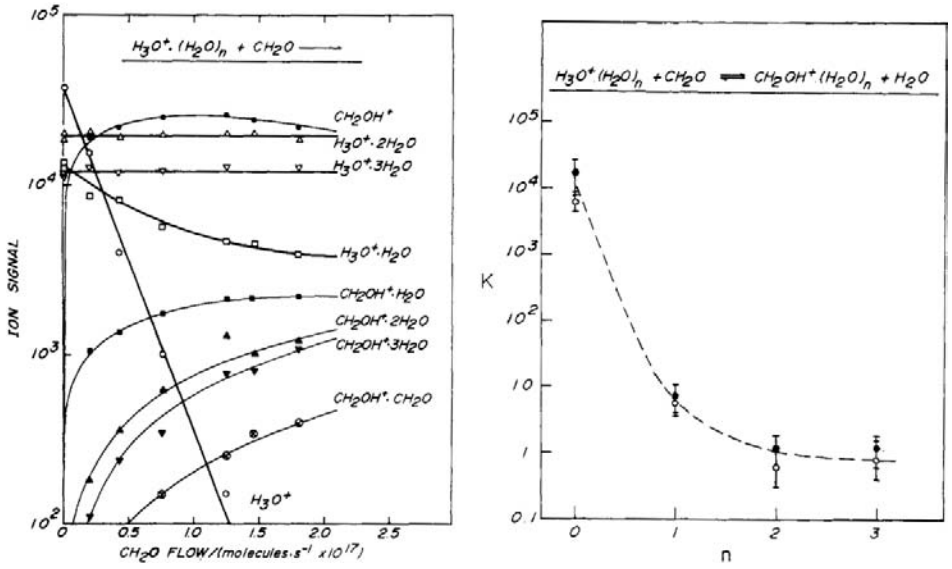

Fig. 8. Variation in the rate coefficient with extent of hydration for proton transfer reactions of the hydrated hydronium ion with several oxygen bases and ammonia at room temperature (16).

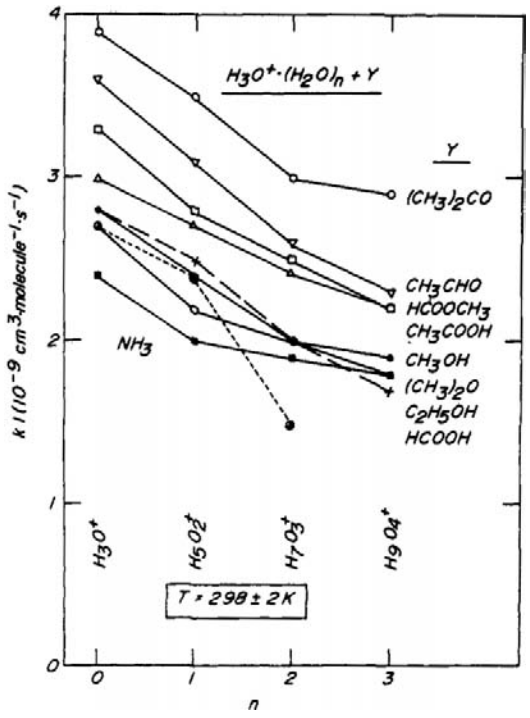

Molecular hydration in the gas phase was observed (20,21) to drop the rate by at least 4 orders of magnitude with the addition of only 3 solvent molecules (see Fig. 9). So there is no intrinsic activation energy at the heart of the reaction; rather, an activation energy emerges upon solvation (see Fig. 10).

These early measurements clearly demonstrate the usefulness and power of flow-tube mass spectrometry in determining intrinsic reactivities of chemical reactions that occur in solution and in tracking changes in reactivity with solvation at the molecular level.

Kinetics, collision theories, and thermodynamics

We have performed extensive kinetic measurements of numerous proton-transfer reactions involving small molecules and ions (unsolvated), to determine both the rate coefficients and the position of equilibrium.

[14] $XH^+ + Y \rightarrow YH^+ + X$

[15] $X^- + YH \rightarrow Y^- + XH$

The rate in the preferred directions of reactions [14] and [15] was observed to be controlled by the thermodynamics of reaction (22, 23): proton transfer was seen to be fast when it was seen to be thermodynamically favoured (exoergic) from equilibrium constant measurements (see Fig. 11).

Because the rate of proton transfer is expected to be collision-controlled, the measurements of the rate coefficients of proton transfer proved to be valuable for testing the various collision theories that evolved at about the same time as the measurements were being made. Collision theories are based on the electrostatic interaction between the colliding ion and the molecule, and this depends on the physical properties of the neutral molecule such as its polarizability, dipole moment, and quadrupole moment. A wide choice in these physical properties is available with the neutral reagents that can be added into the flow tube, and this has allowed extensive testing of the various collision theories. Some representative results are given in Figs. 12 and 13. Figure 12 provides a comparison between experiment and theory for proton-transfer reactions of type [14] and [15] with the dipolar HCN molecule (24) and also reactions of type [14] with quadrupolar acetylene (25). Figure 13 presents results for proton-transfer reactions of H_3O^+ with a variety of polar molecules according to reaction [14] (26). The best agreement for proton-transfer reactions with polar molecules is found with the average dipole orientation theory. The aver-

© 2008 NRC Canada

Fig. 9. (Left) Raw data for the room-temperature reaction between OH^- and methyl chloride in the complete absence of water and for the step-wise hydration with up to three water molecules. (Right) Measured variation in the rate of reaction of various nucleophiles with solvation with up to three molecules of solvent (21).

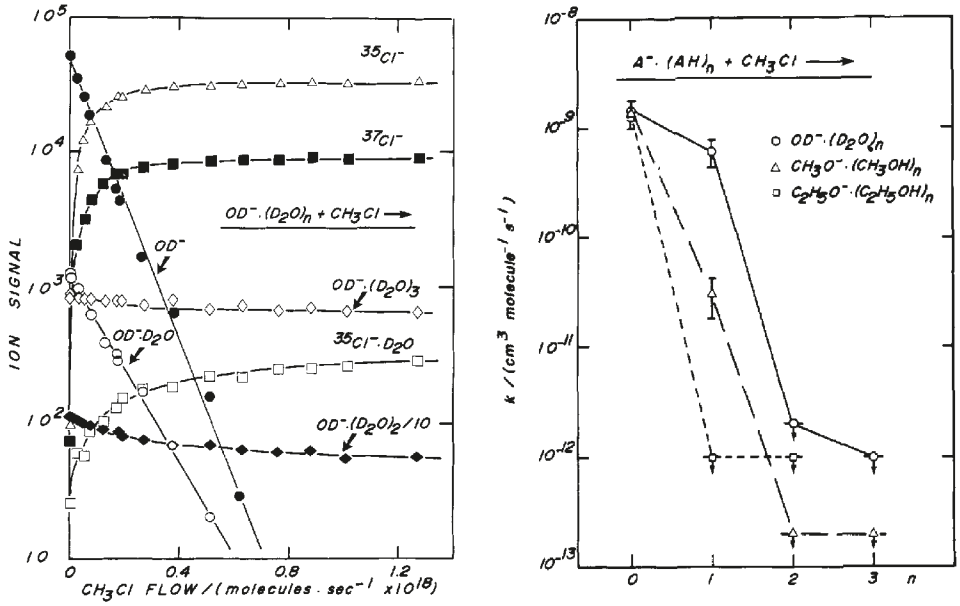

Fig. 10. Sketch of plausible potential energy vs. reaction coordinates for the nucleophilic displacement reaction between OH- and methyl bromide for various degrees of hydration. Barrier heights are ascribed to the transition states to illustrate the transition expected in the reaction kinetics from the gas phase to solution (20).

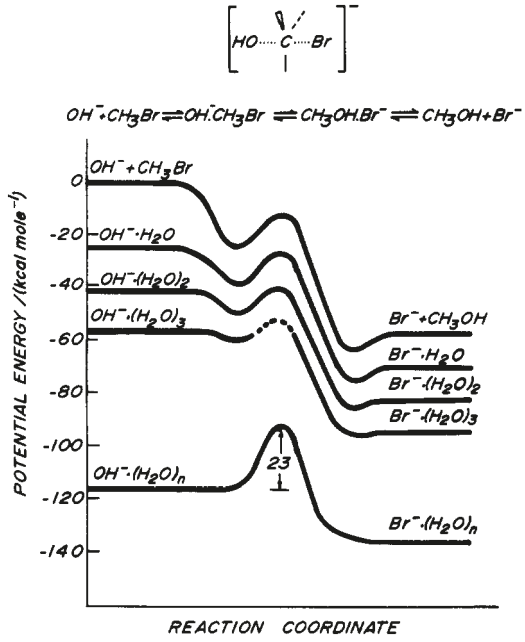

age quadrupole orientation theory provides a good prediction for the protonation of acetylene in which the collision is controlled by ion–quadrupole interaction.

Equilibrium constant measurements and bracketing measurements that establish the preferred direction for reactions of type [14] and [15] have provided the magnitude or sign of the standard free energy change for proton transfer (ΔG^o = –*RT* ln *K*). Equilibrium constants were determined either from measurements of equilibrium concentrations or from measurements of the forward and reverse rate coefficients (27, 28). These measurements provided important new absolute and relative values for gas-phase acidities, basicities and proton affinities of small molecules. For example, we reported very early (1971) measurements of the gas-phase acidities of alcohols (29) and later on of several aliphatic amines (30), and acidity orders for other Brönsted acids and several inorganic acids (31, 32). Some early (1980) definitive values determined for the proton affinities of small molecules and enthalpies of formation of protonated molecules are given in Table 1.

Table 1. Recommended proton affinities, PA, and enthalpies of formation, $\Delta H^o_f(XH^+)$, at 298 K (in kcal mol^{-1}) (22).

X	PA_{298} (X)[a]	$\Delta H^0_{f,298}$ (XH^+)
CO	141.4±0.4	199.4±0.4
N_2O	137.0±1.4	249.8±1.5
CH_4	130.5±2.0	218.8±2.1
CO_2	128.6±21	144.5±2.1
Xe	118.0±0.9	249.2±0.9
N_2	117.4±0.7	249.8±0.7
O	116.1±0.2	310.6±0.2
Kr	101.4±0.8	265.8±0.8
H_2	100.7±0.8	266.5±0.8
O_2	100.4±	266.8±0.4

[a]CO, O, and O_2were used as benchmarks.

Proton transfer to and from a suitable "transporter" molecule also can provide an alternative route for the isomerization of protonated molecules and this was recognized with the notion of proton-transport catalysis (33). Such catalysis is often efficient when the proton affinity of the transporter molecules has

© 2008 NRC Canada

Fig. 11. Variation in reaction efficiency, k_{exp}/k_c, at 298 K with the standard free energy of reaction for proton-transfer reactions of type [14] (left, 22) and with the standard enthalpy of reaction for proton-transfer reactions of type [15] (right, 23).

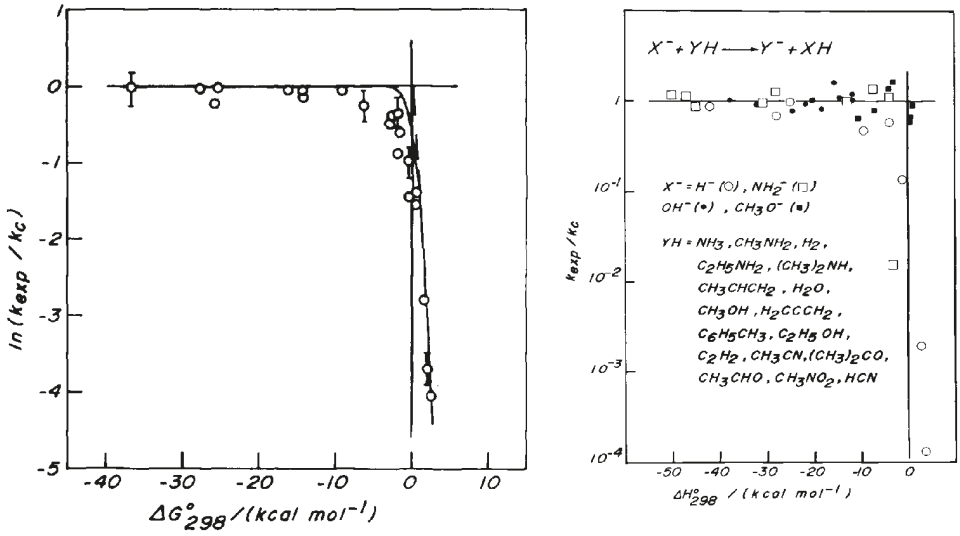

Fig. 12. A comparison of rate coefficients measured for proton-transfer reactions with HCN (24) and C_2H_2 (25) at 297 ± 2 K with collision rate coefficients predicted by various classical collision theories. The polarizability of HCN is 2.59 Å^3 and its dipole moment is 2.98 D. The polarizability of C_2H_2 is 3.33 Å^3 and its quadrupole moment Q = 3.6 × 10^{-26} e.s.u. cm^2. ADO = average dipole orientation. AQO = average quadrupole orientation.

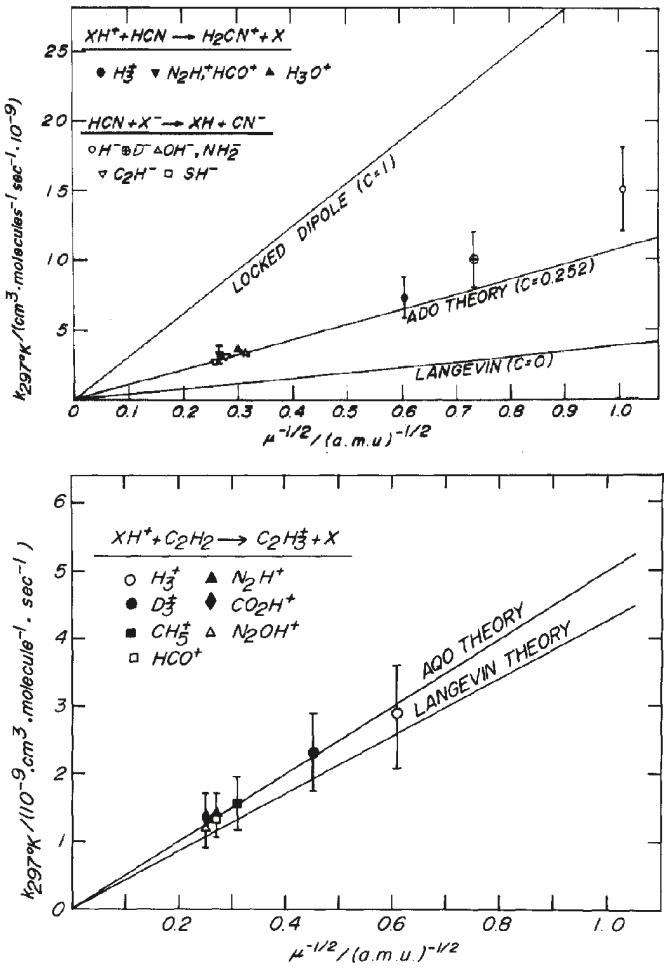

Fig. 13. A comparison of measured rate coefficients with capture rate coefficients predicted by various collision theories for proton transfer reactions of H_3O^+ with polar molecules (26). The solid bars represent the estimated accuracies of the measurements. k_L is the collision rate coefficient determined from the Langevin theory.

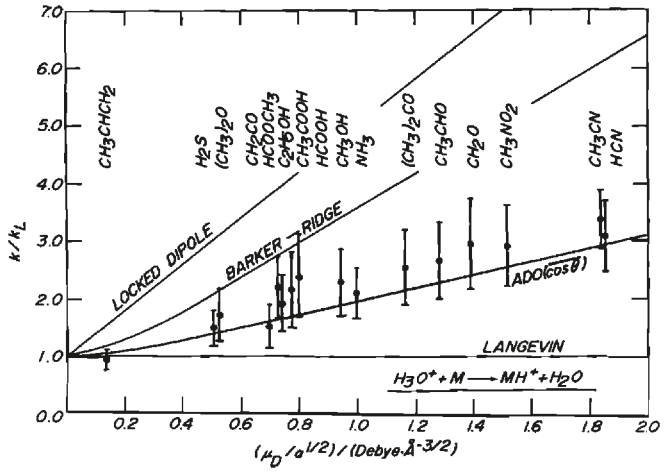

a value in between the proton affinities of the different sites of protonation of the two isomers.

Selected-ion flow tube (SIFT) tandem mass spectrometry

A major advance in flow-tube mass spectrometry was achieved in the late 1970s by two British physicists, Nigel Adams and David Smith, then at the University of Birmingham. They showed in 1976 that ions could be produced and mass-selected *outside* the flow tube and then injected through a Venturi-type interface that is able to maintain the pressure difference across a hole large enough (ca. 5 mm in diameter) to transmit enough ions into the flowing He buffer gas at a pressure of ca. 0.35 Torr (1 Torr = 133.322 Pa) (34). With this innovation, the chemistry of one type of ion could be followed in the absence of other ions, as well as metastable atoms and electrons. The selected-ion flow tube

© 2008 NRC Canada

Fig. 14. Schematic and pictorial views of the selected-ion flow tube (SIFT) tandem mass spectrometer built at York University in 1978 (35).

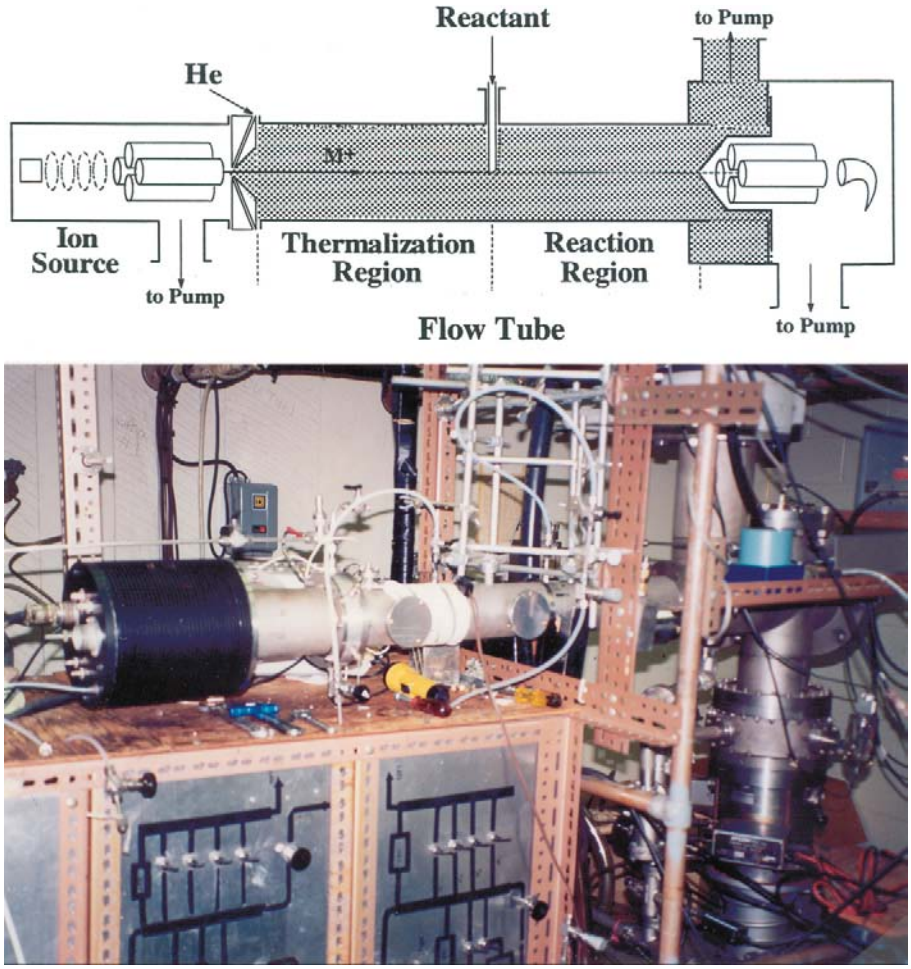

Fig. 15. Observed variations in ion signals recorded for the addition of acetylene (38) and formic acid (41) into the reaction region of the SIFT apparatus in which $Si^+(^2P)$ has been established as the dominant ion in He buffer gas at 0.35 Torr and room temperature. The Si^+ is derived by electron impact of tetramethyl- (left) or tetrachloro- (right) silane with deuterium added to convert the excited $Si^+(^4P)$ to SiD^+.

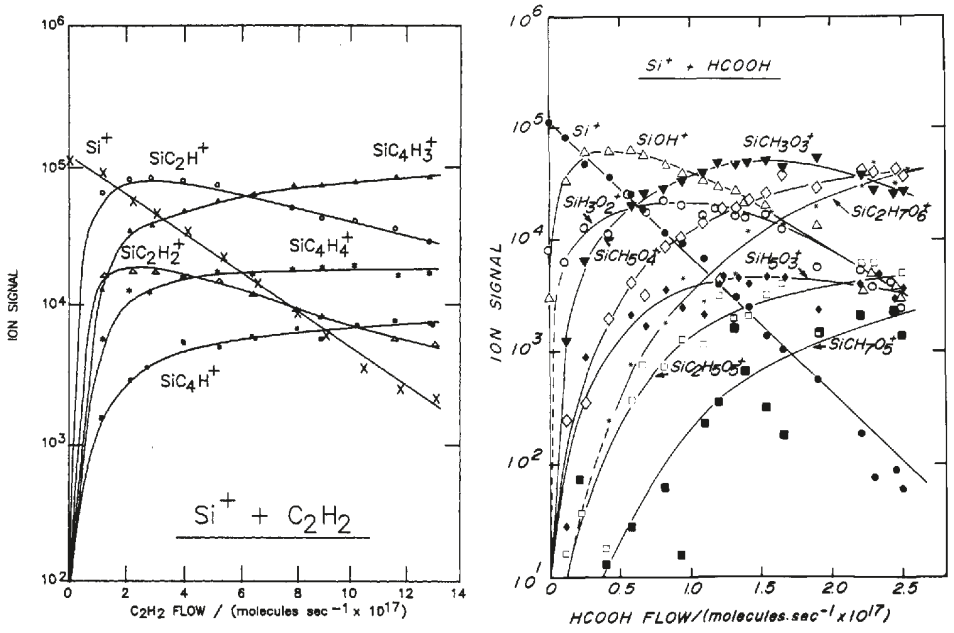

© 2008 NRC Canada

Fig. 16. Observed variations of ions recorded with the addition of diacetylene (left) and methane (right) into the reaction region of a SIFT apparatus in which $C_4H_2^+$ (ionized diacetylene) and C_3H^+, respectively, were established as the predominant upstream ions (56, 57).

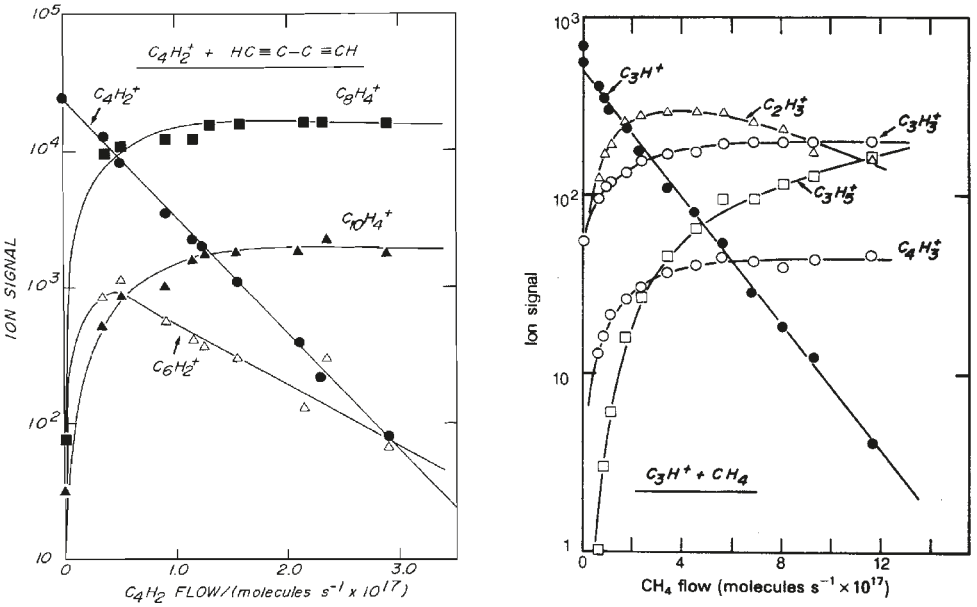

(SIFT) tandem mass spectrometer constructed and operative shortly thereafter at York University is shown in Fig. 14 (35). The SIFT technique proved to be particularly useful for measurements with atomic ions and reactive ion intermediates that are elusive otherwise.

Chemical bond formation initiated by atomic ions

A variety of atomic ions could be produced by electron-impact ionization of appropriate parent molecules and injected into the flow tube. Examples include C^+ (36), S^+ (37), Si^+ (38–42) (see Fig. 15), and the atomic metal ions Mg^+ (43–46) and Fe^+ (47–49). Reactions with the non-metallic ions invariably lead to heavy-atom bond formation and the initiation of ionic growth; atomic metal cations also can mediate bond formation. Ionic growth by successive ion–molecule reactions is useful in neutral molecular synthesis if the grown ions can be neutralized, for example by proton transfer or recombination with electrons, without excessive dissociation.

Thus C^+ was observed to react with hydrocarbons such as methane, ethylene, and acetylene by C–C bond formation to form hydrocarbon ions that may neutralize to form larger hydrocarbons (36); see reaction [16], for example. S^+ was observed to react with diacetylene by C–S bond formation according to reaction [17] to form HC_4S^+, a possible precursor of C_4S in interstellar clouds (37). We also investigated in much detail the rich chemistry initiated by reactions with Si^+ leading to Si–H (41), Si–C (39), Si–O (40), Si–N (42), and Si–S (40) bond formation as in reactions [18] to [22]. A large variety of Si-containing neutrals, including some interesting silicon carbides (38, 39, 42), silicon oxides (40, 41), and silicon hydroxides (41), become accessible to these initiating reactions and these have been described in considerable detail (50, 51). Much of this chemistry is also of great interest in the silicon chemistry of interstellar clouds (52, 53).

[16] $C^+ + C_2H_2 \rightarrow C_3H^+ + H$

[17] $S^+ + C_4H_2 \rightarrow HC_4S^+ + H$

[18] $Si^+ + C_4H_2 \rightarrow C_4H^+ + SiH$

[19] $Si^+ + C_2H_2 \rightarrow SiC_2H^+ + H$

[20] $Si^+ + H_2O \rightarrow SiOH^+ + H$

[21] $Si^+ + NH_3 \rightarrow SiNH_2^+ + H$

[22] $Si^+ + OCS \rightarrow SiS^+ + CO$

Hydrocarbon-ion chemistry and ionic origins of carbenes in space

The value of the SIFT technique is further illustrated by the development in our laboratory of models for the ionic synthesis of hydrocarbon molecules (54) including cyanoacetylenes (55) and carbenes (56) known to be present in regions of ionizing radiation such as the tails of comets, the atmospheres of carbon stars, and cool molecular gas clouds. Figure 16 shows raw data for the reaction of diacetylene with the diacetylene radical cation $C_4H_2^{+\bullet}$ selected from an electron-impact source in which diacetylene was ionized (57) and for the reaction of the carbene cation $:C_3H^+$ derived from the electron impact of propylene (56). The following reaction sequence observed in diacetylene (57) can lead to the growth of carbon-chains.

[23] $C_4H_2^{+\bullet} + C_4H_2 \rightarrow C_4H_2^{+\bullet}(C_4H_2)$
$\rightarrow C_6H_2^{+\bullet} + C_2H_2$

[24] $C_6H_2^{+\bullet} + C_4H_2 \rightarrow C_{10}H_4^{+\bullet}$

One early focus in our laboratory of interstellar and circumstellar ion chemistry was the exploration of possible ionic origins of carbenes such as $:CH_2$, :C=C:, :C=S, :C=O, :C=NH, :C=C=C:, *l,c*-$:C_3H_2$, and $:C_3O$. Figure 17 shows a model scheme for the ionic synthesis of :C=C=C:, *c*-$:C_3H_2$ and $:C=C=C=CH_2$ (56) based, in part, on SIFT measurements of ion–molecule reactions.

© 2008 NRC Canada

Fig. 17. Chemical model for the ionic synthesis of neutral carbenes initiated by atomic carbon cations (56). EIR = electron/ion recombination; PT = proton transfer. Raw data for the reaction of :C=C=CH$^+$ with methane is shown in Fig. 16.

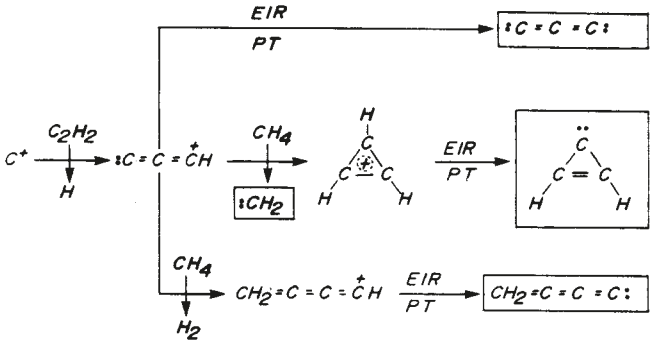

Fig. 18. (Left) Data recorded for the sequential addition of cyanoacetylene to Mg^+ to form $Mg(HC_3N)_n^+$ in a He buffer gas at 294 ± 3 K and 0.35 ± 0.01 Torr (46). (Right) Results of multi-CID experiments (46). The fractional abundance of ion signals for $Mg(HC_3N)_n^+$ are plotted against the nose-cone potential, U_{nc}. The flow of cyanoacetylene is 6.0×10^{17} molecules s^{-1}.

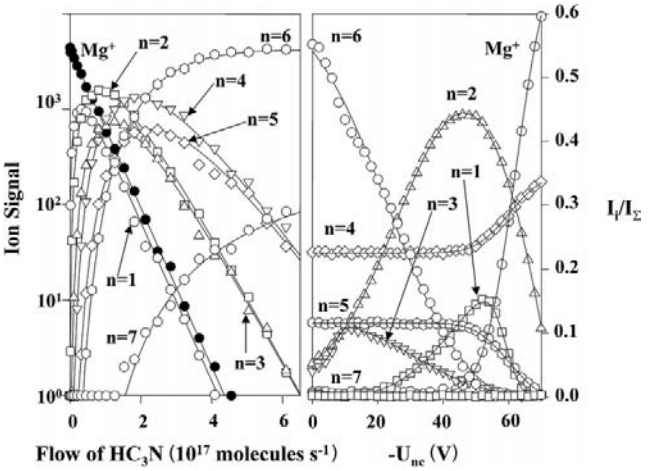

Fig. 19. Proposed routes for the synthesis of amino acids in interstellar environments (59). M and A represent any neutral atom or molecule with an ionization energy suitable for neutralization or ionization by electron transfer. RH^+ represents a proton carrier with PA(R) < PA(NH_2OH).

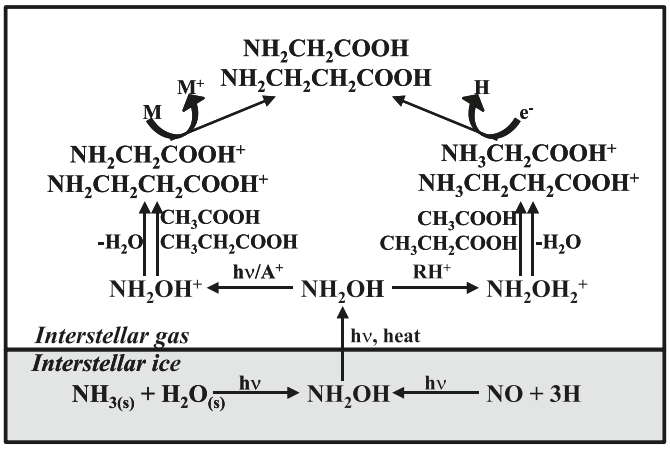

Furthermore, multi-collision induced dissociation experiments using the sampling nose cone in the flow tube as an "ion attractor" (58) pointed toward an extraordinary stability for the fourth adduct, also seen in Fig. 18. Why should this be so? Our molecular orbital calculations with density functional theory showed the existence of at least two very stable isomers of $(HC_3N)_4$, 1,2,5,6-tetracyano-1,3,5,7-cyclooctatetrene and 2,4,6,8-tetracyanosemibullvalene (46). The isomerization of $(HC_3N)_4$ into one of these isomers mediated by $Mg^{+\bullet}$ became an attractive proposition as a consequence. So we have suggested the formation of these exotic ring molecules in extraterrestrial environments by the sequence of radiative association and electron–ion recombination expressed in reactions [26] and [27]. $Mg^{+\bullet}$ ions, cyanoacetylene, and electrons are known to be present in circumstellar envelopes and the atmosphere of Titan.

[25] $Mg(HC_3N)_{n-1}^{+\bullet} + HC_3N \rightarrow Mg(HC_3N)_n^{+\bullet}$,

where n = 1 to 7

[26] $Mg(HC_3N)_{n-1}^{+\bullet} + HC_3N \rightarrow Mg(HC_3N)_n^{+\bullet} + h\nu$

[27] $Mg(HC_3N)_n^{+\bullet} + e \rightarrow (HC_3N)_n + Mg$

The formation of cyclooctatetrene is illustrated in eq. [28].

[28]

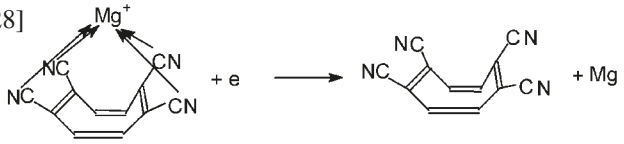

Ions and life

The "holy grail" for many ion chemists is a gas-phase ionic reaction mechanism that leads to the formation of neutral amino acids, the building blocks of life, in outer space. We tried for many years to identify and characterize ion–molecule reactions appropriate for such formation. The SIFT mass spectrometer provided the right tool to do so, but the right chemistry was elusive. Earlier searches for the direct formation of glycine from plausible ionized and molecular fragments of this molecule were hampered by the preference of N–O bond formation over the desired C–C or C–N bond formation. For example, the reactions of $CH_3NH_2^+$ with HCOOH, CO_2, or CO + H_2O, of NH_3^+ with CH_3COOH, and of CH_2COOH^+ with NH_3 all failed to produce glycine. Finally in 2003, we were able to report that ionized glycine and β-alanine are produced in the reactions of hydroxylamine ions, NH_2OH^+, with acetic and propanoic acid, respectively, and the corresponding production of the protonated amino acids from analogous reactions with

© 2008 NRC Canada

protonated hydroxylamine (59). We have since explored the potential energy surfaces of the latter reactions and explained the observed preference for the formation of β-AlaH$^+$ over the α-AlaH$^+$ isomer (60). Figure 19 summarizes our proposed routes for the synthesis of amino acids in interstellar environments (59).

The striking specificity of these syntheses for the β-isomer of alanine suggests that the amino acids of CI chondrites, a class of carbonaceous meteorites, are products of interstellar chemistry and supports the hypothesis that these meteorites are of cometary origin (59). Now we are targeting the formation of larger and more complex biomolecules by ionic synthesis.

Chemistry with buckyballs

Thanks to the generosity of Wolfgang Krätschmer who had produced buckminsterfullerene C_{60} powder for the first time in 1989 in Heidelberg at the Max-Planck Institute for Nuclear Physics (61), I was able to bring a small sample to Canada in 1990. We had just had resounding success at the Technical University of Berlin in the laboratories of Helmut Schwarz (where I was on sabbatical leave) in producing endohedral cluster compounds of He and $C_{60}^{+\bullet}$ at high collision energies (62). So my two postdoctoral fellows at the time, Simon Petrie and Reza Javahery, and I had an unprecedented opportunity to do chemistry here in Canada with this fascinating new molecule whose discovery would lead to a Nobel Prize in 1996. The next three years of research were packed with numerous discoveries and were among the most exciting and rewarding of my entire career (63).

Chemical ionization of fullerenes

We quickly found out that the buckminsterfullerene molecule could undergo completely novel chemical ionizations at room temperature. We first demonstrated the single ionization of C_{60} with metastable atoms (the well-known Penning ionization) (64), reaction [29], but then also observed the occurrence of double ionization by concomitant electron transfer and electron detachment (65), reaction [30], a thermal ionization process that was completely unknown at the time and which we attribute to the metallic character of C_{60}, a cage of 60 C nuclei surrounded by an ocean of electrons. Since then we also have discovered the occurrence of "double-electron transfer / electron detachment" with Ar^{2+} (66), reaction [31].

[29] $\quad He\ (^3S_1,\ ^1S_1) + C_{60} \rightarrow He(^1S_0) + C_{60}^{+\bullet} + e$

[30] $\quad He^{+\bullet} + C_{60} \rightarrow C_{60}^{2+} + He + e$

[31] $\quad Ar^{2+} + C_{60} \rightarrow C_{60}^{3+\bullet} + Ar + e$

Reactions of fullerene cations: Electron transfer and derivatization

Our studies of ion–molecule reactions of mono-, di-, and tri-cations of C_{60} have provided a wealth of new information about the physical and chemical properties of this fascinating molecule and other fullerene relatives. The observation of, or failure to observe, electron transfer to multiply charged fullerene cations from molecules of known ionization energy provided insights into the electron recombination

Fig. 20. Overview of the chemistry of C_{60}^{2+} recorded with our SIFT apparatus at RT and a He bath gas pressure of 0.35 Torr (63).

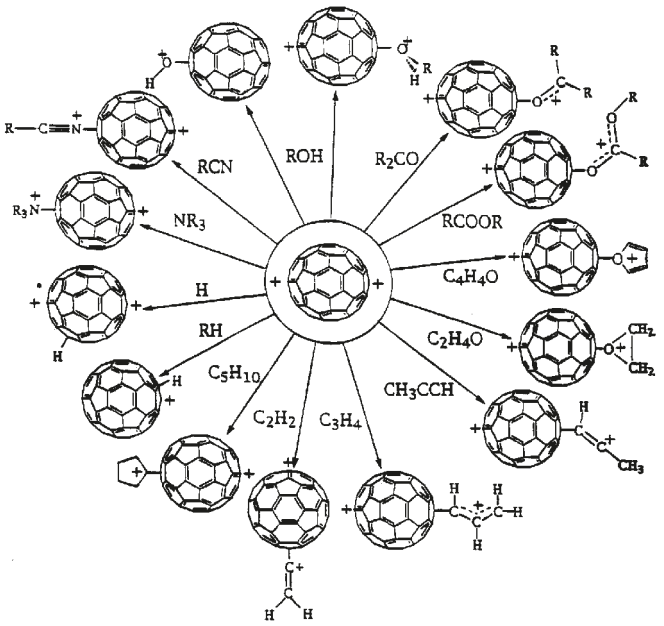

energies of the fullerene cations as well as the magnitude of the barrier to electron transfer that can arise from the Coulombic repulsion between the charged product ions (67). An unprecedented transfer of *two electrons* was observed between triply charged $C_{60}^{3+\bullet}$ cations and the PAHs anthracene, pyrene, corannulene and benzo[rst]pentaphene (68). These reagent molecules have sufficiently low first and second ionization energies to make double-electron transfer thermodynamically and kinetically favourable.

Reactions that lead to chemical bond formation also face an activation barrier (estimated to be 15 kcal mol^{-1}) because a transition is required from largely sp^2 to sp^3 hybridization at the C atom that becomes bonded. This intrinsic activation barrier is overcome with increasing charge on the fullerene cation because of the resulting increase in electrostatic interaction between reactants. Thus, higher charge states tend to exhibit higher chemical reactivity (69–71) and greater efficiency of ligation (72). Figure 20 captures an overview of the chemistry observed with the fullerene dication.

Chemistry as a function of charge state

The extraordinary stability of buckminsterfullerene in multiple charge states provides an extremely rare opportunity to investigate systematically the influence of charge state on chemical reactivity (73). An overview of the results of such investigations in our laboratory is provided in Fig. 21. Experimental results with a large variety of neutral molecules as reagents indicated that chemistry (chemical-bond formation) is increasingly pre-empted by physics (electron transfer) with increasing charge state (63). The competition between electron transfer and bond formation has been monitored quantitatively for reactions of C_{60}^{2+} with ammonia and several amines as displayed in Fig. 22. However, the onset for electron transfer as the dominant channel is delayed by the activation barrier that arises from the Coulomb repulsion between the charged products (73).

© 2008 NRC Canada

Fig. 21. (Left) Stoichiometrically possible channels for the reactions of multiply charged buckminsterfullerene cations with molecules XY. (Right) Trends with charge state in the electron recombination energy, RE, and the observed reaction channels (63).

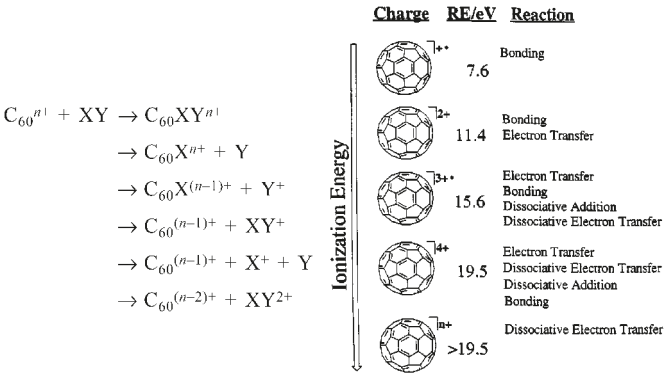

Fig. 22. The competition between electron transfer (dashed line) and ligation (solid line) observed for reactions of C_{60}^{2+} with ammonia and several amines in a SIFT apparatus at 294 K and a He bath gas pressure of 0.35 Torr (63).

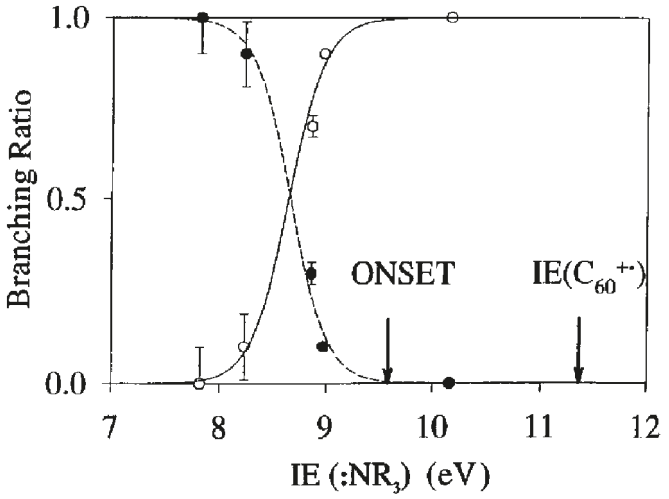

Higher-order fullerene ion chemistry

We have observed higher-order reactions of derivatized fullerene cations that exhibit proton (74) and cation (75) transfer as illustrated in reactions [32] and [33], double and multiple derivatization of the surface of C_{60} (71, 75 and example in Fig. 23) including sequential hydrogenation with hydrogen atoms (76), and cation-induced polymerization of several small unsaturated hydrocarbon monomers by "ball-and-chain" propagation (76). The latter can be assisted by intramolecular Coulomb repulsion.

[32] $C_{60}(XH)_n^{2+} + XH \rightarrow C_{60}(XH)_{n-1}^{+} + XH_2^{+}$

[33] $C_{60}(XCH_3)^{3+} + XCH_3 \rightarrow C_{60}(X)^{2+} + X(CH_3)_2^{+}$

Chemistry and physics in concert

We have found that chemistry and physics can operate in concert in reactions involving multiply charged derivatized fullerene ions, when Coulomb repulsion between the charges drives intramolecular charge transport that enhances charge

Fig. 23. Data recorded for the sequential addition of methyl isocyanide to $C_{60}^{3+\bullet}$ in He buffer gas at 0.35 Torr and 294 K.

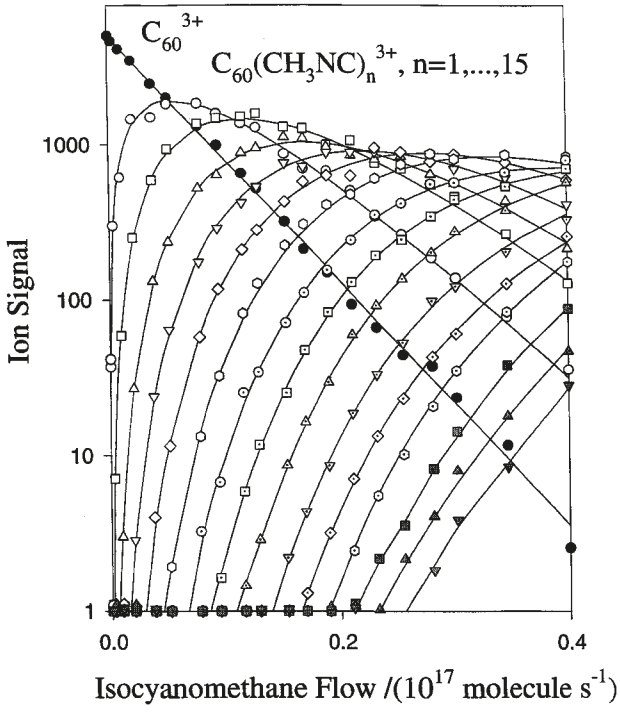

Fig. 24. "Molecular dock mechanism" proposed for the cyclization of cyanoacetylene assisted by C_{60}^{2+}.

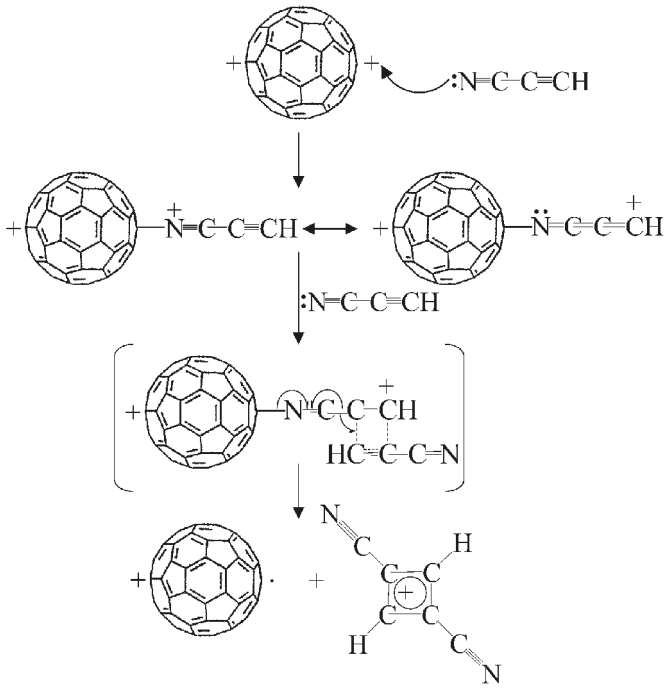

localization on the substituent and so the chemical reactivity of the derivatized ion. This mechanism is illustrated in Fig. 24 and explains the products of the reaction between C_{60}^{2+} and cyanoacetylene that we have observed in our SIFT (77). The 2+2 cyclization that is envisaged leads to the remarkable formation of the derivatized cyclobutadiene isomer

© 2008 NRC Canada

Scheme 1.

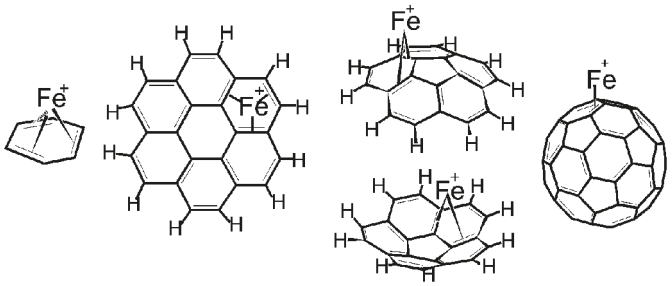

of $(HC_3N)_2^{+\bullet}$ that is not directly accessible to the reaction of ionized cyanoacetylene with cyanoacetylene, as we have shown by the collision-induced dissociation of the isomers formed in these two different ways. The same mechanism, which we have called the "molecular dock mechanism", might well apply to the formation of other derivatized cyclobutadienes from higher homologs of cyanoacetylene and should be applicable more generally to any carbonaceous molecule or particle that can carry multiple charges and provide an atomic site for covalent bonding. The generalized case is illustrated in reaction [34]. We have proposed such reactions as a source of neutral derivatized cyclobutadiene ring molecules in interstellar and circumstellar environments when the cyclic product ion is subsequently neutralized by electron transfer.

[34] $$X^{2+} + 2\ H(C_2)_nCN \rightarrow X^+ + c\text{-}C_4H_2((C_2)_{n-1}CN)_2^+$$

Gas-phase surface chemistry: The influence of curvature

The availability of fullerenes provides an unprecedented opportunity to investigate carbonaceous surface chemistry in the gas phase at the molecular level in the absence of boundary effects and free of contamination and surface imperfections. For example, the influence on the chemistry of individual atomic ions attached (ligated) to various molecular carbonaceous surfaces (here defined as such by their much larger size) can be studied in splendid detail. Our emphasis so far has been on the modification of the reactivity of Fe^+ by the various carbonaceous molecules shown in Scheme 1 (78, 79).

Some progress has been made in investigating the influence of surface features on the chemical reactivity of fullerene cations themselves. Early SIFT investigations of addition reactions of fullerene cations C_{56}^+, C_{58}^+ and C_{60}^+ with NH_3, of addition reactions of C_{56}^{2+}, C_{58}^{2+} and C_{60}^{2+} with C_2H_4 and CH_3CN, and of hydride-transfer reactions of C_{56}^{2+}, C_{58}^{2+} and C_{60}^{2+} with n-C_4H_{10}, revealed an enhanced reactivity for the adjacent-pentagon fullerene ions(80). More recent systematic studies of addition reactions of C_{56}^+, C_{58}^+, C_{60}^+, C_{70}^+, corannulene$^+$, and coronene$^+$ with cyclopentadiene (see Fig. 25) and 1,3-cyclohexadiene indicate that the efficiency of bond formation with these two molecules also depends strongly on the curvature of the carbonaceous surface of the reacting cation (81, 82).

Extraterrestrial fullerene ion chemistry

There are very good reasons to expect the presence of fullerene and derivatized fullerene cations in the interstellar medium and in the circumstellar envelopes of carbon-rich

Fig 25. A correlation between reaction efficiency k_{obs}/k_c with the square of the pi orbital axis vector angle and the strain energy for addition reactions with cyclopentadiene at room temperature and a He pressure of 0.35 ± 0.01 Torr (81). k_{obs} is the measured rate coefficient and k_c is the collision rate coefficient which is estimated to be 10^{-9} cm^3 molecule^{-1} s^{-1}. The dotted line defines the dependence of k_{obs} on strain energy, E_s, which is indicated.

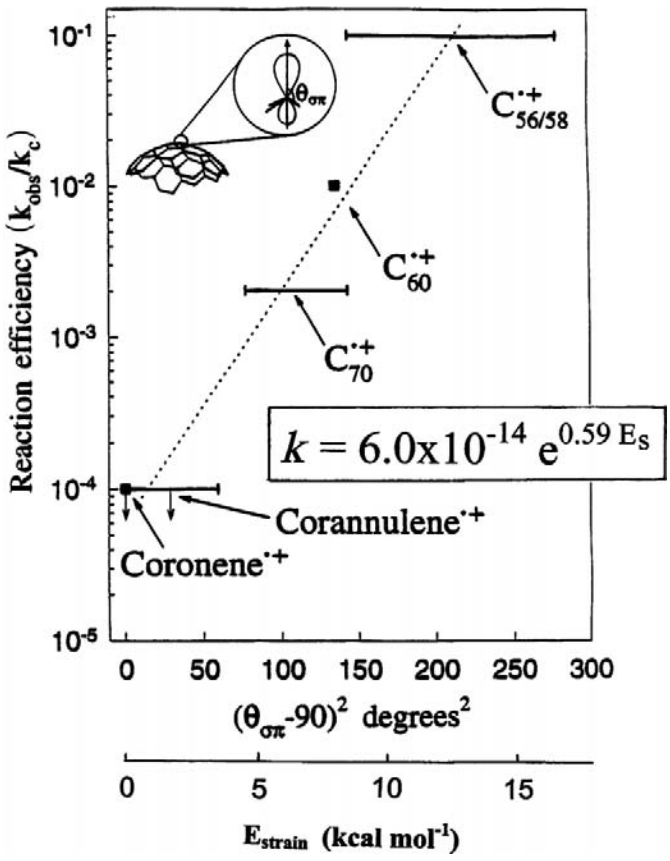

stars, as well as the formation of molecules in these regions that is assisted by fullerene cations (83, 84) including the formation of derivatized cyclobutadienes in the presence of cyanoacetylenes (77). For example, Fig. 26 provides an overview of chemical pathways that we have proposed that can be initiated by doubly charged fullerenes in interstellar or circumstellar environments (84).

The ICP/SIFT/QqQ instrument: Atomic ion chemistry

At the turn of the millennium, I became reconnected with a former graduate student, Scott Tanner, then working at MDS Sciex, a company that manufactures ICP/MS instruments for atomic ion analysis. He and his colleague, Vladimir Baranov, a former postdoctoral fellow of mine, had developed a "dynamic reaction cell" for the chemical resolution of isobaric interferences between atomic ions for use in ICP/MS (85) and they needed information on atomic ion reactivities. We formed a partnership with the Natural Sciences and Engineering Research Council of Canada (NSERC) and the National Research Council Canada and were able to fit a commercial ICP to the front end of the SIFT and so to inject mass selected atomic cations into the

© 2008 NRC Canada

Fig. 26. Schematic view of possible chemical pathways initiated by doubly charged fullerene cations.

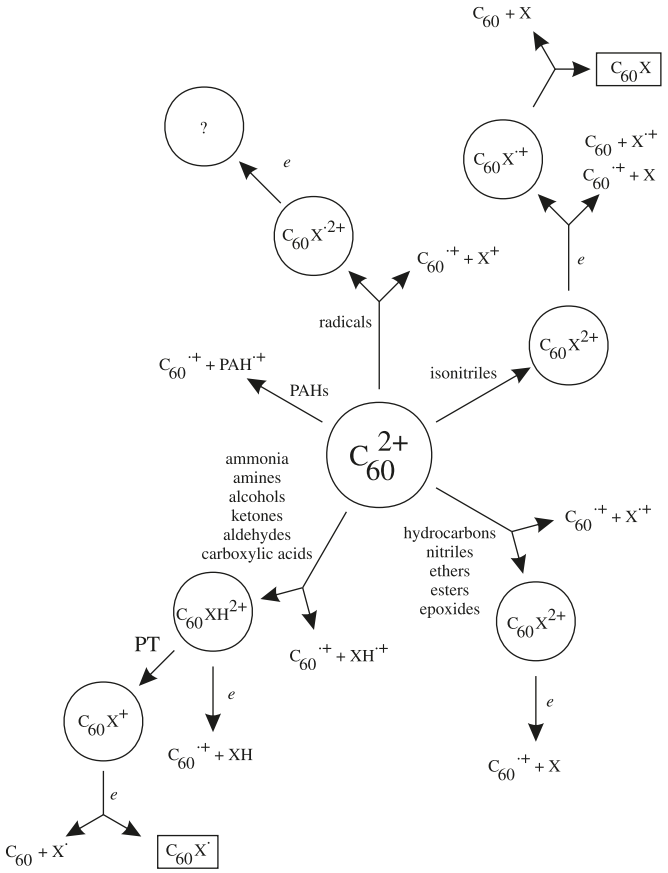

flow tube (86). Schematic and pictorial views of the instrument are shown in Fig. 27.

Fig. 27. Schematic and pictorial views of the ICP/SIFT/QqQ multipole mass spectrometer originally built at York University in 2000, initially with a single rather than a triple quadrupole mass spectrometer as the ion detector (86). Also shown is the "periodic table" of the bottled solutions of atomic cations that were sprayed into the ICP.

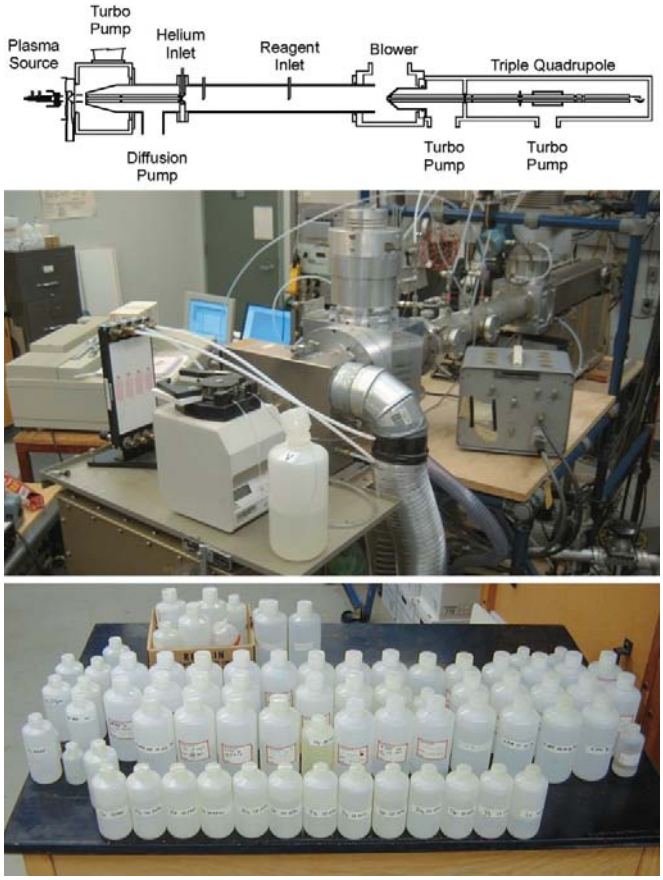

Reactions of atomic cations: Surfing the periodic table

The availability of the ICP as a source of atomic cations has made it possible to thoroughly investigate reactions of some 60 different atomic cations with a large variety of different molecules. Indeed, we now can routinely measure reactions with alkali, alkaline earth, transition metal, main group, and lanthanide atomic cations.

Figure 28 shows an example of some of the more extreme data obtained for the chemistry initiated by atomic niobium cations with nitrous oxide (87). N_2O was found, somewhat surprisingly, to transfer an N atom or an O atom to Nb^+, and both transfers were seen to trigger extensive secondary and higher-order chemistry, including further oxidation and substantial clustering with nitrous oxide.

We have surveyed the reactivity of nitrous oxide with 59 elemental cations and so characterized the periodic behaviour of this reactivity over most of the periodic table as illustrated in Fig. 29 (87). Systematic studies of this type now have been performed for reactions of up to 61 atomic cations with 15 different molecules including O_2, NO, D_2O, CO_2, NO_2, N_2O, OCS, CS_2, NH_3, CH_4, CH_3F, CH_3Cl, C_6H_6, C_6F_6 and SF_6. Except for Mg^+ and Si^+, which were produced only by conventional electron impact ionization of suitable parent gases, all atomic cations were generated using the ICP. A data base is now available on the web that provides measured reaction rate coefficients and product distributions as well as the observed higher order chemistry of almost 1000 reactions that we have investigated.[3]

Periodicities were observed in overall reaction efficiency and these were scrutinized in terms of kinetic constraints that determine chemical reactivity such as overall exothermicity, the presence of an activation barrier in the reaction co-ordinate, and the overall conservation of spin (87). The measured periodic behaviour is especially intriguing for the reactions with lanthanide cations (88).

Often, higher-order reactions have been observed and reported, as have reactions of singly and multiply ligated atomic cations, for example reactions of $M^+(C_6H_6)$ and $M^+(C_6H_6)_2$ (89).

The special case of lanthanide cation reactions: Arrhenius would be interested!

Measured rates for reactions of lanthanide cations with small molecules often were observed to vary from close to

[3] The web address is http://www.chem.yorku.ca/profs/Böhme/research/selection_table.html.

© 2008 NRC Canada

Fig. 28. (Left) Ion profiles recorded with the ICP/SIFT tandem mass spectrometer for the reaction of Nb^+ with N_2O in He buffer gas at 0.35 Torr and 295 K (87). (Right) A summary of the primary and higher-order reactions that explain the measured profiles.

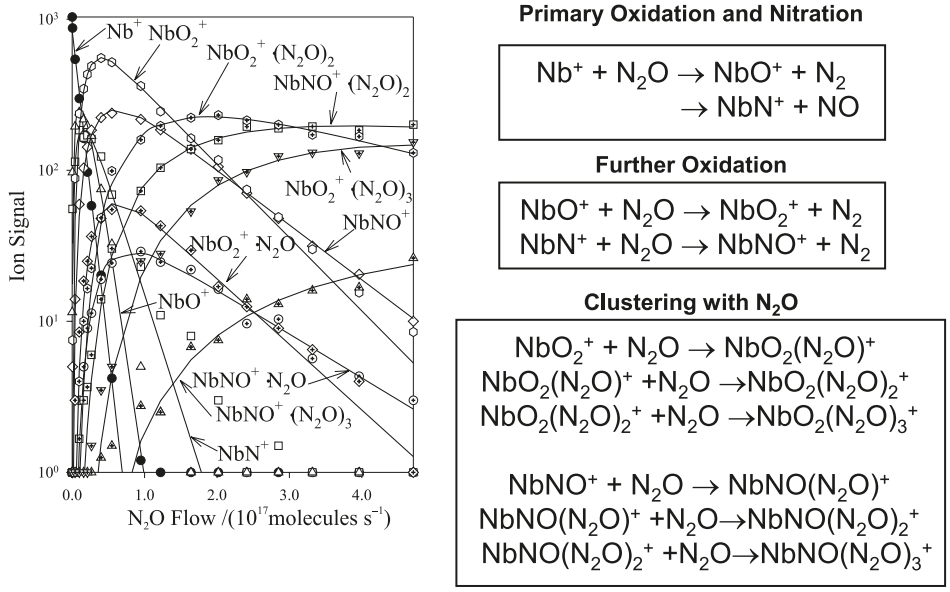

Fig. 29. Periodic variations observed in the efficiencies, k/k_c (represented as solid circles), for reactions of atomic cations with nitrous oxide (87). k represents the measured room-temperature reaction rate coefficient and k_c is the calculated collision rate coefficient. Also indicated are the ground-state electronic configurations of the atomic cations. The different colours designate the different product channels that were observed and the numbers in parentheses give the number of sequential reactions of that type that were recorded.

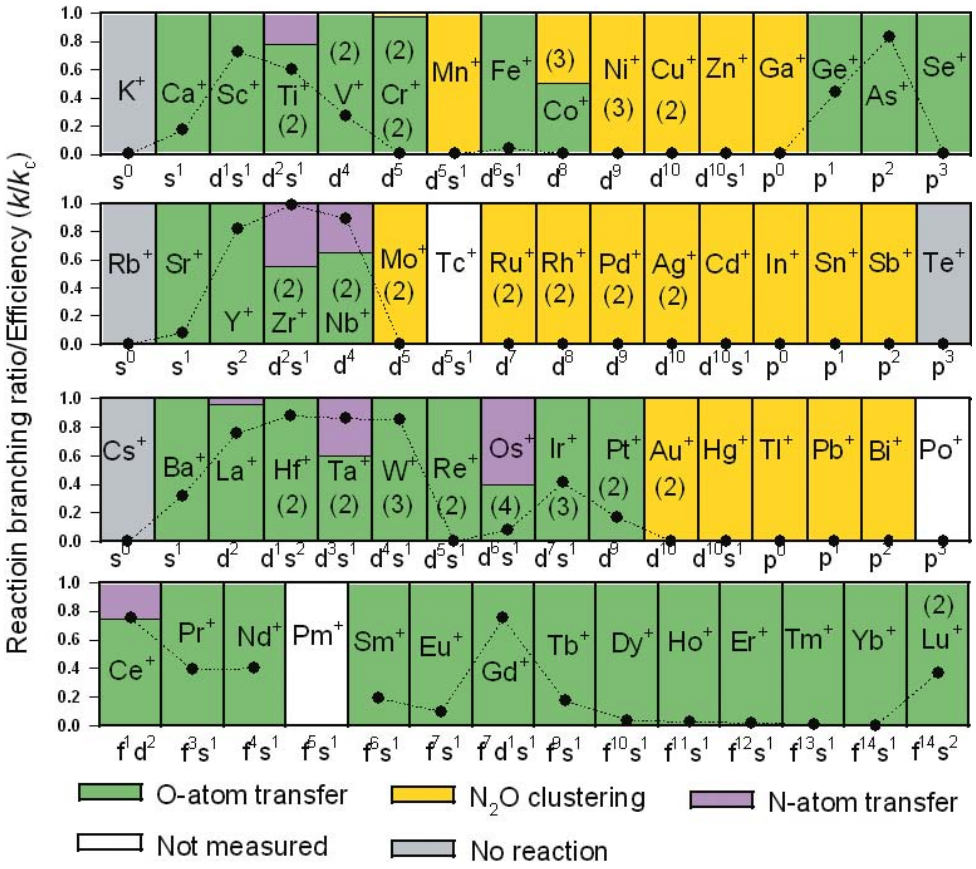

© 2008 NRC Canada

Fig. 30. Reaction-rate coefficient (solid circles and left ordinate axis) and electron-promotion energy of the Ln^+ cation (open circles and right ordinate axis) plotted versus element for lanthanide cations reacting with N_2O (88). There is an apparent correlation between reaction rate and electron-promotion energy.

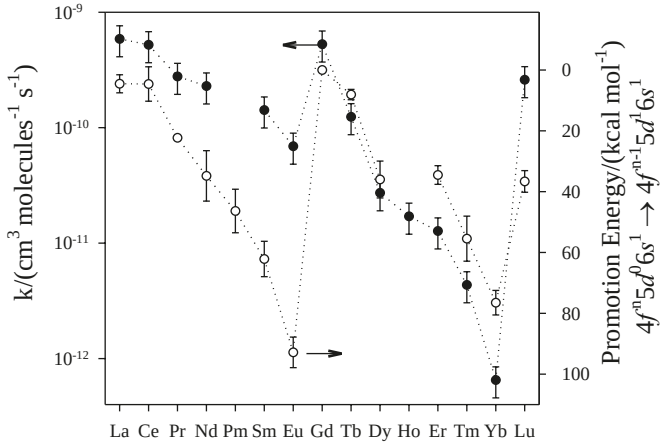

the predicted ion–molecule collision rate down to less than 0.1% efficiency. These observations were rationalized in terms of reaction thermodynamics and electronic structure effects. For example, the efficiency for exothermic reactions with N_2O (88) was found to decrease as the energy required to promote an electron in the lanthanide cation from the $4f^n5d^06s^1$ to the $4f^{n-1}5d^16s^1$ configuration increases (see Fig. 30). Furthermore, remarkably different Arrhenius-like correlations are found in the reactivity of the early and late lanthanide cations with this electro-promotion energy. The correlations for reactions with N_2O are shown in Fig. 31. Here we are using the Arrhenius equation in a novel way: we plot the efficiency for O-atom transfer against promotion energy, using the activation energy rather than T as the variable. The slope of such a plot provides an effective way to measure temperature or energy RT, and differs for the early and late lanthanides. The interpretation of this difference remains a puzzle.

Chemical resolution in elemental analysis

Atomic ion reactions have found application in elemental analysis using ICP/MS (90). Isobaric interferences are resolved chemically in a dynamic reaction cell placed between the ICP and the MS by adding an appropriate gas that reacts selectively with only one of the interfering ions and so moves its signature to another *m/z* that can be easily resolved. A good example is the interference of Rb^+ with Sr^+ at *m/z* = 87 that arises in the use of these two ions for age dating (91). ^{87}Sr arises, in part, from the natural β-decay of ^{87}Rb. This means that the $^{87}Rb/^{87}Sr$ ratio must be measured accurately. The data shown in Fig. 32 indicate that SF_6 can shift the mass of Sr^+ by 19 mass units while leaving the Rb^+ ion untouched. Rb^+ (s^0), which has a rare-gas configuration, is measured to be unreactive while Sr^+ (s^1) reacts rapidly, almost at the collision rate, primarily by F-atom abstraction as indicated in reactions [35] and [36].

[35] $Rb^+ (s^0) + SF_6 \rightarrow NR$
$(k \leq 1 \times 10^{-13}\ cm^3\ molecule^{-1}\ s^{-1})$

Fig. 31. A correlation of reaction efficiency with the electron promotion energy that is proposed to be required for Ln-O^+ bond formation in the reactions of early (solid circles) and late (solid squares) Ln^+ ions with N_2O (88). Lu^+ (open square) clearly is an exception to the trend observed for the late Ln^+ ions.

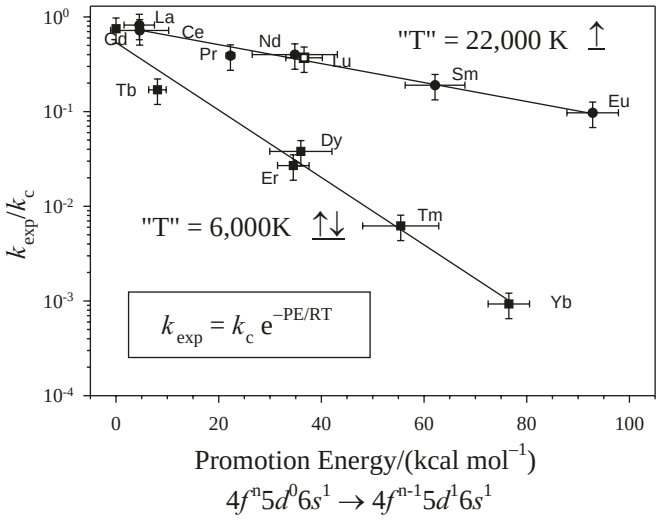

[36] $Sr^+ (s^1) + SF_6 \rightarrow SrF^+ + SF_5$ (97%;
$\rightarrow SrSF_5^+ + F$ (3%)\
$(k = 5.7 \times 10^{-10}\ cm^3\ molecule^{-1}\ s^{-1})$

We have surveyed the general utility of SF_6 for resolving isobaric interferences. The boxes on the periodic table in Fig. 33 encompass adjacent ions with large differences in reactivity that may be used to resolve them.

Atomic ions: The ultimate sites for catalysis

Another potential application of atomic ion chemistry is in the field of catalysis (92). Our measurements have demonstrated that atomic metal cations with appropriate O-atom affinities can serve to transport O-atoms from one neutral molecule to another and so to catalyse the neutral redox reaction. This is illustrated in Fig. 34 for the catalytic reduction of N_xO_y molecules by CO (93).

This computed energy landscape that nicely illustrates the catalytic activity of Fe^+ for the reduction of N_2O by CO is shown in Fig. 35 (94). The two legs of the catalytic cycle that involve ion–molecule reactions follow potential energy surfaces with double minima, with only a very small barrier in the first leg.

Packing atomic metal cations with fullerenes

The atomic cations of Sr and Mo have been observed (95) to add sequentially up to four molecules of C_{60} in He at 0.35 Torr and RT using the ICP/SIFT/QqQ configuration (see Fig. 36). The available center-of-mass energy in collision-induced dissociation experiments within the triple quadrupole provided a *lower* limit to the binding energy of the fourth C_{60} molecule of approximately 1.3 eV. A structure is proposed for $M^+(C_{60})_4$ cations in which the bonding involves η^6 interaction of the metal with the C_{60} ligands and η^2-to-η^2 interactions between the C_{60} ligands (see Fig. 36).

© 2008 NRC Canada

Fig. 32. Observed ion profiles recorded with the ICP/SIFT tandem mass spectrometer for the reactions of Rb^+ and Sr^+ with SF_6 in He buffer gas at 0.35 Torr and 295 K.

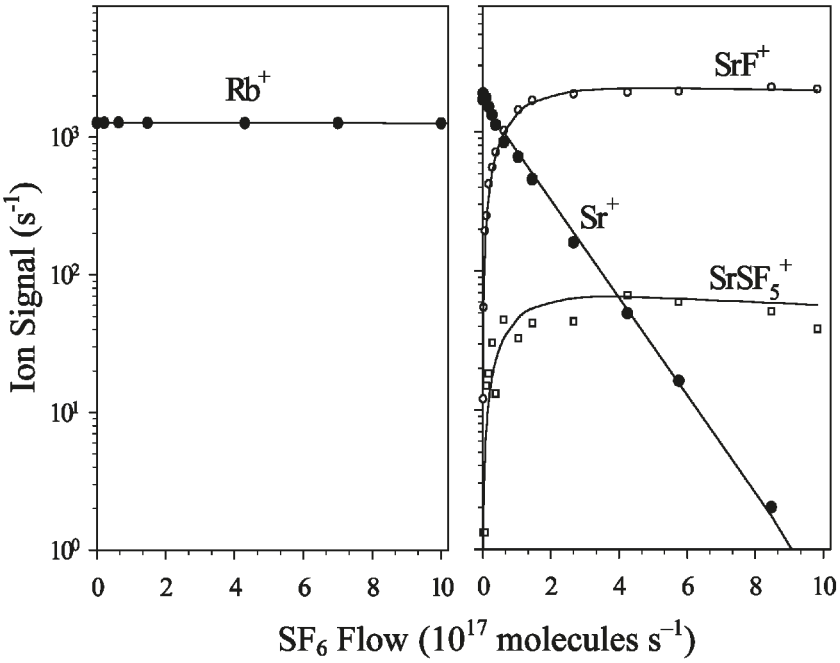

Fig. 33. Periodic variations observed in the efficiencies, k/k_c (represented as solid circles), for reactions of atomic cations with SF_6. k represents the measured room-temperature reaction rate coefficient and k_c is the calculated collision rate coefficient. Also indicated are the ground-state electronic configurations of the atomic cations. The different colours designate the different product channels that were observed.

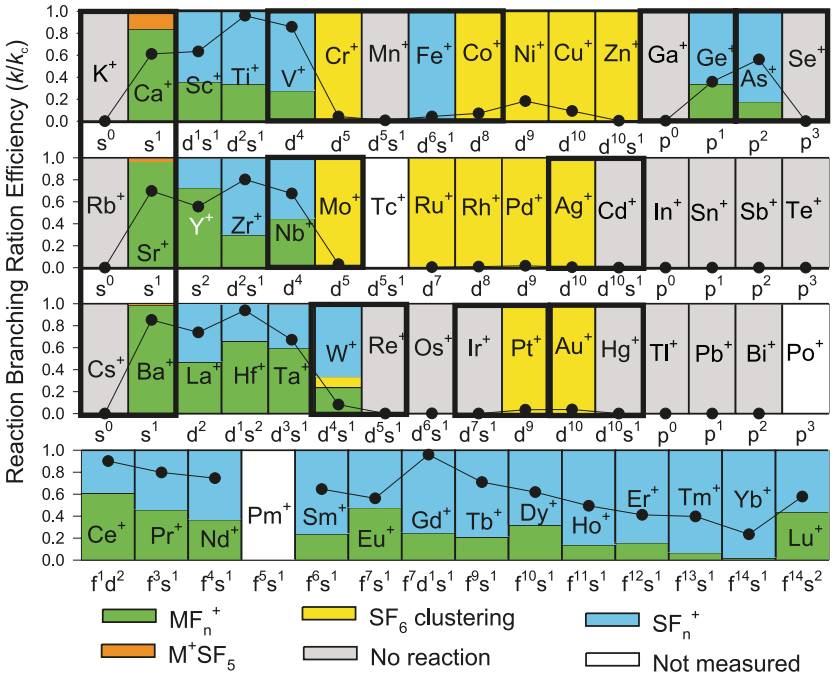

The ESI/qQ/SIFT/QqQ instrument: The ultimate chemical mass spectrometer

Our most recent breakthrough in flow-tube mass spectrometry involved interfacing an ESI source at the front end of the flow tube as shown schematically and pictorially in Fig. 37 (96). The Nobel Prize winning (John B. Fenn, 2002) ESI source is very powerful as it provides a near-universal source for ions: essentially any ion that forms spontaneously in solution, can be sprayed in a droplet into the gas phase and be liberated as a free or solvated ion. The ESI interface in our instrument permits complete desolvation of electrosprayed ions. Moreover, this desolvation region can be used to fragment weaker covalent bonds, further extending the di-

© 2008 NRC Canada

Fig. 34. Reaction cycles for the reduction of NO_2, NO, and N_2O by CO catalyzed by atomic metal cations.

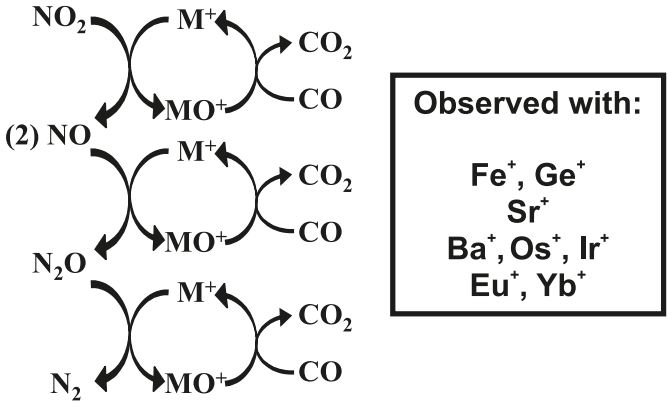

Fig. 35. Potential energy landscape for the reduction of nitrous oxide by carbon monoxide catalysed by Fe^+ (94).

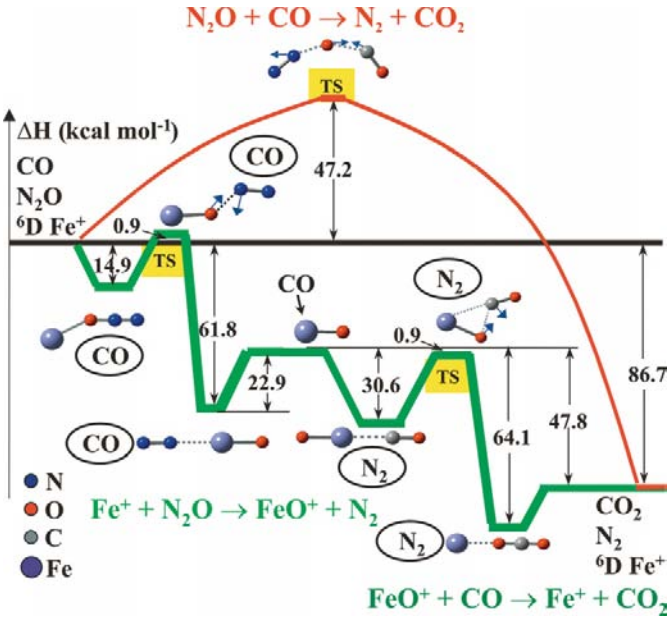

versity of reactant ions generated by the ESI source. Mass selection prior to entering the flow tube removes complications due to charge state distributions and can eliminate complications due to isotope distributions. The operation of the instrument has been demonstrated with a selection of reactivity and kinetic measurements and threshold collision-induced dissociation determinations. Reactions investigated include H–D exchange between protonated bradykinin and deuterated ammonia, the protonation of the oligo-nucleotide anion $[AGTCTG\text{-}5H^+]^{5-}$ with HBr, the ozonolysis of Ca^{2+}, the reaction of protonated phthalic anhydride with dimethyl disulfide, and the Ar collision-induced dissociation of $Ba(C_6H_6)^{2+}$.

The chemistry of atomic metal dications

The ESI source provides access to multiply charged atomic ions that are formed in solution. Recently we have extracted doubly charged atomic cations of the alkaline earth metals from solutions of their salts. An early result shown in Fig. 38 indicates that the oxidation of the calcium dication

Fig 36. ICP/SIFT/QqQ mass spectrum and proposed tetrahedral structure for $Sr(C_{60})_4^+$ (95).

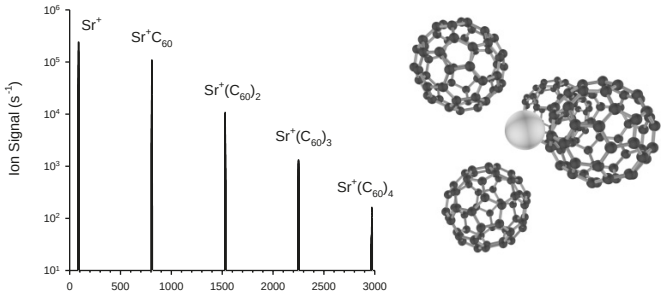

with ozone proceeds first by charge separation and then by sequential O-atom abstraction. The Ba dication on the other hand was observed simply to add up to four ozone molecules to form fascinating ozone clusters such as $Ba(O_3)_4^{2+}$ (97). We are able now to extract singly charged atomic cations from solution and some of their oxides and hydroxides and to measure their reactions as well.

The intrinsic reactivity of multiply charged oligonucleotides

We are now also able to probe, for the first time, intrinsic chemical properties of multiply charged biological ions, including highly charged DNA-like anions, derived by ESI. We have shown that such anions can be produced by ESI, injected into our flow reactor, and exposed to chemical reactions in the gas phase (98). This allows the quantitative measurement for the very first time of *intrinsic* kinetic and thermodynamic properties of reactions of such biological ions at room temperature. We began with studies of the chemistry of the oligo-nucleotide $[AGTCTG\text{-}nH]^{n-}$ anions. Against our wishes, these anions were found generally to be quite unreactive in the gas phase (see Fig. 39), a result that is perhaps not surprising in retrospect because *Mother Nature* wished it so! The oligonucleotide $[AGTCTG\text{-}nH]^{n-}$ anions were found to be intrinsically stable; they could not be oxidized with strong oxidants, were not hydrated with D_2O, and were not easily protonated. No reactions, $k < 10^{-13}$ cm^3 molecule^{-1} s^{-1}, were observed with O_2, N_2O, O_3, D_2O, and benzene, for n = 2, 3, 4, and 5. However, proton transfer from HBr to the $[AGTCTG\text{-}5H]^{5-}$ anion (see Fig. 40) was observed to be rapid, $k = 3.2 \times 10^{-9}$ cm^3 molecule^{-1} s^{-1}, and also to proceed sequentially to produce ultimately the $[AGTCTG\text{-}2H]^{2-}$ anion according to charge-separation reactions of the type indicated in reaction (37).

$$[37] \quad [AGTCTG\text{-}nH]^{n-} + HBr \rightarrow [AGTCTG\text{-}(n-1)H]^{(n-1)-} + Br^-$$

The measured reaction profiles for sequential proton transfer and an overview of the complete chemistry that was identified are shown in Fig. 40. Extensive HBr addition to the oligonucleotide was observed to compete with proton transfer. From 5 to 7 molecules of HBr were observed to add to each of the four charge states of the oligonucleotide anions and this is interpreted as addition to the various basic sites of the nucleobase substituents. HBr is effective in "counting" the number of such available sites (99).

As shown in Fig. 40, the measured reaction rates with HBr increase with increasing charge state from 2– to 5–, but

© 2008 NRC Canada

Fig. 37. Schematic and pictorial views of the ESI/qQ/SIFT/QqQ multipole mass spectrometer built at York University in 2006 (96).

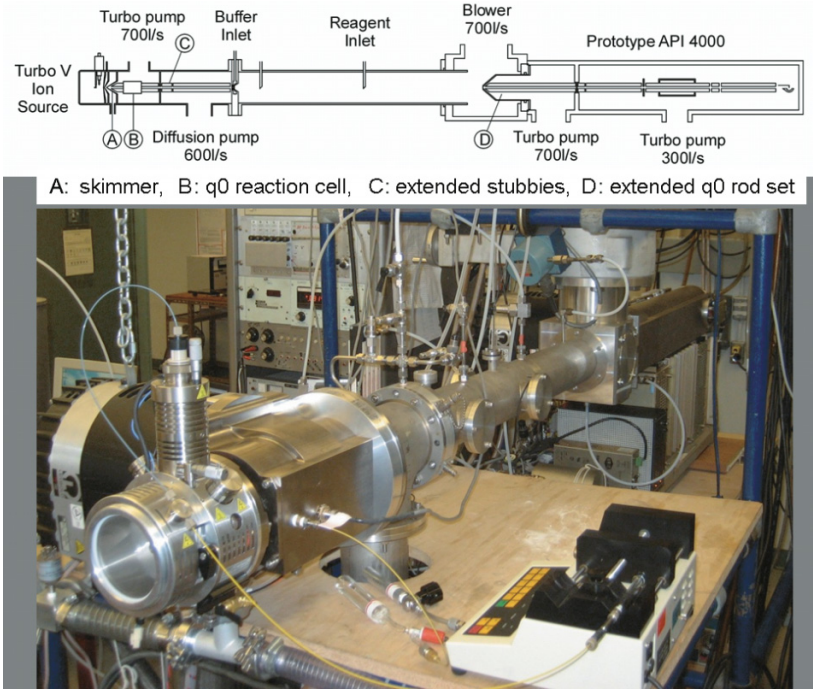

Fig. 38. (Left) Experimental results obtained for the gas-phase ozonolysis of calcium dications in He buffer gas at 0.35 Torr and 295K (97). (Right) The chemical reactions and their kinetics that explain the experimental observations (97). The Ca^{2+} ions were derived from a solution of 100 mM CaAcetate in H_2O/CH_3OH (1/1).

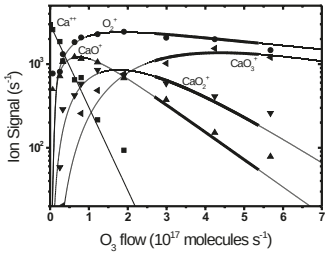

$Ca^{++} + O_3 \rightarrow CaO^+ + O_2^+$
($k = 1.5 \times 10^{-9}$ cm^3 mol^{-1} s^{-1})

$CaO^+ + O_3 \rightarrow CaO_2^+ + O_2$
($k = 5 \times 10^{-10}$ cm^3 mol^{-1} s^{-1})

$CaO_2^+ + O_3 \rightarrow CaO_3^+ + O_2$
($k = 6 \times 10^{-10}$ cm^3 mol^{-1} s^{-1})

the efficiency of reaction, k_{obs}/k_{cap} (where k_{cap} is the computed capture rate coefficient) remains unchanged and equal to 1 within experimental uncertainty. Proton transfer predominates (> 70%) with the two highest charge states, drops to 20% for the 3– charge state, and does not occur with the 2– anion.

Fig. 39. Summary of the intrinsic non-reactivity of [AGTCTG-*n*H]$^{n-}$ observed under SIFT conditions in He at 0.35 Torr and 295 K (98).

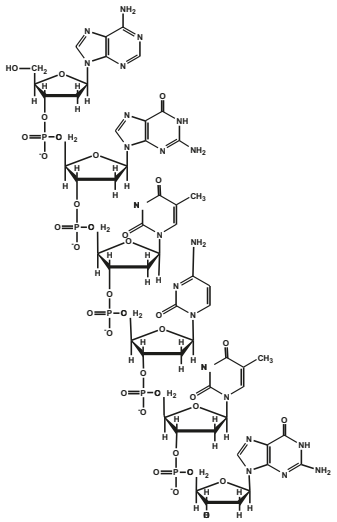

	k_{295} (cm^3 molecule^{-1} s^{-1})	
+ O_3	<10^{-13}	No oxidation
+ O_2	<10^{-13}	
+ N_2O	<10^{-13}	
+ D_2O	<10^{-13}	No hydration
+ C_6H_6	<10^{-13}	No intercalation
+ HBr	fast	Protonation Hydrobromination

New horizons

We are very encouraged with the performance of our new ESI/qQ/SIFT/QqQ instrument and are now extending our measurements in still other directions. For example, we are exploring the influence of metal dications on the reactivity of oligonucleotide anions. Recently we have investigated the influence of Zn^{2+} on the hydrolysis of beta-lactam antibiotics in the gas phase and have explored the oxidation of metal – tetraphenyl porphyrin, bleomycin, fatty acid, and lipid cations in the gas phase.

In a separate study of the kinetics of ion–molecule reactions of potential use in the suppression of chemical noise in mass spectrometry (100), we have used the ESI/qQ/SIFT/QqQ multipole mass spectrometer to explore the reactivity of dimethyl disulphide with a number of chemical background ions commonly observed in atmospheric pressure ionization mass spectrometry along with several model analyte ions such as protonated caffeine and doubly protonated bradykinin. Background ions that were studied include protonated acetonitrile, phosphoric acid, phthalic anhydride, and triphenyl phosphate.

Clearly our newest SIFT mass spectrometer will challenge our ingenuity in the study of new ion–molecule reactions for many years to come. There is much else left to be learned!

© 2008 NRC Canada

Fig. 40. Summary of the chemical kinetics observed for the reactions of $[AGTCTG\text{-}nH]^{n-}$ with hydrogen bromide under SIFT conditions in He at 0.35 Torr and 295 K (98).

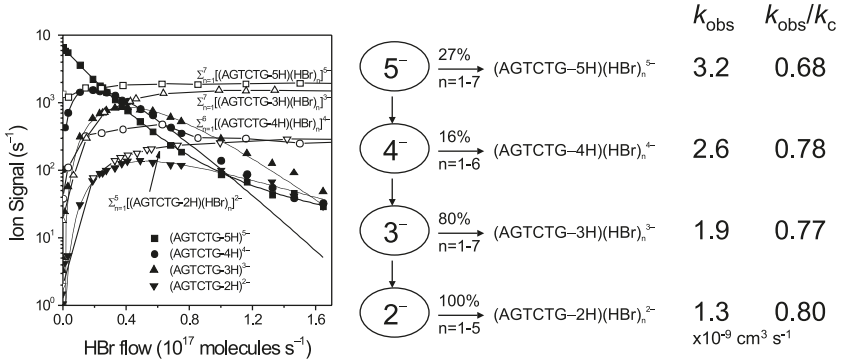

Acknowledgments

First I want to thank John Goodings, my Ph.D. supervisor, and Eldon Ferguson, my postdoctoral mentor, for my formative years as a research scientist. Much of the credit for the achievements in my own research laboratory belongs to the students and postdoctoral fellows that joined my research group over the years, especially Simon Petrie with whom I continue to collaborate, and my research associate, Greg Koyanagi, and I am grateful to all of them for their valued contributions and inspiration. The continuous financial support over the years from the Natural Sciences and Engineering Research Council of Canada (NSERC) is greatly appreciated. Also, I acknowledge support from the National Research Council Canada, the Natural Science and Engineering Research Council, and MDS SCIEXciex in the form of several Research Partnership grants. Timely Research Fellowships from the A.P. Sloan, A.V. Humboldt, and Killam Foundations need to be recognized with thanks. Finally, as holder of a Canada Research Chair in Physical Chemistry, I also acknowledge the contributions of the Canada Research Chair Program to my research over the past seven years.

References

1. K.M. Downard. Mass Spectrom. Rev. **26**, 713 (2007).
2. S. Petrie and D.K. Bohme. Mass Spectrom. Rev. **26**, 258 (2007).
3. S.A. Haider and A. Bhardwaj. Icarus, **177**, 196 (2005).
4. W.D. Pesnell and J.M. Grebowsky. Adv. Space Res. **27**, 1807 (2001).
5. W. Paul and H. Steinwedel. Z. Naturforsch. **8a**, 448 (1953).
6. D.K. Bohme and J.M. Goodings. Rev. Sci. Instr. **37**, 362 (1966).
7. D.K. Bohme and J.M. Goodings. J. Appl. Phys. **37**, 4261 (1966).
8. E.E. Ferguson, F.C. Fehsenfeld, and A.L. Schmeltekopf. Adv. At. Mol. Phys. **5**, 1 (1969).
9. F.C. Fehsenfeld, A.L. Schmeltekopf, and E.E. Ferguson. J. Chem. Phys. **4**6 2802 (1967).
10. E.E. Ferguson. Rev. Geophys. Space Phys. **12**, 703 (1974).
11. E.E. Ferguson, F.C. Fehsenfeld, P.D. Goldan, and A.L. Schmeltekopf. J. Mass Spectrom. **32**, 1273 (1997).
12. D.K. Bohme, E. Lee-Ruff, and L.B. Young. J. Am. Chem. Soc. **93**, 4608 (1971).
13. D.K. Bohme, E. Lee-Ruff, and L.B. Young. J. Am. Chem. Soc. **94**, 5153 (1972).
14. G.I. Mackay and D.K. Bohme. J. Am. Chem. Soc. **100**, 327 (1978).
15. A.B. Raksit and D.K. Bohme. Can. J. Chem. **61**, 1683 (1983).
16. D.K. Bohme, G.I. Mackay, and S.D. Tanner. J. Am. Chem. Soc. **101**, 3724 (1979).
17. G.I. Mackay, S.D. Tanner, A.C. Hopkinson, and D.K. Bohme. Can. J. Chem. **57**, 1518 (1979).
18. D.K. Bohme and L.B. Young. J. Am. Chem. Soc. **92**, 7354 (1970).
19. K. Tanaka, G.I. Mackay, J.D. Payzant, and D.K. Bohme. Can. J. Chem. **54**, 1643 (1976).
20. D.K. Bohme and G.I. Mackay. J. Am. Chem. Soc. **103**, 978 (1981).
21. D.K. Bohme and A.B. Raksit. J. Am. Chem. Soc. **106**, 3447 (1984).
22. D.K. Bohme, G.I. Mackay, and H.I. Schiff. J. Chem. Phys. **73**, 4976 (1980).
23. D.K. Bohme. Trans. Royal Soc. Can. Fourth Series. Volume XIX. 265. (1981).
24. G.I. Mackay, L.D. Betowski, J.D. Payzant, H.I. Schiff, and D.K. Bohme. J. Phys. Chem. **80**, 2919 (1976).
25. G.I. Mackay, K. Tanaka, and D.K. Bohme. Int. J. Mass Spectrom. Ion Phys. **24**, 123 (1977).
26. G.I. Mackay, S.D. Tanner, A.C. Hopkinson, and D.K. Bohme. Can. J. Chem. **57**, 1518 (1979).
27. D.K. Bohme, R.S. Hemsworth, H.W. Rundle, and H.I. Schiff, J. Chem. Phys. **58**, 3504 (1973).
28. R.S. Hemsworth, H.W. Rundle, D.K. Bohme, H.I. Schiff, D.B. Dunkin, and F.C. Fehsenfeld. J. Chem. Phys. **59**, 61 (1973).
29. D.K. Bohme, E. Lee-Ruff, and L.B. Young. J. Am. Chem. Soc. **93**, 4608 (1971).
30. G.I. Mackay, R.S. Hemsworth, and D.K. Bohme. Can. J. Chem. **54**, 1624 (1976).
31. D.K. Bohme, E. Lee-Ruff, and L.B. Young. J. Am. Chem. Soc. **94**, 5153 (1972).
32. D.K. Bohme, L.B. Young, and E. Lee-Ruff. Can.J. Chem. **49**, 979 (1971).
33. D.K. Bohme. Int. J. Mass Spectrom. Ion Processes, **115**, 95 (1992).
34. N.G. Adams and D. Smith. Int. J. Mass Spectrom. Ion Phys. **21**, 349 (1976).
35. G.I. Mackay, G.D. Vlachos, D.K. Bohme, and H.I. Schiff. Int. J. Mass Spectrom. Ion Phys. **36**, 259 (1980).
36. D.K. Bohme, A.B. Rakshit, and H.I. Schiff. Chem. Phys. Lett. **93**, 592 (1982).
37. S. Wlodek, D.K. Bohme, and E. Herbst. Mon. Not. R. Astron. Soc. **235**, 493 (1988).
38. S. Wlodek, A. Fox, and D.K. Bohme. J. Am. Chem. Soc. **113**, 4461 (1991).
39. S. Wlodek and D.K. Bohme. J. Am. Chem. Soc. **111**, 61 (1989).

© 2008 NRC Canada

40. S. Wlodek and D.K. Bohme. J. Chem. Soc. Faraday Trans. 2, **85**, 1643 (1989).
41. S. Wlodek, A. Fox, and D.K. Bohme. J. Amer. Chem. Soc. **109**, 6663 (1987).
42. S. Wlodek and D.K. Bohme. J. Amer. Chem. Soc. **110**, 2396 (1988).
43. R.K. Milburn, V. Baranov, A.C. Hopkinson, and D.K. Bohme. J. Phys. Chem. **102**, 9803 (1998).
44. R.K. Milburn, V. Baranov, A.C. Hopkinson, and D.K. Bohme. J. Phys. Chem. **103**, 6373 (1999).
45. R.K. Milburn, A.C. Hopkinson, and D.K. Bohme. J. Phys. Chem. **104**, 3926 (2000).
46. R.K. Milburn, A.C. Hopkinson, and D.K. Bohme. J. Am. Chem. Soc. **127**, 13070 (2005).
47. V.I. Baranov and D.K. Bohme. Int. J. Mass Spectrom. Ion Processes, **149/150**, 543 (1995).
48. S. Petrie, H. Becker, V. Baranov, and D.K. Bohme. Astrophys. J. **476**, 191 (1997).
49. V.I. Baranov and D.K. Bohme. Int. J. Mass Spectrom. **210/211**, 303 (2001).
50. S. Wlodek and D.K. Bohme. Gas-phase oxidation of atomic silicon ions. *In* Advances in Mass Spectrometry. Vol. 11A. *Edited by* P. Longevialle. Heyden & Son, London. 1989. pp. 538–539.
51. D.K. Bohme. Chemistry initiated by atomic silicon cations. *In* Advances in Gas-Phase Ion Chemistry. Vol. 1. *Edited by* N.G. Adams and L. Babcock. JAI Press, London. 1992. pp. 225–270.
52. E. Herbst, T.J. Miller, S. Wlodek, and D.K. Bohme. Astron. Astrophys. **222**, 205 (1989).
53. S. Wlodek, D.K. Bohme, and E. Herbst. Mon. Not. R. Astron. Soc. **242**, 674 (1990).
54. H.I. Schiff and D.K. Bohme. Astrophys. J. **232**, 740 (1979).
55. D.K. Bohme, S. Wlodek, and A.B. Raksit. Can. J. Chem. **65**, 2057 (1987).
56. D.K. Bohme. Nature, **319**, 473 (1986).
57. S. Dheandhanoo, L. Forte, A. Fox, and D.K. Bohme. Can. J. Chem. **64**, 641 (1986).
58. V. Baranov and D.K. Bohme. Int. J. Mass Spectrom. Ion Processes, **154**, 71 (1996).
59. V. Blagojevic, S. Petrie, and D. K. Bohme. Mon. Not. R. Astron. Soc **339**, L7 (2003).
60. J.L. Snow, G. Orlova, V. Blagojevic, and D.K. Bohme. J. Am. Chem. Soc. **129**, 9910 (2007).
61. W. Krätschmer, L.D. Lamb, K. Fostiropoulos, and D.R. Huffman. Nature **347**, 354 (1990).
62. T. Weiske, D.K. Bohme, J. Hrusak, W. Kraetschmer, and H. Schwarz. Angew. Chem. Int. Ed. Engl. **30**, 884 (1991).
63. D.K. Böhme. Can. J. Chem. **77**, 1453–1464 (1999).
64. G. Javahery, S. Petrie, J. Wang, X. Wang, and D.K. Bohme. Int. J. Mass Spectrom. Ion Processes, **125**, R13 (1993).
65. G. Javahery, S. Petrie, J. Wang, and D.K. Bohme. Chem. Phys. Lett. **195**, 7 (1992).
66. V. Blagojevic, S. Petrie, and D.K. Bohme. Int. J. Mass Spectrom. **233**, 33 (2004).
67. D.K. Bohme. Int. Rev. Phys. Chem. **13**, 163 (1994).
68. J. Javahery, H. Becker, S. Petrie, P.-C. Cheng, H. Schwarz, L.T. Scott, and D.K. Bohme. Org. Mass Spectrom. **28**, 1005 (1993).
69. S. Petrie, G. Javahery, J. Wang, and D.K. Bohme. J. Am. Chem. Soc. **114**, 9177 (1992).
70. R. Javahery, S. Petrie, H. Wincel, J. Wang, and D.K. Bohme. J. Am. Chem. Soc. **115**, 6295 (1993).
71. G. Javahery, S. Petrie, J. Wang, H. Wincel, and D.K. Bohme. J. Am. Chem. Soc. **115**, 9701 (1993).
72. S. Petrie and D.K. Bohme. Can. J. Chem. **72**, 577 (1994).
73. D.K. Bohme. *In* Recent Advances in the Chemistry and Physics of Fullerenes and Related Materials. *Edited by* R.S. Ruoff and K.M. Kadish. Electrochemical Society Proceedings 1995–10. Electrochemical Society, Pennington, NJ. 1995. p. 1465.
74. S. Petrie, G. Javahery, and D.K. Bohme. Int. J. Mass Spectrom. Ion Processes, **124**, 145 (1993).
75. S. Petrie, G. Javahery, H. Wincel, J. Wang, and D.K. Bohme. Int. J. Mass Spectrom. Ion Processes, **138**, 187 (1994).
76. V. Baranov, G. Javahery, J. Wang, S. Petrie, A.C. Hopkinson, and D.K. Bohme. J. Am. Chem. Soc. **119**, 2040 (1997).
77. R.K. Milburn, A.C. Hopkinson, and D.K. Bohme. J. Phys. Chem. **103**, 7528 (1999).
78. D. Caraiman, G. Koyanagi, L.T. Scott, D.V. Preda, and D.K. Bohme. J. Am. Chem. Soc. **123**, 8573 (2001).
79. D. Caraiman and D.K. Bohme. Int. J. Mass Spectrom. **223/224**, 411 (2003).
80. S. Petrie and D.K. Bohme. Nature, **365**, 426. (1993).
81. H. Becker, L.T. Scott, and D.K. Bohme. Int. J. Mass Spectrom. Ion Processes, **167/168**, 519 (1997).
82. C. Lee, J. Kang, S. Soo Park, J. Lee, S.K. Lee, and D.K. Bohme. J. Phys. Chem. A **110**, 11730 (2006).
83. S. Petrie, G. Javahery, and D.K. Bohme. Astron. Astrophys. **271**, 662 (1993).
84. S. Petrie and D.K. Bohme. Astrophys. J. **540**, 869 (2000).
85. S.D. Tanner and V.I. Baranov. J. Am. Soc. Mass Spectrom. **10**, 1083 (1999).
86. G.K. Koyanagi, V.V. Lavrov, V. Baranov, D. Bandura, S. Tanner, J.W. McLaren, and D.K. Bohme. Int. J. Mass Spectrom. **194**, L1 (2000).
87. V.V. Lavrov, V. Blagojevic, G.K. Koyanagi, G. Orlova, and D.K. Bohme. J. Phys. Chem. A **108**, 5610 (2004).
88. G.K. Koyanagi and D.K. Bohme. J. Phys. Chem. A **105**, 8964 (2001).
89. D. Caraiman and D.K. Bohme. J. Phys. Chem. A **106**, 9705 (2002).
90. G.K. Koyanagi, V.I. Baranov, S. Tanner, and D.K. Bohme. J. Anal. At. Spectrom, **15**, 1207 (2000).
91. See, for example, L.J. Moens, F.F. Vanhaecke, D.R. Bandura, V.I. Baranov, and S.D. Tanner. J. Anal. At. Spectrom. **16**, 991 (2001).
92. D.K. Böhme and H. Schwarz. Angew. Chem. Int. Ed. **44**, 2336 (2005).
93. V. Blagojevic, M.J.Y. Jarvis, E. Flaim, G.K. Koyanagi, V.V. Lavrov, and D.K. Bohme. Angew. Chem. Int. Ed. **42**, 4923 (2003).
94. V. Blagojevic, G. Orlova and D.K. Bohme. J. Am. Chem. Soc. **127**, 3545 (2005).
95. G.K. Koyanagi, J. Xu, and D.K. Bohme. Chem. Phys. Lett., **450**, 228 (2008).
96. G.K. Koyanagi, V.I. Baranov, S.D. Tanner, M.J.Y. Jarvis, S. Feil, and D.K. Bohme. Int. J. Mass Spectrom. **265**, 295 (2007).
97. S. Feil, G.K. Koyanagi, A.A. Viggiano, and D.K. Bohme, J. Phys. Chem. A, **111**, 13397 (2007).
98. G.K. Koyanagi, J. Anichina, S. Feil, and D.K. Bohme. J. Am. Chem. Soc. Submitted Dec. 2007.
99. J.L. Stephenson and S.A. McLuckey. Anal. Chem. **69**, 281 (1997).
100. M.J.Y. Jarvis, G.K. Koyanagi, X. Zhao, T.R. Covey, and D.K. Bohme. Anal. Chem. **79**, 4006 (2007).

© 2008 NRC Canada

Highly selective oxidation of toluene using air over [Fe(III)TPP]Cl supported on chitosan

Guan Huang, Chun-Cai Cai, Jin Luo, Hong Zhou, Yong-An Guo, and Shang-Yue Liu

Abstract: The highly selective catalytic oxidation of toluene with air to benzaldehyde and benzyl alcohol in the liquid phase has been studied with the use of iron tetraphenylporphyrin (Fe TPP) supported on chitosan (CTS), (Fe TPP/CTS). The rates of toluene conversion and selectivity (aldehyde + alcohol) were subject to the reaction temperature, air pressure, and amount of iron tetraphenylporphyrin. By the use of the Fe TPP/CTS, containing 2 mg of iron tetraphenylporphyrin as catalyst, toluene oxidation with air under the optimum conditions of 190 °C and 0.6 MPa produced benzaldehyde and benzyl alcohol at 90% selectivity and 5.4% conversion of toluene, the mole turnover of the catalyst was about 6×10^6, and it could be reused efficiently for one more time. It is suggested that the amine groups ($-NH_2$) on the chitosan chain act as a key assistor to the catalysis of Fe TPP for toluene oxidation. Compared with the conventional method of synthesizing benzaldehyde and benzyl alcohol, the new method has the advantages of reduced environmental pollution, higher selectivity for the two main products, and easy recovery of the catalyst.

Key words: chitosan-supported iron porphyrin, catalysis, toluene oxidation, benzaldehyde, benzyl alcohol.

Résumé : Utilisant un catalyseur formé de tétraphénylporphyrine-fer (TPP Fe) déposé sur du chitosane (CTS), (TPP Fe/CTS), on a étudié l'oxydation catalytique hautement sélective en phase liquide du toluène par l'air qui conduit à la formation de benzaldéhyde et d'alcool benzylique. Les vitesses de conversion du toluène et la sélectivité (aldéhyde + alcool) varient avec la température de la réaction, la pression de l'air et la quantité de tétraphénylporphyrine-fer. Lorsqu'on utilise du TPP Fe/CTS contenant 2 mg de tétraphénylporphyrine-fer comme catalyseur, dans les conditions optimales pour l'oxydation du toluène par l'air de 190 °C et de 0,6 MPa, il y formation de benzaldéhyde et l'alcool benzylique avec une sélectivité de 90%, une conversion de 5,4% du toluène et une réutilisation molaire interne du catalyseur d'environ 6×10^6 qui pouvait être réutilisé efficacement au moins une fois. On croit que les groupes amino ($-NH_2$) de la chaîne du chitosane sont des assistants clés pour la catalyse de l'oxydation du toluène par la TPP Fe. Par comparaison avec la méthode conventionnelle de synthèse du benzaldéhyde et de l'alcool benzylique, la nouvelle méthode présente des avantages en raison d'une réduction de la pollution environnementale, d'une grande sélectivité pour les deux produits principaux et de la facilité de récupération du catalyseur.

Mots-clés : porphyrine-fer déposée sur du chitosane, catalyseur, oxydation du toluène, benzaldéhyde, alcool benzylique.

[Traduit par la Rédaction]

Introduction

Benzaldehyde and benzyl alcohol are versatile intermediates in the chemical industry; therefore, much work has been devoted to the selective oxidation of toluene with air to synthesize these industrial products (1–3). Environmentally friendly and clean production processes are urgently required in the chemical industry. Although homogeneous catalysis for the oxidation of hydrocarbons has long been practiced in large-scale oxidation reactions (4), there are problems with corrosion, pollution, and recovery of the catalyst from the reaction mixture. Most of the problems related to the homogeneous catalyst can be solved by supporting the catalyst on an insoluble support (5). For example, impregnation of expensive metalloporphyrin catalysts on insoluble organic and inorganic supports can improve their stability and selectivity because of the support environment, and there are other advantages with respect to recovery and reuse. Supported metallo-porphyrins also provide physical separation of active sites, thus minimizing catalyst self-destruction (6). In the past decade, oxidation of hydrocarbons, catalyzed with molecular oxygen, by supported metalloporphyrins under mild conditions has attracted much interest because of its potential application and the environmentally friendly conditions (7, 8). However, there are few reports concerning the direct oxidation of toluene with air catalyzed by supported metalloporphyrin. When a simple metalloporphyrin (M TPP/CTS) was supported on polysaccharides as a catalyst for oxidation of cyclohexane using air, the best results (higher catalytic activity, better selectivity, and more efficient reuse) were obtained with chitosan as the support (9, 10).

The present work describes a new approach to the heterogeneous liquid-phase oxidation of toluene by air to benzaldehyde and benzyl alcohol; it uses iron tetraphenyl-

Received 30 October 2007. Accepted 18 December 2007. Published on the NRC Research Press Web site at canjchem.nrc.ca on 8 February 2008.

G. Huang,[1] C.-C. Cai, J. Luo, H. Zhou, Y.-A. Guo, and S.-Y. Liu. College of Chemistry and Chemical Engineering, Guangxi University, Nanning 530004, P.R. China.

[1]Corresponding author (e-mail: huangg66@126.com).

 doi:10.1139/V08-002 © 2008 NRC Canada

porphyrin supported on chitosan as catalyst. The system was tested under different temperatures and air pressure values and with different amounts of the catalyst. The data obtained are compared with those obtained with the unsupported catalyst.

Experimental

Instruments and reagents

The instruments used were a PE L-17 spectrometer (UV–vis), a PE-783 spectrometer (IR), a Class-5000 GC–MS spectrometer and an Agilent 1100LC-MS, a Shimadzu GC-16A equipped with a 0.5 mm i.d. × 25 m PEG20000 capillary column and flame ionization detector, and a WDF High Pressure Reactor with a high-speed magnetic agitator.

All reagents and solvents were analytical-grade and were obtained commercially. No impurities were found in the toluene by GC analysis before use. Fe TPP was synthesized according to the documented procedures (11).

Preparation of chitosan-supported Fe TPP

A mixture of 100 mL diluted hydrochloric acid and 4 g chitosan in a three-necked flask with an electro-magnetic stirrer was stirred at room temperature for 10 min. Then, 400 mL of distilled water was added to form the colloidal solution to which 5% NaOH solution was added until it became neutral. Then, 0.1 g of chloro[tetraphenylporphyrinato]iron(III) (Fe TPP) dissolved in 240 mL chloroform was slowly added. The mixture was vigorously stirred for 4 h, the reaction was stopped, and the mixture was filtered by pumping and then washed with distilled water; 3.90 g of brown solid was obtained by means of drying the filter cake at low temperature. This filtrate was used to analyze the amount of Fe TPP in the solid product. The amount of Fe TPP supported per 1 g chitosan was 0.0280 mmol as determined by UV–vis spectrophotometer technique (12).

Characterization of the supported catalyst

The supported catalyst was characterized by UV–vis spectroscopy by the same method (7). The electronic spectrum of the supported Fe TPP was obtained in a glycerol mull in a quartz vessel, and the UV–vis spectrum of Fe TPP/CTS was compared with that of Fe TPP in the region of 300–750 nm (Fig. 1). The chloroform extraction from the powder of the solid catalyst was measured by UV–vis spectrophotometry (Fig. 1*a*).

FTIR spectra were recorded on a PerkinElmer model 783 IR spectrophotometer in the range of 4000–450 cm^{-1} at a resolution of 2 cm^{-1}. Dry chitosan and chitosan-supported iron tetraphenylporphyrin samples were ground into fine powder, mixed with KBr, and then were pressed into their thin pellets, which were placed in the sample holder of the spectrometer to assay their spectra. IR spectra for them were shown in Fig. 2.

Procedure for the catalytic oxidation of toluene

Catalytic oxidation of toluene using air was performed according to the following standard reaction procedures: toluene (350 mL) and Fe TPP/CTS catalyst (containing 2 mg Fe TPP) were placed in a 500 mL autoclave reactor charged with nitrogen at 0.6 MPa. The reaction mixture was heated to 190 °C under stirring, and air was continuously injected at 0.020 m^3/h to maintain the pressure at 0.6 MPa. Subsamples of the reaction mixture were taken at regular intervals and analyzed by GC–MS. The oxygenated products were quantified by GC using chlorobenzene as the internal standard (13). The supported catalyst was recovered by simple separation from the reaction mixture followed by washing with ethanol and drying in air, and it was used in subsequent toluene oxidation.

Fig. 1. UV–vis spectra for the catalysts at room temperature. (*a*) chloroform solution of Fe TPP and (*b*) in glycerol mull Fe TPP on chitosan.

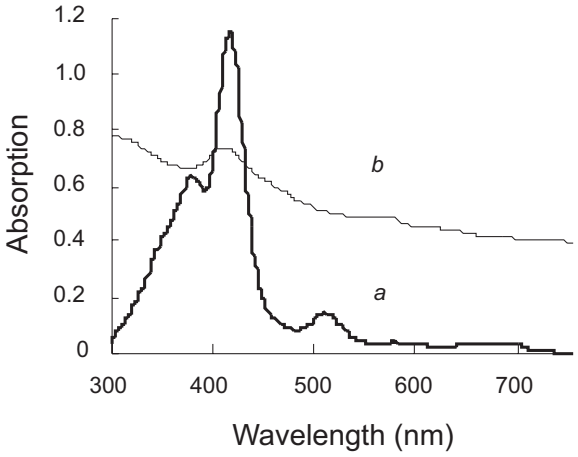

Fig. 2. FTIR spectra of pure chitosan (1) and chitosan-supported iron tetraphenylporpnyrin complex (2) with an effective frequency range of 4000–450 cm^{-1}.

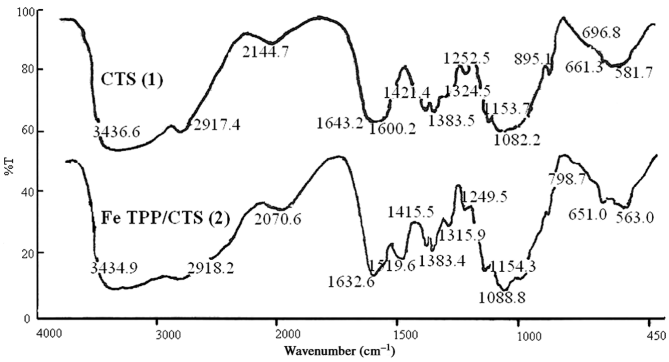

Results and discussion

Characterization of chitosan-supported Fe TPP

Fe TPP was successfully supported on CTS as shown by the UV–vis spectrum of a suspension of the material in a glycerol mull. The spectrum presented the characteristic Soret peak of the metalloporphyrin at 411 nm and the two Q peaks at 572 nm and 622 nm (Fig. 1*b*). The presence of the red-shifted Soret peak and the two Q peaks between 500 and 700 nm was similar to the UV–vis spectra of diamino metalloporphyrins reported by Yoshimura and Kobayashi (14). It indicates that the Fe TPP had been immobilized on the structure of the chitosan. The chloroform extraction from the powder of the solid catalyst presented the same peaks as

© 2008 NRC Canada

those shown in Fig. 1*a*, again showing that the metalloporphyrin had been adsorbed on the support.

The IR spectra of the two samples studied are characterized by the absorption bands of chitosan and its iron tetraphenylporphyrin complex (see Fig. 2): (A) a broad unstructured absorption around 3430 cm^{-1} related to the superposition of stretching vibrations for OH and NH groups; (B) narrow bands of stretching vibrations for CH group at ~2920 cm^{-1} and little shoulder bands near by them, assigned to CH (at ~2920 cm^{-1}) and CH_2 (at 2860–2930 cm^{-1}) fragments, which are similar to the reports (15); and (C) the carbonyl O=C–NHR band, observed at ~1643 cm^{-1}, and the amine $–NH_2$ band, observed at ~1600 cm^{-1}, for their deforming vibrations (see Fig. 2 (**1**)) (16). When iron tetraphenylporphyrins were added to chitosan to form a solid complex, the key bands assigned to chitosan in the complex shifted to lower wavenumbers. The carbonyl band is observed to shift to as low as 1632 cm^{-1} and the amine band to as low as 1519 cm^{-1} (see Fig. 2 (**2**)). These indicate that there is a strong interaction between the nitrogen atom in chitosan and iron tetraphenylporphyrin. It is known that the amine groups ($–NH_2$) on the chitosan chain act as electron donors. The nitrogen electrons present in the amine groups can establish dative bonds with transition-metal ions (17).

Catalysis of Fe TPP and Fe TPP/CTS for toluene oxidation

The role of the main catalysts, containing transition metals, in the partial oxidation of toluene has received much attention (2, 18). High activity and good selectivity for the oxidation of toluene are generally achieved by the Mo-based and V-based oxides (19). However, the chemical oxidation of toluene is not a suitable method for large-scale production of benzaldehyde and benzyl alcohol. Fe_2O_3 has been found to be a catalyst for complete oxidation of toluene under certain reaction conditions (19), and its catalytic activity can be regulated by changing the nature of the chemical bond and the microenvironment of the iron ion. Since Fe TPP and the corresponding chitosan-supported catalyst appeared to be suitable, they were tested as catalysts for toluene oxidation. We found that both could selectively catalyze aerobic oxidation of toluene to benzaldehyde and benzyl alcohol under our reaction conditions. The reaction catalyzed by the supported catalyst, or by the unsupported catalyst, with air is described in Scheme 1.

GC–MS and LC–MS analyses indicated that the by-products of toluene oxidation were chiefly benzoic acid, and to a lesser extent, benzyl benzoate, which can be disregarded. In the absence of the catalysts, toluene can not be oxidized by air under the same conditions.

Figure 3 shows the changes of benzaldehyde, benzyl alcohol, benzoic acid, and selectivity (aldehyde + alcohol) with reaction time for the aerobic oxidation of toluene catalyzed by Fe TPP/CTS and Fe TPP, respectively. The two catalysts had similar effects, i.e., the amounts of benzaldehyde and benzyl alcohol increased with reaction time to a maximum and then fell. First, it was because the desired products were partially oxidized into by-products, as a result, those of benzoic acid increased throughout and more and more. Second, iron tetraporphyrin catalyst suffered from oxidation degradation and lost its catalytic activity. With both catalysts, toluene oxidation is attributable to the iron ion coordinated by the four nitrogen atoms in porphyrin, but there were quantitative differences. Fe^{3+} in the supported catalyst gained more assistance of the nitrogen electrons present in the amine groups in chitosan than those in the unsupported catalyst; this has been explained by the IR spectra of Fe TPP/CTS. It is probable that chitosan had a great effect on Fe TPP or that it changed the original potential of Fe TPP by the action of amino groups, which conferred better activity and selectivity on Fe TPP/CTS. Therefore, after 3 h reaction time, the concentrations of the main products, benzaldehyde and benzyl alcohol, and of the by-product, benzoic acid, and even selectivity for main products were all higher with the supported catalyst than with the unsupported catalyst (Fig. 3). Based on the previous researches (9, 10), we suggest that it is probable that the amino of chitosan took part in the catalytic process, elevating the catalytic activity of the supported catalyst and more increasing the amount of main products, and the results were the increment of the toluene conversion, catalyst turnover, and selectivity for main products shown in Fig. 3 and Table 1 in which the data were obtained when the amount of main products reached the maximum in the oxidation process. At 4.5 h reaction time, the conversion of toluene was up to 5.5%, the selectivity of benzaldehyde and benzyl alcohol was about 91%, which is higher than the corresponding value for Fe TPP (Fig. 3), and the mole turnover of the catalyst reached 6 130 000 for the supported catalyst. Under the same reaction condition, the recovered supported

Scheme 1. The catalytic toluene oxidation over Fe TPP/CTS and Fe TPP.

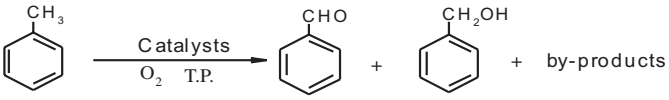

Fig. 3. Changes in mol% of products and selectivity (aldehyde + alcohol) with reaction time for toluene oxidation over Fe TPP/CTS (containing 2 mg Fe TPP) and Fe TPP, respectively. Fe TPP/CTS (◆: benzaldehyde, ■: benzyl alcohol, ▲: benzoic acid, ●: selectivity) and Fe TPP(△: benzaldehyde, □: benzyl alcohol, △: benzoic acid, ○: selectivity). Reaction conditions: 350 ml toluene, 190 °C, 0.6 MPa, and 0.020 m^3/h air flow.

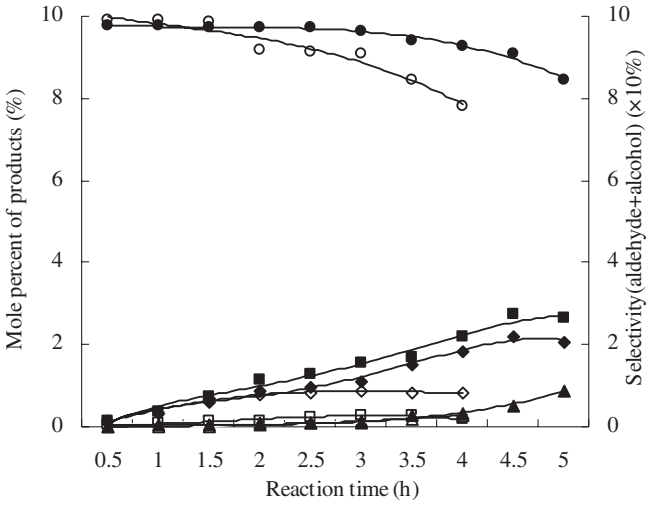

© 2008 NRC Canada

Table 1. The results of toluene oxidation catalyzed by Fe TPP/CTS and Fe TPP.

	Reaction products (mol%)					
Catalysts	Aldehyde	Alcohol	Acid	Selectivity (%)	Conversion (%)	Turnover number ($\times 10^6$)
Fe TPP/CTS	2.21	2.75	0.51	90.7	5.47	6.13
Fe TPP	0.87	0.29	0.12	90.6	1.26	1.44

Note: For reaction conditions, see Fig. 3. Reaction times are 4.5 h and 3 h for Fe TPP/CTS and Fe TPP, respectively.

catalyst catalyzed aerobic oxidation of toluene into main products with 5.2% toluene conversion and 89% selectivity to aldehyde and alcohol for once. The results are better than those for the unsupported catalyst in terms of toluene conversion and turnover number. This is in good agreement with the results of cyclohexane oxidation catalyzed by Fe TPP/CTS (10). Toluene oxidation has potential for the industrial production of benzaldehyde because it requires no more equipment than the conventional method of synthesizing benzaldehyde and benzyl alcohol, needs less extreme reaction conditions, and results in less environmental pollution. It was necessary to assess the effect of reaction temperature, air pressure, and quantity of Fe TPP/CTS catalyst on the toluene conversion and the selectivity for main products.

Influence of reaction temperature on toluene oxidation

Toluene conversion increased with each increment of reaction temperature from 170 to 190 °C, but at 200 °C, toluene conversion decreased (Fig. 4). The reason is that the supported catalyst was partially and gradually burned out in the oxidation process, thereby weakening its power, because when the recovered catalyst was employed to catalyze aerobic oxidation of toluene, no products were detected by GC. At <130 °C, very little benzaldehyde and benzyl alcohol was produced. Not only the toluene conversion but also the changes in selectivity to the main products (aldehyde + alcohol) were influenced by reaction temperature (Fig. 5). In general, the ratio of selectivity to reaction time differed in size in the order 200 °C > 190 °C > 180 °C > 170 °C, especially after a reaction time of 3 h. This indicates that overheating can be detrimental to the selective formation of aldehyde and alcohol, with the excessive temperature and longer reaction time favoring the production of benzoic acid. On the basis of these results for toluene conversion and selectivity, 190 °C was chosen as an optimum reaction temperature for further investigations of the effect of air pressure on the catalysis of Fe TPP/CTS for toluene oxidation.

Influence of air pressure on toluene oxidation

Generally, toluene conversion increased at a different pitch with reaction time (see Fig. 6). Under 0.8 MPa and 0.4 MPa air pressures, the toluene conversion increased with oxidation proceeding, reaching 2.88% and 2.05% at 2.5 h reaction time, respectively, and then the increment of toluene conversion slowed down. Under 0.6 MPa, however, toluene conversion increased at first, and then the increment also slowed down until 5.47% toluene conversion was obtained at 4.5 h reaction time. This indicates that at the highest air pressure tested (0.8 MPa), the dioxygen solubility in the liquid-phase toluene is higher, and the supported catalyst tends partially to break up and lose activity, thereby reducing its catalytic power to a level similar to that seen under 0.4 MPa. In addition, air pressure of 0.8 MPa caused a reduction in selectivity, with many main products being oxidized into benzoic acid (Fig. 7). At the lowest air pressure (0.4 MPa), the activated oxygen atoms in the catalytic reaction system were too few to oxidize toluene into more products, and this directly resulted in low toluene conversion and, since no more activated oxygen was available further to oxidize the main products into by-products, selectivity was high (Fig. 7). The most appropriate air pressure proved to be 0.6 MPa, which allowed not only the highest toluene conver-

Fig. 4. Changes in toluene conversion with reaction time for toluene oxidation over Fe TPP/CTS (containing 2 mg Fe TPP) at different temperatures. ◆: 200 °C, ■: 190 °C, ×: 180 °C, ▲: 170 °C. Reaction conditions: 350 ml toluene, 0.8 MPa, and 0.020 m^3/h air flow.

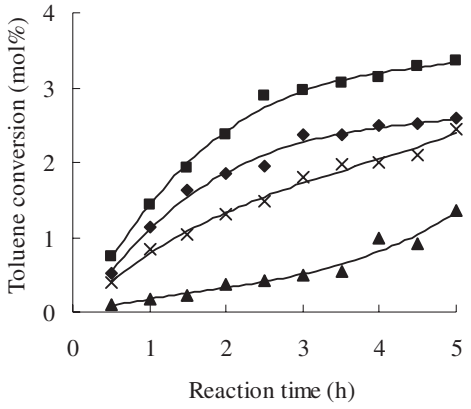

Fig. 5. Changes in selectivity (aldehyde + alcohol) with reaction time for toluene oxidation over Fe TPP/CTS (containing 2 mg Fe TPP) at different temperatures. ◇: 200 °C, □: 190 °C, ×: 180 °C, △: 170 °C. Reaction conditions: see Fig. 4.

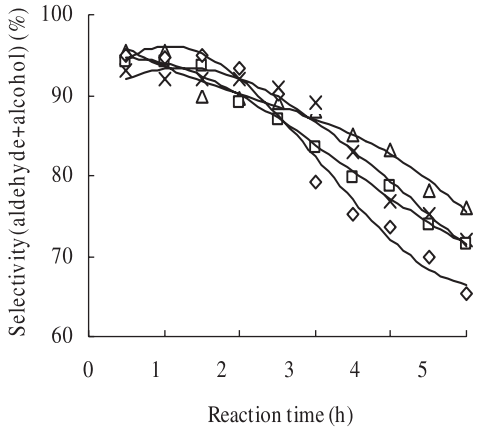

© 2008 NRC Canada

Table 2. The influence of the amount of catalyst on toluene oxidation catalyzed by Fe TPP/CTS.

Catalysts amount[a] (mg)	Reaction products (mol%)			Selectivity (%)	Conversion (%)	Turnover number ($\times 10^6$)
	Aldehyde	Alcohol	Acid			
4	0.79	0.42	0.14	89.6	1.35	0.75
2	2.21	2.75	0.51	90.7	5.47	6.13
1	0.76	0.94	0.21	89.0	1.91	4.24

[a]Containing amount of Fe TPP; Reaction conditions: see Fig. 3; reaction time: 4.5 h.

Fig. 6. Changes in toluene conversion with reaction time for toluene oxidation over Fe TPP/CTS (containing 2 mg Fe TPP) under different pressures. ■: 0.8 MPa, ◇: 0.6 MPa, ▲: 0.4 MPa. Reaction conditions: 350 ml toluene, 190 °C, and 0.020 m^3/h air flow.

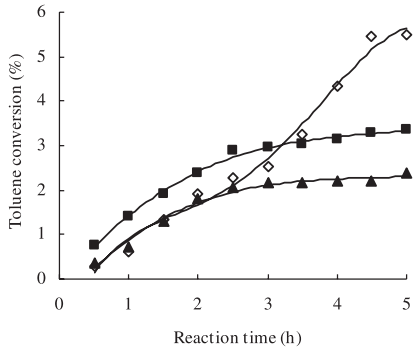

Fig. 7. Changes in selectivity (aldehyde + alcohol) with reaction time for toluene oxidation over Fe TPP/CTS (containing 2 mg Fe TPP) under different pressures. ■: 0.8 MPa, ◆: 0.6 MPa, △: 0.4 MPa. Reaction conditions: see Fig. 6.

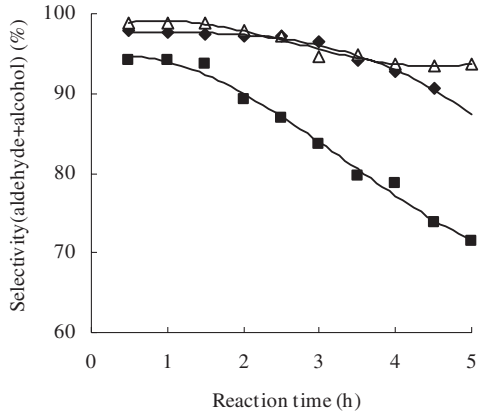

sion (~5.5%; Fig. 5) but also considerable selectivity (90%; Fig. 7).

Influence of the amount of catalyst on toluene oxidation

With a reaction time of 4.5 h at 190 °C and 0.6 MPa, the amount of supported catalyst (1, 2, or 4 mg) had little effect on the product selectivity (Table 2). Toluene conversion increased significantly with an increase in catalyst from 1 to 2 mg but decreased with a further increase in catalyst to 4 mg. A similar phenomenon was observed in our previous work (10). This behavior can be identified with the so-called "catalyst inhibitor conversion" phenomenon already known for some auto-oxidations catalyzed by transition-metal salts in low polar media (20). Obviously, the optimum amount of catalyst is 2 mg.

Conclusions

Chitosan-supported iron(III) tetraphenylporphyrin is a catalyst for aerobic oxidation of toluene with high selectivity to main products and moderate toluene conversion under the optimum reaction conditions. It offers the opportunity to avoid some of the problems experienced with the traditional catalyst with regard to corrosion, pollution, and recovery of catalyst from the reaction mixture. Further studies in our laboratory will consider its high-efficiency reuse for catalytic oxidation of toluene with air under high temperature.

Acknowledgements

We are grateful for the financial supports of Natural Science Foundation of Guangxi province (No. 0728007), the Doctoral Startup Foundation (No. DD040025), and the Experimental Innovation Project Foundation of Guangxi University, P. R. China.

References

1. (*a*) A. Bottino, G. Capannelli, A. Comite, and R. Di Felice. Catal. Today, **99**, 171 (2005); (*b*) K. Gauli, R.N. Ram, and H.P. Soni. J. Mol. Catal. A: Chem. **242**, 161 (2005).
2. H. Gao, G.W. Chen, Q. Yuan, and H.Q. Li. Catal. Today, **110**, 171 (2005).
3. M.A.Gonzalez, S.G. Howell, and S.K. Sikdar. J. Catal. **183**, 159 (1999).
4. F. Quignard and A. Choplin. Comprehensive coordination chemistry. *Edited by* J. Mc Cleverty, A. Mayer, and J. Thomas. Elsevier Ltd. 2004. Chap. 9.
5. (*a*) F. Ciardelli, A. Altomare, G. Conti, G. Arribas, B. Memdez, and A. Ismayel. Macromol. Symp. **80**, 29 (1994); (*b*) M.C. Hausladen, R.C. Cyganovich, H.Y. Huang, and C.R.F. Lund. Appl. Catal. A: Gen. **219**, 1 (2001).
6. Z. Li, C.G. Xia, and X.M. Zhang. J. Mol. Catal. A: Chem. **185**, 47 (2002).
7. J. Haber, L. Matachowski, K. Pamin, and J. Połtowicz. Catal. Today, **91**, 195 (2004).
8. (*a*) J. Połtowicz and J. Haber. J. Mol. Catal. A: Chem. **220**, 43 (2004); (*b*) H.S. Hilal, W. Jondi, S. Khalaf, A. Keilan, M. Suleiman, and A.F. Schreiner. J. Mol. Catal. A: Chem. **113**, 35 (1996); (*c*) T.M. Nenoff, M.C. Showalter, and K.A. Salaz. J. Mol. Catal. A: Chem. **121**, 123 (1997); (*d*) J.W. Huang, W.J.

© 2008 NRC Canada

Mei, J. Liu, and L.N. Ji. J. Mol. Catal. A: Chem. **170**, 261 (2001); (*e*) J. Haber, M. Kłosowski, and J. Połtowicz. J. Mol. Catal. A: Chem. **201**, 167 (2003); (*f*) C.P. Du, Z.K. Li, X.M. Wen, J. Wu, X.Q. Yu, M. Yang, and R.G. Xie. J. Mol. Catal. A: Chem. **216**, 7 (2004).

9. (*a*) G. Huang, S.Y. Liu, A.P. Wang, Y.A. Guo, and H. Zhou. Catal. Comm. **8**, 1183 (2007); (*b*) G. Huang, C.C. Guo, and S.S. Tang. J. Mol. Catal. A: Chem. **261**, 125 (2007).
10. C.C. Guo, G. Huang, X.B. Zhang, and D.C. Guo. Appl. Catal. A: Gen. **247**, 261 (2003).
11. (*a*) A.D. Adler, F.R. Longo, and J.D. Finarelli. J. Org. Chem. **32**, 476 (1967); (*b*) A.D. Adler, F.R. Longo, and F.J. Kampas. Inorg. Nucl. Chem. **32**, 2443 (1970).
12. P.R. Cooke and J.R. Lindsay Smith. J. Chem. Soc. Perkin Trans. **1**, 1913 (1994).
13. C.C. Guo, Q. Liu, X.T. Wang, and H.Y. Hu. Appl. Catal. A: Gen. **282**, 55 (2005).
14. (*a*) T. Yoshimura, H. Toi, S. Inoba, and H. Ogoshi. Bull. Chem. Soc. Jpn. **65**, 1915 (1992); (*b*) H. Kobayashi and Y. Yanagawa. Bull. Chem. Soc. Jpn. **45**, 450 (1972).
15. (*a*) J. Brugnerotto, J. Lizardi, F.M. Goycoolea, W. Argüelles-Monal, J. Desbrières, and M. Rinaudo. Polymer, **42**, 3569 (2001); (*b*) N.V. Kramareva, AY. Stakheev, O.P. Tkachenko, K.V. Klementiev, W. Grünert, E.D. Finashina, and L.M. Kustov. J. Mol. Catal. A: Chem. **209**, 97 (2004).
16. (*a*) D.K. Singh and A.R. Ray. J. Appl. Polym. Sci. **66**, 869 (1997); (*b*) C. Peniche, C. Elvira and J. San Roman. Polymer, **39**, 6549 (1998); (*c*) H.Y. Kweon, I.C. Um, and Y.H. Park. Polymer, **42**, 6651 (2001); (*d*) X. Qu, A. Wirsen, and A.C. Albertsson. Polymer, **41**, 4841 (2000).
17. W.S. Wan Ngah, S.A. Ghani, and A. Kamari. Bioresour. Technol. **96**, 443 (2005).
18. (*a*) M.W. Xue, X.D. Gu, J.P Chen, H.L. Zhang, and J.Y. Shen. Thermochim. Acta, **434**, 50 (2005); (*b*) C. Subrahmanyam, B. Louis, F. Rainone, B. Viswanathan, A. Renken, and T.K. Varadarajan. Catal. Commun. **3**, 45 (2002).
19. W.X. Kuang, Y.N. Fan, K.D. Chen, and Y. Chen. J. Catal. **186**, 310 (1999).
20. J.F. Black. J. Am. Chem. Soc. **100**, 527 (1978).

© 2008 NRC Canada

A novel limonoid from the seeds of *Chisocheton siamensis*

Surat Laphookhieo, Wisanu Maneerat, Sorwaporn Koysomboon, Rattana Kiattansakul, Kan Chantrapromma, and John Keith Syers

Abstract: Analysis of an acetone/hexane (1:1) extract of the seeds of *Chisocheton siamensis* led to the isolation of a novel limonoid, chisosiamensin (**1**), along with five known limonoids, dysobinin (**2**), azadiradione (**3**), mohinin (**4**), epoxyazadiradione (**5**), and 6α-acetoxyepoxyazadiradione (**6**). Their structures were characterized by spectroscopic methods, including UV, IR, NMR, and MS. All isolated limonoids were reported for the first time as secondary metabolites of *C. siamensis*.

Key words: Chisocheton siamensis, Meliaceae, chisosiamensin, limonoids.

Résumé : L'analyse d'un extrait par un mélange acétone-hexane (1:1) de graines de *Chisocheton siamensis* a permis d'extraire un nouveau limonoïde, la chisosiamensine (**1**), aux côtés de cinq limonoïdes connus, la dysobinine (**2**), l'azadiradione (**3**), la mohinine (**4**), l'époxyazadiradione (**5**) et la 6α-acétoxyépoxyazadiradione (**6**). On a caractérisé leurs structures par des méthodes spectroscopiques, incluant l'UV, l'IR, la RMN et la SM. Tous les limonoïdes isolés ont été identifiés pour la première fois comme métabolites secondaires du *C. siamensis*.

Mots-clés : Chisocheton siamensis, Meliaceae, chisosiamensine, limonoïdes.

[Traduit par la Rédaction]

Introduction

Meliaceae plants are known to be rich sources of limonoids. A number of limonoids have been isolated from several genera of Meliaceae and some of these exhibit antimalarial (1, 2), cytotoxic (3, 4), antiprotozoal (5), and antifeedant (6, 7) activities. *Chisocheton siamensis* is one of the Meliaceae plants, which is found in the northern part of Thailand. This plant has been used by local Thai people as anti plant pathogen and antimalarial. In the continuation of our research on secondary metabolites from Thai medicinal plants (8, 9), we have studied an acetone/hexane (1:1) extract of the seeds of *C. siamensis* identified a new limonoid, chisosiamensin (**1**), along with five known compounds (**2**–**6**). In this paper, we describe the isolation and identification of a new and known limonoids isolated from the seeds of *C. siamensis*. The plausible biogenetic pathway of the new compound **1** and limonoids **4**–**6** is also reported.

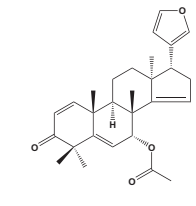

Chisosiamensin (1)

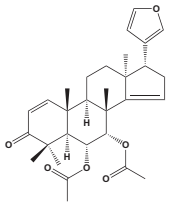

Dysobinin (2)

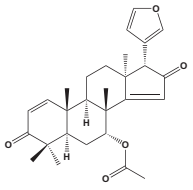

Azadiradione (3)

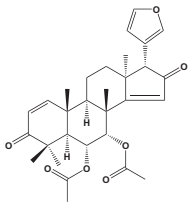

Mohinin (4)

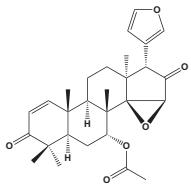

Epoxyazadiradione (5)

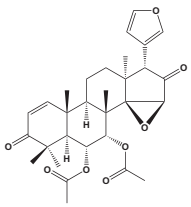

6α-Acetoxyepoxyazadiradione (6)

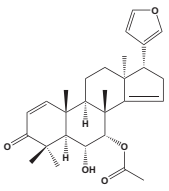

Nimonol (7)

Received 25 September 2007. Accepted 16 December 2007. Published on the NRC Research Press Web site at canjchem.nrc.ca on 1 February 2008.

S. Laphookhieo,[1] W. Maneerat, and J.K. Syers. School of Science, Mae Fah Luang University; Tasud, Muang, Chiang Rai 57100, Thailand.
S. Koysomboon and R. Kiattansakul. Faculty of Arts and Sciences, Prince of Songkla University, Muang, Suratthani 84100, Thailand.
K. Chantrapromma. School of Science, Walailak University, Thaiburi, Thasala, Nakhon Si Thammarat 80160, Thailand.

[1]Corresponding author (e-mail: surat@mfu.ac.th or laphookhieo@yahoo.com).

Results and discussion

Soaking the seeds of *C. siamensis* in acetone/hexane (1:1) for 3 days provided a crude extract. This crude extract was subjected to a succession of chromatographic procedures, in-

 doi:10.1139/V07-155 © 2008 NRC Canada

Table 1. ^{1}H, ^{13}C, and DEPT spectral data of chisosiamensin (**1**) and nimonol (**7**).

	Chisosiamensin		Nimonol		
C/H	δ_C	δ_H (J in Hz)	δ_C	δ_H (J in Hz)	DEPT[a]
1	158.1	7.15 (d, J = 10.2)	157.40	7.12 (d, J = 10.06)	CH
2	125.4	5.84 (d, J = 10.2)	126.14	5.90 (d, J = 10.06)	CH
3	204.6	–	205.96	–	C
4	39.9	–	40.51	–	C
5	158.2	–	49.88	2.21 (d, J = 11.65)	C
6	129.7	5.33 (m)	68.08	4.38 (dd, J = 11.65, 2.37)	CH
7	74.5	5.27 (br m)	79.08	5.36 (d, J = 2.37)	CH
8	44.1	–	45.43	–	C
9	38.6	2.28 (m)	37.13	2.21 (m)	CH
10	42.8	–	43.11	–	C
11	16.5	1.75 (m), 2.03 (m)	16.39	1.82 (m)	CH_2
12	33.0	1.68 (m), 1.95 (m)	32.72	1.82 (m)	CH_2
13	47.1	–	47.08	–	C
14	158.8	–	158.53	–	C
15	119.6	5.37 (br m)	119.55	5.42 (dd, J = 1.82, 2.84)	CH
16	34.3	2.35 (m)	34.30	1.7 (m), 2.4 (m)	CH_2
17	51.6	2.80 (dd, J = 7.8, 10.5)	51.12	2.83 (m)	CH
18	19.0	0.78 (s)	20.84	0.82 (s)	CH_3
19	27.0	1.07 (s)	27.08	1.14 (s)	CH_3
20	124.5	–	124.37	–	C
21	139.6	7.23 (br s)	139.64	7.26 (m)	CH
22	111.0	6.27 (br m)	110.94	6.29 (m)	CH
23	142.5	7.37 (br m)	142.57	7.39 (m)	CH
28	21.1	1.19 (s)	20.23	1.27 (s)	CH_3
29	27.3	1.22 (s)	31.87	1.31 (s)	CH_3
30	20.6	1.07 (s)	20.79	1.41 (s)	CH_3
7-O*CO*CH_3	170.1	–	172.32	–	C
7-O*CO*CH_3	21.2	1.95 (s)	21.16	2.05 (s)	CH_3

[a]The chisosiamensin data were analyzed by DEPT 90° and 135°.

cluding quick column chromatography (QCC) and column chromatography (CC) and crystallization to afford a new limonoid, chisosiamesin (**1**), along with five known limonoids (**2**–**6**).

The ^{1}H NMR spectra of limonoids isolated from the seeds of *C. siamensis* that were tetranortriterpenoids indicated that all compounds contained an α,β-unsaturated ketone at ring A and a β-furan moiety at C-17 of ring D. Three of these were connected with two acetoxyl groups at C-6 and C-7 in ring B, which existed in compounds **2**, **4**, and **6**, whereas limonoids **1**, **3**, and **5** consisted of an acetoxyl group at C-7. In addition, compounds **3** and **4** also contained an additional α,β-unsaturated ketone at ring D, while compounds **5** and **6** had an epoxy ketone instead of an α,β-unsaturated ketone.

Chisosiamensin (**1**) was isolated as a colorless viscous oil with a molecular ion peak at m/z 435.4526 $[M + H]^+$ in HREI–MS, corresponding to the molecular formula $C_{28}H_{34}O_4$. The UV spectrum indicated the presence of α,β-unsaturated ketone at 218 nm, while the IR spectrum of this compound showed two carbonyl functionalities at 1750 and 1680 cm^{-1}. Compound **1** was classified as tetranortriterpenoidal limonoid by the presence of five methyl singlets at δ: 0.78 (Me-18), 1.07 (2 × Me, Me-19, and Me-30), 1.19 (Me-28), and 1.22 (Me-29) and a β-furan moiety at δ: 6.27 (s, H-22), 7.23 (s, H-21), and 7.37 (s, H-23) in the ^{1}H NMR spectrum (10, 11). The ^{1}H NMR and ^{13}C NMR spectral data of **1** (Table 1) were similar to nimonol (**7**), isolated from *Azadirachta indica* (10), except that **1** showed an olefinic proton at δ: 5.33 (m), which was connected to sp^2 carbon at δ: 129.7 (C-6) in the HMQC experiment, instead of the two methine protons (H-5 and H-6) of nimonol (Table 1). These results indicated that compound **1** consisted of a double at C-5/6. Therefore, chisosiamensin was identified as **1**, a dehydrated derivative of nimonol.

The remaining limonoids (**2**–**6**) were characterized as dysobinin (**2**) (12), azadiradione (**3**) (2), mohinin (**4**) (13), epoxyazadiradione (**5**) (14), and 6α-acetoxyepoxyazadiradione (**6**) (15) by the analysis of 1D and 2D NMR data and by comparison with their reported physical and spectroscopic data. It should be noted that the plausible biogenetic pathway of three limonoids (**1**, **4**, and **6**) could be derived from dysobinin (**2**) (Scheme 1). The elimination of AcOH of dysobinin produced chisosiamensin, whereas the hydroxylation at C-16 of dysobinin followed by alcohol oxidation yielded mohinin (**4**). Epoxidation at C-14/15 of mohinin (**4**) gave 6α-acetoxyepoxyazadiradione (**6**). In the case of epoxyazadiradione (**5**), this compound could be de-

© 2008 NRC Canada

Scheme 1. Plausible biogenetic pathway of compounds **1** and **4–6**.

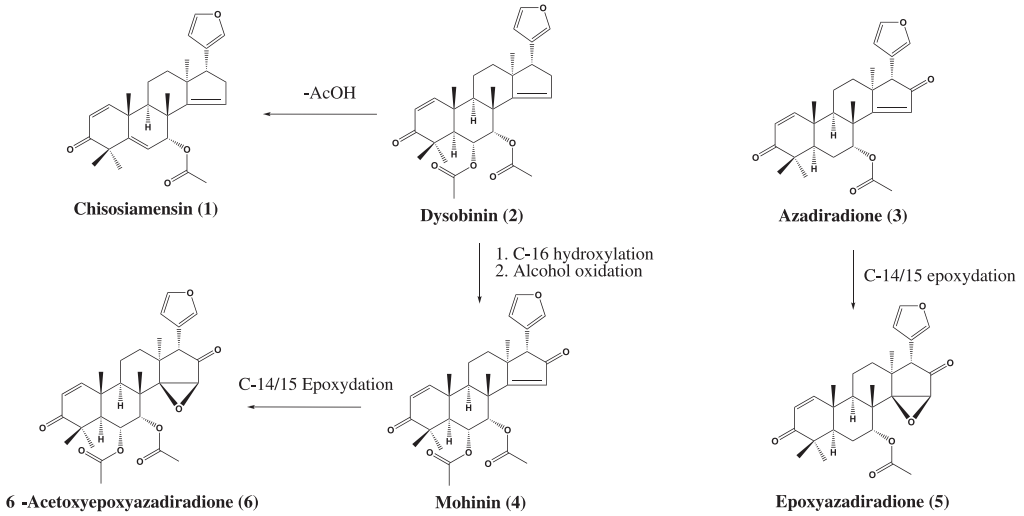

rived from the epoxidation at C-14/15 of azadiradione (**3**) (Scheme 1). Finally, the control experiment of compound **2** (dysobinin) was done. Unfortunately, no compound **1** (chisosiamensin) was observed from this experiment. Therefore, compound **1** was a natural product produced from the seeds of this plant.

It is worth noting that a number of limonoids have been isolated from the Meliaceae species. However, less than 30 compounds have been isolated from the genus *Chisocheton*. In this study, we isolated an additional novel limonoid from the seeds of *C. siamensis* and all isolated limonoids were reported for the first time as secondary metabolites of *C. siamensis*.

Experimental section

General

Melting points were determined using a Fisher–John melting point apparatus. The optical rotation $[\alpha]_D$ values were determined with a JASCO P-1020 digital polarimeter. UV spectra were measured with a UV-160A spectrophotometer (Shimadzu). The IR spectra were measured with a PerkinElmer FTS FT-IR spectrophotometer. The ^{1}H NMR and ^{13}C NMR spectra were recorded using a 300 MHz Bruker FTNMR Ultra Shield spectrometer. Chemical shifts were recorded in parts per million (δ) in $CDCl_3$ with tetramethylsilane (TMS) as the internal reference. The EIMS was obtained from a MAT 95 XL mass spectrometer. Quick column chromatography (QCC) and column chromatography (CC) were carried out on silica gel 60 H (Merck, 5–40 μm) and silica gel 100 (Merck, 63–200 μm), respectively. Precoated plates of silica gel 60 F_{254} were used for the analytical procedure.

Plant material

Seeds of *C. siamensis* were collected from Queen Sirikit Garden, Mae Rim District, Chiang Mai Province, northern Thailand, in February, 2006. The botanical identification was made by Dr. Prachaya Srisanga, botanist at Queen Sirikit Garden. Voucher specimens are deposited in the Herbarium of Queen Sirikit Garden, Mae Rim District, Chiang Mai, Thailand.

Extraction and isolation

Seeds of *C. siamensis* (600 g) were extracted with acetone/hexane (1:1) over the period of 3 days at room temperature. The mixture was filtered and concentrated under reduced pressure to provide the crude extract (62.21 g). This crude extract was subjected to quick column chromatography (QCC, column size: 12 cm × 16 cm) over silica gel and eluted with a gradient of EtOAc/hexane to afford 13 factions (A1–A13). Fraction A2 (435.9 mg) was subjected to column chromatography (CC) using 15% EtOAc/hexane to give compound **1** (51.2 mg). Fraction A4 (4.0 g) upon standing at room temperature yielded compound **2** (3.30 g). Compound **5** (227.0 mg) was obtained from fraction A6 (576.9 mg) after repeated CC with 25% EtOAc/hexane. Purification of fraction A8 (1.01 g) by CC with 25% EtOAc/hexane gave compounds **6** (17.2 mg) and **3** (31.2 mg). Compound **4** (18.2 mg) was obtained from fraction A10 (65.5 mg) by repeated CC using 5% EtOAc/CH_2Cl_2 as eluent.

Control experiment of dysobinin (2)

A solution of dysobinin (10 mg) and 1:1 acetone/hexane (2 mL) was stirred at room temperature for three days. The solution mixture was monitored by TLC (15% EtOAc/hexane) and only dysobinin was observed on the TLC.

Chisosiamensin

Colorless viscous oil. $[\alpha]^{27}_D$ +49.0° (*c* 0.04, MeOH). UV λ_{max} (log ε) (MeOH): 218 (4.37). IR (neat): 1750, 1680. For ^{1}H NMR and ^{13}C NMR see Table 1. EI-MS *m/z*: 435 (87) $[M + H]^+$. HR-EI-MS *m/z*: 435.4526 $[M + H]^+$.

Acknowledgments

Surat Laphookhieo thanks the Bioresources Research Network, National Center for Genetic and Engineering and Biotechnology (grant number BRN 003 G-49), and Mae Fah Luang University for financial support.

© 2008 NRC Canada

References

1. J. Bickii, N. Njifutie, J.A. Foyere, L.K. Basco, and P. Ringwald. J. Ethnopharmacol. **69**, 27 (2000).
2. N. Saewan, J.D. Sutherland, and K. Chantrapromma. Phytochemistry, **67**, 2288 (2006).
3. K. Awang, C.S. Lim, K. Mohamad, H. Morita, Y. Hirasawa, K. Takeya, O. Thoison, and A.H.A. Hadi. Bioorg. Med. Chem. **15**, 5997 (2007).
4. K. Takeya, Z.S. Qiao, C. Hirobe, and H. Itokawa. Phytochemistry, **42**, 709 (1996).
5. S.A. Khalid, G.M. Friedrichsen, A. Kharazmi, T.G. Theander, C.E. Olsen, and S.B. Christensen. Phytochemistry, **49**, 1769 (1998).
6. O. Koul, W.M. Daniewski, J.S. Multani, M. Gumulka, and G. Singh. J. Agric. Food Chem. **51**, 7271 (2003).
7. K.I. Nihei, F.J. Hanke, Y. Asaka, T. Matsumoto, and I. Kubo. J. Agric. Food Chem. **50**, 5048 (2002).
8. S. Laphookhieo, W. Maneerat, and R. Kiattansakul. Can. J. Chem. **84**, 1546 (2006).
9. S. Laphookhieo, P. Promnart, J.K. Syers, A. Kanjana-Opas, C. Ponglimanont, and C. Karalai. J. Braz. Chem. Soc. **18**, 1077 (2007).
10. G. Suresh, N.S. Narasimhan, and N. Palani. Phytochemistry, **45**, 807 (1997).
11. B.S. Siddiqui, F. Afshan, Ghiasuddin, S. Faizi, S.N.H. Naqvi, and R.M. Tariq. Phytochemistry, **53**, 371 (2000).
12. S. Singh, H.S. Garg, and N.M. Khanna. Phytochemistry, **15**, 2001 (1976).
13. S. Kadota, L. Marpaung, T. Kikuchi, and H. Ekimoto. Chem. Pharm. Bull. **38**, 1495 (1990).
14. S. Siddiqui, T.N. Waheed, J. Luecke, and W. Voelter. Chem-Ztg. **99**, 504 (1975).
15. D.A. Mulholland, R. Osborne, S.L. Roberts, and D.A.H. Taylor. Phytochemistry, **37**, 1417 (1994).

© 2008 NRC Canada

Diastereoselective bismuth triflate catalyzed Claisen rearrangement of 2-alkoxycarbonyl-substituted allyl vinyl ethers

Thierry Ollevier and Topwe M. Mwene-Mbeja

Abstract: In the presence of a catalytic amount of bismuth triflate, 2-alkoxycarbonyl-substituted allyl vinyl ethers as a mixture of enol ether double bond isomers were smoothly converted into the β,γ-alkyl-substituted α-keto esters. The isomerization reaction proceeded rapidly to afford smoothly the α-keto esters in good to excellent yields using catalytic amounts of $Bi(OTf)_3 \cdot 4H_2O$ (1 mol%). (*Z,Z*)-2-*iso*-Propyloxycarbonyl-substituted allyl vinyl ethers $\mathbf{3_{Z,Z}}$ afforded the corresponding β,γ-alkyl-substituted α-keto esters **4** with very good *syn* diastereoselectivity.

Key words: bismuth; bismuth(III) triflate; Claisen rearrangement; allyl vinyl ethers.

Résumé : En présence d'une quantité catalytique de triflate de bismuth, les allyl vinyl éthers substitués par un groupement 2-alcoxycarbonyl, et sous la forme d'un mélange d'isomères au niveau de la double liaison de l'éther d'énol, sont facilement convertis en α-céto esters β,γ-alkyl-substitués. La réaction d'isomérisation a lieu rapidement et conduit aux α-céto esters dans des rendements bons à excellents à l'aide de quantités catalytiques de $Bi(OTf)_3 \cdot 4H_2O$ (1 mol %). Les allyl vinyl éthers $\mathbf{3_{Z,Z}}$ substitués par un groupement (*Z,Z*)-2-*iso*-propyloxycarbonyle conduisent aux α-céto esters **4** β,γ-alkyl-substitués correspondants avec une très bonne diastéreosélectivité *syn*.

Mots-clés : bismuth; triflate de bismuth(III), réarrangement de Claisen, allyl vinyl éthers.

[Traduit par la Rédaction]

Introduction

The thermal aliphatic Claisen rearrangement of allyl vinyl ethers has been studied in numerous applications since the first example was reported by Claisen in 1912 (1). A limited number of metal catalysts that accelerate the Claisen rearrangement have been disclosed (2), i.e., lanthanides complexes (3), $TiCl_4$ (4), or Pd^{II} complexes (5). Recently, some precedents have been disclosed regarding metal salts (Cu^{II}, lanthanides(III), Sc^{III}) as catalysts for the Claisen rearrangement of 2-alkoxycarbonyl-substituted allyl vinyl ethers (6). High catalytic activity, low toxicity, moisture, and air tolerance make lanthanide triflates valuable catalysts (7). However, the high cost of some of these catalysts often restrain their use. Bismuth compounds provide a good alternative as they have recently attracted attention because of their low toxicity, low cost, and good stability (8). Bi^{III} salts have been reported as catalysts for the Sakurai reaction (9), opening of epoxides (10), Mukaiyama-aldol reaction (11), Mannich-type reactions (12), formation or deprotection of acetals (13), Friedel–Crafts reactions (14), and Fries rearrangements (15). $Bi(OTf)_3$ is particularly attractive because it is commercially available or can be easily prepared from commercially available compounds (16).

As a part of our ongoing interest in bismuth(III)-catalyzed Claisen rearrangements (17), we report herein our results in bismuth(III)-catalyzed rearrangement of 2-alkoxycarbonyl-substituted allyl vinyl ethers as a mixture of enol ether double bond isomers. They were prepared from **1** according to Hiersemann's method (18). Esters **1** were treated with LDA at –78 °C in THF, followed by the addition of an aldehyde to provide the desired β-hydroxyesters **2** in good yields but low diastereoselectivity. Mesylation of **2**, followed by treatment of the crude mesylate with DBU, afforded the α,β-unsaturated esters **3** in high yields as a mixture of double bond isomers (Scheme 1). *Z/E* Isomer ratio in **3** rose from 87:13 to 95:5, with the exception of a 68:32 ratio in $\mathbf{3b_{E,Z}}$. The use of this type of allyl vinyl ethers offers advantages in terms of synthesis, stability, and reactivity according to previous studies (2*b*, 18). We disclose herein the preparation of various substrates possessing a *n*-Pr group either in a *Z* or *E* stereochemistry at the allylic ether double bond ($\mathbf{3_{Z,Z}}$ and $\mathbf{3_{E,Z}}$ series).

Received 18 November 2007. Accepted 9 December 2007. Published on the NRC Research Press Web site at canjchem.nrc.ca on 5 February 2008.

T. Ollevier[1] and T.M. Mwene-Mbeja. Département de chimie, Université Laval, Québec QC G1K 7P4, Canada.

[1]Corresponding author (email: thierry.ollevier@chm.ulaval.ca).

Results and discussion

Initially, we screened the Claisen rearrangement on differently R^1-substituted (*Z,Z*)-2-*iso*-propyloxycarbonyl-substituted allyl vinyl ethers $\mathbf{3_{Z,Z}}$ (Table 1). The rearrangement occured with 1 mol% of $Bi(OTf)_3 \cdot 4H_2O$ in toluene. While using MeCN as the solvent did not lead to the formation of any product (Table 1, entry 2), toluene and CH_2Cl_2 were both

 doi:10.1139/V07-149 © 2008 NRC Canada

Scheme 1. Preparation of the 2-*iso*-propyloxycarbonyl-substituted allyl vinyl ethers.

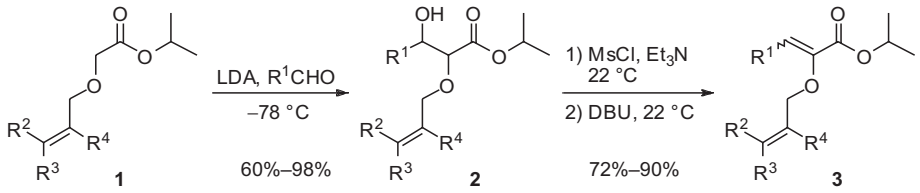

Table 1. $Bi(OTf)_3 \cdot 4H_2O$ catalyzed rearrangement of (*Z,Z*)-2-*iso*-propyloxycarbonyl-substituted allyl vinyl ethers $\mathbf{3_{Z,Z}}$.

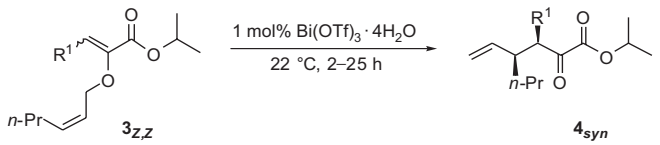

Entry	R^1	*Z,Z*/*Z,E* (**3**)	Solvent	Yield **4** (%)[a]	*Syn*/*anti* (**4**)[b]
1	*i*-Pr	95:5	PhMe	78 (**4a**)[c]	98:2
2	*i*-Pr	95:5	MeCN	–[d]	–
3	Et	89:11	PhMe	85 (**4b**)	90:10
4	Et	89:11	CH_2Cl_2	94 (**4b**)	89:11
5	Ph	93:7	PhMe	80 (**4c**)	73:27
6	*p*-Tol	94:6	CH_2Cl_2	89 (**4d**)	88:12

[a]Isolated yield.
[b]Determined by ^{1}H NMR.
[c]Using 5 mol% of $Bi(OTf)_3 \cdot 4H_2O$.
[d]Recovered starting material.

Table 2. $Bi(OTf)_3 \cdot 4H_2O$ catalyzed rearrangement of (*E,Z*)-2-*iso*-propyloxycarbonyl-substituted allyl vinyl ethers $\mathbf{3_{E,Z}}$.

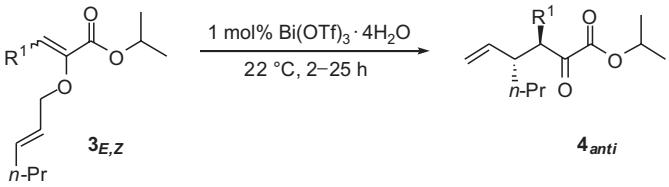

Entry	R^1	*E,Z*/*E,E* (**3**)	Solvent	Yield **4** (%)[a]	*Anti*/syn (**4**)[b]
1	*i*-Pr	90:10	PhMe	82 (**4a**)	41:59
2	*i*-Pr	90:10	PhMe	79 (**4a**)[c]	43:57
3	Et	68:32	CH_2Cl_2	83 (**4b**)	61:39
4	Ph	92:8	PhMe	81 (**4c**)	74:26
5	*o*-Tol	92:8	CH_2Cl_2	98 (**4d**)	72:28
6	*o*-Tol	87:13	CH_2Cl_2	95 (**4e**)	66:34

[a]Isolated yield.
[b]Determined by ^{1}H NMR.
[c]Using 5 mol% of $Bi(OTf)_3 \cdot 4H_2O$.

solvents of choice (Table 1, entries 3 and 4). The β,γ-alkyl-substituted α-keto ester was systematically obtained as the major *syn* diastereoisomer $\mathbf{4_{syn}}$. The diastereoselectivity of the catalyzed rearrangement was high with the various substrates tested, except for the benzaldehyde-derived substrate **3c** leading to **4c** with a moderate *syn*/*anti* ratio (Table 1, entry 5). It should also be pointed out that the diastereoselectivity of the rearrangement was also dependent on the stereoisomeric purity of the substrate **3**.

When substrates in the $\mathbf{3_{E,Z}}$ series ((*E*)-configured allylic ether double bonds) were subjected to the same reaction conditions, the rearrangement produced the β,γ-alkyl-substituted α-keto ester **4** in good to excellent yields (Table 2). The *iso*-propyl-substituted derivative was isolated as the *syn* isomer $\mathbf{4_{syn}}$ in very low diastereoselectivity (Table 2, entries 1 and 2). Increasing the catalyst loading up to 5 mol% led to a slight decrease of yield and diastereoselectivity (Table 2, entry 2). The ethyl-substituted allyl vinyl ether showed a low diastereoselectivity in favor of the *anti* diastereoisomer (Table 2, entry 3). Various aryl-substituted substrates afforded the rearranged product with higher but still moderate diastereoselectivity (Table 2, entries 4–6). *o*-Tolyl- and *p*-tolyl-derived (*E,Z*)-2-*iso*-propyloxycarbonyl-substituted allyl vinyl ethers $\mathbf{3(d, e)_{E,Z}}$ led to excellent yields in rearranged products but with low diastereoselectivity (Table 2, entries 5 and entry 6).

At this point, it clearly appears that the ratio and sense of diastereoselectivity depend on the stereochemistry of the allyl ether double bond (compare Table 1, entry 5 with Table 2, entry 4). More detailed investigations on the mechanism of this transformation are in progress.

Conclusion

As an improvement over other catalytic systems, $Bi(OTf)_3 \cdot 4H_2O$ is a versatile catalyst for the rearrangement of 2-alkoxycarbonyl-substituted allyl vinyl ethers. The reaction affords good to excellent yields in the corresponding β,γ-alkyl-substituted α-keto esters **4** with a very good syn diastereoselectivity starting from the (*Z,Z*)-2-*iso*-propyloxycarbonyl-substituted allyl vinyl ethers $\mathbf{3_{Z,Z}}$. This method offers several advantages including mild reaction conditions, highly catalytic process (1 mol%), and no formation of by-products. The conditions are suitable for a variety of starting materials. Also, the practical use of $Bi(OTf)_3 \cdot 4H_2O$ is highly valuable as an environmentally benign Lewis acid. Because of its numerous benefits, this method for the diastereoselective synthesis of β,γ-alkyl-substituted α-keto esters using $Bi(OTf)_3 \cdot 4H_2O$ catalysis should find utility in the synthesis of biologically active compounds. Research is on its way to demonstrate other significant applications of this $Bi(OTf)_3 \cdot 4H_2O$-catalyzed rearrangement.

Experimental

General procedure for the bismuth triflate catalyzed rearrangement of the (*Z,Z*)- and (*E,Z*)-2-*iso*-propyloxycarbonyl-substituted allyl vinyl ethers 3

The substrate **3** (0.405 mmol) and $Bi(OTf)_3 \cdot 4H_2O$ (0.004 mmol) were mixed together in dry PhMe or CH_2Cl_2 (2 mL) under nitrogen atmosphere. The solution was stirred at 22 °C for 2–25 h. The resulting mixture was quenched with water, extracted with ethyl acetate (3 times), washed

© 2008 NRC Canada

with water (2 times), dried over Na_2SO_4, and concentrated under reduced pressure to afford the crude product. The crude was then purified by column chromatography (eluent hexane/EtOAc 95:5). Spectral data agree with those previously reported in the literature (6*a*, 18).

(3*RS*,4*SR*)-Isopropyl 3,4-diisopropyl-2-oxo-4-vinylheptanoate 4a

Table 1, entry 1. Reagents: (*Z*)-isopropyl 2-((*Z*)-hex-2-enyloxy)-4-methylpent-2-enoate (103 mg, 0.405 mmol) and $Bi(OTf)_3 \cdot 4H_2O$ (14.2 mg, 0.0202 mmol) in toluene (2.0 mL). Work-up followed by purification afforded 80 mg (78%) of the title compound as a mixture of unseparable diastereoisomers (colorless oil). R_f 0.33 (hexane/ethyl acetate 95:5). IR (cm^{-1}) ν: 3076, 2961, 2935, 2874, 2735, 1742, 1724, 1639. ^1H NMR ($CDCl_3$) δ: 5.60–5.67 (m, 1H), 5.08–5.14 (m, 1H), 5.03 (d, *J* = 12.2 Hz, 1H), 4.98 (d, *J* = 18.9 Hz, 1H), 3.31 (dd, *J* = 6.8 Hz, 6.8 Hz, 1H), 2.39–2.47 (m, 1H), 2.00–2.08 (m, 1H), 1.35–1.48 (m, 2H), 1.43 (d, *J* = 6.4 Hz, 6H–maj), 1.33 (d, *J* = 6.4 Hz, 6H–min), 1.10–1.27 (m, 2H), 0,95 (d, *J* = 6.6 Hz, 6H), 0.88 (t, *J* = 6.6 Hz, 3H–maj), 0.84 (t, *J* = 6.6 Hz, 3H–min). ^{13}C NMR ($CDCl_3$) δ: 199.7, 162.2, 138.7, 117.0, 70.6, 56.2, 44.5, 34.8, 28.8, 21.7, 21.5, 20.7, 20.5, 19.7, 14.1.

(3*RS*,4*SR*)-Isopropyl 3-ethyl-2-oxo-4-vinylheptanoate 4b

Table 1, entry 4. Reagents: (*Z*)-isopropyl 2-((*Z*)-hex-2-enyloxy)pent-2-enoate (90 mg, 0.457 mmol) and $Bi(OTf)_3 \cdot 4H_2O$ (3.2 mg, 0.00457 mmol) in dichloromethane (2.3 mL). Work-up followed by purification afforded 85 mg (94%) of the title compound as a mixture of unseparable diastereoisomers (yellowish oil). R_f 0.44 (hexane/ethyl acetate 95:5). IR (cm^{-1}) ν: 3077, 2963, 2935, 2875, 2737, 1723, 1640. ^1H NMR ($CDCl_3$) δ: 5.54–5.63 (m, 1H), 5.09–5.16 (m, 1H), 4.95–5.08 (m, 2H), 3.20–3.24 (m, 1H), 2.27–3.19 (m, 1H), 1.68–1.77 (m, 2H), 1.53–1.62 (m, 2H), 1.35 (d, *J* = 6.2 Hz, 6H–maj), 1.32 (d, *J* = 5.8 Hz, 6H–min.), 1.01–1.29 (m, 2H), 0.88 (t, *J* = 6.3 Hz, 3H), 0.84 (t, *J* = 7.2 Hz, 3H). ^{13}C NMR ($CDCl_3$) δ: 198.5, 161.9, 139.4, 116.9, 70.5, 53.3, 45.7, 33.8, 21.7, 21.6, 21.5, 20.3, 14.0, 13.9, 12.1.

(3*RS*,4*RS*)-Isopropyl 2-oxo-3-phenyl-4-vinylheptanoate 4c

Table 1, entry 5. Reagents: (*Z*)-isopropyl 2-(hex-2-enyloxy)-3-phenylacrylate (0,161 g, 0,656 mmole) and $Bi(OTf)_3 \cdot 4H_2O$ (4.6 mg, 0.00656 mmole) in toluene (3.3 mL). Work-up followed by purification afforded 129 mg (80%) of the titled compound as a mixture of unseparable diastereoisomers (colorless oil). R_f 0.41 (hexane/ethyl acetate 95:5). IR (cm^{-1}) ν: 3079, 3064, 3029, 2981, 2959, 2934, 2873, 1746, 1725. ^1H NMR ($CDCl_3$) δ: 7.18–7.38 (m, 6H), 5.57–5.66 (m, 1H), 5.00–5.13 (m, 3H), 4.45 (d, *J* = 10.3 Hz, 1H–maj), 4.37 (d, *J* = 9.7 Hz, 1H–min), 2.87 (m, 1H), 1.29–1.42 (m, 2H), 1.23 (d, *J* = 6.2 Hz, 6H–maj), 1.20 (d, *J* = 6.2 Hz, 6H–min.), 1.02–1.18 (m, 2H), 0.75 (t, *J* = 7.0 Hz, 3H). ^{13}C NMR ($CDCl_3$) δ: 193.5, 160.8, 139.8, 138.8, 134.9, 130.2, 129.9, 129.0, 127.9, 117.6, 70.7, 59.0, 58.4, 45.6, 35.7, 33.9, 21.7, 20.5, 19.9, 14.0. HRMS calcd. for $C_{18}H_{24}O_3$ ($[M + H]^+$): 289.1798; found: 289.1801.

(3*RS*,4*RS*)-Isopropyl 2-oxo-3-*p*-tolyl-4-vinylheptanoate 4d

Table 1, entry 6. Reagents: (*Z*)-isopropyl 2-((*Z*)-hex-2-enyloxy)-3-*p*-tolylacrylate (157 mg, 0.519 mmol) and $Bi(OTf)_3 \cdot 4H_2O$ (3.6 mg, 0.00519 mmol) in dichloromethane (2.6 mL). Work-up followed by purification afforded 139 mg (89%) of the title compound as a mixture of unseparable diastereoisomers (colorless oil). R_f 0.41 (hexane/ethyl acetate 95:5). IR (cm^{-1}) ν: 3079, 3050, 3024, 2982, 2959, 2873, 2735, 1725, 1640, 1512, 1465, 1457. ^1H NMR ($CDCl_3$) δ: 7.03–7.26 (m, 4H), 5.56–5.65 (m, 1H), 5.01–5.12 (m, 3H), 4.40 (d, *J* = 10.5 Hz, 1H–maj), 4.33 (d, *J* = 9.7 Hz, 1H–min), 2.87 (m, 1H), 2.32 (s, 3H–maj), 2.29 (3H–min), 1.28–1.38 (m, 2H), 1.24 (d, *J* = 6.2 Hz, 6H–maj), 1.21 (d, *J* = 6.2 Hz, 6H–min), 1.01–1.18 (m, 2H), 0.76 (t, *J* = 7.0 Hz, 3H). ^{13}C NMR ($CDCl_3$) δ: 193.5, 160.9, 139.9, 137.6, 131.8, 130.1, 129.7, 129.6, 117.5, 70.7, 58.0, 45.4, 45.3, 35.7, 33.9, 21.7, 21.3, 20.5, 19.9, 14.1. HRMS calcd. for $C_{19}H_{26}O_3$ ($[M + H]^+$): 303.1955; found: 303.1956.

(3*RS*,4*SR*)-Isopropyl 2-oxo-3-*o*-tolyl-4-vinylheptanoate 4e

Table 2, entry 6. Reagents: (*Z*)-isopropyl 2-((*E*)-hex-2-enyloxy)-3-*o*-tolylacrylate (258 mg, 1.027 mmol) and $Bi(OTf)_3 \cdot 4H_2O$ (7.2 mg, 0.01027 mmol) in dichloromethane (5.1 mL). Work-up followed by purification afforded 246 mg (95%) of the title compound as a mixture of unseparable diastereoisomers (colorless oil). R_f 0.49 (hexane/ethyl acetate 95:5). IR (cm^{-1}) ν: 3077, 3020, 2981, 2959, 2934, 2873, 2737, 1746, 1725, 1641, 1491, 1465. ^1H NMR ($CDCl_3$) δ: 7.11–7.19 (m, 4H–maj), 6.98–7.09 (m, 4H–min), 5.61–5.73 (m, 1H), 5.40–5.50 (m, 1H–min), 5.26–5.37 (m, 1H–maj), 5.12 (d, *J* = 16.7 Hz, 1H), 5.06 (d, *J* = 10.3 Hz, 1H), 4.93–4.99 (m, 1H), 4.70–4.80 (m, 1H), 4.65 (d, *J* = 10.1 Hz, 1H–min), 4.59 (d, *J* = 9.9 Hz, 1H–maj), 4.51–4.57 (m, 1H), 2.84–2.91 (m, 2H–min), 2.47 (s, 3H–min), 2.42 (s, 3H–maj), 1.50–2.18 (m, 2H–maj), 1.42–1.49 (m, 2H–min), 1.22–1.40 (m, 2H–maj), 1.19 (d, *J* = 6.6 Hz, 6H–maj), 1.17 (d, *J* = 6.2 Hz, 6H–min), 0.89 (t, *J* = 8.7 Hz, 3H–maj), 0.76 (m, 3H–min). ^{13}C NMR ($CDCl_3$) δ: 193.3, 193.0, 161.3, 140.0, 138.5, 137.9, 133.5, 133.3, 131.1, 131.0, 128.9, 128.8, 128.5, 127.7, 127.6, 126.7, 126.5, 126.4, 122.7, 122.6, 117.7, 127.6, 127.0, 70.7, 67.2, 54.4, 53.7, 46.1, 35.8, 34.5, 22.0, 21.5, 20.7, 20.4, 14.2, 13.9. HRMS calcd. for $C_{19}H_{26}O_3$ ($[M + H]^+$): 303.1955; found 303.1955.

Acknowledgements

This work was financially supported by the Natural Sciences and Engineering Research Council of Canada (NSERC), the Fonds Québécois de la Recherche sur la Nature et les Technologies (FQRNT, Québec, Canada), the Canada Foundation for Innovation, and Université Laval. We thank Rhodia (Lyon, France) for generous gift of chemicals.

References

1. L. Claisen. Ber. Dtsch. Chem. Ges. **45**, 3157 (1912).
2. (*a*) The Claisen Rearrangement. *Edited by* M. Hiersemann and U. Nubbemeyer. Wiley-VCH, Weinheim, Germany. 2007; (*b*) M. Hiersemann and L. Abraham. Eur. J. Org. Chem. 1461 (2002).

© 2008 NRC Canada

3. (*a*) B.M. Trost and F.D. Toste. J. Am. Chem. Soc. **120**, 815 (1998); (*b*) S. Gester, P. Metz, O. Zierau, and G. Vollmer. Tetrahedron, **57**, 1015 (2001).
4. G. Koch, P. Janser, G. Kottirsch, and E. Romero-Giron. Tetrahedron Lett. **43**, 4837 (2002).
5. (*a*) J.L. van der Baan and F. Bickelhaupt. Tetrahedron Lett. **27**, 6267 (1986); (*b*) M. Sugiura and T. Nakai. Chem. Lett. 697 (1995); (*c*) K. Mikami, K. Takahashi, T. Nakai, and T. Uchimaru. J. Am. Chem. Soc. **116**, 10948 (1994).
6. (*a*) L. Abraham, M. Körner, P. Schwab, and M. Hiersemann. Adv. Synth. Catal. **346**, 1281 (2004); (*b*) M. Hiersemann and L. Abraham. Org. Lett. **3**, 49 (2001).
7. S. Kobayashi, M. Sugiura, H. Kitagawa, and W.W.-L. Lam. Chem. Rev. **102**, 2227 (2002).
8. (*a*) Y. Sugihara. Organobismuth chemistry. *Edited by* H. Suzuki and Y. Matano. Elsevier, Amsterdam. 2001; (*b*) H. Gaspard-Iloughmane and C. Le Roux. Eur. J. Org. Chem. 2517 (2004); (*c*) H. Gaspard-Iloughmane and C. Le Roux. Trends Organic Chemistry, **11**, 65 (2006); (*d*) N.M. Leonard, L.C. Wieland, and R.S. Mohan. Tetrahedron, **58**, 8373 (2002).
9. (*a*) P.W. Anzalone, A.R. Baru, E.M. Danielson, P.D. Hayes, M.P. Nguyen, A.F. Panico, R.C. Smith, and R.S. Mohan. J. Org. Chem. **70**, 2091 (2005); (*b*) T. Ollevier and Z. Li. Org. Biomol. Chem. **4**, 4440 (2006); (*c*) T. Ollevier and T. Ba. Tetrahedron Lett. **44**, 9003 (2003); (*d*) T. Ollevier and Z. Li. Eur. J. Org. Chem. 5665 (2007).
10. (*a*) C. Ogawa, S. Azoulay, and S. Kobayashi. Heterocycles, **66**, 201 (2005); (*b*) T. Ollevier and G. Lavie-Compin. Tetrahedron Lett. **45**, 49 (2004); (*c*) T. Ollevier and G. Lavie-Compin. Tetrahedron Lett. **43**, 7891 (2002); (*d*) T. Ollevier and E. Nadeau. Tetrahedron Lett. **49**, asap (2008).
11. (*a*) C. Le Roux, L. Ciliberti, H. Laurent-Robert, A. Laporterie, and J. Dubac. Synlett, 1249 (1998); (*b*) S. Kobayashi, T. Ogino, H. Shimizu, S. Ishikawa, T. Hamada, and K. Manabe. Org. Lett. **7**, 4729 (2005); (*c*) T. Ollevier, V. Desyroy, B. Debailleul, and S. Vaur. Eur. J. Org. Chem. 4971 (2005); (*d*) T. Ollevier, V. Desyroy, C. Catrinescu, and R. Wischert. Tetrahedron Lett. **47**, 9089 (2006); (*e*) T. Ollevier, J.-E. Bouchard, and V. Desyroy. J. Org. Chem. **73**, 331 (2008).
12. (*a*) T. Ollevier and E. Nadeau. J. Org. Chem. **69**, 9292 (2004); (*b*) T. Ollevier, E. Nadeau, and J.-C. Eguillon. Adv. Synth. Catal. **348**, 2080 (2006); (*c*) T. Ollevier, E. Nadeau, and A.-A. Guay-Bégin. Tetrahedron Lett. **47**, 8351 (2006); (*d*) T. Ollevier and E. Nadeau. Synlett, 219 (2006); (*e*) T. Ollevier and E. Nadeau. Org. Biomol. Chem. **5**, 3126 (2007).
13. N.M. Leonard, M.C. Oswald, D.A. Freiberg, B.A. Nattier, R.C. Smith, and R.S. Mohan. J. Org. Chem. **67**, 5202 (2002).
14. (*a*) C. Le Roux and J. Dubac. Synlett, 181 (2002); (*b*) J.R. Desmurs, M. Labrouillère, C. Le Roux, H. Gaspard, A. Laporterie, and J. Dubac. Tetrahedron Lett. **38**, 8871 (1997); (*c*) S. Répichet, C. Le Roux, J. Dubac, and J. R. Desmurs. Eur. J. Org. Chem. 2743 (1998).
15. T. Ollevier, V. Desyroy, M. Asim, and M.-C. Brochu. Synlett, 2794 (2004).
16. S. Répichet, A. Zwick, L. Vendier, C. Le Roux, and J. Dubac. Tetrahedron Lett. **43**, 993 (2002).
17. (*a*) T. Ollevier and T. M. Mwene-Mbeja. Synthesis, 3963 (2006); (*b*) T. Ollevier and T.M. Mwene-Mbeja. Tetrahedron Lett. **47**, 4051 (2006).
18. M. Hiersemann. Synthesis, 1279 (2000).

© 2008 NRC Canada

Prodigiosin synthesis with electron rich 2,2′-bipyrroles

Benoit Jolicoeur and William D. Lubell

Abstract: The prodigiosins possess a linear tripyrrolic scaffold with the A and B pyrrolic rings connected directly in a bipyrrole unit, and the B and C rings joined in a dipyrrin. These red streptomycete metabolites exhibit among other activities, antitumor, antimicrobial, and immunomodulating properties. A new prodigiosin synthesis has been developed that employs electron rich 2,2′-bipyrroles. In particular, undecylprodigiosin and PNU-156804 were synthesized by condensations of 4-methoxy and 4-benzyloxy 2,2′-bipyrroles, **20a** and **20b**, respectively, with 5-undecylpyrrole-2-carboxaldehyde in 75% and 83% yields. The 4-alkoxy-2,2′-bipyrroles were synthesized from 4-alkoxypyrrolyl butenyl ketones (**15a** and **15b**), which were made by a novel one-pot process from 2-acyl-*N*-(PhF)pyrrolidin-4-one (**13**) [PhF = 9-(9-phenylfluorenyl)] using PhFNa in the presence of alkyl halide. A sequence of alkoxy pyrrole **15a** and **15b** protection, olefin oxidation, Paal–Knorr condensation, and deprotection gave the requisite 4-alkoxy-2,2′-bipyrroles (**20**). This route offers utility for making 4-alkoxybipyrroles as well as prodigiosins with diversity at the 6-position of the linear tripyrrolic skeleton.

Key words: prodigiosin, pyrrole, bipyrrole, PNU-156804, undecylprodigiosin.

Résumé : Les prodigiosines possèdent un squelette linéaire comportant trois pyrroles dont les pyrroles A et B sont connectés directement en une unité bipyrrole, et les pyrroles B et C sont joint en une unité dipyrrine. Ces métabolites rouges de streptomycète ont montré entre autre comme activité des propriétés antitumorales, antimicrobiennes et immunomodulatrices. Une nouvelle synthèse de prodigiosine, utilisant des 2,2′-bipyrroles riches en électron, a été développée. Undécylprodigiosine et PNU-156804 ont été synthétisés respectivement par la condensation de 4-méthoxy et 4-benzyloxy 2,2′-bipyrroles **20a** et **20b** avec 5-undécylpyrrole-2-carboxaldéhyde avec des rendements de 75 % et 83 %. Les 4-alkoxy-2,2′-bipyrroles ont été synthétisés à partir de 4-alkoxypyrrolyl butènyl cétones (**15a** et **15b**), lesquels ont été préparés par un nouveau procédé en un pot à partir de 2-acyl-*N*-(PhF)pyrrolidin-4-one (**13**) [PhF = 9-(9-phénylfluorènyl)] en utilisant PhFNa en présence d'un halogénure d'alkyle. Une séquence de protection d'alkoxypyrrole **15a** et **15b**, suivi d'une oxydation de l'oléfine, une condensation de Paal-Knorr et une déprotection a donné les 4-alkoxy-2,2′-bipyrroles (**20**) désirés. Cette route offre la possibilité de synthétiser des 4-alkoxybipyrroles ainsi que les prodigiosines possédant différents substituents en position 6 du squelette linéaire tripyrrolique.

Mots-clés : prodigiosine, pyrrole, bipyrrole, PNU-156804, undecylprodigiosine.

[Traduit par la Rédaction]

Introduction

Prodigiosins (1–4) and structurally related alkaloids (5–8) represent a family of naturally occurring red pigments produced by bacteria, such as *Streptomyces* and *Serratia*. These natural alkaloids, which include prodigiosin (**1**) and undecylprodigiosin (**2**), typically possess a methoxy bipyrrole moiety joined to a third pyrrole by a methene bridge (Fig. 1) (9). They have demonstrated antibacterial, antifungal, immunosuppressive, antimalarial, and cytotoxic properties (10–13). Methoxy bipyrrole alkaloids, such as undecylprodigiosin (**2**, so called prodigiosin 25-C or UP), have, however, exhibited side effects that have restricted their development as drugs such as immunosuppressants (14). To counter side effects, replacement of the 6-methoxy group on the B pyrrole ring of undecylprodigiosin by a 6-benzyloxy group has been used to improve the pharmacological profile in PNU-156804 (15), which has demonstrated potential for treating autoimmune diseases, such as multiple sclerosis and rheumatoid arthritis (16, 17) as well as for preventing solid organ transplant rejection (18). Methodology for modifying the 6-position substituent pattern of prodigiosin analogs has thus been pursued to harness their beneficial properties (19).

Since the pioneering synthesis of Rapoport and Holden (21), 2,2′-bipyrrole-5-carboxaldehyde (**4**) has served as a key precursor for the production of prodigiosins with different substituents on the C-ring pyrrole (Scheme 1) (22). The coupling between a bipyrrole methene triflate (**7**) and pyrrol-2-ylboronic acid (**8**) has offered an alternative method for assembling prodigiosins with other substitution patterns (15, 23). Recently, we prepared the first example of a 6-amino-prodigiosin (**3**) by a third route to the prodigiosin skeleton featuring condensation of an electron rich 4-morphilino-

Received 27 October 2007. Accepted 5 December 2007. Published on the NRC Research Press Web site at canjchem.nrc.ca on 8 February 2008.

B. Jolicoeur and W.D. Lubell.[1] Département de chimie, Université de Montréal, C.P. 6128, Succursale Centre-Ville, Montréal, QC H3C 3J7, Canada.

[1]Corresponding author (e-mail: lubell@chimie.umontreal.ca).

 doi:10.1139/V07-150 © 2008 NRC Canada

Fig. 1. Representative members of the prodigiosin family and synthetic derivatives (nomenclature and numbering are according to ref. 20.

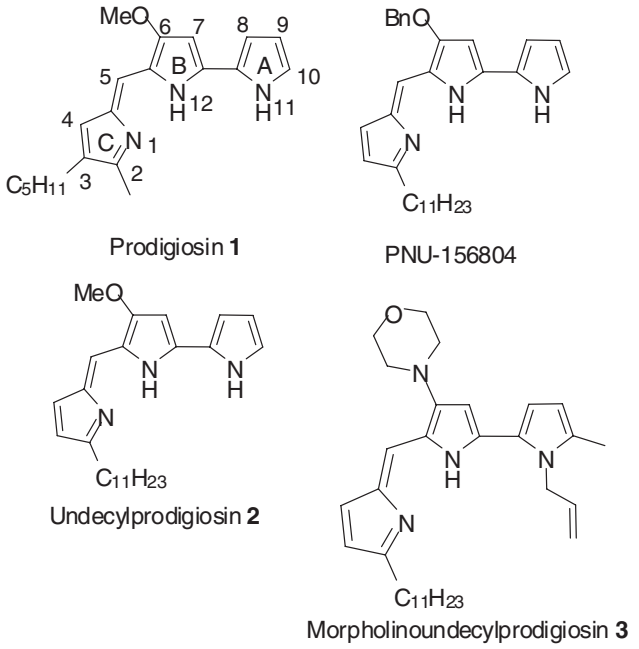

Scheme 1. Synthetic routes to prodigiosins.

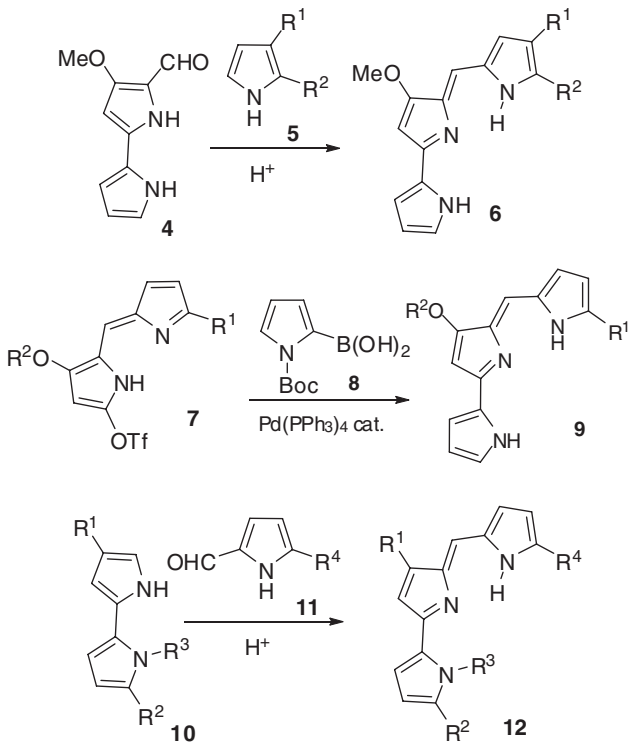

2,2′-bipyrrole (**10**) with a pyrrole-2-carboxaldehyde (**11**) (19, 24). In developing this latter route to synthesize 4-alkoxy-2,2′-bipyrroles (**20**), we have now achieved the syntheses of prodigiosin analogs bearing 6-alkoxy substituents.

In parallel to their use in natural product synthesis, interest in the synthesis of bipyrrole derivatives has been driven by their potential for application in conducting organic materials in microelectronic devices, such as batteries, sensors, and fuel cells (25–27). In contrast to alkylbipyrroles (25), their alkoxy counterparts polymerize usually more readily to produce materials with enhanced conductivity contingent on the substitution pattern (28). Few methods exist, however, for making alkoxy bipyrroles, and many, such as oxidative Ullman-type homocouplings (29), typically provide symmetric materials. Transition metal cross couplings, employing pyrrole boronates and stannanes (23, 30) as well as reactions of donor-acceptor cyclopropanes with 2-cyanopyrroles have provided unsymmetrical bipyrroles, albeit with a limited structural variety (31). Diversity-oriented strategies for creating bipyrroles are thus desired for making innovations in the fields of medicinal chemistry and materials science.

Scheme 2. Synthesis of 4-alkoxypyrroles.

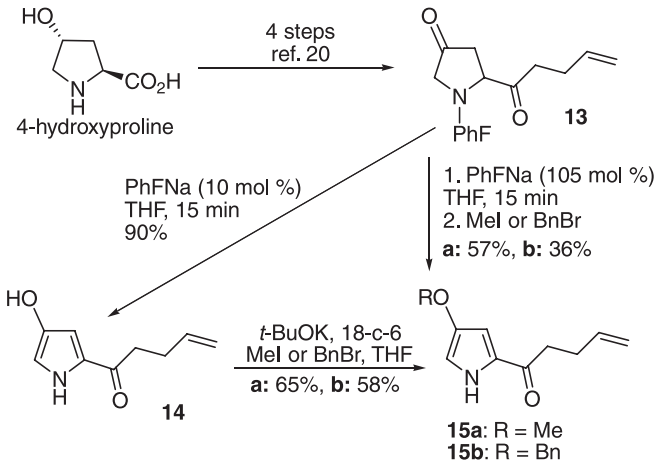

Results and discussion

4-Alkoxy-2,2′-bipyrrole synthesis began with pyrrolidinone **13**, which was prepared from 4-hydroxyproline in 4 steps commencing with protections of the carboxylic acid as a methyl ester and amine with the 9-(9-phenylfluorenyl) (PhF) group (Scheme 2) (19). Dione **13** was prepared by conversion of the carboxylate ester to a γ,δ-unstaturated ketone by a cascade addition of vinyl magnesium bromide (32–34) and oxidation of the 4-position alcohol using DMSO and oxalyl chloride (35).

Exposure of 2-acylpyrrolidin-4-one (**13**) to 10 mol% NaHMDS in THF for 15 min followed by chromatographic purification gave 4-hydroxypyrrole **14** in 89% yield (Scheme 2) (19). 2-Acyl-4-alkoxypyrroles (**15a** and **15b**) were then obtained from alkylation of 4-hydroxypyrrole (**14**) (19). Considering that liberated PhF anion acted as a base to continue the elimination reaction in the synthesis of **14**, pyrrolidinone **13** was treated with 10 mol% of PhFNa to provide **14** in similar yield. 4-Alkoxypyrroles (**15a** and **15b**) were found to also result from a one-pot process featuring treatment of pyrrolidinone **13** with 105 mol% of PhFNa in the presence of iodomethane and benzylbromide, respectively, albeit in 57% and 36% yields.

Attempts to oxidize γ,δ-unstaturated ketone **15** had previously failed due to competitive pyrrole degradation (19). Protection of 4-alkoxypyrrole (**15**) as phenyl sulfonamide (**16**) was necessary and achieved by reacting the pyrrolyl

© 2008 NRC Canada

Scheme 3. Synthesis of 4-alkoxy-2,2′-bipyrroles (yields in parentheses account for recovered starting material).

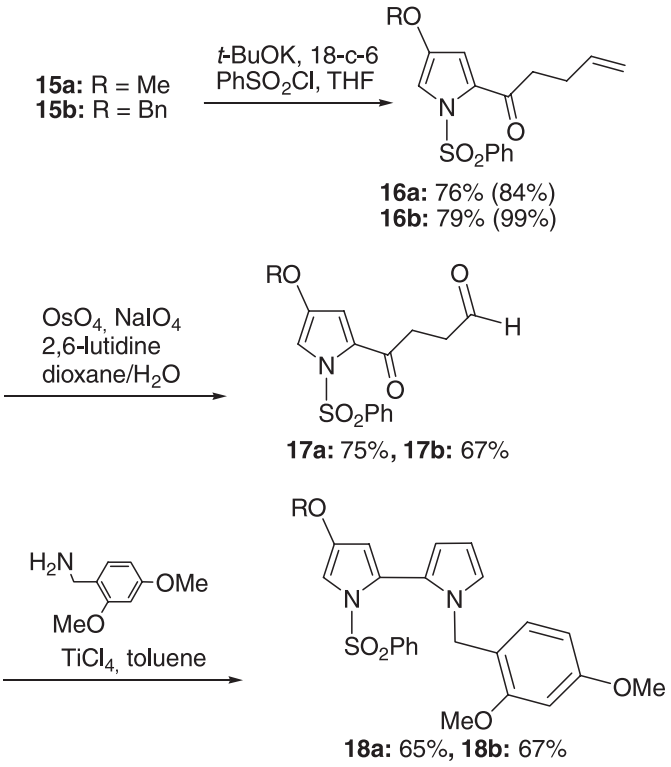

anion, formed with potassium *tert*-butoxide, with phenylsulfonyl chloride in THF (Scheme 3) (36). Oxidations of 1-phenylsulfonyl-4-alkoxy and 4-aminopyrroles were previously achieved using the Tsuji–Wacker process to provide the corresponding diones for Paal–Knorr condensation with an alkyl amine (19). Although attempts to prepare the corresponding δ-keto aldehyde have not been successful in the presence of a 4-amino substituent, oxidation of the olefin of 1-phenylsulfonyl-4-alkoxypyrroles (**16**) has now been achieved using osmium tetraoxide and sodium periodate (37) in dioxane–water to give δ-keto aldehydes (**17**) in 65%–75% yields after purification by chromatography.

With δ-keto aldehyde (**17**) in hand, Paal–Knorr condensations (38, 39) with dimethoxybenzylamine were performed using 100 mol% $TiCl_4$ in toluene (19). 2,2′-Bipyrroles (**18a** and **18b**) were isolated after chromatography in 65% and 67% yields, respectively.

Aiming at minimizing protection in the prodigiosin synthesis, attempts were focussed on employing ammonia in the Paal–Knorr condensation with δ-keto aldehyde (**17**) (Scheme 4). Various Paal–Knorr conditions were screened leading to either no reaction or decomposition (34, 39–41). Success was only obtained using ammonium formate and a catalytic amount of acetic acid in a 10:1 ethanol–acetonitrile solvent mixture. A homogeneous solution of ammonium formate and δ-keto aldehyde (**17**) was obtained using this solvent system, which delivered bipyrroles **19** in 81%–93% yields after purification by filtration through a short silica gel column.

Scheme 4. Synthesis of undecylprodigiosin and PNU-156804.

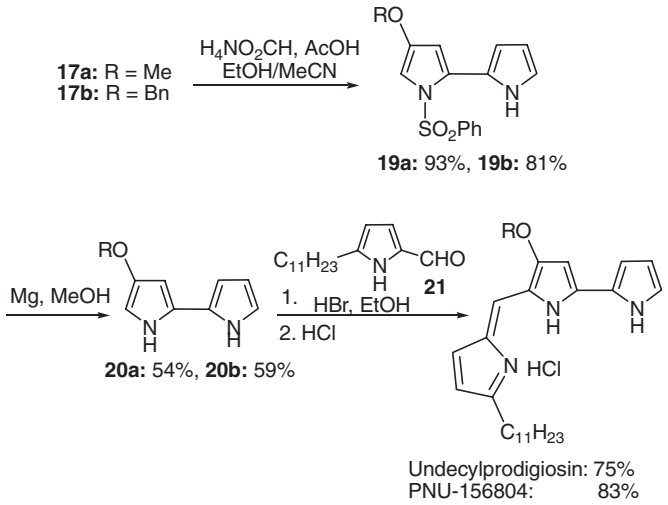

Removal of the sulfonamide group was next achieved by exposure of bipyrrole **19** to magnesium powder in methanol (36). 4-Methoxy and 4-benzyloxy-2,2′-bipyrroles (**20a** and **20b**) were respectively isolated in 54% and 59% yields after chromatography over neutral aluminium oxide.

In the final condensation step, undecylpyrrole-2-carboxaldehyde (**21**) (23) was respectively reacted with bipyrrole **20a** and **20b** in warm EtOH in the presence of aqueous hydrobromic acid to give undecylprodigiosin and PNU-156804 as their free bases after chromatography over neutral aluminium oxide. Treatment of the free bases with 1 mol/L HCl and freeze drying afforded the respective hydrochloride salts in 75% and 83% yields. These yields are notably higher than those reported earlier for condensations of the corresponding 2,2′-bipyrrole-5-carboxaldehyde with alkyl pyrroles (Scheme 1) (10, 21, 42, 43).

In conclusion, we have developed a route for adding diversity at the 6-position of the prodigiosin skeleton. 2-Acyl-4-alkoxypyrroles (**15a** and **15b**) were first obtained from dione **13** by a one-pot alkylative elimination. Access to unsymmetrical 4-alkoxy-2,2′-bipyrroles (**20**) was then achieved by sulfonylation of the nitrogen of 4-alkoxypyrrole (**15**), selective olefin oxidation to δ-oxo aldehyde (**17**), Paal–Knorr condensation with ammonium formate and deprotection. Condensations of bipyrroles **20** with a pyrrole aldehyde C-ring precursor then provided the respective prodigiosin analogs.

Experimental section[2]

General procedure for the one-pot synthesis of 4-alkoxypyrroles (15)

A solution of 9-phenylfluorene (65 mg, 0.27 mmol) and sodium hydride (6 mg, 0.26 mmol) in THF (5 mL) was stirred for 15 min, treated with pyrrolidinone **13** (100 mg, 0.245 mmol), stirred for 30 min, treated with methyliodide (26 μL, 0.42 mmol), stirred for 24 h, and treated with water (7 mL) and EtOAc (7 mL). The layers were separated. The aqueous layer was extracted with EtOAc (2 × 7 mL). The organic layers were combined, washed with brine, dried

[2] Supplementary data for this article are available on the journal Web site (canjchem.nrc.ca) or may be purchased from the Depository of Unpublished Data, Document Delivery, CISTI, National Research Council Canada, Ottawa, ON K1A 0R6, Canada. DUD 3708.

© 2008 NRC Canada

($MgSO_4$), and concentrated to a residue that was purified by column chromatography on silica gel (15%–40% EtOAc–hexane). Evaporation of the collected fractions yielded 4-methoxypyrrole **15a** (25 mg, 57%) (19). 4-Benzyloxypyrrole (**15b**) was prepared in 36% yield from pyrrolidinone **13** (0.98 mmol) using the same procedure and benzylbromide (1.7 mmol) as electrophile.

4-Benzyloxy-2-(pent-4-enoyl)-1-(phenylsulfonyl)pyrrole (16b)

A solution of 4-benzyloxy-2-(pent-4-enoyl)pyrrole (**15b**) (700 mg, 2.74 mmol) in THF (40 mL) was added to a solution of potassium *t*-butoxide (493 mg, 4.39 mmol) and 18-crown-6 (72 mg, 0.27 mmol) in THF (40 mL) at 0 °C. The mixture was stirred for 30 min, and treated with a solution of benzenesulfonyl chloride (0.49 mL, 3.84 mmol). The ice bath was removed and the solution was allowed to warm to room temperature, stirred for 15 h, and treated with water followed by EtOAc. The layers were separated and the aqueous layer was extracted with EtOAc. The organic layers were combined, washed with brine, dried ($MgSO_4$), and concentrated to a residue that was purified by column chromatography on silica gel (40% EtOAc–hexane). Evaporation of the collected fractions yielded **16b** as a clear oil (858 mg, 79%). ^{1}H NMR (400 MHz, $CDCl_3$) δ: 7.96 (d, J = 7.9 Hz, 2H), 7.59 (t, J = 7.5 Hz, 1H), 7.50 (t, J = 8.0 Hz, 2H), 7.42–7.36 (m, 6H), 6.75 (d, J = 2.1 Hz, 1H), 5.74 (m, 1H), 4.94 (m, 4H), 2.71 (t, J = 7.3 Hz, 2H), 2.32 (q, J = 6.6 Hz, 2H). ^{13}C NMR (100 MHz, $CDCl_3$) δ: 188.0, 146.7, 139.1, 136.7, 135.9, 133.5, 131.0, 128.7 (2C), 128.4, 127.9, 127.7, 115.4, 114.0, 111.9, 72.8, 38.5, 28.4. HR-MS calcd. for $C_{22}H_{22}NO_4S$ ([M + H^+]): 396.1264; found: 396.1274. 4-Benzyloxy-2-(pent-4-enoyl)pyrrole (**15b**) was also recovered in 20% yield (137 mg).

General procedure for the synthesis of aldehydes 17 (method A)

*4-(4-Methoxy-1-(phenylsulfonyl)-1*H*-pyrrol-2-yl)-4-oxobutanal (17a)*

To a solution of 4-methoxy-2-(pent-4-enoyl)-1-(phenylsulfonyl)pyrrole (**16a**, 595 mg, 1.86 mmol, prepared according to ref. 19) in dioxane (51 mL) and water (17 mL), 2,6-lutidine (0.43 mL, 3.7 mmol), OsO_4 (0.49 mL, 0.037 mmol), and $NaIO_4$ (1.59 g, 7.44 mmol) were added. The mixture was stirred for 15 h and treated with water followed by DCM. The layers were separated and the aqueous layer was extracted with DCM. The organic layers were combined, washed with brine, dried ($MgSO_4$), and concentrated to a residue that was purified by column chromatography on silica gel (25%–40% EtOAc–hexane). Evaporation of the collected fractions yielded aldehyde **17a** as a white solid (447 mg, 75%); mp 131 °C. ^{1}H NMR (400 MHz, $CDCl_3$) δ: 9.74 (s, 1H), 7.94 (d, J = 7.5 Hz, 2H), 7.59 (t, J = 7.4 Hz, 1H), 7.50 (t, J = 8.0 Hz, 2H), 7.31 (d, J = 2.1 Hz, 1H), 6.79 (d, J = 2.1 Hz, 1H), 3.79 (s, 3H), 2.98 (t, J = 6.5 Hz, 2H), 2.77 (t, J = 6.5 Hz, 2H). ^{13}C NMR (100 MHz, $CDCl_3$) δ: 199.9, 185.8, 147.8, 138.6, 133.3, 130.1, 128.4, 127.5, 113.5, 110.7, 57.7, 37.1, 30.9. HR-MS calcd. for $C_{15}H_{16}NO_5S$ ([M + H^+]): 322.0743; found: 322.0737.

*4-(4-Benzyloxy-1-(phenylsulfonyl)-1*H*-pyrrol-2-yl)-4-oxobutanal (17b)*

The title compound was prepared according to method A from pyrrole **16b** (2.17 mmol). Purification by column chromatography on silica gel (30%–50% EtOAc–hexane) afforded aldehyde **17b** as a beige solid (580 mg, 67%); mp 123 °C. ^{1}H NMR (400 MHz, $CDCl_3$) δ: 9.72 (s, 1H), 7.92 (m, 2H), 7.57 (tt, J = 1.2, 7.5 Hz, 1H), 7.49 (m, 2H), 7.41–7.34 (m, 6H), 6.84 (d, J = 2.1 Hz, 1H), 4.98 (s, 2H), 2.97 (t, J = 6.5 Hz, 2H), 2.75 (t, J = 6.5 Hz, 2H). ^{13}C NMR (100 MHz, $CDCl_3$) δ: 200.2, 186.1, 146.7, 138.8, 135.9, 133.5, 130.3, 128.64, 128.59, 128.3, 127.7, 127.6, 114.3, 112.1, 72.7, 37.3, 31.2. HR-MS calcd. for $C_{21}H_{20}NO_5S$ ([M + H^+]): 398.1057; found: 398.1057.

General procedure for the synthesis of 1′-(2,4-dimethoxybenzyl)-2,2′-bipyrroles (18) (method B)

4-(Methoxy)-1-benzenesulfonyl-1′-(2,4-dimethoxybenzyl)-2,2′-bipyrrole (18a)

A solution of $TiCl_4$ (1 mol/L in toluene, 75 μL, 75 μmol) was added dropwise to a solution of aldehyde **17a** (16 mg, 0.50 mmol) and 2,4-dimethoxybenzylamine (52 μL, 0.35 mmol) in toluene (5 mL). After stirring for 18 h, the reaction was treated with a solution of saturated aqueous NH_4Cl followed by 5 mL of EtOAc. The layers were separated and the aqueous layer was extracted with EtOAc (5 mL × 2). The organic layers were combined, washed with brine, dried ($MgSO_4$), and concentrated to a residue that was purified by column chromatography on silica gel using DCM as eluant. Evaporation of the collected fractions yielded bipyrrole **18a** as a colorless oil (15 mg, 65%). ^{1}H NMR (400 MHz, $CDCl_3$) δ: 7.54 (m, 3H), 7.40 (t, J = 7.6 Hz, 2H), 6.90 (d, J = 2.1 Hz, 1H), 6.69 (t, J = 2.0 Hz, 1H), 6.60 (d, J = 8.3 Hz, 1H), 6.37 (d, J = 2.3 Hz, 1H), 6.33 (dd, J = 2.3, 8.3 Hz, 1H), 6.08 (t, J = 3.0 Hz, 1H), 5.88 (d, J = 2.1 Hz, 1H), 5.85 (dd, J = 1.8, 3.5 Hz, 1H), 4.73 (s, 2H), 3.76 (s, 3H), 3.74 (s, 3H) 3.72 (s, 3H). ^{13}C NMR (100 MHz, $CDCl_3$) δ: 160.3, 157.7, 150.3, 138.3, 133.5, 129.5, 128.6, 127.4, 125.9, 122.9, 121.7, 119.1, 112.8, 111.0, 107.0, 103.9, 103.0, 98.2, 57.5, 55.3, 55.2, 45.7. HR-MS calcd. for $C_{24}H_{25}N_2O_5S$ ([M + H^+]): 453.1479; found: 453.1472.

4-(Benzyloxy)-1-benzenesulfonyl-1′-(2,4-dimethoxybenzyl)-2,2′-bipyrrole (18b)

The title compound was prepared according to method B from aldehyde **17b** (0.25 mmol). Purification by column chromatography on silica gel using DCM as eluant afforded bipyrrole **18b** as a green foam (88 mg, 67%). ^{1}H NMR (400 MHz, $CDCl_3$) δ: 7.57 (t, J = 7.4 Hz, 1H), 7.50 (d, J = 8.1 Hz, 2H), 7.39 (m, 7H), 6.99 (d, J = 2.1 Hz, 1H), 6.74 (t, J = 2.5 Hz, 1H), 6.64 (d, J = 8.3 Hz, 1H), 6.41 (d, J = 2.3 Hz, 1H), 6.36 (dd, J = 2.3, 8.4 Hz, 1H), 6.13 (t, J = 3.4 Hz, 1H), 5.97 (d, J = 2.1 Hz, 1H), 5.90 (dd, J = 1.7, 3.5 Hz, 1H), 4.94 (s, 2H), 4.79 (s, 2H), 3.77 (s, 3H), 3.75 (s, 3H). ^{13}C NMR (100 MHz, $CDCl_3$) δ: 160.3, 157.7, 149.0, 138.1, 136.3, 133.4, 129.4, 128.6, 128.5, 128.1, 127.6, 127.3, 125.9, 122.9, 121.7, 119.0, 112.8, 111.4, 107.0, 104.1, 103.9, 98.1, 72.2, 55.23, 55.16, 45.6. HR-MS calcd. for $C_{30}H_{29}N_2O_5S$ [M + H^+]: 529.1791; found: 529.1778.

© 2008 NRC Canada

General procedure for the synthesis of 2,2′-bipyrroles (19) (method C)

4-(Methoxy)-1-benzenesulfonyl-2,2′-bipyrrole (19a)

Ammonium formate (711 mg, 11.3 mmol) was added to a solution of 4-(4-methoxy-1-(phenylsulfonyl)-1*H*-pyrrol-2-yl)-4-oxobutanal (**17a**) (362 mg, 1.13 mmol) in EtOH–MeCN–AcOH (50 mL–5 mL–50 μL). After stirring for 18 h, the reaction was treated with water followed by EtOAc. The layers were separated and the aqueous layer was extracted with EtOAc. The organic layers were combined, washed with brine, dried ($MgSO_4$), and concentrated to a residue that was purified by filtration on silica gel (30% EtOAc–hexane). Evaporation of the collected fractions yielded bipyrrole **19a** as a dark oil (318 mg) in 93% yield. ^{1}H NMR (400 MHz, $CDCl_3$) δ: 9.10 (br s, 1H), 7.50 (t, *J* = 7.3 Hz, 1H), 7.36 (m, 4H), 6.90 (m, 1H), 6.82 (d, *J* = 2.1 Hz, 1H), 6.16 (m, 1H), 6.07 (m, 1H), 6.02 (d, *J* = 2.1 Hz, 1H), 3.73 (s, 3H). ^{13}C NMR (100 MHz, $CDCl_3$) δ: 150.8, 137.4, 133.7, 128.8, 127.8, 126.8, 121.1, 119.3, 110.9, 108.7, 107.9, 102.6, 57.6. HR-MS calcd. for $C_{15}H_{15}N_2O_3S$ ([M + H^+]): 303.0798; found: 303.0796.

4-(Benzyloxy)-1-benzenesulfonyl-2,2′-bipyrrole (19b)

The title compound was prepared according to method C from pyrrole **17b** (1.16 mmol). Purification by filtration on silica gel (25% EtOAc–hexane) afforded bipyrrole **19b** as a grey solid (355 mg) in 81% yield; mp 107 °C. ^{1}H NMR (400 MHz, $CDCl_3$) δ: 9.10 (br s, 1H), 7.40 (m, 10H), 6.90 (m, 1H), 6.87 (d, *J* = 2.0 Hz, 1H), 6.17 (m, 1H), 6.09 (m, 2H), 4.95 (s, 2H). ^{13}C NMR (100 MHz, $CDCl_3$) δ: 149.5, 137.2, 136.3, 133.6, 128.8, 128.5, 128.1, 127.7, 127.6, 126.8, 121.1, 119.3, 110.9, 108.7, 108.3, 103.8, 72.2. HR-MS calcd. for $C_{21}H_{19}N_2O_3S$ ([M + H^+]): 379.1111; found: 379.1121.

General procedure for the synthesis of 2,2′-bipyrroles (20) (method D)

4-(Methoxy)-2,2′-bipyrrole (20a)

Magnesium powder (255 mg, 10.5 mmol) was added to a solution of 4-(methoxy)-1-benzenesulfonyl-2,2′-bipyrrole (**19a**) (318 mg, 1.05 mmol) in methanol (20 mL). After stirring for 18 h, the reaction was treated with a solution of saturated aqueous NH_4Cl followed by EtOAc. The layers were separated and the aqueous layer was extracted with EtOAc. The organic layers were combined, washed with brine, dried ($MgSO_4$), and concentrated to a residue that was purified by chromatography over neutral aluminium oxide (10%–30% EtOAc–hexane). Evaporation of the collected fractions yielded bipyrrole **20a** as a grey solid (92 mg) in 54% yield; mp 143 °C. ^{1}H NMR (400 MHz, $CDCl_3$) δ: 8.24 (br s, 1H), 7.66 (br s, 1H), 6.76 (s, 1H), 6.30 (s, 1H), 6.23 (s, 1H), 6.22 (s, 1H), 5.94 (s, 1H), 3.75 (s, 3H). ^{13}C NMR (100 MHz, $CDCl_3$) δ: 149.8, 125.8, 124.2, 117.7, 109.4, 103.7, 98.8, 93.4, 57.9. HR-MS calcd. for $C_9H_{11}N_2O$ ([M + H^+]): 163.0869; found: 163.0866.

4-(Benzyloxy)-2,2′-bipyrrole (20b)

The title compound was prepared according to method D from bipyrrole **19b** (0.905 mmol). Purification by column chromatography on neutral aluminium oxide (10%–25% EtOAc–hexane) afforded bipyrrole **20b** as a grey solid (127 mg) in 59% yield; mp 155 °C. ^{1}H NMR (400 MHz, $(CD_3)_2CO$) δ: 10.14 (br s, 1H), 9.59 (br s, 1H), 7.46 (d, *J* = 7.2 Hz, 2H), 7.38 (t, *J* = 7.1 Hz, 2H), 7.31 (t, *J* = 7.2 Hz, 1H), 6.73 (s, 1H), 6.38 (s, 1H), 6.28 (s, 1H), 6.09 (m, 2H), 4.94 (s, 2H). ^{13}C NMR (100 MHz, $(CD_3)_2CO$) δ: 149.1, 138.9, 128.7, 128.0, 127.9, 126.9, 124.9, 117.5, 109.0, 103.4, 100.0, 93.5, 72.5. HR-MS calcd. for $C_{15}H_{15}N_2O$ ([M + H^+]): 239.1179; found: 239.1189.

General procedure for the synthesis of undecylprodigiosins (method E)

*4-Methoxy-5-[(5-undecyl-2**H**-pyrrol-2-ylidene)methyl]-2,2′-bi-1**H**-pyrrole hydrochloride (undecylprodigiosin hydrochloride)*

A solution of 4-(methoxy)-2,2′-bipyrrole **20a** (26.4 mg, 0.163 mmol) and 5-undecylpyrrole-2-carboxaldehyde **21** (44.6 mg, 0.179 mmol) in EtOH (4 mL) was warmed to 50 °C, and treated with concentrated hydrobromic acid (10 μL). The heating bath was removed and the reaction mixture was allowed to cool to room temperature while stirring for 15 h. The reaction mixture was concentrated in vacuo. Chromatography on neutral aluminium oxide (0%–10% EtOAc–hexane) and evaporation of the collected fractions afforded the free base, which was treated with HCl in ether (1 mol/L, 3 mL) and freeze dried to afford undecylprodigiosin hydrochloride as a red film (52 mg) in 75% yield. ^{1}H NMR (400 MHz, $CDCl_3$) δ: 12.5–11.7 (br s, 1H), 10.9–10.0 (br s, 1H), 6.91 (s, 1H), 6.71 (d, *J* = 3.5 Hz, 1H), 6.64 (s, 1H), 6.51 (d, *J* = 3.5 Hz, 1H), 6.14 (m, 2H), 5.86 (d, *J* = 3.5 Hz, 1H), 4.00 (s, 3H), 2.08 (t, *J* = 6.2 Hz, 2H), 1.4–1.1 (m, 18H), 0.95 (t, *J* = 6.6 Hz, 3H). ^{13}C NMR (100 MHz, $CDCl_3$) δ: 169.0, 160.2, 144.8, 128.2, 128.1, 123.0, 121.2, 116.0, 112.9, 109.9, 109.2, 108.5, 95.7, 58.3, 31.9, 29.63, 29.59, 29.47, 29.33, 29.23, 29.15, 29.0, 27.2, 22.7, 14.1. HR-MS calcd. for $C_{25}H_{36}N_3O$ ([M + H^+]): 394.2857; found: 394.2853.

Ref. 15: ^{1}H NMR (400 MHz, $CDCl_3$) δ: 0.9 (m, 3H), 1.1–1.5 (m, 16H), 1.8 (m, 2H), 2.95 (t, *J* = 7.5 Hz, 2H), 4.05 (s, 3H), 6.0 (d, *J* = 1.8 Hz, 1H), 6.2 (dd, *J* = 1.8, 3.9 Hz, 1H), 6.5 (m, 1H), 6.85 (dd, *J* = 3.9, 2.6 Hz, 1H), 7.0 (m, 1H), 7.05 (s, 1H), 7.25 (m, 1H), 12.5–12.7 (2 bs, 2H), 12.9 (bs, 1H).

Ref. 44: ^{1}H NMR ($CDCl_3$) τ: 2.83 (br, 3H), 2.78 (m, 1H), 3.06 (s, 1H), 3.10 (m, 2H), 3.67 (m, 1H), 3.80 (m, 1H), 3.96 (d, 1H), 6.05 (s, 3H), 7.06 (t, 2H), 8.76 (m, 18H), 9.13 (t, 3H).

*4-Benzyloxy-5-[(5-undecyl-2**H**-pyrrol-2-ylidene)methyl]-2,2′-bi-1**H**-pyrrole hydrochloride (PNU-156804)*

The title compound was prepared according to method E from bipyrrole **20b** (0.090 mmol) to afford PNU-156804 hydrochloride as a red film (37 mg) in 83% yield. ^{1}H NMR (400 MHz, $CDCl_3$) δ: 13.0–11.6 (br s, 1H), 11.0–9.7 (br s, 1H), 7.56 (d, *J* = 7.2 Hz, 2H), 7.49 (t, *J* = 7.0 Hz, 2H), 7.44 (t, *J* = 7.2 Hz, 1H), 6.99 (s, 1H), 6.72 (d, *J* = 3.4 Hz, 1H), 6.66 (s, 1H), 6.51 (d, *J* = 3.6 Hz, 1H), 6.23 (s, 1H), 6.15 (t, *J* = 3.2 Hz, 1H), 5.87 (d, *J* = 3.6 Hz, 1H), 5.21 (s, 2H), 2.09 (t, *J* = 7.3 Hz, 2H), 1.40–1.15 (m, 18H), 0.93 (t, *J* = 6.6 Hz, 3H). ^{13}C NMR (100 MHz, $CDCl_3$) δ: 167.8, 160.0, 145.0,

© 2008 NRC Canada

138.3, 135.9, 128.6, 128.4, 128.23, 128.17, 127.8, 123.1, 121.4, 116.3, 112.9, 110.0, 108.7, 96.6, 73.2, 33.4, 31.9, 29.7, 29.64, 29.61, 29.5, 29.3, 29.2, 27.3, 22.7, 14.1. HR-MS calcd. for $C_{31}H_{40}N_3O$ ([M + H^+]): 470.3165; found: 470.3166.

Ref. 15: ^{1}H NMR (200 MHz, $CDCl_3$) δ: 0.9 (m, 3H), 1.2–1.5 (m, 16H), 1.75 (m, 2H), 2.95 (m, 2H), 5.2 (s, 2H), 6.15 (m, 1H), 6.2 (m, 1H), 6.35 (m, 1H), 6.85 (m, 1H), 6.95 (m, 1H), 7.05 (s, 1H), 7.25 (m, 1H), 7.45 (m, 5H), 12.6–12.8 (2 bs, 2H), 12.95 (bs, 1H).

Acknowledgments

We acknowledge Dalbir Sekhon from the Regional Laboratory of Mass Spectrometry at the Université de Montréal for his helpful assistance as well as the Natural Sciences and Engineering Research Council of Canada (NSERC) and Fonds Québécois de la Recherche sur la Nature et les Technologies (FQRNT) for financial support.

References

1. J.W. Bennett and R. Bentley. Adv. Appl. Microbiol. **47**, 1 (2000).
2. A. Fürstner. Angew. Chem. Int. Ed. **42**, 3582 (2003).
3. R.A. Manderville. Curr. Med. Chem.– Anti-Cancer Agents, **1**, 195 (2001).
4. B. Montaner and R. Pérez-Tomás. Curr. Cancer Drug Targets, **3**, 57 (2003).
5. C.M. Baldino, J. Parr, C.J. Wilson, S.C. Ng, D. Yohannes, and H.H. Wasserman. Bioorg. Med. Chem. Lett. **16**, 701, (2006).
6. D.M. Pinkerton, M.G. Banwell, and A.C. Willis. Org. Lett. **9**, 5127 (2007).
7. J.T. Reeves. Org. Lett. **9**, 1879 (2007).
8. S.G. Salamone and G.B. Dudley. Org. Lett. **7**, 4443 (2005).
9. J.Q.H. La, A.A. Michaelides, and R.A. Manderville. J. Phys. Chem. B, **111**, 11803 (2007).
10. D.L. Boger and M. Patel. J. Org. Chem. **53**, 1405 (1988).
11. M. Isaka, A. Jaturapat, J. Kramyu, M. Tanticharoen, and Y. Thebtaranonth. Antimicrob. Agents Chemother. **46**, 1112 (2002).
12. H.S. Kim, M. Hayashi, Y. Shibata, Y. Wataya, T. Mitamura, T. Horii, K. Kawauchi, H. Hirata, S. Tsuboi, and Y. Moriyama. Biol. Pharm. Bull. **22**, 532 (1999).
13. J.E.H. Lazaro, J. Nitcheu, R.Z. Predicala, G.C. Mangalindan, F. Nesslany, D. Marzin, G.P. Concepcion, and B. Diquet. J. Nat. Toxins, **11**, 367 (2002).
14. S. Songia, A. Mortellaro, S. Taverna, C. Fornasiero, E.A. Scheiber, E. Erba, F. Colotta, A. Mantovani, A.M. Isetta, and J. Golay. J. Immunol. **158**, 3987 (1997).
15. R. D'Alessio, A. Bargiotti, O. Carlini, F. Colotta, M. Ferrari, P. Gnocchi, A. Isetta, N. Mongelli, P. Motta, A. Rossi, M. Rossi, M. Tibolla, and E. Vanotti. J. Med. Chem. **43**, 2557 (2000).
16. A. Mortellaro, S. Songia, P. Gnocchi, M. Ferrari, C. Fornasiero, R. D'Alessio, A. Isetta, F. Colotta, and J. Golay. J. Immunol. **162**, 7102 (1999).
17. V. Rizzo, A. Morelli, V. Pinciroli, D. Sciangula, and R. D'Alessio. J. Pharm. Sci. **88**, 73 (1999).
18. S.M. Stepkowski, R.A. Erwin-Cohen, F. Behbod, M.E. Wang, X. Qu, N. Tejpal, Z.S. Nagy, B.D. Kahan, and R.A. Kirken. Blood, **99**, 680 (2002).
19. B. Jolicoeur and W.D. Lubell. Org. Lett. **8**, 6107 (2006).
20. W.R. Hearn, M.K. Elson, R.H. Williams, and J. Medina-Castro. J. Org. Chem. **35**, 142 (1970).
21. H. Rapoport and K.G. Holden. J. Am. Chem. Soc. **84**, 635 (1962).
22. For syntheses of aldehyde **4** see: K. Dairi, S. Tripathy, G. Attardo, and J.-F. Lavallée. Tetrahedron Lett. **47**, 2605 (2006), and refs. cited therein.
23. R. D'Alessio and A. Rossi. Synlett, **6**, 513 (1996).
24. D. Brown, D. Griffiths, M.E. Rider, and R.C. Smith. J. Chem. Soc. Perkin Trans. 1, 455 (1986).
25. T. Benincori, E. Brenna, F. Sannicolo, G. Zotti, S. Zecchin, G. Schiavon, C. Gatti, and G. Frigerio. Chem. Mater. **12**, 1480 (2000).
26. C. Gatti, G. Frigerio, T. Benincori, E. Brenna, F. Sannicolo, G. Zotti, S. Zecchin, and G. Schiavon. Chem. Mater. **12**, 1490 (2000).
27. G. Zotti, S. Zecchin, G. Schiavon, and A. Berlin. Chem. Mater. **14**, 3607 (2002).
28. A. Merz, S. Anikin, B. Lieser, J. Heinze, and H. John. Chem. Eur. J. **9**, 449 (2003).
29. J. Bordner and H. Rapoport. J. Org. Chem. **30**, 3824 (1965).
30. A. Fürstner, J. Grabowski, and C.W. Lehmann. J. Org. Chem. **64**, 8275 (1999).
31. M. Yu, D. Pantos, J.L. Sessler, and B.L. Pagenkopf. Org. Lett. **6**, 1057 (2004).
32. A.A. Dörr and W.D. Lubell. Can. J. Chem. **85**, 1006 (2007).
33. K.A. Hansford, J.E. Dettwiler, and W.D. Lubell. Org. Lett. **5**, 4887 (2003).
34. K.A. Hansford, V. Zanzarova, A. Dorr, and W.D. Lubell. J. Comb. Chem. **6**, 893 (2004).
35. A.J. Mancuso, S.L. Huang, and D. Swern. J. Org. Chem. **43**, 2480 (1978).
36. B. Jolicoeur, E.E. Chapman, A. Thompson, and W.D. Lubell. Tetrahedron, **62**, 11531 (2006).
37. W.S. Yu, Y. Mei, Y. Kang, Z.M. Hua, and Z.D. Jin. Org. Lett. **6**, 3217 (2004).
38. H.S. Broadbent, W.S. Burnham, R.K. Olsen, and R.M. Sheeley. J. Heterocycl. Chem. **5**, 757 (1968).
39. W. Hinz, R.A. Jones, S.U. Patel, and M.H. Karatza, Tetrahedron, **42**, 3753 (1986).
40. M.J. Hall, S.O. McDonnell, J. Killoran, and D.F. O'Shea. J. Org. Chem. **70**, 5571 (2005).
41. F. Lucchesini. Tetrahedron, **48**, 9951 (1992).
42. H.H. Wasserman and L.J. Lombardo. Tetrahedron Lett. **30**, 1725 (1989).
43. H.H. Wasserman, A.K. Petersen, M.D. Xia, and J.J. Wang. Tetrahedron Lett. **40**, 7587 (1999).
44. H.H. Wasserman, G.C. Rodgers, and D.D. Keith. Tetrahedron, **32**, 1851 (1976).

© 2008 NRC Canada

Resolution of non-proteinogenic amino acids via microbial lipase-catalyzed enantioselective transesterification

Toshifumi Miyazawa, Motoe Mio, Yuko Watanabe, and Takashi Yamada

Abstract: A number of non-proteinogenic amino acids bearing aliphatic side chains were resolved with moderate to good enantioselectivities (E = 15–42) through the *Burkholderia cepacia* lipase-catalyzed enantioselective transesterification of the 2,2,2-trifluoroethyl esters of their *N*-benzyloxycarbonyl derivatives with methanol as a nucleophile in diisopropyl ether.

Key words: non-proteinogenic amino acids, microbial lipases, *Burkholderia cepacia* lipase, 2,2,2-trifluoroethyl ester, enantioselective transesterification, enantioselectivity.

Résumé : On a résolu un certain nombre d'acides aminés non-protéinogéniques portant des chaînes latérales aliphatiques, avec des énantiosélectivités allant de modérées à bonnes (E = 15–42), en faisant appel à une transestérification énantiosélective catalysée par la lipase *Burkholderia cepacia* des esters 2,2,2-trifluoroéthyles de leurs dérivés *N*-benzyloxycarbonyles et en utilisant le méthanol comme nucléophile dans l'éther diisopropylique comme solvant.

Mots-clés : acides aminés non-protéinogéniques, lipases microbiennes, lipase *Burkholderia cepacia*, ester 2,2,2-trifluoroéthylique, transestérification énantiosélective, énantiosélectivité.

[Traduit par la Rédaction]

Introduction

Lipases (triacylglycerol hydrolases, EC 3.1.1.3) have been employed as a very attractive group of enzymes for synthetic purposes (1) because they are stable and easy to handle and they have a rather broad substrate specificity. Moreover, as they are easily available from a variety of sources (especially bacteria and fungi), there must be a fair chance of finding a suitable enzyme for each transformation of interest in terms of catalytic activity and (or) selectivity. Since the first discovery of enzymatic activity in anhydrous organic media (2), 1ipase-catalyzed reactions, such as esterification and transesterification, have attracted an increasing attention in the field of organic synthesis. Thus, a large number of reports have dealt with the optical resolution of alcohols through lipase-catalyzed reactions in organic solvents. On the other hand, fewer examples have been accumulated for the resolution of carboxylic acids by means of the lipase-catalyzed esterification or transesterification procedure in organic milieu. We have previously reported on the resolution of 2-substituted carboxylic acids via the microbial lipase-catalyzed irreversible transesterification of their vinyl esters (3). We also have recently reported on the resolution of non-proteinogenic aliphatic amino acids through the *Carica papaya* lipase-catalyzed enantioselective transesterification of their *N*-benzyloxycarbonyl (*Z*) esters (4). In the present paper, we describe the details of our study on the resolution of non-proteinogenic amino acids via the similar enantioselective transesterification procedure mediated by microbial lipases (5). Homochiral non-proteinogenic amino acids are useful as building blocks for the synthesis of analogs of biologically active peptides (6) and as chiral auxiliaries for other synthetic purposes (7). We have already reported on the resolution of non-proteinogenic amino acids via the enantioselective hydrolysis of their *N*-*Z*-protected esters mediated by microbial and mammalian lipases (8) and via the enantioselective hydrolysis of their *N*-unprotected esters catalyzed by microbial lipases (9).

Received 22 October 2007. Accepted 17 December 2007. Published on the NRC Research Press Web site at canjchem.nrc.ca on 13 February 2008.

T. Miyazawa,[1] M. Mio, Y. Watanabe, and T. Yamada. Department of Chemistry, Faculty of Science and Engineering, Konan University, Kobe 658–8501, Japan.

[1]Corresponding author (e-mail: miyazawa@konan-u.ac.jp).

Results and discussion

Initially, the transesterification between *N*-*Z*-DL-norvaline (2-aminopentanoic acid) 2,2,2-trifluoroethyl ester (DL-**1c**) and methanol in diisopropyl ether was chosen as a model reaction (Scheme 1; R = n-C_3H_7; R′ = CH_3), and a dozen lipases of microbial and mammalian origins were screened: *Burkholderia* (*Pseudomonas*) *cepacia* (Amano P), *Rhizopus javanicus* (Amano F), *Mucor javanicus* (Amano M), *Rhizopus japonicus* (Rhilipase A5), *Chromobacterium viscosum* (Asahikasei LP), *Aspergillus niger* (Amano A), *Candida rugosa* (Sigma Type VII, Meito MY, Amano AY), and porcine pancreas (Sigma Type II). Part of the results are summarized in Table 1. We already reported that in the *Carica papaya* lipase-catalyzed enantioselective transesterification the 2,2,2-trifluoroethyl ester was an ester of choice (4). Also in the present case, the transesterification reactions

 doi:10.1139/V07-154 © 2008 NRC Canada

Scheme 1. Microbial lipase-catalyzed enantioselective transesterification between an *N*-*Z*-DL-amino acid 2,2,2-trifluoroethyl ester (DL-**1**) and an alcohol. See Table 4 for R.

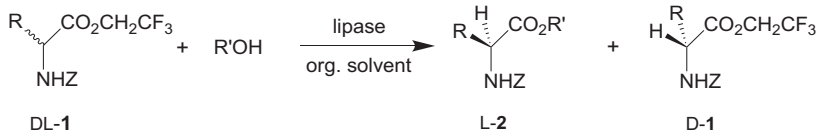

DL-**1** L-**2** D-**1**

Table 1. Enantioselective transesterification between *N*-*Z*-DL-norvaline 2,2,2-trifluoroethyl ester (DL-**1c**) and methanol with different lipases in diisopropyl ether.

Lipase source	Conversion (%)	Time	ee (%)[a]	*E*
Burkholderia cepacia[b]	38	10 h	91	37
Rhizopus javanicus[c]	38	12 h	88	27
Mucor javanicus[d]	41	7 h	67	8.0
Rhizopus japonicus[e]	37	106 h	77	12
Chromobacterium viscosum[f]	43	38.5 h	68	8.4
Aspergillus niger[g]	21	21 d	61	4.9
Porcine pancreas[h]	31	88 d	51	3.8
Candida rugosa[i]	34	92 d	7.6	1.2

Note: Conditions: 0.4 mmol of DL-**1c**, 1.2 mmol of methanol, and 120 mg of a lipase preparation in 0.8 mL of diisopropyl ether at 25 °C.
[a]Enantiomeric excess of the newly formed methyl ester (**2c**).
[b]Amano P.
[c]Amano F.
[d]Amano M.
[e]Rhilipase A5 from Nagase ChemteX Corporation.
[f]Asahi Chemical Industry LP.
[g]Amano A.
[h]Sigma Type II.
[i]Sigma Type VII.

Table 2. *B. cepacia* lipase-catalyzed transesterification of *N*-*Z*-DL-norvaline 2,2,2-trifluoroethyl ester (DL-**1c**) with different alcohols as nucleophiles in diisopropyl ether.

Alcohol	Conversion (%)	Time (h)	ee (%)[a]	*E*
Methanol	38	10	91	37
Ethanol	40	11	90	35
Butanol	37	13	90	32
Heptanol	40	18	88	28
Tetradecanol	43	24	86	26

Note: Conditions: 0.4 mmol of DL-**1c**, 1.2 mmol of an alcohol, and 120 mg of *B. cepacia* lipase in 0.8 mL of diisopropyl ether at 25 °C.
[a]Enantiomeric excess of the newly formed ester.

of other esters, such as the 2-chloroethyl and 2,2,2-trichloroethyl esters, were extremely slow, and moreover, such an active ester as *N*-hydroxysuccinimide ester proceeded with almost no enantioselectivity. As can be seen form Table 1, the rate and enantioselectivity observed varied largely with the enzyme employed, while the stereochemical preference remained unchanged, the preferred absolute configuration of the newly formed methyl ester (**2c**) being L. Among the enzymes tested, 1ipases from *B. cepacia* and *R. javanicus* showed a rather high reaction rate together with a good enantioselectivity, as judged from the value of enantiomeric ratio, *E* (10). With *M. javanicus* lipase, the fastest reaction was accompanied by a poor enantioselectivity. With other lipases, the reactions were slow, and enantioselectivities were practically unacceptable. This includes *C. rugosa* lipase, which is known to show a high enantioselectivity toward carboxylic acids (11).

Next, the effect of alcohols as a nucleophile was examined on the *B. cepacia* lipase-catalyzed transesterification of DL-**1c** in diisopropyl ether. The results are shown in Table 2. The preferred configuration of the newly formed esters was L, irrespective of the alcohol employed. There was almost no difference between methanol and ethanol as the nucleophile in terms of the reaction rate and enantioselectivity. There was a tendency for the enantioselectivity, together with the reaction rate, to decrease with the chain length of the alcohol. This is similar to that observed in the *A. niger* lipase-catalyzed transesterification of vinyl 2-phenoxypropanoate (3), though the differences among the alcohols were rather small in the present case. A reverse tendency, i.e., an increase in enantioselectivity with increasing chain length of the alcohol, has been reported in the *C. rugosa* lipase-catalyzed esterification of 2-(4-chlorophenoxy)propanoic acid (12). The discrepancy may be attributable to the nature of the lipases used and (or) a difference in the type of reactions (transesterification vs. esterification).

Among the external factors influencing the catalytic activity and enantioselectivity of enzymatic reactions, much attention has recently been focused on the solvent effect (2). However, it is still difficult to predict the solvent effect, especially on the enantioselectivity of a certain reaction, and the best way is still to select an appropriate solvent after the screening experiment. Among many solvent parameters proposed so far is the hydrophobicity parameter, log *P* (13), and a correlation has sometimes been observed between the *E* values of an enzymatic resolution carried out in organic solvents and their log *P* values. We also have reported such a correlation, though rough, in the *A. niger* lipase-catalyzed transesterification of vinyl 2-phenoxypropanoate with methanol: the larger the log *P* value, the higher the *E* value (3). A number of solvents having different log *P* values were screened next in the *B. cepacia* lipase-catalyzed transesterification between DL-**1c** and methanol (Table 3). In the table, the solvents are arranged in decreasing order of log *P*. The stereochemical preference remained to be L with all the solvents examined. Good-to-excellent *E* values were obtained in most of the solvents except methanol and *N*,*N*-dimethylformamide. Thus, it is difficult to find a correlation between the *E* value and the log *P* value. The solvent effect on enantioselectivity observed here resembles that reported previously in the transesterification of 1-nitro-2-propanol with vinyl acetate cata1yzed by a lipase from *Pseudomonas* sp. (14) in that tetrahydrofuran, 1,4-dioxane, and benzene give excellent enantioselectivities. In the *A. niger* lipase-catalyzed transesterification of vinyl 2-phenoxypropanoate

© 2008 NRC Canada

Table 3. *B. cepacia* lipase-catalyzed transesterification between *N*-*Z*-DL-norvaline 2,2,2-trifluoroethyl ester (DL-**1c**) and methanol in different solvents.

Solvent	Log P^a	Conversion (%)	Time (h)	% ee^b	*E*
Cyclohexane	3.2	41	6.3	90	36
Toluene	2.5	39	75	90	34
Benzene	2.0	40	71	92	45
Chloroform	2.0	37	14 d	91	36
Diisopropyl ether	1.9	38	10	91	37
Diethyl ether	0.85	36	33	91	35
Pyridine	0.71	30	10 d	77	11
Tetrahydrofuran	0.49	40	129	92	45
Acetonitrile	–0.33	36	15.5	89	28
Methanol	–0.76	37	34	6	1.2
N,*N*-Dimethylformamide	–1.0	43	23	0	1.0
1,4-Dioxane	–1.1	40	95	91	39

Note: Conditions: 0.4 mmol of DL-**1c**, 1.2 mmol of methanol, and 120 mg of *B. cepacia* lipase in 0.8 mL of an anhydrous organic solvent at 25 °C.

[a]Hydrophobicity parameters are cited from ref. 13.

[b]Enantiomeric excess of the newly formed methyl ester (**2c**).

with methanol (3) and the *C. papaya* lipase-catalyzed transesterification of *N*-*Z*-amino acid esters (4), aliphatic hydrocarbons, especially cyclohexane, gave high enantioselectivities. Thus, the solvent effect on the enantioselectivity of lipase-catalyzed transesterifications of carboxylic acid esters is likely to be dependent largely on the lipase source. On the other hand, the solvent had a larger effect on the reaction rate of the present lipase-catalyzed transesterification. The reaction was fast in an aliphatic hydrocarbon, cyclohexane, while it was much slower in the aromatic hydrocarbons. It was extremely retarded in a halogenated methane, chloroform. In the acyclic ethers, the reaction proceeded rather smoothly. Although cyclohexane seemed to be the solvent of choice in terms of the reaction rate as well as enantioselectivity, it had a poor solubilizing power towards some of the substrates examined here. Thus, diisopropyl ether was chosen as the most practical solvent, taking into account not only the reaction rate and enantioselectivity but also the solubility of the substrates.

Based on these results, the transesterification between the 2,2,2-trifluoroethyl esters (DL-**1**) of the *N*-*Z*-derivatives of a number of non-proteinogenic amino acids and methanol in diisopropyl ether was examined using the two microbial lipases, *B. cepacia* lipase and *R. javanicus* lipase. The results are summarized in Tables 4 and 5, respectively, which include also those with proteinogenic amino acids for the purpose of comparison. The *B. cepacia* lipase-catalyzed transesterifications proceeded rather smoothly. The esters (DL-**1**) of amino acids carrying aliphatic side chains reacted generally with high enantioselectivities. One exception is the result with the alanine derivative (DL-**1a**). The enantioselectivity did not depend directly on the length of the side chain of amino acids. As the *E* values were larger than 15 in all these cases except **1a**, the recovered, unreacted substrate can be obtained with a practically high enantiomeric excess (ee) value when the reaction is allowed to proceed near or over ~60% conversion (10). In practice, this was confirmed experimentally in a gram-scale resolution of *N*-*Z*-norvaline mediated by *B. cepacia* lipase as described later. The enantiodiscrimination by *R. javanicus* lipase was poorer than that by *B. cepacia* lipase for each substrate. In comparison with the results with aliphatic amino acids, however, the enantioselectivities observed with aromatic amino acid derivatives were lower in the presence of both the microbial lipases. It is interesting to note that *R. javanicus* lipase showed better enantiodiscrimination than *B. cepacia* lipase for each aromatic substrate. In all the cases mentioned earlier, the preferential reaction of the L-enantiomers was confirmed by comparison with authentic samples prepared from the optically active amino acids, if available, on HPLC or suggested from the regularity of elution order of the enantiomers on HPLC (15). This stereochemical preference is the same as that observed in the lipase-catalyzed hydrolysis of the 2-chloroethyl or 2,2,2-trifluoroethyl esters of the *N*-*Z*-derivatives of amino acids (8) and that observed in the *C. papaya* lipase-catalyzed transesterification of the *N*-*Z*-amino acid 2,2,2-trifluoroethyl esters (4).

Furthermore, a gram-scale resolution of *N*-*Z*-DL-norvaline was carried out via the *B. cepacia* lipase-catalyzed transesterification of DL-**1c** with methanol in diisopropyl ether. After incubation of 9 h (33% conversion), the product methyl ester was isolated by column chromatography on silica gel, which after saponification yielded *N*-*Z*-L-norvaline with 92% ee. In another run, *N*-*Z*-D-norvaline with 97% ee was obtained from the remaining trifluoroethyl ester substrate separated after incubation of 35 h (55% conversion).

In the *C. papaya* lipase-catalyzed transesterification of *N*-*Z*-amino acid 2,2,2-trifluoroethyl esters, excellent enantioselectivities were obtained in cyclohexane. However, the enantioselectivity deteriorated by switching the solvent from cyclohexane to diisopropyl ether in which the starting esters were more soluble (4). On the other hand, although the enantioselectivities observed in the *B. cepacia* lipase-catalyzed transesterification of the same substrates were moderate to good, the fact that diisopropyl ether can be used as a solvent without lowering the enantioselectivity as compared with that in cyclohexane should make the present methodology applicable to more non-proteinogenic amino acids.

© 2008 NRC Canada

Table 4. *B. cepacia* lipase-catalyzed transesterification between *N*-*Z*-DL-amino acid 2,2,2-trifluoroethyl esters (DL-**1**) and methanol in diisopropyl ether.

Compound	R	Conversion (%)	Time (h)	ee (%)[a]	*E*
1a	CH_3	41	2.1	69	8.7
1b	C_2H_5	38	2.5	92	42
1c	*n*-C_3H_7	38	10	91	37
1d	*n*-C_4H_9	38	32	89	30
1e	*n*-C_5H_{11}	35	37	87	23
1f	*n*-C_6H_{13}	36	18	90	31
1g	CH_2=$CHCH_2$	42	2.5	79	15
1h	$C_6H_5CH_2$	42	14	73	11
1i	3-$FC_6H_4CH_2$	37	22	68	7.7
1j	4-$FC_6H_4CH_2$	43	18	55	5.1
1k	4-Thiazolylmethyl	36	11	73	9.5

Note: Conditions: 0.4 mmol of DL-**1**, 1.2 mmol of methanol, and 120 mg of *B. cepacia* lipase in 0.8 mL of diisopropyl ether at 25 °C.
[a]Enantiomeric excess of the newly formed methyl ester (**2**).

Table 5. *R. javanicus* lipase-catalyzed transesterification between *N*-*Z*-DL-amino acid 2,2,2-trifluoroethyl esters (DL-**1**) and methanol in diisopropyl ether.

Compound	Conversion (%)	Time (h)	ee (%)[a]	*E*
1a	37	31	56	4.8
1b	37	32	85	20
1c	38	8	88	27
1d	32	12	90	29
1e	44	18	83	21
1f	37	20	78	13
1g	40	17	79	14
1h	38	14	84	19
1i	38	21	73	9.9
1j	41	14	70	9.1
1k	36	11	73	9.5

Note: Conditions: 0.4 mmol of DL-**1**, 1.2 mmol of methanol, and 120 mg of *R. javanicus* lipase in 0.8 mL of diisopropyl ether at 25 °C.
[a]Enantiomeric excess of the newly formed methyl ester (**2**).

Conclusion

In this paper, we have demonstrated that a number of non-proteinogenic amino acids carrying aliphatic side chains can be resolved with moderate-to-good enantioselectivities through the microbial lipase-catalyzed enantioselective transesterification of the 2,2,2-trifluoroethyl esters of their *N*-*Z* derivatives. Although *C. rugosa* lipase is known to show high enantioselectivity toward carboxylic acids, *B. cepacia* lipase is a preferable enzyme in the present case, with methanol being the nucleophile in diisopropyl ether. This, together with the results reported earlier on the resolution of 2-substituted carboxylic acids via the lipase-catalyzed irreversible transesterification where lipases from *A. niger* and *B. cepacia* were utilized, demonstrates that the microbial lipase-catalyzed transesterification procedure in organic milieu must be useful for the resolution of various racemic carboxylic acids, taking into account that these lipase preparations are available easily and inexpensively.

Experimental

General

Thin-layer chromatography was run on precoated silica gel plates (Merck). Melting points were determined on a Yamato MP-21 apparatus and are uncorrected. Optical rotations were measured with a JASCO DIP-4 digital polarimeter. ^{1}H NMR spectra were obtained at 300 MHz on a Varian Unity 300 spectrometer using chloroform-*d* as a solvent with TMS as an internal standard. The liquid chromatograph employed was a Shimadzu LC-5A instrument, equipped with a Rheodyne 7125 sample injector and a Shimadzu SPD-2A variable wavelength UV monitor. A Shimadzu C-R1A data processor was used for data acquisition and processing.

Chemicals

The racemic amino acids were benzyloxycarbonylated using benzyloxycarbonyl chloride (*Z*-Cl) under the usual Schotten–Baumann conditions (16) to give *N*-*Z*-DL-amino acids, which were purified by recrystallization from appropriate solvents (e.g., ethyl acetate–petroleum ether) (8). They were converted to the 2,2,2-trifluoroethyl, 2-chloroethyl or 2,2,2-trichloroethyl esters by the EDC [l-ethy1-3-(3-dimethylaminopropyl)carbodiimide]-DMAP (4-dimethylaminopyridine) method (17) using the corresponding alcohols. All alcohols and organic solvents employed in this study were obtained commercially, and they were distilled following standard protocols and dried over molecular sieves prior to use.

Enzymes

Lipases from porcine pancreas (Type II) and *Candida rugosa* (Type VII) were purchased from Sigma-Aldrich Chemical Co. (USA). Lipases from *Candida rugosa* (MY), *Chromobacterium viscosum* (LP) and *Rhizopus japonicus* (Rhilipase A5) were supplied by Meito Sangyo Co. (Japan), Asahi Chemical Industry (Japan), and Nagase ChemteX Corporation (Japan), respectively. All other enzymes used were supplied by Amano Pharmaceutical Co. (Japan).

© 2008 NRC Canada

Table 6. TLC and HPLC separations of the 2,2,2-trifluoroethyl esters (**1**) and methyl esters (**2**, R′ = CH_3) of *N*-*Z*-amino acids.

	2,2,2-Trifluoroethyl ester		Methyl ester	
R[a]	TLC, R_f[b]	HPLC, t_R (min)[c]	TLC, R_f[b]	HPLC, t_R (min)[c]
CH_3	0.33	2.39	0.22	2.99
C_2H_5	0.38	2.69	0.29	3.50
n-C_3H_7	0.47	3.21	0.35	4.32
n-C_4H_9	0.50	4.42	0.38	5.78
n-C_5H_{11}	0.54	5.39	0.40	7.86
n-C_6H_{13}	0.52	5.59	0.41	11.37
CH_2=$CHCH_2$	0.45	2.92	0.31	3.86

[a]The side chain of an amino acid [–NHCH(R)CO–].
[b]Solvent: hexane–diethyl ether (2:1, *v*/*v*).
[c]HPLC conditions: column, Cosmosil 5C_{18} (4.6 mm i.d. × 150 mm); eluent, 75% aq. MeOH; flow rate, 1.0 mL min^{-1}; column temperature, 30 °C; detection, UV at 254 nm.

Reactions

General procedure for the lipase-catalyzed transesterification

In a typical experiment, a solution of the 2,2,2-trifluoroethyl ester of a racemic *N*-*Z*-DL-amino acid (DL-**1**; 0.4 mmol) and an alcohol (1.2 mmol) in an anhydrous organic solvent (0.8 mL) was stirred with a lipase preparation (120 mg) at 25 °C. The progress of the reaction was monitored by reversed-phase HPLC on a Cosmosil 5C_{18} column (4.6 mm i.d. × 150 mm; Nacalai Tesque, Japan) using aq. methanol as an eluent. When the desired degree of conversion (~40 % based on the racemic starting ester) had been achieved, the enzyme was filtered off and washed with diethyl ether. The error of conversion determined by the HPLC method was estimated as ~±1%. The filtrate and washing were combined and concentrated to a small volume, and the newly formed ester (**2**) was separated from the unchanged starting ester (**1**) by preparative TLC using hexane–diethyl ether (mainly 2:1, *v*/*v*) as a developing solvent. After the absence of the contaminant starting ester (**1**) had been confirmed by reversed-phase HPLC, the ester formed (**2**) was saponified by 0.1 mol/L NaOH in methanol as usual. The ee value of the resolved *N*-*Z*-amino acids (*Z*-AA) was determined by the following HPLC procedure (18): the obtained *Z*-AA was coupled with Gly-L-Phe-OMe to afford the diastereomeric tripeptide *Z*-AA-Gly-L-Phe-OMe, which was separated by reversed-phase HPLC. The peak area of each diastereomer separated was measured to calculate the ee value of the resolved amino acid. When the amino acid AA bears an aromatic ring, *Z*-AA was converted to *Z*-AA-Sar-L-Phe-OMe (Sar = sarcosine or *N*-methylglycine) for a better diastereomeric separation. The kinetic resolution during the couplings was found to be negligible, probably because achiral Gly or Sar occupies the coupling site in the amino component. When the product of the transesterification was the methyl ester, another procedure was also employed. The enantiomers of the methyl ester product were separated directly by normal-phase HPLC on a chiral column, Chiralcel OD (4.6 mm i.d. × 250 mm; Daicel Chemical Industry, Japan), using hexane–2-propanol as an eluent (15). The ee values obtained by these different procedures were consistent with each other within the experimental error (±2%). The ee value for each compound compiled in Table 4 is that obtained by the HPLC procedure utilizing the diastereomeric separation.

The TLC and HPLC separations of the 2,2,2-trifluoroethyl esters (1) and methyl esters (**2**, R′ = CH_3) of *N*-*Z*-amino acids carrying aliphatic side chains are shown in Table 6.

Gram-scale resolution of N-Z-*norvaline*

The 2,2,2-trifluoroethyl ester of racemic *N*-*Z*-DL-norvaline (DL-**1c**; 1.40 g, 4.2 mmol) was dissolved in diisopropyl ether (8 mL), followed by the addition of methanol (520 µL, 12.8 mmol) and then *B. cepacia* lipase (1.2 g). The reaction mixture was stirred at 25 °C. The reaction was stopped after 9 h (33% conversion) by removing the enzyme powder by filtration. The enzyme was washed with diethyl ether. Evaporation of the solvent in vacuo from the combined filtrate and the washing afforded a pale yellow oil, from which the product (**2c**) was isolated by column chromatography on silica gel (Wakogel C-300) using hexane–diethyl ether (10:1, *v*/*v*) as an eluent. Thus, the unreacted trifluoroethyl ester (**1c**) eluted first, and further elution afforded the methyl ester (**2c**) as a colorless oil. The latter was saponified by 0.1 mol/L NaOH, and the raw material was recrystallized from EtOAc–petroleum ether to give *N*-*Z*-L-norvaline as colorless crystals: 290 mg (27% yield); mp 87–88.5 °C; $[\alpha]_D^{25}$ –4.2° (*c* 1.0, acetone). *N*-*Z*-L-norvaline thus obtained was re-esterified with diazomethane, and the resulting methyl ester was analyzed by HPLC on a Chiralcel OD column: 92% ee. In another run, the reaction was stopped after 35 h (55% conversion), and the unreacted trifluoroethyl ester (**1c**) was separated from the newly formed methyl ester (**2c**) by column chromatography in the same manner as mentioned earlier. The trifluoroethyl ester (**1c**) thus obtained was saponified by 0.1 mol/L NaOH, and the raw material was recrystallized from EtOAc–petroleum ether to give *N*-*Z*-D-norvaline as colorless crystals: 410 mg (39% yield); mp 89.5–90 °C; $[\alpha]_D^{25}$ +4.6° (*c* 1.0, acetone); 97% ee by HPLC. ^{1}H NMR (300 MHz, $CDCl_3$) δ: 0.94 (3H, t. *J* = 7.4 Hz, CH_3), 1.30–1.50 (2H, m, C$H_2$$CH_3$), 1.61–1.95 (2H, m, CHC$H_2$), 4.41 (1H, q-like, CH), 5.12 (2H, apparent s, PhCH_2), 5.27 (1H, d, *J* = 8.1 Hz, NH), 7.26–7.41 (5H, m, Ph), 10.48 (1H, br, OH). Anal. calcd. for $C_{13}H_{17}NO_4$: C, 62.14; H, 6.82; N, 5.57%. Found: C, 62.30; H, 6.89; N, 5.58%.

© 2008 NRC Canada

Acknowledgments

This work was partially supported by the Science Research Promotion Fund from Japan Private School Promotion Foundation. The donation of lipases by Amano Pharmaceutical Co., Meito Sangyo Co., Asahi Chemical Industry, and Nagase ChemteX Corporation is gratefully acknowledged.

References

1. (*a*) U.T. Bornscheuer and R.J. Kazlauskas. Hydrolases in organic synthesis: regio- and stereo-selective biotransformations. 2nd ed. Wiley-VHC, Weinheim, Germany. 2006. p. 84. (*b*) K. Faber. Biotransformations in organic chemistry. 5th ed. Springer, Berlin. 2004. pp. 94–123, 344–367; (*c*) H. J. Gais and F. Theil. *In* Enzyme catalysis in organic synthesis. *Edited by* K. Drauz and H. Waldmann. Wiley-VHC, Weinheim, Germany. 2002. pp. 335–578.
2. A.M.P. Koskinen and A.M. Klibanov (*Editors*). Enzymatic reactions in organic media. Blackie A & P, Glasgow, UK. 1996.
3. T. Miyazawa, S. Kurita, M. Shimaoka, S. Ueji, and T. Yamada. Chirality, **11**, 554 (1999).
4. T. Miyazawa, K. Onishi, T. Murashima, T. Yamada, and S.-W. Tsai. Tetrahedron Asymmetry, **16**, 2569 (2005).
5. T. Miyazawa, M. Mio, Y. Watanabe, T. Yamada, and S. Kuwata. Biotechnol. Lett. **14**, 789 (1992).
6. D.C. Roberts and F. Vellaccio. *In* The peptides. Vo1. 5. *Edited by* E. Gross and J. Meienhofer. Academic Press, New York. 1983. pp. 341–449.
7. G.M. Coppola and H.F. Schuster. Asymmetric synthesis: construction of chiral molecules using amino acids. Wiley, New York. 1987.
8. T. Miyazawa, H. Iwanaga, S. Ueji, and T. Yamada. Biocatal. Biotrans. **17**, 445 (2000).
9. T. Miyazawa, K. Imagawa, H. Minowa, T. Miyamoto, and T. Yamada. Tetrahedron, **61**, 10254 (2005).
10. C.-S. Chen, Y. Fujimoto, G. Girdaukas, and C.J. Sih. J. Am. Chem. Soc. **104**, 7294 (1982).
11. (*a*) I.J. Colton, S.N. Ahmed, and R.J. Kazlauskas. J. Org. Chem. **60**, 212 (1995); (*b*) J.J. Lalonde, C. Govardhan, N. Khalaf, A.G. Martinez, K. Visuri, and A.L. Margolin. J. Am. Chem. Soc. **117**, 6845 (1995).
12. S.-H. Pan, T. Kawamoto, T. Fukui, K. Sonomoto, and A. Tanaka. Appl. Microbiol. Biotechnol. **34**, 47 (1990).
13. C. Laane, S. Boeren, K. Vos, and C. Veeger. Biotechnol. Bioeng. **30**, 81 (1987).
14. K. Nakamura, Y. Takebe, T. Kitayama, and A. Ohno. Tetrahedron Lett. **32**. 4941 (1991).
15. T. Miyazawa, Y. Shindo, and T. Yamada. Chromatographia, **60**, 419 (2004).
16. M. Bodanszky and A. Bodanszky. The practice of peptide synthesis. Springer, Berlin. 1984. p. 12.
17. M.K. Dhaon, R.K. Olsen, and K. Ramasamy. J. Org. Chem. **47**, 1962 (1982).
18. T. Miyazawa, H. Iwanaga, T. Yamada, and S. Kuwata. Chirality, **4**, 427 (1992).

© 2008 NRC Canada

Carbanion reactivity — σ-adduct formation and elimination in the reactions of the carbanion from bis(phenylsulfonyl)methane with 4-nitrobenzofurazan derivatives

Basim H.M. Asghar, Michael R. Crampton, and Chukwuemeka Isanbor

Abstract: ^{1}H NMR studies in [$^2H_6$]-DMSO show that the carbanion **4** from bis(phenylsulfonyl)methane reacts with 4,6-dinitrobenzofuroxan to yield a σ-adduct that undergoes base-catalysed elimination to yield an alkene derivative. Rate constants, measured spectrophotometrically, are reported for the corresponding reactions in methanol of **4** with 4-nitrobenzofurazan and some derivatives that give adducts at the 5-position. The intrinsic rate constant, k_o, for this process has a value of 1.5 ± 0.5. The 5-adducts undergo methoxide-catalysed elimination of phenylsulfinic acid to yield alkene derivatives and rate constants for this process are reported.

Key words: carbanions, 4-nitrobenzofurazan, σ-adducts, elimination reactions.

Résumé : Des études de RMN du ^{1}H dans du [$^2H_6$]-DMSO montrent que le carbanion **4** obtenu à partir du bis(phénylsulfonyl)méthane réagit avec le 4,6-dinitrobenzofuroxane pour donner un adduit σ qui subit une élimination catalysée par les bases pour conduire à la formation d'un alcène. On rapporte les constantes de vitesses, mesurées d'une façon spectroscopique, pour les réactions correspondantes du composé **4** avec le 4-nitrobenzofurazane et quelques dérivés qui conduisent à la formation d'adduits en position 5. La valeur de la constante intrinsèque de vitesse pour ce processus, k_0 = 1,5 ± 0,5. Les adduits en position 5 subissent une élimination d'acide phénylsulfinique catalysée par l'ion méthylate pour conduire à des alcènes et on rapporte les constantes de vitesse de ce processus.

Mots-clés : carbanions, 4-nitrobenzofurazane, adduits σ, réactions d'élimination.

[Traduit par la Rédaction]

Introduction

There is much current interest in quantitatively assessing both nucleophilic and electrophilic reactivities. The nucleophilicities of many carbanions have been measured (1–4) using their reactions with benzhydrylium cations and quinone methides, while the electrophilicities of compounds ranging in reactivity from 1,3,5-trinitrobenzene to 4,6-dinitrotetrazolopyridine have been compared by measuring rate constants for their σ-adduct forming reactions with some standard nucleophiles, such as *N*-methylpyrrole and indole derivatives (5–7).

We have recently used the reactions with 4-nitrobenzofurazan and some derivatives to compare the nucleophilicities in methanol of some nitroalkane anions (8) (**1**) and benzyltriflone anions (9) (**2**). These reactions result initially in the formation of anionic adducts at the 5-position of the nitrobenzofurazans, as shown in the general scheme 1. These results indicate that factors that affect the reactivities include the extent of charge delocalization, high in the case of **1** and low in the case of **2**, in the nucleophiles and steric hindrance to bond formation, which is significant for the reaction of **2**.

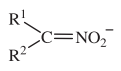

1

R^1,R^2 = H, Me

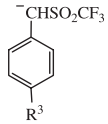

2

R^3 = H, CF_3, CN

It is also of interest that the initially formed adducts may undergo a base-catalysed elimination reaction to produce alkene derivatives.

Following many earlier studies (10–12), there has recently been renewed interest (13) in measuring nucleofugalities of leaving groups. The elimination process shown in Scheme 1 is likely (8, 9) to involve the bimolecular E2 mechanism so that values of the rate constants do not give nucleofugalities directly. Nevertheless, it is useful to examine how the structure of the leaving group Z^- affects the rate of the elimination process.

Received 29 November 2007. Accepted 21 December 2007. Published on the NRC Research Press Web site at canjchem.nrc.ca on 13 February 2008.

B.H.M. Asghar. Department of Chemistry, Umm Al-qura University, P.O. Box 9569, Makkah, Saudi Arabia.
M.R. Crampton.[1] Chemistry Department, Durham University, Durham DH1 3LE, UK.
C.Isanbor. Chemistry Department, University of Lagos, Lagos, Nigeria.

[1]Corresponding author (e-mail: m.r.crampton@durham.ac.uk).

 doi:10.1139/V08-010 © 2008 NRC Canada

Scheme 1.

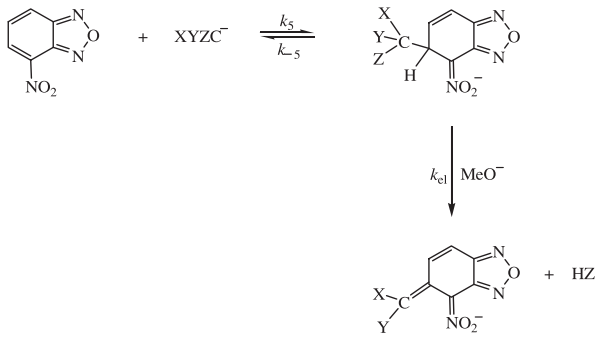

In the present work, we extend our studies to include reactions of the carbanion (**4**) from bis(phenylsulfonyl)methane (**3**). Rate constants in methanol as solvent are reported for the formation of the initial σ-adducts with some 4-nitrobenzofurazan derivatives (**5**), with 4-nitrobenzofuroxan (**6**), and also for the methoxide catalysed elimination of phenylsulfinic acid.

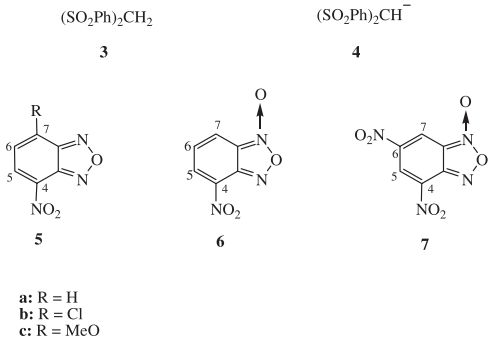

a: R = H
b: R = Cl
c: R = MeO

^{1}H NMR measurements in [$^2H_6$]-DMSO show that reaction of **4** with 4,6-dinitrobenzofuroxan (**7**) results in the initial formation of a σ-adduct at the 7-position followed by elimination of phenylsulfinic acid.

Results and discussion

pK_a Value of bis(phenylsulfonyl)methane 3 in methanol

Since kinetic measurements were made in methanol it was necessary to determine the pK_a value of **3** in this solvent. Reaction of **3** with sodium methoxide in methanol resulted in a strong absorbance band at 280 nm (ε 1.6 × 10^4 dm^3 mol^{-1} cm^{-1}) attributed to formation of the carbanion **4** as indicated in eq. [1]. Absorbance measurements gave a value for K of 40 ± 5 dm^3 mol^{-1}, and the use of eq. [2] leads to a value for pK_a of 15.3 for **3**.

[1] $\mathbf{3} + MeO^- \xleftrightarrow{K} \mathbf{4} + MeOH$

[2] $pK_a = pK_{MeOH} - \log K$

^{1}H NMR spectra

4,6-Dinitrobenzofuroxan **7** is classed as a super-electrophile (14) and will form σ-adducts at the 7-position by reaction with many weakly acidic carbon acids (15–16). ^{1}H NMR spectra in [$^2H_6$]-DMSO of a mixture of **7** (0.1 mol dm^{-3}), **3** (0.1 mol dm^{-3}), and triethylamine (0.1 mol dm^{-3}) provide evidence for the formation of the σ-adduct **8**. Chemical shifts are given in Table 1. Interestingly, the spectrum of **8** shows that the two phenyl rings are not exactly equivalent so that two sets of bands, with equal intensities, are observed for their ring hydrogens. In the presence of excess triethylamine, new bands are observed that are consistent with the formation of the product **9** of the elimination of phenylsulfinic acid. Notably, two singlets due to **9** are observed at δ 8.62 (H5) and δ 7.17 (CH). These results are summarized in Scheme 2. It is known (17) that **7** will react with methanol to give a very stable 7-methoxy adduct, and this precluded kinetic studies of reactions of **7** with **3** in this solvent.

Spectra of 1,3,5-trinitrobenzene in [$^2H_6$]-DMSO containing **3** and triethylamine gave no evidence of strong interaction. After several hours only bands due to the parent molecules were present.

Kinetic measurements

Reactions of the carbanion **4**, generated from **3** and sodium methoxide, with **5a**–**5c** and **6** were investigated spectrophotometrically in methanol. It is known that methoxide ions themselves will react with **5a**–**5c** and **6** to give σ-adducts (18, 19), and in the case of **5b** a substitution product (19). To minimize these reactions, the equilibrium methoxide concentrations were reduced to low levels by working with [**3**] >> [NaOMe] and (or) by using phenolic buffers. Under these conditions the UV–vis spectra of **5a** revealed two processes well separated in time. The first process resulted in a shift in the absorption maximum from 325 nm (ε 8 × 10^3 dm^3 mol^{-1} cm^{-1}) in the parent to 335 nm (ε 1.2 × 10^4 dm^3 mol^{-1} cm^{-1}) and is attributed to σ-adduct formation. The second slower process gave rise to a strong band at 430 nm (ε 2.0 × 10^4 dm^3 mol^{-1} cm^{-1}) and is attributed to the formation of the alkene derivative **11a** by elimination of phenylsulfinic acid from the σ-adduct. The UV–vis spectra of **5b**, **5c**, and **6** similarly showed a fast process, giving a band in the region 330–340 nm. In the case of **5b** and **6**, this was followed by a slower reaction giving an absorption band in the region 430–450 nm. However, with **5c** this process was too slow for measurement. These reactions are shown in Scheme 3.

Our justification for assigning structure **10**, resulting from attack at the 5-position, to the product of the fast reaction is that previous studies with carbanions derived from benzylcyanides (20), nitroalkanes (8), and benzyltriflones (9), have shown that formation of 5-adducts is kinetically favoured relative to the formation of the isomeric 7-adducts. Also in the case of **5b** and of **5c**, reaction at the 7-position is unlikely because of the presence of the 7-substituent (8, 21). That the slower process involves elimination follows by analogy with the behaviour of the nitroalkane adducts (8), which eliminate nitrous acid, and the benzyltriflone adducts (9), which eliminate trifluoromethylsulfinic acid. In these cases, as in the present case, the elimination process involves a shift to longer wavelength in the absorption maximum, consistent with the increased electron delocalization possible in the elimination products. A further analogy is with the behaviour of **8**, which will eliminate phenylsulfinic acid.

Kinetic measurements of the fast reaction were made either with [**3**] and [NaOMe] >> [**5**] or [**6**], or with methoxide

© 2008 NRC Canada

Table 1. ^{1}H NMR data for **3**, **7**, and **8** in [$^2H_6$]-DMSO.

	δ				
Compound	H7	H5	CHn	Ph	J_{57}
3	—	—	5.93(s, CH_2)	7.88(d), 7.63(t), 7.76(t)	—
7	9.26	8.95	—	—	2
8	5.56	8.37	5.91(CH)	7.62(d), 7.46(t), 7.27(t) 7.64(d), 7.47(t) 7.29(t)	<1

Note: J values in Hz. Coupling J = 7.4 Hz is observed between adjacent hydrogens in the phenyl rings.

Scheme 2.

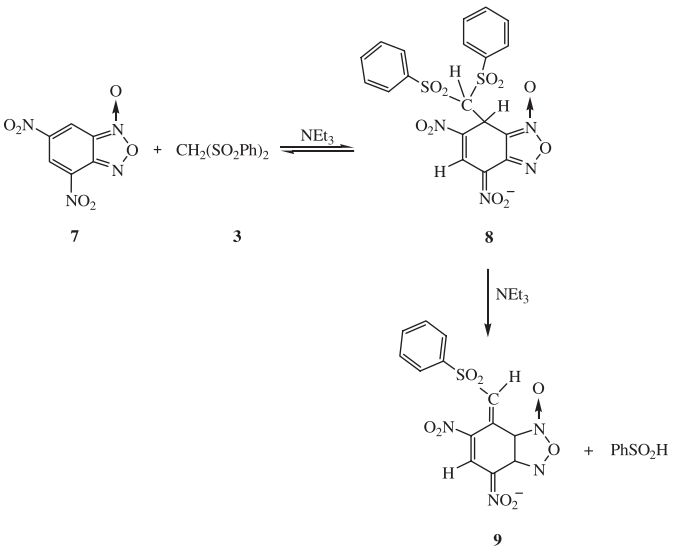

7 3 8 9

Scheme 3.

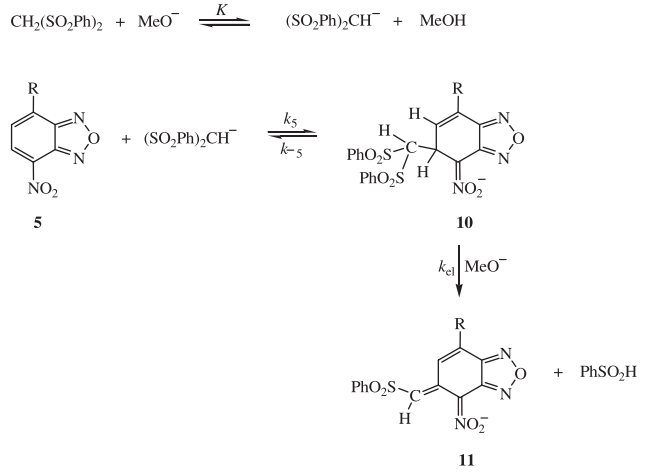

5 10 11

concentration (hence the concentration of **4**) buffered at constant values. Under these conditions, the fast reaction k_{fast} was observed as a first-order process, and eq. [3] will apply. Values of rate constants are given in Table 2. Linear plots of k_{fast} versus the carbanion concentration allowed the evaluation of k_5 and k_{-5}. Since the intercepts of the plots had low values, there are relatively high errors associated with the values of k_{-5} determined in this way. Therefore, measurements were also made, shown in the final three rows of Table 2, using buffered solutions where the concentrations of carbanion were reduced to low levels. Here the k_{-5} term made a large contribution to the overall value of k_{fast}. Using the known values of k_5, values of the term k_5[carbanion] were subtracted from k_{fast} to allow the evaluation of k_{-5}. The good correspondence between experimental and calculated values of k_{fast} (Table 2) gives confidence in the results obtained. Values for k_5, k_{-5}, and K_5, calculated as k_5/k_{-5}, are collected in Table 4.

[3] $$k_{fast} = k_5[(SO_2Ph)_2CH^-] + k_{-5}$$

Kinetic measurements for the slower reaction were made with concentrations of the carbanion **3** that were high enough to ensure that the initial conversion of parent nitrocompounds to adducts **10** was largely complete. In the cases of **5a**, **5b**, and **6**, a first-order process k_{slow} measured at 430–450 nm was observed and is attributed to the elimination of phenylsulfinic acid to give the alkene derivatives **11**. The results in Table 3 show that values of k_{slow} increase linearly with the equilibrium concentrations of methoxide ions, so that eq. [4] is applicable, and there is no dependence on the carbanion concentration. Values obtained for k_{el} were 2.6, 12, and 8 dm^3 mol^{-1} s^{-1} for **5a**, **5b**, and **6**, respectively. In the case of **5c**, this reaction was too slow for convenient measurement.

[4] $$k_{slow} = k_{el}[MeO^-]$$

Comparisons

Results are collected in Table 4. Variations in values among the compounds **5a**–**5c** and **6** are largely in line with data obtained with other nucleophiles (8, 19, 22, 23). Thus the higher value of k_5 found for **5b** compared with **5a** reflects the inductive effect of the chlorine meta to the position of attack. The reduced electrophilicity of **5c** is attributed to resonance stabilization in the parent between the NO_2 and OMe ring-substituents. The N→O functionality (18) in **6** results in increases in values of k_5 and K_5 compared with **5a**.

Although the data is limited, we thought it worthwhile to estimate a value for the intrinsic rate constant k_o, in the Marcus (24–26) sense, for reactions of the carbanion **3** with the nitrobenzofurazan derivatives. A plot, not shown, of the values of log k_5 and log k_{-5} vs. log K_5 gave a value for k_o of 1.5 ± 0.5. The values of intrinsic rate coefficients are thought (26–29) to reflect the amount of electronic–structural reorganisation and solvent reorganisation accompanying a reaction; the more reorganisation required, the lower the reactivity. The value obtained here is significantly higher than that (k_o = 0.05) found (8) for the reaction of nitroalkane anions **1** with nitrobenzofurazans. This suggests that in the carbanions **4**, as with the benzyltriflone anions (4,

© 2008 NRC Canada

Table 2. Kinetic data for the fast reactions of the carbanion **4** with **5a–5c** and **6** in methanol at 25 °C.

[3] (mol dm^{-3})	[NaOMe] (10^{-3} mol dm^{-3})	$[MeO^-]_{eq}$[a] (10^{-4} mol dm^{-3})	$[\mathbf{4}]_{eq}$[a] (10^{-4} mol dm^{-3})	k_{fast}[b,c] (s^{-1})			
				5a	**5b**	**5c**	**6**
0.03	1.0	4.5	5.5	0.30 (0.31)	7.9	0.26 (0.27)	1.0 (0.93)
0.05	1.0	3.3	6.7	0.35 (0.37)	9.8	0.29 (0.31)	1.1 (1.1)
0.05	1.5	5.0	10.0	0.52 (0.54)	12	0.42 (0.43)	1.8 (1.7)
0.05	2.0	6.7	13.3	0.67 (0.70)	21	0.58 (0.55)	2.6 (2.2)
0.022	—	0.54[d]	0.48	0.057 (0.064)	—	—	0.13 (0.13)
0.034	—	0.54[d]	0.73	0.090 (0.080)	—	—	0.18 (0.17)
0.044	—	0.54[d]	0.95	0.098 (0.090)	1.30	0.13 (0.11)	0.21 (0.20)

Note: The concentration of the nitro compounds **5a–5c and 6** is 5×10^{-5} mol dm^{-3}.
[a]Calculated using the value for K of 40 dm^3 mol^{-1} (eq. [1]).
[b]For **5a** and **5b** measured as a forming reaction at 330–340 nm, for **5c** as a forming reaction at 330 nm or fading reaction at 370 nm, and for **6** as a forming reaction at 340 nm or fading reaction at 410 nm.
[c]Values in parentheses were calculated using eq. [3] using the values given in Table 4.
[d]Maintained using bromophenol buffers.

Table 3. Kinetic data for the slow reactions of **5a**, **5b**, and **6** in methanol at 25 °C.

[3] (mol dm^{-3})	[NaOMe] (10^{-3} mol dm^{-3})	$[MeO^-]_{eq}$[a] (10^{-4} mol dm^{-3})	$[\mathbf{4}]_{eq}$[a] (10^{-4} mol dm^{-3})	k_{slow} (10^{-3} s^{-1})		
				5a	**5b**	**6**
0.10	0.5	1.0	4.0	0.28	1.3	1.0
0.05	1.0	3.3	6.7	0.91	3.9	2.6
0.08	1.5	3.6	11.4	—	4.4	2.8
0.10	2.0	4.0	16	0.95	4.8	3.0
0.10	3.0	6.0	24	1.33	7.8	4.6

Note: The concentration of **5a**, **5b**, and **6** is 5×10^{-5} mol dm^{-3}.
[a]Calculated using the value for K of 40 dm^3 mol^{-1} (eq. [1]).

Table 4. Summary of kinetic and equilibrium data for the reactions in Scheme 3.

Compound	k_5 (dm^3 mol^{-1} s^{-1})	k_{-5} (s^{-1})	K_5 (dm^3 mol^{-1})	k_{el} (dm^3 mol^{-1} s^{-1})
5a	500±100	0.04±0.01	$(1.25\pm0.4) \times 10^4$	2.6
5b	$(1.4\pm0.2) \times 10^4$	—	—	12
5c	350±50	0.08±0.02	$(4.4\pm1) \times 10^3$	—
6	$(1.6\pm0.2) \times 10^3$	0.05±0.02	$(3.2\pm1) \times 10^4$	8

9) **2**, the negative charge is more localized on the carbon atom than in the nitroalkane anions. In agreement with this, it should be noted that Hibbert (30, 31) found that little structural reorganisation was involved in ionization of disulfonyl carbon acids in water.

The previous study (9) with carbanions **2** derived from benzyltriflones found evidence for some steric hindrance to the reaction with 4-nitrobenzofurazan derivatives, and the reaction with the more sterically demanding 1,3,5-trinitrobenzene was not observed. The present results suggest that the nucleophilicity of the carbanion **4** from bis(phenylsulfonyl)methane may similarly be reduced by its high steric requirements. Thus again, no reaction is observed with 1,3,5-trinitrobenzene and the values of k_5 for the reaction with 4-nitrobenzofurazan are similar for carbanions **4** and **2** (R3=CN) derived from carbon acids with similar pK_a values. Thus for **4**, k_5 = 500 dm^3 mol^{-1} s^{-1} and pK_a for **3** is 15.3, and for **2** (R3 = CN) k_5 = 1500 dm^3 mol^{-1} s^{-1} and pK_a for 4-cyanobenzyltriflone (9) is 16.0.

Elimination reactions have now been observed from 5-adducts produced from 4-nitrobenzofurazan derivatives and three types of carbanion, i.e., nitroalkane anions (8), benzyltriflone anions (9), and the bis(phenylsulfonyl)methane anion, and it is useful to compare kinetic data in methanol. Values of the rate constant k_{el} for the methoxide-catalysed elimination of nitrous acid from the nitromethane and nitroethane adducts of 4-nitrobenzofurazan **5a** are 3.0 and 1.4 dm^3 mol^{-1} s^{-1}, respectively (8), and are similar to the value of 2.6 dm^3 mol^{-1} s^{-1} found here for the elimination of phenylsulfinic acid from **10**, R = H. In both types of reaction, the presence of the electron-withdrawing 7-chloro substituent in **5c** increases values of k_{el}. Interestingly, in the reactions with the benzyltriflone anion the elimination of trifluoromethylsulfinic acid from the initially formed 5-adducts is faster than their reversal to parent, $k_{el}[MeO^-] > k_{-5}$, so that values of k_{el} are not measurable (9). It might be inferred that the value of k_{el} for the elimination of trifluoromethylsulfinic acid is higher than the corresponding values for the elimination of nitrous acid and phenylsulfinic acid. Indeed, the high nucleofugal character of the SO_2CF_3 group and the possible use of SO_2CF_3 activated carbon acids in vicarious nucleophilic substitutions has been noted previ-

© 2008 NRC Canada

ously (32, 33). Nevertheless, our results (9) do not yield a value for k_{el} for trifluoromethyl sulfinic acid so that a direct comparison is not possible.

In fact, the elimination process is likely (34) to involve the E2 mechanism so that factors other than the nucleofugality of the leaving group are involved. These include steric factors involving the accessibility to the catalysing base of the acidic hydrogen to be removed from the reaction centre in the adducts, such as **10**, and possible steric interaction with the ring nitro-group in the alkene products, such as **11**. For example, the adduct **10**, carrying two phenylsulfonyl groups, is likely to be more sterically demanding than the corresponding adduct produced from the nitromethane carbanion. It should also be noted that in the elimination process in methanol, catalysis has been observed only by the methoxide ion and not by unreacted carbanions, present in excess, which will be more sterically inhibited.

Experimental

Nitro-compounds **5a**–**5c**, **6**, and **7** were available from previous work [9]. Bis(phenylsulfonyl)methane was a commercial sample. Solutions of sodium methoxide were prepared by dissolving clean sodium in AnalaR methanol under nitrogen. Solutions containing very low equilibrium concentrations of methoxide ions were prepared using buffers prepared from 4-bromophenol, whose p*K*a value (35) in methanol is 13.61. All other materials and solvents were the purest available commercial samples.

^{1}H NMR spectra in [$^2H_6$]-DMSO were recorded with a Bruker Avance 400 MHz instrument, UV-vis spectra and kinetic measurements were made at 25 °C with a Shimadzu UV-2101 PC spectrophotometer or an Applied Photophysics SX-17 MV stopped-flow instrument. First-order rate constants, precise to ± 5%, were evaluated using standard methods.

Acknowledgements

BHMA thanks the Ministry of Higher Education, Kingdom of Saudi Arabia for funding. CI thanks the Royal Society of Chemistry for the award of a J.W.T. Jones Travel grant to allow him to spend time in Durham University, U.K.

References

1. H. Mayr, B. Kempf, and A.R. Ofial. Acc. Chem. Res. **36**, 66 (2003).
2. T. Bug, T. Lemek, and H. Mayr. J. Org. Chem. **69**, 7565 (2004).
3. T.B. Phan and H. Mayr. Eur. J. Org. Chem. 2530 (2006).
4. S.T.A. Berger, A.R. Ofial, and H. Mayr. J. Am. Chem. Soc. **129**, 9753 (2007).
5. F. Terrier, S. Lakhdar, T. Boubaker, and R. Goumont. J. Org. Chem. **70**, 6242 (2005).
6. S. Lakhdar, R. Goumont, T. Boubaker, M. Mokhtari, and F. Terrier. Org. Biomol. Chem. **4**, 1910 (2006).
7. S. Lakhdar, R. Goumont, F. Terrier, T. Boubaker, J.M. Dust, and E. Buncel. Org. Biomol. Chem. **5**, 1744 (2007).
8. B.H.M. Asghar and M.R. Crampton. Org. Biomol. Chem. **5**, 1646 (2007).
9. B.H.M. Asghar and M.R. Crampton. J. Phys. Org. Chem. **20**, 702 (2007).
10. R.A. Bartsch and J.F. Bunnett. J. Am. Chem. Soc. **91**, 1376 (1969).
11. C.J.M. Stirling. Acc. Chem. Res. **12**, 198 (1979).
12. D.R. Marshall, P.J. Thomas, and C.J.M. Stirling. J. Chem. Soc. Perkin Trans. 2, 1898 (1977).
13. B. Denegri, A. Streiter, S. Juric, A.R. Ofial, O. Kronja, and H. Mayr. Chem. Eur. J. **12**, 1648 (2006).
14. (*a*) F. Terrier, E. Kizilian, J.-C. Halle, and E. Buncel. J. Am. Chem. Soc. **114**, 1740 (1992); (*b*) R. Goumont, F. Terrier, D. Vichard, S. Lakhdar, J.M. Dust, and E. Buncel. Tetrahedron Lett. **46**, 8363 (2005).
15. F. Terrier. Nucleophilic aromatic displacement. VCH, NY. 1991.
16. (*a*) E. Kizilian, F. Terrier, A.-P. Chatrousse, K. Gzouli, and J.-C. Halle. J. Chem. Soc. Perkin Trans. 2, 2667 (1997); (*b*) F. Terrier, M.-J. Pouet, J.-C. Halle, S. Hunt, J.R. Jones, and E. Buncel. J. Chem. Soc. Perkin Trans. 2, 1665 (1993); (*c*) E. Buncel, R.A. Manderville, and J.M. Dust. J. Chem. Soc. Perkin Trans. 2, 1019 (1997); (*d*) F. Terrier, S. Lakhdar, T. Boubaker, and R. Goumont. J. Org. Chem. **70**, 6242 (2005).
17. F. Terrier, A.-P. Chatrousse, Y. Soudais, and M. Hlaibi. J. Org. Chem. **49**, 4176 (1984).
18. F. Terrier, A.-P. Chatrousse, and F. Millot. J. Org. Chem. **45**, 2666 (1980).
19. L. DiNunno, S. Florio, and P.E. Todesco. J. Chem. Soc. Perkin Trans. 2, 1469 (1975).
20. J.H. Atherton, M.R. Crampton, G.L. Duffield, and J.A. Stevens. J. Chem. Soc. Perkin Trans. 2, 443 (1995).
21. M. Makosza, O. Lobanova, and A. Kwast. Tetrahedron, **60**, 2577 (2004).
22. M.R. Crampton, L.M. Pearce, and L.C. Rabbitt. J. Chem. Soc. Perkin Trans. 2, 257 (2002).
23. M.R. Crampton, R.E.A. Lunn, and D. Lucas. Org. Biomol. Chem. **1**, 3438 (2003).
24. R.A. Marcus. J. Phys. Chem. **72**, 891 (1968).
25. A.O. Cohen and R.A. Marcus. J. Phys. Chem. **72**, 4249 (1968).
26. C.F. Bernasconi. Pure Appl. Chem. **54**, 2335 (1982).
27. C.F. Bernasconi, C.I. Murray, J.P. Fox, and D.J. Carré. J. Am. Chem. Soc. **105**, 4349 (1983).
28. C.F. Bernasconi, A. Laibelman, and J.L. Zitomer. J. Am. Chem. Soc. **107**, 6563 (1985).
29. W.P. Jencks. Chem. Rev. **85**, 511 (1985).
30. F. Hibbert. J. Chem. Soc. Perkin Trans. 2, 1289 (1973).
31. F. Hibbert. J. Chem. Soc. Perkin Trans. 2, 1171 (1978).
32. Z. Wrobel and M. Makosza. Org. Prep. Proced. Int. **22**, 575 (1990).
33. O.N. Chupakhin, V.N. Charushin, and H.C. van der Plas. Nucleophilic aromatic substitution of hydrogen. Academic Press, London, UK. 1994.
34. T. Lemmek, M. Makosza, D.S. Stephenson, and H. Mayr. Angew. Chem. Int. Ed. **42**, 2793 (2003).
35. C.H. Rochester and B. Rossall. J. Chem. Soc. B, 743 (1967).

© 2008 NRC Canada

Bright blue luminescent pyrenyl-containing organosilicon compounds with contrasting charge transport functionality — $SiPh_2$(*p*-C_6H_4-pyrenyl)(*p*-C_6H_4-*N*-benzimidazolyl) and $SiPh_2$(*p*-C_6H_4-pyrenyl)[*p*-C_6H_4-NPh(1-naph)]

Dongren Bai, Shijin Han, Zheng-Hong Lu, and Suning Wang

Abstract: The authors investigated the impact of electron-transport and hole-transport functional groups on the properties and the performance of blue luminescent organosilicon compounds as bifunctional materials in organic light-emitting devices. Two new pyrenyl-containing organosilicon compounds, $SiPh_2$(*p*-C_6H_4-pyrenyl)(*p*-C_6H_4-*N*-benzimidazolyl) (**1**) and $SiPh_2$(*p*-C_6H_4-pyrenyl)[*p*-C_6H_4-NPh(1-naph)] (**2**) were synthesized. Both compounds display bright blue luminescence in solution and in the solid state with a high quantum efficiency, but they have contrasting electroluminescent properties. The presence of the benzimidazolyl group in **1** enables it to function as a bifunctional material (blue emitter and electron transporter) in OLEDs. An efficient triple-layer (CuPc/NPB/**1**) blue OLED (C.I.E. 0.15, 0.14) was fabricated successfully. The presence of the NPh(1-naph) group in **2** enables its use as an effective transparent hole injection material, but not a blue emitter in OLEDs.

Key words: organosilicon compounds, synthesis, luminescence, electroluminescence, devices.

Résumé : On a étudié l'impact des groupes fonctionnels transporteurs d'électron ou de trou sur les propriétés et la performance de composés organosiliciés luminescents dans le bleu comme matériaux bifonctionnels dans les systèmes organiques qui émettent de la lumière (SOEL). On a synthétisé deux nouveaux composés organosiliciés contenant du noyau pyrényle, $SiPh_2$(*p*-C_6H_4-pyrényl)(*p*-C_6H_4-*N*-benzimidazolyle) (**1**) et $SiPh_2$(*p*-C_6H_4-pyrényl)[*p*-C_6H_4-*N*-Ph(1-naphtyle) (**2**). En solution ainsi qu'à l'état solide, chacun de ces composés fournit une intense luminescence bleue, avec une efficacité quantique élevée, mais présentent des propriétés électroluminescentes différentes. La présence, dans le composé **1**, d'un groupe benzimidazolyle lui permet de fonctionner comme matériel bifonctionnel (émettant dans le bleu et transporteur d'électron) dans les SOEL. On a réussi à fabriquer un SOEL bleu à triple couche (CuPc/NPB/**1**) efficace (C.I.E. 0,15, 014). La présence du groupe Nph(1-naphtyle) dans le composé **2** permet de l'utiliser comme un matériel efficace comme trou d'injection transparent, mais il ne peut pas être utilisé comme émetteur dans le bleu dans les SOEL.

Mots-clés : composés organosiliciés, synthèse, luminescence, électroluminescence, systèmes.

[Traduit par la Rédaction]

Introduction

Organic light emitting diodes (OLEDs) have been widely recognized as a promising technology for second-generation flat-panel display because of advantages such as a wide viewing angle, operation over a wide temperature range, and low power consumption (1). Despite the tremendous progress achieved (2–6) since the seminal report (1*a*) by Tang and co-workers, device stability (2) and the lack of blue emitters (3) remain challenging tasks in OLEDs research. Bifunctional molecules, which can act as both emitter and charge-transport material, have recently attracted much attention because of their potential in simplifying OLED device structure and reducing manufacturing cost (4–6). Because most organic molecules can transport holes more effectively than electrons (7), hole-transport emitters constitute the majority of bifunctional emitters reported so far. Therefore emitters, especially blue emitters, with electron-transport capability are still very much in demand.

Saturated organosilicon compounds are attractive because of their high chemical and thermal stability and the possibility of attaching up to four different functional groups to the silicon center (5, 8). Chen and co-workers have demonstrated extensively the effectiveness of a tetraphenylsilane core in enhancing the glass-forming ability of the molecules and the successful use of derivatives with a tetraphenylsilane

Received 6 December 2007. Accepted 7 December 2007. Published on the NRC Research Press Web site at canjchem.nrc.ca on 13 February 2008.

D. Bai and S. Wang.[1] Department of Chemistry, Queen's University, Kingston, ON K7L 3N6, Canada.
S. Han and Z.-H. Lu. Department of Materials Sciences and Engineering, University of Toronto, Toronto, ON M5S 3E5, Canada.

[1]Corresponding author (e-mail: wangs@chem.queensu.ca).

 doi:10.1139/V07-151 © 2008 NRC Canada

core in OLEDs (5). We have also reported previously that homo-functionalizing the silicon center with dipyridylaminoaryl groups can produce blue emitters with good morphological and thermal stability (8). We have also demonstrated that hetero-functionalization of the silicon center by both donor and acceptor groups can result in not only efficient blue emitters but also molecules with dual emission, which has found important applications in fluorescent sensing for fluoride (9). In search of new and highly efficient bifunctional blue emitters, we have investigated several pyrene-functionalized silicon compounds, two of which, $SiPh_2$(*p*-C_6H_4-pyrenyl)(*p*-C_6H_4-*N*-benzimidazolyl) (**1**) and $SiPh_2$(*p*-C_6H_4-pyrenyl)[*p*-C_6H_4-NPh(1-naph)] (**2**), have been found to display bright blue emission in the solid state with contrasting charge transport properties in OLEDs. The details are presented herein.

Experimental

All starting materials were purchased from Sigma-Aldrich Chemical Company and were used without further purification. Solvents were freshly distilled over appropriate drying reagents. All experiments were carried out under a dry nitrogen atmosphere using standard Schlenk techniques unless otherwise stated. TLC was carried out on silica gel. Flash chromatography was carried out on silica (silica gel 60, 70–230 mesh). ^{1}H and ^{13}C NMR spectra were recorded on Bruker Avance 300, 400, or 500 MHz spectrometers. Excitation and emission spectra were recorded on a Photon Technologies International QuantaMaster Model 2 spectrometer. Elemental analyses were performed by Canadian Microanalytical Service Ltd., Delta, British Columbia, Canada. Melting points were determined on a Fisher-Johns melting point apparatus. All DSC measurements were performed on a PerkinElmer Pyris DSC 6 with a heating rate of 10 °C/min and a cooling rate of 20 °C/min. Cyclic voltammetry was performed on a BAS CV-50W analyzer with a scan rate of 100 mV s^{-1}. The electrolytic cell used was a conventional three-compartment cell, with a Pt working electrode, Pt auxiliary electrode, and Ag–AgCl reference electrode. All experiments were performed at room temperature with 0.10 mol/L tetrabutylammonium hexafluorophosphate in CH_2Cl_2 as the supporting electrolyte. The ferrocenium–ferrocene couple was used as the internal standard. High-resolution mass spectra were obtained using electrospray mode with internal calibrants on an Applied Biosystems/MDS-Sciex QSTAR XL spectrometer. The synthesis of $SiPh_2${*p*-[(*N*-(1-naph)ph]Ph}(*p*-Br-Ph) was reported previously by our group (9).

Synthesis of $SiPh_2$(*p*-Br-Ph)(*p*-C_6H_4-*N*-benzimidazolyl) (1a)

Si(*p*-Br-Ph)$_2$$Ph_2$ (2.4 mmol, 1.19 g), benzimidazole (2.0 mmol, 0.241 g), cupric sulfate hydrate (0.025 g), and potassium phosphate (0.300g) were heated at 230 °C for 10 h under nitrogen. After cooling to ambient temperature, the reaction mixture was dissolved in 40 mL of CH_2Cl_2 and washed by water. The water layer was separated and extracted with CH_2Cl_2 (3 × 30 mL). The combined organic layers were dried over $MgSO_4$ and the solvents were evaporated under reduced pressure. The residue was subjected to column chromatography on silica gel (ethyl acetate / hexane as eluent) to afford a colorless solid of **1a** in 31% yield. ^{1}H NMR in $CDCl_3$ (25 °C, ppm) δ: 8.19 (s, 1H), 7.92 (d, *J* = 5.2, 1H), 7.78 (d, *J* = 7.6, 2H), 7.63 – 7.57 (m, 8H), 7.54–7.44 (m, 9H), 7.37 (t, *J* = 4.0, 2H). ^{13}C NMR in $CDCl_3$ (25 °C, ppm) δ: 140.85, 137.07, 136.84, 136.34, 135.25, 134.06, 133.52, 131.83, 131.48, 130.32, 129.14, 127.20, 127.08, 124.10, 123.13, 122.36, 122.22, 119.33, 109.74. HRMS *m/z*: found 531.0866 ([M + H]$^+$, calcd. 531.0892).

Synthesis of $SiPh_2$(*p*-C_6H_4-pyrenyl)(*p*-C_6H_4-*N*-benzimidazolyl) (1)

To a mixture of pyrenyl-1-boronic acid (0.375 mmol, 0.093 g), **1a** (0.25 mmol, 0.135 g), $Pd(PPh_3)_4$ (0.013 mmol, 0.015 g), and Na_2CO_3 (0.500 g) was added degassed EtOH (3 mL), H_2O (3 mL), and toluene (5 mL). The mixture was stirred and heated at reflux for 2 days. The reaction mixture was dissolved in 40 mL of CH_2Cl_2 and washed by water. The water layer was separated and extracted with CH_2Cl_2 (3 × 30 mL). The combined organic layers were dried over $MgSO_4$, and the solvents were evaporated under reduced pressure. The residue was subjected to column chromatography on silica gel (with ethyl acetate / hexane as eluent) to afford a colorless solid **1** in 65% yield. ^{1}H NMR in $CDCl_3$ (25 °C, ppm) δ: 8.31–8. 20 (m, 5H), 8.12 (s, 2H), 8.10–8.03 (m, 3H), 7.98 (d, *J* = 6.4, 1H), 7.94 (d, *J* = 6.8, 2H), 7.88 (d, *J* = 6.4, 2H), 7.80 (d, *J* = 6.0, 4H), 7.75 (d, *J* = 6.8, 2H), 7.68 (d, *J* = 6.8, 1H), 7.62 – 7.54 (m, 8H), 7.41 (t, *J* = 4.8, 2H). ^{13}C NMR in $CDCl_3$ (25 °C, ppm) δ: 143.50, 142.84, 142.30, 138.27, 137.44, 137.30, 136.52, 136.46, 135.03, 133.59, 133.42, 132.30, 131.52, 131.17, 131.00, 130.80, 130.13, 129.88, 128.47, 128.28, 127.67, 127.64, 127.45, 126.13, 125.91, 125.29, 125.21, 125.04, 124.98, 124.94, 124.79, 124.06, 123.26, 120.50, 110.82. HRMS *m/z*: found 653.24130 ([M + H]$^+$, calcd. 653.2412).

Synthesis of $SiPh_2$(*p*-C_6H_4-pyrenyl)[*p*-C_6H_4-NPh(1-naph)] (2)

To a mixture of pyrenyl-1-boronic acid (0.185 g, 0.74 mmol), $SiPh_2$ {*p*-[(*N*-(1-naph)Ph]Ph}(*p*-Br-Ph) (0.310 g, 0.49 mol), $Pd(PPh_3)_4$ (0.025 g, 0.022 mmol), and Na_2CO_3 (1.00 g) was added degassed EtOH (5 mL), H_2O (5 mL), and toluene (10 mL). The mixture was stirred and heated at reflux for 2 days. The reaction mixture was dissolved in 40 mL of CH_2Cl_2 and washed by water. The water layer was separated and extracted with CH_2Cl_2 (3 × 30 mL). The combined organic layers were dried over $MgSO_4$ and the solvents were evaporated under reduced pressure. The residue was subjected to column chromatography on silica gel (with methylene chloride / hexane as eluent) to afford a colorless solid **2** in 55% yield. ^{1}H NMR in $CDCl_3$ (25 °C, ppm) δ: 8.20 (m, 4H), 8.12 (s, 2H), 8.01 (m, 4H), 7.91 (d, 1H), 7.80 (m, 3H), 7.68 (m, 6H), 7.46 (m, 12H), 7.23 (t, 2H), 7.18 (d, 2H), 7.04 (d, 2H), 7.00 (t, 1H). ^{13}C NMR in $CDCl_3$ (25 °C, ppm) δ: 149.80, 147.70, 143.12, 142.31, 137.63, 137.46, 136.55, 136.48, 135.39, 134.82, 133.57, 131.62, 131.55, 131.50, 131.06, 130.72, 130.13, 129.67, 129.28, 128.53, 128.00, 127.71, 127.69, 127.57, 127.55, 127.49, 126.94, 126.63, 126.47, 126.30, 126.08, 125.41, 125.20, 125.05, 124.99, 124.93, 124.88, 124.77, 124.30,

© 2008 NRC Canada

Scheme 1.

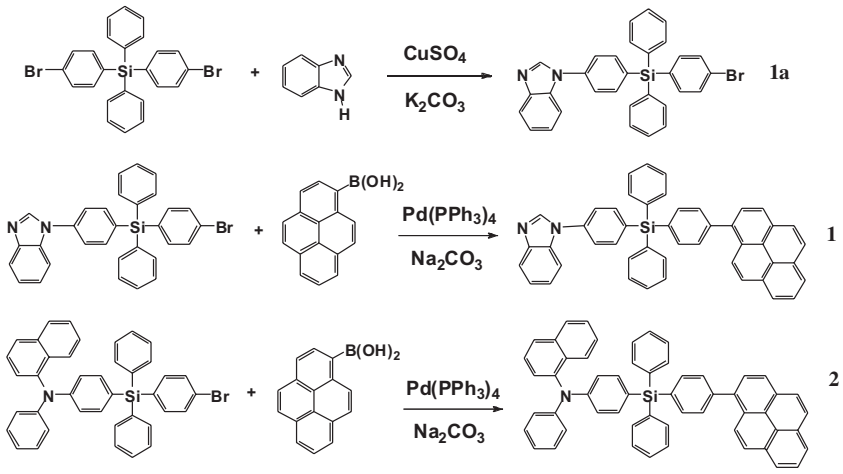

122.95, 122.60, 119.88. HR-MS data *m/z*: found 792.2485 ($[M + K]^+$, calcd. 792.2489).

Solution photoluminescent quantum yield measurements

Emission quantum yields were determined relative to anthracene in CH_2Cl_2 at 298 K ($\Phi_r = 0.36$). The absorbance of all samples and the standard at the excitation wavelength was approximately 0.094–0.114. The quantum yields were calculated by previously reported procedures (10).

Thin-film photoluminescent quantum yield measurements

UV–vis absorption spectra were measured with a Cary 50 Bio (Varian) spectrophotometer. Photoluminescence spectra were recorded using a Horiba Jobin Yvon SPEX FluoroLog equipped with an integrating sphere. The solid-state absolute quantum yields of luminescence efficiencies were obtained using the integrating sphere. Excitation wavelengths of 320 and 330 nm were used for **1** and **2**, respectively.

OLED device fabrication

Electroluminescent (EL) devices were fabricated using a K.J. Lesker OLED cluster tool with six high-vacuum process chambers. For the current experiments, 2 in × 2 in (1 in = 25.4 mm) ITO coated-glass substrates were used. The patterned ITO surface was sequentially cleaned in acetone, methanol, and de-ionized water, and then with UV–ozone treatment. All the testing devices had an active area of 2 mm^2. The base pressures of the organic and metallization chambers were 4×10^{-8} and 1.9×10^{-6} Torr (1 Torr = 133.322 4 Pa), respectively. The pressures during the deposition process in the two chambers were lower than 1.9×10^{-6} Torr. The growth rates were ~1.5 Å s^{-1} for organic materials, 0.2 Å s^{-1} for LiF, and ~1.5 Å s^{-1} for metals (Al and Ag). Luminance – current density – voltage (L–J–V) characteristics were determined in ambient atmosphere using a HP 4140B pA meter and a Minolta LS-110 meter. The dwell time for each testing point was 2 s. EL spectra were recorded using a USB2000-UV-VIS Miniature Fiber Optic Spectrometer.

Results and discussion

Syntheses

The synthetic procedures for intermediate **1a** and final products **1** and **2** are depicted in Scheme 1. Intermediate **1a** was obtained by copper-catalyzed Ullmann condensation between benzimidazole and $SiPh_2(p\text{-Br-Ph})_2$ in 31% isolation yield (11). Due to the low reactivity of the bromide starting material, a high reaction temperature of 220 °C was employed. Excess $SiPh_2(p\text{-Br-Ph})_2$ was used to reduce the formation of di-substituted by-product. Palladium-catalyzed Suzuki–Miyaura cross-coupling between 1-pyrenylboronic acid and **1a** afforded product **1** in 65% yield (12). Similarly, product **2** was obtained from 1-pyrenyl boronic acid and $SiPh_2\{p\text{-}[(N\text{-}(1\text{-naph})Ph]Ph\}(p\text{-Br-Ph})$ via Suzuki–Miyaura cross-coupling in 55% yield.

Physical and electronic properties

Compounds **1** and **2** are stable in solution and the solid state upon extended exposure to air. DSC measurements were carried out to assess the thermal properties of both compounds. As shown in Fig. 1, compound **2** has a glass transition temperature at 110 °C, indicating that it is capable of forming an amorphous phase. The fact that the glass transition is observable after many repeated heating and cooling cycles confirms its excellent morphological and thermal stability, which can be attributed to the presence of the NPh(1-naph) moiety as well as the tetrahedral silicon core. A decomposition temperature of 500 °C from TGA measurement further confirms the outstanding thermal stability of **2**. **1** displays a decomposition temperature ~290 °C, but no glass transition temperature was observed.

Both **1** and **2** exhibit intense absorption bands at $\lambda >$ 380 nm with distinct pyrene features (see Supplementary Data).[2] In addition, the spectra of **1** and **2** have a distinct low-energy absorption band at $\lambda_{max} \approx 350$ nm, which can

[2] Supplementary data for this article are available on the journal Web site (canjchem.nrc.ca) or may be purchased from the Depository of Unpublished Data, Document Delivery, CISTI, National Research Council Canada, Ottawa, ON K1A 0R6, Canada. DUD 3709. For more information on obtaining material refer to cisti-icist.nrc-cnrc.gc.ca/irm/unpub_e.shtml.4

© 2008 NRC Canada

Fig. 1. DSC diagrams of **2**.

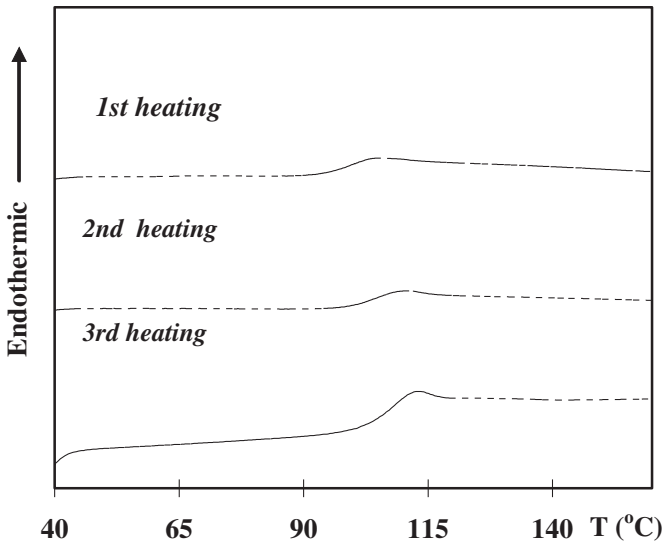

Fig. 2. CV diagrams of **2** and NPB.

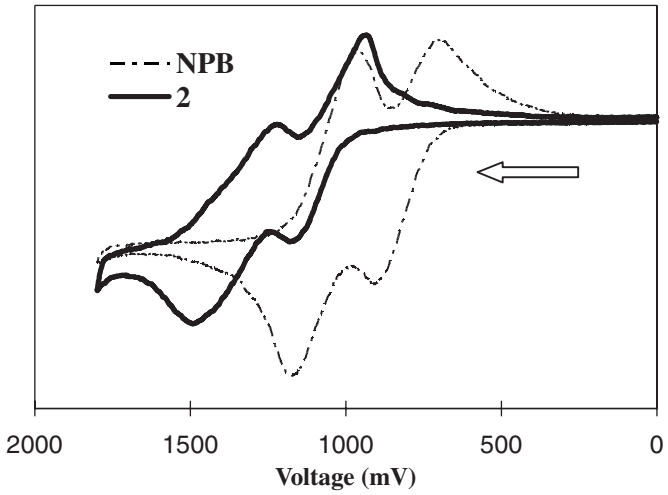

be attributed to the benzimidazolyl group in **1** and the N(1-naph)Ph group in **2**. The redox potentials for **1** and **2** were obtained from cyclic voltammetry measurements. As shown in Fig. 2, there are two reversible oxidation peaks for **2** in CH_2Cl_2. Compared to the CV diagram of (1-naph)PhN-biphenyl-NPh(1-naph), NPB, the first oxidation peak at $E^{1/2}$ = ~1.04 V is assigned to the oxidation of the nitrogen center of the NPh(1-naph) group and the second oxidation peak at $E^{1/2}$ = ~1.36 V to the pyrene ring. No reduction peak was observed for **2** within the range of the solvent limit. In contrast, compound **1** displays an irreversible oxidation peak at E^{p} = ~1.50 V, corresponding to the oxidation of the pyrene ring and a quasi-reversible reduction peak at $E^{1/2}$ ~–1.2 V, which can be assigned to the reduction of the benzimidazolyl moiety. Using the oxidation potentials and the optical energy gaps obtained from the UV–vis absorption edge, the HOMO and LUMO energies were estimated and are provided in Table 1.

The luminescent data for **1** and **2** are summarized in Table 2. Both compounds are blue luminescent as shown in

Table 1. HOMO and LUMO energies of **1** and **2**.

Compound	HOMO[a] (eV)	LUMO[b] (eV)	Optical energy gap (eV)
1	–5.86	–2.76 (–3.10)[c]	3.10
2	–5.36	–2.24	3.12

[a]From the oxidation potential in CH_2Cl_2 ($E^{1/2}$ for $FeCp_2^{0/+}$ = 0.50 V).
[b]From the optical energy gap and the HOMO energy.
[c]From the reduction potential in THF ($E^{1/2}$ for $FeCp_2^{0/+}$ = 0.50 V).

Figs. 3 and 4. In solution, the emission spectrum of **1** does not change significantly with solvent polarity, wheras compound **2** shows solvent-dependant emission, and the Stokes shift of **2** was found to have a linear relationship with the polarity of the solvent (see Supplementary Data), an indication that the emission of **2** originates from intramolecular charge transfer (9, 13).[2] The emission spectra for both compounds in the solid state are considerably red-shifted to the blue region compared with the solution spectra, with λ_{max} = 440 nm for **1** and 455 nm for **2**. Quantum efficiency in CH_2Cl_2 was found to be 0.95 for **1** and 0.83 for **2**, confirming that both are highly emissive in solution. Many blue emitters such as 9,10-diphenylanthracene are known to have a high quantum efficiency in solution. Most of them, however, have much diminished emission quantum efficiencies in the solid state because of strong intermolecular interactions (14). In contrast, the new pyrenyl-containing silicon compounds **1** and **2** maintain a high quantum efficiency in the solid state with Φ = 0.58 for **1** and 0.72 for **2**, respectively. The tetrahedral silicon backbone in **1** and **2** is believed to play a key role in reducing intermolecular interactions in the solid state, thus effectively blocking intermolecular energy-transfer pathways, reducing luminescent quenching, and leading to high emission efficiency in the solid state.

Molecular orbital calculations

Molecular orbital calculations were performed to further understand the electronic and luminescent properties of compounds **1** and **2**. Geometric parameters were obtained from molecular modeling and geometric optimization. The Gaussian suite of programs (Gaussian 98) (15) was employed for the calculations, which were performed with the B3LYT 6–311G** basis set for both compounds. As shown in Fig. 5, both HOMO and LUMO levels for **1** involve orbital contributions from the pyrenyl-phenyl group only. Hence, the lowest electronic transition for **1** should be a π–π * transition centered on the pyrenyl-phenyl group. In contrast, the HOMO level of **2** has contributions nearly exclusively from the π orbitals of the *p*-[*N*(1-naph)ph]phenyl group and its LUMO consists of contributions exclusively from the π* orbitals of pyrenyl-phenyl group. As a result, the lowest electronic transition in **2** is likely charge-transfer from the phenyl-N(naph)Ph group to the pyrenyl-phenyl group, consistent with the observed solvent-dependent emission. The difference between **1** and **2** can be explained by the electron-withdrawing nature of the benzimidazolyl group, which reduces its energy level below that of the pyrene group (HOMO) in **1**. In both compounds, the silicon center is not involved in either HOMO or LUMO; therefore

© 2008 NRC Canada

Table 2. Absorption and luminescent data.

Compd.	UV–vis absorption (nm)	Excitation (nm)	Emission (nm)	Quantum yield (%)	Conditions (298 K)
1	282, 346	280, 349	396	95	CH_2Cl_2
		378	440	58	Thin film
2	282, 346	282, 347	427	83	CH_2Cl_2
		369	455	72	Thin film

Fig. 3. Emission spectra of **1** in various solvents and as neat film.

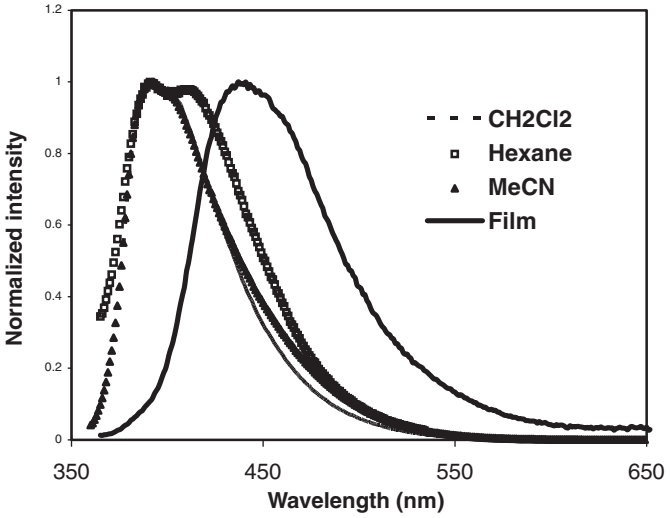

Fig. 4. Emission spectra of **2** in various solvents and as neat film.

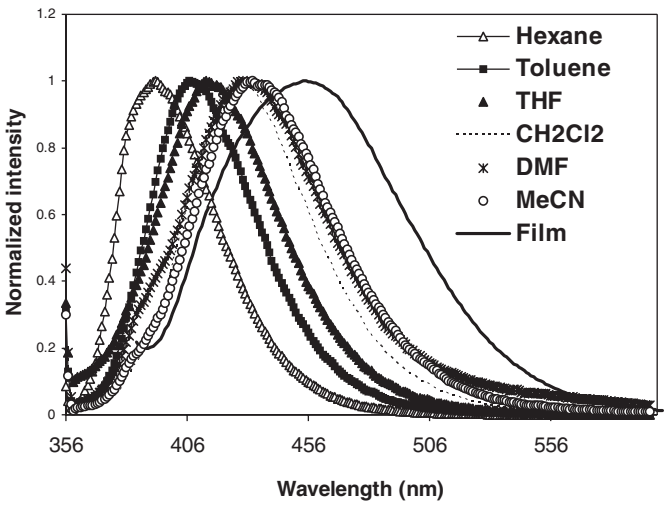

the charge transfer emission in **2** most likely occurs in a through-space manner.

Electroluminescence

Although **1** and **2** are both highly efficient blue emitters, they are expected to display different charge transfer properties. Compound **1** is expected to perform as an electron transport layer (ETL) because of its deep LUMO and HOMO levels and the electronegative nature of the benzimidazolyl ring. In fact, the benzimidazolyl group is responsible for the electron transport property of the well-known electron transport molecule TPBI (16). In contrast, compound **2** is expected to function as either a hole-transport (HTL) or hole-injection material because of its relatively high HOMO level and the presence of the well-known hole-transport group Nph(1-naph) (17). Based on these considerations, a series of devices was fabricated to evaluate the EL performance of **1** as an electron-transport blue emitter and **2** as a hole-transport blue emitter in OLEDs. The device structures and data are presented in Table 3.

Devices A–D were fabricated to evaluate the performance of **1**. Other materials used for these devices include CuPc as the hole-injection layer (HIL), NPB as HTL, and BCP (2,9-dimethyl-4,7-diphenyl-1,10-phenanthroline) and Alq_3 as ETL. Devices A, B, and C employ **1** as the emitter with either Alq_3 or BCP as the ETL. These three devices all produced bright blue emission with the EL maximum (440 nm) matching the PL maximum of **1** (440 nm) very well (Fig. 6), with good color purity (C.I.E. 0.15, 0.14) and maximum brightness up to 3102 cd/m^2, confirming that **1** can indeed function as an efficient blue emitter in OLEDs. Interestingly, the inclusion of CuPc as HIL resulted in a lower maximum brightness and a higher turn-on voltage, as revealed by the performance of devices A and B. Similar phenomena have been noted by Chen et al. (18). Alq_3 appears to be a better ETL than BCP in these devices, based on the performance of devices B and C. Device D has the simplest structure where no conventional ETL material is used and compound **1** is used as both a blue emitter and an ETL layer. Most interestingly, however, as shown in Figs. 7 and 8, device D delivered the best EL performance with the highest maximum brightness of 3562 Cd/m^2 at 8 V and the lowest turn-on voltage at 3.2 V, which unambiguously established the bifunctionality of **1** as both a blue emitter and an effective electron-transport material. The outstanding performance of **1** as an electron-transporting blue emitter can be attributed to its high emission quantum efficiency and to the low LUMO level (–2.76 eV from absorption edge and the oxidation potential or –3.10 eV from the reduction potential). This level is close or comparable to that of TPBI (16), thus facilitating electron injection from the cathode (device D) or the ETL layer to the molecule (device A, B, C). Although the brightness and the device efficiency of D is not yet as good as some of the blue OLEDs known in literature (5), the simplicity of the device structure and the lack of exciplex emission still make compound **1** a very promising new bifunctional material for OLEDs. With further structural optimization, it is very likely that the performance of the device can be further enhanced.

© 2008 NRC Canada

Fig. 5. MO diagrams of **1** and **2**.

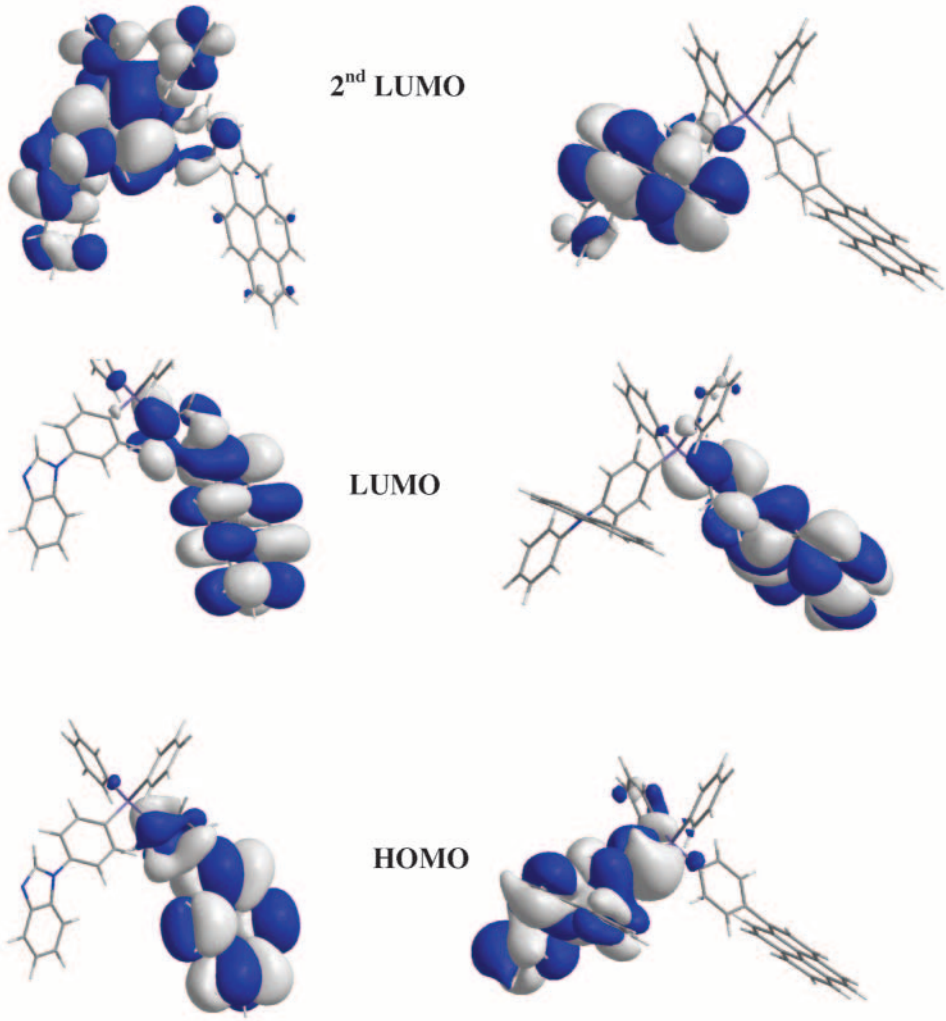

Table 3. Electroluminescent data.

	Structure (thickness, nm)	Turn-on voltage (V)	Max. L (Cd/m^2)	Max. efficiency (Cd/A)/(lm/W)
A	CuPc(25)/NPB(45)/**1** (20)/Alq_3 (20)	3.8	2665	0.6/0.5
B	NPB(60)/**1**(20)/Alq_3(20)	3.4	3102	0.7/0.5
C	NPB(60)/**1**(20)/BCP(20)	3.6	2190	0.8/0.4
D	CuPc(25)/NPB(45)/**1** (40)	3.2	3562	0.9/0.7
E	CuPc(50)/**2** (50)/Alq_3(40)	10	4.8	0.1/0.1
F	NPB(50)/**2**(50)/Alq_3(40)	7.5	388	0.9/0.6
G	**2** (50)/NPB(50)/Alq_3(40)	4.8	16 650	4.6/2.3
H	CuPc(50)/NPB(50)/Alq_3(40)	3.0	19 720	4.1/3.3

Devices E–H were constructed to evaluate the performance of compound **2**. Devices E and F are similar in structure to devices A and B where the silicon compound was intended to function as a blue emitter (F) or a hole-transport blue emitter (E). However, in contrast to the blue-emitting devices A and B, devices E and F produced green emission that is typical of Alq_3, an indication that compound **2** is not an effective blue emitter in these devices, perhaps because of the poor electron transport ability of **2**. Nonetheless, as shown by the performance of devices G and H (Figs. 9 and 10), compound **2** can perform as a very efficient HIL with similar maximum brightness to the most commonly used HIL, CuPc. Although the operating voltage of device G, where **2** is used as the HIL, is much higher than that of the CuPc device H, at low brightness device G has an excellent current efficiency. Furthermore, compared with CuPc which has considerable absorption in the red region (19), **2** is transparent over the entire visible region, making it attractive as a colorless HIL material for full-color OLED devices.

In summary, two bifunctional organosilicon compounds,

© 2008 NRC Canada

Fig. 6. EL of devices A–D and PL of **1**.

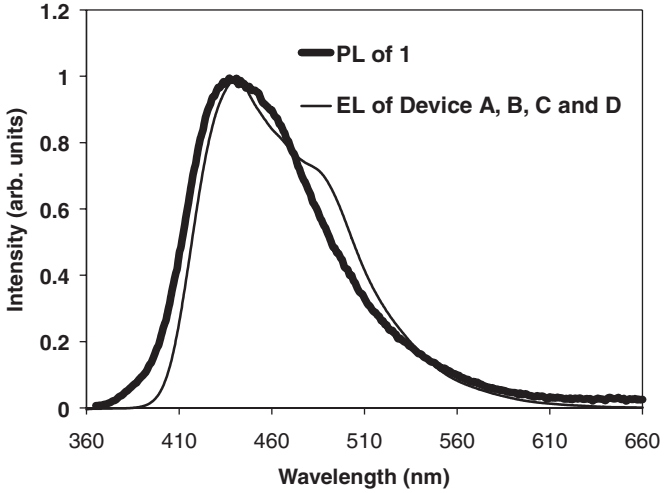

Fig. 7. L-V diagrams of devices A–D.

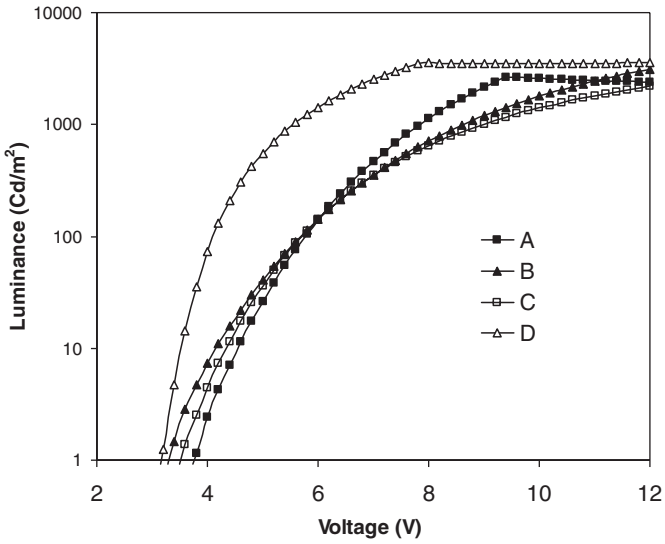

Fig. 8. Current efficiency diagrams of devices A–D.

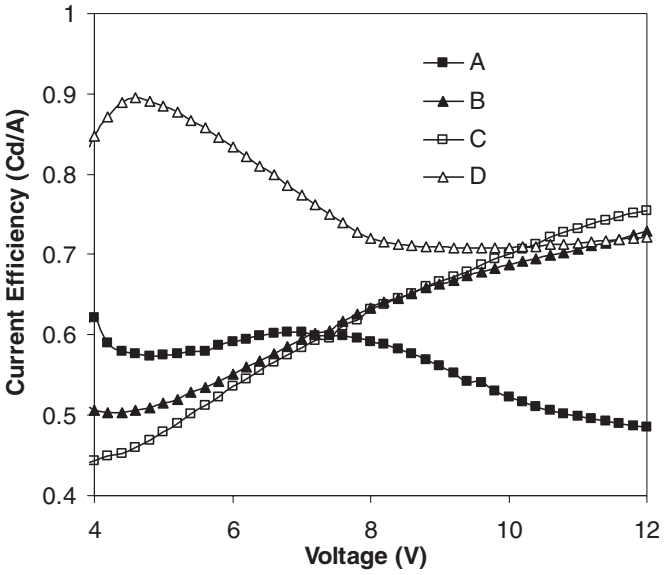

Fig. 9. L-V and J-V diagrams for devices H and G.

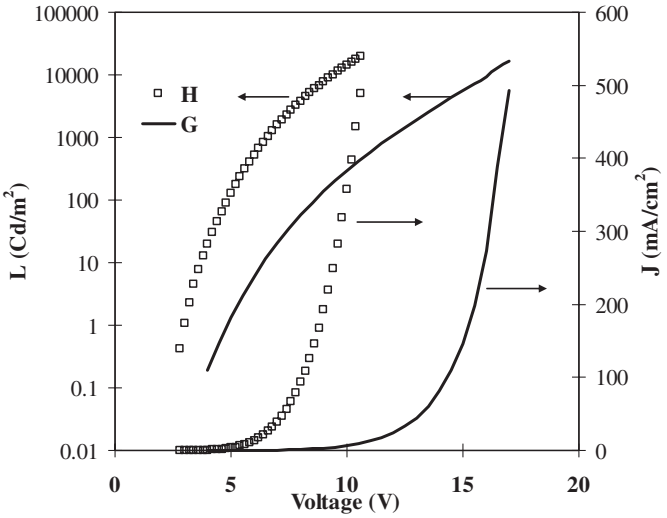

Fig. 10. Current and power efficiency diagrams of devices H and G.

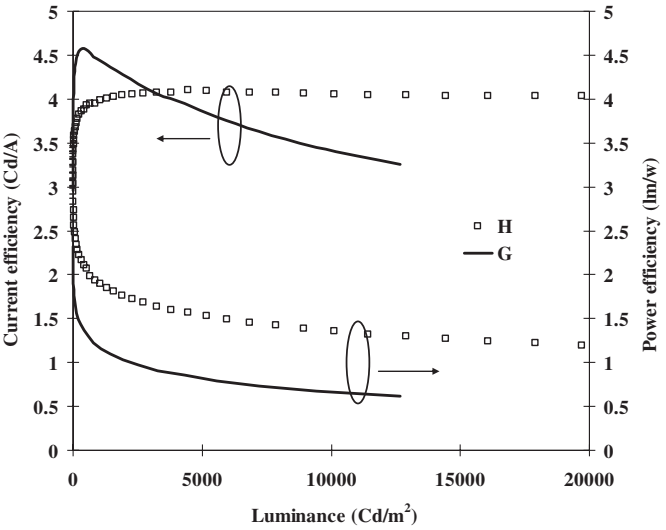

with a tetraphenylsilane core, a pyrene functional group, and either a hole-transport group NPh(1-naph) or an electron-transport benzimidazolyl group, were synthesized. Although both compounds display bright blue photoluminescence, only the molecule that bears the benzimidazolyl group was found to function as an efficient blue emitter as well as a bifunctional electron-transporting blue emitter in OLEDs. The molecule that contains the hole-transporting group NPh(1-naph) was demonstrated to be effective as a hole-injection material, in conjunction with the hole-transport material NPB.

Acknowledgment

We thank the Natural Sciences and Engineering Research Council of Canada for financial support.

© 2008 NRC Canada

References

1. (*a*) C.W. Tang and S.A. VanSlyke. Appl. Phys. Lett. **51**, 913 (1987); (*b*) U. Mitschke and P. BaÈuerle, J. Mater. Chem. **10**, 1471 (2000).
2. H. Aziz and Z.D. Popovic. Chem. Mater. **16**, 4522 (2004).
3. S.-W. Wen, M.-T. Lee, and C.H. Chen. J. Display Technol. **1**, 90 (2005).
4. (*a*) H.C. Yeh, R.H. Lee, L.H. Chan, T.Y.J. Lin, C.T. Chen, E. Balasubramaniam, and Y.T. Tao. Chem. Mater. **13**, 2788, (2001); (*b*) H.C. Yeh, L.H. Jan, R. Lee, and C.T. Chen. *In* Proceedings of SPIE, Organic light-emitting materials and devices IV. Vol. 4105. 2001. p. 348.
5. (*a*) R.H. Lee, H.F. Hsu, L.H. Chan, and C.T. Chen. Polymer, **47**, 7001 (2006); (*b*) L.H. Chan, R.H. Lee, C.F. Hsieh, H.C. Yeh, and C.T. Chen. J. Am. Chem. Soc. **124**, 6469 (2002); (*c*) L.H. Chan, H.C. Yeh, and C.T. Chen. Adv. Mater. **13**, 1637 (2001).
6. (*a*) Q.-D. Liu, M.S. Mudadu, R. Thummel, Y. Tao, and S. Wang. Adv. Funct. Mater. **15**, 143 (2005); (*b*) W.L. Jia, X.D. Feng, D.R. Bai, Z.H. Lu, S. Wang, and G. Vamvounis. Chem. Mater. **17**, 164 (2005); (*c*) W.L. Jia, T. McCormick, Q.D. Liu, H. Fukutani, M. Motala, R.Y. Wang, Y. Tao, and S.N. Wang. J. Mater. Chem. **14**, 3344 (2004); (*d*) W.L. Jia, D.R. Bai, T. McCormick, Q.D. Liu, M. Motala, R.Y. Wang, C. Seward, Y. Tao, and S. Wang. Chem. Eur. J. **10**, 994 (2004).
7. H. Antoniadis, M.A. Abkowitz, and B.R. Hsieh. Appl. Phys. Lett. **65**, 2030 (1994).
8. D.R. Bai and S. Wang. Organometallics, **23**, 5958 (2004).
9. D.R. Bai, X. Liu, and S. Wang. Chem. Eur. J. **13**, 5658 (2007).
10. (*a*) N.J. Demas and G.A. Crosby. J. Am. Chem. Soc. **29**, 7262 (1970); (*b*) I.B. Berlman. Handbook of fluorescence spectra of aromatic molecules. Academic Press, New York. 1971.
11. A. Klapars, J.C.Antilla, X. Huang, and S.L. Buchwald. J. Am. Chem. Soc. **123**, 7727 (2001).
12. (*a*) N. Miyaura. Adv. Met.-Org. Chem. **6**, 187 (1998) and refs. cited therein; (*b*) A. Suzuki. J. Organomet. Chem. **576**, 147 (1999) and refs. cited therein.
13. P. Suppan and N. Ghoneim. Solvatochromism. The Royal Society of Chemistry, Cambridge, UK. 1997.
14. J.R. Lakowicz. Principles of fluorescence spectroscopy. 2nd ed. Kluwer Academic Plenum Publishers, New York. 1999.
15. M.J. Frisch, G. W. Trucks, H. B. Schlegel, G. E. Scuseria, M. A. Robb, J. R. Cheeseman, V. G. Zakrzewski, J. A. Montgomery, Jr., R. E. Stratmann, J. C. Burant, S. Dapprich, J. M. Millam, A. D. Daniels, K. N. Kudin, M. C. Strain, O. Farkas, J. Tomasi, V. Barone, M. Cossi, R. Cammi, B. Mennucci, C. Pomelli, C. Adamo, S. Clifford, J. Ochterski, G. A. Petersson, P. Y. Ayala, Q. Cui, K. Morokuma, D. K. Malick, A. D. Rabuck, K. Raghavachari, J. B. Foresman, J. Cioslowski, J. V. Ortiz, A. G. Baboul, B. B. Stefanov, G. Liu, A. Liashenko, P. Piskorz, I. Komaromi, R. Gomperts, R. L. Martin, D. J. Fox, T. Keith, M. A. Al-Laham, C. Y. Peng, A. Nanayakkara, C. Gonzalez, M. Challacombe, P. M. W. Gill, B. G. Johnson, W. Chen, M. W. Wong, J. L. Andres, M. Head-Gordon, E. S. Replogle and J. A. Pople. GAUSSIAN 98 Revision A.06 [computer program]. Gaussian Inc., Pittsburgh, PA. 1998.
16. (*a*) Z. Gao, C.S. Lee, I. Bello, S.T. Lee, R.M. Chen, T.Y. Luh, J. Shi, and C.W. Tang. Appl. Phys. Lett. **74**, 865 (1999); (*b*) T.D. Anthopoulos, J.P.J. Markham, E.B. Namdas, I.D.W. Samuel, S.C. Lo, and P.L. Burn. Appl. Phys. Lett. **82**, 4824 (2003); (*c*) H.T. Shih, C.H. Lin, H.H. Shih, and C.H. Cheng. Adv. Mater. **14**, 1409 (2002).
17. B.E. Koene, D.E. Loy, and M.E. Thompson. Chem. Mater. **10**, 2235 (1998).
18. R.H. Lee, H.C. Yeh, L.H. Chan, and C.T. Chen. Synth. Met. **137**, 1035 (2003).
19. Y. Yuan, D. Grozea, S.J. Han, and Z.H. Lu. Appl. Phys. Lett. **85**, 4959 (2004).

© 2008 NRC Canada

An unexpected elimination product leads to 4-alkyl-4-deoxy-4-*epi*-sialic acid derivatives

Ivan Hemeon and Andrew J. Bennet

Abstract: A useful, unexpected β,γ-unsaturated-α-keto ester (ethyl (*E*)-5-acetamido-3,4,5-trideoxy-6,7:8,9-di-*O*-isopropylidene-D-*manno*-non-3-en-2-ulosonate **5**) was isolated in 91% yield following ozonolysis and chromatographic purification of its enoate ester precursor ethyl 5-acetamido-2,3,4,5-tetradeoxy-6,7:8,9-di-*O*-isopropylidene-2-methylene-4-nitro-D-*glycero*-D-*galacto*-nononate (**6**). When the 4*R* enoate ester (ethyl 5-acetamido-2,3,4,5-tetradeoxy-6,7:8,9-di-*O*-isopropylidene-2-methylene-4-nitro-D-*glycero*-D-*talo*-nononate, **7**) was subjected to the same conditions, enone **5** was a minor product (18%) while the major product did not eliminate HNO_2 but instead cyclized to form a five-membered ring containing a hemiaminal linkage between C-2 and the amide nitrogen on C-5 (**9**, 70%). Conjugate addition to enone **5** opens up the potential to generate 4-substituted sialic acid derivatives, a general route to such compounds that has not been previously reported. In a preliminary investigation of such a route, diethylzinc and dimethylzinc were added to enone **5** resulting in generation of 4-alkyl-substituted cyclic hemiaminal structures **11** and **13**, which could be deprotected to form 2,7-anhydrosialic acid analogues **14** and **15**. These products could then be converted to peracetylated glycals **16** and **17**, the 4-methyl-substituted compound **17** being finally deprotected to give a 4-methyl-substituted analogue of the glycal of sialic acid (5-acetamido-2,6-anhydro-3,4,5-trideoxy-4-methyl-D-*glycero*-D-*talo*-non-2-enonic acid **18**).

Key words: conjugate addition, dialkylzinc reagent, sialic acid, ozonolysis, inhibitors.

Résumé : À la suite de l'ozonolyse et la purification de son précurseur, l'ester énoate 5-acétamido-2,3,4,5-tétradésoxy-6,7:89-di-*O*-isopropylidène-2-méthylène-4-nitro-D-*glycéro*-D-*galacto*nononate d'éthyle (**6**), on a isolé avec un rendement de 91% le (*E*)-5-acétamino-3,4,5-tridésoxy-6,7:8,9-di-*O*-isopropylidène-D-*manno*-non-3-én-2-ulosonate d'éthyle (**5**), un α-cétoester β,γ-insaturé utile et inattendu. Lorsqu'on soumet l'ester énoate 4*R* [5-acétamino-2,3,4,5-tétradésoxy-6,7:8,9-di-*O*-isopropylidène-2-méthylène-4-nitro-D-*glycéro*-D-*tallo*-nononate d'éthyle (**7**)], aux même conditions, l'énone **5** n'est qu'un produit mineur (18%) alors que le produit majeur n'élimine pas de HNO_2, mais conduit plutôt à un produit de cyclisation comportant un cycle à cinq chaînons et une liaison hémiaminale entre le C-2 et l'azote de l'amide en C-5 (**9**, 70%). Une addition conjuguée sur l'énone **5** donne la possibilité de généré des dérivés de l'acide sialique substitués en position 4 pour lesquels aucune voie de synthèse générale n'avait été proposée antérieurement. Dans une étude préliminaire de cette route, l'addition de diéthylzinc et de diméthylzinc à l'énone **5** conduit à la formation des structures hémiaminales cycliques **11** et **13** portant des substituants alkyles en position 4 qui peuvent être déprotégées pour conduire aux analogues **14** et **15** de l'acide 2,7-anhydrosialique. Ces produits peuvent ensuite être convertis en glycals peracétylés **16** et **17**, le composé 17 portant un groupe méthyle en position 4 étant finalement déprotégé pour fournir un analogue substitué en position 4 de l'acide sialique, l'acide 5-acétamido-2,6-anhydro-3,4,5-didésoxy-4-méthyl-D-*glycéro*-D-*talo*-non-2-énonique, **18**.

Mots-clés : addition conjuguée, réactif dialkylzinc, acide sialique, ozonolyse, inhibiteurs.

[Traduit par la Rédaction]

Introduction

Sialic acid (*N*-acetylneuraminic acid, **1**) is a nine-carbon sugar that is often found α-ketosidically linked to the termini of oligosaccharides on glycoconjugates (1). These linkages can be hydrolyzed by sialidases (neuraminidases, EC 3.2.1.18). Because of their terminal locations on glycoconjugates, sialic acid and the proteins that recognize it are important in many biological events, including cell recognition and pathogen infectivity (1, 2). For instance, influenza virus sialidase activity is critical for viral proliferation (3). The virus first recognizes and binds to sialic acid residues on the surfaces of host-cell glycoconjugates in the upper respiratory tract, an event that initiates the infection cycle. After replication, the newly formed virus particles emerge from the infected cell and become coated in cellular sialic acids that cause the virus particles to clump together. The influenza sialidase then cleaves bound sialic acid residues and thus allows the virus particles to move freely to infect further cells. As a consequence, inhibitors of this enzyme, which include the glycal of sialic acid, 2-deoxy-2,3-didehydro-*N*-acetylneuraminic acid (DANA, **2**) and its 4-guanidinyl derivative

Received 3 November 2007. Accepted 21 December 2007. Published on the NRC Research Press Web site at canjchem.nrc.ca on 19 February 2008.

I. Hemeon and A.J. Bennet.[1] Department of Chemistry, Simon Fraser University, 8888 University Drive, Burnaby, BC V5A 1M5, Canada.

[1]Corresponding author (e-mail: bennet@sfu.ca).

 doi:10.1139/V08-006 © 2008 NRC Canada

Fig. 1. Sialic acid (Neu5Ac, **1**) and structurally similar sialidase inhibitors (**2**–**4**).

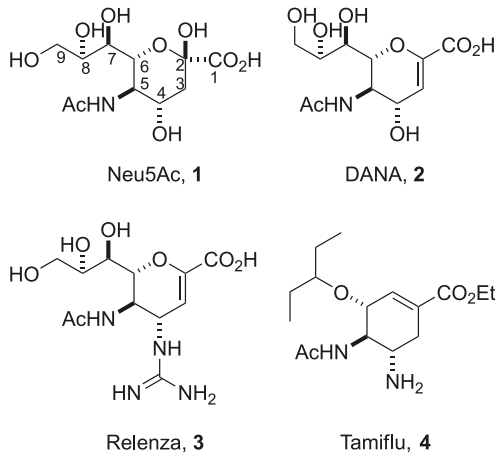

that is marketed as Relenza™ (**3**), are useful biological tools (Fig. 1) (3).

It is important to be able to synthesize analogues of sialic acid to generate selective inhibitors of sialic acid-metabolizing enzymes, which can also be used as probes of the biological pathways. It is therefore advantageous to have access to general synthetic routes that can lead to a number of derivatives for the generation of compound libraries. While there are several positions that can be varied on sialic acid and many derivatives have been made (3, 4), carbon 4 remains a target for derivatization. This is partly due to the fact that variation at this position is tolerated by influenza sialidase as shown by the successful development of 4-substituted sialic acid analogues as influenza sialidase inhibitors, such as Relenza™ (**3**) and Tamiflu™ (**4**) bearing 4-guanidinyl and 4-amino substituents, respectively (Fig. 1) (5, 6).

Design of a general route to 4-modified sialic acid analogues is synthetically challenging. Sialic acid analogues can be made chemoenzymatically using sialic acid aldolase (*N*-acylneuraminate pyruvate lyase, EC 4.1.3.3), which catalyzes the nucleophilic attack of pyruvate on the aldehyde carbon of *N*-acetylmannosamine to form sialic acid. This enzyme is fairly promiscuous with respect to its specificity toward various aldose units, and it can thus be used to make many sialic acid analogues; however, a hydroxyl group is mandatorily installed at the 4-position in the resulting addition product (7). As well, many chemical synthetic routes involve nucleophilic attack of a three-carbon moiety on an aldose carbonyl group, also installing a 4-hydroxyl group (8–10).

While several 4-substituted sialic acid analogues have been synthesized (4), many of these substituents had to be incorporated early in the synthetic route giving intermediate compounds with limited synthetic versatility. Several 4-substituted sialic acid analogues had been synthesized from a common 4-oxo intermediate by Zbiral and co-workers in which the 4-hydroxyl group had been oxidized to a ketone. This could be reduced to give 4-*epi*-sialic acid (11), undergo addition of a nucleophilic methyl group to generate both diastereomers of the 4-methyl addition product (12) and be transformed into the 4-*C*-methylene derivative (12). The 4-*C*-methylene derivative could be reduced to give two 4-epimers of 4-deoxy-4-methylsialic acid (12) and was converted into an epoxide by von Itzstein and co-workers that could be opened with various nucleophiles to generate 4-disubstituted sialic acids (13). As well, several modifications at the 4-position of DANA (**2**) have been made from a common oxazoline intermediate resulting from the $BF_3{\cdot}OEt_2$-promoted displacement of a 4-acetyl group by the carbonyl oxygen of the neighbouring 5-acetamido group. This oxazoline intermediate has been hydrogenated to give 4-deoxy-DANA, hydrolyzed to give 4-*epi*-DANA, and opened with azide to give 4-azido-4-deoxy-DANA that was reduced to 4-amino-4-deoxy-DANA and then transformed into 4-formamido- and 4-acetamido-substituted 4-deoxy-DANA analogues (14). The oxazoline intermediate has also been opened with halogens to generate allylic halides (15), which have been used in palladium(0)-mediated couplings with organotin reagents to install unsaturated functional groups at the 4-position (16). Although these intermediates are useful for synthesizing 4-modified sialic acid analogues, the number of such analogues that can be generated is limited.

Recently, the synthesis of 4-deoxy-4-nitrosialic acid was reported (17), and during the course of that study, an unexpected β,γ-unsaturated-α-keto ester (**5**) was isolated following the ozonolysis of enoate ester **6**. The results described herein report the investigation into this elimination reaction and the use of this enone in conjugate addition reactions for the installation of different substituents at the 4-position in sialic acid analogues.

Results and discussion

Isolation of β,γ-unsaturated α-keto ester 5

A diastereomeric mixture of isopropylidene-protected enoate esters **6** and **7** was synthesized in six steps from D-arabinose as previously reported (17). The intention was to cleave the methylene group of **6** through ozonolysis to install the α-keto ester moiety (**8**), which would allow the molecule to cyclize to the pyranose structure of sialic acid upon removal of the isopropylidene protecting groups. The initial ozonolysis was performed solely on the 4*S* enoate ester **6** rather than on the diastereomeric mixture of **6** and **7** to reduce the complexity of product identification. However, the only product isolated from the reaction, following chromatographic purification, was the β,γ-unsaturated-α-keto ester **5** in 91% yield resulting from oxidative cleavage of the methylene group and elimination of HNO_2 across carbons 3 and 4 (Scheme 1). IR, ^{1}H NMR, and ^{13}C NMR spectra supported the structure of enone **5** because of the presence of signals in the vinylic regions of the NMR spectra, a ketone in the ^{13}C NMR spectrum, and the absence of nitro stretching bands in the IR spectrum. The *trans*-geometry of the double bond was assigned based on the large H3/H4 coupling constant ($J_{3,4}$ = 15.9 Hz).

Isolation of enone **5** was an unexpected result, as no base is present during the ozonolysis of **6** that could effect such an elimination. It was reasoned that the elimination must be occurring post-ozonolysis because if the elimination occurred during ozonolysis, the newly-formed double bond would also be cleaved. The ozonolysis was repeated in the presence of acetic acid to neutralize any possible base generated during the reaction, but enone **5** was again the sole product isolated. Carrying out the ozonolysis in a 1:1

© 2008 NRC Canada

Scheme 1. Ozonolysis of 4*S* enoate ester **6** leads exclusively to unstable α-keto ester **8** that eliminates to enone **5** upon silica chromatography or treatment with DBU, while ozonolysis of 4*R* enoate ester **7** leads predominantly to hemiaminal **9**.

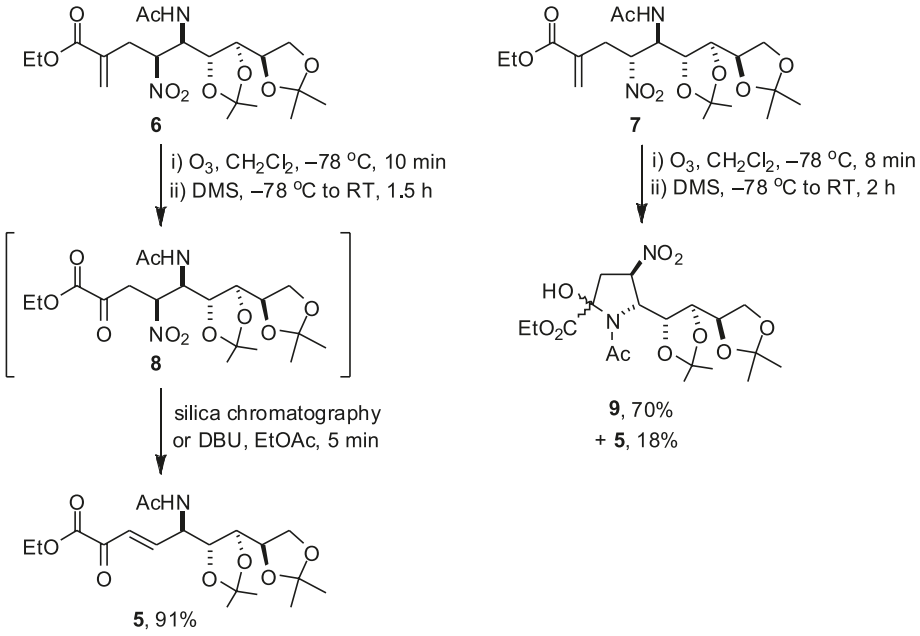

dichloromethane/methanol solvent mixture or using triphenylphosphine as a reducing agent in place of methyl sulfide also had no effect on the reaction outcome.

It was noticed that very little enone was present in the crude ozonolysis product mixture as judged by ^{1}H NMR spectroscopy. In fact, the major compound present in the crude product mixture appeared to be the α-keto ester **8** that had been originally desired (Scheme 1). No elimination had occurred owing to the absence of vinylic signals in the ^{1}H and ^{13}C NMR spectra, and the IR spectrum showed the nitro group was intact. Upon chromatographic purification on silica gel, however, complete elimination to enone **5** was observed, indicating that the elimination of HNO_2 was silica-induced (Scheme 1). Indeed, this silica-induced elimination was not efficient enough to convert α-keto ester **8** into enone **5** completely on larger scales (**5** and **8** are co-polar); thus, the elimination could be induced by treating the crude α-keto ester **8** with DBU (Scheme 1). It was crucial not to allow this elimination to proceed for extended periods, since complete product decomposition was observed after 15 min. Of note, Yao and co-workers noticed a similar silica-induced elimination when synthesizing an α-keto ester similar to **8** that contained a 4-azido group en route to 4-azido-4-deoxysialic acid; this ester eliminated HN_3 upon chromatographic purification (18). These researchers circumvented the problem by using the 4-azido α-keto ester without purification.

It was later noticed that ozonolysis of diastereomeric mixtures of the enoate esters **6** and **7** resulted in isolation of varying yields of enone **5** that reflected the **6/7** ratio, indicating that only one diastereomer may have eliminated HNO_2. When the 4*R* enoate ester **7** was subjected to ozonolysis by itself, enone **5** was isolated in 18% yield, but the major product, isolated in 70% yield, was a saturated product in which the 5-acetamido nitrogen cyclized onto the newly generated 2-keto group to form two five-membered ring hemiaminal anomers (**9**, Scheme 1). These anomers were observed to interconvert in solution by ^{1}H NMR spectroscopy, but only the major anomer could be isolated in sufficient quantities for adequate characterization. The hemiaminal structure was supported by the disappearance of the amide-proton signal around 6.0 ppm from the ^{1}H NMR spectrum and by the appearance of a singlet at 4.8 ppm that disappeared when a drop of D_2O was added to the $CDCl_3$ solution, corresponding to the new 2-hydroxyl group. In addition, an HMBC spectrum showed a correlation between H-5 and C-2, which would not be possible unless the amide nitrogen was bonded to C-2. As well, the IR spectrum indicated the nitro group was intact.

It therefore appears as though the ozonolysis product of the 4*S* enoate ester **6** prefers to eliminate HNO_2 to give enone **5**, while ozonolysis of the 4*R* enoate ester **7** gives rise to a product that cyclizes to a five-membered ring hemiaminal **9** (Scheme 1). Fortunately, the 4*R* enoate ester **7** could be epimerized to a 3:2 mixture of **6**/**7** that was separable by chromatography by treatment with DBU in THF for 40 min, allowing the conversion of **7** to the synthetically useful 4*S* enoate ester **6**. Interestingly, when enoate ester **6** does not have isopropylidene protecting groups, no elimination occurs after ozonolysis; the product spontaneously cyclizes to the sialic acid pyranose (17). This, in addition to the fact that the ozonolysis product of the 4*R* enoate ester **7** prefers to cyclize to a hemiaminal, suggests the possibility that cyclization is faster than elimination for these compounds and elimination is prohibited following cyclization. While the reasons for these differences in reactivity are not apparent, it appears as though something prevents or dramatically slows down cyclization of **8** to a hemiaminal structure, allowing it to undergo facile HNO_2 elimination.

Conjugate addition reactions with enone 5

Although isolation of enone **5** was initially disappointing,

© 2008 NRC Canada

it was quickly realized that this enone could be a useful synthetic intermediate, since a conjugate addition would afford a sialic acid analogue bearing a new substituent in the 4-position. Indeed, these types of enones have been deliberately synthesized for various purposes. Vasella and co-workers synthesized a similar enone from a protected enoate ester similar to **6**/**7** bearing a 4-*O*-acetyl group, eliminating HOAc with sodium bicarbonate during ozonolysis. They then hydrogenated the resulting double bond, leading to 4-deoxysialic acid (19). Shing also synthesized a related 4-deoxysugar by hydrogenation of such an enone resulting from a Wittig reaction between an aldose and a phosphorus ylide containing an α-keto ester moiety (20). As well, this enone was used in alkoxymercuration reactions resulting in installation of alkoxy groups in the 4-position after reduction of the organomercury intermediate (21). However, literature precedent could not be found for conjugate additions being attempted on such enones.

Introduction of a methyl group was attempted via well-known addition reactions using alkylcopper reagents (22). Several conditions were tried for the conjugate addition of a methyl group to enone **5**, including the following: (*i*) Me_2CuLi from 5 equiv. CuI and 10 equiv. MeLi, warming from –78 °C to room temperature while stirring overnight; (*ii*) Me_2CuLi with TMSCl and $BF_3{\cdot}OEt_2$ as promoters; (*iii*) $Me_2CuMgBr$ from MeMgBr instead of MeLi; and (*iv*) $MeCuBF_3$ prepared from 1 equiv. each of CuI, MeLi, and $BF_3{\cdot}OEt_2$. None of these conditions afforded appreciable quantities of conjugate addition products. Also, 1 equiv. of MeLi was added to enone **5** on one occasion, but no 1,2- or 1,4-addition products were observed, and most of the starting material was recovered, indicating the low reactivity of **5** toward these nucleophiles.

Since the conditions for conjugate addition of alkylcopper reagents to enone **5** seemed to be too harsh, conjugate additions of alkyl halides under radical conditions were attempted. These reactions are normally performed with Bu_3SnH/AIBN in refluxing benzene to generate radicals thermally that are added to α,β-unsaturated carbonyl compounds containing electron-withdrawing groups (23, 24). Initially, benzyl bromide was used as an alkylating agent with Bu_3SnH and AIBN in refluxing toluene. This yielded a complex mixture of products, none of which seemed to have incorporated a benzyl group. The same reagents were tried using a 100 W incandescent light source to generate radicals at room temperature but also gave no addition products. These conditions using a 100 W lamp at room temperature were tried with isopropyl iodide and allyl iodide as alkylating agents to try to generate a stable alkyl radical but resulted in decomposition of the enone. Slow addition of a solution containing Bu_3SnH and AIBN over 1 h via syringe pump to a solution of allyl iodide and enone **5** in toluene at 60 °C was attempted to generate radicals more slowly in hopes that they would react with the enone, but this reaction also failed.

Milder conjugate additions were attempted using a dialkylzinc reagent with a copper catalyst, as alkylzinc reagents are less reactive than their alkylcopper counterparts (25). Alexakis and co-workers have screened a number of copper catalysts for use in conjugate addition reactions with dialkylzinc reagents and found that $Cu(OTf)_2$ was one of the most active, and these reactions were greatly accelerated by the addition of a phosphorus ligand, usually PBu_3 or $P(OEt)_3$ (26, 27). Thus, $Cu(OTf)_2$ and $P(OEt)_3$ were mixed with diethylzinc and enone **5** to give a 53% yield of conjugate addition products (Scheme 2). The initial product in the crude reaction mixture appeared to be a single diastereomer of the enol tautomer **10** as observed by ^1H NMR spectroscopy. It was clear that the ethyl group had added due to the presence of two new signals in the ^1H and ^{13}C NMR spectra, and although H-4 had shifted upfield to 2.8 ppm in the ^1H NMR spectrum, H-3 appeared as a doublet integrating to one proton at 5.5 ppm, indicating that it was a vinylic proton. As well, a singlet was observed at 6.5 ppm that disappeared upon addition of a drop of D_2O to the $CDCl_3$ solution, indicating that this was the enol hydroxyl proton. However, the enol could not be purified for proper characterization, since upon silica chromatography, the product tautomerized to form an anomeric mixture of five-membered ring hemiaminal structures, giving **11** in 53% yield (Scheme 2). As with the 4-nitro hemiaminal **9**, the structure of 4-ethyl hemiaminal **11** was assigned based on the disappearance of the amide proton signal in the ^1H NMR and the appearance of a signal for the new hydroxyl group proton around 4.9 ppm that disappeared when a drop of D_2O was added to the $CDCl_3$ solution. An HMBC spectrum showed a correlation between H-5 and C-2, which further supported the five-membered ring structure. As well, the IR spectrum showed absence of an NH stretching band but did show an OH stretch. As with the 4-nitro hemiaminal **9**, only the major anomer of **11** could be purified for adequate characterization, but the two anomers were observed to interconvert when left for extended periods in $CDCl_3$ solution, indicating that they were indeed anomers and not C4-epimers. Since **11** was a five-membered ring, the stereochemistry of the ethyl addition could be probed through a series of 1D NOE difference ^1H NMR spectra. Upon irradiation of the methylene protons of the newly-installed ethyl group, enhancement of the signals for H-5 and H-3a (on the same face) was observed, while irradiation of H-3b (on the opposite face) only enhanced the signal for H-4. These spectra indicate that H-5 and the new ethyl group are on the same face of the ring, which possesses the 4*R*-configuration. The exclusive formation of the 4*R*-diastereomer is unfortunate, since natural sialosides possess the 4*S*-configuration; however, 4-*epi*-sialic acid derivatives can still be useful inhibitors/probes for various sialic acid processing enzymes (28). While there are several possible explanations for this diastereoselectivity, it is likely that the alkylzinc/alkylcopper complex is coordinating to the acetamido group, thus directing nucleophilic attack from the same face to give *cis*-addition.

Several variables were manipulated to try to increase the yield of the 4-ethyl hemiaminal **11**. Specifically, no reaction was observed when THF was used as a coordinating solvent, and when $BF_3{\cdot}OEt_2$ was used to replace $P(OEt)_3$, no reaction products were afforded in either THF or toluene. Moreover, longer reaction times resulted in the formation of increased amounts of other unidentified products, and the use of larger amounts of diethylzinc did not result in increased product yields. Alexakis and co-workers have observed that α,β-unsaturated esters are less reactive toward copper-catalyzed dialkylzinc conjugate additions (26); thus, the 53% yield of 4-ethyl hemiaminal **11** was considered to be satisfactory.

© 2008 NRC Canada

Scheme 2. Conjugate addition of diethylzinc and dimethylzinc to enone **5**, initially affording enol products **10** and **12** that rearrange to five-membered ring hemiaminals **11** and **13** upon chromatography.

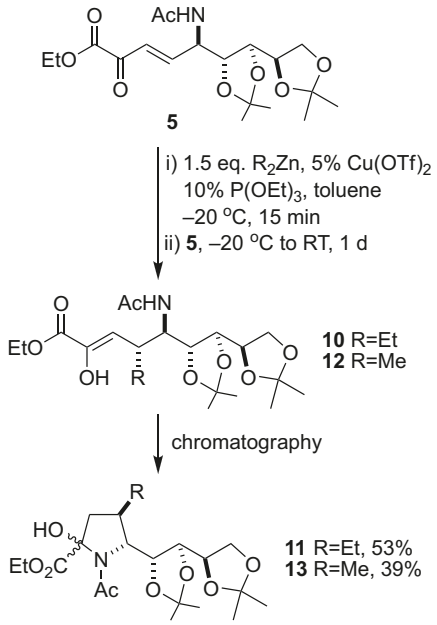

The scope of the copper-catalyzed conjugate addition to enone **5** was examined by testing other dialkylzinc reagents. Commercially available dimethylzinc was added, which also afforded a single diastereomer of the conjugate addition product as its enol tautomer **12** that rearranged to the five-membered ring hemiaminal structure during silica chromatography to give **13** in 39% yield (Scheme 2). Lower product yields were expected, since dimethylzinc is known to be less reactive than diethylzinc (29). The 4-methyl hemiaminal **13** exhibited similar spectral characteristics to its ethyl homologue **11**; notably, a series of 1D NOE difference ^{1}H NMR spectra showed that **13** also had the 4*R*-configuration. Also similarly, the 4-methyl hemiaminal product was obtained as an interconverting mixture of anomers of which only the major anomer could be purified for adequate characterization although NMR spectra were obtained on the minor anomer.

Attempts to perform conjugate addition reactions were made using other alkylzinc reagents that had been synthesized. Benzyl zinc bromide was generated by stirring benzyl bromide with zinc dust in toluene at room temperature for 6 h (30, 31), but it afforded no conjugate addition products when reacted with enone **5** under the standard conditions despite giving a 26% yield of 3-benzylcyclohexanone when reacted with a model enone (2-cyclohexen-1-one). Dibenzylzinc was synthesized by zinc-halogen exchange from the reaction of 1 equiv. dimethylzinc with 2 equiv. benzyl bromide in toluene at –30 °C for 45 min (25, 32). When this was added to 2-cyclohexen-1-one, a 22% yield of 3-benzyl-2-methylcyclohexanone was isolated, as the enolate resulting from the dibenzylzinc conjugate addition was trapped by the in situ generated methyl bromide (33). Despite the generation of electrophilic methyl bromide during the synthesis of dibenzylzinc, these conditions were used with enone **5** but only afforded a very small amount of 4-methyl hemiaminal **13**, likely resulting from addition of unreacted dimethylzinc. The synthesis of diphenylzinc through transmetallation was accomplished by reacting 2 equiv. phenyl magnesium bromide with 1 equiv. $ZnCl_2$ in toluene at –30 °C for 2 h and gave a 68% yield of 3-phenylcyclohexanone when reacted with 2-cyclohexen-1-one. However, no conjugate addition products were obtained when diphenylzinc was added to enone **5**. The failure of benzyl and phenyl groups to add to enone **5** in a conjugate manner suggests that such groups may be too bulky to add to the sterically congested 4-position of this enone. It may also be that impurities generated during the synthesis of the alkylzinc reagents impeded the conjugate addition to enone **5**; thus, it may be useful to purify these alkylzinc reagents prior to performing the addition reactions.

Conversion of 4-alkylhemiaminals to sialic acid analogues

To convert the conjugate addition products **11** and **13** into sialic acid analogues, removal of the isopropylidene protecting groups was necessary to allow rearrangement to the six-membered ring pyranose form of sialic acid. This was achieved by stirring the 4-alkyl hemiaminals **11** and **13** in 90% aq. trifluoroacetic acid. These conditions resulted in removal of the isopropylidene groups, allowing the compounds to cyclize to the pyranose form, but also induced the formation of a 2,7-anhydro linkage to give the 2,7-anhydro-4-ethylsialoside **14** and the 2,7-anhydro-4-methylsialoside **15** (Scheme 3). These 2,7-anhydrosugars were moderately unstable to silica gel chromatography and were normally used in subsequent reactions without purification. The 2,7-anhydro linkage in **15** was assigned based on NMR spectroscopic evidence, as H-5 and H-6 showed very little coupling to any other protons, indicating they were not trans-diaxial, and the frequencies of H-6 and C-2 were shifted downfield from 4.2 to 4.6 ppm and from 94 to 105 ppm, respectively. Zbiral and co-workers noticed similar spectral differences when they made a 4-deoxy-4-*epi*-4-methylsialic acid by deprotecting its precursor under acidic conditions, giving a product that contained a 2,7-anhydro linkage (12). HMBC spectra of **14** and **15** showed correlations between H-7 and C-2, which would only be possible if a 2,7-anhydro linkage existed. Incidentally, these spectra also showed correlations between H-6 and C-2, indicating that the compounds were indeed in their pyranose forms. It therefore seems as though 4-alkyl-4-deoxy-4-*epi*-sialic acid analogues preferentially form such 2,7-anhydro linkages under acidic conditions. Since 2,7-anhydrosialic acids are of interest themselves as conformationally restrained derivatives (34), this synthetic route has the potential to lead to a number of such derivatives.

It was decided to convert the 2,7-anhydro-4-alkylsialosides **14** and **15** into glycals so as to develop a route to give compounds that could be tested as sialidase inhibitors against benchmark compounds such as DANA (**2**). This was accomplished by stirring the crude 2,7-anhydrosugars in acetic anhydride/acetic acid with a catalytic amount of H_2SO_4 followed by stirring in saturated aq. $NaHCO_3$, a reaction sequence that opened the 2,7-anhydro linkage, peracetylated all hydroxyl groups, and eliminated HOAc in one pot (35).

© 2008 NRC Canada

Scheme 3. Conversion of 4-alkyl hemiaminals **11** and **13** into glycals **16** and **17** via their 2,7-anhydrosugars **14** and **15**.

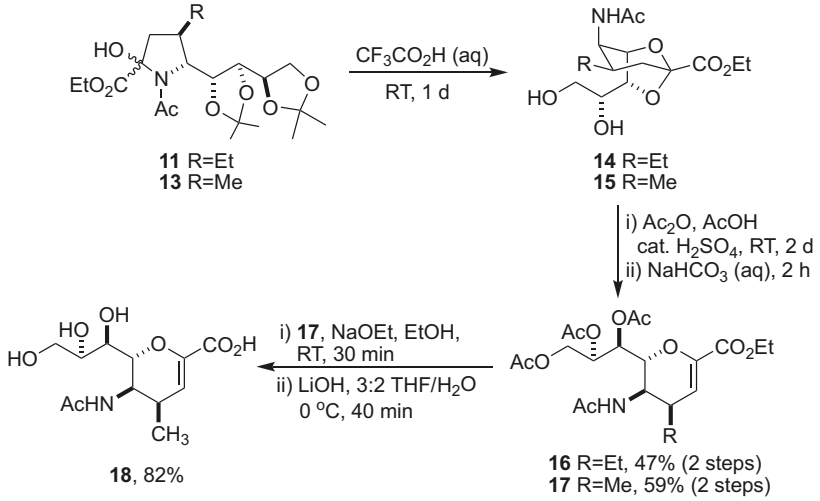

This afforded the peracetylated glycals **16** and **17**, the 4-ethyl-DANA analogue **16** being obtained in 47% yield over two steps from 4-ethyl hemiaminal **11**, and the 4-methyl-DANA analogue being obtained in 59% yield over two steps from 4-methyl hemiaminal **13** (Scheme 3). As with the 2,7-anhydrosialoside precursors, these glycals could be purified by silica chromatography, but their yields decreased significantly despite the crude product mixtures being composed mainly of the glycal products. It was attempted to convert the 4-methyl hemiaminal **13** directly to glycal **17** by performing the deprotection, acetylation, and elimination reactions in one pot, but this did not result in the isolation of any useful products.

The deprotection of 4-deoxy-4-*epi*-4-methyl-DANA **17** was achieved first by removal of the acetyl groups using NaOEt in ethanol, followed by hydrolysis of the ethyl ester using LiOH in 3:2 THF/water to afford the deprotected 4-deoxy-4-*epi*-4-methyl glycal of sialic acid **18** in 82% yield over the two deprotection steps (Scheme 3). A series of 1D NOE difference ^{1}H NMR spectra again confirmed the 4*R*-stereochemical assignment, as irradiation of the 4-methyl group showed a strong contact to H-6 and a weak contact to H-5, indicating that the 4-methyl group and H-6 were on the same face of the six-membered ring. As well, H-4 showed a strong contact to H-5 and virtually no contact to H-6, indicating that H-4 and H-5 are on the same face.

Conclusions

Isolation of an unexpected β,γ-unsaturated α-keto ester **5** led to the development of a synthetic route leading to 4-substituted sialic acid analogues. Ozonolysis of the 4*S* enoate ester **6** led to enone **5** following elimination of HNO_2 during silica chromatography or upon treatment of the crude ozonolysis product with DBU, while ozonolysis of the 4*R* enoate ester **7** led mainly to a five-membered ring hemiaminal structure **9**. Conditions were developed to add alkyl groups to enone **5** through copper-catalyzed conjugate additions of diethylzinc and dimethylzinc. The resulting 4-alkyl-substituted conjugate addition products could be deprotected to generate 2,7-anhydro-4-alkylsialosides **14** and **15** that could then be converted into 4-modified DANA analogues **16** and **17**. Given the functional-group-tolerant nature of dialkylzinc additions, this synthetic route should allow the synthesis of a number of 4-modified sialic acid analogues, including 2,7-anhydrosugars and DANA analogues. Unfortunately, these conjugate addition reactions exclusively afforded the less desirable 4*R*-diastereomer. As well, addition of small nucleophiles from commercially available diethylzinc and dimethylzinc proceeded relatively smoothly, while the addition of bulkier dibenzylzinc and diphenylzinc did not proceed at all. Current work is focusing on attempts to change the diastereoselectivity of the conjugate addition to afford the more desirable 4*S*-diastereomer and on the search for nucleophiles that will participate in conjugate addition reactions with enone **5** to afford more interesting 4-modified sialic acid analogues.

Experimental

Thin-layer chromatography (TLC) was performed on aluminum-backed TLC plates pre-coated with Merck silica gel 60 F_{254}. Compounds were visualized with UV light and (or) staining with phosphomolybdic acid (5% solution in EtOH). Flash chromatography was performed using Avanco silica gel 60 (230–400 mesh). Melting points were recorded on a Gallenkamp melting point apparatus and are uncorrected. Solvents used for anhydrous reactions were dried and distilled immediately prior to use. Ethanol was dried and distilled over magnesium ethoxide. Dichloromethane and toluene were dried and distilled over calcium hydride. Toluene was degassed by repeated freezing, then thawing while under vacuum. Glassware for anhydrous reactions was flame-dried and cooled under a nitrogen atmosphere immediately prior to use. The majority of the NMR spectra were recorded on a Varian Unity 500 MHz spectrometer, while some were recorded on Bruker AMX-400 MHz or Bruker TCI-600 MHz spectrometers. Chemical shifts (δ) are listed in ppm downfield from TMS using the residual solvent peak as an internal reference. ^{1}H and ^{13}C NMR peak assignments are made based on ^{1}H–^{1}H COSY and ^{1}H–^{13}C HMQC experiments. IR spectra were recorded on a Bomem IR spectrometer, and samples were prepared as cast evaporative films on NaCl plates from CH_2Cl_2. Optical rotations were measured

© 2008 NRC Canada

using a PerkinElmer 341 polarimeter and are reported in units of deg cm^2 g^{-1} (concentrations reported in units of g/100 cm^3). Shown in the supporting information are the ^1H NMR and ^{13}C NMR spectra for compounds **14**–**18**.[2]

Ethyl 5-acetamido-3,4,5-trideoxy-6,7:8,9-di-*O*-isopropylidene-4-nitro-D-*glycero*-D-*galacto*-non-2-ulosonate (8)

The 4*S* enoate ester **6** (494 mg, 1.11 mmol) was dissolved in dry CH_2Cl_2 (50 mL) and cooled in a dry ice/acetone bath to –78 °C. The flask was fitted with a $CaCl_2$ drying tube and ozone was bubbled through the solution until a blue color persisted (10 min). The solution was purged with oxygen, and methyl sulfide (1 mL) was added. The colorless solution was allowed to warm to room temperature while stirring for 1.5 h, after which time it was concentrated under reduced pressure to yield a colorless syrup (588 mg) that consisted mainly of DMSO and α-keto ester **8**. The crude material was unstable and could not be fully characterized. IR (cm^{-1}): 1373 (NO_2), 1557 (NO_2), 1673 (amide C=O), 1733 (α-keto ester C=O, one band), 3267 (NH). ^1H NMR ($CDCl_3$, 500 MHz) δ: 1.35 (s, 3H, CMe_2), 1.377 (t, 3H, J = 7.1 Hz, C*H*$_3$CH$_2$O), 1.382 (s, 6H, CMe_2), 1.43 (s, 3H, CMe_2), 2.01 (s, 3H, NHCOC*H*$_3$), 3.46 (dd, 1H, $J_{3a,3b}$ = 19.2 Hz, $J_{3a,4}$ = 6.8 Hz, H-3a), 3.63 (dd, 1H, $J_{3a,3b}$ = 19.2 Hz, $J_{3b,4}$ = 7.3 Hz, H-3b), 3.76 (dd, 1H, $J_{6,7}$ = 5.2 Hz, $J_{7,8}$ = 8.8 Hz, H-7), 3.81 (dd, 1H, $J_{8,9a}$ = 6.7 Hz, $J_{9a,9b}$ = 8.7 Hz, H-9a), 3.98 (dt, 1H, $J_{7,8}$ = 8.8 Hz, $J_{8,9a}$ + $J_{8,9b}$ = 12.9 Hz, H-8), 4.13 (dd, 1H, $J_{5,6}$ = 9.8 Hz, $J_{6,7}$ = 5.2 Hz, H-6), 4.15 (dd, 1H, $J_{8,9b}$ = 6.2 Hz, $J_{9a,9b}$ = 8.7 Hz, H-9b), 4.35 (q, 2H, J = 7.1 Hz, CH$_3$C*H*$_2$O), 4.43 (dt, 1H, $J_{4,5}$ = 2.3 Hz, $J_{5,6}$ + $J_{NH,5}$ = 18.5 Hz, H-5), 5.49 (dt, 1H, $J_{3a,4}$ + $J_{3b,4}$ = 14.1 Hz, $J_{4,5}$ = 2.3 Hz, H-4), 5.96 (d, 1H, $J_{NH,5}$ = 8.7 Hz, N*H*COCH$_3$). ^{13}C NMR ($CDCl_3$, 125 MHz) δ: 13.2 (*C*H$_3$CH$_2$O), 22.2 (NHCO*C*H$_3$), 24.7, 25.8, 26.4, 26.9 (CMe_2 × 2), 38.4 (C-3), 52.3 (C-5), 62.1 (CH$_3$*C*H$_2$O), 66.4 (C-9), 75.9 (C-8), 77.5 (C-6), 80.5 (C-7), 80.7 (C-4), 109.0, 110.2 (*C*Me$_2$ × 2), 158.9 (C-1), 170.3 (NH*C*OCH$_3$), 188.7 (C-2).

Ethyl (*E*)-5-acetamido-3,4,5-trideoxy-6,7:8,9-di-*O*-isopropylidene-D-*manno*-non-3-en-2-ulosonate (5)

The crude α-keto ester **8** from ozonolysis of enoate ester **6** was subjected to flash chromatography (hexanes–EtOAc gradient solvent system from 1:1 *v*/*v* to 100% EtOAc), inducing the elimination reaction to afford enone **5** as a colorless syrup (403 mg, 1.01 mmol, 91%). The elimination could also be effected by stirring **8** with 1 equiv. DBU in EtOAc for 2 min, followed by quenching with saturated aq. ammonium chloride and extraction with Et_2O to afford crude enone **5** that could be purified as described earlier. $[\alpha]^{20}_D$ +18.8 (*c* 1.10, $CHCl_3$). IR (cm^{-1}): 1073 (aliphatic ether C–O–C), 1654 (amide C=O), 1733 (α-keto ester C=O, one band), 3292 (NH). ^1H NMR ($CDCl_3$, 500 MHz) δ: 1.36–1.38 (m, 12H, C*H*$_3$CH$_2$O, CMe_2 × 2), 1.44 (s, 3H, CMe_2), 2.04 (s, 3H, NHCOC*H*$_3$), 3.70 (dd, 1H, $J_{6,7}$ = 7.2 Hz, $J_{7,8}$ = 8.7 Hz, H-7), 3.89 (dd, 1H, $J_{8,9a}$ = 5.8 Hz, $J_{9a,9b}$ = 8.7 Hz, H-9a), 3.99–4.04 (m, 2H, H-6, H-8), 4.17 (dd, 1H, $J_{8,9b}$ = 6.2 Hz, $J_{9a,9b}$ = 8.7 Hz, H-9b), 4.34 (q, 2H, J = 7.1 Hz, CH$_3$C*H*$_2$O), 4.80–4.85 (m, 1H, H-5), 6.16 (d, 1H, $J_{NH,5}$ = 7.9 Hz, N*H*COCH$_3$), 6.85 (dd, 1H, $J_{3,4}$ = 15.9 Hz, $^4J_{3,5}$ = 1.2 Hz, H-3), 7.15 (dd, 1H, $J_{3,4}$ = 15.9 Hz, $J_{4,5}$ = 6.4 Hz, H-4). ^{13}C NMR ($CDCl_3$, 125 MHz) δ: 13.8 (*C*H$_3$CH$_2$O), 23.0 (NHCO*C*H$_3$), 24.9, 26.5, 26.7, 27.0 (CMe_2 × 2), 52.5 (C-5), 62.3 (CH$_3$*C*H$_2$O), 67.7 (C-9), 76.8 (C-8), 79.0 (C-7), 81.3 (C-6), 109.8, 110.3 (*C*Me$_2$ × 2), 126.1 (C-3), 147.9 (C-4), 161.5 (C-1), 169.4 (NH*C*OCH$_3$), 182.6 (C-2). Anal. calcd. for $C_{19}H_{29}NO_8$: C 57.13, H 7.32, N 3.51; found: C 56.82, H 7.17, N 3.76.

Ethyl *N*-acetyl-5-amino-3,4,5-trideoxy-6,7:8,9-di-*O*-isopropylidene-4-nitro-D-*glycero*-D-*talo*-non-2-ulofuranosonate (9)

The 4*R* enoate ester **7** (168 mg, 0.377 mmol) was converted to the 4-nitro hemiaminal **9** (colorless syrup, 118 mg, 0.265 mmol, 70%) under the same conditions used to generate α-keto ester **8** as described earlier. A quantity of enone **5** was also obtained (26.5 mg, 0.066 mmol, 18%). IR (cm^{-1}): 1372 (NO_2), 1562 (NO_2), 1658 (amide C=O), 1753 (ester C=O), 3492 (OH). ^1H NMR ($CDCl_3$, 500 MHz) δ: 1.25 (t, 3H, J = 7.1 Hz, C*H*$_3$CH$_2$O), 1.33 (s, 3H, CMe_2), 1.35 (s, 3H, CMe_2), 1.39 (s, 3H, CMe_2), 1.45 (s, 3H, CMe_2), 2.20 (s, 3H, NHCOC*H*$_3$), 2.97–2.98 (m, 2H, H-3a, H-3b), 3.58 (t, 1H, $J_{6,7}$ = $J_{7,8}$ = 8.6 Hz, H-7), 3.99 (dd, 1H, $J_{8,9a}$ = 4.5 Hz, $J_{9a,9b}$ = 8.9 Hz, H-9a), 4.06–4.11 (m, 1H, H-8), 4.14–4.26 (m, 3H, CH$_3$C*H*$_2$O, H-9b), 4.29 (d, 1H, $J_{6,7}$ = 8.3 Hz, H-6), 4.81–4.83 (m, 2H, H-4, 2-OH), 5.40 (s, 1H, H-5). ^{13}C NMR ($CDCl_3$, 125 MHz) δ: 13.9 (*C*H$_3$CH$_2$O), 22.5 (NHCO*C*H$_3$), 25.0, 26.5, 26.6, 26.9 (CMe_2 × 2), 41.5 (C-3), 62.2 (C-5), 62.3 (CH$_3$*C*H$_2$O), 68.0 (C-9), 77.3 (C-8), 78.4 (C-7), 81.8 (C-6), 84.1 (C-4), 89.2 (C-2), 110.2, 110.7 (*C*Me$_2$ × 2), 169.9 (C=O), 171.1 (C=O). Anal. calcd. for $C_{19}H_{30}N_2O_{10}$: C 51.12, H 6.77, N 6.27; found: C 51.24, H 6.81, N 6.01.

Ethyl 5-acetamido-3,4,5-trideoxy-4-ethyl-6,7:8,9-di-*O*-isopropylidene-D-*glycero*-D-*talo*-non-3-enonate (10)

Copper(II) trifluoromethanesulfonate (10 mg, 0.028 mmol) was suspended in dry, degassed toluene (7 mL), and triethylphosphite (10 μL, 0.058 mmol) was added slowly. The resulting colorless solution was stirred under N_2 at room temperature for 15 min, after which it was cooled to –20 °C, and a solution of diethylzinc in hexanes (1.0 mol/L, 0.90 mL, 0.90 mmol) was added dropwise. After stirring under N_2 for 10 min, a solution of enone **5** (236 mg, 0.59 mmol) in toluene (3 mL) was injected dropwise. The solution was stirred under N_2 overnight as it warmed to room temperature. After 18 h, the reaction was quenched by the addition of saturated aq. NH_4Cl (5 mL). The mixture was diluted with water (15 mL) and extracted with Et_2O (2 × 50 mL). The combined organic layers were dried ($MgSO_4$), filtered, and concentrated under reduced pressure to give a mixture of compounds that contained mainly the enol tautomer of the ethyl addition product **10** as colorless syrup (217 mg). The enol addition product could not be purified for characterization as it rearranged to the five-membered

[2] Supplementary data for this article are available on the journal Web site (canjchem.nrc.ca) or may be purchased from the Depository of Unpublished Data, Document Delivery, CISTI, National Research Council Canada, Ottawa, ON K1A 0R6, Canada. DUD 3711. For more information on obtaining material, refer to cisti-icist.nrc-cnrc.gc.ca/irm/unpub_e.shtml.

© 2008 NRC Canada

ring hemiaminal **11** upon chromatography. ^{1}H NMR ($CDCl_3$, 500 MHz) δ: 0.86 (t, 3H, J = 7.3 Hz, CH_2CH_3), 1.29–1.41 (m, 16H, CMe_2 × 2, OCH_2CH_3, $CH_aH_bCH_3$), 1.51–1.58 (m, 1H, $CH_aCH_bCH_3$), 1.95 (s, 3H, $COCH_3$), 2.82–2.88 (m, 1H, H-4), 3.78–3.83 (m, 3H, H-6, H-7, H-9a), 3.89–3.95 (m, 1H, H-8), 4.06–4.09 (m, 1H, H-9b), 4.23–4.28 (m, 3H, OCH_2CH_3, H-5), 5.50 (d, 1H, $J_{3,4}$ = 10.2 Hz, H-3), 5.73 (d, 1H, $J_{5,NH}$ = 9.4 Hz, NH), 6.54 (s, 1H, OH). ^{13}C NMR ($CDCl_3$, 125 MHz) δ: 12.0 (CH_2CH_3), 14.1 (OCH_2CH_3), 23.4 ($COCH_3$), 24.6 (CH_2CH_3), 25.3, 26.5, 27.2, 27.5 ($C(CH_3)_2$ × 2), 39.1 (C-4), 54.1 (OCH_2CH_3/C-5), 61.8 (OCH_2CH_3/C-5), 67.8 (C-9), 77.0 (C-8), 80.5 (C-6/C-7), 80.7 (C-6/C-7), 109.6, 110.3 ($C(CH_3)_2$ × 2), 113.1 (C-3), 142.3 (C-2), 164.4, 170.1 (C=O × 2).

Ethyl *N*-acetyl-5-amino-3,4,5-trideoxy-4-ethyl-6,7:8,9-di-*O*-isopropylidene-D-*glycero*-D-*talo*-non-2-ulofuranosonate (11)

The crude enol **10** was purified via flash chromatography (hexanes–EtOAc gradient solvent system from 2:1 to 1:2 *v*/*v*) to afford the hemiaminal **11** as a colorless syrup (134 mg, 0.31 mmol, 53%). IR (cm^{-1}): 1648 (amide C=O), 1747 (ester C=O), 3490 (OH). ^{1}H NMR ($CDCl_3$, 500 MHz) δ: 0.97 (t, 3H, J = 7.4 Hz, CH_2CH_3), 1.25 (t, 3H, J = 7.1 Hz OCH_2CH_3), 1.34, 1.35, 1.40, 1.41 (s, 12H, $C(CH_3)_2$ × 2), 1.65–1.71 (m, 2H, CH_2CH_3), 1.89 (d, 1H, $J_{3a,3b}$ = 13.2 Hz, H-3a), 2.14–2.19 (m, 4H, $COCH_3$, H-4), 2.62 (ddd, 1H, $J_{3a,3b}$ = 13.2 Hz, $J_{3b,4}$ = 7.6 Hz, $J_{3b,OH}$ = 1.6 Hz, H-3b), 3.47 (t, 1H, $J_{6,7}$ = $J_{7,8}$ = 8.5 Hz, H-7), 3.93 (dd, 1H, $J_{8,9a}$ = 5.8 Hz, $J_{9a,9b}$ = 8.7 Hz, H-9a), 4.04 (dt, 1H, $J_{7,8}$ + $J_{8,9a}$ + $J_{8,9b}$ = 20.8 Hz, H-8), 4.12 (s, 1H, H-5), 4.14–4.26 (m, 4H, H-9b, H-6, OCH_2CH_3), 4.87 (d, 1H, $J_{3b,OH}$ = 1.5 Hz, OH). ^{13}C NMR ($CDCl_3$, 100 MHz) δ: 12.6 (CH_2CH_3), 14.0 (OCH_2CH_3), 22.5 ($COCH_3$), 25.1, 26.6, 26.8, 27.0 ($C(CH_3)_2$ × 2), 27.3 (CH_2CH_3), 40.5 (C-4), 41.1 (C-3), 61.7 (OCH_2CH_3), 65.3 (C-5), 68.5 (C-9), 77.5 (C-8), 78.9 (C-7), 83.4 (C-6), 90.6 (C-2), 109.8, 110.2 ($C(CH_3)_2$ × 2), 171.4, 171.8 (C=O × 2).

Ethyl *N*-acetyl-5-amino-3,4,5-trideoxy-6,7:8,9-di-*O*-isopropylidene-4-methyl-D-*glycero*-D-*talo*-non-2-ulofuranosonate (13)

Enone **5** (1.02 g, 2.56 mmol) was reacted with dimethylzinc (2.0 mol/L in toluene, 1.9 mL, 3.8 mmol) to generate the 4-methyl hemiaminal **13** (1.4:1.0 anomeric ratio, 373 mg, 0.898 mmol, 35%) using the methods reported earlier for the synthesis of the ethyl-addition product **10**. The major anomer of **13** was purified to analytical standards for complete characterization.

Major anomer

$[\alpha]^{20}_D$ +16.5 (*c* 1.95, $CHCl_3$). IR (cm^{-1}): 1648 (amide C=O), 1746 (ester C=O), 3482 (OH). ^{1}H NMR ($CDCl_3$, 500 MHz) δ: 1.25 (t, 3H, J = 7.1 Hz, CH_3CH_2O), 1.32 (d, 3H, $J_{CH3,4}$ = 7.3 Hz, 4-CH_3), 1.33, 1.34, 1.39, 1.42 (s, 12H, $C(CH_3)_2$ × 2), 1.78 (d, 1H, $J_{3a,3b}$ = 13.1 Hz, H-3a), 2.16 (s, 3H, $COCH_3$), 2.44–2.53 (m, 1H, H-4), 2.66 (dd, 1H, $J_{3a,3b}$ = 13.0 Hz, $J_{3b,4}$ = 7.6 Hz, H-3b), 3.49 (t, 1H, $J_{6,7}$ + $J_{7,8}$ = 17.2 Hz, H-7), 3.99 (dd, 1H, $J_{8,9a}$ = 4.9 Hz, $J_{9a,9b}$ = 8.7 Hz, H-9a), 4.03 (s, 1H, H-5), 4.03–4.07 (m, 1H, H-8), 4.12–4.28 (m, 4H, H-6, H-9b, CH_3CH_2O), 4.91 (s, 1H, OH). ^{13}C NMR ($CDCl_3$, 125 MHz) δ: 14.0 (CH_3CH_2O), 21.3 (4-CH_3), 22.6 ($COCH_3$), 25.1, 26.8 (× 2), 27.0 ($C(CH_3)_2$ × 2), 33.0 (C-4), 43.0 (C-3), 61.8 (CH_3CH_2O), 67.6 (C-5), 68.2 (C-9), 77.5 (C-8), 78.8 (C-7), 83.0 (C-6), 90.8 (C-2), 109.8, 110.1 ($C(CH_3)_2$ × 2), 171.4, 171.7 (C=O × 2). Anal. calcd. for $C_{20}H_{33}NO_8$: C 57.82, H 8.01, N 3.37; found: C 57.52, H 7.90, N 3.59.

Minor anomer

^{1}H NMR ($CDCl_3$, 500 MHz) δ: 1.23 (d, 3H, $J_{CH3,4}$ = 7.5 Hz, 4-CH_3), 1.30 (t, 3H, J = 7.1 Hz, CH_3CH_2O), 1.34, 1.37, 1.42, 1.44 (s, 12H, $C(CH_3)_2$ × 2), 1.97 (d, 1H, $J_{3a,3b}$ = 12.5 Hz, H-3a), 2.14 (s, 3H, $COCH_3$), 2.50–2.60 (m, 2H, H-3b, H-4), 3.57 (t, 1H, $J_{6,7}$ + $J_{7,8}$ = 17.0 Hz, H-7), 3.95 (s, 1H, H-5), 3.98 (dd, 1H, $J_{8,9a}$ = 4.9 Hz, $J_{9a,9b}$ = 8.8 Hz, H-9a), 4.04–4.08 (m, 1H, H-8), 4.17–4.30 (m, 4H, H-6, H-9b, CH_3CH_2O), 4.47 (s, 1H, OH). ^{13}C NMR ($CDCl_3$, 125 MHz) δ: 14.0 (CH_3CH_2O), 21.4 (4-CH_3), 22.1 ($COCH_3$), 25.0, 26.8, 26.90, 26.93 ($C(CH_3)_2$ × 2), 31.9 (C-4), 45.0 (C-3), 62.0 (CH_3CH_2O), 67.6 (C-5), 68.1 (C-9), 77.6 (C-8), 78.8 (C-7), 83.1 (C-6), 90.0 (C-2), 109.8, 110.6 ($C(CH_3)_2$ × 2), 170.5 ($COCH_3$), 171.8 (C-1).

Ethyl 5-acetamido-2,7-anhydro-3,4,5-trideoxy-4-ethyl-D-*glycero*-D-*talo*-non-2-ulopyranosonate (14)

4-Ethyl hemiaminal **11** (239 mg, 0.557 mmol) was dissolved in trifluoroacetic acid (4.0 mL) to which water (0.4 mL) was added. The resulting solution was stirred at room temperature for 15 h and was then concentrated under reduced pressure to give a dark brown syrup (249 mg) that was used directly in the next reaction. A sample for characterization could be purified by flash chromatography (EtOAc–MeOH–H_2O gradient solvent system from 20:3:1 to 10:3:1 *v*/*v*/*v*), giving the 2,7-anhydro-4-ethylsialoside **14** as a light brown foamy syrup. IR (cm^{-1}): 1645 (amide C=O), 1746 (ester C=O), 3328 (OH). ^{1}H NMR (D_2O, 600 MHz) δ: 0.82 (t, 3H, J = 7.4 Hz, CH_2CH_3), 1.24–1.33 (m, 5 H, CH_2CH_3, OCH_2CH_3), 1.65 (t, 1H, $J_{3a,3b}$ = $J_{3a,4}$ = 13.1 Hz, H-3a), 2.02–2.06 (m, 4H, H-3b, $COCH_3$), 2.12–2.17 (m, 1H, H-4), 3.52–3.58 (m, 2H, H-8, H-9a), 3.71 (br d, 1H, $J_{9a,9b}$ = 11.5 Hz, H-9b), 4.05 (dd, 1H, $J_{4,5}$ = 2.0 Hz, $J_{5,6}$ = 4.7 Hz, H-5), 4.21 (d, 1H, $J_{7,8}$ = 7.4 Hz, H-7), 4.29 (q, 2H, J = 7.1 Hz, OCH_2CH_3), 4.59 (d, 1H, $J_{5,6}$ = 1.9 Hz, H-6). ^{13}C NMR (D_2O, 150 MHz) δ: 10.2 (CH_2CH_3), 13.1 (OCH_2CH_3), 21.7 ($COCH_3$), 23.5 (CH_2CH_3), 32.3 (C-4), 34.3 (C-3), 47.9 (C-5), 61.9 (C-9), 63.5 (OCH_2CH_3), 71.3 (C-8), 77.9 (C-7), 79.9 (C-6), 105.0 (C-2), 168.2 (C-1), 173.9 ($COCH_3$). HR–MS (ESI) for $C_{15}H_{25}NO_7$: (MNa^+) calcd: 354.1528; found: 354.1532.

Ethyl 5-acetamido-2,7-anhydro-3,4,5-trideoxy-4-methyl-D-*glycero*-D-*talo*-non-2-ulopyranosonate (15)

4-Methyl hemiaminal **13** (228 mg, 0.548 mmol) was converted into the 2,7-anhydro-4-methylsialoside **15** (263 mg) using the method described earlier for synthesis of the ethyl analogue **14**. The light brown foamy syrup was of adequate purity to be used directly in the next reaction. An analytical sample was purified via flash chromatography (20:3:1 EtOAc–methanol–water *v*/*v*/*v*) to afford the product as a tan solid; mp 117–120 °C (dec). $[\alpha]^{20}_D$ +48 (*c* 0.13, H_2O). IR (cm^{-1}): 1647 (amide C=O), 1741 (ester C=O), 3333 (OH).

© 2008 NRC Canada

^{1}H NMR (D_2O, 500 MHz) δ: 0.87 (d, 3H, $J_{Me,4}$ = 6.8 Hz, 4-CH_3), 1.28 (t, 3H, J = 7.1 Hz, CH_3CH$_2$O), 1.65 (dd, 1H, $J_{3a,3b}$ = 14.0 Hz, $J_{3a,4}$ = 12.3 Hz, H-3a), 1.97 (dd, 1H, $J_{3a,3b}$ = 14.1 Hz, $J_{3b,4}$ = 5.6 Hz, H-3b), 2.06 (s, 3H, COCH_3), 2.34–2.43 (m, 1H, H-4), 3.52–3.59 (m, 2H, H-8, H-9a), 3.71 (dd, 1H, $J_{8,9b}$ = 2.4 Hz, $J_{9a,9b}$ = 11.5 Hz, H-9b), 3.99 (dd, 1H, $J_{4,5}$ = 4.7 Hz, $J_{5,6}$ = 2.0 Hz, H-5), 4.22 (d, 1H, $J_{7,8}$ = 7.4 Hz, H-7), 4.29 (q, 2H, J = 7.1 Hz, CH$_3$CH_2O), 4.60 (d, 1H, $J_{5,6}$ = 1.8 Hz, H-6). ^{13}C NMR (D_2O, 125 MHz) δ: 13.2 (CH_3CH$_2$O), 15.5 (4-CH_3), 21.9 (COCH_3), 26.0 (C-4), 36.0 (C-3), 49.7 (C-5), 62.1 (C-9), 63.7 (CH$_3$CH_2O), 71.5 (C-8), 78.2 (C-7), 80.0 (C-6), 105.1 (C-2), 168.4 (C-1), 174.2 (COCH$_3$). HR–MS (ESI) for $C_{14}H_{23}NO_7$: (MH^+) calcd: 318.1552; found: 318.1564.

Ethyl 5-acetamido-7,8,9-tri-*O*-acetyl-2,6-anhydro-3,4,5-trideoxy-4-ethyl-D-*glycero*-D-*talo*-non-2-enonate (16)

The crude preparation of 2,7-anhydro-4-ethylsialoside **14** from the previous reaction (249 mg) was dissolved in acetic anhydride (2.0 mL) and glacial acetic acid (2.0 mL). Concentrated H_2SO_4 (15 drops) was added, and the resulting solution was stirred at room temperature. After 3 d, the reaction was poured into saturated aq. $NaHCO_3$ (100 mL), which bubbled vigorously, and the resulting basic mixture was stirred for 2 h. The mixture was then extracted with EtOAc (2 × 100 mL), and the combined organic layers were dried ($MgSO_4$), filtered, and concentrated under reduced pressure to give the 4-ethyl-substituted glycal **16** as a light brown syrup (119 mg, 0.261 mmol, 47%). The glycal could be further purified via flash chromatography (hexanes–EtOAc gradient solvent system from 1:2 *v*/*v* to 100% EtOAc) to afford a sample for characterization. $[\alpha]^{20}_D$ +3 (*c* 0.24, $CHCl_3$). IR (cm^{-1}): 1656 (amide C=O), 1747 (ester C=O). ^{1}H NMR ($CDCl_3$, 600 MHz) δ: 1.04 (t, 3H, J = 7.4 Hz, CH$_2$CH_3), 1.31 (t, 3H, J = 7.1 Hz, OCH$_2$CH_3), 1.34–1.39 (m, 1H, CH_aH$_b$CH$_3$), 1.48–1.56 (m, 1H, CH$_a$$H_bCH_3$), 1.97 (s, 3H, COC$H_3$), 2.06 (s, 3H, COC$H_3$), 2.07 (s, 3H, COC$H_3$), 2.11 (s, 3H, COC$H_3$), 2.56–2.60 (m, 1H, H-4), 4.20–4.31 (m, 4H, H-6, H-9a, OCH_2CH$_3$), 4.40 (dd, 1H, $J_{8,9b}$ = 4.4 Hz, $J_{9a,9b}$ = 12.0 Hz, H-9b), 4.55–4.58 (m, 1H, H-5), 5.19 (ddd, 1H, $J_{7,8}$ + $J_{8,9b}$ = 11.4 Hz, $J_{8,9a}$ = 3.2 Hz, H-8), 5.40 (dd, 1H, $J_{6,7}$ = 8.5 Hz, $J_{7,8}$ = 3.1 Hz, H-7), 5.54 (d, 1H, $J_{5,NH}$ = 9.4 Hz, NH), 6.03 (br d, 1H, $J_{3,4}$ = 2.6 Hz, H-3). ^{13}C NMR ($CDCl_3$, 150 MHz) δ: 11.4 (CH$_2$CH_3), 14.1 (OCH$_2$CH_3), 20.66 (COCH_3), 20.72 (COCH_3), 20.9 (COCH_3), 23.2 (CH_2CH$_3$), 23.3 (COCH_3), 33.9 (C-4), 43.7 (C-5), 61.1 (C-9), 61.5 (OCH_2CH$_3$), 68.7 (C-7), 69.3 (C-8), 76.7 (C-6), 112.8 (C-3), 141.1 (C-2), 161.8, 169.7, 170.0, 170.3, 170.6 (C=O × 5). HR–MS (ESI) for $C_{21}H_{31}NO_{10}$: (MH^+) calcd: 458.2026; found: 458.2020.

Ethyl 5-acetamido-7,8,9-tri-*O*-acetyl-2,6-anhydro-3,4,5-trideoxy-4-methyl-D-*glycero*-D-*talo*-non-2-enonate (17)

The crude 2,7-anhydro-4-methylsialoside **15** from the previous reaction (263 mg) was converted into glycal 17 (light brown syrup, 0.144 mg, 0.324 mmol, 59% over 2 steps) using the same conditions described earlier for synthesis of the ethyl analogue **16**. This product could be further purified via flash chromatography (hexanes–EtOAc gradient solvent system from 1:2 *v*/*v* to 100% EtOAc) giving the pure glycal as a colorless syrup (58 mg, 0.13 mmol, 24% over 2 steps). $[\alpha]^{20}_D$ +1.2 (*c* 0.995, $CHCl_3$). IR (cm^{-1}): 1653 (amide C=O), 1683 (trisubstituted C=C), 1748 (ester C=O), 3291 (NH). ^{1}H NMR ($CDCl_3$) δ: 1.08 (d, 3H, $J_{Me,4}$ = 7.1 Hz, 4-CH_3), 1.30 (t, 3H, J = 7.1 Hz, CH_3CH$_2$O), 1.98 (s, 3H, Ac), 2.05 (s, 3H, Ac), 2.06 (s, 3H, Ac), 2.10 (s, 3H, Ac), 2.77–2.83 (m, 1H, H-4), 4.20 (dd, 1H, $J_{5,6}$ = 5.0 Hz, $J_{6,7}$ = 7.1 Hz, H-6), 4.20–4.27 (m, 2H, CH$_3$CH_2O), 4.28 (dd, 1H, $J_{8,9a}$ = 7.1 Hz, $J_{9a,9b}$ = 12.1 Hz, H-9a), 4.48 (dd, 1H, $J_{8,9b}$ = 4.3 Hz, $J_{9a,9b}$ = 12.0 Hz, H-9b), 4.48–4.51 (m, 1H, H-5), 5.21 (br quintet, 1H, $J_{7,8}$ + $J_{8,9a}$ + $J_{8,9b}$ = 14.5 Hz, H-8), 5.43 (dd, 1H, $J_{6,7}$ = 7.1 Hz, $J_{7,8}$ = 3.3 Hz, H-7), 5.55 (d, 1H, $J_{NH,5}$ = 9.6 Hz, NHCOCH$_3$), 5.96 (d, 1H, $J_{3,4}$ = 3.2 Hz, H-3). ^{13}C NMR ($CDCl_3$) δ: 14.1 (CH_3CH$_2$O), 15.6 (4-CH_3), 20.61, 20.67, 20.8, 23.2 (COCH_3 × 4), 27.8 (C-4), 45.1 (C-5), 61.36 (CH$_3$CH_2O), 61.38 (C-9), 68.6 (C-7), 70.0 (C-8), 75.8 (C-6), 114.7 (C-3), 141.3 (C-2), 161.8, 169.7, 170.0, 170.3, 170.5 (C=O × 5). HR–MS (ESI) for $C_{20}H_{29}NO_{10}$: (MH^+) calcd: 444.1869; found: 444.1870.

5-Acetamido-2,6-anhydro-3,4,5-trideoxy-4-methyl-D-*glycero*-D-*talo*-non-2-enonic acid (18)

A 1.2 mol/L solution of sodium ethoxide in ethanol (0.080 mL, 0.096 mmol) was added to a solution of peracetylated 4-methyl-substituted glycal **17** (29 mg, 0.065 mmol) in dry ethanol (3.0 mL). This solution was stirred at room temperature for 30 min, after which time TLC analysis indicated the absence of starting material. The reaction was neutralized with Amberlite™ H^+ resin and filtered. The resin was washed with methanol (30 mL), and the filtrate was concentrated under reduced pressure to give a light yellow syrup (21.1 mg, 0.065 mmol). The de-acetylated product was then dissolved in THF/water (3:2 *v*/*v*, 5 mL) and cooled in an ice bath. Lithium hydroxide monohydrate was added (23.7 mg, 0.565 mmol), and the solution stirred in ice for 30 min, after which time TLC analysis indicated complete de-esterification. The reaction was removed from the cooling bath, diluted with water (5 mL), and neutralized with Amberlite™ H^+ resin to pH 5, which was then filtered and washed with water (30 mL). The combined filtrates were concentrated under reduced pressure to afford the lithium salt of the deprotected glycal **18** as a colorless syrup (16.0 mg, 0.0542 mmol, 82%). $[\alpha]^{20}_D$ –100 (*c* 0.48, H_2O). IR (cm^{-1}): 1645 (amide C=O), 1712 (acid C=O), 3287 (NH), 3340 (OH). ^{1}H NMR (D_2O) δ: 1.04 (d, 3H, $J_{Me,4}$ = 7.2 Hz, 4-CH_3), 2.02 (s, 3H, NHCOCH_3), 2.70–2.76 (m, 1H, H-4), 3.64 (dd, 1H, $J_{8,9a}$ = 6.3 Hz, $J_{9a,9b}$ = 11.9 Hz, H-9a), 3.67 (dd, 1H, $J_{6,7}$ = 2.2 Hz, $J_{7,8}$ = 8.8 Hz, H-7), 3.86 (dd, 1H, $J_{8,9b}$ = 2.8 Hz, $J_{9a,9b}$ = 11.9 Hz, H-9b), 3.90 (ddd, 1H, $J_{7,8}$ = 8.9 Hz, $J_{8,9a}$ = 6.3 Hz, $J_{8,9b}$ = 2.8 Hz, H-8), 4.20 (dd, 1H, $J_{5,6}$ = 8.8 Hz, $J_{6,7}$ = 2.2 Hz, H-6), 4.30 (dd, 1H, $J_{4,5}$ = 5.8 Hz, $J_{5,6}$ = 8.8 Hz, H-5), 6.14 (d, 1H, $J_{3,4}$ = 5.0 Hz, H-3). ^{13}C NMR (D_2O) δ: 15.1 (4-CH_3), 21.9 (NHCOCH_3), 28.9 (C-4), 46.4 (C-5), 63.0 (C-9), 69.0 (C-7), 70.5 (C-8), 72.6 (C-6), 116.7 (C-3), 141.8 (C-2), 166.6 (C=O), 174.1 (C=O). HR–MS (ESI) for $C_{12}H_{18}NO_7$: (M^-) calcd: 288.1083; found: 288.1091.

Acknowledgements

The authors gratefully acknowledge the Natural Sciences and Engineering Research Council of Canada (NSERC) and

© 2008 NRC Canada

Simon Fraser University for financial support of this work. IH thanks the Michael Smith Foundation for Health Research for a Trainee Scholarship. The authors also thank the Saskatchewan Structural Sciences Centre for measuring HR-MS data in a timely manner.

References

1. R. Schauer. Glycoconjugate J. **17**, 485 (2000).
2. G. Taylor. Curr. Opin. Struct. Biol. **6**, 830 (1996).
3. R. Thomson and M. von Itzstein. *In* Carbohydrate-based drug discovery. Vol. 2. *Edited by* C.-H. Wong. Wiley-VCH, Weinheim, Germany. 2003. p. 831.
4. I. Hemeon and A.J. Bennet. Synthesis, 1899 (2007).
5. M. von Itzstein, W.Y. Wu, G.B. Kok, M.S. Pegg, J.C. Dyason, B. Jin, T.V. Phan, M.L. Smythe, H.F. White, S.W. Oliver, P.M. Colman, J.N. Varghese, D.M. Ryan, J.M. Woods, R.C. Bethell, V.J. Hotham, J.M. Cameron, and C.R. Penn. Nature (London), **363**, 418 (1993).
6. C.U. Kim, W. Lew, M.A. Williams, H. Liu, L. Zhang, S. Swaminathan, N. Bischofberger, M. S. Chen, D.B. Mendel, C.Y. Tai, W.G. Laver, and R.C. Stevens. J. Am. Chem. Soc. **119**, 681 (1997).
7. M.-J. Kim, W.J. Hennen, H.M. Sweers, C.-H. Wong. J. Am. Chem. Soc. **110**, 6481 (1988).
8. T.-H. Chan and M.-C. Lee. J. Org. Chem. **60**, 4228 (1995).
9. S. Vorwerk and A. Vasella. Angew. Chem., Int. Ed. Eng. **37**, 1732 (1998).
10. I.A. Kozlov, S. Mao, Y. Xu, X. Huang, L. Lee, P.S. Sears, C. Gao, A.R. Coyle, K.D. Janda, and C.-H. Wong. ChemBioChem, **2**, 741 (2001).
11. M. Hartmann and E. Zbiral. Monatsh. Chem. **120**, 899 (1989).
12. M. Hartmann, R. Christian, and E. Zbiral. Monatsh. Chem. **122**, 111 (1991).
13. D.R. Groves and M. von Itzstein. J. Chem. Soc., Perkin Trans. 1, 2817 (1996).
14. E. Schreiner, E. Zbiral, R.G. Kleineidam, and R. Schauer. Liebigs Ann. Chem. 129 (1991).
15. G.B. Kok, A.K. Norton, and M. Von Itzstein. Synthesis, 1185 (1997).
16. G.B. Kok and M. Von Itzstein. J. Chem. Soc., Perkin Trans. 1, 905 (1998).
17. I. Hemeon and A.J. Bennet. Org. Biomol. Chem. **4**, 2986 (2006).
18. K.G. Liu, S. Yan, Y.L. Wu, and Z.J. Yao. Org. Lett. **6**, 2269 (2004).
19. F. Baumberger and A. Vasella. Helv. Chim. Acta, **69**, 1535 (1986).
20. T.K.M. Shing. Tetrahedron, **48**, 6777 (1992).
21. Z. Pakulski and A. Zamojski. Tetrahedron, **53**, 3723 (1997).
22. B. H. Lipshutz. *In* Organometallics in synthesis: a manual. 2nd ed. *Edited by* M. Schlosser. J. Wiley Sons, Chichester, NY. 2004. p. 665.
23. H. Urabe, K. Kobayashi, and F. Sato. J. Chem. Soc., Chem. Commun. 1043 (1995).
24. H. Urabe, K. Yamashita, K. Suzuki, K. Kobayashi, and F. Sato. J. Org. Chem. **60**, 3576 (1995).
25. E. Nakamura. *In* Organometallics in synthesis: a manual. 2nd ed. *Edited by* M. Schlosser. J. Wiley Sons, Chichester, NY. 2004. p. 579.
26. A. Alexakis, J. Vastra, and P. Mangeney. Tetrahedron Lett. **38**, 7745 (1997).
27. A. Alexakis, C. Benhaim, S. Rosset, M. Humam. J. Am. Chem. Soc. **124**, 5262 (2002).
28. R. Schauer, S. Stoll, E. Zbiral, E. Schreiner, H.H. Brandstetter, A. Vasella, and F. Baumberger. Glycoconjugate J. **4**, 361 (1987).
29. H. Mizutani, S.J. Degrado, A.H. Hoveyda. J. Am. Chem. Soc. **124**, 779 (2002).
30. P. Knochel, M.C.P. Yeh, S.C. Berk, and J. Talbert. J. Org. Chem. **53**, 2390 (1988).
31. S.C. Berk, M.C.P. Yeh, N. Jeong, and P. Knochel. Organometallics, **9**, 3053 (1990).
32. P. Knochel and R.D. Singer. Chem. Rev. **93**, 2117 (1993).
33. X. Rathgeb, S. March, and A. Alexakis. J. Org. Chem. **71**, 5737 (2006).
34. K.G. Liu, H.B. Zhou, Y.L. Wu, and Z.L. Yao. J. Org. Chem. **68**, 9528 (2003).
35. G.B. Kok, D. Groves, and M. Von Itzstein. J. Chem. Soc., Perkin Trans. 1, 2109 (1999).

© 2008 NRC Canada

Synthesis and tautomerization study of pseudonitrosites to 1,2-nitroximes

Ahmad Shaabani, Hamid Reza Bijanzadeh, Ali Reza Karimi, Mohammad Bagher Teimouri, and Kamal Soleimani

Abstract: 4-R-Substituted 2-nitro-1-nitrosoethylbenzenes (R = H, CH_3, OCH_3, Cl, F) have been synthesized under solvent-free conditions and the mechanism of their tautomerization to 2-isonitroso-1-nitro-2-phenylethanes have been investigated by ^{1}H NMR spectroscopy.

Key words: tautomerization, pseudonitrosite, mechanism, 2-nitro-1-nitrosoethylbenzene, ^{1}H NMR spectroscopy.

Résumé : Opérant dans des conditions n'impliquant aucun solvant, on a réalisé la synthèse de 2-nitro-1-nitrosoéthylbenzènes substitués en position 4 par des groupes R = H, CH_3, OCH_3, Cl et F et, faisant appel à la spectroscopie RMN du ^{1}H, on a étudié leur tautomérisation en 2-isonitroso-1-nitro-2-phényléthanes.

Mots-clés : tautomérisation, pseudonitrosite, mécanisme, 2-nitro-1-nitrosoéthylbenzène, spectroscopie RMN du ^{1}H.

[Traduit par la Rédaction]

Introduction

The discovery of important roles of *C*-nitroso compounds in various biological metabolic processes has generated a renewed interest in the general chemical properties of nitrosoarenes (1). For example, identification of the nitrosbenzene adduct of hemoglobin as a product of nitrobenzene poisoning (2, 3) and the realization that some amine containing drugs may metabolize to nitroso derivatives (4–7) led to an increased desire to study the biochemical properties of *C*-nitroso compounds. To this end, many studies have been reported on the fundamental chemistry of *C*-nitroso compounds under conditions that either stabilize the *C*-nitroso functionality or enhance their reactivity toward isomerization or reactivity with substrate.

There is a considerable variety of synthetic routes available for the preparation of *C*-nitroso compounds (1, 8–11). However, a major difficulty in *C*-nitroso chemistry is that the necessary high reactivity of these compounds imposes constraints upon the methods employed for their preparation, particularly with regard to the yield of the desired product. For example, the ease of oxidation of the desired nitroso product to its nitro derivative or its isomerization to corresponding oximes can restrict the choice of solvent for the preparation of these compounds.

Solvent-free reactions are of increasing importance because of their potential use in combinatorial chemistry and because they may result in less environmental impact during industrial applications (12, 13). Since tautomerization of *C*-nitroso compounds to the more stable oximes occurs readily in solutions, we have attempted to find solvent-free reactions that result in selective transformation of the styrene and para-substituted styrenes (**1**) to 2-nitro-1-nitrosoethylbenzenes (**2**) without further tautomerization to 2-isonitroso-1-nitro-2-phenylethanes (**3**). (Scheme 1)

C-Nitroso compounds are characterized as white solid dimers that result from a N-N connection to give diazene dioxides (14). Since 2-nitro-1-nitrosoethylbenzene derivatives are a monomer and has an asymmetric center, the dimer exists in two diastereomeric isomers namely meso (R,S) and racemate (R,R and S,S) (15). When the dimers are dissolved and (or) heated in an inert low polarity solvent, such as CH_2Cl_2 or ether, dissociation into blue (aliphatic) or green (aromatic) monomers usually occurs (1, 16–18).

Received 13 August 2007. Accepted 4 December 2007. Published on the NRC Research Press Web site at canjchem.nrc.ca on 14 February 2008.

A. Shaabani,[1] A.R. Karimi, M.B. Teimouri, and K. Soleimani. Department of Chemistry, Shahid Beheshti University, P.O. Box 19839-4716, Tehran, Iran.
H.R. Bijanzadeh. Department of Chemistry, Tarbiat Modarres University, P.O. Box 14155-4838, Tehran, Iran.

[1]Corresponding author (e-mail: a-shaabani@cc.sbu.ac.ir).

Experimental

Melting points were measured on an Electrothermal 9100 apparatus and are uncorrected. Elemental analyses were performed using a Heraeus CHN-O-Rapid analyzer. NMR spectra were recorded on BRUKER DRX-500 AVANCE spectrometer. Temperatures ranged from 298 to 313 K. Infrared spectra were taken on a Shimadzu IR-470 spectrophotometer. Mass spectra were recorded on a FINNIGAN-MAT 8430 mass spectrometer operating at an ionization potential of 70 eV.

General procedure

Cation exchange resine (Rexyn 101 H obtained from Fisher Scientific, 0.350 g) and sodium nitrite (0.345 g, 5 mmol) were ground separately in a mortar and added to styrene or substituted styrene (2 mmol) in a round-bottomed flask. The reaction mixture was stirred magnetically at room temperature until TLC analysis indicated that all of the sty-

 doi:10.1139/V08-011 © 2008 NRC Canada

Scheme 1.

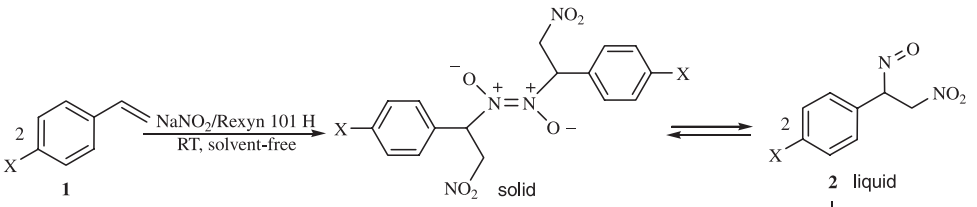

2,3	X	Yeild of 2 (%)
a	H	72
b	CH_3	64
c	OCH_3	62
d	Cl	73
e	F	71

Table 1. Physical and spectral data (IR, ^{1}H, and ^{13}C NMR, MS) of compounds **2b**–**2e** and **3b**–**3e**.

Compound	Selected data
2b	White powder. Mp 119–121 °C. IR (KBr) (υ_{max}, cm^{-1}): 1376 and 1559. ^{1}H NMR (Aceton-d_6) δ_H: 2.33 (3H, s, CH_3), 4.98 (1H, dd, $^2J_{HH}$ = 16.0 Hz, $^3J_{HH}$ = 3.0 Hz, CH*H*), 5.39 (1H, dd, $^2J_{HH}$ = 16.0 Hz, $^3J_{HH}$ = 11.1 Hz, C*H*H), 6.90 (1H, dd, $^3J_{HH}$ = 11.1 Hz, $^3J_{HH}$ = 3.0 Hz, CH), 7.24 and 7.38 (4H, 2d, $^3J_{HH}$ = 7.9 Hz, arom.). ^{13}C NMR (Aceton-d_6) δ_C: 20.29 (CH_3), 67.50 and 73.37 (C-N=O and C-NO_2), 127.69, 129.37, 129.57 and 139.57 (arom.). MS *m*/*z* (%): 194 (M$^+$, 5), 148 (4), 117 (100), 91 (38), 30 (72). Anal. calcd. for $C_9H_{10}N_2O_3$ (194.21) (%): C 55.66, H 5.19, N 14.42; found: C 55.51, H 5.28, N 14.50.
2c	White powder. Mp 124–126 °C. IR (KBr) (υ_{max}, cm^{-1}): 1387, 1560. ^{1}H NMR (Aceton-d_6) δ_H: 3.82 (3H, s, OCH_3), 4.97 (1H, dd, $^2J_{HH}$ = 15.9 Hz, $^3J_{HH}$ = 3.0 Hz, CH*H*), 5.42 (1H, dd, $^2J_{HH}$ = 15.9 Hz, $^3J_{HH}$ = 11.1 Hz, C*H*H), 6.88 (1H, dd, $^3J_{HH}$ = 11.0 Hz, $^3J_{HH}$ = 3.0 Hz, CH), 6.96 and 7.45 (4H, 2d, $^3J_{HH}$ = 9.3 Hz, arom.). ^{13}C NMR (Aceton-d_6) δ_C: 55.36 (OCH_3), 67.69 and 73.27 (C-N=O and C-NO_2), 114.52, 120.61, 129.01 and 160.73 (arom.). MS *m*/*z* (%): 210 (M$^+$, 8),179 (2), 121 (75), 91(45), 30 (100). Anal. calcd. for $C_9H_{10}N_2O_4$ (210.21) (%): C 51.42, H 4.79, N 13.33; found: C 51.52, H 4.90, N 13.30.
2d	White powder. Mp 128–129 °C. IR (KBr) (υ_{max}, cm^{-1}): 1375, 1484 and 1558. ^{1}H NMR (Aceton-d_6) δ_H: 5.08 (1H, dd, $^2J_{HH}$ = 15.8 Hz, $^3J_{HH}$ = 2.5 Hz, CH*H*), 5.58 (1H, dd, $^2J_{HH}$ = 15.8 Hz, $^3J_{HH}$ = 11.0 Hz, C*H*H), 6.88 (1H, dd, $^3J_{HH}$ = 11.0 Hz, $^3J_{HH}$ = 2.5 Hz, CH), 7.23 and 7.34 (4H, 2d, $^3J_{HH}$ = 8.1 Hz, arom.). ^{13}C NMR (Aceton-d_6) δ_C: 67.55 and 72.63 (C-N=O and C-NO_2), 128.42, 128.97, 129.68 and 135.16 (arom.). MS *m*/*z* (%): 214 (M$^+$, 2), 168 (4), 138 (100), 103 (91), 30 (90). Anal. calcd. for $C_8H_7N_2O_3Cl$ (214.63) (%): C 44.77, H 3.29, N 13.05; found: C 44.82, H 3.34, N 13.14.
2e	White powder. Mp 129–131 °C. IR (KBr) (υ_{max}, cm^{-1}): 1390, 1562. ^{1}H NMR (Aceton-d_6) δ_H: 5.03 (1H, dd, $^2J_{HH}$ = 16.0 Hz, $^3J_{HH}$ = 3.0 Hz, CH*H*), 5.45 (1H, dd, $^2J_{HH}$ = 16.0 Hz, $^3J_{HH}$ = 11.1 Hz, C*H*H), 6.96 (1H, dd, $^3J_{HH}$ = 11.1 Hz, $^3J_{HH}$ = 3.0 Hz, CH), 7.20 and 7.61 (4H, 2m, arom.). ^{13}C NMR (Aceton-d_6) δ_C: 66.91 and 73.06 (C-N=O and C-NO_2), 115.84 (d, $^2J_{FC}$ = 22.0 Hz), 126.29 (d, $^4J_{FC}$ = 3.5 Hz), 130.38 (d, $^3J_{FC}$ = 8.8 Hz), and 163.31 (d, $^1J_{FC}$ = 247.3 Hz). MS *m*/*z* (%): 198 (M$^+$, 5), 168 (7), 122 (98), 109 (60), 75 (45), 30 (100). Anal. calcd. for $C_8H_7N_2O_3F$ (198.17) (%): C 48.49, H 3.56, N 14.13; found: C 48.53, H 3.60, N 14.24.
3b	Yellow oil. IR (KBr) (υ_{max}, cm^{-1}): 3100–3500 (O-H), 1669, 1597, and 1551. ^{1}H NMR (Aceton-d_6) δ_H: 2.34 (3H, s, CH_3), 5.84 (2H, s, CH_2), 7.24 and 7.65 (4H, 2d, $^3J_{HH}$ = 8.7 Hz, arom.), 11.40 (1H, s, OH). ^{13}C NMR (Aceton-d_6) δ_C: 20.32 (CH_3), 68.16 (C-NO_2), 125.94, 129.68, 130.35 and 139.38 (arom.), 146.11 (C=N). MS *m*/*z* (%): 194 (M$^+$, 2), 176 (7), 136 (98), 119 (100), 91 (75), 65 (27).
3c	Yellow oil. IR (KBr) (υ_{max}, cm^{-1}): 3100–3500 (O-H), 1549, and 1500. ^{1}H NMR (Aceton-d_6) δ_H: 3.83 (3H, s, OCH_3), 5.84 (2H, s, CH_2), 6.97 and 7.70 (4H, 2d, $^3J_{HH}$ = 9.0 Hz, arom.). 11.24 (1H, s, OH). ^{13}C NMR (Aceton-d_6) δ_C: 67.02 (OCH_3), 73.40 (C-NO_2), 114.81, 121.08, 129.06 and 160.89 (arom.), 139.46 (C=N). MS *m*/*z* (%): 210 (M$^+$, 3), 179 (15), 134 (100), 110(10), 76 (23).
3d	Yellow oil. IR (KBr) (υ_{max}, cm^{-1}): 3100–3500 (O-H), 1652, 1582 and 1548. ^{1}H NMR (Aceton-d_6) δ_H: 5.86 (2H, s, CH_2), 7.46 and 7.78 (4H, 2d, $^3J_{HH}$ = 8.6 Hz, arom.), 11.59 (1H, s, OH). ^{13}C NMR (Aceton-d_6) δ_C: 68.00 (C-NO_2), 127.66, 128.75, 133.19 and 134.99 (arom.), 146.90 (C=N). MS *m*/*z* (%): 214 (M$^+$, 5), 181 (23), 139 (100), 111(75), 75 (61).
3e	Yellow oil. IR (KBr) (υ_{max}, cm^{-1}): 3100–3500 (O-H), 1560 and 1508. ^{1}H NMR (Aceton-d_6) δ_H: 5.89 (2H, s, CH_2), 7.21 and 7.82 (4H, 2m, arom.), 11.35 (1H, s, OH). ^{13}C NMR (Aceton-d_6) δ_C: 67.38 (C-NO_2), 115.72 (d, $^2J_{FC}$ = 23.5 Hz), 125.75 (d, $^4J_{FC}$ = 3.5 Hz), 130.26 (d, $^3J_{FC}$ = 8.9 Hz), 147.07 (C=N), 163.20 (d, $^1J_{FC}$ = 247.3 Hz). MS *m*/*z* (%): 198 (M$^+$, 5), 180 (5), 121 (100), 109(90), 100 (75), 94 (60).

© 2008 NRC Canada

Fig. 1. ^{1}H NMR spectra of the appearance and disappearance of methylene signals of compound **3c** and **2c** at 298 K.

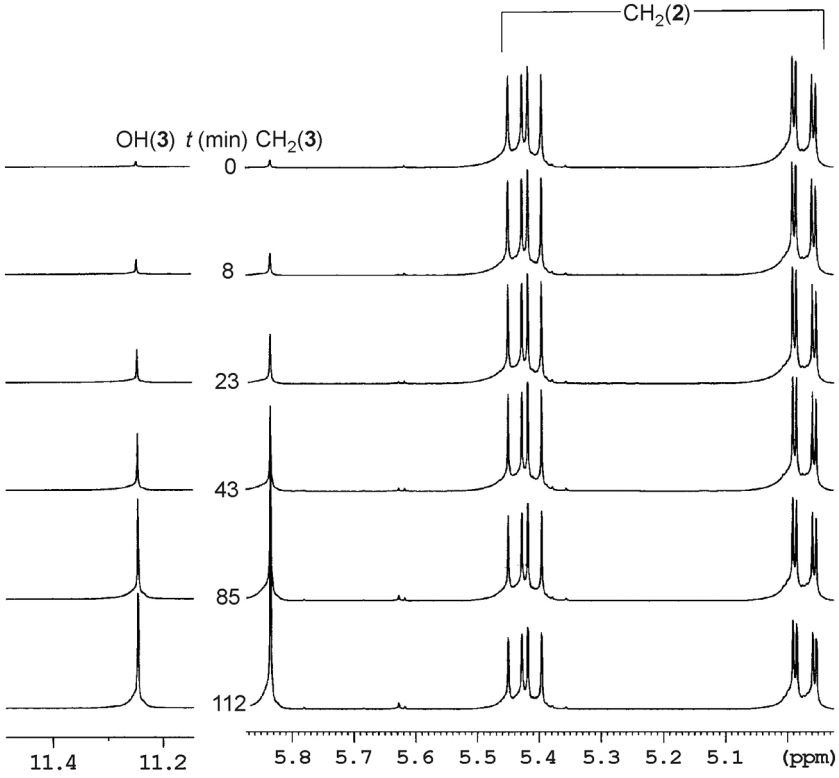

rene or substituted styrene had reacted. The product was separated by washing with acetone (3 × 10 mL) and the filtrate was evaporated to give the product. Compound **2** was obtained as a white solid, which without further purification was used for studying tautomerization.

Results and discussion

Products from the reaction of styrene and para-substituted styrenes

All of the products (except **2a** and **3a** (19)) are new compounds, which were identified from their IR, ^{1}H, and ^{13}C NMR spectra. The mass spectra of these compounds displayed molecular ion peaks at appropriate *m*/*z* values (Table 1).

The ^{1}H NMR spectrum of **2b** exhibited a single sharp line arising from methyl protons (δ 2.33) along with a three-spin AMX system for methylene and methine protons. This leads to a doublet of doublets for each of the protons of H^A, H^M, and H^X at 4.98 (1H, dd, $^2J_{HH}$ = 16.0 Hz, $^3J_{HH}$ = 3.0 Hz, CH_AH), 5.39 (1H, dd, $^2J_{HH}$ = 16.0 Hz, $^3J_{HH}$ = 11.1 Hz, CHH_M), and 6.90 ppm (1H, dd, $^3J_{HH}$ = 11.1 Hz, $^3J_{HH}$ = 3.0 Hz, CH_X), respectively. The aromatic protons appear at 7.24 and 7.38 ppm (4H, 2d, $^3J_{HH}$ = 7.9 Hz). The ^{1}H decoupled ^{13}C NMR spectrum of **2b** showed the distinct resonances in agreement with the proposed structure.

The ^{1}H NMR spectrum of **3b** exhibited two single sharp lines readily recognized as arising from methyl (2.34 ppm) and methylene (5.84 ppm) protons. The 4-substituted phenyl moiety gave rise to characteristic signals in the aromatic region of the spectrum (7.24 and 7.65 ppm, $^3J_{HH}$ = 8.7 Hz). A fairly broad singlet (11.40 ppm) is observed for the OH group, which upon addition of one drop of D_2O to the solution disappeared. The ^{1}H decoupled ^{13}C NMR spectrum of **3b** showed the distinct resonances in agreement with the proposed structure. Partial assignment of these resonances is given in the experimental section.

The ^{1}H and ^{13} C NMR spectra of **2a**, **2c**–**2e** and **3a**, **3c**–**3e** are similar to those of **2b** and **3b**, except for the phenyl groups, which exhibit characteristic signals with appropriate chemical shifts, respectively. The results are summarized in the experimental section.

Kinetics of the reaction of tautomerization

The discovery of new prototropic tautomerization and the study of its mechanism is one of the most important subjects in physical organic chemistry, and investigations on tautomeric processes were surveyed by several reviews (20–28). Tautomerization of 2-nitro-1-nitrosoethylbenzenes to the more stable oximes occurs readily in solution. Oximes are, of course, important synthons in many organic reactions of which Beckman rearrangement is illustrated (29, 30).

For the tautomerization study, a fresh sample of 4-X-substituted of 2-nitro-1-nitrosoethylbenzene (**2**) was dissolved in $(CD_3)_2CO$ (0.01 g in 0.4 mL $(CD_3)_2CO$ in 5 mm NMR tube) and equilibrated at the required temperature. The progress of the tautomerization was monitored by recording the appearance and disappearance of the methylene signal of **3** and **2**, respectively, (Fig. 1). Integration of the area under the methylene signal of **3** with respect to that of the methylene signals of **2** gave the relative concentrations of the species present, [C]. The rate of the reaction is given by rate = $+k[C]^x$, where x is the reaction order. The integrated rate equation for a first order reaction is $\ln[C]_t = kt + \ln[C]_0$. A

© 2008 NRC Canada

Scheme 2.

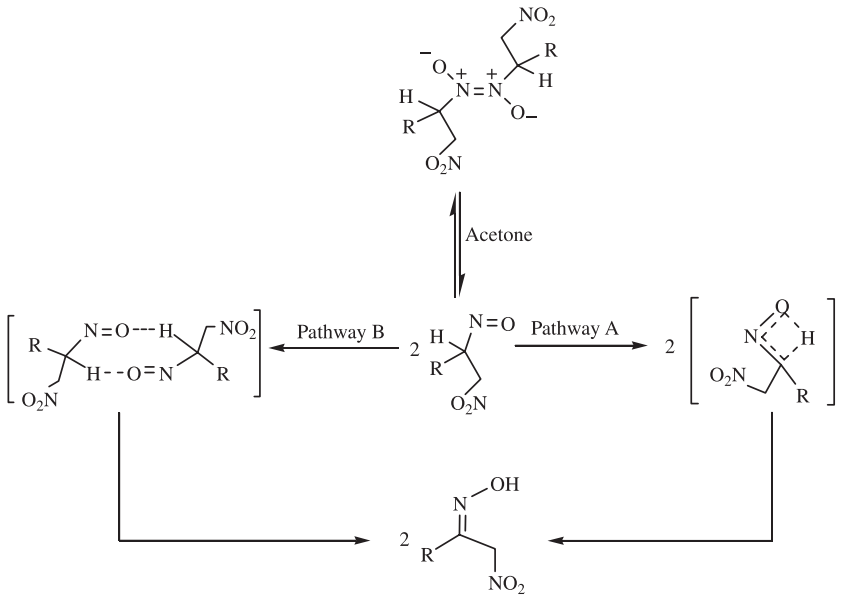

Table 2. Kinetic parameters for the tautomerization of compounds **2** to **3**.

Entry	X	E_{act} (kJ·mol^{-1})	$\Delta S^{\#}$ (J·mol^{-1} K^{-1})	$\Delta H^{\#}$ (kJ·mol^{-1})
2a	H	26.8	–191.8	24.2
2b	CH_3	28.4	–183.4	25.9
2c	OCH_3	34.7	–161.4	32.2
2d	Cl	35.9	–166.1	32.6
2e	F	25.9	–193.6	23.4

Table 3. Rates of tautomerization of **2** to **3** at 298 K in acetone.

Entry	X	k (min^{-1}) × 10^{-2}	σ_p[a]
2a	H	4.5±0.4	0.00
2b	CH_3	4.9±0.4	–0.14
2c	OCH_3	5.7±0.3	–0.28
2d	Cl	3.4±0.4	0.25
2e	F	4.1±0.3	0.15

[a]Ref. 31.

plot of ln[C]$_t$ vs. time should yield a straight line if the reaction is first order. The slope of this line is equal to k. The rate constants were obtained at several temperatures: 298, 303, 308, and 313 K.

By taking the natural logarithm of the Arrhenius equation, the activating energy, E_{act}, was obtained from a plot of ln$k$ vs. 1/T. Enthalpies of activation, $\Delta H^{\#}$, were also obtained from a plot of ln(k/T) vs. 1/T. Furthermore, the intercept in such a correlation gives enthropies of activation, $\Delta S^{\#}$. These data (E_{act}, $\Delta H^{\#}$ and $\Delta S^{\#}$) are given in Table 2.

According to the Hammett equation of $\log(k_x/k_0) = \rho\sigma_p$, where k_x is the rate constant of the tautomerization being studied with a substituted X present and k_0 is the corresponding rate constant of the unsubstituted compound (X = H) (Table 3), a plot of $\log(k_x/k_0)$ vs. σ_p gives the slope of the

Fig. 2. Plot of $\log(k_x/k_0)$ vs. σ_p constant for para-subsituted styrene.

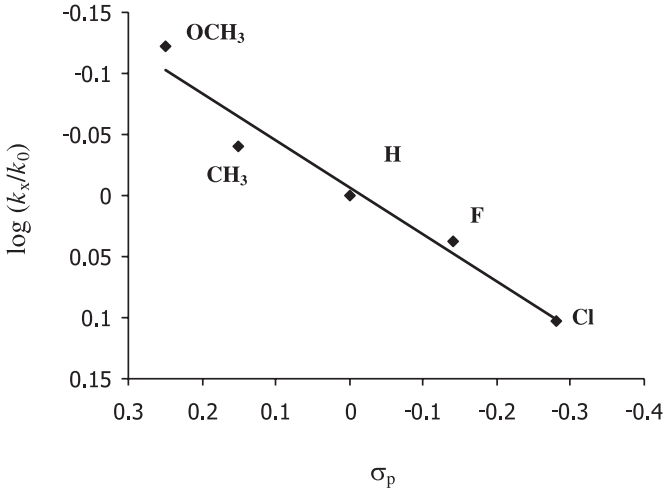

line or reaction constant, ρ. A Hammett plot of these data vs. σ_p (Fig. 2) gives a good straight line through the points for the para-H, CH_3, OCH_3, Cl, and F compounds and a value for $\rho = -0.38 \pm 0.02$ ($R^2 = 0.96$) at 298 K. The very small magnitude of ρ indicates relative insensitivity of the reaction to electronic effects.

The magnitude of the activation parameters, $\Delta H^{\#}$ and $\Delta S^{\#}$, reflects the transition state structure. It can be seen from Table 2 that the relatively low entropy of activation for this tautomerization suggests a mechanism that is compatible with a cyclic activated complex, in which bond-making accompanies bond-breaking. In addition, the fact that the entropies of activation are negative and their magnitudes are relatively large refers to the loss of rotational, translational, and vibrational degrees of freedom associated with highly ordered transition states supporting this complex formation.

In summary, all of the preceding data are fully consistent with and indicative of an intramolecular concerted 1,3-

© 2008 NRC Canada

hydrogen migration involving a four-center transition state (pathway A) or an intermolecular dimeric mechanism (pathway B) where O–H bond formation cannot significantly precede C–H bond-breaking to be consistent with observed $\Delta H^{\#}$ and ρ (Scheme 2).

The results of modern studies have shown that the mechanism of proton transfer through an intramolecular mechanism are sometimes both energetically and geometrically unfavorable (20). From this viewpoint and the negative large magnitude of $\Delta S^{\#}$, the intermolecular dimeric mechanism seems to be more reasonable for the tautomerization of compound **2** to **3**.

Acknowledgement

We gratefully acknowledge the financial support from the Research Council of Shahid Beheshti University.

References

1. B.G. Gowenlock and G.B. Richter-Addo. Chem. Rev. **104**, 3315 (2004).
2. W. Filehne. Arch. Exp. Pathol. Pharmakol. **9**, 329 (1878).
3. R.F. Loeb, A.V. Bock, and R. Fitz. Am. J. Med. Sci. **161**, 539 (1921); Chem. Abstr. **15**, 1761 (1921).
4. J.B. Schenkman, B.J. Wilson, and D.L. Cinti. Biochem. Pharmacol. **21**, 2373 (1972).
5. M.R. Franklin. Mol. Pharmacol. **10**, 975 (1974).
6. D. Mansuy, P. Beaune, T. Cresteil, C. Bacot, J.-C. Chottard, and P. Gans. Eur. J. Biochem. **86**, 573 (1978).
7. J. Lee, L. Chen, A.H. West, and G.B. Richter-Addo. Chem. Rev. **102**, 1019 (2002).
8. S.R. Sandler and W. Karo. In Organic functional group preparations. 2nd ed. Vol. 2. Academic Press, Orlando, Fla. 1986. Chap. 16.
9. C.L.H. Williams. *In* Nitrosation. Cambridge University Press, Cambridge, UK. 1988. Chap. 2 and 3.
10. A.V. Stepanov and V.V. Veselovsky. Russ. Chem. Rev. **72**, 327 (2003).
11. J.H. Boyer. *In* The chemistry of the nitro and nitroso groups. Part 1. *Edited by* H. Feuer. Interscience, New York. 1960. Chap. 5. pp. 215–299.
12. R.S. Varma. Green Chem. **1**, 43 (1999).
13. K. Tanaka and F. Toda. Chem. Rev. **100**, 1025 (2000).
14. Ger. Offen. 2036681 (1971); Chem. Abstr. **74**, 99646c (1971).
15. K.W. Chiu, P. Savage, G. Wilkinson, and D.J. Williams. Polyhedron, **4**, 1941 (1985).
16. J.A. Long, N.J. Harris, and K. Lammertsma. J. Org. Chem. **66**, 6762 (2001).
17. R. Glaser, R.K. Murmann, and C.L. Branes. J. Org. Chem. **61**, 1047 (1996).
18. H. Vancik, V. Simunic-Meznaric, E. Mestrovic, and I. Halasz. J. Org. Chem. **69**, 4829 (2004).
19. A. Shaabani, M. Ameri, and H.R. Bijanzadeh. J. Chem. Res. Synop. 572 (1998).
20. J.A. Kereselidze, T.S. Zarqua, T.J. Kikalishvili, E.J. Churgulia, and M.C. Makaridze. Russ. Chem. Rev. **71**, 993 (2002).
21. A.I. Kol'tsov and G.M. Kheifets. Russ. Chem. Rev. **40**, 773 (1971).
22. G. Klopman and P. Andreozzi. Bull. Soc. Chim. Belg. **86**, 481 (1977).
23. A.R. Katritzky and A.J. Boulton. Advances in heterocyclic chemistry. Suppl. 1. Academic Press, New York. 1976.
24. J. Toullec. Adv. Phys. Org. Chem. **18**, 1 (1982).
25. B.A. Shainyan and A.N. Mirskova. Russ. Chem. Rev. **48**, 107 (1979).
26. H. Schwarz and K. Levsen. In The chemistry of amine, nitroso, and nitro compounds and their derivatives. *Edited by* S. Patai. Wiley, New York. 1982.
27. R. Allman. *In* The chemistry of the hydrazo, azo, and azoxy groups. *Edited by* S. Patai. Wiley, New York. 1975.
28. A.I. Kol'tsov and G.M. Kheifets. Russ. Chem. Rev. **41**, 452 (1972).
29. M.T. Nguyen, G. Raspoet, and L.G. Vanquickenbotne. J. Chem. Soc. Perkin Trans. 2, 1791 (1995).
30. M.T. Nguyen and L.G. Vanquickenbotne. J. Chem. Soc. Perkin Trans. 2, 1969 (1993).
31. M.B. Smith and J. March. Advanced organic chemistry. 5th ed. John Wiley, New York. 2001.

© 2008 NRC Canada

Synthesis, characterization, and X-ray structures of three iridium(III)-hydrido-cyclometallated-imine complexes, including the first reported hydrido-(η^1-imine)-Ir complex

Fabio Lorenzini, Paolo Marcazzan, Brian O. Patrick, and Brian R. James

Abstract: Reactions of *cis*,*trans*,*cis*-[Ir(H)$_2$(PPh$_3$)$_2$(solv)$_2$]PF$_6$ (solv = MeOH or Me$_2$CO) with the imines HN=CPh$_2$, (*o*-HOC$_6$H$_4$)C(Me)=NCH$_2$Ph, and PhC(H)=N(*p*-F-C$_6$H$_4$) in MeOH or acetone under Ar give the complexes [IrH{NH=C(Ph)(*o*-C$_6$H$_4$)}(NH=CPh$_2$)(PPh$_3$)$_2$]PF$_6$ (**3**), [IrH{PhCH$_2$N=C(Me)(*o*-C$_6$H$_3$OH)}(solv)(PPh$_3$)$_2$]PF$_6$, where solv = MeOH (**4**) or Me$_2$CO (**4a**), and [IrH{N(*p*-F-C$_6$H$_4$)=CH(*o*-C$_6$H$_4$)}(Me$_2$CO)(PPh$_3$)$_2$]PF$_6$ (**5a**), which have been isolated and characterized. The imine (C$_6$F$_5$)C(H)=NPh is unreactive toward the Ir precursors. The X-ray structures of **3**, **4**·2MeOH, and **5a**·1/2Me$_2$CO show an η^2-*N*,*C*-imine moiety coordinated via the N atom and an orthometallated-C atom. Complex **3**, which contains both an orthometallated imine and an η^1-imine, is the first structurally characterized hydrido-(η^1-imine)-Ir complex. Comparisons are made with data for the corresponding Rh systems.

Key words: iridium, hydride complexes, imines, fluoroimines, phosphine complexes, orthometallation, crystallography, NMR spectroscopy.

Résumé : Les réactions du *cis*,*trans*,*cis*-[Ir(H)$_2$(PPh$_3$)(solv)$_2$]PF$_6$ (solv = MeOH ou Me$_2$CO) avec les imines HN=CPh$_2$, (*o*-HOC$_6$H$_4$)C(Me)=NCH$_2$Ph et PhC(H)=N(*p*-F-C$_6$H$_4$), en solution dans le MeOH ou l'acétone, sous une atmosphère d'argon, conduit à la formation des complexes [IrH{NH=C(Ph)(*o*-C$_6$H$_4$)}(NH=CPh$_2$)(PPh$_3$)$_2$]PF$_6$ (**3**), [IrH{PhCH$_2$N=C(Me)(*o*-C$_6$H$_3$OH)}(solv)(PPh$_3$)$_2$]PF$_6$ dans lequel solv = MeOH (**4**) ou Me$_2$CO (**4a**) et [IrH{N(*p*-F-C$_6$H$_4$)=CH(*o*-C$_6$H$_4$)}(Me$_2$CO)(PPh$_3$)$_2$]PF$_6$ (**5a**) qui ont été isolés et caractérisés. L'imine (C$_6$F$_5$)CH=NPh n'est pas réactive vis-à-vis les précurseurs Ir. Les structures des composés **3**, **4**·2MeOH et **5a**·1/2Me$_2$CO telles que déterminées par diffraction des rayons X ont permis de montrer la présence d'une portion η^2-*N*,*C*-imine coordinée par le biais de l'atome d'azote et d'un atome de carbone orthométallé. Le complexe **3** qui comporte une imine orthométallée ainsi qu'une η^1-imine est le premier complexe hydrido-(η^1-imine)-Ir à être caractérisée d'un point de vue structural. On a effectué des comparaisons avec des données pour les systèmes correspondants du rhodium.

Mots-clés : iridium, complexes d'hydrure, imines, fluoroimines, complexes de phosphine, organométallation, cristallographie, spectroscopie RMN.

[Traduit par la Rédaction]

Introduction

Since 2003, we have published 10 papers (1), including one review (2), on the hydrogenation of imines catalyzed by the Rh- and Ir-bis(triphenylphosphine) precursor complexes [M(cod)(PPh$_3$)$_2$]PF$_6$ (M = Rh, Ir; cod = 1,5-cyclooctadiene). Much diverse imine-coordination chemistry has been unveiled, important parameters being the structure and physical nature (solid or liquid) of the imine, the imine:metal stoichiometry, the presence of trace water, the nature of the solvent, use of an inert or an H_2 atmosphere, and catalyst poisoning by the amine product. The studies on the Ir systems, because of their lack of catalytic activity, have been more limited than those on the Rh systems. With imines containing an aryl moiety at the imine-C atom, the Ir precursor has generally formed (at 1:1 imine/Ir stoichiometries) monohydrido-Ir^{III} species via orthometallation at an ortho-C atom of an assumed [*trans*-Ir(PPh$_3$)$_2$(η^1-imine)(solv)]$^+$ intermediate, where solv = MeOH or Me$_2$CO (3); this 'standard' chemistry is illustrated in Scheme 1. With use of excess of the imine PhCH$_2$N=CHPh, the presence of trace water results in Ir-promoted hydrolysis of the imine and the generated benzylamine simply replaces the coordinated solvent of the orthometallated species (3). This new paper reports on the reactions of the Ir precursor with three imines, HN=CPh$_2$ (**Im^1**), (*o*-HOC$_6$H$_4$)C(Me)=NCH$_2$Ph (**Im^2**), and PhC(H)=N(*p*-F-C$_6$H$_4$) (**Im^3**) (see Scheme 2), and notes the non-reactivity of (C$_6$F$_5$)C(H)=NPh (**Im^4**). The imines **Im^1** and **Im^2** were chosen for comparison with their known reactivity toward the corresponding Rh precursor species (1), while the fluoro-substituted imines were used in the hope

Received 5 November 2007. Accepted 10 December 2007. Published on the NRC Research Press Web site at canjchem.nrc.ca on 15 February 2008.

F. Lorenzini, P. Marcazzan, B.O. Patrick, and B.R. James.[1] Department of Chemistry, The University of British Columbia, Vancouver, BC V6T 1Z1, Canada.

[1]Corresponding author (e-mail: brj@chem.ubc.ca).

 doi:10.1139/V07-153 © 2008 NRC Canada

Scheme 1. Formation of Ir^{III}-cyclometallated-imine complexes (R, R′ = aryl or alkyl). $[Ir(cod)(PPh_3)_2]^+$ under H_2 is known to generate *cis*,*trans*,*cis*-$[Ir(H)_2(PPh_3)_2(solv)_2]^+$ (solv = Me_2CO or MeOH (refs. 3, 4)).

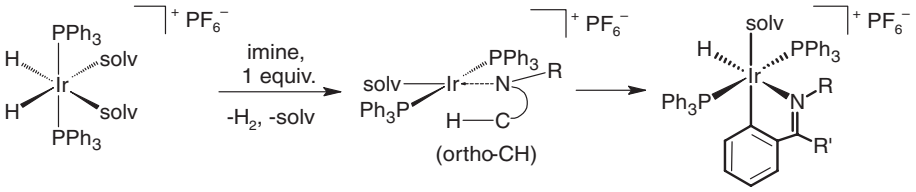

Scheme 2. Reactions of *cis*,*trans*,*cis*-$[Ir(H)_2(PPh_3)_2(solv)_2]PF_6$ (solv = MeOH (**2**) or Me_2CO (**2a**)) with the imines **Im[1]**, **Im[2]**, and **Im[3]** to form the complexes $[IrH\{NH{=}C(Ph)(o\text{-}C_6H_4)\}(\eta^1\text{-}NH{=}CPh_2)(PPh_3)_2]PF_6$ (**3**), $[IrH\{PhCH_2N{=}C(Me)(o\text{-}C_6H_3OH)\}(solv)(PPh_3)_2]PF_6$ (solv = MeOH (**4**) or Me_2CO (**4a**)), and $[IrH\{N(p\text{-}C_6H_4\text{-}F){=}CH(o\text{-}C_6H_4)\}(solv)(PPh_3)_2]PF_6$ (solv = MeOH (**5**) or Me_2CO (**5a**)). **Im[4]** showed no reactivity.

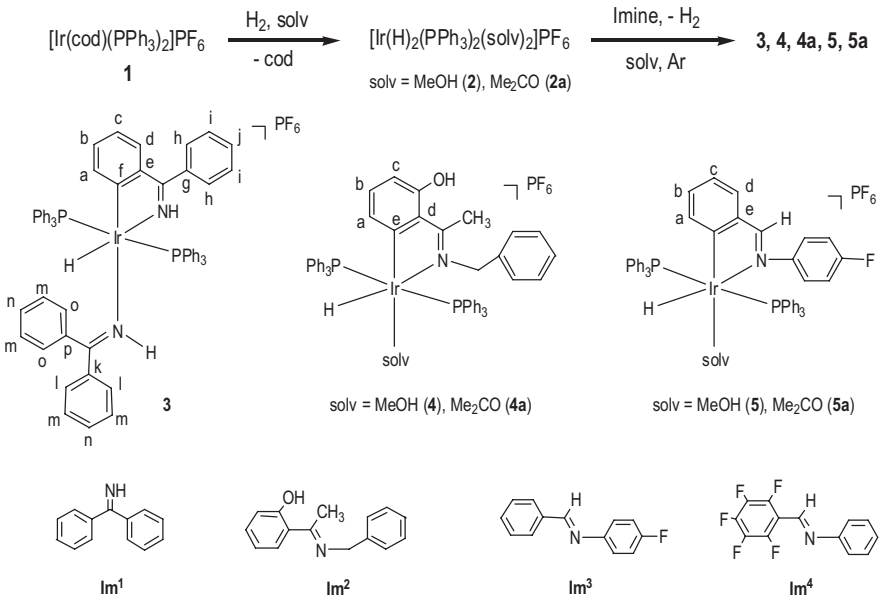

that the product might be a monometallic η^2-C=N (π-bonded) species because electron-withdrawing substituents appear to favour side-on bonding of imines (5). Such species have not been detected in metal complex-catalyzed hydrogenation of imines and whether they play a mechanistic role (as do π-bonded olefins in catalyzed olefin hydrogenations) is an important, unanswered question (6). We find, in fact, that **Im[1]**, **Im[2]**, and **Im[3]** all form hydrido-orthometallated species akin to those shown in Scheme 1, although in the **Im[1]** product the solvent has been replaced by a second η^1-bonded **Im[1]**. The product from the **Im[1]** reaction corresponds to that found earlier for the Rh system (1*b*); however, the structure presented is the first reported for a hydrido-η^1-imine complex of Ir. The product from the **Im[2]** reaction is different from that of the corresponding Rh system, which does not give an orthometallated product (1*a*). Comparisons between the Ir and Rh reactions with **Im[3]** and **Im[4]** systems are also mentioned.

Experimental

All manipulations and synthetic procedures were performed at room temperature (rt, ~20 °C) under an atmosphere of dry Ar or extra-dry H_2 (from Praxair, Edmonton, Alta.) as stated, using standard Schlenk techniques. The liquid imine $HN{=}CPh_2$ was a Sigma-Aldrich product, while the solid imines $(o\text{-}HOC_6H_4)C(Me){=}NCH_2Ph$, $PhC(H){=}N(p\text{-}F\text{-}C_6H_4)$, and $(C_6F_5)C(H){=}NPh$ were synthesized previously in this laboratory (7*a*); recent papers by other groups have also described the syntheses of the solid imines, which involve condensation of the ketones or aldehydes with the appropriate amine (7*b*, 7*c*).

The $[Ir(cod)(PPh_3)_2]PF_6$ complex (**1**) was prepared according to a literature procedure (8) using $IrCl_3{\cdot}3H_2O$ purchased from Colonial Metals Inc. Acetone and MeOH (Fisher Scientific) were dried over K_2CO_3 and Mg/I_2, respectively, and distilled under N_2. Acetone-d_6, CD_2Cl_2, and CD_3OD (Cambridge Isotope Laboratory) were used as received for measuring $^{31}P\{^1H\}$, $^{13}C\{^1H\}$, and ^1H NMR spectra at rt on a Bruker AV400 spectrometer. When necessary, atom assignments were made by means of $^1H\text{-}^{13}C\{^1H\}$ (HSQC and HMBC) and $^1H\text{-}^{31}P\{^1H\}$ (HSQC and HMBC) NMR correlation spectroscopies. Residual protonated species in the deuterated solvents were used as internal references (δ: 2.05 q for acetone-d_6; δ: 5.32 t for CD_2Cl_2; and δ: 3.31 q and 4.87 s for CD_3OD). All shifts are reported in ppm (s = singlet, d = doublet, t = triplet, q = quintet, spt = septet, m = multiplet, br = broad), relative to external $SiMe_4$ or 85% aq. H_3PO_4, with *J* values in Hz. Solid samples of the synthesized complexes were stored at rt under Ar; elemental

© 2008 NRC Canada

analyses were performed on a Carlo Erba 1108 analyzer. ESI-MS were acquired in the positive ion mode on a Bruker Esquire LC ion-trap mass spectrometer equipped with an electrospray ion source; solvents used were acetone/MeOH or CH_2Cl_2/MeOH, and the sample solution of concentration ~25–50 μmol/L was infused into the ion source by a syringe pump at a flow-rate of 700 μL/h. MALDI-MS were obtained on a Bruker Biflex IV MALDI-TOF spectrometer equipped with a nitrogen laser. The samples were dissolved in acetone/MeOH or CH_2Cl_2/MeOH and dithranol was used as matrix. The sample solutions (~1 mg/mL) and the matrix (20 mg/mL) were mixed in a ratio of 1:1 to 1:10, and 1 μL of the mixture was deposited onto the sample target; these spectra were acquired in the positive reflection mode with delay extraction by averaging 100 laser shots, and were calibrated externally using peptides. MS data are reported as *m*/*z* values. IR spectra were measured with a Thermo Nicolet FT-IR Nexus spectrometer using either a KBr pellet or a solution, as stated.

[IrH{NH=C(Ph)(*o*-C_6H_4)}(HN=CPh_2)(PPh_3)$_2$]PF_6 (3)

A red suspension of [Ir(cod)(PPh_3)$_2$]PF_6 (**1**) (61 mg, 0.063 mmol) in MeOH (1.8 mL) was reacted with 1 atm H_2 at rt to generate immediately a brown solution containing *cis*,*trans*,*cis*-[Ir(H)$_2$(PPh_3)$_2$(MeOH)$_2$]PF_6 (**2**) (3, 4). HN=CPh_2 (**Im^1**) (22.0 μL, 0.127 mmol) in MeOH (0.5 mL) was then added under H_2. Stirring the mixture at rt for 90 min resulted in precipitation of a yellow solid that was collected, washed with Et_2O (3 × 5 mL), and dried in vacuo (63 mg, 82% yield). IR (KBr, cm^{-1}): 3429 (ν_{N-H}), 2132 (ν_{Ir-H}), 1589, 1560 ($\nu_{C=N}$). IR (CH_2Cl_2, cm^{-1}): 3340 (ν_{N-H}), 2195 (ν_{Ir-H}), 1583, 1568 ($\nu_{C=N}$). ^{1}H NMR (CD_2Cl_2) (see Scheme 2 for atom-labeling) δ: –15.80 (t, 1H, $^2J_{HP}$ = 14.1, Ir*H*), 10.21 (s, *H*N=C(*o*-C_6H_4)), 9.98 (s, *H*N=CPh_2), 7.58 (t, 1H, $^3J_{HHi}$ ~ 7.6, H_j), 7.43 (d, 1H, $^3J_{HH}$ = 7.3, H_d), 7.39–7.06 (m, 38H, PC_6H_5, H_i, H_m, H_n), 6.86 (d, 2H, $^3J_{HH}$ = 7.7, H_l or H_o), 6.75 (t, 1H, $^3J_{HHa}$ ~ $^3J_{HHc}$ ≅ 7.3, H_b), 6.65 (t, 1H, $^3J_{HHb}$ ~ $^3J_{HHd}$ ~ 7.2, H_c), 6.56 (d, 1H, $^3J_{HH}$ = 7.5, H_a), 6.37 (d, 2H, $^3J_{HH}$ = 7.6, H_h), 6.28 (d, 2H, $^3J_{HH}$ = 7.5, H_l or H_o). ^{13}C{^{1}H} NMR (CD_2Cl_2) δ: 189.40 (s, NH=*C*(*o*-C_6H_4)), 179.32 (s, HN=*C*Ph_2), 151.59 (s, C_f), 147.32 (s, C_e), 142.04 (s, C_d), 137.97 (s, C_k or C_p), 137.01 (s, C_k or C_p), 134.69 and 131.88-127.93 (m, PC_6H_5, C_i, C_m, C_n), 133.82 (s, C_a), 131.18 (s, C_c), 129.86 (s, C_j), 129.43 (s, C_l or C_o), 128.65 (s, C_h), 128.64 (s, C_l or C_o), 121.23 (s, C_b); the C_g signal could not be assigned. ^{31}P{^{1}H} NMR (CD_2Cl_2) δ: 16.93 (s, *P*Ph), –143.70 (spt, $^1J_{PF}$ = 712.0, *P*F_6). ESI-MS: 1080 [M$^+$], 899 [M$^+$-NH=C(Ph)(*o*-C_6H_4)]. Anal. calcd. for $C_{62}H_{52}N_2F_6P_3Ir$: C 60.83, H 4.28, N 2.29; found: C 60.87, H 4.30, N 2.18.

Yellow, X-ray quality tablet crystals of **3** were grown at rt by diffusion of Et_2O into a CH_2Cl_2 solution (1.5 mL) of the complex (25 mg, 20.4 mmol).

[IrH{$PhCH_2$N=C(Me)(*o*-C_6H_3OH)}(solv)(PPh_3)$_2$]PF_6; solv = MeOH (4), Me_2CO (4a)

A red suspension of **1** (60 mg, 0.062 mmol) in acetone (1.0 mL) was reacted with 1 atm H_2 at rt to form a brown solution of *cis*,*trans*,*cis*-[Ir(H)$_2$(PPh_3)$_2$(Me_2CO)$_2$]PF_6 (**2a**).[2] Addition under Ar of (*o*-HOC_6H_4)C(Me)=NCH_2Ph (**Im^2**) (16 mg, 0.069 mmol) in acetone (1.0 mL) and subsequent stirring of the mixture at rt for 1 h generated a yellow solution. Addition of Et_2O (20.0 mL) precipitated a yellow powder that was collected, washed with Et_2O (2 × 10 mL), and dried in vacuo; the product is **4a** (51 mg, 72% yield). IR (KBr, cm^{-1}): 3057 (ν_{O-H}), 2195 (ν_{Ir-H}), 1587, 1579 ($\nu_{C=N}$). IR (acetone, cm^{-1}): 2034 (ν_{Ir-H}), 1581 ($\nu_{C=N}$). ^{1}H NMR (acetone-d_6) (see Scheme 2 for atom-labeling) δ: –15.48 (t, 1H, $^2J_{HP}$ = 17.6, Ir*H*), 8.94 (br s, 1H, O*H*), 7.51 (m, 5H, $CH_2C_6H_5$), 7.39 (m, 15H, PC_6H_5), 7.27 (t, 1H, $^3J_{HHa}$ ~ $^3J_{HHc}$ ~ 7.3, H_b), 7.04 (m, 15H, PC_6H_5), 6.49 (d, 1H, $^3J_{HHb}$ ~ 7.2, H_c), 6.28 (d, 1H, $^3J_{HHb}$ ~ 7.4, H_a), 5.50 (br s, 2H, NCH_2), 2.09 (br s, 3H, CH_3), 2.09 (br m, 6H, (CH_3)$_2$CO). ^{13}C{^{1}H} NMR (acetone-d_6) δ: 183.26 (s, *C*(H)=N), 159.20 (s, C_d), 136.52 (s, *C*-OH), 134.25 (m, PC_6H_5), 133.31 (s, C_a), 132.71 (m, $CH_2C_6H_5$), 128.59 (m, PC_6H_5), 127.94 (s, C_b), 110.83 (s, C_c), 56.99 (s, *C*H_2Ph) 20.66 (s, *C*H_3); the C_e signal could not be assigned. ^{31}P{^{1}H} NMR (acetone-d_6) δ: 17.91 (s, *P*Ph), –142.64 (spt, $^1J_{PF}$ = 707.3, *P*F_6). MALDI-MS: 942 [M-PF_6-Me_2CO]$^+$, 679 [M – H-PF_6-Me_2CO-PPh_3]$^+$.

X-ray quality, yellow prism crystals of **4**·2MeOH, as well as a yellow precipitate of **4**, were obtained at ~273 K from a saturated MeOH (2.0 mL) solution of **4a**; **4** was washed with Et_2O and dried in vacuo. Anal. calcd. for $C_{52}H_{49}N_4O_2F_6P_3Ir$ (**4**): C 55.81, H 4.41, N, 1.25; found: C 55.89, H 4.94, N 1.22.

[IrH{N(*p*-F-C_6H_4)=CH(*o*-C_6H_4)}(Me_2CO)(PPh_3)$_2$]PF_6 (5a)

A red solution of **1** (25 mg, 0.026 mmol) in acetone-d_6 (or acetone) (1.0 mL) was treated as above with H_2 to form a solution of **2a**. Addition under Ar of PhC(H)=N(*p*-F-C_6H_4) (**Im^3**) (6 mg, 0.030 mmol) in acetone-d_6 (or acetone) (0.5 mL) at rt resulted in a yellow solution into which slow diffusion of Et_2O generated overnight a yellow, crystalline powder (**5a**) and X-ray quality, yellow plate crystals of **5a**·1/2Me_2CO. The powder (**5a**) was collected, washed with Et_2O (3 × 5 mL), and dried in vacuo (24 mg, 83% yield). IR (KBr, cm^{-1}): 2206 (ν_{Ir-H}), 1599 ($\nu_{C=N}$). IR (CH_2Cl_2, cm^{-1}): 2217 (ν_{Ir-H}), 1599, 1587 ($\nu_{C=N}$). ^{1}H NMR (acetone-d_6) (see Scheme 2 for atom-labeling) δ: –16.98 (t, 1H, $^2J_{HP}$ = 15.8, Ir*H*), 8.15 (br s, 1H, C(*H*)=N), 7.49 (m, 6H, C_6H_4F, H_a, H_d), 7.40–7.30, 7.19–7.09 (m, 30H, PC_6H_5), 6.87 (br t, 1H, H_b or H_c), 6.55 (dt, 1H, $^3J_{HH}$ ~ 7.6, $^4J_{HH}$ ~ 1.2, H_b or H_c). ^{13}C{^{1}H} NMR (acetone-d_6) δ: 175.07 (s, *C*(H)=N), 146.88 (s, C_e), 131.43 (m, PC_6H_5), 129.42 (s, C_b or C_c), 128.84 (m, C_6H_4F, C_a, C_d), 126.69 (m, PC_6H_5), 119.39 (s, C_b or C_c). ^{31}P{^{1}H} NMR (acetone-d_6) δ: 17.69 (s, *P*Ph), –142.64 (spt, $^1J_{PF}$ = 707.3, *P*F_6). MALDI-MS: 917 [M-H-PF_6-Me_2CO]$^+$. Anal. calcd. for $C_{52}H_{48}NOF_7P_3Ir$: C 55.71, H 4.32, N 1.25; found: C 55.37, H 4.18, N, 1.25.

Attempted reactions with (C_6F_5)C(H)=NPh (Im^4)

Solutions of **2** and **2a** (and the corresponding species with solv = CD_3OD and acetone-d_6, see Scheme 2) were made in the appropriate solvents as described above, but using a smaller quantity of **1** (15 mg, 0.016 mmol) in 0.5 mL of the respective solvents. No rt reactions over several hours were seen on addition of **Im^4** (5 mg, 0.017 mmol), the NMR spec-

[2] All the complexes labelled with an 'a' have coordinated acetone.

© 2008 NRC Canada

Table 1. Crystal data for complexes **3**, **4**·2MeOH, and **5a**·1/2Me_2CO.

Crystal	**3**	**4**·2MeOH	**5a**·1/2Me_2CO
Empirical formula	$C_{62}H_{52}N_2F_6P_3Ir$	$C_{54}H_{57}N_4O_4F_6P_3Ir$	$C_{53.5}H_{49}NO_{1.5}F_7P_3Ir$
Formula weight	1224.17	1183.12	1148
Crystal system	Orthorhombic	Monoclinic	Monoclinic
Space group	$Pna2_1$ (no. 33)	$P2_1/n$ (no. 14)	$P2_1/c$ (no. 14)
Crystal size (mm^3)	0.10 × 0.18 × 0.35	0.12 × 0.20 × 0.50	0.05 × 0.20 × 0.40
a (Å)	27.947(1)	12.1301(5)	23.6030(10)
b (Å)	18.5418(7)	13.4827(7)	14.8451(7)
c (Å)	12.0971(5)	31.115(2)	28.2107(14)
α (°)	90.0	90.00	90.00
β (°)	90.0	95.718(2)	92.489(2)
γ (°)	90.0	90.00	90.00
Volume ($Å^3$)	6268.6(4)	5063.4(4)	9875.4(8)
Z	4	4	8
$D_{calcd.}$ (mg m^{-3})	1.297	1.552	1.544
Abs. μ (mm^{-1})	2.260	2.800	2.868
F(000)	2456.00	2384.00	4592.00
Reflections collected	40 584	64 532	129 567
Unique reflections [*R*(int)]	13 043 [0.051]	12 067 [0.051]	15 224 [0.097]
No. of variables	673	643	1212
GoF on F^2	1.05	1.03	1.20
Final *R* indices ($I > 2\sigma(I)$)	R_1 0.064,[a] wR_2 0.126[b]	R_1 0.048,[a] wR_2 0.065[b]	R_1 0.111,[a] wR_2 0.195[b]
Max. diff. peak/hole (e $Å^{-3}$)	3.84, –2.87	0.99, –1.12	3.87, –5.27

[a] $R_1 = \Sigma||F_o| - |F_c||/\Sigma|F_o|$.
[b] $wR_2 = [\Sigma(w(F_o^2 - F_c^2)^2)/\Sigma w(F_o^2)^2]^{1/2}$.

tra revealing the presence of only **2** or **2a**. ^{1}H NMR (CD_3OD) δ: –29.46 (t, 1H, $^2J_{HP}$ = 17.1, Ir*H*). $^{31}P\{^1H\}$ NMR (CD_3OD) δ: 27.16 (s, *P*Ph), –143.32 (spt, $^1J_{PF}$ = 707.5, *P*F_6). ^{1}H NMR (acetone-d_6) δ: –27.68 (t, 1H, $^2J_{HP}$ = 15.9, Ir*H*). $^{31}P\{^1H\}$ NMR (acetone-d_6) δ: 28.89 (s, *P*Ph), –142.62 (spt, $^1J_{PF}$ = 707.4, *P*F_6). These NMR data are in accord with literature values (3, 4).

X-ray crystallographic analyses of 3, 4·2MeOH, and 5a·1/2Me_2CO

Measurements were made at 173(1) K on a Bruker X8 APEX diffractometer using graphite-monochromated Mo-K α radiation (λ = 0.71073 Å); data were collected and integrated using the Bruker SAINT software package (9) and were corrected for absorption effects using the multi-scan technique (SADABS) (10) with minimum and maximum transmission coefficients of 0.551 and 0.798, respectively, for **3**, 0.434 and 0.715 for **4**·2MeOH, and 0.549 and 0.866 for **5a**·1/2Me_2CO. The data were corrected for Lorentz and polarization effects, and the structures were solved by direct methods (11). For **3**, one phenyl ring appears to be disordered over 2 sites; the 2 rings were thus refined using mild restraints with the major fragment refined anisotropically and the minor fragment isotropically. Located in difference maps and refined isotropically were the imine-H of the orthometallated imine of **3**, and the hydride and the H-atoms of the OH groups of the coordinated MeOH and the C_6H_3 ring of **4**. The hydrides of **3** and **5a** were not located and were thus not included in the models. All other H-atoms of the complexes were placed in calculated positions and were not refined. Some of the crystallographic data are given in Table 1, while selected bond lengths and angles are given in Table 2.

Results and discussion

The new complexes [IrH{NH=C(Ph)(*o*-C_6H_4)}(HN=CPh_2)-(PPh_3)$_2$]PF_6 (**3**), [IrH{$PhCH_2N$=C(Me)(*o*-C_6H_3OH)}(solv)-(PPh_3)$_2$]PF_6, where solv = MeOH (**4**) or Me_2CO (**4a**), and [IrH{N(*p*-F-C_6H_4)=CH(*o*-C_6H_4)}(Me_2CO)(PPh_3)$_2$]PF_6 (**5a**), were obtained by reaction of *cis*,*trans*,*cis*-[$Ir(H)_2(PPh_3)_2$(solv)$_2$]PF_6 (solv = MeOH (**2**) or Me_2CO (**2a**)) with the imine, with co-production of H_2 (Scheme 2); the complexes are of the well-documented hydrido-orthometallated-imine type (Scheme 1). Such complexes have been characterized for many metals (certainly for all the platinum metals; see following and ref. 12), and continue to attract attention because of their wide range of applicability in areas that include asymmetric synthesis, functionalization of C–H bonds, C-C coupling reactions, and biological systems (13).

Complex **3** was readily obtained in 82% yield from reaction in MeOH of **2** with 2 equiv. of benzophenone imine (HN=CPh_2, **Im^1**), and was fully characterized by X-ray analysis, elemental analysis, and NMR, IR, and MS data. Our group recently isolated the analogous Rh complex with essentially the same structure (see later), but the Rh species was formed more slowly via *cis*-[$Rh(PPh_3)_2$(η^1-NH=CPh_2)$_2$]PF_6 in which one imine ligand subsequently undergoes orthometallation (1*b*). No intermediates were detected in the Ir system, the stronger Ir-H bond (vs. Rh-H) presumably promoting the metallation step (14).

The reaction of **2** with (*o*-HOC_6H_4)C(Me)=NCH_2Ph (**Im^2**) in MeOH resulted in a mixture of products that could not be separated. However, a successful isolation of complex **4** was achieved by carrying out a 1:1 reaction of **2a** with **Im^2** in acetone and then recrystallizing the resulting isolated acetone analogue (**4a**) from MeOH. Complex **4a**, obtained in

© 2008 NRC Canada

Table 2. Selected bond lengths and angles for **3**, **4**·2MeOH, and **5a**·1/2Me_2CO.

3		**4**·2MeOH		**5a**·1/2Me_2CO[a]	
Bond lengths (Å)					
Ir(1)—C(1)	2.018(7)	Ir(1)—C(1)	1.998(3)	Ir(2)—C(53)	2.082(15)
Ir(1)—N(1)	2.138(6)	Ir(1)—H(1)	1.27(4)	Ir(2)—N(2)	2.157(12)
Ir(1)—N(2)	2.132(6)	Ir(1)—N(1)	2.151(3)	Ir(2)—O(2)	2.154(10)
Ir(1)—P(1)	2.3308(19)	Ir(1)—O(2)	2.237(2)	Ir(2)—P(3)	2.332(4)
Ir(1)—P(2)	2.331(2)	Ir(1)—P(1)	2.3320(8)	Ir(2)—P(4)	2.316(4)
N(1)—C(7)	1.296(9)	Ir(1)—P(2)	2.3310(8)	C(59)—N(2)	1.294(18)
C(14)—N(2)	1.265(9)	C(7)—N(1)	1.299(4)		
Bond angles (°)					
C(1)-Ir(1)-N(1)	78.7(3)	C(1)-Ir(1)-H(1)	95.9(16)	C(53)-Ir(2)-N(2)	79.3(5)
C(1)-Ir(1)-N(2)	177.1(3)	C(1)-Ir(1)-N(1)	78.27(11)	C(53)-Ir(2)-O(2)	170.4(5)
C(1)-Ir(1)-P(1)	87.3(2)	C(1)-Ir(1)-O(2)	178.07(10)	C(53)-Ir(2)-P(3)	87.3(4)
C(1)-Ir(1)-P(2)	89.6(2)	C(1)-Ir(1)-P(1)	88.04(8)	C(53)-Ir(2)-P(4)	88.3(4)
N(1)-Ir(1)-N(2)	98.6(2)	C(1)-Ir(1)-P(2)	88.95(8)	N(2)-Ir(2)-O(2)	91.1(4)
N(1)-Ir(1)-P(1)	92.21(16)	H(1)-Ir(1)-N(1)	173.8(16)	N(2)-Ir(2)-P(3)	94.6(3)
N(1)-Ir(1)-P(2)	92.40(17)	H(1)-Ir(1)-O(2)	84.6(16)	N(2)-Ir(2)-P(4)	97.2(3)
N(2)-Ir(1)-P(1)	91.70(16)	H(1)-Ir(1)-P(1)	88.6(15)	O(2)-Ir(2)-P(3)	94.5(3)
N(2)-Ir(1)-P(2)	91.58(16)	H(1)-Ir(1)-P(2)	76.7(15)	O(2)-Ir(2)-P(4)	92.0(3)
P(1)-Ir(1)-P(2)	173.88(7)	N(1)-Ir(1)-O(2)	101.26(10)	P(3)-Ir(2)-P(4)	166.37(14)
C(14)-N(2)-Ir(1)	134.7(5)	N(1)-Ir(1)-P(1)	93.26(7)	Ir(2)-O(2)-C(102)	137.6(13)
C(7)-N(1)-H(1n)	127(4)	N(1)-Ir(1)-P(2)	100.84(7)		
Ir(1)-N(1)-H(1n)	118(4)	O(2)-Ir(1)-P(1)	90.12(6)		
		O(2)-Ir(1)-P(2)	92.98(6)		
		P(1)-Ir(1)-P(2)	164.67(3)		
		C(34)-O(2)-Ir(1)	122.7(2)		

[a]Data for one of the two molecules in the asymmetric unit.

72% yield, was well characterized by NMR, MS, and IR data, but a satisfactory elemental analysis could not be obtained, possibly because of the variable acetone solvate content; complex **4** as a yellow powder gave a good elemental analysis for a non-solvated species, while the crystal contained two MeOH solvates per molecule as determined by X-ray analysis (see later).

Of note, the rate of formation of **4a** appears to be dependent on the water content of the solvent (acetone or methanol); in the synthetic work carried out in dried solvents, reaction was complete in ~1 h, but the reaction of **2a** with **Im²**, as monitored by $^{31}P\{^1H\}$ NMR spectroscopy in non-dried acetone-d_6, took ~13 d for completion (Fig. S1, δ_P: 28.89 for **2a** and 17.91 for **4a**).[2] Presumably, water competes with the solvent for a coordination site in **2a** and (or) **4a** and somehow impedes the reaction, although there was no direct evidence for the presence of any aquo species.

Reaction of **2a** with PhC(H)=N(*p*-F-C_6H_4) (**Im³**) at ~1:1 stoichiometry in acetone led to the isolation of **5a** in 83% yield as a mixture of a yellow powder and crystals after slow diffusion of Et_2O into the solution of **5a**; higher yields were obtained when a 2:1 ratio of **Im³**/Ir was used. Elemental analysis of the powder corresponded to unsolvated **5a**, while X-ray analysis of the crystal revealed one-half an acetone solvate per molecule (see below). NMR, MS, and IR data were in accord with the solid state structure. The formation of **5a** is apparently a reversible process as evidenced by monitoring under H_2 an acetone-d_6 solution of isolated **5a** by $^{31}P\{^1H\}$ NMR spectroscopy (Fig. S2)[3]: the δ_P 17.69 resonance of **5a** decays over a week and is partially replaced by the δ_P 28.89 signal of the Ir-dihydride (**2a**, where solv = acetone-d_6). Of note, no formation of **5** (the MeOH/CD_3OD analogue of **5a**) was evident when **2** (solv = CD_3OD) was reacted with ~1 mol equiv. of **Im³** in CD_3OD at rt; in situ $^{31}P\{^1H\}$ NMR spectra over several hours revealed only the δ_P 27.16 resonance of **2**, although over the period of a week this was replaced completely by broad singlets at δ_P 21.00 and 19.68 due to unidentified species (at an **Im³**:Ir ratio of 2, ~15% of **5** was formed over a week as evidenced by a resonance at δ_P 17.66). The complications detected by the NMR experiments may again be symptomatic of water impurity in the deuterated solvents and stresses the need for dry solvents in the synthetic procedures.

As monitored by $^{31}P\{^1H\}$ NMR spectroscopy, there was no reaction at rt of **2** or **2a** with (C_6F_5)C(H)=NPh (**Im⁴**) in the respective solvents at imine:Ir ratios up to 2.

The X-ray structures of the cations of **3**, **4**·2MeOH, and **5a**·1/2Me_2CO are shown in Figs. 1–3, and some geometrical

[2] Supplementary data for this article are available on the journal Web site (canjchem.nrc.ca) or may be purchased from the Depository of Unpublished Data, Document Delivery, CISTI, National Research Council Canada, Ottawa, ON K1A 0R6, Canada. DUD 3710. For more information on obtaining material refer to cisti-icist.nrc-cnrc.gc.ca/irm/unpub_e.shtml. CCDC numbers 670430–670432 contain the crystallographic data for this manuscript. These data can be obtained, free of charge, via www.ccdc.cam.ac.uk/conts/retrieving.html (or from the Cambridge Crystallographic Data Centre, 12 Union Road, Cambridge CB2 1EZ, UK; fax +44 1223 336033; or deposit@ccdc.cam.ac.uk).

© 2008 NRC Canada

Fig. 1. Structure of the $[IrH\{NH=C(Ph)(o\text{-}C_6H_4)\}(HN=CPh_2)(PPh_3)_2]^+$ cation of **3**, with 50% probability ellipsoids.

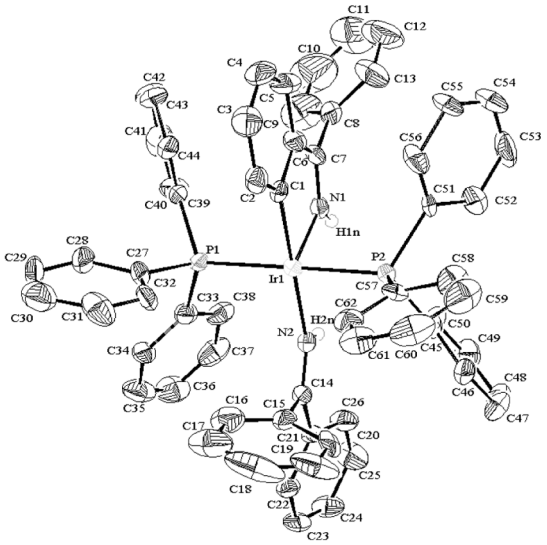

Fig. 2. Structure of the $[IrH\{PhCH_2N=C(Me)(o\text{-}C_6H_3OH)\}(MeOH)(PPh_3)_2]^+$ cation of **4**, with 50% probability ellipsoids.

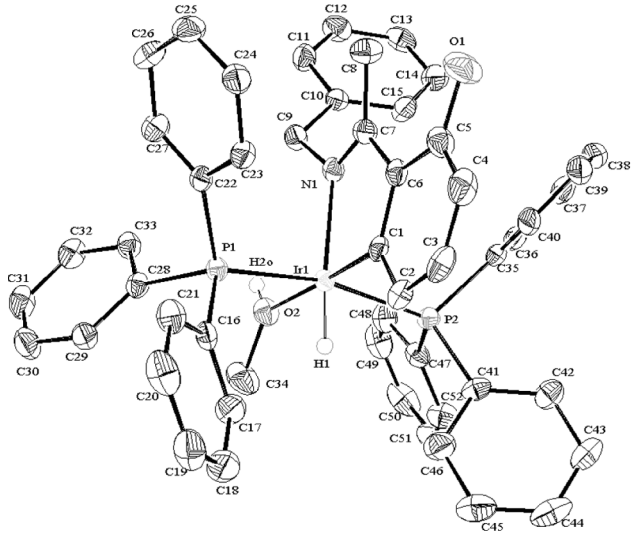

parameters are listed in Table 2. Complexes **3** and **4**·2MeOH crystallize with one molecule in the asymmetric unit, while **5a**·1/2Me_2CO crystallizes as two almost identical, crystallographically independent molecules with one molecule of free acetone in the asymmetric unit. The structures of the three distorted octahedral Ir^{III} cations exhibit similar features, all having five coordination sites occupied by the same arrangement of ligands: an η^2-imine moiety coordinated via the imine-N atom and the orthometallated-C atom (C_{ortho}), a hydride trans to the N-atom, and *trans*-PPh_3 ligands cis to the hydride (cf. Scheme 1), and, while **4** and **5a** respectively have MeOH or Me_2CO coordinated trans to C_{ortho}, **3** has a second imine, η^1-coordinated. The hydride attached to the heavy metal centre was successfully located by X-ray analysis only for **4**, but ^1H NMR data (a high-field triplet at δ_H –17 to –15 with $^2J_{HP}$ ~ 14–18 Hz, and IR data

Fig. 3. Structure of one of the two almost identical molecules of the $[IrH\{N(p\text{-}C_6H_4\text{-}F)=CH(o\text{-}C_6H_4)\}(Me_2CO)(PPh_3)_2]^+$ cation of **5a**, with 50% probability ellipsoids.

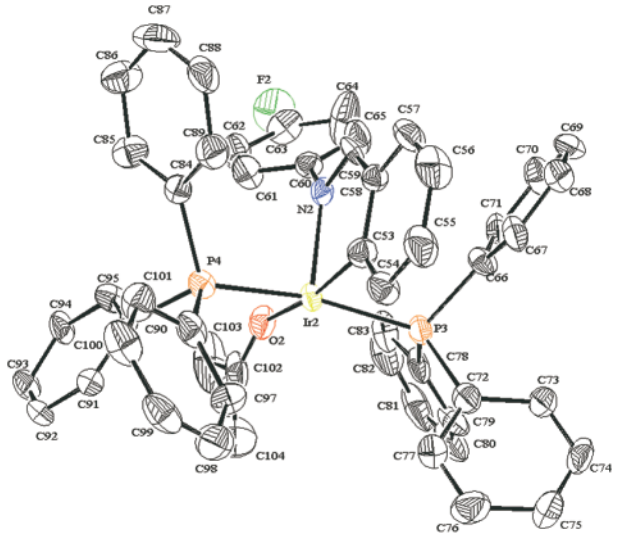

showing $\nu_{Ir\text{-}H}$ 2034–2217 cm^{-1}) unequivocally establish its presence in all three complexes. (Solid state and solution IR data for $\nu_{C=N}$ for **3**–**5**, $\nu_{N\text{-}H}$ for **3**, and $\nu_{O\text{-}H}$ for **4** are also noted). The hydride resonances are very similar to those we found earlier for an analogue of **5a** synthesized in the same manner but using $PhC(H)=NCH_2Ph$ (**3**). The imine-N*H* proton singlets for **3**, at δ 9.98 (for the η^1-imine) and 10.21 (for the η^2-imine), are close to the values reported for the same imine (**Im^1**) similarly coordinated at Ru^{II} and Os^{II} (15) but are ~3 ppm to lower field than those of the Rh analogue $[RhH\{NH=C(Ph)(o\text{-}C_6H_4)\}(HN=CPh_2)(PPh_3)_2]PF_6$ (1*b*). Measurements of 2D HSQC, HMBC $^{31}P\{^1H\}/^1H$, and 2D HSQC, HMBC $^{13}C\{^1H\}/^1H$ NMR spectra have allowed for assignment of all the ^1H NMR resonances of **3**, **4**, and **5a**. The $^{31}P\{^1H\}$ NMR spectra of **3**, **4a**, and **5a** each show a sharp singlet in the δ 18–17 region for the *trans*-phosphines, and a septet at δ ~–143 for the PF_6^- anion. Mass spectral data for complex **3** show the mass fragment of the intact cation, while the highest fragments seen for **4a** and **5a** correspond to $[IrH\{N(CH_2Ph)=C(Me)(o\text{-}C_6H_3OH)\}(PPh_3)_2]^+$ and $[Ir\{N(p\text{-}F\text{-}C_6H_4)=CH(o\text{-}C_6H_4)\}(PPh_3)_2]^+$, respectively.

The five-membered planar metallocycle ring within the complexes is essentially coplanar with the η^1-N atom of the second imine in **3**, the O-C of the MeOH in **4**·2MeOH, and the O-C-C_2 unit of the Me_2CO in **5a**. The N-Ir-C angle of the metallocycle of all three structures (79.3°–78.3°) is very similar to those found in other cyclometallated imine complexes of Ir^{III} (3) and also, for example, of Rh^{III} (16) and Os^{II} (17). The *trans*-PPh_3 ligands are bent slightly towards the hydride as indicated by P-Ir-P angles of 164.7° to 173.9° and other angles at the Ir centre (Table 2); all such hydridobis(phosphine)-orthometallated-imine complexes of Ir (3) and Rh (1*b*, 16) systems display such bending. The Ir-O-C angles of the coordinated MeOH in **4** and coordinated acetone in **5a** are 122.7° and 137.6°, respectively.

The Ir—P, Ir—N, and Ir—C_{ortho} bond lengths (and the C=N bond lengths for the η^2-*C*,*N*-imine) for the three complexes are in the range found previously for the closely re-

© 2008 NRC Canada

lated orthometallated-imine species [IrH{$PhCH_2N{=}CH(o\text{-}C_6H_4)$}$(PPh_3)_2L]PF_6$, where L = Me_2CO or $PhCH_2NH_2$ (3). The geometry of the orthometallated benzophenone ligand of **3** is also very similar to that of the same ligand within the Rh analogue of **3** (1*b*) and within complexes of Ru^{II} (15*d*) and Os^{II} (17). The C=N bond length of the η^1-NH=CPh_2 of **3** is about 0.2 Å shorter than that of the corresponding Rh complex (1*b*) and those found in other Rh^{I}- and Rh^{III}-(η^1-imine) complexes (18).

As far as we are aware, complex **3** is the first structurally characterized Ir(η^1-imine) complex, where the imine is a 'standard one', i.e., containing only alkyl, aryl, or hydrogen substituents at the imine-C and -N atoms; however, other such Ir(η^1-imine) complexes have been isolated, including benzophenone systems (19). Complex **3** is also a relatively rare example of a hydrido-η^1-imine species; except for the Rh analogue of **3** mentioned above (1*b*), all the other examples are η^1-benzophenone derivatives of Ru or Os (15). There is, of course, a vast literature on Ir complexes with 'non-standard' η^1-N=C < moieties within a range of ligands such as imine-ethers, iminols, and amidines (20), diimines (21), pyrazoles (22), imidazoles (22), oxazolines (23), oxazolones (24), anthranil (25), and creatinine (26).

The ketimine **Im^2**, containing an *o*-OH substituent in the imine-C phenyl group, forms complex **4**, a typical hydrido-orthometallated species akin to those we report here and elsewhere (3); however, this is the first type of such a complex derived from this ketimine. In complexes of Cu^{II} (27), Ru^{II} (28), and V^{IV} (29), the ketimine is chelated via the N-atom and the alkoxy-O atom from the hydroxy group. In recent work, on an analogous study of this imine with *cis*,*trans*,*cis*-$[Rh(H)_2(PPh_3)_2(MeOH)_2]PF_6$ (or *cis*-$[Rh(PPh_3)_2(MeOH)_2]PF_6$), we isolated an unique type of zwitterionic complex, namely $[Rh\{\eta^4\text{-}(C_6H_4O)^{(-)}C(Me){=}N^{(+)}(H)CH_2Ph\}(PPh_3)_2]PF_6$, in which the ketimine is coordinated via the C_4 part of the *o*-hydroxy-arene moiety in a quinoid form; this tautomer is generated via proton transfer from the O-atom to the N-atom within the molecular, benzenoid form. Presumably, the strength of the Ir–H bond again promotes the orthometallation.

Complex **5a** formed from **Im^3** is again a typical hydrido-orthometallated species, but we are unaware of any other such structures with this fluorinated imine. Of note, however, a recent structure with this imine, $Ni[^iPr_2P(CH_2)_2P^iPr_2]$-[PhC(H)=N(*p*-F-$C_6H_4$)], reveals the π-bonded **Im^3** (5), and indeed this report prompted us to investigate the reactivity of this particular imine toward Ir. The strength of the Ir–H bond again likely favours formation of **5a**. Of major interest, in a cursory study we have found that the reaction of **Im^3** with the Rh analogue of **2a** forms only a trace of a hydrido-orthometallated species, and the major product has yet to be identified.[3] The fluoro-aldimine $(C_6F_5)C(H){=}NPh$ (**Im^4**) was unreactive toward **2**, **2a**, or the corresponding Rh species; the reactivity of **Im^4** toward the Ni precursor used for the **Im^3** reaction, $[Ni\{^iPr_2P(CH_2)_2P^iPr_2\}]_2(\mu\text{-}H)_2$, was not reported (5). We continue studies with variation of the fluoroimine and the phosphine ligand in the hope of achieving an appropriate electronic and steric environment for formation of a π-bonded imine-Ir or -Rh complex.

Our previous studies have shown that isolated Ir-cyclometallated-imine complexes are stable toward H_2 in acetone or MeOH solution at ambient conditions and are not effective for catalytic hydrogenation of the imine (3, 30), and this has been confirmed recently by the Zaragosa group (31). The new complexes **3**–**5** are similarly inactive. In general, cyclometallated-imine Rh complexes can become active catalysts in MeOH, when they undergo partial reductive elimination of the cyclometallated imine (the reverse of orthometallation — cf. the intermediate shown in Scheme 1) to generate a solvated η^1-imine species that does react with H_2 (2, 16*a*). The Rh analogues of **3** (1*b*) and **5a**[4] are inactive toward H_2, while the Rh analogue of **4** (or **4a**) is unknown (see earlier), and the Ir and Rh complexes derived from **Im^3** in MeOH are not characterized.

Conclusions

Following our earlier work on the reactions between imines and *cis*,*trans*,*cis*-$[Rh(H)_2(PPh_3)_2(solv)_2]^+$ (solv = MeOH or Me_2CO), this article describes reactions of the imines with the corresponding Ir precursor species. The selected imines are $HN{=}CPh_2$, (o-HOC_6H_4)C(Me)=NCH_2Ph, and PhC(H)=N(p-F-C_6H_4), the last one being chosen with the aim of possibly favouring formation of an η^2-C=N (π-bonded) species. However, in each case, the product is a hydrido species containing an η^2-*N*,*C*-imine moiety coordinated via the N atom and an orthometallated-C atom. With benzophenone imine, the product contains also a second imine that is η^1-N coordinated, the product proving to be the first reported, structurally characterized hydrido-(η^1-imine)-Ir complex. The Ir complexes are inactive as precursor hydrogenation catalysts for the imines. Comparisons are made with the products formed in the corresponding Rh systems and significant differences are noted.

Acknowledgment

We thank the Natural Sciences and Engineering Research Council of Canada (NSERC) for financial support via a Discovery Grant.

References

1. (*a*) P. Marcazzan, B.O. Patrick, and B.R. James. J. Mol. Catal. A: Chem. **257**, 26 (2006), and refs. cited therein; (*b*) M.B. Ezhova, B.O. Patrick, and B.R. James. Organometallics, **24**, 3753 (2005), and refs. cited therein.
2. P. Marcazzan and B.R. James. *In* Educ. in Adv. Chem. *Edited by* B. Marciniec. Vol. 10. Wydawnictwo-Poznańskie, Poznań-Wroclaw, Poland. 2006. p. 121, and refs. cited therein.
3. P. Marcazzan, B.O. Patrick, and B.R. James. Russ. Chem. Bull. Int. Ed. **52**, 2715 (2003).
4. (*a*) R.H. Crabtree, P.C. Demou, D. Eden, J.M. Mihelcic, C.A. Parnell, J.M. Quirk, and G.E. Morris. J. Am. Chem. Soc. **104**, 6994 (1982); (*b*) R.R. Schrock and J.A. Osborn. J. Am. Chem. Soc. **98**, 4450 (1976).
5. A.L. Iglesias, M. Muñoz-Hernández, and J.J. García. J. Organomet. Chem. **692**, 3498 (2007), and refs. cited therein.

[3] F. Lorenzini and B.R. James. Unpublished data.

© 2008 NRC Canada

6. (*a*) P. Marcazzan, C. Abu-Gnim, K.N. Seneviratne, and B.R. James. Inorg. Chem. **43**, 4820 (2004); (*b*) B.R. James. Catal. Today, **37**, 209 (1997).
7. (*a*) D.E. Fogg. Ph.D. thesis. Department of Chemistry, University of British Columbia, Vancouver. 1994; (*b*) J. Wagler. Organometallics, **26**, 155 (2007); (*c*) H. Neuvonen, K. Neuvonen, and F. Fülöp. J. Org. Chem. **71**, 3141 (2006).
8. (*a*) R.H. Crabtree and G.E. Morris. J. Organomet. Chem. **135**, 395 (1977); (*b*) L.M. Haines and E. Singleton. J. Chem. Soc. Dalton Trans. 1891 (1972).
9. SAINT. Version 7.03A [computer program]. Bruker AXS Inc., Madison, Wis. 1997.
10. SADABS. Version 2.10 [computer program]. Bruker AXS Inc., Madison, Wis. 2003.
11. A. Altomare, M.C. Burla, M. Camalli, G.L. Cascarano, C. Giacovazzo, A. Guagliardi, A.G.G. Moliterni, G. Polidori, and R. Spagna. J. Appl. Crystallogr. **32**, 115 (1999).
12. (*a*) J. Albert, L. D'Andrea, J. Granell, R. Tavera, M. Font-Bardía, and X. Solans. J. Organomet. Chem. **692**, 3070 (2007), and refs. cited therein; (*b*) H.-F. Klein, S. Camadanli, R. Beck, D. Leukel, and U. Flörke. Angew. Chem. Int. Ed. **44**, 975 (2005), and refs. cited therein; (*c*) K.R. Flower, V.J. Howard, R.G. Pritchard, and J.E. Warren. Organometallics, **21**, 1184 (2002), and refs. cited therein.
13. (*a*) K. Godula and D. Sames. Science (Washington, D.C.), **312**, 67 (2006); (*b*) J. Dupont, C.S. Consorti, and J. Spencer. Chem. Rev. **105**, 2527 (2005); (*c*) F. Kakiuchi and S. Murai. Acc. Chem. Res. **35**, 826 (2002).
14. G.W. Parshall. Acc. Chem. Res. **3**, 139 (1970).
15. (*a*) S. Aime, E. Diana, R. Gobetto, M. Milanesio, E. Valls, and D. Viterbo. Organometallics, **21**, 50 (2002); (*b*) G. Barea, M.A. Esteruelas, A. Lledós, A.M. López, and J.I. Tolosa. Inorg. Chem. **37**, 5033 (1998); (*c*) M.J. Albéniz, M.L. Buil, M.A. Esteruelas, and A.M. López. J. Organomet. Chem. **545–546**, 495 (1997); (*d*) C. Bohanna, M.A. Esteruelas, A.M. López, and L.A. Oro. J. Organomet. Chem. **526**, 73 (1996).
16. (*a*) P. Marcazzan, B.O. Patrick, and B.R. James. Organometallics, **24**, 1445 (2005); (*b*) M.B. Ezhova, B.O. Patrick, K.N. Sereviratne, B.R. James, F.J. Waller, and M.E. Ford. Inorg. Chem. **44**, 1482 (2005); (*c*) M.B. Ezhova, B.O. Patrick, B.R. James, M.E. Ford, and F.J. Waller. Russ. Chem. Bull. Int. Ed. **52**, 2707 (2003); (*d*) L.-Y. Huang, U.R. Aulwurm, F.W. Heinemann, F. Knoch, and H. Kisch. Chem. Eur. J. **4**, 1641 (1998).
17. M.A. Esteruelas, E. Gutiérrez-Puebla, A.M. López, E. Oñate, and J.I. Tolosa. Organometallics, **19**, 275 (2000), and refs. cited therein.
18. (*a*) J. Vicente, M.-T. Chicote, R. Guerrero, I. Vicente-Hernández, M.M. Alvarez-Falcón, P.G. Jones, and D. Bautista. Organometallics, **24**, 4506 (2005), and refs. cited therein; (*b*) A.G. Becalski, W.R. Cullen, M.D. Fryzuk, B.R. James, G.-J. Kang, and S.J. Rettig. Inorg. Chem. **30**, 5002 (1991).
19. H. Werner, M. Müller, and P. Steinert. Z. Anorg. Allg. Chem. **629**, 1337 (2003).
20. C.S. Chin, D. Chong, B. Lee, H. Jeong, G. Won, Y. Do, and Y.J. Park. Organometallics, **19**, 638 (2000).
21. D. Herebian and W.S. Sheldrick. J. Chem. Soc. Dalton Trans. 966 (2002).
22. G. Albertin, S. Antoniutti, J. Castro, S. Garcia-Fontán, and E. Gurabardhi. J. Organomet. Chem. **691**, 1012 (2006), and refs. cited therein.
23. M.B. Ezhova, B.O. Patrick, B.R. James, F.J. Waller, and M.E. Ford. J. Mol. Catal. A: Chem. **224**, 71 (2004), and refs. cited therein.
24. W. Bauer, M. Prem, K. Polborn, K. Sünkel, W. Steglich, and W. Beck. Eur. J. Inorg. Chem. 485 (1998).
25. X. Li, C.D. Incarvito, T. Vogel, and R.H. Crabtree. Organometallics, **24**, 3066 (2005).
26. J.M. O'Connor, K. Hiibner, A.L. Rheingold, and L.M. Liable-Sands. Polyhedron, **16**, 2029 (1997).
27. R.M. Kirchner, G.D. Andreetti, D. Barnhart, F.D. Thomas, D. Welsh, and E.C. Lingafelter. Inorg. Chim. Acta, **7**, 17 (1973).
28. K.D. Keerthi, B.K. Santra, and G.K. Lahiri. Polyhedron, **17**, 1387 (1998).
29. N. Choudhary, D.L. Hughes, U. Kleinkes, L.F. Larkworthy, G.J. Leigh, M. Maiwald, C.J. Marmion, J.R. Sanders, G.W. Smith, and C. Sudbrake. Polyhedron, **16**, 1517 (1997).
30. P. Marcazzan. Ph.D. thesis. Department of Chemistry, University of British Columbia, Vancouver, BC. 2002.
31. M. Martín, E. Sola, S. Tejero, J.L. Andrés, and L.A. Oro. Chem. Eur. J. **12**, 4043 (2006).

© 2008 NRC Canada

Asymmetric nitroaldol reaction with a chiral copper complex derived from D-tartaric acid

Changsheng Gan

Abstract: A novel catalytic enantioselective Henry reaction has been developed using a tetradentate copper complex derived from D-tartaric acid to give β-nitroalkanols in moderate to high enantioselectivities.

Key words: Henry reaction, D-tartaric acid, enantioselective, β-nitroalkanols.

Résumé : On a développé le champ d'application de la nouvelle réaction catalytique énantiosélective d'Henry en utilisant le complexe tétradentate de cuivre de l'acide D-tartrique pour préparer des β-nitroalcanols avec des énantiosélectivités allant de modérées à élevées.

Mots-clés : réaction d'Henry, acide D-tartrique, énantiosélective, β-nitroalcanols.

[Traduit par la Rédaction]

Introduction

The nitroaldol reaction (or Henry reaction) constitutes an important class of C–C bond-forming reactions that provide straightforward access to important synthetic intermediates from readily accessible nitroalkanes and carbonyl compounds (1). Because of its significance in organic synthesis, considerable efforts have been devoted to the development of catalytic asymmetric nitroaldol reactions (2). Several efficient catalysts have been developed, such as BINOL by Shibasaki (3), bis(oxazoline) by Evans and Jørgensen (4), cinchona alkaloid by Deng (5), dinuclear zinc complex by Trost (6), amino alcohol (7), thiourea (8), and Schiff base catalysts (9). Because D-tartaric acid is available very cheaply from natural chiral sources, it has been widely studied in asymmetric catalysis, and different catalysts have been developed for a series of asymmetric reactions (10). We have been studying it for some time. In this article, we report a novel enantioselective Henry reaction catalyzed by a C_2-symmetric tetradentate catalyst **1** derived from D-tartaric acid, which is similar in structure to the salen derivative (11).

Scheme 1 summarizes the synthesis of complex **1** from D-tartaric acid. (4*S*, 5*S*)-(–)-Diethyl 2, 3-*O*-isopropylidene-D-tartarate (**2**) was prepared from D-(–)-tartaric acid using a reported procedure (12, 13). Dropping 25% ammonia into **2** in the presence of ammonium chloride in an ice-salt bath, then stirring overnight, gave diamide **3** in 85% yield. Reduction of the diamide moiety of **3** to diamine **4** with $LiAlH_4$ in refluxing ether for 18 h, followed by condensation with corresponding salicylaldehyde, provided chiral ligand **5**. Finally, mixing **5** and $Cu(OAc)_2 \cdot H_2O$ in methanol followed by the addition of excess sodium hydroxide produced the tetradentate copper complex **1**.

Scheme 1. The synthetic route of complex **1**.

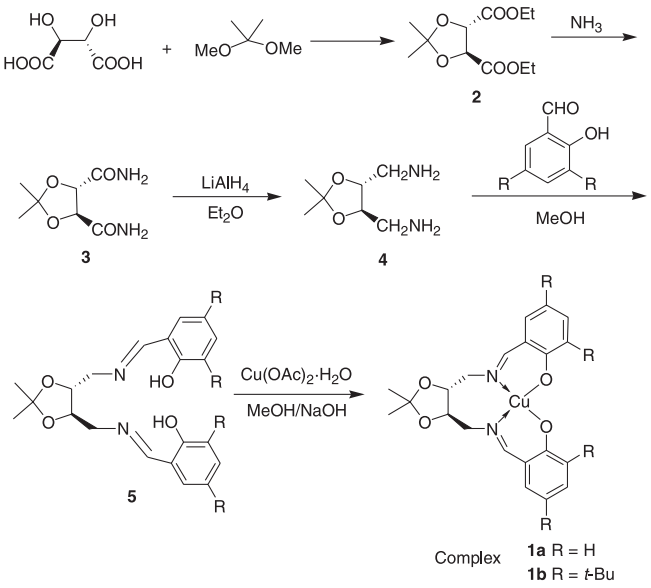

Results and discussions[2]

The complex **1** was added to a mixture of 4-nitrobenzaldehyde and nitromethane (Scheme 2). The results are shown in Table 1. Entries 1 and 2 show that the tetradentate complex **1b**, with a bulky *tert*-butyl substituent,

Received 18 October 2007. Accepted 13 January 2008. Published on the NRC Research Press Web site at canjchem.nrc.ca on 19 February 2008.

C. Gan.[1] Engineering Research Center of Bio-process of Ministry of Education, Hefei University of Technology, Hefei, Anhui 230009, P.R. China.

[1]Contact (e-mail: gancs@mail.ustc.edu.cn).

[2]Supplementary data for this article are available on the journal Web site (canjchem.nrc.ca) or may be purchased from the Depository of Unpublished Data, Document Delivery, CISTI, National Research Council Canada, Ottawa, ON K1A 0R6, Canada. DUD 3715. For more information on obtaining material refer to cisti-icist.nrc-cnrc.gc.ca/irm/unpub_e.shtml.

 doi:10.1139/V08-012 © 2008 NRC Canada

Table 1. Studies on the asymmetric nitroaldol reactions with chiral copper complexes.

Entry	Cat.	Solvent	CH_3NO_2	Time (h)	Yield[a] (%)	Ee[b] (%)
1	**1a**	Tol	2.5 mmol	80	38	12
2	**1b**	Tol	2.5 mmol	80	39	63
3	**1b**	CH_2Cl_2	2.5 mmol	80	42	34
4	**1b**	CH_3CN	2.5 mmol	80	36	23
5	**1b**	THF	0.5 mL	80	75	52
6	**1b**	Tol	0.5 mL	80	67	68
7	**1b**	Tol	1 mL	60	77	44
8	**1b**	EtOH	1 mL	60	79	26
9[c]	**1b**	Tol	0.5 mL	72	68	69
10[d]	**1b**	Tol	0.5 mL	72	66	59
11[e]	**1b**	Tol	1 mL	72	65	72
12[f]	**1b**	Tol	0.5 mL	24	95	11
13[g]	**1b**	Tol	0.5 mL	48	98	25

Note: All reactions were performed with 0.5 mmol 4-nitrobenzaldehyde, nitromethane, and 10 mol% of catalyst **1** in 2 mL solvent at room temperature unless otherwise specified.
[a]Isolated yield.
[b]Determined by chiral HPLC using an OD-H column.
[c]20 mol% of catalyst **1b** was used.
[d]100 mg 4A molecular sieve was added to the reaction mixture.
[e]4 mL toluene and 1 mL nitromethane were used.
[f]20 mol% Et_3N was added to the reaction mixture.
[g]The reaction was carried out at –20 °C in the presence of 20 mol% Et_3N.

Scheme 2. Asymmetric nitroaldol reaction of 4-nitrobenzaldehyde and nitromethane.

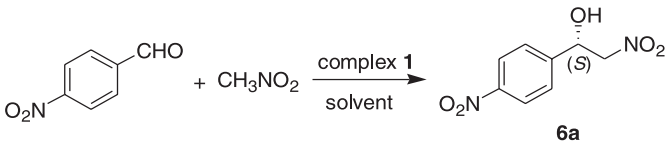

catalyzed the reaction much better than **1a**. Then different solvents were screened. Toluene proved the best, followed by THF, whereas EtOH, CH_2Cl_2, and CH_3CN gave only poor enantioselectivities (entries 2–5, 8). Increasing the amount of CH_3NO_2 to 0.5 mL promoted both the yield and the enantioselectivity (entry 6), but when 1 mL of CH_3NO_2 was used, the enantioselectivity was significantly decreased (entry 7). Neither increasing the amount of catalyst nor adding a molecular sieve to the reaction mixture was effective in improving the enantioselectivity (entries 9 and 10). But diluting the catalyst concentration by doubling the amount of solvent and nitromethane did further improve the enantioselectivity without significant loss of yield (entry 11). Conducting the reaction under lower temperature was then examined. However, very low enantioselectivity was obtained (entry 13). The absolute configuration of the product in Table 1 was determined as *S* by comparing the HPLC elution order of the enantiomers and the optical rotations reported in the literature (4*a*).

With the optimized reaction conditions, the complex **1b** was used to catalyze the addition of nitromethane to a variety of aldehydes (Scheme 3). The results are summarized in Table 2. Moderate enantioselectivities were obtained for the *para*-substituted aromatic aldehydes, such as 4-chlorobenzaldehyde (entry 2), 4-methoxybenzaldehyde (entry 5), and 4-methylbenzaldehyde (entry 8). 2-Chlorobenzaldehyde (entry 6) was shown to produce the highest enantioselectivity among all the substrates examined. When it came to the sterically less-encumbered benzaldehyde (entry 4), the ee value diminished to 48%. As far as aliphatic aldehydes were concerned, the enantioselectivities were only moderate (entries 9–11). The absolute configurations of the products in Table 2 were assigned as *S* based on the data reported in the literature (4, 9, 14), except for **6i**, whose configuration was not determined.

Table 2. Studies on the asymmetric nitroaldol reactions of nitromethane with various aldehydes.

Entry	R	Product	Time (h)	Yield (%)[a]	Ee (%)[b]
1	4-NO_2Ph	**6a**	72	65	72
2	4-ClPh	**6b**	72	64	58
3	1-naphthyl	**6c**	72	66	80
4	Ph	**6d**	72	61	48
5	4-MeOPh	**6e**	84	40	52
6	2-ClPh	**6f**	72	79	84
7	2-MeOPh	**6g**	72	71	70
8	4-MePh	**6h**	72	60	57
9	$PhCH_2$	**6i**	72	59	45[c]
10	*i*-Pr	**6j**	72	56	57
11	*i*-Bu	**6k**	72	60	61

Note: All reactions were performed on a 0.5 mmol scale with 10 mol% of complex **1b** using 1 mL nitromethane in 4 mL toluene. Reactions were run at room temperature for the indicated time.
[a]Isolated yields.
[b]Enantiomeric excess was determined by HPLC using a Chiracel OD-H or OJ-H column.
[c]The absolute configuration was not determined.

© 2008 NRC Canada

Scheme 3. Asymmetric nitroaldol reactions of nitromethane with various aldehydes.

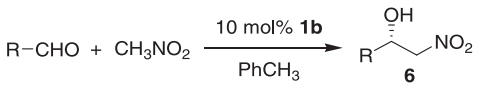

Conclusions

In summary, we have developed a novel and facile enantioselective nitroaldol reaction. It is the first reported use of tartaric acid derivatives in the catalytic enantioselective Henry reaction. Moderate to high enantioselectivities were obtained for the *ortho*-substituted aromatic aldehydes. This reaction works quite well at room temperature, avoiding the use of low temperature. Since the catalyst is very stable in the air, airproof conditions in N_2 or Ar are also unnecessary. Considering that the chiral catalyst can be readily prepared from naturally abundant tartaric acid, this method provides a practical and convenient way to prepare optically active nitroalkanols. Further study is currently in progress to improve the yield and enantiomeric excess and to elucidate the reaction mechanism.

References

1. F.A. Luzzio. Tetrahedron, **57**, 915 (2001).
2. For a recent review of catalytic asymmetric nitroaldol reactions, see: C. Palomo, M. Oiarbide, and A. Mielgo. Angew. Chem. Int. Ed. **43**, 5442 (2004).
3. (*a*) H. Sasai, T. Suzuki, S. Arai, T. Arai, and M. Shibasaki. J. Am. Chem. Soc. **114**, 4418 (1992); (*b*) T. Arai, Y.M.A. Yamada, N. Yamamoto, H. Sasai, and M. Shibasaki. Chem. Eur. J. **2**, 1368 (1996).
4. (*a*) D.A. Evans, D. Seidel, M. Rueping, H.W. Lam, J.T. Shaw, and C.W. Downey. J. Am. Chem. Soc. **125**, 12692 (2003); (*b*) C. Christensen, K. Juhl, R.G. Hazell, and K.A. Jørgensen. J. Org. Chem. **67**, 4875 (2002); (*c*) C. Christensen, K. Juhl, and K.A. Jørgensen. Chem. Commun. 2222 (2001); (*d*) D.M. Du, S.F. Lu, T. Fang, and J.X. Xu. J. Org. Chem. **70**, 3712 (2005); (*e*) S.F. Lu, D.M. Du, S.W. Zhang, and J.X. Xu. Tetrahedron: Asymmetry, **15**, 3433 (2004).
5. H. Li, B. Wang, and L. Deng. J. Am. Chem. Soc. **128**, 732 (2006).
6. B.M. Trost and V.S.C. Yeh. Angew. Chem. Int. Ed. **41**, 861 (2002).
7. (*a*) C. Palomo, M. Oiarbide, and A. Laso. Angew. Chem. Int. Ed. **44**, 3881 (2005); (*b*) Y.-W. Zhong, P. Tian, and G.-Q. Lin. Tetrahedron: Asymmetry, **15**, 771 (2004); (*c*) W. Mansawat, I. Saengswang, P. U-Prasitwong, W. Bhanthumnavin, and T. Vilaivan. Tetrahedron Lett. **48**, 4235 (2007).
8. (*a*) T. Marcelli, R. Haas, J.H. Maarseveen, and H. Hiemstra. Angew. Chem. Int. Ed. 45, 929 (2006); (*b*) Y. Sohtome, Y. Hashimoto, and K. Nagasawa. Adv. Synth. Catal. **347**, 1643 (2005).
9. (*a*) C. Gan, G. Lai, Z. Zhang, Z. Wang, and M.-M. Zhou. Tetrahedron: Asymmetry, **17**, 725 (2006); (*b*) M. Çolak, T. Aral, H. Hoşgören, and N. Demirel. Tetrahedron: Asymmetry, **18**, 1129 (2007); (*c*) G. Blay, E. Climent, I. Fernández, V. Hernandez-Olmos, and J.R. Pedro. Tetrahedron: Asymmetry, **17**, 2046 (2006).
10. (*a*) H.B Kagan and T. Dang. J. Am. Chem. Soc. **94**, 6429 (1972); (*b*) G. Parrinello and J.K. Stille. J. Am. Chem. Soc. **109**, 7122 (1987); (*c*) T. Katstukii and K.B. Sharpless. J. Am. Chem. Soc. **102**, 5976 (1980); (*d*) T. Imai, A. Yamamoto, and S. Masamune. J. Am. Chem. Soc. **108**, 7402 (1986).
11. For reviews on the salen catalyst, see: (*a*) E.M. McGarrigle and D.G. Gilheany. Chem. Rev. **105**, 1563 (2005); (*b*) T.P. Yoon and E.N. Jacobsen. Science, **299**, 1691 (2003).
12. M. Carmack and C.J. Kelly. J. Org. Chem. **33**, 2171 (1968).
13. C. Li. M.Sc. Thesis, Dalian Institute of Chemical Physics, Chinese Academy of Science, Dalian, China, 2000.
14. J. Tian, N. Yamagiwa, S. Matsunaga, and M. Shibasaki. Angew. Chem. Int. Ed. **41**, 3636 (2002).

© 2008 NRC Canada

Synthesis of 2,4,5-trisubstituted imidazoles catalyzed by [Hmim]HSO_4 as a powerful Brönsted acidic ionic liquid

Ahmad R. Khosropour

Abstract: An efficient and green procedure for the synthesis of 2,4,5-trisubstituted imidazoles with various aldehydes using a catalytic amount of 1-methylimidazolium hydrogenesulfate as an active and low cost Brönsted acidic room temperature ionic liquid has been developed. The ionic liquid was easily separated from the reaction mixture and was recycled five times without any loss in activity.

Key words: ionic liquid, 2,4,5-trisubstituted imidazoles, [Hmim]HSO_4, aldehyde, benzil.

Résumé : On a mis au point une méthode efficace et environnementalement correcte pour la synthèse d'imidazoles 2,4,5-trisubstitués utilisant divers aldéhydes et une quantité catalytique d'hydrogénosulfate de 1-méthylimidazolium actif comme acide de Brönsted à la température ambiante et comme liquide ionique de faible coût. On peut facilement séparer le liquide ionique du mélange réactionnel et le recycler au moins cinq fois sans la moindre perte d'activité.

Mots-clés : liquide ionique, imidazoles 2,4,5-trisubstitués, [Hmim]HSO_4, aldéhyde, benzile.

[Traduit par la Rédaction]

Introduction

The imidazole nucleus constitutes the core unit of many natural products (1–3). Also, this moiety is a popular building block for the construction of pharmaceutically interesting compounds and has attracted the attention of synthetic chemists for over a century (4–7). Multi-aryl substituted imidazoles, especially trisubstituted ones, could potentially have novel therapeutic activities (8, 9). In addition, many of the 2,4,5-triarylimidazoles are known as herbicides, fungicides (10), or as inhibitors of IL-1 or P38 MAP kinase (11–13). This class of compounds can be prepared by the condensation of benzil, ammonium acetate, and aldehydes in the presence of either protic or Lewis acids (14–20). However, many of these methods still suffer from some disadvantages, such as the use of toxic or expensive catalysts or reaction media, drastic reaction conditions, unsatisfactory yields, and limited scopes. This is especially true with alkyl aldehydes and some aryl aldehydes, such as nitrobenzaldehydes, that limit these methods. Therefore, the introduction of a new and efficient method for this transformation is still in demand.

Results and discussion

Since there is a growing demand for the development of organic reactions in environmentally friendly media, synthetic manipulations are required to minimize the use of hazardous chemicals, such as replacing toxic catalysts or organic solvents in reactions and their subsequent workup with other nontoxic solvents like water (21) or super critical CO_2 (22). In recent years, ionic liquids have attracted increasing interest in the context of green synthesis (23). Although ionic liquids were initially introduced as alternative green reaction media because of their unique chemical and physical properties of nonvolatility, nonflammability, thermal stability, and controlled miscibility (24–26), today they have evolved beyond this, showing their significant role in controlling reactions as catalysts (27, 28). However, sensitivity to moisture and decomposition of some ionic liquids under normal atmospheric conditions are two major drawbacks to their practical use (29). On the other hand, the high cost of most conventional room temperature (RT) ionic liquids and apprehension about their toxicity (30, 31) have led us to explore the use of more benign salts as practical alternatives. Recently, Binnemans and co-workers (32) reported that 1-methylimidazolium hydrogenesulfate ([Hmim]HSO_4), a powerful Brönsted acidic RT ionic liquid (BARTIL) is relatively nontoxic, readily available at low cost, and fairly stable in water, unlike some ionic liquids (e.g., [bpy]$AlCl_4$) that decompose readily in aqueous media.

Received 2 September 2007. Accepted 9 December 2007. Published on the NRC Research Press Web site at canjchem.nrc.ca on 22 February 2008.

A.R. Khosropour.[1] Catalysis Division, Department of Chemistry, Faculty of Science, University of Isfahan, Isfahan 81746–73441, Iran.

[1]Corresponding author (e-mail: khosropour@chem.ui.ac.ir).

 doi:10.1139/V08-009 © 2008 NRC Canada

Scheme 1.

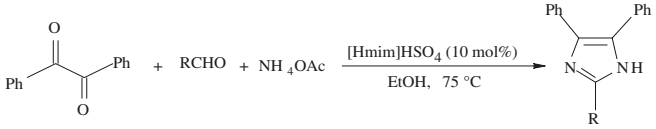

These results, in combination with our recent examination to design new synthetic methodologies (33–41) especially in RT ionic liquid (42–45), led us to develop a simple and efficient procedure for the direct synthesis of 2,4,5-trisubstituted imidazoles with various aldehydes using a catalytic amount of [Hmim]HSO_4 (Scheme 1).

The experimental procedure for this reaction is remarkably simple and does not require the use of toxic or expensive organic solvents or reagents. The reactions were carried out at 75 °C by taking a 1:1:10 mole ratio mixture of aldehydes, benzil, and ammonium acetate, respectively, in the presence of only 10 mol% of [Hmim]HSO_4 in ethanol to give the desired products in high to excellent yields.

It is important to note that the use of 10 mol% of [Hbim]BF_4 instead of [Hmim]HSO_4 resulted in no reaction.

To investigate the influence of the media, temperature, and amount of catalyst in this synthesis, for example, the condensation reaction of benzaldehyde with benzil and ammonium acetate was carried out (Table 1). Among all the systems tested, using 10 mol% of [Hmim]HSO_4 in EtOH (3 mL) at 75 °C proved to be the optimum condition (Table 1, entry 11). Using these optimized conditions, a wide range of substituted and structurally diverse aldehydes were subjected to this procedure to afford the corresponding products in good to excellent yields (Table 2).

The scope and generality of this process are illustrated by a series of 30 trisubstituted imidazoles, as can be seen in Table 2. The high-yield transformations were carried out without any significant amounts of undesirable side products. Unlike previously reported methods, the present method does not require toxic or anhydrous organic solvents to produce the 2,4,5-trisubstituted imidazoles derivatives. All the products were characterized by NMR, IR, and mass spectroscopy and also by comparison with authentic samples. A wide range of aromatic aldehydes were employed and all imidazoles were obtained in high to excellent yields (Table 2, entries 1–22), yielding a general method that tolerates both electron-withdrawing and electron-donating constituents. Another important aspect is that various functionalities such as ether, halide, nitro, nitrile, and hydroxyl, survived under the present reaction conditions.

Also, depending on the reaction times, terephthaldialdehydes can be selectively converted to their corresponding mono- or bis-(4,5-diphenyl)-1*H*-imidazole (Table 2, entries 9 and 10). Interestingly, we achieved that in the case of 4-(diethoxymethyl)benzenaldehyde (Table 2, entry 11); a one-pot deprotection–cyclization reaction was carried out in the reaction conditions. On the other hand, aliphatic aldehydes and unsaturated ones (Table 2, entries 23–30), which normally show extremely poor yields using previous methods, gave the corresponding imidazoles in high yields. The reaction conditions are mild enough not to induce any isomerization for conjugated aldehydes or damage to moieties, such as methoxy that often undergoes cleavage in strongly acidic reaction media (Table 2, entries 16–18, 20, and 23–25).

Table 1. Synthesis of 2-(phenyl)-4,5-diphenylimidazole in the presence of [Hmim]HSO_4 under different conditions.

Entry	[Hmim]HSO_4 (mol%)	Solvent (3 mL)	Temprature (°C)	Yield (%)[a]
1	30	CH_3CN	80	72
2	30	CH_2Cl_2	40	18
3	30	$CHCl_3$	61	36
4	30	CH_3OH	60	86
5	30	CH_3CH_2OH	75	95
6	30	CH_3CH_2OH	70	92
7	30	CH_3CH_2OH	60	89
8	25	CH_3CH_2OH	75	95
9	20	CH_3CH_2OH	75	95
10	15	CH_3CH_2OH	75	95
11	10	CH_3CH_2OH	75	95
12	5	CH_3CH_2OH	75	89

Note: After 3 h.
[a]Isolated yields.

In addition, the synthesis of imidazoles on a large scale (50 mmol) was tested. The reaction was demonstrated to be very efficient on this scale, and the products were obtained in excellent yields using the same reaction conditions. Another advantage of this promoter system is the recycleability of the catalyst; [Hmim]HSO_4 can be reused in five runs without any loss of activity.

In summary, we have developed an efficient, economical, and environmentally friendly procedure for the synthesis of 2,4,5-trisubstituted imidazoles. This involves the use of [Hmim]HSO_4 as an inexpensive, stable, and easily available Brönsted acidic RT ionic liquid. The use of a powerful, easy accessible, and recyclable ionic liquid makes this procedure quite simple, more convenient, and environmentally benign.

Experimental

General experimental procedure

A mixture of aldehyde (1 mmol), benzil (1 mmol), ammonium acetate (10 equiv.), and [Hmim]HSO_4 (0.1 mmol) in ethanol (3 mL) was stirred at 75 °C for the appropriate time, according to Table 1. After completion of the reaction, as indicated by TLC, the mixture was concentrated in vacuo to remove the solvent. The resulting solution was extracted by Et_2O (3 × 10 mL). The organic layer was dried (Na_2SO_4), concentrated under vacuum, and recrystallized by 25% ethyl acetate/petroleum ether to give the corresponding imidazoles in 80%–97% yields.

Recycling of ionic liquid [Hmim]HSO_4

Residual ionic liquid was washed with Et_2O (3 × 10 mL) to remove any organic impurity and dried at 80 °C. Under this procedure, [Hmim]HSO_4 can be reused in five runs without any loss of its activity.

© 2008 NRC Canada

Table 2. Synthesis of 2,4,5-trisubstituted imidazoles catalyzed by 10 mol% of [Hmim]HSO_4 in EtOH.

Entry	Aldehyde	Product[a]	Time (h)	Yield (%)[b]
1	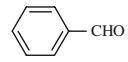	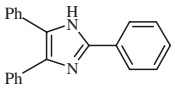	3	95
2	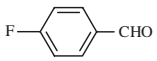	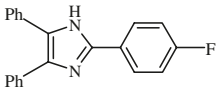	2.5	93
3	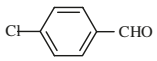	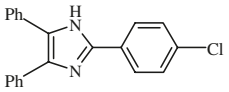	3	80
4	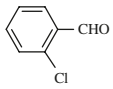	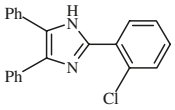	3	85
5	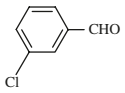	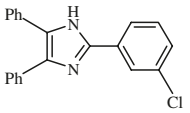	2.5	90
6	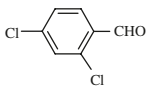	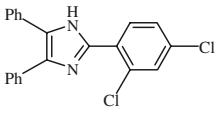	2.5	96
7	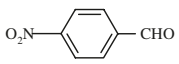	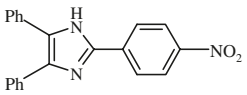	2.5	97
8	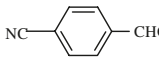	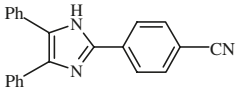	4	93
9	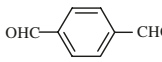	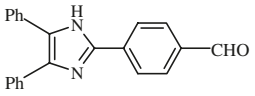	4	97
10	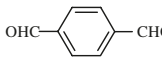	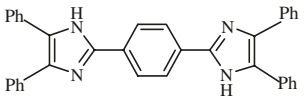	8.5	82
11	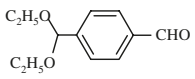	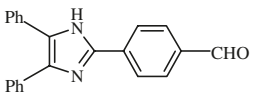	4	96
12	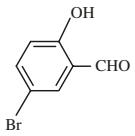	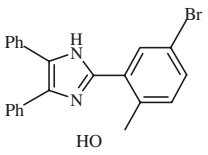	3	89

Spectroscopic data

2-(2,4-dichlorophenyl)-4,5-diphenylimidazole

Table 2, entry 6, mp 174 to 175 °C. IR (KBr, cm^{-1}) ν_{max}: 3427, 3068, 1593, 824, 767, 698. ^1H NMR (400 MHz, DMSO-d_6) δ_H: 12.8 (s, 1H), 7.80 (d, J = 8.4 Hz, 1H), 7.81 (s, 1H), 7.61–7.22 (m, 12H). ^{13}C NMR (100 MHz, DMSO-d_6) δ_C: 126.7, 127.2, 127.4, 127.9, 128.2, 128.2, 128.3, 128.7, 128.8, 129.6, 130.6, 132.4, 132.6, 133.9, 134.8, 137.1, 142.4. EIMS *m*/*z*: 364 (M^+ – 2, 100), 165, 123, 69, 55.

*2,2-(1,4-phenylene)-bis(4,5-diphenyl)-1*H*-imidazole*

Table 2, entry 10, mp > 360 °C. IR (KBr, cm^{-1}) ν_{max}: 3390, 3172, 3054, 1600, 1481, 762, 690. ^1H NMR (400 MHz, DMSO-d_6) δ_H: 12.81 (s, 2H), 8.20 (s, 4H), 7.20–7.72 (m, 20H). ^{13}C NMR (100 MHz, DMSO-d_6) δ_C: 125.2, 126.5, 127.0, 127.7, 128.3, 128.6, 129.5, 129.7, 129.9, 130.9, 135.1, 137.3, 144.9. EIMS *m*/*z*: 514 (M+, 71), 411, 307, 257.

2-(4-methoxyphenyl)-4,5-diphenylimidazole

Table 2, entry 16, mp 230 to 231 °C. IR (KBr, cm^{-1}) ν_{max}:

© 2008 NRC Canada

Table 2 (*continued*).

Entry	Aldehyde	Product [a]	Time (h)	Yield (%) [b]
13		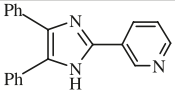	3.5	87
14	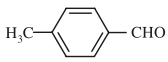	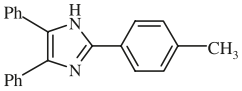	3	92
15	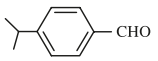	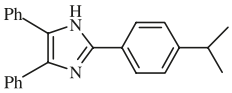	2.5	90
16	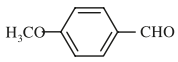	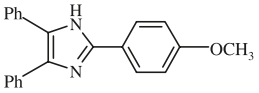	3	91
17	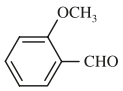	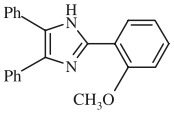	3	94
18	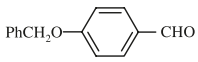	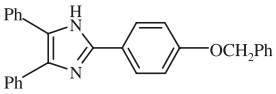	3.5	89
19	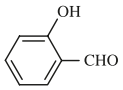	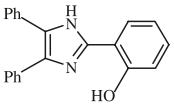	2	92
20	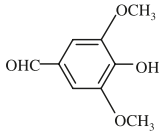	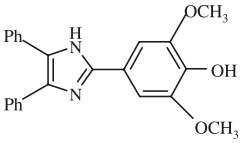	3	88
21	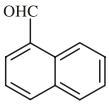	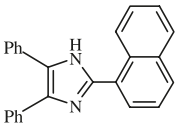	4	86
22	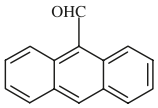	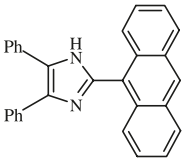	4	81
23	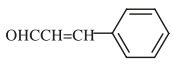	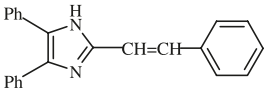	2.5	90
24	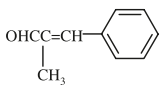	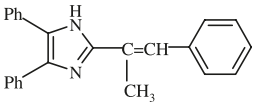	2.5	93
25	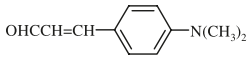	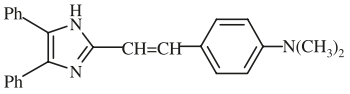	2	95

3400, 3060, 1611, 1490, 1179, 1028, 830, 761. ^{1}H NMR (400 MHz, DMSO-d_6) δ_H: 12.48 (s, Br, 1H), 8.00 (dt, J = 8.8 Hz, 2.0 Hz, 2H), 7.51 (d, J = 7.2 Hz, 4H), 7.35 (t, J = 7.2 Hz, 4H), 7.27 (t, J = 7.2 Hz, 2H), 7.04 (dt, J = 8.8 Hz, 2.0 Hz, 2H), 3.80 (s, 3H). ^{13}C NMR (100 MHz, DMSO-d_6) δ_C: 55.2, 114.1, 122.9, 126.7, 127.0, 127.7, 128.4, 145.6, 159.4. EIMS *m*/*z*: 326 (M+, 100), 311, 283, 235, 97.

© 2008 NRC Canada

Table 2 (*concluded*).

Entry	Aldehyde	Product[a]	Time (h)	Yield (%)[b]
26	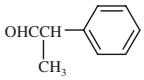	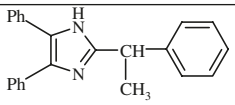	4	80
27	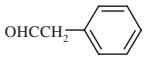	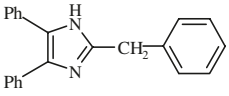	4	79
28	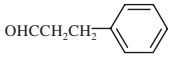	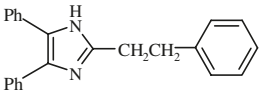	4.5	83
29	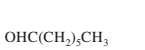	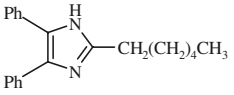	5	81
30	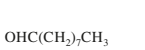	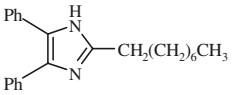	5.5	84
28	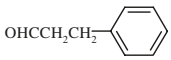	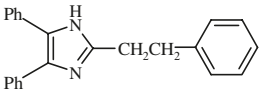	4.5	83
29	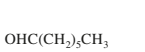	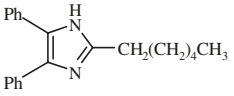	5	81
30	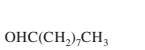	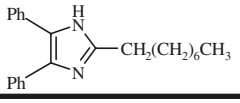	5.5	84

[a]All products wre characterized by ^{1}H NMR, ^{13}C NMR, IR, and mass spectroscopy.
[b]Isolated yields.

Acknowledgement

We are grateful to the Center of Excellence of Chemistry (Catalyst and Fuel Cell), University of Isfahan (CECUI) and also Research Council of University of Isfahan (research project No. 860306) for financial support of this work. In addition, the author thanks Professor Iraj Mohammadpoor-Baltork for his advice.

References

1. G. Haberhauer and F. Rominger. Eur. J. Org. Chem. **16**, 3209 (2003).
2. D.S.V. Vliet, P. Gillespie, and J. Scicinski. Tetrahedron Lett. **46**, 6741 (2005).
3. H.W. Du, Y. He, R. Sivappa, and C.J. Lovely. Synlett, 965 (2006).
4. A. Kumar, S.B. Katiyar, A. Agarwal, and P.M.S. Chauhan. Drugs Future, **28**, 243 (2003).
5. D. Passali, L. Salerni, G.C. Passali, F.M. Passali, and L. Bellussi. Expert Opin. Drug Saf. **5**, 783 (2006).
6. B. Dyck, V.S. Goodfellow, T. Phillips, J. Grey, M. Haddach, M. Rowbottom, G.S. Naeve, B. Brown, and J. Saunders. Bioorg. Med. Chem. Lett. **14**, 1151 (2004).
7. F. Bellina, S. Cauteruccio, S. Monti, and R. Rossi. Bioorg. Med. Chem. Lett. **16**, 5757 (2006).
8. J.C. Lee, J.T. Laydon, P.C. McDonnell, T.T. Gallagher, S. Kumar, D. Green, D. McKulty, M. Blumenthal, J.R. Heys, S.W. Landvatter, J.E. Strikler, M.M. McLaughlin, I.R. Siemen, S.M. Fisher, G.P. Livi, J.R. White, J.L. Adams, and P.R. Young, Nature, **372**, 739 (1994).
9. N.R. Bhat, P.S. Zhang, and S.B. Mohanty. Neurochem. Res. **32**, 293 (2007).
10. T. Maier, R. Schmierer, K. Bauer, H. Bieringer, H. Buerstell, and B. Sachse. U.S. Patent 4-820-335, 11 April 1989; Chem. Abstr. **11**, 19494 (1989).
11. T.F. Gallagher, S.M. Fier-Thompson, R.S. Garigipati, M.E. Sorenson, J.M. Smietana, D. Lee, P.E. Bender, J.C. Lee, J.T. Laydon, D.E. Griswold, M.C. Chabot-Fletcher, J.J.Breton, and J. L. Adams. Bioorg. Med. Chem. Lett. **5**, 1171 (1995).
12. J.C. Boehm, J.M. Smietana, M.E. Sorenson, R.S. Garigipati, T.F. Gallagher, P.L. Sheldrake, J. Bradbeer, A.M. Badger, J.T. Laydon, J.C. Lee, L.M. Hillegass, D.E. Griswold, J.J. Breton, M.C. ChabotFletcher, and J.L. Adams. J. Med. Chem. **39**, 3929 (1996).
13. A. Pesquet, A. Daich, and L. Van Hijfte, J. Org. Chem. **71**, 5303 (2006).
14. M. Kidwai, P. Mothsra, V. Bansal, and R. Goyal. Monatsh. Chem. **137**, 1189 (2006).
15. M.M. Heravi, K. Bakhtiari, H.A. Oskooei, and S. Taheri. J. Mol. Catal. A, **263**, 287 (2006).
16. S.A. Siddiqui, U.C. Narkhede, S.S. Palimkar, T. Daniel, R.J. Lahoti, and K.V. Srinivasan. Tetrahedron, **61**, 3539 (2005).
17. M. Xia and Y.-d. Lu. J. Mol. Catal. A, **265**, 205 (2007).
18. M.M. Heravi, F. Derikvand, and F.F. Bamoharram. J. Mol. Catal. A, **265**, 205 (2007).

© 2008 NRC Canada

19. D.E. Frantz, L. Morency, A. Soheili, J.A. Murry, E.J.J. Grabowski, and R.D. Tillyer. Org. Lett. **6**, 843 (2004).
20. R.B. Sparks and A.P. Combs. Org. Lett. **6**, 2473 (2004).
21. D. Dallinger and C.O. Kappe. Chem. Rev. **106**, 2563 (2007).
22. H. Ohde, M. Ohde, and C.M. Wai. Chem. Comm. (Cambridge), 930 (2004).
23. A.K. Burrell, R.E. Del Sesto, S.N. Baker, T.M. McCleskey, and G.A. Baker. Green Chem. **9**, 449 (2007).
24. R. Sheldon. Chem. Commun. (Cambridge), 2399 (2001).
25. J.S. Wilkes. Green Chem. **4**, 73 (2002).
26. N. Jain, A. Kumar, S. Chauhan, and S.M.S. Chauhan. Tetrahedron, **61**, 1015 (2005).
27. N. Gupta, S. G.L. Kad, and J. Singh. Catal. Commun. **8**, 1323 (2007).
28. S.M. Coman, M. Florea, V.I. Parvulescu, V. David, A. Medvedovici, D. De Vos, P.A. Jacobs, G. Poncelet, and P. Grange. J. Catal. **249**, 359 (2007).
29. T.M. Potewar, S.A. Siddiqui, R.J. Lahoti, and K.V. Srinivasan. Tetrahedron Lett. **48**, 1721 (2007).
30. J.S. Yadav, B.V.S. Reddy, A.K. Basak, and A.Venkat Narsaiah. Tetrahedron Lett. **44**, 1047 (2003).
31. C.-W. Cho, Y.-C. Jeon, T.P.T. Pham, K. Vijayaraghavan, and Y.-S. Yun. Ecotoxicol. Environ. Saf. In press (2007).
32. H. Mehdi, A. Bodor, D. Lantos, I.T. Horváth, D.E. De Vos, and K. Binnemans. J. Org. Chem. **72**, 517 (2007).
33. M.M. Khodaei, A.R. Khosropour, M. Kookhazadeh. Can. J. Chem. **83**, 209 (2005).
34. M. Khodaei, A.R. Khosropour, and J. Abbasi. J. Iranian Chem. Soc. **2**, 289 (2005).
35. A.R. Khosropour, I. Mohammadpoor-Baltork, and M. Jowkar. Heterocylces, **68**, 1551 (2006).
36. I. Mohammadpoor-Baltork, H.R. Memarian, A.R. Khosropour, and K. Nikoofar. Heterocylces, **68**, 1837 (2006).
37. M.M. Khodaei, A.R. Khosropour, and H. Moghanian. Synlett, 6 (2006).
38. I. Mohammadpoor-Baltork, A.R. Khosropour, and S. F. Hojati. Catal. Commun. **8**, 200 (2007).
39. A.R. Khosropour, I. Mohammadpoor-Baltork, M.M. Khodaei, and P. Ghanbary, Z. Naturforsch. B, **62b**, 537 (2007).
40. I. Mohammadpoor-Baltork, A.R. Khosropour, and S.F. Hojati. Catal. Commun. **8**, 1865 (2007).
41. I. Mohammadpoor-Baltork, A.R. Khosropour, and S.F. Hojati. Monatsh. Chem. **138**, 663 (2007).
42. M. Khodaei, A.R. Khosropour, and S. Ghaderi. J. Iranian Chem. Soc. **3**, 69 (2006).
43. A.R. Khosropour, M.M. Khodaei, and S. Ghaderi. Z. Naturforsch. B, **61b**, 326 (2006).
44. A.R. Khosropour, I. Mohammadpoor-Baltork, and H. Ghorbankhani. Catal. Commun. **7**, 713 (2006).
45. A. R. Khosropour, I. Mohammadpoor-Baltork, and H. Ghorbankhani. Tetrahedron Lett. **47**, 3493 (2006).

© 2008 NRC Canada

AWARD LECTURE / CONFÉRENCE D'HONNEUR

The bioorganic chemistry of transglutaminase — from mechanism to inhibition and engineering

Jeffrey W. Keillor, Roberto A. Chica, Nicolas Chabot, Valerio Vinci, Christophe Pardin, Emanuelle Fortin, Steve M.F.G. Gillet, Yukiko Nakano, Mari T. Kaartinen, Joelle N. Pelletier, and William D. Lubell

Abstract: Through a multidisciplinary approach comprising organic synthesis, molecular biology, and physical organic kinetic studies, we have studied the mechanism of transglutaminase-mediated transamidation. More recently, we have applied our understanding of the mechanism to the design of reversible inhibitors and affinity labels for biological application. We have also undertaken the engineering of transglutaminase for its application as a "peptide synthase". Herein, we present a brief overview of previously published work as well as recent results presented at the 2007 Merck–Frosst Centre for Therapeutic Research Award Lecture.

Key words: transglutaminase, enzyme mechanism, enzyme inhibition, protein engineering

Résumé : Nous avons étudié le mécanisme de la transamidation catalysée par la transglutaminase, via une approche multidisciplinaire comprenant la synthèse organique, la biologie moléculaire et les études cinétiques physico-organiques. Plus récemment, nous avons appliqué notre compréhension du mécanisme à la conception d'inhibiteurs réversibles et de marqueurs par affinité pour des applications biologiques. Nous avons également entamé l'ingénierie de la transglutaminase pour son application en tant que « synthase de peptides ». Ici, nous présentons un bref survol des travaux déjà publiés ainsi que des résultats récents présentés à la conférence du Prix 2007 du Centre de recherche thérapeutique de Merck–Frosst.

Mot-clés : transglutaminase, mécanisme enzymatique, inhibition enzymatique, ingénierie des protéines.

[Traduit par la rédaction]

Introduction

While Keillor and co-workers have studied several subjects in bioorganic chemistry ranging from the development of protein labelling methods (1, 2) to the elucidation of transpeptidase mechanisms (3, 4), one of the most long-standing themes represented in their research interests has been their focus on transglutaminase (TGase). Information gleaned from their study of the mechanism of action of this class of enzymes underpins ongoing efforts regarding its inhibition, chemical biology, and engineering. An overview of this research was presented in the context of the 2007 Merck–Frosst Centre for Therapeutic Research Award Lecture and is summarized herein.

TGases (EC 2.3.2.13) are calcium-dependent aminoacyltransferases that catalyze acyl-transfer reactions between peptide-bound glutamine residues as acyl donors and peptide-bound lysine residues as acyl acceptors, leading to the formation of intermolecular ε-(γ-glutamyl)lysine crosslinks (5). While TGases are found in the plasma, tissues, and extracellular media of all vertebrates, our research interests have focused on the ubiquitous tissue TGase (TG2). TG2 is involved in critical physiological processes, such as the stabilization of extracellular matrices, formation of cross-linked cell envelopes, cell-matrix assembly, wound healing, and cellular adhesive processes (5). Its unregulated activity has also been linked to auto-immune gluten intolerance (Celiac disease) (6, 7) and neurodegenerative diseases, such as Hun-

Received 21 November 2007. Accepted 26 January 2008. Published on the NRC Research Press Web site at canjchem.nrc.ca on 10 March 2008.

This article is dedicated to Professors R. Stanley Brown and William P. Jencks, the doctoral and postdoctoral supervisors of J.W.K., respectively.

J.W. Keillor,[1] R.A. Chica, N. Chabot, V. Vinci, C. Pardin, E. Fortin, S.M.F.G. Gillet, J.N. Pelletier, and W. Lubell. Département de chimie, Université de Montréal, Montréal, QC H3C 3J7, Canada.
Y. Nakano, M.T. Kaartinen. Faculty of Dentistry, McGill University, Montréal, QC H3A 2B2, Canada.

[1]Corresponding author (e-mail: jw.keillor@umontreal.ca).

 doi:10.1139/V08-024 © 2008 NRC Canada

Scheme 1. Ping–pong mechanism of TGase.

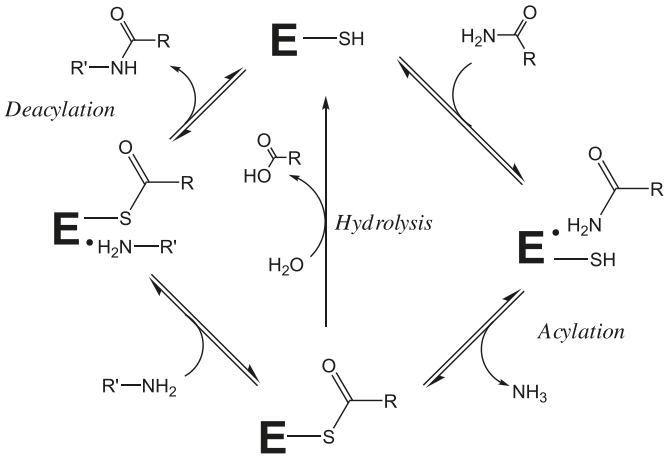

tington's disease (8) and Parkinson's disease (9). Guinea pig liver TG2 (gTG2) is frequently studied as a model of the human enzyme because it is 88% homologous (10) to human TG2 (hTG2) and is readily purified in its recombinant His-tagged form (11). The catalytic acyl-transfer reaction has been known to proceed through a modified ping–pong mechanism (Scheme 1) for almost 40 years (12). According to this mechanism, in the first step of the catalytic cycle, the acyl-donor substrate undergoes nucleophilic attack by the active site thiolate, followed by the release of an equivalent of ammonia. The thiolester acyl-enzyme intermediate thus obtained then undergoes a second nucleophilic attack by the acyl-acceptor substrate, leading to the formation of isopeptide product and the regeneration of free enzyme.

Mechanistic studies of TG2

We have added structural and mechanistic details to our understanding of TG2 function through an approach that comprises the synthesis of substrate analogues, structure–function kinetic studies, and molecular modelling.

The synthesis of simple peptidic acyl-donor substrates **1**–**3** (Fig. 1) permitted the study of the acylation step of the catalytic cycle through pre-steady state (stopped-flow) kinetics (13). Even with substrate analogues of attenuated electrophilicity, acylation is still rapid, confirming that the active-site thiolate is a strong nucleophile.

Peptide ester **1** was also used to study the deacylation step of the TG2 catalytic cycle (14). Using a series of primary amines of varying basicity (nucleophilicity) as acceptor substrates, isotope effects and linear free-energy relationships of the rate-limiting deacylation step were explored. These data implicated the involvement of a general base in the nucleophilic attack of the amine substrate on the acyl-enzyme thiolester.

The compilation of kinetic results obtained in the study of the acylation and deacylation steps are represented in the unified mechanism for TG2-mediated transamidation proposed in Scheme 2.

Reversible TG2 inhibitors

Over the course of the kinetic studies described previously, we remarked upon the ability of the benzoxycarbonyl

Fig. 1. Substrate analogues used to study TG2 acylation.

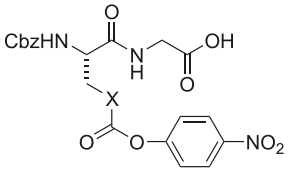

(Cbz) protecting group to confer affinity to small peptidic substrates. Molecular modelling studies suggested the Cbz group may form specific interactions in the donor substrate-binding site that favour binding (15). Subsequently, we explored the structural elements of the Cbz group important for this affinity by preparing and testing series of Cbz analogue derivatives. In doing so, we discovered *trans*-cinnamoyl compounds that serve as rapid, reversible inhibitors (16).

Shown in Fig. 2 are representative examples of these inhibitors, along with their relative IC_{50} values. Briefly, cinammoyl derivative **4** was prepared from *p*-nitrobenzaldehyde via Wittig chemistry to give *p*-nitrocinnamic acid, followed by coupling with hydroxybenzotriazole (16). Azachalcone **5** was obtained by aldol condensation of 3-acetylpyridine with *p*-nitrobenzaldehyde (16). Triazole **6** was made through Huisgen-type [3+2]-cycloaddition reaction of *p*-nitrobenzyl azide and the corresponding ynone (17).

Kinetic studies showed that these cinnamoyl inhibitors are competitive with respect to the acyl-donor substrate (16). More recently, we prepared a derivative of **5** that enabled the photolabelling of TG2 at residues in the donor substrate-binding site (18). Subsequent docking simulations, with a homology model generated for guinea pig liver TG2, support the favourable binding of these derivatives in modes that block access to the active-site tunnel (Fig. 3). Finally, when tested against Factor XIIIa, another TGase, and caspase 3, a similar cysteine protease, *no* inhibition was observed, up to the limits of their solubility. This selectivity bodes well for future in vivo testing.

TG2 affinity labels

Several classes of *irreversible* inhibitors of TG2 have also been developed in our group. In general, these inhibitors have been based on a peptidic scaffold thought to be bound in a peptide backbone-binding groove on the surface of TG2 (15, 19). Our inhibitors present an electrophilic group at the end of a flexible alkyl chain long enough to insert into the active site of TG2. Such inhibitors have been prepared so that they bear various electrophilic groups, such as thiadiazoles (20), epoxides (21), maleimides (22), or α,β-unsaturated amides (23). These amides proved to be the most potent irreversible TG2 inhibitors we have made, and a representative example (**7**) is shown in Fig. 4.

Based on the structure of **7**, we recently designed and prepared a series of TG2 affinity labels, bearing biotin groups or fluorophores via alkyl, PEG, or (cleavable) disulfide linkers (24). The fluorescent affinity labels shown in Fig. 4 were prepared from Cbz-Lys through Boc protection of its ε-

© 2008 NRC Canada

Scheme 2. Unified mechanism of gTG2-mediated transamidation.

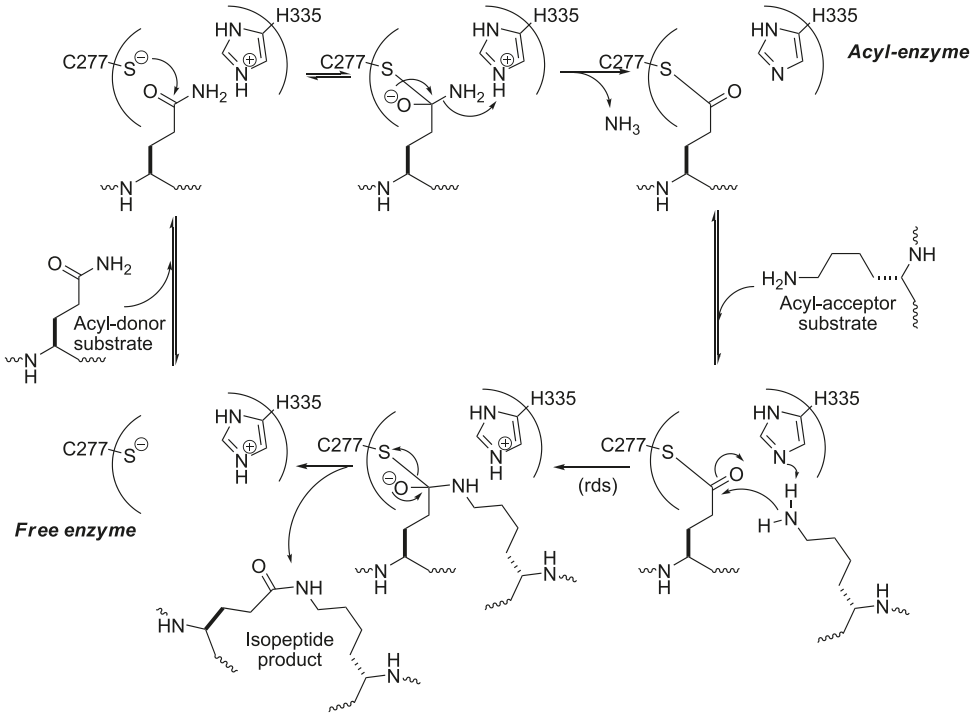

Fig. 2. Representative cinnamoyl inhibitors of gTG2.

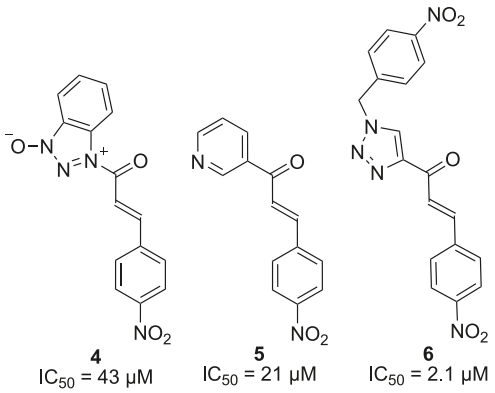

Fig. 3. Homology model of gTG2, showing photolabelled residues (green) adjacent to the mouth of the active-site tunnel (dotted circle).

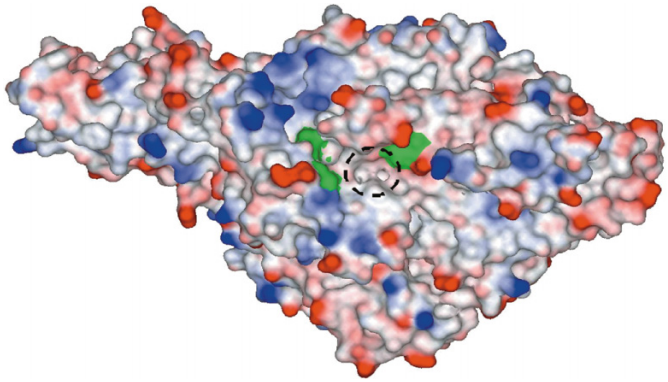

Fig. 4. Irreversible TG2 inhibitor **7** and analogous affinity labels.

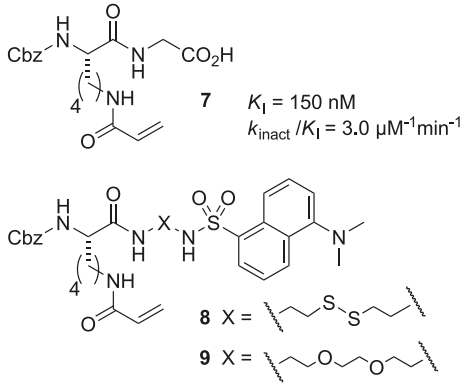

amino group, coupling with the diamine spacer and dansyl chloride, and finally deprotection and acrylation of the pendant amine (see Supplementary Data).[2]

Kinetic characterization of our affinity labels confirmed their efficiency, despite a decrease of roughly two orders of magnitude compared to the parent compound **7**. This decrease was due almost entirely to an increase in K_I, presumably due to the bulk added to the C-terminus of the peptide backbone. For example, for disulfide **8**, K_I = 11 μmol/L and k_{inact}/K_I = 0.030 (μmol/L)$^{-1}$min^{-1} and for the PEG derivative **9**, K_I = 29 μmol/L and k_{inact}/K_I = 0.014 (μmol/L)$^{-1}$min^{-1}.

Inhibitor **9** was then used in a cell culture system to test the role of TG2/TGases in the production of collagenous extracellular matrix. MC3T3-E1 osteoblasts grown for 12 days in the presence of ascorbic acid produce a thick col-

[2] Supplementary data for this article are available on the journal Web site (canjchem.nrc.ca) or may be purchased from the Depository of Unpublished Data, Document Delivery, CISTI, National Research Council Canada, Ottawa, ON K1A 0R6, Canada. DUD 3727. For more information on obtaining material, refer to cisti-icist.nrc-cnrc.gc.ca/irm/unpub_e.shtml.

© 2008 NRC Canada

Fig. 5. Suppression of collagen production and mineralization of MC3T3-E1 osteoblast cultures by inhibitor **9**.

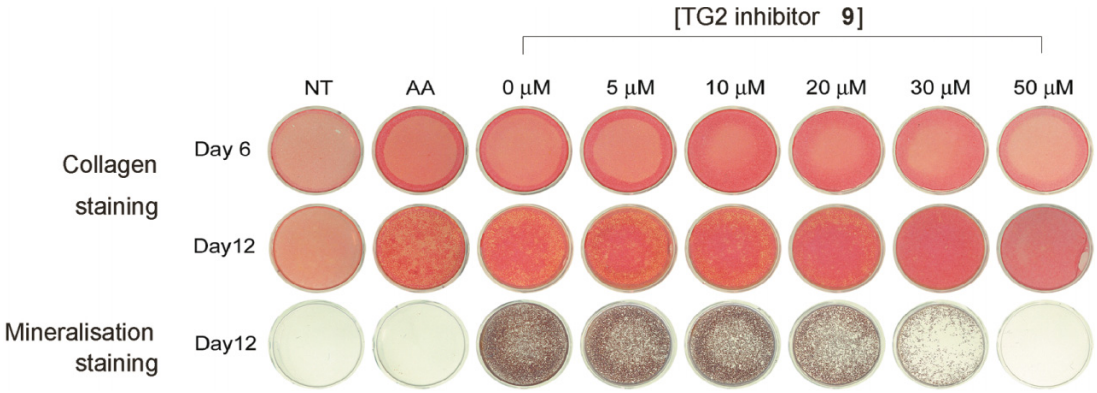

Scheme 3. Isopeptide formation catalyzed by native TG2 and peptide formation to be catalyzed by modified TG2 (TG2*).

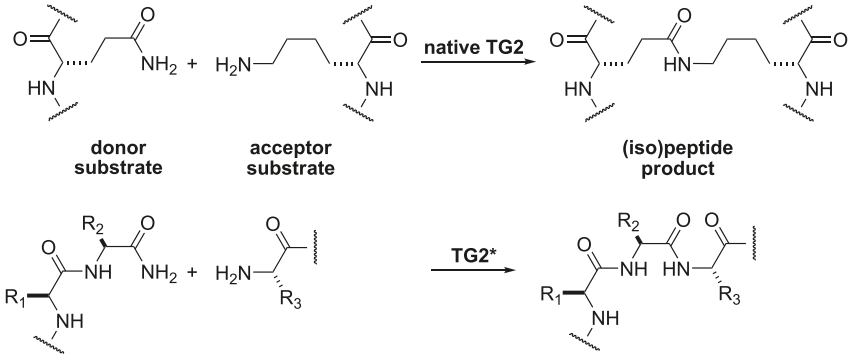

lagen layer, which mineralizes when a phosphate source is provided (in our experiments, β-glycerophosphate, see Supplementary Data).[2] As evident from Fig. 5, inhibitor **9** reduced collagen deposition and blocks mineralization of the cultures in a concentration-dependent manner. Complete inhibition of collagen deposition and mineralization was observed at 50 μmol/L concentration. Furthermore, inhibitor **9** is not toxic to the cells at the concentrations used. Fluorescence microscopy studies are ongoing to determine the localization of inhibitor **9** in the cells and the cellular mechanism of its inhibition.

TG2 engineering

Finally, we have also undertaken the engineering of TG2, with the goal of obtaining variants (TG2*) capable of catalyzing the specific, efficient, and economical formation of amide bonds between various synthetic peptide substrates. Typically, proteases are used for this purpose, but their application can be hindered by their propensity to catalyze the *hydrolysis* of the newly formed amide bond. This limitation can be overcome in part by reducing the activity of water in frozen (25, 26) or organic media (27), or by altering the specificity of the enzyme through engineering (28, 29). However, TGase is already designed to catalyze the desired transamidation reaction. It is thus capable of binding a primary amide, forming a high-energy thiolester intermediate, sequestering it from attack by water and selectively transferring the acyl group to a primary-amine substrate. We have therefore chosen it as a starting point for directed evolution modification, intended to alter its substrate specificity such that branched acyl-donor and acyl-acceptor substrates can be recognized and catalytically coupled (Scheme 3).

Native TG2 is already capable of recognizing a fairly broad range of primary amines as acceptor substrates (14), so our initial goal was to expand the specificity of TG2 with respect to its donor substrate. In this respect, previous modelling studies (15) served to identify residues in the proximity of the active site that may contribute to TG2 specificity.

Libraries of mutant gTG2 were then generated wherein 1–3 amino acids were randomly mutated (Table 1). Briefly, the gene encoding for gTG2 (11) was randomly mutated at each of these positions by cloning with oligonucleotide primers containing degenerate (NNS) codons. Bacterial colonies were transformed with the resulting mutant plasmids, grown on agar plates, then re-picked and grown in 1.5 mL of culture in 96-well plates (see Supplementary Data).[2]

A fluorogenic assay previously developed in the group (30) was then adapted to allow these libraries to be screened for mutant transpeptidase activity. The umbelliferyl ester of

Table 1. Libraries of gTG2 mutants generated through saturation mutation of the indicated residues.

Library	Randomized residue
1	W241
2	H305, D306
3	W332
4	T360, Q362, E363
5	Y519, N520

© 2008 NRC Canada

Table 2. Kinetic parameters measured for the reaction of a series of acceptor substrates with ZGU (25 °C, pH 7.0).

	Wild-type gTG2		W332F mutant	
Acceptor Substrate[a]	k_{cat} (min^{-1})	K_M (mmol/L)	*k*cat (min^{-1})	K_M (mmol/L)
$GlyNH_2$	40.0 ± 3.6	7.0 ±1.6	22.6 ± 1.7	9.6 ± 2.0
$AlaNH_2$	24.0 ± 1.8	32.4 ± 1.4	34.7 ± 1.2	33.7 ± 5.0
ValOMe	27.3 ± 4.8	24.4 ± 6.8	46.6 ± 7.0	28.8 ± 8.8
LeuOMe	26.5. ± 2.6	37.9 ± 9.4	25.0 ± 3.2	47.2 ±13.9
D-LeuOMe	13.2 ± 3.1	78.7 ± 39.0	N.D.[b]	N.D.
SerOMe	15.0 ± 1.0	5.8 ± 1.6	16.5 ± 1.6	6.1 ± 1.9
ThrOMe	N.D.	N.D.	15.6 ± 1.4	16.9 ± 4.2
$AsnNH_2$	N.D.	N.D.	N.D.	N.D.
ArgOMe	12.2 ± 0.9	3.4 ± 1.1	37.4 ± 1.2	4.8 ± 0.6
HisOMe	40.7 ± 4.5	4.8 ± 1.3	49.0 ± 3.6	3.6 ± 0.7
$PheNH_2$	N.D.	N.D.	N.D.	N.D.
TyrOMe	16.6 ± 1.6	4.8 ± 1.1	29.6 ± 3.5	6.4 ± 1.6

Note: Reported errors are from non-linear regression of kinetic data (see Supplementary Data). See Supplementary Data for reaction conditions.[2]

[a]All substrates are of L configuration unless noted otherwise.

[b]Reaction not detected.

Cbz-Gly (Cbz-GlyOUmb, ZGU) was thus synthesized and used as a fluorogenic donor substrate (see Supplementary Data).[2] Initially, this assay was used to characterize the substrate specificity of wild-type gTG2, confirming its remarkable breadth and its capacity to function as a peptide synthase (Table 2).

Libraries 1–5 (Table 1) were then screened for transpeptidation activity, using Ac-Lys-OMe as an acceptor substrate. Two of those libraries gave interesting results. In library 5, many different mutants were found to be active (Table 2S, Supplementary Data), whereas in library 3, only the conservative mutants W332Y and W332F showed transamidation activity.[2] Subsequent expression, purification, and further kinetic characterization of the latter showed that its acceptor substrate specificity differed slightly from that of the wild-type enzyme. For example, as can be seen in Table 2, the W332F mutant is able to recognize ThrOMe as an acceptor substrate. These preliminary results validate efforts to engineer TG2 to create more efficient catalysts for the synthesis and modification of peptides. Currently, more sensitive screening methods, based specifically on *ligation* reaction assays, are currently under development for application to screening different, larger libraries of mutant TG2.

Summary

Our understanding of the mechanism of TG2-mediated transamidation has seen recent application in the design of TG2 inhibitors and affinity labels for the study of the chemical biology of TG2. We have also undertaken the engineering of TG2 as a catalyst for peptide synthesis and modification, and preliminary results validate its potential as a peptide synthase.

Acknowledgements

J.W.K is grateful to the Chemical Society of Canada (CSC) for the 2007 Merck–Frosst Award and to the Merck–Frosst Centre for Therapeutic Research for their sponsorship of the award. This work was funded primarily by the Natural Sciences and Engineering Research Council of Canada (NSERC), the Fonds Québecois de Recherche sur la Nature et les Technologies (FQRNT), and the Canadian Institutes for Health Research (CIHR).

References

1. S. Girouard, M.-H. Houle, A. Grandbois, J.W. Keillor, and S.W. Michnick. J. Am. Chem. Soc. **127**, 559 (2005).
2. J. Guy, K. Caron, S. Dufresne, S. W. Michnick, W.G. Skene and J. W. Keillor. J. Am. Chem. Soc. **129**, 11969 (2007).
3. See R. Castonguay, D. Halim, M. Morin, C. Lherbet, E. Bonneil, A. Furtos, P. Thibault, and J. W. Keillor. Biochemistry, **46**, 12253 (2007); and refs. cited therein.
4. See M. Morin, C. Rivard, and J.W. Keillor. Org. Biomol. Chem. **4**, 3790 (2006); and refs. cited therein.
5. D. Aeschlimann and M. Paulsson. Thromb. Haemostasis, **71**, 402 (1994).
6. O. Molberg, S.N. McAdam, R. Korner, H. Quarsten, C. Kristiansen, L. Madsen, L. Fugger, H. Scott, O. Noren, P. Roepstorff, K.E.A. Lundin, H. Sjostrom, and L.M. Sollid. Nat. Med. **4**, 713 (1998).
7. S. Reif and A. Lerner. Autoimmun. Rev. **3**, 40 (2004).
8. A.J.L. Cooper, K.R. Sheu, J.R. Burke, O. Onodera, W.J. Strittmatter, A.D. Roses, and J.P. Blass. J. Neurochem. **69**, 431 (1997).
9. E. Junn, R.D. Ronchetti, M.M. Quezado, S.-Y. Kim, and M.M. Mouradian. Proc. Natl. Acad. Sci. USA, **100**, 2047 (2003).
10. W. Dietrich, T. Ehnis, M. Bauer, P. Donner, U. Volta, E.O. Riecken, and D. Schupann. Nat. Med. **3**, 797 (1997).
11. S.M.F.G. Gillet, R.A. Chica, J.W. Keillor, and J.N. Pelletier. Prot. Exp. Purif. **33**, 256 (2004).
12. J.E. Folk. J. Biol. Chem. **244**, 3707 (1969).
13. C. Gravel, D. Lapierre, J. Labelle, and J.W. Keillor. Can. J. Chem. **85**, 164 (2007).
14. A. Leblanc, C. Gravel, J. Labelle, and J.W. Keillor. Biochemistry, **40**, 8335 (2001).
15. R.A. Chica, P. Gagnon, J.W. Keillor, and J.N. Pelletier. Prot. Sci. **13**, 979 (2004).

© 2008 NRC Canada

16. C. Pardin, R.A. Chica, J.N. Pelletier, J.W. Keillor, and W.D. Lubell. Submitted (2008).
17. C. Pardin, J.W. Keillor, and W.D. Lubell. Submitted (2008).
18. C. Pardin, R.A. Chica, I. Roy, E. Bonneil, P. Thibault, J.N. Pelletier, J.W. Keillor, and W.D. Lubell. Submitted (2007).
19. J.W. Keillor. Chem. Biol. **12**, 410 (2005).
20. C. Marrano, P. de Macédo, P. Gagnon, D. Lapierre, and J.W. Keillor. Bioorg. Med. Chem. **9**, 3231 (2001).
21. C. Marrano, P. de Macédo, and J.W. Keillor. Bioorg. Med. Chem. **9**, 1923 (2001).
22. D. Halim, K. Caron, and J.W. Keillor. Bioorg. Med. Chem. Lett. **17**, 305 (2007).
23. P. de Macédo, C. Marrano, and J.W. Keillor. Bioorg. Med. Chem. **10**, 355 (2002).
24. C. Pardin. Ph.D. thesis. Université de Montréal. 2007.
25. N. Wehofsky, S.W. Kirback, M. Haensler, J.-D. Wissmann, and F. Bordusa. Org. Lett. **2**, 2027 (2000).
26. S. Gerisch and H.-D. Jakubke. J. Pept. Sci. **3**, 93 (1997).
27. T. Miyazawa, M. Hiramatsu, T. Murashima, and T. Yamada. Biotech. Lett. **24**, 1945 (2002).
28. S. Xu, K. Rall, and F. Bordusa. J. Org. Chem. **66**, 1627 (2001).
29. S. Atwell and J. A. Wells. Proc. Natl. Acad. Sci. USA, **96**, 9497 (1999).
30. S.M.F.G. Gillet, J.N. Pelletier, and J.W. Keillor. Anal. Biochem. **347**, 221 (2005).

© 2008 NRC Canada

Role of solvent nucleophilicity in excess-acidity plots for equilibria in sulfuric acid – water mixtures

T. William Bentley

Abstract: For protonation of a base B to give BH^+ and for reaction of carbocations R^+ with water to give ROH in a range of sulfuric acid – water mixtures, slopes of excess-acidity plots of equilibrium data are discussed. Formal connections between the excess-acidity approach and the Grunwald–Winstein (GW) and extended GW equations, noted previously by Bagno et al., are evaluated. It is proposed that a major factor is variations in the solvent dependence of the rates of reactions of the cations (BH^+ or R^+) with water in the sulfuric acid – water mixtures. Rates of reactions of more stable cations (e.g., Ph_3C^+) with water are more sensitive to changes in solvent nucleophilicity, and the lower nucleophilicity of the water in sulfuric acid – water mixtures leads to an increase in $[BH^+]/[B]$ or $[R^+]/[ROH]$ concentration ratios (and hence to greater slopes m^* in excess-acidity plots).

Key words: excess acidity, sulfuric acid, kinetics, solvent nucleophilicity, solvolysis.

Résumé : On discute des pentes des courbes d'acidité en excès pour les données d'équilibre relatives à la protonation d'une base conduisant à la formation de BH^+ et pour la réaction des carbocations R^+ avec l'eau pour donner du ROH sur une large plage de concentrations pour des mélanges acide sulfurique – eau. On a évalué les corrélations formelles notées antérieurement par Bagno et al. entre l'approche de l'excès d'acidité et les équations de Grunwald–Winstein (GW) normales ou étendues. On suggère que, dans les mélanges d'acide sulfurique – eau, les variations dans la dépendance des vitesses de réaction des cations (BH^+ ou R^+) sur le solvant sont des facteurs importants. Les vitesses de réaction de l'eau avec les cations les plus stables, tel Ph_3C^+, sont beaucoup plus sensibles aux changements dans le caractère nucléophile du solvant et que le caractère nucléophile plus faible de l'eau dans des mélanges acide sulfurique – eau conduit à une augmentation des rapports des concentrations $[BH^+]/[B]$ ou $[R^+]/[ROH]$ et, comme conséquence, à des pentes m^* plus grandes dans les courbes d'acidité en excès.

Mots-clés : acidité en excès, acide sulfurique, cinétique, caractère nucléophile d'un solvant, solvolyse.

[Traduit par la Rédaction]

Introduction

The extent of protonation of a relatively strong base B to give BH^+ (eq. [1]) in dilute aqueous solution allows the calculation of the equilibrium constant pK_{BH^+} from the logarithm of the ratio of molar concentrations (I, eq. [2]) and the pH. However, if B is a weak base, relatively concentrated acid solutions are needed to obtain suitable values of log I. An extrapolation based on the excess-acidity (X) of the acid solution leads to the pK_{BH^+} for aqueous solution ($X = 0$, eq. [3]; the slope m^* depends on the substrate).

$$[1] \quad B + H^+ = BH^+$$

$$[2] \quad \log \{[BH^+]/[B]\} = \log I$$

Received 29 October 2007. Accepted 21 December 2007. Published on the NRC Research Press Web site at canjchem.nrc.ca on 1 February 2008.

This paper is dedicated to the memory of Keith Yates in recognition of his outstanding contributions to physical organic chemistry.

T. W. Bentley.[1] Department of Chemistry, Swansea University, Singleton Park, Swansea, SA2 8PP Wales, UK.

[1]Corresponding author (e-mail: cmsolvol@swansea.ac.uk).

$$[3] \quad \log I - \log [H^+] = m^*X + pK_{BH^+}$$

Important contributions to the mathematical treatment of data for equilibria in acidic solutions were made using the H_o acidity function by Yates and McClelland (1) and using excess acidity by Cox and Yates (2) after earlier work by Marziano et al. (3). The topic has been reviewed recently by Cox (4).

Excess-acidity can also be used in the determination of K_{R^+} for the formation of a carbocation R^+ with water to form an alcohol ROH as in eq. [4]. In this case, the equilibrium constant K_{R^+} is given by eq. [5].

$$[4] \quad R^+ + H_2O = ROH + H^+$$

$$[5] \quad K_{R^+} = [ROH][H^+]/[R^+][H_2O]$$

In eq. [3], I and $[H^+]$ refer to molar concentrations (4), and m^* is usually discussed in terms of activities and activity coefficients (4). Two alternative explanations have also been published (5, 6). Bagno et al. (6) discussed in detail the slope parameter m^* of eq. [3] in terms of the solvation energies of the protonated bases, especially by hydrogen bonding; they also recognized the possible connection between eq. [3] and linear free energy relationships such as the Grunwald–Winstein (GW) eq. [6] (7) and the extended GW

 doi:10.1139/V08-003 © 2008 NRC Canada

eq. [7] (8) for medium effects on kinetic data for solvolysis reactions. In eq. [6], k is the rate constant in any solvent relative to k_o, the rate constant in 80% ethanol–water; Y is the solvent ionizing power (or polarity), defined by the slope parameter m = 1.00 for solvolyses of *t*-butyl chloride at 25 °C (7), and c is the intercept. In eq. [7], l is the substrate sensitivity to N (the solvent nucleophilicity, or cation solvating power).

$$[6] \qquad \log (k/k_o) = mY + c$$

$$[7] \qquad \log (k/k_o) = mY + lN + c$$

Subsequently, many modifications of eqs. [6] and [7] have been devised using different Y and N scales. From solvolyses of tosylates, we have previously obtained Y_{OTs} and N_{OTs} values for mixtures of water and sulfuric acid (up to 60 *w*/*w* in the absence of protonation of substrate) (5), and comparisons will be made with eq. [3] (see later). A good linear correlation leading to a slope and intercept, as in eq. [3], is expected (9) to be more reliable in practice than an equation with extra parameters, as in eq. [7]. Therefore, discussion based on eq. [7] is aimed towards new insights rather than practical applications.

A recent principal-component analysis of solvent effects on a range of equilibrium and kinetic data (10) indicated three recognizable groups of solvent properties, so the success of eq. [3] having only one solvent property (X) is noteworthy (6). Because many factors can contribute to observed solvent effects, identification of only the main factor(s) is the initial objective of the work reported here.

The validity of a "kinetic" approach is supported by the value of K_{R^+} for the triphenylmethyl cation (trityl, **1**) in the aqueous standard state, obtained (11) from the ratio of rate constants for the forward and reverse reactions in eq. [4], which is in satisfactory agreement with the other values of K_{R^+} (4). The possibility of relating other equilibria in acidic media to the rates of the forward and reverse reactions will be explored. Important supporting data will be provided by two types of research on aqueous and alcoholic solvents over a wide range of N: (*i*) the rates of reactions of carbocations investigated by laser flash photolysis (12, 13) and (*ii*) the rates of solvolyses of cationic substrates having neutral leaving groups (14).

The main aim is to try to obtain further insights into the solvation effects revealed in the m^* term of eq. [3] and to strengthen the existing connections (5, 6) between solvolysis research in aqueous and alcoholic media and studies of strongly acidic media. Changes in activities and activity coefficients of B and BH^+ and the effects of changes in ionic strength will not be considered explicitly.

Discussion

In the following sections, it will be assumed that (*i*) the Eigen cation H_3O^+ (not H^+) is reacting as a proton, as in eq. [8], showing nucleophilic substitution reactions of substrates H_3O^+ and BH^+ with B and H_2O representing either nucleophiles or neutral leaving groups (in eq. [8], H_3O^+ replaces H^+ in eq. [1]), and so eq. [9] (in which a_{H_2O} is the water activity) replaces eq. [3]; using eq. [9], m^* = 0.00 for B = H_2O (6);

Fig. 1. Logarithms of water activity (slopes: –0.41 ± 0.02 (r = 0.993) and –0.82 ± 0.04 (r = 0.997)), and (inset) N_{OTs} (slope: –0.51 ± 0.01, r = 0.999) vs. excess acidity (X); data from refs. 4 and 5.

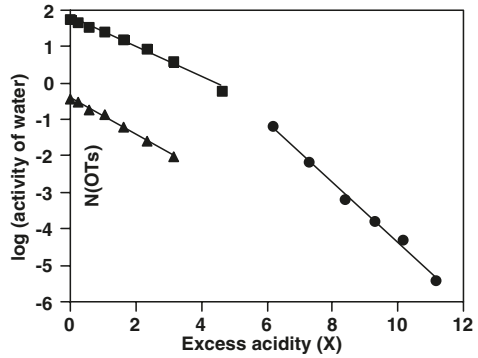

(*ii*) experimental values of log I (eq. [2]) are reliable, although the spectroscopic methods for determining values of I are susceptible to different solvent effects (4) from those to be discussed here using eq. [7].

$$[8] \qquad B + H_3O^+ = BH^+ + H_2O$$

$$[9] \qquad \log I - \log [H^+] = m^* X - \log a_{H_2O} + pK_{BH^+}$$

Why is only one adjustable parameter (m^*) required?

It is well established (4, 6) that only one adjustable parameter (m^*) in eq. [3] is required to correlate the experimental data for log I – log $[H^+]$ in a binary mixture of water and a strong acid. The success of one parameter is remarkable (6) because the m^*X term of eq. [3] could include a large number of possible solvent effects and also a term for log a_{H_2O} (see eq. [9]). A plot of log a_{H_2O} vs. X (Fig. 1) shows two linear regions (slopes of –0.41 and –0.82); although there may be many ranges of log I data spanning only one of the two linear regions, linearity is only approximate over the whole range of X.

The success of eq. [3] is consistent with eq. [7] because, as shown later, the more significant factor is the nucleophilicity (lN) term. Also, a feature of binary mixtures is the tendency for changes in Y to correlate with changes in N for alcohol–water mixtures (15). Data for solvolyses of tosylates show that N_{OTs} values correlate linearly with Y_{OTs} values from water up to 60% *w*/*w* sulfuric acid (5). A plot of N_{OTs} vs. X (Fig. 1) is linear for the limited range of available data, with a similar slope (–0.51) to the log a_{H_2O} plot.

For trityl (**1**) and a variety of benzhydryl cations (**2**) and in acetonitrile–water mixtures (solvents with varying Y, but similar N), rates of nucleophilic attack (eq. [10]) are almost independent of solvent composition (11, 13). Literature data for Y values in acetonitrile–water are based on solvolyses of 1-adamantyl mesylate (16); N values, based on solvolyses of *S*-methylthiophenium ions (17), are almost constant (–0.94–1.06) for 40%–90% acetonitrile–water, and values for 20%–95% range from –0.94 to –1.27 (17). In solvolysis research, the solvent effect of changes in Y can be studied independently of N by examining bridgehead substrates such as

© 2008 NRC Canada

1-adamantyl (**3**) for which rearside nucleophilic attack is prevented by the hydrocarbon framework. Rates of such S_N1 solvolyses of substrates with neutral leaving groups (e.g., **3**) vary less than 20% from 95% to 20% acetone–water (14). These results indicate that the rates of the forward and reverse reactions of the types shown in eqs. [10] and [11] are (to a good approximation) independent of *Y*.

[10] $R^+ + H_2O \rightarrow (ROH_2^+) \rightarrow ROH + H^+$

[11] $RSMe_2^+ \rightarrow R^+ + Me_2S$

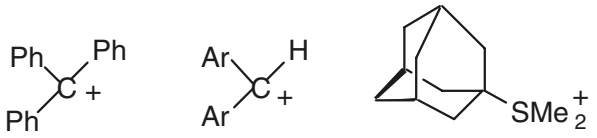

(1) **(2)** **(3)**

Generally, *m* values (eq. [7]) are reduced when nucleophilic attack also occurs (18), and it is assumed that the rates of solvolyses of most substrates (both S_N1 and S_N2) having neutral leaving groups will be independent of the solvent *Y* (19). *By analogy, the solvent effect on the rate of nucleophilic attack on BH^+ by water (the reverse step of eq. [8] in aqueous sulfuric acid) will be independent of Y; therefore, in terms of eq [7], rates will depend mainly on changes in N.*

Factors controlling the magnitude of the slope (*m)**

Values of *m** vary from 0 to about 2.0 (4). As *X* varies from 0.00 in water to about 10 in highly concentrated acid (4), the maximum dependence of K_{BH^+} (eq. [3]) on composition is very large (10^{20}). For all equilibria of the type shown in eq. [8] (except B = water), the value of K_{BH^+} will depend on the water concentration. If this is excluded (as in eq. [1]), then variations in water concentration are included in the *m*X* term, and there will be a substantial contribution to the slope of 0.4–0.8 (Fig. 1).

The next step is to assess how *l* (the sensitivity to *N*, eq. [7]) depends on BH^+. If B = water in eq. [8], the rate of proton transfer in both forward and reverse steps is diffusion-controlled (20). For stronger bases (B), such as ammonia, aniline, and pyridine, the rate of protonation by H_3O^+ is also diffusion-controlled at 25 °C (~10^{10} $M^{-1}s^{-1}$). *Consequently, both the pK_a and the solvent dependence of pK_a are then determined by the rate constant for the dissociation or "hydrolysis" of BH^+ (the reverse reaction of eq. [8]);* as this step refers to a solvolysis with a neutral leaving group (B), the solvent dependence of relative rates will be almost independent of *Y*, but will depend mainly on the response (*l*) of the cation to the lowering of solvent nucleophicity (*N*) when sulfuric acid is added to water (i.e., variations in *m** are then due to changes in *l*, eq. [7] for hydrolysis of BH^+).

Bagno et al. (6) noted a connection between the gas-phase basicity of B and *m** — the least favorable cation H_3O^+ has an *m** of 0, and *m** increases in the order alcohols, ethers, amines — gas-phase proton affinities (the enthalpy change expressed as a positive value when B reacts with H^+) show the same trends (21). Kresge (20*b*) emphasized that large thermodynamic contributions to reaction barriers could lead to relatively slow proton transfers. The tendency for more stable cations (BH^+ or R^+), having smaller values of log *k*, to show a higher sensitivity to *N* is shown (Fig. 2) by the kinetic data for various benzhydryl and other cations (R^+) reacting with water and with 2,2,2-trifluoroethanol (TFE).

Fig. 2. Plots of logarithms of rate constants for reactions of benzhydryl (**2**) cumyl and other cations with acetonitrile–water and with 2,2,2-trifluoroethanol (TFE) at 20 °C vs. N_{OTs} (kinetic data from Table 6 of ref. 12 and N_{OTs} data from ref. 22); the cations can be identified as follows from the order of decreasing rate constants in TFE: $(C_6H_5)_2CH^+$; $4\text{-}MeOC_6H_4C^+(CF_3)_2$; group of three cations: $(4\text{-}MeC_6H_4)_2CH^+$, $4\text{-}MeOC_6H_4C^+(CH_3)_2$, 9-phenyl-9-fluorenyl; $(4\text{-}MeOC_6H_4)(C_6H_5)CH^+$; 2,4,6-trimethoxybenzenonium; $(4\text{-}MeOC_6H_4)_2CH^+$; additional rate constants for reactions of cations in TFE–water mixtures (Table S3 in ref. 13) show a gradual increase in rate constant as water is added to TFE; figure 2 shows k_{water}/k_{TFE} ratios graphically as two-point lines, but the plots would curve if the reactions reach a diffusion-controlled limit (12).

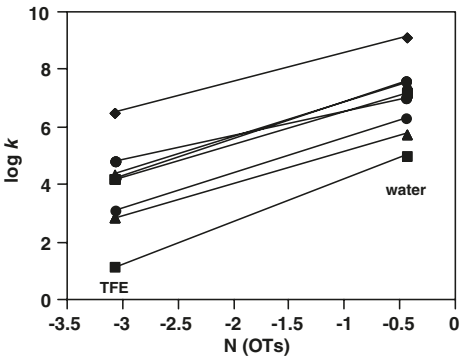

The slopes (*l*) of Fig. 2 can be linked semi-quantitatively to *m** for eq. [4] as follows. On the N_{OTs} scale of solvent nucleophilicity (see Table 5 in ref. 22), the value for 60% sulfuric acid – water of –2.02 is in between the values for water (–0.44) and TFE (–3.07). From a typical slope of Fig. 2 of 1.3 and a difference of 1.58 in N_{OTs}, a rate retardation of 10^2 is calculated for reaction of cations (R^+) with water in 60% sulfuric acid compared with reaction in water alone. Taking *X* = 3.3 for 60% sulfuric acid (4) gives an estimated contribution from the forward reaction in eq. [4] to the slope of 0.6 for *m**.

The slope *m** may also depend on the accessibility of the H in BH^+ to nucleophilic attack (eq. [8]) for the following reason. Extensive data for S_N2 solvolyses, including Et_3O^+ (23) and *S*-methyldibenzo-thiophenium ions (24) as well as many neutral substrates (8), show that *l* (eq. [7]) may also depend on steric effects (*l* increases in the order $Bu^t < Pr^i <$ Et < Me). The carbon atom acting as the site of nucleophilic attack in solvolyses of methyl substrates is the most accessible, and *l* values are highest. Alternatively, stabilization of a developing positive charge is least favorable for methyl substrates, and so there is a greater requirement for nucleophilic assistance. The alkyl effect and the effect of proton affinity of B combine in comparisons of solvolyses Et_3O^+ and *S*-methyldibenzo-thiophenium ions (23, 24) and the ratio of rate constants EtOH:TFE are almost 10-fold greater for the much less reactive *S*-methyldibenzothiophenium ions.

© 2008 NRC Canada

Further contributions to m^* arise from the reverse reaction to eq. [4] when redrawn as eq. [12].

[12] $ROH + H_3O^+ \rightarrow R^+ + 2H_2O \rightarrow$ oxygen exchange

Rate constants for formation of R^+ can be obtained from acid-catalysed oxygen exchange in alcohols (11), thought to occur via a carbocation – water molecule ion pair (25, 26), which is simplified to R^+ in eq. [12]. For 0.005 mol/L HCl, second-order rate constants for oxygen exchange in Ph_3COH increase 10-fold from 90% *v*/*v* acetonitrile–water to water, showing a small but significant dependence of the rate of eq. [12] on *Y*. A further increase in *Y* from water to sulfuric acid – water (5) will also contribute to m^*. The effect of changes in *Y* is consistent with formation of a cationic transition state with a more localized positive charge. In other words, H_3O^+ appears to be acting as a highly delocalized cation, because there is charge delocalization onto at least three hydrogen atoms (27) and extensive hydrogen bonding (6).

The slope of an excess-acidity plot will also include a log a_{H_2O} term because eq. [12] has an additional water molecule (cf. eq. [4]). Further complications arise from the previously mentioned assumption (*i*) that the reacting species is the Eigen cation (H_3O^+) rather than for example a mixture of solvated clusters of $(H_3O^+)(H_2O)_n$, the Zundel cation ($H_5O_2^+$) and solvated clusters $(H_5O_2^+)(H_2O)_n$ (27).

Conclusions

The solvent nucleophilicity term (*lN*) in eq. [7] provides the main connection between the slopes (m^*) of excess-acidity plots for equilibria (eq. [3]) and the Grunwald–Winstein eqs. [6 and 7] for medium effects on solvolyses. It is proposed that the pseudo first-order rate constants for solvolyses of the protonated bases (BH^+, eq. [1]) are more sensitive to changes in *l*, when the base B is more stable (e.g., when the proton affinity of B is lower or for less reactive carbocations (Fig. 2)). Alternatively, if the reaction of BH^+ is considered to be second-order (eq. [8]), rate constants (and hence m^*, eq. [9]) may depend on water activity. Both N_{OTs} and log a_{H_2O} are proportional to the excess-acidity (*X*) from water up to 60% *w*/*w* sulfuric acid (Fig. 1).

Acknowledgements

This work was supported by Science and Engineering Research Council (UK). I am very grateful to R.A. Cox for helpful discussions during a recent visit to Swansea, and to D.N. Kevill for comments on the manuscript.

References

1. K. Yates and R.A. McClelland. J. Am. Chem. Soc. **89**, 2686 (1967).
2. R.A. Cox and K. Yates. Can. J. Chem. **61**, 2225 (1983).
3. N.C. Marziano, G.M. Cimino, and R.C. Passerini. J. Chem. Soc., Perkin Trans. 2, 1915 (1973).
4. R.A. Cox. Adv. Phys. Org. Chem. **35**, 1 (2000).
5. T.W. Bentley and K. Roberts. J. Chem. Soc., Perkin Trans. 2, 293 (1987).
6. A. Bagno, G. Scorrano, and R.A. More O'Ferrall. Rev. Chem. Intermed. **7**, 313 (1987).
7. E. Grunwald and S. Winstein. J. Am. Chem. Soc. **70**, 846 (1948).
8. F.L. Schadt, T.W. Bentley and P.v.R. Schleyer. J. Am. Chem. Soc. **98**, 7667 (1976).
9. T.W. Bentley and M.S. Garley. J. Phys. Org. Chem. **19**, 341 (2006).
10. R.A. Stairs and E. Buncel. Can. J. Chem. **84**, 1580 (2006).
11. N. Mathivanan, R.A. McClelland, and S. Steenken. J. Am. Chem. Soc. **112**, 8454 (1990).
12. R.A. McClelland. Tetrahedron, **52**, 6823 (1996).
13. S. Minegishi, S. Kobayashi, and H. Mayr. J. Am. Chem. Soc. **126**, 5174 (2004).
14. D.N. Kevill and S.W. Anderson. J. Am. Chem. Soc. **108**, 1579 (1986).
15. J. Kaspi and Z. Rappoport. Tetrahedron Lett. 2035 (1977).
16. T.W. Bentley, I.S. Koo, G. Llewellyn, and S.J. Norman. Croat. Chem. Acta, **65**, 575 (1992).
17. D.N. Kevill and S.W. Anderson. J. Chem. Res. 356 (1991).
18. T.W. Bentley and P.v.R. Schleyer. J. Am. Chem. Soc. **98**, 7658 (1976).
19. D.N. Kevill. *In* Advances in quantitative structure – property relationships. No. 1. *Edited by* M. Charton. Jai press, Greenwich, CT. 1996. pp. 81–115.
20. (*a*) M. Eigen. Angew. Chem. Int. Ed. Engl. **3**, 1 (1964); (*b*) A.J. Kresge. Acc. Chem. Res. **8**, 354 (1975).
21. J.E. Szulejko and T.B. McMahon. J. Am. Chem. Soc. **115**, 7839 (1993).
22. T.W. Bentley and G.Llewellyn. Prog. Phys. Org. Chem. **17**, 121 (1990).
23. D.N. Kevill and G.M.L. Lin. J. Am. Chem. Soc. **101**, 3916 (1979).
24. D.N. Kevill and S.W. Anderson. J. Org. Chem. **56**, 1845 (1991).
25. E. Grunwald, A. Heller, and F. S. Klein. J. Chem. Soc. 2604 (1957).
26. M.V. Merritt, D.B. Anderson, K.A. Basu, I.W. Chang, H.J. Cheon, N.E. Mukundan, C.A. Flannery, A.Y. Kim, A. Vaishampayan, and D.A. Yens. J. Am. Chem. Soc. **116**, 5551 (1994).
27. J.M. Headrick, E.G. Diken, R.S. Walters, N.I. Hammer, R.A. Christie, J. Cui, E.M. Myshakin, M.A. Duncan, M.A. Johnson, and K.D. Jordan. Science (Washington, DC), **308**, 1765 (2005).

© 2008 NRC Canada

Triterpenoids from *Saussurea ussuriensis*

Xue-Hu Li, Jia-Tao Feng, and Yan-Ping Shi

Abstract: From an extract of the whole plant of *Saussurea ussuriensis*, three new triterpenoids, 1β-hydroxy-ursa-9(11), 12-dien-3β-yl palmitate (ussuriensin A) (**1**), 1β-hydroxy-oleana-9(11), 12-dien-3β-yl palmitate (ussuriensin B) (**2**), and 28-hydroxy-taraxast-20(30)-ene-3β-yl palmitate (ussuriensin C) (**3**), as well as five known triterpenoids, 11β-hydroxy-urs-12-en-3-one (**4**), 11β-hydroxy-urs-12-en-3β-yl palmitate (**5**), ursa-9(11), 12-dien-3-one (marsformosanone) (**6**), 3β-hydroxy-30-norlupan-20-one (**7**), and taraxast-20(30)-en-3β, 21α-diol (**8**) were isolated. Their structures were characterized by various spectroscopic methods, including 1D NMR, 2D NMR, and HR-ESI-MS.

Key words: Compositae, *Saussurea ussuriensis*, triterpenoids, ursane, oleanane, taraxastane.

Résumé : À partir d'un extrait de la plante complète de *Saussurea ussuriensis*, on a isolé trois nouveaux triterpénoïdes, le palmitate de 1β-hydroxyursa-9(11),12-dién-3β-yle (= ussuriensine A, **1**), le palmitate de 1β-hydroxyoléana-9(11),12-dién-3β-yle (= ussuriensine B, **2**) et le palmitate de 28-hydroxytaraxast-20(30)-én-3β-yle (= ussuriensine C, **3**) ainsi que cinq triterpénoïdes connus, la 11α-hydroxyurs-12-én-3-one (**4**), le palmitate de 11α-hydroxyuras-12-én-3β-yle (**5**), l'ursa-9(11),12-dién-3-one (= marsformosanone, **6**), la 3β-hydroxy-30-norlupan-20-one (**7**) et le taraxast-20(30)-én-3β,21-diol (**8**). Les structures ont été caractérisées par diverses méthodes spectroscopiques, dont la RMN en 1D et en 2D ainsi que par la spectrométrie de masse à haute résolution et ionisation par électronébulisation.

Mots-clés : composition, *Saussurea ussuriensis*, triterpénoïdes, ursane, oléanane, taraxastane.

[Traduit par la Rédaction]

Introduction

The genus *Saussurea* consists of about 400 species distributed throughout Asia and Europe. About 40 species have been investigated on their chemical constituents, and sesquiterpenes and triterpenoids have been reported as the most widespread constituents (1). In the course of our search of bioactive sesquiterpenes and triterpenoids, we selected the plant species, *S. ussuriensis*, which is a perennial herb mainly distributed in northwestern of China and has been used as a traditional folk remedy for the treatment of colds, headache, arthritis, and strain (2). Its chemical constituents have not been previously investigated. In our investigation on phytochemistry, eight steroids have been reported by us (3), and eight triterpenoids (**1**–**8**, Fig. 1) were further isolated from an alcoholic extract of the whole plant of this species. The compounds (**1**–**3**) were previously unreported natural products, and **4**–**8** were known. We report herein the isolation and structural elucidation of these triterpenoids.

Results and discussion

The 95% ethanol extract of the *S. ussuriensis* was subjected to column chromatography to give three new triterpenoids (**1**–**3**) together with five other know triterpenoids (**4**–**8**). Their structures were elucidated using 1D and 2D NMR spectroscopic data and compared with those reported in the literature.

Ussuriensin A (**1**) was obtained as colorless gum. The molecular formula was assigned as $C_{46}H_{78}O_3$ on the basis of HR-ESI-MS (*m/z* 679.6039 $[M + H]^+$). Its IR spectrum showed absorption bands for hydroxyl (3499 cm^{-1}) and ester carbonyl (1732 and 1257 cm^{-1}) groups. The ester group in **1** could be further deduced as a palmitoyl moiety because of the characteristic signal δ_C 173.50 (C-1′) in the downfield region of the ^{13}C NMR spectrum, as well as a saturated long-chain features: a methyl signal δ_H 0.89 (t, J = 6.8 Hz, H-16′), several methlene signals δ_H 1.28 (br s, H-15′ to H-4′, 24H), δ_H 1.75 (m, H-3′), and δ_H 2.31 (t, J = 7.2 Hz, H-2′) in the ^1H NMR spectrum (Table 1) (4–7). In addition to the long-chain ester group, it implied a pentacyclic triterpenes that the left 30 carbon signals (8 × CH_3, 7 × CH_2, 8 × CH, 7 × C) in the ^{13}C NMR combined with DEPT experiment (Table 1) and eight degrees of unsaturation. The deductive results could be demonstrated by the presence of eight methyl groups, in which six singlets (δ_H 0.87, 0.88, 0.90, 0.80, 0.92, 0.93), two doublets (δ_H 0.85, d, J = 6.4 Hz and 0.82, d, J = 6.4 Hz). These results and typical resonances at δ_C 152.08 (C-9), 117.72 (C-11), 123.50 (C-12) and 141.67 (C-13) further indicated a pentacyclic triterpene with an

Received 19 November 2007. Accepted 18 January 2008. Published on the NRC Research Press Web site at canjchem.nrc.ca on 5 March 2008.

X.-H. Li,[1] J.-T. Feng and Y.-P. Shi.[2] Key Laboratory for Natural Medicine of Gansu Province, Lanzhou Institute of Chemical Physics, Chinese Academy of Sciences, Lanzhou 730000, China.

[1]Present address: The Graduate University of Chinese Academy of Sciences, Chinese Academy of Sciences, Beijing 100039, China.
[2]Corresponding author (e-mail: shiyp@lzb.ac.cn).

 doi:10.1139/V08-018 © 2008 NRC Canada

Fig. 1. Molecular structures of the triterpenoids isolated.

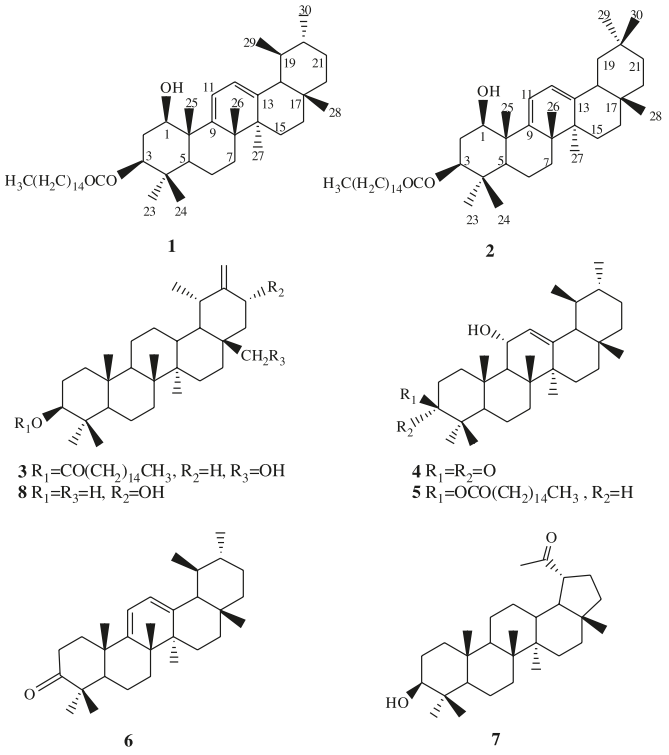

ursa-9(11), 12-diene skeleton (8, 9). This was confirmed by using a COSY experiment: H-11 (δ_H 6.20, d, J = 7.0 Hz) showing correlation with H-12 (δ_H 5.47, d, J = 7.0 Hz), and using a HMBC experiment (Fig. 2): H-11 showing correlation with C-9, C-10, C-12, C-13, and H-12 showing correlation with C-9, C-11, C-13, C-18. The correlation between H-3 (δ_H 4.55, dd, J = 4.4, 12.0 Hz) and C-1′ (δ_C 173.50), C-2 (δ_C 34.74), C-4 (δ_C 38.04) in the HMBC, together with comparison of the chemical shift, peak pattern, and coupling constant of H-3 with those of known triterpenoids in literature (4–7) suggested that the only ester group (palmitoyl) linked at C-3β position. The location of only hydroxyl group was assigned as C-1β using COSY experiment: H-1 (δ_H 3.94, dd, J = 4.4, 11.6 Hz) showing correlation with H-2αβ (δ_H 1.81, 1.94), and HMBC experiment: H-1 (δ_H 3.94) showing correlation with C-9, C-10, and C-25. Hence, compound **1** could be identified as 1β-hydroxy-ursa-9(11), 12-dien-3β-yl palmitate.

Ussuriensin B (**2**) was obtained as colorless gum. Its molecular formula of $C_{46}H_{78}O_3$ was deduced from HR-ESI-MS (*m*/*z* 679.6029 $[M + H]^+$) and indicated that it is an isomer of **1**. The IR spectrum showed strong absorptions for hydroxyl (3413 cm^{-1}) and ester carbonyl (1714, 1222 cm^{-1}) functions, similar to that of **1**. The palmitoyl ester group in **2** was also elucidated by the typical signal δ_C 173.49 (C-1′) and δ_H 2.31 (2H, t, J = 7.2 Hz, H-2′), δ_H 1.75 (2H, m, H-3′), δ_H 1.28 (br s, H-4′ to H-15′, 24H), and δ_H 0.89 (3H, t, J = 7.2 Hz, H-16′) due to saturated long-chain ester group (4–7). The ^1H and ^{13}C NMR spectra (Table 1) of **2** were close to those of **1**. The characteristic resonances at δ_C 151.88 (C-9), 118.28 (C-11), 121.16 (C-12), and 147.42 (C-13) of **2**, different from those of **1**, indicated that ussuriensin **2** was an pentacyclic triterpene with oleana-9(11), 12-diene carbon skeleton (8–10). The locations of the palmitoyl and hydroxyl groups were assigned at C-3β and C-1β, respectively, identical to that of **1**. Therefore, compound **2** was identified as 1β-hydroxy-oleana-9(11), 12-dien-3β-yl palmitate.

Ussuriensin C (**3**) was obtained as colorless oil. Its molecular formula was assigned as $C_{46}H_{80}O_3$ on the basis of EI-MS (*m*/*z* 662 $[M - H_2O]^+$) and ^{13}C NMR spectrum combined with DEPT experiment. Absorption bands for hydroxyl (3352 cm^{-1}), ester carbonyl (1732, 1246 cm^{-1}), and double bond (1653 cm^{-1}) functions were observed in IR spectrum. Detailed inspection of the ^1H (Table 1) and ^{13}C NMR (Table 1) of **3**, and comparison of its spectral data with those of compounds **1**, **2**, and **5** showed that there was a palmitoyl group attaching at C-3β position similar to **1**. Except for the NMR data of palmitoyl ester group, there were 30 carbon signals including six methyls, twelve methlenes, six methines, and six quaternary carbons, and indicating a pentacyclic triterpene. In the ^1H NMR spectrum, there were six methyl groups, in which five singlets (δ_H 0.78, 0.94, 0.85, 0.88, 0.86), one doublet (δ_H 1.03, d, J = 6.4 Hz), and two olefinic protons (δ_H 4.94, br s, 4.91, br s), three oxymethylene protons (δ_H 4.47, dd, J = 5.6, 10.8 Hz, 1H; 4.12, br s, 2H). These spectral data together with the characteristic resonances at δ_C 154.75 (C-20), 106.90 (C-30), and δ_C 48.90 (C-18) suggested that **3** was a taraxast-20(30)-ene type triterpenoid with one hydroxyl group, one palmitoyl ester group, and exocyclic double bond (9–13). By comparison of the ^{13}C NMR data of **3** with those of the known taraxasterol (9, 12) and taraxast-20(30)-ene-3β, 21β-diol (12), taraxast-20(30)-ene-3β, 21α-diol (10, 11), the absence of a methyl peak at δ_C 18.2 (C-28), and the presence of an oxymethylene carbon at δ_C 65.06 noted it was possible to place this hydroxyl group at C-28 position. This was confirmed by the downfield shift from δ_C 34.5 in taraxasterol to δ_C 43.01 in **3** due to the C-28 hydroxyl group. Consequently, compound **3** was elucidated as 28-hydroxy-taraxast-20(30)-ene-3β-yl palmitate. Unfortunately, the molecular composition has not been obtained by HR-ESI-MS like compounds **1** and **2** after trying to do that for several times. Up to now, we do not know the reason for its restricted ionization. However, we believe the structure of **3** must be corrected from NMR and EI-MS spectral data.

The remaining compounds were characterized as 11α-hydroxy-ursa-12-en-3-one (**4**) (14), 11α-hydroxy-urs-12-en-3β-yl palmitate (**5**) (15), ursa-9(11), 12-dien-3-one (marsformosanone) (**6**) (8), 3β-hydroxy-30-norlupan-20-one (**7**) (16), and taraxast-20(30)-en-3β, 21α-diol (**8**) (11) (Fig. 1) by comparison with their reported physical and spectroscopic data.

Experimental

General experimental procedures

Melting points were determined with an X-4 Digital Display Micro-Melting point apparatus and are uncorrected. Optical rotations recorded in $CHCl_3$ using a PerkinElmer 241 polarimeter. UV spectra were measured on a Spect 50-UV–vis instrument (Analytic Jena AG). IR spectra were measured on an FTS 165-IR spectrometer (Bio-Rad, USA). ^1H NMR (400.13 MHz), ^{13}C NMR (100.62 MHz), and 2D NMR were recorded on a Varian INOVA-400 FT NMR spec-

© 2008 NRC Canada

Table 1. ^{1}H NMR (400 MHz) and ^{13}C NMR (100 MHz) spectral data of compounds **1**, **2**, and **3** in $CDCl_3$.

	1		**2**		**3**	
Position	δ_H (*J* in Hz)	δ_C	δ_H (*J* in Hz)	δ_C	δ_H (*J* in Hz)	δ_C
1	3.94 dd (4.4, 11.6)	75.63	3.94 dd (4.4,11.6)	75.61		38.36
2	1.81 m, 1.94 m	34.74		34.74		27.40
3	4.55 dd (4.4, 12.0)	76.81	4.55 dd (4.4, 12.0)	76.75	4.47 dd (5.6, 10.8)	80.57
4		38.04		38.04		37.83
5		48.79		48.92		55.36
6		18.35		18.29		18.18
7		30.98		31.24		34.22
8		43.26		40.80		40.87
9		152.08		151.88		50.28
10		44.15		44.78		37.08
11	6.20 d (5.6)	117.42	6.52 d (5.6)	118.28		21.02
12	5.47 d (6.0)	123.50	5.52 d (6.0)	121.16		26.65
13		141.67		147.42		38.00
14		40.86		42.92		42.79
15		26.24		25.75		23.73
16		28.28		27.25		39.84
17		33.71		32.18		43.01
18		57.30		45.58		48.90
19		39.43		46.80		43.80
20		39.08		31.09		154.75
21		31.21		34.65		31.27
22		41.33		37.02		35.45
23	0.87 s	28.69	0.85 s	28.69	0.78 s	27.96
24	0.88 s	16.25	0.86 s	16.27	0.94 s	15.78
25	0.90 s	18.62	0.93 s	18.54	0.85 s	16.57
26	0.80 s	17.84	0.80 s	20.30	0.88 s	16.16
27	0.92 s	22.17	0.99 s	33.69	0.86 s	14.51
28	0.93 s	27.74	0.93 s	27.78	4.12 brs	65.06
29	0.85 d (6.4)	17.41	0.82 s	33.18	1.03 d (6.4)	17.70
30	0.82 d (6.4)	21.49	0.98 s	21.76	4.94 brs	106.90
1′		173.50		173.49		173.70
2′	2.31 t (7.2)	34.55	2.31 t (7.2)	34.65	2.29 t (7.2)	34.86
3′	1.75 m	25.14	1.75 m	25.15	1.67 m	25.17
4′	1.28 brs	29.2–	1.28 brs	29.2–	1.28 brs	29.2–
13′	1.28 brs	29.8	1.28 brs	29.8	1.28 brs	29.8
14′	1.28 brs	31.92	1.28 brs	31.92	1.28 brs	31.92
15′	1.28 brs	22.68	1.28 brs	22.68	1.28 brs	22.69
16′	0.89 t (7.2)	14.09	0.89 t (7.2)	14.10	0.89 t (7.2)	14.11

Fig. 2. Correlation of HMBC of compound **1**.

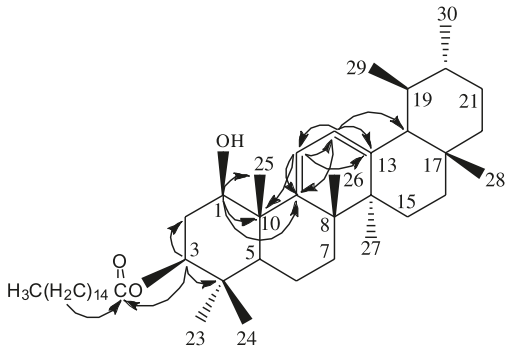

trometer (USA) in $CDCl_3$ with TMS as internal standard. HR-ESI-MS (High resolution electro-spray ionization mass spectrometry) was determined on a Bruker APEX II. EI-MS was determined on a HP 5988A MS (70 eV). Separation and purification were performed by chromatographic column (CC) over silica gel. Silica gel (200–300 mesh) used for CC and silica gel (GF_{254}) for TLC were supplied by the Qingdao Marine Chemical Factory, Qindao, P. R. China. Spots were detected on the TLC under UV light or by heating over 110 °C after spraying with 98% H_2SO_4–EtOH (*v*/*v* 5:95).

Plant material

S. ussuriensis belongs to genus *Saussurea* (Compositae) (17). The whole plant was collected in Zhang county, Gansu province, P. R. China in August 2001 and was identified by adjunct Professor Ji Ma, Faculty of Pharmacy, first Military Medical University of PLA, Guangzhou, P.R. China. A voucher specimen (No. 2001–02) has been deposited at key Laboratory for Natural Medicine of Gansu Province.

© 2008 NRC Canada

Extraction and isolation

The air-dried whole plant of *S. ussuriensis* (5.2 kg) was powdered and extracted with 95% EtOH at room temperature (20 L × 4, each extraction lasted 7 days). The combined extracts were evaporated to dryness under reduced pressure. The residue (240 g) was then suspended in H_2O (1.5 L), extracted with petroleum ether (60–90 °C)(1.0 L × 4), EtOAc (1.0 L × 4) and *n*-BuOH (1.0 L × 4), respectively. The petroleum ether (60–90 °C) extract (94 g) was subjected to column chromatography on silica gel (1000 g) using petroleum ether (60–90 °C) with increasing volume of acetone (*v*/*v* = 40:1, 20:1, 15:1, 10:1, 7:1, 4:1, 2:1, 1:1, each about 4.0 L) as eluent. The fractions A1–A10 were collected according to TLC analysis. Fraction A2 (3.5 g) was further fractionated on a silica gel column (80 g) using petrolemn ether – EtOAc (8:1, 1500 mL) to give impure compound **3** (40 mg) that was purified firstly on a silica gel column (60 g) using $CHCl_3$–Et_2O (30:1, 1000 mL) then on another silica gel column (30 g) with $CHCl_3$–EtOAc (30:1200 mL) to yield pure **3** (5 mg). Fraction A3 (2.4 g) was further fractionated on a silica gel column (70 g), eluting with petroleum ether – EtOAc (10:1, 2000 mL), to give four fractions (fr. A3a, 700 mL; fr. A3b, 200 mL; fr. A3c, 500 mL; and fr. A3d, 600 mL). Fraction A3a (0.8 g) was further subjected to column chromatography on silica gel column (50 g), eluting with $CHCl_3$–acetone (50:1, 2600 mL), to give mixture **1** and **2** (60 mg), and impure **6** (20 mg), that by CC over silica gel (30 g) with petroleum ether – EtOAc (7:1, 300 mL) gave pure **6** (9 mg). The mixture (**1** and **2**) was purified by another silica gel column (25 g), eluting with petroleum ether – EtOAc (4:1, 400 mL), to give pure **1** (8 mg) and **2** (20 mg). Fraction A3b (0.3 g) was purified by CC on silica gel (40 g) using $CHCl_3$ – acetone (50:1, 800 mL) to obtain compound **4** (7 mg), which was further purified by CC (15 g) with petroleum ether – EtOAc (8:1, 200 mL). Fraction A3c (0.5 g) was purified by CC on silica gel (40 g) using petroleum ether – EtOAc (5:1, 1000 mL) to obtain compound **7** (10 mg), which was further purified by CC (20 g) with petroleum ether – EtOAc (8:1, 300 mL). Fraction A3d (0.6 g) was purified using CC on silica gel (50 g) with petroleum ether – EtOAc (8:1, 2000 mL) to yield impure **5** (7 mg) and impure **8** (6 mg), which were further purified by CC on silica gel (20 g) with $CHCl_3$–acetone (40:1, 150 mL) and on silica gel (20 g) with $CHCl_3$–EtOAc (60:1, 200ml), respectively.

1β-Hydroxy-ursa-9(11), 12-dien-3β-yl palmitate (Ussuriensin A)

Colorless gum; [α] +145.0° (*c* 0.33, $CHCl_3$). UV (MeOH) λ_{max} (log ε): 199.4 (3.57). IR (film) ν_{max}: 3499 (OH), 2924, 2854, 1732 (ester carbonyl function), 1460, 1373, 1257, 1176, 1108, 1056, 1028, 985, 876, 840, 803, 723 cm^{-1}. ^1H and ^{13}C NMR: see Table 1. HR-ESI-MS *m*/*z* calcd. for $C_{46}H_{78}O_3$: 679.6024 $[M + H]^+$; found: 679.6039.

1β-Hydroxy-oleana-9(11), 12-dien-3β-yl palmitate (Ussuriensin B)

Colorless gum; [α] +6.0 ° (*c* 0.33, $CHCl_3$). UV (MeOH) λ_{max} (log ε): 199.4 (3.76). IR (film) ν_{max}: 3608, 3526, 3413 (OH), 3004, 2964, 2926, 2577, 2144, 1714 (ester carbonyl function), 1423, 1361, 1222, 1092, 982, 903, 784, 758, 685 cm^{-1}. ^1H and ^{13}C NMR: see Table 1. HR-ESI-MS *m*/*z*: 679.6029 $[M + H]^+$ (Calcd. for $C_{46}H_{78}O_3$: 679.6024).

28-Hydroxy-taraxast-20(30)-ene-3β-yl palmitate (Ussuriensin C)

Colorless oil; [α] +8.0° (*c* 0.17, $CHCl_3$); UV (MeOH) λ_{max} (log ε): 215.6 (3.26), 267.2 (2.72). IR (film) ν_{max}: 3352 (OH), 2924, 2854, 1732 (ester carbonyl function), 1653 (double bond), 1588, 1460, 1373, 1316, 1246, 1172, 1070, 1026, 979, 887 cm^{-1}. ^1H and ^{13}C NMR: see Table 1. EI-MS *m*/*z*: 662 $[M - H_2O]^+$, 647 $[M - H_2O - CH_3]^+$, 424 $[M - C_{15}H_{31}COOH]^+$, 410, 407, 393, 379, 365, 351, 337, 284, 279, 256, 211, 179, 183, 169, 155, 139, 125, 111, 97, 85, 71, and 57.

Acknowledgements

The authors are greatly indebted to adjunct Professor Ji Ma (Faculty of Pharmacy, First Military Medical University of PLA, Gangzhou, P. R. China) for her help in identification of the plant material. This work was supported by the National Natural Science Foundation of China (NSFC 20475057), Natural Science Foundation of Gansu Province (No. 3ZS051-A25–077) and the Foundation for the "Bairen Jihua" of the Chinese Academy of Sciences (CAS) in 2000.

References

1. Y.L. Ren and J.S. Yang. Chin. Pharm. J. **35**, 505 (2000).
2. C. Shih and S.Y. Jin. Flora reipublicae popolaris sinicae. Science Press, Beijing. 1999. p. 173.
3. J.T. Feng and Y.P. Shi. Pharmazie, **60**, 464 (2005).
4. G. Morales and J.L. Mclaughlin. J. Nat. Prod. **52**, 381 (1989).
5. V.S.P. Chaturvedula, J.K. Schilling, J.S. Miller, R. Andriantsiferana, V.E. Rasamison, and D.G.I. Kingston. J. Nat. Prod. **65**, 1222 (2002).
6. S. Öksüz. and G. Topcu. Phytochemistry, **26**, 3082 (1987).
7. M.L. Barreiros, J.M. David, P.A.P. Pereira, M.L.S. Guedes, and J.P. David. J. Braz. Chem. Soc. **13**, 669 (2002).
8. T. Bhaumik, A.K. Dey, P.C. Das, A.K. Mukhopadhyay, and A. Chatterjee. India. J. Chem. **20B**, 664 (1981).
9. S.B. Mahato and A.P. Kundu. Phytohemistry, **37**, 1517 (1994).
10. I. Muhammad, K.A. El-Sayed, J.S. Mossa, M.S. Al-Said, F.S. El-Feraly, and A.M. Clark. J. Nat. Prod. **63**, 605 (2000).
11. S.D. Petrović, M.S. Gorunović, V. Wray, and I. Merfort. Phytochemistry, **50**, 293 (1999).
12. J.Q. Dai, C.Y. Zhao, Q. Zhang, Z.L. Liu, R.L. Zheng, and L.Yang. Phytochemistry, **58**, 1107 (2001).
13. J.Q. Dai, B. Zhou, Y.L. Wang, L. Yang, and Z.L. Liu. Chin. Chem. Lett. **12**, 151 (2001).
14. Z.F. Hou, Z.X. Xie, Y.Q. Tu, and Y. Li. Indian J. Chem. **41B**, 234 (2002).
15. R. Kakuda, K. Machida, Y. Yaotta, M. Kikuchi, and M. Kikuchi. Chem. Pharm. Bull. **51**, 885 (2004).
16. Y. Li, Y.P. Shi, and Y. Li. Pharmazie, **58**, 937 (2004).
17. The editorial board of the plant index of China of Chinese acadamy of science. The plant index of China, Vol 78, Science Press, Beijing. 1999. p. 173.

© 2008 NRC Canada

The Strecker reaction — an examination in terms of no-barrier theory

J. Peter Guthrie and Goonisetty Bhaskar

Abstract: For those examples of the Strecker reaction where information about both rate and equilibrium is available, we have been able to calculate rate constants for the addition of cyanide ion to the iminium ion by the no-barrier theory (NBT) approach. Both experimental and calculated values are for reaction in aqueous solution. Only for the reactions of benzaldehyde with benzyl or allyl amines and HCN are the equilibrium constants and rate constants for the final, rate-determining, step directly available from the literature. For the reactions of acetone with ammonia, methylamine, or dimethylamine and HCN rate constants for the retro-Strecker cleavage and the equilibrium constants for the overall Strecker reaction have been reported. These equilibrium constants, combined with equilibrium constants for iminium ion formation, which can be extracted from information in the literature, allow calculation of the equilibrium constants for the final step of these Strecker reactions. No-barrier theory has already been applied to carbonyl additions, including cyanohydrin formation; this report provides further evidence for the generality of this approach for calculating rate constants without using any kinetic information.

Key words: Strecker reaction, rate constant, equilibrium constant, no-barrier theory, computation.

Résumé : Pour les exemples de la réaction de Strecker pour lesquels on dispose à la fois des vitesses et des équilibres réactionnels, faisant appel à la théorie sans barrière, il nous a été possible de calculer les constantes de vitesse de réaction pour l'addition de l'ion cyanure sur l'ion iminium. Les valeurs expérimentales et les valeurs calculées se rapportent toutes à des réactions en milieu aqueux. Ce n'est que dans le cas des réactions du benzaldéhyde avec les amines benzyliques ou allyliques et le HCN qu'on retrouve dans la littérature les constantes d'équilibre et les constantes de vitesse pour l'étape finale cinétiquement déterminante. Pour les réactions de l'acétone avec l'ammoniac, la méthylamine ou la diméthylamine et le HCN, les constantes de vitesse pour le clivage rétro-Strecker et les constantes d'équilibre pour la réaction globale de Strecker sont aussi connues. Ces constantes d'équilibre combinées avec les constantes d'équilibre pour la formation de l'ion iminium qui peuvent être extraites de données disponibles dans la littérature permettent de calculer les constantes d'équilibre pour l'étape finale de ces réactions de Strecker. La théorie sans barrière a déjà été appliquée à des additions sur des groupes carbonyles, y compris la formation de cyanohydrines; les résultats obtenus dans ce travail permettent de démontrer la généralité de cette approche aux calculs de constantes de vitesse sans faire appel à des informations cinétiques.

Mots-clés : réaction de Strecker, constante de vitesse, constante d'équilibre, théorie sans barrière, calculs.

[Traduit par la Réaction]

Introduction

The Strecker reaction (1, 2) has been used for amino acid synthesis (3, 4) and provides a route to weakly basic amines (5). The reaction is sufficiently complicated that it has been relatively little studied (6–14). In this work, a study is reported of this reaction in terms of no-barrier theory (NBT) (15–22), which permits calculation of rate constants, given only equilibrium constants and distortion energies.

Received 30 November 2007. Accepted 10 January 2008. Published on the NRC Research Press Web site at canjchem.nrc.ca on 6 March 2008.

Dedicated to the memory of Keith Yates, an oustanding physical organic chemist.

J.P. Guthrie[1] and G. Bhaskar. Department of Chemistry, The University of Western Ontario, London, ON N6A 5B7, Canada.

[1]Corresponding author (e-mail: peter.guthrie@uwo.ca).

Both rate and equilibrium constants for the rate-determining step are known for only two Strecker reactions (14). For three additional reactions, the rate constant and the overall equilibrium constant for cyanoamine formation are known (8). All of these studies were carried out in aqueous solution. For these reactions, we now report that the observed rates of reaction can be matched by values calculated by NBT.

Theory

NBT (15–22) asserts that reactions can be analyzed in terms of "simple reaction dimensions" such that for progress along only one such dimension the energy is a quadratic function of the corresponding progress variable. The somewhat paradoxical name "no-barrier theory" was chosen to stress the key idea "if only one thing happens, there is no barrier"; most real reactions involve several simple processes, which must happen simultaneously, and therefore there is a barrier, but the underlying simplicity provides a

 doi:10.1139/V08-014 © 2008 NRC Canada

Table 1. Rate and equilibrium constants for reactions discussed in this work.

	Imine formation	Iminium ion formation	Overall Strecker formation	Cyanide plus iminium ion	Cyanide plus iminium ion	Retro-Strecker reaction
Reaction	log K^a	log K^b	log K^c	log K^d	log k	log k
$C_6H_5CHO + PhCH_2NH_2$				6.86[e]	3.82[e]	–3.04[e]
$C_6H_5CHO + CH_2{=}CHCH_2NH_2$				7.26[e]	4.00[e]	–3.26[e]
$CH_3COCH_3 + NH_3$	–2.19[f]	–5.19[g]	3.02[h]			–2.7[i]
$CH_3COCH_3 + CH_3N_2$	–0.68[j]	–3.68[g]	4.64[h]			–1.5[i]
$CH_3COCH_3 + (CH_3)_2NH$		–6.06[k]	3.61[h]			–0.88[i]

[a]For the reaction: RR′C=O + R″NH_2 ⇌ RR′C=NR″ (+ H_2O); M^{-1}
[b]For the reaction: RR′C = 0 + R″RR‴NH + H^+ ⇌ RR′C=NR″R‴$^+$ (+ H_2O); M^{-2}
[c]For the reaction: RR′C=O + R″R‴NH + HCN ⇌ RR′C(CN)NR″R‴ (+ H_2O)); M^{-2}
[d]For the reaction: RR′C=NR″R‴$^+$ + $^-$CN ⇌ RR′C(CN)NR″R‴; M^{-1}
[e]Reference 14.
[f]Reference 29.
[g]Calculated using an estimated pK_{BH}^+ as described in the text.
[h]Reference 9.
[i]Reference 8.
[j]Reference 31.
[k]Calculated from rate constants for formation (reference 28) and hydrolysis (reference 8) as described in the text.

basis for calculation of the rate constant. Simple reaction dimensions include such things as bond making or breaking involving heavy atoms, geometry change at a reaction center, bond-length change, and proton transfer between electronegative atoms. Each parabolic energy function has a minimum at the low-energy end of the coordinate, which runs from the starting material to the product value. The energies of each of the hypothetical corner species for a Strecker reaction are calculated from distortion energies (based on differences in MO energy between species differing only in geometry), the free energy of encounter complex formation calculated following Hine (23), desolvation of cyanide ion, and ion pairing between cyanide anion and iminium cation calculated by a simple electrostatic model (24). We estimate the desolvation cost of bringing a cyanide ion into contact with a carbon atom as the difference in p*K*a of HCN between water (25) and DMSO (26), assuming that the cyanide ion is predominantly hydrogen-bonded at carbon (15). There is however a problem because interaction of a small exposed $C^{\delta+}$ of the iminium ion should partially replace the interaction with the $H^{\delta+}$ of water, lessening the desolvation cost. It is hard to see how experimental evidence for such a phenomenon could be gathered because it will only be seen for inherently reactive complexes prone to form a covalent bond between $C^{\delta+}$ and $C^{\delta-}$.

Results

The available rate and equilibrium constants from the literature are found in Table 1. In only two cases were rate and equilibrium constants for formation of the Strecker product directly available. In three other cases there were rate constants for breakdown of the Strecker product (8) derived from acetone, and overall equilibrium constants for formation of this product from acetone, HCN, and the appropriate amine (ammonia, methylamine, or dimethylamine) (10).

To determine the equilibrium constant for the final rate-determining step of the Strecker reaction, we require the equilibrium constant for the reaction:

$$(CH_3)_2C{=}O + RR'NH + H^+ \rightleftharpoons (CH_3)_2C{=}NRR'^+$$

For methylamine, the equilibrium constant is known (27), and there is a plausible estimate for pK_{BH}^+ for the imine (27). This allows calculation of the desired equilibrium constant for the final step of Strecker product formation. For dimethylamine, the rate constant for iminium ion formation under conditions where the reaction is uncatalyzed has been reported by Hine et al. (28), and rate constants for the hydrolysis of this iminium ion have been reported by Taillades and Commeyras (8).

Unfortunately, the rate constants reported by Taillades and Commeyras are mostly for the uncatalyzed hydrolysis of the iminium ion, which is the microscopic reverse of the acid-catalyzed dehydration. One point at higher pH is significantly faster than the others, and they report that the reaction was too fast to measure at pH 13.5. Making the assumption that the kinetics should fit the rate law, $k_{obs} = k_{water} + k_{OH}[OH^-]$, and fitting to this rate law, we obtain a value for k_{OH}, which is the microscopic reverse of the process studied by Hine et al., and thus can calculate the equilibrium constant:

$$(CH_3)_2C{=}O + RR'NH \rightleftharpoons (CH_3)_2C{=}NRR'^+ + OH^-$$

Finally, Zuman reported an equilibrium constant for the formation of the imine from acetone and ammonia (29); if we make the same assumption as Bender and Williams, namely that the imininium ion will be three powers of ten more acidic than the corresponding ammonium ion, we can estimate an equilibrium constant for the formation of the iminium ion. All of these equilibrium constants are contained in Table 1.

An additional complication is that the various authors did not all use the same temperature. Hine et al. (28) used 35 °C, and Commeyras and Taillades (8) used 34 °C. The others used 25 °C, and we will report calculations for this temperature. We have approximated the desired rates and equilibria at 25 °C by working with free energies. The free energy, $\Delta G°$ or $\Delta G^‡$, is, for small changes in temperature, insensitive to temperature, because $\Delta G = \Delta H - T\Delta S$, and hence $\Delta\Delta G = \Delta G_{T2} - \Delta G_{T1} = (T_1 - T_2)\,\Delta S = -\Delta T\Delta S$. Now

© 2008 NRC Canada

Fig. 1. Reaction diagram for a Strecker addition. The dimensions are *x*, bond formation; *y*, geometry change; and *z*, bond-length change (exaggerated for clarity).

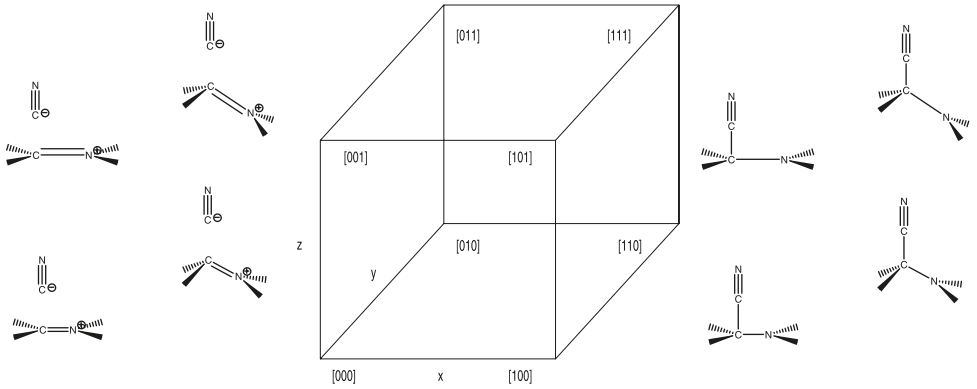

Table 2. Contributions to the corner energy for the final step of the Strecker reaction of benzaldehyde, benzylamine, and HCN.

Corner	GEQUIL[a]	GIP[b]	GENC[c]	GDESOLV[d]	GCORNER[e]
000	0.00	–1.31	2.01	2.60	3.30
100	51.25	0.00	0.00	0.00	51.26
010	42.67	–1.16	2.01	2.60	46.11
001	17.50	–1.28	2.01	2.60	20.83
110	4.98	0.00	0.00	0.00	4.99
101	32.10	0.00	0.00	0.00	32.11
011	52.89	–1.12	2.01	2.60	56.37
111	–9.38	0.00	0.00	0.00	–9.37

[a]Sum of the distortion energy and, for species with the new covalent bond formed, the equilibrium constant for bond formation.
[b]Electrostatic energy of ion-pair formation.
[c]Free-energy change for encounter complex formation
[d]Free-energy cost of partial desolvation of the cyanide nucleophile; half the full desolvation cost was used.
[e]Total corner energy: Sum of the preceding terms.

ΔS is typically 0.03 kcal/K/mol or less so that for ΔT = 10 °C, $\Delta\Delta G$ = 0.3 kcal/mol or less, which is not important for our purposes (1 cal = 4.184 J).

The rates of these reactions were calculated by NBT, using a model for the addition of cyanide ion to the iminium ion involving three dimensions, the formation of the C–C bond, the geometry change at the carbonyl carbon, and the change in length of the C–N bond from that for a double bond to that for a single bond. This model is illustrated in the three dimensional reaction diagram for the Strecker reaction of acetone, dimethyl amine, and cyanide, shown in Fig. 1. The importance of the various terms contributing to the corner energies is shown for one reaction in Table 2; similar tables for all reactions are available as Supplementary Data as are structure files for the initial and final encounter complexes for all reactions.[2] Because of the uncertainty over whether the full potential desolvation cost would be expressed, we carried out calculations with 0.0, 0.5, and 1.0 times the expected full desolvation cost of 5.2 kcal/mol for cyanide in contact with the carbon of an iminium ion. These results are all found in Table 3. The RMS error was larger for zero or full desolvation, though in both cases less than 2 kcal/mol, and lower for 0.5 times the full desolvation cost. Least-squares fitting gave the best value as 0.49, which is not meaningfully different from 0.5. We therefore use the calculations with 0.5 × 5.2 = 2.6 kcal/mol as the best current values. With this model, we calculated the free energies of activation reported in Table 3. The RMS error for all values was 0.65 kcal/mol.

Discussion

It is gratifying that for cyanide addition to iminium ions, as for cyanide addition to carbonyl compounds (15), NBT has been able to predict the rate constants for addition for the range of compounds for which equilibrium data are available. This range is deplorably small, only three powers of ten in equilibrium constant for the rate determining step, in large part because these reactions are potentially complex to study, with three components and three steps, which could be rate-determining (carbinolamine formation, iminium ion formation, and cyanide addition). On top of this, there can be concurrent and competitive cyanohydrin formation. Indeed, some synthetic routes to Strecker adducts begin with

[2]Supplementary data for this article are available on the journal Web site (canjchem.nrc.ca) or may be purchased from the Depository of Unpublished Data, Document Delivery, CISTI, National Research Council Canada, Ottawa, ON K1A 0R6, Canada. DUD 3717. For more information on obtaining material, refer to cisti-icist.nrc-cnrc.gc.ca/irm/unpub_e.shtml.

© 2008 NRC Canada

Table 3. Calculated and observed free energies of activation.

Reaction	$\Delta G°$	ΔG^{*}_{obs}	ΔG^{*}_{calcd}[a]	Diff[a]	$x^{\neq}$	$y^{\neq}$	$z^{\neq}$
$C_6H_5CH{=}NH^{+}CH_2Ph + {}^{-}CN$	–9.38	12.23	10.72	–1.51	0.41	0.47	0.44
			12.28	0.05	0.41	0.50	0.38
			14.14	1.91	0.44	0.38	0.41
$C_6H_5CH{=}NH^{+}CH_2CH{=}CH_2 + {}^{-}CN$	–9.91	11.98	9.61	–2.38	0.38	0.63	0.50
			11.40	–0.59	0.38	0.50	0.38
			13.33	1.33	0.38	0.50	0.25
$(CH_3C){=}NH^{+}_2 + {}^{-}CN$	–11.02	21.89[b]	21.04[c]	–0.85	0.41	0.50	0.38
			22.87[c]	0.98	0.47	0.38	0.22
			23.97[c]	2.08	0.38	0.50	0.50
$(CH_3C){=}NH^{+}CH_3 + {}^{-}CN$	–9.28	19.99[b]	18.81[c]	–1.18	0.50	0.38	0.34
			20.46[c]	0.47	0.50	0.38	0.34
			19.99[c]	2.02	0.38	0.50	0.50
$(CH_3C){=}N{+}(CH_3)_2 + {}^{-}CN$	–6.79	19.01[b]	17.05[c]	–1.96	0.47	0.44	0.34
			18.62[c]	–0.39	0.47	0.41	0.31
			20.34[c]	1.33	0.44	0.34	0.22
RMSE				1.67			
				0.58			
				1.77			

Note: All in aqueous at 25 °C. Dimensions for free energy are kcal/mol.
[a]First value is for desolvation cost set to 0.0; second value is for desolvation cost set to 2.6 kcal/mol; third value is for desolvation cost set to 5.2 kcal/mol. See text.
[b]For the cleavage reaction of the Strecker adduct.
[c]Calculated from the equilibrium free energy change and the calculated free energy of activation for the forward reaction.

the cyanohydrin as source of both carbonyl compound and cyanide (5). We intend to examine a wider range of Strecker reactions to offer predictions of the rate constants for reactions as yet unstudied kinetically, but this requires development of computational methods for calculating the necessary equilibrium constants, which have not been measured.

It is of interest to look at the positions of the transition states found by the NBT approach, even though we have argued that transition-state positions are less well-specified than transition-state energies in these calculations (22).

The key observation is that all the transition states have values for all three coordinates in the range 0.2 to 0.5, i.e., somewhat central but a bit on the early side as is reasonable for exergonic reactions. None of the coordinates is close to either 0 or 1; thus, no lower dimensional transition state is likely to be competitive, and three dimensions are required to describe the reaction.

NBT gives the rate constant/free energy of activation corresponding to a particular detailed mechanism/model for the reaction. This approach requires more detailed models than have usually been proposed and explicit values for interactions often used only qualitatively. We are seeking consistent models over a range of related reactions. Our approach runs into problems where an interaction has not been studied experimentally, as for the question of desolvation of cyanide in contact with an iminium ion. Although we resorted to fitting to see what gave the best results (empirically determining one parameter used for five reactions), we wish to stress that with any plausible value (between 0.0 and 5.2 kcal/mol) for the desolvation energy of cyanide, NBT gave a good fit to the available experimental data. With the optimized fraction of this desolvation energy, the fit is distinctly better; that there should be partial compensation for loss of desolvation in the encounter complex for the Strecker reaction, more so than in cyanohydrin formation, seems reasonable.

Calculations

Methods

All molecular-orbital calculations were carried out using Gaussian 03 (30). Analysis of the reaction to pick out corner energies, creation of structure files for each corner structure, calculation of the distortion energies as differences in MO energies for structures differing only in geometry, calculation of corner energies, and searching for the lowest saddle point were all carried out using computer programs being developed in this laboratory.

Acknowledgments

We thank the Natural Sciences and Engineering Research Council of Canada (NSERC) for financial support of this work and the Shared Hierarchical Academic Research Computing Network (SHARCNET) for computing resources.

References

1. A. Strecker. Justus Liebigs Ann. Chem. **75**, 27 (1850).
2. A. Strecker. Justus Liebigs Ann. Chem. **91**, 349 (1854).
3. E.C. Kendall and B.F. McKenzie. *In* Organic syntheses. Coll. Vol. 1. 1941. p. 21.
4. H.T. Clarke and H.J. Bean. *In* Organic syntheses. Coll. Vol. 2. 1943. p. 29.
5. G.W. Stevenson and D. Williamson. J. Am. Chem. Soc. **80**, 5943 (1958).
6. T.D. Stewart and C.H. Li. J. Am. Chem. Soc. **60**, 2782 (1938).

© 2008 NRC Canada

7. G. Moutou, J. Taillades, S. Benefice-Malouet, A. Commeyras, G. Messina, and R. Mansani. J. Phys. Org. Chem. **8**, 721 (1995).
8. J. Taillades and A. Commeyras. Tetrahedron, **30**, 127 (1974).
9. J. Taillades and A. Commeyras. Tetrahedron, **30**, 2493 (1974).
10. J. Taillades and A. Commeyras. Tetrahedron, **30**, 3407 (1974).
11. M. Bejaud, L. Mion, and A. Commeyras. Bull. Soc. Chim. Fr. 233 (1976).
12. M. Bejaud, L. Mion, and A. Commeyras. Bull. Soc. Chim. Fr. 1425 (1976).
13. R. Arnaud, C. Adamo, M. Cossi, A. Milet, Y. Vallee, and V. Barone. J. Am. Chem. Soc. **122**, 324 (2000).
14. J. Atherton, J. Blacker, M. Crampton, and C. Grosjean. Org. Biomol. Chem. **2**, 2567 (2004).
15. J.P. Guthrie. J. Am. Chem. Soc. **120**, 1688 (1997).
16. J.P. Guthrie. J. Phys. Org. Chem. **11**, 632 (1998).
17. J.P. Guthrie and V. Pitchko. J. Am. Chem. Soc. **122**, 5520 (2000).
18. J. Guthrie. Bioorg. Chem. **30**, 32 (2002).
19. J.P. Guthrie. ChemPhysChem. **4**, 809 (2003).
20. J.P. Guthrie and V. Pitchko. J. Phys. Org. Chem. **17**, 548 (2004).
21. J.P. Guthrie. Can. J. Chem. **83**, 1 (2005).
22. J.P. Guthrie, L. Leandro, and V. Pitchko. Can. J. Chem. **83**, 1654 (2005).
23. J. Hine. J. Am. Chem. Soc. **93**, 3701 (1971).
24. J.P. Guthrie. J. Am. Chem. Soc. **118**, 12886 (1996).
25. W.P. Jencks and J. Regenstein. Physical and chemical data. *In* Handbook of biochemistry and molecular biology. Vol. 1. 3rd ed. *Edited by* G. Fassman. Chemical Rubber Company, Cleveland, OH. 1976. pp. 305–451.
26. C.D. Ritchie and R.E. Uschold. J. Am. Chem. Soc. **89**, 1721 (1967).
27. M.L. Bender and A. Williams. J. Am. Chem. Soc. **88**, 2502 (1966).
28. J. Hine, R.C. Dempsey, R.A. Evangelista, E.T. Jarvi, and J.M. Wilson. J. Org. Chem. **42**, 1593 (1977).
29. P. Zuman. Collect. Czech. Chem. Commun. **15**, 839 (1950).
30. M.J. Frisch, G.W. Trucks, H.B. Schlegel, G.E. Scuseria, M.A. Robb, J.R. Cheeseman, J.A. Montgomery Jr., T. Vreven, K.N. Kudin, J.C. Burant, S.S. Millam, J.M. Iyengar, J. Tomasi, V. Barone, B. Mennucci, M. Cossi, G. Scalmani, N. Rega, G.A. Petersson, H. Nakatsuji, M. Hada, M. Ehara, K. Toyota, R. Fukuda, J. Hasegawa, M. Ishida, T. Nakajima, Y. Honda, O. Kitao, H. Nakai, M. Klene, X. Li, J.E. Knox, H.P. Hratchian, J.B. Cross, C. Adamo, J. Jaramillo, R. Gomperts, R.E. Stratmann, O. Yazyev, A.J. Austin, R. Cammi, C. Pomelli, J.W. Ochterski, P.Y. Ayala, K. Morokuma, G.A. Voth, P. Salvador, J.J. Dannenberg, V.G. Zakrzewski, S. Dapprich, A.D. Daniels, M.C. Strain, O. Farkas, D.K. Malick, A.D. Rabuck, K. Raghavachari, J.B. Foresman, J.V. Ortiz, Q. Cui, A.G. Baboul, S. Clifford, J. Cioslowski, B.B. Stefanov, G. Liu, A. Liashenko, P. Piskorz, I. Komaromi, R.L. Martin, D.J. Fox, T. Keith, M.A. Al-Laham, C.Y. Peng, A. Nanayakkara, M. Challacombe, P.M.W. Gill, B. Johnson, W. Chen, M.W. Wong, C. Gonzalez, and J.A. Pople. *In* Gaussian 03 [computer program], Revision B.04. Gaussian, Inc., Pittsburgh, PA. 2003.
31. A. Williams and M.L. Bender. J. Am. Chem. Soc. **88**, 2508 (1966).

© 2008 NRC Canada

Benzamide hydrolysis in strong acids — The last word[1]

Robin A. Cox

Abstract: Recently it has become apparent that the mechanism of amide hydrolysis in relatively dilute strong acid media is the same as the one observed for ester and benzimidate hydrolysis, two water molecules reacting with the O-protonated amide in the rate-determining step. This is not the whole story, however, at least for benzamide, *N*-methylbenzamide, and *N*,*N*-dimethylbenzamide, since the observed rate constants for these substrates deviate upwards from the observed excess acidity correlation lines at acidities higher than about 60% H_2SO_4, meaning that another, faster, reaction with a different mechanism is taking over at higher acidities. It has never been clear what this latter mechanism was until the work reported in this paper. An exhaustive excess acidity analysis of all the available measured reaction rate constants for the three substrates in three different acidic media, aqueous H_2SO_4, aqueous $HClO_4$, and aqueous HCl, shows that this second mechanism involves a second rate-determining proton transfer to the O-protonated benzamide, followed by (or possibly concerted with) irreversible loss of $^+NH_4$ to give an acylium ion. Subsequent reaction of this with water (or bisulfate, etc.) eventually gives the observed carboxylic acid product. This latter reaction mechanism has never been previously considered for amide hydrolysis, but it may not be uncommon; at least one other reaction with a similar mechanism is known, and another possible case is suggested.

Key words: amides, benzamides, hydrolysis, excess acidity, mechanism, acid media.

Résumé : Il est récemment devenu apparent que le mécanisme d'hydrolyse des amides dans des milieux dilués d'acides forts est le même que celui observé pour l'hydrolyse des esters et des benzamidates et que, dans l'étape cinétiquement déterminante, deux molécules d'eau réagissent avec l'amide protoné sur l'oxygène. Cette conclusion ne correspond toutefois pas à toute l'histoire, au moins pour le benzamide, la *N*-méthylbenzamide et le *N,N*-diméthylbenzamide, puisque les constantes des vitesses observées pour ces substrats, à des acidités supérieures à environ 60% de H_2SO_4, dévient d'une façon positive par rapport aux droites de corrélation des acidités en excès observées; cette observation signifie que, à des acidités plus élevées, une autre réaction plus rapide et avec un mécanisme différent devient prépondérante. La nature de ce dernier mécanisme n'avait jamais été établie avant le présent travail. Un examen exhaustif de l'acidité en excès pour toutes les constantes de vitesses réactionnelles mesurées avec ces trois substrats, dans trois milieux acides différents, H_2SO_4 aqueux, $HClO_4$ aqueux et HCl aqueux montre que ce second mécanisme implique un transfert de proton cinétiquement déterminant vers le benzamide O-protoné qui est suivi par (ou qui se produit possiblement d'une façon conertée) avec une perte irréversible de NH_4^+ qui conduit à la formation d'un ion acylium. Une réaction subséquente de cet ion avec de l'eau ou du bisulfate conduit éventuellement à l'acide carboxylique qui est obtenu comme produit. Ce dernier mécanisme réactionnel n'a jamais été considéré antérieurement pour l'hydrolyse des amides, mais il n'est pas inhabituel; au moins une autre réaction avec un mécanisme semblable est connue et on suggère un autre cas possible.

Mots-clés : amides, benzamides, hydrolyse, excès d'acidité, mécanisme, milieu acide.

[Traduit par la Rédaction]

Introduction

Recently the mechanisms of hydrolysis of benzimidates, esters, and amides in aqueous sulfuric acid were reviewed (1). It was shown that the hydrolysis mechanisms in relatively dilute H_2SO_4 for all of these substrates were the same, rate-determining reaction of the O-protonated substrate with two water molecules, but for benzamides another faster reaction of unknown mechanism became important at the higher acidities. It is the purpose of this paper to delineate this mechanism, which was not possible at the time.

It is highly appropriate that this paper is dedicated to the memory of Keith Yates; his name appears often in the references. He was very interested in amides throughout his ca-

Received 26 November 2007. Accepted 16 January 2008. Published on the NRC Research Press Web site at canjchem.nrc.ca on 6 March 2008.

Dedicated to the memory of Keith Yates, fine chemist, good friend, wonderful human being.

R.A. Cox. 16 Guild Hall Drive, Scarborough, ON M1R 3Z8, Canada (e-mail: robin.a.cox@sympatico.ca).

[1]Part 28 of the series "Mechanistic studies in strong acids" of which part 27 is ref. 1.

 doi:10.1139/V08-015 © 2008 NRC Canada

reer in chemistry, and much of the experimental work used in this paper was carried out by one of his students (2, 3). For many years we thought that the problem of the mechanism of benzamide hydrolysis was solved; rate-determining reaction of the O-protonated amide with three water molecules in the most dilute acid media, followed by reaction with only one as the water activity diminished at the higher acid concentrations, and then with a bisulfate ion at the highest acidities used (4). However, as often happens in science we were overtaken by events; solvent isotope effects in amide hydrolysis are clearly only compatible with two water molecules reacting with the protonated amide in the transition state, not one or three (5), and Guthrie's multidimensional analysis (6) is not consistent with the involvement of three water molecules either. Also, it turns out that we had been using the wrong values for the water activities in the analysis of kinetic data in acid media (7). The values we had been using were based on a standard state of pure water (mole-fraction-based values), whereas all of the other concentrations in these media are based on the hypothetical ideal one molar acid concentration standard state (7). For some reactions, use of the correct water activities makes little difference (for instance ester hydrolysis (7)), but for others it does, and amide hydrolysis is one of these. (This means that Bunnett *w* values (8) and Yates and Stevens *r* values (9) listed in the literature are unlikely to be correct).

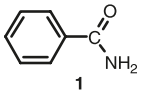

1

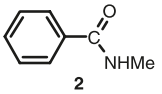

2

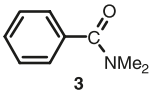

3

It is shown here that the reaction of amides in the stronger acid media is not a hydrolysis as such at all, and so all three of the mechanisms we believed were correct in 1981 (4) are in fact wrong. Every single rate constant in the literature (and there are a lot) for the hydrolysis of benzamide (**1**), its *N*-methylated derivative (**2**), and its *N*,*N*-dimethylated derivative (**3**) were used in the analysis, obtained in aqueous H_2SO_4, in aqueous $HClO_4$, and in aqueous HCl media, and the two proposed mechanisms correlate every one of them. The mechanism at the higher acidities, which is proposed in this paper, has not been previously considered.

Results

Hydrolysis rate constants as a function of sulfuric acid concentration and temperature for benzamide (**1**) are given by Smith and Yates (2, 3), by Rysman de Lockerente et al. (10), and by Bunton et al. (11); as a function of perchloric acid concentration and temperature by Bunton et al. (11), by Leisten (12), by Shingare et al. (13), and by Yamana et al. (14); and as a function of hydrochloric acid concentration and temperature, with some data in DCl/D_2O, by Bunton et al. (11). For *N*-methylbenzamide (**2**), the experimental data used in aqueous H_2SO_4 were obtained from Smith and Yates (2, 3) and from Bunton et al. (11); data at the single temperature of 95.0 °C in aqueous $HClO_4$ are given by Yamana et al. (14), and at the single temperature of 100.4 °C in aqueous HCl by Bunton et al. (11). For *N*,*N*-dimethylbenzamide (**3**) the data in H_2SO_4 come from Smith and Yates (2, 3) and from Bunton et al. (11), in $HClO_4$ from Yamana et al. (14) and Bunton et al. (11), and at the single temperature of 100.4 °C in HCl from Bunton et al. (11).

$$[1]\quad \log k_\psi - \log(C_{SH^+}/(C_{S^+}\,C_{SH^+})) - 2\,\log a_{H_2O} = \log k_0 + (m^\ddagger - 1)m^*X$$

$$[2]\quad \log k_0 = 10.31883 + \log T - (\Delta G^\ddagger/(RT\ln 10)) + (\Delta H^\ddagger/(RT\ln 10))((T-\Theta)/T)$$

These rate constants, k_ψ, were analyzed according to the excess acidity technique (1, 7). The rate equation which is relevant here is eq. [1] (1, 7), where the term $\log(C_{SH^+}/(C_{S^+}C_{SH^+}))$, hereinafter for simplicity called PCT for protonation correction term, is present to correct for the fact that these amides are not fully protonated at the lower acid concentrations. It is obtained from ionization ratios, $I = C_{SH^+}/C_S$, calculated using the excess acidity equation for basicities, $\log I - \log C_{(H^+)_{aq}} = m^*X + pK_{SH^+}$, writing $C_{(H^+)_{aq}}$ for the C_{H^+} used before (7) as this is a better representation of the true state of the proton in aqueous acid media (1). To use this, values for pK_{SH^+} and m^* for the amide substrates are needed; fortunately highly accurate ones are available (15), albeit that I had to develop an entirely new method of separating medium effects on the spectra used to obtain them from the effects due to protonation (16). The values used were: **1**, $pK_{SH^+} = -1.540 \pm 0.020$, $m^* = 0.539 \pm 0.021$; **2**, $pK_{SH^+} = -1.461 \pm 0.009$, $m^* = 0.529 \pm 0.012$; and **3**, $pK_{SH^+} = -0.998 \pm 0.019$, $m^* = 0.581 \pm 0.033$ (15), all measured at 25 °C. The terms m^* and $m^\ddagger$ in eq. [1] are activity coefficient ratios, m^* referring to the protonated substrate and $m^\ddagger$ to the transition state (7). The m^* values are independent of temperature (7), but the pK_{SH^+} values are not; to correct them to the reaction temperature they were converted to free energies via $\Delta G° = (RT\ln 10)pK_{SH^+}$, T being 298.15 K, and then to the reaction temperature T. This correction may not be very accurate, since $\Delta H°$ and $\Delta S°$ values seem to vary randomly for different types of substrate (17), but it is surely better than the often-used assumption that the pK_{SH^+} values are temperature-independent. In practice this method has always appeared to work well (7), and it did so here also. The values of the excess acidity X and $\log C_{(H^+)_{aq}}$ (or $\log C_{H^+}$) were those used previously (18); these and the molarity-based water activity values a_{H_2O} are temperature-corrected as before (7).

In eq. [1], k_0 is the rate constant for the reaction in the standard state at the reaction temperature. With results at different temperatures available, it can be replaced in eq. [1] by eq. [2], where $\Delta G^\ddagger$ is the free energy of activation and $\Delta H^\ddagger$ the enthalpy; the entropy of activation $\Delta S^\ddagger$ can easily be obtained from these via $\Delta G^\ddagger = \Delta H^\ddagger - T\Delta S^\ddagger$. This formulation is due to Clarke and Glew (19); I find it more useful than the usual Eyring formulation (20) as it is more natural to use, giving better numbers with errors that are independent of one another (19). The numerical term in eq. [2] contains the Planck and Boltzmann constants (20), R is the gas constant (1.98589 cal K^{-1} mol^{-1} here; 1 cal = 4.184 J), and Θ the reference temperature for the activation parameters, 298.15 K.

The low acidity mechanism for benzamide hydrolysis is given in Scheme 1; eq. [1] is the rate equation for this mech-

© 2008 NRC Canada

Scheme 1.

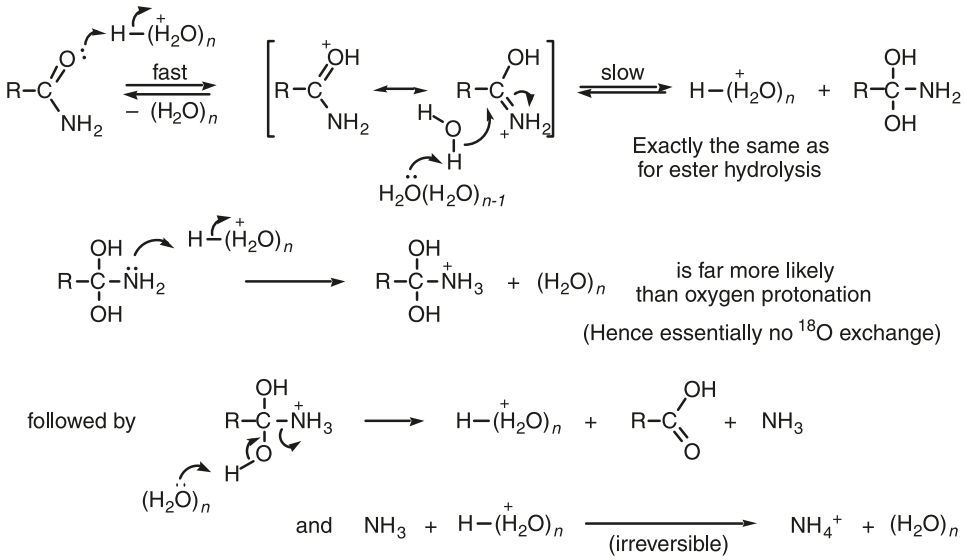

Fig. 1. Excess acidity plots according to eqs. [1] and [2] for the hydrolysis of **1** at several temperatures in relatively dilute sulfuric acid.

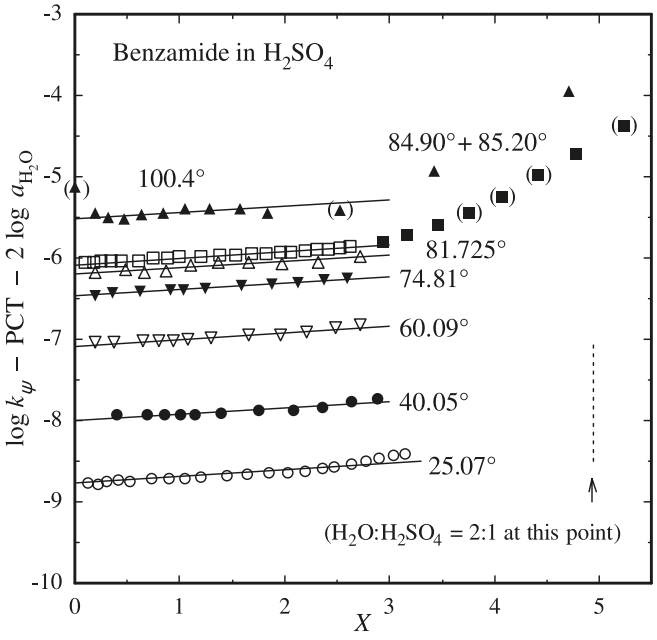

anism. All of the data for benzamide in sulfuric acid are plotted according to eq. [1] in Fig. 1. As can be seen, the data follow the fitted lines precisely up until an X value of about three (about 60% H_2SO_4), where they begin to deviate upwards. There is still plenty of water in the reaction medium at this point, the 2:1 mole ratio H_2O:H_2SO_4 is indicated on Fig. 1.

The only way of dealing with the data after $X = 3$ seemed to be to calculate what the rate constants according to eq. [1] would be at the higher X values, subtract these from the observed rate constants, and plot the resultant in various ways until linearity was achieved. When this was attempted it was soon apparent that a subsequent A1 reaction (21) did not fit the data, and other mechanisms were investigated. When this was done, the only rate equation that correlated all the data was one that included the proton concentration $\log C_{(H^+)_{aq}}$, eq. [3]. This means that the rate-determining step has to include a second proton transfer to the protonated substrate — not really surprising as the rate constants after $X = 3$ are still increasing with the solvent acidity. The proposed mechanism, for which eq. [3] is the rate equation, is given as Scheme 2; this has been proposed before (1) but had not been tested until now.

$$[3]\qquad \log k_\psi - \log(C_{SH^+}/(C_{S^+}C_{SH^+})) - \log C_{(H^+)_{aq}} = \log(k_0)_2 + (m^{\ddagger}_2 - 1)m^*X$$

To illustrate this second mechanism, the data for the hydrolysis of *N*-methylbenzamide in aqueous H_2SO_4 are plotted according to eq. [3] in Fig. 2 (the equivalent plot for benzamide itself does not form such a good illustration). Again, since data at several temperatures are used, the term $\log(k_0)_2$ is replaced according to eq. [2], as before. As can be seen the data approach the correlation lines quite well. For all of the substrates, figures at the higher acidities for the aqueous H_2SO_4, $HClO_4$, and HCl media resemble Fig. 2, and those at the lower acidities for all of these media resemble Fig. 1; for the sake of brevity only one other plot is included here. The correlation lines in these figures result from curve-fitting all of the data simultaneously to eqs. [1] and [3] (including eq. [2]), as before (7, 22). Any data points that do not form part of the data set, to 95% confidence, are rejected from the fit and are in parentheses in the Tables and Figures. Four of the data points for the reaction in the aqueous HCl medium were obtained in D_2O (11), and despite the paucity of data points it proved possible to obtain solvent isotope effects for both mechanisms, by allowing a different intercept for the D_2O data. All of the results for benzamide (**1**) are given in Table 1.

For *N*-methylbenzamide (**2**) and *N*,*N*-dimethylbenzamide (**3**) the results are essentially similar, except that there are fewer data — in some media the reaction was only followed

© 2008 NRC Canada

Scheme 2.

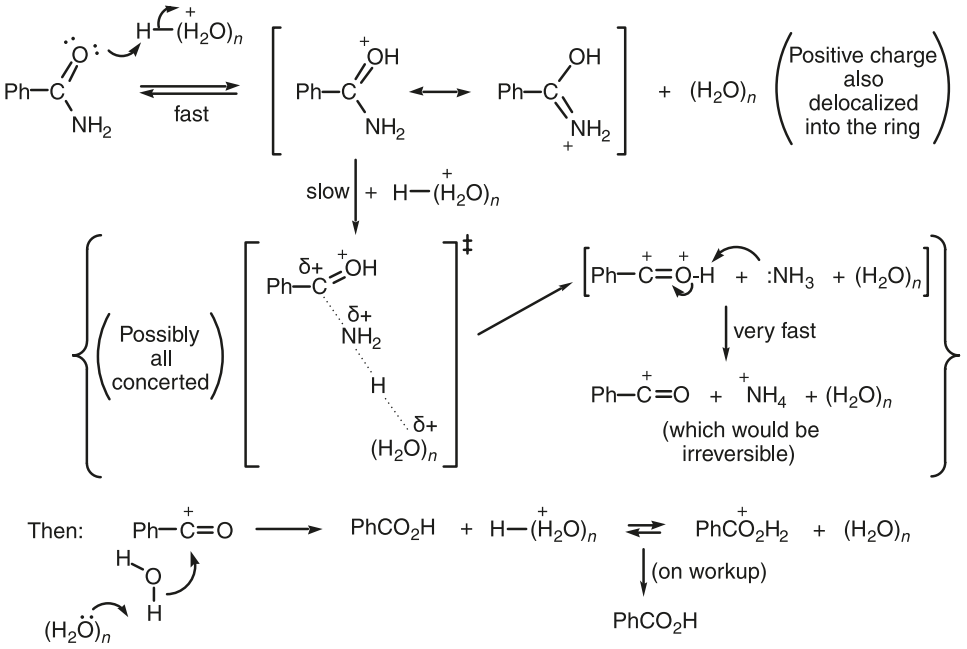

Fig. 2. Excess acidity plots according to eqs. [2] and [3] for the hydrolysis of **2** in sulfuric acid at several temperatures.

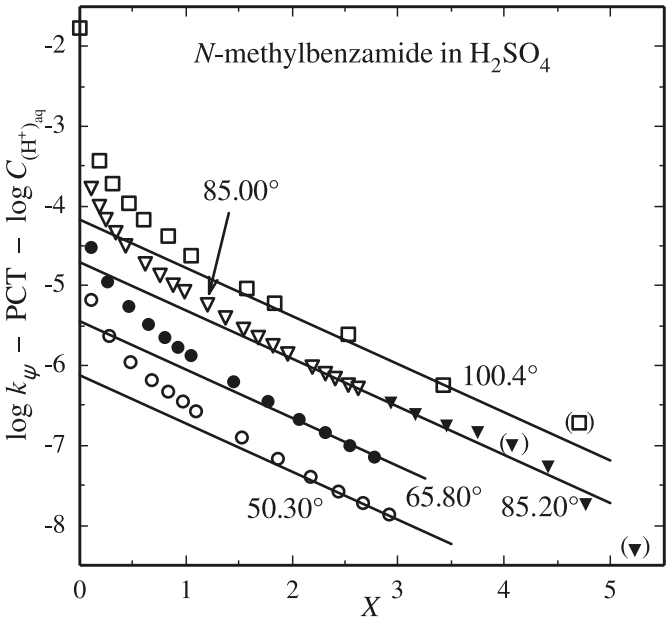

at a single temperature, and there are no results in deuterated media — and for these substrates the second mechanism is relatively more important than is the first. One other plot is given here, Fig. 3 for **3** in HCl at a single temperature, showing both mechanisms. Tables 2 and 3 give the summarized results for **2** and **3**.

Discussion

In the past it had been assumed that the O-protonated amide would somehow switch to an N-protonated one at high acidity, which would then lose ammonia and produce an acylium ion in the rate-determining step (21), which is an A1 reaction. However, this seems unlikely on the face of it. (Why would a perfectly stable O-protonated amide suddenly switch to an unstable N-protonated one in media in which the O-protonated amide would increase in stability?). The analysis of the rate constant results given in this paper is not consistent with an A1 mechanism of any sort, which rules out this "proton reorganization" process. The data are only consistent with Scheme 2 or with its kinetic equivalent.

For benzamide in sulfuric acid, the two data points at the highest acidities were rejected as being off the correlation line; they are above it (faster). It is suggested that here the catalyzing acid switches from $(H^+)_{aq}$ to undissociated H_2SO_4 molecules; for the two points in question, one is at an acidity close to the 1:1 mole ratio H_2O:H_2SO_4 point and the other is above it. We have seen undissociated H_2SO_4 molecules acting as acid catalysts in these media before (23, 24), after all, H_2SO_4 is a stronger acid than is $(H^+)_{aq}$. It is telling that the same thing does not happen in perchloric acid; there the highest acidities used were well short of the 1:1 mole ratio point. However, two points were not enough to quantify this, and so numbers are not given. There is one other systematic trend in the rejected points, involving the data for **2** in sulfuric acid obtained by Smith at 85.2 °C (2) (see Fig. 2). I am inclined to attribute this to some kind of experimental artifact, as these points were rejected whatever correlation scheme was used; perhaps there was some kind of systematic error in the measured sulfuric acid concentrations.

An examination of Table 1 reveals that the intercept rate constants and activation parameters for the low acidity mechanism for **1** are the same for all three acid media, which is gratifying as this is what would be expected if the same mechanism is operating in each case. The equivalent data are too sparse or the errors are too high for **2** and **3** to enable any real conclusion to be drawn. The $m^{\ddagger}$ values are not all the same, but since these are activity coefficient ratios it is at present difficult to know what to expect (7, 25); I will

© 2008 NRC Canada

Table 1. Intercepts, slopes, and activation parameters for benzamide, **1**.

	aq. H_2SO_4	aq. $HClO_4$	aq. HCl
Low acidity mechanism, Scheme 1			
$\log k_0^{25°a}$	–5.2760±0.0089	–5.499±0.051	–5.411±0.025
$\Delta H^{‡}$ (kcal mol^{-1})	21.242±0.066	22.12±0.35	20.72±0.14
$\Delta S^{‡}$ (cal mol^{-1} K^{-1})	–27.32±0.23	–25.4±1.2	–29.69±0.11
$m^{‡}$	1.147±0.043	0.843±0.051	0.689±0.047
k_H/k_D	—	—	0.842±0.076
High acidity mechanism, Scheme 2			
$\log k_0^{25°}$ (1 mol/L acid)[a]	–9.94±0.33	–7.41±0.23	–6.81±0.12
$\Delta H^{‡}$ (kcal mol^{-1})	31.7±1.6	21.04±0.83	[b]
$\Delta S^{‡}$ (cal mol^{-1} K^{-1})	+2.4±5.7	–21.8±3.0	[b]
$m^{‡}$	0.687±0.044	0.238±0.048	[b]
k_H/k_D	—	—	3.3±5.3
$\pm\sigma_y$[c]	0.029	0.059	0.035
N[d]	108(7)	68(2)	24

[a]Intercepts at 25 °C of plots such as Fig. 1. Throughout, the errors given are standard deviations.
[b]Too little data to enable calculation. $HClO_4$ values assumed.
[c]Root-mean-square error between experimental and fitted data points.
[d]Number of data points. The number rejected, if any, are in parentheses (see text).

Fig. 3. Excess acidity plots according to eqs. [1] and [3] for the hydrolysis of **3** in relatively dilute hydrochloric acid at 100.4 °C.

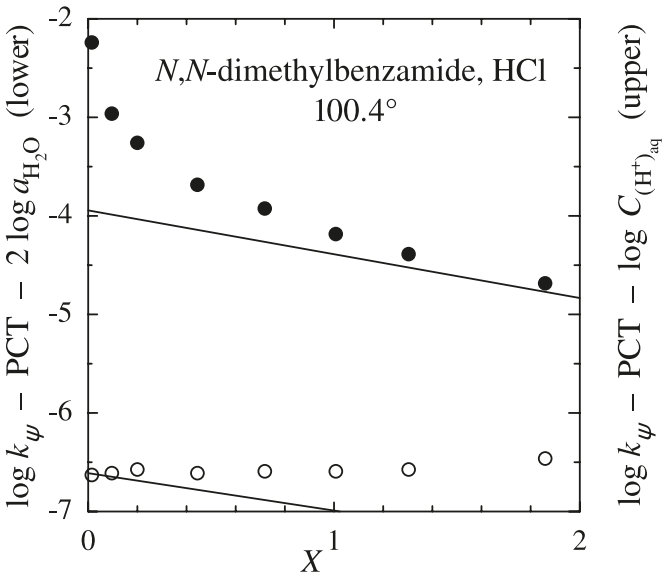

comment that they do not appear to have the utility for mechanistic diagnosis for which I had once hoped (7).

The situation is different for the Scheme 2 results (high acidity mechanism); they are not the same in the three acid media used. This is not surprising insofar as general acid catalysis is involved, with the second proton transfer taking place in the rate-determining step (Scheme 2), and long ago Kresge et al. (26) discussed a similar effect they had observed in aromatic hydrogen exchange and later in alkene hydration (27). The results in Tables 1–3 seem to have no real trends. It is worth commenting that aqueous sulfuric acid is a quite highly structured medium (28), more so than aq. HCl and aq. HClO4, and one might expect a large effect on entropies of activation as the second protonation breaks up the structure of the medium. In Table 1 the entropy of activation for **1** is slightly positive, but the same is certainly not the case for **2** and **3** (Tables 2 and 3).

There were enough data (just) to enable the evaluation of solvent isotope effects for the two mechanisms for benzamide in aqueous HCl. These are in Table 1. For the Scheme 1 mechanism the effect is inverse, which is what would be expected for a pre-equilibrium proton transfer (29), but for the Scheme 2 mechanism it is normal (probably; the error in it is larger than the quantity itself). This is what would be expected for a reaction with a proton transfer involved in the rate-determining step (29).

For benzamide the low acidity reaction is fast by comparison to the high acidity one (compare the log k_0 values), but the opposite is true for **2**, where the high acidity mechanism has a greater relative importance (compare Figs. 1 and 2). This is probably because the electron-donating alkyl groups in **2** and **3** will help to stabilize the partial positive charge on the departing nitrogen in Scheme 2, lowering the overall activation energy for the reaction, as seems to be the case from the $\Delta H^{‡}$ values in Tables 1, 2, and 3. However, by and large there seems to be not very much in the way of trends, which can be rationalized, in many of the results obtained in this work.

The details of the reaction mechanism given in Scheme 2 are a little difficult to draw. I have commented there that all of the steps shown within the braces might be concerted, the proton transfer to nitrogen and the departure of ammonia with a proton so that a diprotonated acylium species does not actually form, but in fact the proton, which the nitrogen takes with it as it leaves, cannot be the same one as was on the carbonyl oxygen because the orbitals are not aligned in such a way as to make this possible. Consequently, proton transfers within the solvent medium must be involved too, one being water (or bisulfate) removing the proton from the carbonyl oxygen and another being the removal of one from the surrounding medium (which is very acidic) by the departing nitrogen. These would all be so fast, however, as to make the whole process *essentially* concerted. I have at-

© 2008 NRC Canada

Table 2. Intercepts, slopes, and activation parameters for *N*-methylbenzamide, **2**.

	aq. H_2SO_4	aq. $HClO_4$	aq. HCl
Low acidity mechanism, Scheme 1			
$\log k_0^{25°}$ [a]	–10.034±0.051	–6.84±0.14[b]	–6.432±0.016[c]
$\Delta H^{‡}$ (kcal mol^{-1})	22.07±0.41	—	—
$\Delta S^{‡}$ (cal mol^{-1} K^{-1})	–30.4±1.4	—	—
$m^{‡}$	0.41±0.10	0.53±0.28	0.19±0.56
High acidity mechanism, Scheme 2			
$\log k_0^{25°}$ (1 mol/L acid)[a]	–7.343±0.072	–5.2±1.6[b]	–4.2±1.8[c]
$\Delta H^{‡}$ (kcal mol^{-1})	20.78±0.30	—	—
$\Delta S^{‡}$ (cal mol^{-1} K^{-1})	–22.4±1.0	—	—
$m^{‡}$	–0.143±0.020	0.13±0.56	–0.13±0.59
$\pm\sigma_y$[d]	0.044	0.024	0.018
N[e]	66(3)	8	11

[a]Intercepts at 25 °C of plots such as Fig. 1. Throughout, the errors given are standard deviations.
[b]Intercepts at 95 °C.
[c]Intercepts at 100.4 °C.
[d]Root-mean-square error between experimental and fitted data points.
[e]Number of data points. The number rejected, if any, are in parentheses (see text).

Table 3. Intercepts, slopes, and activation parameters for *N*,*N*-dimethylbenzamide, **3**.

	aq. H_2SO_4	aq. $HClO_4$	aq. HCl
Low acidity mechanism, Scheme 1			
$\log k_0^{25°}$ [a]	–9.278±0.016	–11.5±2.4	–6.612±0.014[b]
$\Delta H^{‡}$ (kcal mol^{-1})	18.62±0.13	32±16	—
$\Delta S^{‡}$ (cal mol^{-1} K^{-1})	–38.47±0.45	–3±55	—
$m^{‡}$	1.020±0.017	0.51±0.61	0.3±1.7
High acidity mechanism, Scheme 2			
$\log k_0^{25°}$ (1 mol/L acid)[a]	–7.691±0.092	–10.3±1.9	–3.9±1.8[b]
$\Delta H^{‡}$ (kcal mol^{-1})	19.55±0.32	39.7±6.4	—
$\Delta S^{‡}$ (cal mol^{-1} K^{-1})	–28.1±1.1	+28±23	—
$m^{‡}$	0.397±0.020	0.13±0.48	0.24±0.69
$\pm\sigma_y$[c]	0.019	0.037	0.017
N[d]	54(3)	16	8

[a]Intercepts at 25 °C of plots such as Fig. 1. Throughout, the errors given are standard deviations.
[b]Intercepts at 100.4 °C.
[c]Root-mean-square error between experimental and fitted data points.
[d]Number of data points. The number rejected, if any, are in parentheses (see text).

Scheme 3.

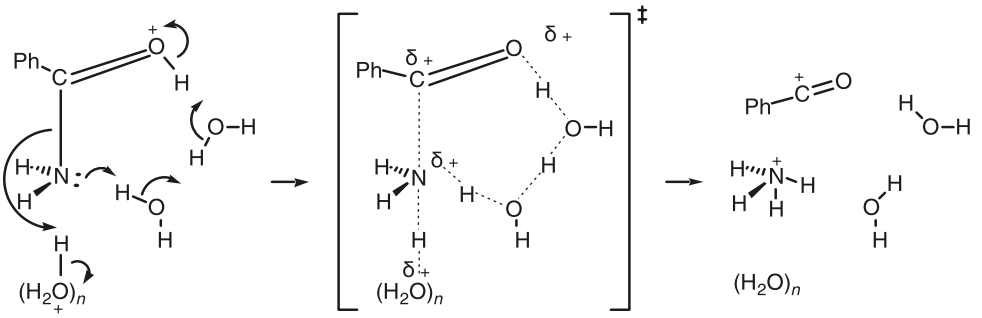

tempted to draw such a process involving surrounding water in Scheme 3, which although rather involved may be a better representation of the high acidity mechanism, if in fact the process really is wholly concerted.

Rate-determining proton transfers are well known to be involved in the Wallach rearrangement of aromatic azoxyarenes (30, 31), shown in Scheme 1 of ref. (31) for comparison with Scheme 2. In fact, diprotonated species in

© 2008 NRC Canada

Scheme 4.

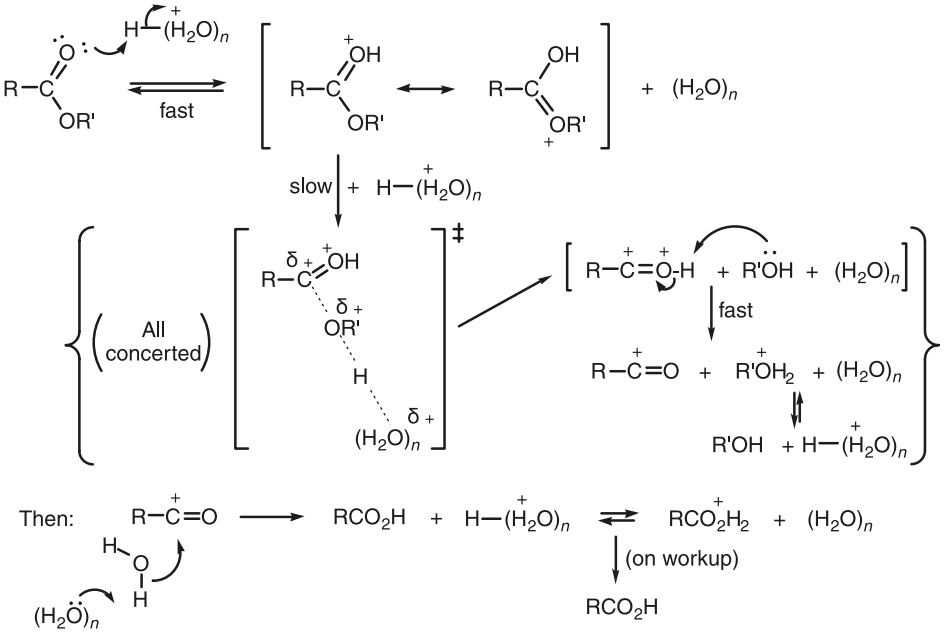

strong acid media are becoming more numerous all the time. For instance, Shudo and co-workers (32) found dications to be important in a Friedel–Crafts type cyclodehydration in CF_3SO_3H; Klumpp and co-workers (33) cited dicationic intermediates as superelectrophiles in similar media; and Olah and his group (34) proposed species like HNO_2^{2+} in superacids.

Another class of reactions that would appear to have mechanisms very similar to Scheme 2 is the hydrolysis of esters in strong acid media. Typically, esters which cannot form stable acylium ions or alkyl cations still hydrolyze quickly in strong acids, with reaction rate constants which increase steeply with acidity (35), and it seems perfectly reasonable that these hydrolyses would have a mechanism like Scheme 4, rather than the proposed A1 process involving a "proton switch" from a stable position on the carbonyl oxygen to an unstable one on the ester oxygen, which subsequently decomposes in an A1 process (35). Again, the process will likely be concerted, but this is difficult to draw.

I have called this paper "the last word" because I have no intention of writing another word on the hydrolyses of **1**, **2**, or **3**. Of course, this does not exclude other amides, ring-substituted benzamides, and so on; there are plenty of available experimental data on some of these, but the results are not as readily accessible as are the data on **1**, **2**, and **3**. The mechanisms of Scheme 1 and Scheme 2 are now expected to apply to all amides, but the Scheme 2 process is only likely to be available to those substrates where the positive charge on the protonated amide can be supported in some way in the acylium ion which is formed. For instance in **1**, **2**, and **3**, it can be delocalized into the aromatic ring. Scheme 4 for esters also remains to be tested.

Acknowledgments

It is a pleasure to acknowledge the many discussions with my colleagues in physical organic chemistry, which have helped to stimulate my thinking in this area, particularly Stan Brown, Peter Guthrie, and Erwin Buncel. And, of course, I owe an immense debt of gratitude to Keith Yates, who got me started on all this over thirty years ago, and acted as friend and mentor for so many of them.

References

1. R.A. Cox. Can. J. Chem. **83**, 1391 (2005).
2. C.R. Smith. Ph.D. thesis, Department of Chemistry, University of Toronto, Toronto. 1971.
3. C.R. Smith and K. Yates. J. Am. Chem. Soc. **93**, 6578 (1971).
4. R.A. Cox and K. Yates. Can. J. Chem. **59**, 2853 (1981).
5. A.J. Bennet, H. Slebocka-Tilk, R.S. Brown, J.P. Guthrie, and A. Jodhan. J. Am. Chem. Soc. **112**, 8497 (1990).
6. J.P. Guthrie. Can. J. Chem. **83**, 1 (2005).
7. R.A. Cox. Adv. Phys. Org. Chem. **35**, 1 (2000).
8. J.F. Bunnett. J. Am. Chem. Soc. **83**, 4956 (1961), and subsequent papers.
9. K. Yates and J.B. Stevens. Can. J. Chem. **43**, 529 (1965), and subsequent papers.
10. S. Rysman de Lockerente, P. van Brandt, A. Bruylants, M. de Buyl-Gaudissart, and D. Hubert. Acad. Roy. Belg. Bull. Cl. Sci. **58**, 180 (1972).
11. C.A. Bunton, S.J. Farber, A.J.G. Milbank, C.J. O'Connor, and T.A. Turney. J. Chem. Soc. Perkin Trans. 2, 1869 (1972).
12. J.A. Leisten. J. Chem. Soc. 765 (1959).
13. M.S. Shingare, D.B. Ingle, and D.D. Khanolkar. J. Indian Chem. Soc. **52**, 599 (1975).
14. T. Yamana, Y. Mizukami, A. Tsuji, and M. Ikuta. Chem. Pharm. Bull. **20**, 1778 (1972).
15. R.A. Cox, L.M. Druet, A.E. Klausner, T.A. Modro, P. Wan, and K. Yates. Can. J. Chem. **59**, 1568 (1981).
16. R.A. Cox and K. Yates. Can. J. Chem. **59**, 1560 (1981).
17. R.A. Cox and K. Yates. Can. J. Chem. **62**, 2155 (1984).
18. R.A. Cox and K. Yates. J. Am. Chem. Soc. **100**, 3861 (1978).
19. E.C.W. Clarke and D.N. Glew. Trans. Faraday Soc. **62**, 539 (1966).

© 2008 NRC Canada

20. K.J. Laidler. Theories of chemical reaction rates. McGraw-Hill, Inc., New York. 1969. Chap. 3.
21. M.I. Vinnik. Izv. Akad. Nauk. SSSR, Ser. Khim. 799 (1978); Engl. Transl. 689 (1978); C.A. Bunton, C.J. O'Connor, and T.A. Turney. Chem. Ind. (London), 1835 (1967); C.J. Giffney and C.J. O'Connor. Aust. J. Chem. **29**, 307 (1976).
22. R.A. Cox. Can. J. Chem. **75**, 1093 (1997), and earlier papers.
23. R.A. Cox. J. Am. Chem. Soc. **96**, 1059 (1974).
24. R.A. Cox and K. Yates. Can. J. Chem. **60**, 3061 (1982).
25. T.W. Bentley. Can. J. Chem. **86** (2008). This issue.
26. A.J. Kresge, L.E. Hakka, S.G. Mylonakis, and Y. Sato. Discuss. Faraday Soc. **39**, 75 (1965).
27. A.J. Kresge, Y. Chiang, P.H. Fitzgerald, R.S. McDonald, and G.H. Schmid. J. Am. Chem. Soc. **93**, 4907 (1971).
28. R.A. Cox, Ü.L. Haldna, K.L. Idler, and K. Yates. Can. J. Chem. **59**, 2591 (1981).
29. F. Ruff and I.G. Csizmadia. Organic reactions: equilibria, kinetics and mechanism. Elsevier, Amsterdam. 1994. p. 239.
30. R.A. Cox, D.Y.K. Fung, I.G. Csizmadia, and E. Buncel. Can. J. Chem. **81**, 535 (2003).
31. S.-R. Keum, S. Rajagopal, E. Kiepek, E. Buncel, and R.A. Cox. Can. J. Chem. **86** (2008). This issue.
32. S. Saito, Y. Sato, T. Ohwada, and K. Shudo. J. Am. Chem. Soc. **116**, 2312 (1994).
33. Y. Zhang, D.J. DeSchepper, T.M. Gilbert, K.K.S. Sai, and D.A. Klumpp. J. Chem. Soc. Chem. Commun. 4032 (2007).
34. G.A. Olah, A. Germain, H.C. Lin, and D. Forsyth. J. Am. Chem. Soc. **97**, 2928 (1975).
35. K. Yates and R.A. McClelland. J. Am. Chem. Soc. **89**, 2686 (1967); K. Yates. Acc. Chem. Res. **4**, 136 (1971).

© 2008 NRC Canada

Wallach rearrangement of azoxypyridines and azoxypyridine *N*-oxides — Charge distributions and dramatic reactivity differences[1]

Erwin Buncel, Sam-Rok Keum, Srinivasan Rajagopal, Eric Kiepek, and Robin A. Cox

Abstract: Extension of our studies of the generic Wallach rearrangement (of azoxybenzene to 4-hydroxyazobenzene) to the heteroaromatic series (azoxypyridines and axoxypyridine *N*-oxides) has revealed some dramatic reactivity differences, particularly for the α and β compounds. We have studied the 3-isomers and the 4-isomers in each series, each with α and β forms, eight compounds in all, in the 100 wt% sulfuric acid region of acidity. In those cases in which a product could be observed, the α and β isomers both give the same one, the corresponding 4′-hydroxyazo compounds. All the compounds react much more slowly than does azoxybenzene itself, presumably because of the extra positive charge present in the substrates, but the β isomers have half-lives of seconds and the α isomers half-lives of hundreds of hours in the 100 wt% H_2SO_4 acidity region. The α compounds have measurable pK_{BH^+} values, but the β compounds do not, exhibiting only a medium effect in the acidity region in which the α compounds protonate. This means that for the β compounds, the protonated intermediates must be much less stable and the postulated reaction intermediates must be much more stable than for the α compounds. To clarify this, we have obtained Mulliken charge distributions for the various species concerned, calculating the charge carried by each half of the molecule, larger charge separations being taken to indicate lesser stability. As far as we can establish, this is the first time that this technique has been used to indicate the stabilities of carbocationic species.

Key words: azoxypyridines, azoxypyridine *N*-oxides, Wallach rearrangement, excess acidity, basicities, theoretical calculations, charge distributions, reactivities.

Résumé : Une extension de nos travaux sur le réarrangement générique de Wallach (de l'azoxybenzène en 4-hydroxyazobenzène) vers les séries hétéroaromatiques - azoypyridines et *N*-oxydes d'azoxypyridines - a mis en évidence des différences de réactivité dramatiques, en particulier avec les composés α et β. Opérant dans la région d'acidité à 100% en poids d'acide sulfurique, on a étudié les isomères 3 et 4 de chacune de ces séries, utilisant dans chaque cas les isomères α et β, soit huit produits en tout. Dans la cas où il était possible d'observer un produit, les isomères α et β conduisent tous les deux au mêmes produits, soit les composés 4'-hydroxyazo correspondants. Tous les composés réagissent beaucoup plus lentement que l'azoxybenzène lui-même, probablement en raison de la charge positive supplémentaire qui est présente dans les substrats, mais les demi-vies des isomères β sont de l'ordre de la seconde alors que celles des isomères α sont de l'ordre de centaines d'heures dans la région d'acidité de 100% en poids de l'acide sulfurique. On peut mesurer les valeurs de pK_{BH^+} des composés α, ce qui n'est pas le cas avec les composés β qui ne présente qu'un faible effet de milieu dans la région d'acidité dans laquelle les composés α se protonent. Ces résultats indiquent que dans le cas des composés β, les intermédiaires protonés doivent être beaucoup moins stables et que les intermédiaires réactionnels postulés doivent être beaucoup plus stables que pour les composés α. Dans le but de clarifier cette conclusion, on a obtenu les distributions de charge de Mulliken pour les diverses espèces concernées en calculant la charge portée par la moitié de la molécule et en faisant l'hypothèse que des séparations de charges plus grandes reflètent une stabilité plus faible. En autant qu'on puisse le savoir, c'est la première fois que cette technique est utilisée pour évaluer les stabilités d'espèces carbocationiques.

Received 29 November 2007. Accepted 14 January 2008. Published on the NRC Research Press Web site at canjchem.nrc.ca on 10 March 2008.

Dedicated to the memory of Keith Yates, fine friend and chemist.

E. Buncel,[2] S.-R. Keum,[2,3] S. Rajagopal, and E. Kiepek.[2] Department of Chemistry, Queen's University, Kingston, ON K7L 3N6, Canada.
R.A. Cox.[2] 16 Guild Hall Drive, Scarborough, ON M1R 3Z8, Canada.

[1]Part 27 of the series "Studies of azo and azoxy dyestuffs" of which part 26 is ref. 7.
[2]Corresponding authors (e-mail: keum@korea.ac.kr; buncele@chem.queensu.ca; robin.a.cox@sympatico.ca).
[3]Present address: Korea University, Department of New Mat. Chem., Jochiwon 339700, South Korea.

 doi:10.1139/V08-016 © 2008 NRC Canada

Mots-clés : azoxypyridines, *N*-oxyde d'azoxypyridines, réarrangement de Wallach, excès d'acidité, basicités, calculs théoriques, distributions de charge, réactivités.

[Traduit par la Rédaction]

Introduction

The Wallach rearrangement, dating from 1880 (1), is the rearrangement of aromatic azoxyarenes, typically azoxybenzene **1**, to hydroxyazo compounds. We have studied the reaction of azoxybenzene itself extensively (2–6) and have recently established the mechanism to be that shown in Scheme 1 (7), in which the calculated geometries of the various species involved are also shown (7).

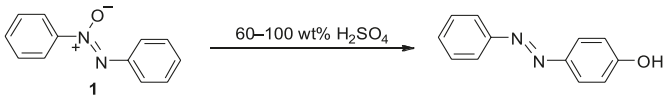

1

We have also studied a number of azoxynaphthalenes (8) and 2,2′,4,4′,6,6′-hexamethylazoxybenzene (9), and in this paper, we extend the study to include a number of azoxypyridines and azoxypyridine *N*-oxides, **2**–**9**. (The trivial and β nomenclature is used here, as it is more easily comprehensible than is the systematic NNO and ONN.)

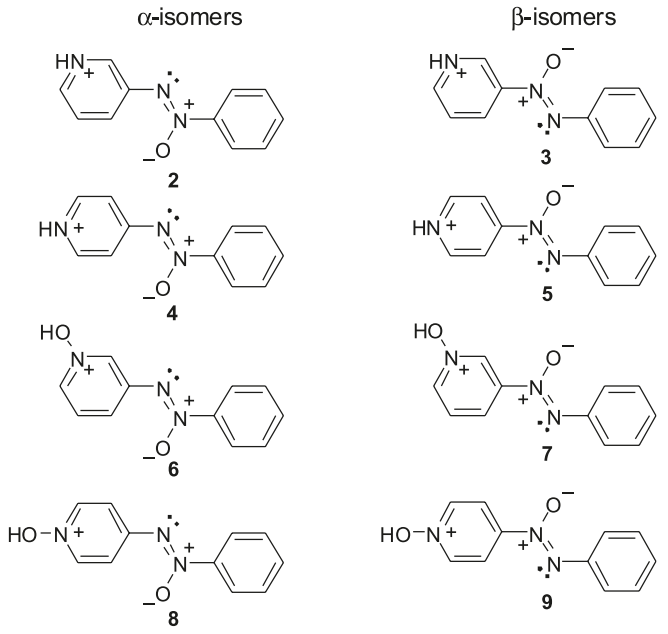

Here, we report the basicities of these compounds as pK_{BH^+} values for the second protonation of the substrates, where measurable (they are all monoprotonated in the pH range, and thus we regard the monoprotonated species **2**–**9** as the true reactants), and their approximate half-lives in about 100 wt% H_2SO_4 if these could be determined. (A preliminary report on the reactivities of **4** and **5** has been published (10)). To explain the observed dramatic differences between the α isomers **2**, **4**, **6**, and **8** (on the left), and the β isomers **3**, **5**, **7**, and **9** (on the right), we found it necessary to perform theoretical calculations on **2**–**9** and various related structures. Most recently, we have reported the results of some detailed theoretical calculations for possible intermediates resulting from **1** and some other substrates (7), following much earlier theoretical studies (11).

Experimental

We have reported the syntheses of **2**–**9** previously (12). In brief, 4- and 3-phenylazopyridines were prepared by condensation of nitrosobenzene with 4- and 3-aminopyridine, according to Brown and Grammeman (13), and purified by column chromatography and recrystallization from hexane. Oxidation of these with *m*-chloroperbenzoic acid according to Badger and Lewis (14) gave the corresponding phenylazopyridine *N*-oxides. Further oxidation of these with H_2O_2/glacial acetic acid following Colonna, Risaliti, and Pentimalli (15, 16) gave mixtures of the α and β phenylazopyridine *N*-oxides, which could be separated by HPLC; these are **6**–**9**. The azopyridines **2**–**5** were obtained from these by selectively deoxygenating them at the *N*-oxide function with PCl_3 according to Pentimalli (16). The identities of the compounds were confirmed by X-ray structure analysis (12).

The basicities were determined in the same way as before (2). UV–vis spectra were obtained at the same substrate concentration, ~5×10^{-5} mol/L, but at differing acidities, using aqueous H_2SO_4, at 25 °C. Examples are given in Fig. 1 for **4** and Fig. 2 for **5**; the relevant experimental data are given as supplementary material, Tables S1–S4 for **2**, **4**, **6**, and **8**, the only compounds for which pK_{BH^+} values could be determined.[4] A PerkinElmer Lambda-5 UV–vis spectrophotometer was used for both the basicity determinations and for kinetic measurements (In Figs. 1 and 2, the unlabelled *y*-axis is the optical density *D*).

The acid solutions used for the kinetic measurements, in the 100 wt% H_2SO_4 range, were carefully prepared from Fisher Reagent Grade 96% sulfuric acid and fuming 30% sulfuric acid, and the concentrations determined accurately by conductivity measurements according to Gillespie and Wasif (17). Reaction rates were determined by the "direct method" (3), either by repeatedly scanning over 350–500 nm, or at a suitable constant wavelength for the faster reactions. Excellent isosbestic points were observed; byproduct formation was minimal. Infinity values after ten half-lives were stable, and were used directly to evaluate the

[4] Supplementary data for this article are available on the journal Web site (canjchem.nrc.ca) or may be purchased from the Depository of Unpublished Data, Document Delivery, CISTI, National Research Council Canada, Ottawa, ON K1A 0R6, Canada. DUD 3720. For more information on obtaining material, refer to cisti-icist.nrc-cnrc.gc.ca/irm/unpub_e.shtml.

© 2008 NRC Canada

Scheme 1.

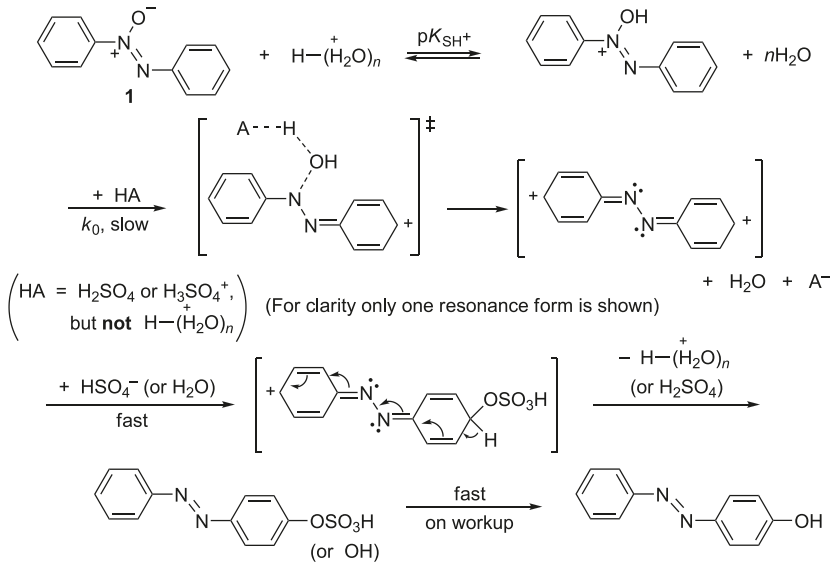

Fig. 1. UV–vis spectra of **4** in aq. H_2SO_4; 1, 82.23%; 2, 89.15%; 3, 91.25%; 4, 93.03%; 5, 94.28%; 6, 95.16%; 7, 96.45%; and 8, 97.17%. The *y*-axis is *D*, optical density.

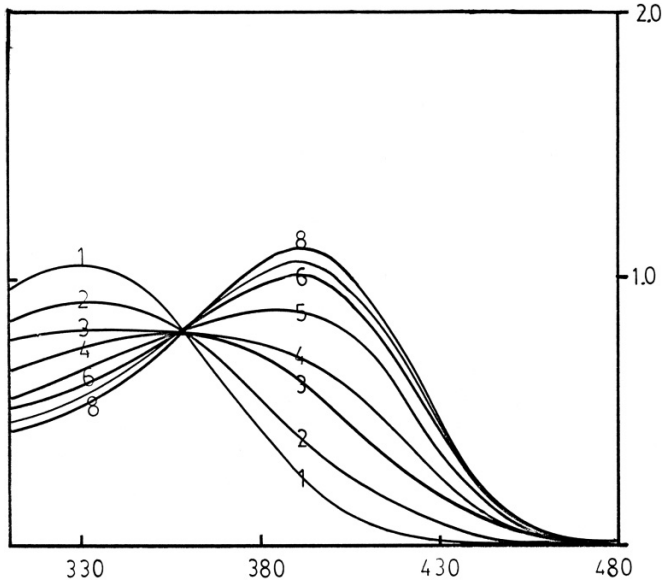

Fig. 2. UV–vis spectra of **5** in aq. H_2SO_4; 1, 83.44%; 2, 87.80%; 3, 91.25%; 4, 93.08%; 5, 94.28%; 6, 95.16%; 7, 96.45%; and 8, 98.45%. The *y*-axis is *D*, optical density.

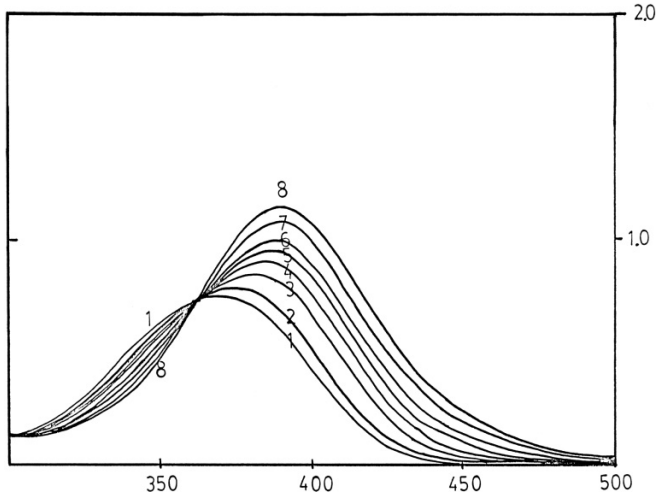

pseudo-first-order rate constants. Reaction products were initially identified by direct isolation as previously (9), and subsequently from a comparison of the final UV–vis spectra with those of the authentic products.

The Mulliken charges at the individual atoms for the various structures were obtained using GAUSSIAN 98, as before (7), at the High Performance Computing Virtual Laboratory of Queen's University.

Results

Basicities

[1] $$pK_{BH^+} = \log I - \log C_{(H^+)_{aq}} - m^*X$$

The basicities that could be obtained for some of the substrates in this work are given in Table 1, together with the observed m^* values, along with the value for azoxybenzene **1** obtained from preexisting data (3) in exactly the same way for comparison. These were obtained using the excess acidity method (18); eq. [1] was curve-fitted directly, with ionization ratio *I* values being obtained from the observed optical density *D* (or extinction ε) differences, $D = (D_B + ID_{BH^+})/(1 + I)$). Differences, usually the *D* (or ε) values at the unprotonated species peak wavelength subtracted from those at the peak wavelength of the protonated species (or vice versa), are used to minimize any errors caused by small differences in substrate concentration in the different acid media. These are given as supplementary information in Tables S1–S4, together with the values of *X* and log $C_{(H^+)_{aq}}$ used (19).[4] ($C_{(H^+)_{aq}}$ is written rather than C_{H^+} as used before (19) because it is a better representation of the actual state of the proton in acid media (20).) This excess acidity treatment

© 2008 NRC Canada

Table 1. Excess acidity pK_{BH^+} and m^* values for **1**, **2**, **4**, **6**, and **8**.

Substrate	pK_{BH^+} [a]	m^* [a]	No. of points	RMS error [b]
1	–5.18±0.17	1.057±0.041	13	±0.019
2	–10.72±0.10	1.122 [c]	7	±0.40
4	–10.43±0.06	1.122 [c]	8	±0.65
6	–10.49±0.77	1.160±0.097	13	±0.57
8	–10.09±0.51	1.149±0.065	13	±0.43

[a]Errors given are standard deviations.
[b]Root-mean-square deviation between experimental and fitted points.
[c]Average of values obtained for **1**, **6**, and **8**. See text.

Scheme 2.

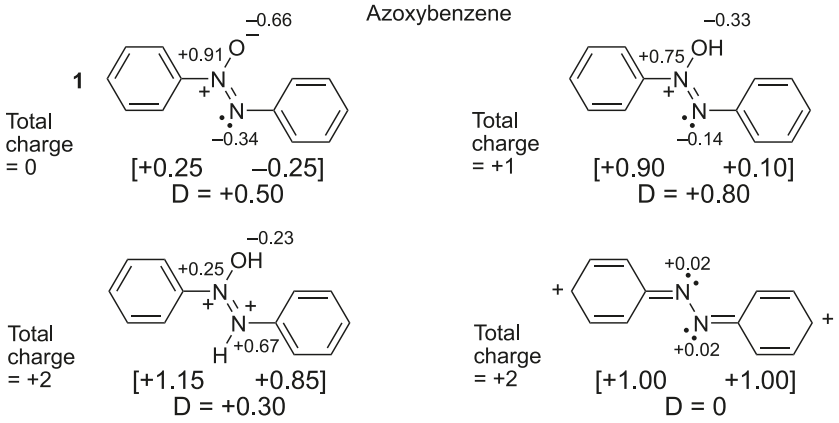

also gives estimated values of D_B and D_{BH^+}, with their errors, so log I values can be easily calculated as well if necessary (the method used actually includes and improves on all existing methods of pK_{BH^+} determination). As is apparent from Table 1, there were not enough data points available to enable calculation of m^* values for **2** and **4**, the numbers obtained having errors larger than the values themselves, so these substrates were assigned the fixed value $m^* = 1.122$, this being the average of that observed for the other three data sets, and the quite reasonable pK_{BH^+} values reported in Table 1 were the result.

Only values of pK_{BH^+} and m^* for the α-isomers could be obtained; examination of Figs. 1 and 2 reveals that only Fig. 1 (**4**) is a protonation equilibrium, with one peak decreasing in intensity while another one increases, clearly indicating a measurable pK_{BH^+}. Figure 2 (**5**) represents only a medium effect on the monoprotonated species — one peak red-shifting as the acidity increases (all of the UV–vis spectra obtained for **2**, **6**, and **8** resemble Fig. 1, and those for **3**, **7**, and **9** resemble Fig. 2; Figs. 1 and 2 are representative). A comparison of Figs. 1 and 2 with Figs. 5 and 6 of ref. 21 shows a remarkable similarity; in ref. 21, an excess acidity method for the reliable separation of medium effects from spectral changes due to protonation was developed, and Fig. 5 of ref. 21 shows the reconstructed spectra due to protonation, and Fig. 6 of ref. 21, the medium effect on the protonated species as the acidity continues to increase (the substrate in that case was *N-tert*-butylbenzamide).

Reactivities

In contrast to the pK_{BH^+} situation, our preliminary results for the rates of the rearrangement reactions of **2**–**9** are essentially the opposite. No reaction at all was observed for the α-compound **2** at 50 °C (and thus, of course, the reaction product could not be determined either); whereas the β-compound **3** has a half-life of about 30 s at this temperature in 99.74 wt% H_2SO_4. Similarly, the α-species **4** gave no reaction, whereas **5** has a half-life of about 96 s in 99.74% H_2SO_4 at 50 °C (10). The *N*-oxides behave similarly; a higher reaction temperature of 65 °C was used for these, and under these conditions the α-isomers **6** and **8** have the very long half-lives of 98 h and 402 h in 99.76 wt% H_2SO_4, respectively. The β compounds **7** and **9** react very much more quickly under these conditions, with half-lives of 42 and 56 s, respectively. For comparison, azoxybenzene **1** itself has a half-life of 5.1 min at 25 °C in 99.59 wt% H_2SO_4 (5).

Charge distributions

To explain these considerable differences in reactivity and pK_{BH^+} value between the α and β isomers, it seemed necessary to examine the charge distributions in **1**–**9** and in the various possible intermediates formed from them on the way to product. We have previously carried out detailed theoretical calculations on the possible intermediates involved in the reaction of **1** and some other compounds (7), and have found that the proposed dicationic reaction intermediate was flat (both phenyl rings in the same plane) and had 120° bond angles at both of the nitrogens (which presumably retain their lone pairs) (7). For the purposes of keeping the calculations simple, it seemed reasonable to constrain the many structures we examined in this work to be flat and bent in the same way also. Mulliken charges at each atom were obtained as before (7), and for simplicity these are summed for the left-hand side and the right-hand side in the structures

© 2008 NRC Canada

Scheme 3.

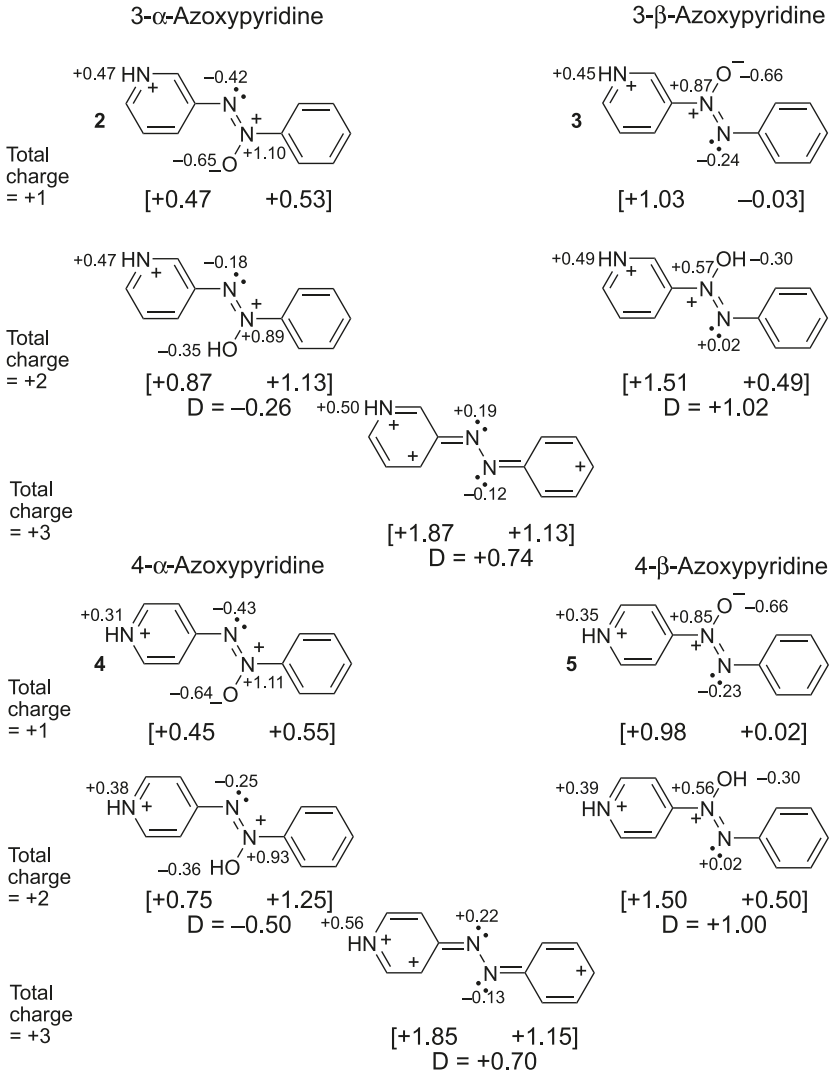

which follow, dividing the molecule into two between the two nitrogen atoms in the middle. Some charges at individual atoms are also given. Azoxybenzene was also calculated for comparison; the resulting numbers were in exact agreement with those obtained before (7). These are given in Scheme 2; the azoxypyridinium cations **2**–**5** are in Scheme 3, and the protonated azoxypyridine *N*-oxides **6**–**9** in Scheme 4.

Discussion

As far as we have been able to establish, this is the first time that charge distributions calculated in this way, by dividing the structures into two halves to calculate charge separations, have been used to estimate the stabilities of cationic species; charge separation is known to be important in carbanionic species (22). A comparison of Scheme 1 with Scheme 2, which gives these calculations for azoxybenzene **1** itself, is instructive. In Scheme 2, the total amount of charge borne by each side of the molecule is given below the structure, and the difference between them is given as Δ, charge on left side minus charge on right side. It would be reasonable to conclude that the smaller this difference, the more stable is the structure, the assumption being that large amounts of charge separation in a structure are destabilizing (this is an assumption that seems to be implicit in physical organic chemistry but does not seem to have been explicitly stated before).

Thus in Scheme 2, protonated azoxybenzene is not particularly stable, with a charge separation of 0.80, but the diprotonated species below it to the left (not actually formed during the course of the reaction, but the transition state does resemble it (7), see Scheme 1), has a charge separation of only 0.30, and in the dicationic intermediate it is zero. Thus, formation of the monoprotonated species is not easy (pK_{BH^+} = –5.18, which is quite a difficult protonation), but once formed, the reaction of it is fairly facile (easily observable reaction at 25 °C) (3, 5). None of the calculated charge separations in Scheme 2 are in accord with what might be expected from drawing simple resonance structures (3, 5).

In Schemes 3 and 4, we present some pertinent charge-distribution data for the azoxypyridine species investigated in this work. Charge densities are given for ring-nitrogen-protonated pyridine species, ring-nitrogen- (or $^{+}$N–OH) and

© 2008 NRC Canada

Scheme 4.

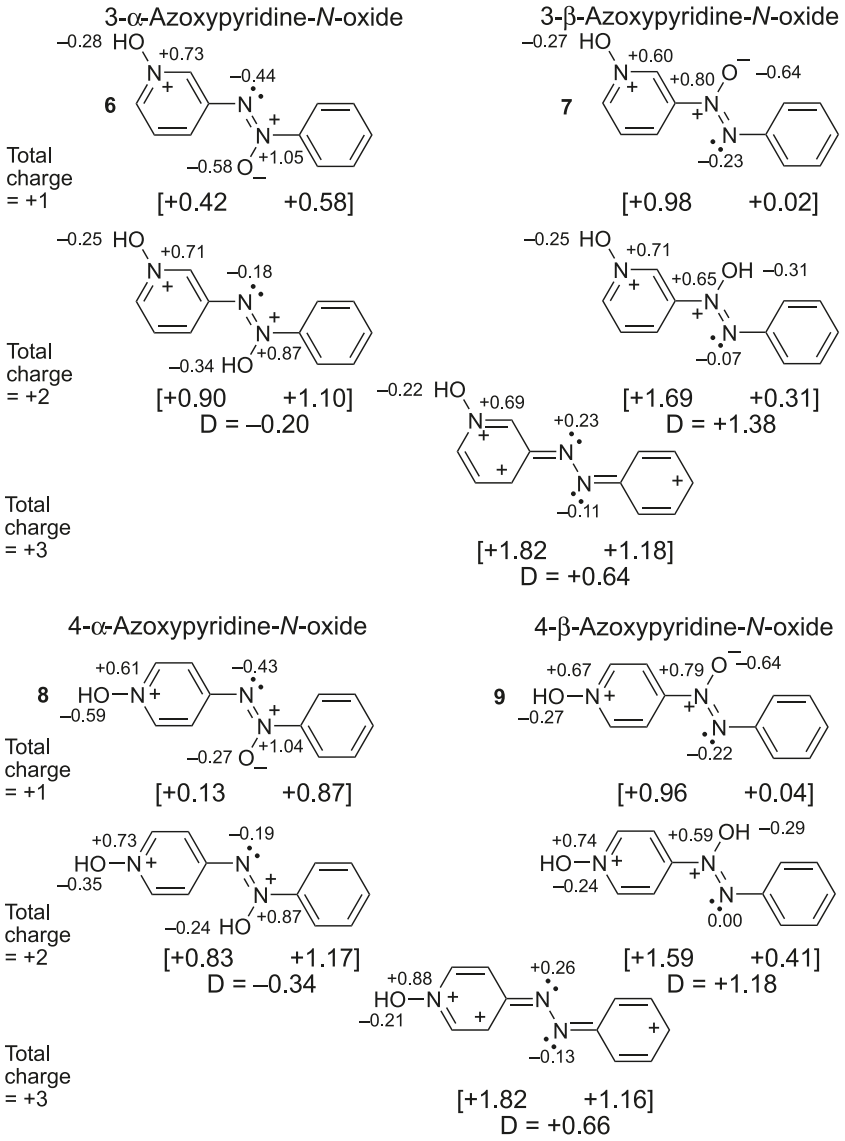

azoxy-oxygen diprotonated species, and for the presumed tripositive intermediates (10). Total charges vary from zero for the parent azoxybenzene **1** (Scheme 2) to +3 for the intermediates derived from the 3- and 4-α- and β-azoxypyridines (Scheme 3) and the 3- and 4-α and β-azoxypyridine *N*-oxides (Scheme 4).

Of particular interest are the fully deoxygenated structures (except for the *N*-oxide OH when present) formed following the loss of the azoxy oxygen in strong H_2SO_4 media. The parent dicationic structure in Scheme 1 was proposed as the key intermediate in the Wallach rearrangement of azoxybenzene (2–6, 23); its geometry was recently subjected to modern theoretical examination (7), resulting in the flat, bent structure for it as given in Schemes 1 and 2. The present study of charge distributions shows that these have a direct bearing on the basicities and reactivities of all of the azoxyarene reactant families.

The results presented in Schemes 2, 3, and 4 reveal some interesting general features. Nitrogens bearing formal positive charges remain, in the main, positively charged, but as the amount of positive charge in the molecule increases, more and more of it is borne by the aromatic rings. For instance, in the dicationic intermediate derived from **1** in Scheme 1, each ring bears 0.98 of a positive charge, leaving only 0.02 for the nitrogen. This undoubtedly explains why the structure can be bent (120° bond angles at nitrogen), and the nitrogens can retain their lone pairs. (In the rings, this positive charge resides mainly on the ring hydrogen atoms, with the carbons remaining essentially neutral). Formally neutral nitrogens remain neutral or can bear negative charge, sometimes a considerable amount. Almost never do they become positive. Oxygen atoms in the structures always retain a considerable amount of negative charge, even when protonated.

For the other azoxyarenes in Schemes 3 and 4, all of the αs (on the left) have a small charge separation, with the right-hand ring more positive than the left-hand one. In contrast, all of the tripositive intermediates formed from them,

© 2008 NRC Canada

presumably in the rate-determining step of the reaction (7), have a LARGER charge separation, with the left-hand ring more positive, as well as having an entire extra positive charge. Thus, the diprotonated species are stable (observable pK_{BH^+}), and are unreactive, because of the large activation energy caused by having to go to a species with greater charge separation. Thus for the αs, reaction is very slow or not observed at all.

For all of the βs (on the right in Schemes 3 and 4), the situation is exactly the opposite. All of the dipositive protonated species have a large charge separation (left-hand side more positive), and thus cannot be very stable (unobservable pK_{BH^+}). On the other hand, once they do form, they will react very quickly (small activation energy) because they are going to a species with a SMALLER charge separation, even though it has one more positive charge. Thus, the considerable reactivity differences in **2–9** can be easily explained on the basis of differing charge separations in the intermediate species.

Other points

The 4-α species have (presumably) better resonance interactions than the 3-αs do (slightly larger negative Δs), and thus have slightly less negative pK_{BH^+} values. As a whole, the azoxypyridine and azoxypyridine *N*-oxide families have pK_{BH^+} values, which are five powers of ten more negative than that of azoxybenzene, simply due to the presence of one more positive charge in these species. The 3-βs react slightly faster than the 4-βs because they gain slightly more charge dispersal in going from the dipositive protonated species to the tripositive intermediate than do the 4-βs. All of them react much more slowly than does azoxybenzene (i.e., the reactions have to be studied at a higher temperature), again because of the extra positive charge. There seems to be little difference between the azoxypyridinium ions and the azoxypyridine *N*-oxides.

Thus, it is apparent that charge distributions have a direct bearing on the basicities and reactivities of **1–9**, and undoubtedly of the entire azoxyarene family. These fascinating molecules continue to provide interesting and useful information about the mechanisms of many other reactions that take place in more dilute acid media (24) and the reactions of superelectrophiles in media such as pure CF_3SO_3H (25), as well as about the Wallach rearrangement itself. Detailed discussion of the reaction rates and mechanisms of **1–9** will follow in a forthcoming publication.

Acknowledgments

Financial support of this research through a grant by the Natural Sciences and Engineering Research Council of Canada (NSERC) (to EB) and to Queen's University via teaching assistantships (to S-RK, SR, and EK) is gratefully acknowledged.

References

1. O. Wallach and E. Belli. Chem. Ber. **13**, 525 (1880).
2. E. Buncel and B.T. Lawton. Chem. Ind. (London), 1835 (1963).
3. E. Buncel and B.T. Lawton. Can. J. Chem. **43**, 862 (1965).
4. E. Buncel, W.M.J. Strachan, R.J. Gillespie, and R. Kapoor. J. Chem. Soc., Chem. Commun. 765 (1969).
5. E. Buncel and W.M.J. Strachan. Can. J. Chem. **48**, 377 (1970).
6. R.A. Cox. J. Am. Chem. Soc. **96**, 1059 (1974).
7. R.A. Cox, D.Y.K. Fung, I.G. Csizmadia, and E. Buncel. Can. J. Chem. **81**, 535 (2003).
8. (*a*) E. Buncel and A. Dolenko. Tetrahedron Lett. 113 (1971); (*b*) A. Dolenko and E. Buncel. Can. J. Chem. **52**, 623 (1974); (*c*) E. Buncel, R.A. Cox, and A. Dolenko. Tetrahedron Lett. 215 (1975); (*d*) R.A. Cox, A.J. Dolenko, and E. Buncel. J. Chem. Soc., Perkin Trans. 2, 471 (1975).
9. (*a*) R.A. Cox and E. Buncel. J. Chem. Soc., Chem. Commun. 1259 (1972); (*b*) E. Buncel and R.A. Cox. Can. J. Chem. **51**, 3143 (1973); (*c*) R.A. Cox and E. Buncel. J. Am. Chem. Soc. **97**, 1871 (1975).
10. E. Buncel and S.-R. Keum. J. Chem. Soc., Chem. Commun. 578 (1983).
11. E. Buncel, A. Dolenko, I.G. Csizmadia, J. Pincock and K. Yates. Tetrahedron, **24**, 6671 (1968).
12. E. Buncel, S.-R. Keum, M. Cygler, K.I. Varughese, and G.I. Birnbaum. Can. J. Chem. **62**, 1628 (1984).
13. E.V. Brown and G.R. Granneman. J. Am. Chem. Soc. **97**, 621 (1975).
14. G.M. Badger and G.E. Lewis. J. Chem. Soc. 2151 (1953).
15. (*a*) M. Colonna, A. Risaliti, and L. Pentimalli. Gazz. Chem. Ital. **86**, 1067 (1956); (*b*) M. Colonna and A. Risaliti. Gazz. Chim. Ital. **85**, 1148 (1955).
16. L. Pentimalli. Ann. Chim. (Rome), **55**, 435 (1965).
17. R.J. Gillespie and S. Wasif. J. Chem. Soc. 213 (1953).
18. R.A. Cox. Adv. Phys. Org. Chem. **35**, 1 (2000).
19. R.A. Cox and K. Yates. J. Am. Chem. Soc. **100**, 3861 (1978).
20. R.A. Cox. Can. J. Chem. **83**, 1391 (2005).
21. R.A. Cox and K. Yates. Can. J. Chem. **59**, 1560 (1981).
22. E. Buncel and J.M. Dust. Carbanion chemistry. Structures and mechanisms. American Chemical Society, WA, and Oxford University Press, Oxford, UK. 2003.
23. (*a*) E. Buncel. *In* Mechanisms of molecular migrations. Vol. 1. *Edited by* B.S. Thyagarajan. Wiley, New York. pp. 61–119. 1968; (*b*) E. Buncel. Acc. Chem. Res. **8**, 132 (1975); (*c*) R.A. Cox and E. Buncel. *In* The chemistry of the hydrazo, azo, and azoxy groups. Vol. 1. *Edited by* S. Patai. Wiley, London. pp. 775–859. 1975; (*d*) R.A. Cox and E. Buncel. *In* The chemistry of the hydrazo, azo, and azoxy groups. Vol. 2. *Edited by* S. Patai. Wiley, London. 1997. pp. 569–602; (*e*) D. Abdallah, M.A.A. Ghani, M.F. Cunningham, P.M. Kazmaier, B. Keoshkerian, and E. Buncel. Can. J. Chem. **82**, 1393 (2004).
24. R.A. Cox. Can. J. Chem. **86**, this issue.
25. (*a*) Y. Zhang, D.J. DeSchepper, T.M. Gilbert, K.K.S. Sai, and D.A. Klumpp. J. Chem. Soc., Chem. Commun. 4032 (2007); (*b*) S. Saito, Y. Sato, T. Ohwada, and K. Shudo. J. Am. Chem. Soc. **116**, 2312 (1994); (*c*) T. Ohwada, T. Ohta, and K. Shudo. J. Am. Chem. Soc. **108**, 3029 (1986).

© 2008 NRC Canada

Adsorption of vapor-phase VOCs (benzene and toluene) on modified clays and its relation with surface properties

C. López-Cortés, G. Osorio-Revilla, T. Gallardo-Velázquez, and S. Arellano-Cárdenas

Abstract: A mexican bentonite was used to prepare three modified clays: an organoclay (OC–CPC) by intercalating cetylpyridinium chloride (CPC), an aluminum-pillared clay (Al-PILC), and an inorganic–organic clay (IOC–CPC) prepared from Al-PILC intercalating CPC. The infrared and thermogravimetric analyses enabled us to differentiate between the structures obtained. Interlayer distance was assessed through X-ray diffraction; the OC–CPC was the clay that showed the highest value (12.4 Å). The natural clay's specific area was 43.5 m^2/g, increasing to 157.2 m^2/g for Al-PILC. The OC–CPC and IOC–CPC specific areas were 13.27 m^2/g and 14.5 m^2/g, respectively. Al-PILC was a microporous material; whereas natural clays, OC–CPC and IOC–CPC were non-porous materials. Toluene and benzene adsorption on OC–CPC was higher than in IOC–CPC and Al-PILC. Natural clay showed no adsorption capacity for these compounds. Comparison of the GC retention times for non polar and low-polarity compounds (octyne and benzene) in columns packed with OC–CPC and a commercial non polar column (squalene) showed that the OC–CPC possessed a higher organophilic (non polar) nature than squalene. This explains the higher benzene and toluene adsorption capacity of the OC–CPC compared with the other modified clays. The toluene and benzene adsorption isotherm for OC–CPC was well-described by the GAB (Guggenheim–Anderson–De Boer) model for the whole range of relative pressure used in this work (0–0.9) describing multilayer adsorption and capillary condensation.

Key words: organoclay, inorgano–organo clay, vapor phase VOC's adsorption, clay surface properties.

Résumé : On a utilisé une bentonite mexicaine pour préparer trois argiles modifiées: une argile organique (AO-CCP) obtenue par intercalation de chlorure de cétylpyridinium (CCP), une argile pillée avec de l'aluminium (APIL-Al) et une argile inorganique organique (AIO-CCCP) préparée en intercalant du CCP dans de l'APIL-Al. Les analyses infrarouges et thermogravimétriques permettent de différencier les structures obtenues. On a évalué les distances intercouches par diffraction des rayons X; la valeur la plus élevée, 12,4 Å, est observée avec l'argile AO-CCP. La surface spécifique de l'argile naturelle est de 43,5 m^2/g et elle atteint 157,2 m^2/g avec l'argile APIL-Al. Les surfaces spécifiques pour les argiles AO-CCP et AIO-CCP sont respectivement 13,27 m^2/g et 14,5 m^2/g. L'argile APIL-Al est un matériau microporeux alors qu'on a démontrer que le l'argile naturelle et les argiles AO-CCP et AIO-CCP sont des matériaux non poreux. En chromatographie gazeuse, une comparaison des temps de rétention de composés non polaires et de faible polarité (octyne et benzène), dans des colonnes contenant de l'argile AO-CCP et une colonne non polaire commerciale (squalène) ont permis de montrer que le caractère organophile (non polaire) de l'argile AO-CCP est plus élevé que celui du squalène. Cette caractéristique explique la capacité d'adsorption du benzène et du toluène plus élevée de l'argile AO-CCP par comparaison avec les autres argiles modifiées. L'isotherme d'absorption du benzène et du toluène pour l'argile AO-CCP est très bien décrite par le modèle GAB (Guggenheim–Anderson–De Boer) pour toute la plage de pressions relatives utilisées dans ce travail (0 à 0,9) décrivant l'adsorption multicouche et la condensation capillaire.

Mots-clés : argile organique, argile inorganique organique, adsorption de composés organiques volatils en phase vapeur, propriétés superficielles d'argiles.

[Traduit par la Rédaction]

Received 11 October 2007. Accepted 25 December 2007. Published on the NRC Research Press Web site at canjchem.nrc.ca on 6 March 2008.

C. López-Cortés, T. Gallardo-Velázquez, and S. Arellano-Cárdenas. Escuela Nacional de Ciencias Biológicas – IPN, Departamento de Biofísica, Laboratorio Central de Instrumentación– Investigación, Prol. de Carpio y Plan de Ayala, Col. Sto. Tomás, Apartado. Postal 42–186, 11340 México.
G. Osorio-Revilla.[1] Departamento de Ingeniería Bioquímica. Prol. de Carpio y Plan de Ayala, Col. Sto. Tomás, Apartado. Postal 42–186, 11340 México.

[1]Corresponding author (e-mail: gosorio@encb.ipn.mx).

 doi:10.1139/V08-017 © 2008 NRC Canada

Introduction

Main air pollutants include gases, such as carbon monoxide, nitrogen oxides, sulfur oxides, partially burned hydrocarbons, and volatile organic compounds (VOCs), the latter constituting the second most abundant and diverse class of emissions after suspended particles. Most VOCs' emissions come from small sources, such as cars, nail enamel bottles, paint containers, solvents, and so forth. These represent a human health risk at high concentrations, mostly in indoor environments, either at home or in work environments, where pollution levels are higher and more hazardous than outdoors. Therefore, there is a need to clean the work environment. The reduction of the concentration of these gases and vapors to acceptable levels can be carried out by a number of methods, including adsorption processes, which use adsorbents like activated carbon and zeolites (1).

A number of studies (2–4) have demonstrated that clay materials having a laminar structure like bentonite, can be chemically modified, changing their physicochemical characteristics, such as interlaminar distance, surface area, pore size, and polarity or chemical affinity. Some studies have focused mainly on obtaining modified clays to be used for the adsorption of organic and inorganic contaminants, which depends on both the nature of the mineral surface and the compound intercalated in the clay's interlayer space (5). Given their hydrophobic nature, organic clays (OC), as well as inorganic–organic clays (IOC), having an intermediate hydrophobicity have been used for the adsorption of toxic organic compounds in liquid phase, e.g., OC–TMAC (OC with tetramethyl ammonium chloride) for phenols and chlorophenols (6); IOC–CPC (IOC with cetylpyridinium chloride) for benzopyrene and chlorophenols (7); OC–TMA (OC with tetramethyl ammonium) for benzene, toluene, and xylene (8); OC–DDA (OC with dimethyl distearyl ammonium) for phenol and trichlorophenol (9); OC–TBA (OC with tetrabutyl ammonium bromide) for chlorobenzene (10); OC–TMPA (OC with trimethyl phenyl ammonium) in aqueous solution for the absorption of benzene, toluene, and ethyl benzene (11); and the removal of aqueous phenolic pollutants using pillared clays (PILC), organic clays (OC), and inorganic–organic clays (IOC) (12), among others. However, only few reports have been published on the use of modified clays for VOCs' adsorption in vapor phase, including trichloroethane, trichloroethylene, methanol, and propane in zeolites and PILCs (13); adsorption of VOCs on mineral clays (14); adsorption of gasoline hydrocarbons (BTEXs) on mineral clays (15); benzene vapor on organobentonites–cetyl trimethyl ammonium (4); and adsorption of benzene and toluene in vapor phase on modified clays (16).

In the present work, the potential use of modified clays in the adsorption of vapor-phase toluene and benzene (VOCs) present in air is investigated. The intercalated compound was cetylpyridinium chloride (CPC), based on the work reported by Keeran et al. (5), but conducting the adsorption of VOCs in the vapor phase. The modified clays OC–CPC, IOC, and Al-PILC were prepared for comparative purposes and were characterized using infrared spectroscopy, themogravimetric analysis, and X-ray diffraction. The surface properties were determined through nitrogen-adsorption isotherms, and the polarity of the organic clay was determined experimentally by gas chromatography. The benzene and toluene adsorption isotherms in modified clays were obtained in a static chamber using the gravimetric method (17).

Experimental

The natural clay used in this study was a Perfobent bentonite (cation exchange capacity CEC = 74 meq/100 g) supplied by Perfobent, Mexico City (a company that extracts minerals from northern Mexico). The natural clay was not refined for pillaring; the only treatment to which it was subjected was grinding to homogenize particle size and sieving through a 65 mesh sieve to obtain a maximum particle diameter of 0.210 mm.

Modified-clays preparation

The aluminum PILC (Al-PILC) was prepared following the method reported by Torkáz and Shabtai (18), preparing the pillaring agent (aluminum polyhydroxycation) with OH:Al molar ratio of 1.85, which is obtained at a pH of 4.35. The pillaring agent was mixed with the natural clay to obtain a ratio of 6 mmol Al/g clay. The inorganic–organic clay (IOC) was prepared mixing the Al-PILC previously prepared with cetylpiridinium chloride (CPC) as carbon source in an amount equivalent to 100% of its cation exchange capacity (5). The organic clay (OC–CPC) was prepared by mixing the natural clay with the organic surfactant CPC (5) in an amount equivalent to 100% of its cation exchange capacity.

IR analysis

Infrared analysis was used to differentiate between the structures obtained by the intercalation of organic and inorganic compounds. This analysis was carried out in a FTIR PerkinElmer 1600 spectrophotometer using the KBr pellet method.

Thermogravimetric analysis

Thermogravimetric analysis was used to evidence the change in chemical structure resulting from the intercalation of the aluminum polymer in Al-PILC and cetylpyridinium in the other modified clays (OC–CPC and IOC), using a Model 1090 AT thermoanalyzer, at 10 °C/min from 25 to 900 °C. The parameters determined were % weight loss as a function of temperature and the differential of this parameter as a function of temperature.

X-ray diffraction

X-ray diffraction was used to obtain the interlaminar distance in each sample, using a Siemens D-500 diffractometer. Nickel filter, Cu radiation Kα = 1.5406 Å operating at 30 kv and 20 mA with a 2θ angle scanning angle ranging from 2 to 64°. The basal distance d_{001} for each sample was calculated and identified using the diffractometer's software.

Nitrogen-adsorption isotherms

Nitrogen adsorption isotherms were obtained at –196 °C with a C.I. Electronics LTD Mark 2 automatic analyzer, from which the specific area was calculated using the Brunauer–Emmett–Teller (BET) model. The mean pore diameter and the micro or mesoporous nature of the

© 2008 NRC Canada

adsorbents were determined using the Lippens and De Boer's *t*-method (19). Determinations were made by replicate and the results averaged.

Experimental adsorption isotherms

The static-chamber method (17) was used to obtain the experimental adsorption isotherms. Each determination was replicated six times, and the result was averaged; the confidence limits were calculated using the *t*-distribution at 95% confidence. This method consisted in preparing a series of solutions having different benzene or toluene concentrations (0–1.0 mol fraction) in a non-volatile and non-reactive mineral oil. The different solutions were placed in 20 mL GC vials, and small aluminum trays containing a known amount of the adsorbent (100–200 mg) were suspended from the vial stopper to expose it to the vapor pressure generated from the oil–toluene or oil–benzene solution. Vials were tightly capped with silicone–Teflon™ stoppers and left at a controlled temperature of 23 °C in a stove until equilibrium, which was reached after 10 days. The amount of the adsorbed solvent per gram of dry solid was then calculated by gravimetry, and the solvent vapor content in the chamber in equilibrium with the solid was determined by GC, using a standard curve for the vapor-phase solvent. A PerkinElmer Sigma 3B gas chromatographer with a FID detector, carbowax 20M (Supelco) packed column, and a constant nitrogen flow rate of 20 mL/min was used. The column temperature was 120 °C with a detector and injector temperature of 140 and 130 °C, respectively. For this determination, 100 μL samples were collected from each vial's vapor atmosphere using a Hamilton syringe for gases, which were injected afterwards in the gas chromatographer. By relating the sample's peak areas with those of the standard curve, the amount of solvent present in the atmosphere of each vial was calculated.

The standard curve was obtained by preparing five solutions (liquid phase) with different toluene–hexane concentrations. The area (arbitrary units) for toluene and benzene present in each sample was determined by GC. The area vs. amount of toluene or benzene (in mg) was plotted and compared with the areas obtained from each vial's atmosphere.

Adsorption mathematical models

Benzene and toluene adsorption isotherms obtained for all modified clays were compared to those predicted by BET and GAB (Guggenheim–Anderson–De Boer) adsorption mathematical models to derive a possible explanation to the behavior observed.

Polarity (chemical affinity)

The polarity (chemical affinity) of the OC–CPC modified clay was determined through GC, obtaining the retention times of different compounds varying in polarity (pentanone, intermediate polarity; octyne, low polarity; and benzene, non-polar) in columns packed with OC–CPC and commercial columns of different polarity (Supelco): carbowax 20M; OV-25 (intermediate polarity), SE 30 (low polarity), and squalene (non-polar). The equipment used was a SIGMA 3B gas chromatographer (GC) with packed column, FID detector, and using nitrogen as carrier (20 mL/min) and a column temperature of 100 °C.

Fig. 1. Infrared spectra of: (*a*) natural and Al-PILC and (*b*) natural clay, OC–CPC, and IOC.

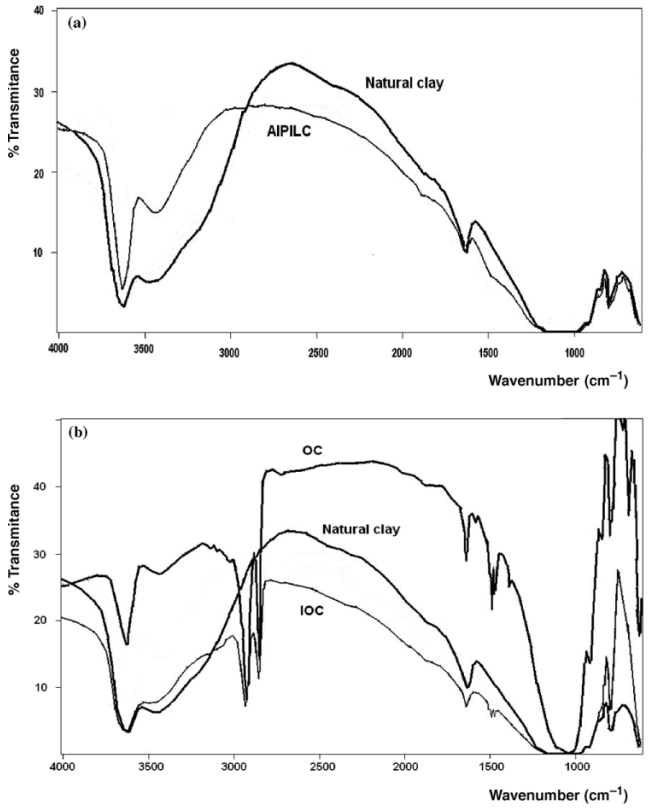

Table 1. % Weight loss of the modified clays and natural clay in the three regions in which the thermogram was divided.

Sample	Region I (30–230 °C)	Region II (230–530 °C)	Region III (530–900 °C)
Natural clay	8.24	0.9	3.12
Al-PILC	8.73	4.29	1.8
IOC	8.73	11.89	1.95
OC–CPC	1.99	21.36	2.13

Results and discussion

Figure 1*a* shows the infrared spectra of natural clay and Al-PILC. Natural clay shows vibration absorption bands of the stretching type of OH groups bound to Al^{3+} and (or) Mg^{2+} near 3600 cm^{-1}. The broad band in the 3000–3500 cm^{-1} region corresponds to the strong OH stretching of water in the interlayer space. This last band appears in Al-PILC, but with a broader and higher intensity peak, due to the presence of additional OH groups from the intercalated aluminum polyhydroxycation. This indicates that the pillaring process was successful. The infrared spectra of OC–CPC and IOC (Fig. 1*b*) also display the OH stretching band of water in the 3000–3500 cm^{-1} region, but the intercalation of the CPC in the OC–CPC caused a considerable decrease of the OH stretching frequency of water from that of the natural clay. The IOC, which was originated from the Al-PILC, shows a similar intensity band to the natural clay due to the OH

© 2008 NRC Canada

Fig. 2. Thermograms of natural clay and modified clays. (*a*) Thermal gravimetric (TG) and (*b*) differential thermal gravimetric (DTG).

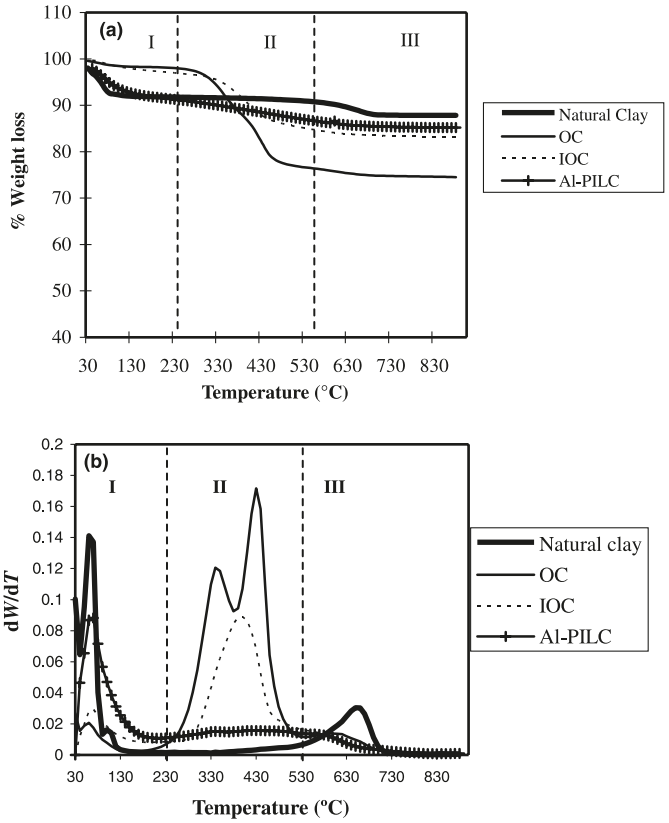

Fig. 3. XRD patterns of natural clay and modified clays: Al-PILC, OC–CPC, and IOC (Cps: intensity in counts per second).

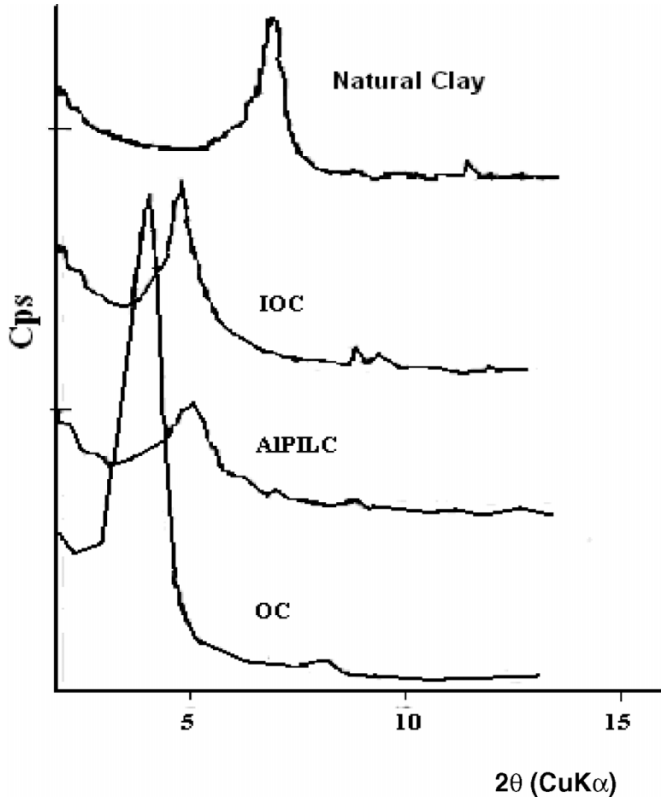

groups from the pillars. The OC–CPC and IOC showed additional bands at 2930, 2848, and 1484 cm^{-1} corresponding to asymmetrical, symmetrical stretching and asymmetric bending vibrations, respectively, of the CH_2 groups (20) of the CPC hydrocarbon chain intercalated into the interlaminar space of the original clay.

The results of the % weight loss as a function of temperature obtained in the thermogravimetric (TG) and diferential thermogravimetric (DTG) analyses for the three selected regions (Fig. 2) are displayed in Table 1. The TG curve (Fig. 2*a*) for natural clay showed the smectites' typical profile (21). An initial weight loss is observed in the 30–230 °C range, corresponding to the evaporation of water adsorbed between silicate layers. Afterwards, a pseudo-plateau occurred between 230–530 °C in which the slight weight loss is related to the removal of OH groups bound to the edges of the clay laminates. Finally, another weight loss was observed between 530 and 900 °C, which corresponds to the total dehydroxylation of the clay structure. This is clearly evident in Fig. 2*b* (DTG). Regarding the weight loss of the Al-PILC in TG, and the peak in the Al-PILC DTG profile in the first region, it corresponds to the loss of water adsorbed on the material, which, as shown in Fig. 2*b*, is lower than that for natural clay due to the lower presence of hydrated exchangeable cations in the interlayer space. In the second and third regions, there is a constant weight loss derived from the dehydroxylation of the polyhydroxycation OH groups and the total dehydroxylation of the structure. The profile of the

Table 2. First-order reflexion d_{001} and interlaminar distance (Δd) of the modified clays and natural clay.

Sample	2θ angle	d_{001} (Å)	Δd (Å)
Natural clay	7.032	12.5	3.0
Al-PILC	5.060	17.4	7.9
IOC	4.841	18.2	8.7
OC–CPC	4.033	21.9	12.4

TG and DTG curves obtained for OC–CPC and IOC shows a considerable difference compared with those of the natural clay for the second region (230–530 °C). The only difference between the natural clay and OC–CPC and IOC lies in the presence of the CPC intercalated in the clay interlaminar space, so it is reasonable to expect that the large weight loss in this region depends on the amount of intercalated CPC in OC–CPC and IOC.

From data on Table 1 and Fig. 2*b*, it can be seen that the thermal stability of the OC–CPC and IOC extends up to 230 °C, which implies that the possible regeneration of the adsorption capacity of these modified clays should be carried out at a temperature lower than 230 °C to ensure the structural integrity of both modified clays.

From the X-ray diffractograms obtained for the different samples (Fig. 3), the interlaminar distance was calculated using Bragg's equation (22) based on the position of the first-order reflection d_{001}, obtaining the basal distance (*d*) from which the montmorillonite layer thickness was subtracted (mean value 0.95 nm) (23). In Bragg's equation,

© 2008 NRC Canada

Table 3. Surface properties of the modified clays.

Sample	S_{total} (m^2/g)	S_{ext} (m^2/g)	S_{mp} (m^2/g)	V_{mp} (cm^3/g)	r_p (Å)
Natural clay	43.5	43.5	0	0	0
Al-PILC	157.2	44.6	112.6	6.29×10^{-2}	11.17
OC–CPC	13.27	13.27	0	0	0
IOC	14.5	14.5	0	0	0

Note: S_{total}: Specific area (evaluated by N_2 isotherms with BET equation); S_{ext}: external specific surface = $S_{total} - S_{mp}$; S_{mp}: microporous specific area; V_{mp}: microporous volume evaluated by ***t*** isotherm; r_p: mean pore radius.

higher values of the 2θ angle correspond to lower basal distance values (*d*). The results obtained are shown in Table 2. Figure 3 shows that the 2θ angle for natural clay is the highest, whereas OC–CPC has the lowest angle. The Al-PILC and IOC show practically the same value of 2θ angle and are located between that for the natural clay and the OC–CPC. This is due to the fact that pillaring caused an increase in the interlayer distance (Δ*d*) lower than that caused by the intercalation of CPC. Table 2 shows that OC–CPC displayed the highest interlaminar distance (12.4 Å). No differences were observed between IOC and Al-PILC in terms of interlaminar distances because the pillaring process fixed the structure in both samples, and therefore the interlayer distance did not change when the organic compound was introduced in the Al-PILC to obtain the IOC.

The surface properties of the modified clays are shown in Table 3. As it can be seen in this table, as a result of the pillaring process, the specific area (S_{total}) of natural clay increased from 43.5 m^2/g to 157.2 m^2/g in Al-PILC. On the contrary, for the OC–CPC clay, a value of 13.27 m^2/g was obtained, which was probably due to the fact that the CPC organic compound occupied available adsorption sites, thereby reducing the adsorption area. The same occurred with IOC, for which a specific area of 14.5 m^2/g was obtained. As regards of porosity, Table 3 shows that Al-PILC had a mean pore radius of 11.17 Å, so that it could be classified as a microporous material (19, 24). The natural clay sample was not porous, as well as the OC–CPC and IOC, because of the previous discussion.

Determination of adsorption isotherms

Figure 4 shows the benzene and toluene adsorption isotherms for the modified clays at 23 °C. This figure illustrates that the organoclay OC–CPC is the one that shows the highest adsorption capacity for both benzene and toluene. This was derived from the strongly organophylic (non-polar) nature that resulted from the introduction of CPC. The natural clay did not adsorb either toluene or benzene because of its hydrophylic nature. The Al-PILC sample showed a very low adsorption capacity for both benzene and toluene, given the low organophylic character developed, while IOC showed a slightly higher adsorption than Al-PILC, since it acquired a more organophylic character (lower polarity) than Al-PILC because of the additional intercalation of CPC.

Since OC–CPC was the sample that showed the highest benzene and toluene adsorption, the BET and GAB adsorption mathematical models were applied to try to understand the OC–CPC adsorption behavior.

The values obtained for the constants of BET and GAB equations are shown in Table 4. Figure 5 shows the experimental adsorption isotherms for benzene and toluene compared with the predictions of both models.

Fig. 4. Adsorption isotherms of modified clays at 23 °C for toluene and benzene. P_i/P_o: relative pressure; a: adsorption in g adsorbed material/dry solid.

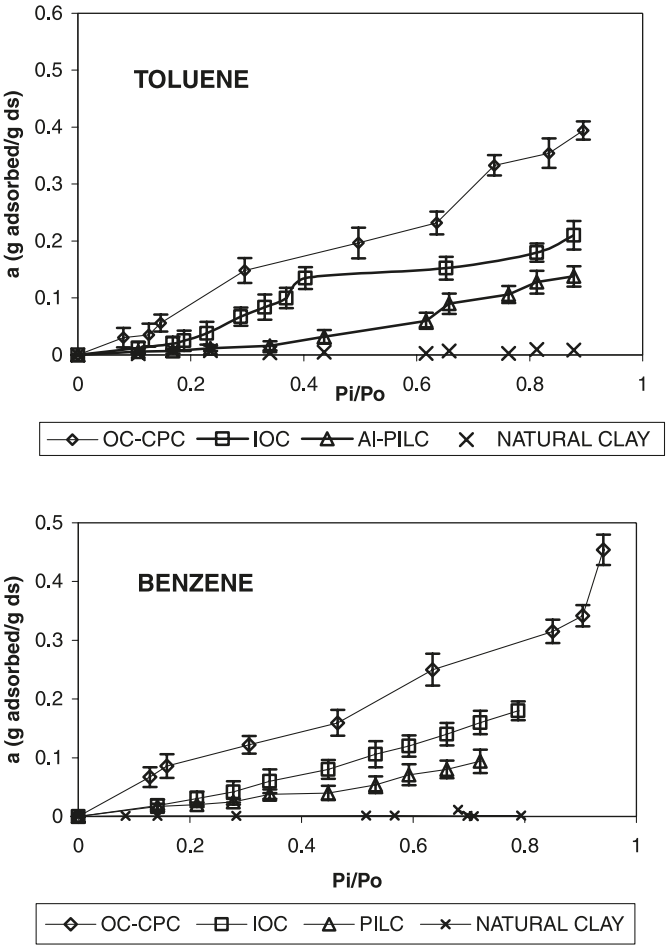

Compliance with the BET model is achieved when the energy of the adsorbate–adsorbent interaction is higher than that of the adsorbate–adsorbate interaction (high *C* values). However, the validity of the BET equation is restricted to low relative pressures, below 0.35 (Fig. 5). At high relative pressures, the BET equation overestimates the amount of adsorbed gas (as observed in Fig. 4), since it considers an infinite number of adsorbed layers (25).

The GAB model was valid in the whole relative pressure range used 0–0.9 (Fig. 5). The determination coefficient (R^2)

© 2008 NRC Canada

Table 4. Constants of BET and GAB equations obtained for adsorption of benzene and toluene on OC–CPC.

	BET (Brunauer–Emmet–Teller)			GAB (Guggenheim–Anderson–de Boer)			
System OC–CPC	C	A_m	R^2	C	A_m	K	R^2
Toluene	25.81	0.1006	0.979	23.24	0.106	0.902	0.905
Benzene	19.96	0.1321	0.941	25.97	0.106	0.804	0.911

Fig. 5. Adsorption isotherms evaluated by BET and GAB models compared with experimental values for toluene and benzene on OC–CPC at 23 °C. P_i/P_o: relative pressure; a: adsorption in g adsorbed material/dry solid.

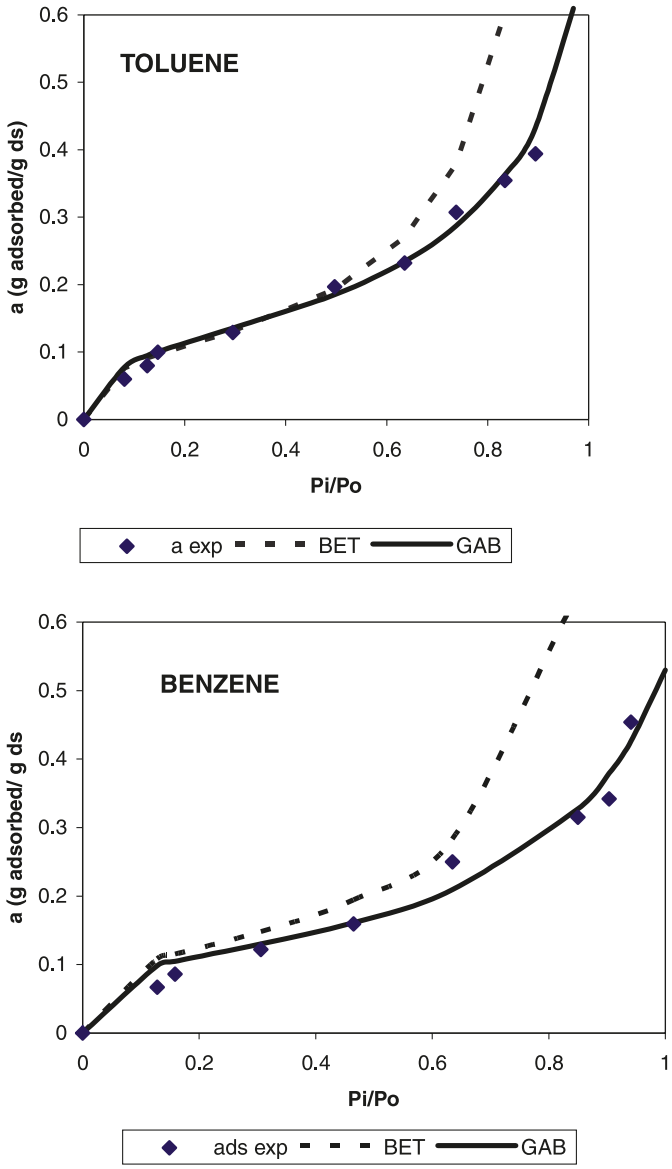

for the model was 0.905 for toluene and 0.911 for benzene. This model can be considered as an extension of the multimolecular BET model, taking into account the modified adsorbate properties in the multilayer region (adsorbate–adsorbent interaction) (26). The constants obtained for this model are also shown in Table 4, evidencing that both benzene and toluene adsorption in OC–CPC produced high C values, which represent a good adsorption capacity with the formation of polylayers. This polylayer formation may cause capillary condensation, mostly at high relative-pressure values. Constant K adopts low values (as in this case, Table 4) when molecules form polylayers accumulate at high relative pressures and may cause volumetric condensation. These results show that the adsorption of both benzene and toluene involves the formation of polylayers, resulting in capillary condensation, which can be explained by the high C values (Table 4).

The adsorption models were applied in an attempt to explain the way in which it takes place. However, considering that adsorption takes place on developed surfaces, and that OC–CPC displayed a low surface area, it is evident that another phenomenon might be occurring as well, which might correspond to partition, as reported by Lizhong and Yuhong (16). These investigators studied benzene adsorption in organobentonites, and reported that a partition phenomenon occurs preferentially in organic clays, which competes with adsorption. This supports the fact that, although the OC–CPC surface area decreases from 43.5 to 13.3 m^2/g through the surfactant intercalation process, it developed a strongly organophylic nature, which caused a strong affinity for toluene and benzene, favoring its absorption in CPC rather than its adsorption.

Polarity determination (chemical affinity) for the modified OC–CPC clay

Given that OC–CPC was the sample with the highest adsorption capacity for benzene and toluene, the polarity determination was conducted only with this modified clay. Retention times of compounds varying in polarity were determined in columns of different polarities. Retention values are a measure of polarity of a given column relative to a non-polar column (squalene).

The retention times obtained, columns used, and solvents studied are shown in Table 5. In physicochemical terms, a chemical compound is polar if it has a dipolar moment (charge separation). In GC, polar compounds are retained for longer times in a polar column compared with a non-polar one (27). Table 5 shows that OC–CPC displayed the highest retention times for non-polar or low-polarity compounds (octyne and benzene), and even higher values compared with the squalene non-polar column. Therefore, this chromatographic method revealed that the organoclay OC–CPC, with which the column was packed, possesses a strong organophylic (non-polar) nature.

Conclusions

Infrared and thermogravimetric analyses (TG and DTG) confirmed the intercalation of the aluminum pillar in Al-

© 2008 NRC Canada

Table 5. Retention times of compounds of various polarity in packed columns with OC and commercial columns of different polarities (Supelco).

	Retention times (min)				
Compounds	Carbowax 20M (P)	OV 25 (PI)	SE 30 (BP)	squalene (NP)	OC
Pentanone (PI)	0.98	0.88	0.88	7.9	18.26
Octyne (BP)	0.52	1.05	1.15	13.7	18.3
Benzene (NP)	0.84	0.82	0.82	15.97	20.5

Note: P = polar; PI = intermediate polarity; BP = low polarity; NP = nonpolar.

PILC and IOC, as well as the introduction of cetylpyridinium in the OC–CPC and IOC. The OC–CPC displayed the highest interlaminar distance (12.4 Å). Al-PILC and IOC showed almost identical interlaminar distances, due to the pillar fixing process prior to the CPC introduction in IOC. The Al-PILC showed the highest surface area, 157 m^2/g, belonging to the group of microporous materials. OC–CPC and IOC are non-porous materials. The reduction of surface area in the organoclays OC–CPC and IOC derived from the blockage of available spaces in clay laminates by the organic compound introduced.

The adsorption studies showed a great affinity of benzene and toluene in gas phase for OC–CPC due to the hydrophobic character that resulted and also to the increase in the interlaminar distance. IOC showed a lower affinity for benzene and toluene, followed by Al-PILC. Natural clay had no affinity for benzene and toluene due to its hydrophylic nature.

The model that best predicted toluene and benzene adsorption in organoclay (OC–CPC) was the GAB model through the whole range of relative pressures used. This indicates monolayer and multilayer adsorption, as well as condensation, depending on the environmental benzene and toluene relative pressure. However, given the low surface area in OC–CPC and the high retention of benzene and toluene content, it is very likely that the phenomenon of partition is also present.

Organoclays, like OC–CPC prepared in this investigation, represent a potential alternative for the adsorption of volatile organic compounds like benzene and toluene present in indoor environments. Given the hydrophobic nature of the OC–CPC, the relative humidity of water vapor in the environment would not affect its adsorption capacity as it is in the case of activated carbon, which is the most commonly used material for the adsorption of VOCs.

Acknowledgment

The financial support of the Secretaría de Estudios de Posgrado e Investigación of the Instituto Politécnico Nacional de México (SIP–IPN) is gratefully acknowledged. The authors are indebted to Dr. Jesus Palacios Gómez of the Department of Material Science (ESFM–IPN) for assistance with the X-ray diffraction analysis.

References

1. H.J. Glynn and G.W. Heinke. Environmental science and engineering. 2nd ed. Prentice Hall Inc., New York. p. 492. 1999.
2. A. Dyer and T. Gallardo. *In* Recent developments in ion exchange 2. *Edited by* P.A. Williams and M.J. Hudson. Elsevier Applied Science, London. 1990. p. 75.
3. P.B. Malla and S. Komarneni. Clays Clay Miner. **38**, 363 (1990).
4. Z. Lizhong and Z. Yuhong. Clays Clay Miner. **50**, 421 (2002).
5. R. Keeran, K.R. Srinvasan, and S. Fogler. Clays Clay Miner, **38**, 277 (1990).
6. T.S. Sheriff, C.J. Sollars, D. Montgomery, and R. Perry. Environ. Technol. Lett. **8**, 501 (1987).
7. R. Keeran, K.R. Srinivasan, and S. Fogler. Clays Clay Miner. **38**, 287 (1990).
8. L. Jiunn, M. Mortland, T. Cary, D.E. Chiou, and S. Boyd. Clays Clay Miner. **38**, 113 (1990).
9. S. Dentel, J. Bottero, and K. Khatib. Water. Res. **29**, 1273 (1995).
10. J.T. Kloprogge, L. Korbijn, and T.P.M. Koster. Appl. Clay Sci. **12**, 85 (1997).
11. W.F. Jaynes and G.F. Vance. Clays Clay Miner. **47**, 358 (1999).
12. A. Tahani, M. Karroua, P. El Farissi, H. Levitz, F. Bergaya, and L. Margulies. J. Chim. Phys. **96**, 464 (1999).
13. J. Pires, A. Carvalho, and M. B. Carbalho. Micropor. Mesopor. Mat. **43**, 277 (2001).
14. G. Kai-Uwe and S.J. Eisenreich. Environ. Sci. Technol., **30**, 2135 (1996).
15. L.Yuncong and G. Gupta. J. Hazard. Mater. **38**, 105 (1994).
16. S. López. Study of the volatile organic compounds (benzene and toluene) vapor-phase adsorption on modified clays. Ph.D. thesis (in spanish). ENCB–IPN, Mexico. 2005.
17. S. López, G. Osorio, T. Gallardo, and S. Arellano. Rev. Soc. Quim. Méx. **46**, 140 (2002).
18. M. Torkaz and J. Shabtai. Clays Clay Miner. **33**, 89 (1985).
19. M. Dubinin. Chem. Rev. **60**, 235 (1960).
20. E. Pretsch, J. Seibl, and W. Simon. Tablas para la determinación structural por métodos espectroscópicos. Springer-Verlag Iberica, Barcelona. p. 238. 1998.
21. N. El-Akkad, N. Flex, S. El-Massary, and S. Naced. Thermochim. Acta **59**, 9 (1982).
22. C. Whiston. X-ray methods. John Wiley and Sons, Chichester. 1987. p. 30.
23. D.J. Greenland and C.J.B. Mott. *In* The chemistry of soil constituents. *Edited by* D.J. Greenland and M.H.B. Hayes. John Wiley and Sons, Chichester. p. 321. 1978.
24. G. Leofanti, M. Padovan, G. Tozzola, and B. Venturelli. Catal. Today **41**, 207 (1998).
25. F. Rouquerol, J. Rouquerol, and K. Sing. Adsorption by powders and porous solids. Academic Press, New York. 1999. p. 191.
26. H. Bizot. *In* Physical properties of foods. *Edited by* R. Jowitt. Applied Science Publishers, London. 1983. p. 43.
27. R.J. Flanagan. *In* Gas chromatography. A practical approach. *Edited by* P. J. Baugh. Oxford University Press, Oxford. 1993. p. 173.

© 2008 NRC Canada

Determination of manganese and nickel in slurry sampling by graphite furnace atomic absorption spectrometry

Luciano Almeida Pereira, Simone Soares de O. Borges, Maurício Costa Castro, Waldomiro Borges Neto, Cláudia Carvalhinho Windmöller, and José Bento Borba da Silva

Abstract: Methods for the determination of manganese and nickel in lake and marine sediment slurries by graphite furnace atomic absorption spectrometry using permanent modifiers are proposed. The slurries were maintained homogeneous with air bubbling with an aquarium pump. For manganese, the best modifier was ruthenium permanent with m_o of 0.9 pg and of 1.0, 1.2, 1.5, and 1.8 pg, for Rh, without modifier, Ir, and Zr, respectively. For nickel, the best modifier was rhodium permanent with m_o of 33 pg, followed by 85, 120, 132, and 240 pg, without modifier, Zr, Ir, and Ru, respectively. After determining manganese and nickel in two certified marine sediment samples (n = 10) from NRCC, PACS-2, and MESS-2, and in the San Joaquin 2079 soil, the results agreed at the confidence level of 95% with the certified value for all analytes studied using aqueous calibration. Calibration curves of all analytes had correlation coefficients R^2 higher than 0.99. Recovery studies made in four levels for each analyte in sediments from Lake Pampulha showed acceptable values. The limits of detection (LODs) were 4.0 and 0.9 μg L^{-1} for manganese and nickel, respectively.

Key words: manganse, nickel, sediments, GF AAS.

Résumé : On a développé de nouvelles méthodes pour déterminer les quantités de manganèse et de nickel présentes dans les boues de sédiments marins et lacustres qui utilisent des modificateurs permanents et qui font appel à la spectroscopie d'absorption atomique avec fournaise de graphite. Les boues sont maintenues à l'état homogène en lui faisant barboter de l'air avec une pompe d'aquarium. Pour le manganèse, le meilleur modificateur est le ruthénium permanent avec m_o de 0,9 pg et respectivement de 1,0, 1,2, 1,5 et 1,8 pg pour le Rh, pour le cas sans modificateur, pour le Ir et le Zr. Pour le nickel, le meilleur modificateur est le rhodium permanent avec m_o de 33 pg, suivi respectivement de 85, 120, 132 et 240, pour le cas sans modificateur, pour le Zr, le Ir et le Ru. Après avoir déterminer les taux de manganèse et de nickel dans deux échantillons certifiés de sédiments marins (n = 10) provenant du NRCC, de PACS-2 et de MESS-2, et dans le sol de San Joaquim, les résultats obtenus en utilisant une calibration aqueuse sont en accord au niveau de confiance de 95% avec les valeurs certifiées pour les analytes étudiés. Les courbes de calibration des tous les analytes ont présenté des coefficients de corrélation R^2 supérieurs à 0,99. Des études de récupération faites à quatre niveaux, pour chacun des analytes dans des sédiments du Lac Pampulha ont présenté des valeurs acceptables. Les limites de détection (LDD) sont respectivement de 4,0 et 0,9 μg L^{-1} pour le manganèse et le nickel.

Mots-clés : manganèse, nickel, sédiments, spectrométrie d'absorption atomique avec fournaise de graphite.

[Traduit par la Rédaction]

Introduction

Manganese is largely distributed as particles in the earth's crust, in water, and in the atmosphere. It is an essential element for humans and animals (1). According to Flores et al. (2), the control of heavy metals in several types of samples (biological tissues, water, soil, foods, etc.) has made the degree of exposure and possible consequences for human health a relevant subject for evaluation.

Nickel is one of the five most abundant elements after iron, oxygen, magnesium, and silicon. The carcinogenicity of nickel is extensively discussed in the literature, being verified in exposed workers and in experimentation animals (3).

Water from rivers, lakes, and the sea contains metals of several origins, such as decomposition of rocks and minerals contained in soils and dry or wet deposition of particulate material. There are several possibilities for the natural origins for metals present in river, lake, and sea water. Some

Received 25 August 2007. Accepted 14 December 2007. Published on the NRC Research Press Web site at canjchem.nrc.ca on 6 March 2008.

L.A. Pereira, S.S. de O. Borges, W. Borges Neto, C.C. Windmöller, and J.B.B. da Silva.[1] Departamento de Química, Universidade Federal de Minas Gerais, Av. Antônio Carlos 6627, 31270–901 Belo Horizonte, MG, Brazil.
M.C. Castro. Setor Físico-químico – Águas tratadas e Poços, Companhia de Saneamento de Minas Gerais (COPASA), Belo Horizonte, MG, Brazil.

[1]Corresponding author (e-mail: bentojb@terra.com.br).

 doi:10.1139/V08-019 © 2008 NRC Canada

examples are weathering of rocks and minerals present in the soil, humid or dry deposition of particulate material from the atmosphere, and anthropogenic action, such as industrial waste water and domestic sewage. These metals can associate to bottom sediments through two mechanisms, with the particulate material that contains the metal deposits with over time or the metal present in the water associates directly to the sediment already deposited through more complex mechanisms. Such mechanisms depend on several factors, such as redox conditions and water pH (4).

The use of slurries to determine metals in sediments has become an attractive technique for its simplicity of sample preparation and the diversity of the means to maintain slurry homogeneity with advantages over other techniques. In addition, the relative standard deviations are compatible with graphite furnace atomic absorption spectrometry (GF AAS), electrothermal vaporization inductively coupled plasma mass spectrometry (ETV ICP MS), and flame atomic absorption spectrometry (FAAS). In spite of this, the literature reports a series of procedures for the determination of metals in sediments. Chemical modifiers were used to avoid interferences caused by the matrix in the reading stage. They can be coinjected along with the sample or applied inside the graphite tube to form a permanent layer (permanent modifiers) (5). Permanent modification is better for allowing shorter furnace programs and for minimizing contamination related problems (6, 7). The elements (or mixtures) most commonly used as permanent modifiers in GF AAS are the carbide-forming ones (W, Zr, Nb, Ta, etc.) and platinum group metals (PGMs) (Pt, Rh, Ir, Ru, etc) (5). The influences of slurry concentration, modifier amount, and the pyrolysis step on the integrated absorbance signals for Pb and Sn in sediment slurry were studied, and it was proposed to coat the integrated platform of a transversely heated graphite atomizer with tungsten carbide–rhodium as a permanent modifier (8, 9).

Ultrasound-assisted extraction was compared with slurry sampling and microwave-assisted acid digestion for the determination of Cd, Pb, and Cu in biological and sediment samples by GF AAS (10). According to the authors, the main advantage of using ultrasound-assisted extraction in comparison with slurry sampling is the doubling of tube lifetime for all analytes.

Barbosa Jr. et al. (11) described a method for the determination of arsenic in sediment and soil slurries by GF AAS, using a W–Rh permanent modifier. In an experiment designed to optimize total tin determination in aqua regia-HF extracts from sediments by GF AAS, palladium was used as chemical modifier (12).

In another work, the use of ultrasonic agitation of the slurry followed by a fast electrothermal program using an Ir–Mg modifier provides the most consistent performance in terms of precision and accuracy for arsenic determination by GF AAS (13). A zirconium–iridium coating is proposed as a permanent modifier for the determination of tin in stream sediment, oyster tissue, and total diet slurries by GF AAS (14). Campillo et al. (15) proposed procedures by slurry preparation from a solution containing 2.5%, 25%, and 50% *v*/*v* of concentrated hydrofluoric acid for chromium, vanadium, and molybdenum determinations, respectively, by GF AAS.

Table 1. Temperature program for Mn and Ni determination in slurry sediment samples by GF AAS using permanent modifiers.

Step	Temperature (°C)	Ramp (s)	Hold (s)	Ar flow rate (mL min^{-1})
1	90	5	10	250
2	140	5	10	250
3	1200[a], 600[b]	10	20	250
4[c]	2500[a,b]	0	5	0
5	2600	1	5	250
6	20	1	5	250

[a]Mn.
[b]Ni.
[c]Read in this step.

Fractionation of Cd and Pb was determined by GF AAS in the BCR (Communities Bureau of Reference of the European Commission, now the Standards, Measuring and Testing Programme) sediment reference material according to the BCR protocol. The use of palladium and magnesium nitrates modifiers in solution and use of Ru and Ir–Rh as permanent modifier were compared and showed similar results (16). Giacomelli et al. (16) studied different permanent modifiers (W, Rh, Ir, Ru, W–Rh, W–Ru, W–Ir) in the determination of arsenic, cadmium, and lead in microwave-digested environmental samples by GF AAS.

In a previous work (7), we developed methods for cadmium, chromium, and lead in marine sediments slurry samples by GF AAS using permanent modifiers.

In this work, some conditions were investigated (no modifier use, iridium, rhodium, ruthenium, and zirconium as permanent modifiers) to determine manganese and nickel in lake and marine sediments from a slurry sampling by GF AAS. The slurry was maintained homogeneous with air introduced by an aquarium pump.

Experimental

Instrumentation

All measurements were carried out with a GBC (Victoria, Australia) 906-AA atomic absorption spectrometer equipped with a graphite furnace and an autosampler PAL 3000 (GBC) with a deuterium arc lamp background correction, operated as recommended by the manufacturer. Integrated absorbance (peak area) was used exclusively for signal evaluation. Hollow cathode lamps from GBC were operated at 5.0 mA, with slit of 0.2 nm in at a wavelength of 279.5 nm for manganese (PN 41–0132–60) and at 4 mA, with a slit of 0.2 nm at 232.0 nm for nickel (PN 41–0136–00). The volume pipetted into the graphite tube was 20 μL for samples and calibration solutions. Argon (99.996%, White Martins, Belo Horizonte, MG, Brazil) was used as sheath gas. Pyrolytic graphite coated tubes without platform (GBC) were used in all studies. The treatment of the graphite tubes with the permanent modifiers was described previously, i.e., by applying 50 μL of a 1000 mg L^{-1} Ru, Ir, Zr, or Rh solution, independently for each modifier and submitting the tube to a specific temperature program (6, 7). This procedure was repeated 10 times to obtain a deposit of 500 μg of the permanent modifier. The graphite furnace temperature pro-

© 2008 NRC Canada

gram for the determination of all metals was optimized and is shown in the Table 1.

Reagents and solutions

All chemicals used were of analytical-reagent grade unless otherwise specified. Water was de-ionized in a Milli-Q system (Millipore, Bedford, Mass., USA). The nitric acid was from Vetec (Rio de Janeiro, Brazil, 022844).

The following 1000 μg mL^{-1} stock solutions were used: ruthenium (Fluka, Buchs, Switzerland, No. 84033), rhodium (Fluka, No. 83722), iridium (Fluka, No. 58195), and zirconium (Sigma-Aldrich, Milwaukee, Wis., USA, No. 27.497–6) all in 1 mol L^{-1} of hydrochloric acid. For the analytes the following 1000 mg L^{-1} solutions were used: all stock solutions for the two analytes were from titrisol Merck (Darmstad, Germany), in nitric acid (~0.5 mol L^{-1}).

Before use, all glasses were washed abundantly with solution of detergent, rinsed with water, maintained in bath with nitric acid (50% *v/v*) for a period of not less than 1 h, and then rinsed several times with deionized water. The autosampler cups were submitted to the same treatment. In all studies, the calibration was accomplished with aqueous solutions in nitric acid (0.5% *v/v*).

The limit of detection (LOD, μg L^{-1}) was calculated using the equation LOD = 3 × S_{BL}/b, where S_{BL} was the standard deviation of ten measurements of the blank (nitric acid, 0.5% v/v) and *b* is the slope of the calibration curve.

The following certified samples were analysed: PACS-S and MESS-2 from National Research of Council of Canada (NRCC) and San Joaquin Soil 2709 from National Institute of Standard and Tech nology (NIST, USA).

Procedure

Samples of lake water (Lake Pampulha, MG, Brazil) were collected with a spatula of polyethylene and transferred to a polyethylene bottle, both decontaminated with nitric acid. Once taken to the laboratory, they were dried at 60 °C overnight, grinded in agate grail, passed consecutively in two screens until particles with grain size smaller than 50 μm were obtained. About 10 to 50 mg of the samples were weighted directly in the autosampler cups and added to a solution of nitric acid (3% *v/v*) and H_2O_2 (10%) until 1.0 g of solution was obtained. The suspension was maintained homogeneous with aid of air introduced by a capillary, produced by an aquarium pump (Big Air Super Pump A 230) (7). The capillary tube was placed into the bottom of the autosampler cups so that the bubbles were collected along with the sample. No problems caused by the introduction of air through the capillary tip of the autosampler were observed. This fact could be proved by the accuracy and precision of the results. For the certified materials, the preparation was made by using an appropriate mass of material and adding to the same solution already described to obtain a sample of 1.0 g.

Results and discussion

Thermal behavior of Mn and Ni in slurry sediments

By comparing the thermal behavior of each element submitted to the furnace temperature program, pyrolysis and atomization temperature curves were obtained for each analyte in sediment slurries using no modifier, iridium, rhodium, ruthenium, and zirconium (independently, 500 μg of each).

Fig. 1. Pyrolysis and atomization temperatures curve for 1 ng of Mn in slurry sediment with different modifiers: Zr (□), Zr′ (●) Rh (△), Rh′ (▽), Ru (◇), Ru′ (◀), Ir (▶), Ir′ (○), no mod (★), no mod′ (☆).

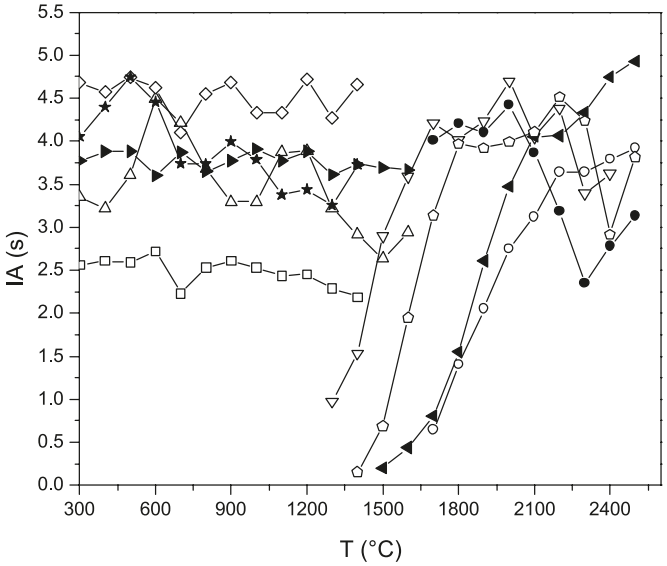

Pyrolysis and atomization temperature curves for manganese in slurry sediment samples are shown in Fig. 1. According to this figure, the best modifier for Mn is ruthenium permanent, with the best pyrolysis and atomization temperatures, respectively, of 1200 and 2500 °C, a characteristic mass of 0.9 pg and of 1.0, 1.2, 1.5, and 1.8 pg, respectively, for Rh, without modifier, Ir, and Zr. For the optimum conditions, the absorption pulses were symmetric, returning to the baseline in 2 s with a corrected background (about 0.1) and were similar to the peaks obtained for the calibration solutions. In the work of Tsalev and Slaveykova (17) on the behavior of ruthenium, rhodium, and palladium, the maximum pyrolysis temperatures for manganese were 1000, 600, and 600 °C for modifiers Ir, Rh, and Zr.

For nickel (Fig. 2), the best modifier was rhodium permanent with m_o of 33 pg, followed by 85, 120, 132, and 240 pg without modifier, Zr, Ir, and Ru, respectively. For this condition, the best pyrolysis and atomization temperatures were 600 and 2400 °C, respectively. For this condition the peak is also very symmetric and with corrected background, about 0.1 integrated absorbance s^{-1}.

Qi et al. (18) also have worked with Rh as a modifier and observed that chlorides of Pt, Rh, and Pd increased sensitivity for nickel only 1.02-fold to 1.09-fold. For ammonium vanadate, this increase was 1.52-fold and is the reason as why this modifier was used for the determination of nickel in plant materials.

Analytical figures of merit

Calibration curves with aqueous solutions were constructed following the procedure described in the Experimental section, applying the temperature programs given in Table 1. Before those curves for aqueous calibration and standard addition were built, similarities were observed for

© 2008 NRC Canada

Table 2. Analytical characteristics for the determination of Mn and Ni in sediment samples by GF AAS using permanent modifiers.

Analyte	Modifier (500 µg)	mo* (pg)	mo (pg) (recommended)	LOD (µg L^{-1})	RSD (%) (n = 10)	R^2	Calibration range (µg L^{-1})
Mn	Ru	0.9	1.0	4.0	< 7.0	0.99978	0.0–100.0
Ni	Rh	33	20	0.9	< 8.8	0.99928	0.0–50.0

Table 3. Comparison between certified and determined values (µg L^{-1}) by GF AAS with the proposed methodologies.

	PACS-2		MESS-2		SAN JOAQUIN SOIL 2709	
Analyte	Certified	Determined	Certified	Determined	Certified	Determined
Mn	49.3±1.8	50.5±0.9	39.5±2.3	41.5±1.2	560±26	538±17
Ni	365±21	357±11	440±19	444±16	79±7	88±5

Fig. 2. Pyrolysis and atomization temperatures curve for 10 ng of Ni in slurry sediment with different modifiers: Ir (▫), Ir′ (●), Rh (▲), Rh′ (▼), Zr (◆), Zr′ (◀), Ru (▶), Ru′ (◇), no mod (★), no mod′ (☆).

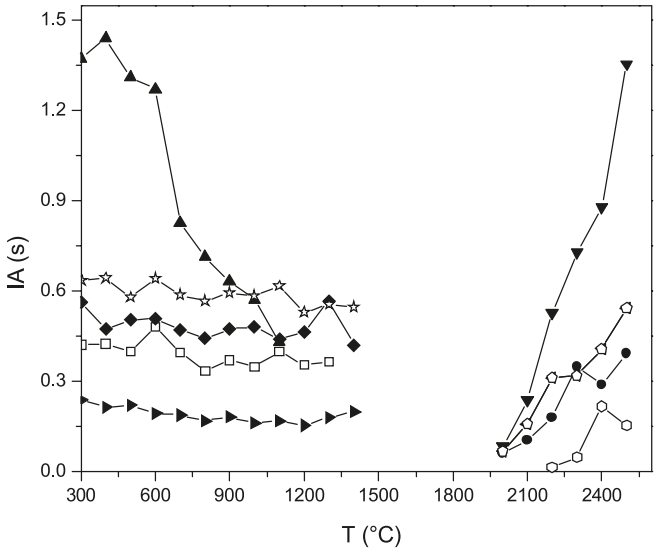

the two analytes, and this way the calibration was accomplished with aqueous solutions. The analytical characteristics for the determination of all analytes are shown in the Table 2.

The calibration curves of all analytes had R^2 greater than 0.99 and were made employing the temperature programs optimized and presented in Table 1. The limits of detection (LODs) were satisfactory for GF AAS. The obtained RSD for all analytes were compatible for slurry GF AAS analysis, showing that the aquarium pump is appropriated for maintaining the stability of the slurry.

Table 3 shows the results obtained with the proposed methodologies for the two analytes (P > 0.05). All values determined were in agreement with the certified values, using aqueous calibration. Table 4 shows the recoveries of the two analytes in real lake sediments (Lake Pampulha, Belo Horizonte, MG, Brazil) in four levels of spike. As can be observed in Table 4, the recoveries showed acceptable values between 100.2% and 110.2% for manganese and 90.62% to 108.14% for nickel (19).

Table 4. Recovery studies of spiked Lake Pampulha sediments.

Expected concentration (µg L^{-1})	Recovery (%)	RSD (n = 5)
Mn		
5	100.2	1.41
7	104.8	1.68
8.5	109.6	1.39
10	110.2	1.88
Ni		
25	108.14	1.32
50	101.68	4.14
75	97.63	5.08
100	90.62	3.36

The lifetime of the graphite tubes was around 600 cycles of atomization. No significant changes in sensitivity were observed throughout the lifetime of the graphite tube.

Conclusions

The determination of manganese and nickel in certified sediment samples can be performed by GF AAS as slurries, using permanent modifiers. For manganese the best modifier was ruthenium and for nickel the best modifier was rhodium. The methodologies applied to the analysis of certified marine sediment samples (PACS-2 and MESS-2) and soil samples (San Joaquin 2079) showed results in agreement with the certified values (with a level of confidence higher than 95%) for all analytes, using aqueous calibration. Recovery studies in the spiked Lake Pampulha sediments showed acceptable values. The limits of detection were 4.0 and 0.9 µg L^{-1} for manganese and nickel, respectively.

Acknowledgements

The authors are thankful to Conselho Nacional de Pesquisas e Desenvolvimento Tecnológico (CNPq), Fundação de Amparo a Pesquisa de Minas Gerais (FAPEMIG), and Companhia de Saneamento do Estado de Minas Gerais (COPASA). JBBS is grateful to CNPq for research grant.

References

1. H.A. Waldron. *In* Metals in the environment. *Edited by* K. Kadish, K.M. Smith, and R. Guilard. Academic Press, New York. 1980.

© 2008 NRC Canada

2. E.M.M. Flores, C.F.L. Bittencourt, V. Laporta, and J.S. Barin. Pharm. Technol. **24**, 9 (2000).
3. F.A. Azevedo and A.M.M. Chasin. Metais: Gerenciamento da Toxicidade. Atheneu. São Paulo, Brazil. 2003. p. 554.
4. M. Bernhard and P.J. Sadler. The importance of chemical speciation in environmental processes. Springer-Verlag, Berlin. 1984.
5. B. Welz and M. Sperling. Atomic absorption spectrometry. 3rd ed. Wiley-VHC, Germany. 1999.
6. J.B.B. Silva, M.A.M. Silva, A.J. Curtius, and B. Welz. J. Anal. At. Spectrom. **14**, 1737 (1999).
7. L.A. Pereira, I. Amorim, and J.B.B. Silva. Talanta, **68**, 771 (2006).
8. V.I. Slaveykova and M. Hoenig. Analyst, **122**, 337 (1997).
9. E.C. Lima, F. Barbosa Jr., and F.J. Krug. J. Anal. At. Spectrom. **14**, 913 (1999).
10. E.C. Lima, F. Barbosa Jr., F.J. Krug, M.M. Silva, and M.G.R. Vale. J. Anal. At. Spectrom. **15**, 995 (2000).
11. F. Barbosa Jr., E.C. Lima, and F.J. Krug. Analyst, **125**, 2079 (2000).
12. I. Arambarri, R. Garcia, and E. Millán. Analyst, **125**, 2084 (2000).
13. E. Vassileva, H. Baeten, and M. Hoenig. J. Anal. Chem. **369**, 159 (2001).
14. N.N. Meeravali and S.J. Kumar. J. Anal. At. Spectrom. **17**, 704 (2002).
15. N. Campillo, I. López-Garcia, P. Viñas, I. Arnau-Jerez, and M. Hernández-Córdoba. J. Anal. At. Spectrom. **17**, 1429 (2002).
16. M.B.O. Giacomelli, M.C. Lima, L.F. Dias, B. Welz, and A.J. Curtius. J. Anal. At. Spectrom.**17**, 1339 (2002).
17. D.L. Tsalev and D.I. Slaveykova. Spectrosc. Lett. **25**, 221 (1992).
18. W. Qi, K. Furuya, and Y. Gohshi. Bunseki Kagaku, **36**, 436 (1987).
19. ISO/AOAC/IUPAC Harmonised Guidelines for the Use of Recovery Information in Analytical Measurement. *Edited by* Michael Thompson, Steven L.R. Ellison, Ales Fajgelj, Paul Willetts and Roger Wood. Pure Appl. Chem. **71**, 337 (1999).

© 2008 NRC Canada

Zinc oxide-tetrabutylammonium bromide tandem as a highly efficient, green, and reusable catalyst for the Michael addition of pyrimidine and purine nucleobases to α,β-unsaturated esters under solvent-free conditions

Abdolkarim Zare, Alireza Hasaninejad, Mohammad Hassan Beyzavi, Abolfath Parhami, Ahmad Reza Moosavi Zare, Ali Khalafi-Nezhad, and Hashem Sharghi

Abstract: An efficient procedure for the synthesis of carboacyclic nucleosides via microwave-assisted Michael addition of pyrimidine and purine nucleobases to α,β-unsaturated esters in the presence of catalytic amounts of zinc oxide (ZnO) and tetrabutylammonium bromide (TBAB) is described. The reactions proceed rapidly in good to excellent yields.

Key words: ZnO–TBAB, green chemistry, Michael addition, nucleobase, solvent-free, microwave.

Résumé : On a mis au point ne méthode efficace de réaliser la synthèse de nucléosides carboacycliques en faisant appel des additions de Michael assistées par les microondes de nucléobases purines et pyrimidines sur des esters α,β-insaturés en présence d'une quantité catalytique d'oxyde de zinc (ZnO) et de bromure de tétrabutylammonium (BTBA). Les réactions se produisent rapidement avec des rendements allant de bons à excellents.

Mots-clés : oxyde de zinc–bromure de tétrabutylammonium, chimie verte, addition de Michael, nucléobase, sans solvant, microonde.

[Traduit par la Rédaction]

Introduction

N-substituted pyrimidine and purine nucleobases have attracted much interest because of their potential use as antineoplastic (1), antiviral (1), and anticancer agents (2). Over the years, extensive efforts have been directed toward the synthesis of new classes of *N*-substituted nucleobases that brought about nucleoside subgroups with potent biological activities, including acyclic (3), carboacyclic (4), carbocyclic (5), aza (6), and thionucleosides (7). These compounds are usually prepared by *N*-alkylation of nucleobases with alkylating agents (8). Carboacyclic nucleosides can also be synthesized via Michael addition of nucleobases to electrophilic alkenes (9). This reaction normally requires a strong base to activate nucleobases. For this purpose, bases such as [bmim]OH (9*a*), 1,4-diazabicyclo[2,2,2]octane (DABCO) (9*b*), NaOEt (9*c*), K_2CO_3 (9*d*, 9*e*), and *t*-BuOK (9*f*) have been used. Moreover, an enzyme can also facilitate this transformation (9*g*).

The methods established for Michael addition of nucleobases to electrophilic alkenes are associated with one or more of the following drawbacks: (*i*) the use of solvents such as DMF or DMSO in which the workup of the reaction is not only cumbersome but also the green aspect of the reaction is annihilated by using DMF, (*ii*) long reaction times, (*iii*) low reaction yields and selectivity, (*iv*) the use of only unsubstituted electrophilic alkenes, and (*v*) the use of stoichiometric amounts of base or reagent.

Recently, mineral oxides have proved to be useful to chemists in the laboratory and industry because of the good activation of adsorbed compounds and reaction rate enhancement, selectivity, easier workup, recyclability of the supports, and the eco-friendly reaction conditions (10, 11). Zinc oxide (ZnO) is certainly one of the most interesting of these oxides that has been applied in different organic transformations (11). The coupling of microwave irradiation with the use of catalysts or mineral-supported reagents provides chemical processes with special attributes, such as enhanced reaction rates, higher yields, better selectivity, and improved ease of manipulation (12).

Having the above facts in mind and also in extension of our previous studies on aza-Michael reactions (9*b*, 10*a*, 11*a*,

Received 23 June 2007. Accepted 24 January 2008. Published on the NRC Research Press Web site at canjchem.nrc.ca on 10 March 2008.

A. Zare.[1] Department of Chemistry, Payame Nour University of Bushehr, Bushehr 1698, Iran.
A. Hasaninejad.[1] Department of Chemistry, Faculty of Sciences, Persian Gulf University, Bushehr 75169, Iran.
M.H. Beyzavi, A. Parhami, A.R. Moosavi Zare, A. Khalafi-Nezhad, and H. Sharghi. Department of Chemistry, College of Sciences, Shiraz University, Shiraz 71454, Iran.

[1]Corresponding authors (e-mail: abdolkarimzare@yahoo.com; ahassaninejad@yahoo.com).

 doi:10.1139/V08-022 © 2008 NRC Canada

Scheme 1. Michael addition of pyrimidine nucleobases to α,β-unsaturated esters.

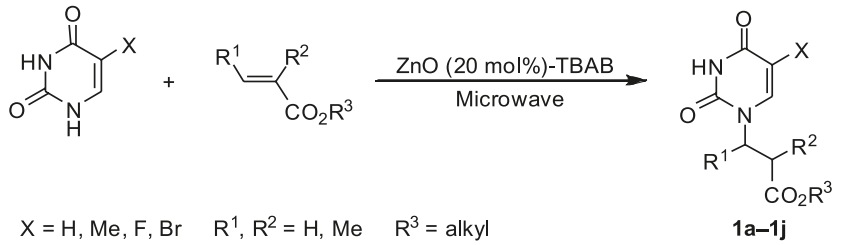

Scheme 2. Michael addition of *N*-(2-oxo-1,2-dihydropyrimidin-4-yl)acetamide to ethyl acrylate.

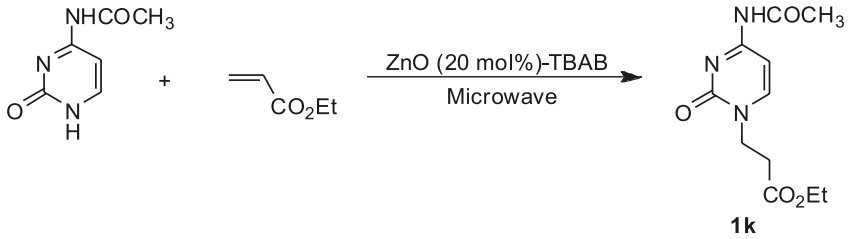

Scheme 3. Michael addition of purine nucleobase adenine to α,β-unsaturated esters.

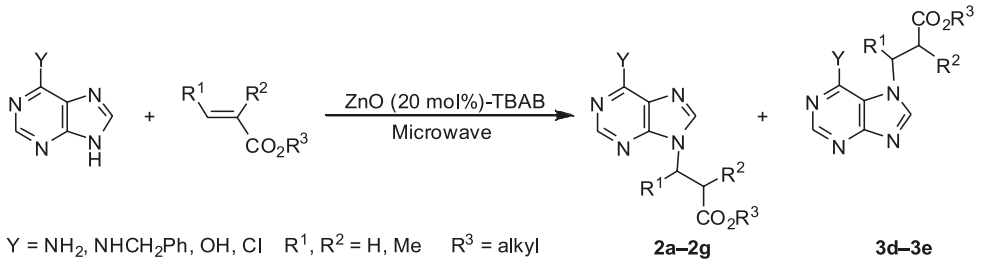

11*b*, 13), solvent-free organic synthesis (8*a*, 9*b*, 13, 14), and nucleoside derivatives synthesis (8*a*, 8*b*, 9*b*, 14*c*, 14*d*, 14*h*, 15), we report herein a clean, facile, and rapid solventless method for Michael addition of pyrimidine and purine nucleobases to α,β-unsaturated esters in the presence of catalytic amount of ZnO–TBAB under microwave conditions (Schemes 1–3).

Results and discussion

To optimize reaction conditions, the reaction of uracil with *n*-butyl acrylate was studied as a model reaction to provide compound **1b**. At first, the catalytic effect of various catalysts in the presence of TBAB was examined under microwave conditions. The results are summarized in Table 1. As shown in Table 1, the best results were obtained when zinc oxide (20 mol%) was used. To understand the role of TBAB in the reaction, Michael addition of uracil to *n*-butyl acrylate was examined in the absence of TBAB under 200 W of microwave power (max. 100 °C). These conditions afforded the product in 39% yield after 40 min (Table 1, entry 8). Increasing the reaction time, the temperature, and the microwave power did not improve the reaction yield. Thus, the presence of TBAB in the reaction media is critically significant. In general, TBAB melts at 100 °C and creates a homogeneous reaction media whose resemblance is not far from that of ionic liquids (8*a*, 9*b*, 11*a*, 13). Moreover, this quaternary ammonium salt absorbs the microwave irradiation as well as generates in situ heat and increases the temperature

Table 1. The influence of different catalysts on Michael addition of uracil to *n*-butyl acrylate promoted by microwave irradiation (200 W, max. 100 °C) under solvent-free conditions.

Entry	Catalyst (mol%)	Time (min)	Yield (%)[a]
1	ZnO (10)-TBAB (20)	30	81
2	ZnO (20)-TBAB (20)	25	93
3	ZnO (50)-TBAB (20)	20	76
4	ZnO (100)-TBAB (20)	15	62
5	CaO (20)-TBAB (20)	30	31
6	MgO (20)-TBAB (20)	30	16
7	Basic Al_2O_3 (20)-TBAB (20)	25	40
8	ZnO (20)	40	39
9	TBAB (20)	25	64

[a]Isolated yield.

higher than its melting point (100–103 °C) (8*a*, 9*b*, 11*a*, 13). TBAB may also act as a phase-transfer catalyst in our reaction (12*a*, 16). The model reaction was also tested in the presence of only TBAB. This reaction afforded the product in 64% within 25 min (Table 1, entry 9). Thus, ZnO and TBAB did not efficiently catalyze the Michael reaction separately; however, these catalysts together (ZnO–TBAB) act as an efficient catalytic system.

In another study, the model reaction was tested in several solvents to compare the efficiency and capacity of the solvent-free conditions with respect to solution conditions.

© 2008 NRC Canada

Table 2. Comparative synthesis of compound **1b** using solution versus the solvent-free conditions in microwave conditions (200 W, max. 100 °C).

Entry	Solvent	Time (min)	Yield (%)[a]
1	DMSO	35	82
2	DMF	35	77
3	HMPTA	35	42
4	*o*-Xylene	35	23
5	Solvent-free	25	93

[a]Isolated yield.

Thus, a mixture of uracil (2 mmol), ZnO (0.4 mmol), TBAB (0.4 mmol), and *n*-butyl acrylate (2.2 mmol) was irradiated in a microwave oven (200 W, max. 100 °C) in different solvents (10 mL) (Table 2). As is clear from Table 2, lower yields and longer reaction times were obtained in solution conditions. Therefore, the solvent-free method is more efficient.

The capability and efficiency of the microwave heating compared to conventional heating on the Michael reaction was also investigated. For this purpose, compound **1b** was prepared via Michael reaction between uracil and *n*-butyl acrylate in the presence of ZnO (20 mol%) and TBAB (20 mol%) under thermal conditions (100 °C). Using these conditions, the Michael adduct (**1b**) was isolated in 71% yield after 150 min. The reaction yield did not improve by increasing the reaction time and the temperature. Therefore, microwave irradiation is an essential factor to promote this reaction.

To establish the generality and applicability of this method, some pyrimidine and purine nucleobases were reacted with structurally diverse α,β-unsaturated esters to furnish the corresponding Michael adducts in good to high yields and short reaction times. The results are displayed in Table 3.

The presence of substituents (Me, F, and Br) on the 5-position of pyrimidine nucleobases had no significant effect on results of the reaction (Table 3, entries 3–5). The structural influence of α,β-unsaturated esters on the reaction was also investigated. Lower yields of products were obtained when both pyrimidine or purine nucleobases were introduced to sterically hindered α,β-unsaturated esters (Table 3, entries 8–10, 17, and 18). In these cases, prolonging the reaction times or increasing the microwave power or the temperature had no effect on the efficiency of the reaction. The bulkiness of alkoxy group (OR) affected the results of the Michael reaction. The yields decreased and the reaction times increased when nucleobase was added to esters possessing bulky alkoxy groups (Table 3, entries 6 and 7). Michael reaction of *N*-(2-oxo-1,2-dihydropyrimidin-4-yl)acetamide was also efficiently achieved (Scheme 2 and Table 3, entry 11).

Interestingly, in our method, pyrimidine nucleobases were regioselectively alkylated at the N1 positions. In these cases, N1,N3-dialkylated pyrimidines were obtained in trace yields. Moreover, pyrimidine nucleobases were not alkylated at the O-positions. Among the purine nucleobases, adenine and *N*-benzyl-9*H*-purin-6-amine were alkylated exclusively at the N9 positions; however, Michael reaction of hypoxanthine and 6-chloropurine afforded N7-adducts together with the N9 products in low yields (Table 3, entries 15 and 16). The sites of N-addition were indicated by ^{1}H and ^{13}C NMR spectral analysis. Several reports from the literature also confirmed these sites of N-addition (8*a*, 9*b*, 17).

Ease of recycling is a useful feature of zinc oxide; for the reaction of uracil with *n*-butyl acrylate no significant loss of product yields was observed when ZnO was used after recycling five times.

In summary, we have introduced an efficient new method for the preparation of carboacyclic nucleosides as biologically interesting compounds via microwave-assisted Michael addition of nucleobases to α,β-unsaturated esters. The advantages of this method are generality, high yields, short reaction times, simplicity, low cost, and matches with green chemistry protocols.

Experimental

All chemicals were purchased from Merck or Fluka chemical companies. ZnO powder (GR for analysis, 99%) from Merck company was used as a catalyst for all reactions. All known compounds were identified by comparison of their melting points and ^{1}H NMR data with the authentic samples. All reactions were carried out using laboratory microwave oven (MW 3000, Landgraf Company, Germany). IR spectra were run on a Shimadzu FTIR-8300 spectrophotometer, ν_{max} in cm^{-1}. The ^{1}H NMR (250 MHz) and ^{13}C NMR (62.5 MHz) were run on a Bruker Avanced DPX-250, FT-NMR spectrometer. Mass spectra were recorded on a Shimadzu GC MS-QP 1000 EX apparatus. Microanalyses were performed on a PerkinElmer 240-B microanalyzer. Melting points were recorded on a Büchi B-545 apparatus in open capillary tubes.

General procedure for the synthesis of compound 1b

To a well ground mixture of uracil (0.224 g, 2 mmol), ZnO (0.033 g, 0.4 mmol), and TBAB (0.129 g, 0.4 mmol) in a microwave vessel was added *n*-butyl acrylate (0.282 g, 2.2 mmol) and mixed carefully with a small rod. The mixture was irradiated in a microwave oven for the powers, the temperatures, and the times reported in Table 3. Afterward, the reaction mixture was cooled to room temperature and suspended in EtOAc (50 mL), filtered, and the filtrate was washed with water (2 × 50 mL) and dried with $MgSO_4$. The solvent was evaporated and the crude product was purified by column chromatography on silica gel eluted with EtOAc–*n*-hexane (2:1). After isolation of the product, the remainder ZnO was reused.

Ethyl 3-(2,4-dioxo-3,4-dihydropyrimidin-1(2*H*)-yl)propanoate (1a)

Column chromathography on silica gel and eluting with EtOAc–*n*-hexane (2:1) gave a colorless solid. Isolated yield: 0.388 g (91%); mp 77–79 °C (lit. (9*b*) value mp 78–80 °C). ^{1}H NMR ($CDCl_3$, ppm) δ: 1.25 (t, 3H, *J* = 7.0 Hz, CH_3), 2.74 (t, 2H, *J* = 6.0 Hz, O = CCH_2), 3.85 (t, 2H *J* = 6.0 Hz, NCH_2), 4.11 (q, 2H, *J* = 7.0 Hz, OCH_2), 5.64 (d, 1H, *J* = 7.9 Hz, H_5 of uracil), 7.26 (d, 1H, J = 7.9 Hz, H_6 of uracil), 10.19 (s, 1H, *NH*).

© 2008 NRC Canada

Table 3. Michael addition of pyrimidine and purine nucleobases to α,β-unsaturated esters in the presence of ZnO (20 mol%) and TBAB (20 mol%) under microwave irradiation.

Entry	Nucleobase	Ester	Product	MW Power (W)	Temperature (°C)	Time (min)	Yield[a] (%)
1		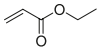	**1a**	200	100	25	91
2		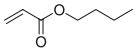	**1b**	200	100	25	93
3		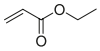	**1c**	200	100	25	89
4		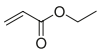	**1d**	200	100	25	91
5		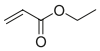	**1e**	200	100	25	90
6		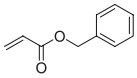	**1f**	200	100	30	86
7	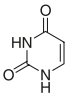	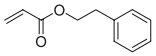	**1g**	200	100	30	84
8		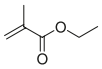	**1h**	300	130	20	48
9		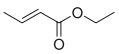	**1i**	400	130	15	41
10		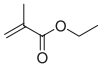	**1j**	300	130	20	45
11	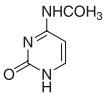	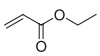	**1k**	200	100	25	83

Butyl 3-(2,4-dioxo-3,4-dihydropyrimidin-1(2*H*)-yl)propanoate (1b)

Column chromathography on silica gel and eluting with EtOAc–*n*-hexane (2:1) gave a colorless solid. Isolated yield: 0.447 g (93%); mp 61–63 °C (lit. (9*b*) value mp 63–65 °C).[1]H NMR ($CDCl_3$, ppm) δ: 0.92 (t, 3H, *J* = 6.8 Hz, CH_3), 1.35 (m, 2H, CH_3CH_2), 1.56 (m, 2H, $CH_3CH_2CH_2$), 2.72 (t, 2H, *J* = 5.9 Hz, O=CCH_2), 3.80 (t, 2H, *J* = 5.9 Hz, NCH_2), 4.09 (t, 2H, *J* = 6.9 Hz, OCH_2), 5.66 (d, 1H, *J* = 7.9 Hz, H_5 of uracil), 7.25 (d, 1H, *J* = 7.9 Hz, H_6 of uracil), 10.22 (s, 1H, *NH*).

Ethyl 3-(5-methyl-2,4-dioxo-3,4-dihydropyrimidin-1(2*H*)-yl)propanoate (1c)

Column chromathography on silica gel and eluting with EtOAc–*n*-hexane (2:1) gave a colorless solid. Isolated yield: 0.403 g (89%); mp 146–148 °C (lit. (9*g*) value mp 149–150 °C). [1]H NMR ($CDCl_3$, ppm) δ: 1.24 (t, 3H, *J* = 7.1 Hz,

© 2008 NRC Canada

Table 3 (*concluded*).

Entry	Nucleobase	Ester	Product	MW Power (W)	Temperature (°C)	Time (min)	Yield[a] (%)
12[b]		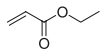	**2a**	300	100	35	70
13		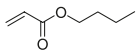	**2b**	300	140	20	74
14		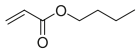	**2c**	300	120	20	89
15[c]		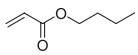	**2d** **3d**	300	120	20	74 18
16[c]		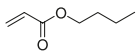	**2e** **3e**	300	120	15	67 23
17		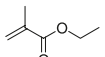	**2f**	400	140	15	37
18		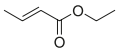	**2g**	400	140	20	29

[a]Isolated yield.
[b]This reaction was carried out at 100 °C because of the lower boiling point of ethyl acrylate.
[c]In this reaction, both N9 and N7 isomers were produced.

CH_2CH_3), 1.88 (s, 3H, CH_3), 2.75 (t, 2H, J = 6.0 Hz, O=CCH_2), 3.83 (t, 2H, J = 6.0 Hz, NCH_2), 4.12 (q, 2H, J = 7.1 Hz, OCH_2), 7.25 (s, 1H, H_6 of thymine), 10.19 (s, 1H, *NH*).

Ethyl 3-(5-fluoro-2,4-dioxo-3,4-dihydropyrimidin-1(2*H*)-yl)propanoate (1d)

Column chromathography on silica gel and eluting with EtOAc–*n*-hexane (2:1) gave a pale yellow solid. Isolated yield: 0.417 g (91%); mp 123–125 °C (lit. (9*g*) value mp 124–126 °C). ^{1}H NMR ($CDCl_3$, ppm) δ: 1.22 (t, 3H, J = 7.1 Hz, CH_3), 2.79 (t, 2H, J = 5.7 Hz, O=CCH_2), 3.80 (t, 2H, J = 5.7 Hz, NCH_2), 4.10 (q, 2H, J = 7.1 Hz, OCH_2), 7.28 (s, 1H, J = 6.7 Hz, H_6 of 5-fluorouracil), 10.25 (s, 1H, *NH*).

Ethyl 3-(5-bromo-2,4-dioxo-3,4-dihydropyrimidin-1(2*H*)-yl)propanoate (1e)

Column chromathography on silica gel and eluting with EtOAc–*n*-hexane (2:1) gave a pale yellow solid. Isolated yield: 0.522 g (90%); mp 140–145 °C (dec.) [(lit. (9*g*) value mp 143–150 °C (dec.)]. ^{1}H NMR ($CDCl_3$, ppm) δ: 1.25 (t, 3H, J = 7.0 Hz, CH_3), 2.79 (t, 2H, J = 5.8 Hz, O=CCH_2), 3.82 (t, 2H, J = 5.8 Hz, NCH_2), 4.12 (q, 2H, J = 7.0 Hz, OCH_2), 7.61 (s, 1H, H_6 of 5-bromouracil), 10.27 (s, 1H, *NH*).

Benzyl 3-(2,4-dioxo-3,4-dihydropyrimidin-1(2*H*)-yl)propanoate (1f)

Column chromathography on silica gel and eluting with EtOAc–*n*-hexane (2:1) gave a pale yellow buff. Isolated yield: 0.470 g (86%). IR (KBr, cm^{-1}): 3157, 3069, 2962, 1732, 1682, 1644. ^{1}H NMR ($CDCl_3$, ppm) δ: 2.73 (t, 2H, J = 5.9 Hz, O=CCH_2), 3.77 (t, 2H, J = 5.9 Hz, NCH_2), 4.89 (s, 2H, OCH_2), 5.56 (d, 1H, J = 7.9 Hz, H_5 of uracil), 7.09–7.23 (complex, 6H, H_1–H_5 of phenyl group and H_6 of uracil), 10.32 (br, 1H, *NH*). ^{13}C NMR ($CDCl_3$) δ: 37.6, 45.3, 66.5, 101.4, 127.9, 128.8, 129.7, 132.0, 144.8, 151.3, 163.3, 171.5. MS *m/z*: 274 [M$^+$]. Anal. calcd. for $C_{14}H_{14}N_2O_4$: C 61.31, H 5.14, N 10.21; found: C 61.45, H 5.30, N 10.09.

Phenethyl 3-(2,4-dioxo-3,4-dihydropyrimidin-1(2*H*)-yl)propanoate (1g)

Column chromathography on silica gel and eluting with EtOAc–*n*-hexane (2:1) gave a pale yellow buff. Isolated

© 2008 NRC Canada

yield: 0.483 g (84%). IR (KBr, cm^{-1}): 3165, 3058, 2956, 1734, 1686, 1651. ^1H NMR ($CDCl_3$, ppm) δ: 2.71 (t, 2H, J = 5.8 Hz, O=CCH_2), 2.86 (t, 2H, J = 7.0 Hz, PhCH_2), 3.81 (t, 2H, J = 5.8 Hz, NCH_2), 4.32 (t, 2H, J = 7.0 Hz, OCH_2), 5.60 (d, 1H, J = 7.9 Hz, H_5 of uracil), 7.11–7.25 (complex, 6H, H_1–H_5 of phenyl group and H_6 of uracil), 10.26 (br, 1H, *NH*). ^{13}C NMR ($CDCl_3$) δ: 34.7, 36.2, 46.4, 65.0, 102.1, 126.3, 128.1, 128.8, 131.9, 145.3, 151.0, 164.1, 170.3. MS *m*/*z*: 288 [M^+]. Anal. calcd. for $C_{15}H_{16}N_2O_4$: C 62.49, H 5.59, N 9.72; found: C 62.40, H 5.72, N 9.87.

Ethyl 3-(2,4-dioxo-3,4-dihydropyrimidin-1(2*H*)-yl)-2-methylpropanoate (1h)

Column chromathography on silica gel and eluting with EtOAc–*n*-hexane (2:1) gave a pale yellow oil (lit. (9*b*) oil). Isolated yield: 0.219 g (48%).^1H NMR ($CDCl_3$, ppm) δ: 1.16–1.21 (complex, 6H, CH_2CH_3 and $CHCH_3$), 2.95 (m, 1H, O=C*CH*), 3.64 (m, 1H, one H of NCH_2), 3.82 (m, 1H, one H of NCH_2), 4.12 (q, 2H, J = 7.0 Hz, OCH_2), 5.63 (d, 1H, J = 7.9 Hz, H_5 of uracil), 7.22 (d, 1H, J = 7.9 Hz, H_6 of uracil), 10.22 (s, 1H, NH),

Ethyl 3-(2,4-dioxo-3,4-dihydropyrimidin-1(2*H*)-yl)butanoate (1i)

Column chromathography on silica gel and eluting with EtOAc–*n*-hexane (2:1) gave a pale yellow solid. Isolated yield: 0.184 g (41%); mp 115–117 °C (lit. (9*b*) vaue mp 116–118 °C).^1H NMR ($CDCl_3$, ppm) δ: 1.22 (t, 3H, J = 7.0 Hz, CH_2CH_3), 1.39 (d, 3H, J = 6.9 Hz, $CHCH_3$), 2.65 (m, 1H, one H of O=CCH_2), 2.86 (m, 1H, one H of O=CCH_2), 4.11 (q, 2H, J = 7.0 Hz, OCH_2), 4.65 (m, 1H, CH_3CH), 5.65 (d, 1H, J = 7.9 Hz, H_5 of uracil), 7.25 (d, 1H, J = 7.9 Hz, H_6 of uracil), 10.24 (s, 1H, *NH*).

Ethyl 2-methyl-3-(5-methyl-2,4-dioxo-3,4-dihydropyrimidin-1(2*H*)-yl)propanoate (1j)

Column chromathography on silica gel and eluting with EtOAc–*n*-hexane (2:1) gave a pale yellow solid. Isolated yield: 0.215 g (45%); mp 40–42 °C. IR (KBr, cm^{-1}): 3170, 3072, 2969, 1732, 1685, 1641. ^1H NMR ($CDCl_3$, ppm) δ: 1.10–1.17 (complex, 6H, $CHCH_3$ and CH_2CH_3), 1.95 (s, 3H, CH_3 of thymine), 2.94 (m, 1H, O=C*CH*), 3.61 (m, 1H, one H of NCH_2), 3.82 (m, 1H, one H of NCH_2), 4.08 (q, 2H, J = 7.0 Hz, OCH_2), 7.16 (s, 1H, H_6 of thymine), 10.21 (br, 1H, *NH*). ^{13}C NMR (62.5 MHz, $CDCl_3$): δ: 13.7, 14.5, 18.9, 39.8, 47.3, 64.7, 109.9, 140.6, 151.2, 164.9, 171.4. MS *m*/*z*: 240 [M^+]. Anal. calcd. for $C_{11}H_{16}N_2O_4$: C 54.99, H 6.71, N 11.66; found: C 55.11, H 6.62, N 11.79.

Ethyl 3-(4-acetamido-2-oxopyrimidin-1(2*H*)-yl)propanoate (1k)

Column chromathography on silica gel and eluting with EtOAc–*n*-hexane (2:1) gave a colorless solid. Isolated yield: 0.421 g (83%); mp 127–129 °C (lit. (9*g*) value mp 130–131 °C). ^1H NMR ($CDCl_3$, ppm) δ: 1.21 (t, 3H, J = 7.0 Hz, CH_2CH_3), 2.19 (s, 3H, O=CCH_3), 2.82 (t, 2H, J = 5.8 Hz, O=CCH_2), 3.97 (t, 2H, J = 5.8 Hz, NCH_2), 4.09 (t, 2H, J = 7.0 Hz, OCH_2), 7.25 (d, 1H, J = 7.3 Hz), 7.73 (d, 1H, J = 7.3 Hz), 9.25 (s, 1H, *NH*).

Ethyl 3-(6-amino-9*H*-purin-9-yl)propanoate (2a)

Column chromathography on silica gel and eluting with EtOAc–*n*-hexane (3:1) gave a colorless solid. Isolated yield: 0.328 g (70%); mp 165–167 (lit. (9*b*) value mp 165–167). ^1H NMR ($CDCl_3$, ppm) δ: 1.19 (t, 3H, J = 6.9 Hz, CH_3), 2.95 (t, 2H, J = 5.9 Hz, O=CCH_2), 4.12 (t, 2H, J = 6.9 Hz, OCH_2), 4.49 (t, 2H, J = 5.9 Hz, NCH_2), 6.41 (s, 2H, NH_2), 7.96 (s, 1H, H_2 of adenine), 8.45 (s, 1H, H_8 of adenine).

Butyl 3-(6-amino-9*H*-purin-9-yl)propanoate (2b)

Column chromathography on silica gel and eluting with EtOAc–*n*-hexane (3:1) gave a colorless solid. Isolated yield: 0.390 g (74%); mp 135–137 °C (lit. (9*b*) value mp 134–136 °C). ^1H NMR ($CDCl_3$, ppm) δ: 0.93 (t, 3H, J = 6.7 Hz, CH_3), 1.36 (m, 2H, CH_3CH_2), 1.58 (m, 2H, $CH_3CH_2CH_2$), 2.93 (t, 2H, J = 5.8 Hz, O=CCH_2), 4.11 (t, 2H, J = 6.8 Hz, OCH_2), 4.53 (t, 2H, J = 5.8 Hz, NCH_2), 6.38 (s, 2H, NH_2), 7.99 (s, 1H, H_2 of adenine), 8.40 (s, 1H, H_8 of adenine).

Butyl 3-(6-(benzylamino)-9*H*-purin-9-yl)propanoate (2c)

Column chromathography on silica gel and eluting with EtOAc–*n*-hexane (1:1) gave a dark yellow oil. Isolated yield: 0.626 g (89%). IR (KBr, cm^{-1}): 3368, 3076, 2947, 1731. ^1H NMR ($CDCl_3$, ppm) δ: 0.89 (t, 3H, J = 6.8 Hz, CH_3), 1.37 (m, 2H, CH_3CH_2), 1.55 (m, 2H, $CH_3CH_2CH_2$), 2.96 (t, 2H, J = 5.7 Hz, O=CCH_2), 4.09 (t, 2H, J = 6.9 Hz, OCH_2), 4.45 (t, 2H, J = 5.7 Hz, NCH_2), 4.78 (s, 2H, $PhCH_2$), 7.14–7.25 (complex, 6H, H_1–H_5 of the phenyl group and *NH*), 7.94 (s, 1H, H_2 of purine nucleobase), 8.45 (s, 1H, H_8 of purine nucleobase). ^{13}C NMR (62.5 MHz, $CDCl_3$) δ: 13.9, 19.5, 30.9, 38.9, 45.2, 46.1, 65.2, 120.8, 127.3, 128.9, 129.6, 131.7, 139.2, 150.4, 151.9, 156.2, 171.9. MS *m*/*z*: 353 [M^+]. Anal. calcd. for $C_{19}H_{23}N_5O_2$: C 64.57, H 6.56, N 19.82; found: C 64.81, H 6.73, N 19.63.

Butyl 3-(6-oxo-1,6-dihydropurin-9-yl)propanoate (2d)

Column chromathography on silica gel and eluting with EtOAc–*n*-hexane (3:1) gave a colorless solid. Isolated yield: 0.389 g (74%); mp 83–85 °C. IR (KBr, cm^{-1}): 3464, 3083, 2958, 1732, 1682. ^1H NMR ($CDCl_3$, ppm) δ: 0.92 (t, 3H, J = 6.8 Hz, CH_3), 1.35 (m, 2H, CH_3CH_2), 1.58 (m, 2H, $CH_3CH_2CH_2$), 2.87 (t, 2H, J = 5.8 Hz, O=CCH_2), 4.12 (t, 2H, J = 6.9 Hz, OCH_2), 4.52 (t, 2H, J = 5.8 Hz, NCH_2), 7.99 (s, 1H, H_8 of hypoxanthine), 8.56 (s, 1H, H_2 of hypoxanthine), 10.43 (s, 1H, *NH*). ^{13}C NMR (62.5 MHz, $CDCl_3$) δ: 14.1, 19.3, 30.4, 39.6, 47.1, 65.4, 122.6, 151.8, 152.2, 152.9, 156.3, 171.3. MS *m*/*z*: 264 [M^+]. Anal. calcd. for $C_{12}H_{16}N_4O_3$: C 54.54, H 6.10, N 21.20; found: C 54.76, H 5.94, N 21.38.

Butyl 3-(6-oxo-1,6-dihydropurin-7-yl)propanoate (3d)

Column chromathography on silica gel and eluting with EtOAc–*n*-hexane (3:1) gave a colorless solid. Isolated yield: 0.097 g (18%); mp 99–102 °C. IR (KBr, cm^{-1}): 3429, 3071, 2946, 1732, 1686. ^1H NMR ($CDCl_3$, ppm) δ: 0.90 (t, 3H, J = 6.8 Hz, CH_3), 1.38 (m, 2H, CH_3CH_2), 1.59 (m, 2H, $CH_3CH_2CH_2$), 2.90 (t, 2H, J = 5.9 Hz, O=CCH_2), 4.08 (t, 2H, J = 6.8 Hz, OCH_2), 4.74 (t, 2H, J = 5.9 Hz, NCH_2), 8.10 (s, 1H, H_8 of hypoxanthine), 8.64 (s, 1H, H_2 of hypoxanthine), 10.48 (s, 1H, *NH*).^{13}C NMR (62.5 MHz, $CDCl_3$) δ: 13.9, 19.6, 31.6, 40.8, 50.8, 65.1, 118.9, 150.7,

© 2008 NRC Canada

152.9, 153.2, 158.0, 171.9. MS *m/z*: 264 [M^+]. Anal. calcd. for $C_{12}H_{16}N_4O_3$: C 54.54, H 6.10, N 21.20; found: C 54.33, H 6.36, N 21.35.

Butyl 3-(6-chloro-9*H*-purin-9-yl)propanoate (2e)

Column chromathography on silica gel and eluting with EtOAc–*n*-hexane (1:1) gave a colorless oil. Isolated yield: 0.381 g (67%). IR (KBr, cm^{-1}): 3090, 2965, 1730. ^1H NMR ($CDCl_3$, ppm) δ: 0.90 (t, 3H, *J* = 6.7 Hz, CH_3), 1.33 (m, 2H, CH_3CH_2), 1.56 (m, 2H, $CH_3CH_2CH_2$), 2.95 (t, 2H, *J* = 5.8 Hz, O=CCH_2), 4.09 (t, 2H, *J* = 6.9 Hz, OCH_2), 4.61 (t, 2H, *J* = 5.8 Hz, NCH_2), 8.52 (s, 1H, H_8 of 6-chloropurine), 8.99 (s, 1H, H_2 of 6-chloropurine). ^{13}C NMR (62.5 MHz, $CDCl_3$) δ: 14.3, 19.8, 30.7, 38.8, 49.7, 65.6, 133.9, 148.3, 150.1, 151.3, 152.7, 172.3. MS *m/z*: 282 [M^+]. Anal. calcd. for $C_{12}H_{15}ClN_4O_2$: C 50.98, H 5.35, N 19.82; found: C 50.82, H 5.56, N 20.04.

Butyl 3-(6-chloro-9*H*-purin-7-yl)propanoate (3e)

Column chromathography on silica gel and eluting with EtOAc–*n*-hexane (1:1) gave a pale yellow solid. Isolated yield: 0.128 g (23%); mp 60–62 °C. IR (KBr, cm^{-1}): 3078, 2973, 1732. ^1H NMR ($CDCl_3$, ppm) δ: 0.93 (t, 3H, *J* = 6.8 Hz, CH_3), 1.35 (m, 2H, CH_3CH_2), 1.60 (m, 2H, $CH_3CH_2CH_2$), 2.99 (t, 2H, *J* = 5.8 Hz, O=CCH_2), 4.11 (t, 2H, *J* = 6.7 Hz, OCH_2), 4.87 (t, 2H, *J* = 5.8 Hz, NCH_2), 8.61 (s, 1H, H_8 of 6-chloropurine), 9.09 (s, 1H, H_2 of 6-chloropurine). ^{13}C NMR (62.5 MHz, $CDCl_3$) δ: 14.1, 19.5, 30.4, 39.7, 52.3, 65.3, 122.0, 142.4, 150.3, 152.2, 161.9, 171.5. MS *m/z*: 282 [M^+]. Anal. calcd. for $C_{12}H_{15}ClN_4O_2$: C 51.07, H 5.35, N 19.82; found: C 50.74, H 5.16, N 20.01.

Ethyl 3-(6-amino-9*H*-purin-9-yl)-2-methylpropanoate (2f)

Column chromathography on silica gel and eluting with EtOAc–*n*-hexane (3:1) gave a colorless solid. Isolated yield: 0.186 g (37%); mp 134–136 °C (lit. (9*b*) value mp 134–137 °C). ^1H NMR ($CDCl_3$, ppm) δ: 1.12–1.21 (complex, 6H, CH_2CH_3 and $CHCH_3$), 3.13 (m, 1H, O=CCH), 4.09 (q, 2H, *J* = 6.9 Hz, OCH_2), 4.22 (m, 1H, one H of NCH_2), 4.43 (m, 1H, one H of NCH_2), 6.24 (s, 2H, NH_2), 7.83 (s, 1H, H_2 of adenine), 8.35 (s, 1H, H_8 of adenine).

Ethyl 3-(6-amino-9*H*-purin-9-yl)butanoate (2g)

Column chromathography on silica gel and eluting with EtOAc–*n*-hexane (3:1) gave a colorless solid. Isolated yield: 0.145 g (29%); mp 102–104 °C (lit. (9*b*) value mp 100–101 °C).^1H NMR ($CDCl_3$, ppm) δ: 1.14 (t, 3H, *J* = 6.8 Hz, CH_2CH_3), 1.66 (d, 3H, *J* = 4.7 Hz, $CHCH_3$), 2.89 (m, 1H, one H of O=CCH_2), 3.15 (m, 1H, one H of O=CCH_2), 4.06 (q, 2H, *J* = 6.8 Hz, OCH_2), 4.97 (m, 1H, NCH), 6.31 (s, 2H, NH_2), 7.80 (s, 1H, H_2 of adenine), 8.27 (s, 1H, H_8 of adenine).

Acknowledgements

We appreciate Payame Nour University of Bushehr, Persian Gulf University, and Shiraz University research councils for financial support of this work.

References

1. (*a*) M. Negwer and H.-G. Scharnow. Organic-chemical drugs and their synonyms. 8th ed. Wiley-VCH, Weinheim. 2001; (*b*) G. Thomas. An introduction to medicinal chemistry. John Wiely & Sons Inc., Chichester, NY. 2000; (*c*) B.G. Katzung. Basic and clinical pharmacology. 8th ed. McGraw-Hill, NY. 2001; (*d*) A. Kleeman, J. Engel, and D.R. Kutscher. Pharmaceutical substances. 3th ed. George Thieme Verlag, Stuttgart. 1999; (*e*) E. De Clercq. Advance in antiviral drug design. Vol. 1. *Edited by* N.G. Johnsson. JAI Press, Greenwich, UK. 1993; (*f*) C. Heidelberger. Cancer medicine. *Edited by* J. Holland and F.E. Frei. Lea & Febiger, Philadelphia, Penn. 1973.
2. (*a*) D.W. Kufe, E. Frei, J.F. Holland, R.R. Weirchesbaum, R.E. Pollock, R.C. Bast, and T.S. Gansler. Holland-Frei cancer medicine. 6th ed. BC Decker Inc, Spain. 2003; (*b*) H. Gao and A.K. Mitra. Synthesis, 329 (2000); (*c*) S. Guillarme, S. Legoupy, N. Bourgougnon, A.-M. Aubertin, and F. Huet. Tetrahedron, **59**, 9635 (2003).
3. (*a*) G. Qu, S. Han, Z. Zhang, M. Geng, and F. Xue. Can. J. Chem. **84**, 819 (2006); (*b*) F. Amblard, S.P. Nolan, I. Gillaizeau, and L.A. Agrofoglio. Tetrahedron Lett. **44**, 9177 (2003); (*c*) L. Naesens, J. Balzarini, and E. De Clercq. Rev. Med. Virol. 147 (1994); (*d*) M.R. Harnden, A. Parkin, M.J. Parratt, and R.M. Perkins. J. Med. Chem. **36**, 1343 (1993); (*e*) E. De Clercq, A. Holy, I. Rosenberg, T. Sakuma, J. Balzarini, and P.C. Maudgal. Nature (London), **323**, 464 (1986).
4. (*a*) C.K. Chu and D.C. Baker (*Editors*). Nucleosides and nucleotides as antitumor and antiviral agents. Plenum, New York. 1993; (*b*) P. Bravo, M. Frigerio, V. Soloshonok, and F. Viani. Tetrahedron Lett. **34**, 7771 (1993); (*c*) G. Gosselin, L. Griffe, J.-C. Meillon, and R. Storer. Tetrahedron, **62**, 906 (2006).
5. (*a*) X.-Q. Yin, W.-K. Li, and S.W. Schneller. Tetrahedron Lett. **47**, 9187 (2006); (*b*) C. Picherit, F. Wagner, and D. Uguen. Tetrahedron Lett. **45**, 2579 (2004); (*c*) O.H. Ko and J.H. Hong. Tetrahedron Lett. **43**, 6399 (2002); (*d*) A.D. Borthwick and K. Biggadike. Tetrahedron, **48**, 571 (1992); (*e*) Y.H. Jin, P. Liu, J. Wang, U. Das, R. Baker, J. Huggins, and C.K. Chu. J. Org. Chem. **70**, 394 (2005); (*f*) Y.-Y. Yang, W.-D. Meng, and F.-L. Qing. Org. Lett. 4257 (2004); (*g*) M.J. Comin, J.B. Rodriguez, P. Russ, and V.E. Marquez. Tetrahedron, **59**, 295 (2003).
6. (*a*) M. Yokoyama and A. Momotake. Synthesis, 1541 (1999); (*b*) M. Koszytkowska-Stawinska and W. Sas. Tetrahedron Lett. **45**, 5437 (2004).
7. (*a*) J.A. Miller, A.W. Pugh, G.M. Ullah, and C. Gutteridge. Tetrahedron Lett. **41**, 10099 (2000); (*b*) M. Yokoyama. Synthesis, 1637 (2000); (*c*) N.A. Van Draanen, G.A. Freeman, S.A. Short, R. Harvey, R. Jansen, and G.W. Szczech. J. Med. Chem. **39**, 538 (1996).
8. (*a*) A. Khalafi-Nezhad, M.N. Soltani Rad, and A. Khoshnood. Synthesis, 583 (2004); (*b*) A. Khalafi-Nezhad, A. Zare, A. Parhami, and M.N. Soltani Rad. Arkivoc, **xii**, 161 (2006); (*c*) A. Khalafi-Nezhad, M.N. Soltani Rad, G.H. Hakimelahi, and B. Mokhtari. Tetrahedron, **58**, 10341 (2002); (*d*) J. Hovinen. Helv. Chim. Acta, **80**, 851 (1997); (*e*) K.K. Ogilvie, S.L. Beaucage, M.F. Gillen, D. Entwistle, and M. Quilliam. Nucl. Acids Res. 1695 (1979); (*f*) H. Singh, P. Aggarwal, and S. Kumar. Synthesis, 520 (1989); (*g*) E.-M. Priego, M.-J. Camarasa, and M.-J. Pérez-Pérez. Synthesis, 478 (2001).
9. (*a*) J.-M. Xu, C. Qian, B.-K. Liu, Q. Wu, and X.-F. Li. Tetrahedron, **63**, 986 (2007); (*b*) A. Khalafi-Nezhad, A. Zarea, M.N. Soltani Rad, B. Mokhtari, and A. Parhami. Synthesis, 419 (2005); (*c*) E.P. Lira and C.W. Huffman. J. Org. Chem. **31**,

© 2008 NRC Canada

2188 (1966); (*d*) H.B. Lazrek, A. Rochdi, H. Khaider, J.-L. Barascut, J.-L. Imbach, J. Balzarini, M. Witvrouw, C. Pannecouque, and E. De Clercq. Tetrahedron, **54**, 3807 (1998); (*e*) H.B. Lazrek, H. Khaider, A. Rochdi, J.-L. Barascut, and J.-L. Imbach. Nucleosides Nucleotides, **13**, 811 (1994); (*f*) H.B. Lazrek, H. Khaider, A. Rochdi, J.-L. Barascut, and J.-L. Imbach. Tetrahedron Lett. **37**, 4701 (1996); (*g*) Y. Cai, X.-F. Sun, N. Wang, and X.-F. Lin. Synthesis, 671 (2004).

10. (*a*) A. Zare, A. Hasaninejad, A. Khalafi-Nezhad, A.R. Moosavi Zare, and A. Parhami. Arkivoc, **xiii**, 105 (2007); (*b*) M.M. Khodaei, K. Bahrami, and M. Khedri. Can. J. Chem. **85**, 7 (2007); (*c*) R.S. Varma. Tetrahedron, **58**, 1235 (2002); (*d*) B.M. Choudary, R.S. Mulukutla, and K.J. Klabunde. J. Am. Chem. Soc. **125**, 2020 (2003); (*e*) T.F. Dossin, M.-F. Reyniers, R.J. Berger, and G.B. Marin. Appl. Catal. B, **67**, 136 (2006); (*f*) B.M. Choudary, L. Chakrapani, T. Ramani, K.V. Kumar, and M.L. Kantam. Tetrahedron, **62**, 9571 (2006); (*g*) B.M. Choudary, M.L. Kantam, K.V.S. Ranganath, K. Mahendar, and B. Sreedhar. J. Am. Chem. Soc. **126**, 3396 (2004).
11. (*a*) A. Zare, A. Hasaninejad, A. Khalafi-Nezhad, A.R. Moosavi Zare, A. Parhami, and G.R. Nejabat. Arkivoc, **i**, 58 (2007); (*b*) A. Zare, A. Hasaninejad, A.R. Moosavi Zare, A. Parhami, H. Sharghi, and A. Khalafi-Nezhad. Can. J. Chem. **85**, 438 (2007); (*c*) H. Sharghi and M. Hosseini. Synthesis, 1057 (2002); (*d*) M. Gupta, S. Paul, R. Gupta, and A. Loupy. Tetrahedron Lett. **46**, 4957 (2005); (*e*) M. Hosseini Sarvari. Synthesis, 787 (2005); (*f*) M. Hosseini Sarvari and H. Sharghi. J. Org. Chem. **69**, 6953 (2004); (*g*) Y.J. Kim and R.S. Varma. Tetrahedron Lett. **45**, 7205 (2004); (*h*) M. Hosseini Sarvari and H. Sharghi. Tetrahedron, **61**, 10903 (2005); (*i*) F. Tamaddon, M.A. Amrollahi, and L. Sharafat. Tetrahedron Lett. **46**, 7841 (2005).
12. (*a*) A. Loupy. Microwaves in organic synthesis. Wiley-VCH, Weinheim, Germany. 2006; (*b*) R.S. Varma. Advances in green chemistry: Chemical synthesis using microwave irradiation. Astra Zeneca Research Foundation, Kavitha Printers, Bangalore, India. 2002; (*c*) K. Tanaka. Solvent-free organic synthesis. Wiley-VCH, GmbH and KGaA, Weinheim, Germany. 2004. (*d*) J. Yin, X. Li, X. Wu, B. Chen, Z. Liu, and Q. Song. Can. J. Chem. **83**, 2140 (2005); (*e*) B.P. Joshi, A. Sharma, and A.K. Sinha. Can. J. Chem. **83**, 1826 (2005); (*f*) S. Singh, M.P.S. Ishar, G. Singh, and R. Singh. Can. J. Chem. **83**, 260 (2005); (*g*) M. Kidwai and R. Mohan. Can. J. Chem. **82**, 427 (2004); (*h*) S. Balalaie, M. Soleiman-Beigi, and F. Rominger. J. Iran. Chem. Soc. **2**, 319 (2005); (*i*) K.G. Desai, J.P. Raval, and K.R. Desai. J. Iran. Chem. Soc. **3**, 233 (2006).
13. (*a*) G.H. Imanzadeh, A. Khalafi-Nezhad, A. Zare, A. Hasaninejad, A.R. Moosavi Zare, and A. Parhami. J. Iran. Chem. Soc. **4**, 229 (2007); (*b*) A. Zare, A. Hasaninejad, A. Khalafi-Nezhad, A. Parhami, and A.R. Moosavi Zare. J. Iran. Chem. Soc. **5**, 100 (2008); (*c*) G.H. Imanzadeh, A. Zare, A. Khalafi-Nezhad, A. Hasaninejad, A.R. Moosavi Zare, and A. Parhami. J. Iran. Chem. Soc. **4**, 467 (2007).
14. (*a*) A. Hasaninejad, A. Zare, H. Sharghi, M. Shekouhy, R. Khalifeh, A. Salimi Beni, and A.R. Moosavi Zare. Can. J. Chem. **85**, 416 (2007); (*b*) A. Hasaninejad and H. Sharghi. Phosphorus, Sulfur Silicon Relat. Elem. **182**, 873 (2007); (*c*) A. Khalafi-Nezhad, A. Zare, A. Parhami, M.N. Soltani Rad, and G.R. Nejabat. Phosphorus, Sulfur Silicon Relat. Elem. **182**, 657 (2007); (*d*) A. Khalafi-Nezhad, A. Parhami, M.N. Soltani Rad, M.A. Zolfigol, and A. Zare. Tetrahedron Lett. **48**, 5219 (2007); (*e*) A. Hasaninejad and A. Zare. J. Sulfur Chem. **28**, 357 (2007); (*f*) A. Khalafi-Nezhad, A. Zare, A. Parhami, M.N. Soltani Rad, and G.R. Nejabat. Synth. Commun. **36**, 3549 (2006); (*g*) A. Khalafi-Nezhad, A. Parhami, M.N. Soltani Rad, and A. Zarea. Tetrahedron Lett. **46**, 6879 (2005); (*h*) A. Khalafi-Nezhad and B. Mokhtari. Tetrahedron Lett. **45**, 6737 (2004); (*i*) A. Khalafi-Nezhad, B. Mokhtari, and M.N. Soltani Rad. Tetrahedron Lett. **44**, 7325 (2003); (*j*) A. Khalafi-Nezhad, F. Alamdari, and N. Zekri. Tetrahedron, **56**, 7503 (2000).
15. (*a*) A. Khalafi-Nezhad, A. Zare, A. Parhami, M.N. Soltani Rad, and G.R. Nejabat. Can. J. Chem. **84**, 979 (2006); (*b*) A. Khalafi-Nezhad, M.N. Soltani Rad, G.H. Hakimelahi, and B. Mokhtari. Tetrahedron, **58**, 10341 (2002).
16. (*a*) W.-Y. Wu, S.-N. Chen, and F.-Y. Tsai. Tetrahedron Lett. **47**, 9267 (2006); (*b*) B.C. Ranu, S.S. Dey, and A. Hajra. Tetrahedron, **59**, 2417 (2003); (*c*) S. Mukhopadhyay, G. Rothenberg, N. Qafisheh, and Y. Sasson. Tetrahedron Lett. **42**, 6117 (2001); (*d*) S. Chatti, M. Bortolussi, and A. Loupy. Tetrahedron Lett. **41**, 3367 (2000); (*e*) S. Chatti, M. Bortolussi, and A. Loupy. Tetrahedron, **56**, 5877 (2000); (*f*) A. Diaz-Ortiz, P. Prieto, A. Loupy, and D. Abenhaim. Tetrahedron Lett. **37**, 1695 (1996); (*g*) J.P. Barnier, A. Loupy, P. Pigeon, M. Ramdani, and P. Jacquault. J. Chem. Soc. Perkin Trans. 1, 397 (1993).
17. (*a*) D. Singh, M.J. Wani, and A. Kumar. J. Org. Chem. **64**, 4665 (1999); (*b*) L.W. Dudycz and G. E. Wright. Nucleosides Nucleotides, **3**, 33 (1984); (*c*) G.E. Wright and L.W. Dudycz. J. Med. Chem. **27**, 175 (1984); (*d*) K.C. Schneider and S.A. Benner. Tetrahedron Lett. **31**, 335 (1990); (*e*) M.-T. Chenon, R.J. Pugmire, D.M. Grant, R.P. Panzica, and L.B. Townsend. J. Am. Chem. Soc. **97**, 4628 (1975); (*f*) M.T. Crimmins, B.W. King, W.J. Zuercher, and A.L. Choy. J. Org. Chem. **65**, 8499 (2000); (*g*) J. Kjellberg and N. G. Johansson. Tetrahedron, **42**, 6541 (1986); (*h*) P. Gamer and S. Ramakanth. J. Org. Chem. **53**, 1294 (1988).

© 2008 NRC Canada

Intramolecular cyclization reaction — Palladium(0)-catalyzed cyclization is more effective than tin hydride mediated reaction

Krishna C. Majumdar, Pradip Debnath, Abu Taher, and Amarta K. Pal

Abstract: Intramolecular CH arylation of pyrone, pyridone, uracil, imidazole, and benzimidazole derivatives are carried out in the presence of a Pd catalyst to form potentially bioactive fused heterocyclic compounds, whereas the *n*-Bu_3SnH-mediated aryl radical cyclization of the precursors **3** afforded mainly halogen-reduced uncyclized products.

Key words: Pd(0) catalyst, CH arylation, intramolecular cyclization, regioselectivity.

Résumé : Opérant en présence d'un catalyseur de palladium, on a réalisé l'arylation intramoléculaire du CH de dérivés de la pyrone, de la pyridone, de l'uracile, de l'imidazole et du benzimidazole pour former des composés hétérocycliques condensés potentiellement bioactifs alors que la cyclisation des précurseurs **3** à l'aide de radicaux aryles, catalysée par le *n*-Bu_3SnH, fournit principalement des produits non cyclisés desquels les halogènes ont été réduits.

Mots-clés : catalyseur de Pd(0), arylation du CH, cyclisation intramoléculaire, régiosélectivité.

Introduction

The synthesis of heteroaromatic compounds by intramolecular cyclizations has received increasing attention in organic chemistry, since a wide variety of such molecules show potential biological activities as pharmaceutical and agrochemical compounds (1). Several intramolecular reactions have been discovered, and their applications in organic chemistry have also been well documented in the literature. The most important ones include the Claisen rearrangement (2), free radical reactions (3), Pd(0)-catalyzed insertion reactions (4), etc. Free radical reactions are one of the most straightforward ways for carbon–carbon bond formation in organic synthesis. Several methods have been devised to effect such radical cyclizations, with *n*-Bu_3SnH- or *n*-Bu_3SnCl-mediated reactions being the most explored. The highly toxic nature of the tin reagent, the difficulties associated with the removal of toxic tin from the reaction products, and reduction of the intermediate carbon centered radical by *n*-Bu_3SnH are frequently highlighted as reasons to avoid these reagents (5). The disadvantages associated with these reagents have led synthetic organic chemists to find alternative methods and (or) reagents to accomplish such reactions. Reagents such as less toxic silanes and germanes have been used as substitutes for *n*-Bu_3SnH and *n*-Bu_3SnCl (6). In recent years, palladium-catalyzed (7) cyclization reactions have been shown to be a highly effective and practical method in organic synthesis. Having established this chemistry, it has been rapidly applied in an intramolecular sense to the synthesis of carbocyclic (8) and heterocyclic (9) compounds. The main advantage is that the reagent is non-toxic and involves an easy workup procedure, and hence can successfully be applied for the synthesis of bioactive molecules.

Recently, there is much interest in the synthesis of 2-pyrone derivatives due to their diverse pharmacological properties (10). Several natural (11) and synthetic (12) 2-pyrones exhibit remarkable biological activity. 3-Deazauridine, a pyridone-based compound, is currently undergoing clinical trials as an anticancer agent (13), and it is also effective against tumor growth (14). Some [1,2-*a*] fused imidazoles are also known to have anti-ulcer, antidepressant, and antimicrobial activity (15). Several [1,2-*a*]fused benzimidazoles have antitumor activity (16). Although Pd-catalyzed intramolecular cyclization is a well-known process, its application on pyrone, pyridone, uracil, imidazole, and benzimidazole systems is much less documented. Recently, the palladium-mediated three component synthesis of 2,3-fused furo-pyridones has been reported (17). An unsuccessful attempt to synthesize the 5-membered fused heterocycles by intramolecular aromatic substitution by an imidazol-2-yl radical has been reported (18). However, Dubois and co-workers (19) reported the synthesis of bioactive 5*H*-imidazol[2,1-*a*]isoindoles by the Pd-catalyzed intramolecular arylation of *N*-benzyl-2-iodoimidazole. Recently, we have successfully demonstrated the radical reaction (20) and a Pd-catalyzed Heck reaction (21) on

Received 14 November 2007. Accepted 30 January 2008. Published on the NRC Research Press Web site at canjchem.nrc.ca on 10 March 2008.

K.C. Majumdar,[1] P. Debnath, A. Taher, and A.K. Pal. Department of Chemistry, University of Kalyani, Kalyani 741235, WB, India

[1]Corresponding author (e-mail: kcm_ku@yahoo.co.in).

 doi:10.1139/V08-023 © 2008 NRC Canada

benzannulated analogues of pyrone and pyridone. Here, we describe a comparative study of radical and Pd(0)-catalyzed cyclizations as a synthetic method to access pyron-, pyridon-, imidazol-, benzimidazol-, and uracil-annulated heterocycles of biological interest.

Results and discussion

For our initial investigation, we have selected compounds **3a**–**3l** as starting materials. These ethers were prepared by the alkylation of 4-hydroxypyrone, 4-hydroxypyridones, 5-hydroxyuracil, imidazole, and benzimidazole with 2-bromobenzyl bromide and 2-bromo-5-methoxybenzyl bromide. Compounds **3a**–**3b** were prepared in 80% and 84% yields, respectively, by using a classical alkylation procedure from 4-hydroxypyrone (**1**) and 2-bromobenzyl bromide (**2a**) or 2-bromo-5-methoxybenzyl bromide (**2b**) in refluxing acetone in the presence of K_2CO_3 (Scheme 1). The compounds **3a**–**3b** were characterized by their elemental analyses and spectroscopic data. Similarly, other substrates **3c**–**3l** were also prepared.

As our goal was to synthesize new heterocycles by C–C bond formation, we first considered *n*-Bu_3SnCl-mediated radical cyclization conditions. The substrate **3a** was subjected to optimal reaction conditions (20), i.e., *n*-Bu_3SnCl, $Na(CN)BH_3$, AIBN in dry toluene under nitrogen atmosphere at 80 °C for 4 h. A single product, solid, mp 92–94 °C, was isolated by column chromatography. The ^1H NMR spectrum of the product revealed that cyclization did not occur. Only the halogen-reduced product **4a** was obtained. We then tried to carry out the cyclization reaction in the presence of *n*-Bu_3SnH, instead of *n*-Bu_3SnCl, in refluxing toluene. But we again failed to achieve the radical cyclization. However, radical cyclization between the precursors **3c**–**3f** and *n*-Bu_3SnH gave the cyclized products **5c**–**5f** in poor yields (4%–7%) with uncyclized reduced products **4c**–**4f** (64%–83%). The use of a stoichiometric amount (22) of radical initiator gave improved yields **5a** (20%), **5b** (17%), **5c** (29%), **5d** (25%), **5e** (27%), and **5f** (31%) respectively, with halogen-reduced products **4a**–**4f** (44%–56%) (Scheme 2).

Aryl radical cyclization onto the benzannulated analogues of these compounds (20), namely coumarins, quinolones, and uracil derivatives (precursors **3g**–**3h**) gave better yields of cyclized product with no reduced product. This may be due to the better stabilization of radical intermediates in the benzannulated series. Aryl radicals are nucleophilic, and electron-withdrawing and (or) radical-stabilizing groups improve the cyclization. The formation of six-membered ring heterocycles at C-3 (not at C-5) may easily be explained by the generation of aryl radical **6**, followed by a 6-*endo trig* cyclization to give allyl radical intermediate **7** (Scheme 2). The oxidative elimination of hydrogen from intermediate **7** may afford **5**. The regioselective formation of compounds **5** from substrates **3** may be attributed to the stability of the intermediate allylic radical **7**. Otherwise, a 6-*endo* attack at C-5 position would give a α-*oxo* radical (**8**), which is unstable.

Attempted five-membered ring aryl radical cyclizations with the azole, imidazole, and benzimidazole radical precursors **3i** and **3k** using *n*-Bu_3SnH gave only reduced uncyclized products **4i** and **4j**, respectively, even with slow addition of the tin reagent (Scheme 3). It is also important to note that attempts to effect the five-membered ring cyclization with a stoichiometric amount of the initiator did not divert the reaction away from dehalogenation. Since radical precursors **3i** and **3k** gave only the reduced products, we did not proceed further with the precursors **3j** and **3l**.

Scheme 1. Reagents and conditions: (*i*) dry acetone, K_2CO_3, reflux, 6 h.

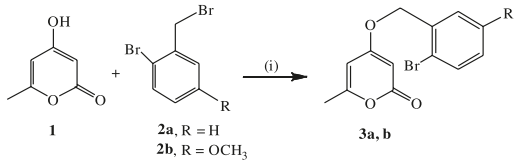

1 **2a**, R = H; **2b**, R = OCH_3 **3a, b**

Cyclizations onto five-membered ring azoles is less favored due to the strain of formation of products with two five-membered rings, one of which is a heteroarene (23). Bowmen and co-workers (24) showed that alkyl radical cyclization onto imidazoles and benzimidazoles, 6-membered ring cyclization, gave better yields than five-membered ring cyclization, whereas aryl radical cyclization gave only reduced products in the case of five-membered ring cyclizations.

To increase the yield of cyclized products, we then utilized Pd(0)-catalyzed cyclization reactions. We have examined the influence of factors such as the nature of the base, the ligand, the solvent, and the reaction temperature, which might influence the efficiency of the reaction. The Heck reaction was carried out at 100 °C in DMF with 10 mol% of $Pd(OAc)_2$, tri-2-tolylphosphine as ligand, and K_2CO_3 as the base with substrate **3a**. Only one product was obtained after 6 h, in 25% yield, along with a large amount of starting material (62%). Increasing the reaction temperature (up to 150 °C) and also the reaction time did not improve the yield of the reaction due to extensive decomposition of the starting material. We have also examined the influence of bases like Cs_2CO_3, KOAc, organic bases like triethylamine, and the ligands triphenylphosphine and tri-4-tolylphosphine. Potassium acetate proved to be the best base with the tri-2-tolylphosphine ligand for this cyclization, improving the yield to 42%. Changing the solvent (DMSO, CH_3CN) did not provide any improvement in the yield. However, the best results were achieved under Jeffery's two phase conditions (25). The reaction conditions for this transformation involved dissolving compound **3a** (0.34 mmol) in dry DMF, followed by the addition of $Pd(OAc)_2$ (10 mmol%), TBAB (0.34 mmol), KOAc (0.85 mmol), and stirring the reaction mixture for 4 h at 95 °C under an inert atmosphere. The reaction was monitored by TLC and an appreciable change was observed. Isolation of the product by flash column chromatography furnished a solid in 87% yield. The product was characterized by elemental analysis and spectral data. Compounds **3b**–**3l**, on similar treatment, furnished compounds **5b**–**5l** in 61%–96% yields (Table 1).

The palladium(0)-catalyzed reaction affords better yields than the tin hydride protocol, except in the case of uracil derivatives, where the yields are comparable with the tin hydride-mediated reaction.

The coupling of the precursors **3a**–**3f** occurs regioselectively at C-3 as in the case of the radical cyclization re-

© 2008 NRC Canada

Scheme 2. Reagents and conditions: (*i*) *n*-Bu_3SnH, AIBN, toluene, reflux, 4–7 h.

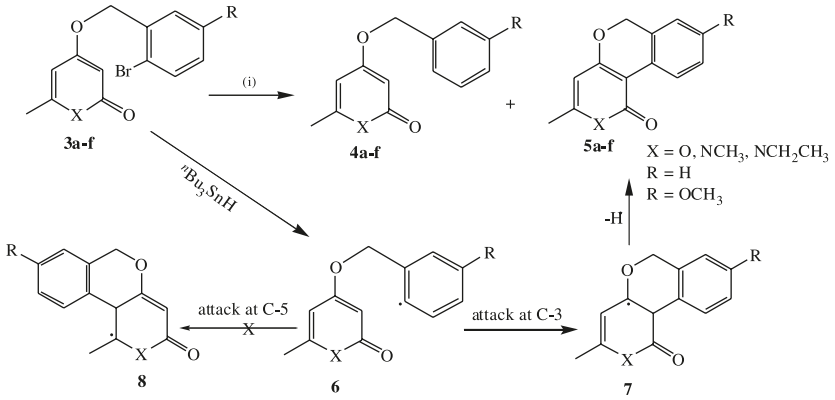

Scheme 3. Radical reactions of imidazole and benzimidazole.

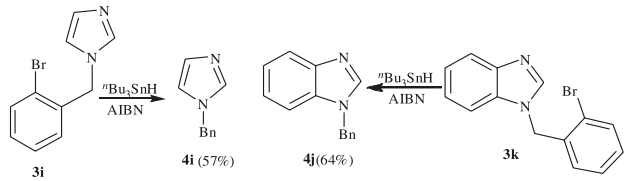

actions. Mori and co-workers (26) also regioselectively synthesized compound **5i** by utilizing $PdCl_2$-$2PPh_3$ in DMSO at 140 °C, but we have achieved better results using Jeffery's protocol in a short reaction time and at a lower temperature.

The proposed mechanism for this annulation process is shown in Scheme 4. Initially, the oxidative addition of compound **3** to palladium may form the arylpalladium intermediate **9**. Complex **9** may then add to the double bond to give a σ–alkylpalladium intermediate **10**, and finally β–hydrogen elimination from intermediate **10** may provide products **5**. Similar mechanisms for the Pd-catalyzed CH-arylation of π-excessive heteroarenes have been reported in the literature (27). Recently, the mechanism of the Pd-catalyzed Heck reaction has been reviewed (28).

Conclusion

In conclusion, we have successfully extended the Pd(0)-catalyzed intramolecular Heck reaction to the regioselective synthesis of potentially bioactive heterocyclic compounds. The process is quite simple, practical, and affords good to excellent yields of the desired products and is far superior to the toxic tin hydride methodology. The mildness of the reaction conditions and the high level of chemoselectivity allow this annulation process to serve as a powerful synthetic tool for the preparation of complex aromatic heterocycles.

Experimental

General

Melting points were determined in open capillaries and are uncorrected. IR spectra were recorded on a PerkinElmer L 120-000A spectrometer (γ_{max} in cm^{-1}) using samples as neat liquids, and solid samples were recorded in KBr disks. ^1H NMR (300 MHz, 400 MHz, 500 MHz) spectra were recorded on a Bruker-300, Bruker DPX-400, and Bruker DRX-500 spectrometers in $CDCl_3$ (chemical shift in δ) with TMS as internal standard. Silica gel [(60–120, 230-400 mesh), Spectrochem, India] was used for chromatographic separation. Silica gel G [E-Merck (India)] was used for TLC. Petroleum ether refers to the fraction boiling between 60 and 80 °C.

Scheme 4.

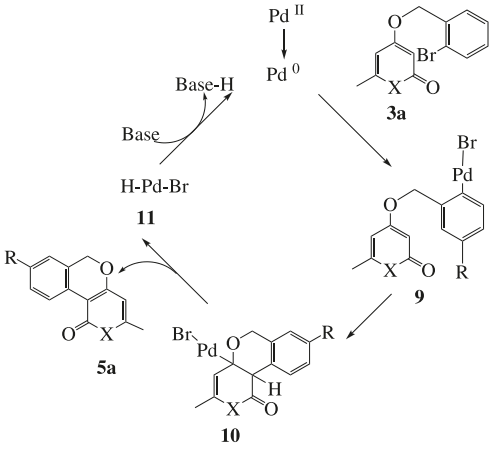

General procedure for the preparation of compounds 3a–3l

A mixture of 4-hydroxy-6-methyl pyrone (**1a**, 0.20 g, 1.59 mmol) 2-bromobenzyl bromide (**2a**, 0.475 g, 1.90 mmol) or 2-bromo-5-methoxybenzyl bromide (**2b**, 0.530 g, 1.90 mmol) and anhydrous potassium carbonate (3 g) were refluxed in dry acetone (75 mL) on a water bath for 5–6 h. The reaction mixture was cooled, filtered, and the solvent was removed. The residual mass was extracted with CH_2Cl_2 (3 × 30 mL). The CH_2Cl_2 extract was washed with water (3 × 30 mL) and dried (Na_2SO_4). The residual mass, after removal of CH_2Cl_2, was subjected to column chromatography over silica gel (60–120 mesh) using petroleum ether – ethyl acetate as the eluant to give compounds **3a–3b.** Similarly, the substrates **3c–3l** were prepared from pyridone, uracil, imidazole, and benzimidazole, respectively. All solid compounds were recrystalized from an acetonitrile–methanol mixture.

© 2008 NRC Canada

Table 1. Pd-catalyzed cyclization of compounds **3a**–**3l**.

Entry	Substrate **3** (%)	Product **5**	Time (h)	Temp. (°C)	Yield (%)[a]
1	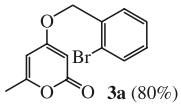 **3a** (80%)	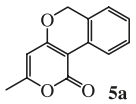 **5a**	4	95	87
2	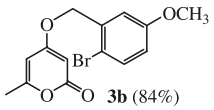 **3b** (84%)	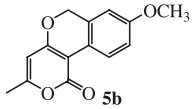 **5b**	4.5	95	94
3	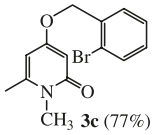 **3c** (77%)	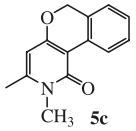 **5c**	5.5	95	88
4	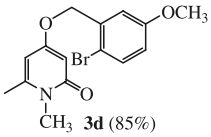 **3d** (85%)	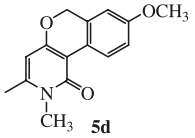 **5d**	5	95	83
5	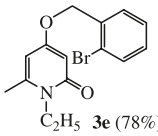 **3e** (78%)	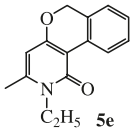 **5e**	7	95	78
6	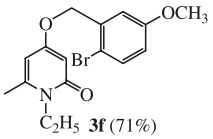 **3f** (71%)	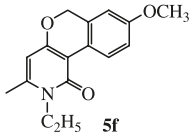 **5f**	6	95	81

4-[(2-Bromobenzyl)oxy]-6-methyl-2*H*-pyran-2-one (3a)

Yield 80%, colorless solid, mp 135–137 °C (acetonitrile–methanol). IR (KBr, cm^{-1}) υ: 2924, 1726, 1248, 1033. ^1H NMR ($CDCl_3$, 400 MHz, ppm) δ_H: 2.20 (s, 3H), 5.01 (s, 2H), 5.48 (d, J = 2.0 Hz, 1H), 5.83 (t, J = 0.8 Hz, 1H), 7.36-7.44 (m, 4H). MS m/z: 294, 296 (M^+). Anal. calcd. for $C_{13}H_{11}BrO_3$: C 52.91, H 3.76; found: C 53.02, H 3.72.

4-[(2-Bromo-5-methoxybenzyl)oxy]-6-methyl-2*H*-pyran-2-one (3b)

Yield 84%, colorless solid, mp 125 to 126 °C (acetonitrile–methanol). IR (KBr, cm^{-1}) υ: 2940, 1733, 1245, 1013. ^1H NMR ($CDCl_3$, 400 MHz, ppm) δ_H: 2.22 (s, 3H), 3.79 (s, 3H), 5.02 (s, 2H), 5.47 (d, J = 2.4 Hz, 1H), 5.85 (t, J = 0.8 Hz, 1H), 6.75 (dd, J = 2.4, 6.6 Hz, 1H), 6.93 (d, J = 2.1 Hz, 1H) 7.44 (d, J = 6.3 Hz, 1H). MS m/z: 324, 326 (M^+). Anal. calcd. for $C_{14}H_{13}BrO_4$: C 51.71, H 4.03; found: C 51.95, H 3.87.

4-[(2-Bromobenzyl)oxy]-1,6-dimethyl-1,2-dihydropyridin-2-one (3c)

Yield 77%, colorless solid, mp 134 to 135 °C (acetonitrile–methanol). IR (KBr, cm^{-1}) υ: 2952, 1658, 1201. ^1H NMR ($CDCl_3$, 400 MHz, ppm) δ_H: 2.29 (s, 3H), 3.44 (s, 3H), 5.01 (s, 2H), 5.86 (s, 1H), 5.89 (s, 1H), 7.15 (t, J = 7.6 Hz, 1H), 7.28 (t, J = 7.6 Hz, 1H), 7.40 (d, J = 7.6 Hz, 1H), 7.54 (d, J = 8.0 Hz, 1H). MS m/z: 307, 309 (M^+). Anal. calcd. for $C_{14}H_{14}BrNO_2$: C 54.56, H 4.58, N 4.55; found: C 54.43, H 4.72, N 4.61.

4-[(2-Bromo-5-methoxybenzyl)oxy]-1,6-dimethyl-1,2-dihydropyridin-2-one (3d)

Yield 85%, colorless solid, mp 148 to 149 °C (acetonitrile–methanol). IR (KBr, cm^{-1}) υ: 2959, 1655, 1238. ^1H NMR ($CDCl_3$, 400 MHz, ppm) δ_H: 2.30 (s, 3H), 3.45 (s, 3H), 3.78 (s, 3H), 4.98 (s, 2H), 5.87 (d, J = 2.2 Hz, 1H), 5.90 (d, J = 2.7 Hz, 1H), 6.72 (dd, J = 3.0, 8.7 Hz, 1H), 6.98 (d, J = 2.8 Hz, 1H), 7.43 (d, J = 8.7 Hz, 1H). MS m/z: 337, 339 (M^+). Anal. calcd. for $C_{15}H_{16}BrNO_3$: C 53.27, H 4.77, N 4.14; found: C 53.53, H 4.86, N 4.26.

4-[(2-Bromobenzyl)oxy]-1-ethyl-6-methyl-1,2-dihydropyridin-2-one (3e)

Yield 78%, colorless solid, mp 102–104 °C (acetonitrile–methanol). IR (KBr, cm^{-1}) υ: 2924, 1645, 1241. ^1H NMR ($CDCl_3$, 400 MHz, ppm) δ_H: 1.26 (t, J = 6.8 Hz, 3H), 2.35

© 2008 NRC Canada

Table 1 (*concluded*).

Entry	Substrate **3** (%)	Product	Time (h)	Temp.(°C)	Yield (%)[a]
7	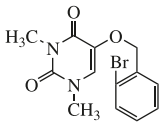 **3g**[20a] (82 %)	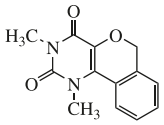 **5g**[20a]	1.5	80	96
8	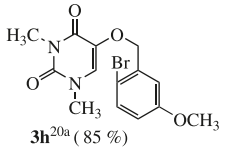 **3h**[20a] (85 %)	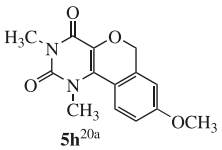 **5h**[20a]	2	80	96
9	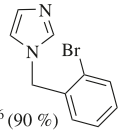 **3i**[26] (90 %)	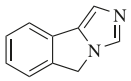 **5i**[26]	5	100	81
10	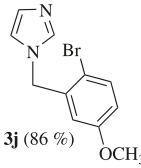 **3j** (86 %)	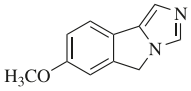 **5j**	4.5	100	84
11	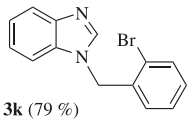 **3k** (79 %)	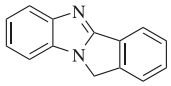 **5k**[24b]	12	120	67
12	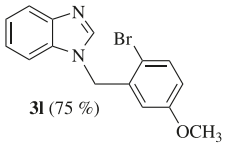 **3l** (75 %)	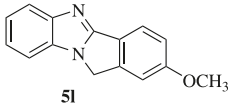 **5l**	12	120	61

Note: Compound **3** (0.34 mmol), $Pd(OAc)_2$ (10 mol%), TBAB (0.34 mmol), KOAc (0.85 mmol), DMF (25 mL).
[a]Isolated yeilds of the Pd(0)-catalyzed cyclized products.

(s, 3H), 4.0 (q, *J* = 7.2 Hz, 2H), 5.03 (s, 2H), 5.84 (d, *J* = 2.8 Hz, 1H), 5.90 (d, *J* = 2.4 Hz, 1H), 7.18–7.22 (m, 1H), 7.30-7.59 (m, 3H). MS *m*/*z*: 321, 323 (M^+). Anal. calcd. for $C_{15}H_{16}BrNO_2$: C 55.92, H 5.01, N 4.35; found: C 55.71, H 5.12, N 4.28.

4-[(2-Bromo-5-methoxybenzyl)oxy]-1-ethyl-6-methyl-1,2-dihydropyridin-2-one (3f)

Yield 71%; gummy mass. IR (KBr, cm^{-1}) υ: 2936, 1651, 1242. ^1H NMR ($CDCl_3$, 400 MHz, ppm) δ_H: 1.25 (t, *J* = 7.1 Hz, 3H), 2.34 (s, 3H), 3.78 (s, 3H), 3.99 (q, *J* = 7.1 Hz, 2H), 4.97 (s, 2H), 5.84 (d, *J* = 2.2 Hz, 1H), 5.89 (d, *J* = 2.6 Hz, 1H), 6.72 (dd, *J* = 3.0, 8.8 Hz, 1H), 6.97 (d, *J* = 3.0 Hz, 1H), 7.43 (d, *J* = 8.8 Hz, 1H). MS *m*/*z*: 351, 353 (M^+). Anal. calcd. for $C_{16}H_{18}BrNO_3$: C 54.56, H 5.15, N 3.98; found: C 54.59, H 5.13, N 4.19.

Compounds 3g and 3h

See ref. 20*a*.

1-(2-Bromobenzyl)-1*H*-imidazole (3i)

See ref. 26.

1-(2-Bromo-5-methoxybenzyl)-1*H*-imidazole (3j)

Yield 86%, colorless solid, mp 118–120 °C (EtOAc – petroleum ether). IR (KBr, cm^{-1}) υ: 2936, 1594, 1241, 729. ^1H NMR ($CDCl_3$, 400 MHz, ppm) δ_H: 3.71 (s, 3H), 5.17 (s, 2H), 6.44 (d, *J* = 2.8 Hz, 1H), 6.73 (dd, *J* = 3.2, 8.8 Hz, 1H), 6.96 (s, 1H), 7.12 (s, 1H), 7.47 (d, *J* = 8.8 Hz, 1H), 7.62 (s, 1H). MS *m*/*z*: 266, 268 (M^+). Anal. calcd. for $C_{11}H_{11}BrN_2O$: C 49.46, H 4.15, N 10.49; found: C 49.70, H 4.12, N 10.52.

1-(2-Bromobenzyl)-1*H*-benzo[d]imidazole (3k)

Yield 79%, colorless solid, mp 108–110 °C (acetonitrile–methanol). IR (KBr, cm^{-1}) υ: 3055, 1613, 749. ^1H NMR ($CDCl_3$, 400 MHz, ppm) δ_H: 5.43 (s, 2H), 6.77-6.81 (m, 1H), 7.15-7.31 (m, 5H), 7.61-7.85 (m, 2H), 7.95 (s, 1H). MS *m*/*z*: 286, 288 (M^+). Anal. calcd. for $C_{14}H_{11}BrN_2$: C 58.56, H 3.86, N 9.76; found: C 58.73, H 3.91, N 9.69.

© 2008 NRC Canada

1-(2-Bromo-5-methoxybenzyl)-1*H*-benzo[d]imidazole (3l)

Yield 75%, colorless solid, mp 94–96 °C (acetonitrile–methanol). IR (KBr, cm^{-1}) υ: 2963, 1614, 739. ^1H NMR ($CDCl_3$, 400 MHz, ppm) δ_H: 3.60 (s, 3H), 5.38 (s, 2H), 6.34 (d, *J* = 2.6 Hz, 1H), 6.71 (dd, *J* = 2.7, 8.7 Hz, 1H), 7.27-7.32 (m, 3H), 7.49 (d, *J* = 8.7 Hz, 1H), 7.82 (d, *J* = 8.0 Hz, 1H), 7.95 (s, 1H). MS *m/z*: 316, 318(M^+). Anal. calcd. for $C_{15}H_{13}BrN_2O$: C 56.80, H 4.13, N 8.83; found: C 57.09, H 4.18, N 8.97.

General procedure for the radical reaction of compounds 3a–3i and 3k

A deoxygenated solution of *n*-Bu_3SnH in toluene (0.12 ml, 0.40 mmol) was added dropwise to a magnetically stirred solution of the precursors **3** (0.34 mmol) and azobis(isobutyro)nitrile (0.056 gm) in dry toluene (10 mL) under a nitrogen atmosphere. The mixture was refluxed for 4–7 h. After completion of the reaction, the solvent was removed under reduced pressure. The residue was dissolved in CH_2Cl_2 (10 mL) and stirred with 10% aq. KF solution (10 mL) for 1 h. The aqueous phase was extracted with CH_2Cl_2 (3 × 25 mL). The combined CH_2Cl_2 extracts were washed with water (2 × 20 mL), brine solution (1 × 20 mL), and dried (Na_2SO_4). The solvent was evaporated under reduced pressure. The crude products were purified by column chromatography over silica gel using petroleum ether – ethyl acetate mixture as eluant. All solid compounds were crystallized from an acetonitrile–methanol mixture.

4-Benzyloxy-6-methyl-2*H*-pyran-2-one (4a)

Eluted from the column with 20% ethyl acetate – petroleum ether mixture as colorless solid (53%), mp 92–94 °C (acetonitrile-methanol). IR (KBr, cm^{-1}) υ: 2923, 1728, 1244, 1035. ^1H NMR ($CDCl_3$, 400 MHz, ppm) δ_H: 2.20 (s, 3H), 4.99 (s, 2H), 5.48 (d, *J* = 2.1 Hz, 1H), 5.82 (t, *J* = 0.8 Hz, 1H), 7.34-7.42 (m, 5H). MS *m/z*: 216 (M^+). Anal. calcd. for $C_{13}H_{12}O_3$: C 72.21, H 5.59; found: C 72.03, H 5.48.

4-[(3-Methoxybenzyl)oxy]-6-methyl-2*H*-pyran-2-one (4b)

Eluted from the column with 20% ethyl acetate – petroleum ether mixture as colorless solid (55%), mp 121 to 122 °C (acetonitrile–methanol). IR (KBr, cm^{-1}) υ: 2943, 1731, 1245, 1012. ^1H NMR ($CDCl_3$, 400 MHz, ppm) δ_H: 2.24 (s, 3H), 3.79 (s, 3H), 5.03 (s, 2H), 5.48 (d, *J* = 2.2 Hz, 1H), 5.84 (t, *J* = 0.8 Hz, 1H) 6.82-7.41 (m, 4H). MS *m/z*: 246 (M^+). Anal. calcd. for $C_{14}H_{14}O_4$: C 68.28, H 5.73; found: C 68.41, H 5.81.

4-Benzyloxy-1,6-dimethyl-1,2-dihydropyridin-2-one (4c)

Eluted from the column with 60% ethyl acetate – petroleum ether mixture as a colorless solid (44%), mp 138–140 °C (acetonitrile–methanol). IR (KBr, cm^{-1}) υ: 2912, 1724, 1244, 1035. ^1H NMR ($CDCl_3$, 400 MHz, ppm) δ_H: 2.28 (s, 3H), 3.42 (s, 3H), 5.00 (s, 2H), 5.86 (s, 1H), 5.88 (s, 1H), 6.99-7.54 (m, 5H). MS *m/z*: 229 (M^+). Anal. calcd. for $C_{14}H_{15}NO_2$: C 73.34, H 6.59, N 6.11; found: C 73.13, H 6.48, N 5.88.

4-[(3-Methoxybenzyl)oxy]-1,6-dimethyl-1,2-dihydropyridin-2-one (4d)

Eluted from the column with 60% ethyl acetate – petroleum ether mixture as a colorless solid (56%), mp 128–130 °C (acetonitrile–methanol). IR (KBr, cm^{-1}) υ: 2931, 1719, 1233, 1011. ^1H NMR ($CDCl_3$, 400 MHz, ppm) δ_H: 2.29 (s, 3H), 3.43 (s, 3H), 3.75 (s, 3H), 4.99 (s, 2H), 5.88 (d, *J* = 2.2 Hz, 1H), 5.90 (d, *J* = 2.7 Hz, 1H), 6.67-7.19 (m, 3H), 7.43 (d, *J* = 8.6 Hz, 1H). MS *m/z*: 259 (M^+). Anal. calcd. for $C_{15}H_{17}NO_3$: C 69.48, H 6.61, N 5.40; found: C 69.45, H 6.66, N 5.33.

4-Benzyloxy-1-ethyl-6-methyl-1,2-dihydropyridin-2-one (4e)

Eluted from the column with 55% ethyl acetate – petroleum ether mixture as a colorless solid (47%), mp 156 to 157 °C (acetonitrile–methanol). IR (KBr, cm^{-1}) υ: 2970, 1723, 1228. ^1H NMR ($CDCl_3$, 400 MHz, ppm) δ_H: 1.24 (t, *J* = 7.0 Hz, 3H), 2.32 (s, 3H), 3.98 (q, *J* = 7.1 Hz, 2H), 4.94 (s, 2H), 5.80 (d, *J* = 2.5 Hz, 1H), 5.88 (d, *J* = 2.6 Hz, 1H), 7.32-7.37 (m, 5H). MS *m/z*: 243 (M^+). Anal. calcd. for $C_{15}H_{17}NO_2$: C 74.05, H 7.04, N 5.76; found: C 74.24, H 7.14, N 5.94.

1-Ethyl-4-[(3-methoxybenzyl)oxy]-6-methyl-1,2-dihydropyridin-2-one (4f)

Eluted from the column with 55% ethyl acetate – petroleum ether mixture as a colorless solid (56%), mp 173 to 174 °C (acetonitrile–methanol). IR (KBr, cm^{-1}) υ: 2945, 1727, 1222. ^1H NMR ($CDCl_3$, 300 MHz, ppm) δ_H: 1.25 (t, *J* = 7.0 Hz, 3H), 2.33 (s, 3H), 3.81 (s, 3H), 3.99 (q, *J* = 7.1 Hz, 2H), 4.94 (s, 2H), 5.83 (d, *J* = 1.9 Hz, 1H), 5.89 (d, *J* = 2.4 Hz, 1H), 6.86-6.96 (m, 3H), 7.26 (dd, *J* = 1.3, 7.7 Hz, 1H). MS *m/z*: 273 (M^+). Anal. calcd. for $C_{16}H_{19}NO_3$: C 70.31, H 7.01, N 5.12; found: C 70.19, H 6.83, N 5.30.

The precursors **3g** and **3h** did not give any reduced uncyclized products (20*a*).

1-Benzyl-1*H*-imidazole (4i)

Eluted from the column with 40% ethyl acetate – petroleum ether mixture as a gummy mass (57%). IR (KBr, cm^{-1}) υ: 2919, 1233. ^1H NMR ($CDCl_3$, 400 MHz, ppm) δ_H: 5.08 (s, 2H), 6.87 (s, 1H), 7.06 (s, 1H), 7.11 (d, *J* = 6.5 Hz, 2H), 7.27-7.35 (m, 3H), 7.51 (s, 1H). MS *m/z*: 158 (M^+). Anal. calcd. for $C_{10}H_{10}N_2$: C 75.92, H 6.37, N 17.71; found: C 75.99, H 6.33, N 17.82.

1-Benzyl-1*H*-benzo[*d*]imidazole (4j)

Eluted from the column with 40% ethyl acetate – petroleum ether mixture as a colorless solid (64%), mp 110–112 °C (acetonitrile–methanol). IR (KBr, cm^{-1}) υ: 2919, 1265. ^1H NMR ($CDCl_3$, 400 MHz, ppm) δ_H: 5.31 (s, 2H), 7.13 (d, *J* = 7.5 Hz, 2H), 7.19-7.32 (m, 6H), 7.79 (d, *J* = 7.5 Hz, 1H), 7.90 (s, 1H). MS *m/z*: 208(M^+). Anal. calcd. for $C_{14}H_{12}N_2$: C 80.74, H 5.81, N 13.45; found: C 80.88, H 5.92, N 13.50.

General procedure for the Heck type of reaction for compounds 3a–3l

To a mixture of **3a–3l** (0.34 mmol), Bu_4NBr (0.113 g,

© 2008 NRC Canada

0.34 mmol), and KOAc (0.083 g, 0.85 mmol) in dry and degassed DMF (25 mL) in a screw-cap sealed tube was added $Pd(OAc)_2$ (0.008 g, 10 mol%) under an inert atmosphere, and the sealed tube was placed in a preheated oil bath at 80–120 °C (Table 1) with stirring for 1.5–12 h (Table 1, for each reaction). The reaction mixture was cooled and diluted with water (50 mL). This was extracted with ethyl acetate (3 × 20 mL). The organic extract was washed with hydrochloric acid (1N, 20 mL), water (3 × 30 mL), and saturated brine solution (25 mL), and dried (Na_2SO_4). The solvent was distilled off. The crude products were purified by column chromatography over silica gel (60–120 mesh) using petroleum ether – ethyl acetate mixture as the eluant to give compounds **5a**–**5l.** All solid compounds were recrystalized from dichloromethane–petroleum ether (60–80 °C).

3-Methyl-1*H*,6*H*-pyran[4,3-*c*]isochromen-1-one (5a)

Eluted from the column with 20% ethyl acetate – petroleum ether mixture as a colorless solid (87%), mp 110–113 °C (dichloromethane–petroleum ether). IR (KBr, cm^{-1}) υ: 2924, 1705, 1240, 1042. ^1H NMR ($CDCl_3$, 400 MHz, ppm) δ_H: 2.26 (s, 3H), 5.22 (s, 2H), 5.90 (d, *J* = 0.6 Hz, 1H), 7.03 (d, *J* = 7.6 Hz, 1H), 7.22-7.26 (m, 1H), 7.33 (t, *J* = 8.0 Hz, 1H), 8.44 (d, *J* = 8.0 Hz, 1H). MS *m*/*z*: 214 (M^+). Anal. calcd. for $C_{13}H_{10}O_3$: C 72.89, H 4.71; found: C 72.82, H 4.75.

8-Methoxy-3-methyl-1*H*,6*H*-pyran[4,3-*c*]isochromen-1-one (5b)

Eluted from the column with 20% ethyl acetate – petroleum ether mixture as a colorless solid (94%), mp 122 to 123 °C (dichloromethane–petroleum ether). IR (KBr, cm^{-1}) υ: 2920, 1704, 1246, 1045. ^1H NMR ($CDCl_3$, 400 MHz, ppm) δ_H: 2.24 (s, 3H), 3.80 (s, 3H), 5.19 (s, 2H), 5.89 (s, 1H), 6.58 (d, *J* = 2.5 Hz, 1H), 6.86 (dd, *J* = 2.6, 8.72 Hz, 1H), 8.39 (d, *J* = 8.7 Hz, 1H). ^{13}C NMR ($CDCl_3$, 125 MHz, ppm) δ_C: 20.4, 55.7, 69.5, 100.2, 100.6, 110.4, 113.7, 119.4, 126.0, 129.0, 159.5, 161.8, 162.2, 165.0. HRMS calcd. for $C_{14}H_{13}O_4^+$(MH): 245.0814, found 245.0807. Anal. calcd. for $C_{14}H_{12}O_4$: C 68.85, H 4.95; found: C 69.08, H 4.89.

2,3-Dimethyl-2,6-dihydro-1*H*-isochromeno[4,3-*c*]pyridin-1-one (5c)

Eluted from the column with 45% ethyl acetate – petroleum ether mixture as a colorless solid (88%), mp 100–102 °C (dichloromethane–petroleum ether). IR (KBr, cm^{-1}) υ: 2916, 1643, 1239. ^1H NMR ($CDCl_3$, 400 MHz, ppm) δ_H: 2.35 (s, 3H), 3.55 (s, 3H), 5.09 (s, 2H), 5.89 (s, 1H), 7.04 (d, *J* = 7.4 Hz, 1H), 7.19-7.37 (m, 2H), 8.77 (d, *J* = 7.5 Hz, 1H). ^{13}C NMR (125 MHz, ppm) δ_C: 16.2, 25.9, 63.9, 95.2, 100.5, 118.6, 119.4, 121.7, 123.1, 123.5, 123.7, 141.2, 157.2, 157.6. MS *m*/*z*: 227 (M^+). Anal. calcd. for $C_{14}H_{13}NO_2$: C 73.99, H 5.77, N 6.16; found: C 74.20, H 5.69, N 6.29.

8-Methoxy-2,3-dimethyl-2,6-dihydro-1*H*-isochromen[4,3-*c*]pyridin-1-one (5d)

Eluted from the column with 45% ethyl acetate – petroleum ether mixture as a colorless solid (83%), mp 98 to 99 °C (dichloromethane–petroleum ether). IR (KBr, cm^{-1}) υ: 2916, 1644, 1251. ^1H NMR ($CDCl_3$, 400 MHz, ppm) δ_H: 2.33 (s, 3H), 3.54 (s, 3H), 3.81 (s, 3H), 5.07 (s, 2H), 5.87 (s, 1H), 6.60 (d, *J* = 2.5 Hz, 1H), 6.86 (dd, *J* = 2.6, 8.7 Hz, 1H), 8.73 (d, *J* = 8.8 Hz, 1H). MS *m*/*z*: 257 (M^+). Anal. calcd. for $C_{15}H_{15}NO_3$: C 70.02, H 5.88, N 5.44; found: C 70.19, H 5.95, N 5.38.

2-Ethyl-3-methyl-2,6-dihydro-1*H*-isochromen[4,3-*c*]pyridin-1-one (5e)

Eluted from the column with 45% ethyl acetate – petroleum ether mixture as a colorless solid (78%), mp 113 to 114 °C (dichloromethane–petroleum ether). IR (KBr, cm^{-1}) υ: 2982, 1644, 1246. ^1H NMR ($CDCl_3$, 400 MHz, ppm) δ_H: 1.32 (t, *J* = 6.9 Hz, 3H), 2.39 (s, 3H), 4.09 (q, *J* = 7.1 Hz, 2H), 5.09 (s, 2H), 5.85 (s, 1H), 7.03 (d, *J* = 7.6 Hz, 1H), 7.18-7.36 (m, 2H), 8.77 (d, *J* = 8.0 Hz, 1H). ^{13}C NMR (125 MHz, ppm) δ_C: 14.2, 20.8, 39.7, 69.3, 100.8, 106.1, 124.0, 124.7, 127.0, 128.5, 128.8, 129.1, 146.0, 162.0, 162.9. HRMS calcd, for $C_{15}H_{16}O_2^+$(MH): 242.1172; found 242.1184. Anal. calcd. for $C_{15}H_{15}NO_2$: C 74.67, H 6.27, N 5.81; found: C 74.62, H 6.04, N 5.99.

2-Ethyl-8-methoxy-3-dimethyl-2,6-dihydro-1*H*-isochromen[4,3-*c*]pyridin-1-one (5f)

Eluted from the column with 45% ethyl acetate–petroleum ether mixture as a colorless solid (81%), mp 105–107 °C (dichloromethane–petroleum ether). IR (KBr, cm^{-1}) υ: 2917, 1643, 1215. ^1H NMR ($CDCl_3$, 400 MHz, ppm) δ_H: 1.30 (t, *J* = 7.0 Hz, 3H), 2.37 (s, 3H), 3.80 (s, 3H) 4.09 (q, *J* = 7.0 Hz, 2H), 5.06 (s, 2H), 5.84 (s, 1H), 6.59 (d, *J* = 2.5 Hz, 1H), 6.86 (dd, *J* = 2.6, 8.7 Hz, 1H), 8.73 (d, *J* = 8.7 Hz, 1H). MS *m*/*z*: 271 (M^+). Anal. calcd. for $C_{16}H_{17}NO_3$: C 70.83, H 6.32, N 5.16; found: C 71.05, H 6.33, N 5.20.

Compounds 5g and 5h

See ref. 20*a*.

5*H*-Imidazole[5,1-*a*]isoindole (5i)

See ref. 26.

8-Methoxy-5*H*-imidazole[5,1-*a*]isoindole (5j)

Eluted from the column with 40% ethyl acetate – petroleum ether mixture as a colorless solid (84%), mp 141 to 142 °C (dichloromethane–petroleum ether). IR (KBr, cm^{-1}) υ: 2932, 1703, 1041. ^1H NMR ($CDCl_3$, 400 MHz, ppm) δ_H: 3.83(s, 3H), 4.96 (s, 2H), 6.88 (dd, *J* = 2.2, 8.4 Hz, 1H), 6.94 (d, *J* = 2.2 Hz, 1H), 7.06 (s, 1H), 7.43 (d, *J* = 8.3 Hz, 1H), 7.67 (s, 1H). ^{13}C NMR ($CDCl_3$, 125 MHz, ppm) δ_C: 49.0, 56.0, 110.3, 114.3, 117.1, 121.3, 123.8, 132.4, 138.9, 142.6, 159.2. MS *m*/*z*: 186 (M^+). Anal. calcd. for $C_{11}H_{10}N_2O$: C 70.95, H 5.41, N 15.04; found: C 70.88, H 5.47, N 15.16.

11*H*-Benzo[4,5]imidazo[2,1-*a*]isoindole (5k)

See ref. 24*b*.

2-Methoxy-11*H*-benzo[4,5]imidazol[2,1-*a*]isoindole (5l)

Eluted from the column with 40% ethyl acetate – petroleum ether mixture as a colorless solid (61%), mp 122 to 123 °C (dichloromethane–petroleum ether). IR (KBr, cm^{-1}) υ: 2920, 1624, 1265. ^1H NMR ($CDCl_3$, 400 MHz, ppm) δ_H:

© 2008 NRC Canada

3.89 (s, 3H), 5.02 (s, 2H), 7.02 (d, J = 8.0 Hz, 1H), 7.09 (s, 1H), 7.24-7.79 (m, 4H), 8.01 (d, J = 8.2 Hz, 1H). MS m/z: 236 (M^+). Anal. calcd. for $C_{15}H_{12}N_2O$: C 76.25, H 5.12, N 11.86; found: C 76.01, H 5.26, N 11.85.

Acknowledgements

We thank the Council of Scientific and Industrial Research (CSIR, New Delhi) for financial assistance. AKP, PD and AT are thankful to the CSIR for their fellowships. We also thank the Department of Science and Technology (DST, New Delhi) for providing UV–vis and IR spectrometers under the DST-FIST program.

References

1. Comprehensive heterocyclic chemistry. Vols. 1-8. *Edited by* A.R. Katritzky, C.W. Rees, E.F.V. Scriven. Pergamon Press, Oxford, UK. 1996.
2. (*a*) R.P. Lutz. Chem. Rev. **84**, 205 (1984); (*b*) U. Kazmaier and A. Krebs. Angew. Chem Int. Ed. Engl. **34**, 2012 (1995); (*c*) T.P. Yoon, V.M. Dong, and D.W.C. MacMillan. J. Am. Chem. Soc. **121**, 9726 (1999); (*d*) K.C. Majumdar and S.K. Chattopadhyay. Can. J. Chem. **84**, 469 (2006).
3. (*a*) B. Giese. Radicals in organic synthesis: Formation of carbon–carbon bonds. Pergamon, New York, 1986; (*b*) K.C. Majumdar, P.K. Basu, and P.P. Mukhopadhyay. Tetrahedron **60**, 6239 (2004); (*c*) K.C. Majumdar and S. Alam. Org. Lett. **8**, 4059 (2006); (*d*) K.C. Majumdar, A. Biswas, and P.P. Mukhopadhyay. Synthesis, 2385 (2003); (*e*) K.C. Majumdar, P.P. Mukhopadhyay, and A. Biswas. Tetrahedron Lett. **46**, 6655 (2005); (*f*) K.C. Majumdar and P.P. Mukhopadhyay. Synthesis, 920 (2003).
4. (*a*) R.F. Heck. J. Am. Chem. Soc. **90**, 518 (1968); (*b*) For the first example using aryl and vinylic halides, see: T. Mizoroki, K. Mori, and A. Ozaki. Bull. Chem. Soc. Jpn. **44**, 44158 (1971); (*c*) T. Mizutani, S. Honzawa, S.U. Tosaki, and K. Shibasaki. Angew. Chem., Int. Ed. **41**, 4680 (2002).
5. (*a*) For a detailed report on the toxicity of tin reagents, see: Occupational exposure to organotin compounds, US Department of Health, Education and Welfare, Washington. Nov. 1976; (*b*) I. J. Boyer. Toxicology, **55**, 253 (1989); (*c*) S. Lee and G. Robinson. Process development: Fine chemicals from grams to kilograms. Oxford University Press, Oxford, UK. 1995.
6. (*a*) D.C. Harrowven, B.J. Sutton, and S. Coulton. Org. Biomol. Chem. **1**, 4047 (2003); (*b*) W. Zhang and G. Pugh. Tetrahedron, **59**, 3009 (2003).
7. (*a*) L.F. Tietze and A. Modi. Eur. J. Org. Chem. 1959 (2000); (*b*) A.D. Lebsack, J.T. Link, L. E. Overman, and B.A. Stearns. J. Am. Chem. Soc. **124**, 9008 (2002); (*c*) N.E. Carpenter, D.J. Kucera, and L.E. Overman. J. Org. Chem. **54**, 5846 (1989).
8. (*a*) M. Shibasaki, T. Mase, and S. Ikegami. J. Am. Chem. Soc. **108**, 2090 (1986); (*b*) T. Ohshima, K. Kagechika, M. Adachi, M. Sodeoka, and M. Shibasaki. J. Am. Chem. Soc. **118**, 7108 (1996); (*c*) K. Kagechika and M. Shibasaki. J. Org. Chem. **56**, 4093 (1991); (*d*) C. S. Nylund, J.M. Klopp, and S.M. Weinreb. Tetrahedron Lett. **35**, 4287 (1994); (*e*) S. Nukul, M. Sodeoka, and M. Shibasaki. Tetrahedron Lett. **34**, 4965 (1993).
9. (*a*) D.J. Hart and Y.M. Tsai. J. Org. Chem. **47**, 4403 (1982); (*b*) K. Kondo, M. Sodeoka, and M. Shibasaki. J. Org. Chem. **60**, 4322 (1995); (*c*) S.P. Maddaford, N.G. Andersen, W.A. Cristofoli, and B.A. Keay. J. Am. Chem. Soc. **118**, 10766 (1996); (*d*) R.V. Rozhkov, and R.C. Larock. Org. Lett. **5**, 797 (2003); (*e*) S. Gracon, S. Vassiliou, M. Cavicchioli, B. Hartmann, N. Monteiro, and G. Balme. J. Org. Chem. **66**, 4069 (2001).
10. (*a*) W.B. Mors, O.R. Gollilieb, and C. Dierassi. J. Am. Chem. Soc. **79**, 4507 (1957); (*b*) W. J. McGahren, G.A. Ellestad, G.O. Morton, M.P. Kunstman, and P. Mullen. J. Org. Chem. **38**, 3542 1973); (*c*) S.A. Sparace, J.B. Mudd, B.A. Bruke, and A.J. Aasan. Phytochemistry, **23**, 2693 (1984); (*d*) R.J. Capon and D.J.J. Faulkner. J. Org. Chem. **45**, 2506 (1984).
11. S. Omura, H. Ohno, T. Saheki, Y. Masakazu, and A. Nakagawa. Biochem. Biophy. Res. Commun. **83**, 704 (1978).
12. W.C. Groutas, M.A. Stanga, M.J. Brubakar, T.L. Huang, M.K. Moi, and R.J. Carrol. J. Med. Chem. 28, 1106 (1985).
13. P. J. Creaven, Y. Rustum, R. Catane, E.S. Henderson, and E. Mihich. 10th International Congress of Chemotherapy, Zurich, 18–23 Sept. 1977. Abstract No. 540. 1977.
14. M.J. Robins and B.L. Currie. Chem. Commun. 1547 (1968).
15. D.Y. Hua, F. Zhang, J. Chen, and P.D. Robinson. J. Org. Chem. **59**, 5084 (1994).
16. E.B. Skibo, I. Islam, W.G. Schulz, R. Zhou, L. Bess, and R. Boruah. Synlett. 297 (1996).
17. E. Bossharth, P. Desbordes, N. Monteiro, and G. Balme. Org. Lett. **5**, 2441 (2003).
18. M.A. Clyne and F. Aldabbagh. Org. Biomol. Chem. **4**, 268 (2006).
19. R.M. de. Figueiredo, S. Thoret, C. Huet, and J. Dubois. Synthesis, 529 (2007).
20. (*a*) K.C. Majumdar, P.K. Basu, P.P. Mukhopadhyay, S. Sarkar, S.K. Ghosh, and P. Biswas. Tetrahedron, **59**, 2151 (2003); (*b*) K.C. Majumdar and P.P. Mukhopadhyay. Synthesis, 97 (2003).
21. K.C. Majumdar, A.K. Pal, A. Taher, and P. Debnath. Synthesis, 1707 (2007).
22. A.L.J. Beckwith, V.W. Bowry, W.R. Bowman, E. Mann, J. Parr, and J.M.D. Storey. Angew. Chem. Int. Ed. **43**, 95 (2004).
23. (*a*) F. Aldabbagh, W.R. Bowman, E. Mann, and A.M.Z. Slawin. Tetrahedron Lett. **40**, 8111 (1999); (*b*) F. Aldabbagh, W.R. Bowman, and E. Mann. Tetrahedron Lett. **38**, 7937 (1997).
24. (*a*) S.M. Allin, W.R. Bowman, M.R.J. Elsegood, V. McKee, and R. Karim. Tetrahedron, **61**, 2689 (2005); (*b*) S.M. Allin, W.R. Bowman, R. Karim, and S.S. Rahman. Tetrahedron, **62**, 4306 (2006).
25. T. Jeffery. Tetrahedron Lett. **26**, 2667 (1985).
26. N. Arai, M. Takahashi, M. Mitani, and A. Mori. Synlett. 3170 (2006).
27. S. Pivsa-Art, T. Satoh, Y. Kawamura, M. Miura, and M. Nomura. Bull. Chem. Jpn. **71**, 467 (1998).
28. C. Amatore and A. Jutand. Acc. Chem. Res. **33**, 314 (2000)

© 2008 NRC Canada

Generation, observation, and reactivity of furyl- and thienylketenes and bisketenes

Nanyan Fu, Annette D. Allen, Winnie Chan, Shinjiro Kobayashi, Thomas T. Tidwell, Daryoush Tahmassebi, Angelica Aguilar, Eduardo Peña Cabrera, and Jazmin Godoy

Abstract: 2- and 3-Furylketenes (**18** and **20**), 2- and 3-thienylketenes (**19** and **21**), and bis(2,5-ketenyl)thiophene (**24**) have been generated as observable reactive intermediates by photochemical Wolff rearrangements. Stabilization energies of the monoketenes **18**–**21** have been determined by DFT computations of isodesmic energy changes, and these ketenes are predicted to be modestly destabilized relative to phenylketene. Rate constants for reaction of **18**–**21** with H_2O and with *n*-$BuNH_2$ have been measured and are similar to those of the 2-, 3-, and 4-pyridylketenes (**1**). The product of reaction of 2-furylketene (**18**) with H_2O is calculated to be stable as an acid enol, and reaction of **18** with the stable free radical TEMPO forms a stable ester enol, consistent with stabilization by intramolecular H-bonding to the furyl oxygen. Bis(thienyl)-1,2-bisketenes **26** and **28** have been generated by photochemical cyclobutenedione ring opening and are highly reactive in ring closure. This is attributed to destabilization of the ketenes and stabilization of the cyclobutenediones by the electron donating aryl groups.

Key words: ketenes, furans, thiophenes, reactive intermediates, photolysis, mechanisms.

Résumé : Faisant appel à des réarrangements de Wolff photochimiques, on a pu générer des 2- et 3-furylcétènes (**18** et **20**), des 2- et 3-thiénylcétènes (**19** et **21**) ainsi que le bis(2,5-cétényl)thiophène (**24**) sous la forme d'intermédiaires réactifs observables. On a calculé les énergies de stabilisation des monocétènes (**18**–**21**) sur la base de la théorie de la fonctionnelle de densité de changements isodesmiques d'énergie et ces calculs permettent de prédire que ces cétènes sont légèrement déstabilisés par rapport au phénylcétène. On a mesuré les constantes de la vitesse de réaction des produits **18**–**21** avec l'eau et avec la butylamine et elles sont similaires à celles observées avec les 2-, 3- et 4-pyridylcétènes (**1**). On a calculé que le produit de la réaction du 2-furylcétène (**18**) devrait être stable sous la forme d'énol acide et la réaction du produit **18** avec le radical libre stable TEMPO forme un ester énolique stable qui est en accord avec la stabilisation par une liaison hydrogène intramoléculaire avec l'oxygène du furyle. On a généré les bis(thiényl)1,2-biscétènes (**26** et **28**) par ouverture photochimique de la cyclobutènedione et ils sont très réactifs vis-à-vis de la réaction de fermeture de cycle. Cette réactivité est attribuée à la déstabilisation des cétènes et à la stabilisation des cyclobutènediones par les groupes aryles électrodonneurs.

Mots-clés : cétènes, furanes, thiophènes, intermédiaires réactifs, photolyse, mécanismes.

[Traduit par la Rédaction]

Introduction

The chemistry of heteroarylketenes provides opportunities for the elucidation of the interaction of the highly electrophilic ketenyl group with heteroaryl groups. 2-Pyridylketene (**3**) was formed by photolysis of the diazo ketone **1** and observed in an Ar matrix at 10 K or in solution as a highly reactive species at 25 °C, along with the pyridyl ylide **2** (eq. [1]) (1). Photolysis of **2** in the matrix forms **3** (1*a*), and substituted analogues **4**–**6** of **2** have been generated and directly observed in solution at 25 °C, and interpreted as possessing antiaromatic character on the basis of the ^{1}H NMR chemical shifts of **4** (R = *i*-Pr_3Si), calculated nucleus independent chemical shifts (NICS), and calculated bond alternations (1*b*).

[1] 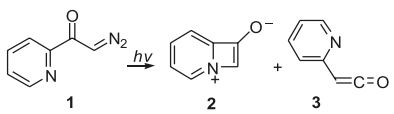

1 2 3

2-Pyridylketene (**3**) forms a dimer **7** by a [4+2] cycloaddition (1*a*), and upon reaction with water (2*a*) and with *n*-$BuNH_2$ (2*b*) forms the dihydropyridine derivatives **8**

Received 7 October 2007. Accepted 25 January 2008. Published on the NRC Research Press Web site at canjchem.nrc.ca on 25 March 2008.

Dedicated to the memory of Keith Yates, a leader in chemistry.

N. Fu, A.D. Allen, W. Chan, S. Kobayashi, and T.T. Tidwell.[1] Department of Chemistry, University of Toronto, Toronto, ON M5S 3H6, Canada.
D. Tahmassebi. Department of Chemistry, Indiana–Purdue University, Fort Wayne, IN 46805, USA.
A. Aguilar, E. Peña Cabrera, and J. Godoy. Facultad de Quimica, Universidad de Guanajuato, Col. Noria Alta S/N, Guanajuato, Gto. 36050, Mexico.

[1]Corresponding author: (e-mail: ttidwell@chem.utoronto.ca).

 doi:10.1139/V08-021 © 2008 NRC Canada

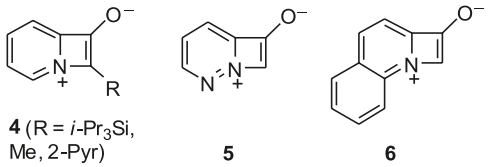

4 (R = *i*-Pr_3Si, Me, 2-Pyr) **5** **6**

and **9**, respectively, as observable reactive intermediates that lead to the corresponding pyridylacetic acid and amide (2*a*, 2*b*). The reactivities of the 3- and 4-pyridylketenes with water and with *n*-$BuNH_2$ have also been examined (2).

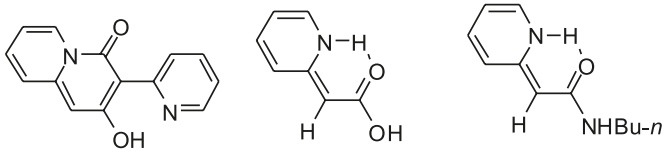

7 **8** **9**

Pyridyl groups are electron poor, and we have also recently reported on the reactivity of electron-rich ferrocenylketenes, including the highly reactive parent **10a** (3*a*) and the triisopropylsilyl derivative **10b**, which is very unreactive because of steric protection and electronic stabilization by the triisopropylsilyl group, and has been isolated as a crystalline solid and characterized by X-ray (3*b*). In studies of bisketene/cyclobutenedione interconversions (3*c*, 3*d*), diferrocenyl-1,2-bisketene **12** was generated by photolysis of the cyclobutenedione **11** (eq. [2]), and the thermal reformation of **11** from **12** was found to be quite rapid, a result attributed to destabilization of the bisketene by the electron-donating ferrocenyl groups, which however stabilize the cyclobutendione **11** (3*a*).

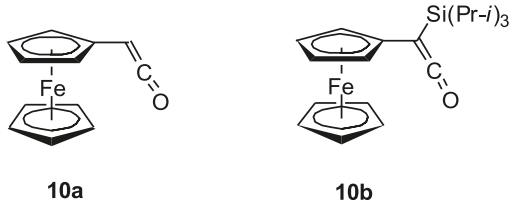

10a **10b**

[2]

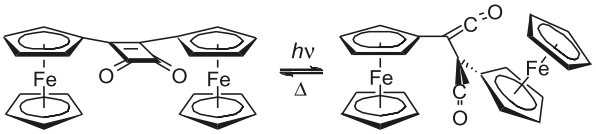

11 **12**

The goal of the present investigation is to extend the examination of electron-rich arylketenes to furylketenes, thienylketenes, and the analogous bisketenes. The chemistry of furyl- and thienylketenes has been recently reviewed (3*e*, 4*a*), and these monoketenes have found significant applications in synthesis (4) and mechanistic studies of their formation (4*m*, 4*n*), but none of these have been characterized by direct observation in solution nor by quantitative reactivity studies. Furylcyclobutenediones have not been previously examined, but reactions of 1,2-bis(2-thienyl)cyclobutenedione with alkynes and carbene precursors have recently been studied (4*o*, 4*p*). Cyclobutenediones have many applications, including use as linkers in DNA analogues (5*a*), chemosensors (5*b*), bioactive compounds with medical applications (5*c*), and receptors for molecular recognition (5*d*). These may also be converted to 1,3-squaraines (**13**), which

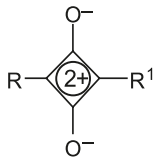

13

have found many uses (6), especially as dyes (6*b*, 6*d*–6*g*), in photodynamic therapy (6*e*), as redox switches (6*f*), and as photoconducting and photoimaging agents (6*f*).

Furyl- and thienyl-ketenes contain electron-rich aryl groups, which are subject to oxidation, and in this respect, resemble ferrocenylketenes but differ from pyridylketenes. Thus, these promise to reveal new types of reactivity not observed with the pyridylketenes. The properties of furyl and thienyl groups may be expressed by their substituent constants, particularly the σ^+_p values, which are significantly more negative than for phenyl, showing their strong electron-donor properties (Table S-1).[2]

2-Furylketene **18** has been reported to form by Wolff rearrangement in a matrix at 10 K, and its structure confirmed by the IR absorption at 2135 cm^{-1} (4*e*), but has not been observed in solution. There is apparently no previous study of 3-furylketene, while 2- and 3-thienylketenes have been generated by dehydrochlorination of the corresponding thienylacetyl chlorides as unobserved intermediates, which reacted by in situ [2+2] cycloaddition with 1,3-cyclohexadiene (4*b*), but have not been directly observed.

Results

For preparation of the 2- and 3-furyl- and thienylketenes **18**–**21**, the known 2- and 3-diazoacetylfurans **14** (4*b*, 4*j*) and **16** (7*a*) and diazoacetylthiophenes **15** (7*b*) and **17** (4*j*) were prepared by the reaction of diazomethane with the corresponding furoyl and thiophenecarbonyl chlorides. Upon photolysis in CH_3CN or hexane of the diazoacetyl furans and thiophenes (eqs. [3] and [4]), formation of the corresponding ketenes was confirmed, as identified by their IR absorptions at 2132 (**18**), 2124 (**19**), 2127 (**20**), and 2122 (**21**) cm^{-1}.

[3]

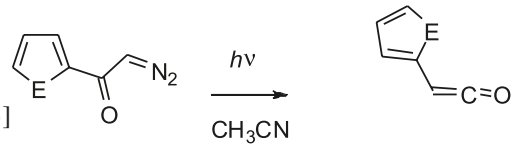

14 (E = O) **15** (E = S)

18 (E = O, IR 2132 cm^{-1}) **19** (E = S, IR 2124 cm^{-1})

[2] Supplementary data for this article are available on the journal Web site (canjchem.nrc.ca) or may be purchased from the Depository of Unpublished Data, Document Delivery, CISTI, National Research Council Canada, Ottawa, ON K1A 0R6, Canada DUD 3725. For more information on obtaining material, refer to cisti-icist-cnrc.gc.ca/irm/unpub_e.shtml.

© 2008 NRC Canada

[4] 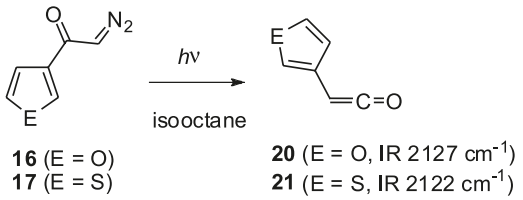

16 (E = O)
17 (E = S)

20 (E = O, IR 2127 cm^{-1})
21 (E = S, IR 2122 cm^{-1})

Previously, we have reported the generation and direct observation of bis(ketenyl)benzenes prepared by dehydrochlorinations or by photochemical Wolff rearrangements (8). To extend this work to the heteroaryl field, 2,5-bis(diazoacetyl)thiophene (**23**) (4*k*, 4*l*) was prepared from the reaction of the bis(acyl choride) **22** with diazomethane, and upon photolysis in CH_3CN presumably gave the bisketene **24**, (eqs. [5] and [6]), as indicated by the ketenyl IR absorption at 2124 cm^{-1} (Fig. 1) and depletion of the diazo and keto absorption at 2112 and 1612 cm^{-1}, respectively. Reaction of both of the diazo ketone groups is not proven, but this was previously found for 1,3-bis(diazoacetyl)benzene (8).

3,4-Di-(2-thienyl)cyclobutenedione **25** (4*o*, 4*p*) and 3,4-di-

[5] 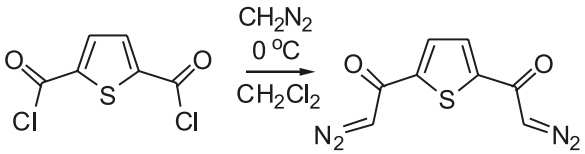

22 **23**

[6] 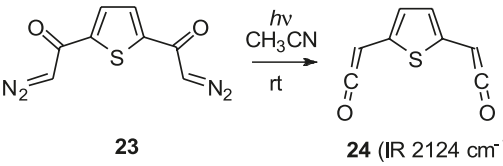

23 **24** (IR 2124 cm^{-1})

(3-thienyl)cyclobutenediones **27** (9) upon photolysis in CH_3CN gave bis(2-thienyl)- and bis(3-thienyl)-1,2-bisketenes **26** and **28**, respectively, as identified by their infrared absorption at 2111 and 2104 cm^{-1}, respectively (eqs. [7] and [8]). Rate constants for thermal ring closure of the bisketenes back to the cyclobutenediones were measured at 25 °C by UV as we have done previously (3*a*, 3*c*, 3*d*) by observing the disappearance of the ketene absorptions and the reformation of cyclobutenedione absorptions. Measured rate constants were obtained in $CDCl_3$ of 5.24 ± 1.20 and 1.51 ± 0.23 s^{-1}, **26** and **28** respectively. These are similar to the rate constant of 2.59 s^{-1} found for the corresponding bis(ferrocenyl) compound **12** (in CH_3CN), and are consistent with the strong electron-donating ability of all these groups (3*a*).

[7] 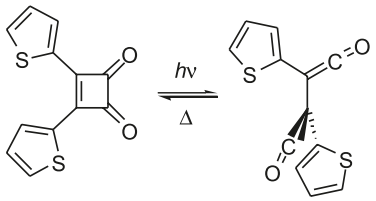

25 **26**

Fig. 1. Ketenyl IR absorption of bisketene **24** in hexane at 2124 cm^{-1} with depletion of diazo ketone absorption at 2112 and 1612 cm^{-1}.

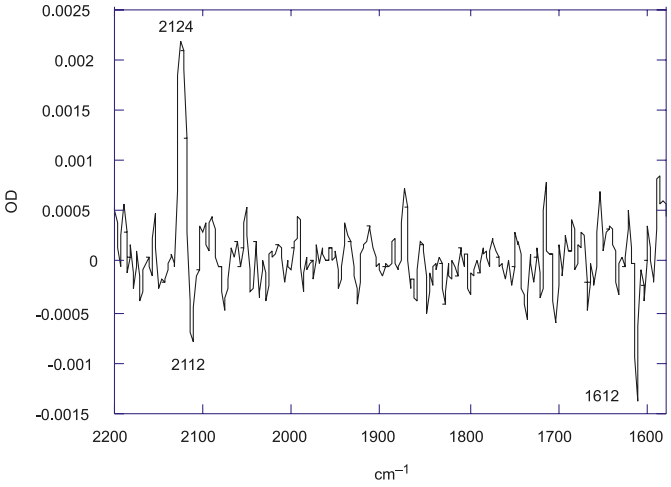

Fig. 2. IR absorption of amide enol **30a** in hexane at 1675 cm^{-1} with depletion of diazo ketone absorption at 2108 and 1606 cm^{-1}.

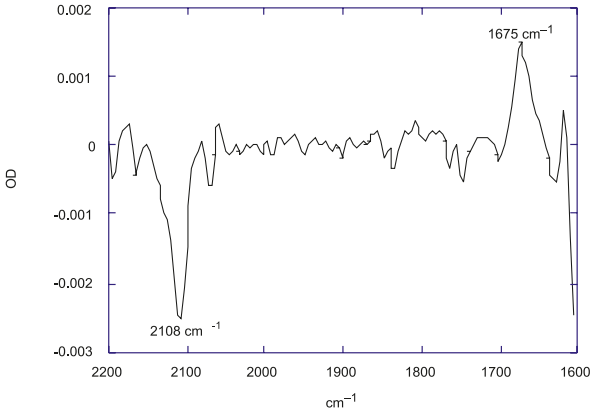

[8] 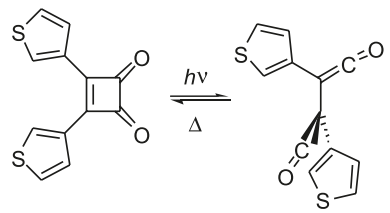

27 **28**

Upon laser flash photolysis (LFP) in CH_3CN in the presence of excess *n*-$BuNH_2$, the diazo ketones **14**–**17** each showed the immediate formation of a transient detected by UV spectroscopy, which decayed with evolution of a second transient, which decayed at a slower rate. As found in previous studies of ketene amination (2*b*,10), the first transients are assigned as the ketenes **18**–**21**, respectively, and the initial observed process rate is formation of the amide enols **29a**–**32a**, while the second step is their conversion to the amides **33a**–**36a** (Scheme 1).

Confirmation of these assignments was obtained by LFP of the 2-furyl- and 2-thienyl diazo ketones **14** and **15**, with

© 2008 NRC Canada

Table 1. Second-order rate constants for amination and first-order rate constants for hydration of furyl- and thienylketenes determined by UV at 25 °C.

Ketene	k_1 *n*-BuNH$_2$ (M^{-1} s^{-1})	k_2 *n*-BuNH$_2$ (M^{-1} s^{-1})	k_1/k_2	k_1(hyd)(s^{-1})	k_2(hyd) (s^{-1})	k_1/k_2[a]
2-Thienyl (**19**)	8.62×10^8	1.16×10^8	7.4	1.32×10^5	2.32×10^4	5.7
3-Thienyl (**21**)	2.19×10^8	1.26×10^7	17	1.58×10^4	6.30×10^3	2.5
4-Pyr[b]	3.7×10^9	6.0×10^8	6.2	5.0×10^4	21	2.4×10^3
3-Pyr[b]	8.9×10^8	2.2×10^8	4.0	2.5×10^4	2.0×10^4	1.2
2-Pyr[b]	2.2×10^8	12.5	1.8×10^7	1.1×10^4	9.8×10^1	1.1×10^2
Ph[b]	5.2×10^8	2.4×10^7	22	3.3×10^4	4.3×10^3	7.7
2-Furyl (**18**)	6.24×10^8	1.07×10^7	58	4.48×10^4	1.66×10^4	2.7
3-Furyl (**20**)	2.94×10^8	7.34×10^6	40	1.19×10^4	5.41×10^3	2.2

Note: k_1 refers to the ketene to enol conversion, and k_2 refers to conversion of the enol.
[a]See text.
[b]Ref. 2*b* for amination; ref. 2*a* for hydration.

Scheme 1. Animation and hydration of furylketenes and thienylketenes.

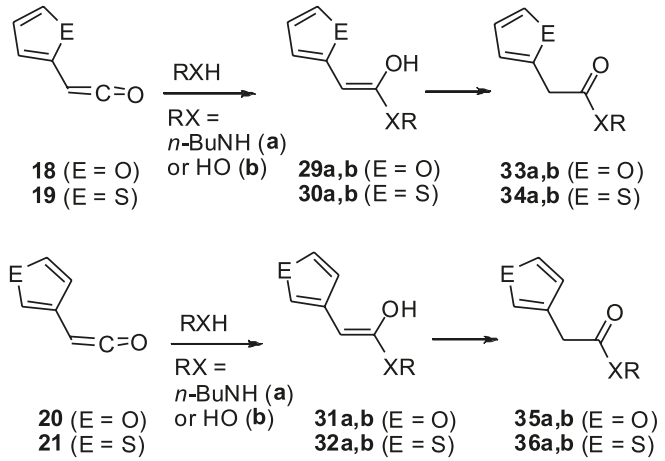

detection of the corresponding ketenes **18** and **19** by observation of the characteristic ketenyl IR absorptions, which formed the respective amide enols **29a** and **30a**, also identified by IR, and finally conversion to the amides **33a** and **34a**, respectively. The IR absorption of the amide enol **30a** from ketene **19** is shown in Fig 2. A representative UV trace for the growth and decay of the UV spectrum of the amide enol **30a** from **19** is shown in the Supplementary data.[2] Rate constants determined by IR for the decay of the ketene absorption and for the formation of the amide enol by IR are in agreement, and also agree with the respective rate constants obtained by UV. Plots of the first-order rate constants obtained by UV vs. [*n*-BuNH$_2$] gave second-order rate constants as reported in Table 1, and the measured rate constants and the plots vs. [*n*-BuNH$_2$] as well as the IR rate data are given in the Supplementary data.[2]

Similarly laser flash photolysis of diazo ketones **14**–**17** in H_2O were monitored by time-resolved UV spectroscopy, and showed the growth of transients absorbing between 240 and 320 nm, followed by a slower decay, and these processes gave first-order rate constants as reported in Table 1. In studies of phenylketene hydration (2*a*, 11), there is some ambiguity in the assignment of these processes, as the identity of the reacting species cannot be confirmed by IR spectroscopic determination. For phenylketene, the growth in the absorption has been assigned to conversion of the acid enol to the acid and the decrease in the absorption to formation of the acid enol from the ketene (11*b*). For the conversion of ketenes **18**–**21** to enols **29b**–**32b** and acids **33b**–**36b** (Scheme 1), the assignments cannot be made with certainty.

For 2-thienylketene (**19**), rate constants for hydration in 80:20 (*v*/*v*) H_2O/CH_3CN were obtained by UV measurement of the decay of the ketenyl absorption at 250 nm and by UV measurement of growth of the acid enol at 300 nm, with good agreement between the two wavelengths.

Photolysis of 2-diazoacetylfuran (**14**) in the presence of 2,2,5,5-tetramethylpiperidinyl-1-oxyl (TEMPO) gave an initial diadduct assigned on the basis of its spectroscopic properties to the structure **37** from 1,2-diaddition of TEMPO to the ketene **18** (eq. [9]). However, upon standing, **37** underwent isomerization to a structure identified as the ester enol **38** (eq. [9]). The analogous reaction of 2-diazoacetylthiophene (**15**) gave the 1,2-addition product **39** (eq. [10]), which was stable over time. Reactions of arylketenes with TEMPO have been previously investigated and found to form 1,2-addition products analogous to **37** (12), but have not previously led to observable enols. The formation of **38** is attributed to the stabilization provided by an intramolecular hydrogen bond to the furyl oxygen shown (see Discussion).

[9]

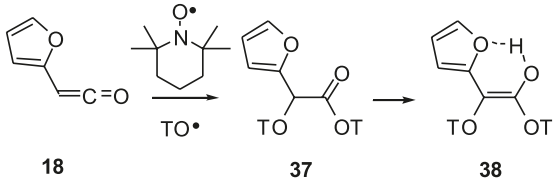

[10]

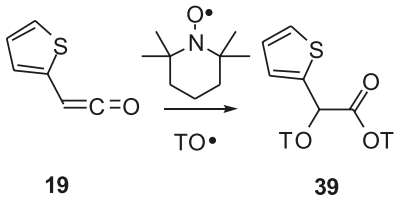

© 2008 NRC Canada

Table 2. B3LYP/6–311++G(d,p) calculated relative minimum and maximum energies (kcal/mol) for conformations of furyl- and thienyl-ketenes.

Ketene	Angle (°)	ΔE (kcal/mol)	Angle (°)	ΔE (kcal/mol)	Angle (°)	ΔE (kcal/mol)
2-Furyl	0.0	0.0	80.0	2.89	180.0	1.00
3-Furyl	20.0	0.86	100.0	2.40	180.0	0.0
2-Thienyl	0.0	0.0	80.0	1.48	160.0	0.13
3-Thienyl	0.0	0.64	100.0	2.86	180.0	0.0

Computational studies

The favored conformations of 2- and 3-furyl-ketenes **18** and **20** and the 2- and 3-thienylketenes **19** and **21** were calculated at the HF/6–31G* and B3LYP/6–311G++(d,p) levels. For each ketene, two minimum energy conformations were found, with coplanar ketenyl and heteraryl groups, and the ring hetero atom *syn* or *anti* to the ketenyl group, as reported in Table 2. For the 2-furyl- and 2-thienylketenes, the *syn* conformations were favored by 1.00 and 0.13 kcal/mol, respectively, while for the 3-furyl- and 3-thienylketenes, the *anti*-conformations were favored by 0.86 and 0.64 kcal/mol, respectively (1 cal = 4.184 J).

Computations at the B3LYP/6–311++G(d,p) level of the structure of the enol **29b** from hydration of 2-furylketene (**18**) found the most stable geometry was a planar structure with the enediol moiety *syn* to the ring oxygen and with an intramolecular hydrogen bond between the oxygen atom in the furan ring and one of the OH groups on the enol (Fig. 3). This was 2.9 kcal/mol more stable than the other minimum energy structure, in which the enediol moiety is *anti* to the ring oxygen, and twisted 30° out of the furan plane. The most stable geometry calculated for the enol **30b** from hydration of 2-thienylketene (**19**) was a non-planar structure with the enediol moiety *anti* to the ring oxygen and twisted 40° out of the thiophene plane (Fig. 3). This was 0.6 kcal/mol more stable than the other minimum energy structure, which had the enediol moiety *syn* to the ring sulfur, and twisted 20° out of the thiophene plane. Details of the computations are given in Table S-2.[2]

2-Furylacetic acid (**40**) is calculated at the B3LYP/6–311++G(d,p) level to be 15.2 kcal/mol more stable than the enol **29b**. For comparison, 2-pyridylactic acid was found to be more stable than the hydrogen bonded enol **41** by 7.0 kcal/mol and more stable than the hydrogen bonded dihydropyridine **8** by 2.1 kcal/mol (2*c*). The comparatively greater stability of **8** and **41** relative to 2-pyridylacetic acid is consistent with the greater basicity of the pyridyl nitrogen.

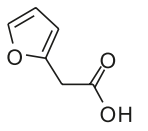

40

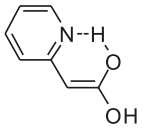

41

Stabilization energies for the furyl- and thienylketenes **18**–**21** were obtained at the B3LYP/6–31G(*d*) level from isodesmic energy comparisons using eq. [11] as done previously (3*a*, 13) and gave values (kcal/mol) of –1.41 (2-furyl-, **18**), –0.61 (3-furyl-, **20**), –1.53 (2-thienyl, **19**), and 0.00 (3-thienyl, **21**). These compare to *SE* values of –0.7 for ferrocenyl and 1.3 for phenyl. The phenyl value was obtained in this work at the B3LYP/6–31G(*d*) level and is close to the value of 0.9 previously (13) obtained at the HF/6–31G* level. The lower stabilization by the furyl, thienyl, and ferrocenyl groups relative to phenyl is modest but is consistent with the previously proposed destabilization of ketenes by strong π-donors.

Fig. 3. B3LYP/6–311++G(d,p) calculated energy minimum structures for 2-furyl enol **29b** (upper) and 2-thienyl enol **30b** (lower).

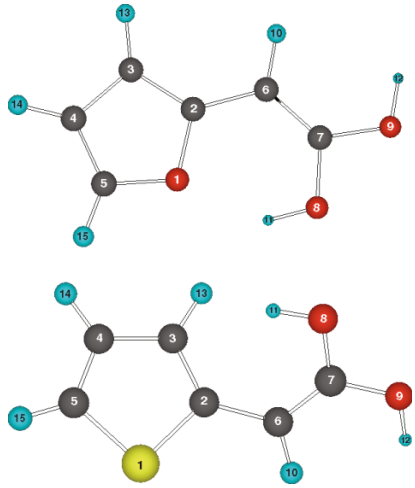

[11] 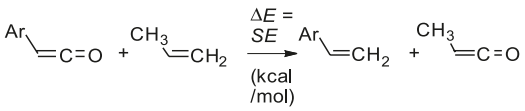

Discussion

2-Furyl- and 2-thienylketene are somewhat more reactive than their 3-isomers in both amination and hydration, with relative rates ranging from 2.1 to 8.4 (Table 1). The Hammett σ_m and σ_p constants (Table S-1)[2] (14) are available for the thienyl derivatives and indicate the 2-isomer is somewhat more electron-withdrawing, and this may cause the difference, as the more electron-withdrawing group would preferentially stabilize a transition state for nucleophilic attack. A direct interaction between the heteroatom and the ketenyl oxygen in the transition state would be expected to be destabilizing, unless there is assistance by hydrogen bonding with the solvent.

There are significant reactivity differences between the initial first step of nucleophilic addition to the ketene, and the second step of conversion of the enol, with k_1/k_2 ratios of 58, 7.4, 40, and 17 for amination of ketenes **18**–**21**, respectively, while for hydration, the corresponding ratios are 2.7,

© 2008 NRC Canada

5.7, 2.2, and 2.5, respectively. For hydration and amination of 2-pyridylketene, corresponding rate ratios for formation and decay of the intermediates **8** (2*a*) and **9** (2*b*) were 110 and 1.8×10^7, respectively. The large rate differences for the 2-pyridyl system were attributed to the formation of dihydropyridine structures with strong intramolecular hydrogen bonds. 2-Furylketene gives a distinctly larger k_1/k_2 ratio in amination compared with 2–thienylketene, and this may also be attributed to formation of an intermediate hydrogen-bonded amide enol **42**. This effect is not observed in hydration, where hydrogen bonding to the solvent may preempt an intramolecular interaction. The B3LYP/6–311++G(d,p) computations suggest that the enol from hydration of 2-furylketene is stabilized by formation of an intramolecular hydrogen bond (Fig. 3), but this computation is for the gas phase, and in H_2O solvent, the formation of intermolecular hydrogen bonds would preclude formation of a long-lived enol. For addition of *n*-$BuNH_2$ in CH_3CN, hydrogen bonding to the solvent is much weaker, and so the enols are relatively longer lived, especially for the amide enol **42** from 2-furylketene.

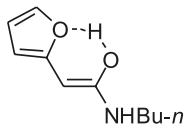

42

As noted for the reaction of 2-furylketene with TEMPO, the final product was an ester enol **38** (eq. [9]), and the stability of this product may be attributed to the formation of an intramolecular hydrogen bond from the enol hydrogen to the furan oxygen, with a possible contribution from steric factors.

The ketene stabilization parameters *SE* (kcal/mol) of –1.41 (2-furyl-, **18**), –0.61 (3-furyl-, **20**), –1.53 (2-thienyl, **19**), and 0.00 (3-thienyl (**21**) do not differ greatly in magnitude, but indicate the 2-furyl- and 2-thienylketenes are less stable than their 3-isomers. However, the rather small variations in the reactivity of these ketenes in amination and in hydration suggest these are not major factors. This may arise because of opposing effects of these aryl groups on the reactant and transition state energies. Overall, the observed differences in reactivity of the heteroarylketenes are consistent with the small differences in the various measures of substituent effects.

The measured rate constants for ring closure of the 2- and 3-thienyl bisketenes **26** and **28** in $CDCl_3$ exceed that of the diphenyl bisketene of 3.89×10^{-2} s^{-1} in isooctane (3*d*) by factors of 130 and 39, respectively. The rate constants for ring closure of other bisketenes to cyclobutenediones have been found to be greater in CH_3CN compared with isooctane by factors of 9 to 16, but **26** and **28** still appear to be more reactive than the diphenyl bisketene, consistent with the ketene destabilizing and cyclobutenedione stabilizing effects of the thienyl substituents.

In summary, the various ketenes and bisketenes reported have been characterized as transient observable intermediates in solution, and quantitative measurements of their reactivities have been made. Contrasting behavior between the furyl- and thienylketenes compared with those of pyridylketenes may be interpreted in terms of the greater electron-acceptor character of the latter. Kinetic studies of ring closure of thienyl substituted bisketenes give quantitative measures of the substituent effects of the thienyl groups. Evidence for intramolecular hydrogen bonding in enols of furylacetic acid derivatives is observed, but not for the corresponding 2-thienyl products. These studies should facilitate the utilization of these intermediates in practical applications.

Experimental

Materials and instruments

Reagents and solvents were the best available commercial grade and were used as received. Time-resolved IR experiments at the University of Toronto were carried out with a Digilab instrument using a 1 mm CaF_2 IR flow cell and laser flash photolysis with a 308 nm excimer laser. The time resolution was 5 μs, and the spectral resolution was 4 cm^{-1}. UV measurements were carried out as described previously (2, 3*a*–3*c*).

2-Diazoacetylfuran (14) (4*j*, 7*b*)

2-Furoyl chloride (493 μL, 653 mg, 5 mmol) in ether (10 mL) was added dropwise to a stirred cooled solution of diazomethane (25 mmol) in ether (40 mL), and the solution was stirred overnight. Excess diazomethane was removed by evacuating with a water aspirator pump, and the remaining solution was concentrated. Chromatography (silica gel, CH_2Cl_2 1% Et_3N) gave the known compound as a yellow oil (457 mg, 67%), which gave yellow crystals on cooling with a mp near room temperature (lit. mp 25 °C) (15*a*). IR (CH_3CN): 2112, 1619 cm^{-1}; IR (hexanes): 2108, 1639 cm^{-1}. ^1H NMR (400 MHz, $CDCl_3$) δ: 7.50 (dd, J = 0.8, 1.6 Hz, 1H), 7.13 (dd, J = 0.8, 3.6 Hz, 1H), 6.54 (dd, J = 1.6, 3.6 Hz, 1H), 5.92 (s, 1H). ^{13}C NMR (100 MHz, $CDCl_3$) δ: 175.5, 151.6, 145.4, 114.5, 112.6, 54.1.

2-Furylketene (18)

Using TRIR detection with LFP of 1.08×10^{-4} mol/L 2-diazoacetylfuran (**14**) in CH_3CN 2-furylketene was detected at 2132 cm^{-1}. Rayonet irradiation of **14** in hexane formed 2-furylketene as identified by the IR absorption at 2134 cm^{-1}.

N-*n*-Butyl 2-furylacetamide (33a)

A solution of **14** (20 mg, 0.15 mmol) and *n*-$BuNH_2$ (1.45 mL, 1.08 g, 14.7 mmol) in hexanes (50 mL) was photolyzed for 10 min with 300 nm light at room temperature. Excess *n*-$BuNH_2$ and solvent was removed at reduced pressure to give a yellow–brown oil. Chromatography (silica gel, EtOAc/hexanes 1:2 *v*/*v*) gave **33a** as a colorless oil (10 mg, 40%), which in the refrigerator gave white crystals, mp 35–36 °C. IR (CH_3CN) 3390 (br), 1678 cm^{-1}. UV–vis (CH_3CN) λ_{max} (ε): 213 nm (1.6×10^4); UV–vis (water) λ_{max} (ε): 220 nm (9.9×10^3). ^1H NMR (400 MHz, $CDCl_3$) δ: 7.39 (dd, J = 0.8, 1.8 Hz, 1H), 6.36 (dd, J = 1.8, 3.2 Hz, 1H), 6.23 (dd, J = 0.8, 3.2 Hz, 1H), 5.65 (s, br, 1H), 3.60 (s, 2H), 3.26–3.21 (m, 2H), 1.47–1.41 (m, 2H), 1.32–1.27 (m, 2H), 0.90 (t, J = 7.2 Hz, 3H). ^{13}C NMR (100 MHz, $CDCl_3$) δ: 168.6, 149.2, 142.8, 111.0, 108.7, 39.7, 36.6, 31.7, 20.2,

© 2008 NRC Canada

13.9. ESI-MS *m/z*: 182 ([M + 1]$^+$). HR-ESI-MS *m/z* calcd. for $C_{10}H_{16}NO_2$: 182.1175, found: 182.1180.

3-Diazoacetylfuran (16) (7*a*)

3-Furoyl chloride (653 mg, 5 mmol) in ether (10 mL) was added dropwise to a stirred cooled solution of diazomethane (25 mmol) in ether (40 mL), and the solution was stirred overnight. Excess diazomethane and solvent were removed under reduced pressure. Chromatography (silica gel, CH_2Cl_2/hexanes 3:1 *v/v* 1% Et_3N) gave **15** as yellow crystals (454 mg, 67%), mp 43.0–43.5 °C. UV–vis (CH_3CN) λ_{max} (ε): 210 nm (1.34×10^4), 287 nm (1.36×10^4); UV–vis (water) λ_{max} (ε): 215 nm (1.10×10^4), 295 nm (1.68×10^4). ^{1}H NMR (400 MHz, $CDCl_3$) δ: 7.93 (dd, *J* = 0.8, 1.5 Hz, 1H), 7.45 (dd, *J* = 1.5, 1.8 Hz, 1H), 6.68 (dd, *J* = 0.8, 1.8 Hz, 1H), 5.64 (s, 1H). ^{13}C NMR (100 MHz, $CDCl_3$) δ: 180.5, 144.9, 144.4, 126.4, 108.4, 54.8. EI-MS *m/z*: 136 (M$^+$, 100), 95 (60), 80 (93). HR-EI-MS *m/z* calcd. for $C_6H_4N_2O_2$: 136.0273, found: 136.0270.

Detection of 3-furylketene (20)

Laser flash photolysis of 5.5×10^{-3} mol/L 3-diazoacetylfuran (**16**) in isooctane gave IR absorption at 2110 cm^{-1} and 1646 cm^{-1}. Irradiation of **16** in a Rayonet reactor with 300 nm light for 2 min gave 80% conversion to ketene. Additional irradiation for 1 min gave only 3-furylketene at 2127 cm^{-1}.

***N*-*n*-Butyl 3-furylacetamide (35a)**

A solution of **16** (20 mg, 0.147 mmol) and *n*-$BuNH_2$ (1.45 mL, 1.075 g, 14.7 mmol) in hexanes (50 mL) was photolyzed for 20 min with 300 nm light at room temperature. Excess *n*-$BuNH_2$ and solvent were removed under reduced pressure to give a yellow oil, and chromatography (silica gel, ethyl acetate/hexanes 1:2 *v/v*) gave **35a** (13 mg, 48%) as white crystals, mp 40–41 °C. IR (CH_3CN): 3389 (br), 1674 cm^{-1}. UV–vis (CH_3CN) λ (ε): 220 nm (4.4×10^3); UV–vis (water) λ (ε): 220 nm (6.1×10^3). ^{1}H NMR (400 MHz, $CDCl_3$) δ: 7.43 (dd, *J* = 0.4, 1.6 Hz, 1H), 7.38 (dd, *J* = 0.8, 1.6 Hz, 1H), 6.34 (dd, *J* = 0.4, 0.8 Hz, 1H), 5.55 (s, br, 1H), 3.39 (s, 2H), 3.25–3.20 (m, 2H), 1.46–1.42 (m, 2H), 1.32–1.26 (m, 2H), 0.90 (t, *J* = 7.2 Hz, 3H). ^{13}C NMR (100 MHz, $CDCl_3$) δ: 170.4, 144.0, 141.0, 118.6, 111.5, 39.6, 33.2, 31.8, 20.2, 13.9. ESI-MS *m/z*: 182 ([M + 1]$^+$). HR-ESI-MS *m/z* calcd. for $C_{10}H_{16}NO_2$: 182.1175, found: 182.1180.

2-Diazoacetylthiophene (15) (7*b*, 15*a*–15*c*)

2-Thienylcarbonyl chloride (144 mg, 1 mmol) in ether (10 mL) was added dropwise to a stirred cooled solution of diazomethane (10 mmol) in ether (20 mL), and the solution was stirred overnight. Excess diazomethane and solvent were removed under reduced pressure, and chromatography (silica gel, CH_2Cl_2/hexanes 1:1 v/v 1% Et_3N) gave **15** as yellow crystals (130 mg, 85%), mp 58–59 °C. IR (CH_3CN): 2108, 1606 cm^{-1}. ^{1}H NMR (400 MHz, $CDCl_3$) δ: 7.59 (dd, *J* = 1.1, 5.0 Hz, 1H), 7.51 (dd, *J* = 1.1, 3.7 Hz, 1H), 7.11 (dd, *J* = 3.7, 5.0 Hz, 1H), 5.82 (s, 1H). ^{13}C NMR (100 MHz, $CDCl_3$) δ: 179.1, 142.7, 132.4, 129.2, 128.2, 54.4. EI-MS *m/z*: 152 (100, M$^+$), 111 (71), 96 (98), 84 (16), 70 (62). HR-EI-MS *m/z* calcd. for $C_6H_4N_2OS$: 152.0044, found: 152.0049. Mp 67–68° (lit. (7b) 67 °C). UV: 216 nm, 309 nm (in methanol).

2-Thienylketene (19)

2-Diazoacetylthiophene (**15**, 1.34×10^{-4} mol/L in CH_3CN) upon LFP gave 2-thienylketene as detected at 2124 cm^{-1}.

***N*-*n*-Butyl 2-thienylacetamide (34a) (15*d*)**

A solution of **15** (20 mg, 0.13 mmol) and *n*-$BuNH_2$ (1.3 mL, 961 mg, 13.2 mmol) in hexanes (50 mL) was photolyzed for 10 min with 300 nm light at room temperature. Excess *n*-$BuNH_2$ and solvent were removed under reduced pressure to give **34a** (24 mg, 92%) as a brown oil. IR (CH_3CN): 1674 cm^{-1}. ^{1}H NMR (400 MHz, $CDCl_3$) δ: 7.25–7.24 (m, 1H), 7.00–6.98 (m, 1H), 6.94–6.93 (m, 1H), 5.65 (s, br, 1H), 3.77 (s, 2H), 3.25–3.20 (m, 2H), 1.45–1.39 (m, 2H), 1.33–1.25 (m, 2H), 0.88 (t, *J* = 7.4 Hz, 3H).

Reaction of 2-furylketene (18) with TEMPO

A solution of 2-diazoacetylfuran (24 mg, 0.18 mmol) in hexane (10 mL) was irradiated with 300 nm light at room temperature with stirring for 9 min, followed by addition of TEMPO (47 mg, 0.30 mmol) dissolved in hexane (0.3 mL). After 2 h stirring, the mixture was filtered and concentrated. Chromatography (silica gel, EtOAc/hexane 1:9 *v/v*, 1% Et_3N) at 4 °C gave material identified as predominantly the unstable TEMPO ester **37** (61 mg, 47%). IR ($CDCl_3$): 1780 cm^{-1}. ^{1}H NMR ($CDCl_3$) δ: 7.40–7.38 (d, 1H), 6.43–6.42 (d, 1H), 6.35 (s, 1H), 5.34 (s, 1H), 1.3–1.75 (m, 12H), 1.24 (s, 3H), 1.22 (s, 3H), 1.14 (s, 3H), 1.08 (s, 3H), 1.04 (s, 3H), 0.92 (s, 3H), 0.80 (s, 3H), 0.67 (s, 3H). On standing 14 h in the NMR tube, the product changed to **38**: IR ($CDCl_3$): 3689, 3607 cm^{-1}. ^{1}H NMR ($CDCl_3$) δ: 7.55–7.54 (d, 1H), 6.61–6.60 (d, 1H), 6.35 (s, 1H), 5.42 (s, 1H), 1.3–1.75 (m, 12H), 1.35 (s, 3H), 1.29 (s, 3H), 1.23 (s, 3H), 1.20 (s, 3H), 1.19 (s, 3H), 1.14 (s, 3H), 1.11 (s, 6H), 1.10 (s, 3H). ^{13}C NMR (100 MHz, $CDCl_3$) δ: 136.4, 127.7, 114.6, 90.3, 88.9, 60.7, 60.7, 60.0, 59.9, 40.4, 39.9, 39.2, 33.7, 33.3, 32.0, 20.7, 20.6, 20.2, 17.2, 17.1. HR-ESI-MS *m/z* calcd. for $C_{24}H_{41}N_2O_4$: 421.3060, found: 421.3078.

3-Diazoacetylthiophene (17) (4*k*)

3-Thienylcarbonyl chloride (733 mg, 5 mmol) in ether (10 mL) was added dropwise to a stirred cooled solution of diazomethane (25 mmol) in ether (40 mL), and the solution was stirred overnight. Excess diazomethane and solvent were evaporated under reduced pressure, and chromatography (silica gel, CH_2Cl_2/hexanes 2:1 *v/v* 1% Et_3N) gave **17** as yellow crystals (468 mg, 62%), mp 59–60 °C. UV–vis (CH_3CN) λ_{max} (ε): 222 nm (1.43×10^4), 257 nm (1.35×10^4), 293 nm (1.50×10^4); UV–vis (water) λ_{max} (ε): 223 nm (1.09×10^4), 257 nm (9.01×10^3), 301 nm (1.88×10^4). ^{1}H NMR (400 MHz, $CDCl_3$) δ: 7.90 (m, 1H), 7.41 (m, 1H), 7.33 (m, 1H), 5.80 (s, 1H). ^{13}C NMR (100 MHz, $CDCl_3$) δ: 180.8, 140.9, 129.3, 126.8, 126.0, 54.7.

3-Thienylketene (21)

3-Diazoacetylthiophene (**17**, 7.7 mmol/L) in iso-octane (IR: 2106 cm^{-1} and 1639 cm^{-1}) upon 1 min irradiation in a Rayonet reactor with 300 nm light gave 50% conversion to

© 2008 NRC Canada

ketene. Additional irradiation for 2 min showed only **21**, IR: 2122 cm^{-1}.

***N*-*n*-Butyl 3-thienylacetamide (36a)**

A solution of **17** (20 mg, 0.13 mmol) and *n*-$BuNH_2$ (1.30 mL, 961 mg, 13.1 mmol) in hexanes (50 mL) was photolyzed for 15 min with 300 nm light at room temperature. Excess *n*-$BuNH_2$ and solvent were evaporated under reduced pressure, and the solid product was purified by chromatography (silica gel, EtOAc/hexanes 1:2 *v*/*v*) to give **36a** (21 mg, 81%) as white crystals, mp 51–53 °C. IR (CH_3CN): 3392, 1673 cm^{-1}. UV–vis (CH_3CN) λ_{max} (ε): 233 nm (6.3×10^3); UV–vis (water) λ_{max} (ε): 235 nm (6.8×10^3). ^1H NMR (400 MHz, $CDCl_3$) δ: 7.34 (dd, *J* = 2.8, 4.8 Hz, 1H), 7.14–7.13 (m, 1H), 7.00 (dd, *J* = 1.2, 4.8 Hz, 1H), 5.55 (s, br, 1H), 3.59 (s, 2H), 3.24–3.19 (m, 2H), 1.44–1.38 (m, 2H), 1.30–1.24 (m, 2H), 0.88 (t, *J* = 7.4 Hz, 3H). ^{13}C NMR (100 MHz, $CDCl_3$) δ: 170.6, 135.2, 128.7, 126.9, 123.6, 39.6, 38.4, 31.7, 20.2, 13.9. EIMS *m*/*z*: 197 (29, M^+), 182 (1), 155 (3), 98 (100), 57 (52). HR-EI-MS *m*/*z* calcd. for $C_{10}H_{15}NOS$: 197.0874, found: 197.0874.

2,5-Bis(diazoacetyl)thiophene (23) (4*k*, 4*l*)

Thiophene-2,5-dicarbonyl chloride (418 mg, 2 mmol) in ether (10 mL) was added dropwise to a stirred cooled solution of diazomethane (20 mmol) in ether (40 mL), and the solution was stirred overnight. Excess diazomethane and residual solvent were evaporated under reduced pressure, and chromatography (silica gel; CH_2Cl_2 1% Et_3N) gave **23** as a pale yellow solid (187 mg, 42%), mp 150 °C (dec.). ^1H NMR (400 MHz, DMSO-d_6 and $CDCl_3$) δ: 7.69 (s, 2H), 6.71 (s, 2H). ^{13}C NMR (100 MHz, DMSO-d_6 and $CDCl_3$) δ: 178.4, 147.0, 129.5, 54.5. EI-MS *m*/*z*: 220 (100, M^+), 108 (100), 95 (57), 82 (28), 69 (47). HR-EI-MS *m*/*z* calcd. for $C_8H_4N_4O_2S$: 220.0055, found: 220.0061.

2,5-Bis(ketenyl)thiophene (24)

Upon LFP of 2,5-bis-diazoacety-thiophene (**23**, 1.82×10^{-5} mol/L in CH_3CN), an absorption at 2124 cm^{-1} with no change in OD for 5 ms was detected.

Photolysis of 3,4-di-(2-thienyl)cyclobut-3-ene-1,2-dione (25) forming 2,3-di-(2-thienyl)-2,3-bisketene (26)

Upon LFP of **25** (1.06×10^{-4} mol/L in CH_3CN), an absorption at 2111 cm^{-1} was detected with no change in OD for 1 ms.

Photolysis of 3,4-di-(3-thienyl)cyclobut-3-ene-1,2-dione (27) forming 2,3-di-(3-thienyl)-2,3-bisketene (28)

Upon LFP of **27** in CH_3CN, absorption at 2104 cm^{-1} was detected with no change in OD for 1 ms.

Reaction of 2-thienylketene (19) with TEMPO

A solution of 2-diazoacetylthiophene (**15**, 15 mg, 0.10 mmol) in pentane (50 mL) was purged with argon for 30 min and then irradiated with 300 nm light at room temperature for 5 min, followed by addition of TEMPO (31 mg, 0.20 mmol) dissolved in pentane (1 mL). After 2 h under Ar, the orange turbid solution was concentrated. Chromatography (silica gel, EtOAc/hexanes 1:10 *v*/*v* 1% Et_3N) gave the bis(TEMPO) adduct as colorless crystals (32 mg, 72 %), mp 37–40 °C, color change at 90–91 °C. IR ($CDCl_3$): 1774 cm^{-1}. ^1H NMR (400 MHz, $CDCl_3$) δ: 7.25 (d, *J* = 0.8 Hz, 1H), 7.11 (d, *J* = 2.9 Hz, 1H), 6.95 (dd, *J* = 5.1, 3.5 Hz, 1H), 5.49 (s, 1H), 1.30–1.75 (m, 12H), 1.24 (s, 3H), 1.23 (s, 3H), 1.14 (s, 3H), 1.08 (s, 3H), 1.05 (s, 3H), 0.92 (s, 3H), 0.75 (s, 3H), 0.61 (s, 3H). ^{13}C NMR (100 MHz, $CDCl_3$) δ: 170.1, 141.6, 126.5, 126.4, 125.7, 83.4, 60.8, 60.7, 60.2, 59.8, 40.5, 40.4, 36.6, 39.4, 33.8, 33.5, 32.1, 31.1, 20.7, 20.3, 20.2, 17.2, 17.0. ESI-MS *m*/*z*: 437 ($[M + 1]^+$). HR-ESI-MS *m*/*z* calcd. for $C_{24}H_{41}N_2O_3S$: 437.2832, found: 437.2844.

Acknowledgement

Financial support by the Natural Sciences and Engineering Research Council of Canada (NSERC) and the Petroleum Research Fund administered by the American Chemical Society is gratefully acknowledged.

References

1. (*a*) A. Kuhn, C. Plüg, and C. Wentrup. J. Am. Chem. Soc. **122**, 1945 (2000); (*b*) N. Fu, A.D. Allen, S. Kobayashi, P. Sequeira, M. Shang, T.T. Tidwell, and M. Mishima. J. Am. Chem. Soc. **129**, 6210 (2007).
2. (*a*) A.D. Allen, A.V. Fedorov, T.T. Tidwell, and S. Vukovic. J. Am. Chem. Soc. **126**, 15777 (2004); (*b*) A.W. Acton, A.D. Allen, L.M. Antunes, A.V. Fedorov, K. Najafian, T.T. Tidwell, and B.D. Wagner. J. Am. Chem. Soc. **124**, 13790 (2002); (*c*) A.V. Fedorov, K. Najafian, T.T. Tidwell, and S. Vukovic. Can. J. Chem. **83**, 1561 (2005).
3. (*a*) A. Aguilar-Aguilar, A.D. Allen, E. Peña-Cabrera, A. Fedorov, N. Fu, H. Henry-Riyad, S. Kobayashi, J. Leuninger, U. Schmid, T.T. Tidwell, and R. Verma. J. Org. Chem. **70**, 9556 (2005); (*b*) N. Fu, A.D. Allen, S. Kobayashi, and T.T. Tidwell. Arkivoc, **3**, 143 (2007); (*c*) N. Fu, A.D. Allen, S. Kobayashi, T.T. Tidwell, S. Vukovic, S. Arumugam, V.V. Popik, and M. Mishima. J. Org. Chem. **72**, 1951 (2007); (*d*) A.D. Allen, J.D. Colomvakos, F. Diederich, I. Egle, X. Hao, R. Liu, J. Lusztyk, J. Ma, M. A. McAllister, Y. Rubin, K. Sung, T.T. Tidwell, and B.D. Wagner. J. Am. Chem. Soc., **119**, 12125 (1997); (*e*) T.T. Tidwell. Ketenes. 2nd ed. Wiley, Hoboken, NJ. 2006.
4. (*a*) T.T. Tidwell. Science of synthesis (Houben-Weyl). Vol. 23, Chap. 12. Thieme, Stuttgart, 2006; (*b*) E.F. Lee-Ruff and J. Ablenas. Can. J. Chem. **65,** 1663 (1987); (*c*) S. France, H. Wack, A.E. Taggi, A.M. Hafez, T.R. Wagerle, M.H. Shah, C.L. Dusich, and T. Lectka. J. Am. Chem. Soc. **126**, 4245 (2004); (*d*) S.L. Wiskur and G.C. Fu. J. Am. Chem. Soc. **127**, 6176 (2005); (*e*) G. Maier, H.P. Reisenauer, and T. Sayrac. Chem. Ber. **115**, 2192 (1982); (*f*) R.L. Danheiser, R.G. Brisbois, J.J. Kowalczyk, and R.F. Miller. J. Am. Chem. Soc. **112**, 3093 (1990); (*g*) J. Bussenius, N. Laber, T. Müller, and W. Eberbach. Chem. Ber., **127**, 247 (1994); (*h*) S.P. Marsden and W.-K. Pung. Chem. Commun. 1199 (1999); (*i*) B.L. Hodous and G.C. Fu. J. Am. Chem. Soc. **124**, 10006 (2002); (*j*) R.L. Danheiser, R.F. Miller, R.G. Brisbois, and S.Z. Park. J. Org. Chem. **55**, 1959 (1990); (*k*) W. Ried and H. Mengler. Angew. Chem., Int. Ed. Engl. **2**, 483 (1963); (*l*) W. Ried and H. Mengler. Justus Liebigs Ann. Chem. **678**, 113 (1964); (*m*) Y.P. Sang, J.C. Eun, J.S. Hyoun, C.K. Ju, H.L. Seok, and R.C. Bong. Bull. Korean Chem. Soc. **28**, 917 (2007); (*n*) B.R. Cho, and S.Y. Pyun. J. Org. Chem. **72**, 1098 (2007); (*o*) V. Nair, A. Deepthi, M. Poonoth, B. Santhamma, S. Vellalath, B.P. Babu,

© 2008 NRC Canada

R. Mohan, and E. Suresh. J. Org. Chem. **71**, 2313 (2006); (*p*) V. Nair, A.N. Pillai, P.B. Beneesh, and E. Suresh. Org. Lett. **7**, 4625 (2005).

5. (*a*) K. Sato, K. Seio, and M. Sekine. J. Am. Chem. Soc. **124**, 12715 (2002); (*b*) N.C. Lim, M.D. Morton, H.A. Jenkins, and C. Brückner. J. Org. Chem. **68**, 9233 (2003); (*c*) G. Verniest, J. Colpaert, K.W. Törnoos, and N. De Kimpe. J. Org. Chem. **70**, 4549 (2005); (*d*) A. Frontera, J. Morey, A. Oliver, M.N. Piña, D. Quiñonero, A. Costa, P. Ballaster, P.M. Deya, and E.V. Anslyn. J. Org. Chem. **71**, 7185 (2006).
6. (*a*) A. Ajayaghosh. Acc. Chem. Res. **38**, 449 (2005); (*b*) H. Meier and R. Petermann. Helv. Chim. Acta, **87**,1109 (2004); (*c*) M. Matsuoka (*Editor*). Infrared absorbing dyes. Plenum Press, New York. 1990; (*d*) H. Meier and R. Petermann. Tetrahedron Lett. **4**1 5475 (2000); (*e*) K. Jyothish, R.R. Avirah, and D. Ramaiah. Org. Lett. **8**, 111 (2006); (*f*) M. Büschel, A. Ajayaghosh, E. Arunkumar, and J. Daub. Org. Lett. **5**, 2975 (2003); (*g*) M. Tian, S. Tatsuura, M. Furuki, Y. Sato, I. Iwasa, and L.S. Pu. J. Am. Chem. Soc. **125**, 348 (2003); (*h*) J.R. Johnson, N. Fu, E. Arunkumar, W.M. Leevy, S.T. Gammon, D. Piwnica-Worms, and B.D. Smith. Angew. Chem., Int. Ed. **46**, 5528 (2007).
7. (*a*) A. Arcoria, S. Fisichella, E. Maccarone, and G. Scarlata. Gazz. Chim. Ital. **105**, 547 (1975); (*b*) H. Ihmels, M. Maggini, M. Prato, and G. Scorrano. Tetrahedron Lett. **32**, 6215 (1991).
8. A.D. Allen, H. Rangwala, K. Saidi, T.T. Tidwell, and J. Wang. Izv. Akad. Nauk Ser. Khim. 1034 (2001); Russ. Chem. Bull. 2130 (2001).
9. (*a*) Preparation of **27**: A. Aguilar-Aguilar, L.S. Liebeskind, and E. Peña-Cabrera. J. Org. Chem. **72**, 8539 (2007); (*b*) Compound **25** has been reported, but without preparative details (4*o*, 4*p*).
10. (*a*) B.D. Wagner, B.R. Arnold, G.S Brown, and J. Lusztyk. J. Am. Chem. Soc. **120**, 1827 (1998); (*b*) N.C. De Lucas, J.C. Netto-Ferreira, J. Andros, and J.C. Scaiano. J. Org. Chem. **66**, 506 (2001).
11. (*a*) A.D. Allen, A.J. Kresge, N.P. Schepp, and T.T. Tidwell. Can. J. Chem. **65**, 1719 (1987); (*b*) Y. Chiang, A.V. Fedorov, A.J. Kresge, I. Onyido, and T.T. Tidwell. J. Am. Chem. Soc. **126**, 9382 (2004).
12. (*a*) A.D. Allen, A. Fedorov, H. Henry-Riyad, and T.T. Tidwell. J. Phys. Org. Chem. **19**, 841 (2006); (*b*) A.D. Allen, B. Cheng, M. H. Fenwick, B. Givehchi, H. Henry-Riyad, V.A. Nikolaev, E.A. Shikova, D. Tahmassebi, T.T. Tidwell, and S.J. Wang. Org. Chem. **66**, 2611 (2001).
13. M.A. McAllister and T.T. Tidwell. J. Org. Chem. **59**, 4506 (1994).
14. C. Hansch, A. Leo, and R.W. Taft. Chem. Rev. **91**, 165 (1991).
15. (*a*) W. Kirmse and L. Horner. Justus Liebigs Ann. Chem. **625**, 34 (1959); (*b*) F.F. Blicke and M.F. Zienty. J. Am. Chem. Soc. **63**, 2945 (1941); (*c*) M. Regitz, A.M. Tawfik, and H. Heydt. Synthesis, 805 (1979); (*d*) Z. Hassen, A. Ben Akacha, and H. Zantour. Phosphorus Sulfur Silicon Relat. Elem. **178**, 2241 (2003).

© 2008 NRC Canada

Kinetic plasticity and the determination of product ratios for kinetic schemes leading to multiple products without rate laws — New methods based on directed graphs

John Andraos

Abstract: This paper presents two new and fast methods of determining product ratios for kinetic schemes leading to more than one product on which the Acree–Curtin–Hammett (ACH) principle is based. The methods involve rewriting a given kinetic scheme as a directed graph with nodes and arrows connecting the nodes and takes advantage of the directionality of the kinetic arrows and the enumeration of paths to the various target product nodes. The first, based on path divergent trees, is computationally simpler but works under a specific set of conditions, whereas the second, based on an adapted version of Chou's graphical method, works for all cases. By means of illustrated examples, both methods are shown to be completely verifiable with conventional more tedious treatments based on rate law determinations. The directed graph concept also works for kinetic schemes that involve entirely equilibrated species. In addition, the paper extends these ideas to variants of the basic ACH scheme, thereby testing the validity of the ACH principle and bringing about a deeper understanding of it. Generalization of the results yields a new parameter, called degree of kinetic plasticity, which completely describes the dynamics of kinetic resolution between the boundary limits of ACH behaviour (100% kinetic plasticity) and anti-ACH behaviour (100% kinetic rigidity). It is shown that this parameter is a good descriptor of all possible scenarios between and including these limits and can be determined experimentally by conducting a new kind of product study that tracks the behaviour of final product excesses as a function of initial substrate excesses. The resulting plot is always linear with a positive slope. The degree of kinetic plasticity is found by simply subtracting the slope from unity. These ideas are tested on complex kinetic schemes exhibiting dynamic kinetic resolution (DKR) by means of organocatalysis.

Key words: physical organic chemistry, kinetics, mechanism, directed graph, Chou digraph, Chou graphical rule, Acree-Curtin-Hammett principle, product ratio, dynamic kinetic resolution, organocatalysis.

Résumé : Dans ce travail on a développé deux nouvelles méthodes rapides pour déterminer les rapports des schémas conduisant à plus d'un produit sur lequel se base le principe d'Acree–Curtin–Hammett (ACH). Les méthodes impliquent une réécriture d'un schéma cinétique donné sous la forme d'un graphique dirigé comportant des nodes et des flèches reliant les nodes et elles tirent avantage du caractère directionnel des flèches cinétiques et de l'énumération des voies vers les divers nodes des produits prévus. La première, qui est basée sur des ramifications divergentes, est la plus simple d'un point de vue des calculs théoriques, mais elle ne s'applique que dans un ensemble spécifique de conditions alors que la deuxième qui est basée sur une version adaptée de la méthode graphique de Chou s'applique à tous les cas. En faisant appel à des illustrations appropriées, on peut démontrer que les deux méthodes peuvent être entièrement vérifier à l'aide de traitements conventionnels plus fastidieux basés sur des déterminations de lois de vitesses. Le concept du graphique dirigé fonctionne aussi pour les schémas cinétiques qui impliquent des espèces entièrement équilibrées. De plus, ce travail permet d'élargir ces idées à des variantes du schéma de base de Acree-Curtin-Hammett qui permet ainsi de vérifier la validité du principe d'ACH et de mieux la comprendre. La généralisation des résultats conduit à un nouveau paramètre, le degré de plasticité cinétique, qui décrit complètement la dynamique de la résolution cinétique entre les limites de la frontière entre le comportement Acree-Curtin-Hammett (100% de plasticité cinétique) et le comportement anti-Acree–Curtin–Hammett (100% de rigidité cinétique). On a montré que ce paramètre permet de bien décrire tous les scénarios entre, et incluant, ces limites et qu'il peut être déterminé expérimentalement en effectuant un nouveau type d'étude de produit qui permet de suivre le comportement des excès de produit final en fonction d'excès de substrats initiaux. La courbe qui en résulte est toujours linéaire avec une pente positive. On détermine le degré de plasticité cinétique en soustrayant la pente de l'unité. On a fait appel à l'organocatalyse pour tester ces idées sur les schémas cinétiques complexes qui présentent de la résolution cinétique dynamique (RCD).

Received 23 October 2007. Accepted 16 January 2008. Published on the NRC Research Press Web site at canjchem.nrc.ca on 25 March 2008.

This paper is dedicated to the memory of Keith Yates.

J. Andraos. Department of Chemistry, York University, Toronto, ON M3J 1P3, Canada (e-mail: jandraos@yorku.ca).

 doi:10.1139/V08-020 © 2008 NRC Canada

Mots-clés : chimie organique physique, cinétique, mécanisme, graphique dirigé, diagramme de Chou, règle graphique de Chou, principe d'Acree–Curtin–Hammett, rapport de produits, résolution cinétique dynamique, organocatalyse.

[Traduit par la Rédaction]

Introduction

The Acree–Curtin–Hammett (ACH) principle is a fundamental concept in mechanistic chemistry that has been used to approximate under simplifying conditions the magnitude of the final product ratio for a pair of products originating from a pair of equilibrating starting materials as shown in Scheme 1. The starting materials may be equilibrating conformers, tautomers, or stereoisomers. Curtin and Hammett demonstrated this principle in the 1950s for products arising from equilibrating conformers (1, 2); however, it had already been described much earlier by Acree in 1907 for products arising from equilibrating tautomers (3). Moreover, Acree's work also derived what would be later known as the Winstein–Holness equation (4). A recent report has described the connections between these works and brought Acree's forgotten work to light (5). Throughout this paper, the principle is therefore referred to as the ACH principle or kinetic theorem to recognize the contributions of the three scientists. It is a concept that is well discussed in several textbooks of mechanistic organic chemistry (6–8), a review (9), and a pedagogical article (10).

Simply stated, the final product ratio $[P_X]$:$[P_Y]$ is equal to the ratio of product forming rate constants k_3:k_4 if the magnitudes of the rate constants k_1 and k_2 involved in the equilibration between X and Y are similar and are very large compared with those of the product forming steps. This independence of the final product ratio on the dynamics of the preceding equilibrium and the amounts of starting materials defines the ACH condition and is a direct result of applying *both* kinetic conditions. When these conditions are not met, an exact analytical solution to the above kinetic scheme becomes necessary to determine the complete form of the final product ratio. Equation [1] yields the complete dependence of the final product ratio on all four rate constants and the starting amounts of X and Y (11).

$$[1] \qquad \frac{[P_X]_\infty}{[P_Y]_\infty} = \left(\frac{k_3}{k_4}\right)\left[\frac{(a+b)\,k_2 + ak_4}{(a+b)\,k_1 + bk_3}\right]$$

where a and b represent the initial amounts of X and Y at time zero. It is easy to verify that the right-hand side of eq. [1] reduces to k_3/k_4 when (*i*) k_1 and $k_2 \gg k_3$ and k_4 and (*ii*) $k_1 = k_2$. Note that if only condition (*i*) holds, then the final product ratio will have a dependence on both the ratio k_3/k_4 and the equilibrium constant $K = k_1/k_2$, according to eq. [2].

$$[2] \qquad \frac{[P_X]_\infty}{[P_Y]_\infty} = \left(\frac{k_3}{k_4}\right)\left(\frac{1}{K}\right)$$

In addition to applying to equilibrating conformers or tautomers, the kinetic scheme shown in Scheme 1 is applicable to the technique of dynamic kinetic resolution (DKR) (12–38) used in synthetic organic chemistry to optimize the synthesis of stereoisomeric products from corresponding enantiomeric or diastereomeric starting materials that are in equilibrium. This is arguably the most important practical application of the ACH principle. In fact, it is this special phenomenon that blends the interests of both mechanistic and synthetic organic chemists. Mechanistic chemists are attracted to reactions that yield multiple products via multiple intermediates but that have the potential to be perturbed to produce one target product under the "right" set of conditions once their corresponding mechanism landscapes are completely elucidated. Synthetic chemists are of course interested in reactions that yield only one target product in high yield and high regio-, stereo-, and chemo-selectivity. Scheme 2 shows an analogous kinetic system to that in Scheme 1 with appropriate stereochemical descriptors R and S for substrates and products.

If a chemical reaction produces enantiomeric or diastereomeric products, and it is desired to carry out a subsequent transformation on one of them, then one is faced with the prospect of first separating or resolving the product mixture from the first reaction, usually racemic, before carrying out the second. Resolution of racemic mixtures by standard methods results in an automatic loss of half the starting material, assuming that the resolution procedure goes to completion. This means that if the individual stereoisomers in the starting racemic mixture are not interconvertible then the maximum amount of desired product formed in the subsequent step is exactly half that of the starting material, and so the maximum yield for this second step is 50%. This situation is designated as anti-ACH behaviour and corresponds to kinetic resolution. If, on the other hand, there is a possibility to have a rapid interchange between starting materials via a racemization process to an extent that the ACH condition applies, then in principle it is possible to shunt all of the starting material toward the product of interest in the subsequent reaction. The more dynamic the equilibration is between S_R and S_S, the more likely this outcome will occur. This situation is designated as ACH behaviour and corresponds to dynamic kinetic resolution.

In a recent report published in 2003, the complete dynamics of Scheme 2 was explored including a full kinetic analysis of the dependence of the initial and final product ratios on all four rate constants and starting amounts of S_R and S_S (11). The method used to derive expressions for these ratios shown in eqs. [3] and [4],

$$[3] \qquad \frac{[P_R]_0}{[P_S]_0} = \left(\frac{a}{b}\right)\left(\frac{k_3}{k_4}\right)$$

$$[4] \qquad \frac{[P_R]_\infty}{[P_S]_\infty} = \left(\frac{k_3}{k_4}\right)\left[\frac{(a+b)\,k_2 + ak_4}{(a+b)\,k_1 + bk_3}\right]$$

where a and b are the initial amounts of S_R and S_S respectively, was the method of Laplace transforms (39). It is important to point out that though there are no products formed initially their ratio extrapolated to zero time is in fact a finite

© 2008 NRC Canada

Scheme 1.

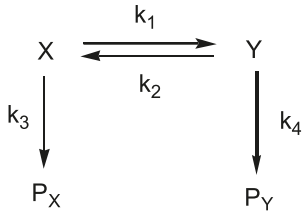

Scheme 2.

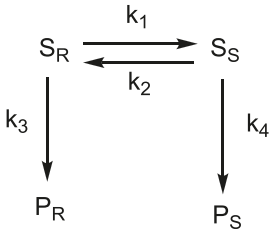

quantity. This observation is entirely consistent with the work of Noyori and co-workers (40, 41) who showed plots of % final enantiomeric excess of product versus % conversion that had well-defined nonzero intercepts. The two expressions given in eqs. [3] and [4] suggested a new kind of experiment that could be carried out that would quantitatively determine the intrinsic efficiency or plasticity of dynamic kinetic resolution that depended only on key rate constant ratios. This parameter was shown to be able to account for all experimentally observed cases between and including the limits of complete dynamic kinetic resolution (ACH conditions) and complete kinetic resolution (anti-ACH conditions) for simple kinetic schemes such as that shown in Scheme 2.

The crux of the new experiment is to determine initial and final product ratios for a *set* of initial substrate ratios covering the full range of possible optical purities of starting materials beyond the simple racemic condition, which is the universal initial composition of starting materials. Hence for a given starting substrate ratio *a*/*b*, one records time-dependent product progress curves, and from these the initial and final product ratios are determined by extrapolation to zero and infinite times. A plot of $[P_R]_0/[P_S]_0$ vs. *a*/*b* yields a slope equal to $r = k_3/k_4$. A plot of final product excess with respect to P_R and pe_∞ vs. initial substrate excess with respect to S_R and $(a–b)/(a+b)$, according to eq. [5],

$$[5] \qquad pe_\infty = \frac{[P_R]_\infty - [P_S]_\infty}{[P_R]_\infty + [P_S]_\infty} = \frac{\dfrac{[P_R]_\infty}{[P_S]_\infty} - 1}{\dfrac{[P_R]_\infty}{[P_S]_\infty} + 1}$$

$$= \frac{1}{rv + u + 1}\left(\frac{a-b}{a+b}\right) + \frac{rv - u}{rv + u + 1}$$

yields a slope equal to $1/(rv + u + 1)$ and an intercept equal to $(rv - u)/(rv + u + 1)$ where $r = k_3/k_4$, $u = k_1/k_3$, and $v = k_2/k_3$. The rate constant ratios *u* and *v* may be determined directly from the slope and intercept of such a plot using eqs. [6] and [7],

Fig. 1. Relationship between final product excess and initial substrate excess according to eq. [8], showing the two limiting slopes corresponding to the Curtin–Hammett condition (zero slope, *u* and $v \to 0$, 100% kinetic plasticity) and anti-Curtin–Hammett condition (unit slope, *u* and $v \to \infty$, 0% kinetic plasticity or 100% kinetic rigidity).

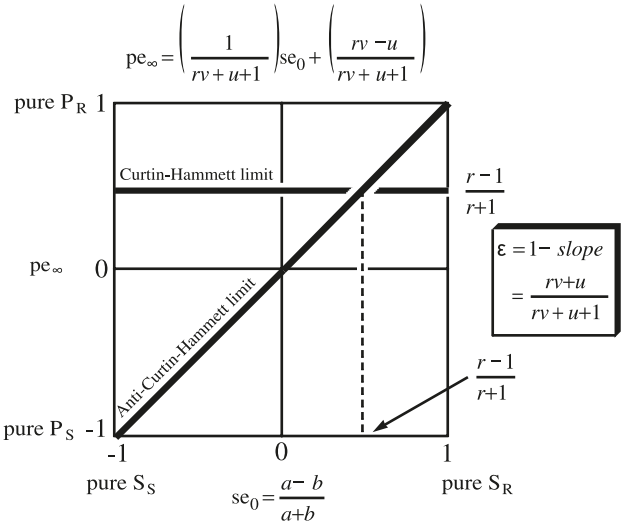

$$[6] \qquad u = \frac{1}{2}\left[\frac{1 - \text{intercept}}{\text{slope}} - 1\right]$$

and

$$[7] \qquad v = \frac{1}{2r}\left[\frac{1 + \text{intercept}}{\text{slope}} - 1\right]$$

An expression for the intrinsic efficiency or degree of kinetic plasticity of dynamic kinetic resolution, ε_{DKR}, may be obtained by examining the full range of possible values for the slope of this plot. In the ACH limit where $u = v \to \infty$ so that $k_1 = k_2$ and k_1, $k_2 \gg k_3$, k_4, the slope reaches a minimum value of zero. This result indicates that the final product ratio is independent of the starting amounts of S_R and S_S. In the anti-ACH limit where $u = v = 0$ so that $k_1 = k_2$ and k_1, $k_2 \ll k_3$, k_4, the slope reaches a maximum value of one. This case indicates that the final product ratio mirrors the initial starting material ratio. From these two boundary conditions, we set $\varepsilon_{DKR} = 1$ to represent the ACH case of 100% efficiency or complete kinetic plasticity and $\varepsilon_{DKR} = 0$ to represent the anti-ACH case of 0% efficiency or complete kinetic rigidity. Hence, we may define the intrinsic efficiency or performance of dynamic kinetic resolution as in eq. [8] to describe the pliability of the equilibrium toward being pulled in either direction by either of the product forming steps.

$$[8] \qquad \varepsilon_{DKR} = 1 - \text{slope} = 1 - \frac{1}{rv + u + 1} = \frac{rv + u}{rv + u + 1}$$

Figure 1 illustrates graphically the two limiting cases described earlier. Equation [5] predicts that experimental data should obey a linear relationship with a positive slope falling between these two limits. The intersection of the two limiting lines suggests that there exists a unique combination of initial substrate amounts that will result in the same final

© 2008 NRC Canada

product ratio, and hence the same final product excess, under both limiting conditions. It should be noted that eq. [5] also predicts that we can never have a plot with a slope of zero and an intercept of zero, i.e., a line falling along the *x*-axis. Such a condition would correspond to the nonsense situation of a completely plastic kinetic system that begins with any combination of substrates and always ends up with a racemic mixture of products. Setting the slope and intercept to be simultaneously zero in eq. [5] leads to a contradiction in the allowable domains of the parameters *u* and *v*, namely, $u, v \to \infty$ for the slope and $u, v \to 0$ for the intercept. A racemic mixture of products can only arise from a racemic mixture of starting materials, which immediately suggests that the kinetic system is 100% rigid and hence the anti-ACH limiting line of unit slope and zero intercept is operative. However, ACH limiting lines with zero slopes and intercepts of +1 or –1 are allowed, i.e., lines falling along the top and bottom edges of the square in Fig. 1. These correspond to the fully dynamic situations where the equilibrium step is fast compared with the product forming steps ($u, v \to \infty$) and $r \to \infty$ (or $k_3 \ggg k_4$) for the case of an intercept of +1, and $r \to 0$ (or $k_3 \lll k_4$) for the case of an intercept of –1. From Scheme 2, the former case essentially corresponds to the case when the step from S_S to P_S is shut down so that the only product formed is P_R, and the latter case corresponds to the opposite situation when the step from S_R to P_R is shut down so that the only product formed is P_S. The plot shown in Fig. 1 may be used as a diagnostic test to verify if a given chemical system obeys ACH kinetic-type schemes.

Equation [8] is applicable to any kinetic scheme that looks like Scheme 1 or 2 regardless of the isomeric relationship of the starting materials so long as their starting ratio is controllable. In the case of isomeric substrates that cannot be easily separated and their initial ratio manipulated as described above, separate kinetic experiments are required to determine individual rate constants so that the kinetic plasticity parameter given in eq. [8] may be determined. To date there has not yet been any experimental verification of this new idea reported in the literature. However, the 2003 report did survey a number of published chemical systems where enough experimental detail was given so that minimum estimates of ε_{DKR} could be made, and thus the validity of eq. [8] was confirmed in principle. In that work, several variant kinetic schemes were examined and their properties and corresponding exact initial and final product ratio expressions were derived. The important point gleaned from that investigation was that all prior work on such kinetic systems *assumed* from the outset that the ACH condition was valid and that Winstein–Holness kinetic behaviour (4) was applicable. These claims were then verified by carrying out *independent* theoretical calculations to determine energy barriers pertaining to the relevant transition states (42). The above analysis clearly shows that the ACH condition may be verified directly from wholly experimentally acquired data without need for further computation. Moreover, even if it turns out that this special condition may not be met for a given chemical system it is still possible to quantify the actual extent of meeting this condition according to the parameter defined in eq. [8].

Having introduced the current understanding of the ACH principle on simple kinetic systems, we now report on further extensions that test the validity of this principle on complex kinetic systems. Extended linear and cyclic kinetic schemes are examined in detail. The concept of kinetic plasticity described above is generalized and the statement of the ACH principle is revised accordingly. In doing so, we also introduce two new time-saving methods of determining the required product ratio expressions for initial and final reaction times that serves as a check for conventional treatments, namely the Laplace transform method. As a bonus, it will be demonstrated that they also circumvent much of the tedious computation that is a consequence of handling complex kinetic systems. Limitations of the methods are also discussed.

Scheme 3.

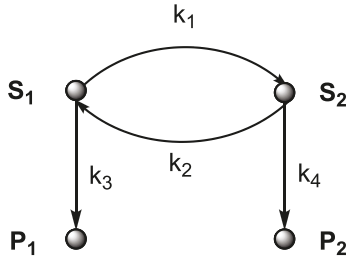

Directed graph method

In this section we introduce easy-to-use algorithms for determining expressions as shown in eqs. [1] and [4], without the use of rate laws. The methods are based on directed graphs, or digraphs (43), and are applicable to competitive-type kinetic schemes leading to multiple products from one or more substrates. The schematic method of King and Altman described in 1956 is a forerunner report describing the use of graphs to derive rate laws for enzyme-catalyzed reactions (44). Chou has previously described powerful algorithms for analyzing non-steady-state and steady-state enzyme kinetics and protein folding kinetics (45–61).

Digraphs are objects that consist of a finite set of vertices and a set of ordered pairs of distinct vertices called arcs. If the ordered pair $\{x, y\}$ is an arc, then the arc is said is to be directed from *x* to *y*. The kinetic schemes shown in Schemes 1 and 2 may be immediately drawn as digraphs, since the chemical entities and reaction arrows are translated as vertices and arcs, respectively, according to the above definitions (see Scheme 3).

The substrate vertices are designated as source nodes and the product vertices as sink nodes. The arrows and rate constant descriptors are retained as before in the usual sense. For the first method based on path divergent trees, beginning with each source node we draw a corresponding divergent tree that enumerates all paths from that node to all product nodes. In doing so, we apply the following rules. For irreversible steps one stops when a product node is reached and for reversible steps one stops when a previously traversed node along that branch is reached. Hence, we have for Scheme 3 the two divergent trees shown in Fig. 2 in which we assign the initial condition that we begin with amounts *a* and *b* for substrates S_1 and S_2.

Next, we write expressions for the expected contribution of each product based on the attenuation of the initial amounts of each source node that lead to each product. This

© 2008 NRC Canada

Fig. 2. Path divergent trees for paths emanating from S1 (A) and S2 (B). See Scheme 3.

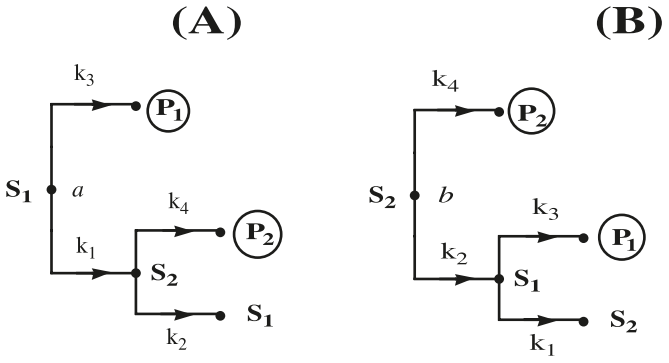

is done following the connectivities between nodes in the path divergent trees. Thus, for paths leading to product P_1 we have eq. [9],

$$[9]\qquad a\left(\frac{k_3}{k_1+k_3}\right)+b\left(\frac{k_3}{k_1+k_3}\right)\left(\frac{k_2}{k_2+k_4}\right)=\left(\frac{k_3}{k_1+k_3}\right)\left[a+b\left(\frac{k_2}{k_2+k_4}\right)\right]$$

The first term in eq. [9] pertains to P_1 originating directly from S_1 along the k_3 branch (see Fig. 2*A*). Note that since there are two branches emanating from S_1, the fraction of starting material a leading to P_1 is $k_3/(k_3 + k_1)$. The second term pertains to P_1 originating from S_1, which in turn originated from S_2 (see Fig. 2*B*). The starting amount of S_2, b, is first split along the k_2 branch and then is split again along the k_3 branch. Hence, we have the corresponding multiplication of fractions.

Similarly, we have for paths leading to product P_2

$$[10]\qquad b\left(\frac{k_4}{k_2+k_4}\right)+a\left(\frac{k_1}{k_1+k_3}\right)\left(\frac{k_4}{k_2+k_4}\right)=\left(\frac{k_4}{k_2+k_4}\right)\left[b+a\left(\frac{k_1}{k_1+k_3}\right)\right]$$

Note that since we have a symmetrical digraph, the pairs of subscripts a and b, 1 and 3, and 2 and 4, are interchangeable in both expressions. This implies that the expression in eq. [10] could have been written at once from eq. [9] using these variable interchanges.

The final product ratio is then given directly by dividing eq. [9] by eq. [10] thus yielding eq. [11],

$$[11]\qquad \frac{[P_1]_\infty}{[P_2]_\infty}=\frac{\left(\frac{k_3}{k_1+k_3}\right)\left[a+b\left(\frac{k_2}{k_2+k_4}\right)\right]}{\left(\frac{k_4}{k_2+k_4}\right)\left[b+a\left(\frac{k_1}{k_1+k_3}\right)\right]}=\left(\frac{k_3}{k_4}\right)\left[\frac{(a+b)k_2+ak_4}{(a+b)k_1+bk_3}\right]$$

which is identical to eqs. [1] and [4]. The initial product ratio is also given directly by eq. [12],

$$[12]\qquad \frac{[P_1]_o}{[P_2]_o}=\frac{ak_3}{bk_4}$$

which is identical to eq. [3]. Note that in eq. [12] the numerator refers to the shortest path from S_1 to P_1 and the denominator refers to the shortest path from S_2 to P_2. This observation turns out to be always true in the determination of expressions for initial product ratios by the digraph method.

It is obvious how facile this method is compared with the standard method of Laplace transforms (39) that becomes more tedious as the number of substrate and product nodes increase and the number of rate constant connections between them increases. It may be recalled that the Laplace transform method involves taking determinants of square matrices whose dimension is equal to the sum of the number of substrates, intermediates, and products involved in the kinetic scheme. In addition, the method relies on tables of inverse transforms that need to be worked out separately, but such tables are readily available (62–64). A key limitation of the method is that it is applicable only to unimolecular or pseudo-unimolecular kinetic systems and not biomolecular ones, since the Laplace transform of a product of functions is not equal to the product of their Laplace transform functions as shown in eq. [13],

$$[13]\qquad L\{f(t)\cdot g(t)\}\neq L\{f(t)\}\cdot L\{g(t)\}$$

Figure 3 summarizes key definitions and the sequence of steps involved in this method. For illustration and comparison with the directed graph method, the Supplementary Data contains a full solution of the kinetic scheme shown in Scheme 3 by the Laplace transform method.[2]

For verification purposes, all of the expressions for initial and final product ratios derived previously (11) were confirmed by the new digraph method. These are also given in the Supplementary Data.[2] Reassuringly, this consistency demonstrates that the present new method also serves as an excellent checking device. However, this method does have its limitations. First, it does not give analytical expressions for the time-dependent substrate and product concentration profiles. For the purposes of determining analytical expressions for product ratios at the beginning and at the end of reactions, paradoxically these are not necessary. Second, like

[2] Supplementary data for this article are available on the journal Web site (canjchem.nrc.ca) or may be purchased from the Depository of Unpublished Data, Document Delivery, CISTI, National Research Council Canada, Ottawa, ON K1A 0R6, Canada DUD 3724. For more information on obtaining material, refer to cisti-icist-cnrc.gc.ca/irm/unpub_e.shtml. The Supplementary Data contains a full solution of the kinetic scheme shown in Scheme 3 by the Laplace transform method, solutions of kinetic schemes described in ref. 11 by both directed graph methods, a modified Chou digraph method applied to Schemes 6 to 10 in sections 6, 7, and 8.

© 2008 NRC Canada

Fig. 4. Example special bimolecular kinetic systems whose initial and final product ratios are determinable exactly by the directed graph method based on path divergent trees.

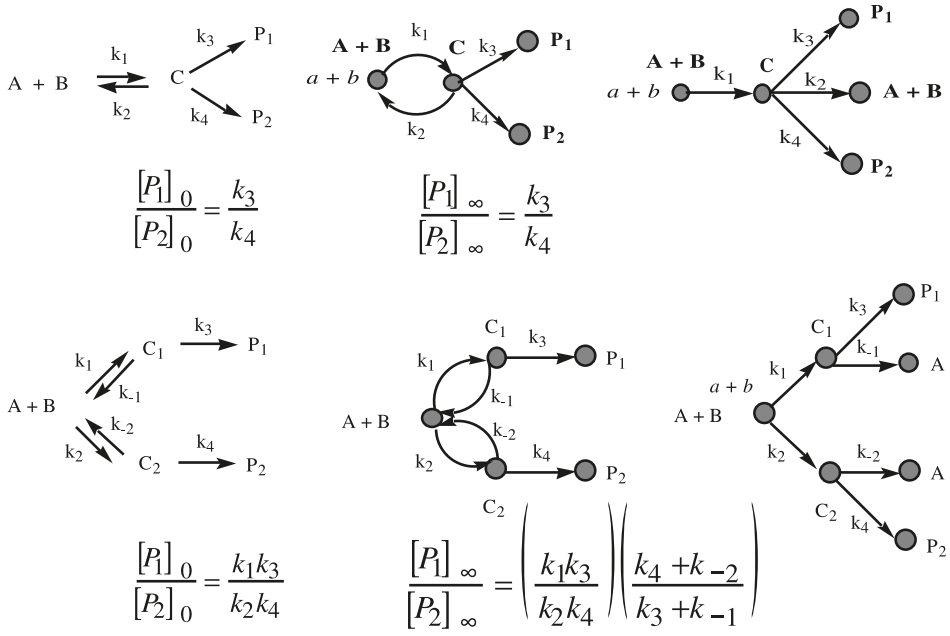

Fig. 3. Key definitions and sequence of steps involved in the Laplace transform method.

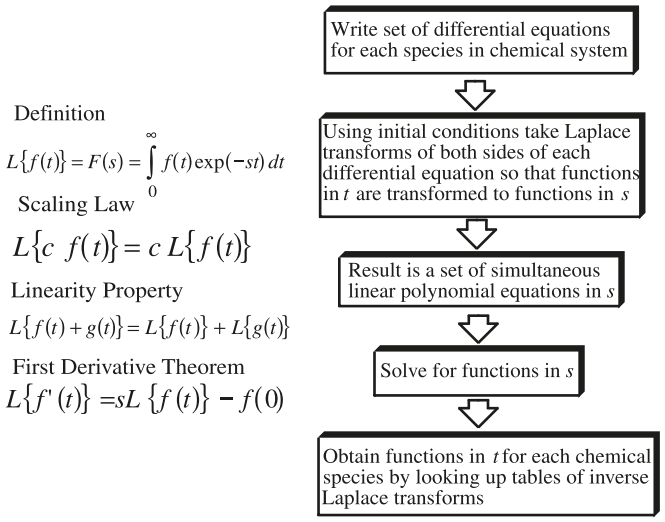

the Laplace transform method, it is applicable to unimolecular and pseudo-unimolecular kinetic systems. However, it can still be applied to special bimolecular systems, such as those shown in Fig. 4 where multiple products arise from a common intermediate via unimolecular steps though that intermediate itself arose from a prior bimolecular step. For these few examples, though time-dependent concentration profiles for products cannot be determined analytically, their product ratios are determinable exactly by the directed graph method.

A key observation from the path divergent trees shown in Fig. 2 is that each tree is composed of two stages or tiers with only one repeat node. For Fig. 2*A* the repeat node is S1 and for Fig. 2*B* it is S2. It turns out that if the construction of path divergent trees from a digraph pertaining to a kinetic

Scheme 4.

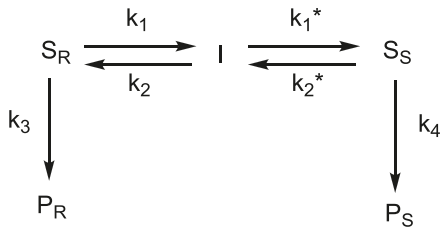

scheme according to the above algorithm leads to trees having more than one repeat node appearing in *different* stages, then the above digraph method does not yield expressions for the product ratio that are consistent with those obtained from the check Laplace transform method. Extra terms appear in the numerator and the denominator for the final product ratio expression, which ultimately yield an apparent dependency on the amounts of equilibrating starting materials when the ACH condition is applied. This would lead to the erroneous conclusion that the ACH principle is violated for such cases. Hence, the third and most important limitation of the above digraph algorithm is that it works only for kinetic schemes having corresponding path divergent trees with only one repeat node or ones with more than one repeat node appearing in the *same* stage or tier.

An example of a kinetic scheme yielding path divergent trees with multiple repeat nodes appearing in different stages or tiers is shown in Scheme 4, which is a more complete representation of the racemization process suggested by Scheme 2. Clearly, racemization between S_R and S_S necessarily takes place via a lower symmetry intermediate that is in equilibrium with both S_R and S_S since loss of chirality takes place via a bond-breaking process.

The corresponding path divergent trees are shown in Figs. 5*A* and 5*B*. Note that in Fig. 5*A* there is a repeat node

© 2008 NRC Canada

Fig. 5. Path divergent trees for paths emanating from SR (A) and SS (B). See Scheme 4.

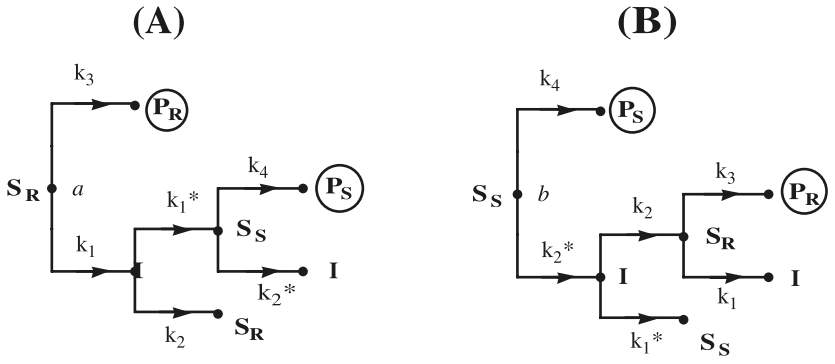

S_R that appears in the second tier and another repeat node I that appears in the third tier. Similarly, repeat nodes in different tiers are observed in Fig. 5*B*. Application of the above digraph algorithm leads to the incorrect expression for the final product ratio shown in eq. [14],

$$[14] \quad \frac{[P_R]_\infty}{[P_S]_\infty} = \left(\frac{k_3}{k_4}\right)\left[\frac{(a+b)\,k_2k_2^* + ak_4(k_2+k_1^*) + ak_1k_1^*}{(a+b)\,k_1k_1^* + bk_3(k_1+k_2^*) + bk_2k_2^*}\right]$$

The correct expression found by the Laplace transform method is shown in eq. [15],

$$[15] \quad \frac{[P_R]_\infty}{[P_S]_\infty} = \left(\frac{k_3}{k_4}\right)\left[\frac{(a+b)\,k_2k_2^* + ak_4(k_2+k_1^*)}{(a+b)\,k_1k_1^* + bk_3(k_1+k_2^*)}\right]$$

Note the extra terms appearing in the numerator and denominator in eq. [14]. The ACH limit applied to eq. [14] leads to eq. [16],

$$[16] \quad \left(\frac{[P_R]_\infty}{[P_S]_\infty}\right)_{ACH} = \left(\frac{k_3}{k_4}\right)\left[\frac{2a+b}{a+2b}\right]$$

which shows a dependency on the starting amounts of S_R and S_S, *a* and *b*. When this limit is applied to eq. [15], however, the result is the expected no dependence on *a* and *b* as shown by eq. [17],

$$[17] \quad \left(\frac{[P_R]_\infty}{[P_S]_\infty}\right)_{ACH} = \frac{k_3}{k_4}$$

A second digraph method based on a variation of the Chou algorithm is found to work for all cases and thus circumvents the third limitation of the above path divergent tree method, as will be shown next. Again using the same kinetic schemes shown in Schemes 1 and 2, the Chou digraph is constructed as shown Scheme 5.

The digraph is similar to that shown in Scheme 3 except that the rate constants connecting the nodes are assigned a negative sign and loops are added to those nodes that have kinetic arrows emanating from them. The rate-constant weights assigned to the loop nodes correspond to the positive sum of the rate constants emanating from them. From this digraph, all subgraphs are enumerated according to the following steps. For a given target product node, draw all paths that lead to it from all starting substrate nodes. All other points not traversed by this path are connected by cycles that neither intersect each other nor intersect the path. Repeat the process for all other target product nodes. The contributing expression to each target product node is given by eq. [18],

Scheme 5.

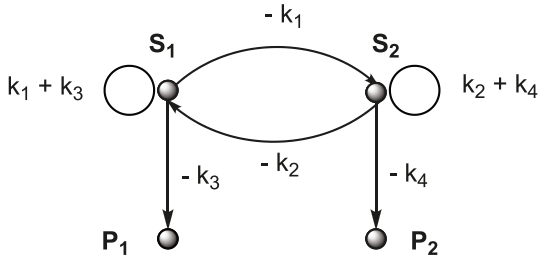

Fig. 6. Subgraphs from digraph shown in Scheme 5: (A) target product P_1; (B) target product P_2.

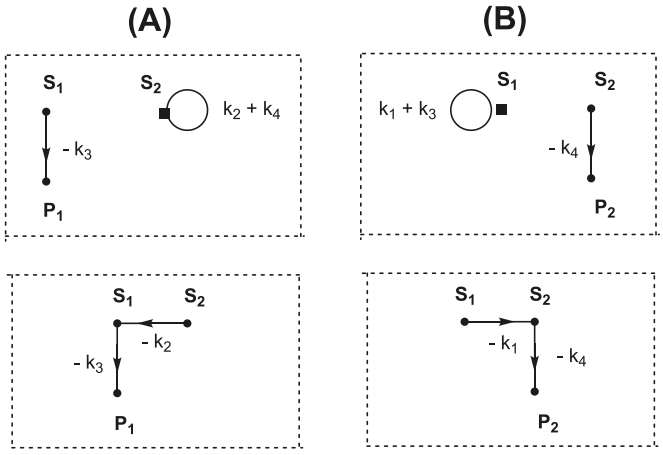

$$[18] \quad P_x \rightarrow \sum_{\text{subgraph}}\left[s_y(-1)^{n+c+1}\left(\prod_j k_j\right)\right]$$

where for a given subgraph, s_y is the starting amount of a starting node, *n* is the total number of nodes in the subgraph, *c* is the number of cycles, the product of rate-constant factors corresponds to all arrow and loop contributions, and the sum is taken over the number of subgraphs leading to common product node P_x. Hence, the subgraphs pertaining to the digraph in Scheme 5 are shown in Fig. 6.

© 2008 NRC Canada

Fig. 7. Digraph and subgraphs pertaining to Scheme 4.

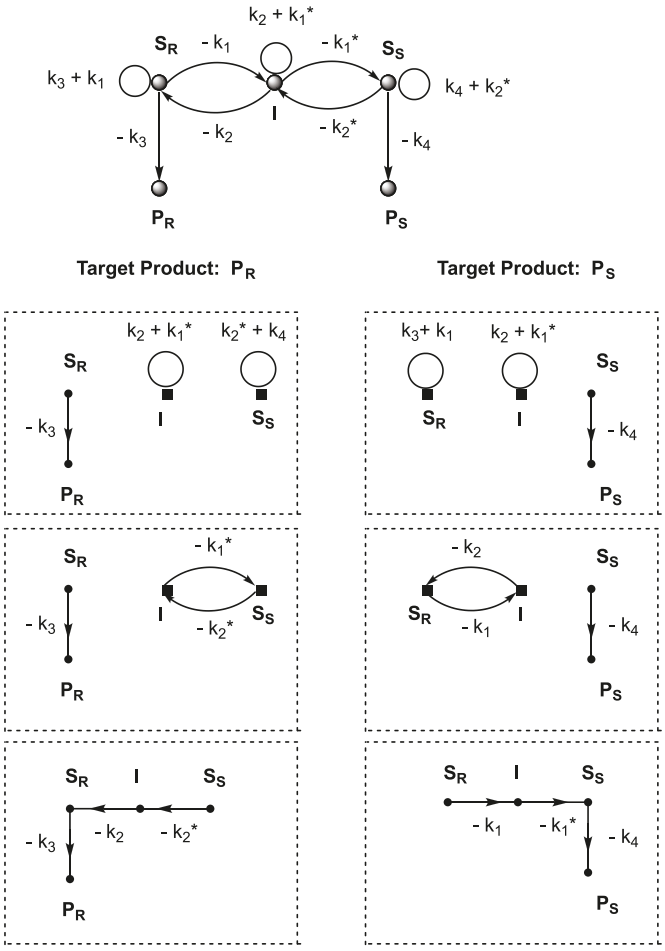

The contributing expression for the P_1 node is,

$$[19]\quad [P_1]_\infty \rightarrow a(-1)^{3+1+1}(-k_3)(k_2 + k_4) + b(-1)^{3+0+1}(-k_2)(-k_3) = k_3[(a + b)k_2 + k_4]$$

and that for the P_2 node is,

$$[20]\quad [P_2]_\infty \rightarrow b(-1)^{3+1+1}(-k_4)(k_1 + k_3) + a(-1)^{3+0+1}(-k_1)(-k_4) = k_4[(a + b)k_1 + k_3]$$

Note the following transposition of variables: $a \leftrightarrow b$, $k_1 \leftrightarrow k_2$, $k_3 \leftrightarrow k_4$. Hence, the final product ratio is found by dividing eq. [19] by eq. [20], which leads immediately to the previous expression given in eq. [11] found by the first digraph method based on path divergent trees. The application of the adapted Chou method to the kinetic scheme shown in Scheme 4 yields the digraph and subgraphs shown in Fig. 7.

The resulting contributing expressions for P_R and P_S are given by eqs. [21] and [22],

$$[21]\quad [P_R]_\infty \rightarrow a[(-1)^{4+2+1}(-k_3)(k_2 + k_1^*)(k_2^* + k_4) + (-1)^{4+1+1}(-k_3k_1^*k_2^*)] + b(-1)^{4+0+1}(-k_2^*k_2k_3) = ak_3(k_2k_2^* + k_2k_4 + k_1^*k_4) + bk_2k_2^*k_3$$

Fig. 8. Example acyclic equilibrium systems.

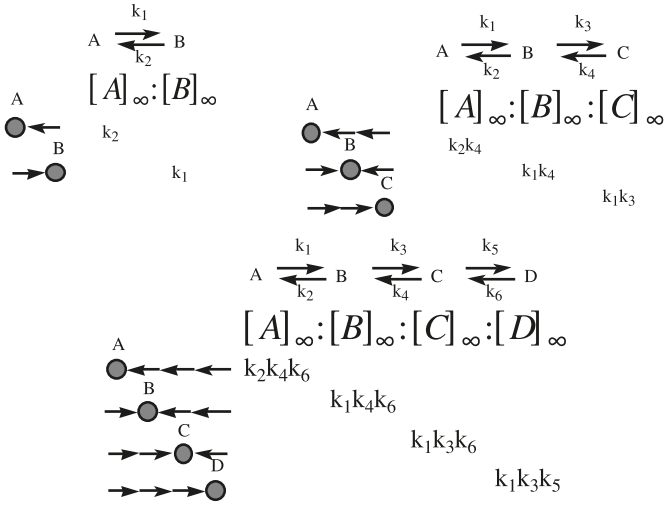

$$[22]\quad [P_S]_\infty \rightarrow b[(-1)^{4+2+1}(-k_4)(k_1 + k_2^*)(k_1^* + k_3) + (-1)^{4+1+1}(-k_4k_2^*k_1^*)] + a(-1)^{4+0+1}(-k_1^*k_1k_4) = bk_4(k_1k_1^* + k_1k_3 + k_2^*k_3) + ak_1k_1^*k_4$$

The ratio of these expressions is in agreement with the expected result given by eq. [15].

It is clear that the present new digraph methods confer key advantages that can be used to tackle rather complex schemes leading to multiple products that would otherwise be daunting to analyze by conventional means as will be shown, vide infra.

Equilibrium systems

The basic idea of keeping track of the arrow directionality in kinetic schemes may be used to full advantage to determine final equilibrium ratios of chemical species connected only by reversible steps by inspection, with almost no work involved. Figure 8 shows the results for acyclic equilibrium systems involving two, three, and four species in a linear arrangement. One can observe key patterns among these examples. If there are N species in an acyclic equilibrium, each term of the product ratio consists of N – 1 rate constants. The final equilibrium concentration expression for each species is determined by a single term equal to a product of rate constants corresponding to the combination of reaction arrows that points towards that species. For example, for the case of four species in an acyclic arrangement, the term for the final concentration of species A consists of a single product of three rate constants with descriptors 2, 4, and 6, which correspond to those that point toward A.

For cyclic equilibrium systems, the situation is more complicated but still can be deduced by the simple technique of following the reaction arrow directionality. Figure 9 shows the results for cyclic equilibrium systems involving three and four species. If there are N species in a cyclic equilibrium, each equilibrium product concentration expression consists of a sum of N terms, each of which consists of a product of N – 1 rate constants. The arrow directionality falls between the limiting clockwise and counter-clockwise

© 2008 NRC Canada

Fig. 9. Example cyclic equilibrium systems.

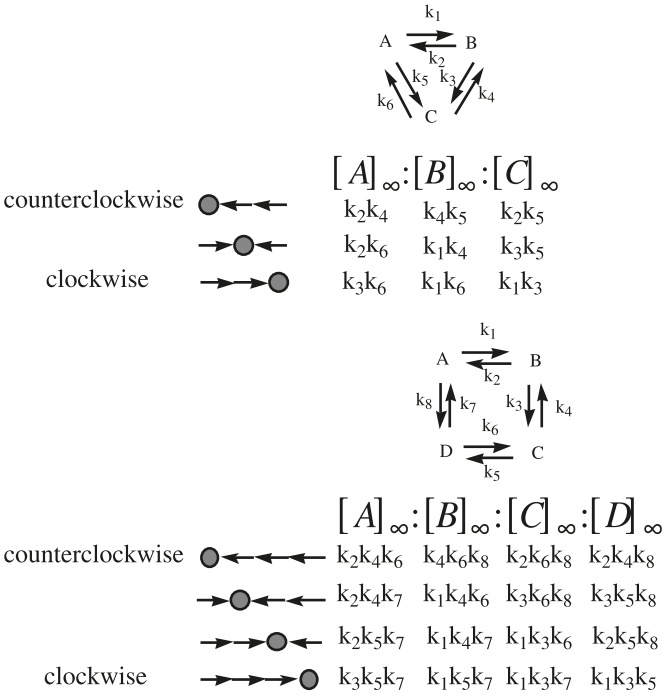

Scheme 6.

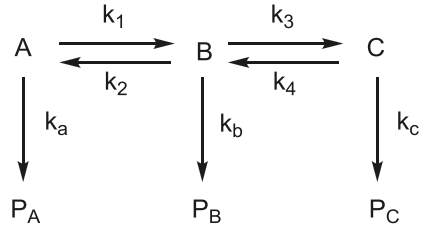

Scheme 7.

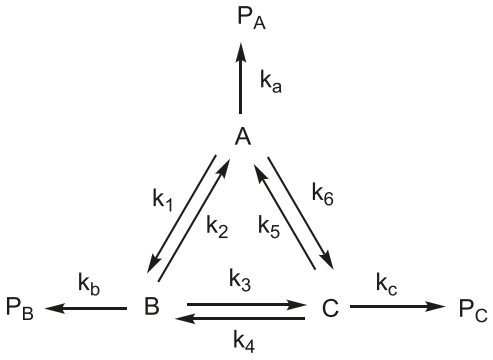

senses. For example, for the case of three species in a cyclic arrangement, the term for the final concentration of species A consists of a sum of three terms, each of which is composed of a product of two rate constants with pairwise descriptors (2,4), (2,6), and (3,6).

Extended variants of ACH kinetic schemes

In this section we examine extended variants of Scheme 1 in acyclic and cyclic arrangements and determine their associated initial and final product ratio expressions by the adapted Chou directed graph method. Consider the linear and cyclic triads shown in Schemes 6 and 7 with initial conditions $[A]_0 = a$, $[B]_0 = b$, and $[C]_0 = c$.

The determination of the final product ratios as given in the Supplementary Data results in the following relationships for the linear and cyclic triads, respectively,[2]

[23] $[P_A]_\infty:[P_B]_\infty:[P_C]_\infty$

$$= k_A\{a[(k_A + k_2)(k_4 + k_C) + k_3k_C] + bk_2(k_4 + k_C) + ck_2k_4\}$$
$$:k_B\{ak_1(k_4 + k_C) + b(k_A + k_1)(k_4 + k_C) + ck_4(k_A + k_1)\}$$
$$:k_C\{ak_1k_3 + bk_3(k_A + k_1) + c[(k_A + k_1)(k_3 + k_C) + k_2k_A]\}$$

[24] $[P_A]_\infty:[P_B]_\infty:[P_C]_\infty$

$$= k_A\{a[(k_B + k_2)(k_4 + k_5 + k_C) + k_3(k_C + k_5)] + b[k_2(k_4 + k_5 + k_C) + k_3k_5] + c[k_5(k_2 + k_3 + k_B)k_2k_4]\}$$
$$:k_B\{a[k_1(k_4 + k_5 + k_C) + k_4k_6] + b[(k_A + k_1)(k_4 + k_5 + k_C) + k_6(k_C + k_4)] + c[k_4(k_A + k_1 + k_6)k_1k_5]\}$$
$$:k_C\{a[k_6(k_2 + k_3 + k_B) + k_1k_3] + b[k_3(k_A + k_1 + k_6) + k_2k_6] + c[(k_A + k_6)(k_2 + k_3 + k_B) + k_1(k_B + k_3)]\}$$

In both cases the initial product ratio based on the shortest paths from A, B, and C to the respective target products is $[P_A]_0:[P_B]_0:[P_C]_0 = ak_A:bk_B:ck_C$. Also, in both cases the ACH limit and the anti-ACH limit lead to final product ratios of $([P_A]_\infty:[P_B]_\infty:[P_C]_\infty)_{ACH} = k_A:k_B:k_C$ and $([P_A]_\infty:[P_B]_\infty:[P_C]_\infty)_{anti\text{-}ACH} = a:b:c$, respectively. These results may be extended to tetrad, pentad, etc. arrangements of chemical species in equilibrium, each producing a unique product in an irreversible product-forming step. We may conclude that the forms of final product ratio expressions for both ACH anti-ACH limiting conditions are universal.

© 2008 NRC Canada

Generalization of kinetic plasticity in DKR systems

As demonstrated for Scheme 3, the key plot needed to determine the degree of kinetic plasticity is that given in Fig. 1, in which the final product excess is plotted against the initial substrate excess. The implication is that kinetic plasticity is defined in a pairwise sense since pairwise comparisons are made between pairs of products and pairs of substrates. For the trivial case of Scheme 3, there is only one pair of products and one pair of substrates. By analogy with the previous analysis based on limiting slopes, we may generalize the expression for kinetic plasticity starting from inequality [25],

[25] $$\text{slope}_{\text{ACH}} < \text{slope}_{\text{exp}} < \text{slope}_{\text{anti-ACH}}$$

Subtracting $\text{slope}_{\text{ACH}}$ from all terms results in

[26] $$0 < \text{slope}_{\text{exp}} - \text{slope}_{\text{ACH}} < \text{slope}_{\text{anti-ACH}} - \text{slope}_{\text{ACH}}$$

Dividing all terms by $(\text{slope}_{\text{anti-ACH}} - \text{slope}_{\text{ACH}})$ results in

[27] $$0 < \frac{\text{slope}_{\text{exp}} - \text{slope}_{\text{ACH}}}{\text{slope}_{\text{anti-ACH}} - \text{slope}_{\text{ACH}}} < 1$$

Using this definition, we may revise the ACH principle simply by stating that a kinetic model in which products are formed from equilibrating substrates satisfies the ACH condition when its degree of plasticity is 100%. For the kinetic model in Scheme 3, $\text{slope}_{\text{ACH}} = 0$ and $\text{slope}_{\text{anti-ACH}} = 1$, which implies by inequality [27] that $0 < \text{slope}_{\text{exp}} < 1$ is satisfied. The kinetic plasticity in this case was defined as $\varepsilon_{\text{DKR}} = 1 - \text{slope}_{\text{exp}}$ to make the zero value and the unit value in inequality [27] correspond to 100% plasticity and 0% plasticity, respectively. Hence for Scheme 3, eq. [8] resulted. Maintaining this sense, the general expression for kinetic plasticity becomes,

[28] $$\varepsilon_{\text{DKR}} = 1 - \frac{\text{slope}_{\text{exp}} - \text{slope}_{\text{ACH}}}{\text{slope}_{\text{anti-ACH}} - \text{slope}_{\text{ACH}}} = 1 - \text{slope}_{\text{exp}}$$

The determination of kinetic plasticity parameters for any kinetic scheme, such as those shown in Schemes 6 and 7, must be done on a pairwise basis such that adjacent pairs of products arising from their corresponding equilibrating substrates are considered. For example, for Scheme 6 there are three substrates leading to three unique products, and there are two pairs of adjacent products to consider in the pairwise analysis. This will result in two kinetic plasticity indices corresponding to the P_AP_B and P_BP_C pairs of products. The global kinetic plasticity for the scheme would be described by this set of two indices. The form of the expression for the kinetic plasticity index would be identical to eq. [8] with $r = k_a/k_b$, $u = k_1/k_a$, and $v = k_2/k_a$ for the P_AP_B pair, and $r = k_b/k_c$, $u = k_3/k_b$, and $v = k_4/k_b$ for the P_BP_C pair. For Scheme 7 there are three adjacent pairs of products to consider, leading to three kinetic plasticity parameters: P_AP_B, P_BP_C, and P_AP_C. Again, eq. [8] applies with $r = k_a/k_b$, $u = k_1/k_a$, and $v = k_2/k_a$ for the P_AP_B pair; $r = k_b/k_c$, $u = k_3/k_b$, and $v = k_4/k_b$ for the P_BP_C pair; and $r = k_a/k_c$, $u = k_6/k_a$, and $v = k_5/k_a$ for the P_AP_C pair. Unfortunately for both Schemes 6 and 7, it is not possible to obtain the kinetic plasticity indices directly by conducting product study experiments by varying in a pairwise fashion the initial substrate ratio as a function of the corresponding final product ratio, since neat expressions of the form of eq. [5] are not obtainable. Instead, the magnitudes of all rate constants need to be determined directly by independent kinetic experiments to make estimates of the above pairs of kinetic plasticity parameters using eq. [8].

Dynamic kinetic resolution by organocatalysis

The emerging field of organocatalysis (65–86) has undergone a rapid growth in recent years and provides several opportunities to test ideas presented in this work. Three examples are presented in which the versatility of the directed graph methods is applied to determine initial and final product ratio expressions. Corresponding expressions for the kinetic plasticity index are also determined in each case. These examples showcase the prowess of the new methods in tackling complex schemes with apparent ease. In addition, the new suggested product study experiment and corresponding linear relationship according to eq. [5] serves as a diagnostic test to verify the proposed kinetic schemes for these chemical systems and offers an opportunity to properly quantify their kinetic plasticities directly from experiment.

The first example (87) shown in Scheme 8 involves a double feed-in reaction that first produces racemizable chiral imine intermediates from chiral aldehydes and aromatic amines, followed by catalytic production of chiral iminium salts that are then finally reduced to their amine analogues via oxidation of Hantzsch dihydropyridine esters to pyridines. Figure 10 shows the corresponding directed graph and Section 6 of the Supplementary Data shows the list of subgraphs to consider with respect to P_1 as the target product by the adapted Chou method.[2] The subgraphs with respect to P_2 as the target product are found using the following transposition of variables: $[A]_0 \leftrightarrow [B]_0$, $k_1 \leftrightarrow k_8$, $k_2 \leftrightarrow k_7$, $k_3 \leftrightarrow k_6$, $k_4 \leftrightarrow k_5$, $k_9 \leftrightarrow k_{10}$, and $k_{11} \leftrightarrow k_{12}$. For the analysis it was assumed that the concentrations of aromatic amine, chiral acids HX*, and Hanzsch dihydropyridine esters were in excess compared with the chiral aldehydes A and B. The expressions for the initial and final product ratios and the final product excess are given by eqs. [29], [30], and [31],

[29] $$\frac{[P_1]_0}{[P_2]_0} = \frac{[A]_0}{[B]_0}\left(\frac{k_1}{k_8}\right)\left(\frac{k_9k_{11}}{k_{10}k_{12}}\right)$$

[30] $$\frac{[P_1]_\infty}{[P_2]_\infty} = \left(\frac{k_9}{k_{10}}\right)\left[\frac{[A]_0\alpha + [B]_0k_4k_6}{[A]_0k_3k_5 + [B]_0\beta}\right]$$

where

$$\alpha = k_4k_6 + k_{10}[HX^*](k_4 + k_5)$$

$$\beta = k_3k_5 + k_9[HX^*](k_4 + k_5)$$

© 2008 NRC Canada

Scheme 8.

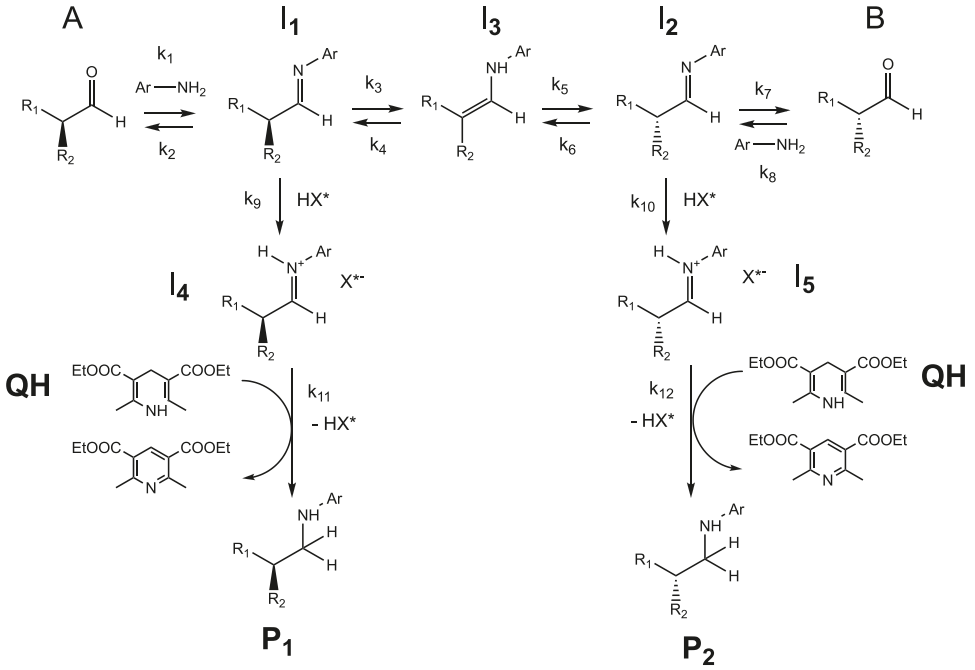

Fig. 10. Chou digraph pertaining to Scheme 8.

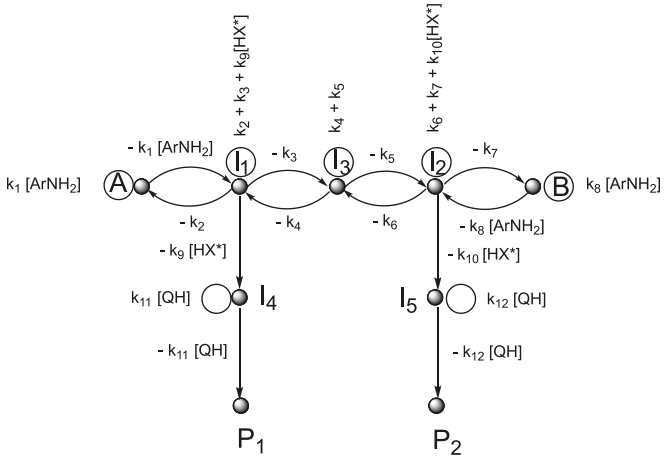

$$[31]\quad pe_\infty = \frac{\left(\frac{k_9}{k_{10}}\right)\left(\frac{[A]_0\alpha + [B]_0 k_4 k_6}{[A]_0 k_3 k_5 + [B]_0\beta}\right) - 1}{\left(\frac{k_9}{k_{10}}\right)\left(\frac{[A]_0\alpha + [B]_0 k_4 k_6}{[A]_0 k_3 k_5 + [B]_0\beta}\right) + 1}$$

$$= \frac{ru_2\nu_1 - u_1\nu_2}{ru_2\nu_1 + u_1\nu_2 + [HX^*](\nu_1 + \nu_2)} + \left(\frac{[A]_0 - [B]_0}{[A]_0 + [B]_0}\right)\left(\frac{[HX^*](\nu_1 + \nu_2)}{ru_2\nu_1 + u_1\nu_2 + [HX^*](\nu_1 + \nu_2)}\right)$$

where $r = k_9/k_{10}$, $u_1 = k_3/k_{10}$, $u_2 = k_6/k_{10}$, $v_1 = k_4/k_{10}$, and $v_2 = k_5/k_{10}$. Note that eq. [31] shows a linear dependence between pe_∞ and se_0. In the ACH limit when $k_i = k$ (for i = 1 to 8) and are very large compared with k_j (for j = 9 to 12), we have,

$$[32]\quad \alpha = k^2 + k_{10}[HX^*]2k$$

$$\beta = k^2 + k_9[HX^*]2k$$

so that the final product ratio becomes,

$$[33]\quad \left(\frac{[P_1]_\infty}{[P_2]_\infty}\right)_{ACH} = \lim_{k\to\infty}\left(\frac{k_9}{k_{10}}\right)\left[\frac{[A]_0(k^2 + k_{10}[HX^*]2k) + [B]_0 k^2}{[A]_0 k^2 + [B]_0(k^2 + k_9[HX^*]2k)}\right]$$

$$= \left(\frac{k_9}{k_{10}}\right)\lim_{k\to\infty}\left[\frac{([A]_0 + [B]_0)k^2 + [A]_0(k_{10}[HX^*]2k)}{([A]_0 + [B]_0)k^2 + [B]_0(k_9[HX^*]2k)}\right]$$

$$= \left(\frac{k_9}{k_{10}}\right)\left(\frac{[A]_0 + [B]_0}{[A]_0 + [B]_0}\right)$$

$$= \frac{k_9}{k_{10}}$$

which shows a dependence only on the product forming rate constants emanating from intermediates I1 and I2.

In the anti-ACH limit when $k_i = k$ (for i = 1 to 8) and are very small compared with k_j (for j = 9 to 12), we have the same relations as in eq. [32] so that the final product ratio becomes,

$$[34]\quad \left(\frac{[P_1]_\infty}{[P_2]_\infty}\right)_{anti\text{-}ACH} = \lim_{k\to 0}\left(\frac{k_9}{k_{10}}\right)\left[\frac{[A]_0(k^2 + k_{10}[HX^*]2k) + [B]_0 k^2}{[A]_0 k^2 + [B]_0(k^2 + k_9[HX^*]2k)}\right]$$

© 2008 NRC Canada

Scheme 9.

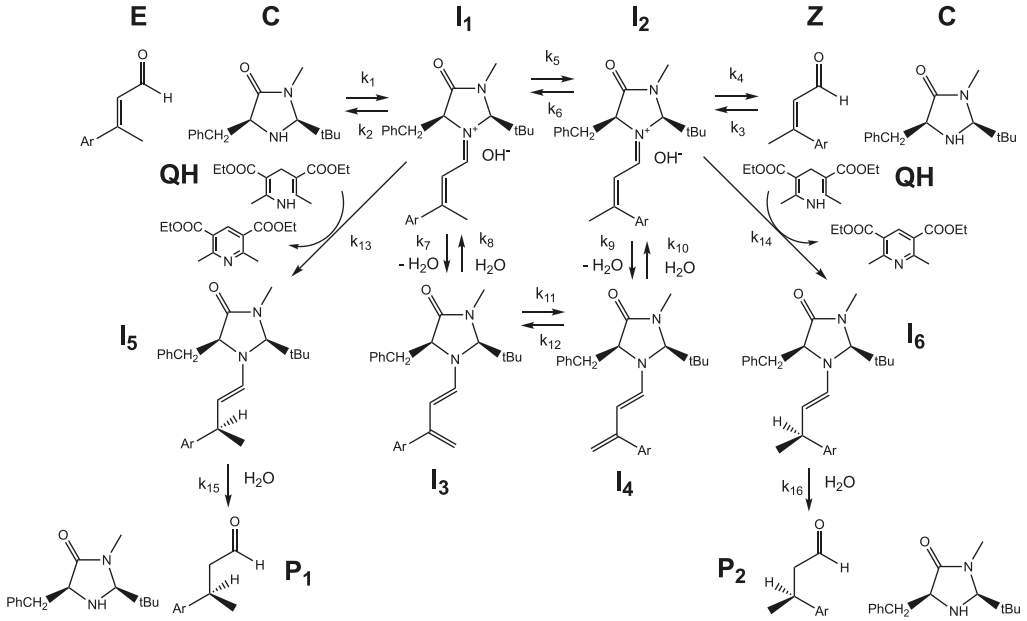

$$= \left(\frac{k_9}{k_{10}}\right) \lim_{k\to 0} \left[\frac{([A]_0 + [B]_0)k^2 + [A]_0(k_{10}[HX^*]2k)}{([A]_0 + [B]_0)k^2 + [B]_0(k_9[HX^*]2k)}\right]$$

$$= \left(\frac{k_9}{k_{10}}\right)\left(\frac{[A]_0}{[B]_0}\right)\left(\frac{k_{10}}{k_9}\right)\left(\frac{2[HX^*]}{2[HX^*]}\right)$$

$$= \frac{[A]_0}{[B]_0}$$

which shows a dependence only on the starting amounts of aldehydes A and B.

The final product excess as a function of initial substrate excess for these two limits is given by eqs. [35] and [36],

$$[35] \quad (\mathrm{pe}_\infty)_{\mathrm{ACH}} = \lim_{\substack{u_i\to\infty \\ \nu_i\to\infty}} \mathrm{pe}_\infty = \frac{r-1}{r+1} = \frac{\dfrac{k_9}{k_{10}} - 1}{\dfrac{k_9}{k_{10}} + 1}$$

$$[36] \quad (\mathrm{pe}_\infty)_{\text{anti-ACH}} = \lim_{\substack{u_i\to\infty \\ \nu_i\to\infty}} \mathrm{pe}_\infty = \mathrm{se}_0$$

where

$$\mathrm{se}_0 = \frac{[A]_0 - [B]_0}{[A]_0 + [B]_0}$$

Using the definition given in eq. [28], the expression for the kinetic plasticity for this kinetic model is given by eq. [37],

$$[37] \quad \varepsilon_{\mathrm{DKR}} = 1 - \frac{\left(\dfrac{\mathrm{d}(\mathrm{pe}_\infty)}{\mathrm{d}(\mathrm{se}_0)}\right)_{\mathrm{exp}} - \left(\dfrac{\mathrm{d}(\mathrm{pe}_\infty)}{\mathrm{d}(\mathrm{se}_0)}\right)_{\mathrm{ACH}}}{\left(\dfrac{\mathrm{d}(\mathrm{pe}_\infty)}{\mathrm{d}(\mathrm{se}_0)}\right)_{\text{anti-ACH}} - \left(\dfrac{\mathrm{d}(\mathrm{pe}_\infty)}{\mathrm{d}(\mathrm{se}_0)}\right)_{\mathrm{ACH}}}$$

$$= 1 - \frac{\left(\dfrac{\mathrm{d}(\mathrm{pe}_\infty)}{\mathrm{d}(\mathrm{se}_0)}\right)_{\mathrm{exp}} - 0}{1 - 0}$$

$$= 1 - \left(\frac{\mathrm{d}(\mathrm{pe}_\infty)}{\mathrm{d}(\mathrm{se}_0)}\right)_{\mathrm{exp}}$$

$$= 1 - \frac{[HX^*](\nu_1 + \nu_2)}{ru_2\nu_1 + u_1\nu_2 + [HX^*](\nu_1 + \nu_2)}$$

$$= \frac{ru_2\nu_1 + u_1\nu_2}{ru_2\nu_1 + u_1\nu_2 + [HX^*](\nu_1 + \nu_2)}$$

The second example (88) shown in Scheme 9 is a more complex variant of Scheme 8. The aim is to stereoselectively reduce a mixture of (*E*/*Z*) α,β-unsaturated aldehydes to their dihydroaldehyde analogs via Hanzsch dihydropyridines and a chiral organocatalyst that produces (*E*/*Z*) iminium intermediates that are interconvertible. Figure 11 shows the corresponding directed graph and Section 7 of the Supplemenatry Data shows the subgraphs with respect to P1 as the target product.[2] As in the previous case, the subgraphs with respect to P_2 are found using the following transposition of variables: $[E]_0 \leftrightarrow [Z]_0$, $k'_1 \leftrightarrow k'_3$, $k_2 \leftrightarrow k_4$, $k_5 \leftrightarrow k_6$, $k_7 \leftrightarrow k_9$, $k'_8 \leftrightarrow k'_{10}$, $k_{11} \leftrightarrow k_{12}$, $k'_{13} \leftrightarrow k'_{14}$, and $k'_{15} \leftrightarrow k'_{16}$.

The expressions for the initial and final product ratios and the final product excess are given by eqs. [38], [39], and [40],

$$[38] \quad \frac{[P_1]_0}{[P_2]_0} = \frac{[E]_0}{[Z]_0}\left(\frac{k_1}{k_3}\right)\left(\frac{k_{13}k_{15}}{k_{14}k_{16}}\right)$$

$$[39] \quad \frac{[P_1]_\infty}{[P_2]_\infty} = \left(\frac{k'_{13}}{k'_{14}}\right)\left(\frac{([E]_0 + [Z]_0)\alpha + [E]_0 k'_{14}\beta}{([E]_0 + [Z]_0)\alpha^* + [E]_0 k'_{13}\beta}\right)$$

where

© 2008 NRC Canada

Fig. 11. Chou digraph pertaining to Scheme 9.

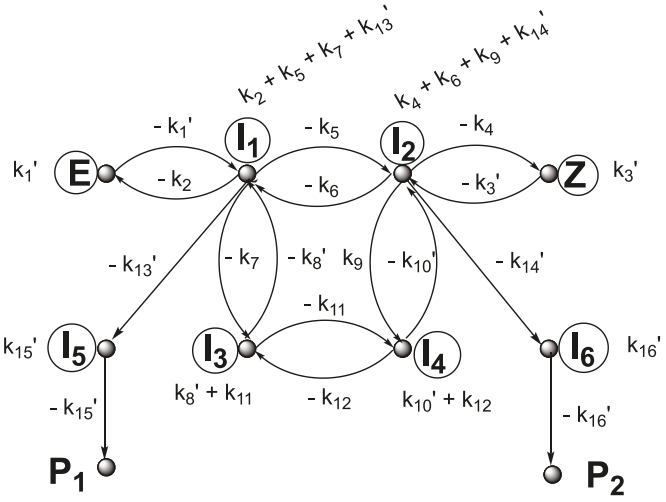

$$\alpha = k_6\beta + k_9k'_8k_{12}$$

$$\alpha^* = k_5\beta + k_7k'_{10}k_{11}$$

$$\beta = k'_8k'_{10} + k'_8k'_{12} + k'_{10}k'_{11}$$

$$k'_1 = k_1[\mathrm{C}],\ k'_3 = k_3[\mathrm{C}],\ k'_8 = k_8[\mathrm{H_2O}],$$

$$k'_{10} = k_{10}[\mathrm{H_2O}]$$

$$k'_{15} = k_{15}[\mathrm{H_2O}],\ k'_{16} = k_{16}[\mathrm{H_2O}],$$

$$k'_{13} = k_{13}[\mathrm{QH}],\ k'_{14} = k_{14}[\mathrm{QH}]$$

[40] $$\mathrm{pe}_\infty = \frac{\left(\frac{k'_{13}}{k'_{14}}\right)\left[\frac{([\mathrm{E}]_0 + [\mathrm{Z}]_0)\alpha + [\mathrm{E}]_0k'_{14}\beta}{([\mathrm{E}]_0 + [\mathrm{Z}]_0)\alpha^* + [\mathrm{E}]_0k'_{13}\beta}\right] - 1}{\left(\frac{k'_{13}}{k'_{14}}\right)\left[\frac{([\mathrm{E}]_0 + [\mathrm{Z}]_0)\alpha + [\mathrm{E}]_0k'_{14}\beta}{([\mathrm{E}]_0 + [\mathrm{Z}]_0)\alpha^* + [\mathrm{E}]_0k'_{13}\beta}\right] + 1}$$

$$= \frac{r\alpha - \alpha^*}{r\alpha + \alpha^* + k'_{13}\beta} + \left(\frac{[\mathrm{E}]_0 - [\mathrm{Z}]_0}{[\mathrm{E}]_0 + [\mathrm{Z}]_0}\right)\left(\frac{k'_{13}\beta}{r\alpha + \alpha^* + k'_{13}\beta}\right)$$

where $r = k'_{13}/k'_{14}$. Note that eq. [40] shows a linear dependence between pe_∞ and se_0. In the ACH limit when $k_i = k$ (for i = 1 to 12) and very large compared with k_j (for j = 13 to 16), we have

[41] $$\alpha \to 4k^3$$
$$\alpha^* \to 4k^3$$
$$\beta \to 3k^2$$

so that the final product ratio becomes,

[42] $$\left(\frac{[\mathrm{P_1}]_\infty}{[\mathrm{P_2}]_\infty}\right)_{\mathrm{ACH}} = \lim_{k\to\infty}\left(\frac{k'_{13}}{k'_{14}}\right)\left[\frac{([\mathrm{E}]_0 + [\mathrm{Z}]_0)4k^3 + [\mathrm{E}]_0k'_{14}3k^2}{([\mathrm{E}]_0 + [\mathrm{Z}]_0)4k^3 + [\mathrm{Z}]_0k'_{13}3k^2}\right]\left(\frac{k'_{13}}{k'_{14}}\right)$$

which shows, as in the previous example, a dependence only on the ratio of product forming rate constants emanating from intermediates $\mathrm{I_1}$ and $\mathrm{I_2}$.

In the anti-ACH limit when k_i — > 0 (for i = 1 to 12), we have the same relations as in eq. [41], so that the final product ratio becomes,

[43] $$\left(\frac{[\mathrm{P_1}]_\infty}{[\mathrm{P_2}]_\infty}\right)_{\text{anti-ACH}} = \lim_{k\to 0}\left(\frac{k'_{13}}{k'_{14}}\right)\left[\frac{([\mathrm{E}]_0 + [\mathrm{Z}]_0)4k^3 + [\mathrm{E}]_0k'_{14}3k^2}{([\mathrm{E}]_0 + [\mathrm{Z}]_0)4k^3 + [\mathrm{Z}]_0k'_{13}3k^2}\right]\left(\frac{[\mathrm{E}]_0}{[\mathrm{Z}]_0}\right)$$

The final product excess as a function of initial substrate excess for these two limits are given by eqs. [44] and [45],

[44] $$(\mathrm{pe}_\infty)_{\mathrm{ACH}} = \frac{r-1}{r+1} = \frac{\frac{k'_{13}}{k'_{14}} - 1}{\frac{k'_{13}}{k'_{14}} + 1}$$

[45] $$(\mathrm{pe}_\infty)_{\text{anti-ACH}} = \mathrm{se}_0$$

where

$$\mathrm{se}_0 = \frac{[A]_0 - [B]_0}{[A]_0 + [B]_0}$$

Using the definition given in eq. [28], the expression for the kinetic plasticity for this kinetic model is given by eq. [46],

[46] $$\varepsilon_{\mathrm{DKR}} = \frac{r\alpha + \alpha^*}{r\alpha + \alpha^* + k'_{13}\beta}$$

The final example (89) shown in Scheme 10 involves stereoselective α-fluorination via an electrophilic "F^+" species of an achiral aldehyde using a chiral proline analogue as an organocatalyst. The two products of interest are $\mathrm{P_1}$ and $\mathrm{P_2}$. The third difluorinated product arises from intermediate $\mathrm{I_4}$ which is in equilibrium with $\mathrm{I_2}$ and $\mathrm{I_3}$. All three products arise from the same source, namely intermediate $\mathrm{I_1}$. Since the products do not arise from different equilibrating starting substrates, kinetic control to produce one of the products over the others will depend on the relative magnitudes of the rate constants and not on the initial amount of starting material. Figure 12 shows the corresponding directed graph and Section 8 of the Supplementary Data shows the subgraphs with respect to $\mathrm{P_1}$, $\mathrm{P_2}$, and $\mathrm{P_3}$ as the target products.[2] The following transposition of variables applies: $k'_3 \leftrightarrow k'_8$, $k_7 \leftrightarrow k_9$, $k'_5 \leftrightarrow k'_8$, and $k'_8 \leftrightarrow k'_{10}$. The initial and final product ratios are given by eqs. [47] and [48], respectively.

[47] $$[\mathrm{P_1}]_0:[\mathrm{P_2}]_0:[\mathrm{P_3}]_0 = k'_3k'_5 : k'_4k'_6 : k'_{11}k'_{12}(k'_3k_7 + k'_4k_9)$$

[48] $$[\mathrm{P_1}]_\infty:[\mathrm{P_2}]_\infty:[\mathrm{P_3}]_\infty$$
$$= k'_5\{k'_3k'_6\,\alpha + k_9(k'_3k'_8 + k'_4k'_8 + k'_3k'_{11})\}$$
$$: k'_6\{k'_4k'_5\,\alpha + k_7(k'_4k'_{10} + k'_4k'_{11} + k'_3k'_{10})\}$$
$$: k'_{11}\{k'_3k_7(k'_6 + k_9) + k'_4k_9(k'_5 + k_7)\}$$

where

© 2008 NRC Canada

Scheme 10.

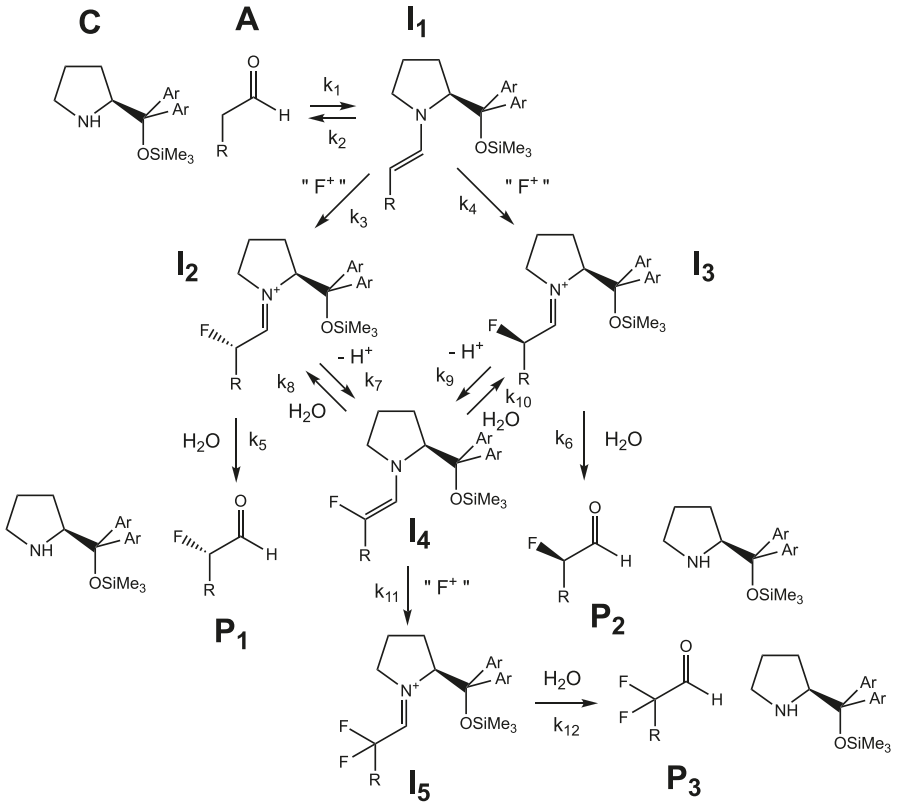

$$\alpha = k'_8 + k'_{10} + k'_{11}$$

$$k_3' = k_3[F^+],\ k'_4 = k_4[F^+],\ k'_{11} = k_{11}[F^+]$$

$$k'_5 = k_5[H_2O],\ k'_6 = k_6[H_2O],\ k'_8 = k_8[H_2O]$$

$$k'_{10} = k_{10}[H_2O],\ k'_{12} = k_{12}[H_2O]$$

In the ACH limit when there is rapid equilibration between intermediates I_2, I_3, and I_4 so that $k_i = k$ (for i = 7 to 10) is very large compared with the product forming rate constants, then the final product ratio becomes,

$$[49]\quad ([P_1]_\infty:[P_2]_\infty:[P_3]_\infty)_{ACH} = k'_5:k'_6:k'_{11} = k_5[H_2O]:k_6[H_2O]:k_{11}[F^+]$$

Again, these are the product-forming rate constants emanating from intermediates I_2, I_3, and I_4. On the other hand, the anti-ACH limit results in a final product ratio given by eq. [50], which predicts the absence of the difluorinated product P_3,

$$[50]\quad ([P_1]_\infty:[P_2]_\infty:[P_3]_\infty)_{anti\text{-}ACH} = k'_3:k'_4:0$$

Since all three products arise from the same source substrate, it is not possible to obtain estimates of kinetic plasticity parameters for this scheme by varying substrate amounts. Direct estimates of the appropriate rate constants need to be made. The two pairs of products to consider are P_1P_3 and P_3P_2 that will lead to two kinetic plasticity indices. They will be of the form of eq. [8] with $r = k'_5/k'_{11}$, $u = k_7/k'_5$, and $v = k'_8/k'_5$ for the P_1P_3 pair and $r = k'_{11}/k'_6$, $u = k'_{10}/k'_{11}$, and $v = k_9/k'_{11}$ for the P_3P_2 pair.

Fig. 12. Chou digraph pertaining to Scheme 10.

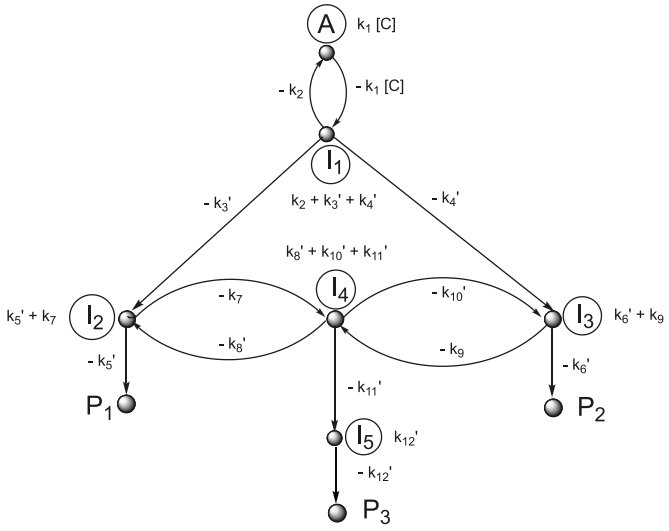

Conclusions

The present work introduces new algorithms based on directed graphs to determine initial and final product ratios for simple and complex kinetic models leading to multiple products for unimolecular transformations and under pseudo-order conditions. These are found to circumvent the tedious and error prone computations that are characteristic of conventional treatments based on rate laws. A degree of kinetic plasticity parameter is introduced and shown to be general in

© 2008 NRC Canada

describing the ACH condition (100% dynamic kinetic resolution), the opposite anti-ACH condition (0% dynamic kinetic resolution), and all other scenarios in between these limits. To empirically probe the full scope of the dynamics of a kinetic system one needs to begin from more than one set of starting substrate conditions. Thus, it is impossible to obtain a full picture by carrying out product studies from one set of starting substrate conditions such as a racemic mixture. For a practicing organic chemist who wishes to understand their kinetic schemes more deeply without having to invoke external assumptions, this means that they must move beyond the confines of racemic mixtures as the only starting point to obtain direct experimental measures of the dynamics of their systems. The determination of the degree of kinetic plasticity is thus based on a key experimental plot that relates final product excess and initial substrate excess in a pairwise fashion. Such a plot is always linear with a positive slope, and the degree of kinetic plasticity is found directly by subtracting the slope from unity. Furthermore, it may be used as a diagnostic test for checking the validity of proposed ACH-type kinetic schemes for a given chemical system. A key bonus of the new methods of obtaining product ratio expressions is that the precise rate constant dependence of the degree of kinetic plasticity is obtained explicitly. Such dependencies may be further checked by direct determination of absolute rate constants from independent kinetic measurements. Examination of extended variants of ACH-type schemes indicates that the ACH principle holds universally and may be elevated to the status of a kinetic theorem. The next challenge for organic chemists is to provide experimental verification of the predictions made in this work.

Acknowledgements

This work was presented at the 90th Canadian Society of Chemistry (CSC) Conference and Exhibition in Winnipeg, Manitoba, Canada (May 26–30, 2007) in honour of the 80th birthday of Prof. Alexander Jerry Kresge and at the 35th Ontario–Quebec Physical Organic Chemistry Mini-Symposium in Waterloo, Ontario, Canada (November 9–11, 2007) honouring the late Prof. Keith Yates. Dedicated to the memory of Keith Yates.

References

1. D.Y. Curtin. Rec. Chem. Prog. **15**, 111 (1954).
2. L.P. Hammett. Physical organic chemistry: reaction rates, equilibria, and mechanisms. 2nd ed. McGraw-Hill, New York. 1970. pp. 119–120.
3. S.F. Acree. Am. Chem. J. **38**, 1 (1907).
4. S. Winstein and N.J. Holness. J. Am. Chem. Soc. **77**, 5562 (1955).
5. J. Andraos. Chemical educator. In press.
6. E.L. Eliel, S.H. Wilen, and L.N. Mander. Stereochemistry of organic compounds. Wiley, New York. YEAR. pp. 647–655.
7. F.A. Carroll. Perspectives in structure and mechanism in organic chemistry. Brooks Cole Publishing Co., New York. 1998. pp. 345–349.
8. F.A. Carey and R.J. Sundberg. Advanced organic chemistry. Part A: structure and mechanism. Plenum Publishing, New York. 1993. pp. 209–216.
9. (*a*) J.I. Seeman. Chem. Rev. **83**, 83 (1983); (*b*) J.I. Seeman and W.A. Farone. J. Org. Chem. **43**, 1854 (1978).
10. J.I. Seeman. J. Chem. Educ. **63**, 42 (1986).
11. J. Andraos. J. Phys. Chem. A, **107**, 2374 (2003).
12. B. Martin-Matute, J.E. Bäckvall. Curr. Opin. Chem. Biol. **11**, 226 (2007).
13. J.E. Bäckvall. *In* Asymmetric catalysis. *Edited by* M. Christmann and S. Braese. Wiley-VCH, Weinheim, Germany. 2007. pp. 171–175.
14. E. Fogassy, M. Nogradi, D. Kozma, G. Egri, E. Palovics, and V. Kiss. Org. Biomol. Chem. **4**, 3011 (2006).
15. U.T. Bornscheuer. Adv. Biochem. Eng. Biotechnol. **100**, 181 (2005).
16. N.J. Turner. Curr. Opin. Chem. Biol. **8**, 114 (2004).
17. O. Pamies and J.E. Bäckvall. Trends Biotechnol. **22**, 130 (2004).
18. H. Pellissier. Tetrahedron, **59**, 8291 (2003).
19. O. Pamies and J.E. Bäckvall. Curr. Opin. Biotechnol. **14**, 407 (2003).
20. N.J. Turner. Curr. Opin. Biotechnol. **14**, 401 (2003).
21. O. Pamies and J.E. Bäckvall. Chem. Rev. **103**, 3247 (2003).
22. B. Schnell, K. Faber, and W. Kroutil. Adv. Synth. Catal. **345**, 653 (2003).
23. D.E.J.E. Robinson and S.D. Bull. Tetrahedron: Asymmetry, **14**, 1407 (2003).
24. M.J. Kim, Y. Ahn, and J. Park. Curr. Opin. Biotechnol. **13**, 578 (2002).
25. J.M.J. Williams, R.J. Parker, and C. Neri. *In* Enzyme catalysis in organic synthesis. Vol. 1. *Edited by* K. Drauz and H. Waldmann. Wiley-VCH, Weinheim, Germany. 2002. pp. 287–312.
26. O. May, S. Verseck, A. Bommarius, and K. Drauz. Org. Process Res. Dev. **6**, 452 (2002).
27. F.F. Huerta, A.B.E. Minidis, and J.E. Bäckvall. Chem. Soc. Rev. **30**, 321 (2001).
28. K. Faber. Chem. Eur. J. **7**, 5005 (2001).
29. G.R. Cook. Curr. Org. Chem. **4**, 869 (2000).
30. U.T. Strauss, U. Felfer, and K. Faber. Tetrahedron: Asymmetry, **10**, 107 (1999).
31. R.S. Ward. Selectivity in organic synthesis. Wiley, New York. 1999. Chap. 6.
32. M.T. El Gihani, J.M.J. Williams. Curr. Opin. Chem. Biol. **3**, 11 (1999).
33. R.J. Parker and J.M.J. Williams. Recent Res. Dev. Org. Bioorg. Chem. **3**, 47 (1999).
34. H. Stecher and K. Faber. Synthesis, 1 (1997).
35. R. Sturmer. Angew. Chem. Int. Ed. Engl. **36**, 1173 (1997).
36. S. Caddick and K. Jenkins. Chem. Soc. Rev. **25**, 447 (1996).
37. R.S. Ward. Tetrahedron: Asymmetry, **6**, 1475 (1995).
38. H.B. Kagan and J.C. Fiaud. *In* Topics in stereochemistry. Vol. 18. *Edited by* E.L. Eliel and S.H. Wilen. Wiley, New York. 1988. pp. 249–330.
39. J. Andraos. J. Chem. Educ. **76**, 1578 (1999) and refs. cited therein.
40. M. Kitamura, M. Tokunaga, and R. Noyori. Tetrahedron **49**, 1853 (1993).
41. R. Noyori, M. Tokunaga, and M. Kitamura. Bull. Chem. Soc. Jpn. **68**, 36 (1995).
42. For a typical example see: R.N. Ben and T. Durst. J. Org. Chem. **64**, 7700 (1999).
43. V.K. Balakrishnan. Schaum's outlines: graph theory. McGraw-Hill, New York. 1997.
44. E.L. King and C. Altman. J. Phys. Chem. **60**, 1375 (1956).
45. K.C. Chou. Eur. J. Biochem. **113**, 195 (1980).
46. K.C. Chou and S. Forsen. Biochem. J. **187**, 829 (1980).

© 2008 NRC Canada

47. K.C. Chou. J. Theor. Biol. **89**, 581 (1981).
48. K.C. Chou and L.W. Min. J. Theor. Biol. **91**, 637 (1981).
49. K.C. Chou and S. Forsen. Can. J. Chem. **59**, 737 (1981).
50. K.C. Chou. Biophys. Chem. **17**, 51 (1983).
51. K.C. Chou. J. Biol. Chem. **264**, 12074 (1989).
52. K.C. Chou. Biophys. Chem. **35**, 1 (1990).
53. K.C. Chou. J. Math. Chem. **12**, 97 (1993).
54. I.W. Althaus, J.J. Chou, A.J. Gonzales, M.R. Diebel, K.C. Chou, F.J. Kezdy, D.L. Romero, P.A. Aristoff, and W.G. Tarpley. J. Biol. Chem. **268**, 6119 (1993).
55. I.W. Althaus, A.J. Gonzales, J.J. Chou, M.R. Diebel, K.C. Chou, F.J. Kezdy, D.L. Romero, P.A. Aristoff, W.G. Tarpley, and F. Reusser. J. Biol. Chem. **268**, 14875 (1993).
56. I.W. Althaus, J.J. Chou, A.J. Gonzales, M.R. Diebel, K.C. Chou, F.J. Kezdy, D.L. Romero, P.A. Aristoff, W.G. Tarpley, and F. Reusser. Biochemistry, **32**, 6548 (1993).
57. I.W. Althaus, J.J. Chou, A.J. Gonzales, M.R. Diebel, K.C. Chou, F.J. Kezdy, D.L. Romero, R.C. Thomas, P.A. Aristoff, W.G. Tarpley, and F. Reusser. Biochem. Pharmacol. **47**, 2017 (1994).
58. S.X. Lin and K.E. Neet. J. Biol. Chem. **265**, 9670 (1990).
59. P. Kuzmic, K.Y. Ng, and T.D. Heath. Anal. Biochem. **200**, 68 (1992).
60. K.C. Chou, F.J. Kezdy, and F. Reusser. Anal. Biochem. **221**, 217 (1994).
61. G.P. Zhou and M.H. Deng. Biochem. J. **222**, 169 (1984).
62. G.E. Roberts and H. Kaufman. Table of Laplace transforms. Saunders, Philadelphia. 1966.
63. F. Oberhettinger and L. Badii. Tables of Laplace transforms. Springer, New York. 1973.
64. M. Healey. Tables of Laplace, Heaviside, Fourier and Z transforms. W. & R. Chambers, Edinburgh. 1967.
65. M.J. Gaunt, C.C.C. Johansson, A. McNally, and T. Vo Ngoc. Drug Discovery Today, **12**, 8 (2007).
66. G. Lelais and D.W.C. Macmillan. *In* New frontiers in asymmetric catalysis. *Edited by* K. Mikami and M. Lautens. Wiley, Hoboken, New Jersey. 2007. pp. 313–358.
67. R.M. de Figueiredo and M. Christmann. Eur. J. Org. Chem. 2575 (2007).
68. N. Marion, S. Diez-Gonzalez, and S.P. Nolan. Angew. Chem. Int. Ed. **46**, 2988 (2007).
69. S.B. Tsogoeva. Eur. J. Org. Chem. 1701 (2007).
70. G. Guillena, D.J. Ramon, and M. Yus. Tetrahedron: Asymmetry, **18**, 693 (2007).
71. D. Enders, C. Grondal, and M. Huettl. Angew. Chem. Int. Ed. **46**, 1570 (2007).
72. K. Maruoka, T. Ooi, and T. Kano. Chem. Commun. (Cambridge, U.K.), 1487 (2007).
73. S.V. Ley. *In* Asymmetric catalysis. *Edited by* M. Christmann and S. Braese. Wiley-VCH, Weinheim, Germany. 2007. pp. 201–206.
74. B. List. *In* Asymmetric catalysis. *Edited by* M. Christmann and S. Braese. Wiley-VCH, Weinheim, Germany. 2007. pp. 161–165.
75. D. Almasi, D.A. Alonso, and C. Najera. Tetrahedron: Asymmetry, **18**, 299 (2007).
76. M. Ikunaka. Org. Process Res. Dev. **11**, 495 (2007).
77. B. List. Chem. Commun. (Cambridge, U.K.), 819 (2006).
78. B. List and J.W. Yang. Science, **313**, 1584 (2006).
79. D. Tejedor, D. Gonzalez-Cruz, A. Santos-Exposito, J.J. Marrero-Tellado, P. de Armas, and F. Garcia-Tellado. Chem. Eur. J. **11**, 3502 (2005).
80. J. Saeyad and B. List. Org. Biomol. Chem. **3**, 719 (2005).
81. P.I. Dalko and L. Moisan. Angew. Chem. Int. Ed. **43**, 5138 (2004).
82. M.L. Clarke. Lett. Org. Chem. **1**, 292 (2004).
83. K.N. Houk and B. List. Acc. Chem. Res. **37**, 487 (2004).
84. P.R. Schreiner. Chem. Soc. Rev. **32**, 289 (2003).
85. N. Gathergood. Austr. J. Chem. **55**, 615 (2002).
86. P.I. Dalko and L. Moisan. Angew. Chem. Int. Ed. **40**, 3726 (2001).
87. S. Hoffmann, M. Nicoletti, and B. List. J. Am. Chem. Soc. **128**, 13074 (2006).
88. J.W. Yang, M.T.H. Fonseca, N. Vignola, B. List. Angew. Chem. Int. Ed. **44**, 108 (2005).
89. J. Franzen, M. Marigo, D. Fielenbach, T.C. Wabnitz, A. Kjaersgaard, and K.A. Jørgensen. J. Am. Chem. Soc. **127**, 18296 (2005).

© 2008 NRC Canada

Correlation of the rates of solvolysis of acetyl chloride and α-substituted derivatives

Malcolm J. D'Souza, Zoon Ha Ryu, Byoung-Chun Park, and Dennis N. Kevill

Abstract: Additional specific rates of solvolysis have been determined for acetyl chloride and diphenylacetyl chloride. These are combined with literature values to carry out correlation analyses, using the extended Grunwald–Winstein equation with incorporation of literature values for solvent nucleophilicity (N_T) and solvent ionizing power (Y_{Cl}). Parallel analysis are carried out using literature values for the specific rates of solvolysis of trimethylacetyl chloride, chloroacetyl chloride, phenylacetyl chloride, and α-methoxy-α-trifluoromethylphenylacetyl chloride (MTPAC). Chloroacetyl chloride and MTPAC react by an addition-elimination pathway, with the addition step rate-determining, over the full range of solvents. Acetyl chloride reacts over the full range of solvents by an ionization pathway, with considerable nucleophilic solvation. The other three substrates can solvolyze with the domination of either mechanism, depending on the properties of the solvent. Reports concerning the use of product selectivity values, kinetic solvent isotope effects, and computational studies as additional probes of the mechanism of solvolysis are discussed.

Key words: Grunwald–Winstein equation, acyl chlorides, mechanism of solvolysis, solvent nucleophilicity.

Résumé : On a déterminé de nouvelles vitesses spécifiques de solvolyse pour le chlorure d'acétyle et le chlorure de diphénylacétyle. Les valeurs ainsi déterminées ont été combinées à celles qu'on peut retrouver dans la littérature pour effectuer une analyse de corrélation, à l'aide de l'équation étendue de Grunwald–Winstein et avec l'incorporation des valeurs obtenues dans la littérature pour le caractère nucléophile du solvant (N_T) et le pouvoir ionisant du solvant (Y_{Cl}). On a effectuer des analyses parallèles à l'aide des valeurs de la littérature pour les vitesses spécifiques de solvolyse du chlorure de triméthylacétyle, du chlorure de chloroacétyle, du chlorure de phénacétyle et du chlorure du α-méthoxy-α-trifluorométhylphénylacétyle (CMTPA). Le chlorure d'acétyle et le CMTPA réagissent par une voie d'addition/élimination dans laquelle l'addition est l'étape cinétiquement déterminante pour l'ensemble des solvants. Pour l'ensemble des solvants, le chlorure d'acétyle réagit par une voie d'ionisation impliquant une forte solvatation nucléophile. Pour les trois autres substrats, les deux mécanismes peuvent être prépondérants suivant les propriétés du solvant. On discute des rapports faisant état de l'utilisation des valeurs de sélectivité du produit, des effets isotopiques cinétiques du solvant et des études théoriques comme sondes additionnelles dans l'étude du mécanisme de solvolyse.

Mots-clés : équation de Grunwald–Winstein, chlorures d'acyles, mécanisme de solvolyse, caractère nucléophile du solvant.

[Traduit par la Rédaction]

Introduction

The extended (two-term) Grunwald–Winstein eq. [1] has been shown to be a useful probe of solvolytic reaction mechanism. In eq. [1], k and k_o are the specific rates (first-order rate coefficients) of solvolysis in a given solvent and in the standard solvent (80% aq. ethanol), respectively, l represents the sensitivity to changes in solvent nucleophilicity (N_T), m represents the sensitivity to changes in the solvent ionizing power (Y_X for a leaving group X), and c is a constant (residual) quantity.

$$[1] \qquad \log k/k_o = lN_T + mY_{Cl} + c$$

The l and m values are closely related to the extent of nucleophilic and electrophilic assistance within the rate-determining step, with solvent polarity and other additional effects being incorporated into the mY_X term. Scales of ionizing power vary somewhat depending on the leaving group, hence the designation Y_X. The scales are available for about a dozen leaving groups, based on the specific rates of solvolysis of 1- and (or) 2- adamantyl derivatives (2). The solvent nucleophilicity (N_T) is based on the specific rates of solvolysis of the *S*-methyldibenzothiophenium ion (3). In addition to its predictive value, the equation can also be useful in establishing the presence of a change in dominant mechanism as the solvent is varied. If the change is towards the middle of the range of solvents and the l and (or) m values differ sufficiently, the two regions can be treated independently in terms of eq. [1].

Received 11 January 2008. Accepted 12 February 2008. Published on the NRC Research Press Web site at canjchem.nrc.ca on 25 March 2008.

This paper is dedicated to the memory of Professor Keith Yates and in recognition of his many contributions to physical organic chemistry.

M.J. D'Souza.[1] Department of Chemistry, Wesley College, 120 N. State Street, Dover, DE 19901-3875, USA
Z.H. Ryu. Department of Chemistry, Dong-Eui University, Busan 614-714, Korea.
B.-C. Park and D.N. Kevill. Department of Chemistry and Biochemistry, Northern Illinois University, DeKalb, IL 60115-2862, USA.

[1]Corresponding author (e-mail: dsouzama@wesley.edu).

 doi:10.1139/V08-028 © 2008 NRC Canada

The mechanisms of nucleophilic substitution at an acyl carbon have been extensively studied. The earlier studies of both haloformate esters (4) and acyl halides (5, 6) have been reviewed. Many of the earlier studies were of chloroformate esters, which solvolyze at a convenient rate at ambient temperatures. Depending on the R group of ROCOCl, the solvolysis can follow bimolecular and (or) unimolecular pathways.

The solvolysis of phenyl chloroformate (PhOCOCl) has been extensively studied (7–10), and there is convincing evidence, independent of the Grunwald–Winstein correlations, that the reaction involves an addition–elimination mechanism, with the addition step being rate-determining. The strongest evidence is that, for the solvolyses of several chloroformates and the corresponding fluoroformates, the two haloformates (including aryl haloformates) react at similar rates, with the fluoroformate frequently faster (11–13). Because of the considerably stronger carbon–fluorine bond, this would be very difficult to reconcile with any mechanism requiring appreciable C–X bond fission within the rate-determining step. The solvolysis of PhOCOCl in 49 solvents, covering a wide range of N_T and Y_{Cl} values, when analyzed (10) in terms of eq. [1], involve an l value of 1.66 ± 0.05 and an m value of 0.56 ± 0.03 (multiple correlation coefficient R of 0.980). The data are very robust and various subsets of values give essentially the same sensitivity values. These values can be taken as typical values for attack at the acyl carbon proceeding by the addition–elimination mechanism, with the addition step rate-determining.

At the other extreme, 1-adamantyl chloroformate containing the tertiary 1-adamantyl cage structure, shows essentially no dependence on solvent nucleophilicity and an unusually low m value (0.47 ± 0.03) for a reaction proceeding with rate-determining ionization. The low value is probably associated with the solvolysis–decomposition nature of the reaction (14), with the ionization accompanied by loss of CO_2 and the formation of the chloride accompanied by ether and (or) alcohol, depending on the solvent. The change from an associative to an ionization rate-determining step can also be brought about, without decomposition, by the substitution of sulfur for one or both oxygens for phenyl chloroformate. For example, for 31 solvents the solvolyses of PhSCSCl show specific rates that can be correlated (15) using eq. [1] with values of 0.69 ± 0.05 for l and 0.95 ± 0.03 for m (R = 0.987). The rather large l value is believed to be due to an appreciable nucleophilic solvation of the developing acylium ion.

Solvolyses of aromatic acyl halides (ArCOCl) also proceed at convenient rates and several specific rate determinations have been made. Recent correlations of the available data using eq. [1] have used data from previous publications in conjunction with a few new values (16). Evidence was again obtained for both addition–elimination and ionization pathways, with the ionization pathway being assisted by nucleophilic solvation of the developing acylium ion. For *p*-nitrobenzoyl chloride solvolyses, with the electron–withdrawing substituent hindering the ionization pathway, the addition–elimination pathway (l = 1.78 ± 0.08, m = 0.54 ± 0.04) was observed over almost the full range of solvents. For solvolyses of *p*-methoxybenzoyl chloride with a powerful electron-supplying substituent, the ionization pathway was dominant over the full range of solvents (l = 0.31 ± 0.05, m = 0.81 ± 0.02). The parent benzoyl chloride and the *p*-chloro derivative both showed a switch-over in the dominant mechanism as one moved across the range of solvents. Other earlier approaches indicating such a change in mechanism, largely from the laboratories of Bentley, are extensively reviewed in this article. In contrast, benzoyl fluoride (17) with the stronger C–F bond retarding the heterolysis required in the ionization pathway followed the addition–elimination pathway over the full range of solvents (l = 1.58 ± 0.09, m = 0.82 ± 0.05).

The solvolyses of aliphatic acyl halides are considerably faster than those for aromatic acyl halides. For example, acetyl chloride solvolyzes about 150 times faster than *p*-methoxybenzoyl chloride over a range of relatively polar hydroxylic solvents (18). For this reason, the early studies were usually done with small concentrations of water or alcohol in the presence of an excess of inert solvent, such as ether, acetone, acetonitrile, or nitrobenzene (5). Studies of the specific rates of methanolysis and phenolysis of acetyl chloride and derivatives, in acetonitrile, led for the methanolyses to the operation of concurrent second-order and third-order pathways. A powerful catalysis by chloride ion was observed, with first-order kinetics in each of the substrate, methanol, and chloride ion. A loose S_N2 transition state was proposed (19, 20) with general base catalysis by solvent, methanol, or chloride ion. Consistent with this picture, modest rate decreases were observed on the introduction of one or two methyl groups, with a larger (about one order of magnitude) reduction on the introduction of a third.

The phenolysis of acetyl chloride (20) and its methyl-substituted derivatives (19) proceeds kinetically by a first-order pathway in each reactant. An alternative pathway was proposed in which the phenol rendered electrophilic assistance to chloride ion removal followed by return of the anionic species at the oxygen when proceeding to product (eq. [2]).

$$[2] \qquad \mathrm{RCOCl + HOPh \rightleftarrows (RCO)^+(ClHOPh)^- \rightarrow RCOOPh + HCl}$$

Consistent with the overall picture, the introduction of one or two chlorine atoms into the methyl group of acetyl chloride accelerated the methanolysis, presumably by superimposing a dominant addition–elimination pathway, but very large rate reductions were observed for the phenolysis, consistent with a large unfavorable electronic effect on the electrophilically assisted ionization reaction.

The kinetics of the solvolyses can be conveniently studied by rapid-response conductivity measurements. The ease with which a homogenous solution of the substrate can be obtained is usually the limiting factor as regards the range of binary aqueous solvents for which meaningful specific rates of solvolysis can be obtained (18).

A study of the ethanolysis of acetyl chloride (21) and a series of derivatives (22) by a rapid-response technique (23, 24) showed, consistent with the studies under nonsolvolytic conditions (19, 20), a faster reaction in presence of a chloro-substitutent, modest rate reductions in the presence of one or two methyl groups or a phenyl group, and a sharp fall-off in rate on the introduction of the third methyl group (22). An

© 2008 NRC Canada

attempted correlation of the effects of the structural changes using the two-term Taft equation (eq. [3]) was only moderately successful ($R = 0.933$).

$$[3] \qquad \log (k/k_o) = \rho^*\sigma^* + \delta E_s$$

In eq. [3], k is the appropriate rate coefficient for the reaction of a member of the series of subtrates, k_o is the corresponding rate coefficient for the standard substrate, ρ^* is the sensitivity to changes in the polar substituent constant σ^*, and δ is the sensitivity to changes in the steric substituent constant E_s. The tabulated substituent constants would only be expected to be valid for a pathway resembling that for the standard system, ester hydrolysis. Since the ethanolysis of the series of acetyl chlorides correlate rather poorly, the addition–elimination pathway, believed to hold for ester hydrolysis, is not supported for all of these formally similar reactions. A change in mechanism at or near the ethanolysis of the parent acetyl chloride was put forward as a possible rationalization.

The effect of the variation of solvent in the solvolyses of aliphatic acyl chlorides has been studied more recently by Bentley and co-workers (18, 25, 26), by Koo and co-workers (27), and by Ryu and co-workers (28–30). The relevant data from these reports will be combined with new data for the solvolyses of acetyl chloride and diphenylacetyl chloride, allowing correlations, in terms of eq. [1], with from 24 to 38 total solvents for each of the subtrates: acetyl chloride, trimethylacetyl chloride, chloroacetyl chloride, phenylacetyl chloride, diphenylacetyl chloride, and α-methoxy-α-(trifluoromethyl)phenylacetyl chloride (MTPAC).

Molecular orbital calculations to predict the pathway for the methanolysis of protonated acetyl chloride, with up to six methanol molecules available, favor an ionization mechanism (31). In contrast, it has been claimed (32) that the methanolyses of a paclitaxel (Taxol) analog bearing a chloroacetyl group at the C2′ position proceeds by a concerted (one-step) substitution process at the acyl carbon with regeneration of the hydroxyl group. Esters of this type are very important in terms of drug design and development because of increases in both stability and water solubility.

Results

The specific rates of solvolysis of acetyl chloride were determined in methanol, ethanol, and 2,2,2-trifluoroethanol (TFE) at 0.0 °C, and the values were found to be in good agreement with literature values. Previously unreported values were obtained at 0.0 °C for solvolyses in three water-1,1,1,3,3,3-hexafluoro-2-propanol (HFIP) solvents. These values are reported in Table 1.

Similarly, the specific rates of solvolysis, at 10.0 °C, of diphenylacetyl chloride were found to be in good agreement with literature values for 100% ethanol, 80% aq. ethanol, and 100% TFE, and new unreported values were obtained for two additional aqueous ethanol compositions, for four aqueous methanol compositions, and for three aqueous acetone compositions. These values are reported in Table 2.

Table 1. Specific rates of solvolysis k of acetyl chloride at 0.0 °C.

Solvent[a]	k (10^2 s^{-1})
MeOH[b]	10.4±0.1
EtOH[c]	1.97±0.05
TFE[d]	2.74±0.04
97% HFIP	8.80±0.07
90% HFIP	19.0±0.7
70% HFIP	57.6±0.8

Note: With associated standard deviations.
[a]On *w*/*w* basis with other component water.
[b]Ref. 18 gives values of 10.8±0.2.
[c]Ref. 18 gives values of 1.83 and ref. 30 gives value of 2.19±0.04.
[d]Ref. 30 gives value of 2.68±0.02.

Table 2. Specific rates of solvolysis k of diphenylacetyl chloride at 10.0 °C.

Solvent[a]	k (10^2 s^{-1})
100% EtOH	1.84±0.03[b]
90% EtOH	3.56±0.07
80% EtOH	4.44±0.08[c]
60% EtOH	6.57±0.15
100% MeOH	7.97±0.20
90% MeOH	13.1±0.6
80% MeOH	18.8±0.8
60% MeOH	16.0±1.6
90% Acetone	0.277±0.008
80% Acetone	0.604±0.008
60% Acetone	1.69±0.02
100% TFE	0.0408±0.0014[d]

Note: With associated standard deviations.
[a]On *v*/*v* basis at 25.0 °C with other component water.
[b]Ref. 29 gives a value of 1.57 ± 0.01.
[c]Ref. 29 gives a value of 4.19 ± 0.06.
[d]Ref. 29 gives a value of 0.0370 ± 0.0010.

Discussion

Solvolyses of acetyl chloride

The literature values (18, 30) for the specific rates of solvolysis, in combination with the HFIP-H_2O values from this study, are used to carry out correlations using eq. [1]. The results are shown in Table 3, together with values for trimethylacetyl chloride and chloroacetyl chloride. The analyses with one or two phenyl substituents present are presented in Table 4.

It has previously been demonstrated that when undergoing solvolysis the parent acetyl chloride shows appreciable sensitivities towards changes in both solvent nucleophilicity and solvent ionizing power over the full range of solvents involved in the studies. The original values, reported as a footnote (18) for only six solvents, were of 0.86 for l and 0.68 for m and these have held up very well. A correlation of data from 20 solvents, with a good representation of TFE-containing solvents, led (30) to values of 0.79 for l and 0.67 for m ($R = 0.988$). The five data points in TFE-EtOH mixtures were excluded from the correlation because, as is often the case (33), they fell below the correlation line. No evi-

© 2008 NRC Canada

Table 3. Correlations of the specific rates of solvolysis of acetyl chloride and trimethylacetyl chloride at 0.0 °C and of chloroacetyl chloride at –10.0 °C.

R in RCOCl	n^a	l	m	c	l/m	R^b	F^c
CH_3	30[d]	0.83±0.06	0.72±0.04	0.00±0.07	1.15±0.10	0.953	134
	25[e]	0.83±0.03	0.70±0.02	0.11±0.04	1.19±0.05	0.989	484
	20[f]	0.85±0.03	0.74±0.03	0.06±0.05	1.15±0.06	0.989	387
	8[g]	0.81±0.08	0.67±0.09	0.14±0.22	1.21±0.20	0.978	54
	8[g,h]		–0.06±0.27	0.03±1.0		0.086	0.04
$(CH_3)_3C$	38[d]	0.69±0.06	0.70±0.04	0.19±0.07	0.99±0.10	0.954	178
	33[e]	0.66±0.05	0.68±0.03	0.26±0.06	0.97±0.09	0.965	203
	28[f]	0.73±0.03	0.84±0.03	–0.07±0.05	0.87±0.05	0.989	540
	8[g]	0.75±0.07	0.92±0.10	–0.31±0.22	0.82±0.12	0.981	63
$ClCH_2$[i]	34[d]	1.40±0.05	0.40±0.03	0.11±0.05	3.50±0.29	0.978	342
	29[e]	1.41±0.06	0.40±0.03	0.14±0.05	3.53±0.30	0.977	276

Note: Using $\log(k/k_o) = lN_T + mY_{Cl} + c$.
[a]Number of solvents.
[b]Multiple correlation coefficient.
[c]*F*-test value.
[d]All available solvents.
[e]Omitting the TFE-EtOH (T-E) solvents.
[f]Omitting T-E, 100% and 90% ethanol and methanol, and 90% acetone.
[g]Using TFE-H_2O and HFIP- H_2O solvents.
[h]Using $\log(k/k_o) = mY_{Cl} + c$.
[i]Footnote to ref. 26 gives values of 1.54 for *l* and 0.45 for *m* (*l*/*m* = 3.42).

Table 4. Correlations of the specific rates of solvolysis of phenylacetyl chloride at 0.0 °C, diphenylacetyl chloride at 10.0 °C, and α-methoxy-α-(trifluoromethyl)phenylacetyl chloride at 25.0 °C.

R in RCOCl	n^a	l	m	c	l/m	R^b	F^c
$PhCH_2$	33[d]	0.72±0.07	0.47±0.05	0.02±0.08	1.53±0.22	0.876	50
	28[e]	0.70±0.07	0.45±0.05	0.40±0.08	1.56±0.23	0.896	51
	24[f]	1.42±0.17	0.56±0.05	0.20±0.08	2.54±0.38	0.926	63
	23[g]	1.59±0.23	0.58±0.05	0.24±0.09	2.74±0.46	0.923	57
	19[h]	1.56±0.31	0.57±0.07	0.25±0.10	2.74±0.64	0.902	35
	10[i]	0.81±0.05	0.88±0.07	–1.12±0.15[j]	0.92±0.09	0.986	119
	9[k]	0.80±0.05	0.83±0.06	–0.94±0.16[j]	0.96±0.09	0.991	160
Ph_2CH	24[d]	0.69±0.11	0.32±0.08	–0.05±0.12	2.16±0.64	0.837	24
	15[l]	1.56±0.20	0.46±0.06	0.24±0.08	3.39±0.59	0.933	40
	9[m]	0.61±0.06	0.72±0.08	–1.63±0.19[j]	0.85±0.13	0.972	51
$PhC(CF_3)(OMe)$	37[d]	1.75±0.09	0.71±0.04	0.31±0.08	2.46±0.19	0.967	245
	33[e]	1.66±0.08	0.66±0.03	0.38±0.07	2.52±0.17	0.973	262

Note: Using $\log(k/k_o) = lN_T + mY_{Cl} + c$.
[a-e]As in Table 3.
[f]Omitting TFE and all TFE-H_2O and HFIP- H_2O solvents.
[g]Omitting those listed under footnote *f* plus 80T-20E.
[h]Omitting those listed under footnote *f* plus all T-E mixtures.
[i]Using those solvents listed as omitted in footnote *g*.
[j]Large negative value because k_o is for a reaction by other reaction channel.
[k]Using those solvents listed as omitted in footnote *f*.
[l]Using 100–80E, 100–60M, 90–60A, and 60T–40E to 20T–80E.
[m]Using all TFE–H_2O and HFIP–H_2O, plus 80T–20E.

dence was obtained for a solvent-induced change in mechanism and a loose S_N2 transition state was proposed (18, 30).

We extended the range of solvents to more ionizing and less nucleophilic types by adding specific rate values in 97%, 90%, and 70% HFIP (*w*/*w*). These values are reported in Table 1. In total there have now been determinations in 30 solvents, which have both N_T and Y_{Cl} values available. Use of all 30 data points leads to *l* and *m* values (Table 3 and Fig. 1) that are essentially unchanged from the two earlier correlations. Sensitivity values are obtained of 0.83 for *l* and 0.72 for *m* (R = 0.953). Omitting the five TFE-EtOH data points does not appreciably change the *l* and *m* values, but it markedly improves the goodness-of-fit parameters (l = 0.83, m = 0.70, R = 0.989).

Two other subsets of correlation values for acetyl chloride solvolysis are reported in Table 3. Of particular interest is the one involving eight TFE-H_2O and HFIP-H_2O solvents. The *l* and *m* values are essentially identical to those for the larger data sets, confirming the absence of any change to a mechanism involving increased importance for ionization

© 2008 NRC Canada

Fig. 1. Plot of log (k/k_o) for solvolyses of acetyl chloride at 0.0 °C against (0.83 N_T + 0.70 Y_{Cl}). The five log (k/k_o) values for the TFE-EtOH mixtures are not included in the correlation; they are added to show the extent of their deviation from the correlation line.

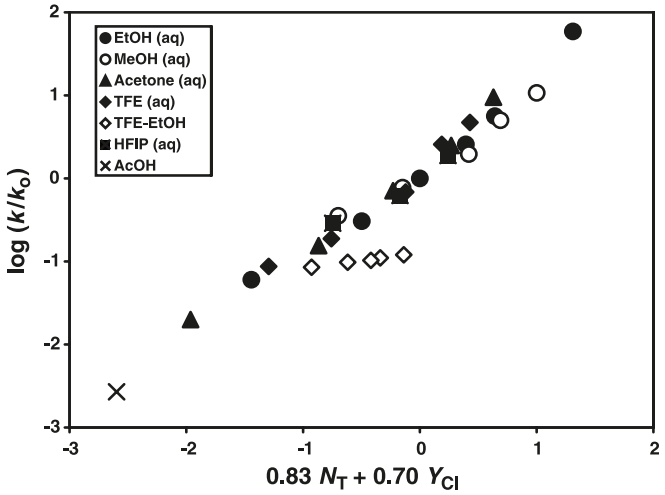

and (or) reduced importance for nucleophilicity in the highly ionizing and low nucleophilicity solvents. However, a correlation of the eight data points using the one-term Grunwald–Winstein equation (eq. [1] without the lN_T term) gives what is essentially a scatter plot with an m value of –0.06 ± 0.27 and a correlation coefficient of 0.086, showing the importance of using the two-term equation when nucleophilic participation is an important component of the mechanism.

The Grunwald–Winstein equation represents only one way in which solvent variation can lead to evidence concerning the mechanism. For example, the kinetic solvent isotope effect (KSIE) can be useful, frequently involving solvolyses in MeOH and MeOD. For acetyl chloride, the KSIE (k_{MeOH}/k_{MeOD}) of 1.29 (18) or 1.32 (29) at 0.0 °C is comparable with that of *p*-methoxybenzoyl chloride (34), which is believed to involve an ionization reaction with moderate nucleophilic solvation (16, 34). The value is significantly lower than the 1.55 for benzoyl chloride (35) or the 2.17 for *n*-propyl chloroformate (36), which are believed to undergo methanolysis by the addition–elimination pathway with a general base catalysis to the nucleophilic attack by a second methanol molecule (26).

A second approach to obtaining evidence that is potentially useful in studying reaction mechanisms for solvolytic reactions is to study the trend in product selectivity values (S) as the composition of a mixture of two hydroxylic solvents, usually water and an alcohol, is varied. Discontinuities indicate the possibility of a change in mechanism at that composition (25, 26). For acetyl chloride, the product selectivities in mixtures of water with ethanol or methanol show slightly increasing S values as the water content increases, with no discontinuity, consistent with the presence of only one mechanism over the full range of 10% to 90% water content (18).

We favor, over the full range of solvents, an ionization reaction with extensive nucleophilic solvation for the solvolysis of acetyl chloride. The l value is quite large, but evidence exists for increased sensitivity for attack at an sp^2 carbon relative to attack at an sp^3 carbon. This evidence has been summarized by Mayr and co-workers (37). The l value is 0.69 for PhSCSCl (15), and solvolyses of carbamoyl chlorides have l values in the 0.4 to 0.7 range (10, 38, 39), systems that are believed to follow an ionization pathway. We cannot, however, argue strongly against the possibility that they should be considered as S_N2 reactions with a very loose transition state (18, 26, 28).

Solvolyses of trimethylacetyl chloride

Based primarily on an early maximum in S values, at 90%–95% alcohol content (as water is progressively added to methanol or ethanol), a duality of mechanism was proposed, with the addition–elimination mechanism dominant only in the solvents of very high alcohol content (25). A curvature in the plots against Y values was considered to give support for the mechanistic change. However when both ionizing power and solvent nucleophilicity terms are important, care must be exercised in interpreting plots against only a solvent ionizing power scale. The detailed behavior will be very dependent upon the relative magnitudes of the l and the m values.

The claim for an ionization pathway being observed for acetyl chloride but not under identical conditions for trimethylacetyl chloride is worthy of further consideration, since electronic factors would suggest a more favorable ionization reaction for the trimethylacetyl chloride. However as mentioned earlier, it undergoes a slower ethanolysis, about one order of magnitude slower than acetyl chloride (22). This suggests that there must be a substantial steric effect towards the nucleophilic solvation, and for the claimed (25) change of mechanism to operate this must be sufficiently strong that the addition–elimination pathway becomes favored for solvolyses of trimethylacetyl chloride in methanol, ethanol, and binary mixtures with water that are rich in alcohol.

This is a situation that can be very nicely investigated using eq. [1] and correlations of available data are reported in Table 3. With the data for the five TFE-EtOH solvents removed, values for 33 solvents of 0.66 for l and 0.68 for m (R = 0.965) are obtained. This correlation is fair, but it can be considerably improved by removing those solvents that appeared to deviate in the consideration of S values: 100% and 90% ethanol and methanol, and also 90% acetone. For the 28 remaining solvents, values are obtained of 0.73 for l and 0.84 for m (R = 0.989). In addition to the improvement in the R value, the F-test value increased from 203 to 540. As with the solvolyses of acetyl chloride, the l and m values obtained using only the eight fluoroalcohol–water solvents are essentially identical to those obtained with a much wider range of solvents.

The observation of a discontinuity at essentially the same solvent compositions, when studied either by product selectivity (S) values or in terms of eq. [1], provides strong support for the view that it is of mechanistic significance.

The KSIE for the solvolyses in methanol or methanol-d has been determined as 1.46. This is intermediate between the values of 1.3 for acetyl chloride (18, 29) and the value of 1.55 for benzoyl chloride (35). It may well be for the solvolyses of trimethylacetyl chloride that the change from the ionization pathway to the addition–elimination pathway

© 2008 NRC Canada

as the water content becomes small is not complete at 100% methanol, and both reaction channels are operating simultaneously (25).

Solvolyses of chloroacetyl chloride

Chloroacetyl chloride reacts faster than acetyl chloride both with small amounts of methanol in acetonitrile (19) and in ethanolysis in 100% ethanol (22). Recently, specific rates of solvolysis were made available at –10.0 °C for 34 solvents, including values in TFE-H_2O and TFE-EtOH (26). Application of eq.[1] led to the values reported in Table 3. With all 34 solvents, values are obtained of 1.40 for l and 0.40 for m (R = 0.978). In this instance, exclusion of the five TFE-EtOH points leads to only minor changes in the values (l = 1.41, m = 0.40, R = 0.977). The magnitudes of the l and the m values suggest an addition–elimination pathway with addition rate-determining, and they are in reasonable agreement with values of 1.54 for l and 0.45 for m given in a footnote to the manuscript (26) presenting the determinations of specific rate. The KSIE (MeOH/MeOD) was determined as 2.18, consistent with the proposed mechanism and the operation of general base catalysis (26).

Solvolyses of phenylacetyl chloride

Values for the specific rates of solvolysis of phenylacetyl chloride are available (26, 30) in 33 solvents at 0.0 °C. The results from the correlations using eq. [1] are shown in Table 4. Both with and without the five TFE-EtOH solvents, poor correlations (R < 0.9) are obtained. The data can, however, be treated in terms of two competing reaction pathways. In TFE and all TFE-H_2O and HFIP-H_2O solvents, plus 80TFE-20EtOH (10 solvents) values are determined of 0.81 for l and 0.88 for m (R = 0.986). In the remaining 23 solvents, values are obtained of 1.59 for l and 0.58 for m (R = 0.923).

The S values (26) are a little ambiguous as regards a change in mechanism in aqueous ethanol or aqueous methanol. In aqueous ethanol, a maximum is observed at around 60% ethanol, but in aqueous methanol the values fall over the full 80%–40% methanol range studied. The Grunwald–Winstein treatment suggests that the addition–elimination pathway is dominant over the full range of aqueous methanol, ethanol, and acetone studied, and only in solvents rich in fluoroalcohol is there a changeover to a dominant ionization pathway. The reported KSIE at 10.0 °C (26, 29) for MeOH/MeOD of 1.40 is unusually low for a reaction following the addition–elimination pathway and it is only slightly greater than the value of 1.3 observed for acetyl chloride at 0.0 °C (18, 29). This suggests that only a weak general base catalysis operates in these solvolyses.

Solvolyses of diphenylacetyl chloride

Earlier studies (29, 30), mainly in TFE-H_2O, TFE-EtOH, and HFIP-H_2O, have been supplemented by measurements in aqueous ethanol, aqueous methanol, and aqueous acetone (Table 2) to give in total 24 data points at 10.0 °C. These have been correlated using eq. [1] and the results are presented in Table 4 and in Figs. 2–4.

As with phenylacetyl chloride, use of all of the data points in the correlations leads to a poor correlation (Fig. 2) and the correlation coefficient is even lower (R = 0.827). Dividing

Fig. 2. Plot of log (k/k_o) for solvolyses of diphenylacetyl chloride against (0.69 N_T + 0.32 Y_{Cl}).

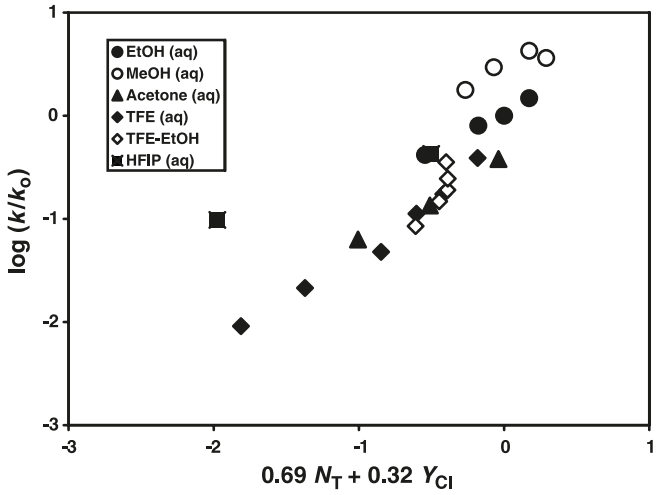

Fig. 3. Plot of log (k/k_o) for solvolyses of diphenylacetyl chloride against (0.61 N_T + 0.72 Y_{Cl}).

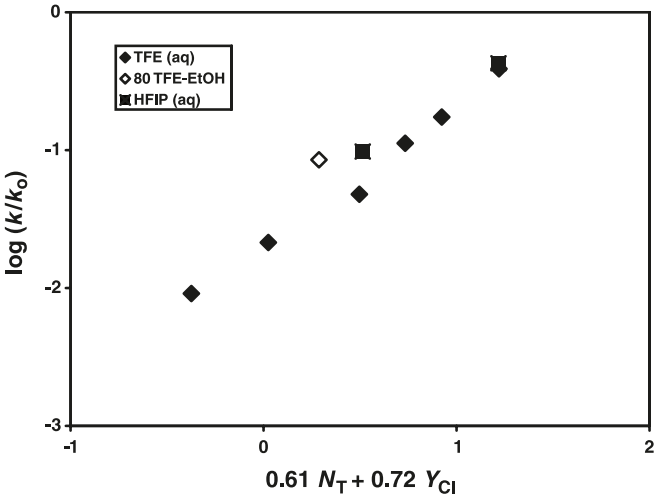

Fig. 4. Plot of log (k/k_o) for solvolyses of diphenylacetyl chloride against (1.56 N_T + 0.46 Y_{Cl}).

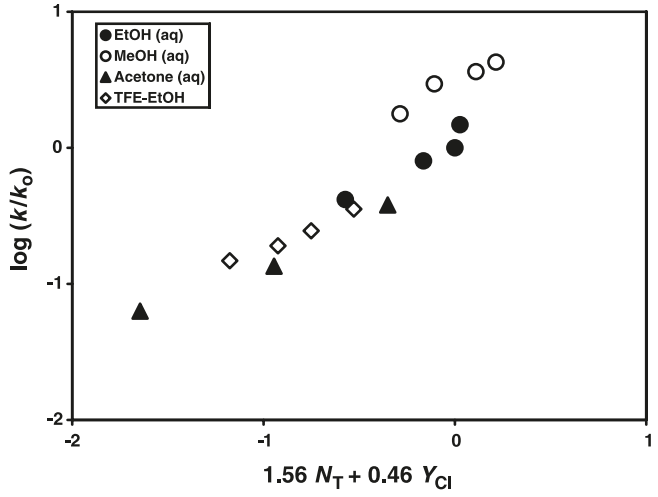

© 2008 NRC Canada

into two subgroups in the identical manner to that used for phenylacetyl chloride, led to values in nine fluoroalcohol-rich solvents of 0.61 for *l* and 0.72 for *m* ($R = 0.972$), as shown in Fig. 3. The remaining 15 solvents give a linear plot (Fig. 4) requiring an *l* value of 1.56 and an *m* value of 0.46 ($R = 0.933$).

The KSIE (MeOH/MeOD) at 10.0 °C is 1.61 (29), compatible with the addition–elimination mechanism, with general base catalysis from a second solvent molecule proposed for the subgroup of solvents that includes methanol.

Solvolyses of α-methoxy-α-trifluoromethylphenylacetyl chloride (MTPAC)

Specific rates of solvolysis are available at 25.0 °C in 37 solvents, including four TFE-H_2O and four TFE-EtOH solvents (27). The TFE-H_2O solvents were prepared on a *v*/*v* basis, and the required N_T and Y_{Cl} values are obtained by interpolation within values for solvents prepared on a *w*/*w* basis. The values obtained are: 97% TFE, $N_T = -3.41$, $Y_{Cl} = 2.82$; 90% TFE, $N_T = -2.73$, $Y_{Cl} = 2.81$; 70% TFE, $N_T = -2.13$, $Y_{Cl} = 2.94$; 50% TFE, $N_T = -1.62$, Y_{Cl} 3.07. The correlations are reported in Table 4. With the use of all data points, values of 1.75 for *l* and 0.71 for *m* ($R = 0.967$) are obtained. These are little changed on removing the four TFE-EtOH solvents, with values of 1.66 for *l* and 0.66 for *m* ($R = 0.973$).

Whereas the "parent" phenylacetyl chloride showed a change in mechanism from addition–elimination to ionization on moving from solvents such as aqueous ethanol or methanol to solvents rich in fluoroalcohol, the insertion on the α-carbon of the powerfully electron-withdrawing methoxy and trifluoromethyl groups severely inhibits the ionization pathway, and as with chloroacetyl chloride, the addition–elimination pathway is observed across the full range of solvents. The KSIE (MeOH/MeOD) at 25.0 °C is of value 2.4 (27), larger than with simple alkyl and arylalkyl groups attached to the carbonyl carbon and comparable to the 2.2 value obtained for chloroacetyl chloride. It has been shown that the KSIE values trend upward as the value for the inductive parameter for R in RCOCl rises (29). This can be interpreted as a more favorable general base catalysis to the solvolysis as the electron-withdrawing power of the R group increases.

Relevance of computational studies to the solvolysis

The extension from computationally favored pathways in the absence of bulk solvents to the reactions as carried out in solution has many potential pitfalls. The observation that the mechanism in solution can, for the hydrolysis component of the solvolysis of several acyl chlorides, be switched between alternative mechanisms by a change of a binary solvent containing water from one of high nucleophilicity and modest ionizing power to one of low nucleophilicity and high ionizing power emphasizes the difficulty involved in making this extension.

A paper by Fox, Bach, and co-workers (31) includes a treatment of the methanolysis of an acetyl chloride molecule with up to six methanol molecules present. Unfortunately, the relevance to the presence study is limited by a prior protonation of the acetyl chloride before the involvement of the methanol molecules. Indeed, for phenolysis where we have proposed (19, 20) electrophilic interaction at the chlorine to generate an acylium ion (eq. [2]), a prior protonation would be very unfavorable to such a pathway. For methanolysis, the perturbation would be expected to be less severe but significant.

When the influence of solvent upon the addition–elimination pathway is considered, it includes both nucleophilic attack at the carbonyl carbon and stabilization of the negative charge developing at the acyl oxygen. The latter effect will be negated by prior protonation, and one can concentrate on nucleophilicity effects. However, the detailed interactions at the transition state will be quite different to those for the neutral substrate.

Nonetheless, the computational analysis leads to essentially the same conclusion as the Grunwald–Winstein treatment of the solvolyses of the neutral (unprotonated) substrate. It is concluded that with either four or six methanol molecules available for possible interaction with the protonated acetyl chloride, the formation of the methyl ester follows a pathway with considerable ionic (S_N1) character in the rate-determining step, consistent with present and previous (18, 26) proposals based on experimental evidence from solvolysis reactions.

Conclusions

It was previously demonstrated (16) that benzoyl chloride and *para*-substituted derivatives react by ionization with modest nucleophilic solvation when a *p*-methoxy substituent is present, and the addition–elimination mechanism, with the addition step rate-determining, becomes of increasing importance as one moves to the parent and on to derivatives with electron-withdrawing substituents. When one arrives at the *p*-nitro derivative, the dominant mechanism is addition–elimination across the full range of solvents, except for the highly ionizing and low nucleophilicity 97% HFIP.

This type of behavior is repeated in the solvolyses of aliphatic acyl chlorides. The parent acetyl chloride is found to follow the ionization pathway with appreciable nucleophilic solvation over the full range of solvents. Various subsets of data points give essentially unchanged *l* and *m* values, showing the correlation to be very robust.

The trimethylacetyl chloride shows similar behavior, except that in methanol, ethanol, 90% MeOH, 90% EtOH, and 90% acetone there is evidence for a superimposed addition–elimination contribution. The incursion of the additional pathway at high organic solvent content is nicely consistent with the evidence, from a reversal in trend of product selectivity (*S*) values, for a change in mechanism at about 90% alcohol content (25).

The consequences of the introduction of powerful electron-withdrawing substituents mirrors the influences of a *para*-nitro substituent introduction into benzoyl chloride. Both chloroacetyl chloride and MTPAC give good correlations over the full range of solvents with *l* and *m* sensitivity values consistent with the addition–elimination pathway.

When all available specific rates of solvolysis are used in the correlations, both phenylacetyl chloride and diphenylacetyl chloride give poor correlations. Acceptable correlations can be obtained when the specific rate data are divided into two subsets. One subset includes the data in TFE, TFE-

© 2008 NRC Canada

H_2O, HFIP-H_2O, and 80%TFE-20%EtOH. The other solvents are assigned to the other subset. The *l* and *m* values for the two subsets are consistent with ionization, with appreciable nucleophilic solvation, and addition–elimination, respectively. Two pathways were also indicated from a maximum in the *S* values for the solvolyses of phenylacetyl chloride in aqueous ethanol (26), but the use of eq. [1] indicates a much more extensive addition–elimination region than that deduced from a consideration of the trend in *S* values.

Literature KSIE values also support the division into two types of reaction channels. Relatively low values of about 1.3 for the methanolysis of acetyl chloride (MeOH/MeOD) increase in value as the addition–elimination pathway takes over and as general base catalysis becomes an increasingly important rate-determining factor. The KSIE value rises to 2.2 for chloroacetyl chloride and 2.4 for MTPAC.

It is probable that the only moderate, at best, success in using the Taft equation (eq. [3]) to correlate the effects of structural change upon the rates of ethanolysis of a series of aliphatic acyl chlorides (22) is due, at least in part, to changes occurring in the dominant mechanism as the structure is changed. For example, the series includes both acetyl chloride (ionization) and chloroacetyl chloride (addition–elimination).

Calculations on reaction of a protonated acetyl chloride molecule with up to six methanol molecules present (31) found that with either four or six methanol molecules an ionization (S_N1-like) mechanism was favored, consistent with the experimental evidence, and no evidence was found for a competitive addition–elimination pathway. The confidence with which this can be considered as support for the experimental findings is, however, tempered by the protonation that is introduced prior to the computations.

The *l*/*m* ratio can be a useful mechanistic indicator. For the correlations believed to be for ionization reactions with nucleophilic solvation, the values from Tables 3 and 4 range from 0.82 to 1.21, and the values for the correlations believed to be for the addition–elimination pathway range from 2.46 to 3.53.

Experimental

Acetyl chloride (Sigma-Aldrich ≥ 99%) and diphenylacetyl chloride (Lancaster >98%) were used as received. Solvents were purified as previously described (40). The determinations of the specific rates reported in Table 1 were carried out by injecting 4.0 μL of a 0.30 mol/L solution of acetyl chloride in acetonitrile into 2.0 mL of the solvent under investigation. Specific rates and the associated standard deviations were determined from a computer analysis (Guggenheim method, ref. 41) of the plots of conductivity against time. The apparatus has been previously described (42).

The determinations of the specific rates reported in Table 2 involved addition of 12 μL of substrate to 25 mL of solvent followed by conductance measurements at appropriate time intervals. The measurements were used in conjunction with the infinity value to obtain the integrated rate coefficients and all values from duplicate runs were averaged to obtain the reported values. The conductivity apparatus consisted of an efficiently stirred cell connected to a TENMA multimeter (72-602 model with a 72-6251 connector), linked to a PC through a RS232C port and with a Simpson 420 function generator.

The multiple regression analyses were performed using commercially available statistical packages.

Acknowledgements

This research was supported by grant number 2 P2O RR016472-07 from the National Center for Research Resources (NCRR), a component of the National Institutes of Health (NIH). Its contents are solely the responsibility of the authors and do not necessarily represent the official views of NCRR or NIH. ZHR thanks Dong-Eui University for support of this work by grant 2006AA089. Acknowledgement is made to the donors of the Petroleum Research Fund, administered by the American Chemical Society, for partial support of this research (postdoctoral fellowship for BCP). The authors thank Dr. T.W. Bentley for helpful discussions.

References

1. S. Winstein, E. Grunwald, and H. W. Jones. J. Am. Chem. Soc. **70**, 846 (1948).
2. T.W. Bentley and G. Llewellyn. Prog. Phys. Org. Chem. **17**, 121 (1990).
3. D.N. Kevill. *In* Advance in quantitative structure–property relationships. Vol. 1. *Edited by* M. Charton. JAI Press, Greenwich, Conn. 1996. pp. 81–115.
4. D.N. Kevill. *In* The Chemistry of acyl halides. *Edited by* S. Patai. Interscience, New York, 1972. Chap. 12.
5. A. Kivinen. *In* The Chemistry of acyl halides. *Edited by* S. Patai. Interscience, New York, 1972. Chap. 6.
6. R.J.E. Talbot. *In* Comprehensive chemical kinetics. Vol. 10. *Edited by* C.H. Bamford and C.F.H. Tipper. Elsevier, Amsterdam. 1972. pp. 226–227.
7. K.H. Yew, H.J. Koh, H.W. Lee, and I. Lee. J. Chem Soc. Perkin Trans. 2, 2263 (1995).
8. D.N. Kevill and M. J. D'Souza. J. Chem. Soc. Perkin Trans. 2, 1721 (1997).
9. I.S. Koo, K. Yang, K. Kang, and I. Lee. Bull. Korean Chem. Soc. **19**, 968 (1998).
10. D.N. Kevill, F. Koyoshi, and M.J. D'Souza, Int. J. Mol. Sci. **8**, 346 (2007)
11. A. Queen and T.A. Nour. J. Chem. Soc. Perkin Trans. 2, 935 (1976).
12. D.N. Kevill and M.J. D'Souza. J. Chem. Soc. Perkin Trans. 2, 240 (2002).
13. J.B. Kyong, C.J. Rhu, Y.-G. Kim, and D.N. Kevill. J. Phys. Org. Chem. **20**, 525 (2007).
14. D.N. Kevill, J.B. Kyong, and F.L. Weitl. J. Org. Chem. **55**, 4304 (1990).
15. D.N. Kevill and M.J. D'Souza. Can. J. Chem. **77**, 1118 (1999).
16. D.N. Kevill and M.J. D'Souza. J. Phys. Org. Chem. **15**, 881 (2002).
17. D.N. Kevill and M.J. D'Souza. J. Org. Chem. **69**, 7044 (2004).
18. T.W. Bentley, G. Llewellyn, and J.A. McAlister. J. Org. Chem. **61**, 7927 (1996).
19. D.N. Kevill and C.-B. Kim. J. Chem. Soc. Perkin Trans. 2, 1353 (1988).
20. D.N. Kevill and C.-B. Kim. Bull. Soc. Chim. Fr. 383 (1988).
21. P.H. Daum and D.F. Nelson. Anal. Chem. **45**, 463 (1973).
22. D.N. Kevill, P.H. Daum, and R. Sapre. J. Chem. Soc. Perkin Trans. 2, 963 (1975).

© 2008 NRC Canada

23. D.E. Johnson and C.G. Enke. Anal. Chem. **42**, 329 (1970).
24. T.W. Bentley and R.O. Jones. J. Chem. Soc. Perkin Trans. 2, 2351 (1993).
25. T.W. Bentley and C.S. Shim. J. Chem. Soc. Perkin Trans. 2, 1659 (1993).
26. T.W. Bentley, H.C. Harris, Z.H. Ryu, G.T. Lim, D.D. Sung, and S.R. Szajda. J. Org. Chem. **70**, 8963 (2005).
27. I.S. Koo, S.I. Lee, S.K. An, K. Yang, and I. Lee. Bull. Korean Chem. Soc. **20**, 1451 (1999).
28. Z.H. Ryu, S.H. Shin, J.P. Lee, G.T. Lim, and T.W. Bentley. J. Chem. Soc. Perkin Trans. 2, 1283 (2002).
29. Y.H. Oh, G.G. Jang, G.T. Lim, and Z.H. Ryu. Bull. Korean Chem. Soc. **23**, 1089 (2002).
30. Z.H. Ryu, G.T. Lim, and T.W. Bentley. Bull. Korean Chem. Soc. **24**, 1293 (2003).
31. J.M. Fox, O. Dmitrenko, L. Liao, and R.D. Bach. J. Org. Chem. **69**, 7317 (2004).
32. W.A. Klis, J.G. Sarver, and P.W. Erhardt. Tetrahedron Lett. **42**, 7747 (2001).
33. D.N. Kevill and B. Miller. J. Org. Chem. **67**, 7399 (2002).
34. T.W. Bentley, I.S. Koo, and S.J. Norman. J. Org. Chem. **56**, 1604 (1991).
35. I. Lee, H.J. Koh, Y.S. Park, and H.W. Lee. J. Chem. Soc. Perkin Trans. 2, 1575 (1993).
36. J.B. Kyong, H. Won, and D.N. Kevill. Int. J. Mol. Sci. **6**, 87 (2005).
37. S. Minegishi, S. Kobayashi, and H. Mayr. J. Am. Chem. Soc. **126**, 5174 (2004).
38. D.N. Kevill, A.J. Oldfield, and M.J. D'Souza. J. Chem. Res. Synop. 122 (1996).
39. D.N. Kevill, A.J. Casamassa, and M.J. D'Souza. J. Chem. Res. Synop. 472 (1996).
40. D.N. Kevill and S.W. Anderson. J. Org. Chem. **56**, 1845 (1991).
41. (*a*) E.A. Guggenheim. Philos. Mag. **2**, 538 (1928); (*b*) A.A. Frost and R.G. Pearson. Kinetics and mechanism. 2nd ed. Wiley, New York. 1961. pp. 49–50.
42. I. Lee, H.W. Lee, T.S. Uhm, D.D. Sung, and Z.H. Ryu. J. Korean Chem. Soc. **32**, 85 (1988).

© 2008 NRC Canada

Chemical functionalization and modification of surface-bound cystamine–glycine monolayers on gold nanoparticles

Mita Dasog, Amir Kavianpour, Matthew F. Paige, Heinz-Bernhard Kraatz, and Robert W.J. Scott

Abstract: Herein, we report the synthesis, characterization, and post-functionalization of Au nanoparticles that have been surface-modified with glycine–cystamine (Gly-CSA) stabilizing groups. We show that Au monolayer protected clusters (MPCs) can be synthesized via the Brust–Schiffrin method using a Boc-Gly–CSA stabilizer, followed by efficient removal of the Boc protecting group with trifluoroacetic acid. The resulting Gly–CSA Au MPCs are characterized via UV–vis, TEM, and ^{1}H NMR, and are stable in solution over long periods of time. Finally, we show that the Gly–CSA Au MPCs can be further functionalized with nearly stoichiometric yields using activated esters of stearic acid and a Bodipy dye derivative. Thus, this work provides an alternative, general approach for the modification of the surface chemistry of MPCs.

Key words: gold nanoparticles, peptide stabilizers, dyes.

Résumé : Dans ce travail, on rapporte la synthèse, la caractérisation et la post-fonctionalisation de nanoparticules d'or dont on a modifié la surface par des groupes stabilisants de glycine–cystamine (Gly–CSA). On démontre que les agrégats protégés de monocouches (APM) d'or peuvent être synthétisés par la méthode de Brust–Schiffrin en utilisant un Boc-Gly–CSA comme stabilisant, suivie par une élimination efficace du groupe protecteur Boc à l'aide d'acide trifluoroacétique. On a caractérisé les agrégats de monocouches d'or protégés par le groupe glycine–cystamine « Gly–CSA Au MPC » par la spectroscopie UV–vis, la microscopie électronique à transmission (MET) et la RMN du ^{1}H et ils sont stables en solution pour de longues périodes de temps. On démontre enfin que les « Gly–CSA Au MPC » peuvent aussi être fonctionnalisés avec des rendements pratiquement stoechiométriques en utilisant des esters activés de l'acide stéarique et un dérivé colorant Bodipy. Ce travail fournit donc une approche alternative générale à la modification de la chimie de surface des APM.

Mots-clés : nanoparticules d'or, stabilisants peptidiques, colorants.

[Traduit par la Rédaction]

Introduction

Modifying the chemical properties of nanoparticle surfaces has been a challenging and active area of research over the past decade (1–6). As the use of metal nanoparticles in biological fields becomes more common for various applications, such as bioimaging, biosensors, drug delivery, and tagging of nucleic acids and proteins, it has become extremely important to control the surface functional groups of these nanoparticles precisely both in vivo and in vitro (7–10). Water soluble, monolayer protected gold clusters (Au MPCs) have attracted a great deal of interest in the field as they are, for the most part, chemically inert (11), and offer a range of chemical functionalities for subsequent modification (12–15). While there have been many examples of propagation reactions on halide and carboxylic acid terminated Au MPCs (12, 16–18), it is highly desirable to directly synthesize stable Au MPCs that have free amine surfaces, as these functional groups are amongst the most useful for further chemical modification. It is our goal to design a synthetic pathway towards stable, monodisperse peptide-stabilized MPCs in which the surface chemistry of the nanoparticle can be further tuned via simple amide coupling reactions with primary amine groups on the surface of the MPC. Such a strategy is complementary to earlier studies by Murray and co-workers who showed further functionalization of tiopronin and mercaptoundanoic acid coated MPCs, which have surface carboxylic acid groups (12, 17). Thus, this work expands the chemical toolbox of peptide-stabilized MPCs whose surface chemistry can be further modified via simple amide coupling reactions.

There are a number of effective strategies, which have been used to functionalize Au nanoparticle surfaces with peptide stabilizers. One popular approach for synthesizing multifunctional, water-soluble Au MPCs is to pre-design a

Received 20 November 2007. Accepted 25 January 2008. Published on the NRC Research Press Web site at canjchem.nrc.ca on 25 March 2008.

M. Dasog, A. Kavianpour, M.F. Paige, and R.W.J. Scott.[1] Department of Chemistry, University of Saskatchewan, 110 Science Place, Saskatoon, SK S7N 5C9, Canada.
H.-B. Kraatz. Department of Chemistry, The University of Western Ontario, Chemistry Building 1151 Richmond Street, London, ON, Canada.

[1]Corresponding author (e-mail: robert.scott@usask.ca).

 doi:10.1139/V08-025 © 2008 NRC Canada

thiol-containing biomolecule, followed by ligand exchange reactions with preexisting Au MPCs. These reactions often involve ligand exchange of thiols onto citrate-stabilized Au nanoparticle surfaces in acidic conditions (13, 19–23), or place-exchange of thiol ligands (1, 24). Another promising route pioneered by the groups of Jacobson (25) and Huo (26–28) is to use solid-phase syntheses to make MPCs with the appropriate arrangement of functional groups. Direct synthetic routes have also been pursued for peptides, such as cysteine (29–32), homocysteine (33), and glutathione (34, 35), and other ligands, such as aminothiophenol (36, 37), which contain both amine and thiol functional groups. However, such bi-functionalized particles often aggregate in solution over time, either because of hydrogen-bonding interactions between particles (13, 29, 30, 33, 37), or the high affinities of both thiols and amines for Au surfaces, leading to cross-linking between particles (36, 38). While these are all effective strategies to design complex peptide-stabilized particles, it can often be difficult to prepare clean, stable amine-terminated particles in solution by these routes. We chose to pursue a direct synthesis route in which amine groups on the peptide were protected during Au nanoparticle synthesis, followed by purification and deprotection of the terminal amine groups.

Herein, we report an effective strategy to synthesize glycine–cystamine-derivatized Au MPCs with protected glycine groups on the exterior surface of the particles, followed by deprotection of the glycine groups to free amine groups. Furthermore, we show that the resulting amine-terminated particles can be effectively coupled with a range of activated ester compounds to give nearly stoichiometric functionalization of the MPCs. More specifically, MPCs were effectively functionalized with activated esters of stearic acid and a Bodipy dye derivative through the formation of amide bonds. In addition, we show that the short distance between the Au surface and terminal amine groups in these particles allows for studies of quenching interactions between particles and covalently attached dyes.

Experimental

Materials

Hydrogen tetrachloroaurate (III) salt ($HAuCl_4 \cdot 3H_2O$) and stearic acid were bought from Alfa Aesar. Triethylamine, trifluoroacetic acid (TFA), cystamine dihydrochloride (CSA), and sodium borohydride ($NaBH_4$) were purchased from Sigma-Aldrich. *N*-Hydroxybenzotriazole (HOBt) and *O*-*b*enzotriazole-*N*,*N*,*N*′,*N*′-tetramethyl-uronium hexafluorophosphate (HBTU) were from Synpep and Boc-glycine (Boc-Gly–OH) and 1-ethyl-3-(3-dimethylaminopropyl) carbodiimide hydrochloride (EDC) were bought from Advanced Chemtech. Sodium bicarbonate ($NaHCO_3$), citric acid, and organic solvents (HPLC grade chloroform, dichloromethane (DCM), and acetonitrile) were from EMD Chemicals Inc. 4,4-Difluoro-5,7-dimethyl-4-bora-3a,4a-diaza-*s*-indacene-3-propionic acid (Bodipy Fl) was purchased from Invitrogen. Deuterated solvents were purchased from Cambridge Isotope Laboratories. All the chemicals were used without further purification. 18 MΩ·cm Milli-Q deionized water (Millipore, Bedford, MA) was used throughout.

Synthesis of Boc-glycine–cystamine (Boc-Gly–CSA)

The amide coupling synthesis was carried out using an established literature synthesis (see Supplementary Data for details) (39).[2]

Synthesis of Boc-glycine–cystamine (Boc-Gly–CSA) Au MPCs

All syntheses and purifications were done under N_2 to avoid oxidation of thiols and Au MPCs (11). $HAuCl_4$ (20 mmol) salt was dissolved in 5 mL chloroform, followed by the addition of Boc-Gly–CSA (40 mmol) in 50 mL of chloroform. After stirring for 30 min, 10 mL of a 0.5 mol/L aqueous $NaBH_4$ solution at 0 °C was then added as a reducing agent. This solution mixture was stirred vigorously for 2 h. The chloroform layer was separated and washed twice with 20 mL of Millipore water. The solvent was removed, and the particles were redissolved in 10 mL of chloroform and dried over anhydrous $CaSO_4$ for 24 h.

Deprotection of the Boc group

To deprotect the Boc group on the Boc-Gly–CSA Au MPCs, the MPCs were dissolved in 5 mL dichloromethane (DCM), followed by the addition of 20 mL of 50% TFA solution in DCM. This solution was stirred for 1 h. Unreacted TFA was completely removed by rotary evaporation. The resulting Gly–CSA Au particles were dissolved in deionized water, and dialyzed for 120 h in deionized water to remove excess peptide not coordinated to the Au MPCs. A similar deprotection procedure was used to synthesize free Gly–CSA ligands. In addition, for IR studies, Gly–CSA was reduced in Zn/HCl to give the corresponding free thiol.

Synthesis of activated esters of stearic acid and Bodipy dye derivative

To activate stearic acid, HBTU (30 mmol), HOBt (30 mmol), and stearic acid (25 mmol) were stirred together for 1 h in 50 mL acetonitrile (40). The activated stearic acid was purified by column chromatography. A similar procedure was used to form the activated ester of the Bodipy dye derivative, except the activated ester of 4,4-difluoro-5,7-dimethyl-4-bora-3a,4a-diaza-*s*-indacene-3-propionic acid was purified by removal of impurities via crystallization at –10 °C.

Amide coupling of Gly-CSA Au MPCs with activated esters

Amide coupling reactions with activated stearic acid were done with 5 mmol of Au MPCs (moles with respect to Au) dissolved in 5 mL of deionized water. Known amounts of the activated stearic acid (the absolute concentration of Gly–CSA was extrapolated via ^{1}H NMR using an internal standard of absolute ethanol), dissolved in 10 mL acetonitrile,

[2] Supplementary data for this article are available on the journal Web site (canjchem.nrc.ca) or may be purchased from the Depository of Unpublished Data, Document Delivery, CISTI, National Research Council Canada, Ottawa, ON K1A 0R6, Canada. DUD 3733. For more information on obtaining material, refer to cisti-icist.nrc-cnrc.gc.ca/irm/unpub_e.shtml.

© 2008 NRC Canada

were added to the nanoparticle solution in the presence of 3 mL of triethylamine. After stirring the reaction mixture for 3 h, the solvent was removed, followed by washing with 5 mL of a saturated $NaHCO_3$ solution and then 5 mL of a 10% citric acid solution. This alternate washing with saturated $NaHCO_3$ and 10% citric acid was done three times, followed by a final wash with 25 mL of deionized water. The Au MPCs were dried over anhydrous $CaSO_4$ over 24 h and dissolved in acetonitrile.

For the activated ester of the dye, the amide coupling reaction was carried out in a similar manner as outlined above. The number of Au MPCs was extrapolated from TEM measurements (see Discussion) given a known concentration of Au (1 μmol); then the required volume of activated Bodipy dye (0.685 mmol/L solution) was added to give 160, 80, 40, 20, 15, 10, 5, and 1 dye molecule(s) per nanoparticle. The Au MPCs were dissolved in acetonitrile to carry out the amide coupling reaction. After 3 h of stirring, the acetonitrile was pumped off and the MPCs were redissolved in chloroform, followed by removal of impurities via crystallization at –10 °C and drying over anhydrous $CaSO_4$ for 24 h. Control samples in which there was no covalent bonding between MPC and dye were synthesized by combining dodecanethiol-derivatized Au MPCs (11) with the activated Bodipy dye.

Characterization

Absorption spectra were recorded on a Varian Cary 50 Bio UV–vis spectrometer with an optical path length of 1.0 cm. Transmission electron micrographs (TEM) were obtained with a Philips 410 microscope operating at 100 keV. Samples were prepared by placing a drop of solution on a holey-carbon-coated Cu TEM grid and allowing the solvent to evaporate in air. In all cases, many TEM images were collected at multiple locations for each sample, and the images shown are representative of the samples. Size distributions from TEM were obtained by measuring the diameters of several hundred particles. ^{1}H NMR were recorded on a Bruker 500 MHz Avance spectrometer; chemical shifts were referenced to the residual protons of the deuterated solvent. FTIR measurements were made on a Bruker Tensor 27 spectrometer. Infrared spectroscopy (FTIR) was done in chloroform and acetonitrile, using KBr windows, and a background spectrum of pure solvent was subtracted from the sample signal. The sample chamber was purged with nitrogen gas for 15 min before analysis and 128 scans per sample were obtained for each spectrum. Fluorescence measurements were performed on a SPEX 212 spectrofluorometer. The emission spectra were collected in the range of 515–600 nm with an excitation wavelength of 508 nm.

Results and discussion

Boc-Gly–CSA Au MPCs were synthesized in a single step using a modified Brust–Schiffrin method (41). The Au MPCs were made in quantitative yield, and no precipitation of particles due to aggregation was seen. As it was difficult to purify the MPCs at this stage by selective precipitation or column chromatography, deprotection of the Boc group was done immediately after synthesis. The Boc deprotection was carried out using 50% TFA to give Gly–CSA derivatized

Scheme 1. Schematic representation of Au MPCs stabilized with Boc-Gly–CSA before and after removal of the Boc group.

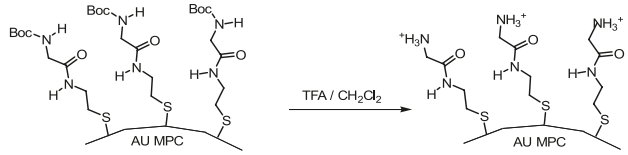

Fig. 1. UV–vis spectra of Boc-Gly–CSA and Gly–CSA Au MPCs.

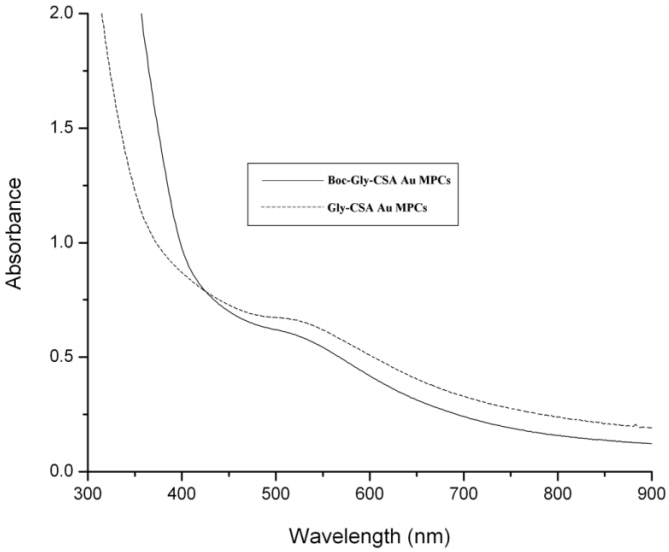

particles, which were soluble in water at pHs between 4 and 5, as shown in Scheme 1. Figure 1 shows the UV–vis spectra of the Boc-Gly–CSA Au MPCs before and after deprotection of the amine group with TFA. The initial Boc-Gly–CSA Au MPCs show a weak plasmon shoulder around 530 nm, suggesting the Au MPCs are above 2 nm in size (42, 43). This plasmon shoulder shifts to 540 nm and increases slightly in intensity for the deprotected Gly–CSA MPCs, suggesting a slight increase in particle size accompanying deprotection. While this shift in the plasmon band could also be the result of particle aggregation, no particle aggregation in solution was seen at acidic pHs between 4 and 5, while reversible aggregation due to H-bonding was seen at pHs near 7. In addition, no aggregates were seen in TEM images of the deprotected samples. Figure 2 shows representative TEM images and particle-size histograms of the Boc-Gly–CSA Au MPCs before and after deprotection; the average particle size increases from 3.2 ± 0.6 nm to 4.4 ± 0.8 nm. We believe that this increase in size may be due to instability of the Gly–CSA Au MPCs in the highly acidic TFA environment. Several other groups have attempted similar Boc deprotections on Au MPCs, though there was no specific mention in either case as to whether any Au nanoparticle growth was seen (12, 24).

The number of Au atoms in the final 4.4 ± 0.8 nm Gly–CSA Au MPCs is estimated to be approximately 2600 atoms using eq. [1] below (44), where n is the number of atoms per particle, R is the particle diameter and V_g is the molar volume of Au, 10.2 cm^3/mole. Hostetler et al. have shown that the percentage thiolate coverage on Au MPCs approaches

© 2008 NRC Canada

Fig. 2. TEM images and size-distribution histograms of (A) Boc-Gly–CSA Au MPCs and (B) Gly–CSA Au MPCs.

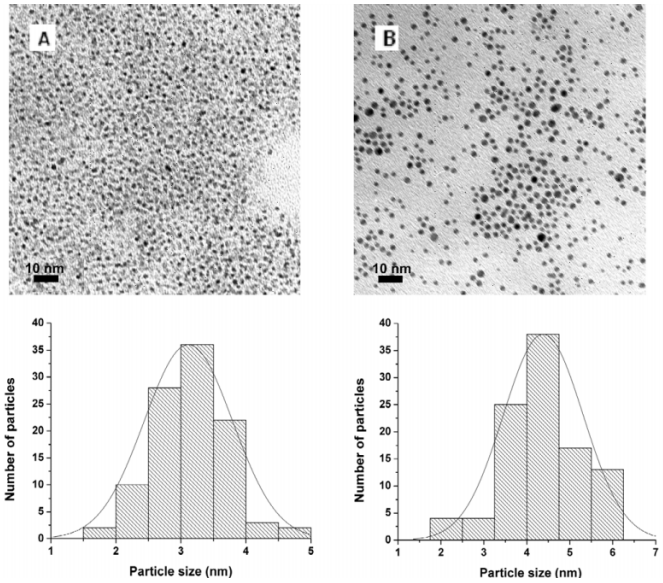

the single-crystal Au(111) limit of 33% as nanoparticles increase in size, with similarly sized particles estimated to have ~42% thiolate coverage on the surface (45). Using this estimate, there are, on average, approximately 350 Gly–CSA groups on each Au nanoparticle surface. Attempts were made to extrapolate more exact ligand–metal ratios from TGA measurements; however, it was extremely difficult to remove chemisorbed water and anions associated with the protonated Gly–CSA ligands. Thus, broad TGA decomposition peaks were seen from 240–340 °C and TGA mass losses were quite high.

$$[1] \qquad n = 4\pi R^3/3V_g$$

The final Gly–CSA Au MPCs are fairly monodisperse and are stable in water at pH between 4 and 5. It should be noted that similar syntheses of Au MPCs using deprotected Gly–CSA stabilizers gave rise to larger particles that had a mixed monolayer; that is, attachment of both amine and thiol groups of the bifunctional Gly–CSA ligand to the Au nanoparticle surfaces was seen by ^{1}H NMR (see Supplementary Data).[2] These particles were unstable in solution and typically precipitated from solution over a period of 6 to 7 days.

The Gly–CSA particles were dialyzed for 120 h to remove excess free peptide and other impurities. Figure 3 shows ^{1}H NMR of the Gly–CSA Au MPCs and free Gly–CSA in D_2O. Note that the α-H signal for the surface-bound Gly–CSA groups is not observed, and the β-H signal at 3.5 ppm is significantly broadened in the pure Au MPCs as a result of their proximity to the Au surface (1). A less-broadened singlet at 3.7 ppm is seen in the Gly–CSA Au MPCs, which corresponds to protons on carbon d in the free Gly–CSA. The lack of significant broadening seen for these protons as compared with the β-H signal indicates it resides further from the Au surface. This is in agreement with the proposed structure for the Gly–CSA Au MPCs in which the thiol group is associated with the Au surface. Further evidence of this bonding arrangement is a broad peak at 10.5 ppm for the Gly–CSA Au MPCs, which corresponds to the protonated amine group; this peak is significantly shifted from the free Gly–CSA peak at 8.3 ppm. This shift is likely due to spatial confinement of protonated amines on the nanoparticle surface (46). We also note the ^{1}H peak for the amide proton (proton c) is not seen for the Gly–CSA Au MPCs, which may be due to extensive H-bonding. FTIR data provide further support for the thiol–Au bonding arrangement, as shown in Fig. 4. The FTIR spectra of the free Gly–CSA thiol and Gly–CSA Au MPCs showed similar N–H stretching vibrations at 3512 cm^{-1} and 3405 cm^{-1} as well as a N–H bending vibration at 1603 cm^{-1}; this indicates that the amine groups are in similar chemical environments for both samples. Also, a weak S–H stretching band can be seen at 2563 cm^{-1} for the free Gly–CSA thiol, and is completely absent in the spectra of Gly–CSA Au MPCs, indicating that all thiols are functionalized on the Au surface.

Coupling reactions with an activated ester of stearic acid were carried out to determine the extent to which the free amine groups could be functionalized on the Gly–CSA Au MPCs. Both the Gly–CSA Au MPCs and the activated stearic acid were completely purified, followed by the addition of stoichiometric amounts of the activated ester to the MPCs. The ^{1}H NMR spectrum of Gly–CSA Au MPCs coupled with stearic acid in a 1:1 ratio shows nearly complete functionalization of all the terminal amine groups (see Supplementary Data).[2] Table 1 shows the quantitative yields of the coupling reactions as determined by ^{1}H NMR for reactions run at different Gly–CSA: stearic acid ratios; nearly stoichiometric yields were typically seen for all coupling reactions. Verification of amide-coupling was seen upon inspection of the FTIR spectrum of the conjugated MPCs (Fig. 4C); a carbonyl stretch at 1678 cm^{-1} corresponding to the new amide group was seen, along with the disappearance of the N–H stretching bands above 3300 cm^{-1}. It should be noted that while the amide conjugation onto the Gly–CSA MPCs was nearly quantitative, TEM images of the final particles after stearic acid conjugation often showed increases in particle size. For example, MPCs synthesized with a 1:1 ratio of Gly–CSA MPCs: stearic acid showed an increase in average nanoparticle size from 4.4 ± 0.8 nm to 6.2 ± 1.4 nm after conjugation, with bimodal distributions of particle sizes emerging (see Supplementary Data).[2] We still do not fully understand the reasons for these size increases, though we believe that it may be due to reagents present in the conjugation and (or) cleaning steps.

Having successfully demonstrated that nearly-quantitative conjugation could be obtained between the terminal surface amine groups of the Gly–CSA MPCs and an activated ester, an activated ester of a Bodipy dye derivative, 4,4-difluoro-5,7-dimethyl-4-bora-3a,4a-diaza-*s*-indacene-3-propionic acid, was synthesized and reacted with the Gly–CSA MPCs. A series of Gly–CSA: dye conjugates was then synthesized; for all solutions the final concentration of dye was kept constant, while the concentration of the Gly–CSA Au MPCs was varied to give loadings of approximately 160, 80, 40, 20, 15, 10, 5, and 1 dye molecules per nanoparticle (note these loadings are all significantly below the earlier estimate of 350 Gly–CSA groups per nanoparticle). Because of the low concentrations of these conjugated systems, ^{1}H NMR and FTIR studies could not be carried out; rather, the conju-

© 2008 NRC Canada

Fig. 3. NMR spectra of free Gly–CSA and Gly–CSA Au MPCs in D_2O (* denotes residual H_2O peak from solvent).

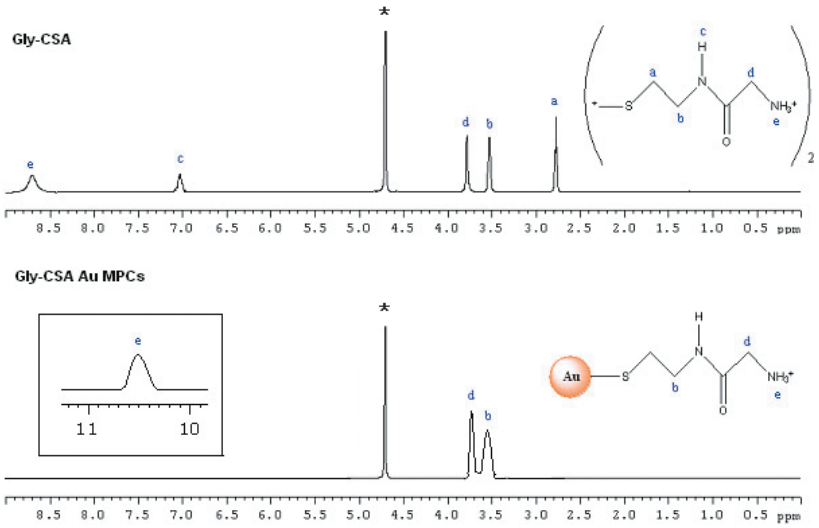

Fig. 4. FTIR spectra of (A) Gly–CSA, (B) Gly–CSA Au MPCs, and (C) stearic acid conjugated Au MPCs.

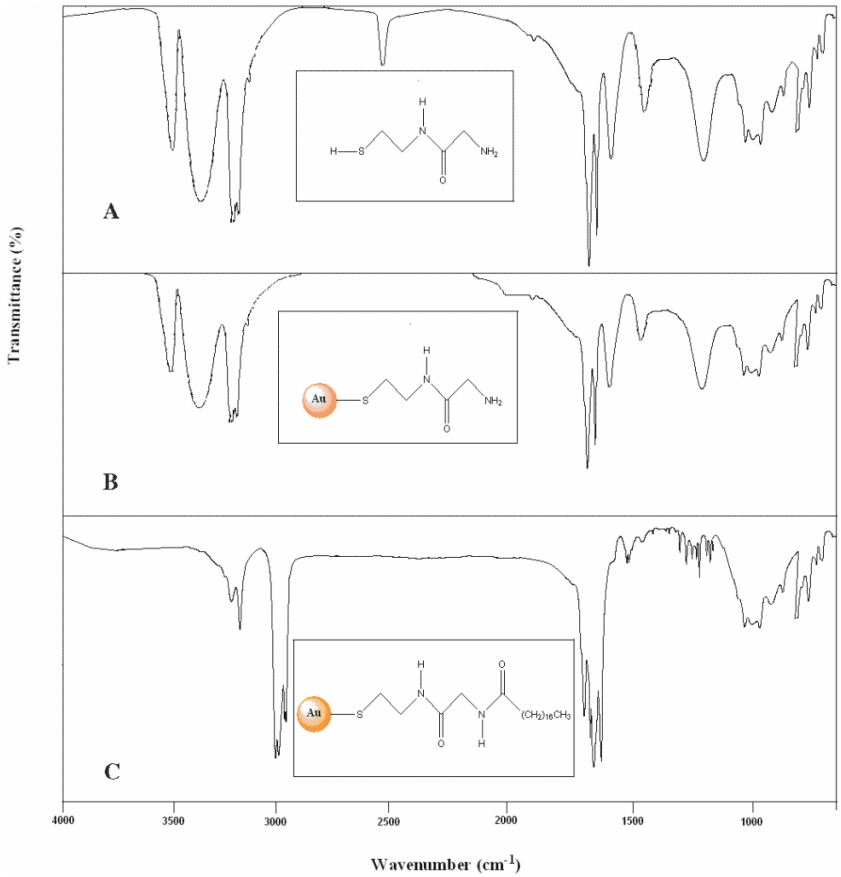

gation reaction was followed by fluorescence emission studies. Figure 5 shows the UV–vis and emission spectra for a series of Bodipy propionic ester samples conjugated with Gly–CSA Au MPCs (Figs. 5A and 5B), and the corresponding UV–vis and emission spectra of non-conjugated Bodipy propionic ester mixed with dodecanethiol Au MPCs (Figs. 5C and 5D). For these experiments, the total amount of Bodipy dye in the mixture was kept constant. As the ratio of dye to Au nanoparticle increased, the absorbance peak height decreased, reflecting the change in concentration of Au MPCs. For the emission studies, it was observed that the fluorescence emission of the dye-conjugated particles was significantly quenched over that of the non-conjugated system.

The quenching of fluorescence emission from fluorophores near metal surfaces has been observed in a number of

© 2008 NRC Canada

Table 1. Theoretical and experimental yields for amide coupling reaction between Gly–CSA Au MPCs and stearic acid.

Gly–CSA/Stearic acid	Theoretical amount of stearic acid w.r.t. Gly–CSA	Experimental amount of stearic acid w.r.t. Gly–CSA
1:1.0	1.00	1.00
1:0.9	0.90	0.90
1:0.8	0.80	0.79
1:0.7	0.70	0.68
1:0.6	0.60	0.59
1:0.5	0.50	0.50

Fig. 5. UV–vis and emission spectra of (A, B) Gly–CSA Au MPCs conjugated with Bodipy dye, and (C, D) dodecanethiol Au MPCs, which are not conjugated with the dye. Note that the dye concentration is kept constant for all samples.

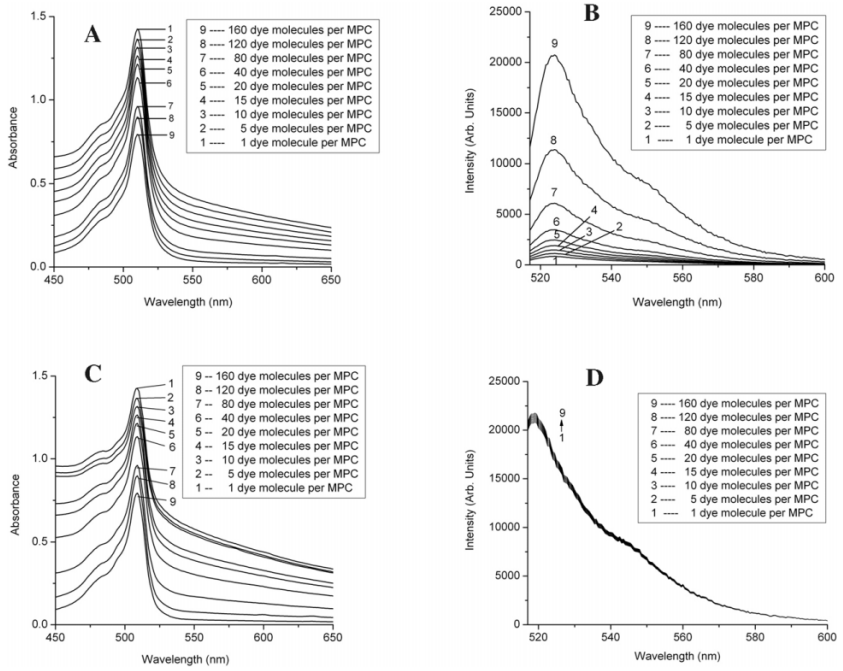

systems, including both planar surfaces and colloidal particles, and has been attributed to a number of different mechanisms, including energy transfer, electron transfer, and others (47). However, for this system, it was observed that the extent of quenching depends strongly on the amount of fluorophore loading. A significant amount of quenching of the fluorescence of the fluorophore that is bound to the Au MPCs is seen at low fluorophore loadings for the Gly–CSA MPCs with conjugated fluorophores as compared with high loadings of 160 dyes per nanoparticle (for an average fluorophore loading of 1 molecule per Au nanoparticle, the emission signal was 4% of that of the 160:1 fluorophore–nanoparticle sample, as determined by the relative areas under the emission curves). Similar effects have been described by Kamat and others for various fluorophore–nanoparticle conjugated systems (48–52). While not direct evidence of amide bond formation, we believe the strong quenching seen in the emission spectra, in conjunction with the stearic acid studies, are indicative of amide bond formation; only weak "collisional" quenching is seen for the non-conjugated system (53). In addition, preliminary single-molecule fluorescence studies of nanoparticles with high dye loadings have shown exponential decay of the fluorescence intensity, which is consistent with multiple fluorophores per Au nanoparticle, and little to no on–off fluorophore blinking of free fluorophores in solution is seen.

The above studies show that amine-terminated Au MPCs can indeed be used as effective precursors for further functionalization of nanoparticles, with nearly stoichiometric reactivity. However, it should be noted that it cannot be assumed that the Au–thiol chemistry is inert under all chemical conditions; particle growth was seen both during the deprotection of Boc groups using TFA and during the amide functionalization/purification of activated esters to the terminal amine groups of the MPCs. This is most likely due to either incomplete steric stabilization of the particles or ligand oxidation of the relatively short Gly–CSA stabilizer used in this work. There are other examples of decomposition of MPCs with short-peptide stabilizers; Tsukuda and coworkers have previously noted that many small glutathione MPCs can spontaneously decompose (54), while Gies et al. have detected the presence of Au–thiolate tetramer species

© 2008 NRC Canada

in samples of tiopronin stabilized MPCs (55). While such problems may often be overcome by carefully adjusting experimental procedures or post-synthesis fractionation of MPCs, it is important to note that there is still much unknown about the chemistry of Au MPCs under different chemical conditions, particularly when the stabilizing ligands do not form a dense, close-packed monolayer.

Conclusion

We have shown that peptide-stabilized Au MPCs can be synthesized via Brust–Schriffin syntheses using protected Boc-Gly–CSA stabilizers, followed by deprotection of the glycine amine groups with trifluoroacetic acid. In addition, we have shown that the surface-modified Au MPCs can be further functionalized by a variety of activated esters with nearly stoichiometric reactivity. In principle, this system allows for facile access to nanoparticle surfaces with multiple functional groups via one-pot syntheses involving activated esters and Gly–CSA MPCs. Further studies are underway to investigate the synthesis of other simple peptide Au and CdSe nanoparticle systems.

Acknowledgements

We thank the Natural Sciences and Engineering Research Council of Canada (NSERC) Nano Innovation Platform and the University of Saskatchewan for financial support of this project and the Saskatchewan Structural Science Centre for access to NMR facilities.

References

1. A.C. Templeton, W.P. Wuelfing, and R.W. Murray. Acc. Chem. Res. **33**, 27 (2000).
2. M.A. El-Sayed. Acc. Chem. Res. **34**, 257 (2001).
3. M. Brust and C. Keily. J. Colloids Surf. A **202**, 175 (2002).
4. G. Schmid and B. Corain. Eur. J. Inorg. Chem. 3081 (2003).
5. J. Zhang, Z. Wang, J. Liu, S. Chen, and G. Liu. Self-assembled nanostructures. Kluwer Academic/Plenum, New York. 2003.
6. M.C. Daniel and D. Astruc. Chem. Rev. **104**, 293 (2004).
7. G. Bilbao, J. Gomez-Navarro, and D.T. Curiel. *In* Gene therapy of cancer. *Edited by* P. Walden. Plenum Press, New York. 1998.
8. R. Kole and P. Sazani. Curr. Opin. Mol. Ther. **3**, 229 (2001).
9. E. Katz and I. Willner. Angew. Chem., Int. Ed. **43**, 6042 (2004).
10. N.L. Rosi and C. Mirkin. Chem. Rev. **105**, 1547 (2005).
11. M. Dasog and R.W.J. Scott. Langmuir, **23**, 3381 (2007).
12. A.C. Templeton, M.J. Hostetler, E.K. Warmoth, S. Chen, C.M. Hartshorn, V.M. Kirshnamurthy, M.D.E. Forbes, and R.W. Murray. J. Am. Chem. Soc. **120**, 4845 (1998).
13. R. Levy, N.T.K. Thanh, R.C. Doty, I. Hussain, R.J. Nichols, D.J. Schiffrin, M. Brust, and D.G. Fernig. J. Am. Chem. Soc. **126**, 10076 (2004).
14. K.A. Stevenson, G. Muralidharan, L. Maya, J.C. Wells, J. Barhen, and T. Thundat. J. Nanosci. Nanotechnol. **2**, 397 (2002).
15. A.C. Templeton, S.W. Chen, S.M. Gross, and R.W. Murray. Langmuir, **15**, 66 (1999).
16. A.C. Templeton, M.J. Hostetler, C.T. Kraft, and R.W. Murray. J. Am. Chem. Soc. **120**, 1906 (1998).
17. A.C. Templeton, D.E. Cliffel, and R.W. Murray. J. Am. Chem. Soc. **121**, 7081 (1999).
18. S. Nuβ, H. Böttcher, H. Wurm, and M.L. Hallensleben. Angew. Chem., Int. Ed. **40**, 4016 (2001).
19. M.S. Wong, J.N. Cha, K.-S. Choi, T.J. Deming, and G.D. Stucky. Nano Lett. **2**, 583 (2002).
20. R. Chakarabarti and A.M. Klibanov. J. Am. Chem. Soc. **125**, 12531 (2003).
21. M.M. Stevens, N.T. Flynn, C. Wang, D.A. Tirrell, and R. Langer. Adv. Mater. **16**, 915 (2004).
22. Z. Wang, R. Lévy, D.G. Fernig, and M. Brust. Bioconjugate Chem. **16**, 497 (2005).
23. H.S. Mandal and H.-B. Kraatz. J. Am. Chem. Soc. **129**, 6356 (2007).
24. J. Fan, S. Chen, and Y. Gao. Colloids Surf. B, **28**, 199 (2003).
25. K.-M. Sung, D.W. Mosley, B.R. Peelle, S. Zhang, and J.M. Jacobson. J. Am. Chem. Soc. **126**, 5064 (2004).
26. J.G. Worden, A.W. Shaffer, and Q. Huo. Chem. Commun. 518 (2004).
27. J.G. Worden, Q. Dai, A.W. Shaffer, and Q. Huo. Chem. Mater. **16**, 3746 (2004).
28. A.W. Shaffer, J.G. Worden, and Q. Huo. Langmuir. **20**, 8343 (2004).
29. S. Mandal, A. Gole, N. Lala, R. Gonnade, V. Ganvir, and M. Sastry. Langmuir, **17**, 6262 (2001).
30. K. Naka, H. Itoh, Y. Tampo, and Y. Chujo. Langmuir. **19**, 5546 (2003).
31. C.J. Ackerson, P.D. Jadzinsky, and R.D. Kornberg. J. Am. Chem. Soc. **127**, 6550 (2005).
32. S. Aryal, B.K.C. Remant, N. Dharmaraj, N. Bhattarai, C.H. Kim, and H.Y. Kim. Spectrochim. Acta A, **63**, 160 (2006).
33. I.-I.S. Lim, W. Ip, E. Crew, P.N. Njoki, D. Mott, C.-J. Zhong, Y. Pan, and S. Zhou. Langmuir, **23**, 826 (2007).
34. T.G. Schaaff, G. Knight, M.N. Shafigullin, R.F. Borkman, and R.L. Whetten. J. Phys. Chem. B, **102**, 10643 (1998).
35. Y. Negishi, Y. Takasugi, S. Sato, H. Yao, K. Kimura, and T. Tsukuda. J. Am. Chem. Soc. **126**, 6518 (2004).
36. J. Sharma, S. Mahima, B.A. Kakade, R. Pasricha, A.B. Mandale, and K. Vijaymohanan. J. Phys. Chem. B, **108**, 13280 (2004).
37. S.R. Johnson, S.D. Evans, and R. Brydson. Langmuir, **14**, 6639 (1998).
38. M. Aslam, L. Fu, M. Su, K. Vijaymohanan, and V.P. Dravid. J. Mater. Chem. **14**, 1795 (2004).
39. W. König and R. Geiger. Chem. Ber. **103**, 788 (1970).
40. M. Bodasky and A. Bodansky. The practice of peptide synthesis. Springer Verlag, Berlin. 1984.
41. M. Brust, J. Fink, D.J. Schiffrin, and C. Keily. J. Chem. Soc., Chem. Comm. 1655 (1995).
42. U. Kreibig and M. Vollmer. Optical properties of metal clusters. Springer, Berlin. 1995.
43. M.M. Alvarez, J.T. Khoury, T.G. Schaaff, M.N. Shafigullin, I. Vezmar, and R.L. Whetten. J. Phys. Chem. B, **101**, 3706 (1997).
44. D.V. Leff, P.C. Ohara, J.R. Heath, and W.M. Gelbart. J. Phys. Chem. **99**, 7036 (1995).
45. M.J. Hostetler, J.E. Wingate, C.-J. Zhong, J.E. Harris, R.W. Vachet, M.R. Clark, J.D. Londono, S.J. Green, J.J. Stokes, G.D. Wignall, G.L. Glish, M.D. Porter, N.D. Evans, and R.W. Murray. Langmuir, **14**, 17 (1998).
46. V. Chechik, R.M. Crooks, and C.J.M. Stirling. Adv. Mater. **12**, 1161 (2000).
47. K.G. Thomas and P.V. Kamat. Acc. Chem. Res. **36**, 888 (2003).
48. B.I. Ipe, K.G. Thomas, S. Barazzouk, S. Hotchandani, and P.V. Kamat. J. Phys. Chem. B, **106**, 18 (2002).
49. P.V. Kamat, S. Barazzouk, and S. Hotchandani. Angew. Chem., Int. Ed. **41**, 2764 (2002).

© 2008 NRC Canada

50. F. Stellacci, C.A. Bauer, T. Meyer-Friedrichsen, W. Wenseleers, S.R. Marder, and J.W. Perry. J. Am. Chem. Soc. **125**, 328 (2003).
51. H. Imahori, M. Arimura, T. Hanada, Y. Nishimura, I. Yamazaki, Y. Sakata, and S. Fukuzumi. J. Am. Chem. Soc. **123**, 335 (2001).
52. A.C. Templeton, D.E. Cliffel, and R.W. Murray. J. Am. Chem. Soc. **121**, 7081 (1999).
53. P.P.H. Cheng, D. Silvester, G. Wang, G. Kalyuzhny, A. Douglas, and R.W. Murray. J. Phys. Chem. B, **110**, 4637 (2006).
54. Y. Negishi, K. Nobusada, and T. Tsukuda. J. Am. Chem. Soc. **127**, 5261 (2005).
55. A.P. Gies, D.M. Hercules, A.E. Gerdon, and D.E. Cliffel. J. Am. Chem. Soc. B, **129**, 1095 (2007).

© 2008 NRC Canada

One-pot preparation of β-amido ketones/esters in a three-component condensation reaction using magnesium hydrogensulfate as an effective and reusable catalyst

Hamid Reza Shaterian, Asghar Hosseinian, and Majid Ghashang

Abstract: A one-pot, three-component condensation of an aryl aldehyde, an enolizable ketone or β-keto ester, acetyl chloride, and acetonitrile or benzonitrile in the presence of magnesium hydrogensulfate as an active, recoverable, and reusable green catalyst is described for the synthesis of β-amido ketones/esters at room temperature. The key features of this methodology are simplicity, mild reaction conditions, and high to excellent yields.

Key words: multi-component reaction, magnesium hydrogensulfate, heterogeneous catalyst, β-amido ketone/ester, mild conditions.

Résumé : On décrit une condensation monotope à trois composants dont un aldéhyde aromatique, une cétone ou un β-cétoester énolisable et du chlorure d'acétyle, de l'acétonitrile ou du benzonitrile, en présence de sulfate acide de magnésium comme catalyseur vert actif, récupérable et réutilizable, pour réaliser la synthèse à la température ambiante la synthèse de β-amidocétones et de β-amidoesters. Les caractéristiques principales de cette méthodologie sont sa simplicité, des conditions réactionnelles douces et des rendements allant d'élevés à excellents.

Mots-clés : réaction à plusieurs composants, sulfate acide de magnésium, catalyseur hétérogène, β-amidocétones, β-amidoesters, conditions douces.

[Traduit par la Rédaction]

Introduction

Today, with the emergence of high-speed parallel synthesis, the multi-component reaction (MCR) is widely employed for the rapid assembly of arrays with high molecular diversity (1). Due to their inherent simple experimental procedures and their one-pot character, they are perfectly suited for automated synthesis. Thus, MCRs have attracted considerable interest owing to their exceptional synthetic efficiency (2–7).

β-Amido ketones are important building blocks and intermediates in synthesis For example, they are important precursors of heterocyclic compounds (8), as well as of β-amino alcohols, which are common units in both natural and synthetic biologically or pharmacologically important compounds (9). The reported one-pot syntheses of the title compounds from aldehydes, enolizable ketones, acetyl chloride, and acetonitrile or benzonitrile are based on some Lewis or Brønsted acid catalysts such as $CoCl_2$ (10, 11), Montmorillonite K-10 clay (12), silica sulfuric acid (13), $BiCl_3$ generated from BiOCl (14), $ZrOCl_2{\cdot}8H_2O$ (15), heteropoly acid (16), sulfuric acid absorbed on silica gel (17), $Sc(OTf)_3$ (18), silica supported $H_3PW_{12}O_{40}$ (19), $K_5CoW_{12}O_{40}{\cdot}3H_2O$ (20), $CeCl_3{\cdot}7H_2O$ (21), ZnO (22), iodine (23), sulfated zirconia (24), iron(III) chloride (25), and *p*-TSA (26). Herein we wish to report an efficient method for the synthesis of β-amido carbonyl compounds in high to excellent yields by employing $Mg(HSO_4)_2$ as an active environmentally friendly heterogeneous catalyst (Scheme 1). We believe that our method is simple, mild, and rapid for the synthesis of the mentioned compounds at room temperature (RT).

Scheme 1. Synthesis of β-amido carbonyl compounds using $Mg(HSO_4)_2$ as an active heterogeneous catalyst.

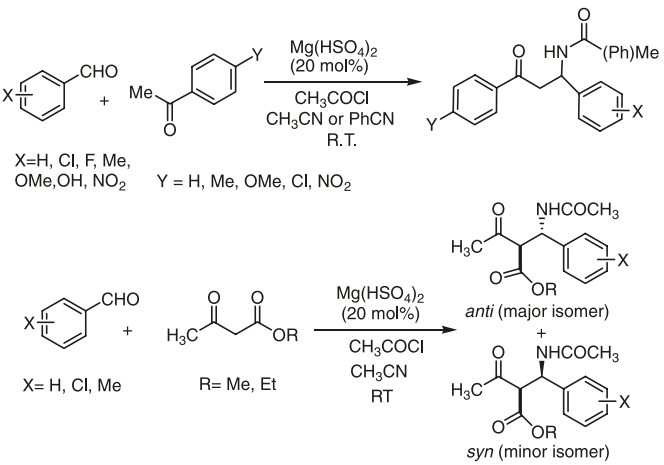

Received 6 December 2007. Accepted 13 January 2008. Published on the NRC Research Press Web site at canjchem.nrc.ca on 27 March 2008.

H.R. Shaterian,[1] A. Hosseinian, and M. Ghashang. Department of Chemistry, Faculty of Sciences, University of Sistan and Baluchestan, Zahedan, Iran.

[1]Corresponding author (e-mail: hrshaterian@hamoon.usb.ac.ir).

 doi:10.1139/V08-013 © 2008 NRC Canada

This catalyst is safe, easy to handle, environmentally benign, presents fewer disposal problems, and is stable in reaction media. Magnesium hydrogensulfate has been used in some organic reactions, such as acetylation and formylation of alcohols (27), cleavage of C=N (28), and oxidation of thiols (29).

Results and discussion

First, we optimized the amount of magnesium hydrogensulfate as catalyst in the reaction among benzaldehyde, acetophenone, acetyl chloride, and acetonitrile (Table 1). The amount of magnesium hydrogensulfate was chosen to be 20 mol%.

Thus, we continued preparation of β-amido ketones in an optimum model experiment: aldehydes (1 equiv.), enolizable ketone or β-keto ester (1 equiv.), acetyl chloride (0.5 mL), and acetonitrile or benzonitrile (reactant, as well as solvent, 2 mL) in the presence of magnesium hydrogensulfate (20 mol%, Table 2).

As shown in Table 2, aromatic aldehydes and acetophenone derivatives with both electron-withdrawing and electron-donating substituents afforded to the corresponding β-amido ketones without the formation of any side products and in high to excellent yields at RT (Table 2, entries 1–22). Phenolic-OH groups under present reaction conditions were converted to acetate (-OAc) groups (Table 2, entries 19, 20).

Under the optimized reaction conditions, by using benzonitrile in place of acetonitrile, aldehydes were transformed to their corresponding β-benzamido ketones in high yields (Table 2, entries 2, 15).

We also studied the multi-component reaction of aromatic aldehydes with other enolizable ketones (methyl acetoacetate, ethyl acetoacetate, and propiophenone) and acetonitrile in the presence of acetyl chloride and $Mg(HSO_4)_2$ as catalyst. In all cases, mixtures of syn and anti diastereomers were obtained. The amount of syn and anti products was determined by ^{1}H NMR spectra, the coupling constant between H-2 and H-3 is 6–9 Hz for an anti isomer and 2–5 Hz for a syn isomer (10-12, 26). As shown in Table 3, anti diastereomers were found to be major products. The conformational preference of these anti diastereomers depend on the intramolecular H-bonding between the acidic proton and the carbonyl oxygen This phenomenon was confirmed by Ghosh et al. (15) with the X-ray crystallographic analysis data. Methyl and ethyl acetoacetate afforded the corresponding β-acetamido esters and the anti/syn diastereoselectivity further increased from 61:39 to 81:19 (Table 3).

In a typical experiment, after a period of time in which the reaction was completed, the mixture was filtered and the heterogeneous catalyst was recovered. Then, the residue solution was poured into the cooled water until a solid crude product was formed. In every experiment all of the magnesium hydrogensulfate was easily recovered from the reaction mixture. The reusability of the catalysts is one of their most important benefits and makes them useful for commercial applications. Thus, the recovery and reusability of magnesium hydrogensulfate was investigated. The separated catalyst can be reused after washing with $CHCl_3$ and drying. The reusability of the catalyst was checked by the reaction of benzaldehyde and acetophenone in the presence of acetyl chloride and acetonitrile using 20 mol% of $Mg(HSO_4)_2$ at RT. The results indicate that the catalyst can be used five times without any loss of its activity (Table 4).

Table 1. Preparation of *N*-(3-oxo-1,3-diphenylpropyl) acetamide in the presence of various amounts of $Mg(HSO_4)_2$ at room temperature.

Entry	$Mg(HSO_4)_2$ (mol%)	Time (h)	Yield (%)[a]
1	5	8	50
2	10	5	60
3	15	3	75
4	20	2.5	89
5	30	2.5	91

[a]Isolated yields.

To show the merit of the present work in comparison with reported results in the literature, we compared results of magnesium hydrogensulfate with BiOCl (14), $ZrOCl_2 \cdot 8H_2O$ (15), $CeCl_3 \cdot 7H_2O$ (21), ZnO (22), and I_2 (23) in the synthesis of β-acetamido ketone derivatives. As shown in Table 5, magnesium hydrogensulfate can act as an effective catalyst with respect to reaction times, yields, and the obtained products.

Conclusion

In summary, we have demonstrated a new and important catalytic activity of magnesium hydrogensulfate as an inexpensive, commercially available, and reusable catalyst for the synthesis of β-amido ketones/esters in high to excellent yields under mild conditions at RT. The simple experimental procedure combined with the easy work-up and high to excellent yields of products are strong features of the presented method.

Experimental

All reagents were purchased from Merck and Sigma-Aldrich and used without further purification. All yields refer to isolated products after purification. Products were characterized by comparison with authentic samples and by spectroscopy data (IR, ^{1}H NMR, ^{13}C NMR spectra). The NMR spectra were recorded on a Bruker Avance DEX 500 and 300 MHz instrument. The spectra were measured in $CDCl_3$ (and DMSO-d_6) relative to TMS (0.00 ppm). Elemental analyses for C, H, and N were performed using a Heraeus CHN-O-Rapid analyzer. IR spectra were recorded on a JASCO FT-IR 460plus spectrophotometer. Mass spectra were recorded on a Agilent technologies 5973 network mass selective detector (MSD) operating at an ionization potential of 70 eV. Melting points were determined in open capillaries with a BUCHI 510. TLC was performed on silica-gel Poly-Gram SIL G/UV 254 plates.

Preparation of magnesium hydrogensulfate

A 500 mL suction flask was equipped with a constant-pressure dropping funnel. A gas outlet was connected to a vacuum system through an adsorbing solution (water) and an

© 2008 NRC Canada

Table 2. Preparation of β-amido ketones from aldehydes and acetophenone derivatives in the presence of acetyl chloride and acetonitrile or benzonitrile catalyzed using $Mg(HSO_4)_2$ at room temperature.

Entry	Aldehyde	Ketone	Product	Time (h)	Yield (%)[a]	Mp, lit. value, ref.
1	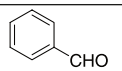	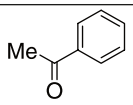	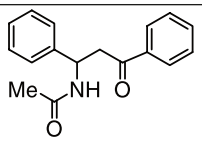	2.5	89	102–104, 103–105, 16
2	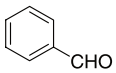	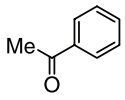	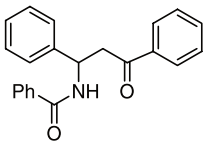	2.5	90	153–155 153–154, 25
3	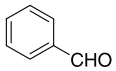	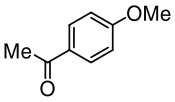	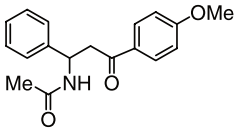	2.5	95	129–131, 130, 14
4	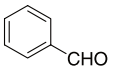	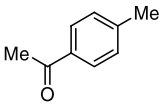	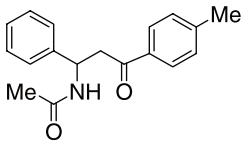	2.5	93	112–115, 121–123, 17
5	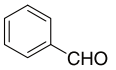	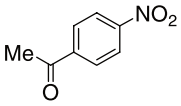	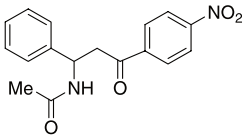	4	79	74–76, 74–76, 16
6	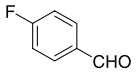	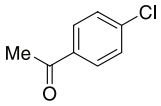	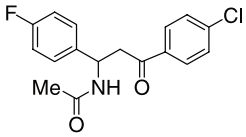	3	87	108–110, 108–110, 17

alkali trap. Anhydrous magnesium chloride (47.6 g, 0.5 mol) was charged into the flask and concentrated sulfuric acid (98.07 g, 1 mol) was added dropwise over a period of 30 min at RT. HCl gas was evolved immediately. After completing the addition of the H_2SO_4, the mixture was shaken for 30 min; meanwhile, the residual HCl was exhausted by suction. A white solid material was thus obtained (108.5 g) (28).

Typical experimental procedure for the one-pot preparation of *N*-(3-oxo-1,3-diphenylpropyl) acetamide (Table 2, entry 1)

A solution of the benzaldehyde (1 mmol), acetophenone (1 mmol), acetyl chloride (0.5 mL), and acetonitrile in the presence of magnesium hydrogensulfate (20 mol%) was stirred at RT for the appropriate time (Table 2). The progress of the reaction was followed by TLC. After completion of the reaction, the reaction mixture was filtered and the heterogeneous catalyst was recovered. Then, the residue solution was poured into 50 mL of ice water, the solid was separated and recrystallized twice using ethyl acetate/petroleum ether, which gave the desired pure *N*-(1,3-diphenyl-3-oxo-propyl) acetamide in 89% yield (Table 2, entry 1). IR (KBr, cm^{-1}): 3286, 3091, 1693, 1650, 1556, 1273, 1066, 753, 691. ^{1}H NMR (300 MHz, $CDCl_3$, ppm) δ: 2.03 (s, 3H), 3.45 (dd, J = 6.0 and 16.9 Hz, 1H), 3.77 (dd, J = 5.2 and 16.9 Hz, 1H), 5.58 (dd, J = 5.6 and 13.1 Hz, 1H), 6.90 (d, J = 6.3 Hz,1H), 7.24-7.60 (m, 8H), 7.91 (d, J = 7.5 Hz, 2H). ^{13}C NMR (75 MHz, $CDCl_3$, ppm) δ: 23.5, 43.3, 50.0, 126.6, 127.5, 128.2, 128.7, 128.8, 133.6, 136.7, 141.6, 169.6, 199.3.

The desired pure product(s) was characterized by comparison of their physical data with those of known β-amido carbonyl compounds (10–26). The spectral data of some representative β-amido ketones/esters are given as follows.

N-(1,3-Diphenyl-3-oxo-propyl) benzamide

Table 2, entry 2. IR (KBr, cm^{-1}): 3306, 3062, 1681, 1634, 1599, 1488, 1357, 981, 754. ^{1}H NMR (300 MHz, $CDCl_3$, ppm) δ: 3.52 (dd, J = 6.0 and 16.4 Hz, 1H), 3.87 (dd, J = 4.8 and 16.8 Hz, 1H), 5.73–5.78 (m, 1H), 7.22 (t, J = 7.2 Hz, 1H), 7.30 (t, J = 7.6 Hz, 2H) 7.37–7.45 (m, 5H), 7.49 (t, J = 7.2 Hz, 2H), 7.55 (t, J = 7.2 Hz, 1H), 7.60 (d, J = 8.0 Hz, 1H), 7.82 (d, J = 8.0 Hz, 2H), 7.90 (d, J = 8.0 Hz, 2H). ^{13}C NMR (75 MHz, $CDCl_3$, ppm) δ: 43.1, 50.4, 126.6, 127.2, 127.6, 128.3, 128.7, 128.8, 128.9, 131.8, 133.8, 134.4, 136.7, 141.1, 166.9, 199.3.

© 2008 NRC Canada

Table 2 (*continued*).

Entry	Aldehyde	Ketone	Product	Time (h)	Yield (%)[a]	Mp, lit. value, ref.
7	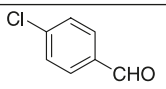	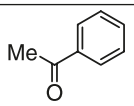	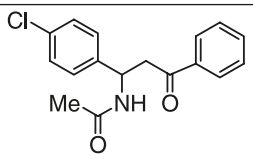	2	92	149–152, 149–150, 15
8	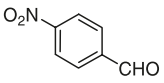	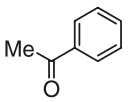	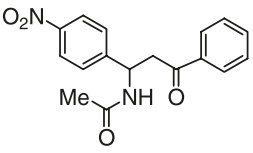	4	81	138–141, 153, 25
9	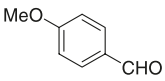	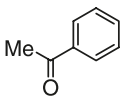	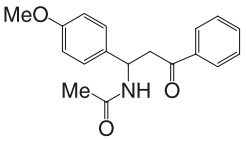	3	85	109–111, 110–112, 15
10	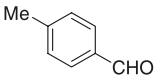	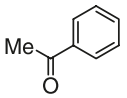	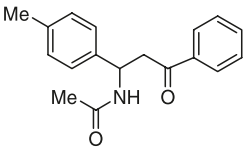	2.5	91	110–112, 112, 15
11	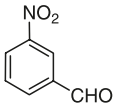	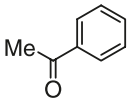	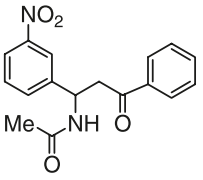	4	84	135–137, 139–140, 15
12	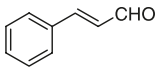	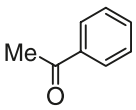	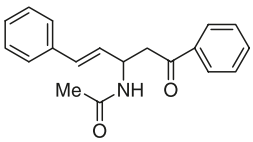	2	91	120–122, 120–121, 25
13	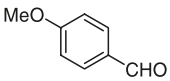	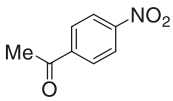	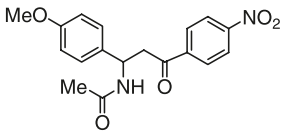	3.5	82	88–90, 87–89, 16

N-[1-Phenyl-3-oxo-3-(4-methoxyphenyl)propyl] acetamide

Table 2, entry 3. IR (KBr, cm^{-1}): 3260, 1680, 1640, 1600, 1570, 1255, 1170, 990, 700. ^1H NMR (300 MHz, $CDCl_3$, ppm) δ: 2.00 (s, 3H), 3.34 (dd, *J* = 5.9 and 16.6 Hz, 1H), 3.67 (dd, *J* = 5.3 and 16.6 Hz, 1H), 3.84 (s, 3H), 5.50–5.57 (m, 1H), 6.86 (s, 1H), 6.89 (d, *J* = 8.8 Hz, 2H), 7.18–7.34 (m, 5H), 7.88 (d, *J* = 8.8 Hz, 2H). ^{13}C NMR (75 MHz, $CDCl_3$, ppm) δ: 23.4, 42.8, 50.0, 55.5, 113.8, 126.4, 127.3, 128.5, 129.7, 130.4, 141.1, 163.8, 169.5, 197.1.

N-[1-(2,5-Dimethoxyphenyl)-3-oxo-3-phenylpropyl] acetamide

Table 2, entry 17. IR (KBr, cm^{-1}): 3296, 3086, 1689, 1649, 1558, 1505, 1774,1296, 1226, 1047, 807, 754. ^1H NMR (500 MHz, $CDCl_3$, ppm) δ: 2.00 (s, 3H), 3.46 (dd, *J* = 6.6 and 15.8 Hz, 1H), 3.56 (dd, *J* = 6.1 and 15.7 Hz, 1H), 3.73 (s, 3H), 3.85 (s, 3H), 5.69 (dd, *J* = 2.3 and 6.5 Hz, 1H), 6.73 (dd, *J* = 3.0 and 8.9 Hz, 1H), 6.79 (d, *J* = 8.9 Hz, 1H), 6.83 (d, *J* = 8.4 Hz, 1H), 6.87 (d, *J* = 3.0 Hz, 1H), 7.43 (t, *J* = 7.6 Hz, 2H), 7.55 (t, *J* = 7.3 Hz, 1H), 7.92 (d, *J* = 7.4 Hz, 2H). ^{13}C NMR (125 MHz, $CDCl_3$, ppm) δ: 23.5, 43.0, 48.0, 55.7, 55.8, 111.7, 112.8, 115.0, 128.2, 128.6, 129.5, 133.2, 136.8, 150.8, 153.6, 169.0, 198.6. MS *m*/*z* (%): 327.2 (M^+, 17), 285.2 (19), 284.2 (100), 237.1 (16), 208.1 (17), 180.2 (27), 166.1 (62), 151.1 (13), 136.1 (12), 105.1 (45), 77.2 (23), 43.2 (14). $C_{19}H_{21}NO_4$ requires (%): C 69.71, H 6.47, N 4.28; found: C 69.56, H 6.39, N 4.34.

© 2008 NRC Canada

Table 2 (*concluded*).

Entry	Aldehyde	Ketone	Product	Time (h)	Yield (%)[a]	Mp, lit. value, ref.
14	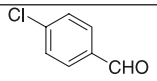	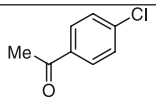	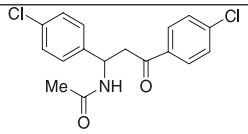	2	90	141–143, 143–145,19
15	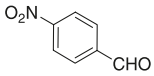	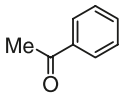	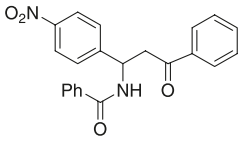	3.5	78	142–145, 142–144,25
16	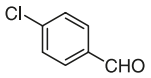	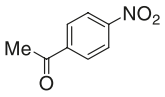	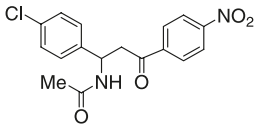	3.5	86	116–118, 116–119,19
17	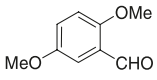	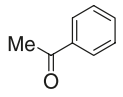	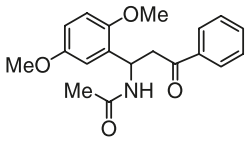	2	92	153–156,—
18	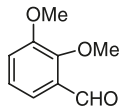	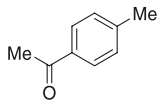	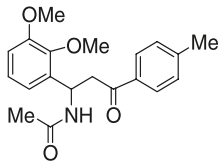	2	90	108–110,—
19	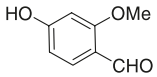	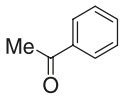	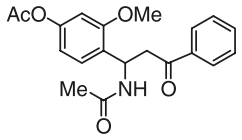	2.5	89	129–132,—
20	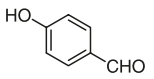	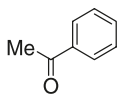	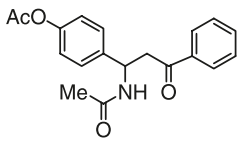	3	84	120–122,—
21	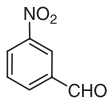	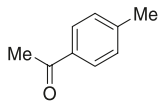	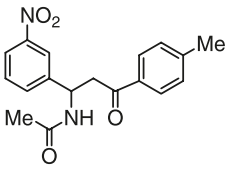	4	80	94–97,—
22	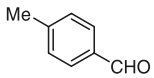	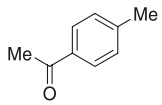	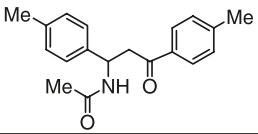	2.5	91	103–105,—

[a]Yields refer to the isolated pure products. All known products have been reported previously inthe literature and were characterized by comparison of mp, IR, and NMR spectra with authentic samples (10–26).

© 2008 NRC Canada

Table 3. Preparation of β-acetamido ketoesters in the presence of $Mg(HSO_4)_2$ as a catalyst at room temperature.

Entry	Enolizable ketone	Aldehyde	Time (h) ,Yield (%)[a]	Products[b] *Anti*	Products[b] *Syn*
1	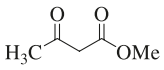	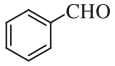	2 , 84	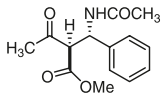 78 %	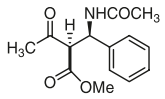 22 %
2	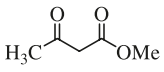	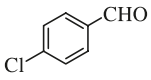	2 , 90	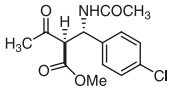 81 %	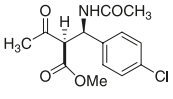 19 %
3	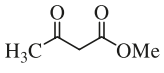	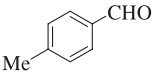	2 , 87	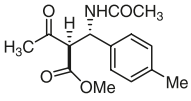 72 %	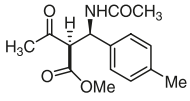 28 %
4	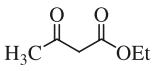	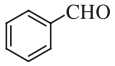	3 , 89	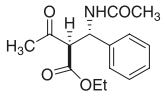 69 %	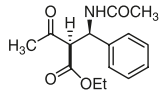 31 %
5	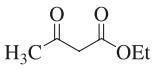	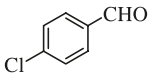	3 , 91	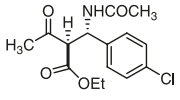 74 %	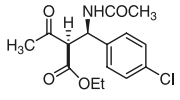 26 %
6		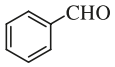	4 , 84	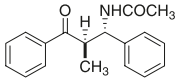 63 %	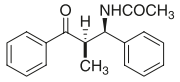 37 %
7		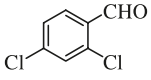	4 , 85	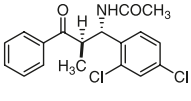 61 (%)	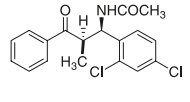 39 (%)

[a]Yields refer to the isolated pure products.

[b]Ratio obtained from 1H NMR of the crude reaction mixture. All syn and anti diastereomers havebeen reported previously in the literature, thus we compared 1H NMR spectra with authenticsamples (10–12, 26).

Table 4. Recyclability of $Mg(HSO_4)_2$ in the synthesis of *N*-(1,3-diphenyl-3-oxopropyl) acetamide.

Run no.	Yield (%)
1	89
2	87
3	88
4	85
5	84

N-[1-(2,3-Dimethoxyphenyl)-3-oxo-3-(4-methylphenyl)propyl] acetamide

Table 2, entry 18. IR (KBr, cm^{-1}): 3301, 3081, 2941, 1686, 1651, 1610, 1552, 1503, 1466,1372, 1284, 1225, 1047, 807, 714. ^1H NMR (500 MHz, $CDCl_3$, ppm) δ: 1.99 (s, 3H), 2.38 (s, 3H), 3.42 (dd, *J* = 6.4 and 15.6 Hz, 1H), 3.51 (dd, *J* = 6.2 and 15.6 Hz, 1H), 3.72 (s, 3H), 3.84 (s, 3H), 5.68 (dd, *J* = 6.4 and 14.8 Hz, 1H), 6.72 (dd, *J* = 2.8 and 8.8 Hz, 1H), 6.78 (d, *J* = 8.8 Hz, 1H), 6.87–6.86 (m, 2H), 7.22 (d, *J* = 7.9 Hz, 2H), 7.82 (d, *J* = 8.0 Hz, 2H). ^{13}C NMR (125 MHz, $CDCl_3$, ppm) δ: 21.6, 23.4, 42.9, 47.9, 55.7, 55.8, 111.7, 112.7, 114.9, 128.3, 129.3, 129.7, 134.3, 144.0, 150.7, 153.6, 169.1, 198.2. MS *m*/*z* (%): 341.2 (M^+, 19), 299.2 (21), 298.2 (100), 251.2 (23), 208.1 (20), 180.2 (30), 166.1 (70), 151.1 (15), 136.1 (13), 119.1 (65), 105.1 (14), 91.2 (27), 77.2 (12), 43.2 (20). $C_{20}H_{23}NO_4$ requires (%): C 70.36, H 6.79, N 4.10; found: C 70.32, H 6.71, N 4.07.

© 2008 NRC Canada

Table 5. Comparison result of magnesium hydrogensulfate with BiOCl (14), $ZrOCl_2 \cdot 8H_2O$ (15), CeCl3 $7H_2O$ (21), ZnO (22), and I_2 (23) in the synthesis of β-acetamido ketones.

Entry	Aldehyde	Enolizable Ketone	Catalyst	Molar ratio:aldehyde / enolizable ketone / catalyst (mol %)	Time (h)	Yield (%)
1	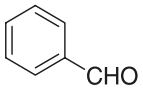	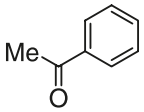	BiOCl	1/1/ (20 mol %)	7	92
			$ZrOCl_2.8H_2O$	1/1/ (20 mol %)	5	90
			$CeCl_3.7H_2O$	1/1/ (10 mol %)	7	96
			ZnO	1/1/ (50 mol %)	6	90
			I_2	1/1/ (10 mol %)	4.5	85
			$Mg(HSO_4)_2$	1/1/ (20 mol %)	2.5	89
2	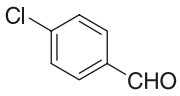	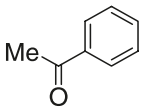	BiOCl	1/1/ (20 mol %)	10	80
			$ZrOCl_2.8H_2O$	1/1/ (20 mol %)	8	91
			$CeCl_3.7H_2O$	1/1/ (10 mol %)	6	98
			ZnO	1/1/ (50 mol %)	5.5	92
			I_2	1/1/ (10 mol %)	4.5	85
			$Mg(HSO_4)_2$	1/1/ (20 mol %	2	92
3	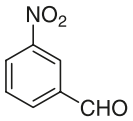	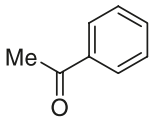	BiOCl	1/1/ (20 mol %)	8	91
			$ZrOCl_2.8H_2O$	1/1/ (20 mol %)	6	92
			$CeCl_3.7H_2O$	1/1/ (10 mol %)	10	90
			ZnO	1/1/ (50 mol %)	5	90
			I_2	1/1/ (10 mol %)	4	85
			$Mg(HSO_4)_2$	1/1/ (20 mol %)	4	84

N-[1-(4-Acethoxy-2-methoxyphenyl)-3-oxo-3-phenylpropyl] acetamide

Table 2, entry 19. IR (KBr, cm^{-1}): 3281, 3096, 1768, 1686, 1653, 1602, 1558, 1511, 1366, 1304, 1279, 1199, 1029, 909, 741. ^1H NMR (500 MHz, $CDCl_3$, ppm) δ: 1.98 (s, 3H), 2.28 (s, 3H), 3.42 (dd, *J* = 6.3 and 16.8 Hz, 1H), 3.69 (dd, *J* = 5.4 and 16.8 Hz, 1H), 3.78 (s, 3H), 5.53 (dd, *J* = 5.9 and 13.8 Hz, 1H), 6.75 (d, *J* = 8.0 Hz, 1H), 6.87–6.97 (m, 3H), 7.45 (t, *J* = 7.6 Hz, 2H), 7.57 (t, *J* = 7.4 Hz, 1H), 7.90 (d, *J* = 8.5 Hz, 2H). ^{13}C NMR (125 MHz, $CDCl_3$, ppm) δ: 20.6, 23.3, 43.2, 49.9, 55.9, 115.5, 118.5, 122.8, 128.1, 128.7, 133.5, 136.6, 139.0, 140.0, 151.1, 169.0, 169.5, 198.4. MS *m/z* (%): 355.2 (M^+, 15), 313.2 (28), 312.2 (57), 271.2 (20), 270.2 (100), 254.2 (19), 208.2 (10), 194.2 (24), 166.2 (35), 152.2 (49), 105.2 (82), 77.2 (31), 43.2 (22). $C_{20}H_{21}NO_5$ requires (%): C 67.59, H 5.96, N 3.94; found: C 67.43, H 5.94, N 3.90.

N-[1-(4-Acethoxyphenyl)-3-oxo-3-phenylpropyl] acetamide

Table 2, Entry 20. IR (KBr, cm^{-1}): 3262, 3085, 2928, 1762, 1699, 1652, 1651, 1509, 1448, 1411, 1365, 1294, 1216, 1200, 911, 759, 691. ^1H NMR (500 MHz, $CDCl_3$, ppm) δ: 2.01 (s, 3H), 2.28 (s, 3H), 3.44 (dd, *J* = 6.1 and 17.0 Hz, 1H), 3.73 (dd, *J* = 5.2 and 17.0 Hz, 1H), 5.56 (dd, *J* = 5.8 and 13.6 Hz, 1H), 6.73 (d, *J* = 8.0 Hz, 1H), 7.03 (d, *J* = 8.5 Hz, 2H), 7.35 (d, *J* = 8.5 Hz, 2H), 7.46 (t, *J* = 7.7 Hz, 2H), 7.58 (t, *J* = 7.4 Hz, 1H), 7.91 (d, *J* = 7.7 Hz, 2H). ^{13}C NMR (125 MHz, DMSO-d_6, ppm) δ: 20.8, 22.6, 44.5, 48.4, 121.5, 127.7, 128.0, 128.7, 133.2, 136.5, 140.5, 149.2, 168.3, 169.2, 197.0. MS *m/z* (%): 352.2 (M^+, 8), 326.2 (2), 282.2 (100), 240.2 (41), 242.2(19), 178.2 (20), 167.1 (26), 149.1 (62), 136.2 (37), 122.2 (55), 105.2 (86), 77.2 (40), 57.2 (16), 43.2 (41). $C_{19}H_{19}NO_4$ requires (%): C 70.14, H 5.89, N 4.31; found: C 70.08, H 5.78, N 4.24.

N-[1-(3-Nitrophenyl)-3-oxo-3-(4-methylphenyl)propyl] acetamide

Table 2, entry 21. IR (KBr, cm^{-1}): 3301, 3069, 1680, 1645, 1606, 1531, 1352, 1202, 1180, 810, 741, 696. ^1H NMR (300 MHz, DMSO-d_6, ppm) δ: 1.97 (s, 3H), 2.36 (s, 3H), 3.43 (dd, *J* = 5.5 and 17.4 Hz, 1H), 3.61 (dd, *J* = 8.3 and 17.4 Hz, 1H), 5.45 (dd, *J* = 7.6 and 13.4 Hz, 1H), 7.31 (d, *J* = 7.9 Hz, 2H), 7.62 (t, *J* = 7.9 Hz, 1H), 7.86–7.75 (m, 3H), 8.08 (d, *J* = 8.0 Hz, 1H), 8.22 (s, 1H), 8.49 (d, *J* = 7.5 Hz, 1H). ^{13}C NMR (75 MHz, DMSO-d_6) δ: 20.7, 22.6, 44.0, 48.5, 121.3, 121.8, 128.1, 129.1, 129.7, 133.7, 133.9, 143.7, 145.6, 147.8, 168.6, 196.1. MS *m/z* (%): 326.3 (M^+, 0.8), 283.2 (20), 267.2 (12), 189.2 (24), 190.2 (17), 165.2 (38), 151.2 (33), 134.2 (13),119.2 (100), 105.2 (12), 91.2

© 2008 NRC Canada

(43), 77.2 (6), 65.2 (14), 43.2 (26). $C_{18}H_{18}N_2O_4$ requires (%): C 66.25, H 5.56, N 8.58; found: C 66.23, H 5.56, N 8.51.

_N_-[1-(4-Methylphenyl)-3-oxo-3-(4-methylphenyl)propyl] acetamide

Table 2, entry 22. IR (KBr, cm^{-1}): 3258, 3069, 1607, 1638, 1605, 1541, 1410, 1326, 1266, 1183, 998, 810, 722. ^1H NMR (300 MHz, DMSO-d_6, ppm) δ: 1.77 (s, 3H), 2.24 (s, 3H), 2.36 (s, 3H), 3.31 (dd, J = 6.1 and 15.9 Hz, 1H), 3.46 (dd, J = 8.0 and 16.7 Hz, 1H), 5.31 (dd, J = 7.7 and 14.2 Hz, 1H), 7.10 (d, J = 7.9 Hz, 2H), 7.21 (d, J = 8.0 Hz, 2H), 7.31 (d, J = 8.0 Hz, 2H), 7.83 (d, J = 8.1 Hz, 2H), 8.25 (d, J = 8.0 Hz, 1H). ^{13}C NMR (75 MHz, DMSO-d_6, ppm) δ: 20.6, 21.1, 22.6, 44.5, 48.8, 126.5, 128.1, 128.7, 129.2, 134.1, 135.8, 140.0, 143.5, 168.2, 196.7. MS m/z (%): 295.2 (M^+, 12), 252.2 (100), 253.2 (21), 221.2 (13), 162.2 (10), 134.2 (49), 120.2 (70), 119.2 (91), 91.2 (44), 65.2 (14), 43.2 (14). $C_{19}H_{21}NO_2$ requires (%): C 77.26, H 7.17, N 4.74; found: C 77.20, H 7.13, N 4.70.

(_R_)-Methyl 2-((_S_)-acetamido(phenyl)methyl)-3-oxobutanoate

Table 3, entry 1 (mixture of diastereomers), data for the major isomer. ^1H NMR (500 MHz, $CDCl_3$, ppm) δ: 1.97 (s, 3H), 2.11 (s, 3H), 3.71 (s, 3H), 4.07 (d, J = 5.5 Hz, 1H), 5.72 (dd, J = 5.5 and 9.0 Hz, 1H), 6.91 (d, J = 8.1 Hz, 1H), 7.22–7.30 (m, 5H).

(_R_)-Methyl 2-((_S_)-acetamido(4-chlorophenyl)methyl)-3-oxobutanoate

Table 3, entry 2 (mixture of diastereomers), data for the major isomer. ^1H NMR (500 MHz, $CDCl_3$, ppm) δ: 1.98 (s, 3H), 2.13 (s, 3H), 3.73 (s, 3H), 4.07 (d, J = 5.5 Hz, 1H), 5.69 (dd, J = 5.5 and 9.0 Hz, 1H), 6.93 (d, J = 8.3 Hz, 1H), 7.20 (d, J = 8.8 Hz, 2H), 7.26(d, J = 7.9 Hz, 2H).

(_R_)-Ethyl 2-((_S_)-acetamido(phenyl)methyl)-3-oxobutanoate

Table 3, entry 4 (mixture of diastereomers), data for the major isomer. ^1H NMR (500 MHz, $CDCl_3$, ppm) δ: 1.20 (t, J = 7.1 Hz, 3H), 1.99 (s, 3H), 2.16 (s, 3H), 4.01 (d, J = 5.9 Hz, 1H), 4.15 (q, J = 7.0 Hz, 2H), 5.76 (dd, J = 6.2 and 8.9 Hz, 1H), 6.99 (d, J = 8.8 Hz, 1H), 7.24–7.33 (m, 5H).

_N_-((1_S_,2_R_)-2-Methyl-3-oxo-1,3-diphenylpropyl)acetamide

Table 3, entry 6 (mixture of diastereomers), data for the major isomer. ^1H NMR (500 MHz, $CDCl_3$, ppm) δ: 1.32 (d, J = 7.2 Hz, 3H), 2.04 (s, 3H), 4.03–4.13 (m, 1H), 5.35 (dd, J = 4.5 and 8.9 Hz, 1H), 6.99–7.27 (m, 9H), 7.79 (d, J = 7.4 Hz, 2H).

Acknowledgments

We are thankful to the Sistan and Baluchestan University Research Council for partial support of this work.

References

1. (*a*) C. Hulme and V. Gore. Curr. Med. Chem. **10**, 51 (2003); (*b*) C. Hulme and T. Nixey. Curr. Opin. Drug Discovery Today, **6**, 921 (2003).
2. Y. Nishiyama, C. Katahira, and N. Sonoda. Tetrahedron Lett. **45**, 8539 (2004).
3. D.E. Portlock, D. Naskar, L. West, R. Ostaszewski, and J.J. Chen. Tetrahedron Lett. **44**, 5121 (2003).
4. A. Fayol and J. Zhu. Org. Lett. **7**, 239 (2005).
5. I. Ugi, A. Dömling, and B. Werner. J. Heterocycl. Chem. **37**, 647 (2000).
6. A. Basso, L. Banfi, R. Riva, and G. Guanti. Tetrahedron Lett. **45**, 587 (2004).
7. A. Basso, L. Banfi, R. Riva, and G. Guanti. J. Org. Chem. **70**, 575 (2005).
8. (*a*) T. Nishio and M. Ori. Helv. Chim. Acta, **84**, 2347 (2001); (*b*) M. Ori and T. Nishio. Heterocycles, **52**, 111 (2000).
9. (*a*) J. Barluenga, A.L. Viado, E. Aguilar, S. Fustero, and B. Olano. J. Org. Chem. **58**, 5972 (1993); (*b*) A.G. Godfrey, D.A. Brooks, L.A. Hay, M. Peters, J.R. McCarthy, and D. Mitchell. J. Org. Chem. **68**, 2623 (2003); (*c*) J.R. Casimir, C. Turetta, L. Ettouati, and J. Paris. Tetrahedron Lett. **36**, 4797 (1995); (*d*) K. Kobinata, M. Uramoto, M. Nishii, H. Kusakabi, J. Nakamura, and K. Isono. Agric. Biol. Chem. **44**, 1709 (1980).
10. M. Mukhopadhyay, B. Bhatia, and J. Iqbal. Tetrahedron Lett. **38**, 1083 (1997).
11. B. Bhatia, M.M. Reddy, and J. Iqbal. J. Chem. Soc. Chem. Commun. 713 (1994).
12. D. Bahulayan, S.K. Das, and J. Iqbal. J. Org. Chem. **68**, 5735 (2003).
13. M.M. Khodaei, A.R. Khosropour, and P. Fattahpour. Tetrahedron Lett. **46**, 2105 (2005).
14. R. Ghosh, S. Maity, and A. Chakraborty. Synlett. 115 (2005).
15. R. Ghosh, S. Maiti, A. Chakraborty, S. Chakraborty, and A.K. Mukherjee. Tetrahedron, **62**, 4059 (2006).
16. E. Rafiee, F. Tork, and M. Joshaghani. Bioorg. Med. Chem. Lett. **16**, 1221 (2006).
17. T. Yakaiah, V.G. Reddy, B.P.V. Lingaiah, B. Narsaiah, and P. Shanthan Rao. Synth. Commun. **35**, 1307 (2005).
18. G. Pandey, R.P. Singh, A. Garg, and V.K. Singh. Tetrahedron Lett. **46**, 2137 (2005).
19. E. Rafiee, F. Shahbazi, M. Joshaghani, and F. Tork. J. Mol. Catal. A: Chem. **242**, 129 (2005).
20. L. Nagarapu, S. Kantevari, V.N. Cheemalapati, S. Apuri, and V. Kumari. J. Mol. Catal. A: Chem. **264**, 22 (2007).
21. A.T. Khan, L.H. Choudhury, T. Parvin, and M. Asif Ali. Tetrahedron Lett. **47**, 8137 (2006).
22. M.T. Maghsoodlou, A. Hassankhani, H.R. Shaterian, S.M. Habibi-Khorasania, and E. Mosaddegh. Tetrahedron Lett. **48**, 1729 (2007).
23. B. Das, K.R. Reddy, R. Ramu, P. Thirupathi, and B. Ravikanth. Synlett. 1756 (2006).
24. B. Das, M. Krishnaiah, K. Laxminarayana, and K.R. Reddy. J. Mol. Catal. A: Chem. **270**, 284 (2007).
25. A.T. Khan, T. Parvin, and L.H. Choudhury. Tetrahedron, **63**, 5593 (2007).
26. B. Das, K.R. Reddy, Y. Srinivas, and R.A. Kumar. Can. J. Chem. **85**, 479 (2007).
27. F. Shirini, M.A. Zolfigol, and B. Mallakpour. Russ. J. Org. Chem. **41**, 625 (2005).
28. F. Shirini, M.A. Zolfigol, B. Mallakpour, S.E. Mallakpour, A.R. Hajipour, and I.M. Baltork. Tetrahedron Lett. **43**, 1555 (2002).
29. F. Shirini, M.A. Zolfigol, B. Mallakpour, I.M. Baltork, and A.R. Hajipour. J. Chem. Res. 28 (2003).

© 2008 NRC Canada

Frontier orbital interactions in the hetero Diels–Alder cycloaddition of diazadienes

Pratibha Sharma, Ashok Kumar, Vinita Sahu, and Jitendra Singh

Abstract: This work deals with the molecular orbital calculation studies performed on different diazadienes to assess their reactivity pattern. The interaction of these diazadienes with various electron-poor and electron-rich dienophiles leads to the formation of diazines and tetrazines as the cycloadducts. The results from frontier orbital interactions were used to rationalize the reactivity and predictability of NDAC and IEDDAC reaction pathways. Correlation studies were also performed to predict reactivity sequence using a number of electronic descriptors, such as electrophilicity index (ω), chemical potential (μ), electronic charge ΔN_{max}, and chemical hardness η. Moreover, these studies exhibit good compatibility with experimental observations.

Key words: AM1, MNDO, PM3, diazadienes, tetrazines, electrophilicity index, chemical potential.

Résumé : Dans ce travail, on rapporte les résultats obtenus lors de calculs d'orbitales moléculaires effectués sur divers diazadiènes dans le but d'évaluer leur mode de réactivité. L'interaction de ces diazadiènes avec divers diénophiles riches et pauvres en électrons conduit, suivant le cas, à la formation de diazines et de tétrazines comme cycloadduits. On a utilisé les résultats d'interactions d'orbitales frontières pour rationaliser la réactivité et pour vérifier si les voies réactionnelles de cycloaddition de Diels–Alder normale et de cycloaddition de Diels–Alder à demande inversée d'électrons peuvent être utilisées pour les prédire. Utilisant un certain nombre de descripteurs électroniques, tel l'indice du caractère électrophile (ω), le potentiel chimique (μ), la charge électronique (ΔN_{max}) et la dureté chimique (η), on a aussi effectué des études de corrélation pour prédire la séquence de réactivité. De plus, ces études présentent une bonne compatibilité avec les observations expérimentales.

Mots-clés : modèle Austin-1 ("AM1"), négligence modifiée du recouvrement différentiel ("MNDO"), modèle paramétrisé numéro 3 ("PM3"), diazadiènes, tétrazines, indice du caractère électrophile, potentiel chimique.

[Traduit par la Rédaction]

Introduction

The Diels–Alder (1) (DA) reaction is one of the most prominent synthetic strategies in organic chemistry to craft annular compounds from small fragments. The DA reactions of 2-azadienes (2) is a very useful method for providing rapid access to a range of highly substituted biologically active heterocyclic system like pyridines, dihydropyridines, and tetrazine (3). The development of synthetic methodologies based on aza-DA reactions to obtain six-membered tetrazines has attracted much interest because of their utility in the field of medicinal chemistry as antitumor drugs and in energetic chemistry as powerful explosives. Hence, the DA reaction is found to be most a promising method for tetrazine synthesis. With the advancement of computational chemistry to predict the fate of a reaction, herein we have tried to incorporate the quantum mechanical results to interpret DA cycloaddition. In this context, the Fukui's FMO method (4) is found to be the most suitable synthetic tool to predict selectivity and reactivity of compounds. A systematic perusal of the literature (5) reveals that the prediction and reactivity of DA reaction are normally based on the strength of HOMO–LUMO interactions between diene and dienophlie. In view of these precedents and as part of our research program devoted to the study of heterocycles (6), we have made an effort to interpret experimental outcomes through normal Diels–Alder cycloaddition (NDAC) and inverse electron-demand Diels–Alder cycloaddition (IEDDAC) pathways. Moreover, we have also incorporated electronic descriptors, such as the electrophilicity index ω, the chemical potential μ, and ΔN_{max}, to interpret cycloaddition reactivity.

A number of diazadienes bearing one or more electron-withdrawing and electron-donating groups have been chosen to initialize these studies using semi-empirical probes (7). These dienes undergo DA reactions with a variety of dienophiles to achieve tetrazines as the final product in appreciable yield under optimum reaction conditions. A judicious selection of the best method to predict the FMO energies of dienes and various dienophiles has been done. A comparative evaluation of different Hamiltonians for various dienes is shown in Table 1, and the AM1 method was found to show good correlation with Fukui's approximations. Hence, we have chosen the AM1 method for further discussion. Moreover, it is to be emphasized here that the MO semi-empirical method allows the study of more complex diazadienes in a very much more facile manner in compari-

Received 29 November 2007. Accepted 19 February 2008. Published on the NRC Research Press Web site at canjchem.nrc.ca on 27 March 2008.

P. Sharma,[1] A. Kumar, V. Sahu, and J. Singh. School of Chemical Sciences, Devi Ahilya University, Takshashila Campus, Indore, MP 452 001, India.

[1]Corresponding author (e-mail: drpratibhasharma@yahoo.com).

 doi:10.1139/V08-035 © 2008 NRC Canada

Table 1. Frontier orbital energies of diazadiene.

	AM1		MNDO		PM3	
Dienes	HOMO	LUMO	HOMO	LUMO	HOMO	LUMO
1	–9.356	0.465	–9.502	0.282	–9.180	0.388
2	–9.903	0.135	–9.982	–0.011	–9.677	0.106
3	–9.998	0.822	–9.691	0.120	–10.157	0.147
4	–9.314	–0.245	–9.310	–0.231	–9.166	–0.552
5	–8.319	–0.036	–9.358	–0.036	–8.544	–0.041
6	–9.794	–1.353	–9.668	–0.915	–9.800	–1.326
7	–8.407	–0.126	–8.812	–0.123	–8.486	–0.501
8	–8.875	–0.237	–8.899	–0.273	–8.864	–0.529
9	–9.456	–0.856	–9.526	–0.327	–9.397	–0.986
10	–9.352	–0.091	–9.440	–0.091	–9.853	–0.574

Fig. 1. Frontier orbital energies for 1,3-butadiene **1**, 2-aza-diene **2**, and diazadiene **3** and **4** (AM1 calculation).

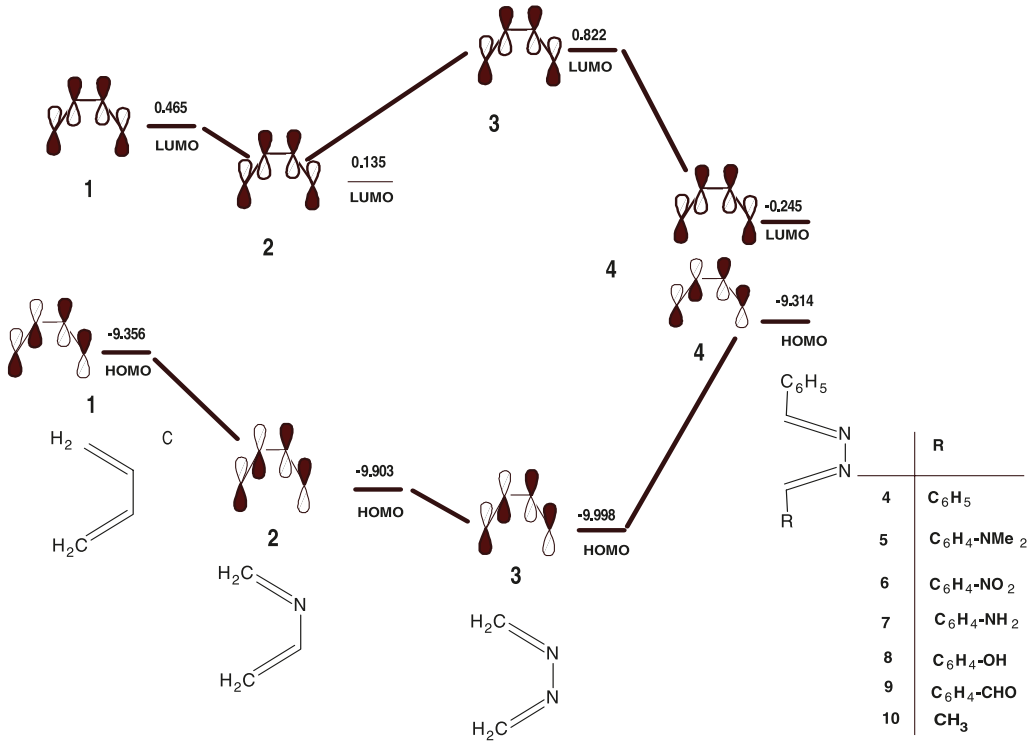

son to ab initio methods. To make a comparative study, we have used some reference dienes and have revealed that 1,3-butadiene (**1**), being an electron-rich diene is prone to undergo NDAC reaction with electron-deficient dienophlie. However, the similar prediction is not easy for heterodienes, because upon substituting one CH moiety of 1,3-butadiene with N, the energy of **2** HOMO–LUMO decreases, while substitution with another N does not show a major decrease in HOMO energy of diene **3** (Figs. 1 and 2).

Furthermore, upon comparing the relative reactivity of diazadienes **4**–**10**, it has been inferred that diazadiene **5**, bearing an electron-donating substituent (i.e., $–NMe_2$) at the phenyl ring, was expected to be more electron-rich compared with **4**, and therefore it is more likely to react with electron-deficient dienophile through the NDAC pathway. On the other hand, **6** takes part in the IEDDAC reaction only with electron-rich dienophile. Similarly, diazadienes **7** and **8**, bearing electron-donating substituents, also show the precedence of the NDAC pathway over IEDDAC with electron-deficient dienophile.

The CH→N substitution in the dienes enhances their reactivity towards electron-rich dienophiles in IEDDAC reactions. However, further decreases in electrophilicity by electron-withdrawing substituent, as in **9** and **6**, makes them more favored species for IEDDAC reactions.

Also, in an attempt to synthesize tetrazines, reference diene **4** was allowed to react with a number of dienophiles **11**–**20** (Figs. 3 and 4) and the experimental results were correlated with theoretical outcomes. The AM1 optimized geometry of cycloadduct **25** is depicted in Fig. 5.

© 2008 NRC Canada

Fig. 2. HOMO and LUMO pictures of dienes **1–3**.

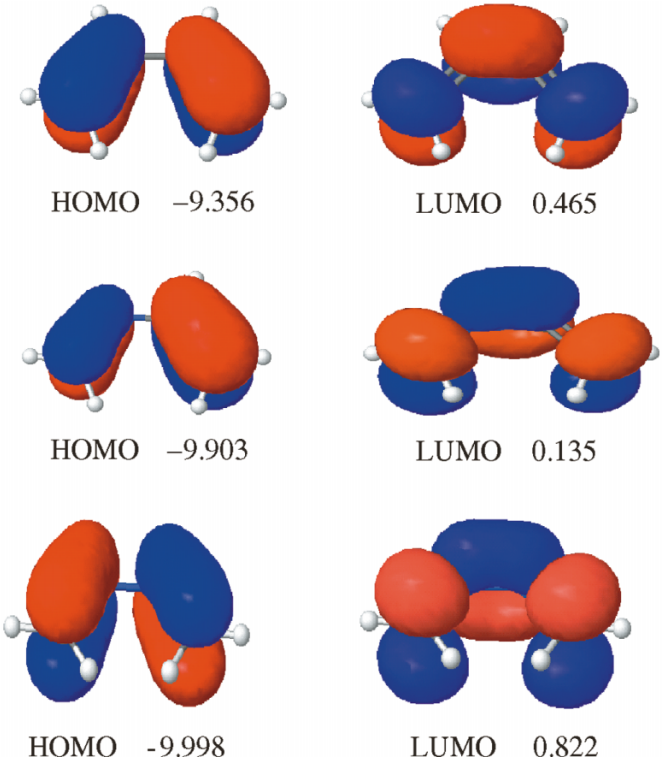

Reactivity of diazadienes 4–10

Table 1 shows the frontier orbital energies of diazadienes **4–10** calculated at the AM1 level. The AM1 calculations described above were performed considering the *S-cis* conformations of dienes.

It is deduced from the aforementioned discussion that HOMO–LUMO energies lowers upon CH→N substitution, making them more reactive species towards electron-rich dienophiles. Substitution of an electron-donating group (–NMe_2) at the phenyl ring raises the HOMO energy by 0.995 eV and lowers the LUMO energy, thereby explaining their preferred participation in NDAC reactions. The calculated HOMO energies of **4**, **6, 9**, and **10** are lower than those of **5**, **7**, and **8**. This explains the lack of reactivity of these diazadienes towards electron-deficient dienophiles (NDAC). On the other hand, the predicted LUMO energies of **4**, **6–10** are lower than that of **5**, pointing to an increased reactivity toward electron-rich dienophiles (IEDDAC). Diazadienes **6**, bearing a nitrophenyl group, has the lowest energy followed by **9**, **10**, and **4**. This indicates that the addition of one nitro group at the 4-position of phenyl ring of diazadienes has a more substantial effect than the introduction of N at the same position.

It can be concluded that on the basis of HOMO energy from AM1 calculations, the reactivity of different diazadienes to participate in inverse electron-demand DA reactions would be in the following order: **6** > **9** > **10** > **4** > **8** > **7** > **5**.

NDAC and IEDDAC

In a view to unravelling the understanding of the mechanistic details of DA cycloaddition, we have taken the Fukui's assumption into consideration and tried to associate the experimental results with computational semi-empirical outcomes. Hence to gain deeper insight into the DA cycloaddition strategy, we proceeded with the treatment of diazadiene **4** with different dienophiles **11–20** and the pertinent results are presented in Tables 2 and 3.

Here we offer an interesting and novel interpretation of eigenfunctions to predict the outcomes of DA reactions. In this context, diazadiene **4**, which is an electron-rich diene, shows similar reactivity with maleic anhydride **16**, bis-4-nitrophenyl diazene **19**, and 4-[4-nitrophenyl]-diazenyl phenol **20**, which are electron-deficient dienophiles. The reaction time required for **4** and dienophiles **16**, **19**, and **20** was found to be approximately similar, favoring NDAC pathway. Moving toward more electron-rich dienophiles, other than **16**, **19**, and **20**, the reaction time increases and sometimes no reaction occurs. 1,2-Ethoxyethene **11** and allyl chloride **18** should take the longest time for reaction with **4**. In actuality, the reactions of **4** with allyl halide **18** requires 13 h, which may be due to the high HOMO–LUMO energy gap for this NDAC reaction, which includes a significant molecular orbital energy gap. A close inspection of eigenfunctions suggests that the dienophile 1,2-ethoxyethene **11**, *N*,*N*-dimethy-4-phenyldiazenyl aniline **12**, and 4-phenyldiazenyl aniline **13**, are likely to undergo IEDDAC reaction, and the experimental results show that dienophiles **11** and **12**, being highly electron-rich dienophiles, remain unreactive with diene **4** after a long time. According to the energy level gap between participating molecular orbitals for dienophiles **12** and 1**3**, both are prone to undergo the IEDDAC pathway, but experimentally no reaction occurs with diazadiene **4** under similar reaction conditions. With dienophile 4-phenyldiazenyl phenol **14**, 1-(dinitrophenyl)-2-phenyldiazene **15**, and diethyl fumarate **17**, reactions proceed according to our expectations, and the experimental results are in agreement with computational outcomes with nearly similar reactivity. It has been experimentally found that the normal DA cycloaddition of diazadiene **4** with allyl chloride **18** provides better yield of the adduct, although the HOMO–LUMO energy gap is larger for these reactions, in contrast with other cycloadditions.

Discussion

A perusal of the calculated energies (Table 2) of the frontier orbitals for the diazadiene **4** and the dienophile points out the significance of the HOMO–LUMO energy gap (Fig. 6). Here Lde-Hdo represents the calculated energy gap (eV) between each dienophile with respect to the LUMO of diene **4**. Ldo-Hde represents the calculated energy gap (eV) between the dienophile's LUMO with respect to the HOMO of diene **4**. The Ldo-Hde energy gap is least (7.695 eV) for diazadiene **4** and maleic anhydride **16**. As **16** is an electron-deficient dienophile, this energy gap favors the NDAC reaction, while the highest energy gap for 1,2-ethoxyethene **11** makes this reaction IEDDAC. Furthermore, it is interesting to note that the energy gap (Lde-Hdo) between diazadiene **4** and *N*,*N*-dimethy-4-phenyldiazenyl aniline **12**, and 4-phenyldiazenyl aniline **13** and 4-phenyldiazenyl phenol **14** dienophiles, are nearly similar, but their reactivities differ markedly, which further emphasizes that the Lde-Hdo en-

© 2008 NRC Canada

Fig. 3. Orbital energies (eV) and geometries of dienophile **11**–**20**.

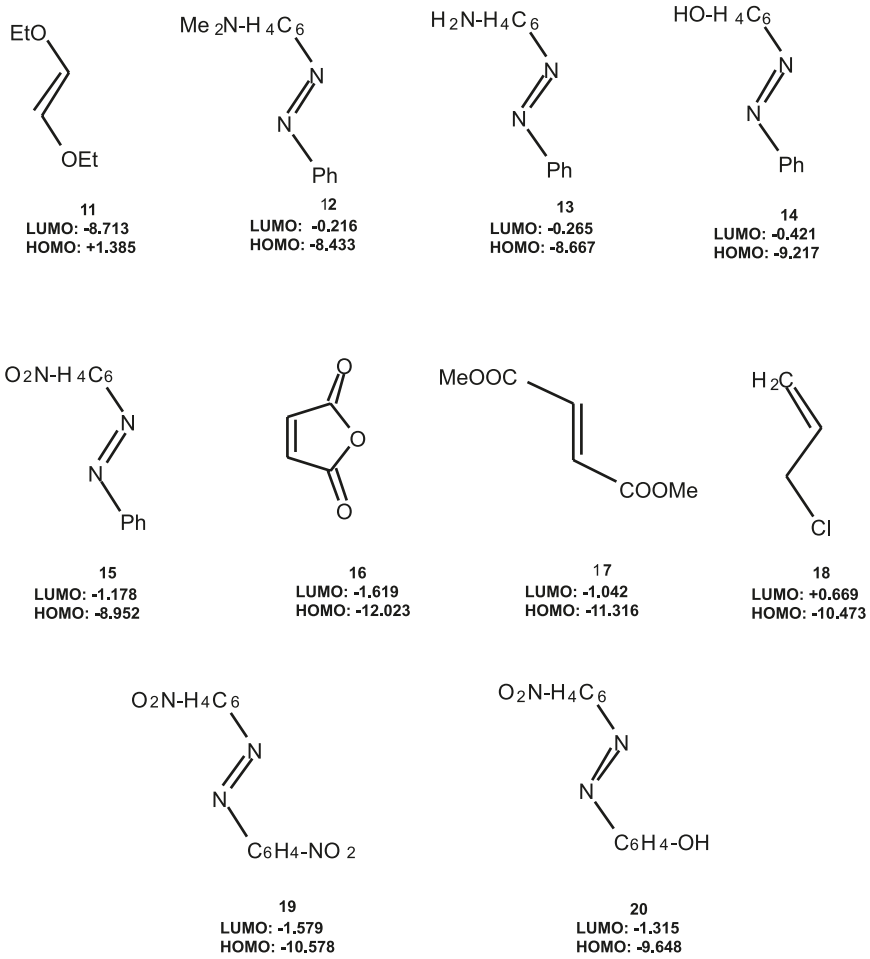

ergy gap is not a reliable tool to predict the reactivity of dienes and dienophiles toward IEDDAC reactions. However, the Ldo-Hde energy gap reasonably predicts the reactivity of dienes and dienophiles. Hence, the NDAC is a more favored pathway for DA reactions than is IEDDAC.

Global electrophilicity index

For a long time Domingo's group has been interested in the study of the molecular mechanism of the polar DA reactions (8–9). Recently, the use of the global electrophilicity index ω proposed by Parr et al. (10), has been reported to classify the global electrophilicity of a series of dienes and dienophiles currently present in DA reactions (11). We found a good correlation between the difference in electrophilicity for the diene and dienophile pair, Δω, and the feasibility of the cycloaddition. Therefore, Δω for a diene–dienophile pair is a valuable tool to predict the polar character of a DA reaction. The global electrophilicity index ω, which measures the stabilization in energy when the system acquires an additional electronic charge N_{max} from the environment, has been given the following simple expression,

$$\omega = \mu^2/2\ \eta$$

where $\mu \approx (I + A)/2$ and $\eta = (A - I)$ are the electronic chemical potential and chemical hardness of the ground state of atoms and molecules, respectively, approximated in terms of the vertical ionization potential (I) and electron affinity (A) using Koopman's theorem. Here, in our calculations $I = E_{HOMO}$ and $A = E_{LUMO}$ were used.

The electrophilicity index encompasses both the propensity of the electrophile to acquire an additional electronic charge driven by μ^2 (the square of the electronegativity) and the resistance of the system to exchange electronic charge with the environment described by η simultaneously. The maximum electronic charge N_{max} is another useful quantity; it is the maximal electronic charge which electron accept from environment, giving a better understanding of Fukui's model.

Table 4 presents an overview of electronic parameters such as electronic chemical potential μ, chemical hardness η, and global electrophilicity index ω. The electronic chemical potential for dienophile **11**–**20** lies in the range –6.821 to –3.664, whereas for diene **4** this value is an intermediate one, –4.779. Dienophiles**11**, **12**, and **13** have higher chemical potentials than **4**, which further suggests that a net charge transfer will take place from electron-rich dienophiles to electron-poor diene **4** in an IEDDAC reaction pathway. In addition, a good correlation can be observed between the substitution pattern on dienophile and the chemical potential μ for the remaining dienophiles **14**–**20**, where charge transfer take place from an electron-rich diene to an electron-deficient dienophile through the NDAC pathway.

© 2008 NRC Canada

Fig. 4. Various cycloadducts **21**–**30**.

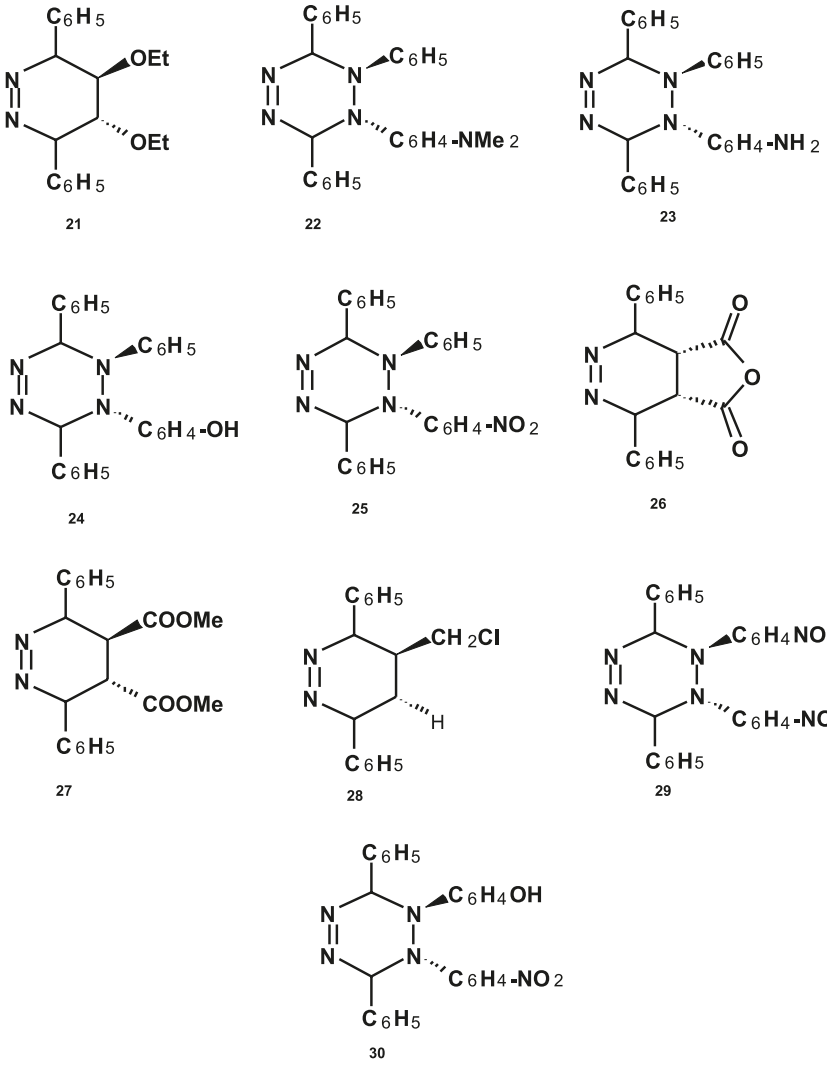

Fig. 5. Optimized geometry of tetrazine cycloadduct **25**.

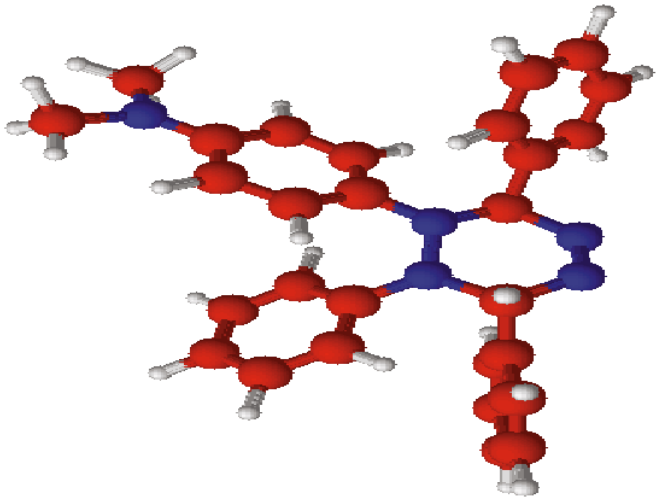

The μ value is found to be lowest for **16** amongst dienohiles **11**–**20**, indicating ease of reaction with the least Ldo-Hde energy gap (7.695) in DA cycloaddition. Experimentally this reaction took the least reaction time to completion (~2 h) in the presence of xylene.

The highest μ value of –3.664 for **11** opens up the possibility of an inverse electron-demand DA reaction in which charge transfer direction is from an electron-rich dienophile to an electron-deficient diene, making this reaction experimentally not feasible under similar reaction conditions. The electrophilicity index ω values for the diene and dienophile falls within the range 18.08–60.84 eV; the highest ω value obtain for **16** illustrates the highly electrophilic nature of this dienophile and is supported by experimental observations. Moreover, the difference in electrophilicity between the diazadiene **4** and dienophiles (Δω) gives a measure of the reactivity of diene and dienophiles in a cycloaddition reaction, where the smallest value of Δω for dienophile **16** suggests the nonpolar synchronous nature of transition states in normal DA cycloaddition.

On the other hand, the highest Δω difference value for the **4a+1** reaction provides an asynchronous polar transition state and IEDDAC pathway, which is experimentally not observable and no reaction occurs at all.

© 2008 NRC Canada

Table 2. Calculated HOMO and LUMO energies of diazadiene **4** and dienophiles **11**–**20**.

S. No.	Diene–dienophile	HOMO	LUMO	Ldo-Hde	Lde-Hdo
1	4	–9.314	–0.245	9.069	9.069
2	11	–8.713	1.385	10.699	8.468
3	12	–8.433	–0.216	9.098	8.188
4	13	–8.667	–0.265	9.049	8.422
5	14	–9.215	–0.421	8.893	8.970
6	15	–8.952	–1.178	8.136	8.707
7	16	–12.023	–1.619	7.695	11.778
8	17	–11.316	–1.042	8.272	11.071
9	18	–10.473	0.669	9.983	10.228
10	19	–10.578	–1.579	7.735	10.333
11	20	–9.648	–1.315	7.999	9.403

Table 3. Experimental results of the **[4+2]** cycloaddition of diene **4** with dienophiles **11**–**20**.

Entry	Dienophile	Adduct	Time to completion (h)	Yield (%)
1	11	21	—	—
2	12	22	—	—
3	13	23	—	—
4	14	24	20	65
5	15	25	8	70
6	16	26	2	85
7	17	27	6.5	75
8	18	28	13	70
9	19	29	4	79
10	20	30	6	78

Fig. 6. Molecular orbital energy gap between diene **4** and dienophile **11** and **16**.

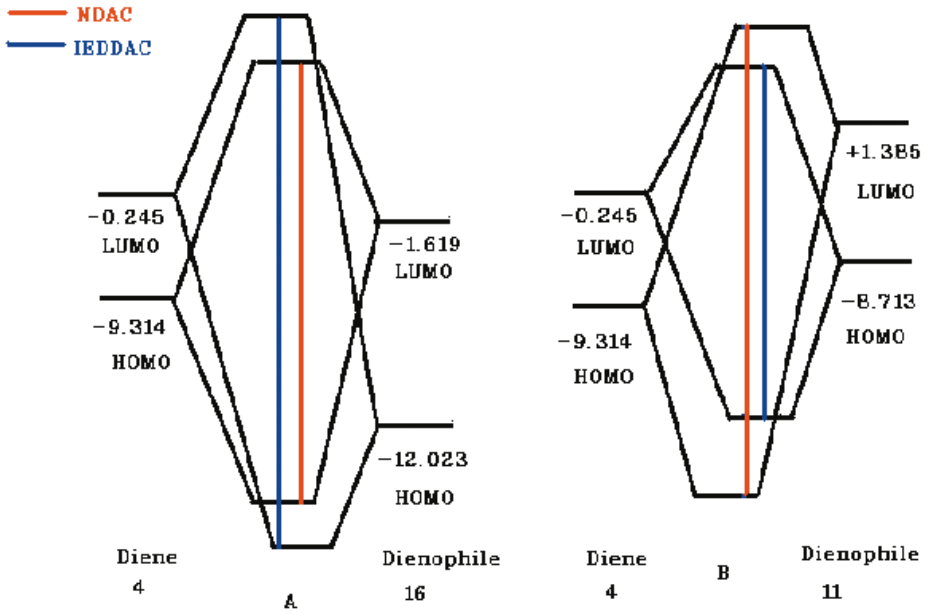

Multiple analysis regression (MAR) data between the electrophilicity index ω and electron affinity EA for 11 compounds (Table 4) shows that the statistical parameters (standard deviation) SD ≈ 0.31 and (correlation co-efficient) $R \approx 0.95$ significantly support excellent correlation (Fig. 7) between the electrophilicity index ω and electron affinity EA.

The stereo- and regio-selectivity of DA cycloadditions are easily rationalized by examining the orbital coefficient values on the molecular orbitals. The preferred regioisomeric transition states in DA cycloadditions depends upon the terminal coefficient of the interacting orbitals. Table 5 shows the orbital coefficient at different carbon atoms of dienes **1**–

© 2008 NRC Canada

Table 4. Global electronic descriptors values of diene and dienophiles.

Entry	Diene/dienophile	HOMO	LUMO	μ (a.u.)	η (a.u.)	ω (eV)	N_{max}	ω (eV)
1	4	–9.314	–0.245	–4.779	9.069	34.26	0.527	0.00
2	11	–8.713	+1.385	–3.664	10.098	18.08	0.363	+16.180
3	12	–8.433	–0.216	–4.324	8.217	30.95	0.526	+3.310
4	13	–8.667	–0.265	–4.466	8.402	32.30	0.532	+1.960
5	14	–9.215	–0.421	–4.818	8.794	35.91	0.548	–1.650
6	15	–8.952	–1.178	–5.065	7.774	44.90	0.652	–10.640
7	16	–12.023	–1.619	–6.821	10.404	60.84	0.656	–26.580
8	17	–11.316	–1.042	–6.179	10.274	50.56	0.601	–16.300
9	18	–10.473	+0.669	–4.902	11.142	29.34	0.440	+4.920
10	19	–10.578	–1.579	–6.078	8.999	55.86	0.675	–21.600
11	20	–9.648	–1.315	–5.482	8.333	49.05	0.660	–14.790

Fig. 7. Correlation graph vs. electrophilicity index ω and electron affinity EA.

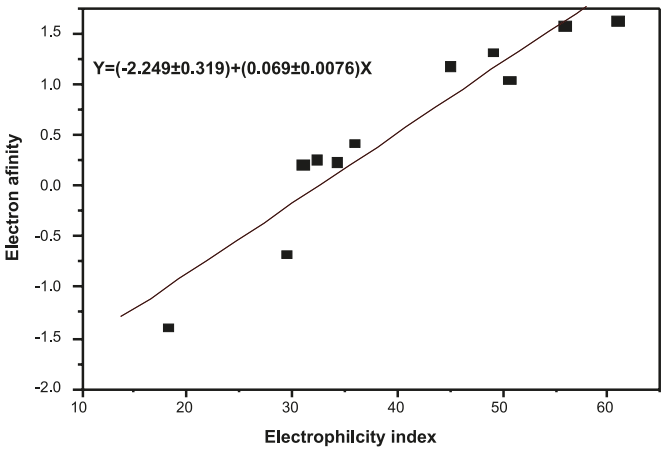

4 and **10**. The results demonstrate that in 1,3-butadiene **1**, the terminal coefficient at C-1 and C-4 of HOMO wave functions are of equal magnitude, but upon CH→N substitution the coefficient magnitude suddenly decreases and so 1-azadienes becomes regiospecific for the unsymmetrical substituted dienophile. Introduction of N in 1,3-butadiene enhances the electrophilicity of the diene, making it a preferred species for IEDDAC reaction. In azadienes, the C-1 position is more polarized than the C-4 position. A similar decrease in orbital coefficient is found upon introducing another N in the diene moiety. A close examination of the orbital coefficients on azadienes **2** and **3** reveals that the magnitude of the orbital coefficients is larger on the C-3/N-3 position than on the C-2/N-2 position, which could play an immense role in the preferred formation of regioisomers through secondary orbital interactions.

An exhaustive exploration of orbital coefficients on different dienophiles (Table 6) provides regioselective understanding toward the DA cycloadduct. The orbital coefficients of the symmetrical molecule (dienophile) are identical in magnitude at terminal atomic centers. These studies show that **D-1** (here **D-1** is taken as reference dienophile to interpret the comparative results of dienophiles **11**–**20** in terms of orbital coefficients, C_6H_5-N=N-C_6H_5) has a similar orbital coefficient at N-1 and N-2 in LUMO, while these values are considerably lower due to the electron-withdrawing phenyl substituent, which makes this species more electron-withdrawing and favorable for NDAC reactions. 1-(Dinitrophenyl)-2-phenyldiazene **15** and 4-[4-nitrophenyl]-diazenyl phenol **20**, having at least one electron-withdrawing moiety attached to the phenyl ring, show the low orbital coefficient at N-2, which is in accordance with literature data. Similarly, 4-phenyldiazenyl aniline **13** and 4-phenyldiazenyl phenol **14**, having electron-releasing substiutents at the phenyl ring, possess larger orbital coefficients at N-1 than at N-2, making these species regiospecific towards unsymmetrical dienes. However, similar predictions cannot be made for *N*,*N*-dimethy-4-phenyldiazenyl aniline **12**, which remains unreactive in DA cycloaddition with diazadiene **4**.

Regioselective studies

When an unsymmetrical diene **10** is allowed to react with a certain range of the aforementioned unsymmetrical dienophiles, the regioselectivity of the cycloadduct was also taken into consideration. We have calculated atomic orbital coefficients at interacting orbitals to check their participation in DA cycloaddition. The orbital coefficient values on diazadienes are very much lower than for their carbon congeners. A close inspection of the coefficients of diene **10** and dienophlie **15** suggest the preferred formation of regioselective **R-31b** over **R-31a**. The experimental results were in accordance with these findings. For a better understanding of regioselectivty in hetero DA reactionsm, diene **10** was also treated with dienophile **20** and preferred formation of **R-32a** rather than **R-32b** was in support of Houk's assumption. Both of these reactions follow the NDAC pathway under similar reaction conditions (Fig. 8).

Furthermore, the role of secondary orbital interactions in deciding the regioselectivity of the product was also envisaged in the case of unsymmetrical diene **10**. It has been revealed that when diazadiene **10** was allowed to react with dienophile **15**, **R-31b** was solely obtained as the regioselective cycloadduct because of primary orbital interactions between terminal orbital coefficients of the HOMO diene and the LUMO dienophile. It has been noticed that preferred regioisomers can still be predicted by considering secondary orbital interactions between the N-2 and N-3 positions of diene **10** and the C_6H_4-NO_2 moiety of dienophlie **15**. A close inspection of the orbital coefficients at N-2 and N-3 in diene **10** show that N-2 has higher orbital coefficient than N-3. Thus, the stabilization of an endo transition state is greater when the C_6H_4-NO_2 group of dienophile **15** is near

© 2008 NRC Canada

Table 5. Orbital coefficient values at different diazadienes.

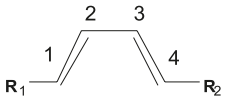

	R_1	R_2
1	H	H
2	H	H
3	H	H
4	Ph	Ph
10	Ph	CH_3

	Orbital coefficient (HOMO)				Orbital coefficient (LUMO)			
Diene	C-1	C-2/N-2	C-3/N-3	C-4	C-1	C-2/N-2	C-3/N-3	C-4
1	0.563	0.427	0.427	0.563	0.566	0.423	0.423	0.566
2	0.328	0.219	0.406	0.550	0.579	0.439	0.368	0.579
3	0.306	0.118	0.391	0.199	0.511	0.4354	0.012	0.021
4	0.230	0.243	0.241	0.044	0.333	0.395	0.030	0.056
10	0.028	0.065	0.038	0.069	0.030	0.081	0.041	0.071

Table 6. Orbital coefficient values at different dienophiles.

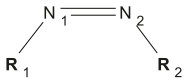

	R_1	R_2
D-1	Ph	Ph
12	Ph	Ph-NMe_2
13	Ph	Ph-NH_2
14	Ph	Ph-OH
15	Ph	Ph-NO_2
20	Ph-OH	Ph-NO_2

	Orbital coefficient (HOMO)		Orbital coefficient (LUMO)	
Dienophile	N-1	N-2	N-1	N-2
D-1	0.119	0.102	0.388	0.370
12	0.164	0.056	0.372	0.293
13	0.189	0.068	0.403	0.332
14	0.146	0.115	0.403	0.327
15	0.125	0.114	0.071	0.024
20	0.059	0.317	0.366	0.278

the secondary position of the diene, yielding the **R-31b** isomer as the favourable product.

Upon similar analysis, the regioselective formation of **R-32a** can be explained by considering the secondary orbital interactions between orbital coefficients at N-2 of diene **10** and the C_6H_4-NO_2 moiety of dienophile **20**. Thus, secondary orbital interactions exerted a significant effect on the regioselectivity of the Diels Alder reaction between unsymmetrically substituted diene and dienophile.

Conclusion

Concluding, we have performed and interpreted FMO interactions with a critical evaluation of the reaction pathways. Highlights of all the studies can be summarized as follows. (*i*) The relative reactivity of different diazadienes in DA reactions was studied in a selective and predictive way. (*ii*) The Ldo-Hde energy gap was found to a be a favored tool to predict DA cycloaddition. These predictions are in good agreement with experimental findings where diene **4** exhibited high reactivity towards **15**, which is a electron-deficient species in NDAC pathway. (*iii*) Synthesis of different substituted tetrazines were achieved via NDAC and IEDDAC DA pathways. (*iv*) All the results were interpreted in terms of electrophilicity index ω and a good correlation was observed between global electronic parameters and experimental findings. Hence, the FMO interactions are the key players to decide the fate of DA reactions. Similar studies on hetero DA reactions are in progress.

Acknowledgements

We are grateful to the Central Drug Research Institute, Lucknow, India for providing spectroanalytical facilities. One of the authors (VS) is also thankful to the Council of Scientific and Industrial Research (CSIR), India, for providing a junior research fellowship.

Experimental

Computational method

The AMl, MNDO, and PM3 approximations to molecular orbital theory have been employed using the MOPAC 2007 computer program (12). The geometries were fully optimized at minimum gradient level (0.01). The minimum energy conformations were used to compute molecular orbital and charge distributions. To explain the results in terms of global electronic parameters viz., electrophlicity index ω, chemical potential μ, etc., the calculations were done at MOPAC 2007 program.

General

All the chemicals used were of AR grade purity. IR spectra were recorded on PerkinElmer model 377 spectrophotometer in KBr pellets. ^{1}H NMR spectra were recorded on a Bruker DRX300 instrument. The FAB mass spectra were recorded on a JEOLSX102/DA–6000 Mass Spectrometer using argon–xenon (6 kv, 10 mA) as the FAB gas. Analytical thin layer chromatography was performed using E. Merck silica gel G (0.50 mm plates, Merck No. 5700). The melting points were determined on an electric melting point apparatus in open capillaries and are uncorrected.

© 2008 NRC Canada

Fig. 8. Predictions of regioselectivity for diazadiene **10** and dienophiles **15** and **20**.

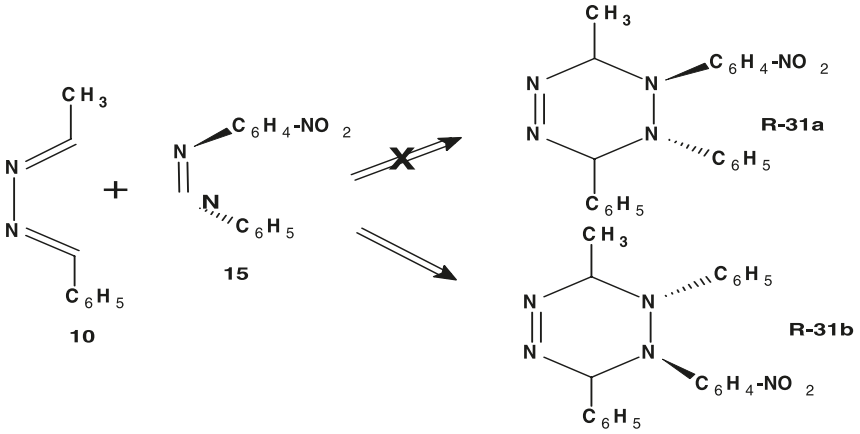

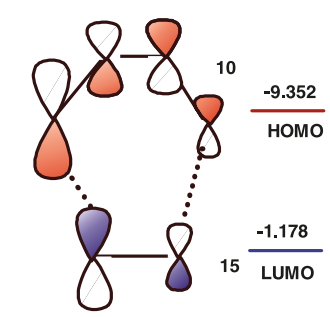

Orbital interactions in diene 10 and dienophile 15 to form R 31b

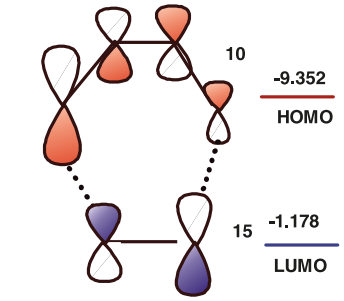

Orbital interactions in diene 10 and dienophile 15 to form R 31a

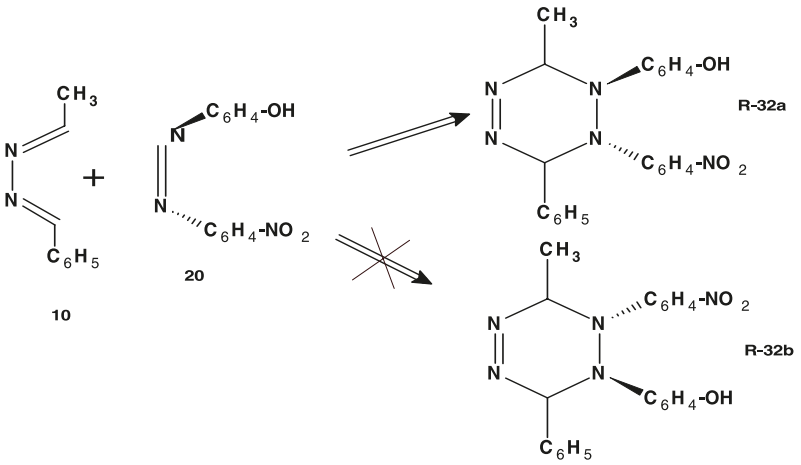

Synthesis of diazadiene 4

The diazadiene **4** was prepared by condensing together dissolving hydrazine hydrate (0.05 mol) into 50% glacial acetic acid (10 mL), and to this solution bezaldehyde (0.10 mol) was added to obtained diazadiene **4** in good yield (80%) as a yellow-green crystalline product. It was washed with cold water and recrystallized from ethanol.

Typical procedure for Diels–Alder reactions

To a solution of diazadiene **4** (0.01 mol) in dry xylene was added dienophile **11**–**20** (0.01 mol) in equimolar quantity. The solution was then refluxed for the required time (Table 3) with constant stirring. At the end of the reaction, solvent were distilled off at reduced pressure from the reaction mixture and the crude cycloadduct was recrystallised and purified by TLC resolution studies on silica gel (E Merck) using ethyl acetate–xylene (4:6, *v*/*v*).

Adduct 24

The reaction was performed according to the general procedure starting with 1.98 gm of **14**. The cycloadduct was isolated in 65% yield, mp 112 °C, decomposed. IR (KBr, cm^{-1}) 3570 (–OH str.), 3033 (=C-H, sp^2), 2986 (C-H, sp^3), 1621 (C=C), 1541 (N=N), 1458, 1371 (C-H, bending, sp^3), 1071 (C-O), 1046 (C-N), 886, 763, 676 (sub. phenyl). ^{1}H NMR (ppm) δ: 3.15 (s, 1H, -CH-Ph), 3.37 (s, 1H, -CH-

© 2008 NRC Canada

Ph), 6.85 (dd, 2H, -C_6H_4-OH, J = 8.5 Hz, J = 2.7 Hz), 7.17 (dd, 2H, –C_6H_4-OH, J = 8.1 Hz, J = 2.8 Hz), 7.21–7.67 (m, 15H, -phenyl), 11.75 (s, 1H, -OH). FAB-MS *m/z*: 407. Anal. calcd. for $C_{26}H_{22}N_4O$: C 76.83, H 5.46, N 13.78; found: C 76.78, H 5.41, N 13.72.

Adduct 25

The reaction was performed according to the general procedure starting with 2.27 gm of **15**. The cycloadduct was isolated in 70% yield, mp 121–122 °C. IR (KBr, cm^{-1}): 3034 (=C-H, sp^2), 2974 (C-H, sp^3), 1623 (C=C), 1544 (N=N), 1535 (–NO_2), 1451, 1361 (C-H, bending, sp^3), 1064 (C-O), 1041 (C-N), 881, 751, 672 (sub. phenyl). ^{1}H NMR (ppm) δ: 3.11 (s, 1H, –CH-Ph), 3.22 (s, 1H, –CH-Ph), 7.45–7.64 (m, 15H, -phenyl), 7.74 (dd, 2H, –C_6H_4-NO_2, J = 8.6 Hz, J = 3.0 Hz), 8.11 (dd, 2H, –C_6H_4-NO_2, J = 9.1 Hz, J = 2.2 Hz). FAB-MS *m/z*: 436. Anal. calcd. for $C_{26}H_{21}N_5O_2$: C 71.71, H 4.86, N 16.08; found: C 71.67, H 4.79, N 16.01.

Adduct 26

The reaction was performed according to the general procedure starting with 0.98 gm of **16**. The cycloadduct was isolated in 85% yield, mp 124–125 °C. IR (KBr, cm^{-1}): 3028 (=C-H, sp^2), 2884 (C-H, sp^3), 1778 (–C=O, anhydride), 1612 (C=C), 1544 (N=N), 1444, 1348 (C-H, bending, sp^3), 1071 (C-O), 1049 (C-N), 761, 688 (sub. phenyl). ^{1}H NMR (ppm) δ: 2.55 (d, 2H, –CH × 2, J = 5.8 Hz), 3.21 (d, 2H, –CH-Ph × 2, J = 6.1 Hz), 6.83–7.81 (m, 10H, –phenyl). FAB-MS *m/z*: 307. Anal. calcd. for $C_{18}H_{14}N_2O_3$: C 70.58, H 4.61, N 9.51; found: C 70.51, H 4.59, N 9.48.

Adduct 27

The reaction was performed according to the general procedure starting with 1.44 gm of **17**. The cycloadduct was isolated in 75% yield, mp 130–132 °C. IR (KBr, cm^{-1}): 3034 (=C-H, sp^2), 2889 (C-H, sp^3), 1771 (–C=O, ester), 1621 (C=C), 1551 (N=N), 1434, 1371 (C-H, bending, sp^3), 1061 (C-O), 1053 (C-N), 775, 669 (sub. phenyl). ^{1}H NMR (ppm) δ: 2.38 (d, 2H, –CH × 2, J = 5.5 Hz), 3.33 (d, 2H, –CH-Ph × 2), 3.80 (s, 6H, –$COOCH_3$), 6.81–7.66 (m, 10H, –phenyl). FAB-MS *m/z*: 353. Anal. calcd. for $C_{20}H_{20}N_2O_4$: C 68.17, H 5.72, N 7.95; found: C 68.14, H 5.67, N 7.89.

Adduct 28

The reaction was performed according to the general procedure starting with 0.76 gm of **18**. The cycloadduct was isolated in 70% yield, mp 78–80 °C. IR (KBr, cm^{-1}): 3032 (=C-H, sp^2), 2891(C-H, sp^3), 1615 (C=C), 1557 (N=N), 1450, 1368 (C-H, bending, sp^3), 550 (C-Cl), 1050 (C-N), 765, 661 (sub. phenyl). ^{1}H NMR (ppm) δ: 2.48 (d, 2H, –CH_2–), 2.61 (d, 1H, –CH-C_6H_5, J = 5.9 Hz), 2.71 (m, 1H, –CH-), 2.78 (d, 1H, –CH-C_6H_5, J = 5.7 Hz), 2.98 (d, 2H, –CH_2-Cl, J = 6.5 Hz), 7.22–7.58 (m, 10H, –phenyl). FAB-MS *m/z*: 285. Anal. calcd for $C_{17}H_{17}ClN_2$: C 71.70, H 6.02, N 9.84; found: C 71.67, H 5.92, N 9.78.

Adduct 29

The reaction was performed according to the general procedure starting with 2.72 gm of **19**. The cycloadduct was isolated in 79% yield, mp 79–80 °C. IR (KBr, cm^{-1}): 3034 (=C-H, sp^2), 2974 (C-H, sp^3), 1623 (C=C), 1544 (N=N), 1535 (–NO_2), 1451, 1361 (C-H, bending, sp^3), 1041 (C-N), 881, 751, 672 (sub. phenyl). ^{1}H NMR (ppm) δ: 3.16 (s, 2H, –CH-Ph × 2), 7.44–7.66 (m, 10H, –phenyl), 7.70 (dd, 4H, –C_6H_4-NO_2, J = 8.5 Hz, J = 2.3 Hz), 8.14 (dd, 4H, –C_6H_4-NO_2, J = 8.8 Hz, J = 2.5 Hz). FAB-MS *m/z*: 481. Anal. calcd. for $C_{26}H_{20}N_6O_4$: C 64.99, H 4.20, N 17.49; found: C 64.91, H 4.18, N 17.45.

Adduct 30

The reaction was performed according to the general procedure starting with 2.43 gm of **20**. The cycloadduct was isolated in 78% yield, mp 128–130 °C. IR (KBr, cm^{-1}): 3556 (–OH str.), 3028 (=C-H, sp^2), 2987 (C-H, sp^3), 1615 (C=C), 1548 (N=N), 1548 (–NO_2), 1467, 1372 (C-H, bending, sp^3), 1061 (C-O), 1044(C-N), 884, 761, 669 (sub. phenyl). ^{1}H NMR (ppm) δ: 3.19 (s, 1H, –CH-Ph), 3.32 (s, 1H, –CH-Ph), 6.78 (dd, 2H, –C_6H_4-OH, J = 7.9 Hz, J = 2.9 Hz), 7.31 (dd, 2H, –C_6H_4-OH, J = 8.1 Hz, J = 3.0 Hz), 7.40–7.63 (m, 10H, –phenyl), 7.75 (dd, 2H, –C_6H_4-NO_2, J = 8.5 Hz, J = 2.8 Hz), 7.91 (dd, 2H, –C_6H_4-NO_2, J = 8.7 Hz, J = 2.9 Hz). FAB-MS *m/z*: 452. Anal. calcd. for $C_{26}H_{21}N_5O_3$: C 69.17, H 4.69, N 15.51; found: C 69.11, H 4.65, N 15.49.

Adduct R-31b

The reaction was performed according to the general procedure starting with 2.27 gm of **15**. The cycloadduct was isolated in 71% yield, mp 110–112 °C. IR (KBr, cm^{-1}): 3033 (=C-H, sp^2), 2981 (C-H, sp^3), 1618 (C=C), 1542 (N=N), 1539 (–NO_2), 1441, 1371 (C-H, bending, sp^3), 1061 (C-O), 1044 (C-N), 880, 749, 671 (sub. phenyl). ^{1}H NMR (ppm) δ: 2.62 (d, 3H, –CH_3), 2.68 (q, 1H, –CH-CH_3), 3.23 (s, 1H, –CH-C_6H_5), 6.91–7.43 (m, 10H, –phenyl), 7.51 (dd, 2H, –C_6H_4-NO_2, J = 8.8 Hz, J = 2.4 Hz), 7.84 (dd, 2H, –C_6H_4-NO_2, J = 8.9 Hz, J = 2.9 Hz). FAB-MS *m/z*: 375. Anal. calcd. for $C_{21}H_{19}N_5O_2$: C 67.55, H 5.13, N 18.76; found: C 67.14, H 5.08, N 18.61.

Adduct R-32a

The reaction was performed according to the general procedure starting with 2.43 gm of **20**. The cycloadduct was isolated as reddish brown solid in 75% yield, mp 135–136 °C. IR (KBr, cm^{-1}): 3549 (–OH str.), 3014 (=C-H, sp^2), 2981 (C-H, sp^3), 1614 (C=C), 1543 (N=N), 1551 (–NO_2), 1457, 1371 (C-H, bending, sp^3), 1059 (C-O), 1041 (C-N), 881, 758, 662 (sub. phenyl). ^{1}H NMR (ppm) δ: 2.30 (d, 3H, –CH_3), 2.53 (s, 1H, –CH-CH_3), 3.32 (q, 1H, –CH-C_6H_5), 6.54 (dd, 2H, –C_6H_4-OH, J = 7.9 Hz, J = 2.9 Hz), 6.79 (dd, 2H, –C_6H_4-OH, J = 8.1 Hz, J = 2.3 Hz), 6.99 (s, 5H, –C_6H_5), 7.75 (dd, 2H, –C_6H_4-NO_2, J = 8.5 Hz, J = 2.8 Hz), 7.92 (dd, 2H, –C_6H_4-NO_2, J = 8.8 Hz, J = 2.7 Hz), 11.16 (s, 1H, –OH) ; FAB-MS *m/z*: 390. Anal. calcd. for $C_{21}H_{19}N_5O_3$: C 64.77, H 4.92, N 17.98; found: C 64.61, H 4.85, N 17.89.

References

1. (*a*) J. Sauer and R. Sustmann. Angew. Chem. Int. Ed. Engl. **19**, 779 (1980); (*b*) K.N. Houk, Y.T. Lin, and F.K. Brown. J. Am. Chem. Soc. **108**, 554 (1986); (*c*) W.T. Borden, R.J. Loncharich, and K.N. Houk. Annu. Rev. Phys. Chem. **39**, 213 (1988).

© 2008 NRC Canada

2. (*a*) D.L. Boger, S.R. Duff, J.S. Panek, and M. Yasuda. J. Org. Chem. **50**, 5790 (1985); (*b*) D.L. Boger, J. Schumacher, M.D. Mullican, M. Patel, and S.Panek, J. Org. Chem. **47**, 2673 (1982); (*c*) H. Neunhoeffer and M. Bachmann. Chem. Ber. **108**, 3877 (1975); (*d*) D.L. Boger, R.S. Coleman, J.S. Panek, and D. Yohannes. J. Org. Chem. **49**, 4405 (1984); (*e*) D.L. Boger, R.S. Coleman, J.S. Panek, F.X. Huber, and J. Sauer. J. Org. Chem. **50**, 5377 (1985); (*f*) D.L. Boger and J.S. Panek. Tetrahedron Lett. **24**, 4511 (1983).
3. (*a*) D.L. Boger, D.R. Soenen, C.W. Boyce, M.P. Hedrick and Q. Jin. J. Org. Chem. **65**, 2479 (2000); (*b*) D.L. Boger and S.E. Wolkenberg. J. Org. Chem. **65**, 9120 (2000); (*c*) D.L. Boger and J. Hong. J. Am. Chem. Soc. **123**, 8515 (2001); (*d*) A. Hamasaki, J.M. Zimpleman, I. Hwang, and D.L. Boger. J. Am. Chem. Soc. **127**, 10767 (2005).
4. (*a*) K. Fukui. Acc. Chem. Res. **4**, 57 (1971); (*b*) R.B. Woodward and R. Hoffmann. J. Am. Chem. Soc. **87**, 4388 (1965); see also the review: R.B. Woodward and R. Hoffmann. The conservation of orbital symmetry. Verlag Chemie, Weinheim, Germany. (1970); (*c*) G. Klopmann. J. Am. Chem. Soc. **90**, 223 (1968); (d) L. Salem, J. Am. Chem. Soc. **90**, 543, 553 (1968).
5. (*a*) G. Ujaque, J.E. Norton, and K.N. Houk. J. Org. Chem. **67**, 7179 (2002); (*b*) L.R. Domingo, M.J. Aurell, M. Arno, and J.A. Saez, J. Org. Chem. **72**, 4220 (2007); (*c*) A. Zhong, C. Rong, and S. Liu. J. Phys. Chem. A, **111**, 3132 (2007); (*d*) D.H. Ess and K.N. Houk. J. Am. Chem. Soc. **129**, 10646 (2007); (*d*) P.R.Campodonico, P. Fuentealba, E.A.Castro, J.G. Santos, and R. Contreras. J. Org. Chem. **70**, 1754 (2005).
6. (*a*) P. Sharma, A. Kumar, and P. Pandey. Phosphorous Sulfur Silicon Relat. Elem. **178**, 583 (2003); (*b*) P. Sharma, A. Kumar, and A. Mandloi. Synth. Commun. **33**, 3 (2003); (*c*) P. Sharma, S. Sharma, and N. Rane. Biorg. Med. Chem. **12**, 3135 (2004); (*d*) P. Sharma, A. Kumar, and M. Sharma. Eur. J. Med. Chem. **41**, 883 (2006); (*e*) P. Sharma, N. Rane, and P. Pandey. Archiv. Pharm. **339**, 572 (2006); (*f*) P. Sharma, A. Kumar, N. Rane, and V. Guarram. Tetrahedron, **61**, 4237 (2005).
7. (*a*) M.J.S. Dewar, S. Olivella, and H.S. Rzepa. J. Am. Chem. Soc. **100**, 56 (1978); (*b*) M. Ortega, A. Oliva, J.M. Lluch, and J.Bertran. Chem. Phys. Lett. **102**, 317 (1983); (*c*) F.K. Brown and K.N. Houk. Tetrahedron Lett. **25**, 4609 (1985).
8. (*a*) L.R. Domingo, R.A. Jones, M.T. Picher, and J. Sepulveda Arques. Tetrahedron, **51**, 8739 (1995); (*b*) L.R. Domingo, M.T. Picher, J. Andres, and V.S. Safont. J. Org. Chem. **62**, 1775 (1997); (*c*) L.R. Domingo, M. Arno, and J. Andres. J. Org. Chem. **64**, 5867 (1999); (*d*) L.R. Domingo. Theor. Chem. Acc. **104**, 240 (2000); (*e*) L.R. Domingo. J. Org. Chem. **66**, 3211 (2001).
9. (*a*) L.R. Domingo, M.T. Picher, J. Andres, V. Moliner, and V.S. Safont. Tetrahedron, **52**, 10693 (1996); (*b*) L.R. Domingo, M.T. Picher, and R.J. Zaragoza. J. Org. Chem. **63**, 9183 (1998); (*c*) L.R. Domingo, M.T. Picher, and M.J. Aurell. J. Phys. Chem. A, **103**, 11425 (1999); (*d*) L.R. Domingo, M. Oliva, and J. Andres. J. Org. Chem.**66**, 6151 (2001); (*e*) L.R. Domingo, J. Andres, and C.N. Alves. Eur. J. Org. Chem. 2557 (2002).
10. R.G. Parr, L. Von Szentpaly, and S. Liu. J. Am. Chem. Soc. **121**, 1922 (1999).
11. L.R. Domingo, M.J. Aurell, P. Perez, and R. Contreras. Tetrahedron, **58**, 4417 (2002).
12. MOPAC2007-DS-DG1, ©2007, Stewart Computational Chemistry.

© 2008 NRC Canada

Efficient syntheses of four chiral phenylcyclopropanes

John E. Baldwin and Stephanie R. Singer

Abstract: An efficient four-step synthetic route from each of four crystalline isotopically labeled (1*R*)-menthyl (1*S*,2*S*)-(+)-2-phenylcyclopropanecarboxyates of better than 99% enantiomeric excess has provided multi-gram quantities of the corresponding chiral phenylcyclopropanes. The key transformation involved a bis[1,3-bis(diphenylphosphino)propane]rhodium chloride that catalyzed a highly stereoselective decarbonylation of a *trans*-2-phenylcyclopropanecarboxaldehyde.

Key words: cyclopropanes chiral thanks to isotopic substituents, catalytic decarbonylations of cyclopropanecarboxaldehydes.

Résumé : Une méthode de synthèse efficace et en quatre étapes pour chacun des quatre (1*S*,2*S*)-(+)-2-phénylcyclopropanecarboxylates de (1*R*)-menthyle isotopiquement marqués avec un excès énantiomérique de plus de 99 % a permis de préparer des quantités supérieures au gramme des phénylcyclopropanes chiraux correspondants. La transformation clé implique une réaction très stéréosélective de décarbonylation d'un *trans*-2-phénylcyclopropanecarboxaldéhyde catalysée par un chlorure de bis[1,3-bis(diphénylphosphino)propane]rhodium.

Mots-clés : cyclopropanes chiraux en raison de substituants isotopiques, décarbonylation de cyclopropanecarboxaldéhydes.

[Traduit par la Rédaction]

Introduction

This article reports the preparation of four chiral isotopically labeled phenylcyclopropanes (**1**-d_i). In the representations of structures **1**-d_i, and elsewhere, the asterisk symbol (*) denotes a carbon-13 atom.

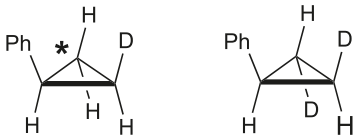

1-d_1 **1**-d_2 **1**-d_3 **1**-d_3'

A long-standing interest in mechanistic questions posed by the thermal chemistry exhibited by relatively simple hydrocarbons, including cyclopropanes (1), led years ago to the preparation and utilization in mechanistic studies of **1**-d_3' and three other isotopically labeled chiral phenylcyclopropanes, (1*S*,2*R*)-**1**-d_1, (1*R*,2*R*)-**1**-d_1 and (1*R*,2*S*,3*R*)-**1**-d_3 (2). The present work extends, and greatly improves upon these earlier synthetic endeavors.

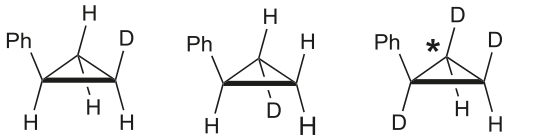

(1*S*,2*R*)-**1**-d_1 (1*R*,2*R*)-**1**-d_1 (1*R*,2*S*,3*R*)-**1**-d_3

To make multi-gram quantities of each of the **1**-d_i compounds (**1**-d_1, **1**-d_2, **1**-d_3, and **1**-d_3') with reasonable efficiency would require thrifty preparations of chiral intermediates of high enantiomeric purity, high stereochemical integrity, and high incorporations of the requisite labels. Once these demands were satisfied, a functional group temporarily used for securing a specific enantiomer of a given diastereomer of high stereochemical purity would need to be replaced by a hydrogen, or possibly a deuterium atom.

The first of these two desiderata has been achieved: each of the four crystalline (1*R*)-menthyl (1*S*,2*S*)-(+)-2-phenylcyclopropanecarboxyates (**2**-d_i) has been prepared efficiently on a 20 g scale (3). No trace of a (1*R*)-menthyl (1*R*,2*R*)-(+)-2-phenylcyclopropanecarboxyate was detected by capillary GC analyses in once recrystallized **2**-d_i compounds.

Received 14 November 2007. Accepted 12 February 2008. Published on the NRC Research Press Web site at canjchem.nrc.ca on 1 April 2008.

In Memoriam, Professor Keith Yates (1928–2006).

J.E. Baldwin[1] and S.R. Singer. Department of Chemistry, Syracuse University, Syracuse, NY 13244, USA.

 doi:10.1139/V08-033 © 2008 NRC Canada

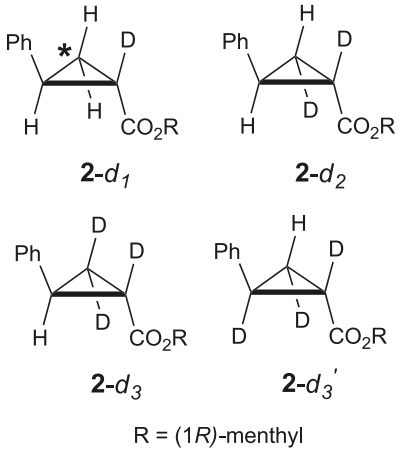

To satisfy the second requirement, a conventional reaction sequence was projected: hydroylysis of a menthyl ester to the corresponding carboxylic acid (4), reduction of the acid to a *trans*-2-phenylcyclopropanemethanol (5), oxidation of the alcohol to an aldehyde with PCC (pyridinium chlorochromate), and finally a Rh-catalyst-promoted decarbonylation. Not surprisingly, the first three steps were easily accomplished, while the decarbonylation proved challenging.

Results and discussion

The reaction sequence used to prepare chiral phenylcyclopropanes (**1**-d_1, **1**-d_2, **1**-d_3, and **1**-d_3') is summarized without full detail in Scheme 1 for unlabeled structures. Earlier preparations of chiral isotopically labeled phenylcyclopropanes, such as **1**-d_3' and stereoisomers (1*S*,2*R*)-**1**-d_1, (1*R*,2*R*)-**1**-d_1, and (1*R*,2*S*,3*R*)-**1**-d_3, depended on this scheme, though two limitations led to far from optimal overall yields (2, 5).

The first limitation was inherent in the presupposition of Scheme 1 that the starting material **2** or at least intermediates **3**, **4**, and **5** would be enantiomerically pure. One enantiomer of acid **3** may be secured through a chiral copper catalyst promoted diastereoselective and enantioselective condensation of racemic menthyl α-deuteriodiazoacetate and styrene or an isotopically labeled styrene, followed by a separation of cis and trans diastereomers, and then fractional crystallization of quinine salts of the trans acids (2, 5). This sequence of steps works, but it is both tedious and inefficient. This first limitation has been overcome by adopting and developing an efficient route to crystalline, enantiomerically pure esters (**2**-d_1, **2**-d_2, **2**-d_3, and **2**-d_3') (3).

The second limitation in earlier work was associated with the decarbonylation step: decarbonylations of *trans*-2-phenylcyclopropanecarboxaldehydes using stoichiometric amounts of chlorotris(triphenylphosphine)rhodium(I) (Wilkinson's catalyst) (6–8) were realized (in 8 reactions) with yields ranging from 42% to 72% (55% ± 12% on average) on scales affording from 124 to 630 mg of a labeled phenylcyclopropane product (330 ± 164 mg on average). Given the investments required to secure 20 g amounts of intermediates **2**-d_1, **2**-d_2, **2**-d_3, and **2**-d_3', and the cost of commercial $RhCl(PPh_3)_3$, a catalytic and more efficacious decarbonylation reaction option seemed essential.

Scheme 1. Reaction sequence to convert (1*R*)-menthyl (1*S*,2*S*)-(+)-2-phenylcyclopropanecarboxyate to phenylcyclopropane (R = (1*R*)-menthyl).

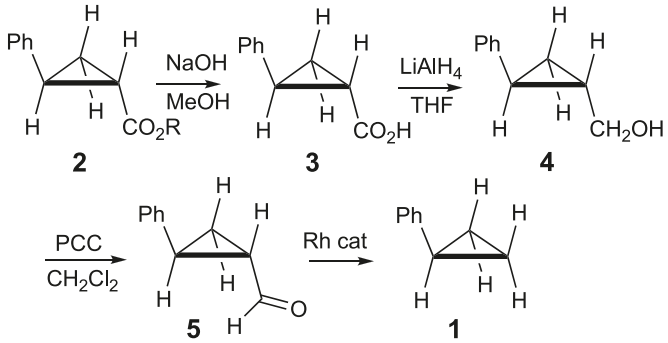

The first three steps outlined in Scheme 1, starting with enantiomerically pure **2**-d_i esters, were implemented without difficulty and in high yields. The two-step hydrolysis-then-reduction sequence converting a **2**-d_i ester to the corresponding colorless distilled **4**-d_i alcohol was completed with an average overall yield of 92% ± 3%.

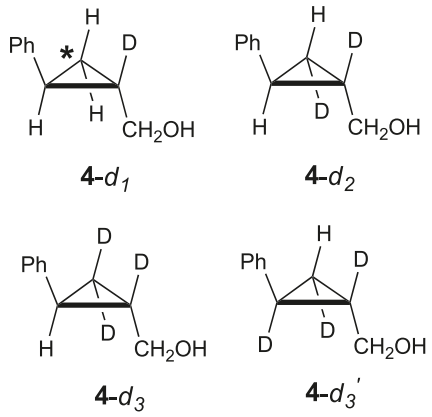

The oxidation of a **4**-d_i alcohol with PCC in CH_2Cl_2 afforded the related aldehyde, essentially quantitatively; it was typically stored briefly under argon and decarbonylated as promptly as possible. The all-important decarbonylation step was not so easily dispatched.

Decarbonylations of aldehydes using $RhCl(Ph_3P)_3$ in stoichiometric proportions are generally successful for aryl, alkenyl, and primary alkyl aldehydes at modest temperatures (8). They involve a reversible dissociation of the reagent to $RhCl(PPh_3)_2$ and PPh_3 as a key step, and usually take place with excellent stereochemical selectivity, with the retention of configuration (9). Other reactions may sometimes intervene, but are not of significant concern in the present context. The co-product of the decarbonylation reaction, $RhCl(CO)(PPh_3)_2$, is relatively stable thermally at normal reaction temperatures; the thermal dissociation of $RhCl(CO)(PPh_3)_2$ to give CO and $RhCl(PPh_3)_2$ is typically too slow to facilitate a catalytic decarbonylation process.

Primary alkyl aldehydes may be decarbonylated catalytically in high yields when combined with only 5% of Wilkinson's catalyst and a stoichiometric portion of diphenylphosphoryl azide, but more sterically crowded aldehydes are relatively inert (10).

© 2008 NRC Canada

Scheme 2. Catalytic decarbonylation of an aldehyde (R-C(O)H) by $[Rh(dppp)_2]^+$.

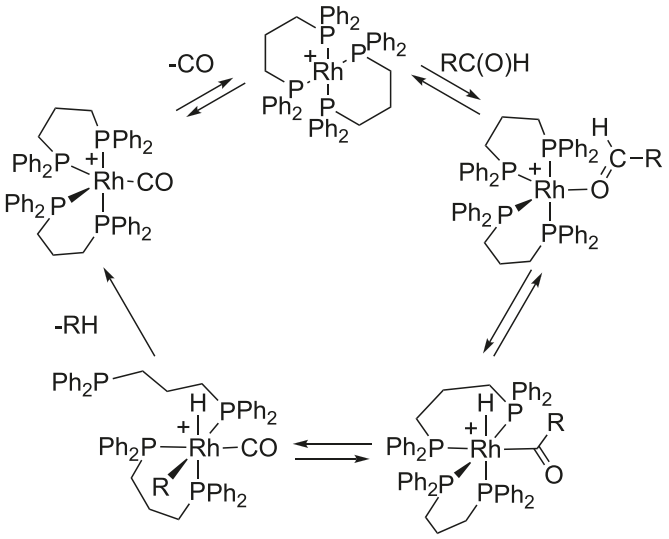

Bisdiphosphine complexes of Rh(I), such as [bis(1,3-bisdiphenylphosphino)propane]rhodium chloride or tetrafluoroborate, $[Rh(dppp)_2]Cl$ or $[Rh(dppp)_2]BF_4$ (11, 12), will decarbonylate an aldehyde following a mechanistic path much like one postulated for Wilkinson's catalyst mediated decarbonylations. The reductive elimination step gives a $[Rh(dppp)_2]^+CO$ complex that dissociates relatively easily to $[Rh(dppp)_2]^+$, and the process can continue, as schematized in the putative mechanistic model outlined in Scheme 2.

The $[Rh(dppp)_2]^+$ structure is probably not square planar but distorted so as to position the two P-Rh-P planes at a dihedral angle approximately midway between 0° and 90°, as has been found for $Rh(PMe_3)_4^+$ and [bis(1,4-bisdiphenylphosphino)butane]rhodium$^+$ (13, 14). The pentacoordinate complexes with CO or an aldehyde are approximately trigonal bipyramidal, though they exhibit considerable conformational flexibility. At room temperature (RT) all four phosphorous atoms are equivalent: $^{31}P\{^1H\}$ NMR spectra exhibit a simple doublet due to P-Rh spin–spin coupling, while at –80 °C an A_2B_2X pattern of multiplets is observed (15).

Kinetic evidence points toward the oxidative addition step being rate-limiting (12). The catalytic cycle is completed through a reverse migration followed by an irreversible reductive elimination to give the decarbonylation product and a carbon monoxide complex, one that can dissociate readily at modest temperatures.

Reported decarbonylations of aryl, alkenyl, and primary alkyl aldehydes with reagents providing a source of $[Rh(dppp)_2]^+$ are impressively efficient, but similar reactions of secondary alkyl aldehydes using these catalysts have not been entirely encouraging: 2-ethylbutanal and a catalytic amount of $[Rh(dppp)_2]BF_4$ at 110 °C for 36 h gave pentane in only 15% yield (12).

The $[Rh(dppp)_2]Cl$ or $[Rh(dppp)_2]BF_4$ catalysts may be prepared in crystalline form. A convenient alternative is to make the former in situ by combining $RhCl(CO)(PPh_3)_2$ with 1,3-bis(diphenylphosphino)propane in a 1:2 ratio, respectively (16). The present work opted for this option. When a labeled aldehyde, **5**-d_i, was combined with a catalyst prepared from 3.6 mol% of $Cl(CO)Rh(PPh_3)_2$ and 7.2 mol% of dppp in anhydrous, degassed toluene, and heated at reflux for about a day, analysis by capillary GC revealed that the decarbonylation reaction was progressing slowly. An additional increment of catalyst was prepared and added, and the reaction mixture was heated at reflux for another day. A third increment of catalyst was prepared and added. After another day at reflux, all of the aldehyde had reacted, according to GC analyses. Following workup, the labeled phenylcyclopropane was secured in good yields, with very little contamination by the side-product α-methylstyrene. In three of the eight decarboxylation reactions, two from each of the labeled phenylcyclopropanecarboxaldehydes, four or five increments of catalyst and additional days of heating the reaction mixture at reflux were invested, prompted by indications of incomplete reactions gained from GC analyses. The annoyingly inconsistent rates of decarbonylation may be associated with various intrusions of adventitious oxygen, which binds reversibly but tightly to $[Rh(dppp)_2]^+$, and stalls but does not shut down the catalytic cycle (17).

Proton NMR spectra of **1**-d_1, **1**-d_2, **1**-d_3, and **1**-d_3' were completely consistent with expectations. For **1**-d_2, for example, the three equal-intensity cyclopropyl H multiplet absorptions were observed at δ 1.97, 1.02, and 0.78 (Fig. 1). In **1**-d_3, the upfield absorption of the H cis to phenyl at δ 0.78 is nearly absent, and the two cyclopropyl H doublets for cis related hydrogens at C1 and C3 are separated by 0.95 ppm. In **1**-d_3', the spectrum has the expected pair of doublets for trans disposed hydrogens at C2 and C3 and no significant absorption intensity at δ 1.97. For **1**-d_1, the spectrum is complicated just as one might anticipate from ^{13}C-H spin–spin couplings.

The eight decarbonylation reactions (Scheme 3), two from each **5**-d_i isotopomer, gave phenylcyclopropanes **1**-d_i in 79% yields, on average, from the precursor alcohols **4**-d_i. The catalytic decarbonylation reactions were slow but effective. The four **1**-d_i chiral phenylcyclopropanes prepared, secured in quantities ranging from 5.4 to 5.9 g, should prove sufficient for projected stereochemical and mechanistic studies.

The synthetic project reported in this work realized its objective, but surely did not validate an optimal experimental protocol for the catalyzed decarbonylation reactions. The goal was to make useful amounts of the required chiral isotopically labeled phenylcyclopropanes efficiently, not to perfect the decarbonylation step. Work in that direction might well find that employing $[Rh(dppp)_2]Cl$ or $[Rh(dppp)_2]BF_4$ directly, rather than making a catalyst in situ, would bring better yields or shorter reaction times; perhaps another solvent at another reaction temperature rather than toluene at reflux would be preferred; perhaps different and more rigorous measures to keep oxygen from the catalyst at every stage would prove beneficial. A systematic optimization effort could be most useful, but even now an efficient (though slow) catalytic decarbonylation procedure for cyclopropanecarboxaldehydes, one that should work for other secondary aldehydes, has been exemplified. Especially for reactions on a multi-gram scale; it should prove a practical and valuable synthetic method, and in certain situations make possible mechanistic studies that otherwise would remain imagined but not undertaken.

© 2008 NRC Canada

Fig 1. ^{1}H NMR spectra of chiral phenylcyclopropanes **1**-d_1, **1**-d_2, **1**-d_3, and **1**-d_3' acquired on a 300 MHz spectrometer; × absorptions = H_2O.

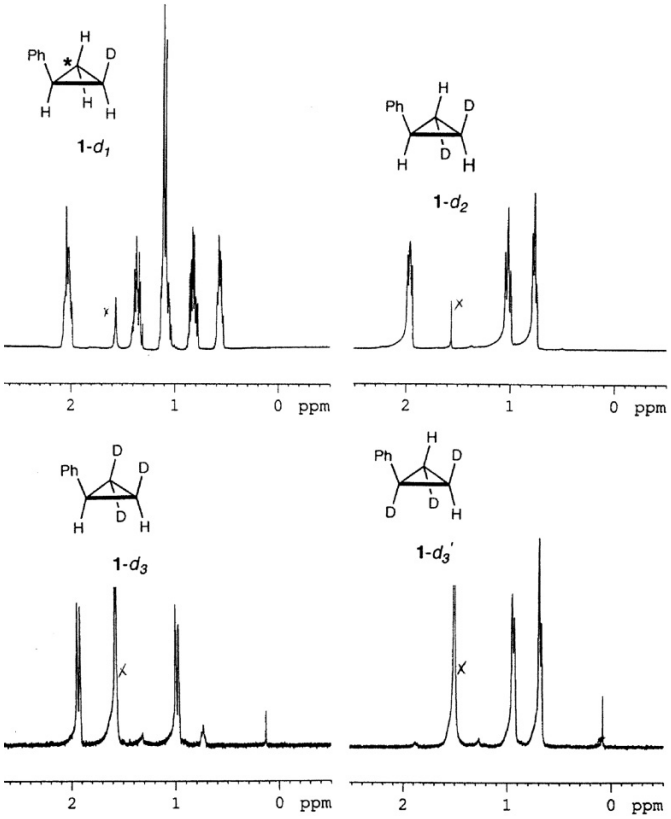

Experimental section

trans-2-Phenylcyclopropanemethanol

The following general procedures for the hydrolysis of (1*R*)-menthyl (1*S*,2*S*)-(+)-2-phenylcyclopropanecarboxylate was used to prepare acids **3**-d_1, **3**-d_2, **3**-d_3, and **3**-d_3' from esters **2**-d_1, **2**-d_2, **2**-d_3, and **2**-d_3', and to reduce these acids to **4**-d_1, **4**-d_2, **4**-d_3, and **4**-d_3'.

(1*R*)-Menthyl (1*S*,2*S*)-(+)-2-phenylcyclopropanecarboxylate (9.65 g, 31.9 mmol) suspended in 300 mL of CH_3OH was stirred for 30 min. Aqueous 25% NaOH (56 g) was added, and the reaction mixture was heated at reflux for 21 h. It was cooled to RT and concentrated by rotary evaporation. The white residue was dissolved in 225 mL of H_2O and the basic solution was extracted with ether (3 × 100 mL). The aqueous layer was separated, acidified with concd HCl (~30 mL), and extracted with ether (4 × 100 mL). The ether extracts were combined, dried ($MgSO_4$), and filtered. The colorless filtrate was concentrated by distillation to remove all but about 30 mL of the ether.

This concentrate was added dropwise by addition funnel along with anhydrous THF (~30 mL, used to rinse out the flask) to a suspension of $LiAlH_4$ (3.03 g, 79.8 mmol) in anhydrous THF (250 mL) under argon. The resulting gray suspension was heated at reflux for 42 h, cooled in an ice bath, and quenched with H_2O (3.0 g), 15% aqueous NaOH (3.03 g), and H_2O (9.09 g), with 5 min of stirring the quenched reaction mixture after each addition. The resulting mixture was stirred for an additional 30 min, dried over K_2CO_3, and filtered through Celite. The solid collected over Celite was washed with THF (~75 mL) and the filtrates were combined and concentrated by distillation. The colorless liquid remaining was purified by Kugelrohr distillation at 75–95 °C under reduced pressure. The colorless oil collected (4.45 g, 93% yield) had a ^{1}H NMR spectrum matching the reference data for *trans*-2-phenylcyclopropanemethanol (5). In **4**-d_2 and **4**-d_3' the C3-H cis to phenyl was seen at δ 0.95 (1H); in **4**-d_1, **4**-d_2, and **4**-d_3 the benzylic H was recorded at δ 1.81–1.85 (1H).

Scheme 3. Stereoselective Rh-catalyzed decarbonylation reactions.

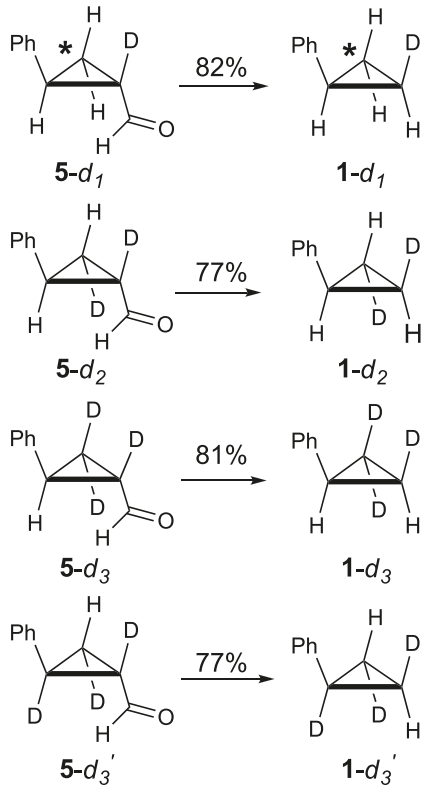

trans-2-Phenylcyclopropanecarboxaldehydes

trans-2-Phenylcyclopropanecarboxaldehydes (**5**-d_i) were prepared as described in this specific example, starting from **4**-d_2. Alcohol **4**-d_2 (4.87 g, 32.4 mmol) in anhydrous CH_2Cl_2 (25 mL) was added dropwise by addition funnel to an orange suspension of PCC (11.18 g, 51.9 mmol) in 100 mL of anhydrous CH_2Cl_2. The flask containing **4**-d_2 and the addition funnel were rinsed with dry CH_2Cl_2 (3 × 5 mL). A dark brown suspension formed immediately, and the reaction mixture was stirred for 4 h at RT under argon. Ether (150 mL) was added and a light brown precipitate was formed. The mixture was stirred for 5 min and then filtered through a short column of Florisil. The reaction flask residue and the Florisil column were rinsed with additional ether (3 × 50 mL). All ethereal material was combined and concentrated by distillation under an aspirator vacuum, and then using a vacuum pump. The residue, a green oil of crude aldehyde **5**-d_2 (4.80 g, ≈100% yield), was stored briefly under argon and subjected to catalytic decarbonation without delay.

© 2008 NRC Canada

Labeled chiral 2-phenylcyclopropanes by catalytic decarbonylation of labeled chiral *trans*-2-phenylcyclopropanecarboxaldehydes

Labeled chiral 2-phenylcyclopropanes (**1**-d_i) by catalytic decarbonylation of labeled chiral *trans*-2-phenylcyclopropanecarboxaldehydes (**5**-d_i) were synthesized as described in this specific example, starting from the sample of crude **5**-d_2 prepared immediately above.

An argon atmosphere was established for an oven-dried 500 mL three-necked round-bottomed flask equipped with an addition funnel, condenser, and a specialized adapter to connect a septum to the flask through a stopcock to protect the septum from toluene at reflux. Then $RhCl(CO)(PPh_3)_2$ (0.78 g, 1.5 mmol) and 1,3-bis(diphenylphosphino)propane (dddp; 1.3 g, 2.5 mmol) were added quickly, and 160 mL of anhydrous, degassed toluene was added by syringe. The resulting mixture was heated to 70–90 °C for 1 h. To the orange solution in the reaction flask was added a yellow solution of **5**-d_2 (4.80 g, 32.4 mmol) in anhydrous, degassed toluene (20 mL) through an addition funnel. The small flask that had contained the aldehyde solution was rinsed with toluene (3 × 5 mL) and the washings were added to the reaction mixture, which was then heated to reflux for 21 h.

A mixture of $RhCl(CO)(PPh_3)_2$ (0.78 g, 1.5 mmol), dddp (1.03 g, 2.5 mmol), and toluene (40 mL) in a separate flask was heated for 1 h at 65–80 °C and then added to the reaction mixture. The small flask was rinsed with toluene (2 × 5 mL) and the washings were added to the reaction mixture, which was then heated to reflux for an additional 24 h. Analysis by GC showed that the aldehyde (**5**-d_2)/phenylcyclopropane (**1**-d_2) ratio was about 1:1. An additional 1.5 mmol of catalyst was prepared and added to the reaction mixture, which was heated to reflux for another 24 h. The (**5**-d_2)/(**1**-d_2) ratio was 0.46:1. Additional toluene (50 mL) was added, and the mixture was heated to reflux for 26 h. Another increment of catalyst (0.49 mmol) was prepared and added, and the reaction mixture was heated to reflux for an additional 44 h, by which time the reaction had gone to completion. Pentane (200 mL) was added to the cooled reaction mixture; the mixture was passed through a silica gel column, followed by 275 mL of pentane. The colorless, clear liquid collected was concentrated by distillation using an efficient teflon spinning band column (a B/R Instrument Corporation 36T 100 system rated at up to 200 theoretical plates with microprocessor controller). The dark yellow pot residue (9.69 g) was characterized by capillary GC: it contained the phenylcyclopropane **1**-d_2 (31.6 weight%, 3.06 g, 79% yield for the two steps from alcohol **4**-d_2), toluene (56.1%, 5.44 g) and α-methylstyrene (1.4%, 0.14 g). Further concentration using a micro spinning band distillation system (B/R 800), followed by a Kugelrohr distillation at 130 °C, afforded a colorless liquid. ^{1}H NMR δ: 0.78 (m, 1H), 1.02 (m, 1H), 1.97 (m, 1H), 7.15–7.37 (m, 5H). ^{13}C NMR δ: 9.25 (1:1:1 triplet), 15.63, 125.78, 126.09, 128.71.

This decarbonylation reaction utilized four additions of catalyst, 12 mol% in all, and 139 h of heating the reaction mixture at reflux. A second preparation of **1**-d_2 starting with 4.70 g of **4**-d_2 used three 3.5 mol% additions of catalyst and keeping the reaction mixture at reflux for 73 h gave 2.83 g (75% yield) of the d_2-phenylcyclopropane.

Other labeled **1**-d_i phenylcyclopropanes were prepared from **4**-d_i alcohols in like fashion. For the eight preparations, times at reflux ranged from 66 to 146 h. Five reactions took three portions of catalyst (10.5% in all); three took four portions (12.5 mol% in total); the 146 h reaction required five portions of catalyst (4 × 3.5% + 2%).

Pure **1**-d_i samples could be secured easily by preparative GC using an Apiezon L column at 125 °C. Under the conditions employed, the retention times for toluene, α-methylstyrene, and a phenylcyclopropane were 2.66, 9.16, and 11.83 min, respectively.

Acknowledgments

We thank the National Science Foundation for support of this work through CHE-0211120 and CHE-0514376.

References

1. J.E. Baldwin. J. Labelled Compd. Radiopharm. **50**, 947 (2007).
2. (*a*) J.E. Baldwin, T.W. Patapoff, and T.C. Barden. J. Am. Chem. Soc. **106**, 1421 (1984); (*b*) J.E. Baldwin and T.C. Barden. J. Am. Chem. Soc. **106**, 5312 (1984); (*c*) J.E. Baldwin and T.C. Barden. J. Am. Chem. Soc. **106**, 6364 (1984).
3. E.J. Keliher, R.C. Burrell, H.R. Chobanian, K.L. Conkrite, R. Shukla, and J.E. Baldwin. Org. Biomol. Chem. **4**, 2777 (2006).
4. K. Furuta, K. Iwanaga, and H. Yamamoto. Org. Syn. Coll. **8**, 141 (1983).
5. J.E. Baldwin and C.G. Carter. J. Am. Chem. Soc. **104**, 1362 (1982).
6. (*a*) J.F. Young, J.A. Osborn, F.H. Jardine, and G. Wilkinson. Chem. Commun. 131 (1965); (*b*) F.H. Jardine, J.A. Osborn, G. Wilkinson, and J.F. Young. Chem. Ind. (London), 560 (1965); (*c*) M.A. Bennett and P.A. Longstaff. Chem. Ind. (London), 846 (1965).
7. (*a*) J. Tsuji and K. Ohno. Tetrahedron Lett. 3969 (1965); (*b*) K. Ohno and J. Tsugi. J. Am. Chem. Soc. **90**, 99 (1968).
8. K. Burgess and W.A. van der Donk. *In* Encyclopedia of reagents for organic synthesis. Vol 2. *Edited by* L.A. Paquette. Wiley, Chichester, NY. 1995. pp. 1253–1261.
9. H.M. Walborsky and L.E. Allen. Tetrahedron Lett. 823 (1970).
10. (*a*) J.M. O'Connor and J. Ma. J. Org. Chem. **57**, 5075 (1992); (*b*) J.M. O'Connor and J. Ma. Inorg. Chem. **32**, 1866 (1993).
11. D.A. Slack and M.C. Baird. J. Organomet. Chem. **142**, C69 (1977).
12. (*a*) D.H. Doughty and L.H. Pignolet. J. Am. Chem. Soc. **100**, 7083 (1978); (*b*) D.H. Doughty, M.F. McGuiggan, H.H. Wang, and L.H. Pignolet. Fundam. Res. Homogeneous Catal. **3**, 909 (1979); (*c*) D.H. Doughty, M.P. Anderson, A.L. Casalnuovo, M.F. McGuiggan, C.C. Tso, H.H. Wang, and L.H. Pignolet. In Catalytic aspects of metal phospine complexes: Based on a symposium sponsored by the ACS and CIC Divisions of Inorganic Chemistry at the 1980 Biennial Inorganic Chemistry Symposium. Guelph, Canada. 5–7 June 1980. *Edited by* E.C. Alyea and D.W. Meek. American Chemical Society, Washington, D.C. 1982. pp. 65–83; (*d*) D.H. Doughty and L.H. Pignolet. *In* Homogeneous catalysis with metal phosphine complexes. *Edited by* L.H. Pignolet. Plenum Press, New York. 1983. pp. 343–375; (*e*) M.A. Aubart and L.H. Pignolet. *In* Encyclopedia of reagents for organic synthesis. Vol. 1. *Edited by* L.A. Paquette. Wiley, Chichester, NY. 1995. pp. 432–434.

© 2008 NRC Canada

13. R.A. Jones, F.M. Real, G. Wilkinson, G.M.R. Gales, M.B. Hursthouse, and K.M.A. Malik. J. Chem. Soc. Dalton Trans. 511 (1980).
14. M.P. Anderson and L.H. Pignolet. Inorg. Chem. **20**, 4101 (1981).
15. B.R. James and D. Mahajan. Can. J. Chem. **58**, 996 (1980).
16. M.D. Meyer and L.I. Kruse. J. Org. Chem. **49**, 3195 (1984).
17. M.G. Banwell, M.J. Coster, A.J. Edwards, O.P. Karunaratne, J.A. Smith, L.L. Lee, and A.C. Willis. Aust. J. Chem. **56**, 585 (2003).

© 2008 NRC Canada

Feasibility of sigmatropic rearrangement on electron-deficient coumarinyl ketones

Lakshmi Narayan Dutta, Banani De, Godhuli Pal, and Amarendra Patra

Abstract: Different alkyl/aryl 7-hydroxy-8-coumarinyl ketones were converted to 7-*O*-allyl and 7-*O*-cyclohexenyl ethers and the study of hitherto unreported sigmatropic rearrangement on 7-*O*-allyl and 7-*O*-cyclohex-2′-ene-1′-ylcoumarinyl ketones prepared is accounted herein. The rearrangement yielded alkyl/aryl 6-allyl-7-hydroxy-8-coumarinyl ketones **3** and alkyl/aryl 6-cyclohex-2′-en-1′-yl-7-hydroxy-8-coumarinyl ketones **7** as the major products. Interestingly, unusual selectivity was observed in the case of alkyl 7-*O*-allylcoumarinyl ketones. Thus alkyl 3-allyl-7-hydroxy-8-coumarinyl ketones **4** and alkyl 8-allyl-7-hydroxy-6-coumarinyl ketones **5** were the outcome from alkyl 7-*O*-allyl-8-coumarinyl ketones and alkyl 4-methyl-7-*O*-allyl-8-coumarinyl ketones, respectively, albeit in minor yields.

Key words: allyloxycoumarinyl ketones, 7-*O*-cyclohex-2′-en-1′-ylcoumarinyl ketones, sigmatropic rearrangement, 3-allylcoumarinyl ketones, 8-allylcoumarinyl ketones.

Résumé : On a transformé diverses alkyl/aryl 7-hydroxy-8-coumarinylcétones en leurs éthers, les oxydes de 7-*O*-allyle et 7-*O*-cyclohexényle correspondants, et on rapporte les résultats obtenus lors des réarrangements sigmatropiques qui n'avaient jamais été rapportés antérieurement et qui ont été effectués sur les 7-*O*-allyl- et 7-*O*-cyclohex-2′-én-1′-ulcoumarinylcétones ainsi préparées. Les produits principaux de ces réactions sont les alkyl/aryl 6-allyl-7-hydroxy-8-coumarinylcétones, **3**, et les alkyl/aryl 6-cyclohex-2′-én-1′-yl-7-hydroxy-8-coumarinylcétones, **7**. On a observé une sélectivité inhabituelle intéressante dans le cal des alkyl 7-*O*-allylcoumarinylcétones. Même s'ils n'ont été obtenus qu'avec de faibles rendements, les alkyl 3-allyl-7-hydroxy-8-coumarinylcétones, **4**, et alkyl 8-allyl-7-hydroxy-6-coumarinylcétones, **5**, sont les produits obtenus à partir respectivement des 7-*O*-allyl-8-coumarinylcétones et alkyl 4-méthyl-7-*O*-allyl-8-coumarinylcétones.

Mots-clés : allyloxycomarinylcétones, 7-*O*-cyclohex-2′-én-1′-ylcoumarinylcétones, réarrangement sigmatropique, 3-allylcoumarinylcétones, 8-allylcoumarinylcétones.

[Traduit par la Rédaction]

Introduction

Coumarins (1, 2) have attracted the attention of synthetic organic chemists (3–5) throughout the globe for building up new exotic molecules owing to their well-established range of biological activities (6–10). In quest of newer synthetic methodologies we have successfully carried out a series of systematic studies on the selectivities of different organometallics (11, 12) and ylids (13) involving typical non-concerted processes on coumarinyl ketones and coumarincarboxaldehydes. Under the scope of concerted process we have extensively applied a sigmatropic reaction in the form of thermal Claisen rearrangement for the synthesis of various natural and unnatural coumarins. In spite of a flurry of activity in the synthesis of coumarin employing Claisen rearrangement (14–20), there is virtually no report on the efficacy of the rearrangement on the coumarin moiety bearing further electron-rich and electron-deficient functionalities. Herein we report the findings of an intense investigation on Claisen rearrangement restricting the functionalisation to the electron-deficient coumarinyl ketones.

Received 26 November 2007. Accepted 22 February 2008. Published on the NRC Research Press Web site at canjchem.nrc.ca on 3 April 2008.

L.N. Dutta,[1] **B. De, G. Pal.** Department of Chemistry, Jadavpur University, Kolkata 700 032, India
A. Patra. Centre of Advanced Studies on Natural Products, Department of Chemistry, University College of Science, Kolkata 700 009, India.

[1]Corresponding author (e-mail: amarendra@satyam.net.in).

Discussion

The starting materials selected for this study, viz. 7-allyloxy-8-coumarinyl alkyl/aryl ketones **2a**–**2h** and 7-cyclohex-2′-en-1′-yloxy-8-coumarinyl alkyl/aryl ketones **6a**–**6h** were prepared from 7-hydroxy-8-coumarinyl alkyl/aryl ketones **1a**–**1h**. The hydroxycoumarinyl ketones could be procured from 7-hydroxycoumarin and 4-methyl-7-hydroxycoumarin, as appropriate, exploiting Fries rearrangement (21). The aforesaid allyl coumarinyl ethers have thus been successfully prepared in good yield by following the usual protocol of refluxing the compounds for 8 h in dry acetone with allyl bromide in the presence of anhydrous K_2CO_3. An initial sigmatropic rearrangement study revealed that the allyl ethers failed to record any positive result in solvents like chlorobenzene and polyethylene glycol 400. Consequent to that, the rearrangement was tried and ultimately became successful in *N,N*-diethylaniline. The C–C bond formations showed typical selectivities by yielding 6-allyl substituted coumarinyl ketones **3** and 3-allyl substituted coumarinyl ketones **4** with 7-allyloxy-8-coumarinyl ketones

 doi:10.1139/V08-037 © 2008 NRC Canada

Scheme 1. Reagents and conditions: (*i*) , anhyd. K_2CO_3, dry Me_2CO, 14 h, and reflux; (*ii*) $PhNEt_2$, 195 °C, and 8 h.

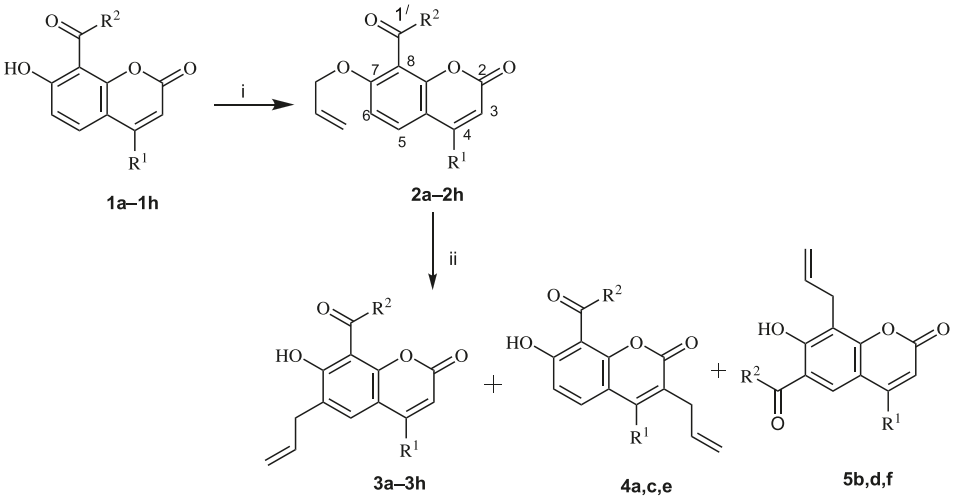

Scheme 2. Reagents and conditions: (*i*) , NEt_3, dry Me_2CO, 4 h, and reflux. (*ii*) Ph_2O, reflux for 10 min.

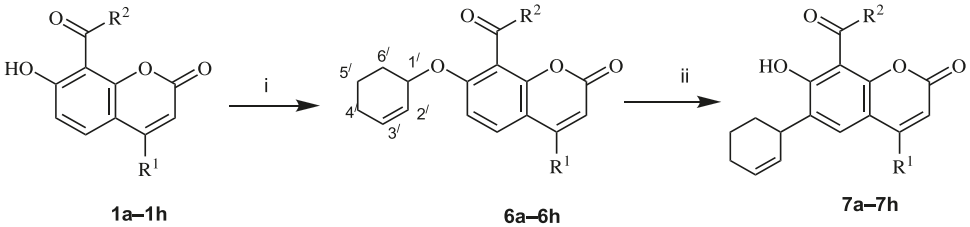

2a, **2c**, and **2e**, whereas the 4-methyl-7-allyloxy-8-coumarinyl ketones **2b**, **2d**, and **2f** resulted in 6-allyl substituted coumarinyl ketones **3** along with 8-allyl substituted 6-coumarinyl ketones **5** as a consequence of unusual acyl migration. The allyl ethers having benzoyl coumarinyl functionality, **2g** and **2h**, did produce only the usual 6-allyl substituted coumarinyl ketones without any trace of other rearranged products (Scheme 1).

It should be noted that attempted cyclohexenylation of hydroxycoumarinyl ketones following the usual protocol of refluxing in dry acetone with 3-bromocyclohexene in the presence of anhydrous K_2CO_3 (22) turned out to be entirely unsuccessful. Finally the problem was overcome through the judicious selection of a base, viz. triethylamine instead of anhydrous K_2CO_3 (Scheme 2). It should be emphasized that the study of Claisen rearrangement turned out to be remarkably successful in diphenyl ether as solvent, while the yield was extremely poor when carried out in chlorobenzene (<5%) and *N,N*-diethylaniline (~10%). The cyclohexenyl ethers on Claisen rearrangement underwent regioselective formation of 6-cyclohex-2′-ene-1′-yl-8-coumarinyl alkyl/aryl ketones **7a**–**7h** in good yields (Table 1). No unusual acyl migration or Claisen rearrangement on other positions of coumarin moiety was observed with cyclohexenyl ethers.

The formation of 6-allyl and 6-cyclohexenyl substituted coumarinyl ketones turned out to be quite obvious via an intermediate **A** (Scheme 3). In the formation of 3-allylcoumarinyl ketones, the intermediate **C** may be visualized as a consequence of a [3,3] Cope rearrangement of the intermediate **B** produced via a [3,3] sigmatropic shift. Alternatively, the genesis of 3-allylcoumarinyl ketones from alkyl 7-allyloxy-8-coumarinyl ketones may be rationalized from the intermediate **C** formed via a [3,3] sigmatropic shift, which further underwent Cope rearrangement with the transfer of allyl functionality at the 4a position, leading to the intermediate **C**. The intermediate **C** follows an itinerary of further [3,3] Cope rearrangement followed by [1,7] tautomeric shift to afford the 3-allyl substituted coumarinyl ketones. The 4-methyl-7-allyloxycoumarinyl ketones prefer to follow from the intermediate **B** as an alternative pathway leading to the anionic intermediate **D**, along with the ejected acylium ion R-C≡O^+ that may exist, most plausibly enjoying the character of an intimate ion pair though the feasibility of a concerted mechanism cannot be ruled out. On further chemical mutation to intermediate **F**, the 6-acyl-8-allylcoumarinyl ketones are being derived via the [1,3] tautomeric shift.

Table 1. Yields of the compounds **2** to **7**.

	Substituents			Yield (%)					
Entry		R^1	R^2	**2**	**3**	**4**	**5**	**6**	**7**
1	**a**	H	Me	83	44	40	—	66	60
2	**b**	Me	Me	83	46	—	33	93	62
3	**c**	H	Et	84	41	26	—	76	62
4	**d**	Me	Et	85	42	—	26	63	65
5	**e**	H	*n*-Pr	84	43	24	—	70	59
6	**f**	Me	*n*-Pr	84	43	—	26	78	61
7	**g**	H	Ph	85	47	—	—	76	59
8	**h**	Me	Ph	85	44	—	—	89	58

© 2008 NRC Canada

Scheme 3.

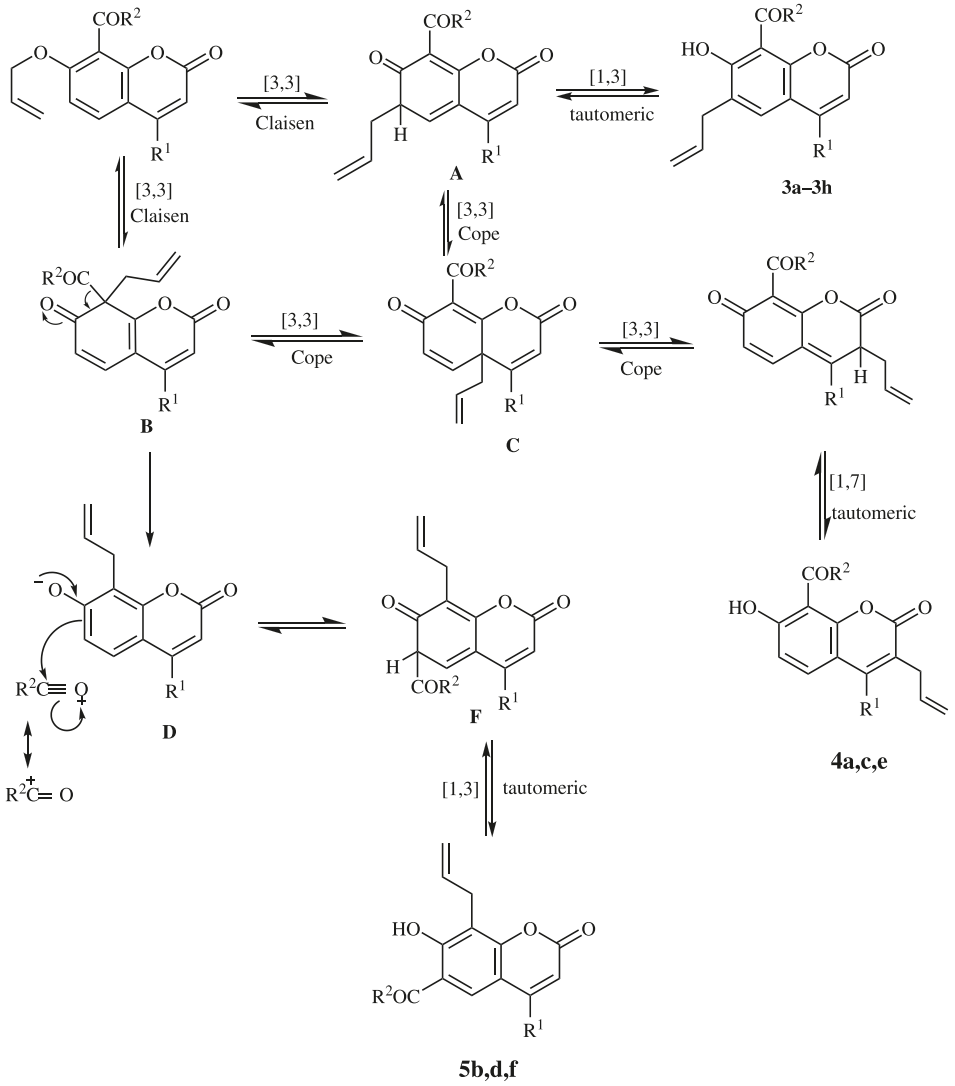

The structures of the compounds were unequivocally settled from elemental analyses and extensive spectroscopic investigations. Assignment of the structures of 6-allyl and 8-allylsubstituted coumarinyl ketones posed an interesting problem and could be unequivocally solved by critical analysis of the ^{1}H NMR and ^{13}C NMR spectra, with particular emphasis on the proton signals of C-5 and carbon signals of C-6 and C-8. The proton signals at the 5-position enjoy more deshielding because of the anisotropic effect offered by the newly arrived adjacent ketocarbonyl functionality. On the contrary, the C-6 carbon signal of 8-allyl substituted compounds are more shielded than those of the 6-allyl substituted compounds (23) (Table 2), and the C-8 signals varied oppositely.

Table 2. Chemical shift (δ) values of C-5 protons and C-6, C-8 carbon signals.

Compound	Location of ketoalkyl functionality	δ Value		
		C-5 proton signal	C-6 carbon signal	C-8 carbon signal
3b	C-8	7.48	126.1	108.6
5b	C-6	7.88	112.4	116.3
3d	C-8	7.43	126.2	108.7
5d	C-6	7.95	112.5	116.0
3f	C-8	7.49	126.1	108.7
5f	C-6	7.95	112.5	116.2

Conclusion

In conclusion, it is worth mentioning that an unusual selectivity was observed in the product formation with the introduction of a methyl group at the 4-position of the 7-allyloxy-8-coumarinyl ketone moiety. The changeover in the character of the minor products with the introduction of methyl group at the 4-position of the 8-coumarinyl ketone moiety may be rationalized either from steric or electronic considerations. The plausible explanation of such selectivity in favor of the electronic and (or) steric effect of methyl group can only be confirmed on further study of Claisen rearrangement on 7-allyloxy-8-coumarinyl ketones with varying substituents (Et, *n*-Pr, *i*-Pr, *t*-Bu, CHO, CN, CO_2Me, CH_2OH) at the 4-position.

© 2008 NRC Canada

Experimental

All melting points were determined in open capillaries and are uncorrected. IR spectra (ν_{max} in cm^{-1}) were recorded in KBr with a PerkinElmer 883-IR and RXI FT IR spectrophotometers. The UV spectra were measured in 95% ethanol using an Hitachi U 2000 and Lamda 20 ELMER spectrophotometers. The elemental analyses were carried out in a PerkinElmer 240C elemental analyzer. The ^1H NMR and ^{13}C NMR spectra were recorded in a Bruker AV300 supercon NMR spectrometer operating at 300.13 MHz for proton and 75.47 MHz for carbon, using $CDCl_3$ as solvent and TMS as an internal standard. Mass spectra were recorded on a Finnigan Mat 1020 C, Shimadzu Model GEMS QP1000A, and LC-MS MS Q-TOF-micro spectrometers and a Q TRAP LC/MS/MS system operative at 70 eV. The column chromatographic separation and filtration were performed with silica gel (mesh size 60–120) prepared by Glaxo (India) Ltd and Merck (India) Ltd. Petroleum ether used had a boiling point 60–80 °C.

Preparation of 7-allyloxycoumarinyl ketones 2a–2h

General procedure

7-Hydroxycoumarinyl ketones (4.3 mmol) dissolved in dry acetone (50 mL) were treated with allyl bromide (4.9 mmol) and anhydrous K_2CO_3 (4.3 mmol) and refluxed under anhydrous conditions on water bath for ~14 h. Excess acetone was distilled off and the residual solid cakelike mass was treated with water (150 mL). The mixture was acidified in cold conditions with cold dil HCl (4 N). The solid separated was filtered out and washed with cold water until it was neutral. The resultant solid was dried and crystallized from EtOAc/petroleum ether to obtain crystals of 7-allyloxycoumarinyl ketones **2a**–**2h**.

Compound 2a

Mp 68 °C. IR (cm^{-1}): 3080, 2980, 1740, 1700, 1620, 1590, 1490, 1400. ^1H NMR δ: 2.57 (sharp s, 3H, 1′-CH_3), 4.73 (d, J = 5.0 Hz, 2H, OCH_2CH=CH_2), 5.34 (d, J = 10.0 Hz, 1H, $OCH_2CH=CH_AH_B$), 5.39 (d, J = 17.0 Hz, 1H, $OCH_2CH=CH_AH_B$), 5.95 (m, 1H, $OCH_2CH=CH_2$), 6.27 (d, J = 9.0 Hz, 1H, 3-H), 6.91 (d, J = 7.2 Hz, 1H, 6-H), 7.45 (d, J = 7.2 Hz, 1H, 5-H), 7.70 (d, J = 9.0 Hz, 1H, 4-H). Anal. calcd. for $C_{14}H_{12}O_4$: C 68.84, H 4.95; found: C 68.79, H 4.90.

Compound 2b

Mp 108 °C. IR (cm^{-1}): 3060, 2995, 1730, 1710, 1605, 1565, 1495, 1380. ^1H NMR δ: 2.32 (d, J = 1.0 Hz, 3H, 4-CH_3), 2.53 (sharp s, 3H, 1′-CH_3), 4.58 (d, J = 6.0 Hz, 2H, OCH_2CH=CH_2), 5.23 (d, J = 10.0 Hz, 1H, $OCH_2CH=CH_AH_B$), 5.32 (d, J = 17.0 Hz, 1H, $OCH_2CH=CH_AH_B$), 5.96 (m, 1H, $OCH_2CH=CH_2$), 6.08 (q, J = 1.0 Hz, 1H, 3-H), 6.80 (d, J = 9.0 Hz, 1H, 6-H), 7.47 (d, J = 9.0 Hz, 1H, 5-H). Anal. calcd. for $C_{15}H_{14}O_4$: C 69.75, H 5.46; found: C 69.72, H 5.41.

Compound 2c

Mp 65 °C. IR (cm^{-1}): 3080, 2970, 1750, 1715, 1610, 1570, 1490, 1405, 1300. ^1H NMR δ: 1.16 (t, J = 7.0 Hz, 3H, 2′-CH_3), 2.86 (q, J = 7.0 Hz, 2H, 1′-CH_2), 4.63 (d, J = 6.0 Hz, 2H, OCH_2CH=CH_2), 5.30 (d, J = 10.0 Hz, 1H, $OCH_2CH=CH_AH_B$), 5.37 (d, J = 17.0 Hz, 1H, $OCH_2CH=CH_AH_B$), 5.98 (m, 1H, $OCH_2CH=CH_2$), 6.24 (d, J = 9.0 Hz, 1H, 3-H), 6.84 (d, J = 9.0 Hz, 1H, 6-H), 7.43 (d, J = 9.0 Hz, 1H, 5-H), 7.63 (d, J = 9.0 Hz, 1H, 4-H). Anal. calcd. for $C_{15}H_{14}O_4$: C 69.75, H 5.46; found: C 69.70, H 5.41.

Compound 2d

Mp 70 °C. IR (cm^{-1}): 3090, 2990, 1745, 1710, 1605, 1570, 1495, 1380. ^1H NMR δ: 1.21 (t, J = 7.0 Hz, 3H, 2′-CH_3), 2.39 (d, J = 1.0 Hz, 3H, 4-CH_3), 2.91 (q, J = 7.0 Hz, 2H, 1′-CH_2), 4.60 (d, J = 5.0 Hz, 2H, OCH_2CH=CH_2), 5.45 (d, J = 10.0 Hz, 1H, $OCH_2CH=CH_AH_B$), 5.52 (d, J = 16.0 Hz, 1H, $OCH_2CH=CH_AH_B$), 6.02 (m, 1H, $OCH_2CH=CH_2$), 6.15 (q, J = 1.0 Hz, 1H, 3-H), 6.88 (d, J = 7.2 Hz, 1H, 6-H), 7.51 (d, J = 7.2 Hz, 1H, 5-H). Anal. calcd. for $C_{16}H_{16}O_4$: C 70.57, H 5.92; found: C 70.60, H 5.88.

Compound 2e

Mp 52 °C. IR : 3080, 2970, 1760, 1710, 1610, 1560, 1490, 1410. ^1H NMR δ: 0.93 (t, J = 5.1 Hz, 3H, 3′-CH_3), 1.68 (tq, J = 5.1 Hz, 5.1 Hz, 2H, 2′-CH_2), 2.77 (t, J = 5.1 Hz, 2H, 1′-CH_2), 4.56 (d, J = 6.0 Hz, 2H, OCH_2CH=CH_2), 5.23 (d, J = 12.0 Hz, 1H, $OCH_2CH=CH_AH_B$), 5.28 (d, J = 18.0 Hz, 1H, $OCH_2CH=CH_AH_B$), 5.90 (ddt, J = 18.0, 12.0, 6.0 Hz, 1H, $OCH_2CH=CH_2$), 6.17 (d, J = 9.0 Hz, 1H, 3-H), 6.78 (d, J = 9.0 Hz, 1H, 6-H), 7.36 (d, J = 9.0 Hz, 1H, 5-H), 7.57 (d, J = 9.0 Hz, 1H, 4-H). Anal. calcd. for $C_{16}H_{16}O_4$: C 70.57, H 5.92; found: C 70.52, H 5.99.

Compound 2f

Mp 70 °C. IR (cm^{-1}): 3060, 2950, 1735, 1720, 1600, 1560, 1485, 1370. ^1H NMR δ: 0.98 (t, J = 7.0 Hz, 3H, 3′-CH_3), 1.73 (tq, J = 7.0 Hz, 7.0 Hz, 2H, 2′-CH_2), 2.38 (d, J = 1.0 Hz, 3H, 4-CH_3), 2.83 (t, J = 7.0 Hz, 2H, 1′-CH_2), 4.63 (d, J = 6.0 Hz, 2H, OCH_2CH=CH_2), 5.28 (d, J = 10.0 Hz, 1H, $OCH_2CH=CH_AH_B$), 5.37 (d, J = 18.0 Hz, 1H, $OCH_2CH=CH_AH_B$), 5.97 (ddt, J = 18.0, 10.0, 6.0 Hz, 1H, $OCH_2CH=CH_2$), 6.13 (q, J = 1.0 Hz, 1H, 3-H), 6.85 (d, J = 9.0 Hz, 1H, 6-H), 7.52 (d, J = 9.0 Hz, 1H, 5-H). Anal. calcd. for $C_{17}H_{18}O_4$: C 71.31, H 6.34; found: C 71.34, H 6.30.

Compound 2g

Mp 102 °C. IR : 3065, 2980, 1725, 1675, 1610, 1565, 1495, 1405. ^1H NMR δ: 4.58 (d, J = 5.0 Hz, 2H, OCH_2CH=CH_2), 5.16 (d, J = 11.0 Hz, 1H, $OCH_2CH=CH_AH_B$), 5.18 (d, J = 17.0 Hz, 1H, $OCH_2CH=CH_AH_B$), 5.83 (m, 1H, $OCH_2CH=CH_2$), 6.24 (d, J = 8.0 Hz, 1H, 3-H), 6.92 (d, J = 8.0 Hz, 1H, 6-H), 7.52 (m, 5H, C_6H_5), 7.77 (d, J = 8.0 Hz, 1H, 5-H), 7.88 (d, J = 8.0 Hz, 1H, 4-H). Anal. calcd. for $C_{19}H_{14}O_4$: C 74.50, H 4.60; found: C 74.45, H 4.65.

Compound 2h

Mp 151 °C. IR : 3090, 2990, 1725, 1680, 1595, 1560, 1490, 1370. ^1H NMR δ: 2.44 (d, J = 1.2 Hz, 3H, 4-CH_3), 4.60 (br d, J = 7.0 Hz, 2H, OCH_2CH=CH_2), 5.15 (d, J = 10.0 Hz, 1H, $OCH_2CH=CH_AH_B$), 5.18 (d, J = 17.0 Hz, 1H, $OCH_2CH=CH_AH_B$), 5.81 (ddt, J = 17.0, 10.0, 7.0 Hz, 1H, $OCH_2CH=CH_2$), 6.14 (q, J = 1.2 Hz, 1H, 3-H), 6.94 (d, J = 9.0 Hz, 1H, 6-H), 7.43 (t, J = 7.8 Hz, 2H, 3′-H and 5′-H), 7.58 (br t, J = 7.8 Hz, 1H, 4′-H), 7.65 (br d, J = 7.8 Hz, 2H,

© 2008 NRC Canada

2′-H and 6′-H), 7.85 (d, J = 9.0 Hz, 1H, 5-H). Anal. calcd. for $C_{20}H_{16}O_4$: C 74.99, H 5.03; found: C 74.94, H 4.98.

Preparation of 6-allyl-8-coumarinyl alkyl/aryl ketones 3a–3h

General Procedure

The allyloxycoumarinyl ketones **2a**–**2h** (2.0 mmol) dissolved in distilled $PhNEt_2$ (30 mL) were heated at 195 °C for 8 h under anhydrous conditions. $PhNEt_2$ was then distilled off and the residual mass left was dissolved in $CHCl_3$ (30 mL). The $CHCl_3$ solution of the mass was washed successively with cold dil. HCl (3 × 15 mL), a saturated brine solution (1x15 mL), followed by a saturated aqueous solution of $NaHCO_3$ (2 × 15 mL), and again with a saturated brine solution (2 × 15 mL). Removal of solvent after drying over anhydrous Na_2SO_4 afforded a semi-solid mass, which was found to be a mixture of three components. Column chromatographic resolution over silica gel yielded the 6-allyl-8-coumarinyl ketones **3a**–**3h** from petroleum ether and EtOAc (99:1) eluate fractions. The products were crystallized from EtOAc/petroleum ether.

Compound 3a

Mp 121 °C. UV–vis (EtOH) λ_{max} (log ϵ): 321.7 (4.78), 270.5 (4.76), 254.5 (4.75). IR (cm^{-1}): 3080, 2920, 1730, 1710, 1610, 1560, 1400, 1365. ^{1}H NMR δ: 2.89 (sharp s, 3H, 1′-CH_3), 3.35 (br d, J = 6.5 Hz, 2H, 6-CH_2CH=CH_2), 5.071 (d, J = 10.0 Hz, 1H, CH_2CH=CH_AH_B), 5.072 (d, J = 18.0 Hz, 1H, CH_2CH=CH_AH_B), 6.01 (m, 1H, CH_2CH=CH_2), 6.20 (d, J = 9.5 Hz, 1H, 3-H), 7.33 (s, 1H, 5-H), 7.57 (d, J = 9.5 Hz, 1H, 4-H), 14.02 (s, 1H, 7-OH). ^{13}C NMR δ: 33.0 (2°, CH$_2$CH=CH_2), 33.7 (1°, 1′-CH_3), 108.7 (4°, C-8), 110.3 (4°, C-4a), 112.0 (3°, C-3), 116.9 (2°, CH_2CH=CH_2), 126.7 (4°, C-6), 133.9 (3°, CH_2CH=CH_2), 135.1 (3°, C-5), 144.2 (3°, C-4), 154.4 (4°, C-8a), 159.6 (4°, C-2), 165.1 (4°, C-7), 204.3 (4°, C-1′). MS-EI (70 eV) m/z: 244 (49.5, M^+), 229 (57.2), 216 (19.6), 211 (25.6), 201 (100), 183(12.8), 173 (41.8), 155 (16.6), 145 (29.4), 131 23.5), 115 (92.5). Anal. calcd. for $C_{14}H_{12}O_4$: C 68.84, H 4.95; found: C 68.89, H 4.99.

Compound 3b

Mp 122 °C. IR (cm^{-1}): 3080, 2980, 1740, 1715, 1610, 1560, 1450, 1395. ^{1}H NMR δ: 2.36 (d, J = 1.0 Hz, 3H, 4-CH_3), 2.90 (sharp s, 3H, 1′-CH_3), 3.38 (br d, J = 6.5 Hz, 2H, CH_2CH=CH_2), 5.06 (d, J = 16.0 Hz, 1H, CH_2CH=CH_AH_B), 5.07 (d, J = 10.0 Hz, 1H, CH_2CH=CH_AH_B), 5.93 (m, 1H, CH_2CH=CH_2), 6.10 (q, J = 1.0 Hz, 1H, 3-H), 7.48 (s, 1H, 5-H), 8.86 (s, 1H, 7-OH). ^{13}C NMR δ: 19.2 (1°, 4-CH$_3$), 33.4 (2°, CH$_2$CH=CH_2), 33.9 (1°, 1′-CH_3), 108.6 (4°, C-8), 111.1 (3°, C-3), 111.3 (4°, C-4a), 116.8 (2°, CH_2CH=CH_2), 126.1 (4°, C-6), 130.6 (3°, CH_2CH=CH_2), 135.3 (3°, C-5), 153.2 (4°, C-4), 153.7 (4°, C-8a), 159.6 (4°, C-2), 164.8 (4°, C-7), 204.7 (4°, C-1′). MS-EI (70 eV) m/z: 258 (60.3), 243 (54.4), 230 (21.5), 215 (34.3), 187 (13.2), 115 (27.4), 91 36.7), 77 (41.6), 65 (43.6), 43 (100). Anal. calcd. for $C_{15}H_{14}O_4$: C 69.75, H 5.46; found: C 69.71, H 5.43.

Compound 3c

Mp 110 °C. IR (cm^{-1}): 3060, 2960, 1730, 1710, 1620, 1580, 1465, 1400, 1310. ^{1}H NMR δ: 1.21 (t, J = 7.0 Hz, 3H, 2′-CH_3), 3.40 (q, J = 7.0 Hz, 2H, 1′-CH_2), 3.47 (br d, J = 7.0 Hz, 2H, CH_2CH=CH_2), 5.04 (d, J = 7.0 Hz, 1H, CH_2CH=CH_AH_B), 5.10 (d, J = 17.0 Hz, 1H, CH_2CH=CH_AH_B), 5.96 (m, 1H, CH_2CH=CH_2), 6.24 (d, J = 10.0 Hz, 1H, 3-H), 7.38 (s, 1H, 5-H), 7.62 (d, J = 10.0 Hz, 1H, 4-H), 14.20 (s, 1H, 7-OH). MS-EI (70 eV) m/z: 258 (62.4), 243 (2.9), 229 (100), 212 (3.4), 201 (33.3), 185 (3.8), 173 (8.9), 145 (3.4), 128 (2.9), 115 (7.2). Anal. calcd. for $C_{15}H_{14}O_4$: C 69.75, H 5.46; found: C 69.71, H 5.49.

Compound 3d

Mp 125 °C. IR (cm^{-1}): 3080, 2960, 1740, 1710, 1610, 1560, 1450, 1395. ^{1}H NMR δ: 1.17 (t, J = 7.0 Hz, 3H, 2′-CH_3), 2.34 (d, J = 1.0 Hz, 3H, 4-CH_3), 3.30 (q, J = 7.0 Hz, 2H, 1′-CH_2), 3.35 (br d, J = 6.5 Hz, 2H, CH_2CH=CH_2), 5.04 (d, J = 17.0 Hz, 1H, CH_2CH=CH_AH_B), 5.05 (d, J = 10.0 Hz, 1H, CH_2CH=CH_AH_B), 5.91 (m, 1H, CH_2CH=CH_2), 6.06 (q, J = 1.0 Hz, 1H, 3-H), 7.43 (s, 1H, 5-H), 14.00 (s, 1H, 7-OH). ^{13}C NMR δ: 8.2 (1°, 2′-CH$_3$), 19.2 (1°, 4-CH$_3$), 33.5 (2°, CH$_2$CH=CH_2), 39.7 (2°, 1′-CH_2), 108.7 (4°, C-8), 111.0 (3°, C-3), 111.3 (4°, C-4a), 116.8 (2°, CH_2CH=CH_2), 126.2 (4°, C-6), 130.3 (3°, CH_2CH=CH_2), 135.3 (3°, C-5), 153.2 (4°, C-4), 153.7 (4°, C-8a), 159.7 (4°, C-2), 164.7 (4°, C-7), 207.8 (4°, C-1′). MS-EI (70 eV) m/z: 272 (49.1), 257 (5.9), 243 (100), 215 (19.6), 201 (2.3), 117 (4.7), 115 (2.5). Anal. calcd. for $C_{16}H_{16}O_4$: C 70.57, H 5.92; found: C 70.60, H 5.87.

Compound 3e

Mp 84 °C. IR (cm^{-1}): 3085, 2970, 1735, 1720, 1625, 1565, 1455, 1400. ^{1}H NMR δ: 1.05 (t, J = 7.2 Hz, 3H, 3′-CH_3), 1.81 (tq, J = 7.2 Hz, 7.2 Hz, 2H, 2′-CH_2), 3.35 (t, J = 7.2 Hz, 2H, 1′-CH_2), 3.42 (br d, J = 6.6 Hz, 2H, CH_2CH=CH_2), 5.13 (d, J = 16.0 Hz, 1H, CH_2CH=CH_AH_B), 5.14 (d, J = 10.0 Hz, 1H, CH_2CH=CH_AH_B), 5.99 (ddt, J = 16.0, 10.0, 6.6 Hz, 1H, CH_2CH=CH_2), 6.27 (d, J = 9.5 Hz, 1H, 3-H), 7.38 (s, 1H, 5-H), 7.62 (d, J = 9.5 Hz, 1H, 4-H), 14.16 (s, 1H, 7-OH). MS-EI (70 eV) m/z: 272 (43), 257 (8), 244 (1), 229 (100), 201 (10), 173 (3), 115 (5). Anal. calcd. for $C_{16}H_{16}O_4$: C 70.57, H 5.92; found: C 70.55, H 5.99.

Compound 3f

Mp 98 °C. IR (cm^{-1}): 3080, 2960, 1740, 1725, 1620, 1560, 1450, 1390. ^{1}H NMR δ: 1.03 (t, J = 7.0 Hz, 3H, 3′-CH_3), 1.78 (tq, J = 7.0 Hz, 7.0 Hz, 2H, 2′-CH_2), 2.40 (d, J = 1.0 Hz, 3H, 4-CH_3), 3.32 (t, J = 7.0 Hz, 2H, 1′-CH_2), 3.43 (br d, J = 6.5 Hz, 2H, CH_2CH=CH_2), 5.08 (d, J = 9.0 Hz, 1H, CH_2CH=CH_AH_B), 5.11 (d, J = 16.0 Hz, 1H, CH_2CH=CH_AH_B), 5.98 (m, 1H, CH_2CH=CH_2), 6.13 (q, J = 1.0 Hz, 1H, 3-H), 7.49 (s, 1H, 5-H), 14.07 (s, 1H, 7-OH). ^{13}C NMR δ: 13.6 (1°, 3′-CH$_3$), 17.7 (2°, 2′-CH$_2$), 19.2 (1°, 4-CH$_3$), 33.4 (2°, CH$_2$CH=CH_2), 46.8 (2°, 1′-CH$_2$), 108.7 (4°, C-8), 111.0 (3°, C-3), 111.2 (4°, C-4a), 116.7 (2°, CH_2CH=CH_2), 126.1 (4°, C-6), 130.2 (3°, CH_2CH=CH_2), 135.3 (3°, C-5), 153.0 (4°, C-4), 153.6 (4°, C-8a), 159.6 (4°, C-7), 164.7 (4°, C-2), 207.3 (4°, C-1′). MS-EI (70 eV) m/z: 286 (61.1), 271 (12.8), 258 (2.9), 253 (8.5), 243 (100), 225 (2.9), 215 (14.5), 201 (2.1), 187 (4.3), 115 (9.8). Anal. calcd. for $C_{17}H_{18}O_4$: C 71.31, H 6.34; found: C 71.25, H 6.30.

© 2008 NRC Canada

Compound 3g

Mp 119 °C. IR (cm^{-1}): 3060, 1730, 1710, 1620, 1575, 1450, 1400, 1345. ^{1}H NMR δ: 3.49 (br d, *J* = 6.6 Hz, 2H, CH_2CH=CH_2), 5.17 (d, *J* = 12.0 Hz, 1H, CH$_2$CH=CH_AH$_B$), 5.18 (d, *J* = 15.0 Hz, 1H, CH$_2$CH=CH$_A$$H_B$), 6.02 (ddt, *J* = 15.0, 12.0, 6.6 Hz, 1H, CH$_2$C*H*=CH$_2$), 6.16 (d, *J* = 9.0 Hz, 1H, 3-H), 7.43 (s, 1H, 5-H), 7.46 (t, *J* = 9.0 Hz, 2H, 3′-H and 5′-H), 7.59 (d, *J* = 9.0 Hz, 1H, 4-H), 7.61 (br t, *J* = 9.0 Hz, 1H, 4′-H), 7.67 (br d, *J* = 9.0 Hz, 2H, 2′-H and 6′-H), 11.56 (s, 1H, 7-OH). Anal. calcd. for $C_{19}H_{14}O_4$: C 74.50, H 4.60; found: C 74.48, H 4.56.

Compound 3h

Mp 180 °C. IR (cm^{-1}): 3060, 1710, 1695, 1590, 1555, 1425, 1365. ^{1}H NMR δ: 2.26 (d, *J* = 1.0 Hz, 3H, 4-CH$_3$), 3.68 (br d, *J* = 6.5 Hz, 2H, CH_2CH=CH$_2$), 5.06 (dq, *J* = 10.0, 1.0 Hz, 1H, CH$_2$CH=CH_AH$_B$), 5.17 (dq, *J* = 16.0, 1.0 Hz, 1H, CH$_2$CH=CH$_A$$H_B$), 5.96 (m, 1H, CH$_2$C*H*=CH$_2$), 6.16 (q, *J* = 1.0 Hz, 1H, 3-H), 7.68 (s, 1H, 5-H), 7.71 (m, 5H, C$_6$H$_5$), 12.76 (s, 1H, 7-OH). Anal. calcd. for $C_{20}H_{16}O_4$: C 74.99, H 5.03; found: C 74.97, H 5.02.

Subsequent elution of the silica column of crude Claisen products from compounds **2a**, **2c**, and **2e** with petroleum ether/EtOAc (96:4, *v*/*v*) afforded the 3-allyl-8-coumarinyl ketones **4a**, **4c**, and **4e**, as appropriate. The products were crystallized from EtOAc/petroleum ether.

Compound 4a

Mp 147 °C. IR (cm^{-1}): 3080, 2960, 1730, 1710, 1610, 1400, 1325. ^{1}H NMR δ: 2.62 (sharp s, 3H, 1′-CH$_3$), 3.55 (br d, *J* = 7.0 Hz, 2H, 3-CH_2CH=CH$_2$), 4.99 (d, *J* = 13.0 Hz, 1H, 3-CH$_2$CH=CH_AH$_B$), 5.00 (d, *J* = 16.0 Hz, 1H, 3-CH$_2$CH=CH$_A$$H_B$), 5.90 (ddt, *J* = 16.0, 13.0, 7.0 Hz, 1H, 3-CH$_2$C*H*=CH$_2$), 6.22 (d, *J* = 9.5 Hz, 1H, 6-H), 7.57 (d, *J* = 9.5 Hz, 1H, 5-H), 7.74 (s, 1H, 4-H), 12.93 (s, 1H, 7-OH). ^{13}C NMR δ: 26.3 (2°, 3-*C*H$_2$CH=CH$_2$), 26.5 (1°, 1′-CH$_3$), 111.3 (4°, C-8), 113.6 (3°, C-6), 115.9 (2°, 3-CH$_2$CH=*C*H$_2$), 116.5 (4°, C-4a), 116.7 (4°, C-3), 129.2 (t, 3-CH$_2$*C*H=CH$_2$), 134.2 (3°, C-5), 143.2 (3°, C-4), 156.7 (4°, C-8a), 159.8 (4°, C-2), 163.5 (4°, C-7), 203.4 (4°, C-1′). MS-EI (70 eV) *m*/*z*: 244 (82.1), 229 (100), 211 (5.9), 201 (55.9), 187 (20.9), 173 (17.9), 155 (3.4), 145 (7.7), 127 (6.4), 115 (29.9). Anal. calcd. for $C_{14}H_{12}O_4$: C 68.84, H 4.95; found: C 68.82, H 4.91.

Compound 4c

Mp 130 °C. IR (cm^{-1}): 3080, 2970, 1735, 1710, 1620, 1560, 1450, 1400, 1360. ^{1}H NMR δ: 1.24 (t, *J* = 7.0 Hz, 3H, 2′-CH$_3$), 3.08 (q, *J* = 7.0 Hz, 2H, 1′-CH$_2$), 3.60 (br d, *J* = 7.0 Hz, 2H, 3-CH_2CH=CH$_2$), 5.02 (d, *J* = 10.0 Hz, 1H, 3-CH$_2$CH=CH_AH$_B$), 5.10 (d, *J* = 17.0 Hz, 1H, 3-CH$_2$CH=CH$_A$$H_B$), 5.95 (m, 1H, 3-CH$_2$C*H*=CH$_2$), 6.28 (d, *J* = 10.0 Hz, 1H, 6-H), 7.64 (d, *J* = 10.0 Hz, 1H, 5-H), 7.84 (s, 1 H, 4-H), 13.12 (s, 1 H, 7-OH). MS-EI (70 eV) *m*/*z*: 258 (35.5), 243 (5.1), 229 (100), 201 (54.7), 185 (2.1), 173 (8.5), 145 (3.8), 128 (4.7), 115 (13.6). Anal. calcd. for $C_{15}H_{14}O_4$: C 69.75, H 5.46; found: C 69.70, H 5.42.

Compound 4e

Mp 132 °C. IR (cm^{-1}): 3090, 2975, 1740, 1725, 1620, 1570, 1470, 1400. ^{1}H NMR δ: 1.04 (t, *J* = 7.2 Hz, 3H, 3′-CH$_3$), 1.80 (tq, *J* = 7.2 Hz, 7.2 Hz, 2H, 2′-CH$_2$), 3.00 (t, *J* = 7.2 Hz, 2H, 1′-CH$_2$), 3.61 (br d, *J* = 6.3 Hz, 2 H, 3-CH_2CH=CH$_2$), 5.02 (d, *J* = 10.0 Hz, 1H, 3-CH$_2$CH=CH_AH$_B$), 5.12 (d, *J* = 17.0 Hz, 1H, 3-CH$_2$CH=CH$_A$$H_B$), 5.97 (ddt, *J* = 17.0, 10.0, 6.3 Hz, 1H, 3-CH$_2$C*H*=CH$_2$), 6.27 (d, *J* = 9.6 Hz, 1H, 6-H), 7.63 (d, *J* = 9.6 Hz, 1H, 5-H), 7.83 (s, 1H, 4-H), 13.16 (s, 1H, 7-OH). MS-EI (70 eV) *m*/*z*: 272 (40), 257 (10), 244 (1.5), 229 (100), 201 (18), 173 (2), 145 (1), 115 (5). Anal. calcd. for $C_{16}H_{16}O_4$: C 70.57, H 5.92; found: C 70.53, H 5.94.

Further elution of the silica column of Claisen product mixture from compounds **2b**, **2d**, and **2f** afforded the 8-allyl-6-coumarinyl ketones **4b**, **4d**, and **4f**, respectively, from later petroleum ether/EtOAc (96:4, *v*/*v*) eluate fractions and subsequent crystallization from the appropriate solvent–solvent mixture.

Compound 5b

Mp 98 °C. IR (cm^{-1}): 3080, 2960, 1730, 1710, 1620, 1590, 1395, 1270. ^{1}H NMR δ: 2.43 (d, *J* = 1.0 Hz, 3H, 4-CH$_3$), 2.69 (sharp s, 3H, 1′-CH$_3$), 3.58 (br d, *J* = 7.0 Hz, 2H, 8-CH_2CH=CH$_2$), 5.00 (d, *J* = 10.0 Hz, 1H, 8-CH$_2$CH=CH_AH$_B$), 5.08 (d, *J* = 17.0 Hz, 1H, 8-CH$_2$CH=CH$_A$$H_B$), 5.94 (m, 1H, 8-CH$_2$C*H*=CH$_2$), 6.16 (q, *J* = 1.0 Hz, 1H, 3-H), 7.88 (s, 1H, 5-H), 12.96 (s, 1H, 7-OH). ^{13}C NMR δ: 18.6 (1°, 4-CH$_3$), 26.4 (2°, 8-*C*H$_2$CH=CH$_2$), 26.5 (1°, 1′-CH$_3$), 112.4 (q, C-6), 112.6 (3°, C-3), 115.7 (2°, 8-CH$_2$CH=*C*H$_2$), 116.1 (4°, C-4a), 116.3 (4°, C-8), 125.7 (3°, 8-CH$_2$*C*H=CH$_2$), 134.2 (3°, C-5), 151.9 (4°, C-4), 156.1 (4°, C-8a), 159.9 (4°, C-2), 163.1 (4°, C-7), 203.5 (4°, C-1′). Anal. calcd. for $C_{15}H_{14}O_4$: C 69.75, H 5.46; found: C 69.72, H 5.44.

Compound 5d

Mp 110 °C. IR (cm^{-1}): 3080, 2960, 1740, 1710, 1620, 1590, 1450, 1395. ^{1}H NMR δ: 1.32 (t, *J* = 7.0 Hz, 3H, 2′-CH$_3$), 2.45 (d, *J* = 1.0 Hz, 3H, 4-CH$_3$), 3.15 (q, *J* = 7.0 Hz, 2H, 1′-CH$_2$), 3.68 (br d, *J* = 7.0 Hz, 2H, 8-CH_2CH=CH$_2$), 5.06 (d, *J* = 10.0 Hz, 1H, 8-CH$_2$CH=CH_AH$_B$), 5.15 (d, *J* = 18.0 Hz, 1H, 8-CH$_2$CH=CH$_A$$H_B$), 5.99 (m, 1H, 8-CH$_2$C*H*=CH$_2$), 6.20 (s, 1H, 4-H), 7.95 (s, 1H, 5-H), 13.20 (s, 1H, 7-OH). ^{13}C NMR δ: 8.2 (1°, 2′-*C*H$_3$), 18.4 (1°, 4-*C*H$_3$), 26.5 (2°, 8-*C*H$_2$CH=CH$_2$), 31.5 (2°, 1′-CH$_2$), 112.5 (4°, C-6), 112.6 (3°, C-3), 115.8 (2°, 8-CH$_2$CH=*C*H$_2$), 116.0 (4°, C-8), 116.6 (4°, C-4a), 124.8 (3°, 8-CH$_2$*C*H=CH$_2$), 134.5 (3°, C-5), 151.7 (4°, C-4), 156.2 (4°, C-8a), 159.7 (4°, C-2), 163.4 (4°, C-7), 206.2 (4°, C-1′). MS-EI (70 eV) *m*/*z*: 272 (58.5),. 257 (10.6), 243 (100), 215 (29.9), 201 (1.6), 187 (7.2), 159 (1.7), 115 (2.5). Anal. calcd. for $C_{16}H_{16}O_4$: C 70.57, H 5.92; found: C 70.95, H 5.90.

Compound 5f

Mp 128 °C. IR (cm^{-1}): 3080, 2960, 1740, 1715, 1620, 1570, 1450, 1390. ^{1}H NMR δ: 1.10 (t, *J* = 8.0 Hz, 3H, 3′-CH$_3$), 1.80 (tq, *J* = 8.0 Hz, 8.0 Hz, 2H, 2′-CH$_2$), 2.50 (d, *J* = 1.0 Hz, 3H, 4-CH$_3$), 3.08 (t, *J* = 8.0 Hz, 2H, 1′-CH$_2$), 3.68 (br d, *J* = 7.0 Hz, 2H, 8-CH_2CH=CH$_2$), 5.08 (d, *J* = 11.0 Hz, 1H, CH$_2$CH=CH_AH$_B$), 5.18 (d, *J* = 18.0 Hz, 1H, 8-CH$_2$CH=CH$_A$$H_B$), 6.00 (m, 1H, 8-CH$_2$C*H*=CH$_2$), 6.24 (s, 1H, 4-H), 7.95 (s, 1H, 5-H), 13.24 (s, 1H, 7-OH). ^{13}C NMR δ: 13.7 (1°, 3′-*C*H$_3$), 18.0 (2°, 2′-*C*H$_2$), 18.7 (1°, 4-*C*H$_3$), 26.5 (2°, 8-*C*H$_2$CH=CH$_2$), 40.1 (2°, 1′-CH$_2$), 112.5(q, C-6), 112.8 (3°, C-3), 115.8 (2°, 8-CH$_2$CH=*C*H$_2$), 116.2 (4°, C-8), 116.6 (4°, C-4a), 125.0 (3°, 8-CH$_2$*C*H=CH$_2$), 134.5 (3°, C-5), 151.7 (4°, C-4), 156.3 (4°, C-8a), 159.8 (4°, C-2), 163.5 (4°,

© 2008 NRC Canada

C-7), 205.8 (4°, C-1′). MS-EI (70 eV) *m/z*: 286 (63.2), 271 (21.3), 258 (3.4), 243 (100), 215 (12.8), 201 (2.5), 187 (8.5), 115 (6.8). Anal. calcd. for $C_{17}H_{18}O_4$: C 71.31, H 6.34; found: C 71.27, H 6.29.

7-*O*(Cyclohex-2′-ene-1′-yl)-8-coumarinyl ketones 6a–6h

General procedure

Pure and dried 7-hydroxy-8-coumarinyl ketone **1a**–**1h** (2.5 mmol) taken in dry acetone (50 mL) were refluxed with 3-bromocyclohexene (0.4 mL, 0.003 mole) and NEt_3 (1 mL, 0.726 g, 0.007 mole) for 4 h. After distilling off acetone, water (10 mL) was added, and the content was acidified with cold dil HCl (4 N, 15 mL). The organic part of the mixture was then extracted with $CHCl_3$ (50 mL), which was washed successively with a saturated brine solution (15 mL), a saturated $NaHCO_3$ solution (2 × 15 mL), and again with a saturated brine solution (3 × 15 mL). The $CHCl_3$ layer was dried over anhydrous Na_2SO_4 for 30 min, filtered, and excess $CHCl_3$ was distilled off to obtain an oily mass. TLC experiment showed that the oily mass was more polar than the starting material on using 5% EtOAc/benzene as developer solvent. The oily mass was then column chromatographically filtered. Crystals of **6a**–**6h** were obtained on eluting with 10% EtOAc/petroleum ether and subsequent crystallization of the products.

Compound 6a

Mp 118 °C. IR (cm^{-1}): 3071, 2925, 1722, 1666, 1607, 1560, 1489, 1436, 1400. ^{1}H NMR δ: 1.66–1.63 (br m, 1H, 6′-H_{ax}), 1.93–1.82 (br m, 3H, 5′-H_2, 6′-H_{eq}), 2.18–2.01 (br m, 2H, 4′-H_2), 2.54 (sharp s, 3H, 8-$COCH_3$), 4.89 (br s, 1H, 1′-H), 5.78 (br d, *J* = 12.3 Hz, 1H, 2′-H), 5.98 (br dt, *J* = 11.1 Hz, 3.8 Hz, 1H, 3′-H), 6.21 (d, *J* = 9.6 Hz, 1H, 3-H), 6.90 (d, *J* = 8.7 Hz, 1H, 6-H), 7.41 (d, *J* = 8.7 Hz, 1H, 5-H), 7.76 (d, *J* = 9.6 Hz, 1H, 4-H). ^{13}C NMR δ: 18.67 (2°, C-5′), 24.90 (2°, C-4′), 28.39 (2°, C-6′), 32.13 (1°, 8-CO*C*H_3), 72.81 (3°, C-1′), 110.16 (3°, C-6), 112.83 (4°, C-4a), 113.72 (3°, C-3), 120.87 (4°, C-8), 124.85 (3°, C-2′), 129.29 (3°, C-5), 133.34 (3°, C-3′), 142.85 (3°, C-4), 151.49 (4°, C-8a), 157.53 (4°, C-2), 159.68 (4°, C-7), 198.53 (4°, 8-*C*OCH_3). Anal. calcd. for $C_{17}H_{16}O_4$: C 71.82, H 5.67; found: C 71.85, H 5.66.

Compound 6b

Mp 90 °C. IR (cm^{-1}): 3418, 3029, 2939, 1724, 1601, 1488, 1378, 1282. ^{1}H NMR δ: 1.70–1.62 (br m, 1H, 6′-H_{ax}), 1.81–1.75 (br m, 3H, 5′-H_2, 6′-H_{eq}), 2.08–2.02 (br m, 2H, 4′-H_2), 2.36 (d, *J* = 1.0 Hz, 3H, 4-CH_3), 2.60 (sharp s, 3H, 8-$COCH_3$), 4.88 (br s, 1H, 1′-H), 5.79 (br dt, *J* = 11.1 Hz, 2.7 Hz, 1H, 2′-H), 5.97 (br dt, *J* = 10.0 Hz, 2.7 Hz, 1H, 3′-H), 6.09 (q, *J* = 1.0 Hz, 1H, 3-H), 6.90 (d, *J* = 8.7 Hz, 1H, 6-H), 7.52 (d, *J* = 8.7 Hz, 1H, 5-H). Anal. calcd. for $C_{18}H_{18}O_4$: C 72.47, H 6.08; found: C 72.48, H 6.05.

Compound 6c

Mp 104 °C. IR (cm^{-1}): 3031, 2937, 1725, 1714, 1605, 1560, 1484, 1406. ^{1}H NMR δ: 1.17 (t, *J* = 7.2 Hz, 3H, 8-$COCH_2CH_3$), 1.64–1.59 (br m, 1H, 6′-H_{ax}), 1.84–1.73 (br m, 3H, 5′-H_2, 6′-H_{eq}), 1.92–1.85 (br m, 2H, 4′-H_2), 2.82 (q, *J* = 7.2 Hz, 2H, 8-$COCH_2CH_3$), 4.87 (s, 1H, 1′-H), 5.78 (br dt, *J* = 7.2 Hz, 3.1 Hz, 1H, 2′-H), 5.97 (br dt, *J* = 7.2 Hz, 3.2 Hz, 1H, 3′-H), 6.20 (d, *J* = 9.6 Hz, 1H, 3-H), 6.89 (d, *J* = 8.7 Hz, 1H, 6-H), 7.40 (d, *J* = 8.7 Hz, 1H, 5-H), 7.61 (d, *J* = 9.6 Hz, 1H, 4-H). ^{13}C NMR δ: 7.55 (1°, 8-$COCH_2CH_3$), 13.73 (3°, C-3), 18.65 (2°, C-5′), 24.93 (2°, C-4′), 28.42 (2°, C-6′), 38.00 (2°, 8-$COCH_2CH_3$), 72.74 (3°, C-1′), 110.14 (3°, C-6), 112.84 (4°, C-4a), 120.85 (4°, C-8), 124.90 (3°, C-2′), 129.10 (3°, C-5), 133.28 (3°, C-3′), 142.85 (3°, C-4), 151.52 (4°, C-8a), 157.54 (4°, C-2), 159.72 (4°, C-7), 201.98 (4°, 8-*C*OCH_2CH_3). Anal. calcd. for $C_{18}H_{18}O_4$: C 72.47, H 6.08; found: C 72.42, H 6.09.

Compound 6d

Mp 89 °C. IR (cm^{-1}): 3035, 2958, 1726, 1668, 1607, 1568, 1490, 1484, 1377. ^{1}H NMR δ: 1.18 (t, *J* = 7.2 Hz, 3H, 8-$COCH_2CH_3$), 1.67–1.61 (br m, 1H, 6′-H_{ax}), 1.96–1.90 (br m, 3H, 5′-H_2, 6′-H_{eq}), 2.14–2.03 (br m, 2H, 4′-H_2), 2.37 (d, *J* = 1.0 Hz, 3H, 4-CH_3), 2.83 (q, *J* = 7.2 Hz, 2H, 8-$COCH_2CH_3$), 4.44 (br s, 1H, 1′-H), 5.80 (br d, *J* = 10.5 Hz, 1H, 2′-H), 5.98 (br d, *J* = 10.0 Hz, 1H, 3′-H), 6.11 (q, *J* = 1.0 Hz, 1H, 3-H), 6.91 (d, *J* = 8.8 Hz, 1H, 6-H) 7.52 (d, *J* = 8.8 Hz, 1H, 5-H). Anal. calcd. for $C_{19}H_{20}O_4$: C 73.06, H 6.45; found: C 73.09, H 6.44.

Compound 6e

Mp 72 °C. IR (cm^{-1}): 3047, 2929, 1727, 1702, 1607, 1560, 1485, 1458. ^{1}H NMR δ: 0.96 (t, *J* = 7.4 Hz, 3H, 8-$COCH_2CH_2CH_3$), 1.67–1.63 (br m, 1H, 6′-H_{ax}), 1.72 (tq, *J* = 7.3 Hz, 7.3 Hz, 2H, 8-$COCH_2CH_2CH_3$), 1.84–1.82 (br m, 3H, 5′-H_2, 6′-H_{eq}), 2.07–2.01 (br m, 2H, 4′-H), 2.81 (t, *J* = 7.2 Hz, 2H, 8-$COCH_2CH_2CH_3$), 4.87 (br s, 1H, 1′-H), 5.79 (br dt, *J* = 10.0 Hz, 2.8 Hz, 1H, 2′-H), 5.97 (br dt, *J* = 10.0 Hz, 3.4 Hz, 1H, 3′-H), 6.20 (d, *J* = 9.5 Hz, 1H, 3-H), 6.87 (d, *J* = 8.7 Hz, 1H, 6-H), 7.39 (d, *J* = 8.7 Hz, 1H, 5-H), 7.60 (d, *J* = 9.5 Hz, 1H, 4-H). ^{13}C NMR δ: 13.64 (1°, 8-$COCH_2CH_2CH_3$), 16.92 (2°, 8-$COCH_2CH_2CH_3$), 18.66 (2°, C-5′), 24.93 (2°, C-4′), 28.40 (2°, C-6′), 46.76 (2°, 8-$COCH_2CH_2CH_3$), 72.70 (3°, C-1′), 110.08 (3°, C-6), 112.81 (4°, C-4a), 113.71 (3°, C-3), 120.95 (4°, C-8), 124.90 (3°, C-2′), 129.98 (3°, C-5), 133.23 (3°, C-3′), 142.85 (3°, C-4), 151.54 (4°, C-8a), 157.55 (4°, C-2), 159.71 (4°, C-7), 201.41 (4°, 8-*C*O$CH_2CH_2CH_3$). Anal. calcd. for $C_{19}H_{20}O_4$: C 73.06, H 6.45; found: C 73.05, H 6.48.

Compound 6f

Mp 64 °C. IR (cm^{-1}): 2952, 1735, 1718, 1611, 1570, 1491, 1434, 1408. ^{1}H NMR δ: 0.95 (t, *J* = 7.4 Hz, 3H, 8-$COCH_2CH_2CH_3$), 1.67–1.63 (br m, 2H, 6′-H_2), 1.71 (tq, *J* = 7.3 Hz, 7.3 Hz, 2H, 8-$COCH_2CH_2CH_3$), 1.92–1.86 (br m, 2H, 5′-H_2), 2.07–2.01 (br m, 2H, 4′-H_2), 2.36 (d, *J* = 1.0 Hz, 3H, 4-CH_3), 2.77 (t, *J* = 7.2 Hz, 2H, 8-$COCH_2CH_2CH_3$), 4.86 (br d, *J* = 2.0 Hz, 1H, 1′-H), 5.78 (br dt, *J* = 10.0 Hz, 2.7 Hz, 1H, 2′-H), 5.96 (br dt, *J* = 10.0 Hz, 3.2 Hz, 1H, 3′-H), 6.07 (q, *J* = 1.0 Hz, 1H, 3-H), 6.89 (d, *J* = 8.9 Hz, 1H, 6-H), 7.50 (d, *J* = 8.9 Hz, 1H, 5-H). Anal. calcd. for $C_{20}H_{22}O_4$: C 73.60, H 6.79; found: C 73.62, H 6.81.

Compound 6g

Mp 99 °C. IR (cm^{-1}): 2934, 1728, 1674, 1605, 1560, 1486, 1448, 1402. ^{1}H NMR δ: 1.43–1.36 (br m, 1H, 6-H′$_{ax}$), 1.76–1.66 (br m, 3H, 5′-$H_{2,\ 6}$′-H_{eq}), 1.90–1.85 (br m, 2H, 4′-H_2), 4.82 (br d, *J* = 3.3 Hz, 1H, 1′-H), 5.69 (br dt, *J* = 11.0 Hz, 3.5 Hz, 1.55 Hz, 1H, 2′-H), 5.83 (br dt, *J* =

© 2008 NRC Canada

10.2 Hz, 3.24 Hz, 1H, 3′-H), 5.85 (d, *J* = 9.5 Hz, 1H, 3-H), 6.20 (d, *J* = 8.7 Hz, 1H, 6-H), 7.38 (t, *J* = 7.4 Hz, 2H, 3′′-H and 5′′-H), 7.50 (d, *J* = 8.7 Hz, 1H, 5-H), 7.54 (br t, *J* = 7.5 Hz, 1H, 4′′-H), 7.65 (d, *J* = 9.5 Hz, 1H, 4-H), 7.83 (br d, *J* = 7.18 Hz, 2H, 2′′-H and 6′′-H). Anal. calcd. for $C_{22}H_{18}O_4$: C 76.29, H 5.24; found: C 76.32, H 5.22.

Compound 6h

Mp 130 °C. IR (cm^{-1}): 3063, 2905, 1730, 1665, 1608, 1575, 1491, 1440, 1381. ^{1}H NMR δ: 1.46–1.41 (br m, 2H, 6′-H_2), 1.78–1.66 (br m, 2H, 5′-H_2), 1.88–2.00 (br m, 2H, 4′-H_2), 2.44 (d, *J* = 1.0 Hz, 3H, 4-CH_3), 4.86 (br s, 1H, 1′-H), 5.72 (br d, *J* = 9.8 Hz, 1H, 2′-H), 5.88 (br d, *J* = 9.9 Hz, 1H, 3′-H), 6.13 (q, *J* = 1.0 Hz, 1H, 3-H), 7.00 (d, *J* = 8.7 Hz, 1H, 6-H), 7.42 (t, *J* = 7.4 Hz, 2H, 3′′-H and 5′′-H), 7.57 (br t, *J* = 7.18 Hz, 1H, 4′′-H), 7.64 (d, *J* = 8.7 Hz, 1H, 5-H), 7.83 (br d, *J* = 7.4 Hz, 2H, 2′′-H and 6′′-H). Anal. calcd. for $C_{23}H_{20}O_4$: C 76.65, H 5.59; found: C 76.68, H 5.58.

6-(Cyclohex-2′-ene-1′-yl)-7-hydroxy-8-coumarinyl ketones 7a–7h

General procedure

Pure and dry 7-(cyclohex-2′-ene-1′-yloxy)-8-coumarinyl ketones **6a**–**6h** (1.8 mmol) were taken in Ph_2O (10 mL) and refluxed for 10 min. The brown viscous liquid formed was less polar than the starting material (as shown by TLC experiment on using 5% EtOAc/benzene as developer). The brown liquid was then charged on a column of silica gel and eluted with petroleum ether and then with EtOAc/petroleum ether (1:9 *v*/*v*). The crystals of pure Claisen products **7a**–**7h** were obtained from the later eluate fraction.

Compound 7a

Mp 120 °C. IR (cm^{-1}): 3080, 2920, 1745, 1725, 1610, 1560, 1440, 1400, 1360. ^{1}H NMR δ: 1.62–1.48 (br m, 4H, 5′-H_2, 6′-H_2), 2.09–2.00 (br m, 2H, 4′-H_2), 2.95 (sharp s, 3H, 8-$COCH_3$), 3.86 (sextet, *J* = 2.8 Hz, 1H, 1′-H), 5.60 (br dt, *J* = 8 Hz, 2.7 Hz, 1H, 2′-H), 5.99 (br dt, *J* = 10.0 Hz, 2.1 Hz, 1H, 3′-H), 6.24 (br d, *J* = 9.5 Hz, 1H, 3-H), 7.42 (s, 1H, 5-H), 7.64 (d, *J* = 9.5 Hz, 1H, 4-H), 14.17 (s, 1H, 7-OH). ^{13}C NMR δ: 20.40 (2°, C-5′), 25.10 (2°, C-4′), 29.36 (2°, C-6′), 33.57 (1°, 8-CO*C*H_3), 33.64 (3°, C-1′), 108.87 (4°, C-4a), 110.27 (4°, C-8), 111.93 (3°, C-3), 128.67 (3°, C-2′), 129.94 (3°, C-5), 132.36 (4°, C-6), 133.19 (3°, C-3′), 144.24 (3°, C-4), 154.45 (4°, C-8a), 159.59 (4°, C-2), 165.03 (4°, C-7), 204.42 (4°, 8-*C*OCH_3). MS *m*/*z*: 285.4 $[M + H]^+$. Anal. calcd. for $C_{17}H_{16}O_4$: C 71.82, H 5.67; found: C 71.85, H 5.66.

Compound 7b

Mp 132 °C. IR (cm^{-1}): 3060, 2920, 1736, 1710, 1610, 1555, 1430, 1390, 1360. ^{1}H NMR δ: 1.53–1.44 (br m, 1H, 6′-H_{ax}), 1.62–1.54 (br m, 3H, 5′-H_2, 6′-H_{eq}), 2.1–1.99 (br m, 2H, 4′-H_2), 2.40 (d, *J* = 1.0 Hz, 3H, 4-CH_3), 2.93 (sharp s, 3H, 8-$COCH_3$), 3.89 (q, *J* = 3.0 Hz, 1H, 1′-H), 5.62 (br d, *J* = 8.1 Hz, 1H, 2′-H), 5.99 (br dd, *J* = 10.0 Hz, 2.2 Hz, 1H, 3′-H), 6.12 (q, *J* = 1.0 Hz, 1H, 3-H), 7.53 (s, 1H, 5-H), 14.70 (s, 1H, 7-OH). ^{13}C NMR δ: 19.04 (1°, 4-CH_3), 20.53 (2°, C-5′), 25.05 (2°, C-4′), 29.46 (2°, C-6′), 33.87 (1°, 8-CO*C*H_3), 33.97 (3°, C-1′), 108.93 (4°, C-4a), 110.96 (3°, C-3), 111.12 (4°, C-8), 128.76 (3°, C-2′), 129.60 (4°, C-6), 129.87 (3°, C-5), 131.81 (3°, C-3′), 153.07 (4°, C-4), 153.80 (4°, C-8a), 159.45 (4°, C-2), 164.61 (4°, C-7), 200.00 (4°, 8-*C*OCH_3). MS *m*/*z*: 299.2 $[M + H]^+$, 321.1 [M + Na]. Anal. calcd. for $C_{18}H_{18}O_4$: C 72.47, H 6.08; found: C 72.45, H 6.09.

Compound 7c

Mp 132 °C. IR (cm^{-1}): 3020, 2975, 1735, 1715, 1610, 1560, 1445, 1400. ^{1}H NMR δ: 1.25 (t, *J* = 7 Hz, 3H, 8-$COCH_2CH_3$), 1.62–1.48 (br m, 4H, 6′-H_2, 5′-H_2), 2.09–1.99 (br m, 2H, 4′-H_2), 3.41 (q, *J* = 7.0 Hz, 2H, 8-$COCH_2CH_3$), 3.87 (q, *J* = 2.7 Hz, 1H, 1′-H), 5.62 (br dt, *J* = 7.7 Hz, 2.3 Hz, 1H, 2′-H), 6.00 (br dt, *J* = 10.0 Hz, 3.4 Hz, 1H, 3′-H), 6.25 (br d, *J* = 9.5 Hz, 1H, 3-H), 7.40 (s, 1H, 5-H) 7.64 (d, *J* = 9.5 Hz, 1H, 4-H), 14.28 (s, 1H, 7-OH). ^{13}C NMR δ: 8.2 (1°, 8-$COCH_2CH_3$), 20.41 (2°, C-5′), 25.10 (2°, C-4′), 29.37 (2°, C-6′), 33.67 (3°, C-1′), 38.52 (2°, 8-$COCH_2CH_3$), 108.64 (4°, C-4a), 110.27 (4°, C-8), 111.61 (3°, C-3), 128.74 (3°, C-2′), 129.90 (3°, C-5), 132.44 (4°, C-6), 132.91 (3°, C-3′), 144.35 (3°, C-4), 154.35 (4°, C-8a), 159.64 (4°, C-2), 165.03 (4°, C-7), 207.63 (4°, 8-*C*OCH_2CH_3). MS *m*/*z*: 299.2 $[M + H]^+$, 321.2 [M + Na]. Anal. calcd. for $C_{18}H_{18}O_4$: C 72.47, H 6.08; found: C 72.43, H 6.07.

Compound 7d

Mp 114 °C. IR (cm^{-1}): 3033, 2980, 1735, 1710, 1610, 1550, 1400, 1320. ^{1}H NMR δ: 1.24 (t, *J* = 7.0 Hz, 3H, 8-$COCH_2CH_3$), 1.49–1.44 (br m, 1H, 6′-H_{ax}), 1.66–1.51 (br m, 3H, 5′-H_2, 6′-H_{eq}), 2.09–2.03 (br m, 2H, 4′-H_2), 2.38 (d, *J* = 1.0 Hz, 3H, 4-CH_3), 3.41 (q, *J* = 7.0 Hz, 2H, 8-$COCH_2CH_3$), 3.89 (br s, 1H, 1′-H), 5.63 (br d, *J* = 9.0 Hz, 1H, 2′-H), 6.00 (br dt, *J* = 10.0 Hz, 2 Hz, 1H, 3′-H), 6.13 (sharp q, *J* = 1.0 Hz, 1H, 3-H), 7.53 (s, 1H, 5-H), 14.20 (s, 1H, 7-OH). ^{13}C NMR δ: 8.29 (1°, 8-$COCH_2CH_3$), 19.14 (1°, 4-CH_3), 20.57 (2°, C-5′), 25.10 (2°, C-4′), 29.51 (2°, C-6′), 33.92 (3°, C-1′), 38.67 (2°, 8-$COCH_2CH_3$), 108.47 (4°, C-4a), 110.93 (3°, C-3), 111.15 (4°, C-8), 128.86 (3°, C-2′), 129.34 (3°, C-5), 129.84 (4°, C-6), 131.92 (3°, C-3′), 153.19 (4°, C-4), 153.73 (4°, C-8a), 159.63 (4°, C-2), 164.64 (4°, C-7), 208.00 (4°, 8-*C*OCH_2CH_3). MS-EI (70 eV) *m*/*z*: 312 (100, M), 283 (81.8), 258 (39), 229 (13.2), 215 (25.5), 203 (9.1), 187 (10), 128 (10), 115 (10), 91 (8.2), 77 (8.2). Anal. calcd. for $C_{19}H_{20}O_4$: C 73.06, H 6.45; found: C 73.09, H 6.46.

Compound 7e

Mp 114 °C. IR (cm^{-1}): 3040, 2970, 1730, 1715, 1610, 1550, 1445, 1405, 1310. ^{1}H NMR δ: 1.05 (t, *J* = 7.4 Hz, 3H, 8-$COCH_2CH_2CH_3$), 1.59–1.53 (br m, 1H, 6′-H_{ax}), 1.64–1.60 (br m, 3H, 5′-H_2, 6′-H_{eq}), 1.81 (tq, *J* = 7.2 Hz, 7.2 Hz, 2H, 8-$COCH_2CH_2CH_3$), 2.10–2.02 (br m, 2H, 4′-H_2), 3.35 (t, *J* = 7.0 Hz, 2H, 8-$COCH_2CH_2CH_3$), 3.86 (br d, *J* = 2.6 Hz, 1H, 1′-H), 5.62 (br dd, *J* = 10.0 Hz, 3.6 Hz, 1H, 2′-H), 5.99 (br dt, *J* = 10.2 Hz, 3.4 Hz, 1H, 3′-H), 6.25 (br d, *J* = 9.5 Hz, 1H, 3-H), 7.41 (s, 1H, 5-H), 7.64 (d, *J* = 9.5 Hz, 1H, 4-H), 14.00 (s, 1H, 7-OH). ^{13}C NMR δ: 13.70 (1°, 8-$COCH_2CH_2CH_3$), 17.95 (2°, 8-$COCH_2CH_2CH_3$), 20.41 (2°, C-5′), 25.10 (2°, C-4′), 29.37 (2°, C-6′), 33.70 (3°, C-1′), 46.92 (2°, 8-$COCH_2CH_2CH_3$), 108.79 (4°, C-4a), 110.27 (4°, C-8), 111.88 (3°, C-3), 128.78 (3°, C-2′), 129.93 (3°, C-5), 132.46 (4°, C-6), 132.97 (3°, C-3′), 144.34 (3°, C-4), 154.32 (4°, C-8a), 159.60 (4°, C-2), 165.15 (4°, C-7), 207.28 (4°, 8-

© 2008 NRC Canada

*C*OCH$_2$CH$_2$CH$_3$). MS *m/z*: 313.6 [M + H]$^+$. Anal. calcd. for $C_{19}H_{20}O_4$: C 73.06, H 6.45; found: C 73.05, H 6.44.

Compound 7f

Mp 89 °C. IR (cm^{-1}): 2958, 1724, 1711, 1603, 1563, 1490, 1448, 1372. ^{1}H NMR δ: 1.04 (t, *J* = 7.4 Hz, 3H, 8-COCH$_2$CH$_2$C*H*$_3$), 1.54–1.50 (br m, 1H, 6′-H$_{ax}$), 1.68–1.55 (br m, 3H, 5′-H$_2$, 6′-H$_{eq}$), 1.80 (tq, *J* = 7.0 Hz, 7.0 Hz, 2H, 8-COCH$_2$C*H*$_2$CH$_3$), 2.19–2.04 (br m, 2H, 4′-H$_2$), 2.40 (d, *J* = 1.0 Hz, 3H, 4-CH$_3$), 3.34 (t, *J* = 7.05 Hz, 2H, 8-COC*H*$_2$CH$_2$CH$_3$), 3.90 (br s, 1H, 1′-H), 5.63 (br d, *J* = 8.1 Hz, 1H, 2′-H), 6.01 (br dt, *J* = 8.0 Hz, 2.2 Hz, 1H, 3′-H), 6.14 (q, *J* = 1.0 Hz, 1H, 3-H), 7.54 (sharp s, 1H, 5-H), 14.17 (s, 1H, 7-OH). ^{13}C NMR δ: 13.67 (1°, 8-COCH$_2$CH$_2$*C*H$_3$), 18.02 (2°, 8-COCH$_2$*C*H$_2$CH$_3$), 19.10 (1°, 4-CH$_3$), 20.60 (2°, C-5′), 25.12 (2°, C-4′), 29.54 (2°, C-6′), 47.04 (2°, 8-CO*C*H$_2$CH$_2$CH$_3$), 108.94 (3°, C-1′), 108.95 (4°, C-4a), 111.00 (3°, C-3), 111.17 (4°, C-8), 128.91 (3°, C-2′), 129.36 (3°, C-5), 129.86 (3°, C-3′), 131.93 (4°, C-6), 153.09 (4°, C-4), 153.71 (4°, C-8a), 159.74 (4°, C-2), 164.71 (4°, C-7), 207.60 (4°, 8-*C*OCH$_2$CH$_2$CH$_3$). MS *m/z*: 327.3 [M + H]$^+$. Anal. calcd. for $C_{20}H_{22}O_4$: C 73.60, H 6.79; found: C 73.63, H 6.77.

Compound 7g

Mp 138 °C. IR (cm^{-1}): 3060, 2950, 1730, 1680, 1565, 1440, 1400, 1340. ^{1}H NMR δ: 1.67–1.54 (m, 3H, 5′-H$_2$, 6′-H$_{ax}$), 2.13–2.05 (br m, 3H, 6′-H$_{eq}$, 4′-H$_2$), 3.93 (br s, 1H, 1′-H), 5.69 (br d, *J* = 9.8 Hz, 1H, 2′-H), 6.04 (br dt, *J* = 10.1 Hz, 2.1 Hz, 1H, 3′-H), 6.16 (br d, *J* = 9.5 Hz, 1H, 3-H), 7.46 (t, *J* = 7.4 Hz, 2H, 3′′-H and 5′′-H), 7.46 (s, 1H, 5-H), 7.61 (br t, *J* = 7.3 Hz, 1H, 4′′-H), 7.62 (d, *J* = 9.3 Hz, 1H, 4-H), 7.68 (br d, *J* = 7.3 Hz, 2H, 2′′-H and 6′′-H), 11.64 (s, 1H, 7-OH). MS *m/z*: 347.4 [M + H]$^+$. Anal. calcd. for $C_{22}H_{18}O_4$: C 76.29, H 5.24; found: C 76.33, H 5.22.

Compound 7h

Mp 175 °C. IR (cm^{-1}): 3444, 2926, 1735, 1685, 1617, 1560, 1498, 1449, 1399. ^{1}H NMR δ: 1.84–1.62 (br m, 3H, 5′-H$_2$, 6′-H$_{ax}$), 2.29–2.15 (br m, 3H, 6′-H$_{eq}$, 4′-H$_2$), 2.43 (d, *J* = 1.0 Hz, 3H, 4-CH$_3$), 3.97 (br s, 1H, 1′-H), 5.73 (br d, *J* = 10.0 Hz, 1H, 2′-H), 6.07 (br d, *J* = 10.0 Hz, 1H, 3′-H), 6.16 (q, *J* = 1.0 Hz, 1H, 3-H), 7.48 (t, *J* = 7.4 Hz, 2H, 3′′-H and 5′′-H), 7.59 (s, 1H, 5-H), 7.61 (br t, *J* = 7.3 Hz, 1H, 4′′-H), 7.70 (br d, *J* = 7.3 Hz, 2H, 2′′-H and 6′′-H), 11.39 (s, 1H, 7-OH). MS-EI (70 eV) *m/z*: 360 (100, M), 339 (12.7), 332 (14.1), 317 (10.9), 306 (22.7), 279 (13.6), 263 (63.6), 215 (8.2), 165 (8.2), 115 (10.4), 105 (38.2), 77 (34.1) Anal. calcd. for $C_{23}H_{20}O_4$: C 76.65, H 5.59; found: C 76.63, H 5.61.

Acknowledgement

Sincere thanks are accorded to the Department of Chemistry, J.U. for IR spectra, CAS Instrumentation Centre, Department of Chemistry, C.U. for various NMR spectra, Indian Institute of Chemical Biology, Kolkata 700032 for mass spectral data, and Indian Association for the Cultivation of Science, Kolkata 700032 for elemental analyses.

References

1. (*a*) R.D.H. Murray. *In* Fortschritte der Chem. Org. Naturstoffe. Vol. 35. *Edited by* W. Herz, G.W. Kirby, and W.C. Steiglich. Springer-Verlag, Wien, Austria. 1978. p. 199; (*b*) R.D.H. Murray, J. Mendez, and S.A. Brown. *In* The natural coumarins, occurrence, chemistry and biochemistry. Wiley, New York. 1982; (*c*) R.D.H. Murray. *In* Fortschritte der Chem. Org. Naturstoffe. Vol. 58. *Edited by* W. Herz, G.W. Kirby, and W.C. Steiglich. Springer-Verlag, Wien, Austria. 1991. p. 83.
2. A.I. Gray and P.G. Waterman. Phytochemistry, **17**, 845 (1975).
3. E. Späth. Ber. Deutsch. Chem. Ges. **70A**, 83, (1937).
4. (*a*) J.R. Johnson. *In* Organic reactions. Vol. 1. *Edited by* R. Adams. Wiley, London, UK. 1942. p. 210; (*b*) S. Sethna and R. Phadke. *In* Organic reactions. Vol. 7. *Edited by* R. Adams. Wiley, London. 1953; (*c*) G. Jones. *In* Organic reactions. Vol. 15. *Edited by* A.C. Cope. Wiley, London. 1967. p. 204.
5. J.A. Joule and K. Mills. *In* Heterocyclic chemistry. Blackwell Publishing, New York. 2000. p. 181.
6. (*a*) H. Cairns, D. Cox, K.J. Gould, A.H. Ingall, and J.L. Suschitzky. J. Med. Chem. **28**, 1832 (1958); (*b*) S.R. Paraskar and P.H. Ladwa. Indian J. Chem. **22B**, 829 (1983).
7. S. Guchi and N. Utsugi. J. Pharm. Soc. Jpn. **73**, 1292 (1953).
8. E.J. Morris. Eur. Pat. Appl. EP 95-316. 30 Nov 1983. Chem. Abstr. **100**, 174665u (1984).
9. H. Nakayma, M. Ishikura, Y. Veda, K. Imai, M.Terajima, and A. Suzui. Jpn. Kokai Tokkoyo Koho JP03 48-674[91-48-6741]. 01 Mar 1991. Chem. Abstr. **115**, 158968z (1991).
10. M.M. Badran, A.K. El-Ansari, and S. El-Meligie. Egypt. J. Pharm. Sci. **30**, 379 (1989).
11. (*a*) L.N. Dutta, N.C. Sinha, and A.K. Sarkar. Indian J. Chem. **30B**, 1112, (1991); (*b*) L.N. Dutta, N.C. Sinha, and A.K. Sarkar. Indian J. Chem, **27B**, 801 (1988).
12. (*a*) L.N. Dutta, M. Bhattacharyya, and A.K. Sarkar. Can. J. Chem. **73**, 1556 (1995); (*b*) L.N. Dutta and M. Bhattacharyya. J. Indian Chem. Soc. **80,** 953 (2003).
13. L.N. Dutta and P.K. De. J. Indian Chem. Soc. **75**, 684 (1998).
14. (*a*) R.D.H. Murray, M.M. Ballantyne, and K.P. Mathai. Tetrahedron Lett. **11**, 243 (1970); (*b*) R.D.H. Murray, M.M. Ballantyne, T.C. Hogg, and P.H. McCabe. Tetrahedron, **31**, 2960 (1975).
15. (*a*) V.K. Ahluwalia, R.P. Singh, and S. Bala. Tetrahedron Lett. **23**, 2049 (1982); (*b*) V.K. Ahluwalia, C. Prakash, and R. Gupta. Synthesis, **48**, 1 (1980).
16. S.K. Ghantwal and S.D. Samant. Indian J. Chem. **38B**, 1242 (1999).
17. (*a*) K.C. Majumdar, A.T. Khan, and D.P. Das. Synth. Commun. **19**, 917 (1989); (*b*) K.C. Majumdar, A.T. Khan, A.K. Gupta, and K. Dey. Synth. Commun. **20**, 1249 (1990); (*c*) K.C. Majumdar and P. Chatterjee. Synth. Commun. **28**, 3633 (1998).
18. D.J. Clarke and R.S. Robinson. Tetrahedron, **58**, 2831 (2002).
19. S.K. Chattopadhyay, S. Maity, and S. Panja. Tetrahedron Lett. **43**, 7781 (2002).
20. K.C. Majumdar, P.K. Basu, and B. Roy. Synth. Commun. **33**, 3621 (2003).
21. A. Gerecs. *In* Friedel–Crafts and related reactions. Part I. Vol. 3. *Edited by* G.A. Olah. Wiley, New York. 1964. p. 499.
22. A. Patra, A.K. Mukhopadhyay, and A.K. Mitra. Indian J. Chem. **25B**, 1167 (1986).
23. G.C. Levy, R.L. Litcher, and G.L. Nelson. *In* Carbon-13 nuclear magnetic resonance for Organic Chemists. 2nd ed. Wiley, New York. 1980. p. 9.

© 2008 NRC Canada

Linear free-energy correlation analysis of the electronic effects of the substituents in the Sonogashira coupling reaction

Christine Gottardo, Thomas M. Kraft, M. Selim Hossain, Peter V. Zawada, and Heidi M. Muchall

Abstract: Relative rate constants (k_{rel}) for the Sonogashira coupling were determined in competitive reactions between iodobenzene and a series of *para*- and *meta*-substituted iodobenzenes and compared to the charge on iodine and the *z*-component of the quadrupole moment of the iodine-bearing carbon. We use an Hammett correlation analysis and the computational data to provide further evidence that the rate limiting step of the Sonogashira reaction is the initial oxidative addition of Pd to the carbon–iodine bond.

Key words: Sonogashira, competitive reactions, Hammett correlation.

Résumé : On a déterminé les constantes de vitesses relatives (k_{rel}) pour le couplage de Sonogashira dans des réactions compétitives entre l'iodobenzène et une série d'iodobenzènes substitués en positions *méta* et *para* et on a les a comparées à la charge sur l'iode et au composant *z* du moment quadripolaire du carbone portant l'iode. On a utilisé une analyse par corrélation de Hammett et des données de calculs théoriques pour obtenir d'autres bases pour établir que l'étape cinétiquement limitante de la réaction de Sonogashira est l'addition initiale oxydante du palladium sur la liaison carbone–iode.

Mots-clés : Sonogashira, réactions compétitives, corrélation de Hammett.

[Traduit par la Rédaction]

Introduction

Preparations of aryl alkynes have been described in the literature using the Sonogashira reaction since 1975 (1). As this coupling reaction has become the most important method for the synthesis of terminal aryl alkynes that have found use as building blocks in materials chemistry and natural product synthesis, amongst others, numerous variations in reaction conditions have been reported (2), and the efforts have culminated in a recent review (3). The original reaction involved the presence of a palladium catalyst, a base, and cuprous iodide. Studies investigating the nature of the aryl halide, the base, the solvent, and the palladium catalyst have all been reported with changes to the reaction that result in improved yields and reduced reaction times (4). In fact, the Sonogashira reaction was developed from earlier reports by Stephens and Castro who used cuprous acetylides to couple with phenyl halides (5). In their report, they indicate that electron-withdrawing groups in the *para*-position increase the ease of substitution with respect to electron-donating groups in the following manner: *p*-nitro > H > *p*-methoxy. Subsequent reports of Sonogashira coupling reactions have described improved yields when electron-withdrawing substituents, such as carboxaldehydes, nitro groups, and esters, are used (6).

The Sonogashira reaction is one of a family of coupling reactions; these reactions are proposed to proceed via an oxidative addition–reductive elimination via the use of d^{10} or d^8 catalysts such as Pd^0 or Pd^{2+} (1, 7, 8) or Ni^0 or Ni^{2+} (9, 10). The mechanisms of other reactions in this family, such as the Heck reaction (11, 12), Stille coupling (13), and Suzuki reaction (8, 9, 14) have been investigated previously, with a focus on the oxidative addition. Those studies focussed primarily on changes in reactivity resulting from changes in *para*-substitution. All but one (11) obtained a positive Hammett ρ value, indicating that the reaction involves an oxidative addition as the rate-determining step. Even in the case where a negative value (ρ = –1.6) was obtained, the researchers suggest that the oxidative addition is rate-limiting (11) and proceeds through a three-center reaction model, based on work presented for a d^9 iridium catalyst (15, 16).

In light of these studies, and having previously reported competitive Sonogashira reactions between iodobenzenes with electron-donating and electron-withdrawing groups in the *para*-position, which support the observations by Stephens and Castro (17), we would like to report on an extension of this research. A kinetic competition experiment between iodobenzene and a large number of *para*- and *meta*-

Received 21 December 2007. Accepted 13 February 2008. Published on the NRC Research Press Web site at canjchem.nrc.ca on 4 April 2008.

C. Gottardo,[1] T.M. Kraft, M.S. Hossain, and P.V. Zawada. Department of Chemistry, Lakehead University, Thunder Bay, ON P7B 5E1, Canada.
H.M. Muchall. Centre for Research in Molecular Modeling and Department of Chemistry and Biochemistry, Concordia University, Montreal, QC H4B 1R6, Canada.

[1]Corresponding author (e-mail: Christine.Gottardo@lakeheadu.ca).

 doi:10.1139/V08-038 © 2008 NRC Canada

substituted iodobenzenes is presented. The majority of studies presented in the literature have focused on *para*-substitution, and we present a number of new *meta*-substituted compounds to extend the scope of the study. Furthermore, a computational study was undertaken to analyze the relationship of the kinetic data with the electron density within the quantum theory of atoms in molecules (18).

Results and discussion

The substituted iodobenzenes were chosen for their availability and to ensure a range of electron-donating and electron-withdrawing substituents. The intermolecular competition was carried out using 1 equiv. each of iodobenzene and the substituted iodobenzene and 0.05 equiv. of the trimethylsilylacetylene. The Pd catalyst and CuI catalyst were present in 0.02 and 0.06 mol equiv., respectively. The choice of reaction conditions (catalyst, solvent, and base) was based on established reaction conditions that allow the Sonogashira coupling to occur for a wide variety of substituents (4). The alkyne was present at a level of 0.05 equiv. to establish pseudo first-order reaction conditions with respect to the aryl iodides. Biphenyl was used as an internal standard in the GC analysis and was added after the desired reaction time. The yields of the aryl alkynes were determined using this internal standard with the relative areas of the GC peaks (aryl alkyne : biphenyl) being compared to the response factors that had been previously obtained using pure samples of the products of known concentrations with known amounts of biphenyl added. To obtain pure samples of the aryl alkynes, samples of each of the aryl alkynes, **3** and **4a**–**4r**, were synthesized using an excess of the alkyne to ensure sufficient yields (Scheme 1). The relative rate constants for the substituted iodobenzenes were determined from the yield of products and are reported in Table 1. No products other than **3** and **4** could be detected by GC. A reaction containing iodobenzene in the presence of the catalysts (no alkyne present) was run to ensure that homocoupling of the aryl iodides did not occur. The products of oxidative homocoupling of the alkyne [bis(trimethylsilyl)butadiyne], Buchwald–Hartwig type amination of **3g** and **3r**, or Ulmann ether coupling could not be detected by GC.

The relative rate constants follow a predictable trend with the exception of the *m*-OH and *m*-NH_2 substituents. In both of these cases, the resonance effects of the substituents greatly overwhelm the inductive effects. Even more strikingly, *m*-OH appears to have a greater electron-donating effect than *p*-OH as evidenced by the relative rate constants, k_{rel} values of 0.0948 and 0.199, respectively. It is interesting to note that the effect of substituting a proton with a methyl group (**4p** to **4o** vs. **4r** to **4q**) has a more pronounced effect for the oxygen-containing substituent than for the nitrogen-containing substituent, with the *p*-OCH_3 group leading to a rate enhancement over the *p*-OH group of 2.6 times, while the rate increase of *p*-$N(CH_3)_2$ is only 1.5 times that of the *p*-NH_2 group. If the anomalous rates for the hydroxyl and primary amino groups are a result of coordination with the metal catalyst, removing two potential bonding sites from **4r** to **4q** vs. one site from **4p** to **4o** should have shown the greater effect. However, the overall effectiveness of the coordination in **4p** must have a greater relative influence on reactivity.

We next correlated the relative rate constants with the Hammett substituent constants (19) and found the best correlation with σ_p (Table 2; Fig. 1). The Hammett reaction constant ρ shows a higher sensitivity to substituent change than with the standard Hammett reaction (dissociation of benzoic acid), which is reasonable for a reaction site directly

Scheme 1.

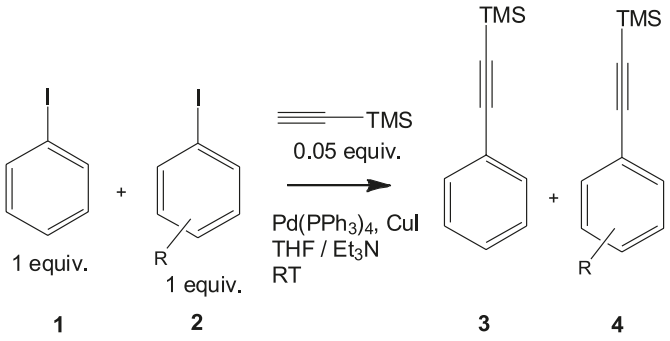

R = a) *m*-NO_2, b) *m*-CN, c) *m*-CO_2CH_3, d) *m*-CH_3, e) *m*-OCH_3, f) *m*-OH, g) *m*-NH_2, h) *p*-NO_2,i) *p*-CN, j) *p*-$C(O)CH_3$, k) *p*-CO_2CH_3 l) *p*-Ph m) *p*-C_2H_5 n) *p*-CH_3, o) *p*-OCH_3, p) *p*-OH, q) *p*-$N(CH_3)_3$, r) *p*-NH_2

Table 1. Relative rate constants of the Sonogashira coupling reaction.

4 (R =)	k_{rel}[a]
a) *m*-NO_2	9.60
b) *m*-CN	6.44
c) *m*-CO_2CH_3	4.03
d) *m*-CH_3	0.904
e) *m*-OCH_3	0.434
f) *m*-OH	0.0948
g) *m*-NH_2	0.0417
h) *p*-NO_2	36.7
i) *p*-CN	22.5
j) *p*-$C(O)CH_3$	3.54
k) *p*-CO_2CH_3	1.41
l) *p*-Ph	0.619
m) *p*-C_2H_5	0.855
n) *p*-CH_3	0.846
o) *p*-OCH_3	0.514
p) *p*-P–OH	0.199
q) *p*-$N(CH_3)_2$	0.035
r) *p*-NH_2	0.023

[a]Relative rate constants k_{rel} are calculated from the GC ratios: See supplementary material for the kinetic treatment.[2]

[2]Supplementary data for this article are available on the journal Web site (canjchem.nrc.ca) or may be purchased from the Depository of Unpublished Data, Document Delivery, CISTI, National Research Council Canada, Ottawa, ON K1A 0R6, Canada. DUD 3737. For more information on obtaining material, refer to cisti-icist.nrc-cnrc.gc.ca/irm/unpub_e.shtml.

© 2008 NRC Canada

Table 2. Hammett correlation data of relative rate (Log k_{rel}).

Substituent constant[11]	ρ^a	$R^{2\ b}$
σ^+_p	1.229	0.854
σ_p	1.803	0.904
σ^-_p	1.089	0.710

Fig. 1. Plot of (*a*) log k_{rel} against σ and (*b*) log k_{rel} against σ^- relationships for *para*-substitution (excluding the point for *p*-NH_2, □).

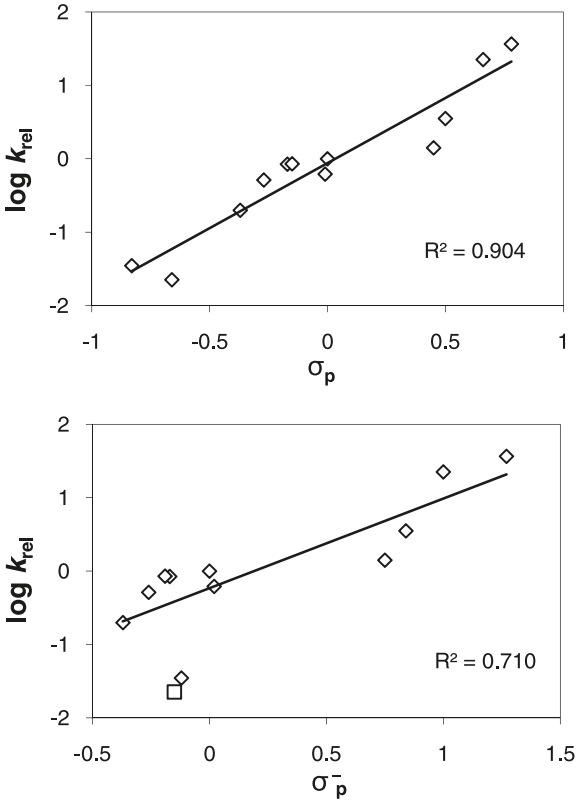

on a ring carbon atom, i.e., closer to the perturbing substituent. The positive value (1.8) indicates an increase in electron density at the rate-limiting step, suggesting a nucleophilic attack. In comparison, this ρ value is closest to that presented by Fauvarque et al. (7). Their conditions are significantly different, having completed an electrochemical kinetic study in which the results were obtained in the absence of copper. In their study, they attribute the rate-limiting step to the oxidative addition of the Pd to the aryl halide (7). In the study by Weissman and Milstein, an investigation of Suzuki coupling with aryl bromides, the best fit was with σ_p^- (R^2 = 0.97) with a ρ value of close to 1, which they attribute to conjugation with electron donors (14). They present data for only four *para*-substituted compounds, one of which is a strong resonance donator (14). Our data stem from a greater range of compounds, including strong resonance withdrawers; we do not see an effect that would indicate a strong direct resonance in either direction, i.e., anomalously high or low values of k_{rel} for withdrawers or donators.

The ease with which a nucleophilic attack on a ring carbon of the iodobenzenes occurs should be reflected in the

Fig. 2. Plot of the log of the rate against the *z*-component of the quadrupole moment of the iodine-bearing carbon for *para*-substitution.

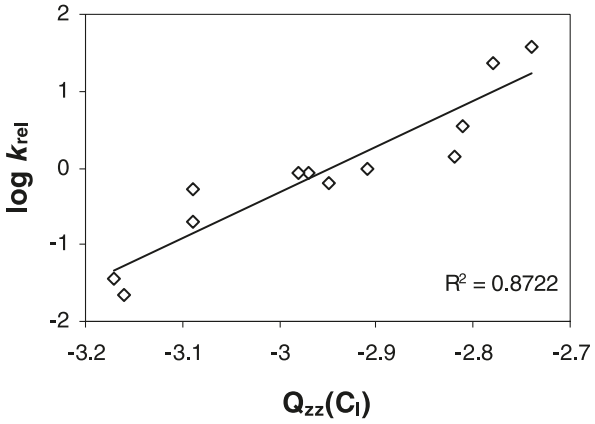

atomic properties of that carbon. Analyzing the electron density within the quantum theory of atoms in molecules (18), we obtained the charge on the ipso-C atom that bears the iodine atom, $q(C_I)$, and the *z*-component of the quadrupole moment of C_I, given as $Q_{zz}(C_I)$, as it has been correlated with the π-density on carbon atoms in aromatic systems (18). For comparison and because the first step in the suggested mechanism (see below) involves the C–I bond of the iodobenzenes, the charge on iodine, *q*(I), and its quadrupole moment component Q_{zz}(I) were obtained as well.

It is known that substituent effects in electrophilic aromatic substitutions cannot be explained through total atomic charges of the carbon atoms, because the σ and π contributions to the density are not affected uniformly by different substituents; while CH_3 is both σ and π electron-donating and CN is both σ and π withdrawing, OH is σ withdrawing and π donating (20). On the other hand, the negative values of Q_{zz}, indicative of a charge accumulation at the atom above and below the molecular plane, i.e., where one would expect π-density, are known to parallel the observed reactivity (20). These findings should also hold for the nucleophilic aromatic substitution. As expected in the iodobenzenes, therefore, while $q(C_I)$ for *meta*- or *para*-substitution does not correlate with a Hammett substituent constant, $Q_{zz}(C_I)$ shows a strong correlation with σ_p (R^2 = 0.9604). In contrast, *q*(I) correlates equally well with both σ_m (R^2 = 0.9060) and σ_p (R^2 = 0.9043). For relationships involving k_{rel} and log k_{rel}, we find that, for *para*-substitution, log k_{rel} correlates only with $Q_{zz}(C_I)$ (Fig. 2), while, for *meta*-substitution, the best correlation is found for k_{rel} with *q*(I) (Fig. 3).

The palladium cycle in the proposed mechanism of the Sonogashira reaction involves an oxidative addition (to give intermediate **5**) followed by a reductive elimination (to give product) (Fig. 4) (1). Electron density on the reactive site is most likely to be impacted in one of these two steps, since addition of the alkyne/ligand exchange on Pd would rely on the electronic effects being transmitted through the metal. Both the correlation of log k_{rel} with σ_p and with $Q_{zz}(C_I)$ indicate that the first insertion step is rate-limiting for the *para*-substituted iodobenzenes. The positive reaction constant of 1.8 indicates an increased electron density in the rate-

© 2008 NRC Canada

Fig. 3. Plot of the rate against the charge of the iodine atom for *meta*-substitution.

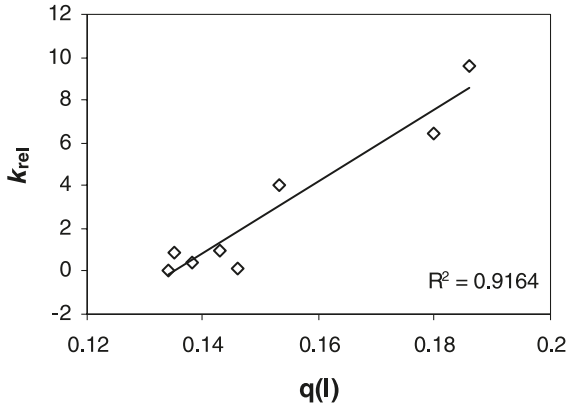

Fig. 4. Proposed mechanism of the Sonogashira reaction (1).

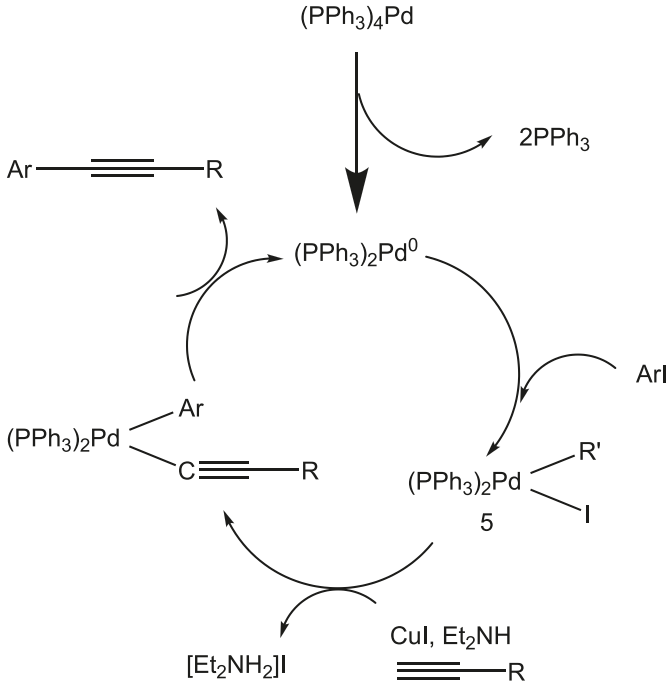

limiting step; the largest increase in electron density at the reaction site, according to Sonogashira's proposed mechanism, would occur to give **5** (Fig. 4). Furthermore, this proposed rate-limiting step is supported by the correlation of the rate with $Q_{zz}(C_I)$, i.e., a strong correlation existing with the undisturbed iodobenzenes. When we turned our attention to the *meta*-substituents, a correlation could be found between k_{rel} and σ_m (R^2 = 0.8849); when log k_{rel} was used, a correlation was not obtained (R^2 = 0.6768). Even though k_{rel} for the *meta*-substituted iodides correlates with q(I), a correlation supporting the first step of the reaction as being rate-determining is not as obvious. Since the final step of the reaction would result in a decreased electron density at the carbon, it should, therefore, result in a reaction constant with a negative value, which was not observed.

Conclusion

Both the experimental and computational results provide evidence that the rate-limiting step of the Sonogashira reaction is the oxidative addition of the metal catalyst. The evidence to support this rate-limiting step is not as compelling with the *meta*-substituted iodobenzenes as with the *para*-substituted iodobenzenes.

Experimental

Solvents and reagents were used as purchased unless otherwise noted. THF was dried over sodium. $Pd(PPh_3)_4$ was synthesized according to literature procedure (21) and stored under nitrogen at –4 °C.

General procedure for the Sonogashira coupling reactions– Preparation of aryl alkynes 3 and 4a–4r for use as standards

Iodobenzene, **1**, or the substituted iodobenzene, **2a**–**2r** (1.0 mmol), $Pd(PPh_3)_4$ (0.02 mmol, 23 mg), CuI (0.06 mmol, 11 mg), triethylamine (0.21 mL), and trimethylsilylacetylene (2.5 mmol, 245 mg, 0.353 mL) were combined in THF (2.5 mL) and stirred under argon at room temperature, 21 °C, overnight. The reaction was filtered through Celite, the solvent removed in vacuo, and the residue was purified by silica gel chromatography (hexanes/EtOAc = 90:10) to give products **3** and **4a**–**4r**. All of the products are known and were characterized or confirmed by spectral data, which is provided along with a Chemical Abstracts number for reference. The pure products were used to determine the detector response factors according to standard methods, using biphenyl as the internal standard.

Trimethyl[(3-nitrophenyl)ethynyl]silane, 4a [Chem. Abstr. 183322-33-0]

^{1}H NMR (200 MHz, $CDCl_3$) δ: 8.32 (s, 1H), 7.75 (dt, J = 7.8, 1.4 Hz, 1H), 7.49 (t, J = 6.6 Hz, 1H), 7.45 (t, J = 6.6 Hz, 1H) 0.26 (s, 9H).

3-[(Trimethylsilyl)ethynyl]benzonitrile, 4b [Chem. Abstr. 190771-22-3]

^{1}H NMR (500 MHz, $CDCl_3$) δ: 7.74 (s, 1H), 7.66 (dt, J = 6.4, 1.2 Hz, 1H), 7.58 (dt, J = 6.4, 1.2 Hz, 1H), 7.42 (t, J = 6.4 Hz, 1H), 0.26 (s, 9H).

Methyl 3-[(trimethylsilyl)ethynyl]benzoate, 4c [Chem. Abstr. 77123-59-2]

^{1}H NMR (500 MHz, $CDCl_3$) δ: 7.88 (s, 1H), 7.71 (d, J = 6 Hz, 1H), 7.31 (d, J = 6 Hz, 1H), 7.12 (t, J = 6 Hz, 1H), 3.92 (s, 3H), 0.27 (s, 9H).

Trimethyl[(3-methylphenyl)ethynyl]silane, 4d [Chem. Abstr. 40230-90-8]

^{1}H NMR (200 MHz, $CDCl_3$) δ: 7.36 (s, 1H), 7.40 (t, J = 7.3 Hz, 1H), 7.18 (d, J = 7.2 Hz, 1H), 7.14 (d, J = 7.1 Hz, 1H), 2.32 (s, 3H), 0.26 (s, 9H).

© 2008 NRC Canada

Trimethyl[(3-methoxyphenyl)ethynyl]silane, 4e [Chem. Abstr. 40230-92-0]

^{1}H NMR (200 MHz, $CDCl_3$) δ: 7.39 (dt, *J* = 9.0, 2.4 Hz, 1H), 7.26 (s, 1H), 7.13 (t, *J* = 9.0 Hz, 1H), 7.06 (dt, *J* = 8.5, 2.4 Hz, 1H), 3.36 (s, 3H), 0.37 (s, 9H).

3-[(Trimethylsilyl)ethynyl]phenol, 4f [Chem. Abstr. 388061-72-1]

^{1}H NMR (500 MHz, $CDCl_3$) δ: 7.16 (t, *J* = 7.5 Hz, 1H), 7.06 (d, *J* = 8.0 Hz, 1H), 6.96 (s, 1H), 6.81 (d, *J* = 6.0 Hz, 1H), 5.10 (s, 1H), 0.27 (s, 9H).

3-[(Trimethylsilyl)ethynyl]aniline, 4g [Chem. Abstr. 110598-30-6]

^{1}H NMR (200 MHz, $CDCl_3$) δ: 7.65 (t, *J* = 8.0 Hz, 1H), 6.86 (dt, *J* = 8.0, 3.0 Hz, 1H), 6.78 (s, 1H), 6.63 (dt, *J* = 8.0, 3.0 Hz, 1H), 3.50 (s, 2H), 0.27 (S, 9H).

Trimethyl[(4-nitrophenyl)ethynyl]silane, 4h [Chem. Abstr. 75867-38-8]

^{1}H NMR (200 MHz, $CDCl_3$) δ: 8.18 (d, *J* = 6.6 Hz, 2H), 7.50 (d, *J* = 6.7 Hz, 2H), 0.31 (s, 9H).

4-[(Trimethylsilyl)ethynyl]benzonitrile, 4i [Chem. Abstr. 75867-40-2]

^{1}H NMR (500 MHz, $CDCl_3$) δ: 7.59 (d, *J* = 6.4 Hz, 2H), 7.53 (d, *J* = 6.4 Hz, 2H), 0.26 (s, 9H).

1-[4-[(Trimethylsilyl)ethynyl]phenyl]ethanone, 4j [Chem. Abstr. 75883-03-3]

^{1}H NMR (500 MHz, $CDCl_3$) δ: 7.89 (d, *J* = 5.2 Hz, 2H), 7.54 (d, *J* = 5.2 Hz, 2H), 2.61 (s, 3H), 0.27 (s, 9H).

Methyl 4-[(trimethylsilyl)ethynyl]benzoate, 4k [Chem. Abstr. 75867-41-3]

^{1}H NMR (500 MHz, $CDCl_3$) δ: 7.97 (d, *J* = 6.8 Hz, 2H), 7.52 (d, *J* = 6.8 Hz, 2H), 3.92 (s, 3H), 0.26 (s, 9H).

([1,1′-Biphenyl]-4-ylethynyl)trimethylsilane, 4l [Chem. Abstr. 75867-42-4]

^{1}H NMR (500 MHz, $CDCl_3$) δ: 7.49 (d, *J* = 6.0 Hz, 2H), 7.44 (m, 4H), 7.34 (t *J* = 6.0 Hz, 2H), 7.26 (t, *J* = 6.0 Hz, 1H), 0.19 (s, 9H). ^{13}C NMR (125 MHz, $CDCl_3$) δ: 141.1, 140.3, 132.4, 128.8, 127.6, 127.0, 126.9, 122.0, 105.0, 94.8, 0.3.

Trimethyl[(4-ethylphenyl)ethynyl]silane, 4m [Chem. Abstr. 393857-27-7]

^{1}H NMR (500 MHz, $CDCl_3$) δ: 7.39 (d, *J* = 8 Hz, 2H), 7.10 (d, *J* = 8 Hz, 2H), 2.62 (q, *J* = 7 Hz, 2H), 1.21 (t, *J* = 7.5 Hz, 3H), 0.27 (s, 9H).

Trimethyl[(4-methylphenyl)ethynyl]silane, 4n [Chem. Abstr. 4186-14-5]

^{1}H NMR (500 MHz, $CDCl_3$) δ:7.11 (d, *J* = 3.2 Hz, 2H), 6.83 (d, *J* = 3.2 Hz, 2H), 2.34 (s, 3H), 0.26 (s, 9H).

Trimethyl[(4-methoxyphenyl)ethynyl]silane, 4o [Chem. Abstr. 3989-14-8]

^{1}H NMR (200 MHz, $CDCl_3$) δ: 7.42 (d, *J* = 8.7 Hz, 2H), 6.81 (d, *J* = 8.7 Hz, 2H), 3.60 (s, 3H), 0.70 (s, 9H).

4-[(Trimethylsilyl)ethynyl]phenol, 4p [Chem. Abstr. 88075-18-7]

^{1}H NMR (500 MHz, $CDCl_3$) δ: 7.35 (d, *J* = 3.5 Hz, 2H), 7.53 (d, *J* = 3 Hz, 2H), 5.30 (s, 1H), 0.23 (s, 9H).

N,N-Dimethyl-4-[(trimethylsilyl)ethynyl]aniline, 4q [Chem.Abstr. 40230-97-5]

^{1}H NMR (500 MHz, $CDCl_3$) δ: 7.31 (d, *J* = 9.0 Hz, 2H), 6.55 (d, *J* = 9.0 Hz, 2H), 2.92 (s, 6H), 0.21 (s, 9H).

4-[(Trimethylsilyl)ethynyl]aniline, 4r [Chem. Abstr. 75867-39-9]

^{1}H NMR (200 MHz, $CDCl_3$) δ: 7.27 (d, *J* = 6.8 Hz, 2H), 6.57 (d, *J* = 6.8 Hz, 2H), 3.80 (bs, 2H), 0.22 (s, 9H).

General procedure for the competitive coupling reactions

The intermolecular competition was carried out using iodobenzene (1.0 mmol, 204 mg, 0.11 mL) and the substituted iodobenzene, **2a**–**2r** (1.0 mmol), $Pd(PPh_3)_4$ (0.02 mmol, 23 mg), CuI (0.06 mmol, 11 mg), triethylamine (0.21 mL), and trimethylsilylacetylene (0.05 mmol, 5 mg, 7 μL) combined in THF (2.5 mL) and stirred under argon at room temperature, 21 °C. After a standard reaction time of 5 h, a GC of the mixture was run (internal standard biphenyl), and the relative rates of reactivity were calculated. The reported rates are an average of a minimum of two experiments.

GC conditions

The reaction mixtures were analyzed by a flame ionization detector (FID) and DB-5 High Temp column. The initial oven temperature was 50 °C, which was ramped by 5 °C/min to the final temperature of 200 °C, which was held for 5 min. At least two GC runs were performed for each sample to ensure reproducibility.

Computational details

All geometry optimizations were performed with Gaussian03 (22), using the Perdew–Burke–Ernzerhof (PBE0) hybrid density functional (23–25) with the 6–31+G(d) basis set for all atoms except for iodine and the Midi! basis set (26) for iodine. All geometries were confirmed to be minima by frequency calculations. In case of rotational isomerism (*m*-CO_2CH_3, *m*-OCH_3, and *m*-OH), the lower-energy conformer, determined through either electronic energies or Gibbs free energies, given in Fig. S2 in the supplementary information was used in the analyses.[2] Wave functions were analyzed with the Proaim module from the AIMPAC (27) series of programs for charges (q) and quadrupole moments (Q_{zz}); both are obtained from integrations of the electron density over the atomic basin. For *p*-C_2H_5 (torsional angle 90°) and *p*-Ph (torsional angle 40°), wave functions were also obtained for the planarized geometries and these were used in the analyses. Total energies as well as the q and Q_{zz} data used in the correlations are given in Table S1 of the supplementary information.[2]

Acknowledgments

Financial support by the Natural Sciences and Engineering Research Council of Canada (NSERC) is gratefully

© 2008 NRC Canada

acknowledged. We thank D. Leach (GC of compounds **4b** and **4i**) and A. Raitsakas (GC of compound **4m**) of Lakehead University for assistance with some analyses. Calculations were performed at the Centre for Research in Molecular Modeling (CERMM), which was established with the financial support of the Concordia University Faculty of Arts and Science, the Ministère de l'Éducation du Québec (MEQ), and the Canada Foundation for Innovation (CFI).

References

1. K. Sonogashira, Y. Tohda, and K. Hagihara. Tetrahedron Lett. **16**, 4467 (1975).
2. E. Negishi and L. Anastasia. Chem. Rev. **103**, 1979 (2003).
3. R. Chinchilla and C. Nájera. Chem. Rev. **107**, 874 (2007).
4. S. Thorand and N. Krause. J. Org. Chem. **63**, 8551 (1998).
5. R.D. Stephens and C.E. Castro. J. Org. Chem. **28**, 3313 (1963).
6. S. Takashi, Y. Kuroyama, K. Sonogashira and N. Hagihara. Synthesis, 627 (1980).
7. J.-F. Fauvarque, F. Pfluger, and M. Troupel. J. Organomet. Chem. **208**, 419 (1981).
8. C. Amatore and F. Pfluger. Organometallics, **9**, 2276 (1990).
9. D. Zim, V.R. Lando, J. Dupont, and A.L. Monteiro. Org. Lett. **3**, 3049 (2001).
10. S. Saito, S. Oh-tani, and N. Miyaura. J. Org. Chem. **62**, 8024 (1997).
11. R. Benhaddou, S. Czernecki, G. Ville, and A. Zegar. Organometallics, **7**, 2435 (1988).
12. A.S. Gruber, D. Zim, G. Ebeling, A.L. Monteiro, and J. Dupont. Org. Lett. **2**, 1287 (2000).
13. D. Milstein and J.K. Stille. J. Am. Chem. Soc. **101**, 4992 (1979).
14. H. Weissman and D. Milstein. Chem. Commun. 1901 (1999).
15. R. Ugo, A. Pasini, A. Fusi, and S. Cenini. J. Am. Chem. Soc. **94**, 7364 (1972).
16. R.J, Mureinik, M. Weitzberg, and J. Blum. Inorg. Chem. **18**, 915 (1979).
17. C. Gottardo and A. Aguirre. Tetrahedron Lett. **43**, 7091 (2002).
18. R.F.W. Bader. Atoms in molecules: A quantum theory. Clarendon Press, Oxford, UK. 1990.
19. Substituent constants were taken from: (*a*) C. Hansch, A. Leo, and R.W. Taft. Chem. Rev. **91**, 165 (1991); (*b*) D.H. McDaniel and H.C. Brown. J. Org. Chem., **23**, 420 (1958).
20. R.F.W. Bader and C. Chang. J. Phys. Chem. **93**, 2946 (1989).
21. F.R. Hartley. The chemistry of platinum and palladium: with particular reference to complexes of the elements. John Wiley & Son, New York. 1973.
22. M.J. Frisch, G.W. Trucks, H.B. Schlegel, G.E. Scuseria, M.A. Robb, J.R. Cheeseman, J.A. Montgomery, Jr., T. Vreven, K.N. Kudin, J.C. Burant, J.M. Millam, S.S. Iyengar, J. Tomasi, V. Barone, B. Mennucci, M. Cossi, G. Scalmani, N. Rega, G.A. Petersson, H. Nakatsuji, M. Hada, M. Ehara, K. Toyota, R. Fukuda, J. Hasegawa, M. Ishida, T. Nakajima, Y. Honda, O. Kitao, H. Nakai, M. Klene, X. Li, J.E. Knox, H.P. Hratchian, J.B. Cross, C. Adamo, J. Jaramillo, R. Gomperts, R.E. Stratmann, O. Yazyev, A.J. Austin, R. Cammi, C. Pomelli, J.W. Ochterski, P.Y. Ayala, K. Morokuma, G.A. Voth, P. Salvador, J.J. Dannenberg, V.G. Zakrzewski, S. Dapprich, A.D. Daniels, M.C. Strain, O. Farkas, D.K. Malick, A.D. Rabuck, K. Raghavachari, J.B. Foresman, J.V. Ortiz, Q. Cui, A.G. Baboul, S. Clifford, J. Cioslowski, B.B. Stefanov, G. Liu, A. Liashenko, P. Piskorz, I. Komaromi, R.L. Martin, D.J. Fox, T. Keith, M.A. Al-Laham, C.Y. Peng, A. Nanayakkara, M. Challacombe, P.M.W. Gill, B. Johnson, W. Chen, M.W. Wong, C. Gonzalez, and J.A. Pople. Gaussian 03 [computer program], Revision C.02. Gaussian, Inc., Wallingford CT. 2004.
23. J.P. Perdew, K. Burke, and M. Ernzerhof. Phys. Rev. Lett. **77**, 3865 (1996).
24. J.P. Perdew, K. Burke, and M. Ernzerhof. Phys. Rev. Lett., **78**, 1396 (1997).
25. J.P. Perdew, M. Ernzerhof, and K.Burke. J. Chem. Phys. **105**, 9982 (1996).
26. R.E. Easton, D.J. Giesen, A. Welch, C.J. Cramer, and D.G. Truhlar. Theor. Chim. Acta **93**, 281 (1996).
27. Available from Professor R.F.W. Bader, McMaster University, Hamilton, ON L8S 4M1, Canada, and from the AIMPAC website (www.chemistry.mcmaster.ca/aimpac, last accessed on February 6, 2008).

© 2008 NRC Canada

Oxyhalogen–sulfur chemistry — Kinetics and mechanism of the bromate oxidation of cysteamine

Moshood K. Morakinyo, Edward Chikwana, and Reuben H. Simoyi

Abstract: The kinetics and mechanism of the oxidation of the biologically important molecule, cysteamine, by acidic bromate and molecular bromine have been studied. In excess acidic bromate conditions, cysteamine is oxidized to N-brominated derivatives, and in excess cysteamine the oxidation product is taurine according to the following stoichiometry: $BrO_3^- + H_2NCH_2CH_2SH \rightarrow H_2NCH_2CH_2SO_3H + Br^-$. There is quantitative formation of taurine before N-bromination commences. Excess aqueous bromine oxidizes cysteamine to give dibromotaurine: $5Br_2 + H_2NCH_2CH_2SH + 3H_2O \rightarrow Br_2NCH_2CH_2SO_3H + 8Br^- + 8H^+$, while excess cysteamine conditions gave monobromotaurine. The oxidation of cysteamine by aqueous bromine is effectively diffusion-controlled all the way to the formation of monobromotaurine. Further formation of dibromotaurine is dependent on acid concentrations, with highly acidic conditions inhibiting further reaction towards formation of dibromotaurine. The formation of the N-brominated derivatives of taurine is reversible, with taurine regenerated in the presence of a reducing agent such as iodide. This feature makes it possible for taurine to moderate hypobromous acid toxicity in the physiological environment.

Key words: cysteamine, hypobromous acid, toxicities, antioxidant.

Résumé : On a étudié la cinétique et le mécanisme de l'oxydation de la molécule biologiquement importante, cystéamine, par le bromate acide et le brome moléculaire. Dans des conditions de bromate acide en excès, la cystéamine est oxydée en dérivés bromés et, dans un excès de cystéamine, le produit d'oxydation est la taurine qui est formée en d'après la stoechiométrie: $BrO_3^- + H_2NCH_2CH_2SH \rightarrow H_2NCH_2CH_2SO_3H + Br^-$. Il y a formation quantitative de taurine avant que la N-bromation commence. Un excès de brome en milieu aqueux provoque une oxydation de la cystéamine avec formation de dibromotaurine: $5Br_2 + H_2NCH_2CH_2SH + 3H_2O \rightarrow Br_2NCH_2CH_2SO_3H + 8Br^- + 8H^+$, alors que les conditions dans lesquelles la cystéamine est en excès conduit à la formation de la monobromotaurine. L'oxydation de la cystéamine par le brome aqueux est effectivement une réaction sous contrôle de la diffusion jusqu'à la formation de la monobromotaurine. La formation subséquente de dibromotaurine dépend des concentrations d'acide alors que les conditions fortement acides inhibent la réaction subséquente pouvant conduire à la formation de la dibromotaurine. La formation des dérivés N-bromés de la taurine est réversible, la taurine pouvant être régénérée en présence d'un agent réducteur, tel un ion iodure. Cette caractéristique fait que la taurine peut réduire le caractère toxique de l'acide hypobromeux dans un environnement physiologique.

Mots-clés : cystéamine, acide hypobromeux, toxicités, antioxydant.

[Traduit par la Rédaction]

Introduction

Sulfur metabolism in biological systems is believed to be the main source of thiols (1, 2). The most important thiols in biological chemistry are cysteine, homocysteine, and glutathione. Glutathione is the most abundant non-protein thiol in mammals, an adult human having about 30 g glutathione widely distributed in most tissues, with levels in the kidney and liver significantly higher (3). In general, thiols are readily oxidized to disulfides in the presence of mild oxidants, and in the presence of more powerful oxidants S-oxygenation can occur, which yields, successively, sulfenic, sulfinic, and sulfonic acids. In some cases, the C–S bond cleaves to give sulfate as the final oxidation product (2, 4). Those thiols without an amino group adjacent to the sulfhydryl group are easily oxidized to sulfate and a mixture of alcohols, aldehydes, and carboxylic acids (depending on the amount and strength of oxidant). α-Aminothiols are very reactive, but will not easily cleave the C–S bond, and can thus be regenerated for further use after oxidation to the S-oxide or the disulfide (5). Sulfinic and sulfonic acids formed from thiols with an amino group on the α or β position have been found to be quite stable (6, 7).

In living systems, S-oxygenation of the thiol group in the physiological environment can be initiated by two microsomal systems: one involving cytochrome P-450 sys-

Received 30 August 2007. Accepted 6 February 2008. Published on the NRC Research Press Web site at canjchem.nrc.ca on 5 April 2008.

M.K. Morakinyo, E. Chikwana,[1] and R.H. Simoyi.[2] Department of Chemistry, Portland State University, Portland, OR 97207-0751, USA.

[1]Present address: Department of Chemistry & Biochemistry, California State University-Chico, CA 95929-0210, USA.
[2]Corresponding Author (e-mail: rsimoyi@pdx.edu).

 doi:10.1139/V08-031 © 2008 NRC Canada

tem of enzymes and the other based on the flavin-containing monooxygenase (8–10). In the presence of these enzyme systems and cofactor-like compounds such as sulfide and hydroxylamine, cysteamine is oxidized to the sulfinic acid derivative, hypotaurine. Most metabolic pathways, however, give hypotaurine as a precursor to taurine (the sulfonic acid). Scheme I encompasses nearly all possible reactions of cysteamine in the physiological environment.

Cysteamine and its major metabolite, hypotaurine, are known to be excellent scavengers of HOCl and other reactive oxygen species (ROS) and are more likely to act as antioxidants in vivo than taurine (3, 11, 12). These ROS can cause damage to DNA, proteins, and lipids in addition to causing radical damage and oxidative stress in animal cells (11, 13, 14). In addition to protection against radical damage in DNA, cysteamine can also act as a repair agent for DNA through the formation of the protective $RSSR^{\bullet -}$, which then reacts with the $DNA^{\bullet +}$ radical ion to regenerate DNA and form cystamine, the cysteamine disulfide (2, 3). The ability of cystamine to reversibly form disulfide links with the sulfhydryl groups at or near the active sites of enzymes is also important in regulation of several essential metabolic pathways (15, 16).

Our research group embarked on a series of studies to elucidate the kinetics and mechanisms of the oxidation of cysteamine and its S-oxides. Previous studies done in our laboratory on the cysteamine sulfinic acid, hypotaurine, have shown that it reacts quite rapidly with chlorite to give a mixture of taurine, monocloro- and dichloro-taurine (17). Oxidation is believed to occur simultaneously at the sulfur center (to give the sulfonic acid) and at the nitrogen center (to give the chloramines). The oxidation of taurine by chlorite (18) and bromate (19) showed that oxidation occurs only on the nitrogen centre to give the corresponding N-derivatives. The reaction was exceedingly slow, even with the most powerful oxidizing agents such as acidic bromate. The formation of *N*-bromo- and *N*-chloro-taurines is suggested as a possible mechanism by which taurine can moderate the oxidative toxicity of halogens and hypobromous and hypochlorous acid in the slightly basic physiological environments (20).

A recent study from our laboratory on the oxidation of cysteamine by iodine and acidic iodate showed that these mild oxidants only oxidized cysteamine to its dimer, cystamine (21). In this study, stronger oxidants bromine and acidic bromate have been used. The aim of the study reported in this manuscript was to investigate whether these oxidants also produced cystamine as a viable product or whether the oxidation proceeded to hypotaurine or all the way to taurine as well as the *N*-bromotaurines. Bromate is a precursor to HOBr, a particularly damaging oxidizing species in the physiological environment. Stimulated granulocytes produce oxidizing agents (especially H_2O_2) and secrete granular proteins into the extracellular medium, which contributes to their antimicrobial, cytotoxic, and cytolytic activities (22). Each group of cells contains a specific peroxidase, which catalyzes the reactions of hydrogen peroxide with halogens. The enzyme, myeloperoxidase, which is abundant in neutrophils, catalyzes the oxidation of Br^- ions by H_2O_2 to yield HOBr as a reactive and oxidatively damaging product (23).

Scheme I.

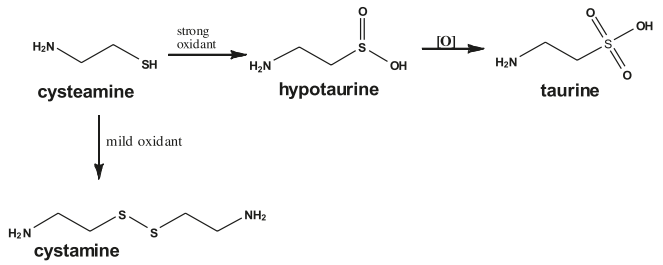

[R1] $H_2O_2 + Br^- + \text{Myeloperoxidase}/H^+ \rightarrow HOBr + H_2O$

Taurine and its precursors, e.g., hypotaurine and cysteamine have been suggested as possible moderators of HOBr toxicity by forming longer-lived and less oxidizing products in their reactions with HOBr (24).

Experimental

Materials

Cysteamine hydrochloride (CA, 2-aminoethanethiol hydrochloride) 98%, cystamine, bromine, potassium iodide, potassium bromide (Sigma-Aldrich), sodium perchlorate (98%) (Acros), sodium bromate, perchloric acid (72%), soluble starch, sodium thiosulfate, and hydrochloric acid (Fisher) were used without further purification. The concentration of bromine was determined by standardization against thiosulfate solution after addition of excess acidic iodide. Spectrophotometry was used as a complementary technique by measuring bromine absorbance at 390 nm where the extinction coefficient had been deduced to be 142 mol^{-1} L cm^{-1}. This standardization was carried out before each series of kinetic experiments owing to the volatile nature of bromine. CA solutions were prepared just before use and not kept for more than 24 h. All solutions were prepared using distilled and deionized water from a Barnstead Sybron Corporation water-purification unit. Inductively coupled plasma mass spectrometry (ICPMS) analysis showed negligible concentrations of iron, copper, and silver and approximately 1.5 ppb of cadmium and 0.43 ppb in lead as the most abundant metal ions, which was not enough to affect the overall reaction kinetics and mechanism (25).

Methods

All experiments were carried out at 25.0 ± 0.1 °C and a constant ionic strength of 1.0 mol/L ($NaClO_4$). CA, sodium perchlorate, and perchloric acid solutions were mixed in one vessel and bromate (or bromine) solutions in another. A PerkinElmer Lambda 25 UV–vis spectrophotometer interfaced to a Pentium IV computer was used for most of the kinetics and stoichiometric determinations. The slower BrO_3^- – CA reactions were monitored on the UV–vis spectrophotometer by monitoring bromine absorbance at 390 nm. Faster reactions were followed on a Hi-Tech Scientific SF61 – DX2 double mixing stopped-flow spectrophotometer.

© 2008 NRC Canada

Results

Stoichiometry

The stoichiometry of the BrO_3^- – cysteamine reaction in acidic medium is very complex. The reaction showed simultaneous oxidations at both the nitrogen and sulfur centers to give N-derivatives of the cysteamine sulfonic acid. Unlike what had been observed with other small organic sulfur molecules subjected to strong oxidizing agents, there is no cleavage of the C–S bond as evidenced by the lack of sulfate production. The reaction gives a mixture of products: $H_2NCH_2CH_2SO_3H$, $Br(H)NCH_2CH_2SO_3H$, and $Br_2NCH_2CH_2SO_3H$, all of which give nearly identical ^1H NMR spectra in the strongly acidic medium necessary for bromate oxidations.

Iodometric titrations in excess bromate conditions gave a reproducible stoichiometry consistent with a $6e^-$ oxidation of the sulfur center to the sulfonic acid, taurine, according to the following stoichiometric ratio:

$$[R2] \quad BrO_3^- + H_2NCH_2CH_2SH \rightarrow H_2NCH_2CH_2SO_3H + Br^-$$

In this titrimetric method, excess acidic bromate was reacted with a fixed amount of cysteamine and the excess oxidizing power left after complete consumption of cysteamine determined by addition of excess acidified iodide followed by a thiosulfate titration. Figure 1*a* shows a plot of thiosulfate titer vs. initial bromate concentrations. The plot is linear, as expected, with the intercept on the bromate concentration axis (zero thiosulfate titer) representing the exact amount of bromate needed to oxidize cysteamine. Data shown in Fig. 1*a* were taken with cysteamine fixed at 0.0020 mol/L. The intercept concentration on the bromate axis is 0.0021 mol/L, which is very close, within statistical error, to the 1:1 stoichiometric ratio of reaction [R2]. The UV spectrum of the product solution, on the other hand, shows a strong absorption peak at 244 nm, which is consistent with the formation of dibromotaurine. This is even more evident when Br^- is deliberately added to the reaction mixture to produce predominantly the dibromotaurine after prolonged standing.

$$[R3] \quad 5BrO_3^- + 3H_2NCH_2CH_2SH + Br^- + 6H^+ \rightarrow 3Br_2NCH_2CH_2SO_3H + 6H_2O$$

Reaction [R3] is preceded by the formation of monobromotaurine:

$$[R4] \quad 4BrO_3^- + 3H_2NCH_2CH_2SH + 3H^+ \rightarrow 3(Br)HNCH_2CH_2SO_3H + Br^- + 3H_2O$$

Direct reaction of cysteamine with aqueous bromine showed a clean 1:5 stoichiometric ratio:

$$[R5] \quad 5Br_2 + H_2NCH_2CH_2SH + 3H_2O \rightarrow Br_2NCH_2CH_2SO_3H + 8Br^- + 8H^+$$

Stoichiometry [R5] was deduced by mixing excess bromine solutions with a fixed amount of cysteamine and measuring the residual absorbance of bromine at 390 nm. None of the mono- or di-bromotaurine products absorb at 390 nm, and so all contribution to the absorbance at this wavelength was attributed solely to bromine. Figure 1*b* shows the data derived from such a series of experiments for a fixed concentration of 3.0×10^{-4} mol/L cysteamine. The intercept concentration of the $[Br_2]_0$ axis is 1.5×10^{-3} mol/L, which represents the exact amount of bromine needed to consume 3×10^{-4} mol/L cysteamine, which confirms the 1:5 stoichiometry.

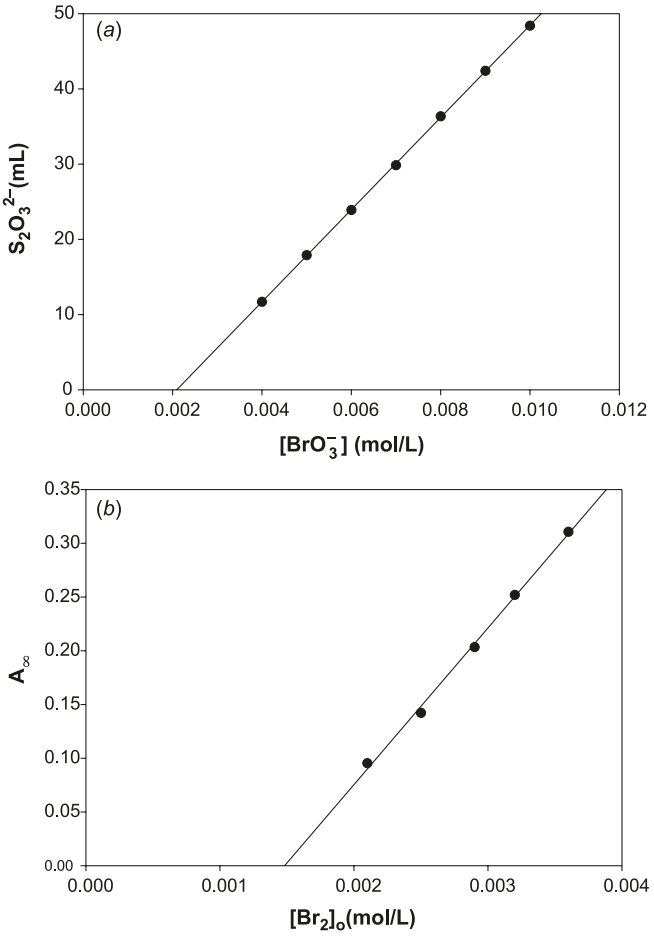

Fig. 1. (*a*) Iodometry titration for stoichiometry analysis of product solutions for a constant $[CA]_o$ and $[H^+]_o$ of 0.002 mol/L and 0.2 mol/L, respectively. $[BrO_3^-]$ = (a) 0.004 mol/L, (b) 0.005 mol/L, (c) 0.006 mol/L, (d) 0.007 mol/L, (e) 0.008 mol/L, (f) 0.009 mol/L, (g) 0.010 mol/L. This intercept represents the maximum amount of bromate tolerated by the reaction system before permanent bromine production is observed. (*b*) Plot of absorbance at infinity (A_∞) vs. $[Br_2]_o$ from the bromine oxidation of cysteamine. The intercept, as expected, is consistent with the stoichiometry equation proposed for the direct Br_2 – CA reaction. [CA] = 0.0003 mol/L, $[Br_2]_{intercept}$ = 0.0015 mol/L.

Monobromotaurine and dibromotaurine can be quantified in the reaction product by their rapid reaction with excess iodide to produce iodine, which could be determined spectrophotometrically and (or) titrimetrically:

$$[R6] \quad (Br)HNCH_2CH_2SO_3H + 2I^- + H^+ \rightarrow H_2NCH_2CH_2SO_3H + I_2\ (aq) + Br^-$$

© 2008 NRC Canada

Reaction [R6] is the reason why iodometric titrations in excess bromate only showed the formation of the sulfonic acid taurine (stoichiometry [R2]), and not the *N*-bromo derivatives. Their formation was masked, since they rapidly oxidized the iodide to iodine.

Product identification

Dibromotaurine was identified by its distinct UV spectrum featuring a sharp strong peak at 244 nm and a weaker peak at 336 nm (26). In addition to a peak also at 336 nm, monobromotaurine has an absorption peak at 288 nm (27) with a weak absorptivity coefficient of only 425 mol^{-1} L cm^{-1}. Bromine oxidations of cysteamine always produced mixtures of the mono- and di-bromotaurines, with the monobromotaurine's peak at 336 nm completely obscured by the contribution from dibromotaurine. Highly acidic environments favored monobromotaurine over dibromotaurine, since the ratio of the absorbance at 288:244 increased with a decrease in pH. This ratio also increased if taurine was added to the stoichiometric solution [R5]. Quantitative formation of monobromotaurine could be achieved by mixing an exact 1:4 ratio of cysteamine to bromine:

$$[R7] \quad 4Br_2 + H_2NCH_2CH_2SH + 3H_2O \rightarrow BrHNCH_2CH_2SO_3H + 7Br^- + 7H^+$$

^{1}H NMR spectra were also used to prove that the cysteamine carbon skeleton of two sets of methylene protons is not disturbed during its oxidation. Figure 2 shows the series of spectra representing the reactants and products. Spectrum A is of pure cysteamine in neutral pH showing the methylene proton triplets centered at 2.78 and 3.15 ppm. Spectrum B is of the product of cysteamine–bromate reaction in acidic medium. The two methylene triplets appear at 3.4 and 4.08 ppm with a larger coupling constant than observed with pure cysteamine. Spectrum C is of pure hypotaurine, while D is of the oxidation product of hypotaurine with acidic bromate. Spectrum E is the standard spectrum of taurine in D_2O at nearly neutral pH. The appearance of the methylene peaks upfield compared with the other spectra is due to the comparatively higher pH conditions utilized in the acquisition of this spectrum. Spectrum F is the product of the taurine–bromate reaction. Spectra B, D, and F are identical, showing that cysteamine, hypotaurine, and taurine are all oxidized by acidic bromate to the same final product. The two smaller triplets appearing on the bromate–taurine spectrum are due to the fact that this reaction produces a mixture of products, which also include the oxime, $H(OH)NCH_2CH_2SO_3H$ (28).

Reaction kinetics

As with all bromate oxidations, this reaction is only viable in highly acidic environments. The reaction could be monitored by following the appearance of bromine in excess bromate conditions. In this configuration, the reaction initially showed a quiescent period with no formation of bromine. We shall call this period the "induction period". The end of the induction period is signaled by the formation of bromine. Figure 3*a* shows a series of typical bromine absorbance traces derived from varying the initial bromate concentrations. At the end of the induction period, there is a

Fig. 2. ^{1}H NMR spectrum showing (A) cysteamine, (B) cysteamine + BrO_3^- + H^+, (C) hypotaurine, (D) hypotaurine + BrO_3^- + H^+, (E) taurine, and (F) taurine + BrO_3^- + H^+.

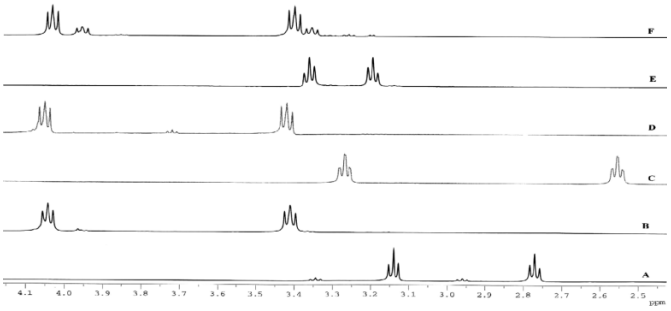

Fig. 3. (*a*) Effect of varying bromate concentration on the oxidation of CA by bromate. There is an increase in the rate of bromine formation as the bromate concentration is increased. $[CA]_o$ = 0.005 mol/L, $[H^+]_o$ = 0.2 mol/L, $[BrO_3^-]$ = (a) 0.05 mol/L, (b) 0.06 mol/L, (c) 0.07 mol/L, (d) 0.08 mol/L, (e) 0.09 mol/L, (f) 0.10 mol/L, (g) 0.11 mol/L. (*b*) Linear plot of reciprocal induction time vs. $[BrO_3^-]$ for data shown in Fig. 3*a*.

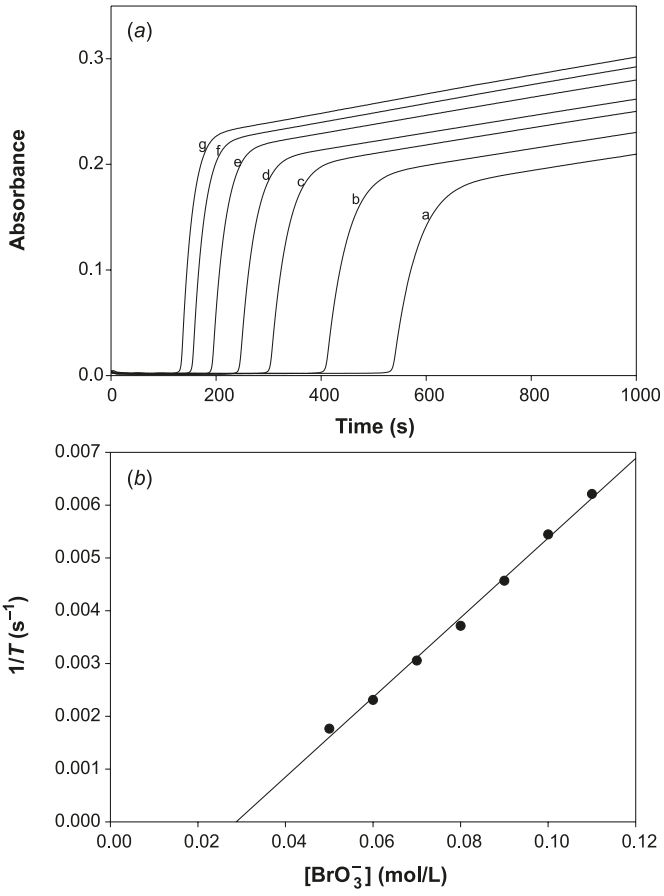

© 2008 NRC Canada

rapid formation of bromine, which eventually gives way to a slower rate of formation until the excess bromate or bromide formed from the reaction mixture has been exhausted, thus shutting down the BrO_3^-/Br^- reaction:

[R8] $BrO_3^- + 5Br^- + 6H^+ \rightarrow 3Br_2 + 3H_2O$

Figure 3*b* shows that the length of this induction period has an inverse linear dependence upon initial bromate concentrations. This would suggest that the precursor reaction to the formation of bromine depends on bromate concentrations to the first power. Figure 4*a* shows the reaction's dependence on acid concentrations, with Fig. 4*b* showing that the induction period follows an inverse squared dependence on acid that tends towards saturation as acid concentrations are further increased. The biphasic bromine formation in Fig. 4*a* is worth noting. Though higher acid concentrations reduce the induction period, they also reduce the amount of bromine formed in the rapid first step. The rate of formation of bromine in the slower phase appeared insensitive to variations in acid concentrations, and they also appear to be zero-order. Figure 5 shows that for as long as $[BrO_3^-]_0 \gg [CA]_0$, then the induction period will be invariant, but the rate and amount of bromine formed after the induction period varies with initial cysteamine concentrations. This trend would be expected, since reaction [R8] is catalyzed by bromide, and higher CA concentrations would produce higher bromide concentrations.

The direct reaction of bromine with CA was so rapid that its rate approached the detection limit of our stopped-flow apparatus. The only way to slow the reaction down so that it could be observed on our stopped-flow ensemble was to flood the reaction with bromide so that the reaction being observed was between CA and tribromide (see Fig. 6) (29, 30).

[R9] $Br_2 + Br^- \rightleftharpoons Br_3^-$; $K_{eq} = 17$

[R10] $3Br_3^- + H_2NCH_2CH_2SH + 3H_2O \rightarrow H_2NCH_2CH_2SO_3H + 6H^+ + 9Br^-$

The reaction involves a very fast initial step that is complete in less that 50 ms followed by a slower step that takes about 1.0 s. The initial step involves the consumption of approximately 3 equiv. of bromine to 1 equiv. of CA. This is equivalent to oxidizing CA to taurine:

[R11] $3Br_2 + H_2NCH_2CH_2SH + 3H_2O \rightarrow H_2NCH_2CH_2SO_3H + 6Br^- + 6H^+$

The formation of bromamines after formation of taurine appears to constitute the slower stage of the reaction. Figure 7 shows a series of experiments in which bromine is in excess of the stoichiometric amounts needed to satisfy reactions [R5] and [R7]. Trace a is a control experiment, which was not flooded with bromide. It shows that the reaction is complete within the mixing time of the stopped-flow instrument. The rest of the other traces show one single rapid step without a slower second step. No acid was added to this series of kinetics runs, and this appears to enhance the normally slower second step. The full 5:1 stoichiometry [R5] is attained within 0.5 s. Acid, however, was not inhibitory enough to allow for the determination of kinetics constants

Fig. 4. (*a*) Effect of progressively increasing $[H^+]$ at constant [CA] and $[BrO_3^-]$. $[CA]_o = 0.005$ mol/L, $[BrO_3^-]_o = 0.05$ mol/L, $[H^+]$ = (a) 0.20 mol/L, (b) 0.25 mol/L, (c) 0.30 mol/L, (d) 0.35 mol/L, (e) 0.40 mol/L, (f) 0.45 mol/L, (g) 0.50 mol/L, (h) 0.60 mol/L. (*b*) Plot showing the linear dependence of induction time on the reciprocal of $[H^+]_o^2$ for data shown in Fig 4*a*.

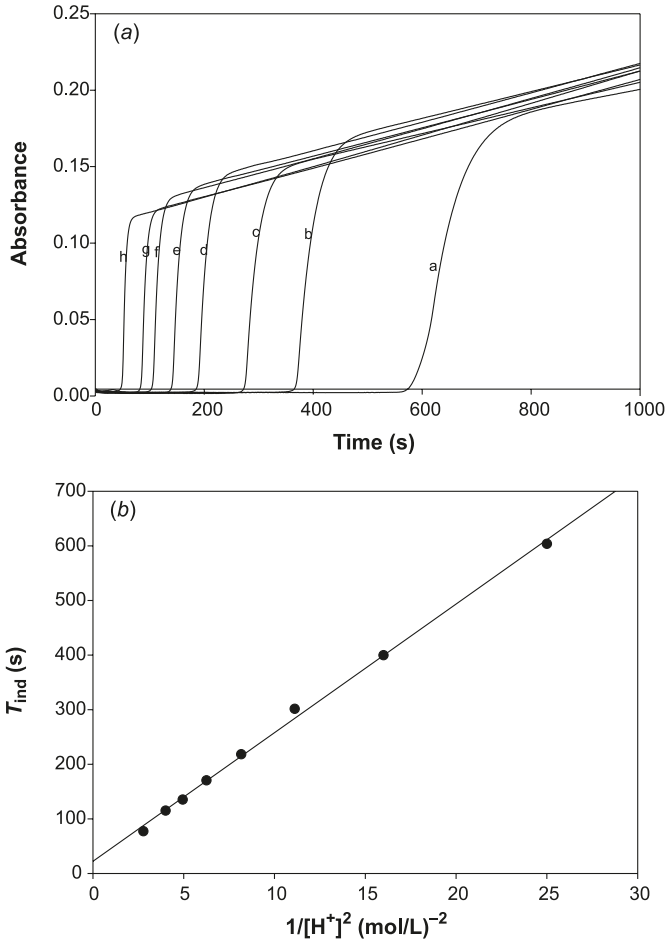

for the Br_2 – CA reaction, but it appeared to stunt the second slower part of the reaction in which bromamines are formed (see Fig. 8).

Mechanism

The rapid Br_2 – CA reaction implies that in both Figs. 1*a* and 3*a*, formation of bromine indicates complete consumption of CA. Any bromine formed in the presence of CA will be rapidly consumed and will not accumulate. The bromine–hypotaurine reaction was also found to be as rapid as the Br_2 – CA reaction; which implies that reaction [R2] has to run its course before bromine production commences.

The inverse bromate dependence and inverse square acid dependence of the induction period implies that the rate-determining step to reaction [R11] is the well-known standard bromate initiation reaction:

[R12] $BrO_3^- + 2H^+ + Br^- \rightleftharpoons HBrO_2 + HOBr$

We base our assertion on the following logic. The direct reaction of bromine and cysteamine (Figs. 6–8) is so rapid (close to diffusion-controlled) and much faster than the reac-

© 2008 NRC Canada

Fig. 5. "Peacock-tail type" traces obtained from variation of $[CA]_o$ in excess $[BrO_3^-]_o$ conditions. The final Br_2(aq) increases with $[CA]_o$, but the induction period does not change. $[BrO_3^-]$ = 0.1 mol/L, $[H^+]$ = 0.2 mol/L, [CA] = (a) 0.005 mol/L, (b) 0.006 mol/L, (c) 0.007 mol/L, (d) 0.008 mol/L, (e) 0.009 mol/L, (f) 0.010 mol/L, (g) 0.011 mol/L.

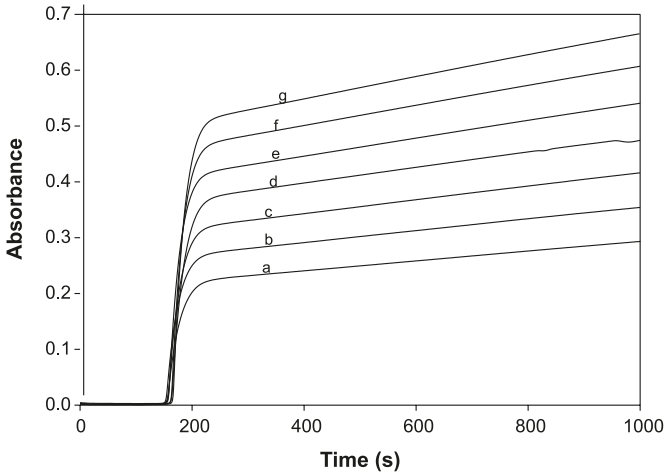

Fig. 6. Effect of varying CA on the direct reaction of Br_2 vs. CA in excess bromide monitored at 390 nm. $[Br_2]$ = 0.00215 mol/L, $[Br^-]$ = 1.0 mol/L, [CA] = (a) 0.0001 mol/L (b) 0.0002 mol/L (c) 0.0003 mol/L (d) 0.0004 mol/L (e) 0.0005 mol/L (f) 0.0007 mol/L.

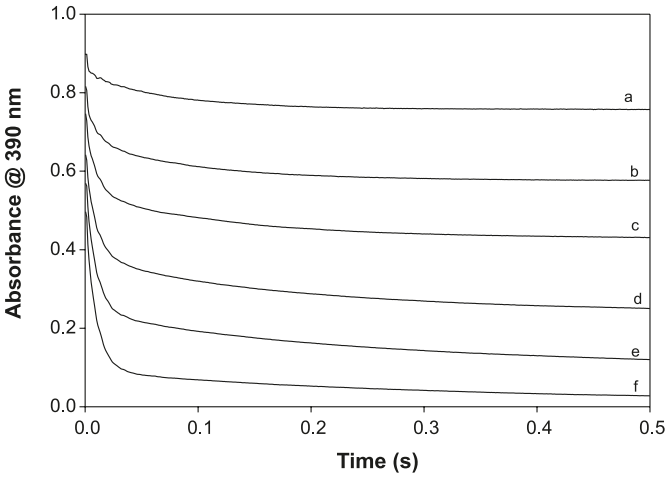

Fig. 7. Effect of varying $[Br_2]_o$ on the direct reaction of Br_2 vs. CA in excess bromide monitored at 390 nm. [CA] = 0.0003 mol/L, $[Br^-]$ = 1.0 mol/L, $[Br_2]$ = (a) 0.001 68 mol/L (no bromide), (b) 0.001 68 mol/L, (c) 0.002 10 mol/L, (d) 0.002 50 mol/L, (e) 0.002 93 mol/L, (f) 0.003 35 mol/L.

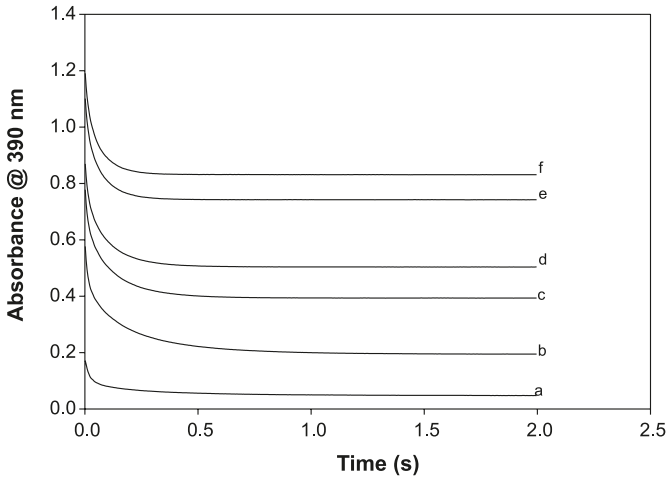

Fig. 8. Effect of acid on the bromine–CA reaction. Acid is mildly inhibitory on the first initial rapid phase of the reaction but shuts down the second slower section of the reaction, which involves formation of bromamines. $[Br_2]_o$ = 0.002 45 mol/L, $[CA]_o$ = 0.0004 mol/L, $[H^+]$ = (a) no acid, (b) 0.006, (c) 0.008, (d) 0.010, (e) 0.012, (f) 0.014 mol/L.

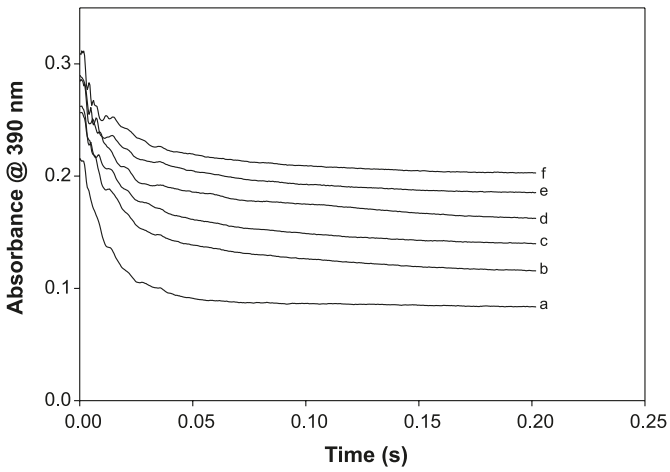

tion of bromate and cysteamine such that formation of bromine should indicate complete consumption of cysteamine. The time taken to achieve complete consumption of cysteamine (the induction period monitored in Figs. 3*b* and 4*b*), is inversely proportional to the rate of reaction (i.e., consumption of cysteamine).

Further reaction can occur between the reactive species $HBrO_2$ and HOBr with CA and its oxidative by-products.

$$[R13]\quad HOBr + H_2NCH_2CH_2SH \rightarrow H_2NCH_2CH_2SOH + Br^- + H^+$$

While $HBrO_2$ can also act as oxidizing agent as in reaction [R13], its rapid disproportionation in the presence of bromide (reaction [R14]) will make its effect as an oxidant negligible.

$$[R14]\quad HBrO_2 + Br^- + H^+ \rightleftharpoons 2HOBr$$

If one re-writes reaction [R13] and substitutes CA with any 2-electron reductant (i.e., the 2 electrons can be supplied by any oxidizable species in the reaction mixture), then a linear combination of R12 + 3R13 + R14 gives an overall reaction stoichiometry that is autocatalytic in Br^-:

$$[R15]\quad BrO_3^- + 6H^+ + Br^- + 6e^- \rightarrow 2Br^- + 3H_2O$$

As long as reaction [R12] is the rate-determining step, Br^- will be an autocatalyst. All bromate solutions contain trace amounts of bromide in the reaction mixture, which have

© 2008 NRC Canada

Table 1.

No.	Reaction	k_f, k_r
M1	$BrO_3^- + 2H^+ + Br^- \rightleftharpoons HBrO_2 + HOBr$	2.1, 1.00×10^{-4}
M2	$HBrO_2 + Br^- + H^+ \rightleftharpoons 2HOBr$	2.00×10^6, 2.00×10^{-5}
M3	$HOBr + Br^- + H^+ \rightleftharpoons Br_2 + H_2O$	8.9×10^9, 1.10×10^2
M4	$2HBrO_2 \rightleftharpoons BrO_3^- + HOBr + H^+$	4.00×10^7, 2.00×10^{-10}
M5	$Br_2 + Br^- \rightleftharpoons Br_3^-$	1.50×10^9, 8.8×10^7
M6	$BrO_3^- + H^+ \rightleftharpoons HBrO_3$	1.00×10^7, 1.00×10^9
M7	$H^+ + HBrO_3 \rightleftharpoons H_2BrO_3^+$	1.00×10^6, 5.0×10^8
M8	$H_2BrO_3^+ + H_2NRSH \rightarrow HBrO_2 + H_2NRSOH + H^+$	6.45
M9	$HBrO_2 + H_2NRSH \rightarrow HOBr + H_2NRSOH$	5.00×10^3
M10	$HOBr + H_2NRSH \rightarrow H^+ + Br^- + H_2NRSOH$	5.00×10^6
M11	$HOBr + H_2NRSOH \rightarrow H^+ + Br^- + H_2NRSO_2H$	5.00×10^5
M12	$HOBr + H_2NRSO_2H \rightarrow H^+ + Br^- + H_2NRSO_3H$	1.00×10^3
M13	$Br_2 + H_2NRSH + H_2O \rightarrow 2H^+ + 2Br^- + H_2NRSOH$	5.00×10^8
M14	$Br_2 + H_2NRSOH + H_2O \rightarrow 2H^+ + 2Br^- + H_2NRSO_2H$	2.50×10^8
M15	$Br_2 + H_2NRSO_2H + H_2O \rightarrow 2H^+ + 2Br^- + H_2NRSO_3H$	1.70×10^3
M16	$Br_2 + H_2NRSO_3H \rightarrow BrHNRSO_3H + H^+ + Br^-$	3.30
M17	$Br_2 + BrHNRSO_3H \rightleftharpoons Br_2HNRSO_3H + H^+ + Br$	7.00×10^{-2}, 1.05×10^{-3}
M18	$2BrHNRSO_3H + H^+ \rightleftharpoons Br_2HNRSO_3H + H_2NRSO_3H$	5.00, 1.00×10^{-2}

Note: The units for the kinetics constants in the third column are derived from the reaction's molecularity except where water is involved, in which case water was ignored.

been measured at approximately 5.0×10^{-6} mol/L. Quantitatively, are these sufficient to initiate the reaction? A computer simulation of the reaction while utilizing these trace bromide concentrations gave much slower reaction kinetics and longer induction periods when compared with the experimental traces. This suggests that there should be another pathway that generates bromide ions, which will initiate reaction [R12]. Another pathway that exists for initial bromide formation involves oxidation by protonated bromic acid (31–33):

[R16] $H^+ + BrO_3^- \rightleftharpoons HBrO_3$

[R17] $H^+ + HBrO_3 \rightleftharpoons H_2BrO_3^+$

[R18] $H_2BrO_3^+ + H_2NCH_2CH_2SH \rightarrow H_2NCH_2CH_2SOH + HBrO_2 + H^+$

[R19] $HBrO_2 + H_2NCH_2CH_2SH \rightarrow H_2NCH_2CH_2SOH + HOBr$

Bromide ions will thus be generated by the successive reduction of bromate to bromide. Adding the sequence R16 + R17 + R18 + R19 + R13 and assuming each reductant can be represented by 2 e's; the overall reaction representing initial bromide formation will be similar to [R15] without the autocatalysis:

[R20] $BrO_3^- + 6H^+ + 6e^- \rightarrow Br^- + 3H_2O$

The autocatalytic route will take over and become dominant as the reaction proceeds and rate of bromide production shifts from the kinetics derived from [R20] to those derived from [R15]. As bromide ions accumulate, their rate of production ceases to be the rate-determining step, and reaction [R12] takes over as the overall rate-determining step. Data shown in Figs. 3*b* and 4*b* strongly suggests that reaction [R12] is rate-determining up to the stage where cysteamine is completely converted to taurine.

All kinetics data collected imply that the oxidation of CA to taurine is much faster than the subsequent N-bromination reactions. Since bromate oxidations are only viable at low pH conditions, in all bromate oxidations of CA studied, the CA should be fully protonated on the amino group:

[R21] $H_2NCH_2CH_2SH + H^+ \rightleftharpoons HSCH_2CH_2NH_3^+$; K_b

The protonation of the amino group should retard the electrophilic bromination of this group:

[R22] $HSCH_2CH_2NH_3^+ + Br_2 \rightleftharpoons HSCH_2CH_2NHBr + Br^- + 2H^+$

An intermediate such as $HSCH_2CH_2NHBr$ should be very unstable and should rapidly hydrolyze to the sulfenic acid, since the thiol group is much more easily oxidizable than the N-containing group:

[R23] $HSCH_2CH_2NHBr + H_2O \rightarrow H_2NCH_2CH_2SOH + Br^- + H^+$

N-bromination of the sulfenic acid and hypotaurine will also be insignificant owing to kinetics factors in which the oxidation of the sulfur group is much more rapid than N-bromination (see Table 1).

N-bromination kinetics

In neutral to slightly basic environments, reaction [R24] should be very rapid and almost diffusion-controlled.

[R24] $HO_3SCH_2CH_2NH_2 + Br_2 \rightarrow HO_3SCH_2CH_2NHBr + Br^- + H^+$

© 2008 NRC Canada

Our stopped-flow ensemble, with a mixing time of 3 ms, could not catch this step, nor the next step that involves formation of the dibromo derivative:

[R25] $HO_3SCH_2CH_2NHBr + Br_2 \rightleftharpoons HO_3SCH_2CH_2NBr_2 + Br^- + H^+$

This reaction is slower in highly acidic medium because reactions of type [R22] are slower than those of type [R24]. Electrophilic attack on the N-center by bromine is retarded by the protonation of the nitrogen center. Kinetics data in Figs. 6 and 7 show first-order kinetics in both bromine and cysteamine. If one was to assume, in a limiting case, that the route of bromination through [R22] is negligible, then the initial rate of N-bromination would be given by the equation,

$$[1] \qquad \text{Rate} = -\frac{d[Br_2]}{dt} = \frac{k_{24}[HO_3SCH_2CH_2NH_2]_T[Br_2]_0}{1 + K_b[H^+]}$$

$[HO_3SCH_2CH_2NH_2]_T$ is the total cysteamine sulfonic acid concentration before it is partitioned into the protonated and unprotonated forms. Retardation by bromide ions can be mathematically handled in the same manner, in which rate of reaction becomes

$$[2] \qquad -\frac{d[Br_2]}{dt} = \frac{k_{24}[HO_3SCH_2CH_2NH_2]_T[Br_2]_0}{\{1 + K_b[H^+]\}\{1 + K_{eq}[Br^-]\}}$$

In none of our experiments were the retardations by Br^- and H^+ effective enough for the use of eqs. [1] and [2] in determining bimolecular rate constant k_{24}. We could only use initial rate data and assuming bimolecular kinetics in Fig. 8 to estimate that k_{24} should be larger than 10^5 mol^{-1} L s^{-1}. Reliable values for k_{24} can be derived from relaxation techniques (34). In the physiological environment and in basic conditions, in general, the major route of N-bromination (reaction [R26]) is through hypobromous acid (35), since the bromine hydrolysis reaction favors hypobromous acid at high pH and aqueous bromine in acidic conditions (36).

[R26] $HO_3SCH_2CH_2NH_2 + HOBr \rightarrow HO_3SCH_2CH_2NHBr + H_2O$

N-bromination in bromate oxidations is predominantly through aqueous bromine, since bromate oxidations only proceed in acidic environments (37).

The acid retardation observed for the reaction shown in Fig. 8 may suggest that reaction [R26] is slower than [R24]. Previous studies have confirmed that the monobromo-and dibromo- derivatives are affected by acid, with highly acidic conditions favoring monobromotaurine (37). This means that while [R24] can proceed quantitatively to the product monobromotaurine, [R25] is an equilibrium condition in which high acid concentrations in the products can swing the equilibrium towards monobromotaurine formation. The addition of taurine to dibromotaurine solutions saw the decrease in the peak at 244 nm (dibromotaurine) and the emergence of a peak at 288 nm (monobromotaurine):

[R27] $HO_3SCH_2CH_2NH_2 + HO_3SCH_2CH_2NBr_2 \rightleftharpoons 2HO_3SCH_2CH_2NHBr$

Scheme II.

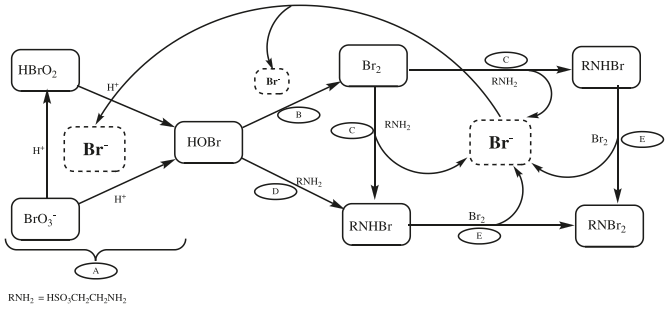

Bromine formation

There is only one reaction in the reaction mixture responsible for bromine formation:

[R28] $HOBr + Br^- + H^+ \rightleftharpoons Br_2(aq) + H_2O$

Since both HOBr and Br_2 react rapidly with cysteamine (and its metabolite, hypotaurine), then formation of bromine is an indicator that cysteamine and its metabolites have all been oxidized to at least the taurine stage. The formation of bromine at the end of the induction period should depend in some manner on the rate of formation of bromide (assuming excess of acidic bromate). The full reaction network responsible for bromine formation is complex, and can be depicted by the network shown in Scheme II. To simplify this scheme, only the relevant reactions after cysteamine has been oxidized to taurine (presented as RNH_2 in the scheme) are included. It is a bromide-controlled network due to bromide's role as an autocatalyst in the reaction network. It provides a positive feedback loop that feeds into reaction A and accelerates the reaction.

This network scheme can explain the rate of bromine formation after the induction period as well as the biphasic nature of bromine production. Without excess bromate the feedback loop cannot exist, since reaction [R12] is a precursor to all autocatalysis. The reaction network relies on process B being fast (reaction [R28]). Our simulations also showed that HOBr does not accumulate to concentrations higher than 10^{-6} mol/L for the duration of the reaction. The fact that process C is faster than E delivers the biphasic bromine formation. Since bromine formation depends on bromide formation, the faster N-bromination of taurine ensures a fast rate of formation of bromide and subsequently a high rate of initial formation of bromine. Higher acid concentrations retard the formation of dibromotaurine. Figure 4*a* illustrates this effect: high acid concentrations catalyze the formation of HOBr, leading to higher bromine formation (processes A + B). This in turn leads to higher bromide formation (process C), which feeds back into process A. Acid catalysis of A is stronger than acid retardation of C. However, acid retardation of E is significant and when most of the monobromotaurine has been formed, the subsequent bromination to dibromotaurine is slower (in high acid), and the equilibrium of reaction [R25] is shifted to the left. With process E slower, bromide formation is slower, and subsequently bromine formation is slow, as observed in the slower bromine formation in the second phase. The zero-order kinetics observed in bromine formation is due to the fact that this section is no longer solely dependent on

© 2008 NRC Canada

Fig. 9. Simulated results (symbols) of traces *a* and *c* (solid lines) from Fig. 3*a* showing the effect of bromate variation on CA oxidation.

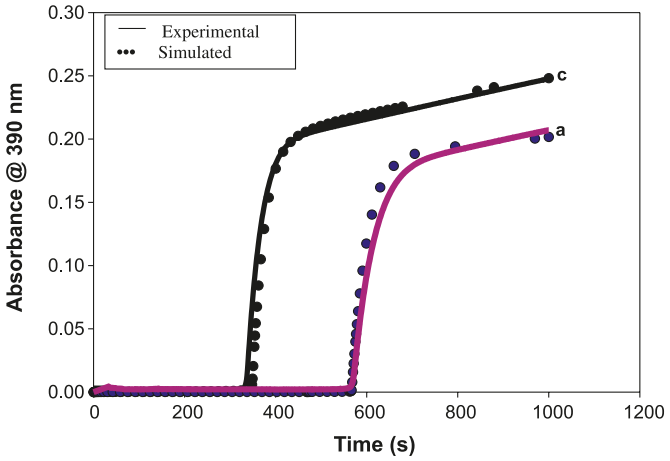

process A, but a much more complex network. Primarily, equilibrium [R25] acts as a valve in the release of bromide and maintains a constant release of bromide ions, as in drug-suspension reactions.

Overall reaction mechanism and simulations

The overall mechanism that can explain the observed global dynamics of the system on the basis of Scheme II is shown in Table 1. The first group of reactions M1–M4 and M5 are the well-known oxybromine reactions whose kinetics constants are well known (31, 33, 39–41). These were not varied during the simulations and were accepted as "fixed". The next set of reactions M6–M10 constitute the initiation reactions whose sole purpose is to produce bromide ions (autocatalytically). Protolytic reactions such as M6 and M7 are normally diffusion-controlled. The use of diffusion-controlled rate constants for these reactions rendered the simulations too stiff, necessitating hours of computer time instead of mere seconds with the use of the kinetics constants used in Table 1. The adopted kinetics constants did not deliver any different simulation results when compared to the use of the diffusion-controlled kinetics constants. The third set of reactions M11–M15 constitute the oxidation of cysteamine to taurine. The major oxidants are HOBr and Br_2. Even though this set of reactions is fast, they are all controlled (after the initiation reactions), by reaction [R12] (M1 in the table). Rapid reaction [R28] (M3 in table) is also controlled by [R12], since production of Br^- is a prerequisite reagent for formation of HOBr. The N-bromination reactions are listed in the last section, M16–M18. We have assumed in all these simulations that we are dealing with a protonated taurine molecule on the amino group, since the pH conditions necessary for the activity of bromate as an oxidant are low enough to protonate that group. Since we did not and could not quantify the degree of acid retardation by the reaction, we felt that this was a reasonable assumption. Reaction M18 was a necessary disproportionation reaction in high-acid conditions. Even in low-acid conditions, reaction M18 ensured that stoichiometry [R7] was attained first before stoichiometry [R5]. The simplicity of the simulations was derived from the bottle-neck offered by reaction M1, irrespective of the other reaction rates. The initiation reactions were important in establishing the time taken before bromine formation commenced, but a few seconds into the reaction reactions M6–M10 ceased to be effective. Since we could not harness the bromination reactions due to their speed, the lower-limit-estimated rate constants were effective, since ultimately, formation of bromine was controlled by M1. Figure 9 shows a reasonably good fit to the data on bromate-dependence data shown in Fig. 3*a*. A good fit was also obtained with acid-dependence traces shown in Fig. 4*a*. The model was able to satisfactorily predict both bromate- and acid-dependence effects with respect to induction period and rate of formation of bromine at the end of this induction period.

Conclusion

The reversible nature of N-bromination of the taurine formed after a full oxidation of cysteamine suggests that cysteamine and its oxidation metabolites are capable of moderating hypobromous acid and hypochlorous acid toxicities by forming these long-lived brominated derivatives. The ease of regeneration of taurine in reducing conditions means that this moderation can proceed indefinitely in a cyclic manner.

Acknowledgement

This work was supported by research grant no. CHE 0614924 from the National Science Foundation.

References

1. Z.M. Bacq. Int. J. Sulfur Chem. B, **6**, 94 (1971).
2. L.D. Buckberry and P.H. Teesdale-Spittle. Sulfur–hydrogen compounds. *In* Biological interactions of sulfur compounds. *Edited by* S. Mitchell. London. 1996. p. 113.
3. P. Wardman. Thiol reactivity towards drugs and radicals: Some implications in the radiotherapy and chemotherapy of cancer. *In* Sulfur-centered reactive intermediates in chemistry and biology. *Edited by* C. Chatgilialoglu and K.D. Asmus. New York. 1990. p. 415.
4. R.J. Cremlyn. An introduction to organosulfur chemistry. John Wiley & Sons, Chichester. 1996.
5. J. Darkwa, R. Olojo, E. Chikwana, and R.H. Simoyi. J. Phys. Chem. A, **108**, 5576 (2004).
6. S.V. Makarov, C. Mundoma, J.H. Penn, J.L. Petersen, S.A. Svarovsky, and R.H. Simoyi. Inorg. Chim. Acta, **286**, 149 (1999).
7. S.V. Makarov, C. Mundoma, J.H. Penn, S.A. Svarovsky, and R.H. Simoyi. J. Phys. Chem. A, **102**, 6786 (1998).
8. A.G. Renwick. Sulfur-containing drugs and related compounds– Chemistry, biology, and toxicology. Ellis Horwood, Chichester, NY. 1987.
9. A.G. Renwick. Sulfur–oxygen compounds. *In* Biological interactions of sulfur compounds. *Edited by* S. Mitchell. London. 1996. p. 42.
10. A.E. Miller, J.J. Bischoff, and K. Pae. Chem. Res. Toxicol. **1**, 169 (1988).
11. O. Aruoma, B. Halliwell, B. Hoey, and J. Butler. Biochem. J. **256**, 251 (1988).
12. D. Becker, S. Summerfield, S. Gillich, and M.D. Sevilla. Int. J. Radiat. Biol. **65**, 537 (1994).

© 2008 NRC Canada

13. A. Del Corso, P.G. Vilardo, M. Cappiello, I. Cecconi, M. Dal Monte, D. Barsacchi, and U. Mura. Arch. Biochem. Biophys. **397**, 392 (2002).
14. M. Hermes-Lima and T. Zenteno-Savin. Comp. Biochem. Physiol. Part C: Toxicol. Pharmacol. **133**, 537 (2002).
15. F. Martin, M.F. Penet, F. Malergue, H. Lepidi, A. Dessein, F. Galland, M. de Reggi, P. Naquet, and B. Gharib. J. Clin. Invest. **113**, 591 (2004).
16. N.B. McDonnell, R.N. DeGuzman, W.G. Rice, J.A. Turpin, and M.F. Summers. J. Med. Chem. **40**, 1969 (1997).
17. B.S. Martincigh, C. Mundoma, and R.H. Simoji. J. Phys. Chem. A, **102**, 9838 (1998).
18. C.R. Chinake and R.H. Simoyi. J. Phys. Chem. B, **101**, 1207 (1997).
19. R.H. Simoyi, K. Streete, C. Mundoma, and R. Olojo. South African J. Chem. (Suid-Afrikaanse Tydskrif Vir Chemie), **55**, 136 (2002).
20. S.T. Test, M.B. Lampert, P.J. Ossana, J.G. Thoene, and S.J. Weiss. J. Clin. Invest. **74**, 1341 (1984).
21. A. Chanakira, E. Chikwana, D. Peyton, and R. Simoyi. Can. J. Chem. **84**, 49 (2006).
22. E.L. Thomas, M.B. Grisham, and M.M. Jefferson. J. Clin. Invest. **72**, 441 (1983).
23. E.L. Thomas, P.M. Bozeman, M.M. Jefferson, and C.C. King. J. Biol. Chem. **270**, 2906 (1995).
24. A.J. Jesaitis and E.A. Dratz. Molecular basis of oxidative damage by leukocytes. CRC Press, Fla. 1992.
25. J. Darkwa, R. Olojo, E. Chikwana, and R.H. Simoyi. J. Phys. Chem. A, **108**, 5576 (2004).
26. R.H. Simoyi, K. Streete, C. Mundoma, and R. Olojo. South African J. Chem. (Suid-Afrikaanse Tydskrif Vir Chemie), **55**, 136 (2002).
27. E.L. Thomas, M.B. Grisham, D.F. Melton, and M.M. Jefferson. J. Biol. Chem. **260**, 3321 (1985).
28. R.H. Simoyi, K. Streete, C. Mundoma, and R. Olojo. South African J. Chem. (Suid-Afrikaanse Tydskrif Vir Chemie) **55**, 136 (2002).
29. M.-F. Ruasse, J. Aubard, B. Galland, and A. Adenir. J. Phys. Chem. **90**, 4382 (1986).
30. Z. Toth and L. Fabian. Inorg. Chem. **43**, 2717 (2004).
31. C.E. Sortes and R.B. Faria. J. Braz. Chem. Soc. **12**, 775 (2001).
32. R.D. Faria, I.R. Epstein, and K. Kustin. J. Phys. Chem. **98**, 1363 (1994).
33. Gy. Rabai, Gy. Bazsa, and T.M. Beck. Int. J. Chem. Kinet. **13**, 1277 (1981).
34. D.H. Turner, G.W. Flynn, N. Sutin, and J.V. Beitz. J. Am. Chem. Soc. **94**, 1554 (1972).
35. E.L. Thomas, P.M. Bozeman, M.M. Jefferson, and C.C. King. J. Biol. Chem. **270**, 2906 (1995).
36. R.C. Beckwith, T.X. Wang, and D.W. Margerum. Inorg. Chem. **35**, 995 (1996).
37. R.H. Simoyi, K. Streete, C. Mundoma, and R. Olojo. South African J. Chem. (Suid-Afrikaanse Tydskrif Vir Chemie), **55**, 136 (2002).
38. R.M. Noyes, R.J. Field, and R.C. Thompson. J. Am. Chem. Soc. **93**, 7315 (1971).
39. R.M. Noyes. J. Am. Chem. Soc. **102**, 4644 (1980).
40. I. Szalai, J. Oslonovitch, and H.D. Forsterling. J. Phys. Chem. A, **104**, 1495 (2000).

© 2008 NRC Canada

Reaction on a solid surface — A simple, economical, and efficient Mannich reaction of azacrown ethers over graphite

Hashem Sharghi and Reza Khalifeh

Abstract: Graphite brings about a rapid Mannich reaction with a range of activated and unactivated phenolic compounds such as *p*-cresol and *p*-nitrophenol. The reactions are carried out with azacrown ether and paraformaldehyde in solvent-free conditions at 100 °C for 20–30 min. The graphite powder can be reused up to three times after simple washing with acetone.

Key words: azacrown ether, lariat ether, graphite, solvent-free, Mannich reaction.

Résumé : Le graphite en poudre permet de réaliser des réactions de Mannich rapides de composés phénoliques activés et non activés, tel le *p*-crésol et le *p*-nitrocrésol, avec un éther azacouronne et le paraformaldéhyde, dans des conditions sans solvant, à 100 °C, pendant 20 à 30 minutes. On peut réutiliser le graphite en poudre jusqu'à trois fois après un simple lavage avec de l'acétone.

Mots-clés : éther azacouronne, éther lariat, graphite, sans solvant, réaction de Mannich.

[Traduit par la Rédaction]

Introduction

Azacrown ethers are often used as precursors for structurally modified macrocyclic ion-complexing agents because of the attachment of pendant groups to the secondary nitrogen atom (1). The major methods for functionalizing azacrown macrocycles with proton-ionizable phenol groups include the treatment of an azacrown ether with a benzyl or benzoyl halide and reductive amination with aromatic aldehydes. These methods are not always convenient because of the difficulties in preparing the starting materials, the need to reduce the carbonyl group if carboxylic acid derivatives are used, and the need to protect the phenolic hydroxy group (2). The Mannich reaction, as a method for modification of azacrown macrocycles with hydroxybenzyl functions, has some advantages when compared to alkylation of the azacrowns by benzyl halides. In fact, aminomethylation of the phenols allows the preparation of azamacrocycles containing both electron-donating and electron-withdrawing groups in the substituent phenolic rings (3). In spite of appreciable interest in the azacrown macrocycles, they are still not readily available for study because they are either very expensive or difficult to prepare. Obviously, the elaboration of general and simple approaches for the synthesis and functionalization of azacrown macrocycles remains a very important problem for researchers working in this field. One of the most important objectives now is to adapt classical processes so that pollution effects are kept to a minimum, with a reduction both in energy and in consumption of raw materials. In this respect, dry-media reactions are promising, and a new approach has been undertaken using graphite chemistry. The exceptional ability of graphite to adsorb organic molecules is well known (4). Diels–Alder and ene reactions (5), decarboxylations (5*a*, 5*b*), decompositions (6), rearrangements (5*a*, 5*b*, 7), keto carboxylation (8), conversion of aldehydes into nitriles (9), Friedel–Crafts acylation of aromatic compounds (10), alkylation of aromatic compounds and alcohols (11*a*), and dehydration of secondary alcohols (11*b*) were all effected using such conditions.

As a part of our continued efforts to utilize surface-mediated reactions for conducting Mannich reaction, here we wish to disclose a very simple, fast, general, highly efficient, and improved one-step method for synthesizing lariat ether containing phenolic groups. The reaction occurs without any solvent in the presence of graphite and gives relatively high yields.

Received 15 September 2007. Accepted 3 February 2008. Published on the NRC Research Press Web site at canjchem.nrc.ca on 8 April 2008.

H. Sharghi[1] **and R. Khalifeh.** Department of Chemistry, College of Sciences, Shiraz University, Shiraz 71454, Iran.

[1]Corresponding author (e-mail: hashemsharghi@gmail.com).

Results and discussion

The Mannich reaction is one of the most important tools for synthesizing new compounds (12). The most important applications of this reaction are in the pharmaceutical chemistry and natural product chemistry (12, 13). Also the Mannich reaction is known to be a powerful method for functionalizing azacrown ethers with additional ligating units (3, 14). The Mannich reaction consist of the condensation of a substrate (R–H) possessing at least one active hydrogen (alkyl ketones, phenols, NH heterocycles, etc) with formaldehyde (or occasionally other aldehydes) and a primary or secondary amine (or occasionally ammonia). Although numerous methods to achieve Mannich reaction are

 doi:10.1139/V08-026 © 2008 NRC Canada

Table 1. Mannich reaction of other azacrown ethers and amines with *p*-cresol

Entry	Substrate	Phenols	Product	Yield (%)
1		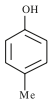	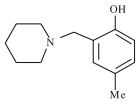 **1**	90
2		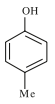	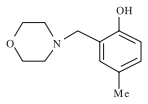 **2**	96
3		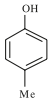	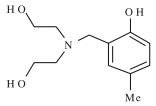 **3**	82
4		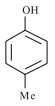	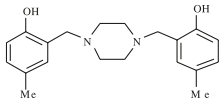 **4**	85
5	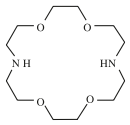	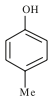	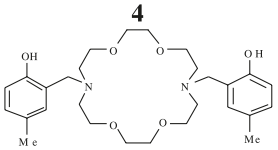 **5**	88
6	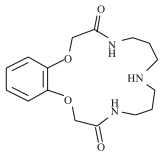 **6**	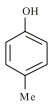	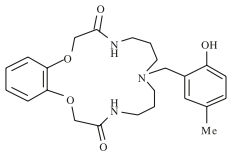 **7**	84
7	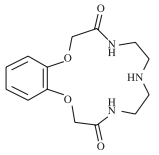 **8**	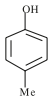	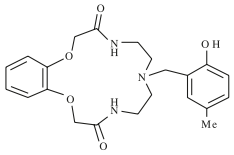 **9**	87

known, newer methods continue to attract attention for their experimental simplicity and effectiveness. We have been interested in the development of methods for Mannich reactions that (a) would avoid the use of added acids, (b) would avoid aqueous workup, (c) are easy to perform, and (d) are economical for application to large-scale preparations.

We have previously shown that azacrown ether **8** can be prepared by a simple and convenient procedure (15). Because graphite has a large surface area, it is a good heat conductor, and the reaction can be carried out under milder conditions (7). During the course of our studies aimed at developing solvent-free procedures (9, 10, 16, 19, 20), we have now discovered that graphite alone promotes a very efficient Mannich reaction of activated and unactivated phenol compounds with azacrown ether **8** and paraformaldehyde at 100 °C in high yields, without any of the environmental disadvantages of using toxic solvents (Scheme 1). In a typical experiment, graphite, azacrown ether **8**, *p*-cresol, and paraformaldehyde were mixed thoroughly. The mixture was heated in an oil bath at 100 °C with stirring for 20 min until

Scheme 1.

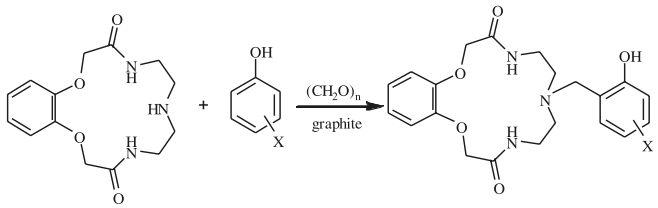

8 **9–19**

the reaction was completed. The product was isolated by simple extraction of the solid mass by acetone followed by the usual workup.

To investigate the generality and versatility of this method, the reaction was extended to various structurally diverse phenols. When the phenols had either electron-donating or electron-withdrawing substituents, the formation of benzylamine bonds occurred very rapidly, within 20–30 min. The results of the Mannich reaction of azacrown ether **8** are collected in Table 1. When *para*-substituted or

© 2008 NRC Canada

Table 1 (*continued*).

Entry	Substrate	Phenols	Product	Yield (%)
8	**8**	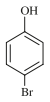	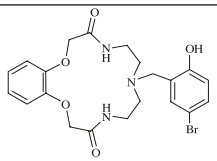 **10**	73
9	**8**	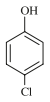	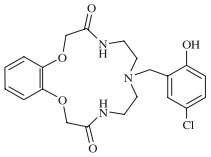 **11**	75
10	**8**	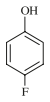	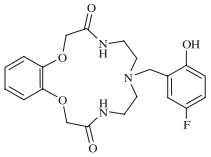 **12**	81
11	**8**	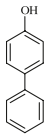	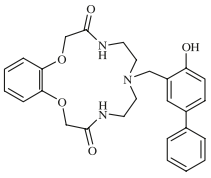 **13**	79
12	**8**		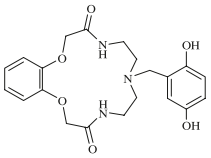 **14**	71
13	**8**	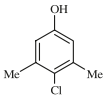	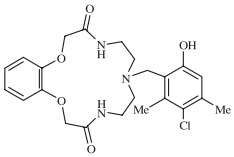 **15**	79
14	**8**		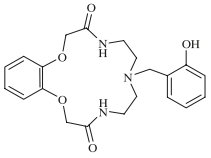 **16**	78

unsubstituted phenols were used for the Mannich reaction with azacrown ether **8** in the presence of paraformaldehyde, macrocyclic ligands **9**–**19** were obtained in relatively high yields (Table 1, entries 7–17), although the yields drop as strongly electron-withdrawing substituents are added, as in **19** (Table 1, entry 17). The moderate yield of **19** is attributed to the relatively weak nucleophilicity of *p*-nitrophenol and its anion (14b). Aminomethylation of phenols by means of the Mannich reaction usually occurs in the position ortho to the phenolic OH group even if the para position is unsubstituted (14a). Possibly the preferential attack on the ortho position is caused by formation of a six-membered transition state where the phenolic proton activates the aminomethylating reagent (17). The free para positions on the benzo units of the final macrocycles are attractive sites for functionalization because of their high reactivity toward electrophilic aromatic substitution.

Additionally a variety of secondary amines were examined using *p*-cresol as the model substrate (Table 1). Interestingly the yield of the reaction was higher when graphite was used as the reaction medium than when the reaction was performed in benzene. For example, with graphite, the reac-

© 2008 NRC Canada

Table 1 (*concluded*).

Entry	Substrate	Phenols	Product	Yield (%)
15	**8**	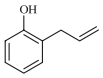	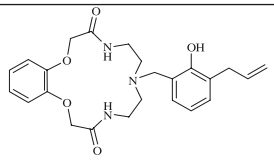 **17**	74
16	**8**	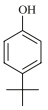	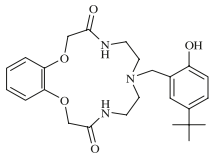 **18**	72
17	**8**	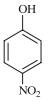	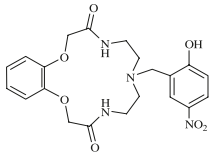 **19**	40

tion of piperazine with *p*-cresol occurred in 85% yield after 20 min at 100 °C. Under reflux conditions in benzene, the same reaction was slower, and afforded the corresponding product only after 24 h in 41% yield (Table 1, entry 4) (14*d*).

Further, the activity of the recovered graphite was examined. As shown in Table 2, the yields of macrocyclic **9** in the second and third uses of the graphite was almost same as that in the first use. In every case >90% of the graphite was easily recovered from the reaction mixture by simple washing with acetone.

A comparison of the present protocol, using graphite, with selected previously known protocols and other inorganic solids that were examined is collected in Table 3 to demonstrate that the present protocol is indeed superior to several of the other protocols. According to Table 3, the Mannich reaction of azacrown ether **8** is completed in 20 min at 100 °C in 87% isolated yield using the present protocol. Most of the other protocols listed either take a longer time for completion, or use toxic solvents with generally reduced isolated yields (entries 1–6) (14). In another study the effect of microwave and inorganic solids as catalysts were investigated and it was found that compound **9** was not produced under these conditions (entry 7, 8, 9) (18, 19, 20). In the absence of graphite (entry 10), the reaction was conducted at 100 °C for 2 h, affording compound **9** only, in 30% yield. The effect of different amounts of graphite on the model compound was studied in another experiment. The result showed that the best yield was obtained when 1 gr of graphite was used. Increasing the amount of graphite had a negligible effect on the efficiency of the reaction. Decreasing the amount of graphite led to a pasty reaction mixture which made the stirring difficult, thus reducing the efficiency of the model reaction.

The Mannich reaction of azacrown ether **8** with *p*-cresol on a 30 mmol scale proceeded just as well as the 1 mmol reaction. The mechanism of the reaction is a subject of a further study. For now, we believe that graphite acts as a dehydration reagent or as a heat-conducting surface for the Mannich reaction.

Table 2. Re-use of graphite.

Number of uses	Yield (%)[a]	Recovery of graphite
1	87	95
2	83	92
3	80	91

[a]Isolated yields.

At the edge of the basal planes of carbon atoms in the graphite structure, where bonding in the plane is terminated, are unsaturated carbon atoms. These sites are associated with high concentrations of unpaired electrons and therefore play a significant role in chemisorption. These carbons may chemisorb oxygen, producing oxygen surface groups. Oxygen surface groups are by far the most important in influencing the surface characteristics and adsorption behavior of graphite (21) (Scheme 2).

The surface groups most often suggested are carboxyl, phenolic hydroxyl, and quinone carbonyl groups. Slightly fewer in number are the reports of ethers, peroxides, ester groups, lactones, carboxylic acid anhydrides, and cyclic peroxides (22). These structures exhibit a high affinity for water (23). As Szymanski et al. reported earlier, the dehydration of secondary alcohols on the carbon catalysts proceeds according to the oxonium mechanism (11*b*).

As described in Scheme 3, we have suggested a mechanism for the solvent-free Mannich reaction of secondary amines that is based on the previously proposed mechanism for dehydration of secondary alcohols.

At the initial stage, the formaldehyde is protonated; then, a secondary amine attacks the activated formaldehyde; finally, a water molecule is lost from the oxonium intermediate (**II**) and the Mannich base (**III**) is formed. The reaction of Mannich base (**III**) with phenol gives the product.

© 2008 NRC Canada

Table 3. Mannich reaction of azacrown ether **8** with *p*-cresol under various conditions.

Entry	Condition	Temp. (°C)	Time	Yield (%)[a]
1	Benzene (14*b*)	reflux	2 h	10
2	Benzene/graphite	reflux	2 h	20
3	CCl_4 (14*a*)	reflux	2 h	7
4	CCl_4/graphite	reflux	2 h	12
5	Toluene (14*c*)	reflux	2 h	15
6	Toluene/graphite	reflux	2 h	22
7	Al_2O_3/MW (18)		1.5 min	no reaction
8	Al_2O_3/CH_3SO_3H (AMA) (19)	100	2 h	no reaction
9	Graphite/CH_3SO_3H (GMA) (20)	100	2 h	no reaction
10	Neat	100	2 h	30
11	Graphite	70	3600 min	81
12	Graphite	100	20 min	87
13	Graphite	130	6 min	85

[a]Isolated yields.

Scheme 2. Some type of oxygen surface groups in graphite.

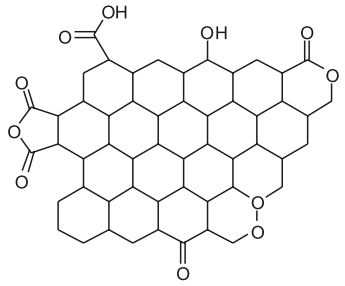

Scheme 3.

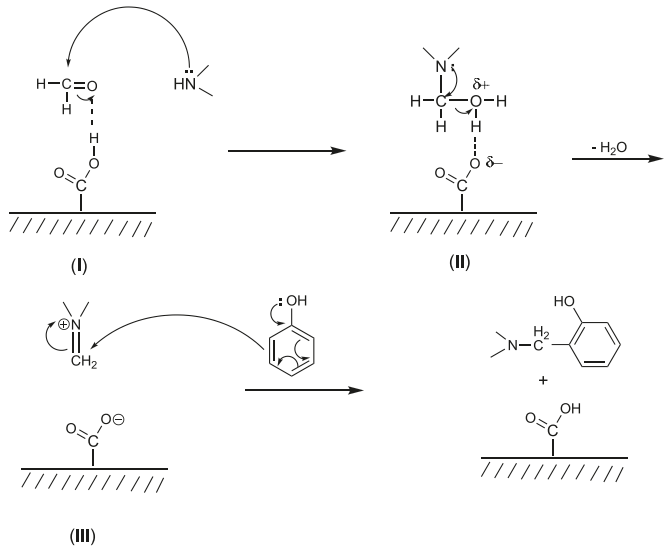

Conclusion

We have described a novel and highly efficient solvent-free protocol for the Mannich reaction of phenol compounds using nontoxic and inexpensive graphite powder. The advantages of this environmentally benign and safe protocol include a simple reaction setup not requiring specialized equipment, mild reaction conditions, high product yields, short reaction times, reusability of graphite, and the elimination of solvents.

Experimental

Instrumentation, analysis, and starting material

NMR spectra were recorded on Bruker Avance DPX-250 (^{1}H NMR 250 MHz and ^{13}C NMR 62.9 MHz) and DRX-500 (^{19}F NMR 470 MHz) spectrometers in pure deuterated solvents with tetramethylsilane (TMS) and trichlorofluoromethane ($CFCl_3$) as internal standards. Infrared spectra were obtained using a Shimadzu FT-IR 8300 spectrophotometer. Mass spectra were determined on a Shimadzu GCMS-QP 1000 EX instrument at 70 or 20 ev. Melting points were determined in open capillary tubes in a Buchi-535 circulating oil melting point apparatus. UV–vis spectra were obtained with an Ultrospec 3000 UV/Visible spectrometer. Elemental analyses were performed at the National Oil Co. of Iran, Tehran Research Center. The purity determination of the substrates and reaction monitoring were accomplished by TLC on silica gel PolyGram SILG/UV 254 plates. Column chromatography was carried out on short columns of silica gel 60 (70–230 mesh) in glass columns (2–3 cm diameter) using 15–30 gram of silica gel per one gram of crude mixture. Chemical materials were either prepared in our laboratories or were purchased from Fluka, Sigma-Aldrich, and Merck Companies.

General procedure

After a mortar was charged with azacrown ether **8** (1 mmol), phenol (1.2 mmol), paraformaldehyde (1.2 mmol), and graphite slurry (1 g) (CAS No.7782–42–5; fine powder extra pure, particle size (<50 μm), pH value 5–6 (50 g/l, H_2O, 20 °C) from Merck), the mixture was ground with a pestle at room temperature. The resulting fine powder was transferred to a round-bottomed flask and stirred on a magnetic stirrer in an oil bath at 100 °C for 20–30 min. After cooling, acetone (3 × 25 mL) was added to the mixture and the graphite was removed by filtration. Evaporation of the solvent under reduced pressure gave the crude product, which was purified by flash column chromathography

© 2008 NRC Canada

(eluent: n-hexane – ethyl acetate 1:1) or recrystallized from ethyl acetate.

4-Methyl-2-(1-piperidinylmethyl)phenol (1)

Purification by plate chromatography, eluted with n-hexane – ethyl acetate (10:2), gave compound **1** in 90% yield; mp 45 °C (Lit. Value: 45 °C (24)). IR (KBr, cm^{-1}) υ_{max} : 3240, 2935, 2804, 1601, 1497, 1338, 1308, 1038, 814, 791, 771. ^1H NMR ($CDCl_3$) δ_H: 10.90 (1H, s), 6.82 (1H, d, J = 8.2 Hz), 6.58 (1H, s), 6.52 (1H, d, J = 8.2 Hz), 3.40 (2H, s), 2.17–2.36 (4H, m), 2.11 (3H, s), 1.17–1.54 (6H, m). ^{13}C NMR ($CDCl_3$) δ_C: 155.7, 129.1, 128.9, 128.2, 121.3, 115.7, 62.2, 54.2, 25.7, 24.3, 20.9. Anal. calcd.. for $C_{13}H_{19}NO$: C 76.06, H 9.33; found: C 76.27, H 9.12.

4-Methyl-2-(4-morpholinylmethyl)phenol (2)

Purification by plate chromatography, eluted with n-hexane – ethyl acetate (10:2), gave compound **2** in 96% yield; mp 49–50 °C (Lit. Value: 48–51 °C (25)). IR (neat, cm^{-1}) υ_{max}: 3160, 2819, 1597, 1304, 1119, 1029, 818. ^1H NMR ($CDCl_3$) δ_H: 9.28 (1H, s), 6.77 (1H, d, J = 7.8 Hz), 6.58 (1H, s), 6.47 (1H, d, J = 7.8 Hz), 3.48 (4H, t, J = 4.2 Hz), 3.40 (2H, s), 2.29 (4H, s), 2.06 (3H, s). ^{13}C NMR ($CDCl_3$) δ_C: 154.5, 128.9, 128.1, 120.4, 116.3, 115.8, 66.6, 61.3, 52.8, 20.7. Anal. calcd. for $C_{12}H_{17}NO_2$: C 69.54, H 8.27; found: C 69.36, H, 8.49.

2-{[Bis(2-hydroxyethyl)amino]methyl}-4-methylphenol (3)

Purification by plate chromatography, eluted with n-hexane – ethyl acetate (10:2), gave compound **3** in 82% yield. (Lit. values, see ref. 26). IR υ_{max} (neat, cm^{-1}): 3356, 2870, 1612, 1481, 1304, 1038, 910, 817, 733. ^1H NMR ($CDCl_3$) δ_H: 6.59–7.05 (5H, m), 3.72 (2H, s), 3.61 (4H, t, J = 5.4 Hz), 2.67 (4H, t, J = 5.4 Hz), 2.14 (3H, s). ^{13}C NMR ($CDCl_3$) δ_C: 154.4, 130.5, 129.1, 122.2, 116.7, 115.5, 58.9, 58.0, 52.8, 20.9. MS *m/z* (%): 227 ([M^+ + 2], 0.1), 226 ([M^+ + 1], 0.5), 225 ([M^+], 1.7), 208 (0.3), 194 (11.6), 162 (1.1), 149 (1.1), 135 (1.4), 121 (34.2), 91 (13.1), 84 (57.4), 74 (100). Anal. calcd. for $C_{12}H_{19}NO_3$: C 63.98, H 8.50; found: C 63.79, H 8.44.

2-{[4-(2-Hydroxy-5-methylbenzyl)-1-piperazinyl]methyl}-4-methylphenol (4)

Rrecrystallization from MeOH gave compound **4** as a colorless powder in 85% yield; mp 225–226 °C (Lit. Value: 225–226 °C (14*d*)). ^1H NMR ($CDCl_3$) δ_H: 10.22 (2H, s), 6.89 (2H, d, J = 8.2 Hz), 6.69 (2H, s), 6.64 (2H, d, J = 8.2 Hz), 3.58 (4H, s), 3.23–2.31 (8H, m), 2.15 (6H, s). ^{13}C NMR ($CDCl_3$) δ_C: 155.1, 129.3, 128.3, 120.5, 115.8, 61.2, 52.4, 20.5. Anal. calcd. for $C_{20}H_{26}N_2O_2$: C 73.59, H 8.03; found: C 73.82, H 7.79.

2-{[16-(2-Hydroxy-5-methylbenzyl)-1,4,10,13-tetraoxa-7,16-diazacyclooctadecan-7-yl]methyl}-4-methylphenol (5)

Purification by flash column chromatography, eluted with n-hexane – ethyl acetate (1:1), gave compound **5** as a colorless powder in 88% yield; mp 113–114 °C (Lit. Value: 114–115 °C (14*b*)). ^1H NMR ($CDCl_3$) δ_H: 6.95 (2H, d, J = 8.2 Hz), 6.72 (2H, d, J = 8.2 Hz), 6.78 (2H, s), 3.77 (4H, s), 3.66 (8H, t, J = 5.4 Hz), 3.61 (8H, s), 2.86 (8H, t, J = 5.4 Hz), 2.23 (6H, s). ^{13}C NMR ($CDCl_3$) δ_C: 155.5, 129.3, 129.1, 122.1, 116.0, 70.7, 69.1, 58.6, 53.6, 20.5. Anal. calcd. for $C_{28}H_{42}N_2O_6$: C 66.91, H 8.42; found: C 66.89, H 8.61.

5,6,7,8,9,10,11,12-Octahydro-2*H*-1,15,4,8,12-benzodioxatriazacycloheptadecine-3,13(4*H*,14*H*)-dione (6)

Rrecrystallization from toluene gave compound **6** as a colorless powder in 70% yield; mp 186 °C (Lit. Value: 187 °C (27)). IR (KBr, cm^{-1}) υ_{max}: 3437, 2924, 2839, 1686, 1543, 1504, 1450, 1254, 1215, 1130, 1049, 818, 760, 582. ^1H NMR ($CDCl_3$) δ_H: 7.46 (2H, s), 6.98–6.84 (4H, m), 4.48 (4H, s), 3.52 (4H, q, J = 6.0 Hz), 2.64 (4H, t, J = 5.7 Hz), 1.78–1.71 (4H, m), 1.04 (1H, br). ^{13}C NMR ($CDCl_3$) δ_C: 167.9, 147.0, 122.7, 113.6, 67.9, 47.2, 36.8, 27.7. MS *m/z* (%): 323 ([M^+ + 2], 5.0), 322 ([M^+ + 1], 26.1), 321 ([M^+], 5.0), 263 (10.3), 236 (7.4), 220 (5.6), 208 (3.4), 180 (3.5), 163 (4.0), 155 (18.9), 135 (10.7), 127 (13.2), 113 (22.1), 100 (24.9), 85 (44.7), 70 (42.1), 56 (70.8), 44 (100). Anal. calcd. for $C_{16}H_{23}N_3O_4$: C 59.80, H 7.21; found: C 59.68, H 7.34.

8-(2-Hydroxy-5-methylbenzyl)-5,6,7,8,9,10,11,12-octahydro-2*H*-1,15,4,8,12-benzodioxatriazacycloheptadecine-3,13(4*H*,14*H*)-dione (7)

Purification by flash column chromatography, eluted with n-hexane – ethyl acetate (1:1), gave compound **7** as a colorless powder in 84% yield; mp 167 °C. IR (KBr, cm^{-1}) υ_{max}: 3329, 2962, 1662, 1550, 1504, 1450, 1254, 1126, 1041, 818, 752. ^1H NMR ($CDCl_3$) δ_H: 7.26 (2H, s), 7.04–6.93 (6H, m), 6.76 (1H, d, J = 8.4 Hz), 4.56 (4H, s), 3.77 (2H, s), 3.42 (4H, q, J = 6.0 Hz), 2.66 (4H, t, J = 5.7 Hz), 2.28 (3H, s), 1.86–1.73 (4H, m). ^{13}C NMR ($CDCl_3$) δ_C: 168.1, 155.2, 147.0, 129.5, 129.2, 123.1, 122.0, 115.9, 114.6, 68.5, 58.1, 50.9, 36.2, 26.0, 20.4. MS *m/z* (%): 334 ([M^+ – 107], 1.2), 333 (9.2), 332 (6.7), 303 (0.5), 291 (1.1), 290 (5.0), 275 (3.9), 261 (2.0), 247 (6.2), 225 (3.4), 220 (3.0), 210 (3.4), 208 (3.6), 183 (12.6), 168 (15.29), 153 (14.8), 140 (28.7), 121 (28.9), 111 (28.7), 98 (62.4), 84 (46.7), 70 (81.4), 56 (100). Anal. calcd. for $C_{24}H_{31}N_3O_5$: C 65.29, H 7.08; found: C 65.84, H 6.87.

7-(2-Hydroxy-5-methylbenzyl)-5,6,7,8,9,10-hexahydro-2*H*-1,13,4,7,10-benzodioxatriazacyclopentadecine-3,11(4*H*,12*H*)-dione (9)

Purification by flash column chromatography, eluted with n-hexane – ethyl acetate (1:1), gave compound **9** as a colorless powder in 87% yield; mp 206 °C. UV–vis (chloroform, nm, (logϵ)) λ_{max}: 271 (3.33), 244 (3.04). IR (KBr, cm^{-1}) υ_{max}: 3400, 3200, 2900, 2860, 2680, 1662, 1598, 1540, 1506, 1438, 1259, 1215, 1047, 1128, 815, 740. ^1H NMR ($CDCl_3$) δ_H: 8.14 (1H, s), 7.56 (2H, s), 7.07–6.87 (6H, m), 6.64 (1H, d, J = 8.0 Hz), 4.51 (4H, s), 3.73 (2H, s), 3.54 (4H, t, J = 5.3 Hz), 2.75 (4H, t, J = 5.3 Hz), 2.22 (3H, s). ^{13}C NMR ($CDCl_3$) δ_C: 168.3, 154.0, 147.6, 131.0, 130.0, 129.5, 123.2, 122.4, 116.1, 114.9, 68.7, 56.0, 53.3, 36.2, 20.8. MS *m/z* (%): 415 ([M^+ + 2], 1.2), 414 ([M^+ + 1], 4.2), 413 ([M^+], 10.0), 396 (2.4), 341 (16.5), 292 (37.7), 225 (41.9), 206 (15.5), 180 (12.3), 176 (23.2), 162 (27.5), 121 (93.3), 91 (85.4), 85 (60.8), 69 (60.0), 56 (86.6), 43 (100.0). Anal. calcd. for $C_{22}H_{27}N_3O_5$: C 63.91, H 6.58; found: C 63.75, H 6.43.

© 2008 NRC Canada

7-(5-Bromo-2-hydroxybenzyl)-5,6,7,8,9,10-hexahydro-2*H*-1,13,4,7,10-benzodioxatriazacyclopentadecine-3,11(4*H*,12*H*)-dione (10)

Rrecrystallization from EtOAc gave compound **10** as a colorless powder in 73% yield; mp 238 °C (decomposed). UV–vis (chloroform, nm (logϵ)) λ_{max}: 374 (1.81), 269 (3.22), 246 (3.08) IR (KBr, cm^{-1}) υ_{max} : 3393, 3200, 2900, 1663, 1590, 1542, 1502, 1464, 1425, 1370, 1258, 1218, 1128, 1106, 1056, 823, 750. ^{1}H NMR (DMSO-d_6) δ_H: 9.81 (1H, s), 7.80 (2H, s), 7.38 (1H, d, J = 1.9 Hz), 7.12–6.95 (5H, m), 6.68 (1H, d, J = 8.6 Hz), 4.44 (4H, s), 3.54 (2H, s), 3.40 (4H, t, J = 5.3 Hz), 2.64 (4H, t, J = 5.3 Hz). ^{13}C NMR (DMSO-d_6) δ_C: 167.2, 155.2, 147.2, 132.3, 130.5, 127.6, 122.2, 117.3, 114.4, 110.3, 68.0, 52.2, 50.1, 35.4. MS *m/z* (%): 479 ([M^+ + 2], 1.5), 477 ([M^+], 1.5), 407 (2.0), 405 (2.0), 292 (29.3), 242 (10.2), 240 (10.2), 225 (27.4), 206 (10.5), 187 (13.4), 185 (13.4), 167 (12.6), 150 (12.5), 121 (22.2), 85 (59.3), 56 (100.0), 43 (89.2). Anal. calcd. for $C_{21}H_{24}BrN_3O_5$: C 52.73, H 5.06; found: C 52.85, H 4.88.

7-(5-Chloro-2-hydroxybenzyl)-5,6,7,8,9,10-hexahydro-2*H*-1,13,4,7,10-benzodioxatriazacyclopentadecine-3,11(4*H*,12*H*)-dione (11)

Recrystallization from EtOAc gave compound **11** as a colorless powder in 75% yield; mp 237 °C (decomposed). UV–vis (chloroform, nm (logϵ)) λ_{max}: 360 (2.97), 292 (3.25), 272 (3.24), 246 (3.13). IR (KBr, cm^{-1}) υ_{max}: 3394, 3250, 2950, 2850, 1662, 1590, 1540, 1500, 1427, 1370, 1245, 1210, 1128, 1056, 823, 756, 653. ^{1}H NMR (DMSO-d_6) δ_H: 9.78 (1H, s), 7.80 (2H, s), 7.27 (1H, d, J = 2.2 Hz), 6.95–7.11 (5H, m), 6.72 (1H, d, J = 8.6 Hz), 4.44 (4H, s), 3.54 (2H, s), 3.40 (4H, t, J = 5.3 Hz), 2.64 (4H, t, J = 5.3 Hz). ^{13}C NMR (DMSO-d_6) δ_C: 167.2, 154.8, 147.2, 129.5, 127.6, 127.0, 122.7, 122.2, 116.8, 114.4, 68.0, 52.2, 50.1, 35.4. MS *m/z* (%): 435 ([M^+ + 2], 0.4), 434 ([M^+ + 1], 0.2), 433 ([M^+], 2.2), 416 (0.3), 361 (2.3), 292 (12.7), 225 (24.3), 196 (11.1), 167 (12.6), 141 (16.9), 121 (19.4), 113 (19.9), 85 (50.9), 77 (60.3), 69 (66.2), 56 (97.9), 43 (100.0). Anal. calcd. for $C_{21}H_{24}ClN_3O_5$: C 58.13, H 5.58; found: C 57.89, H 5.76.

7-(5-Fluoro-2-hydroxybenzyl)-5,6,7,8,9,10-hexahydro-2*H*-1,13,4,7,10-benzodioxatriazacyclopentadecine-3,11(4*H*,12*H*)-dione (12)

Purification by flash column chromatography, eluted with n-hexane – ethyl acetate (1:1), gave compound **12** as a colorless powder in 81% yield; mp 214 °C. UV–vis (chloroform, nm (logϵ)) λ_{max} : 288 (3.21), 270 (3.22), 245 (2.73). IR (KBr, cm^{-1}) υ_{max}: 3404, 3078, 2916, 2822, 1676, 1549, 1506, 1448, 1259, 1219, 1195, 1130, 1057, 818, 748. ^{1}H NMR ($CDCl_3$) δ_H: 8.55 (1H, s), 7.46 (2H, s), 7.06–6.91 (4H, m), 6.87–6.63 (3H, m), 4.51 (4H, s), 3.74 (2H, s), 3.54 (4H, t, J = 5.3 Hz), 2.75 (4H, t, J = 5.3 Hz). ^{13}C NMR ($CDCl_3$) δ_C: 168.1, 158.2, 154.5, 152.1, 147.2, 122.9, 116.8, 116.3, 115.9, 114.8, 68.5, 56.0, 52.8, 35.7. ^{19}F NMR ($CDCl_3$) δ_F: –125.0 (1F). MS *m/z* (%): 418 ([M^+ + 1], 1.0), 417 ([M^+], 2.5), 400 (0.2), 346 (0.2), 345 (3.0), 294 (0.8), 293 (3.8), 292 (19.2), 225 (29.7), 206 (14.1), 180 (31.1), 167 (28.1), 150 (16.7), 125 (36.2), 96 (38.1), 85 (49.0), 69 (50.2), 56 (100). Anal. calcd. for $C_{21}H_{24}FN_3O_5$: C 60.42, H 5.80; found: C 60.57. H 5.74.

7-[(4-Hydroxy[1,1'-biphenyl]-3-yl)methyl]-5,6,7,8,9,10-hexahydro-2*H*-1,13,4,7,10-benzodioxatriazacyclopentadecine-3,11(4*H*,12*H*)-dione (13)

Recrystallization from EtOAc gave compound **13** as a colorless powder in 79% yield; mp 190 °C. UV–vis (chloroform, nm (logϵ)) λ_{max}: 293 (3.28), 253 (3.36). IR (KBr, cm^{-1}) υ_{max}: 3380, 3250, 3030, 2950, 2850, 1672, 1598, 1540, 1506, 1456, 1264, 1225, 1127, 1049, 752. ^{1}H NMR ($CDCl_3$) δ_H: 8.81(1H, s), 7.61 (2H, s), 7.48–7.01 (8H, m), 6.90–6.82 (4H, m), 4.47 (4H, s), 3.82 (2H, s), 3.55 (4H, t, J = 5.3 Hz), 2.78 (4H, t, J = 5.3 Hz). ^{13}C NMR ($CDCl_3$) δ_C: 168.4, 156.0, 147.4, 141.0, 133.4, 129.2, 129.0, 128.1, 127.0, 126.9, 123.0, 116.6, 114.6, 68.4, 54.6, 53.3, 36.2. MS *m/z* (%): 477 ([M^+ + 2], 0.1), 476 ([M^+ + 1], 0.4), 475 ([M^+], 1.0), 403 (1.0), 368 (0.4), 352 (1.1), 313 (0.3), 293 (5.5), 249 (5.3), 225 (68.2), 182 (18.1), 167 (23.4), 150 (21.5), 121 (22.8), 113 (22.9), 85 (47.0), 69 (100.0), 56 (89.7), 43 (87.6). Anal. calcd. for $C_{27}H_{29}N_3O_5$: C 68.19, H 6.15; found: C 68.35, H 6.28.

7-(2,5-Dihydroxybenzyl)-5,6,7,8,9,10-hexahydro-2*H*-1,13,4,7,10-benzodioxatriazacyclopentadecine-3,11(4*H*,12*H*)-dione (14)

Recrystallization from EtOAc gave compound **14** as a colorless powder in 71% yield; mp 170 °C. UV–vis (DMSO, nm (logϵ)) λ_{max}: 301 (3.42), 279 (3.41). IR (KBr,cm^{-1}) υ_{max}: 3394, 2916, 2825, 1663, 1597, 1541, 1504, 1259, 1213, 1126, 1051, 818, 750. ^{1}H NMR (DMSO-d_6) δ_H: 8.71 (1H, s), 8.46 (1H, s), 7.67 (2H, s), 7.04–6.88 (4H, m), 6.47–6.32 (3H, m), 4.37 (4H, s), 3.45 (2H, s), 3.31 (4H, t, J = 5.3 Hz), 2.54 (4H, t, J = 5.3 Hz). ^{13}C NMR (DMSO-d_6) δ_C: 166.9, 149.3, 148.5, 146.5, 123.3, 121.8, 117.2, 115.6, 114.4, 114.0, 67.6, 51.5, 49.9, 35.0. MS *m/z* (%): 416 ([M^+ + 1], 0.2), 294 (1.9), 293 (2.6), 292 (0.7), 249 (5.1), 225 (51.3), 180 (13.3), 167 (18.6), 150 (17.3), 123 (25.6), 121 (23.5), 99 (17.7), 85 (42.4), 69 (83.7), 56 (100). Anal. calcd. for $C_{21}H_{25}N_3O_6$: C 60.71, H 6.07; found: C 60.53, H 5.89.

7-(3-Chloro-6-hydroxy-2,4-dimethylbenzyl)-5,6,7,8,9,10-hexahydro-2*H*-1,13,4,7,10-benzodioxatriazacyclopentadecine-3,11(4*H*,12*H*)-dione (15)

Recrystallization from EtOAc gave compound **15** as a colorless powder in 79% yield; mp 241 °C (decomposed). UV–vis (chloroform, nm (logϵ)) λ_{max}: 271 (3.21), 246 (3.15). IR (KBr, cm^{-1}) υ_{max}: 3375, 3190, 2878, 2806, 1657, 1599, 1541, 1506, 1438, 1211, 1122, 1063, 815, 744. ^{1}H NMR ($CDCl_3$) δ_H: 9.43 (1H, s), 7.41 (2H, s), 7.07–6.91 (4H, m), 6.50 (1H, s), 4.51 (4H, s), 3.83 (2H, s), 3.54 (4H, t, J = 5.3 Hz), 2.75 (4H, t, J = 5.3 Hz), 2.33 (3H, s), 2.26 (3H, s). ^{13}C NMR ($CDCl_3$) δ_C: 168.1, 154.8, 147.3, 139.0, 136.8, 123.0, 118.9, 116.1, 115.1, 68.6, 53.8, 52.8, 35.8, 21.1, 16.9. MS *m/z* (%): 463 ([M^+ + 2], 0.3), 462 ([M^+ + 1],1.2), 461 ([M^+], 3.6), 390 (0.3), 389 (2.4), 294 (5.0), 293 (5.6), 292 (15.4), 225 (50.0), 180 (14.3), 168 (32.8), 150 (18.0), 121 (31.1), 105 (81.7), 85 (64.5), 69 (89.3), 56 (100). Anal.

© 2008 NRC Canada

calcd. for $C_{23}H_{28}ClN_3O_5$: C 59.80, H 6.11; found: C 59.95, H 6.01.

7-(2-Hydroxybenzyl)-5,6,7,8,9,10-hexahydro-2*H*-1,13,4,7,10-benzodioxatriazacyclopentadecine-3,11(4*H*,12*H*)-dione (16)

Purification by flash column chromatography, eluted with n-hexane – ethyl acetate (1:1), gave compound **16** as a colorless powder in 78% yield; mp 190 °C. UV–vis (chloroform, nm (logϵ)) λ_{max}: 267 (3.24), 245 (2.85). IR (KBr, cm^{-1}) υ_{max}: 3398, 3074, 2893, 2849, 1661, 1593, 1504, 1456, 1439, 1257, 1219, 1130, 1061, 818, 744. ^{1}H NMR ($CDCl_3$) δ_H: 8.56 (1H, s), 7.55 (2H, s), 7.14–6.70 (8H, m), 4.48 (4H, s), 3.75 (2H, s), 3.51 (4H, t, J = 5.3 Hz), 2.74 (4H, t, J = 5.3 Hz). ^{13}C NMR ($CDCl_3$) δ_C: 168.0, 156.0, 147.2, 130.1, 129.2, 122.8, 122.1, 119.9, 115.8, 115.4, 114.5, 68.3, 55.4, 52.8, 35.8. MS *m/z* (%): 401 ([M^+ + 2], 0.1), 400 ([M^+ + 1], 0.9), 399 ([M^+], 0.9), 328 (0.9), 327 (6.3), 294 (1.9), 293 (4.6), 292 (18.5), 225 (20.5), 162 (18.8), 148 (18.6), 121 (21.8), 107 (57.7), 85 (55.0), 56 (100). Anal. calcd. for $C_{21}H_{25}N_3O_5$: C 63.14, H 6.31; found: C 62.98, H 6.45.

7-(3-Allyl-2-hydroxybenzyl)-5,6,7,8,9,10-hexahydro-2*H*-1,13,4,7,10-benzodioxatriazacyclopentadecine-3,11(4*H*,12*H*)-dione (17)

Rrecrystallization from EtOAc gave compound **17** as a colorless powder in 74% yield; mp 188 °C. UV–vis (chloroform, nm (logϵ)) λ_{max}: 282 (3.20), 265 (3.26), 246 (3.06). IR (KBr, cm^{-1}) υ_{max}: 3304, 2914, 2824, 1662, 1596, 1545, 1504, 1458, 1439, 1261, 1148, 1121, 1047, 812, 752. ^{1}H NMR ($CDCl_3$) δ_H: 8.89 (1H, s), 7.49 (2H, s), 7.05–6.87 (6H, m), 6.72 (1H, t, J = 7.5 Hz), 5.85–5.69 (1H, m), 4.85 (1H, dd, J = 10, 1.65 Hz), 4.78 (1H, dd, J = 17 Hz, 1.72 Hz), 4.48 (4H, s), 3.74 (2H, s), 3.51 (4H, t, J = 5.3 Hz), 3.12 (2H, d, J = 6.5 Hz), 2.73 (4H, t, J = 5.3 Hz). ^{13}C NMR ($CDCl_3$) δ_C: 168.1, 154.2, 147.3, 136.7, 129.7, 127.6, 126.4, 122.9, 121.7, 119.6, 115.5, 114.9, 68.5, 57.1, 52.6, 35.6, 34.1. MS *m/z* (%): 440 ([M^+ + 1], 1.6), 439 ([M^+], 3.8), 368 (1.9), 367 (6.6), 294 (4.4), 293 (6.4), 292 (25.1), 226 (4.0), 225 (30.2), 206 (10.1), 202 (13.8), 188 (19.3), 167 (14.5), 147 (43.6), 131 (25.1), 117 (25.5), 91 (51.4), 85 (62.2), 69 (63.9), 56 (100). Anal. calcd. for $C_{24}H_{29}N_3O_5$: C 65.59, H 6.65; found: C 65.41, H 6.78.

7-(5-*tert*-Butyl-2-hydroxybenzyl)-5,6,7,8,9,10-hexahydro-2*H*-1,13,4,7,10-benzodioxatriazacyclopentadecine-3,11(4*H*,12*H*)-dione (18)

Rrecrystallization from EtOAc gave compound **18** as a colorless powder in 72% yield; mp 216 °C. UV–vis (chloroform, nm (logϵ)) λ_{max}: 282 (3.19), 267 (3.23), 245 (2.96). IR (KBr, cm^{-1}) υ_{max}: 3377, 3281, 2955, 2906, 1676, 1597, 1539, 1506, 1439, 1346, 1263, 1225, 1128, 1051, 820, 725. ^{1}H NMR ($CDCl_3$) δ_H: 8.44 (1H, s), 7.62 (2H, s), 7.11 (1H, d, J = 8.4 Hz), 7.04 (1H, s), 7.01–6.84 (4H, m), 6.68 (1H, d, J = 8.4 Hz), 4.44 (4H, s), 3.73 (2H, s), 3.52 (4H, t, J = 5.3 Hz), 2.74 (4H, t, J = 5.3 Hz), 1.23 (9H, s). ^{13}C NMR ($CDCl_3$) δ_C: 167.9, 153.6, 147.0, 142.5, 127.1, 125.8, 122.6, 121.4, 115.2, 114.1, 68.0, 54.8, 52.4, 35.7, 33.9, 31.5. MS *m/z* (%): 456 ([M^+ + 1], 0.6), 455 ([M^+], 2.8), 384 (1.7), 383 (6.7), 294 (1.7), 293 (3.9), 292 (28.7), 225 (30.9), 204 (21.9), 163 (48.9), 147 (36.5), 119 (37.1), 85 (72.5), 69 (71.3), 56 (100). Anal. calcd. for $C_{25}H_{33}N_3O_5$: C 65.91, H 7.30; found: C 66.07, H 7.41.

7-(2-Hydroxy-5-nitrobenzyl)-5,6,7,8,9,10-hexahydro-2*H*-1,13,4,7,10-benzodioxatriazacyclopentadecine-3,11(4*H*,12*H*)-dione (19)

Rrecrystallization from EtOAc gave compound **19** as yellow powder in 40% yield; mp 239.5 °C (decomposed). UV–vis (DMSO, nm (logϵ)) λ_{max}: 354 (3.43), 298 (3.45). IR (KBr, cm^{-1}) υ_{max}: 3390, 3200, 2850, 1667, 1600, 1550, 1530, 1500, 1440, 1335, 1295, 1257, 1218, 1128, 1085, 1056, 830, 817, 750. ^{1}H NMR (DMSO-d_6) δ_H: 8.11 (1H, d, J = 2.2 Hz), 7.95 (1H, dd, J = 8.9, 2.3 Hz), 7.80 (2H, s), 7.11–6.96 (4H, m), 6.89 (1H, d, J = 8.9 Hz), 4.40 (4H, s), 3.65 (2H, s), 3.37 (4H, t, J = 5.3 Hz), 2.51 (4H, t, J = 5.3 Hz). ^{13}C NMR (DMSO-d_6) δ_C: 167.4, 162.6, 147.4, 139.7, 126.6, 126.3, 126.0, 124.7, 122.4, 115.6, 114.7, 68.3, 52.4, 50.6, 35.5. MS *m/z* (%): 445 ([M^+ + 1], 0.3), 444 ([M^+], 1.3), 427 (14.3), 414 (0.5), 356 (0.4), 340 (0.4), 292 (4.9), 225 (39.2), 207 (10.6), 193 (5.3), 180 (9.7), 167 (20.5), 150 (19.3), 121 (22.3), 113 (18.0), 85 (48.7), 69 (80.7), 56 (92.4), 43 (100.0). Anal. calcd. for $C_{21}H_{24}N_4O_7$: C 56.75, H 5.44; found: C 56.58, H 5.26.

Acknowledgements

We gratefully acknowledge the support of this work by the Shiraz University Research Council. We are also grateful to Mr. H. Sajedian Fard and Mr. M. S. Darvish Tafvizi for helpful cooperation.

References

1. (*a*) J.S. Kim, O.J. Shon, J.W. Ko, M.H. Cho, I.Y. Yu, and J. Vicens. J. Org. Chem. **65**, 2386 (2000); (*b*) H. Nishida, Y. Katayama, H. Katsuki, H. Nakamura, M. Takagi, and K. Ueno. Chem. Lett. 1853 (1982); (*c*) Y. Katayama, R. Fukuda, T. Iwasaki, K. Nita, and M. Takagi. Anal. Chim. Acta, **204**, 113 (1988); (*d*) S. Alihodzic, M. Zinic, B. Klaic, R. Kiralj, B. Kojic-Prodic, M. Herceg, and Z. Cimerman. Tetrahedron Lett. **34**, 8345 (1993); (*e*) H. Nakamura, K. Nita, M. Takagi, and K. Ueno. Heterocycles, **21**, 762 (1984); (*f*) E. Chapoteau, B.P. Czech, C.R. Gebauer, A. Kumar, K. Leong, D.T. Mytych, W. Zazulak, D.H. Desai, E. Luboch, J. Krzykawski, and R.A. Bartsch. J. Org. Chem. **56**, 2575 (1991); (*g*) H. Tsukube. J. Coord. Chem. **16**, 101 (1987).
2. (*a*) H.Tsukube, J. Uenishi, H. Higaki, K. Kikkawa, T. Tanaka, S. Wakabayashi, and S. Oae. J. Org. Chem. **58**, 4389 (1993); (*b*) D. A. Gustowski, V.J. Gatto, J. Mallen, L. Echegoyen, and G.W. Gokel. J. Org. Chem. **52**, 5172 (1987); (*c*) H. Tsukube, K. Takagi, T. Higashiyama, T. Iwachido, and N. Hayama. J. Chem. Soc. Perkin Trans. 1, 1033 (1986); (*d*) H. Tsukube, K. Yamashita, T. Iwachido, and M. Zenki. Tetrahedron Lett. **29**, 569 (1988); (*e*) H. Nishida, M. Tazaki, M. Takagi, and K. Ueno. Microchim. Acta, 281 (1981); (*f*) A.F. Abdel-Magid, K.G. Carson, B.D. Harris, C.A. Maryanoff, and R.D. Shah. J. Org. Chem. **61**, 3849 (1996); (*g*) R.F. Borch and A.I. Hassid. J. Org. Chem. **37**, 1673 (1972); (*h*) F.J. McEvoy and G.R. Allen. J. Med. Chem. **17**, 281 (1974); (*i*) Zh. Yang, J.S. Bradshaw, X.X. Zhang, P.B. Savage, K.E. Krakowiak, N.K. Dalley, N. Su, R.T. Bronson, and R.M. Izatt. J. Org. Chem. **64**, 3162 (1999).

© 2008 NRC Canada

3. A.V. Bordunov, J.S. Bradshaw, V.N. Pastushok, and R.M. Izatt. Synlett, 933 (1996).
4. (*a*) H.B. Kagan. Pure Appl. Chem. **46**, 177 (1976); (*b*) R. Setton. Intercalation compounds of graphite and their reactions. *In* Preparative Chemistry Using Supported Reagents. Chap. 15. *Edited by* P. Lazlo.,Academic Press, London. 1987. pp. 255–283; (*c*) A. Furstner. Angew. Chem. Int. Ed. Engl. **32**, 164 (1993); (*d*) R. Wiesendanger and D. Anslemetti. Phys. Chem. Mater. Low-Dimens. Struct. **16**, 1 (1992); (*e*) L.L. Madsen, J.F. Joergensen, and K. Camerio. Synth. Met. **55**, 335 (1993).
5. (*a*) M. Audhuy-Peaudecerf, J. Berlan, J. Dubac, A. Laporterie, R. Laurent, and S. Lefeuvre. French Patent 94-09073. 1994; (*b*) M. Audhuy-Peaudecerf, J. Berlan, J. Dubac, A. Laporterie, R. Laurent, and S. Lefeuver. French Patent 2722781. 1996. (Chem. Abstr. **125**, 1370 (1996)); (*c*) R. Laurent. Ph.D. thesis, Université Paul Sabatier, France. 1994; (*d*) C. Laporte. Ph.D. thesis, Université Paul Sabatier, France. 1997; (*e*) B. Garrigues, C. Laporte, R. Laurent, A. Laporterie, and J. Dubac. Liebigs Ann. Chem. 739 (1996); (*f*) B. Garrigues, R. Laurent, C. Laporte, A. Laporterie, and J. Dubac. Liebigs Ann. Chem. 743 (1996); (*g*) P. Garrigues and B. Garrigue. C.R. Acad. Sci. Ser. IIc Chim. **1**, 545 (1998); (*h*) C. Laporte, A. Oussaid, B. Garrigues. C.R. Acad. Sci. Ser. IIc Chim. **3**, 321 (2000).
6. Q. Dabirmanesh, S.I.S. Fernando, and R.M.G. Roberts. J. Chem. Soc. Perkin Trans. 1, 643 (1995).
7. D. Villemin, M. Hachemi, and M. Lalaoui. Synth. Commun. 2461 (1996).
8. J. Marquie, A. Laporterie, J. Dubac, and N. Roques. Synlett, 493 (2001).
9. H. Sharghi and M. Hosseini Sarvari. Synthesis, 243 (2003).
10. H. Sharghi and M. Hosseini Sarvari. Synthesis, 2165 (2004).
11. (*a*) G.A. Sereda.. Tetrahedron Lett. **45**, 7265 (2004); (*b*) G.S. Szymanski, Z. Karpinski, S. Biniak, and A. Swiatkowski. Carbon, **40**, 2627 (2002).
12. M. Tramontini and L. Angiolini. Tetrahedron, **46**, 1791 (1990).
13. (*a*) E.F. Kleinman. The Bimolecular Aliphatic Mannich and Related Reactions. *In* B. M. Trost. Comprehensive Organic Synthesis. Vol. 1. Pergamon Press, Oxford. 1991; (*b*) M. Tramontini and L. Angiolini. Mannich bases: chemistry and uses. CRC Press, Boca Raton, Florida.1994.
14. (*a*) N.G. Lukyanenko, V.N. Pastushok, and A.V. Bordanov. Synthesis, 241 (1991); (*b*) K.W. Chi, H.-C. Wei, T. Kottke, and R.J. Lagow. J. Org. Chem. **61**, 5684 (1996); (*c*) N. Su, J.S. Bradshaw, P.B. Savage, K.E. Krakowiak, R.M. Izatt, S.L. De Wall, and G.W. Gokel. Tetrahedron, **55**, 9737 (1999); (*d*) K.W. Chi, Y.S. Ahn, K.T. Shim, H. Huh, and J.S. Ahn. Bull. Korean Chem. Soc. **23**, 688 (2002).
15. (*a*) H. Sharghi and A. Zare. Synthesis, 999 (2006); (*b*) M. Shamsipur, F. Mizani, A.A. Saboury, H. Sharghi, and R. Khalifeh. Electroanalysis, **19**, 587 (2007).
16. (*a*) H. Sharghi, K. Niknam, and A.R. Massah. J. Heterocyclic Chem. **36**, 601 (1999); (*b*) H. Sharghi and M. Hosseini Sarvari. Synlett, 99 (2001); (*c*) H. Sharghi and M. Hosseini Sarvari. Synthesis, 1057 (2002); (*d*) H. Sharghi and M. Hosseini Sarvari. Tetrahedron, **58**, 10323 (2002); (*e*) H. Sharghi and M. Hosseini Sarvari. J. Chem. Res. (S), 446 (2001); (*f*) H. Sharghi and M. Hosseini Sarvari. J. Chem. Res. (S), 176 (2003); (*g*) F. Kazemi, H. Sharghi, and M.A. Nasseri. Synthesis, 205 (2004); (*h*) H. Sharghi and M. Hosseini Sarvari. J. Iranian Chem. Soc. **1**, 28 (2004), Available from www.ics-ir.org/jics; (*i*) H. Sharghi and M. Hosseini Sarvari. J. Org. Chem. **69**, 6953 (2004); (*j*) H. Sharghi, M. Hosseini Sarvari, and R. Eskandari, J. Chem. Res. (S), 482 (2005); (*k*) H. Sharghi and M. Hosseini Sarvari. Tetrahedron, **61**, 10903 (2005); (*l*) H. Sharghi and M. Hosseini Sarvari. J. Chem. Res. (S), 205 (2006).
17. N.G. Lukyanenko, V.N. Pastushok, A.V. Bordanov, V.I. Vetrogon, N.I. Vetrogon, and J.S. Bradshaw. J. Chem. Soc. Perkin Trans. 1, 1489 (1994).
18. M.M. Mojtahedi, A. Sharifi, F. Mohsenzadeh, and M.R. Saidi. Synth. Commun. **30**, 69 (2000).
19. (*a*) H. Sharghi and B. Kaboudin, J. Chem. Res. (S), 628 (1998); (*b*) H. Sharghi and K. Niknam. Iran. J. Chem. Chem. Eng. **18**, 36 (1999) (Chem. Abstr. **132**, 122357m (2000)); (*c*) H. Sharghi and M. Hosseini Sarvari. J. Chem. Res. (S), 446 (2001); (*d*) H. Sharghi and M. Hosseini Sarvari. J. Org. Chem. **68**, 4096 (2003); (*e*) H. Sharghi, M. Hosseini Sarvari. Synth. Commun. **33**, 205 (2003); (*f*) H. Sharghi and M. Hosseini Sarvari. Teterahedron, **59**, 3627 (2003); (*g*) H. Sharghi and M. Hosseini Sarvari. Synthesis, 879 (2003); (*h*) H. Sharghi and Z. Shahsavari-Fard. J. Iranian Chem. Soc. **2**, 47 (2005) (Available from www.ics-ir.org/jics); (*i*) H. Sharghi and Z. Shahsavari-Fard. Phosphorus Sulfur Silicon Relat. Elem. **180**, 1 (2005).
20. (*a*) H. Sharghi and M. Hosseini Sarvari. Synthesis, 243 (2003); (*b*) H. Sharghi and M. Hosseini Sarvari. Synthesis, 2165 (2004); (*c*) H. Sharghi and Z. Shahsavari-Fard. Helv. Chim. Acta **88**, 42 (2005); (*d*) H. Sharghi and M. Hosseini Sarvari. Helv. Chim. Acta **88**, 2282 (2005); (*e*) H. Sharghi, M. Hosseini Sarvari, and R. Eskandari. Synthesis, 2047 (2006).
21. F. Rodriguez-Reinoso. Carbon, **36**, 159 (1998).
22. (*a*) J.T. Cookson Jr. *In* Carbon adsorption handbook. *Edited by* P.N. Cheremisinoff and F. Ellerbush. Ann Arbor Science Publishers Inc., Ann Arbour. 1978; (*b*) J.S. Mattson and H.B. Mark Jr. Activated carbon: Surface chemistry and adsorption from solution. Marcel Dekker, New York. 1971; (*c*) H.P. Boehm. *In* Advances in catalysis, chemical identification of surface groups. Vol. 16. *Edited by* H. Pines. Academic Press, New York. 1966; (*d*) J.B. Donnet. Carbon, **6**, 161 (1968).
23. F. Rodriguez-Reinoso, M. Molina-Sabio, and M.T. Gonzalez. Langmuir, **13**, 2354 (1997)
24. H. Diery and B. Renger. Liebigs Ann. Chem. 8 1239 (1980).
25. J.-z. Tian, J.-q. Zhang, X. Shen, and H.-x. Zou. J. Organomet. Chem. **584**, 240 (1999).
26. E.R. Alekperov, A.N. Dzhabiev, and A.M. Reznik. Kompleksn. Ispol'z. Miner. Syr'ya **8**, 77 (1992) (Chem. Abstr. **118**, 160047d (1993)).
27. S. Kumar, R. Singh, and H. Singh. J. Chem. Soc. Perkin Trans. 1, 3049 (1992).

© 2008 NRC Canada

Accelerated syntheses of amine-bis(phenol) ligands in polyethylene glycol or "on water" under microwave irradiation

Francesca M. Kerton, Stacey Holloway, Angela Power, R. Graeme Soper, Kristina Sheridan, Jason M. Lynam, Adrian C. Whitwood, and Charlotte E. Willans

Abstract: Pure amine-bis(phenol) ligands are readily accessible in high yield, often >90%, when the Mannich condensation reactions are performed "on water" or in poly(ethyleneglycol) (PEG). Microwave-assisted synthesis dramatically reduces the time and energy required to prepare these molecules, typically from 24 h to 5 min. The approach seems to be widely applicable (7 amines and 5 phenols were tested to yield a diverse set of bis(phenol) ligands). Significant improvements in yield were observed for ligands derived from di-*tert*-amyl and di-*tert*-butyl phenols, possibly resulting from a hydrophobic effect. Single crystal X-ray diffraction data for the ligand derived from *p*-cresol and *N*,*N*′-dimethylethylenediamine is reported.

Key words: amine-phenol, Mannich condensation, on water, microwave, ligand, high-throughput.

Résumé : Les ligands amine-bis(phénol) purs sont facilement accessibles avec des rendements élevés, souvent supérieurs à 90%, lorsqu'on effectue des réactions de condensation de Mannich en présence d'eau ou de poly(éthylèneglycol) (PEG). Les synthèses effectuées à l'aide de microondes réduisent sensiblement le temps et l'énergie requis pour préparer ces molécules, passant généralement de 24 heures à 5 min. Il semble que cette approche peut être applicable d'une façon générale; on a en effet testé sept amines et cinq phénols qui ont conduit à divers types de ligands bis(phénol). On a observé des améliorations sensibles dans les rendements obtenus avec les ligands dérivés des di-*tert*-amyl- et di-*tert*-butylphénols qui résultent peut-être d'un effet hydrophobe. On a obtenu des données de diffractions des rayons X par un cristal unique pour des ligands dérivés du *p*-crésol et de la *N*,*N*′-diméthyléthylènediamine.

Mots-clés : amine-phénol, condensation de Mannich, en présence d'eau, microonde, ligand, grand débit.

[Traduit par la Rédaction]

Introduction

Over the last 20 years, researchers have been exploring a wide range of ligand systems for use in combination with metals as new homogeneous catalysts. N-heterocyclic carbenes have emerged as versatile alternatives to phosphine ligands in late-transition metal-catalysed reactions (1–3). Anionic ligands containing "hard" nitrogen and oxygen donor atoms form a diverse set of ligands that are used as alternatives to cyclopentadienyl ligands, particularly in early transition metal and lanthanide based catalysts (4–9). Of these ligands, amine-bis(phenol) molecules have emerged as versatile, modular, and easily accessible materials (Fig. 1).

Fig. 1. Chelating amine-bis(phenol) ligands.

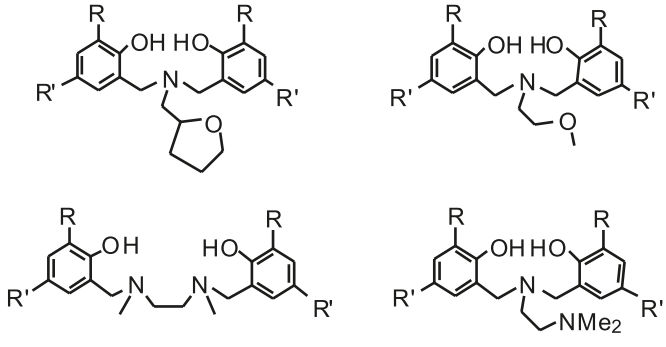

R, R' = H, Me, *t*-Bu, *t*-Am

Primarily, these ligands in combination with metals from throughout the periodic table are active catalysts for alkene polymerization (10–17) and initiators in the ring-opening polymerization of lactones (18–30).

Liquid polymers are emerging as a useful class of nonvolatile solvents and possess valuable, facile separation characteristics. The two most widely used polymers in this area are PEG (polyethylene glycol) and PPG (polypropylene glycol) (31, 32). They have a very low toxicity ranking and have been approved by the US FDA for internal consumption

Received 30 October 2007. Accepted 29 February 2008. Published on the NRC Research Press Web site at canjchem.nrc.ca on 9 April 2008.

F.M. Kerton,[1] S. Holloway, A. Power, R.G. Soper, K. Sheridan. Green Chemistry and Catalysis Group, Department of Chemistry, Memorial University of Newfoundland, St. John's, NL A1B 3X7, Canada.
J.M. Lynam, A.C. Whitwood, and C.E. Willans. Department of Chemistry, University of York, Heslington, York YO10 5DD, UK.

[1]Corresponding author (e-mail: fkerton@mun.ca).

 doi:10.1139/V08-043 © 2008 NRC Canada

(31). The high stability and low toxicity of PEG and PPG allow these molecules to be used in a large number of products and industries. PEGs and PPGs are very similar in structure to glymes, which are used as solvents because of their high chemical and thermal stability, broad pH range, and ability to dissolve polar compounds, such as water and acids, as well as nonpolar compounds, such as hydrocarbons. The polarity of PEG can be compared with the commonly used laboratory solvents CH_2Cl_2 and MeCN, whereas PPG is slightly less polar (32). In terms of laboratory safety, whereas glymes readily form explosive peroxides, PEGs and PPGS do not. The biodegradability of liquid polymers has recently been summarized (32); for example, PEG 400–1500 is >95% biodegraded in 14 days. This makes PEGs and PPGs much safer to use and dispose of than their corresponding class of volatile solvents — the glymes and many other common laboratory solvents.

Recently, cleaner, more benign routes to bis-imine Schiff base ligands have been reported (33). These reactions yielded high-purity ligand under neat reaction conditions or by using polypropylene glycol (PPG) solvent. Inspired by this research, we sought to reduce the amount of solvent used in the preparation of our chosen ligand set and also the time involved. We report herein the rapid, high-yielding synthesis of amine-bis(phenol) ligands on water under microwave irradiation and our journey en route to these results via reactions in PEG solvents.

Results and discussion

In following the work of van den Ancker and co-workers (33), the first modified procedure we attempted (Scheme 1) was the synthesis of amine-bis(phenol)s in PEG and PPG. The phenol reagents dissolved in the warm polymers to form solutions, however the *tert*-amyl and *tert*-butyl substituted phenols were insoluble at room temperature. Vials were loaded with phenol, polymer, solvent, aqueous formaldehyde, and finally the amine was added to the stirred mixture. The reaction of primary amines with formaldehyde and paraformaldehye is exothermic, and therefore care should be taken when adding the amine. The reaction mixtures immediately warmed to around 40 °C and were then heated to 75 °C overnight. Three polymer solvents were studied in this first series of reactions: PEG 400, PPG 400, and PPG 1000. Two concentrations were tested: 1 mmol amine per gram polymer solvent and 2 mmol amine per gram solvent. The amine used was *N*,*N*-dimethylethylenediamine, the phenols were di-*tert*-butyl phenol and di-*tert*-amyl phenol.

Control reactions using ethanol as the solvent were also performed and gave similar yields of products for the same reaction temperatures and times. In this series of reactions (Table 1), yields were similar for all reactions irrespective of the substituted phenol used, but yields were lower at the more dilute concentrations. PEG 400 gave slightly increased yields compared with the other solvents and was therefore used in subsequent experiments. Crystals of the ligand were sometimes obtained upon cooling the reaction mixtures containing PEG and PPG. However, larger crystals of the amine-bis(phenol)s were more readily obtained from saturated ethanol or methanol solutions. As in the work of van den Ancker (33), the polymer solvent could be re-used in subsequent experiments.

Scheme 1. Synthetic route to modular amine-bis(phenol) ligands.

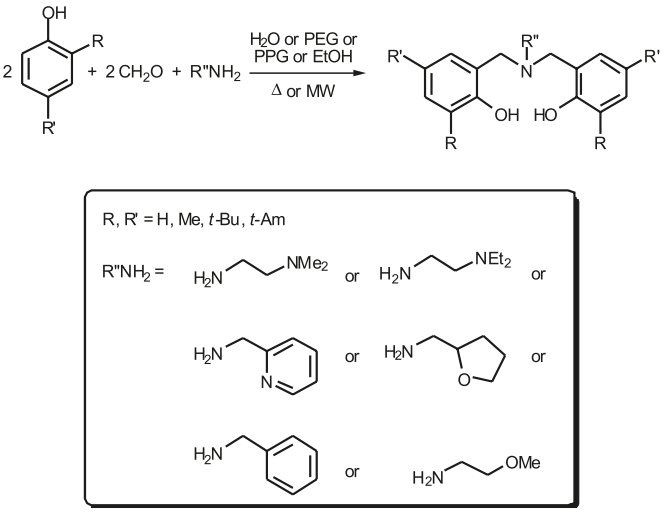

Table 1. Yields of amine-bis(phenol)s from reactions using PEG and PPG solvents.

Entry	Phenol	Solvent[a]	Yield (%)[b]
1	*t*-Bu, *t*-Bu	PPG 400 (dilute)	38
2	*t*-Bu, *t*-Bu	PPG 400	73
3	*t*-Bu, *t*-Bu	PEG 400(dilute)	48
4	*t*-Bu, *t*-Bu	PEG 400	81
5	*t*-Bu, *t*-Bu	PPG 1000 (dilute)	40
6	*t*-Bu, *t*-Bu	PPG 1000	73
7	*t*-Am, *t*-Am	PPG 400 (dilute)	52
8	*t*-Am, *t*-Am	PPG 400	74
9	*t*-Am, *t*-Am	PEG 400 (dilute)	43
10	*t*-Am, *t*-Am	PEG 400	96
11	*t*-Am, *t*-Am	PPG 1000 (dilute)	31
12	*t*-Am, *t*-Am	PPG 1000	76
13	*t*-Am, *t*-Am	Ethanol	72
14	*t*-Am, *t*-Am	Ethanol	79

[a]All reactions were heated to 75 °C, 18 h. Reactions in polymers labelled dilute were performed using 1 mmol amine per gram of polymer; otherwise 2 mmol amine per gram of polymer was used. Reactions in ethanol were performed by starting with a saturated solution of the phenol.
[b]Isolated yields, average of two identical reactions, compounds pure by ^{1}H NMR spectroscopy.

Over the past decade, tremendous advances in organic synthesis (e.g., rate accelerations, enhanced selectivities) have been achieved through the use of microwave irradiation (34–36). A wide variety of microwave-assisted condensation reactions have been studied, and therefore we attempted amine-bis(phenol) syntheses in a household microwave oven. Although there are concerns about the safety and reproducibility of results obtained using these ovens, as long as precautions are taken with safety and interpretation of the data, these ovens act as a good entry point into microwave chemistry (37–39). PEG 400 was used as the solvent in these initial studies. Vials containing the reaction mixtures were prepared as in the conventionally heated experiments. Each vial was heated individually in the microwave at the desired

© 2008 NRC Canada

Table 2. Yields of amine-bis(phenol)s from reactions under microwave irradiation.

Entry	Phenol	Amine	Conditions[a]	Yield (%)[b]
1	*p*-cresol	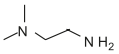	Panasonic, 1200 W, 60 s × 10	43
2	Me, Me	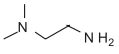	Panasonic, 1200 W, 60 s × 10	67
3	*t*-Bu, Me	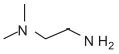	Panasonic, 1200 W, 60 s × 10	58
4	*t*-Bu, *t*-Bu	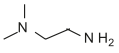	Panasonic, 1200 W, 60 s × 10	73
5	*t*-Am, *t*-Am	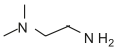	Panasonic, 1200 W, 60 s × 10	48
6	*t*-Am, *t*-Am	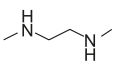	Panasonic, 1200 W, 60 s × 10	77
7	*t*-Am, *t*-Am	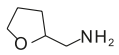	Panasonic, 1200 W, 60 s × 10	58
8	*t*-Am, *t*-Am	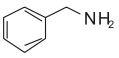	Panasonic, 1200 W, 60 s × 10	92
9	*t*-Am, *t*-Am	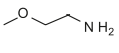	Panasonic, 1200 W, 60 s × 10	76
10	*t*-Am, *t*-Am	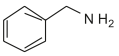	Panasonic, 1200 W, 60 s × 10	30
11	*t*-Bu, Me	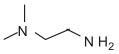	Biotage, 140 °C, 8 g PEG 400	42
12	*t*-Bu, Me	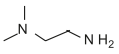	Biotage, 160 °C, 8 g PEG 400	69
13	*t*-Bu, Me	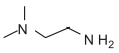	Biotage, 180 °C, 8 g PEG 400	69
14	*t*-Bu, Me	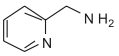	Biotage, 160 °C, 8 g PEG 400	45
15	*t*-Bu, Me	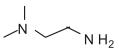	Biotage, 160 °C, 5 mL EtOH	68
16	*t*-Bu, Me	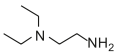	Biotage, 160 °C, 5 mL EtOH	57
17	*t*-Bu, Me	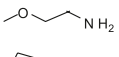	Biotage, 160 °C, 5 mL EtOH	63
18	*t*-Bu, Me	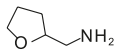	Biotage, 160 °C, 5 mL EtOH	33
19	*t*-Bu, Me	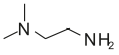	Biotage, 160 °C, 5 mL H_2O	85
20	*t*-Bu, *t*-Bu	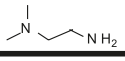	Biotage, 160 °C, 5 mL H_2O	92

[a]Panasonic household microwave oven operated at constant power of 1200 W for 10 × 60 s, reaction scale of 2 g PEG 400, and 0.7 mL aq. CH_2O. Biotage stands for a Biotage Initiator operated at constant temperature mode for 5 min at the indicated temperature, reaction scale of 3 mL aq. CH_2O.

[b]Isolated yields, average of two identical reactions, compounds pure by ^{1}H NMR spectroscopy.

power and for varying lengths of time. Each reaction was then triturated using ethanol, cooled to 0 °C, and the crystalline precipitate collected by filtration. Initial experiments were performed using 60 s microwave pulses at low power settings, 50% power (600 W) or 10% power (120 W). However, as expected, the yields increased with increased reaction time and microwave power setting. Therefore, after preliminary experiments, all amine-bis(phenol) syntheses performed in the household microwave were conducted using ten 60 s full power (1200 W) pulses (Table 2). Reaction temperatures were monitored between pulses and were between 80 and 100 °C. Some reactions were also performed using catalytic amounts of aqueous acid, but this did not increase the yield or rate of reactions.

To confirm the results obtained using a household microwave, selected reactions were repeated using a research grade instrument (Biotage Initiator System, 20 mL reaction volume sealed vessels) (Table 2). In addition to reactions in

© 2008 NRC Canada

Table 3. Yields of amine-bis(phenol)s using water as the reaction medium.

	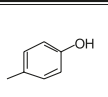		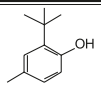	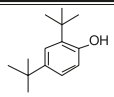	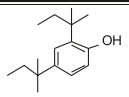
	23	66	76 (85)	94 (92)	98
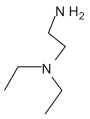	—	51	62	76	83
	25	28	55	72	98
	26	59	86	87	79
	—	94	88	92	89
	—	—	56	99	89
	23	46	33	54	98

Note: Isolated yields, values in parentheses from microwave heated reactions using a Biotage Initiator system, compounds dried in a vacuum desiccator to constant mass and pure by ^{1}H NMR spectroscopy.

PEG 400, reactions were performed using ethanol and water. Yields using ethanol (Table 2, entries 15–18) were comparable with those using PEG 400, but interestingly, excellent yields were obtained using water (Table 2, entries 19 and 20). These reactions can be reproduced using conventional heating, however significantly longer reaction times are needed.

A wide range of reactions using water as the reaction medium have been studied because of their *green* potential (40–42). These include Mannich-type reactions using surfactants to facilitate the acid-catalyzed process (43). Therefore, we decided to prepare a wide range of amine-bis(phenol) ligands in water. Recently, it has been discovered that in some cases when reactants and products are insoluble in water, the reactions occur in a suspension or "on water" (44, 45). Although, we did not see the rate enhancements observed by Sharpless and co-workers (44), as can be seen in Table 3 the yields of these Mannich condensation reactions improve with an increase in hydrophobicity of the phenol. For example, yields using di-*tert*-butyl and di-*tert*-amyl phenol are always significantly higher that those using *para*-cresol or dimethyl phenol as the reagent (Table 3). We tentatively propose that the preferred reaction mechanism for the ligand syntheses is via formation of the iminium ion intermediates from the water-soluble amines and formaldehyde in homogeneous aqueous solution. This is followed by step-wise reactions of these species with two equivalents of phenol via a heterogenous process on the surface of the suspended droplets of liquid phenol. This prevents any alternative reaction pathways occuring, such as reaction of the amine directly with the phenol in homogeneous solution, thus increasing the yields when hydrophobic phenols are used. As phenols can be regarded as enols, when the phenol is water-soluble, some of the amine reagent can react directly with the keto tautomer of the phenol. This reduces the amount of amine available for the desired reaction with formaldehyde and this decreases the yield of amine-bis(phenol) when less sterically demanding reagents such as *p*-cresol are used.

We have also performed this class of reaction on a large scale (50 mL aqueous formaldehyde) using a Morton flask equipped with a condenser, a mechanical stirrer, and a heating mantle. Reactions were performed using 2,4-di-*tert*-butyl phenol or 2,4-di-*tert*-amyl phenol, and *N*,*N*-dimethylethylenediamine, and yields were over 90%. However, care should be taken given the large amount of precipitate that forms, which can affect the stirring mechanism.

© 2008 NRC Canada

During the course of this research, crystals of one ligand suitable for single crystal X-ray diffraction studies were isolated[2]. The molecular structure of **1**, Fig. 2, is significantly different from the previously reported more sterically congested analogue derived from di-*tert*-amyl phenol, although important bond lengths and hydrogen-bond distances are similar (29). The structure of **1** (Table 4) exhibits a twist along the backbone of the ligand, resulting in the phenol OH groups residing on opposite sides of the molecule in the solid state. In contrast, the di-*tert*-amyl derived ligand contains both OH groups on the same side of the molecule (29). The differences in the solid-state molecular structures of these two molecules are presumably due to packing constraints in the solid state, as no significant differences in their solution state structures are observed by ^{1}H NMR spectroscopy.

Fig. 2. Molecular structure of **1**. H atoms omitted for clarity. Thermal ellipsoids are drawn at the 20% probability level. Selected bond lengths (Å) and angles (°): C1–O1 1.3686(14), C7–N1 1.4758(14), C8–N1 1.4693(14), C9–N1 1.4687(15), C8–C8_2 1.520(2), O1–H1 0.91(2), C7-N1-C8 110.75(9), C7-N1-C9 110.79(9), C8-N1-C9 111.28(9).

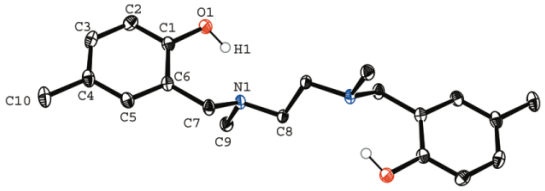

Table 4. Crystallographic data for compound **1**.

Empirical formula	$C_{20}H_{28}N_2O_2$
Formula weight	328.44
Temperature (K)	100(2)
Crystal system	Monoclinic
a (Å)	5.5722(8)
b (Å)	12.6340(19)
c (Å)	12.7270(19)
β (°)	92.380(3)
Space group	$P2_1/n$
Volume (Å^3)	895.2(2)
Z	2
Density$_{calc}$ (g/cm^3)	1.218
Absorption coefficient (mm^{-1})	0.079
θ Range for data collected (°)	2.27 to 28.33
Index ranges	$-7 \le h \le 7$, $-16 \le k \le 16$, $-16 \le l \le 16$
Reflections collected	9049
Independent reflections (R_{int})	2224 (0.0300)
Max. and min. transmission	1.000 and 0.848
Data, restraints, parameters	2224, 0, 115
Goodness-of-fit on F^2	1.061
Final *R* indices [$I > 2\sigma(I)$]	$R_1 = 0.0475$, $wR_2 = 0.1300$
Largest diff. peak and hole (eÅ^{-3})	0.444 and –0.192

Conclusions

In summary, we have reported the synthesis of related amine-bis(phenol) ligands in ethanol, PEG, PPG, or water as the solvent. Yields for these compounds are improved compared with conventional routes and reaction times are dramatically reduced when microwave heating and water are used. Therefore, microwave-assisted synthesis could aid in the synthesis of libraries of these ligands for use in high-throughput catalytic studies, and this approach could potentially be extended to other related ligand syntheses (46–50). Also, even in the absence of a microwave synthesizer, the preferred method of synthesis for the di-*tert*-butyl and di-*tert*-amyl derived ligands, and perhaps other sterically demanding analogues, should be to use water as the reaction medium. During the initial submission period for this article, a communication regarding the syntheses of related amine-phenol ligands using water as the reaction medium has been accepted for publication (51). Therein, data on the relative solubilities of alkyl-substituted phenols is reported. However, further studies are ongoing into the reasons for the increased yields of these ligands when hydrophobic phenol reagents are used during their preparation in aqueous media.

Experimental

General procedures and instrumentation

Amines, phenols, and aqueous formaldehye were purchased from Sigma-Aldrich and Alfa Aesar. Ethanol was purchased from Fisher Scientific. PEG 400, PPG 400, and PPG 1000 were purchased from Alfa Aesar. Microwave heating was achieved using either an unmodified household MW oven (Panasonic NN-S740WA-1200W) or a research grade microwave reactor (Biotage Initiator 2.0). NMR spectra were recorded on a Jeol EX 270, a Tecmag APOLLO 300, or a Bruker Avance 500 instrument (Table 5). ^{1}H NMR spectra were referenced to residual protons in the deuterated solvent and ^{13}C NMR spectra to the ^{13}C atoms therein. EI Mass spectra were recorded on a Fisons Instruments VG Analytical Autospec mass spectrometer, and MALDI-TOF spectra (anthracene matrix) were obtained on an Applied Biosystems DE-RP instrument. Selected data are presented in Table 5. Elemental analyses were performed on several samples to provide additional confirmation of their synthesis at Elemental Microanalysis Ltd., Devon, UK and at Canadian Microanalytical Service Ltd., Delta, B.C., Canada. For example, for $Me_2NCH_2CH_2N[CH_2\text{-}3,5\text{-}Bu_2\text{-}C_6H_2OH_{-2}]_2$ found: C 77.32, H 10.94, N 5.41. $C_{34}H_{56}N_2O_2$ requires: 77.81, H 10.76, N 5.34. However, not all samples were analysed in this way as full characterisation data was obtained on these ligands during their original preparation by Kol and co-workers (10–14). Diffraction data were col-

[2] Supplementary data for this article are available on the journal Web site (canjchem.nrc.ca) or may be purchased from the Depository of Unpublished Data, Document Delivery, CISTI, National Research Council Canada, Ottawa, ON K1A 0R6, Canada. DUD 3742. For more information on obtaining material refer to cisti-icist.nrc-cnrc.gc.ca/irm/unpub_e.shtml. CCDC 658822 contains the crystallographic data for this manuscript. These data can be obtained, free of charge, via www.ccdc.cam.ac.uk/conts/retrieving.html (Or from the Cambridge Crystallographic Data Centre, 12 Union Road, Cambridge CB2 1EZ, UK; fax +44 1223 336033; or deposit@ccdc.cam.ac.uk).

© 2008 NRC Canada

Table 5. Selected NMR and mass spectrometric data of amine-bis(phenol) ligands.

Amine and phenol	Spectroscopic data (^{1}H NMR, ^{13}C{^{1}H} NMR, mass spectra)
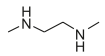 2,4-dimethyl phenol	^{1}H δ: 10.69 (br, 2H, OH), 6.87 (d, $^4J_{HH}$ = 1.1 Hz, 2H ArH), 6.62 (d, $^4J_{HH}$ = 1.1 Hz, 2H ArH), 3.63 (s, 4H, $ArCH_2$), 2.65 (s, 4H, NC_2H_4N), 2.26 (s, 6H, NCH_3), 2.21 (s, 6H, $ArCH_3$), 2.20 (s, 6H, $ArCH_3$). ^{13}C{^{1}H} δ: 153.3 (C), 130.5 (CH), 127.5 (C), 126.5 (CH), 124.6 (C), 120.5 (C), 61.7 (CH_2), 54.0 (CH_2), 20.4 (CH_3), 15.6 (CH_3). *m/z*: 357 (100%) $[MH]^+$, 223 (7%) $[MH\text{-}C_9H_{10}O]^+$, 178 (26%) $[C_{11}H_{16}ON]^+$, 135 (7%) $[C_9H_{11}O]^+$.
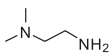 2,4-dimethyl phenol	^{1}H δ: 9.48 (br, 2H, OH), 6.88 (d, $^4J_{HH}$ = 1.9 Hz, 2H ArH), 6.68 (d, $^4J_{HH}$ = 1.9 Hz, 2H ArH), 3.57 (s, 4H, $ArCH_2$), 2.54 (s, 4H, NC_2H_4N), 2.34 (s, 6H, $N(CH_3)_2$), 2.20 (s, 12H, $ArCH_3$). ^{13}C{^{1}H} δ: 152.5 (C), 131.1 (CH), 128.2 (CH), 127.2 (C), 125.3 (C), 121.4 (C), 55.9 (CH_2), 48.9 (CH_2), 44.7 (CH_2), 20.3 (CH_3), 16.1 (CH_3). *m/z*: 357 (100%) $[MH]^+$, 298 (30%) $[MH\text{-}C_3H_9N]^+$, 223 (7%) $[MH\text{-}C_9H_{10}O]^+$, 164 (7%) $[C_{10}H_{14}NO]^+$, 135 (16%) $[C_9H_{11}O]^+$, 58 (17%) $[C_3H_8N]^+$.
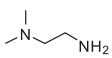 *p*-cresol	^{1}H δ: 9.06 (br, 2H, OH), 6.93 (d, $^3J_{HH}$ = 2.0 Hz, 2H, ArH), 6.83 (d, $^3J_{HH}$ = 2.0 Hz, 2H, ArH), 6.78 (s, 2H, ArH), 3.57 (s, 4H, $ArCH_2$), 2.57 (br, 4H, NC_2H_4N), 2.28 (s, 6H, $N(CH_3)_2$), 2.22 (s, 6H, $ArCH_3$). ^{13}C{^{1}H} δ: 154.7 (C), 130.8 (CH), 129.9 (CH), 128.1 (CH), 122.2 (C), 116.6 (C), 55.3 (CH_2), 48.7 (CH_2), 44.4 (CH_2), 19.9 (CH_3), 19.9 (CH_3). *m/z*: 329 (65%) $[MH]^+$, 270 (29%) $[MH\text{-}C_3H_9N]^+$, 221 (79%) $[MH\text{-}C_7H_8O]^+$, 209 (26%) $[MH\text{-}C_8H_8O]^+$, 121 (12%) $[C_8H_9O]^+$, 58 (100%) $[C_3H_8N]^+$.
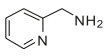 *p*-cresol	^{1}H δ: 9.50 (br, OH), 8.63 (dd, $^3J_{HH}$ = 5.1 Hz, $^4J_{HH}$ = 1.7 Hz, 1H, pyridine CH), 7.68 (dt, $^3J_{HH}$ = 7.7 Hz, $^4J_{HH}$ = 1.7 Hz, 1H, pyridine CH), 7.25 (dd, $^3J_{HH}$ = 7.7 Hz, $^3J_{HH}$ = 5.1 Hz, 1H, pyridine CH), 7.11 (d, $^3J_{HH}$ = 7.7 Hz, 1H, pyridine CH), 6.95 (d, $^3J_{HH}$ = 2.0 Hz, 2H, ArCH), 6.84 (d, $^3J_{HH}$ = 2.0 Hz, 2H, ArCH), 6.78 (s, 1H, ArCH), 6.76 (s, 1H, ArCH), 3.86 (s, 2H, NCH_2), 3.75 (s, 4H, $ArCH_2$), 2.21 (s, 6H, $ArCH_3$). ^{13}C{^{1}H} δ: 156.4 (C), 155.2 (C), 148.5 (CH), 137.9 (CH), 131.1 (CH), 130.1 (CH), 128.4 (CH), 123.7 (CH), 122.9 (CH), 121.4 (C), 116.9 (C), 58.2 (CH_2), 55.6 (CH_2), 20.1 (CH_3). *m/z*: 349 (20%) $[MH]^+$, 256 (10%), $[MH\text{-}C_6H_7N]^+$, 241 (100%) $[MH\text{-}C_7H_8O]$+, 121 (57%) $[C_8H_9O]^+$, 108 (38%) $[C_7H_8O]^+$, 93 (100%) $[C_6H_7N]^+$.
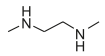 *p*-cresol (**1**)	^{1}H δ: 9.95 (br, OH), 6.96 (d, $^3J_{HH}$ = 1.7 Hz, 2H, ArH), 6.75 (d, $^3J_{HH}$ = 1.7 Hz, 2H, ArH), 6.72 (s, 2H, ArH), 3.63 (s, 4H, $ArCH_2$), 2.63 (s, 4H, NC_2H_4N), 2.25 (s, 6H, NCH_3), 2.22 (s, 6H, $ArCH_3$). ^{13}C{^{1}H} δ: 155.6 (C), 129.4 (CH), 129.3 (CH), 128.3 (C), 121.4 (C), 116.0 (CH), 61.6 (CH_2), 53.8 (CH_2), 41.4 (CH_3), 20.1 (CH_3). *m/z*: 329 (100%) $[MH]^+$, 209 (5%) $[MH\text{-}C_8H_8O]^+$, 164 (19%) $[C_{10}H_{14}NO]^+$, 121 (6%) $[C_8H_9O]^+$.
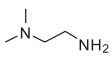 2,4-di-*tert*-amyl phenol	^{1}H δ: 9.62 (br, 2H, OH), 7.07 (d, $^4J_{HH}$ = 2.4 Hz, 2H, ArH), 6.83 (d, $^4J_{HH}$ = 2.4 Hz, 2H, ArH), 3.59 (s, 4H, $ArCH_2$), 2.54 (s, 4H, NC_2H_4N), 2.28 (s, 6H, $N(CH_3)_2$), 1.88 (m, 4H, CH_2), 1.56 (m, 4H, CH_2), 1.33 (s, 12H, CH_3), 1.23 (s, 12H, CH_3), 0.62 (m, 12H, CH_3). ^{13}C{^{1}H} δ: 153.5 (C), 138.5 (C), 134.4 (C), 125.8 (CH), 121.7 (C), 56.4 (CH_2), 55.7 (CH_2), 48.7 (CH_2), 44.5 (CH), 38.3 (C), 36.9 (CH_2), 32.4 (CH_2), 28.3 (CH_3), 27.4 (CH_3), 9.23 (CH_3), 8.86 (CH_3). *m/z* 581 (100%) $[MH]^+$, 522 (32%) $[MH\text{-}C_3H_9N]^+$, 347 (14%) $[MH\text{-}C_{16}H_{26}O]^+$, 247 (5%) $[C_{17}H_{27}O]^+$, 72 (6%) $[C_5H_{12}]^+$, 58 (16%) $[C_3H_8N]^+$. Found: 78.15, H 11.36, N 4.92. $C_{38}H_{64}N_2O_2$ requires: C 78.57, H 11.10, N 4.82.
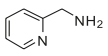 2,4-di-*tert*-amyl phenol	^{1}H δ: 10.39 (br, 2H, OH), 8.67 (dd, $^3J_{HH}$ = 5.0 Hz, $^4J_{HH}$ = 1.7 Hz, 1H, pyridine CH), 7.67 (dt, $^3J_{HH}$ = 7.4 Hz, $^4J_{HH}$ = 1.8 Hz, 1H, pyridine CH), 7.26 (dd, $^3J_{HH}$ = 7.4 Hz, $^3J_{HH}$ = 5.0 Hz, 1H, pyridine CH), 7.13 (d, $^3J_{HH}$ = 7.4 Hz, 1H, pyridine CH), 7.07 (d, $^3J_{HH}$ = 2.4 Hz, 2H, ArH), 6.85 (d, $^3J_{HH}$ = 2.4 Hz, 2H, ArH), 6.57 (s, 1H, ArH), 6.55 (s, 1H, ArH), 3.78 (s, 2H, NCH_2), 3.46 (s, 4H, $ArCH_2$), 1.85 (m, 4H, CH_2), 1.55 (m, 4H, CH_2), 1.32 (s, 12H, CH_3), 1.22 (s, 12H, CH_3), 0.64 (m, 12H, CH_3). ^{13}C{^{1}H} δ: 153.9 (C), 152.1 (CH), 148.5 (C), 141.2 (C), 139.1 (C), 137.6 (CH), 137.6 (CH), 126.0 (CH), 126.0 (CH), 124.3 (CH), 122.7 (CH), 121.4 (C), 115.9 (CH), 56.4 (CH_2), 50.7 (CH_2), 38.4 (C), 37.0 (CH_2), 32.6 (C), 28.3 (CH_3), 27.3 (CH_3), 8.84 (CH_3). *m/z*: 601 (15%) $[MH]^+$, 508 (10%) $[MH\text{-}C_6H_7N]^+$, 367 (24%) $[MH\text{-}C_{16}H_{26}O]^+$, 205 (100%) $[C_{14}H_{21}O]^+$, 93 (17%) $[C_6H_7N]^+$.
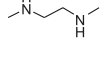 2,4-di-*tert*-amyl phenol	^{1}H δ: 10.60 (br, 2H, OH), 7.06 (d, $^4J_{HH}$ = 2.0 Hz, 2H, ArH), 6.73 (d, $^4J_{HH}$ = 2.0 Hz, 2H, ArH), 3.64 (s, 4H, $ArCH_2$), 2.60 (s, 4H, NC_2H_4N), 2.21 (s, 6H, NCH_3), 1.86 (m, 4H, CH_2), 1.55 (m, 4H, CH_2), 1.34 (s, 12H, CH_3), 1.22 (s, 12H, CH_3), 0.61 (m, 12H, CH_3). ^{13}C{^{1}H} δ: 154.2 (C), 138.8 (C), 134.0 (C), 125.3 (CH), 124.2 (CH), 120.9 (C), 62.5 (CH_2), 53.4 (CH_2), 41.2 (CH_3), 38.3 (C), 36.9 (CH_2), 32.5 (CH_2), 28.2 (CH_3), 27.2 (CH_3), 9.18 (CH_3), 8.74 (CH_3). *m/z*: 581 (100%) $[MH]^+$, 347 (18%) $[MH\text{-}C_{16}H_{26}O]^+$, 290 (40%) $[C_{19}H_{32}NO]^+$, 247 (11%) $[C_{17}H_{27}O]^+$.

© 2008 NRC Canada

Table 5 (*concluded*).

Amine and phenol	Spectroscopic data (^{1}H NMR, ^{13}C{^{1}H} NMR, mass spectra)
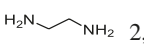 2,4-di-*tert*-amyl phenol	^{1}H δ: 10.57 (br, 2H, OH), 7.08 (d, $^4J_{HH}$ = 2.3 Hz, 2H, ArH), 6.75 (d, $^4J_{HH}$ = 2.3 Hz, 2H, ArH), 3.85 (s, 4H, $ArCH_2$), 3.15 (br, 2H, NH), 2.92 (s, 4H, NC_2H_4N), 1.84 (m, 4H, CH_2), 1.56 (m, 4H, CH_2), 1.35 (s, 12H, CH_3), 1.23 (s, 12H, CH_3), 0.64 (m, 12H, CH_3). ^{13}C{^{1}H} δ: 154.2 (C), 139.2 (C), 134.2 (C), 126.3 (CH), 124.2 (CH), 120.9 (C), 59.0 (CH_2), 51.3 (CH_2), 38.1 (C), 37.0 (CH_2), 33.0 (CH_2), 28.3 (CH_3), 27.3 (CH_3), 9.10 (CH_3), 8.76 (CH_3). *m/z*: 319 (18%) [M-$C_{16}H_{25}O$]$^+$, 234 (16%) [$C_{16}H_{26}O$]$^+$, 219 (6%) [$C_{15}H_{23}O$]$^+$, 205 (100%) [$C_{14}H_{21}O$]$^+$.
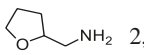 2,4-di-*tert*-butyl phenol	^{1}H δ: 8.87 (br, 2H, OH), 7.20 (d, $^4J_{HH}$ = 2.0 Hz, 2H, ArH), 6.88 (d, $^4J_{HH}$ = 2.0 Hz, 2H, ArH), 4.27 (m, 1H, CHO), 3.89 (m, 2H, CH_2O), 3.77 (m, 4H, $ArCH_2NCH_2Ar$), 2.61(m, 4H, CH_2CH_2), 2.51(m, 2H, NCH_2Furf), 1.40 (s, 18H, $C(CH_3)_3$), 1.27 (s, 18H, $C(CH_3)_3$). ^{13}C{^{1}H} δ: 153.02 (C), 140.63 (C), 136.05 (C), 124.95 (CH), 123.38 (CH), 121.43 (C), 77.54 (CH), 68.28 (CH_2), 57.52 (CH_2), 55.93 (CH_2), 34.99 (CMe_3), 34.10 (CMe_3), 31.67 (CH_3), 29.60 (CH_3), 29.60 (CH_2), 25.21 (CH_2). *m/z*: 537 (100%) [M]$^+$, 466 (47%) [M-THF]$^+$, 410 (9%) [M-THF-Bu]$^+$, 332 (17%) [$C_{21}H_{34}NO_2$]$^+$, 205 (100%) [$C_{14}H_{21}O$]$^+$.
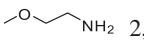 2,4-di-*tert*-butyl phenol	^{1}H NMR δ: 8.39 (br, 2H, OH), 7.20 (d, $^4J_{HH}$ = 1.9 Hz, 2H, ArH), 6.87 (d, $^4J_{HH}$ = 1.9 Hz, 2H, ArH), 3.73 (s, 4H, $ArCH_2$), 3.55 (t, $^3J_{HH}$ = 5.0 Hz, NCH_2), 3.46 (s, 3H, OCH_3), 2.73 (t, $^3J_{HH}$ = 5.0 Hz, 2H, CH_2O), 1.37 (s, 18H, $C(CH_3)_3$), 1.27 (s, 18H, $C(CH_3)_3$). ^{13}C{^{1}H} δ: 152.8(C), 140.7(C), 136.0(C), 124.9(CH), 123.4(CH), 121.6(C), 71.4 ($ArCH_2$), 58.0 (OCH_3), 51.3 (CH_2), 35.0 ($C(CH_3)_3$), 34.1 ($C(CH_3)_3$), 31.6 ($C(CH_3)_3$), 30.1 ($C(CH_3)_3$). *m/z*: 512 (3%) [M]$^+$, 454 (81%) [M-Bu]$^+$, 306 (50%) [$C_{19}H_{32}NO_2$]$^+$, 205 (100%) [$C_{14}H_{21}O$]$^+$.
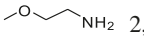 2,4-di-methyl phenol	^{1}H NMR δ: 8.35 (s, 2H, OH), 6.85 (d, $^4J_{HH}$ = 1.8 Hz, 2H, ArH), 6.67 (d, $^4J_{HH}$ = 1.8 Hz, 2H, ArH), 3.72 (s, 4H, $ArCH_2N$), 3.58 (t, $^3J_{HH}$ = 5.0 Hz, 2H, CH_2O), 3.47 (s, 3H, OCH_3), 2.70 (t, $^3J_{HH}$ = 5.0 Hz, 2H, NCH_2), 2.20 (s, 12H, $ArCH_3$). ^{13}C{^{1}H} δ: 152.84 (C), 131.37 (C), 121.24 (C), 127.68 (CH), 127.36 (CH), 125.15 (C), 70.89 (NCH_2CH_2O), 58.17 (OCH_3), 57.04 (NCH_2CH_2O), 50.77 (CH_2Ar), 20.24 (CH_3), 16.03 (CH_3). *m/z*: 343 (21%) [M]$^+$, 320 (100%) [M-Me-H_2O]$^+$, 222 (9%) [$C_{13}H_{20}NO_2$]$^+$, 208 (87%) [$C_{12}H_{18}NO_2$]$^+$.

lected at 100 K on a Bruker Smart Apex diffractometer with Mo Kα radiation (λ = 0.710 73 Å) using a SMART CCD camera. Diffractometer control, data collection, and initial unit cell determination was performed using SMART (52). Frame integration and unit cell refinement software was carried out with SAINT+ (53). Absorption corrections were applied by SADABS (54). Structures were solved by direct methods (SHELXS-97) and refined by full-matrix least-squares based on $|F|^2$ using SHELXL-97 (55, 56).

General procedure for amine-(bis)phenol ligand synthesis in PEG under conventional heating

A capped 10–20 mL vial was loaded with PEG 400 (2.0 g), 37% aq. formaldehyde (0.70 mL), and phenol (8.0 mmol). The mixture was stirred and *N*,*N*-dimethylethylenediamine (0.35 g, 4.0 mmol) was added dropwise. Vials were stirred in a heated block (Chemglass OptiChem) at 75 °C for 18 h. The vial was cooled in an ice bath and filtered. If required, the solid was washed with a minimum amount of ethanol and dried under vacuum to yield the amine-bis(phenol) as a colourless, crystalline solid.

General procedure for amine-(bis)phenol ligand synthesis in PEG under microwave heating

Household microwave oven

A loosely capped 10–20 mL vial was loaded with PEG 400 (2.0 g), 37% aq. formaldehyde (0.70 mL), and phenol (8.0 mmol). Substituted amine (4.0 mmol) was added dropwise. Vials were heated on full power (1200 W) for ten 60 s pulses. The temperature of the reaction mixture in the vial was measured between pulses and temperatures were maintained below 100 °C. Caution: occasionally the reaction mixtures would become very hot and spill out of the container; reactions in a household microwave oven should not be left unattended and safety precautions should be taken. After heating, the vial was cooled in an ice bath and filtered. If required, the solid was washed with a minimum amount of ethanol and dried under vacuum.

Biotage initiator

A 10–20 mL Biotage reaction tube was loaded with PEG 400 (8.0 g), 37% aq. formaldehyde (3.0 mL), substituted phenol (37 mmol), and amine (18 mmol). The tube was sealed with a lid containing a septum and placed in the reaction cavity. The mixture was stirred and heated to the desired temperature for 5 min. During this time, the pressure in the tube was monitored by a pressure sensor on the lid of the tube. The reaction tube was rapidly cooled under a nitrogen flow, and once the pressure in the tube had reduced to near atmospheric the septum was removed. The contents of the tube were filtered, washed with a minimum amount of ethanol, and dried under vacuum.

General procedure for amine-(bis)phenol ligand synthesis in ethanol under conventional heating

Phenol (0.123 mol) was weighed into a 100 mL beaker and ethanol (around 30 mL) added to give a saturated solution. The phenol solution was transferred to a 200 mL round-bottomed flask and 37% aq. formaldehyde (10 mL)

© 2008 NRC Canada

was added. The flask was equipped with a condenser and the amine (0.06 mol) was added. The reaction mixture was stirred and heated at 70 °C for 18 h. The reaction mixture was cooled in an ice bath, filtered, and the residue washed with cold ethanol (2 × 20 mL). The solid was dried under vacuum.

General procedure for amine-(bis)phenol ligand synthesis in ethanol or water under microwave heating

A 10–20 mL Biotage reaction tube was loaded with water or ethanol (5.0 mL), 37% aq. formaldehyde (3.0 mL), substituted phenol (37 mmol), and amine (18 mmol). The tube was sealed with a lid containing a septum and placed in the microwave reaction cavity. The mixture was stirred and heated to the desired temperature for 5 min. During this time, the pressure in the tube was monitored by a pressure sensor on the lid of the tube. The reaction tube was rapidly cooled under a nitrogen flow, and once the pressure in the tube had reduced to near atmospheric the septum was removed. The contents of the tube were filtered, washed with a minimum amount of ethanol, and dried under vacuum.

General procedure for amine-(bis)phenol ligand synthesis in water under conventional heating

Phenol (0.123 mol) was weighed directly into a 200 mL round-bottomed flask, water (80 mL) and 37% aq. formaldehyde (10 mL) were added. The flask was equipped with a condenser and the amine (0.06 mol) was added. The reaction mixture was stirred and heated at 100 °C for 18 h. Upon cooling to room temperature, the product formed a separate phase as either a solid or an oil that could be easily isolated. The product was dried under vacuum, or if significant quantities of water were still present, it was dissolved in an organic solvent and dried over anhydrous magnesium sulfate.

Acknowledgements

We thank Memorial University of Newfoundland, Natural Sciences and Engineering Research Council of Canada (NSERC) (Discovery Grant and Research Tools and Instrument Grant, FMK), WISE-NL Student Summer Employment program (SH), and the EPSRC (Studentship, CEW) for generous funding. We are also grateful to Biotage for access to an Initiator microwave system on a free trial basis.

References

1. O. Kuhl. Chem. Soc. Rev. **36**, 592 (2007).
2. R.H. Crabtree. J. Organomet. Chem. **690**, 5451 (2005).
3. N.M. Scott and S.P. Nolan. Eur. J. Inorg. Chem. 1815 (2005).
4. L.H. Gade. Chem. Commun. (Cambridge), 173 (2000).
5. L.H. Gade. Acc. Chem. Res. **35**, 575 (2002).
6. V.C. Gibson and S.K. Spitzmesser. Chem. Rev. **103**, 283 (2003).
7. H. Kawaguchi and T. Matsuo. J. Organomet. Chem. **689**, 4228 (2004).
8. R. Kempe. Angew. Chem. Int. Ed. **39**, 469 (2000).
9. W.E. Piers and D.J.H. Emslie. Coord. Chem. Rev. **233**, 131 (2002).
10. E.Y. Tshuva, I. Goldberg, M. Kol, H. Weitman, and Z. Goldschmidt. Chem. Commun. (Cambridge), 379 (2000).
11. E.Y. Tshuva, I. Goldberg, M. Kol, and Z. Goldschmidt. Organometallics, **20**, 3017 (2001).
12. E.Y. Tshuva, I. Goldberg, M. Kol, and Z. Goldschmidt. Inorg. Chem. Commun. **3**, 611 (2000).
13. E.Y. Tshuva, I. Goldberg, and M. Kol. J. Am. Chem. Soc. **122**, 10706 (2000).
14. S. Groysman, I. Goldberg, M. Kol, E. Genizi, and Z. Goldschmidt. Organometallics, **22**, 3013 (2003).
15. C. Lorber, F. Wolff, R. Choukroun, and L. Vendier. Eur. J. Inorg. Chem. 2850 (2005).
16. S. Segal, I. Goldberg, and M. Kol. Organometallics, **24**, 200 (2005).
17. S. Gendler, S. Groysman, Z. Goldschmidt, M. Shuster, and M. Kol. J. Polym. Sci. Part A Polym. Chem. **44**, 1136 (2006).
18. X. Lius, X. Shang, T. Tang, N. Hu, F. Pei, D. Cui, X. Chen, and X. Jing. Organometallics, **26**, 2747 (2007).
19. E.E. Delbridge, D.T. Dugah, C.R. Nelson, B.W. Skelton, and A. H. White. Dalton Trans. 143 (2007).
20. S. Gendler, S. Segal, I. Goldberg, Z. Goldschmidt, and M. Kol. Inorg. Chem. **45**, 4783 (2006).
21. A.J. Chmura, M.G. Davidson, M.D. Jones, M.D. Lunn, M.F. Mahon, A.F. Johnson, P. Khunkamchoo, S.L. Roberts, and S.S.F. Wong. Macromolecules, **39**, 7250 (2006).
22. A.J. Chmura, M.G. Davidson, M.D. Jones, M.D. Lunn, and M.F. Mahon. Dalton Trans. 887 (2006).
23. I. Westmoreland and J. Arnold. Dalton Trans. 4155 (2006).
24. Y.M. Yao, M.T. Ma, X.P. Xu, Y. Zhang, Q. Shen, and W.T. Wong. Organometallics, **24**, 4014 (2005).
25. F. Bonnet, A.R. Cowley, and P. Mountford. Inorg. Chem. **44**, 9046 (2005).
26. A. Amgoune, C.M. Thomas, T. Roisnel, and J.F. Carpentier. Chem. Eur. J. **12**, 169 (2005).
27. P. Hormnirun, E.L. Marshall, V.C. Gibson, A.J.P. White, and D.J. Williams. J. Am. Chem. Soc. **126**, 2688 (2004).
28. C.T. Chen, C.A. Huang, and B.H. Huang. Macromolecules, **37**, 7968 (2004).
29. F.M. Kerton, A.C. Whitwood, and C.E. Willans. Dalton Trans. 2237 (2004).
30. C.T. Chen, C.A. Huang, and B.H. Huang. Dalton Trans. 3799 (2003).
31. J. Chen, S.K. Spear, J.G. Huddleston, and R.D. Rogers. Green Chem. **7**, 64 (2005).
32. D.J. Heldebrant, H.N. Witt, S.M. Walsh, T. Ellis, J. Rauscher, and P.G. Jessop. Green Chem. **8**, 807 (2006).
33. T.R. van den Ancker, G.W.V. Cave, and C.L. Raston. Green Chem. **8**, 50 (2006).
34. S.M. Nikles, M. Piao, A.M. Lane, and D.E. Nikles. Green Chem. **3**, 109 (2001).
35. M. Nüchter, B. Ondruschka, W. Bonrath, and A. Gum. Green Chem. **6**, 128 (2004).
36. B.A. Roberts and C.R. Strauss. Acc. Chem. Res. **38**, 653 (2005).
37. R.S. Varma and V.V. Namboodiri. Pure Appl. Chem. **73**, 1309 (2001).
38. V.V. Namboodiri and R.S. Varma. Green Chem. **3**, 146 (2001).
39. V.V. Namboodiri and R.S. Varma. Chem. Commun. (Cambridge), 342 (2002).
40. C.J. Li and L. Chen. Chem. Soc. Rev. **35**, 68 (2006).
41. C.J. Li. Chem. Rev. **105**, 3095 (2005).
42. H.C. Hailes. Org. Proc. Res. Dev. **11**, 114 (2007).
43. J. Itoh, K. Fuchibe, and T. Akiyama. Synthesis, 4075 (2006).
44. S. Narayan, H. Muldoon, M.G. Finn, V.V. Fokin, H.C. Kolb, and K.B. Sharpless. Angew. Chem. Int. Ed. **44**, 3275 (2005).
45. Y.S. Jung and R.A. Marcus. J. Am. Chem. Soc. **129**, 5492 (2007).
46. S. Groysman, I. Goldberg, M. Kol, E. Genizi, and Z. Goldschmidt. Adv. Synth. Cat. **347**, 409 (2005).

© 2008 NRC Canada

47. S. Groysman, I. Goldberg, Z. Goldschmidt, and M. Kol. Inorg. Chem. **44**, 5073 (2005).
48. S. Groysman, E. Sergeeva, I. Goldberg, and M. Kol. Inorg. Chem. **44**, 8188 (2005).
49. A.R.F. Cox, V.C. Gibson, E.L. Marshall, A.J.P. White, and D. Yeldon. Dalton Trans. 5014 (2006).
50. X. Xu, Y. Yao, Y. Zhang, and Q. Shen. Inorg. Chem. **46**, 3743 (2007).
51. K.L. Collins, L.J. Corbett, S.M. Butt, G. Mudhurambal, and F.M. Kerton, Green Chem. Lett. Rev. **1**, 31 (2008).
52. SMART [computer program]. Version v5.625. Program for data collection on area detectors. Bruker Analytical X-ray Systems, Madison, Wisc. 2004.
53. SAINT software users guide. Version 6.22. Bruker Analytical X-ray Systems, Madison, Wisc. 2004.
54. G.M. Sheldrick. SADABS v2.03. Area-detector absorption correction. University of Göttingen, Germany. 1999.
55. G.M. Sheldrick. SHELXS-97 [computer program]. Program for the solution of crystal structures. University of Göttingen, Germany. 1997.
56. G.M. Sheldrick. SHELXL-97 [computer program]. Program for the refinement of crystal structures. University of Göttingen, Germany. 1997.

© 2008 NRC Canada

UV photoelectron spectroscopic and computational study of 7-substituted cycloheptatrienes

T. Bajorek and N. H. Werstiuk

Abstract: The He(I) photoelectron (PE) spectra of cycloheptatriene (**1**), 7-methylcycloheptatriene (**2**), 7-methoxycycloheptatriene (**3**), 7-methylthiocycloheptatriene (**4**), and 7-diemthylaminocycloheptatriene (5) were recorded and interpreted using MO energies and ionization potentials acquired from B3PW91 calculations. Partial simulated PE spectra were in good agreement with the experimental results. The *axial* and *equatorial* conformers have distinct PE spectra as illustrated by simulation. The PE spectra of **2**, **3**, and **5** are representative of the *equatorial* conformers, while the PE spectrum of **4** was in accord with a 1:1 mixture of *equatorial* and *axial* conformational isomers based on spectral simulation. The calculated free energy differences between the *equatorial* and *axial* conformers are in the order of 2 kcal mol^{-1} (1 cal = 4.184 J) for compounds **2**, **3**, and **5**, where the *equatorial* conformational isomer is lowest in energy. In the case of **4**, the *equatorial* conformer was only marginally lower in energy than its *axial* counterpart, where the free energy difference is 0.1 kcal mol^{-1}.

Key words: 7-substituted cycloheptatrienes, He(I) photoelectron spectroscopy, B3PW91, spectral simulation.

Résumé : On a enregistré les spectres photoélectroniques (PE) He(I) du cycloheptatriène (**1**), du 7-méthylcycloheptatriène (**2**), du 7-méthoxycycloheptatriène (3) et du 7-méthylthiocycloheptatriène (4) et on les interprète en faisant appel aux énergies des orbitales moléculaires (OM) et des potentiels d'ionisation obtenus par des calculs B3PW91. Les spectres PE simulés partiels sont en bon accord avec les résultats expérimentaux. Tels qu'illustrés par la simulation, les conformères axiaux et équatoriaux présentent des spectres PE distincts. Les spectres PE des produits **2**, **3** et **5** sont représentatifs de conformères équatoriaux alors que le spectre PE du composé **4** correspond au spectre de simulation d'un mélange 1:1 des isomères conformationnels équatoriaux et axiaux. Les différences d'énergie libre entre les conformères équatorial et axial sont de l'ordre de 2 kcal mol^{-1} pour les conformères équatoriaux des composés **2**, **3** et **5**. Dans le cas du produit **4**, le conformère équatorial n'est que marginalement favorisé par une différence d'énergie de 0,1 kcal mol^{-1} par rapport au conformère axial.

Mots-clés : cycloheptatriènes substitués en position 7, spectroscopie photoélectronique He(I), B3PW91, simulation spectrale.

[Traduit par la Rédaction]

Introduction

Cycloheptatrienes substituted at the 7-position may exist in two conformations, the *axial* and the *equatorial* conformational isomers, illustrated in Fig. 1. 7-Silylcycloheptatriene and 7-methylcycloheptatriene (2) have previously been under computational investigation, where it has been reported that the *axial* conformers were predicted to be more stable than the *equatorial* conformers by nearly 2 kcal mol^{-1} (1) (1 cal = 4.184 J). This was contrary to our calculations that showed that the difference in energy between *axial* and *equatorial* 7-silylcycloheptatriene is nearly nil. In the case of 7-methylcycloheptatriene (**2**), we found the *equatorial* conformational isomer to be lower in energy than the *axial* conformer. The preference of the *axial* conformation in a 7-substituted cycloheptatriene has previously been documented for triphenyl-7-cyclohepta-1,3,5-trienyltin, as evidenced by its crystal structure (2, 3). Given our long-standing interest in studying conformational properties in the gas phase with ultraviolet (UV) photoelectron (PE) spectroscopy (4) and our work on identifying *E,Z* isomers of cyclohepta-2,4-dien-1-one (5) and *N*,*N*-dimethylcyclohepta-1,3,5-trien-1-amine (6), we initiated a computational and UV PE spectroscopic study of cycloheptatriene (**1**), 7-methylcycloheptatriene (**2**), 7-methoxycycloheptatriene (**3**), 7-methylthiocycloheptatriene (**4**), and 7-dimethylaminocycloheptatriene (5) (Fig. 2). We under-

Fig. 1. Schematic representation of *equatorial* and *axial* isomers of cycloheptatrienes.

equatorial *axial*

Received 19 December 2007. Accepted 13 February 2008. Published on the NRC Research Press Web site at canjchem.nrc.ca on 11 April 2008.

This paper is dedicated to the memory of Keith Yates.

T. Bajorek and N.H. Werstiuk.[1] Department of Chemistry, McMaster University, 1280 Main St. West, Hamilton ON L8S 4M1, Canada.
[1]Corresponding author (werstiuk@mcmaster.ca).

 doi:10.1139/V08-041 © 2008 NRC Canada

Fig. 2. 7-Substituted cycloheptatrienes.

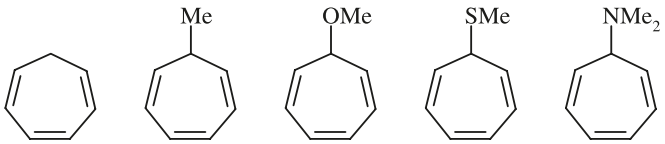

took the study to determine whether it would be possible to distinguish between the *axial* and *equatorial* conformers in the gas phase using PE spectroscopy coupled with DFT calculations and thereby obtain information on the conformational preferences for the compounds, while documenting the PE spectra of **2**–**5** that had not yet been published. In this paper we present and discuss the results of this study.

Results

The experimental UV PE spectra of **1**–**5** as well as the corresponding partial simulated spectra of their *axial* and *equatorial* conformers are shown in Fig. 3. Table 1 lists the B3PW91/6–311+G(2d,p) total energies of **1**, the *axial* and *equatorial* conformational isomers of **2**–**5**, the corresponding radical cations, and the derived first ionization potentials.

Although other methods — time-dependent DFT (TDDFT) (7, 8) and outer valence Green's function (OVGF) (9, 10) — are available for predicting IPs, we preferred to use the method developed in these laboratories (11). In our approach, the first vertical IP, calculated as the difference in energy between ground state and the radical cation fixed in the ground-state optimized geometry, is used to anchor the Kohn–Sham orbital energies. Our approach is also useful for obtaining an estimate of the first-band adiabatic IP simply by optimizing the radical cation. Using our method to obtain the IPs (11) and our program PESPEC (12*a*, 12*b*), we have successfully simulated the PE spectra of a variety of fairly large molecules, some of which exhibit conformational mobility. In our approach, we compare the accuracy of the calculations and the "shapes" of the predicted and experimental spectra. Our method has also been shown to perform very well by other investigators (13). Consequently, we saw no need to do an extensive time-consuming study with all the other computational methods.

Table 2 lists the first five calculated (B3PW91/6–311+G(2d,p)) and first three experimental vertical IPs of compounds **1**–**5**. Overall the differences between the calculated and experimental IPs is <0.4 eV. Given the closeness of the first two IPs, for the case of **3** and **4** we used the average values of the first two IPs given in parentheses in Table 2 for the comparison. We also calculated the first five IPs with OVGF. While the IPs moved to slightly higher values (Table 1S of the Supplementary Data), there are no significant differences in the relative separations of the DFT and OVGF IPs.[2]

Calculated conformational properties

The *equatorial* conformer is the most stable conformational isomer of cycloheptatrienes **2**, **3**, and **5**; the substituent is situated in the plane of the 7-membered ring rather than perpendicular to the ring as in the *axial* conformation, as shown in Fig. 1. For the 7-methylthiocycloheptatriene (**4**), the *axial* conformer is only marginally lower in energy than its *equatorial* counterpart. Of course, the "*equatorial*" and "*axial*" conformations are identical in the case of cycloheptatriene (**1**).

Our B3PW91/6–311+G(2d,p) calculations place the **2**-*axial* conformer 1.9 kcal mol^{-1} higher in energy — based on ΔE_{elec} — than the *equatorial* conformer, which is contrary to previously reported findings (1). Donovan and White have carried out semi-empirical, ab initio, and DFT calculations on 7-methoxycycloheptatriene (**3**), finding that the *equatorial* conformation is favored by 1.2 kcal mol^{-1} at BLYP/6–31G(*d*) (14). Our calculations agree with those of Donovan and White and predict the *equatorial* conformer of **3** to be 1.8 kcal mol^{-1} lower in energy than the *axial* conformer at the B3PW91/6–311+G(2d,p) level. The difference in energy between the *equatorial* and *axial* conformational isomers of **4** is only 0.8 kcal mol^{-1}, with the *axial* conformer only slightly more stable than the equatorial one. If the ZPVE correction is taken into account, then this difference decreases to 0.1 kcal mol^{-1}. Based on free energies, the *equatorial* conformer is marginally lower in energy (–0.2 kcal mol^{-1}) than the *axial* conformer. The *equatorial* conformer of **5** is 1.9 kcal mol^{-1} lower in energy than the *axial* conformer.

Cycloheptatrienes **2**–**5** undergo *axial–equatorial* conformational isomerism. The B3PW91 ZPVE corrected total energies and relative energies (ΔE_0 and ΔG_{298}) of the conformers are shown in Table 3. Cycloheptarienes **2**, **3**, and **5** are predicted to have the *equatorial* conformer lowest in energy; in the case of **4**, the *axial* conformation is marginally lower in energy. Energy barriers for the ring flip from *equatorial* to *axial* are collected in Table 3.

The B3PW91 potential energy surface for the *equatorial* cycloheptatrienes **3** and **4**, obtained by varying the dihedral angle between H-7 and the Me group of –OMe and –SMe, revealed that the *gauche* conformation is lowest in energy in the three cycloheptatrienes, as shown in Fig. 4. It is also the lowest energy conformation in the *axial* conformational isomers with the exception of **4**-*axial* where the *anti* conformation is favored.

Discussion

The PE spectrum of **1**, shown in Fig. 3*a*, exhibits three distinct ionization potential bands at 8.6, 9.5, and 10.9 eV; the calculated IPs and consequently the partial simulated PE spectrum displayed as Fig. 3*b* are in good agreement with the experimental spectrum.

The PE spectra of **2**, **3**, and **5** are representative of mostly the *equatorial* conformers of these compounds. Based on our B3PW91 calculations, the *equatorial* conformers are on the order of 2 kcal mol^{-1} lower in free energy than their *axial*

[2] Supplementary data for this article are available on the journal Web site (canjchem.nrc.ca) or may be purchased from the Depository of Unpublished Data, Document Delivery, CISTI, National Research Council Canada, Ottawa, ON K1A 0R6, Canada. DUD 3739. For more information on obtaining material refer to cisti-icist.nrc-cnrc.gc.ca/irm/unpub_e.shtml.

© 2008 NRC Canada

Fig. 3. Experimental PE spectra: (*a*) **1**, (*c*) **2**, (*g*) **3**, (*k*) **4**, (*o*) **5**; partial simulated (B3PW91) PE spectra: (*b*) **1**, (*d*) **2** *equatorial*, (*e*) **2** *axial*, (*f*) 2 96% *equatorial* – 4% *axial*, (*h*) **3** *equatorial*, (*i*) **3** *axial*, (*j*) 3 96% *equatorial* – 4% *axial*, (*l*) **4** *equatorial*, (*m*) **4** *axial*, (*n*) 4 57% *equatorial* – 43% *axial*, (*p*) **5** *equatorial*, (*q*) **5** *axial*, (*r*) 5 96% *equatorial* – 4% *axial*.

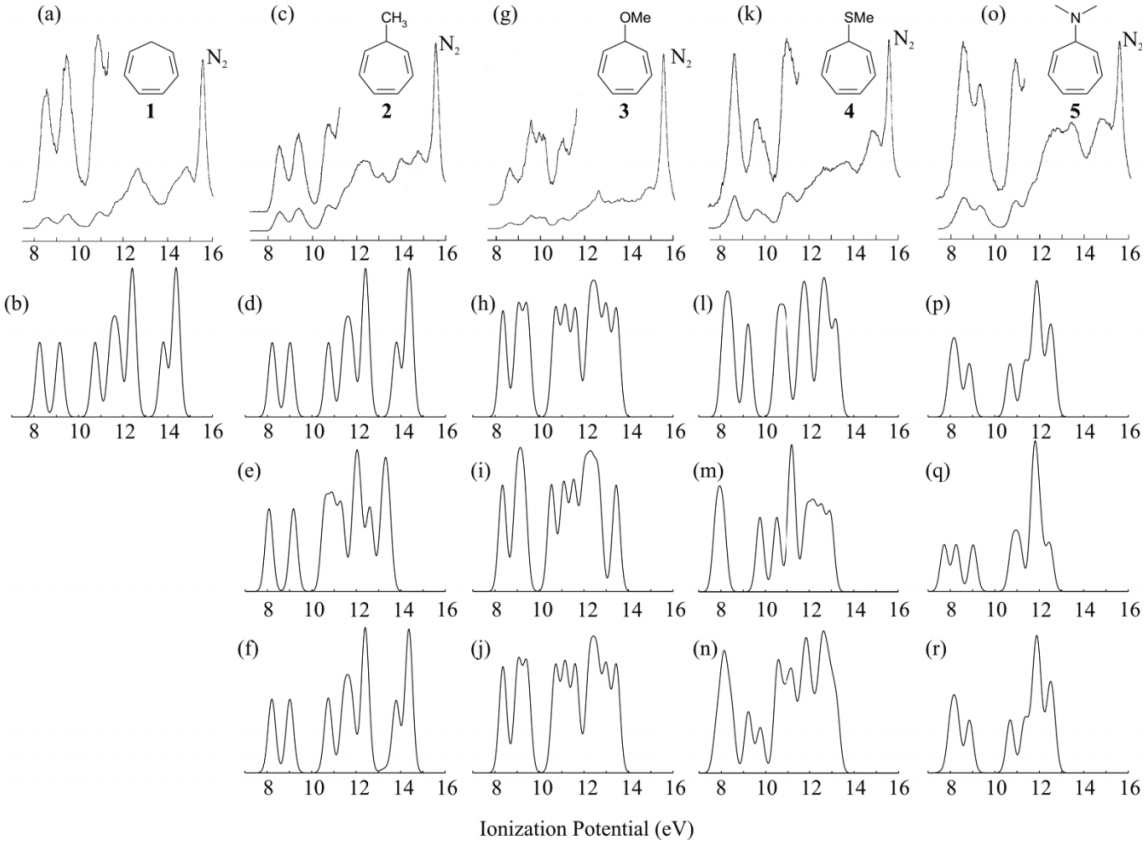

Table 1. Total energies E_{elec} (Hartrees) of *equatorial* and *axial* cycloheptatrienes **1**, **2**, **3**, **4**, and **5** (*N* electrons), their radical cations[a] (*N*-1 electrons), and calculated first IP_v (eV).

	$E_{elec(N)}$ (Hartree)	$E_{elec(N-1)}$[a] (Hartree)	IP_v (eV)
1	–271.481 326	–271.178 032	8.25
2e[b]	–310.793 434	–310.491 535	8.21
2a[c]	–310.790 389	–310.493 891	8.07
3e	–385.989 541	–385.682 710	8.35
3a	–385.986 682	–385.680 381	8.33
4e	–708.954 913	–708.655 627	8.14
4a	–708.956 163	–708.669 426	7.80
5e	–405.428 979	–405.133 707	8.03
5a	–405.425 890	–405.142 044	7.72

[a]Single point energy calculations on the optimized molecule (*N* electrons) geometries with an electron removed.
[b]**e** = *equatorial*.
[c]**a** = *axial*.

counterparts so the *equatorial* conformations are expected to be preferentially populated at equilibrium. The partial simulated PE spectra of the *equatorial* and *axial* conformational isomers as well as the combination of 96% *equatorial* conformer and 4% *axial* conformer — these values are based on the magnitude of the equilibrium constant with ΔG = 2.0 kcal mol^{-1} (15) — of **2** are displayed as Figs. 3*d*, 3*e*, and 3*f*, respectively. Both partial spectra 3*d* and 3*f* (96% *equatorial* + 4% *axial*) correlate well with the experimental spectrum 3*c*.

The partial simulated PE spectra of the *equatorial* and *axial* conformational isomers as well as the combination of 96% *equatorial* conformer and 4% *axial* conformer of **3** are displayed in Figs. 3*h*, 3*i*, and 3*j*, respectively. Although there is a difference in the relative intensities of first bands of the simulated and experimental spectra, the general features of the simulated spectrum 3*j* and the experimental spectrum 3*g* correlate reasonably well.

The experimental spectrum of 7-methylthiocycloheptatriene is displayed as Fig. 3*k*. Figures 3*l* and 3*m* are the simulated spectra of the *equatorial* and axial conformers of **4**, respectively. According to our calculations, the *equatorial* conformer is only marginally (ΔG_{298} = 0.16 kcal mol^{-1}) lower in energy than the *axial* isomer so the *equatorial* conformer should be slightly preferred (55%–60%) at equilibrium (15). In fact, the simulated spectrum 3*n* (57% *equatorial* + 43% *axial*) correlates better with the experimental spectrum than spectra 3*l* and 3*m*.

As far as the PE spectra of **5** are concerned, the simulated spectra of *equatorial* 5 (Fig. 3*p*) and a 94% *equatorial* – 4% *axial* **5** (Fig. 3*r*) correlate superbly with the experimental spectrum displayed in Fig. 3*o*.

To confirm our analysis based on the relative energies of single *equatorial* and *axial* conformers, we computed the barriers for ring flipping to obtain information on the nature of the ring-flipping potential energy surface. This is important because the relative intensities of PE bands can depend on the conformer populations and on the variation in their

© 2008 NRC Canada

Table 2. Experimental and calculated (B3PW91/6–311G(2d,p)) vertical IPs of compounds **1**–**5**.

			IP_v					
1	B3PW91		8.25	9.15		10.74	11.46	11.76
	Experimental		8.6	9.5		10.9		
2	B3PW91	*axial*	8.07	9.17		10.58	10.93	11.32
		equatorial	8.21	9.01		10.55	11.28	11.49
	Experimental		8.5	9.4		10.8		
3	B3PW91	*axial*	8.33	8.98		9.28	10.53	11.08
		equatorial	8.35	9.03		9.43	10.71	11.15
	Experimental		8.6	9.6		10.0	11.1	
4	B3PW91	*axial*	7.80	8.08	7.94[a]	9.75	10.51	11.18
		equatorial	8.14	8.44	8.29[a]	9.21	10.55	10.89
	Experimental		8.7			9.7	11.1	
5	B3PW91	*axial*	7.72	8.26	7.99[a]	9.02	10.79	11.10
		equatorial	8.03	8.29	8.16[a]	8.85	10.68	11.33
	Experimental		8.6			9.4	10.9	

[a]Average of the first and second IPs.

Table 3. Thermochemical parameters for *equatorial* and *axial* cycloheptatriene conformers of **2**–**5** and ring-flip transition states at B3PW91/6–311+G(2d,p) (1 cal = 4.184 J).

	E_{elec}[a] (Hartrees)	ΔE_{elec} (kcal mol^{-1})	E_0[b] (Hartrees)	ΔE_0 (kcal mol^{-1})	G_{298}[c] (Hartrees)	ΔG_{298} (kcal mol^{-1})
2e[d]	–310.793 434	0.00	–310.638 097	0.00	–310.668 974	0.00
TS2	–310.782 074	7.13	–310.626 464	7.30	–310.656 828	7.62
2a[e]	–310.790 389	1.91	–310.634 563	2.22	–310.665 445	2.21
3e	–385.989 541	0.00	–385.829 852	0.00	–385.862 704	0.00
TS3	–385.979 864	6.07	–385.819 853	6.27	–385.852 353	6.50
3a	–385.986 682	1.79	–385.826 454	2.13	–385.859 405	2.07
4e	–708.954 913	0.78	–708.798 947	0.10	–708.833 290	0.00
TS4	–708.947 945	5.16	–708.791 693	4.65	–708.825 011	5.20
4a	–708.956 163	0.00	–708.799 099	0.00	–708.833 039	0.16
5e	–405.428 979	0.00	–405.228 892	0.00	–405.262 984	0.00
TS5[f]	N/A	N/A	N/A	N/A	N/A	N/A
5a	–405.425 890	1.94	–405.225 525	2.11	–405.259 681	2.07

[a]E_{elec} is the uncorrected total energy in Hartrees.
[b]$E_0 = E_{elec}$ + ZPE.
[c]$G = H - TS$; $H = E + RT$; $E = E_0 + E_{vib} + E_{rot} + E_{trans}$.
[d]**e** = *equatorial*.
[e]**a** = *axial*.
[f]Transition state could not be located.

IPs (4*d*, 12*a*, 12*b*, 16). The *equatorial–axial* ring-flipping barriers for **2** and **3** are 7.62 and 6.50 kcal mol^{-1}, respectively, (Table 3). For **4**-*equatorial* to **4**-*axial*, it is 5.20 kcal mol^{-1}. A discrete transition state for the ring flip of **5** could not be located, presumably because of the complexity — inversion at nitrogen is possible — of the potential energy surface. However, after an extensive study we were able to locate a "minimum-energy" geometry 7.64 kcal mol^{-1} higher in energy than **5**, exhibiting a geometry that was close to the TS geometries of **2**, **3**, and **4** with respect to the planarity of the 7-membered ring. The computed low barriers for the ring flip support the fact that **1**–**5** are fluxional molecules (1–3), and that the equilibrium populations of the *equatorial* and *axial* conformations at ambient temperature are determined by ΔG. This validates our analysis based on using the *equatorial* and *axial* conformers; given the nature of the potential energy surfaces, only the *equatorial* and *axia*l conformers and those very closely related to them are significantly populated at ambient temperature and contribute to the PE spectrum.

It should be pointed out that the partial simulated PE spectra of **3** and **4** have been obtained for the lowest energy rotomers. Figures 4*a*–4*d* show the potential energy surfaces for the rotation of the –OMe and –SMe substituents; the *gauche* conformations are lowest in energy in the cases of **3**-*equatorial*, **3**-*axial*, and **4**-*equatorial*. **4**-*Axial* is the lowest-energy conformer in the case of the *anti* orientation. Plots of the orbital energy versus dihedral angle for the five MOs, HOMO–HOMO-4 of **3**-*equatorial* and **4**-*equatorial*, show small energy differences in orbital energies when the substituent is rotated (Fig. 5*a*). The simulation of partial PE spectra based on this angular dependence data and the potential energy surfaces displayed in Figs. 4*a* and 4*b*, using our program PESPEC (12*a*), produced simulated spectra that did not differ significantly — not unexpected given the relative invariance of the MO energy with torsional angle — from

© 2008 NRC Canada

Fig. 4. The B3PW91/6–311+G(2d,p) potential energy surface for the rotation of the –OMe (*a* and *b*) and –SMe (*c* and *d*) substituents in the *equatorial* and *axial* isomers of **3** and **4** (1 cal = 4.184 J).

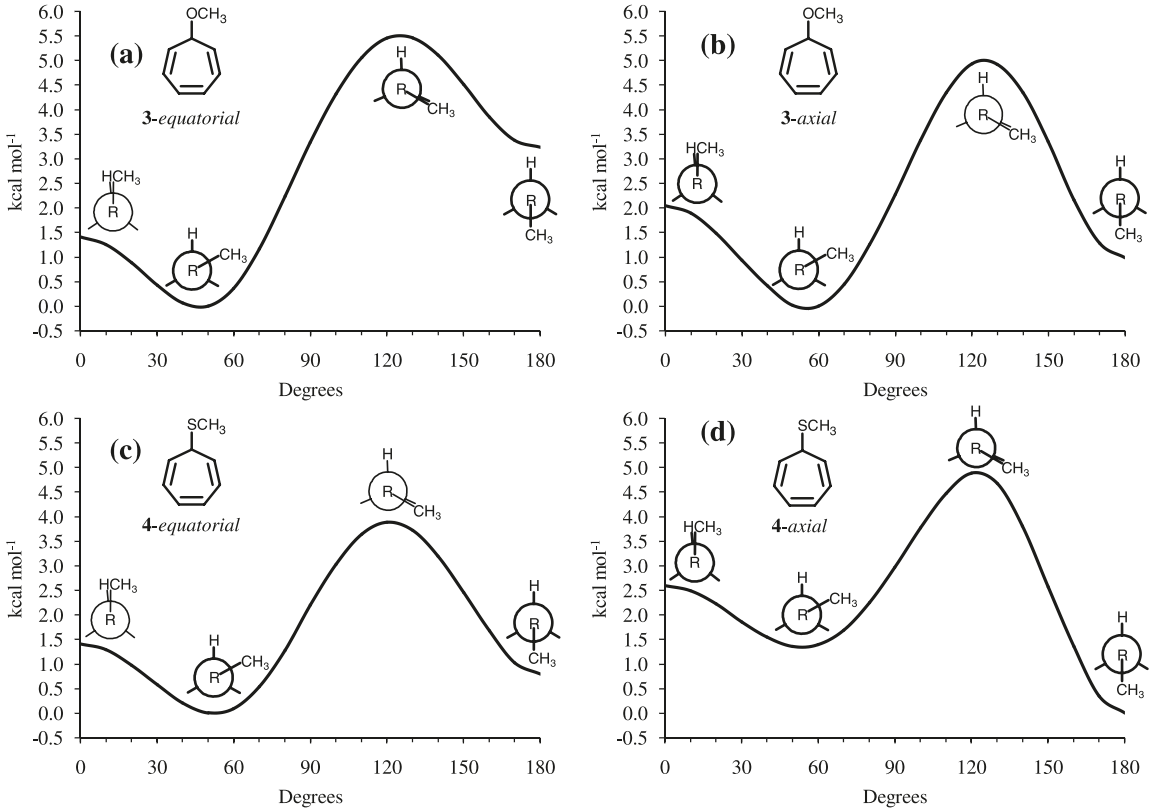

those presented in Fig. 3 and are not reported in this paper. Given the nature of the angular dependences of the MO energies and the torsional potential energy surfaces, the same situation will hold for **4**.

As far as other 7-substituted cycloheptatrienes are concerned, for 7-$SiH_3C_7H_7$ it has been reported that the *axial* conformation is more stable than its *equatorial* counterpart by nearly 2 kcal mol^{-1}, based on computational studies, and the C–Si bond lengths of the two conformers differ (1). Our B3PW91/6–311+G(2d,p) calculations indicate that the *axial* conformational isomer is only marginally more stable than the *equatorial* conformer with ΔG_{298} being 0.05 kcal mol^{-1}. The C–Si bond lengths are slightly different; for *axial* the C–S distance is 1.91 Å and for the *equatorial* conformer it is 1.89 Å. The *axial* conformation in a 7-substituted cycloheptatriene has been experimentally observed in triphenyl-7-cyclohepta-1,3,5-trienyltin (2, 3). Its crystal structure clearly showed the quasi-*axial* orientation of the triphenyltin substituent at position 7 of the cycloheptatriene ring with a carbon–tin bond length of 2.21 Å (2). The trend towards *axial* orientations of the polarizable C–Si and C–Sn bonds suggests that a hyperconjugation interaction plays a role in determining the *axial–equatorial* preference.

Conclusions

The photoelectron spectra of cycloheptatrienes **1**–**5** were recorded and interpreted with the use of calculations at the B3PW91 level of theory. Simulated PE spectra of the *axial* and *equatorial* conformational isomers of all compounds have shown that the experimental PE spectra of compounds **2**, **3**, and **5** are those of mainly the *equatorial* conformers and are in good agreement with experiment. The simulation has also shown that the PE spectrum of **4** is best represented by a nearly 1:1 mixture of the *equatorial* and *axial* conformational isomers, which is supported by our thermochemical calculations on these compounds.

Experimental detail

Computational studies

B3PW91 (17) calculations were performed with Gaussian 03 (18). Calculations on optimized geometries and radical cations were carried out using the TIGHT convergence criteria at B3PW91/6–311+G(2d,p). Two-electron integrals and their derivatives were computed using the ultrafine grid. As it is well established that the correct geometry optimizations of molecules containing chalcogen atoms require the addition of d-polarization functions (19–23), we have used the above triple zeta split valence basis set augmented by two d-polarization functions, one p-polarization function on hydrogen atoms, as well as one diffuse function on hydrogen atoms. The interpretation of the PE spectra was based on our successfully applied method (11, 24, 25, 26) that is basically an extension of Koopman's theorem. The simulated PE spectra of all compounds were obtained by anchoring the Kohn–Sham MO orbital energies to the calculated first IP using our Fortran program PESPEC (12(a)). Band intensities are normalized in simulations involving single structures and (or) conformers. However, in cases where conformations exhibit

© 2008 NRC Canada

Fig. 5. Orbital energy dependence on dihedral angle for the rotation of the substituent in **3**-*equatorial* and **4**-*equatorial*.

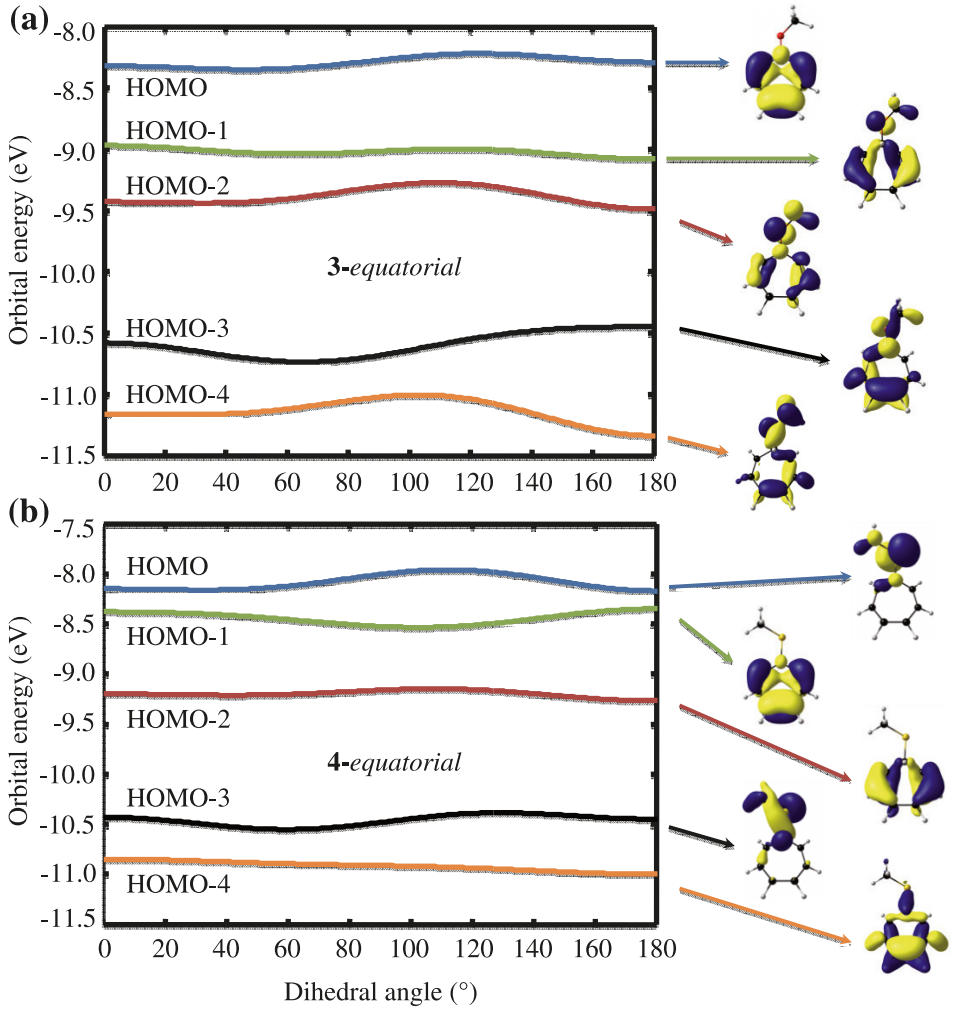

vastly different orbital energies, analyses based on conformational potential energy surfaces yield simulated spectra that exhibit intensity variations in the bands due to the inclusion of conformer populations. Gaussian line shape with a full-width-at-half-height (FWHH) of 0.4 and a temperature set to 300 K was used to simulate the partial PE spectra with ten MO energies, HOMO to HOMO-9.

UV photoelectron spectroscopic studies

A locally built spectrometer (27) was used to acquire the photoelectron (PE) spectra. A sample of the cycloheptatriene was placed in an 8 mm od. A pyrex sample tube was externally attached to the end of a probe. While all spectra were recorded at the ambient temperature (~20 °C) of the spectrometer housing, the temperature of the external sample was controlled to achieve a suitable source pressure (3–8 × 10^{-3} mbar, 1 bar = 100 kPa). The sample temperature for compounds **3**, **4**, and **5** was 0 °C; for **1** it was –30 °C and for **2** –15 °C. To obtain the spectra, the probe was inserted into the spectrometer housing so the tip was located 10 mm from the intersecting photon beam. Twenty scans were averaged to obtain the spectra that were calibrated with N_2 (15.6 eV); linearity of the scale was ensured through calibrations with N_2 and CH_3I (9.54 and 10.16 eV) prior to the experiments. Vertical IPs are accurate to ±0.05 eV. Experimental PE spectra are displayed in Fig. 3.

Synthesis of cycloheptatrienes

Tropylium bromide was synthesized according to the procedure by Doering and Knox (28). Cycloheptatriene (1) was purchased from Sigma-Aldrich and distilled.

7-Methylthiocycloheptatriene (4)

To a solution of 2 g (0.01 mol/L) of tropylium bromide in 10 mL of methanol, a solution of 0.7 g (0.01 mole) of sodiumthiomethoxide in 30 mL of methanol was added. The solution was allowed to stir for 0.5 h. Excess sodiumthiomethoxide was quenched with 50 mL of water. The resulting solution was extracted with diethylether (3 × 30 mL), which was dried with magnesium sulfate. Removal of solvent produced 0.6 g (43%) of 7-methylthiocycloheptatriene. ^{1}H NMR ($CDCl_3$) δ: 2.08 (s, 3 H), 3.43 (t, 1 H), 5.47 (m, 2 H), 6.21 (m, 2 H), 6.50 (m, 2 H). ^{13}C ($CDCl_3$) δ: 13.4, 44.0, 124.6, 126.7, 131.1.

7-Methoxycycloheptatriene (3)

A solution of 2 g (0.01 mol/L) of tropylium bromide in 10 mL of methanol was added to a solution of sodium

© 2008 NRC Canada

methoxide in methanol (1.5 g Na in 20 mL MeOH). The mixture was stirred for 45 min and filtered to remove precipitated sodium bromide. Removal of the solvent afforded yellow oil, which was washed with water and extracted with diethylether (3 × 10 mL) and dried with anhydrous $MgSO_4$. ^{1}H NMR ($CDCl_3$) δ: 3.41 (s, 3 H), 3.41 (t, 1 H), 5.51 (m, 2 H), 6.18 (m, 2 H), 6.67 (m, 2 H). ^{13}C ($CDCl_3$) δ: 56.5, 77.9, 123.2, 125.4, 131.1.

7-Dimethylaminocycloheptatriene (5)

Synthesized according to a procedure by Doering and Knox (17). ^{1}H NMR ($CDCl_3$) δ: 1.86 (t, 1 H), 2.37 (s, 6 H), 5.45 (m, 2 H), 6.17 (m, 2 H), 6.71 (m, 2 H). ^{13}C ($CDCl_3$) δ: 43.2, 65.6, 122.8, 123.5, 130.6.

7-Methylcycloheptatriene (2)

To a vigorously stirred suspension of 2 g. (0.01 mol/L) of tropylium bromide in dry diethylether, a 1.4 mol/L solution of methyllithium in diethylether was added dropwize (100% excess). Exothermic reaction took place upon addition of methyllithium and reflux was observed. The reaction mixture was allowed to stir for additional 30 min, 20 mL of 2N HCl was added with care, the mixture was separated and washed twice with 10 mL portions of 2N NaOH and three 15 mL portions of water. The ethereal layer was dried with anhydrous $CaCl_2$. Removal of solvent afforded 0.15 g (14%) of **5**. ^{1}H NMR ($CDCl_3$) δ: 1.34 (d, 3 H), 1.64 (m, 1 H), 5.12 (m, 2 H), 6.13 (m, 2 H), 6.63 (m, 2 H). ^{13}C NMR ($CDCl_3$) δ: 19.1, 33.5, 124.4, 128.2, 131.1.

Acknowledgments

We thank the Natural Sciences and Engineering Research Council of Canada for financial support and gratefully acknowledge the usage of computational resources of SHARCnet at McMaster University.

References

1. C. Glidewell. J. Organomet. Chem. **266**, 25 (1984).
2. J.E. Weidenborner, R.B. Larrabee, and A.L. Bednowitz. J. Am. Chem. Soc. **94**, 4140 (1972).
3. R.B. Larrabee. J. Organomet. Chem. **74**, 313 (1974).
4. (*a*) N.H. Werstiuk, J. Ma, M.A. McAllister, T.T. Tidwell, and D.-C. Zhao. J. Chem. Soc. Faraday Trans. **90**, (22), 3383 (1994); (*b*) H.M. Muchall, N.H. Werstiuk, J. Ma, T.T. Tidwell, and K. Sung. Can. J. Chem. **75**, 1851 (1997); (*c*) H.M. Muchall, N.H. Werstiuk, J.L. Pitters, and M.S. Workentin. Tetrahedron, **55**, 3757 (1999); (*d*) H.M. Muchall and N.H. Werstiuk. Can. J. Chem. **84**, 1124 (2006).
5. T. Bajorek and N.H. Werstiuk. Chem. Commun. (Cambridge), 648 (2002).
6. T. Bajorek and N.H. Werstiuk, Can. J. Chem. **82**, 80 (2004).
7. M.E. Casida, C. Jamorski, K.C. Casida, and D.R. Salahub. J. Chem. Phys. **108**, 4439 (1998).
8. R.E. Stratmann and G.E. Scuseria. J. Chem. Phys. **109**. 8218 (1998).
9. W. Von Niessen, J. Schirmer, and L.S. Cederbaum. Comput. Phys. Rep. **1**, 57 (1984).
10. J.V. Ortiz. J. Chem. Phys. **89**, 6348 (1988).
11. H.M. Muchall, N.H. Werstiuk, and B. Choudhury. Can. J. Chem. **76**, 221 (1998).
12. (*a*) N.H. Werstiuk, G. Timmins, J. Ma, and T.A. Wildman. Can. J. Chem. **70**, 1971 (1992); (*b*) D. Chmielewski, N.H. Werstiuk, and T.A. Wildman. Can. J. Chem. **71**, 1741 (1993).
13. A. Chrostowska, A. Dargelos, V. Lemierre, J-M. Sotiropoulos, P. Guenot, and J.-C. Guillemin. Angew. Chem. Int. Ed. **43**, 873 (2004).
14. W.H. Donovan and W.E. White. J. Org. Chem. **61**, 969 (1996).
15. E.L. Eliel. Stereochemistry of carbon compounds. McGraw-Hill Book Company Inc., New York. Back cover. 1962.
16. E. Honegger and E. Heilbronner. Chem. Phys. Lett. **81**, 615 (1981).
17. A.D. Becke. J. Chem. Phys. **98**, 5648 (1993).
18. M.J. Frisch, G.W. Trucks, H.B. Schlegel, G.E. Scuseria, M.A. Robb, J.R. Cheeseman, J.A. Montgomery Jr., T. Vreven, K.N. Kudin, J.C. Burant, J.M. Millam, S.S. Iyengar, J. Tomasi, V. Barone, B. Mennucci, M. Cossi, G. Scalmani, N. Rega, G.A. Petersson, H. Nakatsuji, M. Hada, M. Ehara, K. Toyota, R. Fukuda, J. Hasegawa, M. Ishida, T. Nakajima, Y. Honda, O. Kitao, H. Nakai, M. Klene, X. Li, J.E. Knox, H.P. Hratchian, J.B. Cross, V. Bakken, C. Adamo, J. Jaramillo, R. Gomperts, R.E. Stratmann, O. Yazyev, A.J. Austin, R. Cammi, C. Pomelli, J.W. Ochterski, P.Y. Ayala, K. Morokuma, G.A. Voth, P. Salvador, J.J. Dannenberg, V.G. Zakrzewski, S. Dapprich, A.D. Daniels, M.C. Strain, O. Farkas, D.K. Malick, A.D. Rabuck, K. Raghavachari, J.B. Foresman, J.V. Ortiz, Q. Cui, A.G. Baboul, S. Clifford, J. Cioslowski, B.B. Stefanov, G. Liu, A. Liashenko, P. Piskorz, I. Komaromi, R.L. Martin, D.J. Fox, T. Keith, M.A. Al-Laham, C.Y. Peng, A. Nanayakkara, M. Challacombe, P.M. W. Gill, B. Johnson, W. Chen, M.W. Wong, C. Gonzalez, and J.A. Pople. Gaussian 03 [computer program]. Revision C.02. Gaussian, Inc., Wallingford, Conn. 2004.
19. A. Hinchliffe. J. Mol. Struct. **55**, 127 (1979)
20. W.J. Pietro, M.M. Francl, W.J. Hehre, D.J. DeFrees, J.A. Pople, and J.S. Binkley. J. Am. Chem. Soc. **104**, 5039 (1982).
21. C.J. Marsden and B.J. Smith. J. Mol. Struct. (Theochem.) **105**, 385 (1983).
22. A. Yadav, P.R. Surjan, and R.A. Poirier. J. Mol. Struct. (Theochem.) **42**, 297 (1988).
23. E. Magnusson. J. Am. Chem. Soc. **112**, 7940 (1990).
24. H.M. Muchall, N.H. Werstiuk, B. Choudhury, J. Ma, J. Warkentin, and J.P. Pezacki. Can. J. Chem. **76**, 238 (1998).
25. N.H. Werstiuk, H.M.Muchall, J. Ma, and M.T.H. Liu. Can. J. Chem. **76**, 1162 (1998).
26. H.M. Muchall and P. Rademacher. J. Mol. Struc. **435**, 157 (1997).
27. N.H. Werstiuk, D.N. Butler, and E. Shahid. Can. J. Chem. **65**, 760 (1986).
28. W.von E. Doering and L.H. Knox. J. Am. Chem. Soc. **79**, 352 (1957).

© 2008 NRC Canada

Synthesis of constrained aromatic $\beta^{2,3,3}$-amino alcohol scaffolds — Precursors of non-proteinogenic phenylalanine for peptidomimetics

Surinderjit Singh Bhella, Mohan Paul S. Ishar, Gajendra Singh, Rajinder Singh, Gurpinder Singh, and Tilak Raj

Abstract: Novel constrained $\beta^{2,3,3}$-amino alcohol scaffolds (**11a**–**11e**) with varied substitution patterns have been synthesized by reductive cleavage of the N–O bond of isoxazolidines (**10a**–**10e**) derived from intramolecular 1,3-dipolar cycloadditions. A number of methods were probed for reductive cleavage, however, better results were obtained with ammonium formate in the presence of Pd/C or Zn as compared to Zn/acetic acid. The obtained scaffolds (**11a**–**11e**) can serve as valuable building blocks for peptidomimetics.

Key words: $\beta^{2,3,3}$-amino alcohol, peptidomimetics, building blocks, isoxazolidines, reductive cleavage, ammonium formate.

Résumé : En procédant au clivage réducteur de la liaison N–O des isoxazolidines, **10a**–**10e**, obtenues par des cycloadditions 1,3-dipolaires intramoléculaires, on a effectué la synthèse de nouveaux $\beta^{2,3,3}$-aminoalcools, **11a**–**11e**, contraints et en échafauds, et qui portent divers types de substituants. On a étudié un certain nombre de méthodes de clivages réducteurs et on a obtenu de meilleurs résultats par le biais de la réaction du formiate d'ammonium en présence de Pd/C ou de Zn par opposition aux réactions en présence de zinc et d'acide acétique. Les échafauds obtenus, **11a**–**11e**, peuvent être utilizés comme blocs dans la synthèse de produits peptidomimétiques.

Mots-clés : $\beta^{2,3,3}$-aminoalcool, peptidomimétique, bloc dans la synthèse, isoxazolidines, clivage réducteur, ammonium formiate.

[Traduit par la Rédaction]

Introduction

Peptide mimic drugs continue to be in high demand (1). The building block approach is highly appreciated in peptide mimic drug design (2*a*), and advances in preparation of such building blocks have made feasible the synthesis of novel peptidomimetics (2*b*). The design considerations of peptidomimetics include restriction of the torsional angles, ϕ (phi), ψ (psi), and ω (omega), which determine the 3D structure of peptide backbone (3), as well as χ (chi) torsional angles that define the position of side chain functional groups (4) (Fig. 1). An additional torsion angle, θ, responsible for gauche or trans conformations in constrained aromatic β-amino alcohols/β-amino acids is generated by the insertion of methylene units (5). Furthermore, the gauche conformation is more accessible with $\beta^{2,3,3}$ substitution because it leads to: (*i*) confinement of ϕ and ψ in the preferred region and (*ii*) θ is covalently fixed in the gauche position (5*b*, 5*c*). The characteristic torsions of such secondary structure types

Fig. 1.

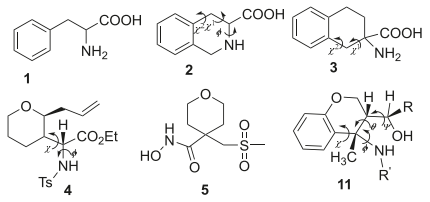

readily reveal that, in general, such a substitution pattern strongly promotes helix formation (5*a*). Moreover, the presence of *N*-methyl residues increases proteolytic stability, membrane permeability (lipophilicity), and alters the conformational characteristics and properties of the amide bond (6). Considerable effort has been focused, particularly, on developing substituted conformationally constrained aromatic precursors because of their importance in protein folding and recognition (7). Consequently, phenylalanine (1) is a key amino acid because it is located in the pharmacophoric region of many bioactive peptides (7*a*–7*c*). The phenylalanine side chain has been constrained, inter alia, by the use of tetrahydroisoquinoline based (**2**, Tic-2) (8) and tetraline-based (**3**, Atc-1) scaffolds (9). On the other hand, the use of pyran rings (**4** and **5**) is an interesting concept in the design of inhibitors of HIV-1 protease and HIV integrase, which requires the use of a scaffold to project hy-

Received 8 January 2008. Accepted 28 February 2008. Published on the NRC Research Press Web site at canjchem.nrc.ca on 11 April 2008.

S.S. Bhella, M.P.S. Ishar,[1] G. Singh, R. Singh, G. Singh, and T. Raj. Bio-organic and Photochemistry Laboratory, Department of Pharmaceutical Sciences, Guru Nanak Dev University, Amritsar, 143 005 Punjab, India.

[1]Corresponding author (e-mail: mpsishar@yahoo.com).

 doi:10.1139/V08-042 © 2008 NRC Canada

Scheme 1.

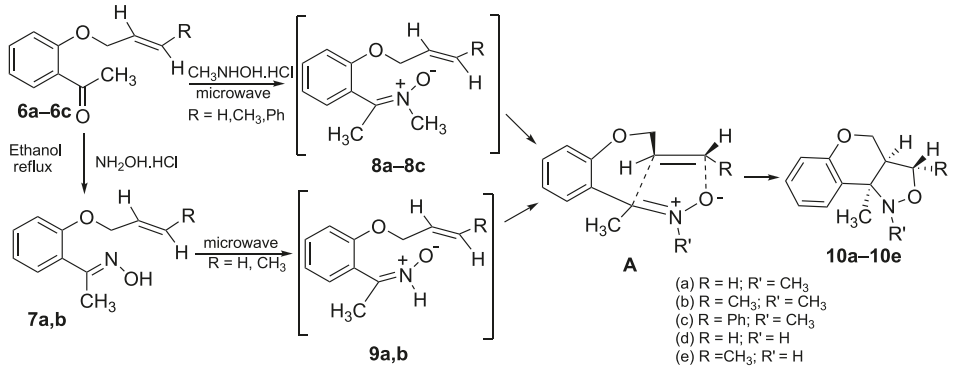

drophobic substituents into the appropriate positions for interaction with the enzyme (10).

Compared to the α-amino acids (**2**–**4**), β-amino acids possess a much greater chemical diversity (11). Consequently, the importance of the synthesis of $\beta^{2,3,3}$-amino alcohol precursors for conformationally constrained $\beta^{2,3,3}$-amino acids (sub-class of β-amino acids) (11*b*, 12, 13) building blocks increases because $\beta^{2,3,3}$ substitutions have a more pronounced influence on the torsional space by reducing the available dihedral angles ϕ and ψ, which in turn influence angle θ (5*a*). Amino alcohols are versatile intermediates in organic synthesis and increasingly important in drugs and pharmaceutics (14), and simple, efficient, and environmentally friendly processes are highly sought for their synthesis.

Herein, we report the synthesis of substituted conformationally constrained $\beta^{2,3,3}$-amino alcohols (**11a**–**11e**), by reductive cleavage of the N–O bond of isoxazolidines (**10a**–**10e**) with ammonium formate using a metal catalyst, such as palladium on charcoal (Pd/C) or zinc dust (Zn). The results are compared with the results obtained by reductive cleavage of the N–O bond of isoxazolidines with Zn/acetic acid. The starting compounds *o*-allyloxy-/crotyloxy-/cinnamyloxy-acetophenones were utilized to achieve $\beta^{2,3,3}$ substitutions in **11a**–**11e**. The obtained scaffolds (**11a**–**11e**) have varied substitution patterns as well as chemical diversity, compared with the compounds reported in the literature (7–9, 13) and these precursors (**11a**–**11e**) of non-proteinogenic phenylalanine can be exploited in peptidomimetic drug designing.

Results and discussion

For targeting the $\beta^{2,3,3}$ substitution in aromatic amino alcohols (**11a**–**11e**), the isoxazolidines (**10a**–**10e**) were synthesized by intramolecular 1,3-dipolar cycloaddition of *N*-methylnitrones (**8a**–**8c**) and nitrones (**9a**, **9b**) generated in situ from oximes (**7a**, **7b**) by starting with *o*-allyloxy-/crotyloxy-/cinnamyloxy-acetophenones (**6a**–**6c**), under microwave irradiation conditions (Scheme 1); the stereochemical outcome is a consequence of π-facial selectivity, which can be rationalized in terms of preferred endo-orientation of R and exo-orientation of -O-CH_2- moiety in the transition state (**A**) (15).

Opening of the obtained isoxazolidines (**10a**–**10e**) by cleavage of the N–O bond was investigated under reductive conditions. Thus, reaction of **10a**–1**0e** with Zn-aq. AcOH, Zn-$HCOONH_4$, and Pd/C-$HCOONH_4$ in a mixture of solvents (THF and methanol) at room temperature (RT) led to $\beta^{2,3,3}$-amino alcohols (**11a**–**11e**) with yields varying from 48% to 52% for Zn-aq. AcOH, 75% to 78% for Zn-$HCOONH_4$, and 90% to 93% for Pd/C-$HCOONH_4$ (Scheme 2 and Table 1). The reaction was monitored by TLC [R_f values for **11a**–**11e** are 0.16–0.15 and for **10a**–**10e** are 0.37–0.35, $CHCl_3$ solvent]. It was observed that the use of ammonium formate ($HCOONH_4$) in THF–MeOH solvent in the presence of Pd/C efficiently cleaved the N–O bond of isoxazolidines (**10a**–**10e**) to β-amino alcohols (**11a**–**11e**) at RT in high yields and in less time than Zn/acetic acid (Table 1); the reaction is also very neat and clean.

Scheme 2.

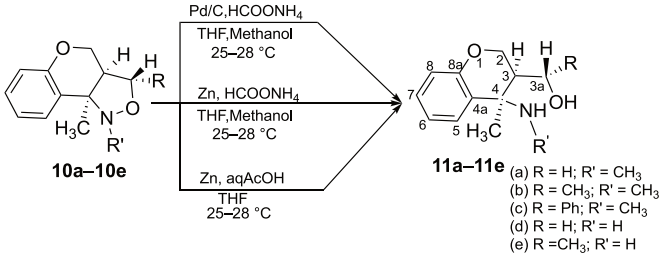

Table 1. Reaction conditions, yields, and times for **11a**–**11e**.

	Zn-aq. AcOH		Zn-$HCOONH_4$		Pd/C-$HCOONH_4$	
Entry	Yield (%)	Time (h)	Yield (%)	Time (h)	Yield (%)	Time (h)
11a	52	11	78	7	93	2
11b	51	12	75	6	92	3
11c	51	12	77	7	93	3
11d	49	11	76	6	91	2
11e	48	12	77	7	90	2

The products were characterized by spectroscopic analysis (IR, ^{1}H, and ^{13}C NMR, including COSY, hetero-COSY, and NOESY 2D NMR measurements, and mass) and microanalytical data. The -O-H and N-H bands of the ring opened products, in the case of **11a**, appeared at 3280 and 3130 cm^{-1}, respectively; their presence was also corroborated by deuterium exchange (on shaking with D_2O, resonances of -O-H and NH in the ^{1}H NMR spectra of the products are suppressed). The changes in the chemical shift values, both in ^{1}H and ^{13}C NMR, in going from isoxazolidines (**10a**–**10e**) to

© 2008 NRC Canada

the corresponding ring-opened products (**11a**–**11e**) are in agreement with the assigned structures. The cis arrangement between C4-CH_3 and C3-H is corroborated by spatial proximity established by the NOESY spectrum in the case of **11a**; this cis arrangement was also established in the case of **10a** through its NOESY spectrum (15), thereby indicating the retention of stereochemical disposition of the isoxazolidines in the ring-opened products. The chemical shift of C3a-H(s) resonances, which indicated the proximity of C3a to the OH function, were easily identified from their multiplicity.

The use of ammonium formate ($HCOONH_4$) as a reductive reagent (16*a*, 16*b*) is very cost effective with good yields under mild conditions compared with the other conventional hydrogenation procedures, which require a special set of apparatus and involve risk associated with the use of hydrogen gas (12, 13). Ammonium formate acts as a hydrogen source in the presence of a metal catalyst, such as palladium on charcoal, zinc dust, etc., and this process offers a valuable alternative, providing greater experimental convenience that avoids many disadvantages and hazards (16*c*). Ammonium formate has advantages of being readily available, inexpensive, stable, and nontoxic. The use of ammonium formate is also a better option than the use of acid for reductive cleavage in the presence of acid sensitive moieties (16*b*).

The obtained $\beta^{2,3,3}$ amino alcohols (**11a**–**11e**) are potentially more useful than α-amino acids (**2–4**) because with the extra carbon atom in the backbone, the presence of *N*-alkyl substituent, and the presence of benzopyran moiety, these scaffolds possess more chemical diversity. The double substitution at C3 and single substitution at C4 in **11a**–**11e** should enhance the gauche conformation (5); such gauche conformations induce the folded structural motifs, such as helices, and turns into peptides (5). The *N*-methyl residue in **11a**–**11c** increases the metabolic stability, improves absorption properties, and also alters the conformational characteristics and properties of the amide bond (6). These constrained scaffolds (**11a**–**11e**) can also project their hydrophobic substituents into the appropriate positions for enzyme interaction.

Conclusion

Facile reductive cleavage of the N–O bond of isoxazolidines (**10a**–**10e**) with ammonium formate in the presences of a Pd/C or Zn metal catalyst have been utilized to obtain novel $\beta^{2,3,3}$-amino-alcohols (**11a**–**11e**), with a substitution pattern having pronounced influence on torsional angles. These compounds (**11a**–**11e**) could serve as valuable scaffolds for peptidomimetics upon which substituents can be mounted to mimic the peptides.

Experimental

General information

Starting materials and reagents were purchased from commercial suppliers and used after further purification (crystallization/distillation). Bruker AC-200FT (200 MHz) and JEOL AL-300FT (300 MHz) spectrometers were used to record ^{1}H NMR and ^{13}C NMR (50 and 75 MHz) spectra. Chemical shifts (δ) are reported as downfield displacements from TMS used as internal standard and coupling constants (*J*) are reported in Hz. IR spectra were recorded with a Shimadzu DR-2001 FT-IR spectrophotometer on KBr pellets. Mass spectra, ESI-method, were recorded on a Bruker Daltonics Esquire 300 mass spectrometers. Elemental analyses were carried out on a PerkinElmer 240C elemental analyzer and are reported in percent atomic abundance. All melting points are uncorrected and measured in open glass-capillaries on a Veego MP-D digital melting point apparatus. Thin layer chromatography (TLC) was carried out on silica gel G-coated (Loba Chemie, containing 13% $CaSO_4$ as a binder) (1 mm thick layer) glass plates.

General procedure for the reaction of 10a–10e with Zn and aq. AcOH to synthesize 11a–11e

A solution of **10a**–**10e** (500 mg) in acetic acid (10 mL), THF (5 mL), and water (5 mL) was stirred at RT (25–28 °C). Activated zinc dust (1.5 g, excess) was added to the above solution. To the stirred mixture (11–12 h) additional amounts of zinc were added until the starting material disappeared; the reaction was monitored by TLC. The reaction mixture was filtered and the residue washed with ether (30 mL). The filtrate was basified with aqueous sodium hydroxide (10%) and extracted with dichloromethane (3 × 50 mL). The combined organic layer was dried over Na_2SO_4 and concentrated under vacuum. Purification of the residue by flash column chromatography (silica gel, ethyl acetate–hexane, 7:3) afforded **11a**–**11e**.

General procedure for the reaction of 10a–10e with Pd/C and $HCOONH_4$ or Zn and $HCOONH_4$ to synthesize 11b–11e

A solution of **10a**–**10e** (500 mg), ammonium formate (3.0 g), methanol (15 mL), and THF (5 mL) was stirred at RT (25–28 °C). Activated 10% palladium on charcoal (1.5 g) or zinc dust (1.5 g, excess) was added to the above solution. The mixture was stirred for 2–3 h for Pd/C–$HOOCNH_4$ and 6–7 h for Zn–$HOOCNH_4$; completion of the reaction was monitored by TLC. The reaction mixture was filtered and the residue washed with ether (30 mL). The filtrate was basified with aqueous sodium hydroxide (10%) and extracted with dichloromethane (3 × 50 mL). The combined organic layer was dried over Na_2SO_4 and concentrated under reduced pressure. Purification by flash column chromatography (silica gel, ethyl acetate-hexane, 7:3) afforded **11a**–**11e**.

(4-Methyl-4-methylamino-chroman-3-yl)-methanol (11a)

Colorless solid, mp 43–45 °C (hexane:chloroform, 2:1). R_f = 0.16 ($CHCl_3$). IR (KBr, cm^{-1}): 3280, 3130, 1577, 1122. ^{1}H NMR ($CDCl_3$, 300 MHz) δ: 7.30 (dd, 1H, *J* = 7.6 and 1.8 Hz, arom.-H), 7.18 (dd, 1H, *J* = 8.4 and 1.6 Hz, arom.-H), 6.92 (dd, 1H, *J* = 7.5 and 1.5 Hz, arom.-H), 6.86 (dd, 1H, *J* = 8.1 and 1.5 Hz, arom.-H), 4.49 (unresolved dd, 1H, *J* = 11.7 Hz, 1H, C3a-Ha), 4.34 (dd, 1H, *J* = 11.7 and 4.5 Hz, C2-Ha), 4.29 (dd, 1H, *J* = 11.8 and 3.6 Hz, 1H, C2-Hb), 3.74 (dd, 1H, *J* = 11.8 and 3.3 Hz, C3a-Hb), 3.42 (broad singlet, 2H, NH, and OH), 2.33 (s, 3H, N-CH_3), 2.00–1.93 (m, 1H, C3-H), 1.61 (s, 3H, C4-Hs, CH_3). ^{13}C NMR ($CDCl_3$, 75 MHz) δ: 153.9 (C8a), 128.7 (CH), 126.4

© 2008 NRC Canada

(C4a), 126.1 (CH), 119.9 (CH), 117.7 (CH), 65.3 (C3a), 61.2 (C2), 54.5 (C4), 43.4 (N-CH_3), 29.8 (C3), 23.5 (C4-CH_3). MS (ESI) *m/z*: 231.9 $(M + Na)^+$. Anal. calcd. for $C_{12}H_{17}NO_2$: C 69.54, H 8.27, N 6.76; found: C 69.48, H 8.13, N 6.64.

1-(4-Methyl-4-methylamino-chroman-3-yl)-ethanol (11b)

Colorless oil. R_f = 0.16 ($CHCl_3$). IR ($CHCl_3$, cm^{-1}): 3458, 3363, 1495, 1132. ^1H NMR ($CDCl_3$, 300 MHz) δ: 7.54 (dd, 1H, *J* = 7.5 and 1.5 Hz, arom.-H), 7.19 (t, 1H, *J* = 7.8 Hz, arom.-H), 6.99 (t, 1H, *J* = 7.8 Hz, arom.-H), 6.83 (d, 1H, *J* = 8.1 Hz, arom.-H), 3.81 (broad singlet, 2H, NH, and OH), 4.16 (dd, 1H, *J* = 11.9 and 3.9 Hz, C2-Ha), 4.05 (dd, 1H, *J* = 12.0 and 3.9 Hz, C2-Hb), 3.97 (dd, 1H, *J* = 11.5 and 3.0 Hz, C3-Hb), 2.62 (s, 3H, N-CH_3), 2.11–2.05 (m, 1H, C3-H), 1.77 (s, 3H, C4-CH_3), 1.40 (d, 3H, *J* = 5.7 Hz, C3a-CH_3). ^{13}C NMR ($CDCl_3$, 75 MHz) δ: 154.4 (C8a), 128.9 (CH), 125.9 (C4a), 122.1 (CH), 121.9 (CH), 117.3 (CH), 65.5 (C3a), 61.9 (C2), 56.11 (C4), 49.3 (N-CH_3), 27.9 (C3), 19.9 (C3a-CH_3), 18.8 (C4-CH_3). MS (ESI) *m/z*: 245.14 $(M + Na)^+$. Anal. calcd. for $C_{13}H_{19}NO_2$: C 70.56, H 8.65, N 6.33; found: C 70.58, H 8.53, N 6.27.

(4-Methyl-4-methylamino-chroman-3-yl)-phenyl-methanol (11c)

Colorless oil. R_f = 0.16 ($CHCl_3$). IR ($CHCl_3$, cm^{-1}): 3404, 3153, 1490, 1110. ^1H NMR ($CDCl_3$, 300 MHz) δ: 7.50 (d, 1H, *J* = 7.5 Hz, arom.-H), 7.44–6.97 (m, 7H, arom.-Hs), 6.87 (t, 1H, *J* = 7.5 Hz, arom.-H), 4.79 (d, 1H, *J* = 8.1, C3a-Ha), 3.68 (broad signal, 2H, NH, and OH), 4.00 (dd, 1H, *J* = 11.8 and 3.6 Hz, C2-Ha), 3.87 (dd, 1H, *J* = 11.7 and 7.5 Hz, C2-Hb), 2.66 (s, 3H, N-CH_3), 2.43–2.37 (m, 1H, C3-H), 1.51 (s, 3H, C4-CH_3). ^{13}C NMR ($CDCl_3$, 75 MHz) δ: 153.9 (C8a), 142.9 (quart), 129.3 (CH), 128.4 (CH), 127.9 (quart), 126.8 (CH), 125.9 (CH), 124.9 (CH), 121.3 (CH), 117.4 (CH), 73.4 (C3a), 65.4 (C2), 58.1 (C4), 46.4 (N-CH_3), 29.6 (C3), 22.5 (C4-CH_3). MS (ESI) *m/z*: 284.1 $(M + Na)^+$. Anal. calcd. for $C_{18}H_{21}NO_2$: C 76.29, H 7.47, N 4.94; found: C 76.21, H 7.40, N 4.87.

(4-Amino-4-methyl-chroman-3-yl)-methanol (11d)

Colorless oil. R_f = 0.15 ($CHCl_3$). IR ($CHCl_3$, cm^{-1}): 3452, 3260, 1585, 1115. ^1H NMR ($CDCl_3$, 300 MHz) δ: 7.32 (dd, 1H, *J* = 8.5 and 1.8 Hz, arom.-H), 7.18 (ddd, 1H, *J* = 9.0, 7.2, and 1.2 Hz, arom.-H), 6.923 (unresolved dd, 1H, *J* ~ 7.2 Hz, arom.-H), 6.86 (dd, 1H, *J* = 9.7 and 2.4 Hz, arom.-H), 4.48 (unresolved dd, 1H, *J* = 11.4 Hz, C3a-Ha), 4.34 (dd, 1H, *J*= 11.7 and 4.8 Hz, C2-Ha), 4.26–4.18 (unresolved dd, 1H, C2-Hb), 3.75 (dd, 1H, *J* = 11.8 and 3.0 Hz, C3a-Hb), 3.67 (broad signlet, 3H, NH_2, and OH), 1.99–1.96 (m, 1H, C3-H), 1.62 (s, 3H, C4-Hs, CH_3). ^{13}C NMR ($CDCl_3$, 75 MHz) δ: 154.6 (C8a), 128.9 (CH), 128.7 (CH), 124.8 (C4a), 121.9 (CH), 117.2 (CH), 72.5 (C3a), 65.4 (C2), 61.1 (C4), 47.7 (C3), 26.3 (C4-CH_3). MS (ESI) *m/z*: 284.1 $(M + Na)^+$. Anal. calcd. for $C_{11}H_{15}NO_2$: C 68.37, H 7.82, N 7.25; found: C 68.40, H 7.78, N 7.20.

1-(4-Amino-4-methyl-chroman-3-yl)-ethanol (11e)

Colorless oil. R_f = 0.15 ($CHCl_3$). IR ($CHCl_3$, cm^{-1}): 3458, 3270, 1490, 1118. ^1H NMR ($CDCl_3$, 300 MHz) δ: 7.48 (d, 1H, *J* = 7.5 Hz, arom.-H), 7.21 (t, 1H, *J* = 7.5 Hz, arom.-H), 6.99 (t, 1H, *J* = 7.5 Hz, arom.-H), 6.85 (d, 1H, *J* = 8.1 Hz, arom.-H), 4.58 (broad singlet, 3H, NH_2, and OH), 4.15–4.03 (m, 3Hs, C3a-H and C2-Hs), 2.09–2.08 (m, 1H, C3-H), 1.77 (s, 3H, C4-CH_3), 1.41 (d, 3H, *J* = 5.7 Hz, C3a-CH_3). ^{13}C NMR ($CDCl_3$, 75 MHz) δ: 153.6 (C8a), 128.7 (CH), 126.1 (CH), 125.8 (C4a), 119.9 (CH), 117.3 (CH), 65.2 (C3a), 61.1 (C2), 54.6 (C4), 42.9 (C3), 29.6 (C4-CH_3), 23.1 (C3a-CH_3). MS (ESI) *m/z*: 230.13 $(M + Na)^+$. Anal. calcd. for $C_{12}H_{17}NO_2$: C 69.54, H 8.27, N 6.76; found: C 69.49, H 8.22, N 6.69.

Acknowledgements

Use of the 300 MHz NMR facilities provided by the Department of Science and Technology, Government of India, at the Chemistry Department, Guru Nanak Dev University, Amritsar, is gratefully acknowledged.

References

1. (*a*) P.D. Bailey. An introduction to peptide chemistry. Wiley, New York. 1990; (*b*) J. Gante. Angew. Chem. Int. Ed. Engl. **33**, 1699 (1994); (*c*) W.A. Loughlin, J.D.A. Tyndall, M.P. Glenn, and D.P. Fairlie. Chem. Rev. **104**, 6085 (2004), and refs. cited therein.
2. (*a*) J.C.M. van Hest and D.A. Tirrell. Chem. Commun. 1897 (2001); (*b*) S. Kotha. Acc. Chem. Res. **36**, 342 (2003), and refs. cited therein.
3. (*a*) G.N. Ramachandran and V. Sasisekharan. Adv. Protein Chem. **23**, 283 (1968); (*b*) H.A. Scheraga. Chem. Rev. **71**, 195 (1971); (*c*) S.M. Bloom, G.D. Fasman, C. deLoze, and E.R. Blout. J. Am. Chem. Soc. **84**, 458 (1961).
4. S.E. Gibson, N. Guillo, and M.J. Tozer. Tetrahedron, **55**, 585 (1999).
5. (*a*) F. Fulop, T.A. Martinek, and G.K. Toth. Chem. Soc. Rev. **35**, 323 (2006); (*b*) T.A. Martinek and F. Fülöp. Eur. J. Biochem. **270**, 3657 (2003); (*c*) D. Seebach, A.K. Beck, and D.J. Bierbaum. Chem. Biodiversity, **1**, 1111 (2004).
6. L. Aurelio, R.T.C. Brownlee, and A.B. Hughes. Chem. Rev. **104**, 5823 (2004), and refs. cited therein.
7. (*a*) C. Cativiela, P. Lopez, and M. Lasa. Eur. J. Org. Chem. 3898 (2004); (*b*) W. Wang and H. Li. Tetrahedron Lett. **45**, 8479 (2004); (*c*) S. Kotha and A.K. Ghosh. Tetrahedron, **60**, 10833 (2004); (*d*) H. Ueki, T.K. Ellis, M.A. Khan, and V.A. Soloshonok. Tetrahedron, **59**, 7301 (2003); (*e*) P. Gerieco, P. Campiglia, I. Gomez-Monterrey, and E. Novellino. Tetrahedron Lett. **43**, 6297 (2002); (*f*) A. Long and S.W. Baldwin. Tetrahedron Lett. **42**, 5343 (2001).
8. (*a*) P. Majer, J. Slaninova, and M. Lebl. Int. J. Pept. Protein Res. **43**, 62 (1994); (*b*) G. Balboni, S. Salvadori, R. Guerrini, L. Negri, E. Giannini, Y. Jinsmaa, S.D. Bryant, and L.H. Lazarus. J. Med. Chem. **45**, 5556 (2002); (*c*)V. Kumar, T.F. Murray, and J.V. Aldrich. J. Med. Chem. **45**, 3820 (2002).
9. (*a*) W. Liu, P. Ray, and S.A. Benezra. J. Chem. Soc. Perkin Trans. 1, **5**, 553 (1995); (*b*) D. Obrecht, C. Spiegler, P. Schoenholzer, K. Mueller, H. Heimgartne, and F. Stierli. Helv. Chem. Acta, **75**, 1666 (1992); (*c*) J.V. Aldrich, Q. Zheng, and T.F. Murray. Chirality, **13**, 125 (2001).
10. (*a*) A.K. Ghosh, C.X. Xu, S.S. Kulkarni, and D. Wink. Org. Lett. **7**, 8 (2005); (*b*) B. Lovejoy, A.R. Welch, S. Carr, C. Luong, C. Broka, R.T. Hendricks, J.A. Campbell, K.A.M. Walker, R. Martin, H.Van Wart, and M.F. Browner. Nat. Struct. Biol. **6**, 217 (1999).

© 2008 NRC Canada

11. (*a*) G. Guichard. *In* Pseudo-peptides in drug discovery. Vol. 33. *Edited by* Peter E. Nielsen. Wiley-VCH, New York. 2004. Chap. 2; (*b*) A.A. Fuller, B. Chen, A.R. Minter, and A.K. Mapp. J. Am. Chem. Soc. **127**, 5376 (2005).
12. (*a*) R. Huisgen, R. Grashey, H. Hauck, and H. Seidl. Chem. Ber. **101**, 2548 (1968); (*b*) R. Huisgen, R. Grashey, H. Seidl, and H. Hauck. Chem. Ber. **101**, 2559 (1968); (*c*) R. Huisgen, H. Hauck, R. Grashey, and H. Seidl. Chem. Ber. **101**, 2568 (1968).
13. G. Broggini, L. Bruche, E. Cappelletti, and G.J. Zecchi. Chem. Res. (S) 36 (1996).
14. (*a*) D.J. Ager, I. Prakash, and D. Schaad. Chem. Rev. **96**, 835 (1996); (*b*) C. Auvin-Guette, S. Rebuffat, Y. Prigent, and B. Bodo. J. Am. Chem. Soc. **114**, 2170 (1992); (*c*) E.J. Corey, R.K. Bakshi, S. Shibata, C.P. Chen, V.K. Singh. J. Am. Chem. Soc. **109**, 7925 (1987); (*d*) J. Takehara, S. Hashiguchi, A. Fujii, S.I. Inoue, T. Ikaria, and R. Nayori. Chem. Commun. 233 (1996); (*e*) J. S. Yadav, B.V.S. Reddy, A.K. Basak, and A.V. Narsaiah. Tetrahedron Lett. **44**, 1047 (2003).
15. S. Singh, M.P.S. Ishar, G. Singh, and R. Singh. Can. J. Chem. **83**, 260 (2005).
16. (*a*) S. Ram and R.E. Ehrenkaufer. Synthesis, 91 (1988); (*b*) A.G.M. Barrett and C.D. Spilling. Tetrahedron Lett. **29**, 5733 (1988); (*c*) B.C. Ranu, A. Sakkar, K.G. Sankar, and K. Ghosh. J. Indian Chem. Soc. **75**, 690 (1998).

© 2008 NRC Canada

Triarylmethyl chlorides as novel, efficient, and mild organic catalysts for the synthesis of *N*-sulfonyl imines under neutral conditions

Ali Khalafi-Nezhad, Abolfath Parhami, Abdolkarim Zare, Amir Nasrolahi Shirazi, Ahmad Reza Moosavi Zare, and Alireza Hassaninejad

Abstract: A highly efficient procedure for the preparation of *N*-sulfonyl imines via condensation of sulfonamides with aldehydes as well as ketones in the presence of triarylmethyl chlorides as metal-free organo-catalysts at 40 °C is described. The advantages of this class of catalysts over the reported ones are their efficiency and possibility of running reactions in neutral media that makes them suitable for acid-sensitive substrates.

Key words: triarylmethyl chloride, *N*-sulfonyl imine, sulfonamide, aldehyde, ketone.

Résumé : On a développé une méthode très efficace pour préparer des *N*-sulfonylimines par le biais d'une condensation à 40 °C de sulfonamides sur des aldéhydes ou des cétones, en présence de chlorures de triarylméthyles agissant comme catalyseurs organiques sans métaux. Les avantages de cette classe de catalyseurs par rapport d'autres qui ont déjà été utilisés sont leur efficacité et la possibilité d'effectuer les réactions dans des milieux neutres appropriés pour les substrats sensibles aux acides.

Mots-clés : chlorure de triarylméthyle, *N*-sulfonylimine, sulfonamide, aldéhyde, cétone.

[Traduit par la Rédaction]

Introduction

N-Sulfonyl imines are versatile intermediates in organic synthesis (1). They are excellent substrates in aza Diels–Alder reactions (2–3), nucleophilic additions (3), and reductions (4), as well as in radical (5) or ene reactions (6). They have been also used in the synthesis of aziridines (7). So far, several synthetic methods for the preparation of *N*-sulfonyl imines have been reported (8–22). Most of those methods involve the condensation of sulfonamides with aldehydes or ketones in the presence of strong Lewis or protic acids, such as sulfamic acid (22). In many cases, strongly acidic conditions are not compatible with other functionalities present in a given substrate. Some methods need two-step procedures or they are expensive methods and generate toxic by-products. Moreover, several methods require prior preparation of precursors, such as oxime, sulfinylimine, or aziridine. Many methods also need harsh reaction conditions. Because of the limitations of the above methods, development of a new method for the synthesis of *N*-sulfonyl imines under neutral conditions in one-step would be desirable.

Recently, organic Lewis acids, such as NBS, trichlorocyanuric acid, and trichloroisocyanuric acid, have been proved to be useful to chemists in the laboratory and industry because of the good activation of carbonyl compounds, selectivity, and mild reaction conditions (23). The use of organic catalysts instead of inorganic Lewis acids have some advantages, including (*i*) the possibility to perform the reactions for acid sensitive substrates, (*ii*) performing the reactions in milder reaction conditions, and (*iii*) the substrates bearing basic functional groups or electron-donating substituents prone to capture the acidic catalysts do not affect the reaction results. Triarylmethyl chlorides (Ar_3CCl) can be introduced as new organic catalysts that are inexpensive and can be obtained commercially or easily prepared by the known procedures (24). These type of compounds has been extensively studied as bulky protective groups for amino and primary hydroxyl functional groups in multi-step organic synthesis (25). Furthermore, triarylmethyl chlorides in combination with metal salts particularly $SnCl_2$ have been employed in a few organic transformations (26); however, the use of triarylmethyl chlorides in the absence of a co-catalyst is really intriguing. To the best of our knowledge, there is no report for the application of triarylmethyl chlorides as catalyst in organic transformations.

Having the above facts in mind and also in continuation of our previous studies on the preparation of *N*-sulfonyl imines (9*a*, 9*b*) as well as catalysis in organic transformations (27), we describe here the first procedure for the application of triarylmethyl chlorides as catalysts in the synthesis of *N*-

Received 9 January 2008. Accepted 24 February 2008. Published on the NRC Research Press Web site at canjchem.nrc.ca on 11 April 2008.

A. Khalafi-Nezhad,[1] **A. Parhami, A.N. Shirazi, and A.R. Moosavi Zare.** Department of Chemistry, College of Sciences, Shiraz University, Shiraz 71454, Iran.
A. Zare. Department of Chemistry, Payame Noor University of Bushehr, Bushehr 1698, Iran.
A. Hasaninejad. Department of Chemistry, Faculty of Sciences, Persian Gulf University, Bushehr 75169, Iran.

[1]Corresponding author (e-mail: ali_khalafinezhad@yahoo.com).

 doi:10.1139/V08-039 © 2008 NRC Canada

Scheme 1. The condensation of sulfonamides with carbonyl compounds.

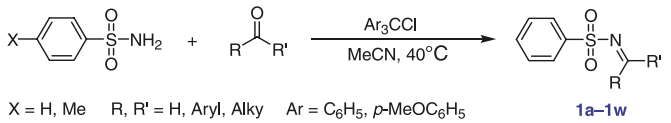

sulfonyl imines via the reaction of sulfonamides with aromatic and aliphatic aldehydes as well as ketones under mild and neutral reaction conditions (Scheme 1).

Results and discussions

To optimize the reaction conditions, first we examined the reaction of benzenesulfonamide (2 mmol) with benzaldehyde (2 mmol) as a model in the presence of DMTrCl [Ph(p-MeOC$_6$H$_4$)$_2$CCl, 0.25 mmol] in MeCN (10 mL) at room temperature. In these conditions, the corresponding *N*-sulfonyl imine **1a** was obtained in 64% yield after 30 min. Increasing the reaction time had no effect on the efficiency of the reaction; however, enhancing the temperature to 40 °C improved the yield to 90%. In another study, the influence of different solvents on the model reaction was investigated. The results are summarized in Table 1. As it can be seen from Table 1, higher yield and shorter reaction time were obtained when MeCN was used. So, MeCN was used as the solvent of choice in all reactions. The reaction of benzenesulfonamide with benzaldehyde was also examined in the absence of solvent in which the product was obtained in 46% within 50 min (Table 1, entry 6). These results indicated the preference of the solvent-phase procedure in comparison with solvent-free conditions. We suggest that it is due to the greater stability of intermediate triphenylcarbonium ions in solvent media.

To select the best triarylmethyl chloride as catalyst, the model reaction was performed using TrCl (Ph$_3$CCl), MMTrCl (Ph$_2$(p-MeOC$_6$H$_4$)Cl), and DMTrCl (Ph(p-MeOC$_6$H$_4$)$_2$Cl) (Table 2). As it is shown in Table 2, there is not a great difference between the catalysts; however; the best yield was obtained using DMTrCl. As expected, the methoxy groups in the catalyst can increase the extent of ionization of triarylcarbenium chloride, thus increasing the amount of Lewis acid in the reaction medium.

To investigate the generality and versatility of the catalyst, the optimized reaction conditions, as described above, were extended to various structurally diverse carbonyl compounds (aldehydes and ketones) and sulfonamides. The results are displayed in Table 3. As Table 3 indicates, the reactions proceeded efficiently, and the desired products were obtained in good to high yields in short reaction times.

In general, higher reaction yields were obtained when benzenesulfonamide was used instead of *p*-toluenesulfonamide. It was observed that the electronic properties of the aromatic ring of aromatic aldehydes can affect the reaction. The results showed that electron-donating substituents improved the reaction yields (Table 3, entries 2, 9, and 10). However, aryl aldehydes possessing electron-withdrawing groups, generally necessitate longer reaction times and decrease the reaction yields (Table 3, entries 3, 11, and 12). Moreover, the presence of a halogen on the aromatic ring of aldehydes slightly decreased the yields and increased the reaction times (Table 3, entries 4, 5, 13, and 14). When the reaction was examined for 4-(dimethylamino)benzaldehyde (Table 3, entry 7), the corresponding bis(indolyl)alkane was obtained in good yield, indicating that the amine function cannot affect the efficiency of the reaction via irreversible complexation with catalyst. *o*-Substituted aromatic aldehydes (Table 3, entry 15) and aliphatic aldehydes (Table 3, entries 18 and 19) needed longer reaction times and afforded lower yields of the products in comparison with the others. The reaction of terphtalaldehyde (2 mmol) with *p*-toluenesulfonamide (4 mmol) afforded the corresponding bis-*N*-sulfonyl imine (Table 3, entry 20) in 51% yield as well as *N*-(4-formylbenzylidene)toluenesulfonamide in 25% yield, which shows the generality and applicability of this method for the synthesis of bis-*N*-sulfonyl imine analogous. Moreover, the reaction of terphtalaldehyde (2 mmol) and *p*-toluenesulfonamide (2 mmol) provided *N*-(4-formylbenzylidene)toluenesulfonamide (Table 3, entry 21) as the product in 76% yield. Generally, aldehydes are more reactive than ketones, since approach of bulky trityl cation is hindered due to the presence of two substituents in ketones. The reaction of ketones with *p*-toluenesulfonamide provided the corresponding *N*-sulfonyl imines in moderate yields (Table 3, entries 22 and 23); however, most of the reported methods were not suitable for the ketones especially enolizable ones.

We suggest that complexes of carbonyl compounds and triarylmethyl cation (**I**, **II**, and **III** for benzaldehyde) were formed (Scheme 2). The cationic intermediates **I**, **II**, and **III** were introduced by Oikawa et al. for the first time (31). These complexes act as activated carbonyl compound and then react with *p*-toluenesulfonamide providing **IV**, which converts to **V** by proton transfer. **V** dissociates to form an

Table 1. The effect of various solvents on the reaction of benzenesulfonamide with benzaldehyde in the presence of DMTrCl at 40 °C.

Entry	Solvent	Time (min)	Yield (%)[a]
1	EtOH	60	48
2	EtOAc	100	65
3	DMF	45	51
4	CH_2Cl_2	80	54
5	MeCN	30	90
6	Solvent-free	50	46

[a]Isolated yield.

Table 2. The influence of different catalysts on the condensation of benzenesulfonamide with benzaldehyde in MeCN at 40 °C.

Entry	Catalyst	Time (min)	Yield (%)[a]
1	TrCl	30	82
2	TrOH	30	12
3	MMTrCl	30	85
4	DMTrCl	30	90

[a]Isolated yield.

© 2008 NRC Canada

Table 3. Preparation of *N*-sulfonyl imines from sulfonamides and aldehydes as well as ketones in the presence of DMTrCl in MeCN at 40 °C.

Entry	R(CO)R'	Product	Time (min)	Yield[a] (%)	Ref.
1	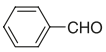	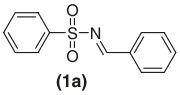 **(1a)**	30	90	19
2	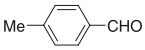	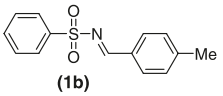 **(1b)**	30	94	16
3	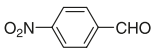	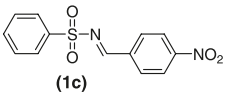 **(1c)**	45	80	21*a*
4	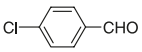	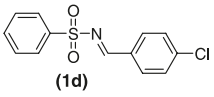 **(1d)**	45	84	16
5	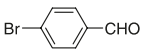	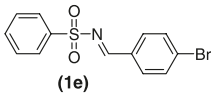 **(1e)**	45	85	10*b*
6	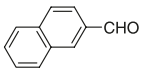	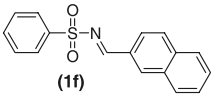 **(1f)**	30	87	18
7	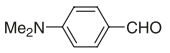	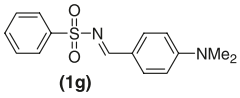 **(1g)**	30	83	10*c*
8	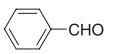	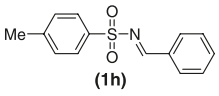 **(1h)**	45	85	17
9	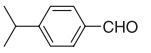	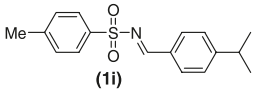 **(1i)**	30	90	10*b*
10	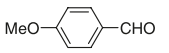	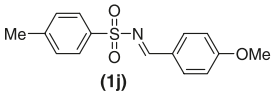 **(1j)**	30	91	9

equilibrating mixture of cations as is shown in Scheme 2. The **VI** eliminates a proton to give the sulfonylimine product, and simultaneously the triarylmethanol is converted to triarylmethyl chloride. The suggested mechanism is confirmed, since the catalyst was completely recovered unchanged, and no triarylmethanol could be identified after the completion of the reaction as it could be observed on TLC by comparison with pure authentic samples. If a base, such as triethylamine or pyridine (in equimolar amount relative to DMTrCl), was added to the model reaction preceding to the addition of DMTrCl, the yield would decrease greatly (9%); moreover, the DMTrCl was not regenerated and DMTrOH was obtained instead. We suggest that this is owing to the ability of base to interfere with the protonation and proton transfer steps in the mechanism. Increasing the amounts of base and DMTrCl had negligible effect on the yield. In another experiment, to examine the applicability of another organo-catalyst for the synthesis of *N*-sulfonyl imines, the reaction was performed using the same amount of 2,4,6-trichloro-1,3,5-triazine instead of DMTrCl and in DMF as the solvent. The results showed that this catalyst is also able to perform the reaction (30% yield in 60 min) and emphasize the role of organo-catalysts for activation carbonyl groups.

In conclusion, this new strategy offers several advantages, including neutral and mild reaction conditions, short reaction times, high yields of products, low catalyst loading as well as simple experimental and isolation procedures, which make it useful for the synthesis of *N*-sulfonyl imines. The

© 2008 NRC Canada

Table 3 (*continued*).

Entry	R(CO)R'	Product	Time (min)	Yield[a] (%)	Ref.
11	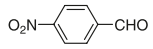	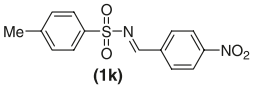 (1k)	50	74	21*b*
12	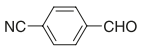	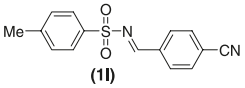 (1l)	50	77	10*a*
13	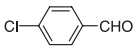	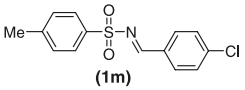 (1m)	50	80	9
14	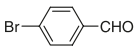	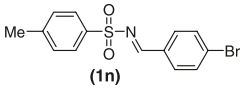 (1n)	50	82	19
15	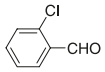	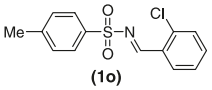 (1o)	50	71	10*a*
16		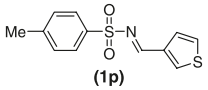 (1p)	40	86	10*a*
17		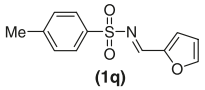 (1q)	40	83	10
18		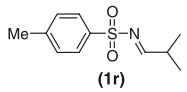 (1r)	50	68	28
19	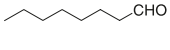	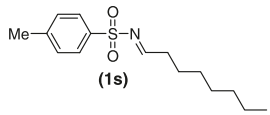 (1s)	50	74	29
20	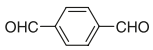	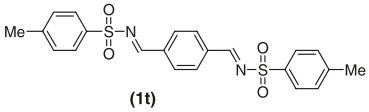 (1t)	60	51[b]	32

selected catalyst is found to be highly efficient, easily available, economical, and recyclable.

Experimental

All chemicals were purchased from Merck or Fluka chemical companies. All known compounds were identified by comparison of their melting points, ^{1}H NMR, and ^{13}C NMR data with the authentic samples. The ^{1}H NMR (250 MHz) and ^{13}C NMR (62.5 MHz) were run on a Bruker Avance DPX-250 FTNMR spectrometer. Mass spectra were recorded on a Shimadzu GC MS-QP 1000 EX apparatus. Microanalyses were performed on a PerkinElmer 240-B microanalyzer. Melting points were recorded on a Büchi B-545 apparatus in open capillary tubes.

General procedure for the synthesis of *N*-sulfonyl imines

To a mixture of sulfonamide (2 mmol), carbonyl compound (2 mmol), and MeCN (10 mL) in a 25 mL round-bottomed flask connected to a reflux condenser was added DMTrCl (0.25 mmol), and the resulting mixture was stirred at 40 °C for the times indicated in Table 3. Subsequently, the solvent was evaporated and to it was added EtOAc (50 mL) and extracted with saturated solution of $NaHSO_3$ (2 × 50 mL) to remove the unreacted carbonyl compound. The organic layer was dried with $MgSO_4$ and concentrated to 5 mL and to it was added gradually *n*-hexane (20–30 mL) and allowed to stand at room temperature until crystals were formed, which then was collected by filtration, washed with *n*-hexane, and dried. The catalyst was recovered by evaporation of the filtrate and subsequent recrystalization in *n*-hexane.

© 2008 NRC Canada

Table 3 (*concluded*).

Entry	R(CO)R'	Product	Time (min)	Yield[a] (%)	Ref.
21	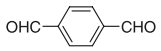	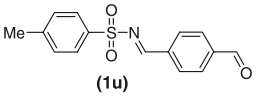 (1u)	50	76[c]	33
22		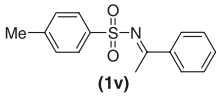 (1v)	60	59	30
23	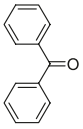	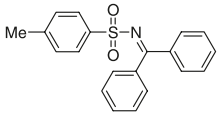 (1w)	70	42	30

[a]Isolated yield.
[b]Molar ratio of $TsNH_2$/terphtalaldehyde is 2:1.
[c]Molar ratio of $TsNH_2$/terphtalaldehyde is 1:1.

Scheme 2. The proposed mechanism for the condensation of sulfonamides with carbonyl compounds.

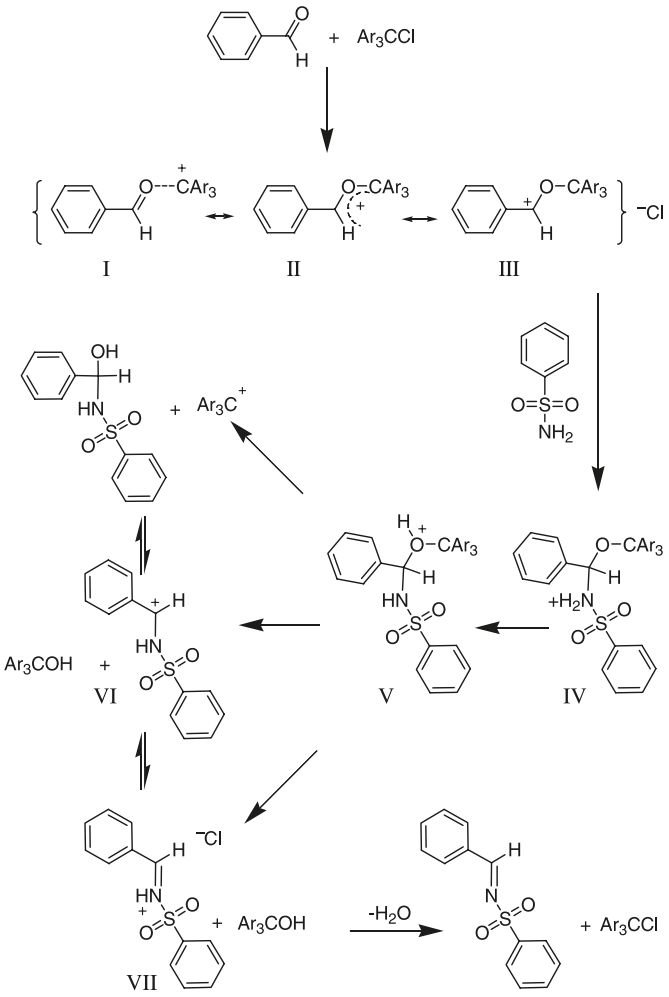

Acknowledgements

We are grateful to the Shiraz University Research Councils for financial support of this work.

References

1. (*a*) S.M. Weinreb. Top. Curr. Chem. **190**, 131 (1997); (*b*) M. Gohain. Synlett, 2097 (2003); (*c*) R. Bloch. Chem. Rev. **98**, 1407 (1998).
2. (*a*) J. Sisko and S.M. Weinreb. Tetrahedron Lett. **30**, 3037 (1989); (*b*) D.L. Boger, W.L. Corbett, T.T. Curran, and A.M. Kasper. J. Am. Chem. Soc. **113**, 1713 (1991).
3. O. Garcia-Mancheno, R. Gomez-Arrayas, and J. C. Carretero. J. Am. Chem. Soc. **126**, 456 (2004); and refs. cited therein.
4. (*a*) M.J. Melnick, A.J. Freyes, and S.M. Weinreb. Tetrahedron Lett. **29**, 3891 (1988); (*b*) K. Yamada, H. Fujihara, Y. Yamamoto, Y. Miwa, T. Taba, and K. Tomioka. Org. Lett. 3509 (2002); (*c*) V. Aggarwal, E. Alonso, M. Ferrar, and S.E. Spey. J. Org. Chem. **67**, 2335 (2002); (*d*) T. Soeta, K. Nagai, H. Fujihara, M. Kuriyama, and K. Tomioka, J. Org. Chem. **68**, 9723 (2003); (*e*) P. Wipf, C. Kendall, and C.R. Stephenson. J. Am. Chem. Soc. **125**, 761 (2003); (*f*) M. Gunter and H.-J. Gais. J. Org. Chem. **68**, 8037 (2003); (*g*) H.-K. Yim and H.N.C. Wong. J. Org. Chem. **69**, 2892 (2004).
5. (*a*) M. Hojo, C. Murakami, A. Fujii, and A. Hosomi. Tetrahedron Lett. **40**, 911 (1999); (*b*) H. Nisikori, R. Yoshihara, and A. Hosomi, Synlett, 561 (2003).
6. K.-I. Yamada, H. Fujihara, Y. Yamamoto, Y. Miwa, T. Taga, and K. Tomioka. Org. Lett. 3509 (2002).
7. M. Yamanaka, A. Nishida, and M. Nakagwa. Org. Lett. 159 (2002).
8. (*a*) R. Hori, T. Aoayama, and T. Shoiri. Tetrahedron Lett. **41**, 9455 (2000); (*b*) L.G. Arini, A. Sinclair, P. Szeto, and R. A. Stockan. Tetrahedron Lett. **45**, 1589 (2004).
9. B.M. Trost and M. Christopher. J. Org. Chem. **56**, 6468 (1991).
10. (*a*) A. Hasaninejad and H. Sharghi. Phosphorus Sulfur Silicon Relat. Elem. **182**, 873 (2007); (*b*) A. Hasaninejad and A. Zare. J. Sulfur Chem. **28**, 357 (2007); (*c*) E. Zieglere and W. Ruef. Z. Naturforsch. **30B**, 946 (1975).
11. K.Y. Lee, C.C. Lee, and J.N. Kim. Tetrahedron Lett. **44**, 1231 (2003); and refs. cited therein.

© 2008 NRC Canada

12. R.N. Ram and A.A. Khan. Synth. Commun. **31**, 841 (2001).
13. G.D. Artman, A. Bartolozzi, R.W. Franck, and S.M. Weinreb. Synlett, 232 (2001).
14. D.L. Boger and W.L. Corbett. J. Org. Chem. **57**, 4777 (1992).
15. J. Wolfe and J.E. Ney. Org. Lett. 4607 (2003).
16. T. Jin, G. Feng, M. Yang, and T. Li. Synth. Commun. **34**, 1277 (2004).
17. F.A. Davis, J. Lamendola, U. Nadir, E.W. Kluger, T.C. Sedergran, T.W. Panunto, R. Billmers, R. Jenkins, I.J. Turchi, W.H. Watson, J.S. Chen, and M. Kimura. J. Am. Chem. Soc. **102**, 2000 (1980).
18. J.L.G. Ruano, J. Aleman, M.B. Cid, and A. Parra. Org. Lett. 179 (2005).
19. A. Vass, J. Dudas, and R. S. Varma. Tetrahedron Lett. **40**, 4951 (1999).
20. G.I. Georg, G.C.B. Harriman, and S.A. Peterson. J. Org. Chem. **60**, 7366 (1995).
21. (*a*) F.A. Davis and S.G. La. J. Org. Chem. **53**, 5004 (1988); (*b*) S.L. Jain. V.B. Sharma, and B. Sain. Mol. Catal. A: Chem. **239**, 92 (2005).
22. Z. Li, X. Ren, P. Wei, H. Wan, Y. Shi, and P. Ouyang. Green Chem. **8**, 433 (2006).
23. (*a*) J.C. Barros. Synlett, 2115 (2005); (*b*) K.P. Haval. Synlett, 2156 (2006); (*c*) T. Kundu. Synlett, 498 (2006).
24. W.E. Bachmann. Org. Synth. Coll. **3**, 841 (1955).
25. T.W. Green and P.G.M. Wuts. Protective groups in organic synthesis. 3rd ed. John Wiley and Sons, New York. 1999.
26. T. Mukaiyama and S. Kobayashi. J. Organomet. Chem. **382**, 39 (1990).
27. (*a*) A. Zare, A. Hasaninejad, A.R. Moosavi Zare, A. Parhami, H. Sharghi, and A. Khalafi-Nezhad. Can. J. Chem. **85**, 438 (2007); (*b*) A. Hasaninejad, A. Zare, H. Sharghi, M. Shekouhy, R. Khalifeh, A. Salimi Beni, and A.R. Moosavi Zare. Can. J. Chem. **85**, 416 (2007); (*c*) A. Zare, A. Hasaninejad, A. Khalafi-Nezhad, A.R. Moosavi Zare, A. Parhami, and G.R. Nejabat. Arkivoc, **i**, 58 (2007); (*d*) A. Khalafi-Nezhad, A. Parhami, M.N. Soltani Rad, M.A. Zolfigol, and A. Zare. Tetrahedron Lett. **48**, 5219 (2007); (*e*) A. Zare, A. Hasaninejad, A. Khalafi-Nezhad, A.R. Moosavi Zare, and A. Parhami. Arkivoc, **xiii**, 105 (2007); (*f*) A. Hasaninejad, A. Zare, H. Sharghi, K. Niknam, and M. Shekouhy. Arkivoc, **xiv**, 39 (2007); (*g*) A. Zare, A. Hasaninejad, A. Khalafi-Nezhad, A. Parhami, and A.R. Moosavi Zare. J. Iran. Chem. Soc. **5**, 100 (2008).
28. A. Milenkovic, F. Fache, R. Faure, and M. Lemaire. Synth. Commun. **29**, 1535 (1999).
29. F. Chelma, V. Hebbe, and J-F. Normant. Synthesis, 75 (2000).
30. D.L. Borger and W.L. Corbett. J. Org. Chem. **57**, 4777 (1992).
31. M. Oikawa, H. Yoshizaki, and S. Kusumoto. Synlett, 757 (1998).
32. Spectral data for unknown compound, 4-methyl-*N*-{(*E*)-[4-((*E*){[(4-methylphenyl)sulfonyl]imino}methyl)phenyl]methylidene}benzenesulfonamide (**1t**): Pale yellow crystals, mp 109–110 °C. ^{1}H NMR (DMSO-d_6, ppm) δ: 2.36 (s, 6H), 7.28 (d, 4H, J = 7.5 Hz), 7.76 (d, 4H), 8.01 (d, 4H, J = 7.5 Hz), 9.31 (s, 2H). ^{13}C NMR (DMSO-d_6) δ: 21.8, 124.7, 128.7, 137.9, 140.2, 141.6, 145.7, 172.5. MS *m/z*: 349 [M^+ – $CH_3C_6H_4$]. Anal. calcd. for $C_{22}H_{20}N_2O_4S_2$: C, 59.98; H, 4.58; N, 6.36. Found: C, 60.17; H, 4.35; N, 6.58.
33. K-C. Yamada, Y. Yamamoto, and K. Tomioka. Org. Lett, **5**, 1797 (2003).

© 2008 NRC Canada

Determination of dissociation constants of *p*-hydroxybenzophenone in aqueous organic mixtures — Solvent effects

M.I. Sancho, A.H. Jubert, S.E. Blanco, F.H. Ferretti, and E.A. Castro

Abstract: The apparent acidity constant of *p*-hydroxybenzophenone, which is a practically insoluble drug in water but of great pharmaceutical interest, was determined by reversed-phase high-performance liquid chromatography in organic solvent – water mixtures (acetonitrile–water, ethanol–water, and methanol–water), varying the reaction medium permittivity in the interval 56 to 70, at constant ionic strength (0.050) and temperature (30 °C). A combined glass electrode calibrated with aqueous standard buffers was used to obtain pH readings based on the concentration scale ($^{s}_{w}$pH). The p*K*a values from chromatographic data were obtained using the Hardcastle–Jano equation. Moreover, excellent linear relationships between the p*K*a values and solvation properties of the reaction medium (relative permittivity and *Acity*) were used to derive acid dissociation constants in aqueous solution. It has been concluded that the p*K*a values extrapolated from such solvent–water mixtures are consistent with each other and with previously reported measurements. In addition, the molecular structures of all the chemical species involved in the acid–base dissociation equilibrium studied were calculated with a B3LYP/6–311++G(d,p) method that makes use of the polarizable continuum model (PCM). Taking into account the theoretical p*K*a values, the conclusions obtained match our experimental determinations.

Key words: solvent effects, *p*-hydroxybenzophenone, acidity constant, solvation parameters, structure, DFT calculation.

Résumé : Faisant appel à la chromatographie liquide à haute performance en phase inversée et opérant à une température de 30 °C, à une force ionique de 0,050 et dans des mélanges de solvants organiques et d'eau (acétonitrile–eau, éthanol–eau et méthanol–eau) dont la permittivité du milieu se situe entre 56 et 70, on a déterminé la constante d'acidité apparente de la *p*-hydroxybenzophénone, un médicament pratiquement insoluble, mais d'un grand intérêt pharmaceutique. On a utilisé une combinaison d'une électrode de verre calibrée avec des tampons aqueux de référence pour obtenir des lectures de pH sur l'échelle de concentration ($^{s}_{w}$pH). On a obtenu les valeurs de p*K*a à partir de données chromatographiques, en utilisant l'équation de Hardcastle–Jano. De plus, on a utilisé les excellentes relations linéaires entre les valeurs de p*K*a et les propriétés de solvatation du milieu réactionnel (permittivité relative et *Acité*) pour obtenir les constantes de dissociation acide en solutions aqueuses. On en conclut que les valeurs de p*K*a extrapolées à partir des mélanges solvants organiques et eau sont en accord entre eux ainsi qu'avec les mesures rapportées antérieurement. De plus, les structures moléculaires de toutes les espèces chimiques impliquées dans l'équilibre de dissociation acide–base étudié ont été calculées à l'aide de la méthode B3LYP/6-311++G(d,p) qui utilise le modèle du continu polarisable (MCP). En prenant en considération les valeurs de p*K*a théoriques, les conclusions obtenues sont en accord avec nos données expérimentales.

Mots-clés : effets de solvant, *p*-hydroxybenzophénone, constante d'acidité, paramètres de solvatation, calculs par la théorie de la fonctionnelle de densité.

[Traduit par la Rédaction]

Received 14 November 2007. Accepted 20 February 2008. Published on the NRC Research Press Web site at canjchem.nrc.ca on 11 April 2008.

M.I. Sancho, S.E. Blanco, and F.H. Ferretti. Area de Química–Física, Facultad de Química, Bioquímica y Farmacia, Universidad Nacional de San Luis, Chacabuco y Pedernera, 5700 San Luis, Argentina.
A.H. Jubert. CEQUINOR, Dpto. de Química, Facultad de Ciencias Exactas, Universidad Nacional de La Plata, 1900 Buenos Aires, Argentina.
E.A. Castro.[1] INIFTA, Dpto. de Química, Facultad de Ciencias Exactas, Universidad Nacional de La Plata, 1900 Buenos Aires, Argentina.

[1]Corresponding author (castro@quimica.unlp.edu.ar).

Introduction

The knowledge of p*K*a values of organic compounds in aqueous solutions with weak acid or basic properties is fundamental to the development of chemical and biological studies, specially those related to chemical stability (1, 2) and preformulation of new pharmaceuticals (3). Numerous compounds with potential biological applications frequently present very low solubility in aqueous media, while in organic solvents the solubility is elevated. Because of this, the determination of the ionization constants in water – organic solvent mixture and the calculation of these constants in pure water by means of extrapolations techniques become very useful (4, 5). It must be noted that the variation of nu-

 doi:10.1139/V08-040 © 2008 NRC Canada

merous physicochemical properties of solutes with the solvent and pH form a very attractive field of research, of great interest and applicability (6–9).

Benzophenones (BPs) are aromatic ketones usually obtained from natural products (10) or by methods of organic synthesis (11). The great importance of these compounds results from the varied biological and physicochemical properties that they possess. Due to these properties, BPs are used in the pharmaceutical industry as sunscreen lotions (12), in medicine (13–15), and in the polymer industry (16). Other applications are the design of optical materials (17), the development of asymmetric catalysts (18), and the preparation of UV-protecting coats (19). The effects of substituents on their conformations (20, 21) and the metal complexing ability in hydroxylic solvents were studied (22, 23) for a better understanding of the physicochemical properties of BPs. Nevertheless, it should be noticed that several structural characteristics of BPs in solution have not been completely defined yet.

In this paper and with the aim of contributing to clarify the influence of solvents on the acid–base properties of *p*(OH)BP, the p*K*a value of the compound was determined by means of high performance liquid chromatography (HPLC) in different organic–aqueous solutions, with a permittivity range of 56–70, and using methanol, ethanol, and acetonitrile as organic modifiers. Also, diverse correlations are proposed between the p*K*a values and solvation parameters of the reaction medium, which allow for a calculation of the p*K*a of the compound in pure water. In addition, the structures of ionized and non ionized *p*(OH)BP in organic solvents and water were calculated by means of a B3LYP/6–311++G(d,p) method (Becke hybrid three-parameter nonlocal exchange functional combined with the Lee–Yang–Parr dynamic correlation functional) (24, 25) that makes use of the PCM model (polarizable continuum model) (26).

Experimental

Chemicals and reagents

p(OH)BP from Fluka was purified by repeated crystallization from ethanol–water. The purity control was performed determining its spectroscopic properties (27). NaH_2PO_4 and $NaHCO_3$ from Merck were used without further purification. Methanol (MeOH), ethanol (EtOH), and acetonitrile (ACN), all HPLC grade, from Merck, were degassed and filtered through 0.22 μm nylon filters (Millipore) before use. Milli-Q water was used to prepare the aqueous buffer solutions. All the solutions were prepared by weighting with an accuracy of ±0.0001 g.

Instrumentation

The HPLC instrument consisted of a Gilson 322 series pump (Gilson Inc., Middleton, WI, USA), a Rheodyne 7725i sample injector (Cotati, CA, USA), and a Gilson 152 UV–vis detector, equipped with a Phenomenex column temperature controller. The system was controlled by UniPoint system software v2.10 (Gilson). The analysis was carried out with a reverse-phase Luna (C_{18} (2), 250mm × 4.6 mm, 5 μm) column from Phenomenex (Torrance, CA, USA). Chromatographic studies were performed under isocratic (actually policratic) elution with a mobile phase of aqueous buffer:organic modifier at different ratios, using amphiprotic solvents (MeOH, EtOH), and a low basic aprotic solvent (ACN) as organic modifier with a flow rate of 1.0 mL/min. Column temperature was maintained at a constant 30 °C. The injection volume was 20 μL, and the detector was set at 280 nm. The capacity factor (k) was measured from chromatographic data in the usual way, that is, $k = (T_R - T_o)/T_o$. The mobile phase holds up times were measured by injecting a solution of $K_2Cr_2O_7$ (0.001 mol/L).

The buffers solutions employed were NaH_2PO_4–Na_2HPO_4 covering the pH range from 4.50 to 8.00 and $NaHCO_3$–Na_2CO_3 covering the pH range from 8.00 to 9.00. The ionic strength was maintained at constant value (0.05 mol/L) by adding appropriate amounts of KCl. The pH measurements were performed on an Orion SA 520 pH meter provided with a 91–01 Orion combined glass electrode.

Special precautions must be taken when the pH is measured in a mixed-solvents mobile phase. It is well-known that when the aqueous buffer is added to the mobile-phase mixed solvent, the measured pH of the mixture will be different from the pH measured in the pure aqueous buffer. This problem was recognized and discussed by Rosés et al. (28), among other authors. When the p*K*a value of ionogenic analytes must be measured, it is advisable to perform the measurement of the pH after mixing aqueous buffers and organic modifiers (29), with the electrode previously calibrated with aqueous standard buffers. Such pH value is denoted as ${}^{s}_{w}$pH, and the respective p*K*a values obtained from data expressed in the ${}^{s}_{w}$pH scale leads to a thermodynamically meaningful dissociation constant, also expressed in the same scale (${}^{s}_{w}$p*K*a). In all the experimental determinations carried out in this work, the pH measurements were made following this recommendation, i.e., the pH of the mobile phase was measured after mixing the aqueous buffers with the organic solvents (MeOH, EtOH, and ACN) with the electrode previously calibrated with aqueous buffers, and the ${}^{s}_{w}$pH scale was used to obtain the experimental ${}^{s}_{w}$p*K*a values.

Calculations

The structure of *p*-hydroxybenzophenone adopted for carrying out the calculations is shown in Fig. 1. The calculations were performed following known procedures (22). The initial molecular geometries were modelled by the AM1 (Austin Model vs. 1) method (30). Afterwards, these initial geometries were optimized with the Gaussian 03 (31) programs package. Since diffuse functions are crucial for theoretical treatment of anions (32), the B3LYP/6–311G++(d,p) method (24, 25) was chosen to perform the final optimization of the molecular structures. To analyse the solvent effects on the optimized structures in the gas phase, the PCM model (26) was used. The corresponding frequencies were calculated to make sure that the obtained structures were true minima. In all the calculations, the default convergence criteria were used.

Results and discussion

Determination of p*K*a

The acid–base equilibrium in aqueous solution studied can be represented by the general equation

© 2008 NRC Canada

Fig. 1. Structure adopted in the calculations of *p*-hydroxybenzophenone.

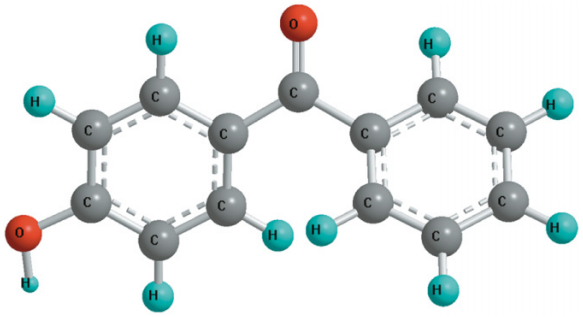

[1] $$AH + H_2O \leftrightarrows A^- + H_3O^+$$

where AH is the weak acid *p*(OH)BP and A^- is the pertinent conjugate base *p*(O^-)BP. The above reaction is characterized by the ionization equilibrium constant (*K*a), conventionally defined as

[2] $$Ka = \frac{a_{A^-} \cdot a_{H_3O^+}}{a_{AH} \cdot a_{H_2O}} = \frac{[A^-][H_3O^+]}{[AH][H_2O]} \cdot \frac{\gamma_{\pm A^-}\gamma_{\pm H_3O^+}}{\gamma_{AH}\gamma_{H_2O}}$$

In this equation, a_{A^-}, $a_{H_3O^+}$, a_{AH} and a_{H_2O} are the activities of the species in equilibrium. The brackets stand for the molar concentration and γ for the molar activity coefficients. The *K*a constant is related to a chromatographic measurable, the capacity factor *k*, by the following equation (33)

[3] $$k = \frac{k_0 + k_1 f_{(1)} Kap\, e^x}{1 + f_{(1)} Kap\, e^x}$$

In the above equation, $x = (\ln 10)pH$, k_0 and k_1 are the limiting capacity factors of *p*(OH)BP and *p*(O^-)BP, respectively, $f_{(1)}$ is the molar activity coefficient ratio between the weak acid and its conjugate base, *K*ap is the apparent equilibrium constant, and the product $Kap \times f_{(1)}$ is the effective acid dissociation constant of the acid AH from eq. [1]. It can be easily demonstrated that $e^x = 1/[H^+]$ and represents the inverse of the proton concentration in the mobile phase. This is the most general equation for the retention factor of the analyzed monoprotic weak acid. Under our experimental conditions (*p*(OH)BP $\approx 1 \times 10^{-4}$ mol/L), the activity coefficient ratios are approximately equal unity, and eq. [3] reduces to eq. [4] (34),

[4] $$k = \frac{k_0 + k_1 Ka\, e^x}{1 + Ka\, e^x}$$

Figure 2 shows the chromatographic results for *p*(OH)BP at different ^s_wpH values with a mobile phase of MeOH : aqueous buffer 39:61 (*v*/*v*). Computer-generated plots of *k* vs. ^s_wpH show typical sigmoidal curves (Figs. 3, 4, and 5) where the ^s_wpH value of the inflection point is the compound ^s_wp*K*a. For the determination of the ^s_wp*K*a value of *p*(OH)BP, eq. [4] was used. The ^s_wp*K*a values were obtained by fitting the data from the measured retention factors as a function of ^s_wpH of the mobile phase, and performing a non-linear least-square iterative procedure. The experimental data were fitted to a rational function equation type 0 [$y = (b + cx)/(1 + ax)$],

Fig. 2. Overlaid chromatograms showing the retention behaviour of *p*-hydroxybenzophenone at different ^s_wpH values (indicated over the peak) in 39% (*v*/*v*) methanol mobile phase, UV detection at 280 nm, flow rate 1 mL/min.

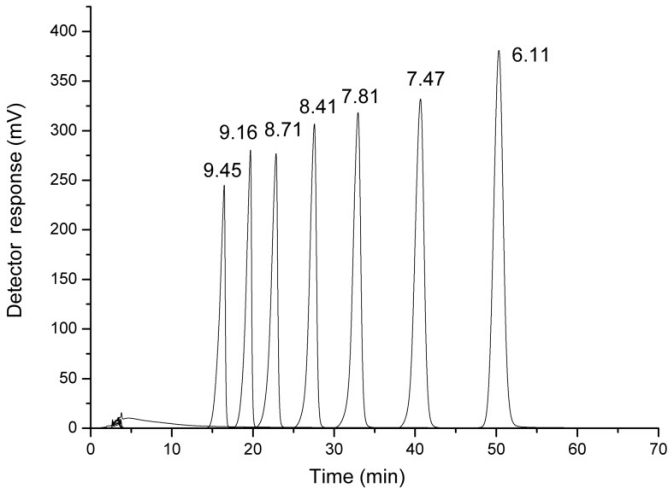

Fig. 3. Measured capacity factors vs. ^s_wpH for *p*-hydroxybenzophenone in methanol:buffer mixtures.

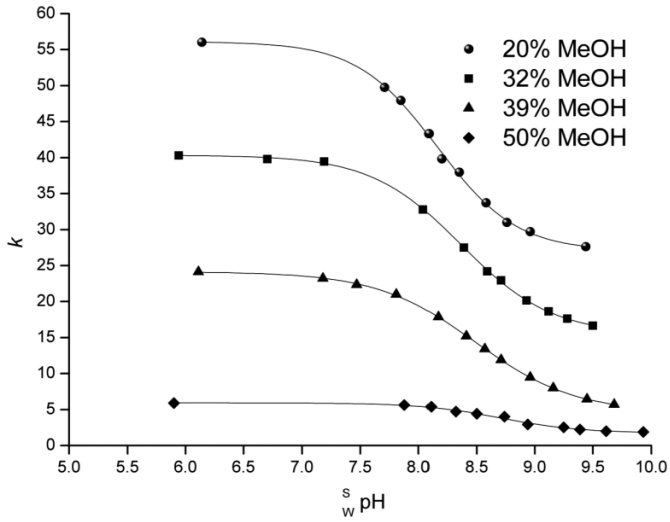

using the software Origin Pro 7.5 (35). Figure 6 shows the results of the fitting process for MeOH:buffer 39:61 (*v*/*v*) mobile phase compositions, and Table 1 reports the ^s_wp*K*a values and limiting capacity factors for *p*(OH)BP obtained in the three solvents under study.

Equation [4] suggests that the retention factor of the solute *k* is a weighted average of the retention factors of the different species that may exist in the mobile phase (34), and this factor may be written as

[5] $$k = X_0 k_0 + X_1 k_1$$

The term X_n ($n = 0, 1$) is the probability that the observed retention factor *k* of the solute is equal to k_n, and it is also the probability of the presence of *p*(OH)BP (if $n = 0$) or the presence of *p*(O^-)BP (if $n = 1$) in the mobile phase expressed as a function of the pH, i.e., it is the relative concentration of the species (the mole fraction) at equilibrium. If $X_0 = 1$, then

© 2008 NRC Canada

Fig. 4. Measured capacity factors vs. $^{s}_{w}$pH for *p*-hydroxybenzophenone in ethanol:buffer mixtures.

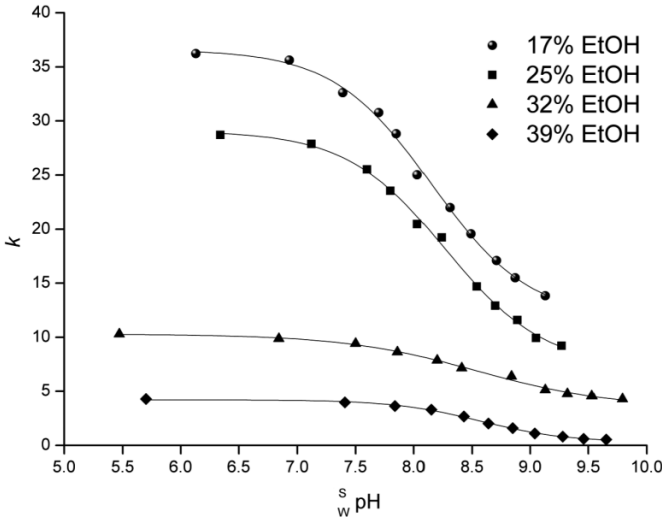

Fig. 5. Measured capacity factors vs. $^{s}_{w}$pH for *p*-hydroxybenzophenone in acetonitrile:buffer mixtures.

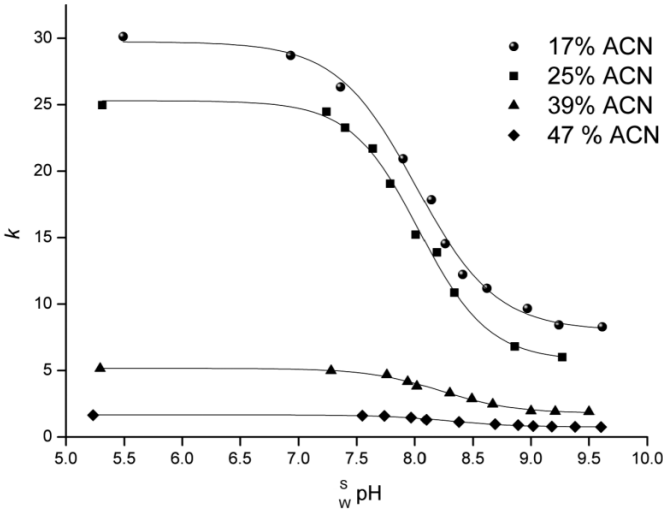

$X_1 = 0$, and only *p*(OH)BP is present in the mobile phase; therefore, the observed retention factor k is exclusively due to the neutral species and equal to k_0. Thus, the distribution of both species at a given pH can be estimated considering that

$$[6] \qquad X_1 = \frac{K\mathrm{a}\,\mathrm{e}^{x}}{1 + K\mathrm{a}\,\mathrm{e}^{x}}$$

and

$$[7] \qquad X_0 = 1 - X_1$$

Figure 7 shows the results of the distribution of both *p*(OH)BP and *p*(O^-)BP at a given pH for two different methanol: buffer mobile phase compositions. It can be observed that when pH ≤ 6 the neutral molecule is the prevailing specie ($X_0 = 0.99$), while at pH ≥ 11, the anion is the prevailing specie in solution ($X_1 = 0.99$).

Fig. 6. Plot of the capacity factor of *p*-hydroxybenzophenone against e^x ($x = 10.\ln(^{s}_{w}\mathrm{pH})$) according to eq. [4].

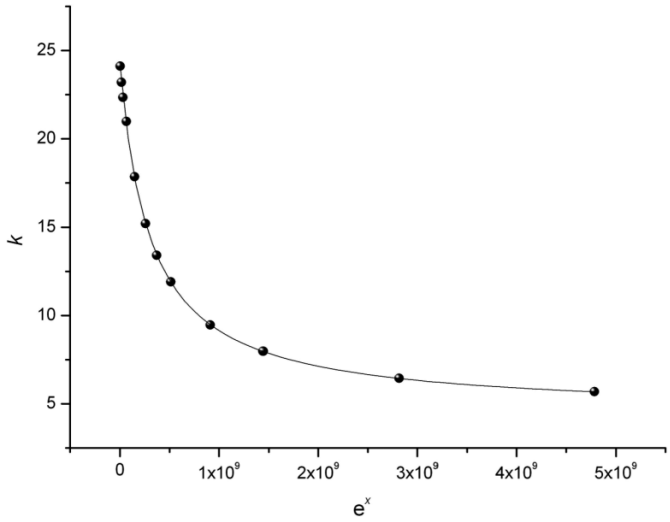

Solvent effects

It is known that one of the most important factors determining the ionization equilibrium constants is the reaction medium. The influence of the solvent upon the specific rate of ion–ion, ion–dipole, or dipole–dipole reactions can be analyzed using the expression by Kirkwood (36, 37).

$$[8] \qquad \ln k = \ln k_0 + \frac{\mathrm{e}^2}{2Dk_\mathrm{B}T}\left[\frac{Z_\mathrm{A}^2}{r_\mathrm{A}} + \frac{Z_\mathrm{B}^2}{r_\mathrm{B}} - \left(\frac{Z_\mathrm{A} + Z_\mathrm{B}}{r_\ddagger}\right)^2\right] + \frac{3}{4Dk_\mathrm{B}T}\left[\frac{\mu_\mathrm{A}^2}{r_\mathrm{A}^3} + \frac{\mu_\mathrm{B}^2}{r_\mathrm{B}^3} - \frac{\mu_\ddagger^2}{r_\ddagger^3}\right]$$

In this equation, k_0 and k are the reaction specific rates for media with infinite and D relative permittivity, e is the unit of electric charge, k_B is Boltzman's constant, T is the absolute temperature, Z_A and Z_B are the charges of the two ions, r is the radius of the involved species, μ stands for the dipolar moments, while the symbol ‡ refers to the activated complex. It is evident that in the acid–base dissociation equilibrium of eq. [1], the forward reaction involves two dipolar molecules, AH and H_2O, while the reverse reaction involves the A^- and H_3O^+ ions. Consequently, applying Kirkwood's equation to these two reactions in equilibrium, eq. [9] was obtained.

$$[9] \qquad {}^{s}_{w}\mathrm{p}K\mathrm{a} = \mathrm{p}K\mathrm{a}^0 + \frac{1}{2.303}\left[\frac{\mathrm{e}^2}{2k_\mathrm{B}T}\left(\frac{1}{r_{\mathrm{A}^-}} + \frac{1}{r_{\mathrm{H_3O^+}}}\right) + \frac{3}{4k_\mathrm{B}T}\left(\frac{\mu_\ddagger^2}{r_\ddagger^3} - \frac{\mu_{\mathrm{AH}}^2}{r_{\mathrm{AH}}^3} - \frac{\mu_{\mathrm{H_2O}}^2}{r_{\mathrm{H_2O}}^3}\right)\right]\frac{1}{D}$$

The $^{s}_{w}$pKa values determined for *p*(OH)BP in MeOH, EtOH, and ACN:water mixtures were plotted against $1/D$ (38, 39) according to eq. [9], and they are shown in Fig. 8. The linear equations included in Fig. 8 indicate that when D

© 2008 NRC Canada

Table 1. ${}^{s}_{w}$p*K*a values and chromatographic parameters obtained for each mobile phase composition at 30 °C (k_0, k_1 = limiting capacity factors of the weak acid *p*(OH)BP and conjugate base *p*(O^-)BP, respectively; *r* = linear regression coefficient). Errors recovered from data fit are in parenthesis.

Organic modifier	Mobile phase composition[a]	${}^{s}_{w}$p*K*a	k_0	k_1	*r*
MeOH	20:80	8.19 (0.04)	57.02 (0.80)	25.04 (0.23)	0.9938
	32:68	8.38 (0.02)	40.59 (0.17)	21.84 (0.04)	0.9993
	39:61	8.49 (<0.01)	24.18 (0.05)	4.48 (0.04)	0.9998
	50:50	8.74 (0.07)	6.07 (0.14)	1.46 (0.41)	0.9883
EtOH	17:83	8.16 (0.03)	36.69 (0.34)	11.41 (0.19)	0.9973
	25:75	8.28 (0.03)	29.13 (0.30)	7.02 (0.20)	0.9976
	32:68	8.46 (0.06)	10.04 (0.14)	4.12 (0.32)	0.9918
	39:61	8.60 (0.03)	4.29 (0.06)	0.10 (0.08)	0.9974
ACN	17:83	7.99 (0.05)	30.56 (0.59)	7.16 (0.30)	0.9926
	25:75	8.08 (0.09)	26.43 (0.81)	3.83 (0.60)	0.9837
	39:61	8.26 (0.07)	5.30 (0.12)	1.51 (0.37)	0.9877
	47:53	8.36 (0.08)	1.71 (0.04)	0.66 (0.39)	0.9856

[a]The mobile phase composition is organic modifier: aqueous buffer (*v*/*v*).

Fig. 7. Variation of X_n with the pH at two different methanol:water mobile phase composition. X_0 is the mole fraction of *p*-hydroxybenzophenone, and X_1 is the mole fraction of the *p*-hydroxybenzophenonate anion.

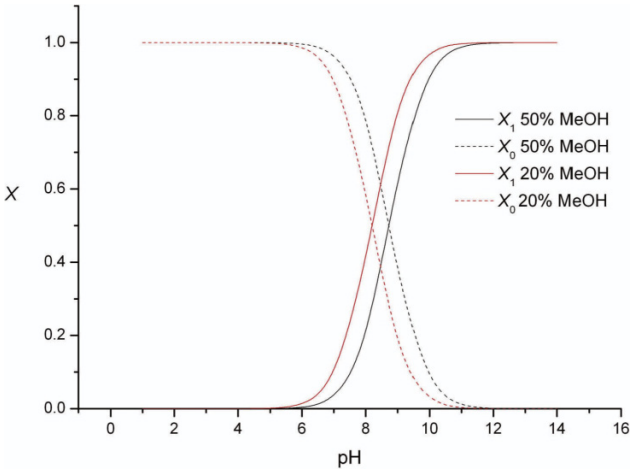

Fig. 8. Plot of the ${}^{s}_{w}$p*K*a of *p*-hydroxybenzophenone against the permittivity of solvent–water solutions at 30 °C, according to eq. [9]. Errors are in parenthesis.

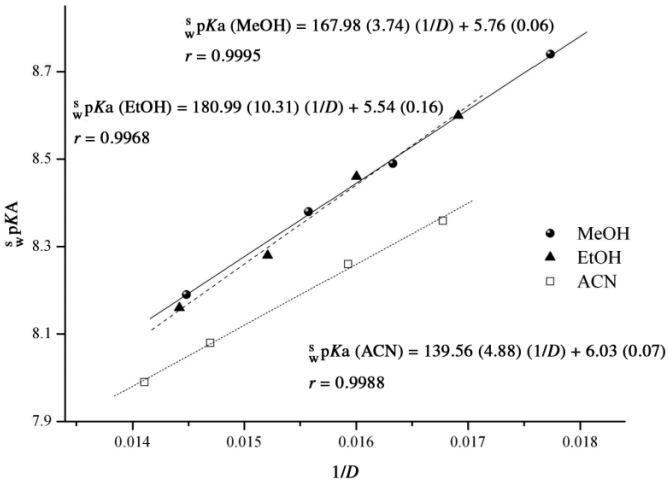

increases, the corresponding ${}^{s}_{w}$p*K*a decreases. As expected, the solvents with greater *D* favour the ionization reaction described by eq. [1]. Although permittivity is important to measure the solvation abilities of solvents, it should be noted that it is not very useful for describing solute–solvent specific interactions. Consequently, we selected the solvation parameter *Acity* (40), which is appropriate for measuring the hydrogen-bond donating ability (HBD capability) of a solvent, i.e., the capability of the solvent to provide a proton. The values of *Acity* determined for ACN, EtOH, MeOH, and water are 0.37, 0.66, 0.75, and 1.00 (41), respectively. The ${}^{s}_{w}$p*K*a values were plotted against the *Acity* parameter of the used organic–aqueous mixtures as shown in Fig. 9. It can be observed that when the *Acity* of the reaction medium increases, the corresponding ${}^{s}_{w}$p*K*a decreases, i.e., the solvents with greater HBD capability favour the acid dissociation reaction of *p*(OH)BP. Moreover, it should also be noted that the limiting capacity factors k_0 and k_1 vary reasonably in a linear way with the *Acity* of the reaction media.

Considering eqs. [10–12] (Fig. 9),

[10] p*K*a (MeOH) = –7.92 (0.49) *Acity* + 15.77 (0.45)

[11] p*K*a (EtOH) = –6.79 (0.39) *Acity* + 14.61 (0.36)

[12] p*K*a (ACN) = –2.20 (0.03) *Acity* + 9.99 (0.02)

and taking into account that *Acity* (H_2O) = 1.00 [41], the ${}^{w}_{w}$p*K*a (p*K*a in pure water) values 7.83, 7.85, and 7.80 were obtained, respectively. These results suggest that the accuracy of the HPLC methodology carried out in this work is very good. In addition, when the obtained ${}^{w}_{w}$p*K*a values are compared with the ${}^{w}_{w}$p*K*a value of 7.51 obtained by means of UV–vis spectroscopy (42), a reasonable agreement is observed.

Table 2 summarizes the calculated Gibbs free energies by means of the B3LYP/6–311++G(d,p) method with the PCM model for all the species involved in the ionization reaction

© 2008 NRC Canada

Fig. 9. Changes of the $^{s}_{w}pK_a$ of *p*-hydroxybenzophenone with the *Acity* parameter of the reaction medium. Errors are in parenthesis.

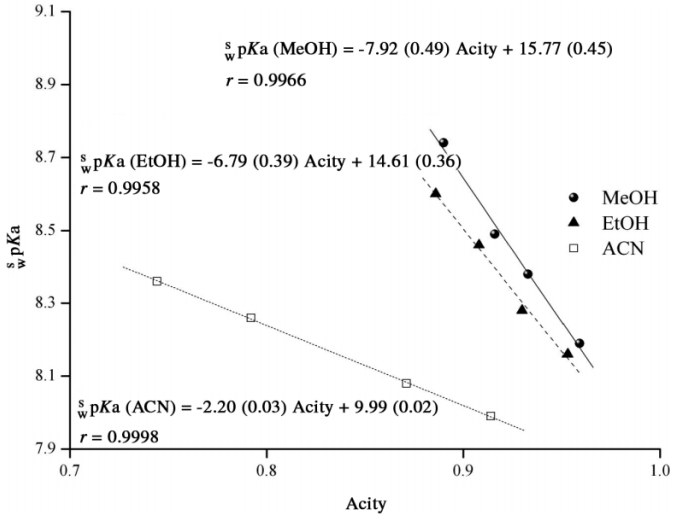

Table 2. Calculated molecular magnitudes for the species involved in the ionization reaction described by eq. [1], using the B3LYP/6–311++G(d,p) method with the PCM model. (G°_{sol} = Gibbs energy in solution, kcal mol^{-1}; *p*(OH)BP = *p*-hydroxybenzophenone; *p*(O^{-})BP = *p*-hydroxybenzophenonate anion; H_3O^+, H^+–ACN, H^+–MeOH, H^+–EtOH = solvated proton with one molecule of water, acetonitrile, methanol, and ethanol, respectively; K_{Theo} = theoretical acidity constant).

Magnitude	G°_{sol}	K_{Theo}	G°_{sol}	K_{Theo}
Solvent	Water		Methanol	
p(OH)BP	–409172.15	4.48×10^{-34}	–409171.36	2.27×10^{-35}
p(O^{-})BP	–408875.83		–408874.35	
H_2O	–47987.14		—	
H_3O+	–48237.97		—	
MeOH	—		–72649.82	
H^+–MeOH	—		–72899.57	
Solvent	Ethanol		Acetonitrile	
p(OH)BP	–409170.94	6.06×10^{-36}	–409171.38	5.36×10^{-37}
p(O^{-})BP	–408873.51		–408874.51	
EtOH	–97329.85		—	
H^+–EtOH	–97579.24		—	
ACN	—		–83336.38	
H^+–ACN	—		–83583.77	

under study. A thermodynamic cycle, shown in Fig. 10, was used to calculate the Gibbs free energy change in solution, ΔG°_{sol}, according to the following equations

[13] $$\Delta G^{\circ}_{gas} = G^{\circ}_{gas}(A^-) + G^{\circ}(H^+S) - G^{\circ}_{gas}(HA) - G^{\circ}_{gas}(S)$$

[14] $$\Delta G^{\circ}_{solv}(X) = G^{\circ}_{solv}(X) - G^{\circ}_{gas}(X) \quad \text{(for X = HA, A}^-\text{, S, and H}^+\text{S)}$$

[15] $$\Delta G^{\circ}_{sol} = \Delta G^{\circ}_{gas} + \Delta G^{\circ}_{solv}(A^-) + \Delta G^{\circ}_{solv}(H^+S) - \Delta G^{\circ}_{solv}(HA) - \Delta G^{\circ}_{solv}(S)$$

Fig. 10. Thermodynamic cycle used to calculate the theoretical acidity constants of *p*-hydroxybenzophenone in solution.

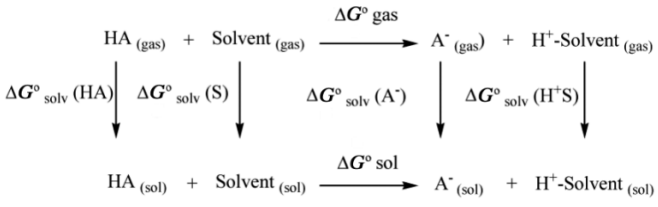

where AH and A$^-$ are *p*(OH)BP and *p*(O$^-$)BP, respectively, S is the solvent molecule, and H^+S is the solvated proton. Equation [15] can be used to calculate ΔG°_{sol}, and therefore p*K*a. The calculated p*K*a (pK_{Theo}) values were

© 2008 NRC Canada

[16] pK_{Theo} (water) = 33.35; pK_{Theo} (MeOH) = 34.64
pK_{Theo} (EtOH) = 35.22; pK_{Theo} (ACN) = 36.27

The above pK_{Theo} values differ from the ones experimentally determined. It must be noted that the calculation of p*K*a values using computational methods is difficult, as there is no simple and accurate way to calculate the Gibbs free energy of the solvated proton. In addition, the pK_{Theo} values are referred to the standard state, which is not the case for the experimental data reported in this paper. Nevertheless, if the calculated pK_{Theo} are analyzed comparatively with each other, it is observed that the theoretical ionization constants vary as the *Acity* parameter of the solvents. This suggests that the conjugate bases are specifically more solvated, according to the *Acity* of the reaction medium, i.e., the pK_{Theo} values of *p*(OH)BP increase when the polarity–polarizability and solvation abilities of the reaction media decrease. This conclusion agrees with experimental observations that indicate that the acid–base equilibria are shifted towards the formations of ions when the polarity–polarizability and HBD capability of the reaction medium increase.

Conclusions

The apparent acidity constant of *p*-hydroxybenzophenone (very slightly soluble drug in water) was determined in diverse organic solvent–water mixtures using a polycratic high-performance liquid chromatographic method based on the Hardcastle–Jano equation. The p*K*a values measured in organic–aqueous solutions were correlated with solvation parameters (relative permittivity and *Acity*) of the reaction medium. Excellent linear equations were proposed from which the p*K*a values in pure water were obtained. The results allowed to infer that the p*K*a values of the compound increase when the polarity–polarizability and solvation abilities of the reaction medium decrease. The molecular structures of all the chemical species involved in the acid–base dissociation equilibria studied were calculated with a B3LYP/6–311++G(d,p) method that makes use of the polarizable continuum model, and the p*K*a values were calculated using a thermodynamic cycle. Considering the theoretical p*K*a values, several conclusions were presented, which are consistent with the experimental determinations. The methodology described in this work is very useful for obtaining the p*K*a of compounds of low solubility in water with adequate accuracy.

Acknowledgements

This work was supported by grants from the National University of San Luis (Argentina). M.I. Sancho thanks Consejo Nacional de Investigaciones Científicas y Técnicas (CONICET) for a Doctoral Fellowship.

References

1. K.A. Connors, V.J. Stella, and G.L. Amidon. Chemical stability of pharmaceuticals: a handbook for pharmacists. 2nd Ed. John Wiley & Sons, New York. 1986.
2. J.T. Cartensen and C.T. Rhodes. Drug stability. 3rd Ed. Marcel Dekker, New York. 1999. pp. 145–189, and 209–260.
3. J.I. Wells. Pharmaceutical preformulation: the physicochemical properties of drug substances. Ellis Harwood, England. 1990. pp. 15 and 80.
4. R. Ruiz, M. Rosés, C. Ràfols, and E. Bosch. Anal. Chim. Acta. **550**, 210 (2005).
5. G. Garrido, C. Ràfols, and E. Bosch. Eur. J. Pharm. Sci. **28**, 118 (2006).
6. M.A.R. Silva, D.C. Silva, V.G. Machado, E. Longhinotti, and V.L.A. Frescura. J. Phys. Chem.: A. **106**, 8820 (2002).
7. N.M. Rageh. Spectrochim. Acta: Part A, **60**, 103 (2004).
8. S.K. Dogra. J. Luminesc. **118**, 45 (2006).
9. T. Stalin and N. Rajendiran. Chem. Phys. **322**, 311 (2006).
10. M. Pecchio, P.N. Solís, J.L. López-Pérez, Y. Vásquez, N. Rodríguez, D. Olmedo, M. Correa, A. San Feliciano, and M.P. Gupta. J. Nat. Prod. **69**, 410 (2006).
11. H.A.M. Hejaz, L.W. Lawrence Woo, A. Purohit, M.J. Reed, and B.V.L. Potter. Bioorg. Med. Chem. **12**, 2759 (2004).
12. E.R.M. Kedor-Hackmann, M.L. De Lourdes Pérez González, A.K. Singh, M.I.R.M. Santoro. Int. J. Cosmet. Sci. **28**, 219 (2006).
13. B. T. Prabhakar, S.A. Khanum, K. Jayashree, B.P. Salimath, and S. Shashikanth. Bioorg. Med. Chem. **14**, 435 (2006).
14. R. Siles, S. Chen, M. Zhou, K.G. Pinney, and M.L. Trawick. Bioorg. Med. Chem. Lett. **16**, 4405 (2006).
15. J.H. Chan, G.A. Freeman, J.H. Tidwell, K.R. Romines, L.T. Schaller, J.R. Cowan, S.S. Gonzales, G.S. Lowell, C.W. Andrews III, D.J. Reynolds, M. St. Clair, R.J. Hazen, R.G. Ferris, K.L. Creech, G.B. Roberts, S.A. Short, K. Weaver, G.W. Koszalka, and L.R. Boone. J. Med. Chem. **47**, 1175 (2004).
16. N.B. Patel, G.P Patel, and J.D. Joshi. Int. J. Polym Mater. **55**, 399 (2006).
17. M. Arivanandhan, C. Sanjeeviraja, K. Sankaranarayanan, S.K. Das, G.K. Samanta, and P.K. Datta. Opt. Mater. **28**, 324 (2006).
18. K. Mikami, K. Wakabayashi, and K. Aikawa. Org. Lett. **8**, 1517 (2006).
19. P.G.Parejo, M. Zayat, and D. Levy. J. Mater. Chem. **16**, 2165 (2005).
20. A. Mantas, S.E. Blanco, and F.H. Ferretti. Internet Electron. J. Mol. Des. **3**, 387 (2004).
21. N. Basaric, D. Mitchell, and P. Wan. Can. J. Chem. **85**, 561 (2007).
22. M.I. Sancho, M.C. Almandoz, S.E. Blanco, and F.H. Ferretti. J. Mol. Struct.: Theochem. **634**, 107 (2003).
23. M.C. Almandoz, M.I. Sancho, and S.E. Blanco. Phys. Chem. Indian. J. **1**, 32 (2006).
24. C. Lee, W. Yang, and R.G. Parr. Phys. Rev.: B, **37**, 785 (1988).
25. A. Becke. Phys. Rev.: A. **38**, 3098, (1988).
26. S. Miertus, E., Scrocco, and J. Tomasi. Chem. Phys. **65**, 239 (1982).
27. J.G. Grasselli and W.M. Ritchey (*Editors*). Atlas of spectral data and physical constants for organic compounds. Vol. III. CRS Press Inc. NY. 1975. pp. b2600–b2664.
28. M. Rosés, I. Canals, H. Allemann, K. Siigur, and E. Bosch. Anal. Chem. **68**, 4049 (1996).
29. M. Roses and E. Bosch. J. Chromatogr. A **982**, 1 (2002).
30. M.J.S. Dewar, E.G. Zoebisch, E.F. Healey, and J.J.P. Stewart. J. Am. Chem. Soc. **107**, 3902 (1985).
31. M.J. Frisch, G.W. Trucks, H.B. Schlegel, G.E. Scuseria, M.A. Robb, J.R. Cheeseman, J.A. Montgomery Jr., T. Vreven, K.N. Kudin, J.C. Burant, J.M. Millam, S.S. Iyengar, J. Tomasi, V. Barone, B. Mennucci, M. Cossi, G. Scalmani, N. Rega, G.A. Petersson, H. Nakatsuji, M. Hada, M. Ehara, K. Toyota,

© 2008 NRC Canada

R. Fukuda, J. Hasegawa, M. Ishida, T. Nakajima, I. Honda, O. Kitao, H. Nakai, M. Klene, X. Li, J.E. Knox, H.P. Hratchian, J.B. Cross, C. Adamo, J. Jaramillo, R. Gomperts, R.E. Stratmann, O. Yazyev, A.J. Austin, R. Cammi, C. Pomelli, J.W. Ochterski, P.Y. Ayala, K. Morokuma, G.A. Voth, P. Salvador, J.J. Dannenberg, V.G. Zakrzewski, S. Dapprich, A.D. Daniels, M.C. Strain, O. Farkas, D.K. Malick, A.D Rabuck, K. Raghavachari, J.B. Foresman, J.V. Ortiz, Q. Cui, A.G. Baboul, S. Clifford, J. Cioslowski, B.B. Stefanov, G. Liu, A. Liashenko, P. Piskorz, I. Komaromi, R.L. Martin, D.J. Fox, T. Keith, M.A. Al-Laham, C.Y. Peng, A. Nanayakkara, M.P. Challacombe, M.W. Gill, B. Johnson, W. Chen, M.W. Wong, C. Gonzalez, and J.A. Pople. Gaussian 03, Revision B.01 [computer program]. Gaussian, Inc., Pittsburgh, Pa. 2003.

32. J.R. Llano, J. Raber, and L.A. Eriksson. J. Photochem. Photobiol., A, **154**, 235 (2003).
33. J. Hardcastle and I. Jano. J. Chromatogr. B **717**, 39 (1998).
34. I. Jano, J.E. Hardcastle, K. Zhao, and R. Vermillion-Salsbury. J. Chromatogr. A, **762**, 63 (1997).
35. Origin (Scientific graphing & analysis software). Ver. 7.5. [computer program]. Available from www.OriginLab.com.
36. J.G. Kirkwood. J. Chem. Phys. **2**, 351 (1934).
37. K.J. Laidler. Chemical kinetics. 3rd Ed. Harper Collins, New York. 1987. pp. 203–204.
38. D.R. Lide. Handbook of chemistry and physics. 78th Ed. CRC Press, New York. 1997–1998. pp. 6–127; 6–173–175.
39. M.C. Grande, H.L. Bianchi, and C.M. Marschoff. J. Argent. Chem. Soc. **92**, 109 (2004).
40. C.G. Swain, M.S. Swain, A.L. Powell, and S. Alunni. J. Am. Chem. Soc. **105**, 502 (1983).
41. Y. Marcus. Chem. Soc. Rev. **22**, 409 (1993).
42. G.T. Castro, O.S. Giordano, and S.E. Blanco. J. Mol. Struct.: Theochem. **626**, 167 (2003).

© 2008 NRC Canada

REVIEW / SYNTHÈSE

Enzymatic processes for biodegradation of poly(hydroxyalkanoate)s crystals[1]

Keiji Numata, Hideki Abe, and Yoshiharu Doi

Abstract: Poly(hydroxyalkanoate)s (PHAs) have attracted much attention as environmentally compatible polymeric materials that can be produced from renewable carbon resources. Biodegradation of PHA materials occurs by the function of extracellular PHA depolymerase secreted from microorganisms. Thus, elucidation of the enzymatic degradation mechanism for PHA materials is important to design PHA materials with desirable properties and controlled biodegradability. The solid PHA polymer is a water-insoluble substrate but PHA depolymerases are soluble in water. Therefore, the enzymatic degradation of PHA materials is a heterogeneous reaction on the material's surface. Two distinct processes are involved during the degradation, namely, adsorption of the enzyme on the surface of PHA material and the subsequent hydrolysis of polymer chains. Atomic force microscopy (AFM) is a powerful tool that has been used for the quantitative analysis of PHA crystal degradation. AFM enables the characterization of the crystal surface nanostructure in a buffer solution. By using in-situ (real-time) AFM observations, we recently succeeded in observing the degradation processes of PHA crystals. Subsequently, we were also able to investigate the degradation rates of PHA crystals using the same technique. In this review, we have attempted to give an overview concerning the direct visualization of the adsorption, as well as the hydrolysis reactions of PHA depolymerases at the nanometer scale. In addition, we present other analytical techniques besides AFM as a complimentary approach to analyze the effect of enzyme adsorption on PHA crystals.

Key words: poly(hydroxyalkanoate) (PHA), enzymatic degradation, lamellar crystal, PHA depolymerase.

Résumé : Les poly(hydroxyalcanoates) (PHA) attirent beaucoup d'attention en raison de la compatibilité avec l'environnement de ces produits polymères qui peuvent être obtenus à partir de ressources renouvelables de carbone. La biodégradation de ces PHA se produit par la fonction de la dépolymérase extracellulaire des PHA qui est sécrétée par les microorganismes. L'élucidation du mécanisme de la dégradation enzymatique des PHA est donc importante pour le développement des matériaux de type PHA comportant des propriétés désirables ainsi qu'un degré contrôlé de biodégradabilité. Le polymère PHA solide est un substrat insoluble dans l'eau alors que la dépolymérase de PHA est soluble dans l'eau. La dégradation enzymatique des matériaux apparentés au PHA est donc une réaction hétérogène sur la surface des matériaux. Deux processus distincts sont impliqués au cours de la dégradation, soit l'adsorption de l'enzyme sur la surface du PHA et une hydrolyse subséquente des chaînes de polymère. On a utilisé la puissance de la technique de microscopie des forces atomiques (MFA) pour faire une analyse quantitative de la dégradation des cristaux de PHA. La MFA permet de caractériser la nanostructure de la surface cristalline en solution tamponnée. En faisant appel à des observations de MFA *in situ* et en temps réel, on a récemment été capable d'observer le processus de dégradation des cristaux de PHA. Faisant appel à la même technique, on a ensuite été en mesure d'étudier les vitesses de dégradation des cristaux de PHA. Dans cette revue, on essaye de donner une vue d'ensemble concernant la visualisation directe de l'adsorption ainsi que les réactions d'hydrolyse des dépolymérases de PHA à l'échelle du nanomètre. On présente de plus de nouvelles techniques analytiques qui complémentent la MFA pour analyser l'effet de l'adsorption de l'enzyme sur les cristaux de PHA.

Mots-clés : poly(hydroxyalcanoate), PHA, dégradation enzymatique, cristal lamellaire, dépolymérase de PHA.

[Traduit par la rédaction]

Received 30 October 2007. Accepted 31 December 2007. Published on the NRC Research Press Web site at canjchem.nrc.ca on 25 March 2008.

K. Numata,[2] H. Abe, and Y. Doi. Department of Innovative and Engineered Materials, Tokyo Institute of Technology, 4259 Nagatsuta, Midori-ku, Yokohama 226-8502, Japan and Polymer Chemistry Laboratory, RIKEN Institute, 2-1 Hirosawa, Wako-shi, Saitama 351-0198, Japan.

[1]This article is part of a Special Issue dedicated to Professor R. Marchessault.
[2]Corresponding author (e-mail: knumata@riken.jp).

 doi:10.1139/V08-004 © 2008 NRC Canada

Introduction

Poly(hydroxyalkanoate)s (PHAs) are synthesized by a variety of bacteria as an intracellular storage material of carbon and energy and their properties have been extensively studied (1–4). Poly[(*R*)-3-hydroxybutyrate] (P(3HB)) was first isolated from *Bacillus megaterium* in 1925 and later identified as a microbial reserve polyester. The identification of hydroxyalkanoate (HA) units, other than the 3HB unit, as constituents of microbial reserve polyesters proved to have a major impact on research and commercial interests in the microbial polyester, since the incorporation of different HA units into P(3HB) can vary its properties (5). Many bacteria have the ability to synthesize optically active homopolymers and copolymers of HA units. The term poly(hydroxyalkanoate) (PHA) is used to refer to the various polyesters derived from these HA units. Recently, Lenz and Marchessault (6) reviewed the history of PHA covering discoveries over a period of 80 years.

One of the unique properties of PHA materials is their biodegradability in various environments (Fig. 1). Since the 1990s, much effort has been redevoted to the investigations of PHA-degrading microorganisms (7–9). PHA is a high molecular weight solid polymer that cannot be transported through the cell wall. Therefore microorganisms, such as bacteria and fungi, excrete extracellular PHA-degrading enzymes (PHA depolymerases) that hydrolyze the solid PHA into the water-soluble monomer and oligomers. These low molecular weight degradation products are then transported into the cell and subsequently metabolized as carbon and energy sources (10).

Unlike the extracellular degradation of crystalline PHA by the PHA depolymerases, the intercellular degradation (also known as mobilization) of PHA granules involves a completely different set of enzymes. Intracellular PHA depolymerase has been studied since the 1960s to elucidate the mechanism of intracellular degradation of the amorphous PHA granules. Merrick and co-workers (11, 12) were the first to study the depolymerization of amorphous P(3HB) granules isolated from *B. megaterium* and they suggested that a thermolabile depolymerase and a thermostable activator are necessary for the depolymerization. In contrast to the intracellular depolymerase, the extracellular depolymerases have received more attention because of the important role they play in the degradation of crystalline PHA in the environment. A number of extracellular PHA depolymerases from various microorganisms have been secreted, and their structure and properties have been studied by many groups (13–24). The PHA-degrading microorganisms and enzymes were first isolated from *Pseudomonas* strains by Chowdhury in 1963 (13). Stinson and Merrick (14) also secreted the extracellular PHA depolymerase from *P. lemoignei* and reported the first biochemical data on PHA depolymerase. In addition, the PHA depolymerases with hydrolytic activity against poly[(*R*)-3-hydroxyvalerate], medium chain-length PHA, and amorphous P(3HB) were also purified and studied (15–17). Analyses of the structural genes of extracellular PHA depolymerases have shown that most of the isolated enzymes have multi-functional domain structures, i.e., a catalytic domain, a substrate-binding domain, and a linker domain, which connects the two domains (18–21). PHA

Fig. 1. Biodegradation process of PHA in a natural environment.

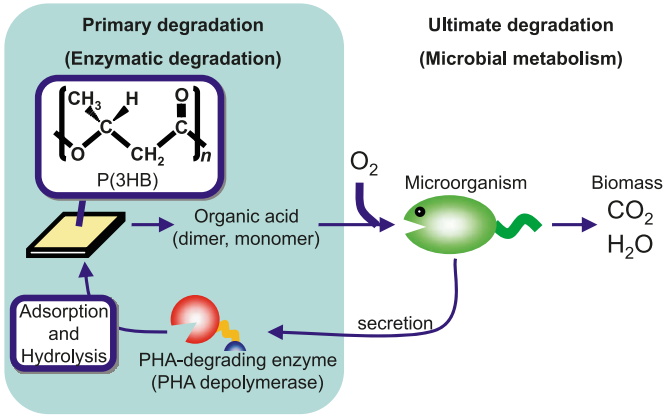

Fig. 2. Typical AFM images of (A) PHA single crystals and (B) melt-crystallized thin films and (C) typical scanning electron micrograph of spherulites in PHA films during enzymatic degradation by PHA depolymerase.

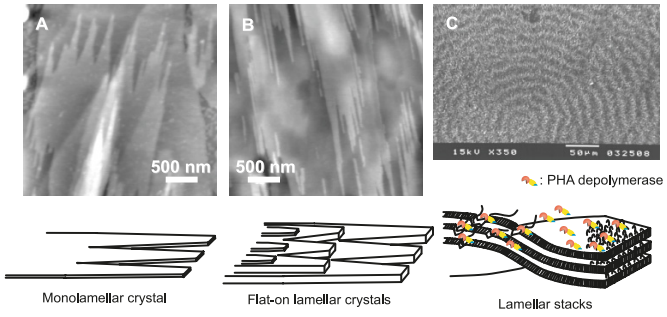

materials in the form of films, thin films, and single crystals have been widely used to elucidate the hydrolytic mechanism of PHA depolymerases (Fig. 2). Besides the hydrolytic mechanism of the catalytic domain, the substrate-binding domain is also of great importance in the degradation process. The effect of the substrate-binding domain on the hydrolytic activity has been studied since the 1980s by several groups (25–27). The hydrophobic substrate-binding domain is an essential component for the adsorption of PHA depolymerase to the hydrophobic surface of PHA.

The substrate specificity of PHA depolymerase was first investigated by using various hydrolases and polymer substrates (28). Substrate-binding specificity, in addition to a substrate-hydrolyzing one was also studied by Doi and coworkers (29). Though the rates of hydrolysis were different among three PHA depolymerases, all PHA depolymerases hydrolyzed the same kinds of films of PHAs that are structurally similar, i.e., P(3HB), poly(3-hydroxypropionate), poly(4-hydroxybutyrate), poly(ethylene succinate), and poly(ethylene adipate). These five polyesters are structurally similar with respect to the number of carbon and oxygen atoms, which is either 3 or 4, in the backbone between two carbonyl groups. In addition to that, the side chain is either a methyl carbon or a hydrogen atom. Therefore, PHA depolymerases show relatively narrow substrate specificity for the hydrolysis reaction of PHAs.

© 2008 NRC Canada

The effects of the chemical structure of second monomer units and copolymer compositions on the rate of enzymatic erosion have been examined through the enzymatic degradation of the solvent-cast films of various PHA copolymers in the presence of PHA depolymerase from *Ralstonia pickettii* T1 (formally *Alcaligenes faecalis* T1) (30). The rate of enzymatic erosion of the solvent-cast PHA films increased markedly with an increase in the fraction of second monomer units, up to 10–20 mol%, to reach a maximum value followed by a decrease in the erosion rate.

The structures and compositions of water-soluble products of PHA copolymers during the enzymatic degradation by PHA depolymerase from *R. pickettii* T1 have been characterized by using high performance liquid chromatography and nuclear magnetic resonance analyses (31, 32). The water-soluble products of random copolymers by the PHA depolymerase showed a mixture of monomers and several oligomers of 3HB and HA units. The water-soluble degradation products of random copolymers have some common chemical structures; the carboxyl-terminus of water-soluble products were always the monomeric units with a main-chain length of 3 or 4 carbon atoms, while the hydroxyl-terminus were always the monomeric units with a side-chain length ranging from 0 to 2 carbon atoms. Based on these results, it was proposed that the active site in the catalytic domain of PHA depolymerase recognizes a sequence of at least three monomeric units as substrate. The rate of enzymatic hydrolysis of an ester bond may be strongly dependent on the chemical structure of the sequential three monomeric units in a polyester chain. This recognition model has been supported by a recent study on the enzymatic hydrolysis of 3HB oligomers by the PHA depolymerase by Bachmann and Seebach (33, 34).

The rate of enzymatic erosion of PHA samples can be regulated not only by the chemical structure of the monomeric units but also by the crystallinity of the polymer. The rate of enzymatic hydrolysis for melt-crystallized P(3HB) films by the PHA depolymerase from *R. pickettii* T1 decreased with an increase in the crystallinity of the P(3HB) film, while the size of spherulites hardly affected the rate of hydrolysis (35). In addition, it was demonstrated that the rate of enzymatic degradation of P(3HB) chains in an amorphous state was approximately 20 times faster than that of P(3HB) chains in a crystalline state.

The thickness of crystalline lamellae for melt-crystallized films also varied with the crystallization conditions. The enzymatic erosion rate of melt-crystallized copolyester films decreased significantly with an increase in the crystallinity. It is suggested that the PHA depolymerase predominantly hydrolyzes polymer chains in the amorphous phase before eroding the crystalline phase (36). In addition, the enzymatic erosion rate of crystalline phases in polyester films was determined from both overall erosion rate and crystallinity. The enzymatic erosion rate of crystalline phases decreased with an increase in the lamellar thickness of the PHA films (30).

PHA depolymerases are water-soluble enzymes. However, the solid P(3HB) polymer is a water-insoluble substrate. Therefore, the enzymatic degradation of P(3HB) material by PHA depolymerase is a heterogeneous reaction, involving two steps, namely, adsorption and hydrolysis; the first step involves the adsorption of the enzyme on the surface of P(3HB) material by the binding domain of enzyme, and the second step involves the hydrolysis of polymer chains by the active site of the enzyme (37–39).

In this review, we have attempted to give an overview of direct atomic force microscopy (AFM) visualization of the adsorption as well as the hydrolysis reactions catalyzed by PHA depolymerases during the degradation process of PHA crystals at the nanometer scale. In addition, we also present other measurement techniques as a complimentary approach to AFM to analyze the enzyme adsorption effect on PHA crystals.

Enzymatic degradation of PHA lamellar crystals

Studies on the enzymatic degradation of films and monolamellar single crystals have shown that the degradation rate of PHA materials is strongly dependent on both the chemical structure of the monomeric unit and on the solid-state structure. With respect to the solid-state structure of PHA materials, the crystallinity and lamellar crystal sizes play a decisive role in the degradation process.

Single crystals, which clearly have a uniform and well-defined structure, are an excellent monolamellar system for studying the enzymatic degradation process. P(3HB) single crystals have been prepared from many kinds of solvents. The surface morphology and crystal structure have been investigated using microscopic analyses (40–47). Typically, P(3HB) forms lath-shaped crystals with dimensions of around 0.3–2 μm and 5–10 μm along the short and long axes, respectively. Based on the electron diffractogram of P(3HB) single crystals, the long axis of P(3HB) single crystals is the crystallographic *a* axis. The thickness of P(3HB) single crystals ranges from 4–10 nm depending on the molecular weight, solvent, and crystallization temperature.

PHA depolymerases from bacteria and fungi have been used to study the enzymatic degradation of P(3HB) single crystals to elucidate the degradation mechanism of the crystalline region for P(3HB). Marchessault and co-workers (40, 41, 44) were the first to perform the enzymatic degradation of P(3HB) single crystals by PHA depolymerases. Hocking et al. (40) carried out the enzymatic degradation of P(3HB) single crystals with PHA depolymerase, and the enzymatic degradation of P(3HB) single crystals was evaluated by turbidimetric and titrimetric assays, as well as by monitoring the changes in molecular weight of the polymer. Nobes et al. (41) used transmission electron microscopy (TEM) to show the conversion of PHA single crystals into needlelike morphologies after enzymatic degradation. Iwata and co-workers (42, 43, 45–47) investigated the enzymatic degradation of single crystals of P(3HB) and its copolymer single crystals by TEM and AFM. All these researchers reported that the single crystals were enzymatically hydrolyzed preferentially at the crystal edges (*ac* plane) and ends (*bc* plane) rather than at the chain-folding surfaces (*ab* plane) of the single crystals. This conclusion was arrived at because the lamellar thickness and molecular weight of P(3HB) crystals remained the same during the enzymatic degradations. The enzymatic reaction produced many narrow cracks and small crystal fragments along the crystal long axis corresponding

© 2008 NRC Canada

to the crystallographic *a* axis of P(3HB) single crystals, which was independent of both surface morphology of the single crystals and the types of PHA depolymerases. As for the single crystals of PHA copolymers, the enzymatic degradation mechanism was found to be the same as in the case of P(3HB) single crystals.

Similar morphological changes in lamellar crystals by enzymatic reaction have been confirmed for the flat-on lamellar crystals formed in melt-crystallized thin films of P(3HB) and its copolymers (Fig. 2B). Following the enzymatic degradation of thin film by a PHA depolymerase, a jagged texture along the crystal long axis could be observed at the ends of crystalline lamellae on the surface of the thin film (48–50).

A scanning electron microscopic observation (Fig. 2C) revealed that the surfaces of melt-crystallized PHA films after enzymatic degradation obviously blemished after the action of PHA depolymerase, whereby a ringed texture of spherulites was detected (30). Two different types of planes, i.e., smooth and rough planes, can be observed on the surface of PHA spherulites after enzymatic degradation. The smooth and rough planes exist alternately along the radial direction of spherulite. As a result, lamellar stacks on the surface of melt-crystallized films have also been hydrolyzed preferentially at the crystal edge by PHA depolymerase.

By using an AFM, we recently performed a quantitative characterization of the dimensions of the fibril-like crystals generated at the edge of lamellar crystals during enzymatic degradation (50, 51). A typical AFM image of the PHA single crystals after enzymatic degradation for 1 h is shown in Fig. 3. The thickness of the major part of the remaining crystals was almost identical with the crystals before degradation, as reported previously (41–43). The thickness at the root of fibril-like crystals (Fig. 3*a*) was almost identical to the thickness of the single crystals before degradation. The thickness of the intermediate region of fibril-like crystals (Fig. 3*b*) was slightly decreased compared to the thickness of the original single crystals. We found that the thickness at the tip of the fibril-like crystals (Fig. 3*c*) was apparently thinner than the thickness of the single crystals before degradation. It is of interest to note that the fibril-like crystals did not taper completely, whereby we did not observe any crystals with dimensions of either less than 1.9 nm thickness or less than 28 nm width for all the PHA samples after degradation at 37 °C for 1 h. These minimum values of thickness and width of fibril-like crystals may mean that the critical dimensions to maintain the crystalline lamellar structure of P(3HB) are by the intermolecular chain-packing.

Based on these results, we have proposed a mechanism for the enzymatic degradation mechanism of fibril-like crystals generated from PHA single crystals, as shown in Fig. 4. The PHA single crystals may consist of both ordered and disordered chain-packing regions that exist in a periodic manner due to the crystallization characteristic of P(3HB) molecules (52–54). PHA depolymerase adsorb homogeneously on the edges, ends, and chain-folding crystalline surfaces. The adsorbed enzymes predominantly hydrolyze the polymer molecules at the disordered chain-packing regions in single crystals from the edges and ends, as shown in Fig. 4B. As a result, the ordered chain-packing regions remain as fibril-like crystals. Figure 4E demonstrates that the

Fig. 3. (A) AFM amplitude images and cross-sections ((*a*), (*b*), and (*c*)) of fibril-like crystals generated from P(3HB) single crystals during enzymatic degradation by PHA depolymerase. White lines in (A) are the distance of the cross-section shown in (*a*), (*b*), and (*c*). (B) Each dimension of the fibril-like crystal is defined as in the schematic representation (ref. 51).

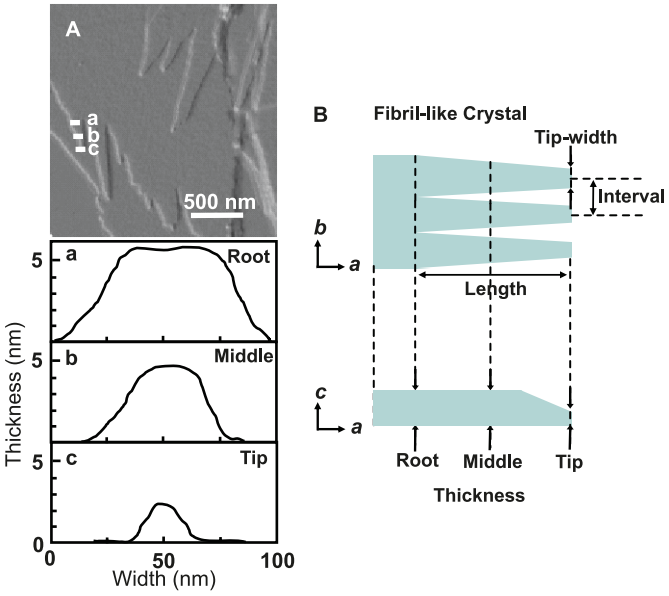

Fig. 4. Schematic model of the enzymatic degradation process of PHA lamellar crystals by the PHA depolymerase from *R. pickettii* T1 (ref. 51).

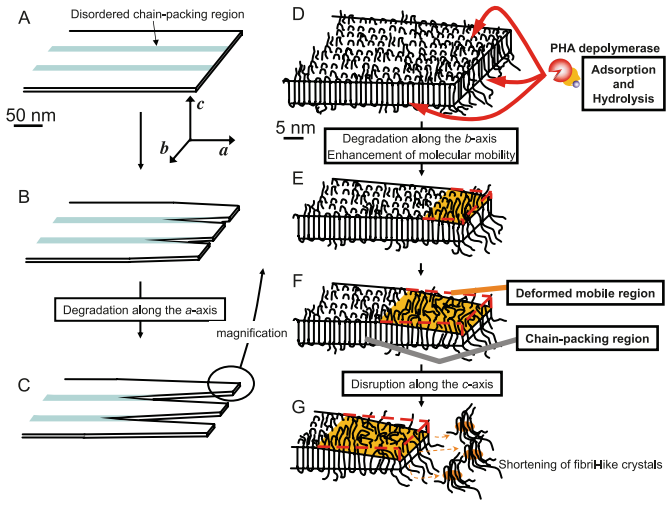

enzymes adsorbed on the fibril-like crystals also erode the ordered chain-packing region from the edge, which results in the tapering of the fibril-like crystals down to a minimum width of approximately 28 nm. In addition, the adsorption of enzyme on the fibril-like crystals may also enhance the molecular mobility in ordered chain-packing regions. Subsequently, the molecular packing structure in the ordered chain-packing region is gradually distorted starting from the chain-folding surface along the crystallographic *c* axis to reach a minimum value (around 1.9 nm), as shown in Fig. 4F. The tapping mode AFM was used for the dimen-

© 2008 NRC Canada

sional analysis of PHA single crystals. The AFM cantilever tip may penetrate the distorted crystalline region on the chain-folding surface that formed following the adsorption of PHA depolymerase. Therefore, the measured thickness may reflect the thickness of the remaining ordered chain-packing region beneath the distorted crystalline region. The remaining ordered chain-packing region will be progressively eroded from the edge by the catalytic action of the enzyme. At the same time, adsorption of the enzyme on the chain-folding region will produce surface distortion. Together, both these effects will reduce the crystal dimensions to the minimum values at which the lamellar structure at the tip of the fibril-like crystal will collapse as is shown in Fig. 4G at the tip of the glacier. As a result of these degradation processes, the tip of the fibril-like crystals will fragment into smaller pieces, which will eventually be hydrolyzed to water-soluble dimers and monomers by the PHA depolymerase.

Direct observations of the enzymatic degradation processes for PHA crystals

As mentioned above, the enzymatic degradation process of lamellar crystals has been characterized mainly by measuring changes in the crystal morphologies of dried samples before and after enzymatic degradation using various microscopic techniques. Although this method has enabled us to determine and understand the factors involved in the degradation process, the molecular mechanism of enzyme adsorption and hydrolysis reaction are still poorly understood. For this, a direct observation method is crucial. To obtain direct information on the enzymatic degradation process of PHA lamellar crystals, the real-time observations of enzymatic degradation have been applied by using AFM under aqueous condition.

Shakesheff and co-workers (55–57) were the first to study the real-time degradation process of aliphatic polyesters at the spherulitic level by using AFM. Kikkawa et al. (49, 58) succeeded in observing the real-time changes in lamellar morphologies during enzymatic degradation of P(3HB) copolymer thin film by AFM. AFM techniques have also been applied to biological studies, e.g., characterization of PHA granules (59–61).

The realtime AFM imaging of the lamellar crystals during enzymatic degradation have been investigated further by our group (50, 51). Figure 5 shows typical real-time AFM height images of P(3HB) single crystals during enzymatic degradation. Enzymatic erosions proceeded from the edges and ends of lamellar crystals, and the fibril-like crystals were obviously generated gradually by the action of PHA depolymerase. Figure 6 shows AFM amplitude images of five types of PHA single crystals after degradation for 1 h. Each of the images in Fig. 6 shows that the fibril-like crystals were formed along the long axis of all single crystals after enzymatic degradation. The results revealed the effect of both the molecular weight and the second-monomer composition on the morphology of fibril-like crystals.

As shown in Fig. 5, the grooves were formed along the crystallographic *a* axis, and the erosions of fibril-like crystals progressed from both the tip of crystals along the *a* axis and the edges along the *b* axis. The eroded distances at the tip and edge of fibril-like crystals and at the point of the grooves were determined from the real-time AFM images by measuring distances from the fixed spot in the images to the edges and ends of eroding crystals. Figure 7 shows the time-dependent changes in eroded distances at the root and tip of PHA fibril-like crystals. The eroded distances along the *a*

Fig. 5. (A) Real-time AFM height images of P(3HB) single crystals before and (B–D) during enzymatic degradation over time by the PHA depolymerase from *R. pickettii* T1 at 37 °C. The first frame (A) was taken in a phosphate buffer solution at 37 °C. The following frames (B–D) were obtained during enzymatic degradation for (B) 4 min, (C) 20 min, and (D) 43 min, respectively, (ref. 51).

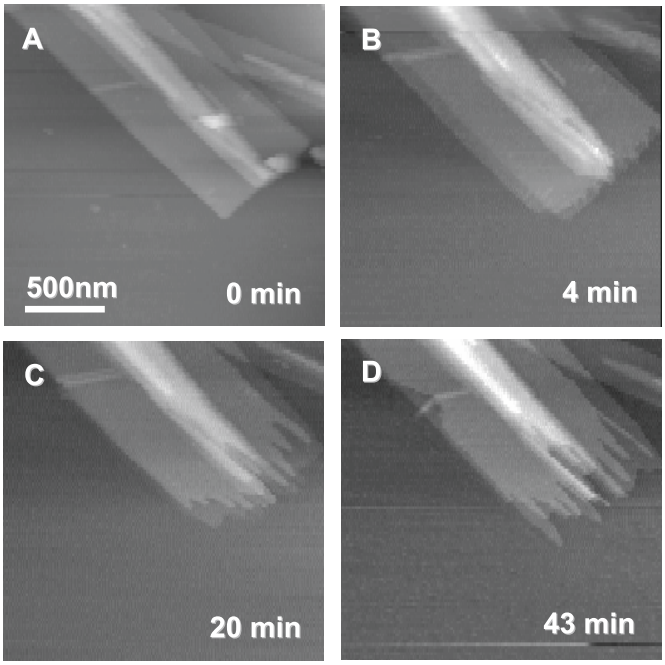

Fig. 6. AFM amplitude images of single crystals for (A) H-P(3HB) (M_n: 240 000), (B) M-P(3HB) (M_n: 55 000), (C) L-P(3HB) (M_n: 8500), (D) P(3HB-co-6 mol% 3HV), and (E) P(3HB-co-14 mol% 3HV) after enzymatic degradation by the PHA depolymerase from *R. pickettii* T1 for 1 h at 37 °C. These images were obtained at 25 °C in air. Each scale bar is 500 nm (ref. 51).

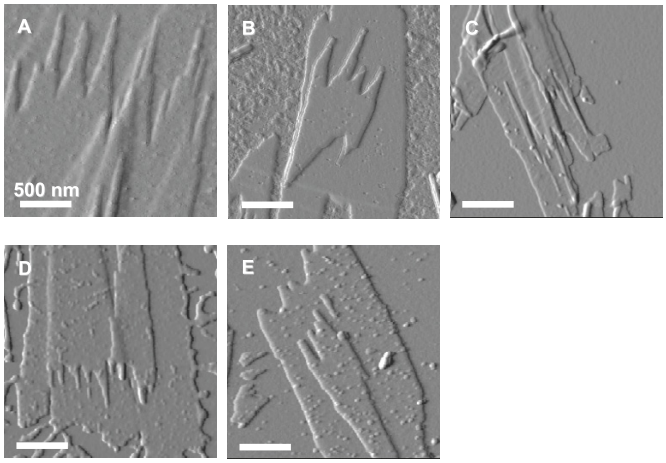

© 2008 NRC Canada

Fig. 7. (*a*) Time-dependent changes in eroded distance along the crystallographic *a* axis at the root and (*b*) and (*c*) along the *a* and *b* axes at the tip of the fibril-like crystal in L-P(3HB) (M_n: 8500) single crystals, respectively. The data in the graphs were calculated from the real-time AFM images during enzymatic degradation by PHA depolymerase *R. pickettii* T1 at 37 °C. The illustration represents the kind of eroded distance in a lamellar crystal as shown in the vertical axis of the graph (ref. 51).

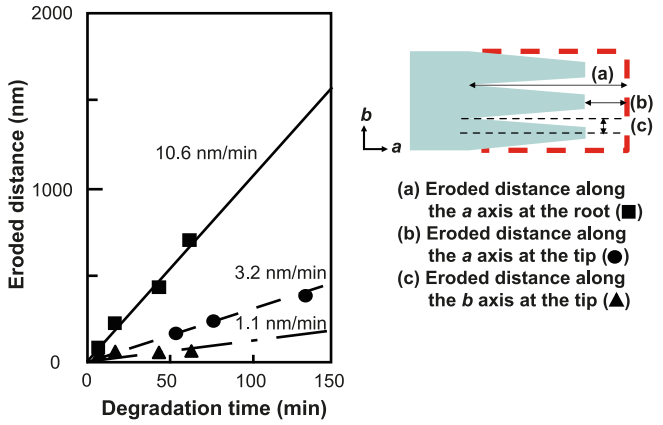

and *b* axes of fibril-like crystals changed linearly with time, and the erosion rates of single crystals were calculated from the slope of the line plot of the eroded distance against time.

Figure 7 shows time-dependent changes in eroded distance along (*a*) the crystallographic *a* axis at the root and (*b*) and (*c*) along the *a* and *b* axes at the tip of the fibril-like crystal in P(3HB) single crystals. Table 1 lists the erosion rates at the tip and edge of fibril-like crystals and the point of the grooves and overall erosion rates of PHA single crystals. For the single crystals of P(3HB) with a molecular weight of 8500, the grooves grew along the crystallographic *a* axis at a rate of 10.6 nm/min. The fibril-like crystals were eroded from the tip of the crystals along the *a* axis at a rate of 3.2 nm/min and from the edges along the *b* axis at a rate of 1.1 nm/min. For the single crystals of P(3HB) with different molecular weights, the erosion rate at the point of the grooves along the *a* axis increased with a decrease in the molecular weight of P(3HB), while those at the tip of fibril-like crystals along the *a* and *b* axes revealed relatively similar values, independent of molecular weight. As mentioned above, the formation of grooves is attributed to the degradation of disordered chain-packing regions in single crystals. As the molecular weight of P(3HB) is decreased, the number of the chain ends increases on the crystalline surface. With an increase in chain end groups, the disordered chain-packing region may become increasingly unstable. In addition, PHA depolymerase easily hydrolyzes the P(3HB) molecules from the chain ends exposed on the surface of single crystals. Therefore, the erosion rate at the grooves (disordered chain-packing region) increased with a decrease in the molecular weight of P(3HB). In contrast, the erosion rates along the *a* and *b* axes at the tip of fibril-like crystals was similar, independent of the molecular weight, for all P(3HB) samples. All the fibril-like crystals consist of highly ordered chain-packing regions. Moreover, the erosion rate along the *a* axis of fibril-like crystals reflected the degradation rate at the tip of the crystals. The packing structure of

Table 1. AFM measurement results on dimensions of the fibril-like crystals generated from PHA single crystals after enzymatic degradation of 1 h at 37 °C, and partial and overall erosion rates along the *a* axis and *b* axis at the tip and root of the fibril-like crystals during enzymatic degradation.

Sample	Length (nm)	Interval (nm)	Width (nm)	Thickness (nm)			Erosion rates (nm/min)[a]				Overall erosion rates (mg/(min·cm^2))
							Root		Tip		
			Tip	Root	Middle	Tip	*a* axis		*a* axis	*b* axis	
H-P(3HB)[b]	326±230	124±66	55±15	6.3±0.7	5.3±0.8	3.5±0.9	3.7		2.6	1.3	0.0007
M-P(3HB)	373±166	125±55	51±18	5.8±0.5	4.9±0.6	2.9±1.0	8.3		3.8	1.3	0.0015
L-P(3HB)	572±340	130±67	64±17	5.4±0.5	4.5±0.6	2.7±0.8	10.6		3.2	1.1	0.0018
P(3HB-co-6 mol% 3HV)	212±63	88±20	39±11	5.8±0.5	4.9±0.7	2.8±0.8	12.4		6.8	2.0	0.0026
P(3HB-co-14 mol% 3HV)	193±72	85±23	39±11	5.7±0.4	5.2±0.5	2.7±0.7	19.7		14.1	2.1	0.0065

[a]Erosion rates were determined from real-time AFM observations seen in Fig. 5.
[b]H-P(3HB), M-P(3HB), and L-P(3HB) mean high molecular weight (M_n: 240 000), middle molecular weight (M_n: 55 000), and low molecular weight P(3HB) (M_n: 8500), respectively.

© 2008 NRC Canada

such highly ordered crystalline regions may be slightly influenced by the number of chain-foldings and chain ends. As shown in Table 1, the morphology of fibril-like crystals formed after enzymatic degradation for 1 h varied with the molecular weight of P(3HB). The length of fibril-like crystals became shorter with an increase in molecular weight. The erosion rates at the grooves of P(3HB) single crystals increased with a decrease in molecular weight, while the erosion rates at the tip of fibril-like crystals were almost similar. Additionally, the erosion rates at the grooves of P(3HB) single crystals were faster than those at the tip of fibril-like crystals, and the length of fibril-like crystals increased with degradation time. Therefore, we concluded that the length of fibril-like crystals is governed by the ratio of the erosion rates at the grooves and at the tip of the crystals (50, 51).

For poly[(*R*)-3-hydroxybutyrate-*co*-(*R*)-3-hydroxyvalerate] (P(3HB-*co*-3HV)) samples, both the erosion rates at the point of the grooves and at the tip of fibril-like crystals along the *a* axis increased significantly with an increase in the 3HV composition, whereas the rates at the edges along the *b* axis were slightly increased by the introduction of 3HV units. However, the lengths and intervals of the fibril-like crystals for P(3HB-*co*-3HV) samples had relatively similar values, independent of the 3HV composition, although all of these values were apparently smaller than those of P(3HB) samples. As shown in Table 1, the difference of erosion rates at the grooves and at the tip of fibril-like crystals for P(3HB-*co*-3HV) was slightly smaller than that of P(3HB). Therefore, the lengths of fibril-like crystals for P(3HB-*co*-3HV) samples became shorter than those of P(3HB) samples. Thus, the morphologies and sizes of fibril-like crystals were established by the erosion rates along the *a* axis at the grooves and tip of the fibril-like crystals (50, 51).

The enzymatic erosion rate of PHA single crystals was also estimated by the volumetric analysis from real-time AFM height images (51). By considering the density of the P(3HB) crystalline region, the changes in the volume of single crystals during enzymatic degradation can be converted into changes in weight. Figure 8 shows the rate of erosion weight for PHA single crystals during enzymatic degradation. The results of overall erosion rates from AFM measurements were comparable to the enzymatic erosion rates of melt-crystallized film, reported by Abe et al. (30), implying that we succeeded in analyzing the overall erosion rate of PHA single crystals during enzymatic degradation by real-time AFM observation. For P(3HB) single crystals, the overall erosion rates increased with a decrease in the molecular weight of P(3HB), similar to the erosion rates at the grooves. The overall degradation rates of P(3HB-*co*-3HV) single crystals were much faster than those of P(3HB) single crystals. Thus, we succeeded in estimating the enzymatic erosion rate of crystalline region from the real-time AFM height images.

Direct observations of PHA depolymerase

Direct observations of PHA depolymerase molecules is important to elucidate the adsorption process of enzymes towards the polymer substrate. Visualization of the PHA

Fig. 8. Enzymatic erosion rates in weight of PHA single crystals by PHA depolymerase from *R. pickettii* T1 at 37 °C. The number averaged molecular weights of high, middle, and low molecular weight P(3HB) are 240 000, 55 000, and 8500, respectively. The values in this graph were calculated from the degraded volume measured from the real-time AFM images.

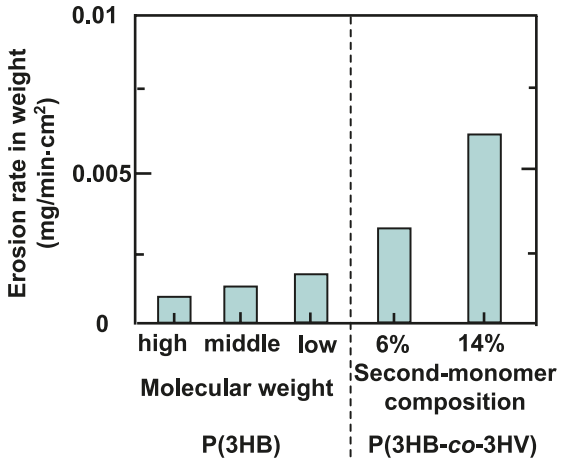

depolymerase adsorbed on the P(3HB) and its copolymers single crystals was performed using immuno-gold labeling techniques by Iwata et al. (42, 43, 45). They demonstrated by TEM that the PHA depolymerase molecules labeled by gold particles were distributed homogeneously on the surfaces of single crystals, and concluded that the enzyme molecules adsorb randomly on the crystal surface.

Kikkawa et al. (62) first observed the molecule of PHA depolymerase adsorbed on the poly(L-lactide) (PLLA) thin film directly by using AFM, and found that the PHA depolymerase appeared elliptic in shape when bound on the surface of the film. They reported that the average dimensions of PHA depolymerase from *R. pickettii* T1 were 2.8 ± 0.5 nm in height and 23 ± 3 nm in width on PLLA thin film in water.

For the purpose of visualizing PHA depolymerase during enzymatic reaction with PHA lamellar crystals, we have characterized the adsorption behaviors of PHA depolymerase from *R. pickettii* T1 on P(3HB) single crystals and silicon wafers by AFM observations in air and in a buffer solution (63, 64). PHA depolymerase adsorbed on the silicon wafer was characterized to determine the single molecular dimension, and it was found that the PHA depolymerase had dimensions of 2.2 ± 0.7 nm high and 16 ± 5 nm wide. The observation of PHA depolymerase adsorbed on P(3HB) single crystals indicated that the enzyme on the crystalline surface in air was 1.2 ± 0.5 nm high and 28 ± 7 nm wide, while dimensions of 2.1 ± 0.6 nm high and 16 ± 7 nm wide were detected in the buffer solution. A comparison of the dimensions of PHA depolymerase in air and in water revealed that the enzyme was squashed in air but not in water, suggesting that the AFM observation in the buffer solution could reveal the native morphology of PHA depolymerase.

We also carried out the real-time AFM observations of PHA depolymerase adsorbed onto P(3HB) single crystals in the enzyme solution (64). Initially, the surface of P(3HB) single crystals in the buffer solution was characterized by

© 2008 NRC Canada

Fig. 9. Real-time AFM height images of the typical enzymatic reaction process onto P(3HB) single crystals by the PHA depolymerase from *R. pickettii* T1. The concentration of the enzyme was 0.5 μg/mL. These images were obtained in a phosphate buffer solution (pH 7.5) at 37 °C (ref. 64).

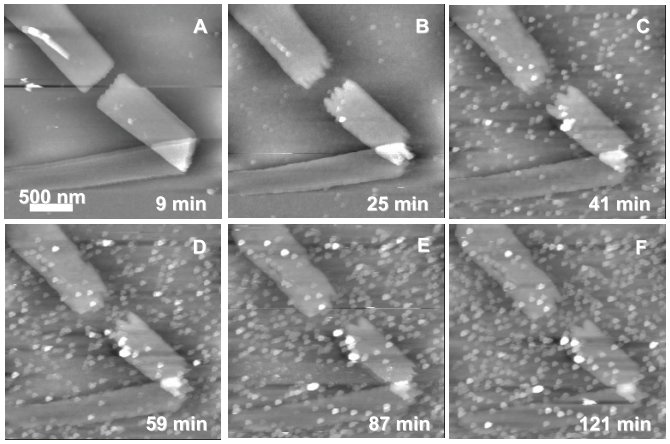

AFM in the absence of PHA depolymerase. As shown in Fig. 9A, small particles were not detected on the surface of P(3HB) single crystals in the buffer solution. Real-time AFM observations of PHA depolymerase adsorbed onto P(3HB) single crystals were recorder after adding concentrated enzyme solution into the buffer solution. Figure 9B–9F shows the AFM height images of PHA depolymerase adsorbed onto P(3HB) crystals. As shown in Fig. 9B–9F, PHA depolymerase adsorbed randomly onto the surface of P(3HB) single crystals without any preference towards crystalline edges, ends, or surfaces.

Adsorption specificity of PHA depolymerase substrate-binding domain

Extracellular PHA depolymerases are typically comprised of three functional domains. It has been suggested that the C-terminal domain acts as a substrate-binding domain for the water-insoluble P(3HB) substrate, since the PHA depolymerase lacking the C-terminal domain lost the hydrolyzing activity towards the water-insoluble P(3HB), while it retained the activity towards water-soluble 3HB oligomers. This is because the binding of PHA depolymerase to substrate is necessary for the degradation of water-insoluble polymer substrate (65).

Kasuya et al. (29) investigated the binding-specificity of three types of PHA depolymerases and the fusion proteins of substrate-binding domains of PHA depolymerases with glutathione *S*-transferase for various polymeric substrates. Based on the adsorption study using PHA depolymerases and fusion proteins, PHA depolymerases were found to have the ability to bind on the surfaces of both enzymatically degradable and non-degradable polyesters, while they hardly bind to the polysaccharides of Avicel or chitin. These results suggest that several specific interactions that facilitate molecular recognition exist between the substrate-binding domain and the surface of polyesters.

Yamashita et al. (66) studied the adsorption of PHA depolymerase from *R. pickettii* T1 onto thin films of PLLA, poly(3-hydroxyoctanoate) (PHO), polystyrene (PS), and polyethylene (PE), using quartz crystal microbalance (QCM) techniques. They reported that the rate of adsorption of PHA depolymerase decreases in the following order: PLLA >> PHO > PS >> PE. It has been suggested that the binding domain has an affinity not only for polyesters but also for PS, indicating that hydrophobic interactions partially contribute to the affinity of the binding domain.

The binding specificity of PHA depolymerase to PHA single crystals has also been evaluated by using immuno-gold labeling techniques (42, 43, 45). In both cases of P(3HB) homopolymer and copolymer single crystals, the adsorption of PHA depolymerase showed a homogeneous distribution on the surfaces of single crystals, suggesting that the substrate-binding domain contributes to the random adsorption of enzyme on P(3HB) crystals. However, the concentrations of adsorbed enzyme on the surface of copolymer single crystals are slightly lower than that of P(3HB) homopolymer single crystals. PHA depolymerase molecules cannot bind tightly to the irregular surface of copolymer crystals by hydrophobic adsorption since the copolymer chains with second monomer units have loose-loop foldings.

To further clarify the binding specificity of the substrate-binding domain of PHA depolymerase, we quantitatively measured the amount of the enzyme molecules adsorbed on single crystals of various polymers by using a catalytically inactive mutant enzyme and AFM (67). The number of enzyme molecules adsorbed on each single crystal was counted from AFM images, and it was found that the quantity of adsorbed enzyme molecules increased in the following order: PE (56 ± 6 enzymes/μm^2) < poly[(*R*)-3-hydroxybutyrate-co-8 mol% (*R*)-3-hydroxyhexanate] (84 ± 13 enzymes/μm^2) << P(3HB) (171 ± 23 enzymes/μm^2) ≈ P(3HB-co-6 mol% 3HV) (183 ± 35 enzymes/μm^2) < poly(D-lactide) (PDLA) (227 ± 26 enzymes/μm^2) ≈ PLLA (253 ± 23 enzymes/μm^2). The mutant enzyme adsorbs onto PE single crystals, but the number of the adsorbed enzymes is significantly lower than the number of enzymes capable of adsorbing onto the P(3HB) single crystals. If the chemical structure and the surface property of PE single crystals are taken into consideration, the mutant enzyme is likely to adsorb onto the surface of PE crystals through non-specific hydrophobic interaction. Equally, this result suggests that the PHA depolymerase binds to polymer crystals, not only by hydrophobic interaction but also by specific interaction between the ester bonds of polyesters and the binding domain. Moreover, the numbers of enzyme molecules adsorbed onto the PLLA and PDLA single crystals were apparently higher compared with those adsorbed onto the P(3HB) and P(3HB-*co*-6 mol% 3HV) single crystals. Based on the hydrophobic characteristics and density of ester bonds at the surface of polyester crystals, the number of adsorbed enzymes may be dependent on the amount of ester bonds rather than the hydrophobicity of crystals.

Adsorption and desorption of PHA depolymerase on crystal surfaces

It has been reported that the rate of enzymatic erosion of P(3HB) by PHA depolymerase is strongly dependent on the concentration of the enzyme (37, 38, 68). The rate of enzymatic hydrolysis increased to a maximum value with the

© 2008 NRC Canada

concentration of PHA depolymerase, followed by a gradual decrease. Accordingly, the kinetic behavior of P(3HB) hydrolysis has been accounted for in terms of a surface-enzymatic reaction.The hydrolysis of P(3HB) chains takes place through the surface reaction between adsorbed enzymes and free adsorption points on the surface. In this kinetic deal, the ratio of the surface-occupation of enzyme molecules is given by the Langmuir adsorption. Based on the kinetic analyses of the enzyme adsorption on the surface of P(3HB), it has been confirmed that the adsorption isotherms of PHA depolymerase are expressed by the Langmuir adsorption equation (69). It has been concluded that at low concentrations of PHA depolymerase the majority of catalytic domains of adsorbed enzyme are able to hydrolyze P(3HB) chains on the surface, while at high concentrations of enzyme the majority of catalytic domains are not accessible to P(3HB) chains on the surface due to a dense coverage of the substrate-binding domains on the surface of P(3HB).

Recently, Yamashita et al. (70) determined the amount of enzyme molecules adsorbed on P(3HB) films using catalytically inactive mutant enzymes by QCM (70). They found that the adsorption isotherm of PHA depolymerase with P(3HB) films could not be satisfied by any set of parameters for the Langmuir equation. Furthermore, they determined the changes in rate of enzymatic degradation of P(3HB) film by the replacement of the wild-type enzyme solution with a pure buffer solution or the mutant enzyme solution. When the wild-type enzyme solution was replaced with the mutant enzyme solution in the middle of the reaction, the degradation rate was remarkably reduced. On the other hand, replacement with a pure buffer solution hardly affected the degradation rate (Fig. 10A). From these results, they suggested that each molecule of PHA depolymerase adsorbs irreversibly on the P(3HB) film surface, while it is easily substituted by the attack of the enzyme molecules in the solution. As a result, it seems that the apparent adsorption isotherms of PHA depolymerase obeys the Langmuir isotherm.

We confirmed the irreversible adsorption manner of PHA depolymerase on the P(3HB) crystals using the technique to visualize enzyme molecules by AFM (64). As shown in Fig. 9 of the continuous AFM images of the reaction process, the enzyme molecule of PHA depolymerase from *R. pickettii* T1 adsorbed on the P(3HB) single crystals remained at the same position during the observation for 121 min. This result suggests that the enzyme molecule of *R. pickettii* T1 interacts strongly with the P(3HB) molecules, and that the adsorption of the enzyme takes place irreversibly.

Brucato and Wong (22) purified and characterized the PHA depolymerase from a strain of *Penicillium funiculosum*. The enzyme has a molecular mass of 37 kDa, and the value is apparently smaller than typical PHA depolymerases from other strains (around 50 kDa). Kasuya and co-workers (23) reported that the PHA depolymerase from *P. funiculosum* degrades P(3HB) and a trimer of 3HB, though the degradation of P(3HB) is less efficient by two orders of magnitude in comparison with the enzyme from *R. pickettii* T1. They speculated that the enzyme from *P. funiculosum* lacks a substrate-binding domain. Although a large number of PHA depolymerases have been discovered, the three-dimensional structure has been obtained only for the enzyme from *P. funiculosum* by Hisano et al. (24). The enzyme is shown

Fig. 10. Time courses of frequency changes (F) observed during enzymatic degradation of P(3HB) thin films by two types of PHA depolymerases from (A) *R. pickettii* T1 and (B) *P. funiculosum* at 37 °C. The concentrations of the enzyme were 1.0 and 5.0 μg/mL, and the pH of the buffer were 7.5 and 6.0, respectively. As indicated by arrow 1, the degradation reaction was started by the injection of enzyme solution at time 0 h. After 2 h of reaction, the enzyme solution was replaced with a pure buffer solution (at the point denoted by arrow 2). The solid line is the frequency changes for the enzymatic degradation without replacement of enzyme solution with a pure buffer (control) (ref. 64).

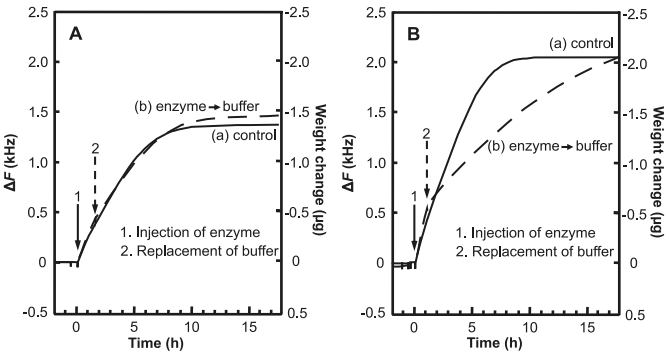

Fig. 11. A molecular surface representation of the PHA depolymerase from *P. funiculosum* centering on the mouth of the crevice. Positions of solvent-exposed hydrophobic residues (purple), as well as polar (green), and catalytic triad (cyan) residues, are indicated. A model of the 3HB trimer bound in the crevice is shown as a yellow stick model (ref. 24).

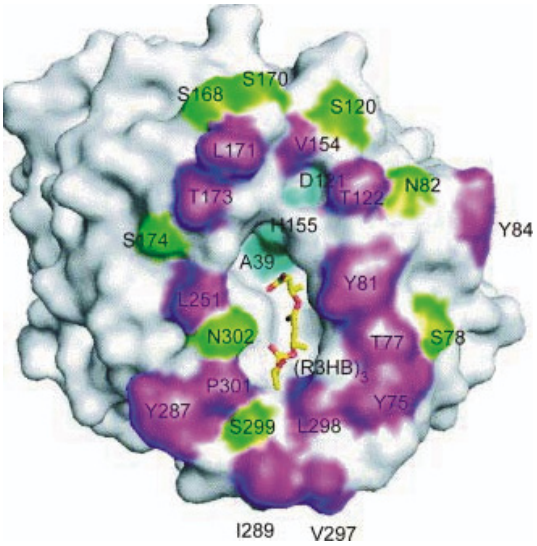

to be a globular molecule with approximate dimensions of 5.2 nm × 4.8 nm × 4.1 nm and with a single domain (Fig. 11). In addition, it was suggested that 13 hydrophobic residues around the active site induce the enzyme to bind onto polymer chains without a substrate-binding domain. Furthermore, a cDNA encoding PHA depolymerase from *P. funiculosum* was cloned, and the homology analysis showed that the enzyme lacks linker and substrate-binding domains (71).

© 2008 NRC Canada

To compare the adsorption mechanisms between the two types of PHA depolymerases with different domain structures, we carried out the real-time AFM observations using P(3HB) single crystals and PHA depolymerase from *P. funiculosum* (64). It has been reported that the catalytic domain of the enzyme from *P. funiculosum* resembles that of *R. pickettii* T1 in the α/β hydrolase folds despite the difference in the position of the lipase box in the catalytic domain of each enzyme (24). Thus, compared with the difference in the binding domain between the two types of PHA depolymerases, the difference in the catalytic domain is considerd to have little influence on the degradation process observed by AFM in this study. Figure 12 shows the typical real-time AFM height images of the enzymatic degradation process of P(3HB) single crystals in a phosphate buffer solution containing the PHA depolymerase from *P. funiculosum*. In Fig. 12B, the white arrow indicates the location where the enzyme degraded initially, and subsequently a hole was generated at the same location. As the reaction progressed, the P(3HB) single crystal was split at the hole along the crystallographic *a* axis, in a manner similar to the case of PHA depolymerase from *R. pickettii* T1. However, no enzyme molecule was observed by AFM around the hole and cleft created by the enzyme. Although many repeated observations were carried out by real-time AFM, we rarely succeeded in visualizing the enzyme molecules from *P. funiculosum* (Fig. 12D–12F). In contrast to the PHA depolymerase from *R. pickettii* T1, the enzyme molecule at (*a*) in Fig. 12E disappeared from the surface of single crystal, even though the crystal that the enzyme adsorbed on was hardly degraded. Here, it should be noted that the enzyme molecules attached on the surface of P(3HB) single crystals were detected in the AFM images obtained in air after enzymatic treatment with PHA depolymerases from *P. funiculosum*. The number of attached enzyme molecules of *P. funiculosum* was relatively the same as that of *R. pickettii* T1. This result indicates that the PHA depolymerase from *P. funiculosum* has the ability to adsorb onto the surface of P(3HB) single crystals.

The adsorption of PHA depolymerase from *P. funiculosum* was also confirmed by QCM measurement (64). Although the replacement of enzyme solution of *P. funiculosum* with a buffer solution reduced the degradation rate of P(3HB) film, the enzymatic erosion of P(3HB) film could be detected continuously (Fig. 10B). This result suggests that the PHA depolymerase from *P. funiculosum* adsorbs onto the surface of P(3HB) thin films to degrade P(3HB) molecules, but the adsorbed enzyme is easily released from the P(3HB) film in aqueous conditions. The occurrence of reversible adsorption and desorption of enzyme molecule makes it difficult to capture the adsorbed enzyme molecules on the P(3HB) single crystals in the real-time AFM images.

Such difference in the binding affinity of two enzymes may be caused by the difference in the domain structure, and is reflected in the adsorption manner of enzymes. The PHA depolymerase from *R. pickettii* T1 is anchored to the substrate surface via the substrate-binding domain by strong affinity towards P(3HB) molecules. The absence of substrate-binding domain decreases the binding affinity of the enzyme from *P. funiculosum* compared to the enzyme from *R. pickettii* T1, resulting in the easy release of the adsorbed enzyme molecule, which is easily released from the substrate surface. Thus, the substrate-binding domain of PHA depolymerase facilitates the interactions of the catalytic domain with the polyester chains.

Fig. 12. Continuous AFM height images of the typical enzymatic reaction process onto P(3HB) single crystals by the PHA depolymerase from *P. funiculosum*. The frames (A) and (D) were recorded before the enzymatic reaction, and the following images were obtained during enzymatic reaction ((B), (C) (E), and (F)). The concentration of the enzyme was 0.5 μg/mL. These images were obtained in a phosphate buffer solution (pH 6.0) at 37 °C. The white arrow and circles denote the hole generated by the enzymatic degradation and enzyme molecules, respectively, (ref. 64).

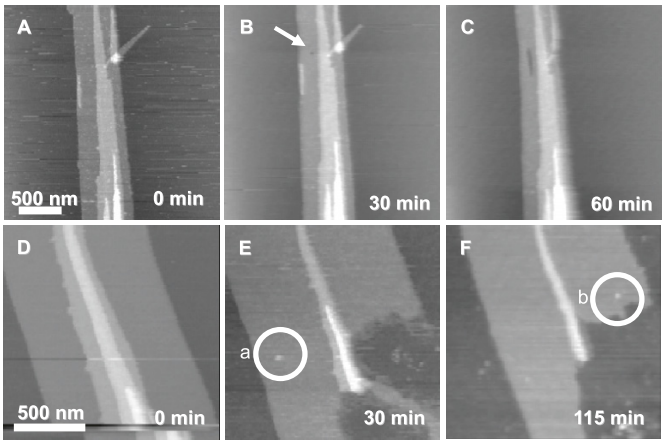

Other functions of the substrate-binding domain of PHA depolymerase

As discussed earlier, the substrate-binding domain is primarily responsible for the adsorption of the PHA depolymerase to the surface of water-insoluble polyester materials. However, in recent years, it has been proposed that the substrate-binding domain has another function in addition to its adsorption role (62, 72). Murase et al. (72) have studied the morphological change of P(3HB) single crystals during the adsorption of the catalytically inactive mutant PHA depolymerase. They showed that the adsorption of the mutant PHA depolymerase contributed to the formation of cracks along the long axis of the P(3HB) single crystals and suggested that the adsorption of PHA depolymerase with the substrate-binding domain disturbs the molecular chain packing in P(3HB) single crystals. Also, Kikkawa et al. (62) observed two types of PHA depolymerases adsorbed on amorphous PLLA films, and demonstrated the formation of small hollows on the PLLA film after removal of the adsorbed enzyme.

We also investigated the morphological changes at the surface of P(3HB) single crystals by the adsorption of PHA depolymerase using real-time AFM observation (63). Figure 13 shows the continuous AFM images of the surface of a P(3HB) single crystal before and after the removal of PHA depolymerase. A PHA depolymerase molecule was observed on a P(3HB) crystal before the removal of the enzyme, subsequently a concavity as wide as the enzyme molecule

© 2008 NRC Canada

Fig. 13. Real-time AFM height images of P(3HB) single crystal degraded by PHA depolymerase for 30 min (A) before and (B) after washing with ethanol solution and then recorded in Milli-Q at 20 °C. (C) and (D) Line profile data of the white lines in (A) and (B), respectively, (ref. 63).

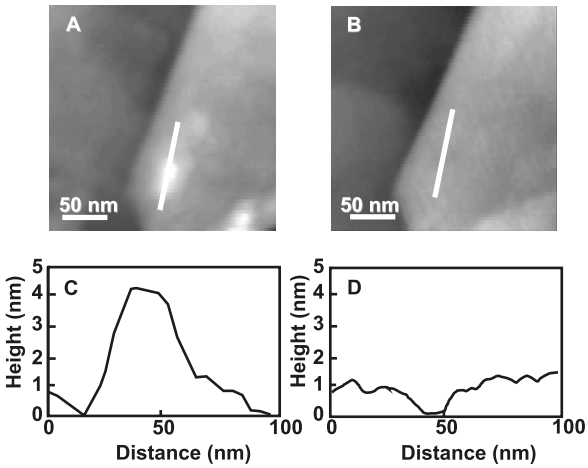

(25 nm in width) was generated after removing the enzyme. To determine the changes in the molecular properties of the crystalline surface due to the adsorption of PHA depolymerase, AFM height and phase images were recorded for the P(3HB) single crystal after removing the enzyme. The concaved area revealed dark contrast in the AFM phase image, indicating that the surface of the concaved area is softer than the surface of the chain-folded crystal. This result suggests that the adsorption of PHA depolymerase causes changes in the molecular state at the surface of P(3HB) single crystals.

To elucidate any additional functions for the substrate-binding domain, we further investigated the changes in surface properties of polymer single crystals after the adsorption of PHA depolymerase by using frictional force microscopy (FFM) (67). Figure 14 shows FFM images and electron diffraction patterns of the P(3HB) single crystals before and after enzymatic treatment with a catalytically inactive mutant enzyme for 1 h. The electron diffraction data revealed that the enzymatic adsorption has little influence on the crystal structure and the molecular packing state within the crystal. However, it was found that the frictional force values after the enzymatic treatment apparently decreased in comparison with those before the enzymatic treatment. The decrease in frictional forces for P(3HB) and its copolymers deduced that the adhesion of PHA depolymerase onto the chain-folding surface containing ester bonds causes partial disordering of the molecular folding at the surface of single crystals. Thus, the adsorption effect will induce the initial step of the enzymatic degradation.

Recently, the binding interaction of PHA depolymerase from *R. pickettii* T1 on P(3HB) and PLLA thin films were investigated by AFM (73). The adhesive forces between polyester substrates and the substrate-binding domain of PHA depolymerase by using AFM cantilever tips immobilized with the substrate-binding domain were measured, and the adhesive force of a single molecule with the substrate-binding domain was estimated to be about 100 pN for both P(3HB) and PLLA. Furthermore, it was suggested that the

Fig. 14. FFM images of single crystals for P(3HB) (A) before and (B) after the enzymatic treatment by mutant PHA depolymerase. These images were obtained at 25 °C under reduced pressure conditions (10^{-5}–10^{-6} torr). Each inset shows the typical electron diffraction pattern of the single crystal after the enzymatic treatment (ref. 67) (1 torr = 133 322 4 Pa).

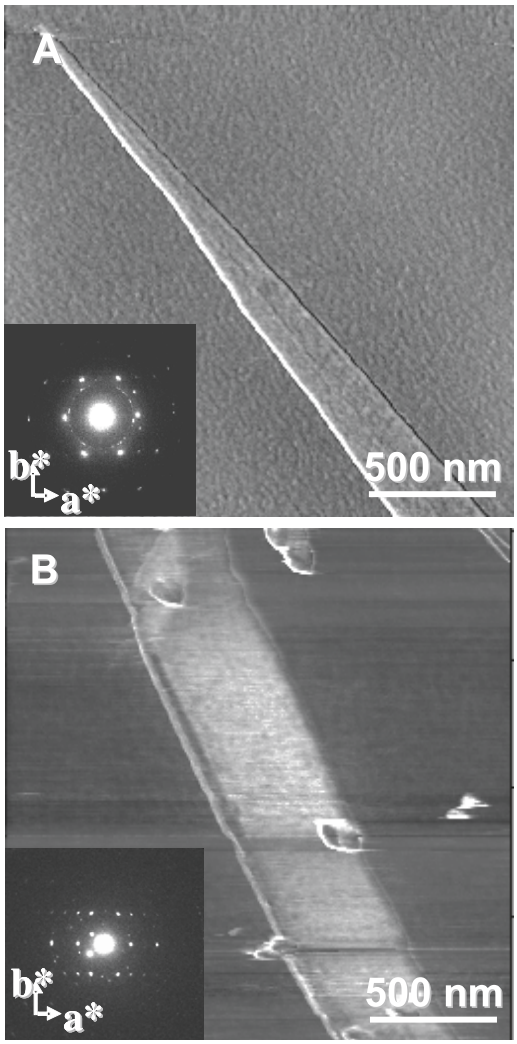

PHA depolymerase interacts specifically with polyester surfaces by electrostatic interaction and hydrogen bonding, in addition to hydrophobic interaction, and that several amino acid residues in the substrate-binding domain take part in the adsorption reaction. In summary, the substrate-binding domain of PHA depolymerase interacts with polyester molecules via various affinities by several amino acid residues, and hence the chain-folding surface of PHA lamellar crystals is disordered and deformed by the adsorption of enzyme molecule.

Conclusion and future perspectives

In this review, the studies on the enzymatic processes for biodegradation of PHA lamellar crystals by microscopic and quantitative analyses were summarized. The information integrated in this review concerning the reaction processes between PHA depolymerases and PHA crystals will enable the

© 2008 NRC Canada

design and synthesis of biodegradable polymers with controlled degradation rates in the natural environment. For the practical use of PHAs as biodegradable materials, their degradation rate should be controlled by chemical structure and solid-state properties. Also, the degradation process of PHA crystals is the rate-determining step, and hence it is important to carry out further investigation on the enzymatic processes and mechanisms for biodegradation of PHA lamellar crystals.

Based on the results obtained to date, it can be proposed that the degradation process of PHA lamellar crystals can be divided into five steps as follows: (*i*) PHA depolymerase adsorbs onto and then deforms the chain-folding surface of PHA crystals, (*ii*) the enzyme attacks the chain-end of PHA molecules composing PHA lamellar crystals, (*iii*) lath-shaped PHA lamellar crystals are degraded into fibril-like crystals, (*iv*) the fibril-like crystals are collapsed into small lamellae and molecular aggregations, and (*v*) the PHA molecules are hydrolyzed into its oligomer, dimer, and monomer. This review has focused especially on steps (*i*) and (*iii*). Step (*ii*), which is the starting reaction of the enzymatic process, is not obvious at the nanometer scale until now because it is not possible to follow the starting reaction by AFM and the other equipment. In the near future, it is essential to investigate step (*ii*) – the initial step of the hydrolysis of PHA lamellar crystals, namely the hydrolysis of the chain end of PHA molecules at the surface of the PHA crystals to control the starting reaction of biodegradation of PHA materials. This is because the practical use of PHAs in various areas would materialize if we can control not only the degradation rate but also the start of the degradation reaction of PHA materials.

Acknowledgments

The authors wish to thank their co-workers Professor T. Iwata, Dr. K. Yamashita, Professor K. Kasuya, Dr. T. Tsuge, Dr. M. Fujita, Dr. Y. Kikkawa, Mr. T. Hirota, and Mr. S. Sato. We deeply appreciate the assistance provided by Dr. K. Sudesh for correcting the English of our manuscript. This work has been supported by SORST (Solution Oriented Research for Science and Technology) from Japan Science and Technology Agency (JST) and the grants of Ecomolecular Science Research from RIKEN Institute, and was completed while KN was a Research Fellow of the Japan Society for the Promotion of Science (JSPS).

References

1. Y. Doi. Microbial polyesters. VCH publishers, New York. 1990.
2. A.J. Anderson and E.A. Dawes. Microbiol. Rev. **54**, 450 (1990).
3. K. Sudesh, H. Abe, and Y. Doi. Prog. Polym. Sci. **25**, 1503 (2000).
4. Y. Doi and A. Steinbüchel (*Editors*). Biopolymers. Polyesters I and II. Vol. 3.Wiley-VCH, Weinheim, Germany. 2001.
5. L.L. Wallen and W.K. Rohwedder. Environ. Sci. Technol. **8**, 576 (1974).
6. R.W. Lenz and R.H. Marchessault. Biomacromolecules, **6**, 1 (2005).
7. D. Jendrossek, A. Schirmer, and H.G. Schlegel. Appl. Microbiol. Biotechnol. **46**, 451 (1996).
8. D. Jendrossek. Polym. Degrad. Stab. **59**, 317 (1998).
9. D. Jendrossek and R. Handrick. Annu. Rev. Microbiol. **56**, 403 (2002).
10. D. Jendrossek. Appl. Microbiol. Biotechnol. **74**, 1186 (2007).
11. J.M. Merrick, D.G. Lundgren, and R.M. Pfister. J. Bacteriol. **89**, 234 (1965).
12. J.M. Merrick. J. Bacteriol. **90**, 965 (1965).
13. A.A. Chowdhury. Arch. Microbiol. **47**, 167 (1963).
14. M.W. Stinson and J.M. Merrick. J. Bacteriol. **119**, 152 (1974).
15. B. Müller and D. Jendrossek. Appl. Microbiol. Biotechnol. **38**, 487 (1993).
16. A. Schirmer, D. Jendrossek, and H.G. Schlegel. Appl. Environ. Microbiol. **59**, 1220 (1993).
17. R. Handrick, S. Reinhardt, M.L. Focarete, M. Scandola, G. Adamus, M. Kowalczuk, and D. Jendrossek. J. Biol. Chem. **276**, 36215 (2001).
18. T. Tanio, T. Fukui, Y. Shirakura, T. Saito, K. Tomita, T. Kaiho, and S. Masamune. Eur. J. Biochem. **124**, 71 (1982).
19. Y. Shirakura, T. Fukui, T. Saito, Y. Okamoto, T. Narikawa, K. Koide, K. Tomita, T. Takemasa, and S. Masamune. Biochem. Biophys. Acta, **880**, 46 (1986).
20. K. Mukai, K. Yamada, and Y. Doi. Polym. Degrad. Stab. **41**, 85 (1993).
21. M. Uefuji, K. Kasuya, and Y. Doi. Polym. Degrad. Stab. **58**, 275 (1997).
22. C.L. Brucato and S.S. Wong. Arch. Biochem. Biophys. **290**, 497 (1991).
23. S. Miyazaki, K. Takahashi, M. Shiraki, T. Saito, Y. Tezuka, and K. Kasuya. J. Polym. Envirom. **8**, 175 (2000).
24. T. Hisano, K. Kasuya, Y. Tezuka, N. Ishii, T. Kobayashi, M. Shiraki, E. Oroudjev, H. Hansma, T. Iwata, Y. Doi, T. Saito, and K. Miki. J. Mol. Biol. **356**, 993 (2006).
25. T. Fukui, T. Narikawa, K. Miwa, Y. Shirakura, T. Saito, and K. Tomita. Biochim. Biophys. Acta, **952**, 164 (1988).
26. T. Ohura, K. Kasuya, and Y. Doi. Appl. Environ. Microbiol. **65**, 189 (1999).
27. A. Behrends, B. Klingbeil, and D. Jendrossek. FEMS Microbiol. Lett. **143**, 191 (1996).
28. K.-E. Jaeger, A. Steinbüchel, and D. Jendrossek. Appl. Environ. Microbiol. **61**, 3113 (1995).
29. K. Kasuya, T. Ohura, K. Masuda, and Y. Doi. Int. J. Biol. Macromol. **24**, 329 (1999).
30. H. Abe, Y. Doi, H. Aoki, and T. Akehata. Macromolecules, **31**, 1791 (1998).
31. Y. Kanesato, N. Tanahashi, Y. Doi, and T. Saito. Polym. Degrad. Stab. **45**, 179 (1994).
32. H. Abe, Y. Doi, H. Aoki, T. Akehata, and Y. Hori. Macromolecules, **28**, 7630 (1995).
33. B.M. Bachmann and D. Seebach. Helv. Chim. Acta, **81**, 2430 (1998).
34. B.M. Bachmann and D. Seebach. Macromolecules, **32**, 1777 (1999).
35. Y. Kumagai, Y. Kanesawa, and Y. Doi. Makromol. Chem. **193**, 53 (1992).
36. G. Tomasi, M. Scandola, B.H. Briese, and D. Jendrossek. Macromolecules, **29**, 507 (1996).
37. K. Mukai, K. Yamada, and Y. Doi. Int. J. Biol. Macromol. **15**, 361 (1993).
38. M.R. Timmins, R.W. Lenz, and R.C. Fuller. Polymer, **38**, 551 (1997).
39. H. Abe, I. Mastubara, and Y. Doi. Macromolecules, **28**, 844 (1995).

© 2008 NRC Canada

40. P.J. Hocking, R.H. Marchessault, M.R. Timmins, R.W. Lenz, and R.C. Fuller. Macromolecules, **29**, 2472 (1996).
41. G.A.R. Nobes, R.H. Marchessault, H. Chanzy, B.H. Briese, and D. Jendrossek. Macromolecules, **29**, 8330 (1996).
42. T. Iwata, Y. Doi, K. Kasuya, and Y. Inoue. Macromolecules, **30**, 833 (1997).
43. T. Iwata, Y. Doi, T. Tanaka, T. Akehata, M. Shiromo, and S. Teramachi. Macromolecules, **30**, 5290 (1997).
44. G.A.R. Nobes, R.H. Marchessault, B.H. Briese, and D. Jengrossek. J. Environ. Polym. Degrad. **6**, 99 (1998).
45. T. Iwata, Y. Doi, S. Nakayama, H. Sasatsuki, and S. Teramachi. Int. J. Biol. Macromol. **25**, 169 (1999).
46. T. Murase, T. Iwata, and Y. Doi. Macromolecules, **34**, 5848 (2001).
47. T. Murase, T. Iwata, and Y. Doi. Macromol. Biosci. **1**, 275 (2001).
48. H. Abe, Y. Kikkawa, T. Iwata, H. Aoki, T. Akehata, and Y. Doi. Polymer, **41**, 867 (2000).
49. Y. Kikkawa, T. Hirota, K. Numata, T. Tsuge, T. Iwata, H. Abe, and Y. Doi. Macromol. Biosci. **4**, 276 (2004).
50. K. Numata, T. Hirota, Y. Kikkawa, T. Tsuge, T. Iwata, H. Abe, and Y. Doi. Biomacromolecules, **5**, 2186 (2004).
51. K. Numata, Y. Kikkawa, T. Tsuge, T. Iwata, Y. Doi, and H. Abe. Biomacromolecules, **6**, 2008 (2005).
52. M. Fujita, T. Iwata, and Y. Doi. Polym. Degrad. Stab. **81**, 131 (2003).
53. R.H. Marchessault and J. Kawada. Macromolecules, **37**, 7418 (2004).
54. J. Kawada and R.H. Marchessault. Biomacromolecules, **6**, 2271 (2005).
55. K. M. Shakesheff, M.C. Davies, C.J. Roberts, S.J.B. Tendler, A.G. Shard, and A. Domb. Langmuir, **10**, 4417 (1994).
56. K.M. Shakesheff, M.C. Davies, A. Domb, D.E. Jackson, C.J. Roberts, S.J.B. Tendler, and P.M. Williams. Macromolecules, **28**, 1108 (1995).
57. M.C. Davies, K.M. Shakesheff, A.G. Shard, A. Domb, C.J. Roberts, S.J.B. Tendler, and P.M. Williams. Macromolecules, **29**, 2205 (1996).
58. Y. Kikkawa, T. Murase, H. Abe, T. Iwata, and Y. Doi. Macromol. Biosci. **2**, 189 (2002).
59. K. Sudesh, A. Maehara, Z. Gan, T. Iwata, and Y. Doi. Polym. Degrad. Stab. **83**, 281 (2004).
60. K. Kuchta, L. Chi, H. Fuchs, M. Pötter, and A. Steinbüchel. Biomacromolecules, **8**, 657 (2007).
61. D. Dennis, V. Sein, E. Martinez, and B. Augustine. J. Bacteriol. J. Bacteriol. **190**, 555 (2008).
62. Y. Kikkawa, M. Fujita, T. Hiraishi, M. Yoshimoto, and Y. Doi. Biomacromolecules, **5**, 1642 (2004).
63. K. Numata, Y. Kikkawa, T. Tsuge, T. Iwata, Y. Doi, and H. Abe. Macromol. Biosci. **6**, 41 (2006).
64. K. Numata, K. Yamashita, M. Fujita, T. Tsuge, K. Kasuya, T. Iwata, Y. Doi, and H. Abe. Biomacromolecules, **8**, 2276 (2007).
65. T. Fukui, T. Narikawa, K. Miwa, Y. Shirakura, T. Saito, and K. Tomita. Biochem. Biophys. Acta, **952**, 164 (1988).
66. K. Yamashita, Y. Aoyagi, H. Abe, and Y. Doi. Biomacromolecules, **2**, 25 (2001).
67. K. Numata, S. Sato, M. Fujita, T. Tsuge, T. Iwata, Y. Doi, and H. Abe. Polym. Degrad. Stab. **92**, 176 (2007).
68. K. Kasuya, Y. Inoue, K. Yamada, and Y. Doi. Polym. Degrad. Stab. **48**, 167 (1995).
69. K. Kasuya, Y. Inoue, and Y. Doi. Int. J. Biol. Macromol. **19**, 35 (1996).
70. K. Yamashita, T. Funato, Y. Suzuki, S. Teramachi, and Y. Doi. Macromol. Biosci. **3**, 694 (2003).
71. K. Kasuya, Y. Tezuka, N. Ishii, Y. Yamagata, M. Shiraki, T. Saito, T. Hisano, T. Iwata, Y. Doi. Macromol. Symp. **249–250**, 540 (2007).
72. T. Murase, Y. Suzuki, Y. Doi, and T. Iwata. Biomacromolecules, **3**, 312 (2002).
73. M. Fujita, Y. Kobori, Y. Aoki, N. Matsumoto, H. Abe, Y. Doi, and T. Hiraishi. Langmuir, **21**, 11829 (2005).

© 2008 NRC Canada

REVIEW / SYNTHÈSE

Polysaccharide nanocrystal reinforced nanocomposites[1]

Alain Dufresne

Abstract: There are numerous examples of animals or plants that synthesize extracellular high-performance skeletal biocomposites consisting of a matrix reinforced by nanosized crystalline domains. Cellulose and chitin are classical examples of these reinforcing elements, which occur as whisker-like microfibrils that are biosynthesized and deposited in a continuous fashion. In many cases, this mode of biogenesis leads to crystalline microfibrils that are almost defect-free, and whose axial physical properties therefore approach those of perfect crystals. During the last decade we have attempted to mimic biocomposites by blending cellulose or chitin whiskers from different sources with polymer matrices. Aqueous suspensions of such nanocrystals can be prepared by acid hydrolysis of the substrate. The object of this treatment is to dissolve away regions of low lateral order so that the water-insoluble, highly crystalline residue may be converted into a stable suspensoid by subsequent vigorous mechanical shearing action. The resulting nanocrystals occur as rod-like particles or whiskers, whose dimensions depend on the nature of the substrate. They are typically a few hundred nm long and between 5 and 20 nm in diameter. Starch can also be used as a source for the production of nanocrystals. The constitutive nanocrystals appear as platelet-like nanoparticles with a length ranging between 20 and 40 nm, a width ranging between 15 and 30 nm, and a thickness ranging between 5 and 7 nm. Since the first announcement of using cellulose whiskers as a reinforcing phase, they have been used extensively as model fillers in several kinds of polymeric matrices, including synthetic and natural ones. Casting mixtures of polysaccharide nanocrystals and lattices led to the production of nanocomposite materials with drastically enhanced mechanical properties, especially at $T > T_g$ of the matrix, by virtue of the formation of a whiskers network, even when the whisker volume fraction was only a few percent. The formation of this rigid network, resulting from strong interactions between whiskers, was assumed to be governed by a percolation mechanism. This hydrogen-bonded network induced a thermal stabilization of the composite up to 500 K, the temperature at which polysaccharides start to decompose. Any factors that perturb the formation of this percolating network directly affect the reinforcing effect of polysaccharide nanocrystals. In addition to some practical applications, the study of these nanocomposite materials can help researchers understand such physical properties as the geometric and mechanical percolation effect.

Key words: nanocomposites, polysaccharide, polymer, cellulose, nanocrystal.

Résumé : Il existe de nombreux exemples d'animaux ou de plantes qui synthétisent des biocomposites haute performance constitués d'une matrice renforcée par des domaines cristallins de taille nanométrique. La cellulose et la chitine sont des exemples classiques de ces éléments de renfort qui se présentent sous la forme de microfibrilles biosynthétisées et arrangées de manière régulière. Ce mode de biogenèse conduit généralement à des microfibrilles cristallines pratiquement exemptes de défauts présentant donc des propriétés physiques axiales proches de celles du cristal parfait. Au cours de la dernière décennie, nous avons tenté de mimer ces biocomposites en mélangeant des whiskers de cellulose ou de chitine de différentes sources avec des matrices polymères. Des suspensions aqueuses de ces nanocristaux peuvent être préparées par hydrolyse acide du substrat. L'objectif de ce traitement est de dissoudre les régions de faible cohésion de sorte que le résidu insoluble fortement cristallin soit transformé en une suspension stable par une action mécanique de cisaillement vigoureuse. Les nanocristaux résultants se présentent sous forme de particules en bâtonnet ou whiskers, dont les dimensions dépendent de la nature du substrat. Leur longueur typique est de l'ordre de 100 nm et le diamètre varie entre 5 et 20 nm. L'amidon peut également être utilisé comme source pour la préparation de nanocristaux. Ces nanocristaux se présentent sous forme de plaquettes de longueur comprise entre 20 et 40 nm, de largeur

Received 27 September 2007. Accepted 18 December 2007. Published on the NRC Research Press Web site at canjchem.nrc.ca on 25 March 2008.

A. Dufresne.[2] Ecole Française de Papeterie et des Industries Graphiques, Institut National Polytechnique de Grenoble (EFPG-INPG), BP 65, 38402 Saint-Martin d'Hères CEDEX, France.

[1]This article is part of a Special Issue dedicated to Professor R. Marchessault.
[2]Corresponding author (e-mail: Alain.Dufresne@efpg.inpg.fr).

 doi:10.1139/V07-152 © 2008 NRC Canada

située entre 15 et 30 nm et d'épaisseur comprise entre 5 et 7 nm. Depuis la première étude sur l'utilisation des whiskers de cellulose comme phase renforçante, ceux-ci ont été largement utilisés comme charge modèle dans différents types de matrice polymère, synthétique ou naturelle. Le mélange de nanocristaux polysaccharide et de latex par coulée permet d'obtenir des matériaux nanocomposites avec des propriétés mécaniques nettement améliorées, notamment à $T > T_g$ de la matrice, grâce à la formation d'un réseau de whiskers, même pour des fractions volumiques de whiskers de quelques pourcents. Il a été proposé que la formation d'un réseau rigide, résultant d'interactions fortes entre whiskers, est gouverné par un mécanisme de percolation. Ce réseau obtenu par liaisons hydrogène conduit à la stabilisation du composite jusqu'à 500 K, température à partir de laquelle les polysaccharides se décomposent. Tout facteur qui perturbe la formation de ce réseau percolant affecte directement l'effet de renfort des nanocristaux polysaccharides. Hormis des applications pratiques, l'étude de ces matériaux nanocomposites peut aider à la compréhension de certaines propriétés physiques comme les phénomènes de percolation géométrique et mécanique.

Mots-clés : nanocomposites, polysaccharide, polymère, cellulose, nanocristal.

[Traduit par la Rédaction]

Introduction

Nanoscience and nanotechnology refer to the science and technology of materials that extend from about 100 nm down to atomic orders of magnitude around 0.2 nm and to the physical phenomena and material properties observed when operating in this size range. Conceptually, nanocomposites refer to multiphase materials where at least one of the constituent phases has one dimension less than 100 nm. This field has attracted the attention, scrutiny, and imagination of both scientist and industrial communities in recent years. A large window of opportunity has opened to overcome the limitations of traditional micrometer-scale composites. Research in this field is exploding because of the intellectual appeal of building blocks on the nanometer scale and because the technical innovations permit the design and creation of new materials and structures which possess unprecedented flexibility, improved physical properties, and significant industrial impact.

Some nanofilled polymer composites such as those filled with carbon black or fumed silica have been used for more than a century. A variety of clays such as montmorillonite and organoclays have been used to obtain unusual nanocomposites, by exploiting the ability of the clay silicate layers to disperse into polymer matrices. The development of new nanocomposite materials is restricted by both the limited availability of nanoparticles and their strong tendency to aggregate, preventing their homogeneous dispersion within a continuous matrix, which is the key step required for high mechanical performances.

A possible source of inspiration is nature and its wonderful nanocomposite structures. Among biologically inspired nanocomposites, polysaccharides are among the most promising sources for the production of nanoparticles. These abundant biorenewable raw materials are increasingly used in non-food applications. They can also be used for the preparation of crystalline nanoparticles with different geometrical characteristics providing a wide range of potential nanoparticle properties. Huge quantities of these nanoparticles are potentially available, often as waste products from agriculture. Moreover, polysaccharides offer significant potential for surface modification using well-established carbohydrate chemistry, allowing researchers to tailor the surface functionality of the nanoparticles. In this field, the scientific and technological challenges are tremendous.

Polysaccharide nanocrystals

Stable aqueous suspensions of polysaccharide nanocrystals can be prepared by acid hydrolysis of the biomass. Throughout this chapter, different descriptors of the resulting suspended colloidal particles will be used, including whiskers, monocrystals, and nanocrystals. The term "whiskers" is used to designate elongated rod-like nanoparticles. These crystallites have also been referenced in the literature as microfibrils, microcrystals, or microcrystallites, despite their nanoscale dimensions. Most of the studies reported in the literature refer to cellulose. A recent review reported the properties and application in the nanocomposite field of cellulosic whiskers (1).

The procedure for the preparation of such colloidal aqueous suspensions is described in detail in the literature for cellulose and chitin (2, 3). The biomass is generally first submitted to a bleaching treatment with NaOH in order to purify the cellulose or chitin by removing other constituents. The bleached material is then disintegrated in water, and the resulting suspension is submitted to a hydrolysis treatment with acid. The amorphous regions of cellulose or chitin act as structural defects and are responsible for the transverse cleavage of the microfibrils into short monocrystals under acid hydrolysis (4, 5). Under controlled conditions, this transformation consists of the disruption of amorphous regions surrounding and embedded within the cellulose or chitin microfibrils while leaving the microcrystalline segments intact. It is ascribed to the faster hydrolysis kinetics of amorphous domains compared to crystalline ones. The resulting suspension is subsequently diluted with water and washed by successive centrifugations. Dialysis against distilled water is then performed to remove free acid in the dispersion. Complete dispersion of the whiskers is obtained by a sonication step. The dispersions are stored in the refrigerator after filtration to remove residual aggregates with the addition of several drops of chloroform. Determination of the whisker content can be done by weighing aliquots of the solution before and after drying.

© 2008 NRC Canada

Table 1. Geometrical characteristics of polysaccharide nanocrystals from various sources: length (L) and cross section (D) of rod-like particles obtained from acid hydrolysis of cellulose or chitin.

Nature	Source	L (nm)	D (nm)	Ref.
Cellulose	Algal (*Valonia*)	>1000	10–20	(6)
	Bacterial	100–several 1000	5–10 × 30–50	(7)
	Cladophora	—	20 × 20	(8)
	Cotton	100–300	5–10	(9)
	Cottonseed linter	170–490	40–60	(10)
	MCC	150–300	3–7	(11)
	Sisal	100–500	3–5	(12)
	Sugar beet pulp	210	5	(13)
	Tunicin	100–several 1000	10–20	(14)
	Wheat straw	150–300	5	(15)
	Wood	100–300	3–5	(16)
Chitin	Crab shell	80–600	8–50	(17)
	Riftia tubes	500–10 000	18	(18)
	Shrimp	50–300	5–70	(19)
	Squid pen	150–800	10	(20)

This general procedure has to be adapted depending on the nature of the substrate. The constitutive nanocrystals occur as elongated rod-like particles or whiskers. The precise physical dimensions of the crystallites depend on several factors, including the source of the cellulose or chitin, the exact hydrolysis conditions, and ionic strength. The typical geometrical characteristics for crystallites derived from different species are reported in the literature are collected in Table 1. The length is generally of the order of a few hundred nanometers and the width is of the order of few nanometers. The aspect ratio of these whiskers is defined as the ratio of the length to the width.

Aqueous suspensions of starch nanocrystals can be prepared according to the "lintnerization" procedure described in the literature (21). Degradation of native starch granules by acid hydrolysis depends on many parameters, including those related to the botanical origin of the starch, namely its crystalline type, granule morphology (e.g., shape, size, and surface state), and relative proportion of amylose and amylopectin. It also depends on the acid hydrolysis conditions, namely the acid type, acid concentration, starch concentration, temperature, hydrolysis duration, and stirring. The kinetics of lintnerization shows two main steps. During the initial step, the hydrolysis kinetics is fast and corresponds to the hydrolysis of amorphous domains. In the second step, the hydrolysis kinetics is slow and corresponds to the hydrolysis of crystalline domains.

The main drawbacks to the use of such hydrolysis residues in composite applications are the duration (40 days of treatment) and the yield (0.5 wt%) of the hydrochloric acid hydrolysis step (21). Response surface methodology was used (22) to investigate the effect of five selected factors on the selective sulfuric acid hydrolysis of waxy maize starch granules in order to optimize the preparation of aqueous suspensions of starch nanocrystals. These predictors were temperature, acid concentration, starch concentration, hydrolysis duration, and stirring speed. With a starch concentration of 14.69 wt%, the preparation of aqueous suspensions of starch nanocrystals was achieved after 5 days of hydrolysis with 3.16 mol/L H_2SO_4 at 40 °C and 100 rpm, with a yield of 15.7 wt%. Waxy maize starch nanocrystals consist of platelet-like particles about 5–7 nm thick, 20–40 nm long, and 15–30 nm wide. The structure of these platelet-like nanoparticles was investigated in detail (23). Such nanocrystals are generally observed in the form of aggregates having an average size around 4.4 μm, as measured by laser granulometry (24).

The stability of resulting suspensions depends on the dimensions of the dispersed particles, their size polydispersity, and the surface charge. The use of sulfuric acid for preparing polysaccharide nanocrystals leads to more stable aqueous suspensions than the use of hydrochloric acid (24). Indeed, the H_2SO_4-prepared nanoparticles present a negatively charged surface while the HCl-prepared nanoparticles are not charged.

Surface modification of nanocrystals

The stability of aqueous suspensions of surface-charged nanocrystals has an electrostatic origin. One of the characteristics of polysaccharide nanoparticles with polar surfaces is their poor dispersibility or compatibility with nonpolar solvents or resins. Reducing their surface energy and improving their level of dispersion in a polymeric matrix are difficult. Strategies have been considered to broaden the number of possible polymer matrices and to allow the processing of nanocomposite materials from organic solvent solutions instead of using aqueous suspensions.

Dispersion of cellulose nanoparticles in low polarity solvents was reported after either coating or chemical modification of the surface of cellulose whiskers. Coating of cotton and tunicin whiskers by a surfactant such as a phosphoric ester of polyoxyethylene nonyl phenyl ether was found to lead to stable suspensions in toluene and cyclohexane (25) or chloroform (11). The dispersion of cellulose whiskers in an apolar solvent allows the application of an electric field for

© 2008 NRC Canada

times sufficient for the visual observation of the orientation and the preparation of aligned dried samples. Indeed, the use of a non-aqueous medium avoids the limitations arising from the high conductivity of water, as reported for tunicin whiskers suspended in cyclohexane (37). Cellulose whiskers orient parallel to an electric field, but perpendicular to a magnetic field. This axial orientation was assumed to originate mainly from a positive dielectric anisotropy of the nanoparticles.

Modifying the surface chemistry of nanocrystals is another way to disperse these nanoparticles in organic solvents. It generally involves reactive hydroxyl groups at the surface. Indeed, polysaccharides bearing a high concentration of hydroxyl groups in each glucose residue offer various possible coupling reactions. Goussé et al. (27) stabilized tunicin microcrystals in tetrahydrofuran (THF) by a partial silylation of their surface. At a low degree of substitution (DS), between 0.6 and 1, the whiskers kept their morphological integrity and became dispersible in solvents of low polarity, leading to stable birefringent suspensions when observed between cross polars. However at a DS greater than one, the core of the whiskers became silylated and it was no longer possible to obtain any birefringent suspension. Grunert and Winter (7) reported the preparation of bacterial cellulose nanocrystals that were topochemically trimethylsilylated. Resulting nanoparticles were dispersed in acetone to produce nanocomposites with a cellulose–acetate–butyrate matrix. Araki et al. (28) prepared original sterically-stabilized aqueous rod-like cellulose microcrystal suspensions by a combination of HCl hydrolysis, oxidative carboxylation, and grafting of poly(ethylene glycol) (PEG) having a terminal amino group on one end using water soluble carbodiimide. The PEG-grafted microcrystals displayed greatly enhanced dispersion stability evidenced through their resistance to the addition of 2 mol/L sodium chloride. They also could be redispersed into either water or chloroform from the freeze-dried state.

Alkenyl succinic anhydride (ASA) can be used for acylating the surface of polysaccharide nanocrystals. ASA is widely used as a sizing agent in papermaking, where it is applied to pulp fibers in aqueous systems. Surface chemical modification of chitin whiskers prepared by acid hydrolysis of chitin from crab shells, waxy maize starch nanocrystals, and tunicin whiskers with ASA was reported by Gopalan Nair et al. (29), Angellier et al. (30), and Yuan et al. (31), respectively. In the first two works, researchers used organic solvents to avoid hydrolysis of ASA. Gopalan Nair et al. (29) achieved acylation of chitin whiskers in a dioxane system with 4-(dimethylamino)pyridine as the catalyst. The reaction was carried out for 1 week at 70 °C. FTIR, TEM, and contact angle measurements were performed to prove the occurrence of the surface modification without any major morphological changes of the nanoparticles associated with the treatment applied. Stable toluene suspensions of the modified whiskers were obtained, showing colloidal behavior when observed between crossed polars. Angellier et al. (30) used the toluene–(dimethylammo)pyridine system to modify starch nanocrystals. Modified nanoparticles were characterized by FTIR and XPS spectroscopy, contact angle measurements, TEM, and X-ray diffraction analysis. The lower polarity of the modified nanocrystals was demonstrated by their migration to the methylene chloride phase from the aqueous phase. Yuan et al. (31) used a drying aqueous emulsion method to obtain acylated tunicin whiskers. The degree of esterification of modified cellulose nanoparticles was evaluated by FTIR and XPS spectroscopy, elemental analysis, and weight gain. The acylated whiskers were found to disperse in medium- to low-polarity solvents. It was shown that by controlling the heating time, whiskers with different dispersibility could be obtained. Isocyanates, such as phenyl isocyanate (PI) and 3-isopropenyl-α-α'-dimethylbenzyl isocyanate (TMI), were also used to chemically modify the surface of chitin whiskers and starch nanocrystals (29, 30).

The creation of stable suspensions of cellulose whiskers in dimethylformamide (DMF) without the addition of a surfactant or any chemical modification was also reported (32, 33). Both the high value of the dielectric constant of DMF and the medium wettability of cellulose whiskers were assumed to control the stability of the suspension. Indeed, the maintenance of the disperse state of cellulose nanoparticles requires the existence of an opposing interparticle repulsion, achieved in this case through electrostatic forces between charged whiskers. Use of DMF should allow researchers to avoid the use of water as a solvent for composites processing and to mask hydroxyl groups from the surface of nanocrystals that play an important role in the reinforcing effect of these nanoparticles, as will be seen below.

A promising new process consists of transforming polysaccharide nanocrystals into a co-continuous material through long-chain surface-chemical modification, based on the use of grafting agents bearing a reactive end group and a long "plasticizing" tail. The general objective of this surface-chemical modification is of course to increase the apolar character of the nanoparticle. From this procedure, biocomposite materials based on fully-renewable resources could be processed by classical methods such as hot-pressing, extrusion, injection molding, or thermoforming from these co-continuous materials. Very little work has been performed in this way.

Thielemans et al. (34) reported the chemical modification of starch-derived nanocrystals with poly(ethylene glycol) methyl ether (PEGME) and stearic acid chloride. Toluene 2,4-diisocyanate (2,4-TDI) was used to graft the PEGME to the starch surface. Successful surface modification was confirmed using FTIR and XPS spectroscopy and differential scanning calorimetry (DSC) as well as contact angle measurements. Efficient and complete surface coverage was confirmed and the starch crystalline structure was not affected. X-ray diffraction showed extensive crystallization of the stearate moieties grafted at the starch nanoparticles surface, forming a crystalline hydrophobic shell around the hydrophilic starch nanocrystal. Both modifications exhibited a large effect on the individualization of the nanocrystals owing to reduced hydrogen bonding and polar interactions between the individual particles.

The described surface modifications clearly change the character of the nanocrystal surfaces and their activity. Long-chain surface modifications can offer some extraordinary possibilities. The surface modifications can act as binding sites for active agents in drug delivery systems or for toxins in purifying and treatment systems. These surface modifications may also be able to interdiffuse, upon heating,

© 2008 NRC Canada

to form a polymer matrix phase. The covalent linkage between reinforcement and matrix will result in near-perfect stress transfer at the interface with exceptional mechanical properties of the composite as a result. The large surface area, inherent in the small size of nanoparticles, guarantees high surface activity and high grafting per unit mass of particles. Their small size also reduces the required chain length for interdiffusion to assure sufficient matrix phase cohesion. The described surface modifications have a layer thickness of the order of magnitude of the thickness of the starch nanoparticles.

In a recent work (35), we reported the possibility of grafting longer polymer chains onto starch nanocrystals. Monocrystalline starch nanoparticles were successfully grafted with polytetrahydrofuran, polycaprolactone, and poly(ethylene glycol) monobutyl ether chains using TDI as the linking agent. Surface grafting was confirmed using FTIR and XPS spectroscopy, DSC and elemental analysis, and contact angle measurements. Transmission electron microscopy (TEM) observations of modified starch nanocrystals showed either the individualization of nanoparticles or the formation of a film, depending on the polymer used. It was shown that grafting efficiency decreased with the length of polymeric chains, as expected.

Processing of nanocomposites

Because of the high stability of aqueous polysaccharide nanocrystal dispersions, water is the preferred processing medium. A high level of dispersion of the filler within the host matrix in the resulting composite film is expected when processing nanocomposites in aqueous medium. Therefore, this restricts the choice of the matrix to hydrosoluble polymers. The use of aqueous dispersed polymers (i.e., latexes) is a first alternative, which allows the use of hydrophobic polymers as matrix and ensures good dispersion of the fillers, indispensable for processing homogenous composites. Dispersing polysaccharide nanocrystals in non-aqueous media is a second alternative and it opens other possibilities for nanocomposites processing.

In the first report of the preparation of polymer nanocomposites reinforced with polysaccharide nanocrystals, a latex, obtained by the copolymerization of styrene and butyl acrylate (poly(S-co-BuA)) and with a glass transition temperature (T_g) around 0 °C, and tunicin whiskers were used (14). Composite materials are generally obtained by casting and evaporation. The dispersion of polysaccharide nanocrystals in nonpolar media can be obtained by chemically modifying their surface.

Microstructure

The easiest way to assess the dispersion of the polysaccharide nanocrystals within the host polymeric matrix is a simple examination with the naked eye. Addition of a filler to a transparent polymeric matrix results in a loss of transparency. Because of the nanoscale dimensions of reinforcing nanoparticles, the nanocomposite film remains transparent and opacity suggests the presence of aggregates of micrometric sizes. Polarized optical microscopy was used to observe and follow the growth of polyoxyethylene (POE) spherulites in films reinforced with tunicin whiskers (36). For the unfilled POE matrix, birefringent spherulites were clearly identified through the characteristic Maltese cross pattern indicating a spherical symmetry. Reinforced with 10 wt% tunicin whiskers, the supermolecular structure was found to be quite different. It was observed that the spherulites exhibited a less birefringent character, most probably due to a weakly organized structure. It was supposed that the cellulosic filler interfered with the spherulite growth and that during growth the whiskers were ejected and then occluded in interspherulitic regions. The high viscosity of the filled medium most probably restricted this phenomenon and limited the size of the spherulites.

Scanning electron microscopy (SEM) is generally employed for the more extensive morphological inspection of polysaccharide nanocrystal reinforced polymers. This technique leads to conclusions about the homogeneity of the composite, the presence of voids, the dispersion level of the nanoparticles within the continuous matrix, the presence of aggregates, sedimentation, and the possible orientation of rod-like particles. By comparing the micrographs showing the surface of fracture of the unfilled matrix and of the composites, polysaccharide nanocrystals can generally be easily identified. In fact, they appear like white dots. Their concentration is a direct function of the polysaccharide composition in the composite. For rod-like nanoparticles, these shiny dots correspond to the transverse sections of the cellulose or chitin whiskers. TEM observations can also be performed to investigate the microstructure and dispersion quality of the nanoparticles in the nanocomposite films. This technique is more difficult to perform because it involves the use of specimens around 50 nm thick prepared by ultramicrotomy.

Small-angle X-ray scattering (SAXS) and small-angle neutron scattering (SANS) are other ways to determine the dispersion of cellulosic whiskers into the matrix. These techniques were used to confirm the isotropic dispersion of tunicin whiskers in plasticized poly(vinylchloride) (PVC) without aggregates (37). Atomic force microscopy (AFM) imaging has been used recently to investigate the microstructure of cellulose nanocrystal reinforced polymer nanocomposites (11).

Thermal properties

In most studies, no change in T_g is reported when increasing the amount of whiskers, regardless of the nature of the polymeric matrix. This result is surprising because of the high specific area of these nanoparticles (around 170 $m^2 \cdot g^{-1}$ for tunicin whiskers, for instance) (38).

In glycerol-plasticized starch-based composites, peculiar effects of tunicin whiskers on the T_g of the starch-rich fraction were reported depending on moisture conditions (39). For low loading level (up to 3.2 wt%), a classical plasticization effect of water was reported. However, an antiplasticization phenomenon was observed for higher whisker content (6.2 wt% and up). These observations were discussed according to the possible interactions between hydroxyl groups on the cellulosic surface and starch, the selective partitioning of glycerol and water in the bulk starch matrix or at the whiskers surface, and the restriction of amorphous starch chain mobility in the vicinity of the starch

© 2008 NRC Canada

crystallite coated filler surface. For glycerol-plasticized starch reinforced with cellulose crystallites prepared from cottonseed linter (10), an increase of T_g with filler content was reported and attributed to cellulose–starch interactions. For tunicin whisker sorbitol plasticized starch (40), T_gs were found to increase slightly up to about 15 wt% whiskers and then to decrease for higher whisker loading. Crystallization of amylopectin chains on the addition of whiskers and migration of sorbitol molecules to the amorphous domains were proposed to explain the observed modifications.

For natural rubber reinforced with waxy maize starch nanocrystals, a decrease in the onset T_g with an increase in the nanoparticle content was reported (41). Using a glycerol-plasticized starch matrix, the temperature of the main relaxation process associated with the glass–rubber transition of amylopectin-rich domains was reported to increase with the increasing of the starch nanocrystals content (42). The reduction in the molecular mobility of matrix amylopectin chains for filled materials was explained by the establishment of hydrogen bonding forces between both components. A similar observation was reported for poly(vinyl acetate) (PVAC) reinforced with sisal cellulose whiskers (12) and carboxymethyl cellulose (CMC) reinforced with cotton cellulose whiskers (43). For waxy maize starch nanocrystals reinforced glycerol plasticized starch, the increase of T_g led to a considerable slowing down of the retrogradation of the matrix (42). This is a very interesting result since retrogradation and crystallization of thermoplastic starch during aging are main drawbacks of this material and lead to an undesired change in thermomechanical properties.

Melting temperature (Tm) values were reported to be nearly independent of the filler content in plasticized starch (39, 40) and in POE-based materials (36, 33, and 44) filled with tunicin whiskers. The same observation was reported for polycaprolactone reinforced with chitin whiskers from *Riftia* tubes (18) and cellulose acetate butyrate (CAB) reinforced with native bacterial cellulose whiskers (7). However, for the latter system, Tm values were found to increase when the amount of trimethylsilylated whiskers increased. The authors ascribed this difference to the stronger filler–matrix interaction in the case of chemically modified whiskers.

A significant increase in the crystallinity of sorbitol plasticized starch (40) was reported when increasing cellulose whiskers content. This phenomenon was ascribed to an anchoring effect of the cellulosic filler, probably acting as a nucleating agent. For POE-based composites the degree of crystallinity of the matrix was found to be roughly constant up to 10 wt% tunicin whiskers (36, 33, 44) and to decrease for higher loading level (36). Incorporation of chitin whiskers from shrimp shells did not have any effect on the crystallinity of PVA (19) or chitosan (45).

It seems that the nucleating effect of cellulosic nanocrystals is mainly governed by surface chemical considerations. Indeed, when untreated or surfactant-coated, whiskers were also reported to be very good nucleating agents for isotactic polypropylene (iPP). The unmodified whiskers have the largest nucleating effect (45). On the other hand, whiskers grafted with maleated polypropylene did not modify the crystallization of iPP. It was shown from both X-ray diffraction and DSC analysis that the crystallization behavior of films containing unmodified and surfactant-modified whiskers displayed two crystalline forms (α and β), whereas the neat matrix and the nanocomposite reinforced with nanocrystals grafted with maleated polypropylene only crystallized in the α form. It was suspected that the more hydrophilic the whisker surface, the more it appeared to favor the appearance of the β phase. It was observed that native bacterial fillers impede the crystallization of the CAB matrix whereas silylated ones help to nucleate the crystallization (7). A decrease in the degree of crystallinity of polycaprolactone was reported when adding chitin whiskers from *Riftia* tubes (18). It was suggested that during crystallization, the rod-like nanoparticles are most probably first ejected and then occluded in intercrystalline domains, hindering the crystallization of the polymer. In iPP reinforced with tunicin whiskers, a mechanical coupling between the polypropylene crystallites and filler–filler interactions was reported (45).

For tunicin whisker filled semicrystalline matrices such as poly(β-hydroxyoctanoate) (PHO) (46) and glycerol plasticized starch (39), a transcrystallization phenomenon was reported. It consists of a preferential crystallization of the amorphous polymeric matrix chains during cooling at the surface of nanoparticles. For glycerol plasticized starch based systems, the formation of the transcrystalline zone around the whiskers was assumed to be due to the accumulation of plasticizer in the cellulose–amylopectin interfacial zones improving the ability of amylopectin chains to crystallize. These specific crystallization conditions were evidenced at high moisture content and high whisker content by DSC and wide angle X-ray scattering (WAXS). It was displayed as a shoulder on the low-temperature side of the melting endotherm and as a new peak in the X-ray diffraction pattern. This transcrystalline zone could originate from a glycerol-starch V structure. In addition, the inherent restricted mobility of amylopectin chains was put forward to explain the lower water uptake of cellulose-starch composites for increasing filler content.

In silk fibroin reinforced with tunicin whisker composites a conformational change of fibroin chains from a random coil to an ordered structure was reported (47). This change was ascribed to the highly ordered surface of cellulosic whiskers. For waxy maize starch nanocrystals that reinforced glycerol plasticized starch, an increase of the degree of crystallinity of the thermoplastic starch matrix was reported (42). It was suggested that crystallization of the matrix occurred at the interface between the filler and the matrix owing to the similar chemical structure of both components.

Mechanical properties

Nanoscale dimensions and impressive mechanical properties make polysaccharide nanocrystals, particularly when occurring as high aspect ratio rod-like nanoparticles, ideal candidates to improve the mechanical properties of the host material. Indeed, these properties are profitably exploited in nature. In the past ten years, there has been great interest in using polysaccharide nanocrystals, especially cellulose whiskers, as a reinforcing phase in a polymeric matrix, evaluating the mechanical properties of the resulting composites,

© 2008 NRC Canada

and elucidating the origin of the mechanical reinforcing effect.

The first demonstration of the reinforcing effect of cellulose whiskers was reported for poly(S-*co*-BuA) reinforced with tunicin whiskers (14). The authors measured a spectacular improvement in the storage modulus after adding the filler even at low content into the host polymer. This increase was especially significant above the glass–rubber transition temperature of the thermoplastic matrix because of its poor mechanical properties in this temperature range. For instance, the rubbery modulus of the composite reinforced with 6 wt% tunicin whiskers was more than two orders of magnitude higher than that of the unfilled matrix. Moreover, the introduction of 3 wt% or more cellulosic whiskers provides outstanding thermal stability of the matrix modulus up to the temperature at which cellulose starts to degrade (500K).

Favier et al. tried to understand the unusual reinforcing effect from the high modulus of cellulose whiskers (14), which was reported to be of the order of 150 GPa (48). They used a classical model for randomly dispersed short-fiber-reinforced composites that is the model of Halpin–Kardos (49). In this mean-field approach, fibers are assumed to be dispersed in a continuous matrix and no interaction between fillers is taken into account. The description of the equations used in this approach can be found elsewhere (15). It was found that the predicted rubbery modulus fails to describe the experimental data. The cellulose whiskers seemed to act as fibers much longer than expected from geometrical observation.

The outstanding properties observed for these systems were ascribed to a mechanical percolation phenomenon (14). Good agreement between experimental and predicted data was reported when using the series–parallel model of Takayanagi modified to include a percolation approach. It was suspected that all the stiffness of the material was due to infinite aggregates of cellulose whiskers. Above the percolation threshold the cellulosic nanoparticles can connect and form a tri-dimensional continuous pathway through the nanocomposite film. For rod-like particles such as tunicin whiskers with an aspect ratio of 67, the percolation threshold is close to 1 vol% (50). The formation of this cellulose network was supposed to result from strong interactions between whiskers, such as hydrogen bonds (51). This phenomenon is similar to the mechanical properties observed for a paper sheet, which result from the hydrogen-bonding forces that hold the percolating network of fibers. This mechanical percolation effect explains both the reinforcing effect and the thermal stabilization of the composite modulus for evaporated films.

Any factor that affects the formation of the percolating whiskers network or interferes with it changes the mechanical performance of the composite (52). Three main parameters were reported to affect the mechanical properties of such materials, the morphology and dimensions of the nanoparticles, the processing method, and the microstructure of the matrix and matrix–filler interactions.

Morphology and dimensions of the nanoparticles

Cellulose and chitin nanocrystals occur as rod-like nanoparticles in contrast to starch nanocrystals that consist of nanometer-scale platelet-like particles. For rod-like particles, the geometrical aspect ratio is of course an important factor since it determines the percolation threshold value. This factor is linked to the source of cellulose or chitin and to the whisker preparation conditions. Fillers with a high aspect ratio give the best reinforcing effect. For instance, the rubbery storage tensile modulus was systematically lower for wheat straw whisker – poly(S-*co*-BuA) composites than for tunicin whisker based materials (52). The following relation was found between the percolation threshold (v_{Rc}) and the aspect ratio of rod-like particles:

$$v_{Rc} = 0.7/(L/d)$$

Also, the flexibility and tangling possibility of the nanofibers plays an important role (13). These authors reported the mechanical properties of poly(S-*co*-BuA) reinforced with cellulose rod-like nanoparticles extracted from sugar beets and submitted to different hydrolysis conditions. Unhydrolyzed cellulose microfibrils were prepared by submitting sugar beet pulp to a chemical treatment consisting of alkali extraction with a sodium hydroxide solution to solubilize most of the pectins and hemicelluloses (53). The resulting insoluble residue was bleached with a sodium chlorite solution, suspended in distilled water, and homogenized by successive passes through a Manton–Gaulin laboratory homogenizer. Individualized flexible cellulose microfibrils, almost 5 nm in width and practically infinite in length, result from this treatment. These microfibrils were submitted to a hydrolysis treatment using different sulfuric acid concentrations. As the acid concentration increased, it was observed that the length of the microfibrils decreased because of the increased probability of removal of the amorphous material with the concentration of acid. For the strongly hydrolyzed material, most of the amorphous domains were hydrolyzed and rigid whiskers were obtained. Linear mechanical measurements performed on poly(S-co-BuA) reinforced with these microfibrils did not show significant differences by varying the strength of the hydrolysis step nor the length and flexibility of the nanoparticles. However, for nonlinear mechanical tensile tests it was observed that, as the hydrolysis strength increased both the modulus and the strength of the composite decreased, whereas the elongation at break increased. This result showed the strong influence of entanglements on the mechanical behavior of the nanocomposites.

Processing method

The processing method governs the possible formation of a continuous nanocrystals network and then the final properties of the nanocomposite material. Slow processes such as casting/evaporation were reported to give materials with the highest mechanical performance compared to freeze-drying/molding and freeze-drying/extruding/molding techniques. This effect was ascribed to the probable orientation of the rod-like nanoparticles during film processing resulting from shear stresses induced by freeze-drying/molding or freeze-drying/extruding/molding techniques.

It was shown that whisker dimensions affect their ability to align within a shear field. Neutron and X-ray scattering data were used to monitor shear alignment of softwood-derived nanocrystals isolated from the same source, but with

© 2008 NRC Canada

different sizes (54). It was shown that as the aspect ratio falls below 20, shear alignment of whiskers and the ability to maintain this alignment drop significantly. In addition, this difference was suggested to be due to the predominance of the whisker–whisker interactions and their contribution to the overall reinforcing effect in the evaporated films in relation to the dispersion of homogeneous fillers into the matrix. During slow water evaporation, because of Brownian motion in the suspension or solution (whose viscosity remains low, up to the end of the process when the latex particle or polymer concentration becomes very high), the rearrangement of the nanoparticles is possible. They have time enough to interact and connect to form a percolating network which is the basis of their reinforcing effect. The resulting structure is completely relaxed and direct contacts between nanocrystals or microfibrils are then created. On the other hand, during the freeze-drying/hot-pressing process, the nanoparticle arrangement in the suspension is first frozen; during the subsequent hot-pressing stage, because of the polymer melt viscosity, the particle rearrangements are strongly limited and contacts can be made through a limited amount of polymer matrix. However, although the freeze-drying/hot-pressing process limits the possibility of creation of hydrogen bonds it is expected that, for high polysaccharide nanoparticles content, some bonds may still be created.

When using a polymeric matrix in latex form, particle size seems to play a predominant role (55). Larger latex particle size results in greater effects on mechanical properties. Indeed, the polymeric particles act as impenetrable domains to polysaccharide nanoparticles during the film formation owing to their high viscosity. Increasing latex particle size leads to an increase in the excluded volume and these geometrical constraints seem to affect the whisker network formation.

Microstructure of the matrix and matrix–filler interactions

The microstructure of the matrix and the resulting competition between matrix–filler and filler–filler interactions also affect the mechanical behavior of the polysaccharide nanocrystal reinforced nanocomposites. Classical composite science tends to prefer the former as a fundamental condition for optimal performance. In polysaccharide nanocrystal based composite materials the opposite trend is generally observed when the materials are processed via the casting/evaporation method. Increasing the affinity between the polysaccharide filler and the host matrix leads to a decrease in mechanical performance. This unusual behavior is ascribed to the reinforcing phenomenon of polysaccharide nanocrystals resulting from the formation of a percolating network due to hydrogen-bonding forces.

Tensile tests performed on silk fibroin – microcrystalline cellulose composites showed a linear trend for the Young's modulus, with additive dependence on the mixing ratio, whereas the tensile strength and elongation at break showed a maximum around 70%–80% cellulose content, reaching five times those of films derived from fibroin alone or cellulose alone (47). Strong interactions between cellulose crystallites prepared from cottonseed linters and between the filler and the glycerol-plasticized starch matrix were reported to play a key role in reinforcing properties (10). In non-percolating systems, for instance for materials processed from freeze-dried cellulose nanocrystals, strong matrix–filler interactions enhance the reinforcing effect of the filler. This observation was reported using poly(ethylene-co-vinyl acetate) (EVA) matrices with different vinyl acetate contents and then different polarities (56).

A higher reinforcing effect was reported for unmodified cellulose whiskers than for trimethylsilylated whiskers (7). Apart from the fact that 18% of the weight of the silylated crystals was due to the silyl groups, they attributed this difference to restricted filler–filler interactions. Similar results and loss of mechanical properties were reported for natural rubber based nanocomposites reinforced with both unmodified and surface chemically modified chitin whiskers (29) and starch nanocrystals (57).

The transcrystallization phenomenon reported for semicrystalline PHO on cellulose whiskers resulted in a remarkable decrease in the mechanical properties (especially above the melting temperature of the matrix) when compared to fully amorphous PHO (46). In these systems, the filler–matrix interactions and distance from the surface at which the molecular mobility of the amorphous PHO phase is restricted were quantified using a physical model predicting the mechanical loss angle (38). The determination of the ratio between experimental and predicted magnitude of the main relaxation process allows one to remove the filler-reinforcement effect keeping only the interfacial effect, using it to calculate the thickness of the interphase. It was shown that when using semicrystalline PHO as the matrix, the molecular mobility of amorphous PHO chains was only slightly affected by the presence of tunicin whiskers, owing to a possible transcrystallization phenomenon leading to the coating of the nanoparticles with the crystalline PHO phase. The thickness of the transcrystalline layer, around 2.7 nm, was found to be independent of the cellulose whisker content. In contrast, when using amorphous PHO as the matrix, the flexibility of polymeric chains in the surface layer is lowered by the conformational restrictions imposed by the cellulose surface. This results in a broader interphase and in a broadening of the main relaxation process of the matrix.

Similar transcrystallization was reported for plasticized starch reinforced with cellulose whiskers (58). This strong loss of performance in the filler–filler interactions demonstrates an effect of outstanding importance to ensuring the mechanical stiffness and thermal stability of these composites. When using unhydrolyzed cellulose microfibrils extracted from potato pulp rather than cellulose nanocrystals to reinforce glycerol plasticized thermoplastic starch, a completely different mechanical behavior was reported (59, 60), resulting in a significant reinforcing effect by the unhydrolyzed microfibrils. It was suspected that the tangling effect contributed to this high reinforcing effect (58). However, for POE-based nanocomposites the formation of the percolating cellulose network is not altered by the crystallization of the matrix and filler–POE interactions (36, 33, 61–63).

Swelling properties

Swelling is a method currently used for composite materials to determine if the filler creates supplementary crosslinks due to specific interactions between the filler and the

© 2008 NRC Canada

matrix. The choice of the solvent used for the experiment is critical. It must be a good solvent for the matrix to allow its swelling or dissolution, but it must not be able to break the eventual links between the matrix and the filler. If this last condition is not respected, the experiments cannot be conclusive.

The kinetics of solvent absorption consists generally of first drying and weighing the sample, and then immersing it in the liquid solvent or exposing it to the vapor medium. The sample is then removed at specific intervals and weighed until an equilibrium value is reached. The swelling rate of the sample can be calculated by dividing the gain in weight by the initial weight. Generally, absorption is fast in the initial stages, whereas at longer times, the kinetics of absorption is low and leads to a plateau, corresponding to the solvent uptake at equilibrium. The diffusion coefficient can be determined from the initial slope of the solvent uptake curve as a function of time.

Water absorption

The resistance to water absorption by glycerol plasticized thermoplastic starch conditioned at 98% RH was reported to increase with increasing cellulose nanocrystals content (10, 39). These experiments were conducted using cellulose whiskers from tunicate and cottonseed linter, respectively. Both the water uptake and the diffusion coefficient of water were found to decrease upon the addition of whiskers. These phenomena were ascribed to the presence of strong hydrogen-bonding interactions between nanoparticles and between the starch matrix and cellulose whiskers. The hydrogen-bonding interactions in the composites tend to stabilize the starch matrix when it is submitted to highly moist atmosphere. Moreover, the high crystallinity of cellulose might be responsible for the decreased water uptake at equilibrium and the decreased diffusion coefficient of the materials. Lower water uptake and dependence on cellulose whisker content were reported when using sorbitol rather than glycerol as the plasticizer for the starch matrix (40). An explanation was proposed based on the chemical structure of both plasticizers, the number of accessible end hydroxyl groups in glycerol being about twice those in sorbitol.

An increase in the water resistance of soy protein isolate (SPI) films when reinforced with cotton cellulose (64) or chitin whiskers from crab shells was also reported (65). Similar results were obtained for shrimp chitin whisker reinforced PVA (19) and chitosan (67), and cotton cellulose whisker reinforced carboxymethyl cellulose (CMC) (43). In addition, it was found that heat treatment decreased the affinity to water of shrimp chitin or cotton cellulose whisker based nanocomposite films.

The water absorption of waxy maize starch nanocrystals reinforced unvulcanized natural rubber when immersed in water was also reported (41). When starch nanoparticles were added to the apolar polymeric matrix, both the water uptake and the diffusion coefficient obviously increased. However, a discontinuity in both parameters as a function of starch content was reported around 10 wt%. It seemed that the formation of a continuous network of starch nanocrystals occurred at this concentration. Although not easily determinable because of the ill-defined geometry of the percolating species, the critical volume fraction of waxy maize starch nanocrystals at the percolation threshold should be around 6.7 vol% (i.e., 10 wt%). It was observed that the water uptake was lower when starch nanocrystals were chemically modified on their surface with ASA and PI compared to their unmodified counterparts. For potato starch nanocrystal reinforced poly(S-*co*-BuA), a linear relationship was reported between the amount of absorbed water and the volume fraction of nanoparticles (67) whereas the diffusion coefficient displayed two well-defined regions with respect to filler content, namely below and above a critical value of 20 vol%. It was concluded that the diffusion coefficient was sensitive to the percolation threshold, unlike the water uptake, which corresponds to an equilibrium state. The connectivity of fillers was supposed to contribute to the creation of diffusion pathways.

Non-aqueous liquid absorption

PVC reinforced with tunicin whiskers was submitted to swelling experiments in methyl ethyl ketone (MEK) (37). A large decrease in swelling of PVC-based samples when immersed in MEK was observed with increasing cellulose whisker content. It was assumed to be due to the existence of an interphase making a link between nanoparticles, thus allowing the formation of a flexible network. The swelling properties of unvulcanized natural rubber reinforced with crab shells chitin whiskers (17) and waxy maize starch nanocrystals (41) when immersed in toluene were also reported. Both fillers caused a decrease in the toluene uptake of natural rubber. It was assumed to be due to the formation of a nanocrystal network through hydrogen bonding between nanoparticles and also to favorable interactions between the matrix and the filler. The diffusion coefficient of toluene was also found to decrease with addition of polysaccharide nanocrystals. It was observed that the toluene uptake was higher with chemically modified polysaccharide nanocrystal surfaces than with unmodified nanoparticles. The effect was ascribed to lower interactions between modified nanocrystals, higher interactions between the filler and the matrix, and higher affinity between the modified filler and toluene.

For crab shell chitin whisker based nanocomposites, a comparison between samples prepared by freeze-drying / hot-pressing and casting/evaporation was reported (17). It was shown that cast/evaporated nanocomposites were more resistant to swelling than freeze-dried / hot-pressed ones because of the presence of a percolating chitin network in the former. The extent of filler–matrix interactions was also determined by calculating the relative weight loss (RWL) and fraction of bounded matrix (FBM) after 48 h immersion of samples in toluene and subsequent drying. For instance, the RWL and FBM values for a 20 wt% filled evaporated sample were 7.5% and 35.3% and that of the corresponding freeze-dried sample were 11.8% and 28.5%, respectively, giving quantitative indication of the effect of the three-dimensional chitin network in evaporated samples.

The swelling behavior in toluene of poly(S-co-BuA) reinforced with unhydrolyzed cellulose microfibrils from *Opuntia ficus-indica* cladodes was also studied (68). The authors reported a strong toluene resistance even at very low filler loading. Although the unfilled matrix completely dissolved in toluene and no residual gel was recovered at the end of the swelling experiment, only 27 wt% of the polymer

© 2008 NRC Canada

could be dissolved when filled with only 1 wt% of cellulose microfibrils. This phenomenon was ascribed to the presence of a three-dimensional entangled cellulosic network which strongly restricted the swelling capability and dissolution of the matrix. The effect was not observed to increase at higher microfibril content because the overlapping of the microfibrils restricted the filler–matrix interfacial area and because the densification of the microfibrils network decreased the entrapping matrix fraction. Similar experiments were conducted with poly(S-*co*-BuA) reinforced with cellulose microfibrils obtained from sugar beet pulp (69). Toluene resistance of nanocomposites was found to be less significant than for microfibrils from *Opuntia ficus-indica* cladodes and to depend upon filler content. It was observed that the cohesion of composites prepared by evaporation was higher than that of freeze-dried / hot-pressed materials. This difference was ascribed to the presence of a hydrogen-bonded network in the former samples. It was concluded that the solvent did not have any effect on the hydrogen bonds of the cellulose network present in evaporated composites. On the other hand, for freeze-dried / hot-pressed materials, less strong interactions supposedly created between microfibrils and polymer chains could be more easily disentangled and dissolved by the solvent.

Barrier properties

The permeability of natural rubber reinforced with waxy maize starch nanocrystals to both water vapor and oxygen was studied (41). The water vapor transmission rate of these materials was found to decrease continuously upon the addition of starch nanoparticles. This unobvious result shows that the hydrophilic nature of starch nanocrystals does not increase the permeability of natural rubber to water vapor. It was also observed that starch nanocrystals reduced oxygen diffusion, as shown from the decrease in the diffusion coefficient when adding the filler, and oxygen permeability. It was confirmed that this phenomenon was mainly due to the structural modification of the film and not to the decrease in the solubility of oxygen. Both observations were ascribed to the nanoscale platelet-like morphology of starch nanocrystals that increases the tortuosity of the diffusion path of molecules.

The water vapor permeability of sorbitol plasticized pullulan films reinforced with starch nanocrystals was also investigated (70). The authors reported no significant differences in water vapor permeability of unfilled samples and those containing up to 20 wt% nanocrystals. For higher filler content, enhanced barrier properties were observed. The water vapor transmission rate of cotton nanocrystals reinforced CMC films was found to decrease slightly in heat-treated nanocomposites compared to materials not undergoing heat treatment (43).

Conclusions

Polysaccharide nanocrystals are building blocks biosynthesized to provide structural properties to living organisms. They can be isolated from biomass through acid hydrolysis with concentrated mineral acids under strictly controlled conditions, varying time and temperature. Acid hydrolysis results in an overall decrease in amorphous material by removing polysaccharide material closely bonded to the crystallite surface and breaks down portions of glucose chains in the most accessible, non-crystalline regions. The degree of polymerization levels off, corresponding to the residual highly crystalline regions of the original material (i.e., cellulose or chitin fiber or starch granule). Dilution of the acid and dispersion of the individual crystalline nanoparticles complete the process and yield an aqueous suspension of polysaccharide nanoparticles. These nanoparticles can occur as rod-like nanocrystals in the case of cellulose- or chitin-based materials, or platelet-like nanoparticles when using starch granules as the raw material. The rod-like nanocrystals can display chiral nematic properties whose liquid crystalline behavior depends on the mineral acid chosen for the hydrolysis.

Polysaccharide nanocrystals are inherently low-cost materials that are available from a variety of natural sources and in a wide variety of aspect ratios (for example, ~200 nm long and 5 nm in lateral dimension for cellulose and up to several microns long and 18 nm in lateral dimension for chitin). They show the advantages of their renewable source materials, such as abundance, renewability and self-assembly into well-defined architectures. As polymer fillers, they have a greater impact on mechanical properties (e.g., strength, modulus and dimensional stability), permeability to gases and water, thermal stability and heat distorsion temperature, surface appearance, and optical clarity than conventional polymer fillers. They are an attractive nanomaterial for a multitude of potential applications in a diverse range of fields. Indeed, nanotechnology has applications across most economic sectors and allows the development of new enabling science with broad commercial potential. Possible and suggested areas of application include optically variable films, ink, and iridescent pigments for security papers. Polysaccharide nanocrystals reinforced polymer nanocomposites display outstanding mechanical properties and can be used to process high-modulus thin films. For instance, nanocomposite polymer electrolytes reinforced with cellulosic nanoparticles were successfully prepared. There are many other appealing expectations regarding their potential. The growing literature studying polysaccharide, mainly cellulose, nanocrystals is a clear indication of this evolution. Practical applications of such fillers and their transition into industrial technology require a favorable balance between the expected performance of the composite materials and their cost. To exploit their potential, research and development investments must be made in the science and engineering that will fully determine the properties and characteristics of polysaccharides at the nanoscale, develop the technologies to manipulate self-assembly and multifunctionnality, and develop these new technologies to the point where industry can produce advanced and cost-competitive polysaccharide nanoscale products. There are still significant scientific and technological challenges to take up.

References

1. M.A.S. Azizi Samir, F. Alloin, and A. Dufresne. Biomacromolecules, **6**, 612 (2005).

© 2008 NRC Canada

2. L.E. Wise, M. Murphy, and A.A. D'Addiecco. Pap. Trade J. **122**, 35 (1946).
3. R.H. Marchessault, F.F. Morehead, and N.M. Walter. Nature, **184**, 632 (1959).
4. O.A. Battista, S.J. Coppick, A. Howsmon, F.F. Morehead, and W.A. Sisson. Ind. Eng. Chem. **48**, 333 (1956).
5. R.H. Marchessault, F.F. Morehead, and M. J. Koch. J. Colloid Sci. **16**, 327 (1961).
6. J.F. Revol. Carbohydr. Polym. **2**, 123 (1982).
7. M. Grunert and W.T. Winter. J. Polym. Environ. **10**, 27 (2002).
8. U.J. Kim, S. Kuga, M. Wada, T. Okano, and T. Kondo. Biomacromolecules, **1**, 488 (2000).
9. T. Ebeling, M. Paillet, R. Borsali, O. Diat, A. Dufresne, J.Y. Cavaillé, and H. Chanzy. Langmuir, **15**, 6123 (1999).
10. Y. Lu, L. Weng, and X. Cao. Macromol. Biosci. **5**, 1101 (2005).
11. I. Kvien, S.T. Bjørn, and K. Oksman. Biomacromolecules, **6**, 3160 (2005).
12. N.L. Garcia de Rodriguez, W. Thielemans, and A. Dufresne. Cellulose, **13**, 261 (2006).
13. M.A.S. Azizi Samir, F. Alloin, M. Paillet, and A. Dufresne. Macromolecules, **37**, 4313 (2004).
14. V. Favier, G.R. Canova, J.Y. Cavaillé, H. Chanzy, A. Dufresne, and C. Gauthier. Polym. Adv. Technol. **6**, 351 (1995).
15. W. Helbert, J.Y. Cavaillé, and A. Dufresne. Polym. Compos. **17**, 604 (1996).
16. S. Beck-Candanedo, M. Roman, and D.G. Gray. Biomacromolecules, **6**, 1048 (2005).
17. K. Gopalan Nair and A. Dufresne. Biomacromolecules, **4**, 657 (2003).
18. A. Morin and A. Dufresne. Macromolecules, **35**, 2190 (2002).
19. J. Sriupayo, P. Supaphol, J. Blackwell, and R. Rujiravanit. Polymer, **46**, 5637 (2005).
20. M. Paillet and A. Dufresne. Macromolecules, **34**, 6527 (2001).
21. O.A. Battista. *In* Microcrystal Polymer Science. McGraw-Hill Book Company, New York. 1975, p. 138.
22. H. Angellier, L. Choisnard, S. Molina-Boisseau, P. Ozil, and A. Dufresne. Biomacromolecules, **5**, 1545 (2004).
23. J.L. Putaux, S. Molina-Boisseau, T. Momaur, and A. Dufresne. Biomacromolecules, **4**, 1198 (2003).
24. H. Angellier, J.L. Putaux, S. Molina-Boisseau, D. Dupeyre, and A. Dufresne. Macromol. Symp. **221**, 95 (2005).
25. L. Heux, G. Chauve, and C. Bonini. Langmuir, **16**, 8210 (2000).
26. D. Bordel, J.L. Putaux, and L. Heux. Langmuir, **22**, 4899 (2006).
27. C. Goussé, H. Chanzy, G. Exoffier, L. Soubeyrand, and E. Fleury. Polymer, **43**, 2645 (2002).
28. J. Araki, M. Wada, and S. Kuga. Langmuir, **17**, 21 (2001).
29. K. Gopalan Nair, A. Dufresne, A. Gandini, and N.M. Belgacem. Biomacromolecules, **4**, 1835 (2003).
30. H. Angellier, S. Molina-Boisseau, M.N. Belgacem, and A. Dufresne. Langmuir, **21**, 2425 (2005).
31. H. Yuan, Y. Nishiyama, M. Wada, and S. Kuga. Biomacromolecules, **7**, 696 (2006).
32. M.A.S. Azizi Samir, F. Alloin, J.Y. Sanchez, N. El Kissi, and A. Dufresne. Macromolecules, **37**, 1386 (2004).
33. N.E. Marcovich, M.L. Auad, N.E. Belessi, S.R. Nutt, and M.I. Aranguren. J. Mater. Res. **21**, 870 (2006).
34. W. Thielemans, M.N. Belgacem, and A. Dufresne. Langmuir, **22**, 4804 (2006).
35. M. Labet, W. Thielemans, and A. Dufresne. Biomacromolecules, **8**, 2916 (2007).
36. M.A.S. Azizi Samir, F. Alloin, J.Y. Sanchez, and A. Dufresne. Polymer, **45**, 4033 (2004).
37. L. Chazeau, J.Y. Cavaillé, G.R. Canova, R. Dendievel, and B. Boutherin. J. Appl. Polym. Sci. **71**, 1797 (1999).
38. A. Dufresne. Compos. Interfaces, **7**, 53 (2000).
39. M.N. Anglès and A. Dufresne. Macromolecules, **33**, 8344 (2000).
40. A.P. Mathew and A. Dufresne. Biomacromolecules, **3**, 609 (2002).
41. H. Angellier, S. Molina-Boisseau, L. Lebrun, and A. Dufresne. Macromolecules, **38**, 3783 (2005).
42. H. Angellier, S. Molina-Boisseau, P. Dole, and A. Dufresne. Biomacromolecules, **7**, 531 (2006).
43. Y.J. Choi and J. Simonsen. J. Nanosci. Nanotechnol. **6**, 633 (2006).
44. M.A.S. Azizi Samir, F. Alloin, W. Gorecki, J.Y. Sanchez, and A. Dufresne. J. Phys. Chem. B, **108**, 10845 (2004).
45. N. Ljungberg, J.Y. Cavaillé, and L. Heux. Polymer, **47**, 6285 (2006).
46. A. Dufresne, M.B. Kellerhals, and B. Witholt. Macromolecules, **32**, 7396 (1999).
47. Y. Noishiki, Y. Nishiyama, M. Wada, S. Kuga, and J. Magoshi. J. Appl. Polym. Sci. **86**, 3425 (2002).
48. I. Sakurada, Y. Nukushina, and T. Ito. J. Polym. Sci. **57**, 651 (1962).
49. J.C. Halpin and J.L. Kardos. J. Appl. Phys. **43**, 2235 (1972).
50. V. Favier, R. Dendievel, G.R. Canova, J.Y. Cavaillé, and P. Gilormini. Acta Mater. **45**, 1557 (1997).
51. V. Favier, G.R. Canova, S.C. Shrivastava, and J.Y. Cavaillé. Polym. Eng. Sci. **37**, 1732 (1997).
52. A. Dufresne. J. Nanosci. Nanotechnol. **6**, 322 (2006).
53. A. Dufresne, J.Y. Cavaillé, and M.R. Vignon. J. Appl. Polym. Sci. **64**, 1185 (1997).
54. W.J. Orts, L. Godbout, R.H. Marchessault, and J.F. Revol. (1998). Macromolecules, **31**, 5717 (1998).
55. D. Dubief, E. Samain, and A. Dufresne. Macromolecules, **32**, 5765 (1999).
56. N. Ljungberg, C. Bonini, F. Bortolussi, C. Boisson, L. Heux, and J.Y. Cavaillé. Biomacromolecules, **6**, 2732 (2005).
57. H. Angellier, S. Molina-Boisseau, and A. Dufresne. Macromolecules, **38**, 9161 (2005).
58. M.N. Anglès and A. Dufresne. Macromolecules, **34**, 2921 (2001).
59. A. Dufresne and M.R. Vignon. Macromolecules, **31**, 2693 (1998).
60 A. Dufresne, D. Dupeyre, and M.R. Vignon. J. Appl. Polym. Sci. **76**, 2080 (2000).
61. M.A.S. Azizi Samir, A. Montero Mateos, F. Alloin, J.Y. Sanchez, and A. Dufresne. Electrochim. Acta, **49**, 4667 (2004).
62. M.A.S. Azizi Samir, F. Alloin, J.Y. Sanchez, and A. Dufresne. Macromolecules, **37**, 4839 (2004).
63. M.A.S. Azizi Samir, L. Chazeau, F. Alloin, J.Y. Cavaillé, A. Dufresne, and J.Y. Sanchez. Electrochim. Acta, **50**, 3897 (2005).
64. Y. Wang, X. Cao, and L. Zhang. Macromol. Biosci. **6**, 524 (2006).
65. Y. Lu, L. Wenig, and L. Zhang. Biomacromolecules, **5**, 1046 (2004).
66. J. Sriupayo, P. Supaphol, J. Blackwell, and R. Rujiravanit. Carbohydr. Polym. **62**, 130 (2005).
67. A. Dufresne and J.Y. Cavaillé. J. Polym. Sci. Part B: Polym. Phys. **36**, 2211 (1998).
68. M.E. Malainine, M. Mahrouz, and A. Dufresne. Compos. Sci. Technol. **65**, 1520 (2005).
69. F. Dalmas, L. Chazeau, C. Gauthier, J.Y. Cavaillé, and R. Dendievel. Polymer, **47**, 2802 (2006).
70. E. Kristo and C.G. Biliaderis. Carbohydr. Polym. **68**, 146 (2007).

© 2008 NRC Canada

Semi-synthesis and proteasome inhibition of D-ring deoxy analogs of (–)-epigallocatechin gallate (EGCG), the active ingredient of green tea extract[1]

Congde Huo, Guoqing Shi, Wai Har Lam, Di Chen, Quizhi Cindy Cui, Q. Ping Dou, and Tak Hang Chan

Abstract: A semi-synthetic route to the D-ring analogs of (–)-epigallocatechin gallate (EGCG) from the relatively abundant (–)-epigallocatechin (EGC), isolated from green tea leaves, is described. A natural product (**13**), found in *Cistus salvifolius*, its acetate (**14**) and analog (**17**) were synthesized by this method. Their inhibitory activities against proteasomes were investigated.

Key words: green tea, (–)-epigallocatechin gallate (EGCG), (–)-epigallocatechin (EGC), proteasome inhibition.

Résumé : On a développé une voie semisynthétique vers des analogues du cycle D du gallate de (–)-épigallocatéchine (GEGC) à partir de la (–)-épigallocatéchine (EGC) qui est relativement abondante et qu'on a isolé des feuilles de thé vert. Faisant appel à cette méthode, on a réalisé la synthèse du produit naturel **13** qu'on retrouve dans *Cistus Salvifolius*, son acétate **14** et son analogue **17**. On a évalué leurs activités inhibitrices vis-a-vis des protéasomes.

Mots-clés : thé vert, gallate de (–)-épigallocatéchine (GEGC), (–)-épigallocatéchine (EGC), inhibition des protéasomes.

[Traduit par la Rédaction]

Introduction

Tea, produced from the plant *Camellia sinensis*, has been consumed by humans for thousands of years. Green tea contains many polyphenols, commonly known as catechins, which constitute about 30%–40% of the water-soluble compounds in brewed green tea (1). The major catechins are: (–)-epigallocatechin-3-gallate (EGCG, **1**), (–)-epigallocatechin (EGC, **2**), (–)-epicatechin-3-gallate (ECG, **3**), and (–)-epicatechin (EC, **4**) (Fig. 1). Of these, EGCG is by far the most abundant and has been reported to have various biological activities that may account for the beneficial effects attributed to green tea (2, 3). Regular drinking of green tea has been associated with reduced risk of several forms of cancer (4), and the effect is attributed mainly to tea polyphenols, in particular EGCG (5).

A critical issue concerning the potential application of EGCG as an anti-cancer agent is its known poor bioavailability (6). The low bioavailability was partly due to poor cellular uptake as well as the instability of EGCG in alkaline or neutral solutions (7, 8). To improve the bioavailability of EGCG, we recently proposed the use of EGCG octaacetate (pro-EGCG, **5**) as a prodrug (9). Compound **5** was found to be more stable to alkaline than EGCG (9) but inactive in vitro as an inhibitor of proteasomes, a presumed key mechanism for the cancer cytotoxicity of EGCG (9). Compound **5** was, however, converted intracellularly into EGCG and active in proteasome inhibition and cancer cell apoptosis (10, 11). Furthermore, intragastric administration of **5** to CF-1 mice resulted in higher bioavailability compared to the administration of equimolar doses of EGCG (10). More importantly, we showed that in vivo for either breast cancer animal model (11) or the androgen-independent prostate cancer animal model (12), **5** showed a significant inhibition of cancer growth compared to EGCG itself (11, 12).

Received 10 October 2007. Accepted 30 November 2007. Published on the NRC Research Press Web site at canjchem.nrc.ca on 22 March 2008.

C. Huo[2] and T.H. Chan.[2,3] Department of Chemistry, McGill University, Montreal, QC H3A 2K6, Canada.
W.H. Lam. Department of Applied Biology and Chemical Technology and the Open Laboratory for Chiral Technology, the Institute of Molecular Technology for Drug Discovery and Synthesis, The Hong Kong Polytechnic University, Hung Hom, Kowloon, Hong Kong SAR, China.
G. Shi,[4] D. Chen, Q.C. Cui, and Q.P. Dou. The Prevention Program, Barbara Ann Karmanos Cancer Institute, and Department of Pathology, School of Medicine, Wayne State University, Detroit, MI 48201, USA.

[1]This article is part of a Special Issue dedicated to Professor R. Marchessault.
[2]Alternative address: Department of Applied Biology and Chemical Technology and the Open Laboratory for Chiral Technology, the Institute of Molecular Technology for Drug Discovery and Synthesis, The Hong Kong Polytechnic University, Hung Hom, Kowloon, Hong Kong SAR, China.
[3]Corresponding author (e-mail: tak-hang.chan@mcgill.ca).
[4]Present address: School of Applied Science, University of Science and Technology Beijing, Beijing, China.

 doi:10.1139/V07-141 © 2008 NRC Canada

Fig. 1. Four major green tea catechins, **1**, **2**, **3**, and **4** and their peracetates, **5**, **6**, **7**, and **8**.

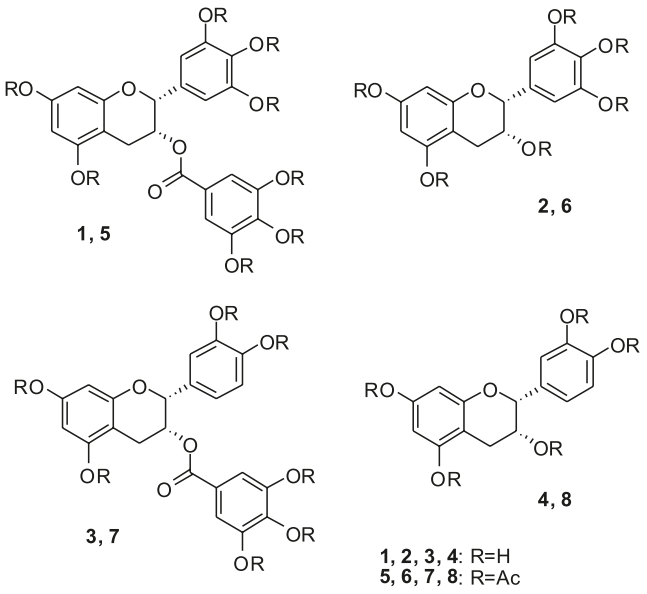

Another factor that affects the bioavailability of EGCG is due to metabolic biotransformation reactions, including methylation, glucuronidation, and sulfonation, resulting in reduced biological activities of EGCG in vivo (13–15). Recently, an epidemiological study of women found that risk of breast cancer did not differ between tea drinkers and non-tea drinkers among those who were homozygous for the high activity catechol-*O*-methyltransferase (COMT) (16). Only women who carried at least one low activity COMT allele and were tea drinkers had a significantly reduced risk of breast cancer compared to non-tea drinkers (16). The hypothesis to explain these results is that tea polyphenols are methylated by COMT and that the methylated tea polyphenols are less cancer-protective. Indeed, EGCG is a substrate of COMT and is converted to methylated EGCGs (17). In support of this hypothesis, we found that methylated EGCGs are much weaker inhibitors of proteasomes (18). A possible approach to circumvent the effect of metabolic methylation is to use analogs of EGCG, which may be poorer substrates of COMT. In this connection, we have recently synthesized compound **13**, a natural compound found in *Cistus salvifolius* and a D-ring deoxy analog of EGCG (19). Interestingly, even though **13** is a poorer inhibitor of proteasome than EGCG itself, the prodrug of **13** (acetate **14**) was found to be a more potent cancer cytotoxic agent than EGCG itself and comparable to **5** (19). A possible explanation of the enhanced activity of **13** (via its prodrug **14**) is that **13** is probably a poorer substrate of COMT than EGCG. To validate this explanation and to perform animal studies, we need substantial quantities of **13** and **14**, which cannot be easily fulfilled with total synthesis (19, 20). We therefore sought a semi-synthetic approach to prepare **13** and **14** as well as the isomeric acetate (**17**).

In 2001, we reported the first total enantioselective synthesis of EGCG (20). Subsequently, many analogs of EGCG have been prepared utilizing the established total synthetic routes (21), including compound **13**, which was prepared via the key intermediate **9** in 12 steps (Scheme 1) (19). Since

Scheme 1.

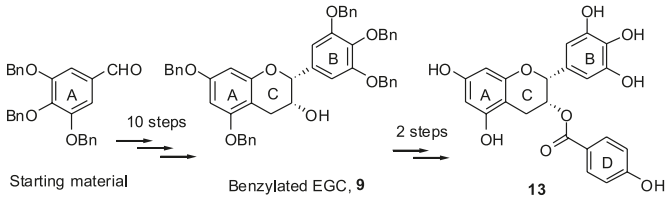

compound **9** is simply the benzylated derivative of EGC, it seems reasonable that EGC can serve as the starting material for the preparation of **9** in a semi-synthesis approach.

Results and discussion

Even though the amounts of catechins, especially that of EGCG and EGC, in green tea leaves are quite high, the purification of individual catechins to high purity (>98%) has not been easy due to the presence of many components with similar water solubility and the structural similarities of the catechins. A US patent described a four-step process involving three column chromatographic separations to isolate catechins from green tea, using expensive reverse phase column fillings (22). A more recent patent application described a process of separating catechins by subjecting a green tea extract to chromatography on a macroporous polar resin with a polar elution solvent under pressure (23). We have devised an alternative method of purifying catechins to high purity by treating comminuted green tea leaves directly or green tea extracts with acetic anhydride in pyridine. This acetylation reaction converted the mixture of catechins into fully acetylated catechins (Fig. 1) and rendered them less hydrophilic and separable by simple column chromatography over silica gel with ethyl acetate/hexane as eluent (see experimental). In this way, EGCG octaacetate (**5**), EGC hexaacetate (**6**), ECG heptaacetate (**7**), and EC pentaacetate (**8**) were obtained as solids with good analytical data. HPLC analysis showed that they can be obtained in >98% purity. The amounts of the four acetates depended on the source of green tea. Using Japanese green tea bags with OSK trademark, EGCG octaacetate (**5**) and EGC hexaacetate (**6**) were obtained respectively in 4.3% and 1.5% of the dry weight of the green tea leaves used. The yields of compounds **7** and **8** were generally less than 1% of dry weight.

With EGC hexaacetate (**6**) readily at hand, we examined the selective hydrolysis of the acetate moieties. We found that ammonium acetate in aqueous methanol (24) was able to selectively hydrolyze the aromatic acetate esters of EGC hexaacetate (**6**) to give compound **10**. Benzylation of **10** gave the protected benzyl ether **11**. Base hydrolysis of **11** removed the aliphatic acetate group to give the key intermediate **9** (Scheme 2).

After benzylated EGC (**9**) was obtained by the above method, esterification of **9** with 4-benzyloxybenzoic acid gave the ester **12**. Catalytic hydrogenolysis of **12** gave compound **13**. Compound **13** is a natural product, which has been identified and isolated in small quantities from *C. salvifolius*, a plant indigenous in the Mediterranean area (25). In Turkey, tea prepared from the leaves of *C. salvifolius* has been used for the treatment of cancer (26). Using this semi-synthetic method, we can obtain **13** from

© 2008 NRC Canada

Scheme 2.

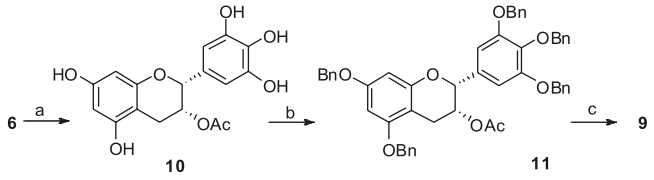

(a) NH_4OAc, MeOH/H_2O (4:1), Rt, 24h; (b) BnCl, K_2CO_3, acetone, reflux, 6h; (c) K_2CO_3, MeOH/$CHCl_3$, Rt, 2h.

Scheme 3.

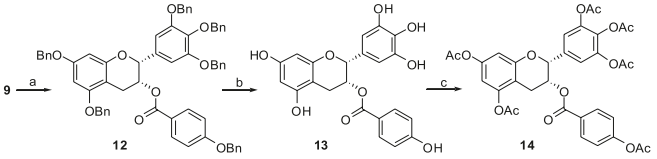

(a) 4-benzyloxybenzoic acid, DCC, DMAP, CH_2Cl_2, 0 °C to Rt, 48h; (b) H_2, Pd/C, THF/MeOH (1:1), Rt, 6h; (c) Ac_2O, pyridine, 45 °C, 8h.

Table 1. Inhibition of the CT-like activity of purified 20S proteasome by D-ring analogs of EGCG.

Compound	IC_{50} (μmol/L)
13	6.61±0.76[a]
14	n.a[b]
17	n.a.[b]

Note: Compounds at 2, 5, 10, 20, and 50 μmol/L were incubated with a purified 20S proteasome (0.1 μg) and the substrate Suc-LLVY-AMC (40 μmol/L) for 2 h, followed by the measurement of the proteasomal CT-like activity.

[a]The data are representatives of independent triplicate experiments.

[b]n.a. represents the inhibition of the CT-like activity of purified 20S proteasome by the indicated compounds at 50 μmol/L to be lower than 50%. Similar results were obtained from three independent experiments.

EGC hexaacetate (**6**) isolated from green tea leaves in 5 steps with an overall yield of 38%. Acetylation of compound **13** afforded the fully acetylated derivative **14** (Scheme 3).

Esterification of **9** with 3-acetoxybenzoyl chloride gave the ester **15**. Catalytic hydrogenolysis followed by acetylation gave compound **17**, the positional isomer of **14** (Scheme 4).

With the synthesis accomplished, the inhibition potency of compound **13**, compound **14**, and compound **17** against the chymotrypsin (CT)-like activity of purified 20S proteasome were investigated. As shown in Table 1, compound **13** was an inhibitor to the CT-like activity of purified 20S proteasome with IC_{50} of 6.61 μmol/L, while **14** and **17** had much less inhibitory effect and could not inhibit 50% of the CT-like activity of purified 20S proteasome at 50 μmol/L. Those results were in accordance with our previous observations (19, 27).

We have previously reported that compound **13** has no obvious inhibition to proteasomal CT-like activity in intact tumor cells (19). To investigate if the acetylated derivative **14** and **17** could exhibit proteasomal inhibition in whole cells,

Scheme 4.

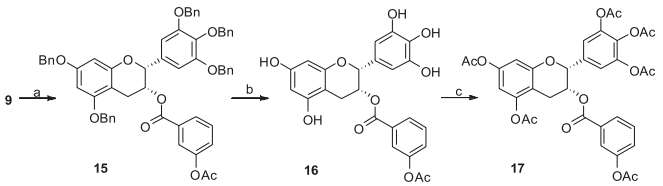

(a) 3-acetoxybenzoyl chloride, DMAP, DCM, Rt, overnight; (b) H_2, Pd/C, THF/MeOH (1:1), Rt, 6h; (c) Ac_2O, pyridine, 45 °C, 8h.

Fig. 2. The inhibition potency of **14** and **17** to the proteasomal chymotrypsin-like activity in Jurkat T cells. Jurkat T cells were treated with each of the indicated compounds at 50 μmol/L for 48 h, and then the proteasomal chymotrypsin-like activity of cell lysate was determined.

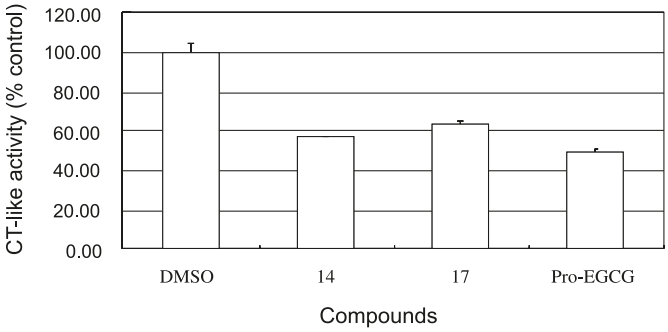

human leukemia Jurkat T cells were treated with each of these compounds at 50 μmol/L for 48 h, using pro-EGCG **5** as a control. As shown in Fig. 2, **14** and **17** exhibit 43% and 37% of proteasome inhibition, respectively, while pro-EGCG **5** inhibited ~50% of the proteasome activity (Fig. 2). Because the per-acetylated EGCG was easier to get into cells than EGCG and the per-acetylated EGCG can be converted to EGCG by the cellular esterase enzymes (9, 11, 27), we believe that **14** and **17** behave as prodrugs in a manner similar to pro-EGCG.

Consistent with the inhibition of proteasomal chymotrypsin-like activity, the accumulation of the proteasome target protein Bax (p21) and ubiquitinated Bax [Bax/(Ub)n, mainly by **5**] by **14**, **17** and **5** were also observed, while expression of Bax (p36), a calpain cleavage product homodimer, was not increased (Fig. 3), indicating that proteasome inhibition by these EGCG analog prodrugs activates the caspase, but not calpain enzyme (see the following paragraph).

In various cancer cells, induction of apoptotic cell death is the consequence of proteasomal CT-like activity inhibition. We thus investigated apoptosis by measuring caspase-3 activity and PARP cleavage. Figure 4 shows that **14** and **17** induced a 13.5- and 15-fold increase of caspase-3 activity, respectively, while pro-EGCG **5** also induced a ~15-fold increase of caspase activity (Fig. 4). Trypan blue assay shows that **14** and **17** induced 36% and 34% of cell death after treatment for 24 h, while pro-EGCG induced 40% of cell death (Fig. 5). Consistent with apoptotic cell death induction, the PARP cleavage fragment p85 was produced by **14**, **17**, and pro-EGCG **5** (Fig. 3). It has been shown that caspase-3/-7 cleaves PARP, generating the p85 PARP frag-

© 2008 NRC Canada

Fig. 3. Compounds **14** and **17** inhibit the proteasome and activate the caspase pathway. Jurkat T cells were treated with 50 μmol/L of each indicated compound or solvent DMSO for 48 h, followed by Western blot analysis of the Bax and PARP. DMSO- and pro-EGCG-treated cells were used as solvent control and positive control, respectively, and Actin was used as a loading control.

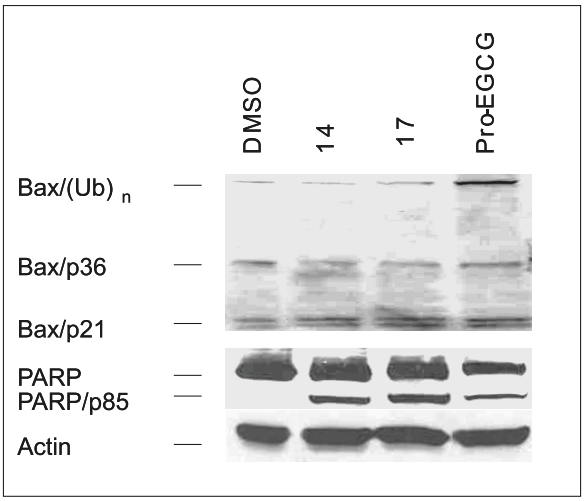

Fig. 4. Induction of caspase-3 activity of Jurkat T cells. These cells were treated with compounds at 50 μmol/L for 48 h, and then the caspase-3 activity of cell lysate was determined.

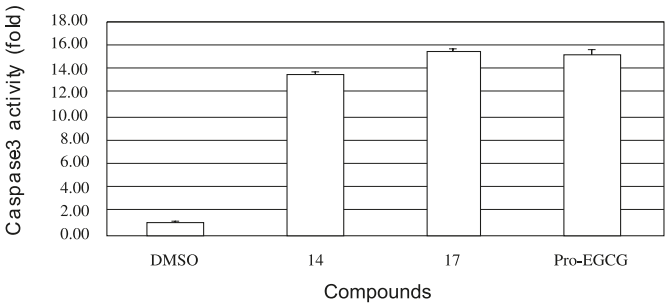

ment (28). The PARP cleavage is consistent with caspase-3 activation.

Conclusion

We have developed an efficient method for the isolation and purification of various catechin acetates from green tea leaves. Using EGC hexaacetate (**6**) as starting material, semi-synthesis of D-ring deoxy analogs of EGCG can be obtained in gram quantities. The acetates of these analogs show cytotoxic activities and proteasomal inhibition after cellular intake.

Experimental

General

The starting materials and reagents, purchased commercially, were used without further purification. Green tea bags with OSK trademark were purchased from SEIYU super-

Fig. 5. Induction of cell death. Jurkat T cells were treated with each of the compounds at 50 μmol/L for 24 h, and then the percentage of death cells was determined.

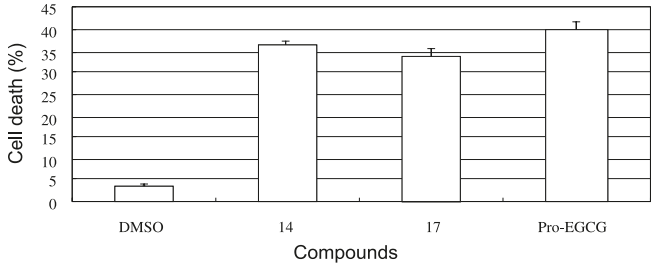

market in Hong Kong. Alternately, Shou Mee green tea leaves were purchased from Ying Kee Tea House, Hong Kong. Anhydrous DMF was distilled under vacuum from CaH_2. Anhydrous DCM was distilled under nitrogen from CaH_2. Anhydrous THF was distilled under nitrogen from sodium benzophenone ketyl. Flash chromatography was carried out using silica gel 60 (70–230 mesh). The melting points were uncorrected. The spectra were run on the following instruments: Varian AS500 spectrometer for ^1H and ^{13}C NMR and VG Micromass 7070F mass spectrometer for MS and HR-MS.

To investigate their proteasome inhibition, compounds **13**, **14**, and **17** were diluted in DMSO to give stock solution of 50 mmol/L and stored in aliquots at –20 °C. Purified rabbit 20S proteasome and fluorogenic peptide substrates, Suc-LLVY-AMC for the proteasomal chymotrypsin-like activity and Ac-DEVD-AMC for caspase-3/-7 activity, were from Calbiochem Inc. (San Diego, Calif.). RPMI 1640, penicillin, and streptomycin were purchased from Invitrogen (Carlsbad, Calif.). Mouse monoclonal antibody against human poly (ADP-ribose) polymerase (PARP) was purchased from BIOMOL International LP (Plymouth Meeting, Penn.). Mouse monoclonal antibodies against Bax (B-9), goat polyclonal antibody against actin (C-11), and HRP labeled secondary antibodies were from Santa Cruz Biotechnology, Inc. (Santa Cruz, Calif.).

Extraction and isolation of the four major green tea catechins peracetates (5, 6, 7, and 8).

Method 1

Comminuted green tea leaves (100 g) were added to a mixture of pyridine (200 mL) and acetic anhydride (100 mL). The resulting mixture was stirred at room temperature for 20 h. The mixture was filtered through a Buchner funnel and washed with ethyl acetate. The filtrate was washed with 0.1 mol/L HCl, saturated $NaHCO_3$ solution, water, and brine. The organic solution was dried over anhydrous magnesium sulfate and evaporated by rotary evaporator. The residue was subjected to chromatography as described later.

Method 2

Green Tea leaves (100 g) were extracted with water (1 L) at 70 °C for 30 min four times. The combined water solution was washed with chloroform three times to remove the low polarity components of green tea. Then the water phase was extracted with ethyl acetate five times. The ethyl acetate so-

© 2008 NRC Canada

lution was dried over anhydrous magnesium sulfate and evaporated by rotary evaporator to give green tea extract as a pale yellow powder after vacuum (10 g, 10%). The powder (10 g) was added to a mixture of pyridine (70 mL) and acetic anhydride (80 mL) with stirring. And the mixture was kept for 20 h at 45 °C in an oil bath. The reaction mixture was then poured into ice-cold water and extracted with ethyl acetate three times. The combined organic layer was washed with 0.1 mol/L HCl, saturated $NaHCO_3$ solution, water, and brine. The organic solution was dried over anhydrous magnesium sulfate and evaporated by rotary evaporator.

The concentrate from method 1 or method 2 was purified by column chromatography over silica gel (EA/*n*-Hex from 2:3 to 3:2) to afford the EC pentaacetate (**8**), EGC hexaacetate (**6**), ECG heptaacetate (**7**), and EGCG octaacetate (**5**), sequentially. TLC performed with Merck pre-coated silica gel 60 F254 plates and with EA/*n*-Hex (*v*/*v* = 2:1) as eluent gave the following R_f values: **8** 0.68, **6** 0.58, **7** 0.46, and **5** 0.32.

EGCG octaacetate (5)

Yield: 4.2%–4.9%. Mp 114.3–115.1 °C. $[\alpha]_D^{20}$ –60.8 (*c* 2.0, $CHCl_3$). ^{1}H NMR ($CDCl_3$, 500 MHz) δ: 7.63 (s, 2H), 7.24 (s, 2H), 6.73 (d, *J* = 2.0 Hz, 1H), 6.61 (d, *J* = 2.0 Hz, 1H), 5.64 (s, 1H), 5.18 (s, 1H), 3.06 (dd, *J* = 18.0 Hz, *J* = 4.5 Hz, 1H), 2.99 (dd, *J* = 18.0 Hz, *J* = 2.5 Hz, 1H), 2.31–2.23 (m, 24H). ^{13}C NMR (CDCl3, 125 MHz) δ: 169.1, 168.7, 167.9, 167.7, 167.0, 166.5, 163.8, 155.0, 150.0, 149.9, 143.7, 143.6, 139.2, 135.3, 134.6, 127.7, 122.6, 119.1, 109.7, 109.3, 108.3, 76.8, 68.3, 26.1, 21.3, 21.0, 20.8, 20.8, 20.4, 20.4. LR-MS (ESI) *m*/*z*: 817.15 (M^+ + Na, 100). HR-MS *m*/*z* calcd. for $C_{38}H_{34}O_{19}Na$: 817.1592; found: 817.1605.

EGC hexaacetate (6)

Yield of dry weight of green tea leaves: 1.5%–2.1%. Mp 192–193 °C. $[\alpha]_D^{20}$ –15.6 (*c* 2.0, $CHCl_3$). ^{1}H NMR ($CDCl_3$, 500 MHz) δ: 7.22 (s, 2H), 6.67 (d, *J* = 2.0 Hz, 1H), 6.57 (d, *J* = 2.0 Hz, 1H), 5.38 (s, 1H), 5.09 (s, 1H), 2.95 (dd, *J* = 18.0 Hz, *J* = 4.5 Hz, 1H), 2.88 (dd, *J* = 18.0 Hz, *J* = 1.5 Hz, 1H), 2.28–2.27.94 (m, 15H), 1.94 (s, 3H). ^{13}C NMR ($CDCl_3$, 125 MHz) δ: 170.8, 169.3, 168.7, 168.0, 167.1, 155.0, 150.0, 149.9, 143.5, 135.7, 134.5, 119.2, 109.8, 109.1, 108.3, 76.7, 66.7, 26.1, 21.3, 21.0, 21.0, 20.9, 20.4. LR-MS (EI) *m*/*z*: 558.14 (M^+, 15). HR-MS *m*/*z* calcd. for $C_{27}H_{26}O_{13}Na$: 581.1271; found: 581.1252.

ECG heptaacetate (7)

Yield: 0.1%–0.8%. $[\alpha]_D^{20}$ –58.8 (*c* 2.0, $CHCl_3$). ^{1}H NMR ($CDCl_3$, 500 MHz) δ: 7.63 (s, 2H), 7.34 (s, 1H), 7.30 (d, *J* = 8.5 Hz, 1H), 7.20 (d, *J* = 8.5 Hz, 1H), 6.73 (d, *J* = 2.0 Hz, 1H), 6.61 (d, *J* = 2.0 Hz, 1H), 5.64 (s, 1H), 5.21 (s, 1H), 3.08 (dd, *J* = 18.0 Hz, *J* = 4.5 Hz, 1H), 2.99 (d, *J* = 18.9 Hz, 1H), 2.29–2.24 (m, 21H). ^{13}C NMR ($CDCl_3$, 125 MHz) δ: 168.9, 168.4, 168.0, 167.9, 167.4, 166.2, 163.5, 154.9, 149.7, 149.6, 143.3, 142.1, 142.0, 138.9, 135.4, 127.4, 124.4, 123.5, 122.3, 121.8, 109.5, 108.9, 108.1, 68.1, 26.0, 21.1, 20.8, 20.6, 20.6, 20.5, 20.1. LR-MS (ESI) *m*/*z*: 759.14 (M^+ + Na, 100). HR-MS *m*/*z* calcd. for $C_{36}H_{32}O_{17}Na$: 759.1537; found: 759.1539.

EC pentaacetate (8)

Yield: 0.1%–1.2%. $[\alpha]_D^{20}$ –12.6 (*c* 2.0, $CHCl_3$). ^{1}H NMR ($CDCl_3$, 500 MHz) δ: 7.35 (s, 1H), 7.27 (d, *J* = 8.5 Hz, 1H), 7.20 (d, *J* = 8.5 Hz, 1H), 6.67 (d, *J* = 1.0 Hz, 1H), 6.57 (d, *J* = 1.0 Hz, 1H), 5.39 (s, 1H), 5.11 (s, 1H), 2.98 (dd, *J* = 17.5 Hz, *J* = 4.0 Hz, 1H), 2.88 (d, *J* = 17.5 Hz, 1H), 2.29 (m, 12H), 1.92 (s, 3H). ^{13}C NMR ($CDCl_3$, 125 MHz) δ: 170.7, 169.3, 168.7, 168.4, 168.3, 155.2, 150.0, 149.9, 142.3, 142.1, 136.1, 124.6, 123.4, 122.3, 109.8, 109.0, 108.3, 76.9, 66.9, 26.3, 21.3, 21.0, 21.0, 20.9. LR-MS (ESI) *m*/*z*: 523.11 (M^+ + Na, 100). HR-MS *m*/*z* calcd. for $C_{25}H_{24}O_{11}Na$: 523.1216; found: 523.1206.

(–)-(2*R*,3*R*)-5,7-Dihydroxy-2-(3,4,5-trihydroxyphenyl)chroman-3-yl acetate (10)

To a solution of **6** (558 mg, 1 mmol) in water/methanol (1:4 *v*/*v*, 50 mL), ammonium acetate (1.54 g, 20 mmol) was added. The resulting mixture was stirred at room temperature and the progress of the reaction was monitored by TLC. After 24 h the mixture was concentrated and water was added, then the mixture was extracted with ethyl acetate. The organic extract was then dried over sodium sulfate and evaporated. The residue was purified by column chromatography over silica gel (EA/*n*-Hex = 3:1) to afford compound **10** (296 mg, 85% yield) as a white solid. ^{1}H NMR (acetone-d_6, 500 MHz) δ: 6.56 (s, 1H), 6.06 (d, *J* = 2.0 Hz, 1H), 5.96 (d, *J* = 2.0 Hz, 1H), 5.37 (s, 1H), 4.96 (s, 1H), 2.96 (dd, *J* = 17.5 Hz, *J* = 4.5 Hz, 1H), 2.78 (dd, *J* = 17.5 Hz, *J* = 2.0 Hz, 1H), 1.88 (s, 3H). ^{13}C NMR (acetone-d_6, 125 MHz) δ: 169.7, 157.1, 156.8, 156.3, 145.6, 132.6, 129.9, 106.1, 98.2, 95.7, 95.1, 77.1, 68.3, 30.0, 25.7, 20.3.

(–)-(2*R*,3*R*)-5,7-Bis(benzyloxy)-2-(3,4,5-tris(benzyloxy)phenyl)chroman-3-yl acetate (11)

A solution of **10** (256 mg, 0.73 mmol) and benzyl bromide (0.48 mL, 4 mmol) in acetone (20 mL) was treated with potassium carbonate (554 mg, 4 mmol), and the resulting mixture was heated under reflux for 6 h. After cooling, the mixture was concentrated and water was added. The mixture was extracted with ethyl acetate. The organic phase was then dried over sodium sulfate and evaporated. The residue was purified by column chromatography over silica gel (EA/*n*-Hex = 1:6) to afford the benzyl protected product **11** (382 mg, 65% yield) as a white solid. Mp 116–118 °C. ^{1}H NMR ($CDCl_3$, 500 MHz) δ: 7.48–7.30 (m, 25H), 6. 82 (s, 2H), 6.35 (s, 1H), 6.34 (s, 1H), 5.47 (s, 1H), 5.19–5.06 (m, 10H), 4.99 (s, 1H), 3.06 (dd, *J* = 17.5 Hz, *J* = 4.5 Hz, 1H), 3.00 (d, *J* = 17.5 Hz, 1H), 1.84 (s, 3H). ^{13}C NMR ($CDCl_3$, 125 MHz) δ: 170.1, 158.7, 157.9, 155.3, 152.7, 138.1, 137.8, 137.0, 136.8, 136.8, 133.3, 128.6, 128.6, 128.5, 128.5, 128.4, 128.1, 128.0, 127.9, 127.9, 127.8, 127.5, 127.4, 127.1, 106.3, 100.8, 94.7, 93.9, 77.3, 75.1, 71.3, 70.1, 69.9, 67.7, 26.0, 21.0.

(–)-(2*R*,3*R*)-5,7-Bis(benzyloxy)-2-(3,4,5-tris(benzyloxy)phenyl)chroman-3-ol (9)

To a solution of **11** (342 mg, 0.43 mmol) in methanol (50 mL), potassium carbonate (119 mg, 0.86 mmol) was added. The resulting mixture was stirred at room temperature and the progress of the reaction was monitored by TLC. After 2 h the mixture was concentrated and water was

© 2008 NRC Canada

added. The mixture was extracted with ethyl acetate. Evaporation of the organic solvent afforded compound **9** (308 mg, 95% yield) as a white solid. Mp 135–137 °C. ^{1}H NMR ($CDCl_3$, 500 MHz) δ: 7.45–7.27 (m, 25H), 6.83 (s, 2H), 6.30 (s, 2H), 5.15 (s, 4H), 5.08 (s, 2H), 5.04 (s, 4H), 4.91 (s, 1H), 4.23 (s, 1H), 3.03 (d, *J* = 17.0 Hz, 1H), 2.93 (dd, *J* = 17.0 Hz, *J* = 4.5 Hz, 1H). ^{13}C NMR ($CDCl_3$, 125 MHz) δ: 159.0, 158.6, 155.3, 153.3, 138.6, 138.1, 137.2, 137.2, 134.0, 128.9, 128.8, 128.8, 128.7, 128.7, 128.7, 128.4, 128.3, 128.2, 128.2, 128.1, 128.1, 127.8, 127.8, 127.5, 106.4, 101.2, 95.0, 94.4, 78.8, 75.5, 71.6, 70.4, 70.2, 66.7, 28.4. LR-MS (ESI) *m*/*z*: 779.28 (M^+ + Na, 100). HR-MS *m*/*z* calcd. for $C_{50}H_{44}O_7H$: 757.3165; found: 757.3177.

4-Benzyloxybenzoic acid

To a suspension of 4-hydroxybenzoic acid (2.0 g, 15.2 mmol) and potassium carbonate (4 g) in dry DMF (40 mL), benzyl bromide (3.6 mL, 30.5 mmol) was added dropwise under a nitrogen atmosphere. The reaction mixture was heated at 80 °C for 6 h. The mixture was evaporated, added to ice water (300 mL) and acidified with 1:1 HCl to a pH of 1. The suspension was filtered, washed three times with water, then dried to give benzyl 4-(benzyloxy)benzoate (3.5 g, 76%) as an off-white solid. To the suspension of the dibenzylated product (2 g, 6.3 mmol) in methanol (20 mL) was added 30% aqueous solution of potassium hydroxide (4 mL) and heated at reflux for 6 h. The solvent was evaporated, added to ice water (100 mL) and acidified to a pH of 1. The white precipitate was filtered, washed thoroughly with water, and dried to give the acid (1.3 g, 91%) as white solid. ^{1}H NMR (CDC_{l3}, 500 MHz) δ: 8.00 (d, *J* = 8.5 Hz, 2H), 7.51 (d, *J* = 8.0 Hz, 2H), 7.42 (t, *J* = 8.0 Hz, 2H), 7.35 (t, *J* = 8.0 Hz, 1H), 7.12 (d, *J* = 8.0 Hz, 2H), 5.23 (s, 2H).

(2*R*,3*R*)-5,7-Bis(benzyloxy)-2-(3,4,5-tris(benzyloxy)phenyl)chroman-3-yl 4-(benzyl-oxy)-benzoate (12)

To a solution of 4-benzyloxylbenzoic acid (34.2 mg, 0.15 mmol) in dry CH_2Cl_2 (10 mL), dicyclohexylcarbodiimide (DCC, 31 mg, 0.15 mmol) was added. The resulting mixture was stirred at room temperature for 4 h and cooled down to 0 °C. 4-Dimethylaminopyridine (DMAP, 1.2 mg, 0.01 mmol.) was added, then a solution of **9** (75.7 mg, 0.1 mol) in dry CH_2Cl_2 (2 mL) was added dropwise. The mixture was refluxed and the progress of the reaction was monitored by TLC. After 24 h the mixture was concentrated and ethyl acetate was added. The resulting mixture was cooled in a refrigerator and the urea byproduct was filtered. The filtrate was evaporated. The resulting residue was purified by column chromatography (EA/*n*-Hex 1:6) to afford compound **12** as a pale yellow amorphous solid (72.5 mg, 75% yield). $[\alpha]_D^{20}$ –42.1 (*c* 0.2, CHCl3). ^{1}H NMR ($CDCl_3$, 500 MHz) δ: 7.96 (d, *J* = 8.0 Hz, 2H), 7.47–7.22 (m, 30H), 6.93 (d, *J* = 8.0 Hz, 2H), 6.81 (s, 2H), 6.36 (d, *J* = 1.5 Hz, 1H), 6.32 (d, *J* = 1.5 Hz, 1H), 5.68 (m, 1H), 5.09–4.96 (m, 11H), 4.79 (d, *J* = 11.5 Hz, 2H), 3.11 (m, 2H). ^{13}C NMR ($CDCl_3$, 125 MHz) δ: 165.3, 162.9, 159.0, 158.2, 155.8, 153.1, 138.5, 138.1, 137.3, 137.2, 137.1, 136.3, 133.6, 132.1, 128.9–122.9 (m, Bn), 114,7, 106.9, 101.2, 95.0, 94.2, 78.1, 75.4, 71.4, 70.4, 70.3, 70.2, 68.2, 26.4. LR-MS (ESI) *m*/*z*: 989.37 (M^+ + Na, 69). HR-MS *m*/*z* calcd. for $C_{64}H_{54}O_9H$: 967.3846; found: 967.3874.

(2*R*,3*R*)-5,7-Dihydroxy-2-(3,4,5-trihydroxyphenyl)chroman-3-yl 4-hydroxy-benzoate (13)

Under a hydrogen atmosphere, palladium hydroxide (5 mg, 20% on carbon) was added to a solution of **12** (48.4 mg, 0.05 mmol) in ethyl acetate (5 mL). The resulting mixture was stirred at room temperature until TLC showed that the reaction was completed in about 2 h. The reaction mixture was filtered to remove the catalyst. The filtrate was evaporated to afford compound **13** (20.4 mg, 96% yield) as white foam. ^{1}H NMR ($CDCl_3$, 500 MHz) δ: 7.78 (d, *J* = 8.0 Hz, 2H), 6.83 (d, *J* = 8.0 Hz, 2H), 6.63 (s, 2H), 6.05 (d, *J* = 2.0 Hz, 1H), 6.03 (d, *J* = 1.5 Hz, 1H), 5.54 (m, 1H), 5.09 (s, 1H), 3.05 (dd, *J* = 17.0 Hz, J = 4.5 Hz, 1H), 2.95 (dd, *J* = 17.0 Hz, J = 2.5 Hz, 1H). ^{13}C NMR ($CDCl_3$, 125 MHz) δ: 165.3, 161.9, 157.1, 156.8, 156.4, 145.6, 131.9, 130.1, 121.9, 115.3, 105.9, 98.2, 95.7, 95.0, 77.4, 68.9, 25.8. LR-MS (ESI) *m*/*z*: 449.08 (M^+ + Na, 74). HR-MS *m*/*z* calcd. for $C_{22}H_{18}O_9H$: 427.1029; found: 427.1028.

(2*R*,3*R*)-5,7-Bis(acetoxy)-2-(3,4,5-tris(acetoxy)-phenyl)chroman-3-yl 4-acetoxy-benzoate (14)

To a solution of **13** (17.1 mg, 0.04 mmol) and acetic anhydride (28.4 μL, 0.30 mmol) in dry MeCN (5 mL) at –40 °C, DMAP (5 mg, 0.04 mmol) was added. The resulting mixture was stirred for 1 h. Saturated $NaHCO_3$ solution was added and the mixture was allowed to warm to room temperature. The mixture was extracted three times with ethyl acetate. The combined organic phase was washed with water and brine, dried over sodium sulfate, and evaporated. The residue was purified by column chromatography over silica gel (EA/*n*-Hex 1:1) to afford the title product **14** (24.4 mg, 90% yield) as a white solid. Mp 109–111 °C. $[\alpha]_D^{20}$ = –60.0 (*c* 0.2, acetone). ^{1}H NMR ($CDCl_3$, 500 MHz) δ: 7.87 (d, *J* = 8.0 Hz, 2H), 7.27 (s, 2H), 7.09 (d, *J* = 8.0 Hz, 2H), 6.74 (d, *J* = 2.0 Hz, 1H), 6.59 (d, *J* = 2.0 Hz, 1H), 5.62 (s, 1H), 5.20 (s, 1H), 3.06 (m, 2H), 2.28 (s, 6H), 2.27 (s, 3H), 2.24 (s, 3H), 2.23 (s, 6H). ^{13}C NMR ($CDCl_3$, 125 MHz) δ: 168.9, 168.6, 168.4, 167.5, 166.7, 165.0, 154.7, 154.4, 149.7, 149.7, 143.4, 135.4, 134.2, 131.4, 126.9, 121.5, 118.6, 109.5, 108.9, 108.0, 76.4, 67.5, 25.9, 21.1, 20.7, 20.6, 20.1. LR-MS (ESI) *m*/*z*: 701.12 (M^+ + Na, 67). HR-MS *m*/*z* calcd. for $C_{34}H_{30}O_{15}Na$: 701.1482; found: 701.1472.

3-Acetoxybenzoyl chloride

A suspension of 3-hydroxybenzoic acid (3.5 g, 25 mmol) was heated in acetic anhydride (5 mL) under reflux for 6 h. The acetic anhydride was evaporated and the resulting residue was triturated in ethyl ether, filtered, and washed with ethyl ether to give 3-acetoxybenzoic acid as a white solid (3.4 g, 74% yield). ^{1}H NMR ($CDCl_3$, 500 MHz) δ: 9.50 (brs, 1H), 8.00 (d, *J* = 7.5 Hz, 1H), 7.84 (s, 1H), 7.50 (t, *J* = 7.5 Hz, 1H), 7.36 (d, *J* = 8.5 Hz, 1H), 2.34 (s, 3H).

To a solution of 3-acetoxybenzoic acid (1 g, 5.5 mmol) in methylene chloride (20 mL), thionyl chloride (10 mL) was added. After the solution was stirred overnight, the solvents were removed under vacuum to give 3-acetoxybenzoyl chlo-

© 2008 NRC Canada

ride as a colorless oil. This was used for the next step without further purification.

(–)-(2*R*,3*R*)-5,7-Bis(benzyloxy)-2-(3,4,5-tris(benzyloxy)phenyl)chroman-3-yl 3-acetoxybenzoate (15)

A solution of 3-acetoxybenzoyl chloride (164 mg, 0.8 mmol) in methylene chloride (2 mL) was added dropwise to a solution of **9** (308 mg, 0.407 mmol) and DMAP (122 mg, 1 mmol) in methylene chloride (15 mL) at 0 °C. The mixture was stirred at room temperature overnight and then saturated $NaHCO_3$ solution was added. The organic layer was separated and the aqueous layer was extracted with methylene chloride. The organic layers were combined, dried over sodium sulfate, and evaporated. The residue was purified by column chromatography over silica gel (EA/*n*-Hex 1:5) to afford the desired compound, **15** (114 mg, 78% yield), as a colorless oil. ^{1}H NMR ($CDCl_3$, 500 MHz) δ: 7.84 (d, *J* = 7.5 Hz, 1H), 7.68 (s, 1H), 7.45–7.19 (m, 27H), 6. 78 (s, 2H), 6.34 (d, *J* = 2.0 Hz, 1H), 6.30 (d, *J* = 2.0 Hz, 1H), 5.66 (s, 1H), 5.13 (s, 1H), 5.05–4.94 (m, 9H), 4.85 (d, *J* = 11.5 Hz, 2H), 3.12–3.10 (m, 2H), 2.21 (s, 3H). ^{13}C NMR ($CDCl_3$, 125 MHz) δ: 169.0, 164.5, 158.8, 157.9, 155.4, 152.8, 150.6, 138.2, 137.7, 136.9, 136.8, 136.7, 133.2, 131.5, 129.3, 128.7, 128.6, 128.5, 128.5, 128.4, 128.0, 128.0, 127.9, 127.8, 127.7, 127.5, 127.5, 127.5, 127.5, 127.2, 126.6, 122.8, 106.4, 100.8, 94.8, 93.9, 77.6, 75.1, 71.2, 70.1, 70.0, 68.8, 26.0, 20.9. LR-MS (ESI) *m*/*z*: 941.34 (M^+ + Na, 17). HR-MS *m*/*z* calcd. for $C_{59}H_{51}O_{10}$: 919.3482; found: 919.3480.

(–)-(2*R*,3*R*)-5,7-Dihydroxy-2-(3,4,5-trihydroxyphenyl)chroman-3-yl 3-acetoxy-benzoate (16)

Under a hydrogen atmosphere, palladium hydroxide (52 mg, 20% on carbon) was added to a solution of **15** (48 mg, 0.052 mmol) in a solvent mixture of THF/MeOH (1:1 *v*/*v*, 8 mL). The resulting mixture was stirred at room temperature until TLC showed that the reaction was completed. The reaction mixture was filtered to remove the catalyst. The filtrate was evaporated to afford compound **16** (22.5 mg, 91% yield) as a white solid. ^{1}H NMR ($CDCl_3$, 500 MHz) δ: 7.77 (d, *J* = 7.5 Hz, 1H), 7.61 (s, 1H), 7. 48 (t, *J* = 7.5 Hz, 1H), 7.34 (d, *J* = 7.5 Hz, 1H), 6.63 (s, 2H), 6.05 (s, 1H), 6.03 (s, 1H), 5.60 (s, 1H), 5.12 (s, 1H), 3.09 (dd, *J* = 18.0 Hz, *J* = 4.5 Hz, 1H), 2.78 (d, *J* = 18.0 Hz, 1H), 2.27 (s, 3H).

(–)-(2*R*,3*R*)-5,7-Bis(acetoxy)-2-(3,4,5-tris(acetoxy)phenyl)chroman-3-yl 3-acetoxy-benzoate (17)

Compound **16** (20 mg, 0.043 mmol) was added to a mixture of pyridine (0.7 mL) and acetic anhydride (0.8 mL) with stirring, and the mixture was kept for 6 h at 45 °C in an oil bath. The solvent was removed under vacuum. The crude product was purified by column chromatography on silica gel with EA/*n*-Hex (1:1) to afford the desired compound, **17** (22 mg, 75% yield), as a white solid. Mp 72–73 °C. ^{1}H NMR ($CDCl_3$, 500 MHz) δ: 7.73 (d, *J* = 7.5Hz, 1H), 7.58 (s, 1H), 7.38 (t, *J* = 7.5 Hz, 1H), 7.27 (s, 2H), 7.25 (d, *J* = 7.5 Hz,1H), 6.75 (d, *J* = 2.5 Hz, 1H), 6.60 (d, *J* = 2.5 Hz, 1H), 5.64 (s, 1H), 5.21 (s, 1H), 3.06 (m, 1H), 2.30 (s, 3H), 2.29 (s, 3H), 2.28 (s, 3H), 2.25 (s, 3H), 2.24 (s, 6H). ^{13}C NMR ($CDCl_3$, 125 MHz) δ: 169.3, 169.2, 168.7, 167.8, 167.0, 165.1, 155.0, 150.7, 150.0, 149.9, 143.7, 135.6, 134.5, 131.1, 129.6, 127.6, 126.9, 123.1, 119.0, 109.8, 109.2, 108.3, 76.8, 67.9, 26.2, 21.4, 21.3, 21.0, 20.8, 20.4. LR-MS (ESI) *m*/*z*: 701.03 (M^+ + Na, 100). HR-MS *m*/*z* calcd. for $C_{34}H_{30}O_{15}Na$: 701.1482; found: 701.1467.

Cell culture and cell extract preparation

Jurkat T cells were from American Type Culture Collection (Manassas, Va.). Cells were grown in RPMI 1640 supplemented with 10% fetal bovine serum, 100 units/mL of penicillin, and 100 µg/mL of streptomycin and were incubated at 37˚C in a humidified incubator with an atmosphere of 5% CO_2. A whole extract was prepared as previously described (29).

Inhibition of chymotrypsin-like activity of purified 20S proteasome

Two µL of each compound's stock DMSO solution was added to 100 µL of 20S proteasome solution (25 mmol/L Tris-HCl buffer, pH 7.5) on the 96-well plate, in the presence of Suc-Leu-Leu-Val-Try-7-amido-4-methyl-coumarin (AMC) (40 µmol/L) fluogenic substrate for 2 h at 37 °C, followed by measurement of hydrolyzed AMC groups using a Victor 3 Multilabel counter with an excitation filter of 380 nm and an emission filter of 460 nm (PerkinElmer).

Proteasome CT-like activity and caspase-3 activity assay in whole cell extracts

The Jurkat T cells were treated with 50 µmol/L of compounds or solvent DMSO for 48 h, harvested, and lysed. Whole cell extracts (10 µg) were incubated with 40 µmol/L of Suc-Leu-Leu-Val-Try-AMC (for the proteasomal CT-like activity) for 2 h or Ac-DEVD-AMC (for caspase-3 activity) for 3 h at 37 °C. The release of the AMC groups was measured as described above.

Trypan blue assay

The trypan blue dye exclusion assay was performed as described previously (30).

Western blot analysis

Western blot analysis using the enhanced chemiluminescence reagent was done as previously described (11).

Acknowledgements

We thank the Areas of Excellence Scheme established under the University Grants Committee of the Hong Kong Administrative Region, China (Project No. AoE/P-10/01) for financial support. Funding support from the Natural Sciences and Engineering Research Council of Canada (NSERC) and the National Cancer Institute (Grant Number: 1R01CA120009 and 5R03CA112625) is gratefully acknowledged.

References

1. E. Haslam. Plant polyphenols: Vegetable tannins revisited. Cambridge University Press, New York. 1989. p. 230.

© 2008 NRC Canada

2. H. Fujiki, M. Suganuma, S. Okabe, N. Sueoka, A. Komori, E. Sueoka, T. Kozu, Y. Tada, K. Suga, K. Imai, and K. Nakachi. Mutat. Res. **402**, 307 (1998).
3. I.E. Dreosti. Nutr. Rev. **54**, S51 (1996).
4. D. Chen, K.G. Daniel, D.J. Kuhn, A. Kazi, M. Bhuiyan, L. Li, Z. Wang, S.B. Wan, W.H. Lam, T.H. Chan, and Q.P. Dou. Front. Biosci. **9**, 2618 (2004).
5. D.J. Kuhn, W.H. Lam, A. Kazi, K.G. Daniel, S. Song, L.M.C. Chow, T.H. Chan, and Q.P. Dou. Front. Biosci. **10**, 1010 (2005).
6. S. Sang, J.D. Lambert, and C.S. Yang. J. Sci. Food Agric. **86**, 2256 (2006).
7. Z.-Y. Chen, Q.Y. Zhu, D. Tsang, and Y. Huang. J. Agric. Food Chem. **49**, 477 (2001).
8. J.D. Lambert and C.S. Yang. Mutat. Res. **523**, 201 (2003).
9. W.H. Lam, A. Kazi, D.J. Kuhn, L.M.C. Chow, A.S.C. Chan, Q.P. Dou, and T.H. Chan. Bioorg. Med. Chem. **12**, 5587 (2004).
10. J.D. Lambert, S. Sang, J. Hong, S.-J. Kwon, M.-J. Lee, C.-T. Ho, and C.S. Yang. Drug Metab. Dispos. **34**, 2111 (2006).
11. K.R. Landis-Piwowar, C. Huo, D. Chen, V. Milacic, G. Shi, T.H. Chan, and Q.P. Dou. Cancer Res. **67**, 4303 (2007).
12. S.-C. Lee, W.-K. Chan, T.-W. Lee, W. Lam, X. Wang, T.-H. Chan, and Y.-C. Wong. Nutr. Cancer. In press.
13. Q.Y. Zhu, A. Zhang, D. Tsang, Y. Huang, and Z.-Y. Chen. J. Agric. Food Chem. **45**, 4624 (1997).
14. K. Okushio, M. Suzuki, N. Matsumoto, F. Nanjo, and Y. Hara. Biosci. Biotechnol. Biochem. **63**, 430 (1999).
15. H. Lu, X. Meng, and C. S. Yang. Drug Metab. Dispos. **31**, 572 (2003).
16. A.H. Wu, C.-C. Tseng, D. Van Den Berg, and M.C. Yu. Cancer Res. **63**, 7526 (2003).
17. D. Chen, C.Y. Wang, J.D. Lambert, N. Ai, W.J. Welsh, and C.S. Yang. Biochem. Pharmacol. **69**, 1523 (2005).
18. K.G. Daniel, K.R. Landis-Piwowar, D. Chen, S.B. Wan, T.-H. Chan, and Q.P. Dou. Int. J. Mol. Med. **18**, 625 (2006).
19. K. Osanai, C. Huo, K.R. Landis-Piwowar, Q.P. Dou, and T.H. Chan. Tetrahedron, **63**, 7565 (2007).
20. L. Li and T.H. Chan. Org. Lett. **3**, 739 (2001).
21. (*a*) S.B. Wan and T.H. Chan. Tetrahedron, **60**, 8207 (2004); (*b*) S.B. Wan, Q.P. Dou, and T.H. Chan. Tetrahedron, **62**, 5897 (2006); (*c*) K. Osanai, K.R. Landis-Piwowar, Q.P. Dou, and T.H. Chan. Bioorg. Med. Chem. **15**, 5076 (2007).
22. D.T. Bailey, R.L. Yuhasz, and B. Zheng. U.S. Patent 6-210-679. 2001.
23. D.C. Burdick, H. Egger, A.G. Gum, I. Koschinski, E. Muelchi, and I. Prevot-Halter. U.S. Patent application 20030083270. 2003.
24. C. Ramesh, G. Mahender, N. Ravindranath, and B. Das. Tetrahedron, **59**, 1049 (2003).
25. G. Attaguile, A. Russo, A. Campisi, F. Savoca, R. Acquaviva, N. Ragusa, and A. Vanella. Cell Biol. Toxicol. **16**, 83 (2000).
26. A. Guevenc, S. Yildiz, A. Oezkan, C. Erdurak, M. Coskun, G. Yilmaz, T. Okuyama, and Y. Okada. Pharmaceut. Biol. **43**, 178 (2005).
27. K.R. Landis-Piwowar, D.J Kuhn, S.B. Wan, D. Chen, T.H. Chan, and Q.P. Dou. Int. J. Mol. Med. **15**, 735 (2005).
28. Y.A. Lazebnik, S.H. Kaufmann, S. Desnoyers, G.G. Poirier, and W.C. Earnshaw. Nature (London), **371**, 346 (1994).
29. B. An and Q.P. Dou. Cancer Res. **56**, 438 (1996).
30. D.M. Smith, Z. Wang, A. Kazi, L.-H. Li, T.-H. Chan, and Q.P. Dou. Mol. Med. **8**, 382 (2002).

© 2008 NRC Canada

Partitioning of charged and neutral dextran-dye derivatives in biphasic cellulose nanocrystal suspensions[1]

Stephanie Beck-Candanedo, David Viet, and Derek G. Gray

Abstract: The partitioning behaviour of dye-labeled dextrans of high molecular weight in aqueous suspensions of native cellulose nanocrystals was studied. Cellulose concentrations lie in the isotropic–nematic coexistence region. Blue dextrans of various molecular weights and degrees of substitution of dye molecules (anionic Cibacron blue 3G-A) were investigated. Increasing the total concentration of blue dextran and degree of dye substitution led to increasing partition coefficients. Increasing dextran molecular weight resulted in higher partition coefficients, in agreement with theory. Partition coefficients were larger than predicted theoretically using a second virial coefficient approximation. Electrostatic and entropic contributions to the partition coefficient of blue dextran are discussed. Dextrans labeled with neutral fluorescein isothiocyanate did not partition preferentially in this system.

Key words: partition coefficient, cellulose nanocrystals, dextrans, degree of substitution, polyelectrolyte.

Résumé : Le comportement de partage préférentiel entre deux phases manifesté par des dextrans de haut poids moléculaire marqués par différents types de colorants dans des suspensions aqueuses de nanocristaux de cellulose a été étudié. Les concentrations en cellulose se situent dans la région de coexistence nématique–isotrope. Des dextrans bleus de divers poids moléculaires et à différents degrés de substitution en colorant (Cibacron bleu 3G-A anionique) ont été étudiés. L'augmentation de la concentration du dextran bleu de même que l'augmentation du degré de substitution du colorant tend à élever le coefficient de partage. En accord avec la théorie, plus on monte en masse molaire, plus le coefficient de partage est haut. Les coefficients de partage sont supérieurs à ceux prédits par la théorie si l'approximation du second coefficient viriel est utilisée. Les contributions électrostatiques et entropiques du dextran bleu sont exposées. Enfin, nous ne dénotons aucun effet de partage sur des dextrans marqués avec des colorants neutres comme l'isothiocyanate de fluorescéine.

Mots-clés : coefficient de partage, nanocristaux de cellulose, dextrans, degré de substitution, polyélectrolyte.

[Traduit par la Rédaction]

Introduction

It is well-established that the drive to maximize entropy can cause ordering (1) and bulk demixing in systems containing components of sufficiently different physical properties, such as shape or flexibility (2). The bulk demixing is predicted to give rise to phases enriched in one of the components of the system (1, 3). Ordered phases of rodlike particles coexisting with random phases, such as aqueous suspensions of cellulose nanocrystals (Fig. 1*a*), have been shown to exclude random coil polymers and spherical particles for several experimental systems (2, 4–10) including cellulose nanocrystals and blue dextran, as shown in Fig. 1*b* (11). Assuming only excluded-volume interactions between the components, Flory predicted the phase separation of a solution containing a rigid rodlike polymer and a flexible randomly coiled polymer and concomitant partitioning to give a rod-rich, coil-poor phase and a coil-rich, rod-poor phase (3). The phase separation is entropy-driven, based on depletion attractions observed in colloid-polymer systems (12). The extent of the partitioning depends on the relative size and concentration of the two components as well as their chemical nature. This has been shown experimentally (6, 8, 9) as well as theoretically (13).

Preliminary results obtained in this laboratory for blue dextran in cellulose nanocrystal suspensions have shown that the partitioning behaviour is not affected by the nature of the phase separation, that is, whether the suspension concentration lies in the isotropic–chiral nematic (I–N) coexistence region or whether phase separation is induced by the addition of a macromolecule to a completely ordered suspension (11). This article further investigates the partitioning behav-

Received 20 September 2007. Accepted 18 December 2007. Published on the NRC Research Press Web site at canjchem.nrc.ca on 26 March 2008.

S. Beck-Candanedo,[3] D. Viet,[4] and D.G. Gray.[2] Department of Chemistry, Pulp and Paper Research Centre, McGill University, Montréal, QC H3A 2A7, Canada.

[1]This article is part of a Special Issue dedicated to Professor R. Marchessault.
[2]Corresponding author (e-mail: derek.gray@mcgill.ca).
[3]Present address: Department of Chemical Pulping, FPInnovations Paprican, 570 Blvd St-Jean, Pointe-Claire, QC H9R 3J9, Canada.
[4]Present address: LGP2-UMR 5518 INPG-CNRS, Laboratory of Pulp & Paper Science, BP #65-461, Rue de la Papeterie, F-38402, Saint-Martin d'Hères, CEDEX, France.

 doi:10.1139/V08-005 © 2008 NRC Canada

Fig. 1. (*a*) Biphasic suspension of cellulose nanocrystals viewed between crossed polars, showing schematic representations of the upper isotropic (random) phase and lower liquid crystalline (chiral nematic) phase. (*b*) Vials of biphasic cellulose nanocrystal suspension containing increasing concentrations from left to right of blue dextran, showing the preferential partitioning of the blue dextran (appears dark in this grey-scale image) into the upper isotropic phase.

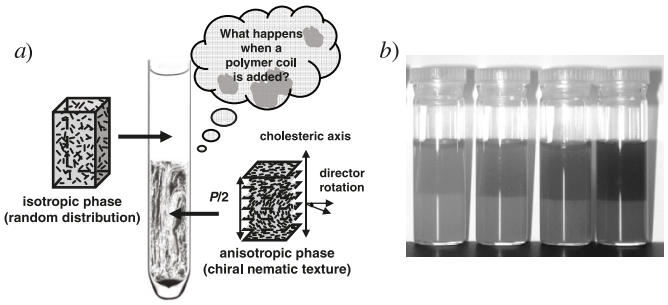

iour of blue dextrans in biphasic cellulose nanocrystal suspensions. It is our goal to clarify the factors driving the partitioning of such polyelectrolytic species, in particular the effect of the ionic charge due to the dye substituents on the partition coefficient.

Experimental

Materials

Whatman ashless cotton cellulose powder was purchased from Cole-Parmer. Sulfuric acid (95%–98%) for hydrolysis was purchased from Fisher Scientific. Cibacron blue 3G-A dye (CB, 55% dye content, MW 840.12 Da), and sodium hydroxide, sodium chloride, and sulfuric acid volumetric standards for conductometric titration were purchased from Sigma-Aldrich. Anhydrous sodium carbonate was purchased from Anachemia. Concentrated hydrochloric acid, ACS reagent grade, was purchased from ACP Chemicals. Methanol, HPLC grade, was purchased from Fisher Scientific. Blue dextran 2000 (nominal M_w 2 000 000 Da) and fluorescein isothiocyanate (FITC)-labeled dextrans 2000, 500, and 150 (M_w 2 000 000, 525 000, 130 000, and 77 000 Da, respectively) were purchased from Sigma-Aldrich. Dextrans (Dx) T-2000, T-500, T-110, and T-70 (M_w 2 000 000, 532 000, 106 000, and 70 000 Da, respectively) were purchased from Pharmacia Fine Chemicals. All water used was purified using a Millipore Milli-Q purification system.

Cellulose nanocrystal suspensions

Suspensions of cellulose nanocrystals were prepared as described in previous publications (14–16). Whatman ashless cotton cellulose powder was hydrolysed for 45 min at 45 °C, using 64 wt% sulfuric acid (17.5 mL per g powder). The reaction mixture was diluted 10-fold with cold distilled water to stop the reaction and washed once by centrifugation. The precipitate was then dialysed until a pH of 4–5 inside the dialysis membrane was reached. Suspensions were sonified (Vibracell, Sonics & Materials, Inc., Danbury, Conn.) in an ice bath to yield colloidal dispersions, which were placed over a mixed-bed ion-exchange resin (Sigma-Aldrich) for several hours and then filtered. The

Scheme 1. Coupling of Cibacron blue 3G-A (I = R-Cl) with dextran (II) to give blue dextran (III), showing the random binding sites of the dye (27).

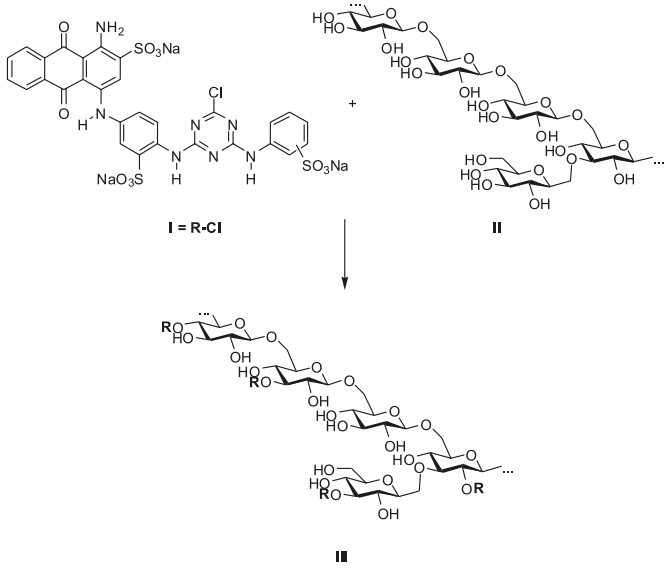

aqueous suspensions, 0.5%–2% cellulose by weight, were evaporated with stirring at ambient conditions to obtain the desired final nanocrystal concentrations.

Conductometric titration and neutralization

Conductometric titration was used to determine the surface charge density of the cellulose nanocrystals associated with surface sulfate ester groups. A Contiburette µ10 (Ing. CAT, Staufen, Germany) was used for all titrations. Titrations were performed under a flow of nitrogen using an Orion conductivity cell 018010 (cell constant $K = 0.987$ cm^{-1}) attached to a Fisher Scientific accumet pH meter 50. Sodium hydroxide was standardized against volumetric standard sulfuric acid. Equivalence points were used to calculate the amount of sodium hydroxide required to convert the suspensions to the sodium form (Na^+ counterions).

Preparation of blue dextrans

Blue dextrans of various molecular weights and ligand densities were prepared using methods adapted from Mayes et al. (17) and Tang et al. (18) (Scheme 1), as described in a previous publication (19). A brief description of the procedure follows: a solution of the dextran is mixed with aqueous solutions of Cibacron blue 3G-A dye and Na_2CO_3 and the mixture is shaken in a water bath at 45 °C. After around 75 h another aliquot of CB is added. An equal volume of ethanol is added to the mixture to precipitate the dextran–dye conjugate. After standing at –20 °C, the precipitate is spun down, rinsed with ethanol, and redissolved in water, and the precipitation step repeated. Following a final resuspension in water, the dextran is dialysed against distilled water to remove any traces of unreacted dye and salt. The final product is lyophilised and stored as a solid.

Acid hydrolysis of dextran T-2000

To obtain dextran fractions of high molecular mass (>500 kDa), degradation by acid hydrolysis was carried out according to starch hydrolysis methods (20, 21) adapted for

© 2008 NRC Canada

Table 1. Properties of blue dextrans and FITC-dextrans.

Dextran–dye conjugate[a]	MW_{Dx} (kDa)[b]	MW (kDa)[c]	Dye ligand density (DS per AGU, 10^{-4})	R (nm)[d]
Blue dextran 2000_7	2000	2007	7	—
Blue dextran 2000_{12}	2000	2010	12	40.8±1.0
Blue dextran 2000_{16}	2000	2017	16	37.9±0.8
Blue dextran 2000_{30}	2000	2031	30	–
Blue dextran 2000_{36}	2000	2038	36	35.1±1.1
Blue dextran 2000_{56}	2000	2058	56	36.9±0.9
Blue dextran 2000_{161}	2000	2167	161	40.2±0.8
Blue dextran 500_{49}	532	545	49	—
Blue dextran 500_{11}	532	535	11	18.4±0.7
Blue dextran 110_{143}	106	114	143	—
Blue dextran 70_{280}	70	80.2	280	<10
Blue dextran 70_{66}	70	72.4	66	<10
Blue dextran d1700	1690[e]	1720	33	40.1±0.4[e]
Blue dextran d1400	1380[e]	1410	27	37.2±0.4[e]
Blue dextran d1200	1180[e]	1200	25	35.4±1.4[e]
Blue dextran d980	980[e]	1000	20	30.9±2.8[e]
FITC-dextran 2000	2000	2065	130	16
FITC-dextran 500	525	543	140	—
FITC-dextran 150	130	134	120	—
FITC-dextran 70	77	79.5	130	—

[a]The designation d indicates acid-degraded dextrans.
[b]Supplier data, unless otherwise indicated.
[c]Molecular weights calculated based on the DS per AGU obtained by UV–vis spectroscopy.
[d]Hydrodynamic radius R_H measured by dynamic light scattering (unpublished results), unless otherwise indicated.
[e]Molecular weight M_w and radius of gyration R_g obtained by GPC coupled with SLS (see text).

dextran by Ioan et al. (22). Dextran T-2000 (1 g) was suspended in 4 mL of methanol to which various amounts of concentrated hydrochloric acid were added (0.02, 0.04, 0.06, and 0.09 mL, which yielded dextrans d1700, d1400, d1200, and d980, respectively). The suspensions were shaken for 4 days, at which point the limiting value was reached (23). The degraded dextrans were neutralized with 1 mol/L NaOH and washed with 1:1 methanol/water. The hydrolysed dextran fractions were dialysed against milliQ water to remove any traces of base or small dextran fragments, lyophilised, and stored as solids. Following characterisation (see later and Table 1), the solid dextrans were reacted with CB dye to give dextran–dye conjugates as described above. It should be noted that the degradation is not fully random; the cleavage rate of the α-(1,6) bonds differs from that of the α-(1,3) bonds and leads to a change in the branching density that may affect the partitioning (24).

Characterisation of blue dextrans

Moisture contents of the dextran–dye conjugates and degraded dextrans were determined by thermogravimetric analysis (TGA, TA Instruments TGA Q500).

The dye content of the dextran–dye conjugates was determined using UV–vis spectroscopy (Varian Cary 300 Bio spectrophotometer). A calibration curve was obtained from solutions of commercially available blue dextran 2000 and adherence to the Beer–Lambert law was established. The molar extinction coefficient for blue dextran 2000 at 609 nm was found to be 8865 $(mol/L)^{-1}cm^{-1}$. The extinction coefficient at 620 nm was 8966 $(mol/L)^{-1}cm^{-1}$ = 0.823 $g^{-1}dm^3cm^{-1}$, which agrees well with the value of 0.812 $g^{-1}dm^3cm^{-1}$ found by Champ et al. (25) for commercially available blue dextran 2000. The ligand density was estimated from absorbance measurements at 609 nm for solutions of the dextran–dye conjugates and calculated in terms of the degree of dye substitution (DS) per anhydroglucose repeat unit (AGU). Absorbance measurements in dilute aqueous solution and in 6 mol/L aq. HCl (17, 26) have shown that negligible intramolecular dye stacking occurs at dye ligand densities, comparable with those reported in this article.

A combination of gel permeation chromatography (GPC) and static light scattering (SLS) was used to obtain molecular weights ($\overline{M}_w$, $\overline{M}_n$), and radii of gyration (R_g) for the hydrolysed dextrans and for FITC-Dx 2000. Dextrans (2 mg/mL) were dissolved in the eluent (pH 7, 0.2 mol/L $NaNO_3$, and 0.01 mol/L NaH_2PO_4 containing 0.2% NaN_3) and filtered using 0.45 μm membranes. Samples (100 μL) were injected onto a GPC column (300 × 75 mm PL aquagel-OH mixed 8 μm, 1×10^2 to 1×10^7 Da separation, Polymer Laboratories) at a flow rate of 1.0 mL/min using a Merck Hitachi AS-2000A autosampler and Waters 510 HPLC pump. The column was coupled to a Wyatt Optilab rEX IR detector (690 nm) and a Wyatt Technology Corporation DAWN EOS light scattering detector. Data were analysed with Astra v5.3.0 18 software (Wyatt Technology Corporation).

Preparation of cellulose suspensions containing dextran–dye conjugate

Solid dextran–dye derivatives were added to samples of biphasic cellulose suspension, which were mixed and al-

© 2008 NRC Canada

Table 2. Sample calculation of the theoretical partition coefficient for blue dextran 2000_{161} in 10.1 wt% cellulose nanocrystal suspension, using eq. [2].

		Isotropic phase [cellulose]		Anisotropic phase [cellulose]			
[Dx] (μmol/L)	[AGU] (μmol/L)	wt%	ϕ	wt%	ϕ	K_{theory}	K_{exp}
0.383	4 700	7.6	0.05	11.3	0.07	1.28	3.11

lowed to re-equilibrate for 24 to 48 h. The concentration of dextran in the dispersions is expressed as AGU molarity, in order that the concentrations of dextrans of different molar masses be comparable among the samples. The more usual volume fraction was not used, as the coil volumes are model-dependent and the dextran concentrations were such that it was not possible to calculate accurate values (the dispersions were not dilute enough).

When phase separation was complete, samples were taken from the upper and lower phases and diluted prior to analysis to minimize scattering caused by the cellulose nanocrystals. Linear correlations between absorbance and concentration were observed for blue dextran 2000 and FITC-dextran 2000 in cellulose suspension. The volume fraction of the phases was determined by measuring the heights of the anisotropic and isotropic phases in each vial.

Determination of partition coefficients

UV–vis absorption spectra were taken and the absorbance measured at 609 nm for blue dextrans and 490 nm for FITC-dextrans. Suspensions of cellulose nanocrystals containing no dextran–dye conjugate, but otherwise identical to the sample suspensions, were used as references. Because calibration measurements showed that measured absorbance is proportional to the concentration of macromolecule, partition coefficients K were calculated from the relative absorbance values A of the isotropic and anisotropic phases,

$$[1] \qquad K = A_{iso}/A_{aniso}$$

The concentration of cellulose in the samples was determined by gravimetry. The number density of the dextran–dye conjugates and dextran molecules in the samples was calculated using the equation,

$$[2] \qquad C_i = \frac{N_i}{V_{tot}} = \frac{N_a}{V_{tot}}\frac{m_i}{M_i}$$

where N_i is the number of molecules of species i, V_{tot} is the volume of the sample, N_a is Avogadro's number, m_i is the mass of species i, and M_i is the molar mass of species i. It should be noted that while number average molecular weight $\overline{M}_n$ should be used in the formula for number density, the molecular weights given for the dextrans are weight average $\overline{M}_w$ (supplier data). The polydispersity $\overline{M}_w/\overline{M}_n$ of the dextrans decreases with decreasing molar mass (28).

Results and discussion

Partition theory

The concentrations of hard core monodisperse rodlike particles in the isotropic and nematic phases are predicted to remain constant across the I–N coexistence region (1). However, because the cellulose nanocrystals contain ionic sulfate groups on their surface, increasing the total cellulose concentration causes the particle densities in the isotropic and anisotropic phases to increase and diverge slightly because of the change in ionic strength in the aqueous medium, as previously observed for this system (11, 29). Partitioning of the blue dextran coils between the coexisting isotropic and nematic or chiral nematic phases causes the rod densities in the phases to diverge further as more polymer coils are added (13). Because the concentration of coils is higher in the isotropic phase, adding blue dextran increases the osmotic pressure of the isotropic phase relative to the nematic phase. To compensate, the rod density decreases in the isotropic phase and increases in the nematic phase, resulting in a widening of the I–N coexistence region of the phase diagram (13).

Sear has studied the phase behaviour of lyotropic mixtures of rodlike and flexible polymers, obtaining an expression for the partition coefficient K of a flexible polymer (13),

$$[3] \quad K = \frac{c_p^I}{c_p^N} \sim \exp[LD^{1/3}R_g^{5/3}(c_r^N - c_r^I)]$$

where c_p^I and c_p^N are the number densities of the polymer in the isotropic and the nematic phases, respectively, L is the rod length, D is the rod diameter, R_g is the radius of gyration of the polymer, and c_r^I and c_r^N are the number densities of the rodlike polymer in the isotropic and nematic phases. The parameters used in the calculation of theoretical K values were as follows: L = 110 nm, D = 10 nm, and R_g = 34 nm (28). A sample calculation is shown in Table 2 (for the last entry in Table 4).

The rodlike polymer is modeled as a hard rod with a diameter much smaller than the radius of the flexible coiled polymer, $D \ll R_g$. Interactions between the rods and coils are based on excluded volume; there are no attractive interactions between the rods, which is required for the suspension to be stable. The equation is valid in the dilute regime, that is, at small volume fractions of polymer (13). It predicts that polymers with larger radii of gyration will partition to a greater extent, while for a given radius of gyration, a larger difference in cellulose rod concentration between the two phases will increase partitioning (i.e., K increases with total cellulose concentration, as previously observed (11)). This expression for K has been used previously to predict blue dextran partitioning in cellulose nanocrystal suspensions; despite the fact that the expression only provides an order of magnitude for K, it predicted an increase in partition coefficient with increasing blue dextran concentration (11).

The critical concentration c^* (at which the semi-dilute regime begins) for blue dextran 2000_{161} is 73 mg/mL in 10 mmol/L of NaCl and 209 mg/mL in 200 mmol/L NaCl

© 2008 NRC Canada

(unpublished results). Sear's theory is valid only in the dilute regime, where the volume fraction of polymers and colloidal rods is small (13). The dextran concentrations used in this study do not exceed 50 mg/mL; Sear's theory is therefore valid for our samples. However, although we are working in the dilute regime for the blue dextran, it should be noted that the cellulose nanocrystals also contribute to the sample viscosity; their volume fraction is fairly low (about 6.5% for 10 wt% nanocrystals with L = 120 nm and D = 10 nm). At high viscosity, kinetic effects likely have important effects on the phase separation and partitioning behaviour. Sear's theory also assumes constant rod concentration across the biphasic region, as predicted by Onsager (1). As stated earlier, this is not the case for suspensions of cellulose nanocrystals, which may contribute to any discrepancy between the theoretical predictions and experimental results.

The partition coefficient K of a macromolecule in a two-phase system can be expressed as

$$[4] \qquad K = K_{hphob} \cdot K_{el} \cdot K_{size} \cdot K_{sol} \cdot K_{aff} \cdot K_o$$

where K_{hphob}, K_{el}, K_{size}, K_{sol}, and K_{aff} represent the contributions to the total partition coefficient of the effects of hydrophobicity, electrostatic forces, size factors, solubility, and affinity, respectively, and K_o represents other effects on partitioning, such as the dimensions of the rodlike particles and their relative concentrations in the two phases (30). These factors may be competing with each other; their relative importance will depend on the composition of the biphasic system and the properties of the molecule being partitioned. The main contributions to K for blue dextran are likely to be K_{el} and K_{hphob} (the sulfonated triazine dye introduces both ionic and hydrophobic elements into the macromolecule). K_{size} is also expected to play a role for blue dextrans of different molecular weights. Because FITC-dextran is electrostatically neutral, K_{el} should not be an important factor in its partitioning behaviour; K_{hphob} may dominate because of the hydrophobic aromatic rings in the FITC dye.

Blue dextran partitioning

The effect of increasing blue dextran 2000_{161} concentration on its partition coefficient is shown in Fig. 2, which also contains data from a previous publication (11). The partition coefficient increases linearly with increasing blue dextran concentration.

The effect of the DS of blue dextran 2000 at constant AGU monomer concentration on its partition coefficient is shown in Table 3. The partition coefficients increased from around 1.3 to greater than 2 when the DS was increased from 7×10^{-4} to 1.61×10^{-2}. A two-fold increase in the AGU concentration did not have a significant effect on the partition coefficients.

The effect of DS of blue dextran 2000 at constant dye concentration on its partition coefficient is shown in Table 4. The partition coefficients increased from 1.1 to greater than 3 when the DS increased from 1.60×10^{-3} to 1.61×10^{-2}. A 2.5-fold increase in the total dye concentration did not have a significant effect on the partition coefficients (they increased slightly).

It can be concluded from the results in Tables 3 and 4 that increasing the DS results in larger K values for blue dextrans

Fig. 2. Partition coefficients of blue dextran 2000_{161} in ~10 wt% cellulose suspension. The line is the best fit to the data. Closed symbols were obtained in 10.1 wt% cellulose nanocrystal suspension; open symbols were obtained in 10.3 wt% cellulose nanocrystal suspension.

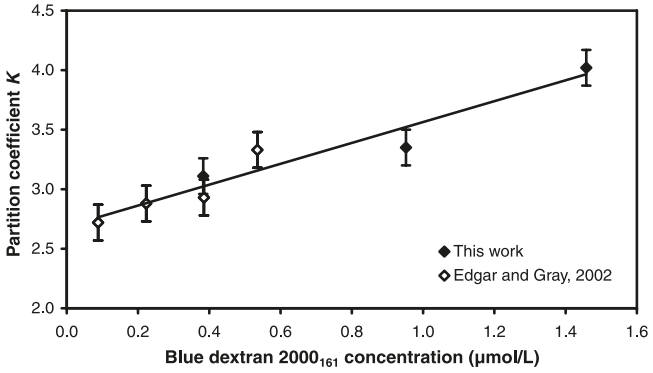

2000 at constant AGU concentration and at constant dye concentration. The DS of the blue dextran 2000 thus determines the magnitude of K in this biphasic system.

Effect of molecular weight on partition coefficient K

The partition coefficients for blue dextrans and FITC-dextrans of various molecular weights and DS are given in Table 5. In this case, it is particularly difficult to separate the effect of the DS of dye ligands (K_{el}) from the effect of the blue dextran molecular weight (K_{size}). For nonhydrolysed blue dextrans with similar DS (shown in italics), K decreases from 1.48 to 1.12 when the molecular weight decreases from 2000 to 70 kDa. Partition coefficients for blue dextrans prepared from acid-hydrolysed dextrans measured at similar AGU and dye concentrations (blue dextrans d1700–d980 contain 0.020 ± 0.001 g dye per g blue dextran) also decrease with decreasing dextran molecular weight. As shown in Fig. 3, this is in qualitative agreement with Sear's partitioning theory in which K is proportional to the exponential of $R_g^{5/3}$ (13). It should be noted that the hydrolysed dextrans are more polydisperse (Ip values for dextrans d1700, d1400, d1200, and d980 are 2.74, 2.98, 2.38, and 2.45, respectively) than the blue dextrans prepared from commercial dextrans, which have Ip values of around 1–1.25 (unpublished results). Lower molecular weight FITC-dextrans appear to partition slightly more strongly into the anisotropic phase, but relatively large error bars make it difficult to differentiate between the lowest experimental partition coefficients of 0.89 and 1.05.

FITC-dextran partitioning

The partition coefficients for FITC-dextrans in the same biphasic system were all around 0.8–1.0, indicating partitioning into the lower anisotropic phase (Table 6). FITC-dextran is neutral at basic pH (32) or at most slightly positive at the pH of 4–5 in the cellulose suspensions, but contains several hydrophobic aromatic rings, similar to blue dextran (Fig. 4).

The observed partitioning behaviour of charged and neutral dye-labeled dextrans suggests that the blue dextran partitioning is partly electrostatic in nature.

© 2008 NRC Canada

Table 3. Partition coefficients of blue dextrans 2000 in 10.1 wt% cellulose nanocrystal suspension at constant anhydroglucose monomer concentration.

Series	Dextran	DS per AGU (10^{-4})	[AGU] (μmol/L)	[Dye] (μmol/L)	[Cellulose] (wt%)	*K*
I	Blue dextran 2000_{16}	16	18	29	10.1	1.46
	Blue dextran 2000_{30}	30		54		1.60
	Blue dextran 2000_{36}	36		65		1.72
	Blue dextran 2000_{56}	56		99		1.83
	Blue dextran 2000_{161}	161		290		4.02
II	Blue dextran 2000_{7}	7	40	29	10.1	1.28
	Blue dextran 2000_{17}	17		70		1.37
	Blue dextran 2000_{30}	30		121		1.47
	Blue dextran 2000_{36}	36		150		1.51
	Blue dextran 2000_{56}	56		228		1.55
	Blue dextran 2000_{161}	161		661		2.01

Table 4. Partition coefficients for blue dextrans 2000 in 10.1 wt% cellulose nanocrystal suspension at constant dye concentration.

Series	Dextran	DS per AGU, 10^{-4}	[AGU] (μmol/L)	[Dye] (μmol/L)	[Cellulose] (wt%)	*K*
III	Blue dextran 2000_{16}	16	123	197	10.1	1.10
	Blue dextran 2000_{36}	36	54	196		1.43
	Blue dextran 2000_{56}	56	35	193		1.41
	Blue dextran 2000_{161}	161	12	189		3.39
IV	Blue dextran 2000_{16}	16	47	78	10.1	1.23
	Blue dextran 2000_{36}	36	21	78		1.45
	Blue dextran 2000_{56}	56	13	76		1.54
	Blue dextran 2000_{161}	161	4.7	78		3.11

Table 5. Partition coefficients for blue dextrans and FITC-dextrans of different molecular weights.

MW (kDa)	Dextran	DS per AGU (10^{-4})	[Dye] (μmol/L)	[AGU] (μmol/L)	[Cellulose] (wt%)	*K*
2167	Blue dextran 2000_{161}	161	997	61 700	10.1	3.38
2058	Blue dextran 2000_{56}	56	344	61 900		1.48
2010	Blue dextran 2000_{12}	12	85	66 000		1.39
2017	Blue dextran 2000_{16}	16	81	49 700		1.13
1722	Blue dextran d1700	33	96	24 400	9.8	1.50
1410	Blue dextran d1400	27	94	24 200		1.45
1202	Blue dextran d1200	25	101	24 000		1.37
1003	Blue dextran d980	20	97	24 500		1.36
545	Blue dextran 500_{49}	49	82	16 600	10.1	1.30
545	Blue dextran 500_{49}	49	86	17 200		1.30
114	Blue dextran 110_{143}	143	79	5 400	10.1	1.09
80.2	Blue dextran 70_{280}	280	55	1 900	10.1	2.04
72.4	Blue dextran 70_{66}	66	110	16 100		1.12
72.4	Blue dextran 70_{66}	66	110	12 400		1.11
2065	FITC-dextran 2000	130	963	74 000	9.8	0.98
543	FITC-dextran 500	140	256	18 300	9.8	0.98
134	FITC-dextran 150	120	58	4 800	9.8	0.88
79.5	FITC-dextran 70	130	36	2 700	9.8	0.81

© 2008 NRC Canada

Table 6. Partition coefficients for FITC-dextrans.

Dextran	DS per AGU (10^{-4})	[AGU] (μmol/L)	[Dye] (μmol/L)	[Cellulose] (wt%)	K
Increasing FITC-dextran concentration					
FITC-dextran 2000	130	9000	117	9.8	1.05
		9900	129		0.90
		14 900	194		1.07
		20 400	265		1.02
		21 000	272		1.02
		42 500	552		0.91
		65 000	846		0.91
		95 400	1240		1.03
Increasing total cellulose nanocrystal concentration					
FITC-dextran 2000	130	27 600	360	7.9	0.90
		21 000	272	9.8	1.02
		27 600	331	9.9	0.97
		27 600	386	11.0	0.89

Fig. 3. Natural logarithm of the measured partition coefficient K_{meas} as a function of $R_g^{5/3}$ for blue dextrans of different molecular weights. Radii of gyration of the dextrans were calculated using the equation $R_g = 0.66\ M_w^{0.43}$, which is valid over the M_w range 400 to 2700 kDa (31).

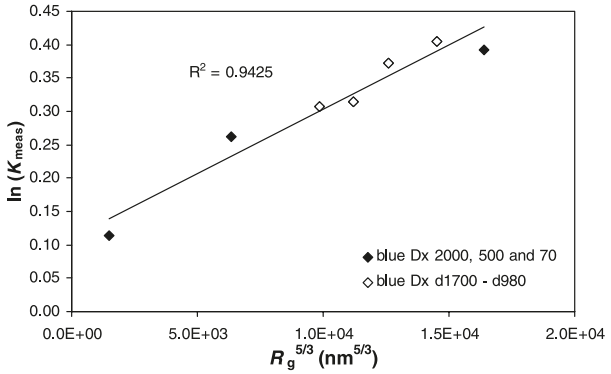

Fig. 4. Structure of FITC-dextran. FITC is assumed to associate randomly with any free hydroxyl group (33).

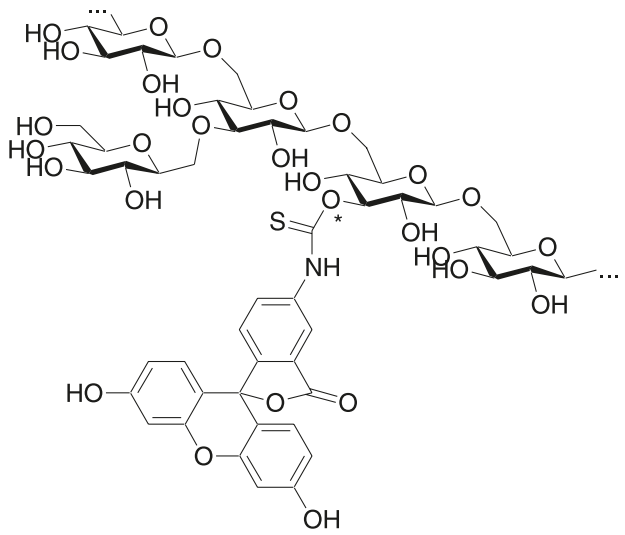

Increasing degree of dye substitution (DS)

Cibacron blue 3G-A dye has been found to adsorb onto the surface of microcrystalline cellulose (MCC, Avicel PH 102) in studies of the hydrolysis of amylase by CB-dyed amylases in the presence of MCC (34). The adsorption of CB dye onto cellulose nanocrystals containing anionic surface sulfate esters was also verified by exhaustively dialyzing cellulose suspensions to which small amounts of CB dye were added. The absorption spectra of the resulting samples showed a peak in the range of 590–630 nm, indicating the presence of CB dye. Free CB dye was not found to partition in biphasic cellulose nanocrystal suspensions. Because CB contains three anionic sulfonate groups per molecule, it is soluble in water and it is therefore conceivable that many dye ligands will be exposed on the surface of a blue dextran molecule in aqueous solution and be available to adsorb onto the surfaces of cellulose nanocrystals. This presumably occurs during the mixing and early equilibration stages of sample preparation. Upon formation of the anisotropic phase, the adsorbed blue dextrans may desorb and be expelled into the isotropic phase, as they are too large and interfere with the chiral nematic structure (excluded volume effect) (19); the entropy gain and the associated reduction in free energy is greater than the reduction in free energy due to adsorption. The increase in K with increasing DS of the blue dextran may be caused by an electrostatic effect: the negatively charged cellulose nanocrystals in the anisotropic phase may be more efficient at expelling the more highly substituted blue dextrans which are more negatively charged. This may explain why the observed blue dextran K values are much higher than predicted by Sear's theory (Fig. 5), which does not take electrostatic factors into account. Using surface charge density values measured by conductometric titration, the ratio of surface charge (and corresponding counterions) between the anisotropic and isotropic phases of 8.7 and 9.8 wt% suspensions was calculated to be around 1.3 for both samples (which differed in nanocrystal surface charge density). There is therefore an electrical potential difference between the phases, which may affect the partitioning behaviour of the negatively

© 2008 NRC Canada

Fig. 5. Theoretical and experimental K values for blue dextrans and FITC-dextrans in cellulose nanocrystal suspension. Inset shows FITC-dextran data points in more detail. The error bars for experimental K values are on the order of the size of the data points.

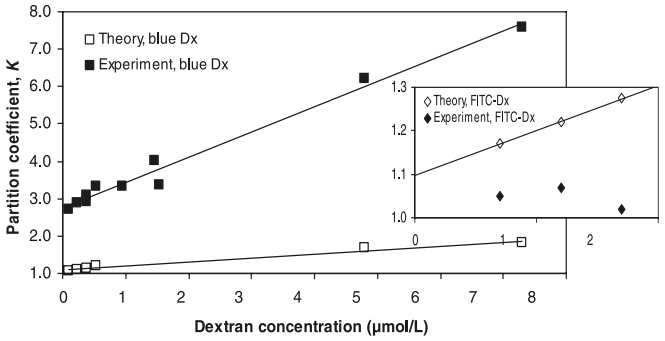

charged blue dextrans. That is, blue dextrans with higher DS may be more strongly repelled by the negatively charged nanocrystals and prefer the more dilute isotropic phase. Thus, K_{el} increases with increasing blue dextran DS (30).

Increasing blue dextran concentration

The divergence in the cellulose concentrations of the two phases (as predicted by Flory (3) and observed by Edgar and Gray (11)), caused by the increase in ionic strength from 0.4 to 7.3 μmol/L due to the increasing concentration of blue dextran dye ligands, is likely too small to affect K according to Sear's theory (13), as increasing the ionic strength from 0 to 2.5 mmol/L was found to cause only a very slight divergence of the isotropic and anisotropic phase concentrations (29). At low concentrations of dextran–dye conjugate, the mixing entropy dominates resulting in a weak driving force for partitioning that increases with increasing polymer concentration. Increasing the total concentration of an ionic dextran–dye conjugate did not have an effect on the value of K in an aqueous two-phase system consisting of dextran and PEG, where such electrostatic and entropic (excluded volume) factors would not be present (35).

Nonionic FITC-dextran vs. anionic blue dextran

In the context of the above observations, the lack of partitioning observed in the FITC-dextran samples is plausible. It has been found that in suspensions of rodlike fd virus suspensions at low ionic strength, neutral FITC-dextran has no effect on the coexistence concentrations of the I–N transition, and no partitioning is observed, in contrast to the strong partitioning predicted theoretically (32). Dogic et al. (32) explained this by stating that the depletion attraction caused by the polymer is screened by long-range electrostatic repulsion of the rods. A similar phenomenon may be occurring here.

In addition, the nonionic FITC dye is more hydrophobic than CB dye and is more likely to be found in the interior of the dextran coil, where it is not available to adsorb onto cellulose nanocrystals. Although free FITC dye has been found to adsorb somewhat onto cellulosic materials (36, 37), there may be a high concentration of nonadsorbed neutral FITC-dextran, which may be better tolerated in the anisotropic phase because it is more mobile and can fit in the defects (although blue dextran also fits in defects) and is not electrostatically repelled by the nanocrystals. If some FITC dye molecules are available for binding, they may not adsorb on cellulose to as great an extent as CB (the binding energy may be weaker for FITC than for CB dye); FITC-dextrans with higher DS may possibly partition more strongly. FITC-dextran 2000 has a radius of gyration of around 16 nm measured by GPC-LS in pH 7 0.20 mol/L $NaNO_3$ + 0.01 mol/L NaH_2PO_4, which is significantly smaller than the radii obtained for blue dextrans 2000 (see Table 1). The smaller size of FITC-Dx is likely caused by its higher hydrophobicity and lack of intramolecular electrostatic repulsions (internal hydrophobic interactions of the aromatic rings cause the macromolecule to contract inwards). FITC-dextran partition coefficient values were found to be slightly lower than predicted theoretically (Fig. 5).

Sear's theoretical calculation considers only the effect of the relative sizes of the rods and coils, in conjunction with the concentration of the rods in each phase, to predict K for a given system (13). The relative concentrations of the two species may also play a role in determining K, particularly in the case of electrostatically charged rods *and* coils, as in the case of blue dextran and cellulose nanocrystals. For blue dextrans, K_{el} (>1) appears to dominate the contribution to K_{meas}, while for FITC-Dx the hydrophobic interactions ($K_{hphob} \leq 1$) of the dye ligands are of greater importance. The theoretical K values for both dextran-dye derivatives therefore lie on the same line (Fig. 5), while their experimental values are very different.

Conclusions

The partitioning behaviour of blue dextrans and FITC-dextrans of high molecular weight in biphasic suspensions of negatively charged cellulose nanocrystals was investigated. Increasing the total concentration of blue dextran increased the partition coefficient by causing a divergence in cellulose concentrations of the isotropic and nematic phases, in agreement with theory and previous experiments conducted in this laboratory. Increased blue dextran–nanocrystal electrostatic repulsions led to larger partition coefficients at higher degrees of CB dye substitution. The effect of CB adsorption onto the cellulose nanocrystal surfaces was discussed. The total concentration of anionic CB dye present in the sample and the DS per AGU affected the electrostatic and entropic contributions to the blue dextran partition coefficient in the cellulose suspension. The divergence between the results presented here and the theoretical prediction of Sear illustrates the influence of the electrostatic charges on the partitioning effect. For blue dextrans and hydrolysed blue dextrans with similar DS at similar total dextran and dye concentrations, the partition coefficient varied linearly with the exponential of $R_g^{5/3}$, in agreement with Sear's partition theory. Dextrans labeled with fluorescein isothiocyanate were found to have partition coefficients of around 1 in this system, possibly because of the lack of electrostatic repulsion and (or) dye adsorption onto cellulose nanocrystals. Blue dextran partition coefficients were larger than predicted theoretically using a second virial coefficient approximation, while FITC-dextran partition coefficients were smaller.

© 2008 NRC Canada

Acknowledgments

We thank Natural Sciences and Engineering Research Council of Canada (NSERC) and FPInnovations (Paprican) for support and the Centre for Self-Assembled Chemical Structures (CSACS) at McGill University for the use of their Varian Cary 300 Bio UV-vis spectrophotometer and TA Instruments TGA Q500. Helpful discussions with Dr. Greg Chauve are gratefully acknowledged. We also thank Julie Boivin at the Université de Montréal for technical assistance with GPC-LS measurements.

References

1. L. Onsager. Ann. N.Y. Acad. Sci. **51**, 627 (1949).
2. M. Adams, Z. Dogic, S.L. Keller, and S. Fraden. Nature, **393**, 349 (1998).
3. P.J. Flory. Macromolecules, **11**, 1138 (1978).
4. M. Takayanagi, T. Ogata, M. Morikawa, and T. Kai. J. Macromol. Sci. Phys. **B17**, 591 (1980).
5. W.-F. Hwang, D.R. Wiff, C.L. Benner, and T.E. Helminiak. J. Macromol. Sci. Phys. **B22**, 231 (1983).
6. E. Bianchi, A. Ciferri, and A. Tealdi. Macromolecules, **15**, 1268 (1982).
7. M. Adams and S. Fraden. Biophys. J. **74**, 669 (1998).
8. K. Inomata, N. Ohara, H. Shimizu, and T. Nose. Polymer, **39**, 3379 (1998).
9. M. Ramzi, J. Borgström, and L. Piculell. Macromolecules, **32**, 2250 (1999).
10. G.H. Koenderink, G.A. Vliegenthart, S.G.J.M. Kluijtmans, A. van Blaaderen, A.P. Philipse, and H.N.W. Lekkerkerker. Langmuir, **15**, 4693 (1999).
11. C.D. Edgar and D.G. Gray. Macromolecules, **35**, 7400 (2002).
12. H.N.W. Lekkerkerker and A. Stroobants. Il Nuovo Cimento, **16D**, 949 (1994).
13. R.P. Sear. J. Phys. II. **7**, 877 (1997).
14. X.M. Dong, J.-F. Revol, and D.G. Gray. Cellulose, **5**, 19 (1998).
15. J.-F. Revol, H. Bradford, J. Giasson, R.H. Marchessault, and D.G. Gray. Int. J. Biol. Macromol. **14**, 170 (1992).
16. J.-F. Revol, L. Godbout, X.M. Dong, D.G. Gray, H. Chanzy, and G. Maret. Liq. Cryst. **16**, 127 (1994).
17. A.G. Mayes, J.D. Moore, R. Eisenthal, and J. Hubble. Biotechnol. Bioeng. **36**, 1090 (1990).
18. M. Tang, R. Zhang, A. Bowyer, R. Eisenthal, and J. Hubble. Biotechnol. Bioeng. **87**, 791 (2004).
19. S. Beck-Candanedo, D. Viet, and D.G. Gray. Langmuir, **22**, 8690 (2006).
20. W.-P. Ma and J.F. Robyt. Carbohydr. Res. **166**, 283 (1987).
21. J.D. Fox and J.F. Robyt. Carbohydr. Res. **227**, 163 (1992).
22. C.E. Ioan, T. Aberle, and W. Burchard. Macromolecules, **33**, 5730 (2000).
23. G. Galinsky and W. Burchard. Macromolecules, **28**, 2363 (1995).
24. C.E. Ioan, T. Aberle, and W. Burchard. Macromolecules, **34**, 3765 (2001).
25. S. Champ, W. Xue, and M.B. Huglin. Macromol. Chem. Phys. **201**, 931 (2000).
26. G.K. Chambers. Anal. Biochem. **83**, 551 (1977).
27. Sigma-Aldrich. Blue dextran molecular weight 2 000 000 product information. Product No. D5751. 1997.
28. M.L. Fishman, W.C. Damert, J.G. Phillips, and R.A. Barford. Carbohydr. Res. **160**, 215 (1987).
29. X.M. Dong, T. Kimura, J.-F. Revol, and D.G. Gray. Langmuir, **12**, 2076 (1996).
30. P.-Å. Albertsson. Partition of cell particles and macromolecules. Wiley-Interscience, New York. 1986.
31. F.R. Senti, N.N. Hellman, N.H. Ludwig, G.E. Babcock, R. Tobin, C.A. Glass, and B.L. Lamberts. J. Polym. Sci. **27**, 527 (1955).
32. Z. Dogic, K.R. Purdy, E. Grelet, M. Adams, and S. Fraden. Phys. Rev. E **69**, 051702-1 (2004).
33. Sigma-Aldrich. Fluorescein isothiocyanate dextran product information. Product No. FD-2000S (1997).
34. D.L. Stevenson, J.F. Kennedy, and C.A. White. Starch, **40**, 433 (1988).
35. G. Johansson and M. Joelsson. J. Chromatogr. **393**, 195 (1987).
36. L. Hildén, G. Daniel, and G. Johansson. Biotechnol. Lett. **25**, 553 (2003).
37. R. Pinto, J. Carvalho, M. Mota, and M. Gama. Cellulose, **13**, 557 (2006).

© 2008 NRC Canada

Occurrence of poly(hydroxyalkanoate) in the gut homogenate of a phylogenetically higher termite: *Macrotermes carbonarius*[1]

Kumar Sudesh, Bee-Yong Tay, and Chow-Yang Lee

Abstract: Gas chromatography analysis of a phylogenetically higher termite-gut homogenate detected the presence of trace amounts of poly(3-hydroxybutyrate) (PHB), a prokaryotic storage material. In addition, the gut homogenate smear, stained with Nile blue A, also suggested the presence of PHB-like granules. Chloroform extracts of both soldier and worker classes of this termite were obtained for further spectroscopic analysis. FTIR, ^{1}H NMR, and 2D ^{1}H-^{1}H NMR analyses confirmed the presence of PHB in both the chloroform extracts. This showed for the first time the occurrence of bacteria capable of accumulating PHB in the termite gut. The results indicated that the physiological environment in the termite gut is suitable for the colonization by PHB-producing bacteria and is probably rich in organic carbon sources, which can be readily assimilated and stored as PHB.

Key words: Macrotermes carbonarius, poly(hydroxyalkanoate), PHB, termite

Résumé : L'analyse par chromatographie gazeuse d'une préparation homogénéisée d'estomac de termites phylogénétiquement plus élevées a permis de détecter la présence de traces de poly(3-hydroxybutyrate) (PHB), un matériel d'emmagasinage prokaryotique. De plus, un frottis d'une préparation homogénéisée d'estomac, teint avec du bleu du Nile A, suggère aussi la présence de granules ressemblant à du PHB. On a aussi obtenu des extraits au chloroforme des classes tant de soldat que de travailleur de cette termite qui ont pu être analysés par des méthodes spectroscopiques. Des analyses par IR à transformée de Fourier, par RMN du ^{1}H et par RMN ^{1}H-^{1}H en 2D ont permis de confirmer la présence de PHB dans chacun de ces extraits chloroformiques. Ces résultats démontrent pour la première fois l'existence de bactéries qui sont capables d'accumuler du PHB dans l'estomac des termites. Ils démontrent aussi que l'environnement physiologique dans l'estomac des termites est approprié pour la colonisation par des bactéries pouvant produire du PHB et qu'il est probablement riche en sources de carbone organique qui peut être facilement assimilé et emmagasiné sous la forme de PHB.

Mots-clés : Macrotermes carbonarius, polyhydroxyalcanonate, PHB; termite.

[Traduit par la rédaction]

Introduction

Poly(hydroxyalkanoate) (PHA) is a carbon- and energy-storage material accumulated by a large number of prokaryotes (1). The synthesis of PHA by bacteria usually occurs when carbon source is abundant. The most common type of PHA found naturally in the environment is poly(3-hydroxybutyrate) (PHB). The ability to accumulate PHB has been shown to enhance the survival of bacteria during prolonged period of starvation and (or) under stress conditions (2). PHB also serves as an electron sink and provides energy for the energy-intensive process of sporulation in some bacteria (3, 4). The occurrence of PHB in an environmental sample provides physiological evidence for the presence of prokaryotic microorganisms capable of synthesizing this storage material (5). In addition, it also indicates suitable growth conditions for bacteria and the presence of sufficiently high concentrations of organic carbon sources that can be assimilated and polymerized into PHB.

The intestine of termites is colonized by a variety of microorganisms (6), which contribute to the biomineralization of lignocellulosic matter ingested by termites. These microorganisms have attracted the attention of microbiologists because of their important and interesting symbiotic association with the termite host for the efficient biorecycling of plant litter (7). A major drawback faced by microbiologists in understanding the physiological aspects of termite gut microbiota is the difficulty to cultivate most of the microorganisms in the laboratory (8). To partially solve this problem, culture independent methods have been used to identify and characterize the various types of microorganisms (7, 9).

The primary objective of this study was to determine if termite-gut environment provides conditions favorable for the colonization by PHA producing bacteria. Although molecular methods have revealed the presence of bacteria that

Received 17 October 2007. Accepted 18 December 2007. Published on NRC Research Press Web site at canjchem.nrc.ca on 1 April 2008.

K. Sudesh,[2] B.Y.Tay, and C.Y. Lee. School of Biological Sciences, Universiti Sains Malaysia, 11800 Penang, Malaysia.

[1]This article is part of a Special Issue dedicated to Professor R. Marchessault.

[2]Corresponding author (e-mail: ksudesh@usm.my).

 doi:10.1139/V08-007 © 2008 NRC Canada

are phylogenetically related to PHA producers (10), there is still no evidence for the occurrence of PHA-producing bacteria in termite gut. Furthermore, it is not known if the nutritive conditions in the termite gut favor the growth of PHA producing bacteria and that substantial amounts of suitable carbon sources are available to the bacteria for the accumulation of PHA. Here, we report for the first time the occurrence of PHA in a phylogenetically higher termite, *Macrotermes carbonarius*. Quantitative monitoring of PHA in the termite gut might be useful in defining the recent nutritional history of the gut microbiota. In addition, knowledge of the microorganisms in the termite gut will provide new insights into the possibility to convert lignocellulosic matter to PHA.

Materials and methods

Live worker and soldier termites of *M. carbonarius* were collected from mound material dug from various locations in Universiti Sains Malaysia. The termites were transported to the laboratory together with their fungus comb. The termites were then separated into workers and soldiers based on their obvious morphological characteristics (11, 12). One hundred workers were cleaned using sterile distilled water and 70 % ethanol before extracting their whole guts for gas chromatography (GC) analysis. The freeze-dried gut homogenate was methanolyzed in a screw-capped test tube at 100 °C for 140 min in a mixture of 2 mL chloroform, 1.7 mL methanol, and 0.3 mL concentrated sulfuric acid. Upon completion, 1 mL of distilled water was added to the cooled mixture and vortexed for 1 min. After phase separation, the organic phase (bottom layer) was subjected to GC analysis. A Shimadzu GC-14B capillary gas chromatograph system equipped with flame-ionization detector (FID) was used along with a fused silica capillary column (SPB^{TM}-1, Supelco) for the analysis.

The remaining workers (1368) and soldiers (706) were homogenized separately prior to lyophilization. A total freeze-dried mass of 14.5 g whole soldier homogenate and 4.5 g whole worker homogenate were obtained and subjected to extraction with hot chloroform for 4 h. The brownish chloroform extracts were then concentrated to approximately 10 mL and added to 100 mL of rapidly stirred cold methanol. This resulted in the formation of a fluffy precipitate, which was recovered by filtration and dried in vacuo before subjecting to spectroscopic analyses. For ^{1}H, ^{13}C NMR, and 2D ^{1}H-^{1}H NMR spectroscopy analyses, the dried precipitate was dissolved in $CDCl_3$, and the spectra were recorded using a Bruker 400 MHz NMR spectrometer. The same solution was used for FTIR analysis. For the latter, a thin layer of film was made on a ZnSe window by evaporating the solvent. After thorough drying, the IR spectrum of the resulting film was recorded using a PerkinElmer System 2000 FTIR. For comparison purposes, pure PHB was synthesized and purified from *Delftia acidovorans* according to a method described recently (13).

Results and discussion

GC analysis of the lyophilized whole-gut extract of *M. carbonarius* workers revealed the presence of trace amounts (<0.5% of the gut dry mass) of PHB. Nile blue A staining of the gut homogenate smear also suggested the presence of PHA-like granules, which showed the typical bright orange fluorescence when viewed under a UV-light microscope (results not shown). These results provided early indication for the presence of PHA in the termite gut. To obtain conclusive evidence, large quantities of lyophilized whole-termite homogenate were subjected to chloroform extraction to dissolve any PHA that may be present. During the precipitation step in methanol, the formation of white fluffy material was a further indication for the presence of relatively high molecular mass PHA. Upon filtration, the white precipitate was co-purified with a brownish pigment. To remove the brownish pigment, the above process of dissolving in chloroform and precipitating in methanol was repeated. This resulted in lesser amount of the brownish pigment, as indicated by its lighter color intensity. However, it also reduced the amount of the white fluffy precipitate. No further attempts were made to remove the brownish pigment, as it may decrease the concentration of any PHA that was extracted.

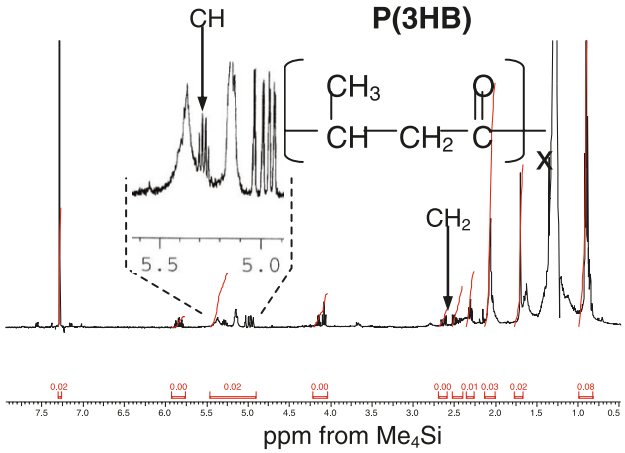

Fig. 1. ^{1}H NMR spectrum of chloroform extract of whole worker homogenate recorded at 25 °C in $CDCl_3$. Inset shows an expanded spectrum in the vicinity of methine proton resonance of PHB.

Figure 1 shows the ^{1}H NMR spectrum of the extract recorded in $CDCl_3$ at 25 °C. The chemical shifts are in ppm from TMS. The predominant peaks at around 0.9 ppm and 1.4 ppm can be attributed to methyl and methylene protons of long-chain alkanes. This is further supported by the symmetric–asymmetric stretching bands of methyl–methylene at around 2900 cm^{-1} in the FTIR spectrum (Fig. 2) of the chloroform extract. The carbonyl (C=O) stretching band at 1724 cm^{-1} (appears as a faint shoulder near the band at 1737 cm^{-1}) is a characteristic band of PHB, as shown in the spectrum obtained from pure PHB. However, the bands at 2900 cm^{-1} are more intense than that at 1724 cm^{-1}, indicating that most of the extracted products may be long-chain alkane compounds. Therefore, the peak from methyl protons of PHB (1.27 ppm) in the NMR spectrum may be overlapping with the peak at 1.4 ppm due to the methylene protons of long-chain alkanes. Because of the significant amount of co-purified long-chain alkane compounds, the presence of PHB could not be confirmed from the FTIR spectrum.

© 2008 NRC Canada

Fig. 2. FTIR spectra of chloroform extract of whole worker homogenate and pure poly(3-hydroxybutyrate) (PHB).

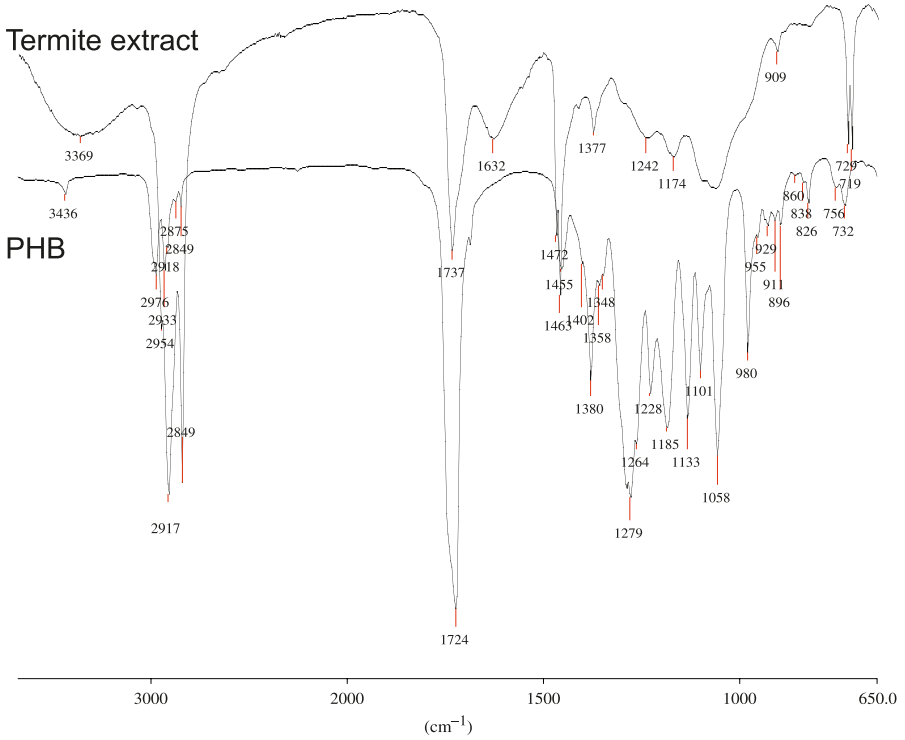

Further clues for the presence of PHB was obtained from a faint peak at around 5.27 ppm in the ^{1}H NMR spectrum (Fig. 1). By comparison with previously reported ^{1}H NMR spectrum of PHB (14), the peak near 5.27 ppm may be a resonance from the methine proton of PHB. In addition, weak resonance peaks (2.45–2.65 ppm) corresponding to the methylene protons of PHB can also be detected from the ^{1}H NMR spectrum (14). The identities of the peaks also were confirmed by comparing with the ^{1}H NMR spectrum of pure PHB sample (see Supplementary Data).[3] To obtain further confirmation, 2D ^{1}H-^{1}H NMR analysis was performed, and the result is displayed in Fig. 3.

Clear correlation peaks were seen between the neighboring protons of methine and methylene. In addition, correlation peaks were also observed between methine and methyl protons showing that they are adjacently located as is in the case of PHB. These results provided strong evidence for the presence of PHB in the chloroform extract of the worker-class termite homogenate.

Another interesting type of PHA has also been identified in many organisms, including eukaryotes. This PHA is characterized by its low molecular mass, because it is consisted of less then 150 monomeric units of either 3-hydroxybutyrate or 3-hydroxyvalerate. Unlike the high molecular mass storage PHA synthesized by most bacteria, the low molecular mass PHA is a non-storage PHA and is usually complexed with other cellular macromolecules; hence they are referred to as complexed PHA (15). It is possible that some of the non-storage PHAs may have been co-extracted from our samples. However, we have also carried out ultrastructural studies on the termite gut, which revealed the presence of many bacterial cells that contained discrete granules resembling PHAs (see Supplementary Data).[3] Based on all these evidences, the PHB detected in this study is most likely the storage PHB accumulated by bacteria in the termite gut.

NMR and FTIR analyses of chloroform extract of the soldier-class termite homogenate also produced similar results (results not shown). Thus, the occurrence of PHB was confirmed in both the soldier and worker homogenates. The results indicated the presence of PHB producing microorganisms in the gut of both soldier and worker classes of this termite. It is known that the soldiers are not capable of feeding themselves because of their huge mandible. The soldiers have to be fed by the workers by a process called trophallaxis. Therefore, the intestinal microbiota of *M. carbonarius* soldiers must have originated from the workers and therefore may be quite similar. The occurrence of PHB in the guts of both these classes provides good evidence for the similarities of gut physiological conditions in workers and soldiers. In addition, this study has also shown that the physiological environment of the guts of both soldiers and workers allow for the growth and proliferation of PHB producing bacteria and that suitable types and concentrations of carbon sources are readily available for PHB biosynthesis. We have since successfully isolated three morphologically different bacteria capable of producing PHB from the gut of *M. carbonarius* (manuscript in preparation). By understand-

[3] Supplementary data for this article are available on the journal Web site (canjchem.nrc.ca) or may be purchased from the Depository of Unpublished Data, Document Delivery, CISTI, National Research Council Canada, Ottawa, ON K1A 0R6, Canada. DUD 3729. For more information on obtaining material, refer to cisti-icist.nrc-cnrc.gc.ca/irm/unpub_e.shtml.

© 2008 NRC Canada

Fig. 3. 2D ^{1}H-^{1}H NMR spectrum of chloroform extract of whole worker homogenate. Signals confirming the presence of poly(3-hydroxybutyrate) (PHB) are circled.

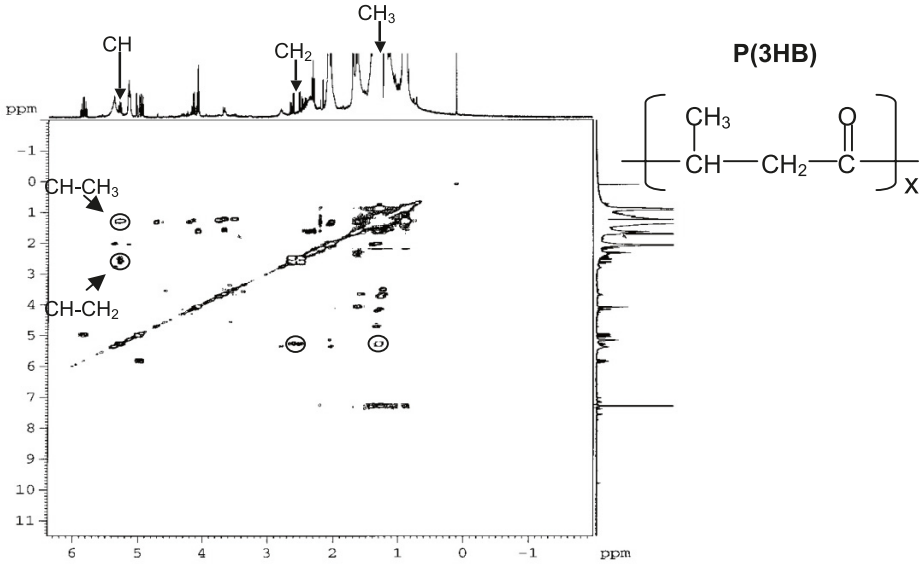

ing the PHB biosynthesis process in these bacteria, it would provide additional insight into the physiological environment of the termite gut. In addition, this knowledge might enable the development of novel processes for the conversion of lignocellulosic wastes into PHB.

Acknowledgements

The authors thank Goh Yik Pheng and Chee Jiun Yee for assisting with the collection and dissection of termites. Dr. Hideki Abe's help with the interpretation of the NMR spectra is gratefully acknowledged. Universiti Sains Malaysia supported this study through the Research University grant.

References

1. A.J. Anderson and E.A. Dawes. Microbiol. Rev. **54**, 450 (1990).
2. J.A. Ruiz, N.I. Lopez, R.O. Fernandez, and B.S. Mendez. Appl. Environ. Microbiol. **67**, 225 (2001).
3. M.A. Cevallos, S. Encarnacion, A. Leija, Y. Mora, and J. Mora. J. Bacteriol. **178**, 1646 (1996).
4. W.J. Page, A. Tindale, M. Chandra, and E. Kwon. Microbiology, **147**, 483 (2001).
5. R.H. Findlay and D.C. White. Appl. Environ. Microbiol. **45**, 71 (1983).
6. A. Brune and M. Friedrich. Curr. Opin. Microbiol. **3**, 263 (2000).
7. M. Ohkuma. Appl. Microbiol. Biotechnol. **61**, 1 (2003).
8. B.S. Stevenson, S.A. Eichorst, J.T. Wertz, T.M. Schmidt, and J.A. Breznak. Appl. Environ. Microbiol. **70**, 4748 (2004).
9. A. Brauman, J. Dore, P. Eggleton, D. Bignell, J.A. Breznak, and M.D. Kane. FEMS Microbiol. Ecol. **35**, 27 (2001).
10. T. Thongaram, Y. Hongoh, S. Kosono, M. Ohkuma, S. Trakulnaleamsai, N. Noparatnaraporn, and T. Kudo. Extremophiles, **9**, 229 (2005).
11. Y.P. Tho. Malayan Forest Records, **36**, 1 (1992).
12. C.Y. Lee, B.T. Forschler, and T.M. Jenkins. Proceedings of the 5th International Conference on Urban Pests, July 9-14, Singapore, 2005. pp. 205-211. ISBN 983 42607 0 9.
13. W.H. Lee, M.N.M. Azizan, and K. Sudesh. Polym. Degrad. Stab. **84**, 129 (2004).
14. Y. Doi, M. Kunioka, Y. Nakamura, and K. Soga. Macromolecules. **19**, 1274-1276 (1986).
15. R.N. Reusch. Non-storage poly-(*R*)-3-hydroxyalkanoates (complexed PHAs) in prokaryotes and eukaryotes. In Y. Doi and A. Steinbüchel (*Editors*). Biopolymers, vol. 3a. Wiley-VCH Verlag GmbH, Weinheim, Germany. p123 (2002).

© 2008 NRC Canada

Thiolysis of poly(3-hydroxybutyrate) — A novel biochemical reaction[1]

K. Uchino and T. Saito

Abstract: An enzyme involved in the degradation of poly(3-hydroxybutyrate) (PHB), PhaZa1 from *Ralstonia eutropha* H16, catalyzes the thiolysis of PHB with coenzyme A. The properties of this novel reaction were investigated in vitro. The active center's cysteine residue was point-mutated to prepare C183S and C183A. The wild type and the two mutants were compared in terms of hydrolytic and thiolytic activity. C183S was as active as the wild type in the hydrolysis, but less active in the thiolysis, of PHB. The cysteine residue was important for the thiolysis of PHB, which may be why it has been conserved in almost all PhaZa1 homologs in various bacteria.

Key words: PHB, thiolysis, PHB depolymerase

Résumé : Un enzyme impliqué dans la dégradation du poly(3-hydroxybutyrate) (PHB), le PhaZa1 obtenu à partir du *Ralstonia eutropha* H16, catalyse la thionolyse du PHB en présence du coenzyme A (CoA). On a étudié les propriétés de cette nouvelle réaction in vitro. On a fait subir une mutation au résidu cystéine du centre actif pour préparer les enzymes C183S et C183A. On a comparé le type original et les deux mutants en termes d'activités hydrolytique et thiolytique. L'activité hydrolytique du mutant C183S est aussi grande que celle du produit original, mais moins active dans la thiolyse du PHB. Le résidu cystéine est important pour la thiolyse du PHB et c'est probablement la raison pour laquelle il a été conservé dans pratiquement tous les homologues du PhaZa1 dans diverses bactéries.

Mots-clés : PHB, thiolyse, dépolymérase du PHB.

[Traduit par la Rédaction]

Introduction

Poly([R]-3-hydroxybutyrate) (PHB) is a natural polyester found in a wide variety of bacteria (1). The bacteria accumulate PHB in their cells and utilize it as a source of energy and carbonlike glycogen or fat. In cells of PHB-producing bacteria, PHB was found as discrete granules (inclusion bodies). Bacteria depositing PHB may be dead and release PHB into the environment. While amorphous in inclusion bodies, PHB becomes semi-crystalline out of the cell. Some bacteria and fungi (2) hydrolyze semi-crystalline PHB to its monomer [R]-3-hydroxybutyrate (3HB) by secreting PHB depolymerases, and PHB-producing bacteria have been believed to hydrolyze stored PHB with intracellular PHB depolymerase (eq. [1]).

$$[1] \qquad (3HB)_n + H_2O \rightarrow (3HB)_{n-1} + 3HB$$

Received 10 November 2007. Accepted 15 February 2008. Published on NRC Research Press Web site at canjchem.nrc.ca on 3 April 2008.

This paper is dedicated to Robert H. Marchessault in recognition of his many contributions to polysaccharide and biopolymer chemistry.

K. Uchino and T. Saito.[2] Department of Biological Sciences, Faculty of Science, Kanagawa University, 2946 Tsuchiya, Hiratsuka, Kanagawa, 259-1293 Japan.

[1]This article is part of a Special Issue dedicated to Professor R. Marchessault.

[2]Corresponding author (e-mail: 43saito-bio@kanagawa-u.ac.jp).

In *Ralstonia eutropha* H16, a model for studying the PHB metabolism of PHB, several proteins such as PHB synthase, PHB depolymerase, phasin, and a regulatory protein, as well as phospholipids, were found on the surface of PHB granules (3–6).

Recently, it was revealed that PHB was thiolyzed with coenzyme A (CoA) to 3-hydroxybutyryl-CoA (3HB-CoA) in *R. eutropha* H16 when PHB granules were incubated in the presence of CoASH (7) (eq. [2]), and it was suggested that an intracellular PHB depolymerase (PhaZa1) is responsible for this novel reaction (8).

$$[2] \qquad (3HB)_n + CoA \rightarrow (3HB)_{n-1} + 3HB\text{-}CoA$$

Since the basic properties of PhaZa1 from *R. eutropha* as a PHB thiolase are not sufficiently understood, we examined the thiolytic reaction of PhaZa1 in vitro. PhaZa1 has a cysteine at the 183rd amino acid residue as the active center, and this residue is conserved in homologous proteins in various bacteria (9). Therefore, the importance of this cysteine residue was also investigated.

Experimental section

The materials used to prepare buffer solutions, the substrates, and all reagents were obtained commercially except PHB, which was prepared from *R. eutropha*. All solutions were prepared from distilled, deionized water. Spectrophotometric measurements were made using a Shimadzu UVmini-1240 or Bio-Rad microplate reader benchmark. The CoA derivatives were analyzed with a HPLC system (Hitachi, Tokyo, Japan) equipped with an L-6200 pump, a D-2500

 doi:10.1139/V08-034 © 2008 NRC Canada

integrator, a L-4200 detector operated at 254 nm, and a Shodex RSpak RP18-415 column (4.6ϕ × 150 mm, Showa Denko, Tokyo, Japan).

PhaZa1 and the mutated PhaZa1 C183S, in which the cysteine at 183 was replaced by serine, and C183A, in which it was replaced by alanine, were prepared from gene-overexpressing *Escherichia coli*, as reported previously (9). The soluble fraction of the *E. coli* cells was used as the crude extract. Artificial amorphous PHB was prepared with deoxycholate as a detergent as previously described (10).

The standard reaction mixture (0.1 mL) containing enzymes, amorphous PHB (deoxycholate-coated, final concentration 0.5 mg/mL, or washed PHB (see below), final concentration 1.0 mg/mL), 50 mmol/L Tris-HCl buffer, pH 8.0, and 1 mmol/L CoA was incubated at 30 °C. Samples were acidified with 10 µL of 1 N HCl to stop the reaction and then centrifuged (15 000g, 5 min). The supernatant was stored on ice or at –20 °C prior to use. For the thiolytic assay, the supernatant was analyzed by HPLC in conditions described previously (8). For the hydrolytic assay, 3HB in the supernatant was measured based on the reduction of NAD^+ with 3HB dehydrogenase as previously reported (9). In other experiments such as the experiment to find the optimum pH, the components or concentrations were modified as written in the following. Enzymes were not stable after purification, therefore crude extracts were used as enzymes for assays. These experiments were performed at least twice.

Results and discussion

PhaZa1 was purified from crude extract of the gene-overexpressing *E. coli* (Fig. 1). When PhaZa1 was incubated with amorphous PHB and CoA, it produced 3HB-CoA (Fig. 2). A previous report showed that crude extract of *E. coli* containing PhaZa1 catalyzed the thiolysis of PHB (8), and this was confirmed using purified enzyme. Phasins, proteins covering PHB inclusion bodies in a living cell, were required in some experiments in the previous report (8), but the present study shows that phasins are not essential for the thiolysis of PHB with PhaZa1. Because the purified enzyme easily lost its activity and the crude extract showed the same activity (Fig. 2) and was stable at –20°C for at least 3 months, the crude extract was used as an enzyme. Some components of the crude extract might stabilize PhaZa1, but no component catalyzed thiolysis, since the *E. coli* extract with only the cloning vector showed no 3HB-CoA production (data not shown).

The optimum conditions for the thiolysis of PHB by PhaZa1 were examined. An important aspect was the preparation of the substrate PHB. Generally, intracellular PHB depolymerase cannot degrade semi-crystalline PHB but can degrade amorphous PHB. In a protein-free system, amorphous PHB was prepared using detergents to stabilize the amorphous state, but the detergents inhibited thiolysis. Therefore, amorphous PHB coated with deoxycholate was washed with water. The washed PHB was active as a substrate for the thiolysis of PHB, and 0.2% deoxycholate inhibited thiolysis completely (Fig. 3). The hydrolysis was also inhibited, but the thiolysis was more sensitive to the detergent. On the other hand, a large volume of crude enzyme showed activity with unwashed substrate, possibly because

Fig. 1. Sodium dodecyl sulfate-polyacrylamide gel electrophoresis of purified PhaZa1. Each protein (1 µg) was loaded onto a 12% gel. Lane 1, protein markers; lane 2, crude extract; lane 3, PhaZa1. Protein was stained with Coomassie brilliant blue R-250.

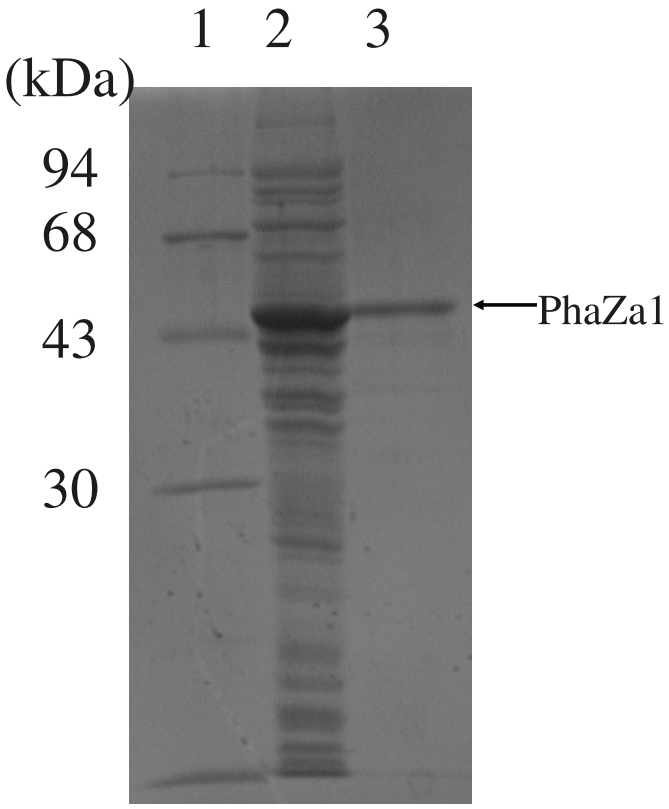

of absorption of the detergent by the crude enzymes. Using washed PHB, the optimum pH was examined. As shown in Fig. 4, pH 8 was optimum. At a pH of less than 6 or higher than 9, this reaction was completely inhibited.

To investigate the importance of the active center residue cysteine, three PhaZa1s were tested: PhaZa1 (wild type), and two mutated PhaZa1s, C183S and C183A. Under the conditions described in the Experimental section, the serine-mutation lowered the thiolytic activity by about 80% compared with the wild type. The alanine mutant hardly produced 3HB-CoA. Table 1 shows the activities of hydrolysis and thiolysis by the respective enzymes. The serine-mutated enzyme showed little change in hydrolytic activity but significantly less thiolytic activity (Table 1). The alanine mutant showed neither hydrolytic nor thiolytic activity (Table 1). These three PhaZa1s differ in only one functional group: thiol (cysteine), hydroxyl (serine), or neither (alanine). Therefore, these results suggest that the thiol group at the active center is necessary for thiolysis. A thioester bond has more energy than an ester bond. When the active center was acylated, PhaZa1 would have formed a thioester bond with the substrate, and C183S an ester bond. The thioester bond can more easily promote the transfer of 3HB from the enzyme to CoA than the ester bond.

The thiolysis of PHB is a paradigmic reaction of the degradation of biopolymers that parallels the hydrolysis of nucleic acid and polysaccharide as cellulose etc. and phosphorylation of glycogen and starch. The thiolysis of

© 2008 NRC Canada

Fig. 2. Chromatograms for thiolysis by (*A*) crude extract and (*B*) purified PhaZa1. The reaction mixture contained 50 mmol/L phosphate pH 7.0, washed PHB, 1 mmol/L CoA, and 0.2 mg of crude extract or 15 μg of purified PhaZa1. After incubation for 30 min, 1N HCl was added and the reaction mixture was centrifuged. The concentration of 3HB-CoA was measured with HPLC. Peaks for CoA and 3HB-CoA are shown. Asterisks show unknown peaks. The other peaks are impurities.

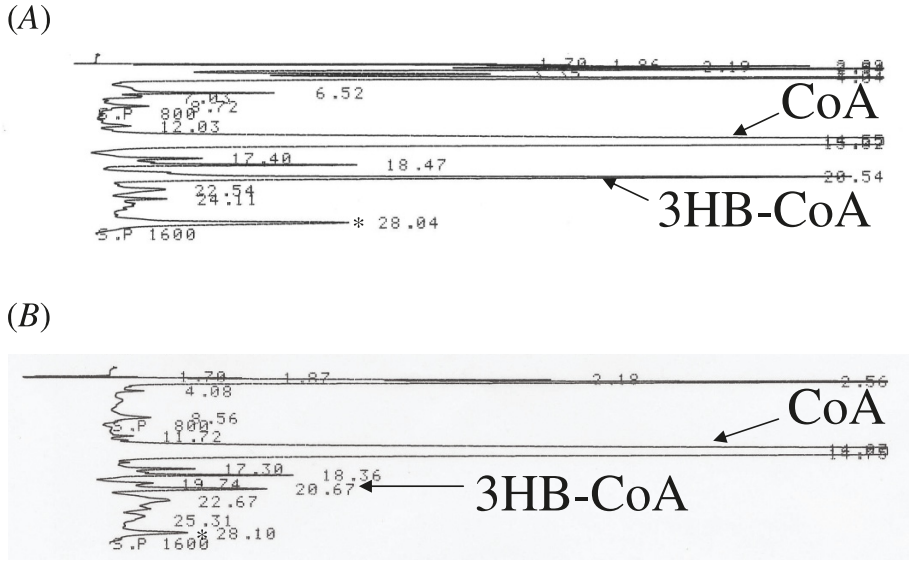

Fig. 3. Inhibition of the thiolysis of PHB by deoxycholate. The reaction mixture contained 0%–0.5% deoxycholate. After incubation for 30 min, 1 N HCl was added and the reaction mixture was centrifuged. The supernatant was analyzed by HPLC.

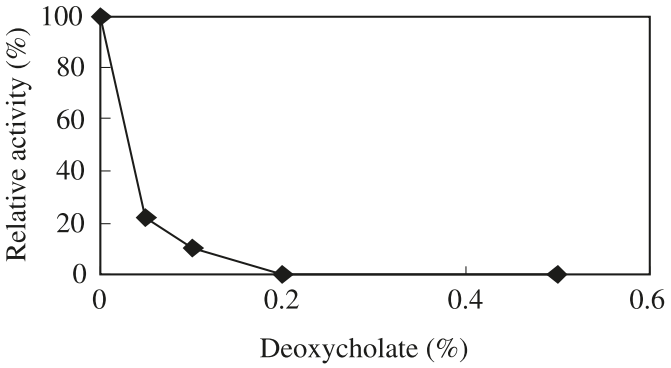

Fig. 4. pH Profile of the thiolysis of PHB. The reaction mixture contained 100 mmol/L buffer: sodium phosphate pH 6–8, Tris-HCl pH 7–9. The reaction was acidified with 1 N HCl at 10 min. The supernatant of the reaction mixture was analyzed with HPLC. The peak height of 3HB-CoA at pH 8 in phosphate buffer was 100%.

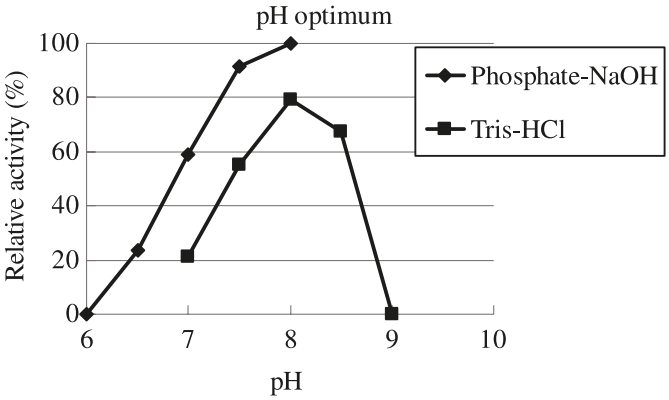

PHB is a novel reaction in the metabolism of PHB. Hitherto, intracellular PHB degradation has been studied only in terms of hydrolysis. However, there have been observations of the turnover of intracellular PHB; PHB is simultaneously synthesized and degraded in *R. eutropha* H16 (11, 12). In the metabolism of PHB, stored PHB has been believed to be hydrolyzed by depolymerases (hydrolases) based on analogy with extracellular PHB depolymerase. Metabolizing 3HB, the product of the hydrolysis, requires an input of energy such as activation with CoA to form 3HB-CoA (eq. 3) or other CoA derivatives as a CoA donor (11).

[3] 3HB + CoA +ATP → 3HB-CoA + AMP + pyrophosphate

Therefore, the simultaneous turnover of PHB occurring in *R. eutropha* H16 wastes a lot of energy. Thiolysis of PHB is much preferable over hydrolysis of PHB in terms of energy, since the energy contained in ester bonds in PHB will be

Table 1. Comparison of hydrolysis and thiolysis.

	3HB Production (mmol/L)	3HB-CoA Production (mmol/L)
PhaZa1	0.55	0.44
C183S	0.34	0.09
C183A	0	0.01

Note: The reaction mixture (100 μL) contained 50 mmol/L Tris-HCl pH 8.0, 1 mmol/L CoA, 2 mg of protein as crude extract. The mixture was incubated for 30 min at 30 °C. The reaction was stopped by the addition of 10 μL of 1 mol/L HCl. After centrifugation, the supernatant of the mixture was analyzed by spectrophotometer for 3HB and by HPLC for 3HB-CoA.

© 2008 NRC Canada

preserved in a thioester bond in 3HB-CoA. Therefore, the thiolysis of PHB is of great significance to the metabolism of PHB in bacteria.

Although PhaZa1 showed both hydrolytic and thiolytic activity toward PHB in vitro, its physiological reaction seems to be the thiolysis of PHB. Thiolysis was catalyzed much more efficiently than hydrolysis with the serine-mutated PhaZa1, C183S (Table 1). PhaZa1 showed almost no hydrolytic activity toward the native PHB granules (8) or in vivo (data not shown). Furthermore, all proteins homologous to PhaZa1 have cysteine at the active center for thiolysis. This shows the importance of the thiolysis of PHB to bacteria since a cysteine residue seems preferable to a serine residue in the thiolytic reaction.

Acknowledgements

We thank J. Oyanagi for technical assistance. This study was supported in part by a grant-in-aid for the High-Tech Research Center Project (2007) from the Ministry of Education, Culture, Sports, Science and Technology of Japan.

References

1. A. J. Anderson and E. A. Daws. Microbiol. Rev. **54**, 450 (1990).
2. D. Jendrossek and R. Handrick. Annu. Rev. Microbiol. **56**, 403 (2002).
3. A. Steinbüchel, K. Aerts, W. Babel, C.Föllner, M. Liebergesell, M.H. Madkour, F. Mayer, U. Pieper-Fürst, A. Pries, H.E. Valentin, and R. Wieczorek. Can. J. Microbiol. **41**, 94 (1995).
4. G.M. York, J. Stubbe, and A. J. Sinskey. J. Bacteriol. **184**, 59 (2002).
5. L. Jurasek and R. H. Marchessault. Biomacromolecules, **3**, 256 (2002).
6. M. Pötter and A. Steinbüchel. Biomacromolecules, **6**, 552 (2005).
7. K. Uchino and T. Saito. J. Biochem. **139**, 615 (2006).
8. K. Uchino, T. Saito, B. Gebauer, and D. Jendrossek. J. Bacteriol. **189**, 8250 (2007).
9. T. Kobayashi and T. Saito. J. Bioeng. Biosci. **96**, 487 (2003).
10. T. Abe, T. Kobayashi, and T. Saito. J. Bacteriol. **187**, 6982 (2005).
11. Y. Doi, A. Segawa, Y. Kawaguchi, and Ml. Kunioka. FEMS Microbiol. Lett. **59**, 165 (1990).
12. B. Taidi, D. Mnasfield, and A. J. Anderson. FEMS Microbiol. Lett. **129**, 201 (1995).

© 2008 NRC Canada

Swelling of *Valonia* cellulose microfibrils in amine oxide systems[1]

Pierre Noé and Henri Chanzy

Abstract: Cellulose microfibrils from *Valonia ventricosa* cell-wall fragments were immersed into molten *N*-methylmorpholine-*N*-oxide monohydrate (NMMO·H_2O), stabilized with *n*-propyl gallate and kept at 80 °C. The resulting ultrastructural modifications, which were followed by transmission electron microscopy and electron diffraction analysis, showed that within minutes the solvent slowly penetrated inside the crystalline microfibrils and progressed as a wedge in between the cellulose chains without cutting them. Prior to dissolution, a longitudinal subfibrillation of the initial microfibrils occurred, leading to the observation of highly swollen microfibrils, which could reach diameters up to three times larger than those of the initial samples. This mode of swelling is compared with those occurring in other systems, where the intracrystalline swelling of cellulose has been described at the ultrastructural level.

Key words: cellulose swelling, *Valonia* cellulose, *N*-methylmorpholine-*N*-oxide.

Résumé : Des microfibrilles en provenance de fragments de paroi de *Valonia ventricosa* ont été immergées à 80 °C dans de la *N*-oxyde de *N*-méthylmorpholine monohydratée (NMMO·H_2O), en présence de gallate de *n*-propyle. La modification de l'ultrastructure de ces microfibrilles a été étudiée par microscopie électronique à transmission et analysée par diffraction des électrons. On observe un gonflement de ces microfibrilles sous l'influence du solvant qui pénètre comme un coin à l'intérieur de celles-ci, en se glissant entre les chaînes cellulosiques. Dans l'étape ultime, avant la dissolution, on remarque des microfibrilles ayant gonflé jusqu'à un diamètre trois fois supérieur au diamètre initial. Ce mode de gonflement est comparé avec d'autres systèmes de gonflement intra-cristallins de la cellulose.

Mots-clés : gonflement de la cellulose, cellulose de *Valonia*, *N*-oxyde de *N*-méthylmorpholine.

[Traduit par la Rédaction]

Introduction

Cellulose can be considered as the archetype of a renewable resource susceptible to yield structural materials of high mechanical properties. For this reason the processing of cellulose into various other products is the focus of never-ending interest. Developed more than a century ago (1), the viscose process has traditionally been the leading method to yield cellulose products, such as yarns, fibers, films, cellular products, etc. Today, however, the viscose process is slowly being abandoned, since it presents serious environmental drawbacks. As a consequence, alternative ways of processing cellulose by finding environmentally friendly solvent systems have been, and still are, the focus of intense research and development.

Among the new cellulose solvents that have been reported, *N*-methylmorpholine-*N*-oxide (NMMO) stands out as being the only organic solvent that has successfully reached the stage of commercialization (2), leading to the development of new cellulose fibers under the trade names of Tencel and Lyocell. Today, these fibers are being successfully incorporated in high class clothing, nonwoven fabrics, as well as in a number of specialty products. As opposed to the viscose process, the dissolution of cellulose in NMMO does not require any derivatization. In this system, the dissolution and regeneration process is derived from the hydrogen-bonding characteristics of the hygroscopic NMMO, which will interact with cellulose if there is a shortage of water, but will reject cellulose if water is in excess. As the melting point of NMMO is inversely related to its water content, the dissolution of cellulose can thus be monitored by temperature and water content. Typical phase diagrams (3, 4) have shown that NMMO monohydrate (NMMO·H_2O: 13.3% water *w*/*w*) acted as a solvent at temperatures in the order of 100 °C, whereas NMMO disesquihydrate (NMMO·2.5 H2O: 28% water *w*/*w*) did not lead to solubilization at any temperature.

Observations of the dissolution of various cellulose fibers into NMMO have shown that if NMMO monohydrate was used at temperatures of 80 °C and above, ramie fibers readily dissolved by breaking down without appreciable swelling (5). On the other hand, if 18–20% *w*/*w* water was present in the system, extensive swelling occurred as the diameter of the fibers could increase several fold without any dissolution. This behavior was also reported for other fibers, such as those of cotton or wood pulp, but the swelling oc-

Received 9 October 2007. Accepted 20 February 2008. Published on NRC Research Press Web site at canjchem.nrc.ca on 4 April 2008.

P. Noé[2] and H. Chanzy.[3] Centre de Recherches sur les Macromolécules Végétales (CERMAV), ICMG-CNRS, BP 53, F-38041 Grenoble Cedex 9, France.

[1]This article is part of a Special Issue dedicated to Professor R. Marchessault.

[2]Present address: Aracruz (Europe), 14 avenue Réverdil, CH-1260 Nyon, Switzerland.
[3]Corresponding author (e-mail: henri.chanzy@cermav.cnrs.fr).

 doi:10.1139/V08-030 © 2008 NRC Canada

curred in the form of ballooning (5), thus revealing the inner organization of the cellulose microfibrils within the cell walls of these fibers. With ramie, as well as with the other fibers, the swelling process took a substantial time to reach its limit, while their dissolution occurred readily when the water concentration conditions were sufficiently low. At the cellulose crystal level, X-ray and ^{13}C NMR studies have shown that in the case of swelling, the NMMO molecules were able to pry open the $(1\bar{1}0)$ crystallographic planes, while the dense equatorial planes, such as the (110) and (200), were less sensitive to the solvent influence (5–7). On the other hand, no crystalline NMMO-cellulose complex could be detected.

Since X-ray data gives only global information, the ultrastructural details of the swelling of the cellulose crystal under the thrust of hydrated NMMO molecules is not known. This work was therefore undertaken to answer this question. For this, we have used *Valonia* cellulose microfibrils and followed their swelling by transmission electron microscopy, together with selected area electron diffraction analysis. Individual *Valonia* microfibrils, which are easily disrupted from *Valonia* cell walls, have such large dimensions that they can be readily observed in their finer details by transmission electron microscopy (8, 9) and analyzed locally by electron diffraction (10, 11), diffraction contrast imaging (12, 13), or high resolution AFM (14, 15). In view of their high crystallinity and perfection, they have become ideal objects to model any solid-state interaction of cellulose with chemical (16, 17) or enzymatic reagents (18, 19). Indeed, these transformations can be unambiguously followed, both in image and diffraction modes, with a transmission electron microscope. It is believed that the observations made on the transformation of *Valonia* cellulose can be transposed to narrower and less organized cellulose, where the microfibrils are too small to be investigated individually by electron microscopy.

Experimental

Chemicals

N-Methylmorpholine-*N*-oxide (NMMO) and *n*-propyl gallate were purchased from Sigma-Aldrich. NMMO was recrystallized in dry acetone in the form of NMMO·H_2O (melting point 80 °C).

Valonia cellulose

Valonia ventricosa single-cell vesicles were harvested in the Lower Keys, Florida. After puncturing the cells, their walls were dried by pressing on tissue paper. The dried cell walls were immersed overnight in 0.5% (*w*/*w*) aqueous HCl to remove the incrusting calcite and then, after adequate washing, were boiled for 2 h in 2% aqueous NaOH solution. After rinsing thoroughly with water, wall fragments were delaminated with a pair of tweezers under a stereomicroscope. The resulting fragments, with individualized microfibrils, were used for subsequent swelling experiments.

Swelling and dissolution

The swelling was achieved by immersing the *Valonia* cell wall fragments into solutions of NMMO·H_2O containing 2% *n*-propyl gallate and kept at 80 °C for times ranging from a few minutes to four hours. The swollen fragments were removed and washed thoroughly with methanol. For the samples, which had dissolved, the corresponding solutions were diluted with DMSO, cooled and then dialyzed against water to yield a flocculent precipitate.

Transmission electron microscopy (TEM)

The swollen samples, as well as the precipitate resulting from dissolution were deposited on carbon-coated grids. Some samples were negatively stained with uranyl acetate for imaging purposes, whereas others, which were investigated by electron diffraction analysis, were kept unstained. Observations were achieved with a Philips EM 400 T electron microscope operated at 80 kV and normal illumination for imaging purposes and at 120 kV and reduced electron beam for electron diffraction experiments. Calibration of the diffraction diagrams was achieved by depositing some specimens on gold sputtered carbon coated grids and comparing the diameters of the gold diffraction rings with those of the diffraction spots of the specimens.

Results and discussion

Confirming known descriptions (9), the initial *Valonia* cellulose fragments that were used here consist of arrays of slender featureless microfibrils having rigorously parallel edges and lengths of many microns. Whereas each microfibril has a constant diameter throughout its length, there is a variation of these diameters, which range from 25 nm for the largest to no more than 15 nm for the narrowest. This distribution is well illustrated in Figure 1*a*, where out of the three microfibrils, two have a diameter of 24 nm whereas the third one is only 18 nm wide. When the *Valonia* fragments were immersed in molten NMMO·H_2O at 80 °C, a slow swelling was observed before total dissolution. Figures 1*b*–1*d* correspond to local images depicting the various aspects of a fragment that was immersed for 10 min. These figures illustrate the heterogeneity of the swelling action of NMMO on these highly crystalline microfibrils; in the same sample some microfibrils were barely affected, whereas others were extensively swollen and perhaps some even dissolved. In Figure 1*b*, the swelling, which is initiated in the middle of a microfibril, produces an initial delamination, and from there the solvent pries open the intact part of the microfibril in both directions. Interestingly, the swelling does not lead to any sectioning of the microfibril but exclusively produces a longitudinal subfibrillation into no more than three or four elements, the thicker one being about 7 nm wide. These subfibrils, which are parallel to one another, are seen without interruption along the whole swollen area. In Figure 1*c*, a bundle of four microfibrils is swelling in unison, starting from the right hand side of the micrograph towards the left. Again, the delamination into subfibrils is clearly visible, and as in Figure 1*b*, the progression of NMMO into the microfibril can be seen to result from a solvent wedge, slowly progressing in the core of the microfibril. The result is a delamination of the microfibril into narrower elements but again without apparent breakage into shorter segments. In Figure 1*d*, three completely swol-

© 2008 NRC Canada

Figure 1. Negatively stained images of (*a*) initial *Valonia* microfibrils and (*b*)–(*d*) aspects of *Valonia* microfibrils after swelling for 10 min in NMMO·H_2O at 80 °C. Figures (*a*)–(*d*) are at the same magnification.

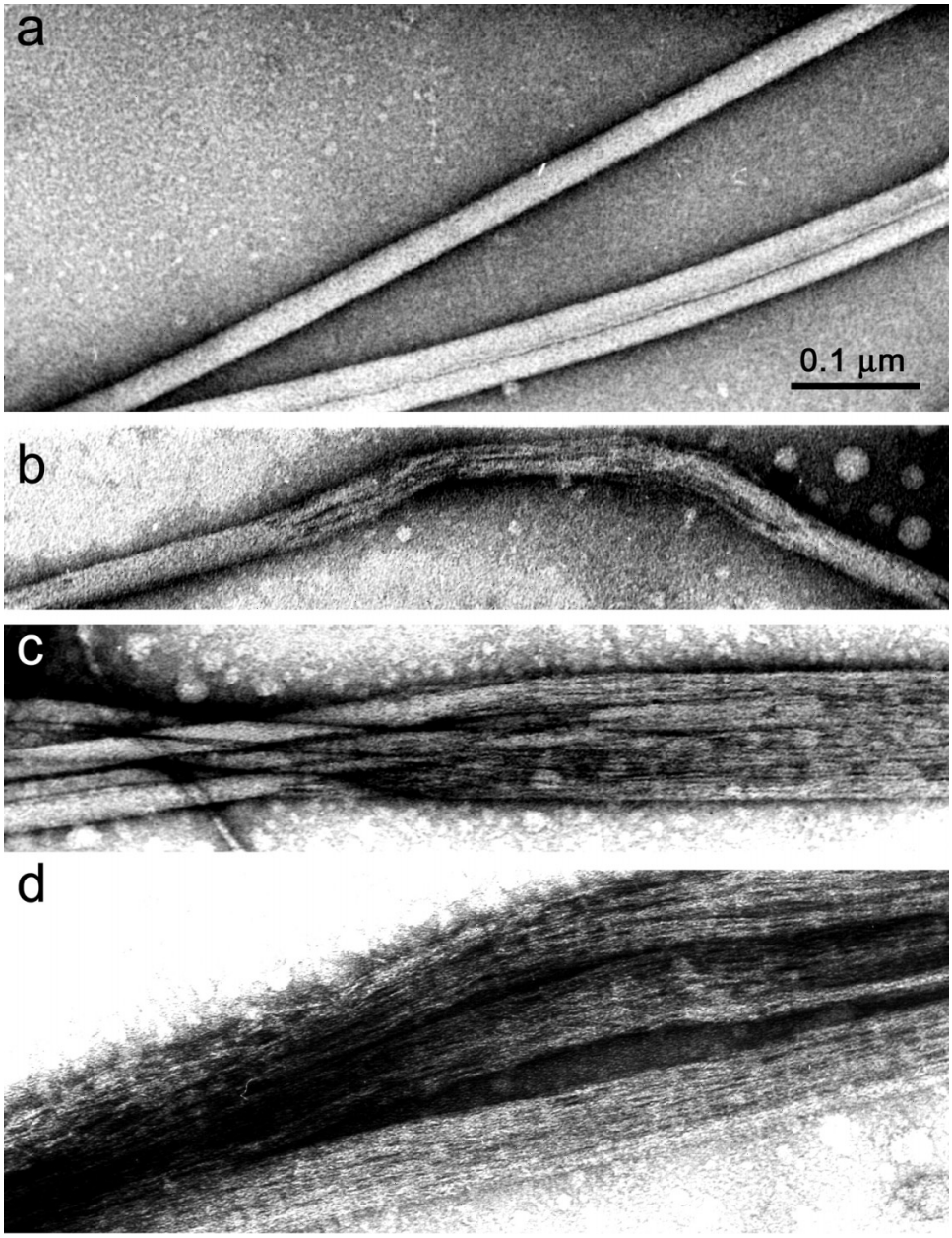

len microfibrils are represented. The widest one has a diameter of 60 nm, i.e., about three times the initial diameter, whereas the other two are respectively 48 and 44 nm wide. Each of these swollen microfibrils now consist of a bundle of about a dozen of undulating subfibrils more or less organized parallel to the microfibril direction but having a diameter no more than 2–3 nm. Whereas the microfibril located at the top of Figure 1*d* shows some trace of dissolution with loosened fibril tips in its upper border, the other two are only swollen and do not present any hint of dissolution or transversal fracturing.

In Figure 2, the state of swelling and its concomitant decrystallization is followed by electron diffraction analysis. Figure 2*a* is typical of a fiber diffraction diagram of a bundle of initial *Valonia* microfibrils aligned vertically. A pattern such as this one contains several hundred diffraction spots extending to a resolution better than 0.1 nm in the fiber direction and 0.2 nm in the equatorial direction. Such wealth of data, which is typical of *Valonia* cellulose (10), denotes a high coherence of large crystalline domains, each of them encompassing the whole width of the corresponding microfibrils. Figure 2*b* corresponds to a bundle of parallel swollen microfibrils, where the subfibrillation is of the type shown in Figure 1*b*, with elements having in the order of 7 nm in width. In this pattern, one still recognizes the main features of the fiber diffraction diagram of native cellulose (cellulose I), but the resolution is much lower than that of the initial pattern. In fact, only the strongest diffraction spots

© 2008 NRC Canada

Figure 2. Electron diffraction diagrams of (*a*) a fragment of an initial bundle of *Valonia* microfibrils oriented vertically, (*b*) as in (*a*) but treated for 10 min in NMMO·H_2O at 80 °C (sample morphology as in Fig. 1*b* or 1*c*), (*c*) as in Fig. 2*b* but from a sample bundle resembling that in Fig. 1*d*, and (*d*) a sample of *Valonia* microfibrils treated for 4 h in NMMO·H_2O at 80 °C. The sample was totally dissolved and re-precipitated.

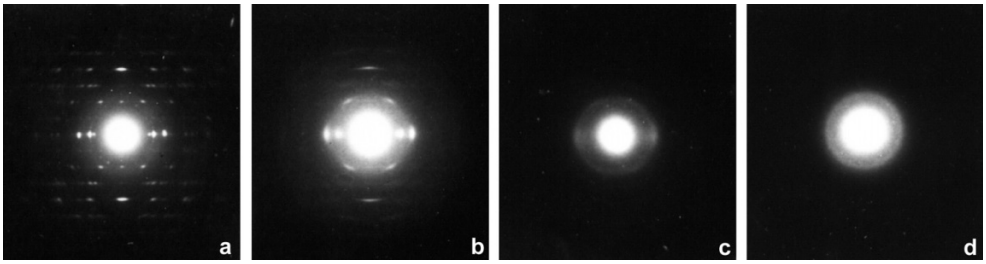

are clearly visible on the equator, the meridian, and the second layer line. This pattern is very similar to a classical electron diffraction diagram of cotton (20), i.e., that of cellulose is made of native crystalline microfibrils having a diameter in the order of 5–6 nm (21). The diagram in Figure 2*c* corresponds to a sample such as the one shown in Figure 1*d*. This diagram consists of only two arced equatorial diffraction spots with *d*-spacings centered at 0.4 and 0.56 nm together with four arced spots on the second layer line, calibrated at 0.43 nm. These features indicate that one is still dealing with native cellulose but with samples of low crystallinity. In fact, the diagram in Figure 2*c* is very similar to that of primary wall cellulose, where the individual microfibrils are fewer than 3 nm wide and one cannot decide whether they belong to the cellulose I or cellulose IV_I crystalline systems (22). Another aspect of the diagram in Figure 2*c* is that unlike samples of primary wall cellulose, it does not present any meridional diffraction spots. This absence reveals that the longitudinal coherence of the crystalline domains along the microfibrils is rather poor, which is in agreement with the undulating aspect of the subfibrils in Figure 1*d*. Figure 2*d* is the diagram of a sample that was left for 4 h in NMMO·H_2O at 80 °C, followed by re-precipitation. Under these conditions, the sample that had been totally dissolved and re-precipitated does not show any hint of left over microfibrils. The diagram, which consists of only one ring at a *d*-spacing of 0.4 nm, can be categorized as belonging to the cellulose II allomorph, but with a rather poor crystallinity.

The results presented in this study are informative since they give ultrastructural details on the progression of NMMO into a crystalline cellulose microfibril prior to its dissolution. The images shown in Figure 1 indicate that once the amine oxide has started to swell a given microfibril, the solvent wedges its way along the microfibril by cutting the hydrogen bonds that hold the cellulose chain together. This mechanism is schematically illustrated in Figure 3, which sketches the penetration of NMMO·H_2O into a typical crystalline *Valonia* microfibril consisting of ~1000 chains. In this sketch, which would correspond to the situations in Figs. 1*b* and 1*c*, the initial microfibril is split into 13 fibrous blocks, each having from ~40 to 100 chains and lateral dimensions ranging from 60 to 110 nm. In addition, the blocks have been drawn with a somewhat narrower dimension along the (110) planes, but wider along the ($1\bar{1}0$) planes of the lattice, which is in agreement with earlier descriptions (5). Obviously, a subsequent penetration of the solvent will further divide these initial blocks, which will thus become narrower and narrower until individual chains are surrounded by the solvent, with the result of total dissolution. Thus, a given microfibril subjected to a solution of NMMO·H_2O at 80 °C will successively lose its "crystalline *Valonia*" characteristic denoted by its well-resolved electron diffraction diagram (Fig. 2*a*) to adopt a cotton-like character (Figs. 1*b* and 2*b*) and then that of a primary-wall cellulose sample (Figs. 1*d* and 2*c*), before being completely dissolved.

Figure 3. Schematic representation of the swelling of one *Valonia* microfibril subjected to NMMO·H_2O at 80 °C for a few minutes. This sketch corresponds to the images shown in either Fig. 1*b* or 1*c*.

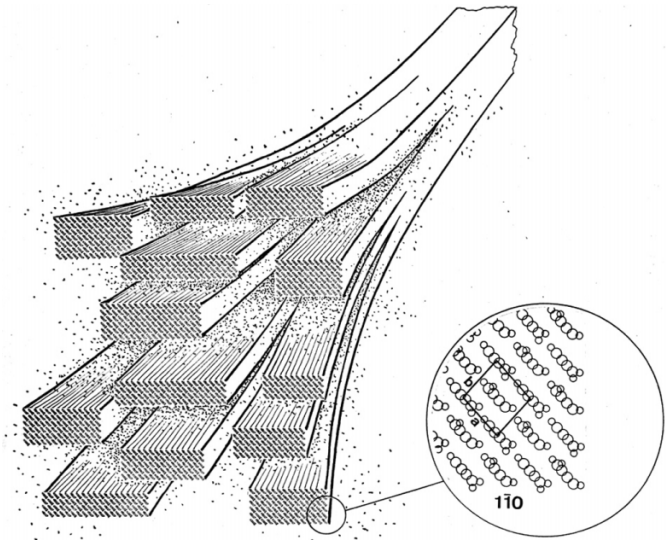

Unlike the case of ramie fibers, which dissolve readily into NMMO·H_2O, it seems that the highly crystalline *Valonia* microfibrils take some time to dissolve at 80 °C, even if there is a large excess of solvent. As aforementioned, all the microfibrils of a given *Valonia* cell wall fragment do not interact with the solvent at the same rate, since in a given preparation there is at the same time a distribution of swollen states, as illustrated in Figs. 1*b* and 1*c*. This distribution may be related to the perfection of the initial microfibrils where the presence or the absence of crystalline defects may or may not govern the extent of swelling at a given time. In related systems where *Valonia* cellulose was swollen in

© 2008 NRC Canada

strong aqueous NaOH solutions, it was shown that no swelling could occur unless some defects could first be created by some acid hydrolysis (23). It was thus clear that to penetrate into the cellulose lattice, the aqueous NaOH had to start from some crystalline defect. A similar mechanism must take place here, but at a much faster rate as NMMO·H_2O is much more aggressive than NaOH at breaking the hydrogen bonds of cellulose.

Another somewhat unexpected result of this study is that in their interaction with NMMO·H_2O, *Valonia* microfibrils do not break down into shorter segments but undergo only a longitudinal splintering. This observation is an indication that the cellulose chains remain intact during the whole process and that the swelling forces are not strong enough to break the cellulose molecules. In fact, cellulose is subject to severe oxidation and chain scission when interacted with NMMO alone, but the use of the antioxidant *n*-propyl gallate protects the molecules and prevents any cellulose chain scission (24). The use of 2% of this antioxidant with respect to NMMO·H_2O may therefore explain why no cellulose chain and consequently no microfibril was split into short elements during the swelling process.

The spectacular images of *Valonia* microfibrils swollen in NMMO·H_2O can be compared with those of other systems where the microfibrils were also swollen under the action of specific intracrystalline swelling agents. Images somewhat reminiscent of the one presented here were obtained when *Valonia* cellulose was converted into cellulose III_I by the addition of ethylenediamine. In such a case as the present one, each microfibril became swollen without intermingling with its neighbors and one observed a longitudinal splintering of the microfibrils (16) but much less pronounced than the one shown in the present case. In fact, the complex of cellulose with ethylenediamine is highly crystalline and possesses a fixed stoichiometry based on one ethylenediamine molecule per glucosyl residue (25). This incorporation of ethylenediamine into the cellulose lattice leads to its lateral expansion of about 1.5 times, and thus to an equivalent increase of the diameter of the microfibril (26). This increase, which is about half of what is observed in Figure 1*d*, explains why the ethylenediamine-swollen microfibrils do not show the unique open subfibrillated structure, which is shown here.

In the case of swelling with concentrated aqueous NaOH, only acid-treated *Valonia* microfibrils could be modified (23, 27). After such a treatment, the swelling of individual microfibrils in a pattern similar to that of ethylenediamine or NMMO·H_2O was not observed. In the case of compact cell wall fragments, the action of NaOH leads to an extensive intermingling of the microfibrils, but no subfibrillation could be observed (27). In the case of individual microfibrils, the swelling action corresponded more to a stripping of the cellulose chains located at the surface of the microfibrils, while the core remained intact (23). Again, the swelling pattern in concentrated NaOH was substantially different from the one observed here, which, so far, appears to be unique in the field of cellulose.

Acknowledgements

This paper is dedicated to Professor R.H. Marchessault, not only for his wonderful guidance as a mentor and a friend through more than four decades but also for his inspiring contributions to the fields of biopolymers, polysaccharides, cellulose, and carbohydrates. The authors are also indebted to Professor P. Smith for the drawing in Fig. 3 and valuable discussions during this work.

References

1. C.F. Cross, E.J. Bevan, and C. Beadle. British Patent 8-700, 8 April 1893.
2. C. Woodings. In Encyclopedia of polymer science and technology. Edited by J.I. Kroschwitz. Wiley-Interscience, Hoboken, N.J. Vol. 5. 2003. pp. 532–569.
3. H. Chanzy, S. Nawrot, A. Peguy, P. Smith, and J. Chevalier. J. Polym. Sci. Polym. Phys. Ed. **20**, 1909 (1982).
4. O. Biganska and P. Navard. Polymer, **44**, 1035 (2003).
5. H. Chanzy, P. Noé, M. Paillet, and P. Smith. J. Appl. Polym. Sci. Appl. Polym. Symp. **37**, 239 (1983).
6. The Miller indices refer to the cellulose unit cell parameters defined in: Y. Nishiyama, P. Langan, and H. Chanzy. J. Am Chem. Soc. **124**, 9074 (2002).
7. M. Michael, R.N. Ibbett, and O.W. Howarth. Cellulose, **7**, 21 (2000).
8. W.W. Franke and H. Falk. Z. Naturforsch. **23B**, 272 (1968).
9. T. Itoh and R.M. Brown, Jr. Planta, **160**, 372 (1984).
10. G. Honjo and M. Watanabe. Nature (London), **181**, 326 (1958).
11. J.-F. Revol and D.A.I. Goring. Polymer, **24**, 1547 (1983).
12. A. Bourret, H. Chanzy, and R. Lazaro. Biopolymers, **11**, 893 (1972).
13. J. Sugiyama, H. Harada, Y. Fujiyoshi, and N. Uyeda. Planta, **166**, 161 (1985).
14. A.A. Baker, W. Helbert, J. Sugiyama, and M.J. Miles. J. Struct. Biol. **119**, 129 (1997).
15. A.A. Baker, W. Helbert, J. Sugiyama, and M.J. Miles. Biophys. J. **79**, 1139 (2000).
16. H. Chanzy, B. Henrissat, M. Vincendon, S.F. Tanner, and P.S. Belton. Carbohydr. Res. **160**, 1 (1987).
17. J.F. Sassi and H. Chanzy. Cellulose, **2**, 111 (1995).
18. H. Chanzy and B. Henrissat. Carbohydr. Polym. **3**, 161 (1983).
19. H. Chanzy and B. Henrissat. FEBS Lett. **184**, 285 (1985).
20. K.M. Paralikar, S.M. Betrabet, and N.V. Bhat. J. Appl. Crystallogr. **12**, 589 (1979).
21. A.N.J. Heyn. J. Appl. Phys. **26**, 519 (1955).
22. H. Chanzy, K. Imada, A. Mollard, R. Vuong, and F. Barnoud. Protoplasma, **100**, 303 (1979).
23. H.D. Chanzy and E.J. Roche. J. Polym. Sci. Polym. Phys. Ed. **13**, 1859 (1975).
24. A. Brandner and H.D. Zengel. U.S. Patent 4-426-228, 17 January 1984.
25. D.M. Lee, K.E. Burnfield, and J. Blackwell. Biopolymers, **23**, 111 (1984).
26. H.Chanzy, B. Henrissat, R. Vuong, J.-F. Revol. Holzforschung, **40(Suppl)**, 25 (1986).
27. H.D. Chanzy and E.J. Roche. Appl. Polym Symp. **28**, 701 (1976).

© 2008 NRC Canada

Mixed-dimer formation in binary systems of 4-substituted benzoic acids and structure considerations[1]

Maren Roman, Annett Kaeding-Koppers, and Peter Zugenmaier

Abstract: The phase behavior of binary systems of 4-substituted benzoic acids is governed by the formation of mixed dimers. This study was conducted to determine the effect of the components' structural difference on mixed-dimer formation in crystalline and liquid-crystalline phases. The phase diagrams of two systems, with 4-[(*S*)-(–)-2-methylbutoxy]benzoic acid (MBOBA) as one component and 4-(hex-5-enoxy)benzoic acid (HOBA) and 4-(dec-9-enoxy)benzoic acid (DOBA), respectively, as the second component, were determined by differential scanning calorimetry, polarized-light microscopy, and X-ray diffraction. The MBOBA-HOBA system exhibited a cholesteric phase, two solid solutions, and above 58 °C for compositions between 40 and 80 mol% HOBA a crystalline phase of mixed dimers. The MBOBA-DOBA system showed a crystalline phase of mixed dimers at all compositions, a cholesteric phase, and a twisted smectic C phase, which was dominated by mixed dimers at 60 and 70 mol% DOBA. We conclude that liquid-crystalline phases are generally dominated by mixed dimers, but in crystalline phases the formation of mixed dimers is promoted by a greater difference in molecular structure. The crystal structure of two of the pure compounds MBOBA and DOBA and comparable compounds have been determined for an evaluation of the arrangements of the molecules in the crystal and liquid-crystalline state.

Key words: benzoic acid, crystal arrangement, phase diagrams, liquid crystal.

Résumé : Le comportement de phase des systèmes binaires d'acides benzoïques substitués en position 4 est régi par la formation de dimères mixtes. On a réalisé cette étude dans le but de déterminer les effets des différences de structure des composants sur la formation de dimères mixtes dans les phases cristallines et à cristaux liquides. Les diagrammes de phase de deux systèmes dans lesquels ont retrouve d'une part, dans tous les deux, de l'acide 4[(*S*)-(–)-2-méthylbutoxy]benzoïque (AMBOB) et, d'autre part, respectivement de l'acide 4-(hex-5-énoxy)benzoïque (AHOB) et de l'acide 4-(dec-9-énoxy)benzoïque (ADOB) en faisant appel à la calorimétrie à balayage différentiel, à la microscopie à lumière polarisée et la diffraction des rayons X. Le système AMBOB/AHOB, on observe une phase cholestérique, deux solutions solides et, au-dessus de 58 °C, pour les compositions entre 40 et 80 mol% d'AHOB, on observe aussi une phase cristalline des dimères mixtes. Le système AMBOB/ADOB, présente une phase cristalline de dimères mixtes pour toutes les compositions, une phase cholestérique et une phase smectique C décalée qui était dominée par les dimères mixtes pour les compositions allant de 60 à 70 mol% d'ADOB. On en conclut que les phases à cristaux liquides sont généralement par les dimères mixtes, but que dans les phases cristallines la formation de dimères mixtes est facilitée par une plus grande différence dans les structures moléculaires. On a déterminé les structures cristallines des composés AMBOB et ADOB et de composés apparentés afin d'évaluer les arrangements des molécules dans le cristal et dans l'état à cristal liquide.

Mots-clés : acide benzoïque, arrangement cristallin, diagrammes de phase, cristal liquide.

[Traduit par la Rédaction]

Introduction

Molecules of benzoic acid and its derivatives generally pair through intermolecular hydrogen bonds and form dimers. The bonding is so strong that, on heating, the dimers persist from the crystalline state through to the isotropic state (1). A dimer has a larger aspect ratio and twice the number of polarizable aromatic rings and carbonyl groups

Received 1 November 2007. Accepted 1 December 2007. Published on the NRC Research Press Web site at canjchem.nrc.ca on 4 April 2008.

M. Roman,[2] A. Kaeding-Koppers,[3] and P. Zugenmaier.[4] Institute of Physical Chemistry, Clausthal University of Technology, Arnold-Sommerfeld-Str. 4, D-38678 Clausthal-Zellerfeld, Germany.

[1]This article is part of a Special Issue dedicated to Professor R. Marchessault.
[2]Present address: Department of Wood Science and Forest Products, 230 Cheatham Hall (0323), Virginia Tech, Blacksburg, VA 24061, USA.
[3]Present address: Wipak-Walsrode GmbH & Co KG, P.O. Box 1661, 29656 Walsrode, Germany.
[4]Corresponding author (e-mail: zugenmaier@pc.tu-clausthal.de).

 doi:10.1139/V08-008 © 2008 NRC Canada

Table 1. Properties of the pure components.

Compound	Molecular structure	Molecule/Dimer length[a] (Å)	*d* Value[b] (Å)	Phase transition temperatures (°C) (above arrow) and enthalpies (kJ·mol^{-1}) (below arrow)
MBOBA	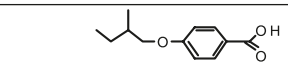	12.2/24.2	8.7–9.0 14.6–14.5	C^{α} $\xrightarrow[6.1]{105.8}$ C^{β} $\xrightarrow[11.5]{110.5}$ I
HOBA	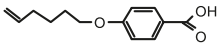	15.2/30.2	16.2–16.0	C $\xrightarrow[15.8]{99.5}$ N $\xrightarrow[1.4]{140.0}$ I
DOBA	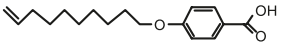	16.7/32.8	24.1–25.0 25.2–26.0 28.1–29.7	C^{α} $\xrightarrow[12.4]{<80}$ C^{β} $\xrightarrow[16.3]{78.4}$ S_C $\xrightarrow[1.2]{115.4}$ N $\xrightarrow[2.1]{137.0}$ I

[a]Determined by the lengths of the molecules in the crystal structure; for HOBA by adding the lengths of appropriate segments.
[b]Change of *d* values upon increase of temperature.

with respect to a single molecule. However, due to the formation of dimers by hydrogen bonding by the carbonyl groups, the dipoles are compensated and an antiparallel arrangement of the molecules is favored. For this reason, most of the 4-substituted benzoic acids with linear substituent groups are liquid-crystalline (2). When 4-substituted benzoic acids are mixed, dimers containing two different molecules can be formed. In studies of binary systems of 4-substituted benzoic acids (3, 4), a number of systems showed deviation from eutectic phase behavior. Mixed-dimer formation is thought to be the reason for the high melting points in these systems.

In this study, crystalline and liquid-crystalline phases of these systems have been investigated with a focus on the formation of mixed dimers. To determine the effect of the difference in molecular structure of the components on mixed-dimer formation, we studied two systems that have one common component and whose second components differ only in the length of the substituent groups. In the first system, the molecular structures of the components are fairly similar so that mutual solubility is expected. In the second system, the molecular structures of the components are distinctly different, which can result in eutectization. The component that both systems have in common is the chiral 4-[(*S*)-(–)-2-methylbutoxy]benzoic acid (MBOBA). This compound is not liquid-crystalline but a tendency to form a mesophase is anticipated because 4-butoxybenzoic acid is mesomorphic. Because of its asymmetric carbon atom, MBOBA is further expected to twist the molecular arrangements in the mesophases of the second components, which are 4-(Hex-5-enoxy)benzoic acid (HOBA) and 4-(Dec-9-enoxy)benzoic acid (DOBA). Further clues for the formation of chiral phases can be provided by consideration of the unusual arrangement of the pure compounds.

Experimental

Materials

MBOBA was synthesized by brominating (*S*)-(–)-2-methylbutan-1-ol (5, 6) with phosphorus tribromide (7, 8) and subsequently reacting the obtained (*S*)-(–)-2-methyl-1-bomobutane with 4-hydroxybenzoic acid. The different alkenoxy benzoic acids used in this study were prepared as described in ref. (9). The properties of the pure components (Table 1) were determined as described in the methods section below. For MBOBA, no liquid-crystallinity was observed; it showed two crystalline phases, C^{α} and C^{β}. HOBA, consisting of longer molecules, exhibited a nematic mesophase. DOBA showed a nematic and a smectic C mesophase. A crystalline phase transition was observed below 80 °C in X-ray measurements. The transition was very slow, which we attributed to impurities (10). As a consequence, the crystalline phase transition of the DOBA was only indirectly revealed by differential scanning calorimetry (DSC): the enthalpy of melting upon cooling was lesser by 12.4 kJ/mol than upon first heating. This decrease implied that in the heating run the crystalline phase transition occurred at the melting temperature and was supercooled below 0 °C in the cooling run. The transition did not occur during the second heating, as the enthalpy of melting was in good agreement with the one for cooling.

Methods

Eleven mixtures were prepared for the MBOBA–HOBA system and nine for the MBOBA–DOBA system by co-dissolving various amounts of the components in warm ethanol. The solvent was allowed to evaporate over a period of one to two weeks after the solutions had cooled to room temperature.

Transition temperatures were determined with a PerkinElmer DSC7. Samples were prepared by weighing 4–6 mg of a mixture into an aluminum pan and then sealing it. Every sample was heated, cooled, and heated again at a rate of 5° min^{-1}.

Mesophases were identified using an Olympus BH-2 polarized-light microscope with a Linkam THM600 hot stage. The crystalline regions were investigated with an Anton Paar Kratky Compact Small Angle System with a KH-R sample heater. Samples were prepared by melting a small amount (about 2 mg) of a mixture on a microscope slide and driving it by capillary action into a quartz capillary, where it recrystallized on cooling.

Crystals of the mixture 65 mol% HOBA in MBOBA, as obtained from solution, were investigated with an in-house flat-film camera equipped with an FP82-Mettler hot stage.

Single crystals suitable for X-ray investigations were obtained by slow crystallization. The data collections was performed on a CAD4 single-crystal diffractometer with Mo K α radiation and the MolEN package (Enraf Nonius, Delft) (11), and (or) the Shelxl-93 program (12) was used for data processing and refinement. The starting models were obtained by SIR97 (13). Here, we concentrate on the conformation and packing arrangement of the molecules only. A full description and discussion of the data will be published

© 2008 NRC Canada

elsewhere. The drawings were obtained with SCHAKAL-92 (14).

Results and discussion

Crystal structures

Almost all benzoic acids, composed of single non-chiral compounds and forming dimers by hydrogen bonds, crystallize in centric space groups with an inversion center between the carbonyl groups (15, 16). However, a 1:1 mixture of two different benzoic acids is devoid of the inversion center and an acentric space group can describe the crystal structure (16) with consequences for the chirality of the liquid-crystalline phases (17).

MBOBA and four benzoic acids with a linear group attached in 4-position of the benzyl ring, namely 4-(but-3-enoxy)benzoic acid (BOBA), 4-(pent-4-enoxy)benzoic acid (POBA), 4-(dec-9-enoxy)benzoic acid (DOBA), and 4-(undec-10-enoxy)benzoic acid (UOBA), have been investigated by single crystal analysis to get insight into the conformation and packing arrangements of these molecules, which are important for a discussion of the liquid crystal phases observed. All five compounds are arranged in antiparallel fashion to compensate the strong dipoles of the molecules and form dimers. They have in common a similar distance of the two C–O bonds of the carbonyl group of which both oxygens are involved in hydrogen bonds and a gauche position of the alkoxy segment of the linear substituent.

The chiral MBOBA crystallizes in the enantiomorphous space group *P*1 and projections representing the conformation and packing arrangement are shown in Fig. 1. The dimer formations are revealed. Both molecules forming the asymmetric unit have similar conformations. The carbon atom of the methyl branch of the substituent lies in plane with the preceding carbon atoms and oxygen, while the alkoxy segment of the linear group is placed in gauche position involving the oxygen attached to the benzene ring. The molecules are placed in a tilted direction in the unit cell, which means that the length of the molecule, which amounts to 12.2 Å, does not agree with the longest unit-cell axis of *c* = 9.4 Å. The molecules pack in planes with the benzene rings lying flat in these planes and they are staggered (Figs. 1A, 1B, 1C).

BOBA crystallizes in the acentric space group *Pa* with two antiparallel molecules in the asymmetric unit, unique axis *b* (Fig. 2). Although the torsion angles of the alkoxy segment have reversed signs, as expected for centrosymmetric arrangements, the torsion angle of the terminal atom does not follow this reversal, and two distinct different molecules form the dimer and cannot crystallize in a centric space group with an inversion center between the carboxyl groups of the dimers. Here, the dimer is tilted in the *a*–*c* plane, and the length of the dimer of ~20 Å is also longer compared with the largest unit-cell parameter *c* = 14.9 Å. According to our experience, the centric or acentric packing of molecules in the crystalline state may also lead to different kinds of arrangement in the liquid-crystalline state.

Surprisingly, the space group of crystalline POBA is $P2_1$, unique axis *b*, which belongs to the optically active space groups and the ones, which may exhibit second-order non-linear properties. The packing arrangement of the dimers formed is represented in Fig. 3 in two projections. Two antiparallel molecules form the asymmetric unit, which by application of a 2_1 screw axis lead to the four molecules within the unit cell. The molecular axes are placed almost perpendicular to the screw axis *b* in contrast to DOBA, to be discussed. The overall arrangement of POBA resembles the one of BOBA. The length of the dimers amounts to 26.8 Å and is much longer than the *c* parameter of the unit cell with 15.4 Å. Here, a the tilt is observed in the *a*–*c* plane. If mesophases are formed, they are expected to be chiral.

Fig. 1. Representation of 4-[(*S*)-(–)-2-methylbutoxy]benzoic acid (MBOBA), which crystallizes in the triclinic two-molecule acentric space group *P*1 in three projections. (A) Projection in [010] direction on the *a*–*c* plane showing the formation of dimers through hydrogen bonding. (B) Projection in [100] direction on the *b*–c plane showing the continuous rod formation. (C) Projection along the continuous rods showing the relative packing arrangement of the molecules.

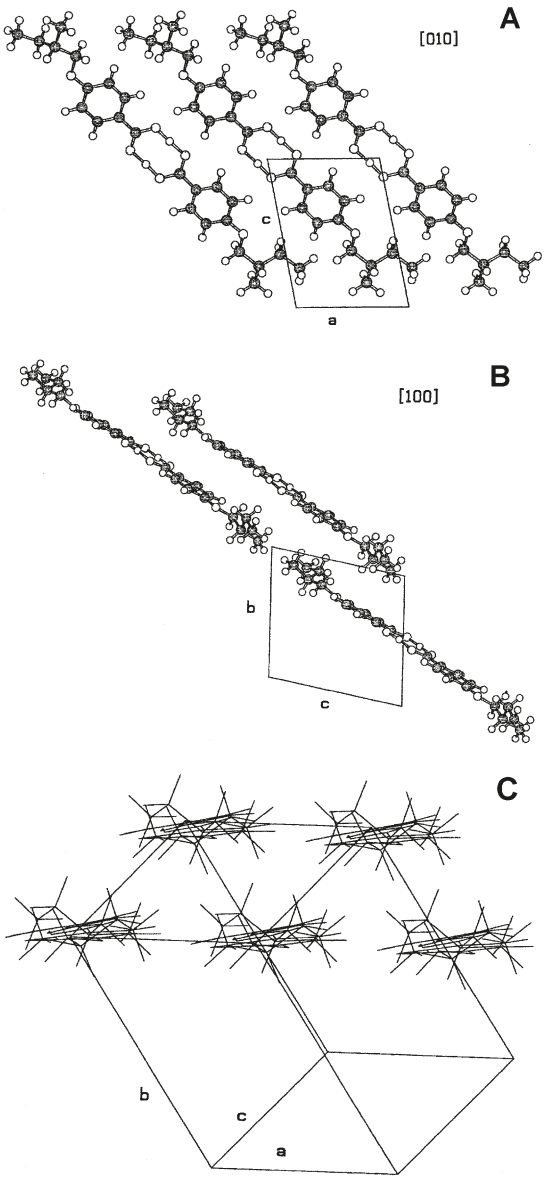

© 2008 NRC Canada

Fig. 2. Representation of 4-(but-3-enoxy)benzoic acid (BOBA), which crystallizes in the monoclinic four-molecule unit cell of the acentric space group *Pa* in three projections. (A) Projection in [010] direction on the *a*–*c* plane showing the formation of dimers through hydrogen bonding. (B) Projection in [100] direction on the *b*–*c* plane showing the overlapping molecules of the plane represented in A. (C) Projection in rod direction showing the lateral packing arrangement of the molecules. The hydrogen atoms at the terminal carbon could not be localized.

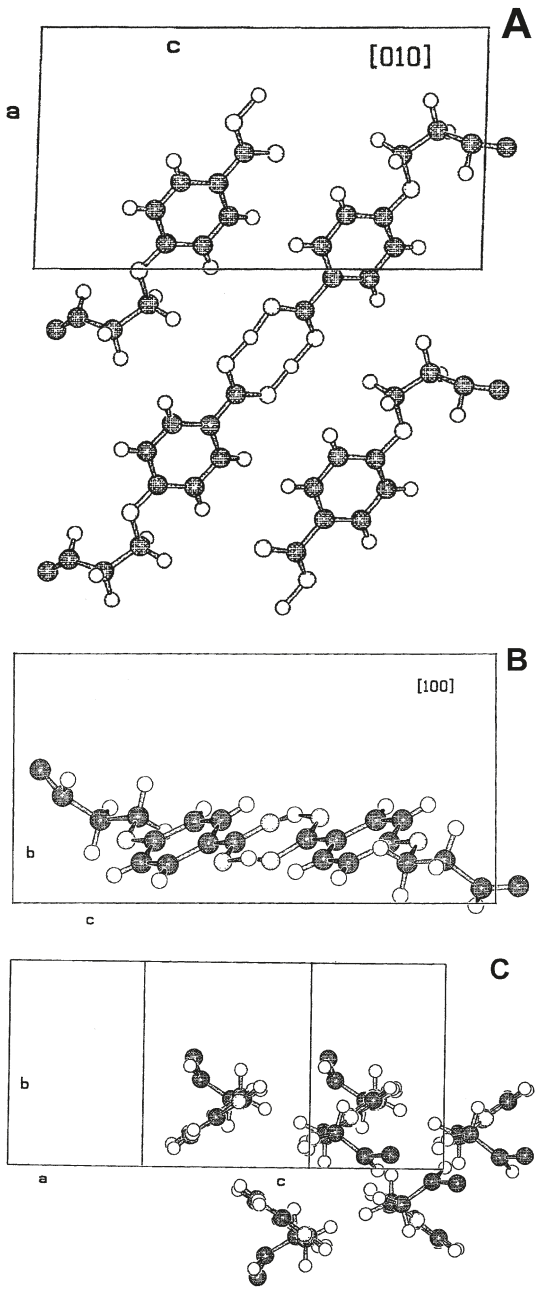

In contrast, centric space groups are found for longer linear chains attached in the 4-position on the benzene ring of benzoic acids as DOBA and UOBA. But again the packing arrangement differs for these two compounds.

UOBA crystallizes in the triclinic space group *P*-1. The unit cell contains two molecules, which are connected by an inversion symmetry element, thus forming the expected

Fig. 3. Representation of 4-(pent-4-enoxy)benzoic acid (POBA), which crystallizes in the monoclinic four molecule unit cell of the acentric space group $P2_1$ (*b* unique axis) in two projections. (A) Projection showing the formation of dimers through hydrogen bonding. (B) Projection in rod direction showing the lateral packing arrangement of the molecules.

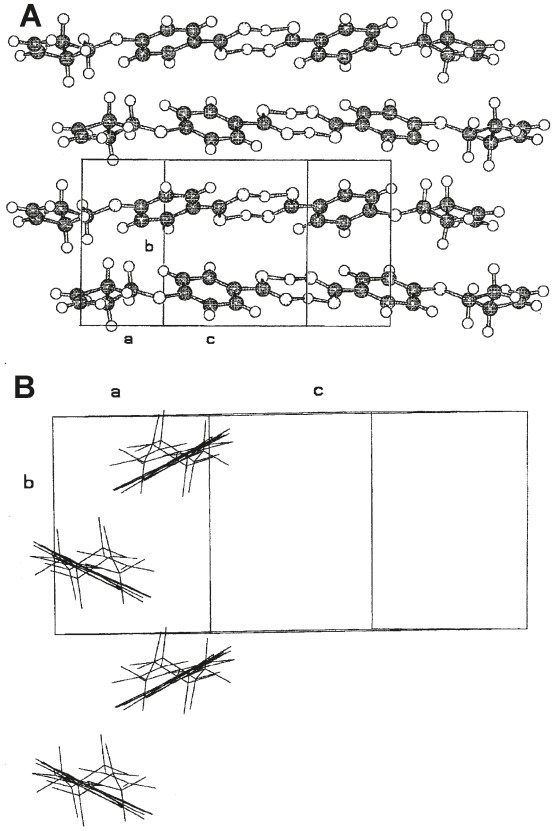

dimer through hydrogen bonds as in almost all benzoic acids (Fig. 4). The gauche conformation of the alkoxy segment forces a change of direction between the central part of the dimer and the linear chain, which exhibits an almost trans conformation. A chain length is difficult to define and amounts to 39.3 Å between the two terminal groups of the dimer and differs considerably, if this length is calculated with a trans conformation of the alkoxy segment.

A similar conformation for the single molecule is found for DOBA as compared to UOBA, but the packing arrangement in the crystalline state differs considerably as shown in Fig. 5. The long dimension *c* is almost doubled due to the centric space group $P2_1/n$, *c* = 41.51 Å for DOBA and *P*-1 with 22.34 Å for UOBA. The unit cell of DOBA has to accommodate two succeeding molecules related by a 2_1 screw axis, which changes the direction of the central part of the dimer in space. Nevertheless, quite similar dimensions of the unit cell are found for the lateral packing of the molecules for DOBA and UOBA. A single molecule represents the asymmetric unit in both structures. A distance between the terminal hydrogen of 32.8 Å was determined for the dimer of DOBA as compared with 39.3 Å for UOBA, and both lengths deviate from a trans conformation of the alkenoxy substituent.

The crystal and molecular structures of the four homologous achiral benzoic acids show a broad variation of possible

© 2008 NRC Canada

Fig. 4. Representation of 4-(undec-10-enoxy)benzoic acid (UOBA), which crystallizes in the triclinic two-molecule unit cell of the centric space group *P*-1 in two projections. (A) Projection in [100] direction on the *b*–*c* plane showing the formation of dimers through hydrogen bonding. (B) Projection in [010] direction on the *a*–*c* plane showing the relative packing arrangement of the molecules.

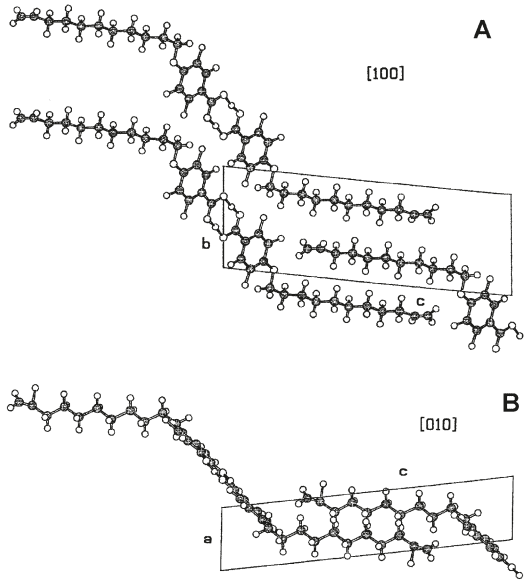

low energy states, which may lead to a variety of arrangements of molecules in the liquid-crystalline state. Moreover, chiral molecules are created when the chiral MBOBA forms dimers with achiral benzoic acid homologues regardless of the conformation of the achiral partner.

MBOBA–HOBA system

All MBOBA–HOBA mixtures were liquid-crystalline (Fig. 6). The only mesophase upon heating revealed an "oily streak" texture in the polarized-light microscope, which is characteristic of the cholesteric phase. As anticipated, the nematic molecular arrangement was twisted by the chiral MBOBA molecules and became cholesteric. The fact that 10 mol% of HOBA was enough to induce a mesophase indicated the expected tendency of MBOBA to show liquid-crystallinity. In accordance, extrapolation of the cholesteric–isotropic transition line to 100 mol% MBOBA gave a value of 101.8 °C for the acid's virtual cholesteric–isotropic transition temperature (T^{V}_{N*I}). This value defines how disruptive the non-mesomorphic compound is towards the mesophase (18). Since the value was close to the melting point of 110.5 °C, the disruptive effect of MBOBA, due to the methyl branch of the substituent group, on the nematic molecular arrangement was small.

The melting curve indicated that the MBOBA–HOBA system was not eutectic. To elucidate the deviation from eutectic behavior, we calculated eutectic melting curves (Fig. 6) on a thermodynamic basis using the Schroeder–vanLaar equations (19, 20). The observed melting temperatures were notably higher than the theoretical temperatures for the mixtures with 20 to 70 mol% HOBA, which suggested solid-solubility of the two components or the formation of phases of mixed dimers. To identify the cause for the

Fig. 5. Representation of 4-(dec-9-enoxy)benzoic acid (DOBA), which crystallizes in the monoclinic four-molecule unit cell of the centric space group $P2_1/n$ (*b* unique axis) in two projections. (A) Projection in [100] direction on the *b*–*c* plane showing the formation of dimers through hydrogen bonding. (B) Projection in [001] direction on the *a*–*b* plane representing the lateral packing arrangement of the molecules.

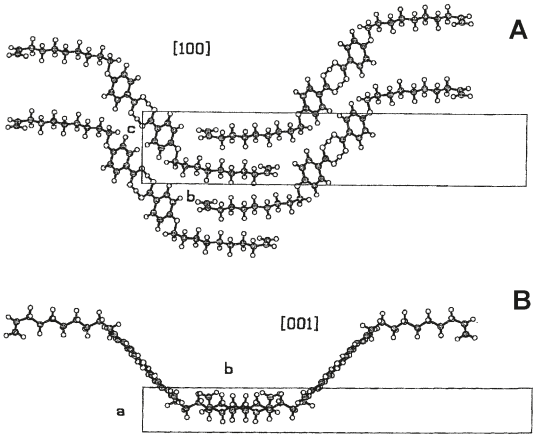

Fig. 6. Crystalline-cholesteric and cholesteric–isotropic transition line for the MBOBA–HOBA system (peak temperatures of the first DSC heating run); T^{V}_{N*I}: virtual cholesteric–isotropic transition temperature (– – –): theoretical melting curves for a eutectic system.

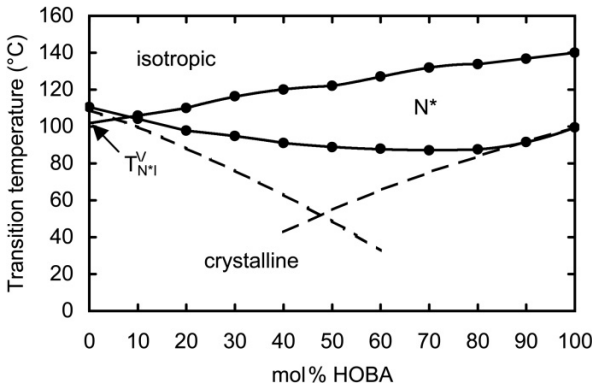

thermal stability of the crystalline region, we investigated the mixtures at different temperatures below their melting temperatures by X-ray diffraction. Below 58 °C two crystalline phases (C^{α}_{A} and C_B) were found, represented by different reflections in the diffraction patterns (Fig. 7). The C^{α}_{A} phase was formed by mixtures containing less than 80 mol% HOBA (Fig. 8). It had a characteristic *d* value equal to the *d* value of MBOBA and was therefore most likely a solid solution of HOBA in MBOBA. The C_B phase was formed by mixtures with more than 65 mol% HOBA and had a *d* value equal to that of HOBA. In this phase, MBOBA molecules or dimers are probably incorporated into the HOBA crystal lattice. In the mixtures with 65 to 80 mol% HOBA, the two phases, C^{α}_{A} and C_B, coexisted.

The high-temperature crystalline phase of the MBOBA, C^{β}_{A}, was found only in the mixtures with a HOBA content less than 20 mol%. For the mixtures containing 40 to 80 mol% HOBA an additional phase (C_{AB}) was found above

© 2008 NRC Canada

Fig. 7. X-ray diffraction patterns of 70 mol% HOBA in MBOBA.

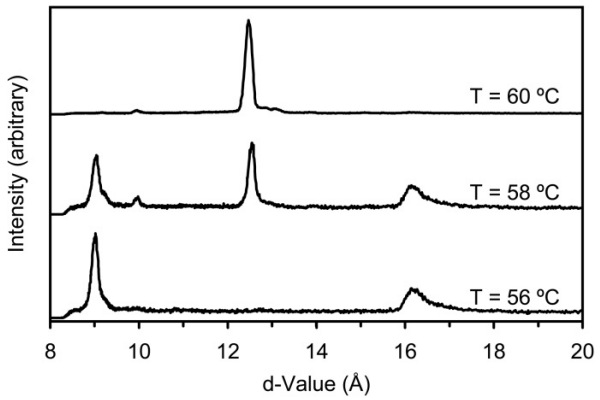

58 °C. The characteristic *d* value (*d* = 12.5 Å) lay between the *d* values of C_A^{α} and C_B and thus indicated the formation of mixed dimers. The *d* value of MBOBA amounts to ~9 Å that of HOBA to ~16 Å. In the crystalline state, the molecular length of the monomer does not correlate with the *d* spacing obtained by X-ray diffraction due to possible tilted positions within the unit cell. The *d* value of MBOBA is confirmed by the longest *d* spacing derived from the unit cell (*d* = 9.12 Å). The length of the mixed dimer was calculated to 27.4 Å as opposed to 24.2 and 30.2 Å for the pure MBOBA and HOBA dimers (Table 1). The *d* value increased slightly with increasing temperature to *d* = 12.6 Å before melting. The phase transition from the two-phase region into the high-temperature phase was clearly evident at 58 °C in X-ray experiments (Fig. 7).

To assure that this high-temperature phase was not a more highly ordered liquid-crystalline phase, we investigated the mixture with 65 mol% HOBA above 70 °C by polarized-light microscopy. We did not observe any fluidity. A flat-film X-ray diffraction pattern of the same mixture, taken at 80 °C, showed discrete Bragg maxima indicating the presence of small crystalline domains. We concluded that this was not a smectic phase of higher order but a fourth crystalline phase dominated by mixed dimers.

The C_A^{α}–C_{AB} or C_B–C_{AB} phase transitions, respectively, in the mixtures with 40 to 90 mol% HOBA were also revealed in DSC measurements as shown for 50 mol% HOBA in MBOBA in Fig. 9. In most mixtures, the transition occurred just below or at the melting temperature in the first heating run and was strongly supercooled in the cooling run. The shift of the crystalline transition to lower temperatures upon cooling differed for the different mixtures. At 40, 50, and 90 mol% HOBA in MBOBA, the transition was supercooled by about 15 °C, 40 °C (Fig. 9), and 50 °C, respectively. In the mixtures with 60, 70, and 80 mol% HOBA, the transition was supercooled below 0 °C and thus not seen in the cooling trace. It occurred in both directions (exotherm and endotherm) during the second heating run for the mixture with 60 mol% HOBA, but the mixtures with 70 and 80 mol% HOBA did not show the transition upon second heating. The different thermal behavior upon cooling reflected that the transition in the mixtures with 40, 50, 60, and 90 mol% HOBA was into a one-phase region; whereas it was into a two-phase region in the mixtures with 70 and 80 mol%. In the latter case, the molecules had to arrange from one crystal lattice into two different crystal lattices.

Fig. 8. Crystalline phase diagram of the MBOBA–HOBA system (temperatures from X-ray diffraction measurements).

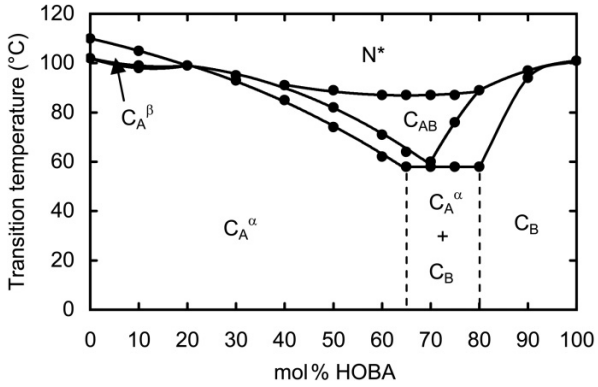

Fig. 9. DSC traces of 50 mol% HOBA in MBOBA; the arrows indicate the C_A^{α}–C_{AB} phase transition.

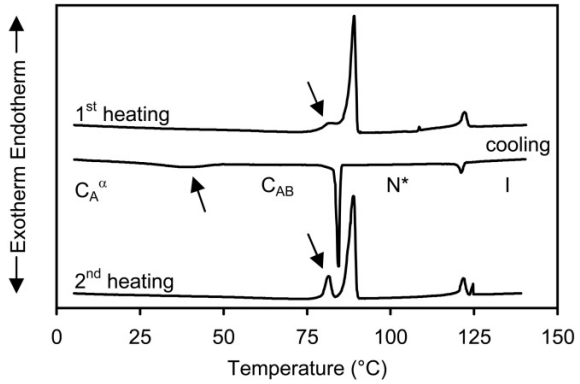

MBOBA–DOBA system

As in the MBOBA–HOBA system, all mixtures exhibited a cholesteric mesophase (Fig. 10). The cholesteric–isotropic transition temperature of the mixture 10 mol% DOBA in MBOBA was 105.1 °C as opposed to 105.9 °C for 10 mol% HOBA in MBOBA, reflecting that the molecular arrangement of the cholesteric phase was only weakly affected by the greater difference in molecular lengths of the components. The cholesteric–isotropic transition line, however, was not as smooth as in the case of the MBOBA–HOBA system. It was straight at the extremes of the composition range and had a local minimum at the composition with a one-to-one ratio of the components. The shape of the cholesteric–isotropic transition line indicated that the cholesteric phase at DOBA contents less than 20 and more than 80 mol% was dominated by pure MBOBA or DOBA dimers, respectively, but that mixed dimers dominated at DOBA contents in between. This conclusion was supported by microscopy results: the textures observed for the cholesteric phase on heating were "oily streak" textures for all mixtures; on cooling, the mixtures with a DOBA content less than 70 mol% showed fan textures; whereas the mixtures with 80 and 90 mol% DOBA showed textures of a cholesteric phase with greater pitch.

© 2008 NRC Canada

Fig. 10. Phase diagram of the MBOBA–DOBA system (peak temperatures of the first DSC heating run); DSC transition peak has a shoulder (○).

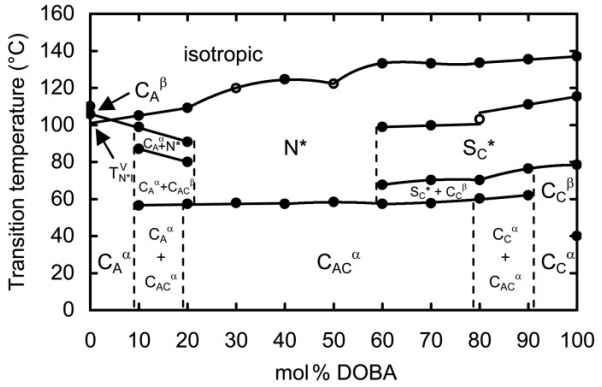

The low thermal stability at 50 mol% DOBA in MBOBA was attributed to the structural difference of the substituent groups of the components. The linear decenoxy group of DOBA allowed a narrower molecular arrangement than the branched 2-methylbutoxy group of MBOBA. The DSC thermogram of the mixture 50 mol% DOBA in MBOBA showed a shoulder peak for the cholesteric–isotropic transition, which implied that the cholesteric phase of this mixture is not homogeneous. It might separate into domains with differently tight molecular arrangements.

The mixtures that contained more than 50 mol% DOBA exhibited a twisted smectic C phase. In the polarized-light microscope the phase appeared in form of a fine Schlieren texture.

To determine whether this phase contained mixed dimers, we analyzed the mixtures by X-ray diffraction at temperatures between their melting points and S_C*–N* transition temperatures. The temperature dependence of the *d* value was similar in all mixtures (Fig. 11*a*) and the absolute value increased with increasing DOBA content (Fig. 11*b*). The increase in *d* value was linear with a discontinuity and change in slope at 80 mol% DOBA. In comparison the longest *d* value calculated from the size of the unit cell depicted in Fig. 5 with interdigitated molecules of DOBA amounts to *d* = 20.82 Å. We concluded that similar to the cholesteric phase, the twisted smectic *C* phase at a DOBA content less than 80 mol% was dominated by mixed dimers, but pure DOBA dimers dominated at a DOBA content higher than 80 mol%. This conclusion was supported by DSC results, which revealed a shoulder peak for the S_C*–N* transition at 80 mol% DOBA in MBOBA, indicating that the S_C* phase in this mixture was not homogenous. The mixed dimers with a length of 28.9 Å did not form a smectic phase on their own. The smectic phase in the mixtures with 60 and 70 mol% DOBA was induced by the dimers of excess DOBA molecules.

At 58 °C, the mixtures with 10 and 20 mol% DOBA showed a phase transition into another mixed phase (C_{AC}^β, Fig. 10). This phase must have a slightly different composition (higher DOBA content), since the crystalline phase of the MBOBA is formed simultaneously with it.

With respect to the crystalline region, X-ray diffraction gave a variety of *d* values (Table 2). We were able to distinguish at least six different crystalline phases. The two phases

Fig. 11. *d* Values of the smectic *C* phases at different MBOBA–DOBA compositions: (*a*) as a function of temperature (numbers indicate DOBA content in mol%), (*b*) at the smectic–nematic transition temperatures.

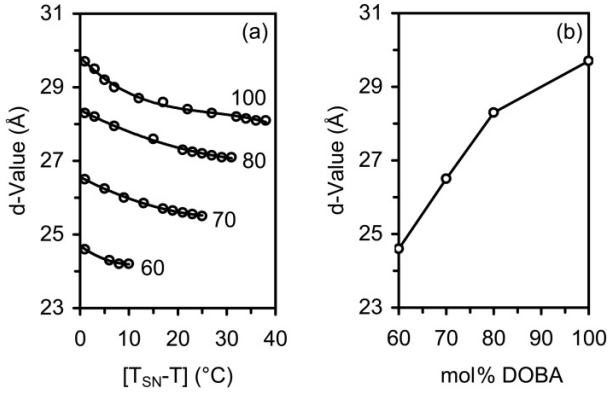

Table 2. *d* Values of the crystalline phases of the MBOBA–DOBA mixtures (at 30 °C for the α-phases and at the temperature of the phase transition for the β-phases).

DOBA content mol%	*d* Value (Å)					
	C^α_A	C^β_A	C^α_{AC}	C^β_{AC}	C^α_C	C^β_C
0	8.7	14.6				
10	8.8		14.6	19.2		
20	8.8[a]		15.1	16.2		
30[b]						
40			17.2			
50			19.8			
60			20.8			25
70			21.7			25.6
80			22.1		23.9	25.9
90[a]						
100					24.1	25.2

[a]Appeared at ~57 °C upon heating.
[b]Values not available.

at the extremes of the composition range (C_A and C_C, Fig. 10) were most likely the crystalline phases of the pure components with a low- and a high-temperature modification (α and β). The C^α_{AC} phase presumably contained different amounts of mixed dimers in the different mixtures, as the *d* value varied with composition. Most of the mixtures (30 to 90 mol% DOBA in MBOBA) melted at about 58 °C. The mixtures with 60 to 90 mol% DOBA separated above 60 °C into a S_C* phase and the high-temperature crystalline phase of DOBA. On melting, the *d* value of the smectic phase showed a distinct shift to higher values, which reflected increasing incorporation of DOBA molecules into the smectic molecular arrangement.

Conclusions

A variety of shapes and packing arrangements was found for crystalline 4-substituted benzoic acids. Achiral pure compounds with longer substituents attached crystallize in acentric and with shorter substituents in centric crystal structures with dimers formed by hydrogen bonding. The symme-

© 2008 NRC Canada

try elements present in the crystalline state also influence the kind of arrangements in liquid crystals.

Regarding the crystalline phases in the mixed systems, the formation of mixed dimers was found to be promoted by a greater difference in molecular structure. The system with the more structurally similar components, the MBOBA–HOBA system, exhibited a crystalline phase of mixed dimers at compositions between 40 and 80 mol% HOBA and temperatures above 58 °C. The system with the greater structural difference in components (the MBOBA–DOBA system) showed crystalline phases containing mixed dimers at room temperature and for all compositions. A greater difference in molecular structure led to a decrease in solubility. Due to the tendency of these systems to form mixed dimers, the region in which mixed dimers were found was enlarged, as opposed to enlarging the region where two crystalline phases coexisted.

The liquid-crystalline phases were found to be dominated by mixed dimers at compositions in the midrange. At the extremes of the composition range, pure dimers dominated the liquid-crystalline phases. Concerning the cholesteric phase, mixed-dimer formation in the composition midrange was indicated by the shape of the cholesteric–isotropic transition line and was more obvious for the system with the more structurally different components. Regarding the twisted smectic *C* phase, the change from mixed-dimer prevalence to pure-dimer prevalence with composition was evident by a discontinuity in the increase of the *d* value with increasing DOBA content.

Acknowledgement

We thank the European Commission's Directorate-General Education and Culture for an ERASMUS scholarship for M.R. and Prof. Corrie T. Imrie at the University of Aberdeen for hosting M.R. during her study abroad. We also thank Mrs. Astrid Peschel for assistance with the DSC measurements.

References

1. D.W. Bruce, D.A. Dunmur, P.M. Maitlis, J.M. Watkins, and G.J.T. Tiddy. Liq. Cryst. **11**, 127 (1992).
2. G.W. Gray. Molecular structure and the properties of liquid crystals. Academic Press, London. 1962.
3. S. Takenaka and M.M. Labes. Mol. Cryst. Liq. Cryst. **90**, 365 (1983).
4. J. Homer and A.R. Dudley. J. Chem. Soc., Chem. Commun. 926 (1972).
5. F.C. Whitmore and J.H. Olewine. J. Am. Chem. Soc. **60**, 2569 (1938).
6. D.H. Brauns. J. Research Natl. Bur. Standards **18**, 315 (1937).
7. G.Y. Brokaw and W.R. Brode. J. Org. Chem. **13**, 194 (1948).
8. R.L. Burwell, Jr. and G.S. Gordon, III. J. Am. Chem. Soc. **70**, 3128 (1948).
9. H. Ringsdorf and A. Schneller. Makromol. Chem. Rapid Commun. **3**, 557 (1982).
10. B. Sternberg, W. Pilz, P. Reich, and H.D. Koswig. Z. Phys. Chemie Leipzig, **264**, 499 (1983).
11. MolEN. An interactive structure solution Procedure, Enraf Nonius, Delft, The Netherlands. 1990.
12. G.M. Sheldrick. SHELX-93 [computer program]. A program for the refinement of single-crystal diffraction data. University of Göttingen, Göttingen, Germany. 1993.
13. A. Altomare, G. Cascarano, C. Giacovazzo, A. Guagliardi, A.G.G. Moliterni, M.C. Burla, G. Polidori, M. Camalli and R. Spagna. SIR97 [computer program]. A package for crystal structure solution by direct methods and refinement. 1997.
14. E. Keller. SCHAKAL-92 [computer program]. A computer program for the graphic representation of molecular and crystallographic models. Kristallographisches Instistut der Universität Freiburg, Germany. 1992.
15. G.M. Frankenbach and M.C. Etter. Chem. Mat. **4**, 272 (1992).
16. P. Zugenmaier, I. Bock, and J. Schacht. Mol. Cryst. Liq. Cryst. **392**, 31 (2003).
17. F. Heinemann and P. Zugenmaier. *In* Chiral liquid crystals. *Edited by* W. Kuczynski. Institute of Molecular Physics, Polish Academy of Sciences, Poznan. 2003. pp. 99.
18. R.J. Diefendorf. Ext. Abstr. Program– Bienn. Conf. Carbon. **16**, 26 (1983).
19. E.C.H. Hsu and J.F. Johnson. Mol. Cryst. Liq. Cryst. **20**, 177 (1973).
20. D. Demus, C.H. Fietkau, R. Schubert, and H. Kehlen. Mol. Cryst. Liq. Cryst. **25**, 215 (1974).

© 2008 NRC Canada

Efficient bioconversion of palm acid oil and palm kernel acid oil to poly(3-hydroxybutyrate) by *Cupriavidus necator*[1]

Yik-Kang Kek, Wing-Hin Lee, and Kumar Sudesh

Abstract: Efficient bioconversion of palm oil by-products to green materials serves as a prominent way to overcome wastage. Generally, major palm oil by-products such as palm acid oil (PAO) and palm kernel acid oil (PKAO) are used for animal feed. This pioneer study investigated the ability of *Cupriavidus necator* H16 (ATCC 17699) (formerly *Ralstonia eutropha*) to biologically convert these by-products to poly(3-hydroxybutyrate) [P(3HB)]. P(3HB) was synthesized when PAO or PKAO was fed as the sole carbon source. However, it was found that PKAO is superior with respect to higher amount of P(3HB) accumulation in 48 h (85 wt% of the dry cell mass). In addition, important culture parameters were identified, such as nitrogen sources and ratio of culture volume to flask volume, which significantly affected the P(3HB) content. The nitrogen concentration in the culture medium is very crucial in promoting the biosynthesis of P(3HB). The highest P(3HB) yield (3.1 g/L) was initiated at 4 mmol/L of urea. Less than 0.4 g/L of P(3HB) was obtained when 30.0 mmol/L or higher urea concentrations were used. This study has identified a suitable process to produce high P(3HB) yield from major palm oil by-products. It is also demonstrated that *C. necator* H16 has suitable metabolic pathways that allow the conversion of palm oil by-products to P(3HB) effectively. Hereby, surplus palm oil by-products can be converted to a relatively high-value and sustainable product.

Key words: poly(3-hydroxybutyrate), palm oil, palm acid oil, palm kernel acid oil, *Cupriavidus necator.*

Résumé : Une bioconversion efficace des sous-produits de l'huile de palme en matériaux verts est une méthode de choix pour éliminer les déchets. En général, les sous-produits majeurs de l'huile de palme, tel l'huile acide de palme (HAP) et l'huile acide de la noix de palme (HANP), sont utilisés comme nourriture pour les animaux. Dans ce travail, on a étudié la possibilité d'utiliser le *Cupriavidus necator* H16 (ATCC 17699) [antérieurement *Ralstonia eutropha*] pour transformer biologiquement ces sous-produits en poly(3-hydroxybutyrate) P(3HB). Il y a synthèse de P(3HB) quand on utilise du HAP ou du HANP comme seule source de carbone. Toutefois, on a observé que, sur une période de 48 heures, le HANP conduit à une accumulation plus élevée de P(3HB) (85% en poids de cellules sèches). De plus, on a identifié des paramètres importants pour la culture, telles les sources d'azote et le rapport du volume de culture au volume du contenant, qui affectent profondément la teneur en P(3HB). La concentration en azote dans le milieu de culture est cruciale pour la biosynthèse du P(3HB). Le rendement le plus élevé de P(3HB) (3,1 g/L) a été obtenu à partir d'une solution contenant 4 mmol/L d'urée. On n'a obtenu qu'un maximum de 0,4 g/L de P(3HB) lorsque les concentrations d'urée étaient supérieures à 30 mmol/L. Cette étude a identifié un processus approprié pour obtenir des rendements élevés de P(3HB) à partir des sous-produits de l'huile de palme. Il a aussi été démontré que le *C. necator* H16 possède les voies métaboliques appropriées pour permettre de transformer effectivement les sous-produits de l'huile de palme en P(3HB). Il est donc possible de transformer les surplus de sous-produits de l'huile de palme en un produit durable et de valeur relativement élevée.

Mots-clés : poly(3-hydroxybutyrate), huile de palme, huile acide de palme, huile acide de la noix de palme, *Cupriavidus necator.*

[Traduit par la Rédaction]

Introduction

A large consortium of bacteria is capable of dispensing excessive carbon source through the formation of intracellular polyester granules under unfavourable growth conditions (1). This family of bacterial polyesters, which could be composed of an enormous range of hydroxyalkanoate (HA) units, is designated as poly(hydroxyalkanoates) (PHA) (2). Plant oils have been identified as feasible feedstocks for PHA biosynthesis using

Received 19 October 2007. Accepted 6 December 2007. Published on the NRC Research Press Web site at canjchem.nrc.ca on 8 April 2008.

Y.K. Kek, W.H. Lee, and K. Sudesh.[2] School of Biological Sciences, Universiti Sains Malaysia, Penang 11700, Malaysia.

[1]This article is part of a Special Issue dedicated to Professor R. Marchessault.
[2]Corresponding author (e-mail: ksudesh@usm.my).

 doi:10.1139/V08-001 © 2008 NRC Canada

various microorganisms (3). Recently, palm kernel oil was determined as suitable carbon source for the biosynthesis of poly(3-hydroxybutyrate) [P(3HB)] and poly(3-hydroxybutyrate-*co*-3-hydroxyhexanoate) [P(3HB-*co*-3HHx)] by *Cupriavidus necator* H16 and its recombinant (4). The idea of using palm oil and its by-products has piqued interest among researchers in Malaysia because of the abundance of these raw materials throughout the country. Impressive growth of the crude palm oil production in the last few decades (7.8 million tonnes per year (1995) to 15 million tonnes in the year 2005) allowed Malaysia to be the largest producer of palm oil in the world (5). Hence, palm oil and its by-product can be counted on as a steady source of raw materials to be used as the carbon feedstock in PHA production. Bioconversion of whey (6–8), molasses (9–12), starch (13, 14), triacylglycerols (15, 16), and other crude carbon substrates from industrial food wastes (17) or industrial by-products (18) to PHA have been investigated.

Cheap, ready availability in bulk quantity and constant supply of the feedstock become crucial factors for large scale and continuous PHA production. The undesirable free fatty acids present in palm oils are removed by using a chemical refining process (saponification) to produce palm acid oil (PAO) and palm kernel acid oil (PKAO), which are derived from crude palm oil (CPO) and crude palm kernel oil (CPKO), respectively. In 2006, there were 51 refineries in operation in Malaysia with the total processing capacity of 18.5 million tonnes per year (5). Thus, those surplus materials from the refinery process are readily available as carbon sources for the viable production of PHA.

In this study, for the first time, efficient bioconversion of two major by-products of the palm oil industry, PAO and PKAO for bacterial growth and PHA production, was evaluated. We report here that these carbon sources are not only suitable for the growth of *C. necator*, but they are also excellent carbon sources for the synthesis and accumulation of P(3HB).

Materials and methods

Bacterial strain, media, and maintenance

Wild type *Cupriavidus necator* H16 (ATCC 17699) [formerly *Ralstonia eutropha*] was used throughout this study. The bacterium was grown in Nutrient-Rich (NR) medium as described previously (19). For maintenance purposes, 12.5 mL of pure glycerol was added into the 50 mL culture after 24 h growth in NR medium to prepare a 20% (*v*/*v*) glycerol stock, which was stored at –20 °C in 1 mL aliquots.

Culture conditions

One-stage batch culture was carried out for the evaluation of PHA biosynthesis. The bacterium was activated by inoculating 1 mL of glycerol stock into 50 mL NR medium and cultivated at 30 °C and 200 rpm. After 24 h cultivation, 3% (*v*/*v*) of the preculture medium was transferred into a 250 mL flask containing 50 mL of nitrogen-limited mineral medium (MM) for PHA accumulation (19). Nitrogen limitation was imposed by supplying various nitrogen sources with a nitrogen molarity of 0.01 mmol/L in the MM. In this study, palm oil by-products PAO and PKAO that were used for growth and biosynthesis of PHA by *C. necator* H16 were supplied by Unitata Ltd, Perak, Malaysia. A total of 5 g/L of these carbon sources were evaluated for the PHA production. PKAO, which is in the liquid form, was autoclaved separately from the culture medium, whereas solid PAO was autoclaved together with the medium. The cultures were cultivated at 30 °C for 48 h and shaken at 200 rpm.

Analytical procedures

At the end of the cultivation period, the cells were harvested by centrifugation (6000*g*) and washed once with hexane/distilled water before lyophilization. The lyophilized cells were subjected to methanolysis in the presence of methanol/sulfuric acid (85:15 *v*/*v*). After heating for 140 min at 100 °C, the resulting methyl esters were then quantified by gas chromatography (GC) with caprylic methyl ester as an internal standard (20). Total cell mass was determined by measuring dry cell mass (DCM). The residual cell biomass was calculated by subtracting the amount of PHA from the total DCM.

Transmission electron microscopy (TEM)

Cells cultivated in MM supplemented with 50 mmol/L and 5 mmol/L urea were harvested and prefixed in McDowell–Trump fixative (21). The cell pellets were then fixed with 1% Osmium tetroxide (OsO_4). To dehydrate the cells, they were subjected to increasing amounts of ethanol (50%, 75%, 95%, and 100%) followed by 100% acetone. Cell embedment was performed in Spurr's low viscosity resin (22). Ultra-thin sections were prepared, mounted on copper grids and stained with uranyl acetate and lead citrate for electron microscope examination at an acceleration voltage of 80 kV (Philip CM 12/ STEM and JLM-2000FX11).

Results

This study shows for the first time the biosynthesis of P(3HB) from palm oil by-products, PAO and PKAO by *C. necator* H16. This bacterium was first screened on PAO and PKAO with the supplementation of various nitrogen sources to determine the bioconversion efficiency of these by-products into P(3HB). Dry cell mass (DCM) and P(3HB) content obtained at 48 and 72 h of cultivations are illustrated in Fig. 1. Varying the nitrogen sources in the culture medium rendered significant effect on cell biomass synthesis and PHA accumulation of this bacterium. Both carbon sources favored cell growth and P(3HB) accumulation, although it seemed that PKAO was a better carbon source. PKAO resulted in a much higher P(3HB) yield than PAO after 48 h of cultivation with all nitrogen sources assayed except urea, whereby approximately 1.9 g/L was synthesized from both carbon sources (Fig. 1*B*). Further incubation up to 72 h often resulted in the reduction of PHA content. Figure 1 also demonstrates that cells cultivated in urea [$(NH_2)_2CO$] achieved higher DCM in a shorter period as compared to other nitrogen sources.

The effect of urea concentration on the cell growth and PHA biosynthesis was also evaluated on both PAO and PKAO as shown in Fig. 2. In this study, the initial concentration of carbon source used was 5 g/L. As expected, it was clear that the reduction in urea stimulated higher P(3HB) accumulation. The highest P(3HB) content was obtained from

© 2008 NRC Canada

Fig. 1. Effects of different nitrogen sources on growth and the level of P(3HB) accumulation from 5 g/L of (*A*) PAO and (*B*) PKAO during cultivation of *C. necator* H16 at 48 and 72 h. Culture medium was supplemented with 10 mmol/L of nitrogen source.

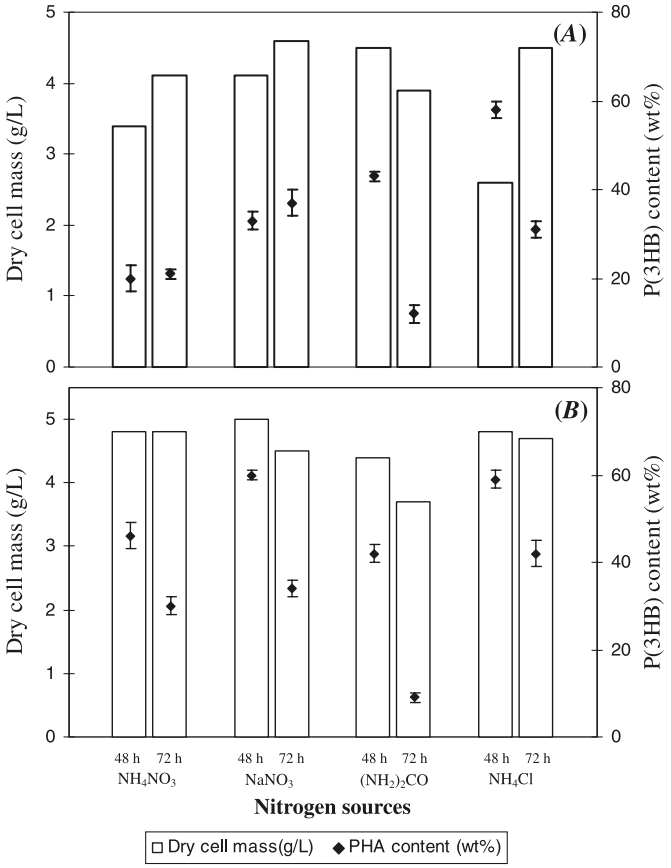

Fig. 2. Comparison of the dry cell mass and P(3HB) content obtained from (*A*) PKAO and (*B*) PAO in mineral medium supplemented with various urea concentrations.

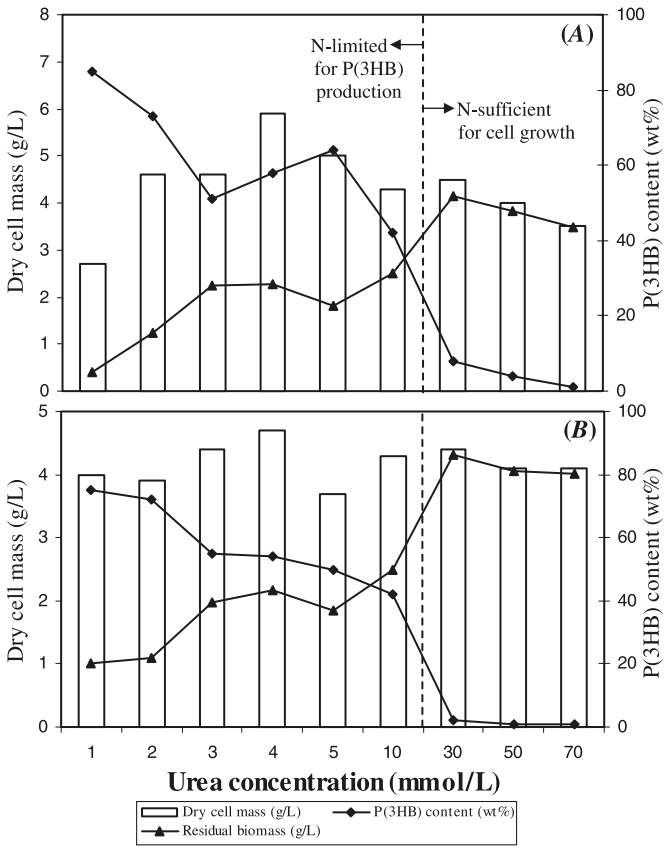

both carbon sources when the cells were supplemented with 1 mmol/L of urea, whereby up to 75 and 85 wt% of P(3HB) was attained at 48 h from PAO and PKAO, respectively. However, at this concentration (1 mmol/L of urea), the cell biomass achieved from PAO (4 g/L) was almost two-fold higher than that obtained from PKAO (2.7 g/L). In general, an increase in the urea concentration resulted in a higher residual biomass. On the other hand, the P(3HB) content was significantly reduced. It is noteworthy that the threshold level of urea concentration for P(3HB) accumulation and cell growth fell between 10 and 30 mmol/L. As shown in Fig. 2, a sharp decrease was observed in the P(3HB) content as the concentration of urea was increased from 10 to 30 mmol/L. P(3HB) content dropped from 42 wt% to 2 and 8 wt% of the DCM for PAO and PKAO, respectively. For all the nitrogen source concentrations assayed, 4 mmol/L of urea was found to support the best growth of *C. necator* H16, whereby 5.4 and 4.7 g/L of DCM was obtained from PKAO and PAO, respectively.

C. necator H16 grown under nitrogen-limited as well as nitrogen-rich conditions were then observed under TEM to study their morphological characteristics. At low concentration of urea (5 mmol/L), *C. necator* H16 was found to be packed with P(3HB) granules at the end of 48 h cultivation. GC results revealed that approximately 65 wt% of P(3HB) was accumulated under such conditions. In addition, the number of P(3HB) granules was in the range of 5–16 per cell. When the urea concentration was increased 10-fold, it was noted that most of the cells were actively dividing (data not shown). Small discrete P(3HB) granules were also noticed in some of the cells. A relatively small amount of those inclusions were produced (not more than five) at such high urea concentration (Fig. 3*A*). This observation corresponded to the GC results obtained in which only 5 wt% of P(3HB) was accumulated.

Generally, an increase in the carbon source concentration will increase the C/N ratio. In this study, the C/N ratio was varied by manipulating the PKAO concentration in the culture medium. As expected, a higher ratio of C/N resulted in higher cell biomass and PHA accumulation. The DCM obtained showed a sixfold increment (0.9 to 5.4 g/L) as the PKAO concentration was increased from 1 to 5 g/L. Supplementation of PKAO at a higher concentration denotes higher quantity of substrate available to cell biomass for its biosynthetic processes, and thus gives better cell growth. Figure 4 clearly shows that high C/N ratio resulted in high level of P(3HB) accumulation by *C. necator* H16. It was found that 5 g/L of PKAO was the optimal concentration for cell growth and also led to the highest P(3HB) yield (3.1 g/L) at 48 h of cultivation. The residual biomass reached its highest value, 2.5 g/L, at PKAO concentration of 5 g/L. However, poorer cell growth was achieved as the PKAO concentration was further increased in the culture medium. Although 9 g/L of PKAO resulted in the highest

© 2008 NRC Canada

Fig. 3. Transmission electron micrographs of P(3HB) granules in *C. necator* H16 cultivated in mineral medium for 48 h at 30 °C. Cells were grown on PKAO under nitrogen-rich or nitrogen-limited conditions: (*A*) Content of intracellular P(3HB) was 5 wt% of total DCM with the supplementation of 50 mmol/L urea. (*B*) High accumulation of P(3HB) contributing to about 65 wt% of DCM was attained using low urea concentration (5 mmol/L). (*C*) and (*D*) Newly formed P(3HB) granules found to be localized around the nucleoid region, which were observed near the center of the cells. Bar represents 200 nm for Figs. 3*B*, 3*C*, and 3*D*.

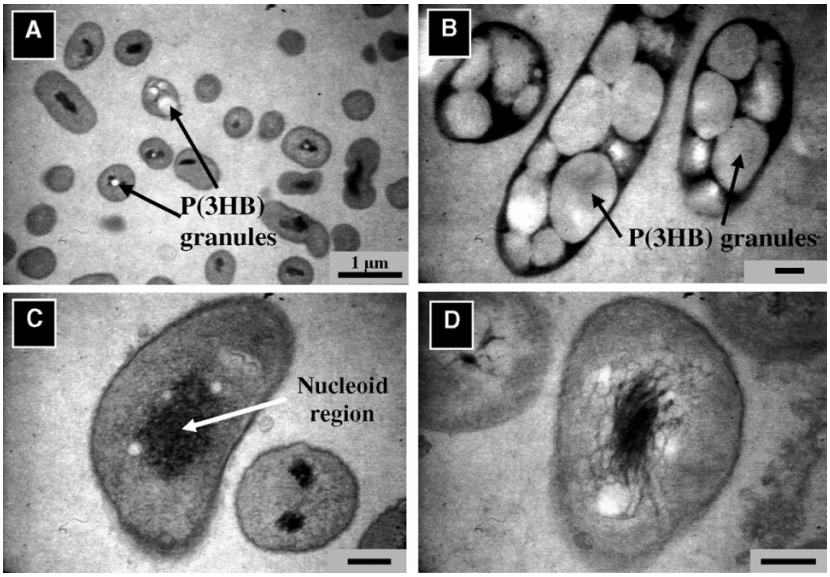

Fig. 4. Effects of PKAO concentration on cell biomass and P(3HB) synthesis by *C. necator* H16. Cells were cultivated for 48 h in mineral medium containing urea with a concentration of 4 mmol/L.

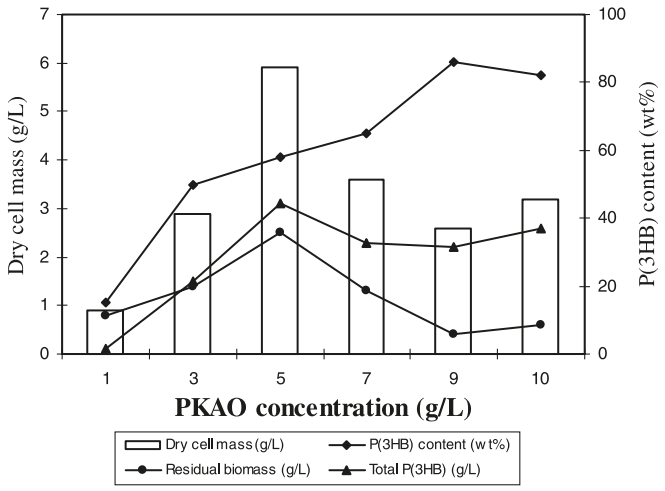

P(3HB) content (86 wt%), it was relatively lower in terms of PHA yield (2.2 g/L).

The culture volume to flask volume ratio is another factor that was found to affect the cell growth and P(3HB) synthesis of this bacterium from PKAO. Cells were cultivated in varying volumes of MM in a 250 mL flask. It was assumed that the increase in culture volume will result in lower oxygenation rate and subsequently promote better P(3HB) accumulation. It is apparent that P(3HB) content could be enhanced by increasing the culture volume (Table 1). Intracellular P(3HB) content was increased from 60 to 77 wt% of DCM as the culture volume was raised from 50 to 100 mL, although the DCM obtained were comparable. Cells grown in 200 mL MM revealed the highest accumulation of P(3HB), resulting in a total of 3.7 g/L P(3HB) at the end of the cultivation period. The P(3HB) yield shows the highest value of 4.1 g/L during cultivation in 100 mL culture medium. Meanwhile, 4.5–5.3 g/L of DCM was obtained from all the culture volumes examined. Low residual biomass was observed in large volume cultures.

Discussion

Previous studies have demonstrated that agricultural and industrial wastes are suitable carbon sources for PHA production in an economically competitive manner (13, 14, 16, 23). With this idea in mind, we have attempted to produce PHA from the main by-products of the palm oil industry, which are PAO and PKAO. The present study has demonstrated that these palm oil by-products are feasible as the carbon source for rapid accumulation of P(3HB) by *C. necator* H16. Approximately 3 g/L of P(3HB) was attained after 48 h of cultivation when ammonium chloride or sodium nitrate was used as the nitrogen source. Increasing the productivity of PHA synthesis (higher PHA yield in a shorter fermentation period) is among the efforts to reduce the overall PHA production costs, particularly equipment-related costs (24, 25). Loo and co-workers have recently reported the P(3HB-*co*-3HH*x*) production with a constant molar fraction of 3HH*x* monomer by recombinant *C. necator* from various palm oil products, however, with the cultivation period of 72 h (26).

Our results showed that PKAO supported better growth and P(3HB) accumulation, compared with PAO as the sole carbon source. This variation can be explained by the differences in fatty acids composition of these by-products. The two most predominant fatty acids in PAO are saturated C16:0 palmitic acid (~45%) and unsaturated C18:1 oleic acid (~40%). Meanwhile, PKAO is mainly comprised of saturated fatty acids (Table 2), which are the preferred carbon

© 2008 NRC Canada

Table 1. Effects of culture volume to flask volume ratio upon the growth and P(3HB) production in *Cupriavidus necator* H16.

Culture volume (mL)[a]	Dry cell mass (g/L)[b]	P(3HB) content (wt%)[c]	P(3HB) yield (g/L)	Residual biomass (g/L)
25	4.5	58±1	2.6	1.9
50	5.2	60±2	3.1	2.1
100	5.3	77±2	4.1	1.2
150	4.6	76±2	3.5	1.1
200	4.7	79±2	3.7	1.0

Note: PKAO, Palm kernel acid oil (5 g/L).
[a]Cells were cultivated for 48 h at 200 rpm and 30 °C in MM containing 4 mmol/L urea as nitrogen source with the initial pH of 7.
[b]Dry cell mass after lyophilization.
[c]PHA content in lyophilized cells was determined by GC analysis.

Table 2. Fatty acid compositions of palm oil products related to this study.

Fatty acid	CPO	PAO	CPKO	PKAO
Saturated				
Caproic (6:0)	—	—	—	—
Caprylic (8:0)	—	—	3.9	2.0
Capric (10:0)	—	—	3.5	2.5
Lauric (12:0)	0.1	0.8	48.5	44.1
Myristic (14:0)	0.9	1.1	16.2	17.8
Palmitic (16:0)	43.8	44.7	7.5	10.8
Stearic (18:0)	4.0	3.7	2.6	3.1
Arachidic (20:0)	—	—	—	—
Unsaturated				
Palmitoleic (16:1)	—	—	—	—
Oleic (18:1)	42.1	40.3	15.7	17.3
Linoleic (18:2)	8.9	9.4	2.1	2.3
Linolenic	0.2	—	—	—

Note: CPO, crude palm oil; PAO, palm acid oil; CPKO, crude palm kernel oil; PKAO, palm kernel acid oil (Source: Unitata Ltd.).

sources for cell growth and PHA accumulation. In a separate study, we have also experimented with CPKO and CPO, which share similar fatty acid compositions to PKAO and PAO, respectively. *C. necator* showed better growth on CPKO when used as the sole carbon source in comparison with CPO (data not shown). Similar results were also obtained by Loo and co-workers whereby the accumulation of P(3HB-*co*-3HH*x*) from crude CPKO was better than that from CPO (26).

There are several strategies to increase the accumulation of PHA in bacterial cells such as by inducing the limitation of phosphorus, nitrogen, and (or) magnesium (27, 28). In this study, we applied nitrogen limitation, which is generally employed for the production of P(3HB) (29).

Several nitrogen sources were evaluated, and urea was selected for subsequent experiments because of its cheaper cost. Figure 2 clearly shows the influences of different urea concentration upon the P(3HB) production using PAO or PKAO as the sole carbon source. A noticeable drop in P(3HB) content was observed when the urea concentration was increased from 10 mmol/L to 30 mmol/L.

It is apparent that 30 mmol/L or higher concentrations of urea hampered P(3HB) synthesis, because *C. necator* H16 entered the balanced growth conditions whereby carbon sources are used mainly for cell growth. This is most probably because acetyl-CoA produced from the metabolism of free fatty acids via β-oxidation pathway flows primarily into the tricarboxylic acid cycle (TCA) for energy generation and formation of cell constituents. Synthesis of P(3HB) from acetyl-CoA generally occurs via a sequence of three enzyme-mediated reactions: condensation of two acetyl-CoA moieties to form acetoacetyl-CoA, followed by stereoselective reduction of acetoacetyl-CoA to (*R*)-3-hydroxybutyryl-CoA, and finally polymerization of (*R*)-3-hydroxybutyryl-CoA to form P(3HB) [Fig. 5]. This pathway is believed to be under the control of the first enzyme 3-ketothiolase, which is inhibited by free coenzyme A (CoASH). Increased flux of acetyl-CoA into TCA cycle during nitrogen-rich conditions will enhance the pool of free CoASH within bacterial cell. It was reported that the CoASH level without PHA synthesis is three times higher than during PHA synthesis in *C. necator* (30). As a consequence, negative regulation of 3-ketothiolase by CoASH leads to a low P(3HB) content (less than 10 wt%) at the end of 48 h cultivation.

Cells for TEM analysis were cultivated on PKAO with the supplementation of low (5 mmol/L) and high (50 mmol/L) concentration of urea, which produced approximately 65 and 5 wt% of P(3HB), respectively. *C. necator* H16 was found to be fully packed with P(3HB) granules at 5 mmol/L of urea, as shown in Fig. 3*B*. To the contrary, we noted that *C. necator* H16 were actively dividing when 50 mmol/L urea was used in the culture medium, and the nucleoid region of the cells could be observed clearly near the center of the cell.

Another interesting observation of TEM analysis is that small and newly synthesized P(3HB) granules were found to be localized around and nearby the nucleoid region (Figs. 3*C* and 3*D*). The nucleoid region was then gradually less apparent as the size of P(3HB) granules increased. A similar observation was reported recently by Tian and co-workers (31, 32). They noticed the presence of a dark-stained mediation elements near the center of *C. necator* cells, where P(3HB) granules were localized. They proposed that these mediation elements may act as nucleation sites for P(3HB) granule initiation.

In addition to the type and concentration of nitrogen source, the dissolved oxygen concentration also affects PHA accumulation. We found that the PHA accumulation by *C. necator* H16 from PKAO was favored by an increase in culture volume to flask volume ratio, as illustrated in Table 1. Poorer aeration in larger culture volumes and the consequent oxygen limitation to the cultures contributed to a higher P(3HB) yield presumably due to a higher $NADH/NAD^+$ ratio within *C. necator* H16. It has been dem-

© 2008 NRC Canada

Fig. 5. Metabolic pathways of P(3HB) biosynthesis in *C. necator* H16 from palm oil products and its regulatory system. Block arrows indicate negative regulatory effects.

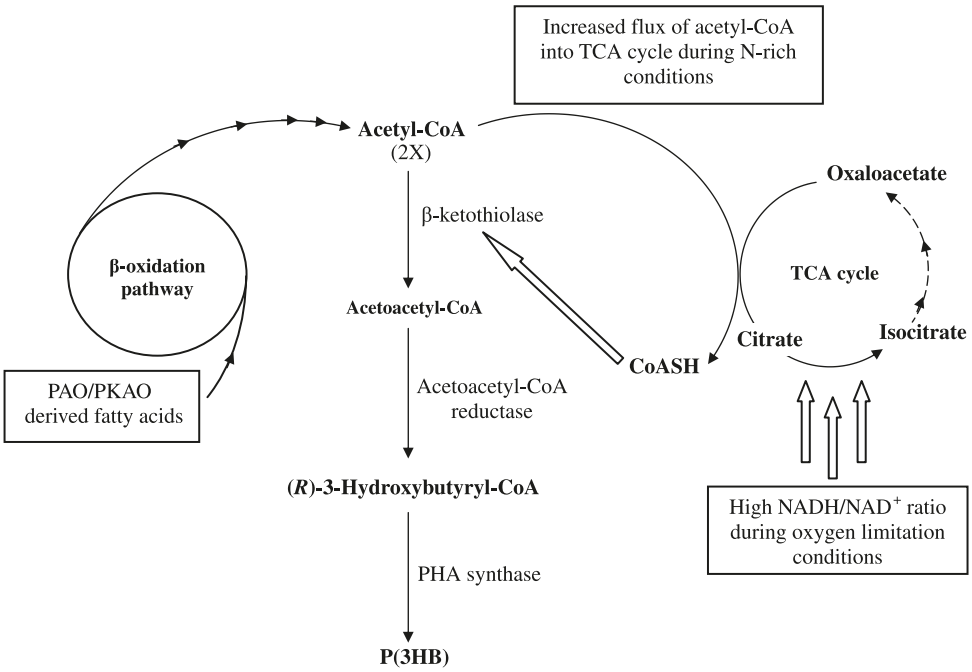

onstrated that the biosynthesis of P(3HB) is stimulated by both high intracellular concentrations of NADH and high ratios of NADH/NAD^+ (33). Key enzymes related to the TCA cycle, such as citrate synthase and isocitrate dehydrogenase, are inhibited by the elevated levels of intracellular NADH and thereby ensure the availability of acetyl-CoA for the condensation reaction mediated by β-ketothiolase (1, 34, 35). In such conditions, re-oxidation of NADH is principally achieved via P(3HB) biosynthesis pathway rather than by electron transport to oxygen as the ultimate electron acceptor (34, 36). As a result, P(3HB) constituted up to 80 wt% of DCM after 48 h of cultivation, resulting in a maximum P(3HB) yield of 4.1 g/L from PKAO. The results in Table 1 surprisingly show that the oxygen limitation due to the increment of culture volume, which promoted better P(3HB) accumulation, did not affect the DCM. Intracellular degradation of fatty acids is an oxidative process, which requires sufficient amounts of oxygen. Here, it seemed that the low oxygen level was still not a limiting factor for the growth of *C. necator* H16 even at high culture volume to flask volume ratio.

Conclusion

This study has demonstrated that the by-products from the palm oil refining process could be efficiently converted to P(3HB) by *C. necator* H16. Up to 85 wt% P(3HB) of the DCM was achieved in 48 h of cultivation. Nitrogen molarity and aeration of the cultures were crucial parameters for high yield production of P(3HB) from PAO and PKAO. P(3HB) synthesis by *C. necator* H16 using these surplus palm oil by-products looks promising, as the adoption of inexpensive and renewable carbon substrate in the PHA production is essential if this green material is to become an economically competitive product.

Acknowledgements

This study was supported in parts by research grants from Ministry of Science, Technology, and Innovation, Malaysia and Universiti Sains Malaysia. Generous supplies of palm oil products by Acidchem International Ltd. and Unitata Ltd. are gratefully acknowledged.

References

1. A.J. Anderson and E.A. Dawes. Microbiol. Rev. **54**, 450 (1990).
2. K. Sudesh, H. Abe, and Y. Doi. Prog. Polym. Sci. **25**, 1503 (2000).
3. T. Fukui and Y. Doi. Appl. Microbiol. Biotechnol. **49**, 333 (1997).
4. P. Kahar, T. Tsuge, K. Taguchi, and Y. Doi. Polym. Degrad. Stab. **83**, 79 (2004).
5. Malaysia oil palm statistics. 26th ed. Malaysia palm oil board. 2006.
6. S.Y. Lee, A.P.J. Middelberg, and Y.K. Lee. Biotechnol. Lett. **19**, 1033 (1997).
7. H.H. Wong and S.Y. Lee. Appl. Microbiol. Biotechnol. **50**, 30 (1998).
8. W.S. Anh, S.J. Park, and S.Y. Lee. Appl. Environ. Microbiol. **66**, 3624 (2000).
9. W.J. Page. FEMS Microbiol. Rev. **103**, 149 (1992).
10. Q. Zhang and C. Wang. J. Appl. Polym. Sci. **54**, 515 (1994).
11. D.K.Y. Solaiman, R.D. Ashby, A.T. Hotchkiss Jr., and T.A. Foglia. Biotechnol. Lett. **28**, 157 (2006).
12. F. Liu, W.Q. Li, D. Ridgway, and T.Y. Gu. Biotechnol. Lett. **20**, 345 (1998).
13. M.A. Hassan, Y. Shirai, A. Kubota, M.I.A. Karim, K. Nakanishi, and K. Hashimoto. J. Fermentation Bioeng. **86**, 57 (1998).
14. J. Yu. J. Biotechnol. **86**, 105 (2001).

© 2008 NRC Canada

15. D.K.Y. Solaiman, R.D. Ashby, and T.A. Foglia. Appl. Microbiol. Biotechnol. **56**, 664 (2001).
16. D.K.Y. Solaiman, R.D. Ashby, and T.A. Foglia. Curr. Microbiol. **44**, 189 (2002).
17. P.H. Hu, H. Chua, A.L. Huang, and K.P. Ho. Appl. Biochem. Biotechnol. **77**, 445 (1999).
18. K.M. Lee and D.F. Gilmore. Process Biochem. **40**, 229 (2005).
19. Y. Doi, S. Kitamura, and H. Abe. Macromolecules, **28**, 4822 (1995).
20. G. Braunegg, B. Sonnleitner, and R.M. Lafferty. Eur. J. Microbiol. Biotechnol. **6**, 29 (1978).
21. E.M. McDowell and B.F. Trump. Arch. Pathol. Lab Med. **100**, 405 (1976).
22. A.R. Spurr. J. Ultrastruct. Res. **26**, 31 (1969).
23. D.K.Y. Solaiman, R.D. Ashby, T.A. Foglia, and W.N. Marmer. Appl. Microbiol. Biotechnol. **71**, 783 (2006).
24. J. Choi and S.Y. Lee. Bioprocess Eng **17**, 335 (1997).
25. S.Y. Lee, J. Choi, and H.N. Chang. *In* Proceeding for the 1996 international symposium on bacterial poly(hydroxyalkanoates). *Edited by* G. Eggink, A. Steinbuchel, Y. Poirier, and B. Witholt. NRC Research Press, Ottawa, ON. pp. 127–136.
26. C.Y. Loo, W.H. Lee, T. Tsuge, Y. Doi, and K. Sudesh. Biotechnol. Lett. **27**, 1405 (2005).
27. H.W. Ryu, S.K. Hahn, Y.K. Chang, and H.N. Chang. Biotechnol. Bioeng. **55**, 28 (1997).
28. S.Y. Lee, J. Choi, and S.H. Lee. Macromol. Symp. **159**, 259 (2000).
29. T. Suzuki, T. Yamane, and S. Shimizu. J. Appl. Microbiol. Biotechnol. **24**, 370 (1986).
30. D.A. Mansfield, A.J. Anderson, and L.A. Naylor. Can. J. Microbiol. **41**(Suppl. 1), 44 (1995).
31. J. Tian, A.J. Sinskey, and J. Stubbe. J. Bacterio. **187**, 3814 (2004).
32. J. Tian, A. He, A.G. Lawrence, P. Liu, N. Watson, A.J. Sinskey, and J. Stubbe. J. Bacteriol. **187**, 3825 (2005).
33. I.Y. Lee, M.K. Kim, H.N. Chang, and Y.H. Park. FEMS Microbiol. Lett. **131**, 35 (1995).
34. P.J. Senior and E.A. Dawes. Biochem J. **125**, 55 (1971).
35. P.J. Senior and E.A. Dawes. Biochem J. **134**, 225 (1973).
36. G.A.F. Ritchie and E.A. Dawes. Biochem. J. **121**, 309 (1969).

© 2008 NRC Canada

Dumbbell-shaped dendrimers — Synthesis and self-assembly[1]

Tatiana Vassilieff and Ashok Kakkar

Abstract: We report on the synthesis and detailed characterization of dendrimers that evolve symmetrically from a linear core of 2-butyne-1,4-diol with 3,5-dihydroxybenzyl alcohol based dendron arms. The divergent layer-by-layer build-up of the dumbbell-shaped dendrimers is based on simple acid–base hydrolytic chemistry of bis(dimethylamino)dimethylsilane with OH-terminated molecules. The self-assembly of these dendrimers in THF and water is significantly influenced by their generation number, the backbone structure, and the solvent.

Key words: dendrimers, divergent synthesis, macromolecules, self-assembly

Résumé : On a effectué la synthèse et une caractérisation totale de dendrimères qui radient à partir d'un noyau linéaire de but-2-yne-1,4-diol avec des ramifications à base d'alcool 3,5-dihydroxybenzylique. La synthèse divergente, faite couche par couche, des dendrimères en forme d'haltère court est basée sur une chimie d'hydrolyse acide–base simple de bis(diméthylamino)diméthylsilanes dans lesquels les molécules se terminent par des groupes OH. L'autoassemblage de ces dendrimères dans un mélange de THF et d'eau est fortement influencé par le nombre de générations, la structure du squelette, et le solvant.

Mots-clés : dendrimères, synthèse divergente, macromolécules, autoassemblage.

[Traduit par la Rédaction]

Introduction

Hyperbranched and monodisperse macromolecules that are commonly referred to as dendrimers are becoming increasingly important in designing smart and efficient nanomaterials for a variety of applications in medicine, catalysis, and electronics (1). A significant effort in the design and syntheses of these globular architectures has been invested, which has led to inside-out (divergent) or outside-in (convergent) methodologies (2). Changing the central core leads to many structural variations and novel types of morphologies in the resulting dendrimers (3). We have been investigating the role of the core, backbone, and linking units in the evolving morphology of the dendrimers, and have established a simple and efficient divergent route to the syntheses of such dendritic macromolecules (4), based on the acid–base hydrolytic chemistry of amino-silanes and -stannanes with organic acids (5). We were intrigued by the possibility of developing hyperbranched structures using symmetric growth on either side of a bifunctional linear core, giving rise to dumbbell-shaped dendrimers. The synthetic elaboration and detailed investigation of the properties of dumbbell-shaped dendrimers have been much less explored than those of globular dendrimers (6). We report herein a route to the synthesis of dumbbell-shaped dendrimers that are constructed from the bifunctional core 2-butyne-1,4-diol using 3,5-dihydroxybenzyl alcohol (DHBA) as wedges. The synthetic elaboration is based on the controlled addition of bis(dimethylamino)dimethylsilane ($Me_2Si(NMe_2)_2$) to the bifunctional core, followed by the addition of DHBA. The process is then repeated with $Me_2Si(NMe_2)_2$) and DHBA in sequence, with amine as the only by-product, and the purification of dendrimers can be easily achieved by simple extraction into deuterium oxide. Self-organization of dendrimers by means of suitable peripheral groups continues to be an area of much significance and provides opportunities for designing nanomaterials for molecular encapsulation and delivery (4, 7, 8). The dumbbell-shaped dendrimers reported here have suitably placed OH groups for interdendrimer interactions, and we have examined their self-assembly through such interactions in THF and water, using UV–vis spectroscopy and transmission electron microscopy. In THF, generations 1–3 require a higher critical aggregation concentration (*cac*) to form aggregates than does generation 4. Because of the open structure in the lower generations, the linear core inhibits self-assembly, whereas in generation 4, the more globular architecture with more prominent hydrogen bonding sites facilitates self-assembly at lower concentrations.

Received 9 November 2007. Accepted 25 January 2008. Published on NRC Research Press Web site at canjchem.nrc.ca on 18 April 2008.

Dedicated to Professor Robert H. Marchessault for his contributions to Science in general and to Macromolecular Chemistry in particular.

T. Vassilieff and A. Kakkar.[2] Department of Chemistry, McGill University, 801 Sherbrooke St. West, Montreal, Quebec H3A 2K6, Canada.

[1]This article is part of a Special Issue dedicated to Professor R. Marchessault.

[2]Corresponding author (e-mail: ashok.kakkar@mcgill.ca).

Results and discussion

Dendrimers were synthesized using a quantitative acid–base hydrolytic reaction of aminosilanes with molecules con-

 doi:10.1139/V08-027 © 2008 NRC Canada

Scheme 1.

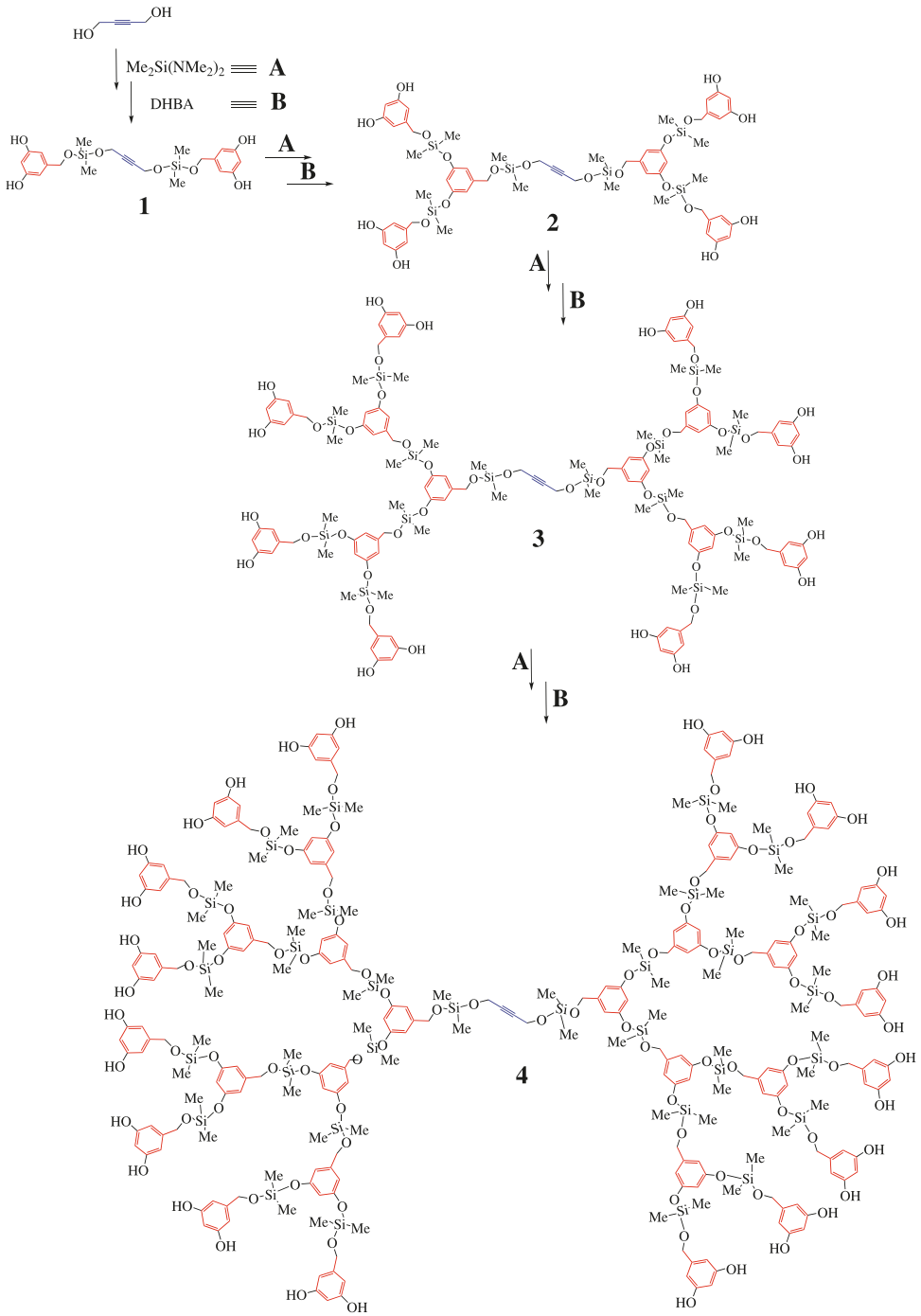

taining terminal OH groups (5). The choice of the linear core around which dendrons are built was based on rigidity, solubility, and commercial availability, and 2- butyne-1,4-diol was considered to be an ideal candidate for developing the desired dendrimers. The dendron backbone was chosen to be 3,5-dihydroxybenzyl alcohol because it has been successfully employed in our laboratory in the past to synthesize globular dendritic architectures (4). For synthesizing the first generation dendrimer, 1 molar equivalent of 2-butyne-1,4 diol was added dropwise over a period of 2 h to an ice-bath-cooled solution of 2 equivalents of bis(dimethylamino)dimethylsilane in THF. The solution was stirred at ice-bath temperature for an additional six hours, and then left to warm to room temperature. The solution was transferred to an addition funnel, and added slowly to a solution of 2 equivalents of DHBA in THF, and stirred overnight. After removal of the solvent in vacuo, the product was extracted into deuterium oxide (D_2O). The solution was filtered and D_2O was then removed under vacuum, to afford a light pink powder **1**. Continuation of this methodology by carrying out reactions under controlled conditions led to the synthesis of dendrimers **2**–**4** in very good yields. Dendrimers were characterized using a combination of

© 2008 NRC Canada

Fig. 1. (*A*) UV–vis absorption spectra of dendrimer **1** at concentrations of 1 to 10 mg/mL in THF and (*B*) plot of absorbance *vs* concentration of dendrimer **1** in THF at 340 nm.

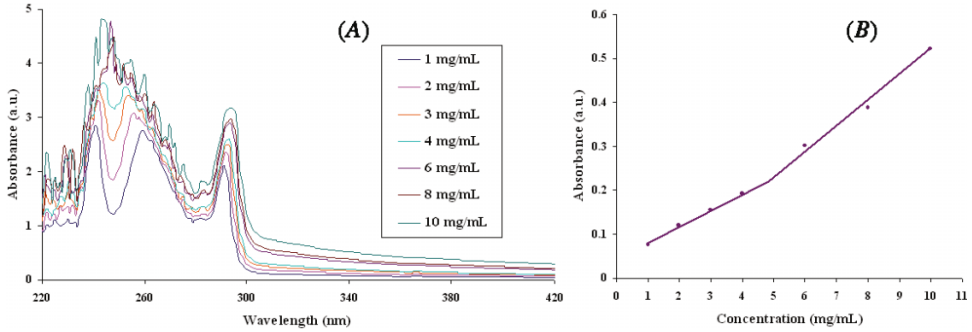

^{1}H and ^{13}C{^{1}H} NMR, matrix-assisted laser desorption/ionization time of flight (MALDI-TOF), and FT-IR spectroscopies, and elemental analyses. These data confirmed the identity of the dendrimers as shown in Scheme **1**.

Self-assembly of dendrimers via intermolecular interactions between peripheral groups is a topic of current interest (7, 8), and we have also investigated the aggregation behaviour of globular DHBA based dendrimers in solution and at interfaces (4). We were intrigued by the self-assembly behaviour of dendrimers in which the linear core as well as the evolving shape of the dendrimers could influence their association. In addition, dendrimers **1**–**4** contain peripheral hydroxyl groups that increase in number exponentially from 4 to 32, and are expected to contribute to enhanced interdendrimer interactions as the generation number increases.

The aggregation behaviour of dendrimers was first investigated using UV–vis spectroscopy at concentrations of 1 to 10 mg/mL in THF. The dendrimers generally depicted three peaks around 240, 260, and 290 nm at 1 mg/mL (Fig. 1*A*), which become broad as the concentrations were increased and the solutions become turbid. The *cac* for each generation was calculated by plotting the intensity of scattered light at a given wavelength against concentration (Fig. 1*B*), and it was found to be 4.9 mg/mL for dendrimers **1**–**3**. The latter is much higher than the globular DHBA based dendrimers of generations 1-3, which was calculated to be 3.7 mg/mL (4g). This suggests that the more open structure of dendrimers, constructed around the linear core, allows more freedom for these molecules. In addition, the central core in these open structures might participate in packing via π–π interactions, and these competing interactions might create an association–dissociation equilibrium which will delay aggregation.

The dendrimer **4** showed a *cac* of 4.1 mg/mL, which was quite comparable to the DHBA based dendrimers, suggesting clearly that the structure was becoming more globular at generation 4. The aggregation of dendrimers through participation of terminal OH groups in hydrogen bonding was also confirmed by FT-IR that showed a broad peak at approximately 3300 cm^{-1} for the terminal OH groups. The latter clearly suggested that terminal OH groups in these dendrimers are strongly hydrogen-bonded at concentrations above *cac*; below this concentration, a peak at around 3500 cm^{-1} is commonly observed, which is indicative of the absence of hydrogen bonds.

Transmission electron microscopy is a useful technique for examining the self-assembly of macromolecules, and can provide essential information related to the morphology of the resulting aggregates (9). We first studied the aggregation behaviour of dendrimers **1**–**4** in THF at concentrations of 4 and 8 mg/mL (concentrations below and above *cac*). At 4 mg/mL, a general globular morphology for the aggregates (Fig. 2) was observed for dendrimers **1**–**4**. The particle size distribution in these aggregates showed that, whereas the size distribution for dendrimer **1** aggregates was found to range between 30 and 135 nm (Fig. 2*A*), dumbbell dendrimers **2**–**4** formed mostly small aggregates of 5 to 25 nm in size, below *cac* (Figs. 2*B*–2*D*). The largest aggregates for those from generation 4, for example, were 55 nm in size. This type of behavior has also been observed earlier (10), and can be explained by considering that, generally, dendrimers of lower generations have a more open structure. This facilitates their interaction with other dendrimers.

When the concentration was increased to 8 mg/mL in THF, it was observed that the globular shape of dumbbell dendrimers **1**–**4** was generally retained. However, there were quite significant differences in particle size distribution of the aggregates from those at 4 mg/mL. For example, dendrimer **1** formed a larger number of smaller aggregates, in the range of 5 to 15 nm in size (Fig. 3). This can be explained by considering that at much higher concentrations, large aggregates can collapse, yielding small-size clusters.

We also studied the aggregation of these dendrimers in a more polar solvent at a concentration of 4 mg/mL and found that aggregation behaviour changed significantly with the change in the solvent from THF to water. The dumbbell-shaped dendrimers possess a hydrophobic interior with polar OH groups at the periphery. In lower generations, there may be hydrophobic–hydrophilic repulsion between dendrimers that enhances their coagulation in water. Water will also compete with interdendritic hydrogen bonding, and it is expected that much smaller aggregates will emerge. The transmission electron microscopy (TEM) study confirmed these expectations, and the effects were quite evident especially in generations 1 and 2 of dendrimers **1** and **2**, which seem to avoid any contact with water, and yield random assemblies of various confirmations (Fig. 4). In addition, the size of these aggregate assemblies was much smaller than in THF at 4 mg/mol.

Self-assembly of dendrimers **3** and **4** in water was found to be quite different from that of first and second generation dendrimers. It suggested that small aggregates of 5 to 25 nm are first formed, which then assemble into larger clusters of 55 to 75 nm size (Fig. 4*D*). This is in agreement with the ob-

© 2008 NRC Canada

Fig. 2. Transmission electron micrographs and particle-size distributions of dendrimers (*A*) **1**, (*B*) **2**, (*C*) **3**, and (*D*) **4** in THF at 4 mg/mL

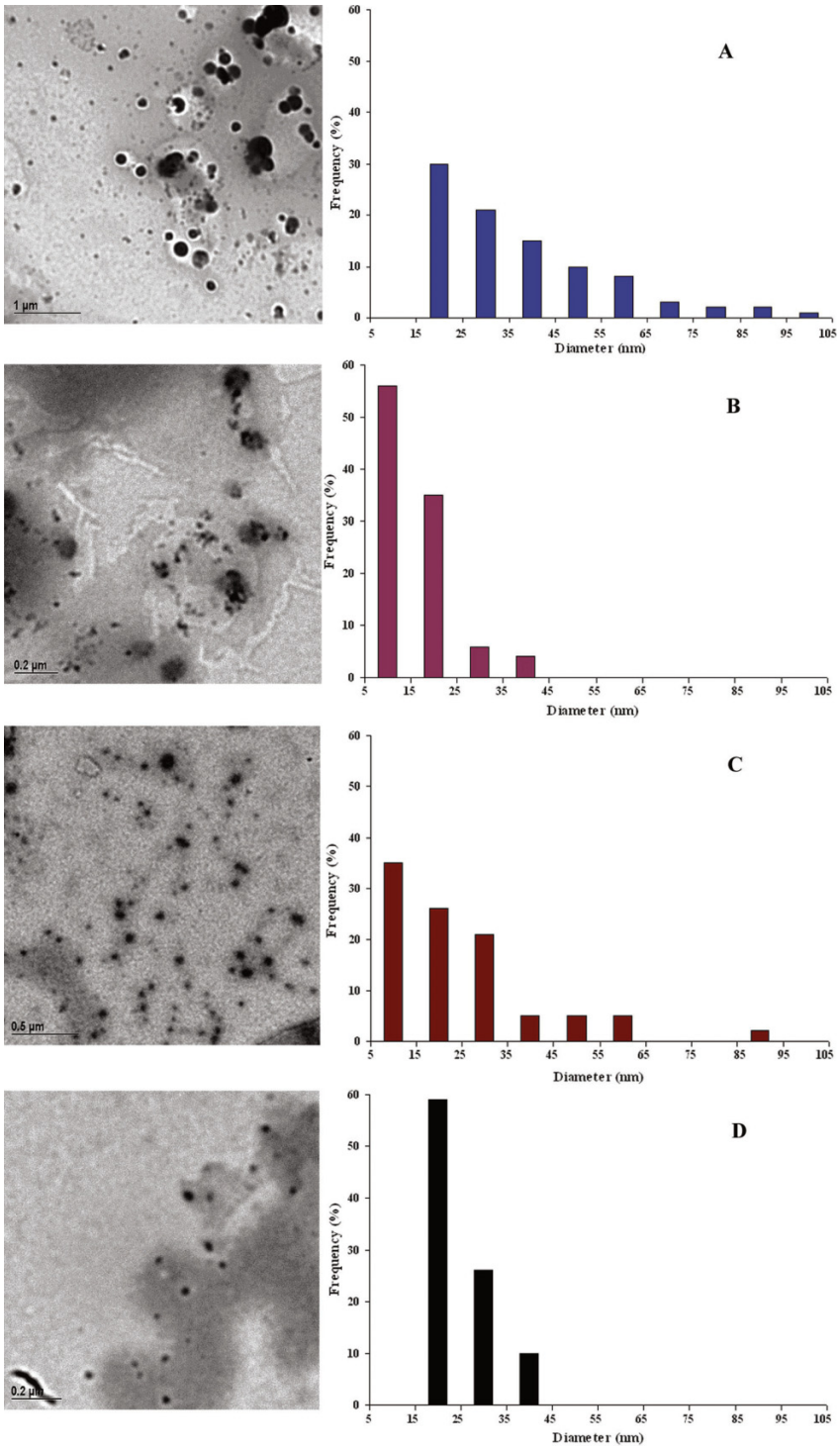

servation that generation 3 and 4 dendrimers will start to adopt a more globular structure, and there will be much less contact of the hydrophobic interior with hydrophilic exterior (water), thereby reducing repulsion.

Conclusions

Symmetric growth of DHBA based dendrons on a linear core has been successfully carried out to construct dumbbell-shaped dendrimers of generations 1–4. These dendrimers evolve from a very open structure in lower generations to a more globular architecture in higher generations. Molecular self-assembly of these dendrimers is influenced by their backbone structure, as indicated by much higher critical aggregation concentration for generations 1–3 in THF, compared to that for globular dendrimer counterparts, and for generation 4. The influence of the solvent in their self-assembly was examined using THF and water; in lower generations, the inability

© 2008 NRC Canada

Fig. 3. Transmission electron micrographs and particle-size distributions of dendrimers (*A*) **1**, (*B*) **2**, (*C*) **3**, and (*D*) **4** in THF at 8 mg/mL.

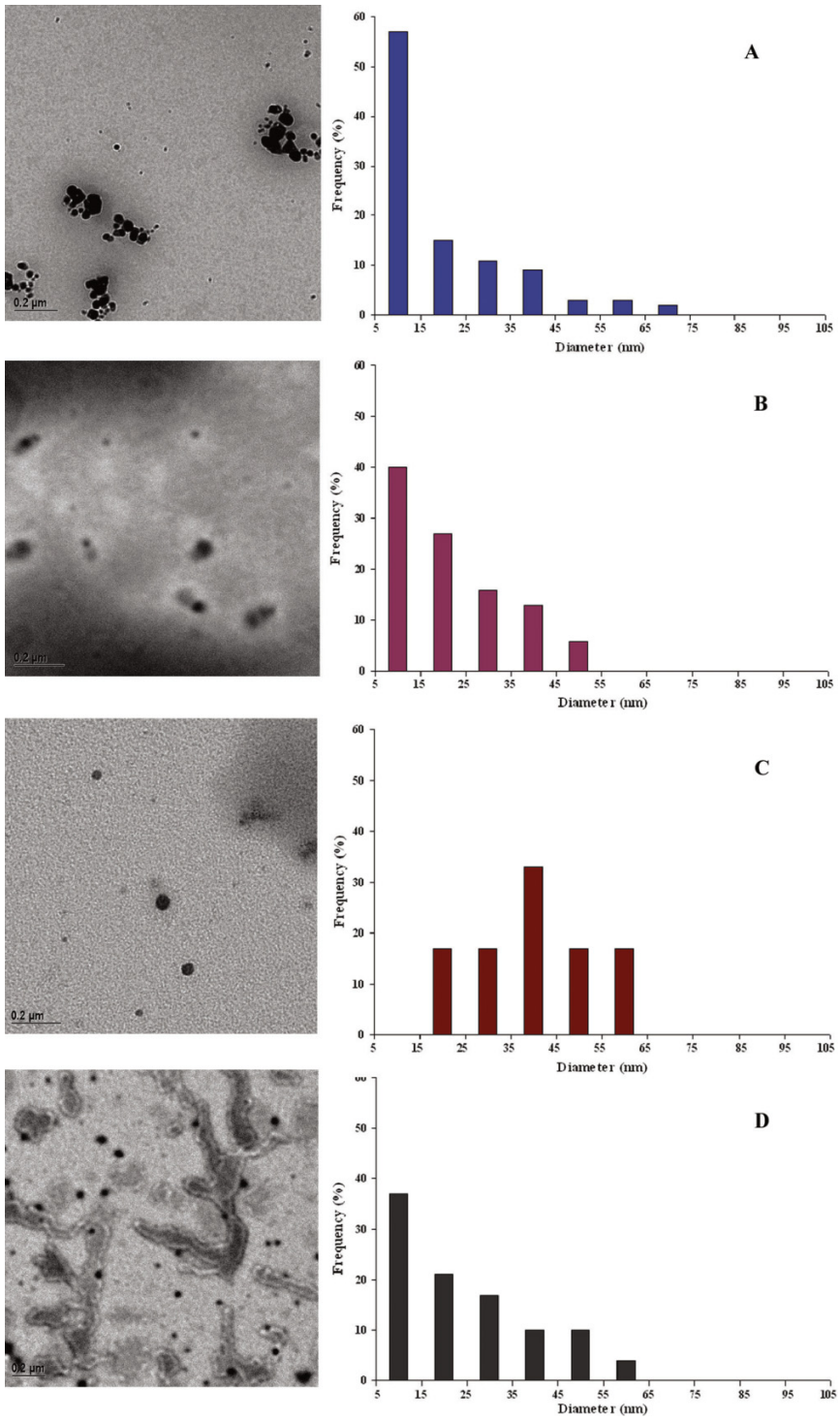

of the more polar solvent to interact with dendrimer backbones leads to aggregates that are formed by minimizing the repulsive forces. In higher generations, the major interaction of the solvent with the dendrimer is at the periphery which has a higher concentration of polar OH groups, and it does not interfere significantly with their ability to self-associate. The influence of the solvent in controlling morphology and sizes of dendrimer aggregates is of interest, as it allows one to tailor their properties for molecular encapsulation and release.

Experimental

Materials and Measurements

2-butyne-1,4-diol (Sigma-Aldrich), 3,5-dihydroxybenzyl alcohol (Sigma-Aldrich), and bis(dimethylamino)dimethylsilane (Gelest) were used as received. All manipulations were performed under a nitrogen atmosphere using either standard Schlenk line techniques or an Innovative Technology (Braun) Labmaster MB-150-M dry box. All solvents were stored un-

© 2008 NRC Canada

Fig. 4. Transmission electron micrographs and particle-size distributions of dendrimers (*A*) **1**, (*B*) **2**, (*C*) **3**, and (*D*) **4** in H_2O at 4 mg/mL.

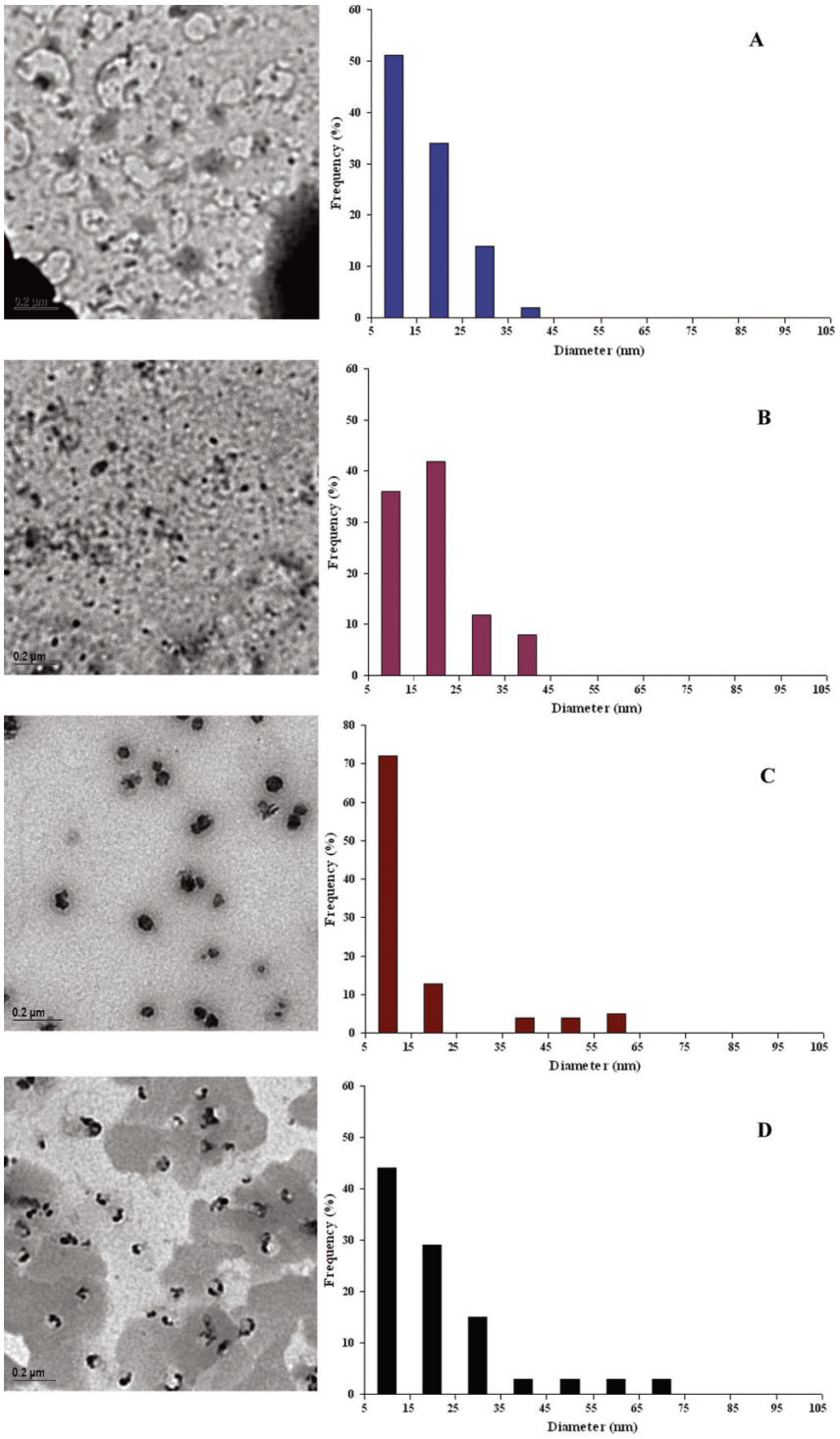

der nitrogen and used after distillation over sodium–benzophenone. NMR spectra were measured on a 270 MHz JEOL spectrometer at ambient temperature. The samples were prepared inside the dry box using deuterated solvents (Cambridge Isotope laboratories, Inc.), and the chemical shifts in ppm are reported relative to tetramethylsilane as an internal standard for ^{1}H and ^{13}C spectra. Mass spectra were obtained on a Hewlett Packard 5973 mass spectrometer and MALDI-TOF spectra on a Kratos Kompact Maldi 3.v.4.0.0 spectrometer using LiBr–dithranol as the matrix. Elemental analyses were performed by Laboratoire d'Analyse Elementaire de l'Université de Montréal. Infrared spectra were measured on a Bruker IFS-48 Fourier transform infrared spectrometer using a standard resolution of 4 cm^{-1} for transmission. UV–vis spectra were recorded in water on a Hewlett Packard 8453 with a resolution of 2 nm. TEM measurements were carried out on a JEOL 2000FX microscope operating at an acceleration voltage of 80 kV.

© 2008 NRC Canada

First generation dendrimer (1)

A solution of 2-butyne-1,4-diol (0.200 g, 2.32 mmol) dissolved in 5 mL of dry THF was added dropwise to a solution of 2 equiv. of bis(dimethylamino)dimethylsilane (0.852 mL, 4.65 mmol) in 5 mL of dry THF cooled to 0°C. Stirring at ice bath temperature was maintained for an additional 6 h, and the resulting solution was subsequently warmed to room temperature. The solution was then added dropwise to a solution of 2 equiv. of DHBA (0.651 g, 4.65 mmol) in 10 ml of dry THF. The resulting solution was stirred overnight, and the THF was then removed under vacuum to afford a sticky gel. D_2O (2–3 mL) was added to the gel and was stirred for 5–10 minutes. The solution was filtered and the D_2O was then removed under vacuum to afford a light pink powder (778 mg, 70%). ^{1}H NMR (270 MHz, D_2O-d_2, ppm) δ 0.05 (s, 12H, OSiMe_2O), 4.11 (s, 4H, OCH_2C), 4.36 (s, 4H, C_6H_3-CH_2O), 6.18 (s, 2H, C_6H_2 para), 6.30 (t, 4H, C_6H_2 ortho).^{13}C NMR (68 MHz, D_2O-d_2) δ –1.7, –0.7 (SiCH_3), 49.7 (OCH_2C), 63.6 (C_6H_3-CH_2), 83.6 (OCH$_2C$), 101.9, 106.4, 143.8, 157.1 (C_6H_3). FT-IR (KBr, cm^{-1}): 3243 (ν_{OH}), 2896 ($\nu_{C\text{-}H\ arom.}$), 1242 ($\delta_{Si\text{-}CH3}$), 1041 ($\nu_{Si\text{-}O}$). EI-MS *m*/*z*: 479.1 (expected: 478.6). Anal. calcd. for $C_{22}H_{30}O_8Si_2$: C 55.21, H 6.32; found: C 55.36, H 5.96.

Second generation dendrimer (2)

A solution of 1 equiv. of 2-butyne-1,4-diol (50 mg, 0.581 mmol) in 10 mL of THF was added to a solution of 2 equiv. of bis(dimethylamino)dimethylsilane (0.213 mL, 1.161 mmol) in 5 mL of THF, and stirred for 6 h at ice bath temperature. The resulting solution was added dropwise over a period of 1h to 2 equiv. of DHBA (163 mg, 1.161 mmol) dissolved in 10 mL of THF. After stirring overnight, the mixture was then added dropwise (1h) to a solution of 4 equiv. of bis(dimethylamino)dimethylsilane (0.426 mL, 2.323 mmol) in 5 mL of THF. The resulting solution was added dropwise (1h) to 4 equiv. of DHBA (325 mg, 2.323 mmol) dissolved in 15 mL of THF, and stirred overnight. The removal of the solvent under vacuum afforded a sticky gel. D_2O (4–5 mL) was added to the gel and stirred for 5–10 minutes. The solution was filtered and the D_2O was then removed under vacuum to afford a light pink powder (455 mg, 62%). ^{1}H NMR (270 MHz, D_2O-d_2) δ 0.05 (m, 36H, OSiMe_2O), 4.15 (s, 4H, OCH_2C), 4.36 (s, 12H, C_6H_3-CH_2O), 6.18 (s, 6H, C_6H para), 6.30 (m, 12H, C_6H_2 ortho). ^{13}C NMR (68 MHz, D_2O-d_2, ppm) δ –1.7, –0.1 (SiCH_3), 50.3 (OCH_2C), 64.3 (C_6H_3-CH_2), 83.6 (OCH$_2C$), 102.6, 107.0, 144.5, 157.8 (C_6H_3). FT-IR (KBr, cm^{-1}): 3378 (ν_{OH}), 2962 ($\nu_{C\text{-}H\ arom.}$), 1262 ($\delta_{Si\text{-}CH3}$), 1084, 890 ($\nu_{Si\text{-}O}$). MALDI-TOF *m*/*z*: 1261.3 (expected 1263.7, including *m*/*z* Li$^+$). Anal. calcd. for $C_{58}H_{78}O_{20}Si_6$: C 55.11, H 6.22; found: C 55.95, H 6.26.

Third generation dendrimer (3)

A similar procedure as described above for the second generation was used to prepare the third generation. A solution of 1 equiv. of 2-butyne-1,4-diol (20 mg, 0.232 mmol) in 10 mL of THF was added to a solution 2 equiv. of bis(dimethylamino)dimethylsilane (0.085 mL, 0.465 mmol) in 5 ml THF, and stirred for 6 h at ice bath temperature. The mixture was added dropwise (1h) to a solution of 2 equiv. of DHBA (65.1 mg, 0.465 mmol) in 10 mL of THF, and stirred overnight at room temperature. It was then added dropwise (1h) to a solution of 4 equiv. of bis(dimethylamino)dimethylsilane (0.170 mL, 0.929 mmol) in 5 mL of THF, and stirred overnight at room temperature. The solution was added dropwise (1h) to a solution of 4 equiv. of DHBA (130 mg, 0.929 mmol) in 10 mL of THF, and after stirring overnight, it was added dropwise (1h) to a solution of 8 equiv. of bis(dimethylamino)dimethylsilane (0.341 mL, 1.858 mmol) in 5 mL of THF, and stirred for 14 h. Finally it was added to a solution of 8 equiv. of DHBA (260 mg, 1.858 mmol) in 15 mL of THF, and stirred overnight. THF was removed under vacuum to afford a gel. D_2O (4–5 mL) was added to the gel and stirred for 5–10 minutes. The solution was filtered and the D_2O was then removed under vacuum to afford a light pink powder (402 mg, 61%). ^{1}H NMR (270 MHz, D_2O-d_2) δ 0.01, 0.05 (m, 84H, OSiMe_2O), 4.10 (s, 4H, OCH_2C), 4.34 (s, 28H, C_6H_3-CH_2O), 6.18 (s, 14H, C_6H para), 6.30 (m, 28H, C_6H_2 ortho). ^{13}C NMR (68 MHz, D_2O-d_2, ppm) δ –1.7, –0.77 (SiCH_3), 49.6 (OCH_2C), 63.6 (C_6H_3-CH_2), 83.5 (OCH$_2C$), 101.8, 106.3, 143.7, 157.0 (C_6H_3). FT-IR (KBr, cm^{-1}): 3378 (ν_{OH}), 2892 ($\nu_{C\text{-}H\ arom.}$), 1154 ($\delta_{Si\text{-}CH3}$), 1042, 954 ($\nu_{Si\text{-}O}$). MALDI-TOF *m*/*z*: 2837.9 (expected 2833.9, including *m*/*z* Li$^+$). Anal. calcd. for $C_{130}H_{174}O_{44}Si_{14}$: C 55.10, H 6.19; found: C 55.12, H 6.38.

Fourth generation dendrimer (4)

A solution of 1 equiv. of 2-butyne-1,4-diol (20 mg, 0.232 mmol) in 10 mL of THF, was added to a solution 2 equiv. of bis(dimethylamino)dimethylsilane (0.085 mL, 0.465 mmol) in 5 ml THF, and stirred for 6 h at ice bath temperature. The mixture was added dropwise (1h) to a solution of 2 equiv. of DHBA (65.1 mg, 0.465 mmol) in 10 mL of THF, and stirred overnight at room temperature. It was then added dropwise (1h) to a solution of 4 equiv. of bis(dimethylamino)dimethylsilane (0.170 mL, 0.929 mmol) in 5 mL of THF, and stirred overnight at room temperature. The latter was added dropwise (1h) to a solution of 4 equiv. of DHBA (130 mg, 0.929 mmol) in 10 mL of THF, and after stirring overnight, it was added dropwise (1h) to a solution of 8 equiv. of bis(dimethylamino)dimethylsilane (0.341 mL, 1.858 mmol) in 5 mL of THF, and stirred for 14 h. Then it was added to a solution of 8 equiv. of DHBA (260 mg, 1.858 mmol) in 15 mL of THF, and stirred overnight. The resulting solution was added dropwise to 16 equiv. of bis(dimethylamino)dimethylsilane (0.681 mL, 3.717 mmol) in 10 mL of THF. Stirring was continued overnight at room temperature. The resulting solution was then added dropwise (1h) to a solution of 16 equiv. of DHBA (521 mg, 3.717 mmol) in 10 mL of THF. The reaction mixture was stirred for 36 h at room temperature. Solvent removal under vacuum afforded a sticky gel. D_2O (4–5 mL) was added to the gel and was stirred for 5–10 minutes. The solution was filtered and D_2O was then removed under vacuum to afford a pink powder (833 mg, 60%). ^{1}H NMR (270MHz, D_2O-d_2) δ –0.06, 0.00, 0.22 (m, 180H, OSiMe_2O), 4.10 (s, 4H, OCH_2C), 4.31 (s, 60H, C_6H_3-CH_2O), 6.15 (s, 30H, C_6H para), 6.25 (m, 60H, C_6H_2 ortho). ^{13}C NMR (68 MHz, D_2O-d_2, ppm) δ –1.54, –1.033, 0.40 (SiCH_3), 49.5 (OCH_2C), 63.9 (C_6H_3-CH_2), 83.7 (OCH$_2C$), 100.5, 105.9, 143.1, 158.8 (C_6H_3). FT-IR (KBr, cm^{-1}): 3379 (ν_{OH}), 2889 ($\nu_{C\text{-}H\ arom.}$), 1263 ($\delta_{Si\text{-}CH3}$), 1042, 970 ($\nu_{Si\text{-}O}$). MALDI-TOF *m*/*z*: 5978.8

© 2008 NRC Canada

(expected: 5974.3, including *m/z* Li^+). Anal. calcd. for $C_{274}H_{366}O_{92}Si_{30}$: C 55.14, H 6.18; found: C 55.26, H 6.31.

Acknowledgments

We would like to thank the Natural Sciences and Engineering Research Council of Canada (NSERC) and the Center for Self-Assembled Chemical Structures (FQRNT, Quebec, Canada) for financial assistance.

References

1. (*a*) P. Antoni, D. Nystrom, C. J. Hawker, A. Hulta, and M. Malkoch. Chem. Comm. 2249 (2007); (*b*) J.K. Vohsa and B. D. Fahlman. New J. Chem. **31**, 1041 (2007); (*c*) M. Gingras, J-M. Raimundo and Y. M. Chabre. Angew. Chem. Int. Ed. **46**, 1010 (2007); (*d*) B. Helms and E. W. Meijer. Science, **313**, 929 (2006); (*e*) G. R. Newkome, C. N. Moorefield, and F. Vögtle. Dendrimers and Dendrons: Concepts, Syntheses and Applications. Wiley-VCH, Weinheim. 2002; (*f*) S. M. Grayson, J. M. J. Fréchet. Chem. Rev. **101**, 3819 (2001); (*g*) D.-L. Jiang and T. Aida. Nature, **388**, 454 (1997); (*h*) Y. Sayed-Sweet, D. M. Hedstrand, R. Spinder, and D. A. Tomalia. J. Mater. Chem. **7**, 1199 (1997).
2. (*a*) Dendrimer and Other Dendritic Polymers. *Edited by* J. M. J. Fréchet and D. A. Tomalia. John Wiley & Sons, West Sussex, UK. 2001; (*b*) D. K. Smith. Chem. Commun. (Cambridge, UK), 34 (2006); (*c*) D. Astruc and F. Chardac. Chem. Rev. **101**, 2991 (2001); (*d*) Y. Ishida, M. Jikei, and M. Kakimoto. Macromolecules, **33**, 3202 (2000).
3. I. Washio, Y. Shibasaki, U. Mitsuru. Macromolecules, **38**, 2237 (2005).
4. (*a*) A. A. Czerniewski, X. J. Liu, O. Rolland, R. Hourani, M. Four, and A.K. Kakkar. J. Mater. Chem. **17**, 2737 (2007); (*b*) R. Hourani, A.K. Kakkar, and M.A. Whitehead. J. Mol.Struct: THEOCHEM, **807**, 101 (2007); (*c*) T. Vassilieff, F. Quist, and A.K. Kakkar. J. Colloid Interface Sci. **297**, 455 (2006); (*d*) R. Hourani, A.K. Kakkar, and M.A. Whitehead. J. Mater. Chem. **15**, 2106 (2005); (*e*) O. Bourrier, J. Butlin, R. Hourani, and A.K. Kakkar. Inorg. Chim. Acta, **357**, 3836 (2004); (*f*) O. Bourrier and A.K. Kakkar. Macromolec. Symp. **209**, 97 (2004); (*g*) O. Bourrier and A.K. Kakkar. J. Mater. Chem. **13**, 1306 (2003); (*h*) A.K. Kakkar. Macromolec. Symp. **196**, 145 (2003); (*i*) M. Dasgupta, M.B. Peori, and A.K. Kakkar. Coord. Chem. Rev. **233–234**, 223 (2002); (*j*) M.B. Peori and A.K. Kakkar. Organometallics, **21**, 3860 (2002); (*k*) M.G.L. Petrucci, V. Guillemette, M. Dasgupta, and A.K. Kakkar. J. Am. Chem. Soc. **121**, 1968 (1999).
5. (*a*) K. Jones and M.F. Lappert. J. Organomet. Chem. **3**, 295 (1965); (*b*) K. Jones and M.F. Lappert. J. Chem. Soc. 1944 (1965); (*c*) A.K. Sawyer. Organotin Compounds, Vol 2. New York, NY. 1971; (*d*) A.G. Davies. Organotin Chemistry, 2nd Ed. Wiley-VCH, Weinheim. 2004.
6. (*a*) Z. Ge, D. Chen, J. Zhang, J. Rao, J. Yin, D. Wang, X. Wan, W. Shi, and S. Liu. J. Polym. Sci. Part A: Polymer Chem. **45**, 1432 (2007); (*b*) B. Huang, A.R. Hirst, D.K. Smith, V. Castelletto, and I.W. Hamley. J. Am. Chem. Soc. **127**, 7130 (2005); (*b*) X.-D. Tang, Q.-Z. Zhang, A.-X. Li, X.-H. Fan, X.-F. Chen, and Q.-F. Zhou. Chin. J. Chem. **23**, 11 (2005); (*c*) M. Lee, Y.-S. Jeong, B.-K. Cho, N.-K. Oh, and W.-C. Zin. Chem. Eur. J. **8**, 876 (2002); (*d*) G. R. Newkome, X. Lin, C. Yaxiong, and G.H. Escamilla. J. Org. Chem. **58**, 3123 (1993).
7. (*a*) A.W. Bosman, H.M. Janssen and E.W. Meijer. Chem. Rev. **99**, 1665 (1999); (*b*) M.J. Laufersweiler, J.M. Rhode, J.-L. Chaumette, D. Sarazin, and J.R. Parquette. J. Org. Chem. **66**, 6440 (2001); (*c*) V. Percec, C.-H. Ahn, T.K. Bera, G. Ungar, and D.J.P. Yeardley. Chem. Eur. J. **5**, 1070 (1999); (*d*) R.-M. Sebastian, G. Margo, A.-M. Caminade, and J.-P. Majoral, Tetrahedron, **56**, 6269 (2000); (*e*) M. Brettreich, S. Burghardt, C. Bottcher, T.S. Bayerl, and A. Hirsch. Angew. Chem. Int. Ed. **39**, 1845 (2000).
8. (*a*) K. Tanaka, S. Dai, and T. Kajiyama. Langmuir, **19**, 1196 (2003); (*b*) V. V. Tsukruk, H. Shulha, and X. Zhai. Appl. Phys. Lett. **82**, 907 (2003); (*c*) M. Sano, J. Okamura, A. Ikeda, and S. Shinkai. Langmuir, **17**, 1807 (2001); (*d*) A. P. H. J. Schenning, C. Elissen-Roman, J.-W. Weener, M. W. P. L. Baars, S. J. van der Gaast, and E. W. Meijer. J. Am. Chem. Soc. **120**, 8199 (1998); (*e*) M. J. Laufersweiler, J. M. Rohde, J. L. Chaumette, D. Sarazin, and J. R. Parquette, J. Org. Chem. **66**, 6440 (2001); (*f*) W. Zhang and E. E. Simanek. Tetrahedron Lett. **42**, 5355 (2001).
9. J. C. H. Spence. Mater. Sci. Eng. R. **26**, 1 (1999).
10. (*a*) K. Esumi, A. Suzuki, A. Yamahira, and K. Torigoe. Langmuir, **16**, 2604 (2000); (*b*) K. Esumi and K. Torigoe. Prog. Colloid Polym. Sci. **80**, 117 (2001); (*c*) C.Y. Bao, M. Jin, R. Lu, T.R. Zhang, and Y.Y. Zhao. Mater. Chem. Phys. **81**, 160 (2003); (*d*) F. Tarazona-Vasquez and P.B. Balbuena. J. Phys. Chem. B, **108**, 1599 (2004); D.-M. Xu, K.-D. Zhang, and C.-L. Zhu. J. Appl. Polym. Sci. **104**, 422 (2007).

© 2008 NRC Canada

REVIEW / SYNTHÈSE

Biological production of functional chemicals from renewable resources[1]

Yutaka Tokiwa and Buenaventurada P. Calabia

Abstract: The development and implementation of renewable feedstocks for the production of multifunctional chemicals has received attention from the food and pharmaceutical industries and also as potential raw materials for the manufacture of biodegradable polymers. A major shift towards renewable resources, however, requires new ways to optimize and evaluate industrial processes. There are several possibilities to replace chemical techniques with biological methods based on renewable resources. This review discusses some examples of process development in which a biotechnological route might be favorable leading to industrial realization. Herein are described the production of biomaterials that can be used as monomers in plastics, such as lactic acid for polylactide (PLA), (*R*)-3-hydroxybutyric acid (*R*-3HB) for poly[(*R*)-3-hydroxybutyrate] (PHB), and succinic acid for poly(butylene succinate) (PBS). Moreover, several species of microorganisms that produce significant quantities of these functional chemicals under specific cultivation conditions from biomass-derived carbohydrates are also reviewed.

Key words: functional chemicals, renewable resources, lactic acid, (*R*)-3-hydroxybutyric acid, succinic acid.

Résumé : Le développement et l'implantation de ressources renouvelables pour la production de produits chimiques multifonctionnels a reçu beaucoup d'attention de la part des industries pharmaceutiques et alimentaires, mais ces ressources présentent aussi de l'intérêt comme matières premières potentielles pour la fabrication de polymères biodégradables. Un déplacement important vers les ressources renouvelables nécessite toutefois de nouvelles façons d'optimiser et d'évaluer les processus industriels. Il y a plusieurs possibilités pour remplacer les techniques chimiques avec des méthodes biologiques assises sur des ressources renouvelables. Cette revue discute de quelques exemples de développement de procédés dans lesquels la voie biotechnologique pourrait être favorable et conduire éventuellement à une réalisation industrielle. On décrit donc la production de matériaux qui peuvent être utilisés comme monomères dans les plastiques, tels l'acide lactique pour le polylactide (PLA), l'acide (*R*)-3-hydroxybutyrique (R-3HB) pour celle du poly[(*R*)-3-hydroxybutyrate] (PHB) et l'acide succinique pour la production du poly(butylènesuccinate) (PBS). De plus, on passe en revue diverses espèces de microorganismes qui produisent des quantités significatives des ces produits chimiques multifonctionnels dans des conditions de cultures spécifiques à partir de carbohydrates dérivés de la biomasse.

Mots-clés : produits chimiques multifonctionnels, ressources renouvelables, acide lactique, acide (*R*)-3-hydroxybutyrique, acide succinique.

[Traduit par la Rédaction]

Introduction

Because of the increasing world demand for energy, diminishing fossil resources, and dramatic increases in the price of petroleum, chemicals from renewable feedstocks are becoming increasingly viable and important alternative resources. Moreover, the biological conversion of biomass into commodity and specialty chemicals have gained interest because these renewable resources do not produce any net contribution of carbon dioxide to the atmosphere, thus re-

Received 3 December 2007. Accepted 3 March 2008. Published on the NRC Research Press Web site at canjchem.nrc.ca on 29 April 2008.

This paper is dedicated to Robert H. Marchessault in recognition of his many contributions to polysaccharide and biopolymer chemistry.

Y. Tokiwa[2] and B.P. Calabia. National Institute of Advanced Industrial Science and Technology (AIST), Tsukuba Central 6, Higashi, Tsukuba, Ibaraki 305-8566, Japan.

[1]This article is part of a Special Issue dedicated to Professor R. Marchessault.
[2]Corresponding author (e-mail: y.tokiwa@aist.go.jp).

 doi:10.1139/V08-046 © 2008 NRC Canada

Fig. 1. Schematic representation for the production of functional materials from food and nonfood renewable resources.

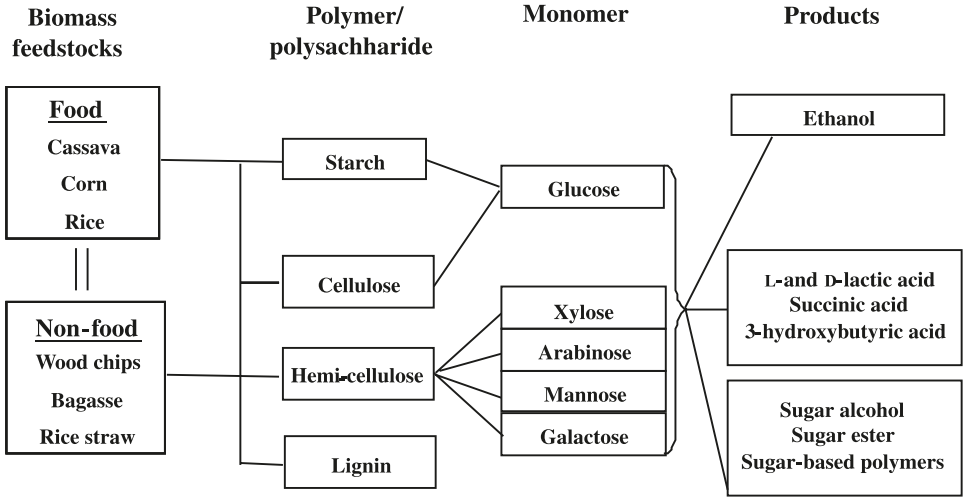

ducing green house gas emissions. A wide range of functional materials derived from renewable resources are being developed as raw materials for the production of biodegradable plastics. As shown in Fig. 1, there are different food and nonfood agricultural products that can be used as potential substrates for the production of biochemicals, biomaterials, or biofuels. These agricultural products are first converted into sugar, which can be readily fermented by microorganisms into the desired products such as ethanol, L- and D-lactic acid, succinic acid, and 3-hydroxybutyric acid. Different strategies must be developed to achieve efficient production of these chemicals to compete with petroleum-based materials. One way to achieve this is to use inexpensive and renewable raw materials for the production of these chemicals. The microorganisms should be able to utilize a wide variety of sugar feedstocks (glucose, sucrose, fructose, xylose, mannose, etc.) with high yield and improved fermentation yield for downstream processing of the products.

Fermentative production of lactic acid

Lactic acid is the most widely occurring hydroxycarboxylic acid that is usually used in the food and pharmaceutical industries. Recently, the production of lactic acid has grown considerably mainly because of its new application as a raw material for biodegradable plastics. Lactic acid can be produced either by chemical process or by microbial fermentation. The most commonly used method in chemical synthesis is based on the hydrolysis of lactonitriles derived from acetaldehyde and hydrogen cyanide. However, this technique is expensive and results in the production of racemic DL-lactic acid, while microbial fermentation produces optically pure D- or L-lactic acid depending on the microorganism. The optical purity of lactic acid is necessary to the physical properties of polylactide (PLA), because when PLA is produced from pure L-isomer or D-isomer, the polymer is crystalline and more stable than the amorphous polymer obtained from a racemic mixture (1).

Lactic acid bacteria (LAB) and some filamentous fungi are the major microbial sources of lactic acid (2). LAB are classified into homofermentative (producing a single product, i.e., lactic acid) and heterofermentative (producing other products such as ethanol, acetic or formic acid, and carbon dioxide along with lactic acid). Some of the major homofermentative LAB are: *Lactobacillus, Carnobacterium*, *Streptococcus*, *Enterococcus*, *Lactococcus*, *Vagococcus*, *Brochothrix*, *Pediococcus*, *Tetragenococcus*, and *Weissella* (3). *Lactobacillus casei*, *L. rhamnosus*, and *Rhizopuz* sp. produce high concentrations of L-lactic acid (1, 4). L. rhamnosus and *Rhizopus* sp. (*R. oryzae* and *R. arrhizus*) are widely accepted producers of lactic acid with high optical purity, however, these microorganisms are categorized as level 2 pathogens. To date, studies on D-lactic acid fermentation are very few and a small number of LAB can produce D-lactic acid with high optical purity. As shown in Table 1, a wild strain of *Lactobacillus delbrueckii* (5, 6, 7) and *L. coryniformis* (8) ferment sugars mainly to D-lactic acid, and among the substrates used, sugarcane juice gave the highest yield. Several microorganisms have been engineered to produce high optical purity D-lactic acid, however the yield of the metabolically engineered microbes are comparable to wild strains (9, 10, 11, 12). It should be noted that lactic acid production should be evaluated in terms of lactic acid concentration (g/L) and not in terms of productivity. High concentration of lactic acid is preferred to minimize the cost of downstream processing.

The most widely used substrates for the production of lactic acid are starch and sugars. When starch is used, it is commonly hydrolyzed either by chemicals or enzymes prior to fermentation. However, there are several LAB that can directly ferment starch into L-lactic acid, thus eliminating the two–step process of saccharification prior to microbial fermentation to make it economical. For instance, *Lactobacillus amylovorus* can directly produce 92.5 g/L of L-lactic acid from 120 g/L of raw starch in 39 h (13). Yumoto and Ikeda (14) reported that 30 and 53.4 g/L of L-lactic acid were obtained from 50 and 100 g of unhydrolyzed soluble starch, respectively, using *Lactobacillus amylophilus*. Moreover, *Streptococcus bovis* 148, which secretes α-amylase, can degrade raw starch and convert it into high optical purity L-lactic acid (15).

© 2008 NRC Canada

Table 1. Comparative evaluation of D-lactic acid production by wild-type and metabolically engineered microorganisms.

Strains	Carbon source	Fermentation mode	Culture time (h)	D-Lactic acid concentration (g/L)	Optical purity (%)	Yield (D-lactic acid) (%)	Productivity (g/L/h)	Ref. No.
Lactobacillus delbrueckii (JCM 1148)	Sugarcane molasses	Batch	72	104	97.2	90	1.48	5
	Sugar cane juice	Batch	72	118	98.3	95	1.66	5
	Sugar beet juice	Batch	72	82.0	97.6	88	1.16	5
L. delbrueckii subsp. *delbrueckii* (IFO 3202)	Defatted rice bran	SSF	36	28.0	95.0	78	0.77	6
L. delbrueckii (LD 0028)	Rice starch	Batch	96	62.6	98.4	70	0.65	7
L. corynitormis subsp. *torquens*	Cellulose	SSF	48	24.0	100	89	0.5	8
E. coli RR1 (*pta, ppc*)	Glucose	Fed-batch	60	62.2	NA	72	1.03	9
E. coli W3110 (*pflB, frdBC, adhE*)	Glucose	Batch	24	50.8	> 99.8	95	2.11	10
E.coli W3110 (*pflB,frdBC,adhE,ackA*)	Sucrose	Batch	36	51.2	> 99.8	97	1.42	11
E. coli (*CSCR, CSCA, CSCKB*)	Molasses	Batch	96	48.7	> 99.8	90	0.50	12
Saccharomyces cerevisiae OC2 (*pdc*1::*Ppdc* l-D-*LDH*(*L. mesenteroides* D-LDH)	Glucose	Batch	72	61.5	99.9	53	0.85	12

Note: SSF = Simultaneous saccharification and fermentation, NA = Data not available.

Refined sugar such as glucose or sucrose, although expensive, are frequently used as raw materials for lactic acid production (1). The production costs could be reduced if glucose or sucrose from by-products of sugar manufacture (i.e., molasses) or from sugar crops (sugarcane, sugar beet, sweet sorghum) could be used instead of refined sugars, especially if the microorganisms can directly ferment these substrates into lactic acid without any pre-treatment. Just recently, we reported an efficient production of D-lactic acid with high optical purity of 97%–98% using sugarcane molasses, sugarcane juice, and sugar beet molasses (5). We also investigated the effect of sugarcane juice concentration on the productivity and yield of lactic acid fermentation using a newly isolated *Lactobacillus* sp. strain FCP2. The productivity and yield obtained in 3% (*w*/*v*) sugarcane juice were higher than in 13% (*w*/*v*) because of shorter fermentation time and no residual sugar (16).

In addition to the above mentioned substrates is inulin, a polysaccharide composed of β-(2→1)-linked fructose units and a reserve carbohydrate in the tubers of plants like chicory, yacon, Jerusalem artichoke, or dahlia. These are promising raw materials for lactic acid fermentation, because inulin can be easily extracted from these tubers. Several lactic acid bacteria (LAB) were screened for their ability to ferment inulin into lactic acid. One lactic acid bacterium was selected as giving the highest lactic acid concentration (17). However, further work is still necessary to improve the performance of the strain and to increase lactic acid concentration.

Most of the reports on lactic acid fermentation have examined the response of LAB to acid stress, including the mechanisms on acid tolerance of the microorganisms (18, 19). On the contrary, there are few studies on the stress response of LAB to alkaline environments to date. There are several alkaliphilic LAB that could grow at > pH 9.5. Among these are *Marinilactibacillus piezotolerans* (20), *M. psychrotolerans* (21), *Halolactibacillus halophilus*, *H. miurensis* (22), *Alkalibacterium olivoapovliticus* (23), and *Enterococcus hirae* (formerly *Streptococcus faecalis*) (24). The biochemical properties and characteristics of these LAB have been examined, but to our knowledge no report on lactic acid fermentation using alkaliphilic microorganisms have been published so far. Batch fermentation of lactic acid by *A. psychrotolerans*, using glucose as carbon source, was performed in a 5 L fermentor with a working volume of 2.5 L. Temperature and agitation were maintained at 30 °C and 150 rpm, respectively. The medium composition was the same as described elsewhere (5). The pH was automatically controlled at 10 by the addition of 6 N NaOH. The final lactic acid accumulation reached 21.2 g/L from a total of 30 g/L glucose in 48 h, with a productivity of 0.44 g/L/h (Fig. 2) (25). More studies are necessary to increase lactic acid concentration using alkaliphilic microorganisms. Research on the isolation, screening, and distribution of alkaliphilic and halophilic LAB in different environments is ongoing in our laboratory.

Production of (*R*)-3 hydroxybutyric acid monomer

(*R*)-3 hydroxybutyric acid (*R*-3HB) is a monomer that can be utilized as a chiral building block for the synthesis of fine

© 2008 NRC Canada

Fig 2. Time course for lactic acid fermentation by an alkaliphilic microorganism *Alkalibacterium psychrotolerans*. Optical density (620 nm, □), colony forming unit (CFU, ●), residual glucose (g/L, ■), lactic acid (g/L, ▲).

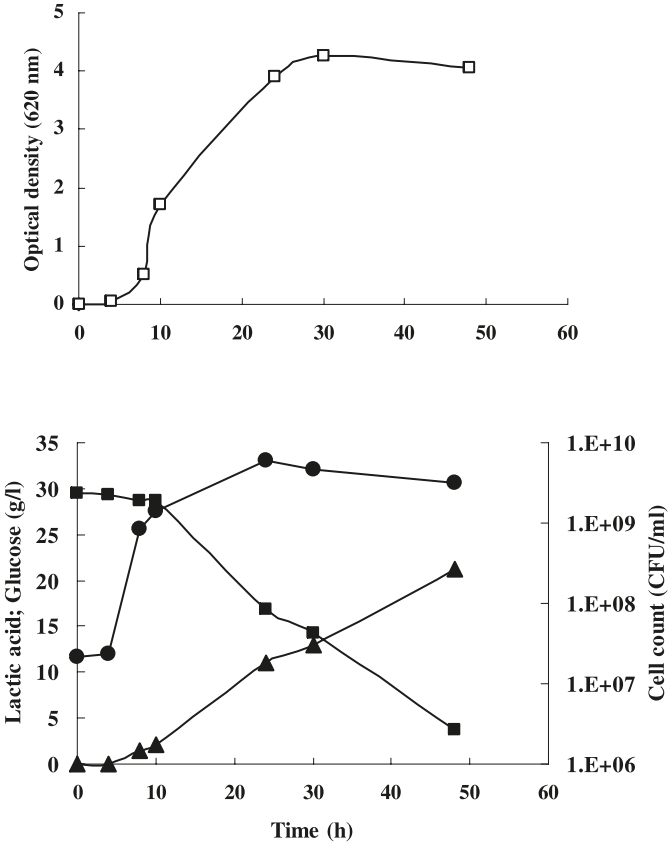

chemicals such as antibiotics, vitamins, aromatics, and pheromones (26, 27, 28). Production of *R*-3HB can be accomplished by chemical synthesis, enzymatic hydrolysis, or by metabolic engineering of strains (29). Although production of *R*-3HB by chemical synthesis is feasible, this method is complicated and expensive for industrial use. Several strategies have been developed to improve the production of *R*-3HB. Lee et al. (30), reported that a high yield of *R*-3HB can be obtained by providing suitable environmental conditions wherein the cells have high activity of intracellular depolymerase and low *R*-3HB dehydrogenase. Moreover, *R*-3HB could be efficiently produced by using metabolically engineered *E. coli* strains harboring a heterologous PHA synthesis and degradation pathway. This method consists of a two plasmid systems, depolymerase gene (high-copy number), and the biosynthesis gene (medium-copy number). *R*-3HB from glucose with high productivity of 9.9 g/L was obtained in 51 h (31). Gao et al. (32) improved the production of *R*-3HB by establishing a new method using the simultaneous expression of genes for β-ketothiolase (*phbA*), acetoacetyl-CoA reductase (*phbB*), phosphor-transbutyrylase (*ptb*), and butyrate kinase (*buk*) in the *E. coli* strain DH5α. Results showed that in shake flasks studies, *E. coli* DH5α that harbored *phbA* and *phbB* genes gave a small amount of *R*-3HB with a concentration of 75 to 400 mg/L. On the other hand, with the addition of *ptb* and *buk* genes the concentration increased to 1.4 g/L. Moreover, the *R*-3HB concentration was increased further to more than 2 g/L when the two plasmids in *E. coli* DH5α contain *phbA* and *phbB* in one plasmid and *ptb* and *buk* in the other. Shiraki et al. (33) reported the use of (*R*)-3-hydroxybutyrate dehydrogenase (BDH) null mutant of *Ralstonia eutropha* and recombinant *E.coli* for the fermentative production of *R*-3HB. They examined the effect of various conditions on the amount of *R*-3HB released into the culture supernatant. The concentration of *R*-3HB was higher in anaerobic (30 mmol/L) than under aerobic (4–10 mmol/L) conditions. The decrease of *R*-3HB in the supernatant under aerobic conditions was presumed to be due to *R*-3HB being metabolized via other metabolic pathways in which BDH does not participate.

Recently, we reported that *R*-3HB could be produced by enzymatic hydrolysis using a thermophilic *Streptomyces* sp. MG. This microorganism could efficiently hydrolyze poly [(*R*)-3-hydroxybutyrate] (PHB) and the main component of the degradation products was *R*-3HB monomer (34). Another alternative method that could be used for the enzymatic synthesis of *R*-3HB is via acetoacetate, wherein *R*-3HB dehydrogenase converts acetoacetate to *R*-3HB in the presence of NADH and H^+ (29).

Ring-opening polymerization (ROP) offers another approach for producing PHB. *R*-3HB can be polymerized via (*R*)-β-butyrolactone to make PHB. In addition to *R*-3HB, other compounds such as lactide, glycolide, caprolactone, and (*R*,*S*)-β-butyrolactone can be co-polymerized with (*R*)-β-butyrolactone for the production of the pure co-polymer of *R*-3HB (Fig. 3). It is expected that using ROP, good properties of synthetic PHB and its co-polyesters (poly[(*R*)-β-butyrolactone-*co*-L-lactide]) could be obtained, such as a high degree of purity and high molecular weight.

Biotechnological production of succinic acid

Succinic acid is a dicarboxylic acid that can be used as a feedstock for the manufacture of various chemicals such as 1,4 butanediol, adipic acid, γ-butyrolactone, tetrahydrofuran, *N*-methylpyrolidone, and linear aliphatic polyesters. To date, most of the commercially available succinic acid has been manufactured by chemical process (35, 36). However, production of succinic acid from petrochemicals is expensive. For this reason, there has been much interest in the production of succinic acid from renewable resources by microbial fermentation. As shown in Table 2, there are several succinate-producing microorganisms such as *Actinobacillus succinogenes*, *Mannheimia succiniciproducens*, *Anaerobiospirillum succiniciproducens*, *Bacteroides fragilis*, and *Enterecoccus flavescens*. Among these, *A. succinogenes* and *A. succiniciproducens* can accumulate succinic acid in significant concentrations. *A.succinogenes* was isolated from bovine rumen (37), while *A. succiniciproducens* was from animal feces (38). *A. succinogenes* has distinct characteristics that produce high concentrations of succinic acid under anaerobic conditions using various carbon sources such as glucose, sucrose, fructose, lactose, maltose, mannose, xylose, cellobiose, arabinose, galactose, sorbitol, manitol, and salicin. It has good tolerance to a high concentration of glucose (160 g/L) (39). Production of succinic acid by *A. succinogenes* is strongly affected by the amount of CO_2;

© 2008 NRC Canada

Fig. 3. Schematic illustration for the synthesis of poly [(*R*)-3-hydroxybutyrate] and its co-polyesters from (*R*)-3-hydroxybutyric acid.

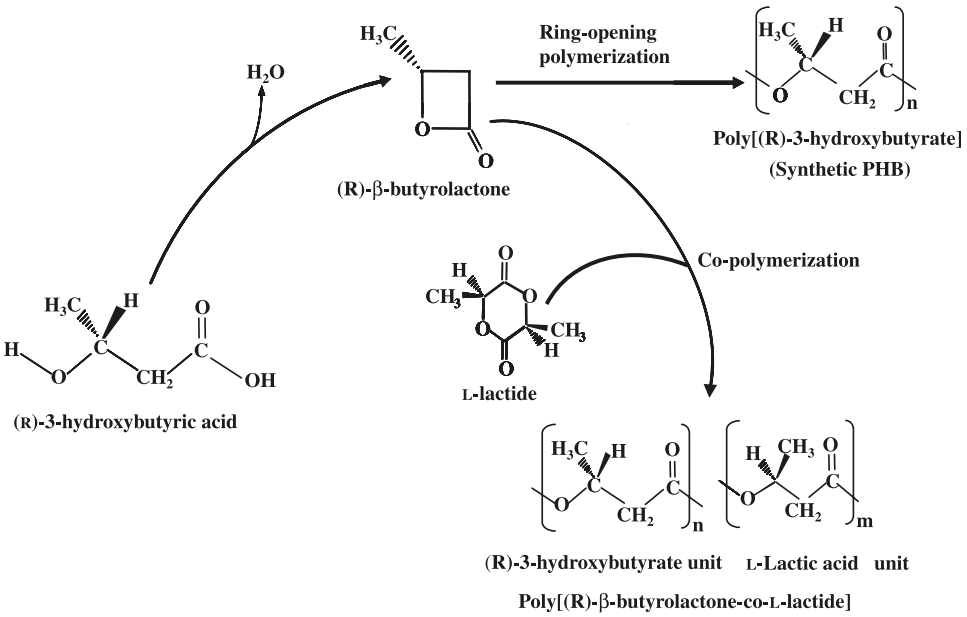

high CO_2 concentration produced higher succinic acid and low ethanol concentration. Furthermore, the addition of H_2 to the gas phase also improved succinic acid production. This is probably due to the increased carboxylization of phosphoenolpyruvate (PEP) to oxaloacetate over the conversion of PEP to pyruvate (40). *A. succinogenes* can also produce succinic acid from pre-treated sugarcane molasses (41). *M. succiniciproducens* was able to produce succinic acid as the major fermentation product in the presence of CO_2, with acetic and formic acids as the minor products. An efficient and economical production of succinic acid was possible by using pre-treated wood hydrolysate. The major sugar contents of wood hydrolysate are glucose and xylose. *M. succiniciproducens* can utilize both as carbon source for succinic acid production (42), while *A. succinoproducens* can only use glucose in wood hydrolysate but not xylose (43).

Although some of the strains are able to produce relatively high succinic acid than other microorganisms, formation of other organic acids (acetic, formic, and lactic acid) becomes a problem because it reduces the succinic acid yield and makes the downstream process difficult and expensive. Several strategies have been used to reduce other by-products and to enhance biotechnological production of succinic acid. One approach is through genetic manipulation technologies. For instance, Lee et al. (44) reported the development of the *M. succiniciproducens* LPK7 strain, wherein the lactate dehydrogenase (ldhA), pyruvate formate lyase (*pflB*), and phosphotransacetylase-acetate kinase (*pta-ackA*) genes were inactivated by metabolic engineering, based on its complete genome sequence. Batch fermentation of wild-type *M. succiniciproducens* using 22.5 g/L glucose produced 10.5 g/L succinic acid, 4.96 g/L acetic acid, 4.10 g/L formic acid, and 3.47 g/L lactic acid. However, metabolically engineered *M. succiniciproducens* LPK7 produced 13.4 g/L of succinic acid from 20 g/L glucose without formic acid and lower lactic acid production. A monofluoroacetate-resistant mutant strain of *A. succinogenes* produced less acetic and formic acids than the parent strain (31). Furthermore, succinic acid could be efficiently produced by redirecting carbon flux from phosphoenolpyruvate (PEP) and pyruvate to the reductive tricarboxylic acid (TCA) by overproducing PEP and pyruvate-carboxylating enzymes. Succinic acid concentration increased significantly from 3 to 10.7 g/L by overexpression of PEP carboxylase (PEPC) in *E.coli* (45).

Evaluation of raw materials used in the production of functional chemicals

Biomass from sugar crops, starch crops, or cellulosic materials provides great potential for sustainable production of biochemicals, biomaterials, or biofuels. Agro-industrial residues such as wood chips, bagasse, rice straw, and rice bran, can also be used as potential raw materials because they are inexpensive or even available at no cost in some cases. Lignocellulosic materials consist of cellulose, hemicellulose, and lignin, which are polymeric and responsible for their physical and chemical properties. Of the 3 components, lignin is the most recalcitrant to degradation whereas cellulose is more resistant to hydrolysis than hemicellulose because of its highly ordered crystalline structure. However, pre-treatment of these substrates is necessary prior to fermentation. Chemical hydrolysis (acid and alkali) have been used to hydrolyze starch and lignocelluloses, but enzyme hydrolysis is more attractive because enzymes do not produce undesirable products and they are environmentally friendly. Thus we established a method in determining the enzymatic degradation of insoluble materials such as polymers, starch, and lignocellulosic materials using a total organic carbon (TOC) analyzer. TOC analyzer measures the amount of total organic carbon present in a liquid sample. A liquid sample is initially introduced to an inorganic carbon (IC) removal stage where acid is added to the sample. At this point the IC is converted into carbon dioxide (CO_2) gas that is stripped out of the liquid by a sparge carrier

© 2008 NRC Canada

Table 2. Comparative evaluation of succinic acid production by wild-type succinic acid producing microorganisms.

Strains	Carbon source	Fermentation mode	Culture time (h)	DCW (g/L)	Succinic acid conc. (g/L)	Yield (%)	Productivity (g/L/h)	Ref. No.
Actinobacillus succinogenes 130Z	Glucose	Batch	84	NA	66.4	67	0.79	(9
A. succinogenes ATCC 55618	Glucose	Repeat-batch	39	NA	33.9	86	0.88	46
A.succinogenes ATCC 55618	Wheat flour	Batch	51	NA	15.9	82	0.31	47
A.succinogenes CGMCC	Sugarcane molasses	Batch	48	OD_{660}= 5.9	46.4	79	0.97	41
A.succinogenes CGMCC	Sugarcane molasses	Fed-batch	48	OD_{660}= 7.0	55.2	NA	1.15	41
Mannheimia succiniciproducens MBEL55E	Glucose	Batch	8	3.44	14.0	70	1.87	48
M. succiniciproducens MBEL55E	Wood hydrolysate	Batch	12	1.97	11.7	56	1.17	43
M. succiniciproducens MBEL55E	Wood hydrolysate	Continuous	D = $0.4h^{-1}$	NA	8.0	55	3.19	43
Anaerobiospirillum succiniciproducens ATCC 29305	Glucose	Batch	30	OD_{660} = 2.0	33.0	93	1.10	49
A. succiniciproducens ATCC 29305	Glucose	Batch	14	OD_{660} = 3.5	17.8	90	1.31	50
A. succiniciproducens ATCC 29305	Glucose + Glycerol	Fed-batch	22	1.5	29.6	97	1.35	51
Bacteroides fragilis	Glucose	Batch	30	OD_{660}= 7.5	12.5	NA	0.42	52
Enterecoccus flavescens	Glucose	Batch	36	NA	14.3	NA	0.40	53

Note: NA = data not available.

Fig. 4. Relationships between the formation of water-soluble total organic carbon (TOC) and reaction time degradation of starch granules by (A) α-amylase from *Bacillus subtilis* (B) gluco-amylase from *Rhizopus niveus* using TOC (○), Somogyi-Nelson (□), and Phenol-H_2SO_4 (△) methods.

gas. The sample is then oxidized and the CO_2 generated from the oxidation process is directly related to the total carbon (TC) in the sample. TOC can be measured by subtracting the IC from TC concentrations.

TOC analyzer, phenol sulfuric, and Somogyi-Nelson methods were compared in the determination of the degradation of starch and wood by enzymes. Glucose, which contains 40% organic carbon in the molecule, was used as a standard for phenol sulfuric and Somogyi-Nelson methods. Figure 4 shows the time course of the enzymatic hydrolysis of starch granules by α-amylase and gluco-amylase. α-Amylase is an end-type enzyme acting randomly in the interior parts of the starch chain. The fragmentation by α-amylase initially leads to a rapid reduction in the molecular size of the starch, with the formation of water soluble dextrins and oligosaccharides. Thus, when TOC analyzer and phenol-sulfuric method were used, the TOC formations were the same because all the degradation products (monomer and oligomer) were measured. On the other hand, the Somogyi-Nelson method is only specific to reducing sugars, therefore the TOC formation based on reducing sugars was lower (Fig. 4*a*). When gluco-amylase was used in the hydrolysis of starch, the TOC formations among the 3 methods used were the same because gluco-amylase is an exo-type enzyme that has the ability to hydrolyze from the terminal to produce glucose (Fig. 4*b*). Furthermore, the formation of TOC in the degradation of various kinds of wood by cellulase from *Trichoderma viride* was also determined. As shown in Fig. 5, the calculated TOC was high when phenol-sulfuric method was used, because the aromatic compound in wood mill reacts with these chemicals (phenol and sulfuric acid) and produced color, thus increasing the TOC value. Phenol-sulfuric and Somogyi-Nelson are the common methods used in the determination of total sugar and reducing sugar, respectively. They are useful also in investigating the degrada-

© 2008 NRC Canada

Fig 5. (A) Relationships between the formation of water-soluble total organic carbon (TOC) and reaction time on degradation of Pinus densiflora wood meal using Phenol-H_2SO_4 (△), TOC (○) and Somogyi-Nelson methods (□) and (B) Degradation of different wood meals powder by cellulase-Onozuka R-10 from *Trichoderma viride* using TOC (solid), Phenol-H_2SO_4 (cross-hatched), and Somogyi-Nelson methods (oblique pattern).

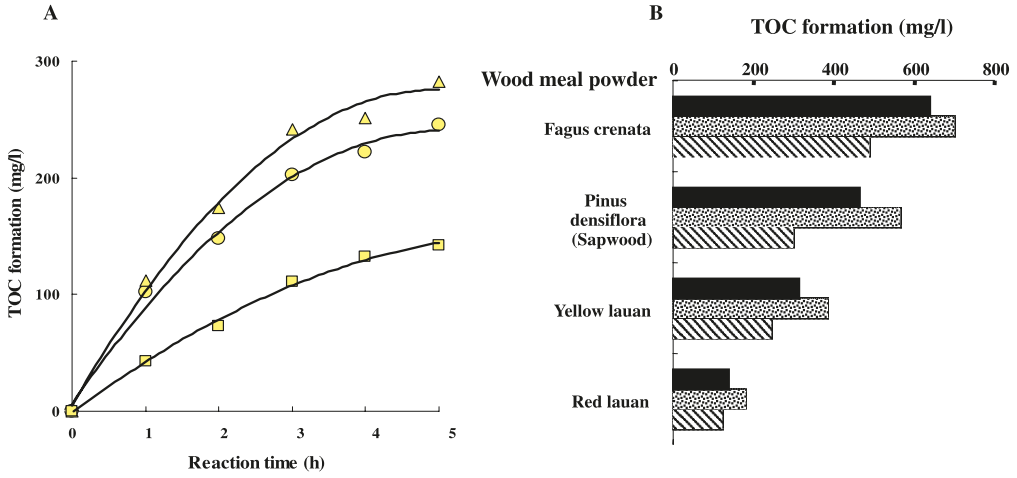

tion mechanisms of cellulose and starch. However, these methods are not applicable in biomass containing lignin such as wood chips, bagasse, and rice straw. The TOC analysis is more appropriate.

Conclusion

Although considerable effort has been made in the development of functional materials from renewable resources, there are still a lot of tasks to be accomplished to make them cost-competitive with petrochemical-based materials. It is important to isolate, screen, or improve novel microorganisms to enhance the microbial production of monomers (lactic acid, (*R*)-3HB, and succinic acid). Genetic engineering is one approach to optimize biotechnological production routes, however recombinant microorganisms are not yet fully accepted because of the unpredictable detrimental effect on the environment. In addition to metabolic engineering, the conventional method, UV mutation, is a practical way of improving microbial strains. Utilization of biomass, such as starch, cellulose, hemicellulose, and lignocellulose, is an attractive approach in the production of functional materials because these raw materials are abundant and inexpensive. In addition, TOC analysis is an effective approach in the determination of the degrading activity of insoluble biomaterials and fermentation activity of biomass because it is reliable, versatile, economical, and user friendly (no chemicals involved).

References

1. K. Hofvendalh and B. Hagerdal-Hahn. Enzyme Microb. Technol. **26**, 87 (2000).
2. J.H. Litchfield. Adv. Appl. Microbiol. **42**, 48 (1996).
3. M.E. Stiles and W.H. Holzapel. Intl. J. Food Microbiol. **36**, 1 (1997).
4. S. Miura, T. Arimura, M. Hoshino, M. Kojima, L. Dwiarti, and M. Okabe. J. Biosci. Bioeng. **96**, 65 (2003).
5. B.P. Calabia and Y. Tokiwa. Biotechnol Lett. **29**, 1329 (2007).
6. T. Tanaka, M. Hoshina, S. Tanabe, K. Sakai, S. Ohtsubo, and M. Taniguchi. Bioresour. Technol. **97**. 211 (2006).
7. K. Fukushima, K. Sogo, S. Miura, and Y. Kimura. Macromol. Biosci. **4**, 1021 (2004).
8. R. Yanez, A.B. Moldes, J.L. Alonso, and J.C. Parajo. Biotechnol. Lett. **25**, 1161 (2003).
9. D.E. Chang, H.C. Jung, J.S. Rhee, and J.G. Pan. Appl. Microbiol. Biotechnol. **65**, 1384 (1999).
10. S. Zhou, T.B. Causet, A. Hasona, K.T. Shanmugan, and L.O. Ingram. Appl. Environ. Microbiol. **69**, 399 (2003).
11. V.B. Shukla, S. Zhou, L.P. Yomano, K.T. Shanmugam, J.F. Preston, and L.O. Ingram. Biotechnol. Lett. **26**, 689 (2004).
12. N. Ishida, T. Suzuki, K. Tokuhiro, E. Nagamori, T. Onishi, S. Saitoh, K. Kitamoto, and H. Takahashi. J. Biosci. Bioeng. **101**, 172 (2006).
13. D.X. Zhang and M. Cheryan. Biotechnol. Lett. **13**, 733 (1991).
14. I. Yumoto and K. Ikeda. Biotechnol Lett. **17**, 543 (1995).
15. J. Narita, S. Nakahara, H. Fukuda, and A. Kondo. J. Biosci. Bioeng. **97**, 6 (2004).
16. W. Timbuntan, K. Sriroth, and Y. Tokiwa. Biotechnol Lett. **28**, 811 (2006).
17. B.P. Calabia and Y. Tokiwa. Paper presented at the annual meeting of Japan Society for Biotechnology. 2007. p. 157.
18. M. De Angelis and M. Gobbetti. Proteomics, **4**, 106 (2004).
19. M. van de Guchte, P. Serror, C. Chervaux, T. Smokvina, S.D. Ehrlich, and E. Maguin. Antonie Van Leewenhoek, **82**,187 (2002).
20. L. Toffin, K. Zink, C. Kato, P. Pignet, A. Bidault, N. Bienvenu, J.L. Birrien, and D. Prieur. Int. J. Syst. Evol. Microbiol. **55**, 345 (2005).
21. M. Ishikawa, K. Nakajima, Y. Itamiya, S. Furukawa, Y. Yamamoto, and K. Yamasato. Int. J. Syst. Evol. Microbiol. **5**3 711 (2003).
22. M. Ishikawa, K. Nakajima, Y. Itamiya, S. Furukawa, Y. Yamamoto, and K. Yamasato. Int. J. Syst. Evol. Microbiol. **55**, 2427 (2005).
23. S. Ntougias and N.J. Russel. J. Syst. Evol. Microbiol. **5**, 1161 (2001).
24. J.A.E. Farrow and M.D. Collins. Int. J. Syst. Evol. Microbiol. **35**, 73 (1985).

© 2008 NRC Canada

25. W. Timbuntan, Y. Tokiwa, and K. Nakajima. Paper presented at the annual meeting of Japan Society for Biotechnology. 2007. p. 156.
26. T. Chiba and T. Nakai. Chem. Lett. 651 (1985).
27. A. Steinbuchel and H.E. Valentin. FEMS Microbiol. Lett. **128**, 219 (1995).
28. D. Seebach, M.Albert, P.I. Arvidsson, M. Rueping, and J.V. Schreiber. Chimia, **55**, 345 (2001).
29. Y. Tokiwa and C.U. Ugwu. J. Biotechnol. **132**, 264 (2007).
30. S.Y. Lee, Y. Lee, and F. Wang. Biotechnol. Bioeng. **65**, 363 (1999).
31. S.Y. Lee and Y. Lee. Appl. Environ. Microbiol. **69**, 3421 (2003).
32. H.J. Gao, Q. Wu, and G.Q. Chen. FEMS Microbiol. Lett. **213**, 59 (2002).
33. M. Shiraki, T. Endo, and T. Saito. J. Biosci. Bioeng. **102**, 529 (2006).
34. B.P. Calabia and Y. Tokiwa. Biotechnol. Lett. **28**, 383 (2006).
35. H. Song and S.Y. Lee. Enz. Microb. Technol. **39**, 352 (2006).
36. G. Zeikus, M.K. Jain, and P. Elankov. Appl. Microbiol. Biotechnol. **51**, 545 (1999).
37. M.V. Guettler, D. Rumler, and M.K. Jain. Int. J. Syst. Bacteriol. **49**, 207 (1999).
38. C.P. Davis, D. Cleven, and J. Brown. Int. J. Syst. Bacteriol. **26**, 498 (1976).
39. M.V. Guettler, M.K. Jain, and D. Rumler. US Patent 5-573-931. 1996.
40. M.J. van der Werf, M.V. Guettler, M.K. Jain, and J.G. Zeikus. Arch. Microbiol. **167**, 332 (1997).
41. Y.P. Liu, P. Zheng, Z.H. Sun, Y. Ni, J.J. Dong, and L.L Zhu. Bioresour. Technol. **99**, 1736 (2008).
42. D.Y. Kim, S.C. Yim, P.C. Lee, W.G. Lee, S.Y. Lee, and H.N. Chang. Enz. Microbiol. Technol. **35**, 648 (2004).
43. P.C Lee, W.G. Lee, S. Kwon, S.Y. Lee SY, and H.N. Chang. Enz. Microbiol. Technol. **24**, 549 (1999).
44. S.J. Lee, H. Song, and S.Y. Lee. Appl. Microbiol. Biotechnol. **72**, 1939 (2006).
45. C.S. Millard, Y.P. Chao, J.C. Liao, and M.I. Donnelly. Appl. Microbiol. Biotechnol. **62**, 1808 (1996).
46. S.E. Urbance, A.L Pometto, A.A. DiSpirito, and Y. Denli. Appl. Microbiol. Biotechnol. **65**, 664(2004).
47. C. Du, S.K.C. Lin, A. Koutinas, R. Wang, and C. Webb. Appl. Microbiol. Biotechnol. **76**, 1263 (2007).
48. P.C. Lee, S.Y. Lee, S.H. Hong, and H.N. Chang. Appl. Microbiol. Biotechnol. **58**, 663 (2002).
49. N.P. Nghiem, B.H. Davison, B.E. Suttle, and G.R. Richardson. Appl. Biochem. Biotechnol. **39**, 352 (2006).
50. P.C. Lee, W.G. Lee, S.Y. Lee, H.N. Chang, and Y.K. Chang. Biotechnol. Bioprocess Eng. **5**, 379 (2000).
51. P.C. Lee, W.G. Lee, S.Y. Lee, and H.N. Chang. Biotechnol. Bioeng. **72**, 41 (2001).
52. J. Isar, L. Agarwal, S. Saran, R. Kaushik, and R.K. Saxena. Anaerobe, **13**, 50 (2007).
53. L. Agarwal, J. Isar, G.K. Meghwanshi, and R.K. Saxen. Enz. Microb. Technol. **40**, 629 (2007).

© 2008 NRC Canada

The crystallization of ultrathin films of polylactides — Morphologies and transitions[1]

Damien Maillard and Robert E. Prud'homme

Abstract: Poly(L-lactide) ultrathin films of thicknesses between 10 and 80 nm were crystallized between 100 and 170 °C. Four different morphologies were obtained: single crystals, hedrites, dendrites, and spherulites. Dendrites were always obtained below 20 nm due to chain diffusion limitations, whereas, at larger thicknesses, the morphology heavily depends on the crystallization temperature. The thickness–temperature morphological map led to the observation of two transition temperatures, at 115 and 145 °C. Other parameters such as the lamellar thickness, melting temperature, and dendricity of the lamellae for 15 nm thick films show significant changes at these two temperatures. Those transitions occur at the same temperatures as Regime III/Regime II, and Regime II/Regime I transitions of the Lauritzen–Hoffman crystallization theory.

Key words: polylactide, ultrathin film, crystalline morphology, single crystal, dendrite, spherulite, transition temperature, regime of crystallization.

Résumé : Des films ultraminces de poly(L-lactide) d'épaisseurs comprises entre 10 et 80 nm ont été cristallisés sur une gamme de températures allant de 100 à 170 °C. Quatre morphologies distinctes ont été observées : monocristaux, hédrites, dendrites et sphérolites. Des dendrites ont été systématiquement observés à des épaisseurs de moins de 20 nm à cause des empêchements à la diffusion des chaînes tandis qu'à plus grande épaisseur, la morphologie dépend de la température de cristallisation. Une représentation morphologique épaisseur/température permet de visualiser deux températures de transition, à 115 et 145 °C. D'autres paramètres tels que l'épaisseur des lamelles cristallines, la température de fusion et la dendricité des lamelles obtenues à partir de films de 15 nm montrent des changements significatifs à ces deux températures. Ces transitions se produisent aux mêmes températures que les transitions entre les régime III/régime II, puis régime II/régime I de la théorie de cristallisation de Lauritzen et Hoffman.

Mots-clés : polylactide, film ultramince, morphologie cristalline, cristal unique, dendrite, sphérulite, température de transition, régime de cristallisation.

Introduction

In general, the crystallization of ultrathin polymer films (thickness ≤ 100 nm) leads to a different behaviour from that in the bulk. For example, the kinetics of crystallization and the final degree of crystallinity decrease with the film thickness below 100 nm (1, 2).

Contrary to the bulk where the lamellae have the possibility to grow in three dimensions, all the lamellae in ultrathin films grow in the same plane; this restriction leads to the observation of phenomena that are impossible to detect in the bulk. For example, Hobbs et al. have observed that the lamellae at the growth front of spherulites, called dominant lamellae, do not grow at a constant rate but can remain dormant for certain periods of time (3). Other studies have shown how the branching of a lamella results from the secondary nucleation of a parent lamella and how lamellae are able to join together during the growth (4–6). In the case of crystallization at low supercooling, polymers like isotactic polystyrene, syndiotactic polypropylene, and poly(ε-caprolactone) (PCL) exhibit "isolated" flat-on single crystals from which it is possible to measure the lamellar thickness or the growth rate along the different sectors (7, 8). Our own studies on PCL ultrathin films have shown that the lamellar thickness of single crystals is only controlled by the crystallization temperature, not the film thickness, even when the melt is much thinner than the lamellar thickness, and have permitted to identify the plasticizer role of the residual solvent in the polymer crystallization (8, 9).

Polylactides are biodegradable and biocompatible chiral polyesters largely studied for their various characteristics. Poly(L-lactide) (PLLA) and poly(D-lactide) (PDLA) are semi-crystalline, whereas poly(DL-lactide) (atactic) is amorphous. The thermal and crystallization behaviours of PLLA were extensively studied in the bulk, its melting temperature (T_m), which varies with the crystallization temperature (T_c) being close to 180 °C (10–12). Several studies have reported

Received 20 November 2007. Accepted 13 February 2008. Published on the NRC Research Press Web site at canjchem.nrc.ca on 25 April 2008.

This paper is dedicated to Robert H. Marchessault in recognition of his many contributions to polysaccharide and biopolymer chemistry.

D. Maillard and R.E. Prud'homme.[2] Département de chimie, Université de Montréal, Succursale Centre-Ville, C.P. 6128, Montréal, QC H3C 3J7, Canada.

[1]This article is part of a Special Issue dedicated to Professor R. Marchessault.

[2]Corresponding author (e-mail: re.prudhomme@umontreal.ca).

 doi:10.1139/V08-045 © 2008 NRC Canada

an exotherm followed by a double melting peak in differential scanning calorimetry (DSC) curves, and that behaviour was recently interpreted as the result of spontaneous recrystallization (13).

Studies on ultrathin films of PLLA led to the observation of truncated lozenge single crystals (with four (110) sectors and two (200) sectors) and of dendritic structures below 20 nm (14–16). Edge-on lamellae able to nucleate new flat-on lamellae were also reported, exhibiting *S* or *Z* shapes, depending on the chain chirality (17).

In the present paper, the crystallization conditions leading, for ultrathin PLLA films, to single crystals and other morphologies will be determined, and using classical and modulated DSC, in addition to atomic force microscopy (AFM), two transitions, at which several crystalline parameters are significantly modified, will be defined at 115 and 145 °C.

Experimental section

Materials

Poly(L-lactide) was provided by Polysciences Inc. and used without further purification. The molecular masses were determined by gel permeation chromatography using a Wyatt light scattering detector: M_n = 110 000 g mol^{-1} and polydispersity (PD) = 1.26.

Sample preparation

Ultrathin films were prepared by spin-coating in dichloromethane solutions at a rotation speed of 3000 rpm for 20 s, following an acceleration of 4000 rpm/s, using a Headway Research Inc. EC-101 apparatus. The film thickness was controlled by the solution concentration; concentrations from 2 to 20 mg/mL were used to obtain thicknesses ranging between 5 and 100 nm. The films were cast onto cleaned Si substrates (p-type single side polished (100) silicon wafers). The wafers were cleaned by immersion in nitrohydrochloric acid for 1 h in an ultrasonic bath to remove any organic contamination and to hydroxylate the native oxide layer, thus making the surface hydrophilic. The substrates were then rinsed with distilled water and dried by spin-coating for 40 s at 3000 rpm, before treatment in a plasma cleaner (Harrick PDC-32G) at 18 W for 20 s. To keep a solvent-saturated atmosphere around the sample and to allow uniform evaporation, a glass dome was placed on top of the sample area during spin-coating. Film thicknesses were measured by AFM.

The films used for the static studies were melted at 190 °C for 2 min and crystallized at the desired temperature (between 100 and 175 °C) in a THMS-600 Linkam hot-stage connected to a TMS-94 temperature controller. After crystallization, samples were placed on an aluminum sheet previously cooled in liquid nitrogen for quickly decreasing the temperature below the glass transition temperatures and freezing the sample.

Atomic force microscopy

A multimode AFM apparatus (Digital Instrument (DI)), equipped with a Nanoscope IIIa controller (DI), a Quadrex extender (DI), and a high temperature heating accessory (DI), operated in tapping mode, was used to capture images. JVH (temperature control, maximal scan size: 130 μm × 130 μm) and J (ambient temperature, maximal scan size 100 μm × 100 μm) scanners were used with silicon nitride probes (MikroMash and Nanosensor).

The temperature-controlled studies were performed directly inside the AFM. The samples were melted at 190 °C for 2 min, and the stage temperature was decreased to the chosen crystallization temperature (between 90 and 165 °C), which was maintained until the beginning of the crystallization. Then, the temperature was increased during the crystallization to obtain specific areas crystallized at defined temperatures. Finally, the temperature was increased by steps of 2 °C, maintained constant at each step for 10 min to obtain AFM pictures, until reaching a complete melted state. During the whole process, the AFM probe was maintained at the same temperature as the sample to avoid any condensation. The scan rate was 1 Hz. Height, amplitude, and phase were collected simultaneously.

Branching density measurements were performed by counting the number of branches on a 10 μm × 10 μm AFM picture completely covered by dendritic flat-on lamellae. The results presented in this paper are averages of observations performed on at least three pictures obtained in the same conditions. The quantitative values are expressed in number of branches/μm^2.

Film and lamellar thicknesses were measured by profilometry using AFM. The films were scratched with a surgical blade to uncover the substrate, and the profile was established on both sides of the scratch; the difference in height between the film area and the uncovered substrate is read. In the case of film thicknesses of 15 nm or below, the lamellae are thicker than the films and emerge from them.

Differential scanning calorimetry

DSC experiments were performed on a TA Q1000 apparatus. The C_p response was calibrated with sapphire, and the temperature response was calibrated with indium. The scan rates were 10 and 0.5 °C/min for the classical and 4 °C/min for the modulated experiments. For modulated DSC, the period was 40 s, and the amplitude was 0.424 °C.

Results

The variety of crystalline morphologies obtained for PLLA as a function of film thickness was investigated at several crystallization temperatures from 100 to 175 °C. Depending on these two parameters, four different morphologies are observed, as illustrated in Fig. 1: single crystals, single-crystal stacks (hedrites), dendrites, and spherulites. At temperatures above 115 °C and thicknesses of 25 nm (Figs. 1*e* and 1*h*), single crystals are observed. In the case of PLLA, single crystals from solution have a lozenge shape, but from the melt they adopt a truncated lozenge shape, geometrically almost a hexagon, due to chain diffusion. In both pictures, dendritic overgrowths are seen on top of the main lamella; this is possible because the thickness of the single crystal is about 18 nm (AFM measurement), making possible the superposition of two crystalline layers because of the 25 nm melt thickness. At temperatures above 145 °C and thicknesses above 50 nm, crystal stacks are observed (Fig. 1*g*). The crystal stack, or hedrite, is a three-dimensional object made of the superposition of flat-on lamellae epitaxially aligned. This superposition can be due

© 2008 NRC Canada

Fig. 1. AFM micrographs of PLLA ultrathin films after crystallization and quenching in liquid nitrogen. The film thicknesses are 80 nm (*a*, *d*, g), 25 nm (*b*, *e*, h), and 15 nm (*c*, *f*, *i*). The crystallization temperatures are 105 °C (*a*, *b*, *c*), 125 °C (*d*, *e*, *f*), and 155 °C (*g*, h, *i*). Note that the scales are not exactly the same on each picture.

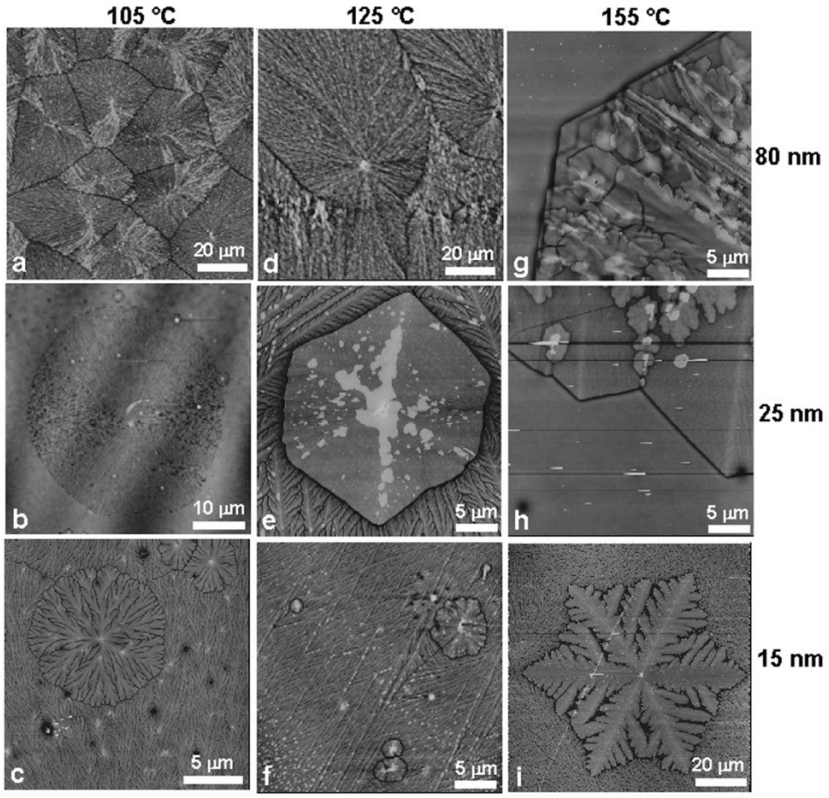

to a secondary nucleation on top of the crystal (crystal stacks) or to a screw dislocation of the primary lamella (hedrite) conducting to a "snail" structure. At 15 nm, in the range of crystallization temperatures investigated, dendrites are observed (Figs. 1*c*, 1*f*, and 1*i*). Their shape ressembles that of single crystals (snow-like crystals or more spherical flower-like crystals), but the growth fronts are broken and branched. Spherulites are systematically observed at temperatures below 115 °C for thicknesses above 20 nm (Figs. 1*a* and 1*b*), and at temperatures between 115 and 145 °C for thicknesses above 50 nm (Fig. 1*d*).

Electron diffraction measurements have confirmed those morphologies. In the case of single crystals, crystal stacks/hedrites, and dendrites, the chain axis is oriented normal to the substrate while the *a* and *b* axes have the same orientation throughout the entity. In contrast, in the case of spherulites, there is very little orientation, the *a*, *b*, and *c* axes being almost randomly distributed.

Additional observations made at several other film thicknesses and crystallization temperatures lead to a "map" of morphologies in terms of those two parameters, as given on Fig. 2.

In this map, there are three morphological sectors in terms of temperature, with significant changes at about 115 and 145 °C. At temperatures below 115 °C, the morphologies are dendritic below 20 nm and spherulitic above 20 nm. Above 145 °C, the morphologies are dendritic and single-crystalline, with a transition thickness at about 30 nm; above 50 nm, the lamellae are able to superpose, leading to

Fig. 2. Morphology map of PLLA films for thicknesses below 100 nm.

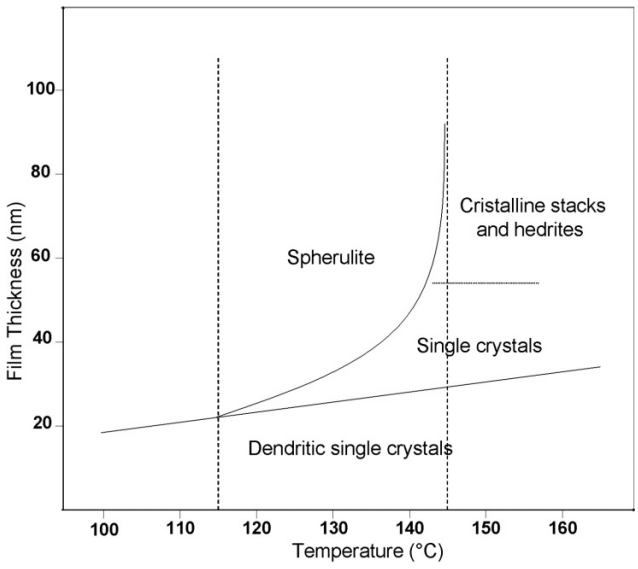

lamellar stacks, or hedrites, which can be considered as a superposition of the single-crystal structures. Between 115 and 145 °C, three morphologies can be obtained: below 25 nm, the crystals and dendritic; above 25 nm, they can be spherulitic (close to 115 °C) or single crystalline (close to 145 °C); above 80 nm, the crystals are always spherulitic.

© 2008 NRC Canada

Below 20 nm, the morphology is always dendritic, as it has been observed for example with poly(ε-caprolactone) below 15 nm (8) because of limitations to the chain diffusion: the lamellae formed (dendrites) are as thick, or even thicker, than the melt from which they grow. However, even if the morphology is always dendritic in this area, there is a notable evolution in branching density because the diffusion of the chains depends not only on the film thickness (spatial restriction) but also on the temperature. Figure 3 shows the variation of the branching density of the dendritic flat-on crystals, for 15 nm thick films, with the crystallization temperature – three representative samples are shown for illustration. Below 115 °C, the dendrites are coarse and tree-like oriented. Above 145 °C, they are flower-like and well-outlined. Finally, between those two temperatures, the branches are fine, regularly aligned, with a fixed distance between them. The curve of the dendricity as a function of T_c shown in Fig. 3 presents a maximum at 112.5 °C.

For the same series of samples, Fig. 4 shows the variation of the lamellar thickness with the crystallization temperature. Our values, between 121 and 152 °C, agree well with those of Kanchanasopa et al. (18), although they are slightly larger because the two techniques of measurement were different. It is seen in Fig. 4 that the thickness does not increase smoothly as a function of temperature. Although the data points can be represented by a curved line, as proposed in the literature (19), they are better described as a succession of three linear lines with inflection points at 121 and 152 °C.

For a deeper understanding of this system, the melting behaviour of PLLA was studied by DSC and AFM during heating scans at two scan rates (Fig. 5). At a scan rate of 10 °C/min and crystallization temperatures below 115 °C, the thermograms exhibit an exotherm before the melting peak (Peak 1) (Fig. 5*a*). At a crystallization temperature of 115 °C, double melting peaks are visible, one at 170 °C (Peak 2) and the other at 176 °C (Peak 1). At crystallization temperatures higher than 115 °C, a single peak is observed (Peak 2), whose position increases with the crystallization temperature. At a scan rate of 0.5 °C/min, the trend is the same, but Peak 1 is present up to 135 °C, where double peaks are detectable (Fig. 5*c*) and, because of the slower scan rate, the peaks are thinner.

Figures 5*b* and 5*d* summarize the transitions observed in DSC scans. At a scan rate of 10 °C/min, below 110 °C, the position of the exotherm shifts slowly to higher temperatures while Peak 1 remains almost constant between 174 and 176 °C. At the same time, Peak 2 shows up at T_c = 105 °C, even below the exotherm, but shifts to higher temperatures upon increasing T_c. It exhibits two inflection points at about 115 and 145 °C. At a scan rate of 0.5 °C/min, the transition temperatures evolve as they do at 10 °C/min, but Peak 1 is visible until 135 °C, and the melting temperatures are a little lower.

To understand the origin of these transitions, we used modulated DSC, a technique that permits to separate reversible and non-reversible events during a thermal scan. With this technique, it is possible to visualize the opposite behaviour of melting and immediate crystallization (an endotherm followed by an exotherm in DSC) that form the recrystallization process.

Fig. 3. Variation of branching density (dendricity) as a function of crystallization temperature for film thicknesses of 15 nm. The inserts show some representative AFM micrographs.

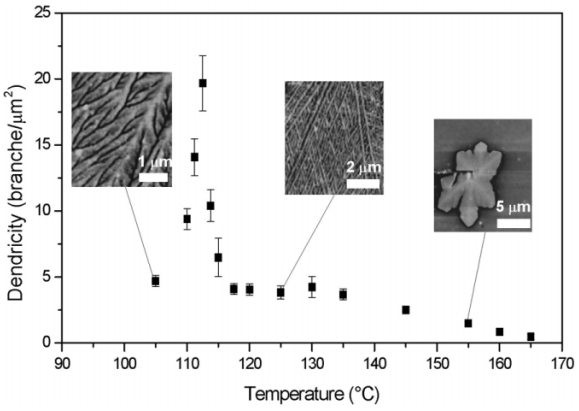

Fig. 4. PLLA lamellar thickness, measured by AFM for films of 15 nm in thickness, as a function of crystallization temperature.

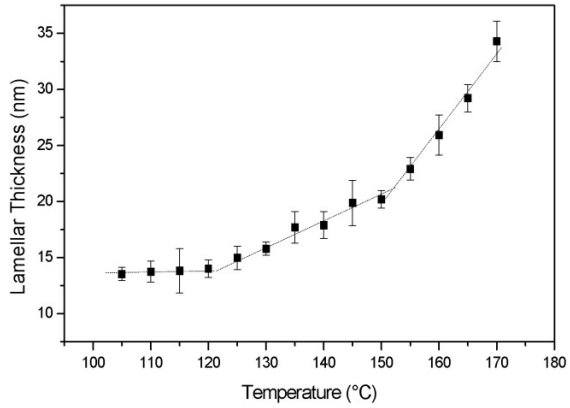

Figure 6 shows a modulated DSC scan of a sample isothermally crystallized at 90 °C. The reversible heat capacity curve exhibits a small melting peak at 156 °C; whereas the non-reversible curve shows two events, a crystallization peak at 157 °C and a melting peak at 174 °C (maximum of the peak). These curves show clearly that opposing events occur in the 150–160 °C range: melting and crystallization occur at the same time (but crystals that melt have a lamellar thickness different from the crystals that are formed). However, since the area of the crystallization exotherm is larger than the area of the corresponding endotherm (melting peak), the final resulting transition, i.e., the sum of the two curves in the resultant heat flow curve, is a small exotherm before the final melting peak. This is the so-called recrystallization process. At higher crystallization temperatures, as shown in Fig. 5, beginning at 110 °C, the melting peak begins to dominate and the exotherm is not anymore visible.

Using AFM, it is possible to go further and to visualize the transitions: recrystallization and melting. For that purpose, samples were crystallized at the desired temperature in the AFM, and the temperature was slowly increased until the observation of melting.

Figure 7 shows two series of measurements made on ultrathin films whose temperature was increased until the

© 2008 NRC Canada

Fig. 5. DSC thermograms (*a* and *c*) of PLLA isothermally crystallized at temperatures between 90 and 160 °C, scanned at (*a*) 10 °C/min and (*c*) 0.5 °C/min. The temperatures of peak 1(□), peak 2 (△), and the exotherms (○) are reported as a function of crystallization temperature in part (*b*) for a scan rate of 10 °C/min and part (*d*) for a scan rate of 0.5 °C/min. Here, the films are thick (about 500 μm).

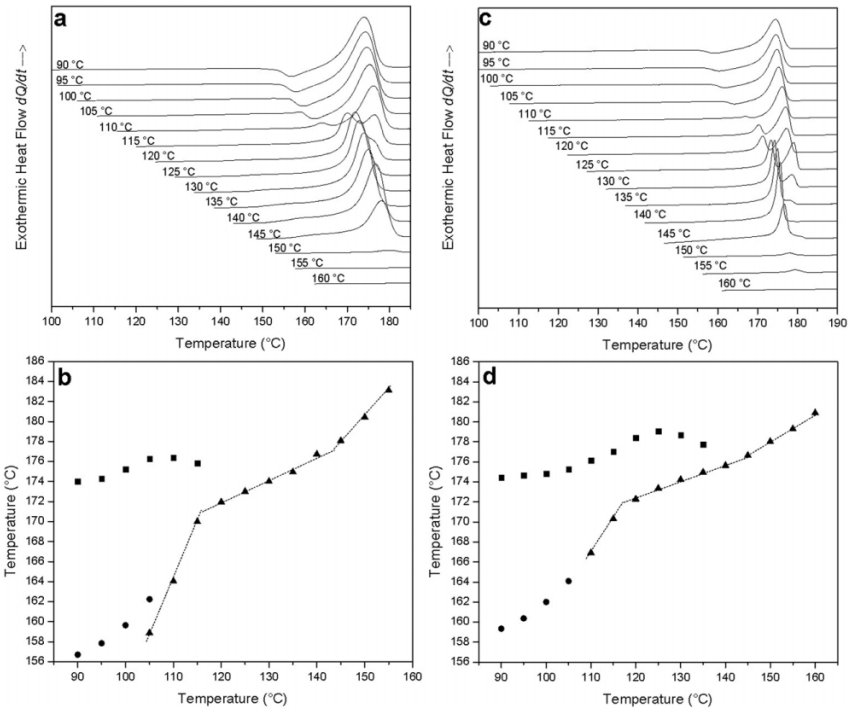

Fig. 6. Modulated DSC thermograms of a sample isothermally crystallized at 90 °C, scanned at 4 °C/min with a period of 40 s and an amplitude of 0.424 °C. The three thermograms represent, respectively, the reversible, the non-reversible, and the total heat capacity as a function of temperature. The main melting temperature (summit of the peak) is 174 °C, the secondary crystallization peak temperature is 157 °C, and the first reversible melting temperature is 156 °C.

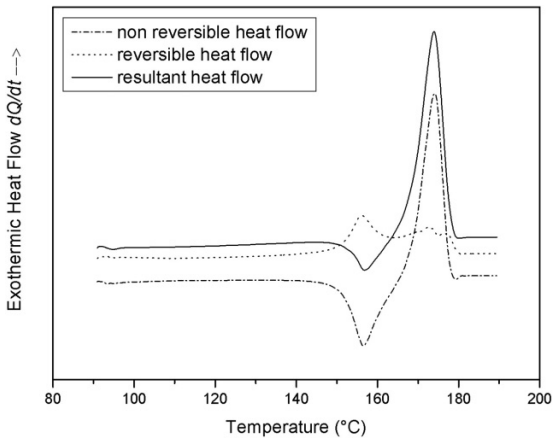

observation of in situ recrystallization and melting. First, a film of 15 nm was crystallized at 110 °C, and the temperature was increased to 145 °C. The left part of Fig. 7*a* is covered by crystals obtained at 110 °C, while the right-hand side of the picture is covered by crystals obtained at 145 °C, whose dendricity is reduced as compared with the crystals obtained at 110 °C. After increasing the temperature to 172 °C (Fig. 7*b*), cheese holes, indicative of annealing, are obtained in the area previously crystallized at 110 °C while the area crystallized at 145 °C does not change. At 175 °C (Fig. 7*c*), the area crystallized at 145 °C is modified and also exhibits cheese holes.

Second, a film of 15 nm was crystallized at 145 °C, and the temperature was increased to 155 °C and maintained there 10 min. At 165 °C (Fig. 7*d*), three areas are distinguished, corresponding to crystallizations at 145, 155, and 165 °C; between those three areas, there is a difference of dendricity and thickness. At 174 °C (Fig. 7*e*), the structure of the area crystallized at 145 °C is modified, exhibiting cheese holes and increased thickness, as observed by AFM height measurements (during that transformation, the crystal continues to grow). At 180 °C (Fig. 7*f*), the areas initially crystallized at 145 and 155 °C begin to melt, but the area crystallized at 155 °C does not exhibit any kind of recrystallization before that temperature.

The thickness of the crystals changes during the recrystallization. From the examples of Fig. 7, the thicknesses measured by AFM are 14.5 nm for a crystallization at 110 °C and 31 nm after annealing at 172 °C. Similarly, the thickness of a film crystallized at 145 °C is found at 21.5 nm before and 41.5 nm after annealing at 174 °C. In general, the thickness after annealing is roughly the double of the initial thickness.

The appearance of cheese holes on the crystal surface is the consequence of a modification of the lamellar thickness. An increase of the thickness (by a factor of two) is obtained by a reorganisation of the chain arrangement leading to a decrease of the number of chain folds. As the total volume of material remains constant, the increase in thickness must be compensated by a decrease of the lateral occupancy, and

© 2008 NRC Canada

Fig. 7. AFM micrographs of 15 nm films crystallized and melted in the AFM. Crystallization at 110 °C, heating to 145 °C for 10 min and observation at (*a*) 145, (*b*) 172, and (*g*) 175 °C. Crystallization at 145 °C, heating at 155 °C for 10 min and observation at (*d*) 165, (*e*) 174, and (*f*) 180 °C.

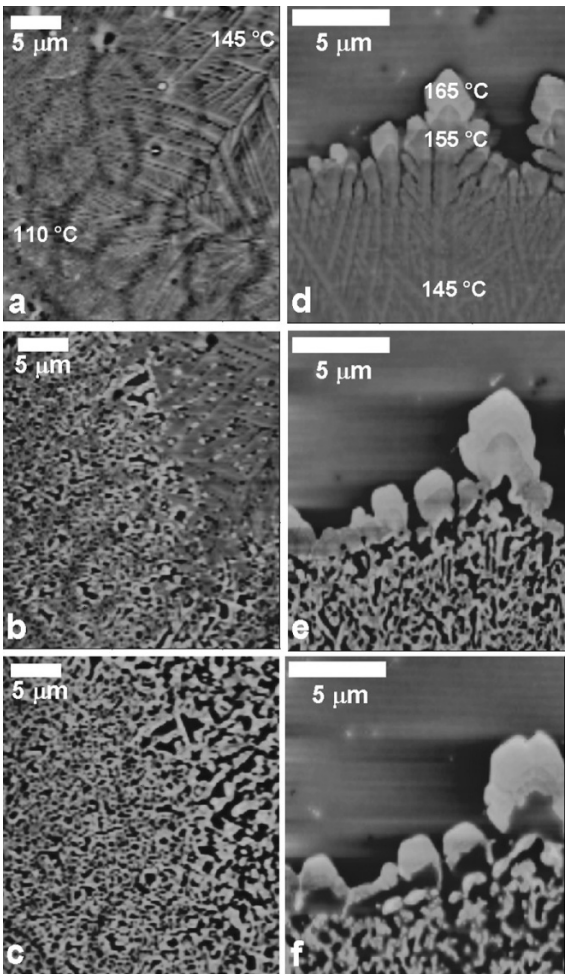

Fig. 8. Recrystallization and melting temperatures (measured by AFM) plotted as a function of the crystallization temperature. DSC results obtained at a scan rate of 0.5 °C/min (lightly shaded) are added for comparison (see Fig. 5 for details).

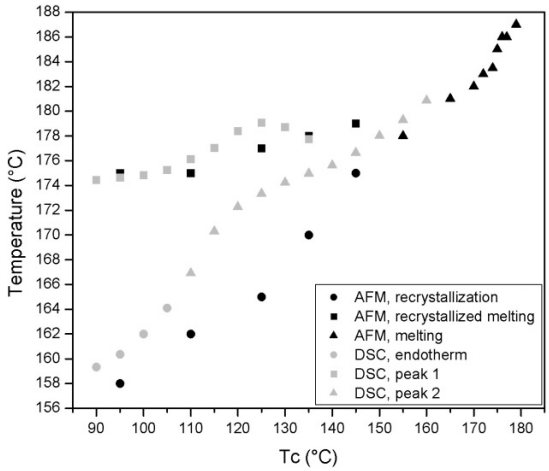

therefore, the cheese holes of Fig. 7 occupy roughly half the surface area.

Figure 8 summarizes the data of recrystallization and melting obtained by AFM from micrographs, such as those shown in Fig. 7, plotting the temperature of the event as a function of T_c. For comparison, the melting temperatures obtained by DSC at a low scan rate, i.e., 0.5 °C/min (conditions similar to the slow increase of temperature during the AFM experiments) were added on the graph. The melting temperatures obtained by DSC and AFM for Peak 1 and Peak 2 agree closely; the recrystallization temperatures, obtained by AFM below T_c = 145 °C, agree with those seen by DSC below 115 °C, and increase almost linearly between 115 and 145 °C in a range of temperatures where the recrystallization process was buried in the DSC curve under the endotherm. Therefore, DSC and AFM measurements are here complementary.

Discussion

The previous section indicates that several significant changes occur at 115 and 145 °C during the crystallization of ultrathin PLLA samples. From AFM measurements (Fig. 2), changes in morphology occur at 115 and 145 °C; from spherulites to single crystals in the first case (film thickness of 25 nm); from spherulites to hedrites in the second one (film thickness ≥ 70 nm). All those morphologies originate from the same crystal structure as shown by electron diffraction, i.e., a pseudo-orthorombic $P2_12_12_1$ unit cell with a = 1.08 and b = 0.63 nm, in agreement with the X-ray values reported in the literature (20–22). In the measurement of the lamellar thickness on films of 15 nm in thickness (Fig. 4), two inflection points are detected at 121 and 152 °C. On bulk samples, DSC measurements (Fig. 5) show that the melting temperature exhibits two inflection points at about 115 and 145 °C.

In the literature, those temperatures correspond to the transitions observed between the three regimes of crystallization in the Lauritzen–Hoffman theory, i.e., at 115 °C, there is a transition between Regimes III and II, and at 145 °C, the transition is between Regimes II and I (23). The difference between these three regimes is the relative value of the radial and lateral growth rates at the lamellar surface (19). In Regime I, the lateral growth rate is larger than the radial growth rate; in Regime II, they are of the same order of magnitude; in Regime III, the radial growth rate is larger than the lateral growth rate.

Transitions between Regimes I, II, and III have been found for many polymers, but in general there is no direct link between regimes and microscopic morphologies. However, there are exceptions. In the case of polyethylene, Regime I is found above 127 °C with an axialite morphology, but in contrast spherulites form below 127 °C and the lamellae grow according to a Regime II kinetics (24). Polylactides appear to behave like polyethylene in this respect, at least at film thicknesses above 20 nm. In polylactides, a transition from spherulites to hexagonal lamellae in thin films (>100 nm) has been reported at a temperature of 150 °C, corresponding to the passage from Regime II to Regime I, but no similar morphological transition was detected between Regime II and Regime III (23). This result agrees with the data shown above (Fig. 2) with a tran-

© 2008 NRC Canada

sition from spherulites to hedrites at 145 °C. However, in addition, we have also seen a morphological transition at 115 °C from spherulites to single crystals, corresponding to the transition from Regime III to Regime II.

When the film thickness is below 20 nm, there is no change in morphology (dendrites are seen throughout the temperature range contrary to the observations in thicker films), but there are transitions in lamellar thickness at the two transition temperatures. This result is unexpected because, according to the Gibbs–Thomson equation (19), an exponential behaviour is expected with an asymptote at T_m^0

$$[1] \qquad T_m = T_m^0 (1 - 2\sigma_e/(l\Delta H))$$

where T_m is the melting temperature, T_m^0 is the equilibrium melting temperature, σ_e is the surface energy of the crystal, l is the thickness of the crystal, and ΔH is the melting enthalpy. To our knowledge, this is the first time that transitions are detected in the evolution of the lamellar thickness with the crystallization temperature (under conditions where there are no changes in morphology). Moreover, the temperature of these transitions correspond to the Regime III/Regime II and Regime II/Regime I transitions in the Lauritzen–Hofman theory.

The dendricity curve (Fig. 3) exhibits a global shape similar to the behaviour of the growth rate – T_c curve observed for polymers. According to the Keith and Padden theory concerning the fibrillation density of lamellae in spherulites, the distance between two lamellae, δ, i.e., the inverse of the dendricity, is proportional to the ratio of the diffusion coefficient, D, to the growth rate, G, i.e., $\delta \approx D/G$ (25). The diffusion coefficient increases linearly with the temperature; in contrast, the growth rate goes through a maximum, being slowed down at low temperatures because of the increase in viscosity of the system and at high temperatures because of a decreased nucleation rate. Therefore, δ goes through a minimum as a function of temperature, i.e., the dendricity goes through a maximum. This is the general behaviour observed in Fig. 3. However, it also shows a sharp maximum at 112.5 °C. This is reminiscent of the growth rate – T_c behaviour reported in the literature for PLLA (23, 26, 27) with a maximum at 113 °C, which has been attributed to a change of regime of crystallization or crystal structure. In this case, there is no change in crystal structure, and this latter explanation must be ruled out.

Many polymers experience recrystallization when they are heated up in a DSC apparatus, i.e., small crystals melt, but at the same time crystallization occurs leading to bigger crystals. This phenomenon leads to DSC curves exhibiting a double melting peak (28, 29). Often, the relative intensity of the two peaks changes with the heating rate. In the case of PLLA, the recrystallization process is particularly intense, since the crystallization during heating often dominates the melting of previously formed crystals leading to an exotherm in the DSC curve (Fig. 5). This competition is clearly seen in Fig. 6 with the reversible heat flow that goes in one direction while the non-reversible signal goes into the other; the addition of these two curves gives an exothermic resultant heat flow.

In summary, we have shown that PLLA, crystallized between 95 and 170 °C, exhibits a variety of morphologies, at thicknesses below 80 nm (spherulites, dendrites, hedrites, and single crystals); even in the case where only one morphology is present, i.e., below 20 nm, there is a clear evolution of dendricity from low to high crystallization temperatures. Moreover, not only morphological observations but also T_m values and lamellar thicknesses show two transitions, at 115 and 145 °C, where the mode of crystallization changes. These temperatures correspond to those where there is a transition from Regime III to Regime II, and from Regime II to Regime I, respectively. This is the first time that the two changes of regimes in crystallization kinetics, in the context of the Lauritzen–Hoffman theory, can be related to simple crystallization characteristics as lamellar thickness and temperature of fusion. This indicates, once again, that studies on thin and ultrathin films can lead to phenomenon that are hardly detected in bulk samples, contributing to a deeper knowledge of the crystallization behaviour of polymers.

Acknowledgements

The authors thank the Natural Sciences and Engineering Research Council of Canada (NSERC) and the Department of Education of the Province of Québec (FQRNT program) for financial support.

References

1. V.H. Mareau and R.E. Prud'homme. *In* Soft materials. *Edited by* A.G. Marangoni. Marcel Dekker, Inc., New York, NY. Vol. 39. 2005.
2. K. Taguchi, A. Toda, and Y. Miyamoto. J. Macromol. Sci. **B45**, 1141, (2006).
3. J.K. Hobbs, T.J. McMaster, M.J. Miles, and P.J. Barham. Polymer, **39**, 2437, (1998).
4. L. Li, C. Chan, J. Li, K. Ng, K. Yeung, and L. Weng. Macromolecules, **32**, 8240, (1999).
5. L. Li, C. Chan, K.L. Y, J. Li, K. Ng, and Y. Lei. Macromolecules, **34**, 316, (2001).
6. J.K. Hobbs, A.D.L. Humphris, and M.J. Miles. Macromolecules, **34**, 5508, (2001).
7. W. Zhou, S.Z.D. Cheng, S. Putthanarat, R.K. Eby, D.H. Reneker, B. Lotz, S. Maganov, E.T. Hsieh, R.G. Geerts, S.J. Palackal, G.R. Hawley, and M.B. Welch. Macromolecules, **33**, 6861, (2000).
8. V.H. Mareau and R.E. Prud'homme. Macromolecules, **38**, 398, (2005).
9. V.H. Mareau and R.E. Prud'homme. Polymer, **46**, 7255, (2005).
10. J.R. Sarasua, R.E. Prud'homme, M. Wisniewski, A.L. Borgne, and N. Spassky. Macromolecules, **31**, 3895, (1998).
11. L. Cartier, T. Okihara, Y. Ikada, H. Tsuji, J. Puiggali, and B. Lotz. Polymer, **41**, 8909, (2000).
12. J. Puiggali, Y. Ikada, H. Tsuji, L. Cartier, T. Okihara, and B. Lotz. Polymer, **41**, 8921, (2000).
13. M. Yasuniwa, K. Iura, and Y. Dan. Polymer, **48**, 5398, (2007).
14. Y. Kikkawa, H. Abe, M. Fujita, T. Iwata, Y. Inoue, and Y. Doi. Biomacromolecules, **2**, 940, (2001).
15. Y. Kikkawa, H. Abe, T. Iwata, Y. Inoue, and Y. Doi. Biomacromolecules, **3**, 350, (2002).
16. Y. Kikkawa, H. Abe, M. Fujita, T. Iwata, Y. Inoue, and Y. Doi. Macromol. Chem. Phys. **204**, 1822, (2003).
17. D. Maillard and R.E. Prud'homme. Macromolecules, **39**, 4272, (2006).

© 2008 NRC Canada

18. M. Kanchanasopa, E. Manias, and J. Runt. Biomacromolecules, **4**, 1203, (2003).
19. J.D. Hoffman, G.T. Davis and J.J.I. Lauritzen. *In* Treatise on solid state chemistry. *Edited by* N.B. Hannay. Plenum, New York. Vol. 3. 1976. p. 497.
20. W. Hoogsteen, A.R. Postems, A.J. Pennings, and G.T. Brinke. Macromolecules, **23**, 634, (1990).
21. T. Miyata and T. Masuko. Polymer, **38**, 4003, (1997).
22. C. Aleman, B. Lotz, and J. Puiggali. Macromolecules, **34**, 4795, (2001).
23. H. Abe, Y. Kikkawa, Y. Inoue, and Y. Doi. Biomacromolecules, **2**, 1007, (2001).
24. J.D. Hoffman, L.J. Frolen, G.S. Ross, and J. J. I. Lauritzen. J. Res. Nat. Bur. Std. **79A**, 671, (1975).
25. H.D. Keith and J.F.J. Padden. J. Appl. Phys.**34**, 2409, (1963).
26. M. Yasuniwa, S. Tsubakihara, K. Iura, Y. Ono, Y. Dan, and K. Takahashi. Polymer, **47**, 7554, (2006).
27. P. Pan, B. Zhu, W. Kai, T. Dong, and Y. Inoue. J. Appl. Polym. Sci. **107**, 54, (2007).
28. B.B. Sauer, W.G. Kampert, E.N. Blanchard, S.A. Threefoot, and B.S. Hsiao. Polymer, **41**, 1099, (1999).
29. K.L. Singfield and N.B. Djogbenou. J. Therm. Anal. Calorim. **86**, 631, (2006).

© 2008 NRC Canada

Decaying exponential feeding of nonanoic acid for the production of medium-chain-length poly(3-hydroxyalkanoates) by *Pseudomonas putida* KT2440[1]

Heather Maclean, Zhiyong Sun, Juliana Ramsay, and Bruce Ramsay

Abstract: Decaying exponential feeding strategies for the production of medium-chain-length poly(3-hydroxyalkanoates) by *Pseudomonas putida* KT2440 have been developed as a method of delaying oxygen limitation that is typically responsible for the termination of high cell density aerobic fermentations. Two feeding strategies were evaluated to control the biomass generation rate and consequently control the oxygen uptake rate of the cells. A linear decaying strategy allowed the production of 90 g L^{-1} dry biomass containing 65% PHA in 31 h with a cumulative productivity of 1.9 g L^{-1} h^{-1}, while a quadratic decaying exponential feeding rate followed by a constant feeding rate produced 109 g L^{-1} of dry biomass containing 63% PHA. The latter methodology improved the cumulative PHA productivity to 2.3 g L^{-1} h^{-1}, which is the highest MCL-PHA productivity ever reported. Analysis of the relationship between the final biomass concentration and the associated maximum cell generation rate (which is directly related to the maximum oxygen transfer rate) indicated that higher biomass levels could be attained by decreasing the substrate feeding rate at high biomass concentrations.

Key words: MCL-PHA, high cell density, decaying exponential feeding, oxygen limitation.

Résumé : Afin de retarder la limitation par l'oxygène responsable de la terminaison des fermentations aérobiques à densité cellulaire élevée, on a mis au point des stratégies de décroissance exponentielle de l'alimentation pour la production de poly(3-hydroxyalcanoates) de longueur de chaîne moyenne par le *Pseudomonas putida* KT2440. On a évalué deux méthodes d'alimentation pour contrôler la vitesse de génération de la biomasse et, en conséquence, contrôler la vitesse d'absorption d'oxygène par les cellules. Une stratégie de décroissance linéaire permet d'obtenir une production de 90 g L^{-1} de biomasse sèche contenant 65% de PHA, dans 31 heures, avec une productivité cumulative de 1,9 g L^{-1} h^{-1} alors qu'une décroissance exponentielle quadratique de la vitesse d'alimentation, suivie par une vitesse d'alimentation constante permet d'obtenir une production de 109 g L^{-1} de biomasse sèche contenant 63% de PHA. Cette dernière méthodologie a permis d'augmenter la productivité cumulative de PHA jusqu'à 2,3 g L^{-1} h^{-1} qui correspond à la valeur la plus élevée jamais rapportée pour une productivité cumulative de PHA. Une analyse de la relation entre la concentration finale de la biomasse et la vitesse maximale de génération de cellule qui lui est associée, qui est directement reliée à la vitesse maximum de transfert d'oxygène, indique que les niveaux les plus élevés de biomasses peuvent être atteints en diminuant la vitesse d'alimentation du substrat aux concentrations élevées de biomasse.

Mots-clés : MCLll-PHA, densité élevée de cellule, décroissance exponentielle de l'alimentation, limitation par l'oxygène

[Traduit par la Rédaction]

Received 16 November 2007. Accepted 15 March 2008. Published on the NRC Research Press Web site at canjchem.nrc.ca on 29 April 2008.

This paper is dedicated to Robert H. Marchessault in recognition of his many contributions to polysaccharide and biopolymer chemistry.

H. Maclean, Z. Sun, J. Ramsay, and B. Ramsay.[2,3]
Department of Chemical Engineering, Queen's University, Kingston, ON K7L 3N6, Canada

[1]This article is part of a Special Issue dedicated to Professor R. Marchessault.
[2]Corresponding author (e-mail: bruce.ramsay@chee.queensu.ca).
[3]Present address: Polyferm Canada Inc., RR1, Harrowsmith, ON K0H 1V0, Canada.

Introduction

Poly(3-hydroxyalkanoates) (PHAs) have attracted great interest as biodegradable and biocompatible substitutes for conventional polymers in recent years. Short-chain-length PHAs (SCL-PHAs), with repeating units containing 4 to 5 carbons, may be brittle due to a high degree of crystallinity. Medium-chain-length PHAs (MCL-PHAs), with repeating units of 6 or more carbons, are thermoelastomers. Potential applications are numerous because PHAs exhibit a wide variety of physical and chemical properties depending on their structure and the nature of covalently bound functional groups (1). Poly(3-hydroxybutyrate) (PHB) and poly(3-hydroxybutyrate-*co*-3-hydroxyvalerate) (PHBHV) are SCL-PHAs that have been produced on a commercial scale under the trade name Biopol. In contrast, MCL-PHAs have not

 doi:10.1139/V08-062 © 2008 NRC Canada

been commercialized. To make their production more commercially viable, strategies for increasing cell density, PHA content, and cumulative productivity have been investigated. High cell density is a prerequisite for achieving high PHA productivity, and high PHA content is important as it reduces separation and downstream processing costs. Fermentation processes for the production of MCL-PHAs have been reviewed recently (2).

MCL-PHA production processes have invariably incorporated a nutrient limitation because of the widely held belief that significant PHA production only occurs in the presence of excess carbon, while nitrogen or phosphorus limits growth. Therefore, many substrate-feeding strategies for fed-batch fermentations have involved an initial stage of rapid cell growth, followed by a nutrient-limited PHA accumulation stage (3, 4). However, some organisms have been shown to accumulate significant amounts of PHA during nutrient unlimited or carbon-limited growth, suggesting that nitrogen or phosphorus limitation is not always a necessity for substantial MCL-PHA accumulation (5, 6). When PHA is accumulated during carbon-limited growth, simple exponential feeding strategies can be applied. Recently, it was shown that *Pseudomonas putida* KT2440 produced large amounts of MCL-PHA during exponential carbon-limited growth on nonanoic acid at various predefined specific growth rates (7). This approach allowed high productivity but oxygen limitation inevitably occurred at high cell density causing nonanoic acid accumulation in the reactor. This led to cell lysis, uncontrollable foaming, and termination of the fermentation.

High oxygen demand is a common problem in high cell density aerobic cultivation (8). To avoid or delay oxygen limitation and therefore achieve higher cell concentrations and productivities, the oxygen uptake rate of the culture should be limited. Since oxygen uptake rate is roughly proportional to the cell generation rate (μX), oxygen limitation could be avoided by controlling μX below a certain critical value. Since cell concentration (X) keeps increasing in a fed-batch fermentation, a gradually decaying specific growth rate (μ) may be imposed to quickly achieve high cell densities, while avoiding the physiological disturbances that would result from rapidly decreasing μ. This work examines the application of two decaying exponential feeding strategies for the production of MCL-PHAs by *P. putida* KT2440.

Experimental

Microorganism and growth medium

P. putida KT2440 (ATCC 47054) was maintained in lyophiles and on nutrient agar plates at 4 °C. The inoculum medium contained (per litre): 4.70 g of $(NH_4)_2SO_4$, 0.80 g of $MgSO_4 \cdot 7H_2O$, 12.00 g of $Na_2HPO_4 \cdot 7H_2O$, 2.70 g of KH_2PO_4, 1.00 g of nutrient broth, and 9.00 g of glucose. The initial culture medium contained (per litre): 4.70 g of $(NH_4)_2SO_4$, 0.80 g of $MgSO_4 \cdot 7H_2O$, 18.00 g of $Na_2HPO_4 \cdot 7H_2O$, 4.05 g of KH_2PO_4, 10 mL trace element solution, and nonanoic acid as indicated in the substrate feeding section. The trace element solution contained (per litre): 10.0 g of $FeSO_4 \cdot 7H_2O$, 3.0 g of $CaCl_2 \cdot 2H_2O$, 2.2 g of $ZnSO_4 \cdot 7H_2O$, 0.5 g of $MnSO_4 \cdot 4H_2O$, 0.30 g of H_3BO_3, 0.20 g of $CoCl_2 \cdot 6H_2O$, 0.15 g of $Na_2MoO_4 \cdot 2H_2O$, 0.02 g of $NiCl_2 \cdot 6H_2O$, and 1.00 g of $CuSO_4 \cdot 5H_2O$. The pH was controlled with 14% (*w*/*v*) NH_4OH, which was also the nitrogen source. Nonanoic acid (NA, 98%, Spectrum Chemicals) was autoclaved and fed to the reactor according to the chosen feeding scheme. Additional $MgSO_4 \cdot 7H_2O$ was fed at a ratio of 0.033 g of $MgSO_4 \cdot 7H_2O$ g nonanoic acid^{-1}.

Fermentation conditions

The inoculum was cultivated in 500 mL shake flasks (100 mL medium) at 30 ± 1 °C and 200 rpm for approximately 12 h. Fed-batch fermentations were performed at 30 ± 1 °C with a 3.0 L initial working volume in a Minifors 5 L stirred tank bioreactor (Infors HT, Bottmingen, Switzerland). Data acquisition (dissolved oxygen, air outlet CO_2, nonanoic acid and base addition, and pH) and control was conducted with LabVIEW 6.1 (National Instruments). pH was controlled at 6.85 ± 0.05. Dissolved oxygen was measured with an Ingold polarographic probe and maintained at or above 40% air saturation by adjusting the agitation speed up to 1200 rpm and by automatically adjusting the mixture of air and pure oxygen via mass flow controllers to maintain a total gas flow at 1 vvm, until oxygen limitation occurred even at 1 vvm of pure oxygen. Exiting CO_2 was measured with an IR CO_2 monitor (Guardian Plus, Topac Inc. Hingham, MA, USA). Feeding of nonanoic acid with peristaltic pumps was automatically controlled based on the mass of the reservoirs.

Substrate feeding and control methods

Nonanoic acid feeding based on a linearly decaying specific growth rate

With an initial 1 g L^{-1} nonanoic acid in the reactor, exponential feeding of nonanoic acid controlled growth at 0.25 h^{-1} (7) until an estimated biomass concentration of 3 g L^{-1} was achieved. Feeding designed to achieve a linearly decaying specific growth rate was then imposed. The specific growth rate model was based on two user-defined parameters: initial specific growth rate, μ_{init}, and the time over which the growth rate would decrease to zero, t_{max}. The imposed specific growth rate followed eq. [1], where the t is the time from the start of the decaying exponential feeding (the dashed line in Fig 1).

$$[1] \qquad \mu = \frac{-\mu_{init}}{t_{max}} t + \mu_{init}$$

where μ_{init} was set at 0.25 h^{-1} with a corresponding t_{max} of 30 h. Biomass concentration was expected to follow eq. [2], where X_0 was estimated as 3 g L^{-1}. Nonanoic acid was fed according to eq. [3] to support this level of growth, based on the yield of biomass from nonanoic acid, $Y_{X/S}$ (0.8 g g^{-1}).

$$[2] \qquad X_t = X_0 e^{\frac{-\mu_{init}}{2t_{max}} t^2 + \mu_{init} t}$$

$$[3] \qquad S_t = \frac{X_t}{Y_{X/S}} = \frac{X_0 e^{\frac{-\mu_{init}}{2t_{max}} t^2 + \mu_{init}}}{Y_{X/S}}$$

© 2008 NRC Canada

Fig. 1. Growth and PHA production of *P. putida* KT2440 on nonanoic acid fed at a linearly decaying specific growth rate. The dashed line indicates the start of automated feeding.

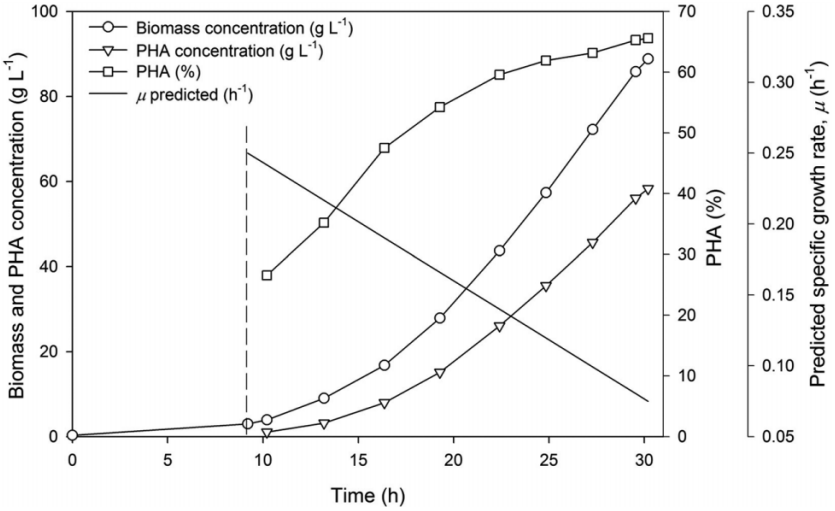

Quadratic decaying specific growth rate followed by constant feeding of nonanoic acid

Initially, 1 g L^{-1} nonanoic acid was added to the reactor and the culture was grown in a batch mode. Depletion of this carbon source was detected by a sudden decrease in CO_2 production. At this time, a quadratic model for the decaying specific growth rate was immediately imposed on the system. The quadratic model, shown as eq. [4], was based on the user defined parameters μ_{init} and t_{max}.

$$[4] \qquad \mu = \frac{-\mu_{init}}{t_{max}^2} t^2 + \mu_{init}$$

The μ_{init} was set as 0.45 h^{-1} and t_{max} was chosen as 15 h (based on simulations) to achieve high productivity while controlling μX below the set point, which was the value expected to cause an oxygen demand that exceeded the oxygen transfer capacity of the bioreactor (based on previous experience). Cell concentration was expected to follow eq. [5], where X_0 was estimated as 0.6 g L^{-1}, with nonanoic acid feeding shown in eq. [6].

$$[5] \qquad X_t = X_0 e^{\frac{-\mu_{init}}{3t_{max}^2} t^3 + \mu_{init} t}$$

$$[6] \qquad S_t = \frac{X_t}{Y_{X/S}} = \frac{X_0 e^{\frac{-\mu_{init}}{3t_{max}^2} t^3 + \mu_{init} t}}{Y_{X/S}}$$

The quadratic feeding strategy continued until the cell generation rate (μX) achieved its maximum set point of 7 g L^{-1} h^{-1}, at which time the system automatically switched to a constant rate of nonanoic acid feeding of 8.75 g L^{-1} h^{-1} of nonanoic acid based on $Y_{X/S}$ (0.8 g g^{-1}), as described previously (10).

Analytical procedures

Cell dry weight was determined after lyophilization of biomass obtained by centrifugation and washing of 5 mL culture broth at 13 000*g* for 15 min. The culture supernatant was saved for analysis of nonanoic acid and other nutrients. Nonanoic acid concentration was determined by gas chromatography analysis with decanoic acid as internal standard following methylation (11). Phosphate was measured via reduction of phosphomolybdate to molybdene blue (12). Ammonium was determined by the phenol-hypochlorite method (13). PHA content and composition was determined as previously described (7).

Results and discussion

Linear decaying exponential feeding

All previous *P. putida* KT2440 fermentations, in which exponential feeding at different constant specific growth rate was applied, ended with oxygen limitation (7). Since $dO_2/dt = Y_{O2/X}$ (dX/dt) and $dX/dt = \mu X$, oxygen limitation occurs when the oxygen transfer rate of the bioreactor cannot meet the high oxygen demand (dO_2/dt, g L^{-1} h^{-1}) caused by a high cell generation rate (dX/dt, or μX, g L^{-1} h^{-1}). To avoid or delay this limitation while still attaining high cell concentration, the specific growth rate can be controlled such that μX (or dX/dt) and consequently dO_2/dt do not exceed a critical value. A sudden decrease in the nonanoic acid feeding rate, which controls the specific growth rate, usually resulted in cell lysis, which in turn caused excessive foaming. Therefore, a gradually decaying specific growth rate should avoid such physiological disturbances. In previous fermentations, which had employed simple exponential feeding to obtain constant specific growth rates of 0.075 (unpublished data), 0.15, and 0.25 h^{-1} (7), before reaching the limit in the system oxygen transfer capacity the μX was 14.0, 10.5, and 6.4 g L^{-1} h^{-1}, with the highest biomass being obtained at the lower value. Based on this information, an upper boundary of in the decaying exponential feeding was set at the relatively conservative value, 7 g L^{-1} h^{-1}.

A linear decaying specific growth rate was imposed to test the effectiveness of a decaying feeding strategy. A biomass concentration of 3 g L^{-1} was initially attained using a proven

© 2008 NRC Canada

Fig. 2. Comparison of predicted and actual growth of *P. putida* KT2440 in decaying exponential fermentations. (*a*) Linearly decaying specific growth rate. (*b*) Quadratic decaying specific growth rate followed by a constant feeding of nonanoic acid.

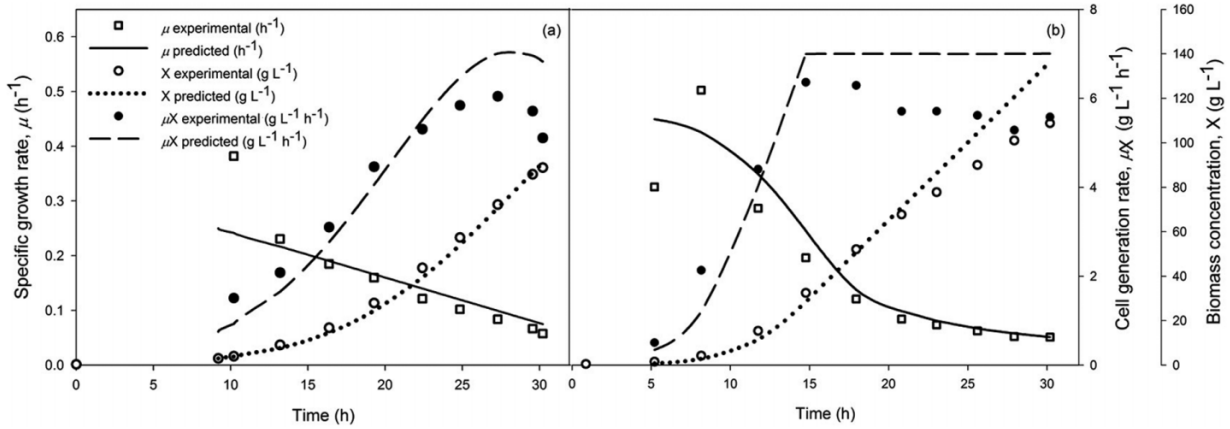

exponential feeding with 0.25 h^{-1} (Fig. 1, 0–9 h), followed by a decaying feeding rate imposed at 9.2 h. The μ_{init} and t_{max} in eqs. [1–3] were set as 0.25 h^{-1} and 30 h, respectively, as these values would never produce a μX greater than 7 g L^{-1} h^{-1}, but should attain a high cell concentration as seen in simulations (Fig. 2*a*, predicted plots). The imposed specific growth rate decreased linearly from the initial value of 0.25 h^{-1} to approximately 0.07 h^{-1} within 21 h (Fig. 1). Nonanoic acid was the only limiting factor throughout the fermentation.

The cell concentration in the reactor increased to a final value of 90 g L^{-1}. There was also substantial PHA accumulation. At the beginning of the fermentation no PHA was detected (data not shown) since the inoculum was grown on glucose and nutrient broth. By the end of the process, the PHA content of the cells had increased to 65%, corresponding to a final concentration of 58 g L^{-1} and a cumulative productivity of 1.9 g L^{-1} h^{-1}. However, the fermentation eventually ended when the dissolved oxygen concentration in the reactor dropped to zero. Oxygen limitation caused the nonanoic acid concentration in the reactor to accumulate to toxic levels, resulting in cell lysis and uncontrollable foaming.

The linear decaying exponential feeding strategy was promising. The actual biomass concentration, specific growth rate, and instantaneous cell generation rate followed the predicted trends quite closely (Fig. 2*a*), indicating that the culture growth was controlled by the feeding strategy. This feeding strategy allowed a higher final cell and PHA concentration than had been previously achieved by feeding at a constant specific growth rate (7). However, the μ_{init} of 0.25 h^{-1} was a conservative choice. A higher μ_{init} is possible if the actual μ of the culture can be determined from CO_2 production data during the initial growth (9). Although the linearly decreasing μ avoided μX from exceeding the upper boundary of 7 g L^{-1} h^{-1} (Fig. 2*a*, μX predicted), the culture grew well below its optimum μ for most of the fermentation. A less rapidly decreasing μ is preferable. Even after reaching the maximum μX set point, an unnecessary decrease in μX (and consequently the oxygen consumption rate) occurred because of the continual decrease in μ. Assuming that the maximum μX set point would avoid oxygen limitation as intended, biomass productivity could be improved if the system could operate at its maximum μX for as long as possible.

Quadratic decaying exponential feeding followed by a constant feed rate

Taking the above considerations into account, a quadratic decaying exponential feeding followed by a constant feed rate was designed to further increase final cell density, PHA concentration, and PHA productivity (Fig. 2*b*, predicted plots). The initial concentration of nonanoic acid in the reactor was 1 g L^{-1}. The μ_{max} during the batch cultivation (Fig. 3, 0–5 h) was estimated by CO_2 analysis to be approximately 0.6 h^{-1}, but to avoid overfeeding, the initial specific growth rate (μ_{init}) in the quadratic decaying feeding model (eqs. [4–6]) was chosen as 0.45 h^{-1}.

In the first stage of the feeding strategy, nonanoic acid was fed at a decreasing specific growth rate according to a quadratic model. The quadratic model allowed the maintenance of a higher specific growth rate than the linear decaying strategy (Fig. 3, 5–15 h). The maximum cell generation rate (7 g L^{-1} h^{-1}) was achieved more quickly using this strategy. These benefits were expected to improve productivity by reducing the total fermentation time. The quadratic decaying feeding strategy took approximately 10 h to attain the predicted maximum cell generation rate. Substrate feeding was then maintained at a constant value of 8.75 g L^{-1} h^{-1} nonanoic acid for the remainder of the fermentation. This constant nonanoic acid feed rate was intended to keep the cell generation rate constant at its maximum value and hence should keep the oxygen uptake rate at a sustainable level. However, after a total of 30 h of operation the dissolved oxygen in the reactor decreased to zero, and the fermentation ended because of oxygen limitation and consequent foaming.

The final biomass concentration in the reactor was 109 g L^{-1} and contained 63% of PHA. The final PHA concentration (68.5 g L^{-1}) corresponded to a cumulative PHA productivity of 2.3 g L^{-1} h^{-1}.

These results show a substantial improvement in the final biomass and also in the PHA productivity. The actual biomass concentration, specific growth rate, and instantaneous biomass productivity once again followed the predicted trends quite closely (Fig. 2*b*), with some deviation that was mostly caused by changes in volume that were not accounted for in the prediction. The cumulative PHA productivity that was attained using the decaying exponential

© 2008 NRC Canada

Fig. 3. Growth and PHA production of *P. putida* KT2440 on nonanoic acid fed at a quadratic decaying specific growth rate followed by a constant nonanoic acid feeding rate. The first dashed line indicates the start of the quadratic decaying specific growth rate model. The second dashed line represents the start of the constant feeding of nonanoic acid.

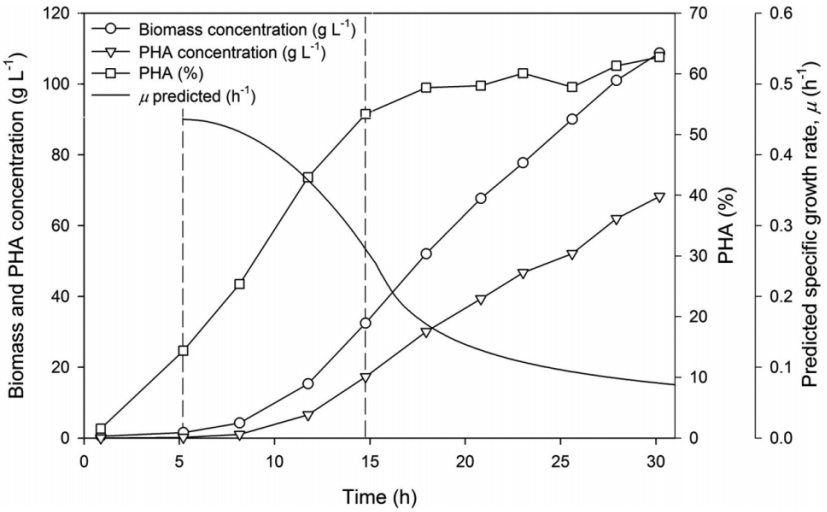

feeding strategy is the highest MCL-PHA productivity ever reported (2). The maximum biomass concentration achieved by conventional exponential feeding on this system was 85 g L^{-1} when the cells were grown at a constant specific growth rate of 0.075 h^{-1} (data not shown). However, the long fermentation time resulted in a low productivity of only 0.55 g L^{-1} h^{-1}. At higher constant growth rates, higher productivities were achieved but oxygen limitation resulted in a lower cell concentration (7). This feeding regime combines the advantages of high and low specific growth rates at appropriate times. The high initial specific growth rate decreased the amount of time required for the initial stage of the fermentation when biomass concentration was quite low and hence oxygen uptake rate was low. This decreased the fermentation time, which improved productivity. The low specific growth rate near the end of the fermentation decreased oxygen demand, which delayed oxygen limitation, and therefore allowed higher biomass concentrations to be attained.

Both feeding regimes produced MCL-PHA containing 62, 35, and 2 mol% hydroxynonanoate, hydroxyheptanoate, and hydroxyvalerate repeating units, respectively, with only 1 mol% of the repeating units containing even numbers of carbon. 3-Hydoxyoctanoate was the most common of the even carbon numbered repeating units, accounting for about 0.7 mol% of the total PHA repeating units. The composition was measured for every sample and did not vary significantly. While the polymer molecular weight was not measured during these fermentations, we have found that for this bacterial strain, it is typically in the range of 80–100 000 Da with a polydispersity index of less than 2.0 (unpublished data).

The relationship between cell concentration and oxygen transfer rate

A maximum cell generation rate of 7 g L^{-1} h^{-1} was chosen for the fermentations in this study based on the results of previous exponential feeding experiments when the culture was grown at constant specific growth rates. In the previous experiments, the cell generation rate increased throughout the fermentation until oxygen limitation was encountered at some maximum μX value. However, oxygen limitation was still encountered in the decaying exponential experiments and could not be avoided completely by this method. Analyzing results from different fermentations demonstrated that the attainable maximum cell generation rate (dX/dt or μX) decreased with the increase in final biomass concentration (Fig. 4), indicating that the maximum oxygen transfer rate also decreased. This relationship between cell density and the oxygen transfer rate has been observed by others. For example, in a high cell density cultivation of recombinant *Escherichia coli*, the oxygen transfer coefficient k_La decreased as the biomass concentration in the reactor increased (14).

There are several ways in which biomass concentration could affect oxygen transfer. Ju and Sundararajan (15) suggested that cells are able to affect oxygen transfer by modification of the medium, by their physical presence as solid particles, or through respiration at the gas–liquid interface. During MCL-PHA production, the appearance of the fermentation broth changed with increasing cell density. The broth became increasingly viscous with a milky yellow colour. Any cell lysis would result in the release of water-soluble macromolecules, such as DNA and RNA, into the fermentation broth. The resultant increase in viscosity would reduce oxygen transfer, which may explain why oxygen limitation occurred at lower cell generation rates when the cell density in the reactor was high.

Conclusions

Decaying exponential feeding strategies were developed in this study to solve the problem of early oxygen limitation resulting from exponential feeding with constant specific growth rate. High cell densities and PHA productivities were achieved by this novel feeding strategy. A cumulative PHA productivity of 2.3 g L^{-1} h^{-1} was obtained, representing the highest MCL-PHA productivity reported in the literature. Despite these improvements, decaying exponential feeding experiments still ended because of oxygen limitation, possibly

© 2008 NRC Canada

Fig. 4. Relationship between final biomass concentration and maximum cell generation rate attained by the current fermentation system with different exponential feeding strategies. Constant μ fermentation data (at 0.15 and 0.25 h^{-1}) are taken from Sun et al. (7).

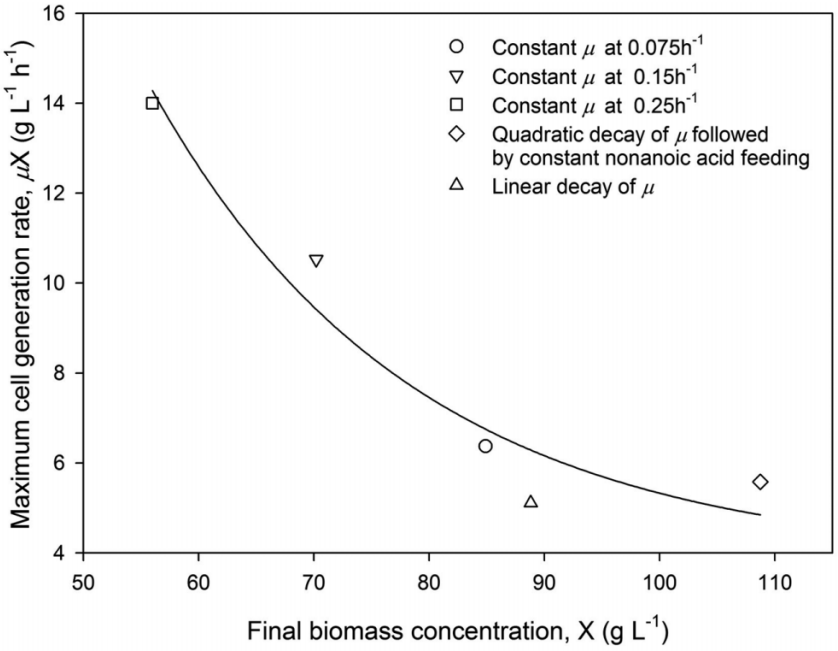

due to decreased oxygen transfer coefficient at high cell densities. An improved strategy would be to decrease the substrate feeding rate in accordance with the decreasing oxygen transfer rates encountered at high biomass concentrations

The final PHA content of 60%–65% in these fermentations was representative of results obtained previously. High PHA content within the cells is essential for cost-efficient separation as well as for further improvements in productivity. Further understanding of the mechanisms by which PHA is produced within the cell during carbon limited growth would give insight into how PHA content could be increased.

Acknowledgements

This research was supported by the Natural Science and Engineering Research Council of Canada and an Ontario Graduate Scholarship to HM.

References

1. B. Hazer, and A. Steinbüchel. Appl. Microbiol. Biotechnol. **74**, 1 (2007).
2. Z. Sun, J.A. Ramsay, M. Guay, and B.A. Ramsay. Appl. Microbiol. Biotechnol. **75**, 475 (2007).
3. S.Y. Lee, H.H. Wong, J.I. Choi, S.H. Lee, S.C. Lee, and C.S. Han. Biotechnol. Bioeng. **68**, 466 (2000).
4. B.S. Kim. Biotechnol. Lett. **24**, 125 (2002).
5. R. Durner, M. Zinn, B. Witholt, and T. Egli. Biotechnol. Bioeng. **72**, 278 (2001).
6. B. Kessler, R. Weusthuis, B. Witholt, and G. Eggink. Adv. Biochem. Eng. Biotechnol. **71**, 159 (2001).
7. Z. Sun, J.A. Ramsay, M. Guay, and B.A. Ramsay. Appl. Microbiol. Biotechnol. **74**, 69 (2007).
8. D. Riesenberg, and R. Guthke. Appl. Microbiol. Biotechnol. **51**, 422 (1999).
9. Z. Sun, J.A. Ramsay, M. Guay, and B.A. Ramsay. Appl. Microbiol. Biotechnol. **71**, 423 (2006).
10. Z. Sun, J.A. Ramsay, M. Guay, and B.A. Ramsay. J. Biotechnol. **132**, 280 (2007).
11. B.A. Ramsay, I. Saracovan, J.A. Ramsay, and R.H. Marchessault. Appl. Environ. Microbiol. **57**, 625 (1991).
12. L.S. Clesceri, A.E. Greenberg, and A.D. Eaton. Standard methods for the examination of water and wastewater. 20th ed. American Public Health Association, Wash. 1999.
13. M.W. Weatherburn. Anal. Chem. **39**, 971 (1967).
14. C.S. Shin, M.S. Hong, and J. Lee. Biotechnol. Lett. **10**, 679 (1996).
15. L.K. Ju and A. Sundararajan. Bioprocess Eng. **13**, 271 (1995).

© 2008 NRC Canada

Graft copolymers containing poly(3-hydroxyalkanoates) — A review on their synthesis, properties, and applications[1]

Sophie Nguyen

Abstract: The use of the poly(3-hydroxyalkanoates) in copolymer synthesis has received much interest, as the microbial polyester segments can bring interesting properties, such as biodegradability and biocompatibility. The synthesis, properties, and applications of graft copolymers containing poly(3-hydroxyalkanoates) as main chain or branches are reviewed here, with emphasis on the different preparation methods, which fit into the three main synthesis strategies of graft copolymers: "grafting onto", "grafting from", and "grafting through" or macromonomer methods.

Key words: poly(3-hydroxyalkanoates), graft copolymer, synthesis, properties, applications.

Résumé : L'utilisation des poly(3-hydroxyalcanoates) dans la synthèse de copolymères a suscité beaucoup d'intérêt, car les segments de polyesters microbiens peuvent apporter des propriétés intéressantes comme la biodégradabilité et la biocompatibilité. La synthèse, les propriétés, et les applications de copolymères greffés comprenant des poly(3-hydroxyalcanoates) comme chaines principales ou pendantes (branches) sont revues ici, en s'intéressant tout particulièrement aux différentes méthodes de préparation qui utilisent l'une ou l'autre des trois principales stratégies de synthèse des copolymères greffés: les méthodes de "greffage sur", "greffage à partir de", "greffage par" ou technique des macromonomères.

Mots-clés : poly(3-hydroxyalcanoates), copolymères greffés, synthèse, propriétés, applications.

[Traduit par la Rédaction]

Introduction

Graft copolymers represent interesting materials as their properties can be controlled by their chemical composition and their architecture, i.e., by the length of the different polymer blocks (1, 2) and the distribution of the grafted chains along the main chain. They can advantageously show properties of one copolymer moiety, while avoiding the macro-scaled phase-separation problems often encountered in binary polymer blends (1, 3, 4). In fact, one application of graft copolymers is their use as compatilizers in such blends (3, 4).

Poly(3-hydroxyalkanoates), PHAs, have received much attention over the past forty years as completely biodegradable plastics available from renewable sources (5–10). They are used by a large number of bacteria as carbon and energy reserve, stored in cytoplasmic granules (5–14), and their production was observed in more than 300 different microorganisms (11). In addition, they are biocompatible, provided sufficient purification from residual proteins, surfactants, or endotoxins has been performed (15). PHAs can be classified according to their side chain length: short chain length PHAs, scl-PHAs, have repeat units containing 3 to 5 carbon atoms; medium chain length PHAs, mcl-PHAs, contain 6 to 14 carbons; long chain length PHAs, lcl-PHAs, contain more than 14 carbon atoms in their repeat units (16, 17). For poly(3-hydroxyalkanoates), which hold the same number of carbon atoms between the ester functions in the main chain, properties vary with the side chain length, with scl-PHAs being hard crystalline polymers and PHAs with longer side chains being elastomers (15).

The present paper reviews the different synthesis methods applied to prepare graft copolymers with poly(3-hydroxyalkanoates) as main chain or grafted branches, with a number of different comonomers, as well as their properties and applications.

Received 20 November 2007. Accepted 3 March 2008. Published on the NRC Research Press Web site at canjchem.nrc.ca on 30 April 2008.

This paper is dedicated to Robert H. Marchessault in recognition of his many contributions to polysaccharide and biopolymer chemistry.

S. Nguyen. Bio Syntech Canada Inc., 475 Armand-Frappier Blvd., Laval, QC H7V 4B3, Canada (e-mail: sophie.nguyen@biosyntech.com).

[1]This article is part of a Special Issue dedicated to Professor R.H. Marchessault.

Synthesis of graft copolymers with PHA segments

Graft copolymers can be prepared by three main methods: "grafting onto", "grafting from", and "grafting through" or macromonomer technique (1). The grafting onto method involves the covalent coupling of reactive sites distributed along the copolymer main chain or trunk with end groups of copolymer segments (1), for example, by amidation (18, 19), esterification (20), or free-radical mechanism (21, 22). In the grafting from synthetic strategy, the polymer trunk is acti-

 doi:10.1139/V08-044 © 2008 NRC Canada

vated at sites along the chain, and grafted chains are grown from these active sites by monomer polymerization (1); for example, the monomer can be copolymerized using the trunk as macroinitiator with multiple initiation sites along its chain (23, 24). Graft copolymers can also be produced by copolymerization of a low molecular weight monomer with a macromonomer (1), defined as a polymer or oligomer bearing at least one polymerizable end group (25, 26). This approach is called the grafting through or macromonomer method, and compared to the grafting onto and grafting from methods, control of the branches can easily be achieved. The macromonomer is selected and prepared prior to copolymerization, and a wide range of chemical structures have been reported in the literature, with the macromonomer being a homopolymer, a random, or block copolymer; the size of the side chains is chosen with the length of the macromonomers; their distribution along the main chain is controlled by the comonomer reactivity ratios (1, 25–28).

Preparation by coupling reaction or the grafting onto technique

Yalpani et al. (18) reported the grafting of bacterial poly(3-hydroxybutyrate), PHB, segments (M_n 10 000) onto different polymers: chitosan (CS), by amidation via the amine group of carbohydrate repeat units; cellulose acetate, by transesterification; and poly(ethylenimine), by amidation (Scheme 1).

In the same fashion, poly(3-hydroxybutyrate-*co*-3-hydroxyvalerate), PHB/V, and poly(3-hydroxyoctanoate), PHO, oligomers (with M_n of ca. 14 700 and 77 300 for PHB/V, and M_n of ca. 19 100 for PHO) were grafted onto chitosan by amidation at the amine group of chitosan, to produce either chitosan-*g*-PHB/V or chitosan-*g*-PHO (Scheme 1) (19).

The "opposite" or "reverse" graft copolymers, PHB-*g*-chitosan and PHB/V-*g*-chitosan, were prepared by treatment of PHB and PHB/V (with 5 wt% of 3-hydroxyvalerate, HV, units) membranes with ozone followed by grafting of acrylic acid, AA, to introduce carboxyl groups along the PHA chains, which were esterified with either chitosan (M_w of 160 000, degree of deacetylation of 75%) or chitooligosaccharide (M_w of 1170) (20).

Free radical chemistry was also used to produce PHA with grafted copolymer branches. Cavallaro et al. (21) reported the production of PHB/V-*g*-poly(ε-caprolactone) by reactive blending of PHB/V (4 mol% of HV) with poly(ε-caprolactone), in the melt at 160 °C with peroxide initiators, either benzoyl peroxide, BPO, or dicumyl peroxide. It was observed that the process also induced free-radical cross-linking of PHB/V (21).

The mcl-PHA poly(β-hydroxynonanoate), PHN, was grafted with polystyrene, PS, by free-radical coupling reaction of PS bearing peroxide groups, obtained by polymerization of styrene with an oligoperoxide initiator, as seen in Scheme 2 (22).

In the same fashion, active PS and poly(methyl methacrylate), PMMA, containing either peroxide or peroxide and azo groups in the main chain were prepared (29). Grafting was achieved by free-radical methods, with the active polymers decomposing into macroradicals, which could abstract the proton at the C-3 carbon (-*C*H(C_6H_{13})-), creating radicals

Scheme 1. Preparation of chitosan-*g*-PHAs by grafting of PHAs onto chitosan (18, 19); AcOH: acetic acid, DMSO: dimethyl sulfoxide, DMF: dimethyl formamide.

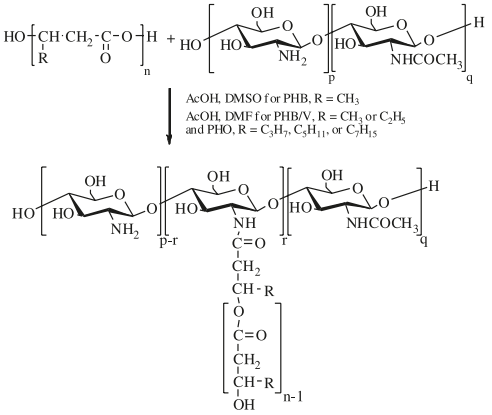

Scheme 2. Synthesis of poly(β-hydroxynonanoate)-*g*-polystyrene by grafting of polystyrene onto poly(β-hydroxynonanoate) (22).

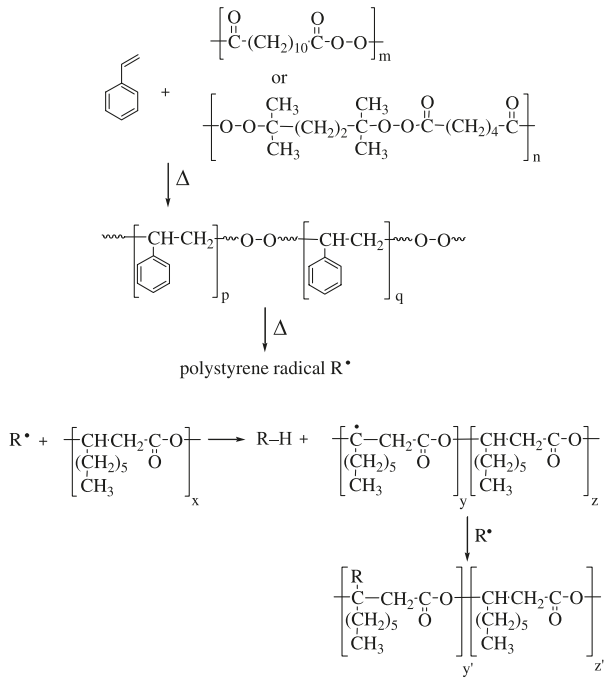

along the PHN main chain (29). Coupling of the macroradicals onto the free-radical sites of PHN produced the graft copolymers; however, homopolymers were also obtained by coupling macroradicals with the same chemical structure. In addition, the free-radical process could lead to PHN chain cleavage, which could produce graft copolymers with different chain lengths and homopolymers of lower molecular mass (29).

Mcl-PHAs with unsaturated side groups, obtained by feeding *Pseudomonas oleovorans* bacterium with mixtures of saturated and unsaturated acids, were also grafted with active oligomers of ethylene glycol (30), PS, and PMMA (31). The low molecular mass poly(ethylene glycol), PEG (400 g/mol), was functionalized at both ends with 4,4′-azobis(4-cyanovaleryl chloride) or 2,2′-azobis(isobutyronitrile), and the

© 2008 NRC Canada

Scheme 3. Poly(3-hydroxyoctanoate-*co*-3-hydroxyundecenoate)-*g*-poly(ethylene glycol) and poly(3-hydroxyoctanoate-*co*-3-hydroxyundecenoate)-*g*-poly(lactic acid) by grafting of poly(ethylene glycol) or poly(lactic acid) onto the PHA (32); DCC: *N*,*N*′-dicyclohexyl carbodiimide, DMAP: 4-(dimethylamino)pyridine.

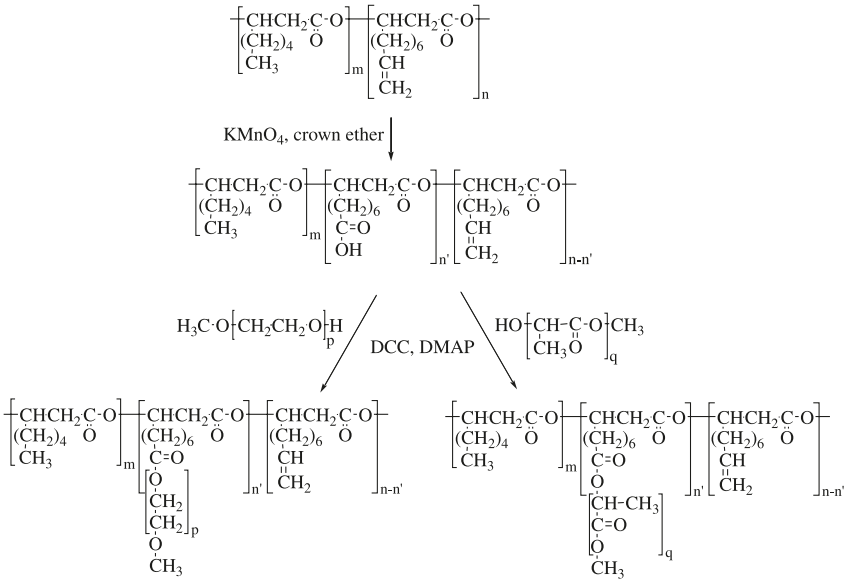

obtained polyazoester was grafted by free-radical reaction onto the unsaturated PHA (30). Active oligomers of styrene and methyl methacrylate, MMA, were obtained by polymerization with an oligo(terephthaloyl peroxide) initiator, to yield polymers with peroxide groups in the polymer chain, and M_w between 36 000 and 57 000 for PS and 52 000 and 76 000 for PMMA (31). These active polymers were then grafted onto the PHA with unsaturated side chains using the peroxy radicals (31).

Graft copolymers of mcl-PHA as the main chain and PEG or poly(lactic acid), PLA, as branches were reported by Renard et al. (32) (Scheme 3). Bacterial poly(3-hydroxyoctanoate-*co*-3-hydroxyundecenoate) was obtained by feeding *P. oleovorans* with sodium octanoate and 10-undecenoic acid, and the unsaturated side groups $-(CH_2)_6-CH=CH_2$ underwent oxidation using potassium permanganate and a crown ether to yield side groups bearing carboxylic acid functions ($-(CH_2)_6-COOH$). PEG or PLA oligomers, with one hydroxyl end and the other end protected, were then coupled onto the PHA by esterification of the carboxylic acid groups on the PHA using carbodiimide activation (32).

More recently, Zhijiang and Zhihong (33) reported the synthesis of graft copolymers of PHB and PEG, using PEG oligomer (M_n of 4000) functionalized at both ends with acryloyl chloride to transform the two hydroxyl ends into photoactive acrylate ($-O-C(=O)-CH=CH_2$) ends. The graft copolymers of PHB and PEG were obtained by UV-irradiation of a concentrated solution of the acrylic PEG and PHB in chloroform (33).

The grafting from technique

Anionic polymerization

Kowalczuk et al. (23) reported the preparation of PMMA-*g*-PHB by anionic polymerization of β-butyrolactone on PMMA chains (Scheme 4). The latter were functionalized to become macroinitiators of β-butyrolactone polymerization by partial saponification yielding randomly distributed carboxylate anions, which were activated by complexation with 18-crown-6 counterion (23). It should be noted that the polymerization produced atactic PHB side chains (23).

Scheme 4. Poly(methyl methacrylate)-*g*-PHB by grafting of PHB from poly(methyl methacrylate) (23); 18-C-6: 18-crown-6 ether, β-BL: β-butyrolactone.

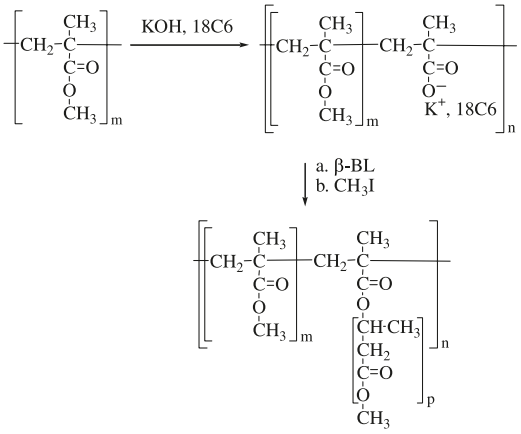

Free radical polymerization (FRP)

Radiation polymerization

Graft copolymers with PHB or PHB/V as the main polymer chain were reported by grafting by gamma radiation polymerization of various monomers: MMA, 2-hydroxyethyl methacrylate, HEMA, styrene, isoprene, and AA (34–39). MMA (35, 38), HEMA (35, 38), and styrene (36, 40) were graft-polymerized on PHB and PHB/V (24 mol% of HV units) by irradiation with ^{60}Co γ-rays at low doses, by two different methods: direct irradiation of the PHA in monomer solution and pre-irradiation of the PHA at –78 °C at a dose

© 2008 NRC Canada

rate of 5 kGy·h^{-1} followed by monomer polymerization on the irradiated PHA. X_g, the degree of grafting, defined as the percent increase of polymer mass based on the original polymer sample mass, was found to increase with increasing pre-irradiation dose and to level off at ca. 5 kGy, and was lower for PHB-*g*-PMMA than for PHB/V-*g*-PMMA, because of the higher crystallinity of PHB compared to PHB/V (38). In the case of PHB-*g*-PS, X_g increased with increasing pre-irradiation dose, from 5 to 15 kGy and grafting temperature from 30 to 80 °C, while for PHB/V-*g*-PS, it was found higher at 50 °C than at 30 or 70 °C (36). Styrene grafting on PHB and PHB/V produced PHA-*g*-PS with X_g lower than for MMA grafting on the same PHAs (36).

Radiation-induced grafting from mcl-PHA was also reported, as PMMA was grafted from poly(β-hydroxynonanoate) by bulk copolymerization of MMA with ^{60}Co γ-rays at 8.5 kGy (41).

Polyisoprene was also grafted on PHB by polymerization of isoprene in methanol, induced by direct irradiation with ^{60}Co γ-rays at 21.62 kGy·min^{-1} (37).

Acrylic acid was polymerized on PHB/V (with 8% of HV units) melt processed disks and solvent cast films to produce PHB/V-*g*-poly(acrylic acid) with ^{60}Co γ-irradiation at a dose rate of ca. 4.5 kGy·h^{-1} (39). It was observed that rather short poly(acrylic acid), PAA, side chains were produced, with cross-linking of PAA with higher irradiation doses (39). The graft copolymerization of AA on PHB induced by pre-irradiation of PHB films was reported by Wada et al. (42). It was observed that increasing the dose level increased X_g and decreased molecular mass of the irradiated PHB films, without cross-linking, contrary to the AA grafting on PHB/V films (39, 42). The same group used pre-irradiation techniques to graft copolymerize vinyl acetate, VAc, from PHB powder or film (43). PHB powder was pre-irradiated with ^{60}Co γ-rays before bulk copolymerization of VAc at 60 °C, while pre-irradiated PHB film was grafted with poly(vinyl acetate), PVAc, branches by emulsion polymerization (43, 44). The PVAc chains were further saponified into poly(vinyl alcohol), PVA, to partially convert the branches of PVAc to PVA (43).

Grafting by plasma glow discharge

Oxygen plasma glow discharge was another method used to induce the graft polymerization of AA on films of PHB/V (with 34 mol% of HV units) (45). The peroxides produced at the PHB/V surface by plasma glow discharge were used to catalyze the monomer polymerization at 75 °C in aqueous solution (45). The grafted PAA chains were further coupled with amino-terminated poly(ethylene oxide), PEO (600 g/mol), by amidation with carbodiimide activation, to produce PHB/V-*g*-(PAA-*b*-PEO) (45).

Grafting induced by ozone treatment

Tesema et al. (46) reported the preparation of PHB/V-*g*-poly(methacrylic acid) to ultimately immobilize collagen on the PHB/V surfaces. PHB/V (with 8 wt% of HV units) films were treated with ozone to produce peroxide groups, which were subsequently grafted with poly(methacrylic acid), PMA, branches produced by polymerization of the monomer in the presence of sulfuric acid and iron sulfate (46).

Scheme 5. PHB-*g*-poly(methyl methacrylate) by grafting of poly(methyl methacrylate) from PHB (3); BPO: benzoyl peroxide.

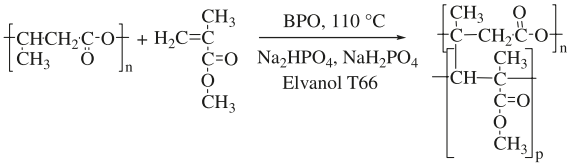

Photografting

Photopolymerization was also used to graft polymer branches on PHB/V films. Acrylamide was polymerized on PHB/V (8% of polyhydroxyvalerate) films using benzophenone as initiator and a high-pressure mercury lamp under nitrogen flow to produce PHB/V-*g*-polyacrylamide (47). Increases in acrylamide monomer concentration and irradiation time were shown to enhance X_g and the grafting efficiency (percentage gain in polymer mass compared to initial acrylamide monomer mass) (47).

Free radical polymerization initiated by benzoyl peroxide

Avella et al. (3) reported the reactive blending of PHB with PMMA with weight ratios PHB/PMMA of either 70/30 or 80/20, where blends of PHB and PMMA containing PHB-*g*-PMMA graft copolymers were formed by free-radical water suspension polymerization of MMA in the presence of PHB (M_w of 540 000) (Scheme 5). MMA was polymerized using BPO as initiator, at 110 °C in an aqueous dispersion of PHB with sodium phosphate dibasic (Na_2HPO_4), sodium phosphate monobasic (NaH_2PO_4), and poly(vinyl alcohol) (Elvanol T66) as suspending agents (3). PMMA homopolymer was found to be the main polymerization product as the produced graft copolymer represented only ca. 5% of the original blend, because of the low accessibility of PHB towards MMA and PMMA growing chains (3). NMR structural analysis of the isolated graft copolymers using 1D-^{1}H NMR and NOESY experiments showed that the PMMA branches were grafted on PHB by covalent bonding between the C-3 carbon (*C*H(CH_3)) of PHB and the vinyl CH (*C*H-C(CH_3)($COOCH_3$)) of MMA repeat unit (3). The grafting mechanism would include both the formation of PHB macroradical at the C-3 atom by chain transfer from a growing PMMA chain to PHB, and the formation of PMMA secondary macroradical within the PMMA chain at one vinyl carbon by chain transfer to PMMA from another growing PMMA chain (3).

Wu (48) reported the grafting of AA onto PHB with free-radical methods using BPO in xylene solution at 85 °C, with a low degree of grafting, at ca. 5.75 wt%. Blending of the grafted PHB with wood flour at 190 °C at 50 rpm for 15 min enabled their covalent coupling by esterication of the carboxyl groups of acrylic acid-funtionalized PHB with the hydroxyl functions of the wood flour (48).

Phenyl vinyl ketone was polymerized on PHB/V dissolved in 1,2-dichloroethane by free-radical polymerization initiated by BPO, producing both the homopolymer, poly(phenyl vinyl ketone) and the graft copolymer PHB/V-*g*-poly(phenyl vinyl ketone) (Scheme 6) (49). Mcl-PHA with unsaturated side chains was also grafted with methyl methacrylate using free-radical methods and BPO as initiator (50).

© 2008 NRC Canada

Scheme 6. Free radical grafting of phenyl vinyl ketone, acrylamide, *N*-vinylpyrrolidone, and 2-hydroxyethyl methacrylate from PHB/V (49, 51–53).

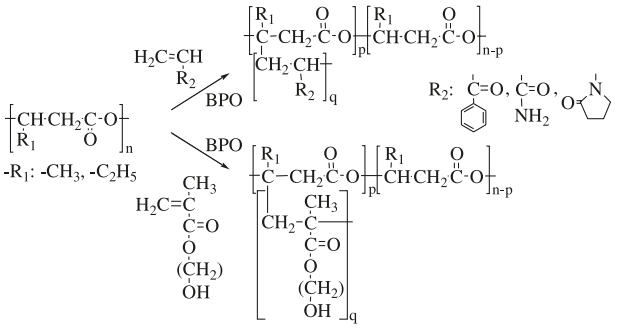

Polyacrylamide was grafted on PHB/V films by bulk polymerization of acrylamide monomer (Scheme 6) (51). In the same fashion, PHB/V films (with 12% of HV units) were grafted with poly(2-hydroxyethyl methacrylate), PHEMA, to increase the surface hydrophilicity and enhance their interaction with cells (Scheme 6) (52). In both cases, the monomer was polymerized in aqueous medium by free-radical methods, initiated by BPO, in the presence of the PHB/V films. The process was performed heterogenously, as the monomers were water soluble (polyacrylamide was water soluble, PHEMA was poorly soluble in water), and BPO and PHB/V were water insoluble. Both the grafts on the films and the homopolymers were obtained, the latter in large amounts (51, 52). Indeed, Lao et al. (52) observed that the homopolymerization was predominant, with ca. 95% of the monomer being homopolymerized and 5% being grafted.

The preparation of PHB/V-*g*-poly(*N*-vinylpyrrolidone) in homogenous medium was also recently reported by Wang and co-workers, using free-radical methods (Scheme 6) (53). *N*-vinylpyrrolidone was graft-copolymerized from PHB/V (3.57 mol% of HV units) in chlorobenzene solution with BPO as initiator, with a maximum X_g reaching 10.48% (53). Again, mixtures of poly(*N*-vinylpyrrolidone) homopolymer and graft copolymers were produced, and they could not be separated from each other (53).

Free radical grafting was possibly produced either by growing from the C-3 carbon (-*C*H(R)-) of the PHA, where the protons could be abstracted by BPO to form the macroradicals, as these protons were the most acidic ones along the PHA chains and (or) by polymer chain radical transfer to the PHA backbone (51–53).

Controlled free-radical polymerization

Brush type graft copolymers, PHB-*g*-PMMA, were reported by Arslan et al. (24) by atom transfer radical polymerization (ATRP) of MMA from PHB oligomers. Solutions of low to medium molecular mass PHB (M_n of ca. 14 900, 77 300, or 93 100) in a mixture of chloroform, $CHCl_3$, and carbon tetrachloride, CCl_4 ($CHCl_3/CCl_4$ volume ratio of 75/25) were exposed to chlorine gas to produce PHB partially chlorinated at the methyl side group, i.e., with a side group $-CH_2X$, X being either H or Cl atom and with decreased molecular mass because of hydrolysis side-reaction. The chlorinated PHB oligomers (M_n from ca. 2 500 to 17 400) were then used as macroinititators in the ATRP of MMA in toluene at 90 °C, with 2,2′-bipyridine and copper(I) bromide as the catalyst system (reversible termination agent for ATRP) to produce the graft copolymers (24).

Scheme 7. Preparation of poly(methyl methacrylate)-*g*-PHB by the macromonomer method (28, 54); AIBN: 2,2′-azobis(isobutyronitrile), HMTETA: 1,1,4,7,10,10-hexamethyltriethylenetetramine.

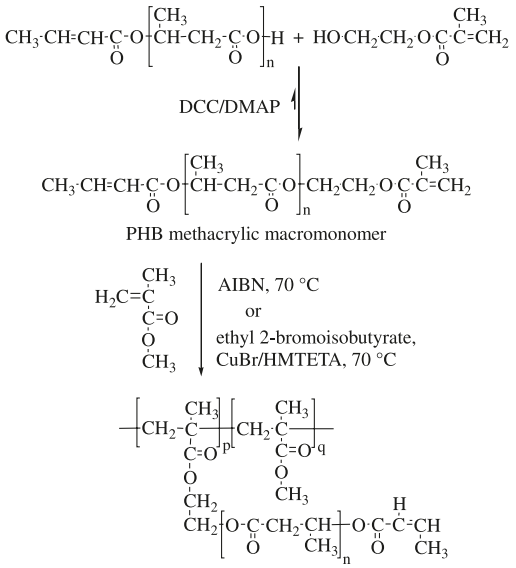

Synthesis by the grafting through or macromonomer technique

Graft copolymers of PMMA with isotactic PHB branches were produced by copolymerization of MMA and methacrylic bacterial PHB macromonomers, with conventional (28, 54) and controlled (ATRP) free-radical polymerization methods (28, 55). Nguyen et al. (56) used isotactic PHB oligomers obtained by thermal degradation; since the unsaturated, crotonate end was not easily polymerizable by free-radical methods (56, 57), the other end, bearing a carboxylic acid, was subsequently esterified with HEMA using carbodiimide chemistry to introduce a methacrylic, polymerizable with free radicals, end group (54). The obtained PHB macromonomers were then copolymerized with methacrylate in anisole solution at 70 °C by conventional free-radical copolymerization and by ATR copolymerization (28, 54). The size of the PHB side chains was determined with ^{1}H NMR spectroscopy with the peak integral ratio of 3-hydroxybutyrate, HB, repeat unit protons to the ones of the crotonate end group and was found to be only 5% different from the one of PHB macromonomers before the copolymerization, confirming that the crotonate groups did not participate in the copolymerization (28). PMMA-*g*-PHB copolymers obtained by conventional FRP displayed rather large polydispersity indexes, as expected, with a random distribution of the PHB branches suggested by the single glass transitions observed (54). ATRP of MMA with PHB macromonomers was found to produce, with limited chain transfer, more monodisperse graft copolymers of lower molecular weight (28) (Scheme 7).

Following the same macromonomer functionalization and ATRP methods as Nguyen and Marchessault (28, 54),

© 2008 NRC Canada

Table 1. Enzymatic degradability of graft copolymers of PHA films, exposed to extracellular PHB depolymerase if not mentionned otherwise.

Graft copolymers	X_g (%)	Weight loss (%)		Type of polymer films (ref.)
		Graft copolymer	PHA homopolymer	
PHB-*g*-PMMA	ca. 50	16	60	Solvent-cast films (38)
PHB/V-*g*-PMMA	ca. 50	13	46	
PHB-*g*-PHEMA	ca. 15	ca. 75	60	
PHB/V-*g*-PHEMA	ca. 20	ca. 50	46	
PHB-*g*-PAA	<5	Extensive decrease compared to PHB[a]	NA[b]	PHB films, which underwent grafting (42)
	≥5	None		
	12	Higher than for PHB[a]		PHB films, which underwent grafting and hot-pressing (42)
PHB-*g*-PVAc	10, 70	None	100	Solvent-cast films of polymer powder (43)
PHB-*g*-PVA	70	ca. 50	100	
PHB-*g*-PVAc, PHB-*g*-PVA	1–5	Extensive decrease compared to PHB[a]	NA[b]	PHB films, which underwent grafting (43)
	≥5	None		
PHB-*g*-PS	4	5	95	Solvent-cast films (40)
PHB/V-*g*-PS	8	90	100	
PHB-*g*-PS	4	30	80	Hot-pressed films (40)
PHB/V-*g*-PS	10	25	90	
PHB-*g*-PEG[c]	22	90	80	(33)

[a]No weight loss % data provided.
[b]Not available.
[c]Degradation by lysozyme.

Neugebauer et al. (55) synthesized graft copolymers of methacrylates with PHB macromonomers. Atactic PHB oligomers were prepared by anionic polymerization of β-butyrolactone, while isotactic PHB oligomers were prepared by two different methods: partial saponification of high molecular mass bacterial PHB, using potassium hydroxide and 18-crown-6 ether according to Adamus (58) and thermal degradation according to Nguyen et al. (56). Copolymerizations by ATRP of the PHB macromonomers were performed with methacrylates of increasing PEG chain length: MMA, ethylene glycol methyl ether methacrylate, and PEG methyl ether methacrylate, with a degree of polymerization of PEG of 5 and 23 (55).

Properties

A comparison of the enzymatic degradability results of PHA graft copolymers is shown in Table 1. Enzymatic degradability studies of PHB-*g*-PMMA, PHB/V-*g*-PMMA, PHB-*g*-PHEMA, and PHB/V-*g*-PHEMA produced by radiation polymerization of the methacrylate monomer on the PHA were reported by Mitomo et al. (38). It was shown that the degradability of solution-cast PHB-*g*-PMMA and PHB/V-*g*-PMMA with PHB depolymerase was significantly reduced compared to the ungrafted PHA polymers. On the contrary, degradability of PHB-*g*-PHEMA and PHB/V-*g*-PHEMA were higher than the corresponding PHA homopolymer at a degree of grafting (X_g) lower than 20%, because of the hydrophilicity of HEMA improving the wettability with the enzyme (38).

The enzymatic degradability of PHB-*g*-PAA and PHB-*g*-PVAc films subjected to PHB depolymerase from *Ralstonia pickettii* T1 was shown to be tuned by the X_g (degree of grafting) of the comonomer branches, and further treatment of the graft copolymers (42, 43). PHB-*g*-PAA and PHB-*g*-PVAc films displayed decreased degradability with increasing X_g, with no degradation observed for films with X_g above 5% as the surface was covered by either non-degradable PAA or hydrophobic PVAc, which screened PHB from the depolymerase enzyme (42, 43). However, when the PHB-*g*-PAA films were thermally remolded by hot-pressing, enzymatic degradability towards the PHB depolymerase was shown to increase with increasing X_g, up to 12%, and then decreased with a X_g higher than 12% (42). The degradability was retrieved by the dispersion of the PAA branches during the thermal remolding, enabling areas of degradable PHB at the surface (42). PHB-*g*-PVAc films were saponified in mild conditions to avoid PHB degradation as a side-reaction and subjected to enzymatic degradability studies (43). Little weight loss was observed when the films were exposed to PHB depolymerase enzyme, because of the coverage of the surface with the saponified branches; however, the saponified PHB-*g*-PVAc films degraded in environmental water while the untreated PHB-*g*-PVAc films did not, as both PVA and PHB were degraded by micro-organisms present in the water (43). This non-degradability of the PHB-*g*-PVAc films also confirmed that the non-degradable branches covered the surface of the films (43).

The enzymatic degradability of graft copolymers of PHB and PEG towards lysozyme was studied by Zhijiang and Zhihong (33). It was shown that the degradability was stronger with increasing PEG graft content, which was attributed to a reduced crystallinity of PHB and the hydrophilicity of PEG (33).

Thermal stability and enzymatic degradability of PHB-*g*-PS and PHB/V-*g*-PS, obtained by radiation grafting of styrene on

© 2008 NRC Canada

the PHAs (36), were studied by Bahari et al. (40). Both graft copolymers displayed higher thermal stability with a low degree of grafting (X_g of 9%) than for the corresponding PHA. Solution-cast PHB-*g*-PS and PHB/V-*g*-PS degraded more slowly than ungrafted PHB when subjected to PHB depolymerase, which, in the same fashion as for films of PHB-*g*-PAA and PHB-*g*-PVAc (42, 43), was because of hydrophobic coating of the surface by the comonomer, which reduced the affinity of the enzyme to the PHAs (40).

PMMA-*g*-PHB graft copolymers with atactic PHB branches were shown to combine the thermal stability behavior of both homopolymers, with thermogravimetric analysis showing two weight losses from the degradation of the two types of polymer segments (4).

Wang et al. (53) reported that the thermal stability of PHB/V-*g*-poly(*N*-vinylpyrrolidone) was dependent on X_g and was significantly improved at X_g of 10.48%; T_m, the melting point, was unchanged with X_g between 0% and 10.48%; T_d, the decomposition temperature, and T_{95}, the temperature at which the residual mass reaches 95% of the original mass, were both found 30 °C higher than for ungrafted PHB/V (53).

Thermal stability of chitosan-*g*-PHB/V and chitosan-*g*-PHO was studied by Arslan et al. (19). Thermogravimetric analysis was performed on the graft copolymers and compared to their corresponding homopolymers. The decomposition temperatures (T_d) were determined to be at 340 °C and ca. 100 °C (small peak) for water loss for chitosan, ca. 300 and 150 °C (small peak) for PHB/V, and 300 °C for PHO. Chitosan-*g*-PHA graft copolymers showed weaker thermal stability than for their corresponding homopolymers, with chitosan-*g*-PHB/V displaying two decomposition temperatures at ca. 255–181 and 160 °C (small peak), and chitosan-*g*-PHO exhibiting three decomposition temperatures, at ca. 260 °C (for PHO), 300 °C (for chitosan), and 70 °C for water loss (small peak) (19).

Biodegradability and antibacterial activity of PHB and PHB/V membranes grafted with acrylic acid, chitosan, CS, and chitooligosaccharide, COS, were assessed by Hu et al. (20). When the polymer membranes were incubated in a medium with *Alcaligenes faecalis* (ATCC 25094) cells, AA-grafted PHAs showed higher degradability then PHV and PHB/V membranes as AA-grafting increased the hydrophilicity of the surfaces, therefore increasing their accessibility to the bacterial attack (20). CS or COS-grafting increased further the hydrophicility of the membranes; however, because of the antibacterial activities of CS and COS, which reduced the number of bacteria, and to smoother surfaces after the grafting, which limited their accessibility to the bacteria, the biodegradability was lower than the ungrafted membranes (20). Antibacterial activity of the CS and COS-grafted PHA membranes was shown to be higher than the ungrafted PHAs for four clinically infectious bacteria: two Gram-negative ones, *Escherichia coli* and *Pseudomonas aeruginosa*, and two Gram-positive ones, methicilin-resistant *Staphyloccocus aureus*, MRSA, and *S. aureus* strain-2. The antibacterial activity of CS and COS-grafted PHAs was observed, from the highest to the lowest, with *E. coli*, *P. aeruginosa*, *S. aureus*-2, and MRSA (20).

Cell compatibility of PHB/V films modified with photografting of polyacrylamide to enable immobilization of bioactive materials, e.g., oligopeptides, proteins, glycosaminoglycan, or growth factors was studied by Ke et al. (47). Marrow stromal cells from sheep were cultured on the grafted and ungrafted films, and it was observed that the cells were well spread on the grafted films with a cell attachment efficiency increasing with the grafting percentage, i.e., with increased concentration of polyacrylamide on the PHB/V films, showing their biocompatibility with this type of cells (47).

Mechanical properties of PHB were found to be improved by subjecting the polyester to reactive blending with PMMA, which produced blends (with either 30 or 20 wt% of PMMA) containing ca. 5% of PHB-*g*-PMMA (3). Flexural testing showed that PMMA acted as a rigid filler, as the flexural modulus was improved for both blends of PHB/PMMA with or without PHB-*g*-PMMA; however, the fracture toughness of the blends, measured with impact testing, was only superior to the one of pure PHB when the graft copolymers were present in the blends, acting as compatibilizer by improving the interfacial adhesion between PHB and PMMA homopolymers (3).

Ceccorulli et al. (4) showed that the addition of 5% of PMMA-*g*-PHB with 67 mol% of HB units improved significantly the ductility of blends of PMMA/PHB containing 30 to 50% of PHB, by inhibition of PHB crystallization. However, no improvement of mechanical properties was observed with PMMA/PHB blends with PHB content higher than 50%, as the graft copolymer presence could not prevent PHB crystallization (4).

The mechanical properties of PHN were found to be improved when grafted with PS in low contents, with both tensile strength and elongation higher than pure PHN (29). It should be noted that graft copolymers with PS contents higher than 20 wt% showed lower elongation. Tensile strength and elongation of PHN grafted with low PS amounts (6 wt%) were measured and compared to the ones of a blend of PHN/PS with the same PS content, as well as the ones of pure PHN; while both the graft copolymer and the blend displayed higher tensile strength and elongation, the graft copolymer showed the highest tensile strength and the blend, the highest elongation (29).

When PHB was replaced by PHB grafted with AA in blends with wood flours, it was found that the latter were coupled to PHB via the carboxyl functions of acrylic acid, ultimately producing a graft copolymer of PHB and wood flours (48). Biodegradability in soil and with α-amylase enzyme, and mechanical performance, with the tensile strength at breakpoint, were studied for the blends of wood flours with either ungrafted or grafted PHB (48). While the biodegradability of PHB grafted with wood flours was found slightly lower than for blends with ungrafted PHB, its tensile strength at breakpoint was higher and remained stable when the wood flours content in the blends was increased, while the tensile strength of blends of PHB with wood flours decreased with increasing wood flours content (48).

Applications

Among the applications of copolymers containing PHA moieties is their use as surfactants or compatibilizers in blends of the corresponding homopolymers (3, 4, 59), as most polymer combinations are immiscible and create

© 2008 NRC Canada

phase-separation into macroscopic domains in their blends, resulting in mechanically weak materials (4). Avella et al. (3) showed that a low amount of PHB-*g*-PMMA copolymers could act as compatiblizer of PHB/PMMA blends containing either 20% or 30% of PMMA (3). Ceccorulli et al. (4) studied the compatibility of blends of PMMA and bacterial PHB in the presence of graft copolymers PMMA-*g*-PHB with atactic PHB branches. It was shown that while PMMA and bacterial PHB are partially miscible up to a PHB content of 20%, blends containing 30%–50% of PHB could be compatibilized with 5% of PMMA-*g*-PHB with 67 mol% of HB units (4).

The ability of PHAs, and especially their oligomers, to enhance in vivo degradability and biocompatibility in a copolymer makes them suitable for developments in pharmaceutical and surgical fields (60). In addition, PHB is piezoelectric so it could promote bone growth, a property that other degradable polymers with faster degradation do not possess, e.g., PLA (61, 62). PHAs have been proposed to be incorporated in formulations of biocompatible and partially or completely biodegradable bone cements (63–66). Acrylic bone cements have been used mainly in total joint replacement surgeries for prosthesis fixation inside the bone and transfer of body weight and service load (67–70). They are prepared by mixing a liquid, mostly composed of MMA monomer with *N*,*N*-dimethyl-*p*-toluidine, with a powder, mainly PMMA-based prepolymer with BPO. The peroxide initiates the free-radical polymerization of MMA when activated by *N*,*N*-dimethyl-*p*-toluidine, producing the cement dough (69, 70). Since one major drawback of the cemented joint implant technique is aseptic loosening, which can decrease the prosthesis lifetime by 30% (69), and classical PMMA-based bone cements are unable to resorb or allow bone ingrowth (71), partially degradable cement with enhanced compatibility were proposed to allow bone ingrowth inside the progressively, partially degraded cement (63–65, 72). Copolymers with PMMA and low molecular mass bacterial PHB hold interesting potential as a component in bone cement formulations, bringing degradability, expected enhancement of the cement biocompatibility, and compatibility with the methacrylic ingredients. PMMA-*g*-PHB copolymers obtained by free-radical copolymerization of MMA with methacrylic PHB macromonomers (28, 54), were incorporated in the powder component of a commercial acrylic bone cement formulation, antibiotic Simplex®, which could contain up to 13.5 wt% of the graft copolymers (66). Formulations with higher graft copolymer content produced unprocessable soft to friable material, probably because of the difference in solubility and swelling capacity of PMMA and graft copolymers when mixed with the liquid MMA monomer component (66). Micropores were observed in the processable modified cements (with up to 13.5 wt% of the graft copolymer) with volumetric porosities ranging from 13.5% to 16.9% (66). However, their ultimate compression strengths, measured at ca. 85 MPa, were similar to the one of unmodified commercial cement and exceeded the ASTM (American society for testing and materials) F451 requirements (minimum value of 70 MPa) (66).

The suitability of PHB/V surfaces to immobilize biomolecules for the design of biomaterials for tissue engineering was shown with glucosamine, (39), insulin (45), and collagen (46). PHB/V surfaces grafted with PAA side chains were functionalized with glucosamine by amidation of carboxyl groups of PAA with the amine function of glucosamine using carbodiimide activation (39). Insulin was grafted onto PHB/V-*g*-PAA and PHB/V-*g*-(PAA-*b*-PEO) using coupling with a carbodiimide catalyst (45). The protein-immobilized surfaces with either PAA or PAA-*b*-PEO as spacer arms were shown to accelerate the proliferation of human fibroblasts when compared to the surfaces without protein (45). PHB/V surfaces were functionalized with collagen by poly(methacrylic acid) grafting followed by amidation of the carboxyl groups of the branches with collagen using carbodiimide activation (46). In vitro studies of cell viability and proliferation of rat osteosarcoma UMR-106 cell line and mouse osteoblastic MC3T3-E1 cell line have been conducted on the collagen grafted PHB/V surfaces, as well as on PHB/V surfaces, both untreated and with physically immobilized collagen, for comparison (46). It was observed that the PHB/V surfaces with covalently fixed collagen showed higher cell activity than the ones with physically immobilized collagen, while the latter showed higher cell activity than the untreated PHB/V surfaces (46).

Conclusions

The preparation of graft copolymers including PHA blocks as main or side chains have been reported, with various preparation methods using either one of the three synthesis strategies of graft copolymers, i.e., the grafting onto, grafting from, and grafting through methods. Various types of copolymers were combined with PHAs: polyethers like poly(ethylene glycol); polysaccharides, for example, chitosan and cellulose acetate; polyesters, e.g., poly(ε-caprolactone) and poly(lactic acid); and numerous vinyl polymers,including polystyrene, poly(methyl methacrylate), and poly(2-hydroxyethyl methacrylate). For a number of the graft copolymers reported, the nature of the copolymer and the graft copolymer composition could control properties such as the thermal stability, mechanical properties, as well as the enzymatic degradability, biodegradability, antibacterial activity, and cell compatibility.

PHA graft copolymers can be used as compatibilizers of polymer blends, but were also proposed as biodegradable additives for bone cement formulations, and have recently received much attention in tissue engineering, with applications as biomolecule-immobilizing surfaces for enhancement of cell proliferation.

References

1. J.M.G. Cowie. *In* Comprehensive polymer science. *Edited by* G. Allen and J.C. Bevington. Pergamon Press, Oxford. 1989. p. 33.
2. K. Vallée-Rehel, V. Langlois, P. Guérin, and A. Le Borgne. J. Environ. Polym. Degrad. **7**, 27 (1999).
3. M. Avella, M.E. Errico, B. Immirzi, M. Malinconico, L. Falcigno, and L. Paolillo. Macromol. Chem. Phys. **199**, 1901 (1998).
4. G. Ceccorulli, M. Scandola, and G. Adamus. J. Polym. Sci. Part B: Polym. Phys. **40**, 1390 (2002).
5. Y. Doi. Microbial polyesters. VCH Publishers, New York. 1990.

© 2008 NRC Canada

6. H.G. Schlegel. General microbiology. Cambridge University Press, Cambridge. 1993.
7. H.-M. Müller and D. Seebach. Angew. Chem. **105**, 483 (1993).
8. D. Seebach, A. Brunner, B.M. Bachmann, T. Hoffmann, F.N.M. Kühnle, and U.D. Lengweiler. Ernst Schering Research Foundation. **28**, 7 (1995).
9. G. Braunegg, G. Lefebvre, and K.F. Genser. J. Biotechnol. **65**, 127 (1998).
10. H. Brandl, R.A. Gross, R.W. Lenz, and R.C. Fuller. *In* Microbial bioproducts: Advances in biochemical engineering/biotechnology. Springer, Berlin. 1990. p. 77.
11. S. Lee. Trends Biotechnol. **14**, 431 (1996).
12. A. Steinbüchel and B. Füchtenbusch. Trends Biotechnol. **16**, 419 (1998).
13. P.J. Hocking and R. H. Marchessault. *In* Biopolymers from renewable resources. *Edited by* D.L. Kaplan. Springer, Berlin. 1998. p. 220.
14. R. Alper, D.G. Lundgren, R.H. Marchessault, and W.A. Cote. Biopolymers, **1**, 545 (1963).
15. S.F. Williams, D.P. Martin, D.M. Horowitz, and O.P. Peoples. Int. J. Biol. Macromol. **25**, 111 (1999).
16. M. Zinn, B. Witholt, and T. Egli. Adv. Drug Deliv. Rev. **53**, 5 (2001).
17. A. Steinbüchel, E. Hustede, M. Liebergesell, U. Pieper, A. Timm, and H. Valentin. FEMS Microbiol. Rev. **103**, 217 (1992).
18. M. Yalpani, R.H. Marchessault, F.G. Morin, and C.J. Monasterios. Macromolecules, **24**, 6046 (1991).
19. H. Arslan, B. Hazer, and S.C. Yoon. J. Appl. Polym. Sci. **103**, 81 (2007).
20. S.-G. Hu, C.-H. Jou, and M.-C. Yang. J. Appl. Polym. Sci. **88**, 2797 (2003).
21. P. Cavallaro, B. Immirzi, M. Malinconico, E. Martuscelli, and M. G. Volpe. Macromol. Rapid Commun. **15**, 103 (1994).
22. B. Hazer. Polym. Bull. **33**, 431 (1994).
23. M. Kowalczuk, G. Adamus, and Z. Jedlinski. Macromolecules, **27**, 572 (1994).
24. H. Arslan, N. Yesilyurt, and B. Hazer. J. Appl. Polym. Sci. **106**, 1742 (2007).
25. P.F. Rempp and E. Franta. Adv. Polym. Sci. **58**, 1 (1984).
26. K. Ito and S. Kawaguchi. Adv. Polym. Sci. **142**, 129 (1999).
27. J.L. Eguiburu, M.J. Fernandez, and J. San Roman. Polymer, **37**, 3615 (1996).
28. S. Nguyen and R.H. Marchessault. Macromolecules, **38**, 290 (2005).
29. B. Hazer. Macromol. Chem. Phys. **197**, 431 (1996).
30. B. Hazer, R.W. Lenz, B. Çakmakli, M. Borcakli, and H. Koçer. Macromol. Chem. Phys. **200**, 1903 (1999).
31. B. Cakmakli, B. Hazer, and M. Borcakli. Macromol. Biosci. **1**, 348 (2001).
32. E. Renard, P.-Y. Tanguy, E. Samain, and P. Guérin. Macromol. Symp. **197**, 11 (2003).
33. C. Zhijiang and W. Zhihong. J. Mater. Sci. **42**, 5886 (2007).
34. A. Södergård. J. Bioact. Compat. Polym. **19**, 511 (2004).
35. H. Mitomo, T. Enjôji, Y. Watanabe, F. Yoshii, K. Makuuchi, and T. Saito. J. Macromol. Sci. Pure Appl. Chem. **A32**, 429 (1995).
36. K. Bahari, H. Mitomo, T. Enjôji, S. Hasegawa, F. Yoshii, and K. Makuuchi. Angew. Makromol. Chem. **250**, 31 (1997).
37. T. Jiang and P. Hu. Polym. J. **33**, 647 (2001).
38. H. Mitomo, Y. Watanabe, F. Yoshii, and K. Makuuchi. Radiat. Phys. Chem. **46**, 233 (1995).
39. L. Grøndahl, A. Chandler-Temple, and M. Trau. Biomacromolecules, **6**, 2197 (2005).
40. K. Bahari, H. Mitomo, T. Enjôji, F. Yoshii, and K. Makuuchi. Polym. Degrad. Stab. **61**, 245 (1998).
41. M.S. Eroğlu, T. Çaykara, and B. Hazer. Polym. Bull. **41**, 53 (1998).
42. Y. Wada, H. Mitomo, K.-i. Kasuya, N. Nagasawa, N. Seko, A. Katakai, and M. Tamada. J. Appl. Polym. Sci. **101**, 3856 (2006).
43. Y. Wada, N. Seko, N. Nagasawa, M. Tamada, K.-i. Kasuya, and H. Mitomo. Radiat. Phys. Chem. **76**, 1075 (2007).
44. A.C. Mesquita, M.N. Mori, and L.G. Andrade e Silva. Radiat. Phys. Chem. **71**, 251 (2004).
45. I.-K. Kang, S.-H. Choi, D.-S. Shin, and S.C. Yoon. Int. J. Biol. Macromol. **28**, 205 (2001).
46. Y. Tesema, D. Raghavan, and J. Stubbs III. J. Appl. Polym. Sci. **93**, 2445 (2004).
47. Y. Ke, Y. Wang, L. Ren, L. Lu, G. Wu, X. Chen, and J. Chen. J. Appl. Polym. Sci. **104**, 4088 (2007).
48. C.-S. Wu. J. Appl. Polym. Sci. **102**, 3565 (2006).
49. J. Park, J.-G. Park, W.-M. Choi, C.-S. Ha, and W.-J. Cho. J. Appl. Polym. Sci. **74**, 1432 (1999).
50. S. Ilter, B. Hazer, M. Borcakli, and O. Atici. Macromol. Chem. Phys. **202**, 2281 (2001).
51. H.S. Lee and T.Y. Lee. Polymer, **38**, 4505 (1997).
52. H.-K. Lao, E. Renard, I. Linossier, V. Langlois, and K. Vallée-Rehel. Biomacromolecules, **8**, 416 (2007).
53. W. Wang, Y. Zhang, and Y. Chen. Iran. Polym. J. **16**, 195 (2007).
54. S. Nguyen and R. H. Marchessault. Macromol. Biosci. **4**, 262 (2004).
55. D. Neugebauer, J. Rydz, I. Goebel, P. Dacko, and M. Kowalczuk. Macromolecules, **40**, 1767 (2007).
56. S. Nguyen, G.-e. Yu, and R.H. Marchessault. Biomacromolecules, **3**, 219 (2002).
57. A. Matsumoto, A. Horie, and T. Otsu. Polym. J. **23**, 211 (1991).
58. G. Adamus. Macromol. Symp. **239**, 77 (2006).
59. M.S. Reeve, S.P. McCarthy, and R.A. Gross. Macromolecules, **26**, 888 (1993).
60. C. Lauzier, J.-F. Revol, E.-M. Debzi, and R.H. Marchessault. Polymer, **35**, 4156 (1994).
61. J.C. Knowles, G.W. Hastings, H. Ohta, S. Niwa, and N. Boeree. Biomaterials, **13**, 491 (1992).
62. J.C. Knowles. J. Med. Eng. Technol. **17**, 129 (1993).
63. C. Bunel, V. Le Saux, and J.-P. Vairon. Science et Medecine, Fr., FR 2670114. 1992.
64. C. Bunel, V. Le Saux, and J.-P. Vairon. Science et Medecine, Fr., FR 2670115. 1992.
65. Y. Jiang and M. Roby. United States Surgical Corporation, USA, US Patent 5-847-046. 1998.
66. S. Nguyen and R.H. Marchessault. J. Biomed. Mater. Res., Part B, **77**, 5 (2006).
67. K.-D. Kühn. Bone cements: Up-to-date comparison of physical and chemical properties of commercial materials. Springer, Berlin. 2000.
68. G. Lewis. J. Biomed. Mater. Res., Part B, **38**, 155 (1997).
69. M. Abboud, S. Vol, E. Duguet, and M. Fontanille. J. Mater. Sci. Mater. Med. **11**, 295 (2000).
70. J.M. Hasenwinkel, E.P. Lautenschlager, R.L. Wixson, and J.L. Gilbert. J. Biomed. Mater. Res., Part A, **47**, 36 (1999).
71. P. Hardouin, F. Grados, A. Cotten, and B. Cortet. Joint Bone Spine, **68**, 216 (2001).
72. I. Espigares, C. Elvira, J.F. Mano, B. Vázquez, J. San Román, and R.L. Reis. Biomaterials, **23**, 1883 (2002).

© 2008 NRC Canada

Diffusion of molecular probes and the effects of their interactions with polymer matrices as studied by pulsed-field gradient NMR spectroscopy[1]

Héloise Thérien-Aubin, Wilms E. Baille, and X.X. Zhu

Abstract: Pulsed-field gradient NMR spectroscopy was used to study the interactions between small molecular probes and polymers bearing interacting groups. The self-diffusion coefficients of ethylene glycol and its oligomers and their methyl ester derivatives in poly(vinyl alcohol) gels were measured to study the effect of hydrogen bonding. The self-diffusion coefficients of small molecular probes containing hydroxyl, amine, and carboxylic acid groups were determined in several polymer matrices including poly(vinyl alcohol), poly(allylamine), and poly(acrylic acid) bearing lateral hydroxyl, amine, and carboxylic acid groups, respectively. The ionic interactions between the functional groups of the diffusants and of the polymers exhibited a marked effect on the diffusion of the molecular probes. For example, the reduced self-diffusion coefficients measured for a diffusant with a carboxylic acid group in a poly(allylamine) matrix were shown to be lower even though the molecular masses of the diffusants are similar.

Key words: pulsed-field gradient NMR spectroscopy, self-diffusion, intermolecular interactions.

Résumé : La spectroscopie RMN à gradient de champ pulsé a été utilisée afin d'étudier les interactions entre des petites molécules et des polymères portant divers groupements fonctionnels. Les coefficients d'auto-diffusion de l'éthylène glycol, de ses oligomères et de leurs esters de méthyle respectifs dans des gels de poly(alcool vinylique) ont été mesurés pour étudier l'effet des interactions de type pont hydrogène. Les coefficients d'auto-diffusion de petites molécules ayant des groupements fonctionnels de type alcool, amine et acide carboxylique ont été mesurés dans le poly(alcool vinylique), le poly(allyl amine) et le poly(acide acrylique), des polymères ayant respectivement des groupements latéraux de type alcool, amine et acide carboxylique. Les interactions ioniques entre les groupements fonctionnels du diffusant et ceux du polymère ont un effet marqué sur la diffusion des sondes moléculaires. Par exemple, le coefficient d'auto-diffusion réduit mesuré pour l'acide acétique dans le poly(allyl amine) est inférieur à celui de l'éthylène glycol bien que la masse molaire et le rayon hydrodynamique des deux sondes soient similaires.

Mots-clés : spectroscopie RMN à gradient de champ pulsé, auto-diffusion, interactions intermoléculaires.

Introduction

The study of the diffusion of molecules in polymer matrices and biological systems is of both fundamental and applied importance (1–3). Diffusion studies in polymer systems give insight to different phenomena such as polymer dynamics (4) and structures or controlled release of drugs (5). Self-diffusion in polymer systems, which is caused by the random walk of the diffusing species in a homogenous sample, can be measured by pulsed-field gradient NMR techniques.

The physical properties of both the diffusant and the polymer matrix can affect the diffusion process. The effects of the molecular mass, size, and shape of the diffusants, concentration of the polymer, solvent conditions, temperature, and diffusant–polymer interactions on the diffusion process have been studied by the use of pulsed-field gradient NMR spectroscopy (6–9). Previously, we have also studied the diffusion of water in biomacromolecules, such as in tablets made of modified starch (5, 10, 11). The effect of the interactions between the diffusant and the polymer on the diffusion process remains to be better understood.

It was shown that coulombic interactions and hydrogen bonding can reduce substantially the diffusion rate of a solute (12–16). For example, the reduced self-diffusion coefficient (D/D_0) of 4-[[4-(dimethylamino)phenyl]azo]benzoic acid (commonly known as *p*-methyl red) decreases in a

Received 31 October 2007. Accepted 20 February 2008. Published on the NRC Research Press Web site at canjchem.nrc.ca on 29 April 2008.

This paper is dedicated to Robert H. Marchessault in recognition of his many contributions to polysaccharide and biopolymer chemistry.

H. Thérien-Aubin, W.E. Baille, and X.X. Zhu.[2]
Département de Chimie, Université de Montréal, C.P. 6128, Succ. Centre-ville, Montréal, Québec, Canada H3C 3J7

[1]This article is part of a Special Issue dedicated to Professor R. Marchessault.

[2]Corresponding author (e-mail: julian.zhu@umontreal.ca).

 doi:10.1139/V08-036 © 2008 NRC Canada

polymer–diffusant–toluene mixture (6 wt% polymer in toluene) when the polymer was changed from polystyrene (PS) (D/D_0 = 0.8) to poly(methyl methacrylate) (PMMA) (D/D_0 = 0.5) and then to poly(vinyl acetate) (PVAc) (D/D_0 = 0.4) (values obtained from the extrapolation of the data of Lee and Chang (16)). The decrease in D between PS and PMMA is related to the presence of the carbonyl group on PMMA participating in hydrogen bonding, the difference between PMMA and PVAc is caused by the enhanced availability of the carbonyl group in PVAc (16). The effect of hydrogen bonding on the diffusion of ethylene glycol in a poly(vinyl alcohol) (PVA) matrix was previously studied (17). The results showed the coexistence of two fractions of ethylene glycol, a bound fraction with a lower self-diffusion coefficient and a free fraction with higher self-diffusion coefficient. It was shown that the fraction of ethylene glycol bound to the PVA matrix increased with the PVA concentration. Recently, the effects of ionic interactions on the diffusion of dendrimers in polymers gels were studied. Ionic interactions significantly reduce the self-diffusion coefficient of the dendrimers and lead to a more complex diffusive behaviour (18). The influence of such interactions on diffusion cannot be easily described by the diffusion models.

In the present study, the self-diffusion coefficients of a series of small molecules bearing different functional group have been selected as diffusion probes and their self-diffusion coefficients have been determined by pulsed-field gradient NMR spectroscopy to elucidate the effects of hydrogen bonding and ionic interactions on the diffusion process in solutions and gels of polymers also bearing interacting functional groups.

Experimental section

Materials

Ethylene diamine (EDA), acetic acid (HAc), ethylene glycol (EG), diethylene glycol (DEG), triethylene glycol (TEG), and their end-capped methyl ether derivatives were purchased from Sigma-Aldrich (Milwaukee, WI). Poly(vinyl acohol) (PVA) (M_n = 52 000 with a degree of hydrolysis of 99%), poly(allylamine) (PAAm) (M_w = 65 000), and poly(acrylic acid) (PAA) (M_w = 100 000) were also purchased from Sigma-Aldrich. D_2O was purchased from C.I.L. (Andover, MA). All chemicals were used as received. The chemical structures of selected diffusants and the polymers are shown in Fig. 1.

Sample preparation

NMR samples were prepared by dissolving the polymer, weighed in a 5 mm NMR tube, in a D_2O solution containing 1 wt% of the diffusing probe. The NMR tubes were then sealed and heated for 24 h. PVA samples were heated at 110 °C while PAA and PAAm sample were heated at 65 °C.

Pulsed-field gradient NMR measurements

Both spin echo (SE: 90°-t_1–180°-t_1-echo) technique developed by Stejskal and Tanner (19) and stimulated echo (STE: 90°-t_1–90°-t_2–90°-t_1-echo) technique developed by Tanner (20) were used to measure the self-diffusion coefficients (D) of solute probes. Measurements were performed on a Bruker DSX-300 NMR spectrometer operating at a frequency of 300.18 MHz for protons. The gradient strength

Fig. 1. Chemical structures of polymers and selected diffusant used to study diffusant–polymer interactions.

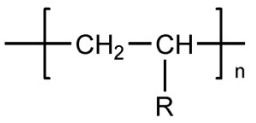

R	Polymer
OH	PVA
COOH	PAA
CH_2NH_2	PAAm

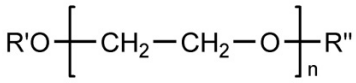

n	R'	R''	Diffusant
1	H	H	EG
	H	CH_3	EGMe
	CH_3	CH_3	$EGMe_2$
2	H	H	DEG
	H	CH_3	DEGMe
3	H	H	TEG
	H	CH_3	TEGMe
	CH_3	CH_3	$TEGMe_2$

was varied in 16 steps between 0.05 and 1 T/m. The duration of the gradient pulse (δ) was set between 1 and 6 ms depending on the characteristics of the samples, and the interval between the gradient pulses was fixed to 100 ms. When the STE pulse sequence is used, the delay t_1 was set to a value of δ + 2.1 ms.

The experiments were performed at several different temperatures (from 15 to 45 °C) (fluctuation ± 0.3 °C). Temperature calibration was done with ethylene glycol as described previously (21).

Diffusion models

The experimental results obtained were fitted to two models of diffusion in an attempt to analyze the influence of the interactions.

The model of Petit et al. (22) is based on the assumption that the diffusion occurs when the diffusing molecule, which resides in a cavity of size ξ, jumps at a frequency k to an adjacent cavity of the transient statistical network. The diffusion coefficient of the molecules varies with the polymer concentration according to

$$[1] \qquad D = \frac{D_0}{1 + \frac{D_o}{k\beta^2} c^{2\nu}}$$

where ν is a the quality of the solvent as defined by de Gennes, a constant characteristic of the polymer–solvent system, the value of ν is expected to be a constant for a given polymer system. β is a system-dependent scaling parameter from de Gennes theory (23), c is the polymer concentration, and k represents the jump frequency over an energy barrier and depends on the temperature, the size, and the shape of the diffusant. Both D_0 and $k\beta^2$ should decrease

© 2008 NRC Canada

with molecular mass of the diffusing molecule. In fact, they are affected by the effective hydrodynamic radius (R_h) of the diffusant, which is related to the self-diffusion coefficient by the Stokes–Einstein equation

$$[2] \qquad D_0 = \frac{k_B T}{6\pi\eta R_h}$$

where D_0 is the self-diffusion coefficient at zero concentration of the polymer, k_B is Boltzmann's constant, and R_h is the effective hydrodynamic radius of the diffusing molecule.

To further characterize the interactions between the diffusant and the polymer, the self-diffusion coefficients were also analyzed with a model based on a more phenomenological approach, the model of Phillies (24–26).

$$[3] \qquad D/D_0 = \exp(-\alpha\phi^{\upsilon})$$

where α and υ are scaling parameters, which are system-dependent (14, 16, 24, 25). The value of α is related to the molecular mass or the hydrodynamic size of the diffusants. The parameter υ may be related to the interactions in the system. Lee et al. found υ equal to 0.62 ± 0.06 and 1.0 ± 0.1 for a diffusion process controlled by hydrogen bonding and hydrodynamic interactions, respectively (27).

Results and discussion

EG, EDA, and HAc were the diffusants chosen to investigate the effect of functional groups on their diffusion in the polymers, since they have similar molecular mass (62.1, 60.1, and 60.1 g/mol, respectively). In the aqueous solutions consisting of the polymers and diffusants, extensive hydrogen bonding should be expected. In addition, between the charged polymers and the diffusant forming a counter-ion, ionic interactions are expected to have even a greater influence. Indeed, the mixing of EDA (1 wt% in D_2O) with PAA caused a precipitation throughout the entire concentration range of polymers. The other ternary systems remained homogenous and were used for the diffusion studies. The interaction between EG and the PVA matrix has been studied previously by the use of NMR spectroscopy (17). Two signals corresponding to free and bound EG were observed in the aqueous PVA solutions (17). Results of EG presented here are those of the unbound fraction. The three different polymer matrices used in this study have different molecular mass (M_r) and polydispersity (PDI). However, a previous study (28) on the effect of M_r and PDI of different PVA and hydroxypropylcellulose sample shows that, in the same range of polymer concentration used here, M_r and PDI of the polymer matrix do not significantly influence the diffusion of small molecules. The differences in the diffusion coefficient observed here should thus be ascribed to the differences in the interactions between the solute and the polymer rather than to an effect of the polymer matrices itself.

Effect of hydrogen bonding

Figure 2A shows the effect of the increasing PVA concentration on the self-diffusion of EG, EDA and HAc. It is known that the self-diffusion coefficient of the diffusants depends on their hydrodynamic sizes. In fact, the self-diffusion coefficient of a diffusant in an aqueous polymer system is largely determined by its self-diffusion coefficient in pure water (D_0). The smaller hydrodynamic radius (R_h) of HAc is the reason that throughout the entire concentration range of PVA the self-diffusion coefficient of HAc remains higher than that of EG and of EDA (Fig. 2A).

The reduced diffusion coefficients (D/D_0) of the three diffusants (EG, HAc, and EDA) in the PVA–water system are quite similar at a given concentration of the polymer (Fig. 2B), even though they have different R_h values. The reduced diffusion coefficient is strongly related to the interaction between the diffusant and the polymer matrix. The lower values of D/D_0 correspond to a stronger interaction between the polymer matix and the diffusant in the systems. Figure 2B shows that the interaction between the diffusant and the PVA matrix is similar in the three systems.

Although the effects of the hydrodynamic radius on the self-diffusion data show the same trend in Figs. 2A (EG, HAc, and EDA) and 3A (EG, DEG, and TEG), the reduced self-diffusion coefficients of these two groups of diffusants show a quite different behaviour (Figs. 2B and 3B). The D/D_0 values are rather similar for EG, HAc, and EDA in PVA (Fig. 2B). By contrast, the D/D_0 values for EG, DEG, and TEG are quite different (Fig. 3B). In this case, the dominant interaction between the diffusants and the PVA matrix is hydrogen bonding. The effect of hydrogen bonding is more pronounced for the diffusion of TEG than for DEG and EG. The apparent reason is the greater number of oxygen atoms on TEG (four oxygen atoms) available to participate in hydrogen bonding in comparison to DEG (three oxygen atoms) and EG (two oxygen atoms).

To further analyze the effect of hydrogen bonding between the diffusants and PVA, the self-diffusion coefficients of EG, DEG, and TEG were compared with their end-capped methyl ether derivatives. The presence of methyl ether end groups should not significantly alter the size (Table 1) and shape of the diffusant, which are known to affect diffusion (9). Figure 4 shows the results obtained for the diffusion of mono-, di-, and tri-ethylene glycol and their methyl esters in the PVA matrix. In all three cases, the reduced self-diffusion coefficients of EG, DEG, and TEG are lower than those of their end-capped methyl ether derivatives, although their molecular masses are correspondingly lower in each case. In these cases, hydrogen bonding is the dominant factor and the effect of molecular mass of the diffusant becomes less significant. The differences observed in the diffusion data are greater than the experimental error estimated at less than 5%. When one of the alcohol end groups is capped by a methyl ether group, the value of D/D_0 increases because of the limitation in the formation of hydrogen bonds between the diffusant and the matrix. A larger increase of the value of D/D_0 should be observed in the case of the diether derivatives. However, the capping of the second alcohol group of the diffusant did not influence the diffusing behaviour of the probe as much as the capping of the first alcohol group. Therefore, similar reduced self-diffusion coefficients were obtained for the interactions of PVA with either the mono- or di-ether species.

Effect of ionic interactions

The effect of functional groups on the diffusion process was studied in the aqueous systems of EG, EDA, and HAc as diffusant probes and polymer matrix containing different functional groups (PVA, PAA, and PAAm). The diffusion of

© 2008 NRC Canada

Fig. 2. Variation of (A) the self-diffusion coefficients and (B) the reduced diffusion coefficients D/D_0 as a function of PVA concentration at 25 °C. Dashed lines are fits to eq. [1]. EG (■); EDA (●); HAc (▲).

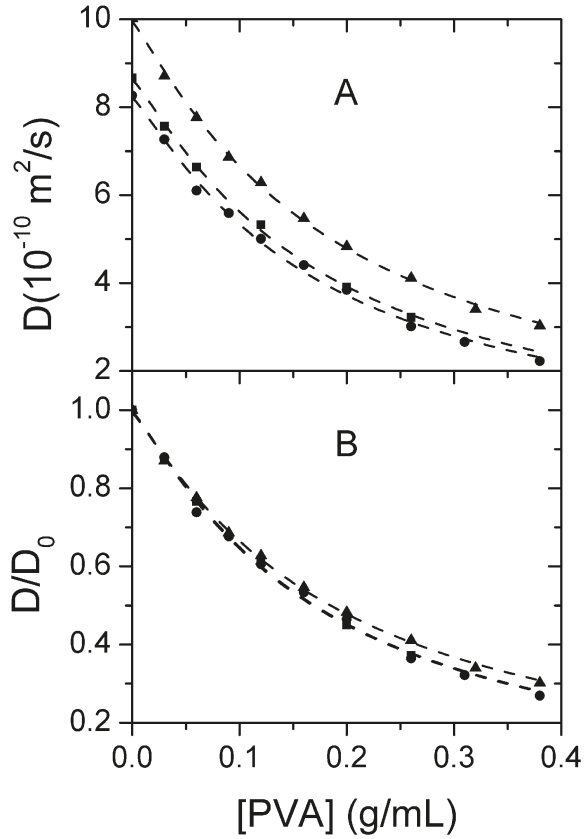

Fig. 3. Variation of (A) the self-diffusion coefficients (B) the reduced diffusion coefficients D/D_0 as a function of PVA concentration at 25 °C. Dashed lines are fits to eq. [1]. EG (■); DEG (●); TEG (▲).

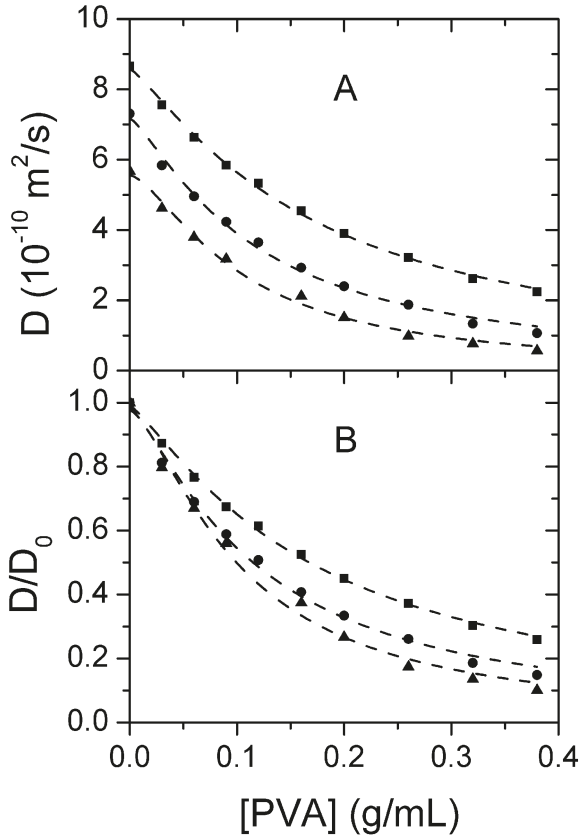

EDA in PAA matix was not studied because of precipitation upon mixing. It should be pointed out that, in the HAc–PAA, HAc–PAAm, and EDA–PAAm systems, the NMR signals of the diffusant overlap with those of the polymer, which may have caused somewhat larger errors in the measured self-diffusion coefficients.

Figure 5A shows the self-diffusion coefficients of EG in the three different polymer matrices. The change of D can be attributed to the difference of interactions (electrostatic interaction and hydrogen bonding) resulting from the functional groups of the diffusant and the polymer. Figure 5A shows that the reduced self-diffusion coefficient of EG in the different polymer matrices (PVA, PAAm, and PAA) vary a lot. Hydrogen bonding between EG and PVA should be more extensive, as shown by the different viscosity of the mixture at the same concentration of polymer. At a polymer concentration of 0.25 g/mL, the viscosities of the polymer solutions are 0.96, 0.27, and 0.08 Pa·s for PVA, PAA, and PAAm, respectively. The viscosity effect could influence the diffusion of EDA and HAc because of the complex nature of the interactions in the different polymer matrices.

Figure 5 shows interactions between the polymer and the diffusants by the differences in the reduced diffusion coefficients of EG, EDA, and HAc in the three-polymer matrices. At the same polymer concentration, the self-diffusion coefficients of HAc are higher in PVA and in PAA than in PAAm. For example, the self-diffusion coefficient of HAc is systematically lower in PAAm than in PAA because of the electrostatic interactions between HAc and PAAm. This result does not mean that the HAc molecules do not interact with the others polymer matrices, but the attractive electrostatic interactions with PAAm are more important than hydrogen bonding between the diffusant HAc and the polymer matrix (PAA). Note that for all three diffusants, their self-diffusion coefficients in PVA are always lower because of the much higher viscosity of the PVA aqueous systems.

Diffusion models

Equation [1] was used to fit the diffusion profiles in Fig. 4, and the results of the fitting parameters are listed in Table 1. The D_0 values obtained from the fitting are almost identical to the experimental values and show a clear dependence on the size of the diffusant. The parameters ν are in the same range as those obtained previously for PVA systems (6, 9). As expected, the $k\beta^2$ value decreases from EG to DEG and then to TEG, since the jump frequency factor k is related to the hydrodynamic size of the molecular probes. In comparision, the $k\beta^2$ value shows an increase instead of a decrease from TEG to TEGMe and then to $TEGMe_2$ (or from EG to EGMe and $EGMe_2$), although the M_r also increases. Obviously, the methyl group at the ends reduces hydrogen bonding between the diffusant and PVA, making the molecules easier to diffuse even though they are larger. It seems that the $k\beta^2$ parameter obtained may serve as an indication to the interactions between the diffusant and the polymer. This model in its present form does not provide a provision for the interactions between the

© 2008 NRC Canada

Table 1. Hydrodynamic radii and fitting parameters values for aqueous PVA systems at 25 °C obtained by the models of Petit et al. and of Phillies.

				Model of Petit et al.[c]		Phillies' model[d]	
Sample	M (g/mol)	R_h[a] (Å)	D_0[b] (10^{-10}m^2/s)	$k\beta^2$ (10^{-10} s/m^2)	ν	α	υ
HAc	60.1	2.4	9.89	1.54±0.05	0.55±0.02	2.8±0.1	0.83±0.04
EDA	60.1	2.9	8.26	1.04±0.04	0.58±0.03	3.1±0.2	0.85±0.02
EG	62.1	2.8	8.66	0.98±0.06	0.62±0.02	3.4±0.1	0.91±0.03
EGMe	76.1	3.1	7.88	1.17±0.05	0.60±0.02	2.7±0.1	0.89±0.03
$EGMe_2$	90.1	3.2	7.56	1.27±0.08	0.56±0.02	2.8±0.3	0.90±0.03
DEG	106.1	3.6	7.31	0.44±0.05	0.65±0.04	4.5±0.1	0.87±0.05
DEGMe	120.1	3.7	6.46	1.0±0.1	0.51±0.06	2.8±0.2	0.84±0.05
TEG	150.1	4.2	5.67	0.21±0.04	0.72±0.04	2.7±0.1	0.83±0.01
TEGMe	164.1	4.7	5.23	0.65±0.03	0.58±0.02	2.8±0.1	0.85±0.02
$TEGMe_2$	178.1	4.8	5.15	0.64±0.05	0.58±0.02	3.0±0.3	0.87±0.03

[a]Calculated from eq. [2].
[b]Experimental values.
[c]Obtained as a fitting parameter from eq. [1].
[d]Obtained as a fitting parameter from eq. [3].

diffusant and the polymer, since the $k\beta^2$ parameter also changes with M_r and shape of the diffusant and the temperature. It remains useful to analyze the experimental diffusion data to account for structural changes to the diffusant.

The model of Phillies was also used to analyze these data, with fitting parameters listed in Table 1. For small molecule diffusants, $\alpha = aR_h^b$ (where a is a constant between 3.03 and 3.20, and b is a constant between 0.53 and 0.59) (14, 29). However, the α values obtained (Table 1) do not show a clear dependence on the hydrodynamic size of the diffusants. The parameter υ decreases with increasing intermolecular interactions and was found to have a slight increasing trend from TEG to TEGMe and $TEGMe_2$ and a decreasing trend from EG to DEG and TEG. The variations in υ observed in this study are not as large as those observed in other systems such as PS and PVAc – methyl red – toluene systems (27).

Table 2 shows the results obtained from the fitting of experimental data of EG, EDA, and HAc in PVA, PAA, and PAAm to both diffusion models. The ionic interactions between the probe and the matrix are evidenced by the variation of the reduced self-diffusion coefficient of the diffusants in the same matrix. It is shown that the interactions between HAc and PAAm are stronger than the interaction between PAAm and either EDA or EG (from both $k\beta^2$ and υ values). However, the direct comparison among the different polymer systems is not straight forward.

The diffusion models do not provide provisions to directly account for the interactions in the system. The $k\beta^2$ parameter in the model of Petit et al. and the υ parameter in the model of Phillies are related to the probe–matrix interaction and are largely affected by the presence of ionic interactions, but the variation of these parameters does not always follow the expected trend. The interaction between HAc and PAAm is clearly shown by the differences in the self-diffusion coefficients, but the $k\beta^2$ value for this diffusant–polymer pair is higher than the $k\beta^2$ values of HAc in PAA and PVA. The parameter β is not a constant and should vary in different polymer systems, but it cannot be measured independently. The $k\beta^2$ values obtained with the model of Petit et al. can only be used to compare results obtained in the same polymer system. The parameter υ is strongly dependent on the interactions present in the system as observed by Lee et al. (27) and generally decreases in the presence of ionic interactions in the system. This parameter, however, is also known to vary with the quality of the solvent for the polymer (30) and this may change when different polymer matrices are used.

Effect of temperature and activation energy

Temperature has an important effect on the diffusion and the apparent activation energy of self-diffusion. The effect of the temperature was studied between 15 and 45 °C for EDA, HAc, and EG in the three different polymer matrices. As previously observed, D increases with increasing temperature (9) as shown in the example of EG in PVA in Fig. 6A. The D/D_0 values, however, are rather similar at a given polymer concentration (Fig. 6B), indicating that the diffusion of EG was largely determined by the initial diffusion in water and the nature of the polymer–diffusant interaction does not vary with temperature. The apparent activation energy for each diffusant has been obtained from the variation of $k\beta^2$ parameter with the reciprocal temperature by the Arrhenius approach. Since β is assumed to be a constant within the temperature range for a given polymer–solvent system, the variation of $k\beta^2$ with temperature reflects the variation of k with temperature.

As β may not be the same in the different systems, a comparison of apparent activation energy E_a values (Table 2) obtained in different polymer systems would not be appropriate. However, for a given polymer system, these values are comparable. In general, the E_a values in Table 2 do not show any significant variation. In both PVA and PAA systems, HAc has the lowest E_a presumably due to its smaller hydrodynamic radius among the diffusants tested. In the PAAm system, where ionic interaction with HAc takes place, HAc seems to have a higher E_a than the other two diffusants or at least a value similar to that of the others.

Conclusion

We have found that the presence of hydrogen bonding and electrostatic interactions between the diffusants and the

© 2008 NRC Canada

Fig. 4. Variation of the reduced self-diffusion coefficients as a function of PVA concentrations at 25 °C (A) for EG (■), EGMe (●), and $EGMe_2$ (▲). (B) for DEG (■) and DEGMe (●). (C) for TEG (■), TEGMe (●), and $TEGMe_2$ (▲). Dashed lines are fits to eq. [1].

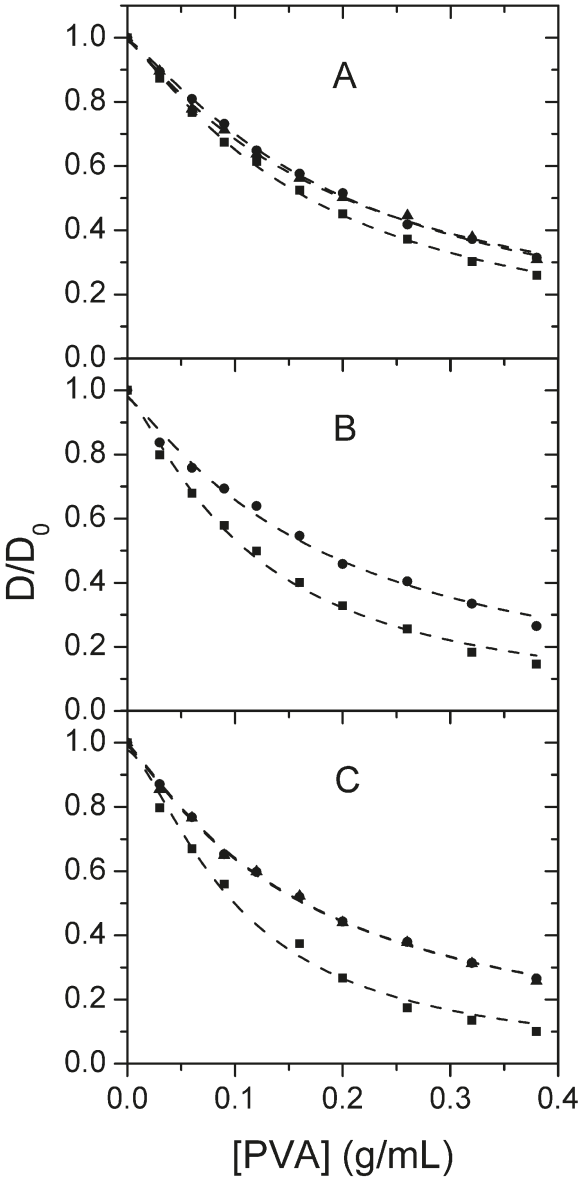

Fig. 5. Self-diffusion coefficients of (A) EG, (B) EDA, and (C) HAc into three-polymer matrices and at different polymer concentrations. PVA (■), PAAm (●), and PAA (▲). Dashed lines are fits to eq. [3].

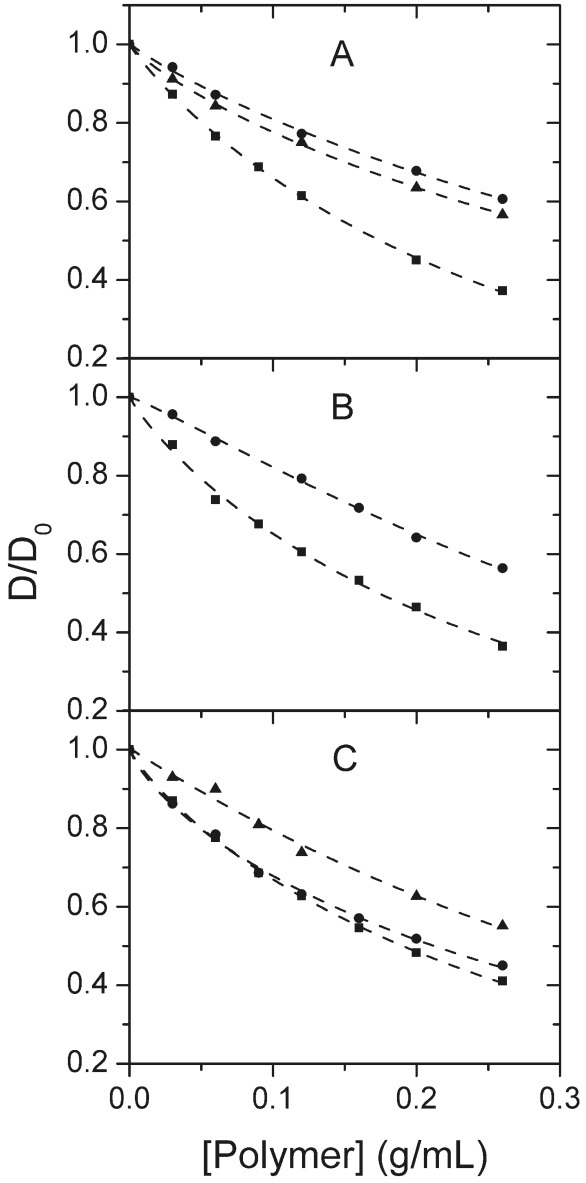

Table 2. Fitting parameters values for the models of Petit et al. and of Phillies for HAc, EDA, and EG in three different polymer matrices.

		Model of Petit et al.			Phillies' model	
Polymer	Probe	ν	$k\beta^2$ (10^{-10} s/m^2)	E_a (kJ/mol)	υ	α
PVA	HAc	0.55±0.02	1.54±0.05	27±1	0.83±0.04	2.8±0.1
	EDA	0.58±0.03	1.04±0.04	34±2	0.85±0.02	3.1±0.2
	EG	0.62±0.02	0.98±0.06	33±1	0.91±0.03	3.4±0.1
PAA[a]	HAc	0.60±0.05	2.4±0.3	21±6	1.01±0.09	2.4±0.3
	EG	0.51±0.02	3.37±0.08	31±3	0.89±0.05	1.7±0.1
PAAm	HAc	0.46±0.04	3.4±0.2	27±5	0.70±0.02	1.7±0.1
	EDA	0.62±0.06	1.9±0.4	24±10	1.05±0.09	2.5±0.4
	EG	0.49±0.01	3.07±0.07	26±2	0.88±0.02	1.8±0.1

[a]Mixing of PAA with aqueous solutions of EDA caused precipitation of the polymer.

© 2008 NRC Canada

Fig. 6. Variation of (A) the self-diffusion coefficients and (B) the reduced diffusion coefficients D/D_0 of the EG as a function of PVA concentrations at 25 (■), 30 (●), 35 (▲), 40 (▼), and 45 °C (◀). Dashed lines are fits to eq. [3]. (C) Semilogarithmic plot of the $k\beta^2$ parameter as a function of reciprocal temperature for EG (■), EDA (●), and HAc (▲).

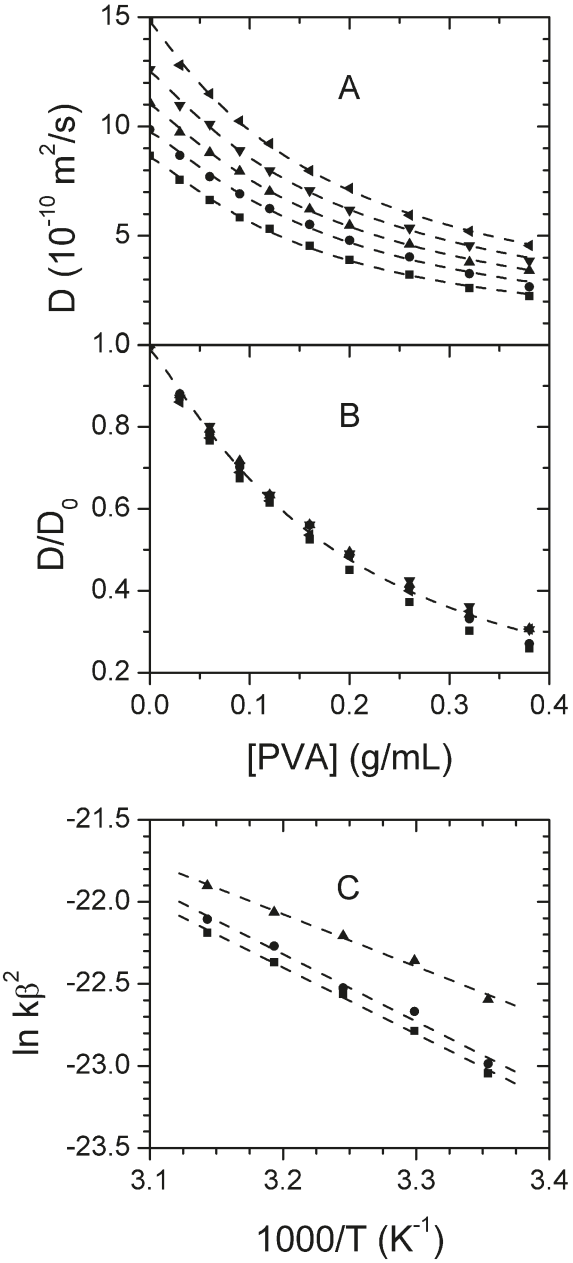

polymers can lower significantly the value of self-diffusion coefficient of small molecules in polymers and considerably reduce or even overwrite the effect of molecular size of the diffusants. The reduced or normalized self-diffusion coefficient (D/D_0) gives a better indication of these interactions. The physical models of diffusion generally describe well the variation of the self-diffusion coefficient with diffusant size, polymer concentration, and temperature, but they still lack adequacy in describing the effects of the interactions in the polymer–water–diffusant systems.

Acknowledgments

The financial support from the Natural Sciences and Engineering Research Council (NSERC) of Canada and the Canada Research Chair program is gratefully acknowledged. We appreciate our continuous collaboration on the study of diffusion in modified starch tablets with Professor Robert H. Marchessault by NMR imaging, whose profound understanding of the biomacromolecules has always been very helpful.

References

1. W. Brown, P. Stilbs, and T. Lindstrom. J. Appl. Polym. Sci. **29**, 823 (1984).
2. X.X. Zhu and P.M. Macdonald. Macromolecules, **25**, 4345 (1992).
3. P.C. Griffiths, P. Stilbs, B.Z. Chowdhry, and M.J. Snowden. Colloid. Polym. Sci. **273**, 405 (1995).
4. S.Z.D. Cheng, J.S. Barley, and E.D. von Meerwall. J. Polym. Sci. Part B: Polym. Phys. **29**, 515 (1991).
5. H. Thérien-Aubin, W.E. Baille, X.X. Zhu, and R.H. Marchessault. Biomacromolecules, **6**, 3367 (2005).
6. J.-M. Petit, X.X. Zhu, and P.M. Macdonald. Macromolecules, **29**, 70 (1996).
7. S. Abrahmsen-Alami and P. Stilbs. J. Colloid Interface Sci. **189**, 137 (1997).
8. S. Kwak and M. Lafleur. Macromolecules, **36**, 3189 (2003).
9. W.E. Baille, X.X. Zhu, and S. Fomine. Macromolecules, **37**, 8569 (2004).
10. W.E. Baille, C. Malveau, X.X. Zhu, and R.H. Marchessault. Biomacromolecules, **3**, 214 (2002).
11. C. Malveau, W.E. Baille, X.X. Zhu, and R.H. Marchessault. Biomacromolecules, **3**, 1249 (2002).
12. H. Walderhaug, F.K. Hansen, S. Abrahmsen, K. Persson, and P. Stilbs. J. Phys. Chem. **97**, 8336 (1993).
13. L. Johansson, U. Skantze, and J.E. Löfroth. J. Phys. Chem. **97**, 9817 (1993).
14. H.S. Park, J.M. Sung, and T.H. Chang. Macromolecules, **29**, 3216 (1996).
15. S. Matsukawa and I. Ando. Macromolecules, **30**, 8310 (1997).
16. H. Lee and T. Chang. Macromolecules, **34**, 937 (2001).
17. L. Masaro and X.X. Zhu. Langmuir, **15**, 8356 (1999).
18. H. Therien-Aubin, X.X. Zhu, C.N. Moorefield, K. Kotta, and G.R. Newkome. Macromolecules, **40**, 3644 (2007).
19. E.O. Stejskal and J.E. Tanner. J. Chem. Phys. **42**, 288 (1965).
20. J.E. Tanner. J. Chem. Phys. **52**, 2523 (1970).
21. C. Ammann, P. Meier, and A.E. Merbach. J. Magn. Reson. **46**, 319 (1982).
22. J.M. Petit, B. Roux, X.X. Zhu, and P.M. Macdonald. Macromolecules, **29**, 6031 (1996).
23. P.-G. de Gennes. Scaling concepts in polymer physics. Cornell University Press, Ithaca, NY. Chap. 3 and 5. 1979.
24. G.D.J. Phillies. Macromolecules, **19**, 2367 (1986).
25. G.D.J. Phillies. Macromolecules, **23**, 2742 (1990).
26. B. Amsden. Polymer, **43**, 1623 (2002).
27. J.Y. Lee, K.J. Park, T.Y. Chang, and J.C. Jung. Macromolecules, **25**, 6977 (1992).
28. L. Masaro, M. Ousalem, W.E. Baille, D. Lessard, and X.X. Zhu. Macromolecules, **32**, 4375 (1999).
29. S.J. Gibbs and C.S. Johnson Jr. Macromolecules, **24**, 6110 (1991).
30. G.D.J. Phillies and D. Clomenil. Macromolecules, **26**, 167 (1993).

© 2008 NRC Canada

Direct analysis of analyte–laden chromatographic stationary phase by induction–heating electrothermal vaporizer with inductively coupled plasma atomic emission spectroscopy[1]

Rebecca Lam and Eric D. Salin

Abstract: We describe the inductively heated electrothermal vaporization of 8-hydroxyquinolate complexes of Cd, Pb, and Zn adsorbed onto C_{18}-bonded silica gel with inductively coupled plasma atomic emission spectroscopic detection. The metal complexes were adsorbed onto the chromatographic stationary phase using a solid-phase extraction procedure. Instead of eluting the complexes from the stationary phase, the solid phase was directly vaporized into the plasma. Absolute detection limits for this method ranged from 0.3 to 3 μg.

Key words: 8-hydroxyquinoline, silica gel, induction heating electrothermal vaporization, inductively coupled plasma atomic emission spectroscopy.

Résumé : Faisant appel à une détection à l'aide de spectroscopie d'émission atomique au plasma avec couplage inductif, on a étudié la vaporisation avec chauffage électrothermique à induction de complexes entre le 8-hydroxyquinoléinate et du Cd, du Pb et du Zn adsorbés sur un gel de silice lié à un C_{18}. Les complexes métalliques ont été adsorbés sur la phase chromatographique stationnaire à l'aide d'une méthode d'extraction en phase solide. Au lieu d'éluer les complexes de la phase stationnaire, la phase solide a plutôt été directement vaporisée dans le plasma. Les limites absolues de détection de cette méthode se situent entre 0,3 et 3 μg.

Mots-clés : 8-hydroxyquinoléine, gel de silice, vaporisation avec chauffage électrothermique à induction, spectroscopie d'émission atomique au plasma avec couplage inductif.

[Traduit par la Rédaction]

Introduction

The use of solid-phase extraction for preconcentration and matrix separation is a powerful tool for trace-metals determination and continues to be an active field of research in atomic spectroscopy (1, 2). For typical solution analysis of the trace metals by inductively coupled plasma atomic emission spectroscopy or mass spectrometry (ICP-AES or ICP-MS), an elution step is required to remove the bound analytes from the solid sorbent by using a solvent. Under some circumstances, it would be desirable to avoid the elution process by directly vaporizing the analyte from the preconcentration material. Higher preconcentration factors may be achieved, as analytes are deposited, concentrated, and then vaporized rather than being diluted in 5–10 mL of eluant. One might also expect better detection limits by direct analysis when considering the low 1%–3% efficiency of nebulizers.

For aqueous samples, an extraction procedure is commonly cited in which metals complexed with 8-hydroxyquinoline are trapped onto chromatographic packing (C_{18}-bonded silica gel) (3–6). 8-Hydroxyquinoline is a powerful chelating agent that is particularly useful for separations because of its low affinity for the alkali metals that can cause matrix effects in ICP spectrometry. Alkali metals and other matrix components that are not chelated are eluted from the column during the washing step while the chelated metal complexes bind to the stationary phase. Silica powder is often used for preconcentration either directly or as a stationary-phase solid support. Direct analysis of the analyte–laden silica powder would eliminate the elution step and consequently should reduce both labor and dilution concerns. Dried precipitates of 8-hydroxyquinoline metal complexes have been directly analyzed by graphite furnace atomic absorption spectrometry (7); however, the direct analysis of 8-hydroxyquinoline chelates laden on chromatographic powder has not been reported.

Despite the popularity of solid-phase extraction, there have been very few reports in the literature describing direct analysis of solid, analyte–laden sorbents, or chelating agents. Metals extracted through various co-precipitation

Received 28 September 2007. Accepted 3 March 2008. Published on the NRC Research Press Web site at canjchem.nrc.ca on 29 April 2008.

This paper is dedicated to Robert H. Marchessault in recognition of his many contributions to polysaccharide and biopolymer chemistry.

R. Lam and E.D. Salin.[2] Department of Chemistry, McGill University, 801 Sherbrooke St. W., Montreal, QC H3A 2K6, Canada.

[1]This article is part of a Special Issue dedicated to Professor R. Marchessault.

[2]Corresponding author (email: eric.salin@mcgill.ca).

 doi:10.1139/V08-055 © 2008 NRC Canada

methods have been electrothermally vaporized as solids for analysis by atomic absorption spectrometry (8, 9). Skinner et al. trapped analyte on activated charcoal and then vaporized the analyte with a direct sample insertion (DSI) system using ICP-AES detection (10). Rattray and Salin also used DSI-ICP-AES for the direct analysis of analytes bound to Chelex-100 resin (11). Van Berkel and Maessen used electrothermal vaporization-ICP-AES to analyze metals trapped with poly(dithiocarbamate) resin (12).

In this report, we describe the use of an induction–heating electrothermal vaporizer (IH-ETV) (13–15) for the direct analysis of 8-hydroxyquinoline complexes adsorbed onto C_{18}-bonded silica. The silica gel containing the trapped chelated analyte is placed in a graphite sample cup inside the IH-ETV, where the analyte is vaporized from the silica gel and detected with inductively coupled plasma atomic emission spectroscopy (ICP-AES). The non-contact heating environment of the IH-ETV reduces the risk of contamination, while the heating of the cups can easily be controlled. In addition to ease of use, the graphite sample cups can be customized in size and shape to potentially hold a large amount of material, thereby suggesting that IH-ETV would be a powerful tool for application with chromatographic materials.

Experimental section

Chemicals

The brand of C_{18}-bonded silica gel used as packing in the columns was either Bondapak Porasil B (37–75 μm, Waters Corporation, Milford, Mass., USA) or Chromabond Sorbenz (mean particle size of 45 μm, Macherey–Nagel, Düren, Germany). The silica gel was not treated prior to placement in the column. An acidified reagent-grade methanol solution, 2% NH_4OH solution and 5% (*w*/*v*) solution of 8-hydroxyquinoline in methanol was prepared as described in the literature (5).

Column

The solid-phase extraction column was constructed inside a micropipette tip (101–1000 μL Fisherbrand, Fisher Scientific, Ottawa, Ont., Canada). A plug of quartz wool was used as a frit in the end of the pipette tip. Approximately, 150 mg of C_{18}-bonded silica gel was slurried with methanol and loaded into the pipette tip to give a packing bed of ~1 cm in height.

Samples

Aqueous samples (20 mL, elemental concentrations ranging from 0.25 to 1 μg g^{-1}) were prepared by diluting and mixing single-element reference solutions of Cd, Pb, and Zn (Fisher Scientific) with distilled, deionized water (Milli-Q system, Millipore Corp., Billerica, Mass., USA). An equivalent volume of distilled, deionized water was prepared as a blank. Prior to the extraction, 0.5 mL of the 5% 8-hydroxyquinoline solution was added to the sample or blank. This was equivalent to 200–600 times the stoichiometric amount of 8-hydroxyquinoline required to chelate the analytes in a given sample. The sample was adjusted to pH 9.0 ± 0.1 with the 2% NH_4OH solution and then manually shaken to ensure good mixing.

Extraction

The basic column washing and extraction procedure followed in this study is described by Skinner and Salin (5), except that the solvents and samples were delivered to the column manually by glass transfer pipettes, and the elution step was not performed. Tygon tubing was attached to the end of the column, and a peristaltic pump was used to drive the solvents or sample through the column at a flow rate of about 5 mL min^{-1}. The chelated analytes formed an easily observed thin green band on top of the column. The column was then rinsed with distilled, deionized water (previously adjusted to pH 9.0) and allowed to air-dry. The dried silica gel with the chelated analytes was removed from the pipette tip and homogenized.

IH-ETV-ICP-AES

The IH-ETV system used in this study has been previously described in detail (15–17). A schematic is provided in the Supplementary Data (Fig. S1).[3] The system was directly coupled to the torch of a Thermo–Jarrell Ash IRIS ICP-AES system.

Commercially available graphite sample cups with boiler caps (Bay Carbon, Bay City, Mich., US) were used to hold the silica samples. A drawing of the cups with dimensions labeled is shown as Fig. S2 in the Supplementary Data.[3] A wad of quartz wool was added inside the cup to prevent silica particles from passing through the hole in the end of the boiler cap. A plug of silica gel weighing 150 mg was used to trap the chelated analytes; however, the cup size used in these experiments could accommodate a maximum of 50 mg (though larger cups are possible). Consequently, a weighed subsample was placed into the cup for analysis.

Ten seconds after the start of the data acquisition, power was applied to the IH-ETV to heat the samples for 45 s to the maximum temperature achieved by the system (1400 °C). Multiple emission lines were monitored for each analyte to show that the peaks were real and not due to spectral interferences. Detailed operating parameters are show in Table 1.

Results and discussion

Figure 1 shows the time profiles of Chromabond and Porasil B silica gels (10 mg subsamples) used to extract multi-element solutions containing a mixture of Cd, Pb, and Zn. The analyte signals were obtained simultaneously for each type of silica gel but are shown on separate plots for clarity. There are several differences between the profiles of the Chromabond samples and the Porasil B samples. The Chromabond silica gel released a large amount of Si when heated, whereas the Porasil B released relatively little Si. The peaks for Zn and Pb also consistently occur a few sec-

[3] Supplementary data for this article are available on the journal Web site (canjchem.nrc.ca) or may be purchased from the Depository of Unpublished Data, Document Delivery, CISTI, National Research Council Canada, Ottawa, ON K1A 0R6, Canada. DUD 3747. For more information on obtaining material, refer to cisti-icist.nrc-cnrc.gc.ca/irm/unpub_e.shtml.

© 2008 NRC Canada

Table 1. ICP-AES operating parameters.

RF power	1350 W
Plasma gas flow rate	14 L min^{-1} Ar
Auxiliary gas flow rate	1 L min^{-1} Ar
Carrier gas flow rate	0.8 L min^{-1} Ar
Wavelengths monitored	C: 193.090 nm
	Si: 212.412 nm, 251.612 nm
	Zn: 206.200 nm, 213.856 nm
	Cd: 214.438 nm, 228.802 nm
	Pb: 220.353 nm, 261.418 nm
Number of time slices	500
Time per slice	0.2 s
Total acquisition time	100 s

onds later in the Porasil B than in the Chromabond sample, indicating that the Porasil B sample may be heating less quickly.

Recoveries for similar extractions have been reported to be near 100% for Cd, Pb, and Zn (4). The eluent collected from several extractions was analyzed by ICP-AES. The measured signals did not vary from levels in eluent collected from the blank extraction, indicating that the extraction efficiency was close to 100%.

A linear response is achieved when a five-point calibration plot is constructed from a 10 mg blank and 10 mg subsamples of analyte-laden Porasil B from separate extractions of four solutions of differing concentrations (20 mL of multi-element aqueous standards containing Cd, Pb, and Zn, corresponding to about 0.2–0.9 μg of analyte in the subsample). The plot is shown as Fig. S3 in the Supplementary Data.[3] A good correlation is shown for the analytes studied (R^2 = 0.99 for Cd, R^2 = 0.98 for Zn, and R^2 = 0.96 for Pb) if the amount of Si is kept constant for each standard.

Differences between the silica gel laden with only a single element (Cd) and silica gel laden with multiple elements (Cd, Pb, and Zn) were noted. First, the time profiles contained several Cd peaks. The multi-element samples of both Porasil B (Fig. 1*a*) and Chromabond (Fig. 1*d*) show a second Cd peak appearing at about the same time as the Zn peak. However, the time profiles for Cd in single-element samples of Porasil B and Chromabond (Fig. 2) only contain one peak that occurs at the same place as the first Cd peak of the multi-element samples.

Second, the integrated peak area for the single Cd peak from a single-element solution was about 20% lower than the total integrated peak area of both Cd peaks from a multi-element solution containing the same amount of Cd. This was seen with either Chromabond or Porasil B as the packing material. However, the peak area for Cd from the single-element solution did match with the integrated area of the first peak of the multi-element solution. Experiments showed that if Cd data from multi-element standards were used to construct a calibration curve, then Cd concentrations would be accurately determined (within 3% accuracy) for a single-element sample if only the peak area of the first Cd peak of the standards was used instead of the total peak area of both peaks. This plot is available as Fig. S4 in the Supplementary Data.[3]

Fig. 1. IH-ETV-ICP-AES time profiles of a Porasil B sample laden with Cd, Pb, and Zn (*a*, *b*, and *c*) and of Chromabond laden with Cd, Pb, and Zn (*d*, *e*, and *f*). Wavelengths shown are Cd = 228.8 nm, Zn = 213.9 nm, Pb = 220.4 nm, and Si = 251.6 nm.

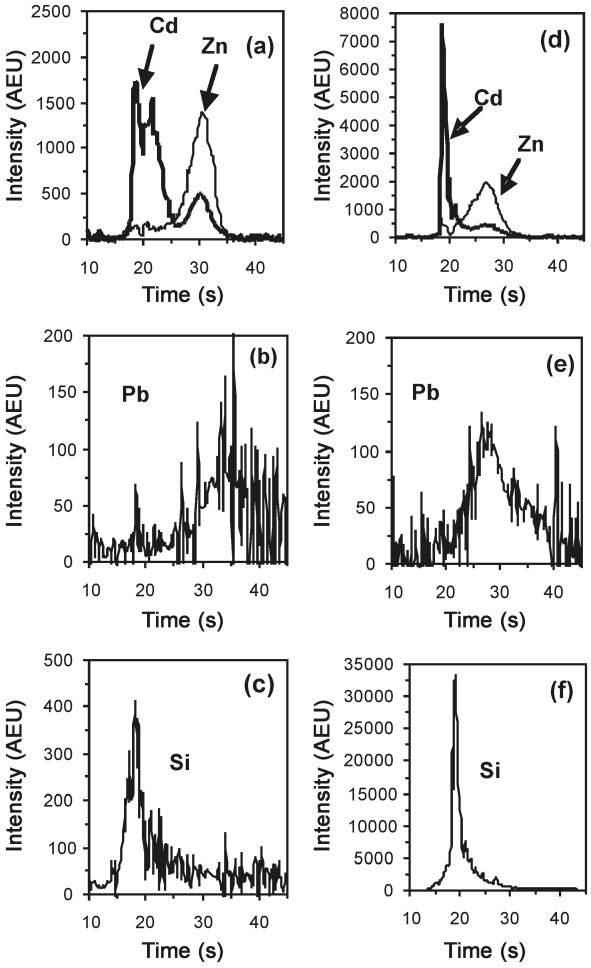

Fig. 2. IH-ETV-ICP-AES time profiles of (*a*) Porasil B sample laden only with Cd and (*b*) Chromabond sample laden only with Cd.

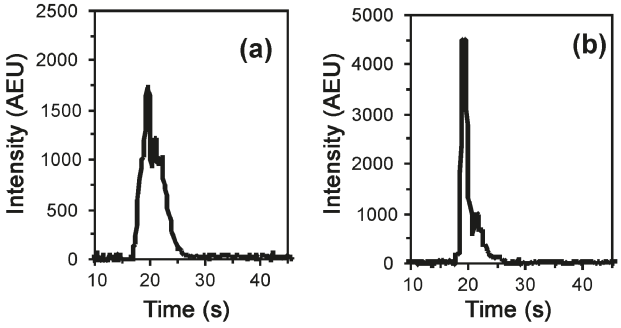

There are several possibilities for the variability in the number of peaks and the integrated peak areas between the single-element and multi-element solution. There may be a mass-transport phenomenon occurring in which some Cd is lost by condensation on the way to the ICP. The deposited Cd could then be picked up by the zinc or lead as it travels to the ICP. It is interesting to note that the first Cd peak appears with the early Si peak, whereas the Zn, Pb, and second

© 2008 NRC Canada

Table 2. Detection limits for the IH-ETV-ICP-AES of chromatographic material.

Element	Absolute (μg)	Relative (ng g^{-1})[a]	Solution nebulization (ng g^{-1})
Cd	0.3	15	80
Pb	1	60	40
Zn	3	150	2

[a]Based on an aqueous sample size of 20 g (about 20 mL) and analyzing only a subsample of total silica gel used in the extraction.

Cd peak all appear at the same time, although later. This suggests that either a different transport or vaporization scheme may be involved with Cd. Metallic Cd is both the lowest melting and boiling of the three metals. It may also be that there is a chemical conversion of the Cd form in which the second form of Cd is only seen or transported when other analytes are present. In any case, it was possible to obtain good analytical results using the procedure described above.

The detection limits (3σ) for Cd, Pb, and Zn are shown in Table 2. Zn, in particular, has a higher detection limit than the others because of a relatively high blank. The Zn contamination likely occurred when handling the graphite cups with latex gloves. Except for Zn, the concentration detection limits are about the same for those obtained for solution nebulization for the same ICP-AES instrument. These detection limits could probably be improved if purified reagents are used. In addition, one might see improvement if the operation conditions were optimized for this particular sample-introduction device (dry vapor) rather than the nebulizer conditions that were used. The performance of the IH-ETV with an ICP-MS system would have to be tested, but complications might be expected because of the high levels of organics vaporized during the analysis.

The concentration detection limit calculated in Table 2 is based on analyzing a 10 mg subsample of the total 150 mg used in the extraction (as was done in most experiments in this study because of the small volume of the graphite cup). If the entire amount of silica gel could be vaporized, then we would expect the detection limit to be roughly 15 times better.

We have shown that the analysis of analyte–laden chromatographic material by IH-ETV-ICP-AES is feasible. The detection limits obtained are useful for many applications. The experiments indicate that it may be possible to make on-column sampling systems that pretreat an aqueous environmental sample on-site in a format that can be followed by direct analysis by IH-ETV-ICP-AES later in the laboratory.

Acknowledgements

The authors wish to thank the Natural Sciences and Engineering Research Council of Canada (NSERC) for support under the Discovery Grant Program.

References

1. V. Camel. Spectrochim. Acta, **58B**, 1177 (2003).
2. E.H. Evans, J. Day, C. Palmer, W.J. Price, C.M.M. Smith, and J.F.J Tyson. Anal. At. Spectrom. **21**, 592 (2006).
3. H. Watanabe, K. Goto, S. Taguchi, J.W. McLaren, S.S. Berman, and D.S. Russell. Anal. Chem. **53**, 738 (1981).
4. R.E. Sturgeon, S.S. Berman, and S.N. Willie. Talanta, **29**, 167 (1982).
5. C.D. Skinner and E.D. Salin. J. Anal. At. Spectrom. **18**, 495 (2003).
6. J. Otero-Romani, A. Moreda-Pineiro, A. Bermejo-Barrera, and P. Bermejo-Barrera. Anal. Chim. Acta. **536**, 213 (2005).
7. K. Akatsuka and I. Atsuya. Fresenius Z. Anal. Chem. **329**, 453 (1987).
8. T. Nakamura, H. Oka, M. Ishii, and J. Sato. Analyst, **119**, 1397 (1994).
9. Q. Zhang, H. Minami, S. Inoue, and I. Atsuya. Fresenius J. Anal. Chem. **370**, 860 (2001).
10. C.D. Skinner, M. Cazagou, J. Blaise, and E.D Salin. Appl. Spectrosc. **53**, 191 (1999).
11. R. Rattray and E.D. Salin. J. Anal. At. Spectrom. **10**, 1053 (1995).
12. W.W. Van Berkel and F.J.M. Maessen. J. Spectrochim. Acta: Part B. **43B**, 1337 (1998).
13. D.M. Goltz and E.D. Salin. J. Anal. At. Spectrom. **12**, 1175 (1997).
14. D.M. Goltz, C.D. Skinner, and E.D. Salin. Spectrochim. Acta: Part B, **53B**, 1139 (1998).
15. M.E. Rybak and E.D. Salin. Spectrochim. Acta: Part B, **56B**, 289 (2001).
16. J.P. Lafleur, R. Lam, H.M. Chan, and E.D Salin. J. Anal. At. Spectrom. **20**, 1315 (2005).
17. J.M. Ren, M.E. Rybak, and E.D. Salin. J. Anal. At. Spectrom. **18**, 485 (2003).

© 2008 NRC Canada

Effect of relative humidity on the morphology of electrospun polymer fibers[1]

Eliton S. Medeiros, Luiz H. C. Mattoso, Richard D. Offeman, Delilah F. Wood, and William J. Orts

Abstract: The effect of relative humidity on the morphology of electrospun fibers of poly(vinyl alcohol), poly(methyl methacrylate), poly(vinyl chloride), polystyrene, and poly(lactic acid) dissolved in solvents such as toluene, *N*,*N*-dimethylformamide, 2,2,2-trifluoroethanol, and deionized water was studied by scanning electron microscopy to investigate the factors that may contribute to pore formation. Results showed that the presence of pores depends on factors such as the type of polymers used, the polymer–solvent combination, molecular weight, and the size of the electrospun structure. The final morphology developed implies a competition between the dynamics of phase separation and the rate of solvent evaporation. In addition, continuous solvent evaporation and constant stretching owing to the electric potential difference give rise to the final shape of porous electrospun fibers.

Key words: electrospinning, relative humidity, porous fibers, polymers.

Résumé : Faisant appel à la microscopie électronique à balayage pour étudier les facteurs qui peuvent contribuer à la formation de pores, on a examiné l'effet de l'humidité relative sur la morphologie de fibres électrofilées du poly(alcool vinylique), du poly(méthacrylate de méthyle), de poly(chlorure de vinyle), de polystyrène et de poly(acide lactique) dissous dans des solvants tel le toluène, le *N*,*N*-diméthylformamide, le 2,2,2-trifluoroéthanol et l'eau déionizée. Les résultats montrent que la présence des pores dépend de facteurs tels que le type de polymère utilizé, la combinaison polymère–solvant, le poids moléculaire et la taille de la structure électrofilée. La morphologie finale qui se développe implique une compétition entre la dynamique de la séparation de phase et la vitesse d'évaporation du solvant. De plus, l'évaporation continue du solvant et l'étirement constant qui résulte de la différence de potentiel conduit à la forme finale des fibres électrofilées poreuses.

Mots-clés : fibres électrofilées, humidité relative, fibres poreuses, polymères.

[Traduit par la Rédaction]

Introduction

A significant number of papers have been published on the electrospinning of micro- and nanostructures in recent years (1–3). However, most of these works do not take into account the fact that the relative humidity (RH) of the spinning environment affects fiber morphology as well as the structure–properties relationship. It has already been established that reproducibility during the production of nanoscale materials can only be obtained by accurate control of parameters governing each electrospinning system (materials and process variables). To study the effect of other process variables, RH must be accurately controlled, a parameter not always discussed.

Recently, some reports have begun to address the effect of RH on the morphology of electrospun fibers and beads (4–11). These works report that electrospinning of certain combinations of polymers and solvents, specifically the highly volatile ones, in humid environments (RH above ca. 30%) produced porous structures whose surface features can be controlled by the appropriate choice of materials and process variables. The porous structure has been attributed to several factors, such as the combined effects of the polymer, the electric force applied, and the fast absorption of oxygen in air by the solvent (5); a temperature decrease at the surface because of fast solvent evaporation, which causes moisture condensation on the surface of the fibers thereby forming the pores and (or) other surface features (6, 7); and phase separation (8, 11, 12).

Furthermore, the production of electrospun fibers by RH-controlled experiments results in porous structures without going through extravagant measures, such as removing the "other" phase with selective solvation (12–14).

Applications of porous materials range from filtration membranes and sensors to controlled release systems and

Received 10 December 2007. Accepted 13 February 2008. Published on the NRC Research Press Web site at canjchem.nrc.ca on 30 April 2008.

This paper is dedicated to Robert H. Marchessault in recognition of his many contributions to polysaccharide and biopolymer chemistry.

E.S. Medeiros, R.D. Offeman, D.F. Wood, and W.J. Orts.[2] USDA Bioproduct Chemistry and Engineering Research Unit, Western Regional Research Center, 800 Buchanan St., Albany, CA 94710, USA.
L.H.C. Mattoso. Laboratório Nacional de Nanotecnologia para o Agronegócio, Embrapa Instrumentação Agropecuária, R. XV de Novembro, 1452, São Carlos, SP, 13560–970, Brazil.

[1]This article is part of a Special Issue dedicated to Professor R. Marchessault.
[2]Corresponding author (email: bill.orts@ars.usda.gov).

 doi:10.1139/V08-029 © 2008 NRC Canada

Table 1. Some physical and chemical properties of the solvents used (17–19).

Solvent	Chemical formula	*MW*	bp (°C)	Solubility in water (g/100 g)	ϵ	vp @ 20 °C (mm Hg)
Water	H_2O	18.02	100	—	78.54	17.5
Toluene	C_7H_8	92.14	110.6	0.05	2.38	21.9
N,*N*-Dimethylformamide (DMF)	C_3H_7NO	73.09	153	Miscible	36.7	2.7
2,2,2-Trifluoroethanol (TFE)	$C_2H_3F_3O$	100	78	Miscible	27.5	52
1,1,1,3,3,3-Hexafluoro-2-propanol (HFP)	$C_3H_2F_6O$	168.1	58.2	Miscible	17.75	102

bone-tissue scaffolds (1, 2, 15). In biomedical applications, such as in bone tissues and wound-dressing, porosity is a requirement that promotes tissue growth and oxygen exchange between the damaged tissues and the external environment (16).

In this work, the morphology of electrospun nanofibers was studied under various relative humidity conditions (between 20% and 80%). Specifically, the fiber morphology of poly(vinyl alcohol) (PVA), poly(methyl methacrylate) (PMMA), poly(vinyl chloride) (PVC), polystyrene (PS), and poly(lactic acid) (PLA) that had been dissolved in solvents such as toluene, *N*,*N*-dimethylformamide (DMF), 2,2,2-trifluoroethanol (TFE), and deionized water, was studied by scanning electronic microscopy (SEM) to describe factors that contribute to pore formation and give an explanation of possible mechanisms involved.

Experimental

Polymers

PVA (97% hydrolyzed, MW = 5–8 × 10^4g/mol, CAS No. 9002–89–5); PMMA (MW = 1.2 × 10^5g/mol, CAS No. 9011–14–7); PVC, (M = 1.1 × 10^5 g/mol, CAS 9002–86–2, inherent viscosity = 1.02); and PS (CAS No.9003–53–6, MW = 4 × 10^5g/mol) were purchased from Sigma-Aldrich (St. Louis, MO, USA), and PLA (Polylactide Resin 4042D, MW = 2–4x10^5) was acquired from NatureWorks LLC (Minnetonka, MN, USA).

Solvents

Toluene, 1,1,1,3,3,3-hexafluoro-2-propanol (HFP), and DMF were purchased from Sigma-Aldrich (St. Louis, MO, USA) and 2,2,2-trifluoroethanol (TFE) was purchased from Alfa Aesar (Ward Hill, MA, USA). The PVA solution was prepared with deionized water. Some physical and chemical properties of these solvents such as solubility in water, boiling point (bp), molecular weight (M_r), dielectric constant (ϵ), and vapor pressure (vp) are listed in Table 1.

Electrospinning

The electrospinning setup used in this study consisted of a 5 mL plastic syringe, a 21G (id: 0.495 ± 0.001mm) or 18G (id:1.194 ± 0.001mm) needle, a grounded collector (stainless steel barrel with controllable rotation speed (ω), a hypodermic syringe pump (KD Scientific, USA) to control the injection rate (β) of the polymer solutions, and a high-voltage supply (Series FC, Glassman High Voltage, Inc., USA), which can generate positive direct current voltages (V) up to 99 kV. The needle was connected to the high-voltage source and positioned at a fixed working distance (WD from the grounded collector, and the polymer solution was injected at a constant rate (see Scheme 1). The experimental conditions used in each polymer–solvent system are listed in Table 2.

Scheme 1. Electrospinning setup: (*a*) Injection pump with hypodermic syringe, (*b*) grounded collector, (*c*) high voltage supply, and (*d*) working distance.

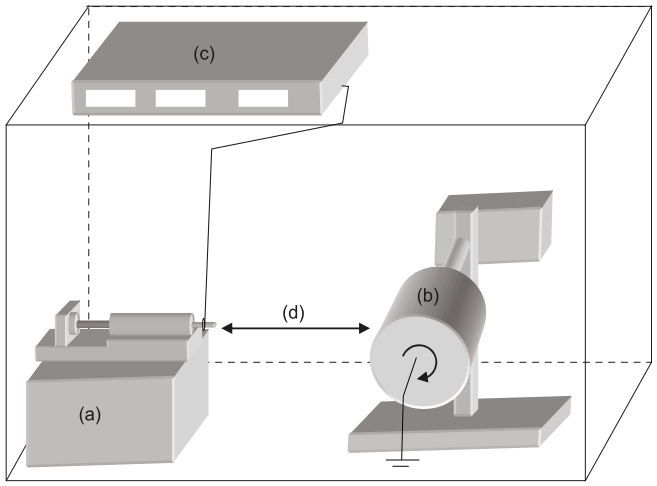

These conditions were based on a prior study in which the electrospinning parameters such as voltage, working distance, and injection rate (results not shown) were varied so that optimized experimental conditions could be used in further experiments.

Scanning electron microscopy (SEM) characterization

Samples were electrospun onto aluminum foil that had been wrapped on the rotating collector, and were collected for SEM analysis after 30 min. SEM samples were coated by gold sputtering for 45 s and analyzed for surface characterization using a Hitachi Scanning Electron Microscope (Model S4700, Hitachi High-Technologies, Japan) at a voltage of 2 kV.

Results

Despite being investigated for the past few years, the mechanisms that lead to the formation of porous fibers during electrospinning are not sufficiently understood. Therefore, to investigate the possible factors that may influence the presence of pores on electrospun fibers, different polymers were electrospun at relative humidity (RH) varying from 20% to 80%. Fibril morphology was analyzed by SEM and correlated to physical and chemical characteristics of

© 2008 NRC Canada

Table 2. Experimental conditions used for the electrospinning of the polymers.

Polymer	Concentration (*w*/*v*%)	Solvent	V (kV)	WD (cm)	β (μL/min)	Needle	ω (rpm)
PS	14	DMF	20	20	6	16 G	600
PMMA	14	DMF	11	20	5	16 G	600
PVC	14	DMF	28	20	5	16 G	600
PLA	12	HFP	11	20	5	16 G	600
PLA	11	TFE	11	20	5	16 G	600
PVA	14	H_2O	28	11.5	6	16 G	600
PMMA	14	Toluene	22	18	2.5	21 G	600

Fig. 1. SEM micrographs of polystyrene (PS) fibers electrospun from DMF solution at (*a*) 20 ± 4; (*b*) 40 ± 4; (*c*) 60 ± 4; and (*d*) 80 ± 4% RH.

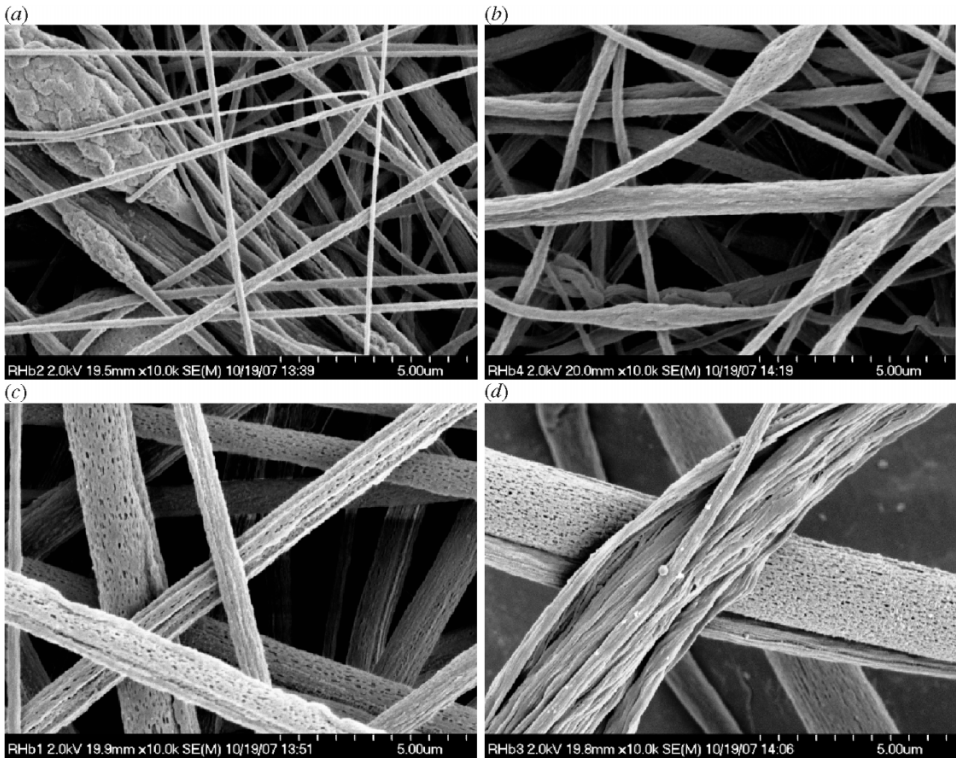

each system such as polymer hydrophobicity, solvent volatility, and solubility in water. Figs. 1, 2, and 3 show the SEM micrographs of PS, PMMA, and PVC electrospun fibers from DMF solutions.

The results of Figs. 1 to 3 show that when the relative humidity is higher than 25%, pores are formed along the electrospun fibers. The relative humidity at which pores form varies somewhat between polymers; for PS it is 40%–60%; for PVC, 60%; and for PMMA, 80%. It is worth observing that not all of the fibers electrospun at the highest RH (80%) are porous; rather, porosity seems to depend on the size of the electrospun structure. For example, the existence of pores can be observed even at 20% RH when large structures are involved as can be seen in the lower left corner of Fig. 1*a*, when beads are also formed among the fibers. It seems that only fibers with a diameter above a certain critical value are porous, whereas those below this value are nonporous.

The intensity of electric field does not affect the pore formation. This makes sense, since the space between the polymer injection and the target is filled up with water molecules in vapor phase, which makes the atmosphere surrounding the electrospinning more conductive because of polarization of the water molecules (19). As a consequence of this increase in conductivity, the effect of the electric field on the fiber surface is less intense and the fibers are thicker, as can be seen in Figs. 1, 2, and 3. Furthermore, these results are in accordance with the literature showing that the applied voltage does not affect the pore size of PS fibers electrospun from tetrahydrofurane (THF) solutions (11).

To verify the effect of solvent volatility on pore formation, PMMA and PS were electrospun from toluene. Figs 4 and 5 show SEM micrographs of these fibers. It can be observed that, when electrospun fibers from DMF and toluene are compared, the ones electrospun from toluene have more defined porous structures (see, e.g., Fig. 5*e*) than those produced from DMF (see, e.g., Fig. 2*e*). Some of these pores, depending on their size, can partially close because polymer chains still have mobility as a consequence of incomplete

© 2008 NRC Canada

Fig. 2. SEM micrographs of poly(methyl methacrylate) (PMMA) fibers electrospun from DMF solution at (*a*) 20 ± 4; (*b*) 40 ± 4; (*c*) 60 ± 4; (*d*) 80 ± 4% RH; and (*e*) detail of fiber surface in (*d*).

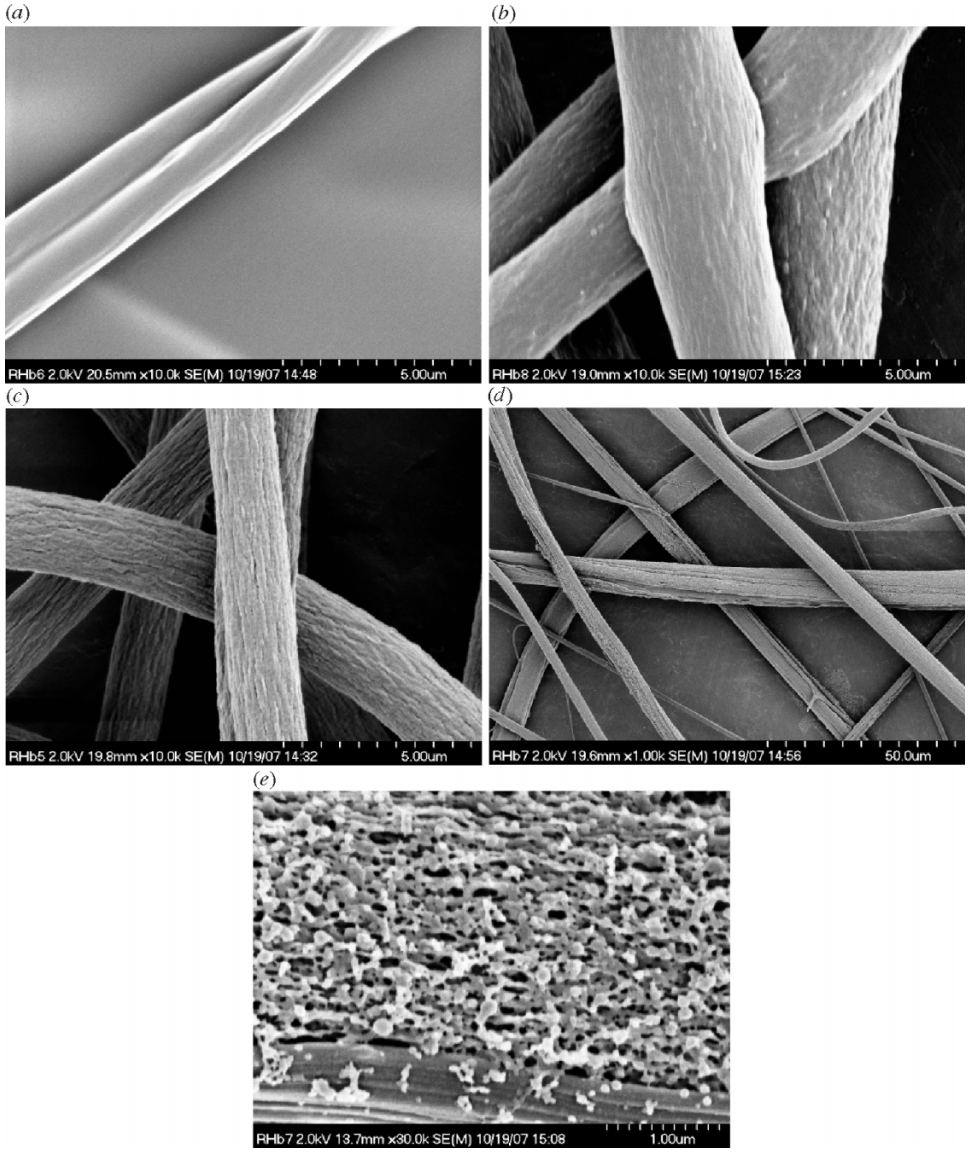

solvent evaporation in the core, while others remain open as shown in Fig. 4*e*. This is a consequence, both of the less volatile DMF whose boiling point is about 40 °C higher than that of toluene and whose vapor pressure is about eight times lower (see Table 1), and of the higher molecular weight of PMMA. When pores are formed, because of solvent volatilization and phase separation, the tendency for pores to coalesce is much reduced because the rapid increase in polymer viscosity forms well-defined porous structures, as will be discussed later.

Fig. 5 also displays wrinkled beads clearly indicating skin formation and collapse. If there is enough time for chain coiling, the droplets acquire a round shape, an effect that clearly depends on factors such as viscosity, working distance, applied voltage, and polymer molecular weight to minimize the surface area in contact with the surrounding atmosphere. Immediate skin formation because of fast evaporation prevents the solvent molecules entrapped in the core from diffusing though the skin. However, when internal pressure (which is dependent on solvent vapor pressure) overcomes skin cohesive forces (which are dependent on its thickness, polymer molecular weight, and surface tension) holes are opened. Then, the skin may or may not collapse depending on several factors such as those mentioned above. Depending on the size of the beads, the collapse may occur either completely, forming fully wrinkled surfaces and cups (see big beads in Fig. 5*a*), or partially as can be observed in Fig. 5*c*. These results are in accordance with the report by Eda and Shivkumar (9) on the bead structure variations during electrospinning of polystyrene dissolved in THF. They found that pore size increased as the polymer molecular weight increased.

The skin formation because of fast solvent evaporation does not fully explain why pores are not formed when PLA is electrospun from TFE and HFP, which are very volatile solvents. Figs. 6 and 7 show the morphologies of PLA fibers electrospun from TFE and HFP solutions. Additionally, to

© 2008 NRC Canada

Fig. 3. SEM micrographs of poly(vinyl chloride) (PVC) fibers electrospun from DMF solution at (*a*) 20 ± 4; (*b*) 40 ± 4; (*c*) 60 ± 4; and (*d*) 80 ± 4% RH.

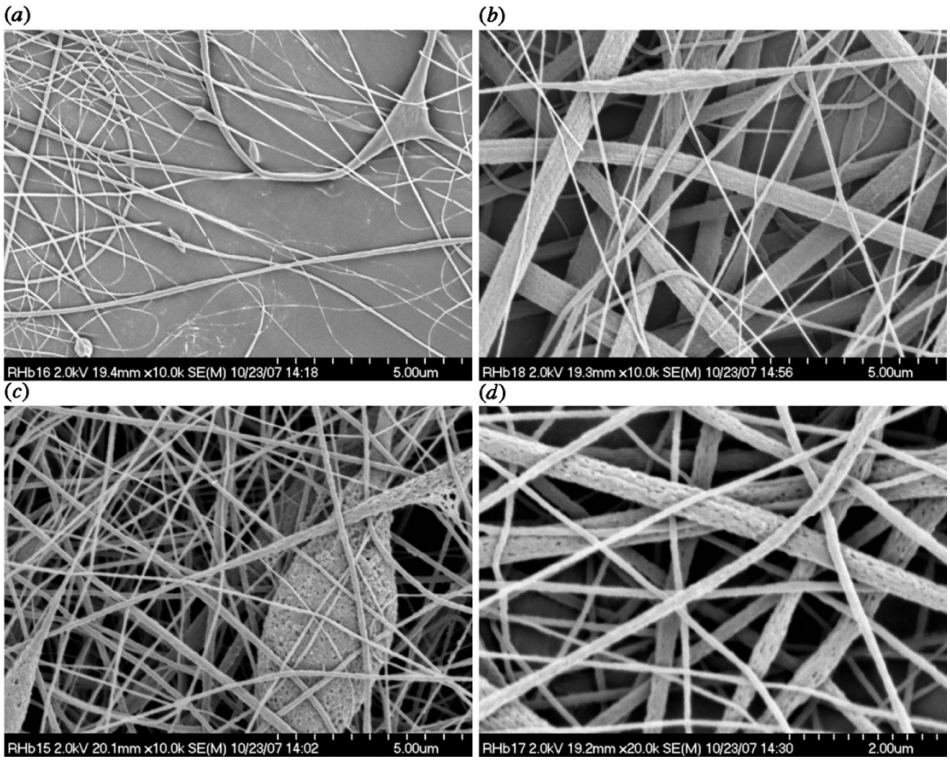

increase the possibility of pore formation on these fibers by producing thicker fibers, the concentration of PLA dissolved in TFE was increased to 15%, 20%, and 25% so that thicker fibers could be obtained while keeping fixed the other experimental parameters (working distance, applied voltage, injection rate, and relative humidity) (see Fig. 8).

These results showed that the fibers do not display any surface features other than slight wrinkles, possibly because of volume reduction caused by solvent evaporation and polymer crystallization. This shows that even when producing thicker fibers using highly volatile solvents, thus increasing the tendency toward the formation of a porous structure because of solvent entrapped in the core, there was no pore formation on their surface as can be seen in Fig. 6.

According to the literature, fast solvent evaporation lowers the temperature at the fiber surface so that water droplets condense, thereby forming the breath figures (6, 7, 11). However, this effect alone cannot explain why pores are formed on PS fibers electrospun from DMF solutions, whereas there is no pore formation when polymers like PLA are electrospun from TFE or THF, which are very volatile solvents that can undergo evaporative cooling because of fast solvent evaporation. To investigate the effect of polymer hydrophilicity on pore formation, PVA was electrospun from aqueous solutions. SEM micrographs are shown in Fig. 9.

The results of Fig. 9 show that PVA electrospun in high humidity environments does not form porous structures, a result which is in agreement with the results for poly(oxyethylene) electrospun from aqueous solution obtained by Magelski et al. (11). Likewise, PLA, a hydrophobic polymer, did not give pore formation. These results indicate that if the polymer is hydrophilic there is no pore formation in high humidity environments. On the other hand, if the polymer is hydrophobic, it does not mean necessarily that there will always be pore formation.

It is important to notice also that the diameter of PVA electrospun fibers decreased as relative humidity increased and beads were formed on the fibers electrospun at 60% and 80% RH. This effect is opposite to that of fibers electrospun from organic solvents such as DMF, THF, and toluene, in which fiber diameter generally increases as the relative humidity increases, as shown in Table 3. Moreover, PVA fibers had a round shape without wrinkles as a consequence of a lower rate of solvent evaporation and no skin formation; this gives enough time for the solvent to evaporate while the fiber contracts more slowly forming a much less rough surface.

When RH increases, the conductivity of the medium increases both because of polarization of the air owing to the high applied electric field with ozone formation (this phenomenon can be detected easily by the ozone odor in the electrospinning box) and because of formation of conductive "paths" owing to water dipoles across the working distance. This reduces the stretch on the fibers, but may also split them because of formation of secondary jets (3, 18). This phenomenon is more evident when the viscosity is low (e.g., Figs. 9*c* and 9*d* show branched fibers of PVA because of this phenomenon).

Whereas fibers of PMMA, PVC, and PS in DMF, or PMMA and PS in toluene were porous when electrospun at relative humidity higher than 30%, fibers of PLA in TFE and HFP, and PVA in water did not exhibit pore formation at any value of relative humidity. Actually, the final morphol-

© 2008 NRC Canada

Fig. 4. SEM micrographs of poly(methyl metacrylate) (PMA) fibers electrospun from toluene soluation at (*a*) 20 ± 4; (*b*) 40 ± 4; (*c*) 60 ± 4; (*d*) 80 ± 4% R.H.; and (*e*) detail of fiber surface in (*d*).

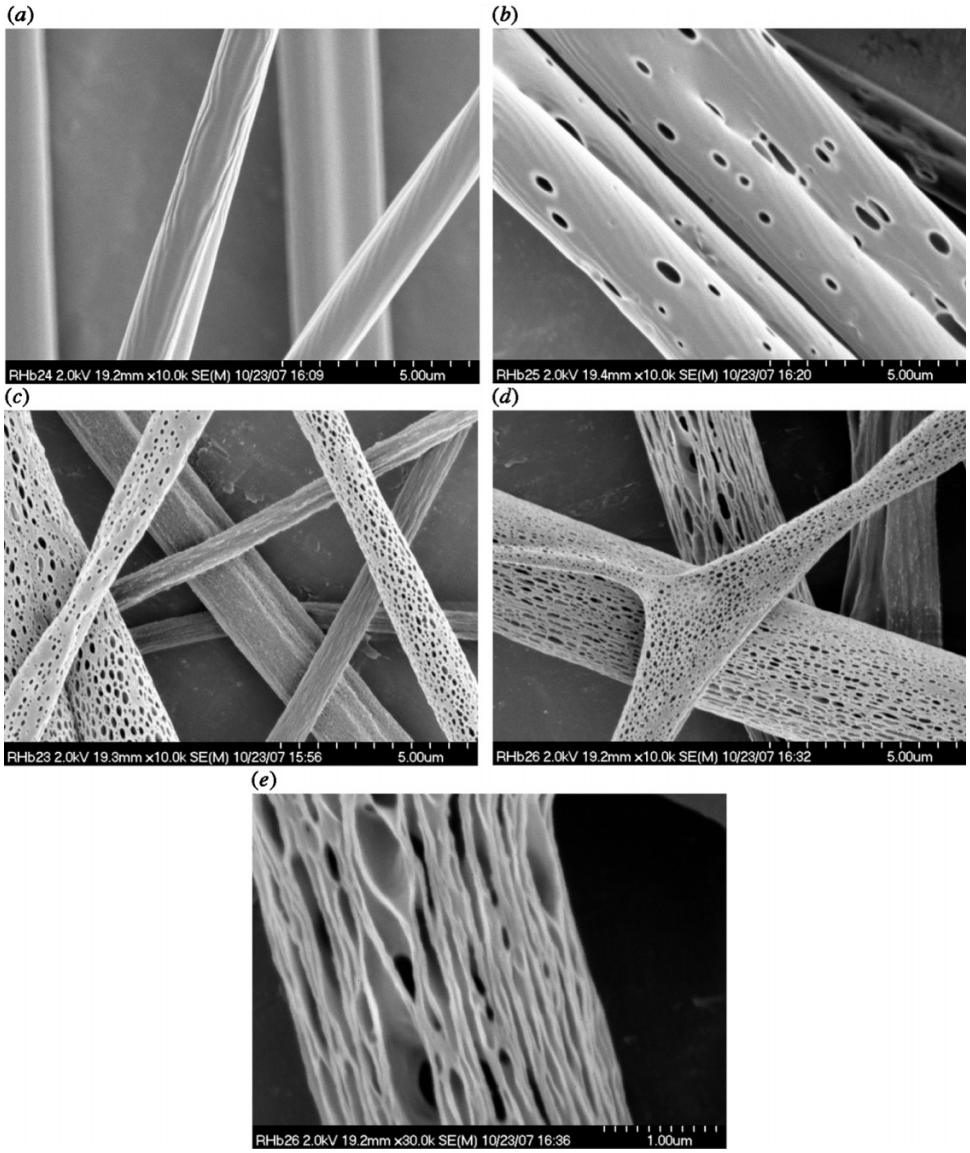

Table 3. Range of fiber diameters as a function of relative humidity for the polymers studied.

	Range of fiber diameter (nm) at RH (%)			
Polymer (solvent)	20%±4%	40%±4%	60%±4%	80%±4%
PS (DMF)	90–600	200–850	300–1800	400–2400
PVC (DMF)	30 190	70–290	60–940	72–500
PMMA (DMF)	1000–1200	2400–3000	1900–2100	1200–5000
PMMA (Tol)	2180–4400	525–8662	404–2928	1811–4380
PVA (H_2O)	230–540	146–550	100–460	100–400
PLA (TFE) – 11%	90–220	90–220	90–210	110–690
PLA (TFE) – 15%	—	—	—	155–460
PLA (TFE) – 20%	—	—	—	238–604
PLA (TFE) – 25%	—	—	—	268–715
PLA (HFP) – 12%	—	—	—	240–2200

© 2008 NRC Canada

Fig. 5. PS fibers electrospun from toluene between 40 and 50% RH. (*a*) Overall structure composed of big beads and fibers; (*b*) close-up showing the smallest beads and fibers; (*c*) details showing the smallest beads; and (*d*) details of a porous fiber.

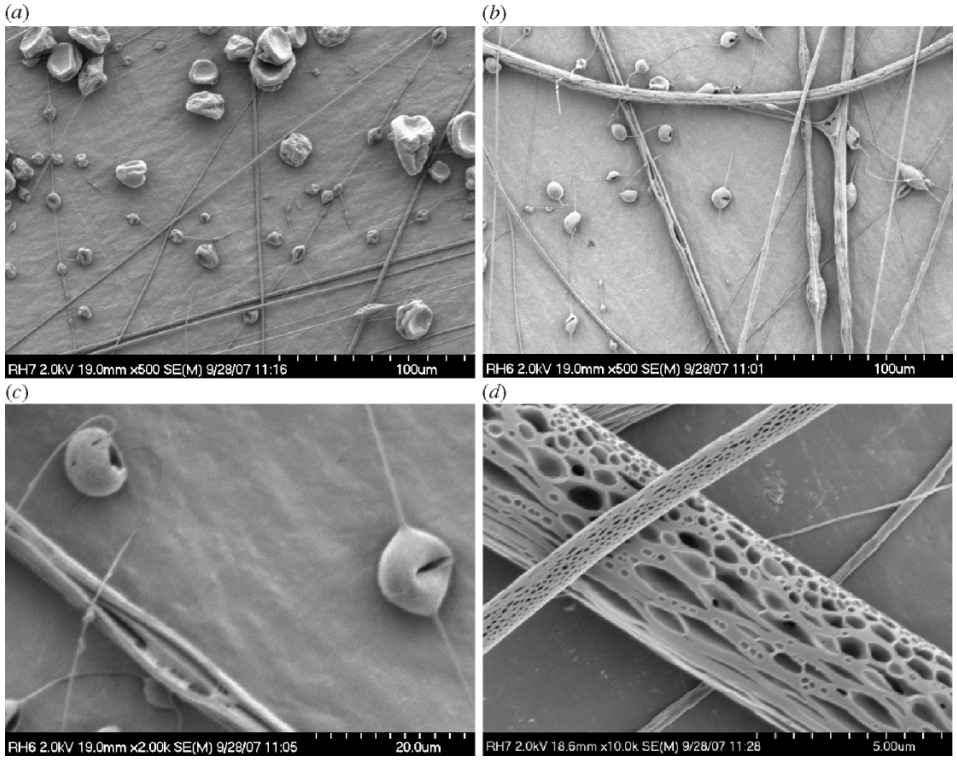

Fig. 6. SEM micrographs of poly(lactic acid) (PLA) fibers electrospun from TFE solution at (*a*) 20 ± 4; (*b*) 40 ± 4; (*c*) 60 ± 4; and (*d*) 80 ± 4% RH.

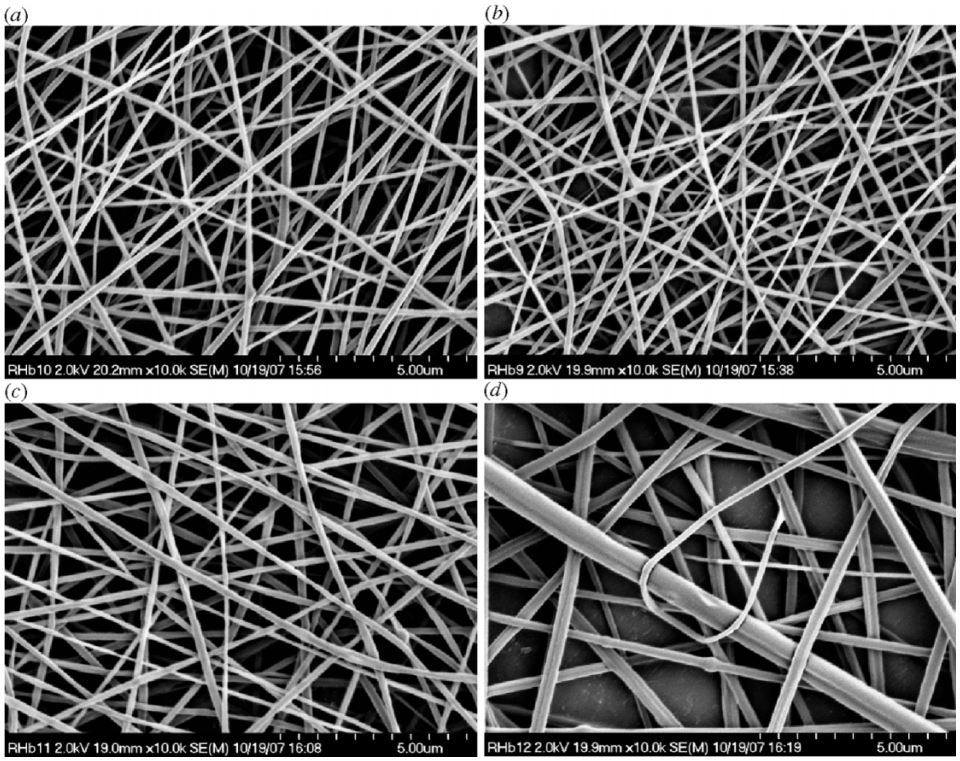

© 2008 NRC Canada

Fig. 7. SEM micrograph of poly(lactic acid) (PLA) fibers electrospun from HFP solution at 80 ± 4% RH.

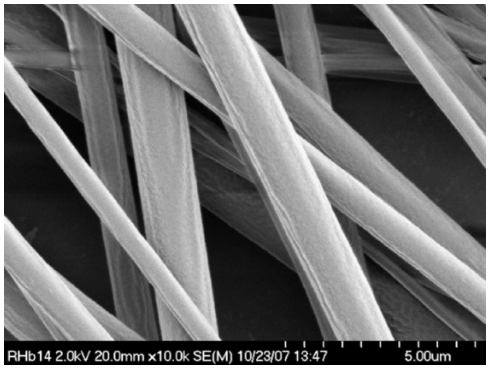

ogy developed during electrospinning is controlled by the solution chemistry of the polymer–solvent system, i.e., there is a competition between the dynamics of phase separation and the rate of solvent evaporation, in a way similar to the casting of porous membranes (20, 21).

The phase separation mechanism is believed to be comprised of two steps, nucleation and growth, and spinodal decomposition, where the interconnected porous structure is generally attributed to phase separation by the spinodal decomposition mechanism. In contrast, closed pores are attributed to the nucleation and growth mechanism (22–25). Since fast solvent evaporation at the external layer or skin of the fibers are being formed, abrupt concentration changes may also take place. If these changes lie within the range of the instability or spinodal decomposition region, phase separation of the components can occur thereby forming a rapidly solidified skin with micro and (or) nanopores (21–25).

When fibers are electrospun from organic solvents like DMF and toluene in a high humidity environment and the polymer is hydrophobic, a skin is formed immediately after the polymer comes into contact with the surrounding environment. This is because the vapor water molecules act as nonsolvent for the polymer–solvent system, which is one of the necessary conditions for a system to undergo phase separation. Although the nonsolvent produces phase separation, not all nonsolvent behaves this way (22). This explains why PLA, being hydrophobic, did not undergo phase separation and hence did not form porous fibers when electrospun from TFE and HFP. However, because PVA is soluble in water, phase separation does not occur in this system; this explains the absence of pores on PVA electrospun fibers.

When the internal pressure due to solvent volatilization and diameter contraction is higher than the surface tension, some of the pores may have their walls broken, thus opening channels though which the solvent evaporates and leaving behind radial pores all over the fiber surface.

If the degree of phase separation is high and the solvent is volatile enough to form a relatively thick skin as the solvent evaporates, an abrupt increase in viscosity can take place restraining polymer mobility and preventing the pores from closing. Otherwise, these pores may eventually coalesce to surface defects (surface pores) rather than through pores (see Scheme 2), as also observed by Megelski et al. [27].

This behavior helps explain why well-defined pores were formed on the surface of PS and PMMA fibers electrospun from toluene. The average pore size, therefore, depends on multiple factors, specifically surface tension, solution viscosity, polymer molecular weight, glass transition (i.e., relative mobility of polymer chains), stretching level imposed by the electric field, solvent diffusion, and polymer–solvent interaction (4, 26, 27). Moreover, as shown in the literature (7, 8, 11) and in this work, the fibers susceptible to pore formation and surface defects are those whose diameters lie at the micron scale. For fibers at the nanoscale, however, the skin as well as the internal core may be so thin that the dynamics of solvent evaporation, phase separation, and skin formation are so fast that there is not enough time to form the surface features.

In addition, as the surface charges overcome the surface tension of the polymer droplet at the needle tip, the droplet is deformed by the action of electrostatic repulsion forces while it is being pushed to the collector by the action of electrical potential difference. At first, when the field intensity is high, the polymer is rapidly stretched in a way analogous to shear stress development when a polymeric melt exits a die of an extruder (28–30). After the development of this step, continuous solvent evaporation and constant stretching, as the jet moves toward the collector help freeze the stretched pores as the fibers are deposited on the collector, thereby giving rise to the final shape of porous electrospun fibers. This is depicted, for example, in SEM micrographs of fiber surface in Figs. 4 and 5.

Conclusions

When the relative humidity is higher than 25%, pores are formed along electrospun fibers, with the RH of initial pore formation varying somewhat from polymer to polymer as a consequence of several factors such as molecular weight and structure. Not all of the fibers electrospun at 80% RH are porous; rather, porosity depends on the size of the electrospun structure. The fibers susceptible to pore formation and surface defects are those whose diameters lie at the micron scale, because at the nanoscale the skin as well as the internal core may be so thin that the dynamics of solvent evaporation, phase separation, and skin formation are too fast to allow enough time to form the surface features.

The final morphology developed during electrospinning is a competition between the dynamics of phase separation and the rate of solvent evaporation, in a way similar to the casting of porous membranes. A water-rich environment helps the fast formation of a skin with well-defined boundaries, while the opposite can cause a semi-diffuse layer allowing easy solvent evaporation.

When a polymer is hydrophobic, water acts as nonsolvent and the skin is more readily formed. This explains why the systems PMMA, PVC, or PS in DMF, or PMMA or PS in toluene exhibited porous fibers when electrospun at relative humidity higher than 30%, whereas PLA in TFE or HFP, and PVA in water did not exhibit pore formation at any value of relative humidity. In addition, continuous solvent evaporation and constant stretching gives rise to the final porous structure of the electrospun fibers.

© 2008 NRC Canada

Fig. 8. SEM micrographs of poly(lactic acid) (PLA) fibers electrospun from TFE at 80% RH. (*a*) 15 *w*/*v*% PLA; (*b*) 20 *w*/*v*% PLA; (*c*) 25 *w*/*v*% PLA; and (*d*) details of fiber surface in (*c*) at higher magnification.

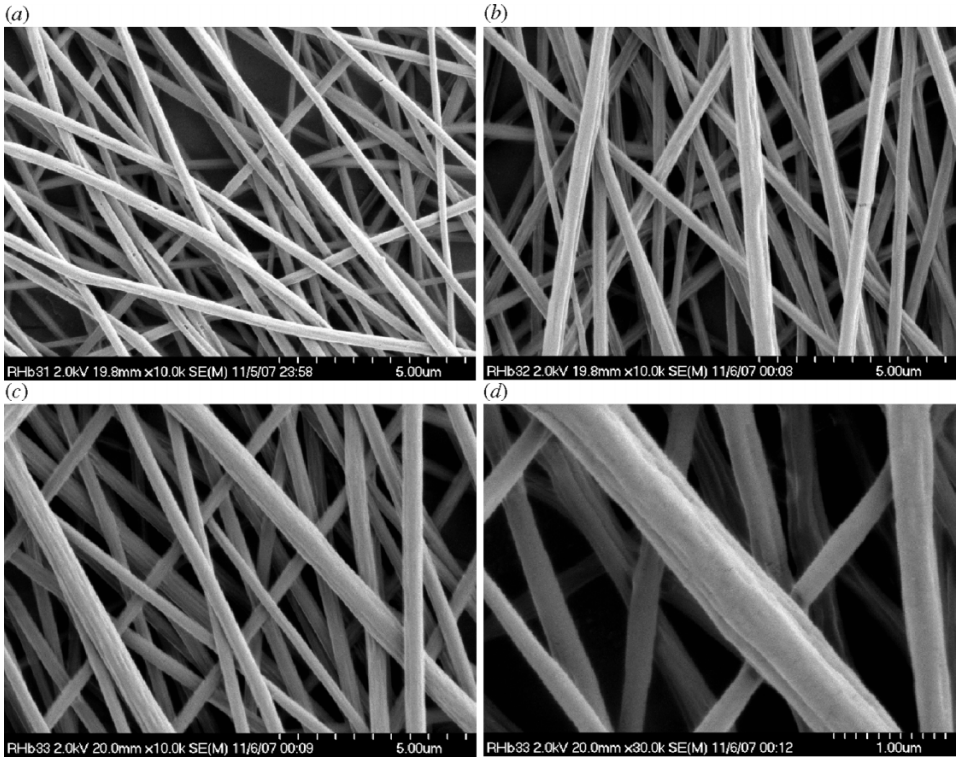

Fig. 9. SEM micrographs of poly(vinyl alcohol) (PVA) fibers electrospun from aqueous solution at (*a*) 20 ± 4; (*b*) 40 ± 4; (*c*) 60 ± 4; and (*d*) 80 ± 4% RH.

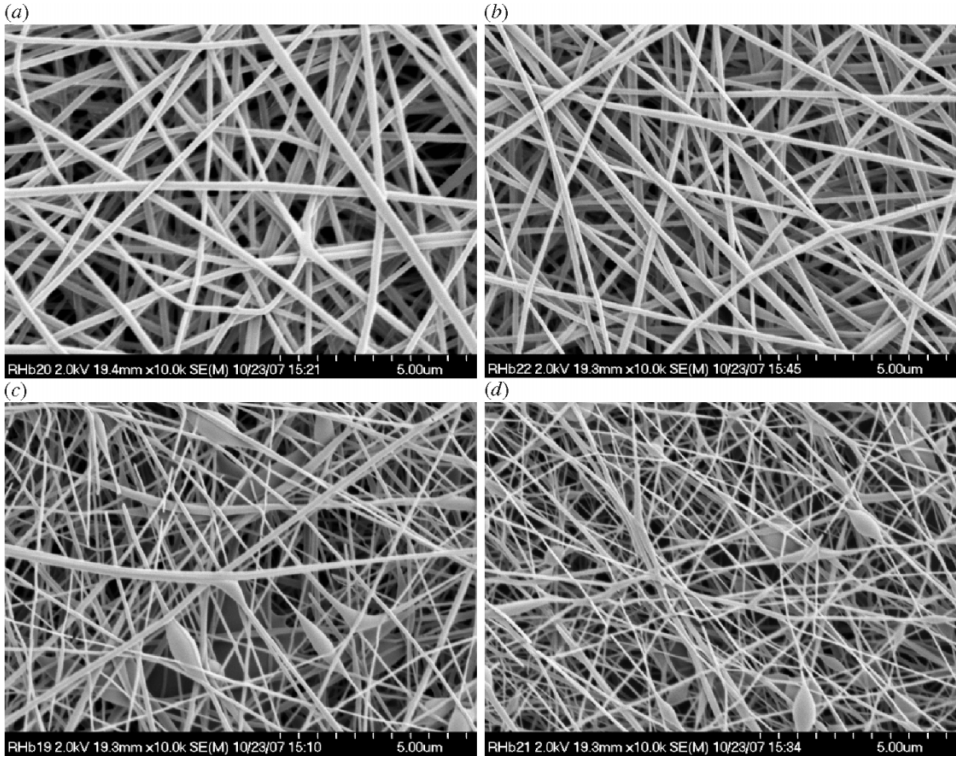

© 2008 NRC Canada

Scheme 2. Mechanism of skin and pore formation. As the skin is formed, polymer concentration increases from its initial concentration (C_0) at the core to ca. 100% at the outer surface of the skin. (*a*) Thin skin with polymer solution entrapped in the core, (*b*) solvent molecules diffusing through the pores, and (*c*) partial closing of the pores to form surface pores.

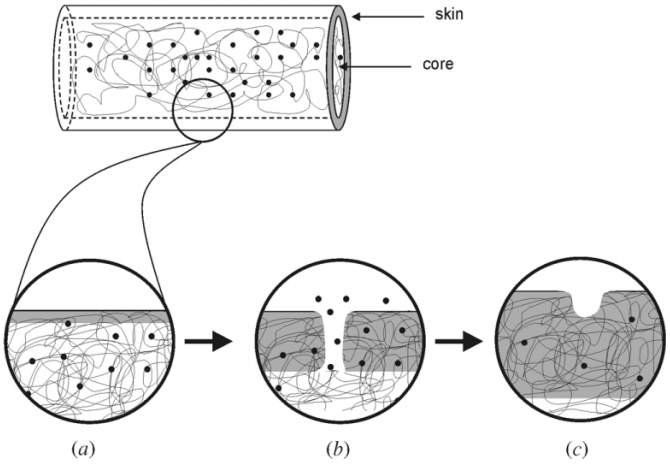

Acknowledgements

The authors would like to thank Tina Williams for superior technical help with SEM and Gregory M. Gray for his many valuable suggestions on electrospinning. Thanks are also due to Dr. J.A. Malmonge and Dr. A.P.Klamczynski for their helpful discussions. One of the authors, L.H.C. Mattoso, would like to thank the National Council for Scientific and Technological Development (CNPq, Brazil) for his financial support. The authors are also indebted to Professor R.H. Marchessault for valuable insights and discussions over the years, and for initiating a persistent interest in nanocomposites. This work is part of a long-term research effort to incorporate cellulose nanocrystals into polymer systems, an idea inspired by the visionary work of Marchessault and colleagues.

References

1. A. Greiner and J.H. Wendorff. Angew. Chem. Int. Ed. **46**, 5670 (2007).
2. T. Subbiah, G.S. Bhat, R.W. Tock, S. Parameswaran, and S.S. Ramkumar. J. Appl. Polym. Sci. **96**, 557 (2005).
3. S. Ramakrishna, K. Fujihara, W.E. Teo, T.C. Lim, and Z. Ma. An Introduction to electrospinning and nanofibers. World Scientific Publishing, Singapore. 2005.
4. C.A. Smolders, A.J. Reuvers, R.M. Boom, and I.M. Wienk. J. Membr. Sci. **73**, 259 (1992).
5. K.H. Lee, H.Y. Kim, H.J. Bang, Y.H. Jung, and S.G. Lee. Polymer, **44**, 4029 (2003).
6. G.T. Kim, J.S. Lee, J.H. Shin, Y.C. Ahn, K.H. Jeong, C.M. Sung, and J.K. Lee. Microsc. Microanal. **10** (Suppl. 2), 554 (2004).
7. G.T. Kim, J.S. Lee, J.H. Shin, Y.C. Ahn, Y.J. Hwang, H.S. Shin, J.K. Lee, and C.M. Sung. Kor. J. Chem. Eng. **22**, 783 (2005).
8. C.L. Casper, J.S. Stephens, N.G. Tassi, D.B. Chase, and J.F. Rabolt. Macromolecules, **37**, 573 (2004).
9. G. Eda and S. Shivkumar. J. Mater. Sci. **41**, 5704 (2006).
10. J.P. Jeun, Y.H. Kim, Y.M. Lim, J.H. Choi, C.H. Jung, P.H. Kang, and Y.C. Nho. J. Ind. Eng. Chem. **13**, 592 (2007).
11. S. Megelski, J.S. Stephens, D.B. Chase, and J.F. Rabolt. Macromolecules, **35**, 8456 (2002).
12. S.O. Han, W.K. Son, J.H. Youk, T.S. Lee, W.H. Park, Y.H. Lee, J.H. Lee, I.G. An, C. Kim, D.S. Lee, Y.K. Lee, and J.D. Nam. Biomaterials, **26**, 3165 (2005).
13. Y. You, S.W. Lee, J.H. Youk, B.M. Min, S.J. Lee, and W.H. Park. Polym. Degrad. Stab. **90**, 441 (2005).
14. Y. You, J.H. Youk, S.W. Lee, B.-M. Min, S.J. Lee, and W.H. Park, Mater. Lett. **60**, 757 (2006).
15. A. Kelly. Philos. Trans. R. Soc. London, Ser.A, **364**, 5 (2006).
16. A.S. Pandit and D.S. Feldman. Wound Rep. Reg. **2**, 130 (1994).
17. D.R. Lide. Handbook of Chemistry and Physics. CRC Press LLC, Boca Raton, FL. 2004.
18. M.M. Demirm, I. Yilgor, E Yilgor, and B. Erman. Polymer, **43**, 3303 (2002).
19. D. Halliday, R. Resnick, and J.Walker. Fundamentals of Physics. 7th ed. John Wiley & Sons, Hoboken, NJ. 2004.
20. P. Neogi. AlChE J. **29**, 402 (1983).
21. I.F. Wang, R.A. Morris, and R.F. Zepf. US Patent No. 6-565-782 B1. May 30, 2003.
22. M. Mulder. Basic Principles of Membrane Technology. Kluwer Academic Publishers, Dordrecht. 1991.
23. P. van de Witte, P.J. Dijkstra, J.W.A. van den Berg, and B.J. Feijn. J. Membr. Sci. **117**, 1 (1996).
24. T. van den Boomgaard, R.M. Boom, and C.A. Smolders. Makromol. Chem. Makromol. Symp. **39**, 271 (1990).
25. H.C. Park, Y.P. Kim, H.Y. Kim, and Y.S. Kang. J. Membr. Sci. **156**, 169 (1999).
26. R.M. Boom, I.M. Wlenk, T. van den Boomgaard, and C.A. Smolders. J. Membr. Sci. **73**, 277 (1992).
27. J.R. Wood and M.G. Bader. J. Mater. Sci. **29**, 844 (1994).
28. D.H. Morton-Jones. Polymer Processing. 1st ed. Chapman & Hall, London. 1989.
29. C. Rauwendaal. Polymer Extrusion. 4th ed. Hanser Gardner Publications, Munich. 2001.
30. Z. Tadmor and C. G. Gogos. Principle of Polymer Processing. John Wiley & Sons, New. York. 1979.

© 2008 NRC Canada

Morphology of a hydrogen-bond mediated self-assembling small molecule in a polycarbonate matrix[1]

Molla Rafiquel Islam and P.R. Sundararajan

Abstract: Dispersing functional small molecules in a polymer matrix is a well-known method of device fabrication for optoelectronic applications. Normally, no specific interactions such as hydrogen bonding occur between the polymer and the small molecule. The latter does not belong to the category of "self-assembling" molecules. When phase separation occurs, the small molecule would diffuse to the surface and crystallize. In this paper, we describe a very different morphological behaviour of hydrogen-bond mediated self-assembling molecules in a polycarbonate matrix. We used a series of biscarbamates with two hydrogen-bonding motifs and alkyl side chain lengths symmetrically varying from C_4 to C_{18}. We infer that the rate of self-assembly is faster than the diffusion of the small molecule to the surface. As a result, crystallization of the small molecule occurs predominantly in the bulk, i.e., sub surface, and not on the surface of the polymer film.

Key words: self-assembly, crystallization, diffusion, phase separation.

Résumé : La dispersion de petites molécules fonctionnelles dans une matrice de polymère est une méthode bien connue de fabrication pour dispositifs pour des applications optoélectroniques. Normalement, il ne se produit aucune interaction spécifique, telles des liaisons hydrogènes, entre la polymère et la petite molécule. Cette dernière n'appartenant généralement pas à la catégorie des molécules donnant lieu à de l'autoassemblage. Lorsqu'il se produit une séparation de phase, la petite molécule à tendance à diffuser vers la surface et à cristalliser. Dans le présent travail, on décrit un comportement morphologique très différent de molécules présentes dans une matrice de polycarbonate qui donnent lieu à un autoassemblage favorisé par des liaisons hydrogènes. On a utilisé une série de bis carbamates avec deux motifs de liaisons hydrogènes et des longueurs de chaînes latérales alkyles symétriques variant de 4 à 18 atomes de carbone. On en déduit que la vitesse d'autoassemblage est plus rapide que la diffusion de la petite molécule vers la surface. En conséquence, la cristallisation des petites molécules se fait dans la masse, c'est-à-dire sous la surface, et non pas à la surface du film de polymère.

Mots-clés : autoassemblage, cristallisation, diffusion, séparation de phase.

[Traduit par la Rédaction]

Introduction

Photo-active and electro-active functional small molecules are widely used in optoelectronic devices as a dispersed phase in polymer matrices (1). Molecular dispersion of such molecules without phase separation is a requirement for the longevity of the device. Polycarbonate is often the preferred polymer for these applications. Thermally induced crystallization of the small molecule is a common cause of defects in, for example, photoreceptors (2) and the delamination of OLED devices (3). Abrasion is also a cause of such crystallization in photoreceptors. In a series of papers, we used thermal annealing as a means of testing the accelerated ageing and phase separation in model composites related to photoreceptors (2, 4, 5).

Fig. 1. The structures of simple carbamates and biscarbamates.

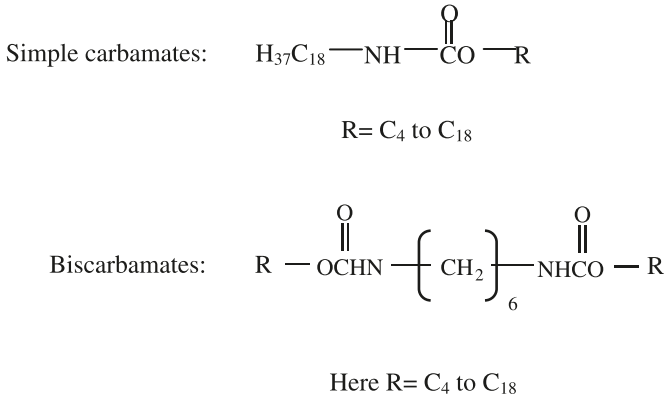

Received 30 November 2007. Accepted 7 April 2008. Published on the NRC Research Press Web site at canjchem.nrc.ca on 1 May 2008.

This paper is dedicated to Robert H. Marchessault in recognition of his many contributions to polysaccharide and biopolymer chemistry.

M.R. Islam and P.R. Sundararajan.[2] Department of Chemistry, Carleton University, 1125 Colonel By Drive, Ottawa, ON K1S 5B6, Canada.

[1]This article is part of a Special Issue dedicated to Professor R. Marchessault.

[2]Corresponding author (e-mail: Sundar@Carleton.ca).

 doi:10.1139/V08-073 © 2008 NRC Canada

Fig. 2. Optical micrographs of polycarbonate films containing (3 wt%) biscarbamates with different alkyl chain lengths.

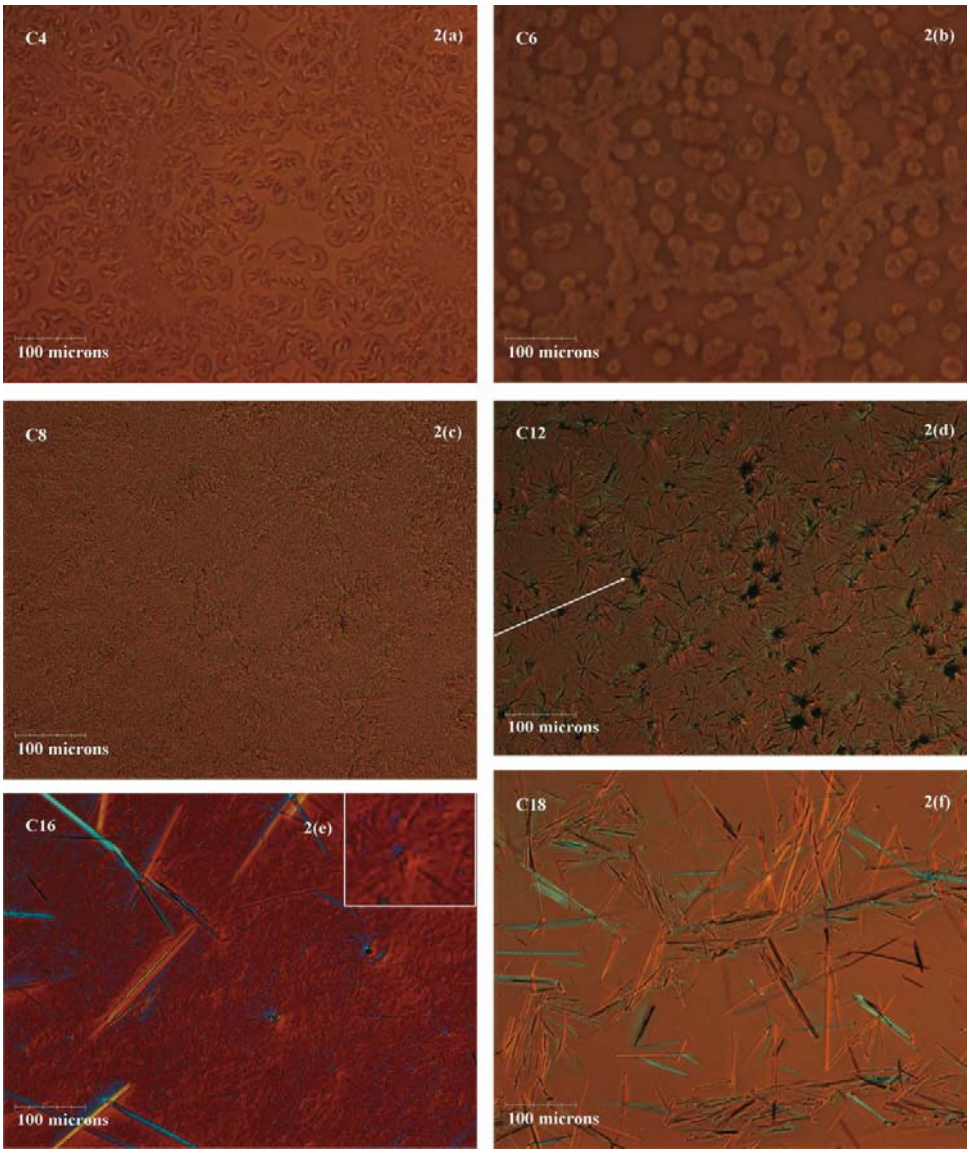

The commonly used functional small molecules in optoelectronic devices, such as the *N,N′*–diphenyl-*N,N′*-bis(3-methylphenyl)-[1,1′-biphenyl]-4,4′-diamine (TBD), tritolyl amine (TTA), etc., are nonplanar and do not have segments that are associated with the term "self-assembly". They do not have hydrogen-bonding or extended π-stacking interactions, although our studies showed some weak molecular interaction in terms of phenyl group overlap between the polycarbonate and these small molecules (2). When phase separation occurs, the small molecules diffuse to the surface of the polymer film and crystallize, forming single crystals of various shapes and habits (2, 4, 5).

The design of supramolecular structures using the self-assembling moieties is an active area of research at this time. Hydrogen bonding, π-stacking, and charge transfer are the common elements used for such design. It was also found to be advantageous to use multiple hydrogen-bonding sites, using A-D-A and D-A-D groups, to control the extended assembly such as building a transient polymer based on noncovalent interactions (6, 7). The nature of the side chain also plays a significant role. In such cases, the crystallization and morphology would depend on the number of such sites. In a recent study, we showed that significant differences are found in the crystallization rate, spherulite growth, etc., between molecules with single or double hydrogen bonding motifs as well as the length of the side chain (8, 9). We used carbamates (one hydrogen-bonding N-H…C=O group, asymmetric alkyl side chain lengths) and biscarbamates (two hydrogen bonds and symmetric side chains) to this end (Fig. 1). These materials are candidates for the ink vehicle for phase change ink jet printing (10).

Given that self-assembly means spontaneous association of the molecules facilitated by the types of interactions mentioned above, it would be of interest to examine the nature of such assembly when such small molecules are dispersed in a polymer matrix. Essentially, they are confined in a polymer matrix. Although the field of polymer dispersed liquid crystals is mature, we are not referring to this case. The molecules under discussion are not liquid crystalline. We found that when simple carbamates were dispersed in the poly-

© 2008 NRC Canada

Fig. 3. Optical micrographs of films that were dried at 50 °C.

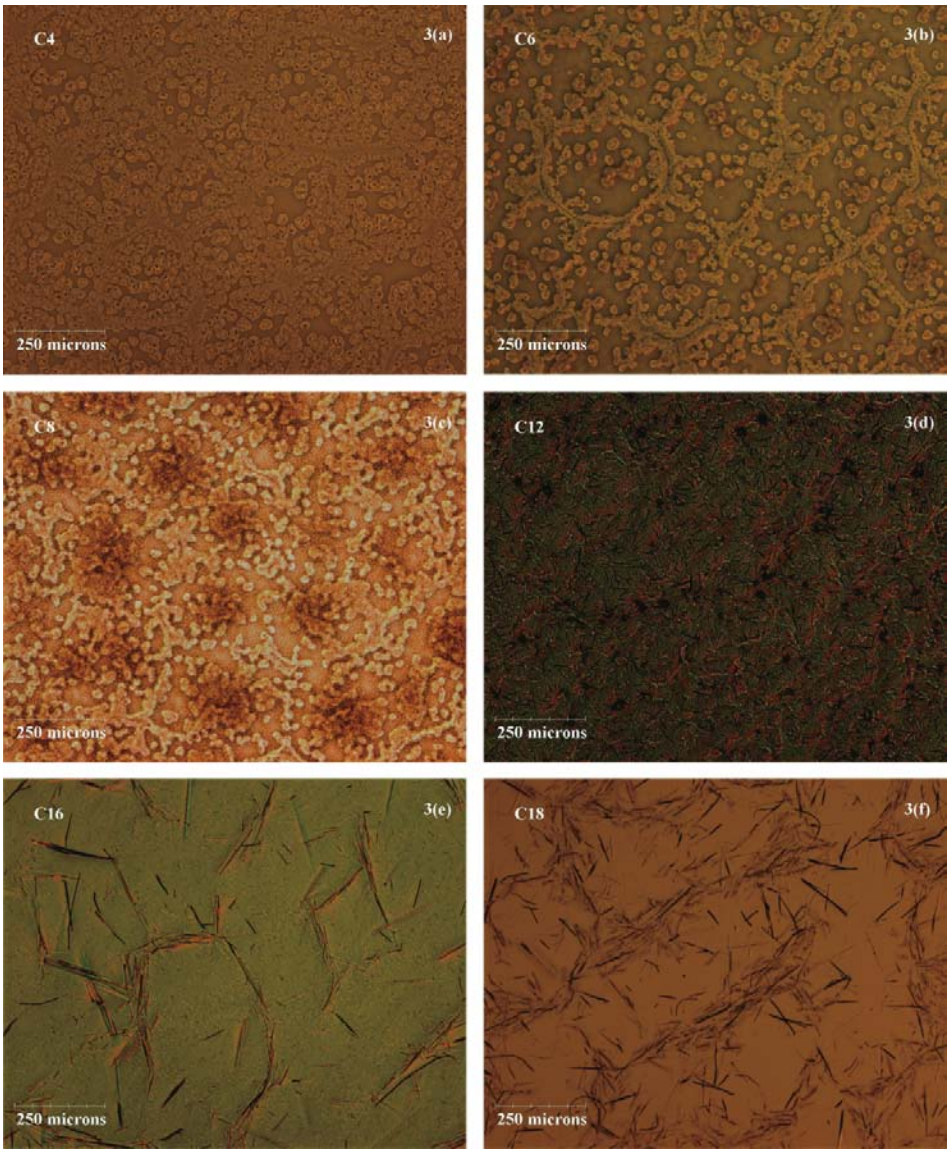

carbonate matrix, they formed colloidal size domains, of uniform size, with the domain size increasing with the relative concentration of the small molecule in the polymer (11). It was also noted that these domains form in the bulk of the polymer and not the surface. This would indicate that the self-assembly and crystallization occur before the molecules diffuse to the surface.

As we found (8, 9) significant differences in the crystallization features between the simple carbamates (with a single hydrogen bond) and the biscarbamates (with double hydrogen bonds), we now examine the nature of assembly when these biscarbamates are dispersed in the polycarbonate matrix. We used biscarbamates with alkyl side chain length varying from C_4 to C_{18}. Note that the concept of dispersion of self-assembling small molecules in a polymer matrix is new.

Experimental

Poly (bisphenol-A-carbonate) (M_w 64 000, GPC) and chloroform were purchased from Sigma-Aldrich Chemical Company Inc. The synthesis of the biscarbamates has been described elsewhere (9). Generally, 3 wt% of C_4, C_6, C_8, C_{12}, C_{16}, or C_{18} biscarbamate in polymer were used. Solutions were prepared by mixing an appropriate amount of the biscarbamate and polycarbonate in chloroform by an electrical shaker for 24 h. Films were coated on a glass substrate using an electrically driven film coater and dried at a very low rate of solvent evaporation at ambient condition for 24 h and then under vacuum for 48 h. This coater was built by Xerox Research Centre of Canada using a motor from Bodine Electric Company, Chicago, USA. The films were made using a spreader made by P.G. and T. Company. This is the same apparatus that is used by Xerox Research Centre of Canada for fabricating model photoreceptors. A set of films were also dried at 50 °C for 48 h to assess the effect of temperature. The thickness of the films was about 10–15 μm. This film thickness was used for all of our previous work on model charge transport layers of photoreceptors and verified by SEM of cross sections (2). Another set of films

© 2008 NRC Canada

Fig. 4. Optical micrographs of polycarbonate films with different concentrations of C_4: (*a*) 0.75%, (*b*) 2%, (*c*) 4%, (*d*) 6%, (*e*) 8%, and (*f*) 10%, respectively.

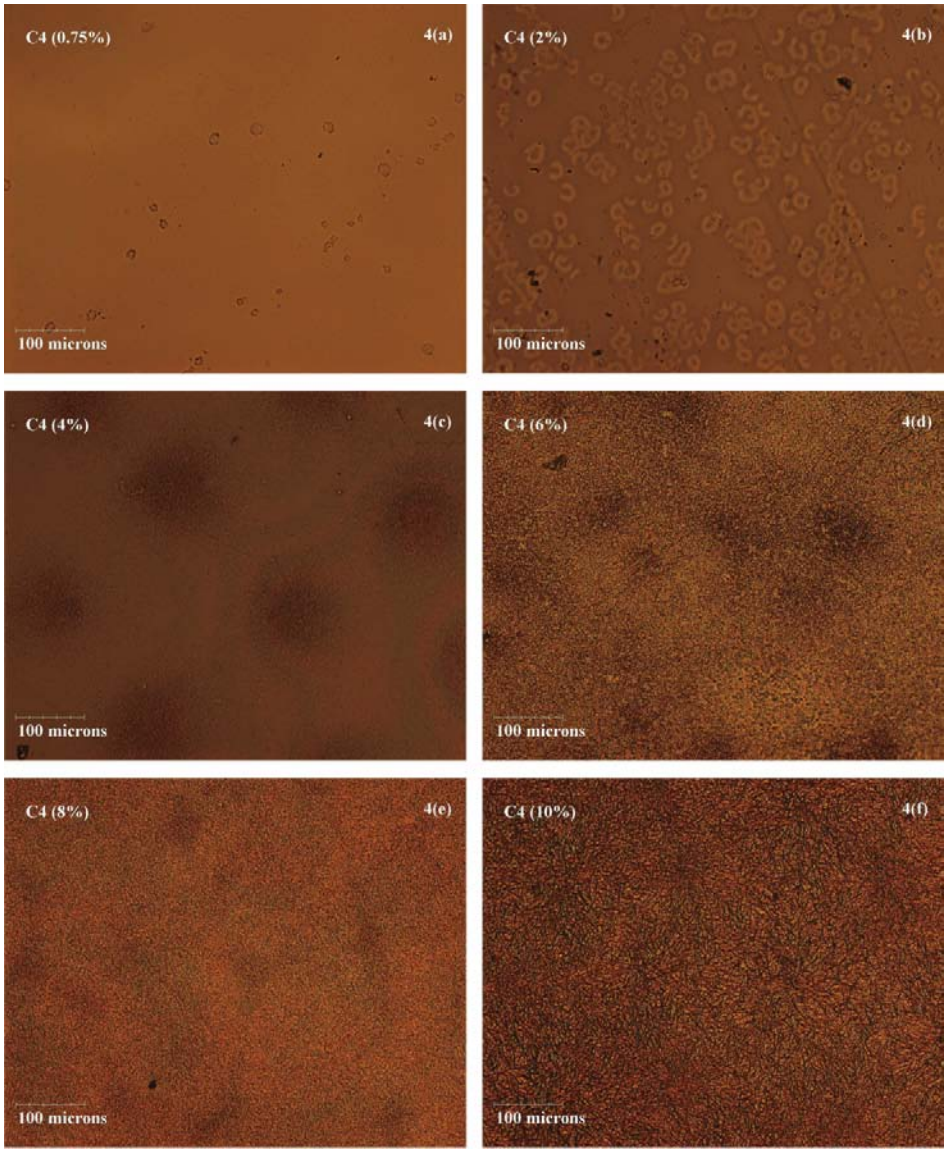

of C_4 and C_6 biscarbamates with concentrations ranging from 0.75 to 10 wt% were also prepared.

A Zeiss Axioplan 2 imaging universal optical microscope with Q-imaging Retiga digital camera was used to record optical micrographs of the films. In addition, a JSM-6400 scanning electron microscope was also used. The surface of the films was coated with a conductive layer for taking the SEM images.

The Fourier transform infrared (FTIR) spectroscopic measurements were performed at ambient conditions using a Michelson M120 BOMEM FTIR spectrometer. The BOMEM GRAMS/386 software was used for data collection. The films were attached to the holder by a small magnet and placed in the path of radiation and the spectra were recorded.

Results and discussion

Polarizing optical microscopy

The solutions and the films were transparent in the cases of C_4 and C_6. The biscarbamates used here do not exhibit specific interactions with polycarbonate. In the IR spectra, we did not observe any absorption peak for the as-prepared films that could be identified with non-hydrogen-bonded C=O and N-H groups of the biscarbamates, although the N-H group showed a peak at 3314 cm^{-1} instead of the usual 3337 cm^{-1} that is assigned to the hydrogen-bonded group. Such a shift just confirms the strength of the interactions between the biscarbamates while in the polymer matrix. Fig 2 shows the optical micrographs of the polycarbonate films containing the various biscarbamates. With C_4 and C_6, the self-assembling small molecules form spherical domains, which almost look like a donut. They aggregate to form a meandering chain. The images are not sharp, as it appears that they are covered with a layer of the polymer. Note that polycarbonate itself is amorphous in this case. This is in contrast to the phase separation and crystallization of other small molecules from the polymer matrix where the crystals form on the surface of the polymer film. These may be com-

© 2008 NRC Canada

Fig. 5. SEM images of the films made with different biscarbamates.

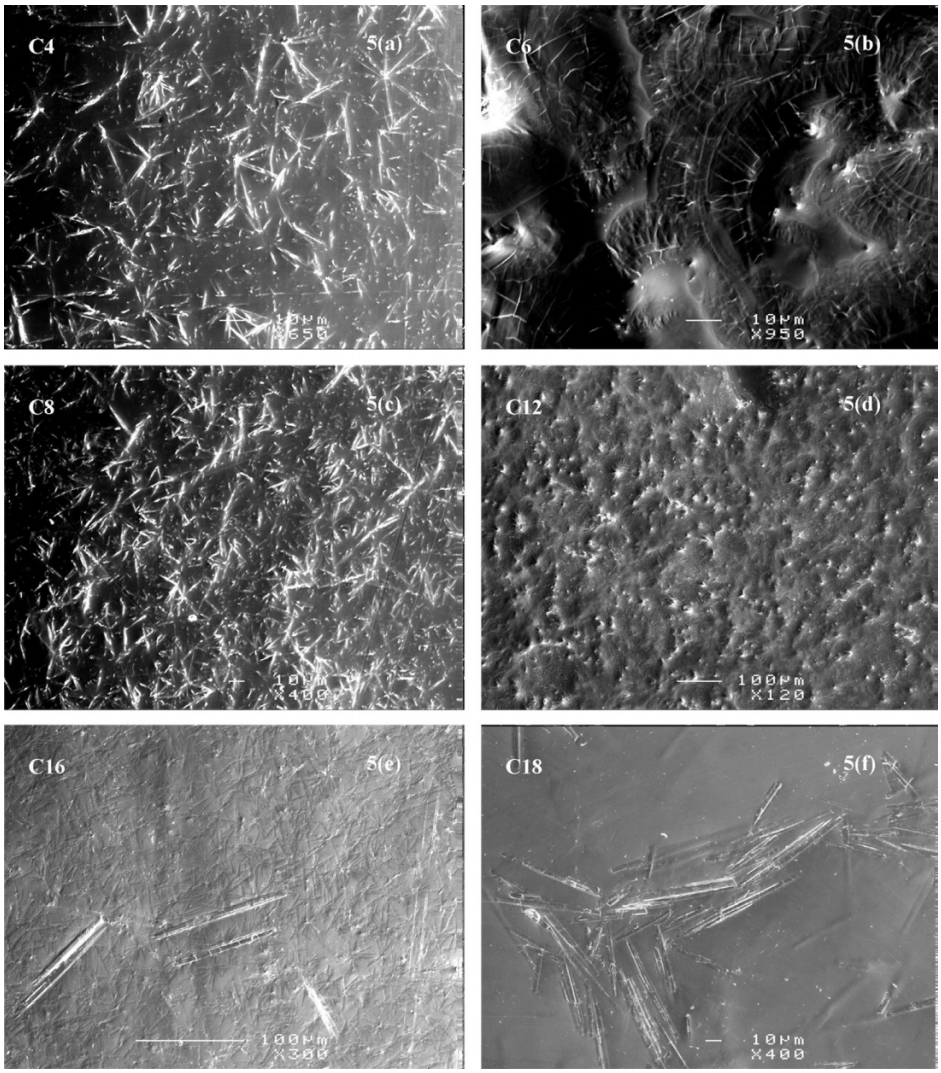

pared with distinct crystals of the charge transport molecules TBD and TTA shown in Fig. 6 of ref. 2*b*, Fig. 3 of ref. 4, and Fig. 11 of ref. 5. As the alkyl chain length increases, the crystals begin to appear, radiating from nodes (as shown by the arrows). It appears that these nodes are protruding crystals that have formed during the diffusion of the small molecule from the bulk (Fig. 2 for C_{12} and C_{16}), but the crystallization had already taken place before the completion of the diffusion step. One of these areas is shown as an inset for C_{16}, which shows radiating lamellae from a protrusion. We have shown before (9) that the rate of spherulite growth is a maximum for C_8, and that of C_{12} is faster than for C_4. Although long needles of crystals are seen in for the case of C_{16}, there are a number of areas that show a bulge and radiating lamellae. It is due to these bulges that we infer that the growth has already taken place before the diffusion of the molecules to the surface.

Similar to the case of polycarbonate – simple carbamates system (11), we see a competition between diffusion of the small molecule from the matrix to the surface and the crystallization in the bulk of the polymer before the diffusion is complete. The rate of crystallization of the simple carbamates by themselves was so fast that we could not study their rates of spherulite formation etc. (8). However, we were able to measure such rates with biscarbamates (9). As discussed before, the rate of self-assembly depends on the length of the alkyl chains and it was seen that the alkyl chains stabilize the structure (9). It was shown using IR spectra that the packing of the alkyl chains is enhanced with the chain length. In the present case with the longer alkyl chain lengths, we see some needle-like crystals on the surface as well as circular asperities that indicate crystals growing in the bulk. As we mentioned before, when small molecules crystallize out of the polymer, they would tend to form crystals of various types of habits that depend on the growth mechanism. In this case the asperities as well as the lamellae radiating from the nodes indicate an irregular spherulite formation. Thus, the faster growth rate of the biscarbamates with shorter alkyl chains result in crystallization below the surface. As the alkyl chain length increases and the growth rate decreases, crystals appear on the surface, as seen in other cases (as in refs. 2, 4, and 5)

Figure 3 shows the micrographs of some of the samples that were dried at 50 °C. The morphologies for C_4, C_6, and

© 2008 NRC Canada

Fig. 6. Optical micrographs of the films heated to the melting temperature of the respective biscarbamate and cooled. The images for samples that were kept at T_m for 2 min (left) and 30 min (right) are shown.

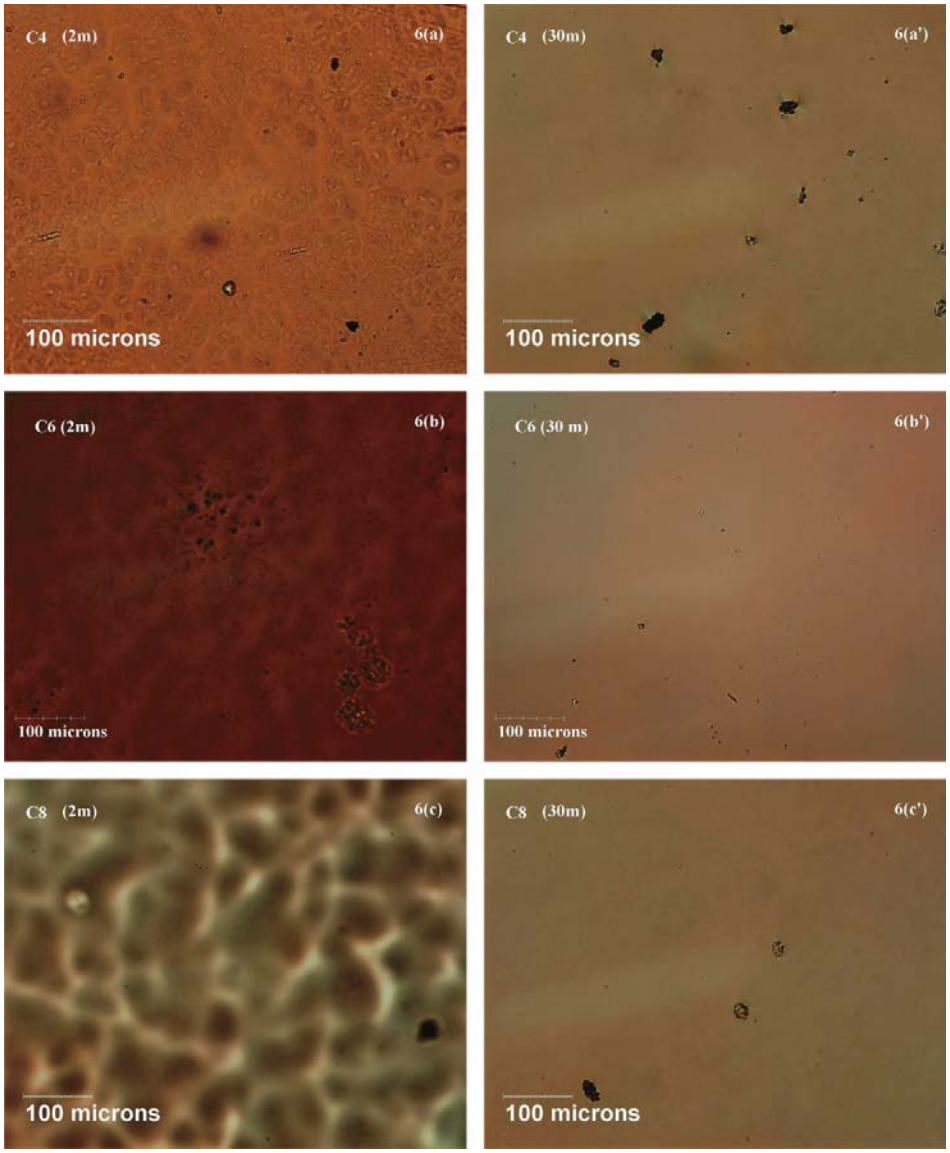

C_{12} are similar to those seen in Fig. 2. For C_8, we observe features similar to those of C_6. Spherical patches are also seen. Perhaps because of the enhanced diffusion to the surface at the higher temperature, C_{16} and C_{18} show crystals on the surface, and the bumps or nodes that were seen in Fig. 2 are not present. Thus the morphology for the biscarbamates with longer alkyl chains differ with this mild thermal treatment. We did not examine this aspect in detail at this time.

The effect of concentration on the domains is shown in Fig. 4 for C_4 biscarbamate. With a concentration of 2%, the morphology is similar to what is shown in Fig. 2. With 4%, "patchy" regions appear that increase in number with concentration. These are the crystalline domains that formed in the bulk of the polymer film. These domains are not clearly seen since these are covered by a layer of the polymer, which is amorphous. However, the polymer film itself shows strain birefringence around these patchy domains. With a high concentration of 10%, dense lamellar growth is seen.

Scanning electron microscopy

The SEM images shown in Fig. 5 illustrate the subsurface growth of the crystalline domains of the biscarbamates. The image for C_4 shows the enlarged view of the morphology of the donuts seen in Fig. 2. It is seen that the domains appear as if covered by a layer of the polymer. This is quite pronounced in the case of C_{12}. Even with C_{16}, the crystalline lamellae are not well above on the surface of the film. Thus, the self-assembly and the fast rate of crystallization give rise to subsurface morphologies. As we investigate this phenomenon further, we plan to study the effect of the thickness of the film and the SEM images of cross sections.

Reversibility

With the polycarbonate – simple carbamate system we found that the domains can be melted and reformed. The T_m of the simple carbamates vary from 61.2 to 86.5 °C as the alkyl chain length increases from C_4 to C_{18}. The T_m of the

© 2008 NRC Canada

Fig. 6. (*concluded*).

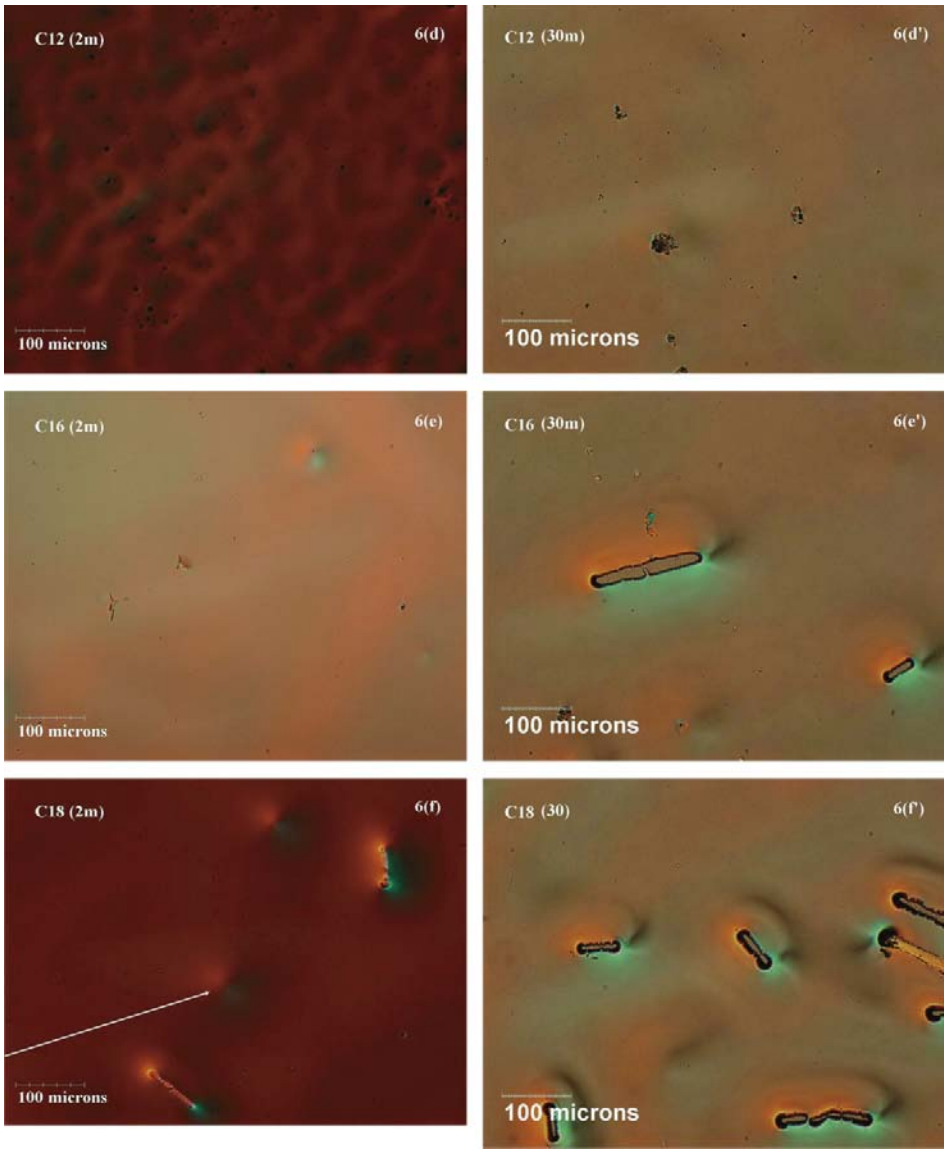

biscarbamates are higher, ranging from 90 to 120 °C (9). Figure 6 shows the micrographs of the polycarbonate–biscarbamate system, which was held at the melting temperature of each of the biscarbamates for two minutes and cooled by removal from the hot plate (all the images on the left side in Fig. 6). Another set of samples was held at the T_m for 30 min and cooled.

The samples that were kept for 2 min at the T_m show morphological features similar to those seen in Fig. 2, but more diffuse. The blur in the images is due to the covering of the polymer layer on the small molecule crystalline domains. The protrusions that were seen for C_{16} in Fig. 2 are seen here for the case of C_{18}. The process of melting and cooling did not result in the crystallization on the surface. We mentioned in the Introduction that the biscarbamates are candidates as vehicles for phase change ink jet inks. Their melt viscosity is only a few centipoises, in the range of 8–12 Cp. The images in Fig. 6 for the samples kept at T_m for two min indicate that the melt of the biscarbamates remained distributed in the bulk and did not form droplets on the surface. Thus, the interfacial tension between the polycarbonate and the melt of biscarbamate has a significant effect on the morphology because of the low melt viscosity of the small molecule. Thus, by heating the composite to the T_m of the biscarbamates and cooling within a short time creates subsurface crystallization

This effect is amplified when the samples are kept at the T_m for 30 min. All the images in Fig. 6 for this case do not show any features. Even with C_{16} and C_{18}, no crystals are observed. It appears that during the 30 min, the melt diffused into the polycarbonate matrix and the crystals did not form again. In the FTIR spectra of these samples, the peaks corresponding to the hydrogen bonded N-H and C=O groups (at about 1684 and 3315 cm^{-1} respectively) were not seen. Instead, a broad peak at about 3450 was seen for the non-hydrogen bonded N-H group. Thus, the 30 min dwell time and subsequent cooling created a molecular dispersion of the biscarbamate in polycarbonate, with no intermolecular hy-

© 2008 NRC Canada

drogen bonded interaction between these molecules, which have the self-assembly motif in their structure.

Conclusions

The morphologies of self-assembling molecules in polymer matrices are different from those of molecules that do not possess self-assembling codes (hydrogen bond, π-interaction, etc.), as seen from this work as well as our previous study on a related system (11). As the small molecules would normally diffuse to the surface of the polymer film and crystallize, we propose that the rate of crystallization due to self-assembly is faster than the diffusion to the surface. This is the cause of the subsurface morphology that was discussed above. The biscarbamates used here do not exhibit specific interactions with polycarbonate. In the IR spectra, we did not observe any absorption peak for the as-prepared films that could be identified with non-hydrogen-bonded C=O and N-H groups of the biscarbamates, although the N-H group showed a peak at 3314 cm^{-1} instead of the usual 3337 cm^{-1} that is assigned to the hydrogen-bonded group. Such a shift just confirms the strength of the interactions between the biscarbamates while in the polymer matrix. There was no shift in the C=O peak of the polycarbonate (1175 cm^{-1}). The T_g of the polycarbonate was reduced to about 125 °C with C_4 and C_6 biscarbamates (3 wt%), but no noticeable change with the longer alkyl side chains.

The longer dwell time of the films at the T_m of the biscarbamates results in the absence of IR peaks due to hydrogen bonded N-H and C=O groups, which indicates the molecular dispersion of the small molecules and the lack of any association between them. Thus, the behavior of self-assembling molecules in a polymer matrix is distinctly different from that of other cases, e.g., the composites of charge transport layers of optoelectronic devices with functional photoactive molecules dispersed in a polycarbonate matrix.

Acknowledgements

Financial support from the Natural Sciences and Engineering Research Council (NSERC) of Canada is gratefully acknowledged.

References

1. (*a*) P.M. Borsenberger and D.S. Weiss. Organic photoreceptors for xerography. Marcel Decker, New York (1998); (*b*) A. R. Melnyk and D. M. Pai. Hard copy and printing materials. Media and Process Proc. SPIE, **1253**, 141 (1990).
2. (*a*) F. Khan, A.M. Hor, and P.R. Sundararajan. J. Phys. Chem. **108**, 117 (2004); (*b*) F. Khan and P.R. Sundararajan, Org. Electron. **7**, 410 (2006).
3. P.F. Smith, P. Gerroir, S. Xie, A.M. Hor, Z. Popovic, and M.L. Hair. Langmuir, **14**, 5946 (1998).
4. F. Khan, A.M. Hor, and P.R. Sundararajan. Pure Appl. Chem. **76**, 1467 (2004).
5. F. Khan, A-M. Hor, and P.R. Sundararajan. Synthetic Metals, **150**, 199 (2005).
6. J.M. Lehn. Supramolecular chemistry. VCH, Germany. 1995.
7. M. Ikeda, T. Nobori, M. Schmutz, and J. M. Lehn. Chem. Eur. J. **11**, 662 (2005).
8. M. Moniruzzaman, B. Goodbrand, and P. R. Sundararajan. J. Phys. Chem. Part B, **107**, 8416 (2003).
9. S. Khanna, M. Moniruzzaman, and P.R. Sundararajan. J. Phys. Chem. Part B, **110**, 15251 (2006).
10. B. Goodbrand, D.C. Boils, P.R. Sundararajan, and R.W. Wong. US Patent 6-414-051. 2002.
11. B. Tuteja, M. Moniruzzaman, and P.R. Sundararajan. Langmuir, **23**, 4709 (2007).

© 2008 NRC Canada

REDOR recoupling in polymer-stabilized liquid crystals undergoing MAS — Two-dimensional NMR applications with strongly aligned proteins[1]

Jean-François Trempe, Ekaterina Pomerantseva, and Kalle Gehring

Abstract: We recently introduced a technique, termed SAD-REDOR, for recoupling residual dipolar couplings in a single-domain polymer-stabilized liquid crystal (PSLC) undergoing magic-angle spinning (MAS). The experiment was demonstrated with ^{1}H–^{15}N dipolar couplings in a small molecule. Here, we show the applicability of the technique to a strongly aligned protein and we describe a novel two-dimensional experiment to generate in-phase and anti-phase (IPAP) doublets in the ^{1}H dimension of an HSQC NMR spectrum. This pulse sequence, SAD-IPAP, was tested on a sample of ^{15}N-labeled ubiquitin (5 mmol/L) in a polyacrylamide-stabilized Pf1 phage liquid crystal (20 mg/mL). ^{15}N–^{1}H residual dipolar couplings (RDCs) were measured with the SAD-IPAP pulse sequence at spinning speeds of 1000 and 1250 Hz. RDSs were also measured using the conventional HSQC-IPAP method in a sample of ^{15}N-ubiquitin dissolved in a solution of Pf1 phage (1 mg/mL). The resulting RDCs were fitted to the solution structure of ubiquitin to estimate the alignment tensor and to determine the accuracy of the measured couplings. The results highlight the benefits of SAD-REDOR for the measurement of RDCs in strongly aligned macromolecules.

Key words: residual dipolar couplings (RDCs), polymer-stabilized liquid crystals (PSLCs), rotational echo double resonance (REDOR) recoupling, magic-angle spinning (MAS), ubiquitin, biomolecular nuclear magnetic resonance (NMR), proteins.

Résumé : Nous avons récemment introduit une technique, nommée SAD-REDOR, pour recoupler des couplages dipolaires résiduels (CDR) dans des cristaux liquides à domaine unique stabilisé par polymérisation (CLSP), en rotation rapide à l'angle magique. Cette technique fut démontrée en recouplant des CDR ^{1}H-^{15}N dans une petite molécule. Dans cet article, nous démontrons l'applicabilité de cette technique pour les protéines fortement alignées. Nous décrivons un nouveau programme d'impulsions bidimensionnel qui génère des doublets en phase et anti-phase dans la dimension ^{1}H d'un spectre de RMN HSQC. Le programme, nommé SAD-IPAP, fut testé sur un échantillon d'ubiquitine enrichie en ^{15}N (5 mmol/L) et mélangé avec un cristal liquide de phages Pf1 (20 mg/mL) stabilisé par de la polyacrylamide. Des CDR ^{15}N-^{1}H furent mesurés avec la méthode SAD-IPAP à des vitesses de rotation de 1000 Hz et 1250 Hz. Des CDR furent aussi mesurés en appliquant la méthode HSQC-IPAP à un échantillon d'ubiquitine-^{15}N dans une solution de bactériophages Pf1 (1 mg/mL). Les CDR expérimentaux furent ajustés à la structure de l'ubiquitine en solution pour estimer le tenseur d'alignement et pour déterminer l'exactitude des couplages mesurés. Les résultats soulignent les bénéfices potentiels des techniques SAD-REDOR pour mesurer des CDR dans des macromolécules fortement alignées.

Mots-clés: couplages dipolaires résiduels, cristaux liquides, phage Pf1, polyacrylamide, recouplage REDOR, rotation à l'angle magique, résonance magnétique nucléaire (RMN), biomoléculaire, protéines, ubiquitine.

Introduction

Liquid crystals have numerous applications in chemistry and biology. Suspensions of fibrous or highly elongated particles can form liquid crystals that align in magnetic fields (1, 2). These aligned liquid crystals can be used to induce orientational order in dissolved molecules for the study of anisotropic interactions such as NMR dipolar and quadrupolar couplings. The orientational order of these liquid crystals can be captured by polymerization of a matrix (3, 4). Our laboratory has taken advantage of polymer-stabilized liquid crystals (PSLC) to measure residual dipolar couplings (RDC) in proteins and small molecules.

Residual anisotropic interactions such as dipolar couplings and chemical shift anisotropies (CSA) measured in dilute liquid crystals are an increasingly important source of NMR structural information in biomolecules (reviewed in

Received 15 November 2007. Accepted 3 March 2008. Published on the NRC Research Press Web site at canjchem.nrc.ca on 1 May 2008.

This paper is dedicated to Robert H. Marchessault in recognition of his many contributions to polysaccharide and biopolymer chemistry.

J.-F. Trempe, E. Pomerantseva, and K. Gehring.[2] Laboratory of Nuclear Magnetic Resonance, Department of Biochemistry, McGill University, 3655 Promenade Sir William Osler, Montreal, QC H3G 1Y6, Canada.

[1]This article is part of a Special Issue dedicated to Professor R. Marchessault.

[2]Corresponding author (e-mail: kalle.gehring@mcgill.ca).

 doi:10.1139/V08-048 © 2008 NRC Canada

refs. 5–8). Incorporation of these parameters improves the accuracy and precision of biomolecular structure determination and extends the molecular weight limit of biomolecules for which solution NMR methods can be applied. Alignment magnitudes on the order of 10^{-3} scale one-bond heteronuclear couplings (~10^4 Hz) and ^{13}C-^{15}N chemical shift anisotropies (80–200 ppm) into a range that can be conveniently measured by liquid-state NMR methods. A variety of pulse sequences have been proposed for measurements of residual dipolar couplings in proteins, including frequency-based (9) and intensity-encoded (10, 11) NMR experiments. These methods require the acquisition of spectra in both isotropic and liquid crystalline media so that the measured spin–spin couplings or chemical shifts can be compared to extract their anisotropic components.

Residual anisotropic interactions arise from the weak induced alignment of biomolecules, which depends on the nature of the interaction between the biomolecule and the alignment medium as well as on the concentration of the alignment medium and its order parameter. Tuning of the alignment tensor magnitude is typically achieved by varying the alignment medium concentration. If the alignment is too weak, the anisotropic interactions will be too small to be accurately measured, whereas if the alignment is too strong, the linewidths of NMR signals will increase owing to many unresolved dipolar couplings. Moreover, strong alignments result in large, variable (*J*+*D*) spin–spin couplings that result in inefficient and unequal INEPT magnetization transfer steps in multidimensional NMR spectra. These experiments rely on the fact that all the one-bond nuclear spin–spin *J* couplings in a molecule have more or less the same value. The ability to study proteins under strong alignment conditions would open the door to measurement of weaker long-range dipolar couplings and chemical shift anisotropies.

Several approaches have been proposed for mitigating problems arising from strong alignments. These can be classified in two groups: selective radiofrequency decoupling and sample-spinning techniques. The former has been used to decouple unresolved ^{1}H–^{1}H RDCs during the acquisition period using selective ^{1}H RF decoupling in ^{15}N–^{1}H HSQC-IPAP experiments (12) or Flip-Flop ^{1}H-decoupling in ^{13}C–^{1}H HSQC of natural products (13). However, RF decoupling does not resolve the problem of uneven spin–spin magnetization transfer in multidimensional liquid-state NMR experiments. Sample-spinning techniques offer the advantage of removing unwanted anisotropic interactions via time averaging of these interactions. These include variable-angle sample-spinning (VASS) (14, 15), switched angle spinning (SAS) (16–18), and dipolar recoupling on-axis with scaling and shape preservation (DROSS) (19).

Our laboratory recently introduced SAD-REDOR (single-alignment domain rotational-echo double resonance) as a novel approach for the measurement of residual anisotropic interactions (20). It consists of spinning a single-domain PSLC at the magic angle while applying REDOR pulses during the acquisition period. The liquid crystal director of the PSLC is immobilized by the polymer matrix and remains independent of the magnetic field and the spinning axis (4). Radiofrequency pulses are applied synchronously with the rotor angular position to recover specific heteronuclear dipolar couplings. This technique has been successfully applied for the measurement of ^{15}N–^{1}H RDCs in ^{15}N-labeled benzamide.

For the study of isotopically labeled biological macromolecules, it is necessary to extend the SAD-REDOR methodology to multidimensional experiments. In the present work, we present a novel 2D NMR experiment based on SAD-REDOR for the measurement of heteronuclear dipolar couplings in strongly aligned biomolecules. The applicability of the technique is demonstrated by measuring ^{15}N–^{1}H RDCs in ^{15}N-enriched ubiquitin in polyacrylamide-stabilized Pf1 phage. The theoretical aspects of the experiment are reviewed, followed by a presentation of the experiment and a comparison of the RDCs obtained by SAD-IPAP with those measured using conventional methods.

Theory

The heteronuclear dipolar Hamiltonian contains the spin–spin component-dependent term $I_{Az}I_{Bz}$ and the orientation-dependent term ($3\cos^2\theta - 1$), as shown in eq. [1]:

$$[1] \qquad H_{dd}^{AB} = \frac{\mu_0}{4\pi}\frac{\gamma_A\gamma_B\hbar}{r_{AB}^3}\overline{\left\langle\frac{3\cos^2\theta-1}{2}\right\rangle}2I_{Az}I_{Bz} = D_{\max}^{AB}\overline{\langle P_2(\cos\theta)\rangle}2I_{Az}I_{Bz}$$

In a PSLC, the polymer fixes the liquid crystal director so that it does not reorient during sample spinning (4). For molecules aligned in the spinning PSLC, anisotropic interactions therefore vary according to the rotor azimuthal angle. Under magic-angle spinning, the dipolar couplings evolve according to eq. [2]:

$$[2] \qquad D^{AB} = D_{\max}^{AB}\left[\frac{4}{3}\sin\alpha - \frac{1}{3}\sin 2\alpha\right]_{\alpha_0}^{\alpha_0+\omega_r t} = D_{\max}^{AB}\, I_{\alpha_0}^{\alpha_0+\omega_r t}$$

where α is the angle describing rotor azimuth position (Fig. 1*A*), α_0 is the rotor angle at the beginning of the pulse sequence, and ω_r is the sample rotation velocity (21). The integral of D^{AB} for a single rotation period during MAS is zero, which accounts for the vanishing of anisotropic interactions in samples undergoing MAS.

The spin component of the dipolar Hamiltonian can be affected by RF pulses applied at certain intervals synchronously with the sample rotation (22). REDOR inversion π pulses interfere with the MAS averaging. The derivation for a single-domain PSLC undergoing MAS was described in our previous work (20) and the final expression describing the recoupled interaction is shown in eq. [3]:

$$[3] \qquad D^{AB} = D_{\max}^{AB}[I_{\alpha_0}^{\alpha_0+2\pi f_1} - I_{\alpha_0+2\pi f_1}^{\alpha_0+2\pi f_2} + I_{\alpha_0+2\pi f_2}^{\alpha_0+2\pi}]$$

where f_1 and f_2 are the fractions of the rotor period T_r where pulses are applied (Fig. 1*B*). The magnitude and the sign of the dipolar couplings depend on the position of the inversion π pulses (f_1 and f_2) and the orientation of the liquid crystal director at the beginning of the recoupling scheme (α_0). The theoretical recoupling efficiency has been calculated for various pulse schemes as a function of the starting azimuthal

© 2008 NRC Canada

Fig. 1. Schematics and principles of the SAD-REDOR experiment. (*A*) Geometry of the PSLC sample undergoing magic-angle spinning. The thick line represents the PSLC director. The dashed line is the rotor axis. θ is the angle between the liquid crystal director and the external magnetic field, and α is the rotor azimuthal angle. (*B*) REDOR π-recoupling pulse train on one RF channel, synchronously with the acquisition period on the other RF channel. T_r is the MAS rotation period, and f_1, f_2 are the fractions of T_r at which recoupling pulses are applied. (*C*) Scaling of *J* couplings and RDCs during SAD-REDOR recoupling with different pulse schemes: f_1 = 0.1, f_2 = 0.9 (short dashes); f_1 = 0.19, f_2 = 0.81 (solid line); f_1 = 0.25, f_2 = 0.75 (long dashes).

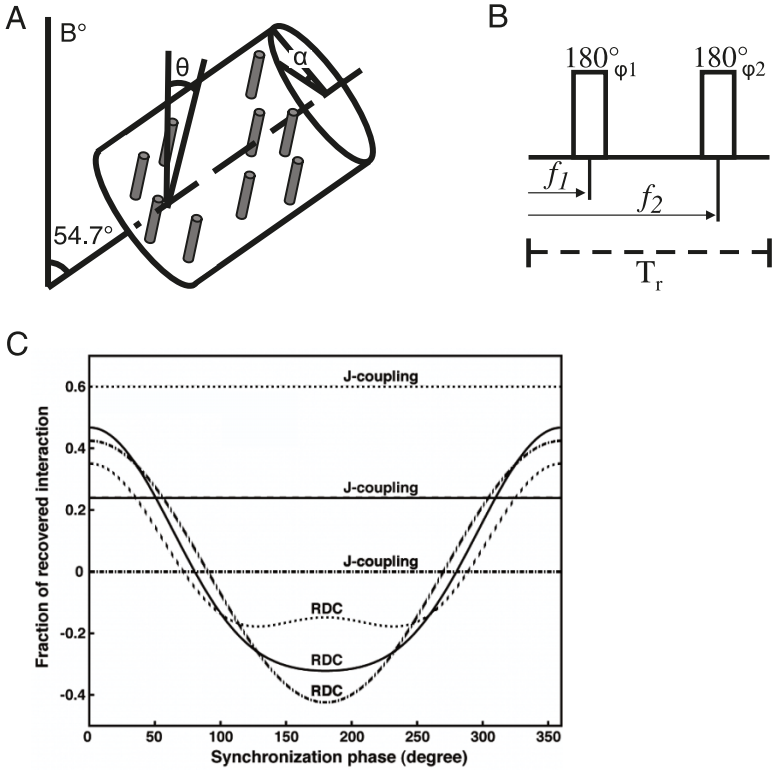

angle α_0 (Fig. 1*C*). The scaling of the isotropic interaction is then optimized by adjusting α_0, within the limits imposed by the choice of f_1 and f_2.

The scalar spin–spin coupling term is also affected by the inversion pulses, but its residual value depends on f_1 and f_2 only, as shown in eq. [4]:

$$[4] \qquad \overline{J_{iso}} = J_{iso}(1 + 2f_1 - 2f_2)$$

where J_{iso} is isotropic scalar coupling, and the overbar denotes the time average of this interaction over a rotor period. Scalar coupling can be eliminated from observation by setting f_1 and f_2 to any combination that differs by 0.5, for example $f_1 = 0.25T_r$ and $f_2 = 0.75T_r$.

Results

To assess the effects of strong alignments on the liquid-state NMR spectra of a protein, we recorded ^{15}N–^{1}H HSQC spectra of ^{15}N-labeled ubiquitin in polyacrylamide-stabilized Pf1 phage in an MAS rotor at different rotor azimuthal positions (Figs. 2*A*–2*C*). Different rotor angular positions correspond to the different orientations of the liquid crystal (LC) director frozen in the polyacrylamide matrix with respect to the external magnetic field. The orientation of the liquid crystal director can be assessed by measuring the residual ^{2}H quadrupolar coupling arising from weakly aligned deuterated water molecules. Dipolar and quadrupolar couplings are both scaled by the term $3\cos^2\theta - 1$, where θ is the angle between the liquid crystal director and the magnetic field (Fig. 1). When the LC director is parallel to the magnetic field, B_0, the maximum ^{2}H residual quadrupolar coupling is detected (14 Hz) and the protein signals disappear (Fig. 2*C*). When the rotor angle is changed such that $0° < \theta < 54.74°$, the protein signal becomes partially observable and a residual quadrupolar coupling of ~5 Hz is measured (Fig. 2*B*). Finally, when the LC director is at the magic angle with respect to the external magnetic field, all second-order anisotropic interactions vanish: the ^{2}H spectrum is a singlet and the ubiquitin ^{15}N–^{1}H HSQC reveals a well-resolved spectrum (Fig. 2*A*). This confirms that the broadening observed in the HSQC of the fully aligned protein originates from anisotropic interactions and not from shorter relaxation times. Anisotropic interactions affect the HSQC spectrum in two ways: the efficiency of the INEPT transfer step is compromised when the total coupling becomes significantly different from the scalar coupling, and the multiple unresolved ^{1}H–^{1}H dipolar couplings broaden the proton signals during the acquisition period. These two effects can be readily eliminated by the use of magic-angle spinning, which averages out dipolar interactions and recovers the HSQC signal (Fig. 2*D*). The MAS spectrum shows improved resolution compared to the static HSQC spectrum acquired at the magic angle due to the improved B_0 homogeneity.

One way to recover dipolar information is to apply a

© 2008 NRC Canada

Fig. 2. Static ^{15}N–^{1}H HSQC spectra of ^{15}N-ubiquitin recorded at different rotor angles corresponding to θ angles of 54.74°, 40° and 0° (*A*, *B*, and *C*, respectively) and under MAS (*D*, spinning speed of 1000 Hz). 1D ^{2}H spectra recorded at the same rotor angular positions are shown to the left of each HSQC spectrum. All spectra were recorded with 32 scans and are shown at the same baseline level.

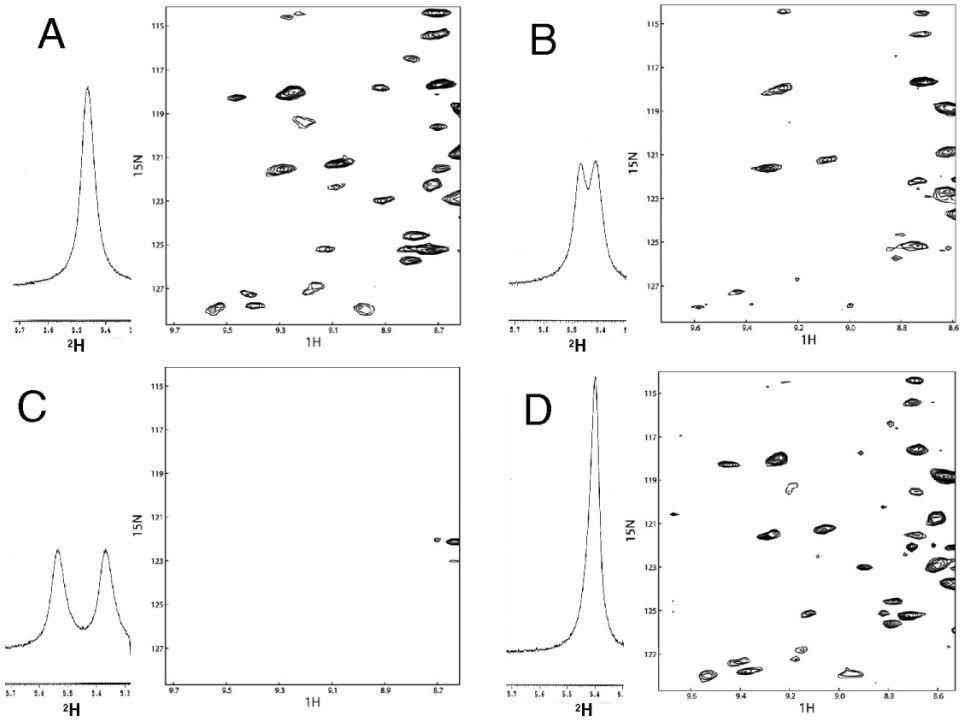

REDOR recoupling pulse train during the acquisition period while MAS is employed throughout the experiment. We took the IPAP approach (23) to generate in-phase and anti-phase magnetizations and named the experiment SAD-IPAP. The pulse scheme of the ^{15}N–^{1}H SAD-IPAP experiment is shown in Fig. 3. The REDOR recoupling pulse train is applied synchronously with the rotor phase on the ^{15}N channel during ^{1}H acquisition. The synchronization is achieved using the Bruker *trigger* command followed by the delay τ*. The delay τ* should be equal to $\tau + t_{1,\,max} - t_1$, where t_1 is the ^{15}N chemical shift evolution period, $t_{1,\,max}$ is the longest t_1 value set in the 2D experiment, and τ is the synchronization delay. In practice, the τ* is set to a large value (larger than the $t_{1,max}$) at the beginning of the experiment and is decreased synchronously as t_1 is increased. This ensures that the rotor phase is always the same during REDOR pulses regardless of the t_1 delay. Furthermore, this ensures that the magnetic field *z*-gradients are always applied at the same rotor azimuthal angle. This is particularly important for the WATERGATE (24) gradients since the magnetization has to be refocused for optimal signal recovery. We applied all gradients for a duration of one rotor period and optimized their strength. As a result of the *z*-gradient adjustment, the overlap of the protein signal with the water spinning side bands was minimized.

The observation of the in-phase and anti-phase components of magnetization can be understood from a product operator description of the experiment. After the INEPT transfer (Fig. 3, point a), $2I_zS_y$ magnetization is generated, where *I* and *S* represent ^{1}H and ^{15}N nuclear spin throughout the text, respectively. During the ^{15}N chemical shift evolution period, t_2, ^{1}H 180° pulse ensures refocusing of the scalar coupling. Thus, at the end of the evolution period (Fig. 3, point b) magnetization evolves into eq. [5]:

$$[5] \qquad 2I_zS_y \cos(\omega_S t_1) - 2I_zS_x \sin(\omega_S t_1)$$

where ω_S is the nitrogen chemical shift. Either term in eq. [5] can generate observable magnetization depending on the phase of the coherence selection pulses. The evolution of the $2I_zS_y \cos(\omega_S t_1)$ term (Fig. 3, point c) is shown in eq. [6]:

$$[6] \qquad 2I_zS_y \cos(\omega_S t_1) \xrightarrow{90^\circ_y\,^1\mathrm{H},\ 90^\circ_x\,^{15}\mathrm{N}} 2I_xS_z \cos(\omega_S t_1)$$

The selection of either in-phase or anti-phase magnetization is achieved by toggling on and off a 180° pulse on the ^{15}N channel (Fig. 3, oblique shaded pulse). When this pulse is present, the magnetization evolves into $I_y \cos(\omega_S t_1)$, which corresponds to the in-phase spectrum. Without the 180° pulse, the term evolves to $2I_xS_z \cos(\omega_S t_1)$ and the anti-phase spectrum is thus recorded. However, since the anti-phase signal is acquired in the dispersion mode, a 90° phase correction is necessary after the Fourier transformation in order to convert the signal into absorption mode.

In-phase and anti-phase spectra were recorded using the SAD-IPAP technique in a PSLC sample (20 mg/mL Pf1) of ^{15}N-ubiquitin at an angular velocity of 1000 Hz. For RDC measurements, the REDOR recoupling scheme with $f_1 = 0.25$, $f_2 = 0.75$ (Fig. 1*B*) was used. This pulse scheme allows recovery of 80% of the RDC measured by comparing an isotropic and anisotropic sample and eliminates the scalar coupling contribution (Fig. 1*C*). The rotor synchronization delay τ* was adjusted so as to maximize the magnitude of the RDCs. Using the IPAP approach, the in-phase and anti-phase spectra were added and subtracted to generate upfield

© 2008 NRC Canada

Fig. 3. Pulse scheme of the ^{15}N–^{1}H SAD-IPAP experiment: two dimensional pulse sequence with the REDOR recoupling pulses applied on the ^{15}N channel during acquisition and synchronized with the angular rotor position. Narrow and wide pulses correspond to 90° and 180° flip angles, respectively, with phase *x*, unless indicated. The WATERGATE water suppression scheme (24) was used. Rectangular gradients (vertically shaded) with the duration of one rotor period were used synchronously with the rotor phase for the most effective suppression of the water signal. The selection of either in-phase (I_y), or anti-phase ($2I_xS_z$) magnetization is done by including or removing 180° pulse on ^{15}N channel (oblique shaded pulse). $\phi_1 = 4(x), 4(-x)$; $\phi_2 = x, -x$; $\phi_3 = 2(x), 2(-x)$; $\phi_4 = 4(x), 4(-x)$.

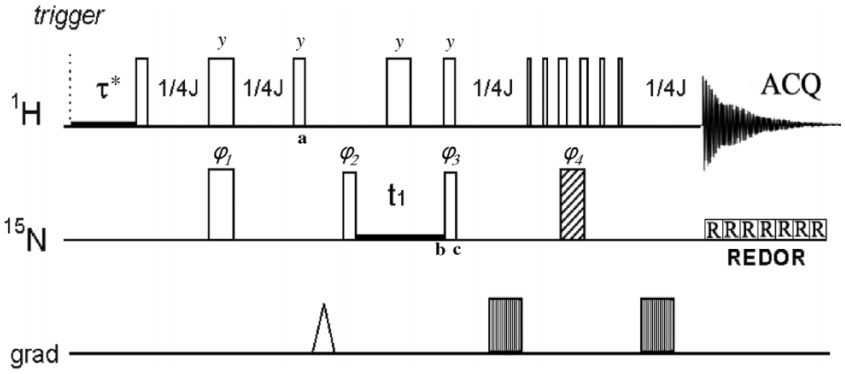

and downfield doublet components (23). The superposition of the resulting spectra is shown in Figs. 4*A* and 4*B*. Residual dipolar couplings can be obtained by subtracting proton frequencies for corresponding peaks in the sum and difference spectra. Figure 4*B* shows a small region of the 2D SAD-IPAP spectra, recorded with the scheme shown in Fig. 3. The sum spectrum is shown in dark grey whereas the difference spectrum is shown in light grey. It is interesting to note that this technique not only allows the measurement of the RDC magnitude, but also reveals the sign of the RDC (Fig. 4*B*).

Because of overlap with the water spinning side bands, only 39 backbone ^{15}N–^{1}H RDCs (out of a total of 69) were accurately measured using the SAD-IPAP experiment at a spinning speed of 1000 Hz. In order to measure additional dipolar constants, we recorded another data set at a spinning speed of 1250 Hz. At different spinning speeds, different spectral regions overlap with the spinning side bands originating from the water signal (Figs. 4*C* and 4*D*). The synchronization delay τ* (Fig. 3) was adjusted to maintain equal splittings for the same peak at both spinning speeds. This allowed the measurement of 57 ^{15}N–^{1}H averaged residual dipolar couplings from both experiments. The remaining missing couplings were either too weak to be measured or severely overlapped.

To overcome the problem of overlapping spinning sidebands, we also measured the recoupled RDCs in the ^{15}N indirect dimension using a SAD-IPAP-indirect experiment (not shown). In this experiment, the REDOR recoupling pulse train is applied on the proton channel synchronously with the rotor during the t_1 (^{15}N) evolution period. This restricts the evolution time to an integer multiple of rotation periods T_r. In practice, the SAD-IPAP-indirect experiment with ^{15}N-ubiquitin yielded broader lines with only 43 measurable couplings and a poor fit (R_{dip} of 34%) to the back-calculated couplings. The reason for the poor accuracy of the RDCs measured in the indirect dimension is still unclear, but it may be explained by a distortion of the PSLC at the high spinning velocity (2000 Hz) required to avoid folding the spectrum in the ^{15}N dimension.

The RDCs measured by the SAD-IPAP-direct technique were fitted to the high-resolution solution structure of ubiquitin (PDB code 1D3Z) by adjusting the principal values of the alignment tensor using the program MODULE (25). To compare the accuracy of the experimental RDCs, backbone ^{15}N–^{1}H residual dipolar couplings for ^{15}N-ubiquitin dissolved in a static 1 mg/mL Pf1 phage liquid crystal were measured using a conventional HSQC-IPAP NMR experiment (23). The quality of the fit was assessed using the quality factor R_{dip}. A fit is considered satisfactory when R_{dip} is below or equal to 20%. The 61 RDCs measured by this conventional method yielded a satisfactory fit with an R_{dip} of 19.2% (Fig. 5*B*). When all 57 RDCs from the SAD-IPAP experiment were fitted, an R_{dip} of 28.1% was obtained. Removal of four outliers (residues 4, 26, 65 and 66) improved the fit significantly, with a resulting R_{dip} of 21.5% (Fig. 5*A*). These outliers correspond to weak peaks in the SAD-IPAP spectra and hence the precision of these measurements is poor with differences between calculated and experimental RDCs above 10 Hz.

Discussion

In this study, we have extended the SAD-REDOR methodology introduced earlier (20) to two-dimensional NMR experiments in order to measure RDCs in biological macromolecules. We developed a new pulse sequence named SAD-IPAP that generates in-phase and anti-phase doublets from which residual dipolar couplings can be directly calculated. This pulse sequence was tested on a strongly aligned protein sample where the largest ^{15}N–^{1}H RDCs would be close to 75 Hz in a static sample, near the size of the scalar coupling (90–95 Hz). Fifty-seven couplings were measured and the accuracy of the RDCs was confirmed by fitting the experimental values to the structure of ubiquitin.

Analysis of the magnitude of the alignment tensor (D_a) suggests that some remaining loss of order still occurs in the spinning PLSC samples. The effective degree of alignment in ^{15}N-ubiquitin as estimated from the *measured* couplings in the SAD-IPAP experiment with a Pf1 concentration of

© 2008 NRC Canada

Fig. 4. Superposition of the sum (dark grey) and the difference (light grey) of the in-phase and anti-phase spectra of PSLC ^{15}N-labeled ubiquitin, recorded with the SAD-IPAP pulse scheme shown in Fig. 3: (*A*) large and (*B*) small regions of the spectrum are shown; in-phase ^{15}N–^{1}H SAD-IPAP spectra of ~5 mmol/L ^{15}N-labelled PSLC ubiquitin recorded under MAS at (*C*) 1000 Hz; and (*D*) 1250 Hz. At different spinning speeds different parts of the ubiquitin spectra overlap with the H_2O spinning side bands (enclosed in dashed boxes).

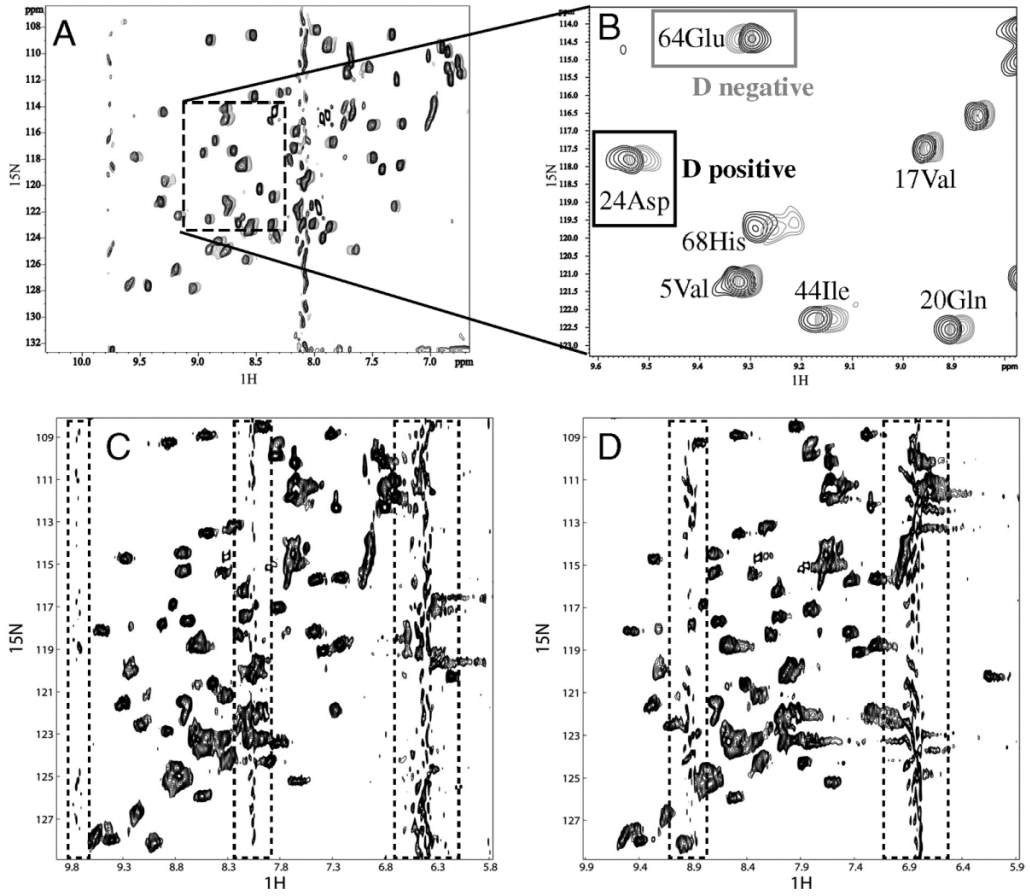

Fig. 5. Correlation plots for $^{1}D_{NH}$ RDCs measured in ^{15}N-ubiquitin. Experimental versus back-calculated RDCs are shown for: (*A*) the MAS SAD-IPAP experiment; and (*B*) conventional static HSQC-IPAP. The principal values of the alignment tensors and fitting statistics are shown as insets in each plot. The high-resolution solution structure of ubiquitin (1D3Z) was used to estimate back-calculated couplings using the program MODULE. The Pf1 phage concentration in the SAD-IPAP experiment was 20 mg/mL, while 1 mg/mL Pf1 phage was used in the conventional HSQC-IPAP experiment.

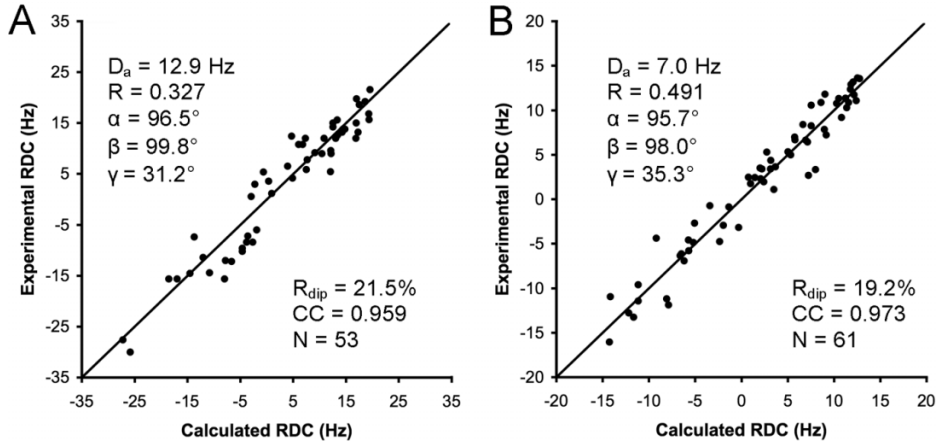

© 2008 NRC Canada

~20 mg/mL was less than twice that of ubiquitin in a 1 mg/mL Pf1 phage suspension. Based on the theoretical coupling efficiency for the pulse scheme (0.4), the degree of alignment in the SAD-IPAP setup would correspond to a D_a value of 32 Hz in a static sample. While polymerization is known to decrease the order parameter of the Pf1 phage liquid crystal (4) (the quadrupolar splitting of the static sample was ~14 Hz and not 20 Hz as expected from the concentration of Pf1 (26)), there remains a 3-fold reduction in the expected alignment magnitude. This presumably originates from distortions in the spinning sample, which reduce the order parameter of the liquid crystal and REDOR recoupling efficiency.

Future work needs to address the mechanical stability of the sample. Polyacrylamide gels made with 7% acrylamide are strong enough to hold the liquid crystal director orientation constant (4) but at angular velocities of several hundred Hz, the gel is subjected to strong centrifugal forces. The presence of air bubbles in the sample can lead to severe mechanical disruption of the gel. As a consequence, the NMR linewidths become larger and the apparent residual dipolar couplings smaller. In the present work, we minimized the formation of air bubbles by slightly changing the rotor cap design—the empty space in the rotor cap was filled with gum. During the sample preparation, the interior volume of the rotor was precisely filled to ensure that there was no air between the cap and the bulk of the polymerizing liquid. This simple modification of the rotor cap improved the stability of the gel and allowed use of spinning speeds of up to 2 kHz compared to 300 Hz used previously (20). The higher spinning speeds led to a better averaging of the interactions and improved spectral resolution.

The SAD-IPAP technique conveniently circumvents the need to measure the isotropic component of the spin–spin coupling and provides the sign of the dipolar coupling. It allows accurate measurement of RDCs in strongly aligned samples where static NMR signals are broadened beyond detection. The method offers the advantages that dipolar couplings are selectively reintroduced, standard instrumentation can be used, and the sensitivity is near that of conventional liquid-state experiments. The mix of solution and solid-state approaches advocated here promises to increase the range of NMR information that can be measured in strongly aligned biomolecules.

Experimental

Protein expression and purification

Uniformly ^{15}N-labelled yeast ubiquitin (K48R) was expressed in the *BL21DE3pLysS E.coli* strain from a *pET3a* plasmid. Cell growth was performed in minimal media M9 (pH 7.0) supplemented with 1 g/L $^{15}NH_4Cl$. The harvested cell pellets were resuspended in 50 mmol/L Tris, 1 mmol/L EDTA, 1 mmol/L PMSF, and 1 mmol/L DTT, buffered to pH 7.5, followed by sonication and centrifugation at 15 000 rpm. The protein was purified by anion exchange chromatography (Mono Q Sepharose) in 20 mmol/L Tris, 0.5 mmol/L EDTA, and 1 mmol/L DTT at pH 8.0, and gel filtration (Superdex-75) in 20 mmol/L HEPES, 40 mmol/L NaCl, 0.5 mmol/L EDTA, and 1 mmol/L DTT at pH 7.0. The protein was concentrated to the appropriate concentration for the NMR expression.

Preparation of the polyacrylamide-stabilized liquid crystal samples

Pf1 phage purification was carried out according to the procedure described previously (26). A solution of 30% acrylamide–bis-acrylamide (37.5:1) was obtained from Bio-Rad Laboratories. A mixture of 5 mmol/L ^{15}N-labelled ubiquitin, 20 mg/mL *w/v* Pf1 phage, 7% *w/v* acrylamide, 0.25% *w/v* 1,9-bisacrylamide, 0.05% *w/v* ammonium persulfate, and 10% D_2O was prepared and polymerization was initiated by the addition of 0.15% *w/v* *N*,*N*,*N*′,*N*′-tetramethylethylenediamine. The samples were rapidly mixed with a vortex and centrifuged to remove the air bubbles, and 40 μL (200 nmole ubiquitin) was immediately transferred into a 4 mm zirconia rotor and polymerized at the magic angle (54.74°) with respect to the external magnetic field $\mathbf{B_0}$, inside the bore 14.1 T magnet for ~12 hrs. The stability of the alignment was monitored by static ^{2}H spectra recorded at different rotor azimuthal angles before and after MAS.

NMR spectroscopy

MAS NMR experiments were performed on a 600 MHz ^{1}H frequency Bruker Avance spectrometer at 303 K with a triple-resonance ^{1}H–^{15}N–^{13}C high-resolution air-driven MAS probe (Bruker Biospin). The synchronization of the pulse program with the rotor phase was achieved using trigger pulse and the optical signal from the rotor that was also used for monitoring the spinning velocity. Typical π/2 pulse lengths were 8.0 and 10.0 μs for ^{1}H and ^{15}N, respectively. The SAD-IPAP experiment was recorded with 256 transients, with 40 complex points and a sweep width of 30 ppm in the ^{15}N dimension, and 512 complex points and a sweep width of 7.5 ppm in the ^{1}H dimension.

Control ^{1}H–^{15}N residual dipolar coupling constants were measured from comparison of HSQC-IPAP experiments (23) recorded on a sample of 0.5 mmol/L ubiquitin with 10% D_2O, with or without 1 mg/mL Pf1 phage, at 303 K. A total volume of 250 μL was used (125 nmole protein). The experiment was recorded in a 5 mm Shigemi NMR microtube on a 600 MHz ^{1}H frequency Bruker Avance spectrometer with 128 transients, with 100 complex points and a sweep width of 34 ppm in the ^{15}N dimension, and 512 complex points and a sweep width of 7.5 ppm in the ^{1}H dimension.

All NMR spectra were processed using either XWINNMR version 2.5 or 3.1 (Bruker Biospin) or NMRPipe (27). Evaluation of spectra and RDC measurements were completed with NMRView (28). Correlation between measured dipolar couplings and couplings calculated back from the structures were performed using MODULE (25). This program was used to evaluate alignment tensor components and Euler angles by minimization of the total χ^2 between calculated and experimental residual dipolar couplings.

Acknowledgements

We thank Dr. Katherine S. Hamilton for providing us with the yeast ubiquitin (K48R) plasmid, and Dr. Guennadi Kozlov and Dr. Alexey Denisov for fruitful discussions. This

© 2008 NRC Canada

work was supported by a Canadian Institutes of Health Research (CIHR) training grant Chemical Biology studentship to E.P. and a Natural Sciences and Engineering Research Council of Canada (NSERC) Discovery grant to K.G.

References

1. R.H. Marchessault, F.F. Morehead, and N.M. Walter. Nature, **184**, 632 (1959).
2. W.J. Orts, L. Godbout, R.H. Marchessault, and J.-F. Revol. Macromolecules, **31**, 5717 (1998).
3. S.A. Riley, J.R. Giuliani, and M.P. Augustine. J. Magn. Reson. **159**, 82 (2002).
4. J.-F. Trempe, F.G. Morin, Z. Xia, R.H. Marchessault, and K. Gehring. J. Biomol. NMR, **22**, 83 (2002).
5. N. Tjandra and A. Bax. Science, **278**, 1111 (1997).
6. J.H. Prestegard, H.M. Al-Hashimi, and J.R. Tolman. Q. Rev. Biophys. **33**, 371 (2000).
7. A. Bax, G. Kontaxis, and N. Tjandra. Methods Enzymol. **339**, 127 (2001).
8. J.-F. Trempe and K. Gehring, Observation and interpretation of residual dipolar couplings in biomolecules. *In* NMR of Ordered Liquids. *Edited by* E.E. Burnell and C.A. de Lange. Kluwer Academic Publishers, Dordrecht. 2003.
9. G.T. Montelione and G. Wagner. J. Am. Chem. Soc. **111**, 5474 (1989).
10. A. Bax, G.W. Vuister, S. Grzesiek, F. Delaglio, A.C. Wang, R. Tschudin, and G. Zhu. Methods Enzymol. **239**, 79 (1994).
11. G.W. Vuister and A. Bax. J. Am. Chem. Soc. **115**, 7772 (1993).
12. C.W. Vander Kooi, E. Kupce, E.R. Zuiderweg, and M. Pellecchia. J. Biomol. NMR, **15**, 335 (1999).
13. J. Farjon, W. Bermel, and C. Griesinger. J. Magn. Reson. **180**, 72 (2006).
14. F. Tian, J.A. Losonczi, M.W. Fischer, and J.H. Prestegard. J. Biomol. NMR, **15**, 145 (1999).
15. G. Zandomeneghi, M. Tomaselli, J.D. van Beek, and B.H. Meier. J. Am. Chem. Soc. **123**, 910 (2001).
16. R.H. Havlin, G.H.J. Park, T. Mazur, and A. Pines. J. Am. Chem. Soc. **125**, 7998 (2003).
17. R.H. Havlin, G.H.J. Park, and A. Pines. J. Magn. Reson. **157**, 163 (2002).
18. G. Zandomeneghi, P.T.F. Williamson, A. Hunkeler, and B.H. Meier. J. Biomol. NMR, **25**, 125 (2003).
19. J.D. Gross, D.E. Warschawski, and R.G. Griffin. J. Am. Chem. Soc. **119**, 796 (1997).
20. J.F. Trempe, A. Denisov, and K. Gehring. J. Magn. Reson. **164**, 329 (2003).
21. M. Maricq and J.S. Waugh. J. Chem. Phys. **70**, 3300 (1979).
22. T. Gullion and J. Schaefer. J. Magn. Reson. **81**, 196 (1989).
23. M. Ottiger, F. Delaglio, and A. Bax. J. Magn. Reson. **131**, 373 (1998).
24. M. Piotto, V. Saudek, and V. Sklenar. J. Biomol. NMR, **2**, 661 (1992).
25. P. Dosset, J.C. Hus, D. Marion, and M. Blackledge. J. Biomol. NMR, **20**, 223 (2001).
26. M.R. Hansen, L. Mueller, and A. Pardi. Nat. Struct. Biol. **5**, 1065 (1998).
27. F. Delaglio, S. Grzesiek, G.W. Vuister, G. Zhu, J. Pfeifer, and A. Bax. J. Biomol. NMR, **6**, 277 (1995).
28. B.A. Johnson and R.A. Blevins. J. Biomol. NMR, **4**, 603 (1994).

© 2008 NRC Canada

Gold-catalyzed efficient regioselective addition of arenes to allenes[1]

Rachid Skouta and Chao-Jun Li

Abstract: An efficient addition of arenes to allenes is developed by using a combination of gold and silver catalysts. The arene addition takes place exclusively at the terminal allenic carbon leading to a highly regioselective carbon–carbon bond formation.

Key words: arenes, allenes, gold, hydroarylation, regioselective, silver.

Résumé : On a mis au point une méthode efficace d'addition d'arènes à des allènes qui fait appel à une combinaison de catalyseurs d'or et d'argent. L'addition de l'arène se fait exclusivement sur le carbone allénique terminal, ce qui conduit à une formation hautement régiosélective de la liaison carbone-carbone.

Mots-clés : arènes, allènes, or, hydroarylation, régiosélective, argent.

[Traduit par la Rédaction]

Introduction

Allenes are three-carbon functional groups possessing a 1,2-diene moiety and serve as potential precursors in the synthesis of highly complex and strained target molecules of biological and industrial importance. Their unique reaction behaviour, where the reactivity is spread over three contiguous carbon atoms, has been successfully applied to the synthesis of pharmaceuticals, dyes, and polymers (1). For example, a nucleophilic addition on allene can occur on any one of the three-carbon atoms depending on the substituents at the terminals of the allene. All three possible regioisomers can be selectively produced by properly substituting at the terminals of the allene (Fig. 1).

Transition metal-catalyzed reactions of allenes have attracted a great deal of interest in recent years (2, 3) because of their highly atom-economical transformations (4). Nucleophilic additions of nitrogen, oxygen, or active methylene toward allenes using transition metals have been extensively studied (5–8).

On the other hand, the addition of arenes to allenes has rarely been studied. Such addition could potentially generate various useful aromatic compounds upon proper controlling of the regioselectivity. It was shown recently that intramolecular addition of arenes to allenes can be activated by Lewis acids such as $BF_3{\cdot}OEt_2$, $TiCl_4$ (9), or a stoichiometric amount of mercury(II) trifluoroacetate (10). In both cases, the addition occurs exclusively at the central sp allenic carbon, generating styrene derivatives (9, 10). On the other hand, Ohno and co-workers (11) reported a synthesis of dihydroquinoline and chromen via gold-catalyzed intramolecular hydroarylation of allenic anilines and phenols. This intramolecular hydroarylation occurs at the terminal sp^2 allenic carbon (11). There is also one report describing the regiospecific intermolecular alkenylation of phenols by 1,1-dimethylallene, at the terminal sp^2 allenic carbon, which can be catalyzed by platinum; however, the reaction is only limited to phenols and always generates a mixture of several products, including ether (due to the oxygen attack), allylation, and cyclization products (12).

In the 1980s, gold and gold salts started to be used in heterogeneous catalysis. Lately, gold-based homogeneous catalyses have been developed rapidly to synthesize fine chemicals (13, 14). Gold is a soft carbophilic Lewis acid, which allows it to activate C–C multiple bonds leading to the formation of the new C–C, C–N or C–O bonds. Moreover, gold catalysts activate C–H bonds, which is the first step in the formation of new bonds (15–23). Recently, we reported a highly efficient gold/silver-catalyzed addition of arenes to imines (24). The unique high efficiency of the arene-imine addition led us to explore the addition of arenes to other compounds, such as allenes (traditionally difficult for Friedel–Crafts type reactions) catalyzed by the gold/silver combination. Furthermore, it is interesting to see what regioselectivity (α, β, or γ) would be obtained for the addition of arenes to allenes with the gold/silver catalyst. Herein

Received 1 November 2007. Accepted March 3 2008. Published on the NRC Research Press Web site at canjchem.nrc.ca on 1 May 2008.

This paper is dedicated to Robert H. Marchessault in recognition of his many contributions to polysaccharide and biopolymer chemistry.

R. Skouta and C.-J. Li.[2] Department of Chemistry, McGill University, 801 Sherbrooke St. West, Montreal, QC H3A 2K6, Canada.

[1]This article is part of a Special Issue dedicated to Professor R. Marchessault.
[2]Corresponding author (e-mail: cj.li@mcgill.ca).

 doi:10.1139/V08-067 © 2008 NRC Canada

Table 1. Reaction of mesitylene with 3-phenylpropa-1,2-diene under various conditions.

Entry	Catalyst (mol%)	Solvent (1 mL)	Time, temp (h, °C)	Yield of **3a** (%)[a]
1	$Ph_3PAuCl(5)$	CH_3NO_2	12, 50	12 (19)
2	$Ph_3PAuCl(5)/AgOTf(5)$	CH_3NO_2	12, 50	19 (31)
3	$AuCl(5)/AgOTf(5)$	$CDCl_3$	12, 50	22 (35)
4	$AuBr(5)/AgOTf(5)$	$ClCH_2CH_2Cl$	12, 80	25 (45)
5	$AuCl(5)/AgOTf(5)$	$ClCH_2CH_2Cl$	12, 80	35 (39)
6	$AuCl(5)/AgOTf(5)$	Dioxane	18, 105	46 (75)
7	$AuCl(10)/AgOTf(10)$	Dioxane	18, 105	55 (65)
8	$AuBr_3(5)/AgOTf(15)$	Dioxane	18, 105	55 (70)
9	$AuCl_3(5)/AgOTf(15)$	Dioxane	18, 105	62 (98)
10	$AuCl_3(10)/AgOTf(30)$	Dioxane	18, 105	65 (75)
11	$AuCl_3(5)/AgOTf(15)$	Dioxane/AcOH (drops)	18, 105	70 (98)
12	$AuCl_3(5)$	Dioxane/AcOH (drops)	18, 105	35 (88)
13	AgOTf(5)	Dioxane/AcOH (drops)	18, 105	30 (81)
14	—	Dioxane/AcOH (0.2 mL)	18, 105	No reaction

Note: Conditions: all reactions were heated in an oil bath at the indicated temperature in sealed tubes under nitrogen with **1a** (0.25 mmol) and **2a** (0.3 mmol) in 1 mL of solvent.

[a]Based on ^1H NMR using an internal standard and conversions are shown in parentheses.

Fig. 1. Three possible nucleophilic additions on allene.

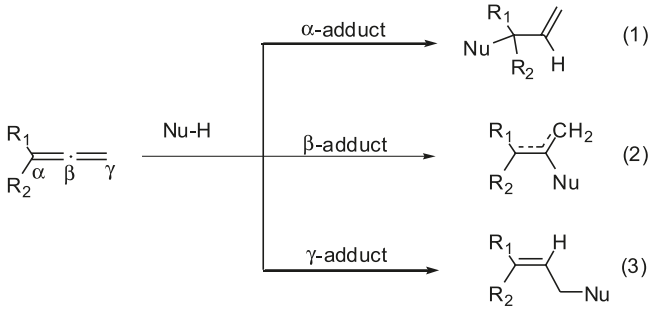

we wish to report an efficient gold/silver-catalyzed addition of arenes to mono-substituted allene, generating exclusive terminal addition products (Scheme 1).

Results and discussions

To begin our study, we examined the reaction of mesitylene (**1a**) with allene **2**, (3-phenylpropa-1,2-diene) (Scheme 1). The 3-phenylpropa-1,2-diene (**2**) can be readily prepared via a Mannich-type reaction followed by a 1,5-hydride shift (25). Initially, mesitylene (**1a**) was reacted with 3-phenylpropa-1,2-diene (**2**) in different solvents, such as nitromethane, 1,2-dichlorethane, chloroform, and dioxane, by using several potential catalysts, such as Ph_3PAuCl, $Ph_3PAuCl/AgOTf$, AuCl/AgOTf, AuBr/AgOTf, $AuBr_3/AgOTf$, and $AuCl_3/AgOTf$ (Table 1). In all cases, the desired product was obtained with varied yields (Table 1, entries 1–11). Low yields were obtained with Ph_3PAuCl and $Ph_3PAuCl/$ AgOTf complexes as catalysts (Table 1, entries 1 and 2). With 5 mol% of AuX (X = Cl, Br)/AgOTf as the catalyst, the effect of solvent was examined (Table 1, entries 3–6). Among solvents being studied, dioxane gave the highest yield (Table 1, entry 6). With dioxane as the optimized solvent, different ratios of gold(I) and gold(III) relative to AgOTf were examined by using the addition of mesitylene with 3-phenylpropa-1,2-diene (**2**), (Table 1, entries 7–10). Reducing

Scheme 1. Gold-catalyzed addition of arenes to allene.

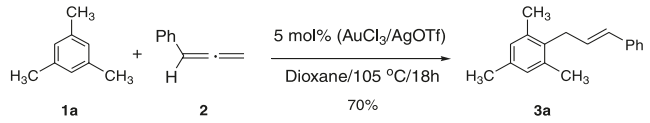

the amount of $AuCl_3/AgOTf$ to 5 mol% and adding traces (1–2 drops) of AcOH gave the best yield (Table 1, entry 11). When using $AuCl_3$ or AgOTf alone as catalyst, low yields of the desired product were obtained (Table 1, entries 12 and 13), whereas with AcOH alone in dioxane, no reaction was observed and the starting materials were recovered completely (Table 1, entry 14).

Subsequently, various arenes, including toluene, anisole, di-, tri-, tetra-, and penta-substituted benzene (**1a**–**1g**), were used for the regioselective addition to 3-phenylpropa-1,2-diene (**2**) by using 5 mol% of $AuCl_3/AgOTf$ as catalyst together with traces (1–2 drops) of AcOH in dioxane. Various arenes were added to the terminal carbon of allene **2** to give the desired products of **3a**–**3g** in good yields (40%–85%) (Table 2, entries 1–4, 6 and 7). However, no reaction was observed in the case of simple benzene (Table 1, entry 9). The use of 1,3,5-triisopropylbenzene (**1e**) and 1,3,5-tri-*tert*-butylbenzene (**1h**) led to lower yields, possibly due to steric effect (Table 2, entries 5 and 8).

Surprisingly, highly electron-rich arenes such as indole **1j** and methyl indole **1k** did not react at all under the present reaction conditions (Scheme 2).

Regarding the reaction mechanism, Yamaguchi and coworkers (26) previously reported an aromatic alkenylation of arenes using an electrophilic organogallium reagent generated from allenylsilane and $GaCl_3$. In this reaction, the silylallene reacts exclusively at the 2-position (Scheme 3, eq. [2]). Alternatively, an initial Friedel–Crafts type addition of the arene to the allene would add to the most stable carbocation formed in the α carbon of the allene (Scheme 3, eq. [1]). However, such a mechanism can be ruled out be-

© 2008 NRC Canada

cause it gives a wrong regioselectivity on the basis of the structure of compound **3a**.

Thus, two plausible mechanisms remain to be considered. (1) Auration of arenes occurs first, as Shi and He (27) reported in the hydroarylation of alkynes (27). The formed arylgold-(III) species could then be added to the allene at the γ-position to give the final products. This step could be aided by the Lewis acid activation of the allene with metal ions or with acid present in the reaction solution, followed by a proton-demetalation (Scheme 4, mechanism 1). (2) Alternatively, gold(III) could simply work as a Lewis acid to activate allene as reported by Reetz and Sommer (28). The cationic gold complex would coordinate to the allene. Nucleophilic attack by the arene from the opposite side and the less sterically hindered terminal site would lead to the formation of a vinylgold intermediate, which would be stereospecifically protonated to form the desired product (Scheme 4, mechanism 2).

Conclusions

In summary, a regioselective and intermolecular addition of arenes to the terminal carbon of mono-substituted allene was developed by using gold and silver catalysts. The scope and mechanism of the reaction are under further investigations.

Experimental

General information

Standard column chromatography was performed on 20–60 mm silica gel using flash-column chromatography techniques (29). Infrared spectra were recorded by an ABB Bomem MB100 instrument. Liquid compounds were recorded as a thin film on NaCl plates and solid compounds as KBr pellets. ^{1}H NMR spectra were recorded on Varian 300, 400, and 500 MHz spectrometers in $CDCl_3$ solution (central peak is 7.26 ppm), and the chemical shifts were reported in parts per million (δ) relative to internal standard TMS (0 ppm). The peak patterns are indicated as follows: s, singlet; d, doublet; t, triplet; dt, doublet of triplet; dd, doublet of doublet; m, multiplet; q, quartet; qt, quintet. The coupling constants, *J*, are reported in Hertz (Hz). ^{13}C NMR spectra were obtained at 75 and 125 MHz and referenced to the internal solvent signals (central peak is 77.00 ppm). MS data were obtained by Agilent 6890N Network GC System/ Agilent 5973 Mass Selective Detector. HR-MS were made by McGill University. Thin layer chromatography was performed using Sorbent Silica Gel 60 F_{254} TLC plates and visualized with ultraviolet light. All reagents were weighed and handled in air, and backfilled under an inert atmosphere of nitrogen at room temperature (RT). Unless otherwise noted all reagents were purchased from Sigma-Aldrich, Strem, and Across and used without further purification.

Preparation of 3-phenylpropa-1,2-diene (2)

Following the general procedure reported in the literature (25), compound **2** was isolated by distillation (bp 80–95 °C at 20 mm Hg (1 mm Hg = 133.322 4 Pa). R_f 0.81 (hexane/ethyl acetate, 40:1). ^{1}H NMR ($CDCl_3$, 400 MHz, ppm) δ: 7.32–7.20 (m, 5H), 6.18 (t, *J* = 7.2 Hz, 1H), 5.16 (d, *J* = 7.2 Hz, 2H). ^{13}C NMR ($CDCl_3$, 75 MHz, ppm) δ: 210.2, 134.3, 129.2, 129.0, 127.1, 94.4, 79.2.

Typical experimental procedure for the preparation of compounds 3a–3g

Allene **2** (34.8 mg, 0.3 mmol) in 1 mL of dioxane was added to a sealed tube containing $AuCl_3$ (3.8 mg, 0.0125 mmol), AgOTf (9.6 mg, 0.0375 mmol), and arenes **1a**–**1h** (0.25 mmol) under an atmosphere of nitrogen. A trace amount (1–2 drops) of AcOH was added to the mixture, which was stirred at RT for 5 min and heated at 105 °C for 18 h under an atmosphere of nitrogen. The reaction mixture was cooled to RT and the solvent was evaporated in vacuo. The residue was purified by flash-column chromatography on silica gel with the appropriate mixture of hexane and EtOAc to give compounds **3a**–**3g**.

2-Cinnamyl-1,3,5-triisopropylbenzene (3e)

Following the above general procedure with 1,3,5-triisopropylbenzene, **1e** (60.5 mL, 0.25 mmol) and allene **2** (34.8 mg, 0.3 mmol), the residue was purified by flash-column chromatography on silica gel. R_f 0.44 (hexane/ethyl acetate, 40:1). IR (neat, NaCl, cm^{-1}) ν_{max}: 3025, 2961, 2927, 2868, 1575, 1495, 1448, 1382, 1362, 966, 876, 730, 691. ^{1}H NMR ($CDCl_3$, 400 MHz, ppm) δ: 7.30–7.16 (m, 5H), 7.03 (s, 2H), 6.37–6.19 (m, 2H), 3.62 (d, *J* = 5.6 Hz, 2H), 3.20 (qt, *J* = 6.8 Hz, 2H), 2.90 (qt, *J* = 6.8 Hz, 1H), 1.28 (s, 3H), 1.27 (s, 3H), 1.24 (s, 6H), 1.23 (s, 6H). ^{13}C NMR ($CDCl_3$, 125 MHz, ppm) δ: 147.3, 147.0, 138.1, 130.7, 130.4, 130.2, 128.6, 127.0, 126.2, 121.2, 34.4, 31.8, 31.0, 29.6, 24.6, 24.3. MS (GC/MS) *m/z* (%): 320 (M^+), 305, 291, 277, 263, 250, 235, 216, 201 (100), 187, 173, 157, 143, 131, 115, 105, 91, 77, 65. HR-MS calcd. for $C_{24}H_{32}$: 320.250 40; found: 320.250 08.

3-Cinnamyl-1,2,4,5-tetramethylbenzene (3f)

Following the above general procedure with 1,2,4,5-tetramethylbenzene, **1f** (33.5 mg, 0.25 mmol) and allene **2** (34.8 mg, 0.3 mmol), the residue was purified by thin-layer chromatography. R_f 0.70 (hexane/ethyl acetate, 40:1). IR (neat, NaCl, cm^{-1}) ν_{max}: 3026, 2963, 2921, 2865, 1468, 1440, 1002, 965, 867, 733, 692. ^{1}H NMR ($CDCl_3$, 500 MHz, ppm) δ: 7.32–7.16 (m, 5H), 6.91(s, 1H), 6.33–6.23 (m, 2H), 3.61 (d, *J* = 5.1 Hz, 2H), 2.26 (s, 6H), 2.22 (s, 6H). ^{13}C NMR ($CDCl_3$, 125 MHz, ppm) δ: 137.9, 136.3, 133.9, 132.9, 130.2, 130.1, 128.6, 128.3, 127.1, 126.2, 33.7, 20,8, 15.8. MS (GC/MS) *m/z* (%): 250 (M^+) (100), 235, 220, 205, 189, 178, 157, 146, 131, 115, 105, 91, 77, 65, 51. HR-MS calcd. for $C_{19}H_{22}$: 250.172 15; found: 250.171 40.

1-Cinnamyl-2,3,4,5,6-pentamethylbenzene (3g)

Following the above general procedure with 1,2,3,4,5-pentamethylbenzene, **1g** (37.0 mg, 0.25 mmol) and allene **2** (34.8 mg, 0.3 mmol), the residue was purified by thin-layer chromatography plate. R_f 0.45 (hexane/ethyl acetate, 40:1). IR (neat, NaCl, cm^{-1}) ν_{max}: 3026, 2960, 2927, 1596, 1447, 1062, 966, 795, 752, 735, 693. ^{1}H NMR ($CDCl_3$, 400 MHz, ppm) δ: 7.36–7.20 (m, 5H), 6.37–6.32 (m, 2H), 3.65 (d, *J* = 5.2 Hz, 2H), 2.31 (s, 6H), 2.30 (s, 3H), 2.29 (s, 6H). ^{13}C NMR ($CDCl_3$, 125 MHz, ppm) δ: 138.0, 133.6, 133.3, 132.8, 132.7, 130.2, 128.8, 128.7, 127.1, 126.2, 34.2, 17,1,

© 2008 NRC Canada

Table 2. Gold catalyzed addition of arene compounds to allene.

Entry	Arene	Product	Yield (%)
1	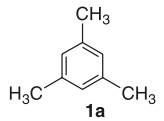 **1a**	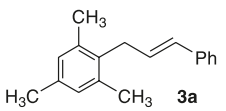 **3a**	70
2	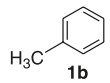 **1b**	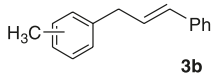 **3b**	40[a]
3	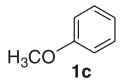 **1c**	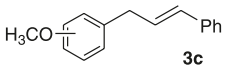 **3c**	55[b]
4	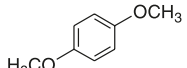 **1d**	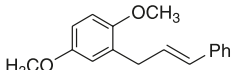 **3d**	69
5	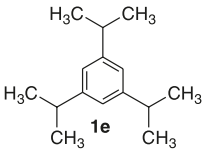 **1e**	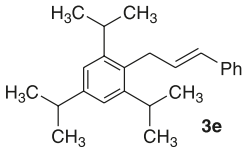 **3e**	45
6	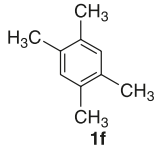 **1f**	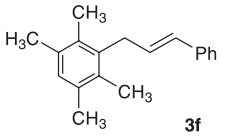 **3f**	73
7	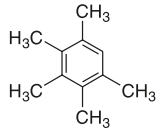 **1g**	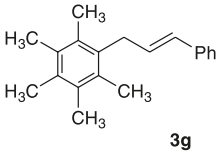 **3g**	85
8	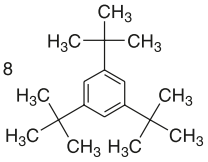 **1h**	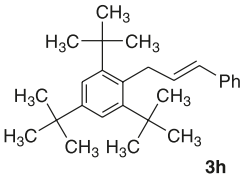 **3h**	traces
9	**1i**	No reaction	—

Note: Conditions: all reactions were carried out at 105 °C, for 18 h, in a sealed tube under an atmosphere of nitrogen, with aryl **1a**–**1h** (0.25 mmol), allene **2** (0.3 mmol), $AuCl_3$ (5 mol%), AgOTf (15 mol%), 1 mL of dioxane, and 1–2 drops of AcOH.

[a]Mixture of p/o not isolated.

[b]Mixture of p/o (16:1) isolated by flash-column chromatography.

Scheme 2.

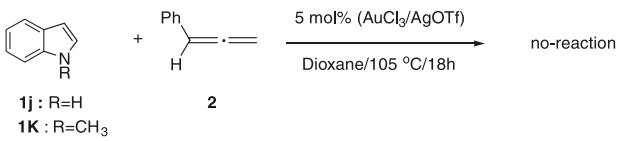

16.8. MS (GC/MS) *m*/*z* (%): 264 (M^+), 249 (100), 234, 219, 203, 171, 160, 145, 129, 115, 105, 91, 77, 65, 51. HR-MS calcd. for $C_{20}H_{24}$: 264.187 80; found: 264.187 57.

Scheme 3.

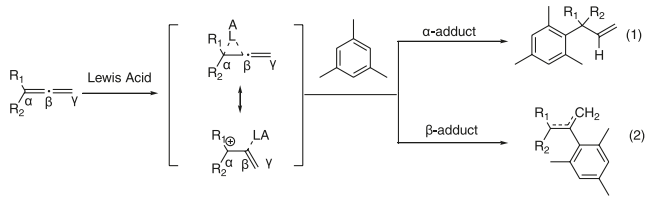

Scheme 4. Tentative mechanisms for the gold-catalyzed addition of mesitylene with allene.

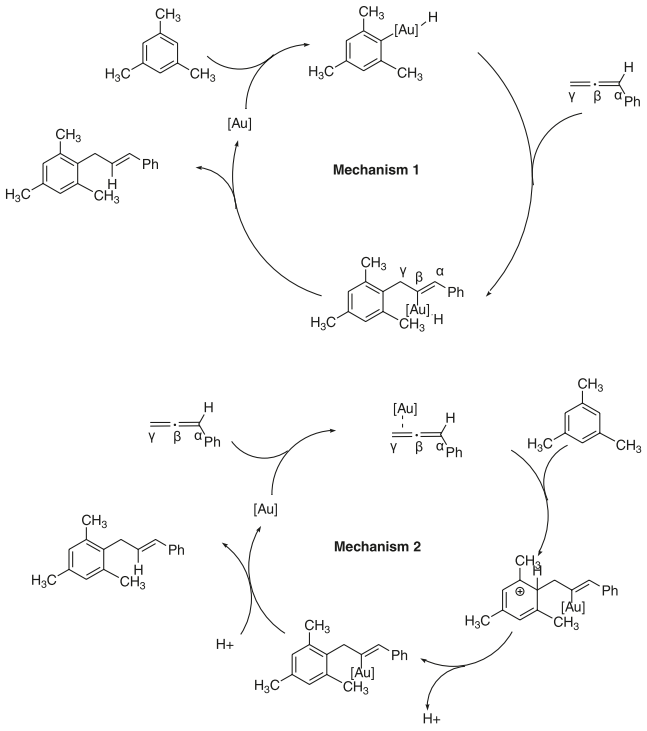

Acknowledgements

We are grateful to the Canada Research Chair (Tier I) Foundation (CJL), the Canadian Foundation for Innovation (CFI), the National Sciences and Engineering Research Council of Canada (NSERC), and McGill University for support of our research. Rachid Skouta would like to thank Mr. Nadim Saade at the Mass Unit and Mr. Frederick Morin at the NMR Unit in the Chemistry Department at McGill University for providing help and support.

References

1. For reviews, see: (*a*) S. Patai (*Editor)*. The chemistry of ketenes, allenes and related compounds. Wiley, New York. 1980; (*b*) S.R. Landor (*Editor*). The chemistry of allenes. Academic Press, London. 1982; (*c*) H.F. Schuster and G.M. Coppola. Allenes in organic syntheses. Wiley, New York. 1984; (*d*) C. Bruneau and P.H. Dixneuf. *In* Comprehensive organic functional group transformations. Vol. 1. *Edited by* A.R. Katritzky, O. Meth-Cohn, and C.W. Rees. Pergamon, Oxford. 1995. Chap. 20.
2. For recent reviews, see: (*a*) R. Zimmer, C.U. Dinesh, E. Nandanam, and F.A. Khan. Chem. Rev. **100**, 3067 (2000);

© 2008 NRC Canada

(*b*) R.W. Bates and V. Satcharoen. Chem. Soc. Rev. **31**, 12 (2002); (*c*) N. Krause and A.S.K. Hashmi (*Editors*). Modern allene chemistry, 2 Vols. Wiley-VCH, Weinheim, Germany. 2004.
3. (*a*) Y. Yamamoto, M. Al-Masum, and N. Asao. J. Am. Chem. Soc. **116**, 6019 (1994); (*b*) For hydroamination of allenes, see: Y. Yamamoto, M. Al-Masum, and N. Fujiwara. J. Chem. Soc. Chem. Commun. 381 (1996); (*c*) Y. Yamamoto, M. Al-Masum, and A. Takeda. J. Chem. Soc. Chem. Commun. 831 (1996); (*d*) Y. Yamamoto, M. Al-Masum, N. Fujiwara, and N. Asao. Tetrahedron Lett. **36**, 2811 (1995); (*e*) Y. Yamamoto and M. Al-Masum. Synlett. 969 (1995); (*f*) M. Meguro, S. Kamijo, and Y. Yamamoto. Tetrahedron Lett. **37**, 7453 (1996); (*g*) For addition of the C–H bond of carbon pronucleophiles to allenes, see: L. Besson, G. Jacques, and B. Cazes. Tetrahedron Lett. **36**, 3853 (1995); (*h*) B.M. Trost and V.J. Gerusz. J. Am. Chem. Soc. **117**, 5156 (1995); (*i*) B.M. Trost, C. Jakel, and B. Plietker. J. Am. Chem. Soc. **125**, 4438 (2003).
4. (*a*) B.M. Trost. Science (Washington, D.C.), **254**, 1471 (1991); (*b*) B.M. Trost. Angew. Chem. Int. Ed. Engl. **34**, 259 (1995); (*c*) B.M. Trost. Acc. Chem. Res. **35**, 695 (2002).
5. (*a*) H. Urabe, T. Takeda, D. Hideura, and F. Sato. J. Am. Chem. Soc. **119**, 11295 (1997); (*b*) K.M. Brummond, H. Chen, P. Sill, and L. You. J. Am. Chem. Soc. **124**, 15186 (2002); (*c*) T. Shiabata, Y. Takesue, S. Kadowaki, and K. Takagi. Synlett. 268 (2003); (*d*) Q. Shen and G.B. Hammond. J. Am. Chem. Soc. **124**, 6534 (2002).
6. (*a*) N. Cadran, K. Cariou, G. Hervé, C. Aubert, L. Fensterbank, M. Malacria, and J. Marco-Contelles. J. Am. Chem. Soc. **126**, 3408 (2004); (*b*) G. Lemiere, V. Gandon, N. Agenet, J.-P. Goddard, A. de Kozak, C. Aubert, L. Fensterbank, and M. Malacria. Angew. Chem. Int. Ed. **45**, 7596 (2006).
7. (*a*) T. Makino and K. Itoh. J. Org. Chem. **69**, 395 (2004); (*b*) S.-K. Kang, B.-S. Ko, and D.-M. Lee. Tetrahedron Lett. **43**, 6693 (2002); (*c*) B.M. Trost and K. Matsuda. J. Am. Chem. Soc. **110**, 5233 (1988).
8. (*a*) J. Franzén and J.E. Bäckvall. J. Am. Chem. Soc. **125**, 6056 (2003); (*b*) K. Närhi, J. Franzén, and J.E Bäckvall. Chem. Eur. J. **11**, 6937 (2005); (*c*) J. Piera, K. Närhi, and J.E. Bäckvall. Angew. Chem. Int. Ed. **45**, 6914 (2006); (*d*) H. Ohno, K. Miyamura, Y. Takeoka, and T. Tanaka. Angew. Chem. Int. Ed. **42**, 2647 (2003); (*e*) H. Ohno, K. Miyamura, T. Mizutani, Y. Kadoh, Y. Takeoka, H. Hamaguchi, and T. Tanaka. Chem. Eur. J. **11**, 3728 (2005).
9. (*a*) Y. Nagao, W.S. Lee, and K. Kim. Chem. Lett. 389 (1994); (*b*) Y. Nagao, W.S. Lee, Y. Komaki, S. Sano, and M. Shiro. Chem. Lett. 597 (1994); (*c*) Y. Nagao, W.S. Lee, I.-Y. Jeong, and M. Shiro. Tetrahedron Lett. **36**, 2799 (1995); (*d*) W.S. Lee, I.-Y. Jeong, M. Shiro, S. Sano, and Y. Nagao. Tetrahedron Lett. **38**, 611 (1997).
10. T. Balasubramanian and K.K. Balasubramanian. Tetrahedron Lett. **32**, 6641 (1991).
11. T. Watanabe, S. Oishi, N. Fujii, and H. Ohno. Org. Lett. **9**, 4821 (2007).
12. A. De Renzi, A. Panunzi, A. Saporito, and A. Vitagliano. J. Chem. Soc. Perkin Trans. 2, 993 (1983).
13. A. Höffmann-Röder and N. Krause. Org. Biomol. Chem. **3**, 387 (2005).
14. (*a*) A. Arcadi and S. Di Giuseppe. Curr. Org. Chem. **8**, 795 (2004); (*b*) G. Bianchi and A. Arcadi. Targets Heterocycl. Syst. **8**, 82 (2004).
15. For selected reviews on gold catalysis, see: (*a*) A.S.K. Hashmi. Angew. Chem. Int. Ed. **43**, 6990 (2005); (*b*) A.S.K. Hashmi. Gold Bull. **37**, 51 (2004); (*c*) G. Dyker. Angew. Chem. Int. Ed. **39**, 4237 (2000).
16. L. Zhang and S.A. Kozmin. J. Am. Chem. Soc. **127**, 6962 (2005).
17. D.J. Gorin, N.R. Davis, and F.D. Toste. J. Am. Chem. Soc. **127**, 11260 (2005).
18. (*a*) Y. Liu, F. Song, Z. Song, M. Liu, and B. Yan. Org. Lett. **7**, 5409 (2005); (*b*) M.H. Suhre, M. Reif, and S. Kirsh. Org. Lett. **7**, 3925 (2005).
19. Z. Shi and C. He. J. Am. Chem. Soc. **126**, 5964 (2004).
20. K. Sato, N. Asao, and Y. Yamamoto. J. Org. Chem. **70**, 8977 (2005).
21. (*a*) C. Wei and C.-J. Li. J. Am. Chem. Soc. **125**, 9584 (2003); (*b*) B. Huang, X. Yao, and C.-J. Li. Adv. Synth. Catal. **348**, 1528 (2006)
22. (*a*) R.-V. Nguyen and C.-J. Li. Org. Lett. **8**, 2397 (2006); (*b*) X. Yao and C.-J. Li. Org. Lett. **8**, 1953 (2006); (*c*) X. Yao and C.-J. Li. J. Am. Chem. Soc. **126**, 6884 (2004).
23. (*a*) R. Skouta and C.-J. Li. Angew. Chem. Int. Ed. **46**, 1117 (2007); (*b*) R. Skouta and C.-J. Li. Synlett. 1759 (2007); (*c*) R. Skouta and C.-J. Li. Tetrahedron Lett. **48**, 8343 (2007).
24. Y. Luo and C.-J. Li. Chem. Commun. 1930 (2004).
25. (*a*) S. Searles, Y. Li, B. Nassim, M.-T.R. Lopes, P.T. Tran, and P. Crabbi. J. Chem. Soc. Perkin. Trans. 1, 747 (1984); (*b*) For recent articles on the preparation of allenes via Pd-catalyzed hydrogen-transfer reactions, see: H. Nakamura, T. Kamakura, and S. Onagi. Org. Lett. **8**, 2095 (2006)
26. Y. Kido, F. Yonehara, and M. Yamaguchi. Tetrahedron, **57**, 827 (2001).
27. (*a*) Z. Shi and C. He. J. Organomet. Chem. **690**, 5049 (2005); (*b*) Z. Shi and C. He. J. Org. Chem. **69**, 3669 (2004); (*c*) Z. Shi and C. He. J. Am. Chem. Soc. **126**, 13596 (2004).
28. M.T. Reetz and K. Sommer. Eur. J. Org. Chem. **18**, 3485 (2003).
29. W.C. Still, M. Khan, and A. Mitra. J. Org. Chem. **43**, 2923 (1978).

© 2008 NRC Canada

Targeted engineering of *Cupriavidus necator* chromosome for biosynthesis of poly(3-hydroxybutyrate-*co*-3-hydroxyhexanoate) from vegetable oil[1]

Jun Mifune, Satoshi Nakamura, and Toshiaki Fukui

Abstract: Previous studies have demonstrated that heterologous expression of PHA synthase from *Aeromonas caviae* ($PhaC_{Ac}$), capable of accepting (*R*)-3-hydroxyacyl-CoA of C_4–C_7 as substrates, could confer the ability to PHA-negative mutant of *Cupriavidus necator* PHB$^-$4 to synthesize poly((*R*)-3-hydroxybutyrate-*co*-(*R*)-3-hydroxyhexanoate) [P(3HB-*co*-3HHx)] from vegetable oils. The mutation point within *pha* operon in PHB$^-$4 was determined to be a single nonsense mutation within the PHA synthase gene ($phaC_{Cn}$), suggesting the much lower β-ketothiolase and NADPH-dependent acetoacetyl-CoA reductase activities observed in this strain would be a polar effect of the mutation. For further efficient biosynthesis of P(3HB-*co*-3HHx) copolyester, *C. necator* wild strain H16 was engineered by homologous recombination targeting the chromosomal $phaC_{Cn}$, and the PHA productivity was compared with previous PHB$^-$4-derived strain harboring $phaC_{Ac}$ on a multi-copy plasmid (PHB$^-$4/pJRDEE32d13). A strain $H16C_{Ac}$, in which $phaC_{Cn}$ was substituted for $phaC_{Ac}$ on the chromosome, could produce P(3HB-*co*-3HHx) from soybean oil with high productivity, but the 3HHx fraction in the accumulated polymer was decreased. Meanwhile, H16ΔC/pJRDEE32d13, that lost region for the original synthase gene and expresses exochromosomal $phaC_{Ac}$, grew and accumulated PHA with similar properties to the PHB$^-$4-derived strain. The results of enzyme assay suggested that low β-ketothiolase activity might be relevant for decrease of growth ability accompanied by increase of 3HHx composition when soybean oil was fed as a sole carbon source.

Key words: poly(hydroxyalkanoates), poly(3-hydroxybutyrate-*co*-3-hydroxyhexanoate), PHA synthase, *Cupriavidus necator*, vegetable oil.

Résumé : Des études antérieures ont démontré que l'expression hétérologue de la synthase de PHA de *Aeromonas caviae* ($PhaC_{Ac}$), qui est capable d'accepter comme substrat du (*R*)-hydroxyacyl-CoA comportant de quatre à sept atomes de carbone, peut conférer l'habilité au mutant PHA-négatif du *Cupriavidus necator* PHB$^-$4 de synthétiser du poly ((*R*)-3-hydroxybutylate-*co*-(*R*)-3-hydroxyhexanonate) [P(3HB-*co*-3HHx)] à partir d'huies végétales. On a déterminé le point de mutation de l'opéron *pha* du PHB$^-$4 en effectuant une seule mutation dans le gène de la synthase de PHA ($phaC_{Cn}$), ce qui suggère que les activités beaucoup plus faible de réductase de l'acétoacétyl-CoA dépendantes sur la β-cétothiolase et la NADPH résultent d'un effet polaire de la mutation. Afin d'améliorer la biosynthèse du copolyester [P(3HB-*co*-3HHx)], on a modifié la source sauvage H16 du *C. necator* par une recombinaison homologue orientée vers le ($phaC_{Cn}$) chromosomique et on a comparé la productivité en PHA avec celle obtenue antérieurement avec la souche dérivée du PHB$^-$4 présentant un ($phaC_{Ac}$) sur un plasmide à plusieurs copies (PHB$^-$4/pJRDEE32d13). Une souche de $H16C_{Ac}$ dans laquelle on a substitué un $phaC_{Ac}$ par un $phaC_{Cn}$ sur le chromosome peut produire du P(3HB-*co*-3HHx) à partir de l'huile de soya avec une productivité élevée, mais la fraction de 3HHx dans le polymère accumulé est diminuée. Par ailleurs, le H16ΔC/pJRDEE32d13, cette région perdue du gène original de la synthase, et du $phaC_{Ac}$ d'expressions exochromosomales ont permis de faire croître et d'accumulé du PHA ayant des propriétés similaires à celles du produit obtenu à partir de la souche dérivée du PHB$^-$4. Les résultats des essais avec les enzymes suggèrent qu'une faible activité β-cétothiolase pourrait jouer un rôle important dans la diminution de la de l'habilité à faire croître qui accompagne l'augmentation de la composition 3HHx quand on utilise uniquement de l'huile de soya comme source de carbone.

Received 14 December 2007. Accepted 4 March 2008. Published on the NRC Research Press Web site at canjchem.nrc.ca on 7 May 2008.

This paper is dedicated to Robert H. Marchessault in recognition of his many contributions to polysaccharide and biopolymer chemistry.

J. Mifune, S. Nakamura, and T. Fukui.[2] Department of Bioengineering, Graduate School of Bioscience and Biotechnology, Tokyo Institute of Technology, B-37 4259 Nagatsuta, Midori-ku, Yokohama 226–8501, Japan.

[1]This article is part of a Special Issue dedicated to Professor R. Marchessault.
[2]Corresponding author (e-mail: tfukui@bio.titech.ac.jp).

 doi:10.1139/V08-047 © 2008 NRC Canada

Mots-clés : polyhydroxyalcanoates, poly(3-hydroxybutyrate-*co*-3-hydroxyhexanonate), synthase de PHA, *Cupriavidus necator*, huile végétale.

[Traduit par la Rédaction]

Introduction

Recent apprehension about huge amounts of waste materials has prompted much interest in bio-based materials. Poly(hydroxyalkanoates) (PHAs), synthesized by a number of bacteria as carbon- and energy-storage materials, are thermoplastics that can be produced from renewable carbon resources and be completely biodegraded to CO_2 and H_2O, so they have come under investigation as potential alternatives to petroleum-based plastics (1, 2).

A homopolymer of (*R*)-3-hydroxybutyrate, P(3HB), is the most abundant PHA in nature, and it is produced by a variety of bacteria. This polyester is usually synthesized from acetyl-coenzyme A (acetyl-CoA) via three-step reactions catalyzed by β-ketothiolase (PhaA), NADPH-dependent acetoacetyl-CoA reductase (PhaB), and PHA synthase (PhaC). In *Cupriavidus necator*, all the three genes form a single operon with the order of *phaC-A-B*, and are constitutively expressed. It has been revealed that the PHA synthase from *C. necator* ($PhaC_{Cn}$) is specific to short-chain-length (*R*)-3-hydroxyacyl-CoA monomers of C_3–C_5. The bacterial P(3HB) generally has molecular mass from 10^5 to 10^6 and is a highly crystalline thermoplastic resembling polyethylene and polypropylene. Nevertheless, the hard and brittle properties of this homopolyester with low elongation before breaking (5%–6%) have hampered its wide range of application (3–5).

To improve mechanical properties of this homopolyester, biosynthesis of random copolyesters consisting of 3HB with a second monomer unit has been attempted (1–5). So far, microbial synthesis of 3HB-based copolyesters, for example, those containing (*R*)-3-hydroxypentanoate or 4-hydroxybutyrate has been demonstrated by feeding the related alkanoates or hydroxyalkanoates into the medium as precursors for the desired second monomer units (6). However, such additional supplement of precursor compounds tends to increase the production cost of PHAs.

Aeromonas caviae, isolated from soil, accumulates flexible poly((*R*)-3-hydroxybutyrate-*co*-(*R*)-3-hydroxyhexanoate) [P(3HB-*co*-3HHx)] from alkanoates of even carbon numbers or vegetable oils as a single carbon source (7, 8). Our research group has cloned a gene ($phaC_{Ac}$) for PHA synthase with unique substrate specificity (C_4–C_7) from this bacterium, and has demonstrated that introduction of $phaC_{Ac}$ into a mutant strain of *C. necator*, PHB$^-$4, could not only restore the PHA negative phenotype but also confer the ability to synthesize P(3HB-*co*-3HHx) copolyester from fatty acids or oils (9–11). This result indicated that the substrate preference of PHA synthase was one of the major factors for determining monomer composition of PHAs, as well as that *C. necator* cells are equipped with channeling pathway(s) for generation of (*R*)-3HHx-CoA via β-oxidation. The recombinant *C. necator* harboring $phaC_{Ac}$ accumulated the copolyester with 4–5 mol% 3HHx up to 76 wt% of dry-cell mass from inexpensive vegetable oils (10). However, in batch cultivation, the copolyester productivity by this recombinant (0.034 g/L·h) was lower than P(3HB) productivity of wild strain H16 (0.077 g/L·h) when 1% olive oil was supplied as a carbon source. This was mainly owing to relatively poor growth of the host strain PHB$^-$4 that had been obtained by chemical mutagenesis (12).

In this study, *C. necator* H16 chromosome was engineered by specific homologous recombination that avoided unintended negative effects of random mutagenesis. We applied $phaC_{Ac}$ for the recombination to achieve biosynthesis of P(3HB-*co*-3HHx) via β-oxidation, and then evaluated PHA productivity of the newly constructed strains.

Results

Identification of a mutation site within *pha* operon in *C. necator* PHB$^-$4.

The PHA-negative mutant of *C. necator* (PHB$^-$4) was frequently used as a host strain for heterologous expression of PHA synthase gene from various sources to evaluate their in vivo polymerizing properties and to construct recombinant strains for the production of copolyesters (9, 10, 13–17). A few reports described that the genotype of this strain was $phaC^-A^-B^-$ based on low activities of the corresponding enzymes (13, 14) (see below). However, to our knowledge, there has been no identification of the mutation site within *pha* operon in PHB$^-$4. We determined nucleotide sequence of a 5.0 kbp fragment containing *pha* operon (amplified with ReP-N and RePhbB-C primers) by direct sequencing. As a result, only one single-nucleotide substitution of G to A was identified, corresponding to TGG coding Trp107 in $PhaC_{Cn}$ protein to TAG stop codon; consequently, the translation of $phaC_{Cn}$ was interrupted after Ala106 by the nonsense mutation. No other mutation was detected within the nucleotide sequence of the remaining region, indicating that the native promoter region and $phaAB_{Cn}$ genes were intact in PHB$^-$4.

Targeted engineering of *C. necator* H16

PHA synthase from *A. caviae* is a unique enzyme that can accept (*R*)-3HHx-CoA in addition to short-chain-length of (*R*)-3HA-CoA of C_4-C_5 as substrates, so the gene $phaC_{Ac}$ is useful for development of P(3HB-*co*-3HHx)-producing recombinant bacteria (9, 10, 16, 17). In particular, *C. necator* PHB$^-$4 strains expressing harboring $phaC_{Ac}$ from plasmids have been demonstrated to be good producers for P(3HB-*co*-3HHx) copolyester from related alkanoates, but the slower growth of the host strain PHB$^-$4 limited the overall PHA productivity on vegetable oils (10). As the decrease of growth ability of PHB$^-$4 was predicted to be caused by unknown mutations induced through chemical mutagenesis, two recombinant strains based on *C. necator* wild strain H16 were constructed by specific homologous recombination targeting the original PHA synthase gene, $phaC_{Cn}$, on the chromosome (Fig. 1A). Markerless recombinant strains $H16C_{Ac}$

© 2008 NRC Canada

Fig. 1. (A) Schematic diagram of genotypes of *C. necator* strains used in this study. Small arrows indicate primers for PCR as below. (B) PCR analysis of recombinant strains of *C. necator* H16C_{Ac} (lanes 1–5), H16ΔC (6–10), and wild strain H16 (11–15) using primer sets of ReP-f2/RePhbB-C (lanes 1, 6, 11), ReP-N/RePhbB-C (2, 7, 12), ReP-f2/RePhbA-Rv (3, 8, 13), AcPhaC-f4/RePhbB-C (4, 9, 14), and RePhbC-f5/RePhbB-C (5, 10, 15). Lane M; molecular mass standard (λ DNA digested with EcoRI and HindIII).

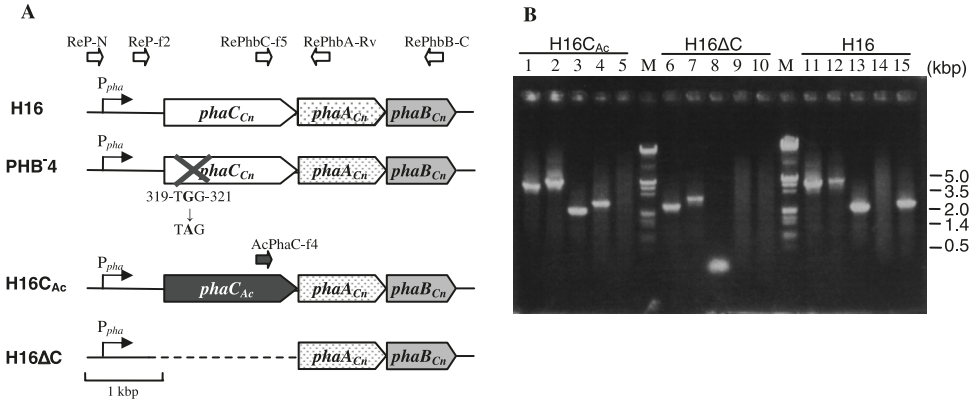

(*phaC*$_{Cn}$::*phaC*$_{Ac}$) and H16ΔC (Δ*phaC*$_{Cn}$) were constructed by substituting chromosomal *phaC*$_{Cn}$ for *phaC*$_{Ac}$ and deleting *phaC*$_{Cn}$ region from the chromosome, respectively, using pop-in – pop-out recombination technique. PCR analysis of each the strains confirmed the occurrence of the desired recombination (Fig. 1B). These strains have no unintended mutation on the chromosome and do not require additional antibiotics to maintain the phenotype. H16ΔC/pJRDEE32d13 was obtained by transconjugation of H16ΔC with *Escherichia coli* S17–1 harboring pJRDEE32d13. This strain possesses multi-copies of *phaC*$_{Ac}$ on the plasmid under the transcriptional control by its native promoter region, distinct from H16C_{Ac} having one copy of *phaC*$_{Ac}$ with *C. necator pha* promoter.

Enzyme assay

Table 1 shows the results of enzyme assay (PHA synthase, β-ketothiolase, and NAD(P)H-acetoacetyl-CoA reductase) in each strain of *C. necator* grown on fructose. As represented in several reports (13–15), the activities in PHB⁻4 were much lower than those in H16 besides NADH-acetoacetyl-CoA reductase. The negligible activity of PHA synthase agreed with the nonsense mutation within *phaC*$_{Cn}$; however, the significant decrease of β-ketothiolase and NADPH-acetoacetyl-CoA reductase was inconsistent with the presence of intact *phaAB*$_{Cn}$ genes. In contrast, only PHA synthase activity was completely lost in H16ΔC, as expected. This strain had similar levels of NADPH- and NADH-acetoacetyl-CoA reductase activities as the wild strain, whereas β-ketothiolase activity (986 U/g) was decreased to one fourth of that in H16 (3677 U/g). H16C_{Ac} showed high activities for all enzymes examined, but the activity of PHA synthase encoded by chromosomal *phaC*$_{Ac}$ (177 U/g) was lower than that in H16 (715 U/g). The transconjugants of PHB⁻4 and H16ΔC harboring pJRDEE32d13 exhibited high PHA synthase activity derived from *phaC*$_{Ac}$ on the multi-copy plasmid, although the reason for much higher activity in PHB⁻4 was unclear. As a result, the strains H16C_{Ac} and H16ΔC/pJRDEE32d13 were confirmed to express *phaC*$_{Ac}$-derived PHA synthase along with NADPH-acetoacetyl-CoA reductase and β-ketothiolase with higher activities than previous recombinant strain PHB⁻4/pJRDEE32d13.

PHA production by engineered strains of *C. necator*

PHA-producing ability of the constructed strains was examined with fructose, octanoate, or soybean oil as a carbon source, and compared with those of wild strain H16 and PHB⁻4/pJRDEE32d13 (Table 2). The strain H16 accumulated P(3HB) homopolymer from all carbon sources examined, where cell growth and P(3HB) accumulation via β-oxidation (on octanoate or soybean oil) were better than glycolysis (on fructose). Unlike H16, PHB⁻4/pJRDEE32d13 could synthesize P(3HB-*co*-3HHx) from octanoate and soybean oil, but the lower cell yield on soybean oil led to lower copolyester production (1.9–2.0 g PHA/L) than P(3HB) biosynthesis by H16 (3.0–3.1 g PHA/L), as seen in a previous study (10). No effect of soybean oil concentration (0.5% or 1.0%) was observed on cell growth and PHA yield for H16 and PHB⁻4/pJRDEE32d13. The strain H16C_{Ac} also exhibited P(3HB-*co*-3HHx)-biosynthetic ability via β-oxidation owing to the function of PHA synthase from *A. caviae*. This strain could grow as well as wild strain on 0.5% soybean oil or octanoate (3.7 g dry cells/L), and interestingly, the final cell yield (5.2 g dry cells/L) reached to 1.4 fold larger than that of H16 on 1% soybean oil. PHA content within the cells was also increased up to 89 wt%, resulted in improved PHA productivity of H16C_{Ac}. However, the 3HHx fraction in the copolyester chains synthesized by H16C_{Ac} (3.9 mol% from octanoate and 0.7 mol% from soybean oil) was decreased when compared with those by PHB⁻4/pJRDEE32d13 (13.0 mol% and 2.5–2.7 mol%, respectively). The strain H16ΔC/pJRDEE32d13 also produced P(3HB) from fructose and P(3HB-*co*-3HHx) from octanoate or soybean oil, and unexpectedly, its growth and PHA-producing properties were very similar to PHB⁻4/pJRDEE32d13 in spite of higher β-ketothiolase and NADPH-acetoacetyl-CoA reductase activities within this strain.

The engineered *C. necator* strains harboring foreign *phaC*$_{Ac}$ accumulated high-molecular-mass PHAs both from fructose and soybean oil (Table 3). The number average molecular mass (M_n) and the polydispersity (M_w/M_n) of

© 2008 NRC Canada

Table 1. Enzyme activities in *C. necator* strains.

Strain	PHA synthase (U/g)[a]	β-Ketothiolase (U/g)[b]	Acetoacetyl-CoA reductase (U/g)[c]	
			NADH	NADPH
H16	715	3677	664	649
PHB$^-$4	1 (2272)	148	726	40
H16C$_{Ac}$	177	3723	707	662
H16ΔC	2 (546)	986	746	705

Note: Cells were cultivated for 36 h at 30 °C in an MB medium containing 0.5% (*w*/*v*) fructose as a sole carbon source.

[a]Polymerization activity for (*R*)-3HB-CoA. The activities in PHB$^-$4 and H16ΔC harboring pJRDEE32d13 were shown in parentheses.

[b]Cleavage activity for acetoacetyl-CoA to acetyl-CoAs.

[c]NAD(P)H-dependent reduction activity for acetoacetyl-CoA.

Table 2. PHA biosynthesis by wild and recombinant strains of *C. necator.*

Strain	Carbon source[a]	DCM[b] (g/L)	PHA[c] (g/L)	Content[c] (wt%)	Composition[c] (mol%)	
					C4	C6
H16	0.5% fructose	2.0±0.17	1.2±0.08	60±2.7	100	0
	0.5% octanoate	4.2±0.05	3.7±0.07	87±0.6	100	0
	0.5% soybean oil	3.6±0.00	3.0±0.04	82±0.6	100	0
	1.0% soybean oil	3.7±0.14	3.1±0.22	84±2.5	100	0
PHB$^-$4/pJRDEE32d13	0.5% fructose	1.9±0.07	1.1±0.10	61±2.0	100	0
	0.5% octanoate	4.4±0.22	3.7±0.29	84±1.6	87.0±0.5	13.0±0.5
	0.5% soybean oil	2.5±0.15	1.9±0.16	77±0.9	97.5±0.0	2.5±0.0
	1.0% soybean oil	2.7±0.04	2.0±0.13	75±2.8	97.3±0.1	2.7±0.1
H16C$_{Ac}$	0.5% fructose	2.0±0.08	1.2±0.05	60±1.0	100	0
	0.5% octanoate	4.5±0.14	3.8±0.09	86±1.3	96.1±0.4	3.9±0.4
	0.5% soybean oil	3.7±0.07	3.1±0.15	85±2.6	99.3±0.0	0.7±0.0
	1.0% soybean oil	5.2±0.32	4.7±0.14	89±3.2	99.3±0.0	0.7±0.0
H16ΔC/pJRDEE32d13	0.5% fructose	1.8±0.24	1.0±0.03	57±1.3	100	0
	0.5% octanoate	4.1±0.20	3.6±0.32	87±2.2	89.2±0.7	10.8±0.7
	0.5% soybean oil	2.6±0.10	1.8±0.13	72±3.1	98.0±0.0	2.0±0.0
	1.0% soybean oil	2.4±0.14	1.7±0.18	73±1.9	98.0±0.1	2.0±0.0

Note: Standard deviation was shown with each value (n = 3). Cells were cultivated for 72 h at 30 °C in an MB medium containing carbon source represented.

[a]0.5% (*w*/*v*) fructose and 0.5%–1.0% (*v*/*v*) soybean oil were added at the start of cultivation, and 0.1% (*w*/*v*) sodium octanoate was added at 12 h intervals from 0 to 48 h.

[b]Dry cell mass.

[c]Determined by methanolysis/GC analysis of the dried cells or ^{1}H NMR analysis of the extracted polymers.

Table 3. Molecular mass of PHAs produced by wild and recombinant strains of *C. necator.*

PHA Sample[a]	Strain	Carbon source[b]	Molecular mass[c]		
			M_n [× 10^5 Da]	M_w [× 10^5 Da]	M_w/M_n
P(3HB)	H16	Fructose	9.1	27.2	2.99
P(3HB)	H16	Soybean oil	5.3	8.6	1.61
P(3HB)	PHB$^-$4/pJRDEE32d13	Fructose	8.2	18.8	2.29
P(3HB-*co*-2.7 mol% 3HHx)	PHB$^-$4/pJRDEE32d13	Soybean oil	4.4	8.7	1.97
P(3HB)	H16C$_{Ac}$	Fructose	8.9	19.6	2.19
P(3HB-*co*-0.7 mol% 3HHx)	H16C$_{Ac}$	Soybean oil	6.9	14.1	2.05
P(3HB)	H16ΔC/pJRDEE32d13	Fructose	8.7	21.7	2.49
P(3HB-*co*-2.0 mol% 3HHx)	H16ΔC/pJRDEE32d13	Soybean oil	6.4	14.4	2.24

[a]PHAs were extracted and purified from the dried cells shown in Table 2.

[b]Concentration of fructose and soybean oil were 0.5% (*w*/*v*) and 1% (*v*/*v*), respectively.

[c]Determined by gel-permeation chromatography.

© 2008 NRC Canada

P(3HB-*co*-3HHx) copolyesters from soybean oil were within 4.4–6.9 × 10^5 and 2.0–2.2, respectively, which were slightly lower than those of P(3HB) homopolymer from fructose (8.2–8.9 × 10^5 and 2.3–2.5, respectively). These values were comparable to those of P(3HB) produced by wild strain of *C. necator*.

Discussion

This study aimed to establish new recombinants for biosynthesis of P(3HB-*co*-3HHx) copolyester, overcoming the drawback of previous PHB⁻4-derived strains. We first found that *pha* operon in PHB⁻4 has a single nonsense mutation within $phaC_{Cn}$. Inactivation of $phaC_{Cn}$ gene by the incomplete translation coincided with the results of enzyme assay (Table 1), and the PHA-negative phenotype of PHB⁻4 was obviously caused by the lack of PHA synthase. Despite the presence of intact $phaAB_{Cn}$ genes, β-ketothiolase and NADPH-dependent acetoacetyl-CoA redutase activities were drastically decreased in PHB⁻4. One feasible explanation for this phenomenon could potentially be a polar effect of the mutation in $phaC_{Cn}$ on expression of downstream $phaAB_{Cn}$ genes. Otherwise, we cannot exclude the possibility that regulation system for expression of *pha* genes or for activities of the corresponding enzymes might be modified by random mutagenesis. It should be considered that β-ketothiolase and NADPH-acetoacetyl-CoA reductase activities were actually low but not completely abolished in PHB⁻4. This strain would be a leaky mutant for expression of $phaAB_{Cn}$, or possess other genes responsible for these activities. Indeed, recent whole-genome analysis of *C. necator* H16 revealed the presence of multiple homologs of *phaA* and *phaB* (18). Interestingly, recombinant PHB⁻4 strains expressing PHA synthase alone still had high ability to produce PHA even from fructose, despite the low thiolase and reductase activities (Table 2 and previous studies (9, 10, 13–15)). These facts suggested that, in *C. necator* cells, such low activities for these two steps were enough to provide (*R*)-3HB-CoA from acetyl-CoA precursor toward PHA biosynthesis.

We initially estimated that the lower growth ability of PHB⁻4 on vegetable oils might be caused by some unintended mutations against genes involved in incorporation and (or) degradation of triacylglycerols, because PHB⁻4/pJRDEE32d13 showed comparable growth and PHA accumulation to H16 on fructose and octanoate. Therefore, $H16C_{Ac}$ was constructed by replacing original PHA synthase gene on *C. necator* chromosome by $phaC_{Ac}$. This strain actually showed excellent growth and PHA productivity on soybean oil, which was assumed to be due to the absence of unknown mutation on the chromosome. However, this assumption was not supported by the fact that the strain H16ΔC/pJRDEE32d13, not having any unintended mutation like $H16C_{Ac}$, showed similar behaviour to PHB⁻4/pJRDEE32d13 in growth and PHA biosynthesis. The common biochemical property of these strains, distinct from H16 and $H16C_{Ac}$, was lower β-ketothiolase activity (Table 1). The activity in H16ΔC (986 U/g) was higher than that in PHB⁻4 (148 U/g), but much lower than those in H16 and $H16C_{Ac}$ (>3000 U/g). Although the reason for the decrease of β-ketothiolase activity in H16ΔC has not been clear, the flanking region between $phaA_{Cn}$ and P_{pha} region created after the $phaC_{Cn}$ deletion may not be suitable for efficient gene expression of $phaA_{Cn}$. The results obtained here suggested that the lower β-ketothiolase activity appeared to be relevant to the diminished growth on vegetable oils. The low interconversion rate between two acetyl-CoA molecules and acetoacetyl-CoA may affect overall efficiency for degradation of long-chain fatty acids through β-oxidation.

In terms of copolyester biosynthesis, $H16C_{Ac}$ and H16ΔC/pJRDEE32d13 accumulated P(3HB-*co*-3HHx) via β-oxidation as well as PHB⁻4/pJRDEE32d13. Among them, $H16C_{Ac}$ incorporated less 3HHx unit into the copolyester chains than the others. That is, the higher β-ketothiolase activity may tend to decrease 3HHx fraction in the copolyester. In *C. necator* cells grown on alkanoates or triacylglycerols, (*R*)-3HHx-CoA would be supplied via β-oxidation by unknown channeling pathway(s), while (*R*)-3HB-CoA can be generated via two possible pathways: channeling from β-oxidation cycles and dimerization of acetyl-CoA. Although flux distribution of the two possible pathways for (*R*)-3HB-CoA formation has not been determined yet in PHA biosynthesis by *C. necator* cells, high β-ketothiolase activity along with high acetoacetyl-CoA reductase activity in $H16C_{Ac}$ was supposed to enhance (*R*)-3HB-CoA formation from acetyl-CoA, leading to relative decrease of (*R*)-3HHx-CoA provision via β-oxidation. Consequently, 3HHx fraction would be decreased in copolyesters produced by $H16C_{Ac}$. Such increase of 3HB fraction was also observed in *Aeromonas hydrophila* and recombinant bacteria harboring *phaC1* from *Pseudomonas* spp. when multi-copies of $phaAB_{Cn}$ were introduced into the cells (19–21). Alternatively, there would be a possibility that low β-ketothiolase activity, which favours thiolysis, may increase intracellular concentration of β-oxidation intermediates of C_6, which would likely promote (*R*)-3HHx-CoA formation via β-oxidation as described previously (22).

The strain $H16C_{Ac}$ constructed here was a superior PHA producer, exhibiting high growth ability on soybean oil, but the physical properties of P(3HB-*co*-3HHx) produced by this strain were inadequate for practical application owing to the too small fraction of longer 3HHx unit. Further metabolic modification is now underway to increase 3HHx fraction into the copolyester chains with the higher productivity.

Materials and methods

Bacterial strains and plasmids

C. necator H16 (DSM428), PHB⁻4 (DSM541) (12), and recombinant strains derived from them were cultivated at 30 °C in a nutrient-rich (NR) medium containing 10 g of meat extract, 10 g of polypeptone, and 2 g of yeast extract in 1 L of distilled water. *E. coli* DH5α and S17–1 (23) were grown at 37 °C on a Luria–Bertani (LB) medium (24). Kanamycin (200 mg/L for *C. necator* and 50 mg/L for *E. coli*) or ampicillin (50 mg/L for *E. coli*) was added to the medium when necessary.

A recombinant plasmid pJRDEE32d13 containing $phaC_{Ac}$ with its native promoter region was reported previously (9). pTA2 (Toyobo) and pK18mobsacB (25) were used for general gene manipulation and homologous recombination of

© 2008 NRC Canada

C. necator, respectively. Transconjugation of *C. necator* with *E. coli* S17–1 harboring mobilizable plasmid was performed as described previously (9).

Construction of recombinant strains

A 5.0 kbp fragment of *pha* operon with its promoter region (P_{pha}-$phaCAB_{Cn}$) and a 1.8 kbp fragment of $phaC_{Ac}$ were amplified using primer sets with *C. necator* H16 genomic DNA and pEE32d1 (9) as a template, respectively. The sequences of primers used are ReP-N, ATGGATCCCGGGCAAGTACCTTGCCGACATC; RePhbB-C, GCCCGGATCCTATGCCCAACAAGGCACTAAG; AcPhaC-Fw2, GGTTCGAATAGTGACGGCAGAGAGACAATCAAATCATGAGCCAACCATCTTATGGC; and AcPhaC-Rv2, AACCTGCAGGCCTGCCGGCGCCGTGCATATGCAAGCGTCATGCGGCGTCCTCCTCTG (underlined sequences indicate BamHI, BamHI, Csp45I, and SbfI, respectively). The amplified fragments were subcloned into pTA2 by using TA-cloning procedure to obtain pTA2CAB (P_{pha}-$phaCAB_{Cn}$) and pTA2C′ ($phaC_{Ac}$). pTA2CAB was digested with Csp45I and SbfI to remove $phaC_{Cn}$ region and then ligated with a 1.8 kbp Csp45I-SbfI restriction fragment of $phaC_{Ac}$ from pTA2C′. The resulting plasmid was digested with BamHI, and the 5.0 kbp fragment containing P_{pha}-$phaC_{Ac}$-$phaAB_{Cn}$ was inserted into pK18mobsacB at the corresponding site to obtain pK18C′AB. For construction of another plasmid pK18AB, Csp45I-SbfI-double digested pTA2CAB was blunted followed by self-ligation and a 3.2 kbp BamHI restriction fragment (P_{pha}-$phaAB_{Cn}$) from the resulting plasmid was inserted into pK18mobsacB.

pK18AB was transferred by conjugation from *E. coli* S17–1 to *C. necator* H16. Transconjugants (pop-in strains), formed by integration of pK18AB into the chromosome by homologous recombination, were selected on Difco Simmons Citrate Agar (BD diagnostics) medium containing 200 mg/L kanamycin at 30 °C for several days. The cells of one isolate were then inoculated onto NR agar medium containing 10% (*w*/*w*) sucrose and cultivated for 48 h at 30 °C for counter selection of pop-out strains after excision of the plasmid region via the second recombination event (25). PCR analysis was carried out to confirm genotype of the sucrose-resistant isolates, and a strain lacking $phaC_{Cn}$, referred as H16ΔC, was selected. The strain $H16C_{Ac}$ with $phaC_{Cn}$::$phaC_{Ac}$ genotype was also constructed from H16ΔC by using pK18C′AB according to the similar procedure. The sequences of primers used for PCR analysis (Fig. 1) are ReP-f2, GTGCGGTCGAGGGCTTCCAG; RePhbA-Rv, CGCGGTGCGGGCGGCGGATA; RePhbC-f5, CTGGGCGATACGTCAAAGCC; and AcPhaC-f4, GCAGGGCATGAAGCTGTTTG.

Production and characterization of PHA

PHA production by *C. necator* strains was carried out on a reciprocal shaker (115 strokes/min) at 30 °C in 500 mL flasks with 100 mL of nitrogen-limited mineral salts (MB) medium, which was composed of 0.9 g of $Na_2HPO_4{\cdot}12H_2O$, 0.15 g of KH_2PO_4, 0.05 g of NH_4Cl, 0.02 g of $MgSO_4{\cdot}7H_2O$, and 0.1 mL of trace-element solution (26) in 100 mL of distilled water. A filter-sterilized solution of fructose or octanoate was added to the medium at a final concentration of 0.5% (*w*/*v*), and kanamycin was added at 50 mg/L when necessary. Soybean oil was directly added to the medium at 0.5 or 1.0% (*v*/*v*). After the cultivation for 72 h, cells were harvested, washed with distilled water, and then lyophilized.

PHA content within cells was determined by gas chromatography (GC) after methanolysis of the dried cells in the presence of 15% sulfuric acid, as described previously (26). The intracellular polymer accumulated was extracted with stirring for 72 h at room temperature, purified by precipitation with methanol, and then filtered with poly(tetrafluoroethylene) (PTFE) membrane to remove the cell debris. Molecular mass measurements by gel-permeation chromatography (17, 27) and ^{1}H NMR analysis were performed as described previously (8).

Enzyme assay

C. necator cells grown on fructose at 30 °C for 36 h were washed and resuspended in 50 mmol/L Tris-HCl buffer (pH 8.0). The cells were disrupted by sonication for 3 min and then centrifuged with low speed (1500g, 5 min, 4 °C) to obtain whole-cell extract containing PHA granules. PHA synthase activity in the whole-cell extracts was determined by a spectroscopic assay using chemically synthesized (*R*)-3HB-CoA and 5,5′-dithiobis(2-nitrobenzoic acid) (28). The whole-cell extract was further centrifuged with high speed (12 000g, 20 min, 4 °C) to obtain soluble protein fraction. β-Ketothiolase was assayed in 400 μL of 50 mmol/L Tris-HCl buffer (pH 8.5) containing 0.1 mmol/L acetoacetyl-CoA, 0.1 mmol/L CoA-3Na, 25 mmol/L $MgCl_2$, and the decrease in absorbance at 304 nm derived from Mg^{2+}-acetoacetyl-CoA complex was recorded (29, 30). Acetoacetyl-CoA reductase was assayed in 400 μL of 50 mmol/L Tris-HCl buffer (pH 8.0) containing 0.1 mmol/L acetoacetyl-CoA, 0.2 mmol/L NAD(P)H, and the decrease in absorbance of NAD(P)H was measured at 340 nm (31). The extinction coefficients of Mg^{2+}-acetoacetyl-CoA complex at 304 nm and NAD(P)H at 340 nm were taken to be 19.5×10^3 mol^{-1} L cm^{-1} and 6.22×10^3 mol^{-1} L cm^{-1}, respectively (29).

Acknowledgements

We thank Dr. T. Tsuge (Department of Innovative and Engineered Materials, Interdisciplinary Graduate School of Science and Engineering, Tokyo Institute of Technology, Japan) for his kind measurement of molecular mass of PHAs by gel-permeation chromatography. This study was supported by Industrial Technology Research Grant Program in 2005 from New Energy and Industrial Technology Development Organization (NEDO), KAKENHI (Grant-in-Aid for Scientific Research) on Priority Areas Applied Genomics from the Ministry of Education, Culture, Sports, Science and Technology, and Research Grant from Institute of Fermentation, Osaka, of Japan.

References

1. Y. Doi. Microbial polyesters. VCH Publishers, New York. 1990.
2. A. Steinbüchel. PHB and other polyhydroxyalkanoic acids. VCH Publishers. Weinheim, Germany. 1996.

© 2008 NRC Canada

3. L.L. Madison and G.W. Huisman. Microbiol. Mol. Biol. Rev. **63**, 21 (1999).
4. K. Sudesh and Y. Doi. Polym. Adv. Technol. **11**, 865 (2000).
5. B.H. Rehm. Biochem. J. **376**, 15 (2003).
6. A. Steinbüchel and H.E. Valentin. FEMS Microbiol. Lett. **128**, 219 (1995).
7. E. Shimamura, K. Kasuya, G. Kobayashi, T. Shiotani, Y. Shima, and Y. Doi. Macromolecules, **27**, 878 (1994).
8. Y. Doi, S. Kitamura, and H. Abe. Macromolecules, **28**, 4822 (1995).
9. T. Fukui and Y. Doi. J. Bacteriol. **179**, 4821 (1997).
10. T. Fukui and Y. Doi. Appl. Microbiol. Biotechnol. **49**, 333 (1998).
11. T. Fukui, T. Shiomi, and Y. Doi. J. Bacteriol. **180**, 667 (1998).
12. H.G. Schlegel, R. Lafferty, and I. Krauss. Arch. Mikrobiol. **71**, 283 (1970).
13. M. Liebergesell and A. Steinbüchel. Eur. J. Biochem. **209**, 135 (1992).
14. M. Liebergesell and A. Steinbüchel. Appl. Microbiol. Biotechnol. **38**, 493 (1993).
15. M. Liebergesell, F. Mayer, and A. Steinbüchel. Appl. Microbiol. Biotechnol. **40**, 292 (1993).
16. T. Fukui, T. Kichise, T. Iwata, and Y. Doi. Biomacromolecules, **2**, 148 (2001).
17. T. Fukui, H. Abe, and Y. Doi. Biomacromolecules, **3**, 618 (2002).
18. A. Pohlmann, W.F. Fricke, F. Reinecke, B. Kusian, H. Liesegang, R. Cramm, T. Eitinger, C. Ewering, M. Pötter, E. Schwartz, A. Strittmatter, I. Voβ, G. Gottschalk, A. Steinbüchel, B. Friedrich, and B. Bowien. Nat. Biotechnol. **24**, 1257 (2006).
19. H. Matsusaki, H. Abe, K. Taguchi, T. Fukui, and Y. Doi. Appl. Microbiol. Biotechnol. **53**, 401 (2000).
20. H. Matsusaki, H. Abe, and Y. Doi. Biomacromolecules, **1**, 17 (2000).
21. Y.Z. Qiu, J. Han, and G.Q. Chen. Appl. Microbiol. Biotechnol. **69**, 537 (2006).
22. D. Dennis, M. McCoy, A. Stangl, H.E. Valentin, and Z. Wu. J. Biotechnol. **64**, 177 (1998).
23. R. Simon, U. Priefer, and A. Pühler. Bio/technology, **1**, 784 (1983).
24. J. Sambrook and D.W. Russell. Molecular cloning: A laboratory manual. 3rd ed. Cold Spring Harbor Laboratory Press. Cold Spring Harbor, New York. 2001.
25. A. Schäfer, A. Tauch, W. Jäger, J. Kalinowski, G. Thierbach, and A. Pühler. Gene, **145**, 69 (1994).
26. M. Kato, H.J. Bao, C.K. Kang, T. Fukui, and Y. Doi. Appl. Microbiol. Biotechnol. **45**, 363 (1996).
27. S. Sato, C.T. Nomura, H. Abe, Y. Doi, and T. Tsuge. J. Biosci. Bioeng. **103**, 38 (2007).
28. H.E. Valentin and A. Steinbüchel. Appl. Microbiol. Biotechnol. **40**, 699 (1994).
29. S. Slater, K.L. Houmiel, M. Tran, T.A. Mitsky, N.B. Taylor, S.R. Padgette, and K.J. Gruys. J. Bacteriol. **180**, 1979 (1998).
30. T. Nishimura, T. Saito, and K. Tomita. Arch. Microbiol. **116**, 21 (1978).
31. G.W. Haywood, A.J. Anderson, L. Chu, and E.A. Dawes. FEMS Microbiol. Lett. **52**, 259 (1988).

© 2008 NRC Canada

REVIEW / SYNTHÈSE

Poly(hydroxyalkanoates): Biorefinery polymers with a whole range of applications. The work of Robert H. Marchessault[1]

William J. Orts, Geoffrey A.R. Nobes, Jumpei Kawada, Sophie Nguyen, Ga-er Yu, and François Ravenelle

Abstract: This review describes the characterization and application of poly(hydroxyalkanoates), PHAs, a remarkable family of natural polyesters with a wide array of useful properties and potential applications. It places specific emphasis on the work of Robert H. Marchessault and his many colleagues outlining how Marchessault's body of work both shaped the field and complemented the work of his contemporaries. Particular attention will focus on the "rediscovery" of poly(β-hydroxybutyrate), PHB, the first PHA to be discovered, from the late 1950s onward, highlighting some of the historical aspects of PHA's path toward commercial applications. It will also cover why this class of materials is so unique, including PHA structure–properties relationships, its unique crystalline behaviour, in vivo – in vitro synthesis and degradation, and PHA-graft-copolymers.

Key words: poly(hydroxyalkanoate), PHA, poly(β-hydroxybutyrate), PHB, biopolymers, bacterial polyester, random copolymers, polymer single crystals, graft copolymers.

Résumé : Dans cette revue, on décrit la caractérisation et l'application des polyhydroxyalcanoates, PHA, une famille remarquable de polyesters naturels qui possèdent une grande variété de propriétés utiles et d'applications potentielles. On met l'accent sur les travaux de Robert H. Marchessault et de ses nombreux collaborateurs, en exposant les grandes lignes de la façon dont ces travaux ont orienté le domaine tout en apportant un complément à ceux de ses contemporains. On porte une attention particulière sur la "redécouverte" du poly(β-hydroxybutyrate), PHB, le premier PHA à être découvert depuis les années 1950 et on met l'accent sur quelques-uns des aspects historiques qui ont conduit les PHA vers des applications commerciales. On explicitera aussi pourquoi cette classe de matériaux est si unique, y compris les relations structure/propriétés des PHA, leur comportement cristallin unique, leur synthèse et leur dégradation in vivo/in vitro ainsi que les copolymères PHA greffés.

Mots clés : polyhydroxyalcanoate, PHA, poly(β-hydroxybutyrate), PHB; biopolymères, polyesters bactéricides, copolymères aléatoires, cristaux uniques de polymères, copolymères greffés.

[Traduit par la Rédaction]

Received 8 December 2007. Accepted 13 February 2008. Published on the NRC Research Press Web site at canjchem.nrc.ca on 13 May 2008.

This paper is dedicated to Robert H. Marchessault in recognition of his many contributions to polysaccharide and biopolymer chemistry.

W.J. Orts[2]. United States Department of Agriculture, ARS, WRRC, 800 Buchanan St., Albany, CA 94710, USA.
G.A.R. Nobes. Tate & Lyle, 2200 East Eldorado Street, Decatur, IL 62525, USA.
J. Kawada. Toyota Central R&D Laboratories, Organic Materials Lab., 41–1, Aza Yokomichi, Nagakute-cho, Aichi-ken 480–1192, Japan.
S. Nguyen. Bio Syntech Canada Inc., 475 Armand-Frappier Blvd., Laval, QC H7V 4B3, Canada.
G. Yu. Advanced Polymer Materials Inc., 5020 Fairway, Suite 224, Montreal, QC H8T 1B8, Canada.
F. Ravenelle. LaboPharm, 480 Boul. Armand-Frappier, Laval, QC H7V 4B4, Canada.

[1]This article is part of a Special Issue dedicated to Professor R. Marchessault.
[2]Corresponding author (e-mail: orts@pw.usda.gov).

 doi:10.1139/V08-050 © 2008 NRC Canada

Introduction

In the late 1980s, Marchessault and colleagues discussed the wide range of potential commercial uses for poly(β-hydroxyalkanoates), PHAs, in a paper that described "biorefinery polymers in search of applications" (1). Like many visionaries, Marchessault was ahead of his time, but his career-long passion and technically advanced view of PHAs have proven prescient. This year, for example, the US firm Metabolix has joined forces with agricultural processing giant, Archer Daniels Midland (ADM), to construct a $200 MM PHA biorefinery in Iowa, with initial commercial production in 2008 set to boost PHA production in the US by 110 million pounds per year (2).

The term "biorefinery", a word not widely used in the 1980s, also hit the mark. Biorefineries have only recently emerged into the public consciousness with the rapid ascent of ethanol production. Bacterial PHA, as Marchessault et al. (1) aptly implied, is the perfect biorefinery complement to ethanol in that it adds much needed flexibility and value to biorefinery operations. The Metabolix–ADM plant not only hedges ADM's bet on ethanol production, but it also meets rising demand for "green plastics", polymers that displace petroleum, minimize greenhouse gases, and are environmentally friendly. PHAs provide biodegradable, sustainable materials from a wide array of biomass sources.

PHAs are a family of polyesters, outlined in Scheme 1, that are generally produced by fermentation, but can also be synthesized or produced in transgenic plants. Their remarkable range of properties results from the variability in the R substituent off the β carbon, which can range from a simple methyl group in the case of poly(β-hydroxybutyrate), PHB, ethyl for poly(β-hydroxyvalerate), PHV, to long chain moieties, including rings, double bonds, and branched chains. As the number of side-chain carbons increases, PHAs become increasingly elastomeric.

The fact that bacteria could produce polyesters was discovered by Lemoigne in the mid-1920s (3, 4) but was virtually unknown to chemists and biochemists until its "rediscovery" in the 1950s and early 1960s. The history of PHAs, and specifically poly(β-hydroxybutyrate), PHB, has been shaped by a series of events (3) or "eras" as follows: (*i*) discovery and characterization of PHB by Lemoigne (4–9), (*ii*) rediscovery of PHB in the 1950s and early 1960s (3), (*iii*) commercial exploitation of PHAs by ICI in the early to mid-1980s (10–11), (*iv*) discovery that PHAs represented a family of more than a 100 different aliphatic polyesters that could be tailored based on feedstock and microbe selection (12–18), (*v*) application of genetic engineering to produce PHAs in *E. coli* and other optimized strains (18–22), and (*vi*) production of PHAs in plant tissue by insertion of genes coded for PHA synthesis (23–24).

The rediscovery of PHA in the 1950s and 1960s paved the way for multiple significant events. For example, the biotechnological advances toward improved microbial production of PHAs in genetically improved *E. coli*, which sparked commercialization efforts by Metabolix and later, Procter and Gamble (25), were the direct offshoot of the elegant biochemistry describing PHA biosynthesis as part of the β-oxidation cycle put forth by Weibull (26), Williamson and Wilkinson (27), Doudoroff and colleagues (28–29), and

Scheme 1. Structure of PHA.

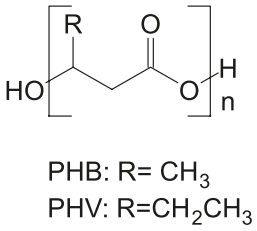

Merrick and colleagues (30–32). Subsequent production of PHAs in transgenic plants by Somerville and colleagues (23–24) and then Monsanto during the 1990s relied on knowledge of PHB synthase enzymes and the specific genes encoded for their production.

This review will not be an all-encompassing overview of the PHA field, a task that could be best described as Herculean, and one that has been covered before (3). Rather, it will focus on the rediscovery of PHB and PHAs from the late 1950s onward, placing specific emphasis on the work of Marchessault and colleagues. Marchessault's body of work both shaped the field and complemented the work of his contemporaries. As such, this review will highlight some of the historical aspects of PHAs rediscovery. It will review why this class of materials is so unique, including PHA structure–properties relationships, its unique crystalline behaviour, in vivo – in vitro synthesis of granules, PHA degradation mechanisms, and PHA graft-copolymers.

Brief history of PHB and its rediscovery

PHB homopolymer was discovered in the mid-twenties by Maurice Lemoigne and summarized in papers that were clearly ahead of their time (4–9). In attempts to discover why certain soil bacteria cause acidification of their media broth during fermentation, Lemoigne obtained material that was characterized as a "polymer of 3-hydroxybutyric acid" (4). This material accumulates in cells during the absence of critical nutrients by converting excess carbon into aliphatic polyester (Scheme 1). During the next 30 years, Lemoigne and co-workers characterized this unique material, correlating properties to its high molecular mass and even suggesting that it was the result of in vivo "dehydration polymerization" (9), concepts that were far-reaching in their scope.

Despite such remarkable vision, the work of Lemoigne remained relatively obscure until the late 1950s and early 1960s. Almost simultaneously, several research groups described the biosynthetic routes toward PHB accumulation within bacterial cells (26–29), while chemists began to discover its unique polymer properties.

A significant part of the re-awakening of PHB-related work stemmed from the discovery by Doudoroff and Stanier at UC Berkeley that poly(β-hydroxybutyrate) was the product of oxidative assimilation of organic substrates that were metabolized via acetate or butyrate (28–29). Michael Doudoroff, a pioneer in microbial bioenergetics (as exemplified by the critical importance of the well-known Entner–Doudoroff pathway describing the fundamentals of glucose-to-pyruvate conversion in bacteria), inspired Joseph Merrick to explore the biosynthesis and breakdown mechanisms of

© 2008 NRC Canada

PHB (30), work that required new substrates and new methodologies. For this work, Merrick (*i*) prepared radioactive PHB by growing cells of *Bacillus megaterium* in the presence of radioactive acetate, (*ii*) isolated labeled β-hydroxybutryic acid, (*iii*) synthesized the CoA derivative by a mixed anhydride procedure, and (*iv*) ultimately used these tools to describe many aspects of enzymatic synthesis of PHB (31–32).

Merrick and Doudoroff established that PHB synthase, which catalyzes the polymerization of PHB from β-hydroxybutyryl-CoA, was located on PHB granules (isolated from either *R. rubrum* or *B. megaterium* in his study). More surprisingly, granules from *R. rubrum* were also "self-digesting", suggesting that these inclusions were acting as carbon sinks, repositories for excess carbon as energy reserve (32), similar in function to starch in plants and fats in mammals.

When Joseph Merrick left Doudoroff's lab at UC Berkeley and moved east to join the Microbiology Department at Syracuse University, he inspired a group of other biochemists and microbiologists within the department – Donald Lundgren, Ralph Schlepecky, and Richard Alper. This group made a concerted effort to advance the fundamental understanding of this carbon-reserve material (33–35), and soon enlisted the help of a relative newcomer to the University, Chemistry Professor R.H. Marchessault, to characterize their "waxy" materials (36). Over the next ten years, this Syracuse "gang of four" provided leading multidisciplinary research on PHB by combining world-class biochemistry and microbiology with important polymer research.

In 1962, Marchessault and colleagues began a program to elucidate the structure–properties relationship of these unique materials (36), a research quest that helped to define Marchessault's career and continues to bear fruit. News of the commercial exploitation of PHB started in 1963 when *Chemistry and Engineering News* published an article concerning the development by W.R. Grace & Co. of a biopolymer thermoplastic material, which was produced by fermentation. The article described how PHB was extracted from bacterial cells in the form of sub-micron granules (1 micron = 1 μm), i.e., "storage polymers", similar to starch granules from corn, wheat, and other small grains. Treatment of dried cells with acetone followed by chloroform extraction resulted in a polymer yield of nearly 80%. As the story goes (36), Francis Werber, VP of Research at Grace and Co. had hired Jim Baptist, their first biochemist, to study fruit ripening inside cartons sealed with polyvinyl films. Instead, Jim Baptist convinced Werber that academic breakthroughs describing stereoregular PHB from bacteria were a source of marketable polyester. PHB was a film-forming, hydrophobic, biocompatible thermoplastic similar to polypropylene, and offered the added benefit of biodegradability (37).

Over the next three to four years. Werber and Baptist took out several patents on PHB (38, 39), produced landmark measurements on the mechanical properties of PHB-derived films and moldings, and showed that PHB is remarkably stereoregular, exhibiting > 99% isotacticity. PHB film properties rivaled those of polypropylene; however, they soon realized that large-scale processing (part-forming) would be hampered by the thermal instability of PHB. With a melting point of 170–180 °C, and a degradation point of ~190 °C, PHB's processing window is very limited, a drawback that ultimately caused termination of the project at Grace.

Despite this setback in establishing PHB as a commodity polyester, researchers in industry and academia frequently pushed its potential in specialty applications, with some stories verging on the heroic. For example, in one verified story (36), Baptist wanted to convince the world that PHB could be applied as a bio-absorbable suture. He created a PHB fiber, slashed his own arm with a scalpel, and then sutured the cut with this fiber. Application of absorbable sutures from PHB was mentioned in a patent by W.R. Grace & Co. (39), establishing PHB as a forerunner to the highly profitable absorbable sutures of polylactide and glycolide that were marketed years later by Ethicon and Davis.

As a result of Grace's inability to establish large markets for PHB, Marchessault and colleagues at Syracuse were given pound quantities of Grace's discarded PHB material. This "leftover" PHB supported multiple research projects for years (33–36). The Syracuse team quickly produced data such as dilute solution molecular masses, optical rotation, differential scanning calorimetery results, X-ray diffractograms, crystalline structures (via molecular modeling), electron micrographs, and electron diffractograms of polymer single crystals (33–36).

One significant result of the biosynthetic origin of PHB is its optical activity (40). When polarized light hits films or solutions of PHB, the plane of the polarized light will rotate a measurable degree. This arises because the β-carbon in every monomer is perfectly stereoregular; nature always aligns this moiety in the *R* (*rectus*) optical configuration. Such stereoregularity leads to a high level of crystallinity, rapid crystallization, and multiple unique properties.

Furthermore, PHB crystals have no center of symmetry; thus, they exhibit piezoelectric properties (41). This means that as PHB crystals are deformed, the direction of their average ensemble dipole moment is changed, resulting in a change in polarization. This in turn changes the surface charge as a direct response to the deformation. In practical terms, this means that PHB materials, when deformed with shear in a voltage field, will alter the electric field significantly (41). Piezoelectricity is typical of many biological systems, but generally not found in most polymers.

The unique crystalline behaviour of PHB and its copolymers

PHB homopolymer is a semi-crystalline thermoplastic material that becomes viscous and moldable above its melting temperature. Upon cooling, it crystallizes rapidly to a plastic material, which exhibits high crystallinity of 60%–80% (42–46) with properties that are often compared to those of polypropylene. PHB homopolymer has had limited commercial success, though, because it is relatively stiff and brittle. Brittleness is largely due to the formation of large, uninterrupted spherulites that create large crystalline domains, i.e., it crystallizes too readily.

X-ray fiber diffraction and data analysis from K. Okamura's thesis (47) from Marchessault's lab in Syracuse established the helical nature and pitch of the PHB crystalline unit cell,

© 2008 NRC Canada

Table 1. PHB unit-cell parameters and packing energy (47–51).

	Cell dimension (nm)			Packing energy (kcal mol^{-1})			
Form	*a*	*b*	*c*	van der Waals	C.E.[a]	Total	Reference
α	5.76	13.20	5.96	–28.7	–13.5	–42.2	(48)
α	5.76	13.20	5.96	–28.5	–14.7	–43.2	(49)
α	5.73	13.14	5.93	–29.1	–47.4	–76.5	(50)
β	—	—	4.6	—	—	—	(51)

[a]C.E.: chemical potential energy field.

Table 2. Properties of P(3HB-*co*-3HV) copolymers (derived from ref. 10 and references therein).

P(3HB-*co*-3HV) mol% HV	T_{melt} (°C)	T_g (°C)	Young's modulus (GPa)	Tensile strength (MPa)	Notched izod impact strength (Jm^{-1})
0	179	10	3.5	40	50
3	170	8	2.9	38	60
9	162	6	1.9	37	95
14	150	4	1.5	35	120
20	145	–1	1.2	32	200
25	137	–6	0.7	30	400

with corresponding two-fold symmetry. No intramolecular hydrogen bonds are needed to stabilize the helix, as in proteins; but, rather, PHB relies on bipolar interaction between continuous anti-parallel helical chains, which are stabilized via their ester moieties.

Four separate structural models have been published over the years (47–50), with close agreement among these differing models, as outlined in Table 1. These data show remarkable agreement in the three unit-cell measurements, *a*, *b*, and *c*, which have been derived from X-ray diffraction as well as electron diffraction (1). Recent analysis of these models by Pazur et al. (51) shows that the Brukner model (50) based on Rietfeld analysis of PHB X-ray powder traces is the most favoured structure. Interestingly, it also confirms how close to the mark Okamura was in his original Syracuse thesis work in 1967 (47), a model that was improved in 1972 by Cornibert and Marchessault (48) via Marchessault's sabbatical work in Strasbourg.

The high degree of crystallinity, high melting temperature, brittleness, and low degradation temperature restricted the commercial potential for PHB. A major breakthrough toward commercialization was the development by ICI of a family of PHA co-polyesters (10–11). Wallen and Rohwedder (12), two researchers from the USDA labs in Peoria, IL, were the first to note that PHB-producing bacteria could generate other related copolymers. In careful analysis of polyester production in wastewater sludge, they noticed other polyester moieties, specifically poly(β-hydroxybutyrate-*co*-β-hydroxyvalerate), P(3HB-*co*-3HV), the valerate-based copolymer of PHB.

P(3HB-*co*-3HV) copolymers, commercialized by ICI in the 1980s, and trademarked under the brand, Biopol©, were derived from *Ralstonia eutropha* (formerly *Alcaligenes eutrophus*). The importance of the ICI copolyester family of products was to show that PHAs could be manufactured with a whole range of properties, varying in toughness, flexibility, melting temperature, impact strength, and processing requirements. The range of properties outlined in Table 2 could be tailored to fit market needs, implying wide commercial applicability. Furthermore, as the biosynthetic pathways became better understood, the importance of oxygen and phosphorous starvation, rather than nitrogen limitation, in the growth medium allowed for higher yields of P(3HB-*co*-3HV), as high as 85%–90% (on a dry mass basis).

ICI's commercialization of Biopol resulted in a new awakening of PHA-related research, with ground-breaking results by P. Barham and colleagues (Bristol, UK), Y. Doi (Riken, Tokyo), and R.H. Marchessault. By the 1980s, the "gang of four" at Syracuse had long broken up, first, with the move of Joe Merrick from Syracuse to a faculty position in Buffalo and then with the death of Lundgren in 1968. Marchessault had also moved on, first to a successful stint at Université de Montréal, and then to the Xerox Research Centre of Canada, XRCC, near Toronto. At XRCC, Marchessault led and mentored a team of diverse senior researchers and was able to remain active in biopolymer research at XRCC by convincing Xerox Corp that someday biodegradable materials were needed as "green alternatives" to inks, paper coatings, and fibers.

The XRCC team, along with prominent collaborators from several Canadian universities, including David Holden (Waterloo), Colin Fyfe (Guelph), and Jim Guillet (Toronto), was the first to define and characterize the unique isodimorphic behaviour of P(3HB-*co*-3HV); research that exemplified the world-class biopolymer research carried out in Canada at that time. Isodimorphism describes co-crystallization, in which P(3HB-*co*-3HV) maintains a high degree of crystallinity throughout all compositions of 3HV comonomer addition (42–43). For most typical random copolymers, the random addition of a "foreign" comonomer would usually disrupt crystallinity, thus lowering melting temperatures and increasing flexibility. Similar to typical random copolymers, P(3HB-*co*-3HV) exhibits a drop in melting temperature and greater flexibility with increasing

© 2008 NRC Canada

3HV composition (see Table 2). However, it also exhibits a high degree of crystallinity (60%–80%) at all comonomer compositions (42–46, 51–53).

P(3HB-*co*-3HV) fits the relatively rare criteria outlined by Allegra and Bassi (54) for isodimorphism. The monomers are similar in size, and their crystalline conformations are roughly similar; thus, the crystalline lattice of PHB can accommodate 3HV comonomer units, and the PHV lattice can accommodate 3HB comonomer units. A statistical model of this behaviour was then presented (55) that describes melting-point depression data that varies depending on the degree to which the "other" comonomer is included in the crystalline domain. For P(3HB-*co*-3HV) isodimorphic random copolymers, it predicts a pseudo-eutectic depression as outlined in Fig. 1.

Figure 1 includes melting temperature (T_m) and heat of fusion (ΔH) data from bacterial and synthetic copolymers over the entire range of 3HV comonomer composition. This figure was derived from data established by Bloembergen et al. (42) who synthesized higher 3HV-containing copolymers, i.e., synthetic analogs of the bacterial copolyesters. The melting temperature trend shows a pseudo-eutectic behaviour, a pattern that was subsequently confirmed in more detail using a full range of bacterial P(3HB-*co*-3HV) samples (45).

In Fig. 1, T_m decreases until roughly 35–40 mol% 3HV and then increases at higher 3HV compositions. On one side of the pseudo-eutectic point, below ~40% 3HV, the crystalline lattice is that of PHB, while at higher 3HV compositions, the crystalline structure is that of PHV.

When isodimorphism was examined for melt-crystallized systems (43) or for solvent-derived crystals (1), the unit-cell parameters varied as 3HV composition varied. The **a**-parameter of the unit cell undergoes a small linear increase with increasing 3HV content up to the pseudo-eutectic point, i.e., it "accommodates" the larger 3HV comonomer into the PHB-type lattice structure with a small expansion in its fundamental dimensions.

How does isodimorphism affect crystallization rates and what factors are involved? Barham and colleagues (56–59) had already utilized PHB as a model system to study homogeneous polymer crystallization and the role of nucleation. Bacterial PHB, with 100% isotacticity, i.e., complete stereoregularity, exhibited ideal homogeneous polymer crystallization based on individual nucleation "events" resulting in large "equilibrium" crystals (57). In contrast, for the random copolymer, P(3HB-*co*-3HV), it was surmised that non-equilibrium crystallization was involved. The partitioning of 3HV units between the crystalline and non-crystalline domains depends on crystallization temperature and the rate of crystallization. The slower the crystallization rate, therefore, the more likely that equilibrium conditions would be attained; thus, energy minimization considerations will work towards excluding the "other" comonomer from the crystalline lattice. This means that at lower 3HV concentrations, below the pseudo-eutectic where the PHB crystal structure is present, the composition of 3HV in the crystalline domain will be lower than the average composition of that entire sample. When the 3HV comonomers are included in the PHB-type lattice, they will result in "less perfect" crystals with more defects (46), smaller crystalline domains, and less brittleness (see Table 2).

Fig. 1. Variation of melting point (T_m) and enthalpy of fusion (ΔH_f) with composition of P(3HB) of bacteria origin (solid circles) and fractionated synthetic samples (open circles).

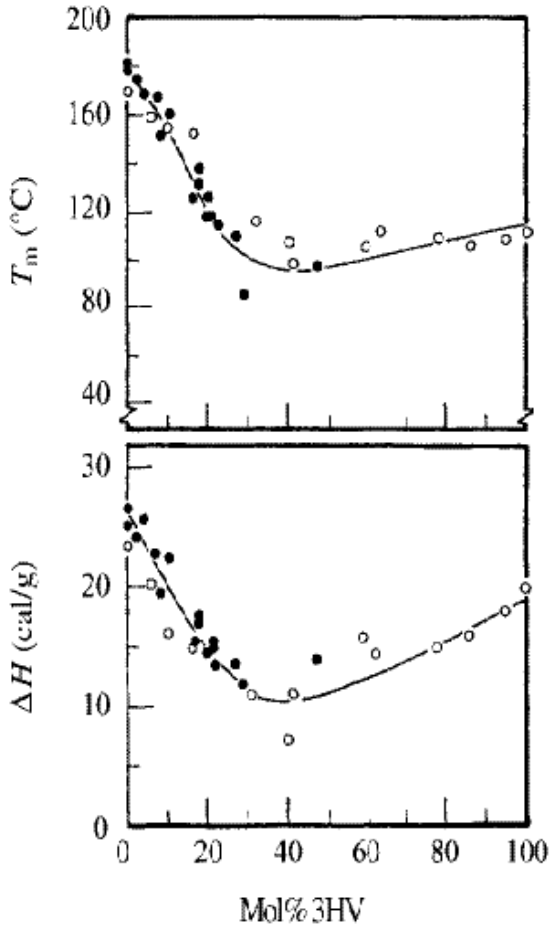

Isodimorphism alters the crystalline structure as outlined by the changes in the spherulites derived from P(3HB-*co*-3HV) samples with varying 3HV content (see Fig. 2). The PHB sample, Fig. 2*a*, exhibits large uninterrupted spherulites presumably because of rapid crystallization relative to the number of nucleation events. At higher 3HV compositions, and thus higher levels of 3HV inclusion, the spherulites are smaller because the rate of crystallization is slower and (or) there are relatively more nucleation sites. Higher 3HV implies a greater number of defects within the crystalline region. In terms of mechanical properties, less perfection in the crystalline domains corresponds to films with greater flexibility and toughness (45, 46).

By the late 1980s, Marchessault had left XRCC for McGill University where his PHA-related research broadened in many different directions. Despite this move, research continued at Xerox for several more years via Marchessault's mentoring. In one example, colleagues at XRCC were studying the implications of isodimorphism in P(3HB-*co*-3HV) by collecting wide angle X-ray diffraction (WAXD) traces of cold-stretched films and fibers. Many WAXD traces of cold-stretched films showed an intense equatorial reflection and a first layer line "streak" that could

© 2008 NRC Canada

Fig. 2. Polarized light micrographs showing spherulitic morphology of (*a*) PHB, (*b*) P(3HB-*co*-3HV): 7% 3HV, and (*c*) P(3HB-*co*-3HV): 21% 3HV.

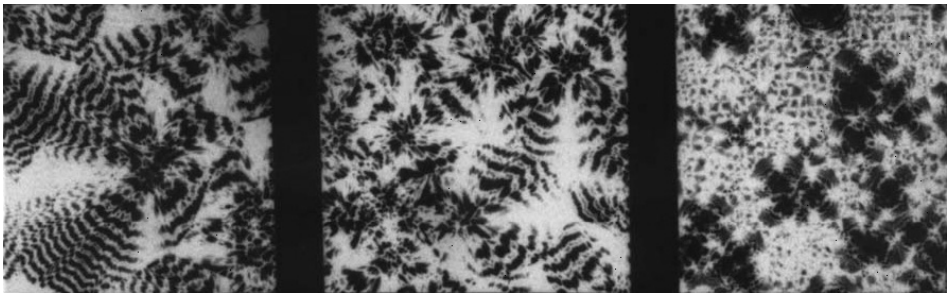

not be assigned to any plane in the orthorhombic crystalline system originally modeled for PHB (47–50). Marchessault immediately recognized this as evidence of the extended-chain, β-crystalline form (51). In the β-crystalline form, chains are arranged in a planar zigzag-type of structure, and the repeat distance along the crystallized chain is shorter than for the helical structure. As shown in Table 1 (last row), the *c* parameter for the β-crystalline form of P(3HB-*co*-3HV) is 4.6, in contrast to 5.96 for the more energy-favourable *a*-helical structure. The best interpretation is that PHB and (or) P(3HB-*co*-3HV), upon cold drawing, stores the energy of deformation in a metastable β-crystalline phase, almost like a coiled spring. Upon heating near the melt, this energy is released. Annealing under high tension makes the molecules in the amorphous region more stretched and increases the fraction of the β-zigzag form (60). Yamane et al. (61) also showed that the β-form crystal, which seems to have less ordered structure, degraded more readily than the α-form.

In another interesting result, Bloembergen et al. (62) created stereoblock synthetic analogs of P(3HB-*co*-3HV). In these samples, stereochemistry is consistent along relatively long stretches of copolymer chain (either all *sinister* or all *rectus*), and then it switches to the other stereoisomer for long stretches. This behaviour has allowed for interesting blends of synthetic and bacterial polyester in which PHB's brittleness was reduced and its toughness increased by intentional introduction of crystalline imperfections (1).

Biomimetic granules of PHA and in vitro synthesis

Beginning in the early 1990s, researchers began to report more extensively on the formation of in vitro synthesized PHA. The first step in these approaches was the development of biomimetic granules. Biomimetic granules were used to theorize about the crystallization dynamics of PHA (63–65). More specifically, intracellular PHB is contained within inclusions or granules, which, to the surprise of many, consist of highly mobile, non-crystalline chains. Prior to the eye-opening studies by Horowitz and Sanders (63), it was assumed that native granules were crystalline, considering how readily PHB crystallizes outside the cell.

Why is native PHB non-crystalline? To answer this, Horowitz and Sanders developed artificial granules to study PHB's rapid crystallization upon isolation, showing the potential effects of nucleation on crystallization kinetics (63). They substituted synthetic surfactant in place of the native granule coating to create submicron-size artificial granules, which were amorphous, stable in suspension, and indistinguishable from native granules in terms of size, morphology, molecular mobility, and density (64–65). When the surfactant coating was removed from the artificial granules, the PHB crystallized rapidly, thus verifying their hypothesis of nucleation-assisted crystallization.

Marchessault et al. also began a more extensive study of granules (66) and then reported (67) in vitro preparation of artificial granules of PHB and poly(β-hydroxyoctanoate), PHO, an elastomeric PHA with a six-carbon side chain. Light-scattering measurements of aqueous suspensions of the artificial granules showed particles with diameters in the range of 90–200 nm. The non-crystalline nature of the granules was shown by high resolution ^{13}C NMR. When the suspensions were allowed to dry, they yielded a continuous film with a low glass transition temperature and low Young's modulus.

Around the same time as in vitro granules from PHB and PHO were reported, the first studies on truly in vitro PHB biosynthesis and granule formation were reported by Gerngross and Martin (68). They combined a chemical and enzymatic procedure to synthesize in vitro macroscopic granules of PHB. When purified PHA-synthase from *Alcaligenes eutrophus* was exposed to synthetically prepared (*R*)-3-hydroxybutyryl CoA, (3HB-CoA) granules formed in a matter of minutes. Such formation proved that enzyme plus monomer was indeed the minimal requirement for PHB granule formation.

The artificial granules from Gerngross and Martin were spherical, with diameters up to 3 μm. This result was significant, since native granules in vivo are in the range of ~0.5 μm. The PHB formed in the in vitro granules was characterized by NMR, GPC, and chemical analysis and shown to have molar mass greater than 10×10^6 Da, an order of magnitude greater than the mass of PHB typically obtained from microorganisms. Gerngross and Martin (68–69) also showed that two different forms of the synthase are active in vitro, granule-bound and soluble PHA-synthase. Granule-bound synthase has a significantly higher specific activity and can be separated from the soluble form by centrifugation.

The Marchessault group, specifically Nobes et al. (70), with the aid of transmission electron microscopy (TEM) and Cryo-TEM, described the growth and kinetics of in vitro PHB granule formation. As discussed earlier, PHA biosynthesis is prompted by conditions of stress, such as the shortage of an essential nutrient (often phosphate or nitro-

© 2008 NRC Canada

gen). The biosynthetic pathway to PHB includes three key enzymes, which catalyze, in turn, carbon–carbon bond formation, chiral reduction, and finally head-to-tail polymerization. The first of the three enzymes, β-ketothiolase, catalyzes the formation of acetoacetyl-CoA from two molecules of acetyl-CoA in a bio-Claisen reaction. The acetoacetyl-CoA is subsequently converted to 3-hydroxybutyryl-CoA by acetoacetyl-CoA reductase. The final enzyme, PHB synthase, converts 3-hydroxybutyryl-CoA to PHB.

Nobes et al. (70) formed in vitro granules from 3HB-CoA in the presence of PHA synthase, yielding spherical granules of rapidly increasing size. After only 2 min of reaction, granules were already > 0.1 μm. While the average granule diameter and volume increased with reaction time, the overall number of granules decreased throughout the reaction owing to coalescence. As in previous studies, it was found that the granules formed by this process were essentially noncrystalline. A computer simulation accounted for kinetic data (71) based on the initial formation of relatively large microporous granules that consolidate by the expulsion of water during polymerization. Marchessault's group thus hypothesized that the initial granules were microporous, i.e., they contained some polymer but were mainly filled with water. Polymerization is, thus, topotactic and is hindered by the surface energy required to expel the hydrophobic polymer into the largely aqueous environment inside the granules. As the granules accumulate PHB, polymerization is increasingly favoured with its rate reaching a predictable maximum.

The biggest drawback to marketable application of in vitro reactions was the inability to recycle the CoA produced during PHA synthesis, an obstacle that appears to be recently overcome by Satoh et al. (72). Significant additional work in the synthesis of in vitro granules was reported by Steinbuchel's group, in which, for example, they reported in vitro formation of PHB granules by using a purified PHA-synthase from *Chromatium vinosum* (73) confirming mechanistic data for PHA synthase.

More recently, in vitro synthesis of PHA has been used to study the relationship between monomer structure and reactivity for PHA synthases, with indications that hydrophobicity in the side chain plays an important role in the reaction (74). The configuration and the position of the hydroxyl group affect the reactivity of a given monomer, suggesting that in vitro systems could be used to tailor entirely novel polymers that may not be obtainable from living cells.

In vitro degradation of PHA

Until the mid-1990s, virtually every published report (75–83) on the in vitro degradation of PHAs involved analysis of only the non-crystalline regions of the PHA. This was the result of the comparatively rapid degradation of amorphous regions and their accessibility to PHA-degrading organisms or enzymes. In studies of PHB degradation, it was found that a bimodal molecular mass distribution played a significant part in the degradation pattern of the polymer film (77). For P(3HB-*co*-3HV), Chaput et al. (80) reported that the mass loss rate due to degradation generally increased with the content of 3HV, presumably because of less perfect crystallization.

Fig. 3. Electron micrographs of PHB single crystals: (*a*) before enzymatic treatment and (*b*) after 24 h of depolymerase-A treatment from *P. Lemoignei* showing broken splinters.

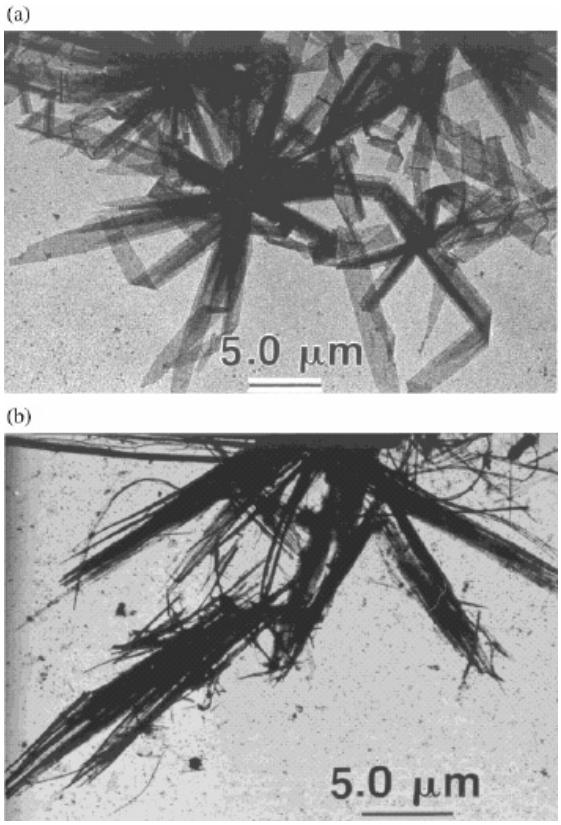

It soon became clear that accounting for the degradation of only the amorphous region would not fully describe the biodegradability of PHAs. Beginning in the mid-1990s, Marchessault group published a series of papers examining the mode of degradation of crystalline PHA. Nobes et al. (84–86) isolated depolymerase enzymes and applied TEM to visualize their action on folded-chain lamellar single crystals of PHB and P(3HB-*co*-3HV). Folded-chain single crystals presented a dual surface for enzymatic attack, i.e., the loops of the fold surface and the crystalline stems at the edge of the single crystal. These reports built upon the previous conclusion by Hocking et al. (83) that single crystals of bacterial PHB degraded completely when exposed to enzymes isolated from *Aspergillus fumigatus* and *Pseudomonas lemoignei*; yet, when they were only partially degraded, no decrease in molecular mass was observed. Results were consistent with preferential degradation from the crystal edges rather than the chain folds of the lamellar surface.

The Marchessault group explained this phenomenon at a molecular level by examining the partial degradation of folded-chain lamellar single crystals of PHB with PHB depolymerase from *P. lemoignei* (84). When observed by TEM, the partially degraded crystals were seen as splintered longitudinally to a needle-like morphology, as shown in Fig. 3.

© 2008 NRC Canada

Fig. 4. Two possible mechanisms of enzyme attack on folded-chain lamellae: (*a*) directional attack along the chain folding edge, removing "one chain at a time", and (*b*) preferred chain cleavage at the fold plane surface with rapid decrease in molecular mass.

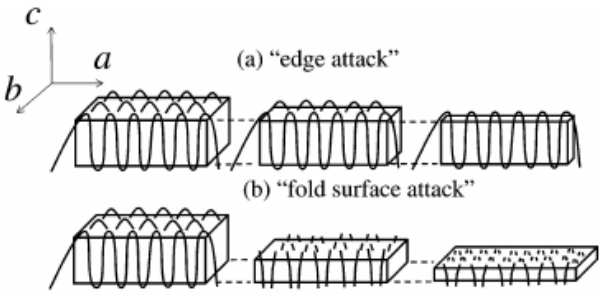

The needle-like splinters of degraded PHB still yield the same crystalline baseplane diffraction pattern, and they are still crystallographically perfect, with an average width of 20 nm (about 1/100 of the original crystal). A mechanistic explanation in subsequent papers (85–87) showed that polymer chains were cleaved by depolymerases acting in the direction of the chain folding plane. As outlined in Fig. 4, splintering of the crystalline laths runs parallel to the direction of the *a* axis of the PHB unit cell. It was hypothesized that the surface of single crystals is imperfectly crystallized because of chain folding; that is, the surface is thought of as amorphous. If the enzymes were to preferentially hydrolyze this surface, depolymerization would be followed by a rapid loss in molecular mass. However, since molecular mass (M_r) is not significantly lower after partial enzymatic degradation (83), PHB crystals must lose "entire chains one at a time", as shown in Fig. 4*a*.

Atomic force microscopy (AFM) can probe the same place in single crystals before and after enzymatic erosion. Analysis of AFM micrographs confirmed that the splinter thickness is unchanged until, perhaps, the last stage of enzymatic erosion. These facts are consistent with the "splintering" model shown in Fig 4*a*.

More recently, Marchessault and Kawada (87) reported that the origin of depolymerase-induced splintering is the precursor lath mode of single-crystal growth. This refinement of the splintering model states that the antiparallel chain packing of PHB, which provides a relatively stable tubular ribbon in the first stages of chain folding, encourages subsequent self assembly of precursor elements. This structure leaves parallel seams of mobile chains susceptible to enzymatic erosion. In this way, parallel arrays of splinters are created. In addition, this phenomenon must have an autocatalytic effect on the enzymatic degradation, since a net increase in accessible surface is created.

As a complement to previous studies of the enzymatic degradation of folded-chain lamellar single crystals of PHAs, single crystals of bacterial P(3HB-*co*-3HV), bacterial PHV, and synthetic PHB with 88% isotactic diads were partially degraded and examined by TEM using a range of PHA depolymerases (86). In contrast to previous results with single crystals of bacterial PHB, the predominant effect observed with most other crystals was a significant narrowing of the lamellae. This suggested an edge-attack mechanism such as outlined in Fig. 4*b*. In a fold-surface attack, depolymerase actions lead to a narrowing of the crystalline lamellae rather than splintering. Mechanistic models were expanded to hypothesize that this behaviour accounts for lateral disorder within the single crystal caused by the introduction of 3HV comonomers or addition of units of opposite stereochemistry.

Fig. 5. Proposed crystallization steps for formation of PHB lath-shaped single crystals: (1) random coil, (2) initial self-folding of chains, (3) formation of precursor laths, (4) self-assembly of precursor laths, and (5) consolidated single crystal with "out of register" regions.

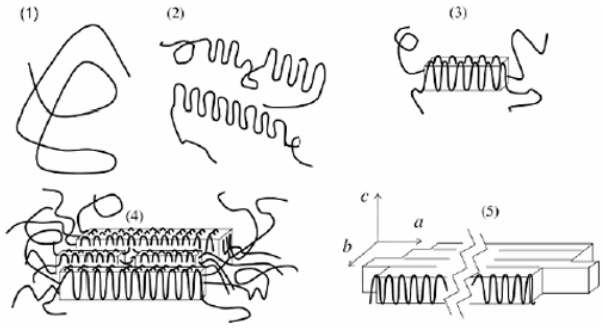

Subsequent to publication of the splintering model proposed by Marchessault group (85, 86), the team of Iwata et al. published a series of papers on the microscopic visualization of partially degraded single crystals of PHAs (88–95). They analyzed PHB single crystals that were degraded via extracellular PHB depolymerase purified from *Pseudomonas stutzeri* YM1006 using TEM, AFM, GPC, and immuno-gold labeling techniques and (*i*) demonstrated a homogeneous distribution of the PHB depolymerase on the surface of crystals, and (*ii*) confirmed the splintering mechanism of degradation.

PHA single crystals — Growth dynamics

Knowledge of degradation mechanisms for single crystals may also be used to gain insight into their formation. Geil (96) suggested that lath-shaped single crystals of PHB initially grow by apposition of chain folded ribbons, one or only a few fold planes wide, as shown schematically in Fig. 5, a cartoon version of the mechanism proposed by Geil. PHB single crystals grow from a dilute solution as follows: (1) random coil chain in dilute solution, (2) the chain folds against itself, (3) pre-folded ribbons form needle-like precursors, (4) self-assembly of the precursors, and (5) lath-shaped single crystals consolidate, leaving "out of register" regions. The needle-like precursors can be detected as protrusions at the single crystal ends during early crystal growth, evidence of the dominance of longitudinal growth (87, 96). Crystallographic support for step (2) in Fig. 5 is the anti-parallel chain packing of PHB chains. As noted by Birley et al. (97), tight chain folds in the crystal that alternate between the [110] and [110] planes result in an average chain-folding plane parallel to the *a*-axis direction (Fig. 6).

Models for crystal degradation and formation suggest a mechanistic relation between the "splintering" mechanism and the parallel seams during crystal formation (Fig. 5). Formation of PHB tubular ribbons by adjacent re-entry chain folding means that PHB stems are anti-parallel, and thus

© 2008 NRC Canada

Fig. 6. Formation of PHB tubular ribbon by adjacent re-entry chain folding. PHB stems are anti-parallel.

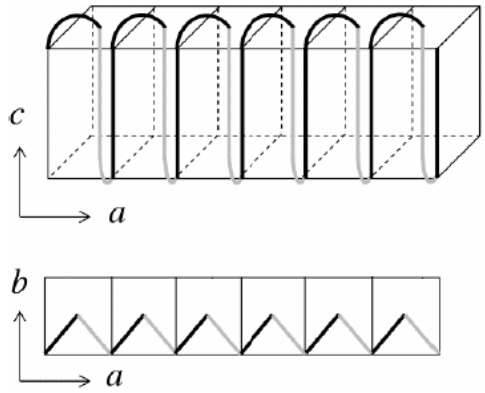

Fig. 7. TEM picture of PHB from a dilute solution (0.01% *w*/*v*) at the early stage of crystallization (30 min crystal growth) in a mixture of $CHCl_3$ and ethanol (1:2 *v*/*v*) at 60 °C.

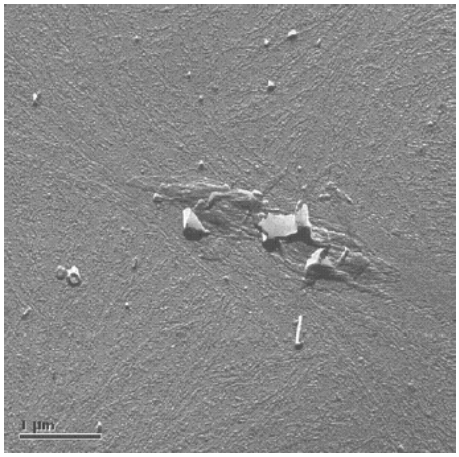

"out of register" as a result of the apposition of precursor laths. Hence, Geil's (96) seminal PHB electron micrographs showing self-assembly of the precursor laths was prescient to the "splintering" discovery for depolymerase action on PHB single crystals.

Figure 7 is an electron micrograph of PHB from a dilute solution (0.01% *w*/*v*) at the early stage of crystallization and self-assembling, with precursors surrounding a growing single crystal. The needle-like precursors are evidence of "out of register" regions between rows. Interestingly, the width of the PHB single-crystal lamellae in Fig. 7 is about 0.5 μm, which is narrower than the mature PHB single crystals (about 1–2 μm).

PHV square single crystals

Single crystals of PHV are square-shaped, as seen in the transmission electron micrographs reported previously (98). This differs from the lath-shaped single crystals of PHB, even though the chemical formula of PHV is similar to that for PHB. The difference in the single-crystal shape is explained by the direction of PHV chain-fold plane, which is perpendicular to the crystal growth direction. In other words, the chain-folding direction for PHV is [110] and perpendicular to the crystal growth direction; whereas that for the PHB is [100] (along the *a* axis) and parallel to the crystal growth.

Fig. 8. TEM pictures of PHV at various crystallization times: (*a*) cooled from 64 to 60 °C, (*b*) crystallized at 50 °C for 1 h and 30 min, (*c*) high magnification of PHV single crystals at 50 °C for 3 h (arrows show centered tips), and (*d*) high magnification of PHV single crystals cooled to room temperature after 3 h crystallization at 50 °C.

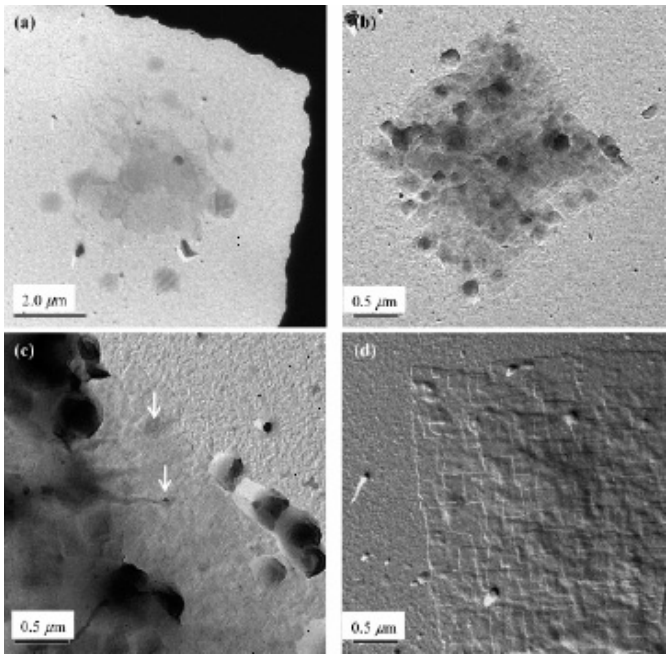

Figure 8*a* shows the early stage of PHV single-crystal growth observed by TEM just as the sample was cooled from 80 to 60 °C, which is close to the equilibrium temperature between the dissolving temperature (64 °C) and crystallization temperature (50 °C). An incipient square crystal is outlined by small primary nuclei, sometimes called "globs", which surround the nucleated crystal. These globs are precursors, which have been observed in previous PHV studies (98, 99). After 1.5 h at 50 °C, the crystals have a better defined square shape, and crystal self-assembly is underway, as shown in Fig. 8*b*. These precursors undergo annealing and self-assembly to form a square-shaped crystal composed of orthogonally arranged predominately as square tiles, although some precursors were still glob-like. The difference between precursors may be the extent of crystallization in solution prior to attachment to the single crystal. In other words, square-type precursors were already crystallized before self-assembly, whereas globs were annealed during self-assembly. Crystals, prepared at 50 °C for 3 h, showed an almost finished crystallization with rows of square-shaped precursors almost attached to the mother crystal, as shown in Fig. 8*c*. One of the squares gives evidence of a centered tip, characteristic of a primary nucleus.

This self-assembly evidence can explain why the surface of PHV single crystals have a tile-like morphology, as in Fig. 8*d*. Specifically, the precursors, which have different degrees of perfection, self-assemble, and grow as shown by Iwata and Doi (99) and Saracovan (100). They reported screw dislocation pairs: right- and left-handed. In the mid-

© 2008 NRC Canada

1980s back at Xerox (XRCC), Pundsack and Bluhm (101) had observed the small square tiles of PHV, which they referred to as mosaic structure, equivalent to edge decoration on a large single crystal. Electron diffraction on the tilted crystals provided the unit-cell parameters, which were confirmed by Marchessault et al. (98) both for natural and synthetic racemic PHV.

PHA oligomers — New functionalities

Marchessault group (at McGill) was among the first to note that PHA oligomers, as more manageable molecules than their high molecular mass equivalents, represent useful tools in the structural understanding of high molecular mass PHA analogues (102, 103). Oligomers had been used by various groups to determine the composition and the sequence distribution of the comonomer units, essentially via mass spectrometry (104–112). They were also used as models for physical characterization (103, 112), as well as model substrates in enzymatic degradation studies (113–118); for example, nearly monodisperse PHB oligomers were used as calibration standards for gel permeation chromatography (112). Ravenelle and Marchessault (119) took this a step further and showed that oligomers also constitute interesting building blocks with their combined properties of biodegradability, biocompatibility, and stereoregularity. Coming from the high molecular mass analogues, they exhibit enhanced solubility and reactivity for chemical modification.

Degradation of high molecular mass PHAs can also yield linear oligomers. Various preparative methods using chemical degradation have been reported in the literature: acid-catalyzed hydrolysis with either hydrochloric acid (120, 121), acetic acid and dimethyl sulfoxide (122), or *p*-toluenesulfonic acid (123); base-catalyzed hydrolysis using sodium hydroxide (120, 123–126); ammonolysis (127); acid-catalyzed alcoholysis or transesterification, with methanolysis using sulfuric acid (128, 129), hydrochloric acid (103, 105, 107, 131), or *p*-toluenesulfonic acid (132) as catalyst, or with diols, using 1,10-decanediol (128), 1,6-hexanediol (133), or 1,4-butanediol with also *p*-toluenesulfonic acid as catalyst (134); base-catalyzed alcoholysis with sodium methoxide in methanol (107); saponification with potassium hydroxide and a crown ether (109–111, 135); and degradation with lithium bases (112). Thermal degradation in the melt has also been reported as a method for preparation of PHA oligomers (136, 137).

The preparation of oligomers of PHB and P(3HB-*co*-3HV) by thermal degradation at 190 °C in the melt, without using a solvent or chemical reagents, was reported by Nguyen et al. (138) with 0, 4, 7, and 21 mol% of 3HV units in the copolymers. Chemical structure was confirmed by proton nuclear resonance spectroscopy and fast atom bombardment mass spectrometry, confirming the same PHA repeat unit as the high molecular mass starting material, with a carboxylic acid end group, and an alkenyl end mostly in the trans configuration (crotonate-type). Variations of 3HV content, reaction temperature, and time were shown to tune the molecular mass of the produced oligomers determined by size-exclusion chromatography. While the thermal degradation followed a random scission model during the first hours of processing, an auto-acceleration was observed, possibly due to an increase of the rate of ester cleavages caused by the inductive effect of the unsaturated end groups on the neighboring ester linkages (138).

PHA graft copolymers

Three main preparation strategies have been reported to produce graft copolymers: (*i*) "grafting from", by growing polymer segments along a polymer chain via monomer polymerization; (*ii*) "grafting onto", by coupling onto a polymer chain blocks of another copolymer; and (*iii*) "grafting through" or macromonomer technique, by copolymerization of a macromonomer, a polymer or oligomer with one or two polymerizable end groups with a low molecular mass comonomer. Marchessault's group has contributed to the field with the synthesis and characterization of graft copolymers of PHB using the two latter methods (122, 139–141).

Bacterial PHB blocks (M_n 10 000) were grafted by Yalpani et al. onto chitosan using amidation, cellulose acetate by transesterification, and poly(ethylenimine) by amidation (122). The same strategy was used to graft oligomers of PHB/V and poly(3-hydroxyoctanoate), PHO (M_n of ~ 14 700 and 77 300 for PHB/V, and M_n of ~ 19 100 for PHO) onto chitosan by amidation, which yielded either chitosan-*g*-PHB/V or chitosan-*g*-PHO (142).

Block copolymers poly([*R*]-3-hydroxybutyrate-block-styrene) synthesized by a coupling reaction were reported by Reeve and co-workers (128, 129). Polystyrene, PS, oligomers (M_n 5 900) with one carboxylic acid end were esterified with PHB oligomers (M_n 2 300) containing one hydroxyl end (produced by methanolysis) (1).

The same authors reported the synthesis of multiblock copolymers by coupling PHB bearing two hydroxyl end groups with poly(tetramethylene glycol) or poly(ethylene glycol), PEG. Marchessault and Yu (130) reported the synthesis of diblock copolymers of PHB and PEG, obtained by coupling monomethoxy-PEG and low molecular mass PHB obtained by the base-hydrolysis of bacterial PHB. In a one-step procedure, high molecular mass, bacterial PHB was degraded and transesterified with low molecular mass monomethoxy-PEG (119).

Nguyen and Marchessault (139, 140) reported the synthesis of graft copolymers of poly(methyl methacrylate), PMMA, with isotactic PHB branches by the "grafting through" method. They copolymerized methyl methacrylate, MMA, with bacterial PHB macro-monomers containing a methacrylate end group. Both conventional free radical polymerization, FRP, methods and controlled FRP methods were used. Macro-monomers were prepared by thermal degradation of bacterial PHB (138), and subsequent esterification of the carboxylic acid end groups (139). As expected, PMMA-*g*-PHB copolymers obtained by conventional FRP displayed rather large polydispersity indexes, with PHB branches randomly distributed. In contrast, the graft copolymers produced via FRP methods were significantly more monodisperse with lower M_w (140). Such copolymers represent interesting additives for acrylic bone cement formulations, as they could increase both their degradability and biocompatibility, while ensuring compatibility between PHB and the methacrylic ingredients of the cements.

© 2008 NRC Canada

Formulations of a commercial acrylic bone cement, antibiotic Simplex®, were modified by adding PMMA-graft-PHB copolymers obtained by free radical methods (141). Cements with up to 13.5 wt% of graft copolymers could be produced, and contained micropores with volumetric porosities ranging between 13.5% and 16.9%, but showed ultimate compression strengths above the ASTM F451 requirements.

In a recent application of the clever synthetic strategy employed by Nguyen and Marchessault (139–141), Neugebauer et al. (143) synthesized graft copolymers of methacrylate with PHB macro-monomers. They produced PHB oligomers of different tacticity and copolymerized them with methacrylates of various sizes of poly(ethylene glycol): methyl methacrylate, ethylene glycol methyl ether methacrylate, and poly(ethylene glycol) methyl ether methacrylate.

Conclusions

This review has covered more than four and a half decades of PHA-related research, highlighting how the work of Robert H. Marchessault and his many colleagues shaped research in this biopolymer area. Marchessault's impacts include the rediscovery of PHA by his Syracuse "gang of four", who were pioneers in defining the biochemistry of PHA biosynthesis and in describing PHAs' unique structure–property relationships. He played a significant role in pushing PHA, and more specifically P(3HB-*co*-HV), toward commercialization, both at Xerox, Canada and later at McGill University. Marchessault and his many varied colleagues were the first to describe isodimorphism of PHAs, a rare event worth fundamental study, and one that also provides a range of unique commercial properties, including biopolymers that rival polypropylene in most mechanical properties. More recent research highlights have included novel in vivo – in vitro PHA synthesis and degradation, and PHA-graft-copolymers.

Marchessault has been noted as describing researchers as having a choice between being "those who plant the flag, the pioneers, vs. those who are content to sweep up around the flagpole later". Bob Marchessault has "planted many flags" in his career and has enriched many lives along the way.

Acknowledgement

All of the contributors to this review were former Marchessault graduate students or post-doctoral research associates. We thank Professor Marchessault for his vision, leadership, creativity, and generosity – with resources and with time. Despite an often busy schedule over the years, he consistently has the time to discuss all realms of science, and to patiently teach his new discoveries to others. His lifelong passion toward research and discovery has left a positive imprint on many students, postdocs, and colleagues.

Thank you, Bob.

References

1. R.H. Marchessault, T.L. Bluhm, Y. Deslandes, G.K. Hamer, W.J. Orts, P.R. Sundararajan, M.G. Taylor, S. Bloembergen, and D.A. Holden. Makromol. Chem. Makromol. Symp. **19**, 235 (1988).
2. G. Reynolds. Sustainable Packaging Coalition Newsletter, **3**, 2 (2007).
3. R.W. Lenz and R.H. Marchessault. Biomacromolecules, **6**, 1 (2005).
4. M.C. R. Lemoigne. Acad. Sci. **176**, 1761 (1923).
5. M.C.R. Lemoigne. Acad. Sci. **178**, 1093 (1924).
6. M.C.R. Lemoigne. Acad. Sci. **179**, 253 (1924).
7. M.C.R. Lemoigne. Acad. Sci. **180**, 1539 (1925).
8. M. Lemoigne. Bull. Soc. Chim. Biol. **8**, 770 (1926).
9. M. Lemoigne. Bull. Soc. Chim. Biol. **9**, 446 (1927).
10. P.A. Holmes. Developments in crystalline polymers. Vol. 2. *Edited by* D.C. Basset. Elsevier Applied Science. London. 1988. pp. 1–65.
11. P.J. Senior and E.A. Dawes. Biochem. J. **134**, 225 (1973).
12. L.L. Wallen and W.K. Rohwedder. Environ. Sci. Technol. **8**, 576 (1974).
13. M.J. de Smet, G. Eggink, B. Witholt, J. Kingma, and H.J. Wynberg. J. Bacteriol. **154**, 870 (1983).
14. R.A. Gross, C. De Mello, R.W. Lenz, and R.C. Fuller. Macromolecules. **22**, 1106 (1989).
15. Y. Doi. Microbial polyesters. VCH Publishers. Weinheim. 1990.
16. Y. Doi, M. Kunioka, Y. Nakamura, and K. Soga. Macromolecules, **21**, 2722 (1988).
17. A. Steinbuchel and H.E. Valentin. FEMS Microbiol. Lett. **128**, 219 (1995).
18. A. Steinbuchel and H. Schlegel. Mol. Microbiol. **5**(3), 535 (1991).
19. S.C. Slater, W.H. Volge, and D.E. Dennis. J. Bacteriol. **170**, 4431 (1988).
20. S. Slater, T. Gallaher, and D. Dennis. Appl. Environ. Microbiol. **58**, 1089 (1992).
21. O.P. Peoples and A.J. Sinskey. J. Biol. Chem. **264**, 15298 (1989).
22. T.V. Gerngross, K.D. Snell, O.J. Peoples, A.J. Sinskey, E. Cauhai, S. Masamune, and J. Stubbe. Biochemistry, **33**, 9311 (1994).
23. Y. Poirier, D.E. Dennis, K. Klomparens, and C. Somerville. Science (Washington, DC), **256**, 520 (1992).
24. Y. Poirier, D.E. Dennis, K. Klomparens, C. Nawrath, and C. Somerville. FEMS Microbiol. Rev. **103**, 237 (1992).
25. I. Noda. I. US Patent 6-569-990. 2003.
26. C.J. Weibull. J. Bacteriol. **66**, 696 (1953).
27. D.H. Williamson and J.F. Wilkinson. J. Gen. Microbiol. **19**, 198 (1958).
28. M. Doudoroff and R.Y. Stanier. Nature (London, UK), **183**, 1440 (1959).
29. R.Y. Stanier, M. Doudoroff, R. Kunisawa, and R. Contopoulou. Proc. Natl. Acad. Sci. USA. **45**, 1246 (1959).
30. J.M. Merrick. Personal communication. 2007.
31. J.M. Merrick and M. Doudoroff. Nature (London, UK), **189**, 890 (1961).
32. J.M. Merrick and M. Doudoroff. J. Bacteriol. **88**, 60 (1964).
33. R. Alper, D.G. Lundgren, R.H. Marchessault, and W.A. Cote. Biopolymers, **1**, 545 (1963).
34. D.G. Lundgren, R. Alper, C. Schnaitman, and R.H.J. Marchessault. J. Bacteriol. **89**, 245 (1965).
35. D. Ellar, D.G. Lundgren, K. Okamura, and R.H. Marchessault. J. Mol. Biol. **35**, 489 (1968).
36. R.H. Marchessault. Personal communication. 2007.
37. (*a*) R.H. Marchessault and G.-E. Yu. Biopolymers: Polyesters II. *Edited by* Y. Doi and A. Steinbüchel. Wiley-VCH, Weinheim. 2002. pp. 157–202; (*b*) J.N. Baptist. US Patent 3-044-942. 1962.

© 2008 NRC Canada

38. J.N. Baptist. US Patent 3-036-959. 1962.
39. J.N. Baptist and F.X. Werber. SPE Trans. **4**, 245 (1964).
40. R.H. Marchessault, K. Okamura, and C.J. Su. Macromolecules. **3**, 735 (1970).
41. E. Fukado and Y.J.Ando. Biol. Macromol. **8**, 361 (1986).
42. S. Bloembergen, D.H. Holden, G.K. Hamer, T.L. Bluhm, and R.H. Marchessault. Macromolecules, **19**, 2865 (1986).
43. T.L. Bluhm, G.K. Hamer, R.H. Marchessault, C.A. Fyfe, and R.P. Veregin. Macromolecules, **19**, 2871 (1986).
44. P.J. Barham, A. Keller, E.L. Otun, and P.A. Holmes. J. Mater. Sci. **19**, 2781 (1984).
45. H. Mitomo, P.J. Barham, and A. Keller. Polym. J. **19**, 1241 (1987).
46. W.J. Orts, D.L. VanderHart, T.L. Bluhm, and R.H. Marchessault. Can. J. Chem. **73**, 2094 (1995).
47. K. Okamura. Physical properties of poly(3-hydroxybutyrate). Ph.D. thesis. State University of New York, College of Forestry, Syracuse, NY. 1967.
48. J. Cornibert and R.H. Marchessault. J. Mol. Biol. **71**, 735 (1972).
49. M. Yokouchi, Y. Chatani, H. Tadokoro, K. Teranishi, and H. Tani. Polymer, **14**, 267 (1973).
50. S. Bruckner, S.V. Meille, L. Malpezzi, A. Cesaro, L. Navarini, and R. Tombolini. Macromolecules, **21**, 967 (1988).
51. W.J. Orts, R.H. Marchessault, T.L. Bluhm, and G.K. Hamer. Macromolecules, **23**, 5368 (1990).
52. R.J. Pazur, S. Raymond, P.J. Hocking, and R.H. Marchessault. Polymer, **39**, 3065 (1998).
53. W.J. Orts, R.H. Marchessault, and T.L. Bluhm. Macromolecules, **24**, 6435 (1991).
54. G. Allegra and L.W. Bassi. Adv. Polym. Sci. **6**, 549 (1969).
55. G. Allegra, R.H. Marchessault, and S. Bloembergen. J. Polym. Sci. B Polym. Phys. **30**, 809 (1992).
56. P.J. Barham, D.A. Jarvis, and A. Keller. J. Polym. Sci. Polym. Phys. Ed. **20**, 1733, (1982).
57. P.J. Barham. J. Mater. Sci. **19**, 3826, (1984).
58. P.A. Barker and P.J. Barham. J. Mater. Sci. Lett. **8**, 1049 (1989).
59. P.A. Barker, P.J. Barham, and J. Martinez-Salazar. Polymer, **38**, 913 (1997).
60. H. Yamanea, K. Teraoa, S. Hiki, and Y. Kimura. Polymer, **42**, 3241 (2000).
61. H. Yamanea, K. Teraoa, S. Hiki, Y. Kimura, and T. Saito. Polymer, **42**, 7873 (2001).
62. S. Bloembergen, D.A. Holden, T.L. Bluhm, G.K. Hamer, and R.H. Marchessault. Macromolecules, **22**, 1656 (1989).
63. D.M. Horowitz and J.K.M. Sanders. J. Am. Chem. Soc. **116**, 2695 (1994).
64. D.M. Horowitz and J.K.M. Sanders. Can. J. Microbiol. **41** (Suppl. 1), 115 (1995).
65. D.M. Horowitz and J.K.M. Sanders. Polymer, **35**, 5079 (1994).
66. C. Lauzier, R.H. Marchessault, P. Smith, and H. Chanzy. Polymer, **33**, 823 (1992).
67. R.H. Marchessault, F.G. Morin, S. Wong, and I. Saracovan. Can. J. Microbiol. **41** (Suppl. 1), 138 (1995).
68. T.U. Gerngross and D.P. Martin. Proc. Natl. Acad. Sci. USA. **92**, 6279 (1995).
69. D.P. Martin and T.u. Gerngross. *In* Proceedings of the international symposium on bacterial poly(hydroxyalkanoates). Davos, Switzerland. Aug. 18–23, 1996. *Edited by* G. Eggink. National Research Council of Canada. Ottawa, ON. 1997. pp. 28–35.
70. G.A.R. Nobes, L. Jurasek, R.H. Marchessault, D.P. Martin, J.L. Putaux, and H. Chanzy. Macromol. Rapid Commun. **21**, 77 (2000).
71. L. Jurasek, G.A.R. Nobes, and R.H. Marchessault. Macromol. Biosci. **1**, 258 (2001).
72. Y. Satoh, F. Murakami, K. Tajima, and M. Munekata. J. Biosci. Bioeng. **99**, 508 (2005).
73. R. Jossek, R. Reichelt, and A. Steinbuchel. Appl. Microbiol. Biotechnol. **49**, 258 (1998).
74. S. Zhang, M. Kamachi, Y. Takagi, R.W. Lenz, and S. Goodwin. Appl. Microbiol. Biotechnol. **56**, 131 (2001).
75. N.D. Miller and D.F. Williams. Biomaterials, **8**, 129 (1987).
76. D.F. Williams and N.D. Miller. *In* Biomaterials and clinical applications. *Edited by* A. Pizzoferrato, P.G. Marchetti, A. Ravaglioli, and A.J.C. Lee. Elsevier, Amsterdam. 1987. pp. 471–476.
77. J.C. Knowles and G.W. Hastings. Biomaterials, **12**, 210 (1991).
78. J.C. Knowles and G.W. Hastings. J. Mater. Sci. Mater. Med. **3**, 352 (1992).
79. J. Mergaert, A. Webb, C. Anderson, A. Wouters, and J. Swings. Appl. Environ. Microbiol. **59**, 3233 (1993).
80. C. Chaput, L.H. Yahia, A. Selmani, and C.-H. Rivard. Natural poly(hydroxybutyrate-hydroxyvalerate) polymers as degradable biomaterials. Res. Soc. Symp. Proc. **394**, 111 (1995).
81. M. Canetti and P. Sadocco. Proceedings of the SPIE — The International Society for Optical Engineering, **3095**, 103 (1997).
82. C. Lauzier, J.-F Revol, E.M. Debzi, and R.H. Marchessault. Polymer, **35**, 4156 (1994).
83. P.J. Hocking, R.H. Marchessault, M.R. Timmins, R.W. Lenz, and R.C. Fuller. Macromolecules, **29**, 2472 (1996).
84. G.A.R. Nobes, R.H. Marchessault, H. Chanzy, B.H. Briese, and D. Jendrossek. Macromolecules, **29**, 8330 (1996).
85. R.H. Marchessault, G.A.R. Nobes, and P.J. Hocking. *In* Proceedings of the international symposium on bacterial poly(hydroxyalkanoates). Davos, Switzerland. Aug. 18–23, 1996. *Edited by* G. Eggink. National Research Council of Canada. Ottawa, ON. 1997. pp. 110–118.
86. G.A.R. Nobes, R.H. Marchessault, B.H. Briese, and D. Jendrossek. J. Environ. Polym. Degrad. **6**, 99 (1998).
87. R.H. Marchessault and J. Kawada. Macromolecules, **37**, 7418 (2004).
88. T. Iwata, Y. Doi, K. Kasuya, and Y. Inoue. Macromolecules, **30**, 833 (1997).
89. T. Iwata, Y. Doi, T. Tanaka, T Akehata, M. Shiromo, and S. Teramachi. Macromolecules, **30**, 5290 (1997).
90. T. Iwata, Y. Doi, S. Nakayama, H. Sasatsuki, and S. Teramachi. Int. J. Biol. Macromol. **25**, 169 (1999).
91. T. Murase, T. Iwata, and Y. Doi. Macromolecules, **34**, 5848 (2001).
92. T. Murase, T. Iwata, and Y. Doi. Macromol. Biosci. **1**, 275 (2001).
93. T. Murase, Y. Suzuki, Y. Doi, and T. Iwata. Biomacromolecules, **3**, 312 (2002).
94. T. Iwata, M. Shiromo, and Y. Doi. Macromol. Chem. Phys. **203**, 1309 (2002).
95. F. Su, T Iwata, F. Tanaka, and Y. Doi. Macromolecules, **36**, 6401 (2003).
96. P.H. Geil. Polymer, **41**, 8983 (2000).
97. C. Birley, J. Briddon, E.K. Sykes, P.A. Barker, S.J. Organ, and P.J. Barham. J. Mater. Sci. **30**, 633 (1995).
98. R.H. Marchessault, E. Debzi, J.-F. Revol, and A. Steinbuchel. Can. J. Microbiol. **41**, 297 (1995).
99. T. Iwata and Y. Doi. Macromolecules, **33**, 5559 (2000).
100. I. Saracovan. Ph.D. thesis. McGill University. 1999.

© 2008 NRC Canada

101. A.L. Pundsack and T.L. Bluhm. J. Mater. Sci. **16**, 545 (1981).
102. R.H. Marchessault, S. Coulombe, H. Morikawa, K. Okamura, and J. F. Revol. Can. J. Chem. **59**, 38 (1981).
103. M.E. Nedea, F.G. Morin and R.H. Marchessault. Polymer Bulletin, **26**, 549 (1991).
104. A. Ballistreri, D. Garozzo, M. Giuffrida, G. Impallomeni, and G. Montaudo. J. Anal. Appl. Pyrol. **16**, 239 (1989).
105. A. Ballistreri, G. Montaudo, G. Impallomeni, R.W. Lenz, Y.B. Kim, and R.C. Fuller. Macromolecules, **23**, 5059 (1990).
106. A. Ballistreri, M. Giuffrida, G. Impallomeni, R.W. Lenz, and R.C. Fuller. Int. J. Biol. Macromol. **26**, 201 (1999).
107. K.A. Saeed, F.O. Ayorinde, B.E. Eribo, M. Gordon, and L. Collier. Rapid Commun. Mass Spectrom. **13**, 1951 (1999).
108. R. Abate, A. Ballistreri, G. Montaudo, D. Garozzo, G. Impallomeni, G. Critchley, and K. Tanaka. Rapid Commun. Mass Spectrom. **7**, 1033 (1993).
109. G. Adamus, W. Sikorska, M. Kowalczuk, M. Montaudo, and M. Scandola. Macromolecules, **33**, 5797 (2000).
110. G. Adamus, W. Sikorska, M. Kowalczuk, I. Noda, and M. M. Satkowski. Rapid Commun. Mass Spectrom. **17**, 2260 (2003).
111. G. Adamus. Macromol. Symp. **239**, 77 (2006).
112. D. Seebach, H.M. Bürger, H.-M. Müller, U.D. Lengweiler, A.K. Beck, K.E. Sykes, P.A. Barker, and P.J. Barham. Helv. Chim. Acta, **77**, 1099 (1994).
113. T. Iwata, Y. Doi, K.-i. Kasuya, and Y. Inoue. Macromolecules, **30**, 833 (1997).
114. Y. Doi. Microbial polyesters. VCH Publishers. New York. 1990.
115. D. Seebach and M. G. Fritz. Int. J. Biol. Macromol. **25**, 217 (1999).
116. B.M. Bachmann and D. Seebach. Macromolecules, **32**, 1777 (1999).
117. T.M. Scherer, R.C. Fuller, S. Goodwin, and R.W. Lenz. Biomacromolecules, **1**, 577 (2000).
118. H. Brandl, B. Aeberli, R. Bachofen, I. Schwegler, H.-M. Müller, M.H. Bürger, T. Hoffmann, U.D. Lengweiler, and D. Seebach. Can. J. Microbiol. **41** (Suppl. 1), 180 (1995).
119. F. Ravenelle and R.H. Marchessault. Biomacromolecules, **3**, 1057 (2002).
120. C. Lauzier, J.-F. Revol, E.-M. Debzi, and R.H. Marchessault. Polymer, **35**, 4156 (1994).
121. G.-e. Yu and R.H. Marchessault. Polymer, **41**, 1087 (2000).
122. M. Yalpani, R.H. Marchessault, F.G. Morin, and C.J. Monasterios. Macromolecules, **24**, 6046 (1991).
123. L. Timbart, E. Renard, M. Tessier, and V. Langlois. Biomacromolecules, **8**, 1255 (2007).
124. B. Hauttecoeur, M. Jolivet, and R. Gavard. C.R. Acad. Sci. Paris, Ser. D. **274**, 2729 (1972).
125. B. Hauttecoeur, M. Jolivet, and R. Gavard. C.R. Acad. Sci. Paris, Ser. C. **274**, 1957 (1972).
126. B. Hauttecoeur, M. Jolivet, and R. Gavard. C.R. Acad. Sci. Paris, Ser. D. **280**, 2801 (1975).
127. M.E. Nedea. Ph.D. thesis. McGill University, Montreal, QC. 1991.
128. M.S. Reeve, S.P. McCarthy, and R.A. Gross. Polym. Prepr. **31**, 437 (1990).
129. M.S. Reeve, S.P. McCarthy, and R.A. Gross. Macromolecules, **26**, 888 (1993).
130. R.H. Marchessault and G.-e. Yu. Polym. Prepr. **40**, 527 (1999).
131. A. Ballistreri, D. Garozzo, M. Giuffrida, G. Impallomeni, and G. Montaudo. Macromolecules, **22**, 2107 (1989).
132. M.I.A. Majid, C.W. Pouton and L.J. Notarianni. J. Pharm. Pharmacol. **39**, 34P (1987).
133. X.M. Deng and J.Y. Hao. Eur. Polym. J. **37**, 211 (2001).
134. Q. Zhao and G. Cheng. J. Mater. Sci. **39**, 3829 (2004).
135. Z. Jedlinski, M. Kowalczuk, G. Adamus, W. Sikorska, and J. Rydz. Int. J. Biol. Macromol. **25**, 247 (1999).
136. M. Kunioka and Y. Doi. Macromolecules, **23**, 1933 (1990).
137. R.S. Lehrle and R.J. Williams. Macromolecules, **27**, 3782 (1994).
138. S. Nguyen, G.-e. Yu, and R.H. Marchessault. Biomacromolecules, **3**, 219 (2002).
139. S. Nguyen and R.H. Marchessault. Macromol. Biosci. **4**, 262 (2004).
140. S. Nguyen and R.H. Marchessault. Macromolecules, **38**, 290 (2005).
141. S. Nguyen and R.H. Marchessault. J. Biomed. Mater. Res. Part B: Appl. Biomater. **77B**, 5 (2006).
142. H. Arslan, B. Hazer, and S.C. Yoon. J. Appl. Polym. Sci. 103, **81** (2007).
143. D. Neugebauer, J. Rydz, I. Goebel, P. Dacko, and M. Kowalczuk. Macromolecules, **40**, 1767 (2007).

© 2008 NRC Canada

BIOGRAPHY / BIOGRAPHIE

Born and raised in Montreal, Robert H. Marchessault earned his B.Sc. from Loyola College (1950) and his Ph.D. from McGill (1954) under the supervision of the renowned colloid chemist, Stanley Mason. After postdoctoral studies at the University of Uppsala in Sweden, he spent several years as a research scientist at American Viscose Corporation in Philadelphia. He then joined the State University of New York (Syracuse) as Professor of Polymer Physical Chemistry. In 1969, he returned to Montreal as Professor and Director of the Department of Chemistry of Université de Montréal. He was also on the Board of Loyola College and played a key role in its merger with Sir George Williams University leading to Concordia University.

From 1978 to 1987, Dr. Marchessault was head of the Xerox Research Centre of Canada in Mississauga, Ontario. This facility serves Xerox Corporation's worldwide materials research needs. Under his direction, this laboratory grew to be recognized as one of Canada's leading industrial research laboratories in the field of organic materials. During his tenure as head of this Centre, Marchessault was a Vice President of Xerox Corporation and Vice President, Research of Xerox Canada Inc. In 1987, Dr. Marchessault returned to McGill University as the Xerox-NSERC Industrial Research Chair. In 1993 he was appointed to the prestigious E.B. Eddy Chair of Industrial Chemistry at McGill, and in 2005 he was promoted to the rank of Emeritus Professor.

His research has been focused on understanding the structure–property relationships of biomacromolecules including cellulose, polyhydroxyalkanoates (PHAs) and carbohydrate polymers. His pioneering 1963 study of the stereochemistry and crystallinity of bacterial polyesters fostered the development of these materials as biodegradable, melt processable plastics with a myriad of uses. He has had a career-long interest in biodegradable commodity plastics and has been a key player in the development of green chemistry. His research program at McGill focused on developing biopolymer materials for imaging, drug delivery, and environmental applications. He has published over 300 refereed papers and is co-inventor on 20 patents.

In 1976, he received the Anselme Payen Award from the Cellulose, Paper, and Textile division of the American Chemical Society, in recognition of his inspiring teaching and dynamic research program. He was also the 1998 recipient of the Chemical Institute of Canada's Macromolecular Science and Engineering Award. Marchessault has been very influential in the overall advancement of scientific research in Canada, serving over the years on several National Research Council of Canada committees and in 1986, on the National Advisory Board on Science and Technology. In 1981, he received the Archambault Award from l'Association canadienne-française pour l'avancement des sciences. The Royal Society of Canada elected Dr. Marchessault to be a fellow and a member of the Canadian Academy of Science in 1982 . In 1984, he was elected to a fellowship of the American Physical Society. Concordia University granted him an honorary D.Sc. in 1982. In 1991, the Canadian Institute of Chemistry recognized his professional and scientific leadership by awarding him the Montréal Medal. In 2000, he was named an Officer in the Order of Canada, and in 2002 was awarded the Queen's Jubilee Medal.

Robert H. Marchessault est né et a grandi à Montréal, où il a obtenu un baccalauréat ès sciences du Collège Loyola (1950) puis un doctorat de l'Université McGill (1954), sous la direction du chimiste de renom, Stanley Mason, spécialiste des colloïdes. Après des études postdoctorales à l'Université d'Uppsala (Suède), il a occupé un poste de chercheur pendant plusieurs années à l'American Viscose Corporation, à Philadelphie. Par la suite, il s'est joint à l'Université d'État de New York (Syracuse) à titre de professeur de chimie physique des polymères. En 1969, il est de retour à Montréal pour occuper à la fois le poste de professeur et celui de directeur du Département de chimie de l'Université de Montréal. Il a également siégé au conseil d'administration du Collège Loyola, et a joué un rôle important dans la fusion du Collège avec l'Université Sir George Williams pour donner lieu à l'Université Concordia.

De 1978 à 1987, M. Marchessault a dirigé le Centre canadien de recherche Xerox, à Mississauga (Ontario). Cet établissement répond aux besoins de la Xerox Corporation en matière de recherche internationale sur les matériaux. Sous sa direction, ce laboratoire a connu une telle expansion qu'il a été reconnu comme l'un des plus importants laboratoires de recherche industrielle au Canada dans le domaine des matériaux organiques. Tout en occupant ses fonctions de directeur, M. Marchessault a été vice-président de la Xerox Corporation et vice-président à la recherche de Xerox Canada inc. En 1987, il est retourné à l'Université McGill à titre de titulaire de la chaire de recherche industrielle CRSNG-Xerox. En 1993, il a été nommé titulaire de la prestigieuse chaire E. B. Eddy de chimie industrielle à la même université, et en 2005, il a été promu au rang de professeur émérite.

Ses travaux de recherche sont axés sur la compréhension des liens entre la structure et les propriétés des macromolécules biologiques, dont la cellulose, les polyhydroxyalcanoates (PHA) et les polymères de glucides. Son étude d'avant-garde de la stéréochimie et de la cristallinité des polyesters bactériens, effectuée en 1963, a favorisé la mise au point de ces matériaux pour en faire des matériaux thermoplastiques biodégradables aux multiples usages. Tout au long de sa carrière, il a manifesté un intérêt soutenu pour les matières plastiques biodégradables, et a joué un rôle important dans l'évolution de la chimie verte. À l'Université McGill, son programme de recherche portait principalement sur la mise au point de biopolymères destinés à des applications touchant l'imagerie, l'administration de médicaments et l'environnement. Il a publié plus de 300 articles dans des revues faisant l'objet d'un examen par des pairs et est cotitulaire de 20 brevets d'invention.

En 1976, il a reçu le prix Anselme-Payen de la division cellulose, papier et textile de l'American Chemical Society, en reconnaissance de son enseignement stimulant et de son programme de recherche dynamique. Également, il a été le récipiendaire du Macromolecular Science and Engineering Award (prix de science et de génie des macromolécules) de l'Institut de chimie du Canada, en 1998. M. Marchessault a exercé une très grande influence sur l'avancement de la recherche scientifique dans son ensemble au Canada, ayant siégé à plusieurs comités du Conseil national de recherches du Canada au fil des années et au Conseil consultatif des sciences et de la technologie en 1986. En 1981, il a reçu le prix Urgel-Archambault de l'Association francophone pour le savoir (anciennement l'Association canadienne-française pour l'avancement des sciences). La Société royale du Canada a élu M. Marchessault membre de l'Académie canadienne des sciences, en 1982. En 1984, il a été élu membre de l'American Physical Society. L'Université Concordia lui a décerné un doctorat honorifique en sciences, en 1982. En 1991, l'Institut de chimie du Canada a reconnu son leadership professionnel et scientifique en lui remettant la Médaille de Montréal. En 2000, il a été nommé officier de l'Ordre du Canada et, en 2002, il a reçu la Médaille du jubilé de la Reine.

© 2008 NRC Canada

AWARD LECTURE / CONFÉRENCE D'HONNEUR

2′F-Arabinonucleic acids (2′F-ANA) — History, properties, and new frontiers

Jonathan K. Watts and Masad J. Damha

Abstract: The development of arabinonucleosides and oligoarabinonucleotides is described, focusing especially on 2′-deoxy-2′-fluoroarabinonucleosides (araF-N) and -oligonucleotides (2′F-ANA). In addition to their chemical and enzymatic synthesis, we discuss various properties of 2′F-ANA: hydrolytic stability (to nucleases, acids, and bases), binding affinity to complementary strands, structure and conformation, and optimization of RNase H activity. We also discuss the use of 2′F-ANA in gene-silencing approaches (antisense, siRNA), and in the stabilization of higher-order structures (such as triplexes and quadruplexes) including aptamers. Finally, we examine several other oligonucleotide derivatives based on 2′F-ANA and look ahead to the future of 2′-fluoroarabinonucleosides and -oligonucleotides.

Key words: arabinonucleic acids, 2′F-ANA, antisense oligonucleotides, siRNA, modified oligonucleotides.

Résumé : On décrit le développement d'arabinonucléosides et d'oligoarabinonucléotides, en portant une attention particulière aux 2′-désoxy-2-fluoroarabinonucléosides (araF-N) et -oligonucléotides (2′F-ANA). En plus de leur synthèse chimique et enzymatique, on discute de diverses propriétés des 2′F-ANA, telles la stabilité hydrolytique (des nucléases, des acides et des bases), l'affinité de fixation à des brins complémentaires, la structure et la conformation et l'optimisation de l'activité RNase H. On discute aussi de l'utilité des 2′F-ANA dans les approches tendant à rendre les gènes silencieux (antisens, siARN) et dans la stabilisation des structures d'ordres supérieurs (triplexes et quadruplexes), y compris les aptamères. Enfin, on examine plusieurs autres dérivés oligonucléotidiques dérivés du 2′F-ANA ainsi que l'avenir des fluoroarabinonucléosides et -oligonucléotides.

Mots-clés : acides arabinonucléiques, 2′F-ANA, oligonucléotides antisens, siARN, oligonucléotides modifiés.

[Traduit par la Rédaction]

Introduction

The synthesis of 2′-deoxy-2′-fluoroarabinonucleosides (2′F-araN) was first reported in 1969 (1, 2). Since then, the study of these compounds and their oligonucleotide derivatives has remained a particularly active area of research. From the very beginning, much of the research has been aimed at therapeutic applications. At least five 2′F-araNs have reached clinical trials, of which only one has been approved for medical use (Table 1). The oligonucleotides (2′-deoxy-2′-fluoroarabinonucleic acids or 2′F-ANAs) are now being studied for both therapeutic and non-therapeutic applications.

This review will summarize the history and development of 2′F-ANA, beginning with several significant 2′-deoxy-2′-fluoroarabinonucleosides. In the interests of space, only those with a true 2′-deoxy-2′-fluoroarabinose sugar will be discussed; many other modified nucleosides and derivatives containing a top-face (β) fluorine at the 2′-position have been omitted but are described elsewhere (3), including the 2′-difluoro cancer drug gemcitabine (4), and the 3′-deoxy adenosine derivative lodenosine (5).

From there, we will move to a review of the properties of 2′F-ANA oligonucleotides, given in historical perspective. The high binding affinity and hydrolytic stability of 2′F-ANA attracted interest early on, along with the ability of 2′F-ANA to elicit RNase H cleavage of a complementary RNA strand. Newer discoveries include the fact that siRNA duplexes tolerate 2′F-ANA modifications, and that 2′F-araN 5′-triphosphates are substrates of various DNA polymerases. We will conclude by looking at various other 2′-fluoroarabinooligonucleotide derivatives inspired by 2′F-ANA.

Received 28 January 2008. Accepted 26 February 2008. Published on the NRC Research Press Web site at canjchem.nrc.ca on 13 May 2008.

J.K. Watts and M.J. Damha.[1] Department of Chemistry, McGill University, 801 Sherbrooke Street West, Montreal, QC H3A 2K6, Canada.

[1]Corresponding author (e-mail: masad.damha@mcgill.ca).

2′-Deoxy-2′-fluoroarabinonucleosides

Several notable 2′-deoxy-2′-fluoroarabinonucleosides

Several factors provided motivation to explore the 2′-deoxy-2′-fluoroarabinonucleosides. Fluorine has a small steric effect but a significant influence on nucleoside confor-

 doi:10.1139/V08-049 © 2008 NRC Canada

Table 1. 2′-deoxy-2′-fluoroarabinonucleosides that have entered human trials.

Compound	Figure	Type	Notes
FMAU	1*a*	D-nucleoside	Potent antiviral and antileukemic activity. A Phase I trial for activity against solid tumors was terminated because of severe neurologic toxicity (11)
L-FMAU (clevudine)	1*b*	L-nucleoside	Performed well in a 2004 Phase II clinical trial against Hepatitis B (18), currently being developed by Pharmasset, Inc.
FIAC (fiacitabine)	1*c*	Base-modified D-nucleoside	Showed good antiviral activity in several Phase I trials (early 1980s) and one Phase I/II trial (against VZV in immunocompromised patients, 1986) (28), but was withdrawn after another Phase I/II trial (1989) showed significant toxicity (22)
FIAU (fialuridine)	1*d*	Base-modified D-nucleoside	Showed good activity against HSV and HBV. A 1993 Phase II trial against HBV was halted on an emergency basis (22, 29)
Clofarabine	2*a*	Base-modified D-nucleoside	Approved by the FDA (in 2004) and the European Union (in 2006) for the treatment of pediatric patients with relapsed or refractory acute lymphoblastic leukemia (ALL) (30, 31)

mation and stability owing to its high electronegativity. For instance, the 2-deoxy-2-fluoroarabinose moiety provides resistance to hydrolytic (acid-catalyzed) or enzymatic (phosphorylase) cleavage of the *N*-glycosidic bond (6, 7). Thymine and other 5-substituted pyrimidine nucleosides exhibit better antiviral activity with 2-fluoroarabinose than with 2-deoxyribose or arabinose sugars (8). Thus FMAU (2′-fluoro-5-methyl-β-D-arabinouridine, Fig. 1*a*) attracted significant attention for its antiviral activity, especially against Herpes Simplex Virus (HSV) (8, 9). Despite its significant antiviral and anticancer activity (10), FMAU caused significant neurotoxicity and myelosuppression at the doses required for activity (11), and was found to be incorporated into DNA by eukaryotic as well as viral enzymes (12, 13). Nevertheless, this family of compounds (2′F-araN) has not been found to cause mutagenesis in bacterial or mammalian cells (14), in contrast with the non-fluorinated nucleoside arabinocytidine (*ara*C) (15). More recently it was discovered that the enantiomer L-FMAU (clevudine, Fig. 1*b*) exhibits a more favorable therapeutic index than D-FMAU against Hepatitis B Virus (HBV) and Epstein-Barr Virus (EBV) (16). The cytosine derivative L-FAC exhibits somewhat lower potency (17). L-FMAU has performed well in phase II clinical trials against HBV (18) and is being developed by Pharmasset, Inc.

A third nucleoside to have been tested in humans is fiacitabine (2′-fluoro-5-iodo-β-D-arabinocytidine (FIAC), Fig. 1*c*). This nucleoside showed much higher activity against HSV than other drugs of its day (19) After performing well in several Phase I and Phase I/II trials, it was eventually abandoned for reasons of toxicity. FIAC was found to be metabolized to FIAU (2′-fluoro-5-iodo-β-D-arabinouridine, Fig. 1*d*) (8, 20). The latter had already demonstrated antiviral activity, and the focus of clinical work shifted to it, hoping to avoid the toxicity associated with FIAC. Indeed, it had a good short-term toxicity profile, but a longer-term, low-dose Phase II trial was cancelled after five patients died of liver failure, probably because of mitochondrial toxicity (21). Clinical development of both FIAC and

Fig. 1. Four 2′-deoxy-2′-fluoroarabinonucleosides that have reached clinical trials.

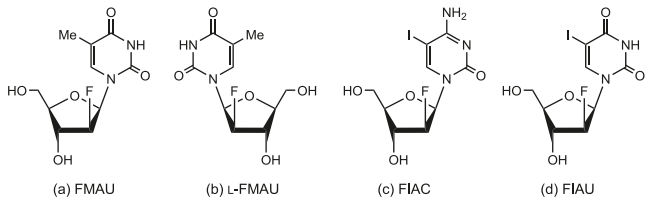

Fig. 2. Clofarabine and the two other drugs from which it was inspired.

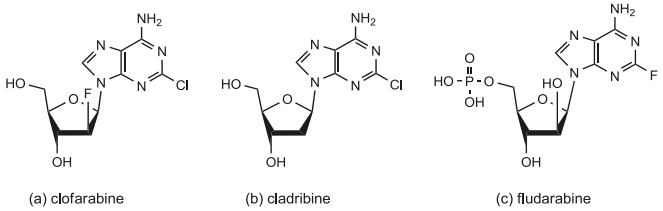

FIAU have been the subject of thorough reviews, to avoid similar outcomes in future (22). Additional details of the antiviral activities of 2′-fluorinated arabinosyl-pyrimidine nucleosides are provided elsewhere (23).

The metabolism and DNA incorporation of other 5-modified 2′-fluoro-β-D-arabinonucleosides are significantly dependent on the 5-substituent (12). FIAU and FEAU (2′-fluoro-5-ethyl-β-D-arabinouridine) (24) have recently found utility in positron emission tomography (PET) (25) and other imaging of experimental tumors and localized bacterial infections (26), because a radiolabeled FIAU or FEAU molecule is preferentially phosphorylated by viral and bacterial kinases within these systems. It is also noteworthy that FEAU is less toxic than other 2′F-araNs (23). On the other hand, because of its greater uptake by eukaryotic DNA polymerases, ^{18}F-FMAU has been used for imaging of DNA synthesis in vivo (27). Because of the very low concentra-

© 2008 NRC Canada

Scheme 1. Synthesis of 2′-fluoroarabinonucleosides is generally approached by coupling the base (normally trimethylsilylated at the carbonyl groups) to a 3,5-di-*O*-acyl-2-deoxy-2-fluoro-D-arabinosyl bromide.

Scheme 2. Pyrimidine O2 rapidly displaces an α-face leaving group at C2′, preventing direct synthesis of 2′-fluoroarabinonucleosides from ribonucleosides.

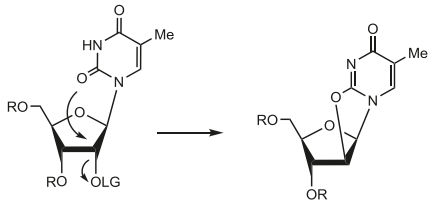

Scheme 3. Various synthetic routes to 1-acetyl or 1-bromo 3,5-di-*O*-acyl-2-deoxy-2-fluoroarabinose, suitable for coupling to nucleobases. Shown are (*a*) the first synthetic route (1, 41); (*b*) an early route amenable to larger scale synthesis (40); and (*c*) the route used for most recent work (38, 44). Reagents and conditions: (*a*) (i) Methyl chloroformate in pyridine–chloroform, 0 ºC, 64h; (ii) TsCl, pyridine, 70 ºC, 6h; (iii) AcOH, Ac_2O, H_2SO_4, 19h; (iv) 1% HCl in MeOH, 19h; (v) NaOMe, MeOH, 47% over 5 steps; (vi) BnBr, Ag_2O, DMF; (vii) KHF_2, ethylene glycol, reflux, 40%; (viii) 1 N H_2SO_4 in dioxane–water, reflux, 4h, ~quant.; (ix) Ac_2O, pyridine, 18h. (*b*) (x) KF, acetamide, 210 ºC, 15 min, 62%; (xi) 0.35% H_2SO_4 in 1:1 methanol–water, rt, 10h; (xii) barium carbonate, reflux, 10 min; (xiii) BzCl, pyridine; (xiv) Amberlite IR-120 (H+), 78%; (xv) potassium metaperiodate, water, overnight; (xvi) NaOMe in MeOH; Ac_2O, pyridine, rt, overnight, 80%; (xvii) 30% HBr in AcOH; (*c*) (xviii) DAST, CH_2Cl_2, 40 ºC, 75%; (xix) 30% HBr, AcOH, CH_2Cl_2, 97%.

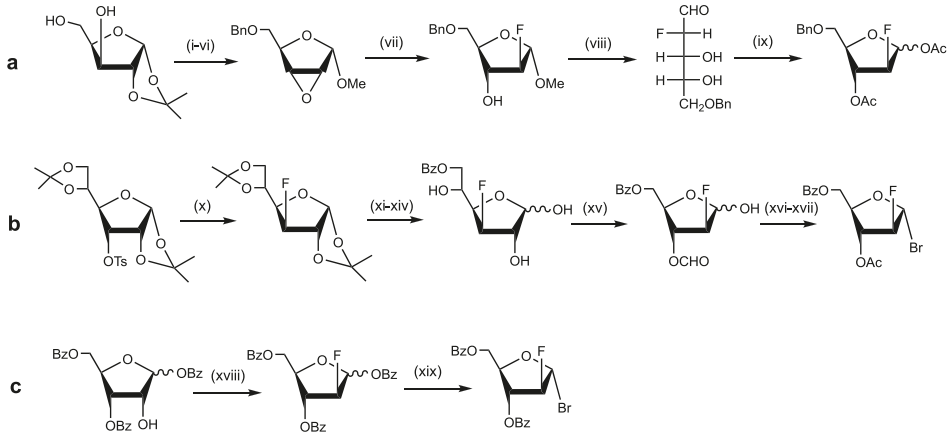

tions required for PET, these nucleosides exhibit "no toxicity" when used for these imaging techniques (26). Studies are underway to move these nucleosides toward clinical trials for this purpose.

The purine nucleosides 2′F-araA and 2′F-araG also show biological activity (32, 33). However in general, the 2′-fluoroarabino purine nucleosides have attracted less attention than their pyrimidine counterparts. The exception is clofarabine (30, 31, 34), one of the most successful 2′-deoxy-2′-fluoroarabinonucleosides, which contains a modified purine, 2-chloroadenine (see Fig. 2*a*). Clofarabine was developed while trying to improve upon the properties of two other adenosine-based anticancer drugs, cladribine and fludarabine (Fig. 2) (35, 36). The 2′-fluoro substitution yielded a glycosidic bond highly resistant to hydrolysis and phosphorylase cleavage (36). Its anticancer activity results from inhibition of DNA polymerases and ribonucleotide reductase (which depletes the dNTP pool, favoring incorporation of clofarabine into DNA), and induction of apoptosis because of DNA damage after clofarabine incorporation (34, 36, 37). Clofarabine was approved for treatment of pediatric acute leukemia by both the FDA (in 2004) and the European Medicines Agency (in 2006). Its side-effect profile is "typically manageable and tolerable" (31), while the drug has significant activity in relapsed or refractory leukemias where other treatments have failed.

2′-Deoxy-2′-fluoroarabinonucleosides have also found use as inhibitors of base-excision repair enzymes (38). The 2-deoxy-2-fluoroarabinose sugar has been used to synthesize mimics of deoxyribose glycosyl phosphates, key intermediates in nucleic acid biosynthesis (39).

Synthesis of 2′-deoxy-2′-fluoroarabinonucleosides

From the earliest work on pyrimidine 2′-deoxy-2′-fluoroarabinonucleosides, the synthetic approach has been based on the coupling of the heterocyclic base to a 3,5-di-*O*-acyl-2-deoxy-2-fluoro-D-arabinosyl bromide (Scheme 1) (8, 40). Occasionally the anomeric acetate has been used instead (1). Direct introduction of top-face fluorine into the 2′ position of a pyrimidine nucleoside by nucleophilic displacement would be very difficult because the carbonyl group at C-2 tends to displace any potential leaving group in the ribose sugar precursor before the fluorination can be carried out (Scheme 2).

Synthesis of the requisite 3,5-di-*O*-acyl-2-deoxy-2-fluoroarabinosyl sugar has been carried out in a variety of ways (Scheme 3). Initial work used a methyl 2,3-anhydroribofuranoside as a key intermediate, which was in turn obtained

© 2008 NRC Canada

from a protected xylofuranose (Scheme 3*a*) (1, 41). Starting from a protected allofuranose reduced the number of separations required, increased the overall yield of product, and was more suitable for large scale synthesis, but required at least eight steps (Scheme 3*b*) (40). 1,3,5-Tri-*O*-benzoylribose (42, 43) is now commercially available and has been used as the starting point for most recent work, thereby simplifying the synthesis tremendously (Scheme 3*c*) (38, 44).

The fluorination step has almost invariably utilized nucleophilic displacement. The first synthesis was based on the opening of a 2′,3′-α-epoxide, but this provided low yields and complex product mixtures (1). Several authors have proposed one-pot (45) or two-step (17, 39, 40, 42, 46, 47) sulfonate displacement reactions, using Bu_4NF (40, 47), KHF_2 (17, 42), or $Et_3N{\cdot}3HF$ (39, 45, 46) as the fluoride source. Diethylaminosulfur trifluoride (DAST), a mild, one-pot fluorinating reagent (48), almost completely avoids dehydration (elimination) during the fluorination reaction. It has been used by many research groups (6, 38, 44). One particular challenge is the scale-up of these reagents, since nucleophilic forms of fluoride such as KHF_2 or $Et_3N{\cdot}3HF$ are difficult to handle and require activation of the displaced hydroxyl group, and reagents such as DAST are too unstable to be useful on large scale. From the many options available (49), Sznaidman et al. have provided a possible solution in the form of a synthesis from arabinose, consisting of electrophilic addition of fluorine to a glycal moiety using the reagent Selectfluor™ (F-TEDA-BF_4) (50). Others have developed protocols that minimize the corrosiveness of the nucleophilic fluorinating agent, and have successfully reached a scale of up to 800 kg (46).

Howell et al. made a major contribution to the glycosylation step by observing that the β-selectivity of the reaction could be made almost complete by carrying out the reaction in nonpolar solvents (51). The reaction is thus forced to follow an S_N2 mechanism from the α-bromo precursor, since the oxygen-C_1-onium ion required for an S_N1 reaction is already destabilized by the 2′-fluoro group, and cannot exist in the absence of solvent stabilization (51). This approach results in high yields of β-nucleosides, which can be purified by crystallization. The mother liquor contains a residual mixture of α and β anomers that is very difficult to separate but can be enzymatically converted to 3′-*O*-benzoyl nucleosides that are separable by chromatography (52).

In the case of the purine 2′-deoxy-2′-fluoroarabinonucleosides, some synthetic work has been undertaken by 2′-fluorination of ribonucleosides (reviewed by Pankiewicz (53); another efficient route has been more recently reported by Maruyama et al. (54)) However, coupling to the fluorinated sugar, as described above for the pyrimidine nucleosides, has the advantage of divergence when both purine and pyrimidine nucleosides are made. In the case of guanine, the synthetic route utilizes a masked base, which is later converted into the desired guanine; initial attempts at this strategy used dichloropurine (55–57) or 2-acetamido-6-chloropurine (32), but the synthesis can be improved and simplified using 2-chlorohypoxanthine instead (58).

Recently published step-by-step protocols may be useful to those wishing to synthesize 2′F-araNs and their phosphoramidite derivatives (57, 59).

Fig. 3. Structures of (*a*) 2′F-ANA and (*b*) ANA, in comparison with (*c*) DNA and (*d*) RNA oligomers.

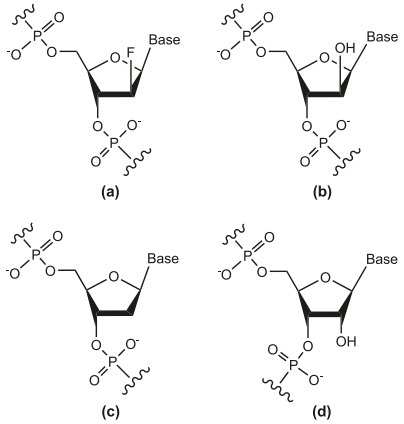

2′-Deoxy-2′-fluoroarabinonucleic acid (2′F-ANA)

The first 2′F-ANA oligomers

Pyrimidine 2′-deoxy-2′-fluoroarabinonucleosides (FMAU, FIAU, FAU, and FAC) were first incorporated into oligonucleotides by Watanabe and co-workers in 1993 (Fig. 3*a*) (60, 61). Oligonucleotide synthesis using 2′-deoxy-2′-fluoroarabino monomers was readily carried out using either phosphoramidite or *H*-phosphonate chemistry (61). Another pair of studies incorporated FMAU into the self-complementary DNA Dickerson–Drew dodecamer (62, 63).

Meanwhile, quite a bit of work had been carried out on the arabinonucleic acids (ANA) (Fig. 3*b*). Initial interest in arabinonucleic acids was somewhat serendipitous. One of us was studying in the group of Professor K.K. Ogilvie at McGill University, and in the course of pursuing Prof. Ogilvie's interest in arabinonucleoside (64) and branched RNA synthesis (65, 66), we discovered that ribonucleoside 2′,3′-*O*-bis-phosphoramidite derivatives exhibited unusual P–P coupling in the ^{31}P NMR spectra (66). It was hypothesized that such coupling ($^5J_{P,P}$ = 10–30 Hz) may arise through space rather than through the five-bond framework (66). To explore this observation further, the corresponding arabino-configured species was synthesized; this compound retained the same P–P bond distance (five), but the disposition of the trans amidite moieties would affect the strength of the putative through-space P–P coupling (67). However, an abundant byproduct in this synthesis, even under forcing conditions, was the arabinonucleoside mono 3′-*O*-phosphoramidite, because steric hindrance reduced the accessibility of the 2′ hydroxyl group (68). After facile acetyl protection at the 2′ position, it was therefore straightforward to begin to explore ANA oligomers.

Thus, initial synthetic work in our group (68) and elsewhere (69) paved the way for investigations into the hybridization and structure of ANA. As well as several hybridization studies of oligonucleotides containing one or two ANA modifications (70), the hybridization of fully modified ANA oligomers to various targets was studied (71).

In most contexts, ANA oligonucleotides bound to RNA target strands with somewhat lower affinity than DNA or

© 2008 NRC Canada

RNA oligonucleotides (71, 72). The difference was even more dramatic in the case of DNA targets, to which very poor binding, or no binding at all, was observed (71, 72). We speculated that the lower binding affinity of ANA might be due to steric hindrance of the top-face 2′-OH, perhaps lowering the efficiency of base-pairing or base-stacking (72). To reduce the steric bulk of the 2′ substituent, we proposed replacing it by fluorine. Thus, we initiated a study of mixed-sequence, fully modified 2′F-ANA sequences containing all four bases, using phosphoramidite chemistry (44, 59, 73). The result was gratifying: the resulting 2′F-ANA·RNA and 2′F-ANA·DNA duplexes were much more stable. The reasons for this change, however, appear to be more complex than we originally thought (see below).

When fully modified ANA or 2′F-ANA strands were annealed with complementary ssRNA, their duplex conformation (as determined by circular dichroism (CD)) closely resembled that of a DNA·RNA duplex (73). This observation prompted investigation of the recognition of the duplexes by RNase H, a ubiquitous enzyme that cleaves the RNA strand of a DNA·RNA duplex. If an antisense oligonucleotide can induce RNase H-mediated RNA cleavage, it becomes a catalyst for the hydrolysis of multiple mRNA strands (74).

Both ANA and 2′F-ANA were able to induce RNase H-directed cleavage of their complementary RNA strand, but the 2′F-ANA strand did so with higher efficiency (73). Prior to 1998, DNA–RNA hybrids were the only reported substrates for RNase H, and thus it was generally perceived that only DNA could support this activity. Thus, ANA and 2′F-ANA represented the first examples of RNase H-competent oligomers that lacked 2-deoxy-D-ribofuranose. These findings also provided a very important advance in understanding the catalytic mechanism and substrate selectivity of RNase H, and underscored the potential of arabinose-based oligomers as gene-silencing agents. The higher efficiency of RNase H induction by 2′F-ANA, along with its higher binding affinity, made it the lead compound for further investigation into gene-silencing applications.

Hydrolytic stability of 2′F-ANA to nucleases, acids, and bases

The improved nuclease stability of 2′F-ANA oligonucleotides has long been appreciated. For example, the first group to work on 2′F-ANA found a 4–8-fold increase in stability to nuclease P1 with respect to DNA (61). Others have also observed increased stability of 2′F-ANA to snake venom phosphodiesterase (SVPDE, a highly active 3′-exonuclease) or serum. Noronha et al. subjected various homopyrimidine sequences to SVPDE hydrolysis and found the following order of stability: PS-DNA > > ANA > 2′F-ANA ≈ RNA > 2′F-RNA > DNA (72). An interesting observation from this study is that arabinonucleic acids (2′-OH or 2′-F) are generally more stable to SVPDE than the corresponding ribonucleic acids (ANA > RNA and 2′F-ANA > 2′F-RNA). Furthermore, enzymatic stability seems to increase as the van der Waals radius of the 2′-substituent increases within each series; i.e., DNA ($2'H_\beta$) < 2′F-ANA ($2'F_\beta$) < ANA ($2'OH_\beta$); and DNA ($2'H_a$) < 2′F-RNA ($2'F_a$) < RNA ($2'OH_a$) (72).

There also appears to be some dependence on base sequence for the hydrolytic stability of 2′F-ANA. In two sequences from a recent study, 2′F-ANA provided little or no advantage over DNA with either phosphodiester (PS) or phosphorothioate (PO) backbones (75). In contrast, a dramatic advantage was observed when 2′F-ANA was used to modify a self-complementary sequence (75). We believe that the higher thermal stability of 2′F-ANA duplexes may provide an extra advantage in terms of nuclease stability simply by holding the duplex more tightly together, thus rendering the individual strands less accessible for nuclease cleavage. Accordingly, Dowler et al. showed that 2′F-ANA modification of one strand of an RNA duplex provided significant additional serum stability to the whole duplex ($t_{1/2}$ ~5 h vs. ~5 min for the unmodified duplex) (76). This could be further enhanced by incorporating 2′F-araN units into the 3′-overhang of the antisense strand as well (76).

2′F-ANA can also confer nuclease resistance to higher order structures. 2′F-ANA-modification of a G-tetrad-containing thrombin-binding aptamer resulted in up to 48-fold greater serum stability compared with the unmodified DNA tetrad (discussed in detail below) (77).

While PO-2′F-ANA does provide some advantages in terms of nuclease stability, it cannot match the dramatic increase in stabilization provided by a PS backbone (78). However, when the two modifications (PS and 2′F-ANA) are combined, the resulting PS-2′F-ANA oligonucleotide is highly resistant to most nucleases. In both PS-DNA and PS-2′F-ANA, one of the diastereomers of the phosphorothioate linkage undergoes nucleolytic cleavage fairly easily, while the other is very stable (75, 79).

Two recent studies have examined the persistence of 2′F-ANA antisense oligonucleotides in cell culture and explored the relationship with gene-knockdown efficacy (80, 81). Kalota et al. observed that chimeric PS-2′F-ANA–DNA oligomers had greater persistence in cultured K562 cells (more than 70% of the oligonucleotide was still recoverable from the cells after 96 h, while very little PS-DNA remained after this time) (80). This suggests either that PS-2′F-ANA is more resistant to nucleases than PS-DNA, or that it is retained by cells to a greater extent. Correspondingly, this study found a lower effective dose and longer duration of action of PS-2′F-ANA oligomers with respect to PS-DNA (80). Another study found that two PS-2′F-ANA sequences were more stable to serum nucleases than most other sequences (with some exceptions) (81). Again, this paralleled excellent activity (luciferase-knockdown in HeLa cells) over extended assay times (81).

The glycosidic bond of 2′F-ANA and 2′F-RNA is also highly resistant to enzymatic cleavage by phosphorylases and glycosylases. Stivers et al. took advantage of this stability to study the mechanism of the DNA repair enzyme uracil DNA glycosylase (UDG), which flips premutagenic uracil bases out of the helix before cleaving them. By replacing a U residue with a 2′F-araU or 2′F-rU, they were able to observe flipping without glycosidic bond cleavage, and even carry out NMR structural characterization (82).

This remarkable stability of the glycosidic bond also means that 2′F-ANA demonstrates remarkable stability to acidic conditions (75). In enzyme-free simulated gastric fluid (pH ~1.2), 2′F-ANA was virtually intact after 2 days incubation at 37 °C. Under the same conditions, DNA was degraded within minutes, PO-RNA within hours, and PS-RNA within days (75, 83). The large difference between DNA and 2′F-ANA

© 2008 NRC Canada

Fig. 4. Mechanism of acid-catalyzed degradation of DNA (84). In the case of 2′F-ANA, the presence of fluorine at the 2′ position destabilizes the oxycarbonium ion intermediate and disfavors depurination, largely preventing this mechanism of degradation.

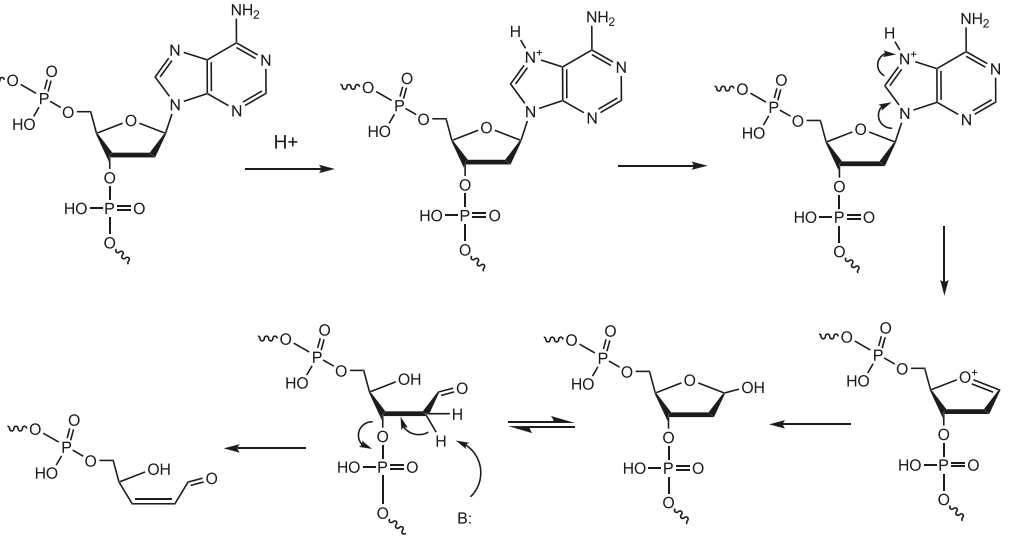

comes because the dominant mechanism for acid-catalyzed degradation of DNA (depurination followed by β-elimination) is disfavored by the presence of electronegative fluorine at the 2′ position (Fig. 4).

As for stability in basic conditions, we have not carried out detailed studies in our laboratory; however, it is clear that 2′F-ANA is much more stable than RNA to strongly basic conditions, as evidenced by the fact that 2′F-ANA strands are routinely deprotected in ammonium hydroxide. These are conditions under which naked RNA and even 2′F-RNA are rapidly degraded. This is, of course, because 2′F-ANA does not have a 2′-OH group to be deprotonated and used to attack the vicinal phosphate linkage. In the case of 2′F-RNA, the O2 atom of the pyrimidine base attacks at the 2′ position to displace the α-oriented fluoride (85, 86). Such a pathway is not possible for 2′F-ANA wherein the pyrimidine and fluorine are both on the top (β) face of the sugar ring.

Binding affinity

When 2′F-ANA pyrimidine-modifed oligonucleotides were first synthesized, their binding to DNA was investigated and the results were somewhat mixed: 2′F-araT units stabilized duplexes but 2′F-araC or 2′F-araU tended to destabilize them, relative to a DNA strand (60, 61). FIAU, when incorporated into oligonucleotides, also conferred stabilization (60). The added stabilization of FMAU and FIAU is consistent with the well-known favorable binding of 5-substituted pyrimidines (87). It has been our experience that 2′F-ANA consistently demonstrates high binding affinity to both DNA and RNA.

A 2′F-ANA·RNA duplex is consistently more thermally stable than a DNA·RNA duplex. Depending on the sequence, the stabilization of fully modified strands ranges from 0.3 °C/bp to 1.8 °C/bp (44, 73, 88, 89). Replacing an all-purine DNA strand with 2′F-ANA (or modifying only the purines of a mixed sequence) tends to yield smaller increases than replacing an all-pyrimidine strand (44), and in some cases no increase at all (56), but does not lead to destabilization as was originally predicted (63). Interestingly, the highest stabilizations observed have been for mixed sequences (for example, up to 1.8 °C/bp for a 10-mer mixed sequence) (89).

In some cases, 2′F-ANA·RNA duplexes are also more stable than RNA·RNA duplexes (44, 89–91). However, this is not always the case, and in other cases 2′F-ANA·RNA duplexes are of slightly lower stability than RNA·RNA duplexes (44,90). Furthermore, in cases where 2′F-ANA·RNA duplexes are in fact more stable than RNA·RNA duplexes, some of the difference can be attributed to the fact that 2′F-ANA typically contains thymine bases while RNA contains uracil (87). For example, duplexes of rT_{18} and 2′FaraT_{18} with rA_{18} were found to have similar melting temperatures (T_m) (51 °C and 52 °C, respectively), but the T_m of rU_{18}·rA_{18} was 17 °C lower (44).

A phosphorothioate backbone reduces the binding affinity of DNA or 2′F-ANA relative to a normal phosphodiester backbone (92). However, PS-2′F-ANA binds to RNA with higher affinity than PS-DNA (about 0.5 °C/bp) (93).

The binding affinity of 2′F-ANA–DNA chimeras has also been studied. For example, so-called "altimers" (Fig. 5) containing alternating stretches of 1, 2, 3, or 6 2′F-ANA nucleotides interspersed with 3 or 6 DNA units had T_m values increased by 0.6–0.8 °C per 2′F-ANA insert (to RNA, with respect to an all-DNA strand). Fully modified 2′F-ANA strands of the same sequences caused a T_m increase of 0.75 °C/bp (88). Thus these architectures cause no major change in the binding affinity of 2′F-ANA on a per-insert basis. This is in contrast to a 2′-OMe-RNA–DNA chimera, for which a 1–1 altimer architecture was significantly destabilized in its binding to RNA (0.8 °C per RNA insert) with respect to an all-DNA strand (88). This demonstrates the compatible conformations of DNA and 2′F-ANA, but the conformational incompatibility of DNA and RNA (the latter apparently inducing multiple AB junctions within the duplex) (62). Another study has shown that these findings are also applicable to the binding affinity of 2′F-ANA–DNA chimeras with phosphorothioate backbones (94).

© 2008 NRC Canada

Fig. 5. Sample architectures of chimeric strands, to illustrate terminology: (*a*) gapmer; (*b*) 1–1 altimer; and (*c*) 3–3 altimer. In a typical 2′F-ANA–DNA chimera, the dark-colored beads would symbolize 2′F-ANA residues and the lighter beads would symbolize DNA.

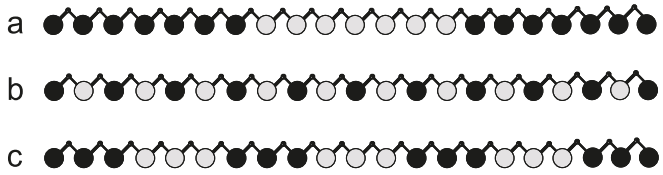

The binding of 2′F-ANA–RNA chimeras is also more favorable than an all-RNA strand, whether binding to an RNA or DNA target strand (91). However, the enhanced binding is particularly strong when the target strand is DNA. This has been shown for various architectures, including a "gapmer"-type structure (a central 2′F-ANA region with RNA wings, see Fig. 5) and siRNA duplexes (91).

Fully modified 2′F-ANA strands, in contrast to ANA, also bind with high affinity to ssDNA. In one study of five 18-mer sequences, 2′F-ANA showed increased binding affinity (to DNA) ranging from 0.2 to 0.9 °C/bp relative to DNA, and 0.4 to 1.7 °C/bp relative to RNA (44).

2′F-ANA also forms stable homoduplexes (that is, 2′F-ANA·2′F-ANA duplexes). While ANA·ANA duplexes tend to be highly unstable (95), 2′F-ANA·2′F-ANA duplexes are more stable even than 2′F-ANA·RNA or RNA·RNA (89, 90)

One important finding related to binding affinity is that 2′F-ANA has a very high base pairing specificity. When a single mismatch was introduced into a DNA target strand, the T_m of the duplex dropped most sharply when the test strand was 2′F-ANA (8.0 °C), followed by RNA (7.2 °C), then DNA (3.9 °C) (44). When using an RNA target strand, introduction of a single mismatch caused the T_m of the duplex to drop most sharply when the test strand was RNA (9.3 °C), followed by 2′F-ANA (6.6 °C), then DNA (5.4 °C) (44) High base pairing specificity is essential for applications such as microarrays and other diagnostics, as well as for therapeutic applications.

2′F-ANA has also been used to increase the inter- and intramolecular binding affinity of triplexes and higher order nucleic acid structures, as discussed below.

We conclude this section by returning to the observation that the binding affinity of 2′F-ANA, to both RNA and DNA target strands, is dramatically higher than that of the related modification ANA. This is especially true when the target strand is DNA; ANA·DNA duplexes are so unstable that they are barely detectable. In a recent study of several 10-mer oligonucleotide duplexes, 2′F-ANA·RNA was the most stable, followed by RNA·RNA (ΔT_m = –4 °C), DNA·DNA (ΔT_m = –14 °C), DNA·RNA (ΔT_m = –18 °C), and finally ANA·RNA (ΔT_m = –19 °C) (89). The dramatic increase in target affinity upon changing OH to F has stimulated numerous studies by our group into the structure of 2′F-ANA and its duplexes, in an attempt to understand the causes of this difference, as described in the following section.

Studies on the structure, conformation, and hydration of 2′F-ANA

Nucleoside conformation

Various groups have undertaken conformational studies of 2′-fluoroarabinonucleosides. Early computational work suggested that the pyrimidine base of FMAU was locked into an *anti* orientation because of the presence of the top-face fluorine at 2′, and that the nucleoside puckered in the south (C2′-*endo*) (96) A study of NMR spectra at various temperatures concluded that FMAU was a relatively rigid nucleoside, with about 65% south character (97).

More recently, quantitative conformational studies have been done using the program PSEUROT (98), which assumes a two-state conformational equilibrium. This has been a key tool in allowing conformational discussions to move beyond vague references to "north" and "south" conformers. We summarize the available quantitative solution-phase parameters in Table 2 and Fig. 7 (structures of canonical and modified purine bases are shown in Fig. 6). Parameters for normal 2′-deoxyribo- and ribonucleosides (dN and rN) are included for comparison.

It becomes clear from Table 2 and Figs. 6 and 7 that there are differences within the literature on the solution-phase conformation of 2′-fluoroarabinonucleosides, specifically 2′F-araA and 2′F-araG. The 2′F-araN conformations, whether with canonical or modified bases, fall into four groupings, in the north, northeast, southeast, and south. Five researchers have found a pair of conformations in the north and southeast for the 2′-fluoroarabinonucleosides, while two others have found a pair of conformations in the northeast and south. For 2′F-araA and 2′F-araG, both of these pairs of conformations have been independently found. One explanation may be that these nucleotides are in fact characterized by a three- or four-state equilibrium, but either of the two pairs is sufficient to reproduce the observed coupling constants. (The PSEUROT program can only resolve equilibria of one or two conformers). Denisov et al. have described an oligonucleotide (hairpin) for which the two-state model adopted by PSEUROT was not adequate to explain the observed NOEs, but a three-state model (explored through molecular modeling) was suitable (105).

One property that emerges very clearly from the data is the presence of eastern conformations for 2′F-araN. All of the nucleosides studied have a predominant population of either the northeast or southeast conformer, with the sole exceptions of those with the unusual 3-bromopyrazolo[3,4-*d*]pyrimidine bases (4f and 4g) and a couple of other more extreme base modifications not included in Table 2 (101, 106). Thus, whichever description of the 2′-araN conformation is correct (north + southeast, northeast + south, or a four-state equilibrium), an eastern shift is observed when comparing 2′F-araN to dN: either the south becomes southeast, or the north becomes northeast, or two new eastern conformations are added to the equilibrium. Consistent with this shift to the east, strong NOE contacts have been observed between H1′ and H4′ of 2′F-araA (44).

Evidence from thermal stabilities

2′F-ANA is a DNA mimic in terms of its effect on helical structure (CD) and binding affinity (T_m). For example, when

© 2008 NRC Canada

Table 2. 2′-Deoxy-2′-fluoroarabinonucleosides for which quantitative solution-phase pseudorotational parameters are available. Purine structures are shown in Fig. 6.

Nucleoside	P_N (ϕ_{max})	P_S(ϕ_{max})	% N	Ref.
Normal nucleosides				
rN (pyrimidine)[a]	15 (43)	165 (43)	59	(99)
rN (purine)[a]	10 (42)	170 (42)	42	(99)
dN (pyrimidine)[a]	13 (41)	167 (41)	42	(99)
dN (purine)[a]	9 (42)	171 (42)	32	(99)
2′-Fluoroarabino nucleosides (canonical bases)				
2′F-araT (FMAU)	–6 (36)	126 (36)	31	(100)
2′F-araG	54 (41)	181 (41)	50	(56)
2′F-araG	66 (43)	173 (43)	57	(101)
2′F-araA	26 (40)	133 (40)	36	(56)
2′F-araA	–9 (40)	128 (40)	32	(102)
2′F-araA	70 (43)	168 (43)	58	(101)
2′F-araA	9 (36)	132 (37)	36	(103)
2′-Fluoroarabino nucleosides (modified bases)				
4a	–2 (41)	129 (41)	35	(104)
4b	10 (41)	130 (41)	34	(104)
4c	–4 (41)	131 (41)	36	(104)
4d	–2 (41)	131 (41)	37	(104)
4e	5 (41)	130 (41)	36	(104)
4f	–2 (37)	108 (42)	98	(101)
4g	–2 (38)	126 (42)	100	(101)

[a]Results for the *anti* base orientation were used since 2′-fluoroarabinonucleosides have a higher proportion of the *anti* orientation than their deoxynucleotide congeners (77, 96).

Fig. 6. 2′-Fluoroarabino purine nucleosides (with canonical and modified bases) for which quantitative solution-phase conformational parameters are available.

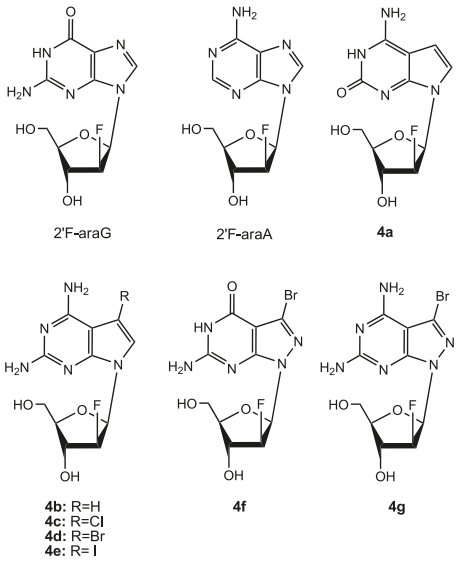

B-DNA was modified with 2′F-ANA units, the thermodynamic stability strongly increased. However, when 2′F-RNA units were used instead, the duplex was destabilized and the presence of an A–B junction was discerned by circular dichroic (CD) spectroscopy (62). Also, thermal stabilities of fully modified oligonucleotides show that 2′F-ANA mimics DNA, as shown by the following example: the known order of stability of the A/T system is dA/dT > rA/dT > rA/rU > dA/rU (107). Replacing the purine strands of 18-nt duplexes with 2′F-ANA and 2′F-RNA results in the order of stabilities 2′F-araA/dT (63.3 °C) > 2′F-rA/dT (48.0 °C) > 2′F-rA/rU (39.2 °C) > 2′F-araA/rU (30.2 °C) (90). Thus, the order is maintained, showing that 2′F-ANA and 2′F-RNA mimic the DNA and RNA structures, respectively.

However, the situation is slightly more complex. As we noted earlier, 2′F-ANA is structurally compatible with *both DNA* (88) *and RNA* (91), in various chimeric structures (as shown by an increase in thermal stability). In contrast, 1:1 DNA–RNA altimers were not compatible in their structures (88). Although the comparison is not perfect since we have not made 1:1 altimers of 2′F-ANA and RNA, it is interesting that while 2′F-ANA appears to be primarily a DNA mimic, it is compatible with RNA as well.

Conformational work on oligonucleotides

General information about the conformation of oligonucleotides can be obtained from CD spectra. CD traces of FANA·RNA and ANA·RNA duplexes are intermediate in form between DNA·RNA (A–B form) and RNA·RNA (A form) CD traces (44). In fact, they have more A-form character than the DNA·RNA hybrid. The CD spectrum of a pure 2′F-ANA·2′F-ANA duplex is also interesting in that it closely resembles the B-form signature above 250 nm, but has strong negative peaks at 207 and 245 nm that are closer to those of an RNA·RNA CD trace (90). These two observations are consistent with the ability of 2′F-ANA to mimic the DNA structure, while being compatible with RNA environments as well.

The first quantitative structural work on 2′F-ANA inserts in a DNA duplex was a crystallographic study that found

© 2008 NRC Canada

Fig. 7. The conformational parameters from Table 2 shown on the pseudorotational wheel. Legend: filled squares, rN; empty squares, dN; filled circles, 2′F-araN with canonical bases; empty circles, 2′F-araN with modified bases. Values for dN and rN are averages for purine and pyrimidine values. Sizes of circles are approximately proportional to the mole fraction of each conformer shown.

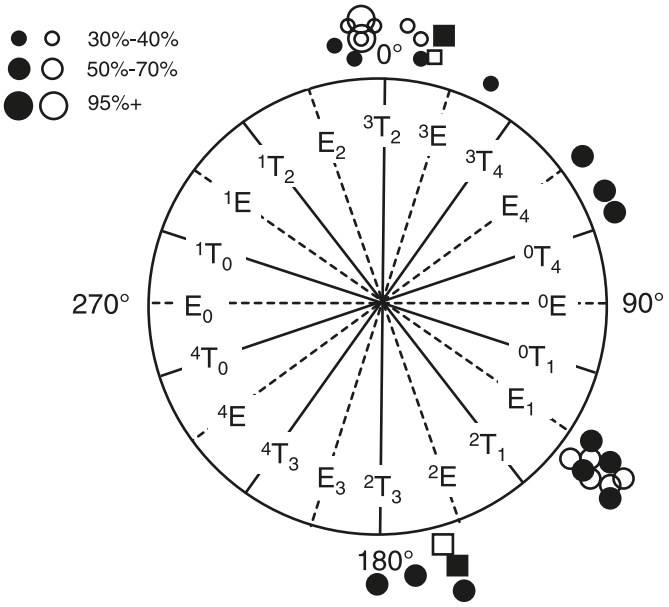

that 2′F-ANA inserts in the Dickerson–Drew dodecamer adopted an O4′-*endo* pucker (63). Significantly, the pucker of the neighboring nucleotides was not greatly affected (63). Thus this rare conformation is fully compatible with the B-form helical environment.

The most important structural study of ANA·RNA and 2′F-ANA·RNA duplexes to date examined short hairpins containing a 4-bp hybrid stem and a 4-nt DNA loop by NMR spectroscopy (105, 108). A third hairpin was studied comprising a DNA·RNA stem, for comparison. The conclusions of this study were as follows:

(*i*) The arabinose sugars of both 2′F-ANA·RNA and ANA·RNA duplexes are strongly preorganized into an O4′-*endo* (east) pucker (105, 108). Very strong H1′–H4′ NOE crosspeaks are observed for both 2′F-ANA and ANA residues (105, 108). In contrast to the deoxyribose sugars of the DNA·RNA duplex, which are very dynamic, the ANA and 2′F-ANA sugars are quite rigid (at least 75% O4′-*endo*, with the other 0–25% made up of northern and (or) southern puckers). The terminal nucleotides are exceptions, presumably because they have more conformational freedom because of end fraying. The rigidity of 2′F-ANA and ANA may explain the slower kinetics of RNase H cleavage of both modified hybrid duplexes (93). However, since both are rigid, it cannot explain the difference in duplex stability (105, 108). Two previous computational studies had also predicted the O4′-*endo* pucker for 2′F-ANA·RNA duplexes, but not for ANA (109,110).

(*ii*) The helical parameters, especially minor groove width, are similar for all three duplexes and are intermediate between A-form and B-form structures (105, 108). This may be the key to the recognition of all three duplexes by RNase H. This finding is consistent with earlier computational work on both duplexes (109).

(*iii*) No evidence for OH2′–O5′ hydrogen bonding was observed in the case of ANA sugars in the ANA·RNA duplex (105). In contrast, previous computational work had attributed the predominant C2′-*endo* sugar pucker observed for ANA sugars in that study to the influence of H-bonding (109).

(*iv*) Very little difference was observed between the conformations of ANA and 2′F-ANA (105). Since no steric hindrance was observed in the case of ANA, and the conformation and flexibility did not differ significantly, it was concluded that the large difference in duplex stability was likely due to differences in hydration.

It is noteworthy that both [3.3.0]bc-ANA and [3.2.0]bc-ANA (Fig. 8) show high affinity pairing to RNA, and the latter also to DNA (110, 111). The reason most commonly advanced for this high affinity is the lack of conformational freedom of the sugar ring. The increased rigidity of the 2′F-ANA (nucleoside and oligonucleotide) means that this reasoning might help explain the increased binding affinity of 2′F-ANA as well. However, ANA oligonucleotides were also observed to be quite rigid when in duplexes with RNA. Thus there may be other reasons for the difference between ANA and its higher affinity cousins 2′F-ANA and bc-ANA. For example, the lack of a hydrogen-bond donor at the 2′ position would change the hydration pattern of the duplex and eliminate the possibility of OH2′-O5′ H-bonding interactions.

Another crystallographic study of single inserts has recently called into question some of the previous results by showing that single 2′F-ANA inserts adopt eastern puckers in the context of a B-form helix but pucker in the north when included in an A-form DNA helix (112). In contrast, ANA inserts maintained a southeastern pucker in both helical environments. The latter result seems to contradict the earlier work on A-like 2′F-ANA·RNA hairpins, and the authors' conclusion that 2′F-ANA "disfavors the southern and south-eastern pucker ranges" (112) also seems to contradict evidence from CD and thermal stability data (see above). We believe caution is essential when interpreting results from single inserts in an oligonucleotide; however, if this interesting result is confirmed in other contexts, it may help explain not only the high thermal stability of 2′F-ANA·RNA duplexes, but also why 2′F-ANA–RNA chimeric structures maintain high binding affinity.

Because of this new result, and the ongoing lack of a satisfactory explanation for the different binding affinities of ANA and 2′F-ANA for RNA, we are currently undertaking another NMR study using 10-mer duplexes (not hairpins) of mixed base composition. We are hopeful that this study will provide further insight into the structure and dynamics of ANA and 2′F-ANA (89).

Hydration

Berger et al. observed an ordered water structure around the 2′-fluorines of FMAU residues incorporated into the Dickerson–Drew dodecamer. However, the contacts were relatively long and argued against strongly stabilizing hydrogen bonds to fluorine (63). More recently, Li et al. observed that the groove regions around 2′F-ANA residues incorporated into DNA oligomers were dry, in contrast with ANA

© 2008 NRC Canada

Fig. 8. Structures of (*a*) [3.2.0]bc-ANA and (*b*) [3.3.0]bc-ANA oligomers.

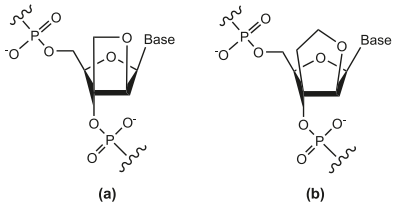

residues that were heavily hydrated (112). To extend this kind of study to the context of fully modified oligonucleotides, we recently made fully modified 2′F-ANA·RNA and ANA·RNA 10-mer duplexes and are currently undertaking a study of the hydration of these duplexes by osmotic stressing (113). Preliminary results indicate that 2′F-ANA·RNA duplexes liberate significantly fewer molecules of ordered water upon melting than do DNA·RNA or ANA·RNA (89). This entails a significant entropic benefit for 2′F-ANA·RNA duplexes (no need to order water molecules) but an enthalpic penalty (H-bonding from ordered water typically makes a significant enthalpic contribution). Interestingly, thermodynamic analysis of this duplex indicated that it was strongly enthalpically favored, even with its low levels of hydration. The low hydration of 2′F-ANA leads to a significant entropic benefit over other strands, and because of its inherently high enthalpy of binding, its low hydration may actually lead to a significant advantage in terms of binding affinity.

Optimization of RNase H activity and recent antisense applications

The combination of high-affinity, specific binding, nuclease stability, and RNase H activation attracted significant interest in 2′F-ANA, and studies were soon undertaken to characterize and optimize its antisense activity (114).

A fully modified 2′F-ANA strand induces RNase H cleavage to a lesser extent than DNA. Lok et al. tested phosphorothioate gapmers (see Fig. 5) containing 2′F-ANA wings and a central DNA gap, and showed that the combination is more active than a strand containing only DNA (93). Furthermore, the potency of the chimera was unchanged for gap sizes ranging from 4 to 10 nucleotides. This was in sharp contrast to chimeras containing RNA wings and a central DNA gap, whose potency dropped below that of all-DNA strands when the DNA gap size dropped below 8 nucleotides (93). It was suggested that the potency of the 2′F-ANA-DNA chimera is related to its increased flexibility with respect to an all-2′F-ANA strand. Accordingly, insertion of an acyclic nucleoside or an alkyl linker into 2′F-ANA oligonucleotides increased their ability to induce RNase H (Fig. 9) (115). This held true even when the AON targeted a highly structured RNA (115). The 2′F-ANA AONs containing butyl linkers comprised the first examples of high potency AONs containing unstructured elements that did not participate in base-pairing (115). A peptide nucleic acid (PNA) insert within a 2′F-ANA strand also provided some improvement in RNase H activation, although not as much as a butyl linker (116). Thus, either DNA–2′F-ANA chimeric constructs or flexible units within a 2′F-ANA AON provided means of improving the ability of 2′F-ANA to activate RNase H.

Another study compared the effects of a variety of single modified inserts into a DNA strand (117). Nucleosides with north, east, and south conformational biases and with varying degrees of steric hindrance and flexibility were studied. The 2′F-arabinonucleosides (T and C bases) were shown to have the most favorable effect on the kinetics of RNase H cleavage. This was attributed to their eastern conformational bias, relatively high conformational flexibility in the context of this oligodeoxyribonucleotide, and favorable sterics in the minor groove (117).

The DNA–2′F-ANA chimeric constructs were also optimized. It was found that a 3–3 altimer construct (Fig. 5) provided the highest potency RNase H-activating AON, equal to or better than a DNA gap surrounded by 2′F-ANA wings (gapmer) (88). Both the altimer and gapmer strand architectures consistently outperformed DNA itself and were applicable to both PO and PS backbones (80, 81, 88, 93). A study on luciferase knockdown in HeLa cells demonstrated that PS-2′F-ANA altimers and gapmers outperform both PS-DNA and PS or mixed backbone DNA–RNA chimeras (81). The PS-2′F-ANA gapmer gave comparable results to the better of two siRNAs targeting luciferase mRNA, in both potency and duration of action (81).

These optimized AONs have seen several recent applications. Lacombe et al. showed that PS-2′F-ANA–DNA chimeras are more effective than PS-DNA AONs in reducing expression levels of Flk-1, a VEGF receptor. However, both chemistries gave comparable levels of VEGF activity (94). Kalota et al. found that both altimer and gapmer architectures of PS-2′F-ANA–DNA chimeras were able to silence expression of c-MYB (a protooncogene involved in various hematologic malignancies) in human leukemia cell line K562 at 20% of the concentration of the corresponding PS-DNA AONs (80). Furthermore, gene silencing using the 2′F-ANA-modified AONs was nearly complete, and lasted twice as long as the unmodified AONs (80). At least part of the improvement was found to be the higher intracellular concentration of the 2′F-ANA-modified AON, because of its greater nuclease resistance (80). This data, along with the studies described below, demonstrates the effectiveness of 2′F-ANA against clinically relevant targets.

2′F-ANA oligomers are close to being clinically validated. TPI-1100, a PS-2′F-ANA–DNA chimera designed to treat chronic obstructive pulmonary disease (COPD), is being developed by Topigen Pharmaceuticals, Inc. Delivered via aerosol, TPI-1100 inhibits the expression of multiple phosphodiesterases (PDEs) considered therapeutic targets for alleviating COPD, a deadly, debilitating disease characterized by inflammation of the airways. Local delivery of TPI-1100 has the advantage that the dose of the oligomer required for efficacy is significantly lower (μg) when delivered directly to lung tissue. Pulmonary delivery also potentially reduces undesirable systemic side effects and overcomes the challenges of systemic delivery of oligonucleotides that target tissues within the body. Phase 1 clinical studies are planned to start in 2009 (118).

© 2008 NRC Canada

Fig. 9. Insertion of (*a*) an acyclic nucleotide or (*b*) a butyl linker into 2′F-ANA oligonucleotides increases their ability to induce RNase H. Adapted from Mangos and Damha (114).

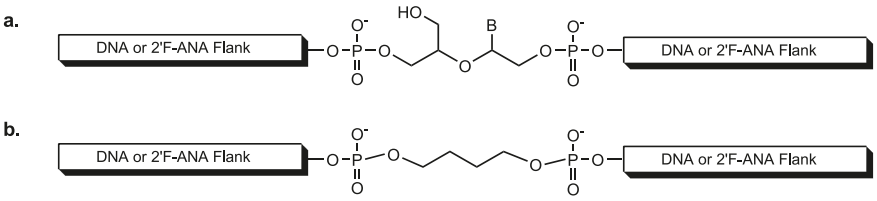

Table 3. Differences between antisense and RNAi strategies.

Antisense	RNAi
Catalytic enzyme is RNase H	Catalytic enzyme is an Argonaute enzyme, part of the RNA-Induced Silencing Complex (RISC).
RNA·DNA duplexes recognized	siRNA (short, double-stranded RNA) recognized
Exogenous oligonucleotide introduced as a single strand	Exogenous oligonucleotides introduced as an siRNA duplex, one strand subsequently incorporated into RISC.
DNA-like modifications required for RNase H activity	RNA-like modifications required for RISC activity

siFANA

While the AON strategy is still an attractive therapeutic option, RNA interference (RNAi) is the gene silencing strategy that has attracted the most attention in recent years, including the 2006 Nobel Prize in physiology or medicine. The two strategies have been compared in various studies (119).

Both approaches involve the cleavage of mRNA by an endonuclease, guided by an exogenous oligonucleotide strand. However, there are several important differences, summarized in Table 3.

Unmodified short interfering RNA duplexes have been used with success for gene silencing; however, chemical modification of one or both of the strands will likely be necessary for therapeutic use (120). Numerous chemical modifications have been tested for effects on siRNA activity, and key benefits have been achieved (including improved biostability, uptake, specificity, and potency) (120, 121). A wide variety of RNA-like modifications can be introduced into siRNA duplexes without perturbing the overall A-form helical structure required for activity. It is not clear yet which chemical modifications will be the most advantageous.

We hypothesized that despite the generally DNA-like properties of 2′F-ANA, siRNA duplexes could be partially 2′F-ANA-modified without compromising their recognition by RISC during the various steps of RNAi. Dowler et al. were the first to show that 2′F-ANA could be incorporated throughout the sense strand, including a fully modified sense strand (76). Watts et al. later showed that the potency of 2′F-ANA-modified sense strands could be significantly improved by including five RNA inserts near the 3′-end of the strand (91). As for antisense strand modifications, a small number of 2′F-ANA inserts are generally well tolerated throughout the strand, although 5′-modified antisense strands should be phosphorylated before introduction into cells to retain high potency (91). Modification of the antisense-strand 3′-overhang with 2′F-ANA brought a significant increase in potency (76). Several of the 2′F-ANA-modified duplexes have been able to surpass the native siRNA in potency (76).

Furthermore, siRNA duplexes with extensive 2′F-ANA modification were found to have a significantly longer serum half-life than unmodified siRNAs. For example, the serum half-life of an siRNA was extended from 15 min to 5 h by replacing the sense strand with 2′F-ANA (76). This is likely why the duration of action of siRNA was found to improve upon 2′F-ANA modification (76).

While it is true that the siRNA duplexes containing entirely 2′F-ANA sense strands are capable of eliciting RNase H activity that would cleave the RNA antisense strands, this activity is not optimal for 2′F-ANA in the absence of DNA units or flexible linkers (as discussed above) and thus allows enough time for the antisense strand to be loaded into the RISC complex.

In summary, 2′F-ANA modified siRNA can have high efficacy, comparable to that of standard siRNAs, but with improved biostability provided by the 2′F-araN nucleotides thus overcoming one of the therapeutic limitations of siRNA.

2′F-ANA in triplexes

One of the earliest studies on 2′F-ANA demonstrated that it can effectively form "pyrimidine motif" triplexes where a pyrimidine-rich third strand binds parallel to the purine strand of a target duplex (122). In general, 2′F-ANA mimics DNA rather than RNA as a triple-helix-forming agent. For example, RNA can form a triple helix with any of the four target duplexes DD, DR, RD, or RR (where the first letter represents the purine strand and the second the pyrimidine strand; thus DR would be a duplex consisting of a purine-rich strand of DNA with a pyrimidine-rich strand of RNA). DNA and 2′F-ANA can only form duplexes with DD and DR target duplexes. The binding affinity of the 2′F-ANA third strand is greater than that of DNA or 2′F-RNA (attributed to favorable preorganization of 2′F-ANA) (122) but less than that of an RNA third strand (attributed to its lack of a 2′-OH group (122), which can interact with interstrand phosphates in the case of an RNA third strand) (123).

© 2008 NRC Canada

2′F-ANA-modified aptamers and higher-order structures

Aptamers, nucleic acid species with binding or catalytic properties, have generated intense interest in recent years because they are so readily available via molecular evolution techniques, often called SELEX (systematic evolution of ligands by exponential enrichement) (124). To make aptamers containing chemical modifications (to improve their properties, especially nuclease resistance), modified triphosphates can be used during the evolution process, or the unmodified aptamer can be carefully modified after determination of its sequence. The latter avenue toward modified aptamers is more challenging, since chemical modifications can affect the structure and properties of the aptamer in a way not accounted for by the selection process. However, it allows modification at selected positions and using nucleotides not amenable to the SELEX process. For example, the first aptamer-based therapeutic, Macugen® (pegaptanib sodium), was approved by the FDA in December 2004. This aptamer was discovered by the SELEX method (including use of some modified nucleoside triphosphates) but was subsequently optimized ("post-SELEX modification") to confer biostability required for in vivo use (125).

Non-evolution-based 2′F-ANA aptamers

More recent work has shown that 2′F-ANA is suitable for use in the modification of aptamers containing G-quartets (77). The top-face fluorine of 2′F-ANA nucleotides favors the *anti*-orientation around the glycosidic bond. Consistent with this, 2′F-ANA modification of *anti*-dG residues of three different G-quartet-containing DNA aptamers led to increased thermal stability as well as increased nuclease resistance. Replacement of the *syn*-dGs, on the other had, led to decreased stability or a total structural transformation. A thrombin-binding aptamer had up to 48-fold greater stability to 10% FBS when modified with 2′F-araN residues (77). As well as the G quartets, 2′F-ANA modification of certain thymines in a loop of this aptamer caused increased thermal stability, nuclease resistance, and binding to thrombin (77).

The i-motif, a C-tetrad structure formed by C-rich DNA sequences (126), has also been modified with 2′F-araN residues. 2′F-ANA modification of all Cs in the hexamer dTCCCCC led to an 8.5 °C decrease in thermal stability at pH 4.5. However, the 2′F-ANA-modified structure was stable over a much wider range of pH (for example, its T_m values were 6.5 °C higher than those of the DNA structure at pH 3.5). Since the i-motif involves C·C$^+$ base pairs (126), this finding can be explained by the lower pK_a of 2′F-araC (3.88) than dC (4.5) (2). This study also demonstrated that the preorganization of 2′F-ANA led to more favorable kinetics for the modified C-tetrads. Improvements in pH range and kinetics are thus two ways in which 2′F-ANA may broaden the scope of applications of aptamers.

In another study, branched oligonucleotides made of dC or araC were shown to associate into the i-motif at acidic pH, unlike the corresponding RNA structures (127), This occurs in spite of the fact that most of the sugar residues in i-DNA tetrads adopt the C3′-*endo* (north) sugar pucker. It was attributed to different steric effects of the 2′-substituent (127).

SELEX using 2′F-ANA

For a modified nucleotide to be compatible with the SELEX process, two conditions are necessary: (*i*) the corresponding nucleoside 5′-triphosphates must be substrates of a polymerase enzyme, able to be incorporated with good fidelity into a PCR-type system, and (*ii*) the modified strand must be able to act as a template for the creation of a corresponding cDNA library. 2′F-araN 5′-triphosphates are indeed substrates of several readily available polymerase enzymes. Surprisingly, in some cases they are incorporated with higher fidelity than dNTPs (128), The biosynthesis of pyrimidine 2′F-ANA and 2′F-RNA triphosphates was later compared using four DNA polymerases. It was found that 2′F-araTTP was significantly better incorporated than 2′F-rUTP, but 2′F-rCTP was slightly preferred over 2′F-araCTP (129).

As for the second condition, it has been shown that a chimeric 2′F-ANA–DNA strand can act as a template for the biosynthesis of a chimeric complementary strand, and in other experiments, that a fully modified 2′F-ANA strand can act as a template for the biosynthesis of a complementary DNA strand (128). Thus, 2′F-ANA appears to have great potential for use within the SELEX process.

Other oligonucleotide derivatives based on 2′F-ANA

The attractive properties of 2′F-ANA have stimulated the development of several other 2′F-ANA-based oligonucleotide derivatives (Fig. 10).

For example, a 2′F-ANA sugar has been tested in combination with P3′–N5′ (130) and N3′–P5′ (85) phosphoramidate linkages. For the P3′–N5′ linkage, the resulting oligonucleotide analogue had lower binding affinity than its phosphodiester counterpart but retained the ability to elicit RNase H activity (130). In fact, the 2′F-ANA phosphoramidate analogue was better able to elicit RNase H activity than a corresponding DNA phosphoramidate oligomer (130). As for the N3′–P5′ phosphoramidate backbone, nucleosides introduced into this backbone appeared to pucker in the north (85). This may be due to the stereoelectronic effect of changing the 3′ group to an amine since the corresponding 2′-deoxy phosphoramidate showed a similar conformation (85). The 2′F-ANA N3′–P5′ phosphoramidate showed increased stability to base with respect to its 2′-epimer, phosphoramidate-linked 2′F-RNA, but lower binding affinity to DNA and RNA (85).

2′F-ANA sugars have been modified with sulfur at the 3′ and 4′ positions. Elzagheid et al. described the synthesis of 2′-deoxy-2′-fluoro-3′-thioarabinothymidine (131). This synthesis has been challenging to repeat, however, since the 3′-SH group (in the precursor to the phosphoramidite) tends to displace the 2′-fluorine, resulting in a 2′,3′-episulfide product (132).

Watts et al. synthesized the 4′-thio analogue of 2′F-ANA and discovered that the change triggers a dramatic conformational shift to the north (3′-*endo*) at the nucleoside level (100) (Fig. 11). This change is carried through to the structure of the corresponding oligonucleotide analogues as well (termed 4′S-FANA), which are rather A-like in character according to CD and as expected lose the ability to elicit

© 2008 NRC Canada

Fig. 10. Other oligonucleotide derivatives based on 2′F-ANA: (*a*) 2′-fluoroarabino P3′–N5′ phosphoramidates (130); (*b*) 2′-fluoroarabino N3′–P5′ phosphoramidates (85); (*c*) 3′S-FANA (131); and (*d*) 4′S-FANA (91).

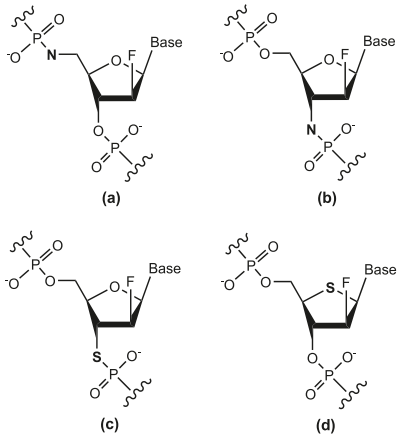

RNase H activity (91). However, the 4′S-FANA derivative is well-tolerated in siRNA duplexes, although it has lower binding affinity than 2′F-ANA itself (91).

Considerations for use of 2′F-ANA in vivo

Given the toxicity of 2′-deoxy-2′-fluoroarabinonucleosides such as FMAU and FIAU, discussed above, any potential in vivo use of 2′F-ANA in therapeutics must provide assurance that the catabolic metabolites (2′F-araN and their nucleotides) will not cause significant side effects. However, the success of the nucleoside analogue clofarabine, the progression toward use of 2′-fluoroarabinonucleosides as PET tracers, and the ongoing pre-clinical studies on 2′F-ANA discussed above makes it clear that 2′F-ANA remains a promising entity for therapeutic use, as long as the in vivo concentrations of the constituent nucleosides remain low. An initial preclinical toxicology study has been performed in mice to compare the toxicological profile of a phosphorothioate 2′F-ANA-containing oligonucleotide (5-gap-4 configuration) and a phosphorothioate DNA oligonucleotide following repeated administrations. The sequence used in the study was that of Monia et al. ISIS 5132, targeting the human c-Raf-1 (133). The oligonucleotides were administered every other day for 28 days (14 doses) at a dose up to 50 mg/kg by iv injection via the lateral tail vein. In line with previous reports, the toxicities observed in this study all appeared to be related to the phosphorothioate chemical class of the oligonucleotides (134). Furthermore, no clear difference could be observed between the two chemistries, suggesting that they are not side effects of 2′F-ANA. Due to the greater efficacy and stability of 2′F-ANA oligos, it is expected that a lower or less frequent dosing will be effective, thus lowering any toxicity.

Summary

2′-Fluoroarabinonucleosides are immensely versatile chemical modifications on their own or in oligonucleotides. 2′F-araNs such as clofarabine are already being used as therapeutics, and other compounds are being studied as drugs

Fig 11. Conformational switch and corresponding change in biological properties, upon changing the ring heteroatom of 2′F-ANA from oxygen to sulfur (100).

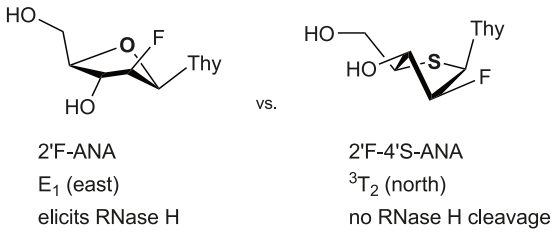

and for in vivo applications such as PET. While 2′F-ANA oligonucleotides form stable duplexes with RNA and these duplexes activate RNase H, additional structural alterations to the backbone further increase the capability to inhibit protein expression. This optimization can be done using gapmer or altimer chimeric constructs, or flexible linkers, according to the target sequence. Different chimeric constructs can also be used in the application of 2′F-ANA to other oligonucleotide approaches (siRNA and aptamers).

2′F-ANA oligonucleotides significantly enhance nuclease resistance, providing lower dosage requirements and the potential for improved systemic administration and safety for oligonucleotide therapeutics including antisense, aptamers, and siRNA. The increased stability exhibited by 2′F-ANA-modified oligonucleotides has the potential to increase their in vivo efficacy. This stability is tunable in that the half life in vivo can be controlled by the extent of 2′F-ANA modification. 2′F-ANA-modified oligomers allow for highly potent, long-lasting gene-silencing effects in both antisense and RNAi approaches. In a series of studies comparing available AON chemistries, 2′F-ANA oligonucleotides showed an improvement in target affinity and duration of gene response while improving efficacy (81). The unique characteristics of 2′F-ANA could be advantageous for a wide variety of therapeutic gene or protein-modifying applications, including topical and systemic administration. A drug candidate is scheduled to enter clinical trials in 2009.

Finally, we note that 2′F-ANA also has potential in the areas of diagnostics and biosensor reagents because of its wide range of pH stability, nuclease resistance, and high binding affinity. Tools can be rationally designed or evolved. Time will tell which of these applications will prove most beneficial. The next forty years of 2′-fluoroarabino nucleosides, nucleotides, and nucleic acids will be no less interesting than the first forty.

Acknowledgments

This work was supported by the Canadian Institutes of Health Research and Topigen Pharmaceuticals, Inc. We thank Dr. John DiMaio and Dr. Nicolay Ferrari for helpful comments regarding this manuscript. JKW is grateful to the Natural Sciences and Engineering Research Council of Canada (NSERC) and Dr. Richard H. Tomlinson for postgraduate fellowships. MJD is the 2007 recipient of the Bernard Belleau Award (Canadian Society for Chemistry).

© 2008 NRC Canada

References

1. J.A. Wright, N.F. Taylor, and J.J. Fox. J. Org. Chem. **34**, 2632 (1969).
2. J.A. Wright, D.P. Wilson, and J.J. Fox. J. Med. Chem. **13**, 269 (1970).
3. See the excellent review by K.W. Pankiewicz, Carbohydr. Res. **327**, 87 (2000), and references therein.
4. L.W. Hertel, G.B. Boder, J.S. Kroin, S.M. Rinzel, G.A. Poore, G.C. Todd, and G.B. Grindey. Cancer Res. **50**, 4417 (1990).
5. A. Graul, J. Silvestre, and J. Castaner. Drugs Future, **23**, 1176 (1998).
6. V.E. Marquez, C.K.H. Tseng, H. Mitsuya, S. Aoki, J.A. Kelley, H. Ford, J.S. Roth, S. Broder, D.G. Johns, and J.S. Driscoll. J. Med. Chem. **33**, 978 (1990).
7. J.D. Stoeckler, C.A. Bell, R.E. Parks, Jr., C.K. Chu, J.J. Fox, and M. Ikehara. Biochem. Pharmacol. **31**, 1723 (1982).
8. K.A. Watanabe, U. Reichman, K. Hirota, C. Lopez, and J.J. Fox. J. Med. Chem. **22**, 21 (1979).
9. (*a*) R.F. Schinazi, J. Peters, M.K. Sokol, and A.J. Nahmias. Antimicrob. Agents Chemother. **24**, 95 (1983); (*b*) M.D. Trousdale, A.B. Nesburn, T.L. Su, C. Lopez, K.A. Watanabe, and J.J. Fox. Antimicrob. Agents Chemother. **23**, 808 (1983).
10. J.H. Burchenal, T.-C. Chou, L. Lokys, R.S. Smith, K.A. Watanabe, T.-L. Su, and J.J. Fox. Cancer Res. **42**, 2598 (1982).
11. J.L. Abbruzzese, S. Schmidt, M.N. Raber, J.K. Levy, A.M. Castellanos, S.S. Legha, and I.H. Krakoff. Invest. New Drugs, **7**, 195 (1989).
12. X.-B. Kong, A.C. Scheck, R.W. Price, P.M. Vidal, M.P. Fanucchi, K.A. Watanabe, J.J. Fox, and T.-C. Chou. Antiviral Res. **10**, 153 (1988).
13. J.L. Ruth and Y.-C. Cheng. Mol. Pharmacol. **20**, 415 (1981).
14. H. Marquardt, J. Westendorf, and H. Marquardt. Carcinogenesis, **3**, 593 (1982).
15. H. Marquardt and H. Marquardt. Cancer, **40**, 1930 (1977).
16. (*a*) C. Chu, T. Ma, K. Shanmuganathan, C. Wang, Y. Xiang, S. Pai, G. Yao, J. Sommadossi, and Y. Cheng. Antimicrob. Agents Chemother. **39**, 979 (1995); (*b*) S. Balakrishna Pai, S. Liu, Y. Zhu, C. Chu, and Y. Cheng. Antimicrob. Agents Chemother. **40**, 380 (1996); (*c*) G.-Q. Yao, S.-H. Liu, E. Chou, M. Kukhanova, C.K. Chu, and Y.-C. Cheng. Biochem. Pharmacol. **51**, 941 (1996).
17. T. Ma, S.B. Pai, Y.L. Zhu, J.S. Lin, K. Shanmuganathan, J. Du, C. Wang, H. Kim, M.G. Newton, Y.C. Cheng, and C.K. Chu. J. Med. Chem. **39**, 2835 (1996).
18. P. Marcellin, H. Mommeja-Marin, S.L. Sacks, G.K.K. Lau, D. Sereni, J.-P. Bronowicki, B. Conway, C. Trepo, M.R. Blum, B.C. Yoo, E. Mondou, J. Sorbel, A. Snow, F. Rousseau, and H.-S. Lee. Hepatology, **40**, 140 (2004).
19. C. Lopez, K.A. Watanabe, and J.J. Fox. Antimicrob. Agents Chemother. **17**, 803 (1980).
20. F.S. Philips, A. Feinberg, T.-C. Chou, P.M. Vidal, T.-L. Su, K.A. Watanabe, and J.J. Fox. Cancer Res. **43**, 3619 (1983).
21. R. McKenzie, M.W. Fried, R. Sallie, H. Conjeevaram, A.M. Di Bisceglie, Y. Park, B. Savarese, D. Kleiner, M. Tsokos, C. Luciano, T. Pruett, J.L. Stotka, S.E. Straus, and J.H. Hoofnagle. N. Engl. J. Med. **333**, 1099 (1995). Also see the helpful editorial by M.N. Swartz. N. Engl. J. Med. **333**, 1146 (1995) and commentary by A. Bari, L. Josephson, A.M. Prince, W. Lewis, F.W. Perrino, M. Gordon, J. Hoofnagle, R. McKenzie, S. Straus, M.N. Swartz, and J.L. Stotka. N. Engl. J. Med. **334**, 1135 (1996).
22. Review of the fialuridine (FIAU) clinical trials. *Edited by* F. Manning and M. Swartz. National Academy Press, Washington, DC. 1995.
23. J.J. Fox, K.A. Watanabe, T.C. Chou, R.F. Schinazi, K.F. Soike, I. Fourel, G. Hantz, and C. Trepo. Antiviral activities of 2′-fluorinated arabinosyl-pyrimidine nucleosides. *In* Fluorinated carbohydrates: chemical and biochemical aspects; ACS symposium series, Vol. 374. *Edited by* N.F. Taylor. American Chemical Society, Washington, DC. 1988. p. 176.
24. (*a*) T.C. Chou, X.B. Kong, M.P. Fanucchi, Y.C. Cheng, K. Takahashi, K.A. Watanabe, and J.J. Fox. Antimicrob. Agents Chemother. **31**, 1355 (1987); (*b*) M.M. Mansuri, I. Ghazzouli, M.S. Chen, H.G. Howell, P.R. Brodfuehrer, D.A. Benigni, and J.C. Martin. J. Med. Chem. **30**, 867 (1987).
25. (*a*) S.S. Gambhir. Nat. Rev. Cancer **2**, 683 (2002); (*b*) A.R. Buursma, V. Rutgers, G.A.P. Hospers, N.H. Mulder, W. Vaalburg, and E.F.J. de Vries. Nucl. Med. Commun. **27**, 25 (2006).
26. C. Bettegowda, C.A. Foss, I. Cheong, Y. Wang, L. Diaz, N. Agrawal, J. Fox, J. Dick, L.H. Dang, S. Zhou, K.W. Kinzler, B. Vogelstein, and M.G. Pomper. Proc. Natl. Acad. Sci. U.S.A. **102**, 1145 (2005).
27. H. Sun, T.J. Mangner, J.M. Collins, O. Muzik, K. Douglas, and A.F. Shields. J. Nucl. Med. **46**, 292 (2005).
28. B. Leyland-Jones, H. Donnelly, S. Groshen, P. Myskowski, A.L. Donner, M. Fanucchi, and J. Fox. J. Infect. Dis. **154**, 430 (1986).
29. R. McKenzie, M.W. Fried, R. Sallie, H. Conjeevaram, A.M. Di Bisceglie, Y. Park, B. Savarese, D. Kleiner, M. Tsokos, C. Luciano, T. Pruett, J.L. Stotka, S.E. Straus, and J.H. Hoofnagle. N. Engl. J. Med. **333**, 1099 (1995).
30. C.-H. Pui, S. Jeha, and P. Kirkpatrick. Nat. Rev. Drug Discov. **4**, 369 (2005).
31. P.L. Bonate, L. Arthaud, W.R. Cantrell, K. Stephenson, J.A. Secrist, and S. Weitman. Nat. Rev. Drug Discov. **5**, 855 (2006).
32. C.K. Chu, J. Matulicadamic, J.T. Huang, T.C. Chou, J.H. Burchenal, J.J. Fox, and K.A. Watanabe. Chem. Pharm. Bull. (Tokyo) **37**, 336 (1989).
33. (*a*) D.S. Shewach, P.E. Daddona, E. Ashcraft, and B.S. Mitchell. Cancer Res. **45**, 1008 (1985); (*b*) V. Verhoef and A. Fridland. Cancer Res. **45**, 3646 (1985).
34. S. Faderl, V. Gandhi, M.J. Keating, S. Jeha, W. Plunkett, and H.M. Kantarjian. Cancer, **103**, 1985 (2005).
35. J.A. Montgomery, A.T. Shortnacy-Fowler, S.D. Clayton, J.M. Riordan, and J.A. Secrist. J. Med. Chem. **35**, 397 (1992).
36. D. Carson, D. Wasson, L. Esparza, C. Carrera, T. Kipps, and H. Cottam. Proc. Natl. Acad. Sci. USA. **89**, 2970 (1992).
37. W.B. Parker, S.C. Shaddix, C.-H. Chang, E.L. White, L.M. Rose, R.W. Brockman, A.T. Shortnacy, J.A. Montgomery, J.A. Secrist III, and L.L. Bennett, Jr. Cancer Res. **51**, 2386 (1991).
38. O.D. Schaerer and G.L. Verdine. J. Am. Chem. Soc. **117**, 10781 (1995).
39. M.-J. Rubira, M.-L. Jimeno, J. Balzarini, M.-J. Camarasa, and M.-J. Perez-Perez. Tetrahedron, **54**, 8223 (1998).
40. U. Reichman, K.A. Watanabe, and J.J. Fox. Carbohydr. Res. **42**, 233 (1975).
41. C.D. Anderson, L. Goodman, and B.R. Baker. J. Am. Chem. Soc. **80**, 5247 (1958).
42. C.H. Tann, P.R. Brodfuehrer, S.P. Brundidge, C. Sapino, and H.G. Howell. J. Org. Chem. **50**, 3644 (1985).
43. P.R. Brodfuehrer, C. Sapino, and H.G. Howell. J. Org. Chem. **50**, 2597 (1985).

© 2008 NRC Canada

44. C.J. Wilds and M.J. Damha. Nucleic Acids Res. **28**, 3625 (2000).
45. J. Yin, D.S. Zarkowsky, D.W. Thomas, M.M. Zhao, and M.A. Huffman. Org. Lett. **6**, 1465 (2004).
46. T.S. Chou, L.M. Becke, J.C. O'Toole, M.A. Carr, and B.E. Parker. Tetrahedron Lett. **37**, 17 (1996).
47. M.M. Alauddin, P.S. Conti, T. Mathew, J.D. Fissekis, G.K. Surya Prakash, and K.A. Watanabe. J. Fluorine Chem. **106**, 87 (2000).
48. W.J. Middleton. J. Org. Chem. **40**, 574 (1975).
49. (*a*) J.A. Wilkinson. Chem. Rev. **92**, 505 (1992); (*b*) R.D. Chambers. Fluorine in organic chemistry. Blackwell Publishing Ltd., Oxford. 2004.
50. M.L. Sznaidman, M.R. Almond, and A. Pesyan. Nucleosides Nucleotides Nucl. Acids, **21**, 155 (2002).
51. H.G. Howell, P.R. Brodfuehrer, S.P. Brundidge, D.A. Benigni, and C. Sapino, Jr. J. Org. Chem. **53**, 85 (1988).
52. J. Garcia, A. Diaz-Rodriguez, S. Fernandez, Y.S. Sanghvi, M. Ferrero, and V. Gotor. J. Org. Chem. **71**, 9765 (2006).
53. K.W. Pankiewicz and K.A. Watanabe. J. Fluorine Chem. **64**, 15 (1993).
54. T. Maruyama, S. Takamatsu, S. Kozai, Y. Satoh, and K. Izawa. Chem. Pharm. Bull. (Tokyo) **47**, 966 (1999).
55. (*a*) J.A. Montgomery, A.T. Shortnacy, D.A. Carson, and J.A. Secrist. J. Med. Chem. **29**, 2389 (1986); (*b*) T. Ma, J.-S. Lin, M.G. Newton, Y.-C. Cheng, and C.K. Chu. J. Med. Chem. **40**, 2750 (1997).
56. T. Tennila, E. Azhayeva, J. Vepsalainen, R. Laatikainen, A. Azhayev, and I.A. Mikhailopulo. Nucleosides Nucleotides Nucl. Acids, **19**, 1861 (2000).
57. M.I. Elzagheid, E. Viazovkina, and M.J. Damha. Synthesis of protected 2′-deoxy-2′-fluoro-β-D-arabinonucleosides. *In* Current protocols in nucleic acid chemistry. *Edited by* S. Beaucage. Vol. 1.7. 2002. p. Unit 1.7.
58. M.I. Elzagheid, E. Viazovkina, and M.J. Damha. Nucleosides Nucleotides Nucl. Acids, **22**, 1339 (2003).
59. E. Viazovkina, M.M. Mangos, M.I. Elzagheid, and M.J. Damha. Synthesis of 2′-fluoroarabino nucleoside phosphoramidites and their use in the synthesis of 2′F-ANA. *In* Current protocols in nucleic acid chemistry. *Edited by* S. Beaucage. Vol. 4.15. 2002. p. Unit 4.15.
60. I. Rosenberg, J.F. Soler, Z. Tocik, W.Y. Ren, L.A. Ciszewski, P. Kois, K.W. Pankiewicz, M. Spassova, and K.A. Watanabe. Nucleosides Nucleotides, **12**, 381 (1993).
61. P. Kois, Z. Tocik, M. Spassova, W.Y. Ren, I. Rosenberg, J.F. Soler, and K.A. Watanabe. Nucleosides Nucleotides **12**, 1093 (1993).
62. H. Ikeda, R. Fernandez, A. Wilk, J.J. Barchi, X.L. Huang, and V.E. Marquez. Nucleic Acids Res. **26**, 2237 (1998).
63. I. Berger, V. Tereshko, H. Ikeda, V.E. Marquez, and M. Egli. Nucleic Acids Res. **26**, 2473 (1998).
64. (*a*) K.K. Ogilvie, D.P.C. McGee, S.M. Boisvert, G.H. Hakimelahi, and Z.A. Proba. Can. J. Chem. **61**, 1204 (1983); (*b*) U.O. Cheriyan and K.K. Ogilvie. Nucleosides Nucleotides **1**, 233 (1982); (*c*) K.K. Ogilvie, G.H. Hakimelahi, Z.A. Proba, and D.P.C. McGee. Tetrahedron Lett. **23**, 1997 (1982); (*d*) S.M. Boisvert. Preparation of novel heterocyclic-ring analogues of BIOLF-62: Application of ^{29}Si NMR nucleosides and the investigation of 2,4-dinitrobenzenesulfenyl as a protecting group for ribonucleotide synthesis. Ph.D. thesis, McGill University, Montreal, Canada. 1986.
65. (*a*) M.J. Damha and K.K. Ogilvie. J. Org. Chem. **53**, 3710 (1988); (*b*) M.J. Damha, R.T. Pon, and K.K. Ogilvie. Tetrahedron Lett. **26**, 4839 (1985).
66. M.J. Damha. Developments in the chemical synthesis of nucleic acids and their analogues. Ph.D. thesis, McGill University, Montreal, Canada. 1987.
67. The arabino-configured bis-phosphoaramidite does show P–P coupling, but the xylo-configured analogue does not. This data could be compatible with either through-space or through-bond origins of the coupling. See: S. Carriero, M.M. Mangos, K.A. Agha, A.M. Noronha, and M.J. Damha. Nucleosides Nucleotides Nucl. Acids, **22**, 1599 (2003).
68. (*a*) M.J. Damha, N. Usman, and K.K. Ogilvie. Tetrahedron Lett. **28**, 1633 (1987); (*b*) M.J. Damha, N. Usman, and K.K. Ogilvie. Can. J. Chem. **67**, 831 (1989).
69. M. Resmini and W. Pfleiderer. Helv. Chim. Acta **76**, 158 (1993).
70. (*a*) T. Mikita and G.P. Beardsley. Biochemistry, **33**, 9195 (1994); (*b*) Y.G. Gao, G.A. Van der Marel, J.H. Van Boom, and A.H.J. Wang. Biochemistry, **30**, 9922 (1991); (*c*) J.M.L. Pieters, E. De Vroom, G.A. Van der Marel, J.H. Van Boom, T.M.G. Koning, R. Kaptein, and C. Altona. Biochemistry, **29**, 788 (1990).
71. P.A. Giannaris and M.J. Damha. Can. J. Chem. **72**, 909 (1994).
72. A.M. Noronha, C.J. Wilds, C.-N. Lok, K. Viazovkina, D. Arion, M.A. Parniak, and M.J. Damha. Biochemistry, **39**, 7050 (2000).
73. M.J. Damha, C.J. Wilds, A. Noronha, I. Brukner, G. Borkow, D. Arion, and M.A. Parniak. J. Am. Chem. Soc. **120**, 12976 (1998).
74. J. Minshull and T. Hunt. Nucleic Acids Res. **14**, 6433 (1986).
75. J.K. Watts, J. Viladoms, and M.J. Damha. Manuscript in preparation.
76. T. Dowler, D. Bergeron, A.-L. Tedeschi, L. Paquet, N. Ferrari, and M.J. Damha. Nucleic Acids Res. **34**, 1669 (2006).
77. C.G. Peng and M.J. Damha. Nucleic Acids Res. **35**, 4977 (2007).
78. F. Eckstein. Antisense Nucleic Acid Drug Dev. **10**, 117 (2000).
79. (*a*) P.M. Burgers, F. Eckstein, and D.H. Hunneman. J. Biol. Chem. **254**, 7476 (1979); (*b*) P.M.J. Burgers and F. Eckstein. Biochemistry, **18**, 592 (1979).
80. A. Kalota, L. Karabon, C.R. Swider, E. Viazovkina, M. Elzagheid, M.J. Damha, and A.M. Gewirtz. Nucleic Acids Res. **34**, 451 (2006).
81. N. Ferrari, D. Bergeron, A.-L. Tedeschi, M.M. Mangos, L. Paquet, P.M. Renzi, and M.J. Damha. Ann. N.Y. Acad. Sci. **1082**, 91 (2006).
82. (*a*) J.T. Stivers, K.W. Pankiewicz, and K.A. Watanabe. Biochemistry, **38**, 952 (1999); (*b*) A.C. Drohat, G. Xiao, M. Tordova, J. Jagadeesh, K.W. Pankiewicz, K.A. Watanabe, G.L. Gilliland, and J.T. Stivers. Biochemistry, **38**, 11876 (1999).
83. On the extra stability provided to RNA by a phosphorothioate backbone, see: M. Ora, M. Oivanen, and H. Lonnberg. J. Org. Chem. **62**, 3246 (1997).
84. (*a*) J.A. Zoltewicz, D.F. Clark, T.W. Sharpless, and G. Grahe. J. Am. Chem. Soc. **92**, 1741 (1970); (*b*) G. Holmquist. Chromosoma, **72**, 203 (1979).
85. R.G. Schultz and S.M. Gryaznov. Tetrahedron Lett. **41**, 1895 (2000).
86. R. Schultz and S. Gryaznov. Nucleic Acids Res. **24**, 2966 (1996).
87. S. Wang and E.T. Kool. Biochemistry, **34**, 4125 (1995).
88. K.-L. Min, E. Viazovkina, A. Galarneau, M.A. Parniak, and M.J. Damha. Bioorg. Med. Chem. Lett. **12**, 2651 (2002).
89. N. Martin-Pintado, J.K. Watts, C. Gonzalez, and M.J. Damha. Manuscript in preparation.

© 2008 NRC Canada

90. C.J. Wilds. Synthesis, physicochemical and biological properties of oligonucleotides containing 2-fluoro-2-deoxy-β-D-arabinose. Ph.D. thesis, McGill University, Montreal, Canada. 1999.
91. J.K. Watts, N. Choubdar, K. Sadalapure, F. Robert, A.S. Wahba, J. Pelletier, B.M. Pinto, and M.J. Damha. Nucleic Acids Res. **35**, 1441 (2007).
92. C.A. Stein, C. Subasinghe, K. Shinozuka, and J.S. Cohen. Nucleic Acids Res. **16**, 3209 (1988).
93. C.-N. Lok, E. Viazovkina, K.-L. Min, E. Nagy, C.J. Wilds, M.J. Damha, and M.A. Parniak. Biochemistry, **41**, 3457 (2002).
94. J. Lacombe, E. Viazovkina, P.N. Bernatchez, A. Galarneau, M.J. Damha, and M.G. Sirois. Can. J. Physiol. Pharmacol. **80**, 951 (2002).
95. A.M. Noronha. Synthesis, physicochemical and biological studies on oligonucleotides containing D-arabinose. Ph.D. thesis, McGill University, Montreal, Canada. 1999.
96. A.M. Sapse and G. Snyder. Cancer Invest. **3**, 115 (1985).
97. N. Hicks, O.W. Howarth, and D.W. Hutchinson. Carbohydr. Res. **216**, 1 (1991).
98. J. van Wijk, C.A.G. Haasnoot, F.A.A.M. de Leeuw, B.D. Huckriede, A.W. Hoekzema, and C. Altona. PSEUROT. Version 6.3 [computer program]. Leiden Institute of Chemistry, Leiden University, Leiden, The Netherlands. 1999.
99. D.B. Davies. Prog. Nucl. Magn. Reson. Spectrosc. **12**, 135 (1978).
100. J.K. Watts, K. Sadalapure, N. Choubdar, B.M. Pinto, and M.J. Damha. J. Org. Chem. **71**, 921 (2006).
101. J. He, I.A. Mikhailopulo, and F. Seela. J. Org. Chem. **68**, 5519 (2003).
102. G.G. Sivets, E.N. Kalinichenko, and I.A. Mikhailopulo. Lett. Org. Chem. **3**, 402 (2006).
103. H. Ford, F. Dai, L. Mu, M.A. Siddiqui, M.C. Nicklaus, L. Anderson, V.E. Marquez, and J.J. Barchi. Biochemistry, **39**, 2581 (2000).
104. X. Peng and F. Seela. Org. Biomol. Chem. **2**, 2838 (2004).
105. A.Y. Denisov, A.M. Noronha, C.J. Wilds, J.-F. Trempe, R.T. Pon, K. Gehring, and M.J. Damha. Nucleic Acids Res. **29**, 4284 (2001).
106. F. Seela, P. Chittepu, J. He, and H. Eickmeier. Acta Crystallogr. Sect. C: Cryst. Struct. Commun. **60**, o884 (2004).
107. F.H. Martin and I. Tinoco, Jr. Nucleic Acids Res. **8**, 2295 (1980).
108. J.-F. Trempe, C.J. Wilds, A.Y. Denisov, R.T. Pon, M.J. Damha, and K. Gehring. J. Am. Chem. Soc. **123**, 4896 (2001).
109. D. Venkateswarlu and D.M. Ferguson. J. Am. Chem. Soc. **121**, 5609 (1999).
110. G. Minasov, M. Teplova, P. Nielsen, J. Wengel, and M. Egli. Biochemistry, **39**, 3525 (2000).
111. N.K. Christensen, M. Petersen, P. Nielsen, J.P. Jacobsen, C.E. Olsen, and J. Wengel. J. Am. Chem. Soc. **120**, 5458 (1998).
112. F. Li, S. Sarkhel, C.J. Wilds, Z. Wawrzak, T.P. Prakash, M. Manoharan, and M. Egli. Biochemistry, **45**, 4141 (2006).
113. E. Rozners and J. Moulder. Nucleic Acids Res. **32**, 248 (2004).
114. The potential of 2′F-ANA as an AON, in the context of other sugar-modified AONs, has been reviewed in: M.M. Mangos and M.J. Damha. Curr. Top. Med. Chem. **2**, 1147 (2002).
115. M.M. Mangos, K.-L. Min, E. Viazovkina, A. Galarneau, M.I. Elzagheid, M.A. Parniak, and M.J. Damha. J. Am. Chem. Soc. **125**, 654 (2003).
116. B.M. Patureau, R.H.E. Hudson, and M.J. Damha. Bioconjugate Chem. **18**, 421 (2007).
117. W.F. Lima, J.G. Nichols, H. Wu, T.P. Prakash, M.T. Migawa, T.K. Wyrzykiewicz, B. Bhat, and S.T. Crooke. J. Biol. Chem. **279**, 36317 (2004).
118. N. Ferrari. TPI ASM8 and TPI 1100 – Multi-targeted antisense oligonucleotide approaches for the treatment of lung inflammatory diseases. EuroTIDES 2007. Berlin, Germany. 2007.
119. (*a*) A. Gruenweller, E. Wyszko, B. Bieber, R. Jahnel, V.A. Erdmann, and J. Kurreck. Nucleic Acids Res. **31**, 3185 (2003); (*b*) T.A. Vickers, S. Koo, C.F. Bennett, S.T. Crooke, N.M. Dean, and B.F. Baker. J. Biol. Chem. **278**, 7108 (2003).
120. D.R. Corey. J. Clin. Invest. **117**, 3615 (2007).
121. M. Manoharan. Curr. Opin. Chem. Biol. **8**, 570 (2004).
122. C.J. Wilds and M.J. Damha. Bioconjugate Chem. **10**, 299 (1999).
123. C. Escudé, J.-C. François, J.-S. Sun, G. Ott, M. Sprinzl, T. Garestier, and C. Hélène. Nucleic Acids Res. **21**, 5547 (1993).
124. (*a*) A.D. Ellington and J.W. Szostak. Nature, **346**, 818 (1990); (*b*) G.F. Joyce. Gene, **82**, 83 (1989); (*c*) C. Tuerk and L. Gold. Science, **249**, 505 (1990).
125. E.W.M. Ng, D.T. Shima, P. Calias, E.T. Cunningham, D.R. Guyer, and A.P. Adamis. Nat. Rev. Drug Discov. **5**, 123 (2006).
126. K. Gehring, J.-L. Leroy, and M. Gueron. Nature, **363**, 561 (1993).
127. S. Robidoux and M.J. Damha. J. Biomol. Struct. Dyn. **15**, 529 (1997).
128. C.G. Peng and M.J. Damha. J. Am. Chem. Soc. **129**, 5310 (2007).
129. C.G. Peng and M.J. Damha. Can. J. Chem. In press. (2008).
130. E. Viazovkina, K.-L. Min, A. Galarneau, and M.J. Damha. Nucleosides Nucleotides Nucl. Acids **22**, 1335 (2003).
131. M.I. Elzagheid, A.L. Tedeschi, and M.J. Damha. Nucleosides Nucleotides Nucl. Acids **22**, 1343 (2003).
132. A.-L. Tedeschi. Synthesis and biological evaluation of oligonucleotides containing 3′- and 5′-*S*-phosphorothiolate internucleotide linkages. M.Sc thesis, McGill University, Montreal, Canada. 2004.
133. B.P. Monia, J.F. Johnston, T. Geiger, M. Muller, and D. Fabbro. Nat. Med. **2**, 668 (1996).
134. For reviews, see: A.A. Levin. Biochim. Biophys. Acta, Gene Struct. Expression **1489**, 69 (1999); and T.L.H. Jason, J. Koropatnick, and R.W. Berg. Toxicol. Appl. Pharmacol. **201**, 66 (2004).

© 2008 NRC Canada

Effectiveness factor of Pt utilization in cathode catalyst layer of polymer electrolyte fuel cells

Zetao Xia, Qianpu Wang, Michael Eikerling, and Zhongsheng Liu

Abstract: In this work, we analyze effectiveness factors of Pt utilization in perfluorosulfonate ionomer (PFSI) bonded thin film cathode catalyst layers of polymer electrolyte fuel cells. We define the effectiveness factor of Pt utilization as the apparent rate of current conversion exhibited by a specific catalyst layer design divided by the ideal rate obtained if all Pt atoms were used equally in electrochemical reactions at the specified electrode overpotential and externally provided reactant concentrations. This definition includes statistical factors at all relevant scales as well as non-uniformities of reaction rate distributions under operation. Our model is based on the random composite agglomerated morphology of the catalyst layer. It accounts for the interplay of transport phenomena and electrochemical kinetics. At the mesoscopic scale, limited effectiveness of Pt utilization in agglomerates is mainly an electrostatic effect. We determined spatial distributions of effectiveness factors of agglomerates in the through-plane direction, and thereafter calculated overall effectiveness factors of the cathode catalyst layer. Our results show that small agglomerate radius, low operating current density, high operating temperature, and high oxygen partial pressure result in high effectiveness factors of Pt utilization. Finally, we compared PFSI-bonded thin film cathode catalyst layers with ultrathin two-phase cathode catalyst layers in terms of effectiveness factors. Including the surface to volume atom ratio of Pt nanoparticles, the two different types of structures exhibit similar effectiveness factors of Pt utilization, which are found to be distinctly below 10%.

Key words: polymer electrolyte fuel cells, fuel cell modeling, cathode catalyst layer, Pt utilization, effectiveness factor.

Résumé : Dans ce travail, on analyse les facteurs d'efficacité de l'utilisation du platine dans un ionomère perfluorosulfonate (IPFS) lié à des couches de catalyseur cathodique en film mince pour des piles à combustible en polymère électrolyte. On a défini le facteur d'efficacité de l'utilisation du platine comme la vitesse apparente de la conversion du courant qui est présentée par un arrangement particulier d'un catalyseur spécifique divisée par la vitesse idéale obtenue si tous les atomes de platine sont utilisés également dans les réactions électrochimiques, au surpotentiel d'électrode spécifié et aux concentrations de réactifs fournies extérieurement. Cette définition inclut des facteurs statistiques à toutes les échelles appropriées ainsi que des distributions de vitesses réactionnelles non uniformes dans les conditions d'opération. Le modèle est basé sur la morphologie agglomérée et composite au hasard de la couche de catalyseur. Il tient compte des interactions des phénomènes de transport et des cinétiques électrochimiques. À l'échelle mésoscopique, l'efficacité limitée de l'utilisation du platine dans les agglomérés résulte principalement d'un effet électrostatique. On a déterminé les distributions spatiales des facteurs d'efficacité des agglomérés dans la direction à travers le plan et on a donc calculé les facteurs d'efficacité globaux de la couche du catalyseur de la cathode. Les résultats montrent que des agglomérés de faible rayon et que l'utilisation d'une faible densité de courant d'opération, une température d'opération élevée et une pression partielle d'oxygène élevée conduisent à des facteurs d'efficacité élevés pour l'utilisation du platine. Enfin, on a comparé les facteurs d'efficacité des couches de catalyseur cathodique en film mince liées à un ionomère de perfulorsulfonate avec ceux de couches de catalyseur cathodique en deux phases ultraminces. Si l'on inclut le rapport surface à volume atomique des nanoparticules de platine, les deux types différents de structures présentent des facteurs d'efficacité d'utilisation du platine qui se ressemblent et qui sont bien en-dessous de 10%.

Mots-clés : piles à combustible en polymère électrolyte, modèle d'une pile à combustible, couche de catalyseur cathodique, utilisation du platine, facteur d'efficacité.

[Traduit par la Rédaction]

Received 6 December 2007. Accepted 11 March 2008. Published on the NRC Research Press Web site at canjchem.nrc.ca on 13 May 2008.

Z. Xia, Q. Wang,[1] M. Eikerling, and Z. Liu. National Research Council, Institute for Fuel Cell Innovation, 4250 Wesbrook Mall, Vancouver, BC V6T 1W5, Canada.
M. Eikerling. Department of Chemistry, Simon Fraser University, Burnaby, BC V5A 1S6, Canada.

[1]Corresponding author (e-mail: qianpu.wang@nrc-cnrc.gc.ca).

Introduction

Polymer electrolyte fuel cells (PEFCs) are considered to be potentially clean power sources for stationary applications, electric vehicles, and portable devices. However, high costs, durability issues, and present insufficient power densities of these electrochemical energy conversion devices impede their rapid commercialization. Prohibitively high costs stem mainly from the polymer electrolyte membrane, Pt-based catalyst, and bipolar plates. With operating tempera-

 doi:10.1139/V08-053 © 2008 NRC Canada

tures <90 °C, only Pt and Pt-alloy catalysts provide acceptable rates of electrocatalytic current conversion in electrodes (1, 2). Due to limited resources and the high cost of Pt, its amount in PEFCs should be as small as possible. Therefore, improving Pt utilization and effectiveness factors in catalyst layers is a major challenge for PEFC research.

Typical catalyst layers in PEFCs are 5–10 μm thick films, sandwiched between a membrane and a gas diffusion layer (GDL, carbon paper or carbon cloth). These random composite media consist of a mixture of proton-conducting perfluorosulfonated ionomer (PFSI) and carbon–Pt particles (3, 4). The generation of electrical current proceeds at Pt nanoparticles, usually 2–4 nm in diameter, which are supported on high surface area nano-to-mesoporous carbon materials. It has been observed that the size of primary carbon particles is 5–20 nm. In colloidal dispersion of carbon–Pt particles and dissolved ionomer molecules, self organization leads to the formation of agglomerates of carbon–Pt, while ionomer domains form a separate phase that binds to the surfaces of those agglomerates (5–14). In a recent work, Malek et al. (15) employed computational modeling based on coarse-grained molecular dynamics (CGMD) to perform a systematic structural analysis of the microphase segregation that occurs during the fabrication process of catalyst layers. The meso-scale simulations provide insights into structural correlations and dynamical behavior of different phases in the catalyst layer composite. Structural analysis of CGMD results (15) and experimental data (10–14) suggest the formation of an agglomerated, phase-segregated morphology with bimodal porous architecture. Primary pores (3–10 nm radius) exist between carbon particles inside agglomerates, and secondary pores (10–50 nm) between agglomerates. Aggregates of PFSI form an interconnected phase in secondary pores, which does, however, not penetrate into primary pores. The network of carbon–Pt provides pathways for electron transport to the reaction sites; the ionomer network provides pathways for protons to reach reaction sites; a network of open pores functions as pathways for the gaseous diffusion of oxygen and water vapor (16).

Based on this structural picture, modeling studies suggest a state of optimal saturation in which primary pores are filled with liquid water to maximize the active area, while secondary pores are open for gaseous transport of reactants (16). In ref. 17 we evaluated two types of agglomerates, viz. ionomer-filled and water-filled agglomerates with distinct compositions and sizes in terms of transport processes, electrochemical reactivity, and effectiveness factors. In water-filled agglomerates, we assumed complete flooding of primary pores.

In ref. 16, Eikerling developed a structure-based model for water management in cathode catalyst layers (CCLs) of PEFCs. In his model, liquid water saturation was studied in relation to pore size distribution, total gas pressure, capillary pressure, and wetting properties of pores. Effects on water production and evaporation were considered. The results demonstrate that pore space is partially saturated with liquid water, and saturation varies with operating conditions and current density. A formalism for calculating the internal wetted pore fraction under stationary operation was provided. In the ideally wetted state, local capillary equilibrium between liquid and gas pressures forces liquid water to retreat to primary pores, which favors large reaction and evaporation rates, and at the same time the majority of secondary pores are open for gaseous transport of reactants and products. It is also postulated that reactions could occur only at interfaces between Pt and liquid water in substrate pores or in ionomer. Pt nanoparticles at Pt–gas contacts are inactive because of the prohibited proton access. Overall, this work highlighted the role of the CCL as a watershed in the fuel cell, which controls water fluxes towards PEM and GDL sides and plays a key-role in converting liquid water into vapor.

Most commonly, definitions can be found that specify Pt utilization as the ratio of the electrochemically active surface area to the total surface area of Pt particles. This definition refers merely to a static property of the medium. Moreover, it relates to surface area ratios and not to ratios of atom numbers or masses of utilized amount of Pt over total amount of Pt. It is, therefore, insufficient for capturing limitations of the catalytic capability of a typical catalyst layer and for assessing the reserves for improvement through advanced structural design. Reduced effectiveness of catalyst utilization is due to statistical inhomogeneities at multiple scales as well as non-uniform distributions of reactants, electrostatic potentials, and rates of electrochemical reactions at agglomerate and CCL levels. To include structural and operational effects at all scales, we define the effectiveness factor of Pt utilization as the apparent rate of current conversion exhibited by a specific catalyst layer design divided by the ideal rate obtained if all Pt atoms were used equally in electrochemical reactions at the specified electrode overpotential and externally provided reactant concentrations. It should be emphasized that this definition includes sensitive dependencies of electrocatalytic reactivities on sizes, composition, and surface structures of nanoparticles, which is an emerging area in fuel cell research (18–22).

The effectiveness factor of Pt utilization is intimately linked to the uniformity of reaction rate distributions. The latter is affected by processes at all levels, including surface transport and kinetics at Pt nanoparticles, as well as transport of reactants and product water at agglomerate level, catalyst layer level, MEA level, unit cell level, and stack level. In the present paper, we explore these contributions only up to the catalyst layer level, by combining our water-filled agglomerate model (17) with the structure-based macrohomogeneous model (16). Further detriments on reaction rate distributions and overall voltage efficiency because of limited transport in gas diffusion layers and flow fields have been neglected. Our calculations focus on the role of transport phenomena and electrochemical reactions inside the CCLs. The structural picture that we exploit is based on TEM pictures (8, 9), measured pore size distributions (9, 12), and coarse-grained MD simulations (15). Moreover, this picture has been successfully applied in systematic optimization studies (6–8, 23, 24).

We will obtain a detailed spatially resolved picture of the effectiveness of Pt utilization, accounting for spatial statistical inhomogeneities and non-uniformities of reaction rate distributions because of transport processes. The overall effectiveness factors will be evaluated for varying structure and operation conditions of the CCLs. The mathematical model is in the form that the water-filled agglomerate model is nested in the macrohomogeneous cathode catalyst layer

© 2008 NRC Canada

model. The water-filled agglomerate model is based on the Nernst–Planck equation of proton transport in water-filled channels, the Poisson equation for proton charge density in agglomerates, Fick's law of oxygen diffusion in water, and the electrochemical source term. The macrohomogeneous catalyst layer model is governed by conservation equations of mass and electrical charges, Ohm's law of proton transport, and Fick's law of gaseous diffusion of oxygen. Assumptions of the combined model are the same as for previous models. Based on the model, effectiveness factors of Pt utilization in typical PFSI-bonded thin film CCLs will be discussed and compared with 3M ultrathin two-phase CCLs (25). To obtain the overall effectiveness factor of Pt utilization, we make use of the assumption that effects at different length scales are well separated. We first focus on the effects at agglomerate and macrohomogeneous scale and in the final evaluation incorporate nanoparticle effects as well.

Pt utilization and effectiveness factor

A plethora of publications in fuel cell research dwell on issues related to Pt utilization in PEFCs. Here we provide a brief survey of representative studies that focused on Pt utilization and effectiveness factors (17, 25–50). In the past, ambiguous definitions of catalyst utilization have been exploited and contradictory values have been reported, which could lead to a wrongful assessment as to how much the performance of fuel cells could be improved by the advanced structural design of catalyst layers. Evidently, the accurate determination of catalyst utilization and effectiveness factors has a major impact on determining priorities in catalyst layer research.

In most studies, Pt utilization is defined as the ratio of the electrochemically active surface area, which is accessible to electrons and protons, to the total surface area of Pt. Pt utilization has been considered under different conditions, viz. in the catalyst powder and in the membrane electrode assembly (MEA). The Pt utilization in the catalyst powder is defined as,

$$[1] \qquad u_{\mathrm{Pt,cat}} = S_{\mathrm{Pt,cat}}/S_{\mathrm{Pt,tot}}$$

Here, the electrochemically active surface area in the catalyst powder, $S_{\mathrm{Pt,cat}}$, was estimated from the charge under the H-adsorption or CO-stripping waves measured by thin-film rotating disk electrode (TF-RDE) voltammetry in H_2SO_4 solution (26–28). The total surface area, $S_{\mathrm{Pt,tot}}$, was calculated from the mean particle size (radius r) determined by XRD experiments (26, 27) or from HR-TEM images (28), based on the assumption that the particles are spheres with surface area $4\pi r^2$. Values of $u_{\mathrm{Pt,cat}}$ were reported to be 109% by Easton and Pickup (26), 125% by Shan and Pickup (27), and 100% by Schmidt et al. (28) for carbon-supported Pt nanoparticles. The fact that the estimated utilization is greater than 100% is usually attributed to contributions from background currents (including that for H_2 evolution) to the measured H-adsorption charge (27).

The purpose of studying Pt utilization in the catalyst powder is to evaluate the electronic connectivity and maximum ionic accessibility of Pt nanoparticles. 100% Pt utilization means that all of the Pt nanoparticles are connected to the electronic conduction network and the entire Pt surface is accessible for protons through the electrolyte. Close to 100% Pt utilization in the catalyst powder of carbon supported Pt, immersed in liquid electrolyte, is possible, since only a negligible fraction of the Pt surface is covered by carbon particles. If Pt nanoparticles were supported by a polymer material such as poly(3,4-ethylenedioxythiphene)/poly(styrene-4-sulfonate), Pt utilization was reported to be only 43%–62%, which is due to poor electronic contact of the Pt nanoparticles with the polymer support and blocking of the Pt surface with the polymer (27).

The Pt utilization in the catalyst layer of an MEA is defined as,

$$[2] \qquad u_{\mathrm{Pt,CL}} = S_{\mathrm{Pt,CL}}/S_{\mathrm{Pt,tot}}$$

where the electrochemically active surface area in catalyst layer of an MEA, $S_{\mathrm{Pt,CL}}$, was estimated from the charge under the H-adsorption waves in cyclic voltammetry (CV) using driven-cell mode (30, 31). For example, to determine the accessible Pt surface area of a cathode, the cathode compartment of a single cell is purged with humidified nitrogen, serving as the working electrode, while the anode compartment is purged with humidified hydrogen, serving as both counter and reference electrode. In some studies, $S_{\mathrm{Pt,tot}}$ was calculated from the mean particle size, and Pt utilization in the cathode was reported to be 34% by Dhathathreyan et al. (32), 45% by Cheng et al. (33), 52% by Sasikumar et al. (34), and 55%–76% by Li and Pickup (35). As mentioned earlier, $S_{\mathrm{Pt,tot}}$ could also be obtained by the TF-RDE method, and Pt utilization in the cathode was reported to be 86%–87% (30) and 90% (36) by Gasteiger et al. Compared with Pt utilization in the catalyst powder, the reduced Pt utilization in catalyst layer of a fully functional MEA originates from two effects. Some Pt nanoparticles may get surrounded by ionomer and therefore loose electronic contact during the fabrication process. The other effect is that a fraction of the Pt particles are neither covered by ionomer electrolyte nor wetted by liquid water, implying that they are disconnected from the proton-supplying network.

The discussed results reveal large uncertainties and inconsistent definitions in determining Pt utilization among different experimental studies. The total charge transferred upon hydrogen adsorption may unintendedly involve non-wetted inactive catalyst surface area or include the catalytically inert substrate surface because of the so-called spillover effect (51). Usually, the active surface area measured by hydrogen adsorption and CO-stripping methods is not characterized under fuel cell operating conditions. Moreover, the values $u_{\mathrm{Pt,CL}}$ provided do not account for non-uniform reaction rate distributions, which arise at finite rates of reactant transport and consumption under stationary fuel cell operation.

The challenges in catalyst layer research can be best explained by considering the exchange current density j^0. It is the major physical property that links structure and activity of the catalyst layer with the working voltage of the fuel cell. A parameterization that relates j^0 to catalyst loading $[m_{\mathrm{Pt}}]$, specific activity of the catalyst with catalyst utilization was proposed in ref. 16.

© 2008 NRC Canada

[3] $j^0 = 2 \times 10^3 [m_{Pt}]\, j^{0*} \Gamma_{stat}$, with

$$\Gamma_{stat} = \varepsilon^{S/V} \Gamma_a g(S_r) \frac{f(X_{PtC}, X_{el})}{X_{PtC}}$$

The factor 2×10^3 approximates the total Pt surface area per real electrode surface area that would be obtained by spreading a catalyst loading of 1 mg cm^{-2} as an ideal monoatomic layer, which could be regarded as the base line for total Pt surface area at the atomistic level. To minimize irreversible voltage losses of the oxygen reduction reaction (ORR) on the cathode side of the cell, j^0 should be as large as possible. On the other hand, cost reduction demands lowest possible $[m_{Pt}]$ (in units mg cm^{-2}). The best compromise of these competing objectives can be achieved if the remaining factors on the right hand side of eq. [3] are maximized. This involves improving the specific activity of the catalyst (j^{0*}) and the statistical utilization of the catalyst, Γ_{stat}, in the random heterogeneous composite. The latter factor specified in eq. [3] involves the surface-to-volume atom ratio of catalyst nanoparticles ($\varepsilon^{S/V}$), the effectiveness factor at the agglomerate level (Γ_a) (17), the wetted fraction of catalyst particles in pores of the CCL ($g(S_r)$) (16), and the statistical fraction of catalyst particles at the triple phase boundary in random composite media ($f(X_{PtC},X_{el})/X_{PtC}$) (5–7). The factors $\varepsilon^{S/V} g(S_r)(f(X_{PtC},X_{el})/X_{PtC})$ define catalyst utilization as the ratio of number of active Pt atoms to total number of Pt atoms, involving effects at a hierarchy of scales, from nanoscale to macroscale (5–7, 16). Additional statistical effects include the possible existence of active sites on the catalyst surface, which could be included in eq. [3] (20, 21). Overall, maximizing the ratio of the $j^0/[m_{Pt}]$ is a joint challenge for electrocatalysis and for understanding statistical inhomogeneity in random composite media with hierarchical structure.

At this point, we would like to point out that the ultimate optimization target of fuel cell developers is not Pt utilization, which is a static statistical property of a catalyst layer, but more importantly the effectiveness factor, which includes as well the effects of non-uniform reaction rate distributions due to electrostatic effects and mass transport phenomena at finite current densities of an operating fuel cell. To account for these effects, effectiveness factors were considered in refs. 37–50. It should be mentioned that the use of this terminology is ambiguous throughout the literature. In some papers, catalyst utilization, or effective catalyst utilization, was used to describe the same concept of effectiveness factors (49, 50).

For a fixed electrode overpotential η_0, the overall effectiveness factor of Pt utilization can be defined by,

[4] $$\Gamma_{CCL} = \Gamma_{stat}\, \Gamma_\delta = \frac{j^0}{2 \times 10^3 [m_{Pt}] j^{0*}} \frac{j_0}{j_0^{id}}$$

where the first quotient on the right hand side, Γ_{stat}, accounts for statistical factors in eq. [3] and the second quotient, Γ_δ, gives the ratio of the actual current density, including transport limitations, relative to the ideal current density j_0^{id} that would be obtained if reaction rates were distributed in an ideal uniform way without any transport limitations (52). The definition of Γ_{CCL} in eq. [4] accounts for effects due to statistical inhomogeneity at multiple scales as well as for non-uniform distributions of electrochemical rates of electrochemical reactions at agglomerate and CCL levels under operation.

In discussions of effectiveness factors, two length scales are usually considered, i.e., the agglomerate scale (~100 nm) and the CCL scale (~10 μm). For ionomer-filled agglomerates on the cathode side with uniform electrostatic potential and non-uniform oxygen distribution inside the agglomerate, the effectiveness factor is described by the well-known Thiele modulus (17, 38–42). As stated in the introduction, we focus on water-filled agglomerates with effectiveness factor Γ_a (see eq. [3]) as explored in our previous modeling work (17, 25). This model involves non-uniform distributions of electrostatic potential, protons, and oxygen at the agglomerate level. At the CCL level, the effectiveness factor accounts for effects of potential gradients in the ionomer electrolyte phase and oxygen concentration gradient along CCL thickness due to the coupled transport of protons, oxygen molecules, liquid water, and water vapor. The model of effectiveness of catalyst utilization at the agglomerate level is embedded into the calculation of the effectiveness factor at the CCL level.

Mathematical model

Since this mathematical model merges our previous two models (16, 17), here we only briefly review the relevant formalisms. The macrohomogeneous model at the CCL level is one-dimensional and isothermal. The main structural parameters of the model are composition, thickness, and pore size distribution (psd). The electrostatic potential in the electronically conducting phase (Pt/C) is assumed to be uniform. The proton concentration is considered to be uniform at the macroscale because of the impregnation with ionomer. The electrostatic potential of the ionomer phase and oxygen concentration are spatially dependent functions. Gas transport in pores is dominated by Knudsen diffusion, since the mean free path of gas molecules is larger than the diameter of secondary pores (10–50 nm) in CCLs. Uniform boundary conditions are assumed at PEM/CCL and CCL/GDL interfaces. In the following equations, the origin ($z = 0$) is at the PEM/CCL interface and the total CCL thickness is L. At the agglomerate level, we consider agglomerates as monodisperse spheres with homogeneously distributed volume fractions of carbon/Pt and water-filled pores. Moreover, we assume that agglomerate radii, R_a, are small compared with the CCL thickness, i.e., $R_a << L$.

Agglomerates are partially covered by ionomer films. In coarse-grained molecular dynamics simulations of structure formation in catalyst layers we found ionomer film thicknesses of ~10 nm. A film of this thickness does not represent a significant diffusion barrier. Moreover, agglomerates are not uniformly covered by an ionomer film, leaving paths for direct transport of oxygen into agglomerate pores. In principle we would have to use complex, heterogeneous boundary conditions for electrostatic potential and concentrations of protons and oxygen on agglomerate surfaces to account for variable thickness and coverage of ionomer films. As a simplification, we will neglect these variations, implying uniform boundary conditions. This simplification was found very insightful in ref. 17. It will have a certain impact on nu-

© 2008 NRC Canada

merical estimates of effectiveness factors but not affect our major conclusions.

In the macrohomogeneous CCL model we only consider operation in the ideally wetted state, in which liquid water fills primary pores, whereas secondary pores are open for gaseous transport of reactants and products, as discussed in ref. 16. Employing this assumption, we will obtain an upper estimate of the effectiveness factor of PFSI-bonded thin film CCL. As shown in ref. 16, effects of the water balance in the CCL do not have to be explicitly accounted for if the CCL is operated in the ideally wetted state. This greatly simplifies the system of differential equations

$$[5] \qquad \frac{d\eta(z)}{dz} = \frac{j(z)}{\sigma_{el}}$$

$$[6] \qquad \frac{dj(z)}{dz} = Q^{ec}(z)$$

$$[7] \qquad \frac{4FD_{O_2}^{eff}}{RT}\frac{dp(z)}{dz} j_0 - j^p(z)$$

Subject to boundary conditions

$$[8] \qquad j|_{z=0} = j_0$$

$$[9] \qquad j|_{z=L} = 0$$

$$[10] \qquad p|_{z=L} = p_L$$

where $\eta(z)$ is the overpotential, $j(z)$ is the proton current density, and $p(z)$ is the oxygen partial pressure.

Proton conductivity σ_{el} in the catalyst layer is assumed to be determined by (5, 6),

$$[11] \qquad \sigma_{el} = \sigma_0 \frac{(X_{el} - X_c)^2}{(1 - X_c)^2}\Theta(X_{el} - X_c)$$

Diffusivity of gaseous oxygen $D_{O_2}^{eff}$ is given by,

$$[12] \qquad D_{O_2}^{eff} = D_{O_2} \frac{[(1 - S_r^{opt})X_p - X_c]^{2.4}}{(1 - X_c)^2(X_p - X_c)^{0.4}}$$

where the residual diffusivity is neglected, since the gas diffusivity is large in the ideally wetted state. The prefactor D_{O_2} in eq. [12] is given by an expression from kinetic gas theory based on the assumption that Knudsen-type diffusion is the main mechanism of gas transport,

$$[13] \qquad D_{O_2} = \frac{2}{3}\sqrt{\frac{8RT}{\pi M_{O_2}}} r_{crit}$$

Assuming that capillary equilibrium prevails in pores, the liquid saturation is given by,

$$[14] \qquad S_r^{opt} = \frac{1}{X_p}\int_0^{r^c} dr' \frac{dX_p(r')}{dr'}$$

where we use a bimodal pore size distribution,

$$[15] \qquad \frac{dX_p(r)}{dr} = \frac{1 - X_{PtC} - X_{el}}{\sqrt{\pi}(\ln s_\mu + \chi_M \ln s_M)}\frac{1}{r} \times \left\{\exp\left[-\left(\frac{\ln(r/r_\mu)}{\ln s_\mu}\right)^2\right] + \chi_M \exp\left[-\left(\frac{\ln(r/r_M)}{\ln s_M}\right)^2\right]\right\}$$

$$[16] \qquad r^c = \frac{2\sigma\cos(\theta)}{p^c}$$

where r^c is the capillary radius of pores in which liquid–gas equilibrium exists. It is the maximum radius of pores that are filled with liquid in a hydrophilic system (wetting angle $\theta < 90°$). Pores of radius less than r^c are filled with liquid water, and pores of radius larger than r^c are filled with gas.

To ensure a good compromise of a high wetted fraction of Pt, high net vaporization rate and good gaseous transport of oxygen and water vapor, r^c should lie in the range between primary pore and secondary pore regions in psds,

$$[17] \qquad r_\mu < r^c < r_M$$

Porous structure and operating pressures should be adjusted to fulfill eq. [17]. In eq. [6], $Q^{ec}(z)$ is the sink term due to electrochemical reaction. It accounts for the reduced effectiveness factor of Pt utilization due to random composition and processes in agglomerates. The value of this term is obtained by integrating the current generated inside the agglomerate and averaging it over the volume of a representative elementary volume element. It is here that the macrohomogeneous model is linked with the agglomerate model.

$$[18] \qquad Q^{ec}(z) = \frac{f(X_{PtC}, X_{el})}{X_{PtC}} g(S_r^{opt}) \frac{3(X_{PtC} + X_\mu)}{R_a^3} \times \int_0^{R_a} j_F^z(r) r^2 dr$$

where r is the radial coordinate inside agglomerates and the local Faradaic current density, $j_F^z(r)$, is determined by the concentrations of dissolved oxygen and protons and by the electrostatic potential inside the agglomerate. Dissolution of oxygen into water-filled pores is implicitly accounted for by using a Henry's law factor in $j_F^z(r)$. In the ideal wetted state, the coefficient that accounts partially saturated porous structure can be calculated by,

$$[19] \qquad g(S_r^{opt}) = \Pi\int_0^{r_{cut}} dr' \frac{dX_p(r')}{dr'}\frac{1}{r'}$$

and Π is a normalization factor that ensures $g \to 1$ in the limit of complete wetting of the layer,

$$[20] \qquad \Pi = \left(\int_0^\infty dr' \frac{dX_p(r')}{dr'}\frac{1}{r'}\right)^{-1}$$

Finally, the effect of reduced Pt utilization due to random three-phase composition is included using percolation theory, which provides a general framework for studying flow and transport in porous composite media, as explained in refs. 5–7. It has proven useful in rationalizing composition-

© 2008 NRC Canada

dependent performance of catalyst layers (53). Systematic experimental studies have been found to be in good agreement with predictions of the model. Percolating pathways must span through the carbon/Pt phase, open pore space, and electrolyte network to provide an adequate supply of all the reactants and removal of the products.

For the effect of random composition on the fraction of active catalyst sites, we adopt a previously suggested parameterization that rests on the theory of active bonds in dual porous composite materials (5–7),

$$[21]\quad f(X_{PtC},X_{el}) = P(X_{el})P(X_{PtC})\{(1-\chi_{ec})(1-[1-P(X_p)]^4)+\chi_{ec}[1-P(X_p)]^4\}$$

with the density of the percolating cluster given by,

$$[22]\quad P(X) = X/\{1+\exp[-53.7(X-X_c)]\}^{3.2}$$

In eq. [21], the factor $P(X_{el})P(X_{PtC})$ takes into account the probability to obtain a meeting point between carbon and ionomer phases with both phases connected to their corresponding infinite clusters. The term $1 - P(X_P)$ takes into account the probability that agglomerate and ionomer have at least one pore as their bond neighbor that belongs to the infinite pore network.

The system of differential equations for water-filled agglomerates is giving by (17),

$$[23]\quad D^{agg}_{H^+}\frac{1}{r^2}\frac{d}{d^2}\left\{r^2\left[\frac{dc^z_{H^+}(r)}{dr}+\frac{F}{RT}c^z_{H^+}(r)\frac{d\phi^z(r)}{dr}\right]\right\} = \frac{j^z_F(r)}{F}$$

$$[24]\quad \varepsilon\varepsilon_0\frac{1}{r^2}\frac{d}{dr}\left[r^2\frac{d\phi^z(r)}{dr}\right] = -Fc^z_{H^+}(r)$$

$$[25]\quad D^{agg}_{O_2}\frac{1}{r^2}\frac{d}{dr}\left[r^2\frac{dc^z_{O_2}(r)}{dr}\right] = \frac{j^z_F(r)}{4F}$$

Subject to uniform boundary conditions

$$[26]\quad \left.\frac{dc^z_{H^+}}{dr}\right|_{r=0} = 0$$

$$[27]\quad c^z_{H^+}\Big|_{r=R_a} = c^{ref}_{H^+}$$

$$[28]\quad \left.\frac{d\phi^z}{dr}\right|_{r=0} = 0$$

$$[29]\quad \phi^z\Big|_{r=R_a} = \eta(z)$$

$$[30]\quad \left.\frac{dc^z_{O_2}}{dr}\right|_{r=0} = 0$$

$$[31]\quad c^z_{O_2}\Big|_{r=R_a} = \frac{p(z)}{RT}H_{O_2}$$

In eqs. [29] and [31], the boundary conditions on agglomerate surfaces correspond to local values (at position z) of electrostatic potential and oxygen partial pressure obtained from the macrohomogeneous model. Equation [31] involves ideal gas law and Henry's law for converting partial pressure of oxygen in the cathodic gas mixture into concentration of dissolved oxygen in agglomerates.

Similar to effective conductivity, we also apply percolation theory to calculate effective proton and oxygen diffusion coefficient in liquid water-filled agglomerates.

$$[32]\quad D^{agg}_{H^+} = D_{H^+}\frac{(X_w-X_c)^2}{(1-X_c)^2}\Theta(X_w-X_c)$$

$$[33]\quad D^{agg}_{O_2} = D^l_{O_2}\frac{(X_w-X_c)^2}{(1-X_c)^2}\Theta(X_w-X_c)$$

where liquid water volume fraction X_w inside the agglomerate is giving by

$$[34]\quad X_w = \frac{X_\mu}{X_{PtC}+X_\mu}$$

Volume fraction of primary pores is giving by

$$[35]\quad X_\mu = \int_0^{r_{cut}} dr'\frac{dX_p(r')}{dr'}$$

The Faradaic current density inside agglomerate is given by

$$[36]\quad j^z_F(r) = 2\times10^3[m_{Pt}]\,j^{0*}\frac{\varepsilon^{S/V}}{L(X_{PtC}+X_\mu)}\frac{c^z_{O_2}(r)}{c^{ref}_{O_2}}\frac{c^z_{H^+}(r)}{c^{ref}_{H^+}}\times\exp\left[\frac{\alpha_c F}{RT}\phi^z(r)\right]$$

The set of governing differential equations (eqs. [23–25]) for the water-filled agglomerate was previously solved numerically using FEMLAB software (17). In this work, the COMSOL script code was generated by COMSOL (an upgraded version of former FEMLAB), which can run in the MATLAB environment. The set of differential equations (eqs. [5–7]) for the entire cathode catalyst layer were solved using MATLAB software. The shooting method converts the boundary value problem into an initial value problem. It takes advantage of the powerful algorithms available for the integration of initial value problems. The iteration procedure is initialized with a guess of the boundary value $\eta|_{z=L}$. The differential equations are integrated forward as a set of simultaneous initial value differential equations. The iteration procedure terminates when the condition $j|_{z=0} = j_0$ is fulfilled, using a small convergence criterion (10^{-3}). Otherwise the value $\eta|_{z=L}$ is adjusted. Each time that eq. [6] is solved, eq. [18] will call the COMSOL script code to solve for $j^z_F(r)$ in the water-filled agglomerate model (eqs. [23–31]), where the boundary conditions (eqs. [29] and [31]) are provided by the catalyst layer model, i.e., eqs. [5] and [7], respectively. Dozens of self-consistency iterations are needed to obtain convergence.

In this paper, we are focusing on discussing the effectiveness factor of Pt utilization. At the agglomerate level, the ef-

© 2008 NRC Canada

Table 1. Constants and parameters representing structure and operating conditions.

Constants	
Faraday's constant	F = 96 485 C mol^{-1}
Universal gas constant	R = 8.314 J mol^{-1} K^{-1}
Molar mass of oxygen	M_{O_2} = 0.032 kg mol^{-1}
Structure parameters	
Thickness of CCL	L = 10 μm
Pt loading	m_{Pt} = 0.4 mg cm^{-2}
Surface-to-volume ratio of atoms in the particles	$\varepsilon^{S/V}$ = 0.3
Volume fraction of Pt/C solid phase in CCL	X_{PtC} = 0.30
Volume fraction of electrolyte in CCL	X_{el} = 0.33
Volume fraction percolation threshold	X_c = 0.10
Factor determining width of micropore distribution	S_μ = 2.0
Factor determining width of mesopore distribution	S_M = 2.0
Characteristic radius of micropore	r_μ = 3.0 nm
Characteristic radius of mesopore	r_M = 30.0 nm
Factor controlling the volume ratio	χ_M = 2.0
Residual activity at nonoptimal reaction spots	χ_{ec} = 0.01
Critical radius based on pore analysis	r_{crit} = 12.0 nm
Operating parameters	
Fuel cell operating temperature	T = 298 K
Reference exchange current density	j^{0*} = 3.03 × 10^{-9} A cm^{-2}
Proton reference concentration	$c^{ref}_{H^+}$ = 1.2 × 10^{-4} mol cm^{-3} (17)
Bulk proton diffusion coefficient in liquid water	D_{H^+} = 9.28 × 10^{-5} cm^2 s^{-1} (54)
Bulk oxygen diffusion coefficient in liquid water	$D^l_{O_2}$ = 2.25 × 10^{-5} cm^2 s^{-1} (55)
Bulk proton conductivity of Nafion	σ_0 = 0.064 S cm^{-1} (56)
Ostwald coefficient in Herry's law	H_{O_2} = 0.031 11 (57)
Relative dielectric constant of liquid water	ε = 80 (17)
Permittivity of vacuum	ε_0 = 8.854 × 10^{-14} C^2 J^{-1} cm^{-1} (17)
Inlet oxygen pressure	p_L = 1 atm
Oxygen reference concentration	$c^{ref}_{O_2} = p_L H_{O2}/RT$
Cathodic transfer coefficient	α_c = 1.0

Note: Unless stated otherwise, the values of parameters comes from ref. 16.

fectiveness factor is defined as the integral current conversion rate divided by the ideal rate that would result if the entire interior surface were exposed to the external conditions prevailing at the agglomerate surface (17).

$$[37] \quad \Gamma_a = \frac{3\int_0^{R_a} j^z_F(r) r^2 dr}{j^z_{F,S} R_a{}^2}$$

where $j^z_{F,S}$ is Faradaic current density on the agglomerate surface.

$$[38] \quad j^z_{F,S} = 2\times10^3 [m_{Pt}]\, j^{0*} \frac{\varepsilon^{S/V}}{L(X_{PtC} + X_\mu)} \frac{p(z) H_{O_2}}{RT c^{ref}_{O_2}} \times \exp\left[\frac{\alpha_c F}{RT}\eta(z)\right]$$

When $\Gamma_a \to 1$, the whole model can be simplified to a pure macrohomogeneous model.

At the catalyst layer level, the effectiveness factor is defined as the integral current conversion rate divided by the ideal rate that would result if the entire catalyst were in the CCL/PEM interface with inlet oxygen concentration.

$$[39] \quad \Gamma_{CCL} = \frac{j_0}{2\times10^3 [m_{Pt}]\, j^{0*}\, p_L \exp\left[\frac{\alpha_c F}{RT}\eta(L)\right]}$$

Note that, after a self-consistent solution, this expression will include effects at the agglomerate level. This parameter is the key parameter to evaluate the performance of CCLs.

Results and discussion

For the purpose of illustration and comparison, we specified most of the parameter values that we have used previously (16). They correspond to state-of-the-art catalyst layer structures described in the literature. Additional parameters related to water-filled agglomerates are given in Table 1. Based on the specified values important parameters can be calculated, which include optimal saturation S_r^{opt} = 0.33, wetted pore fraction $g(S_r^{opt})$ = 0.84, and the utilization factor

© 2008 NRC Canada

due to random three-phase composition, $f(X_{PtC}, X_{el})/X_{PtC}$ = 0.28.

First we discuss the effectiveness factor at the agglomerate level. According to the definition made in this study, Γ_a accounts for the effects from uneven distribution of proton concentration, electrostatic potential, and oxygen concentration inside the agglomerate. Figure 1 shows the distribution of Γ_a as a function of z for varying agglomerate radii R_a, at two distinct overall current densities, j_0 = 1 A cm^{-2} in Fig. 1*a* and j_0 = 0.2 A cm^{-2} in Fig. 1*b*. With the increase of R_a, Γ_a decreases. This is because $c^z_{H^+}(r)$ decreases rapidly toward the center of an agglomerate within a distance corresponding to the Debye length, $\lambda_D = \sqrt{\varepsilon\varepsilon_0 RT/F^2 c^{ref}_{H^+}}$, which is on the order of 10 nm, and is independent of R_a. Thus for larger R_a, a smaller volume portion of the agglomerate is used for reaction.

As shown in Fig. 2*a*, volumetric current densities, j_v, decrease from the CCL/PEM interface towards the CCL/GDL interface. As can be seen in Fig. 2*b*, Γ_a is more markedly reduced in regions in which j_v is high. The more current an agglomerate generates, the more uneven is the distribution of the electrostatic potential $\phi^z(r)$, resulting in a steeper drop of $c^z_{H^+}(r)$ from agglomerate surface towards centre. Because of the same reason, Γ_a increases throughout the layer if the overall current density j_0 decreases, cf. Fig. 1*a* and Fig. 1*b*. Next we discuss the overall effectiveness factor of Pt utilization at the CCL level, Γ_{CCL}, which accounts for effectiveness factors at the agglomerate and nanoparticle levels, as well as reduced Pt utilization due to random composition and partially saturated porous structure. Figure 2*c* shows the effect of agglomerate radius R_a and total current density j_0 on Γ_{CCL}. The larger R_a, the lower Γ_{CCL} will be, which results from low Γ_a. High j_0 will result in low Γ_{CCL} because of the more uneven distribution of reaction rates at agglomerate and CCL levels.

Above we discussed the effect of R_a, which could be used to classify several possible cases. The limiting case of $R_a \to L$ corresponds to ionomer-free CCL, consisting of two functional phases, which have been studied by Wang et al. (25). In this case, the two sets of differential equations can be combined into,

$$[40] \quad D^{eff}_{H^+} \frac{d}{dz}\left[\frac{dc_{H^+}(z)}{dz} + \frac{F}{RT} c_{H^+}(z) \frac{d\eta(z)}{dr}\right] = \frac{j_F(z)}{F}$$

$$[41] \quad \varepsilon\varepsilon_0 \frac{d^2\eta(z)}{dz^2} = -F c_{H^+}(z)$$

$$[42] \quad D^{eff}_{O_2} \frac{dc_{O_2}(z)}{dz^2} = \frac{j_F(z)}{4F}$$

where

$$[43] \quad j_F(z) = 2\times10^3 [m_{Pt}]\, j^{0*} \varepsilon^{S/V} \frac{c_{O_2}(z)}{c^{ref}_{O_2}} \frac{c_{H^+}(z)}{c^{ref}_{H^+}} \times \exp\left[\frac{\alpha_c F}{RT}\eta(z)\right]$$

Fig. 1. Distribution of effectiveness factors of agglomerates along CCL thickness at (*a*) j_0 = 1 A cm^{-2}, (*b*) j_0 = 0.2 A cm^{-2}, R_a is from 50 to 200 nm.

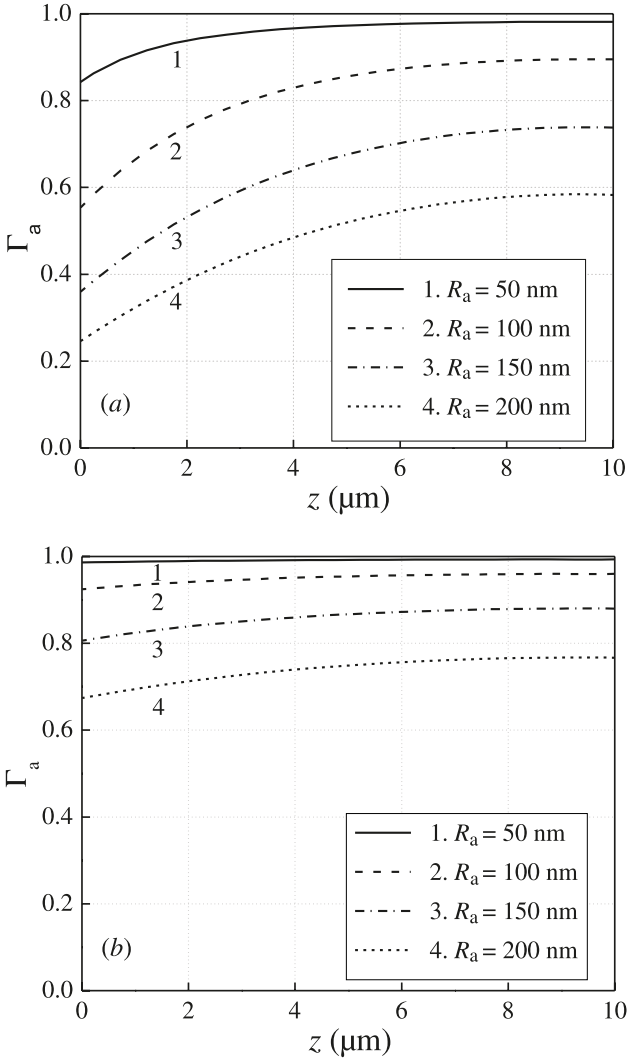

Since the Debye length is only on the order of λ_D ~ 10 nm, i.e., ~1000 times thinner than conventional CCL, only ultrathin layers with L ~ 200 nm provide reasonable values of Γ_{CCL} in this limit.

In the opposite limiting case $R_a \lll$ L, agglomerate effects are negligible and the pure macrohomogeneous approach could be used. In this case, only eqs. [5–7] are relevant and $Q^{ec}(z)$ in eq. [6] is given by,

$$[44] \quad Q^{ec}(z) = 2\times10^3 [m_{Pt}]\, j^{0*} \varepsilon^{S/V} \frac{p(z) H_{O_2}}{RT c^{ref}_{O_2}} \times \exp\left[\frac{\alpha_c F}{RT}\eta(z)\right]$$

For the general case with $R_a << L$ considered in this manuscript, the fully coupled system of equations at agglomerate and CCL levels should be applied to calculate $Q^{ec}(z)$. We would like to use the general model, $R_a <<$ L, to explore the applicability limits of the widely used

© 2008 NRC Canada

Fig. 2. (*a*) Distribution of volumetric current density, (*b*) effectiveness factor at the agglomerate level along CCL thickness at different current densities when R_a = 100 nm, and (*c*) shows effectiveness factors at the CCL level for different current densities and agglomerate sizes.

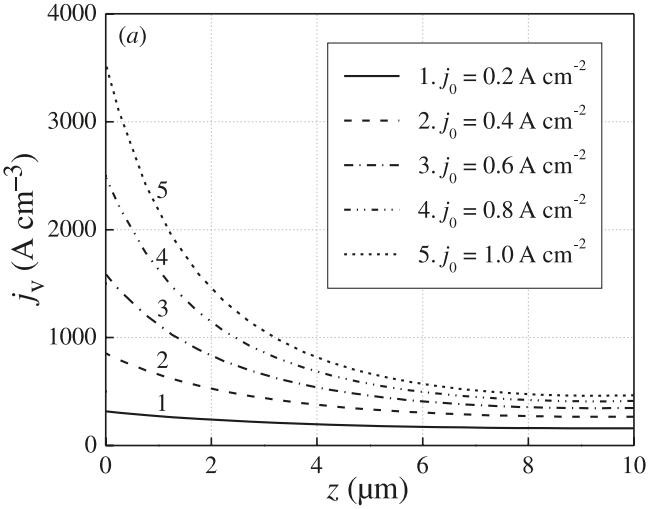

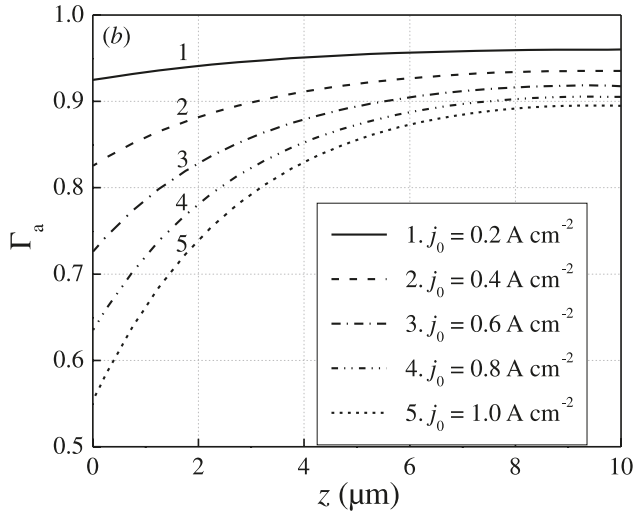

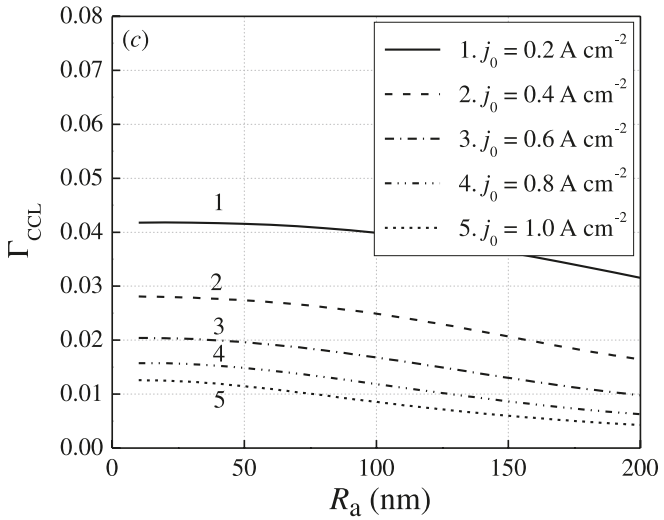

Fig. 3. Critical agglomerate radius that separates the range of validity of the macrohomogeneous model from the macrohomogeneous with agglomerates model.

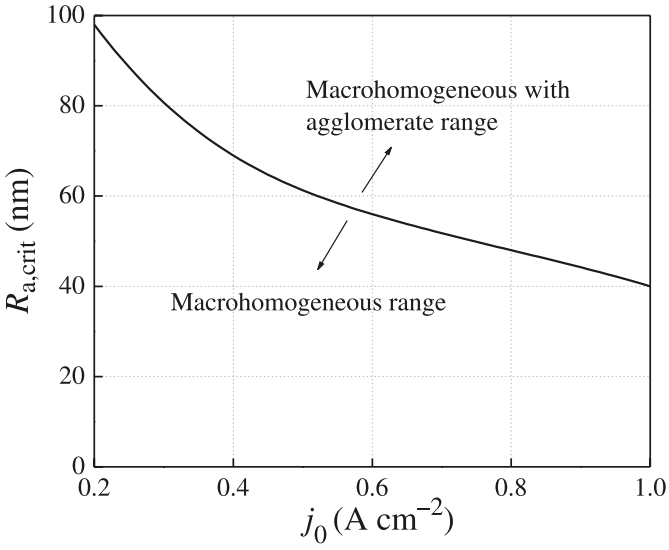

macrohomogeneous approach, $R_a \lll L$. For this purpose, we define a critical agglomerate radius, $R_{a,crit}$, with the condition that for $R_a < R_{a,crit}$, the effectiveness factors in agglomerates is >95%. Under this condition, the macrohomogeneous model provides a reasonably accurate approach. In the other case, $L >> R_a > R_{a,crit}$, the reasonable model should be in the general form of the water-filled agglomerate model nested in the macrohomogeneous cathode catalyst layer model, as introduced in the Mathematical model section. The task is thus to find $R_{a,crit}$ to classify these different cases. To determine $R_{a,crit}$ we define a reference case for which the corresponding Γ_{CCL}^{ref} is calculated under the assumption $\Gamma_a \equiv 1$. Γ_{CCL}^{ref} is the maximum possible effectiveness factor of the CCL for a given thickness, composition, and operating conditions. Next, we consider R_a as a variable parameter and determine its critical value $R_{a,crit}$ at which $\Gamma_{CCL} \equiv 0.95 \times \Gamma_{CCL}^{ref}$. For $R_a < R_{a,crit}$, we will thus have, on average, $\Gamma_a > 0.95$. Figure 3 shows the critical agglomerate radius $R_{a,crit}$ that separates the region in which the macrohomogeneous model is valid, i.e., $R_a < R_{a,crit}$, from the region in which agglomerate effects should be accounted for, i.e., $R_a \geq R_{a,crit}$. $R_{a,crit}$ is determined by operating conditions, such as total current densities, temperature, and oxygen partial pressure. Higher j_0, smaller T, and smaller p_L correspond to smaller values of $R_{a,crit}$.

Increased values of T and p_L result in higher Γ_{CCL}, as demonstrated in Fig. 4. The increase of T improves proton and oxygen diffusion coefficients and proton conductivity of the PFSI phase, leading to more uniform reaction rate distributions. The increase of p_L results as well in more uniform distributions of oxygen in CCLs. A comparison of different operating condition is shown in Fig. 4.

Compared with PFSI-bonded thin film catalyst layers, ultrathin catalyst layers proposed by 3M Company (58) have a different structure in which the Pt catalyst is sputter-deposited onto an ultrathin nanostructured film of oriented crystalline organic whiskers. For the comparison of effectiveness factors of conventional three-phase composite lay-

© 2008 NRC Canada

Fig. 4. Comparison of effectiveness factor at the agglomerate and CCL level at different temperatures and oxygen partial pressures for j_0 = 1 A cm^{-2} [Cases of T = 348 K with their parameters of j^{0*} = 1.023 × 10^{-8} A cm^{-2} (17), D_{H^+} = 1.9 × 10^{-4} cm2 s^{-1} (17), $D^1_{O_2}$ = 9.19 × 10^{-5} cm2 s^{-1} (17), σ_0 = 0.118 S cm^{-1} (56), and H_{O_2} = 0.023 32 (57)].

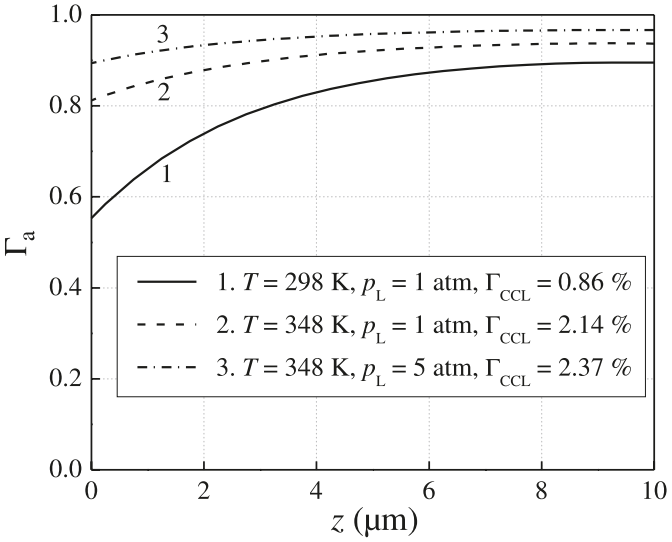

ers, considered predominantly in this publication, and ultrathin two-phase layers, we have to incorporate catalyst utilization at the Pt nanoparticle level, i.e., the surface-to-volume atom ratio $\varepsilon^{S/V}$. This factor is determined by particles or grain sizes of catalyst particles and their surface morphology or roughness. For supported nanoparticle catalysts in PFSI-filled composite CCLs, this ratio can be determined from the particle shape and the particle size. At a typical particle diameter of 4 nm, the corresponding value is $\varepsilon^{S/V}$ = 0.3 (59). For vacuum-deposited catalyst in nano-structured ultrathin film CCL the fraction of catalyst surface atoms is more difficult to estimate. It was suggested in ref. 58 on the basis of cyclic voltammetry measurements that the irregular surface morphology of such catalysts corresponds to grain sizes of ~10 nm with $\varepsilon^{S/V}$ = 0.15 (25, 58). For comparison, we consider the two kinds of CCL at the same Pt loading and operating conditions. From the information provided by Fig. 5*c* of ref. 25, we obtained $\Gamma_{CCL}/\varepsilon^{S/V}$ = 0.21 for the ultrathin layer at the conditions of m_{Pt} = 0.2 mg cm^{-2}, j_0 = 1.0 A cm^{-2}, α_c = 1, T = 348 K, and p_L = 5 atm (1 atm = 101.325 kPa). We applied the same Pt loading and operating conditions to PFSI-bonded thin film CCLs. The thickness was adjusted proportional to the Pt loading to L = 5 μm. Accounting for the distinct values of $\varepsilon^{S/V}$ in both cases, we obtain overall effectiveness factors of Pt utilization of Γ_{CCL} = 3.1% for ultrathin two-phase CCL and Γ_{CCL} = 3.5% for PFSI-bonded thin film CCLs. These rough estimates, which account for statistical inhomogeneities and non-uniformities of reaction rate distributions at relevant scales from nanoscale to macroscale, indicate that the two kinds of CCL exhibit similar effectiveness factors of Pt utilization. All in all, any of the factors is fraught with uncertain error – thus overall, the estimation would be somewhat speculative. On the other hand, the message is clear. The effectiveness of catalyst utilization in currently fabricated CCL, viz. three-phase composite gas diffusion CCL and ultrathin nanostructured CCL, is most likely <10% and not close to 100% as stated recently by Neyerlin et al. (49). This assessment holds out the prospect of tremendous reserves for improvement through structural design.

Conclusions

In this work, we studied the effectiveness factor of Pt utilization for the PFSI-bonded thin film cathode catalyst layer by combining the water-filled agglomerate model with the structure-based macrohomogeneous model. The main goal was the evaluation of effectiveness factor of Pt utilization, a more meaningful parameter than just Pt utilization. It was found that small agglomerate radius, low operating current density, high operating temperature, and oxygen partial pressure result in high effectiveness factors of Pt utilization. When the effectiveness factors at the agglomerate level are close to 1, the pure macrohomogeneous approach is appropriate. The critical agglomerate radii were calculated, which are related to the operating conditions. Finally, the effectiveness factor of Pt utilization in the PFSI-bonded thin film cathode catalyst layer was compared with that in the ultrathin two-phase cathode catalyst layer. Including the estimation of the surface-to-volume atom ratio at the nanoparticle level, the two kinds of catalyst layers exhibit similar effectiveness factors of Pt utilization in the range of ~3% at temperature of 348 K and oxygen pressure of 5 atm. Although any of the factors is fraught with uncertain error, the effectiveness is most likely less than 10%. This suggests that tremendous improvements in specific electrocatalytic activities of Pt in catalyst layers of PEFCS could be harnessed through advanced structural design.

References

1. D. Thompsett. *In* Handbook of fuel cells– Fundamentals, technology, and applications. Vol. 3. *Edited by* W. Vielstich, A. Lamm, and H.A. Gasteiger. John Wiley & Sons Ltd., UK. 2003. Chap. 37. p. 467.
2. L. Zhang, J. Zhang, D.P. Wilkinson, and H. Wang. J. Power Sources, **156**, 171 (2006).
3. M.S. Wilson and S. Gottesfeld. J. Appl. Electrochem. **22**, 1 (1992).
4. M.S. Wilson and S. Gottesfeld. J. Electrochem. Soc. **139**, L28 (1992).
5. M. Eikerling, A.A. Kornyshev, and A.A. Kulikovsky. *In* Encyclopedia of electrochemistry. Vol. 5. *Edited by* A. Bard and M. Stratmann. Wiley-VCH, Weinheim, Germany. 2007. Chap. 8.2. p. 447.
6. M. Eikerling and A.A. Kornyshev. J. Electroanal. Chem. **453**, 89 (1998).
7. M. Eikerling, A.A. Kornyshev, and A. S. Ioselevich. Fuel Cells, **4**, 131 (2004).
8. Z. Xie, T. Navessin, K. Shi, R. Chow, Q. Wang, D. Song, B. Andreaus, M. Eikerling, Z. Liu, and S. Holdcroft. J. Electrochem. Soc. **152**, A1171 (2005).
9. J. Xie, K.L. More, T.A. Zawodzinski, and W.H. Smith. J. Electrochem. Soc. **151**, A1841 (2004).
10. M. Uchida, Y. Aoyama, N. Eda, and A. Ohta. J. Electrochem. Soc. **142**, 463 (1995).

© 2008 NRC Canada

11. M. Uchida, Y. Aoyama, N. Eda, and A. Ohta. J. Electrochem. Soc. **142**, 4143 (1995).
12. M. Uchida, Y. Fukuoka, Y. Sugawara, N. Eda, and A. Ohta. J. Electrochem. Soc. **143**, 2245 (1995).
13. S.J. Shin, J.K. Lee, H.Y. Ha, S.A. Hong, H.S. Chun, and I.H. Oh. J. Power Sources, **106**, 146 (2002).
14. P. Gode, F. Jaouen, G. Lindbergh, A. Lundblad, and G. Sundholm. Electrochim. Acta, **48**, 4175 (2003).
15. K. Malek, M. Eikerling, Q. Wang, T. Navessin, and Z. Liu. J. Phys. Chem. C, **111**, 13627 (2007).
16. M. Eikerling. J. Electrochem. Soc. **153**, E58 (2006).
17. Q. Wang, M. Eikerling, D. Song, and Z. Liu. J. Electroanal. Chem. **573**, 61 (2004).
18. A. Wieckowski, E. Savinova, and C.G. Vayenas (*Editors*). Catalysis and electrocatalysis at nanoparticle surfaces. Marcel Dekker, NY. 2003.
19. F. Maillard, S. Schreier, M. Heinzlik, E.R. Savinova, S. Weinkauf, and U. Stimming. Phys. Chem. Chem. Phys. **7**, 385 (2005).
20. B. Andreaus and M. Eikerling. J. Electroanal. Chem. **607**, 121 (2007).
21. B. Andreaus, F. Maillard, J. Kocylo, E. Savinova, and M. Eikerling. J. Phys. Chem. B, **110**, 21028 (2006).
22. J. Solla-Gullon, P. Rodriguez, E. Herrero, A. Aldaz, and J.M. Feliu. Phys. Chem. Chem. Phys. **10**, 1359 (2008).
23. Q. Wang, M. Eikerling, D. Song, Z. Liu, T. Navessin, Z. Xie, and S. Holdcroft. J. Electrochem. Soc. **151**, A950 (2004).
24. D. Song, Q. Wang, Z. Liu, M. Eikerling, Z. Xie, T. Navessin, and S. Holdcroft. Electrochim. Acta, **50**, 3347 (2005).
25. Q. Wang, M. Eikerling, D. Song, and Z. Liu. J. Electrochem. Soc. **154**, F95 (2007).
26. E.B. Easton and P.G. Pickup. Electrochim. Acta, **50**, 2469 (2005).
27. J. Shan and P.G. Pickup. Electrochim. Acta, **46**, 119 (2000).
28. T.J. Schmidt, H.A. Gasteiger, G.D. Stäb, P.M. Urban, D.M. Kolb, and R.J. Behm. J. Electrochem. Soc. **145**, 2354 (1998).
29. U.A. Paulus, T.J. Schmidt, H.A. Gasteiger, and R.J. Behm. J. Electroanal. Chem. **495**, 134 (2001).
30. H.A. Gasteiger, W. Gu, R. Makharia, M.F. Mathias, and B. Sompalli. *In* Handbook of fuel cells: Fundamentals, technology, and applications. Vol. 3. *Edited by* W. Vielstich, A. Lamm, and H.A. Gasteiger. John Wiley & Sons Ltd., England. 2003. Chap. 46. p. 593.
31. K.C. Neyerlin, H.A. Gasteiger, C.K. Mittelsteadt, J. Jorne, and W. Gu. J. Electrochem. Soc. **152**, A1073 (2005).
32. K.S. Dhathathreyan, P. Sridhar, G. Sasikumar, K.K. Ghosh, G. Velayutham, N. Rajalakshmi, C.K. Subramaniam, M. Raja, and K. Ramya. Int. J. Hydrogen Energy, **24**, 1107 (1999).
33. X. Cheng, B. Yi, M. Han, J. Zhang, Y. Qiao, and J. Yu. J. Power Sources, **79**, 75 (1999).
34. G. Sasikumar, J.W. Ihm, and H. Ryu. J. Power Sources, **132**, 11 (2004).
35. G. Li and P.G. Pickup. J. Electrochem. Soc. **150**, C745 (2003).
36. H.A. Gasteiger, J.E. Panels, and S.G. Yan. J. Power Sources, **127**, 162 (2004).
37. F. Jaouen and G. Lindbergh. J. Electrochem. Soc. **150**, A1699 (2003).
38. W. Sun, B.A. Peppley, and K. Karan. J. Power Sources, **144**, 42 (2005).
39. A.Z. Weber and J. Newman. J. Electrochem. Soc. **152**, A677 (2005).
40. V. Gurau, F. Barbir, and H. Liu. J. Electrochem. Soc. **147**, 2468 (2000).
41. W. Sun, B.A. Peppley, and K. Karan. Electrochim. Acta, **50**, 3359 (2005).
42. M. Secanell, K. Karan, A. Suleman, and N. Djilali. Electrochim. Acta, **52**, 6318 (2007).
43. F. Gloaguen, F. Andolfatto, R. Durand, and P. Ozil. J. Appl. Electrochem. **24**, 863 (1994).
44. F. Gloaguen and R. Durand. J. Appl. Electrochem. **27**, 1029 (1997).
45. F. Gloaguen, P. Convert, S. Gamburzev, O.A. Velev, and S. Srinivasan. Electrochim. Acta, **43**, 3767 (1998).
46. Y. Bultel, P. Ozil, and R. Durand. J. Appl. Electrochem. **29**, 1025 (1999).
47. C.C. Boyer, R.G. Anthony, and A.J. Appleby. J. Appl. Electrochem. **30**, 777 (2000).
48. X. Liu, W. Tao, Z. Li, and Y. He. J. Power Sources, **158**, 25 (2006).
49. K.C. Neyerlin, W. Gu, J. Jorne, A. Clark Jr., and H.A. Gasteiger. J. Electrochem. Soc. **154**, B279 (2007).
50. K. Karan. Electrochem. Comm. **9**, 747 (2007).
51. V.P. Zhdanov and B. Kasemo. Phys. Rev. B, **55**, 4105 (1997).
52. M. Eikerling, K. Malek, and Q. Wang. *In* PEM fuel cell electrocatalysts and catalyst layers. *Edited by* J. Zhang. Springer, New York. In press.
53. A. Ioselevich, A.A. Kornyshev, and W. Lehnert. Solid State Ion. **124**, 221 (1999).
54. L.A. Blumenfeld and A.N. Tikhonov. Biophysical thermodynamics of intracellular processes. Molecular Machines of the Living Cell. Springer-Verlag, NY. 1994.
55. C. Gao. Ph.D thesis, University of Cincinnati, Cincinnati, Ohio. 2005
56. T.E. Springer, T.A. Zawodzinski, and S. Gottesfeld. J. Electrochem. Soc. **138**, 2334 (1991).
57. E. Wilhelm, R. Battino, and R.J. Wilcock. Chem. Rev. **77**, 219 (1977).
58. M.K. Debe. *In* Handbook of fuel cells: fundamentals, technology, and applications. Vol. 3. *Edited by* W. Vielstich, A. Lamm, and H.A. Gasteiger. 2003. p. 576.
59. B. Andreaus and M. Eikerling. *In* Modeling of fuel cells. *Edited by* K. Promislow and S. Paddison. Springer, New York. In press.

© 2008 NRC Canada

Effect of base on alkyltriphenylphosphonium salts in polar aprotic solvents

Julius N. Ngwendson, Cassandra M. Schultze, Jordan W. Bollinger, and Anamitro Banerjee

Abstract: When arylmethyl phosphonium salts are treated with a base (e.g., *t*-BuOK or NaH) they homocouple to form symmetric 1,2-diarylethenes. In some cases, dilution and (or) use of excess base lead to very high yields of the product. This reaction is solvent sensitive: the reaction occurs only when polar aprotic solvents such as acetonitrile or DMSO are used. Other alkyl phosphonium salts (e.g., ethoxycarbonylmethyltriphenylphosphonium bromide and *n*-butyltriphenylphosphonium bromide) form a ylid (when an α-carbonyl group is present) or lose a phenyl group to form alkyldiphenylphosphine oxides when treated with the base. Mechanistic investigation of the homocoupling reaction indicates that the reaction proceeds through a ylid that acts as a nucleophile on an unreacted phosphonium salt. The resulting adduct undergoes elimination to form the observed product. The *E*/*Z* ratio seems to depend on the amount of the base used and the phosphonium salt involved.

Key words: phosphonium salts, homocoupling, 1,2-diarylalkene, Ylids.

Résumé : La réaction des sels d'arylméthylphosphonium avec une base, tel le *t*-BuOK ou le NaH, donne lieu à une réaction d'homocouplage qui conduit à la formation des 1,2-diaryléthènes symétriques. Dans quelques cas, une dilution et/ou un excès de base conduit à des rendements très élevés de ce produit. Cette réaction est sensible aux solvants: la réaction ne se produit que dans les solvants polaires aprotiques, tel l'acétonitrile ou le DMSO. D'autres sels d'alkylphosphonium, tel le bromure d'éthoxycarbonylméthyltriphénylphosphonium ou du bromure de butyltriphénylphosphonium, conduit à la formation d'un ylure quand on est en présence d'un groupe carbonyle en α ou de la perte d'un groupe phényle conduisant à la formation d'oxydes d'alkyldiphénylphosphines quand ils sont traités par des bases. Les études mécanistiques menées sur la réaction d'homocouplage indiquent que la réaction se produit par le biais d'un ylure qui agit comme nucléophile pour le sel de phosphonium qui n'a pas réagi. L'adduit qui en résulte subit une élimination qui conduit à la formation du produit observé. Le rapport *E*/*Z* semble dépendre de la quantité de base utilisée et du sel de phosphonium impliqué.

Mots-clés : sels de phosphonium, homocouplage, 1,2-diaryléthène, ylures.

[Traduit par la Rédaction]

Introduction

1,2-Diarylalkenes undergo reversible *EZ* isomerization or electrocyclic reactions when subjected to thermal or optical stimuli (1). The two isomers (in the case of photoisomerization) or the closed and open forms (in the case of electrocyclic reactions) generally have different absorption spectra (1). This allows for selective formation of one isomer using the appropriate wavelength of light, while using a different wavelength of light to carryout the reverse reaction (2). As a result, these compounds have been used as photochromic compounds (3) and optical switches (4). Specifically, 1,2-dithienylethenes have been widely used as photochromic compounds (4, 5). These compounds show a combination of very good photochromic properties such as high fatigue resistance, short response time, high quantum yields, no thermal isomerization, gated reactivity, and large changes of the absorption wavelength between the isomers. The open and closed forms arising because of the electrocyclic reactions of these compounds also have different electrochemical properties, which is useful in their utility as optical switching materials (6). As the applications of photochromic compounds grow, new diarylalkene-based photochromic compounds are being developed (6, 7). As new 1,2-diarylalkenes are being synthesized for various applications, quick, inexpensive, and convenient routes for their synthesis become more desirable.

Formation of a new C=C bond, using Wadsworth–Horner–Emmons and Wittig reactions (8), is a key step in the synthesis of various 1,2-diaryl alkenes. Other approaches used for the synthesis of these compounds include Heck olefination (9) and Suzuki–Miyaura cross coupling (10). Recently, Blanc and Bochet synthesized 2,2′-dinitrostilbene by the reaction of 2-nitrobenzyl chloride with KOH (11). This homocoupling reaction is however reported only for symmetric dinitrostilbene (12). Opitz and co-workers reported the synthesis of a new C=C bond via a homocoupling of sulfonyl chlorides. In the presence of triethylamine at low

Received 25 July 2007. Accepted 12 March 2008. Published on the NRC Research Press Web site at canjchem.nrc.ca on 13 May 2008.

J.N. Ngwendson, C.M. Schultze, J.W. Bollinger, and A. Banerjee.[1] Department of Chemistry, University of North Dakota, Grand Forks, ND 58202–9024, USA.

[1]Corresponding author (e-mail: abanerjee@chem.und.edu).

 doi:10.1139/V08-056 © 2008 NRC Canada

Scheme 1. Wittig vs. homocoupling solvent dependence.

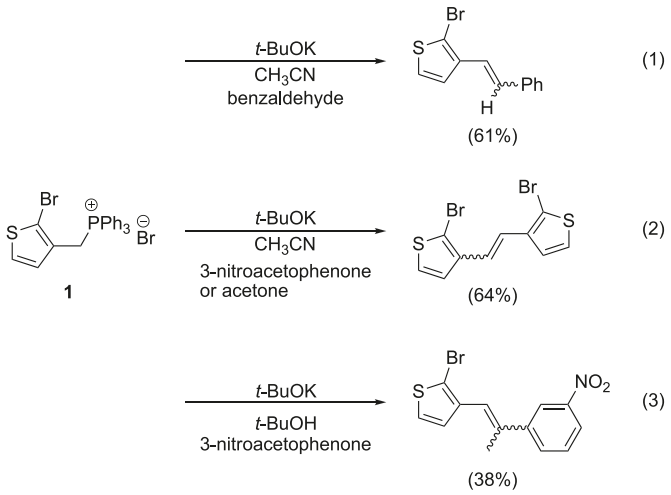

temperatures the sulfonyl chlorides formed thiirane-1,1-dioxide intermediates, which upon thermolysis resulted in the formation of the alkenes (13). Hoeg and Lusk reported homocoupling of benzyl halides by lithiation of the α-hydrogen at low temperatures to form the stilbene derivatives in high yields (14).

Recently we reported a solvent-dependent behavior of arylmethyltriphenyl phosphonium salts in the presence of a base (15). 2-Bromo-3-thienylmethyltriphenylphosphonium bromide (**1**) undergoes a Wittig reaction with benzaldehyde in acetonitrile but undergoes a homocoupling reaction rather than a Wittig reaction when a ketone is used under the same conditions (Scheme 1). The phosphonium salt however undergoes the expected Wittig reaction with ketones when *t*-butanol is used as the solvent. Solvent dependence studies show that the homocoupling reactions occur in polar aprotic solvents with a direct correlation between the yield of the product and the dielectric constant of the solvent (15). This observation complements an earlier report of homocoupling of phosphonium salts to form *trans*-olefins in the presence of *N*-fluoropyridinium salts with THF as the solvent at –30 °C (16). The mechanism proposed for the reaction involved an electron transfer step followed by radical coupling. The resulting dimer then decomposes to form the *trans*-alkene (16). This reaction however is specific to phosphonium salts with electron-withdrawing groups and results in modest yields. When other phosphonium salts were used, only traces of olefins could be detected. In the current study, the homocoupling reaction was found to be effective for arylmethylphosphonium salts when *no* electron withdrawing groups were present. The reaction was also found to be solvent-dependent and resulted in very high yields of the olefin. However, there appears to be no pattern for the *E*/*Z* ratio.

In this article we report the optimized conditions for the homocoupling reaction and explore the generality of this reaction with respect to various arylmethylphosphonium salts and other alkylphosphonium salts. We also report the behavior of diethylarylmethylphosphonates under these conditions.

Results and discussion

The phosphonium salts **3**, **9**, and **10** were obtained commercially, while the rest were synthesized as described

Scheme 2. Reaction of the phosphonium salts with base.

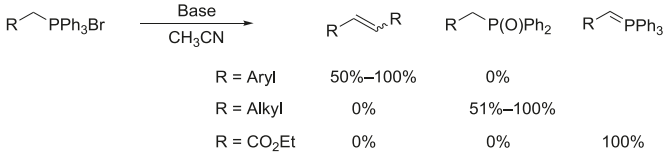

earlier (15). The phosphonium salts were dissolved in acetonitrile (most of the salts were partially soluble, hence forming a suspension). The solution was cooled to 0 °C under ice and the base was added gradually over 5 min. The reaction mixture was allowed to warm up to room temperature (RT) while stirring for 2 h. The formation of the olefin was detected using TLC. After 2 h, the solvent was removed and the resulting mixture was subjected to column chromatography to isolate the product. The product obtained depends on the alkyl group of the phosphonium salts (Scheme 2). Most arylmethylthriphenylphosphonium salts led to the formation of the olefin. In the absence of an aromatic ring on the α-carbon, alkyldiphenylphosphine oxide was formed in quantitative yields. Table 1 lists the isolated yields of the homocoupling reactions under optimized conditions. The phosphonium salts that resulted in 75% or higher yields, as reported in our previous communication, were not optimized and hence are not included in this table. Although we have shown in our previous report that DMSO is more efficient as a solvent for the homocoupling reaction, we optimized this reaction in acetonitrile because of the ease of isolation of the products.

The phosphonium salts **1**, **3**, **4**, and **6** upon treatment with 2 or 3 equivalents of base resulted in 70%–100% yield of the homocoupling product. The choice of the base did not impact the yield nor the *E*/*Z* ratio. A recent study by Ackermann and Berger on Wittig reactions demonstrates the impact of heteroaryl substitutions on phosphorus and *E*/*Z* ratio due to the interaction of the metal ion and the heteroatom (17). In this study, only triphenyl phosphines were used, however similar effects on the *E*/*Z* ratio is possible. Increasing the amount of base resulted in higher yields of the homocoupling product. For example, using 3 equivalents of *t*-BuOK as base improved the yields of **2** to 56% from 21% when only one equivalent of base was used. Similarly, treating **6** with 1, 2, and 3 equivalents of *t*-BuOK resulted in the formation of 2,2′-dimethoxystilbene in 39%, 75%, and 90% yields, respectively. A similar trend was observed when NaH was used as the base. However, 4-methoxybenzyltriphenylphosphonium salt **5** resulted in only 23% yield, irrespective of the amount of base used, whereas the *o*- and *m*-isomers resulted in nearly quantitative yields of the homocoupling products when 2 or 3 equivalents of the base was used. At this time it is difficult to account for this difference in the homocoupling yields for the three isomers.

When an electron-withdrawing nitro group is present in the aromatic ring (**7** and **8**), no product due to the homocoupling reaction could be detected. On the other hand, when alkyltriphenylphosphonium salts (**9**, **10**, and **11**) where subjected to similar conditions, no olefins were detected. In case of **9** and **10**, the action of the base in acetonitrile or DMSO resulted in the loss of a phenyl group to form *n*-butyldiphenylphosphine oxide and methoxymethyldiphenylphosphine oxide, respectively, in good yields. The

© 2008 NRC Canada

Table 1. Reaction of phosphonium salts with a base in acetonitrile.

Phosphonium salt	Base	Product	Yield	*E*/*Z*
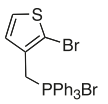 **1**	NaH (2 equiv.)		78%	1:2
	t-BuOK (2 equiv.)		74%	1:1.7
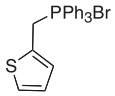 **2**	*t*-BuOK (3 equiv.)	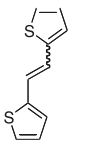	56%	1:0
$PhCH_2PPh_3Br$ **3**	*t*-BuOK (3 equiv.)	Stilbene	74%	1:1.5
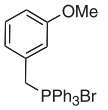 **4**	NaH (2 equiv.)	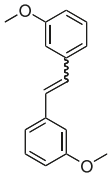	100%	1:1
	t-BuOK (3 equiv.)		89%	1:1
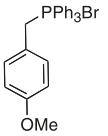 **5**	NaH (3 equiv.)	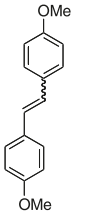	23%	1:3.5
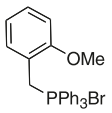 **6**	NaH (3 equiv.)	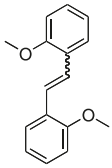	87%	1:4.3
	t-BuOK (3 equiv.)		90%	1:3.8
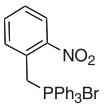 **7**	*t*-BuOK (1 equiv.)	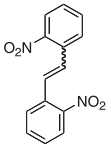	0%	—
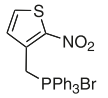 **8**	*t*-BuOK (1 equiv.)	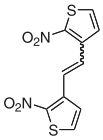	0%	—
n-$BuPPh_3Br$ **9**	NaH (2 equiv.)	n-$BuPOPh_2$	100%	—
	t-BuOK (2 equiv.)		100%	—
$MeOCH_2PPh_3Cl$ **10**	*t*-BuOK (1 equiv.)[a]	$MeOCH_2POPh_2$	51%	—
	t-BuOK (1 equiv.)		84%	—
$EtO_2CCH_2PPh_3Br$ **11**	*t*-BuOK (2 equiv.)	$EtO_2CCHPPh_3$	100%	—

[a]Solvent: DMSO

Scheme 3. Proposed mechanism of the homocoupling reaction.

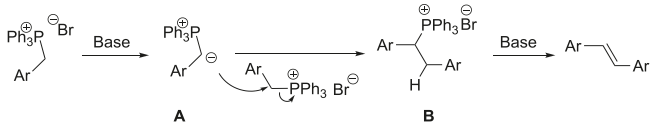

phosphonium salt **11** however formed a stable ylid as expected in acetonitrile.

The proposed mechanism of the homocoupling reaction is described in Scheme 3. Based on the reaction of the phosphonium salt **1** with benzaldehyde in the presence of *t*-BuOK in acetonitrile (Scheme 1, eq. [1]), it can be argued that the first step in the reaction involves the formation of the ylid **A**. The ylid could be trapped by benzaldehyde via a Wittig reaction. However, in the presence of a less reactive substrate like acetophenone or acetone, the ylid reacts with another equivalent of the phosphonium salt to form the intermediate **B**. This is consistent with previous reports of ylid acting as a nucleophile towards alkyl halides (18) and halogens (19). Attempts to detect the intermediate **B** in experiments performed in NMR tubes with CD_3CN as a solvent failed as it revealed a complex mixture. When an electron-withdrawing nitro group is present in the aromatic ring, the ylid is further stabilized by resonance, thereby reducing its reactivity towards homocoupling reaction. It is also possible that the ylid may undergo a single electron transfer resulting in a radical, or eliminate triphenylphosphine to form the corresponding carbene, as observed by Shevchenko and coworkers for phosphanes with orthoquinones (20). Either of these intermediates could couple to form the alkene. However, the absence of any alkene adduct implies that the carbene intermediate is unlikely. The reaction was unaffected by the presence of one equivalent of $CuBr_2$ or n-Bu_3SnH indicating that the existence of a radical intermediate is unlikely. Isolation of triphenylphosphine in 20% yield is consistent with the proposed mechanism. When a mixture of phosphonium salts was treated with a base, a statistical mixture of cross and homocoupling products was detected (see Supplementary data).[2] This result is consistent with the proposed mechanism.

Analysis of the products of the reaction of the phosphonium salts **9** and **10** with base revealed a loss of a phenyl group. While the loss of a phenyl group from triphenylphosphonium salts in the presence of lithium aluminium hydride has been reported in the literature (21), this was an unexpected result in the absence of a reducing agent. Unlike most of the phosphonium salts used in this study, **9** and **10** are readily soluble in acetonitrile. Upon addition of the base, KBr (or KCl) precipitated out of the solution as white solid. The reaction was allowed to continue for about 2 h. The potassium halide salt was filtered out and the solvent was removed under reduced pressure to obtain the products as white solids. ^{1}H NMR, ^{13}C NMR, and HRMS data of the residue indicated that the product was alkyldiphenylphosphine oxide. For example, the ^{1}H NMR of the product resulting from **10** has a doublet (not coupled to any other

[2] Supplementary data for this article are available on the journal Web site (canjchem.nrc.ca) or may be purchased from the Depository of Unpublished Data, Document Delivery, CISTI, National Research Council Canada, Ottawa, ON K1A 0R6, Canada. DUD 3757. For more information on obtaining material refer to cisti-icist.nrc-cnrc.gc.ca/irm/unpub_e.shtml.

© 2008 NRC Canada

aliphatic protons) at δ 4.22 ppm, indicating the presence of phosphorous. Analysis of the aromatic region of this compound shows the presence of only 10 hydrogen atoms indicating the loss of a benzene ring. Surprisingly when NaH was used as the base, a quantitative yield of *n*-butyldiphenylphosphine oxide was obtained as well. Since no known source of oxygen was present in the starting compounds, we believe that *n*-butyldiphenylphosphine was initially formed but was then converted to the phosphine oxide in the presence of air. To test this hypothesis and determine the source of oxygen, we exposed *n*-butyltriphenylphosphonium bromide to NaH in dry acetonitrile under argon atmosphere. After 2 h of stirring, the work-up of the reaction was carefully carried out under argon atmosphere resulting in a pale yellow liquid (22) instead of the white solid. Upon exposure to air the liquid instantaneously turns to a white solid, which shows spectral characteristics of the phosphine oxide. This is consistent with the reported air-sensitivity of alkyldiphenylphosphines (23). NMR analysis of the liquid in dry C_6D_6 under argon atmosphere indicates it to be the phosphine. Change of the reaction solvent to DMSO or extending the reaction time does not affect the result of this reaction. The mechanism of the loss of the phenyl group is not clear to us at this time.

Since the evidence points to the existence of the ylid as an intermediate for the homocoupling reaction, we investigated the possibility of using the ylid from diethyl benzylphosphonate. In the presence of a base, the phosphonate ester produced stilbene in only 5% yield (Scheme 4, eq. [1]). Since the yield of the homocoupling reaction for the phosphonate ester is low in spite of the formation of a reactive ylid, we attempted a cross coupling reaction with the phosphonium salt to synthesize non-symmetric alkenes. Diethyl benzylphosphonate was dissolved in acetonitrile and cooled to 0 °C under ice. The base (*t*-BuOK, 1 equiv.) was added slowly and the reaction mixture was allowed to warm up to RT with stirring for 15 min. The phosphonium salt **1** was added to the reaction mixture and the mixture was stirred for a further 1 h. Another equivalent of the base was then added, stirred for 1 h, and the products were isolated using column chromatography. Only homocoupling products could be isolated from the reaction mixture (Scheme 4, eq. [2]). Only 9% of stilbene was obtained, while unreacted diethyl benzylphosphonate was recovered from the reaction mixture. It is possible that the phosphonate ylid deprotonates the phosphonium salt followed by an adduct formation without undergoing elimination to form the alkene. This would be consistent with the low yields of the homocoupling product of **1** under these conditions. Analysis of the product mixture was inconclusive regarding the formation of an adduct.

Scheme 4. Homocoupling and cross-coupling of diethyl benzylphosphonate with a base.

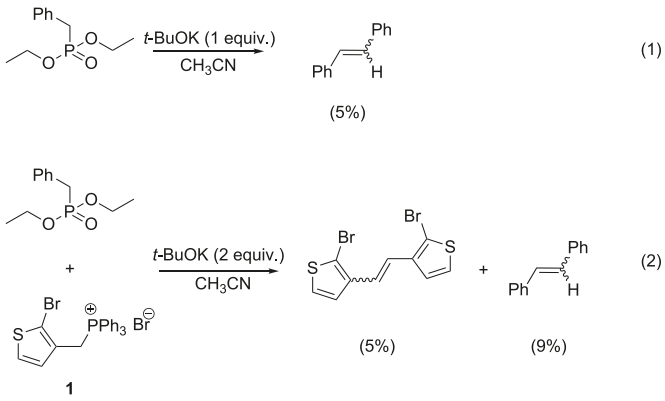

Conclusions

Arylmethyltriphenylphosphonium ions undergo an efficient homocoupling reaction in the presence of a base in polar aprotic solvents. Other alkyltriphenylphosphonium ions that do not form resonance stabilized ylids eliminate an aryl group from the phosphorus under similar conditions. Diethylbenzylphosphonate, which is known to form ylids, also undergoes a homocoupling reaction though the yields are substantially lower. It is possible that other ylids may undergo similar homocoupling reactions in polar aprotic solvents. At this time, it is difficult to rationalize or predict the *E*/*Z* ratio of the alkene.

Materials and methods

Commercially available reagents were obtained from Sigma-Aldrich were used as received. MeCN was distilled over CaH_2, while DMSO was dried over molecular sieves before being used. Reactions were followed with thin-layer chromatography (TLC) and visualized with a UV lamp. Reaction mixtures were purified on prep TLC plates or column chromatography using hexanes as the eluent. GC-MS analysis was done using HP 5890 Series II GC fitted with HP 5971 Series mass selective detector, to confirm the purity of products (selected GC chromatographs are included in the Supplementary Data).[2] ^{1}H, proton decoupled ^{13}C, and proton decoupled ^{31}P NMR spectra were recorded on a Bruker AMX 500 MHz spectrometer at ambient temperature. Triethylphosphite was used as an external standard for ^{31}P NMR and was calibrated to δ 137 ppm. Compounds **4**, **5**, and **6** were synthesized as per procedures described previously (24). High-resolution mass spectral data were obtained on Agilent 61969A TOF high-resolution mass spectrometer using electrospray ionization by direct infusion of the sample in 50% methanol and 1 mmol/L AcOH at 10 mL/min flow rates.

3-Methyl-2-nitrothiophene (25, 26)

3-Methylthiophene (0.49 mL, 0.50 g, 5.1 mmol) was added to 10 mL of acetic anhydride and the solution was stirred at 0 °C in an ice–salt bath. A precooled mixture of 0.320 µL of HNO_3 and 0.320 µL of H_2SO_4 was added to this solution dropwise. The solution turned dark green in the process. The reaction mixture was allowed to warm up to RT while stirring for 2 h. The solution was cooled again and diluted with 10 mL of water and neutralized with NaOH powder to a pH of 8. The resulting brown solution precipitated and was filtered. The brown residue was purified on column chromatography using hexane/ethyl acetate mixtures (4:1) to obtain 0.30 g of the 3-methyl-2-nitrothiophene (43%). ^{1}H NMR ($CDCl_3$) δ: 7.40 (d, J = 5.4 Hz, 1H), 6.91 (d, J = 5.4 Hz, 1H), 2.64 (s, 3H).

© 2008 NRC Canada

Synthesis of phosphonium salts

General procedure

The arylmethylbromides were synthesized as per the literature procedures from the corresponding alkanes (27). The alkane (1.000 g, 1 mmol) was added to 5 mL of dry 1,2-dichloroethane and the solution was heated to reflux. Benzoyl peroxide (2 mg, 0.01 mmol) was added to the refluxing mixture, quickly followed by a mixture of benzoyl peroxide (2 mg, 0.01 mmol) and *N*-bromosuccinimide (0.178 g, 1.00 mmol). The solution was refluxed for 1 h. After cooling to RT, the succinimide was removed by dissolving in hexanes followed by filtration. The solvent was removed under reduced pressure. ^{1}H and ^{13}C NMR of the crude product indicated about 90% conversion of the starting material. The crude product was used for the synthesis of the phosphonium salts. Triphenylphosphane (3.90 g, 14.9 mmol) was dissolved in 10 mL of dry benzene and heated to reflux. The arylmethylbromide (14.9 mmol, 1 equiv.) was dissolved in 5 mL of dry benzene and added to the refluxing mixture. The solution was refluxed for 12 h. After cooling to RT, the white precipitate was filtered off, washed with benzene, and the product was dried under vacuum. The phosphonium salts were recrystallized with dichloromethane-benzene solvent mixtures. The compounds **9**–**11** were purchased from commercial sources (Acros and Alfa Aesar).

2-Bromo-3-thienylmethyltriphenylphosphonium bromide 1 (27)

2-Bromo-3-bromomethylthiophene: yield 1.02 g from 1.00 g of 2-bromo-3-methylthiophene (71%). ^{1}H NMR ($CDCl_3$) δ: 7.39 (d, J = 5.6 Hz, 1H), 7.14 (d, J = 5.7 Hz, 1H), 4.59 (s, 2H).

Yield 5.9 g of **1** from 3.8 g of 2-bromo-3-bromomethylthiophene (77%). Pale yellow crystals. mp 240–241 °C (lit. mp (27) 238–240 °C). ^{1}H NMR ($CDCl_3$) δ: 7.60–7.79 (m, 15H), 7.17 (d, J = 5.7, 1H), 6.86 (dd, J_1 = 5.7 Hz, J_2 = 1.2 Hz, 1H), 5.39 (d, J = 13.7 Hz, 2H).

2-Thienylmethyltriphenylphosphonium bromide 2 (27)

2-Bromomethylthiophene: yield 0.134 g from 0.100 g of 2-methylthiophene (71%). ^{1}H NMR ($CDCl_3$) δ: 7.32 (d, J = 5.0 Hz, 1H), 7.12 (d, J = 3.3 Hz, 1H), 6.95 (t, J = 3.6 Hz, 1H), 4.77 (s, 2H).

Yield: 0.176 g of **2** from 0.142 g of 2-bromomethylthiophene (50%). White crystals. mp > 300 °C. ^{1}H NMR (DMSO) δ: 7.92 (d, J = 5.7 Hz, 3H), 7.78–7.74 (m, 7H), 7.70–7.68 (m, 5H), 7.39–7.36 (m, 2H), 7.25–7.23 (m, 1H), 5.55 (d, J = 14.6 Hz, 2H).

3-Methoxybenzyltriphenylphosphonium bromide 4

Yield 1.081 g of **4** from 1.013 g 3-methoxybenzyl bromide (28%). White crystals, mp 263–265 °C. ^{1}H NMR ($CDCl_3$) δ: 7.76 (dt, J_1 = 1.0 Hz, J_2 = 7.7 Hz, 3H), 7.69–7.63 (m, 12H), 7.35 (dt, J_1 = 2.6 Hz, J_2 = 7.1 Hz, 1H), 7.22 (tt, J_1 = 2.4 Hz, J_2 = 7.6 Hz, 1H), 6.80 (t, J = 7.5 Hz, 1H), 5.20 (d, J = 13.9 Hz, 2H), 3.21 (s, 3H). ^{13}C NMR ($CDCl_3$) δ: 157.4 (d, J = 21.0 Hz), 135.0 (d, J = 11.0 Hz), 134.3 (d, J = 38.5 Hz, 132.9 (d, J = 21.5 Hz), 130.4 (d, J = 15.5 Hz), 130.2 (d, J = 50.0 Hz), 121.4 (d, J = 12.5 Hz), 118.5 (d, J = 339.5 Hz), 115.7 (d, J = 35.5 Hz), 110.5 (d, J = 13.0 Hz), 54.9, 25.7 (d, J = 191.5 Hz).

2-Methoxybenzyltriphenylphosphonium bromide 6

Yield 2.72 g of **6** from 1.46 g 2-methoxybenzyl bromide (83%). Pale yellow crystals, mp 243–244 °C (lit. mp (crude) (28) 210–220 °C). ^{1}H NMR ($CDCl_3$) δ: 7.79–7.73 (m, 9H), 7.66–7.62 (m, 6H), 7.02 (t, J = 7.9 Hz, 1H), 6.81 (b, q, J = 1.7 Hz, 1H), 6.76 (b, dt, J_1 = 2.3 Hz, J_2 = 8.2 Hz, 1H), 6.64 (b, d, J = 7.5 Hz, 1H), 5.37 (d, J = 14.4 Hz, 2H), 3.55 (s, 3H). ^{13}C NMR ($CDCl_3$) δ: 159.9 (d, J = 14.0 Hz), 135.1 (d, J = 12.0 Hz), 134.7 (d, J = 38.5 Hz), 130.3 (d, J = 50.0 Hz), 129.9 (d, J = 13.0 Hz), 128.7, 123.7 (d, J = 22.5 Hz), 118.1 (d, J = 341.5 Hz), 116.5 (d, J = 22.5 Hz), 115.6 (d, J = 15.5 Hz), 55.7, 31.1 (d, J = 186.5 Hz).

2-Nitrobenzyltriphenylphosphonium bromide 7

Yield 0.921 g of **7** from 0.456 g 2-nitrobenzyl bromide (92%). White crystals, mp 248 °C (decomp). ^{1}H NMR ($CDCl_3$) δ: 8.06 (d, J = 5.5 Hz, 1H), 7.94 (d, J = 8.2 Hz, 1H), 7.80 (t, J = 7.3 Hz, 3H), 7.71–7.60 (m, 13H), 7.51 (t, J = 7.5 Hz, 1H), 6.07 (d, J = 14.9 Hz, 2H). ^{13}C NMR ($CDCl_3$) δ: 148.5, 135.5 (d, J = 11.5 Hz), 135.3 (d, J = 20.5 Hz), 135.1 (d, J = 12.5 Hz), 134.5 (d, J = 40.0 Hz), 130.5 (d, J = 50.0 Hz), 130.1 (d, J = 14.0 Hz), 125.9 (d, J = 10.5 Hz), 124.7 (d, J = 36.0 Hz), 117.3 (d, J = 342.5 Hz), 28.7 (d, J = 194.5 Hz).

2-Nitro-3-thienylmethyltriphenylphosphonium bromide 8 (15)

3-Bromomethyl-2-nitrothiophene (25): yield 9 mg from 29 mg of 3-methyl-2-nitrothiophene (20%). ^{1}H NMR ($CDCl_3$) δ: 7.48 (d, J = 5.5 Hz, 1H), 7.19 (d, J = 5.5 Hz, 1Hz), 4.90 (s, 2H).

Yield 45 mg of **8** from 34 mg of 3-bromomethyl-2-nitrothiophene (55%). ^{1}H NMR ($CDCl_3$) δ: 7.84–7.76 (m, 9H), 7.69–7.65 (m, 7H), 7.54 (d, J = 5.5 Hz), 1H, 6.18 (d, J = 15.3 Hz, 2H). ^{13}C NMR ($CDCl_3$) δ: 135.5 (d, J = 11.5 Hz), 134.2, (d, J = 39.5 Hz, 132.5 (d, J = 14.5 Hz), 131.8 (d, J = 11.5 Hz), 130.7 (d, J = 37.5 Hz), 130.5 (d, J = 50.5 Hz), 117.1 (d, J = 344 Hz), 25.5 (d, J = 196 Hz).

Synthesis of homocoupling products

General procedure

The corresponding phosphonium salt was dissolved in 200 mL of dry MeCN and cooled in an ice-water bath while stirring. The base (NaH or *t*-BuOK) was gradually added. Upon completion, the solution was stirred at RT for 2 h. The solvent was evaporated in vacuo. The residue was suspended in ethyl acetate, and the product was isolated by preparative TLC with hexanes as the eluent. When DMSO was used as solvent, about 10 mL of water was added to the reaction mixture and the products were extracted with ethyl acetate. The organic layer was washed a few times with water, dried over anhyd Na_2SO_4, and the solvent was removed under reduced pressure. The product mixture was then subjected to a silica gel column using hexanes as the eluent.

1,2-Di(2-bromo-3-thienyl)ethane (15)

Yield 40 mg from 0.150 g of **1** (78%, *E*/*Z* ratio 1:2) with 2 equiv. of NaH as the base in 200 mL of MeCN. Yield 37 mg

© 2008 NRC Canada

from 0.150 g of **1** (74%, *E*/*Z* ratio 1:1.7) with 2 equiv. of *t*-BuOK as the base in 200 mL of MeCN. ^{1}H NMR ($CDCl_3$) δ: 7.28 (s, 2H), 7.26 (s, 2H), 7.13 (d, J = 5.7 Hz, 2H), 6.72 (s, 2H), 6.72 (d, J = 5.7 Hz, 2H), 6.51 (s, 2H).

1,2-Di(2-thienyl)ethene (E isomer) (15)

Yield 19 mg from 0.150 g of **2** (56%). ^{1}H NMR ($CDCl_3$) δ: 7.19 (d, J = 4.8 Hz, 2H), 7.06 (s, 2H), 7.05 (dd, J_1 = 1.1 Hz, J_2 = 3.5 Hz, 2H), 7.00 (dd, J_1 = 3.6 Hz, J_2 = 5.0 Hz, 2H). ^{13}C NMR ($CDCl_3$) δ: 142.4, 127.6, 126.0, 124.3, 121.5.

Stilbene (15)

Yield 23 mg from 0.150 g of **3** with 200 mL of CH_3CN and 0.076 g of *t*-BuOK (74%, *E*/*Z* ratio 1:1.5). ^{1}H NMR ($CDCl_3$) δ: 7.52 (d, J = 7.4 Hz, 4H), 7.35 (t, J = 7.5 Hz, 6H), 7.27–7.18 (m, 10H), 7.11 (s, 2H), 6.60 (s, 2H). ^{13}C NMR ($CDCl_3$) δ: 130.4, 129.1, 128.9, 128.4, 127.8, 127.6, 127.3, 126.7.

3,3′-Dimethoxystilbene (29)

Yield 35 mg from 0.150 g of **4** (89%, *E*/*Z* ratio 1:1) with 3 equiv. of *t*-BuOK as base in 200 mL of CH_3CN. Yield 40 mg from 0.150 g of **4** (100%, *E*/*Z* ratio 1:1.1) with 2 equiv. of NaH as base in 200 mL of CH_3CN. The purity of the recovered product was confirmed by GC-MS. ^{1}H NMR ($CDCl_3$) δ: 7.30 (d, J = 7.9 Hz, 1H), 7.16 (t, J = 7.9 Hz, 2H), 7.13 (bd, J = 7.7 Hz, 2H), 7.10 (s, 2H), 7.06 (bt, J = 2.3 Hz, 2H), 6.86 (d, J = 7.6 Hz, 2H), 6.83 (dd, J_1 = 2.5 Hz. J_2 = 8.2 Hz, 2H), 6.81 (bt, J = 2.4 Hz, 2H), 6.76 (ddd, J_1 = 0.7 Hz, J_2 = 5.1 Hz, J_3 = 10.5 Hz, 3H), 6.59 (s, 2H), 3.82 (s, 6H), 3,68 (s, 6H).

4,4′-Dimethoxystilbene (E and Z isomers)

Yield 9 mg from 0.150 g of **5** (23%, *E*/*Z* ratio 1:3.5) with 3 equiv. of NaH as base. The purity of the recovered product was confirmed by GC-MS. ^{1}H NMR ($CDCl_3$) δ: 7.44 (d, J = 8.7 Hz, 4H), 7.22 (d, J = 8.7 Hz, 4H), 6.94 (s, 2H), 6.90 (d, J = 8.7 Hz, 4H), 6.78 (d, J = 8.7 Hz, 4H), 6.46 (s, 2H), 3.84 (s, 6H), 3.80 (s, 6H). ^{13}C NMR ($CDCl_3$) δ: 159.2, 158.7, 130.7, 130.3, 130.2, 128.6, 127.6, 126.4, 114.3, 113.8, 55.5, 55.4.

2,2′-Dimethoxystilbene (E and Z isomers) (30)

Yield 15 mg from 0.150 g of **6** (39%, *E*/*Z* ratio 1:3.3) with 1 equiv. of *t*-BuOK as base in 200 mL of CH_3CN. Yield 29 mg from 0.150 g of **6** (75%, *E*/*Z* ratio 1:4.3) with 2 equiv. of *t*-BuOK as base in 200 mL of CH_3CN. Yield 0.035 g from 0.150 g of **6** (90%, *E*/*Z* ratio 1:3.8) with 3 equiv. of *t*-BuOK as base in 200 mL of CH_3CN. Yield 0.034 g from 0.150 g of **6** (87%, *E*/*Z* ratio 1:4.3) with 3 equiv. of NaH as base in 200 mL of CH_3CN. ^{1}H NMR ($CDCl_3$) δ: 7.67 (dd, J_1 = 1.5 Hz, J_2 = 7.6 Hz, 2H), 7.49 (s, 2H), 7.25 (dt, J_1 = 1.6 Hz, J_2 = 8.0 Hz, 2H), 7.18 (dt, J_1 = 1.6 Hz, J_2 = 8.1 Hz, 2H), 7.14 (dd, J_1 = 1.6 Hz, J_2 = 7.6 Hz, 2H), 7.98 (t, J = 7.4 Hz, 2H), 6.91 (d, J = 8.5 Hz, 2H), 6.89 (d, J = 8.2 Hz, 2H), 6.79 (s, 2H), 6.72 (dt, J_1 = 0.6 Hz, J_2 = 7.8 Hz, 2H), 3.89 (s, 6H), 3.85 (s, 6H).

n-Butyldiphenylphosphine

n-Butyltriphenylphosphonium bromide (0.151 g, 0.378 mmol) was dissolved in 15 mL of distilled acetonitrile and the solution was purged with argon for 20 min, followed by cooling in ice. NaH (20 mg, 0.83 mmol) was added and the solution was stirred for 2 h at RT. Filtration of the solution under the atmosphere of argon was followed by removal of the solvent in vacuo. *n*-Butyltriphenylphosphine (87 mg) was obtained as a pale yellow oil (lit. value (31) colorless oil). ^{1}H NMR (C_6D_6) δ: 7.82–7.79 (m, 4H), 7.26–7.13 (m, 6H), 2.10–2.05 (m, 2H), 1.67–1.60 (m, 2H), 1.30–1.28 (m, 2H), 0.80 (t, J = 5.3 Hz, 3H). ^{13}C NMR (C_6D_6) δ: 134.9 (d, J = 411.0 Hz), 131.9 (d, J = 7.5 Hz), 131.4 (d, J = 37.0 Hz), 129.2 (d, J = 46.0 Hz), 30.0 (d, J = 286.7 Hz), 24.6 (d, J = 57.5 Hz), 24.2 (d, J = 15.1 Hz), 14.3. ^{31}P NMR (C_6D_6) (33) δ: 28.7.

n-Butyldiphenylphosphine oxide

n-BuPPh3Br (0.150 g, 0.376 mmol) was dissolved in 10 mL of dry MeCN. The base, *t*-BuOK (84 mg, 0.75 mmol) or NaH (18 mg, 0.75 mmol), was gradually added over 5 min and the solution was stirred for 2 h. The solvent was evaporated under reduced pressure and the products were purified with column chromatography using hexanes and ethyl acetate as eluents. The purity of the recovered product was confirmed by GC-MS. The product was recrystallized with diethyl ether. White solid, mp 92–94 °C (lit. value (32) 94–95 °C). Yield 0.103 g (100%) from *t*-BuOK and 0.110 g (100%) from NaH. ^{1}H NMR ($CDCl_3$) δ: 7.76–7.73 (m, 4H), 7.50–7.44 (m, 6H), 2.30–2.24 (m, 2H), 1.63–1.58 (m, 2H), 1.42 (q, J = 7.4 Hz, 2H), 0.88 (t, J = 7.3 Hz, 3H). ^{1}H NMR (C_6D_6) δ: 7.79–7.77 (m, 4H), 7.06–7.05 (m, 6H), 1.97–1.91 (m, 2H), 1.64–1.59 (m, 2H), 1.20 (q, J = 7.4 Hz, 2H), 0.69 (t, J = 7.4 Hz, 3H). ^{13}C NMR ($CDCl_3$) δ: 133.2 (d, J = 388.5 Hz), 131.7 (d, J = 10.5 Hz), 130.8 (d, J = 36.0 Hz), 128.7 (d, J = 46.0 Hz), 29.5 (d, J = 287.5 Hz), 24.1 (d, J = 60.5 Hz), 23.5 (d, J = 16.0 Hz), 13.6. ^{13}C NMR (C_6D_6) δ: 135.8 (d, J = 381.0 Hz), 131.6 (d, J = 8.5 Hz), 131.4 (d, J = 35.0 Hz), 129.0 (d, J = 45.0 Hz), 30.3 (d, J = 287.0 Hz), 24.7 (d, J = 55.8 Hz), 24.3 (d, J = 15.3 Hz), 14.1. ^{31}P NMR ($CDCl_3$) δ: 17.4. ^{31}P NMR (C_6D_6) δ: 26.0. EI-MS *m*/*z* 229 (7.2), 216 (17.8), 215 (100), 202 (13.7), 201 (42.9), 183 (18.4), 171 (7.9), 155 (10.3), 154 (11.9), 153 (10.7), 152 (10.0), 128 (4.5), 125 (14.4), 91 (5.7), 78 (5.2), 77 (22.8), 51 (16.8). HRMS (ESI) calcd. for $C_{16}H_{20}OP$ [M+H]: 259.1246; found 259.1244.

Methoxymethyldiphenylphosphine oxide

The same procedure was used as with *n*-butyldiphenylphosphine oxide: 0.200 g (0.6 mmol) of **10**, 71 mg (0.59 mmol) of *t*-BuOK, and 8 mL of DMSO were used. The solution was dissolved in dichloromethane and extracted with water. The dichloromethane fraction gave 73 mg (55%) of the product. The purity of the recovered product was confirmed by GC-MS. The product was recrystallized with diethyl ether. Colorless solid, mp 115–116 °C (lit. value (33) 116–117 °C). ^{1}H NMR ($CDCl_3$) δ: 7.84–7.80 (m, 4H), 7.55 (t, J = 6.0 Hz, 2H), 7.54–7.48 (m, 4H), 4.22 (d, J = 6.4 Hz, 2H), 3.45 (s, 3H). ^{13}C NMR ($CDCl_3$) δ: 132.3 (d, J = 10.5 Hz), 131.4 (d, J = 394.5 Hz), 131.6 (d, J = 37.5 Hz), 128.7 (d, J = 47.0 Hz), 71.3 (d, J = 350.5 Hz), 62.0 (d, J = 46.5 Hz). ^{31}P NMR ($CDCl_3$) δ: 11.9. EI-MS *m*/*z* (rel. intensity) 217 (6.8), 216 (58.4), 215 (78.5), 202 (11.5), 201 (100), 199 (8.7), 183 (22.2), 173 (9.2), 171 (17.2), 170 (4.6), 154 (7.3), 153 (15.0), 152 (14.4), 151 (5.8), 133 (4.5), 107 (9.9),

© 2008 NRC Canada

77 (24.4), 51 (9.8). HRMS (ESI) calcd. for $C_{14}H_{16}O_2P$ [M+H]: 247.0882; found 247.0890.

Coupling of ethoxycarbonylmethyltriphenylphosphonium bromide

The compound **11** (0.150 g, 0.350) was dissolved in 10 mL of dry MeCN and cooled to 0 °C. The base *t*-BuOK (78 mg, 0.70 mmol) was added gradually and the solution was stirred for 2 h, while allowing it to warm up to the RT. The insoluble salts were removed by filtration and the solvent was removed under reduced pressure. ^{1}H NMR of the crude filtrate showed the *E*/*Z* ylid. Yield 0.125 g from 0.151 g (100%) of **11**. ^{1}H NMR ($CDCl_3$) δ: 7.68–7.64 (m, 12H), 7.53–7.51 (m, 6H), 7.45–7.42 (m, 12H), 4.03 (q, J = 7.0 Hz, 2H), 3.83 (q, J = 2H), 2.96 (d, J = 21.9 Hz, 1H), 2.69 (d, J = 21.9 Hz, 1H), 1.23 (t, J = 7.1 Hz, 3H), 0.68 (t, J = 7.1 Hz, 3H).

Coupling of diethylbenzylphosphonate

Diethylbenzylphosphonate (184 μL, 0.876 mmol) was dissolved in 10 mL of dry MeCN. The base *t*-BuOK (10 mg, 0.87 mmol) was gradually added over 5 min and the the reaction mixture was stirred overnight. The solvent was removed under reduced pressure. Purification was done with column chromatography using pure hexanes to obtain 4 mg (5%) of stilbene. ^{1}H NMR (CD_3CN) δ: 7.58 (td, J_1 = 1.3 Hz, J_2 = 7.9 Hz, 4H), 7.38 (dt, J_1 = 1.5 Hz, J_2 = 7.1 Hz, 4H), 7.28 (tt, J_1 = 1.2 Hz, J_2 = 7.4 Hz, 2H), 7.22 (s, 2H). ^{13}C NMR (CD_3CN) δ 138.7, 130.0, 129.7, 128.9, 127.7.

Cross-coupling of diethylbenzylphosphonate and 2-bromo-3-methylthiophenetriphenylphosphonium bromide

Di-ethylbenzylphosphonate (184 μL, 0.876 mmol) of was dissolved in 10 mL of dry MeCN and the solution was cooled in an ice-water bath. *t*-BuOK (0.010 g, 0.874 mmol) was added and the solution was stirred at RT for 15 min, followed by the addition of 0.454 g (0.876 mmol) of 2-bromo-3-methylthiophenetriphenylphosphonium bromide. The solution was stirred at RT for another 1 h, after which 10 mg (0.87 mmol) of *t*-BuOK was added and the solution was stirred again at RT for 1 h. The solvent was evaporated and the residue was purified using preparatory thin layer chromatography using hexanes. Only the homocoupled products were isolated: 8 mg (5%) of (*E*/*Z*)-1,2-di-(2-bromothienyl)ethene and 7 mg (9%) of *E*-Stilbene. Isomeric ratios were the same as with homocoupled reactions.

Acknowledgment

The authors thank the Department of Chemistry, University of North Dakota, for financial support. CMS was also supported by the ND EPSCoR AURA program (NSF-EPS-0447679). The authors thank Mr. Leonard Anagho for his help in obtaining phosphorus NMR and Ms. Valeria Stepanova and Dr. Irina P. Smoliakova for their help in isolation of phosphines. We thank Dr. Alena Kubatova for the HRMS data (the funding for the spectrometer was provided by NSF CHE-0216038).

References

1. (*a*) F.B. Mallory, M.J. Rudolph, and S.M. Oh. J. Org. Chem. **54**, 4619 (1989); (*b*) D.H. Waldeck. Chem. Rev. **91**, 415 (1991).
2. T. Hirose, K. Matsuda, and M. Irie. J. Org. Chem. **71**, 7499 (2006).
3. (*a*) J. Saltiel and Y.-P. Sun. Cis-trans isomerization of C=C double bonds. Elsevier, Amsterdam. 1990; (*b*) J.C. Crano and R.J. Guglielmetti. Organic photochromic and thermochromic compounds. Vol. 1. Photochromic Families. Plenum Press, New York. 1999.
4. S.L. Gilat, S.H. Kawai, and J.-M. Lehn. Chem. Eur. J. **1**, 275 (1995).
5. (*a*) M. Irie, O. Miyatake, and K. Uchida. J. Am. Chem. Soc. **114**, 8715 (1992); (*b*) N. Tamai and H. Myasaka. Chem. Rev. **100**, 1875 (2000); (*c*) M. Irie. Chem. Rev. **100**, 1685 (2000); (*d*) S. Kawata and Y. Kawata. Chem. Rev. **100**, 1777 (2000); (*e*) H. Tian, and S. Yang. Chem. Soc. Rev. **33**, 85 (2004).
6. (*a*) A. Mulder, A. Jukovic, J. Huskens, and D. N. Reinhoudt. Org. Biomol. Chem. **2**, 1748 (2005); (*b*) G. Guirado, C. Coudret, M. Hliwa, and J.-P. Launay. J. Phys. Chem. B, **109**, 17445 (2005); (*c*) E. Kim, M. Kim, and K. Kim. Tetrahedron, **62**, 6814 (2006).
7. (*a*) V. Lemieux and N.R. Branda. Org. Lett. **7**, 2969 (2005); (*b*) J.J.D. deJong, T.D. Tiemersma-Wegman, J.H. van Esch, and B.L. Feringa. J. Am. Chem. Soc. **127**, 13804 (2005); (*c*) K. Higashiguchi, K. Matsuda, N. Tanifuji, and M. Irie. J. Am. Chem. Soc. **127**, 8922 (2005); (*d*) H. Choi, H. Lee, Y. Kang, E. Kim, S. O. Kang, and J. Ko. J. Org. Chem. **70**, 8291 (2005); (*e*) S. Pu, T. Yang, G. Li, J. Xu, and B. Chen. Tetrahedron Lett. **47**, 3167 (2006).
8. (*a*) A.K. Singh and S. Kanvah. J. Chem. Soc. Perkin Trans. 2, 395 (2001); (*b*) H. Cho and E. Kim. Macromolecules, **35**, 8684 (2002).
9. L.J. Gooβen and J. Paetzold. Angew. Chem. Int. Ed. **43**, 1095 (2004).
10. G.A. Molander and C.R. Bernardi. J. Org. Chem. **67**, 8424 (2002).
11. A. Blanc and C. G. Bochet. J. Org. Chem. **68**, 1138 (2003).
12. C.-P. Ehrensperger, M. Heberlein, and P. Skrabal. Helv. Chim. Acta, **61**, 2813 (1978).
13. G. Opitz, T. Ehlis, and K. Rieth. Tetrahedron Lett. **30**, 3131 (1989).
14. D.F. Hoeg and D.I. Lusk. J. Organomet. Chem. **5**, 1 (1966).
15. J.N. Ngwendson, W.N. Atemnkeng, C.M. Schultze, and A. Banerjee. Org. Lett. **8**, 4085 (2006).
16. A.S. Kiselyov. Tetrahedron Lett. **35**, 8951 (1994).
17. M. Ackermann and S. Berger. Tetrahedron, **61**, 6764 (2005).
18. H.J. Bestmann, E. Vilsmaier, and G. Graf. J. Liebigs Ann. Chem. **704**, 109 (1967).
19. A.M.d.A.R. Gonsalvez, A. Cabral, T.M.V.D. PinhoeMelo, and T.L. Gilchrist. Synthesis, 673 (1997).
20. I. Shevchenko, V. Andrushko, E. Lork, and G.-V. Röschenthaler. Eur. J. Inorg. Chem. 259 (2007).
21. N. Donoghue and M. J. Gallagher. Chem. Commun. 1973 (1998).
22. E.N. Tsvetkov, N.A. Bondarenko, I.G. Malakhova, and M.I. Kabachnik. Synthesis, 198 (1986).
23. J.A. Davies, J.G. Mierzwiak, and R. Syed. J. Coord. Chem. **17**, 25 (1988).
24. (*a*) S.D. Lorimer, N.B. Perry, and R.S. Tangney. J. Nat. Prod. **56**, 1444 (1993); (*b*) R. Dupont and P. Cotelle. Tetrahedron, **57**, 5585 (2001).

© 2008 NRC Canada

25. H.R. Snyder, L.A. Carpino, J.F. Zack Jr., and J.F. Mills. J. Am. Chem. Soc. **79**, 2556 (1957).
26. M.D. Threadgill, P. Webb, P. O'Neill, M.A. Naylor, M.A. Stephens, I.J. Stratford, S. Cole, G.E. Adams, and E.M. Fielden. J. Med. Chem. **34**, 2112 (1991).
27. W.J. Archer, R. Cook, and R. Taylor. J. Chem. Soc. Perkin Trans. 2, 813 (1983).
28. R.A. Aitkent, M.J. Drysdale, G. Ferguson, and A.J. Lough. J. Chem. Soc. Perkin Trans. 1, 875 (1998).
29. P. Wyatt, S. Warren, M. McPartlin, and T. Woodroffe. J. Chem. Soc., Perkin Trans. 1, 279 (2001).
30. (*a*) M.A. Ali, K. Kondo, and Y. Tsuda. Chem. Pharm. Bull. **40**, 1130 (1992); (*b*) T.W. Wallace, I. Wardell, K.-D. Li, P. Leeming, A.D. Redhouse, and S.R. Challand. J. Chem. Soc. Perkin Trans. 1, 2293 (1995).
31. S. O. Grim and W. McFarlane. Can. J. Chem. **46**, 2071 (1968).
32. Kabachnik and co-workers (ref. 22) reported a melting point of 94–95 °C. However, A.A. Cantrill, H.M.I. Osborn, and J. Sweeney. Tetrahedron, **54**, 2181 (1998) reported a melting point of 85–85.4 °C.
33. S. Trippett. J. Chem. Soc. 2813 (1961).

© 2008 NRC Canada

Asymmetric oxidation of 2-(arylsulfenyl)pyrroles

Alison Thompson, Jose R. Garabatos-Perera, and H. Martin Gillis

Abstract: The asymmetric oxidation of prochiral 2-(arylsulfenyl)pyrroles has been investigated. A marked electronic effect within the substrate significantly influenced the degree of enantioselectivity obtained, with very high enantioselectivity being obtained for 5-(nitrobenzensulfenyl)pyrrole-2-carboxaldehydes using Ti(*i*-PrO)$_4$/(+)-(*R*,*R*)-DET/H_2O/CHP. This result bodes well for optimizing the asymmetric oxidation of other diaryl sulfides, substrates that have previously given only low enantiomeric excesses.

Key words: asymmetric oxidation, sulfide, sulfoxide, pyrrole.

Résumé : On a étudié l'oxydation asymétrique de 2-(arylsulfényl)pyrroles prochiraux. On a noté qu'un effet électronique marqué dans le substrat influence d'une façon significative le degré d'énantiosélectivité obtenu, la plus grande énantiosélectivité étant obtenue avec les 5-(nitrobenzènesulfényl)pyrrole-2-carboxaldéhydes en utilisant le Ti(*i*-PrO)$_4$/(+)-(*R*,*R*)-DET/H_2O/CHP. Les résultats obtenus sont de bon augure pour l'optimisation de l'oxydation asymétrique d'autres sulfures de diaryles, des substrats qui n'ont donné antérieurement que de très faibles excès énantiomériques.

Mots-clés : oxydation asymétrique, sulfure, sulfoxyde, pyrrole.

[Traduit par la Rédaction]

Introduction

The use of chiral sulfoxides as auxiliaries for the asymmetric synthesis of biologically important compounds has found many applications (1, 2). For example, the efficiency of sulfoxides has been demonstrated for controlling the stereoselectivities of alkylation reactions, Michael addition reactions, aldol reactions, cycloaddition reactions, and Pummerer rearrangements (3). Chiral sulfoxides are generally prepared using either organometallic reagents and resolved diastereomeric sulfinates (i.e., chiral sulfinyl transfer reagents) (2, 4–6) or via the asymmetric oxidation of prochiral sulfides (2, 7).

Synthetic strategies involving pyrroles often require the introduction of a deactivating electron-withdrawing group that reduces the electron-rich character of the pyrrole unit. As such, the nucleophilicity of the pyrrolic core may be controlled and undesirable side-reactions minimized (8). Whilst this control has commonly been achieved by the use of carboxylates at the 2-position, the use of a sulfenyl group to mask the 2-position, rather than protect through electron-withdrawal, has recently been demonstrated (9, 10). The utility of 2-(sulfenyl)pyrroles in acylation reactions, nitration reactions, and condensation reactions with various aldehydes, as well as the removal of the sulfenyl group using Raney nickel, highlights the sulfenyl group as a valuable masking/protecting group for pyrrolic compounds. With 2-(arylsulfenyl)pyrroles showing promise for the synthesis of functionalized pyrroles, 2-(arylsulfinyl)pyrroles (11) become of interest.

Chiral 2-(arylsulfinyl)pyrroles of high enantiomeric purity prepared by sulfinylation using diastereomerically pure menthyl arylsulfinates have attracted attention because of their use as removable chiral auxiliaries and as building blocks for macromolecular chemistry (4). While this method has been successfully applied for several 2-(arylsulfinyl)pyrroles (4, 5), it lacks generality because of the difficulty in obtaining a diverse set of diastereomerically pure menthyl aryl- or alkylsulfinates (2). Indeed, the preparation of diastereomerically pure menthyl arylsulfinates requires multiple recrystallizations, and, furthermore, menthyl alkylsulfinates (e.g., menthyl methanesulfinate) are typically oils, which thus prohibits recrystallization as a strategy by which to obtain diastereomerically pure material (12, 13). In this article, we report investigations towards an alternative approach to chiral 2-(arylsulfinyl)pyrroles involving the asymmetric oxidation of prochiral 2-(arylsulfenyl)pyrroles.

Although numerous methodologies have been reported for the asymmetric oxidation of sulfides to sulfoxides (2, 6, 14–16), so far, they have been largely limited to sulfides with two stereochemically different substitutents (i.e., aryl and alkyl). Substrates with similar groups such as dialkyl or diaryl generally lead to little or no asymmetric induction. For example, the asymmetric oxidation of methyl benzyl sulfide using a chiral titanium complex (17, 18), chiral oxaziridine (19), chiral metallo(salen) complex (20), or enzymatic methods (21, 22) gives the desired sulfoxide in modest–excellent yields (50%–97%), but with poor enantioselectivities (14%–58%). Even a recent example for the asymmetric oxidation of sulfides using hydrogen peroxide in water and a homochiral iron(III) catalyst focuses on the oxidation of methyl phenyl sulfide, with a somewhat reduced enantioselectivity being obtained for even ethyl phenyl sulfide (23). Similarly, a very recent novel

Received 3 December 2007. Accepted 19 February 2008. Published on the NRC Research Press Web site at canjchem.nrc.ca on 13 May 2008.

A. Thompson,[1] J.R. Garabatos-Perera, and H.M. Gillis. Department of Chemistry, Dalhousie University, Halifax, NS B3H 4J3, Canada.

[1]Corresponding author (e-mail: Alison.Thompson@dal.ca).

 doi:10.1139/V08-054 © 2008 NRC Canada

Scheme 1. Synthesis of 2-(arylsulfenyl)pyrroles.

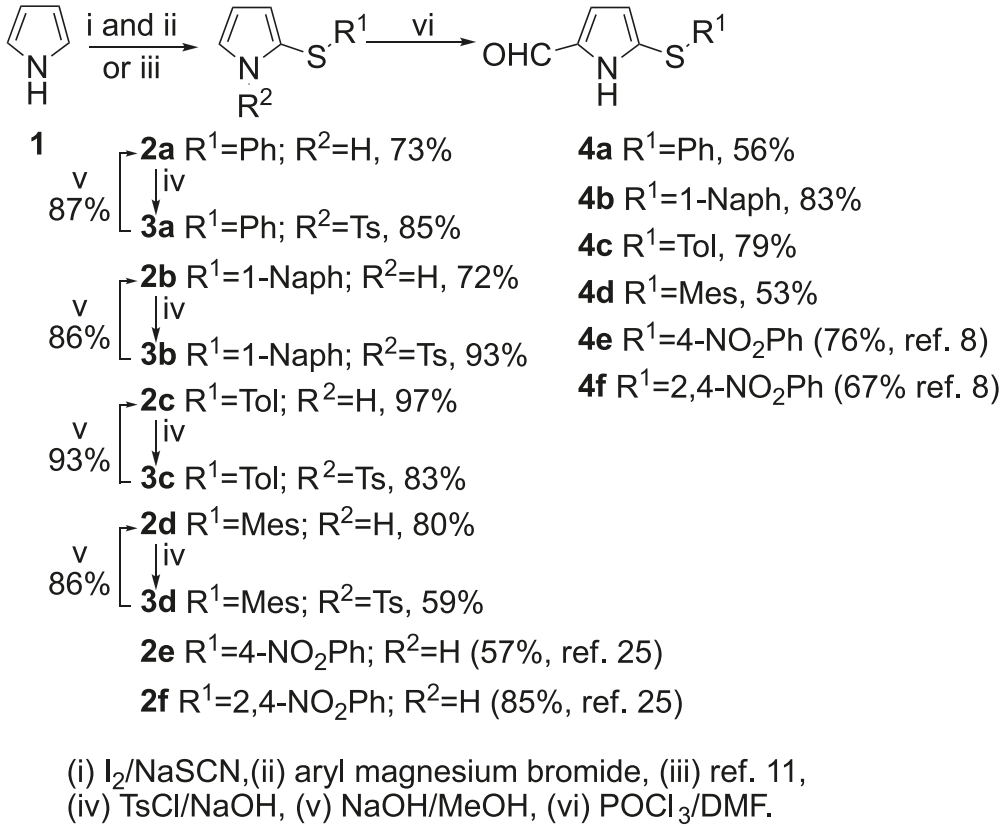

oxaziridinium salt, derived from cholesterol, gives good–excellent enantioselectivity for a variety of aryl alkyl sulfides, but no reports for diaryl sulfides are included (24).

Results and discussion

To probe their asymmetric oxidation, we prepared a series of 2-(arylsulfenyl)pyrroles with various substituents at the 2- and 5-positions. Following an established procedure for the preparation of 2-(phenylsulfenyl)pyrrole **2a** (10, 25) from 2-(thiocyanato)pyrroles (26–28) and phenylmagnesium bromide, a series of 2-(arylsulfenyl)pyrroles **2a**–**2d** were obtained in good yields by simply varying the Grignard reagent used (Scheme 1). We previously reported the preparation of **4e** and **4f** using Vilsmeier–Hack formylation conditions (9), and extension of this work for the 2-(arylsulfenyl)pyrroles **2a**–**2d** provided 5-(arylsulfenyl)pyrrole-2-carboxylaldehydes **4a**–**4d** in moderate to good yields. The excellent directing ability of the arylsulfenyl group for formylation at the vacant α-position emphasizes a general feature of sulfenyl masking groups. In our hands, 2-(arylsulfenyl)pyrroles **2a**–**2d** prepared via this route were found to be unstable to air (9) and were immediately protected as their corresponding *N*-tosyl derivatives **3a**–**3d** for ease of manipulation and storage (8). In all cases, the introduction of an electron-withdrawing group (tosyl or formyl) resulted in enhanced product stability.

With several prochiral 2-(arylsulfenyl)pyrroles available, we investigated their asymmetric oxidation (29–32) using chiral titanium complexes prepared from Ti(*i*-PrO)$_4$ and (+)-(*R*,*R*)-diethyl tartrate (DET), as described by Kagan (17, 33–38) and Modena (18). In our preliminary efforts, the asymmetric oxidation of 2-(phenylsulfenyl)pyrrole **2a** using *tert*-butyl hydroperoxide (TBHP) according to both the Kagan and Modena protocols resulted in essentially racemic sulfoxide **6a** (Table 1, entry 1), albeit in reasonable isolated yield. Under similar conditions, pyrroles **2e** and **2f**, bearing an electron-withdrawing group within the sulfenyl moiety, were oxidized using cumyl hydroperoxide (CHP) at –20 °C and 25 °C with a dramatic improvement of enantioselectivity (Table 1, entries 2 and 3 vs. entry 1). Interestingly, **2e**, bearing one nitro group, gave an enantioselectivity of 29% under these conditions, whereas **2e**, with two nitro groups, gave an enantioselectivity of 78%, and so decreasing the electron-density about the sulfide appeared to result in an increased enantioselectivity. However, the use of **3a** with an electron-withdrawing tosyl group on the pyrrolic nitrogen atom did not result in improved enantioselectivity, despite attempts under various conditions (Table 1, entry 4). Maintaining *N*-tosyl substitution, the introduction of the more sterically demanding naphthyl group within **3b**, rather than a phenyl or tolyl group within **3a** and **3c**, respectively, on the sulfenyl moiety did not significantly affect the oxidation reaction (Table 1, entries 5 and 6A). Furthermore, and significantly, other well-known methods for asymmetric sulfide oxidation resulted in poor yields and enantiopurities with 2-(*p*-tolylsulfenyl)pyrrole-*N*-tosylpyrrole **3c** (Table 1, entry 6; methods C–E). The poor enantioselectivities for **3c** serve to further emphasize that the preparation of enantiopure sulfoxides by the oxidation of diaryl sulfides is far from trivial.

© 2008 NRC Canada

Table 1. Asymmetric and racemic oxidation of 2-(arylsulfenyl)pyrroles.

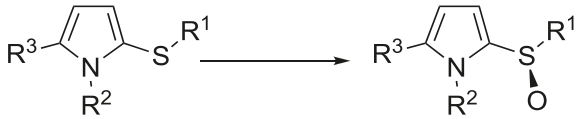

Entry	Substrate	Product	R^1	R^2	R^3	Method[a]	Oxidant	Time (h)	Temperature (°C)	Isolated yield (%)	ee[b] (%)
1	**2a**	**6a**	Ph	H	H	A	TBHP	20	–20	72	0
						B	TBHP	20	–20	98	9
2	**2e**	**6e**	4-NO_2Ph	H	H	A	CHP	48	–20	80	29
3	**2f**	**6f**	2,4-NO_2Ph	H	H	A	CHP	20	25	87	78
4	**3a**	**5a**	Ph	Ts	H	A	CHP	20	–20	0	—
						A	CHP	20	25	77	8[c]
						B	TBHP	20	25	78	7
						F	*m*-CPBA	15 min	0	77	—
5	**3b**	**5b**	1-Naph	Ts	H	A	CHP	20	25	91	12[c]
						F	*m*-CPBA	2	25	72	—
6	**3c**	**5c**	Tol	Ts	H	A	CHP	20	–20	83	16[c]
						C	oxaziridine	48	25	11	31
						D	H_2O_2	48	25	6	0
						E	H_2O_2	48	25	0	—
						F	*m*-CPBA	2	25	45	—
7	**3d**	**5d**	Mes	Ts	H	A	CHP	20	–20	0	—
						A	CHP	48	25	37	27
8	**4a**	**7a**	Ph	H	CHO	A	TBHP	20	–20	62	69
						A	CHP	20	–20	79	54
						B	TBHP	20	–20	95	53
						B	CHP	20	–20	72	53
						B	CHP[d]	20	–20	70[e]	17
9	**4b**	**7b**	1-Naph	H	CHO	A	TBHP	20	–20	87	52
						A	CHP	20	–20	87	53
10	**4c**	**7c**	Tol	H	CHO	A	TBHP	20	–20	78	65
						A	CHP	20	–20	78	54
11	**4d**	**7d**	Mes	H	CHO	A	CHP	48	–20	93	48
12	**4e**	**7e**	4-NO_2Ph	H	CHO	**A**	CHP	48	–20	45	96
						F	*m*-CPBA	2	25	45	—
13	**4f**	**7f**	2,4-NO_2Ph	H	CHO	A	CHP	20	–20	0	—
						A	**CHP**	**20**	**25**	**85**	**98**
						F	*m*-CPBA	2	25	76	—

[a]Method A: Ti(*i*-PrO)$_4$/(+)-(*R*,*R*)-DET/H_2O/TBHP or CHP (1:2:1:2) in CH_2Cl_2. Method B: Ti(*i*-PrO)$_4$/(+)-(*R*,*R*)-DET/TBHP or CHP (1:4:2) in $ClCH_2CH_2Cl$. Method C: (+)-(1*S*)-(10-camphorsulfonyl)oxaziridine (1.05 equiv.) in CH_2Cl_2 (43). Method D: (–)-(*S*)-2-(*N*-3,5-diiodosalicyliden)amino-3,3-dimethyl-1-butanol/[$VO(acac)_2$]/H_2O_2 (1.5 equiv.) in CH_2Cl_2 (20, 44). Method E: chloroperoxidase/H_2O_2 (1.5 equiv.) in 20% acetonitrile and sodium citrate buffer (0.05 mol/L, pH 5) (45). Method F: *m*-CPBA (1.0 equiv.) in CH_2Cl_2.

[b]Determined by chiral HPLC analysis.

[c]Determined by chiral HPLC analysis of the corresponding tosyl deprotected **6c**.

[d]Kinetic resolution of *rac*-**7a** using 0.5 equiv. of CHP.

[e]Recovered **7a**.

Continuing the notion that the introduction of electron-withdrawing groups enhances the stereoselectivity of oxidation (Table 1, entries 2 and 3 cf. 1) the effect of the α-formyl substituent was investigated. Thus, 5-(arylsulfenyl)pyrrole-2-carboxylaldehydes **4a**–**4f** were oxidized in moderate–good yields using the Kagan and Modena protocols, and, in all cases, the enantioselectivities were enhanced (Table 1, entries 8–13) over attempts using analogous pyrroles lacking the formyl group. In particular, the asymmetric oxidation of **4e** and **4f** provided chiral sulfoxides **7e** and **7f**, respectively, in 45% yield (96% ee) and 85% yield (98% ee), respectively (Table 1, entries 12 and 13).

Our results regarding the asymmetric oxidation of 2-(arylsulfenyl)pyrroles possessing substitutents with varying electronic effects allow us to rationalize the effectiveness of the Kagan and Modena protocols for this transformation. Although the Kagan and Modena procedures have been widely used for the oxidation of many prochiral sulfides, the struc-

© 2008 NRC Canada

ture of the reagent responsible for the stereochemical course of the reaction is still unknown (39, 40). In some cases, additives and the preparation of the reagent are crucial in obtaining specific chiral sulfoxides with high enantiopurities and (or) yields (37, 41, 42). More seriously, prochiral sulfides with two sterically different substitutents are generally good substrates for asymmetric oxidation, whereas substrates with similar groups often give products with low enantiopurities. For example, Kagan and co-workers reported the asymmetric oxidation of aryl methyl sulfides using a chiral titanium complex prepared from Ti(*i*-PrO)$_4$/(+)-(*R*,*R*)-DET/H_2O/TBHP (1:2:1:1) to give chiral sulfoxides with good–excellent enantiopurities (i.e., phenyl, 89% ee; *p*-tolyl, 91% ee; *p*-methoxyphenyl, 86% ee; *p*-nitrophenyl, 77% ee); however, the asymmetric oxidation of alkyl methyl sulfides under the same conditions resulted in chiral sulfoxides with reduced enantiopurities (i.e., *n*-octyl, 71% ee, *t*-butyl, 53% ee; cyclohexyl, 54% ee; benzyl, 58% ee) (17). In the face of the poor enantioselectivities that have traditionally been obtained for the asymmetric oxidation of diaryl sulfides, the results from the present study suggest that there is an important electronic effect that can influence this transformation. Although the origin of enantioselectivity is speculative at this point, one factor that could temper the influence of an electronic effect is the substrate–reagent binding affinity. If the mechanism involves a reversible associative step and electron-rich substrates have high association constants, as would be expected, reactions involving electron-rich substrates would give lower enantioselectivities, since these substrates bind more strongly (i.e., high reactivity and less selective). For electron-poor substrates, low association constants would allow for the substrate to dissociate and reassociate before reaction occurs (i.e., low reactivity and more selective). The traditional model used to predict the stereochemical outcome of sulfide oxidation involves the differentiation of sterically different substituents, and electronic effects are not typically considered (17, 39, 40). On the contrary, the results of the study presented herein strongly suggest that electronic effects play an important role in the asymmetric oxidation of diaryl substrates.

Conclusions

We have demonstrated the asymmetric oxidation of 2-(arylsulfenyl)pyrroles using a chiral titanium complex. Our work suggests a strong electronic effect where the incorporation of electron-withdrawing groups to differentiate the two sulfenyl substituents results in an enhancement of enantioselectivity. This method is particularly well-suited for prochiral sulfides bearing two aryl groups and expands the scope of substrates suitable for the Kagan and Modena protocols to include prochiral 2-(arylsulfenyl)pyrroles. Our current research is directed towards the preparation of a range of enantiopure 2-(arylsulfinyl)pyrroles using alternative strategies.

Experimental section

Representative procedures

*2-(*p*-Tolylsulfenyl)pyrrole (2c)*

To a solution of *p*-tolylmagnesium bromide [prepared from *p*-bromotoluene (12.0 mL, 16.8 g, 100 mmol) and magnesium turnings (2.4 g, 100 mmol) in anhydrous THF (150 mL) at 0 °C under N_2], was added dropwise 2-(thiocyanato)pyrrole (4.9 g, 39 mmol) in anhydrous THF (150 mL). After stirring at 0 °C for 30 min, ice-cold water (~100 mL) was added. The mixture was diluted with EtOAc and washed with satd. aqueous NH_4Cl and brine, before being dried over $MgSO_4$ and concentrated to give crude 2-(*p*-tolylsulfenyl)pyrrole **2c**, which was purified using flash column chromatography (CH_2Cl_2 as eluent) to give the title compound **2c** (6.7 g, 38 mmol, 97%).

A solution of 2-(*p*-tolylsulfenyl)pyrrole-*N*-tosylpyrrole **3c** (0.52 g, 1.5 mmol) in 15% *v*/*v* 2 mol/L NaOH (5.5 mL, 11 mmol) in MeOH (35 mL) was heated to reflux for 2 h until no starting material remained (TLC analysis). The mixture was cooled to room temperature and diluted with EtOAc, washed with aqueous 0.1 mol/L NaOH (3×) and brine (3×) before being dried over $MgSO_4$ and then concentrated to give crude 2-(*p*-tolylsulfenyl)pyrrole **2c** (0.25 g, 1.4 mmol, 93%), which was used in the next reaction without further purification. ^{1}H NMR (500 MHz, $CDCl_3$) δ: 8.17 (1H, br s), 7.00–6.97 (2H, m), 6.93–6.91 (2H, m), 6.84–6.82 (1H, m), 6.53–6.52 (1H, m), 6.27–6.26 (1H, m), 2.24 (3H, s). ^{13}C NMR (125 MHz, $CDCl_3$) δ: 135.5 (s), 135.5 (s), 129.9 (d × 2), 126.5 (d × 2), 121.8 (d), 118.4 (d), 116.4 (s), 110.4 (d), 21.0 (q). HRMS *m*/*z* calcd. for $C_{11}H_{11}NS$: 189.0612 (188.0534 for M – H); found: 188.0539 (ESI–).

*2-(*p*-Tolylsulfenyl)pyrrole-*N*-tosylpyrrole (3c)*

TsCl (8.1 g, 43 mmol) was added to a suspension of 2-(*p*-tolylsulfenyl)pyrrole **2c** (6.7 g, 35 mmol) and NaOH (5.6 g, 141 mmol) in 1,2-dichloroethane (130 mL) at 0 °C. The resulting mixture was warmed to room temperature and stirred for 12 h. Water was added, and the mixture was extracted with CH_2Cl_2 (3×). The combined organic layers were washed with brine, dried over $MgSO_4$, and then concentrated to give crude 2-(*p*-tolylsulfenyl)pyrrole-*N*-tosylpyrrole **3c**, which was purified using flash column chromatography (50% CH_2Cl_2 in hexanes as eluent) to give the title compound **3c** (10.0 g, 29 mmol, 83%). ^{1}H NMR (500 MHz, $CDCl_3$) δ: 7.73 (2H, d, *J* = 8.5 Hz), 7.61–7.59 (1H, m), 7.10 (2H, d, *J* = 8 Hz), 6.90 (2H, d, *J* = 8 Hz), 6.76 (2H, d, *J* = 8 Hz), 6.53–6.52 (1H, m), 6.33–6.31 (1H, m), 2.31 (3H, s), 2.24 (3H, s). ^{13}C NMR (125 MHz, $CDCl_3$) δ: 145.1 (s), 135.7 (s), 135.5 (s), 134.1 (s), 129.68 (d × 2), 129.64 (d × 2), 128.2 (d × 2), 127.0 (d × 2), 126.6 (d), 125.8 (d), 121.0 (s), 111.8 (d), 21.7 (q), 21.1 (q). LRMS (EI): 343 ([M]$^+$, 100), 188 (73). HRMS *m*/*z* calcd. for $C_{18}H_{17}NO_2S_2$: 343.0701; found: 342.9792 (EI).

*5-(*p*-Tolylsulfenyl)pyrrole-2-carboxylaldehyde (4c)*

$POCl_3$ (0.28 mL, 0.47 g, 3.1 mmol) was added dropwise to DMF (0.24 mL, 0.23 g, 3.1 mmol) at 0 °C under N_2. The resulting mixture was heated to 100 °C and stirred for 15 min. After cooling to 0 °C, a solution of 2-(*p*-tolylsulfenyl)pyrrole **2c** (0.25 g, 1.4 mmol; 0.05 mol/L in

© 2008 NRC Canada

CH_2Cl_2) was slowly added and then heated at reflux for 1 h. The resulting mixture was cooled to 0 °C, and aqueous 1 mol/L AcONa (50 mL) was added. The resulting suspension was heated to reflux and stirred for 1 h. After cooling to room temperature, the mixture was extracted with CH_2Cl_2 (3×). The combined organic layers were washed with satd. aqueous Na_2CO_3 (3×) and brine, before being dried over $MgSO_4$ and then concentrated to give crude 5-(*p*-tolylsulfenyl)pyrrole-2-carboxylaldehydes **4c** that was purified by flash column chromatography (CH_2Cl_2) to give the title compound **4c** (0.23 g, 1.1 mmol, 79%). ^{1}H NMR (500 MHz, $CDCl_3$) δ: 9.62 (1H, br s), 9.38 (1H, s), 7.20 (2H, d, J = 8 Hz), 7.09 (2H, d, J = 8 Hz), 6.92–6.91 (1H, m), 6.40–6.30 (1H, m), 2.31 (3H, s). ^{13}C NMR (125 MHz, $CDCl_3$) δ: 178.5 (d), 137.1 (s), 135.1 (s), 131.5 (s), 130.6 (d × 2), 130.4 (d × 3), 121.1 (s), 116.6 (d), 21.2 (q). HRMS *m*/*z* calcd. for $C_{12}H_{11}NOS$: 217.0561 (216.0483 for M – H); found: 216.0485 (ESI–).

*2-(*p*-Tolylsulfinyl)pyrrole-*N*-tosylpyrrole (5c)*

Racemic

50% wt% *m*-CPBA (0.22 g, 0.60 mmol) was added to a solution of 2-(*p*-tolylsulfenyl)-*N*-tosylpyrrole **3c** (0.20 g, 0.60 mmol) at room temperature for 2 h. Saturated aqueous $NaHCO_3$ was added, and the mixture was extracted with CH_2Cl_2 (3×). The combined organic layers were washed with brine, dried over $MgSO_4$, and then concentrated to give crude 2-(*p*-tolylsulfinyl)pyrrole-*N*-tosylpyrrole **5c**, which was purified using flash column chromatography (10% ethyl acetate in CH_2Cl_2 as eluent) to give the title compound **5c** (0.092 g, 0.27 mmol, 45%).

Asymmetric

Ti(*i*-PrO)$_4$ (0.14 mL, 0.14 g, 0.50 mmol) was added dropwise to a solution of (+)-(*R*,*R*)-DET (0.17 mL, 0.20 g, 1.00 mmol) and 2-(*p*-tolylsulfenyl)pyrrole-*N*-tosylpyrrole **3c** (0.17 g, 0.50 mmol) in CH_2Cl_2 (2 mL) under argon at room temperature. After 5 min, water (9 μL, 0.50 mmol) was added, and stirring was continued at room temperature for 45 min. 80% wt% Cumylhydroperoxide (0.19 mL, 0.15 g, 1.00 mmol) was then added under argon at –20 °C, and stirring was continued for 20 h. Water was added, and the mixture was allowed to stir for 30 min at room temperature. The resulting mixture was diluted with CH_2Cl_2 and filtered through a pad of silica and eluted with ethyl acetate to give the crude product, which was purified using flash column chromatography (10% ethyl acetate in CH_2Cl_2 as eluent) to give the title 2-(*p*-tolylsulfinyl)pyrrole-*N*-tosylpyrrole **5c** (0.15 g, 40 mmol, 83%, 16% ee; determined by chiral HPLC analysis of the corresponding tosyl deprotected **6c**; see Supplementary Data).[2] ^{1}H NMR (500 MHz, $CDCl_3$) δ: 7.81 (2H, d, J = 8.5 Hz), 7.61 (2H, d, J = 8 Hz), 7.33 (1H, m), 7.29–7.26 (4H, m), 6.62 (1H, dd, J = 2, 4 Hz), 6.31 (1H, dd, J = 3.5, 3.5 Hz), 2.40 (3H, s), 2.39 (3H, s). ^{13}C NMR (125 MHz, $CDCl_3$) δ: 146.0 (s), 142.1 (s), 141.3 (s), 137.0 (s), 135.3 (s), 130.3 (d × 2), 129.9 (d × 2), 127.7 (d × 2), 126.4 (d), 126.0 (d × 2), 118.4 (d), 113.2 (d), 21.8 (q), 21.6 (q). HRMS *m*/*z* calcd. for $C_{18}H_{17}NO_3S_2$: 359.0650 (382.0548 for M + Na); found: 382.0542 (ESI+).

Acknowledgments

This work was supported by the Natural Sciences and Engineering Research Council of Canada (NSERC) and AstraZeneca.

References

1. M.C. Carreno. Chem. Rev. **95**, 1717 (1995).
2. I. Fernandez and N. Khiar. Chem. Rev. **103**, 3651 (2003).
3. G. Hanquet, F. Colobert, S. Lanners, and G. Solladie. ARKIVOC, **7**, 328 (2003).
4. Y. Arai, T. Masuda, and Y. Masaki. J. Chem. Soc. Perkin Trans. 1, 2165 (1999).
5. K. Hiroi, I. Izawa, T. Takizawa, and K.-I. Kawai. Tetrahedron, **60**, 2155 (2004).
6. D.A. Evans, M.M. Faul, L. Colombo, J.J. Bisaha, J. Clardy, and D. Cherry. J. Am. Chem. Soc. **114**, 5977 (1992).
7. H.B. Kagan. Catalytic asymmetric synthesis. *Edited by* I. Ojima. Wiley-VCH, Inc., New York. 2000.
8. B. Jolicoeur, E.E. Chapman, A. Thompson, and W.D. Lubell. Tetrahedron, **62**, 11531 (2006).
9. J.R. Garabatos-Perera, B.H. Rotstein, and A. Thompson. J. Org. Chem. **72**, 7382 (2007).
10. P. Thamyongkit, A.D. Bhise, M. Taniguchi, and J.S. Lindsey. J. Org. Chem. **71**, 903 (2006).
11. A. Thompson, R.J. Butler, M.N. Grundy, A.B.E. Laltoo, K.N. Robertson, and T.S. Cameron. J. Org. Chem. **70**, 3753 (2005).
12. K.K. Andersen, B. Bujnicki, J. Drabowicz, M. Mikolajczyk, and J.B. O'Brien. J. Am. Chem. Soc. **49**, 4070 (1984).
13. K.K. Andersen, W. Gaffield, N.E. Papanikolaou, J.W. Foley, and R.I. Perkins. J. Am. Chem. Soc. **86**, 5637 (1964).
14. F.A. Davis, M.C. Weismiller, C.K. Murphy, R.T. Reddy, and B.-C. Chen. J. Org. Chem. **57**, 7274 (1992).
15. A. Gao, M. Wang, J. Shi, D. Wang, W. Tian, and L. Sun. Appl. Organomet. Chem. **20**, 830 (2006).
16. K. Matsumoto, T. Yamaguchi, and T. Katsuki. Chem. Commun. 1704, (2008).
17. P. Pitchen, E. Duiiach, M.N. Deshmukh, H.B. Kagan. J. Am. Chem. Soc. **106**, 8188 (1984).
18. F.D. Dufria, G. Modena, and R. Seraglia. Synthesis, 325 (1984).
19. F.A. Davis, R.T. Reddy, W. Han, and P.J. Carroll. J. Am. Chem. Soc. 114 (1992).
20. J. Legros and C. Bolm. Chem. Eur. J. 11 (2005).
21. S. Colonna, N. Gaggero, A. Manfredi, L. Casella, M. Gullotti, G. Carrea, and P. Pasta. Biochemistry, **29**, 10465 (1990).
22. S. Colonna, N. Gaggero, P. Pasta, and G. Ottolina. Chem. Commun. 2303 (1996).
23. H. Egami and T. Katsuki. J. Am. Chem. Soc. **129**, 8940 (2007).
24. R.E. del Rio, B. Wang, S. Achab, and L. Bohé. Org. Lett. **9**, 2265 (2007).
25. G. Campiani, V. Nacci, S. Bechelli, SM. Ciani, A. Garofalo, I. Fiorini, H. Wikstrom, P. Boer, Y. Liao, P.G. Tepper, A. Cagnotto, and T. Mennini. J. Med. Chem. **41**, 3763 (1998).
26. Caution: in our hands, 2-thiocyanatopyrrole decomposed very readily and was also extremely liable to pass through multiple layers of latex gloves to cause stains and discomfort of the skin.

[2] Supplementary data for this article are available on the journal Web site (canjchem.nrc.ca) or may be purchased from the Depository of Unpublished Data, Document Delivery, CISTI, National Research Council Canada, Ottawa, ON K1A 0R6, Canada. DUD 3754. For more information on obtaining material, refer to cisti-icist.nrc-cnrc.gc.ca/irm/unpub_e.shtml.

© 2008 NRC Canada

27. R.L.N. Harris. Aust. J. Chem. **25**, 985 (1972).
28. J.S. Yadav, B.V.S. Reddy, S. Shubashree, and K. Sadashiv. Tetrahedron Lett. **45**, 2951 (2004).
29. The asymmetric oxidation of prochiral sulfides presents the opportunity of coupling the initial asymmetric synthesis with a kinetic resolution. While the kinetic resolution of racemic **7a** using the Modena protocol (Table 1, entry 8; 30% conversion, 17% ee) revealed a small kinetic preference ($s = 3$), the results in Table 1 indicate that the enantioselectivity occurred predominantly via the initial asymmetric synthesis.
30. D.E. Ward, Y. Liu, and C.K. Rhee. Can. J. Chem. **72**, 1429 (1994).
31. T. Sugimoto, T. Kokubo, J. Miyazaki, S. Tanimoto, and M. Okano. Bioorg. Chem. **10**, 311 (1981).
32. Z. Dokuzovic, N.K. Roberts, J.F. Sawyer, J. Whelan, and B. Bosnich. J. Am. Chem. Soc. **108**, 2034 (1986).
33. H.B. Kagan, E. Dunach, C. Nemecek, P. Pitchen, O. Samuel, and S.-H. Zhao. Pure Appl. Chem. **57**, 1911 (1985).
34. C. Nemecek, E. Dunach, and H.B. Kagan. New J. Chem. **10**, 761 (1986).
35. J.M. Brunel and H.B. Kagan. Synlett, 404 (1996).
36. J.M. Brunel and H.B. Kagan. Bull. Soc. Chim. Fr. **133**, 1109 (1996).
37. J.M. Brunel, P. Diter, M. Duetsch, and H.B. Kagan. J. Org. Chem. **60**, 8086 (1995).
38. S.H. Zhao, O. Samuel, and H.B. Kagan. Org. Synth. **68**, 49 (1990).
39. P.G. Potvin and B.G. Fieldhouse. Tetrahedron: Asymmetry, **10**, 1661 (1999).
40. A. Massa, V. Mazza, and A. Scettri. Tetrahedron: Asymmetry, **16**, 2271 (2005).
41. M. Seenivasaperumal, H.-J. Federsel, A. Ertanc, and K. Szabo. J. Chem. Commun. 2187 (2007).
42. H. Cotton, T. Elebring, M. Larsson, L. Li, H. Sorensen, and S.V. Unge. Tetrahedron: Asymmetry, **11**, 3819 (2000).
43. F.A. Davis, J.C. Towson, M.C. Weismiller, S. Lal, and P.J. Carroll. J. Am. Chem. Soc. **110**, 8477 (1988).
44. C. Drago, L. Caggiano, and R.F.W. Jackson. Angew. Chem., Int. Ed. **44**, 7221 (2005).
45. H. Fu, H. Kondo, Y. Ichikawa, G.C. Look, and C.-H. Wong. J. Org. Chem. **57**, 7265 (1992).

© 2008 NRC Canada

Vicarious nucleophilic amination of nitroquinolines with 4-amino-1,2,4-triazole

Barbara Szpakiewicz and Maria Grzegożek

Abstract: 3-, 5-, 6-, 7- and 8-Nitroquinolines react with 4-amino-1,2,4-triazole in basic medium (potassium *tert*-butoxide-dimethyl sulfoxide) giving amino products of the vicarious nucleophilic substitution (VNS) of hydrogen, predominantly at ortho position to the nitro group, except 8-nitroquinoline, which reacts at para position. Additionally, furazano[3,4-*f*]- and furazano[3,4-*h*]quinoline were obtained in the case of 5- and 8- nitroquinoline, respectively. 2-Nitroquinoline was aminated to 2-quinolino(1,2,4-triazol-4-yl)amine in these conditions.

Key words: nitroquinolines, vicarious nucleophilic substitution (VNS), 4-amino-1,2,4-triazole.

Résumé : Les 3-, 5-, 6-, 7- et 8-nitroquinoléines réagissent avec le 4-amino-1,2,4-triazole en milieu basique (*tert*-butylate de potassium dans le diméthylsulfoxyde) pour conduire à la formation de produits aminés par le biais d'une substitution nucléophile indirecte (SNI) d'hydrogène, principalement en position ortho du groupe nitro, excepté dans le cas de la 8-nitroquinoléine avec laquelle la substitution se fait en position para. De plus, dans les cas de la 5- et de la 8-nitroquinoléine, on a aussi obtenu respectivement la furazano[3,4-*f*] et la furazano[3,4-*h*]quinoléine.

Mots-clés : nitroquinoléines, substitution nucléophile indirecte (SNI), 4-amino-1,2,4-triazole.

[Traduit par la Rédaction]

Introduction

Many derivatives of aminoquinolines exhibit a wide spectrum of pharmacological and biological activities. Moreover, aminoquinolines are important intermediates in organic synthesis. Some examples of synthesis of aminonitroquinolines have already been described previously. They have been synthesized by the classical method, which is nucleophilic substitution S_NAr of halogen by amines in halogenonitroquinolines (1–3). Another way to obtain compounds mentioned above is dehydroamination of nitroquinolines. It has been carried out as oxidative nucleophilic substitution of hydrogen (ONSH) (4–6) or vicarious nucleophilic substitution (VNS) of hydrogen (7–10). Thus, Woźniak et al. described that mono- and dinitroquinolines undergo selective amination, in liquid ammonia and potassium permanganate at –33 °C, in the ortho position, relative to the nitro group, with moderate to low yields, except 8-nitro- and 2-nitroquinoline (found as unreactive) (4, 5). Additionally, they studied the amination of halogeno and methyl derivatives of nitroquinolines containing the substituents in the benzene ring. The reported amination also undergoes giving selectively ortho substituted products, relative to the nitro group. No amination was observed when the position adjacent to the NO_2 group was occupied by a halogen or a methyl group (6).

Huisgen (7) and Hasegawa et al. (8, 9) described the direct amination of mononitroquinolines with hydroxylamine in basic media, which leads to aminonitroquinolines. Mąkosza suggested that these reactions can be considered as examples of the VNS reaction (10). In these reactions, Hasegawa obtained furazanoquinolines in addition to the known amino derivatives. He obtained furazano[3,4-*f*]quinoline from 5-nitro- and 6-nitroquinoline and furazano[3,4-*h*]quinoline from 7-nitro- and 8-nitroquinoline (7, 8).

For the VNS amination of 5-nitro- and 6-nitroquinoline, Mąkosza and Białecki used sulfenamides. In the first case, they obtained the mixture of 6-amino- and 8-amino-5-nitroquinoline and 6-amino-5-nitrosoquinoline with 90%–98% yield, and in the second case, they obtained only 5-amino-6-nitroquinoline (98% yield) (10).

A variety of regents for the direct amination of nitroarenes and nitrosubstituted heteroaromatic compounds in VNS reactions were described in literature. These are 4-amino-1,2,4-triazole (11–15), *O*-alkylhydroxylamines (16), 1,1,1-trimethylhydrazinium iodide (17–20), and hydroxylamine (7–9) and sulfenamides (10, 21) mentioned above.

In this paper, we report the results of our studies on the amination of nitroquinolines **1** via the vicarious nucleophilic substitution (VNS) of hydrogen with 4-amino-1,2,4-triazole. This is the continuation of our research on the synthesis of amino nitroaromatic compounds (2, 22).

Results and discussion

The amination of the nitroquinolines **1a**–**1e** with 4-amino-1,2,4-triazole was carried out in the presence of potassium *tert*-butoxide-DMSO solution at room temperature. The

Received 20 December 2007. Accepted 28 February 2008. Published on the NRC Research Press Web site at canjchem.nrc.ca on 17 May 2008.

B. Szpakiewicz[1] and M. Grzegożek. Institute of Organic Chemistry and Technology, Cracow University of Technology, ul. Warszawska 24, PL-31155 Kraków, Poland.

[1]Corresponding author (e-mail: bszpak@indy.chemia.pk.edu.pl).

 doi:10.1139/V08-051 © 2008 NRC Canada

Scheme 1.

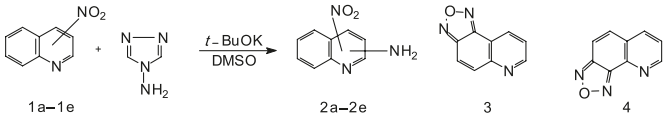

1a 3-NO_2 — **2a** 3-NO_2, 4-NH_2 (52%)

1b 5-NO_2 — **2b** 5-NO_2, 6-NH_2 (15%)

2b′ 5-NO_2, 8-NH_2 (19%); **3** (35%)

1c 6-NO_2 — **2c** 6-NO_2, 5-NH_2 (98%)

1d 7-NO_2 — **2d** 7-NO_2, 8-NH_2 (84%)

1e 8-NO_2 — **2e** 8-NO_2, 5-NH_2 (47%); **4** (23%)

structures of these products were determined on the basis of their physical properties (mp, spectral data: ^{1}H NMR, IR, and MS) and comparison with data from literature or with reference samples in some cases. The results of amination are compiled in Scheme 1.

The reaction of nitroquinolines **1a**–**1e** with 4-amino-1,2,4-triazole proceeds in accordance with vicarious S_NAr^H mechanism, described by Mąkosza (23), which we present as an example of amination of 5-nitroquinoline (**1b**) (Scheme 2).

The reaction occurs between 5-nitroquinoline (**1b**) and the anion generated from 4-amino-1,2,4-triazole, in presence of a strong base (potassium *tert*-butoxide). In the first step, addition of the anion to the 5-nitroquinoline (**1b**) results in formation of σ adducts, type of Meisenheimer complexes, in ortho and para positions relative to the nitro group. Immediate formation of an intense dark-red colour was observed. The σ adducts undergo base-induced β-elimination of 1,2,4-triazole to form carbanions, which are protonated during the work up procedure, giving 6-amino-5-nitro- (**2b**) and 8-amino-5-nitroquinoline (**2b′**). Amination of 3- (**1a**), 6- (**1c**) and 7-nitroquinoline (**1d**) occurs regioselectively giving products of substitution at ortho position to the nitro group: 4-amino-3-nitro- (**2a**), 5-amino-6-nitro- (**2c**), 8-amino-7-nitroquinoline (**2d**) with moderate to high 52%, 98%, and 84 % yields, respectively.

Amination of 5-nitro- (**1b**) and 8-nitroquinoline (**1e**) with 4-amino-1,2,4-triazole in DMSO in the presence of *t*-BuOK at room temperature afforded furazanoquinolines beside the corresponding substituted aminonitroquinolines. In the case of **1b**, we obtained the products of ortho and para substitution of hydrogen: 6-amino-5-nitro- (**2b**) and 8-amino-5-nitroquinoline (**2b′**), as given above, together with furazano[3,4-*f*]quinoline (**3**) with 15%, 19%, and 35% yields, respectively (Scheme 1). On the other hand, 8-nitroquinoline (**1e**) gave 5-amino-8-nitroquinoline (**2e**) (47%) and furazano[3,4-*h*]quinoline (**4**) (23%) under the same conditions.

To explain the formation of furazanoquinolines **3** and **4**, we propose the mechanism for synthesis of furazano[3,4-*f*]quinoline (**3**) from 5-nitroquinoline (**1b**) in Scheme 3. This mechanism is in accordance with the one suggested by Hasegawa for similar reaction (8).

In the first step, addition of 4-amino-1,2,4-triazole anion at the ortho position to the nitro group gives the σ adduct, in which the ortho ring hydrogen undergoes shifting to the oxygen of the nitro group. Subsequently, elimination of hydroxyl group leads to 4-(5-nitroso-6-quinolylamino)-

Scheme 2.

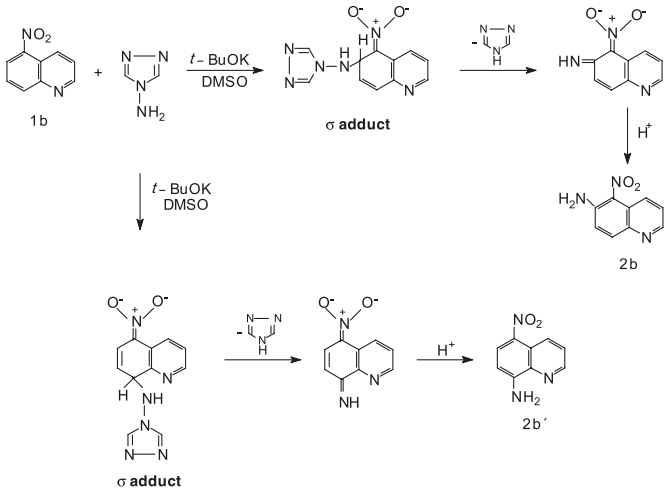

Scheme 3.

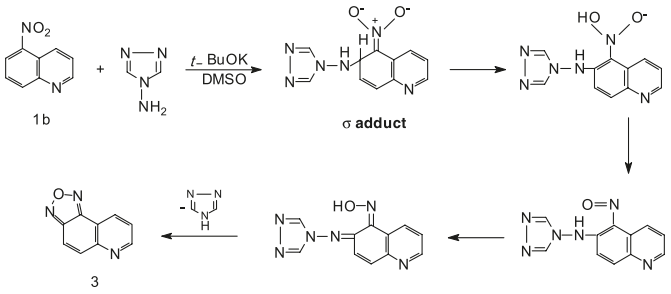

Scheme 4.

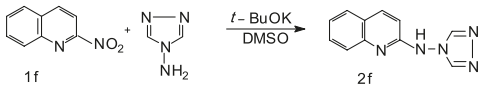

1,2,4-triazole that, by intramolecular cyclization, forms furazano[3,4-*f*]quinoline (**3**).

In the case of 8-nitroquinoline (**1e**), the reaction progress, monitored by thin layer chromatography, indicates the formation of furazano[3,4-*h*]quinoline (**4**) after 5 min of the reaction time. The quick formation of furazane proves that σ adduct undergoes intramolecular transformation more readily than β-elimination of 1,2,4-triazole. This confirms the presented mechanism of reaction and explains why we did not obtain ortho amino isomer instead of only para isomer, as a product of amination.

2-Nitroquinoline (**1f**), in contrast to other studied nitroquinolines **1a**–**1e**, does not undergo vicarious amination by 4-amino-1,2,4-triazole but only displacement of the 2-nitro group occurs, giving 2-quinolino(1,2,4-triazol-4-yl)amine (**2f**) (Scheme 4).

Apparently, the nucleophilic displacement of the highly labile nitro group at C-2 position of the pyridine ring in **1f**, takes place more easily than the vicarious nucleophilic substitution of hydrogen by amino group at another carbon atom. A similar behaviour of 2-nitroquinoline was observed for oxidative methylamination reaction (2).

© 2008 NRC Canada

Summary

In conclusion, we have presented the direct amination of 3-, 5-, 6-, 7- and 8-nitroquinolines (**1a**–**1e**) with 4-amino-1,2,4-triazole under the VNS reaction conditions. Using the 4-amino-1,2,4-triazole permits to obtain aminonitroquinolines in a short time, with moderate to high yields, substituted mainly in ortho position to the nitro group. 5-Nitroquinoline (**1b**) gave, besides the ortho amino product, the para isomer, and in the case of 8-nitroquinoline (**1e**), only the para amino product was obtained. In both cases, as the products of transformation of ortho σ adducts, furazano[3,4-*f*]- (**3**) and furazano[3,4-*h*]quinoline (**4**) were also obtained.

2-Nitroquinoline (**1f**) reacted with replacement of the nitro group, giving 2-quinolino(1,2,4-triazol-4-yl)amine (**2f**).

Experimental

Melting points (uncorrected) were determined on a Boetius melting point apparatus. The ^{1}H NMR spectra were recorded on Tesla BS-587A (80 MHz) spectrometers using TMS as internal standard. Chemical shifts are expressed in parts per million (ppm). The infrared spectra were recorded on Bio-Rad FTS-175C spectrometer (in potassium bromide pellets). Mass spectra (EI) were recorded with a Varian-MAT 112 spectrometer at 70 eV. Elemental analysis was performed on a PerkinElmer 2400 analyser. The reaction products were analysed by thin-layer chromatography (TLC) on silica gel or aluminium oxide plates (Merck 60F_{254}). The progress of reactions was monitored by TLC on silica gel using dichloromethane as eluent. Aluminium oxide type 507 C was used for column chromatography.

Synthesis of starting and reference compounds

3-Nitro-(**1a** (24)), 2-nitro-(**1f** (5)) were prepared according to the literature procedures. 5-(**1b**), 6-(**1c**), 7-(**1d**), and 8-Nitroquinoline (**1e**) were obtained by Skraup reaction from the respective aminonitrobenzenes (25). Other reagents, 4-amino-1,2,4-triazole, *t*-BuOK, and DMSO were commercial products from Merck and Aldrich and were dried before use, except *t*-BuOK.

Amination of nitroquinolines 1a–1f with 4-amino-1,2,4-triazole

General procedure

The mixture of the respective nitroquinolines **1a**–**1f** (174 mg, 1 mmol) and 4-amino-1,2,4-triazole (100–126 mg, 1.2–1.5 mmol) in dimethyl sulfoxide (3–5 mL) was added at room temperature to a stirred suspension of *t*-BuOK (280 mg, 2.5 mmol) in dimethyl sulfoxide (2 mL), except **1e**, where 522 mg (3 mmol) of **1e** and respective amount of remaining reagents were used. The reaction mixture was stirred vigorously for 0.25–0.7 h, and 4 h in the case of 2-nitroquinoline (**1f**), at room temperature. The resulting red-brown solution was poured into saturated NH_4Cl, the precipitate was filtered off, washed with water, and dried. The filtrate was periodically extracted with dichloromethane or chloroform (3 × 25 mL) in some cases. After evaporation of the solvent, the residue was combined with the obtained precipitate and was worked up in the manner described below.

Amination of 3-nitroquinoline (1a)

4-Amino-3-nitroquinoline (**2a**): orange precipitate 98 mg (52%) with mp 258–260 °C (subl.) (without purification, chromatographically pure) and after recrystallization from EtOH: yellow needles with mp 265–266 °C (lit. (1) 261 °C; (4) 274–275 °C; (2) 270–272 °C). IR (ν_{max}) (cm^{-1}): 3385, 3304, 3175 (NH), 1537 (NO_2, as), 1337 (NO_2, s). ^{1}H NMR (DMSO-d_6) δ: 9.18 (s, 2-H), 9.01 (br s, NH_2), 8.58 (dd, 5-H or 8-H), 7.96–7.51 (m, 6-H, 7-H and 5-H or 8-H), $J_{6,7}$ = 4.40, $J_{5,6} = J_{7,8}$ = 8.56, $J_{5,7} = J_{6,8}$ = 1.24 Hz.

Amination of 5-nitroquinoline (1b)

The yellow residue was separated on the chromatographic column using chloroform as eluent. The first fraction gave 60 mg (35%) of furazano[3,4-*f*]quinoline (**3**) colourless needles, mp 132–134 °C (lit.(8) 138–139 °C; (26) 134 °C). ^{1}H NMR ($CDCl_3$) δ: 9.03 (dd, 2-H), 8.85 (dd, 4-H), 7.91 (s, 7-H, 8-H), 7.63 (dd, 3-H), $J_{2,3}$ = 4.60, $J_{2,4}$ = 1.68, $J_{3,4}$ = 8.80 Hz. MS *m*/*z* (%): 171 [M^+] (100), 141 [M^+ – NO].

The second fraction, after removing of the eluent by evaporation, gave 36 mg (19%) of 8-amino-5-nitroquinoline (**2b′**) as orange needles with mp 201–202 °C (lit. (8) 197–198 °C; (2) 194–195 °C). IR (ν_{max}) (cm^{-1}): 3402, 3308, 3212 (NH), 1524 (NO_2, as), 1392 (NO_2, s). ^{1}H NMR ($CDCl_3$) δ: 9.40 (dd, 4-H), 8.79 (dd, 2-H), 8.52(d, 6-H), 7.64 (dd, 3-H), 6.79 (d, 7-H), 5.97 (br s, NH_2), $J_{2,3}$ = 4.16, $J_{2,4}$ = 1.56, $J_{3,4}$ = 8.80, $J_{6,7}$ = 8.92 Hz. The compound **2b′** showed properties identical to the reference sample obtained independently (22).

From the third fraction was isolated 28 mg (15%) 6-amino-5-nitroquinoline (**2b**) as yellow needles, after recrystallization from toluene, mp 176–178 °C (lit. (10) 173–175 °C, (5) 176–178 °C). IR (ν_{max}) (cm^{-1}): 3437, 3412, 3295, (NH), 1511 (NO_2, as), 1300 (NO_2, s). ^{1}H NMR ($CDCl_3$) δ: 9.12 (dd, 4-H), 8.72 (dd, 2-H), 8.05 (d, 8-H), 7.54 (dd, 3-H), 7.16 (d, 7-H), 6.69 (br s, NH_2), $J_{2,3}$ = 4.20, $J_{2,4}$ = 1.60, $J_{3,4}$ = 8.80, $J_{7,8}$ = 9.28 Hz.

Amination of 6-nitroquinoline (1c)

5-Amino-6-nitroquinoline (**2c**): yellow solid 185 mg (98%) with mp 283–284 °C (without purification, chromatographically pure) and after recrystallization from toluene: yellow needles, mp 285–286 °C subl. (lit. (7) 283–284.5 °C; (5) 287–288 °C subl.). IR (ν_{max}) (cm^{-1}): 3404, 3295, 3168 (NH), 1584 (NO_2, as), 1324 (NO_2, s). ^{1}H NMR (DMSO-d_6) δ: 9.10–8.90 (m, 2-H, 4-H), 8.74 (br s, NH_2), 8.22 (d, 7-H), 7.61 (dd, 3-H), 7.15 (d, 8-H), $J_{2,3}$ = 4.40, $J_{3,4}$ = 8.00, $J_{7,8}$ = 9.64 Hz.

Amination of 7-nitroquinoline (1d)

8-Amino-7-nitroquinoline (**3d**): orange crystals 159 mg (84%) with mp 189–190 °C (without purification, chromatographically pure) (lit. (5) 188–189 °C; (1) 185–185.5 °C). The compound showed properties identical (mp, IR spectrum, and coefficient R_f (TLC)) with those of the reference samples. IR (ν_{max}) (cm^{-1}): 3477, 3359 (NH), 1523 (NO_2, as), 1321 (NO_2, s). ^{1}H NMR (DMSO-d_6) δ: 8.91 (dd, 2-H), 8.43 (s, NH_2), 8.34 (dd, 4-H), 8.04 (d, 6-H), 7.76 (dd, 3-H), 7.93 (d, 5-H), $J_{2,3}$ = 4.16, $J_{3,4}$ = 8.16, $J_{2,4}$ = 1.76, $J_{5,6}$ = 9.36 Hz.

© 2008 NRC Canada

Amination of 8-nitroquinoline (1e)

The yellow residue was dissolved in 50 mL of dichloromethane, and the insoluble precipitate was filtered off. The orange precipitate: 232 mg (41%) was analyzed as 5-amino-8-nitroquinoline (**2e**) with mp 250–251 °C (without purification, chromatographically pure) (lit. (2) 252–253 °C). IR (ν_{max}) (cm^{-1}): 3456, 3438, 3324, 3204 (NH), 1576 (NO_2, as), 1298 (NO_2, s). ^{1}H NMR (DMSO-d_6) δ: 8.97 (dd, 2-H), 8.70 (dd, 4-H), 8.19 (d, 7-H), 7.54 (dd, 3-H), 7.39 (br s, NH_2), 6.67 (d, 6-H), $J_{2,3}$ = 4.12, $J_{3,4}$ = 8.68, $J_{2,4}$ = 1.52, $J_{6,7}$ = 8.8 Hz.

The filtrate, after condensation, was separated on the chromatographic column using dichloromethane as eluent. The first fraction gave 120 mg (23%) of furazano[3,4-*h*]quinoline (**4**), colourless plates, mp 176–177 °C (lit. (8) 177.5–178 °C). ^{1}H NMR ($CDCl_3$) δ: 9.04 (dd, 2-H), 8.17 (dd, 4-H), 7.84–7.58 (m, 3-H, 5-H, 6-H), $J_{2,3}$ = 4.56, $J_{2,4}$ = 1.62, $J_{3,4}$ = 8.08 Hz. MS *m*/*z* (%): 171 [M^+] (100), 141 [M^+ – NO] (79), 114 [M^+ – NO – HCN] (30).

The second fraction, after removing of the eluent by evaporation, afforded additional 36 mg compound, which showed the same properties, mp and coefficient R_f, as 5-amino-8-nitroquinoline (**2e**). Total yield of **2e** is 47%.

Amination of 2-nitroquinoline (1f)

2-Quinolino(1,2,4-triazol-4-yl)amine (**2f**): colourless crystals, 171 mg (81%), after recrystallization from methanol, mp 258–259 °C. IR (ν_{max}) (cm^{-1}): 3437 (NH), 1650 (δ NH (s)). ^{1}H NMR (CD_3OD) δ: 8.67 (s, 2H-triazole), 8.11 (d, 4-H), 7.79–7.28 (m, 5–8-H, NH), 6.85 (d, 3-H), $J_{3,4}$ = 8.72 Hz. MS *m*/*z* (%): 211 [M^+] (19), 129 (100). Anal. calcd. for $C_{11}H_9N_5$ (211.23): C 62.55, H 4.29, N 33.16; found: C 62.20, H 4.17, N 32.76.

Acknowledgements

Autors wish to thank Dr. E.Cholewka for measuring the ^{1}H NMR and IR spectra.

References

1. M. Colonna and F. Montanari. Gazz. Chim. Ital. **81**, 744 (1951).
2. M. Woźniak and M. Grzegożek. Liebigs Ann. Chem. 823 (1993).
3. J.F. Gerster. US Patent 4 689 338. 1987.
4. H. Tondys, H.C. van der Plas, and M. Woźniak. J. Heterocycl. Chem. **22**, 353 (1985).
5. M. Woźniak, A. Barański, K. Nowak, and H.C. van der Plas. J. Org. Chem. **52**, 5643 (1987).
6. M. Woźniak, K. Nowak, and H. Poradowska. Polish J. Chem. **65**, 1077 (1991).
7. R. Huisgen. Liebigs Ann. Chem. **559**, 142 (1948).
8. M. Hasegawa and T.O. Kamoto. Yakugaku Zasshi. **93**, 1019, 1024 (1973); **93**, 1024 (1973).
9. M. Hasegawa, T. Takabatake, and T. Miyazawa. Yakugaku Zasshi. **121**, 379 (2001).
10. M. Mąkosza and M. Białecki. J. Org. Chem. **63**, 4878 (1998).
11. A.R. Katrizky, K.S. Laurenzo, and R.D. Schmidt. J. Org. Chem. **51**, 5039 (1986).
12. A.R. Katrizky and K.S. Laurenzo. J. Org. Chem. **53**, 3978 (1988).
13. M. Mąkosza and R. Podraza. Eur. J. Org. Chem. **2000**, 193.
14. J.M. Bakke, H. Svensen, and R. Trevisan. J. Chem. Soc. Perkin Trans. I. 376 (2001).
15. A.R. Mitchell, P.F. Pagoria, and R.D. Schmidt. US Patent 5 633 406. 1997.
16. S. Seko and K. Miyake. J. Synth. Org. Chem. Jpn. **61**, 192 (2003).
17. P.F. Pagoria, A.R. Mitchell, and R.D. Schmidt. J. Org. Chem. **61**, 2934 (1996).
18. R.D. Schmidt, G.S. Lee, P.F. Pagoria, A.R. Mitchell, and R.Gilardi. J. Heterocycl. Chem. **38**, 227 (2001).
19. V.V. Rozhkov, S.A. Shevelev, I.I. Chervin, A.R. Mitchell, and R.D.Schmidt. J. Org. Chem. **68**, 2498 (2003).
20. M. Mąkosza, P.W. Osiński, and S. Ostrowski. Polish J. Chem. **75**, 275 (2001).
21. M. Mąkosza and M. Białecki. J. Org. Chem. **57**, 4784 (1992).
22. (*a*) M. Woźniak, A. Barański, and B. Szpakiewicz. Liebigs Ann. Chem. 875 (1991); (*b*) M. Woźniak and B. Szpakiewicz. Polish J. Chem. **65**, 1303 (1991); (*c*) M. Woźniak, A. Barański, and B. Szpakiewicz. Liebigs Ann. Chem. 7 (1993); (*d*) M. Woźniak and B. Szpakiewicz. PL Patent 162 466, B1. 1993; (*e*) M. Woźniak, M. Grzegożek, and K. Nowak. Indian J. Heterocycl. Chem. **4**, 75 (1994); (*f*) M. Woźniak, M. Grzegożek, W. Roszkiewicz, and B. Szpakiewicz. Recl. Trav. Chim. Pays-Bas, **114**, 13 (1995); (*g*) B. Szpakiewicz and M. Woźniak. J. Prakt. Chem. 341 (1999); (*h*) M. Woźniak and M. Grzegożek. Khim. Geterotsikl. Soedin. **7**, 967 (1998); (*i*) B. Szpakiewicz and M. Grzegożek. Russ. J. Org. Chem. **40**, 829 (2004).
23. M. Mąkosza and K. Wojciechowski. Liebigs Ann. Chem. **1997**, 1805.
24. (*a*) A. Albert, D.J. Brown, and H. Duewell. J. Chem. Soc. 1284 (1948); (*b*) G.R. Clemo and G.A. Swan. J. Chem. Soc. 867 (1945).
25. J. Filippi. Bull. Soc. Chim. Fr. 259 (1968).
26. K. Kostanecki and M. Reicher. Ber. **24**, 159 (1891).

© 2008 NRC Canada

Substituent effects, Arrhenius activation parameters, and rate constants for the photo–Claisen rearrangement of allyl aryl ethers

Carlos M. Gonzalez and James A. Pincock

Abstract: The temperature-dependence of fluorescence quantum yields in both methanol and methylcyclohexane has been used to obtain the rate constants of reaction for the activated process that converts the singlet excited state S_1 of a set of ring-substituted aryl allyl ethers to an intermediate radical pair in the photo–Claisen rearrangement. These rate constants are correlated with the O–H bond dissociation energy of the corresponding ring-substituted phenols; that is, electron-donating groups (CH_3, OCH_3) accelerate the reaction relative to electron-withdrawing groups (CF_3, CN). The rate constants obtained span two orders of magnitude, from 5.4×10^7 s^{-1} for X = 3–CN to 800×10^7 s^{-1} for X = 4–OCH_3, in methylcylcohexane. Moreover, the rate constants are similar in the two solvents, methanol and methcyclohexane, indicating that radical pairs, not ion pairs, are the reactive intermediates, as expected on the basis of previous mechanistic proposals for the photo–Claisen rearrangement. Finally, the rate constants obtained by this temperature-dependent method are in good agreement with those previously reported from a method using the corresponding unreactive anisoles as a model.

Key words: allyl aryl ethers, photo–Claisen rearrangement, substituent effects, activation parameters.

Résumé : La relation de dépendance entre la température les rendements quantiques de fluorescence, tant dans le méthanol que dans le méthylcyclohexane, a été utilisée pour déterminer les constantes de vitesse de réaction pour les processus activés au cours desquels l'état excité singulet S_1 d'un ensemble d'oxydes d'allyle et d'aryles substitués sur le noyau aromatique se transforme en une paire radicalaire dans un réarrangement photo–Claisen. On a établi une corrélation entre ces constantes de vitesse et l'énergie de dissociation de la liaison O–H des phénols correspondants portant les mêmes substituants sur leur noyau, à savoir que les groupes électrodonneurs, tel le CH_3 ou le OCH_3, accélèrent la réaction par rapport aux groupes électroaffinitaires, tels les groupes CF_3 ou C≡N. Dans le méthylcyclohexane, les constantes de vitesse s'étalent sur deux ordres de grandeur, soit de $5{,}4 \times 10^7$ s^{-1} pour X = 3–CN à 800×10^7 s^{-1} pour X = 4–OCH_3. De plus, les constantes de vitesse sont semblables dans les deux solvants, méthanol et méthylcyclohexane, ce qui indique que les intermédiaires réactifs sont des paires de radicaux et non des paires d'ions, tel qu'on pouvait le prévoir sur les bases mécanistiques développées antérieurement pour le réarrangement de photo–Claisen. Enfin, les constantes de vitesse obtenues par cette méthode qui dépend de la température sont en bon accord avec ceux rapportés antérieurement à l'aide d'une méthode qui faisait appel à un modèle impliquant des anisoles non réactifs.

Mots-clés : oxydes d'allyle et d'aryle, réarrangement de photo–Claisen, effets de substituant, paramètres d'activation.

[Traduit par la Traduction]

Introduction

Recently, we reported (1) on the rate constants of reaction in both methanol and cyclohexane from the excited singlet state S_1 of a set of 11 substituted aryl allyl ethers **1** which undergo an efficient photo–Claisen rearrangement, Scheme 1, via a radical pair **2**, to the products **3**. This project was one in a continuing series exploring the effect that substituents on the aryl ring have on the photochemical reactivity of systems of the general structure Ar-X-Y. As in this article, the focus has been on the X–Y bond cleavage. For benzylic systems (X = CH_2), Y is normally a typical leaving group (halide, carboxylate, thiolate, etc.), and the reactions can then be photosolvolysis in polar protic solvents (alcohols, water) proceeding through benzylic carbenium ions. Usually, radical-derived products are formed along with the ion-derived ones and the factors that control the competition between these two pathways have been recently reviewed (2). In contrast, the photo–Claisen reaction has been proposed to involve only radical pairs as intermediates (3), and this suggestion was confirmed by the similar rate constants we obtained in both the polar protic solvent, methanol, and the non-polar one, cyclohexane. The rate constants spanned almost two orders of magnitude, those with electron-drawing groups (CN, CF_3) reacting much more slowly than those

Received 4 December 2007. Accepted 14 March 2008. Published on the NRC Research Press Web site at canjchem.nrc.ca on 23 May 2008.

Dedicated to the memory of Keith Yates in acknowledgment of the importance of his influence on my (JAP) career in science.

C.M. Gonzalez and J.A. Pincock.[1] Department of Chemistry, Dalhousie University, Halifax, NS B3H 4J3, Canada.

[1]Corresponding author (e-mail: james.pincock@dal.ca).

 doi:10.1139/V08-057 © 2008 NRC Canada

Scheme 1. The photo–Claisen reaction of the ring-substituted allyl ethers **1** and the corresponding phenols **4** and anisoles **5**.

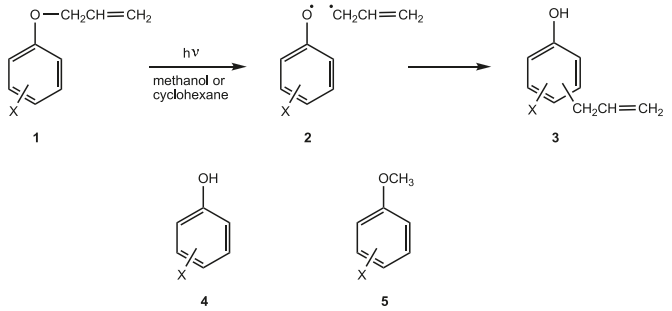

with electron-donating groups (CH_3, OCH_3). Because of the polarity of the O–C bond that was breaking, a reasonable expectation was that the transition state would also be polarized $O^{\delta-}\cdots C^{\delta+}$. If that were the case, a correlation of the rates of the bond cleavage with σ_{ex}, the substituent constants for the excited state pK_a's of substituted phenols (4, 5, 6), might be expected. Surprisingly, the rate constants were correlated reasonably well with σ^+. This counterintuitive observation was resolved by the realization that the rate constants were strongly correlated by the bond dissociation energy (O–H BDE) of the corresponding phenols **4** (7), which also correlate with σ^+, those compounds with weaker bonds reacting with the greater rate constants in both methanol and cyclohexane.

These results were obtained by comparing the fluorescence quantum yield and (or) the fluorescence lifetime of the reactive allyl ethers with the identically substituted, but unreactive model compounds, anisoles **5**. The basic idea was that the decrease in either the excited singlet state lifetime or the quantum yield of fluorescence when comparing a substituted **1** with its analogue **5** could be quantitatively used to determine the rate constant for the excited state bond cleavage of **1**. This idea was questioned (1) with the suggestion that an additional mode of excited state decay, other than reaction, was available for the allyl ethers **1**, namely intramolecular exciplex formation, which was unavailable to the anisoles **5**. At the time, we provided strongly suggestive, but not conclusive, evidence that this was not the case.

We now report on the temperature dependence of the fluorescence quantum yield for the allyl ethers **1** that provides considerably more convincing evidence that the initially reported rate constants were reliably determined.

Results and discussion

Recently we have used, following the examples from the Lewis (8) and Zacchariasse (9) laboratories, a method that allows the direct determination of the rate constant of reactivity of S_1 by the temperature dependence of either the fluorescence lifetime or the fluorescence quantum yield. The basic concept is shown in Scheme 2. The total rate of decay, k_t, the reciprocal of the lifetime τ of S_1, is given by eq. [1]. Two of the terms in this equation are photophysical processes (k_f, fluorescence; k_{isc}, intersystem crossing) and are assumed to be temperature independent. Moreover, k_{ic} can be ignored because the rate of internal conversion from the Frank–Condon state of S_1 of benzene derivatives is known

Scheme 2. Rate constants for the reactions of an excited state S_1 and a reactive intermediate (RI).

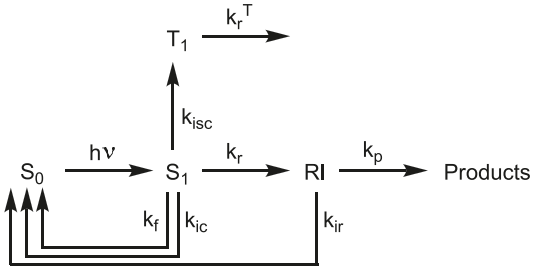

(10) to be negligibly slow relative to other decay modes because of the large energy gap between S_1 and S_0. Therefore, eq. [1] simplifies to eq. [2], where k_r, the photochemical reaction, is assumed to be temperature dependent and follow an Arrhenius' relationship.

$$[1] \qquad k_t = k_f + k_{ic} + k_{isc} + k_r$$

$$[2] \qquad k_t = k_f + k_{isc} + A\ \exp(-E_a/RT)$$

$$[3] \qquad \Phi_f = k_f/[k_f + k_{isc} + A\ \exp(-E_a/RT)]$$

The assumption that k_{isc} is temperature independent and the details of applying this method have been discussed in detail by Lewis (8), Zacchariasse (9) and us (11). An important point to mention is that this method gives k_r from S_1 and any reactivity from T_1 is invisible. Internal return from any reactive intermediate is also not detected. However, a comparison of the quantum yield of formation of the reactive intermediate, $\Phi_{ri} = k_r/k_t$, and that for the products, $\Phi_{products} = \Phi_{ri} \times (k_p/k_p + k_{ir})$ (Scheme 2) will give a measure of the importance of internal return, a process that has been observed in many experiments which have been designed to detect it (11, 12).

Experimentally, either the rate constant of decay k_t or the quantum yield of fluorescence Φ_f as a function of temperature, can be used. For the former, the data obtained is analyzed by eq. [2] with the number of unknowns reduced from four to three by independently determining $k_f = \Phi_f$ (25.0 °C) × k_t (25.0 °C). For the latter, eq. [3] is used, again using an experimental value of k_f. This method is considerably faster because quantum yields of fluorescence over a temperature range from –25 to +95 °C can be determined over a period of several hours from a single sample. Details are given in the Experimental section.

A comment is necessary here about the values of k_f that could only be obtained experimentally for those compounds for which the total rate of decay, τ, was longer than 0.5 ns, the time resolution of our flash lamp, single photon counting spectrometer. These are given in the third column of Table 1 with the corresponding k_f values in the fourth column. Fortunately rate constants of fluorescence, k_f, have been reliably calculated in the past from the Strickler–Berg relation, eq. [4] (13).

$$[4] \qquad k_f = 2.88 \times 10^{-9}\ n^2 < \bar{\nu} >^{-1} \int \varepsilon\ d\ \ln\ \bar{\nu}$$

This equation is a general theoretical relationship between the radiative lifetime ($\tau_f = 1/k_f$) and the absorbance spectrum

© 2008 NRC Canada

Table 1. Rate constants and Arrhenius activation parameters for the reaction of the excited singlet state S_1 of the allyl aryl ethers **1** in methanol (M) and methylcylohexane (MC).

Cmpd (X)[a]/S[b]	Φ_f[c]	τ[d]/ns	$k_f = \Phi_f/\tau$ (10^7 s^{-1})	k_f from eq. [4] (10^7 s^{-1})	k_{isc} from eq. [3] (10^7 s^{-1})	A from eq. [3] (10^{11} s^{-1})	E_a from eq. [3] (kJ mol^{-1})	k^e_r from eq. [3] (10^7 s^{-1})	k^f_r from ref. (1) (10^7 s^{-1})
1a (H)/M	0.012	–	–	2.5	66	2.2	13	130	195
1a (H)/MC	0.0056	–	–	2.9	66	3.1	11	450	500
1b (4-OCH3)/M	0.0069	–	–	4.1	130	4.0	9.7	480	530
1b (4-OCH3)/MC	0.0054	–	–	5.1	110	3.0	10	800	690
1c (3-OCH3)/M	0.0095	0.63	4.0	3.1	26	7.1	14	300	290
1c (3-OCH3)/MC	0.0095	–	–	3.7	27	5.5	12	360	350
1d (4-CH3)/M	0.0065	–	–	2.9	9.1	1.7	9.7	350	510
1d (4-CH3)/MC	0.0053	–	–	3.2	15	1.9	9.1	490	820
1e (3-CH3)/M	0.0088	–	–	2.3	34	2.0	11	220	370
1e (3-CH3)/MC	0.0074	–	–	2.8	31	1.6	9.6	340	570
1h (4-CF3)/M	0.028	1.5	1.9	–	20	5.5	18	46	46
1h (4-CF3)/MC	0.021	0.93	2.3	–	26	5.9	16	81	80
1i (3-CF3)/M	0.067	2.0	3.3	4.0	21	7.3	20	24	48
1i (3-CF3)/MC	0.064	1.6	3.9	4.0	24	8.5	20	31	32
1j (4-CN)/M	0.048	2.4	2.0	–	15	4.0	18	25	12
1j (4-CN)/MC	0.044	2.5	1.8	–	13	3.3	18	26	16
1k (3-CN)/M[g]	0.10	3.1	3.2	4.6	6.6	0.019	7.3	–	–
1k (3-CN)/MC	0.16	3.9	4.1	4.6	16	1.0	19	5.4	6.0

[a]Substituent.
[b]M is methanol, MC is cyclohexane for the fluorescence measurements at 25 °C and methylcyclohexane for the temperature dependent studies
[c]Quantum yield of fluorescence relative to anisole in methanol (0.24) and cyclohexane (0.29), estimated error ±10%.
[d]Singlet lifetime by nanosecond single photon counting. No value indicates that the lifetime was lass than 0.5 ns.
[e]Calculated at 25 °C from the activation parameters.
[f]Calculated at 25 °C from the unreactive anisole model method (see text).
[g]For the 3-cyano compound **3k** in methanol, the change in fluorescence quantum yield with temperature was very small. The activation parameters obtained are of a magnitude expected for activated intersystem crossing.

where n is the refractive index of the solvent, ν is the expectation value for the frequency of the fluorescence spectrum and the final term is the integrated absorbance spectrum. The constant gives k_f in units of s^{-1} if the frequency values are expressed in wavenumber (cm^{-1}) and molar absorptivity ϵ in the usual units ((mol/L^{-1}) cm^{-1}). This equation is derived on the basis of the oscillator strength model and the important assumption that the excited singlet state and the ground state have similar geometries. It has been successfully applied many times to, for example, simple aromatic compounds like benzene, toluene and *ortho*-xylene (14), and by us for the ring-substituted anisoles **5** (1) and aromatic nitriles, boronate esters, and trifluoromethyl derivatives (11). More importantly for the current work, a comparison of the experimentally determined and calculated values for the ethers **1** are in good agreement where both are available (columns 3 and 4 for the trifluoromethyl and cyano substituted cases) giving us confidence that that the calculated values are reliable for the other substituents.

An example of the fluorescence spectrum as a function of temperature for the 4-CN allyl ether **1j** in methylcyclohexane (this hydrocarbon solvent was chosen over cyclohexane because it has a wider temperature range as a liquid) is given in Fig. 1. A plot of the data according to eq. [3], using the experimental value of k_f is given in Fig. 2. As indicated by the correlation coefficient and the errors in the fitted parameters, the fit is excellent even though the

Fig. 1. Temperature dependence of the quantum yield of fluorescence from –25 °C to 95 °C for **1j**: X = 4–CN in methylcyclohexane.

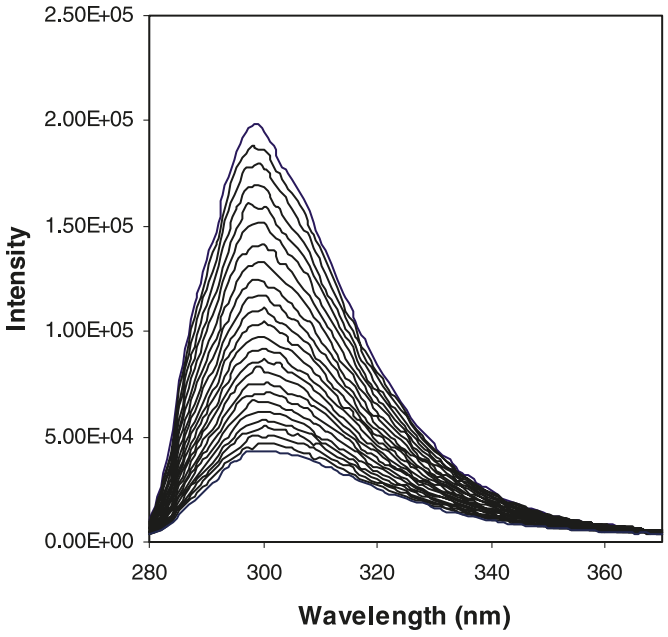

© 2008 NRC Canada

Fig. 2. A fit of the data from Fig. 1 to eq. [3].

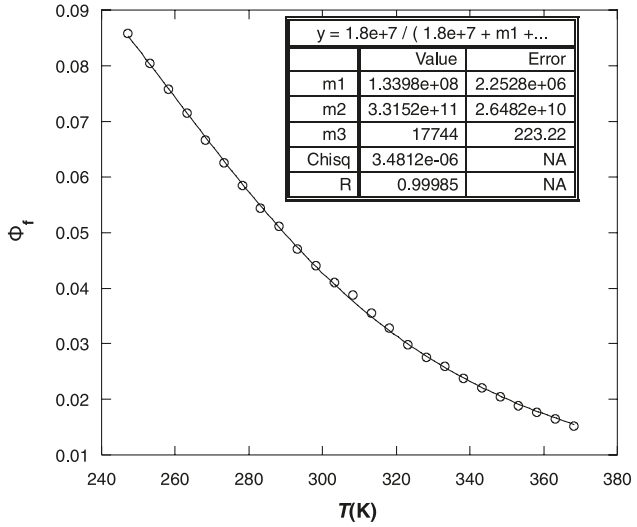

available temperature range is limited. The values of of k_{isc}, A and E_a from the fit are given in Table 1, along with those obtained in the same way for the other substituted allyl ethers **1** in both methanol and methylcyclohexane. Also given are k_r values, calculated from the Arrhenius parameters at 25 °C, the rate constant for the activated photochemical step, the cleavage of the carbon–oxygen bond to give the radical pair **2**.

The k_r values obtained by the two methods, the Arrhenius' one from the temperature dependence of fluorescence and the anisole unreactive model one (1), are plotted against one another in Figs. 3*a* (hydrocarbon solvent) and 3*b* (methanol solvent). As indicated by the correlation coefficients, these linear plots should best be regarded as trends. The reason for the large deviations from the best-fit lines could be real but are more likely a result of the large systematic errors in obtaining the rate constants. The anisole reference method (1) relies on accurate measurements of quantum yields of fluorescence. This is not problematic for the anisoles **5**, which have relatively large values, but is problematic for the allyl ethers **1**. The high reactivity for the methyl and methoxy substituted cases results in very low fluorescence quantum yields and a consequent difficulty in determining them reliably. Moreover, the temperature dependence of fluorescence method ideally requires a measurement over a significantly wider temperature range than is available to us in order that the activation parameters can be obtained with high accuracy (9).

Nevertheless, the trends in the plots are obvious, i.e., slopes near unity in both methylcyclohexane and methanol. This observation confirms that the rate constants obtained for the photo–Claisen reaction and discussed in detail previously (1) are reliable. Therefore, the conclusion reached is that the rate constants for the reaction do correlate with the O-H BDE of the corresponding phenols (7) and, as well, the O-C BDE of the anisoles (15). In other words, those compounds with the weaker bonds react faster, as shown in Fig. 4. This conclusion is reinforced by the trends in the activation parameters from Table 1. The pre-exponential factors vary only from a low of 1.0 to a high of 8.5, a factor of only 8.5, although the rate constants vary over more than

Fig. 3. (*a*) The linear correlation for the reaction rate constant k_r for the bond cleavage from S_1 of the allyl ethers. The horizontal axis gives the values in methylcyclohexane from the Arrhenius equation as described herein. The vertical axis gives the values in cyclohexane from the unreactive model method from reference (1), listed in the last column in Table 1. The substitutents are identified on the right vertical axis. (*b*) The same correlation for the results in methanol.

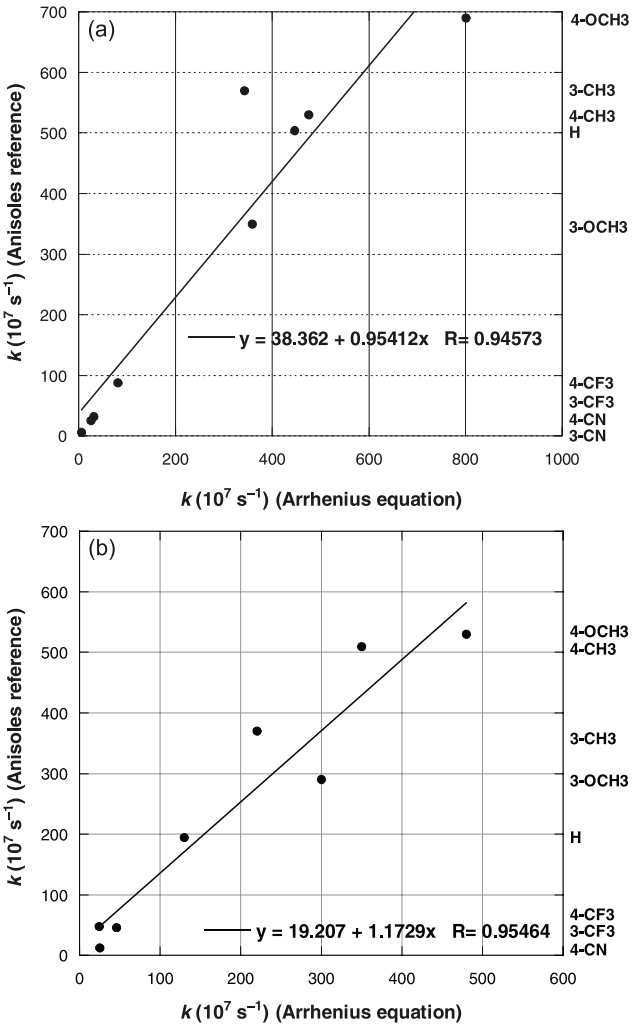

two orders of magnitude. The reason is that the large changes in the BDE are reflected in the changes in the E_a values from a low of ~9 kJ mol^{-1} for the reactive compounds (X = 4–OCH_3 and 4–CH_3) to a high of ~19 kJ mol^{-1} for the least reactive (X = CF_3 and CN). Other factors such as the polarity of the transition state as correlated by Hammett $\rho\sigma$ relationships must be contributing in only a minor way. Multiple parameter fits to assess these other minor contributions were not attempted because they were not warranted by the accuracy of the data.

Experimental

The synthesis and characterization of the allyl ethers has been described previously (1). The solvents, methanol and

© 2008 NRC Canada

Fig. 4. The linear correlation for the reaction rate constant k_r in cyclohexane with the O–H BDE of the corresponding phenols. The values given are relative to a value for phenol itself equal to 371.3 kJ/mol (1).

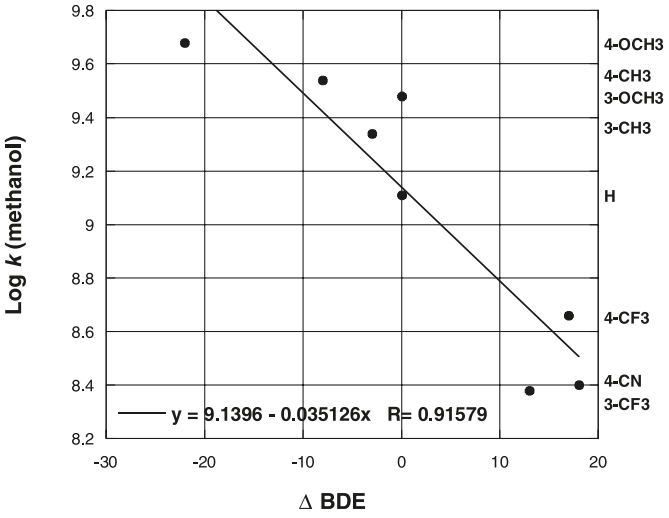

methylcyclohexane, both Aldrich spectrophotometric grade, were used without further purification.

Fluorescence measurements

All samples were degassed by three freeze-pump-thaw cycles and then thermostated at the appropriate temperature. Fluorescence intensity measurements were done using a PTI–210M fluorescence spectrometer with dual Model 101 monochromators, a 75W Xenon lamp and a Model 814 photomultiplier detector. Corrected spectra were obtained. Fluorescence quantum yields were determined using solutions of matched absorbance by comparison with the known fluorescence quantum yield of 0.24 (for anisole in methanol. For temperature dependent quantum yield measurements, a 1 cm cuvette was thermostated (±0.1 °C) with stirring in a cuvette holder equipped with a Quantum Northwest TLC 50 temperature controller that allows relative fluorescence measurements at 5 °C intervals from –25 to 95 °C over a 3 h time span. Normally, intensity measurements at the λ_{max} of the fluorescence spectrum at each temperature were determined. For illustrative purposes, as shown in Fig. 1, scans over the entire fluorescence spectrum could be recorded. However, these required rapid scans to avoid photochemical degradation of the sample. This resulted in noisy spectra, as shown in Fig. 1. The stability of the lamp over this time period was normally confirmed by rerunning the fluorescence spectrum at 25 °C at the end.

Singlet lifetimes were measured at 25 °C by monitoring fluorescence decay using a PRA time correlated single photon counting apparatus with a hydrogen flash lamp of pulse width about 1.8 ns. The temperature was controlled (±0.5 °C) by circulating methanol from an external constant temperature bath.

Acknowledgements

We thank NSERC of Canada and the Killam Trust for financial support. We also thank Sepracor Canada, Ltd., Windsor, Nova Scotia for their generous gift of chemicals. CG thanks the Department of Chemistry and the Faculty of Graduate Studies at Dalhousie University for graduate student scholarships.

References

1. A.L. Pincock, J.A. Pincock and R. Stefanova. J. Am. Chem. Soc. **124**, 9768, (2002).
2. S.A. Fleming and J. A. Pincock. Organic Molecular Photochemistry. *Edited by* V. Ramamurthy and K.S. Schanze. Marcel Dekker, New York. Vol. 3, 211. 1999.
3. W. Gu, M. Warrier, B. Schoon, V. Ramamurthy, and R.G. Weiss. Langmuir, **16**, 6977, (2000) and refs. cited therein.
4. E.L. Wehry and L. B. Rogers. J. Am. Chem. Soc. **87**, 4234, (1965).
5. P.J. Baldry. J. Chem. Soc. 951, (1979).
6. S.C. Shim, J.W. Park, H.-S. Ham, and J.-S. Chung. Bull. Korean Chem. Soc. **4**, 45, (1983) and refs. cited therein.
7. R.M. Borges dos Santos and J. A. Simoes. J. Phys. Chem. Ref. Data **27**, 707, (1998).
8. (*a*) F.D. Lewis and X. Zuo. J. Am. Chem. Soc. **125**, 8806, (2003); (*b*) F.D. Lewis and X. Zuo. J. Am. Chem. Soc. **125**, 2046, (2003); (*c*) F.D. Lewis, X. Zuo, R.S. Kalgutkar, J.M. Wagner-Brennan, M.A. Mirnada, E. Font-Sanchis, and J. Perez-Orieto, J. Am Chem. Soc. **123**, 11883, (2001).
9. S.I. Druzhinin, A. Demeter, V.A. Galievsky, T. Yoshihara, and K.A. Zachariasse. J. Phys. Chem. **107**, 8075, (2003).
10. N. Nijegorodov, V. Ramachandran, and D.P. Winkoun. Spectrochem Acta Part A, **53**, 1813, (1997).
11. C. Gonzalez and J. A. Pincock. Photochem. Photobiol. **82**, 301, (2006).
12. J.M. Kim and J.A. Pincock. Can. J. Chem. **73**, 885, (1995).
13. S.J. Strickler and R.A. Berg. J. Chem. Phys. **37**, 814, (1962).
14. R.B. Cundall and L.C. Periera. J. Chem. Soc. Faraday Trans. **68**, 1152 (1972).
15. D.A. Pratt, J.S. Wright, and K.U. Ingold. J. Am. Chem. Soc. **121**, 4877, (1999).
16. G. Kohler, G. Kittel, and N. Getoff. J. Photochem. **18**, 19, (1982).

© 2008 NRC Canada

Synthesis, X-ray structure, and binding properties of a new fluorescent molecular clip derived from diethoxycarbonyl glycoluril

Sheng-Li Hu, Guo-Dong Yin, Yu-Zhou Wang, and An-Xin Wu

Abstract: A new fluorescent molecule clip derived from diethoxycarbonyl glycoluril with two 2,5-diphenyl-furan sidewalls was designed and synthesized. Its structure and conformation was confirmed by single-crystal X-ray diffraction. Its binding properties, investigated by fluorescence spectroscopey, showed that it can selectively bind Fe^{3+} with fluorescence quenching.

Key words: diethoxycarbonyl glycoluril, molecular clip, fluorescence, Fe(III).

Résumé : On a développé une méthode de synthèse pour une nouvelle pince moléculaire fluorescente qui est dérivée du diéthoxycarboxylglycoluril et qui comporte deux 2,5-diphénylfuranes comme murs latéraux. On a confirmé sa structure et sa conformation sur la base de la diffraction des rayons X par un cristal unique. Ses propriétés de fixation étudiées par spectroscopie de fluorescence montrent qu'elle peut se fixer sélectivement avec le Fe^{3+} avec désactivation de la fluorescence.

Mots-clés : diéthoxycarbonylglycoluril, pince moléculaire, fluorescence, Fe(III).

[Traduit par la Rédaction]

Introduction

Development of fluorescent chemosensors, capable of recognizing metal ions, anions, and neutral molecules, is of interest because of their high sensitivity and low-cost instrumentation (1). In general, fluorescence chemosensors are composed of two covalently linked components: a recognition site that binds the target substance and a transducer (fluorophore) that signals the binding (2–4).

Glycoluril is an important building block for supramolecular chemistry, and its derivatives have been used as the basis for molecular clips (5), molecular capsules (6), anion-binding receptors (7), xerogels (8), and the cucurbit[*n*]uril (CB[*n*]) family (9). However, few studies have been carried out to explore its utilization as a platform for the synthesis of fluorescent chemosensors for ionic guest in recent years (10).

In the previous work, we had reported a pair of molecular clips derived from diethoxycarbonyl glycoluril with two 1,2-dihydro-indazol-3-one moieties as sidewall and developed their function as selective fluorescent chemsensors for Fe^{3+} (11). In continuing our research to develop new fluorescent chemsensors based on glycoluril, we designed a new molecular clip **5**, which has two 2,5-diphenyl-furan fluorescent moieties used as the signaling subunit in its two sidewalls and two carbonyl oxygen atoms of glycoluril ring used as the potential binding sites in its cavity. We assume that such crown-ether derivatives can be used as a fluorescent chemsensor for alkali or alkaline earth metal cations. In this paper, we report its synthesis, X-ray structure, and binding study with different metal ions. Interestingly, the new fluorescent clip molecule **5** also exhibited selective recognition to Fe^{3+} over the other tested metals ions, including alkali and alkaline earth metal cations. This experimental result shows that the two polarized carbonyl groups oxygen atoms of glycoluril ring may be an effective recognition position for Fe^{3+}.

Received 6 December 2007. Accepted 24 March 2008. Published on the NRC Research Press Web site at canjchem.nrc.ca on 23 May 2008.

S.-L. Hu,[1, 2] G.-D. Yin, Y.-Z. Wang, and A.-X. Wu. Key Laboratory of Pesticide and Chemical Biology, Ministry of Education, Central China Normal University, Wuhan 430079, China.

[1]Corresponding author (e-mail: chwuax@mail.ccnu.edu.cn).
[2]Present address: Hubei Key Laboratory of bioanalytical techniques (Hubei Normal University), Huangshi 435002, China.

Results and discussion

Fluorescent molecule clip **5** was prepared by reacting diethoxycarbonyl glycoluril (**3**) with 3,4-bis-bromomethyl-2,5-diphenyl-furan (**4**) using *t*-BuOK as base in anhyd. DMSO (Scheme 1), and the product was further characterized by NMR spectra. The ^{1}H NMR spectrum of **5** in $CDCl_3$ shows two pairs of well-defined doublets with equal intensity for the protons of methylene at δ = 5.28 ppm (J = 16.0 Hz) and δ = 4.36 ppm (J = 16.0 Hz), indicating that the molecules possess good symmetry and the four bridging methylenes have the same chemical environment. The IR and MS spectra for the product are in good agreement with the title compound. In addition, its structure and conformation were confirmed by single-crystal X-ray diffraction, as

 doi:10.1139/V08-058 © 2008 NRC Canada

Scheme 1. Synthesis of molecular clip **5**.

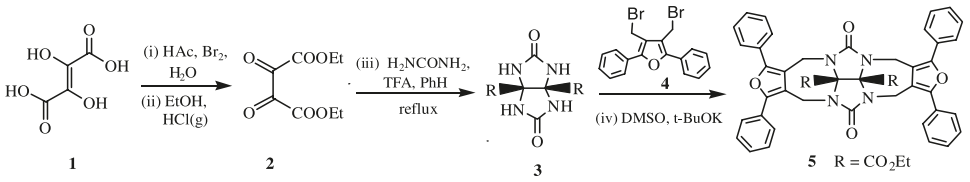

Fig. 1. X-ray crystal structure of compound **5**. Hydrogen atoms and minor components are omitted for clarity.

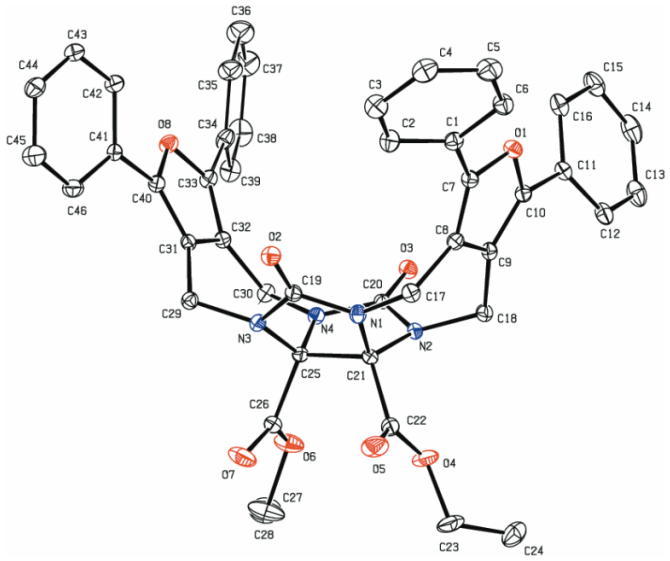

shown in Fig. 1. Its crystal data and details of structure determinations were summarized in Table 1.

The crystal structure of **5** clearly reveals that it has well-defined geometry because of the rigidity that the fused rings confer on the molecule. However, two phenyl rings of the sidewall are twisted away from the furan ring. The phenyl ring (C1–C6) and phenyl ring (C11–C16) form dihedral angles of 41.47° and 35.40°, respectively, with the furan ring (O1–C10). The phenyl ring (C34–C39) and phenyl ring (C41–C46) form dihedral angles of 34.31° and 28.33°, respectively, with the (O8–C40) furan ring. The dihedral angle between them is 34.76°. The dihedral angle between two furan rings is 38.61°, and the distance between the centroids of two furan rings is 6.603 Å. The distances between the two oxygen atoms (O1–O8) of two furan rings and two carbonyl oxygen atoms (O2–O3) of glycoluril ring amount to 7.494 Å and 5.722 Å, respectively.

The binding properties of the clip molecule **5** with various metal ions were investigated through fluorescence-spectroscopy titration experiments. Changes of the fluorescence properties of 1×10^{-5} mol/L of **5** in DMF/CH_3OH (50:1, *v*/*v*) solution caused by 15 equiv. of various metal ions (K^+, Na^+, Mg^{2+}, Hg^{2+}, Cd^{2+}, Fe^{3+}, Zn^{2+}, Co^{2+}, Ni^{2+}, Cu^{2+}, Pb^{2+}, Cr^{3+}, and Mn^{2+}) were measured once their emission intensity were constant. The result showed that Fe^{3+} produced significant quenching in the fluorescent emission of **5**; the other tested metals only show relatively insignificant

Table 1. Crystal structure data for **5**.

Empirical formua	$C_{46}H_{38}N_4O_8$
Formula mass	774.80
Temperature (K)	294(2)
Wavelength (Å)	0.71073
Crystal system	Monoclinic
Space group	*P*2(1)/*n*
a (Å)	12.7623(9)
b (Å)	11.5771(8)
c (Å)	26.5023(19)
α	90°
β	96.1500(10)°
γ	90°
V(Å^3)	3893.2(5)
Z	4
Density$_{calcd.}$ (Mg/m^3)	1.322
Index ranges	$-15 \le h \le 15$, $-13 \le k \le 13$, $-31 \le l \le 31$
F(000)	1624
Crystal size	0.20 mm × 0.10 mm × 0.04 mm
θ range for data collection	1.55–25.00°
Reflections collected	33604
Independent reflections	6862 [$R_{(int)}$ = 0.1084]
Data, restraints, parameters	6862, 0, 526
Goodness-of-fit on F^2	1.000
Absorption correction	None
>2σ(*I*)	3472
Final *R* indices ($I > 2\sigma(I)$)	R_1 = 0.0761, wR_2 = 0.1782
R indices (all data)	R_1 = 0.1563, wR_2 = 0.2090
Largest diff. peak and hole (e Å^{-3})	0.312 and –0.246

changes (Fig. 2). So, it can be concluded that **5** has higher selectivity for the recognition of Fe^{3+}.

The sensitivity of the fluorescence emission response of **5** towards Fe^{3+} was also examined under the same conditions with various Fe^{3+} concentrations (Fig. 3). The fluorescence intensity (λ_{em} = 365 nm) of **5** was decreased continually upon addition of Fe^{3+} with no significant change in the position of the emission maxima. When the concentration of Fe^{3+} increased to 15 equiv., the fluorescence intensity of **5** was reduced to 24% of the initial one. From the Stern–Volmer plot (the fluorescence quenching followed the Stern–Volmer equation) (12), host **5** formed 1:1 stoichiometry complex with Fe^{3+}, and the association constant was estimated 2.24×10^4.

Actually, quenching of electronically excited state of aromatic hydrocarbons by Fe^{3+} chelates is a known

© 2008 NRC Canada

Fig. 2. Fluorescence emission changes of **5** (1×10^{-5} mol/L) in DMF–MeOH (50:1 *v*/*v*) in the presence of 15×10^{-5} mol/L various metal ions (excitation at 305 nm).

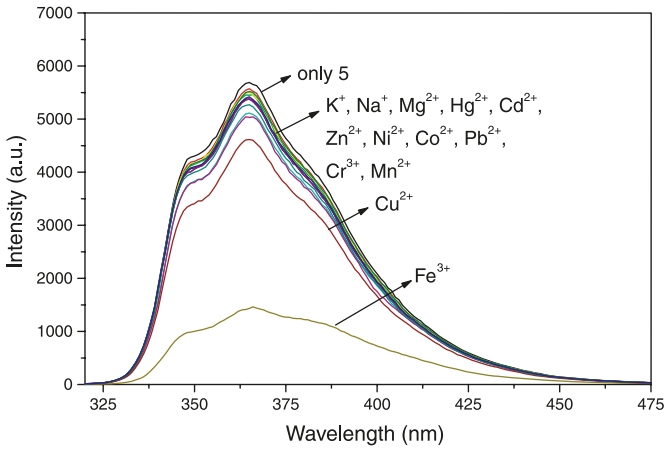

Fig. 3. Fluorescence emission spectra (excitation at 305 nm) of **5** (1×10^{-5} mol/L) in DMF–MeOH (50:1 *v*/*v*) in the presence of $Fe(H_2O)_6Cl_3$. The concentration of Fe^{3+}: 0, 1.0, 2.0, 3.0, 4.0, 5.0, 6.0, 7.0, 8.0, 9.0, 10.0, 11.0, 12.0, 13.0, 14.0, and 15×10^{-5} mol/L. Inset: Stern–Volmer plot of the emission data.

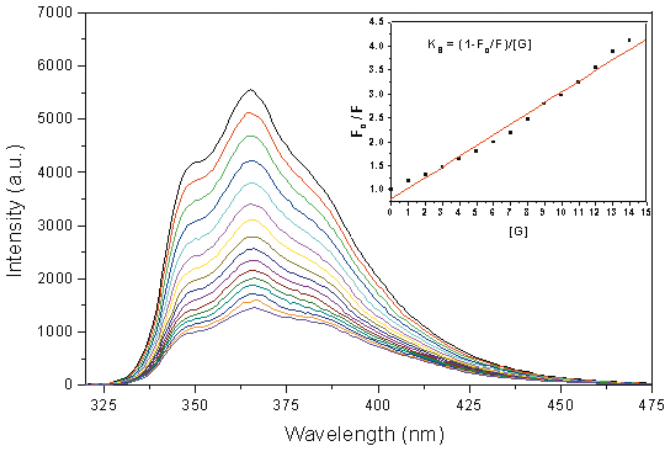

phenomenom that has been the subject of extensive investigations. It has been suggested that two main pathways could account for the efficient radiationless deactivation of the singlet excited state, i.e., electron transfer from the excited aromatic chromophore to the metal and (or) energy transfer from the excited aromatic chromophore to low-lying metal-centered energy states (13). Such processes could be particularly effective in the complex of **5** with Fe^{3+}, due probably to the fact that the chelated metal cation is held very close to two excited 2,5-diphenyl-furan chromophores. Additionally, because molecular clip **5** has different sidewalls but same binding properties compared with previously reported molecular clips (11), we may draw a conclusion that the two polarized carbonyl groups of the glycoluril ring play a crucial role in the recognition of Fe^{3+}.

Conclusion

A new fluorescent molecule clip **5** derived from diethoxycarbonyl glycoluril with two 2,5-diphenyl-furan sidewalls was designed and synthesized. Its binding properties, investigated by fluorescence spectroscopy, showed that it can selectively bind Fe^{3+} with fluorescence quenching.

Experimental

General

Melting point was determined on an XT4A Meltemp apparatus and is uncorrected. IR was recorded on a Perkin–Elmer PE–983 infrared spectrometer as KBr pellets with absorption in cm^{-1}. NMR was recorded in $CDCl_3$ on a Varian Mercury 400 spectrometer. MS was measured on a Finnigan Trace MS spectrometer. Fluorescence spectra were determined on a Hitachi F-4500.

Synthesis

Diethoxycarbonyl glycoluril **3** (14) and 3,4-bis-bromomethyl-2,5-diphenyl-furan **4** (15) were synthesized according to the previously reported procedures.

Compound **3** (0.72 g, 2.5 mmol) was dissolved in anhyd. DMSO (50 mL) under N_2, and *t*-BuOK (1.12 g, 10.0 mol) was added. After stirring for 15 min, compound **4** (2.22 g, 5.5 mmol) was added in one portion, and stirring was continued for 3 h. The reaction mixture was poured into 0.1 N HCl (500 mL) and extracted with EtOAc (3×200 mL). The extracts were washed with brine (2×150 mL) and dried over anhyd. $MgSO_4$. After filtration and rotary evaporation, the residue was purified by flash chromatography (SiO_2, $CHCl_3$/MeOH, 50:1) to give compound **5** (0.31 g, 40%) as a white solid. Mp > 300 °C. IR (KBr, cm^{-1}): 3059, 2983 w, 2898 w, 1758 s, 1722 s, 1653 w, 1464 s, 1428 s, 1255 s, 910 s, 764 s, 695 s. ^{1}H NMR (400 MHz, $CDCl_3$) δ: 7.75–7.74 (m, 8H), 7.50–7.35 (m, 8H), 7.32–7.31 (m, 4H), 5.28 (d, J = 16.0 Hz, 4H), 4.36 (d, J = 16.0 Hz, 4H), 4.28 (q, J = 7.2 Hz, 4H), 1.30 (t, J = 7.2 Hz, 6H). ^{13}C NMR (100 MHz, $CDCl_3$) δ: 165.5, 156.1, 148.7, 130.0, 128.8, 128.1, 126.8, 118.7, 81.3, 63.6, 37.4, 14.0. EI-MS *m*/*z*: 774.0, 778 $[M + 4H]^{4+}$.

X-ray crystallography

A single crystal suitable for X-ray crystallographic analysis was obtained from a slow evaporation of the dichloromethane and methanol solution. Crystallographic measurement of compound **5** was carried out using a Bruker SMART CCD diffractometer. The SMART (version 5.628) program was used for collecting data frames, and SAINT Plus (version 6.45) was used for integration of the intensity of reflections and scaling. SADABS was used for absorption correction (16). The structure was solved by direct methods using the program SHELXS-97 and refined by full-matrix least-squares against all F^2 data using Bruker SHELXTL (17). The phenyl ring (C34–C39) was found to be disordered over two orientations; the site-occupancy factor for the two orientations were refined giving 0.67(8) and 0.33(8) for the major and minor components, respectively. All non-H atoms

© 2008 NRC Canada

were refined anisotropically. Hydrogen atoms were constrained to the ideal geometries.[3]

Binding studies

The solvents for the fluorescence measurement were all of spectroscopic grade. Stock solutions of compound **5** was prepared by dissolution in DMF/MeOH (50:1, *v*/*v*) (1.0×10^{-5} mol/L). The solutions of metal ions were prepared from $Pb(NO_3)_2$ and the chlorides of K^+, Na^+, Mg^{2+}, Hg^{2+}, Cd^{2+}, Fe^{3+}, Cu^{2+}, Zn^{2+}, Co^{2+}, Ni^{2+}, Pb^{2+}, Cr^{3+}, and Mn^{2+}, respectively, and were dissolved in methanol (3.0×10^{-3} mol/L). Fluorescence titration was performed by filling 3 mL solution of **5** in a quartz cell of 1 cm optical path length and adding different stock solutions of cations into the quartz cell portionwise using a micro-syringe each time. Both excitation and emission bands were set at 5 nm.

Acknowledgments

We thank the Central China Normal University, the National Natural Science Foundation of China (Grant No. 20472022 and Grant No. 20672042) for financial support, and Dr Xiang-Gao Meng for the X-ray data collection.

References

1. A.P. de Silva, H.Q.N. Gunaratne, T. Gunnlaugsson, A.J.M. Huxley, C.P. McCoy, J.T. Rademacher, and T.E. Rice. Chem. Rev. **97**, 1515 (1997).
2. A.B. Descalzo, R. Martinez-Manez, R. Radeglia, K. Rurack, and J. Soto. J. Am. Chem. Soc. **125**, 3418 (2003).
3. C. Goze, G. Ulrich, L. Charbonniere, M. Cesario, T. Prange, and R. Ziessel. Chem. Eur. J. **9**, 3748 (2003).
4. B. Turfan and E.U. Akkaya. Org. Lett. **4**, 2857 (2002).
5. (*a*) A.E. Rowan, J.A.A.W. Elemans, and R.J.M. Nolte. Acc. Chem. Res. **32**, 995 (1999); (*b*) Q.S. Liu, S.L. Gong, Y. Ding, Y.Y. Chen, and X.J. Wu. Synlett, **13**, 2385 (2004); (*c*) Y.-T. Li, G.-D. Yin, H.-Z. Guo, B.-H. Zhou, A.-X. Wu. Synthesis, **17**, 2897 (2006); (*d*) B.H. Zhou, L.P. Cao, G.D. Yin, M. Gao, and A.X. Wu. Can. J. Chem. **85**, 586 (2007).
6. F. Hof, S.L. Craig, C. Nuckolls, and J. Rebek, Jr. Angew. Chem., Int. Ed. **41**, 1488 (2002).
7. J. Kang, J.-H. Jo, and S. In. Tetrahedron Lett. **45**, 5225 (2004).
8. M. Kölbel and F.M. Menger. Chem. Commun. 275 (2001).
9. (*a*) J. Kim, I.-S. Jung, S.-Y. Kim, E. Lee, J.-K. Kang, S. Sakamoto, K. Yamaguchi, and K. Kim. J. Am. Chem. Soc. **122**, 540 (2000); (*b*) A. Day, A.P. Arnold, R.J. Blanch, and B. Snushall. J. Org. Chem. **66**, 8094 (2001).
10. J. Kang and J. Kim. Tetrahedron Lett. **46**, 1759 (2005).
11. S.-L. Hu, N.-F. She, G.-D. Yin, H.-Z. Guo, A.-X. Wu, and C.-L.Yang. Tetrahedron Lett. **48**, 1591 (2007).
12. (*a*) T. Tsukube, H. Furuta, A. Odani, Y. Takeda, Y. Kudo, Y. Inoue, Y. Liu, H. Sakamoto, and K. Kimura. *In* Comprehensive supramolecular chemistry. *Edited by* J.-M. Lehn, J.L. Atwood, J.E.D. Davies, D.D. MacNicol, and F. Vögtle. Pergamon. New York. Vol. 8. 1996. p. 425; (*b*) R. Miao, Q.-Y. Zheng, C.-F. Chen, and Z.-T. Huang. Tetrahedron Lett. **46**, 2155 (2005).
13. (*a*) G.L. Hug, and B. Marciniak. J. Phys. Chem. **98**, 7523 (1994); (*b*) R.P. Foss, D.O. Cowan, and G.S. Hammond. J. Phys. Chem. **68**, 3747 (1964); (*c*) F. Wilkinson and A. Farmillo. J. Chem. Soc., Faraday Trans. **72**, 604 (1976).
14. C.A. Burnett, J. Logona, A. Wu, J.A. Shaw, D. Coady, J.C. Fettinger, A.I. Day, and L. Isaacs. Tetrahedron, **59**, 1961 (2003).
15. P.S. Bailey, S.S. Bath, W.F. Thomsen, H.H. Nellon, and E.E. Kawas. J. Org. Chem. **21**, 297 (1956).
16. (*a*) SHELXTL [computer program] (version 5.10); SMART [computer program] (version 5.054); (*b*) SAINT [computer program] (version 6.01). Bruker AXS Inc., Madison, WI. 1997.
17. G.M. Sheldrick. SHELXS-97 and SHELXL-97 [computer programs]. University of Göttingen, Germany. 1997.

[3] Supplementary data for this article are available on the journal Web site (canjchem.nrc.ca) or may be purchased from the Depository of Unpublished Data, Document Delivery, CISTI, National Research Council Canada, Ottawa, ON K1A 0R6, Canada. DUD 3758. For more information on obtaining material, refer to cisti-icist.nrc-cnrc.gc.ca/irm/unpub_e.shtml. CCDC 668714 contains the crystallographic data for this manuscript. These data can be obtained, free of charge, via www.ccdc.cam.ac.uk/conts/retrieving.html (Or from the Cambridge Crystallographic Data Centre, 12 Union Road, Cambridge CB2 1EZ, UK; fax +44 1223 336033; or deposit@ccdc.cam.ac.uk).

© 2008 NRC Canada

Localized-orbital locator (LOL) profiles of chemical bonding

Heiko Jacobsen

Abstract: We examine a recently introduced descriptor of chemical bonding, the localized-orbital locator (LOL), which is based on the kinetic-energy density (τ). Examples are presented for prototypical chemical bonds, such as single, double, and triple bonds, for bonding in transition metal complexes, for three-center two-electron bonds, as well as for hypervalent molecules. The topology of LOL is analyzed in terms of (3,–3) attractors (Γ). The influence of core electrons for chemical bonding is investigated, and a LOL-VSEPR (valence shell electron pair repulstion) relationship is established. Further, we compare LOL to the related electron localization function (ELF).

Key words: chemical bonding, kinetic-energy density, localized-electron locator, VSEPR theory.

Résumé : On a examiné un descripteur proposé récemment pour la liaison chimique, le positionnement d'une orbitale localizée (POL), qui est basée sur la densité d'énergie cinétique, τ. On présente des exemples de prototypes de liaisons chimiques, telles des liaisons simple, double et triples qui donnent lieu à des liaisons dans des complexes de métaux de transition, pour les liaisons à deux électrons et à trois centres ainsi que pour des molécules hypervalentes. La topologie du positionnement d'une orbitale localizée est analysée en fonction d'attracteurs (3,–3) (Γ). On a examiné l'influence des électrons à coeur sur la liaison chimique et on a établi une relation POL-VSEPR. On a de plus comparé le positionnement d'une orbitale localizée à la fonction apparentée de localization, ELF.

Mots-clés : liaison chimique, densité de l'énergie cinétique, positionnement d'un électron localizé, théorie VSEPR.

[Traduit par la Rédaction]

Introduction

The field of chemical bonding is in the midst of a renaissance, and the nature of the chemical bond remains an active field of ongoing chemical research. Although the "electronic structure revolution" initiated by the work of Lewis resulted in a picture of the chemical bond that by now has become a fundamental part of the freshmen chemistry curriculum, it is evident that many open questions remain in the quest for a unified and complete understanding of the true nature of the chemical bond (1). The complexity of this subject manifests itself in the ongoing discussion whether a description of chemical bonding is to be based on orbital or electron density concepts, molecular orbital theory not to be mistaken by the orbital approach and providing a common link between these two fundamentally different descriptions (2).

The success of density functional theory (DFT) of electronic structure (3) has provided new impetus for a density-based description of chemical bonding, and led to the development of new descriptors for old problems of chemical bonding, such as the electron localization function (ELF) introduced by Becke and Edgecombe (4). The problem of electron localization and delocalization constitutes one of the main aspects of the nature of the chemical bond. For density-based descriptions of chemical bonding, various partitioning schemes, mainly based on topological methods, have been proposed that address this very problem. Bader's quantum theory of atoms in molecules (QTAIM) analyzes the gradient field of the one-electron density and characterizes the nature of a chemical bond through a topology analysis of the Laplacian distribution $\nabla^2(\rho)$ of the underlying density, ρ (5). In particular, the topology of the function, L, where $L = -\nabla^2(\rho)$, provides valuable information about the nature of the chemical bond (6). An alternative approach has been proposed by Silvi and Savin, who work with ELF as potential function and partition the molecular space into basins of attractors that have a clear chemical meaning (7). Other recently developed descriptors for electron localization are the electron localizability indicator (ELI) (8, 9) and the localized-orbital locator (LOL) (10, 11), which is the main subject of the present work. Another descriptor that both in spirit and in form is related to LOL, is the local temperature, T (12). Local temperature, T, results from an analysis of thermodynamic elements of DFT, and it has been explored for whether local temperature can be used as a more fundamental descriptor of molecular electronic structure (13).

One aspect that makes density approaches towards chemical bonding particularly attractive is the direct relationship with experiment; X-ray charge densities not only reveal molecular structure but also contain information about chemical bonding through Laplacian analysis (14). Other bonding descriptors, such as LOL, are also accessible from experi-

Received 17 January2008. Accepted 7 March 7 2008. Published on the NRC Research Press Web site at canjchem.nrc.ca on 23 May 2008.

H. Jacobsen.[1] KemKom, Libellenweg 2, 25917 Leck, Nordfriesland, Germany (e-mail: jacobsen@kemkom.com).

[1]Present address: Tulane University, Department of Chemistry, New Orleans, LA 70118, USA.

 doi:10.1139/V08-052 © 2008 NRC Canada

mental electron densities. This requires constructing the kinetic-energy density directly from the experimentally determined electron density, which is achieved by using the second-order gradient expansion (15). Despite the fact that the gradient expansion diverges near the nuclei, an experimentally constructed LOL is accessible, since the regions around the nuclei may be omitted without significant loss of information (16).

Although much progress has been made in recent years in bond description based on experimental electron densities, the main conclusion that is drawn from experimental work is the same as obtained from theoretical studies: the characterization of the chemical bond is not a closed subject (17).

Schmider and Becke (11) have pointed out that LOL gives simple, recognizable patterns in classic chemical bonds, and they expressed their hope that "LOL will prove useful in interpreting the structures of exotic materials, and the classic examples of freshman chemistry texts as well" (10). Becke and Schmider have chosen graphical representations as the most evident way to analyze LOL. However, one has to take into consideration that even a three-dimensional function is not easy to visualize. In practice, one considers 2D-cuts, or plots of iso-surfaces, and often, several plots have to be shown to provide all the significant elements. Here, we use a topology analysis of LOL and characterize this function by determining the positions in space where LOL is maximal. We will briefly elucidate the theoretical background of our analysis before we present our results in more detail.

Theoretical background

The central property on which the localization descriptors ELF and LOL are built is the kinetic-energy density, τ:

$$[1] \qquad \tau = \frac{1}{2}\sum_i (\Delta\psi_i \cdot \Delta\psi_i^*)$$

We note that like other energy densities, the kinetic-energy density is not unique. Two important forms of the kinetic-energy density either depend on the Laplacian of the Kohn-Sham orbitals $-\tau^L-$, or are defined as being positive definite, $-\tau$ (18).

The kinetic energy plays a major role in the description of a chemical bond, since the driving force of covalent bonding is a lowering of the quantum kinetic-energy density by orbital sharing (19, 20). What might look like a violation of the virial theorem can be understood when the kinetic energy of a molecule is partitioned into *intra-atomic* and *inter-atomic* contributions. Upon formation of a covalent bond, the kinetic energy of motion normal to the bond direction increases accordingly; along the bond direction, however, the decrease in kinetic energy predominates. The increase in the kinetic energy is purely intra-atomic and has nothing to do with what happens in the bonding region where the decrease in the inter-atomic kinetic energy is the decisive effect (21).

Since the contributions to the kinetic energy from the bond regions usually decrease, it is desirable to use a measure of the local kinetic energy as an indicator of bond effects. The kinetic-energy density, τ, is quite suitable, although it has a few drawbacks. Kinetic-energy densities, τ, are usually monotonic for atoms, and the structural features of τ are less pronounced than one would wish. Regions with high charge density tend to dominate so strongly that salient features of bonding become invisible. To circumvent this problem, the kinetic-energy density, τ, is compared with some suitable reference value, τ_0. Both ELF and LOL take as a reference the homogeneous spin-neutral electron gas with electron density, ρ, and $\tau_0 = (3/10)\cdot(3\pi^2)^{2/3}\rho^{5/3}$. LOL analysis then defines the dimensionless variable, t:

$$[2] \qquad t = \tau_0/\tau$$

The ratio t is bounded by zero from below, but it is not bounded from above. To lower the semi-infinite range of the variable t, the localized-orbital locator, LOL, which is referred to as ν, is a measure of t in a mapping onto the finite range [0, 1]:

$$[3] \qquad \nu = \frac{t}{1+t} = \frac{\tau_0/\tau}{1+\tau_0/\tau} = \frac{1}{1+\tau_0/\tau}$$

Schmider and Becke (10, 11) have analyzed the localized-electron locator, ν, in much detail. We briefly summarize five important features of this bonding descriptor:

(*i*) LOL reveals electronic shell structure in a simple and clear manner.

(*ii*) The mapping $t \rightarrow \nu$ preserves topological features of t, since it is monotonically increasing. The value $t = 1$ corresponds to regions where the local kinetic energy of electrons is the same as for a uniform electron gas with the local density, ρ, and is mapped onto $\nu = 1/2$. Values of $\nu < 1/2$ indicate "fast" electrons that have a higher kinetic energy than expected from their local density. Regions with a larger value of ν are characterized by relatively "slow" electrons.

(*iii*) A covalent bond is expressed in ν as a local maximum between the bound centers. The $\nu = 1/2$ surface enclosing the maximum has an increasingly concave shape in multiple bonds.

(*iv*) The localized-orbital locator, ν, attains large values (above 1/2) in regions where the electron density is dominated by a single localized orbital.

(*v*) Lone electron pairs are resolved as local maxima in the center of a characteristically shaped $\nu = 1/2$ surface.

The chemical content of the localized-orbital locator, LOL, is similar to that of the electron localization function, ELF, which is also dependent on the kinetic-energy density, τ. However, whereas ELF is founded on consideration of the electron pair density, LOL simply recognizes that gradients of localized orbitals are maximized when localized orbitals overlap. Moreover, LOL has a simpler interpretation in terms of fast and slow electron regions, and always falls to zero asymptotically, whereas ELF sometimes does not.

Borrowing ideas from the topological analysis of electron charge density (5), we locate critical points and in particular (3,–3) attractors, Γ, in the gradient vector field of LOL. Each nucleus-position is associated with one attractor, Γ, but as we shall see, LOL also features attractors, Γ, between connected atoms and in molecular regions associated with lone pairs. We refer to attractors between connected atoms and in lone-pair regions as Γ_{CA} and Γ_{LP}, respectively. It is the Γ topology of LOL and its associated ν_Γ-values that serve as a

© 2008 NRC Canada

Fig. 1. Γ_{CA} and Γ_{LP} attractors and associated ν_Γ-values of (*a*) ethane (C_2H_6), (*b*) ethylene (C_2H_4), (*c*) acetylene (C_2H_2), (*d*) methanol (CH_3OH), (*e*) carbon dioxide (CO_2), and (*f*) carbon monoxide (CO).

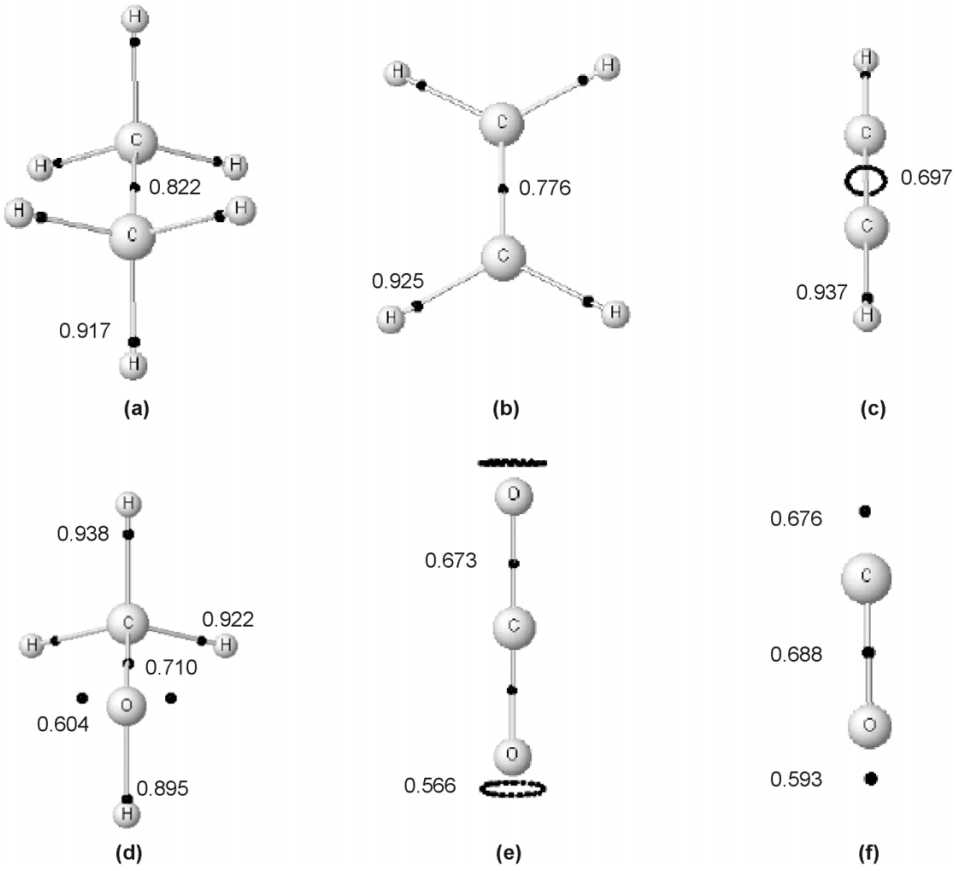

criterion to describe the nature of chemical bonding in molecular systems.

The topologies of *L* and ELF have been studied in much detail (6), and it was found that localized pairs of electrons, bonding or non-bonding, are not only evident in ELF but also in *L*, which is homeomorphic to ELF with few exceptions. It was further noted that critical points other than the (3,–3) attractors also carry valuable information about the nature of a chemical bond. However, a complete topology analysis in terms of *L* even for a small molecule such as water results in an extended picture of bewildering complexity (22). In the spirit of LOL, which "is a simpler function than ELF" (10), we restrict our analysis to the (3,–3) bonding attractors, Γ.

LOL profiles of chemical bonds

Schmider and Becke (10, 11) have analyzed the localized-electron locator for a variety of systems displaying prototypical single and multiple bonds, such as C_2H_4, N_2, and F_2, as well as for cases where the bonding situation is not prototypical and sometimes not straightforward, such as ClF_3, $Cr(CO)_6$, and B_4H_4. They base their analysis on an evaluation of contour line diagrams of LOL in representative molecular planes that contain a particular bond under investigation. Here, we shall construct LOL profiles based on Γ_{CA} and Γ_{LP} attractors. We note that in the figures to follow, bond lines between atoms are derived from standard geometric connectivity arguments and are not to be mistaken for bond paths as obtained from a topological analysis of the electron charge density.

Exemplary single, double, and triple bonds

We begin with examples of what are commonly considered prototypical single and multiple bonds and investigate the LOL profiles of ethane (C_2H_6), ethylene (C_2H_4), acetylene (C_2H_2), methanol (CH_3OH), carbon dioxide (CO_2), and carbon monoxide (CO). Locations and LOL values of Γ_{CA} and Γ_{LP} attractors are depicted in Fig. 1.

Ethane displays seven Γ_{CA} attractors, one for each C–H and C–C bond. The LOL values are above 0.8 and indicate that the bonds are dominated by a single localized orbital. The C=C double bond in ethylene is also characterized by the presence of one, and not two Γ_{CA} attractors. The LOL picture still shows one attractor for each bond, independent of the formal bond multiplicity. We note that the ν_Γ-value at Γ_{CA}(CC) is smaller for the double bond in C_2H_4 than it is for the single bond in C_2H_6. The picture obtained from our LOL analysis is in agreement with the common consensus that double bonds are more delocalized than single bonds. This trend continues when we turn to acetylene (C_2H_2) that formally has a C≡C triple bond. The ν_Γ-value at Γ_{CA}(CC) further decreases, and an increase in bond multiplicity leads to an increase in delocalized bonding character and thus to a decrease in ν_Γ. A similar trend has been found in an ELF analysis, and Bader et al. (6) report ELF values at (3,–3)

© 2008 NRC Canada

Fig. 2. Γ_{CA} and Γ_{LP} attractors and associated ν_Γ-values of the diatomic molecules (*a*) F_2, (*b*) Cl_2, (*c*) N_2, and (*d*) P_2.

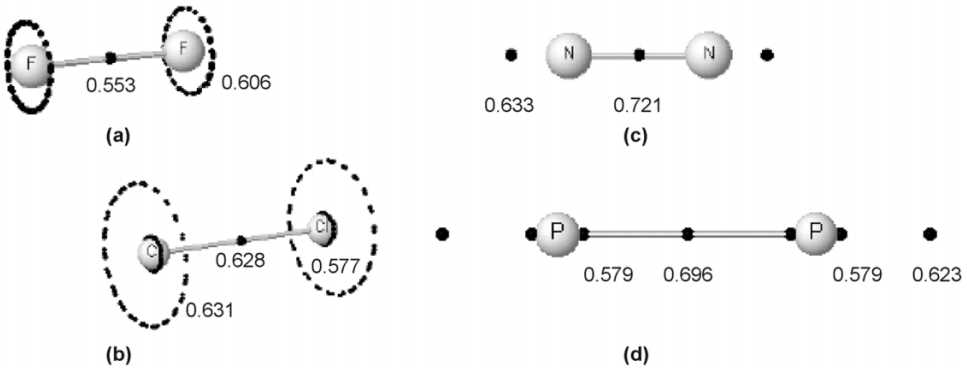

critical points for C–C single, double, and triple bonds as 0.9685 (C_2H_6), 0.9412 (C_2H_4), and 0.8906 (C_2H_2). ELF also contains a mapping of values onto the [0, 1] interval, and it seems that the LOL mapping results in clearer separation of ν_Γ for bonds of different multiplicities. We further note that for all systems Γ_{CA}(CH) is large with values above 0.9.

For the ELF function, it has been recognized that gradient field attractors can be circles and spheres if the system belongs to a continuous symmetry group (23). LOL bears similarities to ELF, and for acetylene, belonging to the continuous symmetry group $D_{\infty h}$, we see the appearance of a ring-shaped Γ_{CA}(CC) attractor, a connected set of (2,–2) critical points. We will further comment on ring-shape attractors at a later point in our discussion.

When we proceed to systems having a carbon-oxygen linkage, we now encounter atomic centers that have additional lone-pairs. The LOL profile of methanol not only displays, as expected, three Γ_{CA}(CH), one Γ_{CA}(CO), and one Γ_{CA}(OH) attractor, but it also shows two Γ_{LP} attractors around oxygen. We note for the bonding geometry around oxygen that the ν_Γ values for O-C and O-H connectors are larger that the ν_Γ values of the oxygen lone pairs. The bonding structure around oxygen is dominated by bonding domains rather than by lone pair domains. For carbon dioxide, we find that the formal C=O double bond again displays a smaller ν_Γ-value than the C–O single bond in CH_3OH. The oxygen lone pairs appear as ring-shaped Γ_{LP} attractors with ν_Γ-value smaller than the Γ_{CA}(CO) attractor.

Although carbon monoxide belongs to the continuous symmetry group, $C_{\infty v}$, no ring shape attractors are found in the LOL profile of CO. A further requirement for the appearance of a ring shape attractor is the presence of an inversion center that renders the two different atomic centers equivalent. The lone pair attractor at carbon displays a larger ν_Γ-value (0.676) than the lone pair attractor at oxygen (0.573) and is further separated from the C-nucleus (d = 100 pm) than its counterpart is separated from the O-nucleus (d = 76 pm). This observation is consistent with the dipole moment of CO with its negative end on the carbon atom.

We note that describing the electronic structure and the nature of the chemical bond of carbon monoxide is not a trivial task because of its unusual chemical and physical properties. Frenking et al. (24) have presented a detailed bonding analysis of CO as "an exercise in modern chemical bonding theory". The authors use an evaluation of the graphical representation of the Laplacian distribution, $-L$, to illustrate some physical properties of CO. The LOL-profile of CO faithfully recovers the analysis of Frenking et al. (24), and puts it on a more quantitative basis.

Atomic shells and chemical bonds

The localized-orbital locator does reflect atomic shell structure, similar to the electron localization function. This feature is partially recovered in the LOL profile of molecules, and we discuss the diatomic molecules F_2, Cl_2, N_2, and P_2 as illustrative examples. Γ_{CA} and Γ_{LP} attractors are depicted in Fig. 2.

For F_2, besides attractors found at the position of the nuclei, we have one valence shell bonding attractor and two ring shaped lone pair attractors. For Cl_2, which contains atoms with electron occupancy in the K, L, and M shells, we see one additional ring shape core attractor around each chlorine center. Similar observations are made when comparing the LOL profiles of N_2 and P_2. For dinitrogen, we find one valence shell Γ_{CA} attractor and two valence shell Γ_{LP} attractors. For diphosphorus, the extended electronic core structure manifests itself in two additional attractors located in close vicinity to each phosphorus atom.

Although the dinitrogen molecule is of $D_{\infty h}$ symmetry, only one Γ_{CA}(NN) single point attractor is found, and not a ring-shaped Γ_{CA}(NN) attractor as one might have expected in comparison to the isoelectronic and isosymmetric HCCH molecule. Similar observations have been made in an analysis of ELF, and with reference to N_2 it was noted that a "disturbing feature is that sometimes, when one would expect separated maxima, just a single maximum appears" (25). However, this somewhat unexpected result can be understood if one considers the fact that the LOL profile of a chemical bond reflects to a major part the character of the highest energy orbital that contributes to that particular bond. The ground state valence configuration of N_2 is $(2\sigma_g^+)^2(2\sigma_u^+)^2(1\pi_g)^4(3\sigma_u^+)^2$, and the structure of LOL is dominated by the HOMO, a single σ_g^+ orbital that extends along the atom-connecting line, and that gives rise to the presence of one single Γ_{CA}(NN) attractor. On the other hand, for acetylene, the valence shell configuration is $(2\sigma_g^+)^2(2\sigma_u^+)^2(3\sigma_g^+)^2\ (1\pi_u)^4$. The HOMO consists of a set of two degenerated π_u orbitals that extend perpendicular to the C-C connecting line and merge together due to the presence of the C_∞-symmetry axis, therefore giving rise to a ring-shaped Γ_{CA}(CC) attractor.

© 2008 NRC Canada

Fig. 3. Γ_{CA} and Γ_{LP} attractors and associated ν_Γ-values of (*a*) chlorine trifluoride, (*b*) tetraborane(4), and (*c*) chromium hexacarbonyl.

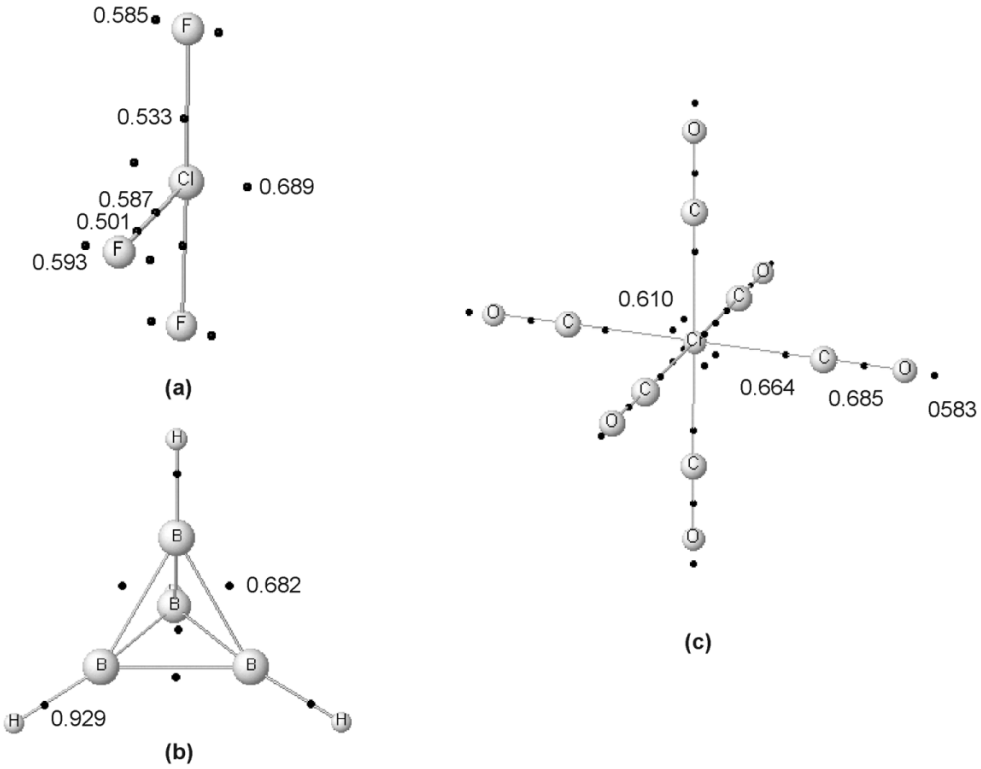

Non-prototypical bonds

Schmider and Becke (11) have presented a LOL analysis for a set of molecules where the bonding situation is not prototypical and sometimes not straightforward. They mainly analyzed LOL via its graphical representation. Here, we select three representative examples out of their set of test molecules, namely ClF_3, B_4H_4, and $Cr(CO)_6$, and examine LOL in terms of Γ attractors. LOL profiles for these molecules are shown in Fig. 3.

Chlorine trifluoride (ClF_3) is often chosen as representative example for hypervalency. We point out that the concept of hypervalency in connection with the octet rule is often misunderstood and misinterpreted (26). All that can safely be attributed to a hypervalent molecule is the fact that it contains an atom forming more than four electron pair bonds, and that the bonds in hypervalent molecules are very similar to those in corresponding non-hypervalent molecules (27). To remove any connection to the nature of the chemical bond, it had been suggested to use the term hypercoordinate, rather than hypervalent, since this provided an empirical characterization of their experimentally observed molecular structures without the necessity of having to endorse a particular view concerning the theoretical description of the chemical nature of a hypervalent bond (28).

The LOL profile of hypercoordinated ClF_3 displays three Γ_{CA}(ClF) attractors. In comparison to regular single and multiple bonds as discussed before, these attractors show fairly small ν_Γ-values. Around each atom, two additional Γ_{LP} attractors are found. The ν_Γ-values of the lone pair attractors, and in particular those of Γ_{LP} around chlorine are larger than those of the Γ_{CA} attractors. Thus, the bonding structure in ClF_3 is dominated by lone pair domains rather than by bonding domains. Distinctive is the fact that Γ_{LP} attractors have larger ν_Γ-values than Γ_{CA} attractors. This, is not a property of hypervalent molecules only, but is related to the nature of the particular bonds present in a hypercoordinated molecule. It does, however, indicate the potential for a coordination sphere expansion beyond four electron groups.

Schmider and Becke (10) have noted before that the localized-electron locator leads to a bonding picture that reflects the basic rules embodied in the valence shell electron pair repulsion (VSEPR) model of molecular geometry. The present study corroborates this result, and for ClF_3 we find a faithful mapping of the Γ_{CA} and Γ_{LP} attractors with the number, relative size, and angular orientation of the bonded and non-bonded electron pair domains assumed in VSEPR (29). Furthermore, the dominance of lone pairs is reflected by the fact that Γ_{LP} attractors have larger ν_Γ-values than Γ_{CA} attractors. We will further explore the LOL-VSEPR relationship in the next section.

Boranes comprise a large group of compounds with the generic formulae of B_xH_y and contain bonds that are characterized by a deficiency of electrons. Thus, the bonding in boranes has stipulated a wide variety of theoretical studies, including an ELF analysis of *closo*-boron clusters of the type B_4X_4 and $B_6X_6^{2-}$ (30). Schmider and Becke (11) have selected B_4H_4 as the simplest representative of an E-E-E three-center two-electron bond, which is a structural element required to explain the existence of most of the closo clusters. The LOL-profile faithfully represents the presence of B-B-B three-center two-electron bonds. Four attractors Γ are located substantially outside the central boron tetrahedron on top of the center of the triangular faces.

For chromium hexacarbonyl as representative example of molecules with metal-ligand bonds, Becke and Schmider (11) note that the LOL picture of $Cr(CO)_6$ is relatively clear

© 2008 NRC Canada

Fig. 4. Γ_{CA} and Γ_{LP} attractors and associated ν_Γ-values of (*a*) SH_2, (*b*) SF_2, (*c*) SF_4, and (*d*) SH_4.

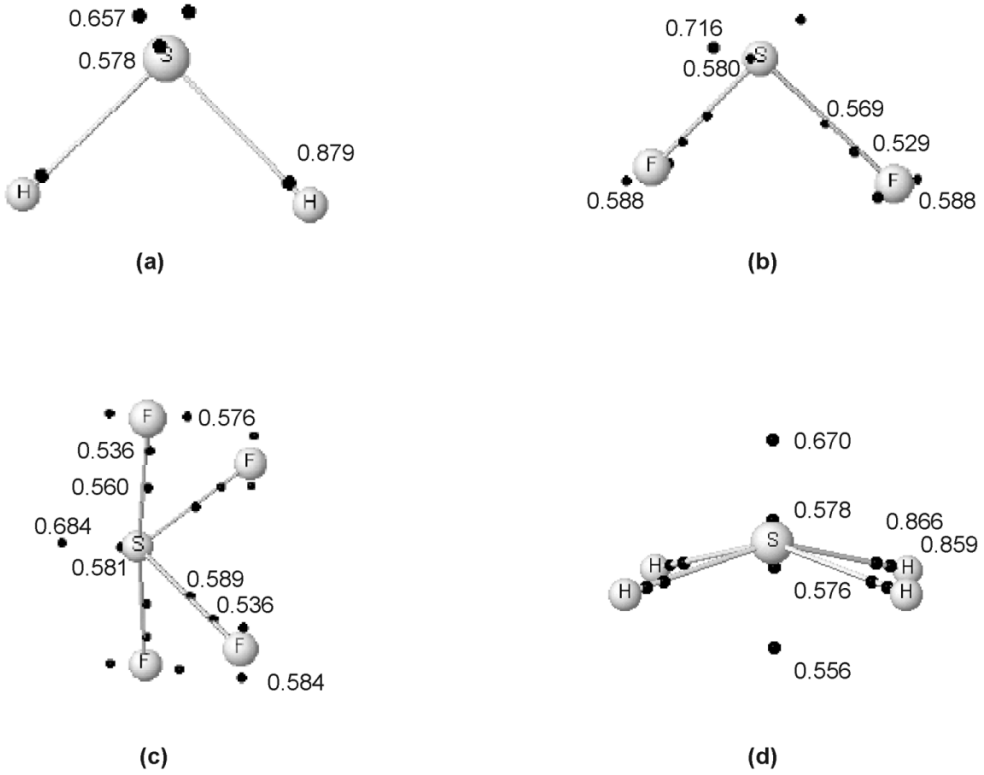

and suggests a ''closed-shell" picture of metal–ligand bonding. The carbonyl groups point their carbon lone pair towards the metal atom but a significant localization-deformation in that direction does not occur. They point out that "the lone-pair region is rather somewhat thinner compared to the free ligand" and that "in the vicinity of the chromium atom there are local maxima on the C_3-symmetry axes of the molecule that point towards the triangular faces of the molecular octahedron", which "should be considered as belonging to the core region". The Γ-attractor profile for $Cr(CO)_6$ is consistent with this analysis. The $\Gamma_{LP}(C)$ attractor is 56 pm away from the carbon atom, compared to 53 pm for the free ligand. The ν_Γ-value decreases from 0.676 for free CO to 0.664 in the bonded ligand. We further see an octet of Γ_{LP} attractors around chromium located on the C_3-symmetry axes. These attractors are 40 pm away from the metal center, which is the same separation as reported by Schmider and Becke (11) for local maxima in vicinity of the transition metal center.

LOL, core electrons, and VSEPR

A comparison of sulfur fluorides with the corresponding hydrogen sulfides demonstrates the importance of core electrons for chemical bonding and elucidates the LOL-VSEPR relationship. LOL profiles of SH_2, SF_2, SF_4, and SH_4 are depicted in Fig. 4.

For SH_2, we find two $\Gamma_{CA}(SH)$ and two $\Gamma_{LP}(S)$ attractors. We note that the ν_Γ-value for the bond attractors is larger than that for the lone pair attractors; the electronic structure of SH_2 is dominated by bond pairs, rather than lone pairs. In addition, we find two core attractors Γ_{core} around sulfur due to its extended electronic shell-structure. We note that the electronic core is accordingly profiled upon formation of a chemical bond. If we proceed to SF_2, we again find two $\Gamma_{CA}(SF)$ attractors, $\nu_\Gamma = 0.569$, and two $\Gamma_{LP}(S)$ attractors, $\nu_\Gamma = 0.716$. In addition, we see lone pair attractors around F, as well as core attractors. Also, for sulfur, $\Gamma_{core}(SH_2)$ and $\Gamma_{core}(SF_2)$ are of similar size. What is important is the fact that for SF_2 the ν_Γ-value for the lone pair attractors is larger than that for the bond attractors, and the electronic structure of SF_2 is dominated by lone pair domains rather than bond pair domains. A similar picture is found for SF_4; the dominant attractor around sulfur again is the lone pair attractor $\Gamma_{LP}(S)$ with $\nu_\Gamma = 0.716$.

Hydrogen does not possess an electronic core, and as a consequence its nucleus is located inside the bond region of any X–H bond. The $\Gamma_{CA}(XH)$ bond maximum is close to the H atom and might even merge with the nucleus position. The absence of an electronic core at hydrogen renders X–H bonds highly localized, and in SH_2 for example, the degree of localization measured by LOL is larger than any lone pair localization around sulfur.

The importance of core orbitals for a bond description based on descriptors of electron localization has been recognized before. For example, the electron localization function, ELF, shows too-high values when computed from valence densities only instead of using the total density (31), and for transition metal systems the ELF analysis needs to involve the atomic core regions as well to reveal a more detailed insight into the bonding situation (32).

The recognition that bonds towards the coreless H are especially localized also has structural consequences. It has been known for a long time that SH_4, a hypothetical molecule, the existence of which remains subject of theoretical

© 2008 NRC Canada

investigations (33), does not adapt a C_{2v} see-saw structure as predicted by VSEPR theory, but rather possesses a C_{4v}-geometry (34), Marsden and Smart (35) have offered an explanation for the origin of the unusual C_{4v}-structure predicted for SH_4 based on atomic charge arguments. Here, we suggest an explanation based on LOL values and VESPR theory.

The valence shell electron pair repulsion (VSEPR) model has for many years provided a useful basis for understanding and rationalizing molecular geometry and has gained widespread acceptance as a pedagogical tool. In its original formulation, the fundamental rule states that pairs of electrons in a valence shell adopt an arrangement that maximizes their distance apart (36). A recent extended version uses the concept of electron domains, the space occupied by valence shell electrons or electron pairs, and places emphasis on the relative sizes and shapes of these domains (27). It has been noted that the topologies of ELF and *L* exhibit a remarkable correspondence with the number and arrangement of the localized electron domains assumed in the VSEPR model of molecular geometry (6), and Schmider and Becke (10, 11) have shown that the same holds true for LOL as well.

VESPR geometries are derived from the realization that pairs of electrons tend to occupy positions in space that minimize repulsions and maximize the distance of separation between them. Electron groups are classified as lone pairs (lp) and bond pairs (bp), and it is generally assumed that lone pairs occupy more space than bonding electron pairs, and that the electron pair repulsion decreases as lp←lp > lp←bp > bp←bp.

We propose that the ν_Γ-value of (3,–3) Γ-attractors can be taken as a measure for the spatial requirement and repulsion potential of an electron group. An intial geometry is constructed according to the points-on-a-sphere model of VSEPR, in which all electron groups are treated equivalent. Then, geometries are determined based on ν_Γ-value of (3,–3) Γ-attractors.

Both SF_4 and SH_4 have five electron domains and therefore take on a geometry derived from a trigonal bipyramid. As we noted before, the Γ_{LP}-attractor of SF_4 has the largest ν_Γ–value, and the lone pair is therefore located in an equatorial position. As a result, SF_4 adopts a C_{2v} disphenoidal geometry. For SH_4, the Γ_{LP}-attractor has the smallest ν_Γ-value, and the lone pair therefore initially adopts an axial position. The remaining four Γ_{CA}-attractors rearrange into a geometry in which the distance of separation between them is maximized. As a consequence, SH_4 takes on a C_{4v}-structure, derived from a square pyramidal arrangement of electron groups around sulfur. This structural rearrangement further creates an additional vacant coordination space for additional electron localization.

The positions of the Γ attractors in SF_4 and SH_4 provide support for our arguments (compare Figs. 4*c* and 4*d*). We also note that SH_4 displays a second Γ_{LP}-attractor in opposite position to the dominant lone-pair domain, thus utilizing the additional coordination space for electron localization.

We conclude this section with a brief comparison of ELF and LOL-values. Bader et al. (6) have reported ELF values for SH_2, SF_2, and SF_4, and their results together with present data are compiled in Table 1.

Table 1. Values of (3,–3) attractors in ELF and LOL for SH_2, SF_2, and SF_4, and radial distances, r_{ELF} and r_{LOL}, to the S atom (in pm).

Molecule	ELF	r_{ELF}	LOL	r_{LOL}	Type[a]
SH_2	0.9694	99	0.657	77	*n*
	0.9998	134	0.879	117	*b*
SF_2	—[b]	—[b]	0.716	75	*n*
	0.8178	99	0.569	83	*b*
SF_4	0.9961	95	0.684	74	*n*
	0.8348	87	0.589	80	*b* to F_e
	0.8178	111	0.560	82	*b* to F_a

[a]*n* denotes a non-bonded maximum, *b* a bonded one.
[b]No values reported in ref. 6.

The ELF and LOL analyses give qualitatively comparable results. SH_2 shows larger attractor values for bonding domains as opposed to sulfur fluorides. Lone pairs are in closer vicinity to the sulfur center than bond pairs. However, the LOL values are spread out more in the [0, 1] array of values, and ν_Γ-values for different type of electron groups are better separated in LOL than they are in ELF. The localized-orbital locator, LOL, seems to provide a clearer and more decisive picture than the electron localization function, ELF.

Computational details

Density functional calculations have been carried out with the Gaussian03 system of programs (41). The molecular density used in topology analyses was obtained from pure density functional calculations within the generalized gradient approximation as proposed by Perdew, Burke, and Ernzerhof, PBE (42). A valence triple-ζ basis augmented by one polarization function (TZVP) was used for all atoms (43). Densities used in topology analyses were taken from optimized gas-phase structures. Topological analyses of molecular electron densities employed a modified version of the program MORPHY (44). 3-D pictures were generated using the graphical package Jmol (45).

Conclusion

Our analysis of molecules with prototypical as well as unusual chemical bonds has shown that the localized-orbital locator, LOL, represents a conceptually simple, but efficient tool in characterizing a chemical bond. In particular, the analysis of LOL in terms of (3,–3) Γ-attractors provides an easy access to meaningful bond profiles. The chemical content of LOL is similar to that of the electron localization function, ELF, but a comparison of both methods suggests that the picture of a chemical bond generated by LOL is more decisive and easier to interpret. The topology of LOL clearly displays the locations of the classic VSEPR electronic groups. LOL nicely illustrates the role of core orbitals, which are an essential element of chemical bonding. Not only does LOL faithfully represent atomic shell structure, it further emphasizes the influence of core electrons on valence localization.

Extracting chemical information from molecular electron density contributions continues to be a main topic in bond-

© 2008 NRC Canada

ing analysis, and more rigorous but also more computational demanding model based on maximum probability domains are currently being developed (37, 38). Compared to more sophisticates approaches, LOL has the advantage of being more accessible not only with respect to the computational approach but also with respect to an intuitive interpretation of the results.

Besides the exemplary studies of Schmider and Becke (10, 11), only a few applications of LOL to molecular problems of chemical bonding and chemical reactivity have appeared in the literature (39, 40), which all utilize graphical representations of LOL. The location of Γ attractors and the evaluation of ν_Γ-values puts the LOL analysis on quantitative basis and facilitates the clear formulation of the nature of a chemical bond. It is hoped that the present work will promote the recognition of the localized-electron locator as a valuable tool in the analysis of chemical bonding.

Acknowledgements

KemKom acknowledges Professor L. Cavallo for granting access to the MoLNaC Computing Facilities at Dipartimento di Chimica, Università di Salerno.

References

1. G. Frenking and S. Shaik. J. Comput. Chem. **28**, 1 (2007).
2. F. Cortés-Guzmán and R.F.W. Bader. Coord. Chem. Rev. **249**, 633 (2005).
3. W. Kohn, A.D. Becke, and R.G. Parr. J. Phys. Chem. **100**, 12974 (1996).
4. A.D. Becke and K.E. Edgecombe. J. Chem. Phys. **92**, 5397 (1990).
5. R.F.W. Bader. Atoms in molecules: A quantum theory. Oxford University Press, Oxford. 1990.
6. R.F.W. Bader, S. Johnson, T.-H. Tang, and P.L.A. Popelier. J. Phys. Chem. **100**, 15398 (1996).
7. B. Silvi and A. Savin. Nature (London), **371**, 683 (1994).
8. M. Kohout. Int. J. Quantum Chem. **97**, 651 (2004).
9. M. Kohout. Faraday Discuss. **135**, 43 (2007).
10. H.L. Schmider and A.D. Becke. J. Mol. Struct: THEOCHEM, **527**, 51 (2000).
11. H.L. Schmider and A.D. Becke. J. Chem. Phys. **116**, 3184 (2002).
12. P.W. Ayers, R.G. Parr, and A. Nagy. Int. J. Quantum Chem. **90**, 309 (2002).
13. P.W. Ayers and A. Nagy. J. Chem. Phys. **126**, 144108 (2007).
14. T.S. Koritsanszky and P. Coppens. Chem. Rev. **101**, 1583 (2001).
15. V. Tsirelson. Acta Crystallogr. **B58**, 632 (2002).
16. V. Tsirelson and A. Stash. Acta Crystallogr. **B58**, 780 (2002).
17. P. Coppens. Angew. Chem. Int. Ed. **44**, 6810 (2005).
18. J.P. Perdew and L.A. Constantin. Phys. Rev. B, **75**, 155109 (2007).
19. T. Bitter, K. Ruedenberg, and W.H.E. Schwarz. J. Comput. Chem. **28**, 411 (2007).
20. K. Ruedenberg and M.W. Schmidt. J. Comput. Chem. **28**, 391 (2007).
21. W. Kutzelnigg. Angew. Chem. Int. Ed. Engl. **12**, 546 (1973).
22. P.L.A. Popelier. Coord. Chem. Rev. **197**, 169 (2000).
23. S. Noury, F. Colonna, A. Savin, and B. Silvi. J. Mol. Struct. **450**, 59 (1998).
24 G. Frenking, D. Loschen, A. Krapp, S. Fau, and S.H. Strauss. Comput. Chem. **28**, 117 (2007).
25. A. Savin. J. Mol. Struct: THEOCHEM, **727**, 127 (2005).
26. R.J. Gillespie and B. Silvi. Coord. Chem. Rev. **233**, 53 (2002).
27. S. Noury, B. Silvi, and R.J. Gillespie. Inorg. Chem. **41**, 2164 (2002).
28. W.B. Jensen. J. Chem. Educ. **83**, 1751 (2006).
29. R.J. Gillespie and E.A. Robinson. Angew. Chem. Int. Ed. Engl. **35**, 495 (1996).
30. A. Burkhardt, U. Wedig, H.G. von Schnering, and A. Savin. Z. Anorg. Allg. Chem. **619**, 437 (1993).
31. M. Kohout and A. Savin. J. Comput. Chem. **18**, 1431 (1997).
32. M. Kohout, F.R. Wagner, and Y. Grin. Theor. Chem. Acc. **108**, 150 (2002).
33. A. Wittkopp, M. Prall, P.R. Schreiner, and H.F. Schaefer. Phys. Chem. Chem. Phys. **2**, 2239 (2000).
34. Y. Yoshioka, J.D. Goddard, and H.F. Schaefer. J. Chem. Phys. **74**, 1855 (1981).
35. C.J. Marsden and B.A. Smart. Aust. J. Chem. **47**, 1431 (1994).
36. R.J. Gillespie. Molecular geometry. Van Nostrand Reinhold, London. 1972.
37. E. Cances, R. Keriven, F. Lodier, and A. Savin. Theor. Chem. Acc. **111**, 373 (2004).
38. A. Scemama, M. Caffarel, and A. Savin. J. Comput. Chem. **28**, 442 (2007).
39. H. Jacobsen and J.P. Donahue. Can. J. Chem. **84**, 1567 (2006).
40. H. Jacobsen and M.J. Fink. Inorg. Chim. Acta, **360**, 3511 (2007).
41. M.J. Frisch, G.W. Trucks, H.B. Schlegel, G.E. Scuseria, M.A. Robb, J.R. Cheeseman, J.A. Montgomery, Jr., T. Vreven, K.N. Kudin, J.C. Burant, J.M. Millam, S.S. Iyengar, J. Tomasi, V. Barone, B. Mennucci, M. Cossi, G. Scalmani, N. Rega, G.A. Petersson, H. Nakatsuji, M. Hada, M. Ehara, K. Toyota, R. Fukuda, J. Hasegawa, M. Ishida, T. Nakajima, Y. Honda, O. Kitao, H. Nakai, M. Klene, X. Li, J.E. Knox, H.P. Hratchian, J.B. Cross, V. Bakken, C. Adamo, J. Jaramillo, R. Gomperts, R.E. Stratmann, O. Yazyev, A.J. Austin, R. Cammi, C. Pomelli, J.W. Ochterski, P.Y. Ayala, K. Morokuma, G.A. Voth, P. Salvador, J.J. Dannenberg, V.G. Zakrzewski, S. Dapprich, A.D. Daniels, M.C. Strain, O. Farkas, D.K. Malick, A.D. Rabuck, K. Raghavachari, J.B. Foresman, J.V. Ortiz, Q. Cui, A.G. Baboul, S. Clifford, J. Cioslowski, B.B. Stefanov, G. Liu, A. Liashenko, P. Piskorz, I. Komaromi, R.L. Martin, D.J. Fox, T. Keith, M.A. Al-Laham, C.Y. Peng, A. Nanayakkara, M. Challacombe, P.M.W. Gill, B. Johnson, W. Chen, M.W. Wong, C. Gonzalez, and J.A. Pople. Gaussian 03 [computer program]. Revision C.02. Gaussian, Inc., Wallingford, Conn. 2004.
42. J.P. Perdew, K. Burke, and M. Ernzerhof. Phys. Rev. Lett. **77**, 3865 (1996).
43. A. Schäfer, C. Huber, and R. Ahlrichs. J. Chem. Phys. **100**, 5829 (1994).
44. P.L.A. Popelier. Comput. Phys. Commun. **93**, 212 (1996).
45. Jmol: an open-source Java viewer for chemical structures in 3D. Available from http://www.jmol.org.

© 2008 NRC Canada

Titania encapsulation of flat gold nanoparticles — A simple route to Au@TiO_2 core-shell nanosheets

Jeffrey J. McDowell, J. Ian McKelvey, Laura A. Richard, and Jeffrey T. Banks

Abstract: We report the attachment of a uniform coating of a thin layer of amorphous TiO_2 to flat gold nanoparticles via a simple sol–gel process. Coatings of variable thickness ranging from 5 to 100 nm have been produced. Activation of the Au particles was unnecessary. However, the ability to coat the flat gold nanoparticles was dependent on the method used for their synthesis. In addition, the amorphous TiO_2 shell was hydrothermally treated to induce crystallization to the anatase polymorph. The desired nanocrystalline anatase morphology was obtained by heating in water at 70 °C for 1 week. A similar result was also obtained when the material was heated to 130 °C for 5 min in a microwave reactor. These new Au@TiO_2 nanosheets were characterized by TEM, EDX, and SAED.

Key words: core-shell, titanium dioxide, anisotropic nanoparticles, semiconductor thin films, nanocomposite material.

Résumé : Faisant appel à un processus simple sol–gel, on a fixé une couche mince uniforme de TiO_2 amorphe à des nanoparticules planes d'or. On a produit des couches dont l'épaisseur varie de 5 à 100 nm. On a trouvé qu'il n'est pas nécessaire d'activer les particules d'or. Toutefois, l'habilité à fixer des nanoparticules planes d'or dépend de la méthode utilisée pour leur synthèse. De plus, on a traité la coquille de TiO_2 d'une façon hydrothermique afin d'induire la cristallisation sur le polymorphe d'anatase. On a obtenu la morphologie désirée d'anatase nanocristalline par chauffage dans l'eau à 70 °C, pendant une semaine. On a aussi obtenu des résultats semblables par chauffage à 130 °C, pendant cinq minutes, dans un réacteur à microondes. On a fait appel aux techniques de TEM, EDX et SAED pour caractériser ces nouveaux feuillets de Au@TiO_2.

Mots-clés : couche à coeur, dioxyde de titane, nanoparticules anisotropes, films minces semiconducteurs, matériaux nanocomposites.

[Traduit par la Rédaction]

Introduction

Nanosized metals, semiconductors, and dielectrics have become an intense area of research over the past few decades because of their attractive size- and shape-dependant properties. More recently, there has been significant interest in nanomaterials made from two or more distinctly different constituents. The properties of such nanocomposite materials depend not only on the properties of their individual components but also on their morphology and interfacial characteristics. Because of this, modern materials chemists seek the ability to design, fabricate, and manipulate nanostructured systems to achieve well-tailored chemical and physical characteristics for advanced applications. The more naive among us may believe that this will eventually lead to Drexler's chimerical utopia where molecular assemblers reign supreme (1). However, serious proponents of nanotechnology must remain realistic, and it is far more likely that an arsenal of synthetic approaches will be required to further develop this area of contemporary science. Indeed, much progress has already been made. For example, an abundance of wet chemical procedures have been developed to produce a variety of nanoparticles with varied composition and shape (2–11). Also, nanoparticles have been further modified by encapsulation in another different material and represent a class of nanocomposite materials now known as core-shell nanoparticles (12–18). The core-shell motif is a popular architecture for metal – metal oxide nanocomposite materials, and potential applications range from biosensors (19) to nanocapacitors (20). Metal oxide shells are typically used to act as protective sheaths for metal nanoparticles (18, 21–24). One of the more popular desired outputs for these materials is as a durable and photoactive catalyst (25–32).

The discovery of a material or system of materials with rectification efficiencies approaching that of photosystems I and II is essential to the design of a catalyst with sufficient redox power for photoelectrolysis of water or carbon fixation by reduction of CO_2 to methanol. The products of such reactions are the focal point of two suggested alternative fuel economies (33). Charge separation is a fundamental requirement for effectively mimicking natural photosynthesis. However, following excitation of materials such as crystalline TiO_2, recombination of e^-/h^+ pairs is the most thermodynamically favoured pathway in the absence of molecules used to scavenge either photogenerated electrons or holes. It has been estimated that <5% of charges in these systems can actually be utilized to induce redox reactions at the interface (31). This is a problem inherent to all large-band-gap metal

Received 1 February 2008. Accepted 1 April 2008. Published on the NRC Research Press Web site at canjchem.nrc.ca on 27 May 2008.

J.J. McDowell, J.I. McKelvey, L.A. Richard, and J.T. Banks.[1] Department of Chemistry, University of New Brunswick, Fredericton, NB, Canada.

[1]Corresponding author (e-mail: jbanks@unb.ca).

 doi:10.1139/V08-064 © 2008 NRC Canada

oxides currently being explored as UV active photocatalysts. Incorporation of noble metal nanoparticles of Au, Ag, and Pt into semiconducting metal oxides has been shown to enhance photocatalytic activity (28, 34–36). Subramanian et al. (27) propose that the noble metals mediate the photocatalytic process by storing and shuttling photogenerated electrons from the semiconductor to an acceptor. Further work by Kamat and co-workers has shown that the surface plasmon resonance (SPR) band of an ethanol suspension of titanium dioxide coated silver nanoparticles ($Ag@TiO_2$) shifts from 460 to 420 nm upon UV irradiation (26). The authors suggest this is the result of Fermi level equilibration between the metal core and the metal oxide shell, which causes significant accumulation of electrons in the core. Ung et al. (37) have shown that the SPR absorption band of colloidal silver undergoes a blue shift when the electron density is increased. Perhaps the most interesting finding of Kamat is that the $Ag@TiO_2$ nanoparticles can maintain this charge separation in the absence of light until discharged by the addition of an appropriate oxidizing agent, such as thionine (26, 38). Core charging has also been observed by chemical reduction of $Au@SiO_2$ nanoparticles (39). These results suggest a mechanism that explains the enhanced photocatalytic efficiencies of metal–TiO_2 nanocomposite materials over conventional titania systems.

Conventional wisdom suggests that increasing catalyst surface area by decreasing particle size maximizes catalytic efficiency (40–42). However, for core-shell systems, one could speculate that the volume of the metal is important, since it acts as an electron reservoir that is needed to balance the positively charged shell of the polarized core-shell nanoparticle. If this were to be the case, it is likely that there would be a trade off between increased surface area and decreased core volume. Furthermore, it is not clear that the metal needs to be of nanoscale dimensions in every axis to perform as an electron sink. As mentioned above, there have been numerous studies on metal core@semiconductor shell systems with all three dimensions in the nano regime (i.e., 'spherical' nanoparticles). This has not been extended to systems that are constrained to the nanoscale in one (nanosheets) or two (nanowires) dimensions. To date, there have been several syntheses of metal@semiconductor nanowires reported (17, 19, 43–45). Very few examples of anisotropic core-shell particles can be found in the literature. One recent example of this type is the synthesis of SiO_2 coated Ag nanoprisms by Xue et al. (46).

Our aim is to synthesize novel anisotropic multicomponent nanoparticles through simple methods. A common feature of oxide-encapsulated metal nanoparticles is the requirement for an organic linking group between core and shell (15, 18, 19, 21, 46). We speculated that, in the case of sol–gel synthesis, a linking group should not be necessary, thereby increasing the simplicity of the route to complex nanoparticle structures. We report herein a simple sol–gel method for the encapsulation of flat gold nanoparticles (FGNPs) by amorphous titanium dioxide without the need for a linking agent. The foundation for the new particles presented here are flat gold nanoparticles. FGNPs provide a high surface area while being quite large (100 nm – 10 μm) in comparison with most nanoparticles. The single-crystalline nature of FGNPs and the ease of their synthesis makes them ideal candidates for functionalization. To date, there have been no examples of core-shell structures using FGNPs. This procedure allows good control over shell thickness for the $Au@TiO_2$ nanosheets. As well, subsequent hydrothermal reactions have been used to crystallize the amorphous sheath to the anatase polymorph of TiO_2.

Experimental section

Hydrogen tetrachloroaurate(III) trihydrate, titanium(IV) butoxide 97% (TnB), ethylene glycol (EG), aniline +99%, anhyd. ethanol, (3-mercaptopropyl)trimethoxy silane (MPTMS) 95%, and 1-dodecanethiol (DDSH) 98% were obtained from Sigma-Aldrich and were used without further purification with the exception of aniline. Aniline was twice distilled over zinc metal. The amphiphilic block copolymer Pluronic P123 ($EO_{20}PO_{70}EO_{20}$, M_n = 5800) was generously donated by BASF and used as received.

Synthesis of flat gold nanoparticles

The initial FGNPs were synthesized in Pluronic 123 hexagonal liquid crystals using a modified procedure described by Wang et al. (47). Typically, 10.3 g of Pluronic P123 was heated at 70 °C until completely liquefied. Then, 0.230 g of CTAB and 25 mL 0.03 mol/L $HAuCl_4$ were added with stirring. The mixture was left to cool and then covered with parafilm and kept in the dark for 3 days. The reaction mixture was taken up in ethanol and heated to dissolve the P123. Au nanosheets were collected by centrifugation and washed with ethanol.

The majority of FGNPs in this work were synthesized using a modification of the procedure described by Gu and coworkers (48). In a typical procedure, an initial 50 mL EG solution of 0.72 mmol/L $HAuCl_4 \cdot 3H_2O$ was heated in a water bath at 95 °C for 20 min with moderate stirring. Then, 0.72 mL of a 0.1 mol/L aniline EG solution was added slowly over 1 min, and the mixture was left without stirring at 95 °C for an additional 3 h. The final product was a metallic, golden precipitate suspended in a dark purple mother liquor. Allowing the solid to settle and decanting the excess liquid accomplished separation of the product plates from the liquid. Residual product was washed twice with ethanol to remove residual ethylene glycol.

A third set of FGNPs were made according to the procedure described by and Huang and co-workers (49).

SAM functionalization

FGNPs were suspended in 25 mL of 5 mmol/L of MPTMS or DDSH in anhyd. ethanol and stirred for 24 h. The nanosheets were then washed three times with copious amounts of anhyd. ethanol.

Synthesis of FGNP@TiO_2 particles

The procedure used to form the FGNP@TiO_2 particles began with a 20 mL suspension of previously synthesized gold nanosheets in anhyd. ethanol. In a typical experiment, TnB (neat) was added with rapid stirring to form a 0.3 to 5 mmol/L solution, followed by the addition of 0.275 mL of HPLC-grade H_2O. The suspension was allowed to stir for 1 h at room temperature. Over this period, the solution became cloudy white as TnB was hydrolyzed. The final prod-

© 2008 NRC Canada

uct was centrifuged multiple times and the mother liquor decanted to remove extraneous TiO_2 as a fine white suspension. Complete elimination of extraneous TiO_2 was impossible, but the majority of Au product was visibly isolated. The golden pellet obtained after centrifugation could be resuspended without signs of aggregation between particles. It should be noted that a 34 mmol/L TnB concentration was used to produce the sample that was cross-sectioned.

Hydrothermal crystallization

Au nanosheets coated with amorphous TiO_2 films (thickness ~30–40 nm) were suspended in HPLC-grade H_2O in a capped glass vial and placed in an oven heated to 70 °C for 1 week.

Microwave-induced hydrothermal crystallization

Au nanosheets coated with amorphous TiO_2 films (thickness ~30–40 nm) were suspended in HPLC-grade H_2O in a capped glass vial. The vial was placed in a CEM laboratory microwave, and the solution was heated to 130 °C for 5 min.

TEM analysis and cross sectioning

A diluted portion of the products in ethanol was dropped onto a 200 mesh copper grid. TEM images were obtained using a JEOL 2011 scanning transmission electron microscope operating at 200 kV and equipped with an EDAX (Genesis) energy dispersive X-ray system. To obtain cross-sections of FGNPs, the sample was dried and put into a mold with L R White resin and cured overnight at 60 °C. Embedded blocks were trimmed with a razor blade, a small block face area was necessary for cutting thin sections. The block was then sectioned using a Leica Ultramicrotome. The sections were floated onto water and collected on a 200 mesh copper grid. The section thickness achieved was in a range from 40 to 50 nm.

Results and discussion

During the past few years, several methods have been developed for the preparation of Au nanosheets (11, 47–54). They typically consist of single Au crystallites with triangular and truncated triangular geometries. Edge lengths have been reported from about 100 nm to several tens of microns. We chose sheets in the size range of ~1 to 5 μm on edge. The idea being that Au@TiO_2 nanosheets of this size would be more easily separated from colloidal titanium dioxide by centrifugation, while still having a core thickness of only a few tens of nanometers. FGNPs were made from P123 hexagonal liquid crystals, and results were similar to those described by Wang. (47). The sheets ranged from about 500 nm to 5 μm on edge with basal Au surfaces that were predominantly {111}, as indicated by the select area electron diffraction pattern (SAED). There was also a significant amount of nanoparticles that proved to be polyhedra with diameters of ~120 nm. It should be noted that there was a considerable amount of extraneous material associated with the Au particles, even after several ethanol washings. Energy dispersive X-ray spectrometry (EDX) of this material suggest it to be carbonaceous. Metal@semiconductor core-shell particles are usually made by activating the surface of the metal with a surfactant (15–18, 21, 26, 55, 56). However, encapsulation by direct precipitation of nanoparticles from a metal oxide sol has also been described in the literature (23, 32, 43). We first tried to encapsulate these FGNPs by suspending the as prepared sheets (i.e., without activation) in a titania sol as described in the Experimental section. This proved to be unsuccessful. Thiols are well-known to bind to gold surfaces, and MPTMS has been found to activate Au nanoparticles towards encapsulation by silica (15). As well, Dahanayaka et al. (57) have shown that alkanethiol SAMs readily form on FGNPs. We then exposed the FGNPs to a 5.0 mmol/L solution of MPTMS in anhyd. ethanol for 24 h prior to exposure to the titania sol. However, this also proved to be unsuccessful. We speculate that the carbonaceous material associated with the Au particles is unremoved P123 and blocks adhesion of the TiO_2 sol to the Au surface. If this is the case, it is seemingly tightly bound, since it could not be easily removed by washing nor displaced by thiols (vide supra).

Fig. 1. Representative FGNP (*a*) before modification and (*b*) coated with an amorphous TiO_2 film.

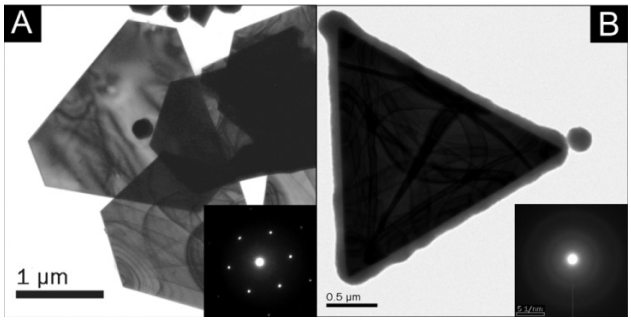

At this point, we decided to try a "cleaner" FGNP synthesis. The method described by Gu and co-workers proved to be straightforward and reliable (48). Simply, adding aniline to a heated ethylene glycol solution of hydrogen tetrachloroaurate produced large amounts of hexagonal plates. Figure 1*a* shows a typical TEM image of FGNPs produced by this method. Bending contours and transparency decorating the surface of the plates indicate reduced plate thickness. This reduced thickness was confirmed by cross-sectioning experiments (vide supra), and on average, sheets were ~40 nm thick. Lateral edge lengths typically ranged from 1 to 5 μm with basal Au surfaces that were predominantly {111}, as indicated by SAED pattern shown in the inset of Fig. 1*a*. A thin film of titanium dioxide via the sol–gel procedure easily encapsulated these sheets as can be seen in Fig. 1*b*. The surrounding light grey layer in Fig. 1*b* is comprised of TiO_2, as indicated by elemental analysis conducted via EDX (Fig. 2). EDX analysis suggested this layer covered the entire surface of the Au sheet and gave strong Ti and O peaks for X-rays collected at any spot over the Au surface. SAED taken on regions of the film show that TiO_2 is amorphous, as indicated by the lack of definition in the diffuse ring pattern (inset, Fig. 1*b*). Although extraneous, unattached TiO_2 nanoparticles were often carried along in the syntheses, this material could be almost completely removed by multiple centrifugation/washing cycles.

MPTMS was initially used to activate these FGNPs, but it was found to be unnecessary. Given that encapsulation of the previously described FGNPs was seemingly blocked by

© 2008 NRC Canada

Fig. 2. Representative EDX spectrum taken on the overhanging TiO_2 layer indicated by the arrow in the inset.

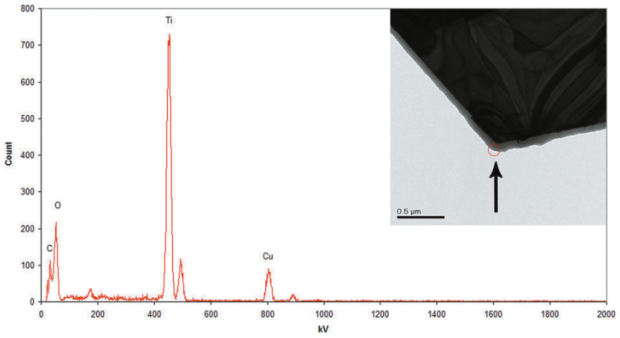

P123 that had remained on the surface, we reasoned that it might be possible to protect the "cleaner" FGNPs from encapsulation by protecting them with an alkanethiol SAM. These sheets were treated with 1-dodecanethiol (DDSH), and SAM formation was supported by absorptions at 2900 and 2800 cm^{-1} in the FTIR spectrum (these absorptions were absent in the parent FGNPs). However, the DDSH-treated FGNPs were also successfully encapsulated by titanium dioxide. In the case of these nanosheets, the TiO_2 coating was the same regardless of SAM functionalization. The ineffectiveness of DDSH as a blocking agent leads us to believe that, in this case, the method of attachment of TiO_2 is simply through adhesion during the slow sol–gel process. A strong encapsulating layer is formed, and the coated nanosheets are robust.

To insure that the sol–gel encapsulation procedure was not specific to the aniline – ethylene glycol FGNP synthesis, a third set of FGNPs were synthesized by the aqueous citrate reduction of hydrogen tetrachloroaurate in the presence of CTAB as described by Chu et al. (49). These sheets were readily encapsulated without activation. We expect this procedure to be general, but it seems proper choice of the FGNP synthesis is important.

To further assess the degree of film coverage, sheets with amorphous films were cross-sectioned. Figure 3 shows TEM images of cross-sectioned samples. TiO_2 films were homogenous and had thicknesses on the order of 100 nm in this particular sample. The thickness of TiO_2 layers showed considerable variation dependent on reaction conditions (primarily TnB concentration). The results obtained by increasing TnB concentration over the range 0.3–5.0 mmol/L, keeping all other quantities constant, showed a proportional increase in film thickness.

TiO_2 can be crystallized hydrothermally to yield the photocatalytically active anatase structure (58–61). Crystallization of the amorphous TiO_2 layer to yield the anatase form would be desirable for these FGNP@TiO_2 particles to be photocatalytically efficient. This is also an important factor when considering the possibility of adding other functionalities to the TiO_2 surface. Light-sensitive dyes, metal nanoparticles, and other catalysts have been shown to have useful properties when bonded to anatase TiO_2. We have experimented with several crystallization techniques to create a new class of composite nanoparticles that could serve as a foundation for more complex nanostructures.

Fig. 3. Cross-sections of FGNPs with amorphous TiO_2 films. Inset shows a close-up where the thickness of the Au plate and the surrounding TiO_2 layer can easily be measured.

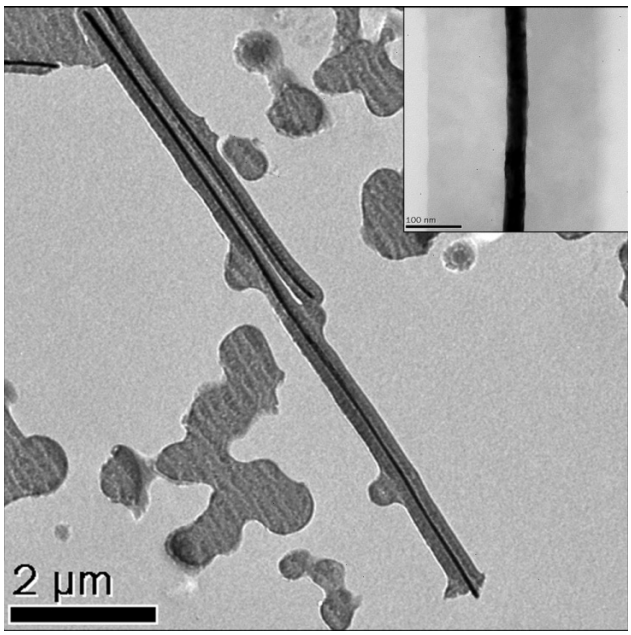

Fig. 4. Contrast between (*a*) amorphous TiO_2 and (*b*) crystalline TiO_2 obtained by heating in water at 70 °C for 1 week.

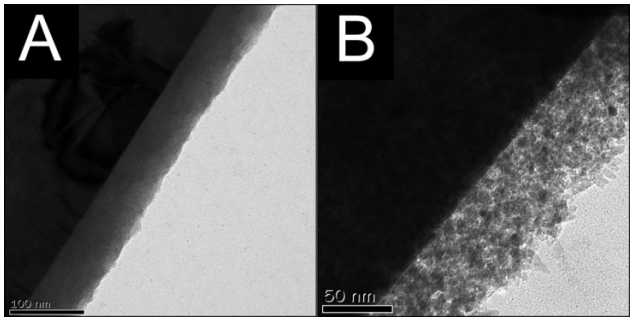

Polycrystalline TiO_2 films were formed by mildly heating an aqueous suspension of FGNPs coated with amorphous titania. HRTEM imaging and SAED showed conclusively that anatase was the dominant crystal morphology in the product. Figure 4 shows the difference in appearance between amorphous TiO_2 and the nanocrystallite films. Figure 5 clearly shows lattice fringes that occur as a result of diffracting crystal planes; the existence of which has also lead to the multi-ring SAED pattern shown in the inset. Comparison of experimental *d* spacing with tabulated values for anatase TiO_2 reveals a number of common values (notably $d = 3.5$ Å and 1.9 Å corresponding to the (101) and (200) crystallographic faces, respectively). Alternatively, no spacings are closely shared between experimental and those of rutile.

Microwave heating to 130 °C of an aqueous suspension of amorphous FGNP@TiO_2 particles also converted the thin TiO_2 film to the anatase phase, but this method only required heating for five minutes. Figure 6 contrasts the starting material and product. Further analysis of the nanocrystallite film by electron diffraction showed the multiple ring pattern

© 2008 NRC Canada

Fig. 5. Lattice fringing in titania-coated FGNPs heated at 70 °C. SAED shown in the inset also indicates polycrystalline TiO_2.

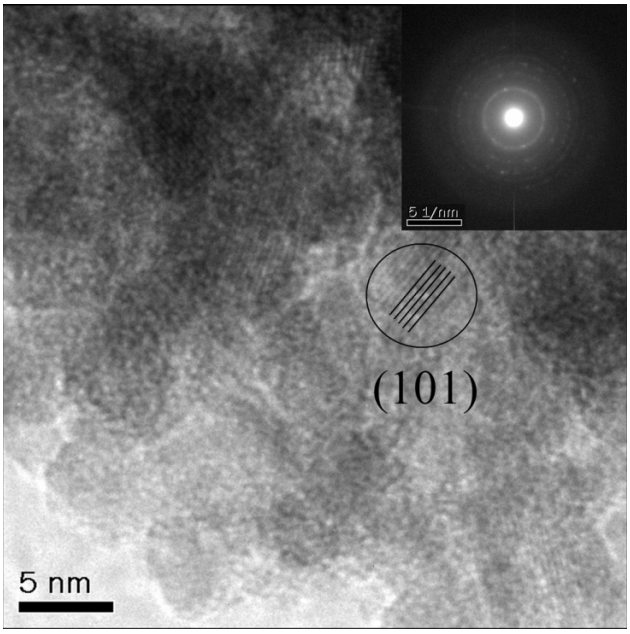

Fig. 6. Contrast between (*a*) amorphous TiO_2 and (*b*) crystalline TiO_2 obtained by heating in water at 130 °C for 5 min.

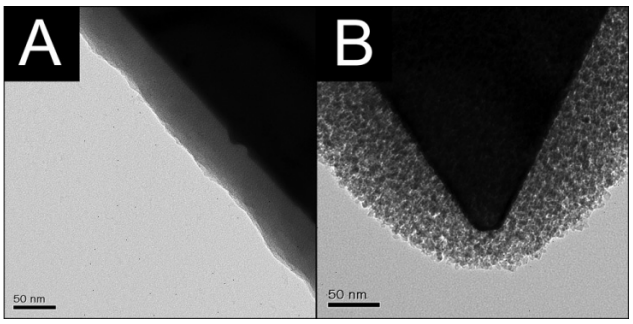

expected for anatase TiO_2. Again, HRTEM images clearly show lattice fringes of diffracting crystallites and at much higher concentration and clarity than analogous polycrystalline films generated in the oven (Fig. 7). Microwave heating significantly reduced crystallization times from hours to minutes under very mild, aqueous conditions. It is possible that interactions between microwaves and FGNPs results in hot spots localized at the metal core, ultimately increasing the rate of the phase change beginning at the metal surface and propagating outward.

Overall, the crystallization of TiO_2 on FGNPs was quite straightforward. Good polycrystallinity was seen and distinguished as anatase. We do not see significant loss of TiO_2 from the nanoplate during the crystallization process. FGNPs coated with crystalline TiO_2 are also quite robust and withstand frequent centrifugation, washing, and sonication.

Conclusion

FGNPs were demonstrated as flat, modifiable platforms onto which TiO_2 could be layered. Provided proper choice of

Fig. 7. Lattice fringing in microwaved TiO_2. SAED shown in the inset also indicates polycrystalline TiO_2.

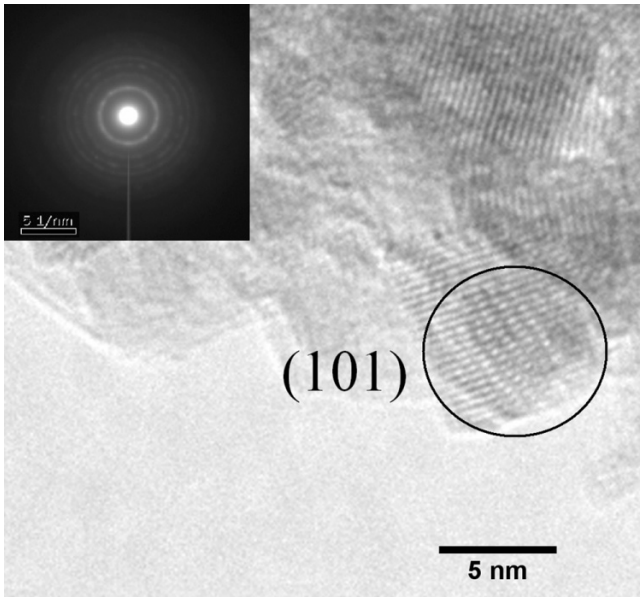

FGNP synthesis, this procedure is possible without the addition of any linking organic groups. The crystallization of TiO_2 was performed conventionally and with microwave heating, and the latter proved to be quite advantageous. At the present time, we continue to investigate many possibilities for bonding of other materials to FGNPs and Au@TiO_2 nanosheets as well as their photocatalytic properties.

Acknowledgement

Thanks to Jenna Holt for repeating some of the intial experiments. Thanks to Dr. Louise Weaver, Douglas Hall, and colleagues at UNB's Microscopy and Microanalysis Facility and to the Natural Sciences and Engineering Research Council of Canada (NSERC), NBIF, and UNB for the generous financial support.

References

1. K.E. Drexler. Engines of creation. Fourth Estate, London. 1990.
2. K. Xu, C.J. Mao, J. Geng, and J.J. Zhu. Nanotechnology, **18**, 315604 (2007).
3. Y. Xiong, W.B.J., and Y. Xia. Angew. Chem., Int. Ed. **46**, 7157 (2007).
4. L.Y. Wang, X. Chen, Y.C. Chai, and J.C. Hao. Colloids Surf. A. **293**, 95, (2007).
5. F. Wang, J. Jiu, L. Pei, K. Nakagawa, S. Isoda, and M. Adachi. Mater. Lett. **61**, 488 (2007).
6. J.L. Zhang, J.M. Du, B.X. Han, Z.M. Liu, T. Jiang, and Z.F. Zhang. Angew. Chem., Int. Ed. **45**, 1116 (2006).
7. H. Xu, W. Wang, and W. Zhu. Mater. Lett. **60**, 2203 (2006).
8. W.Z. Wang, B. Poudel, Y. Ma, and Z.F. Ren. J. Phys. Chem. B, **110**, 25702 (2006).
9. M. Yamamoto, Y. Kashiwagi, T. Sakata, H. Mori, and M. Nakamoto. Chem. Mater. **17**, 5391 (2005).
10. W.Z. Wang, B. Poudel, J. Yang, D.Z. Wang, and Z.F. Ren. J. Am. Chem. Soc. **127**, 13792 (2005).

© 2008 NRC Canada

11. Y. Chen, X. Gu, C.G. Nie, Z.Y. Jiang, Z.X. Xie, and C.J. Lin. Chem. Commun. 4181 (2005).
12. J. van Embden, J. Jasieniak, D.E. Gomez, P. Mulvaney, and M. Giersig. Aust. J. Chem. **60**, 457 (2007).
13. D.K. Yi, S.S. Lee, G.C. Papaefthymiou, and J.Y. Ying. Chem. Mater. **18**, 614 (2006).
14. V. Salgueirino-Maceira and M. A. Correa-Duarte. J. Mater. Chem. **16**, 3593 (2006).
15. N.G. Liu, B.S. Prall, and V.I. Klimov. J. Am. Chem. Soc. **128**, 15362 (2006).
16. C. Graf, D.L.J. Vossen, A. Imhof, and A. van Blaaderen. Langmuir, **19**, 6693 (2003).
17. S.O. Obare, N.R. Jana, and C.J. Murphy. Nano Lett. **1**, 601 (2001).
18. L. M. Liz-Marzan, M. Giersig, and P. Mulvaney. Langmuir, **12**, 4329 (1996).
19. C.G. Wang, Z.F. Ma, T.T. Wang, and Z.M. Su. Adv. Funct. Mater. **16**, 1673 (2006).
20. G. Oldfield, T. Ung, and P. Mulvaney. Adv. Mater. **12**, 1519 (2000).
21. P. Botella, A. Corma, and M.T. Navarro. Chem. Mater. **19**, 1979 (2007).
22. J. Li and H. C. Zeng. Angew. Chem., Int. Ed. **44**, 4342 (2005).
23. R.T. Tom, A.S. Nair, N. Singh, M. Aslam, C.L. Nagendra, R. Philip, K. Vijayamohanan, and T. Pradeep. Langmuir, **19**, 3439 (2003).
24. C.J. Zhong and M.M. Maye. Adv. Mater. **13**, 1507 (2001).
25. P.V. Kamat. J. Phys. Chem. C. **111**, 2834 (2007).
26. T. Hirakawa and P.V. Kamat. J. Am. Chem. Soc. **127**, 3928 (2005).
27. V. Subramanian, E.E. Wolf, and P.V. Kamat. J. Am. Chem. Soc. **126**, 4943 (2004).
28. V. Subramanian, E.E. Wolf, and P.V. Kamat. Langmuir, **19**, 469 (2003).
29. M. Jakob, H. Levanon, and P.V. Kamat. Nano Lett. **3**, 353 (2003).
30. P.V. Kamat, M. Flumiani, and A. Dawson. Colloids Surf. A. **202**, 269 (2002).
31. A. Dawson and P. V. Kamat. J. Phys. Chem. B, **105**, 960 (2001).
32. A. Kumbhar and G. Chumanov. J. Nanosci. Nanotech. **4**, 299 (2004).
33. G.A. Olah. Angew. Chem., Int. Ed. **44**, 2636 (2005).
34. V. Iliev, D. Tomova, L. Bilyarska, and G. Tyuliev. J. Mol. Catal. A: Chem. **263**, 32 (2007).
35. E. Szabo-Bardos, H. Czili, and A. Horvath, J. Photochem. Photobiol. A. **154**, 195 (2003).
36. S. Ikeda, N. Sugiyama, B. Pal, G. Marci, L. Palmisano, H. Noguchi, K. Uosaki, and B. Ohtani. PCCP, **3**, 267 (2001).
37. T. Ung, M. Giersig, D. Dunstan, and P. Mulvaney. Langmuir, **13**, 1773 (1997).
38. T. Hirakawa and P.V. Kamat. Langmuir, **20**, 5645 (2004).
39. T. Ung, L.M. Liz-Marzan, and P. Mulvaney. J. Phys. Chem. B, **103**, 6770 (1999).
40. L.Y. Zou, Y.G. Luo, and E.J. Hu. J. Adv. Oxid. Technol. **10**, 31 (2007).
41. D. Gumy, A.G. Rincon, R. Hajdu, and C. Pulgarin. Sol. Energy, **80**, 1376 (2006).
42. S. Anandan and M. Yoon. J. Photochem. Photobiol. C. **4**, 5 (2003).
43. I. Pastoriza-Santos, J. Perez-Juste, and L.M. Liz-Marzan. Chem. Mater. **18**, 2465 (2006).
44. J.M. Du, J.L. Zhang, Z.M. Liu, B.X. Han, T. Jiang, and Y. Huang. Langmuir, **22**, 1307 (2006).
45. A. Borras, A. Barranco, F. Yubero, and A.R. Gonzalez-Elipe. Nanotechnology, **17**, 3518 (2006).
46. C. Xue, X. Chen, S.J. Hurst, and C.A. Mirkin. Adv. Mater. **19**, 4071 (2007).
47. L.Y. Wang, X. Chen, J. Zhan, Y.C. Chai, C.J. Yang, L.M. Xu, W.C. Zhuang, and B. Jing. J. Phys. Chem. B, **109**, 3189 (2005).
48. Z. Guo, Y. Zhang, Y. DuanMu, L. Xu, S. Xie, and N. Gu. Colloids Surf. A. **278**, 33 (2006).
49. H.C. Chu, C.H. Kuo, and M.H. Huang. Inorg. Chem. **45**, 808 (2006).
50. H.Z. Huang and X.R. Yang. Biomacromolecules, **5**, 2340 (2004).
51. J.U. Kim, S.H. Cha, K. Shin, J.Y. Jho, and J.C. Lee. Adv. Mater. **16**, 459 (2004).
52. C. Lofton and W. Sigmund. Adv. Funct. Mater. **15**, 1197 (2005).
53. Y. Shao, Y.D. Jin, and S.J. Dong. Chem. Commun. 1104 (2004).
54. M. Zhou, S.H. Chen, and S.Y. Zhao. J. Phys. Chem. B, **110**, 4510 (2006).
55. S.H. Liu, Z.H. Zhang, and M.Y. Han. Adv. Mater. **17**, 1862 (2005).
56. O.G. Tovmachenko, C. Graf, D.J. van den Heuvel, A. van Blaaderen, and H.C. Gerritsen. Adv. Mater. **18**, 91 (2006).
57. D.H. Dahanayaka, J.X. Wang, S. Hossain, and L.A. Bumm. J. Am. Chem. Soc. **128**, 6052 (2006).
58. M. Gopal, W.J.M. Chan, and L.C. DeJonghe. J. Mater. Sci. **32**, 6001 (1997).
59. A.B. Corradi, F. Bondioli, B. Focher, A. M. Ferrari, C. Grippo, E. Mariani, and C. Villa. J. Am. Ceram. Soc. **88**, 2639 (2005).
60. J.N. Hart, D. Menzies, Y.B. Cheng, G.P. Simon, and L. Spiccia. Sol. Energy Mater. Sol. Cells, **91**, 6 (2007).
61. G.J. Wilson, A.S. Matijasevich, D.R.G. Mitchell, J.C. Schulz, and G.D. Will. Langmuir, **22**, 2016 (2006).

© 2008 NRC Canada

PMA/SiO_2 — An efficient recyclable heterogeneous catalyst for the synthesis of homoallyl alcohols and amines under solvent-free conditions[1]

Biswanath Das, Rathod Aravind Kumar, Ponnaboina Thirupathi, Kanaparthy Suneel, and Pothkan Sunitha

Abstract: Aldehydes and imines can efficiently undergo nucleophilic addition reaction with allyltributylstannane in the presence of phosphomolybdic acid supported on silica (PMA/SiO_2) under solvent free-conditions to form the corresponding homoallyl alcohols and amines respectively at room temperature in excellent yields. The catalyst can be easily recovered and re-used.

Key words: homoallyl alcohol, homoallyl amine, phosphomolybdic acid, heterogeneous catalyst, allyltributylstannane, solvent-free conditions.

Résumé : Opérant à la température ambiante et des conditions sans solvant, les aldéhydes et les imines peuvent donner lieu à des réactions efficaces d'addition nucléophile avec l'allyltributylstannane, en présence d'acide phosphomolybdique supporté sur de la silice (APM/SiO_2) pour conduire à la formation respectivement d'alcools et d'amines homoallyliques avec d'excellents rendements. Le catalyseur peut facilement être récupéré et réutilisé.

Mots-clés : alcool homoallylique, amine homoallylique, acide phosphomolybdique, catalyseur hétérogène, allyltributylstannane, conditions sans solvant.

[Traduit par la Rédaction]

Introduction

Homoallylic alcohols (1) and amines (2) are important building blocks for the construction of various biologically active compounds, and hence the syntheses of these compounds are highly useful. Lewis acid promoted nucleophilic addition of allyltin reagent to carbonyl compounds and imines is one of the straightforward methods for the synthesis of homoallyl alcohols and amines. Various Lewis acids such as metal halides (3), metal triflates (4), I_2 (5), (bromodimethyl)sulfonium bromide (6), and cyanuric chloride (7) can catalyze this reaction. However, most of the methods employing these catalysts suffer from certain disadvantages such as high temperature, prolonged reaction times, harsh reaction conditions, and the use of hazardous and expensive acid catalysts. Some of the catalysts are extremely moisture sensitive and can cause inconvenience in performing the reaction. In recent years, the use of solid acids as heterogeneous catalysts has gained tremendous interest in different areas of organic synthesis. These catalysts are advantageous over conventional homogeneous acid catalysts as they can be easily recovered from the reaction mixture by simple filtration and can be re-used after activation or without activation, thereby making the process more economically viable. Here we report the utilization of a solid acid as a catalyst for the preparation of homoallylic alcohols and amines.

Received 19 November 2007. Accepted 13 March 2008. Published on the NRC Research Press Web site at canjchem.nrc.ca on 27 May 2008.

B. Das,[2] R.A. Kumar, P. Thirupathi, K. Suneel, and P. Sunitha. Organic Chemistry Division-1, Indian Institute of Chemical Technology, Hyderabad 500 007, India.

[1]Part 150 in a series of studies on novel synthetic methodologies.

[2]Corresponding author (e-mail: biswanathdas@yahoo.com).

Results and discussion

In continuation of our work (8) on the application of heterogeneous catalysts for the development of useful synthetic methodologies, we have observed that phosphomolybdic acid supported on silica (PMA/SiO_2) (9) is very suitable to catalyze the allylation of aldehydes and imines with allyltributylstannane to form the corresponding homoallyl alcohols and amines at room temperature (RT) under solvent-free conditions (Scheme 1). This catalyst possesses excellent activity, low toxicity, and high stability towards humidity. It can be recovered from the reaction mixture and recycled.

Initially we studied the reaction of benzaldehyde, aniline, and allyltributylstananne in CH_3CN in the presence of PMA/SiO_2 at RT. The desired homoallylamine was obtained in good yield (85%) within 80 min (Table 1, entry a). In absence of the catalyst the product was not formed. We studied the effect of different solvent systems such as THF, Et_2O, MeOH, CH_3CN, CH_2Cl_2, and $CHCl_3$ for the reaction, but the conversion proceeded best in the absence of any solvent. A wide variety of aromatic and aliphatic aldehydes

 doi:10.1139/V08-060 © 2008 NRC Canada

Table 1. Preparation of homoallylic amines using PMA/SiO_2.

Entry	Aldehyde (**1**)	Amine (**2**)	Product (**3**)	Time (min)	Isolated yield (%)
a	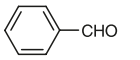	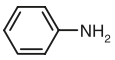	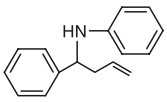	35	92
b	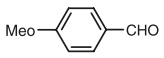	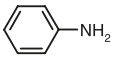	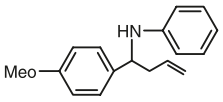	30	96
c	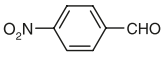	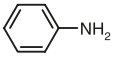	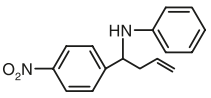	45	87
d	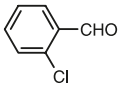	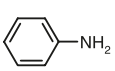	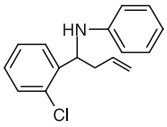	45	89
e	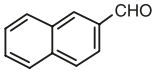	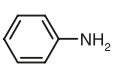	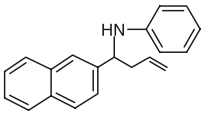	30	93
f	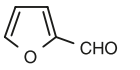	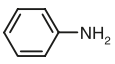	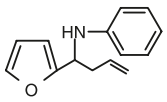	55	84
g	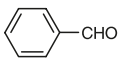	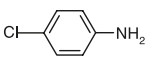	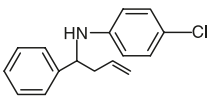	40	90
h	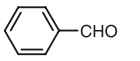	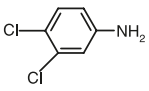	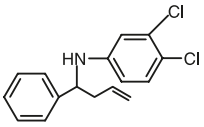	45	88
i	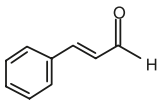	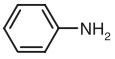	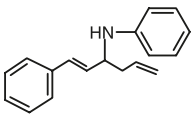	50	87

Scheme 1. Preparation of homoallylic amines using PMA/SiO_2.

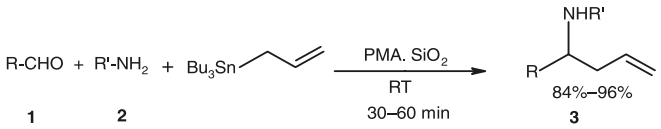

Scheme 2. Preparation of homoallylic alcohols using PMA/SiO_2.

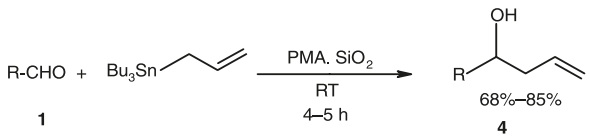

containing electron-donating (Table 1, entries b and l) and electron-withdrawing substituents (Table 1, entries c and d) underwent the transformation smoothly. An acid sensitive aldehyde such as α,β-unsaturated aldehydes (Table 1, entry i), furfuraldehyde (Table 1, entry f), and a sterically hindered aldehyde such as 2-naphthaldehyde (Table 1, entry e) worked well to produce their corresponding homoallylic amines. The imines (formed in situ from aldehydes and amines in the presence of the catalyst) underwent facile reaction with allyltributylstannane to form these compounds. Previously, some methods were found to be unsuitable for the preparation of homoallylic amines from enolizable aldehydes. Interestingly the reaction of aldehydes, benzylcarbamate ($CbzNH_2$), and allyltributylstannane yielded the corresponding Cbz-protected allylamines in excellent yield (79%–83%) (Table 1, entries k and l).

The other application of the present method is the preparation of homoallyl alcohols from the corresponding aldehydes on treatment with allyltributylstannane using

© 2008 NRC Canada

Table 1 (*concluded*).

Entry	Aldehyde (**1**)	Amine (**2**)	Product (**3**)	Time (min)	Isolated yield (%)
j	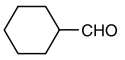	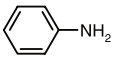	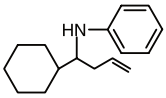	50	86
k	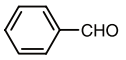	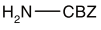	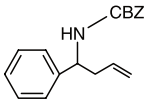	45	79
l	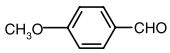	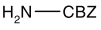	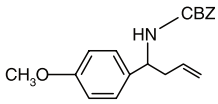	45	83
m	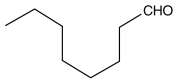	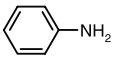	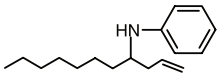	60	87

Note: The structures of the homoallylic amines were settled from their spectral (^{1}H NMR and MS) data.

PMA/SiO_2 under solvent- free conditions (Scheme 2). The reaction proceeded at RT and the products were formed within 4–5 h (Table 2). Both aromatic and aliphatic aldehydes were used for the preparation of homoallylic alcohols. The aldehydes containing electron-donating (Table 2, entry b) and electron-withdrawing groups (Table 2, entry c) in the aromatic rings were found to undergo the conversion smoothly. Acid-sensitive aldehydes such as furfural (Table 2, entry f) and cinnamaldehyde (Table 2, entry e) also smoothly reacted to afford the corresponding homoallyl alcohols.

We extended this method for the conversion of ketones and carried out the reaction using acetophenone, cyclohexanone, and β-ketoesters. None of the ketones gave homoallylic alcohols and amines even after prolonging the reaction times. The chemoselectivity of the present allylation method is remarkable, providing allylation of only aldehydes in the presence of ketones (Table 2, entries i–k). The times required for the preparation of homoallylic alcohols (4–5 h) are somewhat more than those required for the preparation of homoallylic amines (30–60 min).

Conclusion

In conclusion, we have developed a simple and efficient method for the allylation of aldehydes and amines using PMA/SiO_2 as a heterogeneous catalyst. The main features of this methodology are (*i*) operational simplicity, (*ii*) short reaction times, (*iii*) mild reaction conditions, (*iv*) excellent yields, (*v*) application of an inexpensive heterogeneous catalyst, (*vi*) high chemoselectivity, (*vii*) high stability towards humidity, and (*viii*) reusability of the catalyst.

Experimental

Preparation of PMA/SiO_2 catalyst (9)

Slica gel (100–200 mesh, 450 mg) was added slowly to a solution of $H_3PMo_{12}O_{40}{\cdot}24H_2O$ (50 mg) in methanol (5 mL). The mixture was stirred at RT for 6 h. Methanol was evaporated under reduced pressure to attain the catalyst (PMA/SiO_2) as an yellowish powder.

General experimental procedure for the synthesis of homoallyl amines

To a mixture of an aldehyde (2 mmol), amine (2 mmol), and allyltributylstannane (2.5 mmol), PMA/SiO_2 (113 mg) was added under solvent-free conditions at RT. The mixture was stirred and the reaction was monitored by TLC. After completion of the reaction, the mixture was filtered and the catalyst was recovered quantitatively after washing the residue with dry methanol (2 × 5 mL). The filtrate (containing the product in methanol) was concentrated and the residue was subjected to column chromatography (silica gel, hexane) to obtain pure homoallyl amine. The recovered catalyst was re-used three times subsequently for the same reaction without affecting the yield of the product.

General experimental procedure for the synthesis of homoallyl alcohols

To a mixture of an aldehydes (2 mmol) and allyltributylstannane (2.5 mmol), PMA/SiO_2 (113 mg) was added under solvent-free conditions at RT. The mixture was stirred and the reaction was followed by TLC. After completion, the mixture was filtered and the residue was washed with dry methanol (2 × 5 mL) to recover the catalyst quantitatively. The filtrate (containing the product in methanol) was concentrated and the viscous mass was subjected to column chromatography (silica gel, 35% EtOAc and hexane) to afford pure homoallyl alcohol. The recovered catalyst was re-used three times subsequently in this case also for the same reaction without affecting the yield of the product.

All the prepared compounds (except **3b**, **3f**, and **4b**) are known (3*c*, 3*d*, 4*b*, 4*c*, and 6). The spectral and analytical data of representative products are given below.

© 2008 NRC Canada

Table 2. Preparation of homoallylic alcohols using PMA/SiO_2.

Entry	Aldehyde (**1**)	Product (**4**)	Time (h)	Isolated yield (%)
a	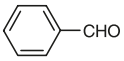	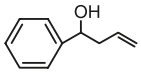	4.0	85
b	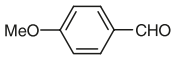	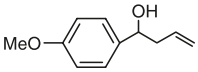	4.0	85
c	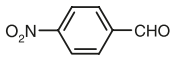	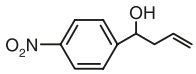	5.0	68
d	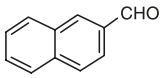	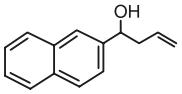	4.5	80
e	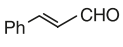	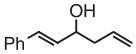	5.0	78
f	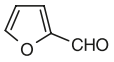	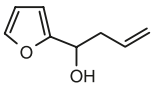	5.0	74
g	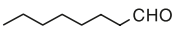	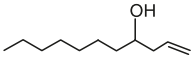	5.0	69
h	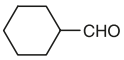	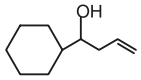	4.0	70
i	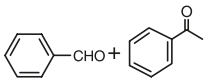	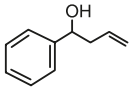	4.0	85
j	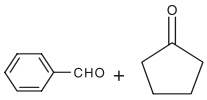	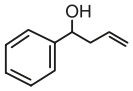	4.0	83
k	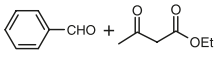	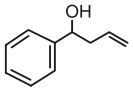	4.0	85

Note: The structures of the homoallylic alcohols were settled from their spectral (^{1}H NMR and MS) data.

3b

Oil. ^{1}H NMR ($CDCl_3$, 200 MHz) δ: 7.27 (2H, d, J = 8.0 Hz), 7.03 (2H, t, J = 8.0 Hz), 6.82 (2H, d, J = 8.0 Hz), 6.59 (1H, t, J = 8.0 Hz), 6.42 (2H, d, J = 8.0 Hz), 5.75 (1H, m), 5.21–5.09 (2H, m), 4.31 (1H, td, J = 5.5, 1.5 Hz), 4.03 (1H, m), 3.78 (3H, s), 2.61–2.40 (2H, m). FABMS m/z: 254 (M^+ + 1). Anal. calcd. for $C_{17}H_{19}$ NO: C 80.63, H 7.50, N 5.53; found: C 80.58, H 7.54, N 5.49.

3f

Oil. ^{1}H NMR ($CDCl_3$, 200 MHz) δ: 7.30 (1H, d, J = 1.8 Hz), 7.06 (2H, t, J = 8.0 Hz), 6.64 (1H, t, J = 8.0 Hz), 6.52 (2H, d, J = 8.0 Hz), 6.23 (1H, dd, J = 2.0, 1.8 Hz), 6.09 (1H, d, J = 2.0 Hz), 5.72 (1H, m), 5.20–5.08 (2H, m), 4.52 (1H, t, J = 5.5 Hz), 3.89 (1H, brs), 2.64 (2H, t, J = 5.5 Hz). FABMS m/z: 214 (M^+ + 1). Anal. calcd. for $C_{14}H_{16}NO$: C 78.50, H 7.47; found: C 78.56, H 7.51.

4b

Oil. ^{1}H NMR ($CDCl_3$, 200 MHz) δ: 7.20 (2H, d, J = 8.0 Hz), 6.80 (2H, d, J = 8.0 Hz), 5.67–5.80 (1H, m), 5.08 (2H, m), 6.42 (1H, t, J = 12.5, 6.0 Hz), 3.77 (3H, s), 2.43 (2H, J = 12.5, 6.5 Hz), 2.08 (brs, OH). FABMS m/z: 179 (M^+ + 1). Anal. calcd. for $C_{11}H_{14}O$: C 74.15, H 7.86; found: C 74.22, H 7.80.

Acknowledgements

The authors thank Council for Scientific and Industrial Research (CSIR) and University Grants Commission (UGC), New Delhi for financial assistance.

References

1. (*a*) K.R. Hoenberer, C.L. Hamblet, and J.L. Leighton. J. Am.

© 2008 NRC Canada

Chem. Soc. **122**, 12894 (2000); (*b*) K.C. Nicolaou, D.W. Khim, and R. Baati. Angew. Chem., Int. Ed. **41**, 3701 (2002).
2. (*a*) R.D. Enders and U. Reinhold. Tetrahedron: Asymmetry, **8**, 1895 (1997); (*b*) R. Bloch. Chem. Rev. **98**, 1407 (1998).
3. (*a*) T. Akiyama, J. Iwai, Y. Onuma, and H. Kagoshima. J. Chem. Soc. Chem. Commun. 2191 (1999); (*b*) T. Akiyama and Y. Onuma. J. Chem. Soc. Perkin Trans. 1, 1157 (2002); (*c*) J.S. Yadav, B.V.S. Reddy, G. Kondaji, and S.S.J. Redyy. Tetrahedron, **61**, 879 (2005); (*d*) N.V. Lingaaih, G. Ezikiel, T. Yakaaih, G.V. Reddy, and P.S. Rao. Tetrahedron Lett. **47**, 4315 (2006).
4. (*a*) S. Kobayashi, T. Busujima, and S. Nagayama. J. Chem. Soc. Chem. Commun. 19 (1998); (*b*) H.C. Aspinall, J.S. Bissett, N. Greeves, and D. Levin. Tetrahedron Lett. **43**, 323 (2002); (*c*) J.S. Yadav, B.V.S. Reddy, and A.K. Raju. Synthesis, 883 (2003); (*d*) T. Ollevier and T. Ba. Tetrahedron Lett. **44**, 9003 (2003); (*e*) H.C. Aspinall, J.S. Bissett, N. Greeves, and D. Levin. Tetrahedron Lett. **43**, 319 (2002).
5. H. Nakamura, H. Iwama, and Y. Yamamoto. J. Am. Chem. Soc. **118**, 6641 (1996).
6. B. Das, B. Ravikanth, P. Thirupathi, and B.V. Rao. Tetrahedron Lett. **47**, 5041 (2006).
7. B. Das, K. Laxminarayana, B. Ravikanth, and B. Rama Rao. Tetrahedron Lett. **47**, 9103 (2006).
8. (*a*) B. Das, B. Ramu, B. Ravikanth, and K.R. Reddy. Tetrahedron Lett. **47**, 779 (2006); (*b*) B. Das, P. Thirupathi, V.S. Reddy, and Y.K. Rao. J. Mol. Catal. A Chem. **247**, 233 (2006); (*c*) B. Das, A. Majhi, J. Benerjee, N. Chowdhury, K.H. Kishore, and U.S.N. Murty. Chem. Pharm. Bull. **54**, 403 (2006).
9. G.D. Kishore Kumar and S. Basakaran. J. Org. Chem. **70**, 4520 (2005).

© 2008 NRC Canada

Exploring the reaction of formaldehyde with α-*N*-protected amino acid hydrazides

Giancarlo Verardo, Paola Geatti, Marta Mancuso, and Paolo Strazzolini

Abstract: The reaction of formaldehyde with enantiomerically pure α-*N*-protected amino acid hydrazides is described. The system has been investigated in different solvents, including both aqueous formaldehyde and paraformaldehyde, with the aim of simplifying the final reaction mixture. Aqueous formaldehyde in refluxing THF proved to be the best combination, affording mainly the corresponding monomeric *N*-methylene and 1,3,5-trisubstituted-1,3,5-hexahydrotriazine derivatives. The monomeric form was the only one present at high temperature, as evidenced by ^{1}H and ^{13}C NMR spectroscopy.

Key words: amino acid hydrazides, formaldehyde, condensation reactions, monomeric *N*-methylene derivatives, oligomers.

Résumé : On décrit la réaction du formaldéhyde avec des hydrazides d'acides aminés α-*N*-protégés énantiomériquement purs. Afin d'obtenir un mélange réactionnel final aussi simple que possible, on a étudié le système dans divers solvant, en utilizant aussi bien du formaldéhyde aqueux que du paraformaldéhyde. Le formaldéhyde aqueux dans du THF au reflux semble la meilleure combinaison et elle conduit principalement aux dérivés correspondants monomères *N*-méthylène et 1,3,5-hexahydrotriazine 1,3,5-trisubstitués. Sur la base de la spectroscopie RMN du ^{1}H et du ^{13}C, la forme monomère est la seule qui soit présente à haute température.

Mots-clés : hydrazides d'acides aminés, formaldéhyde, réactions de condensation, dérivés *N*-méthylène monomères, oligomères.

[Traduit par la Rédaction]

Introduction

In recent years, considerable effort has been directed towards the synthesis of peptidomimetics having different structural features (1). Among them, a notable interest concerns hydrazides, in particular those bearing an *N*-methyl substituent in the 2-position (2). The syntheses reported in the literature to date are essentially based on the direct or mediated condensation between the terminal carboxy function of the peptide unit and *N*-methylhydrazine, free or protected at the methylated nitrogen, affording the corresponding 2-methylhydrazide in moderate yields and after tedious separations (3). The easy, high-yielding access to the hydrazido derivatives of α-*N*-protected amino acid recently described (4) prompted us to consider the possibility of transforming them into the corresponding methylene-imines (5) by direct interaction with formaldehyde. In fact, such methylidene intermediates might in turn be useful precursors, after $NaBH_4$ reduction (6), to the desired *N*-protected α-amino acid 2-methylhydrazides. In addition, this approach should also allow, simply using suitable reagents, the introduction of one or three deuterium atoms to the methyl substituent (6).

It is well-known that the interaction of formaldehyde with primary amines (**1**) in inert solvents invariably gives rise to polymeric adducts (**2**), the favourite oligomeric form of the resulting products being strictly dependent on the nature of **1** (Scheme 1) (7).

Although it is well documented that the reaction of formaldehyde with monosubstituted hydrazines under neutral conditions produces the corresponding hydrazones (8), the same reaction involving carboxylic acid hydrazides has received much less attention so far, perhaps because the reaction products are various and not easily explainable (9). Therefore, taking all these reasons into account, we set out to explore the reaction of formaldehyde with enantiomerically pure α-*N*-protected amino acid hydrazides under different conditions to get an optimized protocol for the production of any valuable intermediates.

Results and discussion

The reaction of aqueous formaldehyde with α-*N*-protected amino acid hydrazides **3** might give rise to a variety of products, as outlined in detail in Scheme 2. With the exception of *N*-hydroxymethyl derivatives, which are unstable intermediates, the other products are expected to be all, or in part, present in the reaction mixture. For this reason, we set out to investigate this complex reaction with the aim of finding the most suitable conditions for reducing the complexity of the final mixture.

Received 14 January 2008. Accepted 28 March 2008. Published on the NRC Research Press Web site at canjchem.nrc.ca on 29 May 2008.

G. Verardo,[1] P. Geatti, M. Mancuso, and P. Strazzolini. Department of Chemical Sciences and Technology, University of Udine, I-33100 Udine, Italy.

[1]Corresponding author (e-mail: giancarlo.verardo@uniud.it).

 doi:10.1139/V08-061 © 2008 NRC Canada

Scheme 1.

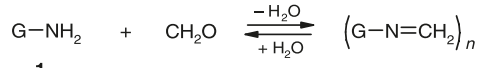

Scheme 2.

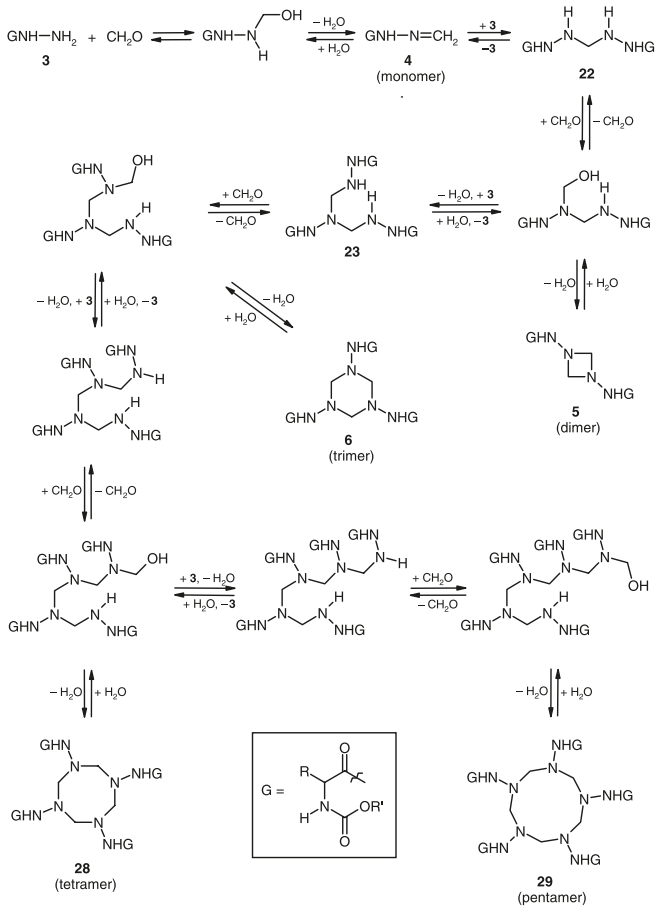

To this end, *N*-ethoxycarbonylphenylalaninohydrazide (**3ab**, Table 1) was used as the model substrate and the corresponding reaction products were carefully identified and quantified by means of ESI–MS and MS–MS experiments. On the basis of previous results (10), we first carried out the reaction in EtOH at 50 °C, using 1.6 equiv. of aq formaldehyde (Table 2, Entry 1). The ESI–MS analysis of the intact reaction mixture showed the presence of the monomer **4ab** (16%), the dimer **5ab** (7%), and the trimer **6ab** (60%) (Scheme 2), as well as the 3,5-disubstituted-1,3,5-oxadiazinone **7** (17%, Scheme 3). The large excess of formaldehyde reacting with the intermediate **8** allowed the formation of the *N*,*N*-di(hydroxymethyl) derivative **9** which, in turn, easily lost water to afford the heterocycle **7** (Scheme 3).

When the same reaction was carried out with less formaldehyde (1.3 equiv.; Table 2, Entry 2), the observed conversion into compound **7** was lower (12%) but, in addition to monomer **4ab** (33%), dimer **5ab** (6%), and trimer **6ab** (15%), the ESI–MS analysis showed the presence of five new compounds (Scheme 4), namely, ethyl 2-*N*-(ethoxycarbonyl)-2′,2′-bis(ethoxymethyl)phenylalaninohydrazide (**10**, 10%), 2′-(ethoxymethyl)-2′,2″-methylenebis[2-*N*-(ethoxycarbonyl)phenylalaninohydrazide] (**11**, 4%), 2′,2″-bis(ethoxymethyl)-2′,2″-methylenebis[2-*N*-(ethoxycarbonyl)phenylalaninohydrazide] (**12**, 16%), 2′-(ethoxymethyl)-2′,2″-({2-[*N*-(ethoxycarbonyl)phenylalanyl]hydrazine-1,1-diyl}bismethylene)bis[2-*N*-(ethoxycarbonyl)phenylalaninohydrazide] (**13**, 2%) and 2′,2″-bis(ethoxymethyl)-2′,2″-({2-[*N*-(ethoxycarbonyl)phenylalanyl]hydrazine-1,1-diyl}bismethylene)bis-[2-*N*-(ethoxycarbonyl)phenylalaninohydrazide] (**14**, 2%).

Table 1. Starting hydrazides (**3**).

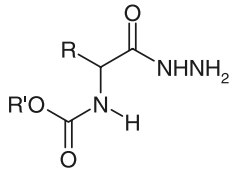

3

3	R	R′	**3**	R	R′
aa	$PhCH_2$	Me	**cd**	$(CH_3)_2CHCH_2$	$PhCH_2$
ab	$PhCH_2$	Et	**dc**	Proline	*t*-Bu
ac	$PhCH_2$	*t*-Bu	**dd**	Proline	$PhCH_2$
ad	$PhCH_2$	$PhCH_2$	**ea**	Ph	Me
bb	$(CH_3)_2CH$	Et	**eb**	Ph	Et
bc	$(CH_3)_2CH$	*t*-Bu	**ec**	Ph	*t*-Bu
bd	$(CH_3)_2CH$	$PhCH_2$	**fa**	1*H*-indol-3-CH_2	Me
cb	$(CH_3)_2CHCH_2$	Et	**fb**	1*H*-indol-3-CH_2	Et

This result is definitely not surprising taking into account the capability of formaldehyde to react not only with the NH_2 groups but also with EtOH yielding ethoxymethanol (**15**, Scheme 4). Therefore, as the reaction proceeds, the amount of formaldehyde decreases and the reaction of amino groups with **15** becomes effectively competitive. We did not observe any significant variation by performing the reaction either at room temperature (1.3 equiv. of aqueous formaldehyde; Table 2, Entry 3) or at 80 °C (1.6 equiv. of aqueous formaldehyde; Table 2, Entry 4) whereas, when it was carried out in MeOH at 50 °C using 1.3 equiv of aq formaldehyde (Table 2, Entry 5) the amount of all the corresponding alkoxymethyl derivatives **16–20** (Scheme 4) and, more significantly, **16** (46%) and **18** (23%), increased. This outcome was not unexpected considering that MeOH gives the corresponding hemiacetal **21** more easily than does EtOH: therefore, the quantity of free formaldehyde available was still smaller than in the case of entry 2.

The use of 1.6 equiv. of paraformaldehyde in refluxing EtOH (Table 2, Entry 6) did not produce the aminoacetals **10–14** (Scheme 4) but, in addition to **4ab** (48%), **5ab** (5%), and **6ab** (2%), the ESI–MS analysis showed the presence of some unreacted starting hydrazide **3ab** (31%), accompanied by 2′,2″-methylenebis[2-*N*-(ethoxycarbonyl)phenylalaninohydrazide] (**22ab**, 8%) and 2′,2″-({2-[*N*-(ethoxycarbonyl)phenylalanyl]hydrazine-1,1-diyl}bismethylene)bis[2-*N*-(ethoxycarbonyl)phenylalaninohydrazide] (**23ab**, 6%) (Scheme 2). This pattern gives a clear indication that there was not enough free formaldehyde at hand, because the temperature (80 °C) was too low for obtaining an efficient depolymerization of paraformaldehyde. Therefore, to achieve a suitably high temperature, the reaction was carried

© 2008 NRC Canada

Table 2. Study of the reaction between *N*-ethoxycarbonylphenylalaninohydrazide (**3ab**) and formaldehyde.

Entry	CH_2O[a] (equiv.)	Solvent	Temp. (°C)	Time (h)	Product (%)[b] **3ab**	**4ab**	**5ab**	**6ab**	**7**	**10** or **16**	**11** or **17**	**12** or **18**	**13** or **19**	**14** or **20**	**22ab**	**23ab**	**25**	**26**
1	AF (1.6)	EtOH	50	2		16±3	7±1	60±5	17±3									
2	AF (1.3)	EtOH[c]	50	2		33±4	6±1	15±2	12±1	10±1[c]	4±1[c]	16±1[c]	2.0±0.5[c]	2.0±0.4[c]				
3	AF (1.3)	EtOH[c]	Amb.	24		31±4	7±1	25±3	13±1	8±1[c]	4±1[c]	8±1[c]	2.0±0.2[c]	2.0±0.3[c]				
4	AF (1.6)	EtOH[c]	80	2		38±3	10±2	19±2	15±2	6±1[c]	4±1[c]	6±1[c]	1.0±0.2[c]	1.0±0.3[c]				
5	AF (1.3)	MeOH[d]	50	2		14±2	2.0±0.2	1.0±0.3		46±4[d]	7±1[d]	23±2[d]	3.0±0.5[d]	4±1[d]				
6	PF (1.6)	EtOH	80	2	31±4	48±5	5±1	2.0±0.3							8±1	6±1		
7	PF (1.6)	Toluene	110	0.5		59±4	7±1								21±3	10±2	3.0±0.2	
8	PF (2.0)	Toluene	110	0.5		58±4	7±1	23±3									12±2	
9	AF (1.6)	Toluene	80	2		52±3	7±1	18±2	8±1								9±1	6±1
10	AF (1.1)	Toluene	80	2		56±4	6±1	19±2	9±1								8±1	2.0±0.2
11	AF (1.3)	THF	70	1		69±5	7±1	14±2	10±2									
12	AF (1.05)	THF	70	0.5		74±5	3±1	23±3										

[a]AF: aqueous formaldehyde; PF: paraformaldehyde.
[b]Mean and standard error of mean of triplicate measurements obtained from the relative percentages of the corresponding $[M+Na]^+$ ions produced by direct infusion of the diluted reaction mixture into the ESI source. It was considered that all compounds had the same ESI–MS response.
[c]In this instance the compounds are **10**–**14** in Scheme 4.
[d]In this instance the compounds are **16**–**20** in Scheme 4.

Scheme 3.

Scheme 4.

out in refluxing toluene, in the presence of 1.6 equiv. of paraformaldehyde (Table 2, Entry 7). Under these conditions, after 0.5 h the starting hydrazide **3ab** was entirely consumed, but in addition to **22ab** (21%) and **23ab** (10%) still present, the ESI–MS analysis showed the presence of 2,4,7-tris[*N*-(ethoxycarbonyl)phenylalaninamido]-1,2,4,5,7-pentaazabicyclo[3.3.1]nonane (**24**, 3%, Scheme 5). Since the longer reaction times (1–2 h) produced a more complex reaction mixture because of the formation of a number of unidentified side-products, we increased the amount of paraformaldehyde (2.0 equiv.; Table 2, Entry 8) while still applying the conditions previously described (0.5 h).

Under these conditions, compounds **22ab** and **23ab** were not observed (Scheme 2) but some 12% of the bicyclic derivative **25** was formed (Scheme 5). When the reaction was performed in toluene, at 80 °C for 2 h, using 1.6 equiv. of aq formaldehyde (Table 2, Entry 9), besides **4ab** (52%), **5ab** (7%), **6ab** (18%), and **25** (9%), the formation of the heterocycle **7** (8%, Scheme 3) was observed, as well as that of a new bicyclic derivative, namely diethyl 1,1′-{[9-(2-ethoxycarbamoyl-3-phenylpropanamido)-4-oxa-1,2,6,7,9-pentaazabicyclo[5.3.1]-undecan-2,6-diyl]bis(1-oxo-3-phenylpro-

© 2008 NRC Canada

Scheme 5.

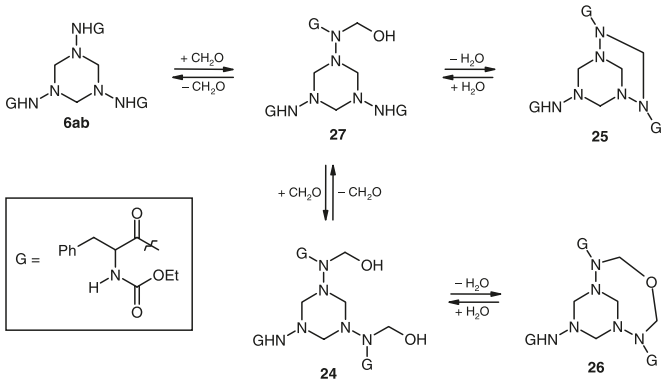

pane-2,1-diyl)}dicarbamate (**26**, 6%, Scheme 5). Under these reaction conditions, formaldehyde reacts rapidly with the NH groups yielding the *N*-hydroxymethyl intermediates **8** (Scheme 3) and **27** (Scheme 5) which are stabilized by internal hydrogen bonding, thus making the loss of water more difficult. Therefore, **8** and **27** survive enough to react with an additional molecule of formaldehyde producing **9** (Scheme 3) and **24** (Scheme 5), which, in turn, are precursors of compounds **7** (Scheme 3) and **26** (Scheme 5), respectively. We did not observe any significant variation in the composition of the final reaction mixture when less aqueous formaldehyde was employed (1.1 equiv.; Table 2, Entry 10).

In conclusion, the reaction of **3ab** carried out in alcohols yielded, besides the usual polymeric structures, the heterocycle **7** either alone or together with the aminoacetals **10**–**14**, **16**–**20** (Scheme 4) depending on whether there is a large or a slight excess of aqueous formaldehyde, respectively. Paraformaldehyde depolymerization occurred efficiently in toluene at 110 °C but not in EtOH at 80 °C; nevertheless, in the aprotic solvent at high temperature some of the formed free formaldehyde distilled off from the reaction mixture. For this reason, it was difficult to correctly estimate the amount of paraformaldehyde available, leading either to an uncomplete conversion or, alternatively, to the formation of the bicyclic derivative **25** (Scheme 5). On the other hand, the use of the more reactive aqueous formaldehyde in toluene yielded, in addition to **25**, the bicyclic derivative **26** (Scheme 5) and the heterocycle **7** (Scheme 3).

To circumvent all these drawbacks, we investigated the reaction in refluxing THF, a solvent able to dissolve both the starting hydrazide **3ab** and the aqueous formaldehyde, without giving rise to side-products as in the case of alcohols. In this medium, after 1 h and using 1.3 equiv. of aqueous formaldehyde (Table 2, Entry 11), compounds **4ab** (69%), **5ab** (7%), and **6ab** (14%) were still formed along with a minor amount of the heterocycle **7** (10%). The latter species completely disappeared when the reaction was carried out with a shorter reaction time (0.5 h) and a lower amount (1.05 equiv.) of aqueous formaldehyde (Table 2, Entry 12), giving rise to a significantly less complex reaction mixture.

This optimized protocol (refluxing THF, 0.5 h, 1.05 equiv. of aqueous formaldehyde) was extended to a number of different α-*N*-protected amino acid hydrazides **3** (Table 1). After evaporation of THF, the reaction of aqueous formaldehyde with all the hydrazides of phenylalanine **3aa**–**3ad** and valine **3bb**–**3bd**, regardless of the α-amino protection present, yielded a solid residue which was triturated in Et_2O and collected by filtration (Table 3, Method A). The ESI–MS analysis of the residues showed the presence of the corresponding monomer **4**, dimer **5**, and trimer **6**. Under the same conditions, all the other tested hydrazides **3** invariably gave an oil which eventually solidified after 1 h at 70 °C in vacuo (oil pump). The obtained solid was triturated in Et_2O and separated by filtration (Table 3, Method B); alternatively, when soluble, the resulting solution was added to pentane dropwise under stirring, obtaining a solid which was collected as above (Table 3, Method C). The ESI–MS analysis of all these residues evidenced, in addition to compounds **4**, **5**, and **6**, the presence of variable amounts of the corresponding tetramer **28** and pentamer **29** (Scheme 2).

Table 3. Treatment of the residue obtained from the reaction of α-*N*-protected amino acids hydrazides **3** and aqueous formaldehyde.

Starting hydrazide	Residue	Treatment[a]	Yield (%)[b]
3aa	Solid	A	87
3ab	Solid	A	79
3ac	Solid	A	77
3ad	Solid	A	64
3bb	Solid	A	68
3bc	Solid	A	70
3bd	Solid	A	63
3cb	Oil	B	67
3cd	Oil	C	66
3dc	Oil	C	63
3dd	Oil	B	67
3ea	Oil	B	70
3eb	Oil	B	78
3ec	Oil	C	68
3fa	Oil	C	75
3fb	Oil	B	81

[a]Method A: after evaporation of THF, the solid residue was triturated in Et_2O and filtered. Method B: after evaporation of THF, the oily residue was heated at 70 °C for 1 h under vacuum, and the obtained solid was triturated in Et_2O and filtered. Method C: after evaporation of THF, the oily residue was heated at 70 °C for 1 h under vacuum, and the obtained solid was dissolved in Et_2O. The clear solution was added dropwise under stirring to pentane and the solid, which separated off, was collected by filtration.

[b]Isolated yield taking the starting hydrazide **3** as the reference and considering the monomeric species **4** as it were the only one present.

To estimate the percentage of the different oligomers present in the above solids, the samples were analysed by LC–ESI–MS. The results (Table 4) showed that the monomer **5** was the main component in all of the mixtures obtained from the hydrazides **3** tested, ranging from a maximum when the substrate was α-*N*-Z-protected to a relative minimum when α-*N*-Boc-protection was present; however, in the last ones, the formation of the trimeric form **6** was favoured. Finally, variable amounts of tetramer **28** and pentamer **29** were always present when the residue, obtained after removal of THF, was an oil (Table 3).

Any attempt to resolve these mixtures by fractional crystallization or absorption chromatography was unsuccessful. Specifically, TLC performed on silica gel or aluminium oxide was found to cause complete hydrolysis to the starting

© 2008 NRC Canada

Table 4. Composition of the mixtures obtained from the reaction of α-*N*-protected amino acids hydrazides **3** and aqueous formaldehyde.

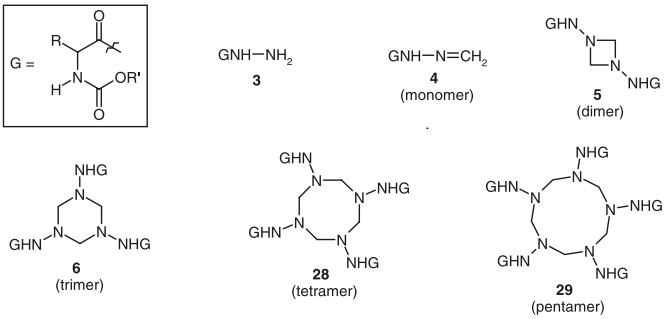

3	**4** (%)	**5** (%)	**6** (%)	**28** (%)	**29** (%)
aa	65±5	3±1	32±4		
ab	75±5	2.0±0.3	23±3		
ac	50±4	3±1	47±5		
ad	87±6	3±1	10±2		
bb	73±4	3±1	24±4		
bc	55±3	2.0±0.2	43±5		
bd	83±6	3±1	14±2		
cb	86±5	2.0±0.4	9±1	2.0±.1	1±0.1
cd	80±6	3±1	7±1	5±1	4±1
dc	53±4	3±1	37±4	7±1	
dd	80±5	3±1	11±2	6±1	
ea	67±2	3±1	19±2	8±1	3±1
eb	88±5	2.0±0.3	7±1	3±1	
ec	53±3	1.0±0.1	44±3	1.0±0.3	1.0±0.2
fa	63±3	3±1	30±2	4±1	
fb	72±4	3±1	17±2	8±1	

Note: Reported percentages, mean, and standard error of mean of triplicate measurements were determined from the areas of chromatographic peaks of the corresponding $[M+Na]^+$ ions (ESI–MS).

α-*N*-protected amino acid hydrazides **3**. The same problems were encountered in trying to resolve the complex mixtures obtained in all cases during the study of the reaction between *N*-ethoxycarbonylphenylalaninohydrazide (**3ab**) and formaldehyde (Table 2).

Data pertinent to the reaction mixtures obtained from the reaction of hydrazides **3** and formaldehyde are collected in Supplementary Data.[2] In this context, it is noteworthy to mention that the ^{1}H and ^{13}C NMR spectra of all the collected residues, recorded in DMSO-d_6 at 40 °C, showed the presence of two main products, namely, the monomer **4** and the trimer **6**. When NMR experiments were performed at high temperature (90–135 °C), a single species was invariably present. In particular, ^{1}H NMR spectra exhibited a single set of signals for each proton, namely two doublets centered at ca. 6.5 and 7.1 ppm with a coupling constant of ca. 12 Hz (two multiplets at 40 °C in the range 6.4–6.6 and 6.9–7.2 ppm), which are typical of *N*-methylene protons, thus confirming the presence of the monomeric form **4**. An identical spectral simplification was observed in the ^{13}C NMR experiments, where the *N*-methylene carbon appeared as a broad signal at ca. 136 ppm (two signals at 40 °C at ca. 135 and 138 ppm).

To check the stereochemical stability of the configuration of the chiral substrates through the whole process, the obtained compounds were hydrolysed under acidic conditions affording the corresponding hydrazides **3**, which were found to be identical to the starting materials, as evidenced by chiral HPLC analysis.

Conclusions

We have reported the detailed study of the interaction of enantiomerically pure α-*N*-amino acid hydrazides with formaldehyde. Aqueous formaldehyde in refluxing THF proved to be the best combination, affording a mixture of the monomeric condensation product and higher-order oligomers in very good isolated yield but, as evidenced by NMR analysis, at high temperature (90–135 °C) only the monomeric precursor was present. Therefore, under suitable conditions, it is possible to obtain reactive *N*-methylene derivatives containing a natural amino acid moiety which could be usefully involved in further reactions, such as $NaBH_4$ reduction to the corresponding *N*-methyl derivatives, as evidenced by preliminary experiments carried out in our laboratory (11).

Experimental section

General

All reagents were of commercial quality (Sigma-Aldrich, Fluka) and used without further purification. The α-*N*-protected amino acids hydrazides **3** were prepared as previously described (4). The reactions were monitored by ESI–MS in the positive ion mode with a Finnigan LXQ (linear trap). The intact reaction mixture was diluted with MeCN and the obtained solution was directly infused into the ion source with the aid of a syringe pump. The identities of the detected compounds were confirmed by ESI–MS–MS experiments (see Supplementary data).[2] The LC–ESI–MS analyses were obtained with the same instrument coupled with a Finnigan Surveyor LC Pump Plus equipped with an Agilent Zorbax Extend-C18 column (150 × 2.1 mm) using MeCN as the mobile phase. Chiral HPLC (hexane-2-propanol, 50:50 *v*/*v*; flow rate 0.5 mL/min; UV detector 254 nm) was performed on a Waters M-45 apparatus using a Daicel Chiracel OD column (0.46 cm I.D. × 25 cm). Direct inlet mass spectra (DI–MS) were obtained with a Fisons TRIO 2000 gas chromatograph – mass spectrometer, working in the positive ion 70 eV electron impact mode. Spectra were recorded in the range 35–450 u. Temperatures between 150 and 250 °C were found suitable to volatilise all the compounds into the ion source (see Supplementary Data).[2] IR spectra were obtained with a Nicolet FT–IR Magna 550 spectrophotometer using the KBr technique for solids and recorded in the range 4000–400 cm^{-1} (see Supplementary Data).[2] ^{1}H and ^{13}C NMR spectra were recorded on a Bruker AC-F 200 spectrometer at 200 and 50 MHz, respectively, using DMSO-d_6 as solvent at different temperatures (see Supplementary

[2] Supplementary data for this article are available on the journal Web site (canjchem.nrc.ca) or may be purchased from the Depository of Unpublished Data, Document Delivery, CISTI, National Research Council Canada, Ottawa, ON K1A 0R6, Canada. DUD 3760. For more information on obtaining material refer to cisti-icist.nrc-cnrc.gc.ca/irm/unpub_e.shtml.

© 2008 NRC Canada

Data).[2] Elemental analyses were performed with a Carlo Erba Mod. 1106 elemental analyser and found satisfactory (see Supplementary Data).[2] Melting points were determined with an automatic Mettler (Mod. FP61) melting point apparatus and are uncorrected (see Supplementary Data).[2] Reported values have to be considered merely indicative as referring to mixtures of monomeric and higher-order condensation products.

Reaction of the α-*N*-protected amino acids hydrazides 3 and aqueous formaldehyde

Aqueous formaldehyde (37%, 1.34 mmol, 0.10 mL) was added in one lot to a refluxing solution of the appropriate α-*N*-protected amino acid hydrazide **3** (1.28 mmol) in THF (3.6 mL), and the resulting mixture was kept under reflux for 0.5 h. After this time, the solvent was evaporated off under reduced pressure and the obtained crude mixture treated following one of the reported procedures, depending on the nature of the residue (Table 3).

Method A. After evaporation of THF, the solid residue was triturated in Et_2O and collected by filtration.

Method B. After evaporation of THF, the oily residue was heated at 70 °C for 1 h under vacuum, and the obtained solid was triturated in Et_2O and collected by filtration.

Method C. After evaporation of THF, the oily residue was heated at 70 °C for 1 h under vacuum, and the obtained solid was dissolved in Et_2O. The clear solution was added dropwise under stirring to pentane and the solid which separated was collected by filtration.

Acknowledgements

Financial support was obtained from MIUR (FURD 2001–2003 to GV). The authors are grateful to Dr. P. Martinuzzi for recording ^1H and ^{13}C NMR spectra, Dr. A. Callea for MS measurements, and Mr P. Padovani for expert instrumental maintenance.

References

1. J. Gante. Angew. Chem., Int. Ed. **33**, 1699 (1994).
2. J. Gante. Synthesis, 405 (1989).
3. (*a*) H. Gutmann, B. Hegedues, and P. Zeller. Ger. Patent 1-089-390 (1960) [Chem. Abstr. **56**, 4860a (1962)]; (*b*) I.Z. Siemion. Rocz. Chem. **42**, 237 (1968) [Chem. Abstr. **69**, 36424 (1968)]; (*c*) A.R. Fersht and Y. Requena. J. Am. Chem. Soc. **93**, 7079 (1971); (*d*) A.S. Dutta and J.S. Morley. J. Chem. Soc. Perkin Trans. 1, 1712 (1975); (*e*) S.A. Dutta, B.J.A. Furr, and M.B. Giles. Ger. Patent 2-720-245 (1977) [Chem. Abstr. **88**, 136991 (1978)]; (*f*) A.S. Dutta, J.J. Gormley, C.F. Hayward, J.S. Morley, and G.J. Stacey. Ger. Patent 2-715-803 (1978) [Chem. Abstr. **89**, 197970 (1978)]; (*g*) J.C. Powers, R. Boone, D.L. Carroll, B.F. Gupton, C.M. Kam, N. Nishino, M. Sakamoto, and P.M. Tuhy. J. Biol. Chem. **259**, 4288 (1984); (*h*) U. Neumann, T. Steinmetzer, A. Barth, and H.U. Demuth. J. Enzym. Inhib. **4**, 213 (1991); (*i*) C. Giordano, R. Calabretta, C. Gallina, V. Consalvi, and R. Scandurra. Farmaco, **46**, 1497 (1991); (*j*) C. Giordano, R. Calabretta, C. Gallina, V. Consalvi, R. Scandurra, F. Chiaia Noya, and C. Franchini. Eur. J. Med. Chem. **28**, 297 (1993); (*k*) R. Xing, and R.P. Hanzlik. J. Med. Chem. **41**, 1344 (1998); (*l*) S.M. Halbert, S.K. Thompson, and D.F. Veber. US Patent 5-998-470 (1999) [Chem. Abstr. **132**, 426 (2000)].
4. G. Verardo, P. Geatti, and B. Lesa. Synthesis, 559 (2005).
5. (*a*) G. Verardo, S. Cauci, and A.G. Giumanini. J. Chem. Soc. Chem. Commun. 1787 (1985); (*b*) A.G. Giumanini, G. Verardo, and M. Poiana. J. Prakt. Chem. **330**, 161 (1988).
6. A.G. Giumanini, G. Verardo, and M.H. Gei. J. Labelled Comp. Radiopharm. **24**, 255 (1987).
7. (*a*) A.G. Giumanini, G. Verardo, L. Randaccio, N. Bresciani-Pahor, and P. Traldi. J. Prakt. Chem. **327**, 739 (1985); (*b*) E. Zangrando, G. Poggi, A.G. Giumanini, and G. Verardo. J. Prakt. Chem. **329**, 195 (1987); (*c*) A.G. Giumanini, G. Verardo, E. Zangrando, and L. Lassiani. J. Prakt. Chem. **329**, 1087 (1987); (*d*) A.G. Giumanini, G. Verardo, F. Gorassini, T. Scubla, P. Strazzolini, F. Benetollo, and G. Bombieri. J. Chem. Soc. Perkin Trans. 2, 1771 (1995); (*e*) G. Verardo, F. Gorassini, A.G. Giumanini, T. Scubla, M. Tolazzi, and P. Strazzolini. Tetrahedron, **51**, 8311 (1995).
8. (*a*) H.M.A. Hartmans. Recl. Trav. Chim. Pays-Bas, **65**, 468 (1946); (*b*) S. Veibel. Acta Chem. Scand. **1**, 54 (1947); (*c*) S.S. Joshi, and D.S. Deorha. J. Indian Chem. Soc. **29**, 46 (1952); (*d*) S. Olsen and C. Rutland. Chem. Ber. **86**, 361 (1953); (*e*) A.T. Blomquist and J.C. Westfahl. J. Am. Chem. Soc. **75**, 2304 (1953); (*f*) J. Klosa. Arch. Pharm. **289**, 211 (1956); (*g*) S.S. Joshi, and D. S. Deorha. J. Indian Chem. Soc. **34**, 14 (1957); (*h*) M. Leonte. Analele Stiint. Univ. AI. I. Cuza Iasi, **4**, 197 (1958) [Chem. Abstr. **56**, 4645e (1962)]; (*i*) R. Delaby, S. Danton, and P. Chabrier. Bull. Soc. Chim. Fr. 2061 (1961); (*j*) S.S. Joshi and D. S. Deorha. J. Indian Chem. Soc. **38**, 31 (1961); (*k*) W. Schulze and G. Letsch. J. Prakt. Chem. **17**, 21 (1962); (*l*) H.H. Stroh and H.E. Nikolajewski. Chem. Ber. **95**, 562 (1962); (*m*) D.S. Deorha and H.L. Sharma. J. Indian Chem. Soc. **40**, 1047 (1963); (*n*) J. Strumillo and S. Grudzinski. Acta Pol. Pharm. **30**, 127 (1973) [Chem. Abstr. **79**, 78345 (1973)]; (*o*) K. Sato, A. Okumura, A. Kurata, and M. Nakamura. Nippon Nogei Kagaku Kaishi **50**, 369 (1976) [Chem. Abstr. **85**, 194106 (1976)].
9. (*a*) P. Chen. J. Chin. Chem. Soc. **3**, 251 (1935) [Chem. Abstr. **29**, 7229f (1935)]; (*b*) P.P.T. Sah and H.-M. Wang. J. Chin. Chem. Soc. **14**, 31 (1946) [Chem. Abstr. **43**, 6973b (1949)]; (*c*) J.G. Lockemann and J. Kalikowsky. Chem. Ber. **82**, 183 (1949); (*d*) O. Isler, H. Gutmann, O. Straub, B. Fust, E. Bohni, and A. Struder. Helv. Chim. Acta **38**, 1046 (1955); (*e*) H.H. Fox. Brit. Patent 720-787 [Chem. Abstr. **49**, 8334c (1955)]; (*f*) R.L. Hinman. J. Am. Chem. Soc. **79**, 414 (1957); (*g*) G.M. Rosen, F.Q. Gemmill, E.O. Snoke, and F.D. Popp. J. Heterocyclic Chem. **12**, 619 (1975); (*h*) A. Csiba, A. Samu, and E. Vari. Kiserletes Orvostudomany, **32**, 299 (1980) [Chem. Abstr. **93**, 215281 (1980)]; (*i*) M. El-Kerdawy, H. Eisa, A. Barghash, and A. Marouf. Sulfur Letters, **10**, 57 (1989). (*j*) I.V. Melikhov, S.S. Berdonosov, F.N. Gonsales, and B.I. Kharisov. Zh. Fiz. Khim. **69**, 614 (1995) [Chem. Abstr. **123**, 284983 (1995)]; (*k*) S.S. Berdonosov, O.I. Buzin, I.V. Melikhov, and A.G. Bogdanov. Vestn. Mosk. U. Khim. **39**, 134 (1998) [Chem. Abstr. **130**, 168071 (1999)]; (*l*) S. Kobayashi, T. Hamada, and K. Manabe. Synlett. 1140 (2001); (*m*) P. Appelblad, K. Irgum, and E. Ponten. Int. Appl. Patent WO 02-094-769 [Chem. Abstr. **137**, 392710 (2002)]; (*n*) D.J. Benstead, A.N. Hulme, H. McNab, and P. Wight. Synlett. 1571 (2005).
10. (*a*) G. Verardo, N. Toniutti, A. Gorassini, and A.G. Giumanini. Eur. J. Org. Chem. 2943 (1999); (*b*) G. Verardo, P. Geatti, P. Martinuzzi, M. Merli, and N. Toniutti. Eur. J. Org. Chem. 3840 (2003).
11. G. Verardo, P. Strazzolini. In press.

© 2008 NRC Canada

An efficient procedure for the TEMPO-catalyzed oxidation of alcohols to aldehydes and ketones using ferric chloride hexahydrate as terminal oxidant

R. Senthil Kumar, K. Karthikeyan, and Paramasivan T. Perumal

Abstract: A simple, efficient procedure for the oxidation of alcohols by catalytic 2,2,6,6-tetramethyl-piperidyl-1-oxy (TEMPO) was developed using $FeCl_3 \cdot 6H_2O$ as the terminal oxidant. The reaction gives high yield of the corresponding aldehydes and ketones with no over oxidation to the acid.

Key words: oxidation, TEMPO, $FeCl_3 \cdot 6H_2O$.

Résumé : On a développé une méthode simple et efficace d'oxydation catalytique 2,2,6,6-tetramethyl-piperidyl-1-oxy (TEMPO) d'alcools faisant appel au $FeCl_3 \cdot 6H_2O$ comme oxydant terminal. La réaction donne des rendements élevés des aldéhydes et des cétones correspondants sans suroxydation vers l'acide.

Mots-clés : oxydation, TEMPO, $FeCl_3 \cdot 6H_2O$.

[Traduit par la Rédaction]

Introduction

Oxidation of alcohols to aldehydes and ketones is one of the important synthetic transformations that is widely employed in various simple and complex syntheses of organic compounds (1). Therefore, it is not suprising to note a number of new oxidants emerge in the literature claiming superiority over the others in terms of cost, ready availability, selectivity, and yield. These factors assume importance especially when the oxidations are performed on a larger scale. Traditional oxidants, mainly inorganic in nature, include CrO_3, $KMnO_4$, MnO_2, SeO_2, and so forth. Moreover, the derivatives of chromium based oxidants, like PCC (2) and PDC (3) that are still in use, are often required in excess stoichiometric amounts and hence result in considerable amount of chromium waste by-products. Also, since these reagents are used in two- or three-fold excess of the substrate, the cost factor also needs to be addressed.

The nitroxyl radical, 2,2,6,6-tetramethyl-piperidyl-1-oxy (TEMPO), is a stable free radical employed in various oxidations of primary and secondary alcohols (4). However, owing to the high cost of TEMPO, most protocols employ it in catalytic amount together with a stoichiometric re-oxidant. Examples include TEMPO with $NaIO_4$ (5), I_2 (6), NBS (7), polyoxometalate (8), hypochlorite (9), Oxone (10), oxygen, or air (11*a*–11*c*). Derivatives of TEMPO, such as 4-hydroxy TEMPO, 4-acetamido TEMPO, have also been reported (11*d*). Not only TEMPO oxidations were carried out in ionic liquids (12*a*) but also a task-specific TEMPO derived ionic liquid was developed (12*b*). To achieve facile separation of product from TEMPO, solid supported reagents like silica-supported TEMPO (13) and polyamine immobilized piperidinyl oxyl (PIPO) (14) were developed owing to their heterogeneous nature; they can be separated by simple filtration.

Received 30 January 2008. Accepted 19 March 2008. Published on the NRC Research Press Web site at canjchem.nrc.ca on 29 May 2008.

R.S. Kumar, K. Karthikeyan, and P.T. Perumal.[1] Organic Chemistry Division, Central Leather Research Institute, Chennai 600 020, India.

[1]Corresponding author (e-mail: ptperumal@gmail.com).

Scheme 1. Oxidation of primary and secondary alcohols with TEMPO/$FeCl_3 \cdot 6H_2O$.

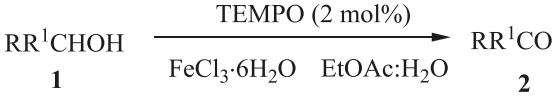

R = alkyl, H
R^1 = alkyl, aryl

Results and discussion

The development of new terminal oxidants for TEMPO-mediated oxidations still continues to be an interesting area of research. The use of ferric chloride hexahydrate for its oxidising properties has been reported only in a few instances, including one by us (15). In continuing our interest in ferric chloride hexahydrate oxidation, we supposed that it could act as terminal oxidant in the TEMPO oxidation of alcohols (Scheme 1).

Accordingly, reaction of benzyl alcohol with catalytic TEMPO and stoichiometric ferric chloride hexahydrate was conducted at room temperature in CH_2Cl_2/H_2O as solvent. The reaction proceeded smoothly giving 75% of benzal-

 doi:10.1139/V08-059 © 2008 NRC Canada

Table 1. Oxidation of alcohols by TEMPO/$FeCl_3 \cdot 6H_2O$

Entry	Alcohol	Aldehyde/Ketone	Time (hours)	Yield[a] (%)
1	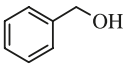	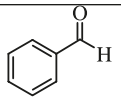	6	90
2	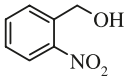	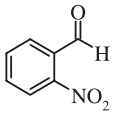	8	85
3	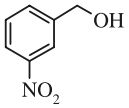	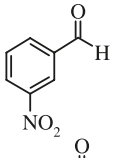	8	68
4	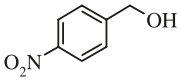	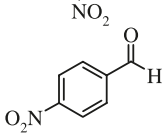	6	88
5	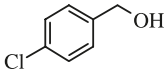	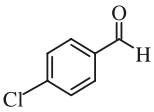	3	80
6	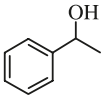	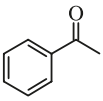	10	95
7	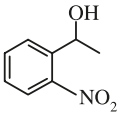	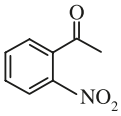	10	96
8	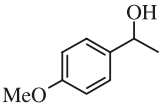	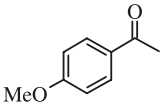	5	96
9	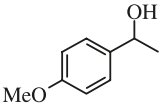	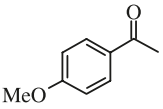	5	98[b]
10	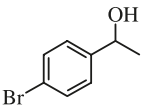	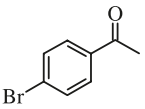	5	85

dehyde with no over oxidation to benzoic acid. Increasing the stoichiometry of $FeCl_3 \cdot 6H_2O$ to 1.30 equiv. increased the yield to 90%. Also, EtOAc/H_2O solvent system was found to give better result than CH_2Cl_2/H_2O. Various primary and secondary alcohols were oxidized to the corresponding aldehydes and ketones in good yield using this protocol (Table 1). 1-Phenyl ethanol gave 95% yield of acetophenone. Similarly, 4-methoxy-1-phenyl ethanol gave the corresponding acetophenone derivative in very good yield. Reaction of 9-anthryl alcohol at room temperature was incomplete; however, on refluxing conditions, it gave quantitative yield of 9-anthraldehyde. Additives like NaBr or NaOAc had no substantial effect (Table 1, entry 9). Similarly, 2-cyclopentenol, 2-cyclohexenol, and 2-cycloheptenol were oxidized to the corresponding ketones in good yield. In all cases, little or no oxidation was observed in the absence of TEMPO.

Oxidation of pyrazolyl alcohols

Pyraxzolyl aldehydes are important precursors for various pyrazole compounds, such as bispyrazolylmethane (16) and pyrazolyl quinolines (17) that display useful biological properties. Pyrazolyl alcohol and its substituted derivatives were oxidized to the corresponding pyrazolyl aldehyde using this protocol in good yield. (Scheme 2, Table 2).

© 2008 NRC Canada

Table 1 (*concluded*)**.**

Entry	Alcohol	Aldehyde/Ketone	Time (hours)	Yield[a] (%)
11	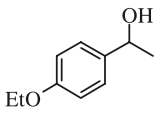	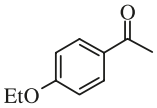	5	95
12	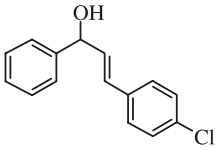	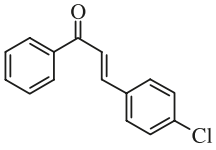	3	80
13	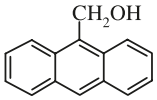	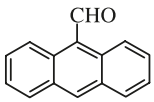	1	98[c]
14			1.5	90
15		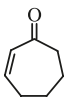	2	80
16			2	78
17	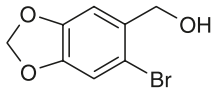	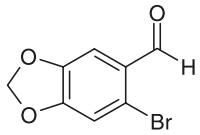	3	75[c]

[a]Isolated yields.
[b]NaBr and NaOAc (0.5 equiv.) were added.
[c]Under reflux condition.

Scheme 2. Oxidation of pyrazolyl alcohols by TEMPO/$FeCl_3 \cdot 6H_2O$.

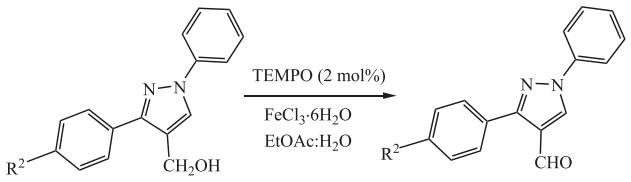

Conclusion

In sumary, a protocol for the efficient oxidation of various primary and secondary alcohols was developed using catalytic TEMPO and $FeCl_3 \cdot 6H_2O$ as co-oxidant. The procedure is operationally simple, as it requires no dry solvent or inert atmosphere and economical, as it employs the low cost $FeCl_3 \cdot 6H_2O$ in stoichiometric amount. Also, since the aldehydes and ketones are obtained in good to excellent yield, we hope this protocol will have good application in organic synthesis.

Table 2. Oxidation of pyrazolyl alcohols by TEMPO/$FeCl_3 \cdot 6H_2O$.

Entry	R^2	Product	Time (h)	Yield (%)
1	H	4a	4	85
2	Br	4b	4.5	50
3	Cl	4c	4	65
4	OEt	4d	5	60

Experimental

Materials and general

All chemicals were purchased from s.d. fine-chem ltd. and Spectrochem. All melting points are uncorrected. ^{1}H and

© 2008 NRC Canada

^{13}C NMR spectra were recorded in $CDCl_3$ and DMSO-d_6 using TMS as an internal standard on a JEOL spectrometer at 500 MHz and 125 MHz, respectively. Mass spectra were recorded on a Thermo Finnigan LCQ Advantage MAX 6000 ESI spectrometer. Column chromatography was performed on silica gel (100–200 mesh, SRL, India). Analytical TLC was performed on precoated aluminium sheets of silica gel G/UV-254 of 0.2 mm thickness (Merck, Germany).

Representative procedure for oxidation of primary and secondary alcohols to aldehydes and ketones

To 1.30 mmol of 3-(4-chlorophenyl)-1-phenylprop-2-en-1-ol in ethylacetate/water (7:3) (10 mL) was added TEMPO (0.02 equiv.), and the reaction mixture was stirred at room temperature. After 5 min, $FeCl_3 \cdot 6H_2O$ (1.69 mmol) was added, and stirring continued, following the progress of the reaction by TLC. After completion of the reaction, ethyl acetate layer was separated, and the aqueous layer was extracted with ethyl acetate (3 × 3 mL). Organic layers were combined and dried with sodium sulphate, filtered, and concentrated under reduced pressure.The residue thus obtained was purified by column chromatography to obtain the (2*E*)-3-(4-chlorophenyl)-1-phenylprop-2-en-1-one.

Benzaldehyde (100–52–7)

Colourless liquid. ^{1}H NMR (500 MHz, $CDCl_3$) δ: 7.49 (t, *J* = 7.7 Hz, 2H), 7.59 (t, *J* = 6.9 Hz, 1H), 7.84 (d, *J* = 7.7 Hz, 2H), 9.98 (s, 1H). ^{13}C NMR (125 MHz, $CDCl_3$) δ: 129.08, 129.81, 134.56, 136.45, 192.52. MS *m*/*z* = 106 M^+.

2-Nitrobenzaldehyde (552–89–6)

White solid (toluene/petroleum ether); mp 43 °C (lit. (18) 43–44 °C). ^{1}H NMR (500 MHz, $CDCl_3$) δ: 7.73–7.78(m, 2H), 7.91 (d, *J* = 9.5 Hz, 1H), 8.09 (d, *J* = 8.0 Hz, 1H), 10.38 (s, 1H). ^{13}C NMR (125 MHz, $CDCl_3$) δ: 124.58, 129.71, 131.40, 133.84, 134.21, 149.63, 188.29. MS *m*/*z* = 151 M^+.

3-Nitrobenzaldehyde (99–61–6)

Yellow solid (toluene/petroleum ether); mp 56 °C (lit. value (18) 58 °C). ^{1}H NMR (500 MHz, $CDCl_3$) δ: 7.76 (t, *J* = 8.4 Hz, 1H), 8.22 (d, *J* = 7.5 Hz, 1H), 8.47 (d, *J* = 7.0 Hz, 1H), 8.69 (d, *J* = 1.5 Hz, 1H), 10.11 (s, 1H). ^{13}C NMR (125 MHz, $CDCl_3$) δ: 124.53, 128.69, 130.51, 134.80, 137.45, 148.83, 189.90. MS *m*/*z* = 151 M^+.

4-Nitrobenzaldehyde (555–16–8)

Pale yellow solid (ethyl acetate/petroleum ether); mp 105 °C (lit. value (19) 104–106 °C). ^{1}H NMR (500 MHz, $CDCl_3$) δ: 8.06 (d, *J* = 8.4 Hz, 2H), 8.36 (d, *J* = 8.4 Hz, 2H), 10.14 (s, 1H). ^{13}C NMR (125 MHz, $CDCl_3$) δ: 124.38, 130.58, 140.13, 151.18, 190.49. MS *m*/*z* = 151 M^+.

4-Chlorobenzaldehyde (104–88–1)

White solid (petroleum ether); mp 45 °C (lit. (19) 45–46 °C). ^{1}H NMR (500 MHz, $CDCl_3$) δ: 7.49 (d, *J* = 8.6 Hz, 2H), 7.80 (d, *J* = 8.0 Hz, 2H), 9.95 (s, 1H). ^{13}C NMR (125 MHz, $CDCl_3$) δ: 129.53, 130.99, 134.77, 141.02, 190.97. MS *m*/*z* = 141 M^+.

Acetophenone (98–86–2)

Colourless liquid. ^{1}H NMR (500 MHz, $CDCl_3$) δ: 2.56 (s, 3H), 7.42 (t, *J* = 7.5 Hz, 1H), 7.52 (d, *J* = 8.0 Hz, 2H), 7.92 (d, *J* = 7.5 Hz, 2H). ^{13}C NMR (125 MHz, $CDCl_3$) δ: 26.69, 128.38, 128.66, 133.21, 137.16, 198.30. MS *m*/*z* = 120 M^+.

2-Nitroacetophenone (577–59–3)

Yellow liquid. ^{1}H NMR (500 MHz, $CDCl_3$) δ: 2.51 (s, 3H), 7.41 (dd, *J* = 1.5, 7.6 Hz, 1H), 7.55–7.58 (m, 1H), 7.69 (dt, *J* = 1.5, 7.6 Hz, 2H), 8.02 (d, *J* = 8.4 Hz). ^{13}C NMR (125 MHz, $CDCl_3$) δ: 30.18, 124.40, 127.43, 130.81, 134.37, 137.88, 145.82, 200.00. MS *m*/*z* = 165 M^+.

4-Methoxyacetophenone (100–06–1)

Colourless solid (petroleum ether); mp 36 °C (lit. (18) 38–39 °C). ^{1}H NMR (500 MHz, $CDCl_3$) δ: 2.56 (s, 3H), 3.87 (s, 3H), 6.94 (d, *J* = 8.4 Hz, 2H), 7.94 (d, *J* = 8.4 Hz, 2H). ^{13}C NMR (125 MHz, $CDCl_3$) δ: 26.48, 56.62, 113.84, 127.42, 130.72, 163.60, 196.92. MS *m*/*z* = 150 M^+.

4-Bromoacetophenone (99–90–1)

White solid (petroleum ether); mp 51 °C (lit. (20) 51–52 °C). ^{1}H NMR (500 MHz, $CDCl_3$) δ: 2.58 (s, 3H), 7.60 (d, *J* = 8.4 Hz, 2H), 7.81 (d, *J* = 8.4 Hz, 2H). ^{13}C NMR (125 MHz, $CDCl_3$) δ: 26.64, 128.40, 129.93, 131.99, 135.91, 197.14. MS *m*/*z* = 198 M^+.

4-Ethoxyacetophenone (1676–63–7)

Colourless solid (petroleum ether); mp 39 °C (lit. (18) 36–37 °C). ^{1}H NMR (500 MHz, $CDCl_3$) δ: 1.42 (t, *J* = 6.9 Hz, 3H), 2.56 (s, 3H), 4.08 (q, *J* = 6.9 Hz, 2H), 6.90 (d, *J* = 9.1 Hz, 2H), 7.91 (d, *J* = 8.4 Hz, 2H). ^{13}C NMR (125 MHz, $CDCl_3$) δ: 14.75, 26.42, 63.83, 114.19, 130.22, 130.68, 163.00, 196.90. MS *m*/*z* = 164 M^+.

(2E)-3-(4-Chlorophenyl)-1-phenylprop-2-en-1-one

White solid (absolute ethanol); mp 110 °C (lit. (21) 111–113 °C). ^{1}H NMR (500 MHz, $CDCl_3$) δ: 7.48 (d, *J* = 6.9 Hz, 2H), 7.53 (t, *J* = 6.9 Hz, 2H), 7.63 (t, *J* = 6.9 Hz, 1H), 7.70 (d, *J* = 16.0 Hz, 1H), 7.88–7.94 (m, 3H), 8.12 (d, *J* = 7.6 Hz, 2H). ^{13}C NMR (125 MHz, $CDCl_3$) δ: 123.27, 129.11, 129.33, 129.48, 131.13, 133.77, 134.15, 135.66, 137.96, 143.07, 189.60. MS *m*/*z* = 243 M^+. Anal. calcd. for $C_{15}H_{11}ClO$ (242.70): C, 74.23; H, 4.57; Cl, 14.61. Found: C, 74.28; H, 4.52; N, 14.69.

9-Anthraldehyde (642–31–9)

Yellow solid; (aq. acetic acid); mp 104 °C (lit. (18) 104–105 °C). ^{1}H NMR (500 MHz, $CDCl_3$) δ: 7.54 (t, *J* = 6.9 Hz, 2H), 7.67 (t, *J* = 7.6 Hz, 2H), 8.04 (d, *J* = 8.4 Hz, 2H), 8.66 (s, 1H), 8.97 (d, *J* = 9.2 Hz, 2H), 11.50 (s, 1H). ^{13}C NMR (125 MHz, $CDCl_3$) δ: 123.62, 124.77, 125.79, 129.23, 129.38, 131.15, 132.22, 135.35, 193.12. MS *m*/*z* = 206 M^+.

2-Cyclohexenone (930–68–7)

Brown liquid. ^{1}H NMR (500 MHz, $CDCl_3$) δ: 1.90–1.95 (m, 2H), 2.24–2.28 (m, 2H), 2.31–2.34 (m, 2H), 5.90–5.92 (m, 1H), 6.89–6.93 (m, 1H). ^{13}C NMR (125 MHz, $CDCl_3$) δ: 22.73, 25.69, 38.10, 129.85, 150.92, 199.86. MS *m*/*z* = 96 M^+.

© 2008 NRC Canada

2-Cycloheptenone (1121–66–0)

Pale brown liquid. ^{1}H NMR (500 MHz, $CDCl_3$) δ: 1.74–1.79 (m, 4H), 2.38–2.42 (m, 2H), 2.53–2.56 (m, 2H), 5.95 (d, J = 12.2 Hz, 1H), 6.50–6.55 (m, 1H). ^{13}C NMR (125 MHz, $CDCl_3$) δ: 21.78, 26.19, 30.31, 43.59, 132.55, 146.67, 204.53. MS m/z = 110 M^+.

2-Cyclopentenone (930–30–3)

Colourless liquid. ^{1}H NMR (500 MHz, $CDCl_3$) δ: 2.20–2.22 (m, 2H), 2.56–2.59 (m, 2H), 6.05–6.06 (m, 1H), 7.62–7.63 (m, 1H). ^{13}C NMR (125 MHz, $CDCl_3$) δ: 28.97, 33.99, 134.46, 165.11, 210.61. MS m/z = 82 M^+.

6-Bromopiperonal (15930–53–7)

White solid (absolute ethanol); mp 128 °C (lit. (22) 132–135 °C). ^{1}H NMR (500 MHz, DMSO-d_6) δ: 6.17 (s, 2H), 7.22 (d, J = 1.5 Hz, 1H), 7.35 (d, J = 1.5 Hz, 1H), 10.00 (s, 1H). ^{13}C NMR (125 MHz, DMSO-d_6) δ: 103.85, 107.92, 113.77, 121.25, 127.88, 148.62, 153.97, 190.51. MS m/z = 228 M^+.

Representative procedure for oxidation of pyrazolyl alcohol

To 1.30 mmol of pyrazolyl alcohol in ethylacetate:water (7:3) (10 mL) was added TEMPO (0.02 equiv.), and the reaction mixture was stirred at room temperature. After 5 min, $FeCl_3 \cdot 6H_2O$ (1.69 mmol) was added, and the stirring continued, following the progress of the reaction by TLC. After completion of the reaction, ethyl acetate layer was separated from water, and water layer was extracted with ethyl acetate (3 × 3 mL). Organic layers were combined and dried with sodium sulphate, filtered, and concentrated at reduced pressure. The residue thus obtained was purified by column chromatography to obtain the pyrazole aldehyde.

1,3-Diphenyl-1*H*-pyrazole-4-carbaldehyde (4a)

Yellow solid (absolute ethanol); mp 138 °C (lit. (23) 140 °C). ^{1}H NMR (500 MHz, $CDCl_3$) δ: 7.37 (t, J = 7.5 Hz, 1H), 7.47–7.49 (m, 5H), 7.78 (d, J = 8.0 Hz, 2H), 7.82 (d, J = 6.8 Hz, 2H), 8.53 (s, 1H) 10.03(s, 1H). ^{13}C NMR (125 MHz, $CDCl_3$) δ: 119.82, 122.58, 128.06, 128.87, 129.07, 129.41, 129.77, 131.16, 131.42, 139.07, 154.85, 185.32. MS m/z = 248 M^+.

3-(4-Bromophenyl)-1-phenyl-1*H*-pyrazole-4-carbaldehyde (4b)

Pale green solid (absolute ethanol); mp 140 °C (lit. (24) 142–143 °C). ^{1}H NMR (500 MHz, $CDCl_3$) δ: 7.40 (t, J = 7.6 Hz, 1H), 7.51 (t, J = 7.6 Hz, 2H), 7.63 (d, J = 8.4 Hz, 2H), 7.76 (t, J = 7.6 Hz, 4H), 8.52 (s, 1H) 10.02(s, 1H). ^{13}C NMR (125 MHz, $CDCl_3$) δ: 119.83, 122.57, 123.83, 128.23, 129.84, 130.37, 130.54, 131.99, 132.13, 138.96, 153.31, 184.5. MS m/z = 326 M^+.

3-(4-Chlorophenyl)-1-phenyl-1*H*-pyrazole-4-carbaldehyde (4c)

Yellow solid (absolute ethanol); mp 114 °C (lit. (25) 110–113 °C). ^{1}H NMR (500 MHz, $CDCl_3$) δ: 7.39 (t, J = 7.5 Hz, 1H), 7.45 (d, J = 8.0 Hz, 2H), 7.50 (t, J = 7.5 Hz, 2H), 7.76 (d, J = 8.0 Hz, 2H), 7.81 (d, J = 8.0 Hz, 2H), 8.51 (s, 1H), 10.01 (s, 1H). ^{13}C NMR (125 MHz, $CDCl_3$) δ: 119.80, 122.56, 128.20, 129.01, 129.82, 129.93, 130.28, 132.18, 135.51, 138.95, 153.24, 184.57. MS m/z = 282 M^+.

3-(4-Ethoxyphenyl)-1-phenyl-1*H*-pyrazole-4-carbaldehyde (4d)

Yellow solid (absolute ethanol); mp 142 °C. ^{1}H NMR (500 MHz, $CDCl_3$) δ: 1.44 (t, J = 6.8 Hz, 3H), 4.10 (q, J = 6.8 Hz, 2H), 7.01 (d, J = 8.4 Hz, 2H), 7.37 (t, J = 7.6 Hz, 1H), 7.50 (t, J = 7.6 Hz, 2H), 7.77 (t, J = 2.3 Hz, 4H), 8.51 (s, 1H), 10.03 (s, 1H). ^{13}C NMR (125 MHz, $CDCl_3$) δ: 14.89, 63.66, 114.81, 119.80, 122.42, 123.73, 127.95, 129.75, 130.33, 131.19, 139.14, 154.69, 160.02, 185.35. MS m/z = 292 M^+. Anal. calcd. for $C_{18}H_{16}N_2O_2$ (292.33): C, 73.95; H, 5.52; N, 9.58. Found: C, 73.86; H, 5.56; N, 9.69.

Acknowledgments

Two of the authors, RSK and KKK, thank Council of Scientific and Industrial Research (CSIR), New Delhi, India for financial support.

References

1. (*a*) M. Hudlicky. Oxidations in organic chemistry. Monograph 186. American Chemical Society, Washington, DC. 1990; (*b*) K.E. Harding, L.M. May, and K.F. Dick. J. Org. Chem. **40**, 1664 (1975).
2. E.J. Corey and J.W. Suggs. Tetrahedron Lett. **16**, 2647 (1975).
3. E.J. Corey and G. Schmidt. Tetrahedron Lett. **20**, 339 (1979).
4. (*a*) H. Adam, C.R. Saha-Moller, and P.A. Ganghpure. Chem. Rev. **101**, 3499 (2001); (*b*) R.A. Sheldon, I.W.C.E. Arends, G.-J. ten Brink, and A. Dijksman. Acc. Chem. Res. **35**, 774 (2002).
5. M. Lei, R.-J. Hu, and Y.-G. Wang. Tetrahedron, **62**, 1 (2006).
6. R.A. Miler and R.S. Hoerrner. Org. Lett. **5**, 285 (2003).
7. J. Einborn, C. Einborn, F. Ratajczak, and J.-L. Pierre. J. Org. Chem. **61**, 7454 (1996).
8. R. Ben-Daniel, P. Alsters, and R. Neumann. J. Org. Chem. **66**, 8650 (2001).
9. S.D. Nwauka and P.M. Keehn. Tetrahedron Lett. **23**, 3131 (1982).
10. C. Bolm, S. Angelika, S. Magnus, and J.P. Hildebrand. Org. Lett. **2**, 1173 (2000).
11. (*a*) G. Mehta and S. Roy. Org. Lett. **6**, 2389 (2004); (*b*) G. Mehta and K. Islam. Org. Lett. **6**, 807 (2004); (*c*) R. Liu, X. Liang, C. Dong, and X. Hu. J. Am. Chem. Soc. **124**, 4112 (2004); (*d*) N. Jiang and A.J. Ragauskas. J. Org. Chem. **71**, 7087 (2006).
12. (*a*) J. Dupont, R.F. de Souza, and P.A.Z. Suarez. Chem. Rev. **102**, 3667 (2002); (*b*) X.E. Wu, L. Ma, M.X. Ding, L.X. Gao. Synlett. 607 (2005).
13. T. Fey, H. Fischer, S. Bachmann, K. Albert, and C. Bolm. J. Org. Chem. **66**, 8154 (2001).
14. A. Dijksman and I. Arends. Chem. Commun. 271 (2000).
15. K. Hemanth Kumar, D. Muralidharan, and P.T. Perumal. Tetrahedron Lett. **45**, 7903 (2004).
16. R. Murugan, M. Karthikeyan, P.T. Perumal, and B.S.R. Tetrahedron, **61**, 12275 (2005).
17. R. Sridhar and P.T. Perumal. Can. J. Chem. **84**, 464 (2006).
18. Dictionary of organic compounds. 4th ed. Eype and Spottiswoode, London. 1965.
19. M. Lei, R.-J. Hu., and Y.G. Wang. Tetrahedron, **62**, 8928 (2006).

© 2008 NRC Canada

20. I.P. Beletskaya, A.S. Sigeev, A.S. Peregudov, and P.V. Petrovskii. Synthesis, 2534 (2007).
21. D.R. Palleros. Green Chem. **81**, 1345 (2004).
22. G. Poli and G.J. Giambastiani. Org. Chem. **67**, 9456 (2002).
23. M.A. Kira, M.O. Abdul-Raeman, and K.Z. Gadalla. Tetrahedron Lett. **30**, 109 (1989).
24. M. Bernard. Pharmazie, **41**, 560 (1986).
25. O. Prakash, K. Pannu, and A. Kumar. Molecules, **11**, 43 (2006).

© 2008 NRC Canada

The unambiguous assignment of NMR spectra of *per-O*-methylated 6-mono and 6,6-diamino-β-cyclodextrins

Eduardo Díaz T., Christopher K. Jankowski, Celine Hocquelet, Federico del Rio P., and Héctor Barrios

Abstract: The step-by-step analysis of high-resolution proton and ^{13}C NMR spectra of *per-O*-methylated 6-monoamino and 6,6-diamino-A,D-β-cyclodextrins is described. Selected 2-D experiments (COSY, NOESY, HSQC, DEPT, and HMBC) allowed us to challenge the current interpretation. The full assignment of the proton and carbon-13 NMR spectra of these two compounds was performed enabling us to complete the assignment of NMR spectra acquired at 500 and 800 MHz for these important synthetic intermediates.

Key words: COSY, NOESY, HSQC, DEPT, HMBC, NMR, 6-amino-β-cyclodextrins, 6,6-diamino-β-cyclodextrins.

Résumé : On décrit l'analyse étape par étape des spectres RMN à haute résolution du ^{1}H et du ^{13}C de 6-monoamino-cyclodextrine et des 6,6-diamino-A,D-β-cyclodextrines *per-O*-méthylées. Des expériences bidimensionnelles choisies (COSY, NEOSY, HSQC, DEPT et HMBC) ont permis de mettre en doute l'interprétation actuelle. L'attribution complète des spectres RMN du ^{1}H et du ^{13}C de ces deux produits a été réalisée et elle permet de faire une attribution complète des spectres RMN obtenus à 500 et 800 MHz pour ces importants intermédiaires de synthèse.

Mots-clés : COSY, NEOSY, HSQC, DEPT, HMBC, RMN, 6-amino-β-cyclodextrines, 6,6-amino-β-cyclodextrines.

Traduit par la Rédaction]

Introduction

One of the most versatile by-products in the functionalization of β-cyclodextrins (CDs) is 6-aminocyclodextrin (**1**) (1–3). Attaching substituents to the primary faces of these molecules is both appealing and relatively easy. One can perform inclusion reactions into its cavity, using this group as an anchor; the use of linkers of various lengths from the amino group allows the design of many new syntheses (4–6). The general good reactivity of this group is extended to the whole family of CDs: α, β, and γ, as well as to their derivatives (e.g., *per*-2-hydroxypropylated CD).

Despite their easy synthesis (Scheme 1), knowledge of several polyamino CDs suffers from the lack of detailed analysis of their NMR spectra because of numerous problems resulting from the number of isomers, which leads to signal overlapped even at higher NMR fields. As a result, although the abundant literature on these molecules has often mentioned their complex spectra, there have been few attempts of any specific and complete assignment of the signals (7–10).

Scheme 1. Synthesis of *per-O*-methylated amino-β-cyclodextrins.

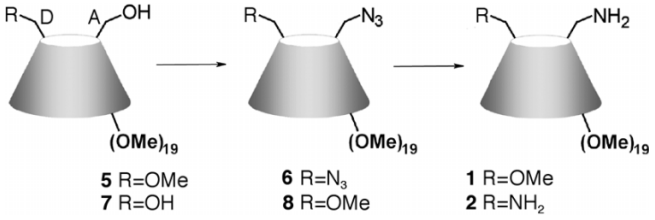

In this work, we report the NMR assignment of two *per-O*-methylated amino-β-CD: the monoamino 6-amino-*per-O*-methyl-β-CD (**1**) and the diamino 6,6-diamino-*per-O*-methyl-β-CD (**2**) (Fig. 1), as a challenging system for isomeric sugar signal assignment and as an exercise for elimination of isomeric structures for amino sugars using 1-D and 2-D proton and carbon NMR on both 500 and 800 MHz instruments.

The syntheses of *per-O*-methylated mono- and di-amino-β-CD were realized, as described in the experimental section (11), and the double amination of the CD in principle leads to the A,D-6,6-diamino-β-CD (**2**) (case 3, Fig. 2). For simplicity, in this paper we will label the glucose unit of cyclodextrins as A, B, C, etc., starting from the sugar bearing the amino group, instead of labeling the glucose units as I, II, etc. The formation of the second amino group on the D sugar moiety (the fourth sugar, relative to the first

Received 15 May 2007. Accepted 17 March 2008. Published on the NRC Research Press Web site at canjchem.nrc.ca on 6 June 2008.

E. Díaz T.,[1] F. Del Rio P., and H. Barrios. Instituto de Química, Universidad Nacional Autónoma de México, Cd Universitaria, Delegación Coyoacan, 04510 México, D.F., México.
C.K. Jankowski[2] and C. Hocquelet. SCM, DRECAM, Centre d'études de Saclay, 91191 Gif-sur-Yvette, France.

[1]Corresponding author (e-mail: maudiaz@servidor.unam.mx).
[2]Present address: Département de chimie et biochimie, Université de Moncton, Moncton, NB E1A 3E9, Canada.

 doi:10.1139/V08-063 © 2008 NRC Canada

Fig. 1. Cyclodextrin structures **1** and **2**.

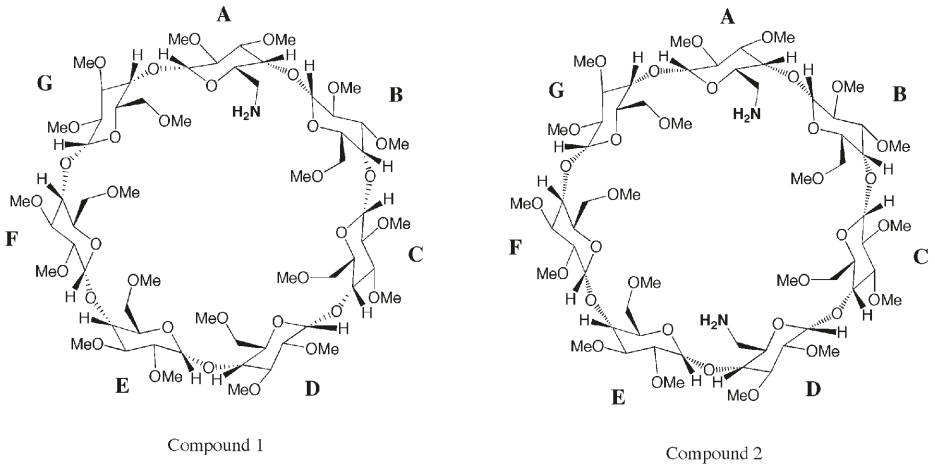

Fig. 2. Analysis of diamino-β-CD structures.

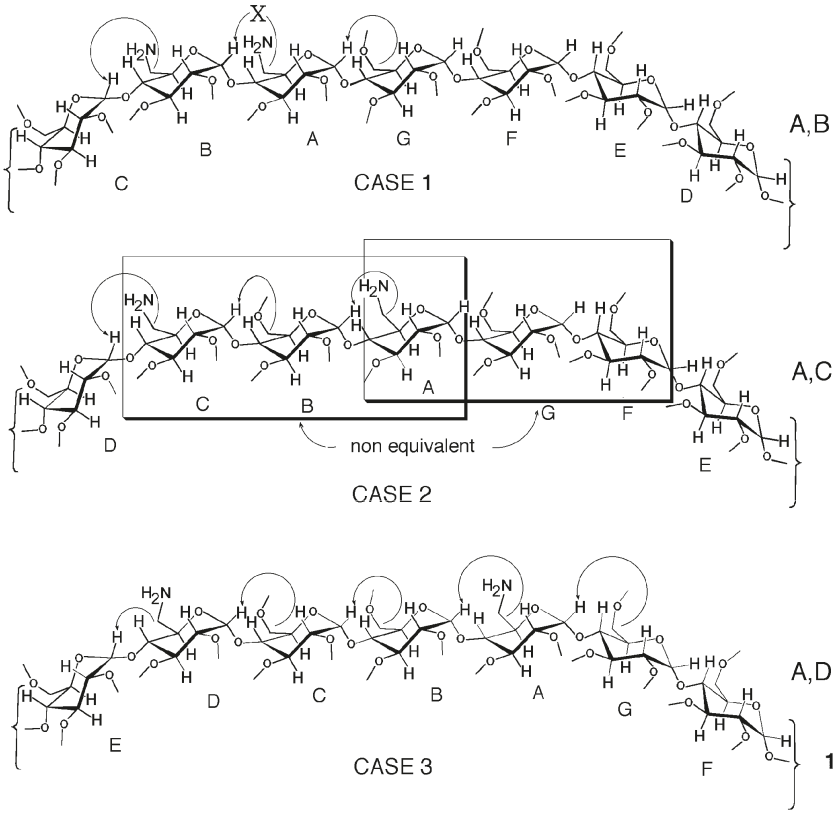

amination) led to the search for the isomeric diamino structure, as well as to the confirmation by the NMR of that diamine structure is substituted on the A and D rings. The A,D-disubstituted structure could also be discussed in a step-by-step method by elimination of the A,B or A,C (case 1 or case 2 in Fig. 2) structures; it leaves the two amino-bearing sugars separated by, respectively, two and three glucose.

Arrows indicate possible NOE interaction; X means absence of this interaction.

It is important to note that we do not want to undermine the assignment (11) of the 6,6-diamino-β-CD as being A,D-substituted; however, the particular chemical shifts of protons and carbons were not described in detail. Nevertheless, several other authors (12) have used NMR to study the methoxy-CDs, as well as their perbenzylated and peracetylated derivatives.

The mono-amino-β-CD (**1**) was used as a model compound for developing the methodology to study the diamino-β-CD NMR systems. As a basis for the assignment, previously recorded high-resolution H-1 and C-13 1-D spectra allowed us to assign some signals. We chose the A-ring, an amino-substituted glucose, as a starting point for selected

© 2008 NRC Canada

2-D experiments (COSY, NOESY, HSQC, and HMBC), which allowed us to complete the interpretation; the full assignment of the proton and carbon-13 NMR spectra of this compound is presented in Table 1. The step-by-step identification of the proton and carbon signals was achieved through the NOE between the protons that are closely related in space, namely, the C-6 methylene protons toward the anomeric signal of the neighbouring glucose unit (e.g., from glucose A to glucose B).

As an example of the analysis, some interesting details are presented from the spectral identification of compound **1**.

Results and discussion

500 MHz determinations

To begin the NMR proton spectra interpretation within the 500 MHz resolution constraints, it was necessary to set the following conditions:

(*i*) The first step was to use the information obtained from the COSY and NOESY spectra (Figs. 3*a* and 4) where the protons of the glucose units (A–G) displayed chemical shifts summarized in Table 1. The COSY spectrum yielded some important information about the proton–proton couplings; however, only two types of sugar rings were observed: as indicated in Fig. 4 and detailed in Fig. 5, all rings except A display the same COSY proton–proton coupling patterns, and even at 500 MHz they remain only weakly resolved.

(*ii*) The anomeric protons of the amino group bearing glucose (A) display their ^{1}H NMR signals at a higher field (δ = 5.063, d, $^3J_{H1\text{-}H2}$ = 3.5 Hz) than those of ring B (δ = 5.14 ppm) having OCH_3 on the C-6. The ratio of the integrated intensity for these two signals compared to the signals at δ = 5.03 ppm from the remaining anomeric protons is 1:1:5.

(*iii*) The C-6 methylene signal for the A ring protons appears at a higher field (2.88 ppm) than do the signals for the other C-6 methylenes at C-6 with the usual attached methoxy (δ = 3.70, 3.45, and 3.50) as detected by DEPT and HSQC experiments.

(*iv*) Through the NOESY experiments, we observed cross-peak correlations between the amino methylene protons on C-6 of ring A and the anomeric proton of ring B, at δ = 5.14, as well as with the signals at δ = 3.70, 3.50, and 3.45. The signal of the anomeric proton at δ = 5.14 also enabled us to observe a dipolar correlation to the doublet of doublets at δ = 3.04 ppm ($^3J_{H1\text{-}H2}$ = 3.5 and $^3J_{H2\text{-}H3}$ = 10.5 Hz). These couplings are assigned for the methine at C-2 of ring B. The remaining C-2 protons for each glucose unit were observed at δ = 3.06 (6H) as a doublet of doublets, ^3J = 3.5, 10.5 Hz.

The diagonal peak due to all H-2 present on glucose units of rings A–G (δ = 3.06) displayed cross peaks with the anomeric proton of ring A (δ = 5.063) and with the anomeric proton of ring B (δ = 5.14) showing the remaining five anomeric protons from glucose units of rings C–G overlapping at δ = 5.03. The additional cross peaks from the signal at δ = 3.06 was with that of the methoxy groups at δ = 3.38 and with that of the methine at C-3 (δ = 3.30).

Table 1. Proton and ^{13}C chemical shifts (ppm) for 6^A-amino-6^A-deoxy-*per*-*O*-methylated-β-cyclodextrin (**1**). IUPAC name: 6^A-amino-6^A-deoxy-2^A,3^A-di-*O*-methylhexakis-(2$^{A–G}$,3$^{B–G}$,6$^{B–G}$-tri-*O*-methyl)-cyclomaltoheptaose (**1**).

Ring	Position	δ_H	δ_C
A	C_1-H	5.063	97.60
	C_2-H	3.06	81.22
	C_3-H	3.30	81.60
	C_4-H	3.57	79.60
	C_5-H	3.55	71.70
	C_6-H	2.88	41.60
B	C_1-H	5.14	97.50
	C_2-H	3.04	81.35
	C_3-H	3.30	81.62
	C_4-H	3.45	79.60
	C_5-H	3.70	70.26
	C_6-H	3.45	70.88
C	C_1-H	5.03	97.68
	C_2-H	3.06	81.22
	C_3-H	3.30	81.60
	C_4-H	3.45	79.42
	C_5-H	3.70	70.29
	C_6-H	3.50	71.08
D	C_1-H	5.03	97.68
	C_2-H	3.06	81.22
	C_3-H	3.30	81.60
	C_4-H	3.45	79.40
	C_5-H	3.70	70.35
	C_6-H	3.50	71.08
E	C_1-H	5.030	97.68
	C_2-H	3.06	81.18
	C_3-H	3.30	81.60
	C_4-H	3.45	79.60
	C_5-H	3.70	70.35
	C_6-H	3.50	71.08
F	C_1-H	5.03	97.68
	C_2-H	3.06	81.18
	C_3-H	3.3	81.60
	C_4-H	3.45	79.60
	C_5-H	3.70	70.35
	C_6-H	3.50	71.08
G	C_1-H	5.03	97.77
	C_2-H	3.06	81.18
	C_3-H	3.30	81.60
	C_4-H	3.45	79.10
	C_5-H	3.70	70.45
	C_6-H	3.70	71.22

Note: Methyl group signals: 7 × [CH_3-O-C-2] 4 peaks δ(^{1}H): 3.387 (3H), 3.382 (3H), 3.375 (12H), 3.373 (3H), 5 peaks δ(^{13}C): 57.86 (2C), 57.80 (1C), 57.78 (1C), 57.76 (2C) 57.72 (1C); 7 × [CH_3-O-C-3] 3 peaks δ(^{1}H): 3.487 (6H), 3.484 (9H), 3.481 (6H), 2 peaks δ(^{13}C): 60.61 (6C), 60.54 (1C); 6 × [CH_3-O-C-6] 5 peaks δ(^{1}H): 3.234 (3H), 3.232 (3H), 3.229 (3H), 3.224 (6H), 3.220 (3H), 4 peaks δ(^{13}C): 58.3 (1C), 58.10 (3C), 58.07 (1C), 58.05 (1C).

© 2008 NRC Canada

Fig. 3. COSY spectra (500 MHz, DMSO-d_6) of compounds (*a*) **1** and (*b*) **2**, respectively.

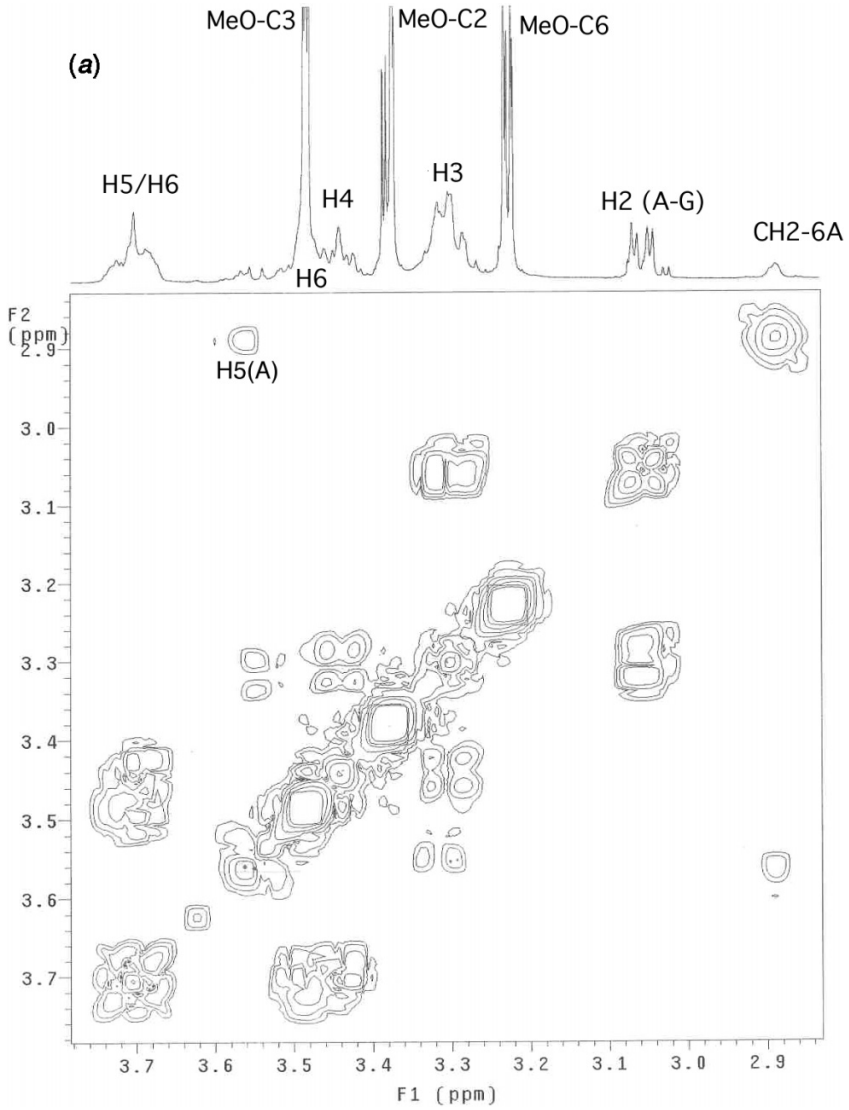

Having assigned this first NOE, we did the same for the remaining methylenes NOEs toward the next sugar (n + 1) units; the other NOEs are shown in Figs. 4 and 5.

It is interesting to note the important NOEs present for the anomeric proton of the A sugar unit were toward the H-4 of the sugar G as well as to the methoxy protons attached to C-2 (ring A) and methylene protons attached on the C-6 due to sugar G.

The signals of the methoxy groups of monoamino cyclodextrin (**1**) must be considered. The methoxy singlets partially overlapped at δ ~3.23 can be expanded to singlets at δ = 3.234 (3H), 3.232 (3H), 3.229 (3H), 3.224 (6H), and 3.220 (3H) and they were assigned for the methoxy groups attached to C-6 methylene of glucose units B–G.

On the other hand, the signal assigned to methoxy groups attached to C-2 (δ ~3.38) from the glucose units A–G was expanded to singlets at δ = 3.387 (3H), 3.382 (3H), 3.375 (12H), and 3.373 (3H). These methoxy groups displayed dipolar correlations with the methoxy groups attached to C-3 (δ = 3.48) as well as C-2 protons at δ = 3.06 in the NOESY spectrum.

Finally, the methoxy groups attached to C-3 displayed a broad peak at δ ~3.48, which upon expansion were poorly resolved into signals at δ = 3.487 (6H), 3.484 (9H), and 3.481 (6H). On the NOESY spectrum these groups also show several dipolar cross peaks with the methoxy groups at δ ~3.38 (attached on C-2), and all H-3, H-4, due to the presence of glucose units at δ = 3.30 and 3.45.

The assignment of ^{1}H and ^{13}C signals for the monoamino product **1** as determined from this analysis is presented in Table 1. From this analysis there are clearly three types of glucose present for compound **1**: aminoglucose unit A, with separate signals for H-1 (A), H-4 (A), and H-5 (A); two glucose from the amino group side of the glucose B and from its anomeric carbon side, glucose G. Glucose B also displayed for their ring protons separate signals for H-1 (B) and H-2 (B). However, the remaining glucose signals are not as well resolved because of their equivalence and similar neighbourhood, just as occured with those nitrogen free glucoses.

The HSQC ($^{1}J_{H\text{-}C}$) experiments for compound **1** allow us to confirm and assign the carbon resonance. In the last series

© 2008 NRC Canada

Fig. 3 (*concluded*).

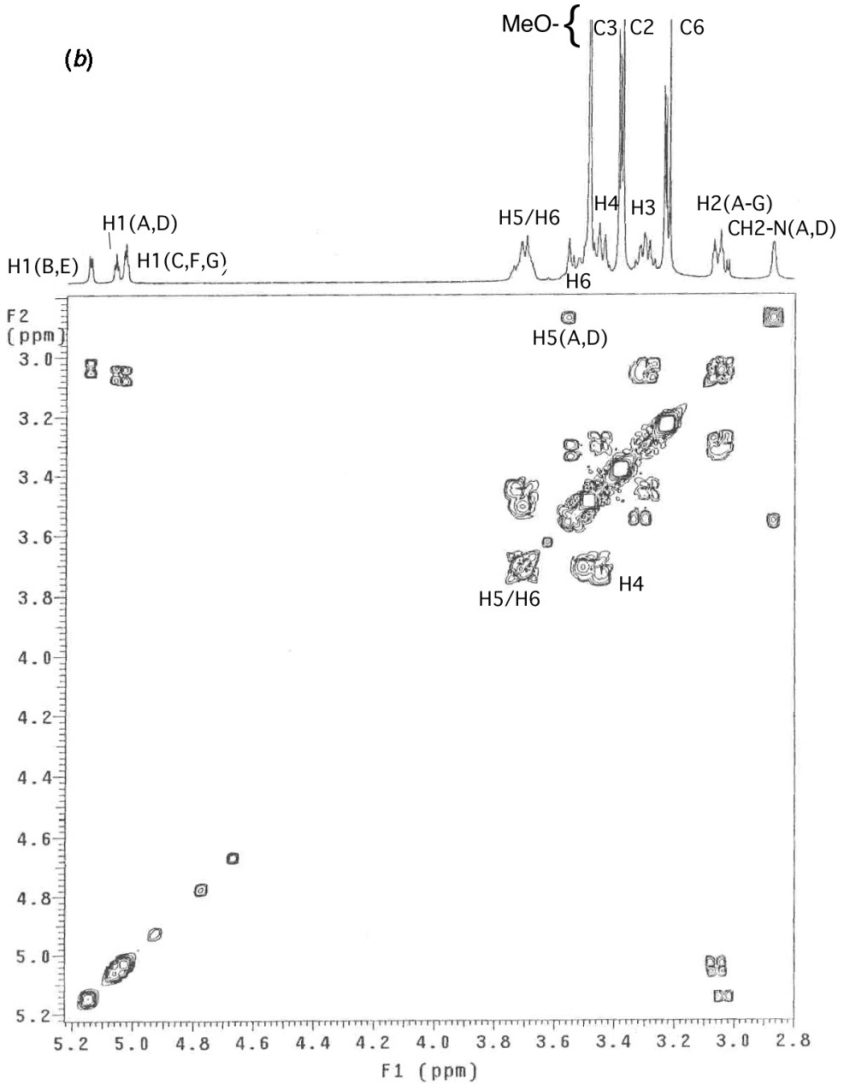

of 2-D experiments, HMBC was performed to confirm the $^{2}J_{\text{H-C-C}}$ and $^{3}J_{\text{H-C-C-C}}$ coupling patterns (see Fig. 5, HMBC).

The complete ^{1}H and ^{13}C assignments of molecules of cyclodextrins discussed here were achieved by means of proton–proton and proton–carbon correlation experiments, an HSQC experiment that allowed all the one-bond proton carbon correlations to be identified, and the HMBC spectrum that allowed sufficient long range correlations to be detected to complete the assignments included in Tables 1 and 2; these are consistents for both compounds **1** and **2**.

The analysis of the high-resolution NMR spectra of compound **2** was done using the methodology developed for the mono 6-amino-β-CD (**1**), discussed in the previous section. In particular, we discuss the interpretation assuming the hypothetical formation of two other isomeric 6,6-diamino-β-CDs (case 1) with A,B-substituted sugar residues, and case 2 with A,C-substituted sugar residues (Fig. 2) as compared to the actual 6,6-diamino A,D-β-CD (11, 12). Such methodology enabled us to obtain the characteristic NMR patterns in the 2-D spectra, which should be absent for the specific structure of compound **2**.

As a first step of our analysis, we considered the NOE for C-6 methylene and for anomeric protons of the (n + 1) sugar unit, as well as the number of the equivalent sugar units in a given isomer.

The key element for the structure elucidation of 6,6-diamino-cyclodextrin comes from the symmetry considerations as well as from the shielding behaviour of anomeric protons observed in its ^{1}H NMR.

The analysis of the diamino CD (**2**) at 500 or 800 MHz begins with the doublet at δ = 5.148 ppm (^{3}J = 3.5 Hz) for the anomeric protons of equivalent sugar rings B and E. In particular, its correlation to the C-6 methylenes in rings A and D through the NOESY spectrum is striking. One triplet at δ = 5.065 (2H, ^{3}J = 3.5 Hz) is assigned to anomeric protons of ring A and D respectively. Then, the doublet at δ = 5.031 (2H, ^{3}J = 3.5 Hz) was assigned to both anomeric protons from glucose units C and G. Finally, the doublet at δ = 5.024 (1H, ^{3}J = 3.5 Hz) was assigned to the anomeric proton of sugar ring F.

The C-6 amino group with protons at δ = 2.87 displayed a broad singlet of 4H, compared to the strong well-defined

© 2008 NRC Canada

Fig. 4. Expanded NOESY for compound **1**, 500 MHz.

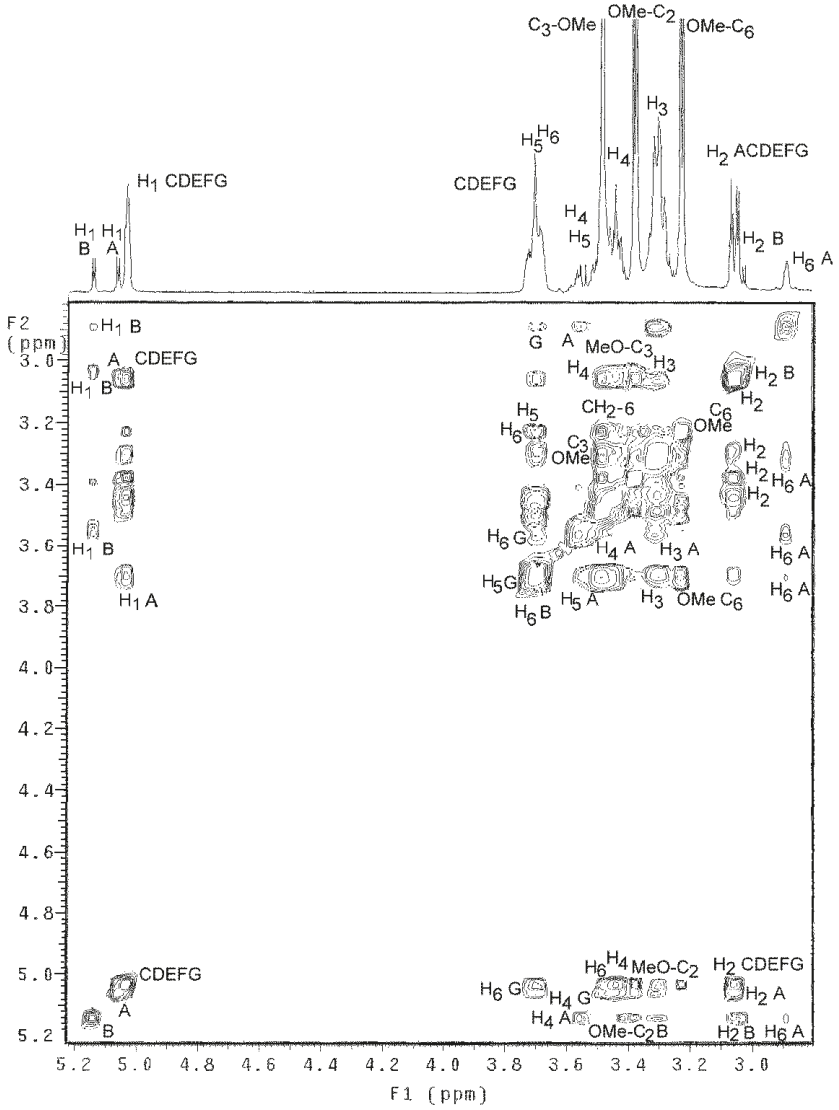

doublet of doublets of five protons of the C-2 methine of rings A, C, D, F, and G (δ = 3.06), leaving the doublet of doublets at δ = 3.03 assigned to C-2 protons for rings B and E.

Through the COSY connectivity, we were able to assign the C-6 aminomethylene signals at δ = 2.87 with the multiplet at δ = 3.55 (4H) assigned to the methines C-5 and C-4 of rings A and D.

Using the signals at δ = 3.06 and 3.03 of protons on C-2 methines from rings A–G, it was possible to use the COSY spectrum to assign the C-3 methine protons of sugars rings A–G at δ = 3.30. From the diagonal peaks at δ = 3.30, it was possible to evaluate the chemical shift of C-4 methine of rings A–G at δ = 3.45 and from the diagonal peaks at δ = 3.45; we also assigned the remaining protons of C-5 and C-6 carbons of the rings B and C as well as those corresponding to the sugars E, F, and G (Table 2). Through the NOESY experiment using the diagonal peaks corresponding to the aminomethylene protons at C-6 of rings A and D (δ = 2.87), we were able to confirm the methyne signals of C-1 at δ = 5.148 (rings B and E), the C-5 methine protons (2H) at δ = 3.55 and C-4 protons at δ = 3.55.

The B and E ring protons at C-1 at δ = 5.148 displayed cross-peaks to the C-6 aminomethylene protons of C-6 for rings A and D. The δ = 3.30 for C-3 methines of rings B and E, the C-4 methines of rings A and D at δ = 3.55, and the D ring protons of C-5 methines of rings A and D were identified similarly.

The methoxy groups attached to the C-2, C-3, and C-6 carbons of rings A–G were also assigned from the diagonal peaks at C-2 methines at δ = 3.06 to the corresponding signals at δ = 3.387 (6H), 3.381 (3H), 3.380 (3H), and finally 3.373 (9H) of rings A–G. Using similar identification criteria, the methoxy groups attached to C-3 (ring A–G, δ = 3.484 for 21H) and those attached to the C-6 of rings B, C, E, F, and G were assigned [δ = 3.236 (3H), 3.233 (3H), 3.228 (3H) and 3.217 (6H)].

Clearly, the case 1 for 6,6-diamino-β-cyclodextrine AB shown in Fig. 2 is not consistent with the NOESY spectrum and can be easily ruled out since only the dipolar correlation between 6-aminomethylene on ring B with anomeric proton of glucose unit C is observed. In support of this observation, no dipolar correlation was observed between aminomethylene

© 2008 NRC Canada

Fig. 5. 2-D NMR experiments on compound **2**, arrows show the interactions determined from COSY, NOESY, and HMBC spectra as discussed in the text.

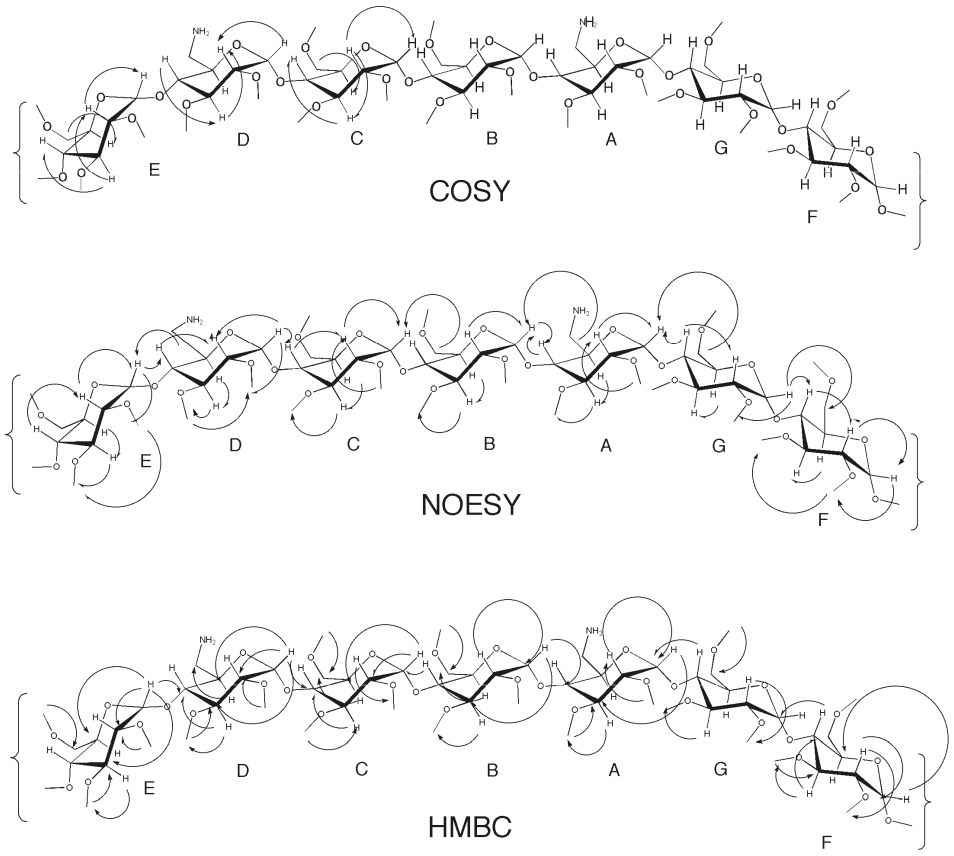

on ring A and the anomeric proton of aminoglucose ring B at δ = 5.057.

The second hypothetical case, A,C-6,6-diamino-β-CD (case 2), can also be ruled out, since it should display twice the discussed NOE of CH_2-N toward the (n + 1) ring than is observed. Here there would be two different sugar triads, amino-glucose/glucose/amino-glucose (e.g., ABC) and aminoglucose/glucose/glucose (e.g., AGF).

Comparison of the ABC and AGF triads in case 2 shows that the sugar ring B may not be magnetically equivalent to sugar ring G in both different triads causing different magnetic environments on the B and G rings and consequently the C-1 proton on ring B should not be equivalent to the correspondig C-1 proton at ring G. Based on symmetry arguments discussed above this A,C substitued isomer is thus discarded from consideration.

From the above discussion, analysis of the spectrum from the *per-O*-methylated 6,6-diamino-β-cyclodextrine AD isomer (case 3) shows two types of triads in addition to three glucose triad EFG, which does not aid in the assignment as follows: ABC (and its equivalent DEF) and GAB (and its equivalent CDE). The difference is that, in GAB, the aminated sugar unit is surrounded by two glucoses, while ABC has a similar behavior with the monoamino-β-CD sequence of aminoglucose followed by two glucose units.

Rings A and D have methylene N-CH_2-6 protons correlated to the anomeric proton of the next sugar (B and E), and as a result, both protons are magnetically equivalent.

Following this analysis, COSY, NOESY, HMBC, and HSQC spectra were interpreted; the results allowed the identification of proton and carbon signals as presented in Table 2.

For both amines, the key to the analysis was the anomeric carbon chemical shift differences as seen through HSQC experiments. Because the anomeric protons in rings A and D appear at δ = 5.065, they were easily assigned to carbon methine signals at δ = 97.67. The anomeric protons from rings B and E (δ = 5.148) were assigned to the anomeric carbons at higher fields (δ = 97.47 and 97.52). The remaining anomeric protons from rings C, F, and G appears overlapped at δ ~ 5.031 and 5.024 displaying heteronuclear correlations with carbons at δ = 97.67.

The C-6 carbons of the A and D rings were easily assigned, since the proton chemical shift at δ = 2.87 correlates to the carbon at a higher field, δ = 41.7. The C-6 signals of the methylene of glucose B, C, E, F, and G were assigned respectively to δ = 71.2 (2C), 71.06 (1C), and 70.88 (2C) from DEPT experiments and these signals correlate with protons at δ = 3.50, 3.70, and 3.45, respectively. The methoxy groups attached to the C-6 were assigned as follows: the singlets at δ = 3.236 (3H), 3.233 (3H), 3.228 (3H), and 3.217 (6H) were correlated with carbon signals at δ = 58.30 (1C), 58.22 (1C), 58.07 (1C), and 58.10 (2C), respectively. Finally, the corresponding C-4 proton methine signals at δ = 3.45 were correlated with carbons at δ = 79.7 (2C), 79.44 (2C), 79.38 (1C), 79.21 (1C) and 79.06 (1C).

© 2008 NRC Canada

Fig. 6. NOESY spectra for compound **2** (*a* and *b*, details, 800 MHz).

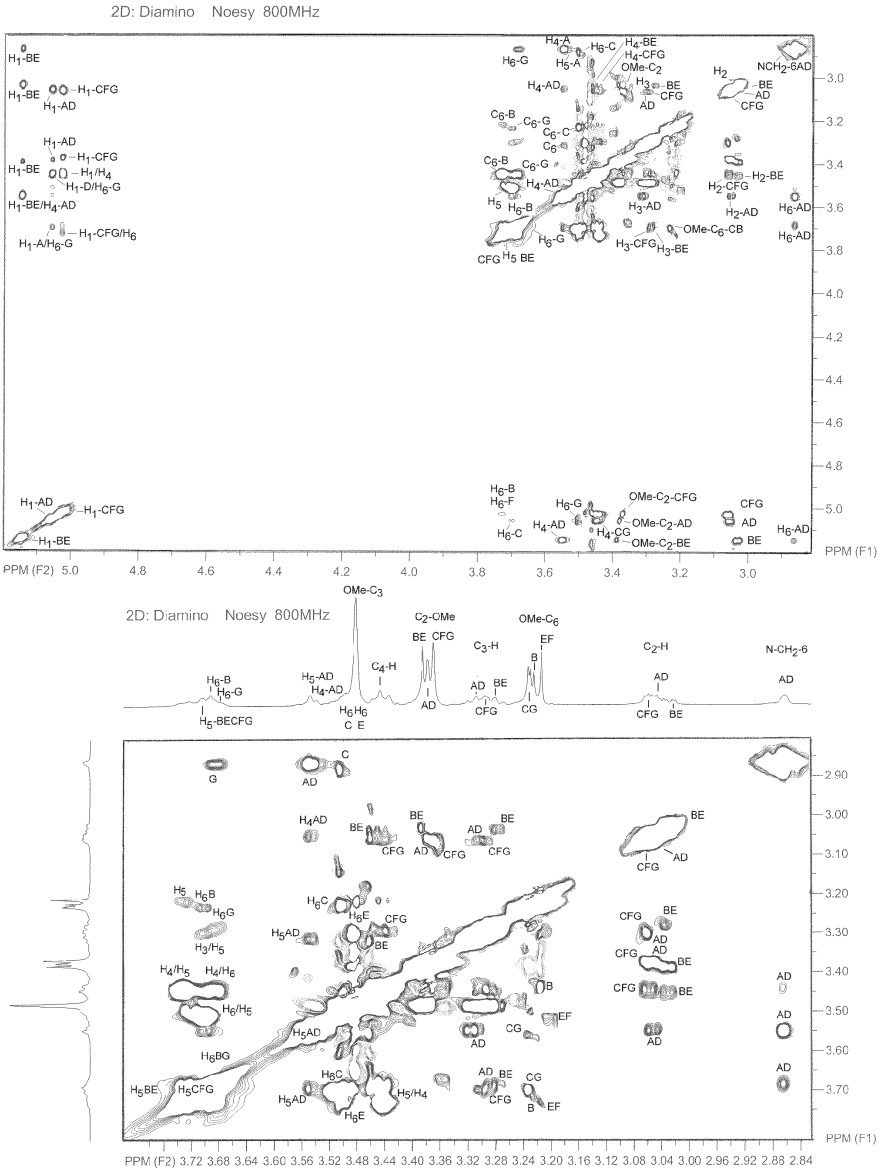

The protons attached to C-3 at δ = 3.30 ppm were correlated to carbon signals δ = 81.6 (4C), 81.58 (2C), and 81.54 (1C), however, their further identification was not possible. The unambiguous assignment of several methoxy signals was possible from HMBC experiments. For example, the methine protons at the C-2 of rings A–G at δ = 3.06 ppm, δ_c = 81.4 and 81.2 ppm were correlated through three σ bonds with methoxy carbons at δ = 57.92 (2C), 57.90 (1C), 57.82 (1C), 57.73 (2C), and 57.70 (1C). The singlet at δ = 3.484 ppm corresponded to the methoxy attached to C-3, and it correlated through three σ bonds to C-3 methine at δ = 81.62 (3C), 81.58 (3C), and 81.54 (1C) ppm. Having in hand this complete identification of proton spectra, the carbon-13 spectrum was assigned as in Table 2; HSQC and HMBC experiments were particularly useful for these assignments. The DEPT and HSQC experiments play an important role for assigning the proton and carbons of C-6. Using the carbon signals at δ = 71.2 (2C), 71.06 (1C), and 70.88 (2C) ppm it was possible to identify the corresponding proton chemical shifts at δ = 3.70 (4H), 3.50 (1H), and 3.45 (4H).

800 MHz determinations

To improve our 500 MHz observations, we have recorded the diamino CD (**2**) spectra at 800 MHz ^{1}H NMR (1-D and 2-D NOESY experiments, DMSO-d_6). Basically, the 1-D spectrum looks similar to that recorded at 500 MHz. However, several relevant details were picked out, particularly from the 800 MHz NOESY spectrum. In principle, through the diagonal peaks from anomeric protons at δ = 5.148, 5.063, and 5.031 we could achieve the complete C_2-OMe assignment as observed in Table 2. Using the diagonal peak at δ = 5.148, the cross peak from C_2-OMe for rings B and E at δ = 3.387 was observed. Then, from the diagonal peak at δ = 5.063 due to the anomeric protons of rings A and D, through the cross peaks at δ = 3.381 and 3.380 of the methoxy groups attached to C-2 from rings A and D, and similarly

© 2008 NRC Canada

Table 2. Proton and ^{13}C chemical shifts (ppm) for 6^{A},6^{D}-diamino-6^{A},6^{D}-deoxy-*per*-*O*-methyl-β-cyclodextrin (**2**). IUPAC name: $6^{A,D}$-diamino-$6^{A,D}$-deoxy-$2^{A,D}$,$3^{A,D}$-di-*O*-methylhexakis-($2^{B–G}$,$3^{B–G}$,$6^{B,C,E,F,G}$-tri-*O*-methyl)-cyclomaltoheptaose (**2**). (DMSO-d_6; 500 or 800 MHz).

Ring	Position	δ_H	δ_C
A	C_1-H	5.065	97.67
	C_2-H	3.05	81.20
	C_3-H	3.30	81.58
	C_4-H	3.55	79.44
	C_5-H	3.55	71.90
	C_6-H	2.87	41.70
B	C_1-H	5.148	97.52
	C_2-H	3.03	81.40
	C_3-H	3.28	81.54
	C_4-H	3.45	79.70
	C_5-H	3.70	70.30
	C_6-H	3.68	70.88
C	C_1-H	5.031	97.67
	C_2-H	3.06	81.20
	C_3-H	3.30	81.62
	C_4-H	3.47	79.50
	C_5-H	3.70	70.44
	C_6-H	3.50	71.20
D	C_1-H	5.065	97.67
	C_2-H	3.05	81.20
	C_3-H	3.30	81.58
	C_4-H	3.55	79.38
	C_5-H	3.55	71.85
	C_6-H	2.87	41.70
E	C_1-H	5.148	97.47
	C_2-H	3.03	81.40
	C_3-H	3.28	81.58
	C_4-H	3.45	79.70
	C_5-H	3.70	70.30
	C_6-H	3.45	70.88
F	C_1-H	5.024	97.67
	C_2-H	3.06	81.20
	C_3-H	3.30	81.62
	C_4-H	3.47	79.23
	C_5-H	3.70	70.34
	C_6-H	3.45	71.06
G	C_1-H	5.031	97.67
	C_2-H	3.065	81.20
	C_3-H	3.30	81.54
	C_4-H	3.47	79.07
	C_5-H	3.70	70.25
	C_6-H	3.70	71.20

Note: Methyl signals: 7 × [CH_3-O-C-2] 4 peaks δ_H: 3.387 (6H, rings B and E), 3.381 (3H), 3.380 (3H, rings A and D), 3.373 (9H, rings C, G, and F), 5 peaks δ_C: 57.92 (2C), 57.90 (1C), 57.82 (1C), 57.73 (2C), 57.70 (1C); 7 × [CH_3-O-C-3] 1 peak δ_H: 3.484 (21H), 3 peaks δ_C: 60.70 (4C), 60.62 (1C), 60.5 (2C); 5 × [CH_3-O-C-6] 4 peaks δ_H: 3.236 (3H), 3.233 (3H), rings G and C, 3.228 (3H) ring B, 3.217 (6H), rings E and F, 4 peaks δ_C: 58.3 (1C), 58.22 (1C), 58.10 (2C), 58.07 (1C).

using the signal at δ = 5.031 we assigned the MeO-C_2- for rings CFG. Other relevant correlations obtained from the NOESY spectrum were those performed for C-2 and C-3 methine protons for rings A–G, just as detailed on Table 2.

The H-5 and H-4 for rings A and D were assigned through dipolar correlation with N-CH_2-6 (δ = 2.87). The complete assignment for the diamino-β-CD (**2**) protons extracted from 800 MHz spectrum are displayed in Figs. 6*a* and 6*b*.

Conclusions

With these complete data, we have presented an the improved interpretation and assignment of spectra of both amino-β-CDs. Data presented here may be used to perform other different CD assignments, assuming substitution of the alcohol groups by esterification or etherification, either of which greatly improves the solubility in organic solvents. It is clear, however, that even with the spectra acquired at 800 MHz, it cannot resolve the highly overlapped signals. Future analysis may be improved by taking into account the minor conformational distortions of glucose rings (which are further reduced in solution), to have a full assignment for all proton and carbon-13 signals of these interesting compounds. In particular, comparison of X-ray data and NMR proton data will improve the knowledge about these molecules.

Using a 1-D and 2-D ^1H and ^{13}C NMR spectroscopy on 6-amino-*per*-*O*-methylated and 6,6-diamino-(AD)-*per*-*O*-methylated-β-cyclodextrins (**1** and **2**), we were able to rationalize the structure of these fascinating compounds. The COSY and NOESY spectra were particulary useful in obtaining relevant information concerning ^1H-^1H couplings and ^1H-^1H dipolar correlations. On the other hand, DEPT, HSQC, and HMBC experiments enabled us to select $^1J_{C\text{-}H}$ correlations, and also to detect long-range (^2J,^3J) ^1H/^{13}C correlations in the sugar unit as well as those due to inter-rings correlations.

Experimental

As a NMR reference during this study, two permethoxylated model derivatives of β-CD were used:

Heptakis(2,3,6-tri-*O*-methyl)-β-cyclodextrin, (Trimeb) **3**: ^1H NMR (DMSO): 5.12, 3.18, 3.50, 3.60, 3.79, and 3.83 (H-1 to H-6 respectively), OCH_3: 3.50, 3.64, and 3.32 (CH_3 on C-2, C-3, and C-6, respectively); ^{13}C NMR: 98.4, 81.6, 82.4, 79.7, 70.5, and 71.0 (C-1 to C-6, respectively), CH_3: 58.0, 60.9, and 58.4 (CH_3 on C-2, C-3, and C-6, respectively) (10).

Heptakis(2,6-di-*O*-methyl)-β-cyclodextrin, (Dimeb) **4**: ^1H NMR (DMSO): 4.95, 3.38, 3.6, 3.5, 3.7 (approx.), 3.95 (H-1 to H-6, respectively), OCH_3: 3.6 and 3.4 (CH_3 on C-2 and C-6, respectively); ^{13}C NMR: 101.3, 83.6, 73.1, 82.1, 70.9, and 71.4 (C-1 to C-6, respectively), CH_3: 60.3 and 58.7 (CH_3 on C-2 and C-6, respectively).

The 6-amino-CD (**1**) was synthesized according to the reported general procedure (11*b*) from products **7** and **8**.

The 6,6-diamino-CD (**2**) was obtained as a result of a two-step procedure described by Lee and co-workers (12*a*) from the dihydroxypermethylated β-cyclodextrin (**5**), which was

© 2008 NRC Canada

obtained as described by Sinay and co-workers (12*b*) via the diazide **6**.

The starting cyclodextrins were obtained from Roquette Frères (France). Most of the reagents and solvents used in this study were obtained from the Sigma-Aldrich and used without further purification. TLC was performed on Silica Gel 60 F_{254} plates (E. Merck) followed by charring with 10% (*v*/*v*) H_2SO_4 or UV.

High resolution ^{1}H and ^{13}C NMR spectra were recorded using a Varian INOVA 500 MHz spectrometer operating at 500 MHz for ^{1}H and 125.0 MHz for ^{13}C. The ^{1}H and ^{13}C chemical shifts are given in (δ) ppm relative to tetramethyl silane (TMS). The experiments were performed using an inverse detection 5 mm probe. The COSY, NOESY, DEPT, HSQC, and HMBC spectra were recorded in DMSO-d_6 solution (25 °C) using the VARIAN software. For HSQC experiments the INOVA program for short range coupling (less than 140 Hz for $^1J_{C\text{-}H}$) was used. The long range proton–carbon experiments (HMBC) were recorded with a Varian INOVA pulse program optimized for long range couplings ($^3J_{C\text{-}H}$ = 9 Hz). The 800 MHz NOESY spectra was recorded in DMSO-d_6 using a Bruker DRX 800 instrument operating on 200 MHz for ^{13}C and 800 MHz for ^{1}H and equipped with a ^{1}H/^{13}C/^{15}N/ cryoprobe. Measurements were performed at 25 °C. The spectrometer is situated in the Centre National de la Recherche Scientifique (CNRS) facilities at Gif-Sur-Yvette, France.

Synthesis

The purity of starting compounds **5** and **6** was comfirmed by the following analysis.

*6^A,6^D-Dihydroxyheptakis(2,3,6-tri-*O*-methyl)-β-cyclodextrin (5)*

^{1}H NMR ($CDCl_3$, 400 MHz, ppm): 5.24 (d, $J_{H1,\ H2}$ = 4.0 Hz, 1H, H-1), 5.22 (d, $J_{H1,\ H2}$ = 3.9 Hz, 1H, H-1), 5.10 (d, $J_{H1,\ H2}$ = 3.4 Hz, 1H, H-1), 5.05 (d, $J_{H1,\ H2}$ = 3.3 Hz, 2H, H-1), 5.01 (d, $J_{H1,\ H2}$ = 3.5 Hz, 1H, H-1), 4.98 (d, $J_{H1,\ H2}$ = 3.5 Hz, 1H, H-1), 3.67–3.97 (m, H-5/H-6), 3.39–3.66 (m, H-3/H-4/H-6/OCH_3), 3.33–3.39 (m, OCH_3), 3.16–3.21 (m, 7H, H-2). ^{13}C NMR ($CDCl_3$, 100 MHz, ppm): 98.61, 98.83, 98.87, 98.94, 98.98, 99.25 (7′ C-1), 80.28, 80.82, 80.91, 81.06, 81.09, 81.35, 81.46, 81.49, 81.63, 81.68, 81.76, 81.89, 82.02, 82.07, 82.34, 82.44 (C-2/C-3/C-4), 77.88, 78.13 (2′ C-4), 71.77 (C-6), 71.66 (2′ C-5), 71.47 (C-6), 71.44 (C-5), 71.38 (C-6), 71.32 (C-5), 71.27 (C-6), 71.22 (C-5), 71.11 (C-6), 71.07 (2′ C-5), 61.70 (OCH_3-6), 61.49, 61.56 (C-6A/C-6D), 60.86, 60.92, 61.45, 61.51 (OCH_3-6), 58.02, 58.16, 58.26, 58.36, 58.52, 58.94, 59.02, 59.05, 59.07, 59.09, 59.16, 59.29 (OCH_3-2/OCH_3-3). ESI-MS + *m*/*z*: 1401.7 $[M + Na]^+$

*6^A,6^D-Diazidoheptakis(2,3,6-tri-*O*-methyl)-β-cyclodextrin (6)*

Diol permethylated, **5** (713 μmol) was dissolved in 20 mL of anhydrous pyridine, 528 mg of DMAP (4.3 mmol) was added and the mixture was cooled to 0 °C. Mesylate chloride (446 μL), dissolved in 10 mL of pyridine was added dropwise. After 3 h of stirring, the mixture was evaporated to dryness, diluted in CH_2Cl_2, and washed twice with water. Organic phases were dried on $MgSO_4$, filtered, and evaporated to dryness. The residue was then dissolved in 50 mL of DMF and 1.3 g of sodium azide (20 mmol) were added, the mixture was stirred for 18 h at 65 °C. Evaporated to dryness, diluted in CH_2Cl_2, and extracted with water, the product was then purified using silica gel column chromatography (ethyl acetate then ethyl acetate–ethanol, 20:1 and 10:1) to yield 880 mg of product **6** as a white powder. Yield: 85%. R_f = 0.5 (AcOEt/EtOH/H_2O, 45:5:3). IR (KBr, cm^{-1}): 2100 (N3). ^{1}H NMR ($CDCl_3$, 400 MHz, ppm): 5.12 (d, $^3J_{H1,\ H2}$ = 3.3 Hz, 5H, H-1), 5.07 (d, $J_{H1,\ H2}$ = 3.6 Hz, 1H, H-1). 5.06 (d, $J_{H1,\ H2}$ = 7 Hz, 1H, H-1), 3.70–3.97 (m, H-5/H-6), 3.42–3.70 (m, H-3/H-4/H-5/H-6/OCH_3), 3.37–3.39 (OCH_3-2), 3.14–3.20 (m, 7H, H-2). ^{13}C NMR ($CDCl_3$, 100 MHz, ppm): 98.33, 98.37, 98.97, 99.10, 99.21, 99.27 (C-1), 80.43–82.09 (C-2/C-3/C-4), 80.15, 80.21, 80.27 (C-4), 71.08, 71.27, 71.59 (C-6), 70.77–70.95 (C-5), 61.28, 61.40, 61.43, 61.53, 61.56, 61.58 (OCH_3-6), 58.45–59.00 (OCH_3-2/OCH_3-3), 51.99, 52.04 (C-6A, C-6D).

*6^A,6^D-Diamino-6^A,6^D-didesoxy-2^{A,D},3^{A,D}-di-*O*-methylhexakis(2$^{B\text{-}G}$,3$^{B\text{-}G}$,6^{B,C,E,F,G}-tri-*O*-methyl)cyclomaltoheptaose (2)*

The diazido compound (880 mg, 606 μmol) was dissolved in 10 mL of dioxane and triphenyl phosphine (954 mg, 3.63 mmol) was added. After 4 h, 2.4 mL of ammonia was added. After overnight stirring, 150 mL of water was added and the pH adjusted to 4.0 with a 1 mol/L HCl solution. Aqueous phase was then extracted five times with toluene and made basic with a 2 mol/L NaOH solution. The resulting aqueous phase was extracted five times with CH_2Cl_2. Organic phases were dried on $MgSO_4$, filtered, and evaporated to give 790 mg of product as a white powder. Yield: 93%. R_f = 0.5 (CH_2Cl_2/MeOH, 9:1). The overall yield for diamino-β-CD (**2**) from dihydroxy-β-CD was 77%.

Acknowledgments

We would like to thank the Nuclear Research Centre of Saclay in France and the University of Moncton for constant support of this project. One of us (CH) is indebted to Dr. J.M. Mallet (École Normale Supérieure (ENS), Paris, France) for his guidance and helpful discussion on the synthesis of diamino-CD. We also thank Hector Rios, M.Sc. from Instituto de Química, Universidad Nacional Autónoma de México (UNAM), for technical NMR assistence. Many others should also be thanked.

References

1. P.R. Ashton, R. Königer, and J.F. Stoddart. J. Org. Chem. **61**, 903 (1996).
2. (*a*) K.J. Jensen and J. Brask. Biopolymers, 747 (2005); (*b*) W. Muderawan, T.T. Ong, T.C. Lee, D.J.Young, C.B. Ching, and S.C. Ng. Tetrahedron Lett. **46**, 7905 (2005).
3. T. Carofiglio, M. Cordioli, R. Fornasier, L. Jicsinszky, and U. Tonellato. Carbohydr. Res. **339**, 1361 (2004).
4. (*a*) C.K. Jankowski, C. Hocquelet, J. Blu, S. Arseneau, D. Buisson, and L. Mauclaire. Tetrahedron, **62**, 11963 (2006); (*b*) C. Fraschi and M. Vigneron. Carbohydr. Res. **328**, 585 (2000); (*c*) T. Hardei and M. Bols. J. Chem. Soc. Perkin Trans. 1, 2880 (2002).

© 2008 NRC Canada

5. (*a*) C. Péan, C. Créminon, A. Wijkhuisen, J. Grassi, P. Guenot, P. Jéhan, J.P. Dalbiez, B. Perly, and F. Djedaïni-Pilard. J. Chem. Soc. Perkin Trans. 1, 853 (2000); (*b*) Z. Chen, J.S. Bradshaw, Y.F. Shen, Y. Habata, and M.L. Lee. J. Org. Chem. **62**, 8529 (1997).
6. (*a*) Y. Liu, Y. Chen, L. Li, G. Huamg, C. You, H.Y. Zang, T. Wada, and Y. Inoue. J. Org. Chem. **66**, 7209 (2001); (*b*) A. Mulder, T. Auletta, A. Sartori, S. DelCiotto, A. Casnati, R. Ungaro, J. Huskens, and D. Reinhoudt. J. Am. Chem. Soc. **126**, 8827 (2004) and refs. on cyclodextrins of D. Reinhoudt and co-workers cited therein.
7. K. Takeo. Carbohydr. Res. **200**, 481 (1990).
8. Z. Chen, J.S. Bradshaw, and M.L. Lee. Tetrahedron Lett. **37**, 6831 (1996).
9. P. Ashton, S. Boyd, G. Gattuso, E. Hartwell, R. Koniger, N. Spencer, and J.F. Stoddart. J. Org. Chem. **60**, 3898 (1995).
10. J.R. Johnson, N. Shankland, and I.H. Sadler. Tetrahedron, **41**, 3149 (1985).
11. (*a*) D. Armspach, D. Matt, F. Peruch, and P. Lutz. Eur. J. Inorg. Chem. 805, (2003); (*b*) R.C. Petter, J.S. Salek, C.T. Sikorski, G. Kumaravel, and F.T. Lin. J. Am. Chem. Soc. **112**, 3860 (1990).
12. (*a*) Z. Chen, J.S. Bradshaw, Y.F. Shen, Y. Habata, and M.L. Lee. J. Org. Chem. **62**, 8529 (1997); (*b*) T. Lecourt, J.M. Mallet, and P. Sinay. Carbohydr. Res. **338**, 2417 (2003); (*c*) C.M. Spencer, J.F. Stoddart, and R. Zarzycki. J. Chem. Soc. Perkin Trans. 2, 1323 (1987).

© 2008 NRC Canada

QTAIM–DI–VISAB computational study on the Diels–Alder reaction of cyclopentadiene — On the nature of the so-called secondary orbital interactions

Nick Henry Werstiuk and Wojciech Sokol

Abstract: We have undertaken a QTAIM–DI–VISAB computational study of the dimerization of cyclopentadiene (**1**), the archetypal example of a Diels–Alder reaction that has been studied experimentally and computationally. Secondary orbital interactions (SOIs) that have gained acceptance in the interpretation of stereoselectivities seen in many cycloaddition reactions have been used to account for the fact that the endo isomer was the kinetic product of the reaction. To this point, "classical" MO analyses along with a variety of arbitrarily assigned solid and dashed lines (solid lines and bold dashes for "primary" interactions and dashed and dotted lines to differentiate between different SOI schemes) have been used in an attempt to describe the bonding of the transition states. Yet, the existence of SOIs has been challenged. Our interest in applying QTAIM to fundamental chemical problems in physical organic chemistry, with the goal of refining our knowledge of the bonding in transition-states and ground-state molecules while obviating the need to use a variety of confusing arbitrarily assigned dashed and dotted lines, led us to a QTAIM–DI–VISAB computational study of the endo and exo dimerizations of **1** at the DFT B3PW91 and MPW1PW91 levels. We have characterized the bonding interactions between cyclopentadiene rings in the various transition states and show that "normal" bonds are present where SOIs have been considered to exist. There is no need to use different types of dashed and dotted lines. An analysis of the changes in atom energies revealed that the significant destabilization of the carbon atoms in achieving the TSs (potentially leading to a very high barrier) is ameliorated by a stabilization of the hydrogen atoms leading to the relatively low barrier for the D–A reaction.

Key words: cyclopentadiene dimerization, bispericyclic transition states, DFT calculations, QTAIM–DI–VISAB analysis, bonding, atom energy analysis.

Résumé : Utilisant l'approche combinant la théorie quantique des atomes dans les molécules (TQADM) avec les indices de délocalisation (ID) et la visualisation de la proximité des bassins atomique (VPBA), on a entrepris une étude théorique de la dimérisation du cyclopentadiène (**1**), l'exemple type d'une réaction de Diels–Alder qui a déjà été abondamment étudiée tant d'un point de vue expérimental que théorique. On a fait appel aux interactions d'orbitales secondaires (IOS), qui gagnent en popularité dans l'interprétation des stéréosélectivités observées dans plusieurs réactions de cycloaddition, pour expliquer le fait que l'isomère endo est le produit cinétique de la réaction. Jusqu'à maintenant, pour essayer de décrire les liaisons dans les états de transition, on a utilisé des analyses classiques des orbitales moléculaires en combinaison avec une variété des lignes solides ou pointillées attribuées d'une façon arbitraire, telles des lignes continues et des traits gras pour les interactions primaires et des lignes pointillées pour les divers schémas d'IOS. Malgré tout, l'existence même des IOS a été mise en doute. Notre intérêt dans l'application de la théorie quantique des atomes dans les molécules aux problèmes chimiques fondamentaux de la chimie organique physique dans le but d'affiner notre connaissance de la liaison dans les états de transitions et fondamentaux des molécules tout en évitant d'utiliser une variété de traits solides ou pointillés attribués d'une façon arbitraire nous a conduit à une étude théorique de type "TQADM-ID-VPBA" des dimérisations endo et exo du produit **1** aux niveaux B3PW91 et MPW1PW91 de la théorie de fonctionnelle de densité. On a caractérisé les interactions de liaison entre les noyaux cyclopentadiènes dans les divers états de transition et on a montré qu'il existe des liaisons normales dans les cas où on a envisagé l'existence d'interactions d'orbitales secondaires. Il n'y a aucune nécessité d'utiliser des types différents de traits solides ou pointillés. Une analyse des changements dans les énergies atomiques révèle que la déstabilisation significative des atomes de carbone afin d'atteindre les états de transition, pouvant conduire à une barrière très élevée, est améliorée par une stabilisation des atomes d'hydrogène conduisant à une barrière relativement basse pour la réaction de Diels–Alder.

Received 15 February 2008. Accepted 7 April 2008. Published on the NRC Research Press Web site at canjchem.nrc.ca on 11 June 2008.

This paper is dedicated to the memory of Keith Yates.

N.H. Werstiuk[1] and W. Sokol. Department of Chemistry, McMaster University, Hamilton, ON, L8S 4M1, Canada.

[1]Corresponding author (e-mail: werstiuk@mcmaster.ca).

 doi:10.1139/V08-070 © 2008 NRC Canada

Mots-clés : dimérisation du cyclopentadiène, états de transition bispéricycliques, calculs d'après la théorie de la fonctionnelle de densité, analyse "TQADM-ID-VPBA", liaison; analyse de l'énergie atomique.

[Traduit par la Rédaction]

Introduction

To assist us in devising a new synthesis of bicyclo[2.2.1]hept-5-ene-2,2-diylbis(trimethylsilane) via a Diels–Alder reaction, we modeled the reaction of cyclopentadiene (**1**) with a series of dieneophiles at the DFT level focusing on reaction barriers and enthalpies of reaction. To check the accuracy of the computed barriers, we studied the dimerization of **1**, the archetypal example of a

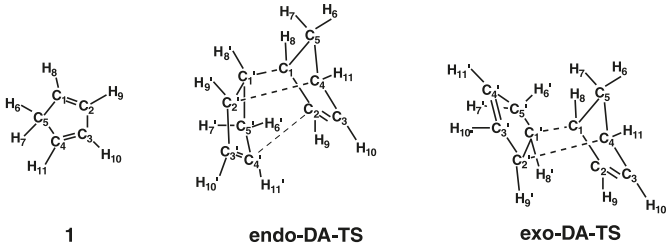

Diels–Alder (D–A) reaction for which an experimental activation energy is available. This reaction, which was studied extensively by Alder and Stein (1), yields the endo dimer exclusively as the kinetic product, although on heating, it isomerizes to the exo isomer. Secondary orbital interactions (SOIs), now firmly entrenched in the chemical literature, have gained acceptance in the interpretation of stereoselectivities seen in many cycloaddition reactions (2) and are used to account for the fact that the endo isomer was the kinetic product. Yet, their existence was challenged by Garcia et al. in a review article in 2000 (2*d*); the authors proposed that "A combination of well-known mechanisms (such as solvent effects, steric interactions, hydrogen bonds, electrostatic forces, and others) can be invoked to justify the endo/exo selectivity of Diels–Alder reactions." In the final sentence of the conclusions, they stated that "Until the hypothesis of SOI is unequivocally demonstrated, however, we believe that Occam's razor should be used to eliminate them from the chemical literature". These proposals clearly illustrate the state of confusion that exists in the field. In 2002, Caramella et al. found that the transition state (TS) for the endo dimerization of **1** (the authors used the term bispericyclic) exhibits C_2 symmetry (3) showing that the situation was more complicated than is described in contemporary textbooks. The authors defined the PE surface at the B3LYP/6–31G(d) level showing that it exhibited a bifurcation point where the endo C_2 TS proceeded to enantiomeric dimers as well as a crest that led to a so-called Cope TS that also could yield products. The authors used a classical MO analysis as well as solid and "cross-hatched" lines to indicate partial "single" bonds along with a variety of dashed lines (bold dashes to refer to primary SOI interactions and dashed and dotted lines to differentiate between different SOI schemes) in an attempt to describe the bonding of the TSs. The question arises at what bond order (0.5, 0.6, 0.7, or other) should the solid or cross-hatched lines be invoked and when should dashed or dotted lines be used to represent bonding interactions. Currently, it appears that the selection is purely arbitrary. A standard "dashed-line" representation that is usually used in attempts to describe the bonding of the TSs is used in **endo-DA-TS** and **exo-DA-TS**.

We also found that **endo-DA-TS** exhibited C_2 symmetry during our modeling studies on the reaction of cyclopentadiene (**1**) at the DFT level. Given our long-standing interest in applying the quantum theory of atoms and molecules (QTAIM) (4) to fundamental chemical problems in physical organic chemistry (SOIs certainly must be considered as one) with the goal of refining our knowledge of the bonding in TSs and ground state molecules led us to a QTAIM–DI–VISAB computational study of the endo and exo dimerizations of **1**. In addition to using molecular graphs to define *molecular* structure and examining the properties at extrema in the topology of the density (bond critical points (CPs), ring CPs, and cage CPS), we recently showed that a combination of a normal QTAIM analysis coupled with an evaluation of delocalization indexes (DIs), and a visualization of the closeness of atomic basins (VISAB) is especially useful for characterizing the bonding in molecules at their equilibrium geometries (5–7).

There are two physical measures of bond order n. One is determined by fitting the value of ρ_b, the value of the density at a bond critical point (CP), to an empirical two-parameter expression that yields orders of 1.0, 1.6, and 2.0 for the C|C bond paths in ethane, benzene, and ethene, respectively; $n = \exp[A(\rho_b - B)]$ (4). Nevertheless, it is convenient to use values of $\rho(r)$ at bond CPs to qualitatively assess relative bond strengths. The second is determined by the pair density and expressed in terms of the delocalization index, DI(A|B), that determines the extent of exchange of electrons between two atomic basins A and B. The DI for pairs of atoms yields the number of "shared electron pairs" with values being 1.035, 1.399, and 1.935 for the C|C pairs of ethane, benzene, and ethene, respectively, in qualitative agreement with the Lewis model. DI(A|B) is an important parameter because the possibility exists to have a significant degree of delocalization and (or) sharing of electrons without having a bond path linking the atomic basins. Clearly, this is important in characterizing the so-called SOIs.

Bond ellipticity is also a useful parameter in discussing bonding. The electron density of a bond that in an orbital model possesses π character, is elliptically disposed about the bond path, being preferentially accumulated in a plane that in ethene is perpendicular to the plane of the nuclei, the plane determined by the major axis of the ellipse. The extent of this accumulation is determined by the ellipticity defined as $\varepsilon = \lambda_1/\lambda_2 - 1$ where λ_1 and λ_2 are the negative eigenvalues of the Hessian, that is, the curvatures of the density at the bond cp perpendicular to the bond path, with $|\lambda_1| > |\lambda_2|$, λ_2 being the curvature along the major axis of the ellipse, that

© 2008 NRC Canada

is, the direction of the "soft" curvature. The ellipticities of the C–C bonds in ethane, benzene, and ethylene are 0.0, 0.197, and 0.346, respectively, at B3PW91/6–31+G(d). The ellipticity has the property of determining the presence of a π-like component to the density, even in situations where the bond order is less than unity. However, this parameter is available only in cases where a bond path connects two atoms.

Finally, the ability to define the energy of an atom in a molecule enables one to determine the degree to which atoms of a reactant are stabilized or destabilized in achieving various TSs. QTAIM energies of carbon atoms bonded to hydrogen are in line with the hybridization model, with increasing "s over p character" leading to an increase in stabilization and electronegativity, as reflected in an increasing withdrawal of electrons from a bonded H. The carbon atom energies (hartrees) of ethane, ethene, and ethyne (–38.065 360, –38.087 560, –38.112 920) yield a near linear relationship (E = 35.980 45 + 0.346 × population) with respect to their electron populations (6.0284, 6.0848, 6.1650) at B3PW91/6–311+G(2d,p) with a regression coefficient of 0.998 (8). Such a "linear charge/energy relationship" enables one to determine the extent to which a carbon atom is stabilized or destabilized in a system with electron delocalization. We present only data for ethane and ethene and selected carbon atoms of **endo-C_2-TS**, **Cope-C_2-TS**, and **exo-C_2-TS** at the B3PW91/6–31+G(d) level in this case. Very important is the fact that a carbon in benzene, with a population intermediate between that in ethane and ethene for example, is more stable than that predicted by the linear charge/energy relationship by 17 kcal mol^{-1} (1 cal = 4.184 J) at B3PW91/6–311+G(2d,p). If the C–H group is used, the increased stability of a |CH group in benzene over the same non-conjugated group in cyclohexene or *cis*-butadiene as determined by QTAIM, yields stabilization or "resonance" energies of 41 and 39 kcal mol^{-1}, respectively, for benzene that are remarkably close to the generally accepted values of 37–41 kcal mol^{-1}, the higher values obtained from heats of combustion.

In this paper, we report and discuss the results of a QTAIM–DI–VISAB study and an analysis of the changes of the energies of the atoms on the dimerization of **1**.

Computational methods

Density functional theory (DFT) calculations were performed with hybrid functionals B3PW91 and MPW1PW91 as implemented in GAUSSIAN 03 (G03) (9). Our previous experiences with DFT calculations on carbocations (10–13) clearly showed that the B3PW91 hybrid functional is superior to B3LYP in computing the geometries of delocalized so-called nonclassical species. Consequently, we used B3PW91, and for the purposes of a comparison, also decided to employ MPW1PW91 developed by Adamao and Berone (14) to better account for van der Waals forces. ChemCraft (15) and GaussView 3.0 (16) were used to fix symmetry where necessary. Finding the Cope TS to be very close to exhibiting C_2 symmetry, we also fixed its symmetry to C_2 as well. Geometries of all structures including TSs were first optimized using the default convergence criteria at the 6–31+G(d) level and re-optimized with OPT=TIGHT to obtain the wave functions. UB3PW91 and B3PW91 yielded identical results. Cartesian coordinates of the optimized geometries of **1**, **endo-C_2-TS**, **Cope-C_2-TS**, and **exo-C_2-TS** obtained with the G03 default convergence criteria at B3PW91/6–31+G(d) are collected in Tables 1S–4S (Supplementary Data).[2] To evaluate the effect of increasing the size of the basis set, transition states were also optimized at the B3PW91/6–311+G(2d,p) with OPT=TIGHT and wave functions written. Selected calculated internuclear distances of **1**, **endo-C_2-TS**, **Cope-C_2-TS**, and **exo-TS** are collected in Table 5S (Supplementary Data).[2]

Vibrational analyses were performed for all structures at the 6–31+G(d) level to confirm minima and transition states and evaluate reaction barriers. Thermochemical data are included in Tables 1S–4S. While we computed ($\Delta E^{\ddagger}_{\text{elec}}$, $\Delta E^{\ddagger}_{0}$, $\Delta E^{\ddagger}_{298}$, $\Delta H^{\ddagger}_{298}$, and $\Delta G^{\ddagger}_{298}$ for the reactions, only $\Delta E^{\ddagger}_{\text{elec}}$ and $\Delta H^{\ddagger}_{298}$ are included in the discussion. The results on of calculations on ethane and ethene are not reported.

Results of QTAIM analyses carried out with AIM 2000 (17) are collected in Table 6S (Supplementary Data).[2] Delocalization indexes (DIs) for selected atom pairs were obtained with LI–DICALC (18–20) are listed in Tables 7S–9S (Supplementary Data).[2] Molecular graphs of **endo-C_2-TS**, **Cope-C_2-TS**, and **exo-C_2-TS** are displayed in Figs. 1*a*, 1*b*, and 1*c*, respectively, and re-orientated (Figs. 2*a* and 2*b*) so the C_2 symmetries of **endo-C_2-TS** and **Cope-C_2-TS** are clearly seen. Selected atomic basins obtained with AIM 2000 a contour value of 0.005 (this includes greater than 95% of the electrons) using a mesh grid size of 0.125 and plotted with a sphere size of 0.15 are displayed in Figs. 3*a*–3*f* (**endo-C_2-TS** and **Cope-C_2-TS**) and Figs. 4*a*–4*f* (**exo-C_2-TS**). AIMALL97 (21) was used for QTAIM integrations to obtain atom energies (Table 1) and atomic overlap matrices required for calculating DIs.

Results and discussion

As mentioned, we initially undertook a study of the dimerization of **1** to validate the accuracy of our calculations on a range of D–A reactions because an experimental E_a was available. That our computed barrier at B3PW91/6–31+G(d) for endo dimerization ($\Delta E^{\ddagger}_{\text{elec}}$ = 17.5 kcal/mol and $\Delta H^{\ddagger}_{298}$ = 18.6 kcal/mol) is in very good agreement with the experimental E_a of 16.7 ± 0.6 kcal/mol validates the level of theory used to obtain wave functions for this study. For exo dimerization, $\Delta E^{\ddagger}_{\text{elec}}$ and $\Delta H^{\ddagger}_{298}$ were 20.8 and 21.8 kcal/mol, respectively, nicely in keeping with the fact that the endo dimer is the kinetic product.

QTAIM–DI–VISAB analysis

The molecular graphs of **endo-C_2-TS**, **Cope-C_2-TS**, and **exo-TS** along with the atom numbers and selected internuclear distances are displayed as Figs. 1*a*, 1*b*, and 1*c*, respectively. Figure 2 shows the molecular graphs rotated in

[2] Supplementary data for this article are available on the journal Web site (canjchem.nrc.ca) or may be purchased from the Depository of Unpublished Data, Document Delivery, CISTI, National Research Council Canada, Ottawa, ON K1A 0S2, Canada. DUD 3759. For more information on obtaining material, refer to http://cisti–icist.nrc–cnrc.gc.ca/irm/unpub_e.shtml.

© 2008 NRC Canada

Fig. 1. Molecular graphs of (*a*) **endo-C_2-TS**, (*b*) **Cope-C_2-TS**, and (*c*) **exo-TS**. Carbon and hydrogen atoms shown as black and gray spheres, respectively. Red spheres are bond Cps, yellow spheres are ring Cps, and green spheres are cage Cps. Selected internuclear distances (Å) are displayed in italics.

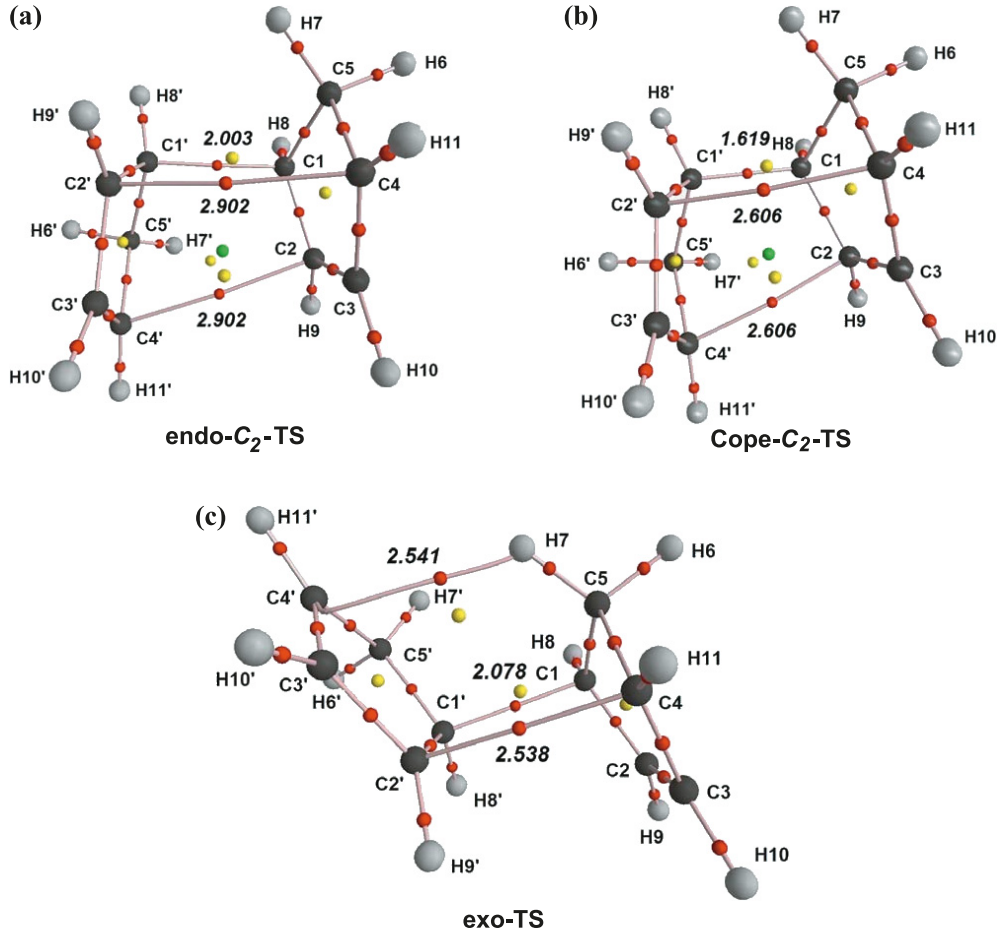

space to better show the C_2 symmetries; the C_2 axes lie along a line defined by the ring CP (yellow sphere), cage CP (green sphere), and C1|C1′ bond CP (red sphere) as labeled with an arrow in the case of **Cope-C_2-TS**. Values of ρ(r) at the bond CPs, ellipticities (italics), and delocalization indexes (underlined) associated with the appropriate atom pairs are also displayed in Fig 2. Values of ρ(r) and ε at selected bond CPs and the DIs are also collected in Table 6S and Tables 7S–9S, respectively.[2] The first obvious result is that **endo-C_2-TS** and **Cope-C_2-TS** exhibit *three normal* albeit weak bonds between the five-membered rings. *Clearly there is no need to arbitrarily differentiate the three bonds with solid, cross-hatched, dashed or dotted lines, to invoke SOIs, and to attempt to characterize SOI schemes with different types of dashed lines*.

In the case of **endo-C_2-TS**, all the bonds are weak; the C2|C4′ and C4|C2′ bonds are the weakest with the ρ(r) and DI values being 0.0161 and 0.124, respectively. The nominal C1|C1′ "single" bond that was represented with a cross-hatched line rather than a dashed line by Caramella et al. (3) is also weak; a ρ(r) value of 0.0871 and a DI of 0.472 indicate that it is roughly four times as strong as the C2|C4′ and C4|C2′ bonds and half the strength of a "normal" single bond that exhibits a DI of ~1.0. The C1|C1′ and C2|C4′ (C4|C2′) bonds exhibit vastly different ellipticities. As seen from the data collected in Table 7S, the DIs are essentially independent of the level of theory used; they are virtually identical at B3PW91/6–31+G(d), MPW1PW91/6–31+G(d), and B3PW91/6–311+G(2d,p).[2] Selected atomic basins of **endo-C_2-TS** obtained at the B3PW91/6–31+G(d) level are displayed as Figs. 3*a*–3*c*. Figure 3*a* shows the C4|C2′ basins, and Fig. 3*b* shows the C2′ basin that clearly shows the flattened atomic surface shared with the C4 basin. The DI is 0.124, substantially lower than the DI of ~1.0 expected for a "normal" single bond. The relatively small shared surface of C2′ seen in Fig. 3*b* is in accord with the smaller DI found for the C4′|C2 pair. As a point of reference, Fig. 3*c* shows the C3|C3′ basins that do not impinge on each other and do not exhibit a bond path (the C3|C3′ internuclear distance is 3.395 Å) while exhibiting a miniscule DI of 0.029.

The **Cope-C_2-TS** also exhibits bond paths between C1|C1′, C2|C4′, and C4|C2′, so there is no need to invoke SOIs and use different types of lines (in this case, the C1|C1′ bond was represented with a cross-hatched line by Caramella et al. (3) line rather than a dashed line) to describe the bonding. The three bonds are stronger (roughly by a factor of two) than the inter-ring bonds of **endo-C_2-TS**. The ρ(r) values of the C1|C1′, C2|C4′, and C4|C2′ bonds are 0.1992, 0.0287, 0.0287, and the DIs 0.829, 0.232, and 0.232, respectively. These results are in accord with the C1|C1′,

© 2008 NRC Canada

Fig. 2. Molecular graphs of (*a*) **endo-C_2-TS**, (*b*) **Cope-C_2-TS**, and (*c*) **exo-TS** including the values of ρ(r) and the ellipticity (in italics) at bond Cps and the delocalization index (underlined) for pair of atoms.

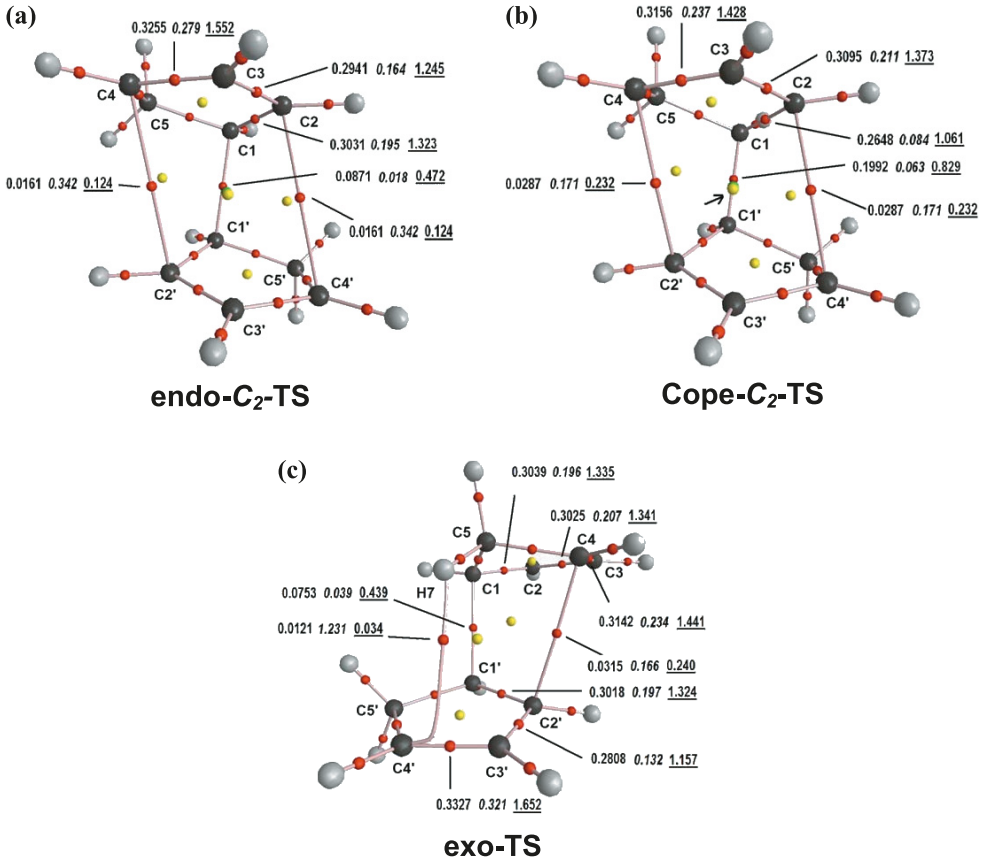

Fig. 3. (*a*) C2 and C4′ basins of **endo-C_2-TS**, (*b*) C4′ basin of **endo-C_2-TS**, (*c*) C3 and C3′ basins of **endo-C_2-TS**: **Cope-C_2-TS**, and (*c*) ***exo*-TS**: (*d*) C2 and C4′ basins of **Cope-C_2-TS**, (*e*) C4′ basin of **Cope-C_2-TS**, (*f*) C3 and C3′ basins of **Cope-C_2-TS**.

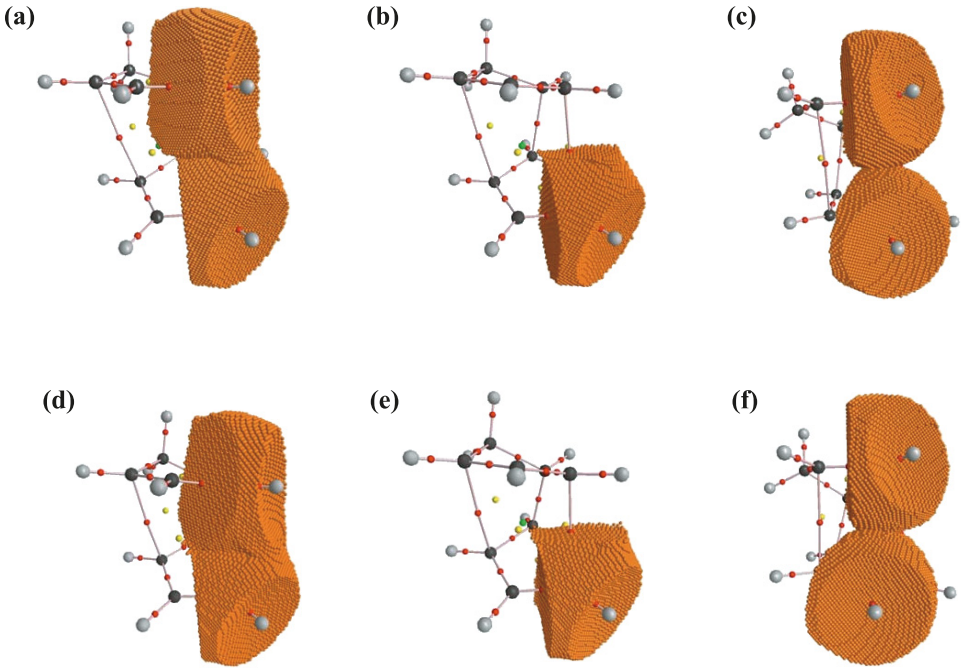

© 2008 NRC Canada

Fig. 4. (*a*) C4 and C2′ basins of **exo-TS**, (*b*) C2′ basin of **exo-TS**, (*c*) H7 and C4′ basins of **exo-TS**, (*d*) C4′ basin of **exo-TS**, (*e*) H7 basin of **exo-TS**, and (*f*) H7, C3′, and C4′ basins of **exo-TS**.

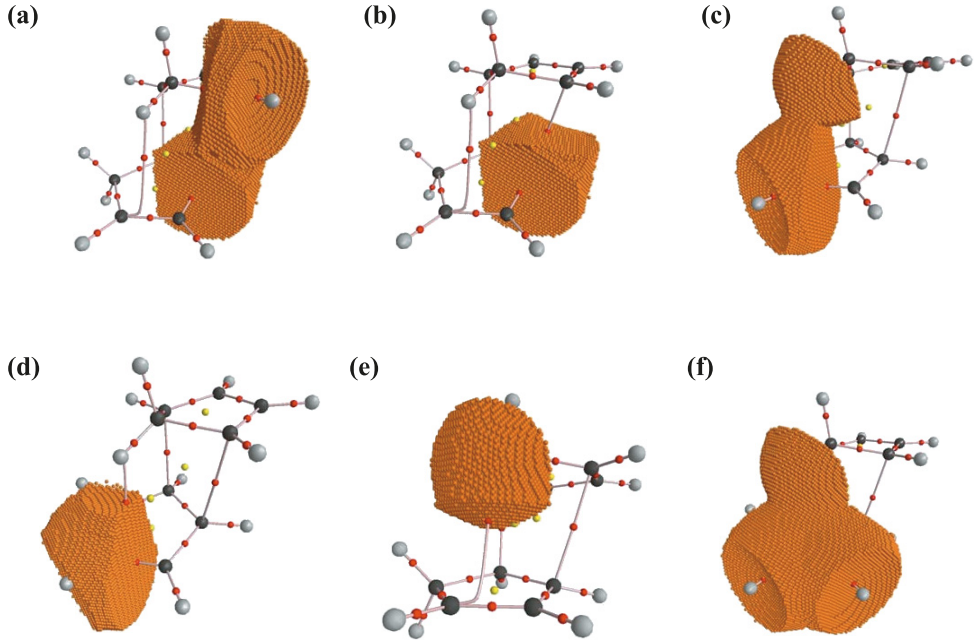

Table 1. Atom energies of **1**, **endo-C_2-TS**, **Cope-C_2-TS**, and **exo-TS** at B3PW91/6–31+G(d).

ATOM	**1**	**endo-C_2-TS**	$\Delta E('\Omega)$ (kcal mol^{-1})	**Cope-C_2-TS**	$\Delta E('\Omega)$ (kcal mol^{-1})	**exo-TS**	$\Delta E('\Omega)$ (kcal mol^{-1})
C1	–38.103 709	–38.067 733	22.57	–38.055 580	30.20	–38.073 426	19.00
C2	–38.100 556	–38.098 254	1.44	–38.092 097	5.31	–38.110 486	–6.23
C3	–38.100 556	–38.104 838	–2.69	–38.111 549	–6.90	–38.108 264	–4.84
C4	–38.103 709	–38.092 987	6.73	–38.084 425	12.10	–38.083 590	12.62
C5	–38.089 794	–39.075 967	8.68	–38.074 490	9.60	–38.095 404	–3.52
H6	–0.587 444	–0.595 548	–5.08	–0.604 837	–10.91	–0.591 042	–2.26
H7	–0.587 444	–0.608 016	–12.91	–0.613 143	–16.13	–0.598 467	–6.92
H8	–0.589 523	–0.602 492	–8.14	–0.612 390	–14.35	–0.599 307	–6.14
H9	–0.591 832	–0.591 379	0.28	–0.589 712	1.32	–0.594 117	–1.43
H10	–0.591 832	–0.593 905	–1.30	–0.594 811	–1.87	–0.594 171	–1.47
H11	–0.589 523	–0.591 044	–0.95	–0.592 531	–1.89	–0.591 284	–1.10
C1′	—	–38.067 729	22.58	–38.055 600	30.19	–38.056 335	29.73
C2′	—	–38.098 266	1.44	–38.092 095	5.31	–38.081 474	11.97
C3′	—	–38.104 824	–2.68	–38.111 563	–6.91	–38.104 659	–2.57
C4′	—	–38.093 005	6.72	–38.084 378	12.31	–38.106 081	–1.49
C5′	—	–38.075 969	8.67	–38.074 489	9.50	–38.069 547	12.70
H6′	—	–0.595 548	–5.08	–0.604 837	–10.91	–0.595 537	–5.08
H7′	—	–0.608 016	–12.91	–0.613 143	–16.13	–0.602 776	–9.62
H8′	—	–0.602 492	–8.14	–0.612 391	–14.35	–0.604 291	–9.27
H9′	—	–0.591 379	0.28	–0.589 712	1.33	–0.593 683	–1.16
H10′	—	–0.593 905	–1.30	–0.594 811	–1.87	–0.593 683	–1.13
H11′	—	–0.591 044	–0.95	–0.592 531	–1.88	–0.590 888	–0.86
$\Sigma(\Omega)$	*–194.035 926*	*–388.044 539*	*17.54*	*–388.051 120*	*12.99*	*–388.038 471*	*20.94*
E_{elec}	–194.035 846	–388.043 736	17.76	–388.050 942	13.01	–388.038 593	20.76

C4|C2′, and C2C4′ internuclear distances that are smaller (1.619, 2.606, 2.606 Å, respectively) than the corresponding internuclear distances (2.003, 2.902, 2.902 Å) of **endo-C_2-TS**. It is noteworthy that the inter-ring bonds are considerably stronger in **Cope-C_2-TS** than in **endo-C_2-TS** yet the Cope TS is only 4.5 kcal mol^{-1} lower in energy than the endo TS. A possible reason for this result is discussed in the section on atom-energy analysis. As far as the ellipticities are concerned, C1|C1′ of **Cope-C_2-TS** exhibits a higher ellipticity than C1|C1′ of **endo-C_2-TS** while C2|C4′, and C4|C2′ exhibit lower ones. Based on the ρ(r) and DI values, the C2|C3 and C3|C4 bonds are stronger than the C1|C2

© 2008 NRC Canada

bond. By symmetry, the same situation holds for the C2′|C3′, C3′|C4′, and C1′|C2′ bonds of ring B. Based on the ρ(r) and DIs values, the C1|C2, C2|C3, and C3|C4 the π electrons are more delocalized in the case of the Cope TS (0.2648, 1.061; 0.3095, 1.373; 0.3156, 1.428) than in the endo TS (0.3031, 1.323; 0.2941, 1.245; 0.3255, 1.522). The C1|C2 bond of the Cope TS exhibits a higher ellipticity (0.063) than the C1|C2 bond of the endo TS suggesting that it is involved to a greater degree in a hyperconjugative interaction than in the case of the endo TS. Again, as seen from the data collected in Table 8S the DIs are essentially independent of the level of theory used; they are virtually identical at B3PW91/6–31+G(d), MPW1PW91/6–31+G(d), and B3PW91/6–311+G(2d,p).[2]

Selected atomic basins of **Cope-C_2-TS** obtained at the B3PW91/6–31+G(d) level are displayed as Figs. 3*d*–3*f*. Figure 3*d* shows the C4|C2′ basins, and Fig. 3*e* shows the C2′ basin that clearly shows its flattened atomic surface shared with the C4 basin. In this case, the shared surface with C4 is larger than the shared surface of **endo-C_2-TS** in accord with the fact that the DI is 0.232, almost two times as large as the DI of the C4|C2′ pair of **endo-C_2-TS**. The C4|C2′ internuclear distance (2.602 Å) of **Cope-C_2-TS** is less than the C4|C2′ internuclear distance (2.902 Å) of **endo-C_2-TS**. Figure 3*f* shows the C3|C3′ basins for which the C3|C3′ internuclear distance (2.952 Å) is marginally smaller than in the case of **endo-C_2-TS**. As in the case of **endo-C_2-TS**, the basins do not impinge on each other (the DI is marginally larger at 0.035) and do not exhibit a bond path.

The TS for exo dimerization **exo-TS** not only exhibits C1|C1′ and C4|C2′ bond paths but also a highly curved one between H7 and C4 that exhibits a ρ(r) value of 0.0121 at the bond CP; the DI is small at 0.034. The C1|C1′ ρ(r) and DIs values (0.0753 and 0.439) are similar to the values for the **endo-C_2-TS** (0.0871 and 0.472), so the C1|C1′ bond of **exo-TS** is slightly weaker than the C1|C1′ bond of **endo-C_2-TS**. However, the C4|C2′ bond is almost twice as strong (the ρ(r) and DIs values are 0.0315 and 0.240) as the C2|C4′(C4|C2′) bonds (values 0.0181 and 0.124) of **endo-C_2-TS** but of comparable strength to each of the C2|C4′ and C4|C2′ bonds (values 0.0287 and 0.232) of **Cope-C_2-TS**. C1|C2 (values 0.3039 and 1.335), C2|C3 (0.3025, 1.341), and C3|C4 (0.3142, 1.441) of ring A of **exo-TS** exhibit very similar double-bond characters. Based on the ρ(r) and DI values, ring B of **exo-TS** exhibits a greater degree of π density localization (C1′|C2, 0.3018 and 1.324: C2′|C3′, 0.2808 and 1.157; C3′C4′, 0.3327, 1.652) than ring A. The C4|C2′ basins are displayed as Fig. 4*a*. Figure 4*b* shows how the C2′ basin is flattened in sharing its interatomic surface with C4. Figure 4*c* shows the H7|C4′ basins. Figures 4*d* and 4*e* show how the C4 basin and H7 basins are "deformed" in impinging on each other. It is interesting to note that from a visual standpoint based on the deformation of the H7 basin, the same interaction occurs between H7 and C3′ (the DI is 0.024) except that there is no bond path generated.

Atom-energy analysis

The atom energies ($E(\Omega)$) of **1** (CPD), **endo-C_2-TS**, **Cope-C_2-TS**, and **exo-TS** along with the $\Delta E(\Omega)$s in going from **1** to **endo-C_2-TS**, **Cope-C_2-TS**, and **exo-TS** are collected in Table 1. Also included at the bottom of the table are the sums $\Sigma E(\Omega)$s and the uncorrected total energies (E_{elec}) obtained from the G03 calculations along with the corresponding barriers; $\Delta E^{\ddagger}(\Omega) = 2 \times [\Sigma E(\Omega)_{CPD} - \Sigma E(\Omega)_{TS}]$ and $\Delta E^{\ddagger}_{elec} = 2 \times E_{elecCPD} \times E_{elecTS}$. First, it is important to note that $\Sigma E(\Omega)$ and E_{elec} of **1** ($\Sigma E(\Omega) - E_{elec} = -0.05$ kcal mol^{-1}), **endo-C_2-TS** (–0.50), **Cope-C_2-TS** (–0.16), and **exo-TS** (+0.08) differ only marginally from each other. These results clearly validate the AIMALL97 integration data. Consequently, the $\Delta E^{\ddagger}(\Omega)$ and $\Delta E^{\ddagger}_{elec}$ values are also close to each other; 17.54 and 17.26 kcal mol^{-1} for **endo-C_2-TS**; 12.99 and 13.01 for **Cope-C_2-TS**; 20.95 and 20.74 for **exo-TS**. These results validate an analysis based on changes in atom energies.

endo-C_2-TS

It is seen that except for C3 that is slightly stabilized (–2.69 kcal mol^{-1}), the carbon atoms of **1** are *destabilized* (a total of +73.46 kcal mol^{-1} or 36.73 per ring) in achieving **endo-C_2-TS**. C1 and C1′ are destabilized to the largest degree (each by +22.6 kcal mol^{-1}). Except for H9 and H9′ that are very slightly destabilized (each by +0.28 kcal mol^{-1}), the 10 hydrogens of **endo-C_2-TS** that gain charge are *stabilized* by a total of –56.20 kcal mol^{-1} relative to the corresponding Hs of two cyclopentadienes. Given that the carbon atoms are *destabilized* by +73.46 kcal mol^{-1}, it is the *stabilization* of the H atoms that leads to a huge lowering of the potentially high barrier for the dimerization of **1**; H7(–12.91), H7′(–12.91), H8(–8.14), and H8′(–8.14) are stabilized to the greatest degree in achieving **endo-C_2-TS**. C1 and C1′ undergo the largest sp^2 to sp^3-like change in hybridization in achieving the TS and thereby are destabilized to the greatest degree. The hydrogens attached to the sp^2-hybridized Cs are stabilized because charge is transferred from C to H as the carbon atoms undergo rehybridization. The methylene Hs also gain charge and are stabilized in all the transition states. As far as the energies of the carbon atoms of **endo-C_2-TS** are concerned relative to the relationship between population and energy for sp^3- and sp^2-hybridized carbons seen in Fig. 1S, only C3 exhibits a significant deviation.[2] Based on its population, it is stabilized by ~20 kcal mol^{-1}. This may be due in part to the fact that there is an increase in the C2–C3–C4 delocalization in **endo-C_2-TS** over **1**; the sum (2.897) of the C2|C3 and C3|C4 DIs is slightly larger for **endo-C_2-TS** than the sum (2.833) of the C2|C3 and C3|C4 DIs of **1**.

Cope-C_2-TS

While C3 is slightly stabilized (–6.90 kcal mol^{-1}), the C atoms of **1** overall are *destabilized to a greater degree* (the total is +100.62 kcal mol^{-1} or 50.31 per ring) in achieving **Cope-C_2-TS** than in the case of **endo-C_2-TS**. C1 and C1′ undergo a greater degree of rehybridization in achieving the transition state than in the case of **endo-C_2-TS** and consequently are destabilized (each by +30.2 kcal mol^{-1}) more than C1 and C1′ of **endo-C_2-TS**. Except for H9 and H9′ that are very slightly destabilized (each by +1.32), the remaining 10 Hs of **Cope-C_2-TS** are *dramatically stabilized* (–87.66 kcal mol^{-1}, 43.83 per set of five of each ring) relative to two cyclopentadienes. It is the differential stabilization of the H atoms that yields a lower energy for

© 2008 NRC Canada

Cope-C_2-TS than **endo-C_2-TS**; H7 (–16.13), H7′ (–16.13), H8 (–14.35), and H8′ (–14.35) are stabilized to the greatest degree in achieving the TS. The destabilization of C1 and C1′ is due to the fact that there is a significant sp^2 to sp^3-like change in hybridization in achieving the **Cope-C_2-TS**. Again, the hydrogens are stabilized because charge is transferred from C to H as rehybridization of the carbon atoms takes place.

exo-TS

The C atoms of **1** are not destabilized to the same degree in achieving the **exo-TS** (a total of +67.37 kcal mol^{-1}) as in the case of **endo-C_2-TS** and **Cope-C_2-TS**. Moreover, the carbon atoms of ring B are destabilized significantly more (the total is +50.34 kcal mol^{-1}) than the carbon atoms of ring A (+17.03). Surprizingly, C1′ is destabilized more (+29.73) than C1 (+19.00). Nevertheless, these atoms together are not destabilized to the same extent as in the case of **endo-C_2-TS** and **Cope-C_2-TS** because the C1–C1′ incipient bond is weaker in the case of **exo-TS** than in **endo-C_2-TS** and **Cope-C_2-TS**. Consequently, the sp^2 to sp^3-like rehybridization at C1 and C1′ is smaller in achieving **exo-TS** than in the case of **endo-C_2-TS** and **Cope-C_2-TS**. The H atoms of ring B are stabilized (–27.12 kcal mol^{-1}) more than the H atoms of ring A (–19.32).

As far as energies of the carbon atoms of the TSs are concerned relative to the relationship between population and energy (Fig. 1S), only the energies of the C3s deviate significantly (they are more stable than expected based on their populations).[2] This may be a consequence of the fact that there is a greater degree of delocalization in the TSs than in the starting material.

Conclusions

Based on the results of this work, a QTAIM–DI–VISAB study coupled with atom-energy analysis should be considered as the method of choice for detailing the nature of the bonding in transition states of cycloaddition reactions exhibiting diastereoselectivities and facial selectivities, and we plan to study several other examples. This approach obviates the need for invoking secondary orbital overlap and arbitrarily selecting and (or) using solid, cross-hatched, dashed, or dotted lines to represent bonding in cycloaddition reactions.

Acknowledgement

We gratefully acknowledge financial support by the Natural Sciences and Engineering Research Council of Canada (NSERC). We thank SHARCNET (Shared Hierarchical Academic Research Computing Network (of Ontario) for providing computing resources at McMaster University.

References

1. (*a*) K. Alder and G. Stein. Liebigs Ann. Chem. **504**, 210 (1933); (*b*) K. Alder and G. Stein. Angew. Chem. **47**, 837 (1934); (*c*) K. Alder and G. Stein. Angew. Chem. **50**, 514 (1937).
2. (*a*) R. Hoffmann and R.B. Woodward. J. Am. Chem. Soc. **87**, 4388 (1965); (*b*) R. Hoffmann and R.B. Woodward. The conservation of orbital symmetry. Academic Press, New York; 1970; (*c*) I. Fleming. Frontier orbital and organic chemical reactions. Wiley, New York. 1967; (*d*) D. Ginsburg. Tetrahedron, **39**, 2095 (1983); (*d*) J.I. Garcia, J.A. Mayoral, and L. Salvatells. Acc. Chem. Res. **33**, 658 (2000).
3. P. Caramella, P. Quadrelli, and L. Toma. J. Am. Chem. Soc. **124**, 1130 (2002).
4. R.F.W. Bader. Atoms in molecules: A quantum theory. Oxford University Press, Oxford, UK. 1990.
5. T. Bajorek and N. H. Werstiuk. Can. J. Chem. **83**, 1352 (2005).
6. D.A. Poulsen and N.H. Werstiuk. J. Chem. Theory. Comput. **2**, 77 (2006).
7. N.H. Werstiuk. J. Chem. Theory. Comput. **3**, 2258 (2007).
8. E. Brown, R.F.W. Bader, and N.H. Werstiuk. Can. J. Chem. Manuscript in preparation.
9. M.J. Frisch, G.W. Trucks, H.B. Schlegel, G.E. Scuseria, M.A. Robb, J.R. Cheeseman, J.A. Montgomery, Jr., T. Vreven, K.N. Kudin, J.C. Burant, J.M. Millam, S.S. Iyengar, J. Tomasi, V. Barone, B. Mennucci, M. Cossi, G. Scalmani, N. Rega, G.A. Petersson, H. Nakatsuji, M. Hada, M. Ehara, K. Toyota, R. Fukuda, J. Hasegawa, M. Ishida, T. Nakajima, Y. Honda, O. Kitao, H. Nakai, M. Klene, X. Li, J.E. Knox, H.P. Hratchian, J.B. Cross, V. Bakken, C. Adamo, J. Jaramillo, R. Gomperts, R.E. Stratmann, O. Yazyev, A.J. Austin, R. Cammi, C. Pomelli, J.W. Ochterski, P.Y. Ayala, K. Morokuma, G.A. Voth, P. Salvador, J.J. Dannenberg, V.G. Zakrzewski, S. Dapprich, A.D. Daniels, M.C. Strain, O. Farkas, D.K. Malick, A.D. Rabuck, K. Raghavachari, J.B. Foresman, J.V. Ortiz, Q. Cui, A.G. Baboul, S. Clifford, J. Cioslowski, B.B. Stefanov, G. Liu, A. Liashenko, P. Piskorz, I. Komaromi, R.L. Martin, D.J. Fox, T. Keith, M.A. Al-Laham, C.Y. Peng, A. Nanayakkara, M. Challacombe, P.M.W. Gill, B. Johnson, W. Chen, M.W. Wong, C. Gonzalez, and J. A. Pople. Gaussian 03 [computer program]. Revision C.02. Gaussian, Inc., Wallingford CT. 2004.
10. N.H. Werstiuk and H.M. Muchall. J. Mol. Struct. (Theochem.) **463**, 225 (1999).
11. N.H. Werstiuk and H.M. Muchall. J. Phys. Chem. A, **103**, 6599 (1999).
12. N.H. Werstiuk and H.M. Muchall, J. Phys. Chem. A, **104**, 2054 (2000).
13. N.H. Werstiuk, H.M. Muchall, and S.J. Noury. J. Phys. Chem. A, **104**, 11601 (2000).
14. C. Adamo and V. Barone. J. Chem. Phys. **108**, 664 (1998).
15. ChemCraft [computer program]. Version 1.5. Available from http://www.chemcraftprog.com.
16. R. Dennington II, T. Keith, J. Millam, K. Eppinnett, W.L. Hovell, and R. Gilliland. GaussView [computer program]. Version 3.09. Semichem, Inc., Shawnee Mission, Kans. 2003.
17. F. Biegler-Konig. AIM 2000 [computer program]. University of Applied Science, Bielefeld, Germany. 1998–2000.
18. Y-G. Wang and N.H. Werstiuk. J. Comput. Chem. **24**, 379 (2003).
19. Y-G. Wang, C. Matta, and N.H. Werstiuk. J. Comput. Chem. **24**, 1720 (2003).
20. Y-G. Wang, K.B. Wiberg, and N.H. Werstiuk. J. Phys. Chem. A, **111**, 3592 (2007).
21. T.A. Keith. AIMALL97 Package (B3) for WINDOWS [computer program]. Available from aim@tkgristmill.com.

© 2008 NRC Canada

Carbon and silicon substitution in (4, 4) aluminum nitride nanotube — Density functional study of ^{27}Al and ^{14}N electric field gradient tensors

Ahmad Seif, Mehran Aghaie, and Hossein Aghaie

Abstract: A computational study at the level of density functional theory (DFT) was performed to investigate the influence of Si and C substitution on the ^{14}N and ^{27}Al quadrupole coupling constants (C_Q) in the armchair single-walled aluminum nitride nanotube (SWAlNNT). To this aim, a 1 nm AlNNT consisting of 28 Al and 28 N atoms was considered in which both mouths of the nanotube are capped by hydrogen atoms. Additionally, two other forms of this model of AlNNT were considered in which five Si and five C atoms were substituted in place of the five Al and five N atoms, with two rings in the length of nanotube, like a wire, in the first form; and three Si and three C atoms were substituted in place of three Al and three N atoms as a central ring on the surface of the AlNNT in the second form. The calculated C_Q values for three optimized AlNNT systems (raw and Si- and C-substituted) reveal diverse electronic environments in the above-mentioned systems. All the calculations were carried out using the Gaussian 98 software package.

Key words: armchair nanotube, density functional theory, nuclear quadrupole resonance.

Résumé : On a effectué une étude théorique au niveau de la théorie de la densité fonctionnelle (TAF) afin d'évaluer l'influence de substitutions par le carbone et le silicium sur les constantes de couplage quadripolaire (CQ) du ^{14}N et du ^{27}Al dans un nanotube d'azoture d'aluminium en chaise berçante à une paroi (SWAlNNT). À cette fin, on a considéré un nanotube d'azoture d'aluminium de 1-nm de longueur formé de 28 atomes d'aluminium et de 28 atomes d'azote dans lequel les deux extrémités d'un nanotube sont fermées par des atomes d'hydrogène. On a considéré de plus deux autres formes de nanotubes dont l'une dans laquelle on a remplacé cinq atomes d'aluminium et cinq atomes d'azotes par cinq atomes de silicium et cinq atomes de carbone en forme de cycles, tels des fils, dans la longueur du nanotube et une autre dans laquelle on a remplacé trois atomes d'aluminium et trois atomes d'azotes par trois atomes de silicium et trois atomes de carbone sous la forme de noyau central dans la surface du nanotube. Les valeurs calculées de C_Q pour les trois systèmes de nanotube d'azoture d'aluminium optimisés (le système de base et les systèmes avec des substitutions par du carbone et du silicium) révèlent l'existence d'environnements électroniques divers dans ces systèmes. On a effectué tous les calculs à l'aide d'un programme à Gaussian 98.

Mots-clés : nanotube en forme de chaise berçante, théorie de la densité fonctionnelle, résonance quadripolaire nucléaire.

[Traduit par la Rédaction]

Introduction

The astonishing discovery of carbon nanotubes (CNTs) by Ijimia (1) caused a rapid development in the field of nanoscale materials. In the subsequent years, extensive efforts were made to synthesize tubular or spherical nanotubes of several non-carbon inorganic materials, e.g., boron nitride (2), silica (3), and alumina (4). Chemical and physical characteristics of these novel materials, dependant on the size and shape of the nanostructures, differ from fullerenes and carbon nanotubes (5). Coaxial cubic aluminum nitride-boron nitride composite nanotubes have been already synthesized (6). Recently, the non-layered structure of hexagonal AlN nanotubes (AlNNTs) has been synthesized without template (7). Theoretical studies have demonstrated that faceted AlNNTs are energetically more favorable than the single-walled AlNNT models (8–9), while thick-walled AlNNTs are energetically comparable to AlN nanowires (AlNNWs) of similar diameter (10). However, single-walled AlNNTs have not been synthesized yet. The pioneering theoretical study of Zhang and Zhang proposed smooth and uniform diameter AlNNTs (11). Infinite armchair and zigzag AlNNTs (12), AlN fullerene cages (13), and open-ended armchair and zigzag AlNNTs nanotubes (14) have also been studied theoretically. The electronegativity of N (eN = 3.04) is con-

Received 10 January 2008. Accepted 2 April 2008. Published on the NRC Research Press Web site at canjchem.nrc.ca on 30 May 2008.

A. Seif and H. Aghaie.[1] Department of Chemistry, Science and Research Campus, Islamic Azad University, P.O. Box 14515–775 Tehran, Iran.
M. Aghaie. Faculty of Chemistry, North Tehran Branch, Islamic Azad University, Tehran, Iran.

[1]Corresponding author: (e-mail: hm_Aghaie@yahoo.com).

 doi:10.1139/V08-066 © 2008 NRC Canada

siderably larger than that of Al (eAl = 1.61) (15), leading to a charge transfer from Al to N, yielding asymmetric electronic charge density distribution along the AlN bond. Hence, Al atoms act as cations while N atoms act as anions in AlNNTs. The AlNNTs are suggested for optoelectronics applications (16).

Nuclear quadrupole resonance (NQR) spectroscopy is an insightful technique to study the physical properties of matter in the solid phase (17). The NQR measurable parameters are the quadrupole coupling constant (C_Q) and the asymmetry parameter (η_Q), which are both also reproduced by quantum chemical calculations of the electric field gradient (EFG) tensors. Nuclei with spin angular momentum (I) greater than one half (I > 1/2) have a nuclear electric quadrupole moment (eQ) that interacts with the EFG tensors originated at the site of quadrupole nuclei (18). The spin angular momenta are 2.5 and 1 for ^{27}Al and ^{14}N (19), respectively. Hence, the electronic densities at the sites of these nuclei are very sensitive and feel changes by any perturbation.

In this theoretical work, we study the influence of Si and C substitution on the ^{27}Al and ^{14}N NQR parameters in the (4, 4) armchair single-walled AlNNTs (Figs. 1–3) to indicate the electronic structure properties of armchair AlNNTs in the Si- and C-substituted forms. Recently, the EFG tensors were studied in a representative model of raw (6, 0) zigzag single-walled AlNNT (20), however, to the best of our knowledge, there are no available experimental NQR data for the considered AlNNTs structures in the literature. The calculated C_Q and η_Q parameters are presented in Tables 1–3. Though we can study the electrostatic properties of the considered nanotubes using the calculated data, these quantities may compared with future experimental data. To our knowledge, this work is the only theoretical quadrupole coupling constant calculation.

Computational procedure

All quantum chemical calculations were performed at the level of the density functional theory (DFT) using the Gaussian 98 software package (21). Five models of (4, 4) armchair single-walled AlNNTs with a length of 1 nm were considered. In each of the five models, both mouths of the nanotubes were capped by hydrogen atoms to saturate the boundary dangling to stabilize the models and also to simulate the effect of a longer tube. Model No. 1 (raw) consisted of 28 Al and 28 N atoms. Model No. 2 consisted of a wire-like substituted model in which five Si and five C atoms in the two rings along the length of nanotube are placed in place of five Al and five N atoms. Model No. 3 is a ring-substituted model in which three Si and three C atoms are substituted for three Al and three N atoms as a central ring on the surface of the Si- and C-substituted AlNNT. Model No. 4 is a Si- and C-substituted model in which one Si and one C atom are substituted in place of one Al and one N atom. Model No. 5 is a Si- and C- substituted model in which two Si and two C atoms are substituted in place of two Al and two N atoms (See Figs 1–5).

First, the models were allowed to fully relax during geometrical optimization using the B3LYP exchange functional method (22–23) and the 6–31G (d) standard basis set (14).

Fig. 1. The 2D view of raw AlNNT model, front side (left) and back side (right).

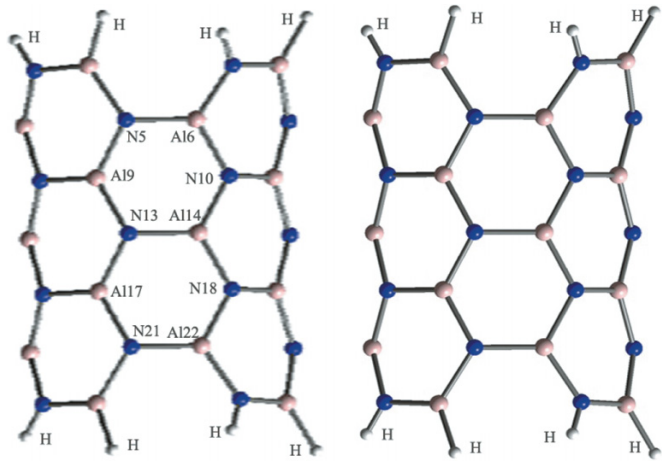

Fig. 2. The 2D view of the Si- and C-substituted AlNNT model, front side (left) and back side (right).

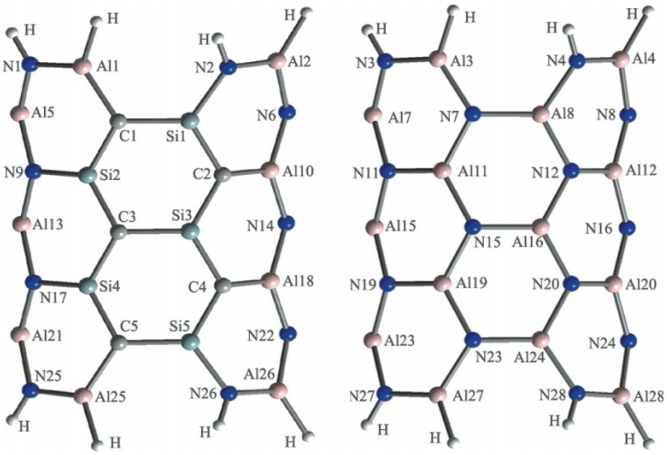

Fig. 3. The 2D view of the Si- and C-substituted (ring-substituted) AlNNT model, front side (left) and back side (right).

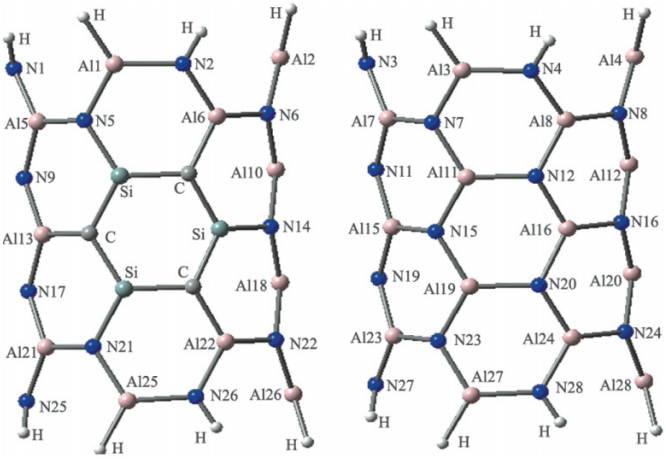

Second, the quantum chemical calculations were performed on the three geometrically optimized models by the B3LYP method and the 6–31+G** standard basis set to evaluate the

© 2008 NRC Canada

Table 1. The NQR Parameters in the raw AlNNT model.

	^{27}Al		^{14}N	
Layers	C_Q (Mhz)	η_Q	C_Q (MHz)	η_Q
Layer 1	28.44	0.08	2.04	0.83
Layer 2	25.52	0.04	0.39	0.74
Layer 3	25.45	0.05	0.31	0.64
Layer 4	25.45	0.08	0.30	0.75
Layer 5	25.45	0.05	0.32	0.60
Layer 6	25.53	0.04	0.39	0.74
Layer 7	28.45	0.08	2.04	0.83

Note: See Fig 1. The average values in each layer are reported.

Table 2. The NQR parameters in the Si- and C-substituted AlNNT model (wire-like).

	^{27}Al			^{14}N		
Layers	Nuclei	C_Q (Mhz)	η_Q	Nuclei	C_Q (Mhz)	η_Q
Layer 1	Al 1	28.40	0.17	N 1	2.01	0.80
	Al 2	29.03	0.27	N 2	2.08	0.95
	Al 3	28.44	0.07	N 3	2.05	0.80
	Al 4	28.47	0.09	N 4	2.03	0.79
	Al 5	26.00	0.06	N 5	—	—
Layer 2	Al 6	—	—	N 6	0.44	0.67
	Al 7	25.92	0.12	N 7	0.40	0.60
	Al 8	25.52	0.05	N 8	0.42	0.91
	Al 9	—	—	N 9	0.86	0.35
Layer 3	Al 10	25.44	0.03	N 10	—	—
	Al 11	25.49	0.14	N 11	0.36	0.60
	Al 12	25.73	0.03	N 12	0.30	0.52
	Al 13	25.57	0.07	N 13	—	—
Layer 4	Al 14	—	—	N 14	0.26	0.89
	Al 15	26.39	0.14	N 15	0.29	0.07
	Al 16	25.42	0.02	N 16	0.37	0.77
	Al 17	—	—	N 17	0.86	0.60
Layer 5	Al 18	25.44	0.03	N 18	—	—
	Al 19	25.73	0.03	N 19	0.36	0.70
	Al 20	25.49	0.13	N 20	0.29	0.52
	Al 21	25.73	0.01	N 21	—	—
Layer 6	Al 22	—	—	N 22	0.40	0.67
	Al 23	26.38	0.25	N 23	0.39	0.60
	Al 24	25.49	0.06	N 24	0.47	0.91
	Al 25	28.40	0.17	N 25	2.05	0.80
Layer 7	Al 26	29.03	0.27	N 26	2.08	0.95
	Al 27	28.46	0.07	N 27	2.01	0.79
	Al 28	28.51	0.10	N 28	2.02	0.80

Note: See Fig. 2. The dashes in the table refers to the Si and C atoms in the model.

^{14}N and ^{27}Al NQR parameters (Tables 1–3). Since the EFG tensors are quantum chemically calculated in the principal axes system (PAS) ($|qzz| > |qyy| > |qxx|$), directly relating with experiments, they are converted to measurable NQR parameters, quadrupole coupling constant C_Q and asymmetry parameter η_Q. C_Q refers to the interaction energy of the nuclear electric quadrupole moment (eQ) and the EFG tensors at the site of quadrupole nucleus, while η_Q is a measure of the EFG tensors deviation from a cylindrical system at the site of the quadrupole nucleus. Equations presented in a previous work (20) are used to directly relate the calculated EFG tensors with the measurable parameters of C_Q and η_Q.

Table 3. The NQR parameters in the Si- and C-substituted AlNNT model (ring-substituted).

	^{27}Al			^{14}N		
Layers	Nuclei	C_Q (Mhz)	η_Q	Nuclei	C_Q (Mhz)	η_Q
Layer 1	Al 1	28.44	0.08	N 1	2.01	0.82
	Al 2	28.45	0.09	N 2	2.02	0.82
	Al 3	28.45	0.07	N 3	2.05	0.80
	Al 4	28.44	0.09	N 4	2.02	0.83
	Al 5	26.00	0.06	N 5	2.68	0.99
Layer 2	Al 6	27.51	0.31	N 6	0.44	0.80
	Al 7	25.92	0.05	N 7	0.40	0.70
	Al 8	25.58	0.07	N 8	0.42	0.72
	Al 9	—	—	N 9	0.40	0.65
Layer 3	Al 10	25.61	0.08	N 10	—	—
	Al 11	25.20	0.05	N 11	0.36	0.60
	Al 12	25.52	0.03	N 12	0.30	0.58
	Al 13	27.21	0.07	N 13	—	—
Layer 4	Al 14	—	—	N 14	0.66	0.66
	Al 15	25.29	0.14	N 15	0.31	0.31
	Al 16	25.42	0.02	N 16	0.27	0.27
	Al 17	—	—	N 17	0.41	0.64
Layer 5	Al 18	25.62	0.03	N 18	—	—
	Al 19	25.20	0.03	N 19	0.37	0.61
	Al 20	25.51	0.13	N 20	0.29	0.58
	Al 21	25.93	0.01	N 21	2.68	0.99
Layer 6	Al 22	27.53	0.33	N 22	0.45	0.67
	Al 23	25.90	0.05	N 23	0.39	0.68
	Al 24	25.558	0.06	N 24	0.45	0.72
	Al 25	28.43	0.17	N 25	2.00	0.80
Layer 7	Al 26	28.43	0.27	N 26	2.02	0.82
	Al 27	28.45	0.07	N 27	2.01	0.81
	Al 28	28.44	0.10	N 28	2.02	0.83

Note. See Fig. 3. The dashes in the table refer to the Si and C atoms in the model.

Fig. 4. The 2D view of the Si- and C-substituted (one pair) AlNNT model, front side.

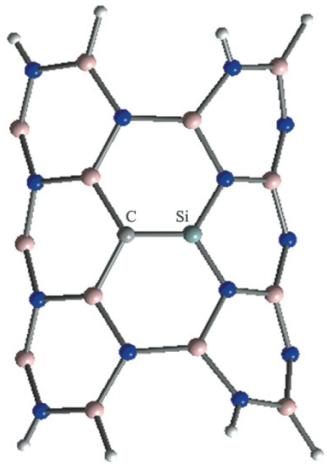

© 2008 NRC Canada

Fig. 5. The 2D view of the Si- and C-substituted (two pairs) AlNNT model, front side.

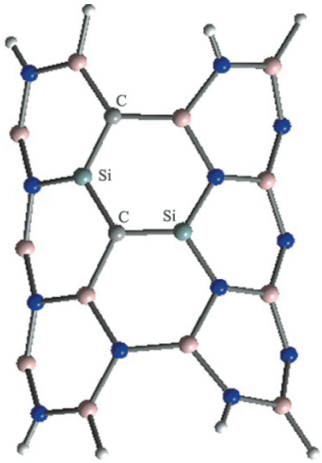

The evaluated NQR parameters at the sites of various ^{14}N and ^{27}Al nuclei for the raw and various Si- and C-substituted models of the considered AlNNT are exhibited in Tables 1–3.

Results and discussion

Geometry optimizations

At the first step of this study to calculate the minimum energy (Table 4), we performed optimization at the level of the B3LYP DFT method and 6–31G(d) standard basis set on each of raw and Si- and C-substituted models of the considered AlNNT. The results indicate that the Si- and C-substituted AlNNT in the wire-like form is more stable than other considered models. In the two-atom substitution form, one Si and one C, we found that even at the best possible position (Fig. 4), this model is more energetically unfavorable than the ring form of substitution. When we gradually add Si and C atoms to the nanotube, we observe that these patterns are more energetically unfavorable than the wire-like substitution pattern. Moreover, in the wire-like substituted pattern, the bond lengths of Al–C and N–Si around the wire are 1.90 and 1.72 Å, respectively. But the bond lengths of Al–C and N–Si in the ring-substituted model are 1.96 and 1.80 Å, respectively. On the other hand, in the wire-like substituted model, the bond lengths of Al–C and N–Si are shorter than those of other substituted patterns. Our study shows that Si and C have alternative positions because when we substitute six Si atoms for three Al and three N atoms in the ring-substituted form of AlNNT, the ring will open and the nanotube structure will disarrange.

C_Q parameters

In this work, the influence of Si- and C-substitution on the electronic structure properties of armchair AlNNTs is studied by DFT calculations of the EFG tensors at the sites of various ^{27}Al and ^{14}N nuclei in three models of raw and Si- and C-substituted (4, 4) single-walled AlNNTs (Figs. 1–3). In the Si- and C-substituted models, although the wire-like substituted form is energetically stable, we also considered the ring-substituted model for a better comparison. First, the models were optimized and then the NQR (C_Q and η_Q) calculations were carried out on the three optimized structures (Tables 1–3). In the following, the evaluated NQR parameters at the sites of the ^{27}Al and ^{14}N nuclei in the raw and Si- and C-substituted models of the considered (4, 4) AlNNT are discussed.

Table 4. The energy values for raw and Si- and C-substituted AlNNTs.

Models	Energy (KeV)
Raw	–226.759
Si- and C-substituted (wire-like)	–230.891
Si- and C-substituted (ring)	–225.858
Si- and C-substituted (one pair)	–224.220
Si- and C-substituted (two pairs)	–224.210

The raw AlNNT model

This section focuses on the calculated EFG tensors at the sites of various ^{27}Al and ^{14}N nuclei in the raw (4, 4) AlNNT model (Table 1 and Fig. 1). The results reveal that the nuclei are divided into seven layers with equivalent electrostatic properties in each layer. Since there is almost no significant difference in the calculated NQR parameters at the sites of nuclei in each layer, the average values in each layer are reported in Table 1 for ^{27}Al and ^{14}N nuclei. There are three kinds of chemical bonds in this model including Al–N, N–H, and Al–H bonds in different positions of the nanotube. The N–H and Al–H bonds are located at the mouths of the nanotube, and the Al and N nuclei contributing to these bonds in layers 1 and 7 have the largest magnitudes of C_Q among other the nuclei, in which the larger C_Q refers to the higher electron density at the sites of the nuclei. In contrast with Zigzag AlNNTs having two different mouths with similar Al and N atoms (Al-mouth and N-mouth), the armchair AlNNTs have two similar mouths, but each one consists of different Al and N atoms. Therefore, similar NQR parameters are calculated for the two mouths of the considered model (layers 1 and 7). Furthermore, the magnitudes of C_Q for each of the ^{27}Al and ^{14}N nuclei in layers 1 and 7 are the largest; in moving to the middle of the nanotube, the magnitudes are reduced; in layer 4 C_Q has the smallest magnitude. Almost parallel results are also observed for changes of η_Q along the length of the considered AlNNT.

The Si- and C-substituted AlNNT models (wire-like and ring-substituted patterns)

The Si and C atoms substitution of the considered (4, 4) AlNNT model is the focus in this section (Tables 2 and 3 and Figs. 2 and 3). Five Si and five C atoms are substituted in place of five Al and five N atoms to create two rings along the length of the nanotube in the wire-like substituted pattern, while three Si and three C atoms are substituted in place of three Al and three N atoms as a central ring on the surface of the nanotube in a ring-substituted pattern. In both of Si- and C-substituted models, there are six kinds of chemical bonds including Al–N, Al–H, N–H, Al–C, Si–C, and N–Si, which makes the front side of the raw and Si- and C-substituted AlNNT models completely different. The optimization process yielded an average Al–N bond length of 1.81 Å in the raw model, and this value is also observed for the back side of the substituted models in which the Al and N atoms are located far from the substituted Si and C atoms. However, on the front side, the bond length of Al–C for both

© 2008 NRC Canada

of the substitution models, wire-like and ring-substituted, are increased to almost 1.90 and 1.96 Å, respectively, and that of N–Si is reduced to almost 1.72 and almost 1.80 Å, respectively, yielding different electronic properties at the sites of those Al and N nuclei directly contributing to these bonds and also to the neighborbonds. In addition, since Al and N play cation and anion roles in AlNNTs, substituting Si and C for one of them in Al–N makes significant changes in the electronic density at the sites of these nuclei. Tables 2 and 3 exhibit the calculated NQR parameters for ^{27}Al and ^{14}N nuclei in the considered models. Only $C_Q(^{14}N)$ at the sites of those nitrogen nuclei, which are directly bonded to Si, are significantly increased in the wire-like substituted form; however, this parameter at the sites of both ^{14}N and ^{27}Al nuclei that are directly bonded to Si and C are significantly increased in the ring-substituted form of AlNNT. Furthermore, since N has a lone pair of electrons in the valance shell, the nucleus feels more electron density compared with Al. Therefore, in the two Si and C-substituted models, the NQR parameters of ^{14}N undergo more significant changes than those of ^{27}Al. Meanwhile, the change of C_Q values at the sites of the ^{14}N nuclei, which are directly bonded to Si in the ring-substituted model of AlNNT, is more significant rather than that of the ^{14}N nuclei, which are directly bonded to Si in the wire-like substituted form of the considered AlNNT model. It is noted that other nuclei in the back side of the Si- and C-substituted models do not exhibit any changes because of Si- and C-substitution. As mentioned earlier, the magnitude of the NQR parameters is the largest at the nanotube mouths, meaning that the highest electron density at the sites of Al and N nuclei is located at the mouths. Therefore, since the NQR parameters at the sites of N nuclei (for both of substituted models) and at the sites of Al nuclei (for ring-substituted), which are directly bonded to Si and C, are significantly increased, then the Si and C-substituted form of AlNNT model may be expected to be more useful in those applications of AlNNTs in which mouth properties are important. This trend means that the active sites of AlNNT are increased by Si and C-substitution in the Si and C-substituted AlNNT models. The values of η_Q are also increased at the sites of the Al and N nuclei directly bonded to C and Si, meaning that the EFG tensors at the sites of these nuclei are more deviated from cylindrical symmetry.

Conclusion

We performed a DFT study to investigate the influence of Si and C-substitution on the electronic structure properties of AlNNTs by calculating the NQR parameters at the sites of ^{27}Al and ^{14}N nuclei. The calculated minimum energies reveal that the wire-like substituted model is energetically more favorable than other substituted patterns. In addition, by the calculated NQR parameters at the sites of various ^{27}Al and ^{14}N nuclei in the three forms of raw, wire-like substituted, and ring-substituted of the considered (4, 4) AlNNT, some remarkable trends were discovered. First, the calculated EFG tensors reveal that various Al and N nuclei along the length of the raw AlNNT are divided into some layers with equivalent electrostatic properties in each layer. Furthermore, the magnitude of C_Q is largest for both Al and N nuclei located at the mouths of the nanotube; however, this magnitude is the smallest for those nuclei located at the middle of the nanotube. Second, the NQR parameters of the middle layer of the raw AlNNT may be extended to the longer armchair AlNNTs. Third, the optimization process yielded an average Al–N bond length of 1.81 Å in the raw and back side of Si- and C-substituted forms of the considered model of AlNNT, however, the bond lengths of Al–C and N–Si undergo changes to 1.90 and 1.72 Å for wire-like and 1.96 and 1.80 Å for ring–substituted forms of AlNNT. Fourth, in addition to having the largest C_Q magnitudes of Al and N nuclei located at the mouths in the wire-like substituted pattern, the N nuclei, which are directly bonded to Si, also have C_Q magnitudes as large as those at the mouths of the nanotube. Fifth, in addition to the largest C_Q magnitudes of Al and N nuclei at the mouths, in the ring-substituted pattern, the Al and N nuclei that are directly bonded to C and Si also have C_Q magnitudes as large as those at the mouths of the nanotube. This trend means that because they have more active sites, the Si and C-substituted models may be expected to be more appropriate for those applications in which the mouth properties are important.

References

1. S. Iijima. Nature (London), **354**, 56 (1991).
2. N.G. Chopra, R.J. Luyken, K. Cherrey, V.H. Crespi, M.L. Cohen, S.G. Louie, and A. Zetel. Science (Washington, DC), **296**, 966 (1995).
3. H. Nakamura and Y. Matsui. J. Am. Chem. Soc. **117**, 2651 (1995).
4. L. Pu, X. Bao, J. Zou, and D. Feng. Angew. Chem. Int. Ed. **40**, 1490 (2001).
5. P.J.F. Harris. Carbon nanotubes and related structure. Cambridg University Press, Cambridge, UK. 1999.
6. L.W. Yin, Y. Bando, Y.C. Zhu, D. Golberg, and M.S. Li. Adv. Mater. **16**, 929 (2004).
7. Q. Wu, Z. Hu, X. Chen, H. Xu, and Y. Chen. J. Am. Chem. Soc. **125**, 10176 (2003).
8. X. Chen, J. Ma, Z. Hu, Q. Wu, and Y. Chen. J. Am. Chem. Soc. **127**, 17144 (2005).
9. Z. Zhou, J.J. Zhao, Y.S. Chen, Pv.R. Schleyer, and Z.F. Chen. Nanotechnology, **18**, 424023 (2007).
10. M.W. Zhao, Y.Y. Xia, X.D. Liu, Z.Y. Tan, B.D. Huang, C. Song, and L.M. Mei. J. Phys Chem. B, **110**, 8764 (2006).
11. D. Zhang and R.Q. Zhang. Chem. Phys. Lett. **371**, 426 (2003).
12. M. Zhao, Y. Xia, D. Zhang, and L. Mei. Phys. Rev. B, **68**, 235415 (2003).
13. R.R. Zope and B.I. Dunlap. Phys. Rev. B, **72**, 045439 (2005).
14. S. Hou, J. Zhang, Z. Shen, X. Zhao, and Z. Xue. Physica E, **27**, 45 (2005).
15. P.S. Adrian. Electronic structure of materials. Oxford University Press, New York, USA. 1996.
16. I. Vurgaftman and J.R. Meyer. Appl. J. **94**, 3575 (2003).
17. T.P. Das and E.L. Han. Nuclear quadrupole resonance spectroscopy. Academic Press, New York, USA. 1958.
18. W.C. Bailey. Chem. Phys. **252**, 57 (2000).
19. R.K. Harris. Pure Appl. Chem. 1800 (2001).
20. A. Seif, M. Mirzaei, M. Aghaie, and A. Boshra. Z Naturforsch. **62a**, 711 (2007).
21. M.J. Frisch, G.W. Trucks, H.B. Schlegel, G.E. Scuseria M.A. Robb, J.R. Cheeseman, V.G. Zakrzewski, J.A. Montgomery Jr., R.E. Stratmann, J.C. Burant, S. Dapprich, J.M. Millam, A.D.

© 2008 NRC Canada

Daniels, K.N. Kudin, M.C. Strain, O. Farkas, J. Tomasi, V. Barone, M. Cossi, R. Cammi, B. Mennucci, C. Pomelli, C. Adamo, S. Clifford, J. Ochterski, G.A. Petersson, P.Y. Ayala, Q. Cui, K. Morokuma, D.K. Malick, A.D. Rabuck, K. Raghavachari, J.B. Foresman, J. Cioslowski, J.V. Ortiz, B.B. Stefanov, G. Liu, A. Liashenko, P. Piskorz, I. Komaromi, R. Gomperts, R.L. Martin, D.J. Fox, T. Keith, M.A. Al-Laham, C.Y. Peng, A. Nanayakkara, C. Gonzalez, M. Challacombe, P.M.W. Gill, B. Jhnson, W. Chen, M.W. Wong, J.L. Andres, C. Gonzalez, M. Head-Gordon, E.S. Replogle, and J.A. Pople. Gaussian 98 [computer program]. Gaussian, Inc., Pittsburgh, PA. 1998.

22. A.D. Becke. J. Chem. Phys. **98**, 5648 (1993).
23. C. Lee, W. Yang, and R.G. Parr. Phys. Rev. B, **37**, 785 (1988).

© 2008 NRC Canada

Hydrolysis of dimethylphenyltin(IV) and triphenyltin(IV) chlorides in different aqueous ethanol solutions

Morteza Jabbari, Farrokh Gharib, Mostafa Mohammadpour Amini, and Amirreza Azadmehr

Abstract: The hydrolysis of $[(Me)_2(Ph)Sn(IV)]^+$ and $[(Ph)_3Sn(IV)]^+$ has been investigated at 25 °C and different aqueous solutions of ethanol, using a combination of spectrophotometric and potentiometric techniques. The species formed together with their formation constants have been determined using the computer program Squad over a wide pH range of 1 to 11. The hydrolysis constants in different media were analyzed in terms of Kamlet and Taft parameters. Single-parameter correlation of the formation constants, K_{11} and K_{12}, versus α (hydrogen-bond donor acidity), β (hydrogen-bond acceptor basicity), and π* (dipolarity/polarizability) for both cases are relatively poor in all solutions, but multiparameter correlation represents significant improvement with regard to the single-parameter models. In this work, we have also used the normalized polarity parameter, E_T^N, alone and in combination with the Kamlet–Taft parameter to find a better correlation of the formation constants in different aqueous ethanol solutions.

Key words: dimethylphenyltin(IV) chloride, triphenyltin(IV) chloride, hydrolysis constant, aqueous ethanol solutions, solvent effect.

Résumé : On a étudié l'hydrolyse des cations $[(Me)_2(Ph)Sn(IV)]^+$ et $[(Ph_3)Sh(IV)]^+$ en faisant appel à une combinaison de techniques spectrophotométriques et potentiométriques et en opérant à 25 °C, dans diverses solutions aqueuses d'éthanol. Faisant appel au programme informatique Squad, on a déterminé la nature des espèces qui se forment ainsi que leurs constantes de formation pour une plage de pH allant de 1 à 11. Les constantes d'hydrolyse dans les divers milieux ont été analysées en fonction de paramètres de Kamlet et de Taft. Dans les deux cas, les corrélations de paramètres uniques des constantes de formation, K_{11} et K_{12} en fonction d'α (acidité d'une liaison hydrogène donneur), de β (basicité d'une liaison hydrogène accepteur) et de π* (caractère dipolaire/polarisabilité) sont relativement mauvaises pour toutes les solutions; toutefois, les corrélations à plusieurs paramètres présentent des améliorations sensibles par rapport aux modèles à un seul paramètre. Dans ce travail, on a aussi utilisé le paramètre de polarité normalisée, E_T^N, seul ou en combinaison avec le paramètre de Kamlet–Taft, pour déterminer une meilleure corrélation des constantes de formations dans les diverses solutions aqueuses d'éthanol.

Mots-clés : chlorure de diméthylphénylétain(IV), chlorure de triphénylétain(IV), constante d'hydrolyse, solutions aqueuses d'éthanol, effet de solvant.

[Traduit par la Rédaction]

Introduction

Organotin(IV) complexes have been found to exhibit relatively high antitumour activity (1–15). Several authors have tried to elucidate many aspects of these complexes, such as their structures, stability constants, binding sites, chelating donor atoms of a ligand, and so forth (1–15). The structures adopted by the di- and tri-alkyltin(IV) ions in aqueous solutions appear to have linear C-Sn-C and planar skeletons, respectively (16–17). Information pertaining to the structure and behavior of these ions in solution at different pHs has been the subject of many recent papers. These ions have rather unusual effects on the structure in water as a solvent. There should be a particularly pronounced ordering of water molecules in the equatorial plane of the dialkyltin(IV) ions because of the strong electrostatic field near the tin atom. In addition, the hydrophobic nature of the alkyl groups will tend to force more hydrogen bonding in the solvent around the axial positions.

Owing to antitumour activity, we have recently begun to investigate several reaction equilibria of organotin(IV) species with some ligands, particularly those of biological interest, such as amino acids, peptides, and nucleotides. The main objectives of the research are to establish the stoichiometries, structures, and stability constants of the reactions of organotin ions with a range of ligands having a variety of donor atoms. The effect of varying reaction media, such as ionic strength, ionic media, and using different aqueous–organic solvents on the stability, hydrolysis, and protonation constants are also investigated.

Received 5 December 2007. Accepted 11 April 2008. Published on the NRC Research Press Web site at canjchem.nrc.ca on 9 June 2008.

M. Jabbari, F. Gharib,[1] M.M. Amini, and A. Azadmehr. Chemistry Department, Shahid Beheshti University, Tehran, Evin, Iran.

[1]Corresponding author (e-mail: f-gharib@cc.sbu.ac.ir).

 doi:10.1139/V08-079 © 2008 NRC Canada

Now we have extended our work to triorganotin(IV) with mixed alkyl and aryl substitution bonded to tin for complexation framework study. Accepting the hypothesis that R_2Sn^{2+} and R_3Sn^+ are the usual active species for antitumour action of organotins (18), a good antitumour agent should be easily dissociable following administration. This requires weak bonds between tin and the donor atom of the coordinated ligands, which are readily hydrolysable. If the compound is hydrolytically unstable, the R_2Sn^{2+} and R_3Sn^+ moieties will be released too soon, and if it is too stable it may be released too slowly and consequently lower activity will be observed. Therefore, there is a relationship between the stability of the organotin compounds and their antitumour activity.

Organotin cations are considered to be acids, in the Lewis scale, of different hardness, depending on the groups bonded to the tin(IV). Consequently, they show a strong tendency to hydrolysis in aqueous solution, as demonstrated by several authors (5–9). Other studies on the interactions of organotin cations with O-donor ligands have been recently reported, confirming the results obtained previously in the hydrolysis investigations (19–21).

This work deals with the study of hydrolysis of $(CH_3)_2C_6H_5Sn(IV)$ and $(C_6H_5)_3Sn(IV)$ to investigate the effect of a changing dielectric constant on the hydrolysis of triorganotin(IV).

Experimental section

Chemicals

Sodium perchlorate was obtained from Merck as an analytical reagent grade material and was dried under vacuum at room temperature for at least 72 h before use. The NaOH solution was prepared from a titrisol solution (Merck) and its concentration was determined by several titrations with standard HCl solution. Perchloric acid, ethanol (absolute), and triphenyltin(IV) were obtained from Merck and Fluka, respectively, as analytical reagent grade materials and were used as supplied. Dilute acid solution was standardized against standard NaOH solution. Dimethylphenyltin(IV) chloride was synthesized following the procedure described before (18). All dilute solutions were prepared from double-distilled water with specific conductance equal to $1.3 \pm 0.1\ \mu\Omega^{-1}\ cm^{-1}$.

Apparatus

A Jenway research pH-meter, model 3520 (with a precision of 0.001 units), was used for pH measurements. The hydrogen ion concentration was measured with a combination electrode (Jenway). Spectrophotometric titrations were performed on a UV–vis Shimadzu 2100 spectrophotometer (with a precision of 0.0002 units) combined to a Pentium 4 computer and using thermostated matched 10 mm quartz cells. The measurement cell was of flow type. A Masterflex pump allowed circulation of the solution under study from the potentiometric cell to the spectrophotometric cell. So, the absorbance and pH of the solution could be measured simultaneously.

Measurements

All measurements were carried out at 25 °C. The ionic strength was maintained with sodium perchlorate, 0.1 mol dm^{-3}, as supporting electrolyte. The pH-meter was calibrated for the relevant H^+ concentration with a solution of 0.01 mol dm^{-3} of $HClO_4$ solution containing 0.09 mol dm^{-3} sodium perchlorate (for adjusting the ionic strength to 0.1 mol dm^{-3}). We set $-\log[H^+] = 2.0$ (22). Junction potential corrections have been calculated from eq. [1]

$$[1] \qquad -\log[H^+]_{real} = -\log[H^+]_{measured} + a + b[H^+]_{measured}$$

where a and b were determined by measuringthe hydrogen ion concentration for two different solutions of perchloric acid with sufficient sodium perchlorate to adjust the ionic strength.

Procedure

Acidic solution (50 mL) of dimethylphenyltin(IV) or triphenyltin(IV) chlorides, ($1.0–2.0 \times 10^{-3}$ mol dm^{-3}), was titrated with an alkali solution, 0.1 mol dm^{-3} NaOH with the same ionic strength and mole fraction of ethanol. Due to insolubility of triorganotin(IV) in water, aqueous ethanol solution has been used. The $-\log[H^+]$ and absorbance were measured after addition of a few drops of titrant, and this procedure was extended up to the required $-\log[H^+]$. To exclude carbon dioxide from the system, a stream of purified nitrogen was passed through a sodium chloride solution and then bubbled slowly through the reaction solution. In all cases, the procedure was repeated at least three times and the resulting average values and corresponding standard deviation are shown in the text and tables.

Calibration of the glass electrode

The glass electrode potential in an aqueous solution differs from that in a solution of mixed solvents, and a liquid-junction potential of uncertain magnitude may affect the results. To overcome this difficulty, it was necessary to calibrate the glass electrode in different solvent mixtures. The experimental method outlined by Van Uitert and Hass (23) and the proposed eq. [2] were employed for this purpose.

$$[2] \qquad -\log[H^+] = B + \log\mu_H^\circ + \log\gamma_\pm$$

Where B is the actual pH-meter reading, $\gamma_\pm$ the mean activity coefficient of perchloric acid in the solvent mixture at the same temperature and ionic strength, and μ_H° is the correction factor. Values of B (pH-meter readings) were recorded in various aqueous solvent mixtures ranging from 50% to 80% (*v*/*v*) ethanol containing a known concentration of perchloric acid and sufficient sodium perchlorate to give a constant ionic strength of 0.1 mol dm^{-3}. The difference between the logarithm of the known hydrogen ion concentration and the corresponding values of B was used to calculate values of the correction term, $\log\mu_H^\circ$.

Results and discussion

Organotin(IV) generally hydrolyzes to form a series of mono- and poly-nuclear hydroxo complexes. The hydrolysis reaction, in general, could be as

© 2008 NRC Canada

[3] $pM^{n+} + q(OH)^- \leftrightarrows M_p(OH)_q^{(np-q)+}$

with the hydrolysis constant, K_{pq},

[4] $K_{pq} = [M_p(OH)_q^{(np-q)+}] / [M^{n+}]^p[OH^-]^q$

In the case of dimethyltin(IV), as reported earlier (1), the following mono- and di-nuclear complex species were considered $[M(OH)]^+$, $[M(OH)_2]$, $[M(OH)_3]^-$, $[M_2(OH)_2]^{2+}$, and $[M_2(OH)_3]^+$, where M represents $(CH_3)_2Sn^{2+}$. The investigation was performed in the pH range of 1 to 11 employing a nonlinear curve fitting method, with this notation that the dinuclear hydroxo species never exceeded 6% of the total dimethyltin(IV) (1).

To the best of our knowledge there have been no reports on determination of the hydrolysis constant of dimethylphenyltin(IV) species. Using again eq. [3], the hydroxo complex species of the triorganotin ions were studied. The hydrolysis constant values, K_{pq}, were determined spectrophotometrically on the basis of the relation $A = f(pH)$. Absorbance, A, and $-\log[H^+]$ were measured for a solution containing $(CH_3)_2C_6H_5Sn^+$ or $(C_6H_5)_3Sn(IV)^+$ with sufficient NaOH solution, as described before. Treatment of the spectrophotometric data in the range of 230 to 280 nm (with an interval of 1 nm) was obtained during the titrations as a function of H^+ concentration analyzed by the computer program Squad (24). The final selection of the species resulting from the computer program was based on graphical fitting. In addition, the various statistical criteria, i.e., sums of the squared residuals and the difference of total concentration of the metal ion existing experimentally in solution from the calculated ones, were considered.

The program allows calculation of the hydrolysis constant for different stoichiometry models. Different models including $[M(OH)]$, $[M(OH)_2]^-$, and several polynuclear species with various hydroxyl groups were tested by the program, where M is $(CH_3)_2C_6H_5Sn^+$ or $(C_6H_5)_3Sn^+$. As expected, polynuclear species were rejected by the program, as were $M_2(OH)$, $M(OH)_3$, $M_2(OH)_2$, and M_2O (charges are omitted for simplicity). Values of these parameters for $M_2(OH)$ were also calculated for both systems, but the species was not considered further because the estimated error in its formation constant was unacceptable and its inclusion does not improve the goodness of the fit. The species finally chosen were $M(OH)$ and $M(OH)_2^-$, resulting in a satisfactory graphical fitting. The average values of the computed hydrolysis constant of the metal ions for the wavelengths range used in this study and different runs at various media are listed in Table 1 and their mole fractions are plotted in Fig. 1 versus $-\log[H^+]$.

The hydrolysis of triphenyltin(IV) ion in dioxane–water solution was previously investigated (25) and only one hydrolytic species had been characterized. For clarification, we applied the computer program in two ways: first calculating only one hydrolysis and second calculating two hydrolysis equilibria of triphenyltin(IV). The estimated error resulting from the computer program for the first assumption is about 100 times more than that for the second one. It is also interesting to note that log K_{11} obtained from the first method (in the solution of ethanol–water 70:30 by volume) resulted in the value of 5.43, which is very close to the value reported before in 75% dioxane–water solution, 5.71.

Table 1. Average values of hydrolysis constants for $Me_2PhSn(IV)$ and $Ph_3Sn(IV)$ species in different aqueous solutions of ethanol at 25 °C and an ionic strength of 0.1 mol dm^{-3} ($NaClO_4$).

Ethanol (% *v*/*v*)	pK_{11} (Me_2PhSn)	pK_{12} (Me_2PhSn)	pK_{11} (Ph_3Sn)	pK_{12} (Ph_3Sn)
50	0.86±0.02	6.41±0.05	0.84±0.02	5.53±0.04
55	0.65±0.01	6.35±0.04	0.68±0.03	5.25±0.05
60	0.48±0.03	6.32±0.06	0.57±0.03	5.07±0.05
65	0.50±0.02	6.33±0.05	0.73±0.02	5.20±0.06
70	0.56±0.03	6.4±0.06	0.98±0.04	5.49±0.05
80	—	—	1.10±0.03	5.95±0.04

Fig. 1. The equilibrium distribution of the hydrolyzed species of (*a*) dimethylphenyltin(IV) and (*b*) triphenyltin(IV) in 70% ethanol (by volume) as a function of $-\log[H^+]$ at 25 °C and ionic strength 0.1 mol dm^{-3} ($NaClO_4$).

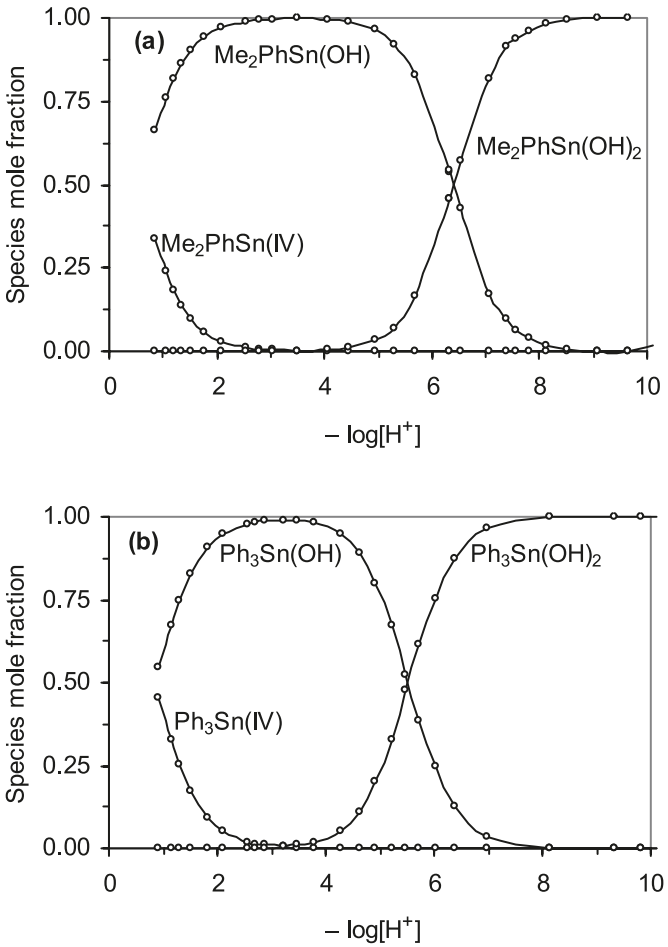

The hydrolysis of the organotins(IV) were studied carefully to determine whether any singly-bridged dimers analogous to those observed with trialkyltin(IV) were formed. Some association might be expected because the hydroxide itself has been reported to be somewhat associated with organic solvents (26). While two bridging hydroxo groups are more probable with coordination compounds, single OH bridges are observed rarely. However, no appreciable concentration of such a dimer was found to exist in the range of

© 2008 NRC Canada

concentrations used in this work, which is in agreement with results of other homologous triorganotin(IV) systems reported before (27).

Solvent effect

To obtain a quantitative method for determination of the solvent effect on physical properties, many empirical solvent scales have been devised during the last two decades (28–29). Among these scales (more than 40), the most comprehensive are the solvatochromic ones, but only a few of them have found a wider application in the correlation analysis of solvent effects. A quantitative measurement of the solvent polarity has been introduced by Kamlet, Abboud, Abraham, and Taft (KAT) (30–31). The KAT equation contains nonspecific as well as specific solute–solvent interactions separately, and the latter should be subdivided into solvent Lewis-acidity interactions (hydrogen-bond accepter, HBA, solute and hydrogen-bond donor, HBD, solvent) and solvent Lewis-basicity interactions (HBD solute–HBA solvent). This approach has been widely and successfully applied in the correlation analysis of many solvent-dependent processes (28). Using the solvatochromic solvent parameters, α, β, and π*, which have been introduced in previous reports (32–35), the multiparametric equation, eq. [5], has been proposed for use in the so-called linear solvation energy relationship.

$$[5] \qquad pK = A_0 + a\alpha + b\beta + p\pi^*$$

where A_0 represents the regression value and π* is the index of the solvent dipolarity/polarizability, which is a measure of the ability of a solvent to stabilize a charge or a dipole by its own dielectric effects. The π* scale was selected to run from 0.0 for cyclohexanone to 1.0 for dimethylsulfoxide. The α coefficient represents the solvent hydrogen-bond donor (HBD) acidity, in other words it describes the ability of a solvent to donate a proton in a solvent to a solute hydrogen bond. The α scale extends from 0.0 for nonHBD solvents to about 1.0 for methanol. The β coefficient is a measure of a solvent hydrogen-bond acceptor (HBA) basicity and describes the ability of a solvent to accept a proton in a solute to solvent hydrogen bond. The β scale was selected to extend from 0.0 for nonHBA solvents to about 1.0 for hexamethylphosphoric triamide. The empirical values of the solvatochromic solvent parameters (α, β, and π*) for pure ethanol and water were found in the literature (28). However, the solvatochromic parameters for the different binary aqueous mixtures of ethanol were calculated with the procedure proposed by Blanco et al. (36) (eq. [6]),

$$[6] \qquad P_{mixture} = P_{EtOH}X_{EtOH} + P_{H_2O}X_{H_2O}$$

where P is the property of interest and X is the mole fraction of the component in the solution. The calculated values of solvatochromic parameters used for different aqueous mixtures of ethanol are listed in Table 2.

In eq. [5], the discontinuous polarizability correction term is omitted because of the solvent used in this work containing no chlorine atoms. The regression coefficients, a, b, and p, measure the relative susceptibilities of the solvent-dependent log K to the indicated solvent parameters.

To explain the obtained log K values through the KAT solvent parameter, the formation constants were correlated with solvent properties by means of single and multiple linear regression analysis by a suitable computer program (37). We used the Gauss–Newton linear least-squares method in the computer program to refine the pK by minimizing the error squares sum from eq. [7]. Single-parameter correlations of log K_{11} and log K_{12} in terms of individually with α, β, or π* did not give a good result for both cases.

Table 2. The solvatochromic and normalized polarity parameters of different aqueous solutions.

Ethanol (% *v*/*v*)	Dielectric constant	α	β	π*	E_T^N
50	65.67	1.097	0.536	0.960	0.918
55	63.63	1.085	0.547	0.939	0.905
60	61.34	1.072	0.559	0.916	0.891
65	58.76	1.057	0.572	0.890	0.874
70	55.84	1.040	0.587	0.860	0.855
80	48.64	0.999	0.625	0.786	0.809

$$[7] \qquad S = \sum (pK_{exp} - pK_{cal})^2$$

So, we thought it would be interesting to correlate log K versus a multiparametric equation involving α, β, and π*. However, the results from eq. [5], multiparametric equation, indicate significant improvement with regard to the single-parameter models, eqs. [8] and [9] for dimethylphenyltin(IV) and triphenyltin(IV), respectively.

$$[8a] \qquad pK_{11} = 353.79 + 219.86\alpha - 464.73\beta - 359.40\pi^*$$

$$[8b] \qquad pK_{12} = 78.37 + 207.05\alpha - 181.24\beta - 210.36\pi^*$$

($n = 5$, $r^2 = 0.9983$ and 0.9994, respectively)

$$[9a] \qquad pK_{11} = 551.80 + 154.92\alpha - 618.97\beta - 405.36\pi^*$$

$$[9b] \qquad pK_{12} = 560.77 + 592.52\alpha - 859.30\beta - 775.68\pi^*$$

($n = 6$, $r^2 = 0.9997$ and 0.9994, respectively)

The coefficients of π*, α, and β in eqs. [8]–[9] are very different from each other and are almost in the order of β > π* > α. This indicates the hydrogen-bond acceptor basicity parameter of the solvent is the most important, the polarity parameter plays a relatively small role, and finally, the hydrogen-bond donor acidity parameter has less significance in changing the hydrolysis constant of tin(IV) systems in the proposed various aqueous solutions of ethanol.

The solvent polarity parameter of the media, π*, increases with increasing the mole fraction of water in aqueous solutions of ethanol. If the π* of the media was the only factor for the solvent effect on the complexation, it may be expected that the log K in a solution with a higher dielectric constant should be greater than those of all the other aqueous solutions of ethanol. However, the hydrolysis constants increase with increasing the solvent hydrogen-bond acceptor basicity parameter, β, and decreases with increasing the solvent polarity, π*, and the hydrogen-bond donor acidity parameter of the solvents, α, for different ethanol–water mixtures, Table 1.

We have also tried to use the polarity scale proposed by Reichardt (28, 38), E_T, based on the solvatochromic behavior of pyridinium *N*-phenoxide betaine dye. This dye is the most solvatochromic compound reported to date. This scale has

© 2008 NRC Canada

Table 3. The percentage contribution of KAT and normalized polarity parameters on the effect of different media on hydrolysis of the species at 25 °C and an ionic strength of 0.1 mol dm^{-3} ($NaClO_4$).

		In terms of eqs. [10] and [11]			In terms of eqs. [8] and [9]		
Different species	E_T^N	α	β	π*	α	β	π*
$(CH_3)_2C_6H_5Sn(OH)$	0.2	18.9	46.6	34.3	21.1	44.5	34.4
$(CH_3)_2C_6H_5Sn(OH)_2^-$	0.4	32.7	31.9	35.1	34.6	30.3	35.1
$(C_6H_5)_3Sn(OH)$	2.8	11.0	51.7	34.5	13.1	52.5	34.4
$(C_6H_5)_3Sn(OH)_2^-$	3.3	28.4	35.9	32.4	26.6	38.6	34.8

now been revised and normalized to E_T^N, known as normalized polarity parameter, due to the introduction of SI units. E_T^N has the value of zero for tetramethylsilane, the least polar solvent, and 1.0 for water, the most polar solvent. The E_T^N value is related to the ability of a solvent to stabilize charge separation in the dye, a correlation between the E_T^N and dielectric constant might be expected (28).

The hydrolysis constants again were correlated with E_T^N as a single linear regression analysis and then with the multiple regression one with Kamlet and Taft's (33) parameters besides E_T^N. Single parameter correlation of pK in terms of E_T^N did not again give good results. However, the multiparametric equation involving E_T^N, α, β, and π* showed very significant improvement with regard to the single-parameter model, eqs. [10]–[11] for dimethylphenyltin(IV) and triphenyltin(IV), respectively.

$$[10a] \quad pK_{11} = 375.83 + 1.99E_T^N + 191.19\alpha - 471.46\beta - 347.74\pi^*$$

$$[10b] \quad pK_{12} = 89.70 + 2.01E_T^N + 186.83\alpha - 182.08\beta - 200.52\pi^*$$

($n = 5$, $r^2 = 0.9989$ and 1.0, respectively)

$$[11a] \quad pK_{11} = 583.89 + 34.91E_T^N + 139.21\alpha - 652.46\beta - 435.51\pi^*$$

$$[11b] \quad pK_{12} = 491.68 - 73.27E_T^N + 622.31\alpha - 785.57\beta - 708.84\pi^*$$

($n = 6$, $r^2 = 1.0$ and 0.9999, respectively)

To show the efficiency of the suggested multiparameter correlations, experimental values of log K are plotted versus their calculated ones from eqs. [10–11], for the different aqueous ethanol solutions. It can be seen, Fig. 2, that the experimental and calculated values of log K are in good agreement with each other, with $r^2 > 0.99$ in both cases. From the values of the regression coefficients, the contribution of each parameter on a percentage basis was calculated and is listed in Table 3.

Conclusions

The combined potentiometric and spectrophotometric measurements were used to characterize the hydrolytic species formed in dimethylphenyltin(IV) and triphenyltin(IV) chlorides in various aqueous ethanol solutions. Our data reveal that the two coordinated water molecules on triorganotin(IV) are able to release two protons to form two hydrolytic species at pH ≅ 3 and 8, respectively. The determined hydrolysis constants in different aqueous ethanol solutions are analyzed in terms of Kamlet and Taft parameters (33). Single-parameter correlation of the formation constants in both cases are poor, but multiparameter correlation represents significant improvement with regard to the single-parameter models. Using the normalized polarity parameter in combination with Kamlet–Taft parameters results in a better correlation of the formation constants in the different medias used.

Fig. 2. The plots of the experimental values of pK vs the calculated ones for triphenyltin(IV) for (*a*) pK_{11} and (*b*) pK_{12}.

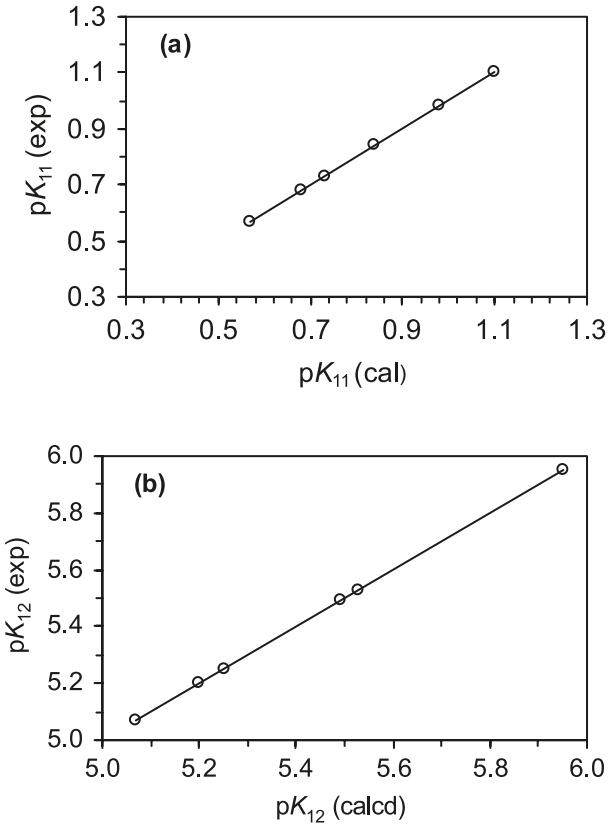

Acknowledgement

One of us (MJ) gratefully acknowledges a research grant from the Research Council of Shahid Beheshti University.

© 2008 NRC Canada

References

1. F. Gharib, M.M. Amini, and A. Haghgou. Main Group Met. Chem. **26**, 381 (2003).
2. F. Gharib, E. Farzad, and M.M. Amini. Can. J. Chem. **84**, 1534 (2006).
3. R. Barbieri, G. Alonzo, and R. Herber. J. Chem. Soc. Dalton Trans. 789 (1987).
4. M. Gielen, M. Biesemans, D. De Vos, and R. Willem. Inorg. Biochem. **79**, 139 (2000).
5. A. Jancso, B. Henry, P. Rubini, G. Vanko, and T. Gajda. J. Chem. Soc. Dalton Trans. 1941 (2000).
6. P. Yang and M. Guo. Coord. Chem. Rev. **185**, 189 (1999).
7. N. Buzas, T. Gajda, L. Nagy, E. Kuzmann, and A. Vertes. Inorg. Chim. Acta, **274**, 167 (1998).
8. A. Szorcsik, L. Nagy, J. Sletten, G. Szalontai, E. Kamu, T. Fiore, L. Pellerito, and E. Kalman. J. Organomet. Chem. **689**, 1145 (2004).
9. O. Al-Flaijj, M.R. Shehata, M.M. Mohamed, and M.M. Shoukry. Monatsh. Chem. **132**, 349 (2001).
10. R. Barbieri. Inorg. Chim. Acta, **191**, 253 (1992).
11. M.M. Mohamed, E.M. Abd-Alla, and A. El-Sayed. J. Organomet. Chem. **692**, 1735 (2007).
12. K. Gajda-Schrantz, A. Jancso, C. Pettinari, and T. Gajda. J. Chem. Soc. Dalton Trans. 2912 (2003).
13. M. Gielen, M. Biesemans, and R. Willem. Appl. Organomet. Chem. **19**, 440 (2005).
14. M. Gielen, M. Biesemans, R. Willem, and E.R.T. Tiekink. Eur. J. Inorg. Chem. 445 (2004).
15. M. Gielen. J. Braz. Chem. Soc. **14**, 870 (2003).
16. H.L. Singh and A.K. Varshney. Appl. Organomet. Chem. **15**, 762 (2001).
17. L. Pellerito, F. Maggio, T. Fiore, and A. Pellerito. Appl. Organomet. Chem. **10**, 393 (1996).
18. M. Gielen and S. Simon. Bull. Soc. Chim. Belg. **86**, 589 (1977).
19. G. Arena, R. Pellerito, R. Purrello, E. Rizzarelli, A.Gianguzza, and L. Pellerito. J. Chem. Soc. Dalton Trans. 773 (1989).
20. G. Arena, A. Gianguzza, S. Musumeci, L. Pellerito, and R. Rizzarelli. J. Chem. Soc. Dalton Trans. 2603 (1990).
21. V. Cucinotta, A. Gianguzza, G. Maccarrone, L. Pellerito, R. Purrello, and E. Rizzarelli. J. Chem. Soc. Dalton Trans. 2299 (1992).
22. P. Lagrange, M. Schneider, K. Zare, and J. Lagrange. Polyhedron, **13**, 861 (1994).
23. L.G. Van Uitert and C.G. Hass. J. Am. Chem. Soc. **75**, 451 (1953).
24. M. Meloun, M. Javurek, and J. Havel. Talanta, **33**, 513 (1986).
25. M.M. Shoukry and M.M.H. Mohammad. J. Coord. Chem. **43**, 217 (1998).
26. R.S. Tobias, H.N. Farrer, M.B. Hughes, and B.A. Nevett. Inorg. Chem. **5**, 2052 (1966).
27. V. Cannizzaro, C. Foti, A. Gianguzza, and F. Marrone. Anal. Chim. **88**, 45 (1998).
28. C. Reichardt. Solvents and solvent effects in organic chemistry. 3rd ed. VCH, New York. 2004.
29. K. Izutsu. Electrochemistry in nonaqueous solutions. Wiley-VCH, Weinheim. 2002.
30. R.W. Taft, J.L.M. Abboud, and M.J. Kamlet. J. Org. Chem. **49**, 2001 (1984).
31. M.J. Kamlet, J.L.M. Abboud, M.H. Abraham, and R.W. Taft. J. Org. Chem. **48**, 2877 (1983).
32. F. Gharib. J. Chem. Eng. Data, **50**, 196 (2005).
33. F. Gharib and F. Sadeghi. Appl. Organomet. Chem. **21**, 218 (2007).
34. F. Gharib, K. Zare, and B. Mohammadi. J. Mol. Liq. **124**, 63 (2005).
35. F. Gharib, T. Kheradmand, and P. Amani. Anal. Sci. **21**, 945 (2005).
36. S.E. Blanco, E.I. Gasull, and F.H. Ferretti. Spectrochim. Acta Part A, **59**, 2985 (2003).
37. D.C. Harris. J. Chem. Educ. **75**, 119 (1998).
38. C. Reichardt. Chem. Rev. **94**, 2319 (1994).

© 2008 NRC Canada

New xanthones from *Cratoxylum cochinchinense*

Surat Laphookhieo, Wisanu Maneerat, Taweesak Buatip, and J. Keith Syers

Abstract: Investigation of the dried fruits of *Cratoxylum cochinchinense* led to the isolation of three new oxygeranyl xanthones, cochinxanthone A-C (**1**–**3**), together with seven known compounds (**4**–**10**). Their structures were characterized using spectroscopic methods including UV, IR, NMR, and MS.

Key words: cochinxanthone A-C, *Cratoxylum cochinchinense*, Clusiaceae.

Résumé : Une étude sur les fruits secs de *Cratoxylum cochinchinense* a permis d'isoler trois nouvelles oxygéranylxanthones, les cochinxanthones A-C (**1**–**3**), en plus de sept produits connus (**4**–**10**). On a caractérisé leurs structures par des méthodes spectroscopiques, dont l'UV, l'IR, la RMN et la spectrométrie de masse.

Mots-clés : cochinxanthones A-C, *Cratoxylum cochinchinense*, Clusiaceae.

[Traduit par la Rédaction]

Introduction

Cratoxylum cochinchinense (Clusiaceae) is a shrub tree distributed in southeast Asian countries. Several parts of this plant have been used by the local Thai people in folk medicine. For example, the decoction of *C. cochinchinense* roots and stems has been used as diuretic drug. Also, the leaves, roots, barks, and latex of this plant have been used for the treatment of fever, cough, diarrhea, itching, and ulcers. In addition, the young fruit are used as a spice for cooking, and the young leaves are used a substitute for tea. *Cratoxylum* plants are known to be rich sources of xanthones (1–6) and antraquinones (4, 7, 8). Some of these compounds showed significant pharmacological activity, such as antimalaria (2), cytotoxicity (2, 4), and antibacteria (3, 7, 8). We have previously reported the isolation, structure determination, and biological evaluation of a number of xanthones from the roots of *C. cochinchinense* (2). In a continuation of our study of this plant, we describe the isolation and structure elucidation of three new oxygeranyl xanthones (**1**–**3**) along with seven known compounds (**4**–**10**) (Fig. 1) from the dried fruit of *C. cochinchinense*.

Results and discussion

The crude hexane and EtOAc extracts of the dried fruit of *C. cochinchinense* were subjected to chromatographic procedures and afforded three new xanthones, named cochinxanthone A-C (**1**–**3**), together with seven known compounds (**4**–**10**). Their structures were elucidated using spectroscopic data and by comparison with those reported in the literature.

Received 16 February 2008. Accepted 16 April 2008. Published on the NRC Research Press Web site at canjchem.nrc.ca on 9 June 2008.

S. Laphookhieo,[1] W. Maneerat, T. Buatip, and J.K. Syers. School of Science, Mae Fah Luang University, Tasud, Muang, Chiang Rai 57100, Thailand.

[1]Corresponding author (e-mail: laphookhieo@yahoo.com).

The new xanthones (**1**–**3**) were oxygeranyl xanthones, which showed characteristic UV absorption bands in ranges of 204–258 and 307–368 nm, while the IR spectra exhibited characteristic conjugated carbonyl and hydroxyl functionalities in the ranges of 1638–1646 and 3435–3446 cm^{-1}, respectively. Also, all new xanthones showed a chelated hydroxyl proton at ca. δ: 12.8–13.0 ppm in the ^1H NMR spectrum. Moreover, the 1D NMR and 2D NMR spectral data suggested that all isolated new xanthones contained the 1,3,7-oxygenated xanthone skeleton.

Cochinxanthone A (**1**) was isolated as a pale yellow solid with a molecular formula of $C_{23}H_{24}O_6$, on the basis of $[M]^+$ ion at *m/z* 396.3709 in the HREI-MS. The ^1H NMR spectral data of **1** (Table 1) showed a downfield hydroxyl proton resonance at δ: 13.00 together with two sets of aromatic protons. The first set was a typical pattern of a 1,2,4-trisubstituted benzene ring and appeared at δ: 7.55 (1H, d, *J* = 2.7 Hz, H-8), 7.39 (1H, d, *J* = 9.3 Hz, H-5), and 7.33 (1H, dd, *J* = 9.3, 2.7 Hz, H-6). The other set displayed two *meta*-coupled protons and appeared at δ: 6.32 (1H, d, *J* = 1.8 Hz, H-4) and 6.19 (1H, d, *J* = 1.8 Hz, H-2). With the combination of COSY, HMQC, and HMBC spectra, a 6-hydroxy-3,7-dimethylocta-2,7-dienyloxy moiety (*O*-geranyl moiety) was evident from ^1H NMR signals at δ: 5.48 (1H, t, *J* = 6.6 Hz, H-2′), 4.96 (1H, s, H-8′a), 4.75 (1H, s, H-8′b), 4.65 (2H, d, *J* = 6.6 Hz, H-1′), 3.98 (1H, t, *J* = 6.6 Hz, H-6′), 2.13 (2H, m, H-4′), 1.82 (3H, s, H-9′), 1.70 (3H, s, H-10′), and 1.63 (2H, m, H-5′) (9). This moiety was also supported by the fragment ion peak at *m/z* 243 ($[M\text{-}C_{10}H_{17}O]^+$) in the EI-MS spectrum. The *O*-geranyl moiety was placed at C-7 because of the correlation of H-1′ (δ: 4.65), H-8 (δ: 7.55) and H-6 (δ: 7.33) to C-7 (δ: 155.2) in the HMBC spectral data (Fig. 1). In addition, the interaction between H-1′ (δ: 4.65) and H-8 (δ: 7.55) in the NOSEY spectrum (Fig. 2) also confirmed the location of *O*-geranyl moiety. Therefore, cochinxanthone A was identified as 1,3-dihydroxy-7-(6-hydroxy-3,7-dimethylocta-2,7-dienyloxy)-xanthen-9-one (**1**).

Cochinxanthone B (**2**) had the same molecular formula as **1**, $C_{23}H_{24}O_6$, (*m/z* 396.3748 $[M^+]$).^1H NMR and ^{13}C NMR signals (Table 1) of **2** were almost identical to those of **1** ex-

 doi:10.1139/V08-076 © 2008 NRC Canada

Fig. 1. Structures of compounds **1–10**.

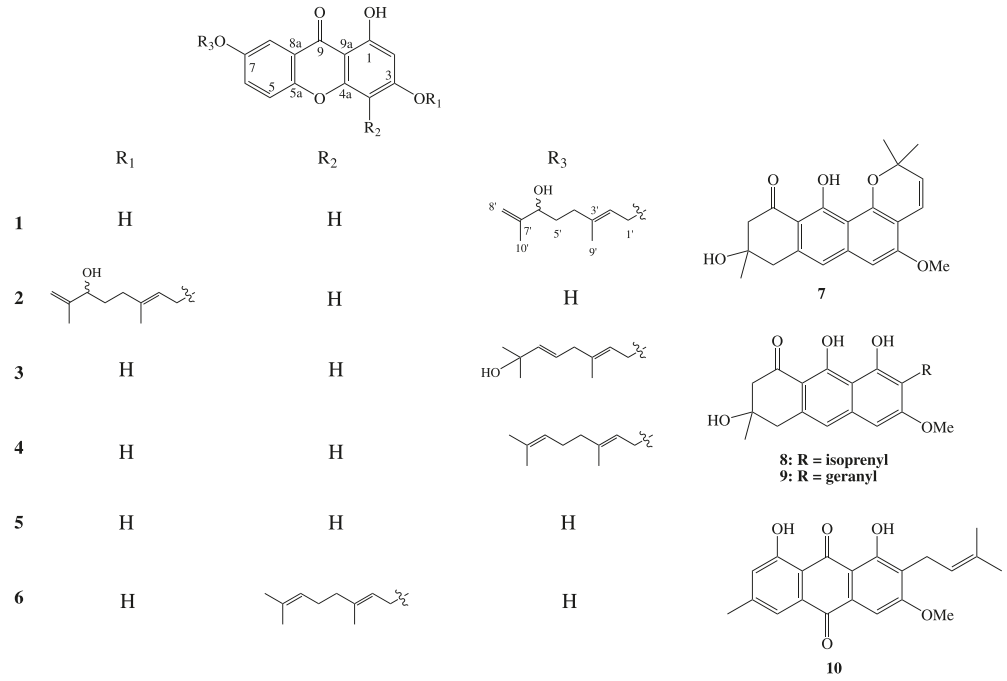

Table 1. ^{1}H NMR and ^{13}C NMR spectral data of compounds **1–3** (300 MHz).

	1[a]		**2**[a]		**3**[b]	
Position	^{1}H	^{13}C	^{1}H	^{13}C	^{1}H	^{13}C
1		163.1		162.8		162.8
2	6.19 (1H, d, *J* = 1.8 Hz)	97.7	6.28 (1H, br s)	97.1	6.24 (1H, s)	99.0
3		165.9		166.1		166.2
4	6.32 (1H, d, *J* = 1.8 Hz)	93.7	6.45 (1H, br s)	92.7	6.29 (1H, s)	94.8
4a		158.1		157.9		157.7
5a		150.6		149.9		150.3
5	7.39 *d* (1H, d, *J* = 9.3 Hz)	118.8	7.37 (1H, d, *J* = 8.7 Hz)	118.6	7.23 (1H, d, *J* = 9.0 Hz)	118.6
6	7.33 (1H, dd, J = 9.3, 2.7 Hz)	124.9	7.26 (1H, dd, *J* = 8.7, 2.4 Hz)	124.1	7.17 (1H, dd, *J* = 9.0, 2.1 Hz)	124.7
7		155.2		153.9		154.8
8	7.55 (1H, d, *J* = 2.7 Hz)	106.3	7.59 (1H, d, *J* = 2.4 Hz)	108.1	7.44 (1H, d, *J* = 2.1 Hz)	106.0
8a		120.4		120.8		120.3
9		180.3		180.6		179.8
9a		102.4		103.0		102.5
1′	4.65 (2H, d, *J* = 6.6 Hz)	65.2	4.62 (1H, d, J = 6.6 Hz)	65.2	4.53 (1H, d, *J* = 6.6 Hz)	65.4
2′	5.48 (1H, t, *J* = 6.6 Hz)	119.4	5.47 (1H, t, *J* = 6.3 Hz)	118.8	5.47 (1H, t, *J* = 6.6 Hz)	119.9
3′		141.3		141.7		140.3
4′	2.13 (2H, m)	35.3	2.10 (2H, m)	35.2	2.75 (2H, d, *J* = 3.6 Hz)	42.0
5′	1.63 (2H, m)	32.7	1.64 (2H, m)	32.7	5.65 (1H, dd, *J* = 13.8, 3.6 Hz)	124.2
6′	3.98 (1H, t, *J* = 6.6 Hz)	74.7	4.00 (1H, t, *J* = 6.3 Hz)	74.6	5.67 (1H, d, *J* = 13.8 Hz)	140.0
7′		147.2		147.2		70.9
8′	4.75 (1H, s); 4.96 (1H, s)	110.4	4.86 (1H, s), 4.95 (1H, s)	110.3	1.33 (3H, s)	29.7
9′	1.82 (3H, s)	15.6	1.82 (3H, s)	15.5	1.72 (3H, s)	16.7
10′	1.70 (3H, s)	17.0	1.71 (3H, s)	16.3	1.33 (3H, s)	29.7
1-OH	13.00 s		12.80 s		12.82 s	

[a]Recorded in $CDCl_3$ and CD_3OD.
[b]Recorded in $CDCl_3$.

cept that the chemical shift values of aromatic and chelated hydroxyl protons were different (Table 1). In addition, the R_f value on the TLC of **2** (R_f = 0.33, 2.5% acetone–DCM) was also different from **1** (R_f = 0.40, 2.5% acetone–DCM). These results suggested that **2** contained the same *O*-geranyl moiety as **1** and was located at C-3 on the basis of HMBC

© 2008 NRC Canada

Fig. 2. Selective HMBC and NOESY correlations of **1**.

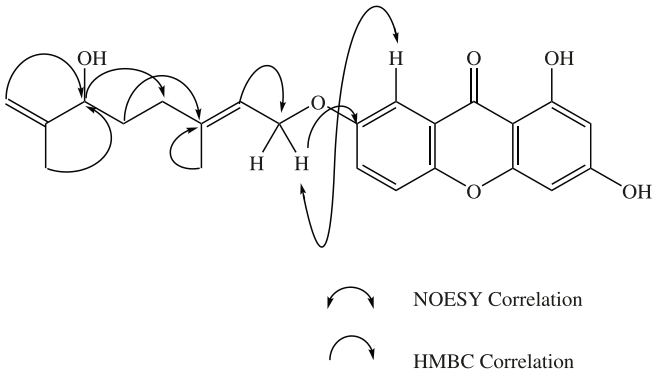

correlations (Fig. 3). Therefore, cochinxanthone B was identified as 1,7-dihydroxy-3-(6-hydroxy-3,7-dimethylocta-2,7-dienyloxy)-xanthen-9-one (**2**), structural isomer of **1**.

Cochinxanthone C (**3**) was obtained as a pale yellow solid. The HREI-MS gave a M-H_2O ion peak at *m*/*z* 378.1453 $[M\text{-}H_2O]^+$ consistent with the molecular formula $C_{23}H_{26}O_6$. All aromatic protons of **3** (Table 1) were similar to those of **1**. The main difference in ^1H NMR signals between **3** and **1** were observed on the *O*-geranyl moiety. Compound **3** appeared as a 7-hydroxy-3,7-dimethylocta-2,5-dienyloxy unit [δ: 5.67 (1H, d, *J* = 13.8 Hz, H-6′), 5.65 (1H, dd, 13.8, 3.6 H-5′), 5.47 (1H, t, *J* = 6.6 Hz, H-2′), 4.53 (2H, d, *J* = 6.6 Hz, H-1′), 2.75 (2H, d, *J* = 3.6 Hz, H-4′), 1.72 (3H, s, H-9′), and 1.33 (6H, s, H-8′ and H-10′)] (7) instead of the 6-hydroxy-3,7-dimethylocta-2,7-dienyloxy moiety in **1** (Table 1). The geometry of the double bond at C-5′/6′ was identified as *E*-geometry because of the large amount of *J* value of H-6′ (13.8 Hz) (7). Thus, cochinxanthone C (**3**) was identified as 1,3-dihydroxy-7-(7-hydroxy-3,7-dimethylocta-2,5-dienyloxy)-xanthen-9-one.

The remaining known compounds were characterized as 7-geranyloxy-1,3-dihydroxyxanthone (**4**) (4), 1,3,7-trihydroxyxanthone (**5**), fuscaxanthone E (11), vismione B (**7**) (10), vismione E (**8**) (7, 10), vismione F (**9**) (12), and vismiaquinone C (**10**) (13). It should be noted that the genus of *Cratoxylum* of the family Clusiaceae has been known to be rich in xanthones with more than 50 compounds being identified (1–7). In the present study, we also isolated and identified three new oxygeranyl xanthones from the dried fruit of *C. cochinchinense*. Also, all the remaining compounds (**4**–**10**) were isolated from this species for the first time.

Experimental

General experimental procedures

Melting points were determined using a Fisher-John melting point apparatus. The optical rotation $[\alpha]_D$ values were determined with a JASCO P-1020 polarimeter. UV spectra were recorded with a UV-160A spectrophotometer (Shimadzu). The IR spectra were recorded with a PerkinElmer FTS FT-IR spectrophotometer. The ^1H NMR and ^{13}C NMR spectra were recorded using 300 MHz Bruker FTNMR Ultra Shield spectrometer. Chemical shifts were recorded in parts per million (δ) in $CDCl_3$ and (or) CD_3OD with tetramethylsilane (TMS) as an internal reference. The EI-MS

Fig. 3. Selective HMBC correlations of **2**.

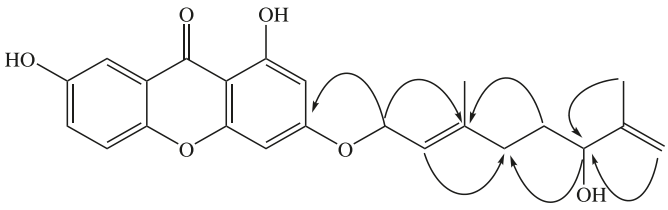

was obtained from a MAT 95 XL mass spectrometer. Quick column chromatography (QCC) and column chromatography (CC) were carried out on silica gel 60 H (Merck, 5–40 μm) and silica gel 100 (Merck, 63–200 μm), respectively. Precoated plates of silica gel 60 F_{254} were used for analytical purposes.

Plant material

The dried fruits of *C. cochinchinense* were collected from Mae Fah Luang University, Tasud, Muang, Chiang Rai province, in the northern part of Thailand in December 2006. Botanical identification was achieved by comparison with a voucher specimen No. SL-1 (PSU) (2) in the herbarium collection of Department of Biology, Prince of Songkla University, Songkhla, Thailand.

Extraction and isolation

The dried fruits of *C. cochinchinense* (1 kg) were extracted with hexane and EtOAc, respectively, over a period of 3 days each at room temperature and evaporated under reduced pressure to provide crude hexane (16 g) and EtOAc extracts (66 g).

The hexane extract (16 g) was subjected to quick column chromatography (QCC) over silica gel and eluted with a gradient of hexane–EtOAc (100% hexane to 50% EtOAc–hexane) to provide sixteen fractions (H1–H16). Fraction H3 (2.1 g) was subjected to column chromatography (CC) using a 5% EtOAc–hexane mixture to afford seventeen subfractions (H3A–H3Q). Subfraction H3F was taken to dryness under reduced pressure to yield an orange solid, which was washed with hexane to afford compound **10** (2.3 mg). Purification of subfraction H14 (329 mg) was performed by CC with 25% acetone–hexane, yielding ten fractions (H14A–H14J). Fraction H14I (43.5 mg) was subjected to repeated CC with 15% acetone–hexane to yield compound **8** (8.4 mg).

The EtOAc extract (66 g) was chromatographed by QCC over silica gel and eluted with a gradient of hexane–EtOAc (100% hexane to 100% EtOAc) to afford twenty fractions (E1–E20). Upon evaporating under reduced pressure, fraction E9 gave a yellow solid, which was washed with hexane and DCM, affording fraction E9a. This fraction, E9a, (352.7 mg) was further subjected to repeated CC with 100% DCM to yield compound **4** (74.8 mg). Fraction E14L (82.9 mg) was subjected to repeated CC using 2.5% MeOH–DCM to yield compound **6** (13.5 mg). Fraction E16 (555.5 mg) was purified by CC with gradient mixtures of acetone–hexane (5% acetone–hexane to 20% acetone–hexane) to afford nineteen subfractions (E16a–E16s). Subfractions E16p, upon evaporating under reduced pressure gave a solid, which was washed with hexane and DCM to give

© 2008 NRC Canada

compound **5** (6.4 mg). Subfraction E16j (43.5 mg) was further purified by preparation of TLC with 15% acetone–hexane to give compound **9** (28.5 mg). Fraction E17 (3.1461 g) was fractionated by CC using 20% acetone–hexane to afford 20 subfractions (E17a–E17t). Subfraction E17o (98.3 mg) was subjected to repeated CC with 2.5% acetone–chloroform to give compound **7** (3.2 mg). Repeated CC of fraction E17q (299.6 mg) with 20% acetone–hexane yielded compounds **1** (5.2 mg) and **2** (5.7 mg). Fraction E17r (33.9 mg) was subjected to repeated preparation of TLC with 2.5% MeOH–chloroform to afford compound **3** (11.9 mg).

Cochinxanthone A (1)

Pale yellow solid, mp 160–162 °C. $[\alpha]_D^{25}$ +112.6 (*c* 0.025, MeOH). UV λ_{max} (log ε) (MeOH): 368 (3.88), 309 (4.14), 258 (4.53), 235 (4.51), 204 (4.30). IR ($CHCl_3$, cm^{-1}): 3436, 1646. For ^1H NMR and ^{13}C NMR ($CDCl_3$ + CD_3OD) spectra, see Table 1. HREI-MS *m/z*: 396.3709 $[M]^+$ (calcd. for $C_{23}H_{24}O_6$: 396.1523).

Cochinxanthone B (2)

Pale yellow solid, mp 154–155 °C. $[\alpha]_D^{25}$ +116.4 (*c* 0.03, MeOH). UV λ_{max} (log ε) (MeOH): 374 (3.67), 307 (4.06), 258 (4.42), 235 (4.32), 203 (4.20). IR ($CHCl_3$, cm^{-1}): 3435, 1638. For ^1H NMR and ^{13}C NMR ($CDCl_3$ + CD_3OD) spectra, see Table 1. HREI-MS *m/z* 396.3709 $[M]^+$ (calcd. for $C_{23}H_{24}O_6$: 396.1523).

Cochinxanthone C (3)

Pale yellow solid, mp 131–132 °C. UV λ_{max} (log ε) (MeOH): 368 (3.62), 309 (3.90), 257 (4.28), 234 (4.27), 204 (4.08). IR ($CHCl_3$, cm^{-1}): 3446, 1647. For ^1H NMR and ^{13}C NMR ($CDCl_3$) spectra, see Table 1. HREI-MS *m/z* 378.1453 $[M\text{-}H_2O]^+$ (calcd. for $C_{23}H_{22}O_5$: 378.1467).

Acknowledgements

SL thanks the Thailand Research Fund and the Commission on Higher Education for a research grant No. MRG5080135. We are indebted to the Mae Fah Luang University for partial financial support. We also thank Associate Professor Dr. Chatchanok Karalai, Department of Chemistry, Faculty of Science, Prince of Songkla University for providing authentic samples, compound **8**, and valuable suggestions. Special thanks are addressed to Dr. S. Koysomboon and Dr. S. Cheenpracha for recording some ^1H NMR and UV spectra.

References

1. W. Mahabusarakam, W. Nuangnaowarat, and W.C. Taylor. Phytochemistry, **67**, 470 (2006).
2. S. Laphookhieo, J.K. Syers, R. Kiattansaku., and K. Chantrapromma. Chem. Pharm. Bull. **54**, 745 (2006).
3. S. Boonsri, C. Karalai, C. Ponglimanont, A. Kanjana-opas, and K. Chantrapromma. Phytochemistry, **67**, 723 (2006).
4. E.-K. Seo, N.-C. Kim, M.C. Wani, M.E. Wall, H.A. Navarro, J.P. Burgess, K. Kawanishi, L.B. S. Kardono, S. Riswan, W.C. Rose, C.R. Fairchild, N.R. Farnsworth, and A.D. Kinghorn. J. Nat. Prod. **65**, 299 (2002).
5. L.H.D. Nguyen and L.J. Harrison. Phytochemistry, **50**, 471 (1999).
6. A. Kijjoa, M. Jose, T.G. Gonzalez, M.M.M. Pinto, A.M. Damas, I. Mondranondra, A.M.S. Silva, and W. Herz. Phytochemistry, **49**, 2159 (1998).
7. N. Boonnak, C, Karalai, S. Chantrapromma, C. Ponglimanont, H.K. Fun, A. Kanjana-Opas, and S. Laphookhieo. Tetrahedron, **62**, 8850 (2006).
8. N. Boonnak, C. Karalai, S. Chantrapromma, C. Ponglimanont, A. Kanjana-Opas, K. Chantrapromma, and H.K. Fun. Can. J. Chem. **85**, 341 (2007).
9. Y.-J. Xu, Y.-H. Lai, Z. Imiyabir, and S.-H. Goh. J. Nat. Prod. **64**, 1191 (2001).
10. B. Botta, F.D. Monache, G.D. Monache, G.B.M. Bettolo, and J.U. Oguakwa. Phytochemistry, **22**, 539 (1983).
11. C. Ito, M. Itoigawa, T. Takakura, N. Ruangrungsi, F. Enjo, H. Tokuda, H. Nishino, and H. Furukawa. J. Nat. Prod. **66**, 200 (2003).
12. B. Botta, F.D. Monache, G.D. Monache, G.B.M. Bettolo, and J.D. Msonthi. Phytochemistry, **24**, 827 (1985).
13. T.J. Nagem and D.J.T. Faria. Phytochemistry, **29**, 3362 (1990).

© 2008 NRC Canada

F 1s spectroscopy and ionic fragmentation of trifluoropropyne[1]

John J. Neville, Narayana P. Appathurai, Yongheng Fan, Samuel Odoh, and Liu Yang

Abstract: The F 1s excitation spectroscopy and ionic fragmentation of 3,3,3-trifluoro-1-propyne have been studied using synchrotron radiation and ion time-of-flight mass spectrometry. The total ion yield spectrum and photoionization branching ratios in the vicinity of the F 1s ionization threshold are reported. Core excited state calculations using the static exchange approximation are used to aid in the interpretation of the experimental results. The F 1s excitation spectrum consists of a number of broad overlapping bands below threshold, attributed to excitations to mixed σ*(C-F)/π*(C-C) molecular orbitals and unresolved Rydberg states, and a continuum shape resonance 12.5 eV above threshold. Ionic fragmentation following F 1s excitation or ionization results overwhelmingly in singly charged ionic fragments, primarily via cleavage of bonds to the fluorinated carbon atom adjacent to the core-excited atom.

Key words: F 1s excitation, XANES, photoelectron-photoion coincidence, ionic fragmentation, static exchange approximation.

Résumé : Utilisant un rayonnement de synchroton et faisant appel à la spectrométrie de masse en temps de vol, on a étudié la spectroscopie d'excitation 1s du fluor et la fragmentation ionique du 3,3,3-trifluoroprop-1-yne. On a déterminé le spectre en rendement ionique total et les rapports de ramification au voisinage du seuil d'ionisation 1s du fluor. On a effectué des calculs de l'état excité du coeur en faisant appel à l'approximation d'échange statique pour avoir un support dans l'interprétation des résultats expérimentaux. Le spectre d'excitation 1s du fluor est formé d'une région en dessous du seuil où on retrouve un certain nombre de bandes larges qui se chevauchent et qui sont attribuées à des excitations à des niveaux d'orbitales moléculaires mixtes σ*(C-F)/π*(C-C) et à des états de Rydberg non résolus; à 12,5 eV au-dessus du seuil, on observe une résonance de forme continue. La fragmentation ionique qui suit l'excitation 1s du fluor ou l'ionisation conduisent à la formation grandement majoritaire des fragments ioniques à charges uniques qui résultent principalement du clivage des liaisons vers l'atome de carbone fluoré adjacent de l'atome excité à coeur.

Mots-clés : excitation 1s du fluor, XANES, coïncidence photoélectron–photoion, fragmentation ionique, approximation d'échange statique.

[Traduit par la Rédaction]

Introduction

Resonant core excitation by absorption of soft X-ray radiation creates a highly localized perturbation of molecular electronic structure. Rapid electronic relaxation of these high-energy core-hole states typically leads to ionization and bond dissociation. Study of these processes is important for an understanding of radiation damage in materials and also provides information about the electronic and chemical properties of the materials investigated. Detailed investigation of these processes is possible for small molecules, where the initial site of the core hole can often be precisely controlled by selection of the appropriate excitation wavelength and many or all fragmentation products can be detected and characterized.

We have studied the core excitation spectroscopy and subsequent ionic fragmentation of 3,3,3-trifluoro-1-propyne. The three chemically inequivalent carbon centres in principle allow for site-specific core-hole formation, as do the fluorine atoms. It is of interest to investigate the extent to which the localized core-hole site is reflected in the subsequent electronic relaxation and ionic fragmentation processes. The C 1s excitation spectroscopy has been reported elsewhere (1). Here, the focus is on the excitation spectroscopy and ionic fragmentation at the F 1s edge.

The F 1s excitation spectrum of trifluoropropyne has been measured previously by electron energy loss spectroscopy (EELS); the data are available for download but the spec-

Received 16 October 2007. Accepted 9 April 2008. Published on the NRC Research Press Web site at canjchem.nrc.ca on 13 June 2008.

J.J. Neville,[2] N.P. Appathurai,[3] Y. Fan, S. Odoh, and L. Yang. Department of Chemistry and Centre for Laser, Atomic and Molecular Sciences, University of New Brunswick, Fredericton, NB E3B 6E2, Canada.

[1]This is part of a Special Issue (Vol. 85, issue 10) dedicated to Professor G. Michael Bancroft.

[2]Corresponding author (e-mail: jneville@unb.ca).

[3]Present address: Canadian Synchrotron Radiation Facility, Synchrotron Radiation Center, 3731 Schneider Dr., Stoughton, WI 53589-3097, USA.

 doi:10.1139/V08-071 © 2008 NRC Canada

Fig. 1. 3,3,3-Trifluoro-1-propyne, with carbon atom numbering as used in the text.

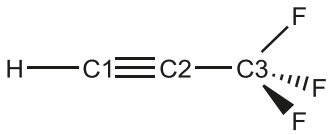

trum is unpublished (2). The F 1s EELS spectrum of the chemically related perfluoro-2-butyne has been reported along with the spectra of a number of other fluorinated hydrocarbons in a study of the perfluoro effect (3). Studies at the C 1s edge indicate considerable site-specificity in the ionic fragmentation of trifluoropropyne following C 1s excitation (4). However, no previous studies of the ionic fragmentation of trifluoropropyne following F 1s excitation have been reported.

For convenience in the following discussion, we refer to the three chemically distinct carbon atoms as C1, C2 and C3, where C1 is the terminal π-bonded carbon, C2 is the central carbon, and C3 is the fluorinated carbon atom, as illustrated in Fig. 1.

Experimental method

The experiments were performed with the spherical grating monochromator (SGM) beamline (11-ID.1) of the Canadian Light Source (CLS). This 45 mm planar undulator beamline provides monochromatic photons in the range 250–2000 eV with a resolving power on the order of 10^4 (5). For this work, the 1100 lines/mm medium energy grating was used with entrance and exit slit settings of 5 μm, providing an estimated photon bandwidth of 70 meV near the F 1s edge. The photon flux was monitored via both a gold mesh upstream of the experimental chamber and a silicon photodiode at the end of the beamline. The two monitors were found to provide equivalent results. The photon energy scale was calibrated using the SF_6 F 1s resonant excitation spectrum and the excitation energies reported by Francis et al. (6).

Total ion yield (TIY) and photoelectron–photoion coincidence (PEPICO) measurements were performed using a Wiley–McLaren type ion time-of-flight (TOF) mass spectrometer mounted perpendicular to the incident photon beam and an electron detector mounted opposite the TOF (7, 8). The time between electron and ion detection is characteristic of the mass-to-charge ratio of the fragment ions. A 1 s dwell time was used for the TIY measurements. A 60 s dwell time was used for the majority of the PEPICO measurements; additional measurements with a 20 min dwell time were made at selected photon energies. The gaseous sample was admitted into the chamber in a continuous flow via an effusive gas inlet. The 3,3,3-trifluoro-1-propyne was purchased from Sigma-Aldrich and used without further purification.

Computational method

Ab-initio molecular orbital (MO) calculations were performed to estimate the transition energies and intensities of the core hole states. The ground-state equilibrium geometry of trifluoropropyne was determined at the HF/6-311G(d,p) level using GAMESS (9). This geometry was used for all subsequent calculations. The F 1s excitation energies and transition probabilities (oscillator strengths) were determined using Kosugi and Kuroda's GSCF3 program (10). These calculations proceeded in three steps: first, a HF calculation of the ground state was performed; second, the F 1s ionized state was calculated with explicit consideration of the core hole; finally, the F 1s excited states were obtained by the improved virtual orbital (IVO) method (11). This approach, also known as the static exchange method or STEX, accounts for the significant alterations in the electronic structure that occur due to relaxation of the valence shell MOs in the presence of the core hole but neglects the core-hole screening effect of the open-shell excited electron (12). This is typically a small error for Rydberg excited states with their large spatial extent but can result in the overestimation of excitation energies to more compact unoccupied valence MOs by as much as a few eV, depending on the extent of interaction between the singly-occupied MO and the remaining valence MOs (1, 12).

Three sets of core excited state calculations were performed employing somewhat different basis sets. In each case, primitive basis functions were taken from (73/7) contracted Gaussian-type functions for carbon and fluorine and (411) for hydrogen (13). Polarization functions were added to carbon (ζ_d = 0.626), fluorine (ζ_d = 1.75), and hydrogen (ζ_p = 0.75) (14). The contraction schemes, indicating (s/p/d) functions, were (4111111/31111/1) for the F 1s excited fluorine, (721/511/1) for the other fluorine atoms and carbon, and (411/1) for hydrogen. This is referred to as Basis 1 in the following discussion. Following the approach of Ueda et al. (15), Basis 1 was supplemented using a set of 6s, 6p, and 6d diffuse functions, proposed initially by Kaufmann et al. (16), to describe 3s–5s, 3p–5p, and 3d–5d Rydberg orbitals: ζ_s = 0.075, 0.02530, 0.01141, 0.00589, 0.00334, and 0.00204; ζ_p = 0.0440, 0.01970, 0.01013, 0.00573, 0.00349, and 0.00224; and ζ_d = 0.02820, 0.01447, 0.00817, 0.00496, 0.00319, and 0.00214. Basis 2 refers to the addition of these Rydberg diffuse functions to the core excited fluorine atom.

It was noted in the calculation of the F 1s ionized state using Basis 1 that charge delocalization in the core-ionized state leads to the majority of the +1 charge localized on the adjacent carbon atom rather than the site of the F 1s core hole (formal charges of +0.77 and +0.36 on the fluorinated carbon and core-ionized fluorine, respectively). Therefore, an additional variation on the core-excited state calculations was performed in which the Rydberg diffuse functions described above were placed on the fluorinated carbon atom instead of on the core-excited fluorine atom. This is referred to as Basis 3.

Results and discussion

F 1s total ion yield spectrum

The TIY spectrum of trifluoropropyne in the vicinity of the F 1s edge is shown in Fig. 2. The spectrum consists of several broad and overlapping resonances superimposed on the F 1s ionization threshold at 694.75 eV (17), with an absence of any sharp resonance features. The spectrum has been fitted with five Gaussian functions to determine band positions and an arctan function to represent the F 1s edge

© 2008 NRC Canada

Table 1. F 1s excitation features of trifluoropropyne.

Pk	Energy (eV)	TV[a] (eV)	Area	Width (eV)	Assignment
1	689.44(10)	5.31	19.8(5)	2.18(1)	σ* C3-F/π* C1-C2(a′)
2	692.58(15)	2.17	26.6(18)	3.44(4)	σ* C3-F/π* C1-C2(a″) & 3p Ryd
IP	694.75[b]				F 1s IP
3	694.83(27)	–0.08	12.8(15)	3.8(2)	Rydberg and σ* C-F
4	697.3(15)	–2.5	3.5(14)	7.2(30)	
5	707.24(85)	–12.45	1.3(1)	7.1(16)	Shape res.

Note: From the least squares fit to the TIY data. Fit uncertainties in the final digits of the reported values are shown in parentheses. Peak numbers (Pk) correspond to those in Fig. 2.

[a]Term value; IP-transition energy.

[b]Ref. 17.

Fig. 2. F 1s total ion yield spectrum of trifluoropropyne (squares). The result of a least-squares fit of five Gaussian functions and an arctan function fixed at the reported energy of the F 1s ionization threshold (17) are also shown. The peak numbering corresponds to that used in Table 1.

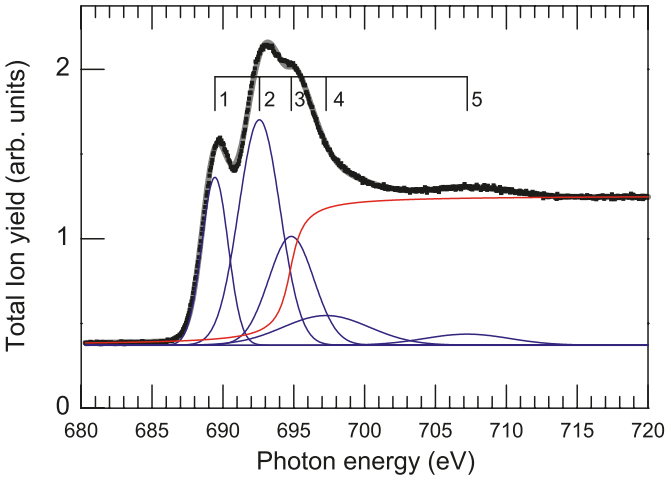

jump. The position of the edge jump was fixed at the literature ionization threshold (17); all other peak positions, widths, and amplitudes were allowed to vary freely. The fit results and assignments are listed in Table 1. Assignments are based on comparison with the F 1s excitation spectra of other fluorinated hydrocarbons and on the core-excited state calculations, as discussed below.

The general features of the spectrum are in good agreement with those determined by EELS for trifluoropropyne (2) and the chemically related perfluoro-2-butyne (3) and are generally consistent with the F 1s spectra of other fluorinated hydrocarbons (3, 18). In general, for fluorinated hydrocarbons with a π-bonding functional group adjacent to the fluorination site (e.g., CF_3CN, $(CF_3)_2CO$), a three-band structure is observed in the F 1s excitation spectra, the bands having term values of ~5, 2, and 0 eV, as is observed here for trifluoropropyne. Because the core excitation originates from a localized F 1s MO, only excitations to valence MOs with appreciable σ* C-F character are expected to have sufficient oscillator strength to be observed.

The first band at 689.4 eV can be assigned by consideration of the F 1s excitation spectra of other fluorinated hydrocarbons. An intense band with a similar term value is not observed in the F 1s spectra of molecules such as CF_4 and CF_3H that lack any π bonds (19–21) but is observed in those having an adjacent π-bonding functional group, such as CF_3CN and perfluoro-2-butyne (3). Band 1 is therefore attributed to excitations into a mixed-character σ* C3-F/π* C1-C2 unoccupied valence orbital. In contrast, strong features corresponding to bands 2 and 3 are observed in other fluorinated hydrocarbons independent of the presence of any π-bonding; these are therefore attributed to excitations to σ* C-F and Rydberg orbitals. Whereas Rydberg series consisting of sharp resonance features are readily identified in the high resolution C 1s excitation spectra of small alkyl fluorides, such features are not evident in the corresponding F 1s excitation spectra (19). This has been attributed in part to the energetic similarity of the Rydberg and C-F σ* excitation features. Fluorination is expected to lower the energy of the σ* C-F orbitals into the energy region below the ionization threshold typically associated with Rydberg excited states. Combined with the greater lifetime broadening for F 1s excitation and significant vibrational excitation (discussed further below), the failure to observe clear Rydberg series in the experimental F 1s excitation spectra is not surprising.

A weak continuum resonance is observed at 707.2 eV, 12.5 eV above threshold. This is consistent with F 1s continuum shape resonances observed in other fluorinated hydrocarbons, e.g., at 709.4 eV (TV = –13.9 eV) in CF_4 (21) and at 708 eV (–13.5 eV) in perfluoro-2-butyne (3).

It was necessary to include a fifth Gaussian (band 4) in the fit to adequately account for the intensity observed just above the ionization threshold. It is not clear whether this should be attributed to discrete electronic excitations just above threshold, to extensive vibrational excitation associated with the F 1s → σ* (C-F) band at 694.8 eV, or whether it simply accounts for a small decrease in the F 1s ionization cross-section with increasing photon energy.

All of the fitted bands are greater in width than expected from instrumental and lifetime broadening, indicating significant vibrational excitation following the creation of a core hole at a fluorine atom. This can be attributed to symmetry lowering, resulting from the creation of a localized F 1s core hole and the electron density contraction expected in the vicinity of the core hole. In the equivalent core model, core excited F is equivalent to Ne, leading to a prediction of dissociation of the bond between carbon and the core-excited fluorine atom, or at least a bond lengthening for the duration of the core hole lifetime. Evidence for ultrafast dissociation in other fluorides has been found in recent resonant Auger

© 2008 NRC Canada

Table 2. Calculated F 1s transitions of trifluoropropyne.

Basis set 1 (no Ryd fcts)			Basis set 2 (Ryd on F*)			Basis set 3 (Ryd on C3)			Description
TV (eV)	n^* [a]	Osc. str. × 100	TV (eV)	n^* [a]	Osc. str. × 100	TV (eV)	n^* [a]	Osc. str. × 100	
			2.955	2.15	0.0009	2.955	2.15	0.0009	3s (a′)
2.233	2.47	0.2443	2.261	2.45	0.2001	2.260	2.45	0.1988	σ* C3-F/π* C1-C2 (a′)
			2.129	2.53	0.0677	2.117	2.54	0.0652	$3p_y$ (a″)
			2.121	2.53	0.0520	2.118	2.53	0.0512	$3p_z$ (a′)
			1.955	2.64	0.0218	1.958	2.64	0.0161	$3p_x$ (a′)
1.763	2.78	0.0869	1.817	2.74	0.0361	1.844	2.72	0.0326	σ* C3-F/π* C1-C2 (a″)
			1.487	3.02	0.0043	1.503	3.01	0.0031	$3d_z^2$/4s (a′)
			1.329	3.20	0.0039	1.327	3.20	0.0044	$4s/3d_{x^2-y^2}$ (a′)
			1.312	3.22	0.0001	1.310	3.22	0.0000	$3d_{xy}$ (a″)
			1.308	3.22	0.0028	1.308	3.23	0.0088	$3d_{x^2-y^2}$ (a′)
			1.279	3.26	0.0330	1.273	3.27	0.0320	$3d_{xz}$ (a′)
			1.241	3.31	0.0083	1.214	3.35	0.0113	$3d_{yz}$ (a″)
			1.066	3.57	0.0050	1.066	3.57	0.0047	$4p_z$ (a′)
			1.036	3.62	0.0011	1.038	3.62	0.0010	$4p_y$ (a″)
			1.015	3.66	0.0070	1.016	3.66	0.0061	$4p_x$ (a′)
			0.830	4.05	0.0023	0.833	4.04	0.0018	$5s/4d_z^2$ (a′)
0.792	4.14	0.0631							Delocalized nonbonding (a′)
			0.771	4.20	0.0010	0.766	4.21	0.0011	$4d_{x^2-y^2}$/5s (a′)
			0.770	4.20	0.0004	0.766	4.21	0.0002	$4d_{xy}$ (a″)
			0.764	4.22	0.0029	0.763	4.22	0.0051	$4d_{x^2-y^2}$ (a′)
			0.756	4.24	0.0062	0.747	4.27	0.0070	$4d_{xz}$ (a′)
			0.747	4.27	0.0007	0.730	4.32	0.0016	$4d_{yz}$ (a″)
			0.642	4.60	0.0027	0.641	4.61	0.0024	$5p_z$ (a′)
			0.632	4.64	0.0013	0.632	4.64	0.0013	$5p_y$ (a″)
			0.615	4.70	0.0042	0.619	4.69	0.0039	$5p_x$ (a′)
			0.505	5.19	0.0011	0.508	5.17	0.0007	$5d_{z^2}$ (a′)
			0.487	5.29	0.0001	0.485	5.30	0.0003	$5d_{x^2-y^2}$ (a′)
			0.487	5.29	0.0003	0.484	5.30	0.0002	$5d_{yz}$ (a″)
			0.480	5.32	0.0015	0.472	5.37	0.0037	$5d_{xz}$ (a′)
			0.474	5.36	0.0002	0.461	5.43	0.0006	$5d_{xy}$ (a″)

[a] n^* is the effective principle quantum number, n-δ, where δ is the quantum defect. $n^* = \sqrt{R_\infty/\text{TV}}$.

spectroscopy and Auger electron-fragment ion coincidence studies of CF_4, CH_3F, SiF_4, and SF_6 (22–26). Fast dissociation of the bond to the core excited F occurs in these molecules following the lowest energy F 1s → σ* resonant excitation; this is followed by atomic-like Auger decay of the dissociating F 1s excited fragment. Evidence for significant vibrational excitation in the remaining CF_3 and SF_5 fragments following fast dissociation of F 1s excited CF_4 and SF_6 has also been observed (22, 24, 26).

The relative intensities of the spectral features of the TIY spectrum of trifluoropropyne are in good agreement with those of the previous EELS measurement (2) up to ~695 eV. However, the relative TIY intensity above threshold is greater than the photoabsorption cross section determined by EELS, indicating an increase in ionization efficiency with F 1s ionization. This is consistent with an increase in the number of ion-pair processes resulting from normal Auger decay and charge separation above threshold and suggests that resonant Auger decay below threshold is leading to a significant amount of single ion formation.

Computational results

The results of our F 1s core excited state calculations are summarized in Table 2 for the three basis sets described above: (*i*) without inclusion of diffuse Rydberg functions, (*ii*) with diffuse Rydberg functions added to the core excited F only, and (*iii*) with diffuse Rydberg functions added to the fluorinated C only. Only resonant excitations below the F 1s IP are included in the table. The molecule was oriented with the C_{3v} symmetry axis along the *z* axis and the core-excited F atom in the *xz* plane. The same calculated F 1s IP of 693.43 eV is obtained from the three calculations, indicating that inclusion of Rydberg diffuse functions in the basis set is not necessary for accurate modelling of the F 1s core ionized state. The calculated IP is in fair agreement with the experimental IP of 694.75 eV (17).

The calculations without diffuse Rydberg functions (Basis 1) predict three states below threshold. The valence MOs singly occupied in these F 1s excited states are shown in Fig. 3. Each of the MOs has some σ* (C-F) character. The first two of these also have significant C1-C2 π* antibonding

© 2008 NRC Canada

Fig. 3. Singly-occupied valence MOs in the F 1s excited states of trifluoropropyne calculated with Basis 1. The F atom above the symmetry axis is the site of core excitation. Top: σ* C3-F/π* C1-C2 (a′); Middle: σ* C3-F/π* C1-C2 (a″); Bottom: delocalized nonbonding (a′).

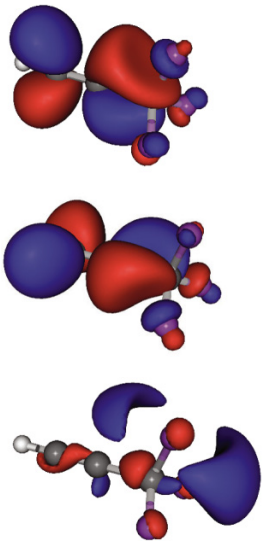

character and C2-C3 π bonding character. These two MOs can be described as a mixing of the C1-C2 π* and C3-F σ* valence orbitals of appropriate symmetries. The lowest energy and most intense transition (TV = 2.233) is to an MO that involves π character in the *xz* plane containing the core excited F (a′ in the C_s symmetry of the core-excited state); the C-F σ* character involves primarily the core-excited F atom with small contributions from the other two F atoms. The next transition, with TV = 1.763, involves mixing of the π* MO perpendicular to the plane containing the core-excited F with a C-F antibonding MO that has much greater contributions from the non-core-excited F atoms. This MO, a″ in C_s symmetry, has a nodal plane through the core-excited F; it is antibonding between C3 and the core-excited F, but in a pseudo-π* sense. The weaker contribution from the core-excited F in this second MO is reflected in the lower oscillator strength and term value of this transition; generally, term values are larger for excitations to MOs with greater character on the core-excited atom because those MOs will experience greater electronic relaxation upon formation of a core hole at that site.

Transitions corresponding to these two lowest energy excitations in the Basis 1 calculations can be readily identified in the two calculations performed with the inclusion of Rydberg basis functions, in which transitions to MOs with the same mixed C1-C2 π* and C3-F σ* character as described above are observed at very similar excitation energies. The calculated intensities of these transitions are less in the Basis 2 and Basis 3 calculations, as would be expected when using basis sets that can model a greater number of excitations in this energy range — the total oscillator strength is distributed over a greater number of transitions. The consistency of the calculated results for these two intense transitions, with and without inclusion of Rydberg basis functions, affirms their assignment as excitations to valence antibonding MOs with no significant Rydberg character.

It is interesting to note that in the ground state, the unoccupied π* MOs are degenerate (as they must be in C_{3v} symmetry) and have much less F character than do the corresponding MOs in the presence of a F 1s core hole. Creation of a core hole on F not only lowers the molecular symmetry to remove the degeneracy of the π* MOs, but electronic relaxation and contraction of the C-F σ* MOs in the presence of the F 1s core hole also allows for increased mixing of the C-C π* and C-F σ* character. This same mixing does not occur when the core hole is on one of the carbon atoms (1).

The calculations with Basis 1 predict a third bound F 1s excited state involving excitation to an MO delocalized throughout the molecule, with significant character from all atoms. Although there is some σ* antibonding character among all pairs of neighbouring atoms, interactions are weaker than in the first two MOs and a nonbonding description appears more appropriate. As can be seen in Fig. 3, this MO is more extended in the vicinity of the core excited fluorine. In contrast to the two lower energy F 1s excited states discussed above, there is no clear counterpart to this excitation in the Basis 2 and Basis 3 calculations. Instead, a number of weak excitations to 4d Rydberg-type MOs are predicted in this energy range (TV ~ 0.8 eV). This suggests that this third F 1s excited state predicted at TV = 0.79 eV in the Basis 1 calculations is the result of an attempt to model a Rydberg excited state with an inadequate basis set.

Comparing the results of the Basis 2 and Basis 3 calculations, it is apparent that, below threshold, placement of Rydberg functions on either the core-excited F or the neighbouring centre of positive charge, C3, gives essentially the same result. Therefore, either choice appears adequate for modelling the more spatially extended F 1s-excited states of trifluoropropyne.

When diffuse Rydberg functions are included in the basis set, the calculations place the three F 1s → Rydberg 3p excitations between the first two valence σ* (C-F) excitations and with appreciable intensity. The calculated quantum defects of ~0.4 are reasonable for p-type Rydberg states. The energies and character of the remaining F 1s excited states predicted in the Basis 2 and Basis 3 calculations are consistent with higher order Rydberg states, as indicated in Table 2. The calculated oscillator strengths of these higher energy Rydberg states are comparatively low. Therefore, it is only in aggregate that they are likely to give rise to sufficient intensity to be observed.

Comparing the calculated results with the experimental F 1s excitation spectrum of Fig. 2 and Table 1, the calculations significantly underestimate the term value of the first transition, predicting 2.3 eV versus the observed term value of 5.3 eV. The underestimation of term values for core excitations to valence MOs is expected with the STEX method, as the core-hole screening by the excited electron is neglected. This error will be most significant for more compact valence excited states having a significant contribution from the core-excited atom and will be considerably smaller for more spatially extended and delocalized excited states. For example, in a study of the C 1s excited states of propyne, trifluoropropyne, and propargyl alcohol, differences of ~1.7 eV were observed between experimental term values and those calculated by the STEX method for C 1s → π*

© 2008 NRC Canada

transitions, but only a few tenths of an electronvolt for transitions to Rydberg states (1). A similar effect is expected here, with the error being largest for the F 1s → σ*(C3-F)/π*(C1-C2) a′ excitation, smaller for the F 1s → σ*(C3-F)/π*(C1-C2) a″ excitation, where the calculations indicate the open shell valence MO is more extended than the a′ MO of the first excitation and the amount of character from the core-excited F atom is less, and much smaller for the excitations to Rydberg states. Therefore, the first peak in the experimental spectrum at 689.44 eV is assigned to the F 1s → σ*(C3-F)/π*(C1-C2) a′ excitation and the second, broader peak at 692.58 eV to a combination of the F 1s → σ*(C3-F)/π*(C1-C2) a″ and F 1s → 3p Rydberg excitations. The broad, third peak fitted to the experimental spectrum near the F 1s ionization threshold is attributed to strongly overlapping higher order Rydberg states with significant vibrational excitation. By analogy with the F 1s excitation spectroscopy of other fluorinated hydrocarbons, discussed above, a contribution from an additional σ* (C-F) MO also seems reasonable in this energy region. However, no clear evidence for this is found in our core excitation calculations, suggesting that any σ* (C-F) character in the excitations near threshold is well-mixed with Rydberg states.

The computational results with the three basis sets are much less consistent above threshold. This is not unexpected, as the goal of the calculations was to describe the electronic states present below the F 1s ionization threshold. However, the calculations with the three basis sets all do predict a relatively intense transition to a high *l* state 10.8–12.5 eV above threshold, consistent with the assignment of peak five as a continuum shape resonance, as indicated in Table 1. The higher energy of 12.5 eV above threshold is predicted by the Basis 2 calculations, in which the diffuse Rydberg basis functions are centred on the core-excited F, in perfect agreement with the experimental observation. The calculations with the other two basis sets place this feature at slightly lower excitation energy.

Ionic fragmentation

A total of 16 ions have been identified in the PEPICO mass spectra collected near the F 1s edge. Ions differing by one mass unit could not be distinguished because of the resolution of the TDC and the widths of the ion peaks resulting from their generally high kinetic energies. Photoionization branching ratios (BR) as a function of photon energy have been derived from the PEPICO data by determining the intensity of each fragment ion in each PEPICO mass spectrum relative to the total signal arising from all ions observed in the mass spectrum. The branching ratios are shown in Figs. 4–6.

The branching ratios of the eight most abundant ions are shown in Fig. 4. These ions account for >92% of the total ion yield throughout this photon energy range. All are singly charged ions, indicating a tendency for charge separation following multiple ionization rather than the production of stable multiply charged ions. The absence from this group of any fragment ions containing at least two carbon atoms and at least one fluorine atom indicate the preference for bond dissociation between C2 and C3 and between C3 and F. Charge separation processes leading to one F^+ ion and a $C_2F_n^+$ or $C_3F_n^+$ ion are not observed following F 1s excitation. Instead, ionic fragmentation processes in which either dissociation of the C2–C3 bond or dissociation of *all* C–F bonds, or both processes, occur.

Fig. 4. Photoionization branching ratios of the eight most abundant fragment ions of trifluoropropyne near the F 1s ionization threshold. The positions of the peaks fitted to the TIY spectrum are indicated by vertical bars and the ionization threshold by a dashed line. The open symbol data were collected with a 60 s dwell time while the solid symbol data were measured separately with a 20 min dwell time.

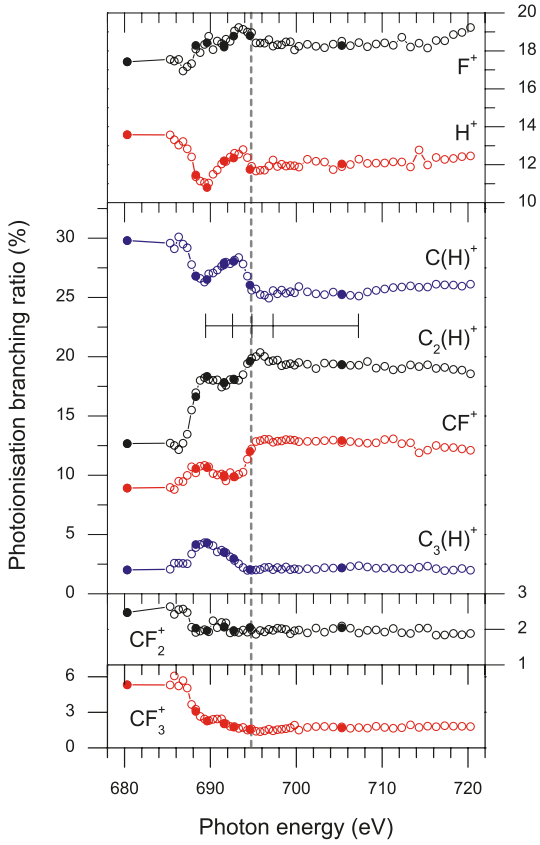

$C(H)^+$ is the most abundant ion throughout the F 1s region, although its BR drops significantly with F 1s excitation or ionization. The CF_3^+ and CF_2^+ BR also drop with the onset of F 1s excitation. This suggests that these ions are being produced via direct valence ionization or C 1s continuum ionization rather than F 1s excitation or ionization. In contrast, the $C_2(H)^+$ and CF^+ BR show corresponding increases while the $C_3(H)^+$ BR increases with F 1s resonant excitation but then decreases again with F 1s ionization. Similar decreases in CF_3^+ and CF_2^+ BR and a corresponding increase in CF^+ have been observed following F 1s resonant excitation in CF_3CH_3 (27), CF_3Cl (28), $CF_3C(O)CH_3$ (18), and CF_3SF_5 (29). The $C_3(H)^+$ behaviour is consistent with the assignment of the first two F 1s near edge features as excitations largely to σ* (C-F) molecular orbitals. These σ* MOs are delocalized over the entire CF_3 group, so that population of these MOs gives rise to the state-specific dissociation of all three C–F bonds. F^+ is the second most abundant ion throughout this photon energy range. A relatively small increase in the F^+ BR is observed with F 1s resonant excitation but no further increase is observed with F 1s ionization.

© 2008 NRC Canada

Fig. 5. Photoionization branching ratios of the four least abundant singly charged fragment ions of trifluoropropyne near the F 1s ionization threshold. The positions of the peaks fitted to the TIY spectrum are indicated by vertical bars and the ionization threshold by a dashed line. The open symbol data were collected with a 60 s dwell time while the solid symbol data were measured separately with a 20 min dwell time.

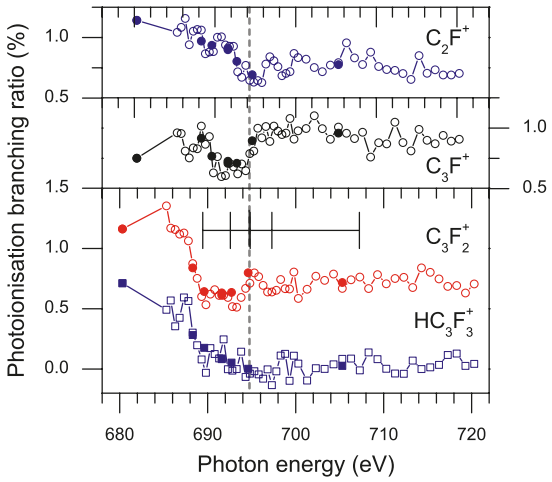

Fig. 6. Photoionization branching ratios of the four multiply charged fragment ions of trifluoropropyne observed near the F 1s ionization threshold. The positions of the peaks fitted to the TIY spectrum are indicated by vertical bars and the ionization threshold by a dashed line. The open symbol data were collected with a 60 s dwell time while the solid symbol data were measured separately with a 20 min dwell time.

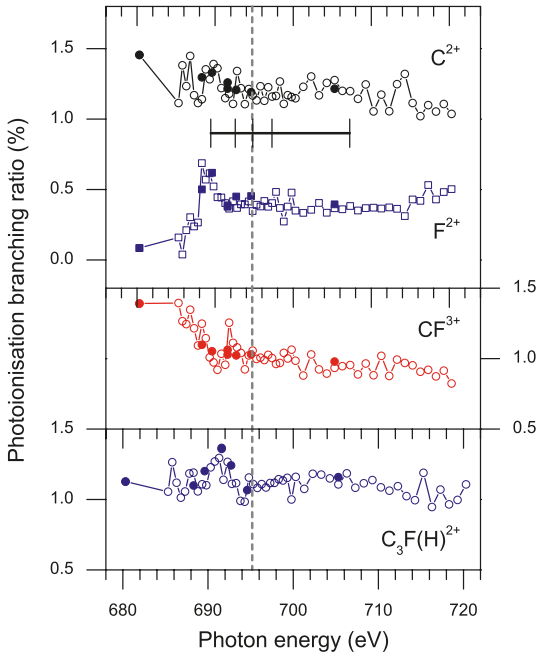

While there is certainly a degree of site-specificity to the ionic fragmentation at the F 1s edge, the data suggest a tendency for some charge delocalization to the rest of the molecule and in particular to the fluorinated carbon atom, resulting in cleavage of multiple bonds to the fluorinated carbon. The high F^+ BR below the onset of F 1s excitation (i.e., in the valence and C 1s ionization continua) may also be partially attributed to charge redistribution following core hole formation in trifluoropropyne, in this case with core hole formation at carbon.

The BR of the low abundance singly charged ions are shown in Fig. 5 while those of the observed multiply charged ions are shown in Fig. 6. All of these ions have BR < 1.5% and exhibit less variation with photon energy than do the more abundant ions shown in Fig. 4. The low abundance singly charged ions all contain at least two carbon atoms and one fluorine atom. With the exception of C_3F^+, which exhibits a small enhancement at the F 1s ionization threshold, there is a tendency with the ions shown in Fig. 5 for a decrease in their BR with F 1s excitation, indicating these ions are produced primarily via C 1s and valence continuum ionization. The drop in the BR of the parent ion $HC_3F_3^+$ with the onset of F 1s excitation indicates that resonant Auger decay of F 1s excited states to yield bound states of the parent ion does not occur to any significant extent.

The multiply charged ions shown in Fig. 6 also exhibit little variation with photon energy, supporting the observation made previously that F 1s excitation and ionization in trifluoropropyne favours charge separation over the formation of multiply charged ions. The one minor exception is F^{2+}, which has an increased (albeit still small) yield, particularly at the lowest energy F 1s resonant excitation. This is suggestive of atomic Auger decay of core-excited fluorine atoms produced via ultrafast dissociation of core-excited trifluoropropyne, as has been observed in resonant F 1s excitation of other fluorinated molecules (22–26).

Conclusions

The core excitation spectroscopy and ionic fragmentation of 3,3,3-trifluoropropyne have been investigated at the F 1s edge using synchrotron radiation, time-of-flight mass spectrometry, and coincidence techniques. The F 1s TIY spectrum exhibits several broad and overlapping resonances involving C-F σ* antibonding orbitals mixed with C-C π* character superimposed on the F 1s ionization threshold. Core excited state calculations also suggest numerous unresolved excitations to Rydberg states below threshold. The broad nature of the observed features is attributed to a combination of overlapping electronic excitations and considerable vibrational excitation following core-hole formation at F. The dominant fragmentation channels exhibit a clear dependence on the atomic site of initial core hole formation. F 1s excitation or ionization favours HC_2–CF_3 bond dissociation as well as C–F bond dissociation, indicating a tendency for charge delocalization from core-excited F to the adjacent C. Charge separation to yield multiple singly charged ions is favoured over the formation of multiply charged ions.

Acknowledgements

The research in this work was performed in part at the Canadian Light Source (CLS), which is supported by the Natural Sciences and Engineering Research Council of Canada (NSERC), the National Research Council Canada (NRC), the Canadian Institutes of Health Research (CIHR),

© 2008 NRC Canada

and the University of Saskatchewan. We thank the CLS staff and in particular Tom Regier, Ian Coulthard, and Robert Blyth for assistance with the beamline operation and experimental measurements. NSERC and the University of New Brunswick provided financial support for this work.

References

1. L. Yang and J.J. Neville. J. Phys. Chem. A, **109**, 11163 (2005).
2. A.P. Hitchcock and J. Stöhr. Unpublished. *In* A.P. Hitchcock and D.C. Mancini. J. Electron Spectrosc. Relat. Phenom. **67**, 1 (1994). Available from http://unicorn.mcmaster.ca/corex/cedb-title.html [accessed 5 June 2008].
3. M.B. Robin, I. Ishii, R. McLaren, and A.P. Hitchcock. J. Electron Spectrosc. Relat. Phenom. **47**, 53 (1988).
4. K. Okada, S. Tanimoto, T. Ibuki, Y. Haga, T. Gejo, K. Saito, and K. Ohno. Chem. Phys. **304**, 273 (2004).
5. T. Regier, J. Paulsen, G. Wright, I. Coulthard, K. Tan, T.K. Sham, and R. Blyth. AIP Conf. Proc. **879**, 473 (2007).
6. J.T. Francis, C.C. Turci, T. Tyliszczak, G.G.B. de Souza, N. Kosugi, and A.P. Hitchcock. Phys. Rev. A, **52**, 4665 (1995).
7. A.P. Hitchcock and J.J. Neville. *In* Chemical applications of synchrotron radiation. *Edited by* T.K. Sham. World Scientific, Singapore. 2002. pp. 154–227.
8. A.C.O. Guerra, J.B. Maciel, C.C. Turci, R.C. Bilodeau, and A.P. Hitchcock. Can. J. Chem. **82**, 1052 (2004).
9. M.W. Schmidt, K.K. Baldridge, J.A. Boatz, S.T. Elbert, M.S. Gordon, J.H. Jensen, S. Koseki, N. Matsunaga, K.A. Nguyen, S.J. Su, T.L. Windus, M. Dupuis, and J.A. Montgomery. J. Comput. Chem. **14**, 1347 (1993).
10. N. Kosugi and H. Kuroda. Chem. Phys. Lett. **74**, 490 (1980).
11. W.J. Hunt and W.A. Goddard III. Chem. Phys. Lett. **3**, 414 (1969).
12. V. Kimberg and N. Kosugi. J. Chem. Phys. **126**, 245101 (2007).
13. S. Huzinaga, J. Andzelm, M. Klobukowski, E.R. Andzelm, Y. Sakai, and H. Tatewaki. Gaussian basis sets for molecular calculations. Elsevier, Amsterdam. 1984.
14. R. Krishnan, J.S. Binkley, R. Seeger, and J.A. Pople. J. Chem. Phys. **72**, 650 (1980).
15. K. Ueda, M. Okunishi, H. Chiba, Y. Shimizu, K. Ohmori, Y. Sato, E. Shigemasa, and N. Kosugi. Chem. Phys. Lett. **236**, 311 (1995).
16. K. Kaufmann, Ch. Nager, and M. Jungen. Chem. Phys. **95**, 385 (1985).
17. R.G. Cavell. J. Electron Spectrosc. Relat. Phenom. **6**, 281 (1975).
18. T. Ibuki, K. Okada, M. Takahashi, S. Samori, T. Goya, Y. Senba, H. Yoshida, A. Hiraya, and K. Ohno. J. Electron Spectrosc. Relat. Phenom. **143,** 21 (2005).
19. K. Ueda, Y. Shimizu, H. Chiba, M. Okunishi, K. Ohmori, Y. Sato, E. Shigemasa, and N. Kosugi. J. Electron Spectrosc. Relat. Phenom. **79**, 441 (1996).
20. M. de Simone, M. Coreno, M. Alagia, R. Richter, and K.C. Prince. J. Phys. B: At. Mol. Opt. Phys. **35**, 61 (2002).
21. T. Ibuki, Y. Shimada, S. Nagaoka, A. Fujii, M. Hino, T. Kakiuchi, K. Okada, K. Tabayashi, T. Matsudo, Y. Yamana, I.H. Suzuki, and Y. Tamenori. Chem. Phys. Lett. **392**, 303 (2004).
22. K. Ueda, M. Kitajima, A. De Fanis, T. Furuta, H. Shindo, H. Tanaka, K. Okada, R. Feifel, S.L. Sorensen, H. Yoshida, and Y. Senba. Phys. Rev. Lett. **90**, 233006 (2003).
23. M. Kitajima, A. De Fanis, K. Okada, H. Yoshida, M. Hoshino, H. Tanaka, and K. Ueda. J. Electron Spectrosc. Relat. Phenom. **144-147**, 199 (2005).
24. G. Prümper, K. Ueda, Y. Tamenori, M. Kitajima, N. Kuze, H. Tanaka, C. Makochekanwa, M. Hoshino, and M. Oura. Phys. Rev. A, **71**, 052704 (2005).
25. X.J. Liu, G. Prümper, E. Kukk, R. Sankari, M. Hoshino, C. Makochekanwa, M. Kitajima, H. Tanaka, H. Yoshida, Y. Tamenori, and K. Ueda. Phys. Rev. A, **72**, 042704 (2005).
26. G. Prümper, X.J. Liu, K. Ueda, and Y. Temenori. Radiat. Phys. Chem. **75**, 2019 (2006).
27. K. Müller-Dethlefs, M. Sander, L.A. Chewter, and E.W. Schlag. J. Phys. Chem. **88**, 6098 (1984).
28. I.H. Suzuki, N. Saito, and J.D. Bozek. Bull. Chem. Soc. Jpn. **68**, 1119 (1995).
29. T. Ibuki, Y. Shimada, R. Hashimoto, S. Nagaoka, M. Hino, K. Okada, I.H. Suzuki, Y. Morishita, and Y. Tamenori. Chem. Phys. **314**, 119 (2005).

© 2008 NRC Canada

Bismuth-triflate-catalyzed Prins–Ritter reaction — An efficient synthesis of 4-amidotetrahydropyrans

J.S. Yadav, B.V. Subba Reddy, D.N. Chaya, G.G.K.S. Narayana Kumar

Abstract: Bismuth(III) triflate is found to be an effective Lewis acid in catalyzing a three-component reaction of homoallylic alcohol, carbonyl compound, and nitrile at ambient temperature via the Prins–Ritter sequence to furnish 4-amidotetrahydropyrans in high yields, all with cis selectivity. Spirocyclic 4-amidotetrahydropyrans are obtained in case of cyclic ketones.

Key words: Prins cyclization, bismuth(III) triflate, homoallyl alcohol, 4-amidotetrahydropyrans.

Résumé : On a trouvé que le triflate de bismuth(III) agit comme acide de Lewis efficace dans la catalyse de la réaction à trois composantes d'un alcool homoallylique, d'un composé carbonylé et d'un nitrile à la température ambiante, par le biais d'une séquence de Prins–Ritter, qui conduit à la formation de 4-amidotétrahydropyranes, avec des rendements élevés et une sélectivité complètement *cis*. Dans les cas où le produit de départ est une cétone cyclique, le produit obtenu est un 4-amidotétrahydropyrane spirocyclique.

Mots-clés : cyclisation de Prins, bismuth(III), triflate, alcool homoallylique, 4-amidotétrahydropyranes.

[Traduit par la Rédaction]

Introduction

Recently, multicomponent one-pot synthesis has received considerable attention because of its wide range of applications in medicinal chemistry for the production of structural scaffolds and combinatorial libraries in drug discovery (1). The 4-aminotetrahydropyran ring system is found in many biologically active natural products, such as ambruticins VS, glycamino acid, and others (2, 3). Tetrahydropyran derivatives are usually prepared by the Prins cyclization using acid catalysis (4, 5) or by intramolecular hetero-Michael reaction (6). However, the use of Ritter amidation to terminate Prins cyclization is scarce (7); hence, an efficient and practical methodology for the Prins–Ritter-type reaction would be of great importance for the synthesis of natural products (8).

Lanthanide triflates are unique Lewis acids that are currently of great interest (9). The high catalytic activity, low toxicity, moisture and air tolerance, and their recyclability make lanthanide triflates attractive alternatives to conventional Lewis acids (10). However, lanthanide triflates are rather expensive and their use in large-scale synthesis is limited. Therefore, cheaper and more efficient catalysts are desirable. In this direction, bismuth triflate has evolved as remarkable Lewis acid catalyst for effecting various organic transformations (11). Compared with lanthanide triflates, bismuth triflate is cheap and is easy to prepare, even on a multi-gram scale, from commercially available bismuth oxide and triflic acid (12). However, there have been no reports on the use of bismuth triflate for the synthesis of tetrahydropyrans.

Received 20 February 2008. Accepted 18 April 2008. Published on the NRC Research Press Web site at canjchem.nrc.ca on 17 June 2008.

J.S. Yadav,[1] B.V. Subba Reddy, D.N. Chaya, G.G.K.S. Narayana Kumar. Division of Organic Chemistry, Indian Institute of Chemical Technology, Hyderabad 500 007, India.

[1]Corresponding author (e-mail: yadavpub@iict.res.in).

Scheme 1.

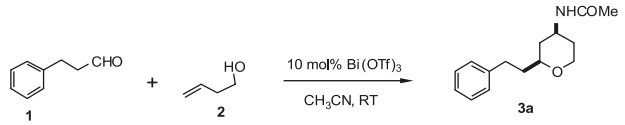

Results and discussion

In this article, we describe a direct and efficient method for the synthesis of 4-amidotetrahydropyrans via the Prins–Ritter sequence using bismuth triflate. In a preliminary study, 3-phenylpropanal (**1**) was treated with but-3-en-1-ol (**2**) in acetonitrile in the presence of 10 mol% of bismuth triflate. The reaction went to completion in 4.5 h at room temperature, and the product 4-acetamidotetrahydropyran **3a** was obtained, instead of tetrahydropyranyl-4-triflate, in 93% yield with cis selectivity (Scheme 1).

This result encouraged us to study the reaction with various aldehydes, homoallylic alcohols, and nitriles. Interestingly, 3-buten-1-ol reacted smoothly with cyclohexanecarboxaldehyde, isobutyraldehyde, *trans*-cinnamaldehyde, 1-naphthaldehyde, 3,4-dichlorobenzaldehyde, 3,4,5-trimethoxybenzaldehyde, and *m*-nitrobezaldehyde in acetonitrile to produce the corresponding 4-acetamidotetrahydropyrans in high yields (Table 1, entries **b**–**h**,). The substituted homoallylic alcohols like 1-phenylbut-en-1-ol and 1-cyclohexylbut-en-1-ol also participated well in this transformation (Table 1, entries **o** and **p**). This reaction proceeded well even with cyclic ketones such as cyclopentanone, cyclohexanone, and 4-phenyl-1-cyclohexanone to give spirocyclic-4-acet-

 doi:10.1139/V08-080 © 2008 NRC Canada

Table 1. Preparation of 4-amidotetrahdyropyrans via the Prins–Ritter reaction sequence.

Entry	Homoallyl alcohol	Carbonyl compound	Nucleophile	Amidopyrans	Time (h)[a]	Yield (%)[b]
a		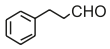	CH_3CN	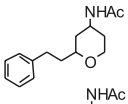	4.5	93
b			CH_3CN		5.0	90
c			CH_3CN		4.0	91
d		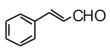	CH_3CN	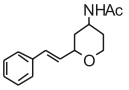	4.5	88
e			CH_3CN	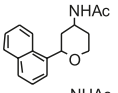	6.5	87
f		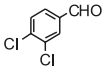	CH_3CN	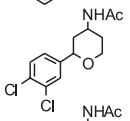	7.0	85
g		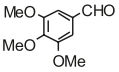	CH_3CN	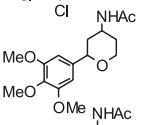	8.5	82
h			CH_3CN	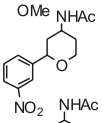	8.5	80
i			CH_3CN		9.0	86
j			CH_3CN		7.5	88
k		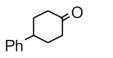	CH_3CN	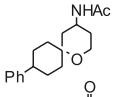	8.0	86
l			$PhCH_2CN$	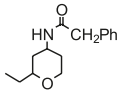	7.0	86
m			Me_3CCN	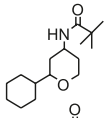	7.5	88
n			PhCN	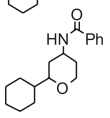	8.5	82
o		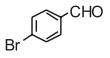	CH_3CN	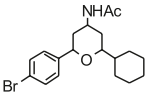	7.5	90
P		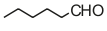	CH_3CN	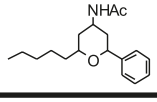	8.0	86

[a]All products were characterized by ^1H NMR, ^{13}C NMR, IR, and mass spectroscopy.
[b]Isolated and unoptimized yields.

amidotetrahydropyrans comparably in good yields (Table 1, entries **i**–**k**; Scheme 2).

The reaction succeeded with other nitriles such as 2-phenyl acetonitrile, 3,3-dimethylbutanenitrile, and benzonitrile (Table 1, entries **l**–**n**). In the absence of bismuth triflate, the

Scheme 2.

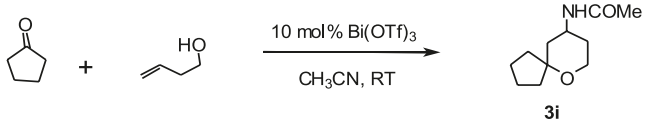

3i

© 2008 NRC Canada

Scheme 3.

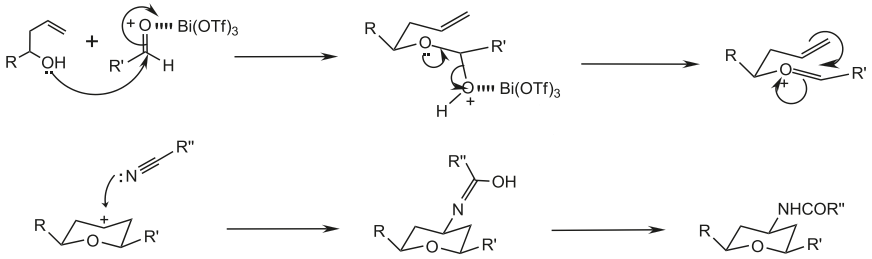

reaction did not proceed even after a long reaction time (16 h). The reactions were clean, and the products were obtained at room temperature in excellent yields and with high diastereoselectivity as determined from the NMR spectra of the crude products. Only one diastereoisomer was obtained in each case, the structure of which was confirmed on the basis of coupling constants and also by nOe experiments (8e). The formation of the products could be explained by hemi-acetal formation followed by Prins cyclization and subsequent Ritter amidation (Scheme 3).

A tentative reaction mechanism to realize the cis selectivity could be explained by assuming the formation of an (*E*)-oxocarbenium ion via a chairlike transition state, which has an increased stability relative to the open oxocarbenium ion owing to delocalization. The optimal geometry for this delocalization places the hydrogen atom at C-4 in a pseudo-axial position, which favours equatorial attack of the nucleophile (13). The effects of various metal triflates such as $In(OTf)_3$, $Yb(OTf)_3$, $Sm(OTf)_3$, $Dy(OTf)_3$, and $Ce(OTf)_3$ were examined in this reaction. Of these, bismuth triflate was found to be efficient in terms of conversion. The scope and generality of this process is illustrated with respect to various carbonyl compounds, homoallylic alcohols, and nitriles, and the results are presented in Table 1. It is noteworthy to highlight that both aromatic and aliphatic substrates worked well for this transformation.

Conclusion

In summary, we described a novel and efficient Prins–Ritter reaction to produce highly substituted 4-amidotetrahydropyrans in high yields, all with cis selectivity. The use of inexpensive and readily available bismuth triflate makes this procedure simple, convenient, and practical. In addition to its simplicity, efficiency, and milder reaction conditions, this method provides an easy access for 4-amidotetrahydropyran derivatives in a single-step operation.

Experimental

Melting points were recorded on Buchi R-535 apparatus and are uncorrected. IR spectra were recorded on a PerkinElmer FTIR 240-c spectrophotometer using KBr optics. ^{1}H, ^{13}C NMR spectra were recorded on Gemini-200 spectrometer in $CDCl_3$ using TMS as internal standard. Mass spectra were recorded on a Finnigan MAT 1020 mass spectrometer operating at 70 eV. TLC was monitored on 0.25 mm pre-coated silica-gel plates (60F-254).

General procedure

A mixture of but-3-en-1-ol (1 mmol), 3-phenylpropanal (1.2 mmol), and bismuth triflate (10 mol%) in acetonitrile (5 mL) was stirred at 23 °C for a specified time (Table 1). After completion of the reaction as indicated by TLC, the reaction mixture was quenched with water and extracted with ethyl acetate (2 × 10 mL). The combined organic layers were dried over anhyd. Na_2SO_4. Removal of solvent followed by purification on silica gel (Merck, 100–200 mesh, ethyl acetate/hexane, 4:6) gave pure 4-amidotetrahydropyran. The products thus obtained were characterized by IR and NMR spectroscopy. Characterization data was found to be consistent with that of authentic samples (6).

a: *N*-(2-phenethyltetrahydro-2*H*-4-pyranyl)acetamide

Pale yellow solid, mp 90–92 °C. IR (KBr) ν: 3308, 2923, 2852, 1648, 1543, 1368, 1083, 946, 745 cm^{-1}. ^{1}H NMR (300 MHz, $CDCl_3$) δ: 1.26 (m, 2H), 1.31 (dq, 1H, *J* = 4.2, 12.2 Hz), 1.36 (q, 1H, *J* = 12.0 Hz), 1.85 (t, 2H, *J* = 7.5 Hz), 1.93 (s, 3H), 2.66 (ddt, 1H, *J* = 2.2, 4.2, 12.0 Hz), 2.74 (ddq, 1H, *J* = 2.2, 12.0, 12.0 Hz), 3.28 (m, 1H), 3.44 (dt, 1H, *J* = 1.5, 12.0 Hz), 3.89 (m, 1H), 4.13 (m, 1H), 5.28 (d, 1H, *J* = 8.3 Hz), 7.07–7.26 (m, 5H). ^{13}C NMR (75 MHz, $CDCl_3$) δ: 23.1, 31.4, 32.5, 37.7, 38.3, 45.9, 66.3, 75.4, 125.6, 127.8, 128.1, 141.7, 169.5. LC-MS: *m*/*z* (%): (M + Na) 270. HR-MS calcd. for $C_{15}H_{21}NO_2Na$: 270.1469. Found: 270.1478.

b: *N*-(2-cyclohexyltetrahydro-2*H*-4-pyranyl)acetamide

Colourless solid, mp 148–150 °C. IR (KBr) ν: 3280, 3089, 2944, 2930, 2822, 1648, 1543, 1422, 1373, 1091, 966, 804 cm^{-1}.^{1}H NMR (300 MHz, $CDCl_3$) δ: 0.89–1.38 (m, 10H), 1.56–1.90 (m, 5H), 1.93 (s, 3H), 3.04 (m, 1H), 3.41 (dt, 1H, *J* = 2.0, 12.0 Hz), 3.86 (m, 1H), 3.90 (m, 1H), 5.36 (d, 1H, *J* = 7.5 Hz). ^{13}C NMR (75 MHz, $CDCl_3$) δ: 169.4, 80.9, 66.2, 46.4, 35.6, 32.8, 32.7, 28.6, 28.4, 25.1, 23.2. LC-MS: *m*/*z* (%): (M + Na) 248. HR-MS calcd. for $C_{13}H_{23}NO_2Na$: 248.1626. Found: 248.1636.

c: *N*-(2-isopropyltetrahydro-2*H*-4-pyranyl)acetamide

Colourless solid. mp 74–76 °C. IR (KBr) ν: 3320, 2928, 2838, 1412, 1370, 1256, 1140, 1088, 1046, 986, 876 cm^{-1}. ^{1}H NMR (300 MHz, $CDCl_3$) δ: 0.88 (d, 3H, *J* = 6.7 Hz), 0.91 (d, 3H, *J* = 6.7 Hz), 1.06 (m, 1H), 1.23–1.42 (m, 2H), 1.64 (m, 1H), 1.76–1.93 (m, 1H), 1.94 (s, 3H), 3.01 (dq, 1H, *J* = 1.5, 6.7 Hz), 3.41 (dt, 1H, *J* = 1.5, 12.0 Hz), 3.84–4.00 (m, 2H), 6.47 (d, 1H, *J* = 7.5 Hz). ^{13}C NMR (75 MHz, $CDCl_3$) δ: 169.4, 81.4, 66.4, 46.3, 35.1, 32.8, 32.7, 23.1, 18.2, 18.0. LC-MS: *m*/*z*: (M + Na) 208. HR-MS calcd. for $C_{10}H_{19}NO_2Na$: 208.1313. Found: 208.1322.

© 2008 NRC Canada

d: *N*-2-[2-phenyl-(*E*)-1-ethenyl]tetrahydro-2*H*-4-pyranylacetamide

Yellow solid, mp 114–116 °C. IR (KBr) ν: 3294, 2956, 2926, 2230, 1648, 1553, 1366, 1087, 1042, 802, 730 cm^{-1}. ^1H NMR (300 MHz, $CDCl_3$) δ: 1.18–1.50 (m, 2H), 1.94 (m, 1H), 1.98 (s, 3H), 2.13 (m, 1H), 3.60 (dt, 1H, *J* = 1.5, 12.0 Hz), 4.02–4.15 (m, 3H), 5.37 (d, 1H, *J* = 6.8 Hz), 6.14 (dd, 1H, *J* = 5.3, 15.8 Hz), 6.57 (d, 1H, *J* = 15.8 Hz), 7.18–7.40 (m, 5H). ^{13}C NMR (75 MHz, $CDCl_3$) δ: 169.4, 131.2, 130.3, 129.5, 128.3, 127.4, 126.1, 77.3, 66.6, 46.1, 38.9, 32.9, 23.2. LC-MS: *m*/*z*: (M + Na) 268. HR-MS calcd. for $C_{15}H_{19}NO_2Na$: 268.1313. Found: 268.1305.

e: *N*-[2-(1-naphthyl)tetrahydro-2*H*-4-pyranyl]acetamide

Pale yellow solid, mp 130–132 °C. IR (KBr) ν: 3294, 2956, 2926, 1648, 1553, 1366, 1087, 1042, 802, 730 cm^{-1}. ^1H NMR (300 MHz, $CDCl_3$) δ: 1.42–1.67 (m, 2H), 1.97 (s, 3H), 2.04 (m, 1H), 2.42 (m, 1H), 3.84 (dt, 1H, *J* = 2.2, 12.0 Hz), 4.24–4.38 (m, 2H), 5.12 (dd, 1H, *J* = 1.7, 11.3 Hz), 5.27 (d, 1H, *J* = 7.5 Hz), 7.42 (m, 3H), 7.79 (m, 4H). ^{13}C NMR (75 MHz, $CDCl_3$) δ: 169.4, 137.4, 133.7, 130.2, 128.8, 128.1, 126.1, 125.5, 125.4, 123.1, 122.9, 75.9, 67.2, 46.6, 39.7, 33.0, 23.4. LC-MS: *m*/*z*: (M + Na) 292. HR-MS calcd. for $C_{17}H_{19}NO_2Na$: 292.1313. Found: 292.1320.

f: *N*-[2-(3,4-dichlorophenyl)tetrahydro-2*H*-4-pyranyl]acetamide

Pale yellow solid. mp 110–112 °C. IR (KBr) ν: 3316, 2945, 2852, 1643, 1543, 1376, 1077, 942, 812, 735 cm^{-1}. ^1H NMR (300 MHz, $CDCl_3$) δ: 1.23–1.55 (m, 2H), 1.95 (m, 1H), 1.99 (s, 3H), 2.22 (m, 1H), 3.67 (dt, 1H, *J* = 2.2, 12.0 Hz), 4.07–4.23 (m, 2H), 4.38 (dd, 1H, *J* = 1.7, 11.3 Hz), 5.34 (d, 1H, *J* = 7.5 Hz), 7.24 (m, 3H). ^{13}C NMR (75 MHz, $CDCl_3$) δ: 169.8, 131.7, 131.2, 130.4, 130.2, 127.7, 124.9, 77.0, 66.8, 46.2, 40.4, 32.3, 23.2. LC-MS: *m*/*z*: (M + Na) 311. HR-MS calcd. for $C_{13}H_{15}Cl_2NO_2Na$: 310.0377. Found: 310.0380.

g: *N*-[2-(3,4,5-trimethoxyphenyl)tetrahydro-2*H*-4-pyranyl]acetamide

Yellow solid, mp 210–212 °C. IR (KBr) ν: 3296, 2944, 2936, 1648, 1548, 1376, 1078, 1042, 814, 720 cm^{-1}. ^1H NMR (300 MHz, $CDCl_3$) δ: 1.32 (q, 1H, *J* = 12.4 Hz), 1.38 (dq, 1H, *J* = 4.5, 12.4 Hz), 1.93 (s, 3H), 2.06 (ddq, 1H, *J* = 12.6, 4.5, 2.2 Hz), 2.12 (ddt, 1H, *J* = 12.6, 4.5, 2.2 Hz), 3.63 (dt, 1H, *J* = 2.4, 12.2 Hz), 3.77 (s, 9H), 4.06 (m, 1H), 4.11 (m, 1H), 4.32 (dd, 1H, *J* = 2.0, 11.3 Hz), 5.30 (d, 1H, *J* = 7.5 Hz), 7.15–7.26 (m, 2H). ^{13}C NMR (75 MHz, $CDCl_3$) δ: 169.2, 153.0, 137.4, 137.1, 102.7, 78.3, 68.1, 66.2, 60.7, 55.9, 42.9, 35.2, 23.2. LC-MS: *m*/*z*: (M + Na) 332. HR-MS calcd. for $C_{16}H_{23}NO_5Na$: 332.1473. Found: 332.1484.

h: *N*-[2-(3-nitrophenyl)tetrahydro-2*H*-4-pyranyl]acetamide

Yellow solid, mp 188–190 °C. IR (KBr) ν: 3308, 2956, 2926, 1648, 1625, 1515,1456, 1102, 1032, 812, 726 cm^{-1}. ^1H NMR (300 MHz, $CDCl_3$) δ: 1.22 (q, 1H, *J* = 12.3 Hz), 1.44 (dq, 1H, *J* = 4.4, 12.3 Hz), 1.95 (s, 3H), 2.20 (ddq, 1H, *J* = 12.3, 4.5, 2.4 Hz), 2.26 (ddt, 1H, *J* = 12.3, 4.5, 2.3 Hz), 3.67 (dt, 1H, *J* = 1.8, 12.0 Hz), 4.12 (m, 1H), 4.20 (m, 1H), 4.49 (dd, 1H, *J* = 2.0, 11.2 Hz), 5.23 (d, 1H, *J* = 7.0 Hz), 7.50–8.08 (m, 4H). ^{13}C NMR (75 MHz, $CDCl_3$) δ: 169.4, 148.2, 144.0, 131.7, 129.1, 122.3, 120.5, 77.1, 66.9, 46.1, 40.4, 32.2, 23.2. LC-MS: *m*/*z*: (M + Na) 287. HR-MS calcd. for $C_{18}H_{26}O_2Na$: 287.1007. Found: 287.1010.

i: *N*-(6-oxaspiro[4.5]dec-9-yl)acetamide

Light yellow solid, mp 112–114 °C. IR (KBr) ν: 3335, 2954, 2922, 2851, 1632, 1536, 1367, 1206, 1083, 821, 743 cm^{-1}.^1H NMR (200 MHz, $CDCl_3$) δ: 1.24–1.75 (m, 12H), 1.87 (s, 3H), 3.45–3.71 (m, 2H), 3.91 (m, 1H), 5.81 (d, 1H, *J* = 8.0 Hz). ^{13}C NMR ($CDCl_3$, 75 MHz) δ: 23.1, 24.5, 33.1, 41.1, 42.1, 44.3, 61.0, 83.9, 169.2 ppm. LC-MS: *m*/*z* (%): (M + H^+) 198. HR-MS calcd. for $C_{11}H_{20}NO_2$: 198.1494. Found: 198.1505.

j: *N*-[1-oxaspiro[5.5]undec-4-yl]acetamide

Colourless solid, mp 148–150 °C. IR (KBr) ν: 3350, 2954, 2922, 2851, 1632, 1536, 1367, 1206, 1083, 821, 743 cm^{-1}. ^1H NMR (300 MHz, $CDCl_3$) δ: 1.20–1.71 (m, 12H), 1.85 (dq, 1H *J* = 4.6, 12.0 Hz), 1.93 (s, 3H), 2.04 (ddq, 1H, *J* = 12.0, 4.4, 2.2 Hz), 3.63 (dt, 1H, *J* = 2.2, 12.0 Hz), 3.68 (m, 1H), 4.11 (m, 1H), 5.10 (d, 1H, *J* = 6.7 Hz). ^{13}C NMR (75 MHz, $CDCl_3$) δ: 169.3, 138.4, 137.2, 129.0, 125.6, 78.5, 66.9, 46.4, 40.6, 32.8, 23.4, 21.0. LC-MS: *m*/*z* (%): (M + Na) 234. HR-MS calcd. for $C_{12}H_{21}NO_2Na$: 234.1469. Found: 234.1476.

k: *N*-[9-phenyl-1-oxaspiro[5.5]undec-4-yl]acetamide

Colourless solid, mp 172–174 °C. IR (KBr) ν: 3434, 3320, 2926, 2860, 1645, 1543, 1446, 1375, 1078, 971, 759, 701 cm^{-1}. ^1H NMR (200 MHz, $CDCl_3$) δ: 1.13–1.38 (m, 3H), 1.32–1.77 (m, 6H), 1.84–1.98 (m, 5H), 2.39–2.55 (m, 2H), 3.64 (dt, 1H, *J* = 2.2, 12.0 Hz), 3.77 (ddd, 1H, *J* = 1.5, 5.2, 12.0 Hz), 4.15 (m, 1H), 5.58 (d, 1H, *J* = 7.5 Hz), 7.08–7.25 (m, 5H). ^{13}C NMR (75 MHz, $CDCl_3$) δ: 169.3, 146.9, 128.1, 126.7, 125.7, 71.8, 59.3, 43.9, 43.5, 42.4, 39.8, 33.0, 29.4, 28.6, 28.0, 23.3. LC-MS: *m*/*z* (%): (M + Na) 310. HR-MS calcd. for $C_{18}H_{25}NO_2Na$: 310.1782. Found: 310.1788.

l: *N*-(2-ethyltetrahydro-2*H*-4-pyranyl)-2-phenylacetamide

Light yellow solid, mp 90–92 °C. IR (KBr) ν: 3434, 3320, 2926, 2860, 1645, 1543, 1446, 1375, 1078, 971, 759, 701 cm^{-1}. ^1H NMR (200 MHz, $CDCl_3$) δ: 1.13–1.38 (m, 3H), 1.32–1.77 (m, 6H), 1.84–1.98 (m, 5H), 2.39–2.55 (m, 2H), 3.64 (dt, 1H, *J* = 2.2, 12.0 Hz), 3.77 (ddd, 1H, *J* = 1.5, 5.2, 12.0 Hz), 4.15 (m, 1H), 5.58 (d, 1H, *J* = 7.5 Hz), 7.08–7.25 (m, 5H). ^{13}C NMR (75 MHz, $CDCl_3$) δ: 179.6, 134.6, 130.8, 128.2, 127.0, 76.5, 66.4, 46.1, 38.1, 32.9, 28.9, 23.3, 9.6. LC-MS: *m*/*z* (%): (M + Na) 270. HR-MS calcd. for $C_{18}H_{25}NO_2Na$: 270.1469. Found: 270.1478.

m: *N*-(2-cyclohexyltetrahydro-2*H*-4-pyranyl)-2,2-dimethylpropanamide

Colourless solid, mp 136–138 °C. IR (KBr) ν: 3434, 3320, 2926, 2860, 1645, 1543, 1446, 1375, 1078, 971, 759, 701 cm^{-1}. ^1H NMR (300 MHz, $CDCl_3$) δ: 1.13–1.38 (m, 3H), 1.32–1.77 (m, 6H), 1.84–1.98 (m, 5H), 2.39–2.55 (m, 2H), 3.64 (dt, 1H, *J* = 2.2, 12.0 Hz), 3.77 (ddd, 1H, *J* = 1.5, 5.2, 12.0 Hz), 4.15 (m, 1H), 5.58 (d, 1H, *J* = 7.5 Hz), 7.08–

© 2008 NRC Canada

7.25 (m, 5H). ^{13}C NMR (75 MHz, $CDCl_3$) δ: 177.7, 80.9, 66.6, 46.2, 35.5, 33.1, 28.8, 27.4, 26.4, 26.1, 26.0, 25.3. LC-MS: *m/z* (%): (M + Na) 290. HR-MS calcd. for $C_{18}H_{25}NO_2Na$: 290.2095. Found: 290.2089.

n: 2-cyclohexyl-4-phenylcarboxamidotetrahydro-2*H*-pyran

Pale brown solid, mp 112–114 °C. IR (KBr) ν: 3434, 3320, 2926, 2860, 1645, 1543, 1446, 1375, 1078, 971, 759, 701 cm^{-1}. ^{1}H NMR (200 MHz, $CDCl_3$) δ: 1.13–1.38 (m, 3H), 1.32–1.77 (m, 6H), 1.84–1.98 (m, 5H), 2.39–2.55 (m, 2H), 3.64 (dt, 1H, *J* = 2.2, 12.0 Hz), 3.77 (ddd, 1H, *J* = 1.5, 5.2, 12.0 Hz), 4.15 (m, 1H), 5.58 (d, 1H, *J* = 7.5 Hz), 7.08–7.25 (m, 5H). ^{13}C NMR (75 MHz, $CDCl_3$) δ: 166.8, 134.4, 131.4, 128.4, 126.8, 80.9, 68.5, 46.8, 35.7, 35.4, 28.8, 26.1, 26.0, 25.2. LC-MS: *m/z* (%): (M + Na) 310. HR-MS calcd. for $C_{18}H_{25}NO_2Na$: 310.1782. Found: 310.1786.

o: *N*-[2-(4-bromophenyl)-6-cyclohexyltetrahydro-2*H*-4-pyranyl]acetamide

Pale yellow solid, mp 186–188 °C. IR (KBr) ν: 3278, 2923, 2848, 1643, 1553, 1488, 1369, 1154, 1085, 1010, 812 cm^{-1}. ^{1}H NMR (300 MHz, $CDCl_3$) δ: 0.95–1.32 (m, 5H), 1.12 (m, 1H), 1.24 (m, 1H), 1.49 (m, 1H), 1.63– 1.85 (m, 5H), 1.94 (s, 3H), 2.00 (ddt, 1H, *J* = 2.0, 4.2, 2.0 Hz), 2.16 (ddt, 1H, *J* = 12.0, 4.2, 2.0 Hz), 3.30 (ddd, 1H, *J* = 11.0, 6.2, 2.0 Hz), 4.11 (ddt, 1H, *J* = 4.4, 8.5, 12.0 Hz), 4.35 (dd, 1H, *J* = 1.4, 11.0 Hz), 5.23 (d, 1H, *J* = 7.3 Hz), 7.18 (d, 2H, *J* = 8.5 Hz), 7.41 (d, 2H, *J* = 8.5 Hz). ^{13}C NMR ($CDCl_3$, 75 MHz) δ: 23.4, 26.2, 26.5, 28.7, 34.8, 40.4, 42.8, 46.7, 77.5, 80.7, 121.0, 127.3, 131.3, 141.6, 169.4 ppm. LC-MS: *m/z* (%): (M + H$^+$) 381. HR-MS calcd. for $C_{19}H_{27}BrNO_2$: 380.1225. Found: 380.1234

p: *N*-(2-pentyl-6-phenyltetrahydro-2*H*-4-pyranyl)acetamide

Pale yellow solid, mp 164–166 °C. IR (KBr) ν: 3434, 3320, 2926, 2860, 1645, 1543, 1446, 1375, 1078, 971, 759, 701 cm^{-1}. ^{1}H NMR (300 MHz, $CDCl_3$) δ: 0.89 (t, 3H, *J* = 7.0 Hz), 0.98–1.64 (m, 10H), 1.94 (s, 3H), 2.02 (m, 1H), 2.19 (m, 1H), 3.53 (dt, 1H, *J* = 2.2, 12.0 Hz), 4.11 (m, 1H), 4.40 (m, 1H), 5.35 (d, 1H, *J* = 7.5 Hz), 7.14–7.33 (m, 5H). LC-MS: *m/z* (%): (M + Na) 312. HR-MS calcd. for $C_{18}H_{27}NO_2Na$: 312.1939. Found: 312.1944.

Acknowledgements

DNC, GGKSNK thank CSIR, New Delhi for the award of fellowships and also thank DST for the financial assistance under J.C. Bose fellowship scheme.

References

1. (*a*) J. Zhu and H. Bienayme. Multicomponent reactions. Wiley. Weinheim, Germany. 2005; (*b*) H.J. Prins. Chem. Weekbl. **16**, 1072 (1919); (*c*) D.R. Adams and S.P. Bhatnagar. Synthesis, 661 (1977); (*d*) S. Chandrasekhar and B.V.S. Reddy. Synlett, 851 (1998).
2. K.C. Nicolaou and E.J. Sorensen. Classics in total synthesis. VCH. Weinheim, Germany. 1996.
3. (*a*) Z.Y. Wei, J.S. Li, D. Wang, and T.H. Chan. Tetrahedron Lett. **28**, 3441 (1987); (*b*) F. Perron, and K.F. Albizati. J. Org. Chem. **52**, 4128 (1987); (*c*) Z.Y. Wei, D. Wang, J.S. Li, and T.H. Chan. J. Org. Chem. **54**, 5768 (1989); (*d*) L. Coppi, A. Ricci, and M. Taddei. J. Org. Chem. **53**, 911 (1988).
4. (*a*) J. Yang, G.S. Viswanathan, and C.J. Li. Tetrahedron Lett. **40**, 1627 (1999); (*b*) J. Yang and C.J. Li. Synlett, 717 (1999); (*c*) K.P. Chan and T.P. Loh. Tetrahedron Lett. **45**, 8387 (2004); (*d*) G. Sabitha, K.B. Reddy, M. Bhikshapathi, and J.S. Yadav. Tetrahedron Lett. **47**, 2807 (2006).
5. (*a*) G.S. Viswanathan, J. Yang, and C.J. Li. Org. Lett. **1**, 993 (1999); (*b*) P.O. Miranda, D.D. Diaz, J.I. Padron, M.A. Ramirez, and V.S. Martin. J. Org. Chem. **70**, 57 (2005); (*c*) J.S. Yadav, B.V.S. Reddy, T. Maity, and G.G.K.S.N. Kumar. Tetrahedron Lett. **48**, 7155 (2007); (*d*) J.S. Yadav, B.V.S. Reddy, T. Maity, and G.G.K.S.N. Kumar. Tetrahedron Lett. **48**, 8874 (2007); (*e*) M.S.R. Murty, K. Rajasekhar, V. Harikrishna, and J.S. Yadav. Heteroatom Chem. **19**, 104 (2008); (*f*) B. Sreedhar, V. Swapna, Ch. Sridhar, D. Saileela, and A. Sunitha. Syn. Commun. **35**, 1177 (2005).
6. M. Reiter, H. Turner, and V. Gouverneur. Chem. Eur. J. **27**, 7190 (2006).
7. (*a*) E.H. Al-Mutairi, S.R. Crosby, J. Darzi, J.R. Harding, R.A. Hughes, C.D. King, T.J. Simpson, R.W. Smith, and C.L. Willis. Chem. Commun. 835 (2001); (*b*) F. Perron and K.F. Albizati. J. Org. Chem. **52**, 4128 (1987); (*c*) O.L. Epstein, and T. Rovis. J. Am. Chem. Soc. **128**, 16480 (2006); (*d*) J.S. Yadav, B.V. Subba Reddy, G.G.K.S. Narayana Kumar, and M.G. Reddy. Tetrahedron Lett. **48**, 4903 (2007).
8. (*a*) J.S. Yadav, M.S. Reddy, P.P. Rao, and A.R. Prasad. Tetrahedron Lett. **47**, 4397 (2006); (*b*) J.S. Yadav, M.S. Reddy, and A.R. Prasad. Tetrahedron Lett. **47,** 4937 (2006); (*c*) J.S. Yadav, M.S. Reddy, and A.R. Prasad. Tetrahedron Lett. **47,** 4995 (2006); (*d*) J.S. Yadav, B.V. Subba Reddy, G.G.K.S. Narayana Kumar, and T. Swamy. Tetrahedron Lett. **48**, 2205 (2007); (*e*) J.S. Yadav, B.V. Subba Reddy, S. Aravind, G.G.K.S. Narayana Kumar, C. Madhavi, and A.C. Kunwar. Tetrahedron, **64**, 3025 (2008).
9. (*a*) T. Imamoto. Lanthanides in organic synthesis. Academic Press. London, UK. 1994. (*b*) G.A. Molander. Chem. Rev. **92**, 29 (1992).
10. (*a*) S. Kobayashi. Synlett 689 (1994); (*b*) S. Kobayashi. J. Synth. Org. Chem. Jpn. **53**, 370 (1995); (*c*) S. Kobayashi. Eur. J. Org. Chem. 15 (1999).
11. M.N. Leonard, L.C. Wieland, and R.S. Mohan. Tetrahedron **58**, 8373 (2002).
12. S. Repichet, A. Zwick, L. Vendier, C. Le Roux, J. Dubac. Tetrahedron Lett. **43**, 993 (2002).
13. (*a*) R.W. Alder, J.N. Harvey, and M.T. Oakley. J. Am. Chem. Soc. **124**, 4960 (2002); (*b*) J. Ramesh, S.D. Rychnovsky. Org. Lett. **8**, 2175 (2006); (*c*) U. Biermann, A. Lutzen, and J.O. Metzger. Eur. J. Org. Chem. 2631 (2006).

© 2008 NRC Canada

Mass spectrometric detection of proteins in non-aqueous media — The case of prion proteins in biodiesel

Michelle D. Douma, Gina M. Kerr, R. Stephen Brown, Bernd O. Keller, and Richard D. Oleschuk

Abstract: Limitations in efficient extraction, minimization of media interferences, and suitable sample preparation methods pose significant challenges to the successful detection of protein traces in non-aqueous media. Here we present a filtration method, employing filter disks with embedded C_8-modified silica particles, that allows the capture of proteins from non-aqueous sample volumes. The extraction process is followed by elution of the protein from the filter disk and by either direct mass spectrometric detection or tryptic digestion followed by peptide mapping and MS/MS fragmentation of protein-specific peptides. The method is applied to spiked biodiesel samples for the detection of prion proteins. The tryptic peptide with sequence YPGQGSPGGNR is specific for prion proteins and can be used for unambiguous identification. The developed extraction method has the potential application to be used for large-scale testing of protein impurities in non-aqueous media, for instance as a safety and quality control tool in the animal tallow-based biodiesel production process.

Key words: protein detection, MALDI, non-aqueous media, filtration

Résumé : Les limitations dans l'extraction efficace, la minimisation des interférences des milieux et les méthodes appropriées de préparations des échantillons présentent des défis importants lorsqu'on veut détecter avec succès la présence de traces de protéines dans des milieux non-aqueux. Dans ce travail, on propose une méthode de filtration dans laquelle on utilise des disques du filtre dans lesquels des particules de silice modifiées avec C_8 sont implantées qui permettent de capturer les protéines à partir des volumes d'échantillons non-aqueux. Le processus d'extraction est suivi d'une élution de la protéine à partir du disque du filtre et par une détection soit directe par spectrométrie de masse ou par une digestion tryptique suivie d'une cartographie des peptides et une fragmentation SM/SM des peptides spécifiques pour une protéine. On a appliqué la méthode à des échantillons de biodiésel trafiqués pour la détection des protéines de prion. Le peptide tryptique comportant la séquence YPGQGSPGGNR est spécifique pour les protéines de prion et peut être utilisé pour une identification non ambiguë. La méthode d'extraction développée possèdel'application potentielle d'être utilisée pour évaluer à une grande échelle les impuretés de protéine dans un milieu non-aqueux, par exemple, comme outil de contrôle de la qualité et de la sécurité dans le processus de production de biodiésel à base suif d'animal.

Mots-clés : détection de protéine, "MALDI", milieu non-aqueux, filtration.

[Traduit par la Rédaction]

Introduction

Proteomics focuses on the identification and quantitation of protein species from a variety of biological matrices such as blood, urine, or cellular and tissue samples (1). As a result, most analysis and synthetic protocols have been developed and optimized to examine and determine proteins and peptides stemming from aqueous samples (2). Mass spectrometry (MS) has often become the detection method of choice because of its ability to provide precise molecular mass information for the proteins of interest. In combination with proteolytic digestion strategies, peptide mapping, and peptide fragmentation (MS/MS), mass spectrometry can provide unambiguous protein identification (1).

With increasing interest in the detection of proteinaceous impurities in pharmaceutical production processes (3), advancements of biocatalysis in non-aqueous systems (4), and the proliferation of fuels derived from biomass sources (5), there is an evolving need to develop novel protein detection and quantification methods that are effective for the associated non-aqueous matrices. An important example is the potential prion protein contamination in biodiesel produced from animal-based sources such as tallow (5). Transmissible

Received 3 March 2008. Accepted 21 April 2008. Published on the NRC Research Press Web site at http://canjchem.nrc.ca on 18 June 2008.

M.D. Douma, G.M. Kerr, R.S. Brown, B.O. Keller,[1] R.D. Oleschuk.[2] Department of Chemistry, Queen's University, Kingston, ON K6L 3N6, Canada.

[1]Present address: University of British Columbia, Dept. Pathology and Laboratory Medicine, Child & Family Research Institute, Vancouver, BC V5Z 4H4, Canada.
[2]Corresponding author (e-mail: oleschuk@chem.queensu.ca).

 doi:10.1139/V08-083 © 2008 NRC Canada

spongiform encephalopathy (TSE), a fatal disease that affects the nervous system, has become a growing concern, especially in the cattle industry where the disease is referred to as bovine spongiform encephalopathy (BSE) or mad cow disease (5). It is hypothesized that prion proteins are the causative agent of TSE (6). A normal form of the protein (PrP^C) is thought to misfold into an amyloidogenic beta-sheet structure that has the ability to convert PrP^C into the infective prion protein (PrP^{Sc}) (6). There is concern that biodiesel produced from specified risk materials (SRMs), including brain, inner organs, or spinal cord, could be a source of infectious prion proteins (5). For inactivation of infectious proteins to occur, both high temperatures and high pressures are needed. Several recent reports have stated that rendering procedures and biodiesel production processes are safe and pose a negligible risk in terms of TSE infectivity, even under worst-case scenarios (7–9). Nevertheless, one report also points out that because of the variability of current rendering and biodiesel production processes, individual assessments for each specific case may be necessary (9). Further scientific research into the matter is desirable, both to add additional levels of safety (5) and to expand our knowledge of protein stability outside their natural environments, for example in non-aqueous media (2).

Bioassays are currently the preferred method for detection of TSE infectivity in biological tissues or organisms (10). Samples are administered to test animals via injection or oral intake. After an incubation period or the onset of clinical signs of the disease, the host animal is euthanized and the brain is examined for TSE. A drawback to this testing method is the long incubation time of up to 30 months. The use of transgenic mice has shortened analysis times to 150–196 days (11). However, biodiesel cannot be directly administered in such bioassays because of its toxicity to the test animals. Furthermore, the average shelf life of biodiesel is in the range of 6–8 months (12), and thus any meaningful tests require detection methods with a shorter turnaround time. Other detection methodologies that rely on affinity interactions such as Western blot analysis can also be ruled out for direct biodiesel monitoring because of organic matrix interferences that would alter affinity binding either through solvent interactions or denaturation (10). In addition, the presence of organic solvents can affect the activity of proteins. For instance, enzyme activity has been enhanced in the presence of organic solvents (13), but over the time of several hours can also decrease enzyme activity (14). Thus, even if organic solvents were not an incompatible matrix for the desired analysis techniques, the tests could provide inconclusive results due to altered protein interactions in organic solvents.

The detection of prion proteins in biodiesel has been carried out using a combination of chloroform and methanol extraction, gel electrophoresis separation, and immunoassay detection (8). Here, we present a novel approach using biodiesel filtration through special filter disks combined with matrix-assisted laser desorption/ionization (MALDI) mass spectrometry. The use of a C_8-embedded membrane to filter and preconcentrate biodiesel samples is attractive due to its applicability for a wide variety of proteins and for different sample media, both aqueous and non-aqueous. Another feature is the ability to filter large sample volumes (15), a major advantage compared with tedious liquid–liquid extraction methods applicable only to small sample batches.

Previously, membranes such as polyurethane (PU) (16), poly(tetrafluoroethylene) (17), nitrocellulose (18), polyethylene (19), polyvinyldifluoride (PVDF) (20), and nylon (21) have been used as sample supports for direct analysis of proteins by MALDI-MS. Proteins are adsorbed to the membrane surface and washing steps can be incorporated without significant loss of protein. Depending on the nature and abundance of the proteins, it may be possible to perform MALDI-MS directly on the disk. This enables sensitive analysis methods optimized for aqueous samples to be employed (e.g., MS and Western blot).

In the present study, we developed an extraction technique using a mixture of acetonitrile, non-ionic detergent, and water that allows for PrP to be removed from an extraction filter disk containing C_{18}- or C_8-modified particles after filtration of a spiked biodiesel sample. This extraction procedure has proven effective for other proteins, including bovine serum albumin (BSA) and cytochrome c, and can also be applied for filtrations involving water or isooctane. Subsequent tryptic digestion of the extracted prion protein either on-disk or after re-suspension in water yields a peptide with a prion-specific sequence YPGQGSPGGNR, allowing unambiguous identification via MS/MS analysis. This method should be generally applicable for any large scale testing for proteinaceous impurities both in aqueous and non-aqueous media.

Experimental

Reagents and materials

Methanol (MeOH), 2-propanol, and acetonitrile (ACN) (all ACS reagent grade) were obtained from Fisher Scientific (Fair Lawn, New Jersey, USA). Bovine serum albumin (BSA), horse heart cytochrome c, bovine trypsin (TPCK treated for deactivation of chymotrypsin activity), 2,2,4-trimethylpentane (isooctane), and octyl-β-D-glycopyranoside (*n*-OGP) were purchased from Sigma-Aldrich (Oakville, Ontario, Canada). Ammonium bicarbonate (bioChemika Ultra), sinapic acid, and α-cyano-4-hydroxycinnamic acid (HCCA) were obtained from Fluka (Buchs, Switzerland). Trifluoroacetic acid (TFA) was purchased from Sigma-Aldrich Chemicals (Milwaukee, Wisconsin, USA). Glacial acetic acid (98%) was obtained from Fisher Scientific (Ottawa, Ontario, Canada). All chemicals were used without further purification.

Biodiesel from animal and plant sources was donated from Environment Canada (Ottawa, Ontario, Canada). A refolded murine (of the rat and mouse family) prion protein (PrP) was expressed according to the protocol of Hornemann et al. (22) and received from the Saskatchewan Research Council (SRC, Saskatoon, Saskatchewan, Canada). The PrP stock solution was received at a concentration of 0.725 mg/mL in *tris*-acetate buffer (pH 6.5) and was stored at –80 °C. Refolded PrP, according to the protocol of Jackson et al. (3), resulted in the β-folded murine prion protein (PrP^*), which was received from the SRC as a precipitate and stored at –80 °C. A MilliQ apparatus (Millipore, Bedford, Massachusetts, USA) was used to purify water (18.2 MΩ cm). 3M Empore extraction disks (47 mm diameter) em-

© 2008 NRC Canada

bedded with either octyl (C_8) or octadecyl (C_{18}) coated absorbent particles were purchased from Fisher Scientific (Ottawa, Ontario, Canada). C_{18} and C_4 ZipTips were from Millipore (Bedford, Massachusetts, USA).

Filtration and whole protein extraction

Filtrations were performed under vacuum by air aspiration using a regular laboratory filtration apparatus. Either 3M Empore C_8 or C_{18} extraction disks were used. Proteins studied by filtration included BSA as a surrogate and PrP. Prior to filtration, the medium of interest was spiked with protein. To help the solubility of the PrP stock solution in biodiesel, a 1:10 solution of PrP stock and methanol was used for spiking. The biodiesel solution was continuously stirred or agitated during the filtration process to ensure uniform dispersion across the extraction disk. After filtration of PrP spiked media such as water, isooctane, or biodiesel, a piece of dry extraction disk, approximately 2 mm × 2 mm, was immersed in a 1:1 solution of acetonitrile and 0.5% *n*-OGP in deionized H_2O to remove the protein from the disk for subsequent MALDI analysis. The extraction was performed for a period of 20 to 30 min while sonicating. It should be noted that initial attempts to employ a Millipore filtration unit (Labscale TFF System, Model #XX42LSS11) failed. Unknown corrosive ingredients present in the biodiesel partially dissolved plastic parts of this equipment and rendered it unusable. As a consequence, any contact of biodiesel with plastic laboratory equipment was avoided.

Protein digestion — trypsin

Tryptic digests in solution were performed using a modified protocol from that of Qin et al. (7). A 1:2 solution of protein stock in 0.1 mol/L NH_4HCO_3 was prepared to a total volume of 15 μL. A 1 μL aliquot of a 1 mg/mL solution of trypsin was added to the vial, and the vial was incubated in a Fisher Scientific dry bath incubator (Ottawa, Ontario) at 37 °C for 2 h. Tryptic digestions were also performed directly on extraction disks. Samples of biodiesel spiked with proteins were filtered through a C_8 or C_{18} extraction disk. After the disk was dried, a piece of extraction disk was cut and spotted with 1 μL of a 1:10 solution of trypsin (1 μg/μL) and 0.1 mol/L NH_4HCO_3. The piece of extraction disk was then placed into a weigh boat inside a plastic container. A wet sponge was also placed into the container to minimize evaporation. The container was placed on top of an incubator for 30 min at 37 °C.

Another approach was to submerge pieces of extraction disks in a 1:10 solution of trypsin (1 μg/μL) and 0.1 mol/L NH_4HCO_3. The solution with the extraction disk was then incubated for 2 h at 37 °C, and the supernatant analyzed for peptides.

Microwave-assisted acid digestion of PrP

Microwave-assisted acid digestion for PrP in solution was accomplished using a modified protocol adopted from Zhong et al. (23). A 50 μL sample of PrP stock solution was concentrated under nitrogen to approximately 10 μL, and 5 μL of 98% TFA was added. The solution was then sealed with Teflon tape in a 1.5 mL propylene Eppendorf vial and microwaved on high for 10 min in a conventional microwave oven (max. 700 watts). A minimal volume (<20 μL) was critical to withstand the vapour pressure created during the microwaving process. A container of water was placed beside the Eppendorf vial of protein and acid to absorb any excess microwave energy (23). After the TFA digest was performed, the microwave was unplugged and cooled to room temperature before opening. The vial was then carefully opened in a fume hood and 0.1 mol/L NH_4HCO_3 was added to neutralize the acid.

Sample preparation for mass spectrometry was either done with protein–peptide solutions, extracts, or directly from extraction disks. In the latter case, the small pieces of the disks were carefully glued onto MALDI target plates using 3M spray adhesive.

Mass spectrometric analysis of whole proteins

For exact molecular weight determination, a 10 μL aliquot of the PrP stock solution was purified using a C_4 ZipTip and eluted with sinapic acid solution according to the protocol of Dai et al. (24). For whole protein detection from C_8 or C_{18} extraction disks, small pieces of the extraction disk (~2 mm × 2 mm) were placed into an Eppendorf tube and extracted with a 1:1 solution of acetonitrile and 0.5% *n*-OGP. This solution was then further prepared, employing a novel sensitive three-layer matrix preparation method reported by Keller and Li (25).

MALDI-TOF analysis was performed on a Voyager DE STAR biospectrometry workstation (Applied Biosystems, Framingham, Massachusetts, USA) in positive linear mode. This instrument is equipped with a 337 nm nitrogen laser. Several hundred laser shots were summed for spectra collection. BSA and cytochrome c were used as standard proteins for calibration.

Mass spectrometric analysis of protein digests

Peptide mixtures resulting from protein digests were first purified and concentrated employing a C_{18} ZipTip and further prepared according to the two-layer matrix preparation method of Dai et al. (24). Peptide maps were obtained on the above-mentioned Voyager instrument in positive reflectron mode. MS/MS analysis of specific peptides was done either with a post-source decay method on the Voyager instrument or from solution after purification with a C_{18} ZipTip and elution with a 70% MeOH and 0.1% acetic acid solution, by employing a static nanospray setup on a QSTAR XL QqTOF mass spectrometer (Applied Biosystems, MDS-Sciex, Toronto, Ontario, Canada).

Results and discussion

PrP characterization

PrP was expressed according to the protocol by Hornemann et al. (22). The PrP sequence is shown in Fig. 1 (209 amino acid residues). The addition of a serine residue at the C-terminus is intended to minimize proteolytic degradation, and the protein contains one disulfide linkage between its two cysteine residues. From the above sequence, the average mass of the protein with all methionine residues oxidized as ensured by the protocol (22) is calculated to be 23 115 Da. Figure 2 shows the mass spectrum of the whole murine PrP protein. The signals at *m*/*z* 23 113 and at 11 553 result from the singly and doubly protonated ions of PrP, re-

© 2008 NRC Canada

Fig. 1. Sequence of murine PrP. All methionies (**M**) are oxidized and a disulfide linkage exists between **C**ys157 and **C**ys192. The theoretical average molecular mass is 23 115 Da.

```
1   KKRPKPGGWN TGGSRYPGQG SPGGNRYPPQ GGGTWGQPHG GGWGQPHGGG  50
51  WGQPHGGGWG QPHGGGWGQG GGTHNQWNKP SKPKTNMKHM AGAAAAGAVV  100
101 GGLGGYMLGS AMSRPMMHFG NDWEDRYYRE NMNRYPNQVY YRPVDQYNNQ  150
151 NNFVHDCVNI TIKQHTVTTT TKGENFTETD IKIMERVVEQ MCTTQYQKES  200
201 QAYYDGRRS
```

Fig. 2. MALDI-TOF mass spectrum of PrP after (ZipTip) purification. Below *m*/*z* 11 000 there are a several protein fragments or contaminating proteins observable.

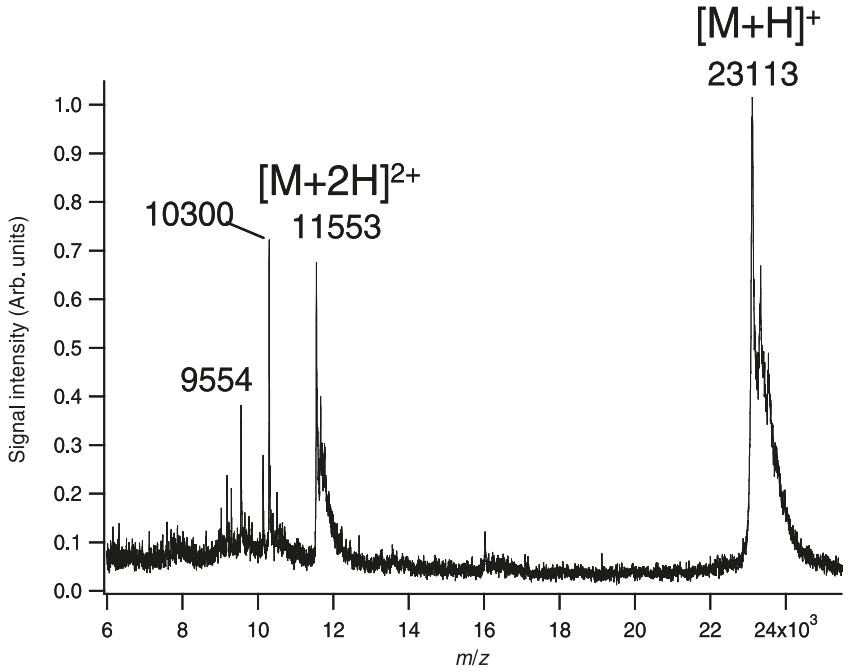

spectively. The observed signal at 23 113 Da is within 3 Da of the calculated *m*/*z* for the singly charged ion (*m*/*z* 23 116) and within the expected accuracy of the instrument at this mass range for external calibration (150 ppm or 3.5 Da). Several protein fragments or protein contaminants below *m*/*z* 11 000 are also observed.

Tryptic digestion of PrP (both unfolded and refolded forms) directly from the stock solutions yielded two peptides with sequence YYR (127–129; *m*/*z* 501) and YPGQGSPGGNR (16–26; *m*/*z* 1089), respectively. The smaller peptide with sequence YYR has little diagnostic value because of its short sequence, which is not specific for prion proteins. The YPGQGSPGGNR peptide (*m*/*z* 1089) is unique for prion proteins and is a conserved sequence found in more than 50 different species (MASCOT sequence search at www.matrixscience.com), such as bovine, deer, and sheep. Since this sequence is specific to the prion protein it can be used as a biomarker for unambiguous identification of prion proteins (26, 27). The YPGQGSPGGNR peptide is located very close to the protein's N-terminus, even before the four octapeptide repeat units involved in copper binding (28). The N-terminal region up to amino acid residue 121 is the so-called non-structured, flexible or "random coil-like" region of the protein and is not involved in alpha-helix or beta-sheet formation (29). Circular dichroism (CD) and fourier-transform infrared (FTIR) experiments have shown that PrP^{C} contains 40% alpha-helix and minimal beta-sheets, whereas PrP^{Sc} contains 30% alpha-helix and 45% beta-sheets (30, 31). The increased beta-sheets present in PrP^{Sc} presumably do not inhibit enzymatic digestion where this peptide is located. Figure 3 shows an electrospray MS/MS fragmentation spectrum of this peptide.

Microwave-assisted acid digestion also yielded specific peptide signals for PrP in the mass range >3000 Da, as is shown in Fig. 4. However, the spectra were generally dominated by several peptides in the mass range below 3000 Da that possibly originated from the protein contaminants in the PrP stock solutions. The observed peptides specific for PrP are in a mass range too high for efficient MS/MS fragmentation (> *m*/*z* 3000) and thus have limited suitability for specific PrP detection in complex mixtures. In addition, the required protein amounts for effective microwave-assisted digestion are in the microgram range (23), thus limiting this method's employability in sensitive protein detection. Microwave-assisted acid digestion experiments with filter disk pieces spiked with prion protein solution were not successful.

Filtration of spiked biodiesel, extraction of filter disks, and protein analysis

Although direct analysis of protein on the extraction disk is possible, the analysis sensitivity is improved when protein is extracted back into solution. With the extract, a recently developed three-layer matrix preparation method for MALDI-MS can be applied that allows the detection of pro-

© 2008 NRC Canada

Fig. 3. Electrospray MS/MS spectrum of the peptide with sequence YPGQGSPGGNR with *m*/*z* for $[M + 2H]^{2+}$ = 545.3.

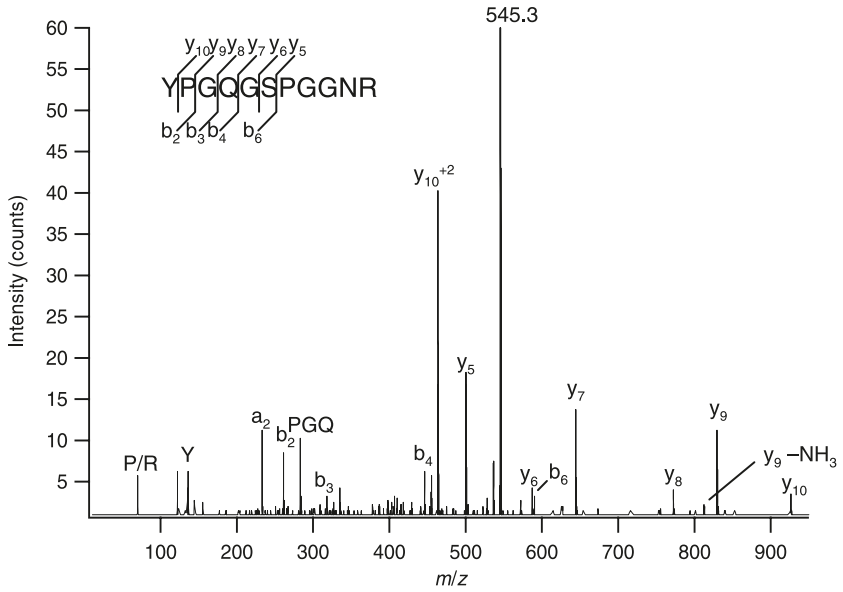

Fig. 4. MALDI-TOF mass spectrum of a microwave-assisted acid (TFA) digest of PrP. The resulting peptides specific for PrP are shown in the insert in the upper right corner. All the arrows indicate a loss of a glycine residue (57 Da), which is typical for TFA digests (23). Peaks below *m*/*z* 2600 are probably from digested contaminant protein fragments.

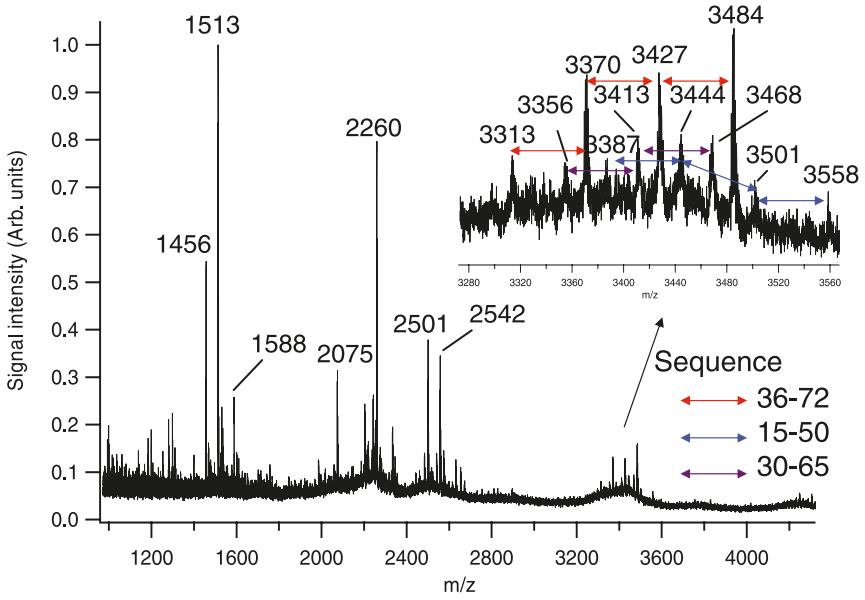

teins in low nanomolar concentrations (25). Furthermore, extracting the protein back into solution provides a medium that is compatible, after removal of acetonitrile, for other analysis techniques, including enzymatic digestion and immunoassay. After filtration of a protein spiked sample, the extraction method of 1:1 acetonitrile and *n*-OGP effectively removed the protein from the extraction disk.

To illustrate that the majority of the PrP was transferred to the extraction disk, a water-spiked sample was analyzed before and after filtration. PrP was detected in the water sample as well as after extraction from the disk, however PrP was not detected in the filtrate (data not shown). The acetonitrile and *n*-OGP extraction procedure is applicable after the filtration of a variety of media including water, isooctane (data not shown), and biodiesel. The mass spectra of whole PrP from the extract of a C_8-disk used to filter 25 mL of a 60 nmol/L PrP biodiesel sample is shown in Fig. 5. Extraction disks with embedded C_8-modified silica particles were found to be superior in terms of protein recovery for biodiesel filtrations and were thus used for all subsequent analysis. This observation is consistent with Engelhardt and Mueller's 1984 report in which C_8-modified bonded phase showed optimal protein recovery in reverse phase high performance liquid chromatography analysis (32).

Difficulties were encountered during the filtration process with older batches of biodiesel that presumably became contaminated with bacterial growth over time. As a result, if the biodiesel was aged a pre-filtration step had to be used to re-

© 2008 NRC Canada

Fig. 5. MALDI-TOF mass spectrum of the extract of PrP from a C_8 extraction disk used to filter 25 mL of biodiesel containing PrP (60 nmol/L). Extraction performed in a 1:1 solution of ACN and 0.5% *n*-OGP for 20 min.

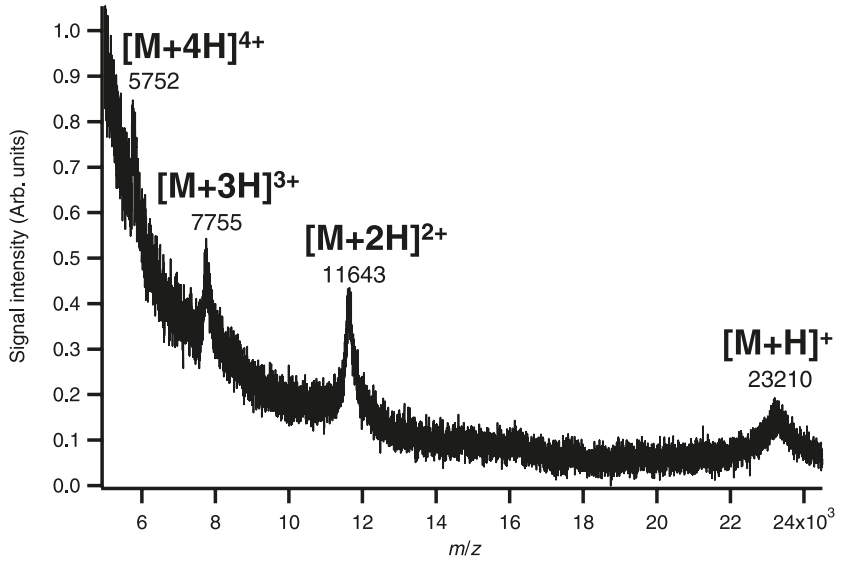

Fig. 6. MALDI-TOF mass spectrum achieved by post source decay to sequence the 1089 peptide achieved from a 2 h tryptic digest performed on a piece of C_8 extraction disk, used to filter 25 mL of biodiesel containing PrP (60 nmol/L). The sample was passed through a C_{18} ZipTip prior to analysis and eluted with HCCA matrix solution.

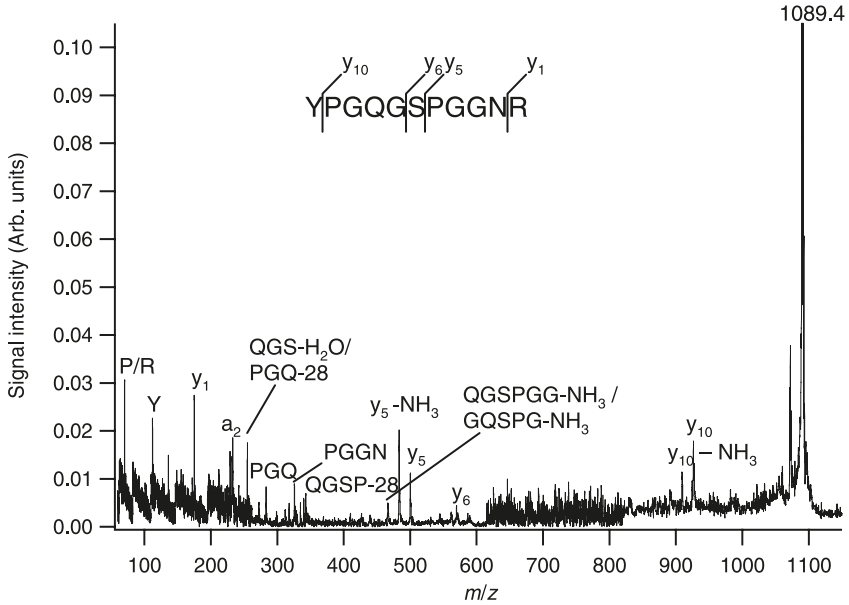

move any particulate interference. For applicability of this technique to large scale analysis of the biodiesel production process, the biodiesel samples should be analyzed within a few months of production because of their limited shelf life (12).

Digestion of proteins can be performed directly on the extraction disk after filtration of a protein spiked sample, and we successfully analyzed BSA and cytochrome c in such a manner (data not shown). For PrP, however, we found this approach not to be suitable, since this protein required a longer digestion time of more than 2 h and thus the trypsin solution dried up before the enzymatic digestion was complete. To circumvent this problem, after filtration a small piece of the extraction disk was immersed directly in a trypsin solution, and the resulting peptide mixture contained both the *m/z* 501 and 1089 peptides. The MS/MS of the 1089 peptide obtained from a tryptic digest of a piece of extraction disk used to filter 25 mL of a 60 nmol/L PrP–biodiesel sample is shown in Fig. 6. In this case, we chose to use MALDI post source decay for peptide fragmentation (as compared with nano-ESI employed for peptide marker screening in Fig. 3.), because of better sensitivity and compatibility with impurities. As can be seen from Fig. 6, this approach allows also for unambiguous PrP identification. These results confirm that PrP can be effectively extracted from biodiesel and unambiguously identified by MS/MS.

Our 25 mL biodiesel sample with 60 nmol/L PrP contains a total amount of ~60 μg PrP. The effective area of our filter

© 2008 NRC Canada

disk is approximately 960 mm^2 since only about 35 mm of its total 47 mm diameter is exposed to filtration solution. Assuming uniform distribution and complete capture of PrP on the extraction disk after the biodiesel filtration, approximately 250 ng (~10 picomole) of PrP is expected on a 2 mm × 2 mm (4 mm^2) piece of extraction disk. Considering potential losses during the filtration process and irreversible protein adsorption to glass surfaces as well as complications incurred by the complex biodiesel sample matrix, it is clear that this approach cannot match the 20–30 attomole detection limit achievable by direct analysis of a pure PrP standard (33). Nevertheless, the spiked amount of PrP is comparable to traditional initial extraction experiments performed for BSA as a carrier protein in lipid media (~1 μg BSA/mL) (8). The question if such a detection limit is adequate for "real" samples cannot be readily answered, since each application's requirements will differ and need individual comprehensive assessments. For applications where a more detailed method development is warranted and affordable, application of stable-isotope labeled standards and testing of dilution series will eventually establish the linear dynamic range and absolute detection limits. In this respect, it should be noted that the extraction disks and extracts obtained from our method allow transfer of the captured proteins to aqueous media and potentially allow employment of more sensitive and quantitative immunoassays (e.g. Western blot) and can also be used in bioassays for testing of infectivity.

Conclusions

The detection and characterization of proteinaceous impurities in non-aqueous media is a new emerging field and currently faces enormous challenges due to the lack of adequate methods. In our present studies, we successfully employed extraction disks with embedded C_8-modified silica particles to extract proteins from both aqueous and non-aqueous media. The ruggedness is demonstrated through the application of this method for a "difficult" protein (i.e. prion protein) in a corrosive medium (i.e. biodiesel), and thus this approach should be applicable to a wide range of potential samples where proteinaceous impurities are of interest. Mass spectrometry has proven to be an efficient detection tool for extracted proteins, and, in combination with enzymatic digestion, peptide extraction, and MS/MS, analysis allowed for unambiguous identification of the proteins. Although mass spectrometry is an invaluable tool in the method development process, current achievable detection limits might not always be sufficient in real world applications. However, the presented protein extraction method allows for recovery of the extracted proteins into aqueous media that also allow for ultrasensitive detection methods such as immunoassays. We anticipate that because of its ruggedness and simplicity, the general principle of this method should be easily adaptable to large-scale production processes in pharmaceutical or other industries, and it represents a realistic alternative to small-batch liquid-liquid extraction methods.

Acknowledgements

We thank Advanced Technologies & Fuels Canada, Natural Resources Canada, the Ontario Innovation Trust, the Canadian a Foundation for Innovation, the Natural Sciences and Engineering Research Council of Canada, and Queen's University for their funding. We also thank the Saskatchewan Research Council (Amy Friesen), Saskatoon, for providing the PrP samples and Environment Canada, Ottawa, for supplying the biodiesel.

References

1. D.C. Liebler. *In* Introduction to proteomics. Humana Press, Totowa, N.J., USA. 2002. Chaps. 1 and 2.
2. C.L. Stevenson. Curr. Pharm. Biotechnol. **1**, 165 (2000).
3. M. Swartz and I. Krull. LCGC North America, **25**, 1196 (2007).
4. N. Krieger, T. Bhatnagar, J.C. Baratti, A.M. Baron, V. M. de Lima, and D. Mitchell. Food Technol. Biotechnol. **42**, 279 (2004).
5. A. Baribeau, R. Bradley, P. Brown, J. Goodwin, U. Kihm, E. Lotero, D. O'Connor, M. Schuppers, and D. Taylor. *In* Biodiesel from specified risk material tallow: An appraisal of TSE risks and their reduction. Advanced Technologies and Fuels Canada, Ottawa, Canada. 2006. pp. 15–76.
6. S.B. Prusiner. Proc. Natl. Acad. Sci. U.S.A. **95**, 13363 (1998).
7. H. Mueller, L. Stitz, and D. Riesner. Eur. J. Lipid Sci. Technol. **108**, 812 (2006).
8. M. Mittelbach, B. Pokits, H. Mueller, M. Mueller, and D. Riesner. Eur. J. Lipid Sci. Technol. **109**, 79 (2007).
9. B. Seidel, M. Alm, R. Peters, W. Koerdel, and A. Schaeffer. Environ. Sci. & Pollut. Res. **13**, 125 (2006).
10. R.S. Brown, B.O. Keller, and R.D. Oleschuk. Detection of prion proteins and TSE infectivity in the rendering and biodiesel manufacture processes. Vol. 2. Advanced Technologies and Fuels Canada, Ottawa, Canada. 2006. pp. 1–17.
11. J. Castilla, A.A. Gutierrez, A. Brun, B. Pintado, M.A. Ramirez, B. Parra, D. Doyle, M. Rogers, F.J. Salguero, C. Sanchez, J.M. Sanchez-Vizcaino, and J.M. Torres. Arch. Virol. **148**, 677 (2003).
12. K.S. Tyson and R.L. McCormick. Biodiesel handling and use guide. Third ed. US Department of Energy Office of Scientific and Technical Information, Oak Ridge, TN, USA. September 2006. pp. 1–69. Available from www.nrel.gov./docsfy06osti/40555/pdf/ (accessed 17 February 2008).
13. B. Castillo, V. Bansal, A. Ganesan, P. Halling, F. Secundo, A. Ferrer, K. Griebenow, and G. Barletta. BMC Biotechnol. **6**, 51 (2006).
14. A.M. Klibanov. Nature (London), **409**, 241 (2001).
15. G. Hess. Chem. Eng. News. **85**, 35 (2007).
16. M.E. McComb, R.D. Oleschuk, D.M. Manley, L. Donald, and A. Chow. Rapid Commun. Mass Spectrom. **11**, 1716 (1997).
17. K.C. Hung, H. Ding, and B. Guo. Anal. Chem. **71**, 518 (1991).
18. J. Bai, M.G. Qian, Y. Liu, X. Liang, and D.M. Lubman. Anal. Chem. **67**, 1705 (1995).
19. J.A. Blackledge and A.J. Alexander. Anal. Chem. **67**, 843 (1995).
20. C. Chang, H. Liao, C. Juo, S. Chen, and Y. Chen. Anal. Chim. Acta, **556**, 237 (2006).
21. E.J. Zaluzec, D.A. Gage, J. Allison, and J.T. Watson. J. Am. Soc. Mass Spectrom. **5**, 230 (1994).
22. S. Hornemann, C. Korth, B. Oesch, R. Riek, G. Wider, K. Wuthrich, and R. Glockshuber. FEBS Lett. **413**, 277 (1997).
23. H. Zhong, S.L. Marcus, and L. Li. J. Am. Soc. Mass Spectrom. **16**, 471 (2005).
24. Y. Dai, R.M. Whittal, and L. Li. Anal. Chem. **71**, 1087 (1999).
25. B.O. Keller and L. Li. J. Am. Soc. Mass Spectrom. **17**, 780 (2006).

© 2008 NRC Canada

26. N.R. Deleault, B.T. Harris, J.R. Rees, and S. Supattapone. Proc. Natl. Acad. Sci. U.S.A. **104**, 9741 (2007).
27. N. Morel, O. Andreoletti, J. Grassi, and G. Clement. Rapid Commun. Mass Spectrom. **21**, 4093 (2007).
28. K. Qin, D. Yang, Y. Yang, M.A. Chishti, L. Meng, H.A. Kretzschmar, C.M. Yip, P.E. Fraser, and D. Westaway. J. Biol. Chem. **275**, 19121 (2000).
29. R. Riek, S. Hornemann, G. Wider, R. Glockshuber, and K. Wuthrich. FEBS Lett. **413**, 282 (1997).
30. K.M. Pan, M. Baldwin, J. Nguyen, M. Gasset, A. Serban, D. Groth, I. Mehlhorn, Z. Huang, R.J. Fletterick, and F.E. Cohen. Proc. Natl. Acad. Sci. U.S.A. **90**, 10962 (1993).
31. P. Pergami, H. Jaffe, and J. Safar. Anal. Biochem. **236**, 63 (1996).
32. H. Engelhardt and H. Mueller. Chromatographia, **19**, 77 (1984).
33. B. Onisko, I. Dynin, J.R. Requena, C.J. Silva, M. Erickson, and J.M. Carter. J. Am. Soc. Mass Spectrom. **18**, 1070 (2007).

© 2008 NRC Canada

Palladium-catalyzed aerobic alcohol oxidation supported by a new type of α-diimine ligands

Jin Zhou, Xiaoyan Li, and Hongjian Sun

Abstract: A series of new ionic sulfonated α-diimine ligands were prepared and employed as supporting ligands for the palladium-catalyzed aerobic alcohol oxidation. The electronic properties, rigidity, and steric hindrance of ligands have remarkable influences upon the catalytic activity of the palladium complexes. The best catalytic result could be achieved using ligand **9** with an electron-withdrawing sulfonyl substituent together with bulky groups (*iso*-propyl in 2,6-positions). This diimine/palladium-catalyzed system is highly efficient for the oxidation of various benzylic alcohols, and showed moderate yields for the secondary aliphatic alcohols and cyclic alcohols.

Key words: α-diimine, palladium, aerobic oxidation, alcohol.

Résumé : On a préparé une série de nouveaux ligands ioniques α-diimines sulfonées et on les a utilisés comme ligands de support pour des réactions d'oxydation aérobiques d'alcools catalysées par le palladium. Les propriétés électroniques, la rigidité et l'empêchement stérique des ligands influencent profondément l'activité catalytique des complexes du palladium. Le meilleur résultat catalytique a été obtenu en utilisant le ligand **9** qui porte un substituant électroaffinitaire sulfonyle avec des substituants volumineux, isopropyles, dans les positions 2 et 6. Ce système de diimine catalysée par le palladium est très efficace pour l'oxydation de divers alcools benzyliques et donne des rendements modérés avec les alcools aliphatiques ou cycliques secondaires.

Mots-clés : α-diimine, palladium, oxydation aérobique, alcool.

[Traduit par la Rédaction]

Introduction

The oxidation of alcohols to the corresponding aldehydes or ketones is one of the most important functional group transformations in organic synthesis. Recently, the use of molecular oxygen as terminal oxidant has received great attention for both economic and environmental benefits, and many highly efficient systems have been developed for catalytic aerobic alcohol oxidation using Fe (1), Ru (2–5), Co (6), Cu (7, 8), Mn (9), Ni (10), and Pd (11,12) catalysts or even a transitional-metal-free catalyst system(13). Homogeneous palladium catalysts are particularly effective for the oxidation of alcohols (14–24). Of these reports, the first significant breakthrough was reported by Peterson and Larock, who employed the $Pd(OAc)_2$/DMSO catalyst system for oxidation of a wide range of benzylic and allylic alcohols with molecular oxygen as the sole oxidant (25). Furthermore, the reported Uemura $Pd(OAc)_2$/pyridine system (26, 27), Sheldon's $Pd(OAc)_2$/phananthroline aqueous system (28), Sigman's $Pd(OAc)_2/NEt_3$ (29), and $Pd(OAc)_2$/*N*-heterocyclic carbene catalyst systems (30) are remarkable catalyst systems and could give a norm for the performance of new catalysts.

The mechanism of palladium-catalyzed aerobic oxidation has been comparatively studied (31–33). Recently, Stahl and co-workers reported a mechanistic study of $Pd(OAc)_2$/DMSO catalyst system (34) and indicated that oxidation of palladium(0) might be the turnover-limiting step. In contrast to the $Pd(OAc)_2$/DMSO catalyst system, Stahl's mechanistic studies of $Pd(OAc)_2$/pyridine catalyst system indicated a palladium(II) resting state with turnover-limiting oxidation of the alcohol substrate, which is similar to the other catalyst systems that employ nitrogen ligands (35, 36). An oxidase-style mechanism was proposed for the aerobic oxidation of alcohols (37, 38). The oxidation proceeds in two independent, sequential stages. Palladium(II) is the real oxidant for the oxidation of alcohol. The role of molecular oxygen is to oxidize the palladium(0) species to palladium(II). The ligands facilitate the activation of dioxygen by increasing the electron density on Pd(0). Experimental evidence, supporting this hypothesis, has been presented by Stahl and coworkers while examining olefin-substitution reactions with bathocuproine–Pd(0) complexes (39, 40).

Herein, we give attention to the famous diimine ligands family, which has been applied in many catalytic processes, such as the notable olefin polymerization (41, 42) and cross-coupling reactions (43, 44). We have synthesized a series of new α-diimine ligands and employed these ligands for the aerobic oxidation of alcohols. The catalytic efficiency of alcohol oxidation could be optimized by the rigidity, steric, and electronic properties of the ligands, which could be ad-

Received 22 January 2008. Accepted 12 April 2008. Published on the NRC Research Press Web site at canjchem.nrc.ca on 2 July 2008.

J. Zhou, X. Li, and H. Sun.[1] School of Chemistry and Chemical Engineering, Shandong University, Shanda Nanlu 27, 250100 Jinan, Shandong Province, P.R. China.

[1]Corresponding author (email: hjsun@sdu.edu.cn).

 doi:10.1139/V08-075 © 2008 NRC Canada

justed through variation of the backbone and the substituents of the *N*-phenyl rings.

Experimental section

Materials and methods

All solvents and reagents were used after standard purification. Sodium salts of alkyl substituted sulfanilic acid (45, 46), DAB^{H}–Ar^{iPr}, DAB^{Me}–Ar^{Me}, DAB^{Me}–Ar^{iPr}, BIAN–Ar^{iPr} (ligands **10**–**13**) (47, 48), and BIAN–$Ar^{(3,5-CF_3,)}$ (ligand **14**) (49) as well as BmimCl (1-*n*butyl-3-methyl-imidazolium chloride), $BmimBF_4$ (1-*n*butyl-3-methyl-imidazolium tetrafluoroborate), and $BmimPF_6$ (1-*n*butyl-3-methyl-imidazolium hexafluorophosphate) (50) were prepared according to the literature methods.

^{1}H NMR and ^{13}C NMR were recorded on a Bruker 300 or 400 MHz. GC–MS was carried out on a Shimadzu QP-5050A. GC was Zheda Zhida 9790. Elemental analyses were carried out on an Elementar Vario EL III.

Synthesis of new diimine ligands

DAB^{H}–Ar^{Me}(4-SO_3Na) (Ligand 1)

Sodium salt of 3,5-dimethyl sulfanilic acid (2.23 g, 10.0 mmol) and 40% aq. glyoxal (0.80 g, 5.50 mmol) were dissolved in 30 ml of anhyd. methanol. Five drops of formic acid were added into this solution. The mixture was stirred at 40 °C for 48 h. After cooling to room temperature, the deposit was isolated and washed by 5 ml of cold methanol. The solid was recrystallized from MeOH and dried over an aspirator for 10 h. Ligand **1** was isolated as a yellow powder. (1.54g, 66%). ^{1}H NMR (300 MHz, DMSO-d_6) δ: 8.14 (s, 2 H), 7.34 (s, 4 H), 2.11 (s, 12 H). ^{13}C NMR (75.5 MHz, DMSO-d_6) δ: 164.19, 150.05, 136.06, 125.60, 119.49, 49.07. Anal. calcd. for $C_{18}H_{18}N_2Na_2O_6S_2$: C, 46.15; H, 3.87; N, 5.98. Found: C, 46.35; H, 3.99; N, 5.60.

DAB^{H}–Ar^{Me}(4-SO_3Na) (Ligand 2–9)

Ligands **2**–**9** were synthesized according to the method given above for ligand **1**. All the ligands were analyzed by ^{1}H NMR and elemental analysis. Melting points could not be obtained because the ligands were sodium salt of sulfonic.

DAB^{H}–Ar^{Et}(4-SO_3Na) (Ligand 2)

Yield: 56.6%. ^{1}H NMR (CD_3OD, 400 MHz) δ: 8.14 (s, 2 H), 7.62 (s, 4 H), 2.55 (m, 8 H), 1.16 (t, 12 H). ^{13}C NMR (100 MHz, CD_3OD) δ: 163.15, 150.08, 140.96, 131.64, 126.14, 49.0, 23.78. Anal. calcd. for $C_{22}H_{26}N_2Na_2O_6S_2$: C, 50.37; H, 5.00; N, 5.34. Found: C, 50.05; H, 4.79; N, 5.25.

DAB^{H}–Ar^{iPr}(4-SO_3Na) (Ligand 3)

Yield: 55%. ^{1}H NMR (300 MHz, DMSO-d_6) δ: 8.17 (s, 2 H), 7.44 (s, 4 H), 2.86 (m, 4 H), 1.15(d, 24 H). ^{13}C NMR (75.5 MHz, DMSO-d_6) δ: 163.91, 148.34, 145.22, 135.63, 120.89, 49.06, 28.06, 23.75. Anal. calcd. for $C_{26}H_{34}N_2Na_2O_6S_2$: C, 53.78; H, 5.90; N, 4.82. Found: C, 53.68; H, 6.12; N, 4.70.

DAB^{Me}–Ar^{Me}(4-SO_3Na) (Ligand 4)

Yield: 76%. ^{1}H NMR (300 MHz, DMSO-d_6) δ: 7.35 (s, 4 H), 1.98 (s, 6 H,), 1.96 (s, 12 H). ^{13}C NMR (75.5 MHz, DMSO-d_6) δ: 168.28, 148.63, 143.33, 125.72, 123.78, 17.86, 16.19. Anal. calcd. for $C_{20}H_{22}N_2Na_2O_6S_2$: C, 48.38; H, 4.47; N, 5.64. Found: C, 48.24; H, 4.23; N, 5.35.

DAB^{Me}–Ar^{Et}(4-SO_3Na) (Ligand 5)

Yield: 52%. ^{1}H NMR (400 MHz, CD_3OD) δ: 7.62 (s, 4 H), 2.42 (q, 8 H), 2.05 (s, 6 H), 1.17 (t, 12 H). ^{13}C NMR (100 MHz, CD_3OD) δ: 163.15, 150.08, 140.96, 131.64, 126.14, 49.0, 23.78. Anal. calcd. for $C_{24}H_{30}N_2Na_2O_6S_2$: C, 52.16; H, 5.47; N, 5.07. Found: C, 51.93; H, 5.60; N, 5.17.

DAB^{Me}–Ar^{iPr}(4-SO_3Na) (Ligand 6)

Yield: 67%. ^{1}H NMR (400 MHz, CD_3OD) δ: 7.79 (s, 4 H), 2.15 (s, 6 H), 2.84 (m, 4 H), 1.34 (d, 12 H), 1.28 (d, 12 H). ^{13}C NMR (100 MHz, CD_3OD) δ: 163.15, 150.08, 140.96, 131.64, 126.14, 49.0, 23.78. Anal. calcd. for $C_{28}H_{38}N_2Na_2O_6S_2$: C, 55.25; H, 6.29; N, 4.60. Found: C, 55.12; H, 6.50; N, 4.50.

BIAN–Ar^{Me}(4-SO_3Na) (Ligand 7)

Yield: 50%. ^{1}H NMR (300 MHz, DMSO-d_6) δ: 8.16 (d, 2 H), 7.61 (t, 2 H), 7.49 (s, 4 H), 6.73 (d, 2 H,), 2.06 (s, 12 H). ^{13}C NMR (75.5 MHz, DMSO-d_6) δ: 160.51, 149.22, 144.10, 140.19, 131.29, 130.24, 129.32, 126.26, 123.61, 122.34, 119.48, 18.45. Anal. calcd. for $C_{28}H_{22}N_2Na_2O_6S_2$: C, 56.75; H, 3.74; N, 4.73. Found: C, 56.37; H, 4.00; N, 4.56

BIAN–Ar^{Et}(4-SO_3Na) (Ligand 8)

Yield: 51%. ^{1}H NMR (400 MHz, CD_3OD) δ: 1.13 (t, 12 H), 8.07 (d, 2 H), 7.77 (s, 4 H), 7.47 (t, 2 H), 6.81 (d, 2 H), 2.57 (q, 4 H), 2.50 (q, 4 H). ^{13}C NMR (100 MHz, CD_3OD) δ: 162.16, 150.39, 142.21, 141.89, 132.07, 130.90, 129.53, 129.04, 125.50, 125.21, 124.28, 25.55, 13.76. Anal. calcd. for $C_{32}H_{30}N_2Na_2O_6S_2$: C, 59.25; H, 4.66; N, 4.32. Found: C, 59.10; H, 4.79; N, 4.10.

BIAN–Ar^{iPr}(4-SO_3Na) (Ligand 9)

Yield: 73 %. ^{1}H NMR (400 MHz, CD_3OD) δ: 7.85 (s, 4 H), 7.49 (t, 2 H), 6.80 (d, 2 H), 6.08 (d, 2 H), 3.00 (m, 4 H), 1.26 (d, 12 H), 1.04 (d, 12 H). ^{13}C NMR (100 MHz, CD_3OD) δ: 160.77, 147.79, 140.95, 140.55, 135.08, 130.90, 129.61, 127.94, 127.42, 123.16, 121.10, 28.28, 21.40, 21.33. Anal. calcd. for $C_{36}H_{38}N_2Na_2O_6S_2$: C, 61.35; H, 5.43; N, 3.97. Found: C, 61.04; H, 5.55; N, 4.16.

Typical experimental procedure

$Pd(OAc)_2$ (0.05 mmol) and ligand (0.05 mmol) were dissolved in DMA (5 ml) in a 25 mL two-necked flask. The flask, equipped with a magnetic stirring bar, was purged with oxygen gas. Oxygen gas was introduced into the flask from an O_2 balloon under atmospheric pressure, and the mixture was stirred at 40 °C for 10 min or stirred for 30 min at room temperature. Then alcohol (1 mmol) and K_2CO_3 (1 equiv.) was added, and the reaction mixture was stirred for appropriate time at 100 °C under oxygen. The oxidation product was analyzed by GC–MS. The reaction yields were determined by GC analysis using *n*-heptane as an internal standard. Recoveries were 100 ± 2% with this procedure. The purified products could be obtained by flash chromatography on a short silica-gel column eluting with a mixture of ethyl acetate and petroleum ether.

© 2008 NRC Canada

General procedure for catalyst-recycling trials

$Pd(OAc)_2$ (0.05 mmol) and ligand **9** (0.05 mmol) were dissolved in DMA (5 ml) in a 25 mL two-necked flask under oxygen gas. Oxygen gas was introduced into the flask from an O_2 balloon under atmospheric pressure, and the mixture was stirred at 40 °C for 10 min. Then, benzyl alcohol (1 mmol) and K_2CO_3 (1 equiv.) was added, and the reaction mixture was stirred for 5 h at 100 °C under oxygen. An aliquot of 0.02 mL of reaction mixture was taken out for the GC analysis. The volatiles of reaction mixture were removed under vacuum. The residual was washed with *n*-pentane for three times, and was applied to the next reaction cycle.

Results and discussions

Synthesis of new α-diimine ligands

At first, 2,6-dialkylaniline was sulfonated with concentrated sulphuric acid at 200 °C, followed by neutralization with NaOH or $NaOCH_3$ to yield the sodium salts. The new α-diimine ligands were prepared by condensation of the α-dione (2,3-butanedione, acenaphthenequinone, or 40% aqueous glyoxal) and the corresponding anilines in anhyd. methanol with a catalytic amount of formic acid (Scheme 1). A small amount of the sulfonated anilines was found in the crude product. This impurity could be removed by recrystallization from methanol or methanol/diethyl ether. These new sulfonated ligands are all easily diffluent and stable in polar organic solvents, such as DMF, DMA, and DMSO, as well as in water, but slowly hydrolyze in the latter when heated.

Influence of solvents on aerobic benzyl alcohol oxidation

Initially, the goal of this work was to develop a new Pd/ionic α-diimine catalytic system with the introduction of sulfonic group for aerobic oxidation in ionic liquid medium where immobilization of the catalysts was expected. That catalytic system could be profitable in the recycling of the catalyst and in the separation of products. Unfortunately, the combination of Pd/α-diimine showed no catalytic activity for oxidation of aerobic alcohols in ionic liquids, such as BmimCl, $BmimBF_4$, and $BmimPF_6$. Therefore, our attention was transferred to the catalytic activity of this $Pd(OAc)_2$/α-diimine system in other solvents.

Six solvents were examined, excluding the ionic liquid, for the aerobic oxidation of benzyl alcohol (Table 1). The use of toluene as the solvent led to complete conversion of the starting alcohol and afforded the desired aldehyde in 99% yield, but a great deal of Pd-black was produced. High pressure of O_2 (10 atm, 1 atm = 101.325 kPa) was employed for the reactions in aqueous phase or ionic liquid to increase the solubility of O_2. Using low loading of catalyst, catalytic reactions in water or DMSO/H_2O mixed solvent showed higher TON value compared with other solvents, but the conversions were low or moderate because of the Pd-colloid produced (Table 1, entries 2 and 3). Increasing the loading of catalyst of 5 mol% did not markedly improve the conversions. The employment of DMA (*N*,*N*-dimethyl acetamide) gave excellent yield without any Pd-black (Table 1, entry 4), while DMF and dioxane displayed moderate results (Table 1, entries 5 and 6). In conclusion, DMA appears to be the most effective solvent under given reaction conditions.

Scheme 1. Preparation of sulfonated α-diimine ligands **1**–**9**.

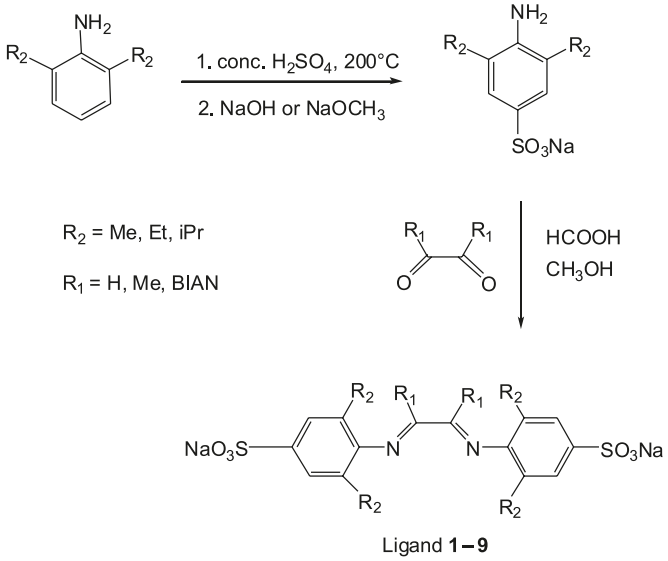

Table 1. Optimization of solvents.

Solvent	Yield[f]
$PhCH_3$[a]	99
H_2O[b]	25[g], 30[h]
H_2O/DMSO[c]	45[i], 52[h]
DMF	74
Dioxane	50
DMA	99
DMA[d]	30
ILs[e]	0

Note: Reaction conditions: 5 mol% $Pd(OAc)_2$ and ligand **9**, K_2CO_3 (1 equiv.), benzyl alcohol (1 mmol), solvent (5 ml), 1 atm O_2 (1 atm = 101.325 kPa), and 100 °C for 5 h.

[a]Pd black occurred.

[b]25 mL, 10 atm O_2, NaOAc, and 10 h.

[c]25 mL H_2O/DMSO (1:1), 10 atm O_2, NaOAc, and 10 h.

[d]No ligand.

[e]Ionic liquid, including BmimCl, $BmimBF_4$, and $BmimPF_6$, and 10 atm O_2.

[f]GC yield, average of two runs.

[g]1 mol% $Pd(OAc)_2$ and ligand **9**.

[h]5 mol% $Pd(OAc)_2$ and ligand **9**.

[i]0.5mol% $Pd(OAc)_2$ and ligand **9**.

Electronic and steric effects of diimine ligands

Benzyl alcohol was selected as a model substrate to investigate the electronic and steric effects of ligands on diimine/palladium(II)-catalyzed aerobic oxidation of alcohol (Scheme 2).

Table 2 showed us the catalytic activities of various ligands for the aerobic oxidation. We recognized that no palladium black was produced in most of the experiments except when ligands **2** and **3** were used. The use of ligands increased the electron density on Pd(0) and facilitated the acti-

© 2008 NRC Canada

Table 2. Influence of various ligands for aerobic oxidation of benzyl alcohol.

Ligand	Structure	Abbreviation	Yield[a] (%)
1	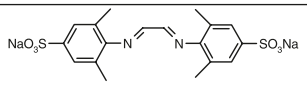	DAB^{H}-Ar^{Me}(4-SO_3Na)	60
2	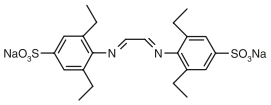	DAB^{H}-Ar^{Et}(4-SO_3Na)	90[b]
3	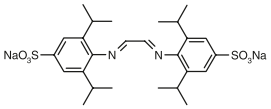	DAB^{H}-Ar^{iPr}(4-SO_3Na)	91[b]
4	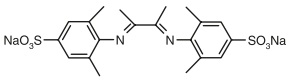	DAB^{Me}-Ar^{Me}(4-SO_3Na)	50
5	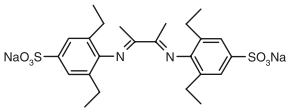	DAB^{Me}-Ar^{Et}(4-SO_3Na)	51
6	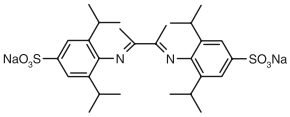	DAB^{Me}-Ar^{iPr}(4-SO_3Na)	92
7	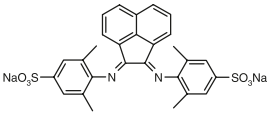	BIAN-Ar^{Me}(4-SO_3Na)	62
8	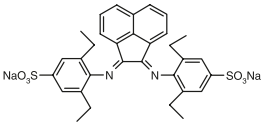	BIAN-Ar^{Et}(4-SO_3Na)	86
9	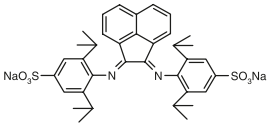	BIAN-Ar^{iPr}(4-SO_3Na)	99
10	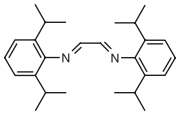	DAB^{H}-Ar^{iPr}	48

Scheme 2. Palladium-catalyzed oxidation of benzyl alcohol.

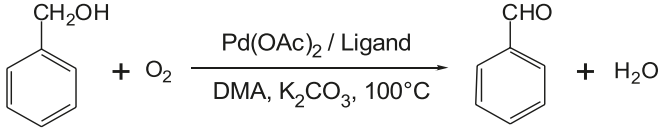

vation of dioxygen. Then, the palladium(0) species could be smoothly re-oxidized to palladium(II) without evident aggregation when supported by the diimine ligands. An interesting electronic effect seems to arise in the series of diimine ligands. It was shown that in runs employing α-diimine ligands with a strongly electron-withdrawing sulfonic group showed much higher yields were obtained than in those employing normal α-diimine ligands (ligands **10**–**15**) in equal reaction times. This electron-deficiency facilitates the oxidation of alcohol because the overall rate of oxidation increased. Faster oxidation was also achieved by using ligand **14** with the strongly electron-withdrawing trifluoromethyl groups (Table 2, entry 14). A similar observation that electron-withdrawing substituents on the ligand increase the reaction rate in alcohol oxidation was reported by Sheldon

© 2008 NRC Canada

Table 2 (*concluded*).

Ligand	Structure	Abbreviation	Yield[a] (%)
11	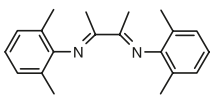	DAB^{Me}-Ar^{Me}	52
12	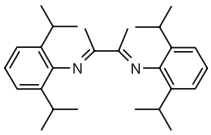	DAB^{Me}-Ar^{iPr}	55
13	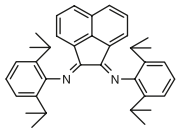	BIAN-Ar^{iPr}	45
14	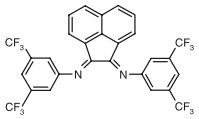	BIAN-$Ar^{(3,5\text{-}CF_3)}$	71
15	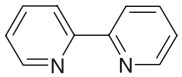	Bipy	31

Note: Reaction conditions: $Pd(OAc)_2$ (0.05 mmol), ligand (0.05 mmol), benzyl alcohol (1.0 mmol), K_2CO_3 (1 equiv.), DMA (5 ml), O2 1atm, 100 °C, and 5 h.
[a]GC yield with *n*-heptane as an internal standard, average of two runs.
[b]Pd black pruduced.

and co-workers in the studies of a range of 4,4-disubstituted-2,2-bipyridines as ligands for the palladium-catalyzed aerobic oxidation of 2-hexanol (51). Variation of the electron density on the diimine ligand changes the redox properties of the catalyst. Therefore, this variation should provide evidence for whether an oxidation step or a reduction step is rate-limiting. The re-oxidation step of Pd(0) to Pd(II) should be facilitated by electron-donating substituents. On the other hand, if the reduction step is rate-limiting, then the reaction should be facilitated by electron-withdrawing substituents in the ligands. The electronic effect of diimine ligands indicated that the reduction step is slow.

Comparing catalytic results of BIAN/diimine ligands **7**–**9** (Table 2, entries 7–9), it was shown that bulky groups on 2 and 6 positions of the *N*-phenyl ring facilitated the oxidation of benzyl alcohol. The same trend is observed in a series of DAB^{Me}/diimine ligands **4**–**6** (Table 2, entries 4–6). A similar conclusion is reported by Sheldon and co-workers (52) for the Pd/phenanthroline system. It was reported that the methyl groups in 2 and 9 positions of the phenanthroline ligands clearly increase the TOF value by raising the cleavage rate of dimeric palladium catalyst species. Generally, the BIAN/diimine ligands (ligands **7**–**9**) showed higher rates of oxidation as compared with the DAB/diimine ligands (ligands **1**–**6**). A more stable coordination and a longer lifetime of the active palladium species in the catalytic cycle (53) was achieved by using a rigid ligand backbone (BIAN). In a word, the bulky group on arene of ligands and the more rigid backbone of ligand effectively prevent aggregation of palladium(0) species and facilitates the re-oxidation of palladium(0).

Scheme 3. Oxidation of the other alcohol.

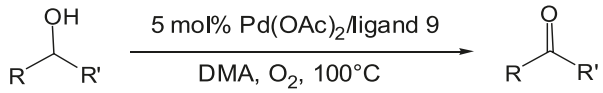

Everntually, the optimized catalytic combination for the aerobic oxidation of alcohol was found to be $Pd(OAc)_2$/ligand **9**/K_2CO_3/DMA/O_2/100 °C.

Oxidation of various alcohols

The scope of this optimized procedure for the oxidation of the other alcohols (Scheme 3) was listed in Table 3. The primary benzylic alcohols were converted to the corresponding aldehydes in 87%–99% yields (Table 3, entries 1–8 and 13). An electronic effect seems to exist for these benzylic systems. Comparing benzyl alcohol (Table 3, entry 1) with the benzylic alcohols with electron-donating substituents (Table 3, entry 2), we found that the reaction times for the electronic-rich arenes were significantly shorter. It was also shown that the benzylic alcohols with electron-withdrawing groups (Table 3, entries 3 and 4) gave lower yields in the same reaction times with benzyl alcohol and required longer reaction times for complete conversion. It is noteworthy that the primary benzylic alcohols with electron-withdrawing

© 2008 NRC Canada

Table 3. Oxidation of the other alcohols.

Entry	Substrate	Product	t (h)	Yield[a] (iso. yield)
1	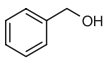	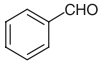	4	87
			5	99
			8	96 [b]
			20	90 [c]
2	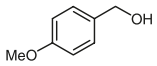	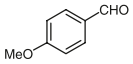	3.5	99
3	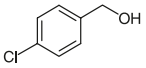	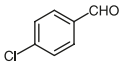	5	85
			8	94 (90)
4	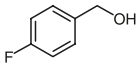	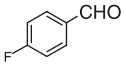	5	62
			12	94
5	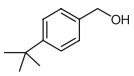	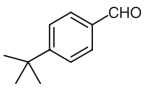	5	96
6	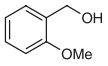	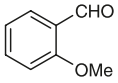	10	90
7	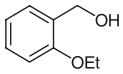	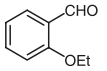	10	90
8	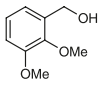	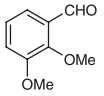	10	89 (87)
9			8	39
10	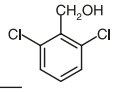	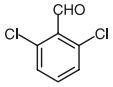	24	15

group at ortho position (Table 3, entries 9 and 10) showed much lower reaction activities. The secondary benzylic substrates generally gave very clean reactions with high yields (Table 3, entries 11, 12, and 14). About 3% yield of 3-formylbenzyl alcohol as halfway product of oxidation was determined by GC and GC–MS for the oxidation of 1,3-benzenedimethanol (Table 3, entry 18) with 94% yield of *iso*-phthalaldehyde. It is noticable that the oxidation of hydrobenzoin (Table 3, entry 19) gave 87% yield with no benzoin produced and a trace of benzaldehyde formed by oxidative C=C cleavage, possibly of an intermediate benzoin. As expected, benzaldehyde was also found in the oxidation of benzoin by GC–MS (Table 3, entry 20).

The secondary aliphatic alcohols and cyclic alcohol (Table 3, entries 15–17) could be transformed into the corresponding aldehydes or ketones in moderate yields. The catalytic system showed no activities for the oxidation of primary aliphatic alcohols (Table 3, entries 21 and 22) because of the decreased electron density on the primary aliphatic alcohols.

So far, our catalytic system is limited in scope to benzylic or secondary aliphatic alcohols, needing higher reaction temperature (100 °C) and longer reaction times (3–12 h for benzylic alcohols) compared with other excellent catalytic systems for aerobic alcohol oxidation, such as the Pd/pyridine and Pd/NEt_3 systems. But one certain advantage is their modularity because the electronic and steric properties could be modulated independently to optimize the catalytic activities. We believe that further investigation of the diimine ligands is worthwhile.

© 2008 NRC Canada

Table 3 (*concluded*).

Entry	Substrate	Product	t (h)	Yield[a] (iso. yield)
11			15	85
12	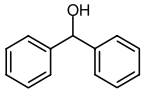	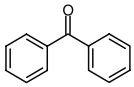	12	96 (92)
13	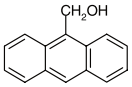	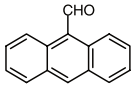	15	87 (85)
14	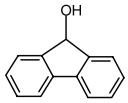	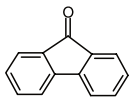	5	100 (97)
15	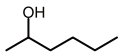	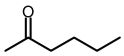	24	60
16			24	46
17	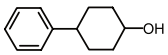	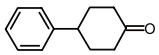	24	31
18	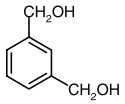	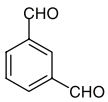	12	95 (93) [d,e]
19	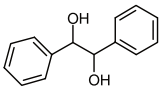	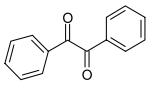	12	87 (85) [f]
20	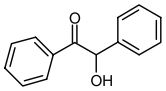	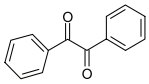	12	85 (84)
21	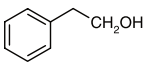	-	48	0
22	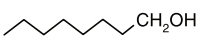	-	48	0

[a]Yield determined by GC.
[b]Run 2.
[c]Run 3.
[d]10 mol% catalyst used.
[e]3% yield of 3-formylbenzyl alcohol.
[f]Trace benzaldehyde was observed.

It is confirmed that the $Pd(OAc)_2$/ligand **9** catalytic system could be recycled three times, while allowing for extended reaction times: 8 h for second cycle and 20 h for third cycle were required after the first run.

Mechanistic discussion

Generally, the mechanism of the palladium-catalyzed aerobic alcohol oxidation mimics the palladium–oxidase pathway (38). This process is composed of two independent steps: substrate oxidation and catalyst oxidation. The trend of the activities of the $Pd(OAc)_2$/dimine system for alcohol oxidation is in contrast with that for the diimine/palladium-catalyzed Suzuki cross-coupling reaction reported by Nolan and co-workers (44). The observation that electron-

© 2008 NRC Canada

withdrawing substituents on the ligand increase the reaction rate in alcohol oxidation is a strong indication that the reduction step (substrate oxidation) is slow and that under these conditions re-oxidation of (diimine)Pd(0) is facile (51), which is similar to other palladium catalyst systems with nitrogen-containing ligands (21–31). A bulky substituent on the arene group in the ligand effectively prevents aggregation of palladium(0) species and facilitates the re-oxidation of palladium(0), still allowing an approach of the substrate alcohol to the catalytic species. An anionic base, such as K_2CO_3, can significantly enhance the rate of alcohol oxidation. Complete conversion of benzyl alcohol could be achieved using only 0.1 equiv. of the base. More mechanistic investigation is clearly desired.

Conclusions

A series of new ionic sulfonated α-diimine ligands were prepared and employed as supporting ligands for the palladium-catalyzed aerobic oxidation of alcohols. The electronic properties, rigidity, and steric hindrance of ligands have remarkable influence upon the catalytic activity of the palladium catalysts. The best catalytic results could be achieved by using ligand **9** with an electron-withdrawing sulfonyl substituent together with bulky groups (*iso*-propyl in 2,6-positions). This diimine/palladium system is highly efficient for the catalytic oxidation of various benzylic alcohols but shows only moderate yields for the secondary aliphatic alcohols and cyclic alcohols. The observation that electron-withdrawing substituents on the ligand increase the reaction rates of alcohol oxidation strongly indicates that the reduction of Pd(II) is a slow step.

Acknowledgements

This work was supported by Natural Science Foundation of China No. 20372042, the Doctoral Program of Ministry of Education No. 20050422010 and 20050422011, Shandong Scientific Plan 032090105, and the Science Foundation of Shandong Y2006B18.

References

1. S.E. Martin and D. Suarez. Tetrahedron Lett. **43**, 4475 (2002).
2. I.E. Marko, P.R. Giles, M. Tsukazaki, C.J. Urch, and S.M. Brown. J. Am. Chem. Soc. **119**, 12661 (1997).
3. A. Dijksman, A. Marino-Gonzalez, I. Mairata, A. Payeras, I.W.C.E. Arends, and R.A. Sheldon. J. Am. Chem. Soc. **123**, 6826 (2001).
4. A. Miyata, M. Murakami, R. Irie, and T. Katsuki. Tetrahedron Lett. **42**, 7067 (2001).
5. A. Wolfson, S. Wuyts, D.E. De Vos, I.F.J. Vankelecom, and P.A. Jacobs. Tetrahedron Lett. **43**, 8107 (2002).
6. T. Iwahama, Y. Yosino, T. Keitoku, S. Sakaguchi, and Y. Ishii. J. Org. Chem. **65**, 6502 (2000).
7. P. Gamez, I.W.C.E. Arends, R.A. Sheldon, and J. Reedijk. Adv. Synth. Catal. **346**, 805 (2004).
8. I.E. Marko, A. Gautier, R. Dumeunier, D. Kanae, F. Philippart, S.M. Brown, and C.J. Urch. Angew. Chem., Int. Ed. **43**, 1588 (2004).
9. M.L. Kantama, T. Ramania, L. Chakrapani, and B.M. Choudary. J. Mol. Catal. A: Chem. **274**,11 (2007).
10. B.M. Choudary, M.L. Kantam, A. Rahman, C.V. Reddy, and K.K. Rao. Angew. Chem., Int. Ed. **40**, 763 (2001).
11. R.A. Sheldon, I.W.C.E. Arends, G.-J. ten Brink, and A. Dijksman. Acc. Chem. Res. **35**, 774 (2002).
12. J. Muzart. Tetrahedron, **59**, 5789 (2003).
13. R. Liu, X. Liang, C. Dong, and X. Hu. J. Am. Chem. Soc. **126**, 4112 (2004).
14. W.G. Lloyd. J. Org. Chem. **32**, 2816 (1967).
15. T.F. Blackburn, and J. Schwartz. J. Chem. Soc., Chem. Commun. **157** (1977).
16. K. Hallman and C. Moberg. Adv. Synth. Catal. **343**, 260 (2001).
17. B. Ganchegui, S. Bouquillon, F. H in, and J. Muzart. Tetrahedron Lett. **43**, 6641 (2002).
18. B. Karimi, A. Zamani, and J.H. Clark. Organometallics, **24**, 4695 (2005).
19. T. Iwasawa, M. Tokunaga, Y. Obora, and Y. Tsuji. J. Am. Chem. Soc. **126**, 6554 (2004).
20. E.M. Ferreira and B.M. Stoltz. J. Am. Chem. Soc. **123**, 7725 (2001).
21. D.R. Jensen, J. S. Pugsley, and M.S. Sigman. J. Am. Chem. Soc. **123**, 7475 (2001).
22. D. Jensen and R.; M.S. Sigman. Org. Lett. **5**, 63 (2003).
23. S.K. Mandal and M.S. Sigman. J. Org. Chem. **68**, 7535 (2003).
24. J.T. Bagdanoff, B.M. Stoltz. Angew. Chem., Int. Ed. **43**, 353 (2004).
25. K.P. Peterson and R.C. Larock, J. Org. Chem. **63**, 3185 (1998).
26. T. Nishimura, T. Onoue, K. Ohe, and S. Uemura. Tetrahedron Lett. **39**, 6011 (1998).
27. T. Nishimura, T. Onoue, K. Ohe, and S. Uemura. J. Org. Chem. **64**, 6750 (1999).
28. G.J. ten Brink, I.W.C.E. Arends, and R.A. Sheldon. Science (Washington, DC), **287**, 1636 (2000).
29. M.J. Schultz, C.C. Park, and M.S. Sigman. Chem. Commun. 3034 (2002).
30. M.J. Schultz, S.S. Hamilton, D.R. Jensen, and M.S. Sigman. J. Org. Chem. **70**, 3343 (2005).
31. M.J. Schultz, R.S. Adler, W. Zierkiewicz, T. Privalov, and M.S. Sigman. J. Am. Chem. Soc. **127**, 8499 (2005).
32. T. Privalov, C. Linde, K. Zetterberg, and C. Moberg. Organometallics, **24**, 885 (2005).
33. J.A. Mueller and M.S. Sigman. J. Am. Chem. Soc. **125**, 7005 (2003).
34. B.A. Steinhoff, S.R. Fix, and S.S. Stahl. J. Am. Chem. Soc. **124**, 766 (2002).
35. B.A. Steinhoff and S.S. Stahl. Org. Lett. **4**, 4179 (2002).
36. B.A. Steinhoff, L.A. Guzei, and S.S. Stahl. J. Am. Chem. Soc. **126**, 11268 (2004).
37. S.S. Stahl. Science (Washington, DC), **309**, 1824 (2005).
38. S.S. Stahl. Angew. Chem., Int. Ed. **43**, 3400 (2004).
39. S.S. Stahl, J.L. Thorman, N. Silva, L.A. Guzei, and R.W. Clark. J. Am. Chem. Soc. **125**, 12 (2003).
40. S.S. Stahl, J.L. Thorman, R.C. Nelson, and M.A. Kozee. J. Am. Chem. Soc. **123**, 7188 (2001).
41. S.A. Svejda, K.J. Lynda, and M. Brookhart. J. Am. Chem. Soc. **121**, 10634 (1999).
42. B.S. Williams, M.D. Leatherman, P.S. White, and M. Brookhart. J. Am. Chem. Soc. **127**, 5132 (2005).
43. G.A. Grasa, A.C. Hillier, and S.P. Nolan. Org. Lett. **3**, 1077 (2001).
44. G.A. Grasa, R.Singh, E.D. Stevens, and S.P. Nolan. J. Organomet. Chem. **687**, 269 (2003).
45. A. Courtin, H.R. Tobel, and P. Doswald. HeIv. Chim. Acta, **61**, 3079 (1978).
46. F. Kanetani and H. Yamaguchi. Bull. Chem. Soc. Jpn. **54**, 3048 (1981).

© 2008 NRC Canada

47. M. Svoboda, H. T. Dieck. J. Organomet. Chem. **191**, 321 (1980).
48. H.T.Dieck., M. Svoboda, and T.Z Greiser. Naturforsch, **36b**, 823 (1981).
49. L.Johansson, O.B. Ryan, and M. Tilset. J. Am. Chem. Soc. **121**, 1974 (1999).
50. J. Dupont, C.S. Consorti, P.A. Z. Suarez, and R.F. de Souza. Org. Syn. **10**, 184 (1933).
51. J. Brink, I.W.C.E. Arends, M. Hoogenraad, G. Verspui, and R.A. Sheldon. Adv. Synth. Catal. **345**, 497 (2003).
52. G.J. ten Brink, I.W.C.E. Arends, and R.A. Sheldon. Adv. Synth. Catal. **345**, 1341 (2003).
53. G.-J. Brink, I.W.C.E. Arends, and R.A. Sheldon. Adv. Synth. Catal. **344**, 355 (2002).

© 2008 NRC Canada

The photochemistry of *trans*-isohumulone, a bitter flavouring component of beer

Alan C. Weedon and John S. Morrison

Abstract: Methanolic solutions of *trans*-isohumulone (**2**), a major bitter flavouring component in beer, were irradiated with UV light of 313 nm wavelength and yielded four primary products containing an enolized cyclic β-triketone moiety: *cis*-isohumulone (**3**), humulone (**1**), *dehydro*-isohumulone (**7**), and *dehydro*-humulinic acid (**5**). The last of these products results from loss of the 4-methyl-3-pentenoyl side chain of *trans*-isohumulone. Nine volatile products derived from this side chain were identified and quantitated. The identifications of all photoproducts were confirmed by independent preparation of authentic samples. No evidence of either intramolecular or intermolecular 2+2 cyclo-addition was observed. This work clarifies previous contradictory reports of the products of isohumulone photolysis and provides an example of unexpected photochemistry of an alkenyl-substituted enolized cyclic β-triketone.

Key words: trans-isohumulone, photo-degradation, cyclic β-triketone.

Résumé : La *trans*-isohumulone (**2**), un des constituants de la bière qui lui donne son goût amer, en solution dans le méthanol a été soumise à une irradiation UV à 313 nm et a conduit à la formation de quatre produits primaires qui contiennent une portion β-tricétonique cyclique énolisée: la *cis*-isohumulone (**3**), l'humulone (**1**), la *déhydro*isohumulone (**7**) et l'acide *déhydro*humulinique. Le dernier de ces produits résulte de la perte de la chaîne latérale 4-méthylpent-3-énoyle de la *trans*-isohumulone. On a aussi identifié la nature et quantifié neuf produits volatils dérivés de cette chaîne latérale. Les identifications de tous les photoproduits ont été confirmées par la préparation d'échantillons authentiques. On n'a pas pu mettre en évidence de cycloadditions 2+2 intramoléculaire ou intermoléculaire. Ces résultats permettent de clarifier des rapports antérieurs contradictoires relatifs à la photolyse de l'isohumulone et ils fournissent un exemple de photochimie inattendue d'une β-tricétone cyclique énolisée et substituée par une chaîne alcényle.

Mots-clés : trans-isohumulone, photodégradation, β-tricétone cyclique.

[Traduit par la Rédaction]

Introduction

Beer is brewed by the yeast-mediated fermentation of an aqueous solution of malted barley to which hops (flowers of the plant *Humulus lupulus*) have been added. The hops are a source of water soluble, bitter-tasting compounds (known as alpha acids) of which humulone (**1**) is the major component. During the brewing process, the alpha acids undergo thermal isomerization to so-called iso-alpha acids that are responsible for the bitter flavour of beer (1). Thermal conversion of the hop alpha-acid humulone (**1**) to the iso-alpha acids *cis*-isohumulone (**3**) and *trans*-isohumulone (**2**) is illustrated in Scheme 1.

The NMR and UV spectra of isohumulone in various solvents reveal it to be enolized, and three tautomers are, in principle, possible. The tautomer illustrated in Scheme 1 is drawn throughout this paper for consistency, but this should not be taken to imply that the other tautomers are not present in solution. The enolized cyclic β-triketone of isohumulone is acidic with a p*K*a of 3.1 in aqueous ethanolic solutions (2), and thus is only partially ionized.[2,3]

Beer develops an off-flavour when exposed to light because of the formation of trace amounts of 3-methyl-2-butene thiol (**4**), and it has been shown that the iso-alpha acids must be present for this to occur (3–5). This thiol has a taste threshold in beer of about 10^{-11} mol/L, and so extremely small amounts formed by photolysis of iso-alpha acids can generate an off-flavour (6–8). In the brewing industry, beer so afflicted is termed "light-struck" and more colloquially as "skunky", since the thiol has an odor similar to that associated with skunks.

In beer, degradation of the iso-alpha acids is initiated either by direct absorption of UV light or indirectly by sensitization. In the latter case, components of the beer such as flavins mediate the light-struck reaction through absorption of both UV and visible light. The light-struck reaction can

Received 30 September 2007. Accepted 3 March 2008. Published on the NRC Research Press Web site at canjchem.nrc.ca on 2 July 2008.

A.C. Weedon and J.S. Morrison.[1] Department of Chemistry, University of Western Ontario, London, ON N6A 5B7, Canada.

[1]Corresponding author (e-mail: john.morrison@bms.com).

[2]The p*K*a was confirmed experimentally (details provided in the Supplementary Data).

[3]Supplementary data for this article are available on the journal Web site (canjchem.nrc.ca) or may be purchased from the Depository of Unpublished Data, Document Delivery, CISTI, National Research Council Canada, Ottawa, ON K1A 0R6, Canada. DUD 3767. For more information on obtaining material refer to cisti-icist.nrc-cnrc.gc.ca/irm/unpub_e.shtml.

 doi:10.1139/V08-072 © 2008 NRC Canada

Scheme 1.

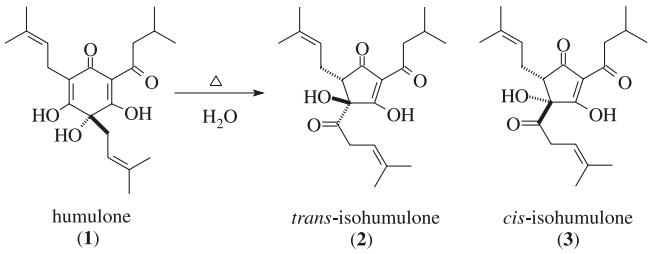

Scheme 2.

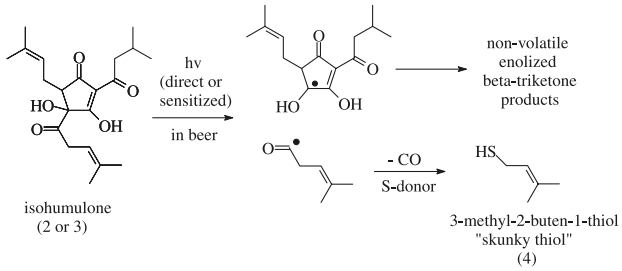

be inhibited by appropriate packaging to block or filter light (hence the common use of green tinted or brown glass for beer bottles). Alternatively, the beer can be brewed with iso-alpha acids that have been extracted from hops and chemically modified. For example, protection from the light-struck reaction can be achieved by the use of iso-alpha acids in which the alkene or carbonyl function of the 4-methyl-3-pentenoyl side chain has been reduced (9, 10). While the mechanism of the light-struck reaction is not entirely known, the evidence suggests it proceeds as indicated in Scheme 2.

Interest in understanding and hence suppressing the light-struck reaction in beer has led to a number of studies of the photochemistry of the iso-alpha acids. In many of these studies *trans*-isohumulone is used as a model, since it can be produced and isolated as a single stereoisomer from natural humulone extracted from hops (11). In one such study, photolysis of *trans*-isohumulone to high conversion was reported to generate *dehydro*-humulinic acid (**5**) in nearly quantitative yield (12, 13), as illustrated in Scheme 3.

However, it has also been reported that a variety of products result from high conversion photolysis of *trans*-isohumulone, or of an iso-alpha–acid mixture, with a significant product being the decarbonylated *dehydro*-isohumulone (**6**), as illustrated in Scheme 4 (14–16).

It is well-known that enones (17–19) and enolized β-diketones (20–25) undergo efficient 2+2 photocycloaddition reactions with alkenes. This reaction is especially efficient for systems containing the enone and the alkene function within the same molecule. It is therefore surprising that no products of photocycloaddition have been reported for isohumulone. This fact, and the inconsistencies in the reported products of photolysis of isohumulone, led us to examine in detail the products of the photochemistry of *trans*-isohumulone. The result of this study is reported here. In view of its importance in the brewing industry, we have also examined the mechanism of this reaction. The results of that work will be reported separately.

In a further report, the headspace over an aqueous solution

Scheme 3.

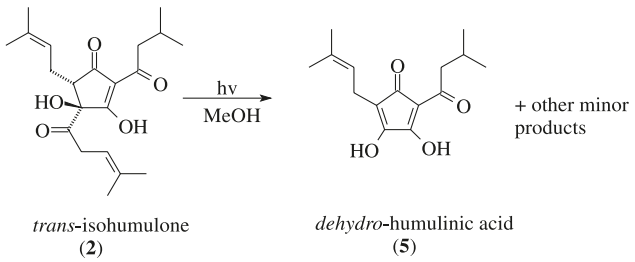

Scheme 4.

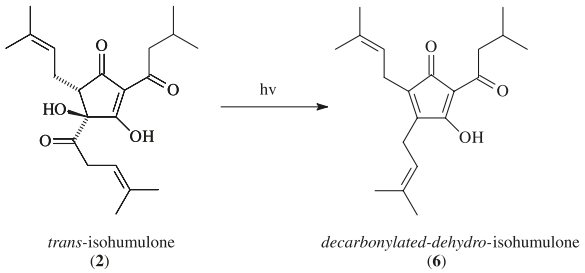

(Reported but unobserved product)

Scheme 5.

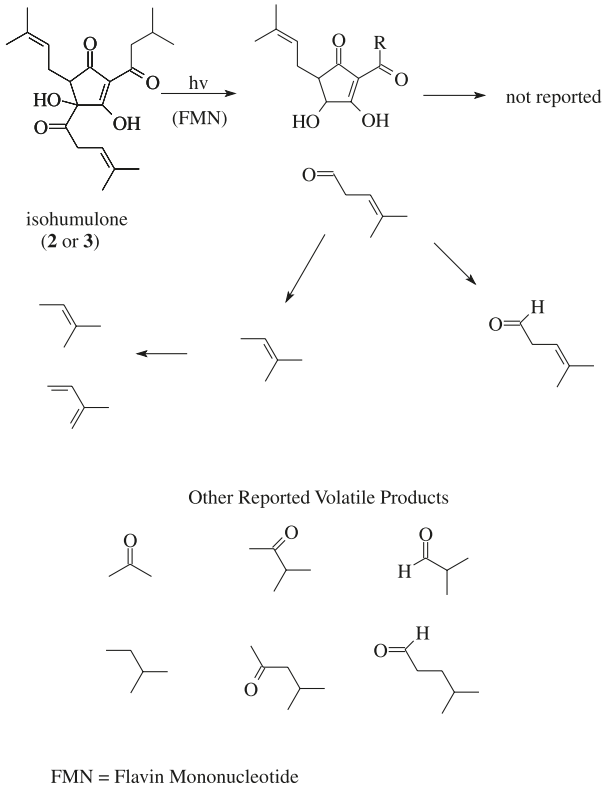

FMN = Flavin Mononucleotide

containing a mixture of iso-alpha acid potassium salts and a flavin sensitizer has been examined after exposure of the solution to visible light (26). This study attempted to determine the fate of any side chains cleaved from isohumulone and found several, which are illustrated in Scheme 5.

The formation of 2-methyl-2-butene, isoprene, and 4-methyl-3-pentenal are consistent with the intermediacy of a

© 2008 NRC Canada

Scheme 6.

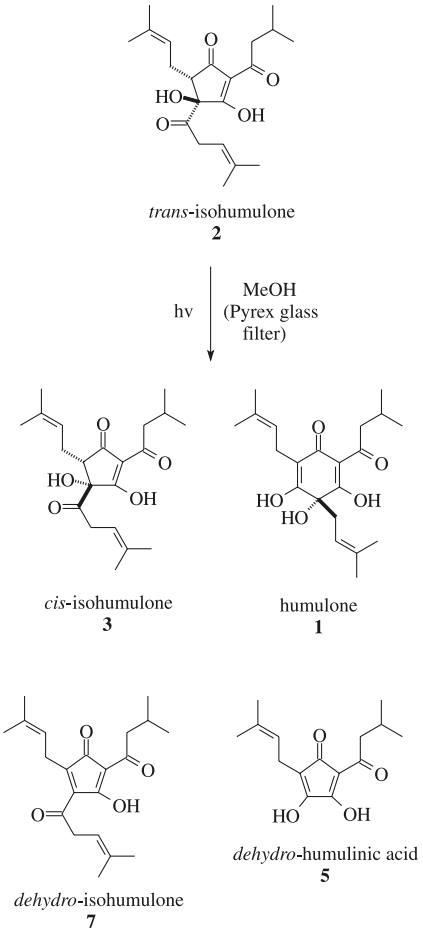

4-methyl-3-pentenoyl radical. The other observed volatile compounds illustrated in Scheme 5 are not. These other products appear to be consistent with degradation of the other side chains of the iso-alpha acid, suggesting further sensitized degradation of the primary enolized cyclic β-triketone products.

Results and discussion

Identification of the enolized cyclic β-triketone-containing photoproducts of *trans*-isohumulone

Solutions of *trans*-isohumulone in methanol were exposed to light of 313 nm wavelength. At conversions of less than 15%, four nonvolatile photoproducts containing the enolized cyclic β-triketone moiety were generated, as illustrated in Scheme 6.

Each product was isolated by semi-preparative HPLC and characterized by one-dimensional (^{1}H NMR and ^{13}C NMR) and two-dimensional (gCOSY, gHSQC, and gHMBC) NMR spectroscopy, as well as electron ionization and chemical ionization mass spectrometry (GC-MS).[3] The identifications were confirmed by independent preparation of an authentic sample of each compound. These results confirm the literature reports that *dehydro*-humulinic acid (**5**), *cis*-isohumulone (**3**), and humulone (**1**) are photoproducts of *trans*-isohumulone (**2**) (12–16). No evidence for the formation of the *decarbonylated-dehydro*-isohumulone (**6**) was found (14, 16). In the previous reports where (**6**) was identified as a product, the identification appears to have been based on HPLC-MS evidence; the product was apparently not isolated such that its ^{1}H and ^{13}C NMR spectra could be recorded, which may account for the observation.

We have also examined the photochemistry of *trans*-isohumulone in aqueous ethanolic solutions as well as in aqueous solutions buffered at a pH of 2.1 and 4.7.[3] In all cases only these four nonvolatile photoproducts were observed when conversions were kept below 15%. This suggests that both the enol and enolate forms of *trans*-isohumulone exhibit similar photochemistry and suggests that the tautomeric form adopted by isohumulone is also not a critical factor in its photochemistry.[3] Futhermore, no evidence of products of intramolecular or intermolecular 2+2 cycloaddition was observed for *trans*-isohumulone.

Fig. 1. Variation with time of *trans*-isohumulone concentration and total photoproduct concentration (enolized cyclic β-triketone products only) for an UV light irradiation conducted in methanol.

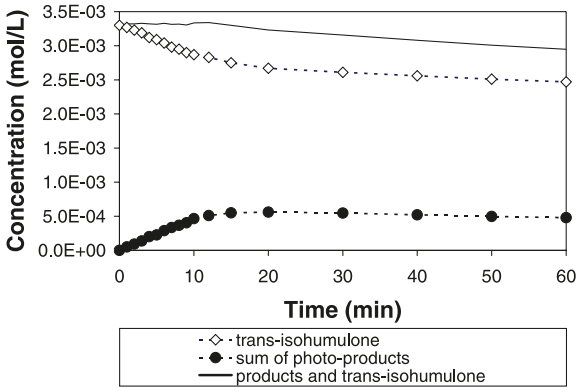

Fig. 2. Variation with time of the concentration enolized cyclic β-triketones produced for the UV light irradiation of *trans*-isohumulone in methanol.

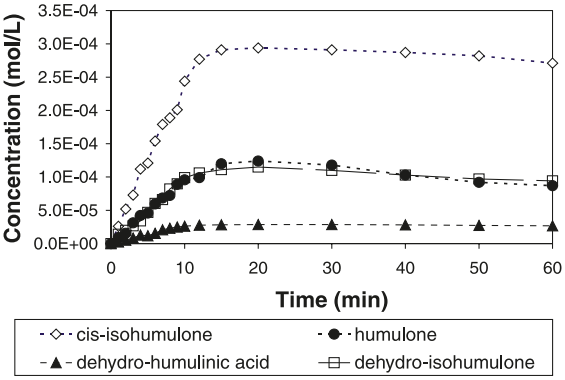

Yields of the enolized cyclic β-triketone products formed by UV light irradiation of *trans*-isohumulone

The conversion of *trans*-isohumulone and the yields of the enolized cyclic β-triketone products were determined as a function of irradiation time. The results are shown in Figs. 1 and 2.

The data illustrated in Figs. 1 and 2 suggest that at conversions below 15% the photochemistry of *trans*-isohumulone follows zero-order kinetics and that the four

© 2008 NRC Canada

Table 1. Yields of enolized cyclic β-triketones formed in the UV light irradiation of *trans*-isohumulone in methanol solution.

Enolized cyclic β-triketone photoproduct	Yield (%)
cis-Isohumulone	50 ± 4
Humulone	20 ± 1
dehydro-Isohumulone	22 ± 1
dehydro-Humulinic acid	6 ± 0.5
Total	98 ± 6.5

enolized cyclic β-triketone products isolated are primary products. At conversions above 15% the conversion of *trans*-isohumulone becomes less efficient and the products themselves decline in yield. This suggests that at these conversions the concentrations of the products are high enough for them to absorb light directly, or to quench the *trans*-isohumulone excited state, and hence undergo secondary photolysis. We were unable to identify the products of secondary photolysis because of their complexity and the low yield of each component. Some previous studies have led to reports of the formation of complex mixtures of products when isohumulone is photolysed to high conversion (13–16).

The gradients of the initial linear portions of the reaction profiles, shown in Figs. 1 and 2, allow the determination of the yield of each primary product based on converted *trans*-isohumulone. These yields are shown in Table 1.

The sum of the yields in Table 1 reveals that all of the converted *trans*-isohumulone has been accounted for, and that there are no other major primary photoproducts, apart from those derived from the cleavage of the pentenoyl side chain en route to *dehydro*-humulinic acid.

Identification and yields of the *trans*-isohumulone side chain photoproducts

The formation of *dehydro*-humulinic acid from the photolysis of *trans*-isohumulone must also yield one or more products resulting from the cleaved 4-methyl-3-pentenoyl side chain, as indicated in Scheme 7.

Deoxygenated diethyl ether solutions of *trans*-isohumulone were exposed to light of 313 nm wavelength and directly analyzed by GC-MS at low conversions. The yields of the primary enolized cyclic β-triketone photoproducts were also determined by GC-MS and are given in Table 2.

The product yields shown in Table 2 are comparable with those determined when methanolic solutions of *trans*-isohumulone were photolysed and analyzed by HPLC (Table 1). This indicates that the change in solvent did not influence the reaction outcome. The identities of the photoproducts derived from the cleaved 4-methyl-3-pentenoyl side chain were determined by GC-MS. Their identities were confirmed by comparison with independently prepared authentic samples. The product structures are given in Fig. 3.

Each of the products is a branched chain of either five carbons (compounds **8**, **9**, **11**, **12**, and **13**) or six carbons (compounds **10**, **14**, **15**, and **16**) and appear therefore to be products formed both prior to and following decarbonylation of an initially produced 4-methyl-3-pentenoyl radical. Several of these photoproducts contain oxygen (compounds **11**, **12**, **13**, **14**, **15**, and **16**), which was not present in the 4-methyl-3-pentenoyl side chain. This observation is consistent with a radical intermediate trapped by reaction with molecular oxygen. The structures of the remaining products are consistent with hydrogen atom transfer (from ether, to oxygen, or via disproportionation, etc.) both before and after decarbonylation of the initially produced 4-methyl-3-pentenoyl radical. The various pathways are summarized in Scheme 8.

To our knowledge, there is only one published investigation of the volatile products of *trans*-isohumulone photochemistry; this involved analysis of the headspace of a riboflavin sensitized reaction of *trans*-isohumulone and led

Scheme 7.

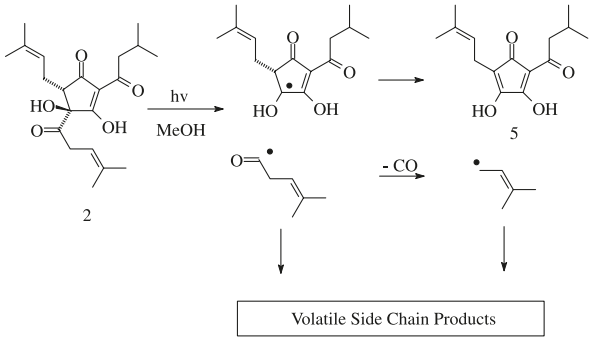

Table 2. Yields of primary enolized cyclic β-triketone products produced from UV light irradiation of *trans*-isohumulone in diethyl ether solution.

Enolized cyclic β-triketone photoproduct	Yield (%)
cis-Isohumulone	50 ± 3
Humulone	19 ± 2
dehydro-Isohumulone	21 ± 2
dehydro-Humulinic acid	5.8 ± 0.6
Total	96 ± 7

Fig. 3. Photoproducts derived from side chain cleavage in the photolysis of *trans*-isohumulone.

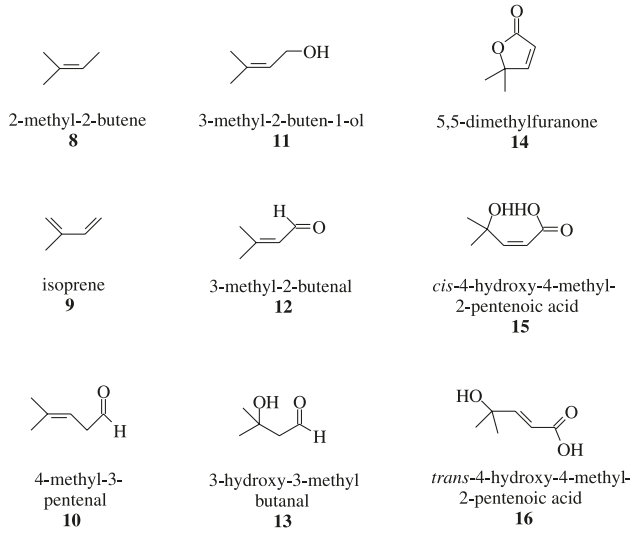

© 2008 NRC Canada

Scheme 8.

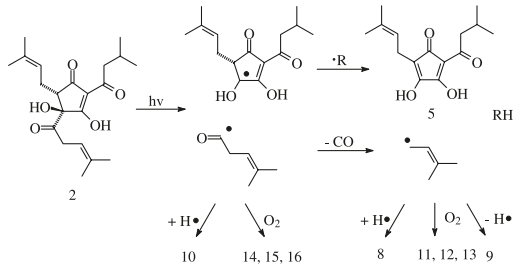

volatile product structures 8-16 are illustrated in Figure 3

to the identification of compounds **8**, **9**, and **10** (26). The yields of each of the products **8–16** found in our work were calculated relative to the amount of *dehydro*-humulinic acid formed and are presented in Table 3.

The dominant fate of the 4-methyl-3-pentenoyl side chain intermediate appears to be the addition of oxygen, despite measures taken to remove the dissolved oxygen from the solution prior to irradiation (The freeze-pump-thaw method of degassing is a well-known procedure often utilized for oxygen sensitive reactions.) (27). If this is the case, the relative yields of these products would increase in solutions containing ambient concentrations of dissolved oxygen. To test this, irradiations of *trans*-isohumulone were conducted with 313 nm light using diethyl ether solutions containing ambient levels of dissolved oxygen. The product yields obtained presented in Table 4.

The data in Table 4 show that within the experimental error, a mass balance was achieved for side chain product formation in the ambient oxygen containing solution. The incomplete recovery of the side chain derived compounds in deoxygenated solutions may reflect reaction of radical intermediates with the solvent to give undetected compounds. In the presence of oxygen, the radicals are trapped and these side reactions are avoided. Since no new volatile products were observed in the ambient oxygen solution, it is reasonable to conclude that the oxidation products formed in both solutions resulted from reaction of a radical intermediate with molecular oxygen.

Conclusions

As noted in the Introduction to this paper, previous reports of the products of photolysis of *trans*-isohumulone are contradictory. For example, in one study *dehydro*-humulinic acid (**5**) was reported as the only product (12, 13), while in another decarbonylated *dehydro*-isohumulone (**6**) was identified as a major product (14–16). In these reports, the products are not isolated or fully characterized, nor are their yields reported. In the work reported here the primary products formed by direct UV light irradiation of *trans*-isohulumone have been isolated and identified by ^{13}C and ^{1}H NMR spectroscopy and by mass spectroscopy, their yields have been determined, and a complete mass balance has been obtained. We find that *dehydro*-isohumulinic acid (**5**) is not the sole product. Rather, three modes of reaction occur. These are isomerization, dehydration, and side chain cleavage to give humulone (**1**), *cis*-isohumulone (**3**), *dehydro*-isohumulone (**7**), as well as *dehydro*-humulinic acid (**5**). No evidence was found for the formation of decarbonylated *dehydro*-isohumulone (**6**). Also, and surprisingly given the normal reactivity of enones when irradiated with UV light in the presence of alkenes, no evidence was found for products of intra- or intermolecular 2+2 photocycloaddition. The formation of *dehydro*-humulinic acid requires the loss of the 4-methyl-3-pentenoyl side chain of *trans*-isohumulone. Previous studies of the fate of this 4-methyl-3-pentenoyl side chain were performed using mixtures of iso-alpha acids under conditions where secondary photochemistry could occur. In the work reported here, the primary products of side chain cleavage have been identified, their yields have been determined, and a complete mass balance has been obtained. In addition to the formation of *dehydro*-humulinic acid, we found that the side chain cleavage leads to products derived from the interception of 4-methyl-3-pentenoyl radicals and methylbutenyl radicals. This is compatible with the observation that isohumulones and light lead to the formation of very low concentrations of 3-methyl-2-butene thiol in a beer matrix and suggests that the thiol is produced by interaction of a photochemically generated methylbutenyl radical with a sulfur donor.

Table 3. Percent yields of *trans*-isohumulone side chain derived products in deoxygenated diethyl ether solution.

Side chain product	Yield (%)
2-Methyl-2-butene	1.0 ± 0.2
Isoprene	0.9 ± 0.2
4-Methyl-3-pentenal	2.3 ± 0.3
3-Methyl-2-buten-1-ol	8.4 ± 0.9
3-Methyl-2-butenal	3.9 ± 0.5
3-Hydroxy-3-methylbutenal	11 ± 1
trans-4-Hydroxy-4-methyl-2-pentenoic acid	23 ±2
cis-4-Hydroxy-4-methyl-2-pentenoic acid	12 ± 1
5,5-Dimethylfuranone	12 ± 1
Total product yield	75 ± 8

Table 4. Percent yields of the identified side chain products from *trans*-isohumulone photolysis in diethyl ether in the presence of ambient oxygen.

Side chain product	Yield (%)
2-Methyl-2-butene	—
Isoprene	—
4-Methyl-3-pentenal	—
3-Methyl-2-buten-1-ol	11 ± 1
3-Methyl-2-butenal	8.0 ± 0.7
3-Hydroxy-3-methylbutenal	14 ± 1
trans-4-Hydroxy-4-methyl-2-pentenoic acid	27 ± 3
cis-4-Hydroxy-4-methyl-2-pentenoic acid	16 ± 1
5,5-Dimethylfuranone	17 ± 1
Total product yield	93 ± 8

Experimental

General

All the solvents used for irradiations, spectrometry, and chromatography were obtained from the Sigma-Aldrich chemical company and were of spectrophotometric quality.

© 2008 NRC Canada

UV irradiations of *trans*-isohumulone were conducted with a 450 W Hanovia medium pressure mercury lamp, surrounded by an aqueous solution of potassium chromate (1.44×10^{-3} mol/L) and sodium carbonate (1.25×10^{-2} mol/L) (27). Methanolic solutions were purged with nitrogen gas for 20 min prior to light exposure and maintained under nitrogen during the irradiation to minimize oxygen contamination. The solutions were stirred throughout the irradiation procedures. Samples were withdrawn from the irradiation vessel via syringe through a Teflon stopcock. Diethyl ether was freshly distilled immediately prior to use. Solutions prepared in diethyl ether were degassed by the freeze-pump-thaw method (27). Sampling of these ether solutions was performed at the conclusion of the irradiation to minimize molecular oxygen contamination and loss of volatile compounds.

Qualitative analyses of products

Semi-preparative HPLC separations were accomplished with a Waters instrument, employing a 10 mm × 300 mm Supelco C_{18}-nucleosil semi-preparative column. Samples were introduced with a 500 uL sample loop and separated with an eluent mixture of 80% acetonitrile, 20% water and 0.1% concentrated phosphoric acid. The NMR spectra were obtained in $CDCl_3$ with a Varian Mercury 400 NMR spectrometer at 400.09 MHz for ^{1}H and 100.69 MHz for ^{13}C. The ^{1}H and ^{13}C NMR assignments were correlated with the two-dimensional NMR techniques of gCOSY, gHSQC, and gHMBC.

Quantitative analyses of products

Samples were analyzed using an isocratic Waters HPLC system with a tunable absorbance detector set to 270 nm. Samples were introduced via a 10 uL injection loop and separated with a 250 mm × 4.6 mm Supelco ODS nucleosil analytical column. The eluent system, composed of a mixture of 600 mL of acetonitrile, 400 mL of distilled water, and 2 mL of concentrated phosphoric acid. Calibration curves were prepared for each analyte using five different concentrations (ranging from 1% to 25% of the starting *trans*-isohumulone concentration). The GC-MS analyses were performed with a Varian Saturn 4-D GC-MS, equipped with a DB-5 capillary column and a splitless injector. The temperature program of the GC began at 50 °C for 2 min, with the temperature increased to 180 °C at 15 °C/min, then to 200 °C at 4 °C/min and finally to 230 °C/min at 1 °C. The mass spectrometer scanned over the mass range of 33 to 550 mass units at 1 s intervals. Samples were analyzed in freshly distilled, spectrophotometric grade diethyl ether. Calibration curves were prepared for the analytes, using five different concentrations (ranging from 0.5% to 50% of the typical *dehydro*-humulinic acid concentration).

Preparation of compounds

Humulone

Humulone was isolated from a commercially available non-isomerized hop extract provided by from the Research and Development department of the Labatt Brewing Company. The procedure used is a literature method (11).

^{1}H NMR δ: 0.97 (d, *J* = 7.0 Hz, 3H), 1.01 (d, *J* = 7.0 Hz, 3H), 1.53 (s, 3H), 1.69, (s, 6H), 1.74 (s, 3H), 2.15 (m, *J* = 7.0 Hz, 1H), 2.49 (dq, *J* = 7.0 Hz, 2H), 2.77 (dd, *J* = 7.0 Hz, 2H), 3.06 (dq, *J* = 7.0 Hz, 2H), 5.00 (t, *J* = 7.0 Hz, 1H), 5.14 (t, *J* = 7.0 Hz, 1H). ^{13}C NMR δ: 17.9, 22.7, 25.4, 25.7, 26.1, 30.2, 46.0, 84.2, 110.1, 113.7, 115.4, 116.2, 135.2, 137.7, 175.8, 186.9, 191.1, 198.2. GC-MS: 363 (76%), 345 (78%), 327 (6%), 307 (3%), 295 (6%), 266 (3%), 223 (3%), 197 (3%), 166 (3%), 137 (4%), 109 (7%), 97 (7%), 85 (5%), 69 (100%), 57 (16%).

trans-*Isohumulone*[3]

Humulone was photo-isomerized by a literature method (11) utilizing UV light from a medium pressure mercury lamp that had passed through a uranium oxide glass filter. The course of the irradiation was monitored by analytical HPLC. Analysis by HPLC and GC-MS indicated the purity to be greater than 97% after recrystallization.

^{1}H NMR δ: 0.88 (d, *J* = 6.6 Hz, 3H), 0.91 (d, *J* = 6.6 Hz, 3H), 1.47 (s, 3H), 1.51 (s, 3H), 1.63 (s, 3H), 1.67 (s, 3H), 2.08 (m, 6.6, 1H), 2.27 (dt, *J* = 7.1 & 15 Hz, 1H), 2.52 (dt, *J* = 7.1 & 15 Hz, 1H), 2.65 (d, *J* = 7.1 Hz, 2H), 2.98 (dd, *J* = 6.8 & 6.9 Hz, 1H), 3.27 (d, *J* = 7.2 Hz, 2H), 5.08 (t, *J* = 7.1Hz, 1H), 5.14 (t, *J* = 7.1 Hz, 1H). ^{13}C NMR δ: 18.2, 18.7, 22.5, 23.1, 23.6, 25.9, 26.3, 38.8, 44.3, 55.8, 91.2, 110.6, 114.7, 120.3, 135.2, 136.4, 195.7, 198.2, 205.3, 207.1. GC-MS: 363 (52%), 345 (44%), 327 (3%), 293 (15%), 277 (7%), 266 (5%), 238 (3%), 209 (5%), 197 (9%), 109 (3%), 97 (8%), 85 (5%), 69 (66%), 57 (11%), 41 (100%).

cis-*Isohumulone*

Humulone was isomerized to *cis*-isohumulone by a literature method (28). The material was isolated as a light yellow oil from the reaction mixture and was purified by semi-preparative HPLC.

^{1}H NMR δ: 0.94 (d, *J* = 6.2 Hz, 3H), 0.96 (d, *J* = 6.2 Hz, 3H), 1.52 (s, 3H), 1.56 (s, 3H), 1.59 (s, 3H), 1.63 (s, 3H), 2.13 (m, *J* = 6.2 Hz, 1H), 2.41 (dt, *J* = 7.2 Hz, 1H), 2.47 (dt, *J* = 7.1 Hz, 1H), 2.60 (d, *J* = 7.1 Hz, 2H), 3.20 (dd, *J* = 7.1 Hz, 1H), 3.30 (d, *J* = 7.0 Hz, 2H), 5.01 (t, *J* = 7.0 Hz, 1H), 5.12 (t, *J* = 7.0 Hz, 1H). ^{13}C NMR δ: 18.0, 18.3, 22.6, 22.7, 25.6, 59.9, 26.3, 37.1, 46.0, 50.3, 55.5, 87.7, 110.7, 114.7, 119.8, 119.9, 135.4, 136.9, 195.5, 200.6, 206.3, 206.9. GC-MS: 363 (84%), 346 (51%), 295 (11%), 266 (7%), 197 (19%), 137 (4%), 109 (3%), 97 (5%), 85 (9%), 69 (80%), 57 (14%), 41 (100%).

Dehydro-*humulinic acid*

A sample of *trans*-isohumulone was used to prepare *dehydro*-humulinic acid by a literature method (29).

^{1}H NMR δ: 0.95 (d, *J* = 7.0 Hz, 3H), 0.96 (d, *J* = 7.0 Hz, 3H), 1.63 (s, 3H), 1.70 (s, 3H), 2.11 (m, *J* = 7.0 Hz, 1H), 2.58 (d, *J* = 7.1 Hz, 1H), 3.02 (d, *J* = 7.0 Hz, 2H), 5.21 (t, *J* = 7.0 Hz, 1H). ^{13}C NMR δ: 17.7, 23.8, 25.2, 25.6, 48.9, 110.8, 116.7, 121.7, 136.2, 158.1, 161.3, 193.5, 198.1. GC-MS: 265 (100%), 247 (9%), 209 (10%), 190 (13%), 175 (6%), 152 (10%), 95 (8%), 81 (13%), 79 (13%), 69 (19%), 55 (21%).

Preparation of side chain products

PCC oxidations of primary alcohols to aldehydes

The pyridinium chlorochromate reagent was prepared by a literature method (30).

© 2008 NRC Canada

3-Methyl-2-butenal

About 0.5 g of 3-methyl-2-buten-1-ol was dissolved in 5 mL of CH_2Cl_2 and added to a suspension of 1.5 g of the PCC reagent in 20 mL of CH_2Cl_2. The mixture was stirred at room temperature for about 2 h. Three 25 mL portions of diethyl ether were used to wash the mixture. The organic extracts were combined, dried with $MgSO_4$, and the solvent removed by rotary evaporation at room temperature. Isolation of the compound and final purification were accomplished by vacuum distillation.

^{1}H NMR δ: 1.95 (s, 3H), 2.12 (s, 3H), 5.54 (d, J = 7.1 Hz, 1H), 9.67 (d, J = 7.2 Hz, 1H). ^{13}C NMR δ: 21.3, 27.6, 124.8, 158.7, 192.6. GC-MS: 84, 69, 55.

4-Methyl-3-pentenal

About 0.6 g of 4-methyl-3-penten-1-ol was dissolved in 5 mL of CH_2Cl_2 and added to a suspension of 1.5 g of the PCC reagent in 20 mL of CH_2Cl_2. The mixture was stirred at room temperature for about 2 h. Three 25 mL portions of diethyl ether were used to wash the mixture. The organic extracts were combined, dried with $MgSO_4$, and the solvent removed by rotary evaporation at room temperature. Isolation of the compound and final purification were accomplished by vacuum distillation.

^{1}H NMR δ: 1.63 (s, 3H), 1.74 (s, 3H), 3.21 (d, J = 7.1 Hz, 2H), 5.31 (d, J = 7.1 Hz, 1H), 9.82 (s, 1H). ^{13}C NMR δ: 18.7, 25.3, 36.8, 115.8, 138.4, 201.4. GC-MS: 98, 83, 70, 54, 44.

3-Methyl-3-hydroxybutanal

The 3-methyl-3-hydroxybutanal was prepared from 3-methyl-2-butenal by a literature method (31). Isolation of the compound and final purification were accomplished by semi-preparative HPLC.

^{1}H NMR δ: 1.42 (s, 6H), 2.54 (s, 2H), 4.21 (s, 1H), 9.78 (s, 1H). ^{13}C NMR δ: 27.2, 54.8, 79.1, 205.4. GC-MS: 102, 87, 85, 73, 58, 44.

4-Hydroxy-4-methyl-2-pentenoic acid derivatives

The 4-hydroxy-4-methyl-2-pentenoic acid derivative compounds were prepared by a literature method from UV irradiation of propargylic acid in isopropanol (32). The resulting yields of each product were approximately 26% for *trans*-4-hydroxy-4-methyl-2-pentenoic acid, 14% for *cis*-4-hydroxy-4-methyl-2-pentenoic acid, and 9% for 5,5-dimethylfuranone. The products were separated and purified by semi-preparative HPLC.

trans-*4-Hydroxy-4-methyl-2-pentenoic acid*

^{1}H NMR δ: 1.31 (s, 6H), 4.92 (s, 1H), 5.82 (d, J = 15 Hz, 1H), 7.28 (d, J = 15 Hz, 1H), 11.03 (s, 1H). ^{13}C NMR δ: 27.8, 69.7, 123.6, 158.4, 172.3. GC-MS: 130, 115, 113, 85, 71, 59, 45.

cis-*4-Hydroxy-4-methyl-2-pentenoic acid*

^{1}H NMR δ: 1.49 (s, 6H), 5.48 (s, 1H), 5.87 (d, J = 12 Hz, 1H), 6.43 (d, J = 12 Hz, 1H), 10.91 (s, 1H). ^{13}C NMR δ: 29.2, 76.4, 121.2, 153.3, 170.8. GC-MS: 130, 115, 113, 85, 71, 59, 45.

5,5-Dimethyl furanone

^{1}H NMR δ: 1.27 (s, 6H), 5.82 (d, J = 5.7 Hz, 1H), 7.28 (d, J = 5.8 Hz, 1H). ^{13}C NMR δ: 27.4, 90.8, 122.1, 165.2, 175.2. GC-MS: 112, 97, 95, 70, 68.

dehydro-*Isohumulone preparation*

A 500 mg sample of *trans*-isohumulone was dissolved in 50 mL of freshly distilled anhydrous diethyl ether. A 1.5 mL aliquot of acetic anhydride and 0.5 mL of triethylamine were added and the mixture was stirred at room temperature for 3 h. The mixture was washed with three portions of sodium bicarbonate solution (1.25 g in 300 mL) and with three 100 mL portions of water. The organic layer was dried with magnesium sulphate, and the solvent removed by rotary evaporation. *Dehydro*-isohumulone was separated as an oil from the reaction mixture and further purified by semi-preparative HPLC.

^{1}H NMR δ: 0.88 (d, J = 7.0 Hz, 3H), 0.90 (d, J = 7.0 Hz, 3H), 1.60 (s, 6H), 1.71 (s, 6H), 2.12 (m, J = 7.0 Hz, 1H), 2.92 (d, J = 7.0 Hz, 2H), 3.47 (d, J = 7.0 Hz, 2H), 3.52 (d, J = 7.0 Hz, 2H), 4.94 (t, J = 7.0 Hz, 1H), 5.24 (t, J = 7.0 Hz, 1H). ^{13}C NMR δ: 18.3, 22.6, 22.7, 24.1, 25.9, 40.3, 52.4, 113.9, 118.7, 125.8, 133.9, 134.2, 137.9, 153.7, 158.4, 176.7, 195.4, 198.6. GC-MS: 345 (100%), 247 (7%), 147 (3%), 119 (7%), 91 (9%), 77 (7%), 69 (20%), 53 (14%).

Acknowledgements

The authors would like to thank Labatt Breweries for their funding and support of the initial stages of this work. The authors thank the Natural Sciences and Engineering Research Council of Canada for continuing support of this work.

References

1. W. Hardwick. Handbook of brewing. Marcel Dekker Inc., New York. 1995.
2. W.J. Simpson. J. Inst. Brew. **99**, 317 (1993).
3. C. Lintner, Kehrbuch der Beirbrauerei, Verlag Vieweg und Sohn, Braunschweig, 1875, as cited in J. Templar, K. Arrigan, and W. Simpson. Brewer's Digest, **5**, 18 (1995).
4. Y. Kuroiwa and H. Hashimoto. Rep. Res. Lab, Kirin Brew Co. Ltd. **4**, 35 (1961).
5. Y. Kuroiwa and H. Hashimoto. Rep. Res. Lab, Kirin Brew Co. Ltd. **5**, 20 (1962).
6. J. Kaplan. Nature (London), **196**, 950 (1962).
7. J. Kaplan. J. Gen. Physiol. **47**, 103 (1963).
8. F. Gunst and M. Verzele. J. Inst. Brew. **84**, 291 (1978).
9. A. Khokher and M. Verzele. Bull. Soc. Belg. Chim. **76**, 101 (1967).
10. M. Verzele and A. Khokher. J. Inst. Brew., **73**, 255, (1967).
11. F. Sharpe and H. Ormrod. J. Inst. Brew. **97**, 33 (1991).
12. D. De Keukeleire and G. Bondeel. J. Chem. Soc. Perkin Trans. 1, **143**, 2715 (1987).
13. C.S. Burns, A. Heyerich, D. De Keukeleire, and M. D. Forbes. Chem. Eur. J. **7**, 4554 (2001).
14. A. Heyerick, Y. Zhao, P. Sandra, K. Huvaere, F. Roelens, and D. De Keukeleire. Photochem. Photobio. Sci. **2**, 306 (2003).
15. A. Heyerick, Y Zhao, P. Sandra, K. Huvaere, F. Roelens, and D. De Keukeleire. Photochem. Photobio. Sci. **3**, 854 (2004).
16. D. De Keukeleire. The Spectrum, **14**, 1 (2001).
17. J.E. Pauw and A. C. Weedon. Tetrahedron Lett. **23**, 5485 (1982).

© 2008 NRC Canada

18. D. Maradyn and A. C. Weedon. J. Am. Chem. Soc. **117**, 5359 (1995).
19. A.R. Matlin, C.F. George, S. Wolff, and W.C. Agosta. J. Am. Chem. Soc. **108**, 3385 (1986).
20. M.C. Pirrung and N.J.G. Webster. J. Org. Chem. **52**, 3603 (1987).
21. T.S. Cantrell, W.S. Haller, and J.C. Williams., J. Org. Chem. **34**, 509 (1969).
22. T.S. Cantrell. Tetrahedron, **27**, 1227 (1971).
23. P. De Mayo and H. Takeshita. Can. J. Chem. **41**, 440 (1963).
24. B. Challand, H. Hikino, G. Kornis, G. Lange, and P. de Mayo. J. Org. Chem. **34**, 794 (1969).
25. B.W. Disanayaka and A.C. Weedon. J. Org. Chem. **52**, 2905 (1987).
26. K. Huvaere, B. Sinnaeve, J. Van Boexlaer, and D. De Keukeleire. Photochem. Photobio. Sci. 854 (2004).
27. S. Murov. Handbook of photochemistry. Marcel Dekker Inc., New York. (1991).
28. B. Clarke. J. Inst. Brew. **71**, 26 (1965).
29. P. James and T Tynan. J Inst. Brew. **96**, 137 (1990).
30. E.J. Corey and W. Suggs. Tetrahedron Lett. **31**, 2647 (1975).
31. G. Vassilikogiannakis. J. Am. Chem. Soc. **120**, 9911 (1998).
32. L. Kostochka. J. Org. Chem. USSR, **9**, 1635 (1973).

© 2008 NRC Canada

Glycine-promoted rapid synthesis of novel xanthene derivatives in ionic liquid

Mazaahir Kidwai, Kavita Singhal, and Shuchi Kukreja

Abstract: A green route for the synthesis of multi-substituted 2,3-dihydro-xanthenone derivatives using ionic liquid as solvent and amino acid as promoter is described. The reaction is simple and proceeds well at room temperature and devoid of the use of any harmful catalyst or solvent. This is an efficient technique.

Key words: xanthene, ionic liquid, glycine, room temperature.

Résumé : On décrit une méthode verte de synthèse de dérivés multisubstitués de la 2,3-dihydroxanthénone qui s'effectue dans un liquide ionique comme solvant, en présence d'un acide aminé comme catalyseur. La réaction est simple; elle s'effectue à la température ambiante et elle ne fait appel à aucun catalyseur ou solvant nocifs. Il s'agit d'une technique efficace.

Mots-clés : xanthène, liquide ionique, glycine, température ambiante.

Introduction

Xanthene-based fluorescent dyes are widely used in chemical biology to detect biological substances, such as proteins, DNAs, and sugars with high sensitivity and selectivity (1). This is attributed to the high electron density in the xanthene skeleton. The emission from the charge-transfer state of xanthenes has also been studied using nanoparticle chemistry (2). Numerous reports have been patented and have delineated the antiviral (3), antibacterial (4), and anti-inflammatory effects (5) and antimalarial activities with the inhibitory action towards *Trypanothione reductase* enzyme (6). Furthermore, they have also been found as good candidates in photodynamics (7) and laser technology (8). A number of such type of compounds are also available from natural sources (e.g., in the form of Santalin pigment) (9).

The large interest in medicinally important molecules stimulates the development of new and more efficient syntheses of this class of compounds. So far, the reported classical synthetic approaches to xanthenes involve the reaction of β-naphthol with formaldehyde (10), with aldehyde acetals under acidic conditions (11), and with 2-naphthol-1-methanol (12) and the reaction of aryloxymagnesium halides with triethyl orthoformate (13). Synthetic alternatives are many, varied, and have resorted to harsh conditions (e.g., the use of catalysts such as *p*-TSA (14), polyaniline-*p*-toluenesulfonate salt (15), sulfamic acid (16), glacial acetic acid (17), AcOH–H_2SO_4, amberlyst-15 (18), and so forth). Many of them often involve the use of hazardous organic solvents, tedious work-up, acidic conditions, which may not be the preferred choices in view of green chemistry.

Because of the increasing demands of environment legislation for the development of organic reactions in environment-friendly media, synthetic manipulations have to be made to minimize the use of hazardous chemicals. One example is replacing the traditional organic solvents in reactions and their subsequent work-up with non-toxic solvents. In this regard, interest is being manifested in the use of room temperature ionic liquids as promising alternative volatile organic solvents (19). These ambient temperature ionic liquids, especially those based on 1,3-dialkyl imidazolium cations, have been emerging as leading green reaction medium for the past decades (20) and also referred as "designer solvents", as their physical and chemical properties could be adjusted by a careful choice of cations and anions.

In our ongoing efforts to investigate the range of organic reactions possible in ionic liquid and developing a more versatile route to biodynamic lead compounds by adopting the principles of "green chemistry" (21), we, for the first time, sought to develop a process of synthesizing xanthene derivatives executed in ionic liquid – glycine system that is robust as well as eco-friendly.

Results and discussion

In view of the emerging relevance of the imidazole-based ionic liquid as reaction media, we explored the condensation reaction for the synthesis of xanthenes using [bmim]PF_6 ionic liquid as green solvent. First, the reaction of 2-hydroxy aldehyde (salicaldehyde) **2a** with 5,5-dimethylcyclohexane-1,3-dione (dimedon) **1a** using glycine with [bmim]PF_6 ionic liquid was selected as a model reaction (Scheme 1). The reaction went into completion in ~3 h at room temperature, and 3,3-dimethyl-xanthene-1-one was obtained efficiently in good yields (Table 1). There are several papers, which re-

Received 25 October 2007. Accepted 19 March 2008. Published on the NRC Research Press Web site at canjchem.nrc.ca on 3 July 2008.

M. Kidwai,[1] K. Singhal, and S. Kukreja. Green Chemistry Research Laboratory, Department of Chemistry, University of Delhi, Delhi 110007, India.

[1]Corresponding author (email: kidwai.chemistry@gmail.com).

 doi:10.1139/V08-069 © 2008 NRC Canada

Scheme 1. Synthesis of dihydroxanthene-1-one derivatives in ionic liquid.

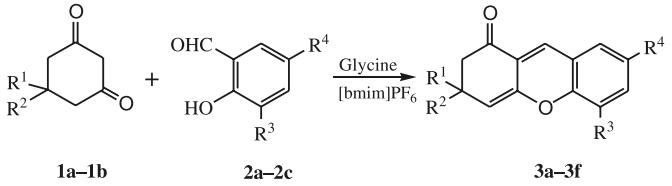

$R^1 = R^2 = CH_3$

$R^3 = Cl$

$R^4 = OMe$

Table 1. Synthesis of Xanthenone derivatives **3a**–**3f**.

Entry	R^1	R^2	R^3	R^4	Time (h)	Yield (%)
1	CH_3	CH_3	H	H	3.5	82
2	CH_3	CH_3	Cl	H	3.5	80
3	CH_3	CH_3	H	OMe	3.2	83
4	H	H	H	H	3.5	78
5	H	H	Cl	H	4.0	82
6	H	H	H	OMe	3.8	82

ported the synthesis of xanthenes using α,β-unsaturated ketones; however, no report adopting ketones and diketones as the starting material is exemplified in the literature.

The absence of glycine requires more reaction time to yield the desired product and also resulted in low yields, and then the presence of glycine as promoter is essential here. Later, we tried to study the effect of different amino acids on the synthesis of **3a**, and the results are outlined in Table 2. Glycine was found to be the best catalyst out of the used amino acids, and thus for the synthesis of other derivatives, glycine was taken under optimal conditions. As the removal of water molecule in the second last step of mechanism (Fig. 1) needs some driving force, the role of glycine played in the reaction is important here, which is attributed to its basicity and helped in the trapping of water molecule.

As a test case, **3a** was synthesized under different reaction conditions using various solvents. Acetonitrile was almost ineffective for this condensation reaction; both DMF and DMSO were found to be effective in affording the products. Two neutral imidazoline-based ionic liquids were screened as the reaction medium, and it seemed that both the ionic liquids were suitable for the preparation of xanthene in good-to-excellent yields. Moreover, among these two ionic liquids tested, $[bmim]PF_6$ was chosen owing to the high yields with shorter reaction time, and then the rest of the reactions were carried out in this ionic liquid. It is important to note here that the use of ionic liquid leads to easy work-up.

Having established $[bmim]PF_6$ as the best solvent, we started to study the effect of temperature for this condensation reaction of 2-hydroxy aldehyde with dimedon, and the results are presented in Table 3. When the reaction temperature was raised, maximum yield was reached soon. However, 3 h of reaction time was found to be sufficient to complete this condensation under room temperature, so the reaction

Table 2. The effect of different a-aminoacids in the synthesis of xanthenone derivative **3a**.

Entry	Amino acid	Yield[a] (%)	Time (h)
1	L-Histidine	76	6.8
2	L-Lysine	72	6.8
3	L-Alanine	70	6.0
4	Glycine	82	3.5

Note: Reaction conditions: ionic liquid $[Bmim]PF_6$, glycine, 25 °C.
[a] Isolated yields.

Fig. 1. Probable mechanism for the synthesis of xanthene-1-one derivative **3a**.

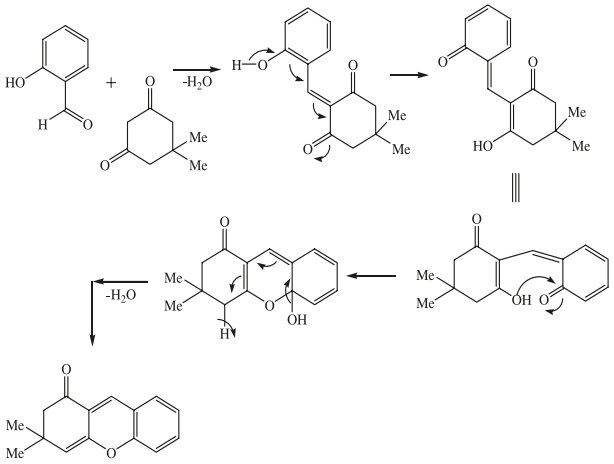

Table 3. Effect of temperature on the synthesis of **3a** using optimal conditions in an ionic liquid system.

Entry	Temp. (°C)	Reaction time (h)	Yield (%)
1	25	3.5	82
2	50	2.5	82
3	75	1.8	80

was ultimately carried out at 25 °C to meet the requirement of minimization of energy consumption.

A plausible mechanism for this protocol is presented in Fig. 1. Initially, we suspected that the self condensation of the 2 mol of 1,3-dicarbonyl compound with 1 mol of aldehyde would possibly yield a compound with the substitution of aryl group at ninth position. Indeed, mass spectra and ^1H NMR spectra clearly ruled out the formation of that compound. Finally, the compound was confirmed on the basis of ^{13}C NMR spectral analysis. Further, to strengthen the mechanism and generality of the reaction, using the above-said optimized reaction conditions described above, we explored the possibility of usage of various cyclic diketones and 2-hydroxyl aldehydes. According to the mechanism, considering the case 1b as reactant, the aromatization is expected in the last step led to the formation of reduced ring system with the hydroxyl group at position 1. But on completion, the reaction furnishes **3d** as product, which was analyzed, and the peaks in ^1H NMR and correspondingly in ^{13}C NMR spectra confirmed the product. All of the compounds are hitherto unknown in chemical literature.

© 2008 NRC Canada

Table 4. Xanthenone derivative (**3a**) obtained in a recycled [Bmim]PF_6 ionic liquid – glycine system using the standard conditions.

Run	Yield (%)
1	82
2	82
3	80
4	80

The ionic liquid used could be typically recovered by extracting out the product and filtering the suspension to remove the residual solid. This separation will not remove glycine as it got immobilized in IL, and the same glycine-immobilized IL has been used further for the rest of the derivatives. Interestingly, glycine can be removed after the aqueous neutralization. Finally, the products obtained were of the same purity as in the first reaction, and there was appreciable consistency in the product yields (Table 4).

Conclusion

In summary, we have devised a facile, eco-benign, and highly efficient protocol for the synthesis of 2,3-dihydroxanthenone derivatives bearing three points of diversity in IL–glycine system at room temperature using suitably substituted 2-hydroxy aromatic aldehydes and 1,3-diketones. This method provides several advantages, such as easy synthesis, simple work-up, sufficient yields, accelerated reaction rates, and low consumption of solvent. Another attractive part of this report is the satisfactory recovery and re-use of ionic liquid with no diminution of product yields, which demonstrates ionic liquid as a greener, economically viable catalyst cum solvent, which can interest the chemical community for the synthesis of interesting library of biologically relevant heterocyclic moieties.

Experimental section

All the chemicals and reagents were of analytical grade. Ionic liquids were prepared according to the literature procedure (22). Melting points were taken on a Thomas Hoover melting-point apparatus and are uncorrected. IR (in Nujol) were recorded on a model PerkinElmer FTIR-1710 spectrophotometer. ^{1}H NMR and ^{13}C NMR were recorded on a Bruker Avance Spectrospin 300 using TMS as internal standard. Mass spectra were recorded on a KC455 Waters TOF MS spectrometer. TLC was run on the silica-gel-coated aluminium sheets (Silica gel 60 F_{254}, E. Merck, Germany) and visualized in UV light (254 nm). Temperature of the reaction mixture was measured through AZ, Mini Gun Type, non-contact IR Thermometer, Model No. 8868.

General procedure for the synthesis of xanthen-1-one derivatives (3a–3f)

To a mixture of 1,3-diketone **1a**–**1b** (1 mmol), 2-hydroxy aromatic aldehyde **2a**–**2c** (1 mmol), and glycine, [bmim]PF_6 (2 mL) was added in a 10 mL flask equipped with a magnetic stirrer. The reaction mixture was stirred vigorously at room temperature, and the progress of the reaction was monitored by TLC. Upon completion of the reaction, the content was extracted with ethyl acetate (3 × 3 mL). The product obtained was further purified by column chromatography [column of SiO_2; pre-adsorption of the residue at SiO_2 (~8 g) with ethylacetate; elution with ether – ethylacetate, 90:10 (*v*/*v*)].

Procedure to recover the ionic liquid

The reaction mixture was filtered to recover ionic liquid through the Whatman no. 3 filter paper under suction. The filtrate was extracted with ethyl acetate (2 × 3 mL). The ionic liquid left after the extraction was concentrated in vacuo to remove traces of organic solvent and used as such in the subsequent reactions.

Compound (3a)

Mp 200–202 °C. IR ν_{max} (cm^{-1}, Nujol): 2960, 2713, 1629, 1573, 1480, 1377, 1271, 1233, 1183, 1152, 1074, 1012, 822, 780. ^{1}H NMR (Me_4Si, 300 MHz, DMSO-d_6) δ: 0.93 (3H, s, CH_3), 1.09 (3H, s, CH_3), 3.32 (2H, s, CH_2), 5.08 (1H, s, C_4–H), 6.88 (1H, d, J = 7.8 Hz, Ar–H), 6.96 (2H, t, Ar–H), 7.06 (1H, d, J = 7.8 Hz, Ar–H), 7.09 (1H, s, C_9–H). ^{13}C NMR (75 MHz, DMSO-d_6) δ: 195.71, 164.56, 154.67, 148.51, 131.25, 127.84, 127.62, 127.51, 126.89, 117.31, 111.84, 50.21, 29.18, 25.01. MS: *m*/*z*: 226.72 (M^+, 100).

Compound (3b)

Mp 218–220 °C. IR ν_{max} (cm^{-1}, Nujol): 2962, 2713, 1628, 1576, 1489, 1373, 1269, 1234, 1185, 1152, 1079, 1020, 856, 775. ^{1}H NMR (Me_4Si, 300 MHz, DMSO-d_6) δ: 0.96 (3H, s, CH_3), 1.04 (3H, s, CH_3), 3.40 (2H, s, CH_2), 5.03 (1H, s, C_4–H), 6.92 (1H, s, C_9–H), 7.01 (2H, d, J = 8.7 Hz, Ar–H), 7.16 (1H, dd, J = 8.7 Hz, J' = 2.1 Hz, Ar–H). ^{13}C NMR (75 MHz, DMSO-d_6) δ: 195.64, 164.17, 154.67, 146.29, 130.96, 129.06, 127.91, 126.89, 126.72, 116.84, 113.25, 51.90, 26.70, 25.01. MS: *m*/*z*: 260.52 (M^+, 100).

Compound (3c)

Mp 244–246 °C. IR ν_{max} (cm^{-1}, Nujol): 2956, 2710, 1628, 1576, 1490, 1368, 1271, 1230, 1177, 1150, 1079, 1010, 843, 775. ^{1}H NMR (Me_4Si, 300 MHz, DMSO-d_6) δ: 1.01 (3H, s, CH_3), 1.11 (3H, s, CH_3), 3.32 (2H, s, CH_2), 3.81 (3H, s, OCH_3), 5.03 (1H, s, C_4–H), 6.69–7.01 (4H, m, Ar–H + C_9–H). ^{13}C NMR (75 MHz, DMSO-d_6) δ: 196.91, 163.70, 149.12, 148.84, 142.01, 131.25, 126.82, 124.47, 117.35, 111.84, 110.39, 57.40, 50.36, 29.06, 28.98, 24.66. MS: *m*/*z*: 256 (M^+).

Compound (3d)

Mp 196–198 °C. IR ν_{max} (cm^{-1}, Nujol): 2950, 2882, 2360, 1642, 1557, 1486, 1373, 1297, 1237, 1199, 1184, 1149, 1063, 985, 842, 775. ^{1}H NMR (Me_4Si, 300 MHz, DMSO-d_6) δ: 1.94–2.21 (2H, m, C_3–H, C_3–H), 2.41–2.66 (2H, m, C_2–H, C_2–H), 4.73 (1H, t, C_4–H), 6.90–7.13 (m, 5H, Ar–H + C_9–H). ^{13}C NMR (75 MHz, DMSO-d_6) δ: 197.01, 167.14, 150.82, 149.52, 129.78, 127.91, 127.62, 126.88, 119.36, 116.70, 112.01, 35.97, 19.84. MS: *m*/*z*: 198 (M^+).

Compound (3e)

Mp 178–180 °C. IR ν_{max} (cm^{-1}, Nujol): 2952, 2896, 2360, 1638, 1573, 1486, 1375, 1274, 1234, 1184, 1132, 1074, 999,

© 2008 NRC Canada

826, 778. ^{1}H NMR (Me_4Si, 300 MHz, DMSO-d_6) δ: 1.86–2.15 (2H, m, C_3–H, C_3–H), 2.39–2.76 (2H, m, C_2–H, C_2–H), 4.67 (1H, t, C_4–H), 6.97 (2H, d, J = 8.7 Hz, Ar–H), 7.16 (1H, dd, J = 8.7 Hz, J' = 2.1 Hz, Ar–H) 7.21 (s, 1H, C_9–H). ^{13}C NMR (75 MHz, DMSO-d_6) δ: 197.04, 168.78, 150.82, 149.49, 129.43, 127.72, 127.52, 126.46, 119.31, 116.82, 111.92, 36.94, 19.52. MS: *m*/*z*: 232 (M^+).

Compound (3f)

Mp 212–214 °C. IR ν_{max} (cm^{-1}, Nujol): 2952, 2902, 1632, 1573, 1490, 1375, 1284, 1232, 1188, 1150, 1063, 856, 775. ^{1}H NMR (Me_4Si, 300 MHz, DMSO-d_6) δ: 1.91–2.14 (2H, m, C_3–H, C_3–H), 2.42–2.81 (2H, m, C_2–H, C_2–H), 3.83 (3H, s, OCH_3), 4.72 (1H, t, C_4–H), 6.78 –7.12 (4H, m, Ar–H + C_9–H). ^{13}C NMR (75 MHz, DMSO-d_6) δ: 197.04, 164.70, 150.46, 144.21, 130.65, 127.91, 126.56, 124.70, 119.31, 116.02, 109.98, 57.11, 36.89, 19.33. MS: *m*/*z*: 228.4 (M^+).

Acknowledgements

One of the authors, Kavita Singhal, acknowledges the senior research fellowhip as financial assistance by the Council of Scientific and Industrial Research (CSIR), New Delhi.

References

1. G.S. Jiao, J.C. Castro, L.H. Thoresen, and K. Burgess. Org. Lett. **5**, 3675 (2003).
2. G. Ramakrishna and H.N. Ghosh. J. Phys. Chem. B, **105**, 7000 (2001).
3. R.W. Lambert, J.A. Martin, J.H. Merrett, K.E.B. Parkes, and G. J. Thomas. PCT Int. Appl. WO 9 706 178. 1997.
4. T. Hideao. Jpn. Tokkyo Koho JP 56-005-480. Chem. Abstr. **95**, 80922 (1981).
5. J.P. Poupelin, G. Saint-Rut, O. Foussard-Blanpin, G. Narcisse, G. Uchida-Ernouf, and R. Lacroix. Eur. J. Med. Chem. **13**, 67 (1978).
6. K. Chibale, M. Visser, D.V. Schalkwyk, P.J. Smith, A. Saravanamuthu, and A.H. Fairlamb. Tetrahedron, **59**, 2289 (2003).
7. R.M. Ion, O. Sirkecioglu, and N. Talinli, The third internet conference on photobiology. 2000. Available from http://www.photobiology.com/ photobiology2000/rodica2/index.htm
8. M. Ahmed, T.A. King, K.K. Do, B.H. Chan, and J. Lee. J. Phys. D: Appl. Phys. **35**, 1473 (2002).
9. J. Kinjo, H. Uemura, T. Nohara, M. Yamashita, N. Marubayashi, and K. Yoshihira. Tetrahedron Lett. **36**, 5599 (1995).
10. P. Papini and R. Cimmarusti. Gazz. Chim. Ital. **77**, 142 (1947).
11. J.A. Van Allan, D.D. Giannini, and T.H. Whitesides. J. Org. Chem. **47**, 820 (1982).
12. R.N. Sen and N. Sarkar. J. Am. Chem. Soc. **47**, 1079 (1925).
13. G. Casiraghi, G. Casnati, M. Catellani, and M. Corina. Synthesis, 564 (1974).
14. A.R. Khosropour, M.M. Khodaei, and H. Moghannian. Synlett, 955 (2005).
15. A. John, P.J.P. Yadav, and S. Palaniappan. J. Mol. Cat. A, **248**, 121 (2006).
16. B. Rajitha, B.S. Kumar, Y.T. Reddy, P.N. Reddy, and N. Sreenivasulu. Tetrahedron Lett. **46**, 8691 (2005).
17. A. Jha and J. Beal. Tetrahedron Lett. **45**, 8999 (2004).
18. S. Ko and C.-F. Yao. Tetrahedron Lett. **47**, 8827 (2006).
19. J.D. Holbrey and K.R. Seddon. Clean Prod. Process. B, **1**, 232 (1999).
20. (*a*) J. Dupont, R.F. De Souza, and P.A.Z. Suarez. Chem. Rev. **102**, 3667 (2002); (*b*) P. Wasserscheid and W. Keim, Angew. Chem., Int. Ed. **39**, 3772 (2000).
21. (*a*) M. Kidwai and S. Rastogi. Lett. Org. Chem. **3**, 149 (2006); (*b*) M. Kidwai, V. Bansal, and P. Mothsra. J. Mol. Cata. A, **76**, 268 (2006); (*c*) M. Kidwai Priya, K. Singhal, and S. Rastogi. Heterocycles, **71**, 569 (2007); (*d*) M. Kidwai, N.K. Mishra, V. Bansal, A. Kumar, and S. Mozumdar. Cat. Commun. In press.
22. J.S. Wilkes, J.A. Levisky, R.A. Wilson, and C.L. Hussey. Inorg. Chem. **21**, 1263 (1982).

© 2008 NRC Canada

Amine-tethered *N*-heterocyclic carbene complexes of rhodium(I)

Howard Jong, Brian O. Patrick, and Michael D. Fryzuk

Abstract: A new family of rhodium-diene based complexes has been developed that incorporates an *N*-heterocyclic carbene ligand with an N-donor tether. The ligand is denoted ^{Mes}[CNH] **2** (where ^{Mes}[CNH] is 2,4,6-$Me_3C_6H_2NC_3H_2NCH_2CH_2NH$-2,4,6-$Me_3C_6H_2$) and ^{Mes}[CN] for the amido form. The synthesis of the ^{Mes}[CNH] ligand involves reaction of *N*-mesitylimidazole with 2-chloroethyl-*N*-mesitylamine under melt conditions, followed by deprotonation with $KN(SiMe_3)_2$. The reaction of ^{Mes}[CNH] with $[(diene)RhCl]_2$ results in the formation of the monodentate complexes, ^{Mes}[CNH]Rh(diene)Cl (where diene = 1,5-cyclooctadiene (COD): **3a**; diene = 2,5-norbornadiene (NBD): **3b**). Bidentate variants could be isolated as either a neutral species, ^{Mes}[CN]Rh(diene) **4a**–**4b**, via deprotonation, or an ionic analogue such as $[^{Mes}$[CNH]Rh(diene)$]BF_4$ **5a**–**5b** by reaction with $NaBF_4$. Compounds **4**–**5** are the first examples of rhodium compounds that contained a bidentate NHC ligand with a pendant amino or amido donor. Complexes **3**–**5** were characterized fully and the solid-state single crystal X-ray structures of **3a**, **4a**, and **5b** are discussed. The utility of these complexes as catalyst precursors for hydrogenation reactions was examined and it was determined that these systems are not significantly more active than colloidal rhodium when parallel reactions were run. Various methods of transfer hydrogenations were also investigated with **3a**, which did not yield an appreciable conversion of either benzophenone or *N*-benzylideneaniline as substrates.

Key words: rhodium, *N*-heterocyclic carbene, catalysis, hydrogenation.

Résumé : On a développé une nouvelle famille de complexes à base de rhodium-diène qui incorpore un ligand carbène *N*-hétérocyclique comportant une une chaîne latérale avec un donneur azoté, ^{Mes}[CNH], **2**, dans lequel ^{Mes}[CNH] = 2,4,6-$Me_3C_6H_2NC_3H_2NCH_2CH_2NH$-2,4,6-$Me_3C_6H_2$ alors que ^{Mes}[CN] correspond à sa forme amido. La synthèse du ligand ^{Mes}[CNH] implique la réaction du *N*-mésitylmidazole avec la 2-chloroéthyl-*N*-mésitylamine à l'état fondu, suivie d'une déprotonation à l'aide du $KN(SiMe_3)_2$. La réaction du ^{Mes}[CNH] avec le $[(diène)RhCl]_2$ conduit à la formation des complexes ^{Mes}[CNH]Rh(diène)Cl (dans lesquels diène = 1,5-cyclooctadiène (COD), **3a**; 2,5-norbornadiène (NBD), **3b**). Des variantes bidentates peuvent aussi être isolées sous la forme d'espèces neutres, ^{Mes}[CN]Rh(diène), **4a**–**4b**, via une déprotonation, ou sous la forme d'un analogue ionique, tel le $\{^{Mes}$[CNH]Rh(diène)$]\}BF_4$, **5a**–**5b**, par réaction avec le $NaBF_4$. Les composés **4** et **5** sont les premiers exemples de composés du rhodium contenant un ligand bidentate NHC comportant une chaîne latérale donneur amino ou amido. On a effectué une caractérisation complète des complexes **3 - 5** et on discute des structures cristallines des composés **3a**, **4a** et **5b** établies par diffraction des rayons X à l'état solide sur des cristaux uniques. On a examiné l'utilité que pourraient avoir ces complexes comme précurseurs de catalyseurs pour les réactions d'hydrogénation et on a déterminé que, dans des réactions parallèles, l'activité de ces systèmes ne dépasse pas d'une façon significative celle du rhodium colloïdal. On a aussi examiné diverses méthodes d'hydrogénation par transfert à l'aide du composé **3a**, mais elles ne conduisent pas à des rendements appréciables de conversion de la benzophénone ou de la *N*-benzylidèneaniline utilisées comme substrats.

Mots-clés : rhodium, carbène *N*-hétérocyclique, catalyse, hydrogénation.

[Traduit par la Rédaction]

Introduction

New innovations in homogeneous catalysis are constantly being uncovered. Much of this revolves around ligand design, which when combined with an appropriate transition metal precursor can generate an active catalytic system for a particular process. Phosphine ligands have been studied exhaustively throughout the past few decades and have found wide applicability in numerous transformations (1, 2). However, more recently, *N*-heterocyclic carbenes (NHCs) have gained much attention as an alternative ligand set to their phosphine counterparts (3). NHCs are similar to phosphines since they are both good σ-donor ligands (4–6), with NHCs being perhaps even stronger σ-donors than phosphines, but lacking π-accepting character (7). NHCs are also very thermally stable and less prone to oxidation compared to phosphine ligands, which is beneficial in the development of robust catalysts.

NHCs have been found to be very effective spectator ligands for palladium and nickel-based C-C coupling catalysts,

Received 9 January 2008. Accepted 27 February 2008. Published on the NRC Research Press Web site at http://canjchem.nrc.ca on 5 July 2008.

H. Jong, B.O. Patrick, and M.D. Fryzuk.[1] Department of Chemistry, The University of British Columbia, Vancouver, BC V6T 1Z1, Canada.

[1]Corresponding author (e-mail: fryzuk@chem.ubc.ca).

 doi:10.1139/V08-082 © 2008 NRC Canada

where they have been proven to be superior to their phosphine competitors (3, 8, 9). More impressive however, has been the improvement in catalytic activity for ruthenium-based olefin metathesis systems (10). Late transition metal-NHC complexes have found applicability in many other kinds of transformations such as hydrosilylation, amination, C–H bond activation, hydroformylation, hydrogenation as well as transfer hydrogenation. The NHC ligand sets used to perform the transformations are often monodentate variants of the original IAd (1,3-diadamantylimidazol-2-ylidene) system developed by Arduengo et al. (11). Substitution at the 1,3-positions of the imidazole unit range from alkyl groups (methyl, isopropyl, *tert*-butyl) to substituted aryl systems such as mesityl (2,4,6-trimethylphenyl) and DIPP (2,6-diisopropylphenyl). Similarly, chelating NHC pincer ligands have also been synthesized in bidentate and tridentate forms (12, 13).

Crabtree's catalyst (14), $[Ir(COD)PCy_3(py)]PF_6$, has become a catalyst benchmark for hydrogenation displaying very high activity for simple as well as substituted olefinic substrates (15). This work has prompted other groups to pursue developments of analogous catalytic systems using NHCs to match or even augment activity and improve the reaction stability that Crabtree's complex does not posses (3, 14). For example, substitution (16) of PCy_3 with SIMes (1,3-dimesityl-4,5-dihydroimidazole-2-ylidene) does provide improved thermal stability of the catalyst but at the expense of a slight reduction in activity at room temperature (RT).

Various derivatives of Crabtree's catalyst incorporating NHC ligands have also been investigated by other groups (17). For example, the first air-stable, pincer bis(NHC) rhodium(III) complex that exhibits good activity for transfer hydrogenation of aryl ketones and imines has been developed (18), and improved hydrogen transfer activity with their next generation iridium analogues has also been reported (19). A chelating pyridine functionalized NHC system coordinated to rhodium (20) has been reported and is capable of performing transfer hydrogenation at good turnover numbers (TONS) at moderate temperatures.

This report focuses on the synthesis of a hemilabile mixed-donor NHC ligand and its coordination chemistry with rhodium(I) diene derivatives. The NHC unit incorporates an amino tether that can bind either as an amine or as an amido donor, after deprotonation. Such a bidentate coordination motif could augment the thermal stability of the resultant Rh complexes with respect to monodentate NHC-bound derivatives (21–24).

Results and discussion

We have previously reported the preparation of a tridentate NHC ligand with flanking amino tethers by melting an imidazole with the appropriate 2-chloroethyl-*N*-arylamine (25). A similar approach can be used to generate a bidentate analog in good yield; the reaction of neat mesityl imidazole with 2-chloroethyl-*N*-mesitylamine in a sealed vessel at 150 °C generates the imidazolium salt **1**, which we denote as ^{Mes}[HCNH]Cl. Deprotonation of **1** with potassium hexamethyldisilazide (KHMDS) results in the formation of the free carbene ^{Mes}[CNH], **2** (Scheme 1). A similar approach to generate tertiary amine side-arm donors has recently been reported (26). Successful conversion to compound **2** can be clearly observed in the ^{1}H NMR spectrum as the iminium proton resonance at δ 10.7 of **1** disappears and a new ^{13}C NMR signal is observed at δ 215.6, due to the carbene carbon (11).

Scheme 1.

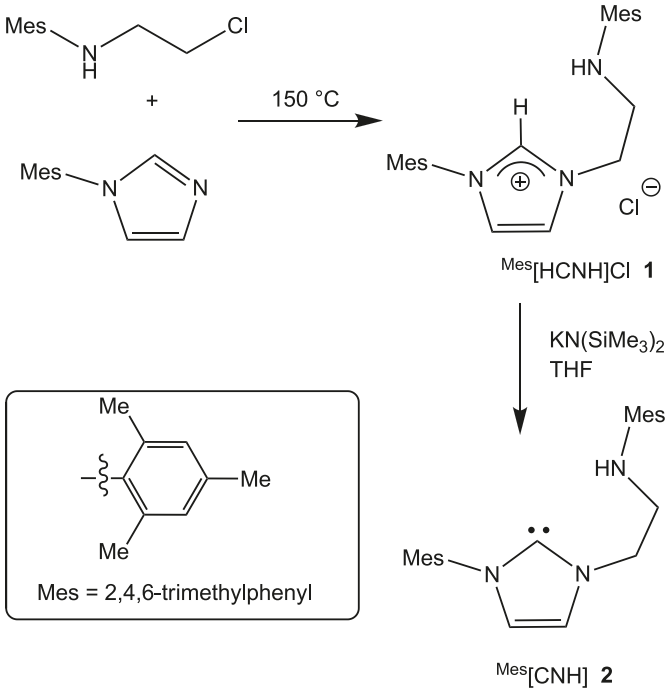

Scheme 2.

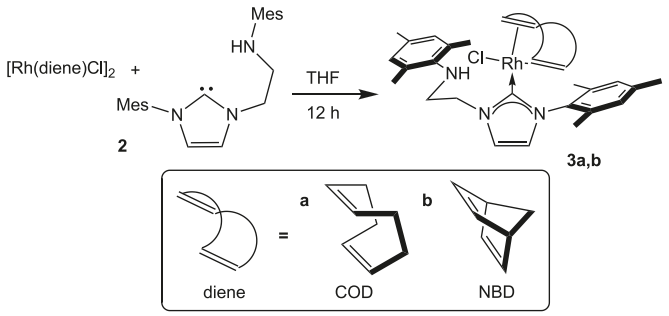

Incorporation of the NHC **2** to rhodium(I) can be accomplished by the addition of ^{Mes}[CNH] to 0.5 equiv. of $[Rh(diene)Cl]_2$ (diene = 1,5-cyclooctadiene (COD) or 2,5-norbornadiene (NBD)) in a solution of THF at RT over a period of 8 h. Both complexes, **3a** and **3b**, are isolated as air-stable yellow powders in good yield (Scheme 2). The resultant NHC-Rh-diene complexes were characterized by ^{1}H and ^{13}C NMR spectroscopy; for example, a weak doublet ($^1J_{Rh\text{-}carbene}$ = 58 Hz) near δ 184 in the ^{31}C NMR spectrum can be assigned to the NHC carbene carbon and confirms the presence of the Rh-carbene bond for each of the diene derivatives.

Figure 1 depicts the solid-state single crystal X-ray structure of **3a**; selected bond distances and angles are given in Table 1; crystallographic data are given in Table 2. The structure shows a mildly distorted square planar geometry about the rhodium(I) center, and the rhodium–carbene dis-

© 2008 NRC Canada

Table 1. Selected bond lengths (Å) and angles (°) for compounds **3a**, **4a**, and **5b**.

3a		**4a**		**5b**	
Bond lengths (Å)					
Rh1–C2	2.0387(18)	Rh01–C02	2.037(3)	Rh01–C02	2.042(4)
Rh1–Cl1	2.3904(6)	Rh01–N03	2.048(3)	Rh01–N03	2.183(3)
Rh1–COD(trans)$_{cent}$	2.072	Rh01–COD(trans)$_{cent}$	2.093	Rh01–NBD(cis)$_{cent}$	1.993
Rh1–COD(cis)$_{cent}$	1.989	Rh01–COD(cis)$_{cent}$	2.009	Rh01–NBD(trans)$_{cent}$	2.081
Bond angles (°)					
C2-Rh–Cl1	89.84(6)	C02-Rh01-N03	87.98(12)	C02-Rh01-N03	91.05(13)
C2-Rh1-COD(cis)$_{avg}$	93.58	C02-Rh01-COD(cis)$_{avg}$	94.09	C02-Rh01-NBD(cis)$_{avg}$	100.5
C2-Rh1-COD(trans)$_{avg}$	161.7	C02-Rh01-COD(trans)$_{avg}$	161.9	C02-Rh01-NBD(trans)$_{avg}$	160
Cl1-Rh1-COD(cis)$_{avg}$	89.17	N03-Rh01-COD(cis)$_{avg}$	93.37	N03-Rh01-NBD(cis)$_{avg}$	95.37
Cl1-Rh1-COD(trans)$_{avg}$	160.4	N03-Rh01-COD(trans)$_{avg}$	160.8	N03-Rh01-NBD(trans)$_{avg}$	155.8

Fig. 1. ORTEP view of **3a**, ^{Mes}[CNH]Rh(COD)Cl, with thermal ellipsoids depicted at 50% probability. All hydrogen atoms (except for H3a attached to N3) have been omitted for clarity.

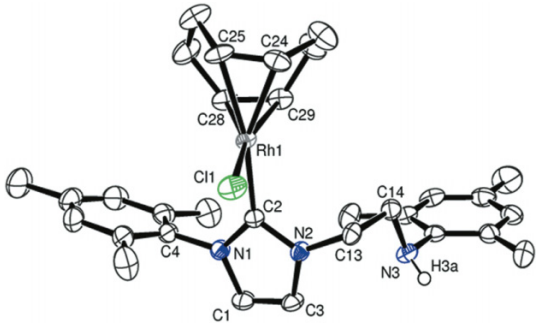

tance (Rh1–C2) of 2.0387(18) Å is well within the range reported for similar Rh(I) derivatives (26). The Rh–COD bond distances (calculated from the distance between the metal to the centroid of the olefinic fragment) are inequivalent with respect to its coordination being in either cis or trans positions relative to the C2 of the carbene (cis = 1.989 Å, trans = 2.072 Å). This inequivalence in bond length is expected and corroborates the trans disposed C=C fragment being less activated and less strongly bound to the rhodium center as is shown in the C=C bond distances of the COD (trans = 1.375(3) Å, cis = 1.395(3) Å) fragment due to the strong trans influence imparted by the NHC ligand.

To coordinate the pendent amine arm to rhodium, potassium hexamethyldisilylamide (KHMDS) can be added to compounds **3a** and **3b**. Alternatively, the bidentate amido carbene-rhodium complexes, **4a** and **4b**, can be synthesized in very good yields in one step by deprotonating imidazolium salt **1** with 2.2 equiv. of KHMDS followed by an in situ reaction with 0.5 equiv. of a rhodium-diene dimer at reduced temperatures. Complexes **4a** and **4b** maintain a slightly distorted square planar geometry and are characterized by a weak doublet resonance (J = 56 Hz) at approximately δ 180 in the ^{13}C NMR spectrum (Rh-carbene carbon).

Interestingly, the single crystal X-ray structure of **4a** (Fig. 2) shows a nearly identical Rh01–C02 bond distance of 2.037(3) Å compared to that of **3a** (2.0387(18) Å); other selected bond distances and angles are given in Table 1; crystallographic data are given in Table 2. The Rh–olefin distances (to the centroid of the C=C bond) for **4a** are 2.009 and 2.093 Å, respectively, for the cis and trans orientations. These values compare to **3a** (cis = 1.989, trans = 2.072 Å), which suggests that COD coordination may be slightly tighter for the chloro complex **3a** as compared to the amido derivative **4a** (Scheme 3).

Cationic analogues can be synthesized with the addition of a halide extraction agent such as sodium tetrafluoroborate to **3a** or **3b** to cleanly yield the corresponding compounds **5a** and **5b** (Scheme 4). The ^{1}H NMR spectrum shows a slight upfield shift of the methylene protons on the ethylene spacer of **3a** (δ 4.83, 3.48) as compared to **5a** (δ 4.76, 3.47), where the upfield shift is larger for the NBD pair: δ 4.93, 3.64 for **3b** versus δ 4.65, 3.25 for **5b**. The N-H resonance in the ^{1}H NMR spectrum does shift downfield slightly upon coordination; for example, in **3a** the uncoordinated N-*H* resonance is found at δ 3.18 whereas upon coordination in **5a**, this resonance shifts to δ 3.26.

The single crystal X-ray diffraction structure depicts **5b** (Fig. 3) with a distorted square planar geometry. Bond distances from the rhodium center to the cis and trans coordinated olefinic fragments of the norbornadiene ligand were found to be 1.993 and 2.081 Å, respectively (measured to the center of the C=C centroid), which is typical of Rh-NBD complexes (27–29). These values are also akin to those of **3a** and **4a**, which suggests that the norbornadiene unit is similarly bound to the rhodium center as the cyclooctadiene unit; other bond distances and angles are given in Table 1, while crystallographic data are listed in Table 2.

Upon inspection of the ^{13}C NMR data of the COD and NBD derivatives, one observes that all of the complexes exhibit very similar metal-carbene chemical shifts, in a range from approximately δ 174 to 185, with the cationic derivative **5b** being most upfield shifted to δ 174.6. Thus, there does not seem to be much change in the Rh-NHC interaction as a function of the amine tether being coordinated or dangling.

We examined the reaction of the cationic complex **5b** with pyridine and PMe_3 to examine the relative binding ability of the tethered amine; addition of excess pyridine did not result in decoordination of the amine arm on **5b**, while addition of PMe_3 did result in the formation of the phosphine adduct **6** (Scheme 5).

© 2008 NRC Canada

Table 2. Crystal data and structural refinement for compounds **3a**, **4a**, and **5b**.

	3a	**4a**	**5b**
Formula	$C_{34}H_{44}ClN_3Rh$	$C_{31}H_{40}N_3Rh$	$C_{30}H_{37}BF_4N_3Rh$
Mass	633.08	557.57	629.35
CCDC	673254	673255	673256
λ (Å)	0.71069	0.71073	0.71073
Crystal system	Triclinic	Monoclinic	Triclinic
Space group	$P\bar{1}$	$P21/n$	$P\bar{1}$
a (Å)	10.1543(6)	15.8359(18)	10.8567(11)
b (Å)	12.0573(7)	8.7280(9)	11.1437(10)
c (Å)	13.9204(7)	20.572(2)	13.3437(10)
α (°)	86.436(2)	90	71.425(4)
β (°)	70.448(2)	105.789(6)	84.597(4)
γ (°)	87.218(2)	90	66.204(4)
V (Å^3)	1602.25(16)	2736.1(5)	1399.1(2)
Z	2	4	2
$D_{calcd.}$ (g cm^{-1})	1.312	1.354	1.494
μ (mm^{-1})	0.642	0.648	0.662
F(000)	662	1168	648
Crystal size (mm^3)	0.25 × 0.25 × 0.1	0.3 × 0.2 × 0.1	0.35 × 0.15 × 0.04
θ_{max} (°)	27.97	22.53	23.15
Reflections collected	31972	16325	16270
Independent reflections [*R*(int)]	7531 [0.0407]	3490 [0.0546]	3926 [0.0591]
Max. and min. transmission	0.0642 and 0.0555	1.0000 and 0.9582	0.97387 and 0.79159
Data/restraints/parameters	7531/0/362	3490/0/346	3926/0/386
Goodness-of-fit on F^2	1.076	0.979	1.014
R_1 [$I > 2\sigma(I)$]	0.0312	0.0267	0.0342
wR_2 (all data)[a]	0.0754	0.0667	0.0676

[a]Least-squares function minimized: $\Sigma w(F_o^2 - F_c^2)^2$.

Fig. 2. ORTEP view of **4a**, ^{Mes}[CN]Rh(COD), with thermal ellipsoids depicted at 50% probability. All hydrogen atoms have been omitted for clarity.

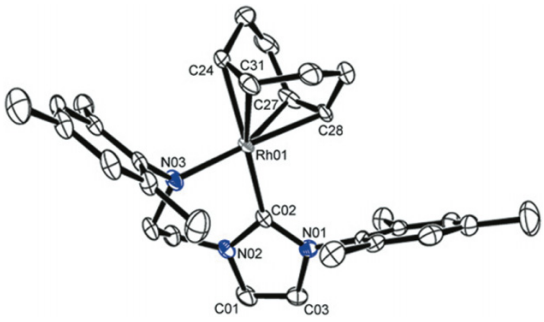

Scheme 3.

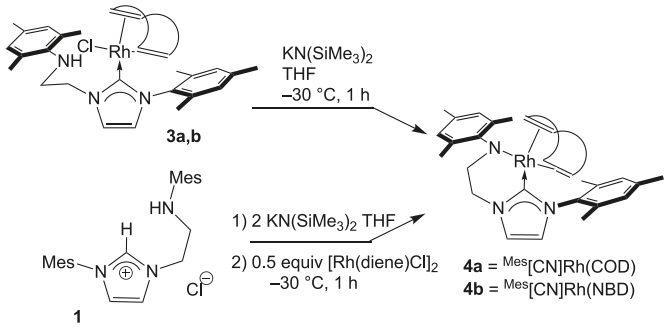

Scheme 4.

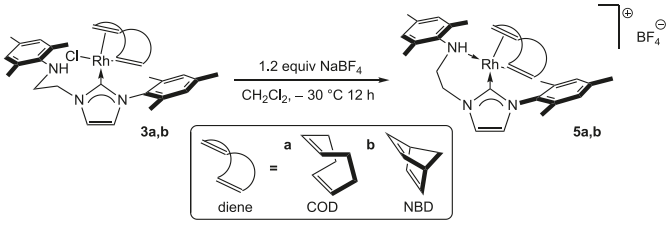

Catalytic test reactions

Hydrogenation test reactions were performed with complexes **3**–**5** using simple cyclic alkenes as substrates; cyclohexene and 1-methyl-cyclohexene were selected as they have been used frequently as benchmark substrates to test hydrogenation activity of later metal catalysts (14, 30). None of the catalysts were able to hydrogenate the substituted cyclohexene substrate beyond 40% after 72 h with the exception of complexes **4a** and **4b** that recorded conversions greater than 90%.

Transfer hydrogenation reactions with ketone and imine substrates were attempted with **3a** as well. Various common literature methods (18, 20, 31, 32) were attempted on benchmark test substrates such as benzophenone and *N*-

© 2008 NRC Canada

Scheme 5.

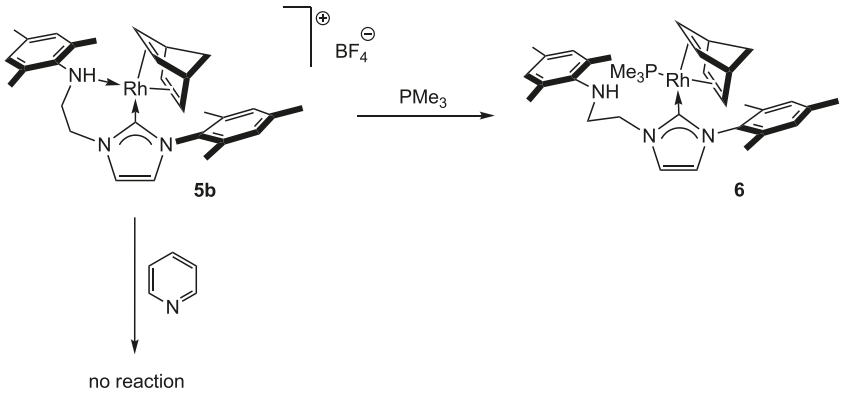

Fig. 3. ORTEP view of **5b**, [^{Mes}[CNH]Rh(NBD)]BF_4, with thermal ellipsoids depicted at 50% probability. All hydrogens (with the exception of H1a attached to N03) have been omitted for clarity. H1a was located and refined isotropically.

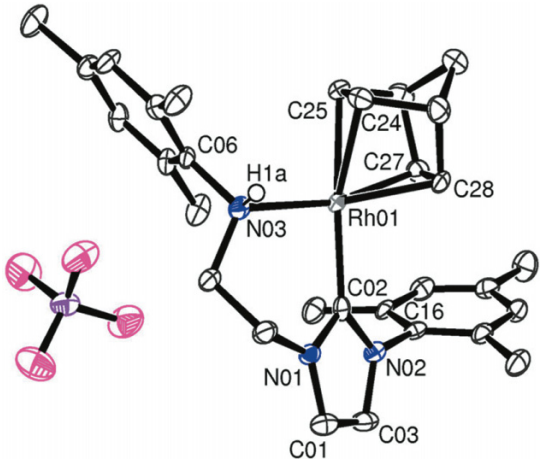

benzylideneaniline. Of the four routes attempted, none of them produced a positive indicator despite being allowed to run for and extended period of time (>12 h). From ^{1}H NMR analysis, it appeared that the precursor was stable and reluctant to become activated in solution.

From the less than satisfactory results of the hydrogenation and transfer hydrogenation studies, it was determined that the induction period of our catalyst precursors **3**–**5** was long and the timescale at which conversions were recorded overlapped with those resulting from simple colloidal rhodium hydrogenations of parallel substrates.

Efforts to determine the reactivity of the precursor complexes **3**–**5** were attempted by reaction with 1 atm H_2 in the absence of a substrate; unfortunately, the results parallel the catalytic runs in that these complexes remained largely unchanged on the basis of NMR spectroscopy; in addition, attempts to detect small amounts of hydride species, which should show resonances upfield of δ 0 were unsuccessful, contrary to characteristic behavior of active Rh precursors (33–37).

Conclusions

The ability of an amine-tethered NHC to coordinate to rhodium(I) diene complexes in either a monodentate or bidentate mode has been investigated. The synthetic protocols to generate each class of compounds are straightforward and illustrate the versatility of this ligand in its binding aptitudes. Given the variable complexes accessible, we examined their ability to act as catalyst precursors for the hydrogenation of cyclic alkenes. Unfortunately, regardless of the bonding mode or form of the tether (i.e., amine versus amide), none of these complexes were especially active in hydrogenation. In addition, the neutral and cationic amine tethered NHC complexes, **3** and **5**, were tested for their ability to act as transfer hydrogenation precatalysts; here again, no positive results were obtained. It would appear that the diene ligands are too firmly bound to any of these complexes, regardless of the tether binding mode, so much so that neither substrates nor H_2 activation can occur. Further studies are ongoing with iridium and ruthenium systems that incorporate these versatile amine-tethered NHCs.

Experimental section

General considerations

Unless otherwise specified, all experimental procedures were performed in a dry, oxygen-free nitrogen or argon atmosphere by Schlenk or glovebox techniques. 2,4,6-$Me_3C_6H_2NHC(O)CH_2Cl$ (38), 2,4,6-$Me_3C_6H_2NHCH_2CH_2Cl$ (39), 2,4,6-trimethylphenylimidazole (40), $[Rh(COD)Cl]_2$ (41), $[Rh(NBD)Cl]_2$ (42), and $[Rh(COE)_2Cl]_2$ (43) were prepared from literature methods. All other chemicals were purchased commercially and used as received. Methylene chloride was dried by refluxing over CaH_2 overnight under nitrogen. Anhydrous toluene, hexanes, pentane, and tetrahydrofuran were purchased from Sigma-Aldrich, sparged with nitrogen, and passed through columns containing activated alumina and Ridox catalyst. Deuterated benzene (C_6D_6) was purified via three freeze-pump-thaw cycles and then refluxed overnight in a sealed vessel, which contained sodium/potassium alloy, and vacuum transferred into a glass bomb. Deuterated methylene chloride (CD_2Cl_2) was purified in a similar manner using CaH_2 as the drying agent. ^{1}H and ^{13}C NMR spectra were obtained by a Bruker AVANCE 300 or 400 MHz spectrometer. Elemental analysis and mass spectrometry (EI/MS) were performed at the Department of Chemistry at the University of British Columbia.

© 2008 NRC Canada

Synthesis of 1-(2,4,6-$Me_3C_6H_2$)-3-(2-(2,4,6-$Me_3C_6H_2NH$)ethyl)imidazolium chloride, ^{Mes}[HCNH]Cl (1)

A glass reactor fitted with a Kontes valve was charged with 3.00 g (55.2 mmol) of 2,4,6-$Me_3C_6H_2NHCH_2CH_2Cl$ and 2.83 g (55.2 mmol) of 2,4,6-trimethylphenylimidazole, and the resultant mixture heated to 150 °C for 1.5 h. The reaction was allowed to cool to RT and the tough air-stable brown solid was filtered and washed with THF to produce the desired cream-colored solid (5.10 g, 90% yield). ^{1}H NMR (CD_2Cl_2, 400 MHz) δ: 2.04 (s, 6H, -*o*-ArC*H*$_3$), 2.09 (s, 6H, -*o*-ArC*H*$_3$), 2.16 (s, 3H, -*p*-ArC*H*$_3$), 2.32 (s, 3H, -*p*-ArC*H*$_3$), 3.23 (t, *J* = 5 Hz, 2H, -N_{Ar}C*H*$_2$), 4.99 (t, *J* = 5 Hz, 2H, -N_{imid}C*H*$_2$), 6.72, 6.99 (s, 2H, -Ar*H*), 7.12 (s, 1H, -imid*H*), 8.12 (s, 1H, -imid*H*), 10.7 (s, 1H, -NC*H*N). ^{13}C NMR (CD_2Cl_2, 100 MHz) δ: 17.89, 18.52 (-*o*-ArC*H*$_3$), 20.80, 21.31 (-*p*-ArC*H*$_3$), 48.08 (-N_{Ar}C*H*$_2$), 50.05 (-N_{imid}C*H*$_2$), 122.78, 124.24 (-imid*C*), 129.6, 130.2, 131.5, 131.9, 132.6, 134.9 (-Ar*C*), 140.3 (-N*C*HN) 141.6, 142.8 (-*ipso*-Ar*C*). EI-MS: 347 [M$^+$]. Anal. calcd. for $C_{23}H_{30}N_3Cl$ (%): C 71.95, H 7.88, N 10.94; found: C 71.87, H 7.62, N 11.30.

Synthesis of (2,4,6-$Me_3C_6H_2$)-3-(2-(2,4,6-$Me_3C_6H_2NH$)ethyl)imidazole-2-ylidene, ^{Mes}[CNH] (2)

$KN(SiMe_2)_2$ (3.12 g, 15.6 mmol) was dissolved in 20 mL of THF and added dropwise to a stirring THF suspension containing 5.00 g (13.0 mmol) of **1** at RT. The mixture was stirred for 1.5 h and dried in vacuo to leave a beige powder. Colorless needle crystals suitable for X-ray grade were grown by slow evaporation from a solution of toluene (4.10 g, 91% yield). ^{1}H NMR (C_6D_6, 400 MHz) δ: 2.08 (s, 6H, -*o*-ArC*H*$_3$), 2.14 (s, 3H, -*p*-ArC*H*$_3$), 2.18 (s, 3H, -*p*-ArC*H*$_3$), 2.23 (s, 6H, -*o*-ArCH_3), 3.29 (t, *J* = 5 Hz, 2H, -N_{Ar}C*H*$_2$), 3.91 (t, *J* = 5 Hz, 2H, -N_{imid}C*H*$_2$), 4.18 (s, 1H, -N*H*), 6.36 (d, *J* = 2 Hz, 1H, -imid*H*), 6.45 (d, *J* = 2 Hz, 1H, -imid*H*), 6.78 (s, 2H, -Ar*H*), 6.80 (s, 2H, -Ar*H*). ^{13}C NMR (C_6D_6, 100 MHz) δ: 18.49, 19.19, 21.13, 21.33 (-ArCH_3), 49.62 (-N_{Ar}C*H*$_2$), 51.93 (-N_{imid}C*H*$_2$), 120.0, 120.9 (-imid*C*), 129.5, 130.2, 130.6, 131.4, 135.7, 137.6, 139.6, 144.6 (-Ar*C*), 215.6 (-N*C*N). EI-MS: 347 [M$^+$]. Anal. calcd. For $C_{23}H_{29}N_3$·2/5C_4H_8O (%): C 78.51, H 8.62, N 11.17; found: C 78.26, H 8.50, N 11.55.

Synthesis of ^{Mes}[CNH]Rh(COD)Cl (3a)

^{Mes}[CNH] (2.82 g, 8.12 mmol) was dissolved in 10 mL of THF and added dropwise to a stirring transparent yellow solution of 2.00 g (4.06 mmol) of $[Rh(COD)Cl]_2$ in 10 mL of THF. The reaction was stirred overnight at RT and the solvent was removed, which resulted in the desired yellow powder. Yellow crystals suitable for X-ray analysis were grown by slow evaporation in methylene chloride (2.12 g, 88% yield). ^{1}H NMR (C_6D_6, 400 MHz) δ: 1.50–1.80 (m, -COD), 1.69 (s, 3H, -ArC*H*$_3$), 1.90–2.30 (m, -COD), 2.15 (s, 3H, -ArC*H*$_3$), 2.19 (s, 3H, -ArC*H*$_3$), 2.23 (s, 6H, -ArC*H*$_3$), 2.67 (s, 3H, -ArC*H*$_3$), 3.18 (s, 1H, -N*H*), 3.35 (m, -COD), 3.47 (t, *J* = 6 Hz, 2H, -N_{Ar}C*H*$_2$), 4.83 (t, *J* = 6 Hz, 2H, -N_{imid}C*H*$_2$), 5.26 (m, 1H, -COD), 5.36 (m, 1H, -COD), 6.00 (d, *J* = 1 Hz, 1H, imid*H*), 6.46 (d, *J* = 1 Hz, 1H, imid*H*), 6.70 (s, 2H, Ar*H*), 6.81 (s, 4H, Ar*H*), 6.86 (s, 2H, Ar*H*). ^{13}C NMR (C_6D_6, 100 MHz) δ: 18.13 (-*p*-CH_3), 19.04 (-*o*-CH_3), 20.63 (-*p*-CH_3), 21.13, 21.37 (-*o*-CH_3), 28.93, 29.79, 32.57, 34.71 (-COD), 49.01 (-N_{Ar}C*H*$_2$), 52.38 (-N_{imid}C*H*$_2$), 67.48, 67.28 (d, *J* = 14 Hz, -RhC_{COD}H), 97.81, 98.61 (d, *J* = 7 Hz, -RhC_{COD}H), 121.7 (-imid*C*), 122.9 (-imid*C*), 130.2, 130.6, 130.7 (-Ar*C*N_{Ar}), 131.9, 134.7, 137.2, 138.3, 139.0 (-Ar*C*N_{imid}), 143.9 (-Ar*C*N_{imid}), 184.2 (d, *J* = 52 Hz, RhC_{NCN}). EI-MS: 593 [M$^+$]. Anal. calcd. for $C_{31}H_{41}N_3ClRh$ (%): C 62.68, H 6.96, N 7.07; found: C 62.61, H 7.30, N 7.32.

Synthesis of ^{Mes}[CNH]Rh(NBD)Cl (3b)

The synthetic procedure is as described for **3a**. Yellow crystals suitable for X-ray analysis were grown by slow evaporation in methylene chloride. ^{1}H NMR (CD_2Cl_2, 400 MHz) δ: 1.14 (s, 2H, -NBD), 2.02 (s, 6H, -ArC*H*$_3$), 2.22 (s, 3H, -ArC*H*$_3$), 2.28 (s, 6H, -ArC*H*$_3$), 2.41 (s, 3H, -ArC*H*$_3$), 3.40 (s, 2H, -NBD), 3.46 (s, 2H, -NBD), 3.64 (m, 2H, -N_{Ar}C*H*$_2$), 4.93 (m, 2H, -N_{imid}C*H*$_2$), 6.73 (d, *J* = 1.6 Hz, -imid*H*), 6.83 (s, 2H, -Ar*H*), 7.05 (s, 2H, -Ar*H*), 7.13 (d, *J* = 1.6 Hz, -imid*H*). ^{13}C NMR (CD_2Cl_2, 100 MHz) δ: 18.51, 18.76 (-*C*H$_3$), 20.86, 21.48 (-NBD), 49.51 (-N_{Ar}C*H*$_2$), 51.27 (d, *J* = 2.5 Hz, -RhC_{NBD}H), 52.12, (-N_{imid}C*H*$_2$), 63.43 (d, *J* = 5.2 Hz, -RhC_{NBD}H), 122.2, 123.1 (-imid*C*), 129.5, 129.9, 130.8 (-Ar*C*), 132.3, 136.1, 136.7 (-Ar*C*), 139.5, 143.4 (-Ar*C*), 183.9 (d, *J* = 58 Hz, RhC_{NCN}). EI-MS: 577 [M$^+$]. Anal. calcd. for $C_{30}H_{37}N_3ClRh$ (%): C 62.34, H 6.45, N 7.27; found: C 62.56, H 6.83, N 7.59.

Synthesis of ^{Mes}[CN]Rh(COD) (4a)

1 (300 mg, 0.781 mmol) was suspended in 5 mL of THF. To this mixture, 343 mg (1.72 mmol) of $KN(SiMe_3)_2$, dissolved in 2 mL of THF, was added dropwise at RT. The yellow-brown solution was stirred for 1 h and then cooled to –30 °C. $[Rh(COD)Cl]_2$ (193 mg, 0.391 mmol) was dissolved in 10 mL of THF and was added dropwise at –30 °C. The solution was warmed to RT and stirred for 1 additional hour that resulted in an orange-brown mixture. The THF was removed under vacuum and the product was extracted with toluene and filtered through Celite. Under reduced pressure, the toluene was removed and the product was washed with hexanes to give a golden orange powder. Cooling a concentrated benzene solution to –30 °C produced orange crystals suitable for X-ray analysis (393 mg, 90% yield). ^{1}H NMR (C_6D_6, 400 MHz) δ: 1.55–1.88 (m, -COD), 2.05–2.25 (m, -COD), 2.10 (s, 3H, -ArC*H*$_3$), 2.21 (s, 6H, -ArC*H*$_3$), 2.32 (s, 3H, -ArC*H*$_3$), 2.71 (s, 6H, -ArC*H*$_3$), 2.99 (m, 2H, -N_{Ar}C*H*$_2$), 3.04 (m, 2H, -COD), 3.85 (m, 2H, -COD), 4.12 (m, 2H, -N_{imid}C*H*$_2$), 5.91 (d, *J* = 2 Hz, 1H, imid*H*), 6.10 (d, *J* = 2 Hz, 1H, imid*H*), 6.74 (s, 2H, Ar*H*), 7.13 (s, 2H, Ar*H*). ^{13}C NMR (C_6D_6, 100 MHz) δ: 18.93, 20.10 (Ar*C*H$_3$), 21.32, 21.53 (-Ar*C*H$_3$), 30.45, 34.05 (-COD), 54.14 (-N_{Ar}C*H*$_2$), 57.35 (-N_{imid}C*H*$_2$), 64.35 (d, *J* = 11 Hz, -RhC_{COD}H), 94.54 (d, *J* = 8 Hz, -RhC_{COD}H), 120.4 (-imid*C*), 122.0 (-imid*C*), 128.9, 129.5, 129.7, 129.9, 130.4 (-Ar*C*), 135.9, 136.4, 138.3, 138.6, 157.9 (-Ar*C*), 180.8 (d, *J* = 56 Hz, -RhC_{NCN}). EI-MS: 557 [M$^+$]. Anal. calcd. for $C_{31}H_{40}N_3Rh$ (%): C 66.78, H 7.23, N 7.54; found: C 66.46, H 7.23, N 7.40.

Synthesis of ^{Mes}[CN]Rh(NBD) (4b)

The synthetic procedure is as described for **4a**. ^{1}H NMR (C_6D_6, 400 MHz) δ: 1.03 (b, 1H, -NBD), 1.09 (b, 1H, -NBD), 2.04 (s, 3H, -ArC*H*$_3$), 2.10 (s, 6H, -ArC*H*$_3$), 2.30 (s, 3H, -ArC*H*$_3$), 2.39 (b, 2H, -NBD), 2.77 (s, 6H, -ArC*H*$_3$),

© 2008 NRC Canada

3.17 (m, 2H, -$N_{Ar}CH_2$), 3.38 (m, 2H, -$N_{imid}CH_2$), 3.77 (b, 4H, -NBD), 5.85 (b, 1H, -imid*H*), 6.11 (b, 1H, -imid*H*), 6.70 (s, 2H, Ar*H*), 7.07 (s, 2H, Ar*H*). ^{13}C NMR (C_6D_6, 100 MHz) δ: 18.43, 20.16 (-Ar*C*H_3), 21.38, 21.56 (-Ar*C*H_3), 39.99, 40.08 (-NBD), 50.45 (-$N_{imid}CH_2$), 53.15 (-$N_{imid}CH_2$), 56.70 (-NBD), 63.30 (d, *J* = 4 Hz, -NBD), 74.11 (d, *J* = 7 Hz, -NBD), 120.6 (-imid*C*), 120.8 (-imid*C*), 129.1, 129.4 (-Ar*C*), 130.4, 136.2, 136.3, 137.4 (-Ar*C*), 138.8, 156.9 (-Ar*C*), 178.3 (d, *J* = 61 Hz, -RhC_{CNC}). EI-MS: 539 [M^+]. Anal. calcd. for $C_{30}H_{36}N_3Rh{\cdot}2/3CH_2Cl_2$ (%): C 61.47, H 6.45, N 7.01; found: C 61.73, H 6.42, N 7.07.

Synthesis of ^{Mes}[CNH]Rh(COD]BF_4 (5a)

3 (1.00 g, 1.68 mmol) was dissolved in 10 mL of CH_2Cl_2 and cooled to –30 °C. $NaBF_4$ (222 mg, 2 mmol) was ground and was slowly introduced to the solution at –30 °C. The mixture was warmed to RT and stirred overnight. The reaction was carefully monitored for the first 2 h to control the effervescing solution. Once complete, the mixture was filtered through Celite and the solvent was removed under reduced pressure to leave the desired yellow product (867 mg, 80% yield). ^{1}H NMR (CD_2Cl_2, 400 MHz) δ: 1.40–2.40 (m, -COD), 1.84 (s, 3H, -*p*-ArCH_3), 2.20 (s, 3H, -*p*-ArCH_3), 2.21 (s, 6H, -*o*-ArCH_3), 2.37 (s, 3H, -*o*-ArCH_3), 2.39 (s, 3H, -*o*-ArCH_3), 3.00 (m, 1H, -COD), 3.26 (s, 1H, -N*H*), 3.46 (m, 2H, -$N_{Ar}CH_2$), 3.60 (m, 1H, -COD), 4.69 (m, 1H, COD), 4.77 (m, 2H, -$N_{imid}CH_2$), 5.14 (m, 1H, -COD), 6.80 (s, 2H, -Ar*H*), 6.81(s, 1H, -Ar*H*), 6.94 (s, 1H, imid*H*), 7.10 (s, 1H, imid*H*), 7.16 (s, 1H, -Ar*H*). ^{13}C NMR (CD_2Cl_2, 100 MHz) δ: 18.11 (-*p*-ArCH_3), 18.69 (-*o*-ArCH_3), 20.01, 20.85, 21.37 (-ArCH_3), 28.50, 29.69, 31.99, 34.61 (-COD), 49.13 (-$N_{Ar}CH_2$), 52.46 (-$N_{imid}CH_2$), 68.13, 69.13 (d, *J* = 15 Hz, -RhC_{COD}H), 97.25, 97.33 (d, *J* = 3 Hz, -RhC_{COD}H), 121.8, 123.8 (-imid*C*), 128.8, 129.9 (-ArCN_{Ar}), 130.0 (-ArCN_{imid}), 130.7 (-ArCN_{Ar}), 132.2, 135.0, 136.8, 137.5 (-ArCN_{imid}), 139.3, 143.4 (-ArC_{ipso}), 183.1 (d, *J* = 51 Hz, -RhC_{NCN}). EI-MS: 558 [M^+]. Anal. calcd. For $C_{31}H_{41}N_3BF_4Rh{\cdot}1/5C_5H_{12}$ (%): C 58.25, H 6.63, N 6.37; found: C 58.63, H 6.94, N 6.44.

Synthesis of ^{Mes}[CNH]Rh(NBD)]BF_4 (5b)

The synthetic procedure is as described for compound **5a**. Slow evaporation in a concentrated solution of CH_2Cl_2 produced yellow X-ray grade platelets. ^{1}H NMR (CD_2Cl_2, 400 MHz) δ: 1.13 (s, 2H, -NBD), 2.03 (s, 6H, -*o*-ArCH_3), 2.22 (s, 3H, -*p*-ArCH_3), 2.35 (s, 6H, -*o*-ArCH_3), 2.40 (s, 3H, -*p*-ArCH_3), 3.47 (s, 2H, -NBD), 3.55 (m, 4H, -NBD), 3.64 (s, 1H, -N*H*), 3.72 (m, 2H, -$N_{Ar}CH_2$), 4.92 (m, 2H, -$N_{imid}CH_2$), 6.72 (d, 1H, -imid*H*), 6.84 (s, *J* = 1 Hz, 2H, -Ar*H*), 7.04 (s, 2H, -imid*H*), 7.17 (d, *J* = 1 Hz, 1H, -imid*H*). ^{13}C NMR (CD_2Cl_2, 100 MHz) δ: 17.95, 19.04 (-*o*-ArCH_3), 20.59, 21.15 (-*p*-ArCH_3), 49.65 (-$N_{Ar}CH_2$), 51.11 (-$N_{imid}CH_2$), 51.47 (d, *J* = 1.8 Hz, -NBD), 64.06 (d, *J* = 5.1 Hz, -NBD), 122.6, 122.9 (-imid*C*), 129.6, 130.2, 130.6, 135.6, 139.8, 140.8 (-Ar*C*), 174.6 (d, *J* = 59 Hz, -RhC_{NCN}). EI-MS: 539 [M^+]. Anal. calcd. for $C_{30}H_{37}N_3BF_4Rh{\cdot}/3C_6H_{14}$ (%): C 58.37, H 6.43, N 6.38; found: C 58.18, H 6.03, N 6.03.

Synthesis of ^{Mes}[CNH]Rh(NBD)PMe_3 (6)

PMe_3 (32 mg, 0.421 mmol) was mixed with 3 mL of benzene and added dropwise to an orange suspension containing 218 mg (0.346 mmol) of **5b** in 5 mL of benzene. Immediately after the addition, the solution becomes transparent and then becomes a suspended orange mixture after 5 min. The reaction was allowed to stir for 30 min before the solution was concentrated under rotary evaporation. The addition of pentane resulted in the precipitation of an orange powder, which was collected and dried under vacuum (212 mg, 87% yield). ^{1}H NMR (CD_2Cl_2, 400 MHz) δ: 1.28, (d, 2H, -NBD), 1.43 (br, 9H, -P(CH_3)$_3$), 1.51 (s, 3H, -*o*-ArCH_3), 1.79 (s, 3H, -*o*-ArCH_3), 2.22 (s, 9H, -ArCH_3), 2.44 (s, 3H, -*p*-ArCH_3), 2.98 (br, 2H, -NBD), 3.32 (m, 2H, -$N_{Ar}CH_2$), 3.46, 3.50 (br, 2H, -NBD), 3.63 (m, 1H, -$N_{imid}CH_2$), 4.16 (br, 1H, -NBD), 4.67 (br, 1H, -NBD), 4.91 (m, 1H, -$N_{imid}CH_2$), 6.80 (d, 1H, -imid*H*), 6.85 (s, 2H, -Ar*H*), 7.14 (s, 2H, -Ar*H*), 7.50 (d, 1H, -imid*H*). ^{13}C NMR (CD_2Cl_2, 100 MHz) δ: 18.22 (-*o*-ArCH_3), 19.0 (-ArCH_3), 20.8 (m, -P(CH_3)$_3$), 21.9 (-*p*-ArCH_3), 42.2, 46.2 (-NBD), 49.9 (-$N_{Ar}(CH_2)$, 51.7 (-$N_{imid}(CH_2)$, 53.4 (-NBD), 61.7 (d, $J_{Rh\text{-}NBD}$ = 3 Hz, -NBD), 66.1 (d, $J_{Rh\text{-}NBD}$ = 5 Hz, -NBD), 67.5 (d, $J_{Rh\text{-}NBD}$ = 4 Hz, -NBD), 77.4 (d, $J_{Rh\text{-}NBD}$ = 6 Hz, -NBD), 123.1, 125.3 (-imid*C*), 130.5, 130.8, 133.4, 136.4, 140.8, 143.2 (-Ar*C*), 183.8 (d, $J_{Rh\text{-}NCN}$ = 58 Hz -RhN*C*N). ^{31}P{^{1}H} NMR (CD_2Cl_2, 162 MHz) δ: –12.91 (d, $J_{Rh\text{-}P}$ = 122 Hz, *P*(CH_3)$_3$). EI-MS: 539 [M^+-PMe_3]. Anal. calcd. for $C_{33}H_{46}N_3BF_4Rh{\cdot}/2C_6H_{14}$ (%): C 57.77, H 7.14, N 5.61; found: C 57.83, H 6.89, N 5.59.

Hydrogenation procedures

The reactions were performed in thick-walled glass vessels, which were charged with a substrate, 5 mol% catalyst, 2 mL of methylene chloride, and pressurized with either 1 or 4 atm of hydrogen gas. The reactions with cyclohexene as the substrate were truncated at *t* = 15 min, 1, 4, and 12 h where an aliquot was taken from the vessel to determine conversion via ^{1}H NMR spectroscopy. From our preliminary results, significant conversions to hydrogenated substrates were not observed prior to the 4 and 12 h mark using 4 and 1 atm of H_2 pressure, respectively. When employing 1-methyl-cyclohexene as the substrate, it was found that the conversions were appreciably lower and the transformations occurred much more slowly. Select reactions were run with 1 atm of H_2 pressure for 12 h and resulted in conversions no greater than 20%. Reactions at 4 atm were performed with aliquots extracted and analyzed at *t* = 12 h, 72 h, and 1.5 weeks.

X-ray crystallographic analysis[2]

All crystals were mounted on a glass fiber and measured on a Bruker X8 diffractometer with graphite monochromated

[2] Supplementary data for this article are available on the journal Web site (canjchem.nrc.ca) or may be purchased from the Depository of Unpublished Data, Document Delivery, CISTI, National Research Council Canada, Ottawa, ON K1A 0R6, Canada. DUD 3768. For more information on obtaining material refer to cisti-icist.nrc-cnrc.gc.ca/irm/unpub_e.shtml. CCDC 673254, 673255, and 673256 contain the crystallographic data for this manuscript. These data can be obtained, free of charge, via www.ccdc.cam.ac.uk/conts/retrieving.html (Or from the Cambridge Crystallographic Data Centre, 12 Union Road, Cambridge CB2 1EZ, UK; fax +44 1223 336033; or deposit@ccdc.cam.ac.uk).

© 2008 NRC Canada

Mo Kα radiation. The data was collected at a temperature of –100.0 ± 0.1 °C with the Bruker APEX II CCD area-detector set at a distance of 36.00 mm. Data was collected and integrated using the Bruker SAINT (44) software package and corrected for absorption effects using the multiscan technique (SADABS (45)). The data was corrected for Lorentz and polarization effects and the structure was solved by direct methods (46). All nonhydrogen atoms were refined anisotropically, while all hydrogen atoms except those coordinated to the amino tether were placed in calculated positions but were not refined. Amino protons were located in a difference map and refined isotropically. The final cycle of the full-matrix least-squares refinement on F^2 is shown in Table 2. Neutral atom scattering factors were taken from Cromer and Waber (47). Anomalous dispersion effects were included in $F_{calcd.}$ (48); the values for Δf' and Δf" were those of Creagh and McAuley (49). The values for the mass attenuation coefficients are those of Creagh and Hubbell (50). All refinements were performed using the SHELXTL (51) crystallographic software package of Bruker-AXS.

Acknowledgements

We thank the Natural Sciences and Engineering Research Council (NSERC) of Canada for funding on this project.

References

1. R. Noyori. Angew. Chem. Int. Ed. Engl. **41**, 2008 (2002).
2. E. Peris and R.H. Crabtree. Coord. Chem. Rev. **248**, 2239 (2004).
3. W.A. Herrmann. Angew. Chem. Int. Ed. Engl. **41**, 1290 (2002).
4. M. Regitz. Angew. Chem. Int. Ed. Engl. **35**, 725 (1996).
5. A.J. Arduengo III and R. Krafczyk. Chemie unserer Zeit, **32**, 6 (1998).
6. A.J. Arduengo III. Acc. Chem. Res. **32**, 913 (1999).
7. M.-T. Lee and C.-H. Hu. Organometallics, **23**, 976 (2004).
8. C.M. Crudden and D.P. Allen. Coord. Chem. Rev. **248**, 2247 (2004).
9. N.M. Scott and S.P. Nolan. Eur. J. Inorg. Chem. 1815 (2005).
10. T.M. Trnka and R.H. Grubbs. Acc. Chem. Res. **34**, 18 (2001).
11. A.J. Arduengo III, R.L. Harlow, and M. Kline. J. Am. Chem. Soc. **113**, 361 (1991).
12. J.A. Mata, M. Poyatos, and E. Peris. Coord. Chem. Rev. **251**, 841 (2007).
13. D. Pugh and A.A. Danopoulos. Coord. Chem. Rev. **251**, 610 (2007).
14. R. Crabtree. Acc. Chem. Res. **12**, 331 (1979).
15. R.H. Crabtree, H. Felkin, and G.E. Morris. J. Organomet. Chem. **141**, 205 (1977).
16. H.M. Lee, T. Jiang, E.D. Stevens, and S.P. Nolan. Organometallics, **20**, 1255 (2001).
17. L.D. Vazquez-Serrano, B.T. Owens, and J.M. Buriak. Inorg. Chim. Acta, **359**, 2786 (2006).
18. M. Albrecht, R.H. Crabtree, J. Mata, and E. Peris. Chem. Commun. 32 (2002).
19. M. Albrecht, J.R. Miecznikowski, A. Samuel, J.W. Faller, and R.H. Crabtree. Organometallics, **21**, 3596 (2002).
20. A.A. Danopoulos, S. Winston, and W.B. Motherwell. Chem. Commun. 1376 (2002).
21. E. Mas-Marza, M. Poyatos, M. Sanau, and E. Peris. Inorg. Chem. **43**, 2213 (2004).
22. M. Poyatos, E. Mas-Marza, J.A. Mata, M. Sanau, and E. Peris. Eur. J. Inorg. Chem. 1215 (2003).
23. A.H. Hoveyda, A.W. Hird, and M.A. Kacprzynski. Chem. Commun. 1779 (2004).
24. V. César, S. Bellemin-Laponnaz, H. Wadepohl, and L.H. Gade. Chem. Eur. J. **11**, 2862 (2005).
25. L.P. Spencer and M.D. Fryzuk. J. Organomet. Chem. **690**, 5788 (2005).
26. M.V. Jiménez, J.J. Perez-Torrente, M.I. Bartolomé, V. Giertz, and L.A. Oro. Organometallics, **27**, 224 (2008).
27. X.-Y. Yu, B.O. Patrick, and B.R. James. Organometallics, **25**, 2359 (2006).
28. M. Stradiotto, J. Cipot, and R. McDonald. J. Am. Chem. Soc. **125**, 5618 (2003).
29. S. Sjoevall, M. Johansson, and C. Andersson. Organometallics, **18**, 2198 (1999).
30. L.D. Vazquez-Serrano, B.T. Owens, and J.M. Buriak. Chem. Commun. 2518 (2002).
31. S. Burling, M.K. Whittlesey, and J.M.J. Williams. Adv. Synth. Catal. **347**, 591 (2005).
32. J.R. Miecznikowski and R.H. Crabtree. Organometallics, **23**, 629 (2004).
33. J.S. Parent, N.T. McManus, and G.L. Rempel. Ind. Eng. Chem. Res. **35**, 4417 (1996).
34. C. O'Connor and G. Wilkinson. J. Chem. Soc. A, **11**, 2665 (1968).
35. J.A. Osborn, F.H. Jardine, J.F. Young, and G. Wilkinson. J. Chem. Soc. A, **12**, 1711 (1966).
36. D.P. Fairlie and B. Bosnich. Organometallics, **7**, 936 (1988).
37. B.J. Holliday, P.A. Ulmann, C.A. Mirkin, C.L. Stern, L.N. Zakharov, and A.L. Rheingold. Organometallics, **23**, 1671 (2004).
38. T.J. Reilly. J. Chem. Educ. **76**, 1557 (1999).
39. R. Bird, A.C. Knipe, and C.J.M. Stirling. J. Chem. Soc. Perkin Trans. 2, **9**, 1215 (1973).
40. A.J. Arduengo, F.P. Gentry, P.K. Taverkere, and H.E. Simmons. U.S. Patent 6-177-575 to E.I. du Pont de Nemours and Company, 23 January 2001.
41. J. Chatt and L.M. Venanzi. J. Chem. Soc. 4735 (1957).
42. E.W. Abel, M.A. Bennett, and G. Wilkinson. J. Chem. Soc. 3178 (1959).
43. A. van der Ent and A.L. Onderdelinden. Inorg. Synth. **28**, 92 (1990).
44. Bruker AXS Inc. SAINT. Version 7.03A [computer program]. Bruker AXS Inc., Madison, Wis. 1997–2003.
45. Bruker AXS Inc. SADABS. Version 2.05 [computer program]. Bruker AXS Inc., Madison, Wis. 2003.
46. A. Altomare, M.C. Burla, M. Camalli, G.L. Cascarano, C. Giacovazzo, A. Guagliardi, A.G.G. Moliterni, G. Polidori, and R. Spagna. J. App. Crystallogr. **32**, 115 (1999).
47. D.T. Cromer and J.T. Waber. International tables for X-ray crystallography. Vol. IV. The Kynoch Press, Birmingham, England. 1974.
48. J.A. Ibers and W.C. Hamilton. Acta Crystallogr. **17**, 781 (1964).
49. D.C. Creagh and W.J. McAuley. International tables for crystallography. Vol. C. *Edited by* A.J.C. Wilson. Kluwer Academic Publishers, Boston, Mass. 1992. Table 4.2.6.8. pp. 219–222.
50. D.C. Creagh and J.H. Hubbell. International tables for crystallography. Vol. C. *Edited by* A.J.C. Wilson. Kluwer Academic Publishers, Boston, Mass. 1992. Table 4.2.4.3. pp. 200–206.
51. G.M. Sheldrick. SHELXL suite of programs for crystal structure analysis (Release 97-2). Institüt für Anorganische Chemie, Tammanstrasse 3, D-3400, Göttingen, Germany. 1998.

© 2008 NRC Canada

Reaction of gaseous mercury with molecular iodine, atomic iodine, and iodine oxide radicals — Kinetics, product studies, and atmospheric implications

Farhad Raofie, Graydon Snider, and Parisa A. Ariya

Abstract: Mercury is present in the Earth's atmosphere mainly in elemental form. The chemical transformation of mercury in the atmosphere may influence its bioaccumulation in the human food chain as well as its global cycling. We carried out the first kinetic and product studies of the reactions of gaseous mercury with molecular iodine, atomic iodine, and iodine oxide radicals at tropospheric pressure (~740 Torr) and 296 ± 2 K in air and in N_2 (1 Torr = 133.322 4 Pa; 0 °C = 273.15 K). Atomic iodine was formed using UV photolysis of CH_2I_2. IO radicals were formed by the UV photolysis of CH_2I_2 in the presence of ozone The reaction kinetics were studied using absolute rate techniques with gas chromatographic and mass spectroscopic detection (GC–MS). The measured rate coefficient for the reaction of Hg^0 with I_2 was ≤ $(1.27 \pm 0.58) \times 10^{-19}$ cm^3 $molecule^{-1}$ s^{-1}. The reaction products were analyzed in the gas phase from the suspended aerosols and from deposits on the walls of the reaction chambers using six complementary methods involving chemical ionization and electron impact mass spectrometry, GC–MS, a MALDI-TOF mass spectrometer, a cold vapor atomic fluorescence spectrometer (CVAFS), and a high-resolution transmission electron microscope (HRTEM) coupled to an energy dispersive spectrometer (EDS). The major reaction products identified were HgI_2, HgO, and HgIO or HgOI. The implications of the results are discussed with regards to both the chemistry of atmospheric mercury and its potential implications in the biogeochemical cycling of mercury.

Key words: mercury, molecular iodine, atomic iodine, iodine oxide radicals kinetics, product study, atmospheric chemistry.

Résumé : Dans l'atmosphère terrestre, le mercure est principalement présent sous la forme élémentaire. La transformation chimique du mercure dans l'atmosphère peut influencer sa bioaccumulation dans la chaîne alimentaire de l'homme ainsi que sur son cycle global. On a effectué les premières mesures cinétiques ainsi que les premières études sur la nature des produits des réactions du mercure gazeux avec l'ion moléculaire, l'iode atomique et les radicaux d'oxyde d'iode, à la pression de la troposphère (environ 740 Torr, 1 Torr = 133.322 4 Pa), à 296 ± 2 K, dans l'air et dans l'azote. L'iode atomique a été obtenu par photolyse UV du CH_2I_2. Les radicaux IO ont été formés par la photolyse UV du CH_2I_2 en présence d'ozone. On a étudié la cinétique des réactions par les techniques de vitesses absolues en utilisant une combinaison des techniques de la chromatographie en phase gazeuse et de la spectrométrie de masse (CG-SM). La valeur du coefficient de vitesse mesuré pour la réaction du Hg^0 avec le I_2 est inférieure à $(1{,}27 \pm 0{,}58) \times 10^{-19}$ cm^3 $molécule^{-1}$ s^{-1}. Les produits de la réaction ont été analysés par chromatographie gazeuse, à partir d'aérosols en suspension ainsi qu'à partir des dépôts recueillis des parois des chambres réactionnelles en faisant appel à six techniques complémentaires impliquant la spectrométrie de masse avec ionisation chimique ainsi que l'ionisation avec impact électronique, la CG-SM et la spectrométrie de masse à temps d'envol avec ionisation par désorption au laser assistée par une matrice (IDLAM), un spectromètre à fluorescence atomique avec vapeur froide (SFAVF) et un microscope à transmission d'électron à haute résolution (MTEHR) couplé à un spectromètre à dispersion d'énergie (SDE). Les produits principaux qui ont pu être identifiés sont le HgI_2, le HgO et le HgIO ou HgOI. On discute des implications de ces résultats en regard tant de la chimie du mercure atmosphérique que de ses implications potentielles dans le cycle biogéochimique du mercure.

Mots-clés : mercure, iode moléculaire, iode atomique, radicaux d'oxyde d'iode, cinétique, étude de produits, chimie de l'atmosphère.

[Traduit par la Rédaction]

Received 19 December 2007. Accepted 25 April 2008. Published on the NRC Research Press Web site at canjchem.nrc.ca on 5 July 2008.

F. Raofie, G. Snider, and P.A. Ariya.[1] Departments of Chemistry and Atmospheric and Oceanic Sciences, McGill University, 801 Sherbrooke St. W., Montreal, QC H3A 2K6, Canada.

[1]Corresponding author (e-mail: parisa.ariya@mcgill.ca).

 doi:10.1139/V08-088 © 2008 NRC Canada

Introduction

Gaseous elemental mercury is a toxic element of concern because of its accumulation in the aquatic food chain (via methylation), leading to mercury deposits found in consumable freshwater and marine species (1). Mercury is released into the atmosphere from a variety of natural (2–6) and anthropogenic sources (7–10). It has been shown that 60% to 80% of present mercury emissions into the atmosphere are of anthropogenic origin, and that about 50% of anthropogenic mercury emissions enter a global cycle of contamination (11). The concentration of atmospheric mercury in the northern hemisphere is between 1.6 to 4.7 ng m^{-3}, with an average of 2.5 ng m^{-3}, which is mainly elemental (12). Atmospheric mercury undergoes various chemical and physical transformations before being deposited on the ground. Unexpectedly rapid depletion of elemental mercury has been observed in the high Arctic (13), Arctic (14, 15), and sub Arctic (16) during springtime, concomitant with ozone depletion. It has been shown that chain reactions of halogen species in the Arctic are responsible for ozone and mercury depletion (17–21). The speciation and chemical transformations of mercury in the atmosphere strongly influence its deposition and global cycling. Hg^0 can be transported back to the earth mainly through dry deposition. Mercury(II) oxides are nonvolatile species and precipitate to the ground much more rapidly than Hg^0 via dry and wet processes (22).

Experimental and theoretical research of gas-phase reactions of mercury with halogen species under atmospheric conditions are relatively new, most of which have only been published within the last decade. Schroeder et al. (23) proposed several possible reactions between gaseous mercury and a variety of atmospheric oxidants and reductants using their thermodynamic data. They suggest that O_3 and Cl_2 may be important for oxidation of Hg^0, while SO_2 and CO are important for the reduction of Hg(II). It has since been found that bromine species play an important role in the rapid Arctic depletion of mercury. In warmer climates, however, oxidation by ozone becomes the most relevant pathway. In our laboratory, we have studied products of the gas-phase reaction of elemental mercury with O_3 (24), BrO (25, 26), and HO (27) radicals; atomic Cl and Br; and molecular Cl_2 and Br_2 (28). We have also considered previous thermochemical calculations of reactions between Hg and halogens (29).

The atmospheric chemistry of iodine is important for several reasons, including the influence of iodine oxides on the oxidizing capacity of the troposphere, the formation of new particles, the enrichment of iodine in marine aerosols, and transport of this essential dietary element to the continents (30). The identified natural sources of iodine are CH_3I, CH_2I_2, C_2H_5I, CH_2ICl, and I_2 from seawater (31–33) that photochemically can release reactive iodine species. Iodine, however, is also released into the atmosphere from industrial activity. The photolysis of many iodine species produces iodine atoms, and hence IO radicals through reaction with O_3 (34). Iodine oxide was observed in the marine boundary layer by several researchers (35, 36). The iodine oxide radicals are involved in ozone depleting cycles in the troposphere (33, 37) and stratosphere (38) as well as reaction with dimethyl sulfide emitted by phytoplankton in the ocean (39). However, there is no available literature on the experimental kinetic and product of molecular iodine, atomic iodine, and iodine oxide radicals with elemental mercury (see Calvert and Lindberg for simulations of iodine kinetics (40)).

The purpose of this work is to study the products of the gas-phase reaction of elemental mercury with molecular iodine, atomic iodine, and iodine oxide radicals and kinetics of the gas-phase reaction of elemental mercury with molecular iodine at tropospheric pressures and ambient temperatures.

Experimental section

Experimental procedure

Experiments were carried out in N_2 and in air at room temperature and near-atmospheric pressure. Reaction chambers included 1 to 50 L Teflon bags and 1 to 5 L Pyrex double-wall flasks equipped with magnetic stirrers to assure homogeneous mixing. The reaction chamber temperature was maintained at 296 ± 2 K (0 °C = 273.15 K) by circulating water through the outer jacket using a Neslab RTE 111 circulator.The reaction chamber was washed a minimum of four times with concentrated nitric acid (12 mol/L), Mili-Q water, and acetone and dried at high temperature (398 K) overnight. The inside walls of the reaction flask were coated with halocarbon wax (Supelco) to prevent unwanted wall reactions (41). A vacuum system was used to prepare gaseous reactant mixtures. Gaseous reactants were transferred directly into the reaction mixture using a 10 or 250 μL syringe (Hamilton series 1800 gas tight). Liquid substrates were injected with a 2 or 10 μL syringe (Hamilton series 700). Ozone was produced using an ozone generator (Model OL 100/DS, Ozone Services Inc.) by a silent discharge technique and was trapped on silica gel cooled to 200 K in a dry ice – acetone mixture. Ozone was then transferred to an evacuated flask (~10^{-7} bar) (1 bar = 100 kPa), and the concentration of ozone was monitored by a UV–vis spectrometer (Varian Cary-50-Bio). A given amount of ozone was injected into the reaction flask (1 to 5 L) using a gas-tight syringe. Molecular iodine vapor was produced by mixing iodine with silica gel and heating to 323 K. Iodine radicals were generated in situ upon UV photolysis of diiodomethane ($300 \leq \lambda \leq 400$ nm).

IO radicals were generated in situ upon UV photolysis of diiodomethane ($300 \leq \lambda \leq 400$ nm) in the presence of ozone (42).

[R1] $CH_2I_2 + h\upsilon\ (300 \leq \lambda \leq 400\ nm) \rightarrow CH_2I^{\cdot} + I^{\cdot}$

[R2] $I^{\cdot} + O_3 \rightarrow IO + O_2$

$$k_{R2} = 8 \times 10^{-13}\ cm^3\ molecule^{-1}\ s^{-1}$$

The initial concentration of Hg^0 was ~0.5 ppm, and the concentration of I_2 was 130 ppm. In the course of ozone addition, we used scavengers such as trimethyl benezene for OH radicals (41) that are formed via side reactions in the presence of organic matter, such as CH_2I_2 or any undesired impurities or production of other undesired oxidants in the course of experiments. We did not observe any organomercury or halo-organo-mercury products using six different analytical methods. The reaction of gaseous mercury with O_3 is too slow [$(6.2 \pm 1.1) \times 10^{-19}$ cm^3 $molecule^{-1}s^{-1}$ (43)]

© 2008 NRC Canada

to observe. Oxidation of gaseous mercury by O_3 was negligible under the reaction conditions.

Analytical procedure for the product analysis

The reactions

[R3] $Hg^0_{(g)} + I_{2\,(g)} \rightarrow$ products

[R4] $Hg^0_{(g)} + I_{(g)} \rightarrow$ products

and

[R5] $Hg + IO^{\cdot}_{(g)} \rightarrow$ products

were carried out in 1 to 50 L Teflon bags and 1 to 5 L Pyrex flasks. The products were analyzed by the methods described below.

Direct mass spectrometry

Reaction products were collected using two methods. In the first method, the reaction products were passed through a 1.1 mm i.d. × 10 cm length Pyrex tube (Corning) immersed in liquid nitrogen. In the second method, the walls of the reaction flask were washed with concentrated HCl. A sample of the collected products (50 μL) was transferred in a 1.1 i.d. × 10 cm length Pyrex tube and was covered immediately with a piece of glass wool. Extra HCl was evaporated by slow heating in a water bath. Finally, the collected products in the tube were evaporated at stepwise elevated temperatures to the chemical and electron impact ion source of a Kratos MS25RFA mass spectrometer.

Cold vapor atomic fluorescence spectrometry (CVAFS)

Samples were prepared by washing the walls of the reaction chamber, a Teflon filter (0.45 μm), and the coiled Pyrex trap, with a mixture of 20 mL HNO_3 and 0.5 mL 30% H_2O_2, diluted to 50 mL with Milli-Q water. The samples were heated to 350 K for 1 h to decompose excess H_2O_2, diluted further to 100 mL in a volumetric flask with Milli-Q water, and analyzed using a cold vapor atomic fluorescence spectrometer (Tekran 2600).

Derivatization

This method is based on chemical transformation of Hg^{2+} to $HgCl_2$ and then to a more volatile organomercury compound, *n*-Bu_2Hg. Samples were prepared by washing the walls of the reaction flask with HCl, which transformed Hg^{2+} to $HgCl_2$. The sample was heated to remove extra HCl, which resulted in the formation of a white residue. Derivatization was performed using previously reported method (44, 45). 2 mL of toluene and 0.4 mL of 2 mol/L *n*-butylmagnesium chloride in tetrahydrofuran were added to the white residue. The mixture was then centrifuged at 0 °C for 10 min with occasional shaking. To quench the excess derivatizing agent, 0.4 mL of 0.6 mol/L HCl was added the mixture that was then centrifuged, allowing for collection of the organic phase for analysis.

[R6] $Hg^{2+} + 2\ HCl \rightarrow HgCl_2 + 2H^+$

[R7] $HgCl_2 + 2\ n\text{-}BuMgCl \rightarrow n\text{-}Bu_2Hg + 2MgCl_2$

Fig. 1. Typical absolute-rate data for reaction of Hg + I_2, [Hg] = 0.5 ppm, [I_2] = 3.2 × 10^{15} molecule cm^{-3}; kinetic runs were performed at 298 K in nitrogen.

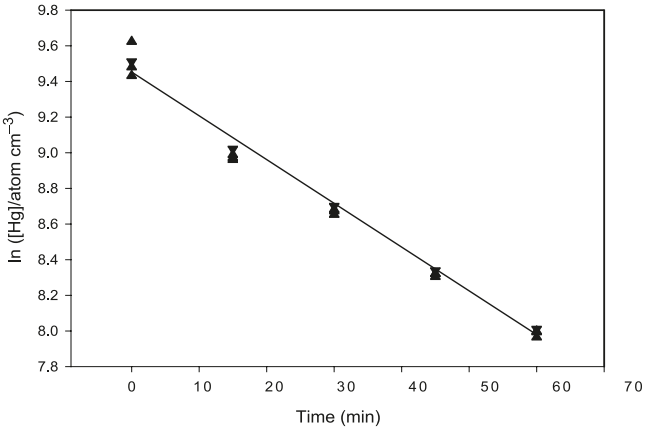

Transmission electron microscopy (TEM)

Reaction products were collected by two different methods. The first technique involved placing carbon-coated Cu grids on the surface of the reaction flask, and the Cu grids were later collected upon completion of the reaction. The second method involved the collection of reaction products in a capillary Pyrex tube, which was immersed in liquid nitrogen. Collected products were analyzed using a high-resolution transmission electron microscope (JEOL 2000 FX TEM). The elemental composition was qualitatively determined by energy dispersive spectroscopy (EDS; JEOL 2000).

Matrix-assisted laser desorption ionization time-of-flight mass spectrometry (MALDI-TOF-MS)

The reaction products were collected in capillary Pyrex tubes, which were immersed in liquid nitrogen. The collected products were analyzed using Kratos Kompakt MALDI-TOF-MS in reflectron mode. Dithranol and lithium bromide were used as matrix and cationization agent, respectively. The matrix has resonance absorption at laser wavelength of 337 nm. This rapid heating results in expulsion and soft ionization of the sample molecules without major fragmentation (46).

Chemicals and materials

Mercury (99.99% purity) and *n*-butyl magnesium chloride (2 mol/L solution in tetrahydrofuran) were supplied by Sigma-Aldrich. Nitrogen (99.998%), argon (99.999%), helium (99.999%), nitric oxide (99.99%), and extra-dry oxygen were obtained from Matheson. Toluene (99.9%), hydrogen peroxide (30%), hydrochloric acid (trace-metal grade), Iodine (99.9%), and nitric acid (trace-metal grade) were purchased from Fisher. Tin (II) chloride (99.999%) and diiodomethane (99%) were obtained from Aldrich. Milli-Q water of 18.2 MΩ cm resistivity was used for all experiments. The nitric and hydrochloric acids used in the course of experiments were 70 wt% and 38 wt% assays, respectively.

© 2008 NRC Canada

Fig. 2. Mass spectra of products formed in the reaction of Hg^0 with molecular iodine.

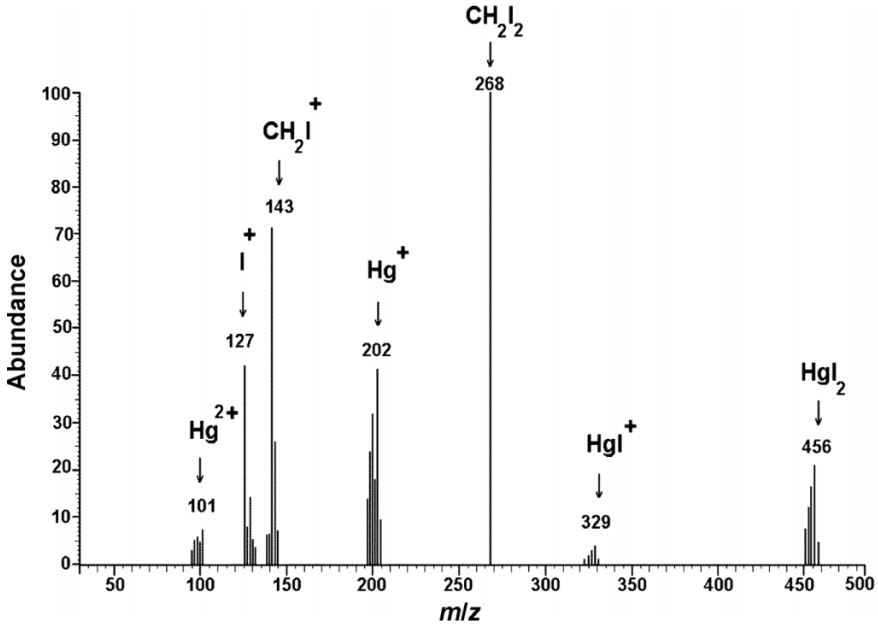

Fig. 3. Mass spectra of products formed in the reaction of Hg^0 with IO radicals.

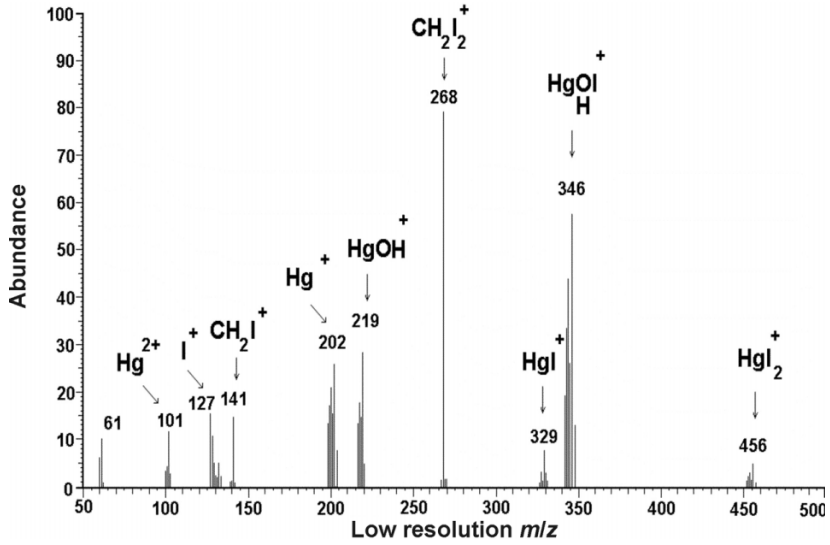

Results and discussion

Kinetic study

The absolute-rate technique was used to study the kinetics of the I_2-initiated reaction of Hg^0 (47). Experiments were carried out in 1 to 5 L Pyrex flask at room temperature in air and nitrogen. To prevent wall reaction, the walls of reaction flask were coated with halocarbon wax. In addition, to minimize the effect of adsorption on the kinetic results, the reaction mixture was kept at equilibration for 2 h before injecting I_2. To inject I_2 as a gas into the reaction chamber, molecular I_2 was first mixed with silica gel (~ 1:50) in 1 L flask. The mixture was evacuated to 7×10^{-3} Torr. The temperature of the flask was increased to 60 °C by slow heating. A given amount of I_2 was injected into the reaction chamber using gas-tight syringe. To prevent dissociation of I_2, the reaction chamber was completely dark. The reaction of gaseous mercury with I_2 was studied under pseudo first-order conditions by monitoring the MS signal of mercury vs. time. Figure 1 shows semi logarithmic plots of data obtained for the reaction of Hg^0 with I_2 in air. The upper-limit rate coefficient calculated from the curve was $\leq (1.27 \pm 0.58) \times 10^{-19}$ cm^3 $molecule^{-1}s^{-1}$. Because we observed the formation of particulate matter, we cannot rule out the possibility of heterogeneous reactions; and hence, this rate coefficient value should represent only an upper limit for the gas-phase-initiated oxidation of elemental mercury with iodine molecule.

Product studies

The products of reactions [R3–R5] have been studied in the gas phase from suspended aerosols and from the walls of

© 2008 NRC Canada

Fig. 4. Mass spectra of $HgCl_2$ and HgI_2, reaction products in reaction of Hg^0 with atomic iodine.

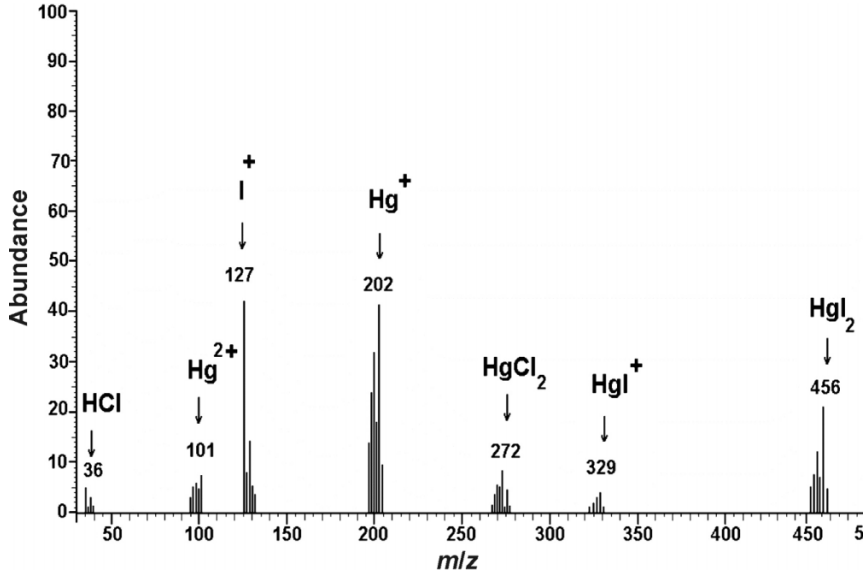

the reaction chambers. Six complementary analytical methods have been employed to identify the reaction products of molecular iodine, atomic iodine, and iodine radicals initiated oxidation of $Hg^0_{(g)}$.

In the first method, after the reaction was completed, the reaction products from the gas–aerosol phase were collected in a liquid-nitrogen-cooled capillary tube. The chemical structure of the reaction products mixture was identified using a direct MS instrument equipped with an electron impact and chemical ionization ion source with probe temperature elevated to 430 K. Figure 2 represents mass spectra of HgI_2. The isotopic ratios for HgI_2 (33.6:56.4:77.5:44.3:100.0:22.8) corresponded well with the anticipated *m*/*z* ratios 452, 453, 454, 455, 456, and 458, respectively; thus further supporting the identified mercury compounds. The *m*/*z* ratio of 268 is assigned to CH_2I_2, which had been used as the iodine radical source. Other *m*/*z* ratios in the mass spectrum represent the fragmentation of HgI_2 or CH_2I_2. Hence, our results identify HgI_2 as the major product of the gas–aerosol reaction: $Hg^0 + I_2$. For $Hg^0 + I^{\cdot}$, the same product was observed. For $Hg^0 + IO^{\cdot}$, chemical ionization of NH_3 was used as an ion source, so the observed mass spectra of the ion (M^+) should be increased by one. We identified the products HgOI or HgIO, HgI_2, and HgO (Fig. 3). The *m*/*z* ratio of each peak was shifted by one. Moreover, the observed isotopic ratios for HgI_2 (33.6:56.4:77.5:44.3:100.0:22.8) corresponded well with the anticipated *m*/*z* ratios of 452, 453, 454, 455, 456, and 458, respectively. The isotopic ratios of 33.5, 56.3, 77.5, 44.4, 100.0, and 23.0 correspond well with those for the *m*/*z* ratios 341, 342, 343, 344, 345, and 347, respectively. The isotopic ratios 33.5:56.3:77.4:44.4:100.0:23.0 matched *m*/*z* ratios of 214, 215, 216, 217, 218, and 220, repectively, illustrating the presence of HgO, which further supports the identified mercury compounds. The *m*/*z* ratio of 268 is assigned to CH_2I_2, which had been used as an iodine radical source. From product analysis, we were unable to distinguish the chemical structure of Hg-, I-, and O-containing species. Other *m*/*z* ratios in the mass spectrum represent either fragmentation of HgI_2, HgO, HgIO (HgOI), or CH_2I_2 in the ion source of the mass spectrometer. The results show that the major products in the gas–aerosol phase of reaction $Hg^0_{(g)} + IO^{\cdot}$ are HgIO or HgOI, HgI_2, and HgO.

In the second method, the walls of the reaction flask were washed with concentrated HCl. Samples of the collected products (50 μL) were transferred in a 1.1 i.d. × 10 cm length Pyrex tube and immediately covered with a piece of glass wool. Extra HCl was evaporated by slow heating in a water bath. Finally, the collected products in the tube were evaporated at stepwise elevated temperatures to the chemical and electron impact ion source of a Kratos MS25RFA mass spectrometer. Figure 4 represents the mass spectra of $HgCl_2$ and HgI_2. The isotopic ratios for $HgCl_2$ (22:37:65:52:100:22:62:16) corresponded well with the anticipated *m*/*z* ratios of 268, 269, 270, 271, 272, 273, 274, and 276, respectively. The *m*/*z* ratio of 456 is assigned to HgI_2, which is slightly soluble in concentrated HCl. Hence, we conclude the existence of HgI_2 as a reaction product on the walls. Similar results were observed for the $Hg^0 + I^{\cdot}$ and $Hg^0 + IO^{\cdot}$ reactions.

In the third method, to confirm the presence of Hg^{2+} on the walls of the reaction chamber, the products on the walls were converted to di(*n*-butyl mercury). The derivatized sample was analyzed using GC–MS. Figure 5 illustrates a chromatogram and mass spectrum of the derivatized mercury. Hg^0 and Hg^{+1} were not targeted in derivatization analysis, so their existence cannot be evaluated using the Grignard reagent. This experiment confirmed the presence of Hg^{2+} (here, HgI_2) on the walls of reaction chamber. Similar results were observed for the $Hg^0 + I^{\cdot}$ and $Hg^0 + IO^{\cdot}$ reactions.

In the fourth method, MALDI-TOF-MS was used to identify the reaction products of molecular iodine, atomic iodine, and iodine oxide radicals. Figure 6 is an example of a MALDI-TOF-MS spectrum. The peak at mass 454 is assigned to HgI_2 in the reaction of Hg with both I_2 and I. No other oxidized forms of mercury were detected. Figure 7 is an example of MALDI-TOF-MS spectrum for the reaction

© 2008 NRC Canada

Fig. 5. Gas chromatogram and the corresponding mass spectrum of the derivatized mercury (di-*n*-butylmercury) eluted at 12.25 min.

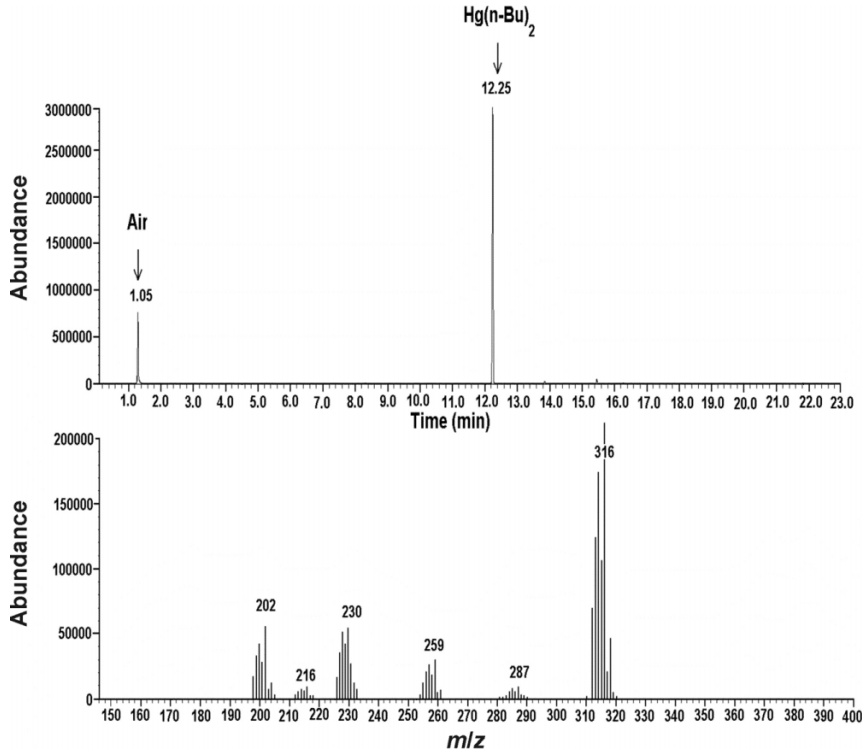

Fig. 6. MALDI-TOF mass spectrum of products formed in the reaction of Hg^0 with molecular iodine.

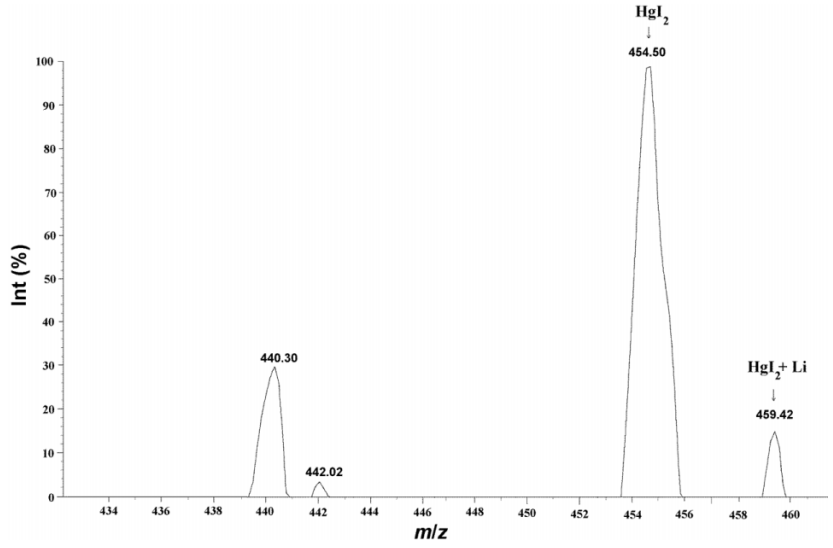

of Hg^0 + IO˙. The peak at mass 357 is assigned to HgIO or HgOI. Other peaks arise from the matrix itself under our experimental conditions.

In the fifth method, we attempted to identify the shape, size, and elemental composition of reaction products from the gas–aerosol phase and on the walls of the reaction chamber using HRTEM coupled to an EDS detector. Figure 8*a* illustrates the TEM image of air-dried products of the reaction Hg^0 + I_2 collected from the gas–aerosol mixture. The size of the particles in the gas–aerosol mixture was approximately 0.2 μm. The EDS spectrum of the chemical composition of the products in the gas–aerosol mixture showed that the gas–aerosol mixture should contain mercury and iodine. Combining evidence from MALDI-TOF-MS and EDS, we believe that the observed aerosol contains HgI_2. Figure 8*b* depicts TEM image of collected products of the reaction of Hg^0 + I_2 from the walls of the reaction chamber. The size and chemical composition of the particles collected from the walls of the reaction chamber exhibit similar features to those observed from gas–aerosol. TEM images of air-dried Hg^O + I reaction products were collected from the gas-aerosol mixture. The size of the particles in the gas–aerosol

© 2008 NRC Canada

Fig. 7. MALDI-TOF mass spectrum of products formed in the reaction of Hg^0 with iodine oxide radicals

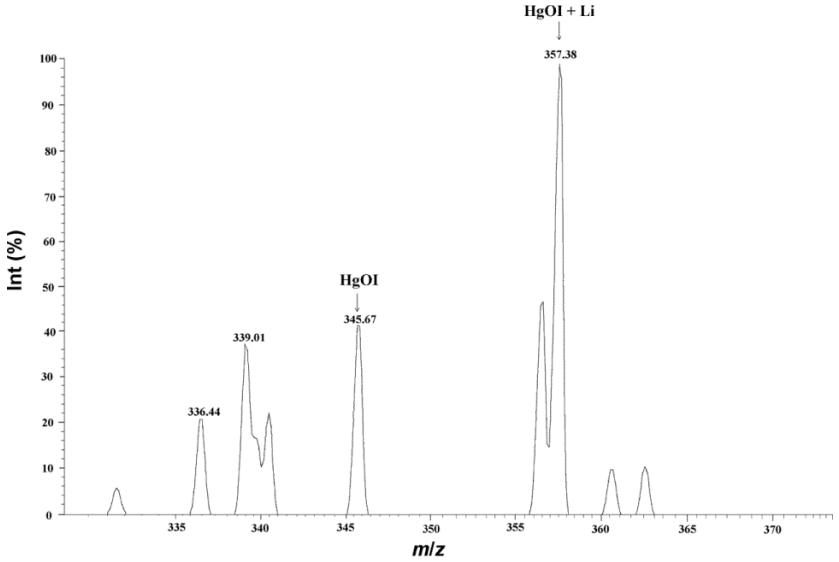

Fig. 8. (*a*) EDS spectrum shows the chemical composition of the product collected from the gas–aerosol in the reaction of Hg^0 with molecular iodine dispersed onto carbon-supported Cu grid. Inset shows HRTEM image of air-dried product collected from the gas–aerosol. (*b*) EDS spectrum shows the chemical composition of the product collected from the walls of the reaction chamber in the reaction of Hg^0 with molecular iodine dispersed onto carbon-supported Cu grid. Inset shows an HRTEM image of air-dried product collected from the walls of the reaction chamber.

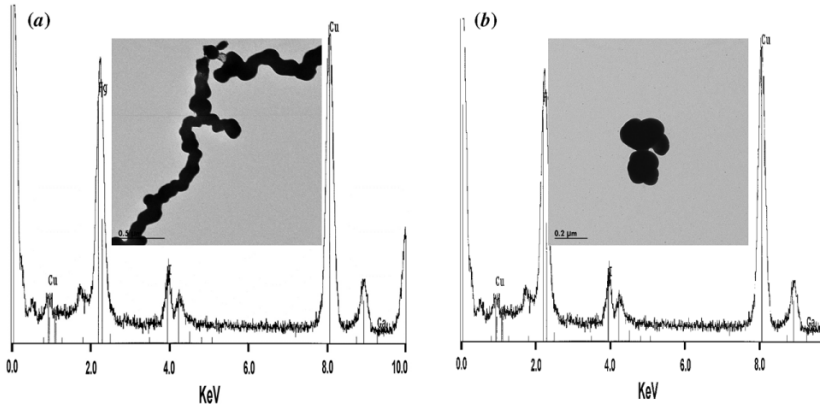

mixture was approximately 0.2 μm (Fig. 9*a*). The EDS spectrum of the chemical composition of the products in the gas–aerosol mixture showed that the gas–aerosol mixture contained mercury and iodine. Because of the chemical composition of the reaction products, we believe that the observed aerosol contains HgI_2. A TEM image of collected products of the reaction of $Hg^0 + I^{\cdot}$ from the walls of the reaction chamber is illustrated in Fig. 9*b*. The size and chemical composition of the particles collected from the walls of the reaction chamber exhibited similar features to those observed from gas–aerosol. Figure 10*a* illustrates the TEM image of air-dried products of the reaction of $Hg^0 + IO^{\cdot}$ that were collected from the gas–aerosol mixture. Particles in the gas–aerosol mixture were observed to be approximately 0.5 μm. The EDS spectrum of the chemical composition of the products in the gas–aerosol mixture revealed the presence of mercury, iodine, and oxygen. Because of the elemental composition of the reaction products, we believe that the observed aerosol contains Hg, O, and I. Collected products from the walls of the reaction chamber are found to have similar size and elemental composition to those observed from the gas–aerosol mixture (Fig. 10).

In the sixth method, we used CVAFS to quantify mercury products in the gas phase, aerosol, and as deposit on the walls of the reaction chamber. Upon completion of the reaction (confirmed by disappearance of MS peak due to Hg^0), the reaction flask was evacuated through a 0.45 μm Teflon filter to a residual pressure of ~0.0007 bar. The filter was treated with a HNO_3/H_2O_2 mixture. CVAFS analysis indicated that ~ (10 ± 1)% of total mercury (relative to the amount of Hg^0 loaded in the flask) was converted to mercury compounds in the aerosol phase. In another set of experiments, products were collected in a cooled coiled Pyrex trap, treated with the HNO_3/H_2O_2 mixture and further analyzed using CVAFS upon completion of the reaction. By subtracting the total mercury collected from the gas and aerosol mixtures and the amount of aerosol mercury collected on the filters, we obtained only ~ (10 ± 3)% of total mercury remaining in the gas phase. This analysis recovered (20 ± 4)% of the mercury in the gas–aerosol phase. Finally, the reaction

© 2008 NRC Canada

Fig. 9. (*a*) EDS spectrum shows the chemical composition of the product collected from the gas–aerosol in the reaction of Hg^0 with atomic iodine dispersed onto carbon-supported Cu grid. Inset shows an HRTEM image of air-dried product collected from the gas–aerosol. (*b*) EDS spectrum shows the chemical composition of the product collected from the walls of the reaction chamber in the reaction of Hg^0 with atomic iodine dispersed onto carbon-supported Cu grid. Inset shows an HRTEM image of air-dried product collected from the walls of the reaction chamber.

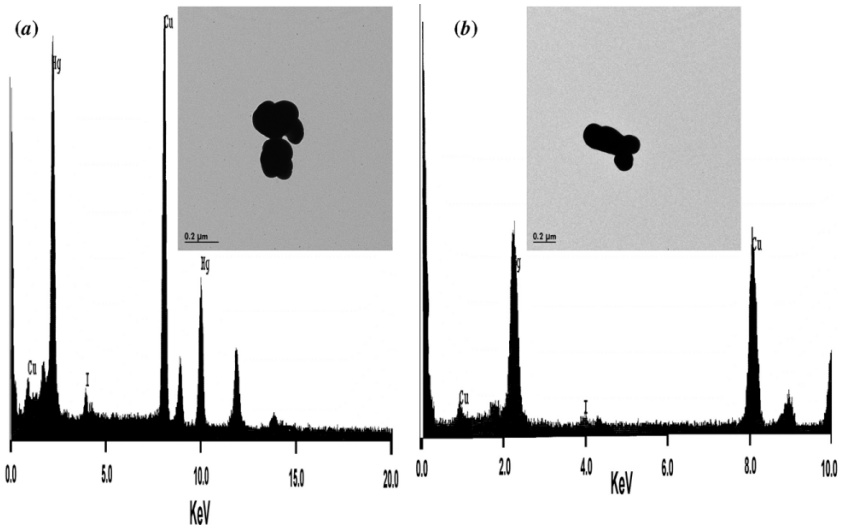

Fig. 10. (*a*) EDS spectrum shows the chemical composition of the product collected from the gas–aerosol in the reaction of Hg^0 with iodine oxide radicals dispersed onto carbon-supported Cu grid. Inset shows an HRTEM image of air-dried product collected from the gas–aerosol. (*b*) EDS spectrum shows the chemical composition of the product collected from the walls of the reaction chamber in the reaction of Hg^0 with iodine oxide radicals dispersed onto carbon-supported Cu grid. Inset shows an HRTEM image of air-dried product collected from the walls of the reaction chamber.

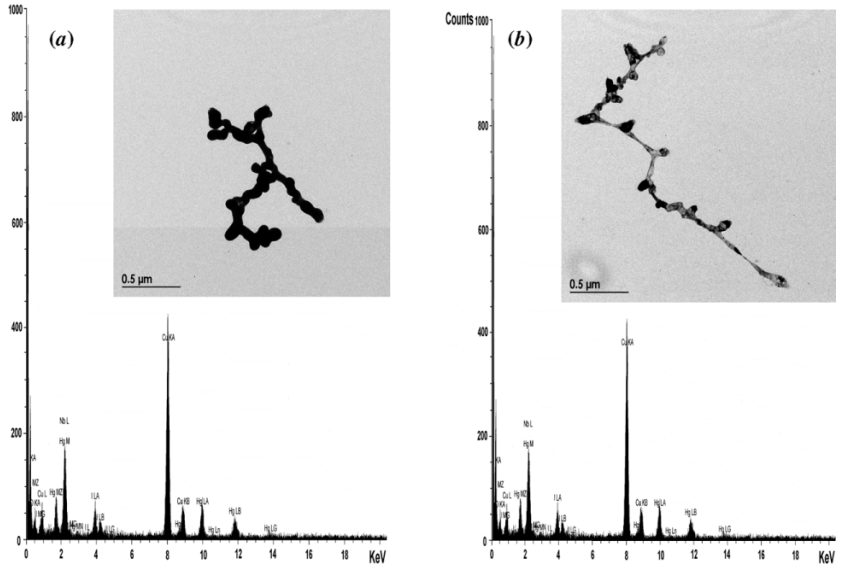

products were collected from the reaction flask walls by washing with a HNO_3/H_2O_2 mixture, and analyzed by CVAFS. Overall, (70 ± 5)% of Hg was recovered from the walls (Table 1). The dominant reaction products were found as adsorbed deposits on the walls of the reaction chamber (85 ± 2)% or as aerosols ~ (14 ± 1)% leaving only ~ (4 ± 1)% of the total mercury existing in the gas phase, as illustrated in Table 1.

As shown in Table 1 for [R5], ~ (25 ± 3)% of total mercury remains in the gas–aerosol phase with ~ (5 ± 2)% of total mercury recovered from the gas phase. Recovery of Hg from the walls of the reaction chamber was (75 ± 4)%. Our results therefore showed that the reaction products were predominantly found adsorbed on the walls of the reaction chamber as deposits or existed as aerosols. Under our experimental conditions, we did not observe any difference in identified mercury compounds in N_2 or air, noting that our nitrogen diluent (99.998%) gas was still not entirely oxygen free.

Potential reactions mechanism

Products of the oxidation of Hg^0 by I_2, I, and IO can be formed by reactions [R3] to [R5]

© 2008 NRC Canada

Table 1. Quantification of mercury in the reaction vessel for I_2-, I˙-, and IO˙-initiated reaction of gaseous mercury using a 0.45 μm Teflon filter.

	Mercury species								
	I_2			I			IO		
	Gas + aerosols	Aerosols	Wall deposits	Gas + aerosols	Aerosols	Wall deposits	Gas + aerosols	Aerosols	Wall deposits
Yield (%)	30±3	20±4	75±5	18±1	14±3	85±2	30±2	25±3	75±2
Char. Width (μm)	~0.2	~0.2	~0.5	~0.2	~0.2	~0.2	~0.5	~0.5	~0.5

[R1] $CH_2I_2 + h\upsilon\ (300 \leq \lambda \leq 400\ nm) \rightarrow CH_2I^{\cdot} + I^{\cdot}$

[R2] $I^{\cdot} + O_3 \rightarrow IO^{\cdot} + O_2$

[R3*a*] $Hg + I_2 \rightarrow HgI_2$

[R4*a*] $Hg + I^{\cdot} \rightarrow HgI$

[R4*b*] $HgI + I^{\cdot} \rightarrow HgI_2$

[R5*a*] $Hg + IO^{\cdot} \rightarrow HgOI/HgIO$

[R5*b*] $Hg + IO^{\cdot} \rightarrow HgO + I^{\cdot}$

[R5*c*] $Hg + IO^{\cdot} \rightarrow HgI + O$

[R5*d*] $HgI + IO^{\cdot} \rightarrow HgI_2 + O$

We identified HgI_2, HgIO or HgOI, HgO, and HgI by direct mass with a chemical ionization ion source. There are two possible sources for HgI, either as a product in the chamber or a fragmentation product of HgI_2 in the ion source of the mass spectrometer. Shepler et al. (48) have estimated the enthalpies of the above reaction at 0 K. This theoretical study used the ab initio CCSD(T) method with basis sets including detailed treatment of core–valence correlation, scalar reactivity, spin–orbit coupling, and the Lamb shift. The values of ΔH_r(0 K) for reactions [R5*a*–R5*d*] have been shown to be –51.2, 191.5, 209.2, and –28.6 kJ mol^{-1}, respectively. Regarding the results for ΔH_r(0 K), HgIO but not HgI and HgO cannot be formed by reactions [R5*b*] and [R5*c*], respectively. HgO can, however, be formed by reaction [R5*b*], and we did observe the existence of HgO with different types of mass spectrometry and HRTEM-EDS. The value of ΔH_r(0 K) = –146.4 kJ/mol for reaction [R3*a*] for the I_2-initiated reaction of gaseous mercury indicates this pathway is possible in the formation of HgI_2. We can indeed observe HgI_2, as confirmed by the different types of mass spectrometry technique used in this study.

Because we observed aerosols, and although we have modified the surface-to-volume ratios and the properties of the surfaces, and used different oxidant and reactant concentration regimes, we cannot rule out the possibility of heterogeneous reactions.

Summary and future work

We have studied the products of the reactions of gaseous mercury with molecular iodine, atomic iodine, and iodine oxide radicals at atmospheric pressure and room temperature in air and in N_2. For the first time, HgI_2, HgO, and HgOI/HgIO are identified as reaction products in the gas and in the aerosol phase, as well as on the walls of the reaction chamber. Our upper-limit rate constant for reaction of Hg^0 with molecular iodine is found to be $\leq (1.27 \pm 0.58) \times 10^{-19}$ cm^3 molecule^{-1} s^{-1}. It remains a possibility that during springtime in the Arctic and Antarctica, the iodine reactions have some significance. The reaction of molecular iodine is apparently too slow for the rapid depletion of elemental mercury in the boundary layer. We suspect that based on the formation rates of products in the course of I + Hg(0) reactions, the reactions of I are slower or at most comparable to the reactions of elemental mercury with Br (40, 49). However, the impact of iodine and iodine oxide in the production of oxidized mercury in atmospheric depletion should be further studied.

Acknowledgements

We would like to cordially thank Dr. Paterson for his valuable insights. We thank the Natural Sciences and Engineering Research Council of Canada (NSERC), Le Fonds québecois de la recherche sur la nature et les technologies (FQRNT), the Canadian Foundation for Innovation (CFI), the COMERN project, Canadian Foundation for Climate and Atmospheric Sciences (CFCAS), and Environment Canada for financial support. We would also like to thank Jackie Johnstone for proof reading the manuscript.

References

1. C.J. Lin and S.O. Pehkonen. Atmos. Environ. **33**, 2067 (1999).
2. S.M. Siegel and B.Z. Siegel. Nature (London, UK), **309**, 146 (1984).
3. Z.F. Xiao, J. Munthe, W.H. Schroeder, and O. Lindqvist. Tellus B. **43**, 267 (1991).
4. R.P. Mason, W.F. Fitzgerald, and F.M.M. Morel. Geochim. Cosmochim. Acta **58**, 3191 (1994).
5. S.E. Lindberg, K.H. Kim, T.P. Meyers, and J.G. Owens. Environ. Sci. Technol. **29**, 126 (1995).
6. N. Pirrone and K. Mahaffey. Dynamics of mercury pollution on regional and global scales. Springer. 2005.
7. R. Ferrara, B.E. Maserti, H. Edner, P. Ragnarson, S. Svanberg, and E. Wallinder. Atmos. Environ. Gen. Top. **26**, 1253 (1992).
8. N. Pirrone, G.J. Keeler, and J.O. Nriagu. Atmos. Environ. **30**, 2981 (1996).
9. A. Carpi and S.E. Lindberg. Environ. Sci. Technol. **31**, 2085 (1997).
10. L.D. Lacerda. Water Air Soil Pollut. **97**, 209 (1997).
11. J.T. Dvonch, J.R. Graney, G.J. Keeler, and R.K. Stevens. Environ. Sci. Technol. **33**, 4522 (1999).
12. F.J.G. Laurier, R.P. Mason, L. Whalin, and S. Kato. J. Geophys. Res. Atmos. **108** (2003).
13. W.H. Schroeder, K.G. Anlauf, L.A. Barrie, J.Y. Lu, A. Steffen, D.R. Schneeberger, and T. Berg. Nature (London, UK), **394**, 331 (1998).

© 2008 NRC Canada

14. J.Y. Lu, W.H. Schroeder, L.A. Barrie, A. Steffen, H.E. Welch, K. Martin, L. Lockhart, R.V. Hunt, G. Boila, and A. Richter. Geophys. Res. Lett. **28**, 3219 (2001).
15. S.E. Lindberg, S. Brooks, C.J. Lin, K.J. Scott, M.S. Landis, R.K. Stevens, M. Goodsite, and A. Richter. Environ. Sci. Technol. **36**, 1245 (2002).
16. L. Poissant and M. Pilote. J. Phys. IV. **107**, 1079 (2003).
17. L.A. Barrie, J.W. Bottenheim, R.C. Schnell, P.J. Crutzen, and R.A. Rasmussen. Nature (London, UK), **334**, 138 (1988).
18. B.J. Finlayson-Pitts, F.E. Livingston, and H.N. Berko. Nature (London, UK), **343**, 622 (1990).
19. K.L. Foster, R.A. Plastridge, J.W. Bottenheim, P.B. Shepson, B.J. Finlayson-Pitts, and C.W. Spicer. Science (Washington, DC), **291**, 471 (2001).
20. C.W. Spicer, R.A. Plastridge, K.L. Foster, B.J. Finlayson-Pitts, J.W. Bottenheim, A.M. Grannas, and P.B. Shepson. Atmos. Environ. **36**, 2721 (2002).
21. P.A. Ariya, A.P. Dastoor, M. Amyot, W.H. Schroeder, L. Barrie, K. Anlauf, F. Raofie, A. Ryzhkov, D. Davignon, J. Lalonde, and A. Steffen. Tellus B, **56**, 397 (2004).
22. S.E. Lindberg and W.J. Stratton. Environ. Sci. Technol. **32**, 49 (1998).
23. W.H. Schroeder, G. Yarwood, and H. Niki. Water Air Soil Pollut. **56**, 653 (1991).
24. B. Pal and P.A. Ariya. Phys. Chem. Chem. Phys. **6**, 572 (2004).
25. F. Raofie and P.A. Ariya. J. Phys. IV. **107**, 1119 (2003).
26. F. Raofie and P.A. Ariya. Environ. Sci. Technol. **38**, 4319 (2004).
27. B. Pal and P.A. Ariya. Environ. Sci. Technol. **38**, 5555 (2004).
28. P.A. Ariya, A. Khalizov, and A. Gidas. J. Phys. Chem. A, **106**, 7310 (2002).
29. A.F. Khalizov, B. Viswanathan, P. Larregaray, and P.A. Ariya. J. Phys. Chem. A, **107**, 6360 (2003).
30. A. Saiz-Lopez and J.M.C. Plane. Geophys. Res. Lett. **31** (2004).
31. J.E. Lovelock and R.J. Maggs. Nature (London, UK), **241**, 194 (1973).
32. J.A. Garland and H. Curtis. J. Geophys. Res. Oceans Atmos. **86**, 3183 (1981).
33. D. Davis, J. Crawford, S. Liu, S. McKeen, A. Bandy, D. Thornton, F. Rowland, and D. Blake. J. Geophys. Res. Atmos. **101**, 2135 (1996).
34. L.J. Carpenter, W.T. Sturges, S.A. Penkett, P.S. Liss, B. Alicke, K. Hebestreit, and U. Platt. J. Geophys. Res. Atmos. **104**, 1679 (1999).
35. B. Alicke, K. Hebestreit, J. Stutz, and U. Platt. Nature (London, UK), **397**, 572 (1999).
36. B.J. Allan, G. McFiggans, J.M.C. Plane, and H. Coe. J. Geophys. Res. Atmos. **105**, 14363 (2000).
37. G. McFiggans, R.A. Cox, J.C. Mossinger, B.J. Allan, and J.M.C. Plane. J. Geophys. Res. Atmos. **107** (2002).
38. S. Solomon, R.R. Garcia, and A.R. Ravishankara. J. Geophys. Res. Atmos. **99**, 20491 (1994).
39. Y. Nakano, S. Enami, S. Nakamichi, S. Aloisio, S. Hashimoto, and M. Kawasaki. J. Phys. Chem. A, **107**, 6381 (2003).
40. J.G. Calvert and S.E. Lindberg. Atmos. Environ. **38**, 5105 (2004).
41. S. Coquet and P.A. Ariya. Int. J. Chem. Kinet. **32**, 478 (2000).
42. M.E. Jenkin, R.A. Cox, and D.E. Candeland. J. Atmos. Chem. **2**, 359 (1985).
43. G. Snider, F. Raofie, and P.A. Ariya. Phys. Chem. Chem. Phys. In press. (2008).
44. E. Bulska, H. Emteborg, D.C. Baxter, W. Frech, D. Ellingsen, and Y. Thomassen. Analyst, **117**, 657 (1992).
45. J. Snell, J. Qian, M. Johansson, K. Smit, and W. Frech. Analyst, **123**, 905 (1998).
46. M. Karas and R. Kruger. Chem. Rev. **103**, 427 (2003).
47. F. Raofie and P.A. Ariya. American Geophysical Union, Spring Meeting, San Francisco, CA, USA. 2006.
48. B.C. Shepler, N.B. Balabanov, and K.A. Peterson. J. Phys. Chem. A, **109**, 10363 (2005).
49. D.L. Donohoue, D. Bauer, B. Cossairt, and A.J. Hynes. J. Phys. Chem. A, **110**, 6623 (2006).

© 2008 NRC Canada

Biotransformation of caffeic acid by *Momordica charantia* peroxidase

Xiang Wan, Haili Liu, Xuefeng Huang, Jianguang Luo, and Lingyi Kong

Abstract: Biotransformation of caffeic acid with H_2O_2/*Momordica charantia* peroxidase at pH 5.0, 25 °C in the presence of acetone has resulted in the isolation of three caffeic acid trimers **1**–**3**, five caffeic acid dimers **4**–**8**, and one monomer **9**. Among them, seven (**1**–**7**) are new compounds, and two (**8** and **9**) are known compounds, including one compound (**9**), which was obtained by biotransformation for the first time. The structures were established by 2D NMR techniques, such as HSQC, HMBC, and NOESY measurements. The possible mechanism for the formation of the products is also discussed. This is the first time that caffeic acid trimers have been obtained through the biotransformation of catalyzed by peroxidase in vitro. Compound **5** has shown much stronger anti-oxidative activity than the other caffeic acid polymers obtained.

Key words: Momordica charantia peroxidase, caffeic acid, polymers of caffeic acid, biotransformation, antioxidant activity.

Résumé : La biotransformation de l'acide caféique sous l'effet du H_2O_2 et de la peroxydase *momordica charantia*, à un pH de 5,0, à 25°C et en présence d'acétone conduit à la formation de trois dimères de l'acide caféique, **1**–**3**, à cinq dimères de l'acide caféique, **4**–**8**, et à un monomère, **9**. De ces produits, sept (**1**–**7**) sont des nouveaux produits alors que deux (**8** et **9**) sont des produits connus, dont le produit **9** qui a été obtenu par biotransformation pour la première fois. On a déterminé les structures par des spectres RMN en 2D, telles des mesures de HSQC, HMBC et NEOSY. On discute aussi du mécanisme possible pour la formation des produits. C'est la première fois que des trimères de l'acide caféique ont pu être obtenus par une biotransformation catalysée par une peroxydase in vitro. On a montré que le composé **5** présente une activité antioxydante beaucoup plus élevée que celle des autres polymères de l'acide caféique obtenus.

Mots-clés : peroxydase *Momordica charantia*, acide caféique, polymères de l'acide caféique, biotransformation, activité antioxydante.

[Traduit par la Rédaction]

Introduction

Momordica charantia peroxidase (MCP) is a novel plant peroxidase with high acidic amino acid purified from the fruits of *Momordica charantia* (1). Compared with other peroxidases such as horseradish peroxidase, the enzyme had several unique characteristics, including enzyme pH stability (pH 3.8–8.0) and thermostability (20–45 °C) (2). According to the unique characteristics, we have applied purified MCP to transform ferulic acid, sinapic acid, and *p*-coumaric acid into some oxidation products, which have not been obtained by other peroxidases or chemosynthesis (2–4).

Caffeic acid (CA), which exists in many plants, exhibits a lot of activities, such as anti-apoptotic activity, anti-cancer, anti-inflammatory, anti-atherogenic effect, and antioxidant activity (5–8). Compared with the structures of other substrates that we had used, the structure of caffeic acid contains two hydroxyls; therefore, the reaction sites are different from those of others and the dimers of caffeic acid maybe have powerful antioxidant activity (9, 10). Recently, some dehydrodimers and higher oligomers of caffeic acid had been isolated from some plants; however, only a few dehydrotrimer and higher oligomers had been obtained by biotransformation with peroxidases (11–16). For these reasons, we can expect to obtain some novel skeleton polymers that may have more powerful activities.

Caffeic acid was subjected to biotransformation with H_2O_2/MCP at pH 5.0, 25 °C in the presence of acetone. Nine products have been obtained, including three new CA trimers (**1**–**3**), four new dimers (**4**–**7**), and two known compounds (**8**, **9**). Herein, we reported on the biotransformation of CA by MCP, the isolation and structure identification of the oxidation products **1**–**9**, as well as the possible biotransformative mechanism of **1**–**9**.

Received 1 February 2008. Accepted 4 May 2008. Published on the NRC Research Press Web site at canjchem.nrc.ca on 9 July 2008.

X. Wan, H.L. Liu, X.F. Huang, J.G. Luo, and L.Y. Kong.[1] Department of Natural Medicinal Chemistry, China Pharmaceutical University, 24 Tong Jia Xiang, Nanjing 210009, P.R. China.

[1]Corresponding author (e-mail: cpu_lykong@126.com).

 doi:10.1139/V08-090 © 2008 NRC Canada

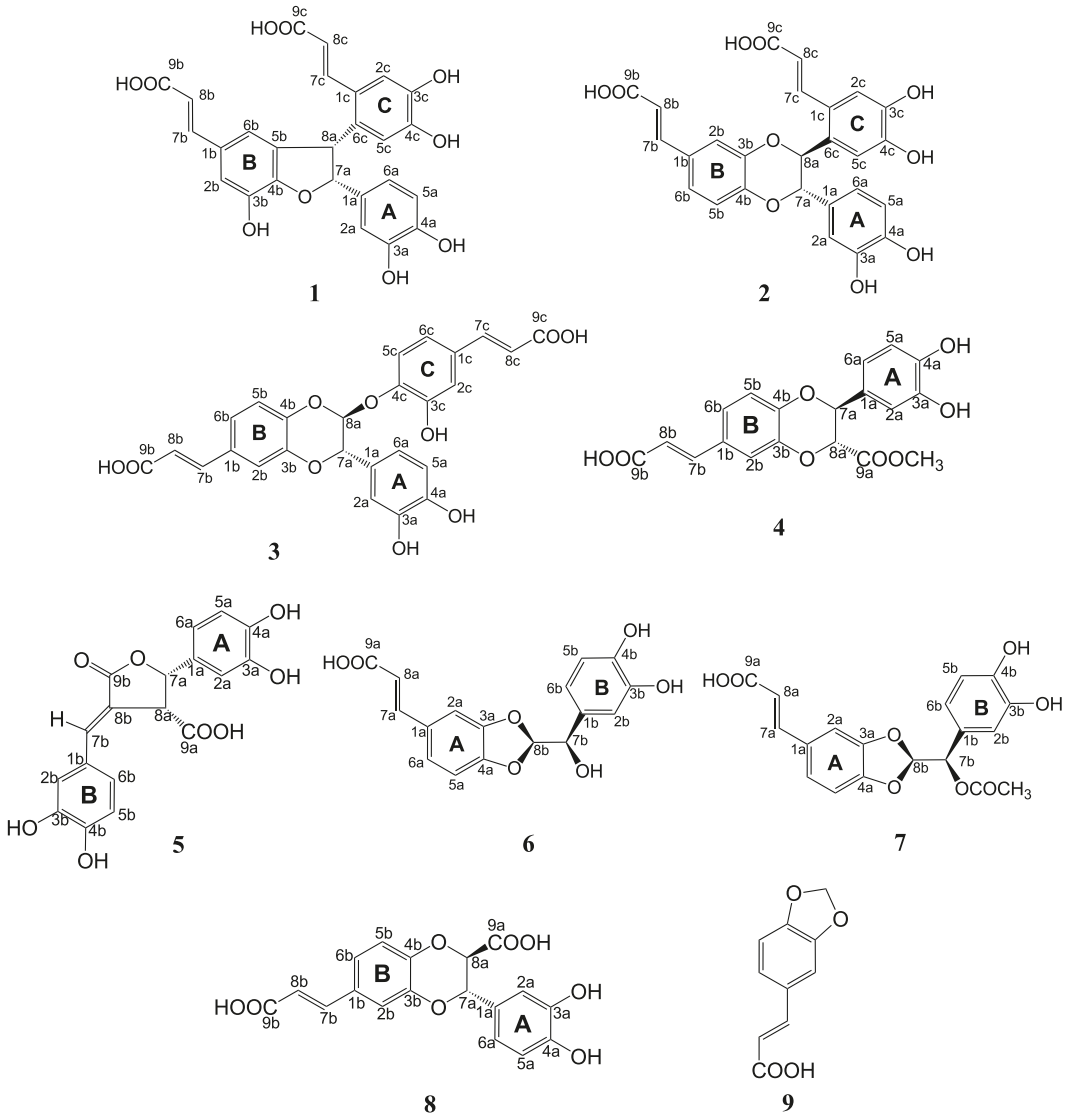

Results and discussion

Compound **1** was obtained as a white powder. Its molecular formula was determined as $C_{26}H_{21}O_{10}$ by positive HR-FABMS spectrometric analysis, indicating the formation of a caffeic acid trimer. The IR spectrum exhibited absorption bands of hydroxyl (3104 cm^{-1}), carbonyl (1683 cm^{-1}), and phenyl (1606, 1515 cm^{-1}) groups. In the ^{1}H and ^{13}C NMR spectra (see Table 1), one 1,3,4-tri-substituted aromatic fragment (**A**), one 1,3,4,5-tetra-substituted aromatic fragment (**B**), one 1,3,4,6-tetra-subsituted aromatic fragment (**C**), two trans double bonds, and two saturated H protons were observed. Twenty-six carbon signals were observed, including two acrylic acids, six oxygen-substituted aromatic carbons, four carbon-substituted aromatic carbons, seven C–H aromatic carbons, and two saturated carbons.

All the signals of protons and carbons of **1** were assigned by a detailed analysis of the ^{1}H and ^{13}C NMR data associated with HSQC and HMBC spectra. The correlations of H-7b to C-2b and C-6b, H-2b, and H-6b to C-7b, H-8b to C-1b, H-7c to C-2c and C-6c, H-2c and H-6c to C-7c, and H-8c to C-1c suggested that two di-substituted double bonds were ascribed to aromatic fragments **B** and **C**. From the long-range correlations H-7a to C-2a and C-6a, H-2a and H-6a to C-7a, we could confirm that the saturated CH–CH fragment was connected with aromatic fragment **A** through C-1a. The signals H-5c to C-8a and H-7a to C-6c demonstrated that the aromatic fragment **C** was connected to CH through C-6c. No signals were obtained about fragment **B** to CH; besides, the chemical shift of C-8a at δ_C 54.1 suggested that fragment **B** was connected to CH through C-5b. Meanwhile, the chemical shift of C-7a (δ_C 95.9) revealed fragment **B** was connected to CH through an oxygen atom. The conclusion could be proved by the NOESY correlation of H-6b to H-8a. The relative configuration of C-7a and C-8a was determined to be cis, because NOE correlation peaks of H-7a to H-8a, H-2a and H-6a to H-5c, and H-5a to H-2c were observed in the NOESY spectrum (see Fig. 1). According to the above analysis, the structure of **1** was elucidated as *cis*-3-[6-[5-[(*E*)-2-carboxyethenyl]-2,3-dihydro-2-(3,4-dihydroxy-phenyl)-7-hydroxy-3-benzofuranyl]-3,4-dihydroxyphenyl]-(*E*)-2-propenoic acid. Compound **1** is a new compound.

© 2008 NRC Canada

Table 1. ^{1}H and ^{13}C NMR spectral data for compounds **1–3** (500 MHz and 125 MHz, respectively).

	1[a]		**2**[b]		**3**[b]	
Position	^{1}H[c]	^{13}C[c]	1H[c]	^{13}C[c]	^{1}H[c]	^{13}C[c]
1a		132.6		129.0		127.3
2a	6.81 (1H, d, *J* = 2.0 Hz)	114.2	6.44 (1H, d, *J* = 2.0 Hz)	116.2	6.92 (1H, d, *J* = 2.0 Hz)	116.6
3a		146.6		146.6		147.3
4a		146.9		147.2		147.5
5a	6.74 (1H, d, *J* = 8.2 Hz)	116.4	6.54 (1H, d, *J* = 8.1 Hz)	116.5	6.73 (1H, d, *J* = 8.5 Hz)	116.7
6a	6.65 (1H, dd, *J* = 8.2 2.0 Hz)	119.3	6.40 (1H, dd, *J* = 8.1, 2.0 Hz)	120.8	6.79 (1H, dd, *J* = 8.5, 2.0 Hz)	121.2
7a	5.34 (1H, d, *J* = 8.4 Hz)	95.9	4.74 (1H, d, *J* = 8.0 Hz)	79.0	5.91 (1H, d, *J* = 3.0 Hz)	76.7
8a	4.97 (1H, d, *J* = 8.4H)	54.1	5.15 (1H, d, *J* = 8.0 Hz)	82.3	6.45 (1H, d, *J* = 3.0 Hz)	112.8
1b		130.4		130.1		128.0
2b	7.05 (1H, d, *J* = 1.5 Hz)	116.5	7.23 (1H, d, *J* = 2.0 Hz)	118.0	6.92 (1H, d, *J* = 2.0 Hz)	115.4
3b		142.7		146.1		146.9
4b		151.0		147.8		150.3
5b		133.9	6.98 (1H, d, *J* = 8.5 Hz)	119.0	6.69 (1H, d, *J* = 8.3 Hz)	116.9
6b	6.76 (1H, br, s)	117.9	7.14 (1H, dd, *J* = 8.5, 2.0 Hz)	123.7	6.73 (1H, dd, *J* = 8.3, 2.0 Hz)	124.0
7b	7.54 (1H, d, *J* = 15.8 Hz)	146.0	7.58 (1H, d, *J* = 16.0 Hz)	146.6	7.24 (1H, d, *J* = 16.0 Hz)	148.3
8b	6.24 (1H, d, *J* = 15.8 Hz)	117.4	6.32 (1H, d, *J* = 16.0 Hz)	118.1	6.12 (1H, d, *J* = 16.0 Hz)	114.8
9b		171.2		171.2		168.0
1c		126.8		127.5		130.7
2c	7.10 (1H, s)	114.1	6.86 (1H, s)	114.2	7.14 (1H, br s)	107.6
3c		146.0		147.5		150.6
4c		149.5		149.5		151.8
5c	6.62 (1H, s)	116.3	6.82 (1H, s)	116.7	6.73 (1H, d, *J* = 8.3 Hz)	109.5
6c		134.9		129.7	6.98 (1H, dd, *J* = 8.3, 2.0 Hz)	126.0
7c	7.63 (1H, d, *J* = 15.6 Hz	142.9	7.58 (1H, d, *J* = 16.0 Hz)	143.1	7.55 (1H, d, *J* = 16.0 Hz)	146.7
8c	6.07 (1H, d, *J* = 15.6 Hz	118.9	5.82 (1H, d, *J* = 16.0 Hz)	118.4	6.29 (1H, d, *J* = 16.0 Hz)	117.8
9c		170.8		171.1		171.2

Note: Chemical shifts were given in δ values and followed by multiplicities and *J* values (in Hz). The ^{1}H and ^{13}C signals were assigned by HSQC and HMBC spectra.

[a]Recorded in DMSO-d_6.

[b]Recorded in CD_3OD.

[c]δ in ppm.

Fig. 1. Key NOESY for compounds **1–3**.

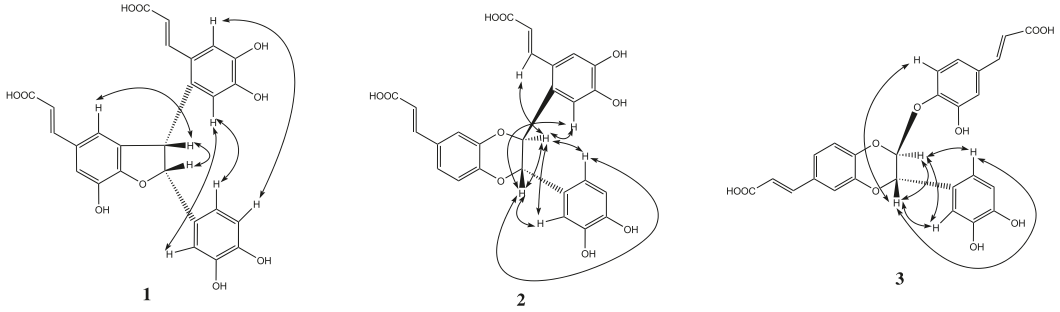

Compound **2** was obtained as a yellow powder. Its molecular formula was determined as $C_{26}H_{21}O_{10}$ by positive HR-FABMS spectrometric analysis, indicating the formation of a caffeic acid trimer. The IR spectrum exhibited absorption bands of hydroxyl (3373, 3256 cm^{-1}), carbonyl (1684 cm^{-1}), and phenyl (1607, 1508 cm^{-1}) groups. The ^{1}H and ^{13}C NMR spectral data (see Table 1) of **2** were very similar to those of **1**. Compared with the ^{13}C NMR spectral data of **1**, the chemical shift of C-7a decreased from δ_C 95.9 to δ_C 79.0, and the chemical shift of C-8a increased from δ_C 54.1 to δ_C 82.3. In addition, compared with the ^{1}H NMR of **1**, the fragment **B** was changed from 1,3,4,5-tetra-substituted aromatic fragment to 1,3,4-tri-substituted aromatic fragment. Besides, the correlation peak of H-8a to C-3b could be observed in HMBC spectra. So, it could be inferred that C-8a was connected with to fragment **B** through an oxygen atom. By detailed analysis of the ^{1}H and ^{13}C NMR data associated with HSQC and HMBC spectra, all the H and C signals could be assigned. The correlations of H-7b to C-2b and C-6b, H-2b, and H-6b to C-7b, H-8b to C-1b, H-7c to C-2c and C-6c, H-2c and H-6c to C-7c, and H-8c to C-1c suggested that two di-substituted double bonds were ascribed to aromatic frag-

© 2008 NRC Canada

ments **B** and **C**. From the long-range correlations H-7a to C-1a, C-2a and C-6a, H-2a and H-6a to C-7a, and H-8a to C-1a, we could confirm that the saturated CH–CH fragment was connected with to the aromatic fragment **A** through C-1a. The signals H-8a to C-1c and C-5c, H-5c to C-8a, and H-7a to C-6c demonstrated that aromatic fragment **C** was connected with to CH through C-6c. NOE correlation peaks of H-7a to H-5c, H-2a, H-6a, and H-8a as well as H-8a to H-2a, H-6a, H-7a, and H-7c were observed in NOESY (see Fig. 1). So, the relative configuration was determined to be trans. According to the above analysis, the structure of **2** was elucidated as *trans*-3-[6-[6-[(*E*)-2-carboxy-ethenyl]-3-(3,4-dihydroxyphenyl)-2,3-dihydro-2-(1,4-ben-zodioxin)]-3,4-dihy-droxyphe-nyl]-(*E*)-2-propenoic acid. Compound **2** is a new compound.

Compound **3** was obtained as a white powder. Its molecular formula was determined as $C_{26}H_{19}O_{10}$ by positive HR-FABMS spectrometric analysis, indicating the formation of a caffeic acid trimer. The IR spectrum exhibited absorption bands of hydroxyl (3410 cm^{-1}), carbonyl (1686 cm^{-1}), and phenyl (1605, 1522 cm^{-1}) groups. In the ^{1}H and ^{13}C NMR spectra (see Table 1), three 1,3,4-tri-substituted aromatic fragments (**A**, **B**, and **C**), two trans olefinic acids, and two saturated H protons were observed. The ^{1}H and ^{13}C NMR spectral data of **3** were similar to those of **2**. Compared the with ^{13}C NMR spectral data of **2**, the chemical shift of C-7a decreased from δ_C 79.0 to δ_C 76.7, and the chemical shift of C-8a increased from δ_C 82.3 to δ_C 112.8. Compared with the ^{1}H NMR of **2**, the fragment **C** was changed from 1,3,4,6-tetra-subsituted aromatic fragment to 1,3,4-tri-substituted aromatic fragment. So, it could be inferred that C-8a was connected to fragment **C** through oxygen atom. HSQC and HMBC experiments established all ^{1}J and ^{3}J ^{1}H, ^{13}C connectivities and allowed to combine these partial structures to those of **3**. The correlations of H-7b to C-2b and C-6b, H-2b and H-6b to C-7b, H-8b to C-1b, H-7c to C-2c and C-6c, H-2c and H-6c to C-7c, and H-8c to C-1c suggested that two di-substituted double bonds were ascribed to aromatic fragments **B** and **C**. The signals H-7a to C-1a, C-2a and C-6a, H-2a and H-6a to C-7a, and H-8a to C-1a demonstrated that aromatic fragment **A** was connected to CH through C-1a. Besides, the correlations H-8a to C-4b and C-4c demonstrated that C-4b and C-4c were connected to CH through an oxygen atom. NOE correlation peaks of H-7a to H-5c, H-2a, H-6a, and H-8a as well as H-8a to H-2a, H-6a, and H-7a were observed in NOESY (see Fig. 1). So, the relative configuration of H-7a/H-8a should be trans. According to the above analysis, the structure of **3** was elucidated as *trans*-3-[4-[[6-[(*E*)-2-carboxy-ethenyl]-3-(3,4-di-hydroxyphenyl)-2,3-dihydro-2-(1,4-benzodioxin)]oxy]-3-hydroxyphenyl]-(*E*)-2-propenoic acid. Compound **3** is a new compound.

Compound **4** was obtained as a white powder. Its molecular formula was determined as $C_{19}H_{16}O_8$ by positive HR-FABMS spectrometric analysis, indicating the formation of a caffeic acid dimer. The IR spectrum exhibited absorption bands of hydroxyl (3435 cm^{-1}), ester carbonyl (1730 cm^{-1}), carbonyl (1686 cm^{-1}), and phenyl (1624, 1512 cm^{-1}) groups. In the ^{1}H and ^{13}C NMR spectra (see Table 2), two 1,3,4-tri-substituted aromatic fragments (**A** and **B**), one trans olefinic acid, two saturated H protons, and one methoxyl group were observed. In HMBC spectra, according to the signals of H-7a to C-4b, C-2a and C-6a, H-2a and H-6a to C-7a, H-8a to C-3b, H-7b to C-2b and C-6b, H-2b and H-6b to C-7b, and H-8b to C-1b, it could be confirmed that compound **4** was a caffeic acid dimer including 1,4-benzodioxin skeleton. The long-range correlation of OMe to C-9a was observed, so COOH (C-9a) was methylated. Because the coupling constant of H-7a and H-8a ($J_{7a,8a}$ = 5.5 Hz) and [α] –5.7° (*c* = 0.18, MeOH), compared with ref. 15, the relative configuration of **4** was trans. According to the above analysis, the structure of **4** was elucidated as *trans*-7-[(1*E*)-2-carboxyethenyl]-3-(3,4-dihydroxy-phenyl)-2,3-dihydro-1,4-benzodioxin-2-carboxlic acid, Me ester. Compound **4** is a new compound.

Compound **5** was obtained as a white powder. Its molecular formula was determined as $C_{18}H_{14}O_8$ by positive HR-FABMS spectrometric analysis, indicating the formation of a caffeic acid dimer. According to the ^{1}H NMR spectra (see Table 2), two AMX systematical aromatic protons and one ABX systematical aromatic proton were observed. In the ^{13}C NMR spectra (see Table 2), 18 carbon signals could be found, including two carbonyl groups, four oxygen-substituted aromatic carbons, two carbon-substituted aromatic carbons, six C–H aromatic carbons, two unsaturated carbons, and two saturated carbons. According to the chemical shift of H-7b (δ_H 7.52), the plane constitution of **5** should be (4)*E*, on the other hand, if the plane constitution were (4)*Z*, the chemical shift should shift to upfield. This conclusion could be confirmed by NOESY spectra. Compared with the reference of Phellinsin A, the coupling constant of H-7a/H-8a of **5** ($J_{7a,8a}$ = 7.6 Hz) was different from that of Phellinsin A ($J_{7a,8a}$ = 2.5 Hz); combined with the NOESY spectra, the relative configuration was cis (18). According to the above analysis, the structure of **5** was elucidated as *cis*-(4)*E*-2-(3,4-dihydroxyphenyl)-4-[(3,4-dihydroxy-phenyl)-methylene]tetrahydro-5-oxo-3-furancarboxylic acid. Compound **5** is a new compound.

Compound **6** was obtained as a white powder. The molecular mass was 330 by ESI-MS analysis, indicating the formation of a caffeic acid dimer. According to the ^{1}H NMR spectra (see Table 2), one AMX systematical aromatic proton, one ABX systematical aromatic proton, one trans double bond, and two saturated H protons were observed. In the ^{13}C NMR spectra (see Table 2), 17 carbon signals could be found, including one C=O signal, four oxygen-substituted aromatic carbons, two carbon-substituted aromatic carbons, six C–H aromatic carbons, one trans double bond, and two saturated carbon. In HMBC spectra, according to the signals of H-7a to C-2a and C-6a, H-2a and H-6a to C-7a, and H-8a to C-1a, we could confirm that the trans double bond was connected to aromatic fragment **A**. The correlations of H-7b to C-2b, C-6b and C-1b, H-2b and H-6b to C-7b, and H-8b to C-1b suggested that aromatic fragment **B** was connected to C-7a though C-1b. The long-range correlations of H-8b to C-3a and C-4a, and the chemical shift of C-8b suggested that aromatic fragment **A** was connected to CH (C-8a) though C-3a and C-4a. Compared with the references, the relative configuration of the chiral carbons (C-7b and C-8b) could be elucidated as cis by the coupling constant ($J_{7a,8a}$ = 3.8 Hz) (19–22). According to the above analysis, the

© 2008 NRC Canada

Table 2. ^{1}H and ^{13}C NMR spectral data for compounds **4**–**9** (500 MHz and 125 MHz, respectively).

	4[a]		**5**[b]		**6**[c]		**7**[c]	
Position	^{1}H[d]	^{13}C[d]	^{1}H[d]	^{13}C[d]	^{1}H[d]	^{13}C[d]	^{1}H[d]	^{13}C[d]
1a		128.1		128.6		130.0		131.2
2a	6.96 (1H, d, *J* = 2.0 Hz)	115.2	6.91 (1H, d, *J* = 1.6 Hz)	114.7	7.10 (1H, d, *J* = 1.6 Hz)	107.0	7.03 (1H, d, *J* = 1.6 Hz)	107.4
3a		146.0		146.8		150.3		150.2
4a		146.7		146.2		151.5		151.1
5a	6.84 (1H, d, *J* = 8.2 Hz)	116.1	6.79–6.78 (2H, m)	116.7	6.81 (1H, d, *J* = 8.2 Hz)	109.0	6.71 (1H, d, *J* = 8.1 Hz)	109.4
6a	6.81 (1H, dd *J* = 8.2, 2.0 Hz)	119.9		119.2	7.03 (1H, dd, *J* = 8.2, 1.6 Hz)	125.4	6.96 (1H, dd, *J* = 8.1, 1.6 Hz)	125.5
7a	5.21 (1H, d, *J* = 5.5 Hz)	76.4	5.69 (1H, d, *J* = 7.6 Hz)	81.7	7.58 (1H, d, *J* = 15.8 Hz)	146.4	7.43 (1H, d, *J* = 15.9 Hz	144.7
8a	4.98 (1H, d, *J* = 5.5 Hz)	77.2	4.46 (1H, dd, *J* = 7.6, 1.7 Hz)	54.1	6.29 (1H, d, *J* = 15.8 Hz)	116.9	6.27 1H, d, *J* = 15.9 Hz	120.3
9a		168.5		174.5		170.7		171.8
1b		129.7		127.3		131.0		127.1
2b	7.28 (1H, *d*, *J* = 2.0 Hz)	117.6	7.09 (1H, d, *J* = 2.1 Hz)	116.0	6.95 (1H, d, *J* = 1.9 Hz)	115.9	6.87 (1H, d, *J* = 2.0 Hz)	116.7
3b		145.2		146.7		146.2		146.8
4b		144.2		149.7		146.5		147.6
5b	6.99 (1H, d, *J* = 8.4 Hz)	118.2	6.85 (1H, d, *J* = 8.3 Hz)	118.3	6.76 (1H, d, *J* = 8.0 Hz)	116.1	6.71 (1H, d, *J* = 8.0 Hz)	116.7
6b	7.24 (1H, dd, *J* = 8.4, 2.0 Hz)	123.2	7.03 (1H, dd, *J* = 8.3, 2.1 Hz)	125.0	6.80 (1H, dd, *J* = 8.0, 1.9 Hz)	120.3	6.74 (1H, d, *J* = 8.0, 2.0 Hz)	121.3
7b	7.59 (1H, d, *J* = 16.0 Hz)	144.9	7.52 (1H, d, *J* = 1.7 Hz)	140.1	4.72 (1H, d, *J* = 3.8 Hz)	75.0	5.82 (1H, d, *J* = 3.5 Hz)	76.3
8b	6.41 (1H, d, *J* = 16.0 Hz)	117.7		123.1	6.24 (1H, d, *J* = 3.8 Hz)	114.3	6.26 (1H, dd, *J* = 3.5 Hz)	112.4
9b		167.8		173.3				170.9
9a–OMe	3.65 (3H, s)	52.8	—				—	
–$COCH_3$	—		—				1.97 (3H, s)	173.0
								21.2

Note: Chemical shifts were given in δ values and followed by multiplicities and *J* values (in Hz). The ^{1}H and ^{13}C signals were assigned by HSQC and HMBC spectra.

[a]Recorded in acetone-d_6.
[b]Recorded in DMSO-d_6.
[c]Recorded in CD_3OD.
[d]δ in ppm.

structure of **6** was elucidated as *cis*-3-[2-[1-(3,4-dihydroxyphenyl)-1-hydroxymethyl]-1,3-ben-zodioxol-5-yl]-(*E*)-2-propenoic acid. Compound **6** is a new compound.

Compound **7** was obtained as a white powder. The molecular mass was 372 by ESI-MS spectrometric analysis, indicating the formation of a caffeic acid dimer. In the ^{1}H and ^{13}C NMR spectra (see Table 2), two 1,3,4-tri-substituted aromatic fragments, one trans double bond, two saturated H protons, and one acetyl fragment were observed. The long-range correlations of H-8b to C-3a, C-4a and C-1b, H-7b to C-2b, C-6b and C-1b, and H-2b and H-6b to C-7b suggested that compound **7** was caffeic acid dimer including 1,3-benzodioxin skeleton. Compared with the spectral data of **6**, compound **7** contained on acetyl group. In the HMBC, the correlation of C-7b to C=O and the chemical shift of C-7b was downshift, suggesting that OH connected to C-7b was acetylated. Compared with the references, the relative configuration of the C-7b and C-8b could be elucidated as cis by the coupling constant ($J_{7a,8a}$ = 3.5 Hz) (19–22). According to the above analysis, the structure of **7** was elucidated as *cis*-3-[2-[1-(3,4-dihydroxy-phenyl)-1-acetoxymethyl]-1,3-benzodioxol-5-yl]-(*E*)-2-propenoic acid. Compound **7** is a new compound. This was the first time that caffeic acid dimers 1,3-benzodioxin skeleton were obtained by biotransfomation.

The known compounds, *trans*-6-[(1*E*)-2-carboxyethenyl]-3-(3,4-dihydroxyphenyl)-2,3-dihydro-1,4-benzodioxin-2-carboxlic acid (**8**) and 3-(1,3-benzodioxol-5-yl)-2-propenoic acid (**9**), were identified by comparing their physical and spectroscopic data with those reported in the literature (17, 23).

A novel peroxidase (*Momordica charantia* peroxidase, MCP) was purified from the fruit of Momordica charantia. We applied the purified MCP to catalyze in the presence of H_2O_2 to transformation of caffeic acid (CA). During our present research, three novel trimers, four novel dimers, and

© 2008 NRC Canada

Scheme 1. Proposed mechanism of the formation of **1**.

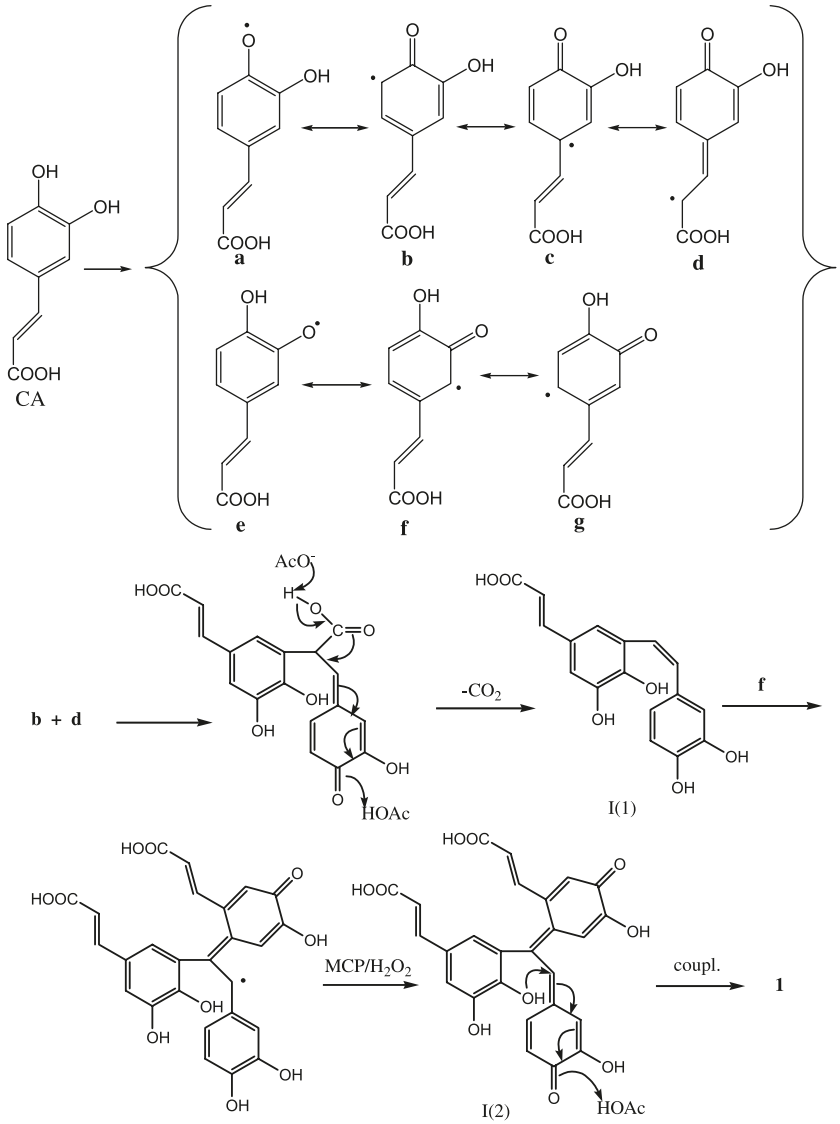

two known compounds were identified from MCP-catalyzed oxidation of CA. The proposed reaction mechanism for the formation of compound **1** is shown in Scheme 1. It is reasonable to assume that the CA radicals (b) and (d) combine, followed by acid–base catalyzed decarboxylation, driven by aromatization of the quinomethane part, to yield I (1). Then, the attack of monomeric CA radical (f) on the vinylic bond of I (1), followed by MCP/H_2O_2 catalysis, leads to I (2). Through intramolecular rearrangement, catalyzed by acid–base, **1** is formed from I (2). Compounds **2** and **3** contain a decarboxylated moiety. A possible mechanism of their formation involves the combination of the CA radicals (e) and (d), followed by decarboxylation, to yield I (4). Then, the attack of CA radical (f) on the vinylic bond of I (4), followed by MCP/H_2O_2 catalysis, leads to I (5). Through an intramolecular rearrangement, catalyzed by acid, **2** is formed from I (5), and the attack of monomeric CA radical (*a*) on the vinylic bond of I (4), followed by MCP/H_2O_2 catalysis, leads to I (6). Through intramolecular rearrangement, catalyzed by acid–base, **3** is formed from I (6), see Scheme 2.

The possible formation mechanisms of **4**–**9** are also discussed (see Scheme 3). The intermediate I (3), catalyzed by acid, undergoes an intramolecular rearrangement, followed by methyl esterification, to yield **4**. The CA radicals (d) combine, followed by acid–base catalyzed decarboxylation, driven by intramolecular rearrangement, to yield I (7). I (7) is catalyzed by MCP/H_2O_2, followed by decarboxylation to yield **5**. The CA radicals (*a*) and (d) combine, followed by acid–base catalysis, to yield I (8). I (8) is catalyzed by MCP/H_2O_2, followed by intramolecular rearrangement and decarboxylation, to yield **6**. I (8) is oxidized by MCP/H_2O_2, followed by intramolecular rearrangement, to give the corresponding intermediate, which then undergoes decarboxylation and ethyl esterification to yield **7**. Compounds **8** and **9** are obtained through intramolecular rearrangement, catalyzed by acid–base from I (8), respectively.

In the pharmacological research, compound **5** has shown much stronger anti-oxidative activity than the other caffeic acid polymers obtained, according to the inhibition ratio, see Table 3. According to our previous reported research, combined with our present study, it was easy to conclude that the dimers that contained the skeleton of 5-phenyl-3-

© 2008 NRC Canada

Scheme 2. Proposed mechanism of the formation of **2** and **3**.

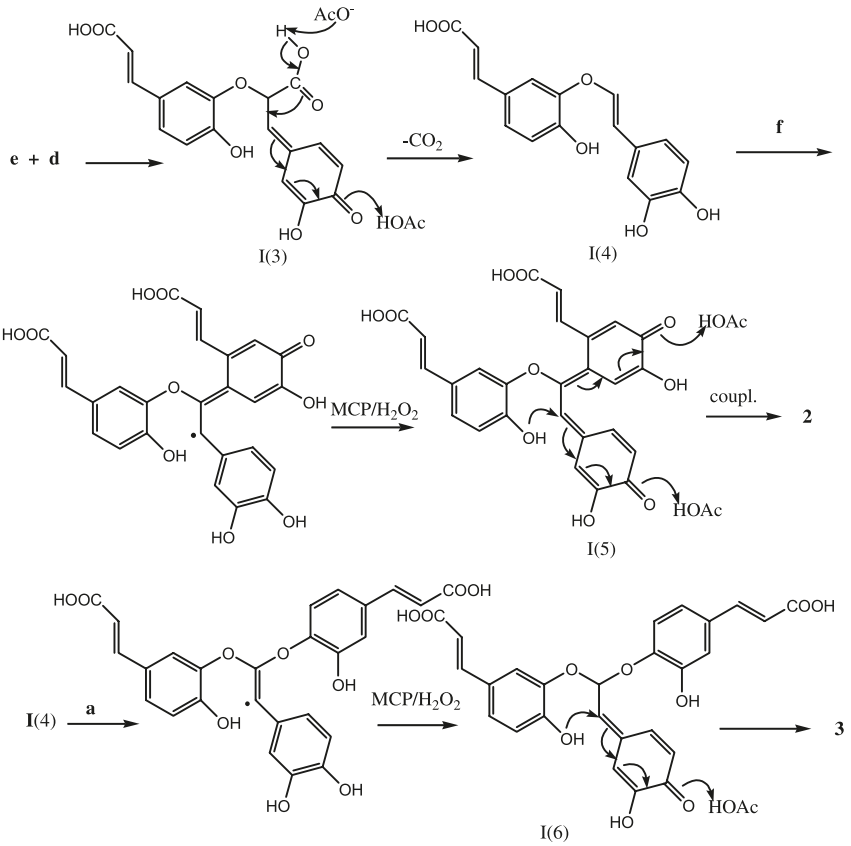

Table 3. The inhibition ratio of the subjects to MDA.

Compound	Mean ± SD[a,b]
CA	59.7±2.9
2	49.5±7.4
5	**64.5±3.3**
10	28.4±7.5
11	13.3±2.5

[a]Final concentration of all compounds was 1×10^{-4} mol/L

[b]The inhibition ratio was defined according to the following equation: Inhibition ratio = (the absorbance of vehicle – the absorbance of tested compound)/the absorbance of vehicle ×100%.

(phenylmethylene)-2(3*H*)-furanone (3, 4) may have higher anti-oxidative activity than other reaction products.

Experimental section[2]

General experimental procedures

Positive-ion HR-FABMS was recorded with a JEOL HX-110 spectrometer using *m*-nitrobenzyl alcohol as a matrix. Negtive-ion HR-ESIMS was recorded with an Agilent TOF MSD 1946D spectrometer. UV and IR spectra were recorded with Shimadzu UV-2501PC and Nicolet Impact 410 spectrometers, respectively. ^{1}H and ^{13}C NMR, HSQC, HMBC, and NOESY spectra were taken with Bruker ACF-500 and ACF-600 spectrometers (1D NMR 500 MHz and 125 MHz, 2D NMR 600 and 150 MHz, respectively) in acetone-d_6, DMSO-d_6, or CD_3OD; chemical shifts are reported in ppm as δ relative to Me_4Si (internal standard). Column chromatography was carried out with Sephadex LH-20 (20–100 μ, Pharmacia) (1 μ = 1 μm) and ODS-C18 (100–200 μ, Waters). L-Cysteine Hydrochloride (High Pure Grade) was purchased from AMRESCO. Caffeic acid and DMSO were purchased from Sigma. The malondialdehyde (MDA) kit was provided by Nanjing Jiancheng Bioengineering Institute. Other reagents and solvents used were of analytical grade and were purchased from reliable commercial sources.

Plant material

Fruits of *M*. charantia were collected at a suburb of Nanjing, China, and identified by Dr. Mingjian Qin, China Pharmaceutical University. A voucher specimen (No. 000804) was deposited in the Department of Natural Medicinal Chemistry, China Pharmaceutical University.

Purification of MCP

MCP from fruits of *Momordica charantia* was purified to electrophoretic homogeneity by consecutive treatment of ammonium sulfate fractionation, ion exchange chromatography on DEAE-Sepharose FF, affinity chromatography on

[2] Supplementary data for this article are available on the journal Web site (canjchem.nrc.ca) or may be purchased from the Depository of Unpublished Data, Document Delivery, CISTI, National Research Council Canada, Ottawa, ON K1A 0R6, Canada. DUD 3771. For more information on obtaining material, refer to cisti-icist.nrc-cnrc.gc.ca/irm/unpub_e.shtml.

© 2008 NRC Canada

Scheme 3. Proposed mechanism of the formation of **4**–**9**.

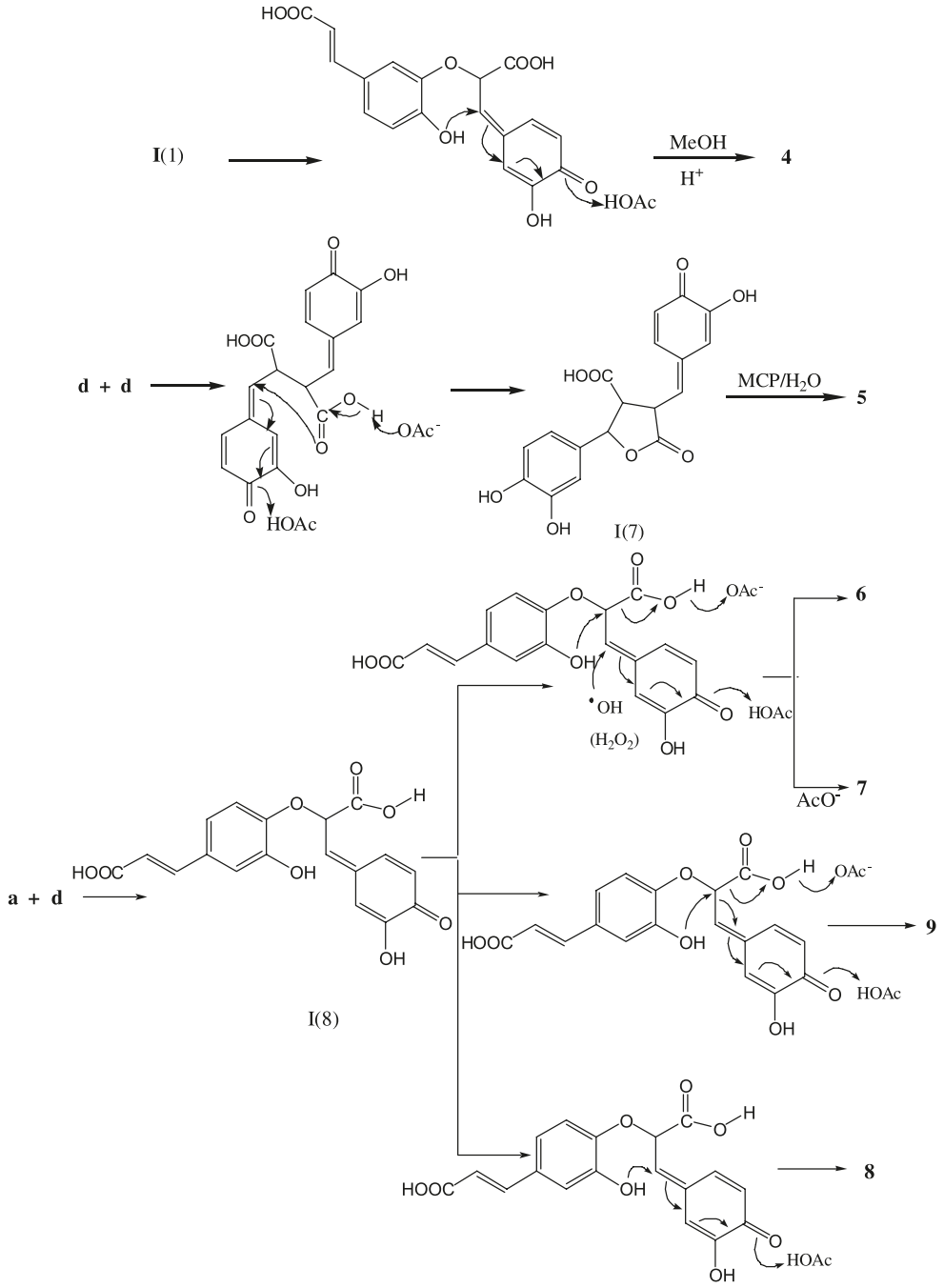

Con A Sepharose, and gel filtration on Sephadex G-150 as described in our previous report (1). The purified MCP exhibited a specific activity of 7757 E.U. of peroxidase per mg of protein, which was 46 fold higher than that of the crude extract.

Biotransformation of caffeic acid in aqueous acetone

A solution of caffeic acid (2.4 g) in acetonitrle (200 mL) and a solution of MCP (4 × 103 U) in buffer (100 mmol/L NaOAc–HOAc, pH 5.0, 400 mL) were mixed and treated with hydrogen peroxide (0.3%, 120 mL) at 25 °C and stirred for 8 h, during which time the mixture gradually turned brownish red.

Isolation and identification

The reaction mixture was evaporated to dryness at 40 °C under reduced pressure. The extractum was dissolved with water. Then, the aqueous mixture was extracted with ethyl acetate and *n*-butanol, successively. The extract was washed with water, dried with anhyd. Na_2SO_4, and evaporated to dryness at 40 °C under reduced pressure. The combined ethyl acetate layer was concentrated to afford a red powder (2.1 g), which was subjected to RP-C18 column chromatography (i.d. 3.0 × 50, 80 g) eluted with MeOH/H_2O (20:80 to 50:50, *v*/*v*) to afford fraction 1 (0.7 g), fraction 2 (0.3 g), fraction 3 (0.5 g), and fraction 4 (0.4 g). Fraction 1 was subjected to Sephadex LH-20 column chromatography (i.d.

© 2008 NRC Canada

1.5 × 100, 70 g, 8 mL each) eluted with MeOH. The elution of 9 to 12 fractions (86 mg) was submitted to RP-C18 column chromatography (i.d. 1.5 × 30, 40 g) eluted with MeOH/H_2O (20:80, *v*/*v*) to give **1** (10 mg). The elution of 15 to 16 fractions (35 mg) was submitted to RP-C18 column chromatography (i.d. 1.5 × 30, 40 g) eluted with MeOH/H_2O (20:80, *v*/*v*) to give **4** (4 mg). The elution of 18 to 22 fractions (103 mg) was submitted to RP-C18 column chromatography (i.d. 1.5 × 30, 40 g) eluted with MeOH/H_2O (20:80, *v*/*v*) to give **5** (48 mg). Fraction 2 was subjected to Sephadex LH-20 column chromatography (i.d. 1.5 × 100, 70 g, 8 mL each) eluted with MeOH/$CHCl_3$ (1:1, *v*/*v*). The elution of 8 to 10 fractions (35 mg) was submitted to RP-C18 column chromatography (i.d. 1.5 × 30, 40 g) eluted with MeOH/H_2O (35:65, *v*/*v*) to give **6** (20 mg). The elution of 13 to 14 fractions (12 mg) was submitted to RP-C18 column chromatography (i.d. 1.5 × 30, 40 g) eluted with MeOH/H_2O (30:70, *v*/*v*) to give **8** (6.5 mg), and the elution of 17 to 19 fractions (20 mg) was submitted to RP-C18 column chromatography (i.d. 1.5 × 30, 40 g) eluted with MeOH/H_2O (30:70, *v*/*v*) to give **9** (11 mg). Fraction 3 was subjected to Sephadex LH-20 column chromatography (i.d. 1.5 × 100, 70 g, 8 mL each) eluted with MeOH/$CHCl_3$. (1:1, *v*/*v*). The elution of 13 to 15 fractions (178 mg) was submitted to RP-C18 column chromatography (i.d. 1.5 × 30, 40 g) eluted with MeOH/H_2O (50:50, *v*/*v*) to give **2** (120 mg). The elution of 18 to 20 fractions (45 mg) was submitted to RP-C18 column chromatography (i.d. 1.5 × 30, 40 g) eluted with MeOH/H_2O (35:65, *v*/*v*) to give **7** (20 mg). Fraction 4 was subjected to Sephadex LH-20 column chromatography (i.d. 1.5 × 100, 70 g, 8 mL each) eluted with MeOH/$CHCl_3$ (1:1, *v*/*v*). The elution of 11 to 15 fractions (66 mg) was submitted to RP-C18 column chromatography (i.d. 1.5 × 30, 40 g) eluted with MeOH/H_2O (50:50, *v*/*v*) to give **3** (25 mg).

cis-*3-[6-[5-[(E)-2-Carboxyethenyl]-2,3-dihydro-2-(3,4-dihydroxyphenyl)-7-hydroxy-3-benzofuranyl]-3,4-dihydroxyphenyl]-(E)-2-propenoic acid (1)*

White amorphous powder. [α] +17.3° (*c* = 0.12, MeOH). IR (KBr): 3418, 1747, 1684, 1622, 1612, 1242, 1126, 999, 839. ^{1}H (500 MHz, DMSO-d_6) and ^{13}C NMR (125 MHz, DMSO-d_6): see Table 1. HR-ESI-MS (positive ion mode): 493.1137 $[M + H]^+$ ($C_{26}H_{21}O_{10}$ calcd.: 445.1135).

trans-*3-[6-[6-[(E)-2-Carboxyethenyl]-3-(3,4-dihydroxyphenyl)-2,3-dihydro-2-(1,4-benzodioxin)]-3,4-dihydroxyphe-nyl]-(E)-2-propenoic acid (2)*

Yellow amorphous powder. [α] 0.4° (*c* = 0.24, MeOH). UV λ_{max} (MeOH) nm (log ε): 320, 300, 240, 222. IR (KBr) ν: 3373, 3256, 1684, 1607, 1508, 1273, 1192, 1117, 1059, 972 cm^{-1}. 1H NMR (CD_3OD, 500 MHz) δ: Table 1. ^{13}C NMR (CD_3OD, 125 MHz) δ: Table 1. HR-ESI-MS (positive ion mode): 493.1133 $[M + H]^+$ ($C_{26}H_{21}O_{10}$ calcd.: 493.1135).

trans-*3-[4-[[6-[(E)-2-Carboxy-ethenyl]-3-(3,4-di-hydroxyphenyl)-2,3-dihydro-2-(1,4-benzodioxin)]oxy]-3-hydroxyphenyl]-(E)-2-propenoic acid (3)*

White amorphous powder. [α] –8.5° (*c* = 0.28, MeOH). UV λ_{max} (MeOH) nm (log ε): 328, 392, 236, 216. IR (KBr) ν: 3410, 1686, 1628, 1605, 1522, 1497, 1450, 1354, 1256, 1159, 1113, 978 cm^{-1}. ^{1}H NMR (CD_3OD, 500 MHz) δ: Table 1. ^{13}C NMR (CD_3OD, 125 MHz) δ: Table 1. HR-ESI-MS (negtive ion mode): 491.0981 $[M - H]^-$ ($C_{26}H_{19}O_{10}$ calcd.: 491.0983).

trans-*7-[(1E)-2-Carboxyethenyl]-3-(3,4-dihydroxyphenyl)-2,3-dihydro-1,4-benzodioxin-2-carboxlic acid, Me ester (4)*

White amorphous powder. [α] –5.7° (*c* = 0.18, MeOH). UV λ_{max} (MeOH) nm (log ε): 320, 288, 236, 220. IR (KBr) ν: 3435, 1730, 1686, 1624, 1512, 1445, 1277 cm^{-1}. ^{1}H NMR (CD_3COCD_3, 500 MHz) δ: Table 2. ^{13}C NMR (CD_3COCD_3, 125 MHz) δ: Table 2. HR-ESI-MS (negative ion mode): 371.0781 $[M - H]^-$ ($C_{19}H_{15}O_8$ calcd.: 371.0772).

cis-*(4)E-2-(3,4-Dihydroxyphenyl)-4-[(3,4-dihydroxyphenyl)-methylene]tetrahydro-5-oxo-3-furancarboxylic acid (5)*

White amorphous powder. [α] 1.6° (*c* = 0.20 MeOH). UV λmax (MeOH) nm (log ε): 336. IR (KBr) ν: 3414, 3242, 1718, 1699, 1643, 1601, 1529, 1225, 1200, 1111, 1007 cm^{-1}. ^{1}H NMR (CD_3OD, 500 MHz) δ: Table 2. ^{13}C NMR (DMSO-*d*6 125 MHz) δ: Table 2. HR-ESI-MS (positive ion mode): 381.0583 $[M + Na]^+$ ($C_{18}H_{14}O_8Na$ calcd.: 381.0580).

cis-*3-[2-[1-(3,4-Dihydroxy-phenyl)-1-hydroxymethyl]-1,3-benzodioxol-5-yl]-(E)-2-propenoic acid (6)*

White amorphous powder. [α] –2.9° (*c* = 0.39 MeOH). UV λ_{max} (MeOH) nm (log ε): 332, 288, 232. IR (KBr) ν: 3420, 1663, 1624, 1605, 1499, 1450, 1252, 1105 cm^{-1}. ^{1}H NMR (CD_3OD, 500 MHz) δ: Table 2. ^{13}C NMR (CD_3OD, 125 MHz) δ: Table 2. ESI-MS *m*/*z*: 329$[M - H]^-$.

cis-*3-[2-[1-(3,4-Dihydroxy-phenyl)-1-acetoxymethyl]-1,3-benzodioxol-5-yl]-(E)-2-propenoic acid (7)*

White amorphous powder. [α] +49.8° (*c* = 0.22 MeOH). UV λ_{max} (MeOH) nm (log ε): 328, 288, 232. IR (KBr) ν: 3443, 3427, 1740, 1616, 1499, 1256, 1115, 1041, 980 cm^{-1}. ^{1}H NMR (CD_3OD, 500 MHz) δ: Table 2. ^{13}C NMR (CD_3OD, 125 MHz) δ: Table 2. ESI-MS *m*/*z*: 371$[M - H]^-$.

trans-*6-[(1E)-2-Carboxyethenyl]-3-(3,4-dihydroxyphenyl)-2,3-dihydro-1,4-benzodioxin-2-carboxlic acid (8)*

White amorphous powder. [α] +4.8° (*c* = 0.03 MeOH). UV λ_{max} (MeOH) nm (log ε): 324, 288, 240, 220. IR (KBr) ν: 3425, 1666, 1616, 1589, 1508, 1425, 1263, 1217, 1103, 970 cm^{-1}. ^{1}H NMR (DMSO-d_6, 500 MHz) δ: 8.96 (2H, br s, 2 × –ArOH), 6.83 (1H, d, *J* = 1.8 Hz, H-2a), 6.57 (1H, d, *J* = 8.2 Hz, H-5a), 6.67 (1H, dd, *J* = 8.2, 1.8 Hz, H-6a), 5.49 (1H, d, *J* = 2.6 Hz, H-7a), 4.57 (1H, br s, H-8a), 7.16 (1H, br s, H-2b), 6.90 (1H, d, *J* = 8.4 Hz, H-5b), 7.12 (1H, br d, *J* = 8.4 Hz, H-6b), 7.43 (1H, d, *J* = 16.1 Hz, H-7b), 6.32 (1H, d, *J* = 16.1 Hz, H-8b). ^{13}C NMR (DMSO-d_6, 125 MHz) δ: 127.91 (C-1a), 115.0 (C-2a), 145.2 (C-3a), 145.7 (C-4a), 115.0 (C-5a), 119.0 (C-6a), 75.5 (C-7a), 76.6 (C-8a), 168.7 (C-9a), 127.8 (C-1b), 115.6 (C-2b), 144.8 (C-3b), 143.2 (C-4b), 117.3 (C-5b), 121.5 (C-6b), 143.3 (C-7b), 116.2 (C-8b), 168.4 (C-9b). ESI-MS *m*/*z* 357 $[M - H]^-$.

3-(1,3-Benzodioxol-5-yl)-2-propenoic acid (9)

White amorphous powder. UV λ_{max} (MeOH) nm (log ε): 326, 292, 238, 216. IR (KBr) ν: 3447, 3431, 1693, 1674, 1626, 1603, 1495, 1448, 1421, 1317, 1250, 1217, 1038, 926 cm^{-1}. ^{1}H-NMR (CD_3OD, 500 MHz) δ: 7.16 (1H, d, *J* = 1.6

© 2008 NRC Canada

Hz, H-2), 6.86 (1H, d, J = 8.0 Hz, H-5), 7.09 (1H, dd, J = 8.0, 1.6 Hz, H-6), 7.60 (1H, d, J = 16.0 Hz, H-7), 6.33 (1H, d, J = 16.0 Hz, H-8), 4.78 (2H, s, H-10). ^{13}C NMR (CD_3OD, 125 MHz) δ: 130.3 (C-1), 109.5 (C-2), 150.0 (C-3), 151.2 (C-4), 107.5 (C-5), 125.6 (C-6), 146.2 (C-7), 117.2 (C-8), 170.6 (C-9), 103.1 (C-10). ESI-MS m/z: 191[M – H]$^-$.

Measurement of anti-oxidative activity

Male Sprague–Dawley SD rats (8–9 weeks old) were used. They were purchased from the Experimental Animal House of China Pharmaceutical University (Nanjing, China). All rats were maintained with free access to pellet food and water in plastic cages at 20 ± 2 °C and kept on a 12 h light–dark cycle. The animal study protocol was in compliance with the guidelines of China for animal care, which conforms to the internationally accepted principles in the care and use of experimental animals. A rat was sacrificed by bloodletting and was perfused in situ via the portal vein with phosphate buffered saline (PBS). Liver tissue was collected and cut into species. After being weighed, the tissue was homogenized with PBS (1:4) using a high speed homogenizer for 10 s each time at 0 °C, and the operation was repeated for 4 to 5 times. The homogenates (25%) were then centrifuged at 5 000g for 20 min. The supernatants were collected and again centrifuged at 5 000g for 60 min. The supernatants were discarded and the microsomal pellet was suspended in 10-volume PBS containing 30% glycerol (glycerol:PBS, 30:70 (*v*/*v*)). Microsomal suspensions were stored in small portions at –80 °C and thawed before lipid peroxidation assay. Microsomal protein was determined by the biuret method.

Lipid peroxidation was induced in rat liver microsomes by $FeSO_4$–cysteine. A mixture of the microsomal suspension (10%, 100 μL), $FeSO_4$ solution (1 mmol/L, 50 μL), L-cysteine hydrochloride (10 mmol/L, 20 μL), the sample solution (finial concentration of 10^{-4} mol/L, 10 μL) or vehicle (DMSO, 10 μL), and PBS (0.01 mol/L, pH 7.4, 820 μL) was incubated at 37 °C for 30 min. Each reaction mixture was stopped at 4 °C. The concentration of MDA (malondialdehyde), the second derivative of lipid peroxidation, in the above-mentioned reaction mixture was determined using the commercial kit according to the guidelines provided (24). 100 μL reaction mixture above mentioned was incubated at 95 °C for 30 min. The reaction was stopped by cooling over ice and contents centrifuged at 800 g for 10 min. The absorbance of the supernatant was recorded at 532 nm. The value for non-specific absorbance at 600 nm was subtracted. The inhibition ratio was defined according to the following equation:

Inhibition ratio = (the absorbance of vehicle – the absorbance of tested compound)/the absorbance of vehicle ×100%.

Acknowledgements

This investigation was supported by Specialized Research Fund for the Doctoral Program of Higher Education (No. 20040316002), P.R. China. We thank Dr. Bin Ma in School of Pharmacy, Shandong University, China for 2D NMR experiments.

References

1. L. Ou, L.Y. Kong, X.M. Zhang, and M. Niwa. Biol. Pharm. Bull. **26**, 1511 (2003).
2. H.L. Liu, L.Y. Kong, Y. Takaya, and M. Niwa. Chem. Pharm. Bull. **53**, 816 (2005).
3. H.L. Liu, X. Wan, X.F. Huang, and L.Y. Kong. J. Agric. Food Chem. **55**, 1003 (2007).
4. H.L. Liu, X.F. Huang, X. Wan, and L.Y. Kong. Helv. Chim. Acta, **90**, 1117 (2007).
5. K.L. Khanduja, P.K. Avti, S. Kumar, N. Mittal, K.K. Sohi, and C.M. Pathak. Biochim. Biophys. Acta, **1760**, 283 (2006).
6. G.D. Norata, P. Marchesi, S. Passamonti, A. Pirillo, F. Violi, and A.L. Catapano. Atherosclerosis, **191**, 265 (2007).
7. S.H. Bhat, A.S. Azmi, and S.M. Hadi. Toxicol. Appl. Pharmacol. **218**, 249 (2007).
8. İ. Gülçin. Toxicology, **217**, 213 (2006).
9. J. Kawabata, H. Tazaki, K. Tanaka, H. Kawakami, and T Fujita. Jap. Patent 2-212-175. 2002.
10. G. Motouri, S. Aoe, T. Fujita, and H. Tazaki. Jap. Patent 2-000-273-452. 2000.
11. I. Agata, H. Kusakabe, T. Hatano, S. Nishibe, and T. Okuda. Chem. Pharm. Bull. **41**, 1608 (1993).
12. I. Agata, T. Hatano, S. Nishibe, and T. Okuda. Phytochem, **28**, 2447 (1989).
13. T. Tanaka, A. Nishimura, I. Kouno, G.I. Nonaka, and T.J. Young. J. Nat. Prod. **59**, 843 (1996).
14. T. Tanaka, A. Nishimura, I. Kouno, G.I. Nonaka, and C.R. Yang. Chem. Pharm. Bull. **45**, 1596 (1997).
15. B.H. Monien, B.L. Henry, A. Raghuraman, M. Hindle, and U.R. Desai. Bioorg. Med. Chem. **14**, 7988 (2006).
16. B.L. Henry, B.H. Monien, P.E. Bock, and U.R. Desai. J. Biol. Chem. **282**, 31891 (2007).
17. K. Matsumoto, H. Takahashi, Y. Miyake, and Y. Fukuyama. Tetrahedron Lett. **40**, 3185 (1999).
18. E.I. Hwang, B.S. Yun, Y.K. Kim, B.M. Kwon, H.G. Kim, H.B. Lee, W.J. Jeong, and S.U. Kim. J. Antibiotics, **53**, 903 (2000).
19. F. Cottet, L. Cottier, and G, Descotes. Can. J. Chem. **68**, 1251 (1990).
20. K. Xiao, L.J. Xuan, Y.M. Xu, D.L. Bai, and D.X. Zhong. Chem. Pharm. Bull. **50**, 605 (2002).
21. K. Ishimaru, G.I. Nonaka, and I. Nishnika. Phytochem, **26**, 1147 (1987).
22. C.H. Ludwig, E.J. Nist, and J.L. McCarthy. J. Am. Chem. Soc. **86**, 1186 (1964).
23. A. Patra and G. Ghosh. Magn. Reson. Chem. **25**, 734 (1987).
24. S.Y. Sun and R. Han. Acta Academiae Medicinae Sinicae, **15**, 59 (1993).

© 2008 NRC Canada

$H_3PW_{12}O_{40}$ — A selective, environmentally benign, and reusable catalyst for the preparation of methoxymethyl and ethoxymethyl ethers and their deprotections under mild conditions

Iraj Mohammadpoor-Baltork, Majid Moghadam, Shahram Tangestaninejad, Valiollah Mirkhani, and Arsalan Mirjafari

Abstract: Different types of primary and secondary alcohols were efficiently transformed to their corresponding methoxymethyl (MOM) and ethoxymethyl (EOM) ethers in the presence of catalytic amounts of $H_3PW_{12}O_{40}$ at room temperature under solvent-free conditions. Selective protection of primary and secondary alcohols in the presence of phenols and tertiary alcohols was achieved by this method. Deprotection of these ethers to their parent alcohols was also performed using this catalyst in ethanol under reflux conditions. We have also found that primary and secondary MOM- and EOM-ethers are selectively deprotected in the presence of phenolic and tertiary ones, methyl and benzyl ethers, esters, and trimethylsilyl ethers by this catalyst. The notable advantages of this protocol are high yields, short reaction times, easy work-up, non-toxicity, easy availability and handling, eco-friendly, and reusability of the catalyst.

Key words: methoxymethylation, ethoxymethylation, protection, deprotection, heteropoly acid.

Résumé : Opérant à la température ambiante, dans des conditions sans solvant et en présence de quantités catalytiques de $H_3PW_{12}O_{40}$, il est possible de transformer d'une façon efficace divers types d'alcools primaires et secondaires en éthers méthoxyméthyle (MOM) ou éthoxyméthyle (EOM) correspondants. Utilisant cette méthode, on a pu effectuer la protection sélective d'alcools primaires et secondaires en présence de phénols et d'alcools tertiaires. On a effectué la déprotection de ces éthers pour régénérer les alcools de départ en utilisant le même catalyseur, dans l'éthanol au reflux. On a aussi trouvé que le même catalyseur permet de déprotéger sélectivement les éthers MOM et EOM en présence d'éthers phénoliques ou tertiaires, d'éthers méthyliques et benzyliques, d'esters et d'éthers triméthylsilyles. Les avantages notables de ce protocole sont les rendements élevés, les courts temps de réaction, la facilité de l'extraction et le fait que le catalyseur est non toxique, qu'il est de disponibilité et de maniement facile, respectueux de l'environnement et réutilisable.

Mots-clés : méthoxyméthylation, éthoxyméthylation, protection, déprotection, acide hétéropolaire.

Introduction

Recently, green chemistry has received considerable importance in organic synthesis. Due to environmental issues affecting all societies, emphasize on the "green" aspects of chemical processes will be appreciated. Thus, catalysts that are eco-friendly and simply recycled in the reaction mixture have attracted a considerable attention.

One important class of solid catalysts is heteropoly acids (HPAs), having both redox and acid properties (1). Among heteropoly acids, polytungstic acids are the most widely used catalysts because of their high acid strengths, thermal stability, and low reducibility. Heteropoly acid catalysts have many advantages over the liquid acid catalysts, which are harmless to the environment with respect to corrosiveness, safety, and quantity of waste. Solid heteropoly acids have attracted much attention in organic synthesis owing to easy work-up procedure, easy filtration, and minimization of cost and waste generation due to reuse and recycling of the catalysts (2). A variety of organic reactions, such as alcohol dehydration, acetylation, alkylation, isomerization, oxydehydrogenation (1, 3), acylation (4), estrification (5), synthesis of 1,4-dihydropyrimidones (6), oxidation of alkylarenes (7), Friedel–Crafts acylation (8), Fries rearrangement of arylesters (9), epoxidation of allylic alcohols (10), reactions of oxiranes with carbonyl compounds (11), ring opening of epoxides (12), conversion of THP ethers into acetates (13), α-glycosidation (14), and preparation of oximes (15), have been reported in the presence of heteropoly acid catalysts.

To synthesize more complicated molecules, chemists have developed satisfactory protective groups and also effective methods for the formation and cleavage of these compounds. The selective protection and deprotection of hydroxyl group have occupied a unique position in organic synthesis be-

Received 31 December 2007. Accepted 19 March 2008. Published on the NRC Research Press Web site at canjchem.nrc.ca on 9 July 2008.

I. Mohammadpoor-Baltork,[1] M. Moghadam, S. Tangestaninejad, V. Mirkhani, and A. Mirjafari. Department of Chemistry, Catalysis Division, University of Isfahan, Isfahan 81746-73441, Iran.

[1]Corresponding author (email: imbaltork@sci.ui.ac.ir).

 doi:10.1139/V08-068 © 2008 NRC Canada

cause of the fundamental importance of hydroxyl groups and their roles in the multi-step synthesis of complex natural products (16). Transformation of hydroxyl groups to their alkoxymethyl ethers is a commonly used protective process for alcohols (17). These derivatives are frequently prepared by the reactions of alcohols with a excess amount of formaldehyde dimethyl acetal (FDMA) or formaldehyde diethyl acetal (FDEA) (18–25). Deprotection of these ethers to their parent alcohols is also an important process in synthetic organic chemistry, and several methods and catalysts have been reported for these transformations (23, 26–33). However, some of these methods suffer from drawbacks, such as harsh reaction conditions, high reaction temperature, tedious work-up procedures, long reaction times, and the use of expensive and toxic reagents. Consequently, introduction of efficient and selective methods for the preparation of alkoxymethyl ethers and their deprotection using inexpensive, relatively non-toxic, easy handling, and environment-friendly catalysts is still in demand.

In continuation of our studies on protection and deprotection reactions (34), we now report $H_3PW_{12}O_{40}$ as an efficient, relatively non-toxic, recycable, and air-stable catalyst for the preparation of methoxymethyl (MOM) and ethoxymethyl (EOM) ethers at room temperature under solvent-free conditions and also deprotection of these ethers in a green solvent, ethanol, under reflux conditions (Scheme 1).

Scheme 1.

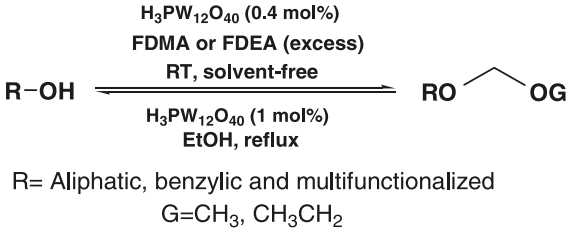

Scheme 2.

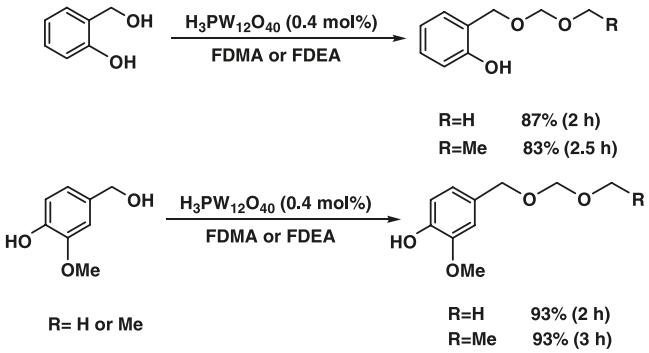

Results and discussion

First, we investigated the ability of $H_3PW_{12}O_{40}$ in the methoxymethylation and ethoxymethylation of benzyl alcohol with FDMA and FDEA, respectively. The results showed that in the presence of 0.4 mol% of this catalyst, the MOM and EOM ethers were obtained in high yields. Both protection reactions were carried out at room temperature and under solvent-free conditions. Primary and secondary, benzylic and saturated alcohols were efficiently converted to their corresponding MOM- and EOM-ethers in high yields (Table 1). Allylic alcohols, such as cinnamyl alcohol, were also transformed to the corresponding MOM- and EOM-ethers efficiently (Table 1, entry 20).

Under the same reaction conditions, phenols and tertiary alcohols did not react even under reflux conditions, and the starting materials remained intact after 24 h. Therefore, a set of competitive reactions was conducted between primary or secondary alcohols and phenols or tertiary alcohols (Table 2). Also in compounds containing both benzylic and phenolic hydroxyl groups, only benzylic hydroxyl groups were converted to their corresponding ethers with excellent chemoselectivity (Table 1, entries 7 and 10; Scheme 2). The results indicated that the present protocol is potentially applicable for the chemoselective conversion of primary and secondary alcohols to their MOM- and EOM-ethers in the presence of phenols and tertiary alcohols.

The actual mechanism of these protection reactions is not clear at present. However, a plausible explanation is that FDMA or FDEA is first activated by catalyst to afford **1**. Alcohol attacks **1** to give **2**, which in turn converts to the final product **3** and releases the catalyst for the next catalytic cycle (Scheme 3).

Scheme 3.

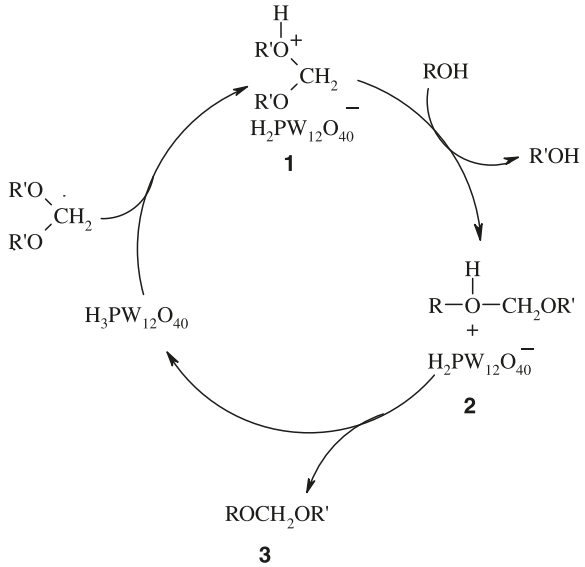

The deprotection reactions of MOM- and EOM-ethers with $H_3PW_{12}O_{40}$ were also investigated (Scheme 1). We optimized the experimental conditions for the cleavage of MOM- and EOM-ethers of benzyl alcohol, and the best results were achieved when 1 mmol of MOM- or EOM-ether was treated with 1 mol% of catalyst in refluxing EtOH. Under these conditions, various MOM- or EOM-ethers of primary and secondary benzylic, allylic, and saturated alcohols were deprotected to their parent alcohols in high yields. The results of deprotection reactions are illustrated in Table 3. Also, a mechanism has been proposed for the deprotection of these ethers (Scheme 4).

© 2008 NRC Canada

Table 1. Preparation of MOM- and EOM-ethers from alcohols catalyzed by $H_3PW_{12}O_{40}$ at room temperature under solvent-free conditions.

Entry	Alcohol	Formation of EOM-ethers (**a**)		Formation of MOM-ethers (**b**)	
		Time (h)	Yield (%)[a]	Time (h)	Yield (%)[a]
1	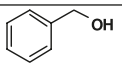	3	89	3	91
2	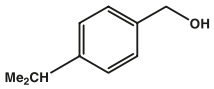	3.5	86	3.5	88
3	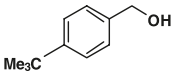	3.5	93	3	93
4	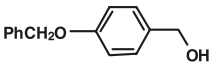	3	89	4	91
5	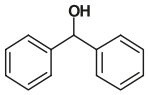	4.5	97	4	87
6[b]	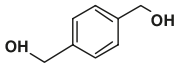	4	81	4	91
7	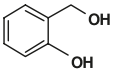	2.5	83	2	87
8	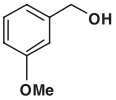	2.5	73	3.5	80
9	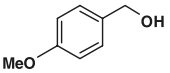	3.5	91	3	82
10	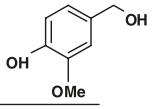	3	93	2	93

To extend the scope and utility of this catalytic system, we have performed several competitive deprotection reactions. As can be seen, interesting selectivities were observed. Primary and secondary MOM- and EOM-ethers are deprotected in the presence of phenolic and tertiary ones with high selectivity (Table 4). Also, chemoselective deprotection of these ethers in the presence of other hydroxyl protecting groups such as benzyl and methyl ethers (Table 3, entries 7–10), acetates and trimethylsilyl ethers (Table 5) is achieved using this catalytic system. These selectivites can be considered as useful practical achievements in deprotection reactions.

The reusability of the catalyst was examined using sequential reactions of benzyl alcohol with FDMA and FDEA (Table 1, entry 1). At the end of the reaction, Et_2O was added, and the catalyst was separated by simple filtration. The organic layer was washed with water, and the water was evaporated to afford the remaining catalyst. The recovered catalyst was reused for five cycles. The reactions were preceded smoothly with 88%–91% yields. The results indicated that the catalyst could be used several times without loss of its activity.

In conclusion a mild, selective, and efficient protocol for the preparation of MOM- and EOM-ethers at room temperature under solvent-free conditions and deprotection of these ethers in refluxing EtOH in the presence of catalytic amounts of $H_3PW_{12}O_{40}$ has been established. The use of this inexpensive, easily available, and reusable catalyst makes this protocol practical, environment-friendly, and economically attractive. Mild reaction conditions, high product yields, easy work-up procedures, and non-toxicity of the catalyst are other noteworthy advantages of this method.

Experimental

All materials were commercial reagent-grade, and alcohols, etherification reagents, and catalyst were purchased from Merck chemical company. The products were identified by comparison of their spectra and physical data with those of authentic samples. Melting points were determined

© 2008 NRC Canada

Table 1 (*concluded*)**.**

Entry	Alcohol	Formation of EOM-ethers (**a**)		Formation of MOM-ethers (**b**)	
		Time (h)	Yield (%)[a]	Time (h)	Yield (%)[a]
11	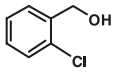	1.5	93	2	85
12	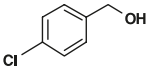	1.5	96	2	83
13	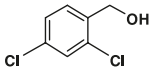	4.5	83	4	91
14	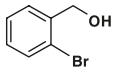	1.5	94	2	93
15	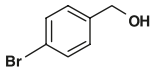	1.5	97	2	93
16	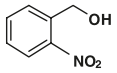	4.5	68	5	64
17	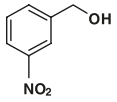	6	64	5	61
18	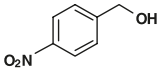	4.5	70	4.5	66
19	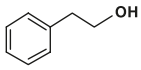	2	90	2	93
20	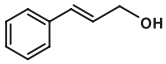	2	88	2	90
21	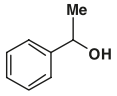	5	83	4.5	87
22	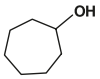	3.5	90	3	85
23	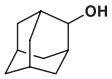	6	87	5.5	83
24	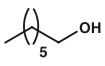	4	93	3	93
25	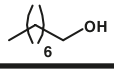	4	92	3	90

[a]Isolated yields.
[b]0.8 mol% of the catalyst was used.

© 2008 NRC Canada

Table 2. Competitive protection of alcohols and phenol catalyzed by $H_3PW_{12}O_{40}$.

Entry	Substrates	Product [a]	R	Yield (%) [b]
1	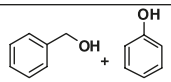	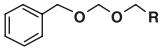	H	89
			Me	91
2	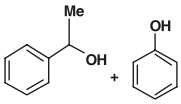	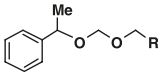	H	83
			Me	87
3	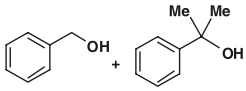	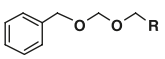	H	88
			Me	89
4	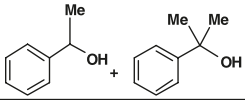	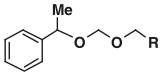	H	80
			Me	86

[a]Phenol and tertiary alcohol remained intact in the reactions mixture.
[b]Isolated yields.

using Stuart Scientific SMP2 apparatus. ^{1}H NMR was recorded on a Bruker AC 500 MHz spectrometer. IR spectra were recorded on a Shimadzu IR-435 spectrophotometer.

General procedure for the preparation of EOM- and MOM-ethers

To a solution of alcohol (1 mmol) in FDEA (5 mmol) or FDMA (7 mmol), $H_3PW_{12}O_{40}$ (0.004 mmol) was added and stirred at room temperature for the appropriate time according to Table 1. After completion of the reaction (TLC analysis), the excess FDMA or FDEA was removed by rotary evaporator. Et_2O (20 mL) was added, and the mixture was filtered. The organic layer was washed with water (10 mL) and dried over anhyd. Na_2SO_4. Evaporation of the solvent followed by chromatography on a short column of silica gel (*n*-hexane – ethyl acetate, 4:1) afforded the pure product (Table 1). In the case of solid materials, the products were recrystallized form *n*-hexane – diethyl ether.

General procedure for the deprotection of MOM- and EOM-ethers

A mixture of alkoxymethyl ether (1 mmol) and $H_3PW_{12}O_{40}$ (0.01 mmol) in EtOH (8–10 mL) was stirred under reflux conditions. After completion of the reaction (TLC analysis), the solvent was evaporated, Et_2O (20 mL) was added and filtered. The organic layer was washed with water (10 mL) and dried over anhyd. Na_2SO_4. The solvent was evaporated and the crude product was purified by a short column of silica gel (eluent: *n*-hexane – ethyl acetate, 4:1) to afford the pure product (Table 3).

Selected physical and spectroscopic data

(Ethoxymethoxy)methyl benzene (Table 1, entry 1a)

Oil. IR ν_{max} (KBr, cm^{-1}): 2800, 1380, 1160, 1100, 1040, 730, 680. ^{1}H NMR (500 MHz, $CDCl_3$) δ_H: 1.35 (t, *J* = 7.20 Hz, 3H, OCH_2CH_3), 3.70 (q, *J* = 7.10 Hz, 2H, OCH_2CH_3), 4.73 (s, 2H, OCH_2O), 4.92 (s, 2H, $PhCH_2$), 7.37–7.43 (m, 5H, Ar).

4-iso-Propyl–1-(ethoxymethoxy)methyl benzene (Table 1, entry 2a)

Oil. IR ν_{max} (KBr, cm^{-1}): 3000, 1350, 1100, 1040, 800, 790. ^{1}H NMR (500 MHz, $CDCl_3$) δ_H: 1.26 (d, *J* = 6.61 Hz, 6H, $CH(CH_3)_2$), 1.27 (t, *J* = 6.68 Hz, 3H, OCH_2CH_3), 2.92 (m, 1H, $CH(CH_3)_2$), 3.67 (q, *J* = 7.09 Hz, 2H, OCH_2CH_3), 4.59 (s, 2H, OCH_2O), 4.78 (s, 2H, $ArCH_2$), 7.24 (d, *J* = 8.05 Hz, 2H, Ar), 7.31 (d, *J* = 8.03 Hz, 2H, Ar).

4-tert-Butyl–1-(ethoxymethoxy)methyl benzene (Table 1, entry 3a)

Oil. IR ν_{max} (KBr, cm^{-1}): 2900, 1360, 1090, 1030, 750, 700. ^{1}H NMR (500 MHz, $CDCl_3$) δ_H: 1.26 (t, *J* = 7.13 Hz, 3H, OCH_2CH_3), 1.34 (s, 9H, $C(CH_3)_3$), 3.67 (q, *J* = 7.05 Hz, 2H, OCH_2CH_3), 4.60 (s, 2H, OCH_2O), 4.78 (s, 2H, $ArCH_2$), 7.31 (d, *J* = 8.15 Hz, 2H, Ar), 7.40 (d, *J* = 8.21 Hz, 2H, Ar).

1-Benzyloxy-4-((ethoxymethoxy))methylbenzene (Table 1, entry 4a)

Mp 69–72 °C. IR ν_{max} (KBr, cm^{-1}): 3000, 1190, 1080, 1040, 1020, 750, 740, 690. ^{1}H NMR (500 MHz, $CDCl_3$) δ_H: 1.26 (t, *J* = 6.99 Hz, 3H, OCH_2CH_3), 3.68 (q, *J* = 7.05 Hz, 2H, OCH_2CH_3), 4.47 (s, 2H OCH_2O), 4.57 (s, 2H, $ArCH_2$), 5.09 (s, 2H, $PhCH_2$), 6.98 (d, *J* = 8.55 Hz, 4H, Ar), 7.29–7.47 (m, 5H, Ar).

(Ethoxymethoxy)methylene dibenzene (Table 1, entry 5a)

Mp 90–93 °C. IR ν_{max} (KBr, cm^{-1}): 3000, 1210, 1080, 1010, 1000, 810. ^{1}H NMR (500 MHz, $CDCl_3$) δ_H: 1.11 (t, *J* = 7.10 Hz, 3H, OCH_2CH_3), 3.41 (q, *J* = 7.06 Hz, 2H, OCH_2CH_3), 4.42 (s, 2H, OCH_2O), 5.43 (s, 1H, CH), 7.26–7.40 (m, 12H, Ar).

1,4-Bis(ethoxymethoxy)methyl benzene (Table 1, entry 6a)

Mp 69–70 °C. IR ν_{max} (KBr, cm^{-1}): 2800, 1220, 1170, 1100, 1080, 1030, 810. ^{1}H NMR (500 MHz, $CDCl_3$) δ_H: 1.24 (t, *J* = 7.06 Hz, 6H, 2 × CH_3), 3.65 (q, *J* = 7.07 Hz, 4H, 2 × CH_2), 4.65 (s, 4H, 2 × OCH_2O), 4.76 (s, 4H, 2 × $ArCH_2$), 7.34 (s, 4H, Ar).

1,4-Bis(methoxymethoxy)methyl benzene (Table 1, entry 6b)

Mp 68–70 °C. IR ν_{max} (KBr, cm^{-1}): 2800, 1210, 1080, 1010, 1000, 810. ^{1}H NMR (500 MHz, $CDCl_3$) δ_H: 4.55 (s, 6H, 2 × CH_3), 4.64 (s, 4H, OCH_2O), 4.70 (s, 4H, 2 × $ArCH_2$), 7.37 (s, 4H, Ar).

© 2008 NRC Canada

Table 3. Deprotection of MOM- and EOM-ethers catalyzed by $H_3PW_{12}O_{40}$ in refluxing ethanol.

Entry	Ethers	Cleavage of EOM-ethers R: CH_2OEt		Cleavage of MOM-ethers R: CH_2OMe	
		Time (h)	Yield (%) [a]	Time (h)	Yield (%) [a]
1	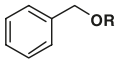	3	91	3	92
2	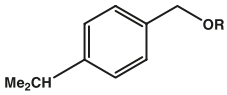	5	83	5.5	81
3	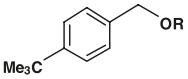	4	90	3.5	84
4	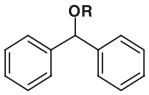	2	93	2.5	94
5[b]	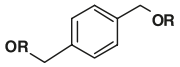	2.5	90	3	93
6	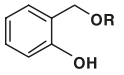	3.5	90	2	96
7	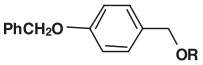	3.5	89	2	95
8	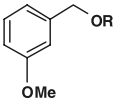	3	93	3	89
9	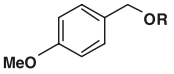	4	97	2	87
10	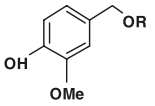	3	91	4	81
11	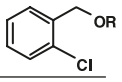	4.5	81	4.5	89

Scheme 4.

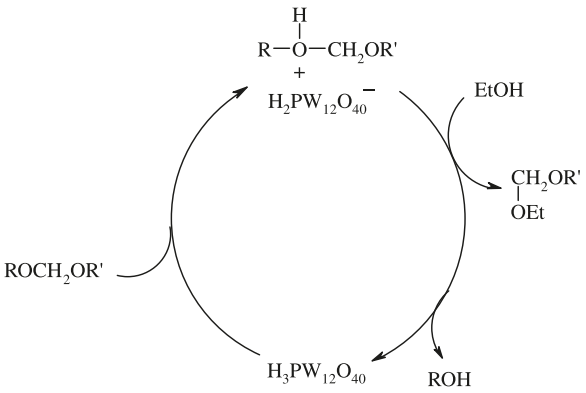

2-(Ethoxymethoxy)methyl phenol (Table 1, entry 7a)

Oil. IR ν_{max} (KBr, cm^{-1}): 3400, 2800, 1330, 1280, 1100, 1050, 740, 680. ^1H NMR (500 MHz, $CDCl_3$) δ_H: 1.26 (t, J = 7.11 Hz, 3H, OCH_2CH_3), 3.56 (s, 2H, OCH_2O), 4.66 (q, J = 7.03 Hz, 2H, OCH_2CH_3), 4.87 (s, 2H, $ArCH_2$), 7.00–7.71 (m, 4H, Ar).

2-(Methoxymethoxy)methyl phenol (Table 1, entry 7b)

Oil. IR ν_{max} (KBr, cm^{-1}): 3400, 2800, 1310, 1270, 1100, 1050, 730, 700. ^1H NMR (500 MHz, $CDCl_3$) δ_H: 1.98 (s, 3H, OCH_3), 2.02 (s, 2H, OCH_2), 3.98 (s, 2H, $ArCH_2$), 7.28–7.34 (m, 4H, Ar).

3-Methoxy-1-(ethoxymethoxy)methyl benzene (Table 1, entry 8a)

Oil. IR ν_{max} (KBr, cm^{-1}): 2900, 1200, 1100, 1000, 800. ^1H NMR (500 MHz, $CDCl_3$) δ_H: 1.27 (t, J = 6.40 Hz, 3H,

© 2008 NRC Canada

Table 3 (*concluded*).

Entry	Ethers	Cleavage of EOM-ethers R: CH_2OEt		Cleavage of MOM-ethers R: CH_2OMe	
		Time (h)	Yield (%) [a]	Time (h)	Yield (%) [a]
12	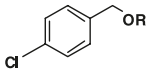	4.5	87	4.5	87
13	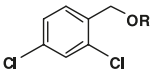	1	97	2	95
14	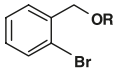	5.5	82	6	71
15	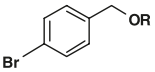	5.5	82	6	73
16	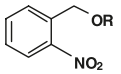	2	89	2	86
17	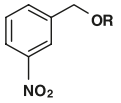	2	97	2	82
18	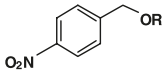	2	93	1.5	97
19	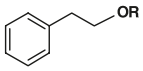	4	81	3	97
20	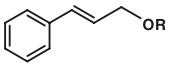	3.5	84	3	87
21	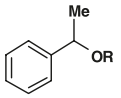	2	91	2	87
22	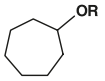	2.5	90	2.5	89
23	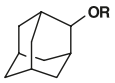	2	89	4.5	88
24	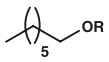	3.5	86	3.5	90
25	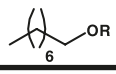	3.5	83	3.5	92

[a]Isolated yields.
[b]2 mol% of the catalyst was used.

OCH_2CH_3), 3.67 (q, J = 7.70 Hz, 2H, OCH_2CH_3), 3.82 (s, 3H, *m*-OCH_3), 4.60 (s, 2H, OCH_2O), 4.66 (s, 2H, $ArCH_2$), 6.83–7.30 (m, 4H, Ar).

4-Methoxy-1-(Ethoxymethoxy)methyl benzene (Table 1, entry 9a)

Oil. IR ν_{max} (KBr, cm^{-1}): 2800, 1240, 1170, 1100, 1030, 810. ^1H NMR (500 MHz, $CDCl_3$) δ_H: 1.24 (t, J = 6.28 Hz, 3H, OCH_2CH_3), 3.78 (q, J= 7.03 Hz, 2H, OCH_2CH_3), 3.82 (s, 3H, *p*-OCH_3), 4.45 (s, 2H, OCH_2O), 4.69 (s, 2H, $ArCH_2$), 6.88 (d, J = 6.78 Hz, 2H, Ar), 7.28 (d, J = 7.07 Hz, 2H, Ar).

4-((Ethoxymethoxy)methyl)-2-methoxy phenol (Table 1, entry 10a)

Mp 75–77 °C. IR ν_{max} (KBr, cm^{-1}): 3400, 2900, 1270, 1100, 1030, 790, 750. ^1H NMR (500 MHz, $CDCl_3$) δ_H: 1.22

© 2008 NRC Canada

Table 4. Competitive deprotection of MOM- and EOM-ethers of alcohols and phenol in the presence of $H_3PW_{12}O_{40}$.

Entry	Substrates	Products	Time (h)	Yield (%)[a]
1	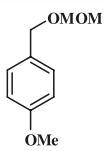 + 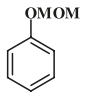	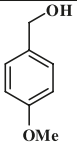 + 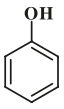	2	88 7
2	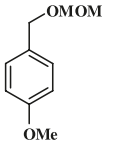 + 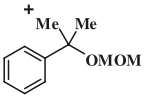	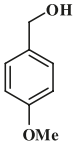 + 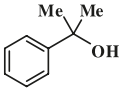	2	87 9
3	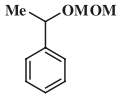 +	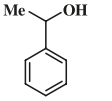 +	2	86 11
4	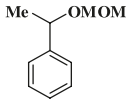 + 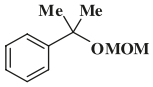	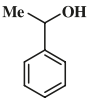 + 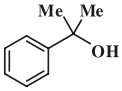	2	87 10
5	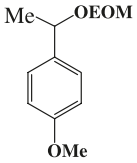 + 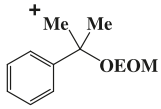	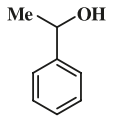 + 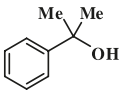	4	89 10
6	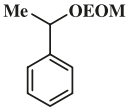 +	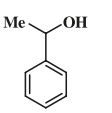 +	2	91 8

[a]Isolated yields.

Table 5. Competitive deprotection of MOM- and EOM-ethers, acetates, and trimethylsilyl ethers in the presence of $H_3PW_{12}O_{40}$.

Entry	Substrates	Products	Time (h)	Yield (%)[a]
1	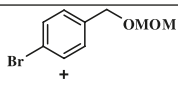 + 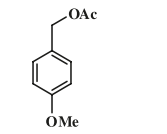	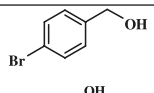 + 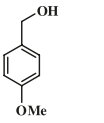	6	73 14
2	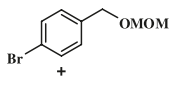 + 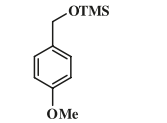	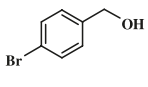 + 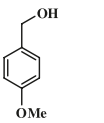	6	73 8
3	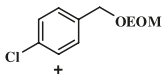 + 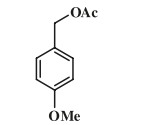	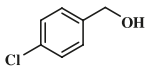 + 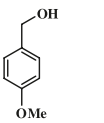	4.5	87 13
4	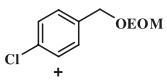 + 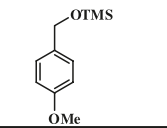	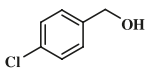 + 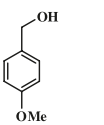	4.5	87 9

[a]Isolated yields.

(t, J = 7.11 Hz, 3H, OCH_2CH_3), 3.72 (s, 3H, *o*-OCH_3), 3.75 (q, J = 7.07 Hz, 2H, OCH_2CH_3), 5.31 (s, 2H, OCH_2O), 5.44 (s, 2H, $ArCH_2$), 6.43–7.26 (m, 3H, Ar).

2-Methoxy-4-((methoxymethoxy)methyl) phenol (Table 1, entry 10b)

Mp 71–73 °C. IR ν_{max} (KBr, cm^{-1}): 3300, 2900, 1200, 1000, 1060, 820, 790. ^1H NMR (500 MHz, $CDCl_3$) δ_H: 4.12 (s, 3H, OCH_3), 4.56 (s, 2H, OCH_2O), 4.66 (s, 3H, *o*-OCH_3), 4.84 (s, 2H, $ArCH_2$), 7.26–7.36 (m, 3H, Ar).

2-Chloro-1-(ethoxymethoxy)methyl benzene (Table 1, entry 11a)

Mp 61 °C. IR ν_{max} (KBr, cm^{-1}): 2800, 1250, 1120, 1050, 1020, 840, 740. ^1H NMR (500 MHz, $CDCl_3$) δ_H: 1.25 (t, J = 7.07 Hz, 3H, OCH_2CH_3), 3.67 (q, J = 7.08 Hz, 2H, OCH_2CH_3), 4.71 (s, 2H, OCH_2O), 4.81 (s, 2H, $ArCH_2$), 7.23–7.48 (m, 4H, Ar).

4-Choloro-1-(ethoxymethoxy)methyl benzene (Table 1, entry 12a)

Mp 69 °C. IR ν_{max} (KBr, cm^{-1}): 2900, 1320, 1280, 1100, 840, 760. ^1H NMR (500 MHz, $CDCl_3$) δ_H: 1.18 (t, J = 7.05 Hz, 3H, OCH_2CH_3), 3.55 (q, J = 7.04 Hz, 2H, OCH_2CH_3), 4.62 (s, 2H, OCH_2O), 4.86 (s, 2H, $ArCH_2$), 7.29 (d, J = 7.44 Hz, 2H, Ar), 7.34 (d, J = 6.42 Hz, 2H, Ar).

© 2008 NRC Canada

2,4-Dichloro-1-(ethoxymethoxy)methyl benzene (Table 1, entry 13a)

Mp 59–60 °C. IR ν_{max} (KBr, cm^{-1}): 2800, 1340, 1160, 1100, 1050, 820, 800, 730. ^1H NMR (500 MHz, $CDCl_3$) δ_H: 1.21 (t, *J*= 7.00 Hz, 3H, OCH_2CH_3), 3.60 (q, *J* = 7.01 Hz, 2H, OCH_2CH_3), 4.76 (s, 2H, OCH_2O), 4.92 (s, 2H, $ArCH_2$), 7.30 (s, 1H, Ar), 7.50 (d, *J* = 8.62 Hz, 1H, Ar), 8.20 (d, *J* = 8.90 Hz, 1H, Ar).

2-Bromo-1-(ethoxymethoxy)methyl benzene (Table 1, entry 14a)

Mp 60–62 °C. IR ν_{max} (KBr, cm^{-1}): 2800, 1360, 1100, 1050, 1020, 740. ^1H NMR (500 MHz, $CDCl_3$) δ_H: 1.25 (t, *J* = 7.05 Hz, 3H, OCH_2CH_3), 3.68 (q, *J* = 7.10 Hz, 2H, OCH_2CH_3), 4.76 (s, 2H, OCH_2O), 4.82 (s, 2H, $ArCH_2$), 7.15–7.55 (m, 4H, Ar).

4-Bromo-1-(ethoxymethoxy)methyl benzene (Table 1, entry 15a)

Mp 61–64 °C. IR ν_{max} (KBr, cm^{-1}): 2800, 1400, 1160, 1060, 1010, 790. ^1H NMR (500 MHz, $CDCl_3$) δ_H: 1.27 (t, *J* = 5.90 Hz, 3H, OCH_2CH_3), 3.63 (q, *J* = 5.84 Hz, 2H, OCH_2CH_3), 4.56 (s, 2H, OCH_2O), 4.76 (s, 2H, $ArCH_2$), 7.22 (d, *J* = 8.38 Hz, 2H, Ar), 7.48 (d, *J* = 6.29 Hz, 2H, Ar).

2-Nitro-1-(ethoxymethoxy)methyl benzene (Table 1, entry 16a)

Mp 71–73 °C. IR ν_{max} (KBr, cm^{-1}): 2800, 1500, 1320, 1120, 1100, 1050, 830, 740. ^1H NMR (500 MHz, $CDCl_3$) δ_H: 1.30 (3H, t, *J*= 7.07 Hz, OCH_2CH_3), 3.70 (2H, q, *J*= 7.07 Hz, OCH_2CH_3), 4.75 (2H, s, OCH_2O), 4.82 (2H, s, $ArCH_2$), 7.51 (t, *J* = 8.39 Hz, 2H, Ar), 8.19 (d, *J* = 8.56 Hz, 2H, Ar).

3-Nitro-1-(ethoxymethoxy)methyl benzene (Table 1, entry 17a)

Oil. IR ν_{max} (KBr, cm^{-1}): 2800, 1500, 1120, 1100, 1030, 820, 730. ^1H NMR (500 MHz, $CDCl_3$) δ_H: 1.24 (t, *J* = 7.09 Hz, 3H, OCH_2CH_3), 3.65 (q, *J* = 7.08 Hz, 2H, OCH_2CH_3), 4.59 (s, 2H, OCH_2O), 4.77 (s, 2H, $ArCH_2$), 6.84 (d, *J* = 8.26 Hz, 1H, Ar), 6.92 (d, *J* = 7.62 Hz, 2H, Ar), 7.26 (t, *J* = 7.90 Hz, 1H, Ar).

4-Nitro-1-(ethoxymethoxy)methyl benzene (Table 1, entry 18a)

Mp 88–90 °C. IR ν_{max} (KBr, cm^{-1}): 2800, 1500, 1320, 1160, 1100, 1040, 840, 790. ^1H NMR (500 MHz, $CDCl_3$) δ_H: 1.30 (t, *J* = 7.08 Hz, 3H, OCH_2CH_3), 3.70 (q, *J* = 7.06 Hz, 2H, OCH_2CH_3), 4.59 (s, 2H, OCH_2O), 4.83 (s, 2H, $ArCH_2$), 7.24 (d, *J* = 8.2 Hz, 2H, Ar), 7.50 (d, *J* = 8.55 Hz, 2H, Ar).

2-(Ethoxymethoxy)ethyl benzene (Table 1, entry 19a)

Oil. IR ν_{max} (KBr, cm^{-1}): 2800, 1380, 1110, 1060, 1020, 740, 690. ^1H NMR (500 MHz, $CDCl_3$) δ_H: 1.22 (t, *J* = 7.05 Hz, 3H, OCH_2CH_3), 2.89 (t, *J* = 7.02 Hz, 2H, $PhCH_2$), 3.59 (q, *J* = 7.03 Hz, 2H, OCH_2CH_3), 3.78 (t, *J* = 7.02 Hz, 2H, $PhCH_2CH_2O$), 4.67 (s, 2H, OCH_2O), 7.17–7.31 (m, 5H, Ar).

1-(Ethoxymethoxy)ethyl benzene (Table 1, entry 21a)

Oil. IR ν_{max} (KBr, cm^{-1}): 2800, 1420, 1100, 1030, 720, 680. ^1H NMR (500 MHz, $CDCl_3$) δ_H: 1.23 (t, *J* = 7.04 Hz, 3H, OCH_2CH_3), 1.42 (d, *J* = 10.29 Hz, 3H, $PhCHCH_3$), 2.05 (s, 2H, OCH_2O), 3.49 (q, *J* = 7.01 Hz, 2H, OCH_2CH_3), 4.13 (q, *J* = 7.01 Hz, 1H, PhCH), 7.28–7.35 (m, 5H, Ar).

2-(Ethoxymethoxy)cycloheptane (Table 1, entry 22a)

Oil. IR ν_{max} (KBr, cm^{-1}): 2900, 1370, 1090, 1030. ^1H NMR (500 MHz, $CDCl_3$) δ_H: 1.19 (t, *J* = 7.65 Hz, 3H, OCH_2CH_3), 1.49–1.88 (m, 12H, $-(CH_2)_6-$), 3.57 (q, *J* = 7.1 Hz, 2H, OCH_2CH_3), 3.69–3.73 (m, 1H, OCH), 4.66 (s, 2H, OCH_2O).

2-(Ethoxymethoxy)methyl adamentane (Table 1, entry 23a)

Mp 270–274 °C. IR ν_{max} (KBr, cm^{-1}): 2800, 1360, 1240, 1100, 1040. ^1H NMR (500 MHz, $CDCl_3$) δ_H: 1.21 (t, *J* = 11.56 Hz, 3H, OCH_2CH_3), 1.49–2.06 (m, 14H, adamentyl), 3.68 (q, *J* = 8.55 Hz, 2H, OCH_2CH_3), 3.78 (d, *J*= 12.27 Hz, 1H, OCH), 4.82 (s, 2H, OCH_2O).

2-(Ethoxymethoxy)heptane (Table 1, entry 24a)

Oil. IR ν_{max} (KBr, cm^{-1}): 2800, 1380, 1240, 1100, 1040, 820. ^1H NMR (500 MHz, $CDCl_3$) δ_H: 0.87 (t, *J*= 7.06 Hz, 3H, CH_3), 1.20 (t, *J* = 7.10 Hz, 3H, OCH_2CH_3), 1.24–1.57 (m, 10H, $-(CH_2)_5-$), 3.51 (t, *J* = 6.66 Hz, 2H, CH_2O), 3.58 (q, *J* = 7.09 Hz, 2H, OCH_2CH_3), 4.65 (s, 2H, OCH_2O).

2-(Ethoxymethoxy)octane (Table 1, entry 25a)

Oil. IR ν_{max} (KBr, cm^{-1}): 2800, 1380, 1240, 1100, 1040, 820. ^1H NMR (500 MHz, $CDCl_3$) δ_H: 0.88 (t, *J* = 7.39 Hz, 3H, CH_3), 1.24 (t, *J* = 7.16 Hz, 3H, OCH_2CH_3), 1.26–1.49 (m, 12H, $-(CH_2)_6-$), 3.41 (t, *J* = 5.49 Hz, 2H, CH_2O), 3.60 (q, *J* = 7.06 Hz, 2H, OCH_2CH_3), 4.67 (s, 2H, OCH_2O).

Acknowledgements

We are thankful to the Centre of Excellence of Chemistry of University of Isfahan (CECUI) and Office of the Graduate Studies for financial support of this work.

References

1. (*a*) M.T. Pope. Heteropoly and isopoly oxometalates. Springer-Velag, Berlin, Germany. 1993; (*b*) N. Mizuno and M. Misono. Chem. Rev. **98**, 199 (1998); (*c*) H. Firouzabadi and A.A. Jafari. J. Iran. Chem. Soc. **2**, 85 (2005).
2. M.A. Schwenger, H. Van Bekkum, and N. Munck. Appl. Catal. **74**, 191 (1991).
3. N. Mizuno and M. Misono. J. Mol. Catal. A: Chem. **86**, 319 (1994).
4. V. Mirkhani, S. Tangestaninejad, M. Moghadam, B. Yadollahi, and L. Alipanah. Monatsh. Chem. **135**, 1257 (2004).
5. E. Rafiee, S. Tangestaninejad, M.H. Habibi, and V. Mirkhani. Bull. Korean Chem. Soc. **25**, 599 (2004).
6. R. Fazaeli, S. Tangestaninejad, H. Aliyan, and M. Moghadam. Appl. Catal. A: General, **309**, 44 (2006).
7. A.M. Khenkin and R. Neurnann. J. Am. Chem. Soc. **124**, 4198 (2002).
8. J. Kaur, K. Griffin, B. Harrison, and I.V. Kozhevnikov. J. Catal. **208**, 448 (2002).

© 2008 NRC Canada

9. E.F. Kozhenikova, E. Rafiee, and I.V. Kozhenikov. Appl. Catal. A: Chem. **260**, 25 (2004).
10. Y.M.A. Yamada, H. Tabata, H. Takahashi, and S. Ikegami. Synlett, 2031 (2002).
11. V. Mirkhani, S. Tangestaninejad, B. Yadollahi, and L. Alipanah. Catal. Lett. **91**, 129 (2003).
12. (*a*) S. Tangestaninejad, M. Moghadam, V. Mirkhani, B. Yadollahi, and S.M.R. Mirmohmmadi. Monatsh. Chem. **137**, 235 (2006); (*b*) V. Mirkhani, S. Tangestaninejad, B. Yadollahi, and L. Alipanah. Tetrahedron, **59**, 8213 (2003).
13. E. Rafiee, S. Tangestaninejad, M.H. Habibi, I. Mohammadpoor-Baltork, and V. Mirkhani. Russian J. Org. Chem. **41**, 393 (2005).
14. E. Rafiee, S. Tangestaninejad, M.H. Habibi, and V. Mirkhani. Bioorg. Med. Chem. Lett. **14**, 3611 (2004).
15. R. Fazaeli, S. Tangestaninejad, and H. Aliyan. Catal. Commun. **8**, 205 (2007).
16. (*a*) M. Schelhaas and H. Waldmann. Angew. Chem., Int. Ed. Engl. **35**, 2056 (1996); (*b*) C.J. Salmon, E.G. Mata, and O.A. Marscaretti. Tetrahedron, **49**, 3691 (1993).
17. (*a*) T.W. Greene and P.G.M. Wuts. Protective groups in organic synthesis. Wiley, New York. 1991. Chap. 2. p. 5; (*b*) P.J. Kocienski. Protecting gourps. Georg Thieme, New York. 1994.
18. G.A. Olah, A. Husain, B.G.B. Gupta, S.C. Narang. Synthesis, 896 (1983).
19. M.L. Kantam and P.L. Santhi. Synlett, 429 (1993).
20. R.L. Danheiser, K.R. Romines, H. Koyama, S.K. Gee, C.R. Johnson, and J. R. Medich. Org. Synth. **71**, 133 (1992).
21. B.P. Bandgar, C.T. Hajare, and P.P. Wadgaonkar. J. Chem. Res. (S), 90 (1996).
22. T.-S. Jin, T.-S. Li, and Y.-T. Gao. Synth. Commun. **28**, 837 (1998).
23. G.V.M. Sharma, K.L. Reddy, P.S. Lakshmi, and P.R. Krishna. Tetrahedron Lett. **45**, 9229 (2004).
24. B. Karimi and L. Ma'mani. Tetrahedron Lett. **44**, 6051 (2003).
25. (*a*) K. Niknam, M.A. Zolfigol, A. Khorramabadi-Zad, R. Zare, and M. Shayegh. Catal. Commun. **7**, 494 (2006); (*b*) M.A. Zolfigol and M. Shiri. Mendeleev Commun. 165 (2005); (*c*) K. Niknam, M.A. Zolfigol, M. Shayegh, and R. Zare. J. Chinese Chem. Soc. **54**, 1067 (2007).
26. B.F. Marcune, S. Karady, U.H. Dolling, and T. Novak. J. Org. Chem. **64**, 2446 (1999).
27. D.A. Goff, R.N. Harris, J.C. Bottaro, and C.D. Bedford. J. Org. Chem. **51**, 4711 (1986).
28. T.R. Boehlow, J.J. Harburn, and C.D. Spilling. J. Org. Chem. **66**, 3111 (2001).
29. E.J. Corey, D.H. Hua, and S.P. Seitz. Tetrahedron Lett. **25**, 3 (1984).
30. A.S.-Y. Lee, Y.-J. Hu, and S.-F. Chu. Tetrahedron, **57**, 2121 (2001).
31. J.P. Deville and V. Behar. J. Org. Chem. **66**, 4097 (2001).
32. C. Ramesh, N. Ravindranath, and B. Das. J. Org. Chem. **68**, 7101 (2003).
33. J.M. Keith. Tetrahedron Lett. **45**, 2739 (2004).
34. (*a*) I. Mohammadpoor-Baltork and H. Aliyan. J. Chem. Res. (S) 272 (1999); (*b*) I. Mohammadpoor-Baltork and H. Aliyan. Synth. Commun. **29**, 2741 (1999); (*c*) I. Mohammadpoor-Baltork and H. Aliyan. Indian J. Chem. **38B**, 1223 (1999); (*d*) I. Mohammadpoor-Baltork, M.K. Amini, and S. Farshipoor. Bull. Chem. Soc. Jpn. **73**, 2775 (2000); (*e*) H. Firouzabadi, I. Mohammadpoor-Baltork, and S. Kolagar. Synth. Commun. **31**, 905 (2001); (*f*) I. Mohammadpoor-Baltork, B. Kharamesh, and S. Kolagar. Synth. Commun. **32**, 1633 (2002); (*g*) A. Bamoniri, M.A. Zolfigol, I. Mohammadpoor-Baltork, and B.F. Mirjalili. J. Iranian Chem. Soc. **3**, 85 (2006); (*h*) I. Mohammadpoor-Baltork, M.M. Khodaei, and H. Ahankar. Lett. Org. Chem. **3**, 768 (2006).

© 2008 NRC Canada

An efficient method for the silylation of hydroxyl groups with hexamethyldisilazane (HMDS) catalyzed by aluminum tris(dihydrogen phosphate) under solvent-free and ambient conditions

Hamid Reza Shaterian, Majid Ghashang, Nassrin Tajbakhsh Riki, and Manijeh Asadi

Abstract: A highly efficient and mild procedure for the trimethylsilylation of a wide variety of alcohols, including primary, benzylic, secondary, hindered secondary, tertiary, phenols, and oximes with hexamethyldisilazane (HMDS), using $Al(H_2PO_4)_3$ as a recyclable heterogeneous catalyst at room temperature in a few minutes with excellent yields under solvent-free conditions is described.

Key words: trimethylsilylation, hexamethyldisilazane, aluminum tris(dihydrogen phosphate) [$Al(H_2PO_4)_3$], solvent-free, hydroxyl groups.

Résumé : On a mis au point une méthode douce et très efficace de triméthylsilylation d'une grande variété d'alcools, y compris les alcools primaires, benzyliques, secondaires, secondaires empêchés et tertiaires, ainsi que des phénols et des oximes, qui implique l'utilization de l'hexaméthyldisilazane (HMDS) en présence de $Al(H_2PO_4)_3$ comme catalyseur hétérogène réutilizable et qui s'effectue en quelques minutes à la température ambiante, avec d'excellents rendements et des conditions sans solvant.

Mots-clés : triméthylsilylation, hexaméthyldisilazane, tris(phosphate diacide) d'aluminium [$Al(H_2PO_4)_3$], sans solvant, groupements hydroxyles.

[Traduit par la Rédaction]

Introduction

Trimethylsilylation of organic compounds having labile hydrogen atoms is an important organic transformation. It is a frequently used protection method in multi-step sequence synthesis of natural products due to the enhanced stability under a variety of conditions, solubility in nonpolar solvents, thermal stability, and the ease of removal, which is simply accomplished by acid- or base-induced hydrolysis giving only unreactive siloxane as the by-product (1). It is also used extensively for the hydroxyl compounds to increase their volatility for gas chromatography and mass spectrometry (1, 2). Several methods have been reported for this conversion, including the reaction of an alcohol with trimethylsilylhalides in the presence of a stoichiometric amount of a tertiary amine (3), with trimethylsilyl triflate and trimethylsilylmethallylsulfinates, which are more reactive than the chloride (4), allylsilanes in the presence of a catalytic amount of *p*-toluenesulfonic acid (4) iodine (5), trifluoromethanesulfonic acid (6), and $Sc(OTf)_3$ (7). Hexamethyldisilazane (HMDS) is frequently used for the trimethylsilylation of hydroxyl groups. HMDS is an inexpensive and commercially available reagent. Its handling does not require special precautions and the workup is not time-consuming because the by-product of the reaction is ammonia, which is simple to remove from the reaction medium. The low silylation power of HMDS is the main drawback to its application. Therefore, there are a variety of catalysts for activating this reagent, such as $(CH_3)_3SiCl$ (8), K-10 montmorillionite (9), sulfonic acids (10), zirconium sulfophenyl phosphonate (11), $ZnCl_2$ (12), Envirocat EPZGO (13), tungstophosphoric acid (14), iodine (15), lithium perchlorate (16), cupric sulfate pentahydrate (17), H–β Zeolite (18), $MgBr_2$ (19), lithium perchlorate supported on silica gel (20), $Al(HSO_4)_3$ (21), $Al(OTF)_3$ (22), magnesium triflate (23), copper triflate (24), $ZrCl_4$ (25), silica-$HClO_4$ (26), lanthanum trichloride (27), trichloroisocyanuric acid (28), and sulfonic acid-functionalized ordered nanoporous silica (29). However, in most cases a long reaction time, drastic reaction conditions, or tedious workup is needed. In addition, trimethylsilyl azide is expensive and toxic. We now show that O-trimethylsilylated compounds can be produced using $Al(H_2PO_4)_3$ (30) as an efficient, recyclable heterogeneous catalyst at room temperature under solvent-free conditions (Scheme 1).

This catalyst is safe, easy to handle, environmentally benign, presents fewer disposal problems, and is stable in reaction media.

Received 2 February 2008. Accepted 1 May 2008. Published on NRC Research Press Web site at canjchem.nrc.ca at 9 July 2008.

H.R. Shaterian,[1] M. Ghashang, N.T. Riki, and M. Asadi. Department of Chemistry, Faculty of Sciences, University of Sistan and Baluchestan, Zahedan, Iran.

[1]Corresponding author (e-mail: hrshaterian@hamoon.usb.ac.ir).

 doi:10.1139/V08-086 © 2008 NRC Canada

Scheme 1. Preparation of trimethylsilyl ethers.

$$2\ \text{R-OH} + \text{Me}_3\text{SiNHSiMe}_3 \xrightarrow[\text{Solvent-free}]{\text{Al(H}_2\text{PO}_4)_3} 2\ \text{R-OSiMe}_3 + \text{NH}_3$$

R= aryl, primary, secondary, tertiary and benzylic alcohol, oxime

Results and discussion

First, silylation of benzyl alcohols with HMDS in the presence of solid aluminum tris(dihydrogen phosphate) as catalyst in various solvents and also under solvent-free conditions at room temperature was investigated. The results were summarized in Table 1. As shown in Table 1, the solvent-free condition is obviously the best choice for these reactions. Solvent-free reactions promise to be an essential facet of 'Green Chemistry'. This type of organic reaction possesses some advantages over traditional reactions in organic solvents. Solvent-free reactions make it possible to reduce the consumption of environmentally unfriendly solvents and lead to new environmentally benign procedures to save resources and energy.

To determine the optimum quantity of $Al(H_2PO_4)_3$, the reaction of benzyl alcohol (1 equiv.) and HMDS (0.8 equiv.) was carried out under the solvent-free conditions using different quantities of catalyst at room temperature. The use of 50 mg of catalyst resulted in the highest yield in 5 min (Table 2).

Thus, we prepared a range of O-trimethylsilylated compounds under the optimized reaction conditions (Table 3).

A wide range of structurally diverse and functionalized phenols, alcohols, and oximes underwent silylation by this procedure to provide the corresponding TMS ethers (trimethysilyl ethers) in good to excellent isolated yields as shown in Table 3 (entries 1–24, 26, 28). Primary alcohols mostly reacted faster than secondary and tertiary alcohols. Generally, in all cases of benzyl, primary, secondary, and tertiary alcohols the reactions were completed within less than 65 min in solvent-free conditions accompanied by evolution of NH_3 gas from the reaction mixture. Inspection of the data in Table 3 clearly shows that different types of hindered secondary and tertiary alcohols were successfully converted to the corresponding silyl ethers at ambient conditions (Table 3). Amines (Table 3, entries 26, 27) and thiols (Table 3, entry 25) remained unaffected under the reaction conditions. To examine the functional group compatibility, we tested some more alcohols having other functional groups such as carbonyl group, amino group, alkene, and ethers. Alcohols were successfully converted to the corresponding silyl ethers, whereas, other functional groups were intact (Table 3, entries 2, 16, 26, 28).

The suggested mechanism of the $Al(H_2PO_4)_3$ catalyzed silylation of hydroxyl groups is shown in Scheme 2. $Al(H_2PO_4)_3$ can act as Brønsted acid and also Lewis acid owing to the empty aluminum *p*-orbital. Thus, in this mechanism, the operation process chart (OPC) of the catalyst in this works is unknown but according to observations such as the evolution of NH_3 in the reaction conditions, we have suggested that an acid–base interaction in $Al(H_2PO_4)_3$ as catalyst and nitrogen in HMDS polarizes the N–Si bond of HMDS to produce a reactive silylating agent (I). A rapid reaction with alcohol then ensues, leading to the ammonium silylating species (II) with concomitant release of the corresponding silyl ether. Irreversible cleavage of (II) with alcohol leading to the fast evolution of ROTMS (trimethysilyl ethers) and also formation of the unstable complexes of $Al(H_2PO_4)_3$ with ammonia (III). Cleavage of this complex with HMDS leads to the fast evolution of NH_3. Release of $Al(H_2PO_4)_3$ as catalyst from the intermediate (III) re-enters the catalytic cycle (Scheme 2).

Table 1. Preparation of benzyl trimethylsilyl ether using aluminum tris(dihydrogen phosphate) (0.05 g) as the catalyst under solvent and solvent-free conditions at room temperature.

Entry	Solvent	Time (min)	GC yield (%)	Yield (%)[a]
1	Dichloromethane	27	100	89
2	Chloroform	20	100	93
3	Ethyl acetate	35	100	91
4	*n*-Hexane	35	100	92
5	Acetonitrile	15	100	89
6	Solvent-free	5	100	98

[a]Isolated yield and the product gave satisfactory IR and NMR spectra.

Table 2. Optimization of the catalyst in the synthesis of benzyl trimethylsilyl ether.

Entry	Catalyst (g)	Time (min)	Isolated yield (%)
1	0.1	3	94
2	0.05	5	98
3	0.025	50	90
4	0.01	75	86

$Al(H_2PO_4)_3$ is an inexpensive and nonhazardous solid acid catalyst, which can be handled easily and removed from the reaction mixtures by simple filtration. The recovered catalyst was reused five times without any loss of activity (Table 4).

To show the merit of the present work in comparison with reported results in the literature, we compared reactions of $Al(H_2PO_4)_3$ with iodine (15), lithium perchlorate (16), cupric sulfate pentahydrate (17), magnesium triflate (23), and copper triflate (24) in the synthesis of trimethylsilyl ethers. As shown in Table 5, $Al(H_2PO_4)_3$ is a better catalyst with respect to reaction times and yields of the obtained products. Thus, the present protocol with $Al(H_2PO_4)_3$ as catalyst is convincingly superior to the reported catalytic methods.

The catalyst stability was assessed to evaluate if the catalyst could be disturbed by solvent or not. In a controlled experiment, preparation of 2-naphthyl trimethylsilyl ether in CH_2Cl_2 as solvent was examined (Table 3, entry 20), after 7 min, the catalyst was removed by simple filtration. The reaction was continued further and it was observed that the reaction stopped (GC monitoring) in absence of solid catalyst particles (Fig. 1). This suggests to us that the catalyst is heterogeneous and stable in reaction medium. When the separated catalyst was transferred to this media, the reaction was progressed and completed. To reconfirm that there were no active catalyst species in solution or to show that the process

© 2008 NRC Canada

Table 3. Silylation of alcohols, phenols, naphthols, and oximes with HMDS in the presence of solid aluminum tris(dihydrogen phosphate) as the catalyst (0.05 g) under solvent-free conditions at room temperature.

Entry	Substrate	Time (min)	Yield (%)[a]
1	Benzyl alcohol	5	98
2	4-Methoxybenzyl alcohol	4	96
3	2-Phenyl ethanol	7	98
4	Diphenyl methanol	9	93
5	1-Phenyl ethanol	8	92
6	1-Butanol	6	83
7	3-Methyl-1-butanol	8	87
8	Cyclohexanol	19	94
9	*tert*-Butanol	65	89
10	Tetrahydro-2-furylmethanol	12	96
11	5-Methyl-2-(1-ethylmethyl) cyclohexanol	9	96
12	1,4-Butandiol	7	91
13	Tricyclo[3,3,1,$1^{3,7}$] doc-1-ol	56	97
14	1-Octanol	9	94
15	2-Octanol	11	95
16	(3β)-Choest-4-en-3-ol	10	98
17	Phenol	6	97
18	4-Methylphenol	6	96
19	1-Naphthol	7	94
20	2-Naphthol	6	95
21	4,4′-Biphenol	6	96
22	Acetophenone oxime	6	95
23	Benzaldehyde oxime	5	93
24	4-Methyl acetophenone oxime	6	90
25	1,3-Propanditiol	7	—
26	4-Aminophenol	7	92
27	Aniline	7	—
28	Benzoin	21	80

[a]The pure isolated products were characterized by comparison of their physical data with those of known compounds (8–30).

Scheme 2. The suggested mechanism of the $Al(H_2PO_4)_3$ catalyzed silylation of hydroxyl groups.

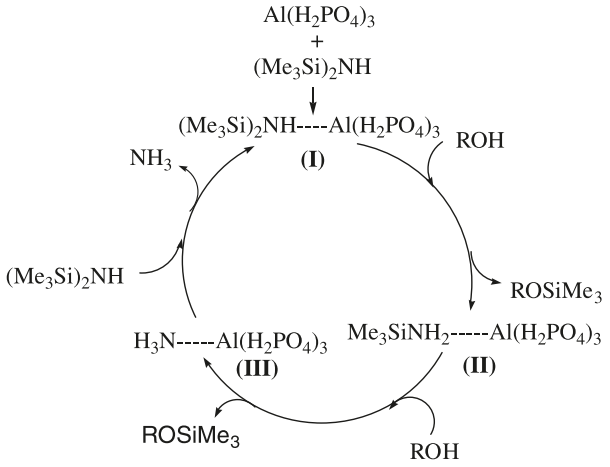

is truly heterogeneous, the catalyst was subjected to vigorous stripping in CH_2Cl_2 for 30 min. The catalyst was filtered and the filtrate was used as reaction medium. No noticeable transformation of 2-naphthyl trimethylsilyl ether confirmed

Table 4. Reusability of the catalyst based on the preparation of benzyl trimethylsilyl ether.

Entry	Run no.	Yield (%)
1	Cycle 1	97
2	Cycle 2	96
3	Cycle 3	96
4	Cycle 4	95
5	Cycle 5	94

heterogeneity of the catalyst in the reaction conditions. This evidence showed that the process is heterogeneous and no leaching occurs.

Conclusion

In conclusion, a reliable, rapid, and environmentally benign method for the preparation of trimethylsilyl ethers in a high to excellent yield under solvent-free and ambient conditions has been developed, which involves the use of recyclable $Al(H_2PO_4)_3$. In addition to the purity of the products, the short reaction times and ease of work-up make the method

© 2008 NRC Canada

Table 5. Comparison of our results with results obtained by some metal salts.

Entry	Catalyst	Conditions [molar ratio of catalyst]	Time, yield (%)
1	Iodine	CH_2Cl_2, RT [0.01]	—
2	$LiClO_4$	Solvent-free, RT [0.5]	20 min, 96
3	Cupric sulfate pentahydrate	CH_3CN, RT [0.01]	1.5 h, 95
4	$Cu(OTf)_2$	CH_3CN, RT [0.01]	120 min, 70
5	$Mg(OTf)_2$	Solvent-free, RT [0.01]	60 min, 70
10	$Al(H_2PO_4)_3$	Solvent-free, RT [0.16]	6 min, 97

Note: Based on phenol/HMDS (1:0.8 equiv.).

Fig. 1. Evaluation of the catalyst stability in the preparation of 2-naphthyl trimethylsilyl ether.

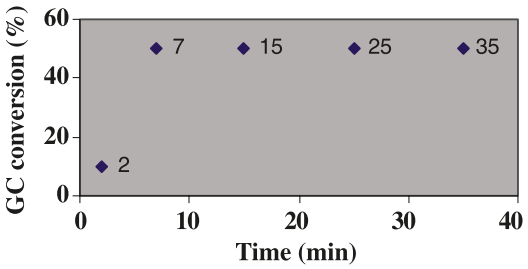

advantageous. We are currently exploring further applications of $Al(H_2PO_4)_3$ for other types of functional group transformations in our laboratories.

Experimental

General

All reagents were purchased from Merck and Sigma-Aldrich and used without further purification. $Al(H_2PO_4)_3$ was prepared according to the reported procedure (30). All yields refer to isolated products after purification. Products were characterized by comparison with authentic samples and by spectroscopy data (IR, ^{1}H NMR spectra). The NMR spectra were recorded on a Bruker Avance DPX 300 and 500 MHz instrument. The spectra were measured in $CDCl_3$ relative to TMS (0.00 ppm). GC analysis was run with Shimadzu GC-14A. IR spectra were recorded on a JASCO FT-IR 460plus spectrophotometer. TLC was performed on Silica-gel polygram SIL G/UV 254 plates.

Preparation of $Al(H_2PO_4)_3$ (30)

The catalyst was prepared by taking a mixture of alumina (neutral) and concentrated phosphoric acid (88%) in a silica boat maintaining the molar ratio of alumina–H_3PO_4 as 1:3 and heating at 200–220 °C on a hot sand bath. The mixture was stirred at the stipulated temperature until the swampy mass solidified and then the temperature was reduced to around 100 °C. The whole was then placed in a vacuum desiccator and cooled to ambient temperature. The catalyst thus prepared was finally transferred and stored in an air tight sample vial. The catalyst has been reported previously in the literature and was characterized by comparison of IR spectroscopy and the powder XRD with known samples (30). IR spectrum and powder XRD pattern matched well with the literature ($Al(H_2PO_4)_3$: 317.84 g mol^{-1}).

$$Al_2O_3 + H_3PO_4 \xrightarrow{\text{Heat}} Al(H_2PO_4)_3 + H_2O \uparrow$$

General procedure for silylation of alcohols using HMDS catalyzed with $Al(H_2PO_4)_3$

$Al(H_2PO_4)_3$ (0.05 g) was added to a stirred solution of alcohol (1 mmol) and HMDS (0.7 mmol) and the mixture was stirred at room temperature for the time specified in Table 3. The reaction was followed by GC and TLC (*n*-hexane–EtOAc, 9:1). After completion of the reaction, *n*-hexane was added and the heterogeneous catalyst was filtered and the resulting mixture was passed through a short pad of silica gel. Then, the pad column was washed with *n*-hexane (2 × 10 mL). Evaporation of the solvent under reduced pressure gave pure product(s) (Table 3). The separated catalyst was washed by ethyl acetate and dried in oven at 100 °C for 3 h. The desired pure product(s) was characterized by comparison of their physical data with those of known compounds (8–30).

Acknowledgements

We are thankful to the Sistan and Baluchestan University Research Council for the partial support of this work.

References

1. T.W. Greene and P.G.M. Wuts. Protective groups in organic synthesis. 3rd ed. Wiley, New York. 1999.
2. G. Sartori, R. Ballini, F. Bigi, G. Bosica, R. Maggi, and P. Righi. Chem. Rev. **104**, 199 (2004).
3. M.A. Brook. Silicon in organic, organometallic, and polymer chemistry. Wiley, New York. 2000.
4. (*a*) T. Morita, Y. Okamoto, and H. Sakurai. Tetrahedron Lett. **21**, 835 (1980); (*b*) T. Veysoglu and L.A. Mitscher. Tetrahedron Lett. **22**, 1299 (1981).
5. A. Hosomi and H. Sakurai. Chem. Lett. 85 (1981).
6. G.A. Olah, A. Husain, B.G.B. Gupta, G.F. Salem, and S.C. Narang. J. Org. Chem. **46**, 5212 (1981).
7. T. Suzuki, T. Watahiki, and T. Oriyama. Tetrahedron Lett. **41**, 8903 (2000).
8. J. Cossy and P. Pale. Tetrahedron Lett. **28**, 6039 (1987).
9. Z.H. Zhang, T.S. Li, F. Yang, and C.G. Fu. Synth. Commun. **28**, 3105 (1998).
10. D. Boerner, G. Koerner, F. Spieker, and M. Wiemann. German Patent, DE 2757936. 1978.
11. M. Curini, F. Epifano, M.C. Marcotullio, O. Rosati, and U. Costantino. Synth. Commun. **29**, 541 (1999).
12. H. Firouzabadi and B. Karimi. Synth. Commun. **23**, 1633 (1993).

© 2008 NRC Canada

13. B.P. Bandgar and P.P. Wadgaonkar. Synth. Commun. **27**, 2069 (1997).
14. H. Firouzabadi, N. Iranpoor, K. Amani, and F. Nowrouzi. J. Chem. Soc. Perkin Trans. 1, 2601 (2002).
15. B. Karimi and B. Golshani. J. Org. Chem. **65**, 7228 (2000).
16. N. Azizi and M.R. Saidi. Organometallics, **23**, 1457 (2004).
17. B. Akhlaghinia and S. Tavakoli. Synthesis, 1775 (2005).
18. V.H. Tillu, V.H. Jadhav, H.B. Borate, and R.D. Wakharkar. ARKIVOC, 83 (2004).
19. M.M. Mojtahedi, H. Abbasi, and M.S. Abaee. J. Mol. Catal. A: Chem. **250**, 6 (2006).
20. N. Azizi, R. Yousefi, and M.R. Saidi. J. Organometallic Chem. **691**, 817 (2006).
21. F. Shirini, M.A. Zolfigol, and M. Abedini. Bull. Chem. Soc. Jpn. **78**, 1982 (2005).
22. H. Firouzabadi, N. Iranpoor, S. Sobhani, and S. Ghassamipour. Synthesis, 595 (2005).
23. H. Firouzabadi, N. Iranpoor, S. Sobhani, and S. Ghassamipour. J. Organometallic Chem. **689**, 3197 (2004).
24. H. Firouzabadi, N. Iranpoor, S. Sobhani, S. Ghassamipour, and Z. Amoozgar. Tetrahedron Lett. **44**, 891 (2003).
25. F. Shirini and E. Mollarazi. Catal. Commun. **8**, 1393 (2007).
26. H.R. Shaterian, F. Shahrekipoor, and M. Ghashang. J. Mol. Catal. A: Chem. **272**, 142 (2007).
27. A.V. Narsaiah. J. Organometallic Chem. **692**, 3614 (2007).
28. A. Khazaei, M.A. Zolfigol, A. Rostami, and A. Ghorbani Choghamarani. Catal. Commun. **8**, 543 (2007).
29. D. Zareyee and B. Karimi. Tetrahedron Lett. **48**, 1277 (2007).
30. (*a*) S.K. Bharadwaj, S. Hussain, M. Kar, and M.K. Chaudhuri. Catal. Commun. **9**, 919 (2007); (*b*) F. d'Yvoire. Bull. Soc. Chim. Fr. 2277 (1961). pdf file no.00-014-0546.

© 2008 NRC Canada

Radical-mediated cyclization reaction — Regioselective synthesis of pyrimidine- and coumarin-annulated [6,6]-fused oxygen heterocycles

Krishna C. Majumdar, Pradip Debnath, and Pradip K. Maji

Abstract: The *n*-Bu_3SnH-AIBN mediated aryl radical cyclization of various 8-[(2-bromophenoxy)methyl]-1,3-dimethyl-2,3,4,6-tetrahydro-1*H*-pyrano[3,2-*d*]pyrimidine-2,4-diones and 1-[(2-bromophenoxy)methyl]-3,5-dihydropyrano[2,3-*c*]coumarins was investigated with the formation of [6,6]-fused oxygen heterocycles as a single regioisomer.

Key words: *n*-Bu_3SnH-AIBN, aryl radical cyclization, 6-endo-trig, oxygen heterocycles, coumarin derivatives, pyrimidine derivatives

Résumé : On a effectué une étude le la régiochimie de la cyclisation arylique radicalaire catalysée par le *n*-Bu_3Sn-AIBN de diverses 8-[2-bromophénoxy]méthyl-1,3-diméthyl-2,3,4,6-tétrahydro-1*H*-pyrano[3,2-*d*]pyrimidine-2,4-diones et de 1-[(2-bromophénoxy)méthyl]-3,5-dihydropyrano[2,3-*c*]coumarines qui conduit à la formation d'hétérocycles oxygénés à fusion [6,6] sous la forme d'un seul régioisomère.

Mots-clés : *n*-Bu_3Sn-AIBN, cyclisation arylique radicalaire, 6-endo-trig, hétérocycles oxygénés, dérivés de la coumarine, dérivés de la pyrimidine.

[Traduit par la Rédaction]

Introduction

Coumarin and its derivatives are important heterocyclic compounds that are found in many natural products (1), many of that exhibit remarkable physiological and biological activities (2). Many compounds containing the coumarin skeleton have shown antihelmintic, hypnotic, insecticidal, anti-coagulant, and antifungal properties (3). Some pyrimidine derivatives are active against cancer (4), viral disease (5), and the AIDS virus (6). Several efforts have been made to synthesize them. In the interest of synthesizing new coumarin and pyrimidine ring systems of biological interest, we previously reported the synthesis of several novel five- and six-membered coumarin- and pyrimidine-annulated heterocycles by the application of sigmatropic rearrangements (7) and radical cyclization strategy (8).

In recent years, intramolecular aryl radical cyclization has revolutionized the construction of various types of cyclic compounds via carbon–carbon bond-forming processes (9). In particular, the intramolecular addition of carbon-centered radical intermediates to arene and aromatic heterocycles has gained considerable prominence (10). It provides a mild and often high-yielding route to condensed aromatic ring systems. It has been rationalized that a stereoelectronically favored 5-exo cyclization is generally preferred over a 6-endo cyclization in those systems having an alkenic bond at the 5-position relative to the radical center. However, regiochemistry of the radical cyclization can be influenced, and even reversed, to favor the formation of six-membered rings by factors other than stereoelectronic control (11). The extensive investigations of the 5-hexenyl radical revealed that there are three factors, namely the substitution pattern at C-5, vinyl radical cyclization, and ring strain, that can direct 6-endo cyclization over 5-exo cyclization (12). In this context, we recently reported the synthesis of pyrone- and coumarin-annulated [6,6]-fused sulfur and oxygen heterocycles, respectively, based on the regioselective 6-endo-trig radical cyclization, wherein a mixture of diastereoisomers was obtained in some cases (13). More recently, we have shown that *n*-Bu_3SnH-mediated cyclization of sulfur and sulfone precursors derived from coumarin afforded a mixture of [6,6]-fused and (or) spiro heterocycles (14). All these previous investigations have influenced us to undertake a study of the radical cyclization on *o*-bromoaryl enol ethers, using 8-[(2-bromophenoxy]methyl]-1,3-dimethyl-2,3,4,6-tetrahydro-1*H*-pyrano[3,2-*d*]pyrimidine-2,4-diones **5a**–**5f**, and 1-[2-bromophenoxy) methyl]-3,5-dihydropyrano[2,3-*c*]coumarin **5g**–**5l** as the starting materials, with a view to synthesize the

Received 22 February 2008. Accepted 23 April 2008. Published on the NRC Research Press Web site at canjchem.nrc.ca on 11 July 2008.

K.C. Majumdar[1], P. Debnath, and P.K. Maji. Department of Chemistry, University of Kalyani, Kalyani 741235, West Bengal, India.

[1]Corresponding author (e-mail: kcm_ku@yahoo.co.in).

 doi:10.1139/V08-087 © 2008 NRC Canada

Scheme 1. Reagents and conditions: (*i*) K_2CO_3, NaI, acetone, reflux, 6–10 h; (*ii*) chlorobenzene, reflux, 3–5 h.

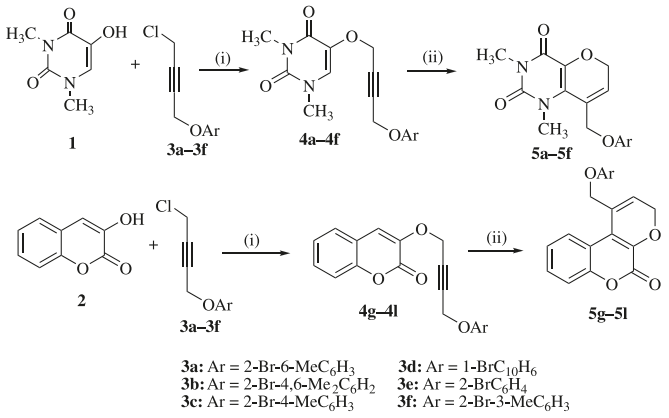

polycyclic pyrimidine and coumarin derivatives, respectively. Here, we report the results of our investigation.

Results and discussion

As radical precursors for our present study, we have prepared 8-[(2-bromophenoxy)methyl]-1,3-dimethyl-2,3,4,6-tetrahydro-1*H*-pyrano[3,2-*d*]pyrimidine-2,4-diones (**5a**–**5f**) and 1-[(2-bromophenoxy)methyl]-3,5-dihydropyrano[2,3-*c*]coumarins (**5g**–**5l**), by the thermal rearrangement of 1,3-dimethyl 5-(4-aryloxybut-2-ynyloxy) uracils (**4a**–**4f**) and 3-(4-aryloxybut-2-ynyl)coumarins (**4g**–**4l**) in 81%–89% and 84%–90% yields, respectively. The compounds **4a**–**4l** were, in turn, prepared by the classical alkylation of 1,3-dimethyl-5-hydroxy uracil (**1**) or 3-hydroxycoumarin (**2**) with different 1-aryloxy-4-chlorobut-2-ynes (**3a**–**3f**) according to our earlier published procedure (7) (Scheme 1).

As our aim was to synthesize [6,6]-fused oxygen heterocycles, we examined the scope of C–C bond formation of compounds **5** by *n*-Bu_3SnH–AIBN (azobis-isobutylnitrile) mediated radical cyclization. Compound **5a**, when heated with *n*-Bu_3SnH (1.1 equiv.) and AIBN (0.5 equiv.) in dry benzene at 80 °C for 5 h, yielded a solid product. The ^1H NMR spectrum of the product revealed that the cyclization did not occur. Only the halogen-reduced product was obtained. However, by changing the solvent to toluene under the same reaction conditions, we were able to obtain regioselectivly the cyclized product **6a** in 89% yield.

It has already been established that a very high level of diastereoselectivity could be obtained when the concentration of the reactant is reduced from 0.1 to 0.01 mol/L (15). These observations have been attributed to the reversibility of the cyclization and the decreased availability of the tin hydride. We then tried to carry out the cyclization reaction in highly dilute conditions. The conditions for the *n*-Bu_3SnH-AIBN procedure were optimized for the six-membered radical cyclizations of the substrates **5**. Substrate **5a** (0.01 mol/L) was refluxed in degassed dry toluene under nitrogen atmosphere with *n*-Bu_3SnH (1.0 equiv.) for 3.5 h. The cyclization of **5a** under dilute conditions gave **6a** in 81% yield (Scheme 2). The high field ^1H NMR (500 MHz in $CDCl_3$) spectrum of the compound **6a** displayed one proton double triplet at δ 3.28 (*J* = 3.8 Hz and 11.6 Hz) and another

Scheme 2. Reagents and conditions: (*i*) Toluene (0.01 mol/L), *n*-Bu_3SnH, AIBN, reflux, 3.5 h.

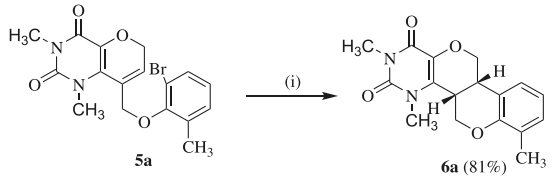

Scheme 3.

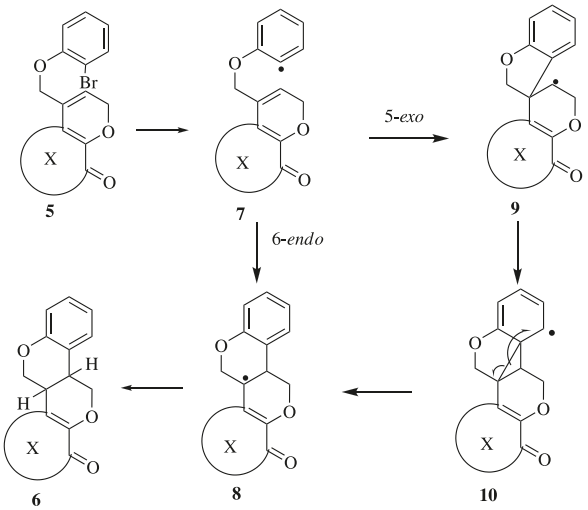

one proton double triplet at δ 3.36 (*J* = 3.8 Hz and 11.7 Hz), owing to ring-juncture protons. The stereochemistry of the ring-juncture protons can be surmised from the molecular model (Dreiding model), which showed a strain-free cis-arrangement. Compared with the literature results (7,13), the small coupling constant value (*J* = 3.8 Hz) of the ring juncture protons of **6a** also indicated the cis stereochemistry.

On the basis of this promising result, the tin hydride mediated cyclization of the precursors **5a**–**5f** was conducted. The results are summarized in **Table 1**. From **Table 1** it is observed that other substrates **5b**–**5f** give exclusively the [6,6] pyranopyran derivatives **6b**–**6f** in 76%–89% yields. Encouraged by the results of radical cyclization of pyrimidines, we have investigated similar radical cyclization reactions of substrates containing a coumarin moiety. Substrate **5g** was subjected to radical cyclization under the aforesaid reaction conditions. Unfortunately, we were unable to obtain any cyclized product because the starting material decomposed under the reaction conditions. However, by changing the solvent to benzene and lowering the reaction temperature to 75 °C, we eliminated the decomposition of the starting material. It was observed that when the substrates **5g**–**5l** were treated with *n*-Bu_3SnH (1.0 equiv) and AIBN in benzene, cyclization proceeded affording the cyclized product **6g**–**6l** in 75%–90% yields (Table 1).

The formation of the products **6** from **5** may be explained by the generation of aryl radical **7**, which may undergo either a 5-exo trig or a 6-endo-trig cyclization at the double bond of the pyran moiety as described in Scheme **3**. A 6-endo-trig cyclization of radical **7** may produce the intermediate radical **8** while a 5-exo-trig cyclization may give the

© 2008 NRC Canada

Table 1. Tin hydride-mediated radical cyclization of compounds **5a**–**5l**.

Substrate (**5**)	Product (**6**)	Yield (%)
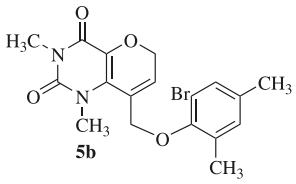 **5b**	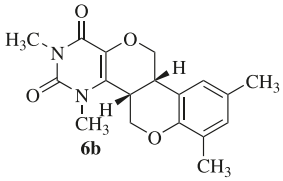 **6b**	86
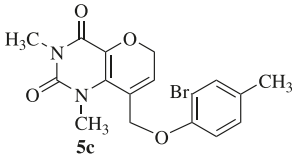 **5c**	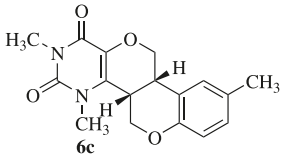 **6c**	85
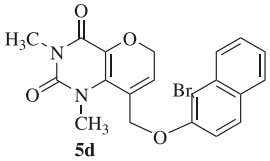 **5d**	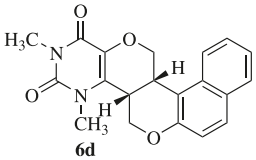 **6d**	76
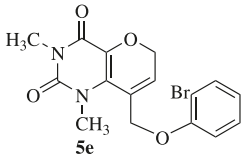 **5e**	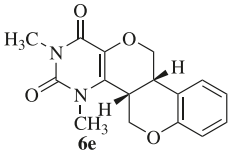 **6e**	89
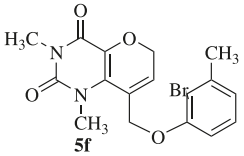 **5f**	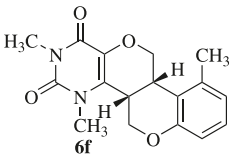 **6f**	81
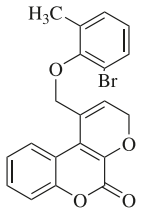 **5g**	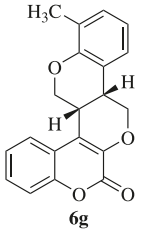 **6g**	75

spirocyclic radical **9** (not isolated), followed by neophyl rearrangement (16) to radical intermediate **10**. Abstraction of a hydrogen from *n*-Bu_3SnH by radical intermediate **7** may give the [6,6]-fused cyclized products **6**.

Aryl radical cyclization normally gives a high 5-exo : 6-endo ratio indicating a stronger preference for exo cyclization than for alkyl radical cyclization. However, suitably substituted 5-hexenyl radicals are known to undergo 6-endo cyclization to give six-membered rings. It is interesting to note that six-membered rings are formed regioselectively in all cases we have studied at present. Earlier we had reported the synthesis of the [6,6]pyranopyrans by sequential Claisen rearrangement of the 4-aryloxy-2-ynyloxy derivatives of uracil and coumarin (7). This radical cyclization protocol is found to give the polycyclic heterocycles in better yields under mild conditions.

Conclusion

In conclusion, we have successfully extended the *n*-Bu_3SnH mediated radical cyclization reaction to the regioselective synthesis of coumarin- and pyrimidine-annulated [6,6]-fused heterocycles. The process is quite general and regioselective and afforded the desired products in good-to-excellent yields. The mildness of the reaction conditions and high level of regioelectivity allow this radical cyclization to serve as a powerful synthetic tool for the preparation of complex aromatic heterocycles.

Experimental

Melting points were determined in an open capillary and are uncorrected. IR spectra were recorded on a

© 2008 NRC Canada

Table 1 (*concluded*).

Substrates (**5**)	Products (**6**)	Yield (%)
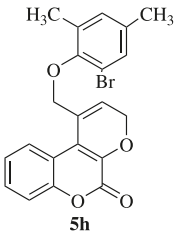 **5h**	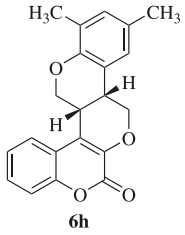 **6h**	82
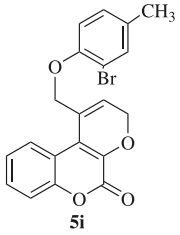 **5i**	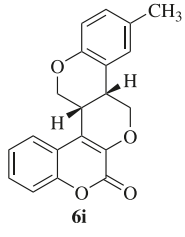 **6i**	76
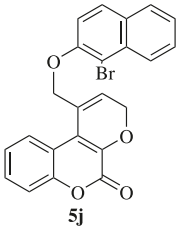 **5j**	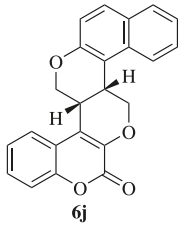 **6j**	90
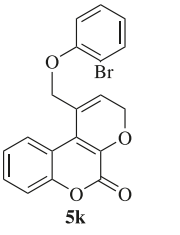 **5k**	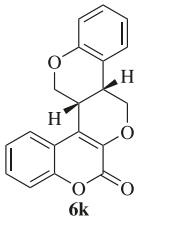 **6k**	86
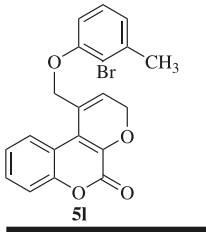 **5l**	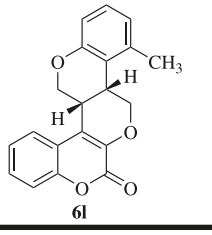 **6l**	85

Note: Reagent conditions: *n*-Bu_3SnH, AIBN, toluene, reflux, 3–4 h; *n*-Bu_3SnH, AIBN, benzene, 75 °C, 3–4 h.

PerkinElmer L 120-000A spectrometer (ν_{max} in cm^{-1}) on KBr disks. ^1H NMR (300 MHz, 400 MHz, and 500 MHz) and ^{13}C NMR (125.7 MHz) spectra were recorded on a Bruker DPX-300, Varian-400 FT–NMR, Bruker DPX-500 and spectrometer in $CDCl_3$ (chemical shift in δ) with TMS as internal standard. Silica gel [(60–120 mesh), Spectrochem, India] was used for chromatographic separation. Petroleum ether refers to the fraction boiling between 60 and 80 °C.

General procedure for the preparation of compounds 4a–4l

The compounds **4a–4l** were synthesized according to the earlier published procedure (7).

5-({4-[(2-Bromo-6-methylphenyl)oxy]but-2-ynyl}oxy)-1,3-dimethyl-1,2,3,4-tetrahydropyrimidine-2,4-dione (4a)

Yield 91%; colorless solid; mp 161–163 °C (acetonitrile–methanol). IR (KBr, cm^{-1}): 2923, 1707, 1648. ^1H NMR (400 MHz, $CDCl_3$) δ_H: 2.56 (s, 3H, $ArCH_3$), 3.61 (s, 6H, $-NCH_3$), 4.94 (s, 2H, $-OCH_2$), 4.99 (s, 2H, $-OCH_2$), 7.51 (m, 3H), 7.76 (s, 1H, C_6H). MS *m/z*: 392, 394 (M^+). Anal. calcd. for $C_{17}H_{17}N_2O_4Br$: C 51.92, H 4.36, N 12; found: C 52.06, H 4.31, N 7.14.

5-({4-[(2-Bromo-4,6-dimethylphenyl)oxy]but-2-ynyl}oxy)-1,3-dimethyl-1,2,3,4-tetrahydropyrimidine-2,4-dione (4b):

Yield 90%; colorless solid; mp 122–123 °C (acetonitrile–methanol). IR (KBr, cm^{-1}): 2982, 1706, 1642. ^1H NMR

© 2008 NRC Canada

(400 MHz, $CDCl_3$) δ_H: 2.24 (s, 3H, $ArCH_3$), 2.27 (s, 3H, $ArCH_3$), 3.34 (s, 3H, -NCH_3), 3.35 (s, 3H, -NCH_3), 4.65 (s, 2H, -OCH_2), 4.73 (s, 2H, -OCH_2), 6.90 (s, 1H), 7.01 (s, 1H), 7.17 (s, 1H, C_6H). MS *m/z*: 406, 408 (M^+). Anal. calcd. for $C_{18}H_{19}N_2O_4Br$: C 53.08, H 4.70, N 6.88; found: C 53.24, H 4.76, N 6.91.

5-({4-[(2-Bromo-4-methylphenyl)oxy]but-2-ynyl}oxy)-1,3-dimethyl-1,2,3,4-tetrahydropyrimidine-2,4-dione (4c)

Yield 93%; colorless solid; mp 155–157 °C (acetonitrile–methanol). IR (KBr, cm^{-1}): 2948, 1700, 1642. ^1H NMR (400 MHz, $CDCl_3$) δ_H: 2.27 (s, 3H, $ArCH_3$), 3.22 (s, 3H, -NCH_3), 3.36 (s, 3H, -NCH_3), 4.73 (s, 2H, -OCH_2), 4.76 (s, 2H, -OCH_2), 7.08 (s, 1H, C_6H), 7.24–7.29 (m, 3H). MS *m/z*: 392, 394 (M^+). Anal. calcd. for $C_{17}H_{17}N_2O_4Br$: C 51.92, H 4.36, N 7.12; found: C 51.85, H 4.41, N 7.10.

5-({4-[(1-Bromonaphthalene-2-yl)oxy]but-2-ynyl}oxy)-1,3-dimethyl-1,2,3,4-tetrahydropyrimidine-2,4-dione (4d)

Yield 87%; colorless solid; mp 118–120 °C (acetonitrile–methanol). IR (KBr, cm^{-1}): 2979, 1701, 1638. ^1H NMR (400 MHz, $CDCl_3$) δ_H: 3.05 (s, 3H, -NCH_3), 3.29 (s, 3H, -NCH_3), 4.72 (s, 2H, -OCH_2), 4.93 (s, 2H, -OCH_2), 6.80 (s, 1H, C_6H), 7.30 (d, J = 8.9 Hz, 1H), 7.42 (d, J = 7.3 Hz, 1H), 7.56 (t, J = 7.6 Hz, 1H), 7.76 (m, 2H), 8.20 (d, J = 8.5 Hz, 1H). MS *m/z*: 428, 430 (M^+). Anal. calcd. for $C_{20}H_{17}N_2O_4Br$: C 55.96, H 3.99, N 6.53; found: C 56.26, H 4.05, N 6.62.

5-({4-[(2-Bromophenyl)oxy]but-2-ynyl}oxy)-1,3-dimethyl-1,2,3,4-tetrahydropyrimidine-2,4-dione (4e)

Yield 96%; colorless solid; mp 104–106 °C (acetonitrile–methanol). IR (KBr, cm^{-1}): 2979, 1705, 1639. ^1H NMR (400 MHz, $CDCl_3$) δ_H: 3.32 (s, 3H, -NCH_3), 3.35 (s, 3H, -NCH_3), 4.72 (s, 2H, -OCH_2), 4.80 (s, 2H, -OCH_2), 6.86–6.99 (m, 2H), 7.06 (s, 1H, C_6H), 7.47 (d, J = 8.0 Hz, 1H), 7.53 (d, J = 7.8 Hz, 1H). MS *m/z*:378, 380 (M^+). Anal. calcd. for $C_{16}H_{15}N_2O_4Br$: C 50.68, H 3.99, N 7.39; found: C 50.58, H 4.02, N 7.37.

5-({4-[(2-Bromo-3-methylphenyl)oxy]but-2-ynyl}oxy)-1,3-dimethyl–1,2,3,4-tetrahydropyrimidine-2,4-dione (4f)

Yield 88%; colorless solid; mp 110–111 °C (acetonitrile–methanol). IR (KBr, cm^{-1}): 2950, 1707, 1661. ^1H NMR (400 MHz, $CDCl_3$) δ_H: 2.40 (s, 3H, $ArCH_3$), 3.20 (s, 3H, -NCH_3), 3.32 (s, 3H, -NCH_3), 4.72 (s, 2H, -OCH_2), 4.78 (s, 2H, -OCH_2), 6.77–6.84 (m, 1H), 6.92 (s, 1H, C_6H), 7.08–7.12 (m, 1H), 7.35–7.43 (m, 1H). MS *m/z*: 392, 394 (M^+). Anal. calcd. for $C_{17}H_{17}N_2O_4Br$: C 51.92, H 4.36, N 7.12; found: C 52.16, H 4.37, N 7.23.

3-({4-[(2-Bromo-6-methylphenyl)oxy]but-2-ynyl}oxy)-2H-chromen-2-one (4g)

Yield: 81%; colorless solid; mp 148–149 °C (dichloromethane–hexane). IR (KBr, cm^{-1}): 2920, 1732, 1629. ^1H NMR (400 MHz, $CDCl_3$) δ_H: 2.27 (s, 3H), 4.71 (s, 2H), 4.85 (s, 2H), 6.97 (s, 1H), 7.18–7.43 (m, 7H). MS *m/z*: 398, 400 (M^+). Anal. calcd. for $C_{20}H_{15}BrO_4$: C 60.17, H 3.79; found: C 60.38, H 3.86.

3-({4-[(2-Bromo-4,6-dimethylphenyl)oxy]but-2-ynyl}oxy)-2H-chromen-2-one (4h)

Yield: 79%; colorless solid; mp 133–134 °C (dichloromethane–hexane). IR (KBr, cm^{-1}): 2928, 1730, 1621. ^1H NMR (500 MHz, $CDCl_3$) δ_H: 2.19 (s, 3H), 2.26 (s, 3H), 4.71 (s, 2H), 4.86 (s, 2H), 6.84 (s, 1H), 7.00–7.10 (m, 2H), 7.27–7.44 (m, 4H). MS *m/z*: 412, 414 (M^+). Anal. calcd. for $C_{21}H_{17}BrO_4$: C 61.03, H 4.15; found: C 60.17, H 4.10.

3-({4-[(2-Bromo-4-methylphenyl)oxy]but-2-ynyl}oxy)-2H-chromen-2-one (4i)

Yield: 69%; colorless solid; mp 107–109 °C (dichloromethane–hexane). IR (KBr, cm^{-1}): 2916, 1731, 1632. ^1H NMR (400 MHz, $CDCl_3$) δ_H : 2.20 (s, 3H), 4.78 (s, 2H), 4.86 (s, 2H), 7.04 (s, 1H), 7.21–7.44 (m, 7H). MS *m/z*: 398, 400 (M^+). Anal. calcd. for $C_{20}H_{15}BrO_4$: C 60.17, H 3.79; found: C 60.40, H 3.85.

3-({4-[(1-Bromonaphthalene-2-yl)oxy]but-2-ynyl}oxy)-2H-chromen-2-one (4j)

Yield: 77%; colorless solid; mp 103–105 °C (dichloromethane–hexane). IR (KBr, cm^{-1}): 2916, 1730, 1627. ^1H NMR (400 MHz, $CDCl_3$) δ_H: 4.83 (s, 2H), 4.93 (s, 2H), 6.84 (s, 1H), 7.04–7.14 (m, 10H). MS *m/z*: 434, 436 (M^+). Anal. calcd. for $C_{23}H_{15}BrO_4$: C 63.47, H 3.47; found: C 63.79, H 3.51.

3-({4-[(2-Bromophenyl)oxy]but-2-ynyl}oxy)-2H-chromen-2-one (4k)

Yield: 78%; colorless solid; mp 128–130 °C (dichloromethane–hexane). IR (KBr, cm^{-1}): 2917, 1734, 1617. ^1H NMR (400 MHz, $CDCl_3$) δ_H: 4.73 (s, 2H), 4.85 (s, 2H), 6.94 (s, 1H), 7.14–7.44 (m, 8H). MS *m/z*: 384, 386 (M^+). Anal. calcd. for $C_{19}H_{13}BrO_4$: C 59.24, H 3.40; found: C 59.36, H 3.37.

3-({4-[(2-Bromo-3-methylphenyl)oxy]but-2-ynyl}oxy)-2H-chromen-2-one (4l)

Yield: 80%; colorless solid; mp 163–165 °C (dichloromethane–hexane). IR (KBr, cm^{-1}): 2919, 1739, 1629. ^1H NMR (400 MHz, $CDCl_3$) δ_H: 2.31 (s, 3H), 4.77 (s, 2H), 4.86 (s, 2H), 6.84 (s, 1H), 7.03–7.43 (m, 7H). MS *m/z*: 398, 400 (M^+). Anal. calcd. for $C_{20}H_{15}BrO_4$: C 60.17, H 3.79; found: C 60.03, H 3.88.

General procedure for the preparation of compounds 5a–5l.

The compounds **5a–l** were synthesized according to the earlier published procedure (7).

8-{[(2-Bromo-6-methylphenyl)oxy]methyl}-1,3-dimethyl-2,3,4,6-tetrahydro-1H-pyrano[3,2-d]pyrimidine-2,4-dione (5a)

Yield 89%; colorless solid; mp 139–141 °C (acetonitrile–methanol). IR (KBr, cm^{-1}): 2957, 1696, 1648. ^1H NMR (400 MHz, $CDCl_3$) δ_H: 2.23 (s, 3H, $ArCH_3$), 3.40 (s, 3H, -NCH_3), 3.54 (s, 3H, -NCH_3), 4.58 (d, J = 4.8 Hz, 2H, -OCH_2), 4.71 (s, 2H, -OCH_2), 6.30 (t, J = 4.8 Hz, 1H), 7.25–754 (m, 3H). MS *m/z*: 392, 394 (M^+). Anal. calcd. for $C_{17}H_{17}N_2O_4Br$: C 51.92, H 4.36, N 7.12; found: C 52.09, H 4.45, N 7.09.

© 2008 NRC Canada

8-{[(2-Bromo-4,6-dimethylphenyl)oxy]methyl}-1,3-dimethyl-2,3,4,6-tetrahydro-1H-pyrano[3,2-d]pyrimidine-2,4-dione (5b)

Yield 83%; colorless solid; mp 175–177 °C (acetonitrile–methanol). IR (KBr, cm^{-1}): 2942, 1698, 1651. ^1H NMR (400 MHz, $CDCl_3$) δ_H: 2.21 (s, 3H, $ArCH_3$), 2.28 (s, 3H, $ArCH_3$), 3.39 (s, 3H, $-NCH_3$), 3.52 (s, 3H, $-NCH_3$), 4.58 (d, J = 4.8 Hz, 2H, $-OCH_2$), 4.69 (s, 2H, $-OCH_2$), 6.33 (t, J = 4.8 Hz, 1H), 6.92 (s, 1H), 7.20 (s, 1H). MS *m/z*: 406, 408 (M^+). Anal. calcd. for $C_{18}H_{19}N_2O_4Br$: C 53.08, H 4.70, N 6.88; found: C 53.36, H 4.54, N 6.93.

8-{[(2-Bromo-4-methylphenyl)oxy]methyl}-1,3-dimethyl-2,3,4,6-tetrahydro-1H-pyrano[3,2-d]pyrimidine-2,4-dione (5c)

Yield 81%; colorless solid; mp 105–108 °C (acetonitrile–methanol). IR (KBr, cm^{-1}): 3001, 2940, 1693, 1654. ^1H NMR (400 MHz, $CDCl_3$) δ_H: 2.26 (s, 3H, $ArCH_3$), 3.39 (s, 3H, $-NCH_3$), 3.48 (s, 3H, $-NCH_3$), 4.57 (d, J = 4.8 Hz, 2H, $-OCH_2$), 4.83 (s, 2H, $-OCH_2$), 6.26 (t, J = 4.8 Hz, 1H), 6.72 (d, J = 8.2 Hz, 1H), 7.02 (d, J = 8.1 Hz, 1H), 7.36 (s, 1H). MS *m/z*: 392, 394 (M^+). Anal. calcd. for $C_{17}H_{17}N_2O_4Br$: C 51.92, H 4.36, N 7.12; found: C 52.11, H 4.39, N 7.19.

8-{[(1-Bromonaphthlene-2-yl)oxy]methyl}-1,3-dimethyl-2,3,4,6-tetrahydro-1H-pyrano[3,2-d]pyrimidine-2,4-dione (5d)

Yield 86%; colorless solid; mp 115–117 °C (acetonitrile–methanol). IR (KBr, cm^{-1}): 3009, 1697, 1654. ^1H NMR (500 MHz, $CDCl_3$) δ_H: 3.40 (s, 3H, $-NCH_3$), 3.55 (s, 3H, $-NCH_3$), 4.59 (d, J = 4.9 Hz, 2H, $-OCH_2$), 5.02 (s, 2H, $-OCH_2$), 6.32 (t, J = 4.9 Hz, 1H), 7.16 (d, J = 7.2 Hz, 1H), 7.43 (t, J = 8.5 Hz, 1H), 7.57 (t, J = 8.3 Hz, 1H), 7.77 (m, 2H), 8.20 (d, J = 8.5 Hz, 1H). MS *m/z*: 428, 430 (M^+). Anal. calcd. for $C_{20}H_{17}N_2O_4Br$: C 55.96, H 3.99, N 6.53; found: C 55.87, H 4.03, N 6.59.

8-{[(2-Bromophenyl)oxy]methyl}-1,3-dimethyl-2,3,4,6-tetrahydro-1H-pyrano[3,2-d]pyrimidine-2,4-dione (5e)

Yield 85%; colorless solid; mp 133–135 °C (acetonitrile–methanol). IR (KBr, cm^{-1}): 2929, 1704, 1656. ^1H NMR (400 MHz, $CDCl_3$) δ_H: 3.40 (s, 3H, $-NCH_3$), 3.56 (s, 3H, $-NCH_3$), 4.59 (d, J = 4.8 Hz, 2H, $-OCH_2$), 4.82 (s, 2H, $-OCH_2$), 6.38 (t, J = 4.8 Hz, 1H), 6.90 (t, J = 8.0 Hz, 2H), 7.51 (d, J = 8.0 Hz, 2H). MS *m/z*: 378, 380 (M^+). Anal. calcd. for $C_{16}H_{15}N_2O_4Br$: C 50.68, H 3.99, N 7.39; found: C 50.95, H 3.92, N 7.41.

8-{[(2-Bromo-3-methylphenyl)oxy]methyl}-1,3-dimethyl-2,3,4,6-tetrahydro-1H-pyrano[3,2-d]pyrimidine-2,4-dione (5f)

Yield 81%; colorless solid; mp 101–104 °C (acetonitrile–methanol). IR (KBr, cm^{-1}): 3012, 2953, 1697, 1654. ^1H NMR (400 MHz, $CDCl_3$) δ_H: 2.40 (s, 3H, $ArCH_3$) 3.39 (s, 3H, $-NCH_3$), 3.47 (s, 3H, $-NCH_3$), 4.58 (d, J = 4.8 Hz, 2H, $-OCH_2$), 4.85 (s, 2H, $-OCH_2$), 6.30 (t, J = 4.8 Hz, 1H), 6.68 (d, J = 8.0 Hz, 1H), 6.92 (d, J = 8.0 Hz, 1H), 7.16 (t, J = 8.0 Hz, 1H, ArH). MS *m/z*: 392, 394 (M^+). Anal. calcd. for $C_{17}H_{17}N_2O_4Br$: C 51.92, H 4.36, N 7.12; found: C 51.99, H 4.38, N 7.23.

1-[(2-Bromo-6-methylphenyl)oxy]-3,5-dihydropyrano[2,3-c]chromen-5-one (5g)

Yield: 85%; colorless solid; mp 166–168 °C (dichloromethane – petroleum ether). IR (KBr, cm^{-1}): 2920, 1729, 1608. ^1H NMR (500 MHz, $CDCl_3$) δ_H: 2.29 (s, 3H), 4.80 (d, J = 4.2 Hz, 2H), 4.98 (s, 2H), 6.27 (t, J = 4.3 Hz, 1H), 7.21–7.64 (m, 7H). MS *m/z*: 398, 400 (M^+). Anal. calcd. for $C_{20}H_{15}BrO_4$: C 60.17, H 3.79; found: C 60.01, H 3.84.

1-[(2-Bromo-4,6-dimethylphenyl)oxy]-3,5-dihydropyrano[2,3-c]chromen-5-one (5h)

Yield: 90%; colorless solid; mp 145–147 °C (dichloromethane – petroleum ether). IR (KBr, cm^{-1}): 2923, 1725, 1608. ^1H NMR (500 MHz, $CDCl_3$) δ_H: 2.26 (s, 3H), 2.32 (s, 3H), 4.76 (d, J = 4.1 Hz, 2H), 4.99 (s, 2H), 6.23 (t, J = 4.1 Hz, 1H), 7.28–7.53 (m, 6H). MS *m/z*: 412, 414 (M^+). Anal. calcd. for $C_{21}H_{17}BrO_4$: C 61.03, H 4.15; found: C 61.32, H 4.24.

1-[(2-Bromo-4-methylphenyl)oxy]-3,5-dihydropyrano[2,3-c]chromen-5-one (5i)

Yield: 86%; colorless solid; mp 153–154 °C (dichloromethane – petroleum ether). IR (KBr, cm^{-1}): 2931, 1723, 1611. ^1H NMR (500 MHz, $CDCl_3$) δ_H: 2.30 (s, 3H), 4.78 (d, J = 4.3 Hz, 2H), 4.95 (s, 2H), 6.25 (t, J = 4.0 Hz, 1H), 7.21 (s, 1H), 7.26–7.52 (m, 5H), 8.07 (d, J = 7.9 Hz, 1H). MS *m/z*: 398, 400 (M^+). Anal. calcd. for $C_{20}H_{15}BrO_4$: C 60.17. H 3.79; found: C 60.27, H 3.83.

1-{(1-Bromonaphthalen-2-yl)oxy}-3,5-dihydropyrano[2,3-c]chromen-5-one (5j)

Yield: 86%; colorless solid; mp 190–192 °C (dichloromethane – petroleum ether). IR (KBr, cm^{-1}): 2864, 1721, 1605. ^1H NMR (500 MHz, $CDCl_3$) δ_H: 4.79 (d, J = 4.6 Hz, 2H), 5.14 (s, 2H), 6.36 (t, J = 4.5 Hz, 1H), 7.22 (d, J = 8.9 Hz, 1H), 7.25–7.28 (m, 1H), 7.36 (dd, J = 1.2, 8.2 Hz, 1H), 7.39–7.60 (m, 3H), 7.79–7.82 (m, 2H), 7.88 (dd, J = 1.0, 8.0 Hz, 1H), 8.22 (d, J = 8.5 Hz, 1H). MS *m/z*: 434, 436 (M^+). Anal. calcd. for $C_{23}H_{15}BrO_4$: C 63.47, H 3.47; found: C 63.54, H 3.50.

1-[(2-Bromophenyl)oxy]-3,5-dihydropyrano[2,3-c]chromen-5-one (5k)

Yield: 88%; colorless solid; mp 140–141 °C (dichloromethane – petroleum ether). IR (KBr, cm^{-1}): 2907, 1724, 1610. ^1H NMR (500 MHz, $CDCl_3$) δ_H: 4.81 (d, J = 4.1 Hz, 2H), 4.92 (s, 2H), 6.31 (t, J = 4.2 Hz, 1H), 7.20–7.71 (m, 8H). MS *m/z*: 384, 386 (M^+). Anal. calcd. for $C_{19}H_{13}BrO_4$: C 59.24, H 3.40; found: C 59.41, H 3.51.

1-[(2-Bromo-3-methylphenyl)oxy]-3,5-dihydropyrano[2,3-c]chromen-5-one (5l)

Yield: 84%; colorless solid; mp 169–171 °C (dichloromethane – petroleum ether). IR (KBr, cm^{-1}): 2909, 1720, 1620. ^1H NMR (400 MHz, $CDCl_3$) δ_H: 2.30 (s, 3H), 4.76 (d, J = 4.2 Hz, 2H), 4.93 (s, 2H), 6.27 (t, J = 4.1 Hz, 1H), 7.18–7.69 (m, 7H). MS *m/z*: 398, 400 (M^+). Anal. calcd. for $C_{20}H_{15}BrO_4$: C 60.17, H 3.79; found: C 60.30, H 3.72.

© 2008 NRC Canada

General procedure for the radical cyclization of compounds 5

A suspension of the compounds **5** (0.30 mmol, 0.01mol/L), *n*-Bu_3SnH (0.08 mL, 0.30 mmol), and AIBN (25 mg) in dry degassed toluene (for **5a**–**f**) or benzene (for **5g**–**l**) were heated for 3–4 h under N_2. After the completion of the reaction the solvent was removed under reduced pressure. The residue was dissolved in CH_2Cl_2 (15 mL) and stirred with 10% aqueous KF solution (10 mL) for 1 h. The aqueous phase was extracted with CH_2Cl_2 (3 × 10 mL). The combined CH_2Cl_2 extract was washed with water (2 × 20 mL) and then brine solution (1 × 20 mL), and was dried (Na_2SO_4). The solvent was removed and the residual mass was subjected to column chromatography over silica gel using petroleum ether – ethyl acetate as eluant to give **6a**–**l**. Compounds **6a**–**f** were recrystallized from acetonitrile–methanol mixture and compounds **6g**–**l** were recrystalized from dichloromethane – petroleum ether (60–80 °C).

2,4,7-Trimethyl-1,2,3,4,4b,5,10b,11-octahydrochromeno[3′,4′:4,5]pyrano[3,2-d]pyrimidine-1,3-dione (6a)

Yield: 81%; colorless solid; mp 171–172 °C (acetonitrile–methanol). IR (KBr, cm^{-1}): 1655, 1633. ^1H NMR (500 MHz, $CDCl_3$) δ_H: 2.20 (s, 3H, $ArCH_3$), 3.24 (dt, *J* = 3.8, 11.6 Hz, 1H), 3.36 (dt, *J* = 3.8, 11.7 Hz, 1H), 3.41 (s, 3H, -NCH_3), 3.52 (s, 3H, -NCH_3), 3.90 (t, *J* = 11.2 Hz, 1H), 4.00 (t, *J* = 11.3 Hz 1H), 4.46 (ddd, *J* = 1.8, 4.3, 11.6 Hz, 1H), 4.53 (ddd, *J* = 1.3, 4.3, 11.6 Hz, 1H), 6.87 (t, *J* = 7.5 Hz, 1H), 7.00 (d, *J* = 7.5 Hz, 1H), 7.07 (d, *J* = 7.2 Hz, 1H). MS *m*/*z*: 314 (M^+). Anal. calcd. for $C_{17}H_{18}N_2O_4$: C 64.96, H 5.77, N 8.91; found: C 65.18, H 5.85, N 8.99.

2,4,7,9-Tetramethyl-1,2,3,4,4b,5,10b,11-octahydrochromeno[3′,4′:4,5]pyrano[3,2-d]pyrimidine-1,3-dione (6b)

Yield: 86%; colorless solid; mp 190–192 °C (acetonitrile–methanol). IR (KBr, cm^{-1}): 1657, 1633. ^1H NMR (500 MHz, $CDCl_3$) δ_H: 2.21 (s, 3H, $ArCH_3$), 2.32 (s, 3H, $ArCH_3$), 3.23 (dt, *J* = 4.4, 11.6 Hz, 2H), 3.41 (s, 3H, -NCH_3), 3.51 (s, 3H, -NCH_3), 3.90 (t, *J* = 11.2 Hz, 1H), 3.93 (t, *J* = 11.4 Hz, 1H), 4.47 (ddd, *J* = 1.3, 4.1, 11.3 Hz, 1H), 4.55 (ddd, *J* = 1.8, 4.1, 11.4 Hz, 1H), 6.79 (s, 1H), 6.89 (s, 1H). ^{13}C NMR (75.5MHz, $CDCl_3$): δ_C 16.2, 20.8, 28.9, 31.3, 31.8, 32.9, 65.7, 67.7, 117.7, 126.7, 127.4, 127.9, 130.7, 131.5, 132.2, 150.8, 151.1, 158.7. MS *m*/*z*: 328 (M^+). Anal. calcd. for $C_{18}H_{20}N_2O_4$: C 65.84. H 6.14, N 8.53; found: C 66.02, H 6.11, N 8.56.

2,4,9-Trimethyl-1,2,3,4,4b,5,10b,11-octahydrochromeno[3′,4′:4,5]pyrano[3,2-d]pyrimidine-1,3-dione (6c)

Yield: 85%; colorless solid; mp 130–132 °C (acetonitrile–methanol). IR (KBr, cm^{-1}): 1651, 1627. ^1H NMR (500 MHz, $CDCl_3$) δ_H: 2.29 (s, 3H, $ArCH_3$), 3.30 (dt, *J* = 4.4, 11.7 Hz, 2H), 3.41(s, 3H, -NCH_3), 3.50 (s, 3H, -NCH_3), 3.91 (t, *J* = 11.2 Hz, 2H), 4.44 (ddd, *J* = 1.7, 4.5, 11.3 Hz, 2H), 6.78 (d, *J* = 8.2 Hz, 1H), 6.95 (s, 1H), 7.01 (t, *J* = 8.1 Hz, 1H). MS *m*/*z*: 314 (M^+). Anal. calcd. for $C_{17}H_{18}N_2O_4$: C 64.96, H 5.77, N 8.91; found: C 65.19, H 5.79, N 8.88.

2,4-Dimethyl-1,2,3,4,4b,5,12c,13-octahydrobenzo[5′,6′]chromeno[3′,4′:4,5] pyroano[3,2-d]pyrimidine-1,3-dione (6d)

Yield: 76%; colorless solid; mp 156–157 °C (acetonitrile–methanol). IR (KBr, cm^{-1}): 1654, 1631. ^1H NMR (500 MHz, $CDCl_3$) δ_H: 3.35 (dt, *J* = 3.8, 11.0 Hz, 1H), 3.44 (s, 3H, -NCH_3), 3.54 (s, 3H, -NCH_3), 3.88 (dt, *J* = 3.9, 11.4 Hz, 1H), 4.00 (t, *J* = 11.4 Hz, 1H), 4.16 (t, *J* = 11.3 Hz, 1H), 4.57 (dd, *J* = 2.4, 11.6 Hz, 1H), 4.86 (dd, *J* = 3.2, 11.8 Hz, 1H), 7.06 (d, *J* = 8.9 Hz, 1H), 7.39 (t, *J* = 7.6 Hz, 1H), 7.54 (t, *J* = 8.2 Hz, 1H), 7.71 (t, *J* = 8.9 Hz, 1H), 7.80 (d, *J* = 8.1 Hz, 1H), 7.90 (d, *J* = 8.5 Hz, 1H). MS *m*/*z*: 350 (M^+). Anal. calcd. for $C_{20}H_{18}N_2O_4$: C 68.56, H 5.18, N 8.00; found: C 68.73, H 5.22, N 8.13.

2,4-Dimethyl-1,2,3,4,4b,5,10b,11-octahydrochromeno[3′,4′:4,5]pyrano[3,2-d]pyrimidine-1,3-dione (6e)

Yield: 89%; colorless solid; mp 200-202 °C (acetonitrile–methanol). IR (KBr, cm^{-1}): 1651, 1623. ^1H NMR (300 MHz, $CDCl_3$) δ_H: 3.17–3.36 (m, 2H), 3.41 (s, 3H, -NCH_3), 3.51 (s, 3H, -NCH_3), 4.00 (dt, *J* = 4.1, 11.1Hz, 2H), 4.47–4.50 (m, 2H), 6.89–7.36 (m, 4H). MS *m*/*z*: 300 (M^+). Anal. calcd. for $C_{16}H_{16}N_2O_4$: C 63.99, H 5.37, N 9.33; found: C 64.08, H 5.45, N 9.49.

2,4,10-Trimethyl-1,2,3,4,4b,5,10b,11-octahydrochromeno[3′,4′:4,5]pyroano[3,2-d]pyrimidine-1,3-dione (6f)

Yield: 81%; colorless solid; mp 144–146 °C (acetonitrile–methanol). IR (KBr, cm^{-1}): 1667, 1624. ^1H NMR (500 MHz, $CDCl_3$) δ_H: 2.35 (s, 3H, $ArCH_3$), 3.24 (dt, *J* = 4.1, 11.1 Hz, 2H), 3.41(s, 3H, -NCH_3), 3.50 (s, 3H, -NCH_3), 3.88 (t, *J* = 11.5 Hz, 1H), 4.01 (t, *J* = 11.3 Hz 1H), 4.49 (dd, *J* = 4.3, 11.6 Hz, 1H), 4.56 (dd, *J* = 1.8, 11.6 Hz, 1H), 6.74–7.14 (m, 3H). MS *m*/*z*: 314 (M^+). Anal. calcd. for $C_{17}H_{18}N_2O_4$: C 64.96, H 5.77, N 8.91; found: C 65.01, H 5.89, N 8.98.

9-Methyl-6c,7,12b,13-tetrahydro-1H-chromeno[3′,4′:4,5]pyrano[2,3-c]chromen-1-one (6g)

Yield: 75%; colorless solid; mp 124–125 °C (dichloromethane – petroleum ether). IR (KBr, cm^{-1}): 2919, 1731, 1623. ^1H NMR (500 MHz, $CDCl_3$) δ_H: 2.23 (s, 3H), 3.34 (dt, *J* = 4.4, 10.4 Hz, 1H), 3.56 (dt, *J* = 4.0, 11.0 Hz, 1H), 3.97 (t, *J* = 11.5 Hz, 1H), 4.18 (t, *J* = 11.6 Hz, 1H), 4.61 (dd, *J* = 4.5, 12.6 Hz, 1H), 4.74 (dd, *J* = 2.0, 11.6 Hz, 1H), 6.84–7.10 (m, 3H), 7.33–7.71 (m, 4H). MS *m*/*z*: 320 (M^+). Anal. calcd. for $C_{20}H_{16}O_4$: C 74.99, H 5.03; found: C 75.23, H 5.18.

9,11-Dimethyl-6c,7,12b,13-tetrahydro-1H-chromeno[3′,4′:4,5]pyrano[2,3-c]chromen-1-one (6h)

Yield: 82%; colorless solid; mp 181–183 °C (dichloromethane – petroleum ether). IR (KBr, cm^{-1}): 2921, 1737, 1623. ^1H NMR (500 MHz, $CDCl_3$) δ_H: 2.20 (s, 3H), 2.28 (s, 3H), 3.33 (dt, *J* = 4.2, 10.2 Hz, 1H), 3.57 (dt, *J* = 4.1, 11.3 Hz, 1H), 3.93 (t, *J* = 11.3 Hz, 1H), 4.16 (t, *J* = 11.7 Hz, 1H), 4.60 (dd, *J* = 4.3, 11.5 Hz, 1H), 4.71 (dd, *J* = 2.6, 11.5 Hz, 1H), 6.84 (s, 1H), 6.91 (s, 1H), 7.33–7.70 (m, 4H). MS *m*/*z*: 334 (M^+). Anal. calcd. for $C_{21}H_{18}O_4$: C 75.43, H 5.43; found: C 75.50, H 5.38.

© 2008 NRC Canada

***11-Methyl-6c,7,12b,13-tetrahydro-1*H-*chromeno[3′,4′:4,5]pyrano[2,3-c]chromen-1-one (6i)**

Yield: 76%; colorless solid; mp 141–144 °C (dichloromethane – petroleum ether). IR (KBr, cm^{-1}): 2930, 1735, 1624. ^{1}H NMR (500 MHz, $CDCl_3$) δ_H: 2.31 (s, 3H), 3.34 (dt, J = 4.4, 10.7 Hz, 1H), 3.59 (dt, J = 4.0, 11.0 Hz, 1H), 3.94 (t, J = 11.3 Hz, 1H), 4.17 (t, J = 11.7 Hz, 1H), 4.61 (dd, J = 4.1, 11.6 Hz, 1H), 4.67 (dd, J = 2.6, 12.6 Hz, 1H), 6.82 (d, J = 8.2 Hz, 1H), 7.00 (s, 1H), 7.03 (d, J = 8.3 Hz, 1H), 7.33–7.46 (m, 3H), 7.65 (d, J = 7.7 Hz, 1H). MS m/z: 320 (M^+). Anal. calcd. for $C_{20}H_{16}O_4$: C 74.99, H 5.03; found: C 75.12, H 5.09.

***4c,5,12c,13-Tetrahydro-7*H-*benzo[f]chromeno[4′,3′:5,6]pyrano[4,3-c]chromen-7-one (6j)**

Yield: 90%; colorless solid; mp 201–202 °C (dichloromethane – petroleum ether). IR (KBr, cm^{-1}): 2916, 1727, 1620. ^{1}H NMR (500 MHz, $CDCl_3$) δ_H: 3.69 (dt, J = 4.2, 11.3 Hz, 1H), 3.95 (dt, J = 4.1, 11.4 Hz, 1H), 4.20 (t, J = 11.5 Hz, 1H), 4.24 (t, J = 11.5 Hz, 1H), 4.77 (dd, J = 3.7, 11.6 Hz, 1H), 5.00 (dd, J = 3.0, 12.0 Hz, 1H), 7.10 (d, J = 8.1 Hz, 1H), 7.35–7.59 (m, 5H), 7.68 (d, J = 7.7 Hz, 1H), 7.72 (d, J = 6.7 Hz, 1H), 7.81 (d, J = 8.0 Hz, 1H), 7.95 (d, J = 8.5 Hz, 1H). MS m/z: 356 (M^+). Anal. calcd. for $C_{23}H_{16}O_4$: C 77.52, H 4.53; found: C 77.76, H 4.63.

***6c,7,12b,13-Tetrahydro-1*H-*chromeno[3′,4′:4,5]pyrano[2,3-c]chromen-1-one (6k)**

Yield: 86%; colorless solid; mp 176–177 °C (dichloromethane – petroleum ether). IR (KBr, cm^{-1}): 2919, 1725, 1621. ^{1}H NMR (500 MHz, $CDCl_3$) δ_H: 3.38–3.43 (m, 1H), 3.61–3.65 (m, 1H), 3.98 (t, J = 11.4 Hz, 1H), 4.19 (t, J = 11.8 Hz, 1H), 4.62 (dd, J = 4.5, 11.6 Hz, 1H), 4.68 (dd, J = 2.8. 11.6 Hz, 1H), 6.93 (d, J = 8.1 Hz, 1H), 6.98 (t, J = 7.3 Hz, 1H), 7.21–7.46 (m, 5H), 7.65(d, J = 7.8 Hz, 1H). ^{13}C NMR (125 MHz, $CDCl_3$) δ_c: 30.0, 31.6, 66.0, 68.6, 117.6, 117.8, 118.9, 119.5, 120.9, 121.9, 122.4, 125.4, 129.2, 129.5, 130.4, 140.5, 149.8, 155.3, 156.9. MS: m/z = 306 (M^+). Anal. calcd. for $C_{19}H_{14}O_4$: C 74.50, H 4.61; found: C 74.81, H 4.72.

***12-Methyl-6c,7,12b,13-tetrahydro-1*H-*chromeno[3′,4′:4,5]pyrano[2,3-c]chromen-1-one (6l)**

Yield: 85%; colorless solid; mp 143–145 °C (dichloromethane – petroleum ether). IR (KBr, cm^{-1}): 2917, 1735, 1619. ^{1}H NMR (300 MHz, $CDCl_3$) δ_H: 2.23 (s, 3H), 3.38–3.41 (m, 1H), 3.61–3.65 (m, 1H), 3.96 (t, J = 10.9 Hz, 1H), 4.17 (t, J = 11.2 Hz, 1H), 4.62 (dd, J = 3.9, 11.4 Hz, 1H), 4.74 (dd, J = 2.5, 11.2 Hz, 1H), 6.90–7.70 (m, 7H). MS m/z: 320 (M^+). Anal. calcd. for $C_{20}H_{16}O_4$: C 74.99, H 5.03; found: C 74.85, H, 5.07.

Acknowledgements

We thank the Council of Scientific and Industrial Research (CSIR), New Delhi, and the Department of Science and Technology (DST), New Delhi, for financial assistance. PKM and PD are thankful to the University Grants Commission (UGC), New Delhi, and CSIR for their respective fellowships.

References

1. Coumarin biological activities: For an extensive bibliography, see: J. Wu, Y. Liao, and Z. Yang J. Org. Chem. **66**, 3642 (2001).
2. (*a*) A.A. Deans. J. Med. Chem. **26**, 580 (1983); (*b*) M. Gordon, S.H. Grover, and J.B. Strothers. Can. J. Chem. **51**, 2092 (1973); (*c*) E. Wenkert and B.L.J. Buckwalter. J. Am. Chem. Soc. **94**, 4367 (1972). (*d*) D. Guilet, J.J. Helesbeux, D. Seraphin, T. Sevenet, P. Richomme, and J. Bruneton J. Nat. Prod. **64**, 563 (2001); (*e*) O. Thastrup and B. Fjalland. J. Lemmich Acta Pharmacol. Toxicol. **52**, 246 (1983); (*f*) S.Y. Kang, K.Y. Lee, S.H. Sung, M.J. Park, and Y.C. Kim J. Nat. Prod. **64**, 683 (2001).
3. (*a*) F.M. Dean. Naturally occurring oxygen ring compounds. Butterworths, London. 1963; (*b*) P. Von. Lauger and H. Motrin. Helv. Chem. Acta, **27**, 892 (1944) (*c*) T.O. Soine. J. Pharm. Soc. **53**, 231 (1964).
4. C. Heidelberger. Pyrimidine and Pyrimidine Antimetabolites. *In* Cancer Medicine, 2nd ed. *Edited by* J.F. Holland and E. Frei III. Lea & Febiger. Philadelphia, PA. 1984. p. 801.
5. (*a*) E. De Clercq, J. Descamps, P. De Somer, P.J. Barr, A.S. Jones, and R.T. Walker. Proc. Natl. Acad. Sci. USA **76**, 2957 (1979); (*b*) C. Heidelberger and D.H. King. *In* Antiviral Agents in Pharmacology and Therapeutics. Vol. 6. *Edited by* D. Shugar. Pergamon, Oxford. 1979. p. 427.
6. (*a*) C. Macllwain. Nature, **365**, 378 (1993); (*b*) R.C. Gallo. Sci. Am. **255**, 78 (1986); (*c*) R.C. Gallo. Sci. Am. **256**, 38 (1987).
7. (*a*) K.C. Majumdar and U. Das. J. Org. Chem. **63**, 9997 (1998); (*b*) K.C. Majumdar, P. Chatterjee, and S. Saha. Tetrahedron Lett. **39**, 7147 (1998).
8. (*a*) K.C. Majumdar, P. Debnath, and P.K. Maji. Tetrahedron Lett. **48**, 5265 (2007); (*b*) K.C. Majumdar, P.K. Basu, P.P. Mukhopadhyay, S. Sarkar, S.K. Ghosh, and P. Biswas. Tetrahedron **59**, 2151 (2003).
9. (*a*) B. Giese. *In* Radicals in organic synthesis: Formation of Carbon–Carbon Bonds. Pergamon, Oxford. 1986; (*b*) *In* Radicals in organic synthesis. Vol. 1. *Edited by* P. Renaud and M. Sibi. Wiley-VCH, Weinheim. 2001; (*c*) M. Malacria. Chem. Rev. **96**, 289 (1996); (*d*) C.P. Jasperse, D.P. Curran, and T.L. Fevig. Chem Rev. **91**, 1237 (1991); (*e*) K.C. Majumdar and P.K. Basu. Heterocycles, **57**, 2413 (2002); (*f*) W.R. Bowman, A.J. Fletcher, and G.B.S. Pots. J. Chem. Soc. Perkin Trans. 1, 2747 (2002); (*g*) K.C. Majumdar, P.K. Basu, and P.P. Mukhopadhyay. Tetrahedron, **60**, 6239 (2004); (*h*) D.P. Curran. Synthesis, 417 (1988).
10. (*a*) V. Snieckus. Bull. Soc. Chim. Fr. 67 (1988); (*b*) D.C. Harrowven. Tetrahedron Lett. **34**, 5653 (1993); (*b*) M.L.E.N. Da Mata, W.B. Motherwell, and F. Ujjainwalla. Tetrahedron Lett. **38**, 141, (1997); (*c*) D.C. Harrowven and R. Browne. Tetrahedron Lett. **35**, 5301 (1994); (*d*) D.C. Harrowven, B.J. Sutton, and S. Coulton. Tetrahedron, **58**, 3387 (2002); (*e*) R.J. Sundberg and R.J. Cherney. J. Org. Chem. **55**, 6028 (1990); (*f*) O. Tsuge, T. Hatta, and H. Tsuchiyama. Chem. Lett. 155 (1998); (*g*) A. Fiumana and K. Jones. Tetrahedron Lett. **41**, 4209 (2000); (*h*) E. Bonfand, L. Forslund, W.B. Motherwell, and S. Vazquez. Synlett, 475 (2000).
11. (*a*) H. Ishibashi. Chem. Rec. 6, 23 (2006); (*b*) J. Cassayre, F. Gagosz, and S.Z. Zard. Angew. Chem. Int. Ed. **41**, 1783 (2002); (*c*) H. Ishibashi, I. Kato, Y. Takeda, M. Kogure, and O. Tamura. Chem. Commun. (Cambridge), 1527 (2000); (*d*) E.W. Della and S.D.J. Graney. J. Org. Chem. **69**, 3824 (2004) (*e*) A.A. Ponaras and O. Zaim. Tetrahedron Lett. **41**, 2279 (2000).

© 2008 NRC Canada

12. (*a*) A.L.J. Beckwith, I.A. Blair, and G. Philipou. Tetrahedron Lett. **15**, 2251 (1974); (*b*) A.L. J. Beckwith, and D.M. O'Shea. Tetrahedron Lett. **27**, 4525 (1986); (*c*) U. Albrecht, R. Wartchow, and H.M.R. Hoffmann. Angew. Chem. Int. Ed. **31**, 910 (1992).
13. (*a*) K.C. Majumdar and S. Muhuri. Synthesis, 2725 (2006); (*b*) K. C. Majumdar and M. Jana Synth. Commun. **37**, 1735 (2007).
14. K.C. Majumdar, P. Debnath, A.K. Pal, S.K. Chattopadhyay, and A. Biswas. Can. J. Chem. **85**, 445 (2007).
15. (*a*) E.J. Enholm and K.S. Kinter. J. Org. Chem. **60**, 4850 (1995); (*b*) E.J. Enholm, E.J. Prasad, and K.S. Kinter. J. Am. Chem. Soc. **113**, 7784 (1991).
16. A.N. Abeywickrema, A.L.J. Beckwith, and S. Gerba. J. Org. Chem. **52**, 4072 (1987).

© 2008 NRC Canada

REVIEW / SYNTHÈSE

Mechanistic principles and applications of resonance energy transfer

David L. Andrews

Abstract: Resonance energy transfer is the primary mechanism for the migration of electronic excitation in the condensed phase. Well-known in the particular context of molecular photochemistry, it is a phenomenon whose much wider prevalence in both natural and synthetic materials has only slowly been appreciated, and for which the fundamental theory and understanding have witnessed major advances in recent years. With the growing to maturity of a robust theoretical foundation, the latest developments have led to a more complete and thorough identification of key principles. The present review first describes the context and general features of energy transfer, then focusing on its electrodynamic, optical, and photophysical characteristics. The particular role the mechanism plays in photosynthetic materials and synthetic analogue polymers is then discussed, followed by a summary of its primarily biological structure determination applications. Lastly, several possible methods are described, by the means of which all-optical switching might be effected through the control and application of resonance energy transfer in suitably fabricated nanostructures.

Key words: FRET, Förster energy transfer, photophysics, fluorescence, laser.

Résumé : Dans une phase condensée, le transfert de l'énergie de résonance est le mécanisme primaire pour la migration de l'excitation électronique. Bien connu dans le contexte particulier de la photochimie moléculaire, c'est un phénomène dont la prévalence beaucoup plus grande tant dans les matériaux naturels que ceux de synthèse n'a été appréciée que lentement et pour laquelle la théorie fondamentale et sa compréhension ont fait des progrès importants au cours des dernières années. Avec la maturité croissante de bases théoriques solides, les derniers développements ont conduit à une identification complète des principes fondamentaux. Le présente revue décrit d'abord le contexte et les caractéristiques générales du transfert d'énergie avant de passer à une mise au point de ses caractéristiques électrodynamiques et photophysiques. On discute ensuite du rôle particulier que joue le mécanisme dans les matériaux photosynthétiques et les polymères synthétiques analogues et puis on résume ses applications principalement dans la détermination des structures biologiques. Enfin, on décrit plusieurs méthodes potentielles à l'aide desquelles il serait possible d'effectuer des commutations complètement optiques par le biais du contrôle et de l'application du transfert de l'énergie de résonance dans des nanostructures fabriquées d'une façon appropriée.

Mots-clés : « FRET », transfert d'énergie Förster, photophysique, fluorescence, laser.

[Traduit par la Rédactions]

1. Introduction

In a variety of complex materials, the close juxtaposition of basic units with suitable spectral character leads to a remarkable phenomenon: the absorption of light by one molecular species produces fluorescence unambiguously attributable to another. The effect is most readily apparent in chemical systems comprising two or more light-absorbing components (chromophores) with well-characterized absorption and fluorescence bands at broadly similar, but experimentally differentiable wavelengths. Observations of such phenomena illustrate the operation of a fundamental mechanism (the transfer of energy between molecules or chromophores) known as resonance energy transfer (RET) (1–3).[1] It is a mechanism that is found to operate across a chemically diverse and extensive range of systems, encompassing protein complexes, doped crystals, and solutions, to name but a few. Moreover, it also operates in systems where the end re-

Received 3 April 2008. Accepted 25 April 2008. Published on the NRC Research Press Website at canjchem.nrc.ca on 17 July 2008.

D.L. Andrews. School of Chemical Sciences, University of East Anglia, Norwich NR4 7TJ, United Kingdom (e-mail: d.l.andrews@uea.ac.uk).

[1]Also electronic energy transfer (EET); both terms are widely used.

 doi:10.1139/V08-099 © 2008 NRC Canada

Fig. 1. Typical spectral discrimination between the fluorescence from donor and acceptor species (here, notionally based on a cyan fluorescent protein donor and a yellow fluorescent protein acceptor): (*a*) the transmission characteristics of a short-wavelength filter ensure initial excitation of only the donor; a dichroic beam-splitter and another narrow emission filter ensuring that only the (Stokes-shifted) fluorescence from the donor reaches a detector; (*b*) in the same system, a longer-wavelength emission filter ensures capture of only the acceptor fluorescence, following RET.

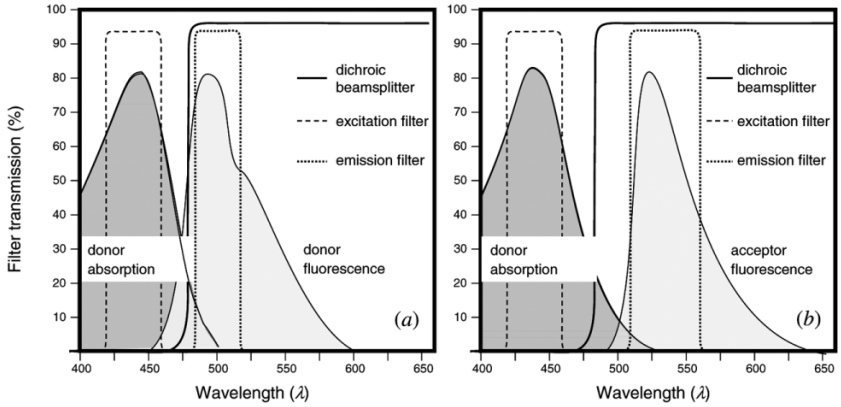

sult of optical absorption is not the release of energy in the form of fluorescence but optical frequency up-conversion or excitation capture in the form of chemical energy.

The singular properties of RET allow the flow of energy to exhibit a directed character (4–7). In complex multi-chromophore materials this effect contributes to a crucial, property-determining characteristic for the channeling of electronic excitation in photosynthetic systems (8), and the same principles are emulated in synthetic energy-harvesting systems such as the fractal polymers known as "dendrimers" (9). However, the observation and applications of RET extend well beyond the technology of light harvesting into numerous areas, several of which will be illustrated in later sections of this review. The phenomenon has an important function in the operation of organic light-emitting diodes (OLEDs) and luminescence detectors (10–14): in crystalline solids and glasses doped with transition metal ions, mechanisms based on RET are also engaged for laser frequency conversion (15–19). In the fields of optical communications and computation, a number of optical-switching and logic-gate devices are founded on the same principle (20–22). In the realm of molecular biology, the determination of protein structures and the characterization of dynamical processes is furthered by studies of the transfer of energy between intrinsic or "tag" chromophores (23–28); other ultra-sensitive molecular-imaging applications are again based on the same underlying principle (29–31). Further applications include the study of polymer interfaces (32), energy-transfer systems designed to act as sensitizers for photodynamic therapy (33), and as analyte-specific sensors (34–36).

The structure of the review is as follows: Section 2 describes the nature and general features of RET, focusing on its optical and photo-physical characteristics, and its uses in molecular structure determination: the underlying electromagnetic mechanism is addressed in more detail in Section 3. In Section 4, the particular role that energy transfer plays in photosynthetic materials and synthetic analogue polymers is discussed. Several possible methods are then described, in Section 5, for exerting optical control over RET, leading into a more general discussion of novel applications and nano-devices in the concluding Section 6.

2. Nature and characteristics of resonance energy transfer

To begin, it is appropriate to review the major features of RET. In this section, where the common attributes are first identified, "chromophore" is used as a generic term for the individual particles between which energy is exchanged. In crystalline, semi-crystalline, or glassy media, these centers of photon absorption (and subsequent energy release) may in fact take the form of ions, atoms, or colour centers; in other types of medium they may be small molecules, electronically distinct parts of large molecules, or nanoparticles, such as quantum dots. For their role in each transfer event, the participating chromophores in any such medium are designated "donor" and "acceptor", though it should be understood that any single chromophore acting in the capacity of acceptor for one transfer event may subsequently become the donor for a subsequent RET process.

A. Migration of electronic excitation in the condensed phase

When resonant ultraviolet or visible radiation impinges on any non-homogeneous dielectric material, the primary result of photon absorption is the population of electronic excited states in individual atomic, molecular, or other nanoscale centers. Typically, such absorption is followed immediately by a rapid but partial degradation of the acquired energy; the associated losses (largely due to vibrational dissipation) ultimately to be manifest in the form of heat. However, if any nearby chromophore has a suitably disposed electronic state, of a similar or slightly lower energy, that neighbour may acquire the major part of the electronic excitation through resonance energy transfer (a process that takes place well before thermal degradation of the excited state energy nears completion). The process is most commonly studied through spectrometric differentiation of fluorescence emerging from the initially excited energy donor and from the energy acceptor species, as illustrated in Fig. 1.

As will be shown in the following, the propensity for energy to be transferred between any two chromophores is severely restricted by distance, and if no suitable acceptor is

© 2008 NRC Canada

within reach, the donor will generally shed its energy by fluorescence or local dissipation. Conversely, any flow of energy that extends beyond conventional molecular dimensions will usually comprise a series of small-scale hops between near-neighbours. Pair interactions are therefore not only important in systems where the absorption of optical energy leads by direct transfer to the excitation of acceptor species; such interactions are also significant as representative components of the overall flow in complex, multichromophore systems. As such, it is appropriate to focus on the detailed character of these pair-transfer events.

B. Spectral overlap and the Förster equation

Though other possibilities exist, most transitions of donor decay and acceptor excitation are electric-dipole-allowed. Accordingly, the theory of pair transfer, beyond any region of wavefunction overlap, is traditionally based on electrodynamical coupling between transition dipoles. The first such formulation of the theory, which identified the inverse sixth power distance dependence (now often considered a hallmark of the transfer process) was made by Förster (37). Subsequently recast in quantum mechanical terms and experimentally verified by Latt et al. (38), this early theory of "radiationless" energy transfer remains widely applicable. Nonetheless, the Förster theory is subject to some conditions that were not originally appreciated, and it is not uncommon to find literature on the subject still perpetuating initial overstatements. Certain sources (see, for example, iupac.org) wrongly treat Förster "radiationless" energy transfer as exact, distinct, and separable from "radiative" energy transfer (the latter signifying successive but independent processes of fluorescence emission by a donor and capture of the ensuing photon by an acceptor). Although that certainly is the observed character of resonance energy transfer over relatively long distances, as for example between donor and acceptor components in a dilute solution, it is now known that both radiative and Förster transfer are simply the long- and short-range limits of one powerful, all-pervasive mechanism, as will be discussed in Section 3.

With this caution in mind, let us proceed to consider the pairwise transfer of excitation between two chromophores *A* and *B*. In the context of this elementary mechanism (potentially one RET component of a complex, multi-step migration process), *A* is designated the donor and *B* the acceptor. Specifically, let it be assumed that prior excitation of the donor generates an electronically excited species *A**. Forward progress of the energy is then accompanied by donor decay to the ground electronic state. Acquiring the energy, *B* undergoes a transition from its ground to its excited state. The complete RET process may be expressed by the following chemical equation:

$$[1] \qquad A^* + B \xrightarrow{\text{RET}} A + B^*$$

The excited acceptor, *B**, subsequently decays either in a further transfer event, or by another means, such as fluorescence. Because the *A** and *B** excited states are real, with measurable lifetimes, the core process of energy transfer itself is fundamentally separable from the initial electronic excitation of *A* and the eventual decay of *B*; the latter processes do not, therefore, enter into the theory of the pair transfer.

Fig. 2. Energetics and spectral overlap features (top) for energy transfer from *A* to *B* (and below, potentially backward transfer from *B* to *A*). For each chromophore, *F* denotes the fluorescence spectrum and σ the absorption. Wavy downward lines denote vibrational dissipation.

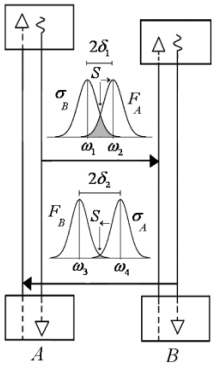

To delve more deeply into the nature of the process, it needs to be recognized that eq. [1] tells only part of the story, dealing as it does with only electronic excitations. In general, other dissipative processes are engaged (such features will be discussed in detail in later sections). In a solid, the linewidth of optical transitions manifests the influence of local electronic environments, which, in the case of strong coupling, may lead to the production of phonon sidebands. Similar effects in solutions or disordered solids represent inhomogeneous interactions with a solvent or host, while the broad bands exhibited by chromophores in complex molecular systems signify extensively overlapped vibrational levels, including those associated with skeletal modes of the superstructure. In each case, the level broadening allows pair transfer to occur at any energy level within the region of overlap between the donor emission and acceptor absorption bands, as illustrated in Fig. 2 (39).

For any donor–acceptor separation, *R*, substantially smaller than the wavelengths of visible radiation, the Förster theory gives the following expression for the rate of pairwise energy transfer w_F, for systems where the common host material for the donor and acceptor has refractive index *n*, at the optical frequency corresponding to the mean transferred energy (40):

$$[2] \qquad w_F = \frac{9\kappa^2 c^4}{8\pi\tau_{A^*} n^4 R^6} \int F_A(\omega)\sigma_B(\omega)\frac{d\omega}{\omega^4}$$

In this expression, $F_A(\omega)$ is the normalized fluorescence spectrum of the donor, τ_{A^*} is the associated radiative decay lifetime (related to the measured fluorescence lifetime τ_{fl} through the fluorescence quantum yield $\eta = \tau_{fl}/\tau_{A^*}$), $\sigma_B(\omega)$ is the linear absorption cross-section of the acceptor, ω is an optical frequency in radians per unit time, and *c* is the speed of light. The spectral functions F_A and σ_B are mathematically defined and discussed in detail in Section 3. As is evident from Fig. 2, the propensity for forward transfer is usually significantly greater than that for backward transfer owing to a sizeable difference in the spectral overlaps for the two processes. This feature, which is highly important in

© 2008 NRC Canada

Fig. 3. Relative orientations and positions of the donor and acceptor and their transition moments: (*a*) angles θ_A and θ_B subtended by donor and acceptor transition moments (not necessarily in the plane of the drawing) against the inter-chromophore displacement vector; (*b*) in-plane angle θ_T between the transition moments.

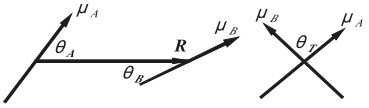

determining the efficiency of energy harvesting materials, is to be discussed in detail in Section 4.

The κ factor in [2] depends on the orientations of the donor and acceptor, both with respect to each other, and with respect to their mutual displacement unit vector $\hat{\boldsymbol{R}}$, as follows:

$$[3] \qquad \kappa = (\hat{\boldsymbol{\mu}}_A \cdot \hat{\boldsymbol{\mu}}_B) - 3(\hat{\boldsymbol{R}} \cdot \hat{\boldsymbol{\mu}}_A)(\hat{\boldsymbol{R}} \cdot \hat{\boldsymbol{\mu}}_B)$$

For each chromophore, $\hat{\boldsymbol{\mu}}$ designates a unit vector in the direction of the appropriate transition dipole moment (see Section 3). The possible values of κ^2, as featured in eq. [2], lie in the range (0, 4). It is evident that in the case of fixed chromophore positions and orientations, the result delivered by eq. [3] is a function of three independent angles as shown and defined in Fig. 3,

$$[4] \qquad \kappa = \cos\theta_T - 3\cos\theta_A \cos\theta_B$$

Unfavourable orientations can thus reduce the rate of energy transfer to zero; other configurations, including many of those found in nature, optimize the transfer rate. The angular disposition of chromophores is therefore a very important facet of energy transfer, and one that invites careful consideration in the design of light-harvesting materials. Note that transfer is not "necessarily" precluded when the transition moments lie in perpendicular directions (provided that neither is orthogonal to $\boldsymbol{R}$ (= $R\hat{\boldsymbol{R}}$)).

In any, at least partially, fluid or disordered system the relative orientation of all donor–acceptor pairs may not be identical, and it is then the distributional average of κ^2 that determines the overall measured response. In the isotropic case (completely uncorrelated orientations), the κ^2 factor averages to 2/3; departures from this value signify a degree of orientational correlation. In molecules of sufficiently high symmetry, it can also happen that either the donor or the acceptor transition moment is not unambiguously identifiable with a particular direction in the corresponding chromophore reference frame. Specifically, the electronic transition may then relate to a transition involving a degenerate state (as can occur with square-planar complexes, for example) (41). Alternatively, the same observational features might indicate rapid but orientationally confined motions. The considerable complication, which each of these effects brings into the trigonometric analysis of RET, has been extensively researched and reported by van der Meer (42).

C. Functional group separation and conformation diagnostics

One obvious field of applications for RET, based on its strong distance dependence, is the identification of motions in molecules, or parts of molecules, that can bring one chromophore into the proximity of another. There are many examples in biology, such as the molecular traffic across a cell membrane and protein folding (43–45). These and other similar processes can be registered by selectively exciting one chromophore using laser light and monitoring either the decrease in fluorescence from that species or the rise in the generally longer-wavelength fluorescence from the other chromophore as it adopts the role of acceptor. The judicious use of optical dichroic filters can make this fluorescence RET or "FRET" technique perfectly straightforward (see Fig. 1). In cases where the two material components of interest do not have suitable overlapped display absorption and fluorescence features in an appropriate wavelength range, molecular tagging with site-specific "extrinsic" (i.e., artificially attached) chromophores can solve the problem. Lanthanide ions, with their characteristically prominent and line-like absorption features, prove particularly useful in this connection (46).

In some applications, the actual distance between the chromophore groups is of specific interest. When the same two chromophores feature, in spatially different configurations, in the chemical composition of two different systems (again, a common feature in biology), then the relative displacements of the chromophores can be quantitatively assessed on the basis of comparisons between the corresponding RET efficiencies (23–28, 47). Such a technique is popularly known as a "spectroscopic ruler". Such elucidations of molecular structure usually lack information on the relative orientations of the groups involved, and as such, the calculations usually ignore the kappa parameter (see eq. [3]). The apparent crudeness of this approach becomes more defensible on realizing that even if it were to introduce a factor of two inaccuracy, the deduced group spacing would still be in error by only 12% (since $2^{1/6} = 1.12$). Refinements to the theory to accommodate the effect of fluctuations in position or orientation of the participant groups introduces considerable complexity, though progress is being made in several areas (48–50).

In experimental studies of RET, it is usually significant that the electronically excited donor can in principle release its energy by spontaneous decay, the ensuing fluorescence being amenable to detection by any suitably placed photodetector. Since the alternative possibility (that of energy being transferred to another chromophore within the system) has such a sharp decline in efficiency as the distance to the acceptor increases, it is commonplace to introduce the concept of a critical distance R_0 (a separation at which the theoretical rates of RET and spontaneous emission by the donor are equal, now known as the Förster distance). The Förster rate eq. is often cast in an alternative form, exactly equivalent to eq. [2], explicitly exhibiting this critical distance (51).

$$[5] \qquad w_F = \frac{3\kappa^2}{2}\frac{1}{\tau_{A^*}}\left(\frac{\overline{R}_0}{R}\right)^6$$

Here, $\overline{R}_0$ is defined as the Förster distance for which the orientation factor κ^2 assumes its isotropic average value, 2/3 (52). For complex systems the angular dependence is quite commonly disregarded, and the following, simpler expression employed

© 2008 NRC Canada

$$[6] \qquad w_F = \frac{1}{\tau_{A^*}}\left(\frac{R_0}{R}\right)^6$$

leading to a transfer efficiency Φ_T expressible as

$$[7] \qquad \Phi_T = \frac{1}{1+(R/R_0)^6}$$

Typical values of the Förster radius range over a few nanometers. Thus, when a given electronically excited chromophore is within a distance R_0 of a suitable acceptor, RET will generally be the dominant decay mechanism; conversely, for distances beyond R_0, spontaneous decay will be the primary means of donor deactivation.

Before continuing, it is nonetheless worth observing that other forms of coupling are also possible, although less relevant to most systems of interest in the following account. For example, the transfer of energy between particles or units with significantly overlapped wavefunctions is usually described in terms of Dexter theory (53), where the coupling carries an exponential decay with distance, directly reflecting the radial form of overlapping wavefunctions and electron distributions. Compared to materials in which the donor and acceptor orbitals do not spatially overlap, such systems are of less use for either device or analytical applications largely because the coupled chromophores lose their electronic and optical integrity. This is the main reason why complex light-harvesting systems are commonly designed with "non-conjugated" linkages or spacer units between the chromophores, or else with the latter held on a host superstructure preventing direct chromophore contact. Parallels can be drawn with the way a dielectric layer operates in a simple electrical capacitor. In the alternative scenario, where spacer units act as a "conductive" bridge through delocalization and mixing of their orbitals with the donor or acceptor orbitals, energy transfer is specifically expedited by the operation of a special "superexchange" mechanism (54, 55), which, despite efficiency gains, compromises diagnostic applications.

D. Decay kinetics and polarization features

When linearly polarized laser light is used to excite any specific species within a complex disordered solid or liquid system, the probability for excitation of any particular molecule is proportional to $\cos^2\theta$, where θ is the angle between the appropriate excitation transition moment and the electric polarization vector of the input radiation. Consequently, the population of excited molecules has a markedly anisotropic distribution, a phenomenon associated with the term "photoselection". If radiative decay were to ensue instantaneously, i.e., from precisely the same excited level, then the fluorescence would carry the full imprint of that anisotropy and itself exhibit a degree of polarization (the highest value possible). Accounting for the necessary three-dimensional rotational average (56), it is readily shown that the fluorescence intensity components polarized parallel to and perpendicular to the polarization of the excitation beam, $I_\parallel$ and $I_\perp$ respectively, would then lie in the ratio 3:1. Commonly observed departures from this result thus signify the extent to which the orientation of the emission dipole differs from that of the prior, initial excitation, which may be due to intervening decay, molecular motion, or intermolecular energy transfer. The two most widely used quantitative expressions of this effect are the "fluorescence anisotropy", r, or the "degree of polarization", P, defined and related as follows

$$[8] \qquad r = \frac{I_\parallel - I_\perp}{I_\parallel + 2I_\perp}, \qquad P = \frac{I_\parallel - I_\perp}{I_\parallel + I_\perp} \quad \Rightarrow \quad r = \frac{2P}{3-P}$$

When the donor and acceptor have transition dipole moments oriented in parallel, then $r = 0.4$ and $P = 0.5$.

The key factor determining any loss in polarization is the angle θ between the directions of the absorption and emission transition dipole moments. In terms of this indicator, the case where internal decay intervenes between excitation and fluorescence decay, within a single molecule, is no different from that of a donor–acceptor pair where the absorption and emission processes are spatially separated (provided the donor and acceptor have a fixed mutual orientation, and the orientation of the pair is random). The following result, derived by Levshin (57) and Perrin (58), can be applied in both cases

$$[9] \qquad P = \frac{3\cos^2\theta - 1}{3 + \cos^2\theta}$$

In the case of a donor–acceptor pair, θ is to be interpreted as the angle θ_T shown in Fig. 3. Equation [9] thus allows direct calculation of this microscopic parameter through measurement of the macroscopic quantity P. Moreover, when P proves to exhibit a time-dependent decay, a study of the kinetics provides information on the extent of rotational motion intervening between the absorption and emission events.

Very different behaviour is observed for RET systems in which the donor and acceptor are orientationally uncorrelated, i.e., where they are both, independently, randomly oriented. In such cases, there is a very rapid loss of polarization "memory", and it transpires that the associated degree of anisotropy is precisely 1/25, i.e., $r = 0.04$ (1); two or more energy-transfer jumps will therefore usually, to all intents and purposes, totally destroy any polarization in any ensuing fluorescence. However, it should be noted that there is a surprising recovery in the anisotropy at distances approaching the transfer wavelength, as will be shown in Section 3C. The effect is sufficiently strong to warrant attention in dilute solution studies.

3. Electromagnetic mechanism

In each area of application, RET measurements exploit key features that originate in the detailed electromagnetic origins of RET coupling. To elicit these features, it is necessary to look more closely at the fundamental nature of the interactions involved.

A. Transition dipole coupling

The spectral functions featured in eq. [2] can be expressed in terms of the electronic transition properties of the chromophores, taking into account their vibrational structure. Although each transition spans a range of frequencies within the overall spectral bandwidth, it can be assumed under the conditions of the Born–Oppenheimer approximation that the vibrational factors in the transition dipole moments

© 2008 NRC Canada

factor out as Franck–Condon factors. The mathematical definitions of $F_A(\omega)$ and $\sigma_B(\omega)$ are then expressible as follows, using Dirac notation

$$[10] \quad F_A(\omega) = \frac{\omega^3 \tau_{A*} \mu_A^2}{3\varepsilon_0 \pi c^3} \sum_{n,r} \rho_{A*}^{(n)} \left| \left\langle \varphi_A^{(r)} \middle| \varphi_{A*}^{(n)} \right\rangle \right|^2 \delta(E_{A_n^*} - E_{A_r} - \hbar\omega)$$

$$[11] \quad \sigma_B(\omega) = \frac{\pi\omega \mu_B^2}{3\varepsilon_0 c} \sum_{m,p} \rho_B^{(m)} \left| \left\langle \varphi_{B*}^{(p)} \middle| \varphi_B^{(m)} \right\rangle \right|^2 \delta(E_{B_p^*} - E_{B_m} - \hbar\omega)$$

Here, μ_A and μ_B are the transition electric dipole moments for the donor decay and acceptor excitation, specifically given by

$$[12] \quad \boldsymbol{\mu}_A = \left\langle \psi_A \middle| \boldsymbol{\mu} \middle| \psi_{A*} \right\rangle, \quad \boldsymbol{\mu}_B = \left\langle \psi_{B*} \middle| \boldsymbol{\mu} \middle| \psi_B \right\rangle$$

where the μ is the dipole operator and each ψ is an electronic-state wavefunction. The indices *m*, *n*, *p*, and *r* in eq. [11] are generic labels denoting vibrational sub-levels, with each φ representing an associated wavefunction and *E* the corresponding energy; ρ denotes a population distribution function for the initial state of each species. Comparing the above results with eqs. [2] and [3] reveals the intrinsic quadratic dependence of the energy transfer rate on a coupling of the form

$$[13] \quad C = \frac{\left|\boldsymbol{\mu}_A\right| \left|\boldsymbol{\mu}_B\right|}{4\pi\varepsilon_0 R^3} [(\hat{\boldsymbol{\mu}}_A \cdot \hat{\boldsymbol{\mu}}_B) - 3(\hat{\boldsymbol{R}} \cdot \hat{\boldsymbol{\mu}}_A)(\hat{\boldsymbol{R}} \cdot \hat{\boldsymbol{\mu}}_B)$$

isomorphous with the usual formula for the interaction of two static dipoles. However, the result given by eq. [13] is an off-diagonal quantum amplitude connecting different initial and final states (only a diagonal quantum amplitude can directly signify energy). This is one of several important distinctions, the significance of which becomes more apparent when the quantum electrodynamical theory is developed.

Before continuing, it is worth emphasizing that the familiar inverse sixth power distance dependence of RET rate in the short range specifically owes its origin to the quadratic rate dependence on a coupling of transition electric *dipoles*. The result is, of course, applicable only when both the donor-decay and acceptor-excitation transitions are electric dipole (*E*1) allowed. In general, the coupling is effected by the lowest orders of multipole, electric or magnetic, that can support the necessary donor and acceptor transitions. In the Förster range, the distance dependence exhibits the form $R^{-(P+Q+1)}$ for the coupling of two transition electric multipoles *EP-EQ*, or two magnetic multipoles *MP-MQ*; whilst for the coupling of an electric with a magnetic multipole, *EP-MQ*, the distance dependence is $R^{-(P+Q)}$ (59, 60). For example, the coupling of an electric dipole decay with an electric quadrupole excitation, *E*1-*E*2, has an R^{-4} distance dependence within the Förster range. However, it should be borne in mind that each unit increase in multipolar order and each substitution of an electric transition by a magnetic counterpart lowers the strength of the coupling by a factor of two to three orders of magnitude. The decreasing efficiency of successive multipole orders increasingly disfavours the role of RET in the decay of the donor, compared with other decay mechanisms.

B. Near-field and long-range behaviour

As mentioned above, Förster theory is subject to several limitations. It is a theory specifically applicable under near-field conditions, i.e., over donor–acceptor distances significantly less than the optical wavelength for the energy being transferred, and this is a constraint that is effective for the coupling between any order of multipolar transitions. This condition is not always satisfied; however, there are numerous systems in which typical donor–acceptor distances approach or even exceed such wavelengths. Under those circumstances, new "retardation" features emerge, reflecting the finite time for the propagation of energy between molecular sites.

To ascertain rate expressions that correctly represent both short- and long-range transfer requires a fundamentally rigorous, quantum mechanical basis that delivers properly retarded solutions. The most suitable framework is afforded by quantum electrodynamics (QED) (61, 62) whose wider successes, such as its correct predictions of the magnetic moment of the electron, the Lamb shift, and the Casimir effect, are well-known (63). Less well-known is the fact that QED alone provides a satisfactory mechanistic explanation for the much more familiar process of spontaneous emission, or that even the use of electric and magnetic multipoles is ultimately defensible only in the context of a fully quantum electrodynamical theory (64). In connection with the theory of resonance energy transfer, the development of a theory based on QED began in pioneering work by Avery, Gomberoff, and Power (65, 66), culminating in a unified theory (67) whose ramifications continue to be explored today (68). A concise exposition is presented below.

A suitable starting point is the following Hamiltonian, for the simple RET system comprising chromophores A and B

$$[14] \quad H = H_A + H_B + H_{int}(A) + H_{int}(B) + H_{rad}$$

Here, the first two terms are the unperturbed Hamiltonian operators for the chromophores, and the two H_{int} operators represent interactions of the radiation field with A and B. The final term, H_{rad}, is the radiation Hamiltonian, which, as befits an operator, is always part of the sum even when there are no photons present. No term in eq. [14] directly links A with B, in other words, there is no static or "longitudinal" coupling; any form of coupling between the two chromophores can only be mediated by their individual interactions with the radiation field. This is an exact feature of any development in terms of multipole transitions (true not only for electric dipole interactions but for every other order of electric and magnetic multipole).

In the electric-dipole approximation, each $H_{int}(\xi)$ is given by the usual dipole coupling formula

$$[15] \quad H_{int}(\xi) = -\sum_{\xi} \boldsymbol{\mu}(\xi) \cdot \boldsymbol{e}^{\perp}(\boldsymbol{R}_{\xi})$$

where the electric-dipole moment operator, $\mu(\xi)$, operates on matter states, and the transverse electric field operator, $\boldsymbol{e}^{\perp}(\boldsymbol{R}_{\xi})$ on electromagnetic radiation states; $\boldsymbol{R}_{\xi}$ is the position vector of the chromophore labeled ξ. By standard methods, the electric field operator can be cast in the form of a summation over optical modes, each mode characterized by wavevector and polarization. Every operation of H_{int} is then asso-

© 2008 NRC Canada

ciated with the creation or annihilation of a photon from one of these modes. Throughout the usual pairwise process of RET, there is no applied radiation involved (the initial photoexcitation and any fluorescence being physically separable events); hence, the lowest order process that can couple the donor-decay and acceptor-excitation transitions is one involving the creation and annihilation of a "virtual" photon. Such photons are not physically observed; the quantum theory accordingly requires a sum to be taken over all radiation modes (i.e., all possible wave-vectors and polarizations). Since $H_{\rm int}$ must feature twice (once to create the virtual photon and the second time to annihilate it), the quantum amplitude $M_{\rm fi}$ for RET is determined by second-order perturbation theory

$$[16] \qquad M_{\rm fi} = \sum_r \frac{\langle f|H_{\rm int}|r\rangle\langle r|H_{\rm int}|i\rangle}{(E_i - E_r)}$$

where i, f, and r denote initial, final, and intermediate states of the system, respectively, and E signifies an energy. Two possible interaction sequences arise: (*a*) the virtual photon is created at A (effecting the decay of the donor excited state) and subsequently annihilated at B (effecting the acceptor excitation); (*b*) the virtual photon is created at B (along with the acceptor excitation) and annihilated at B (with the donor decay). These two possibilities are both represented within a state-sequence diagram as shown in Fig. 4. The counter-intuitive nature of case (*b*) does not preclude its inclusion in the calculation; it can be understood that exact energy conservation is not imposed during the interval between creation and annihilation of the virtual photon, i.e., the ultrashort photon flight-time. This, a key feature of virtual photon behaviour, is consistent with the time-energy Uncertainty Principle. When the whole system enters its final state, the balance of energy conservation is once again restored.

The explicit evaluation of eq. [16] by any of several standard techniques requires a considerable amount of algebra and calculus; details can be found in the original papers and subsequent reviews (69, 70). The result emerges in a form concisely expressible as follows

$$[17] \qquad M_{\rm fi} = \mu_{{\rm A}i} V_{ij}(k,\boldsymbol{R}) \mu_{{\rm B}j}$$

where the subscript indices i and j stand for Cartesian components, and the convention of summation over repeated indices is implicit. The value of k is $2\pi/\lambda$, where λ is the wavelength associated with the transfer energy. In eq. [17], the two transition dipole moments, for the donor-decay and acceptor-excitation transitions, are coupled by an $E1 - E1$ coupling tensor defined by

$$[18] \qquad V_{ij}(k,\boldsymbol{R}) = \frac{e^{ikR}}{4\pi\varepsilon_0 R^3}\{(\delta_{ij} - 3\hat{R}_i\hat{R}_j) - (ikR)(\delta_{ij} - 3\hat{R}_i\hat{R}_j) - (kR)^2(\delta_{ij} - \hat{R}_i\hat{R}_j)\}$$

Before considering the rate equation that ensues from the above QED treatment, some features of physical significance can be identified directly from the quantum amplitude. First,

Fig. 4. State-sequence diagram for RET, progressing from the initial system state of the left, through intermediate states, to the final state on the right. In each box, the two circles designate the states of *A* and *B*, black indicating the ground state; ϕ denotes a virtual photon. The lower route (*a*) and the upper route (*b*) signify the two quantum pathways.]

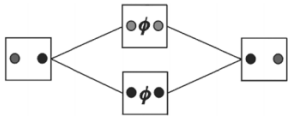

it is important to note that for short-range distances where $k\boldsymbol{R} << 1$ (signifying a length significantly smaller than the wavelength of the donor decay), eq. [18] couples with the transition dipoles in [17] to deliver a result that equates exactly with the classical expression for the coupling, eq. [13]. The additional terms in [18], identified by QED, come into play at larger distances (signifying the accommodation of retardation principles). These are features that reflect the finite interval over which the energy exchange between A and B can be accomplished which is restricted by the photon propagation time, in accordance with relativistic causality.[2]

To appreciate the range-dependent character of the RET rate on its own merits, let it be assumed for simplicity that the donor and acceptor have isotropically averaged orientations, and that the refractive index of the medium is unity. It then follows that the distance-dependence of the transfer rate factorizes out in the following form (67, 71) (one that also identifies it with the tensor inner product of the coupling tensor in eq. [18]).

$$[19] \qquad \langle A(k,R)\rangle = \frac{1}{8\pi^2\varepsilon_0^2 R^6}\{3 + (kR)^2 + (kR)^4\} = V_{ij}(k,\boldsymbol{R})\overline{V}_{ij}(k,\boldsymbol{R})$$

This orientationally averaged transfer function is a scalar characterizing the distance dependence of $E1$-$E1$ coupling in RET. A key property of the result is that as the distance R increases into the range where it substantially exceeds the wavelength for the transfer energy, i.e., where $k\boldsymbol{R} >> 1$, the third term in eq. [19] begins to dominate, and the overall dependence on R assumes an inverse-square form. Detailed calculations reveal that the limiting result tallies exactly with radiative emission by the donor, followed by acceptor absorption of the ensuing radiation. In other words, the photons involved in the energy transfer lose their virtual character and become real, as is consistent with their acquiring a finite (and in principle measurable) time of flight. This change in character of RET with distance is neatly illustrated by a plot of the isotropically averaged excitation transfer function, as shown in Fig. 5. This figure gives a readily comprehensible representation of the Förster radiationless and radiative transfer processes as short- and long-range asymptotes, respectively, shown by the change in gradient of the log–log plot between the short- and long-range regions.

The discovery that Förster radiationless and radiative coupling are components of a single mechanism that operates seamlessly over *all* distances beyond wavefunction overlap

[2] Equally when $k = 0$ (essentially the transfer of an infinitesimal energy with infinitely long wavelength) the result (see eq. [18]) reduces to a form in which the near-field term alone operates out to infinity, duly corresponding to a coupling of "static" dipoles.

© 2008 NRC Canada

Fig. 5. Log–log plot of the RET excitation transfer function $\langle A(k,R)\rangle$, as defined by eq. [19], against log R (in meters), for $k = 9 \times 10^6$ m^{-1} (corresponding to a wavelength at the red end of the visible region). The dotted line shows the radiative asymptote (slope –2).

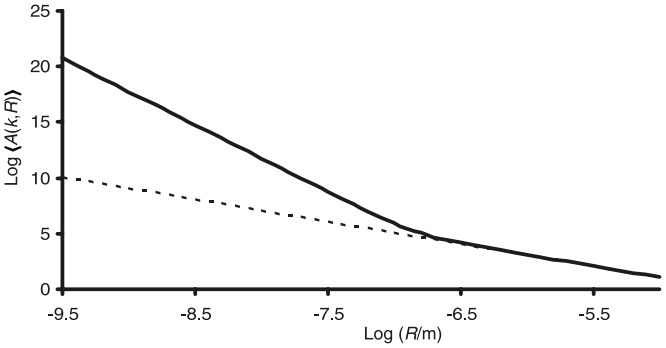

resulted in a paradigm shift in the understanding of RET, and it is the reason why the QED theory has been termed a "unified" theory (67). This theory is valid over a span ranging from the nanoscale up to indefinitely large distances; Förster energy transfer is the short-range asymptote and radiative transfer the long-range asymptote. One consequence of this discovery is that it has become meaningless to entertain any notion of competition between these processes. Recently, a revisitation of the QED theory has enabled the individual contributions associated with each of the two quantum pathways to be disentangled (72), proving that the long-range R^{-2} behaviour is completely identifiable with the physically more intuitive sense of propagation, the lower pathway in Fig. 4. In the same regime, the contribution from the upper pathway unexpectedly drops off as R^{-8}. Nonetheless in the near-zone, both run as R^{-6}. However, it should be emphasized that the unified theory establishes more than this; it also addresses donor–acceptor separations in an intermediate range where neither the radiative nor the Förster mechanism is truly valid. An experimental verification of the behaviour in this region remains a currently unfulfilled objective, a point we shall return to shortly.

The majority of applications of RET relate to the Förster regime, i.e., they involve systems in which stepwise energy transfer events occur between chromophores separated by less than the Förster distance, and as such they are also usually operating within the short-range, $k\boldsymbol{R} << 1$. Systems in which the mean transfer distance might fall in the long-range regime, $k\boldsymbol{R} >> 1$, would necessarily require the optically relevant species to be present in low concentrations; moreover, any diffusion processes that could produce transient short-range donor–acceptor juxtapositions should also have a timescale significantly longer than the donor decay time, or else diffusion-limited Förster transfer would result. The radiative transport that ensues in the latter case is exhibited in a variety of systems, such as dilute dye solutions, and it leads into a distinct branch of the theory where multiple scattering must also be taken into account. A detailed account is given by Berberan-Santos et al. (73).

C. Orientational and refractive effects

It is not only the effective power law governing distance that changes form as donors and acceptors move further apart, but also their functional dependence on orientation changes. To fully describe this feature, it is expedient to introduce the following generalization of the κ factor earlier defined by eq. [4]

Fig. 6. Variation with distance of the fluorescence anisotropy following RET between freely and independently rotating (or randomly oriented) donor and acceptor chromophores. Plot shows the acceptor fluorescence anisotropy r as a function of distance, represented on the abscissa scale as values of kR.

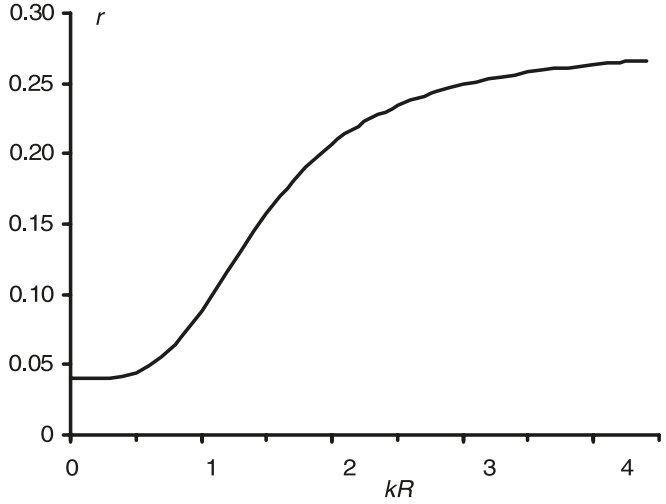

$$[20] \qquad \kappa_n = \cos\theta_T - n\cos\theta_A\cos\theta_B$$

Then, it can be shown that the excitation transfer function, whose isotropic average was given as eq. [19], more generally takes the form

$$[21] \qquad A(k,R) = \frac{9}{16\pi^2\varepsilon_0^2 R^6}\{\kappa_3^2 + (\kappa_3^2 - 2\kappa_1\kappa_3)(kR)^2 + \kappa_1^2(kR)^4\}$$

Equation [21] applies in the case of chromophores that are fixed, or have limited orientational freedom. Although most configurations will exhibit a variation in their orientational dependence with any significant change in donor–acceptor separation, it is the case that when $\mu_A \perp \mu_B$ and one of these transition dipoles is also orthogonal to $\boldsymbol{R}$, RET is entirely dipole forbidden "at all" distances. It is also notable that, although different kappa factors characterize the terms in R^{-6}, R^{-4}, and R^{-2}, both κ_3 and κ_1 feature in the expression for R^{-4}. This is the main reason why the intermediate term has eluded experimental identification, because it is technically difficult to envisage any circumstances in which its contribution could be isolated.

An interesting interplay of distance and orientational factors does however arise in connection with fluorescence polarization measurements, and this might afford the best means of identifying the onset of retardation effects. Calculations show that the fluorescence anisotropy in a system of freely and independently rotating donors and acceptors dramatically increases from its usual value $r = 0.04$, for transfer distances beyond the usual near-zone. The result, shown in Fig. 6, exhibits a long-range asymptote of precisely $r = 0.28$ (74). The reason for this behaviour is best understood as reflecting a "decreased" anisotropy in the short range (where

© 2008 NRC Canada

the transfer is effected by a photon whose virtual character means its propagation is not specifically aligned to the interchromophore direction) (69). Consequently its communication of polarization information is also less precise than is the case for the increasingly real-character photons that become involved in propagation over larger distances. Significant though the result is, its interpretation in any solution study would be significantly complicated by the need to accommodate an ensemble distribution of transfer distances.

To finally secure a completely general and rigorous result for RET requires that due consideration be given to the electronic influence of other material in the vicinity of the donor and acceptor. For optically dense systems, such matter could comprise other potential donor or acceptor species; in doped solids, it would be the host crystal that exerts the primary electronic influence; in the case of solutions, the surroundings would mostly comprise solvent, whereas in photobiological materials, it would usually be a protein superstructure and solvation, for example. Scholes et al. have recently performed extensive quantum chemical calculations quantifying such effects in a host of photosynthetic light-harvesting systems (75, 76).

A more comprehensive and general representation of media effects in each of these systems can be secured from the premise that the bulk material exerts an influence over resonance energy transfer by its effect on real or virtual photon propagation. The detailed form of this influence is duly accommodated in the theory by the introduction of an effective radiation field operator whose eigenstates signify modes in which photons are "dressed" by the electromagnetic influence of the host (77). Strictly, these dressed photons are "polaritons", though the distinction is not important if one is dealing with frequencies at which the host is relatively transparent. By a lengthy development, it transpires that the effect of making this correction is for the coupling tensor in eq. [18] to emerge in the following modified form, assuming Lorentz local field factors are assimilated into the expressions for the spectral functions $F_A(\omega)$ and $\sigma_B(\omega)$.

$$[22]\quad V_{ij}(k,\boldsymbol{R}) = \frac{1}{n^2(\omega)}\frac{e^{in(\omega)kR}}{4\pi\varepsilon_0 R^3}\{(\delta_{ij}-3\hat{R}_i\hat{R}_j) - (in(\omega)kR)(\delta_{ij}-3\hat{R}_i\hat{R}_j) - (n(\omega)kR)^2(\delta_{ij}-\hat{R}_i\hat{R}_j)\}$$

Here, $n(\omega)$ is the complex refractive index for optical frequency $\omega = ck$. The imaginary part of this index leads, through its inclusion in the phase factor in eq. [22], to dissipative losses, which properly increase with distance.

In its final and most general form, consistent with eqs. [21] and [22], it emerges that the RET rate can be written as follows (78)

$$[23]\quad w = w_F + w_I + w_{rad}$$

$$[24]\quad \left.\begin{aligned} w_F &= \frac{9\kappa_3^2 c^4}{8\pi\tau_{A^*}R^6}\int F_A(\omega)\sigma_B(\omega)\frac{d\omega}{\omega^4 n^4(\omega)} \\ w_I &= \frac{9c^2}{8\pi\tau_{A^*}R^4}(\kappa_3^2-2\kappa_i\kappa_3)\int F_A(\omega)\sigma_B(\omega)\frac{d\omega}{\omega^2 n^2(\omega)} \\ w_{rad} &= \frac{9\kappa_i^2}{8\pi\tau_{A^*}R^2}\int F_A(\omega)\sigma_B(\omega)\,d\omega \end{aligned}\right\}$$

The first term of eq. [24] is the usual Förster rate, identical to eq. [1] if the refractive index is taken as a constant. The second contribution, w_I, is a correction that comes into play at distances beyond the near-field, where the assumption $k\boldsymbol{R} << 1$ no longer holds. The third term, w_{rad}, which dominates over both other contributions when $k\boldsymbol{R} >> 1$, equates to radiative transfer. For donor–acceptor distances in the hundreds of nanometers range, where $k\boldsymbol{R} \approx 1$ to the nearest order of magnitude, all three terms of eq. [24] significantly contribute to resonance energy transfer.

4. Role in energy-harvesting materials

A. Optical energy collection and directed transfer

Many of the most widely studied and well-characterized theatres of operation for RET are to be found in connection with light-harvesting materials (both naturally occurring biological systems and synthetic structures). Following the capture of a photon by any such system, the transfer mechanism dictates that the migration of the acquired energy from the site of the initial photoabsorption through to the site of its utilization is at every stage subject to an inverse sixth-power dependence on distance. As a result, energy migration over distances beyond the Förster radius mostly operates through a series of short hops rather than one long one. Moreover, a "spectroscopic gradient" is commonly associated with these hops (79), the term signifying progressively longer wavelengths for absorption and fluorescence in successively visited chromophores (recall Section 2B). This property contributes significantly to the high efficiency of photosynthetic and allied energy-harvesting systems.

In considering the effectiveness of a preferred direction to the traffic between any two chromophores involved in such a sequence of energy transfer steps, it will be immediately apparent that there is a close similarity of form between the eqs. for "forward" and "backward" transfer between any given pair of electronic levels. The distance aspects for forward and backward transfer are obviously the same; moreover, since the unit displacement vector becomes $-\hat{\boldsymbol{R}}$ for back-transfer, its quadratic involvement in the orientation factor κ^2 means the latter is also identical. By reference to eqs. [10] and [11], and considering their counterparts for the inverse transfer process, it is in fact clear that the key to imposing directedness principally lies in exploiting differences in the relative spectral profiles. To quantify the relative rates or propensities for forward and backward transfer, it has been found convenient to introduce a dimensionless relative directional efficiency, ε, defined by

$$[25]\quad \varepsilon = \frac{\tau_B\int F_A(\omega)\sigma_B(\omega)\omega^{-4}d\omega}{\tau_A\int F_B(\omega)\sigma_A(\omega)\omega^{-4}d\omega}$$

The spectral curves illustrated in Fig. 2 exhibit typical implications for the spectral overlaps in the numerator and denominator of eq. [25]. For each chromophore, the fluorescence peak is Stokes-shifted to a lower frequency with respect to its absorption counterpart. Moreover, in the majority of cases of interest the peak of the acceptor absorption curve lies at a lower frequency than that of the donor emission. Thus, it becomes clear that forward transfer in any one step is generally favoured because (with reference to the

© 2008 NRC Canada

parameters shown in Fig. 2) $\omega_4 - \omega_3 > \omega_2 - \omega_1$, signifying that δ_2 will exceed δ_1.

In a recent study accommodating both symmetric and asymmetric lineshapes, detailed analytical results have been determined for the directional efficiency ε (39). In the case of Gaussian spectra, a particularly simple result applies if the two species possess similar fluorescence lifetimes, and if their absorption and fluorescence curves have similar heights and full-widths at half maximum, ω_{FWHM}. Under these conditions, the following result emerges

$$[26] \quad \varepsilon \cong e^{2k(\delta_2^2 - \delta_1^2)}$$

where $k = (4 \ln 2)\omega_{FWHM}^{-2}$. Equation [26] exhibits a transfer efficiency that strongly increases with δ_2 and decreases with δ_1, as might qualitatively be anticipated. Furthermore, if the Stokes shifts for A and B are equivalent and represented by $\omega_S = \omega_4 - \omega_2 = \omega_1 - \omega_3 = \delta_2 - \delta_1$, and the shift characterizing the spectroscopic gradient is defined as $\omega_G = \omega_4 - \omega_1 = \omega_2 - \omega_3 = \delta_1 + \delta_2$, then the directional efficiency is expressible in its simplest form

$$[27] \quad \varepsilon = e^{2k\omega_G\omega_S}$$

It is notable that this result shows the same functional dependence on the spectroscopic gradient and the Stokes shift; both are equally important in determining the directedness of the energy transfer. In an energy-harvesting system consisting of a number of chemically or environmentally different fluorophores, a progressive spectroscopic gradient operating at every energy transfer step thus ensures an overall directionality of flow, a characteristic summarized in the term "energy funnel".

B. Excitons and excitation pooling in photosynthetic systems

To achieve their primary purpose in green plants, leaf structures contain numerous copies of the complex molecular apparatus for synthesizing sugars from carbon dioxide and water. Further to these photosynthetic reaction centres, simpler and more numerous antenna pigments are additionally required to absorb incident light. However, many other structural elements have also to be present; crucially, there must be components that deliver H_2O, CO_2, and photoexcitation energy to the reaction centres, and still others to take the sugars off to where they are required as building materials for new plant tissue. To optimize the overall photosynthetic efficiency of the organism, a trade-off is therefore necessary between the density and arrangements of pigments and reaction centres. Such organizational criteria are further complicated by a consequence of simple chemical energetics; the fact that several visible photon energies are required to effect the synthesis of each carbohydrate unit. Photosynthesis thus also requires a gathering of the necessary energy into one location.

To most effectively utilize the sunlight that falls upon them, photosynthetic organisms typically have a system of antenna complexes surrounding the reaction centers where photosynthesis takes place (80–83). The antenna complexes absorb light, and the acquired energy is transferred onwards through a series of short-range, radiationless energy-transfer steps as illustrated in Fig. 7. Specific channelling to the reaction centres is cleverly accomplished by connectivity between spectroscopic and kinetic features, i.e., a correlation of the spatial locations of the chromophores with a progressive spectroscopic gradient. In the overall migration of energy from the site of its initial deposition to the site of its chemical action, this directionality obviates what would otherwise be random diffusion; on the contrary, it means that energy is quickly and efficiently directed to the site of its chemical utilization. Not only does this allow an organism to harvest light incident on a large surface area but also by pooling energy from a large number of antenna chromophores, energy of a higher equivalent frequency can be produced.

Fig. 7. Schematic energy flow in a bacterial photosystem for the oxidation of water.

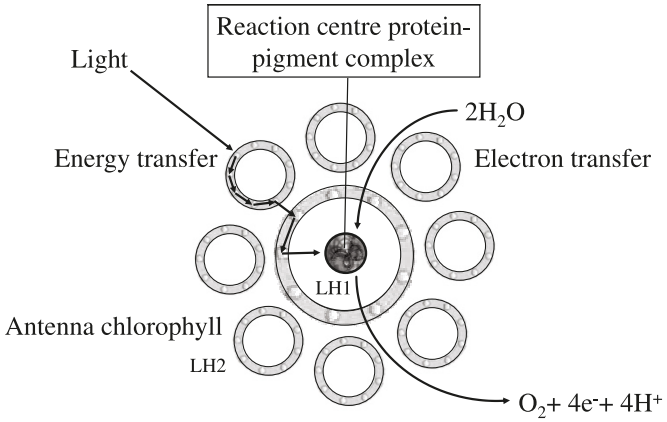

Not only the spectroscopic properties of the chromophores determine the character and direction of energy flow, but the chromophore positioning and orientation are also important. Two-dimensional optical spectroscopy can unveil the intricate interplay between spectral and spatial overlap features in light-harvesting complexes, as beautifully exhibited in a recent study on bacteriochlorophyll (84). Interrogating the system with a sequence of ultrashort laser pulses, the optical response reveals linear absorption processes as well as couplings between the chromophores and dynamical aspects of the energy transfer. The results show that excitation relocation does not simply proceed by stepwise transfer from one energy state to another of nearest energy, but it depends on strong coupling between chromophores (as determined by the extent of their spatial overlap), further limiting any residual randomness in direction of the energy transfer. In other studies on photosynthetic systems, it has also emerged that energy transfer can propagate with a wave-like motion due to quantum coherence (85).

Fluorescence polarization measurements are a powerful means of eliciting other structural information. Because photosynthetic systems are relatively rigid systems with chromophores held at fixed positions and orientations relative to each other, then even when there are several successive energy jumps, any resulting emitted fluorescence is generally polarized. The extent of this polarization affords invaluable information about the internal orientational structure, as was outlined in Section 2D.

C. Energy-harvesting dendrimers

The proven efficiency of photosynthetic units and the elucidation of the responsible mechanisms have stimulated the

© 2008 NRC Canada

design of a variety of synthetic light-harvesting systems (86–88). The materials that have received most attention are dendrimers (89–92) (macromolecules consisting of molecular units repeatedly branching out from a central core designed to act as an excitation trap, exemplified by the structure in Fig. 8).

The outward branching leads to successive generations of structures, each with an increased number of peripheral antenna chromophores. In ideal cases, the requisite spectroscopic gradient is established through chemically similar chromophores in generationally different locations (93, 94). Most recent work on dendrimers has utilized branching motifs of vertex degree three and four, based on tri-substituted benzene (90) and porphyrin rings (95), respectively.

Modelling the multi-step flow of energy in dendrimers presents a considerable challenge (96, 97), and a variety of calculational methods have been brought to bear on the problem. Often, simplifying assumptions are required; for example, in work by Blumen et al. (98) an exact solution has been derived for fractal polymers in which all chromophores have the same absorption cross-section and all rates of transfer between nearest neighbours are considered equal. More radical approaches to the problem have also been attempted, such as modeling the diffusion of the excitation under a constant force as a continuum process (99), or using the Eyring (membrane permeation) model to treat the energy flux as diffusion in a potential energy landscape with thermal barriers (100).

One recently developed method that shows promise is an operator approach developed from an "adjacency matrix" representation, based on the chemical connectivity between individual chromophores (101–103). Here, a square matrix, whose order equals the number of chromophores, represents the propensities (probabilities associated with a specific time interval) for energy migration between the chromophores. This matrix operates upon a vector representation of the population conditions, each iteration representing an advance in time. Considerable simplification is effected, without compromising the fidelity of the model, by collapsing the representation into a reduced basis whose order is generational number of the dendrimer. For a three-generation dendrimer, for example, the RET propensity matrix in the shell basis may be written as follows

$$[28] \qquad \tilde{\mathbf{C}} = \begin{pmatrix} 1-a_3 & 2\varepsilon_3^{-1}a_3 & 0 & 0 \\ a_3 & 1-a_2-2\varepsilon_3^{-1}a_3 & 2\varepsilon_2^{-1}a_2 & 0 \\ 0 & a_2 & 1-a_1-2\varepsilon_2^{-1}a_2 & 3\varepsilon_1^{-1}a_1 \\ 0 & 0 & a_1 & 1-3\varepsilon_1^{-1}a_1-\xi \end{pmatrix}$$

where a_i is the propensity for transfer from a chromophore in the ith shell to another, to which it is chemically bonded, in the $(i-1)^{\text{th}}$ shell (or to the core, if $i = 1$); ε_i is the ratio of efficiencies for inward and outward energy transfer between the same pair of chromophores (the latter usually expressible through eq. [27] as a simple function of the chromophore lineshapes and spectroscopic gradients). Lastly, ξ signifies losses associated with emission or irreversible energy utilization at the core. One advantage of the above representation is that it obviates any assumption of symmetry that chemical connectivity would suggest; this is a facet of particular relevance when issues of folding are to be entertained.

Fig. 8. Fifth-generation polyphenylether dendrimer, centred on a lanthanide ion such as Er^{3+} or Tb^{3+}. The threefold branching is formally described by a vertex degree $r = 3$. Such planar depictions misrepresent the three-dimensional folding that increasingly takes place with successive generations.

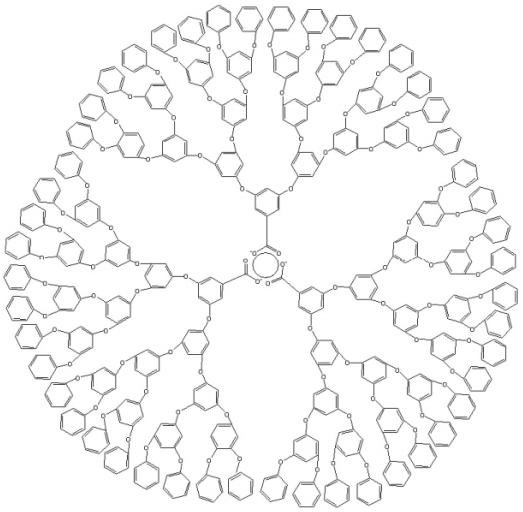

Results based on this model have already indicated a promising potential for representing the time-dependent energy flow towards the core, as indicated in Fig. 9*a*, lending a new capacity to interpret experimentally determined kinetic data in terms of physically meaningful quantities with a clear molecular interpretation. The significance of inter-shell directional transfer efficiency is readily exhibited by results such as that shown in Fig. 9*b*, where the increasingly strong dependence with successive generations of dendrimer growth are dramatically illustrated. In the more extensive results reported elsewhere (103), the effects of spectroscopic gradient and Stokes shift are also detailed.

In other recent developments of the theory based on molecular QED (104, 105), attention has become focused on optically "nonlinear" mechanisms for RET in dendrimers. Such mechanisms naturally fall into two classes: those in which two-photon absorption by individual donors is followed by a direct transfer of their acquired energy to an acceptor, and other processes wherein the excitation of two electronically distinct but neighbouring donor groups is followed by a collective migration of their energy to a suitable acceptor. These two types of transfer process are subject to markedly different forms of dependence on energy level structures, laser coherence factors, chromophore selection rules and architecture, possibilities for the formation of delocalized excitons, spectral overlap features, and the overall distribution of donors and acceptors. With such an array of measures to choose between, experimental differentiation of the mechanisms should prove relatively straightforward, and the first experimental results are awaited with keen interest.

5. Optical control of resonance energy transfer

A. Laser-assisted resonance energy transfer

The pace of development in nanofabrication techniques has promoted an increasing interest in the specific effects of

© 2008 NRC Canada

Fig. 9. (*a*) Extent of core excitation in a single-generation dendrimer of vertex degree ρ = 3, plotted as a function of time, for different values of the parameters *a*, ξ, and ε. (*b*) Core excited-state population (scaled by the number of chromophores) in dendrimers of vertex degree = 3, as a function of the inter-shell transfer efficiency, for third-, fourth- and fifth-generation dendrimers. Adapted from (103).

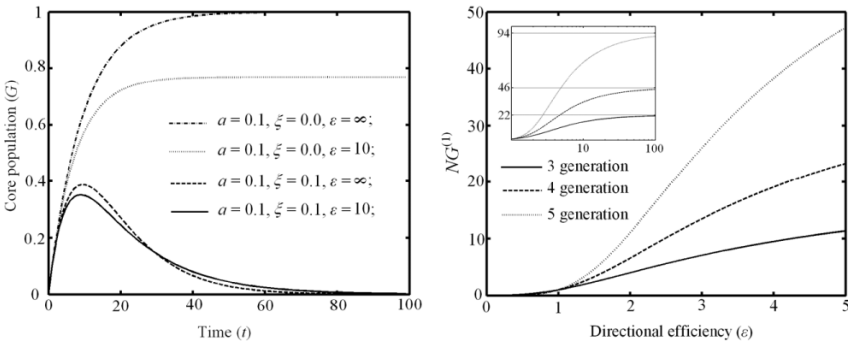

donor and acceptor placement in nanoscale geometries and periodic structures. However, the possibility of influencing the operation of RET by an optical field only recently began to receive notice. Specifically, attention has become focused on possible means to enhance energy transfer, or even switch it on and off, through the controlled input of an off-resonant, auxiliary beam of laser radiation, as schematically illustrated in Fig. 10. The first work in this area considered amplification effects that might be induced by such an auxiliary beam in systems where energy transfer will occur spontaneously (following initial excitation of the donors). It was shown that, at the levels of intensity currently available from mode-locked solid-state lasers, significant enhancements of the transfer rate could be expected (106). The discovery led to a coining of the term "LARET" to denote laser-assisted RET.

The quantum electrodynamical mechanism for LARET involves fourth-order time-dependent perturbation theory. Each interaction is linear in the electric field operator, see eq. [15], and thus entails the absorption or emission of a photon. Specifically, in addition to the two virtual photon events (creation and annihilation) of normal RET, this process involves the absorption and the stimulated re-emission of a photon from the throughput, off-resonant, laser light; each of these real photon events may also occur at either the donor or the acceptor. In general, all four of the resulting possible combinations contribute to the overall quantum amplitude; moreover, each has 24 different time-orderings associated with it. State-sequence representations (107, 108), such as the one illustrated in Fig. 11 (compare Fig. 4), represent a tractable basis for QED calculations that lead to the following eq. for the transfer probability at time *t*

$$[29]\qquad P(t) = \frac{\rho_f}{32\hbar c^2 \pi \varepsilon_0^4 R^6} \left| e_i \alpha_{lk}^{A}(-k')(\delta_{jk} - 3\hat{R}_j\hat{R}_k)\,\alpha_{lk}^{B}(k')\bar{e}_l + \bar{e}_i \alpha_{ij}^{A}(k')(\delta_{jk} - 3\hat{R}_j\hat{R}_k)\,\alpha_{lk}^{B}(-k')e_l \right|^2 \int_0^t I^2(t)\,\mathrm{d}t$$

Here, the α tensors are generalized polarizabilities (61) and $I(t)$ signifies the time-dependent pulses of irradiance delivered by the off-resonant beam; notice the recurrence of the characteristic short-range R^{-6} dependence on distance. Model calculations based on eq. [29] suggest that prominent departures from the normal kinetic behaviour of RET can be expected, as indicated in Fig. 12.

Fig. 10. General schematic of laser-assisted or optically controlled resonance energy transfer.

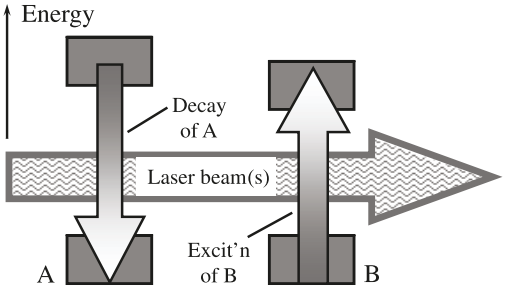

Fig. 11. One of four state-sequence diagrams for LARET. There are 24 pathways from the initial state on the left (excited *A*, ground state *B*) to the final state on the right left (ground state *A*, excited *B*), each progressing through three virtual intermediate states. In each case, ω denotes the off-resonant throughput radiation; in intermediate state boxes where the symbol is absent, a photon has been absorbed, while two ω symbols signify that stimulated emission has added an additional photon into the throughput. As with RET, ϕ denotes a virtual photon.

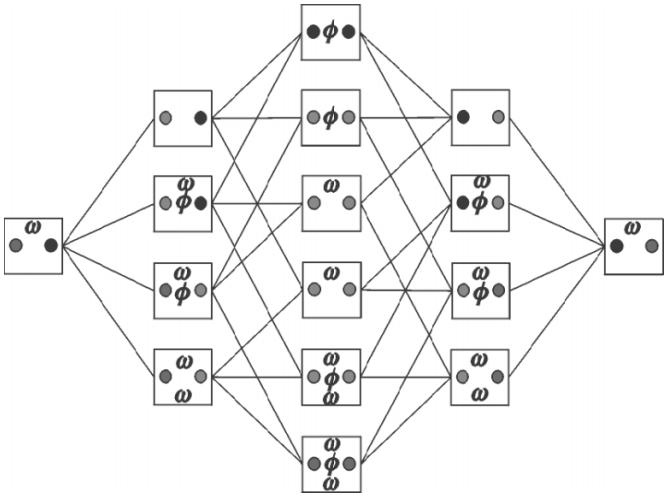

B. Optical switching in array devices

Recently, further interest has focused on structures that can be tailored to exploit the laser-assisted phenomenon. Specifically, consideration has been turned to systems in

© 2008 NRC Canada

Fig. 12. Profiles illustrating the effects of LARET on the kinetics of fluorescence, (*a*) from a donor and (*b*) acceptor, produced by introducing a square pulse of off-resonance laser radiation (dashed line) 100 ps after the initial donor excitation. The solid line shows the LARET behaviour, departing from the usual RET trace shown by the dotted segment. The pulse duration is 100 ps, and its intensity is 5×10^{12} W cm^{-2}. Adapted from (106).

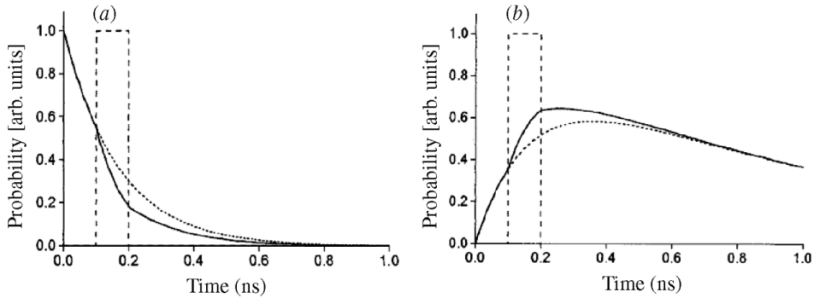

which each donor–acceptor pair has optical properties that satisfy the spectral overlap condition, but for which RET is designedly precluded by a customized geometric configuration (109). For example, as was observed in Section 3C, both short- and long-range RET is forbidden when the donor and acceptor undergo electric dipole transitions whose transition moments are perpendicular both to each other and also to the donor–acceptor displacement vector. For any such donor–acceptor pair, the LARET mechanism offers a means by which the throughput of non-resonant laser pulses can facilitate energy transfer when it would otherwise be rigorously forbidden. This optical switching of energy transfer, which has acquired the acronym OCRET (optically controlled resonance energy transfer), thus achieves the functionality of an optical transistor, with the electronic excitation representing a signal whose throughput is switched on by one or two auxiliary beams (110, 111).

The laser systems most capable of delivering the necessary levels of irradiance prove to be precisely those that will also offer directly controllable, ultrafast speeds of switching. Auspicious results have been obtained from detailed calculations on a prototype implementation of OCRET in planar nano-arrays (Fig. 13); results are illustrated by 3D plots in Fig. 14.

C. Implementation issues and applications

Results such as those shown in Fig. 14 encourage a view that the OCRET mechanism affords a realistic basis for a configuration of optical switches with parallel processing capability, operating without significant cross-talk. To address possible applications, a detailed analysis (112) has recently focused on the critical issue of transfer fidelity, defined as the efficiency of direct energy relocation, from an excited donor to its designated partner in the acceptor array, compared to the summed efficiencies for transfer to any other molecules within either array. The square-planar configuration proves to afford a significantly higher level of transfer fidelity than other likely contenders. It has also emerged that for optimal exploitation of the transition selection rules, the donor and acceptor molecules should belong to one of two common symmetry point groups, D_2 and C_{2v}. For such systems, through judicious choice of the relative values of the array spacing and lattice constant and the laser intensity, cross-talk can be driven down to arbitrarily low levels.

Generally, it may prove expedient to construct the donor and acceptor arrays as film layers, separated by a suitably

Fig. 13. Array implementation of OCRET: (*a*) overhead view of closely separated layers; the upper is a square-planar array of uniformly oriented donors, and the lower is a similarly constructed and registered array of acceptors. Black arrows represent donor transition dipoles in the upper layer, and grey arrows represent acceptor transition dipoles in the lower array; open arrows show an excited donor and its corresponding ground-state acceptor; (*b*) artist's impression of the view between the layers; the separation is exaggerated for clarity; (*c*) inter-layer depiction of the transition-moment orientations.

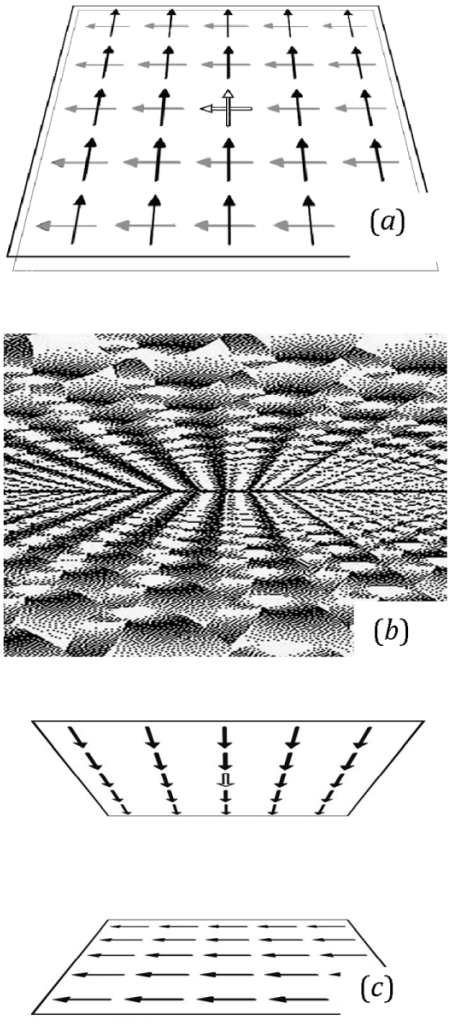

© 2008 NRC Canada

Fig. 14. Contour graphs depicting on a logarithmic scale the probability of energy transfer to the array of acceptors in the absence (left) and presence (right) of laser light. Efficiency of energy transfer is represented by the vertical scale, and dots indicate the locations of each acceptor.

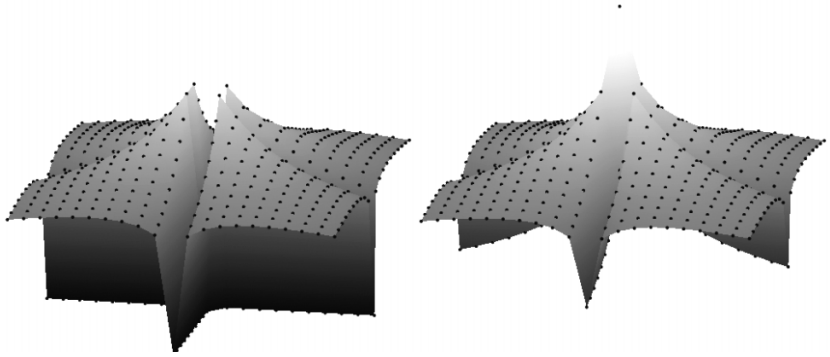

transparent ultra-thin spacer material. Organic dyes represent an extensive range of possibilities for the donor and acceptor species; the use of quantum dots is also conceivable, though their relative isotropy could make it difficult to preclude conventional RET unless spin-imprinted excitation and excitation transfer were to be engaged (113, 114). Two techniques that could offer promise for the deposition and tailoring of the molecular components in each active layer are dip-pen nanolithography and thermochemical nanolithography, in each of which the potential to order and chemically modify molecular units is now established (115–118).

The achievement of RET-based optical switching in an extensive parallel-processing unit introduces a number of potential applications beyond simple switching. The array results signify that, for example, pixel-based images, written by donor excitation, could be transferred with high fidelity to the acceptor film. In the realm of optical communications, possibilities might be built on the obvious capacity of such a system to act as an ultrafast information buffer; the high level of interest in such devices has already prompted others to explore "slow-light" methods, where a host of more problematic limitations apply (119, 120). In the longer term, OCRET may prove a significant channel of progress towards reliable systems for use in optical computing and communications routing.

6. Conclusion

Resonance energy transfer is a fundamental mechanism widely operative in complex multi-component systems. In this review, it has been shown how an increasingly diverse range of applications and devices can exploit features of the process, such as its dependence on the degree of spectral overlap between donor and acceptors, the sharp distance dependence, and transfer selectivity determined by the orientation of transition moments. Attention has been drawn to a number of novel schemes for the control and application of energy transfer, offering particularly bright new prospects for energy-harvesting and all-optical switching.

Acknowledgements

It is a pleasure to acknowledge the involvement of past and present members of my group in the unified theory developments at the University of East Anglia, and I gladly acknowledge their contributions. In particular, I must thank Philip Allcock, David Bradshaw, Richard Crisp, Gareth Daniels, Luciana Dávila Romero, Robert Jenkins, Gediminas Juzeliūnas, Justo Rodríguez, and Brad Sherborne. I gratefully acknowledge funding from the Engineering and Physical Sciences Research Council, the Leverhulme Trust, and the Royal Society.

References

1. V.M. Agranovich and M.D. Galanin. Electronic excitation energy transfer in condensed matter. Elsevier/North-Holland. Amsterdam, The Netherlands. 1982.
2. B.W. van der Meer, J. Coker, III, and S.-Y.S. Chen. Resonance energy transfer: theory and data. VCH. New York, NY, USA. 1982.
3. D.L. Andrews and A.A. Demidov (*Editor*s). Resonance energy transfer. Wiley. New York, NY, USA. 1999.
4. K. Sienicki. J. Chem. Phys. **94**, 617 (1991).
5. M.N. Berberan-Santos, J. Pouget, B. Valeur, J. Canceill, L. Jullien, and J.-M. Lehn. J. Phys. Chem. **97**, 11376 (1993).
6. M.R. Shortreed, S.F. Swallen, Z.-Y. Shi, W. Tan, Z. Xu, C. Devadoss, J.S. Moore, and R. Kopelman. J. Phys. Chem. B, **101**, 6318 (1997).
7. D.L. Andrews and R.G. Crisp. J. Fluorescence **16**, 191 (2006).
8. H. van Amerongen, L. Valkunas, and R. van Grondelle. Photosynthetic excitons. World Scientific. Singapore. 2000.
9. D.M. Guldi. Chem. Soc. Rev. **31**, 22 (2002).
10. M. Halim, J.N.G. Pillow, I.D.W. Samuel, and P.L. Burn. Synth. Metals, **102**, 922–923 (1999).
11. A.W. Freeman, S.C. Koene, P.L. Malenfant, M.E. Thompson, and J.M.J. Fréchet. J. Am. Chem. Soc. **122**, 12385 (2000).
12. T.D. Anthopoulos, J.P.J. Markham, E.B. Namdas, J.R. Lawrence, I.D.W. Samuel, S.-C. Lo, and P.L. Burn. Org. Electronics **4**, 71 (2003).
13. P. Furuta, J. Brooks, M.E. Thompson, and J.M.J. Fréchet. J. Am. Chem. Soc. **125**, 13165 (2003).
14. P.L. Burn, S.-C. Lo, and I.D.W. Samuel. Adv. Mater. **19**, 1675 (2007).
15. T. Miyakawa and D.L. Dexter. Phys. Rev. B, **1**, 70 (1970).
16. F. Auzel. J. Lumin. **45**, 341 (1990).
17. M. Chua and P.A. Tanner. J. Lumin. **66–7**, 203 (1995).
18. D.L. Andrews. J. Raman Spectrosc. **31**, 791 (2000).
19. D.L. Andrews and R.D. Jenkins. J. Chem. Phys. **114**, 1089 (2001).

© 2008 NRC Canada

20. B.W. Lovett, J.H. Reina, A. Nazir, B. Kothari, and G.A. Briggs. Phys. Lett. A, **315**, 136 (2003).
21. A.O. Govorov. Phys. Rev. B, **68**, 075315 (2003).
22. S. Sangu, K. Kobayashi, A. Shojiguchi, and M. Ohtsu. Phys. Rev. B, **69**, 115334 (2004).
23. P.R. Selvin. Nature Struct. Biol. **7**, 730 (2000).
24. S. Hohng, C. Joo, and T. Ha. Biophys. J. **87**, 1328 (2004).
25. S. Rüttinger, R. Macdonald, B. Krämer, F. Koberling, M. Roos, and E. Hildt. Biomedical Optics, **11**, 024012 (2006).
26. S.V. Koushik, H, Chen, C. Thaler, H.L. Puhl, III, and S.S. Vogel. Biophys. J. **91**, L99 (2006).
27. G. Boas. Biophotonics Int. **14** (2) 30 (2007).
28. J. Zhang and M.D. Allen. Mol. Biosystems, **3**, 759 (2007).
29. E.A. Jares-Erijman and T.M. Jovin. Nature Biotechnol. **21**, 1387 (2003).
30. M. Elangovan, H. Wallrabe, Y. Chen, R.N. Day, M. Barroso, and A. Periasamy. Methods, **29**, 58 (2003).
31. S.K. Sekatskii. Phil. Trans. R. Soc. A – Math. Phys. Eng. Sci. **362**, 901 (2004).
32. J.P.S. Farinha and J.M.G. Martinho. Springer Ser. Fluoresc. **4**, 215 (2008).
33. V. Bagalkot, L. Zhang, E. Levy-Nissenbaum, S. Jon, P.W. Kantoff, R. Langer, and O.C. Farokhzad. Nano Lett. **7**, 3065 (2007).
34. I.L. Medintz, A.R. Clapp, H. Mattoussi, E.R. Goldman, B. Fisher, and J.M. Mauro. Nature Materials, **2**, 575 (2003).
35. H. Zhang and D.M. Rudkevich. Chem. Commun. 1238 (2007).
36. X. Fan, A. Majumder, S.S. Reagin, and E.L. Porter. J. Biomed. Opt. **12,** 03407 (2007).
37. T. Förster. Annalen. Phys. **2**, 55 (1948).
38. S.A. Latt, H.T. Cheung, and E.R. Blout. J. Am. Chem. Soc. **87**, 995 (1965).
39. D.L. Andrews and J. Rodríguez. J. Chem. Phys. **127**, 084509 (2007).
40. A.A. Demidov and D. L. Andrews. *In* Encyclopedia of chemical physics and physical chemistry. Vol. 3. J. H. Moore and N. D. Spencer (*Editor*s). Institute of Physics. Bristol. 2001. pp. 2701–2715.
41. C. Galli, K. Wynne, S.M. Lecours, M.J. Therien, and R.M. Hochstrasser. Chem. Phys. Lett. **206**, 493 (1993).
42. B.W. van der Meer. *In* Resonance energy transfer. D.L. Andrews and A.A. Demidov (*Editors*). Wiley. New York, NY, USA. 1999. pp. 151–172.
43. C.G. dos Remedios and P.D.J Moens. J. Struct. Biol. **115**, 175 (1995).
44. G. Ramanoudjame, M. Du, K.A. Mankiewicz, and V. Jayaraman. Proc. Natl. Acad. Sci. USA. **103**, 10473 (2006).
45. X. You, A.W. Nguyen, A. Jabaiah, M.A. Sheff, K.S. Thorn, and P.S. Daugherty. Proc. Natl. Acad. Sci. USA. **103**, 18458 (2006).
46. P.R. Selvin. Annu. Rev. Biophys. Biomol. Struc. **31**, 275 (2002).
47. B. Schuler. Chem. Phys. Chem. **6**, 1206 (2005).
48. F. Tanaka. J. Chem. Phys. **109**, 1084 (1988).
49. Z.G. Yu. J. Chem. Phys. **127**, 221101 (2007).
50. M. Isaksson, N. Norlin, P.-O. Westlund, and L.B.-Å. Johansson. Phys. Chem. Chem. Phys. **9**, 1941 (2007).
51. J.R. Lakowicz. Principles of fluorescence spectroscopy. 2nd ed. Kluwer Academic. New York, NY, USA. 1999. Chap. 10.
52. B. Valeur. Molecular fluorescence. Principles and aapplications. Chapter 9. Wiley-VCH. Weinheim, Germany. 2002.
53. D.L. Dexter. J. Chem. Phys. **21**, 836 (1953).
54. G.D. Scholes and K.P. Ghiggino. J. Phys. Chem. **98**, 4580 (1994).
55. E.K.L. Yeow and K.P. Ghiggino. J. Phys. Chem. A, **104**, 5825 (2000).
56. D.L. Andrews and T. Thirunamachandran. J. Chem. Phys. **67**, 5026 (1977).
57. W.L. Levshin. Z. Angew. Phys. **32**, 307 (1925).
58. F. Perrin. Ann. de Phys. **12**, 169 (1929).
59. G.D. Scholes and D.L. Andrews. J. Chem. Phys. **107**, 5374 (1997).
60. A. Salam. J. Chem. Phys. **122**, 044112 (2005).
61. D.P. Craig and T. Thirunamachandran. Molecular quantum electrodynamics. Dover. New York, NY, USA. 1998.
62. R.G. Woolley. Int. J. Quantum Chem. **74**, 531 (1999).
63. P.W. Milonni. The quantum vacuum. Academic Press. Boston, MA. 1994.
64. R.G. Woolley. Proc. R. Soc. London, Ser A, **456**, 1803 (2000).
65. J.S. Avery. Proc. Phys. Soc. **88**, 1 (1966).
66. L. Gomberoff and E.A. Power. Proc. Phys. Soc. **88**, 281 (1966).
67. D.L. Andrews. Chem. Phys. **135**, 195 (1989).
68. G.J. Daniels, R.D. Jenkins, D.S. Bradshaw, and D.L. Andrews. J. Chem. Phys. **119**, 2264 (2003).
69. D.L. Andrews and B.S. Sherborne. J. Chem. Phys. **86**, 4011 (1987).
70. G. Juzelinas and D.L. Andrews. Adv. Chem. Phys. **112**, 357 (2000).
71. L. Novotny and B. Hecht. Principles of nano-optics. University Press, Cambridge, UK. 2006. pp. 285–293.
72. R.D. Jenkins, G.J. Daniels and D.L. Andrews. J. Chem. Phys. **120**, 11442 (2004).
73. M.N. Berberan-Santos, E.J.N. Pereira and J.M.G. Martinho. J. Chem. Phys. **107**, 10480 (1997).
74. D. L. Andrews and G. Juzeliūnas. J. Chem. Phys. **95**, 5513 (1991).
75. G.D. Scholes, C. Curutchet, B. Mennucci, R. Cammi, and J. Tomasi. J. Phys. Chem. B, **111**, 6978 (2007).
76. C. Curutchet, G.D. Scholes, B. Mennucci, and R. Cammi. J. Phys. Chem. B, **111**, 13253 (2007).
77. G. Juzeliūnas and D.L. Andrews. Phys Rev. B, **49**, 8751 (1994).
78. D.L. Andrews and G. Juzelinas. J. Chem. Phys. **96**, 6606 (1992).
79. C. Devadoss, P. Bharathi, and J.S. Moore. J. Am. Chem. Soc. **118**, 9635 (1996).
80. X. Hu and K. Schulten. Phys. Today, **50** (8) 28 (1997).
81. R. van Grondelle and V. Novoderezhkin. Biochem. **40**, 15057 (2001).
82. T. Renger, V. May, and O. Kühn. Phys. Rep. **343**, 138 (2001).
83. R.J. Cogdell, A. Gall, and J. Kohler. Quart. Rev. Biophys. **39**, 227 (2006).
84. T. Brixner, J. Stenger, H.M. Vaswani, M. Cho, R.E. Blankenship, and G.R. Fleming. Nature (London, UK), **434**, 625 (2005).
85. G.S. Engel, T.R. Calhoun, E.L. Read, T.-K. Ahn, T. Mancal, Y.-C. Cheng, R.E. Blankenship, and G.R. Fleming. Nature (London, UK), **446**, 782 (2007).
86. P. Ball. Nanotechnol. **13**, R15 (2002).
87. D.L. Andrews. *In* Introduction to complex mediums for optics and electromagnetics. W.S. Weiglhofer and A. Lakhtakia (*Editors*). SPIE. Bellingham, WA, USA. 2003. pp 141–163.
88. D.L. Andrews (*Editor*). Energy harvesting materials. World Scientific. Singapore. 2005.
89. A. Bar-Haim, J. Klafter, and R. Kopelmann. J. Am. Chem. Soc. **119**, 6197 (1997).
90. A. Archut and F. Vögtle. Chem. Soc. Rev. **27**, 233 (1998).

© 2008 NRC Canada

91. A. Adronov and J. M. J. Fréchet. Chem. Commun. 1701 (2000).
92. A. Nantalaksakul, D.R. Reddy, C.J. Bardeen, and S. Thayumanavan. Photosynth. Res. **87**, 133 (2006).
93. C. Devadoss, P. Bharathi, and J.S. Moore. J. Am. Chem. Soc. **118**, 9635 (1996).
94. S.F. Swallen, Z.-Y. Shi, W. Tan, Z. Xu, J.S. Moore, and R. Kopelman. J. Lumin. **76–7**, 193 (1998).
95. P.G. van Patten, A.P. Shreve, J.S. Lindsey, and R.J. Donohoe. J. Phys. Chem. B, **102**, 4209 (1998).
96. M. Nakano, M. Takahata, H. Fujita, S. Kiribayashi, and K. Yamaguchi. Chem. Phys. Lett. **323**, 249 (2000).
97. J.L. Bentz and J.J. Kozak. J. Lumin. **121**, 62 (2006).
98. A. Blumen, A. Volta, A. Jurjiu, and Th. Koslowski. Physica A, **356**, 12 (2005).
99. S.M. Vlaming, D.J. Heijs, and J. Knoester. J. Lumin. **111**, 349 (2005).
100. D. Rana and G. Gangopadhyay. J. Chem. Phys. **11**8 434 (2003).
101. D.L. Andrews and S. Li. *In* Nanomodeling II. A. Lakhtakia and S.A. Maksimenko (*Editors*). Proc. SPIE **6328**, 63280V (2006).
102. D.L. Andrews and S. Li. Chem. Phys. Lett. **433**, 239 (2006).
103. D.L. Andrews, S. Li, J. Rodríguez, and J. Slota. J. Chem. Phys. **127**, 134902 (2007).
104. D.L. Andrews and D.S. Bradshaw. J. Chem. Phys. **121**, 2445 (2004).
105. D.L. Bradshaw and D.L. Andrews. Chem. Phys. Lett. **430**, 191 (2006).
106. P. Allcock, R.D. Jenkins, and D.L. Andrews. Phys. Rev. A, **61**, 023812 (2000).
107. R.D. Jenkins, D.L. Andrews, and L.C. Dávila Romero. J. Phys. B: Atom. Molec. Opt. Phys. **35**, 445 (2002).
108. B.W. Alligood and A. Salam. Mol. Phys. **105**, 395 (2007).
109. D.L. Andrews and R.G. Crisp. J. Opt. A: Pure Appl. Opt. **8**, S106 (2006).
110. D.L. Andrews, R.G. Crisp, and S. Li. J. Chem. Phys. **127**, 174702 (2007).
111. D.L. Andrews. Phys. Rev. Lett. **99**, 023601 (2007).
112. D.S. Bradshaw and D.L. Andrews. J. Chem. Phys. **128**, 144506 (2008).
113. B.W. Lovett, J.H. Reina, A. Nazir, and G.A.D. Briggs. Phys. Rev. B, **68**, 205319 (2003).
114. G.D. Scholes and D.L. Andrews. Phys. Rev. B, **72**, 125331 (2005).
115. R.D. Piner, J. Zhu, F. Xu, S.H. Hong, and C.A. Mirkin. Science (Washington, DC), **283**, 661 (1999).
116. C.A. Mirkin, S.H. Hong, and L. Demers. Chem. Phys. Chem. **2**, 37 (2001).
117. N.P. Reynolds, S. Janusz, M. Escalante-Marun, J. Timney, R.E. Ducker, J.D. Olsen, C. Otto, V. Subramaniam, G.J. Leggett, and C.N. Hunter. J. Am. Chem. Soc. **129**, 14625 (2007).
118. R. Szoszkiewicz, T. Okada, S.C. Jones, T.D. Li, W.P. King, S.R. Marder and E. Riedo. Nano Lett. **7**, 1064 (2007).
119. R.W. Boyd and P. Narum. J. Mod. Opt. **54**, 2403 (2007).
120. K.L. Tsakmakidis, A.D. Boardman, and O. Hess. Nature (London, UK), **450**, 397 (2007).

© 2008 NRC Canada

Convenient synthesis of ferrocene amines via Cu-catalyzed coupling reaction

Jinsheng Wu, Xiaolong Li, Mingyu Yang, Yujie Gao, Qianru Lv, and Baohua Chen

Abstract: An efficient copper-catalyzed Ullmann-type cross-coupling reaction without ligand of iodo-ferrocene with amines has been reported. In this process, a range of ferrocenyl amine compounds have been prepared in moderate to good yields.

Key words: amines, iodo-ferrocene, cross-coupling, copper, Ullmann coupling.

Résumé : On a mis au point une méthode efficace de l'iodoferrocène avec des amines qui est catalysée par le cuivre, mais ne donne pas lieu à une réaction de couplage croisé de type Ullmann avec le ligand. Dans ce procédé, on a préparé une grande variété de ferrocénylamines avec des rendements allant de modérés à bons.

Mots-clés : amines, iodoferrocène, couplage croisé, cuivre, couplage d'Ullmann.

[Traduit par la Rédaction]

Introduction

During the past few decades, a wide range of substituted ferrocene derivatives have been synthesized and studied. The ferrocenyl moiety has played a useful role, either as backbone or substituent in ancillary ligands (1). In addtion, it is a metal–organic nonlinear optical material used as a donor moiety (2) and in functional polymers with unusual properties (3).

Although ferrocenes are classical aromatic compounds, they can have rather unique properties due to their particular electronic and geometric features. As an example, the synthetic availability of heteroatom-substituted (oxygen, nitrogen) ferrocene is rather limited, since many methods for the functionalization of aromatics are unsuitable for modifying ferrocene derivatives. Typically, a few reports have been published concerning the synthesis of amino and diaminoferrocene derivatives (4).

Although it is well-known that the Ullmann reaction (copper-catalyzed N-arylation of amines) (5) predates the palladium-catalyzed amination methodology by many decades and that its applications in academic and industrial laboratories are well-documented (6), the methods have some deficiencies. For example, it is necessary to use temperatures as high as 210 °C, highly polar solvents, and often large amounts of copper reagents, to produce only modest yields (7). Without doubt, these factors have limited its usability in this field. Important alternatives have been reported recently, using the Ullmann-type methodology for the N-arylation of iodobenzene with a CuI/glycine/K_3PO_4/dioxane catalyst system (8) and that of iodobenzene using a CuI/K_3PO_4/PPAPM/DMF catalyst system (9). Özçubukçu et al. reported that ferrocenyl amides could be obtained from iodo-ferrocene and amides, pyrazole, imidazole, and triazole in the presence of copper (I) iodide and *t*–BuOK (10).

In the present work, we wish to report a rapid and convenient method for the synthesis of ferrocenyl amines via a Cu-catalyzed Ullmann-type coupling reaction of amines and iodo-ferrocene.

Received 29 February 2008. Accepted 15 May 2008. Published on the NRC Research Press Web site at canjchem.nrc.ca on 28 June 2008.

J. Wu,[1] X. Li, M. Yang, Y. Gao, Q. Lv, and B. Chen. State Key Laboratory of Applied Organic Chemistry Lanzhou University, Lanzhou 730000 P. R. China.

[1]Corresponding author (e-mail: chbh@lzu.edu.cn).

Result and discussion

In the first stage of the study, we focused on the coupling reaction between 2-nitrobenzenamine and iodo-ferrocene. We examined the effects of various copper salts, bases, solvents, and reaction time on the yields of the coupling reaction. The results are shown in Scheme 1 and Table 1.

It can be seen from Table 1 that the effect of the base on the coupling reaction was significant. In general, K_2CO_3 gives superior yields to those obtained by *t*–BuOK, K_3PO_4, and Et_3N (Table 1, entries 2–4). Further optimization of the reaction conditions reveals that the use of xylene is more effective than other solvents, such as toluene, DMSO, DMF, and benzene (Table 1, entries 4–7). In addition to Cu, we also used CuI, Cu(acac)$_2$, Cu_2O, CuCl, $CuCl_2$, CuBr, and $CuBr_2$ as the catalysts. However, the yields given by these other seven copper catalysts are much lower than those produced with Cu. Thus, it is obvious that the inexpensive Cu is the most desirable catalyst of this reaction.

On the basis of the above results, we consider that Cu powder (10 mol%) /K_2CO_3/xylene is a very suitable catalyst system for N-arylation (Scheme 2 and Table 2).

As expected, we have prepared a series of aminoferrocenes via this process. We have not found any side product formation, such as biferrocene, bisarylamines, etc. It seems that the electron-poor amines (e.g., Table 2, entries 1, 4–8, 10) react fairly well in the coupling. The substituted amines having an electron-rich (Table 2, entry 14) group at

 doi:10.1139/V08-096 © 2008 NRC Canada

Scheme 1.

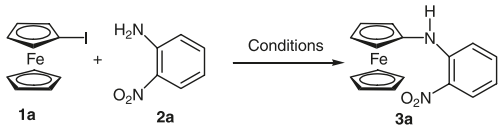

Table 1. Cu-catalyzed cross-coupling of iodo-ferrocene with amines under different conditions.

Entry	Catalyst	Solvent	Time (h)	Base	Yield (%)
1	Cu	Toluene	6	K_3PO_4	35
2	Cu	Toluene	6	K_2CO_3	52
3	Cu	Toluene	6	$(Et)_3N$	Trace
4	Cu	Toluene	6	^{t}–BuOK	Trace
5	Cu	Xylene	6	K_2CO_3	85
6	Cu	DMSO	6	K_2CO_3	0
7	Cu	DMF	6	K_2CO_3	45
8	CuI	Xylene	6	K_2CO_3	0
9	CuCl	Xylene	6	K_2CO_3	50
10	$CuCl_2$	Xylene	6	K_2CO_3	36
11	CuBr	Xylene	6	K_2CO_3	70
12	$CuBr_2$	Xylene	6	K_2CO_3	28
13	CuO	Xylene	6	K_2CO_3	61
14	Cu_2O	Xylene	6	K_2CO_3	72
15	Cu	Xylene	10	K_2CO_3	86

Note: Reactions were carried out on a 0.25 mmol scale in 1.0 mL of solvent under argon for the specified period of time, with 1.0 equiv. of **1a**, 1.2 equiv. of **2a**, 2.0 equiv. of base, and 0.10 equiv. of [Cu].

Scheme 2.

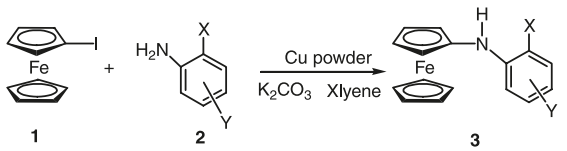

Y=0, X=-NO_2, -Br, -COMe, -CHO,-CO_2Me, Cl;
X=-COPh,Y=4-Cl, 4-CH_3; X=*p*-C_6H_4CO, Y=4-Cl;
X=NO_2, Y=5-CH_3, 5-NO_2; X=Br, Y=4-Br; X=Cl, Y=4-Cl;

the ortho position are often more difficult, compared with those having an electron-poor group, and those having electron-poor groups at the para positions (Table 2, entry 15) give no reaction. We also found that the substituent at the para and ortho positions cannot be tolerated either (Table 2, entries 12 and 13). The mechanism could not be completely elucidated from these results.

In summary, we have described a simple and efficient method for the preparation of a range of N-substituted valuable ferrocene derivatives via Ullmann-type coupling reaction mediated by Cu powder. Attractive features of this protocol are that the reactions are carried out easily in the given conditions, the operation is simple, the reagents used are inexpensive (metal salt and base), and the yields are satisfactory.

Table 2. Ullmann-type coupling of iodo-ferrocene with amines.

Entry	Coupling component	Product	Yield[a] (%)
1		**3a**	85
2		**3b**	46
3	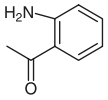	**3c**	92
4	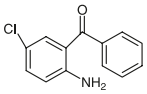	**3d**	89
5	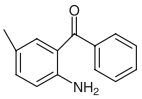	**3e**	84
6	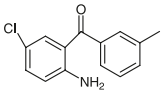	**3f**	86
7	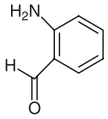	**3g**	96
8	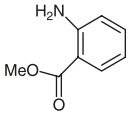	**3h**	81
9	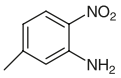	**3i**	89
10		**3j**	94
11	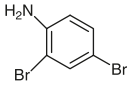	**3k**	38
12	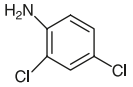	**3l**	—[b]
13	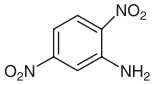	**3m**	—[b]
14	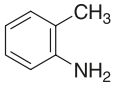	**3n**	—[b]
15	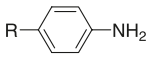 R=OCH_3, CH_3, Br, Cl, $COOCH_3$ CF_3, NO_2	**3o**	—[b]

Note: Reaction conditions: iodo-ferrocene (0.25 mmol), amine (0.3 mmol), Cu (10 mol%), K_2CO_3 (0.5 mmol), and xylene (1 mL) at 140 °C under a ballon pressure of Ar. Reactions were carried out in 6 h.
[a]Isolated yield based on iodo-ferrocene.
[b]No reaction.

© 2008 NRC Canada

Experimental

NMR spectra were recorded in $CDCl_3$ using TMS as internal standard on a Varian Mercury 300 spectrometer (at 300 and 75 MHz for ^1H and ^{13}CNMR spectra, respectively). IR spectra were carried out on a Nicolet Nexus 670 FT/ IR spectrometer. FAB-MS were obtained on a ZAB-HS mass spectrometer. Elemental analysis was performed by an Elementar Vario EL analyzer.

The substituted amines (Table 2, entries 5, 6, and7), as well as iodo-ferrocene (11), were prepared according to the literature. All other starting materials were obtained from commercial suppliers and used without further purification.

Typical procedure for the preparation of of *N*-ferrocenyl-2-nitrobenzenamine (3a)

In a Erlenmeyer flask, xylene (1 mL), iodo-ferrocene (0.25 mmol), amines (0.3 mmol), Cu powder (10 mol%), and K_2CO_3 (0.5 mmol) were added successively under argon atmosphere with stirring. The mixture was reacted at 140 °C until complete consumption of iodo-ferrocene, as monitored by TLC. After cooling, the mixture was extracted with ethyl acetate (3 × 10 mL), the combined organic layer was washed with water and brine, then dried ($MgSO_4$), filtered, and concentrated in vacuo. The residue was purified by column chromatography, petroleum/ethyl acetate. Red solid (**3a**) was obtained; mp 104–105 °C. IR (neat, cm^{-1}) ν: 489, 1265, 1614, 3039, 3379. ^1H NMR (300 MHz, $CDCl_3$) δ: 4.26 (s, 5H), 4.37 (s, 2H), 4.17 (s, 2H) 6.65–6.70 (t, *J* = 6.9 Hz, 1H), 7.09–7.12 (d, *J* = 7.5 Hz, 1H), 7.32–7.36 (t, *J* = 7.2 Hz, 1H), 8.14–8.17 (d, *J* = 7.8 Hz, 1H), 9.12 (s, 1H). ^{13}C NMR (75 MHz, $CDCl_3$) δ: 65.8, 66.1, 69.6 94.2, 115.9, 116.4, 126.3, 132.2, 135.6, 145.2. Anal. calcd. for $C_{16}H_{14}FeN_2O_2$: C 59.65, H 4.38, N 8.70; found: C 59.86, H 4.58, N 8.60. FAB-MS *m*/*z*: 322 [M^+].

Characterization data for products

N-*Ferrocenyl-2-bromobenzenamine (3b)*

Yellow solid, mp 110–112 °C. IR (neat, cm^{-1}) ν: 742, 1521, 1592, 3405. ^1H NMR (300 MHz, $CDCl_3$) δ: 4.14 (s, 2 H), 4.24 (s, 5H), 4.35 (s, 2H), 5.43 (s, 1H), 6.60–6.62 (d, 1H), 7.03 (m, 1H), 7.1 (m, 1H), 7.42–7.45 (m, 1H). ^{13}C NMR (75 MHz, $CDCl_3$) δ: 65.3, 69.4, 114.4, 119.1, 128.0, 132.2. Anal. calcd. for $C_{16}H_{14}BrFeN$: C 53.97, H 3.96, N 3.93; found: C 53.87, H 4.01, N 3.98. FAB-MS *m*/*z*: 355[M^+].

1–Ferrocenylamino-2-phenyl ethanone (3c)

Yellow solid, mp 57–59 °C. IR (neat, cm^{-1}) ν: 745, 1244, 1636, 3092, 3271. ^1H NMR (300 MHz, $CDCl_3$) δ: 2.61 (s, 3H), 4.17 (s, 5H), 4.31 (s, 2H), 4.08 (s, 2H), 6.61–6.66 (t, *J* = 7.8 Hz, 1H), 7.05–7.08 (d, *J* = 7.8 Hz, 1H), 7.26–7.31 (t, *J* = 7.5 Hz, 1H), 7.72–7.75 (d, *J* = 8.1 Hz, 1H), 10.06 (s, 1H). ^{13}C NMR (75 MHz, $CDCl_3$) δ: 28.3, 65.4, 65.7, 69.6, 96.1, 114.4, 115.5, 118.1, 132.6, 134.9, 150.6, 201.4. Anal. calcd. for $C_{18}H_{17}FeNO$: C 67.73, H 5.37, N 4.39; found: C 67.95, H 5.19, N 4.51. FAB-MS *m*/*z*: 319 [M^+].

(5-Chloro-2-(ferrocenylamino)phenyl) (phenyl)methanone (3d)

Yellow solid, mp 114–116 °C. IR (neat, cm^{-1}) ν: 744, 1242, 1510, 1625, 3447. ^1H NMR (300 MHz, $CDCl_3$) δ: 4.14 (s, 2H), 4.26 (s, 5H), 4.36 (s, 2H), 7.08–7.17 (m, 1H), 7.15–7.18 (m, 1H), 7.27 (s, 1H), 7.46–7.47 (m, 3H), 7.59–7.67 (m, 2H), 9.62 (s, 1H). ^{13}C NMR (75 MHz, $CDCl_3$) δ: 65.4, 65.7, 69.4, 115.7, 128.1, 128.3, 129.1, 130.9, 131.4, 1333.6, 134.4, 134.5, 135.6, 199.3. Anal. calcd. for $C_{23}H_{18}ClFeNO$: C 66.45, H 4.36, N 3.37; found: C 66.32, H 4.58, N 3.41. FAB-MS *m*/*z*: 415 [M^+].

(5-Methyl-2-(ferrocenylamino)phenyl) (phenyl)methanone (3e)

Orange solid, mp 87–89 °C. IR (neat, cm^{-1}) ν: 745, 1250, 1625, 3449. ^1H NMR (300 MHz, $CDCl_3$) δ: 2.20 (s, 3H), 4.18 (s, 2H), 4.24 (s, 5H), 4.40 (s, 2H), 7.06–7.09 (m, 1H), 7.16–7.19 (m, 1H) 7.29 (s, 1H), 7.45–7.60 (m, 3H), 7.64–7.67 (m, 2H), 9.50 (s, 1H). ^{13}C NMR (75 MHz, $CDCl_3$) δ: 64.5, 65.3, 69.4, 114.4, 117.6, 124.2, 128.1, 129.1, 130.9, 134.5, 135.6, 140.4, 148.8, 199.3. Anal. calcd. for $C_{24}H_{21}FeNO$: C 72.93, H 5.35, N 3.54; found: C 73.14, H 5.12, N 3.62. FAB-MS *m*/*z*: 395 [M^+].

5-Chloro-2-(ferrocenylamino)phenyl) (m-tolyl)methanone (3f)

Red solid, mp 110–112 °C. IR (neat, cm^{-1}) ν: 734, 1255, 1504, 1625, 3093, 3304. ^1H NMR (300 MHz, $CDCl_3$) δ: 2.42 (s, 3H), 4.12 (s, 2H), 4.25 (s, 5H), 4.33 (s, 2H), 7.05–7.08 (m, 1H), 7.22–7.23 (m, 1H), 7.25–7.26 (m, 1H), 7.35 (s, 1H), 7.37 (s, 1H), 7.40–7.42 (m, 1H) 7.46–7.47 (m, 1H), 9.68 (s,1H). ^{13}C NMR (75 MHz, CDCl3) δ: 21.4, 65.0, 65.6, 69.4, 95.5, 118.4, 119.5, 126.2, 128.1, 129.4, 132.1, 133.6, 134.3, 138.2, 139.5, 149.6, 198.6. Anal. calcd. for $C_{24}H_{20}ClFeNO$: C 67.08, H 4.69, N 3.26; found: C 66.85, H 4.88, N 3.41. FAB-MS *m*/*z*: 429 [M^+].

2-(Ferrocenylamino)benzaldehyde (3g)

Yellow solid, mp 107–109 °C. IR (neat, cm^{-1}) ν: 750, 1654, 3306, 3452. ^1H NMR (300 MHz, $CDCl_3$) δ: 4.11 (s, 2H), 4.24 (s, 5H), 4.35 (s, 2H), 6.72–6.77 (t, *J* = 7.2 Hz, 1H), 7.07–7.10 (d, *J* = 8.4 Hz, 1H), 7.32–7.36 (t, *J* = 7.8 Hz, 1H), 7.47–7.49 (d, *J* = 7.5 Hz, 1H), 9.49 (s, 1H), 9.9 (s,1H). ^{13}C NMR (75MHz, $CDCl_3$) δ: 64.6, 65.5, 69.3, 113.2, 116.0, 118.7, 135.4, 136.2, 149.8, 194.1. Anal. calcd. for $C_{17}H_{15}FeNO$: C 66.91, H 4.95, N 4.59; found: C 67.12, H 4.98, N 4.29. FAB-MS *m*/*z*: 305[M+].

Methyl-2-(ferrocenylamino) benzoate (3h)

Yellow solid, mp 56–58 °C. IR (neat, cm^{-1}) ν: 748, 1246, 1682, 3330. ^1H NMR (300 MHz, $CDCl_3$) δ: 3.89 (s, 3H), 4.09 (s, 2H), 4.23 (s, 5H), 4.32 (s, 2H), 6.60–6.65 (t, *J* = 7.2 Hz, 1H), 7.01–7.04 (d, *J* = 8.7 Hz, 1H), 7.26–7.30 (t, *J* = 6.9 Hz, 1H), 7.89–7.91 (t, *J* = 7.5 Hz, 1H), 8.92 (s, 1H). ^{13}C NMR (75 MHz, $CDCl_3$) δ: 51.6, 64.8, 64.8, 69.2, 110.4, 113.7, 115.7, 134.1, 150.3, 169.1. Anal. calcd. for $C_{18}H_{17}FeNO_2$: C 64.50, H 5.11, N 4.18; found: C 64.27, H 5.33, N 4.32. FAB-MS *m*/*z*: 335 [M^+].

N-*Ferrocenyl-5methyl-2-nitro-benzenamine (3i)*

Orange solid, mp 89–91 °C. IR (neat, cm^{-1}): 744, 914, 1519, 3381. ^1H NMR (300 MHz, $CDCl_3$) δ: 2.26 (s, 3H), 4.15 (s, 2H), 4.19 (s, 5H), 4.24 (s, 2H), 7.04–7.07 (d, *J* = 8.7 Hz, 1H), 7.16–7.19 (d, *J* = 8.7 Hz, 1H), 7.95 (s, 1H), 9.01 (s, 1H). ^{13}C NMR (75 MHz, $CDCl_3$) δ: 20.0, 65.5, 66.0, 69.5, 94.8, 116.0, 125.5, 126.1, 132.0, 137.1. Anal. calcd. for

© 2008 NRC Canada

$C_{17}H1_6FeN_2O_2$: C 60.74, H 4.80, N 8.33; found: C 60.87, H 4.98, N 8.02. FAB-MS *m*/*z*: 336 [M^+].

N-*Feerocenyl-2-chlorobenzenamine (3j)*

Yellow solid, mp 94–96 °C. IR (neat, cm^{-1}) ν: 744, 1524, 1595, 3415. ^1H NMR (300 MHz, $CDCl_3$) δ: 4.12 (s, 2H), 4.23 (s, 5H), 4.33 (s, 2H), 5.45 (s, 1H), 6.67–6.70 (m, 1H), 7.09–7.14 (m, 2H), 7.24–7.29(s, 1H). ^{13}C NMR (75 MHz, $CDCl_3$) δ: 65.2, 69.2, 114.2, 118.5, 127.4, 129.6. Anal. calcd. for $C_{16}H_{14}ClFeN$: C 61.67, H 4.53, N 4.50; found: C 61.56, H 4.69, N 4.72. FAB-MS *m*/*z*: 311 [M+].

N-*Ferrocenyl-2,5-dibromobenzenamine (3k)*

Yellow solid, mp 83–85 °C. IR (neat, cm^{-1}) ν: 744, 1514, 1584, 3403. ^1H NMR (300 MHz, $CDCl_3$) δ: 4.14 (s, 2H), 4.25 (s, 5H), 4.31 (s, 2H), 5.52 (s, 1H), 6.72–6.75 (d, J = 7.8 Hz, 1H), 7.25 (s, 1H), 7.28–7.30 (d, J = 7.2 Hz, 1H). ^{13}C NMR (75 MHz, $CDCl_3$) δ: 65.5, 69.3, 116.7, 120.5, 121.5, 130.4, 133.1, 134.0. Anal. calcd. for $C_{16}H_{13}Br_2FeN$: C 44.18, H 3.01, N 3.22; found: C 44.32, H 2.86, N 3.34. FAB-MS *m*/*z*: 435 [M+].

Acknowledgements

We are grateful to the project-sponsored by SRF for ROCS, SEM.

References

1. (*a*) A. Togni and T. Hayashi (*Editors*). Ferrocenes. VCH, Weinheim, Germany. 1995. Chaps. 1–3; (*b*) A. Togni. Angew. Chem., Int. Ed. Engl. **35**, 1475 (1996); (*c*) A. Togni, N. Bieler, U. Burckhardt, C. Köllner, G. Pioda, R. Schneider, and A. Schnyder. Pure Appl. Chem. **7**, 1531 (1999); (*d*) U. Nettekoven, M. Widhalm, P.C.J. Kamer, P.W.N.M. van Leeuwen, K. Mereiter, M. Lutz, and A.L. Spek. Organometallics, **19**, 2299 (2000).
2. (*a*) M.L.H. Green, S.R. Marder, M.E. Thompson, J.A. Bandy, D. Bloor, P.V. Kolinsky, and R.J. Jones. Nature (London), **330**, 360 (1987); (*b*) H.S. Nalwa and S. Miyata. *In* Nonlinear optical effects in molecules and polymers, and refs. cited therein. CRC Press, New York. 1997; (*c*) J. Jeck, S. Dabek, T. Meyer-Friedrichsen, and H. Wong. Coord. Chem. Re. **190**, 1217 (1999).
3. (*a*) I. Manners. Adv. Organomet. Chem. **37**,131 (1995); (*b*) P. Gómez-Elipe, R. Resendes, P.M. Macdonald, and I.J. Manners. J. Am. Chem. Soc. **120**, 8348 (1998); (*c*) J. Tsuji and T. Mandai. Synthesis, 1 (1996).
4. For aminoferrocene and derivatives thereof, please see: (*a*) E.M. Acton and R.B.J. Silverstein. Org. Chem. **24**,1487 (1959); (*b*) A.N. Nesmeyanov, V.A. Sazonova, and V.I. Romanenko. Doklady Akademii Nauk SSSR. **157(4)**, 922 (1964); (*c*) M. Herberhold, M. Ellinger, and W. Kremnitz. J. Organomet. Chem. **24**, 1227 (1983); (*d*) M. Herberhold, M. Ellinger, and L. Haumaier. *In* Organometallic syntheses. Vol. 3. *Edited by* R.B. King and J.J. Eisch. Elsevier, Amsterdam, 1996; (*e*) M. Sato and S. Ebine. Synthesis, 472 (1981); (*f*) M. Herberhold, M. Ellinger, and W. Kremnitz. J. Organomet. Chem. **241**, 227 (1983); (*g*) C.A. Fleckenstein and H. Plenio. Organometallics, **26**, 2758 (2007); (*h*) V.H. Purecha, N.S. Nandurkar, B.M. Bhanage, and J.M. Nagarkar. Tetrahedron Lett. **49**, 1384 (2008).
5. For N-arylation of anilines, please see: (*a*) F. Ullmann. Ber. Dtsch. Chem. Ges. **36**, 2382 (1903); (*b*) S. Gauthier and J.M.J. Fréchet. Synthesis, 383 (1987); (*c*) R. Gujadhur, D. Venkataraman, and J.T. Kintigh. Tetrahedron Lett. **42**, 4791(2001). For N-arylation of alkylamines, please see: (*d*) D. Ma, Y. Zhang, J. Yao, S. Wu, and F. Tao. J. Am. Chem. Soc. **120**, 12459 (1998); (*e*) J.B. Arterburn, M. Pannala, and A.M. Gonzalez. Tetrahedron Lett. **42**, 1475 (2001); (*f*) F.Y. Kwong, A. Klapars, and S.L. Buchwald. Org. Lett. **4**, 58 (2002).
6. For a review, see: J. Lindley. Tetrahedron, **40**, 1433 (1984).
7. T. Yamamoto and Y. Kurata. Can. J. Chem. **61**, 86 (1983).
8. For amino acid-mediated Goldberg reactions, plase see: W. Deng, Y.-F. Wang, Y. Zou, L. Liu, and Q.-X. Guo. Tetrahedron Lett. **45**, 2311 (2004).
9. H. Rao, Y. Jin, H. Fu, Y. Jiang, and Y. Zhao. Chem. Eur. J. **12**, 3636 (2006).
10. For the synthesis of nitrogen-substituted ferrocenes, please see: S. Özçubukçu, E. Schmitt, A. Leifert, and C. Bolm. Synthesis. **3**, 389 (2007).
11. F.S. Kamounah and J.B. Christensen. J. Chem. Res. Synopses, **4**, 150 (1997).

© 2008 NRC Canada

A novel and efficient synthesis of *bis*(benzofuranyl)methanes and 2-benzofuran-1-nitroalkanes catalyzed by $Bi(OTf)_3$

Ren Er Chen, Yan Li Wang, Zhi Wei Chen, and Wei Ke Su

Abstract: Bismuth (III) triflate-catalyzed Friedel–Crafts reactions between benzofuran and aldehydes in different solvents were investigated. Bis(benzofuranyl)methanes were obtained with good yields when acetonitrile was used as solvent, while in the case of nitromethane the multi-component reaction products, 2-benzofuran-1-nitroalkanes, were formed under similar conditions. A plausible mechanism is given.

Key words: benzofuran, aldehyde, bis(benzofuranyl)methanes, $Bi(OTf)_3$, 2-benzofuran-1-nitroalkane.

Résumé : On a étudié les réactions de Friedel–Crafts catalysées par le triflate de bismuth(III) et effectuées entre le benzofurane et les aldéhydes dans divers solvants. Avec l'acétonitrile comme solvant, on obtient de bons rendements de bis(benzofuranyl)méthanes alors que dans le nitrométhane, dans des conditions semblables, il y a formation de 2-benzofurane-1-nitroalcanes, des produits qui résultent de réactions entre plusieurs réactifs. On propose un mécanisme plausible.

Mots-clés : benzofurane, aldéhyde, bis(benzofuranyl)méthanes, $Bi(OTf)_3$, 2-benzofurane-1-nitroalcanes.

[Traduit par la Rédaction]

Introduction

Most natural and synthetic compounds with benzofuran moieties exhibit broad bioactivities (1, 2) such as antitumor, antifungal, antivirus activities, 5-lipoxygensase and 5α-reductase inhibitory activity (3–5). Moreover, they are also key intermediates for constructing some natural bioactive quinines (6). Though there are some reports of bis(benzofuranyl)methanones (7) and macrocyclic trimer (8), which were prepared from activated benzofurans, bis(benzofuranyl)methanes were only reported in one article (9). In that article, an environmentally harmful mineral acid was chosen as catalyst.

Recently, metal triflates have been widely used as Lewis acids that have low toxicity, low cost, high stability, are easy to handle and recover from water (10–13). In our ongoing green chemistry research program, investigating the use of environmentally friendly reagents, catalysts, and processes for organic reactions, we wish to study the activities of metal triflates in catalyzing the Friedel–Crafts alkylation and multi-component reaction. Herein, we wish to introduce $Bi(OTf)_3$ as a mild, highly efficient, and environmentally benign catalyst for the preparation of benzofuran derivatives. An effective, convenient, and economic method for the synthesis of bis(benzofuranyl)methanes was developed. Additionally, the first three-component synthetic procedure of 2-benzofuran-1-nitroalkane derivatives are reported here. The catalyst could be recovered easily after the reactions and reused without evident loss of activity.

Received 31 January 2008. Accepted 1 May 2008. Published on the NRC Research Press Web site at canjchem.nrc.ca on 8 July 2008.

R.E. Chen, Y.L. Wang, Z.W. Chen, and W.K. Su.[1] Key Laboratory of Pharmaceutical Engineering (Zhejiang University of Technology), Ministry of Education, College of Pharmaceutical Sciences, Zhejiang University of Technology, Hangzhou 310014, P. R. China.

[1]Corresponding author (e-mail: suweike@zjut.edu.cn).

Results and discussion

The condensation between benzofuran (2 equiv.) and benzaldehyde **1a** (1 equiv.) in CH_3NO_2 at refluxing temperature was used as a model reaction (Scheme 1) for the screening of a suitable metal triflate catalyst, and the results are summarized in Table 1. It can be seen that all metal triflates, with the exception of $Mg(OTf)_2$ and $Sr(OTf)_2$, showed good catalytic effects. $Sc(OTf)_3$ and $Bi(OTf)_3$ were particularly effective for this Friedel–Crafts alkylation reaction in short reaction times (Table 1, entries 1–8). Considering its low cost, $Bi(OTf)_3$ was chosen as reaction catalyst. The amounts of metal triflate were also examined in CH_3NO_2. When $Bi(OTf)_3$ and $Sc(OTf)_3$ were used as catalysts, 1 mol% was enough to finish the reaction in 1 h. There is no obvious influence on the yield on increasing the amount of $Bi(OTf)_3$ and $Sc(OTf)_3$ (Table 1, entries 6 and 9).

Solvents such as DMF, CH_3CN, EtOH, and PhMe (Table 1, entries 10–13) were also tested. Acetonitrile was found to give maximum yield followed by nitromethane. Reaction temperature was also explored in CH_3CN. No product was found at room temperature after 3 h. When the reaction temperature was increased to reflux, the yield was obviously improved. In light of this, subsequent studies were carried out under the following optimized conditions: 1 mol% $Bi(OTf)_3$ at refluxing temperature in CH_3CN. In this reac-

 doi:10.1139/V08-091 © 2008 NRC Canada

Scheme 1.

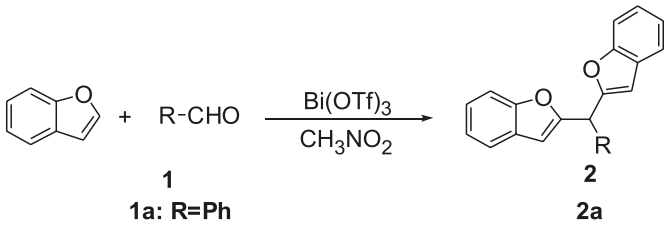

Table 1. The synthesis of bis(benzofuranyl)methanes under different reaction conditions.

Entry	Catalyst	Solvent	Loading (mol%)	Yield (%)[a]
1	$Cu(OTf)_2$	CH_3NO_2	10	65
2	$Zn(OTf)_2$	CH_3NO_2	10	55
3	$Mg(OTf)_2$	CH_3NO_2	10	0
4	$Yb(OTf)_3$	CH_3NO_2	10	46
5	$Sc(OTf)_3$	CH_3NO_2	1	75
6	$Sc(OTf)_3$	CH_3NO_2	5	76
7	$Sr(OTf)_2$	CH_3NO_2	10	0
8	$Bi(OTf)_3$	CH_3NO_2	1	76
9	$Bi(OTf)_3$	CH_3NO_2	5	77
10	$Bi(OTf)_3$	DMF[b]	1	0
11	$Bi(OTf)_3$	CH_3CN[b]	1	77
12	$Bi(OTf)_3$	EtOH[b]	1	65
13	$Bi(OTf)_3$	PhMe[b]	1	60
14	No catalyst	CH_3CN[b]	0	0

Note: General conditions: benzofuran (2 equiv.), benzaldehyde (1 equiv), and catalyst (0.01–0.1 equiv.) at 101 °C; reaction time 1.5 h.
[a]Isolate yields based on benzaldehyde.
[b]Reaction temperature: refluxing temperature.

tion, $Bi(OTf)_3$ could be reused three times without obvious loss of activity (Table 2, entry 1).

To extend the scope of the metal triflate-catalyzed method for the synthesis of bis(benzofuranyl)methanes, a series of aldehydes were investigated (Table 2). Both aromatic and aliphatic aldehydes were applicable to this reaction, except for **1q** and **1r**. The results indicated that a spacial steric effect had an obvious influence on the reaction (Table 2, entries 14–17). Furthermore, the substituted groups on the aromatic ring also had evident influence on the reaction. The aromatic ring-bearing electron-withdrawing groups only required short times with high yields, excluding the sterically hindered 2-nitrobenzaldehyde **1o**. The *m*-substituted benzaldehyde with electron-withdrawing groups were more beneficial to the reactions (Table 2, entries 6, 7, 9, and 11). To our surprise, good yield was also obtained when 3-hydroxybenzaldehyde was used as substrate (Table 2, entry 10). Considering the good reaction activity of aldehydes, benzophenone, acetone, and cyclohexanone were chosen as substrates. Trace reactions took place as indicated by TLC.

The formation of 2-benzofuran-1-nitroalkane derivatives was discovered serendipitiously. During the preparation of bis(benzofuranyl)methanes in nitromethane, another product was detected by TLC and identified as compound **3** (Scheme 2) by ^1H NMR, ^{13}C NMR, and MS. Thus, the catalytic activity of $Bi(OTf)_3$ was explored for the multicomponent condensation using 4-hydroxybenzaldehyde as model substrate. 4-Hydroxybenzaldehyde, benzofuran, and nitromethane were stirred at room temperature for 4 h at the molar ratio of 1:1:1 in CH_3CN. No product was found, as monitored by TLC. But when it was heated to refluxing temperature, contrary to our expectation, compound **2** were obtained instead of compound **3**. We also carried out the condensation of 4-hydroxybenzaldehyde, benzofuran, and nitromethane in CH_3NO_2. Interestingly, compound **3** was obtained as major product along with compound **2** as minor product (Table 3, entry 2). To extend the scope of the metal triflate-catalyzed method for the synthesis of 2-benzofuran-1-nitroalkane derivatives, we also tried other aldehydes. The results are summarized in Table 3. It can be seen that this condensation was only suitable for the aromatic aldehydes bearing strong electron-donating groups (Table 3, entries 2–5).

Table 2. The Friedel–Crafts alkylation of benzofuran with aldehydes catalyzed by $Bi(OTf)_3$ in CH_3CN.

Entry	R	Compound **2**	Yield (%)[a]
1	*n*-C_6H_5	**2a**	77, 76, 75, 75[b]
2	4-OH-C_6H_4	**2b**	65
3	3-CH_3O-4-OH-C_6H_3	**2c**	63
4	4-CH_3O-C_6H_4	**2e**	70
5	4-Cl-C_6H_4	**2f**	70
6	3-Cl-C_6H_4	**2g**	80
7	3-F-C_6H_4	**2h**	83
8	2-F-6-Cl-C_6H_3	**2i**	81
9	3-NO_2-C_6H_4	**2j**	87
10	3-OH-C_6H_4	**2k**	78
11	3-Br-C_6H_4	**2l**	78
12	H	**2m**	70
13	*n*-C_4H_9	**2n**	73
14	2-NO_2-C_6H_4	**2o**	45
15	2-OH-C_6H_4	**2p**	38
16	2,4-$(CH_3O)_2$-C_6H_3	**2q**	0
17	2-OCH_3-C_6H_5	**2r**	0

Note: Reaction condition: aldehyde (1 mmol), benzofuran (2 mmol), and $Bi(OTf)_3$ (1 mol%) in acetonitrile at refluxing temperature.
[a]Isolated yields based on aldehyde.
[b]Catalyst was reused three times.

Scheme 2.

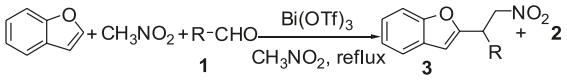

A possible mechanism for the formation of bis(benzofuranyl)methanes and 2-benzofuran-1-nitroalkane derivatives is proposed in Scheme 3 (paths A and B). When CH_3CN was used as reaction solvent, intermediate [**a**] was formed, which was easily attacked by another benzofuran in the presence of $Bi(OTf)_3$ (14). Furthermore, the aromatic ring-bearing electron-withdrawing group was more beneficial to the formation of compound **2,** except for 3-hydroxybenzaldehyde. To our surprise, when CH_3NO_2 is utilized as reaction media there may exist another reaction mechanism

© 2008 NRC Canada

Table 3. The synthesis of 2-benzofuran-1-nitroalkane derivatives catalyzed by $Bi(OTf)_3$ in CH_3NO_2.

Entry	R	Compound	Yield (%)[a]
1	*n*-C_6H_5	**3a**	0
		2a	38
2	4-OH-C_6H_4	**3b**	83
		2b	8
3	3-CH_3O-4-OH-C_6H_3	**3c**	80
		2c	7
4	2,4-$(CH_3O)_2$-C_6H_3	**3d**	85
		2d	0
5	4-CH_3O-C_6H_4	**3e**	82
		2e	8
6	3-Cl-C_6H_4	**3g**	0
		2g	40
7	3-NO_2-C_6H_5	**3j**	0
		2j	43
8	3-OH-C_6H_4	**3k**	0
		2k	40
9	H	**3m**	0
		2m	36
10	*n*-C_4H_9	**3n**	0
		2n	38

Note: Reaction condition: aldehyde (1 mmol), benzofuran (1 mmol), and $Bi(OTf)_3$ (1 mol%) in nitromethane at refluxing temperature.
[a]Isolated yields based on aldehyde.

Scheme 3.

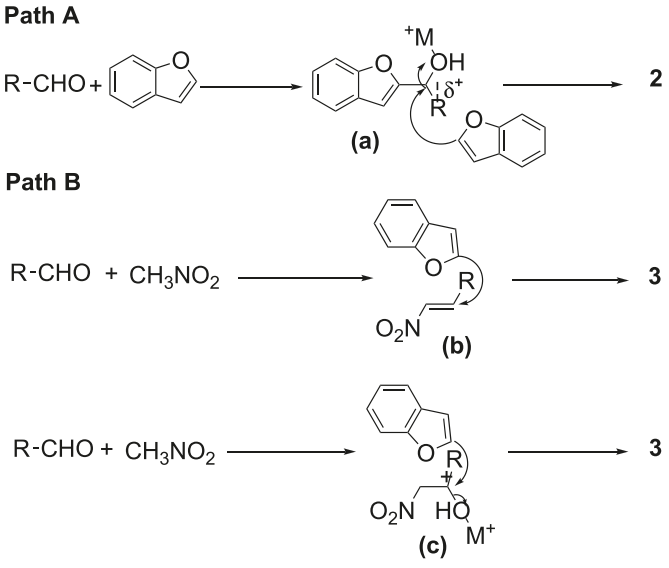

(path B). Compound **3** was synthesized via two possible processes. Intermediate [**b**] was attacked by benzofuran to obtain the Michael adduct **3**. Intermediate [**c**] suffered a nucleophilic attack by benzofuran to give compound **3**. We predicted the mechanism by performing the following reactions. The condensation of **1** and nitromethane in CH_3CN at the molar ratio of 1:1 at refluxing temperature, catalyzed by $Bi(OTf)_3$, gave no product. But when this reaction proceeded in CH_3NO_2 at refluxing temperature, a henry product was obtained with high yield. The aromatic ring-bearing electron-donating groups were apt for the synthesis of the henry product. This may be explained because the electron-donating groups are crucial to the stability of intermediate [**b**]. We also tried the condensation of benzofuran and the henry reaction. Only the aromatic ring-bearing strong electron-donating groups can react easily, which helped us explain the result in Table 3.

Conclusion

In summary, we have developed a simple, convenient, and efficient synthetic protocol for bis(benzofuranyl)methanes using a catalytic amount of $Bi(OTf)_3$ in CH_3CN. Additionally, $Bi(OTf)_3$ efficiently promotes three-component coupling reactions of aldehyde, benzofuran, and nitromethane. The simplicity, efficiency, easy work-up, and the need for only a small amount of $Bi(OTf)_3$ makes it the preferred procedure for the preparation of different kinds of 2-benzofuran-1-nitroalkane derivatives. This class of compounds may be used to construct some bioactive compounds.

Experimental section[2]

General method

All reagents are commercially available. Bismuth(III) triflate was prepared from triphenylbismuth and triflic acid (15). Melting points were measured on a digital melting point apparatus WR-1B and were uncorrected. ^1H NMR and ^{13}C NMR spectra were recorded on a Varian 400 MHz or Bruker Anance III (500 MHz) instrument using $CDCl_3$ as the solvent, and chemical shifts were expressed in parts per million (ppm) using TMS as an internal standard. Mass spectra were measured with a Trace Finnigan DSQ. High-resolution mass spectral (HRMS) analyses were measured on an Agilent 6210 TOF LC/MS using APCI and EI (electrospray ionization) techniques. IR measurements were carried out with a Nicolet Aviatar-370 instrument. Elemental analysis was performed on a VarioEL-III instrument. All spectral data of the products were identical to authentic samples.

General procedure for the preparation of bis(benzofuranyl)methanes

A mixture of benzofuran (2 mmol), benzaldehyde (1 mmol), and $Bi(OTf)_3$ (0.01 mmol) in CH_3CN (1 mL) was heated at refluxing temperature for 1 h. Then water was added, and the mixture was extracted with ethyl acetate (3 × 10 mL). The combined organic phases were dried over Na_2SO_4 and concentrated under reduced pressure. The crude product was purified by flash chromatography (silica gel, petroleum ether / methylene chloride *v*/*v* 16:1) to afford the adduct. The aqueous layer was washed by ethyl acetate and concentrated in vacuo to give white crystals [$Bi(OTf)_3$],

[2] Supplementary data for this article are available on the journal Web site (canjchem.nrc.ca) or may be purchased from the Depository of Unpublished Data, Document Delivery, CISTI, National Research Council Canada, Ottawa, ON K1A 0R6, Canada. DUD 3773. For more information on obtaining material refer to cisti-icist.nrc-cnrc.gc.ca/irm/unpub_e.shtml.

© 2008 NRC Canada

which was finally heated at 180 °C for 48 h in vacuo to afford $Bi(OTf)_3$ as a colorless crystal.

General procedure for the preparation of 2-benzofuran-1-nitroalkane derivatives

$Bi(OTf)_3$ (0.01 mmol) was added to a solution of benzofuran (1 mmol), 4-hydroxybenzaldehyde (1 mmol) in 2 mL of nitromethane. The reaction mixture was stirred at 101 °C for 2 h and then cooled to room temperature. Water (10 mL) was added and the mixture was extracted with ethyl acetate (3 × 10 mL). The combined organic phases were dried over Na_2SO_4, evaporated, and the crude product was purified by flash chromatography (silica gel, petroleum ether / ethyl acetate *v*/*v* 4:1) to afford the corresponding products. The aqueous layer was washed by ethyl acetate and concentrated in vacuo to give white crystals [$Bi(OTf)_3$], which was finally heated at 180 °C for 48 h in vacuo to afford $Bi(OTf)_3$ as a colorless crystal.

2a

Viscous oil. IR (neat, cm^{-1}) ν_{max}: 3133, 1637, 1400, 1253, 748. ^1H NMR (400 MHz, $CDCl_3$) δ: 7.49–7.16 (m, 13H, ArH), 6.46 (s, 2 H, furan-H), 5.70 (s, 1H, CH). ^{13}C NMR (100 MHz, $CDCl_3$, ppm) δ: 155.1, 154.3, 138.1, 128.8, 127.7, 127.5, 124.5, 124.1, 123.9, 120.9, 111.3, 105.2, 45.9. MS (EI) *m*/*z* (%): 324 (100), 247 (64). HRMS (EI) calcd. for $C_{23}H_{16}O_2$: 324.1150; found: 324.1151.

2b

Viscous oil. IR (neat, cm^{-1}) ν_{max}: 3412, 3132, 1614, 1400, 1252, 748. ^1H NMR (500 MHz, $CDCl_3$) δ: 7.48 (d, *J* = 8.0 Hz, 2H, ArH), 7.42 (d, *J* = 7.5 Hz, 2H, ArH), 7.27–7.17 (m, 6H, ArH), 6.81 (d, *J* = 7.5 Hz, 2H, ArH), 6.45 (s, 2H, furan-H), 5.64 (s, 1H, CH), 5.42 (s, 1H, OH). ^{13}C NMR (125 MHz, $CDCl_3$, ppm) δ: 157.1, 155.3, 155.1, 130.1, 129.9, 128.4, 124.0, 122.8, 120.8, 115.6, 111.2, 105.0, 45.1. MS (EI) *m*/*z* (%): 340 (100), 247 (35). HRMS (APCI) calcd. for (M – 1) $C_{23}H_{16}O_3$: 339.1021; found: 339.1016.

3b

Light yellow crystal, mp 92.8–94.6 °C. IR (KBr, cm^{-1}) ν_{max}: 3410, 3171, 1614, 1551, 1337, 1210, 749. ^1H NMR (400 MHz, $CDCl_3$) δ: 7.49 (d, *J* = 8.0 Hz, 1H, ArH), 7.43 (d, *J* = 8.4 Hz, 1H, ArH), 7.28–7.18 (m, 4H, ArH), 6.82 (d, *J* = 8.8 Hz, 2H, ArH), 6.48 (s, 1H, furan-H), 5.15–5.10 (m, 1H, $CHNO_2$), 5.00 (t, *J* = 7.6 Hz, 1H, CH), 4.89–4.83 (m, 1H, $CHNO_2$), 1.58 (s, 1H, OH). ^{13}C NMR (100 MHz, $CDCl_3$, ppm) δ: 155.5, 155.1, 154.9, 129.3, 128.2, 127.9, 124.3, 123.0, 120.9, 116.0, 111.1, 104.3, 77.8, 43.1. MS (EI) *m*/*z* (%): 283 (5), 236 (100). $C_{16}H_{13}NO_4$: calcd. C 67.84, H 4.63, N 4.94; found C 67.89, H 4.70, N 4.94.

2c

Viscous oil. IR (neat, cm^{-1}) ν_{max}: 3416, 3132, 1617, 1400, 1253, 747. ^1H NMR (500 MHz, $CDCl_3$) δ: 7.49 (d, *J* = 7.5 Hz, 2H, ArH), 7.42 (d, *J* = 8.0 Hz, 2H, ArH), 7.28–7.20 (m, 4H, ArH), 6.92–6.87 (m, 3H, ArH), 6.47 (s, 2H, furan-H), 5.63 (s, 1H, CH), 5.60 (s, 1H, OH), 3.84 (s, 3H, OCH_3). ^{13}C NMR (125 MHz, $CDCl_3$, ppm) δ: 157.0, 155.1, 146.7, 145.2, 129.9, 128.3, 124.4, 124.0, 122.8, 121.6, 120.8, 114.6, 111.2, 105.0, 56.0, 45.6. MS (EI) *m*/*z* (%): 370 (100), 247 (48). HRMS (APCI) calcd. for (M – 1) $C_{24}H_{18}O_4$: 369.1127; found: 369.1130.

3c

Yellow crystal, mp 83.5–84.2 °C. IR (KBr, cm^{-1}) ν_{max}: 3410, 3130, 1610, 1400, 1253, 746. ^1H NMR (400 MHz, $CDCl_3$) δ: 7.49 (d, *J* = 8.4 Hz, 1H, ArH), 7.42 (d, *J* = 8.0 Hz, 1H, ArH), 7.27–7.18 (m, 2H, ArH), 6.90–6.82 (m, 3H, ArH), 6.49 (s, 1H, furan-H), 5.68 (s, 1H, OH), 5.13–5.08 (m, 1H, $CHNO_2$), 4.97 (t, *J* = 7.8 Hz, 1H, CH), 4.88–4.83 (m, 1H, $CHNO_2$), 3.85 (s, 3H, OCH_3). ^{13}C NMR (100 MHz, $CDCl_3$, ppm) δ: 155.2, 154.9, 146.8, 145.6, 127.9, 127.8, 124.3, 123.0, 122.7, 120.9, 120.8, 114.9, 111.1, 104.3, 77.8, 55.9, 43.6. MS (EI) *m*/*z* (%): 313 (14), 266 (100). $C_{17}H_{15}NO_5$: calcd. C 65.17, H 4.83, N 4.47; found C 65.21, H 4.85, N 4.47.

3d

Viscous oil. IR (neat, cm^{-1}) ν_{max}: 3130, 2925, 2851, 1613, 1554, 1377, 1254, 752. ^1H NMR (400 MHz, $CDCl_3$) δ: 7.49 (d, *J* = 8.0 Hz, 1H, ArH), 7.42 (d, *J* = 8.0 Hz, 1H, ArH), 7.27–7.18 (m, 2H, ArH), 7.05 (d, *J* = 8.8 Hz, 1H, ArH), 6.53 (s, 1H, ArH), 6.49 (s, 1H, furan-H), 6.43 (d, *J* = 8.0 Hz, 1H, ArH), 5.42–5.38 (m, 1H, $CHNO_2$), 5.01 (t, *J* = 7.6 Hz, 1H, CH), 4.93–4.88 (m, 1H, $CHNO_2$), 3.84 (s, 3H, OCH_3), 3.78 (s, 3H, OCH_3). ^{13}C NMR (125 MHz, $CDCl_3$, ppm) δ: 160.8, 157.8, 155.4, 154.8, 129.6, 128.2, 124.0, 122.8, 120.8, 116.8, 111.1, 104.6, 104.2, 99.0, 77.3, 55.6, 55.4, 37.6. MS (EI) *m*/*z* (%): 327 (10), 280 (74), 265 (100), 131 (50). $C_{18}H_{17}NO_5$: calcd. C 66.05, H 5.23, N 4.28; found C 66.10, H 5.26, N 4.28.

2e

White crystal. mp 106.9– 107.1 °C. IR (KBr, cm^{-1}) ν_{max}: 3128, 1632, 1400, 1250, 752. ^1H NMR (500 MHz, $CDCl_3$) δ: 7.48 (d, *J* = 7.5 Hz, 2H, ArH), 7.47–7.13 (m, 8H, ArH), 6.88 (t, *J* = 7.5 Hz, 2H, ArH), 6.45 (s, 2H, furan-H), 5.65 (s, 1H, CH), 3.78 (s, 3H, OCH_3). ^{13}C NMR (125 MHz, $CDCl_3$, ppm) δ: 159.2, 157.3, 155.2, 130.3, 129.8, 128.5, 124.1, 122.9, 121.0, 114.3, 111.4, 105.2, 55.3, 45.3. MS (EI) *m*/*z* (%): 354 (100), 247 (20). $C_{24}H_{18}O_3$: calcd. C 81.34, H 5.12; found C 81.40, H 5.16.

3e

Viscous oil. IR (neat, cm^{-1}) ν_{max}: 3130, 2920, 2850, 1615, 1550, 1345, 748. ^1H NMR (400 MHz, $CDCl_3$) δ: 7.49 (d, *J* = 7.2 Hz, 1H, ArH), 7.43 (d, *J* = 8.0 Hz, 1H, ArH), 7.31–7.19 (m, 4H, ArH), 6.90 (d, *J* = 8.8 Hz, 2H, ArH), 6.48 (s, 1H, furan-H), 5.16–5.11 (m, 1H, $CHNO_2$), 5.01 (t, *J* = 7.6 Hz, 1H, CH), 4.89–4.84 (m, 1H, $CHNO_2$), 3.80 (s, 3H, OCH_3). ^{13}C NMR (100 MHz, $CDCl_3$, ppm) δ: 155.2, 155.1, 154.7, 129.0, 128.2, 127.9, 124.3, 123.1, 120.8, 115.8, 111.1, 104.3, 77.6, 54.7, 43.1. MS (EI) *m*/*z* (%): 297 (15), 250 (100). $C_{17}H_{15}NO_4$: calcd. C 68.68, H 5.09, N 4.71; found C 68.64, H 5.15, N 4.72.

2f

Viscous oil. IR (neat, cm^{-1}) ν_{max}: 3124, 1637, 1402, 1253, 747. ^1H NMR (400 MHz, $CDCl_3$) δ: 7.50–7.21 (m, 12H, ArH), 6.47 (s, 2H, furan-H), 5.67 (s, 1H, CH). ^{13}C NMR (100 MHz, $CDCl_3$, ppm) δ: 155.0, 143.6, 136.6, 133.6,

© 2008 NRC Canada

130.0, 129.0, 128.2, 124.2, 122.9, 120.9, 111.3, 105.4, 45.3. MS (EI) *m/z* (%): 360 (33), 358 (100), 247 (47). $C_{23}H_{15}ClO_2$: calcd. C 76.99, H 4.21; found C 76.94, H 4.26.

2g

Viscous oil. IR (neat, cm^{-1}) ν_{max}: 3125, 1632, 1400, 1252, 756. ^1H NMR (400 MHz, $CDCl_3$) δ: 7.51 (t, *J* = 7.0 Hz, 2H, ArH), 7.43 (t, *J* = 8.0 Hz, 2H, ArH), 7.37 (s, 1H, ArH), 7.30– 7.23 (m, 5H, ArH), 7.21–7.19 (m, 2H, ArH), 6.50 (s, 2H, furan-H), 5.68 (s, 1H, CH). ^{13}C NMR (100 MHz, $CDCl_3$, ppm) δ: 155.8, 155.1, 140.0, 134.6, 130.0, 128.8, 128.2, 127.9, 126.9, 124.2, 122.9, 120.9, 111.3, 105.4, 45.5. MS (EI) *m/z* (%): 360 (34), 358 (100), 247 (100). $C_{23}H_{15}ClO_2$: calcd. C 76.99, H 4.21; found C 76.94, H 4.25.

2h

Viscous oil. IR (neat, cm^{-1}) ν_{max}: 3123, 1614, 1590, 1400, 1253, 748. ^1H NMR (400 MHz, $CDCl_3$) δ: 7.52–7.50 (m, 2H, ArH), 7.44 (d, *J* = 7.5 Mz, 2H, ArH), 7.35–7.16 (m, 6H, ArH), 7.12–7.08 (m, 1H, ArH), 7.04–7.02 (m, 1H, ArH), 6.50 (s, 2H, furan-H), 5.71 (s, 1H, CH). ^{13}C NMR (100 MHz, $CDCl_3$, ppm) δ: 163.0 (*J* = 250 Hz), 155.9, 155.1, 143.6, 130.3, 130.2, 128.2, 124.3, 122.9, 120.9, 115.7 (*J* = 22.5 Hz), 114.7 (*J* = 21.0 Hz), 111.2, 105.3, 45.5. MS (EI) *m/z* (%): 342 (98), 247 (100). $C_{23}H_{15}FO_2$: calcd. C 80.69, H 4.42; found C 80.62, H 4.48.

2i

Viscous oil. IR (neat, cm^{-1}) ν_{max}: 3117, 1636, 1400, 1249, 745. ^1H NMR (400 MHz, $CDCl_3$) δ: 7.50–7.10 (m, 11H, ArH), 6.61 (s, 2H, furan-H), 6.34 (s, 1H, CH). ^{13}C NMR (100 MHz, $CDCl_3$, ppm) δ: 162.0 (*J* = 250.0 Hz), 154.8, 154.3, 135.4, 129.7, 129.6, 128.4, 125.9, 124.0, 122.8, 120.8, 115.2 (*J* = 23.7 Hz), 111.2, 104.9, 39.3. MS (EI) *m/z* (%): 378 (33), 376 (100), 247 (76). $C_{23}H_{14}ClFO_2$: calcd. C 73.31, H 3.74; found C 73.28, H 3.78.

2j

Viscous oil. IR (neat, cm^{-1}) ν_{max}: 3120, 1616, 1529, 1400, 1348, 1252, 747. ^1H NMR (400 MHz, $CDCl_3$) δ: 8.29 (s, 1H, ArH), 8.18 (d, *J* = 7.2 Hz, 1H, ArH), 7.73 (d, *J* = 8.8 Hz, 1H, ArH), 7.53 (d, *J* = 7.6 Hz, 3H, ArH), 7.44 (d, *J* = 7.6 Hz, 2H, ArH), 7.29–7.21 (m, 4H, ArH), 6.56 (s, 2H, furan-H), 5.81 (s, 1H, CH). ^{13}C NMR (100 MHz, $CDCl_3$, ppm) δ: 155.1, 154.9, 148.5, 140.2, 134.7, 129.7, 128.0, 124.5, 123.7, 123.1, 122.8, 121.1, 111.3, 105.7, 45.5. MS (EI) *m/z* (%): 369 (100), 247 (63). $C_{23}H_{15}NO_4$: calcd. C 74.79, H 4.09, N 3.79; found C 74.75, H 4.12, N 3.75.

2k

Viscous oil. IR (neat, cm^{-1}) ν_{max}: 3415, 3128, 1630, 1400, 1250, 753. ^1H NMR (500 MHz, $CDCl_3$) δ: 7.49 (d, *J* = 7.5 Hz, 2H, ArH), 7.42 (d, *J* = 8.0 Hz, 2H, ArH), 7.29–7.17 (m, 5H, ArH), 6.93 (d, *J* = 7.5 Hz, 1H, ArH), 6.83 (s, 1H, ArH), 6.82–6.75 (m, 1H, ArH), 6.48 (s, 2H, furan-H), 5.65 (s, 1H, CH), 5.17 (s, 1H, OH). ^{13}C NMR (125 MHz, $CDCl_3$, ppm) δ: 156.5, 155.9, 155.1, 139.8, 130.0, 128.3, 124.1, 122.8, 121.1, 120.9, 115.6, 114.7, 111.3, 105.2, 45.7. MS (EI) *m/z* (%): 340 (100), 247 (40). $C_{23}H_{16}O_3$: calcd. C 81.16, H 4.74; found C 81.12, H 4.80.

2l

Viscous oil. IR (neat, cm^{-1})ν_{max}: 3120, 1615, 1525, 1400, 1347, 1250, 745. ^1H NMR (400 MHz, $CDCl_3$) δ: 7.54–7.50 (m, 3H, ArH), 7.46–7.43 (m, 3H, ArH), 7.32 (s, 1H, ArH), 7.28–7.19 (m, 5H, ArH), 6.50 (s, 2H, furan-H), 5.67 (s, 1H, CH). ^{13}C NMR (100 MHz, $CDCl_3$, ppm) δ: 155.8, 155.1, 140.3, 131.6, 130.9, 130.3, 128.2, 127.3, 124.2, 122.9, 122.8, 120.9, 111.3, 105.4, 45.5. MS (EI) *m/z* (%): 404 (26), 402 (26), 248 (46), 247 (100). $C_{23}H_{15}BrO_2$: calcd. C 68.50, H 3.75; found C 68.48, H 3.78.

2m

Melting point 70.1–71.2 °C. (lit. value (16) 73–74 °C). IR (KBr, cm^{-1}) ν_{max}: 3120, 2930, 1600, 1252, 750. ^1H NMR (400 MHz, $CDCl_3$) δ: 7.50–7.18 (m, 8H, ArH), 6.57 (s, 2H, furan-H), 4.29 (s, 2H, CH_2). ^{13}C NMR (100 MHz, $CDCl_3$, ppm) δ: 154.9, 153.7, 128.6, 123.8, 122.7, 120.6, 111.0, 104.1, 28.4. MS (EI) *m/z* (%): 248 (100), 247 (80).

2n

Viscous oil. IR (neat, cm^{-1}) ν_{max}: 3127, 2956, 2928, 2860, 1617, 1453, 1400, 1252, 747. ^1H NMR (500 MHz, $CDCl_3$) δ: 7.57–7.17 (m, 8H, ArH), 6.56 (s, 2H, furan-H), 4.30 (t, *J* = 8.0 Hz, 1H), 2.23–2.18 (m, 2H, CH_2), 1.39–1.36 (m, 4H, 2 CH_2), 0.89 (t, *J* = 7.0 Hz, 3H, CH_3). ^{13}C NMR (125 MHz, $CDCl_3$, ppm) δ: 157.9, 154.7, 128.6, 123.6, 122.6, 120.6, 111.1, 103.2, 39.8, 32.1, 22.5, 22.4, 13.9. MS (EI) *m/z* (%): 304 (15), 247 (100). HRMS (EI) calcd. for: $C_{21}H_{20}O_2$ 304.1463; found: 304.1466.

2o

Viscous oil. IR (neat, cm^{-1}) ν_{max}: 3128, 1617, 1400, 1347, 1252, 748. ^1H NMR (500 MHz, $CDCl_3$) δ: 8.06 (d, *J* = 7.0 Hz, 1H, ArH), 7.59 (t, *J* = 7.5 Hz, 1H, ArH), 7.53–7.47 (m, 4H, ArH), 7.43 (t, *J* = 8.0 Hz, 2H, ArH), 7.31–7.27 (m, 2H, ArH), 7.23–7.20 (m, 2H, ArH), 6.63 (s, 1H, ArH), 6.54 (s, 2H, furan-H). ^{13}C NMR (125 MHz, $CDCl_3$, ppm) δ: 155.1, 154.8, 148.5, 133.4, 132.7, 131.3, 128.7, 128.1, 125.3, 124.3, 123.0, 121.1, 111.3, 105.6, 40.8. MS (EI) *m/z* (%): 369 (100), 247 (60). $C_{23}H_{15}NO_4$: calcd. C 74.79, H 4.09, N 3.79; found C 74.82, H 4.11, N 3.79.

2p

Viscous oil. IR (neat, cm^{-1}) ν_{max}: 3413, 3130, 1617, 1400, 1252, 748. ^1H NMR (500 MHz, $CDCl_3$) δ: 7.49 (d, *J* = 7.0 Hz, 2H, ArH), 7.43 (t, *J* = 8.0 Hz, 2H, ArH), 7.26–7.18 (m, 6H, ArH), 6.93 (t, *J* = 7.5 Hz, 1H, ArH), 6.83 (d, *J* = 7.0 Hz, 1H, ArH), 6.50 (s, 2H, furan-H), 6.09 (s, 1H, ArH), 5.08 (s, 1H, OH). ^{13}C NMR (125 MHz, $CDCl_3$, ppm) δ: 156.2, 155.1, 153.2, 129.9, 129.0, 128.3, 124.6, 124.0, 122.8, 121.3, 120.8, 116.1, 111.2, 105.2, 39.6. MS (EI) *m/z* (%): 340 (100), 247 (45). $C_{23}H_{16}O_3$: calcd. C 81.16, H 4.74; found C 81.13, H 4.79.

Acknowledgement

We are grateful to the National Natural Science Foundation of China (No. 20676123) for financial support.

© 2008 NRC Canada

References

1. A.H. Banskota, Y. Tezuka, K. Midorikawa, K. Matsushige, and S. Kadota, J. Nat. Prod. **63**, 1277 (2000).
2. K.S. Song and I. Raskin. J. Nat. Prod. **65**, 76 (2002).
3. B.S. Yun, H.C. Kang, H. Koshino, S.H. Yu, and I.D. Yoo. J. Nat. Prod. **64**, 1230 (2001).
4. C.L. Kao and J.W. Chern. J. Org. Chem. **67**, 6772 (2002).
5. G.A. Kraus, N. Zhang, J.G. Verkade, M. Nagarajan, and P.B. Kisanga. Org. Lett. **2**, 2409 (2000).
6. J. Lee, J. Tang, and J.K. Snyder. Tetrahedron Lett. **28**, 3427 (1987).
7. (*a*) S. Mahboobi, A.U.C. Cenac, A. Sellmer, E. Eichhorn, S. Elz, F.D. Böhmer, and S. Dove. Bioorg. Med. Chem. **15**, 2187 (2007); (*b*) C. Kirilmis, M. Koca, A. Cukurovali, M. Ahmedzade, and C. Kazaz. Molecules, **10**, 1399 (2005).
8. (*a*) D.S.C. Black, D.C. Craig, N. Kumar, and R. Rezaie. Tetrahedron, **55**, 4803 (1999); (*b*) D.S. Black, D.C. Craig, and R. Rezaie. Chem. Commun. **8**, 810 (2002).
9. A. Bianco, M. Guiso, R.A. Mazzei, and G. Nano. Gazz. Chim. Ital. **127**, 37 (1997).
10. W.K. Su, J.X. Chen, H.Y. Wu, and C. Jin. J. Org. Chem. **72**, 4524 (2007).
11. J.X. Chen, H.Y. Wu, Z.G. Zheng, C. Jin, X.X. Zhang, and W.K. Su. Tetrahedron Lett. **47**, 5383 (2006).
12. W.K. Su, J.J. Li, Z.G. Zheng, and Y.C. Shen. Tetrahedron Lett. **46**, 6037 (2005).
13. W.K. Su and C. Jin. Org Lett. **9**, 993 (2007).
14. A.S.K. Hashmi, L. Schwarz, P. Rubenbauer, and M.C. Blanco. Adv. Synth. Catal. **348**, 705 (2006).
15. J.R. Desmurs, Tetrahedron Lett. **38**, 8871 (1997).
16. A. Kasahara, T. Izumi, A. Suzuki, and T. Takeda. Bull. Chem. Soc. Jpn. **49**, 3711 (1976).

© 2008 NRC Canada

Probing DNA polymerase activity with stereoisomeric 2′-fluoro-β-D-arabinose (2′F-araNTPs) and 2′-fluoro-β-D-ribose (2′F-rNTPs) nucleoside 5′-triphosphates

Chang G. Peng and Masad J. Damha

Abstract: 2′-Deoxy-2′-fluoro-β-D-ribonucleosides (2′F-rN) and 2′-deoxy-2′-fluoro-β-D-arabinonucleosides (2′F-araN) differ solely in the stereochemistry at the 2′-carbon of the furanose sugar ring. 2′F-rN 5′-triphosphates (2′F-rNTPs) are among the most commonly used sugar-modified nucleoside 5′-triphosphates (NTPs) for in vitro selection; however, the epimeric 2′F-araN 5′-triphosphates (2′F-araNTPs) have only recently been applied to polymerase-directed biosynthesis [C.G. Peng and M.J. Damha. J. Am. Chem. Soc. **129**, 5310 (2007)]. The present study describes primer extension assays that compare, for the first time, the incorporation efficiency of the two isomeric NTPs, namely, 2′F-araNTPs or 2′F-rNTPs, by four DNA polymerases [Deep Vent (*exo*-), 9°N_m, HIV-1 RT, and MMLV-RT]. Under the conditions used, incorporation of 2′F-araTTP proceeded more efficiently relative to 2′F-rUTP, while the incorporation of 2′F-araCTP is comparable or slightly less efficient than that observed with 2′F-rCTP. Interestingly, these preferences were observed for all four of the DNA polymerases tested. Unexpected differences in NTP incorporation were observed for 2′F-rCTP vs. rCTP. Despite their seemingly similar conformation, they behaved striking differently in the in vitro polymerization assays. 2′F-rCTP is a much better substrate than the native counterpart (rCTP), an observation first made with human DNA polymerases [F.C. Richardson, R.D. Kuchta, A. Mazurkiewicz, K.A. Richardson. Biochem. Pharmacol. **59**, 1045 (2000)]. In contrast, 2′F-rUTP behaved like rUTP, providing poor yield of full-length products. Taken together, this indicates that 2′F-rCTP is very unusual with regard to enzyme/substrate recognition; an observation that can be exploited for the production of DNA oligomers enriched with both ribose and arabinose modifications. These findings are timely given the significant interest and growing need to develop chemically modified oligonucleotides for therapeutic and diagnostic research. By examining the structure–activity relationship (SAR) of the ribose and arabinose sugar, this study furthers our understanding of how the nature of the 2′ substituent (e.g., α vs. β; F vs. OH) and the heterocyclic base affect NTP selection (specificity) by DNA polymerases.

Key words: 2′F-rNTPs, 2′F-araNTPs, DNA polymerases, biosynthesis, modified nucleoside triphosphates.

Résumé : Les 2′-désoxy-′2-fluoro-β-D-ribonucléosides (2′F-rN) et les 2′-désoxy-2′-fluoro-β-D-arabinonucléosides (2′F-araN) ne diffèrent que par la stéréochimie au niveau du carbone 2′ du furanose du noyau du sucre. Les 5′-triphosphates de 2′F-rN (TP de 2′F-rN) les 5′-triphosphates de nucléosides (TPN) de sucres modifiés les plus fréquemment utilisés pour des sélections in vitro; toutefois, les 5′-triphosphates de 2′F-araB épimères (TP de 2′F-araN) n'ont que récemment été appliqués à la biosynthèse dirigée par une polymérase [C.G. Peng et M.J. Damha. J. Am. Chem. Soc. **129**, 5310 (2007)]. La présente étude décrit les premiers essais d'extension qui comparent pour la première fois l'efficacité d'incorporation de deux TPN isomères, à savoir le TP de 2′F-araN et le TP de 2′F-rN par quatre polymérases d'ADN [Deep Ven (exo-), 9°N_m, HIV-1 RT et MMLV-RT]. Dans les conditions utilisées, l'incorporation du TP de 2′F-araN se fait d'une façon plus efficace que celle du TP de 2′F-rU alors que celle du TP de 2′F-araN est comparable ou légèrement inférieure à celle observée avec le TP de 2′F-rC. Il est intéressant de noter que cette préférence a été observée avec chacune des quatre polymérases d'ADN qui ont été utilisées. On a observé des différences inattendues dans l'incorporation de TPN pour le TP de 2′F-rC par rapport au TP de rC. Malgré leurs conformations qui semblent semblables, ils se comportent de façons totalement différentes dans les essais de polymérisation in vitro. Le TP de 2′F-rC est un meilleur substrat que son pendant natif (TP de rC), une observation qui a été faite pour la première fois avec des polymérases d'ADN humain [F.C. Richardson, R.D. Kuchta, A. Mazurkiewicz, K.A. Richardson. Biochem. Pharmacol. **59**, 1045 (2000)]. Par ailleurs, le TP de 2′F-rU se comporte comme le TP de rU et il fournit de

Received 23 January 2008. Accepted 25 March 2008. Published on the NRC Research Press Web site at canjchem.nrc.ca on 16 July 2008.

C.G. Peng[1] and M.J. Damha.[2] Department of Chemistry, McGill University, Montreal, QC H3A 2K6, Canada.

This paper is dedicated to Dr. Victor E. Marquez on the occasion of his 65th birthday.

[1]Present address: Alnylam Pharmaceuticals, Boston, MA, USA.
[2]Corresponding author (e-mail: masad.damha@mcgill.ca).

 doi:10.1139/V08-089 © 2008 NRC Canada

faibles rendements de produits pleine grandeur. Si on prend l'ensemble de ces résultats en considération, on peut en déduire que le TP de 2′F-rC présente des caractéristiques inhabituelles par rapport à la reconnaissance enzyme/substrat et que cette observation peut être exploitée pour la production d'oligomères d'ADN enrichis de modifications tant de ribose que d'arabinose. Ces observations arrivent à point compte tenu de l'intérêt significatif qu'elles présentent et du besoin croissant de développer des oligonucléotides chimiquement modifiés pour la recherche thérapeutique et diagnostique. En examinant la relation structure activité (RSA) des sucres ribose et arabinose, cette étude permet de plus d'étendre notre compréhension de la façon dont la nature du substituant 2′ (par exemple, α versus β ou F versus OH) et la base hétérocyclique affectent la sélection du TPN (spécificité) par les polymérases d'ADN.

Mots-clés : 2′-désoxy-′2-fluoro-β-D-ribonucléosides (2′F-rN), 2′-désoxy-′2-fluoro-β-D-arabinonucléosides (2′F-araN), polymérases d'ADN, biosynthèse, triphophosphate de nucléoside modifié.

[Traduit par la Rédaction]

Introduction[3]

Nucleoside 5′-triphosphates (NTPs) (Fig. 1) are extensively used as probes to elucidate mechanistic details of DNA biosynthesis, and they represent the active form of several approved and pre-clinical antiviral and anticancer agents (1–3). Chemically-modified NTPs are also of great importance in the development of aptamers as research, therapeutic, and diagnostic agents (4, 5). Aptamers are generally obtained from the process of systematic evolution of ligands by exponential enrichment (SELEX) (6–8) and have gained recognition with the recent FDA approval of Macugen, a 2′F/2′-OMe ribose-modified oligonucleotide indicated for the treatment of neovascular age-related macular degeneration (9).

Modified NTPs can serve either as substrates or inhibitors of polymerases depending on the structural changes introduced through modifications to the base, phosphate, and (or) sugar moieties relative to the natural NTPs (i.e., deoxyribonucleoside 5′-triphosphates (dNTPs) and ribonucleoside 5′-triphosphates (rNTPs)) (2). Introducing a fluorine (F) atom into the sugar moiety of nucleosides, particularly at C2′, has a strong impact on the sugar ring conformational equilibrium (10). When the 2′-fluorine atom is "up" (or β) in 2′-deoxy-2′-fluoro-β-D-arabinonucleic acid (2′F-ANA), the arabinofuranose sugar ring predominantly puckers in the south/east (C2′/O4′-*endo*) conformation (11, 12), whereas a "down" (or α) fluorine in 2′-deoxy-2′-fluoro-β-D-ribonucleic acid (2′F-RNA) steers the ribofuranose ring into the north (C3′-*endo*) conformation (13–15). These C2′-modified sugars in turn dictate the conformation of the corresponding oligonucleotides (2′F-ANA and 2′F-RNA).

A fluorine atom at C2′ significantly impacts the thermodynamic stability and biological activity of duplexes. For example, oligonucleotides modified with 2′F-RNA units have enhanced binding affinity with mRNA (~+2 °C/nt) relative to the unmodified counterparts (16–19). The incorporation of 2′F-ANA units also raises the T_m of different systems, i.e., duplexes (~+1 °C/nt) (20), triplexes (~+0.8 °C/nt) (21), C-rich tetrads (~+1 °C/nt, pH < 4.0) (22), and G-rich tetrads (~+2 °C/nt) (23). Pyrimidine-based 2′F-RNAs were introduced into hammerhead ribozymes (24) or siRNAs (25) and exhibited increased or maintained activity. Antisense DNA or siRNA strands containing a significant 2′F-ANA content displayed gene-silencing efficacy in the low nanomolar range (26, 27).

Fig. 1. (A) 1-(2-Deoxy-2-fluoro-β-D-arabinofuranosyl)thymine 5′-triphosphate (2′F-araTTP); (B) 1-(2-deoxy-2-fluoro-β-Darabinofuranosyl) cytosine 5′-triphosphate (2′F-araCTP); (C) 1-(2-deoxy-2-fluoro-β-D-furanosyl)uracil 5′-triphosphate (2′F-rUTP); (D) 1-(2-deoxy-2-fluoro-β-D-ribofuranosyl)cytosine 5′-triphosphate (2′F-rCTP).

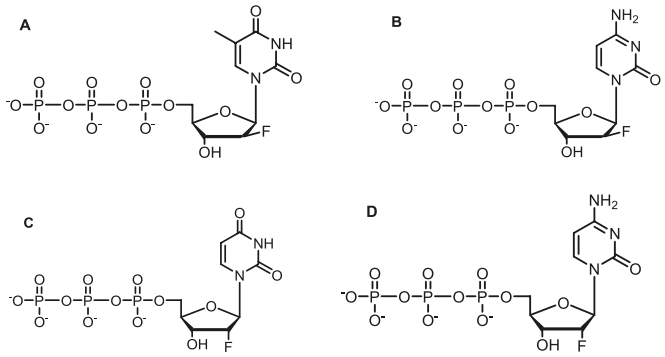

Given that 2′-deoxy-2′-fluoro-β-D-ribonucleoside 5′-triphosphates (2′F-rNTPs) are good substrates for T7 RNA polymerase (28), they are among the most commonly used in RNA-based SELEX (29–31) and, most recently, siRNAs generated by polymerase-catalyzed biosynthesis (32). A few studies have shown that 2′F-rNTPs are also substrates for DNA polymerases (33, 34). Richardson et al. reported that all four 2′F-rNTPs are substrates of human DNA pol γ, and DNA poly α can accept 2′F-rUTP, 2′F-rCTP, and 2′F-rGTP, but not 2′F-rATP (35). Furthermore, the incorporation efficiency of 2′F-rCTP by pol α is 17 fold higher compared to that of 2′F-rUTP (35). Thermostable DNA polymerases [Pfu (*exo*-), Vent (*exo*-), Deep Vent (*exo*-), and UlTma] are also able to incorporate 2′F-rUTP and 2′F-rCTP with reasonable efficiency (36).

2′-Deoxy-2′-fluoro-β-D-arabinonucleoside analogues have been studied for antiviral and anticancer applications. The recently approved anticancer drug clofarabine (37) is 2-

[3] Abbreviations and textual footnotes: 2′F-araN, 2′-deoxy-2′-fluoro-β-D-arabinonucleoside; 2′F-rN, 2′-deoxy-2′-fluoro-β-D-ribonucleoside; NTP, nucleoside 5′-triphosphate; 2′F-araNTP, 2′-deoxy-2′-fluoro-β-D-arabinonucleoside 5′-triphosphate; 2′F-rNTP, 2′-deoxy-2′-fluoro-β-D-ribonucleoside 5′-triphosphate; dNTP, deoxyribonucleoside 5′-triphosphate; rNTP, ribonucleoside 5′-triphosphate; 2′F-ANA, 2′-deoxy-2′-fluoro-β-D-arabinonucleic acid; 2′F-RNA, 2′-deoxy-2′-fluoro-β-D-ribonucleic acid.

© 2008 NRC Canada

Table 1. Base sequence of primer and templates.

Code	Type	Sequence*
PF01	Primer	5′-*TAATACGACTCACTATA*-3′
PF02	DNA temp.	5′-TTTGCCAACTCTTCTCCC*TATAGTGAGTCGTATTA*-3′
PF03	DNA temp.	5′-TTACCGGGCTCTTCTCCC*TATAGTGAGTCGTATTA*-3′
PF04	DNA temp.	5′-CTCTATGTGCACGCACTCTTCTCCC*TATAGTGAGTCGTATTA*-3′

Note: Italized sequence: primer binding sequence and primer (17 nt); underlined sequence: a running start (10 nt).

chloro-2′F-araA. Once triphosphorylated at their 5′ end, 2′F-araNTPs can be incorporated into eukaryotic as well as viral DNA (38–40). One of clofarabine's mechanisms of action, in fact, is the induction of strand breaks after incorporation into cellular DNA (41). 2′F-araNTPs incorporating a ^{18}F radionuclide ($t_{1/2}$ = 110 min) allows for the non-invasive imaging of tumors through positron emission tomography (PET) (42, 43). The successful application of these NTPs in PET relies on the ability of DNA polymerase to largely (and more selectively) incorporate these NTPs in tumor cells (44). 2′F-araNTPs have not been extensively investigated for in vitro selection/amplification processes (45).

Our group has recently shown that thermostable Family A DNA polymerases such as Deep Vent (*exo*-) (DV), 9°N$_m$ (9N), Therminator, and Phusion (46), accept both purine and pyrimidine 2′F-araNTPs as substrates and are able to synthesize long (30 nt) stretches of 2′F-ANAs with high efficiency and fidelity. In addition, these enzymes are capable of synthesizing DNA on a 2′F-ANA template, and can drive the formation of 2′F-ANA/2′F-ANA base pairs on chimeric 2′F-ANA-DNA templates (47).

In this follow-up study, we first assessed the incorporation of contiguous pyrimidine 2′F-araNTPs (i.e., 2′F-araTTP or 2′F-araCTP) into a DNA strand. Then, we compared, for the first time, the incorporation efficiency of pyrimidine 2′F-araNTPs to that of the corresponding 2′F-rNTP stereoisomers by two retroviral DNA polymerases, namely, HIV-1 reverse transcriptase (RT) and Moloney Murine Leukemia (MMLV)-RT, and two thermostable DNA polymerases, namely, DV and 9N. Finally, we also compared the incorporation efficiency of various combinations of pyrimidine 2′F-araNTP, 2′F-rNTP, and native rNTP along with dATP and dGTP. These studies further our understanding of how the nature (and stereochemistry) of the 2′ substituent and the heterocyclic base affect NTP selection (specificity) by DNA polymerases.

Results

Incorporation of three contiguous 2′F-araTTPs and 2′F-araCTPs

Primer extension assays were used to assess the incorporation of three contiguous 2′F-araTTPs on the DNA template PF02 (Table 1). Under the conditions used, all of the polymerases studied generated full-length products, although to different extents (Fig. 2). Pausing was observed for *Taq*, MMLV-RT, DV, 9N, and *Bst*. Remarkably, the thermophilic

Fig. 2. DNA-template directed polymerization of three contiguous 2′F-aratTs by DNA polymerases. (A) All reactions at 37 °C, 20 μL reaction volume, 1 μL polymerase, dNTPs, and 2′F-araTTP concentrations: 0.2 mmol/L for Taq, DV, 9N, and H1V-1 RT; 0.5 mmol/L for MMLV; and 0.033 mmol/L for Kf; (B) reactions at 55 °C, 20 μL reaction volume, 2 μL Bst and 0.4 μL Ph, and 0.2 mmol/L triphosphates; **P**: full-length product control; **H**: products formed through a chain termination assay with 0.1mmol/L dATP, dGTP, dTTP, dTTP+ddTTP (1:1 molar ratio), 0.4 μL HIV-1 RT in 20 μL reaction volume, on the same template PF02.

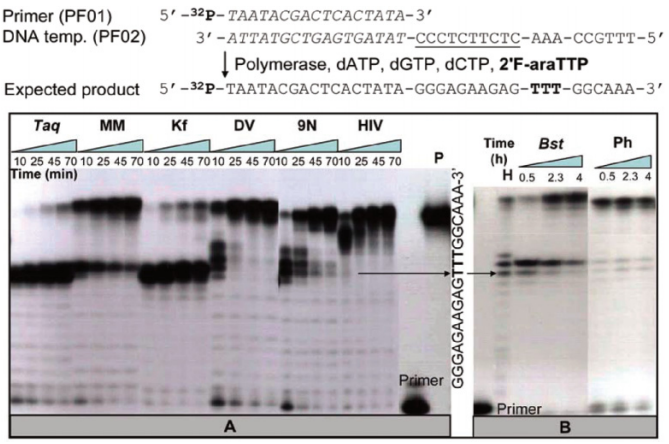

enzymes DV, 9N, and *Taq* were able to incorporate three 2′F-araTTPs even at 37 °C (Fig. 2A). Ph could afford full-length products without any pausing at 55 °C.

The same primer extension assays were used to assess the incorporation of three 2′F-araC units on the DNA template PF03 (Fig. S1, Supplementary Data).[4] MMLV-RT, Kf, and HIV-1 RT all gave full-length products (Fig. S1A).[4] Thermophilic enzymes DV and *Taq* could incorporate three consecutive 2′F-araCTPs at 37 °C; however, the rate of polymerization was significantly slower and some premature products (pausing) were observed. 9N and *Bst* failed to generate full-length products at 37 °C (Fig. S1A, Supplementary Data) but were able to incorporate three 2′F-araCTPs and gave the expected full-length products at higher temperature (55 °C) (Fig. S1B and S1C, Supplementary Data).[4] The high-fidelity enzyme Ph also easily provided a full-length product at 55 °C. Overall, all the DNA polymerases tested were able to incorporate three 2′F-araTTPs and 2′F-araCTPs into a DNA strand and afforded full-length products. 9N and DV could incorporate 2′F-araTTP better than 2′F-araCTP (Table 2).

[4] Supplementary data for this article are available on the journal Web site (canjchem.nrc.ca) or may be purchased from the Depository of Unpublished Data, Document Delivery, CISTI, National Research Council Canada, Ottawa, ON K1A 0R6, Canada. DUD 3788. For more information on obtaining material, refer to cisti-icist.nrc-cnrc.gc.ca/irm/unpub_e.shtml.

© 2008 NRC Canada

Table 2. Polymerase used and efficiency of three 2′F-araT(C)TP incorporations.

Polymerases[a]	Short name	Incorporation of three 2′F-araTTPs[b]	Incorporation of three 2′F-araCTPs
Thermophilic DNA polymerases (assays conducted at 55 °C except otherwise indicated)			
Deep Vent (3′→ 5′ exo-) DNA polymerase	DV	++++ (37 °C)	+++ (37 °C) ++++
9° N_m DNA polymerase	9N	++++ (37 °C)	+ (37 °C) ++++
Bst DNA polymerase large fragment	*Bst*	++ (37 °C) +++	+ (37 °C) ++++
Taq DNA polymerase	*Taq*	++ (37 °C)	++ (37 °C) ++++
Phusion High-Fidelity DNA polymerase	Ph	++++	++++
Mesophilic DNA polymerase (assays conducted at 37 °C)			
Klenow fragment DNA polymerase (3′→ 5′ exo-)	Kf	++	++
Reverse transcriptase DNA polymerases (assays conducted at 37 °C)			
HIV-1 RT (recombinant)	HIV-1	++++	++++
Moloney Murine Leukemia Virus RT	MMLV	+++	++++

[a]Enzyme sources: all from New England Biolabs (NEB) except for Ph from Finnzymes (distributed by NEB); HIV-1 RT from Worthington Biochemical Corp.; Polymerases can be classified into different enzyme families such as family A (*Bst*, *Taq*, Kf), family B (DV, 9N, Ph) and family RT (MMLV, HIV-1) (46).

[b]++++: excellent (full-length products and no pausing observed); +++: very good (full-length products with slight pausing); ++: good (full-length products with significant pausing); +: No full-length products obtained.

Incorporation efficiency of 2′F-araTTP vs. 2′F-rUTP

Once the conditions of the primer extension assays were established, the incorporation efficiencies of 2′F-araNTPs and 2′F-rNTPs by viral reverse transcriptases (HIV-1 RT and MMLV-RT) on a DNA template (PF02) were compared. As shown in Fig. 3A, 2′F-araTTP was an excellent substrate of HIV-1 RT and its incorporation proceeded more efficiently compared to 2′F-rUTP and rUTP. Interestingly, different pausing patterns were observed. In the absence of 2′F-modifed NTPs, the expected full-length DNA product was obtained from DNA-primed (PF01) reverse transcription on the DNA template PF02. Addition of an equivalent amount of the dideoxynucleoside 5′-triphosphate (ddTTP) led to the formation of three new bands resulting from chain termination directly opposite the d(AAA) residues present in the template strand (Fig. 3, lane **H**). These bands served as "markers" facilitating the identification of products formed in the 2′F-modifed NTP-based assays. The replacement of dTTP with either 2′F-rUTP or rUTP strongly inhibited RT-catalyzed synthesis of full-length product, as evidenced by the appearance of significant amounts of products resulting from chain termination after incorporation of one or two rNTPs. Even the incorporation of the first rUTP or 2′F-rUTP unit proceeded with difficulty as evidenced by the band patterns observed after 5 min. These truncated products represented more than 94% of the total polymerization products even after 1 h incubation with the enzyme. In sharp contrast, polymerization in the presence of 2′F-araTTP provided a significant amount of the full-length product after 30 min. However, the appearance of a significant amount of two shorter products, 5′-[DNA primer]-2′F-ara(TpTpT)-dGG-3′ and 5′-[DNA primer]-2′F-ara(TpTpT)-dGGC-3′, was observed during the first 5–20 min of reaction. This suggests that while the arabinose units do not cause significant chain termination as observed with both 2′F-rUTP and rUTP, the efficiency of subsequent steps, particularly the addition of subsequent dNTPs, is somewhat hindered following incorporation of 2′F-araTTPs. In other words, "delayed pausing" was observed in this case.

Similar results were obtained with MMLV-RT. This enzyme was able to incorporate 2′F-araTTP more efficiently than 2′F-rUTP and rUTP (Figs. S2 and S3, Supplementary Data).[4] Similarly, pausing was observed "after" the first incorporation of 2′F-araTTP, and "before" the first incorporation of 2′F-rUTP and rUTP. By analyzing the second incorporations of modified triphosphates in Fig. S3, it is clear that 2′F-araTTP is a better substrate than 2′F-rUTP.

We also wished to compare the efficiency of incorporation of 2′F-araTTP and 2′F-rUTP by thermostable polymerases DV and 9N, as these enzymes were previously found to be the most effective at polymerizing 2′F-araNTP units (47). With DV, incorporation of 2′F-araTTPs proceeded efficiently giving nearly quantitative yield of full-length product after 5 min. Accumulation of an intermediate band corresponding to 5′-[DNA primer]-2′F-ara(TpTpT)-dG-3′ was observed in the first 2 min (Fig. 4A). With 2′F-rUTP, however, abrupt pausing was observed after the first and second 2′F-rUTP incorporation, yielding only 20% of the desired full-length product after 9.5 h (Fig. 4A). The same trends were observed with 9N DNA polymerase (Fig. S4A, Supplementary Data).[4] Incorporation efficiencies of 2′F-araTTP and dTTP were comparable and ~100% full-length products were generated within 2 min and without pausing, whereas the reaction with 2′F-rUTP paused after one incorporation producing little of the expected full-length product (~20% after 1 h).

Incorporation efficiency of 2′F-araCTP vs. 2′F-rCTP

The same primer extension assays were used to evaluate the efficiency of DNA-template (PF03) directed incorporation of the cytosine NTPs by HIV-1 RT and MMLV-RT. Remarkably, 2′F-rCTP was found to be a significantly better

© 2008 NRC Canada

Fig. 3. Efficiency of incorporation of (A) 2′F-araTTP vs. 2′F-rUTP through the DNA template PF02, and (B) 2′F-araCTP vs. 2′F-rCTP through the DNA template PF03 mediated by HIV-1 RT DNA polymerization. (C) is a plot of time-course of full-length product (%). Reactions conducted at 37 °C in a 40 μL reaction volume, with 0.66 μL (18 units) enzyme; triphosphate concentrations were shown; products shown on lane **H** were formed through a chain termination assay with 0.1 mmol/L dATP, dGTP, dCTP, dTTP+ddTTP (1:1 molar ratio) on the template PF02 (A), or 0.1 mmol/L dATP, dGTP, dTTP, dCTP+ddCTP (1:1 molar ratio) on the template PF03 (B), respectively; 0.4 μL HIV-1 RT in 20 μL reaction volume at 37 °C. **P**: full-length product control.

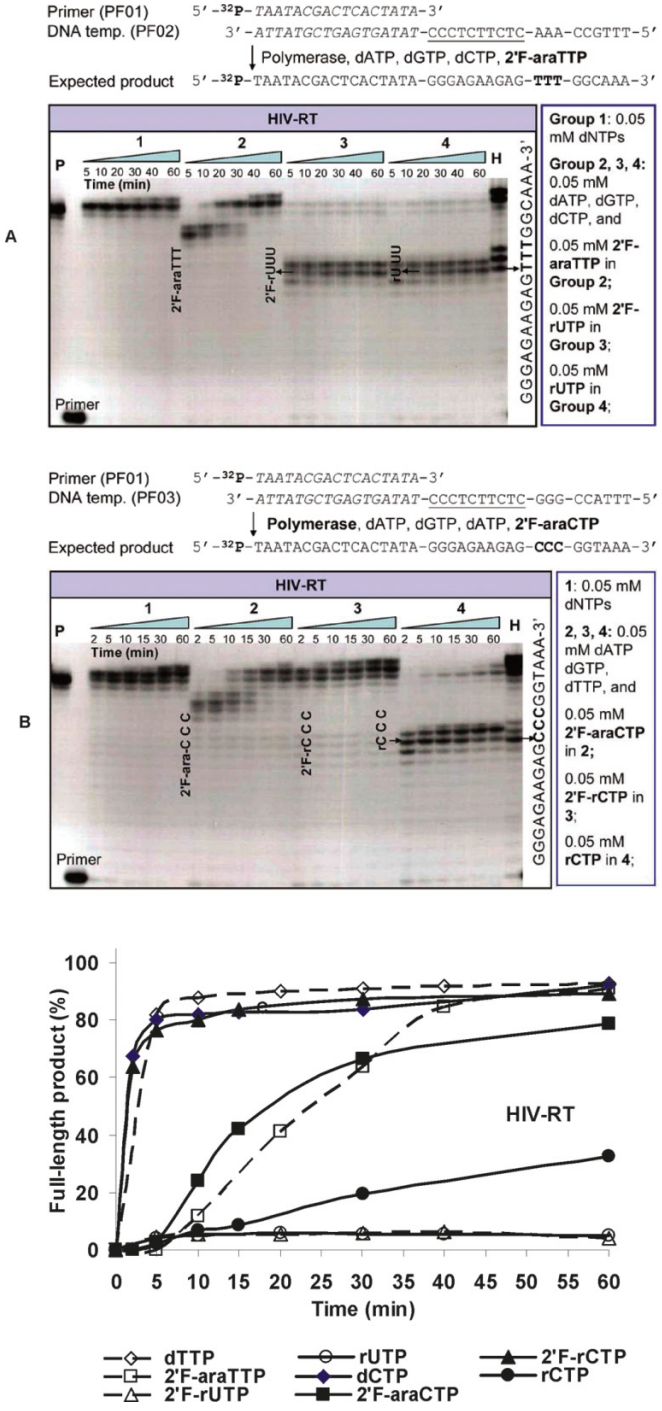

Fig. 4. Efficiency of incorporation of (A) 2′F-araTTP vs. 2′F-rUTP through the DNA template PF02, and (B) 2′F-araCTP vs. 2′F-rCTP through the DNA template PF03 mediated by DV DNA polymerization. (C) is a plot of time-course of full-length product (%). Reactions conducted at 55 °C in a 60 μL reaction volume, with 1.5 μL (3 units) enzyme; triphosphate concentrations were shown; products shown on lane **H** were formed through a chain termination assay with 0.1 mmol/L dATP, dGTP, dCTP, dTTP+ddTTP (1:1 molar ratio), 0.4 μL HIV-1 RT in 20 μL reaction volume on the template PF02 at 37 °C; products shown on lane **M** were formed through a chain termination assay with 0.2 mmol/L dATP, dGTP, dTTP, dCTP+ddCTP (1:1 molar ratio), 0.4 μL MMLV-RT in 20 μL reaction volume on the template PF03 at 37 °C. P: full-length product control.

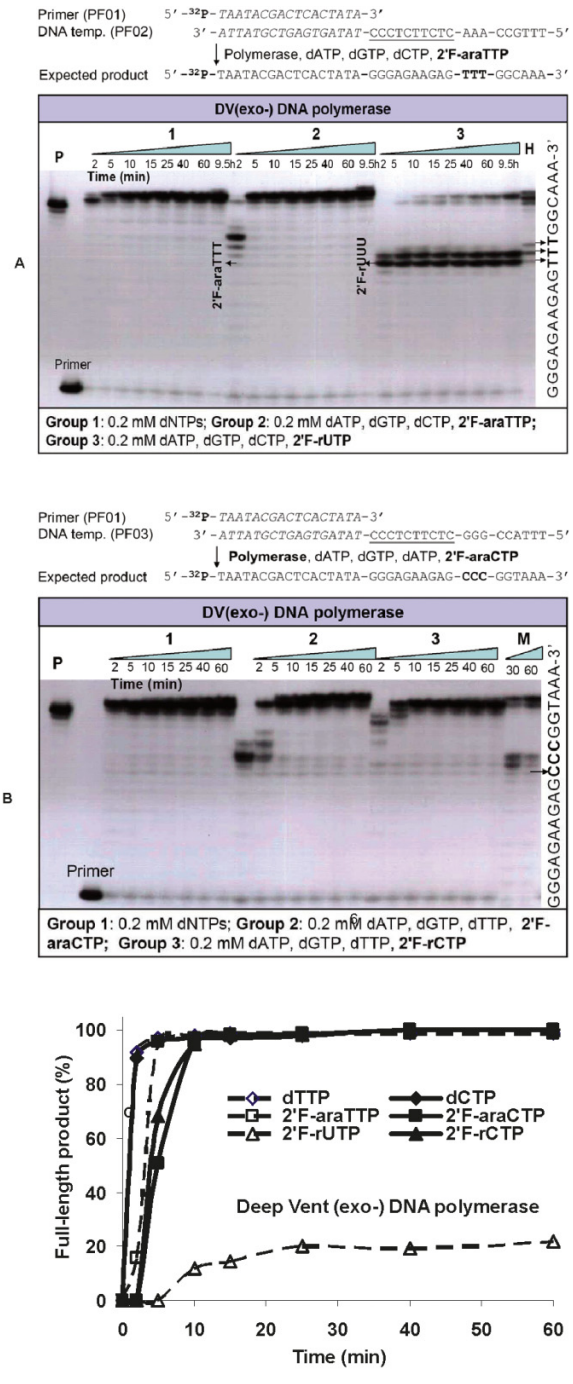

© 2008 NRC Canada

Fig. 5. Efficiency of incorporation of 2′F-araCTP vs. 2′F-rCTP through DNA template PF03 mediated by MMLV-RT DNA polymerization. Lower figure is a plot of time-course of full-length product (%). Reactions conducted at 37 °C, in a 40 μL reaction volume, with 0.6 μL (12 units) enzyme; triphosphate concentrations were shown; products shown on lane **H** were formed through a chain termination assay with 0.1 mmol/L dATP, dGTP, dTTP, dCTP+ddCTP (1:1 molar ratio) on the template PF03, 0.4 μL HIV-1 RT in 20 μL reaction volume at 37 °C. **P**: full-length product control.

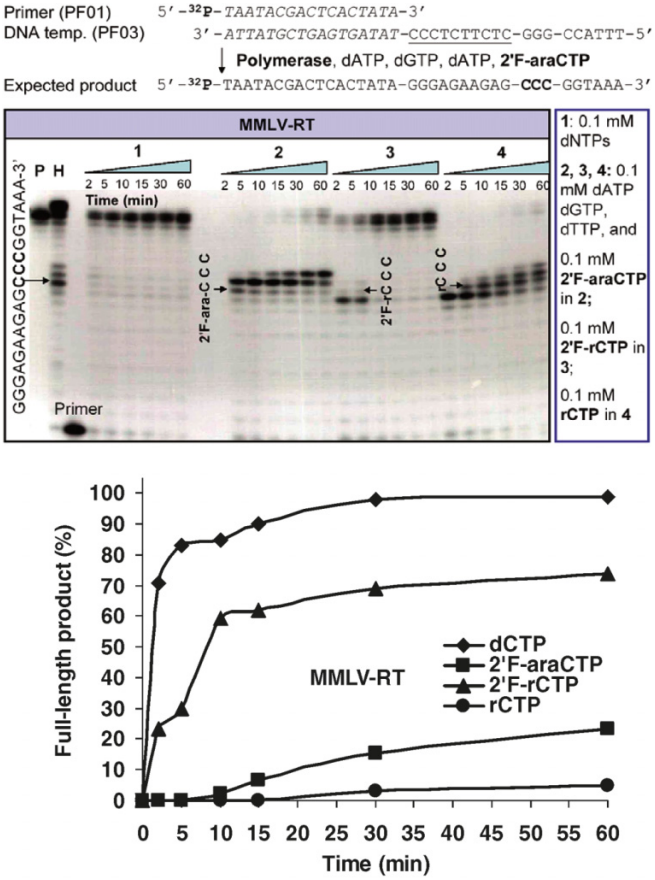

substrate than rCTP. In fact, with rCTP significant pausing was observed before the first rCTP incorporation (Fig. 3B and Fig. 5).

Generally, the incorporation efficiency of 2′F-araCTP by HIV-1 RT and MMLV-RT is comparable to or slightly less efficient than that observed with 2′F-rCTP. Binding of 2′F-araCTP at the active site of MMLV-RT appears to occur more readily over its isomeric counterpart 2′F-rCTP, since pausing was observed "after" the first 2′F-araCTP incorporation but "before" the first 2′F-rCTP incorporation (Fig. 5). Further elongation beyond the first 2′F-araC unit, however, seemed very difficult and mainly premature products (~90%) were observed after 60 min; in contrast, once the first 2′F-rCTP was incorporated, synthesis proceeded readily giving rise to almost 100% of full-length product (Fig. 5).

DV and 9N were able to incorporate 2′F-araCTP as well as 2′F-rCTP under the conditions studied here (Fig. 4B; Fig. S4B in Supplementary Data).[4]

Table 3. The order of incorporation efficiency of 2′F-araT(C)TP vs. 2′F-rU(C)TP.

Polymerases	Order of incorporation efficiency[a]	Figures
HIV-1 RT	dTTP > 2′F-araTTP > 2′F-rUTP > rUTP	3A
	dCTP ≈ 2′F-rCTP ≥ 2′F-araCTP > rCTP	3B
MMLV-RT	dTTP > 2′F-araTTP > 2′F-rUTP > rUTP	S2; S3
	dCTP ≈ 2′F-rCTP ≥ 2′F-araCTP > rCTP	5
DV	dTTP ≈ 2′F-araTTP > 2′F-rUTP	4A
	dCTP ≈ 2′F-rCTP ≈ 2′F-araCTP	4B
9N	dTTP ≈ 2′F-araTTP > 2′F-rUTP	S4A
	dCTP ≈ 2′F-araCTP ≈ 2′F-rCTP	S4B

[a]Incorporation efficiency is evaluated by the percentage of full-length products from primer extension assays.

Fig. 6. DNA-template (PF04)-mediated DNA polymerization assay catalyzed by 9N DNA polymerase comparing the efficiency of incorporation of dATP, dGTP in the presence of various pyrimidine NTP combinations, namely: 2′F-araTTP/2′F-araTTP; 2′FaraTTP/2′F-rCTP; 2′F-rUTP/2′F-rCTP; and rUTP/rCTP. Reactions were carried out at 55 °C; 40 μL reaction volume, 9N enzyme (2 μL; 4 units); 0.2 mmol/L triphosphates; products shown on lane **H1** were formed through a chain termination assay with 0.1 mmol/L dATP, dGTP, dCTP, dTTP+ddTTP (1:1 molar ratio), 0.4 μL HIV-1 RT in 20 μL reaction volume on the same template PF04; bottom figure is a plot of time-course of full-length product (%).

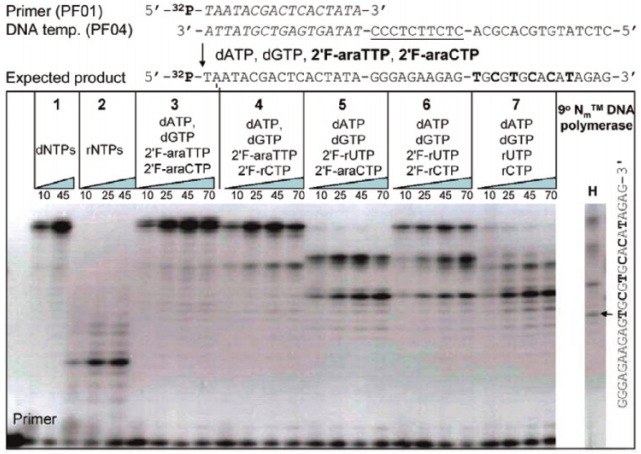

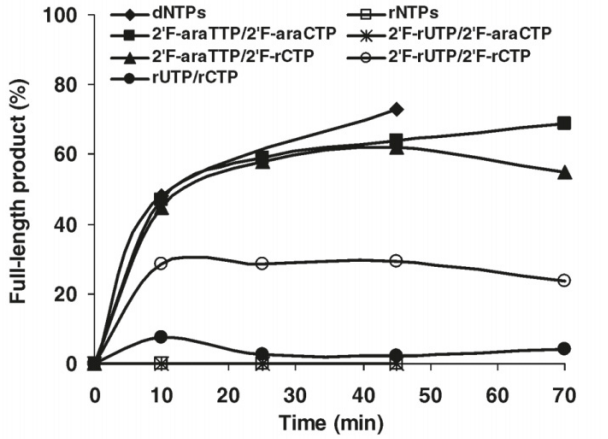

© 2008 NRC Canada

Table 4. The order of incorporation efficiency of different triphosphate pairs.

Polymerase	Order of incorporation efficiency	Figures
9N	all four dNTPs (Group 1) > 2′F-araTTP/2′F-araCTP (Group 3) ≈ 2′F- araTTP/2′F-rCTP (Group 4) > 2′F-rUTP/2′F-rCTP (Group 6) > 2′F-rUTP/2′F-araCTP (Group 5) ≈ rUTP/rCTP (Group 7) >> all four rNTPs (Group 2)	Fig. 6
DV	all four dNTPs (Group 1) ≈ 2′F-araTTP/2′F-araCTP (Group 3) ≈ 2′F-araTTP/2′F-rCTP (Group 4) > 2′F-rUTP/2′F-rCTP (Group 6) > 2′F-rUTP/2′F-araCTP (Group 5) > rUTP/rCTP (Group 7) > all four rNTPs (Group 2)	Fig. S5, Supplementary Data[4]
HIV-1 RT	all four dNTPs (Group 1) >> 2′F-rUTP/2′F-rCTP (Group 6) > 2′F-araTTP/2′F-rCTP (Group 4) > 2′F-araTTP/2′F-araCTP (Group 3) > 2′F-rUTP/2′F-araCTP (Group 5) ≈ rUTP/rCTP (Group 7) > all four rNTPs (Group 2)	Fig. S6, Supplementary Data[4]

In summary, incorporation of 2′F-araTTP proceeded more efficiently relative to 2′F-rUTP. Incorporation of 2′F-araCTP at the 3′-end of a DNA primer strand also proceeded more readily than incorporation of 2′F-rCTP. However, once the first 2′F cytosine unit was incorporated, synthesis proceeded more efficiently from the DNA primer containing the 3′ terminal 2′F-rCTP unit. While the substrate specificities towards the 2′F-rUTP and rUTP pair were similar, a different specificity towards the corresponding cytosine pair (i.e., 2′F-rCTP and rCTP) was observed. The order of incorporation efficiency of 2′F modified pyrimidine NTPs is summarized in Table 3.

Incorporation efficiency of pairs of modified triphosphates

Next, we conducted primer extension assays on the DNA template PF04 to synthesize for the first time chimeric (ribo/arabino/deoxy) oligonucleotides using 9N, DV, and HIV-1 RT DNA polymerases. The monomers consisted of dATP, dGTP, and one of five different pyrimidine pairs: 2′F-araTTP/2′F-araCTP (Group 3 in Fig. 6), 2′F-araTTP/2′F-rCTP (Group 4), 2′F-rUTP/2′F-araCTP (Group 5), 2′F-rUTP/2′F-rCTP (Group 6), and rUTP/rCTP (Group 7). Control reactions with the native dNTPs and rNTPs were carried out as well (Group 1 and 2 in Fig. 6). Incorporation efficiency was measured either as the percentage of full-length products, or the number of nucleotides incorporated if no full-length products were obtained. With 9N and DV, incorporation efficiencies followed the same trend (Table 3). Interestingly, HIV-1 RT produced opposite results for Groups 3, 4, and 6 (Table 4). Generally, dNTPs are the best and rNTPs are the worst substrates; the combination of 2′F-modified NTPs showed different incorporation efficiencies. The results are summarized in Table 4, and possible explanations for these results are discussed below.

Discussion

Nucleoside analogues have been studied extensively from the standpoint of the biochemical consequences of these analogues on DNA polymerase activity. Much is also known about the structural effects of nucleoside analogues when incorporated into DNA duplexes (10, 11), but relatively little information is available concerning the impact of 2′-isomeric modified NTPs on polymerase function. The biochemical experiments presented herein represent the first results obtained with the isomeric 2′F-rNTP and 2′F-araNTPs.

The data obtained show that DNA polymerases can incorporate contiguous pyrimidine 2′F-araNTPs into a growing DNA strand to afford full-length products (Table 2), consistent with data reported in our recent preliminary study. For example, incorporation of three contiguous 2′F-araTTP units proceeded more efficiently relative to three contiguous 2′F-rUTPs, but this was not the case for the 2′F-araCTP/2′F-rCTP pair where equal efficiencies were observed with DV and 9N polymerases (Table 3). With the RT enzymes, incorporation of the first 2′F-araCTP unit proceeded more efficiently relative to its 2′-isomeric counterpart. However, further elongations proceeded more efficiently with 2′F-rCTP. Furthermore, when comparing polymerization patterns, 2′F-rUTP behaved like rUTP, but surprisingly the same was not true for the cytosine pair, 2′F-rCTP and rCTP. Below, we attempt to rationalize these interesting results.

Co-crystallization of HIV-1 RT with a double-stranded DNA template–primer (binary complex: RT-dsDNA) (48), and with dsDNA and dNTP (ternary complex: RT-dsDNA-dNTP) (49) suggest that the dsDNA adopts an A-like (North) structure near the polymerase active site, which gradually converts to the B-form conformation (south) as this DNA region moves away from polymerase active site. Therefore, it is expected that incoming NTPs with an A-like

© 2008 NRC Canada

conformation should be favoured for binding at the active site. Other factors such as steric interactions between incoming NTPs and the polymerase amino acid residues also help dictate the specificity of NTP binding. For instance, models based on crystal structures suggest that Phe155 in MMLV-RT (or Tyr-115 in HIV-1 RT) acts as a "steric gate" that discriminates between the 2′H of a dNTP and the 2′OH group of an NTP (49–51). Studies reported by Marquez and coworkers on conformationally biased NTP analogues and HIV-1 RT fully support this hypothesis (52, 53). They explained the contrasting inhibitory behaviour of αFddATP and (the more potent) βddATP stereoisomer through molecular dynamics simulations that revealed unfavourable steric interaction between "north" puckered αFddATP and Tyr115 (HIV-1-RT) (analogous to the interaction of 2′-OH of rNTPs with Tyr115) (52). Our observation that 2′F-araTTP is incorporated more efficiently than 2′F-rUTP is consistent with these studies (52), suggesting that when the fluorine is on the same face of the ring as the 5 carbon (i.e., β-F) as in 2′F-araTTP, the steric interaction with Tyr115 in HIV-1 RT is avoided. 2′F-araTTP, however, must pay an energy penalty, since it must switch to the "north" conformation to bind at the active site of RT. Such conformation is possible and precedented for some arabinonucleosides (54). The more flexible dTTP thus shows the highest efficiency of incorporation.

Nucleoside analogues that do not block DNA synthesis at the point of incorporation, but only after additional incorporations of normal dNTPs have been termed "delayed chain terminators", which have been shown to be relatively resistant to excision by HIV-1 RT mutant, one of HIV-1 RT's drug-resistance mechanisms (55). The noticeable delayed pausing observed with 2′F-araTTPs may be due to the inclusion of three contiguous 2′F-araT in the dsDNA. The more rigid arabinose units likely affects the A/B form conformational change in the RT–primer–template complex, which should result in a diminished rate of dNTP incorporation or, in the dissociation of RT from the primer–template duplex resulting in abortive products. The pausing observed "before" the incorporation of 2′F-rUTP or rUTP (Fig. 3A) indicates that 2′F-rUTP or rUTP has difficulty in binding at the active site of RT, consistent with the proposal of steric gate control. Similar pausing "patterns" are observed for 2′F-rUTP and rUTP, consistent with the fact that 2′F-rUTP is a mimic of rNTPs and are both excellent substrates for T7 RNA polymerase (28).

Similar results are obtained for MMLV-RT, DV, and 9N (Table 3). One can speculate that these enzymes use the same discrimination mechanism (conformational preference and steric gate) to distinguish between dTTP, 2′F-araTTP, 2′F-rUTP, and rUTP during incorporation. Our finding that the incorporation efficiency of 2′F-araTTP is higher than that of 2′F-rUTP by HIV-1 RT, MMLV-RT, DV, and 9N is not surprising, since 2′F-araTTP is a dTTP mimic (and thus favoured by DNA polymerases) and does not have an α-substituent at C2′, while 2′F-rUTP is a rUTP mimic (with α-substituents at C2′) and should be more favoured by RNA polymerases. A similar pattern was observed among the cytosine series and the thermostable enzymes DV and 9N.

Surprisingly, a more complex pattern of incorporation efficiency was observed among dCTP, 2′F-araCTP, 2′F-rCTP, and rCTP in the primer extension reactions catalyzed by HIV-1 RT and MMLV RT. Based on the pausing patterns observed, binding of 2′F-araCTP at the active site of MMLV-RT seemed to be more advantageous over its ribose counterpart, 2′F-rCTP (Fig. 5). This is again consistent with steric gate control for NTP binding (52). The further elongation observed, however, indicates that other factors play important roles in single-base incorporation, aside from the steric gate factor and conformational bias of sugar pucker. Previous studies on the fidelity of base incorporation have shown that the rate-limiting step could be different among multiple molecular checkpoints involved in DNA-polymerase-directed polymerization (56, 57). Our experiments simply measure the overall result of all possible factors governing base incorporations. The factors governing the specificity and efficiency of base incorporation by DNA polymerases are complex and not completely understood (58). Preferential geometry (1), sugar pucker (53), topology, and size of the polymerase active site (1) are all important considerations. In our screening experiments, we found that the efficiency of incorporation of 2′F-araCTP < 2′F-araTTP in same primer extension conditions with some DNA polymerases (e.g., DV and 9N). For 2′F-rCTP, the literature has shown that the incorporation rate of 2′F-rCTP is much higher than that of 2′F-rUTP by human polymerases α and γ (35). We therefore propose that the observed incorporation efficiency of 2′F-rCTP ≥ 2′F-araCTP is the superposition of two factors: first, the overall incorporation efficiency of 2′F-rCTP may be higher than 2′F-rUTP by HIV-1 RT and MMLV-RT; second, the incorporation efficiency of 2′F-araCTP is lower than that of 2′F-araTTP. As to why 2′F-rCTP differs strikingly from rCTP remains an unsolved question in this work and requires further study. For example, it may be worthwhile in future studies to examine the structure of modified DNA primers differing only in the nature of their 3′-terminal unit (e.g., 2′F-rC vs. and rC). It is conceivable that the north–south population of the fluorinated nucleoside, once incorporated, remains highly biased towards the North, but that of the natural nucleoside resembles that of rU 5′-phosphate in solution, which in fact has an slight excess of the south conformer (N:S ratio < 1) (59, 60).

Delayed pausing was often observed with the incorporation of 2′F-araTTP and 2′F-araCTP (Figs. 3, 4, 5, and Fig. S2 in Supplementary Data).[4] These results are somewhat consistent with studies previously reported by our group, in which a DNA primer strand containing a single 3′-arabinocytidine unit (araC; in this case the 2′-substituent is an OH group) was found to serve as a primer of DNA synthesis. However, significant pausing of HIV-1 RT was observed after extension with 4 × dNTP units (61).

The order of the incorporation efficiency of the NTP mixtures shown in Table 4 is an overall effect of the incorporation efficiencies of individual modified NTPs (Table 3). The first modified NTP incorporated is either 2′F-araTTP or 2′F-rUTP, so the rate-limiting step could be the incorporation of the first NTP. This seems to be the case for 9N and DV. For example, the order of incorporation efficiency Group 3 ≈ Group 4 > Group 6 > Group 5 (Table 4) can be explained by the general trend of incorporation efficiency 2′F-araTTP > 2′F-rUTP and 2′F-rCTP ≥ 2′F-araCTP. The other combinations of rNTPs (Group 2 and Group 7) were not favoured by

© 2008 NRC Canada

9N in this primer extension assay, consistent with the poor incorporation of rNTPs by DNA polymerases (Table 3).

Interestingly, the 2′F-rUTP/2′F-rCTP pair (Group 6) was incorporated by HIV-1 RT more efficiently than the 2′F-araTTP/2′F-rCTP pair (Group 4) (Table 4; Fig. S6 and Supplementary Data)[4], suggesting that 2′F-rUTP is favoured over 2′F-araTTP. However, when comparing 2′F-araTTP/2′F-araCTP (Group 3) with 2′F-rUTP/2′F-araCTP (Group 5), the order of efficiency of incorporation observed suggests that 2′F-araTTP is the better substrate, consistent with the findings shown on Fig. 3A. The greater incorporation efficiency of 2′F-araTTP/2′F-rCTP (Group 4) vs. 2′F-araTTP/2′F-araCTP (Group 3) is also fully consistent with the finding that elongation with 2′F-araCTP seems less efficient than with 2′F-rCTP (Fig. 3B). Taken together, these results indicate that that the rate-limiting step in HIV-1 RT may be different from DV and 9N, since incorporation of 2′F-modified CTPs seems more important in determining the yield of the full-length products.

Conclusion

2′F-araTTP and 2′F-araCTP are substrates of all the DNA polymerases tested in the present study. DV and 9N were the most efficient at incorporating 2′F-araTTP and 2′F-araCTP and afforded good yields of full-length chimeric oligonucleotide products. Our comparative studies of the efficiency of incorporation of 2′F-araNTPs vs. 2′F-rNTPs by four DNA polymerases demonstrate that, under the conditions used, incorporation of 2′F-araTTP proceeded much more efficiently relative to 2′F-rUTP, while the incorporation of 2′F-araCTP was comparable or slightly less efficient than that observed with 2′F-rCTP (Table 3). Generally, dNTPs were found to be better substrates than rNTPs; 2′F-rUTP behaves much like rUTP but 2′F-rCTP is strikingly different from rCTP. Furthermore, we demonstrate that mixtures of 2′F-araNTPs and 2′F-rNTPs can be used to generate 2′F-r/2′F-ara-oligonucleotides through template-directed DNA polymerization reactions. The 2′F-araTTP and 2′F-rCTP pair gave excellent results with the DNA polymerases tested. Considering the potential advantages of these modifications in oligonucleotide-based gene-silencing approaches (16–27), our studies suggest that it should be possible to generate chimeric 2′F-arabinose/ribose oligonucleotide aptamers through an in vitro selection (SELEX) process. By examining the structure–activity relationship (SAR) of the ribose and arabinose sugar, this study also contributes to the understanding of how C2′ stereochemistry, the nature of the 2′subsitutent (F vs. OH), and heterocyclic base affect NTP selection (specificity) by DNA polymerases.

Experimental

Nucleotides

dNTPs were purchased from Fermentas. 2′-Deoxy-2′-fluoro-β-D-arabinonucleosides were obtained from Topigen Pharmaceuticals, Inc. The introduction of the 5′-triphosphate moiety was conducted by Rasayan, Inc. 2′F-rUTP and 2′F-rCTP were purchased from Rasayan, Inc. The structures of the fluorinated nucleoside 5′-triphosphates are shown in Fig. 1.

Template and primer design

DNA and 2′F-ANA-DNA templates and primers used in this study are shown in Table 1. The primer (PF01) is a 17 nt DNA sequence 5′-*TAATACGACTCACTATA*-3′. Each template strand comprises three sequence segments: a 17 nt primer binding sequence 5′-*TATAGTGAGTCGTATTA*-3′, a 10 nt running start sequence 5′-CTCTTCTCCC-3′ (62, 63), and a variable DNA "test sequence". The oligomers were designed to test the incorporation of three 2′F-araT units on the DNA template PF02, three 2′F-araC units on the DNA template PF03, and six mixed 2′F-araT and 2′F-araC units on the DNA template PF04. DNA sequences were obtained from Integrated DNA Technologies (IDT).

Primer extension reactions

We adapted primer extension assays (62, 63) to first screen eight DNA polymerases (Table 2) for their ability to incorporate three consecutive 2′F-araT and 2′F-araC units. Enzyme activity and default reaction buffer conditions suggested by the manufacturers are shown in Table S1 (Supplementary Data).[4] All reaction buffers were provided by the manufacturers except the HIV-1 RT buffer, which was prepared in-house. The DNA primer (PF01) was first labeled by a radioactive phosphorus probe (^{32}P) at the 5′-hydroxyl terminus according to a published procedure (64). Unlabeled DNA primer was also used to adjust the primer concentration. The final concentrations were 85 nmol/L for the primer and 255 nmol/L for the template in the screening experiments, and 100 nmol/L for the primer and the template in the comparison studies. The primer and template were heated at 95 °C for 5 min and annealed at 4 °C at least 2 h before use. In a microtube, the mixture of buffer, triphosphates (different combinations of four dNTPs, 2′F-araNTPs, 2′F-rNTPs, and (or) rNTPs), water, primer, and template was prepared according to pre-calculated reaction volume and concentrations. Mineral oil (20 μL) was used to prevent evaporation for assays running at 55 °C. A polymerase was added to initiate the primer extension reaction. Time points were obtained by removing 4 μL or 8 μL aliquots from the reaction mixture and quenching with an equal volume of a stopping dye solution (98% deionized formamide, 10 mmol/L EDTA, 1 mg/mL bromophenol blue, and 1 mg/mL xylene cyanol). The product pattern was analyzed by 12% denaturing polyacryamide gel electrophoresis (PAGE) and subsequent autoradiography analysis.

Acknowledgements

This work was supported through a grant from the Canadian Institutes of Health Research (CIHR) and Topigen Pharmaceuticals, Inc. We thank J. Watts, R. Donga, and A. Wahba for several helpful discussions, and J. Watts for assistance with the preparation of this manuscript. CGP acknowledges support from a FQRNT fellowship and a Clifford Wong McGill Major Fellowship. M.J.D. is the recipient of the Bernard Belleau Award (Canadian Society for Chemistry, CSC).

References

1. E.T. Kool. Annu. Rev. Biochem. **71**, 191 (2002).

© 2008 NRC Canada

2. G.E. Wright and N.C. Brown. Pharmacol. Ther. **47**, 447 (1990).
3. R.A. Smith, R.W. Sidwell, and R.K. Robins. Annu. Rev. Pharmacol. Toxicol. **20**, 259 (1980).
4. E.N. Brody and L. Gold. Rev. Mol. Biotechnol. **74**, 5 (2000).
5. S.M. Nimjee, C.P. Rusconi, and B.A. Sullenger. Annu. Rev. Med. **56**, 555 (2005).
6. A.D. Ellington and J.W. Szostak. Nature (London, UK), **346**, 818 (1990).
7. C. Tuerk and L. Gold. Science (Washington, DC), **249**, 505 (1990).
8. G.F. Joyce. Gene, **82**, 83 (1989).
9. E.W.M. Ng, D.T. Shima, P. Calias, E.T. Cunningham, D.R. Guyer, and A.P. Adamis. Nat. Rev. Drug Discov. **5**, 123 (2006).
10. C. Thibaudeau and J. Chattopahyaya. Stereoelectronic effects in nucleosides and nucleotides and their structural implications. Uppsala University Press Uppsala, Sweden. 1999.
11. I. Berger, V. Tereshko, H. Ikeda, V.E. Marquez, and M. Egli. Nucleic Acids Res. **26**, 2473 (1998).
12. J.-F. Trempe, C.J. Wilds, A.Y. Denisov, R.T. Pon, M.J. Damha, and K. Gehring. J. Am. Chem. Soc. **123**, 4896 (2001).
13. W. Guschlbauer and K. Jankowski. Nucleic Acids Res. **8**, 1421 (1980).
14. J.C. Catlin and W. Guschlbauer. Biopolymers, **14**, 51 (1975).
15. H. Ikeda, R. Fernandez, A. Wilk, J.J. Barchi, Jr., X. Huang, and V.E. Marquez. Nucleic Acids Res. **26**, 2237 (1998).
16. B.P. Monia, E.A. Lesnik, C. Gonzalez, W.F. Lima, D. Mcgee, C.J. Guinosso, A.M. Kawasaki, P.D. Cook, and S.M. Freier. J. Biol. Chem. **268**, 14514 (1993).
17. A.M. Kawasaki, M.D. Casper, S.M. Freier, E.A. Lesnik, M.C. Zounes, L.L. Cummins, C. Gonzalez, and P.D. Cook. J. Med. Chem. **36**, 831 (1993).
18. D.M. Williams, F. Benseler, and F. Eckstein. Biochemistry, **30**, 4001 (1991).
19. M. Manoharan. BEB Acta-Gene Structure and Expression, **1489**, 117 (1999).
20. C.J. Wilds and M.J. Damha. Nucleic Acids Res. **28**, 3625 (2000).
21. C.J. Wilds and M.J. Damha. J. Bioconjug. Chem. **10**, 299 (1999).
22. C.J. Wilds. Ph.D. thesis. McGill University, Montreal. 2000.
23. C.G. Peng and M.J. Damha. Nucleic Acids Res. **35**, 4977 (2007).
24. W.A. Pieken, D.B. Olsen, D.M. Williams, H. Aurup, F. Benseler, and F. Eckstein. Biol. Chem. Hoppe-Seyler, **372**, 731 (1991).
25. J. Capodici, K. Kariko, and D. Weissman. J. Immunol. **169**, 5196 (2002).
26. T. Dowler, D. Bergeron, A.L. Tedeschi, L. Paquet, N. Ferrari, and M.J. Damha. Nucleic Acids Res. **34**, 1669 (2006).
27. A. Kalota, L. Karabon, C.R. Swider, E. Viazovkina, M. Elzagheid, M.J. Damha, and A.M. Gewirtz. Nucleic Acids Res. **34**, 451 (2006).
28. H. Aurup, D.M. Williams, and F. Eckstein. Biochemistry, **31**, 9636 (1992).
29. M.F. Kubik, C. Bell, T. Fitzwater, S.R. Watson, and D.M. Tasset. J. Immunol. **159**, 259 (1997).
30. J. Ruckman, L.S. Green, J. Beeson, S. Waugh, W.L. Gillette, D.D. Henninger, L. Claesson-Welsh, and N. Janjic. J. Biol. Chem. **273**, 20556 (1998).
31. N.C. Pagratis, C. Bell, Y.-F. Chang, S. Jennings, T. Fitzwater, D. Jellinek, and C. Dang. Nat. Biotechnol. **15**, 68 (1997).
32. R.A. Blidner, R.P. Hammer, M.J. Lopez, S.O. Robinson, and W.T. Monroe. Chem. Biol. Drug Des. **70**, 113 (2007).
33. H. Aoyama, L.S. Cottin, L. Tarragolitvak, S. Litvak, and W. Guschlbauer. Biochim. Biophys. Acta, **824**, 218 (1985).
34. W.B. Helfman, S.S. Hendler, D.H. Shannahoff, and D.W. Smith. Biochemistry, **17**, 1607 (1978).
35. F.C. Richardson, R.D. Kuchta, A. Mazurkiewicz, and K.A. Richardson. Biochem. Pharmacol. **59**, 1045 (2000).
36. T. Ono, M. Scalf, and L.M. Smith. Nucleic Acids Res. **25**, 4581 (1997).
37. J.A. Montgomery, A.T. Shortnacyfowler., S.D. Clayton, J.M. Riordan, and J.A. Secrist. J. Med. Chem. **35**, 397 (1992).
38. X.B. Kong, A.C. Scheck R.W. Price, P.M. Vidal, M.P. Fanucchi, K.A. Watanabe, J.J. Fox, and T.C. Chou. Antiviral Res. **10**, 153 (1988).
39. J.L. Ruth and Y.C. Cheng. Mol. Pharmacol. **20**, 415 (1981).
40. E.C. Mar, J.F. Chiou, Y.C. Cheng, and E.S. Huang. J. Virol. **56**, 846 (1985).
41. S. Faderl, V. Gandhi, M.J. Keating, S. Jeha, W. Plunkett, and H.M. Kantarjian. Cancer, **103**, 1985 (2005).
42. H.H. Sun, A. Sloan, T.J. Mangner, U. Vaishampayan, O. Muzik, J.M. Collins, K. Douglas, and A.F. Shields. Eur. J. Nucl. Med. Mol. I **32**, 15 (2005).
43. P.S. Conti, M.M. Alauddin, J.R. Fissekis, B. Schmall, and K.A. Watanabe. Nucl. Med. Biol. **22**, 783 (1995).
44. A.F. Shields. Mol. Imaging Biol. **8**, 141 (2006).
45. C.G. Peng and M.J. Damha. *In* Proceedings of the International Roundtable on Nucleosides, Nucleotides, and Nucleic Acids. Bern, Switzerland. *Edited by* D.L. Haenni. 2006. p. 287.
46. D.K. Braithwaite and J. Ito. Nucleic Acids Res. **21**, 787 (1993).
47. C.G. Peng and M.J. Damha. J. Am. Chem. Soc. **129**, 5310 (2007).
48. A. Jacobomolina, J.P. Ding, R.G. Nanni, A.D. Clark, X.D. Lu, C. Tantillo, R.L. Williams, G. Kamer, A.L. Ferris, P. Clark, A. Hizi, S.H. Hughes, and E. Arnold. Proc. Natl. Acad. Sci. USA. **90**, 6320 (1993).
49. H. Huang, R. Chopra, G.L. Verdine, and S.C. Harrison. Science (Washington, DC), **282**, 1669 (1998).
50. J.P. Ding, K. Das, Y. Hsiou, S.G. Sarafianos, A.D. Clark, A. Jacobo-Molina, C. Tantillo, S.H. Hughes, and E. Arnold. J. Mol. Biol. **284**, 1095 (1998).
51. P.L. Boyer, S.G. Sarafianos, E. Arnold, and S.H. Hughes. Proc. Natl. Acad. Sci. USA. **97**, 3056 (2000).
52. L. Mu, S.G. Sarafianos, M.C. Nicklaus, P. Russ, M.A. Siddiqui, H. Ford, Jr., H. Mitsuya, R. Le, E. Kodama, C. Meier, T. Knispel, L. Anderson, J.J. Barchi, Jr., and V.E. Marquez. Biochemistry, **39**, 11205 (2000).
53. V.E. Marquez, A. Ezzitouni, P. Russ, M.A. Siddiqui, H. Ford, Jr., R.J. Feldman., H. Mitsuya, C. George, and J.J. Barchi, Jr. J. Am. Chem. Soc. **120**, 2780 (1998).
54. F. Li, S. Sarkhel, C.J. Wilds, Z. Wawrzak, T.P. Prakash, O.M. Manoharan, and M. Egli. Biochemistry, **45**, 4141 (2006).
55. P.L. Boyer, J.G. Julias, V.E. Marquez, and S.H. Hughes. J. Mol. Biol. **345**, 441 (2005).
56. R. Radhakrishnan, K. Arora, Y.L. Wang, W.A. Beard, S.H. Wilson, and T. Schlick. Biochemistry, **45**, 15142 (2006).
57. C.M. Joyce and S.J. Benkovic. Biochemistry, **43**, 14317 (2004).
58. T.A. Kunkel. J. Biol. Chem. **279**, 16895 (2004).
59. S. Yokoyama, T. Watanabe, K. Murao, H. Ishikura, Z. Yamaizumi, S. Nishimura, and T. Miyazawa. Proc. Natl. Acad. Sci. USA. **82**, 4905 (1985).

© 2008 NRC Canada

60. M.J. Damha and K.K. Ogilvie. Biochemistry, **27**, 6403 (1988).
61. G. Borkow, D. Arion, A. Noronha, M. Scartozzi, M.J. Damha, and M.A. Parniak. Int. J. Biochem. Cell Biol. **29**, 1285 (1997).
62. J.C. Chaput and J.W. Szostak. J. Am. Chem. Soc. **125**, 9274 (2003).
63. Y. Kato, N. Minakawa, Y. Komatsu, H. Kamiya, N. Ogawa, H. Harashima, and A. Matsuda. Nucleic Acids Res. **33**, 2942 (2005).
64. A. Galarneau, K.-L. Min, M.M. Mangos, and M.J. Damha. Methods Mol. Biol. (Totowa, NJ, United States), **288**, 65 (2005).

© 2008 NRC Canada

Chemical-constituent diversity of *Tridax procumbens*

Wen-Hao Chen, Xing-Ming Ma, Quan-Xiang Wu, and Yan-Ping Shi

Abstract: Three new phytochemicals, a polyacetylene, 1,2-dihydrodendroarboreol B (**1**), an ionone derivative, (3*S*,5*R*,6*S*,7*E*)-3-tetradecanoate-5,6-epoxy-β-ionone (**4**), and a flavonol diglycoside, quercetagetin-3,6,4′-trimethoxy-7-*O*-neohesperidoside (**38**), along with 35 known compounds with diverse structures, were isolated from the EtOH extract of the aerial parts of *Tridax procumbens*. The structures of **1**, **4**, and **38** were determined on the basis of comprehensive methods including UV, IR, NMR, HR-ESI-MS, and CD, and by comparison of the spectroscopic data with those reported for structurally related compounds. Compounds **4**, (3*S*,5*R*,6*S*,7*E*)-5,6-epoxy-3-hydroxy-7-megastigmene-9-one (**5**), and icariside B_1 (**12**) were tested for their abilities to inhibit SGC-7901 and HL-60 cells. The antioxidant activities of quercetagetin-3,6,4′-trimethoxyl-7-*O*-β-D-glucopyranoside (**36**), quercetin-3-methoxyl-4′-*O*-β-D-glucoside (**37**), and **38** were evaluated by measuring their free-radical-scavenging effects, using the DPPH free-radical method.

Key words: Tridax procumbens, polyacetylene, ionone, flavonol, cytotoxicity, antioxidant activities.

Résumé : L'extraction des parties aériennes du *Tridax procumbens* à l'aide d'éthanol a permis d'isoler trois nouveaux produits phytochimiques, un polyacétylène, le 1,2-dihydroendroarboréol B (**1**), un dérivé de l'ionone, la (3*S*,5*R*,6*S*,7*E*)-3-tétradécanoate-5,6-époxy-β-ionone (**4**) et un diglycoside de flavonol, la quercétagénine-3,6,4′-triméthoxy-7-*O*-néohespéridoside (**38**) aux côtés de 35 produits connus de structures diverses. Les structures des composés **1**, **4** et **38** ont été déterminées sur la base de méthodes spectroscopiques, telle l'UV, l'IR, la RMN, la DC et la spectrométrie de masse à haute résolution avec ionisation par électronébulisation ainsi que par comparaison des données spectroscopiques avec celles rapportées pour des composés apparentés d'un point de vue structural. On a évalué les capacités du composé **4**, de la (3*S*,5*R*,6*S*,7*E*)-5,6-époxy-3-hydroxy-7-mégastigmène-9-one (**5**) et de l'icariside B_1 (**12**) à inhiber des cellules SGC-7901 et HL-60. On a évalué les activités antioxydantes du quercétagénine-3,6,4′-triméthoxy-7-*O*-β-D-glucopyranoside (**36**) et des quercétine-3-méthoxy-4′-*O*-β-D-glucosides (**37**) et (**38**) en mesurant leurs effets comme pièges à radicaux libres à l'aide de la méthode au radical libre DPPH.

Mots-clés : Tridax procumbens, polyacétylène, ionone, flavonol, cytotoxicité, activités antioxydantes.

[Traduit par la Rédaction]

Introduction

Tridax procumbens (Compositae) is the only species of *Tridax* L. genus distributed in China, but is a native plant in tropical America, Asia, and Australia (1). It is used in Indian traditional medicine as anti-coagulant, hair tonic, antifungal, insect repellent, also against bronchial catarrh, diarrhea, dysentery, and wound healing (2–4). To the best of our knowledge, not much attention has been detailed to the chemical constituents of *T. procumbens*, as only fumaric acid (5), β-sitosterol and tannin (6), flavone glycosides, and bergenin derivatives (7, 8) have been reported as constituents of the plant. The medicinal importance and the unusual distribution of this species promoted us to undertake phytochemical studies systematically, which resulted in the isolation and structure elucidation of a new polyacetylene (**1**), a new ionone derivative (**4**), and a novel flavonol diglycoside (**38**), together with 35 known secondary metabolites belonging to various classes of compounds, from the EtOH extract of the aerial parts of *T. procumbens* collected from Wenchang town, Hainan Island, China.

The known compounds were identified by comparing ^{1}H NMR, ^{1}H–^{1}H COSY, ^{13}C NMR (DEPT), MS, CD, and optical rotation data with published values (9–36). The present paper deals with the structure elucidation of **1**, **4**, and **38**. Compounds **4**, **5**, and **12** were tested for their abilities to inhibit human gastric carcinoma (SGC-7901) and human promyelocytic leukemia (HL-60) cells, while **36**–**38** were examined for their antioxidant activities in the free-radical 1,1-diphenyl-2-picrylhydrazyl (DPPH) test.

Received 6 March 2008. Accepted 6 May 2008. Published on the NRC Research Press Web site at canjchem.nrc.ca on 31 July 2008.

W.-H. Chen, Q.-X. Wu, and Y.-P. Shi.[1] State Key Laboratory of Applied Organic Chemistry, College of Chemistry and Chemical Engineering, Lanzhou University, Lanzhou 730000, P. R. China.
X.-M. Ma. School of Basic Medical Sciences, Lanzhou University, Lanzhou 730000, P. R. China.
Y.-P. Shi. Key Laboratory for Natural Medicine of Gansu Province, Lanzhou Institute of Chemical Physics, Chinese Academy of Sciences, Lanzhou 730000, P. R. China.

[1]Corresponding author (e-mail: shiyp@lzb.ac.cn).

 doi:10.1139/V08-097 © 2008 NRC Canada

Fig. 1. Structures of some isolated compounds.

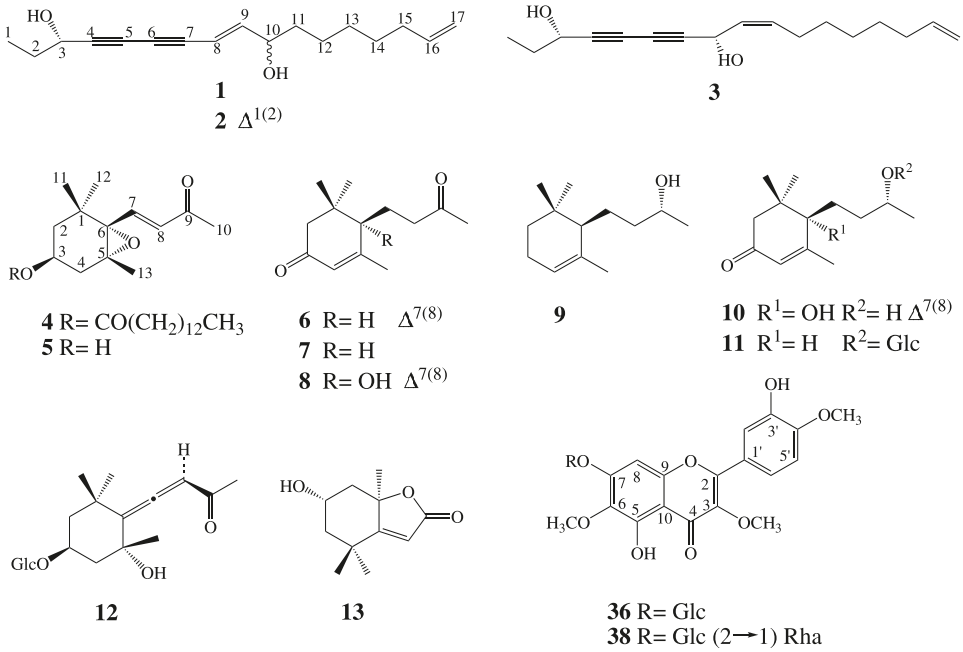

Results and discussion

Structure elucidation

Compound **1** (Fig. 1) was obtained as yellow optically active oil, which showed [α] = –10 (*c* 0.2, $CHCl_3$). The molecular formula of **1** was determined to be $C_{17}H_{24}O_2$ based on its HR-ESI-MS (*m/z* 278.2117 $[M + NH_4]^+$) and the ^{13}C NMR data (Table 1), implying six degrees of unsaturation. The UV spectrum showed typical absorption bands for a conjugated ene-3,5-diyne chromophore (λ_{max} at 215, 241, 253, 268, and 284 nm) (37). Its IR spectrum showed the presence of hydroxy (br 3374 cm^{-1}), alkyne (2232 and 2212 cm^{-1}), and double bond (1640 cm^{-1}) functional groups.

The ^{13}C NMR (Table 1) spectrum with DEPT experiment indicated four nonprotonated acetylene resonances as well as a terminal olefin (δ_C 138.9 (d), 114.4 (t)). Another olefin (δ_C 108.2 (d), 149.6 (d)) accounted for the last unsaturation as the conjugated ene-3,5-diyne, that inherent in the molecular formula. ^1H NMR (Table 1) analyses indicated that the other terminus consisted of a spin system that began with a methyl triplet (δ_H 1.02). The ^1H–^1H COSY experiment showed that H-1 was coupled to H-2 that was further coupled to H-3, making the end of the spin system. Partial structures were linked by the HMBC experiment (Fig. 2). Key correlations included those observed between H-3 and C-4 and C-5, H-2 and C-3 and C-4. On the opposite side of the ene-3,5-diyne, we observed a correlation between H-10 and C-8, C-9, C-11, and C-12. All data (Table 1 and Experimental section) and compared with the isolated compounds **2** and **3,** was consistent with assignment of compound **1** as the analogue of diynene. The paucity of **1** precluded the possibility of defining its absolute configuration. Thus, compound **1** was elucidated as 1,2-dihydrodendroarboreol B (Fig. 1).

Compound **4** was obtained as colourless optically active needles, with [α] = –40 (*c* 0.2, $CHCl_3$). The molecular formula of **4** was determined to be $C_{27}H_{46}O_4$ based on its HR-ESI-MS (*m/z* 457.3293 $[M + Na]^+$) and the ^{13}C NMR (Table 2) data, implying five degrees of unsaturation. The UV spectrum showed an absorption maximum at 229 nm, suggesting an α,β-unsaturated ketone, and the IR spectrum showed the presence of ester carbonyl (1732 cm^{-1}), α,β-unsaturated carbonyl (1672 cm^{-1}), and a long straight-chain aliphatic unit $[(CH_2)_n\ n \geq 4]$ (719 cm^{-1}).

The ^1H NMR (Table 2) spectrum revealed the presence of five methyl groups at δ_H 0.88 (3H, t, H-14′), 0.99 (3H, s, H-12), 1.19 (3H, s, H-13), 1.21 (3H, s, H-11), and 2.29 (3H, s,

Table 1. NMR spectral data of **1** and **2** in $CDCl_3$.

	1[a]		**2**[b]
Position	δ_H (*J* in Hz)	δ_C (DEPT)	δ_C (DEPT)
1	1.02 (t, 6.9)	9.3 q	117.2 t
2	1.74 (m)	30.6 t	135.9 d
3	4.41 (t, 6.6)	64.3 d	63.6 d
4	—	82.9 s	80.4 s
5	—	70.3 s	70.8 s
6	—	73.6 s	73.5 s
7	—	77.9 s	77.5 s
8	5.75 (br d, 15.9)	108.2 d	108.1 d
9	6.31 (dd, 15.9, 6.0)	149.6 d	149.8 d
10	4.19 (ddt, 6.0,1.2, 6.8)	72.0 d	72.0 d
11	1.5 (q, 6.8)	36.8 t	36.7 t
12	1.31 (m)	25.0 t	25.0 t
13	1.31 (m)	29.0 t	28.9 t
14	1.37 (m)	28.8 t	28.7 t
15	2.02 (q, 7.0)	33.6 t	33.6 t
16	5.78 (ddt, 16.8, 10.4, 7.0)	138.9 d	138.9 d
17	4.94 (br d, 10.4); 4.98 (br d, 16.8)	114.4 t	114.3 t

[a]Recorded at 400 and 100 MHz for ^1H and ^{13}C NMR, respectively.
[b]Recorded at 75 MHz for ^{13}C NMR.

© 2008 NRC Canada

Fig. 2. Important HMBC and NOESY correlations for **1**, **4**, and **38**.

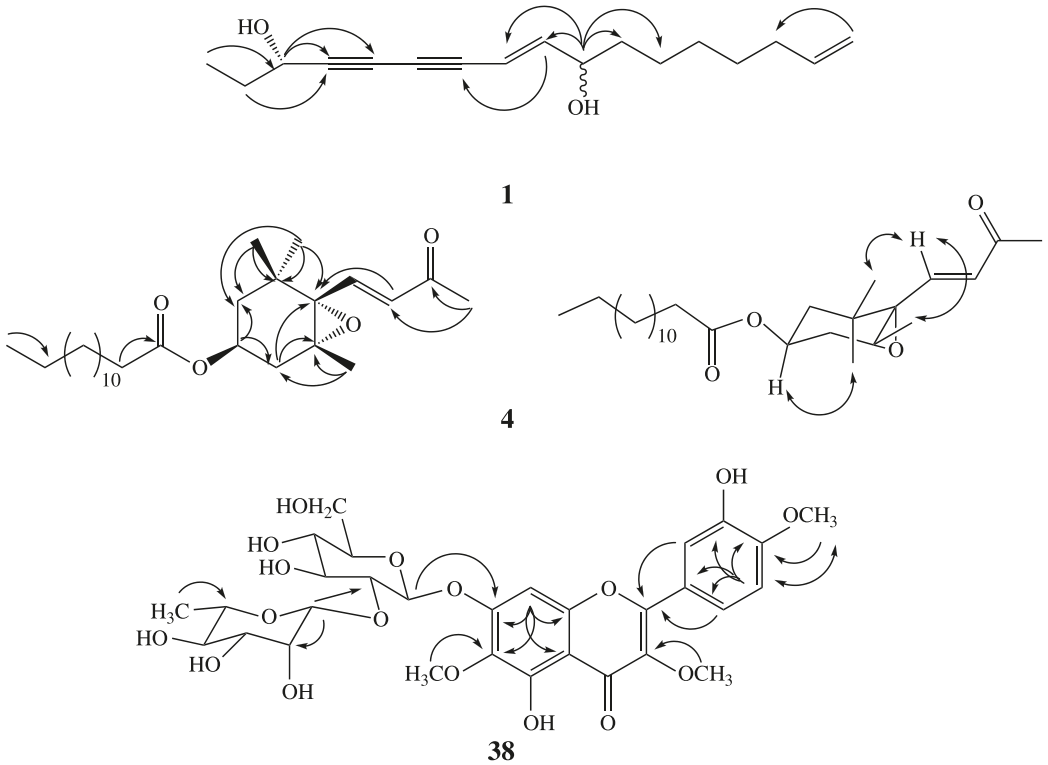

Table 2. NMR spectral data of **4** and **5** in $CDCl_3$.

	4[a]		**5**[b]
Position	δ_H (J in Hz)	δ_C (DEPT)	δ_C (DEPT)
1	—	34.5 s	35.1 s
2	1.67 (ddd, 1.2, 2.8, 13.2); 1.38 (dd, 8.4, 13.2)	41.1 t	40.5 t
3	4.94 br s	66.9 d	64.0 d
4	2.41 (ddd, 1.2, 4.8, 15.2); 1.79 (dd, 6.8, 15.2)	36.5 t	46.6 t
5	—	65.9 s	67.3 s
6	—	69.7 s	69.4 s
7	7.04 (d, 15.6)	141.7 d	142.4 d
8	6.32 (d, 15.6)	132.7 d	132.5 d
9	—	197.3 s	197.5 s
10	2.29 (s)	28.5 q	29.3 q
11	1.21 (s)	25.6 q	24.9 q
12	0.99 (s)	28.4 q	28.3 q
13	1.19 (s)	20.1 q	19.8 q
1′	—	173.1 t	—
2′	2.26 (t, 7.6)	34.6 t	—
3′	1.60 (m)	24.9 t	—
4′–11′	1.27 (m)	29.1–29.7 t	—
12′	—	31.9 t	—
13′	—	22.7 t	—
14′	0.88 (t, 6.4)	14.1 q	—

[a]Recorded at 400 and 100 MHz for ^1H and ^{13}C NMR, respectively.
[b]Recorded at 75 MHz for ^{13}C NMR.

H-10), the last one being due to a methyl ketone. The signals of δ_H 0.88 (3H, t, H-14′) and 1.27 (16H, m, H-(4′–11′)) suggested the presence of a long-chain hydrocarbon. The ^{13}C NMR spectrum of **4** showed signals characteristic of an long-chain ester (δ_C 173.1 and 14.1) moiety and the remaining 13 signals, including those of four methyl groups, indicating that the alcohol part of the ester was a derivative of megastigmane, a pair of trans-double-bond proton signals at δ_H 6.32 (1H, d, J = 15.6 Hz) and 7.04 (1H, d, J = 15.6 Hz) must be present at $\Delta^{7(8)}$ in the side chain, and the attachment point of the fatty-acid chain was assigned to the C-3 position by comparing the ^1H NMR chemical shift of H-3 (δ_H 4.94) with those of 3-acetoxy-5,6-epoxy-β-ionone (δ_H 4.87) (38) and compound **5** (δ_H 3.93, H-3), which must be in an axial orientation ($J_{H\text{-}2\alpha,\ H\text{-}3}$ = 13.2 Hz) on the basis of ^1H NMR and ^1H–^1H COSY experiment. The position of C-5 and C-6, were thus available for two quaternary carbons, each bearing an oxygen function, as demanded by the elemental composition. This premise was really satisfied by the presence of an epoxy ring between the C_5- and C_6-position, which was supported by the HMBC experiment (Fig. 2) and comparison with the data of the related compound 3β-acetoxy-5α, 6α-epoxy-β-ionone (38).

The NOE effect between H-13 and H-7 confirmed a cis stereochemistry for this epoxy. Furthermore, NOESY interactions between H-11 and H-7, H-12 and H-3 revealed the relative stereostructure of **4** as shown in Fig. 1. Finally, The CD spectrum (Fig. 3) showed a negative CE, $\epsilon_{232\ nm}$ –20, confirming the absolute configurations as *S*, *R*, and *S* for C-3, C-5, and C-6, respectively, as previously discussed (38). On the basis of the above data, compound **4** was deduced unambiguously as (3*S*,5*R*,6*S*,7*E*)-3-tetradecanoate-5,6-epoxy-β-ionone (see Fig. 1).

Compound **38** was obtained as yellow amorphous powder, which showed [α] = –56 (*c* 0.5, CH_3OH). The HR-ESI-MS

© 2008 NRC Canada

Fig. 3. The CD spectrum of **4**.

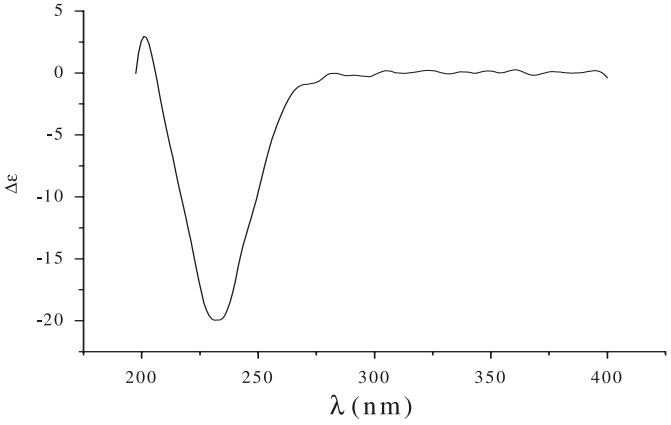

m/z $[M + Na]^+$ 691.1839 indicated its molecular formula to be $C_{30}H_{36}O_{17}$. The UV spectrum was characteristic for flavonoids showing UV maxima at 347 and 258 nm. The IR spectrum showed the presence of hydroxyl (3394 cm^{-1}), chelated hydroxyl (2931 cm^{-1}), conjugated carbonyl (1657 cm^{-1}), and aromatic (1598 cm^{-1}) functional groups. The ^1H NMR spectrum also showed **38** was a flavonoids derivative with the expected signals for the aromatic protons at δ_H 7.54 (1H, br s), 7.52 (1H, d, J = 8.0 Hz), and 7.07 (1H, d, J = 8.0 Hz) for H-2′, H-6′, and H-5′, respectively, the remaining downfield singlet at δ_H 6.96 (1H, s) was due to H-6 or H-8 of ring A. The proton signals for three methoxyl groups were observed at δ_H 3.82, 3.76, and 3.74 (3H, each, s), and the signal at δ_H 12.65 indicated the presence of chelated 5-hydroxyl group. The anomeric protons appeared at δ_H 5.34 (1H, d, J = 7.6 Hz) and 5.25 (1H, br s) with 1.08 (3H, d, J = 5.6 Hz) in ^1H NMR spectrum and ^{13}C NMR data (δ_C 98.5 and 100.6) showed the presence of a β-D-glucose and a α-L-rhamnose, and the α-L-rhamnose moiety was attached to the C-2″ of glucose, judging from the downfield shift of the C-2″ and the upfield shift of C-1″, respectively, from those of **36** (Table 3). The EI-MS showed base peak at *m/z* 360 (100%), a large peak at *m/z* 359 (50%) typical of C-3 methoxylate flavonoids (39), and a strong peak at *m/z* 345 (32%) consistent with the presence of a methoxyl group at C-6 or C-8 (40). The locations of the different groups were made possible through ^1H and ^{13} C NMR data compared with those of **36**.

The proposed structure of **38** was further confirmed by the HMBC experiment (Fig. 2). The correlations between H (δ_H 6.96) and C-6 (δ_C 133.2) as well as C-7 (δ_C 156.6), C-9 (δ_C 151.9), and C-10 (δ_C 107.0) indicated that the aromatic proton was at C-8 (δ_C 94.8). Furthermore, HMBC correlation between H-1″ (δ_H 5.34) and C-7 indicated that the Glc unit was located at C-7. The methoxyl protons δ_H 3.76, 3.74, and 3.82 showed ^3J interactions with C-3 (δ_C 138.6), C-6 (δ_C 133.2) and C-4′ (δ_C 147.1), respectively. Further support for the location of the methoxyl δ_H 3.82 at C-4′ but not C-3′ was derived from a significant NOE correlation between H-5′ and OMe-4′, and compared the physical data with its isomeric compound quercetagetin-3,6,3′-trimethoxy-7-*O*-neohesperidoside (41). Thus, from the above data, the structure of **38** was elucidated as quercetagetin-3,6,4′-trimethoxy-7-*O*- neohesperidoside (see Fig. 1).

Table 3. NMR spectral data of **38** and **36** in DMSO-d_6.

	38[a]		**36**[b]
Position	δ_H (J in Hz)	δ_C (DEPT)	δ_C (DEPT)
2	—	156.6 s	156.7 s
3	—	138.6 s	138.6 s
4	—	179.0 s	179.0 s
5	—	152.7 s	152.7 s
6	—	133.2 s	132.8 s
7	—	156.5 s	157.2 s
8	6.96 (s)	94.8 d	94.7 d
9	—	151.9 s	152.0 s
10	—	107.0 s	106.9 s
1′	—	122.9 s	122.8 s
2′	7.54 (br s)	112.5 d	112.5 d
3′	—	151.0 s	151.0 s
4′	—	147.1 s	147.0 s
5′	7.07 (d, 8.0)	115.8 d	115.7 d
6′	7.52 (d, 8.0)	121.1 d	121.2 d
3-OCH_3	3.76 (s)	60.4 q	60.4 q
6-OCH_3	3.74 (s)	60.9 q	61.0 q
4-OCH_3	3.82 (s)	56.3 q	56.3 q
Glc 1″	5.34 (d, 7.6)	98.5 d	100.7 d
2″	—	76.6 d	73.8 d
3″	—	78.1 d	77.3 d
4″	—	70.4 d	70.2 d
5″	—	77.7 d	77.9 d
6″	—	61.1 t	61.2 t
Rha 1‴	5.25 (br s)	100.6 d	—
2‴	—	71.0 d	—
3‴	—	71.1 d	—
4‴	—	72.6 d	—
5‴	—	69.2 d	—
6‴	1.08 (d, 5.6)	18.7 q	—

[a]Recorded at 400 and 100 MHz for ^1H and ^{13}C NMR, respectively.
[b]Recorded at 75 MHz for ^{13}C NMR.

The known compounds isolated were as following: two polyacetylenes, dendroarboreol B (**2**) (9) and dendroarboreol A (**3**) (9); nine norisoprenoids, (3*S*,5*R*,6*S*,7*E*)-5,6-epoxy-3-hydroxy-7-megastigmene-9-one (**5**) (10), (6*R*,7*E*)-4,7-megastigmadien-3,9-dione (**6**) (11), 4-megastigmene-3,9-dione (**7**) (12), *S*-(+)-dehydrovomifoliol (**8**) (13), 7,8-dihydro-α-ionol (**9**) (14), vomifoliol (**10**) (15), byzantionoside B (**11**) (16), icariside B_1 (**12**) (17), and loliolide (**13**) (18); one sequiterpene, isopterocarpolone (**14**) (19); three diterpenes, phytol (**15**) (20), α-tocopherylquinone (**16**) (21), and phytene-1,2-diol (**17**) (22); four triterpenes, β-amyrin (**18**) (23), oleanolic acid (**19**) (23), cycloeucalenol (**20**) (24), and cycloart-23*Z*-ene-3β,25-diol (**21**) (25); nine steroids, 24-hydroxy-24-vinylcholesterol (**22**) (26), exgoster-5α,8α-peroxide (**23**) (27), 7-oxositosterol (**24**) (28), 7α-hydroxysitosterol (**25**) (28), 7β-hydroxysitosterol (**26**) (28), 6β-hydroxyenone (**27**) (28), 3β,6α-dihydroxy-4-cholestene (**28**) (29), β-sitosterol (**29**) (28), and β-daucosterol (**30**) (30); one coumarin, (–)-8-methoxyobliquin (**31**) (31); three benzenoids, 4-hydroxybenzaldehyde (**32**) (32), 2-hydroxybenzaldehyde (**33**) (33), and benzyl glucoside (**34**) (17); one adenosine, adenosine A (**35**) (34); two flavonoid glycosides, quercetagetin-3,6,4′-trimethoxyl-7-*O*-β-D-glucopyranoside (**36**)

© 2008 NRC Canada

(35) and quercetin-3-methoxyl-4-*O*-β-D-glucoside (**37**) (36), as well as their structures relative new compounds **1**, **4**, and **38** were showed in the Fig. 1.

Activity evaluation

Compounds **4**, **5**, and **12** were tested for their abilities to inhibit SGC-7901 and HL-60 cells using MTT (3-(4,5-dimethylthiazol-2-yl)-2,5-diphenyltetrazolium bromide) method (42,43). Compared with 5-fluorouracil (5-Fu), unfortunately, none of them exhibited significant inhibitory effects with IC_{50} values over 100 μmol/L against SGC-7901 and HL-60 cells.

Compounds **36**, **37**, and **38** were tested for their antioxidant activities using the DPPH test, with VE (vitamin E) as positive control (44, 45). In the DPPH system, the free-radical-scavenging activity of tested samples was expressed as IC_{20}. Compounds **38** and **36** (46) showed limited antioxidant capacity with $IC_{20} > 100$ μmol/L, which indicated that the additional presence of a α-L-rhamnose group in position C-2″ of **38** does not influence its radical-scavenging activity, as expected. On the other hand, **37** showed slight activity with $IC_{20} = 95.57$ μmol/L, when compared with the $IC_{20} = 7.60$ μmol/L of the reference, VE.

Experimental section

General experimental procedures

DPPH was obtained from Sigma-Aldrich Chemical Co. (St. Louis, MO, USA). Silica gel GF_{254} (10–40 μm; Qingdao Marine Chemical Factory) was used for TLC. Column chromatography (CC) experiments were carried out on silica gel (200–300 mesh; Qingdao Marine Chemical Factory). Melting points were determined on a X-4 Digital Display Micro-melting point apparatus, uncorrected. UV and IR spectra were recorded on a Shimadzu UV-260 and a Nicolet *NEXUS-670* FT-IR spectrophotometer, respectively. Optical rotations were recorded on a PerkinElmer 341 polarimeter; CD spectra were recorded on an Olis DSM 1000 spectrophotometer; ^1H and ^{13}C NMR spectra were recorded on a Varian INOVA-400 spectrometer at 400 MHz (for ^1H) and 100 MHz (for ^{13}C) or a Varian INOVA-300 spectrometer 300 MHz (for ^1H) and 75 MHz (for ^{13}C) with TMS as internal reference (δ 0); and EI-MS and HR-ESI-MS were measured on a VG ZABHS and a Bruker APEX-mass spectrometer, respectively.

Plant material

The air-dried aerial parts of *Tridax procumbens* were collected in Wenchang town (latitude 19° 61 N; longitude 110° 72 E), Hainan Province, P. R. China, in August 2004, and were identified by adjunct Professor Huan-Yang Qi. A voucher specimen (No. 2004002) has been deposited in the State Key Laboratory of Applied Organic Chemistry, Lanzhou University, P. R. China.

Extraction and isolation

The air-dried powder of the aerial parts of *T. procumbens* (3.9 kg) was extracted with 95% EtOH (3 × 7 d) at room temperature. After concentration under reduced pressure, the extract (400 g) was suspended in water and fractionated by successive partitioning with petroleum ether (60:90), EtOAc, and *n*-BuOH. After removal of the solvents in vacuo, the following residues were obtained: Rp (73.8 g), Re (8.5 g), Rb (19.3 g). Rp was fractionated on a silica-gel column eluting with a petroleum ether–EtOAc gradient system and then with acetone to give six main fractions (Fr. Rp1–Rp6). Fr. Rp1 mainly contained fatty materials, while the last fraction (Fr. Rp6, eluted with acetone) was a complex mixture. Fr. Rp2 was rechromatographed with petroleum ether – EtOAc (35:1) followed by petroleum ether–actone (25:1) to give **4** (10 mg), **15** (20 mg), **18** (20 mg), and **29** (180 mg), respectively. Fr. 3 was subjected to CC (SiO_2; $CHCl_3$:EtOAc, 30:1) to provide **1** (2 mg). The compounds were eluted in the following order: **20** (15 mg), **16** (20 mg), **19** (2 mg), **3** (30 mg), **21** (4 mg), **2** (7 mg), **22** (10 mg), **23** (6 mg), **27** (5 mg), **17** (11 mg), **24** (10 mg), **8** (10 mg), **5** (15 mg), **6** (2 mg), **7** (2 mg), **14** (5 mg), **26** (15 mg), **28** (3 mg), **25** (15 mg), and **30** (120 mg). From the Re residue, compounds **9** (2 mg), **31** (18 mg), **32** (4 mg), **13** (15 mg), **33** (3 mg), and **10** (5 mg) were isolated using silica-gel chromatography and preparative TLC. From the Rb residue, compounds **36** (30 mg), **11** (10 mg), **34** (5 mg), **37** (15 mg), **35** (15 mg), **12** (12 mg), and **38** (20 mg) were isolated after repeated column chromatography and recrystallization.

Bioassays

Tests of cytotoxicity against tumor SGC-7901 and HL-60 cells

A MTT [3-(4,5-dimethylthiazol-2-yl)-2,5-diphenyltetrazolium bromide] colourimetric assay was performed in 96-well culture plates. The assay was based on reduction of MTT by the mitochondrial dehydrogenase of viable cells to yield a blue formazan product that could be measured spectrophotometrically. In the experiment, the negative controls were isochoric normal saline, 1% DMSO or 0.1% DMSO; positive control was 5-Fu at concentrations of 25, 50, 100, and 200 μmol/L. SGC-7901 and HL-60 cells at a log phase of their growth cycle (1×10^4 cell/mL) were added to each well (90 μL/well), then treated in four replicates at various concentrations of the drugs with six vacant reference wells set in one plate (100 μL cultured madia in each well) and incubated for 44 h at 37 °C in a humidified atmosphere of 5% CO_2. After 44 h, 10 μL of MTT solution (5 mg/mL) was added to each well, which was incubated for another 4 h, after which a solution of 10% sodium dodecyl sulfate (SDS) was added to each well (100 μL/well). Twelve hours later at room temperature, the optical density (O.D.) of each well was recorded on an ELISA reader (Bioteck EL-340) at one wavelength of 578 nm.

Scavenging activity of DPPH radicals

The antioxidant activities of the pure compounds were assessed on the basis of the radical-scavenging effect of the stable DPPH free radical. Aliquots of 30 μL of an ethanol solution containing each pure compound were added to 3 mL of 100 μmol/L ethanol solution of DPPH. Absorbance at 517 nm was determined after 30 min at room temperature, and the percent antioxidant activity (AA) was calculated using the following formula: $AA\% = 100\{[(Abs_{sample} - Abs_{blank}) \times 100]/Abs_{control}\}$.

© 2008 NRC Canada

Ethanol (3 mL) was used as a blank. 100 μmol/L of DPPH ethanol solution (3 mL) was used as a negative control. The IC_{20} value was the concentration of test sample required to scavenging 20% DPPH free radicals. VE was used as positive control.

Spectral data

1,2-Dihydrodendroarboreol B (1)

Yellow oil. [α] = –10 (*c* 0.2, $CHCl_3$). UV (MeOH, nm) λ_{max} (log ε): 215 (2.26), 241 (0.85), 253 (1.22), 268 (1.56), 284 (1.28). IR (KBr plate, cm^{-1}) ν_{max}: 3374, 3076, 2927, 2232, 2212, 1640, 969, 911. ^1H and ^{13}C NMR: see Table 1. HR-ESI-MS *m/z*: 278.2117 ($[M + NH_4]^+$, $C_{17}H_{28}NO_2^+$ calcd. 278.2115).

(3S,5R,6S,7E)-3-Tetradecanoate-5,6-epoxy-β-ionone (4)

Colourless needles; mp 46–47 °C. [α] = –40 (*c* 0.2, $CHCl_3$). CD (*c* 0.0023, MeOH): $[\theta]_{232nm}$ = –8680. UV (MeOH, nm) λ_{max} (log ε): 229 (0.76). IR (KBr plate, cm^{-1}) ν_{max}: 2918, 1732, 1715, 1672, 719. ^1H and ^{13}C NMR: see Table 2. HR-ESI-MS *m/z*: 457.3293 ($[M + Na]^+$, $C_{27}H_{46}O_4Na^+$ calcd. 457.3288).

Quercetagetin-3,6,4-trimethoxy-7-O-neohesperidoside (38)

Yellow amorphous powder; mp 177–179 °C. [α] = –56 (*c* 0.5, CH_3OH). UV (MeOH, nm) λ_{max} (log ε): 212 (0.48), 258 (0.25), 274 (0.23), 347 (0.26). IR (KBr plate, cm^{-1}) ν_{max}: 3394, 2931, 2851, 1657, 1598, 1469, 1360, 1273, 1075. ^1H and ^{13}C NMR: see Table 3. EI-MS (probe 70 eV *m/z*): 360 ($[M – Glc(2\rightarrow1)Rha + H]^+$, 100%), 359 (50%), 345 (32%), 317 (31%). HR-ESI-MS *m/z*: 691.1839 ($[M + Na]^+$, $C_{30}H_{36}O_{17}Na^+$ calcd. 691.1845).

Acknowledgments

The authors are greatly indebted to adjunct Professor Huan-Yang Qi (Key Laboratory of Natural Medicine for Gansu Province, Lanzhou Institute of Chemical Physics, Chinese Academy of Sciences, P. R. China) for her help in identification of the plant material. This work was supported by National Natural Science Foundation of China (NSFC 20621091).

References

1. Publications and Information Directorate (CSIR). The wealth of India: A dictionary of Indian raw materials and industrial products raw materials. New Delhi. 1995. p. 292.
2. S.L. Srivastav, V.K. Kediyal, and R.C. Sundriyal. J. Environ. Biol. **5**, 217 (1984).
3. S.L. Udupa, A.L. Udupa, and D.R. Kulkarni. Fitoterapia, **62**, 146 (1991).
4. S. Saraf and V.K. Dixit. Fitoterapia, **62**, 534 (1991).
5. K.V. Ram and M.G. Madan. Phytochemistry, **27**, 459 (1988).
6. T.S. Raju and E.A. Davidson. Carbohydr. Res. **258**, 243 (1994).
7. M. Ali, E. Ravinder, and R. Ramachandram. Fitoterapia, **72**, 313 (2001).
8. E. Akbar, A. Malik, N. Afza, and S.M. Abdul Hai. Heterocycles, **57**, 733 (2002).
9. M.W. Bernart, J.H. Cardellina, II, M.S. Balaschak, M.R. Alexander, R.H. Shoemaker, and M.R. Boyd. J. Nat. Prod. **59**, 748 (1996).
10. B.D. Abrosca, M.D. Greca, A. Fiorentino, P. Monaco, P. Oriano, and F. Temussi. Phytochemistry, **65**, 497 (2004).
11. A.J. Asen, B. Kimland, and C.R. Enzell. Acta. Chem. Scand. **27**, 2107 (1973).
12. N. Ito and T. Etoh. J. Chem. Soc. Perkin Trans. 1. **19**, 2397 (1996).
13. T. Kato, M. Tsunakawa, N. Sasaki, H. Aizawa, K. Fujita, Y. Kitahara, and N. Takahoshi. Phytochemistry, **16**, 45 (1977).
14. Y.-X Tang and T. Suga. Phytochemistry, **37**, 737 (1994).
15. C.A.L. Bercht, H.M. Samrah, R.J.J.C. Luosberg, H. Theuns, and C.A. Salemink. Phytochemistry, **15**, 830 (1976).
16. Y. Takeda, H.-J Zhang, T. Masuda, G. Honda, H. Otsuka, E. sezik, E. Yesilada, and H.-D. Sun. Phytochemistry, **44**, 1335 (1997).
17. T. Miyase, A. Ueno, N. Takizawa, H. Kobayashi, and H. Karasawa. Chem. Pharm. Bull. **35**, 1109 (1987).
18. N. Okada, K. Shirata, M. Niwano, H. Koshino, and M. Uramoto. Phytochemistry, **37**, 281 (1994).
19. N. Kumar, B. Ravindranath, and T.R. Seshadri. Phytochemistry, **13**, 633 (1974).
20. R.A. Goodman, E. Oldfield, and A. Allerhand. J. Am. Chem. Soc. **95**, 7553 (1973).
21. J.D.P. Teresa, J.G. Urones, I.S. Marcos, J.F. Ferreras, A.M.L. Bertelloni, and P. Basabe Barcala. Phytochemistry, **26**, 1481 (1987).
22. G.D. Brown. Phytochemistry, **36**, 1553 (1994).
23. S.B. Mahato and A.P. Kundu. Phytochemistry, **37**, 1517 (1994).
24. F. Khuong-Huu, M. Sangare, V.M. Chari, A. Bekaert, M. Devys, M. Bareier, and G. Lukacs. Tetrahedron Lett. **22/23**, 1787 (1975).
25. M.D. Greca, A. Fiorentino, P. Monaco, and L. Previtara. Phytochemistry, **35**, 1017 (1994).
26. M. Guyot, D. Davoust, and C. Belaud. Tetrahedron Lett. **23**, 1905 (1982).
27. A.A.L. Gunatilaka, Y. Gopichand, F.J. Schmitz, and C. Djerassi. J. Org. Chem. **46**, 3860 (1981).
28. M.D. Greca, P. Monaco, and L. Previtera. J. Nat. Prod. **53**, 1430 (1990).
29. Z.-Q You and K. Masato. Tetrahedron Lett. **34**, 2745 (1993).
30. Y.-P Shi, Z.-J Jia, L. Jamil, and S. Sadiq. Phytochemistry, **40**, 1219 (1995).
31. W. Herz and M. Bruno. Phytochemistry, **25**, 1913 (1986).
32. Sadtler research laboratories. Sadtler research laboratories Sadtler stand NMR spectra [Z], Philadelphia (USA). 1970. p. 7349.
33. R.M. Benjamin, P.C. Thomas, and B.R. Paul. Phytochemistry, **26**, 1361 (1987).
34. A.J. Jones, D.M. Grant, M.W. Winkley, and R.K. Robins. J. Am. Chem. Soc. **92**, 4079 (1970).
35. C. Long, P. Sauleau, B. David, C. Lavaud, V. Cassabois, F. Ausseil, and G. Massiot. Phytochemistry, **64**, 567 (2003).
36. T. Iwasshima, S. Ootani, and K. Hayashi. Bot. Mag. **97**, 23 (1984).
37. F. Bohlmann, T. Burkhardt, and C. Zedero. Naturally occurring acetylenes. Academic Press. London. 1973. p. 4.
38. K. Mori. Tetrahedron, **30**, 1065 (1974).
39. D.G.I. Kingston. Tetrahedron, **27**, 2691 (1971).
40. J.N. Roitman and L.F. James. Phytochemistry, **24**, 835 (1985).
41. M. Singh and J. Singh. Planta Medica. **51**, 525 (1985).

© 2008 NRC Canada

42. X.-M Niu, S.-H Li, S.-X Mei, Z. Na, Q.-X Zhao, Z.-W Lin, and H.-D Sun. J. Nat. Prod. **65**, 1892 (2002).
43. K. Toume, M. Takahashi, K. Yamaguchi, T. Koyano, T. Kowithayakorn, M. Hayashi, K. Komiyama, and M. Ishibashi. Tetrahedron, **60**, 10817 (2004).
44. C.-H Chen, C.-Y Shaw, C.-C Chen, and Y.-C Tsai. J. Nat. Prod. **65**, 740 (2002).
45. Y.-L Huang, P.-Y Yeh, C.-C Shen, and C.-C Chen. Phytochemistry, **64**, 1277 (2003).
46. I. Parejo, J. Bastida, F. Viladomat, and C. Codina. Phytochemistry, **66**, 2356 (2005).

© 2008 NRC Canada

Ytterbium(III) triflate catalyzed synthesis of calix[4]pyrroles in ionic liquids

Anil Kumar, Israr Ahmad, and M. Sudershan Rao

Abstract: Ytterbium(III) triflate has been utilized as a mild Lewis-acid catalyst for the synthesis of various calix[4]pyrroles by the condensation of pyrrole with different ketones in ionic liquids. The calix[4]pyrroles were obtained in high yield under ecofriendly, economical, and noncorrosive conditions, and the catalyst was recovered and recycled.

Key words: calix[4]pyrrole, ionic liquid, ytterbium triflate.

Résumé : On a utilisé le triflate d'ytterbium(III) comme catalyseur acide de Lewis doux pour la synthèse de divers calix[4]pyrolles par condensation du pyrrole avec diverses cétones dans des liquides ioniques. Les calix[4]pyrolles ont été obtenus avec des rendements élevés dans des conditions économiques, non corrosives et respectueuses de l'environnement alors que le catalyseur peut être récupéré et recyclé.

Mots-clés : calix[4]pyrolle, liquide ionique, triflate d'ytterbium.

[Traduit par la Rédaction]

Introduction

Calix[4]pyrroles, a class of tetrapyrrolic macrocyclic molecules, have been known for a long time but recently have become the subject of intensive research because of their properties for binding with anions, transition metals, and neutral molecules (1). Their anion-binding properties has been extensively studied as a result of their potential biological applications (2). Calix[4]pyrroles were first synthesized over a century before by the condensation of acetone and pyrrole in the presence of hydrochloric acid (3). Since then various methods have been developed to increase the yield and selectivity of the products (4–6). The disadvantages of these methods are that the acid catalysts are corrosive in nature and the workup procedure is tedious and it involves neutralization. Moreover, the yields of calix[4]pyrrole are low and they are accompanied by a mixture of linear oligomers. There is a need to develop a method for the synthesis of calix[4]pyrroles that is ecofriendly, economic, and noncorrosive.

To meet the increasing demands of environmental legislation for the development of organic reactions in environmentally friendly media, synthetic manipulations have to be made to minimize the use of hazardous chemicals, such as replacing the traditional organic solvents in reactions and their subsequent workup with nontoxic solvents. In this regard, ionic liquids, especially those based on 1,3-dialkylimidazolium cations (Fig. 1), have gained considerable interest as a green alternative to volatile organic solvents (VOS) in recent years (7). Their nonvolatile nature and lack of any detectable vapour pressure gives them a significant advantage in minimizing solvent consumption and also addresses the problem of the emission of VOS into the atmosphere, thus making these solvents an environmentally attractive alternative to classical organic solvents (8). The recoverability and reusability of the catalysts immobilized in ionic liquids are key features required to develop economical, efficient, and green chemical processes (9).

Fig. 1. Imidazolium ionic liquid.

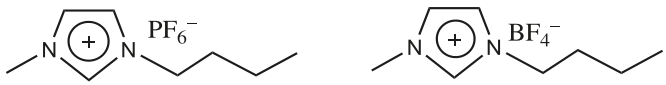

[bmim][PF_6] [bmim][BF_4]

Lanthanide(III) trifluromethanesulfonates, $Ln(OTf)_3$, have enjoyed extensive applications in a variety of Lewis acid catalyzed organic reactions (10). The growing interest in the use of these salts is due to their ease of handling, noncorrosiveness, reusability, and unique reactivity and selectivity. Ytterbium(III) *tris*-trifluromethanesulfonate, $Yb(OTf)_3$ (commonly called ytterbium triflate), is known to be a useful mild Lewis acid and has gained importance in organic synthesis in recent years (11). It was first used by Forsberg et al. (12) and since then it has found a wide utility in organic synthesis (13). Lanthanide triflates immobilized in ionic liquids have been used as efficient and recyclable catalysts for different organic reactions. The chemistry of lanthanides and actinides in ionic liquids was recently reviewed by K. Binnemans (14).

As a part of our ongoing research, we became interested in ionic liquids as an alternative reaction media for various organic transformations (15). We also reported $Yb(OTf)_3$ catalyzed synthesis of 1,3-oxathiolanes in ionic liquids (16). Herein, we report for the first time the synthesis of calix[4]pyrroles catalyzed by $Yb(OTf)_3$ in ionic liquids

Received 21 April 2008. Accepted 20 June 2008. Published on the NRC Research Press Web site at canjchem.nrc.ca on 31 July 2008.

A. Kumar,[1] I. Ahmad, and M.S. Rao. Department of Chemistry, Birla Institute of Technology and Science, Pilani 333 031, Rajasthan, India.

[1]Corresponding author (e-mail: anilkadian@gmail.com).

 doi:10.1139/V08-121 © 2008 NRC Canada

Scheme 1. Synthesis of calix[4]pyrroles in ionic liquid.

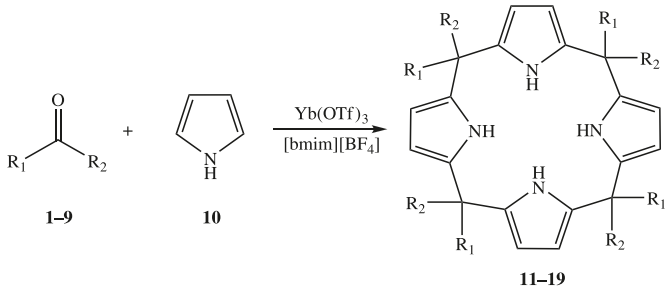

(Scheme 1), which is superior to previous Brønsted and Lewis acid catalyzed methods and overcomes the problems encountered with classical Lewis acids.

Results and discussion

The cyclocondensation of acetone (**1**) and pyrrole (**10**) at room temperature in ionic liquid [bmim][BF_4] containing 20 mol% $Yb(OTf)_3$ gave 100% conversion of acetone after 10 h as monitored by GC analysis. After completion of the reaction, the product was extracted with an ethyl acetate – hexane mixture and purified by column chromatography to give pure *meso*-octamethyl calix[4]pyrrole (**11**) in 92% yield (Table 1, entry 1). The ^{1}H NMR spectrum of **11** showed a broad singlet at δ 9.23 for NH protons and a singlet at δ 5.67 and δ 1.50 for 8 β-pyrrolic protons and 24 *meso*-methyl protons, respectively. It showed a $[M + H]^+$ ion peak at *m/z* 429.2360 in the positive ion mode HRMS (ESI-MS) spectrum. In the IR spectra of **11**, a peak appeared at 3438 cm^{-1} for N–H stretching.

The reaction was also carried out in a more hydrophobic ionic liquid, [bmim][PF_6], and an almost equal yield of calix[4]pyrrole (**11**) was obtained under these conditions. Therefore, we chose [bmim][BF_4] as the solvent of choice for further reactions. After the success of this reaction, the synthesis of *meso*-substituted calix[4]pyrroles (**12**–**19**) was also studied by the condensation of different cyclic and acyclic ketones with pyrrole catalyzed by $Yb(OTf)_3$ in ionic liquid and the results are shown in Table 1. The products were characterized by IR, HR-MS, and ^{1}H NMR spectroscopy. Higher cyclic ketones and substituted acyclic ketones produced slightly less yields as compared with acetone (Table 1). The reaction of unsymmetrical ketones produced a mixture of isomers, but αααα-isomer was in the majority. We did not observe the formation of N-confused calix[4]pyrroles under these conditions, which are reported to be accompanied in minor amounts, along with calix[4]pyrrole in a recently reported amberlyst 15 catalyzed synthesis of calix[4]pyrroles (6*d*).

To study the reusability, the recovered ionic liquid containing $Yb(OTf)_3$ was reused for the synthesis of **16**. After extraction of calix[4]pyrrole from the ionic liquid with an ethyl acetate – hexane mixture, the ionic liquid containing $Yb(OTf)_3$ was dried under vacuum for 30 min. To this dried ionic liquid containing $Yb(OTf)_3$, pyrrole and acetophenone (**6**) were added and stirred at room temperature for 12 h. The reaction mixture was extracted by the ethyl acetate – hexane mixture and the combined organic layer was evaporated to give **16**. This cycle was repeated five times. The catalysts showed good reactivity and yield even after five cycles with little deterioration in catalytic activity as shown in Table 2. The slight deterioration in catalytic activity may be due to a slight decomposition of the ionic liquids because of the release of water in the reaction. Generally, ionic liquids based on imidazolium cation with either tetrafluoroborate or hexafluorophosphate as anions are water insensitive; however, the exposure to moisture for a long time can cause some changes in their physical and chemical properties (17). The products obtained were of the same purity as in the first reaction.

Conclusion

In conclusion, we have developed an efficient, simple, economical, noncorrosive, and ecofriendly method for the synthesis of various calix[4]pyrroles catalyzed by ytterbium(III) triflate in ionic liquids. This method provides several advantages such as easy synthesis, simple workup, and satisfactory recovery and reuse of the ionic liquid immobilized ytterbium triflate with no diminution of product yields.

Experimental section

All the chemicals and reagents were of analytical grade. Ketones and pyrrole were purchased form S.D. Fine and Spectrochem, India. Sodium tetrafluoroborate and 1-methylimidazole were purchased from Sigma-Aldrich. Ionic liquid [bmim][BF_4] was prepared according to an earlier reported procedure (15*a*, 15*b*). The ^{1}H NMR spectra were recorded on a Bruker Avance II 400 (400 MHz) spectrophotometer using TMS as internal standard and $CDCl_3$ as solvent, and the chemical shifts were expressed in ppm. The IR spectra were recorded using KBr pellets on a Shimadzu Prestige-21 FTIR spectrophotometer and ν_{max} was expressed in cm^{-1}. Mass spectra were recorded on a KC455 Waters TOF MS spectrometer. TLC was run on silica gel coated aluminium sheets (silica gel 60 F_{254}, E. Merck, Germany) and visualized in UV light at 254 nm.

General procedure for the synthesis of calix[4]pyrrole in ionic liquid catalyzed by $Yb(OTf)_3$

To a 10 mL round bottom flask containing ionic liquid [bmim][BF_4] (3.0 mL) was added acetone (110 μL, 1.49 mmol), freshly distilled pyrrole (103 μL, 1.49 mmol), and $Yb(OTf)_3$ (20 mol%, 46.2 mg). The reaction mixture was stirred at room temperature for 10 h. Twenty microlitres of the reaction mixture were removed after every 1 h interval and analyzed by TLC and GC. After completion of the reaction, the reaction mixture was extracted with hexane – ethyl acetate (2 × 5 mL, 1:1 *v*/*v*). Ionic liquid containing ytterbium triflate was recovered and dried under vacuum. The combined organic layer was evaporated under reduced pressure. The residue was column chromatographed over silica gel 60–120 mesh using hexane – ethyl acetate as eluent to give pure **11** (146 mg, 92%). The calix[4]pyrrole obtained was characterized by IR, ^{1}H NMR, ^{13}C NMR, and HRMS spectroscopic data.

© 2008 NRC Canada

Table 1. Synthesis of calix[4]pyrroles from different ketones catalyzed by 20 mol% $Yb(OTf)_3$ in ionic liquids

Entry	Ketone	Product	Time (h)	Conversion (%)[a,b]
1	$R_1 = R_2 = CH_3$	**11**	10	100 (92)
2	$R_1 = C(CH_3)_3$, $R_2 = CH_3$	**12**	10	98 (84)
3	R_1-R_2 = -$(CH_2)_4$-	**13**	10	99 (88)
4	R_1-R_2 = -$(CH_2)_5$-	**14**	10	95 (85)
5	R_1-R_2 = -$(CH_2)_7$-	**15**	12	93 (79)
6	R_1 = Ph, $R_2 = CH_3$	**16**	12	97 (85)
7	R_1 = 4-Me-Ph, $R_2 = CH_3$	**17**	12	98 (84)
8	R_1 = 4-Cl-Ph, $R_2 = CH_3$	**18**	15	95 (78)
9	R_1 = 3-NO_2-Ph, $R_2 = CH_3$	**19**	15	96 (75)

[a]The isolated yield provided by column chromatography on silca gel is in parentheses.
[b]All products were characterized by IR, ESI-MS, ^{1}H NMR, and ^{13}C NMR spectra.

Table 2. Reusability of recovered $Yb(OTf)_3$ in ionic liquid for the synthesis of *meso*-tetramethyl tetraphenyl calix[4]pyrrole (**16**).

Run	Conversion (%)	Product yield (%)
1	98	85
2	95	81
3	90	80
4	88	75
5	84	72

Spectroscopic data of selected calix[4]pyrroles

meso-Octamethyl calix[4]pyrrole (11)

^{1}H NMR (Me_4Si; 400 MHz, DMSO-d_6) δ 9.23 (s, 4H), 5.67 (s, 8H), 1.5 (s, 24H). ^{13}C NMR (100 MHz, DMSO-d_6) δ 35.4, 41.2, 111.3, 132.6. HRMS *m/z* calcd. for $C_{28}H_{36}N_4$: 428.2940; found: 429.2360 $[M + H]^+$.

meso-Tetrakis(spirocyclopentane) calix[4]pyrrole (13)

^{1}H NMR (Me_4Si; 400 MHz, DMSO-d_6) δ 9.16 (s, 4H), 5.72 (s, 8H), 2.14 (t, J = 7.6 Hz, 16H), 1.59 (t, J = 7.6 Hz, 16H). ^{13}C NMR (100 MHz, DMSO-d_6) δ 21.5, 26.5, 36.1, 40.3, 111.3, 132.6. HRMS calcd. for $C_{36}H_{44}N_4$: 532.3566; found: 533.1338 $[M + H]^+$.

meso-Tetramethyl-tetrakis(3′-nitrophenyl) calix[4]pyrrole (19)

^{1}H NMR (Me_4Si; 400 MHz, DMSO-d_6) δ 10.47 (s, 4H), 8.09 (m, 4H), 7.72 (m, 4H), 7.58 (m, 4H), 7.48 (m, 4H), 5.92 (s, 8H), 1.99 (s, 12H). ^{13}C NMR (100 MHz, DMSO-d_6) δ 32.8, 39.8, 111.6, 118.3, 121.4, 128.5, 131.7, 132.1, 136.3, 143.2. HRMS calcd. for $C_{48}H_{40}N_8O_8$: 856.2969; found: 857.1823 $[M + H]^+$.

Acknowledgements

This work was supported by the Department of Science and Technology, New Delhi (SR-FTP-CS-34-2007). IA is thankful to the Birla Institute of Technology and Science, Pilani, for an institutional research fellowship.

References

1. (*a*) P.A. Gale, J.L. Sessler, V. Kral, and V. Lynch. J. Am. Chem. Soc. **118**, 5140 (1996); (*b*) J.L. Sessler, P. Anzenbacher, Jr., K. Jursikova, H. Miyaji, J.W. Genge, N.A. Tvermoes, W.E. Allen, and J.A. Shiver. Pure Appl. Chem. **70**, 2401 (1998).
2. H. Miyaji, W. Sato, and J. L. Sessler. Angew. Chem. Int. Ed. **39**, 1777 (2000).
3. A. Baeyer. Ber. Dtsch. Chem. Ges. **19**, 2184 (1886).
4. J.A. Sessler, P. Anzenbacher, J.A. Shriver, K. Jursikova, V. Lynch, and M. Marquez. J. Am. Chem. Soc. **122**, 12061 (2000).
5. S. Shao, A. Wang, M. Yang, S. Jiang, and X. Yu. Synth. Commun. **31**, 1421 (2001).
6. (*a*) M.R. Kishan, N. Srinivas, K.V. Raghavan, S.J. Kulkarni, J.A.R.P. Sarma, and M. Vairamani. Chem. Commun. 2226 (2001); (*b*) M.R. Kishan, V.R. Rani, M.R.V.S. Murty, P.S. Devi, N. Srinivas, S.J. Kulkarni and K.V. Raghavan. J. Mol. Catal. Chem. A, **223,** 203 (2004); (*c*) A.J.F.N. Sobral. J. Chem. Educ. **82**, 618 (2005); (*d*) S.M.S. Chauhan, B. Garg, and T. Bisht. Molecules, **12**, 2458 (2007); (*e*) S. Dey, K. Pal, and S. Sarkar. Tetrahedron Lett. **47**, 5851 (2006).
7. For reviews on ionic liquids see (*a*) N. Jain, A. Kumar, S. Chauhan, and S.M.S. Chauhan. Tetrahedron, **61**, 1015 (2005); (*b*) C.E. Song. Chem. Commun. 1033 (2004).
8. (*a*) M. Freemantle. Chem. Eng. News, **76**, 32 (1998); (*b*) G.-h. Tao, L. He, N. Sun, and Y. Kou. Chem. Commun. 3562 (2005); (*c*) M.S. Rasalkar, S.V. Bhilare, A.R. Deorukhkar, N.B. Darvatkar, and M.M. Salunkhe. Can. J. Chem. **85,** 77 (2007).
9. V.I. Parvulescu and C. Hardacr. Chem. Rev. **107**, 2615 (2007).
10. (*a*) S. Kobayashi. Synlett, 413 (1994); (*b*) S. Kobayashi, M. Sugiura, H. Kitagawa, and W.W.L. Lam. Chem. Rev. **102**, 2227 (2002).
11. R. Ding, K. Katebzadeh, L. Roman, K.-E. Bergquist, and U.M. Lindstrom,.J. Org. Chem. **71**, 352 (2006).
12. J. Forsberg, T. Balasuramanian, and V. Spaziano. J. Chem. Soc. Chem. Commun. 1060 (1976).
13. (*a*) S. Kobayashi, I. Hachiya, T. Takahori, M. Araki, and H. Ishitani. Tetrahedron Lett. **33**, 6815 (1992); (*b*) M. Yamanaka, A. Nishida, and M. Nakagawa. J. Org. Chem. **68**, 3112 (2003); (*c*) R.J. Lu, D. Liu, and R.W. Giese. Tetrahedron Lett. **41**, 2817 (2000); (*d*) M. Curini, F. Epifano, F. Maltese, and M.C. Marcotullio. Eur. J. Org. Chem. 1631 (2003); (*e*) I. Hachiya and S. Kobayashi. J. Org. Chem. **58**,

© 2008 NRC Canada

6958 (1993); (*f*) T. Akiyama and J. Iwai. Tetrahedron Lett. **38**, 853 (1997); (*g*) S. Anjaiah, S. Chandrasekhar, and R. Grée. J. Mol. Catal. A: Chem. **214**, 133 (2004); (*h*) G.V.M. Sharma and A. Ilangovan. Synlett,1963 (1999).
14. K. Binnemans. Chem. Rev. **107**, 2592 (2007).
15. (*a*) S.M.S. Chauhan, A. Kumar, and K.A. Srinivas. Chem. Commun. 2348 (2003); (*b*) K.A. Srinivas, A. Kumar, and S.M.S. Chauhan. Chem. Commun. 2456 (2002); (*c*) A. Kumar, N. Jain, and S.M.S. Chauhan. Synth. Commun. **34**, 2835 (2004).
16. A. Kumar, N. Jain, S. Ranam, and S.M.S. Chauhan. Synlett, 2785 (2004).
17. J.S. Wilkes and M.J. Zaworotko. J. Chem. Soc. Chem. Commun. 965 (1992).

© 2008 NRC Canada

Strategic efficiency — The new thrust for synthetic organic chemists

Fayang Qiu

Abstract: A standard for gauging the efficiency of synthetic strategies has been proposed. Synthetic efficiency is correlated to the molecular-complexity index, which is the cumulative total number of chiral centers, independent functional groups, and rings contained in a molecule. The number of reaction steps for an efficient synthetic design must be smaller than that of molecular-complexity index. This standard will motivate organic chemists to work harder on the synthetic design prior to execution.

Key words: strategic efficiency, total synthesis, synthetic design, complexity index.

Résumé : On propose un standard pour évaluer l'efficacité des stratégies de synthèse. On établit une corrélation entre l'efficacité d'une synthèse et l'indice de complexité moléculaire qui est la somme totale du nombre de centre chiraux, de groupes fonctionnels indépendants et de cycles contenus dans une molécule. Le nombre d'étapes réactionnelles dans une synthèse efficace devrait être plus petit que l'indice de complexité moléculaire. Ce standard motiverait les organiciens à réfléchir plus longuement avant de se lancer dans une synthèse.

Mots-clés : efficacité stratégique, synthèse totale, planification d'une synthèse, indice de complexité.

[Traduit par la Rédaction]

Introduction

Since Wöhler's conversion of ammonium cyanate into urea, numerous synthetic reactions have been discovered, many synthetic methodologies have been invented, and a wealth of detailed reaction mechanisms has been understood. These discoveries and inventions, combined with the mechanistic understanding of reaction pathways, have enabled organic chemists to meet many challenges in the synthesis of complex molecules. When Corey proposed retrosynthetic analysis (1), he enabled the entire synthetic community to deduce synthetic strategies. Since then, the bar for organic synthesis has been raised to a new level and retrosynthetic analysis has become the most powerful tool for synthetic chemists to arrive at proper commercial or readily accessible starting materials.

Although there is plenty of information about the available synthetic methodologies, useful chemical reactions, and reaction mechanisms, not much can be found in the literature about how to define an efficient synthetic strategy. Therefore, many synthetic chemists would ask: Of the many possible synthetic strategies for a given structure, how does one know if the one in hand is efficient? To answer such a question, one needs to have a standard that defines what an efficient strategy is. Surprisingly, the synthetic community has been interested mostly in the structural challenges of the target molecules. For example, chemists have been trying to claim the first synthesis of a new structure, while efficient synthetic design has been overlooked or has not received as much attention as it deserves.

In a recent paper, Corey pointed out that there is little in the existing literature to define an effective strategy of synthesis (2). Thus, in this paper, a standard for strategic efficiency assessment by correlating the molecular-complexity index with the number of reaction steps in the longest reaction sequence of a synthetic design is proposed.

Results and discussion

Synthetic efficiency can be divided into two parts: tactical efficiency and strategic efficiency. While tactical efficiency refers to the efficiency of the individual steps in a reaction sequence, strategic efficiency deals with the entire synthetic design. Since tactical efficiency depends mostly on the optimization of the reaction conditions and has been addressed under the term of atom economy and ideal synthesis (3), in this paper we will only discuss the strategic efficiency of a synthesis because such efficiency can be enhanced through the improvement of the synthetic design prior to execution.

Thanks to Corey's retrosynthetic analysis, at present, even an undergraduate student knows how to do synthetic designs. However, according to the literature, only a small group of synthetic chemists can design highly efficient synthetic strategies through the creative application of the principle of retrosynthetic analysis and new powerful synthetic methodologies. Thus, it is the right time to raise the bar again for organic synthesis so that the entire synthetic community can do efficient synthesis by integrating the knowledge of reaction mechanisms and conformational analysis into the synthetic design in a way that is more creative than ever before.

Received 13 November 2007. Accepted 24 June 2008. Published on the NRC Research Press Web site at canjchem.nrc.ca on 1 August 2008.

F. Qiu. Laboratory of Natural Product Chemistry, Guangzhou Institute of Biomedicine and Health, The Chinese Academy of Sciences, The Science Park of Guangzhou, Guangdong 510 663, P. R. China (e-mail: qiu_fayang@gibh.ac.cn).

 doi:10.1139/V08-120 © 2008 NRC Canada

To work on an efficient synthetic strategy, chemists need a tool to do efficiency assessment for the design prior to its execution. Unfortunately, strategic efficiency is not clearly defined. Offhand, one may think of using the overall yield of a reaction sequence as a measure of the efficiency of a synthetic strategy. This is not appropriate because reaction yields can only be obtained after the execution of a strategy. Therefore, we should only consider those reactions that are mechanistically sound as a standard element of strategic efficiency. Even so, the evaluation of strategic efficiency is totally dependent upon the personal interest and experience of the individual who is carrying out the evaluation. For example, consider the synthesis of Taxol. Some chemists may claim that a thirty-step synthesis is very efficient, while others may believe that only a strategy with less than twenty reaction steps can be considered efficient. Obviously, they have different standards. Hence, it is necessary to set a generally acceptable and reasonably high standard for the assessment of strategic efficiency.

In reality, this task is difficult because different molecules possess different types of structural features, which present different levels of challenge and require different synthetic strategies. Even for the same molecule, one may come up with several synthetic strategies at the same time. It is difficult to compare the efficiency of different strategies for the same molecule because each strategy may have its own advantages and drawbacks. It is more difficult to compare the synthetic strategies for different molecules. Nevertheless, since diverse structural features represent the degree of molecular complexity and the levels of synthetic challenge, if we can define molecular complexity and use it as a frame of reference for the analysis of strategic efficiency, we will be able to establish a standard to perform efficiency assessment for every synthetic strategy.

Although there are some reports about molecular complexity and analysis of synthetic strategies in the literature (4–12), all of them were trying to either describe or analyze how a change in molecular complexity had occurred along a sequence of chemical reactions. So far, no one has indicated how molecular complexity can be used as a standard to determine whether a synthetic design is strategically efficient or not without comparing with other people's synthetic designs. This is important for the large majority of synthetic chemists because even though they can compare their own different strategies and tell which is more efficient, they would very likely have no clue if their design is still efficient when compared to another one, possibly from a top chemist.

Given the fact that every reaction may be optimized in a sufficiently long period of time, we can treat every mechanistically sound reaction to be equivalent, i.e., assume that they are the standard reactions. Therefore, the total number of chemical transformations is the only variable in the determination of strategic efficiency. Obviously, the fewer the total number of reaction steps in a synthetic design, the higher the level of strategic efficiency.

For the sake of convenient calculation to synthetic chemists, molecular complexities are described with three elements: chiral centers, functional groups, and rings. These elements have different weights in different treatments. Among the many different weighting factors in molecular complexity, we believe that the one proposed by Fuchs (4) best fits our needs with a slight modification (see below).

At present, even though an undergraduate knows that different arrangement of functional groups, ring sizes, or chiral centers in a molecule represent different levels of synthetic challenge, it is reasonable for us to assume that the formation of each of these complexity elements will require at least one chemical transformation. The challenge is that we do not allow more than one chemical transformation for the introduction of any complexity element, regardless of the difficulty one may face when introducing it. As a result, the efficiency of a synthetic design can be directly correlated to the number of reaction steps in a synthetic strategy. Thus, we can consider the total number of reaction steps as a measure of strategic efficiency. Here, we propose that an efficient synthetic strategy for any given structure should satisfy this inequality

$$[1] \qquad Ns < I = C + (F - O) + R$$

where Ns is the number of reaction steps in the "longest" reaction sequence starting from "commercial materials"; I is the molecular-complexity index defined as the sum of the following elements: C, the number of chiral centers in a molecule; F, the number of functional groups, including heteroatoms and non-aromatic unsaturations; O, the number of overlaps between C and F; and R, the number of rings.

Note that molecular complexity only refers to the structural features associated with the major backbone of a molecule. Very often, a functional group may also be part of a chiral center. In any case, each atom, if counted, can only be counted once. One convenient way to calculate molecular complexity is to first count the number of chiral centers, followed by the number of hetero atoms that are "not" connected to a chiral center, and then count the number of other functional groups and rings. The sum will be the molecular-complexity index. The allowed number of reaction steps for an efficient synthetic design of a target molecule will be smaller than the index number.

Generally speaking, if a reaction needs a "separation" to isolate the desired product, then the reaction is counted as one step; if no separation is involved in a series of chemical operations, e.g., tandem reactions, then these reactions are "not" counted until a separation is involved. *A higher degree of challenge will be to count each reaction as one step whether or not a separation is involved, excepting tandem and cascade reactions.* Although the idea of starting from a known but not commercially available intermediate is acceptable, the number of reaction steps for the synthesis of that intermediate should be included if it is in the longest reaction sequence.

Although some syntheses have already met or even surpassed the proposed standard (13–21), the large majority of the published syntheses are far from being efficient. The purpose of this paper, however, is not to defeat or embarrass those people whose synthetic strategies did not meet the proposed standard but to provide a guideline for future syntheses. For example, when designing a synthetic strategy for a challenging molecular structure such as Taxol, a chemist would first calculate the complexity index for the molecule: the number of chiral centers contained in Taxol is nine; the

© 2008 NRC Canada

number of functional groups that are not a part of a chiral center includes four ester functional groups, one ketone, and one alkene functional groups. Here, the side chain as a whole is counted as one ester group, while the cyclic ether of the four-membered ring is counted as one functional group. Thus, the total number of functional groups is seven, and the number of rings is four. Thus, the molecular-complexity index for Taxol is

[2] $I = C + (F - O) + R = 9 + 7 + 4 = 20$

Therefore, an efficient synthetic strategy for Taxol will be 19 operational steps or less. If the number of reaction steps in his design is larger, then the chemist is motivated to design a more efficient route and count the number of reaction steps again. This process is repeated until he comes up with a strategy that meets or exceeds the standard. The reward for this effort is that when the strategy possesses the desired efficiency, it will be close to the limit of the state-of-the-art. If the current state-of-the-art cannot meet this standard, he will have to consider creating some new reactions or new methodologies for the synthetic strategy. Hence, the proposed standard also calls for creativity in the search of new chemical reactions and the development of new synthetic methodologies.

Some selected efficient synthetic strategies

Although the proposed standard for strategic efficiency assessment is simple to understand, it is difficult to practice. Nevertheless, there are many examples of synthetic designs in the literature (13–21) whose efficiency has already met or even surpassed the proposed standard, though only three examples are listed below for educational purposes.

A. Progesterone

This molecule contains six chiral centers: $C = 6$; three functional groups that are not a part of a chiral center: two C=O and one C=C, $(F - O) = 3$; and four rings: $R = 4$. Thus, the molecular-complexity index for progesterone is $I = 13$. W.S. Johnson (1971) (14) synthesized the molecule in 11 steps from methacrolein, 5-bromo-2-pentyne, 1,4-dibromobutane, and 2-methylfuran. A brief scheme is outlined below.

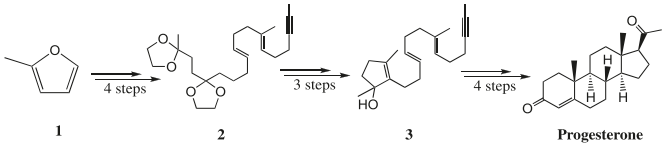

The key features of this synthesis include a highly convergent approach to quickly put the four smaller molecules together and arrange those functional groups in a way such that the functional groups are well-positioned to undergo a biomimetic cascade reaction sequence. The stereochemical outcome of the cascade reaction is predicted on the basis of the chair-like transition-state structures.

B. Carpanone

The number of chiral centers: $C = 5$; the number of functional groups that are not a part of a chiral center: two C=C, one C=O, and two OCH_2O. Since the two pairs of O atoms are each a part of a ring, they are not counted, $(F - O) = 5$; the number of rings: $R = 6$. Thus, the molecular-complexity index for carpanone is $I = 16$. O.L. Chapman (1971) (15) achieved the synthesis in four steps starting from the commercial 3,4-methylenedioxyphenol and allyl bromide as is shown below.

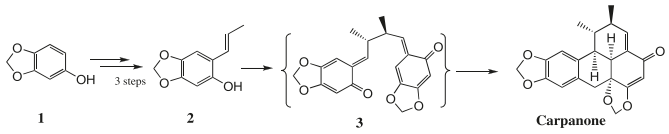

This synthesis is convergent as well as biomimetic. The oxidative coupling of intermediate **2** through the phenolic palladium salt and the subsequent intramolecular Diels–Alder reaction is a remarkable transformation, which establishes two rings, five chiral centers, and one double bond. This synthesis has demonstrated the power of organopalladium chemistry in organic synthesis.

C. Ginkgolide B

Ginkgolide B is a molecule that is composed of 11 chiral centers, $C = 11$; three carbonyl groups and one *t*-butyl group (a quaternary carbon is counted as one if it is not a part of a chiral center), $(F - O) = 4$; and six rings, $R = 6$. Thus, the molecular-complexity index is $I = 21$. Ginkgolide B is a molecule of ultimate challenge for synthesis because the functional groups are highly densely distributed in the molecule. There are four consecutive quaternary bridge-head carbon centers. E.J. Corey (1988) (16) not only successfully synthesized Ginkgolide B, but he also achieved a high level of strategic efficiency (20 steps).

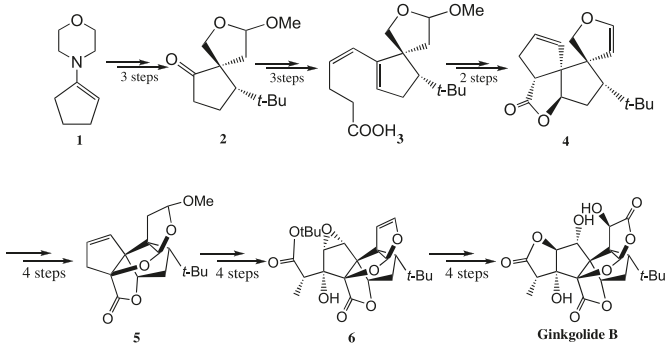

In this synthesis, introduction of the *tert*-butyl group furnished the first chiral center, which was then used to control the configuration of all other chiral centers. There are several major challenges in this synthesis. The first one is the intramolecular [2+2] ketene-olefin cycloaddition, which involves facial selectivity; the most challenging problem, however, is perhaps the subsequent Baeyer–Villiger oxidation of the cyclobutanone in which the regiochemistry is difficult to control; the third challenge is the diastereoselective addition of an enolate generated from *tert*-butyl propionate to the sterically congested ketone carbonyl group. In this synthesis, Corey has extensively applied the knowledge of reaction mechanisms and conformational analysis to solve the selectivity problems.

All the above examples have demonstrated that the proposed standard for strategic efficiency assessment is practi-

© 2008 NRC Canada

cally achievable. However, these strategies are not selected because they have represented a first total synthesis or have dealt with a very complex synthetic target, but because they possess the key features that, in addition to solving the structural challenges, have enhanced the strategic efficiency to the desired level.

Conclusion

The proposed standard for efficient synthetic design invites competition for all chemists in the field on a more equal basis than any other means. Every chemist can thus fully exercise his intellectual power. Being the first in a total synthesis is important and desirable, but it is often associated with the amount of allocated resources; being the best in a total synthesis is more admirable because it creates more value and represents true intellectual progress. Overall, the synthetic community should present more creativity in the practice of organic synthesis and meet the challenge of the proposed standard.

Acknowledgement

The author is grateful to all the reviewers who have made good points and suggestions before finalizing this manuscript.

References

1. (*a*) E.J. Corey, M. Ohno, P.A. Vatakencherry, and R.B. Mitra. J. Am. Chem. Soc. **83**, 1251 (1961); (*b*) E.J. Corey and X.-M. Cheng. The logic of chemical synthesis. John-Wiley and Sons. New York. 1989.
2. C.S. Mushti, J.-H. Kim, and E.J. Corey. J. Am. Chem. Soc. **128**, 14050 (2006).
3. B.M. Trost. Angew. Chem., Int. Ed. Engl. **34**, 259 (1995).
4. P.L. Fuchs. Tetrahedron, **57**, 6855 (2001).
5. (*a*) S.H. Bertz and C. Ruecker. Croat. Chem. Acta **77**, 221 (2004); (*b*) S.H. Bertz. New J. Chem. **27**, 870 (2003); (*c*) S.H. Bertz. New J. Chem. **27**, 860 (2003).
6. R. Barone and M.J. Chanon. Chem. Info. Comput. Sci. **41**, 269 (2001).
7. (*a*) G.A. Gamziani. Zh. Org. Khim. **31**, 31 (1995); (*b*) G.A. Gamziani. Zh. Org. Khim. **31**, 35 (1995).
8. S. Nikolic, I.M. Tolic, N.B.I. Trinajstic, and I. Baucic. Croat. Chem. Acta **73**, 909 (2000).
9. W.H. Whitlock. J. Org. Chem. **63**, 7982 (1998).
10. (*a*) J.B. Hendrickson. J. Am. Chem. Soc. **99**, 5439 (1977); (*b*) J.B. Hendrickson, D.L. Grier, and A.G. Toczko. J. Am. Chem. Soc. **107**, 5228 (1985).
11. W.L. Jorgensen, E.R. Laird, A.J. Gushurst, J.M. Fleischer, S.A. Gothe, H.E. Helson, G.D. Paderes, and S. Sinclair. Pure Appl. Chem. **62**, 1921 (1990).
12. A.K. Lang and J.C. Kappos. J. Chem. Info. Comput. Sci. **34**, 915 (1994).
13. (*a*) R.B. Woodward, F.E. Bader, H. Bickel, A.J. Frey, and R.W. Kierstead. J. Am. Chem. Soc. **78**, 2023 (1956); (*b*) R.B. Woodward, F.E. Bader, H. Bickel, A.J. Frey, and R.W. Kierstead. J. Am. Chem. Soc. **78**, 2657 (1956).
14. W.S. Johnson, M.B. Gravestock, and B.E. McCarry. J. Am. Chem. Soc. **93**, 4332 (1971).
15. O.L. Chapman, M.R. Engel, J.P. Springer, and J.C. Clardy. J. Am. Chem. Soc. **93**, 6696 (1971).
16. E.J. Corey, M.-C. Kang, M.C. Desai, A.K. Ghosh, and I.N. Houpis. J. Am. Chem. Soc. **110**, 649 (1988).
17. R.B. Ruggeri, M.M. Hansen, and C.H. Heathcock. J. Am. Chem. Soc. **110**, 8734 (1988).
18. D.A. Evans, S.W. Kaldor, T.K. Jones, J. Clardy, and T.J. Stout. J. Am. Chem. Soc. **112**, 7001 (1990).
19. T. Matsumoto, T. Hosoya, and K. Suzuki. J. Am. Chem. Soc. **114**, 3568 (1992).
20. M.A. Avery, W.K.M. Chong, and C. Jennings-White. J. Am. Chem. Soc. **114**, 974 (1992).
21. F. He, Y. Bo, J.D. Altom, and E. J. Corey. J. Am. Chem. Soc. **121**, 6771 (1999).

© 2008 NRC Canada

Friedel–Crafts alkylation of indoles with nitroolefins in the presence of β-cyclodextrin in water under neutral conditions

Vydyula Pavan Kumar, Regati Sridhar, Boga Srinivas, Mendu Narender, and Kakulapati Rama Rao

Abstract: Various indolyl nitroalkanes were prepared by the reaction of indoles with nitroolefins in the presence of β-cyclodextrin in water under neutral conditions. β-Cyclodextrin can be recovered and re-used several times without loss of activity.

Key words: β-cyclodextrin, nitroolefins, indoles, neutral conditions, water.

Résumé : On a préparé divers nitroalcanes d'indolyle par réaction d'indoles avec des nitrooléfines, en présence de cyclodextrine, dans des conditions aqueuses neutres. On peut récupérer la β-cyclodextrine et la réutiliser un certain nombre de fois sans perte d'activité.

Mots-clés : β-cyclodextrine, nitrooléfines, indoles, conditions neutres, eau.

[Traduit par la Rédaction]

Introduction

Indoles are present in many biologically active and naturally occurring compounds (1) and are also important intermediates for the synthesis of drugs and pharmaceuticals (2). Many indole alkaloids were synthesized utilizing the increased nucleophilic reactivity of the 3-position of the indole ring (3). The addition of indoles to electron-deficient alkenes, which in many respects is considered as Friedel–Crafts reaction (4), is a reaction of considerable synthetic utility, and the adducts resulting from the reaction are key intermediates for the synthesis of many biologically active compounds (5). However, the synthesis of 3-substituted indoles in the classical methodologies utilized indolylgrignard reagent (6), whereas the later reports involved either acid or base catalysts (7). These methods suffer from various disadvantages, such as drastic reaction conditions, longer reaction times, lower yields, and undesirable side products due to polymerization (8). Thus, there is a need to develop mild and environmentally benign Friedel–Crafts synthesis of these high value 3-substitued indoles in water under neutral conditions with a recyclable catalyst. The use of aqueous medium as solvent under neutral conditions reduces the harmful effects of organic solvents and also precludes the use of either acid or base. This becomes further sophisticated if these reactions can be performed under supramolecular catalysis. Though there are reports in aqueous media with Lewis-acid catalysts (9), there are no reports under neutral conditions in water. The fundamental problem in performing these reactions in water is that many organic substrates are hydrophobic and are insoluble in water. Therefore, we made an attempt at the Friedel–Crafts synthesis of 3-substituted indoles in water through supramolecular catalysis using β-cyclodextrin (β-CD) under neutral conditions.

The choice towards cyclodextrins was dictated by the fact that many interactions are dominated by hydrogen bonding in organocatalysis. Recently, metal-free hydrogen-bonding based catalysts have been put on a rational basis (10). Hydrogen-bonding motif is becoming a powerful tool in organocatalysis for the activation of carbonyl groups and related compounds through weak hydrogen-bond interactions (11). It is well-known that substituents of aromatic rings capable of hydrogen bonding can bind the OH groups of the cyclodextrin edges (12). Cyclodextrins, which are cyclic oligosaccharides, exert micro-environmental effects leading to selective reactions (13). They catalyze reactions by supramolecular catalysis through noncovalent bonding as seen in enzymes. Complexation depends on the size, shape, and hydrophobicity of the guest molecules. These attractive features of cyclodextrins and our earlier expertise in the biomimetic modeling of chemical reactions (14) prompted us to examine their utility in Friedel–Crafts reaction of indoles with nitroolefins.

Results and discussion

In general, the reactions were carried out by the in situ formation of the β-CD complex of the indole in water followed by the addition of nitroolefin and stirring for 1–3 h at 50 °C to give the corresponding products (Scheme 1). Alkylated indoles were formed as single products with high

Received 18 February 2008. Accepted 21 May 2008. Published on the NRC Research Press Web site at canjchem.nrc.ca on 5 August 2008.

V. Pavan Kumar, R. Sridhar, B. Srinivas, M. Narender, and K. Rama Rao.[1] Organic Chemistry Division-I, Indian Institute of Chemical Technology, Uppal Road, Hyderabad 500–007 India.

[1]Corresponding author (e-mail: drkrrao@yahoo.com).

 © 2008 NRC Canada

Scheme 1.

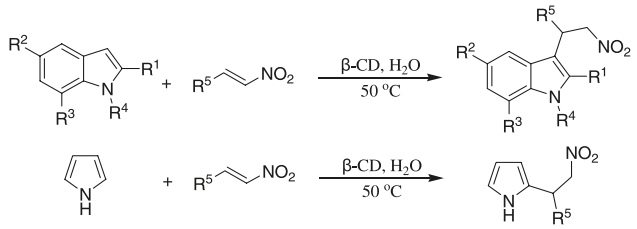

degree of conversion (Table 1). This methodology is also compatible with various substituted indoles and nitroolefines. Several examples illustrating this simple and practical methodology are summarized in Table 1. All the products were characterized by ^{1}H NMR, IR, mass spectroscopy, and elemental analysis. No asymmetric induction was observed in these reactions. The catalyst β-CD can be easily recovered and re-used. To see the further application of this reaction, it was also extended to pyrrole heterocycle (Table 1, entries 17 and 18).

The reaction also occurs at room temperature, but longer reaction times (48 h) are required and the isolated yields of products obtained are also low (1%–15%). All compounds listed in Table 1 failed to react with nitroolefins in water at 50 °C without the presence of β-cyclodextrin. Use of a catalytic amount of β-CD (0.1 mmol per mole of the substrate) at 50 °C had no impact on the reaction. These experiments indicate the substantial role of cyclodextrin. However, the reaction did not proceed when substituents such as bromo and nitro were present in the 5-position of indole ring, whereas the presence of other functionalities improved the reaction, which explains the important role of electron density on heterocycle. It is observed that the reaction did not proceed with alkyl substituted nitroolefins such as ((*E*)-2-nitrovinyl)cyclohexane and (*E*)-1-nitrobut-1-ene. The importance of this methodology can be seen in the case of 5-hydroxy indole (Table 1, entries 9 and 10), which reacts with nitroolefins in very good yields, whereas the reported methodologies utilize either acidic or basic catalysts leading to low yields even after prolonged reaction times because of the interaction of the indolyl hydroxyl group with the catalyst (4*d*, 7*f*).

Inclusion complexes of indole with β-cyclodextrin have been studied by Galian et al. (15). In this model, it was proposed that the indole is included in the β-cyclodextrin cavity in such a way that the pyrrole moiety of indole ring is directed towards primary face of β-cyclodextrin and a hydrogen bonding formed between indolic proton and oxygen of the primary hydroxyl (C_6–O) of β-cyclodextrin. This hydrogen bonding enhances the nucleophilicity of indole. Under the present reaction conditions of supramolecular catalysis, this type of positioning of indole in the cyclodextrin cavity facilitates the complexation of nitroolefin from the primary side, which can be activated by hydrogen bonding with C_6–OH of cyclodextrin for further reaction with indole. This is depicted in Fig. 1. However, in the case of *N*-substituted indoles (Table 1, substrates **1g** and **1h**), longer reaction times are required, since the hydrogen bonding is not possible in these cases. This clearly explains the importance of the presence of free indolic NH group.

The evidence for this mechanistic approach (Fig. 1) was deduced from ^{1}H NMR spectroscopy. The studies were carried out with indole (**1a**) and 2-((*E*)-2-nitrovinyl)furan (**2b**) as representative examples. NMR spectroscopy is one of the most important techniques used for the characterization of inclusion complexes. The formation of an inclusion complex results in the shift changes in the resonances of the host cyclodextrin and the guest protons (16). A comparison of the ^{1}H NMR spectra (D_2O) of β-CD, β-CD : indole complex, and freeze-dried reaction mixture of β-CD : indole complex with the nitroolefin **2b** at 1 h were studied. It is observed from Fig. 2 that there is an upfield shift of H_3 (0.03 ppm) and H_5 (0.05 ppm) protons of cyclodextrin in the β-CD : indole complex as compared with β-CD, indicating the formation of an inclusion complex of indole with β-CD from the secondary side of cyclodextrin. It is further observed from the spectra of the reaction mixture of β-CD : indole complex with the nitroolefin **2b** at 1 h that there is also an upfield shift of H_6 proton by 0.06 ppm. This indicates the complexation of the nitroolefin **2b** from the primary side of cyclodextrin for the reaction to proceed (Fig. 2). This clearly demonstrates that the nitroolefin is elegantly set for the addition reaction with the indole in the hydrophobic microenvironment of β-cyclodextrin cavity.

Thus, we have demonstrated for the first time an operationally simple and efficient aqueous phase Friedel–Crafts synthesis of indolyl nitroalkanes and pyrrolyl nitroalkanes by using β-cyclodextrin under neutral conditions. β-Cyclodextrin, apart from being nontoxic is also considered metabolically safe (17). In contrast with the existing methodologies using many acidic and basic catalysts, this method is very simple, high-yielding, and environment-friendly. Further potential applications of this reaction are under study.

Experimental

General

Melting points were recorded on a Buchi R-535 apparatus and are uncorrected. IR spectra were recorded on a PerkinElmer FTIR 240-c spectrometer using KBr optics. ^{1}H NMR spectra were recorded on Gemini-200 spectrometer in DMSO using TMS as internal standard. Mass spectra were recorded on an Agilent 1200 spectrometer. Starting materials were obtained commercially from Aldrich, Lancaster and were used without purification.

General procedure for the synthesis of indolyl nitroalkanes and pyrrolyl nitroalkanes

β-CD (1 mmol) was dissolved in water (20 mL) by warming to 50 °C until a clear solution was formed. Then, indole/pyrrole (1 mmol) dissolved in methanol (0.5 mL) was added dropwise, followed by nitroolefin (1 mmol), and the mixture was stirred at 50 °C until the reaction was complete (as monitored by TLC) (Table 1). The mixture was extracted with ethyl acetate, and the extract was filtered. The organic layer was dried over anhyd. Na_2SO_4, the solvent was removed under reduced pressure, and the resulting product was further purified by column chromatography. The aqueous layer was cooled to 5 °C to recover β-CD by filtration.

© 2008 NRC Canada

Table 1. Freidel–Crafts reaction of indoles and pyrrole with nitroolefins in the presence of β-CD in water at 50 °C.

Entry	Substrate	R^1	R^2	R^3	R^4	Nitroolefin	R^5	Product[a]	Time (h)	Yield[b] (%)
1	**1a**	H	H	H	H	**2a**	Ph	**3a**[c]	3.0	88
2	**1a**	H	H	H	H	**2b**	2–Furyl	**3b**[c]	3.2	86
3	**1b**	Me	H	H	H	**2a**	Ph	**3c**[c]	2.1	92
4	**1b**	Me	H	H	H	**2b**	2-Furyl	**3d**[d]	2.4	93
5	**1c**	Ph	H	H	H	**2a**	Ph	**3e**[d]	2.5	90
6	**1c**	Ph	H	H	H	**2b**	2-Furyl	**3f**	3.0	89
7	**1d**	COOH	H	H	H	**2a**	Ph	**3g**	2.4	85
8	**1d**	COOH	H	H	H	**2b**	2-Furyl	**3h**	2.5	86
9	**1e**	H	OH	H	H	**2a**	Ph	**3i**[d]	3.4	91
10	**1e**	H	OH	H	H	**2b**	2-Furyl	**3j**	3.5	90
11	**1f**	H	H	Et	H	**2a**	Ph	**3k**	2.2	93
12	**1f**	H	H	Et	H	**2b**	2-Furyl	**3l**	2.4	94
13	**1g**	H	H	H	Me	**2a**	Ph	**3m**[c]	5.3	82
14	**1g**	H	H	H	Me	**2b**	2-Furyl	**3n**[c]	5.5	84
15	**1h**	H	H	H	Bn	**2a**	Ph	**3o**[e]	6.2	81
16	**1h**	H	H	H	Bn	**2b**	2-Furyl	**3p**[e]	6.3	80
17	Pyrrole	—	—	—	—	**2a**	Ph	**3q**[c]	3.3	89
18	Pyrrole	—	—	—	—	**2b**	2-Furyl	**3r**[c]	3.4	92

[a]All the products were characterized by ^{1}H NMR, IR, and mass spectroscopy.
[b]Isolated yields after purification.
[c]Ref. 7*g*.
[d]Ref. 9*b*.
[e]Ref. 7*h*.

Fig. 1.

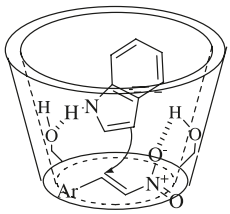

Characterization data for new compounds

*3-(1-(Furan-2-yl)-2-nitroethyl)-2-phenyl-1*H*-indole (3f)*

Light yellow solid; mp 125–127 °C. IR: 3429, 3057, 2924, 1456 cm^{-1}. ^{1}H NMR ($CDCl_3$, 300 MHz) δ: 8.13 (s, 1H), 7.59–7.04 (m, 10H), 6.35–6.27 (m, 1H), 6.14 (d, 1H, *J* = 3.21 Hz), 5.35 (t, 1H, *J* = 7.74 Hz), 5.22 (dd, 1H, *J* = 12.46, 7.55 Hz), 4.93 (dd, 1H, *J* = 12.46, 7.93 Hz). ^{13}C NMR ($CDCl_3$, 75 MHz) δ: 152.58, 142.16, 136.98, 135.97, 131.90, 129.08, 128.73, 126.72, 122.59, 120.25, 119.82, 111.32, 110.46, 107.37, 107.31, 77.12, 35.48. ESI-MS *m*/*z*: 333 (M + 1). Anal. calcd. for $C_{20}H_{16}N_2O_3$: C, 72.28; H, 4.85; N, 8.43. Found: C, 72.02; H, 4.98; N, 8.56.

*3-(2-Nitro-1-phenylethyl)-1*H*-indole-2-carboxylic acid (3g)*

White solid; mp 198–200 °C. IR: 3367, 2961, 1556 cm^{-1}. ^{1}H NMR ($CDCl_3$ + DMSO-d_6, 200 MHz) δ: 11.15 (s, 1H), 7.53–7.07 (m, 8H), 6.96 (t, 1H, *J* = 7.32 Hz), 6.08 (t, 1H, *J* = 8.05 Hz), 5.47–5.12 (m, 2H). ^{13}C NMR ($CDCl_3$ + DMSO-d_6, 75 MHz) δ: 168.43, 156.72, 146.14, 141.83, 132.52, 130.65, 128.31, 125.64, 122.84, 122.31, 121.74, 121.43, 120.58, 80.74, 41.27. EI-MS *m*/*z*: 310 (M^+). Anal. calcd. for $C_{17}H_{14}N_2O_4$: C, 65.80; H, 4.55; N, 9.03. Found: C, 66.04; H, 4.43; N, 9.12.

Fig. 2. ^{1}H NMR spectra of (*a*) β-CD, (*b*) β-CD : indole complex, and (*c*) reaction mixture after 1 h. The spectra were obtained in D_2O at 25 °C.

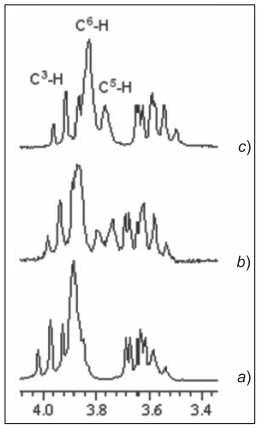

*3-(1-(Furan-2-yl)-2-nitroethyl)-1*H*-indole-2-carboxylic acid (3h)*

Brown solid; mp 201–203 °C. IR: 3506, 2972, 1574 cm^{-1}. ^{1}H NMR ($CDCl_3$ + DMSO-d_6, 200MHz) δ: 11.44 (b s, 1H), 7.65–6.84 (m, 5H), 6.39–6.06 (m, 3H), 5.27 (dd, 1H, *J* = 12.50, 8.59 Hz), 5.02 (dd, 1H, *J* = 13.28, 7.03 Hz). ^{13}C NMR ($CDCl_3$ + DMSO-d_6, 75 MHz) δ: 168.16, 157.41, 146.52, 141.19, 130.93, 129.84, 129.67, 125.66, 125.10, 121.53, 117.76, 115.38, 111.79, 81.81, 39.48. ESI-MS *m*/*z*: 301 (M + 1). Anal. calcd. for $C_{15}H_{12}N_2O_5$: C, 60.0; H, 4.03; N, 9.33. Found: C, 60.23; H, 4.11; N, 9.24.

© 2008 NRC Canada

3-(1-(Furan-2-yl)-2-nitroethyl)-1*H*-indol-5-ol (3j)

Oil. IR: 3419, 1550 cm^{-1}. ^1H NMR ($CDCl_3$, 200MHz) δ: 10.18 (s, 1H), 7.21–6.95 (m, 2H), 6.88–6.80 (m, 1H), 6.76–6.59 (m, 2H), 6.32–6.22 (m, 1H), 6.13 (d, 1H, *J* = 2.94 Hz), 5.16–4.78 (m, 3H). ^{13}C NMR ($CDCl_3$, 75 MHz) δ: 150.62, 141.04, 131.04, 126.19, 123.40, 113.62, 112.27, 112.0, 110.18, 109.47, 106.87, 102.43, 77.23, 35.57. ESI-MS *m/z*: 273 (M + 1). Anal. calcd. for $C_{14}H_{12}N_2O_4$: C, 61.76; H, 4.44; N, 10.29. Found: C, 61.51; H, 4.57; N, 10.17.

7-Ethyl-3-(2-nitro-1-phenylethyl)-1*H*-indole (3k)

Oil. IR: 3422, 3058, 2965, 1550 cm^{-1}. ^1H NMR ($CDCl_3$, 200 MHz) δ: 7.94 (b s, 1H), 7.41–7.17 (m, 6H), 7.06–6.87 (m, 3H), 5.25–4.77 (m, 3H), 2.83 (q, 2H, *J* = 7.39 Hz), 1.35 (t, 3H, *J* = 7.39 Hz). ^{13}C NMR ($CDCl_3$, 75 MHz) δ: 139.23, 135.36, 128.86, 127.74, 127.48, 126.77, 125.83, 121.23, 121.14, 120.23, 116.60, 114.83, 79.49, 41.63, 23.84. 13.68. ESI-MS *m/z*: 295 (M + 1). Anal. calcd. for $C_{18}H_{18}N_2O_2$: C, 73.45; H, 6.16; N, 9.52. Found: C, 73.68; H, 6.29; N, 9.40.

7-Ethyl-3-(1-(furan-2-yl)-2-nitroethyl)-1*H*-indole (3l)

Oil. IR: 3417, 3018, 2929, 1552 cm^{-1}. ^1H NMR ($CDCl_3$, 300 MHz) δ: 7.98 (b s, 1H), 7.39–7.31 (m, 2H), 7.08–6.95 (m, 3H), 6.29–6.24 (m, 1H), 6.13–6.09 (m, 1H), 5.19 (t, 1H, *J* = 7.74 Hz), 4.99 (dd, 1H, *J* = 12.46, 7.93 Hz), 4.86 (dd, 1H, *J* = 12.46, 7.36 Hz), 2.81 (q, 2H, *J* = 7.74 Hz), 1.35 (t, 3H, *J* = 7.74 Hz). ^{13}C NMR ($CDCl_3$, 75 MHz) δ: 142.23, 140.56, 132.41, 129.71, 128.52, 123.47, 121.20, 120.43, 117.61, 116.46, 112.23, 107.36, 77.84, 35.81, 22.70, 13.73. ESI-MS *m/z*: 285 (M + 1). Anal. calcd. for $C_{16}H_{16}N_2O_3$: C, 67.59; H, 5.67; N, 9.85. Found: C, 67.82; H, 5.78; N, 9.72.

Acknowledgement

We thank Council of Scientific & Industrial Research (CSIR), New Delhi, India, for fellowships to VPK, RS, BS, and MN.

References

1. (*a*) R.J. Sunberg. The chemistry of indoles. Academic Press, New York. 1969. p. 113; (*b*) L.G. Thomas. *In* Heterocyclic chemistry. 3rd Ed. Vol. 11. Longman. England. 1997. Parts 1, 2, and 5.
2. (*a*) A. Kleeman, J. Engel, B. Kutscher, and D. Reichert. Pharmaceutical substances. 4th Ed. Thieme, New York. 2001; (*b*) J.F. Austin and D.W.C. MacMillan. J. Am. Chem. Soc. **124**, 1172 (2002).
3. (*a*) R.A. Moore, C. Cheuk, X.Q.G. Yang, G.M.L. Patterson, R. Bonjoukalian, T.A. Smitka, J.S. Mynderse, R.S. Foster, N.D. Jones, J.K. Skiartzendruber, and J.B. Deeter. J. Org. Chem. **52**, 1036 (1987); (*b*) R.L. Garnick, S.B. Levery, and P.W. Le Quesne. J. Org. Chem. **43**, 1226 (1978); (*c*) R.E. Moore, C. Cheuk, and G.M.L. Patterson. J. Am. Chem. Soc. **106**, 6456 (1984).
4. (*a*) M. Bandini, A. Melloni, S. Tommasi, and A. Umani-Ronchi. Synlett, 1199 (2005); (*b*) M. Bandini, M. Fagioli, and A. Umani-Ronchi. Adv. Synth. Catal. **346**, 545 (2004); (*c*) Z.-P. Zhan and K. Lang. Synlett, 1551 (2005); (*d*) G. Bartoli, M. Bosco, S. Giuli, A. Giuliani, L. Lucarelli, E. Marcantoni, L. Sambri, and E. Torregiani. J. Org. Chem. **70**, 1941 (2005); (*e*) G. Bartoli, M. Bartolacci, M. Bosco, G. Foglia, A. Giuliani, E. Marcantoni, L. Sambri, and E. Torregiani. J. Org. Chem. **68**, 4594 (2003).
5. (*a*) H. Harada, Y. Hirokawa, K. Suzuki, Y. Hiyama, M. Oue, H. Kawashima, H. Kato, N. Yoshida, Y. Furutani, and S. Kato. Chem. Pharm. Bull. **53**, 184 (2005); (*b*) E.D. Cox, H. Diaz-Arauzo, Q. Huang, M.S. Reddy, C. Ma, B. Harris, R. McKernan, P. Skolnick, and J.M. Cook. J. Med. Chem. **41**, 2537 (1998).
6. W.E. Noland, G.M. Christensen, G.L. Sauer, and G.G.S. Dutton, J. Am. Chem. Soc. **77**, 456 (1955).
7. (*a*) T. Koike, M. Hagiwara, N. Takeuchi, and S. Tobinaga. Heterocycles, **45**, 1271 (1997); (*b*) S. Mahboobi, W. Wiegrebe, and A. Popp. J. Nat. Prod. **62**, 577 (1999); (*c*) T. Koike, N. Takeuchi, M. Hagiwara, K. Yamazaki, and S. Tobinaga. Heterocycles, **51**, 1271 (1999); (*d*) M. Bandini, M. Fagioli, and A.U. Ronchi. Adv. Synth. Catal. **346**, 545 (2004); (*e*) C. Lin, J. Hsu, M.N.V. Sastry, H. Fang, Z. Tu, J.-T. Liu, and Y.C. Fa. Tetrahedron, **61**, 11751 (2005); (*f*) R. Ballini, R.R. Clemente, A. Palmieri, and M. Petrini. Adv. Synth. Catal. **348**, 191 (2006); (*g*) L.-T. An, J.-P. Zou, L.-L. Zhang, and Y. Zhang. Tetrahedron Lett., **48**, 4297 (2007); (*h*) G. Srihari, M. Nagaraju, and M. M. Murthy. Synth. Commun. **38**, 100 (2008).
8. (*a*) M. Chakrabarty, R. Basak, and N. Ghosh. Tetrahedron Lett. **41**, 8331 (2001); (*b*) I. Komoto and S. Kobayashi. Org. Lett. **4**, 1115 (2002).
9. (*a*) K. Manabe, N. Aoyama, and S. Kobayashi. Adv. Synth. Catal. **343**, 174 (2001); (*b*) M. Bandini, P. Melchiorre, A. Melloni, and A. Umani-Ronchi. Synthesis, 1110 (2002); (*c*) M. Bandini, P.G. Cozzi, M. Giacomini, P. Melchiorre, S. Selva, and A. Umani-Ronchi. J. Org. Chem. **67**, 3700 (2002); (*d*) H. Firouzabadi, N. Iranpoor, and F. Nowrouzi. Chem. Commun. 789 (2005); (*e*) N. Azizi, F. Arynasab, and M. R. Saidi. Org. Biomol. Chem. **4**, 4275 (2006); (*f*) R.S. Kumar and P.T. Perumal. J. Heterocycl. Chem. **43**, 1383 (2006); (*g*) Y. Gu, C. Ogawa, and S. Kobayashi. Org. Lett. **9**, 175 (2007).
10. (*a*) P.R. Schreiner and A. Wittkopp. Org. Lett. **4**, 217 (2002); (*b*) A. Wittkopp and P. Schreiner. Chem. Eur. J. **9**, 407 (2003); (*c*) P.R. Schreiner. Chem. Soc. Rev. **32**, 289 (2003); (*d*) P.M. Pihko. Angew. Chem., Int. Ed. **43**, 2062 (2004); (*e*) C.S. Wilcox, E.-I. Kim, D. Romano. L.H. Kuo, A.L. Burt, and D.P. Curran. Tetrahedron, **51**, 621 (1995).
11. R.P. Herrera, V. Sgarzani, L. Bernardi, and A. Ricci. Angew. Chem., Int. Ed. **44**, 6576 (2005).
12. (*a*) G.G. Gaitano, P.R. Sainz-Rozas, J.R. Isasi, M. Sanchez, and G. Tardajos. J. Phys. Chem. **108A**, 392 (2004); (*b*) A. Sytnik and C.D. Valle. J. Phys. Chem. **99**, 13028 (1995); (*c*) T. Stalin and N. Rajendiran. J. Photochem. Photobiol. A, **182**, 137 (2006); (*d*) B. Manunza, S. Deiana, M. Pintora, and C. Gessa. J. Mol. Graphics Mod. **15**, 79 (1997).
13. (*a*) V.B. Sheshanath and V.B. Sidhanath. Mini-Rev. Org. Chem. **4**, 231 (2007); (*b*) K. Liu, D. Haeussinger, and W.-D. Woggon. Synlett, **14**, 2298 (2007); (*c*) V. Ramamoorthy, C. Meenakshi, S. Muthusubramanian, and S. Sivasubramanian. J. Inclusion Phenom. Macrocyclic Chem. **36**, 425 (2000).
14. (*a*) M. Narender, M.S. Reddy, V. Pavan Kumar, V.P. Reddy, Y.V.D. Nageswar, and K.R. Rao. J. Org. Chem. **72**, 1849 (2007); (*b*) K. Surendra, N.S. Krishnaveni, A. Mahesh, and K.R. Rao. J. Org. Chem. **71**, 2532 (2006); (*c*) N.S. Krishnaveni, K. Surendra, and K.R. Rao. Chem. Commun. 669 (2005); (*d*) K. Surendra, N.S. Krishnaveni, M.A. Reddy, Y.V.D. Nageswar, and K.R. Rao. J. Org. Chem. **68**, 2058 (2003).
15. R.E. Galian and A.V. Veglia. J. Photochem. Photobiol. A, **187**, 356 (2007).

© 2008 NRC Canada

16. (*a*) S.-Y. Jia, Y.-Q. Hao, L.-N. Li, K. Chen, Y. Wu, J. Liu, L. Wu, and Y.-H. Ding. Chem. Lett. **34**, 1248 (2005); (*b*) H.J. Schneider, F. Hacket, V. Rudiger, and H. Ikeda. Chem. Rev. **98**, 1755 (1998); (*c*) P.V. Demarco and A.L. Thakkar. J. Chem. Soc. Chem. Commun. 2 (1970); (*d*) H. Yamamura, Y. Yamada, R. Miyagi, K. Kano, S. Araki, and M. Kawai. J. Inclusion Phenom. Macrocyclic Chem. **45**, 211 (2003).
17. K. Uekama, F. Hirayama, and T. Irie. Chem. Rev. **98**, 2045 (1998).

© 2008 NRC Canada

Metal-induced facile synthesis of a tricyclic system — 10-Methyl-12-thia-2,9-diaza-tricyclo[8.3.1.0^{3,8}]tetradeca-3,5,7-triene-1-carbonitrile. Formation of an intramolecular carbon–carbon bond

Santokh S. Tandon and C. Robert Lucas

Abstract: The reaction between 4-thiaheptane-2,6-dione and 1,2-diaminobenzene in the presence of nickel(II) perchlorate results in the formation of a nickel(II) complex of a novel new heterotricyclic system: 1-methoxy-10-methyl-12-thia-2,9-diaza-tricyclo[8.3.1.0^{3,8}]tetradeca-3,5,7-triene, which on treatment with potassium cyanide gives 10-methy-12-thia-2,9-diaza-tricyclo[8.3.1.0^{3,8}]tetradeca-3,5,7-triene-1-carbonitrile, a case of metal-induced carbon–carbon bond formation.

Key words: nickel-induced carbon–carbon bond formation, intramolecular cyclization, tricyclic formation.

Résumé : La réaction de la 4-thiahpeptane-2,6-dione avec le 1,2-diaminobenzène, en présence de perchlorate de nickel(II), conduit à la formation d'un complexe de nickel(I) d'un nouveau système hétérotricyclique, le 1-méthoxy-10-méthyl-12-thia-2,9-diazatricyclo[8.3.1.0^{3,8}]tétradéca-3,5,7-triène, qui par traitement avec du cyanure de potassium fournit le 10-méthyl-12-thia-2,9-diazatricyclo[8.3.1.0^{3,8}]tétradéca-3,5,7-triène-1-carbonitrile, un cas de formation d'une liaison carbone-carbone induite par un métal.

Mots-clés : formation d'une liaison carbone–carbone induite par le nickel, cyclisation intramoléculaire, formation d'un tricycle.

[Traduit par la Rédaction]

Introduction

This paper reports the observation of the unexpected and useful synthetic reaction shown in eq. [1]. Reaction of 4-thiaheptane-2,6-dione (**1**) with 1,2-diaminobenzene (**2**) in presence of nickel(II) perchlorate results in formation of a nickel(II) complex of a novel new heterotricyclic system: 1-methoxy-10-methyl-12-thia-2,9-diaza-tricyclo[8.3.1.0^{3,8}]tetradeca-3,5,7-triene (**3**), which on treatment with potassium cyanide, gives 10-methyl-12-thia-2,9-diaza-tricyclo[8.3.1.0^{3,8}]tetradeca-3,5,7-triene-1-carbonitrile (**4**), a case of metal-induced intramolecular carbon–carbon bond formation.

The use of transition-metal ions as catalysts in the synthesis of organic compounds with anti-tumoral and anti-viral activities and in the formation of carbon–carbon or carbon–heteroatom (N, S, or O) bonds has attained prominence in recent years (1). Medium-sized heterocyclic benzodiazepines constitute an important class of therapeutic compounds because of their special affinity for serotonin (5-HT2) and acetylcholine receptors. The benzodiazine skeleton is commonly found in compounds exhibiting a wide range of biological properties (2), such as inhibition of tyrosine kinase (3), anti-malarial (4), anti-convulsive (5), anti-hypertensive (6), hypolipidemic (7), anti-tumoral (8), and anti-viral activity (9). More than a dozen benzodiazepines are available by prescription (10), while similar compounds, such as pyrido[2,3-*b*]benzodiazepinones, have been screened as cardioselective muscarinic receptor antagonists and as po-

[1]

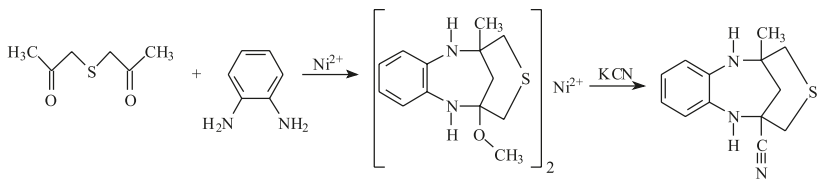

1 2 3 4

Received 26 March 2008. Accepted 9 May 2008. Published on the NRC Research Press Web site at canjchem.nrc.ca on 12 August 2008.

S.S. Tandon. Department of Chemistry, Kent State University, Salem Campus, Salem, OH 44460, USA.
C.R. Lucas.[1] Department of Chemistry, Memorial University of Newfoundland, St. John's, NL A1B 3X7, Canada.

[1]Corresponding author (e-mail: rlucas@mun.ca).

 doi:10.1139/V08-100 © 2008 NRC Canada

tential HIV-1 reverse transcriptase inhibitors (11). Pyrrolo[2,1-*c*][1,4]benzodiazepines and other tricyclics are well-known antibiotics (12) and anti-tumor agents (13). It has been proposed that the cytotoxicity and anti-tumour activity of these compounds result from the formation of a covalent bond between the azomethine unit of the diazepine ring and the C(2)-amino group guanine nucleus in the minor groove of the DNA double spiral (14). Benzothiodiazepinones are used as anti-herpetic agents (15). Recently, the synthesis and in vitro anti-hepatitis B and C virus activities of ring-expanded compounds containing the imidazo[4,5-*e*][1,3]diazepine-4,8-dione ring system have been reported (16). Interest, associated with the pharmacological activities of medium-sized heterocyclics and tricyclics, justifies a continuation of work on novel synthetic methodologies for compounds of these types. However, the difficulties involved in synthesis of tricyclics have prevented in-depth studies on these systems. In this report, we describe a facile, one-step synthesis (see eq. [1]) of a novel heterotricyclic system involving the 1,4-benzodiazepine ring system that has very substantial pharmaceutical implications.

Experimental

Commercially available reagents were obtained from the Aldrich Chemical Co. Inc. and were used without further purification. Spectroscopic data were obtained by using the following instruments: IR, Mattson Polaris FT; UV–vis Carey model 17; NMR, General Electric 300 NB. Analyses were performed by Canadian Microanalytical Service Ltd.[2]

Synthesis of $[Ni(TCS)_2](ClO_4)_2$ (3)

4-Thiaheptane-2,6-dione (2 mmol, 0.29 g), prepared by the reported method (18), was dissolved in dry methanol (10 mL). This solution was added dropwise to a hot methanolic solution (10 mL) of $Ni(ClO_4)_2{\cdot}6H_2O$ (1 mmol, 0.37 g) with stirring. A green solution thus formed was refluxed for ~10 min, and to it, while refluxing, was added dropwise over a period of 10 min a solution of 1,2-diaminobenzene (2 mmol, 0.22 g) in the same solvent (10 mL). The colour of the reaction mixture changed from green to brownish green. The resulting mixture was stirred under reflux, and after ~15 min, a purplish-brown solid separated. The reaction mixture was further refluxed for ~4 h and kept at ambient temperature overnight. The purplish-brown solid was filtered off, washed with dry methanol (3 × 5 mL), and dried under vacuum at room temperature for 12 h. Yield: 0.62 g (82%). Crystals suitable for X-ray studies were obtained by slow diffusion of diethyl ether into a solution of the complex in a mixture of methanol:dimethylformamide (1:1). UV–vis in *N*,*N*-dimethylformamide λ nm (ε $dm^3\ mol^{-1}\ cm^{-1}$): 341 (3620), 267 (6970). UV–vis (Nujol mull, λ nm): 970 mb, 880 mb, 520 sh, 341 vs. IR (Nujol mull, cm^{-1}) υ: 3246 s (N–H). Anal. calcd. for $C_{26}H_{36}N_4Cl_2NiO_{10}S_2$: C 41.18, H 4.79, N 7.39, Ni 7.74; found: C 41.08, H 5.12, N 6.97, Ni 7.68.

Isolation of 10-methyl-12-thia-2,9-diaza-tricyclo[8.3.1.$0^{3,8}$]tetradeca-3,5,7-triene-1-carbonitrile (4)

To a solution of $[Ni(TCS)_2](ClO_4)_2$ (3) (0.92 mmol, 0.70 g), dissolved in a mixture of dimethylformamide:methanol (10 + 20 mL), was added a solution of potassium cyanide (31 mmol, 2.0 g) in water (50 mL). The reaction mixture was stirred for ~10 min. After adding water (100 mL), the mixture was stirred for another 5 min. A yellowish-white solid separated and was extracted with chloroform (100 mL). The chloroform extract was washed with distilled water (4 × 150 mL) and dried over anhyd. sodium sulphate. The extract was filtered, and the solvent was removed at a rotary evaporator. A dirty white solid was obtained and was dissolved in chloroform and treated with activated charcoal. The mixture was filtered, and the filtrate was left at ambient temperature for slow evaporation of solvent. After 24 h, nearly colourless needles suitable for X-ray structure determination had formed. Diethyl ether (5 mL) was added, and the needles were separated by filtration. Yield: 0.37 g (80%). IR (Nujol mull, cm^{-1}) υ: 3301 s and 3317 s (N–H), 2273 m (CN). ^{1}H NMR ($CDCl_3$) δ: 1.28 (s, 3H, CH_3), 1.68 (d, J = 15 Hz, 1H, CH_3CCH_aH), 2.27 (d, J = 15.0 Hz, 1H, CH_3CCH_bH), 2.48 (d, J = 14.0 Hz, $NCCCH_aH$), 2.86 (d, J = 14.0 Hz, $NCCCH_bH$), 2.88 (d, J = 12.0 Hz, 1H, bridge CH_aH), 3.13 (s, 1H, NH_a), 3.18 (d, J = 12.0 Hz, bridge CH_bH), 3.82 (s, NH_b), 6.75 (d, J = 7.0 Hz, 1H, C_6H_4), 6.94 (d, J = 3.5 Hz, 1H, C_6H_4), 6.99 (m, 2H, C_6H_4). ^{13}C{^{1}H} NMR ($CDCl_3$) δ: 31.81 (CH_3), 38.04 (bridge CH_2), 40.11 (S–C_aH_2), 40.35 (S–C_bH_2), 49.51 (C_{Ar}), 50.87 (C_{Ar}), 121.79 ($C_{Ar}H$), 122.14 (*C*N), 123.28 ($C_{Ar}H$), 123.75 ($C_{Ar}H$), 125.58 ($C_{Ar}H$), 134.49 ($C_{Ar}H$), 138.52 ($C_{Ar}H$). Anal. calcd. for $C_{13}H_{15}N_3S$: C 63.64.18, H 6.16, N 17.13, S 13.07; found: C 63.40, H 6.10, N 17.38, S 12.53.

X-ray study

A summary of crystallographic data for 10-methyl-12-thia-2,9-diaza-tricyclo[8.3.1.$0^{3,8}$]tetradeca-3,5,7-triene-1-carbonitrile (**4**) is found in Table 1. X-ray diffraction data were collected by using a Rigaku AFC6S diffractometer. All measurements were made with graphite monochromated Cu Kα radiation (λ = 1.54178 Å) and the ω-2θ scan technique at a scan rate of 4°/min (in ω). Weak reflections ($I < 10.0\sigma(I)$) were rescanned (maximum of five scans), and the counts were accumulated to ensure good counting statistics. Stationary background counts were recorded on each side of the reflection. The ratio of peak counting time to background counting time was 2:1. The intensities of three representative reflections were measured after every 150 reflections and no significant crystal decay was detected. Cell constants and an orientation matrix for data collection, obtained from a least-squares refinement using the setting angles of 25 carefully centered reflections in the range 55.22° <2θ <59.02°, corresponded to a primitive orthorhombic cell with dimensions as shown in Table 1. The space group was determined by systematic absences, a statistical analysis of intensity distribution, packing considerations, and the successful solution and refinement of the structure. Of the 1115 reflections collected, 1096 were unique. The data were corrected for Lo-

[2] Perchlorate salts are often treacherously explosive (see ref. 17), and although we have been unable to cause the compound described to detonate from shock or heat, we recommend suitable precautions be taken whenever perchlorates are handled.

© 2008 NRC Canada

Table 1. Crystallographic data for compound **4**.

Empirical formula	$C_{13}H_{15}N_3S$
Formula mass	245.34
Crystal colour, habit	Colourless, trigonal rod
Crystal dimensions, mm	0.30 × 0.20 × 0.20
Crystal system	Orthorhombic
Space group	$P2_12_12_1$ (#19)
Z	4
a (Å)	10.478(3)
b (Å)	14.108(4)
c (Å)	8.476(3)
T (°C)	26
V (Å^3)	1253.0(6)
$D_{calcd.}$ (g cm^{-3})	1.300
λ (Å)	1.54178
μ (cm^{-1})	21.276
F(0,0,0) electrons	520.00
2θ (max.) (°)	120.0
No. reflections measured	1115
No. unique reflections	1096
No. variable parameters	156
$R1$ ($I > 2.00\sigma(I)$)	0.0304[a]
$wR2$ (all refl.)	0.0754[b]
Last D-map	
Deepest hole (e/Å^3)	–0.13
Highest peak (e/Å^3)	0.12

Note: Throughout this work, esd's are in parentheses and refer to the last digit printed.
[a] $R1 = \sum\|F_o| - |F_c\|/\sum|F_o|$.
[b] $wR2 = [\sum(w(F_o^2 - F_c^2)^2)/\sum w(F_o^2)^2]^{1/2}$

rentz and polarization effects, and a correction for secondary extinction was applied (coefficient = 0.001 040). The linear absorption coefficient, μ, for Cu Kα radiation is 21.276 cm^{-1}.

The structure was solved by direct methods (19) and expanded using Fourier techniques (20). The non-hydrogen atoms were refined anisotropically. Hydrogen atoms were refined using the riding model. The final cycle of full matrix least-squares refinement on F^2 was based on 1096 observed reflections and 156 variable parameters and converged with unweighted and weighted agreement factors $R1 = \sum\|F_o| - |F_c\|/\sum|F_o|$ and $wR2 = [\sum(w(F_o^2 - F_c^2)^2)/\sum w(F_o^2)^2]^{1/2}$ equal to 0.0304 and 0.0754, respectively. Unit weights were used. Neutral atom scattering factors were taken from the usual source (21). Anomalous dispersion effects were included in $F_{calcd.}$ (22); the values for $\Delta f'$ and $\Delta f''$ were those of Creagh and McAuley (23). The values for the mass attenuation coefficients are those of Creagh and Hubbell (24). All calculations were performed using the CrystalStructure (25, 26) crystallographic software package except for refinement, which was performed using SHELXL-97 (27). A description of the experimental procedure, anisotropic thermal parameters and a full listing of bond lengths and bond angles are available as Supplementary Data.[3] Figure 1 shows a view of the structure and its numbering scheme.

Fig. 1. ORTEP of compound **4**. Thermal ellipsoids are shown at the 50% probability level.

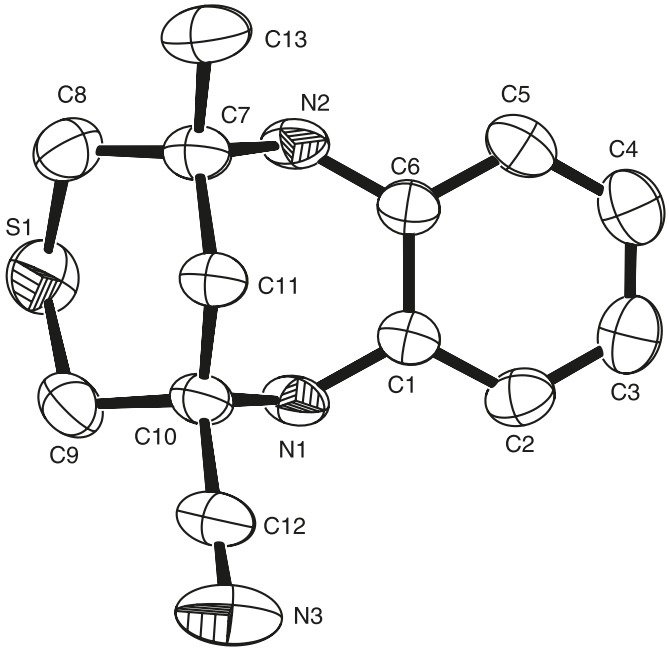

Results and discussion

Earlier, we reported (28) that condensations of diphenacyl sulfide (**1** but with R = Ph) with 1,2-diaminoethane, 1,2-diaminopropane, and 1,3-diaminopropane result in the formation of 5,8a-diphenyl-2,3,8,8a-tetrahydro-1*H*-imidazo[2,1-*c*][1,4]thiazine, 5,8a-diphenyl-2,3,8,8a-tetrahydro-2-methyl-1*H*-imidazo[2,1-*c*][1,4]thiazine (two isomeric products differing in the orientation of the methyl group at position 2 with respect to the plane of the molecule) and 6,9a-diphenyl-1,2,3,4,9,9a-hexahydropyrimido[2,1-*c*][1,4]thiazine, respectively (See eqs. [2—4]).

Likewise, treatment of 4-thiaheptane-2,6-dione (**1**) with triethylenetetramine results in formation of a novel heterocycle 1,1′-ethylenebis[5,8-dimethyl-2,3,8,8a-tetrahydro-1*H*-imidazo[2,1-*c*][1,4]thiazine] (18) as shown in eq. [5].

[2]

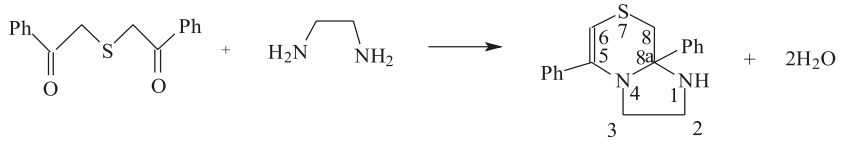

[3] Supplementary data for this article are available on the journal Web site (canjchem.nrc.ca) or may be purchased from the Depository of Unpublished Data, Document Delivery, CISTI, National Research Council Canada, Ottawa, ON K1A 0R6, Canada. DUD 3781. For more information on obtaining material, refer to cisti-icist.nrc-cnrc.gc.ca/irm/unpub_e.shtml. CCDC 656791 contains the crystallographic data for this manuscript. These data can be obtained, free of charge, via www.ccdc.cam.ac.uk/conts/retrieving.html (Or from the Cambridge Crystallographic Data Centre, 12 Union Road, Cambridge CB2 1EZ, UK; fax +44 1223 336033; or deposit@ccdc.cam.ac.uk).

© 2008 NRC Canada

[3] 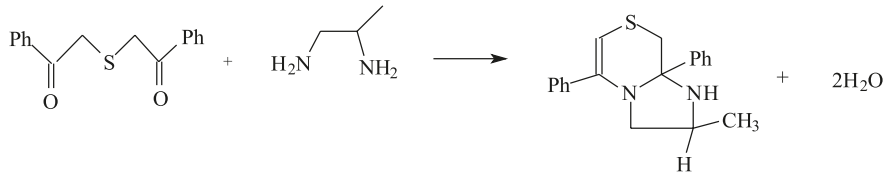

[4] 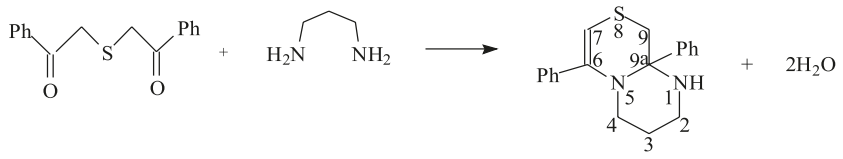

[5] 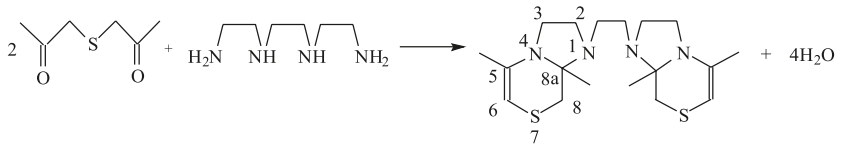

However, attempts to prepare 1,4,7-thiadiazonine by reacting 4-thiaheptane-2,6-dione (**1**) with 1,2-diaminobenzene (**2**) with or without catalytic amounts of acid or base result only in a multitude of products, none of which is present in isolable amount. On the other hand, in presence of nickel(II) perchlorate, this reaction unexpectedly provides a nickel(II) complex (**3**) of a novel tricyclic system, 1-methoxy-10-methyl-12-thia-2,9-diaza-tricyclo[8.3.1.$0^{3,8}$]tetradeca-3,5,7-triene, in which an intramolecular carbon–carbon bond has been formed.

Compound **3** has been characterized through spectroscopic and analytical data, and on treatment with potassium cyanide, it reacts to form **4**, which has been characterized using multinuclear NMR, mass spectroscopy, and single-crystal X-ray studies. Multinuclear 1D and 2D NMR (HETCOR and COSY) experiments, IR, analytical, and mass spectral data confirm that the structure of **4**, determined in the solid state by single-crystal X-ray crystallography, is maintained in solution. The structure of **4** and its numbering scheme in the context of the structural study are shown in Fig. 1.

The bond lengths and angles of **4** are unexceptional and lie in the range observed in similar medium-sized heterocycles and heterobicycles. For example, the angle C10–C11–C7 is 115.1(3)°, N1–C10–C9 is 110.6(3)°, C8–S1–C9 is 98.62(18)°, and C1–N1–C10 is 120.6(3)°. The distance S1—C9 is 1.788(4) Å, C10—C11 is 1.521(4) Å, C10—C12 is 1.494(5) Å, and C10—N1 is 1.455(4) Å.

Because compounds **3** and **4** might not be expected a priori to have the tricyclic organic structures as shown in Fig. 1, their characterization warrants some discussion. Compound **3** has been unequivocally characterized by conventional means not including X-ray structural methods. Notwithstanding that X-ray quality crystals of **3** are relatively easily grown and several samples from independent syntheses were submitted to several different crystallographic laboratories, the structural results obtained in every case were similar and were not completely satisfactory. In every case, despite apparently reasonable residuals, goodness-of-fit and other conventional evidence for satisfactory solution of the structure, an unexplained residual electron density in the vicinity of the methoxyl group in **3** and unacceptably large thermal ellipsoids in the same part of the structure occurred that could not be modelled in a chemically or structurally sensible way. However, because the structure of **3** is relevant to an appreciation of the overall process and notwithstanding the unsatisfactory nature of its X-ray structural study, its ORTEP is nonetheless presented but should be used for general guidance only (Fig. 2), as should details of its coordination sphere (Table 2).

Table 2. Selected bond angles and lengths of compound **3**.

Bond lengths (Å)	
Ni—N(1)	2.141(7)
Ni—S(1)	2.4055(11)
Ni—N(2)	2.170(7)
Bond angles (°)	
N(1)–Ni–N(1A)	105.3(4)
N(1A)–Ni–N(2)	179.4(3)
N(1)–Ni–S(1A)	93.8(2)
N(2)–Ni–S(1A)	94.55(18)
S(1A)–Ni–S(1)	179.69(16)
N(1)–Ni–N(2)	74.78(14)
N(2)–Ni–N(2A)	105.2(4)
N(1A)–Ni–S(1A)	86.0(2)
N(2A)–Ni–S(1a)	85.64(18)

In the light of this experience and in an attempt to separate the ligand from its metal for independent study, **3** was treated with potassium cyanide to sequester the nickel. Although this did successfully separate the nickel from the organic portion of the complex, it was readily apparent that at the same time the ligand had also reacted to become **4**. Compound **4** has also been unequivocally characterized by conventional means, including X-ray structural analysis. The formation of a tricyclic system only in the presence of nickel and the apparent ease with which the methoxyl group of **3** is replaced by a cyano group raises two questions. First, what is the probable mechanism for the formation of the tricyclic system? And second, is the mechanism by which cyano replaces methoxyl related to it? A plausible mechanism for the formation of the intramolecular carbon–carbon bond and the tricyclic system is suggested in Fig. 3. Based upon the structure of compound **3** (Fig. 2), it would be reasonable to as-

© 2008 NRC Canada

Fig. 2. ORTEP of **3**. Thermal ellipsoids are shown at the 50% probability level.

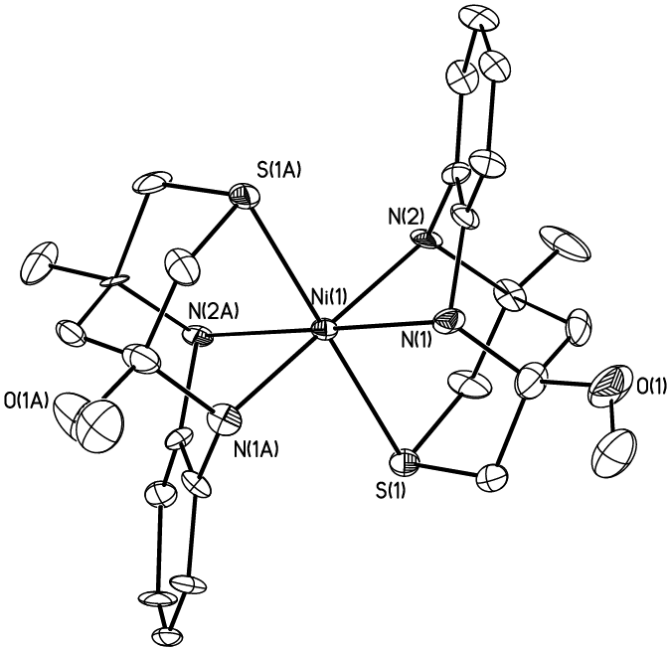

sume the role of the metal is, inter alia, to hold the bridge-forming methyl carbon in appropriate proximity to the other methyl-bearing carbon atom so that they may bond by the sequence shown in Fig. 3 to form the bridge.

One can also easily imagine a process involving CN^- instead of CH_3OH in the latter part of the mechanism in Fig. 3 that would account for conversion of the ligand of **3** into **4** in the presence of potassium cyanide.

Conclusions

Herein, we report a facile, one-step synthesis of a novel heterotricyclic system involving the 1,4-benzodiazepine ring system that has immense pharmaceutical implications. The importance of this work lies in the fact that by using easily available thiodiketone and benzodiamine reagents, a new tricyclic system can be obtained in high yield in a one-step reaction. We are currently collaborating with other research groups for testing the anti-tumor and anti-viral activity of this and similar compounds.

Acknowledgements

The authors are grateful to Dr. Paul Sampson, Kent State University, and Dr. Graham Bodwell, Memorial University of Newfoundland, for useful discussions, and to Mr. D.O. Miller of Memorial University for assistance with the X-ray structure determination. Funding for this work was provided by the Natural Sciences and Engineering Research Council of Canada (NSERC), by Memorial University of Newfoundland, and by Kent State University, Salem and East Liverpool campuses.

Fig. 3. Proposed mechanism for the formation of the ligand of **3**.

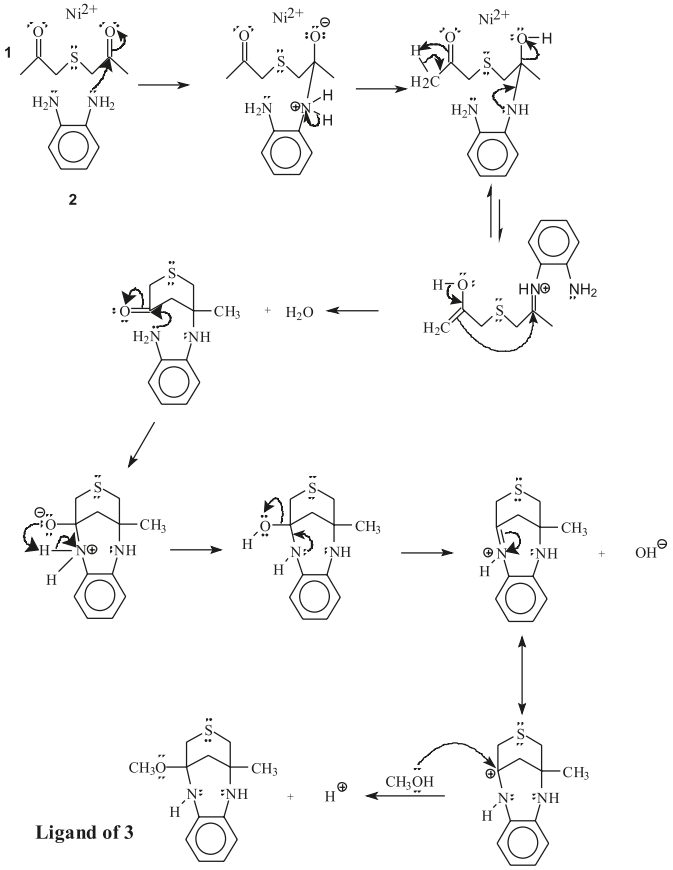

References

1. (*a*) F. Kakiuchi and N. Chatani. Adv. Synth. Catal. **345**, 1077 (2003); (*b*) P.J. Stang (*Editor*). Handbook of C–H transformation. Vols. 1 and 2. *Edited by* G. Dyker. Wiley-VCH Verlag GmbH & Co. KgaA. Weinheim, Germany. 2005; (*c*) B.M. Trost. *In* Advances in natural product chemistry. *Edited by* Atta-Ur-Rahman. Hardwood Academic Publishers. Hardwood. 1992. pp 19–34; (*d*) B.M. Trost and M.L. Crawley. Chem. Rev. **103**, 2921 (2003); (*e*) S. Burling, M.F. Mahon, R.E. Powell, M.K. Whittesey, and J.M.J. Williams. J. Am. Chem. Soc. **128**, 13702 (2006); (*f*) T. Ohmura, H. Taniguchi, and M. Suginome. J. Am. Chem. Soc. **128**, 13682 (2006); (*g*) N. Sasamoto, C. Dubs, Y. Hamashima, and M. Sodeoka. J. Am. Chem. Soc. **128**, 14010 (2006); (*h*) Y. Chen and C. Lee. J. Am. Chem. Soc. **128**, 15598 (2006); (*i*) Z. Gu and S. Ma. Angew. Chem., Int. Ed. **45**, 6002 (2006); (*j*) M. Suginome, M. Shirakura, and A. Yamamoto. J. Am. Chem. Soc. **128**, 14438 (2006); (*k*) X. Chen, C.E. Goodhue, and J. Yu. J. Am. Chem. Soc. **128**, 12634 (2006); (*l*) O. Piechaczyk, C. Thoumazet, Y. Jean, and P.L. Floch. J. Am. Chem. Soc. **128**, 14306 (2006); and references cited therein; (*m*) S.K. Padhi and S.K. Manivannan. Inorg. Chem. **45**, 7994 (2006); (*n*) R. Zimmer, C.U. Dinesh, E. Nandanan, and F.A. Khan. Chem. Rev. **100**, 3067 (2000).
2. (*a*) L. Sandford Goodman, L.E. Limbird, P.B. Milinoff, R.W. Ruddon, and A. Goodman Gilman (*Editors*). Goodman & Gilman's the pharmacological basis of therapeutics. 9th Ed. McGraw Hill. New York. 1996; (*b*) O.H. Drummer. Forensic Sci. Rev. **14**, 1 (2002); (*c*) D.J. Brown. The chemistry of

© 2008 NRC Canada

heterocyclic compounds. Wiley. New York. 1996; (*d*) T.K. Joergensen, K.E. Andersen, H.S. Andersen, R. Hohlweg, P. Madsen, and U.B. Olsen. Patent No. WO 9-631-497. Novo Nordisk A/s, Den. 1996; Chem. Abstr. **126**, 8 146 (1997); (*e*) H. Ohkuma and S. Kobaru. US Patent 94-249-518. Bristol-Myers-Squibb Company. 1996; Chem. Abstr.**125**, 140 671 (1996); (*f*) E.K. Grigorseva, N.V. Kaverina, A.M. Likhosherstov, V.V. Lyskovtsev, A.P. Skoldinov, A.V. Stavrovskaya, E.A. Tolmacheva, G.G. Chichkanov, and R. Barch. Patent No. RU 2-026-862. Nauchno-Issiedovateiski Institut Farmakologi RAMN, Russia. 1995; Chem. Abstr. **124**, 106 663 (1996); (*g*) H. Heinisch, and H. Frank. *In* Progress in medicinal chemistry. *Edited by* G.P. Ellis and G.G. West. Elsevier. Amsterdam. 1990.

3. (*a*) G.W. Rewcastle, W.A. Denny, A.J. Bridges, H. Zhou, D.R. Cody, A. McMichael, and D.W. Fry. J. Med. Chem. **38**, 3482 (1995); (*b*) A. Gazit, H. App, G. McMahon, J. Chen, A. Levitzki, and F.D. Bohmer. J. Med. Chem. **39**, 2170 (1996).
4. F.H.S. Curd, J.K. Landquist, and F.L. Rose. J. Chem. Soc. 775 (1947).
5. (*a*) V.K. Rastogi, S.S. Parmar, S.P. Singh, and T.K. Akers. J. Heterocycl. Chem. **15**, 497 (1978); (*b*) J.F. Wolfe, T.L. Rathman, M.C. Sleevi, J.A. Campbell, and T.D. Greenwood. J. Med. Chem. **33**, 161 (1990); (*c*) M. Hori, R. Iemura, H. Hara, A. Ozaki, T. Sukamoto, and H. Ohtaka. Chem. Pharm. Bull. **38**, 681 (1990); (*d*) A. Melikian, G. Schlewer, J.P. Chambon, and C.G. Wermuth. J. Med. Chem. **35**, 4092 (1992).
6. (*a*) S.J. Lee,Y. Konishi, D.T. Yu, T.A. Miskowski, C.M. Riviello, O.T. Macina, M.R. Frierson, K. Kondo, M. Sugitani, J.C. Sircar, and K.M. Blazejewski. J. Med. Chem. **38**, 3547 (1995); (*b*) J.I. Levin and A.M. Venkatesan. US Patent 5-284-853 A. 1994.
7. Y. Kurogi, Y. Inoue, K. Tsutsumi, S. Nakamura, K. Nagao, H. Yoshitsugu, and Y. Tsuda. J. Med. Chem. **39**, 1433 (1996).
8. J.B. Jiang, D.P. Hesson, B.A. Dusak, D.L. Dexter, G.J. Kang, and E. Hamel. J. Med. Chem. **33**, 1721 (1990).
9. U. Sehlstedt, P. Aich, J. Bergman, H. Vallberg, B. Norden, and A. Graslund. J. Mol. Biol. **278**, 31 (1998).
10. Harvard mental health letter. Vol. 22. 2005.
11. G. Schmidt. US Patent 3-406-168. Boehringer Ingelheim G.m.h.H. 1968.
12. D.E. Thurston, B.D. Subhas, P.W. Howard, T.C. Jenkins, A. Leoni, P.G. Baraldi, A. Guiotto, B. Cacciari, L.R. Kelland, M. Follope, and S. Rault. J. Med. Chem. **42**, 1951 (1999).
13. V. Lisowski, F. Fabis, A. Pierre D.H. Caignard, P. Renard, and S. Rault. J. Enzyme Inhib. Med. Chem. **17**, 403 (2002) and references cited therein.
14. (*a*) L.H. Hurley and R.L. Petrusek. Nature (Lonodon, UK), **282**, 529 (1979); (*b*) S. Cheatham, A. Kook, L.H. Hurley, M.D. Barkley, and W.J. Remers. J. Med. Chem. **31**, 583 (1988); (*c*) J.J. Wang, G.C. Hill, and L.H. Hurley. J. Med. Chem. **35**, 2995 (1992); (*d*) J.A. Montzouris, J.J. Wang, D.E. Thurston, and L.H. Hurley. Med. Chem. **37**, 3132 (1994).
15. H.W. Hamilton, G. Nishiguchi, S.E. Hagen, J.D. Domagala, P.C. Weber, S. Gracheck, S.L. Boulware, E.C. Nordby, H. Cho, T. Nakamura, S. Satoru Ikeda, and W. Watanabe. Bioorg. Med. Chem. Lett. **12**, 2981 (2002).
16. (*a*) J.K. Gill, L. Wang, M. Bretner, R. Newman, N. Kyprianou, and R.S. Hosmane. Nucleosides Nucleotides Nucleic Acids, **20**, 1043 (2001); (*b*) P. Peng, N. Zhang, B.E. Korbab, and R.S. Hosmane. Bioorg. Med. Chem. Lett. **15**, 5397 (2005).
17. W.C. Wosley. J. Chem. Ed. **50**, A335 (1973).
18. S.S. Tandon and L.F. Larkworthy. J. Heterocycl. Chem. **22**, 475 (1985).
19. A. Altomare, M. Cascarano, C. Giacovazzo, and A. Guagliardi. J. Appl. Cryst. **26**, 343 (1993).
20. P.T. Beurskens, G. Admiraal, G. Beurskens, W.P Bosman, R. de Gelder, R. Israel, and J.M.M. Smits. *In* Technical report 1994. Crystallographic Laboratory, Toernooiveld, 6525 Ed. Nijmegen, Netherlands. 1994.
21. D.T. Cromer and J.T. Waber. *In* International tables for X-ray crystallography. Vol. IV. The Kynoch Press. Birmingham, England. 1974. p. 99. Table 2.2 A.
22. J.A. Ibers and W.C. Hamilton. Acta Crystallogr. **17**, 781 (1964).
23. D.C. Creagh and W.J. McAuley. *In* International tables for crystallography. Vol C. *Edited by* A.J.C. Wilson. Kluwer Academic Publishers. Boston. 1992. pp. 219–222. Table 4.2.6.8.
24. D.C. Creagh and J.H. Hubbell. *In* International tables for crystallography. Vol C. *Edited by* A.J.C. Wilson. Kluwer Academic Publishers. Boston. 1992. pp. 200–206. Table 4.2.4.3.
25. CrystalStructure 3.7.0 [computer program]. Rigaku and Rigaku/MSC. 9009 New Trails Dr. The Woodlands TX. 2000–2005.
26. D.J. Watkin, C.K. Prout, J.R. Carruthers, and P.W. Betteridge. CRYSTALS [computer program] Issue 10. Chemical Crystallography Laboratory. Oxford, UK. 1996
27. G.M. Sheldrick. SHELX97 [computer program]. 1997.
28. (*a*) S.S. Sandhu, S.S. Tandon, and H. Singh. Indian J. Chem. **15B**, 664 (1977); (*b*) S.S. Sandhu, S.S. Tandon, and H.J. Singh. Synthesis, 46 (1979); (*c*) S.S. Sandhu, S.S. Tandon, and H.J. Singh. Synthesis, 623 (1979); (*d*) S.S. Sandhu, S.S. Tandon, and H.J. Singh. Chem. **19B**, 1023 (1980); (*e*) S.S. Sandhu, S.S. Tandon, and H. Singh. Chem. **20B**, 985 (1981); (*f*) S.S. Tandon and L.F. Larkworthy. Synthesis, 481 (1983).

© 2008 NRC Canada

First-order parallel and consecutive reaction mechanisms — Isosbestic points criterium

A.E. Croce

Abstract: A criterium for the selection of reaction mechanism derived from a condition for isosbestic points occurrence is presented. Analytical relationships involving the molar absorption coefficients of the species, which participate in a mechanism of parallel first-order reactions and the corresponding rate coefficients, are also reported. A model system of four species that present overlapping absorption spectra may correspond to the reactant and products of a system of parallel or consecutive first-order reactions. In the first case, under experimental conditions in which the absorbances are additive, the presence of an isosbestic point in the spectrum of the reaction mixture at a given wavelength leads to a time-independent ratio of the degree of advancement of reaction variables. From this, relevant kinetic information may be extracted, namely, the ratio of the reaction rate coefficients. Moreover, the occurrence of isosbestic points allows discarding the second mechanism. This conclusion is independent of the number of absorbing species. Model calculated examples show the application of the equations here derived. The resolution for the general case of mechanisms of N first-order reactions is provided.

Key words: chemical kinetics, time-resolved absorption spectra, reaction mechanism.

Résumé : On propose un critère pour la sélection des mécanismes réactionnels qui est dérivé d'une condition pour la présence de points isosbestiques. Les relations analytiques impliquées dans les coefficients d'absorption molaire de l'espèce qui participe dans un mécanisme de réactions du premier ordre parallèles et on rapporte aussi les coefficients de vitesse correspondants. Un système modèle de quatre espèces qui présentent des chevauchements dans leurs spectres d'absorption peut correspondre aux réactifs et aux produits d'un système de réactions du premier ordre parallèles ou consécutives. Dans le premier cas, sous des conditions expérimentales dans lesquelles les absorbances sont additives, la présence d'un point isosbestique dans le spectre du mélange réactionnel, à une longueur d'onde donnée, conduit à un rapport indépendant du temps du degré d'avancement des variables réactionnelles. À partir de ceci, on peut relever les informations cinétiques qui présentent de l'intérêt, soit le rapport des coefficients de vitesse des réactions. De plus, la présence d'un point isosbestique permet d'éliminer le deuxième mécanisme. Cette conclusion est indépendante du nombre d'espèces absorbantes. Des exemples calculés à l'aide de ce modèle montrent les domaines d'application des équations dérivées dans ce travail.

Mots-clés : cinétique chimique, spectre d'absorption résolu en fonction du temps, mécanisme réactionnel.

[Traduit par la Rédaction]

Introduction

Many photochemical and thermal reaction systems in solution are investigated employing UV–vis spectrophotometry (1). Successive scans of the spectrum of the reaction mixture are performed: the initial spectrum usually corresponds to a light-absorbing reactant, and as the reaction proceeds the total absorbance of the mixture changes with time, following the changes in composition (2, 3). The application of such transient absorption methods requires that the Beer–Lambert law applies, and the resulting absorbance for a system of N species absorbing in a given spectral region be given by $A = \sum_i \varepsilon_i c_i l$ (i = 1, 2, …, N) where ε_i is the molar absorption coefficient of the i component, c_i is the corresponding molar concentration, and l is the path length. Therefore, in a reacting system at constant temperature and volume, A becomes a function of two relevant variables, namely, wavelength and time.

Frequently, isosbestic points constitute a feature of such transient absorption spectral families. When the spectra of two or more species participating in a reaction overlap, the total absorbance of the reaction mixture may remain invariant with respect to time during the course of the reaction at certain wavelengths, which define the isosbestic points (4). It is generally asserted that the occurrence of an isosbestic point in a reaction system requires that the changes in the concentrations of the various components are linearly related (1) at one or more crossing points of the spectra of the single contributors (5). Operative criteria have been developed: the existence of an isosbestic point is believed to prove the existence of only two absorbing species (6). It is easily proven that this is true in the case of a single absorbing species A

Received 4 March 2008. Accepted 9 May 2008. Published on the NRC Research Press Web site at canjchem.nrc.ca on 12 August 2008.

Dedicated to Esther Oliveros on the occasion of her forthcoming birthday.

A.E. Croce. Instituto de Investigaciones Fisicoquímicas Teóricas y Aplicadas (INIFTA), Departamento de Química, Facultad de Ciencias Exactas, Universidad Nacional de La Plata, CCT La Plata — CONICET, La Plata, Argentina; (e-mail: acroce@inifta.unlp.edu.ar).

 doi:10.1139/V08-098 © 2008 NRC Canada

converting into a single absorbing B; at the λ at which both spectra cross, an isosbestic point will certainly appear (7).

Exhaustive theories for the interpretation of the occurrence of isosbestic points in chemical analytical systems (8) and useful correlations between isosbestic wavelength shift and composition (9) are based mainly on two-absorbing-species systems. An extensive treatment that employs the tools of linear algebra has been performed by Mauser and Gauglitz (10). More recently, the particular case of constant absorption by two absorbing species has been used for the determination of quantum efficiency (11). However, no reference to competing reaction mechanisms involving several absorbing species has been made to date in formal kinetic treatments.

The appearance of isosbestic points in time-resolved spectra can be easily recognized in absorbance difference representations in which the difference between the absorbance A at time t and A_0, the initial value at $t = 0$, $\Delta A = A - A_0$, is plotted against the wavelength. In this kind of plot, an isosbestic point satisfies the condition

$$[1] \qquad \Delta A_{ip} = 0$$

as it is defined by the wavelength, λ_{ip}, at which the absorbance of the mixture is independent of time. In the following, the subscript ip indicates the correspondence to an isosbestic point. The high sensitivity of difference spectra has been demonstrated even in radiation chemistry of DNA studies (12).

Moreover, the graphs of A or ΔA as a function of λ present an inflection point at the isosbestic point, at which the mathematical condition

$$[2] \qquad (\partial^2 A/\partial\lambda^2)_{ip} = 0$$

has to be fulfilled. Besides, eq. [1] implies that

$$[3] \qquad (\partial \Delta A/\partial t)_{ip} = 0$$

at each λ_{ip}.

For a given reaction mechanism, which governs the increase and decay of the concentrations of the components of a reaction system as a function of time, the application of the above given conditions leads to general criteria related to the presence and number of isosbestic points in families of time-resolved absorption spectra. A detailed kinetic analysis is presented here for mechanisms involving first-order reactions.

A recent study, the experimental investigation of the acid-catalyzed intramolecular attack of β-phenylthioureido group on amide function (13), provides a nice illustration of the present discussion.

Results and discussion

Case I: parallel reactions mechanism

The final criteria derived in the following are valid independent of the order of the reactions for a parallel reaction mechanism. However, for the sake of mathematical simplicity, the particular case of first-order reactions will be discussed.

A system of N parallel first-order reactions such as $Y_1 \rightarrow \nu_{Y_i} Y_i$ ($i = 1, 2, \ldots, N$) is considered. The type of product being irrelevant from the kinetics standpoint, only one for each reaction has been chosen. The molar concentrations at a given reaction time are given by

$$[4] \qquad c_{Y_i} = c_{Y_{i0}} - \sum_i \nu_{Y_i} x_i$$

which takes the form $c_{Y_i} = \nu_{Y_i} x_i$ for the products. ν_{Y_i} represents the stoichiometric coefficient of each product Y_i, and x_i the degree of advancement variable for reaction i (14). In this case, $\nu_{Y_1} = 1$ for the reactant Y_1 and $c_{Y_{10}}$ the initial concentration, such that $c_{Y_1} = \sum_i x_i$. The reaction rate eq. can be expressed as

$$[5] \qquad dc_{Y_i}/dt = d(\textstyle\sum_i x_i)/dt = \sum_i k_i c_{Y_1}$$

where k_i represent the reaction rate coefficient for reaction i. These eqs. lead to

$$[6] \qquad \textstyle\sum_i (dx_i/dt) = \sum_i (c_{Y_{10}} - \sum_i x_i)\, k_i = (c_{Y_{10}} - \sum_i x_i) \sum_i k_i$$

which can be expressed in terms of a single variable y

$$[7] \qquad dy/dt = (c_{Y_{10}} - y)\textstyle\sum_i k_i$$

taking $y = \sum_i x_i$. The solutions (15)

$$[8] \qquad x_j(t) = (k_j c_{Y_{10}} / \textstyle\sum_i k_i)[1 - \exp(-t \sum_i k_i)]$$

yield time independent $x_h(t)/x_j(t)$ ratios, and therefore ratios of the form $x_h/x_j = k_h/k_j$ are obtained.

The above treatment may be easily applied to the case of four species, which absorb light additively at a given wavelength, linked by a two first-order parallel reactions mechanisms: (I) $R \rightarrow \nu_B B + \nu_C C$ and (II) $R \rightarrow \nu_D D$.

The total absorbance A at a given reaction time t is given by

$$[9] \qquad A = \varepsilon_R c_R l + \varepsilon_B c_B l + \varepsilon_C c_C l + \varepsilon_D c_D l$$

where c_i denotes molar concentrations, l the optical path length, and ε_i the respective molar absorption coefficients at a given wavelength. Let's assume that the time-resolved spectra present an isosbestic point at λ_{ip}.

Assuming $c_{R_0} \neq 0$ and $c_{B_0} = c_{C_0} = c_{D_0} = 0$ for the initial concentrations of the reactant and products, and replacing the concentrations given by eq. [4] in the difference absorbance ΔA, the condition

$$[10] \qquad \Delta A_{ip} = x_I(\nu_B \varepsilon_B^{ip} + \nu_C \varepsilon_C^{ip} - \varepsilon_R^{ip}) + x_{II}(\nu_D \varepsilon_D^{ip} - \varepsilon_R^{ip}) = 0$$

is obtained at the isosbestic point, λ_{ip}, according to eq. [1].

As the extent of reaction variables are $x_i > 0$ for any reaction time, in the case of only two absorbing species, namely, R and D, and a single reaction leading to the transformation of R, then $\nu_D \varepsilon_D^{ip} = \varepsilon_R^{ip}$, in agreement with the particular though universally accepted (7) conclusion that the existence of an isosbestic point indicates that two and only two species are responsible for the absorption. The condition given by eq. [10] will be fulfilled in trivial cases, which do not lead to any kinetic information, such as $\nu_B \varepsilon_B^{ip} + \nu_C \varepsilon_C^{ip} - \varepsilon_R^{ip} = 0$, giving rise to isosbestic points at which $\nu_D \varepsilon_D^{ip} = \varepsilon_R^{ip}$.

However, if for example, $\nu_B \varepsilon_B^{ip} + \nu_C \varepsilon_C^{ip} - \varepsilon_R^{ip} \neq 0$, the condition $\Delta A_{ip} = 0$ leads to

© 2008 NRC Canada

Fig. 1. Model spectra for the reactant R (solid line) and the products B (– – –), C (–·–·–), and D (·····). The arrows point to the wavelengths of the isosbestic points.

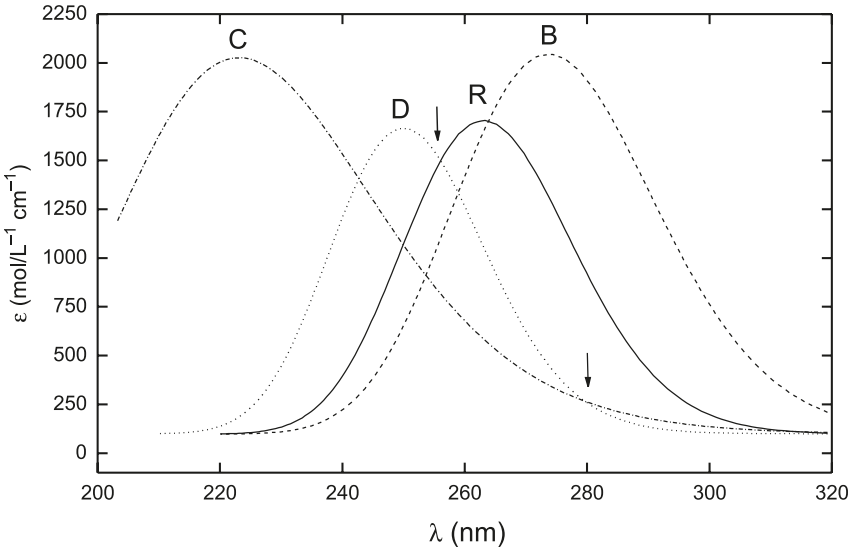

[11] $x_I/x_{II} = (\varepsilon_R^{ip} - \nu_D\,\varepsilon_D^{ip})/(\nu_B\,\varepsilon_B^{ip} + \nu_C\,\varepsilon_C^{ip} - \varepsilon_R^{ip})$

Even though the right hand term of eq. [11] will clearly vary according to the identity and the number of absorbing species, this term will remain constant at an isosbestic point. Therefore, the ratio x_I/x_{II} should be time-independent to observe an isobestic point at a given wavelength.

Equation [10] together with the condition imposed by eq. [3] $(\partial\Delta A/\partial t)_{ip} = (\nu_B\,\varepsilon_B^{ip} + \nu_C\,\varepsilon_C^{ip} - \varepsilon_R^{ip})\,(dx_I/dt) + (\nu_D\,\varepsilon_D^{ip} - \varepsilon_R^{ip})(dx_{II}/dt) = 0$ leads to the relationship

[12] $x_I(dx_{II}/dt) = x_{II}(dx_I/dt)$

which must hold if an isosbestic point is possible.

As a consequence, the eq.

[13] $(\varepsilon_R^{ip} - \nu_D\,\varepsilon_D^{ip})/(\nu_B\,\varepsilon_B^{ip} + \nu_C\,\varepsilon_C^{ip} - \varepsilon_R^{ip}) = k_I/k_{II}$

results. Even though x_I and x_{II} depend on time (eq. [8]) the ratio x_I/x_{II} remains time-independent. Consequently, the first member of eq. [13], which is constant at the isosbestic points, takes the same value k_I/k_{II} at every λ_{ip}. Therefore, if the spectra of the components of the reaction mixture and the stoichiometric coefficients of the products are known and one or more isosbestic points are observed, the first member of eq. [13] can be calculated at λ_{ip}, such that the ratio k_I/k_{II} can be obtained.

In the particular case of the photochemical decomposition of a single reactant R through two competing pathways, in the absence of secondary reactions involving R and the products of steps (I) and (II), eq. [13] leads to the ratio of the respective quantum yields, $x_I/x_{II} = (\varepsilon_R^{ip} - \nu_D\,\varepsilon_D^{ip})/(\nu_B\,\varepsilon_B^{ip} + \nu_C\,\varepsilon_C^{ip} - \varepsilon_R^{ip}) = \Phi_I/\Phi_{II}$, with the additional constraint $\Phi_I + \Phi_{II} = 1$, within the experimental error limits.

Another important example of parallel mechanisms is represented by a system of two or more emissive species formed from a single precursor. In fact, iso-emissive points are observed in the time-resolved area-normalized emission spectroscopy (TRANES) approach to time-resolved fluorescence studies (16).

Model example

The absorption cross-sections (σ base *e* in cm^2 molecule^{-1}), for each hypothetical absorbing species R, B, C, and D participating in reactions (I) and (II), are taken as Gaussian functions of the wavenumber in cm^{-1} (15). After the transformation of σ into molar absorption coefficients (ε base 10 in mol^{-1} L cm^{-1}), these have been represented as a function of wavelength as shown in Fig. 1. These values have been employed to calculate the total absorbance at three given reaction times. To this end, the concentration of each species has been calculated by numerical integration of the kinetic eq. [5] employing the Runge–Kutta method. For simplicity, $\nu_B = \nu_C = \nu_D = 1$ has been assumed. The results for $c_{R_0} = 10^{-4}$ mol/L, $k_I = 10^4$ mol^{-1} L s^{-1}, and $k_{II} = 2 \times 10^4$ mol^{-1} L s^{-1}, and $l = 1$ cm are shown in Fig. 2*a*. Thus, the difference spectra depicted in Fig. 3*a* show two isosbestic points. The isosbestic point condition (1) leads to eq. [11], which therefore should yield finite values for x_I/x_{II}, precisely at the isosbestic points. Figure 4 shows the dependence of $(\varepsilon_R^{ip} - \varepsilon_D^{ip})/(\varepsilon_B^{ip} + \varepsilon_C^{ip} - \varepsilon_R^{ip})$ on wavelength, according to the shape of the individual spectra. However, only positive values of this ratio have a physical interpretation as x_I/x_{II}. This fact precludes that isosbestic points appear at wavelengths at which eq. [11] is not fulfilled. In the present example, for the arbitrarily chosen ratio $k_I/k_{II} = 0.5$, two isosbestic points are predicted at the wavelengths at which they appear in Fig. 3*a*. More generally, the range of wavelengths at which isosbestic points may appear is restricted by the ratio k_I/k_{II}, and the number of possible isosbestic points may be already extracted from the known spectra of the reactants and products, as shown in Fig. 4.

Conversely, from the known spectra of the reactants and products and the "experimental" isosbestic points from Fig. 3*a*, the ratio k_I/k_{II} can be determined using Fig. 4.

Moreover, k_I and k_{II} may depend on temperature in a way that the ratio also depends on temperature. In contrast to the ample variation of absorption coefficients for numerous species observed between room temperature and shock wave conditions (17), no detectable dependence is expected in

© 2008 NRC Canada

Fig. 2. (*a*) Calculated concentrations for R (·····), B or C (solid line), and D (– – –), with $k_I = k_{II}/2 = 10^4$ (mol/L)$^{-1}$ s^{-1}and $[R]_o = 10^{-4}$ mol/L for the parallel reactions mechanism. (*b*) Calculated concentrations for R (solid line), B (– – –), and C (◦◦◦), or D (▽▽▽), with $k_I = k_{II}/2 = 10^4$ (mol/L)$^{-1}$ s^{-1}and $[R]_o = 10^{-4}$ mol/L for the consecutive reactions mechanism.

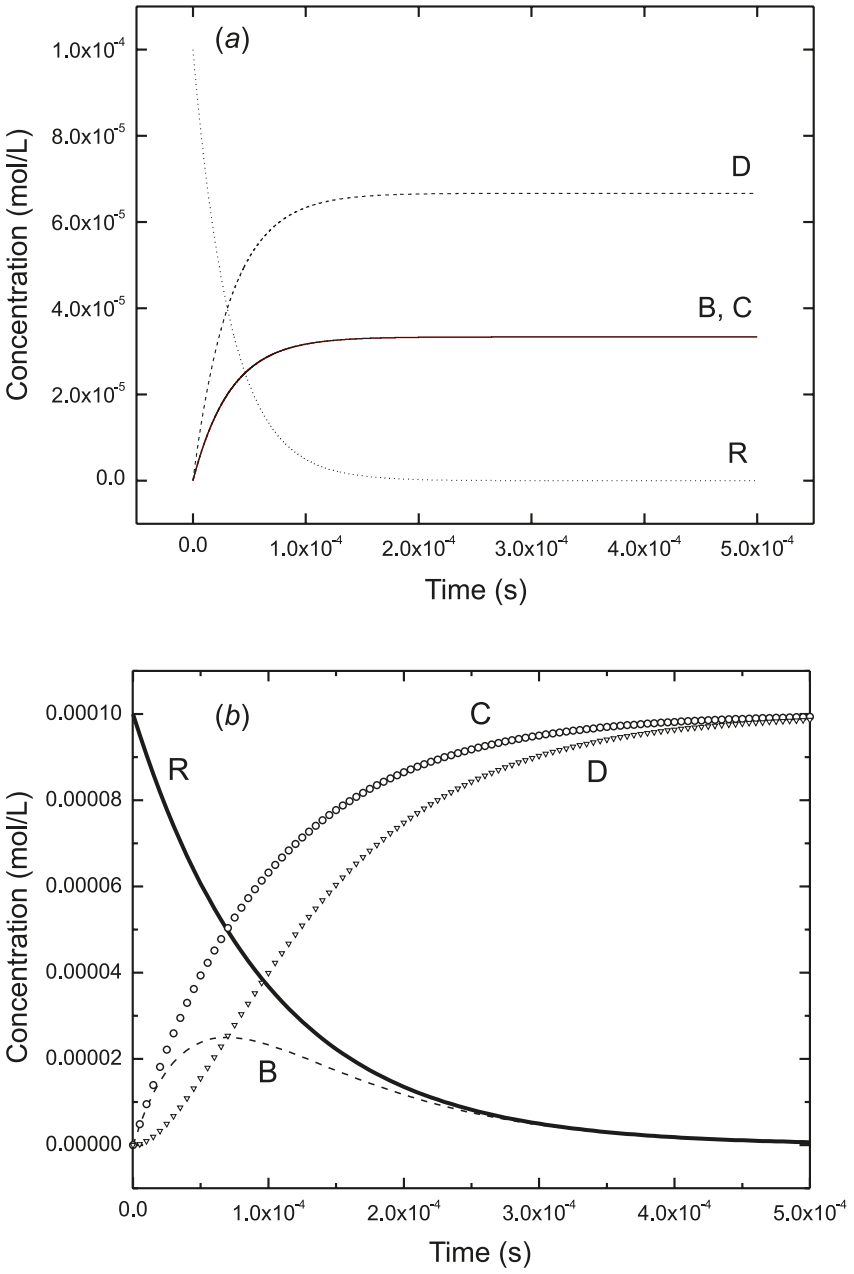

conditions close to the room temperature or below the boiling point of the usual solvents. However, if k_I/k_{II} depends on temperature, the numerical value of the quotient $(\varepsilon_R^{ip} - \varepsilon_D^{ip})/(\nu_B \varepsilon_B^{ip} + \varepsilon_C^{ip} - \varepsilon_R^{ip})$ will change such that a shift of the isosbestic points is expected. In the present example, the behaviour shown in Fig. 4 will not persist; the number and position of the isosbestic points will vary accordingly, leading to the temperature coefficient of the ratio of the rate constants involved.

In a similar way to that presented above, a mechanism of three parallel first-order reactions with at least four absorbing species will lead to $x_I/x_{II} = k_I/k_{II}$, $x_I/x_{III} = k_I/k_{III}$, and $x_{II}/x_{III} = k_{II}/k_{III}$, and more generally, for N parallel reactions, there are N^2 possible $x_i(t)/x_j(t)$ ratios from which $\sum_i i = N(N + 1)/2$ (14) are either unity (for $i = j$) or the inverse of another, namely, $(x_j(t)/x_i(t))$, such that $N(N + 1)/2$ linearly independent relationships $x_i/x_j = k_i/k_j$ with $i, j = 1, 2, 3, \ldots, N$ are obtained. However, the kinetic information becomes less available from the resulting relationships as the number of elementary steps increases.

Case II: consecutive reactions mechanism

On the contrary, a mechanism involving two first-order consecutive steps: (I) $R \rightarrow \nu_{BI}B + \nu_C C$ and (II′) $B \rightarrow \nu_D D$ will not lead to an isosbestic point at λ_{ip}. Should this be the case, then the condition

© 2008 NRC Canada

Fig. 3. Difference spectra as a function of the reaction time. (*a*) Parallel reactions from 0 (solid line) to 20 μs (···), 50 μs (– – –), 100 μs (–•–•–), and 200 μs (–·–·–). (*b*) Consecutive reactions from 0 (solid line) to 20 μs (– – –), 40 μs (·····) and 80 μs (–·–·–).

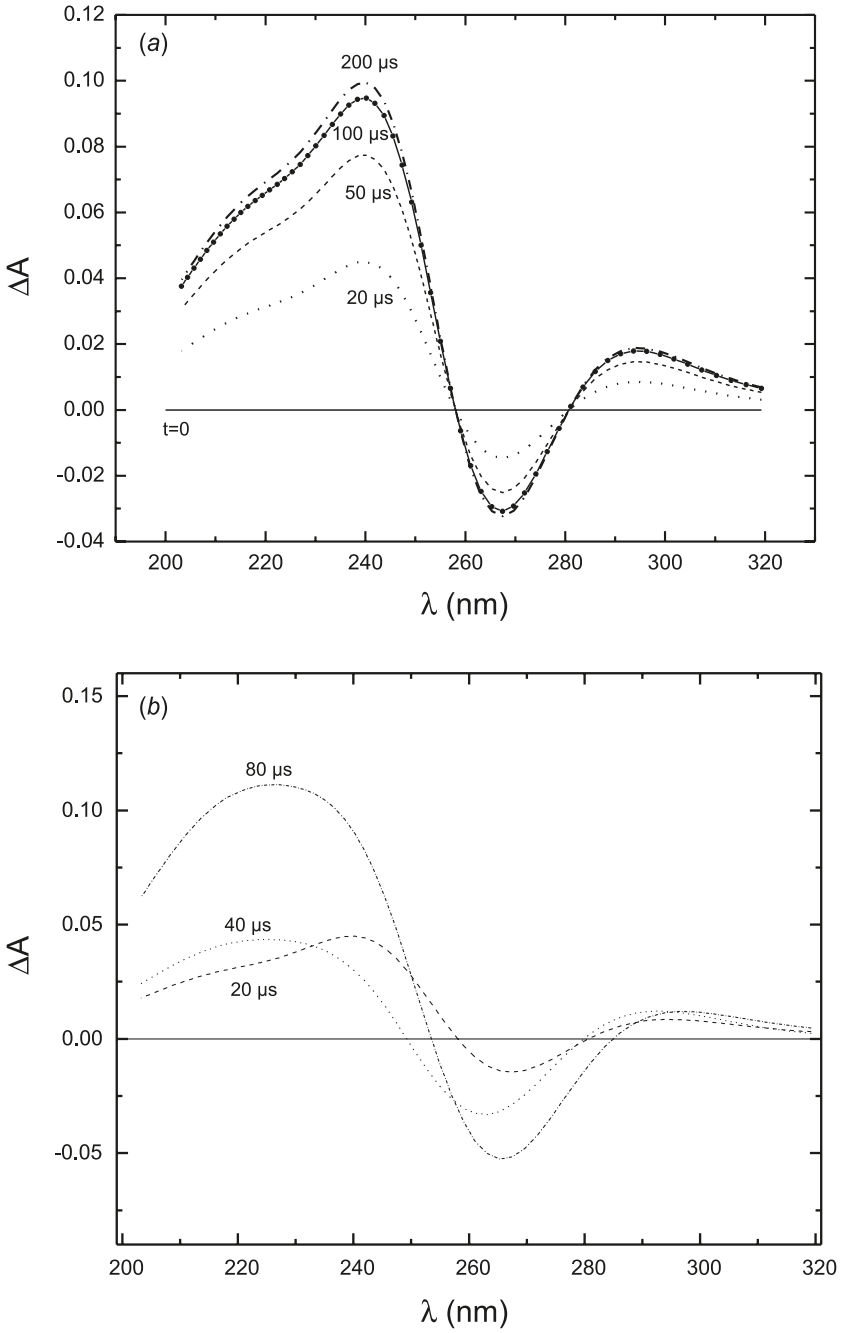

[14] $$\Delta A = x_I(\nu_{BI}\,\varepsilon_B^{ip} + \nu_C\,\varepsilon_C^{ip} - \varepsilon_R^{ip}) + x_{II}(\nu_D\,\varepsilon_D^{ip} - \varepsilon_B^{ip}) = 0$$

would imply

[15] $$x_I/x_{II} = (\varepsilon_B^{ip} - \nu_D\,\varepsilon_D^{ip})/(\nu_{BI}\,\varepsilon_B^{ip} + \nu_C\,\varepsilon_C^{ip} - \varepsilon_R^{ip})$$

namely, a time-independent $x_I/x_{II'}$ ratio.

Also in this case, the extent of reaction variables are $x_I > 0$ and $x_{II'} > 0$ for any reaction time, and the condition of eq. [14] will be fulfilled in the trivial case of $\varepsilon_B^{ip} = \nu_D\,\varepsilon_D^{ip}$ such that $\nu_{BI}\,\varepsilon_B^{ip} + \nu_C\,\varepsilon_C^{ip} - \varepsilon_R^{ip} = \nu_D\,\varepsilon_D^{ip} - \varepsilon_B^{ip}$, which does not lead to any kinetic information.

Equation [15] is analogous to eq. [11], which is yielded from the parallel reaction mechanism.

The mechanism (I) – (II′) is a particular case of (1): $Z \rightarrow \nu_{Y_i}\,Y_1$ for $(i + 1)$: $Y_i \rightarrow \nu_{Y_{i+1}}\,Y_{i+1}$, and for (N): $Y_{N-1} \rightarrow \nu_{YN}\,Y_N$.

If, for the sake of simplicity, $\nu_{Yi} = 1$ is assumed the concentrations are given by

[16] $$c_{Yi} = x_i - x_{i+1} \qquad (i = 1, 2, \ldots, N - 1)$$

which takes the form $c_{YN} = x_N$ for the last product, and $c_Z = c_{Z_0} - x_1$ for the reactant Z. The reaction rate equations in terms of the degree of advancement variables can be expressed as

© 2008 NRC Canada

Fig. 4. Dependence of x_1/x_2 on wavelength for the spectra of Fig. 1. The arrows point to wavelengths for which the ratio $k_I/k_{II} = 0.5$.

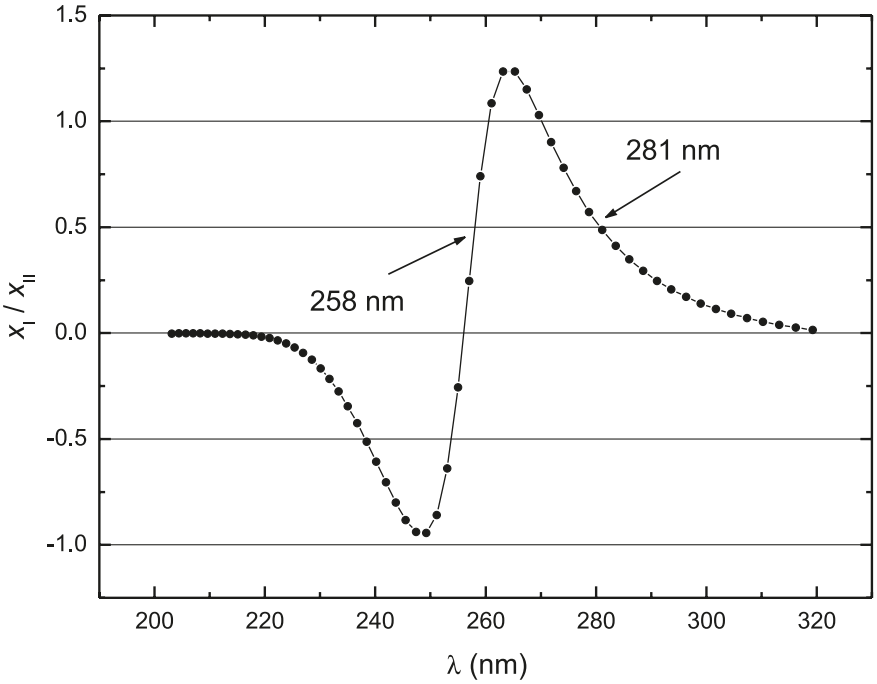

[17] $dx_1/dt = -k_1(c_{Z_0} - x_1)$

[18] $dx_i/dt - dx_{i+1}/dt = k_i(x_{i-1} - x_i) - k_{i+1}(x_i - x_{i+1})$

[19] $dx_N/dt = k_N(x_{N-1} - x_N)$

where all the variables have the same meanings as above.

In the case of the mechanism (I) – (II′), with $\nu_{BI} = \nu_C = \nu_D = 1$, these eqs. lead to solutions of the form

[20] $x_I = c_{R_0}[1 - \exp(-k_I t)]$

and

[21] $x_{II'} = [c_{R_0}/(k_{II'} - k_I)][k_I \exp(-k_{II'} t) - k_{II'} \exp(-k_I t)]$

In contrast to the parallel first-order reactions mechanism, in this case, a time-dependent $x_I/x_{II'}$ is obtained

[22] $x_I/x_{II} = [1/(k_{II'} - k_I)][1 - \exp(-k_I t)]/[k_I \exp(-k_{II'} t) - k_{II'} \exp(-k_I t)]$

Therefore, the first member in eq. [15] would be a function of time clearly contradicting the isosbestic point condition and the relationship $x_I(dx_{II'}/dt) = x_{II'}(dx_I/dt)$ will not hold. This result expresses that the presence of isosbestic points allows the rejection of a consecutive reactions mechanism.

Figure 3*b* shows the difference spectrum at three different reaction times for the mechanism of two consecutive first-order reactions involving the four absorbing species of Fig. 1, for $\nu_{BI} = \nu_C = \nu_D = 1$.

For more complex mechanisms, the occurrence of isosbestic points may not lead to kinetic information; the integration of the corresponding differential equations may not be available. However, the isosbestic-point condition (1) will always allow relating the degree of advancement of reaction variables, the stoichiometric coefficients, and the molar absorption coefficients of the participating species, in a similar way as eqs. [11] and [15] were obtained for two elementary reaction steps.

Conclusions

The detailed discussion given so far leads to general criteria based on the isosbestic point occurrence in difference spectra, which may be formulated as follows. Let a set of two or more species absorbing in a given wavelength range in which the spectra overlap. Let one of them participate as the reactant of two first-order reaction steps.

(*i*) Then, the occurrence of one or more isosbestic points in the time-resolved difference spectra allows the rejection of a consecutive reaction mechanism.

(*ii*) The wavelength of isosbestic points in the time-resolved difference spectra is determined by the ratio of the reaction rate coefficients.

A practical procedure may be outlined as follows. If the spectra of the reactant and products are known, x_I/x_{II} may be calculated using eq. [11] and a figure similar to Fig. 4 may be constructed. In the case of a parallel mechanism, the positive values of the ordinates correspond to the ratios k_I/k_{II}, which lead to isosbestic points. Then, if isosbestic points appear in the experimental ΔA vs. λ graphs, we conclude that the reactions are parallel. Moreover, the experimental λ_{ip} leads to k_I/k_{II}, or Φ_I/Φ_{II}.

Unfortunately for the laboratory worker, not all the absorption coefficients are known or even what the products are, but the occurrence of isosbestic points shows that parallel reactions mechanisms independent of the number of species involved are operating.

The course of the spectral changes observed in a recent study on the acid-catalyzed intramolecular attack of β-phenylthioureido group on amide function provides an illustration of the first conclusion given above (13). The kinetics

© 2008 NRC Canada

follows two mechanistically different stages, each involving three species with overlapping spectra. A system of pseudo first-order reactions A $\leftrightarrow$ B, A $\rightarrow$ C, and B $\rightarrow$ C operates, where A stands for *cis*-2-(3-phenylthioureido)cyclopentanecarboxiamide, B for 4-imino-2-thiooxopyrimidine, and C for *cis*-4-oxo-2-thiooxopyrimidine. Starting the reaction either from A or B, an equilibrium is established, while concomitantly A and B convert into C. In a first stage, e.g., starting from A, the kinetic system behaves as two parallel reactions of A into B and A into C, and isosbestic points are observed. When B accumulates, the isosbestic points are lost because a consecutive reactions mechanism is settled.

Acknowledgements

This research was supported by the Universidad Nacional de La Plata, the Consejo Nacional de Investigaciones Científicas y Técnicas (CONICET), the Agencia Nacional de Promoción Científica y Tecnológica (ANPCyT), and the Max Planck Institute for Biophysical Chemistry Goettingen through the "Partner Group for Chlorofluorocarbons in the Atmosphere". The author wishes to thank Professor I.G. Pojarlieff for providing a decisive test for one of the conclusions of this work.

References

1. J.W. Moore and R.G. Pearson. Kinetics and mechanism. 3rd Ed. John Wiley and Sons Inc. New York. 1981.
2. A.H. Thomas, G. Suárez, F. Cabrerizo, R. Martino, and A.L. Capparelli. J. Photochem. Photobiol. A: Chemistry, **135**, 147 (2000).
3. F. Pina, M.J. Melo, M. Maestri, R. Ballardini, and V. Balzani. J. Am. Chem. Soc. **119**, 5556 (1997).
4. IUPAC compendium of chemical terminology. 2nd Ed. 1997.
5. M.D. Cohen and E. Fisher. J. Chem. Soc. **1962**, 3044 (1962).
6. J.P. Cornard, L. Dangleterre, and C. Lapouge. Chem. Phys. Lett. **419**, 304 (2006).
7. Ch. Chylewski. Angew. Chem., Int. Ed. **10**, 195 (1979).
8. M.-F. Pouët, E. Baures, S. Vaillant, and O. Thomas. Appl. Spectrosc. **58,** 486 (2004).
9. B.S. Berlett, R.L. Levine, and E.R. Stadtman. Anal. Biochem. **287**, 329 (2000).
10. H. Mauser and G. Gauglitz. Photokinetics, theoretical fundamentals and applications. *In* Comprehensive chemical kinetics. *Edited by* R.G. Compton and G. Hancock. Elsevier, Amsterdam. 1998. Vol. 36.
11. Y. Han and L.H. Spangler. J. Phys. Chem. A, **106**, 1701 (2002).
12. C.N. Trumbore, C.T. Hyde, R.D. Hudson, L.A. Turman, A.G. Gehring, and J.K. Masselink. Int. J. Radiat. Biol. **56**, 923 (1989).
13. I.G. Pojarlieff, I.B. Blagoeva, M.M.Toteva, E. Atay, V.T. Angelova, N.G. Vassilev, and A.H. Koedjikov. J. Phys. Org. Chem. **21**, 14 (2008).
14. A.E. Croce. J. Chem. Ed. **79**, 506 (2002) and references cited therein.
15. I.S. Gradsteyn and I.M. Ryzhik. Table of integrals, series and products. 5th Ed. *Edited by* Alan Jeffrey. Academic Press Ltd. London, UK. 1994.
16. A.S.R. Koti and N. Periasamy. J. Chem. Phys. **115**, 7094 (2001).
17. D.C. Astholz, A.E. Croce, and J. Troe. J. Phys. Chem. **86**, 696 (1982).

© 2008 NRC Canada

Reactions of 6-aminouracils — A novel and highly efficient procedure for preparation of some new spiro pyridodipyrimidines under classical or microwave-assisted solvent-free conditions

Mohammad R. Mohammadizadeh, Javad Azizian, Fatemeh Teimouri, Ali A. Mohammadi, Ali R. Karimi, and Esmail Tamari

Abstract: A versatile and highly efficient procedure has been introduced for preparation of spiro pyridodipyrimidines during the investigation of the reaction of 1,3-dimethyl-6- aminouracil with isatin derivatives, ninhydrin, and acenaphthoquinone under classical or microwave-assisted solvent-free conditions.

Key words: isatin, ninhydrin, acenaphtoquinone, 1,3-dimethyl-6-aminouracil, solvent-free.

Résumé : Dans le cadre d'une étude de la réaction du 1,3-diméthyl-6-aminouracil avec des dérivés de l'isatine, la ninhydrine et l'acénaphtoquinone dans des conditions classiques ou des conditions sans solvant, assistées par des microondes, on a développé une méthode versatile et très efficace de préparation de spiropyridodipyrimidines.

Mots-clés : isatine, ninhydrine, acénaphtoquinone, 1,3-diméthyl-6-amino-uracile, sans solvant.

[Traduit par la Rédaction]

Introduction

Synthetic heterocycles have widespread interest as herbicides, insecticides, dyes, organic conductors, and drugs. Nitrogen-containing heterocycles are of broad synthetic and pharmaceutical interest. This fact justifies continuing efforts in the development of structure–activity relationships as well as new synthetic strategies in these series of compounds (1). There is an enormous interest in the synthesis of new heterocyclic rings, stimulated by recent reports showing anti-tumor activity in a wide range of polyheterocyclic compounds isolated from marine organisms (2). Compounds containing a fused pyrimidine ring have significant biological activities, particularly in cancer and virus research (3). Among these heterocycles, pyridopyrimidine derivatives are of particular importance in pharmaceutical discovery research. Several reports have been sited for the preparation of these fused heterocycles, claiming that these derivatives are useful as bronchodilators (4), vasodilators (5), anti-allergic (4, 6), anti-hypertensive (7), and anti-cancer (4) agents. Therefore, considerable efforts have been directed towards the synthetic manipulation of uracils for preparing these complex molecules. A number of reports have appeared in the literature that usually describe forcing conditions, long reaction times, and complex synthetic pathways (8). Considerable attention has been paid to the new simple and rapid routes for the synthesis of the heterocycles.

Recently, we have studied the reaction of 6-aminouracils with aromatic aldehydes (9). As a continuation of our previous report, in this work we investigate the reaction of 6-aminouracils with reactive cyclic ketones and introduce a novel and highly efficient method for preparation of some spiro pyridodipyrimidines.

Received 29 April 2008. Accepted 17 June 2008. Published on the NRC Research Press Web site at canjchem.nrc.ca on 12 August 2008.

M.R. Mohammadizadeh[1]. Department of Chemistry, Faculty of Sciences, Persian Gulf University, Bushehr 75 169, Iran.
J. Azizian and A.A. Mohammadi. Department of Chemistry, Faculty of Sciences, Shahid Beheshti University, P.O. Box 19 395–4 716, Tehran, Iran.
F. Teimouri. Department of Chemistry, Islamic Azad University, Saveh Branch, P.O. Box 39 187–366, Saveh, Iran.
A.R. Karimi. Department of Chemistry, Arak University, Arak 38156, Iran.
E. Tamari. Payame Noor University, Asadabad Center, Iran.

[1]Corresponding author (e-mail: mrmohamadizadeh@pgu.ac.ir).

Results and discussion

According to the hard–soft acid–base (HSAB) theory, first introduced by Pearson in 1963 (10, 11), and later developed by Mendez (12), softer nucleophiles react with softer centers, whereas harder nucleophiles preferably react with harder electrophiles (13). Some fundamental studies about this behaviour were performed by Klopman (14, 15).

From a literature survey, we found that 1,3-dimethyl-6-aminouracil **1** may show an ambident nucleophilic character (16, 17). It has two reactive centers (Fig. 1), which can interact with electrophiles: the NH_2 group (16) and C-5 position (17). Such centers can be classified according to the HSAB principle as the amino group, which is a harder nucleophile as a result of its smaller atomic size and its higher charge density and the C-5 carbon position, which is a softer

 doi:10.1139/V08-117 © 2008 NRC Canada

Fig. 1. Nucleophilic positions of 6-aminouracil **1** and its condensation product **2** with aromatic aldehydes.

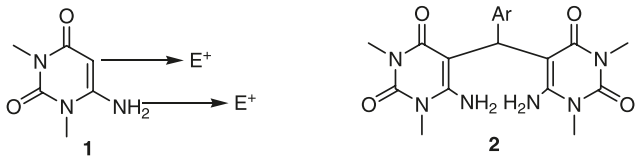

nucleophile because of its lower electronegativity and its higher atomic size.

In our previous investigation (9), we studied condensation reaction of 6-aminouracils and aromatic aldehydes, and consequently we reported a microwave-accelerated procedure for the synthesis of bis(6-aminopyrimidonyl)methanes **2** under solvent-free conditions. We found that 6-aminouracil attacked aldehydes from the C-5 position as a result of more favourable soft–soft interaction between C-5 and the carbonyl groups of aldehydes (Fig. 1). It is worth considering that the carbonyl groups of aldehydes are usually thought of as hard centers in comparison with relatively softer electrophilic centers (13, 15).

In this study, we choose isatin derivatives **3**, which supply more positive and hence harder carbonyl groups for condensation with 6-aminouracil **1**. It is found that 6-aminouracil **1** reacts with isatins **3** to give spiro pyridodipyrimidine derivatives **4** (Scheme 1). The reaction goes to completion at 80 °C in ethanol over 4–5 h, and the pure products were obtained in good yields by simple filtration of the reaction mixture (Table 1).

The possible mechanism for the formation of product **4** is shown in Scheme 2. It is conceivable that the initial event is the formation of iminium **5** from 6-aminouracil **1** and isatin **3**. Intermediate **6** is then produced by nucleophilic attack of another 6-aminouracil **2** to iminium **5**. Finally, cyclization is accomplished by nucleophilic attack of one 6-aminourcil moiety of intermediate **6** to other one to produce compound **4**.

The isolated spiro pyridodipyrimidines **4a**–**4d** were unambiguously characterized on the basis of IR, ^{1}H and ^{13}C NMR spectroscopy, mass spectrometry, and elemental analysis. The mass spectrum of **4a** displayed the molecular ion (M^+) peak at *m*/*z* 422, which is 17 mass units lower than **6**, the initial 1:2 adduct of isatin **3** and 6-aminouracil **1**, confirming elimination of an ammonia molecule. The IR spectrum of **4a** shows absorptions at 3436 and 3284 cm^{-1}, indicating the presence of N–H, and 1699 and 1645 cm^{-1} due to carbonyl of amide functionalities. The ^{1}H NMR spectrum of **4a** exhibited four sharp distinct singlets at δ = 2.97, 3.04, 3.36, and 3.43 ppm due to four methyl groups along with characteristic signals with appropriate chemical shifts for the four aromatic protons. Two relatively broad signals at δ 9.31 and 11.51 ppm were observed for the two N–H protons. In the ^{13}C NMR spectrum of **4a**, four methyl groups distinctly resonated at δ = 27.8, 28.3, 30.9, and 32.3 ppm, and the signal for spiro carbon was evident at δ = 51.7 ppm. These signals together with the other 15 separated signals all are in agreement with the proposed structure.

Two major differences are found between reaction of 6-aminouracil with aromatic aldehydes (9) and isatin derivatives: firstly, one molecule of 6-aminouracil regioselectively

Scheme 1. Synthesis of spiro pyridodipyrimidines.

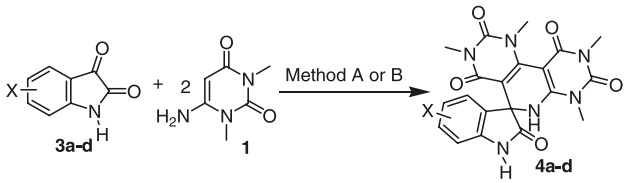

Method A: ethanol, 80 °C, 4–5 h; Method B: solvent-free, MW, 3 min.

Table 1. The yields of pyridodipyrimidines **4** under various conditions.

4	X	Time (h)[a]	Yield (%)[b]	Yield (%)[c]
a	H	4.3	70	90
b	5-Br	4.2	75	93
c	5-NO_2	4	65	88
d	5,7-diBr	4	77	90

[a]Time for reactions based on method A.
[b]Pure isolated yields of products **4** from method A.
[c]Pure isolated yields of products **4** from method B.

Scheme 2. Mechanistic representation for synthesis of spiro pyridodipyrimidines **4**.

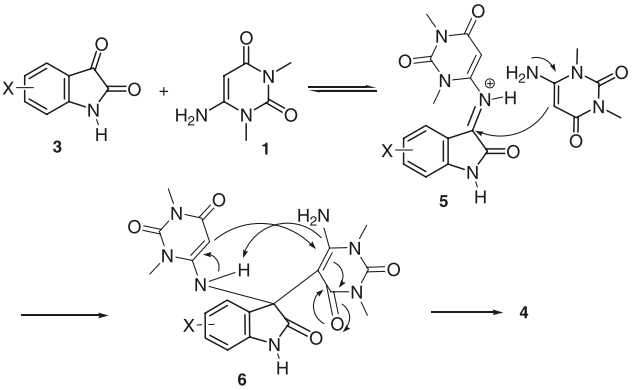

reacted from its NH_2 group, as a result of more favourable hard–hard interaction of the nitrogen and the highly positive carbonyl group; secondly, due to the lower torsional freedom of aminouracil moieties in intermediate **6** with respect to **2**, the C-5 positions get very close to each other and consequently the reaction goes ahead via the cyclization of intermediate **6** to produce the final product **4**.

Microwave-assisted organic synthesis is an increasingly popular field as indicated by numerous publications in the past few years owing to several advantages such as enhanced reaction rates and increase in yields under milder conditions (18). The combination of solvent-free reaction conditions and microwave irradiation leads to large reduction in reaction times, enhancement in conversion, and sometimes in selectivity with several advantages of the eco-friendly approach, termed green chemistry (19). In the context of our general interest in the use of microwave technology in synthetic organic reactions (20), we have also considered the microwave-assisted reaction of 6-aminouracils with cyclic dicarbonyls under solvent-free conditions (Scheme 1, method B). When a homogenous mixture of 6-amino-1,3-

© 2008 NRC Canada

dimethyluracil **1** and cyclic dicarbonyls **3**, **7**, or **9** was wetted with a few drops of dimethylsulfoxide (DMSO) and then irradiated in a microwave oven, the condensation reaction proceeds more efficiently, and it takes only 3 min to complete the reaction. We observed that yields were significantly increased, as can be easily seen from the results mentioned in Table 1.

To explore the synthetic utility of the process, we have investigated the reactivity pattern of 6-amino-1,3-dimethyluracil **1** with ninhydrin **7** in ethanol at reflux temperature as well as under microwave-assisted conditions in the solid state. This reaction was found to proceed in a smooth manner providing spiro pyridodipyrimidines **8** in good yield (Scheme 3). Ninhydrin is a relatively unstable, highly reactive compound, and adducts bearing ninhydrin moiety are prone to undergo rearrangement (21). Consequently, when the reaction was run under more vigorous microwave radiation, the yield of spiro pyridodipyrimidine **8** was lower than that of thermal condition. The structure of this product was confirmed from spectroscopic data and elemental analysis. The ^{1}H NMR spectrum showed the four characteristic signals at δ 3.00, 3.04, 3.20, and 3.28 for the methyl groups of pyrimidine rings.

In a similar way, treatment of 6-amino-1,3-dimethyluracil **1** with acenaphthoquinone **9** under classical or microwave-assisted solvent-free conditions afforded spiro pyridodipyrimidine **10** in good yields (Scheme 4).

However, under the same conditions, this reaction almost could not be observed when the phenanthrenedione **11** and naphthoquinone **12** were used as starting diketones (Scheme 5). This is probably due to the lesser reactivity of sp^2 carbons of six-membered rings with nucleophiles in comparison to five-membered rings (22).

Conclusion

A versatile and highly efficient procedure has been introduced for the preparation of some new spiro pyridodipyrimidines during the investigation of the reaction of 1,3-dimethyl-6-aminouracil with isatin derivatives, ninhydrin, and acenaphthoquinone under classical or microwave-assisted solvent-free conditions. Besides the extension of the chemistry of 6-aminouracils, this work is a further example of the utility of microwaves in organic synthesis.

Experimental section

Melting points were measured on an Electrothermal 9100 apparatus and are uncorrected. IR spectra were recorded as KBr pellets on on a Shimadzu FTIR-8300. ^{1}H NMR and ^{13}C NMR spectra were determined on a Bruker DRX-300 Avance instrument in $CDCl_3$ using TMS as internal standard. The reactions were carried out using CEM MARS 5™ microwave oven. Mass spectra were recorded on a Shimadzu GC MS-QP 1000 EX apparatus. The purity of the obtained spiro compounds was tested by the CHN analysis using a Heraus CHN rapid analyzer.

Scheme 3. Synthesis of spiro pyridodipyrimidine **8**.

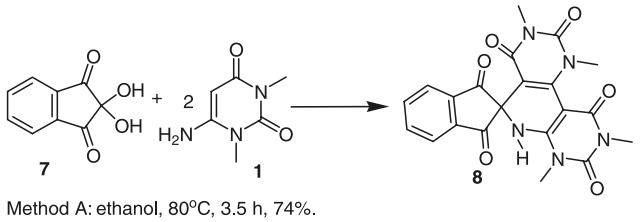

Method A: ethanol, 80°C, 3.5 h, 74%.
Method B: solvent-free, MW, 3 min, 60%.

Scheme 4. Synthesis of spiro pyridodipyrimidine **10**.

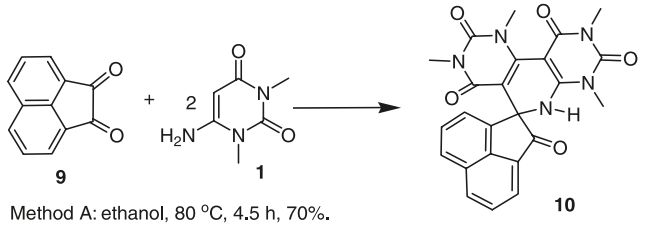

Method A: ethanol, 80 °C, 4.5 h, 70%.
Method B: solvent-free, MW, 3 min,78%.

Scheme 5. No condensation reaction was acquired between aminouracil **1** and cyclic diketones **11** and **12**.

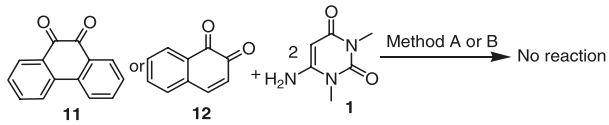

Representative procedure for the synthesis of spiro pyridodipyrimidines

Method A

A solution of the cyclic ketone **3**, **7**, or **9** (1 mmol) and 6-amino-1,3-dimethyluracil **1** (2 mmol) in ethanol (10 mL) was refluxed for an appropriate time (Table 1 and (or) Schemes 3 and 4). Completion of the reaction was evidenced by TLC analysis. The reaction mixture was cooled to room temperature, filtered, and solids washed with 10 mL of hot water. Recrystallization of products from a 1:1 mixture of ethanol/DMSO gave the pure products.

Method B

Appropriate amounts of cyclic ketone **3**, **7**, or **9** (1 mmol) and 6-amino-1,3-dimethyluracil **1** (2 mmol) were wetted with 2–3 drops of DMSO, mixed thoroughly, put in an open vessel, and exposed to microwave irradiation (CEM MARS 5™, 300 W) for 3 min in a three step mode with interval (1 min – 30 s – 1 min). Then, the reaction mixture was allowed to cool down, 20 mL water was added, and the resulting solid was filtered off, washed with 10 mL of hot water, and recrystallized from 1:1 mixture of ethanol/DMSO.

1,3,5,7-Tetramethyl-1*H,5H-*9,10-dihydro-spiro[pyrido[2,3-e:4,5-*d*]pyrimidine-9.3′-indoline]-2,2′,4,6,8-pentaone (4a)

White solid, mp > 300 °C. IR (KBr): 3436, 3284, 1699, 1645 Cm^{-1}. ^{1}H NMR (300 MHz, DMSO-d_6) δ: 2.97 (s, 3H, N–CH_3), 3.04 (s, 3H, N–CH_3), 3.36 (s, 3H, N–CH_3), 3.43 (s,

© 2008 NRC Canada

3H, N–CH_3), 6.97–7.23 (m, 4H, arom), 9.31 (br s, 1H, N–H), 11.51 (s, 1H, N–H). ^{13}C NMR (75 MHz, DMSO-d_6) δ: 27.8, 28.3, 30.9, 32.0, 51.7, 83.6, 98.2, 117.6, 121.8, 124.5, 127.0, 128.9, 146.8, 151.1, 153.0, 157.7, 160.6, 182.2. MS (EI, 70 eV) *m/z* (%) = 422 (M^+, 5), 420 (17), 378 (35), 268 (100). Anal. calcd. for $C_{20}H_{18}N_6O_5$ (422.13): C, 56.87; H, 4.30; N, 19.90. Found: C, 56.69; H, 4.18; N, 20.08.

1,3,5,7-Tetramethyl-1*H,5H-*9,10-dihydro-spiro[pyrido[2,3-e:4,5-d]pyrimidine-9.3′-5′-bromoindoline]-2,2′,4,6,8-pentaone (4b)

White solid, mp > 300 °C. IR (KBr): 3438 (br), 1695, 1645 cm^{-1}. ^{1}H NMR (300 MHz, DMSO-d_6) δ: 3.02 (s, 3H, N–CH_3), 3.08 (s, 3H, N–CH_3), 3.40 (s, 3H, N–CH_3), 3.49 (s, 3H, N–CH_3), 7.14 (br, 1H, arom), 7.25 (br m, 1H, arom), 7.38 (br m, 1H, arom), 9.48 (s, 1H, N–H), 11.60 (s, 1H, N–H). ^{13}C NMR (75 MHz, DMSO-d_6) δ: 27.9, 28.3, 31.0, 32.2, 51.5, 83.6, 97.7, 116.0, 119.8, 124.1, 129.4, 132.1, 136.0, 146.6, 151.1, 152.0, 153.2, 157.7, 160.6, 181.8. MS (EI, 70 eV) *m/z* (%) = 502 (27) $[M + 2)]^+$, 500 (24) $[M]^+$, 471 (73), 473 (72), 348 (98), 346 (100), 321 (22), 261 (27). Anal. calcd. for $C_{20}H_{17}BrN_6O_5$ (500.04): C, 47.92; H, 3.42; N, 16.76. Found: C, 47.79; H, 3.58; N, 16.89.

1,3,5,7-Tetramethyl-1*H,5H-*9,10-dihydro-spiro[pyrido[2,3-e:4,5-d]pyrimidine-9.3′-5′-nitroindoline]-2,2′,4,6,8-pentaone (4c)

White solid, mp > 300 °C. IR (KBr): 3417, 3282, 1706, 1641 cm^{-1}. ^{1}H NMR (300 MHz, DMSO-d_6) δ: 2.97 (s, 3H, N–CH_3), 3.07 (s, 3H, N–CH_3), 3.31 (s, 3H, N–CH_3), 3.38 (s, 3H, N–CH_3), 7.48 (s, 1H, arom), 7.71 (br, 1H, arom), 8.06 (br, 1H, arom), 9.96 (br s, 1H, NH), 11.77 (br s, 1H, NH). ^{13}C NMR (75 MHz, DMSO-d_6) δ: 27.9, 28.5, 31.3, 32.2, 51.4, 84.4, 98.2, 118.3, 122.6, 123.2, 125.0, 142.4, 143.8, 146.4, 150.9, 151.8, 153.1, 157.7, 160.6, 181.6. MS (EI, 70 eV) *m/z* (%) = 467 (3) $[M^+]$, 78 (69), 45(100). Anal. calcd. for $C_{20}H_{17}N_7O_7$ (467.12): C, 51.39; H, 3.67; N, 20.98. Found: C, 51.21; H, 3.80; N, 19.96.

1,3,5,7-Tetramethyl-1*H,5H-*9,10-dihydro-spiro[pyrido[2,3-e:4,5-d]pyrimidine-9.3′-5′,7′-dibromoindoline]-2,2′,4,6,8-pentaone (4d)

White solid, mp > 300 °C. IR (KBr): 3382, 3249, 1696, 1646 cm^{-1}. ^{1}H NMR (300 MHz, DMSO-d_6) δ: 3.01 (s, 3H, N–CH_3), 3.06 (s, 3H, N–CH_3), 3.53 (s, 3H, N–CH_3), 3.55 (s, 3H, N–CH_3), 7.22 (s, 1H, arom), 7.82 (s, 1H, arom), 9.52 (s, 1H, NH), 11.75 (s, 1H, NH). ^{13}C NMR (75 MHz, DMSO-d_6) δ: 27.9, 28.4, 30.5, 32.2, 51.9, 85.9, 97.26, 113.1, 116.4, 126.6, 1293, 134.1, 134.6, 147.0, 151.1, 151.9, 153.6, 157.7, 160.5, 181.2. Anal. calcd. for $C_{20}H_{16}Br_2N_6O_5$ (580.19): C, 41.40; H, 2.78; N, 14.49. Found: C, 51.26; H, 3.79; N, 21.17.

1,3,5,7-Tetramethyl-1*H,5H-*9,10-dihydro-spiro[pyrido[2,3-e:4,5-d]pyrimidine-9.2′-indene]-1′,2,3′,4,6,8-hexaone (8)

White solid, mp > 300 °C. IR (KBr): 3320, 1710, 1699, 1655 cm^{-1}. ^{1}H NMR (300 MHz, DMSO-d_6) δ: 3.00 (s, 3H, N–CH_3), 3.04 (s, 3H, N–CH_3), 3.20 (s, 3H, N–CH_3), 3.28 (s, 3H, N–CH_3), 7.01–7.87 (m, 4H, arom), 9.93 (s, 1H, NH). ^{13}C NMR (75 MHz, DMSO-d_6) δ: 28.1, 28.7, 30.7, 32.0, 99.2, 104.4, 109.4, 115.4, 141.8, 145.8, 147.9, 156.4, 156.6, 163.6, 166.5, 176.1, 192.5. MS (EI, 70 eV): *m/z* (%) = 435 (25) $[M]^+$, 434 (100), 378 (23). Anal. calcd. for $C_{21}H_{17}N_5O_6$ (435.39): C, 57.93; H, 3.94; N, 16.09. Found: C, 57.81; H, 3.95; N, 16.20.

1,3,5,7-Tetramethyl-1*H,2′H,5H-*9,10-dihydro-spiro[pyrido[2,3-e:4,5-d]pyrimidine-9.1′-acenaphthylene]-2,2′,4,6,8-pentaone (10)

White solid, mp > 300 °C. IR (KBr): 3320, 1711, 1692, 1642 cm^{-1}. ^{1}H NMR (300 MHz, DMSO-d_6) δ: 3.15 (s, 3H, N–CH_3), 3.17 (s, 3H, N–CH_3), 3.20 (s, 3H, N–CH_3), 3.22 (s, 3H, N–CH_3), 7.47 (m, 2H, arom), 7.65 (m, 2H, arom), 7.76 (m, 1H, arom), 8.31 (s, 1H, arom), 9.03 (s, 1H, NH). MS (EI, 70 eV): *m/z* (%) = 457 (37) $[M^+]$, 456 (100). Anal. calcd. for $C_{24}H_{19}N_5O_5$ (457.44): C, 63.02; H, 4.19; N, 15.31. Found: C, 62.93; H, 4.06; N, 15.39.

Acknowledgment

Financial support by the research council of Persian Gulf University is gratefully acknowledged.

References

1. R.J. Ife, T.H. Brown, P. Blurton, D.J. Keeling, C.A. Leach, M.L. Meeson, and M.E. Parsons. J. Med. Chem. **38**, 2763 (1995).
2. (*a*) M.L. Bourguet-Kondracki, M.T. Martin, and M. Guyot. Tetrahedron Lett. **37**, 3457 (1996); (*b*) M. Kobayashi, Y-J Chen, S. Aoki, Y. In, T. Ishida, and I. Kitagawa, Tetrahedron, **51**, 3727 (1995); (*c*) K.L. Rinehart, J. Kobayashi, G.C. Harbour, J. Gilmore, M. Mascal, T.G. Holt, L.S. Shield, and F. Lafargue. J. Am. Chem. Soc. **109**, 3378 (1987); (*d*) Y. Take, Y. Inouye, S. Nakamura, H.S. Allaudeen, and A.J. Kubo. Antibiot. **42**, 107 (1989); (*e*) S.E. Kane. Adv. Drug Res. **28**, 181 (1996).
3. (*a*) A.S. Jones, J.R. Sayers, R.T. Walker, and E.J. De Clercq. J. Med. Chem. **31**, 268 (1988); (*b*) H. Griengl, E. Wanek, W. Schwarz, W. Streicher, B. Rosenwirth, and E. De Clercq. J. Med. Chem. **30**, 1199 (1987); (*c*) E. De Clercq and R. Bernaerts. J. Biol. Chem. **262**, 14905 (1987); (*d*) M. Baba, R. Pauwels, P. Herdewijn, De E. Clercq, J. Desmyter, and M. Vandeputte. Biochem. Biophys. Res. Commun. **142**, 128 (1987); (*e*) E. De Clercq. J. Med. Chem. **29**, 1561 (1986); (*f*) E. De Clercq. Anticancer Res. **6**, 549 (1986).
4. (*a*) W.J. Coates. Eur. Patent 351-058. 1990; (*b*) Chem. Abstr. **113**, 40711 (1990); (*c*) A.A. Ramsey. US Patent 3-830-812. 1974; (*d*) Chem. Abstr. **81**, 136174 (1974).
5. (*a*) E.C. Taylor, R.J. Knop, R.F. Meyer, A. Holmes, and M.L. Hoefle. J. Am. Chem. Soc. **82**, 5711 (1960); (*b*) J.D. Figueroa-Villar, C.L. Carneiro, and E.R. Cruz. Heterocycles, **34**, 891 (1992).
6. N. Kitamura and A. Onishi. Eur. Pat. 163-599. 1984; (*b*) Chem. Abstr. **104**, 186 439 (1984).
7. (*a*) P. Raddatz and R. Bergmann. Ger. Patent 360-731. 1988; (*b*) Chem. Abstr. **109**, 54786 (1988).
8. (*a*) K. Singh, J. Sing, and H. Singh. Tetrahedron, **54**, 935 (1998); (*b*) D. Prajapati and A.J. Thakur. Tetrahedron Lett. **46**, 1433 (2005); (*c*) I. Devi, B.S.D. Kumar, and P.J. Bhuyan. Tetrahedron Lett. **44**, 8307 (2003); (*d*) D. Prajapati, M. Gohaina, and A. Thakur. J. Bioorg. Med. Chem. Lett. **16**, 3537 (2006).
9. J. Azizian, M.R. Mohammadizadeh, F. Teimouri, A.A. Mohammadi, and A.R. Karimi. Synth. Commun. **36**, 3631 (2006).
10. R.G. Pearson. J. Am. Chem. Soc. **85**, 3533 (1963).

© 2008 NRC Canada

11. R.G. Pearson and J. Songstad. J. Am. Chem. Soc. **89**, 1827 (1967).
12. J.L. Gazquez and F.J.J. Mendez. Phys. Chem. **98**, 4049 (1994).
13. H. Tse-Lok. Chem. Rev. **75**, 1 (1975).
14. G. Klopman. Chemical reactivity and reaction paths. John Wiley and Sons. New York. 1974.
15. G. Klopman. J. Am. Chem. Soc. **90**, 223 (1968).
16. (*a*) D. Prajapatia and A. J. Thakur. Tetrahedron Lett. **46**, 1433 (2005); (*b*) J.L. Shim, R. Niess, and A.D. Broom. J. Org. Chem. **37**, 578 (1972); (*c*) D. Prajapati, M. Gohaina, and A. Thakur. Bioorg. Med. Chem. Lett. **16**, 3537 (2006).
17. (*a*) I. Devi, B.S.D. Kumar, and P.J. Bhuyan. Tetrahedron Lett. **44**, 8307 (2003); (*b*) D.M. Volochnyuk, A.N. Kostyuk, A.M. Pinchuk, and A.A. Tolmachev. Tetrahedron Lett. **44**, 391 (2003); (*c*) S. Kumar, V. Kumar and S.S. Chimni. Tetrahedron Lett. **44**, 2110 (2003).
18. (*a*) L. Perreux and A. Loupy. Tetrahedron, **57**, 9199 (2001); (*b*) S. Caddick. Tetrahedron, **51**, 10403 (1995).
19. R.S. Varma. Green Chem. **1**, 43 (1999).
20. (*a*) J. Azizian, A.R. Karimi, Z. Kazemizadeh, A.A. Mohammadi, and M.R. Mohammadizadeh. Tetrahedron Lett. 46, 6155 (2005); (*b*) J. Azizian, A.R. Karimi, and A.A. Mohammadi. Synth. Commun. **33**, 415 (2003); (*c*) J. Azizian, A.R. Karimi, Z. Kazemizadeh, A.A. Mohammadi, and M.R. Mohammadizadeh. J. Org. Chem. **70**, 1471 (2005).
21. (*a*) D.B. Hansen and M.M. Joullié. Chem. Soc. Rev. **34**, 2005 (408); (*b*) D.J. McCaldin. Chem. Rev. **60**, 391(960).
22. (*a*) J.E. Dubois, M. El-Alaoui, and J. Toullec. J. Am. Chem. Soc. **103**, 5393 (1980); (*b*) Y. Zhu, G. Chuah, and S. Jaenicke. J. Catal. **227**, 1 (2004); (*c*) G. I. Nikishin and G.V. Somov. Russ. Chem. Bull. **14**, 845 (1965).

© 2008 NRC Canada

AWARD LECTURE / CONFÉRENCE D'HONNEUR

Inside the black box — Perspectives on transformations in catalysis

Deryn E. Fogg

Abstract: Tandem catalysis and olefin metathesis are powerful tools in the development of sustainable synthetic practices. This Award Lecture describes our advances in designing new tandem metathesis-hydrogenation methodologies for the synthesis of "designer materials" and Ru-pseudohalide metathesis catalysts that amplify opportunities for tuning catalyst activity, selectivity, and lifetime. Also discussed is the operation of a previously unrecognized oligomerization-backbiting pathway in ring-closing metathesis of conformationally flexible α,ω-dienes, which has important implications for the sustainable synthesis of medium and large rings.

Key words: tandem catalysis, green chemistry, olefin metathesis, ring-closing metathesis, mechanism.

Résumé : La catalyse en tandem et la métathèse d'oléfines sont de puissants outils dans le développement de pratiques synthétiques renouvelables. Dans cette présentation on décrit les développements réalisés dans nos laboratoires dans la conception de nouvelles méthodologies de tandems catalyse/métathèse qui permettent d'obtenir des produits ciblés ainsi que des catalyseurs de métathèse à base de ruthénium et d'un pseudohalogène qui amplifient les opportunités d'ajustement de l'activité, de la sélectivité et du temps de vie du catalyseur. On discute aussi de l'opération d'une voie réactionnelle antérieurement inconnue d'oligomérisation "par transfert de chaîne interne" dans la métathèse de la fermeture de cycle de α,ω-diènes conformationnellement flexibles qui présente d'importantes implications pour la synthèse renouvelable de cycles de tailles moyennes ou grandes.

Mots-clés : catalyse en tandem, chimie verte, métathèse d'oléfine, métathèse de fermeture de cycle, mécanisme.

[Traduit par la Rédaction]

Introduction

Efficiency is a central challenge in chemical synthesis. It is also a central concept in "green chemistry" initiatives directed at development of environmentally more benign chemical practices, grounded in appropriate stewardship of chemical resources. Green chemistry advocates, in part, the efficient conversion of molecular precursors into products via convergent, atom–economic transformations that minimize energy consumption and production of waste (1). Despite committed industrial interest (2), these principles have made slow headway in fine chemicals and pharmaceutical synthesis, where lower production volumes and the value-added nature of the products have historically shielded manufacturing inefficiencies. Pharmaceutical synthesis, still heavily reliant on stoichiometric technologies and batch processes, is characterized by particularly high environmental "*E* factors" (25–100 vs. <1–5 for bulk chemicals synthesis), where *E* = kg of waste per kg of product (1). Increased pressure on profits, stemming from a decline in new drug approvals and exacerbated by the withdrawal of blockbuster drugs, is now bringing the economics of efficiency into sharper focus.

Selective catalysis offers important opportunities to reduce both waste and energy consumption. (While energy expenditures impose less stringent demands in fine chemicals and pharmaceutical synthesis than the commodity sector, the industry is nevertheless vulnerable to spiralling energy costs). Catalysis is especially valuable where coupled with convergent methods of assembly, which reduce total process stages and time, while improving yields and diversity. Olefin metathesis, as an exceptionally powerful method for the convergent assembly of C=C bonds, offers major opportunities in the "greening" of the chemical industry (1), as indeed noted by the Swedish Academy in awarding the 2005 Nobel Prize to Chauvin, Schrock, and Grubbs. Process rationalization is likewise under scrutiny. Coupled, one-pot synthetic procedures are increasingly important as a way of minimizing work-up demands: their efficiencies are further enhanced for coupled catalytic reactions, and this drives the tremendous interest in tandem catalysis.

Our research centers on the design of new catalysts and methodologies for the efficient construction of organic molecules and specialty polymer materials, with a particular fo-

Received 13 April 2008. Accepted 21 May 2008. Published in the NRC Research Press Web site at canjchem.nrc.ca on 3 September 2008.

D.E. Fogg. Department of Chemistry, and Center for Catalysis Research and Innovation, University of Ottawa, 10 Marie Curie, Ottawa ON K1N 6N5, Canada. (e-mail: dfogg@uottawa.ca).

 doi:10.1139/V08-103 © 2008 NRC Canada

cus on olefin metathesis and tandem catalysis. This article summarizes our progress in these areas. Realization of their full potential rests on a detailed understanding of the underlying inorganic chemistry. We recently described simple adaptations of MALDI-TOF mass spectrometry that create a powerful tool for insight into the identity, speciation, and reactions of transition metal complexes (3). Anaerobic charge-transfer MALDI-MS is highly complementary with electrospray mass spectrometry (4). Of particular value is its capacity to aid in the identification of charged, neutral and even insoluble complexes. A detailed discussion of this topic, however, is deferred for reasons of space.

Discussion

Tandem catalysis

One-pot reactions are of compelling interest in development of sustainable synthetic practices, owing to the significant process efficiencies that result from eliminating unnecessary work-up stages, as noted above (1*c*, 5). Minimizing solvent wastes is a key aspect of this efficiency. Increasingly recognized as a critical issue in fine chemicals and pharmaceutical manufacturing, inefficient solvent use is a major contributor to high *E* factors and process costs (1*c*). The scale of the problem is highlighted by a recent GSK estimate that puts solvents at 85%–90% of the total mass of chemicals used in pharmaceutical manufacturing (6). Tandem catalysis, an important subclass of one-pot reactions, combines the advantages inherent in such processes with reduced catalyst and purification costs. In its most powerful form, tandem catalysis exploits the tremendous catalytic versatility of certain transition metals. The central idea is very simple: where two sequential catalytic steps are required to elaborate a substrate, catalyst consumption and product purification can be minimized if the catalyst used in the first reaction can also promote the second.

Most users of homogenous catalysis have probably been struck by the similarity sometimes evident between catalysts that enable widely different transformations. In the extreme, a single versatile catalyst can promote sequential elaboration of a substrate through multiple, distinct reaction types (Fig. 1*a*). We have termed such processes "spontaneous" or "auto-tandem" catalysis (7). A classic example in industrial use was the formation of long-chain alcohols as a key sequence in the Shell oxo process: here the $HCo(CO)_3(P^nBu_3)$ catalyst promoted both hydroformylation of α-olefins and subsequent hydrogenation of the aldehyde products (8). More commonly, the active site must be modified using a trigger that toggles the catalyst from one chemical manifold to another (Fig. 1*b*, "assisted tandem" catalysis). Either of these processes enables multistep, one-pot elaboration of substrates via sequential, distinct catalytic operations, using a single catalyst precursor, without intermediate work-up. Advantages and limitations of each are inherent in the concurrent (autotandem) or consecutive (assisted tandem) nature of the macroscopic processes. Autotandem catalysis, for example, is attractive for its "walk-away" efficiency: reactions can be set up and left to evolve, because the product from one catalytic cycle automatically enters as substrate into a second. However, the demand for orthogonality between the two processes is often incompletely met. This means, in part, that the substrate for either process may be consumed in the other, undermining product selectivity. As well, because both reaction types proceed concurrently, it is not possible to independently optimize reaction conditions for each, and elimination of incompatible species can be challenging.

Fig. 1. Schematic illustrations of (*a*) spontaneous (autotandem) catalysis and (*b*) assisted tandem catalysis.

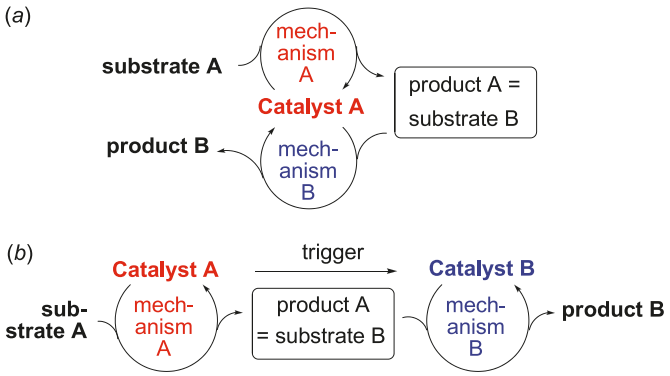

While incompatibility between species that are concurrently present must likewise be addressed in assisted tandem catalysis, greater control results from the temporal segregation of different catalytic processes. Because the second transformation cannot occur until the trigger is added, each process can be independently optimized. Such strategies form part of an emerging paradigm in homogeneous catalysis (7, 9). The startlingly high number of Ru-based processes is in part due to the exceptional catalytic scope (10) of this metal, as well as its relatively low cost, Ru historically trading at 1/20 to 1/30 of the price of Rh (11). Much attention has focused on metathesis-hydrogenation, particularly in the context of materials design (7, 12–14). Tandem processes of ring-opening metathesis polymerization (ROMP) and hydrogenation offer major opportunities, as noted below. However, the macromolecular nature of the hydrogenation substrates presents greater technical challenges than hydrogenation of small molecules. Advances in this area are therefore of added interest for their relevance to ring-closing metathesis (RCM)-hydrogenation and cross-metathesis (CM)-hydrogenation (15–18).

ROMP is one of the most powerful methods now in use for the molecular-level design of macromolecular materials (19). Despite its versatility, a limitation lies in the vulnerability of unsaturated sites in the polymer backbone to thermal or photochemical cross-linking and oxidative degradation (20, 21), which compromise the control over chain lengths that represents a core advantage of ROMP materials. Reduction of ROMP polymers has thus received much attention as a potentially straightforward route to functionalized polyolefins (7, 9), a long-standing goal in Ziegler–Natta catalysis, with enormous implications for materials design. Efficient access of the metal to these sterically encumbered olefinic sites necessitates use of homogeneous catalysis, ideally, in terms of process costs and efficiency, tandem catalysis. The opportunity crystallized with Grubbs' 1995 report of **1** (Chart 1), the first readily accessible, highly active ruthenium catalyst for olefin metathesis (22).

I was then a postdoc with Dick Schrock, designing quantum dot-ROMP polymer composites for device applications

© 2008 NRC Canada

Chart 1. Selected examples of Mo (Schrock-class) and Ru (Grubbs-class) metathesis catalysts.

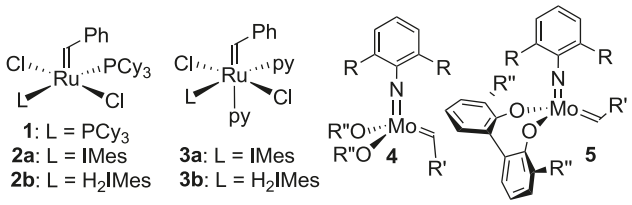

(using strictly group 6 catalysts in the ROMP chemistry!). Device fabrication is a demanding test for polymer materials, and this experience gave me a greater familiarity than I necessarily desired with cross-linking issues. The limitations of then-current, forcing, diimide and heterogeneous reduction methods were becoming evident (23, 24), while the potential opportunities of homogeneous hydrogenation methods (25) were familiar to me from my Ph.D. background with Brian James. The structural resemblance between the new Grubbs catalyst and known Ru hydrogenation catalysts (five-coordinate, square pyramidal complexes with an apical, high-trans-influence active site) led me to wonder about the possibility of transforming the metathesis-active ruthenium alkylidenes into hydrogenation-active ruthenium hydrides (Scheme 1). The concepts of tandem catalysis shown in Fig. 1 were then incompletely formulated (and the term "sustainable chemistry" was itself newly coined), but this struck me as a potentially elegant and economical solution to the problem of hydrogenating ROMP polymers, and it formed the basis for one of the research proposals with which I interviewed for faculty positions.

In the event, my first year at Ottawa saw the seminal report by McLain, Brookhart, and co-workers of precisely such a procedure, in which cyclooctene monomers were transformed into functionalized polyolefins via sequential processes of Ru-catalyzed ROMP, then hydrogenation (12*a*). However, the conditions were forcing (135 °C, 400 psi of H_2, 1 psi = 6.894 757 kPa), the high temperatures being of particular concern because of the risk that thermally induced cross-linking could compete with hydrogenation (20, 21). We took a different approach to the problem, focusing on clarifying the nature of the transformation in the belief that this could aid in designing a more efficient process. In a mechanistic study of the first-generation Grubbs catalyst **1** (26), we showed that the key step is H_2 hydrogenolysis of the [Ru]=CHR functionality to liberate alkane and the Ru(IV) dihydride **6**, which exists in equilibrium with its dihydrogen tautomer **7** (Scheme 2). The more reactive, and more robust, hydridochloro catalyst **8** was obtained by adding base to abstract a chloride ligand, this enabling reduction of cyclooctene-based ROMP polymers at 60 °C and 100 psi H_2 (13, 27). (Of great interest in this connection is subsequent work by the Schmidt group, in which post-metathesis addition of NaH enabled hydrogenation of cyclopentenols at ambient temperature and under 14.6 psi (1 atm, 1 atm = 101.325 kPa) H_2 (17, 18). While the difference in substrates precludes direct comparison, the strikingly mild conditions point toward greater efficiency in the **1**–**8** transformation; i.e. a high concentration of the hydrogenation-active species.)

Another advance, however, resulted in a yet more active catalyst. In the course of patenting this methodology, we en-

Scheme 1.

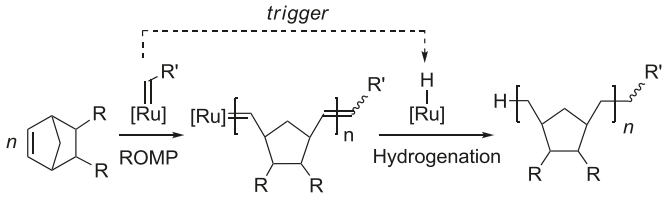

Scheme 2. One-pot procedure for transformation of Ru alkylidenes (e.g., **1**) into hydrogenation-active Ru hydride catalysts by use of appropriate triggers (H_2, base, MeOH).

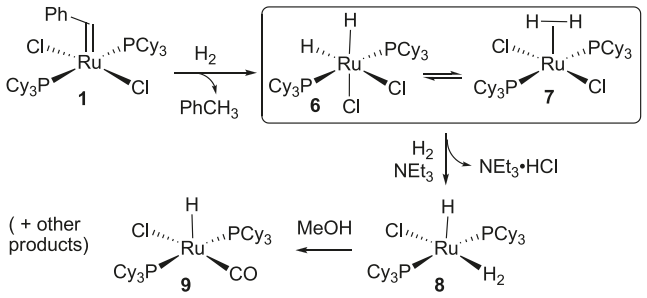

countered at a late stage a "submarine" patent (i.e., one that emerged from examination days before we were to file), which described synthesis of saturated ROMP polymers, albeit without base and in an "inert solvent", at pressures as low as 2 atm of H_2 (28). This drove us to try a number of less obvious potential improvements to reduce the pressure limit, the most successful of which we subsequently described (13, 27) as the "unorthodox expedient" of adding methanol as a co-solvent in the hydrogenation step. We were inspired to do so by scattered literature precedents that suggested curious effects of alcohols on hydrogenation rates, sometimes detrimental but sometimes beneficial (29). The unorthodoxy lies in the fact that organic polymers are rarely methanol-soluble; indeed, methanol is typically added to precipitate such polymers from solution. As well, though this had not been established at the time, the Grubbs catalysts do not tolerate alcohols well (see later). Indeed, methanol is much more inimical to Ru ROMP than has been generally recognized, particularly in terms of control over chain lengths: decomposition of the metathesis-active metal endgroup competes with chain growth unless the monomer is very highly reactive (30). In view of these hazards, we took a cautious approach, adding methanol only once ROMP was complete and only at levels that maintained polymer solubility during and following reduction. Despite the relatively low proportion of MeOH (maximum 20% in CH_2Cl_2), a dramatic increase in hydrogenation activity resulted, which allowed us to reduce the pressure of H_2 to as little as 1 atm for polyoctene hydrogenation (13,27).

Under these modified conditions, we described partial conversion of the Ru species present into the known, potent (20, 31) hydrogenation catalyst **9**. While the activating effect of the CO ligand in **9** was well-established, many will find this difficult to reconcile with its *deactivating* effect in hydrogenation via arylphosphine complexes of Ru, Rh, and Ir (25), and with the much higher hydrogenation activity of electron-rich alkylphosphine catalysts, vs. their arylphos-

© 2008 NRC Canada

phine analogues (32), which suggests the importance of an electron-rich metal centre. While potential explanations come to mind, the uncertainty of the origin of the activating effect continued to trouble us, and we recently undertook a collaborative computational study of model $RuHCl(L)(P^iPr)_2$ systems (L = CO (33), PH_3) with Tom Woo's group at Ottawa. Consistent with our original chemical intuition, the energetic pathway for ethylene hydrogenation was systematically higher for the π-acid CO system, vs. the σ-donor PH_3 complex (34). We suspect that the outstanding performance of **9**, despite these higher barriers, indicates superior productivity rather than superior activity. Indeed, ongoing experimental studies of **8** and **9** (aided by an improved synthesis of **9** (35)) suggest that the basis for the enhanced activity of the latter may be its longer lifetime. The very strong binding of the carbonyl ligand may thus be important chiefly for its non-lability and its capacity to stabilize the catalyst, leading to higher total productivity.

Also important for the efficiency of hydrogenation, as noted above, is the efficiency with which **1** or its derivatives undergo conversion into **9**. The procedure in Scheme 2 effects ca. 60% conversion of **1** into **8** and **9** (ratio 2:1), among other unidentified products. Subsequent to this study, the Mol and Grubbs groups showed that transformation of first- and second-generation Grubbs catalysts into the corresponding hydridocarbonyl complexes (among other products) can be effected by reaction with alcohols alone, i.e., in the absence of added H_2 or base (36–38). Dinger and Mol showed that the proportion of **9** could be increased to 70% by use of *n*-propanol and NEt_3 base (36). Given that our experimental protocol involves, for simplicity, near-simultaneous addition of H_2, NEt_3, and methanol, followed by heating to 60 °C, it is highly probable that conversion to **9** involves both Ru-alkylidene and Ru-hydride precursors, i.e., methanolysis, as well as hydrogenolysis. Other reagents, including vinyloxytrimethylsilane and ethyl vinyl ether, also trigger the alkylidene-hydridocarbonyl transformation (39, 40). In related work, the Cossy group recently utilized silanes as triggers to turn on hydrogenation activity (41). We are presently assessing the relative efficiency of these methods and variants on the Schmidt protocol (17, 18), under controlled conditions, to determine whether we can improve performance further. Beyond metathesis-hydrogenation, this would advance our efforts in developing other tandem catalysis procedures, now under exploration, that exploit the remarkable catalytic versatility of **9** (35).

Our methodology, though a breakthrough in terms of materials design, has some important limitations. A major one is the fact that it can only be applied to monomers that are efficiently polymerized by the first-generation Grubbs initiator **1**. Our appreciation for this problem was driven home by a collaboration with researchers at the Ottawa Eye Institute, directed at the development of an innervated, cell-based artificial cornea (42). In this work, we sought to cross-link a jelly-like collagen matrix with carbohydrate-functionalized ROMP polymers, to develop strong, flexible, and biocompatible corneal transplants with the porosity required for cell in-growth (43). The galactose groups are designed to enable controlled cross-linking of the lysine residues in the collagen fibrils, while also ensuring biocompatibility (galactose groups being native to the collagenous stroma of the cornea (44)). The problem lies in the bulk of the monomers, which impedes ROMP. Two galactose groups are required on each norbornene repeat unit to confer water-solubility on the reduced polymers, and their bulk is further increased by the carbohydrate protecting groups. ROMP of the unprotected monomers, while nominally attractive, is ruled out on the basis of the very poor control over polymer chain lengths characteristic of ROMP of sterically encumbered norbornenes in aqueous (or, worse, methanolic) media (30).

Scheme 3.

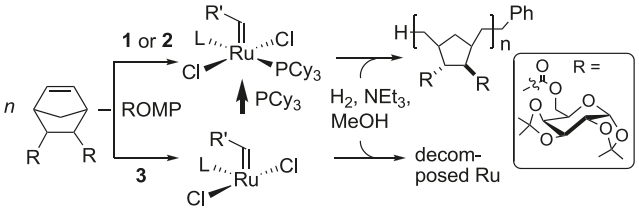

Such bulky 5,6-disubstituted norbornene monomers are polymerized very slowly by **1** (days (14)). While ROMP is rapid using second- or third-generation Grubbs catalysts containing an activating NHC ligand (Chart 1, e.g., **2**, **3**; NHC = *N*-heterocyclic carbene), this levies an unacceptable price: for **2**, control over polymer chain lengths (19); for **3**, activity in the hydrogenation step. In short, none of the existing metathesis catalysts offers all three features — high ROMP activity, controlled polymerization, and high hydrogenation activity — essential to transform sterically demanding monomers into saturated polymers with well-defined chain lengths. However, the problem of instability that limits **3** seems much more readily addressed than the problems of low activity or poor initiation efficiency that plague **1** and **2**, and we therefore turned our attention to devising ways to stabilize the polymer-bound Ru center derived from **3**. The high stability of **2** vs. **3**, clearly a function of the PCy_3 ligand present in the former, afforded a powerful clue. Our ultimate solution is represented in Scheme 3. Here, use of **3** as ROMP initiator affords well-defined polymer chains with excellent control over the chain lengths. Addition of PCy_3 once ROMP is complete effectively transforms the Ru endgroup on the polymer into that generated from **2** itself. This stabilizes the Ru complex under conditions of hydrogenolysis and hydrogenation, restoring hydrogenation activity to the level found with **2a** as initiator. We were thus able to retain the ROMP activity and precision of the third-generation catalyst **3**, without sacrificing the hydrogenation efficiency of the more robust initiator **2** (14).

The approach summarized in Scheme 3 answers a pressing need in materials design, reconciling the requirement for high reactivity in demanding ROMP and hydrogenation reactions, with that for precise control over polymer chain lengths. It is thus likely to find widespread application in the burgeoning area of ROMP-based "designer materials" (19). It also represents an expansion of our perspective on tandem catalysis, beyond manipulation of the active site, to consideration of the ligand architecture and properties best suited to meeting the demands unique to each stage of catalysis, including those of robustness and lifetime. Beyond hydrogenation, this approach holds promise for improving catalyst

© 2008 NRC Canada

efficiency in tandem metathesis-functionalization reactions, emerging applications of which include RCM-oxidation (45, 46) and RCM-cyclopropanation (47, 48) methodologies.

Catalyst design in Ru-promoted olefin metathesis

A second major theme in our research program centers on the design of robust, stereoselective, and tunable catalysts for olefin metathesis. When we began this work in 1997, the power of olefin metathesis in materials chemistry was well-established, but its applications in synthetic organic chemistry were just beginning to take off. This balance has now reversed (49). The tremendous expansion in uptake of metathesis methodologies in organic synthesis was due largely to the advent of robust, easily handled (and commercially available) ruthenium catalysts, of which the first- and second-generation Grubbs catalysts **1** and **2** remain most prominent. The Schrock Mo catalysts of type **4** and **5**, while superior in terms of their exquisite selectivity, ease of tuning, and very high reactivity (as well as a brilliantly conceived ligand architecture, which maximizes tunability while inhibiting bimolecular decomposition), have been less popular with organic chemists because of their thermal instability and their high sensitivity to traces of air or water, and protic or aldehydic functional groups.

Persuaded of the opportunities of the Ru catalysts (including the remarkable catalytic versatility of this metal noted above, with the attendant opportunities in tandem catalysis), but with a keen appreciation for the elegance and design strengths of the Schrock catalysts, we embarked on a program directed at integrating the best features of both. At the time, and indeed until very recently, the overwhelming focus in design of new Ru metathesis catalysts was on improving reactivity, largely by modification of the neutral, L-donor ligands on **1** and later in its second-generation derivative **2**. Following the unexpected finding that the lability of the phosphine ligand in **2** is *lower* than that in the less active complex **1** (50), an intensive, global effort focused on synthesis of derivatives of **2** containing a donor more labile than PCy_3. Examples include Grubbs' pyridine derivatives **3** (51), Grela's and Blechert's modified "Hoveyda"-type catalysts **10**, containing a sterically or electronically weakened ether chelate (52, 53), and, in the extreme, Piers' remarkable four-coordinate phosphonium alkylidene **11** (54) (Chart 2).

While this concerted effort resulted in impressive increases in metathesis activity, it also highlighted the fundamental limitations in catalyst lifetime already established for **1** and **2** (55). Within these catalysts, higher metathesis reactivity is offset by accelerated catalyst decomposition, because metathesis and deactivation proceed via the same 14-electron intermediate, $RuCl_2(NHC)(=CHR)$ **12**. This intermediate is identical to that formed from **2** itself; despite the structural diversity of the precatalysts, therefore, common decomposition routes (as well as selectivity) can be anticipated (56).[1] Concurrent work in our group was connecting the problems of lifetime and selectivity as common design issues. We were struck by the high catalyst loadings required in RCM and CM reactions, especially given that robustness

Chart 2.

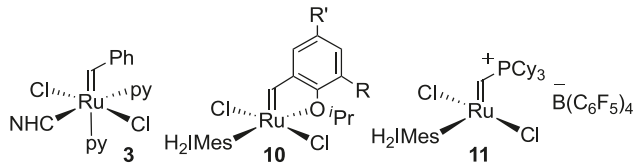

was widely regarded as one of the major assets of the Ru systems. For many industrial applications, prohibitively high catalyst costs could be anticipated from the low catalyst productivity (at that time, routinely 5-20 turnovers). In pursuing a design solution, we began by seeking insight into the nature of the problem. In 2002, we described a chloride-mediated decomposition pathway implicated in the short lifetimes of Grubbs-type alkylidene catalysts (58, 59). Triply chloride bridged diruthenium species result from bimolecular coupling of the alkylidene complexes, consistent with the kinetics data earlier reported (55). Decomposition of the methylidene complexes, in contrast, appears to be unimolecular, though a later report proposed a bimolecular, chloride-mediated deactivation pathway for methylidene species as well (60). The contribution of each pathway to overall catalyst lifetime depends on the extent of initiation and thus on the catalyst, the substrate, and the reaction conditions.

The ability of the chloride ligands to participate in catalyst deactivation is compounded by the isotropic nature of these donor groups, which offers little aid in steric definition of the active site. The potential to modulate not only catalyst lifetime, but tunability and selectivity, we viewed as a powerful case for exploring "pseudohalide" catalysts. While the role of the neutral donor ligands in Ru-catalyzed olefin metathesis has received much attention, as noted above, the role and optimum properties of the anionic ligands have been examined in much less detail. We analyzed the design limitations that have resulted in low activity for the majority of Ru-pseudohalide complexes studied (19, 56). These can be summed up as: (*i*) excessive steric crowding, which hinders the approach of substrate, (*ii*) the absence of a labile neutral ("placeholder") ligand, which impedes substrate binding, or (*iii*) the absence of a strong, activating donor (such as an alkylphosphine or NHC group) among the ligands present in the active catalyst. It was clear that none of these limitations is inherent, and that highly active $RuX_2LL'(CHR)$ catalysts might be accessible if the appropriate anionic ligands could be identified. We sought pseudohalide ligands that could be readily tuned for selectivity, solubility, etc., and that confer minimal inessential three-dimensional bulk. Aryloxide ligands derived from phenols satisfy both criteria.

An initial challenge in installing aryloxide ligands within our target environments was the ease with which the aryloxide ligand undergoes $\sigma \rightarrow \pi$ isomerization in coordinatively unsaturated or labile Ru complexes. Despite the strength of the Ru–OAr bond (61), the reservoir of electron density in the aryloxide ring, in conjunction with the accessibility of three coordination sites on the metal, enables

[1] "Boomerang" strategies involving recapture of the active species may extend the lifetime of the *precatalyst*, replenishing the reservoir for regeneration of the active catalyst. The efficiency of this approach is determined by the relative rates of both recapture and release. Rates of recapture by bulky or electron-deficient styrene ethers may be low in Ru systems (57).

© 2008 NRC Canada

Scheme 4.

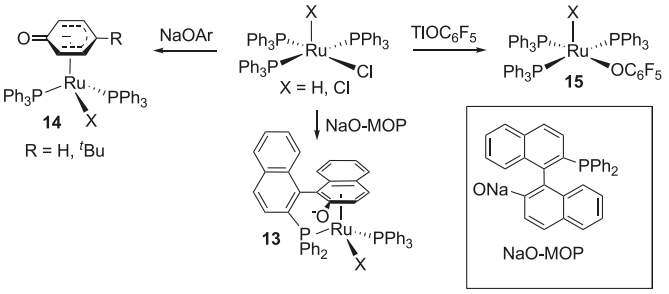

rapid isomerization to piano-stool complexes (62, 63). Model studies with $RuHCl(PPh_3)_3$ showed this behaviour for both monodentate aryloxides and for aryloxides that form seven-membered chelate rings (Scheme 4, see **13** and **14**).

In these model studies, use of an electron-deficient monodentate aryloxide enabled us to curb isomerization; see **15** (64, 65). Alternatively, smaller, more rigid chelates can be used (66). We have now developed a large family of pseudohalide catalysts, of which three important examples are shown in Scheme 5. These complexes are prepared from **3**, the essentially two-dimensional nature of the pyridine and NHC ligands removing the steric driving force for α-elimination (67), which otherwise culminates in Ru-alkylidyne products (64, 68). Use of thallium aryloxides was dictated by the instability of **3** over the timescale required for reaction with the alkali metal salts.

Perfluoroaryloxide catalyst **17**, the first highly active Ru-pseudohalide metathesis catalyst, effects RCM of the benchmark substrate diethyldiallyl malonate **S1** at loadings 10^4 times lower than those conventionally employed (64). Lower overall productivity (maximum TON 21 000), but dramatically increased activity, was found for perbromophenoxide derivative **18**, in which one chloride ligand is retained (a function of the increased aryloxide bulk). Catalyst **18** exhibits particularly high efficiency in RCM and enyne metathesis (Fig. 2).

The range of activity within the pseudohalide catalysts is important in enabling tuning of catalyst reactivity to match the demands of the reaction under study. In ROM–CM reactions of norbornenes such as **S8**, for example, excessive catalyst reactivity leads only to ROMP, and the lower reactivity of **17** is critical to achieving the desired selectivity. In other cases, high activity is essential; in recent work, not yet published, we have been able to achieve efficient RCM of enyne substrates (e.g., **S7**) to yield challenging tetrasubstituted olefins. Tuning of reactivity, of steric demands, and of electronic properties is particularly important for developing versatile methodologies for asymmetric catalysis. The amplified "tunability" of these pseudohalide catalysts is clearly an asset in this regard, complementing the many advances in development of chiral NHC ligands in recent years (70). Building on these advances, we have now incorporated chiral NHC ligands into the aryloxide catalysts and are presently exploring their utility in asymmetric metathesis.

Perhaps most significant in the currently established metathesis behaviour of the Ru-aryloxide catalysts, however, is their performance in RCM synthesis of medium and macrocyclic rings. Detailed examination of this behaviour, and comparison with the Grubbs systems, revealed unexpected insights into the mechanism by which such conformationally unbiased substrates undergo metathesis (71).

Scheme 5. Highly active Ru-pseudohalide metathesis catalysts. Initiation efficiency can be increased further by the use of 3-bromopyridine in place of pyridine (69).

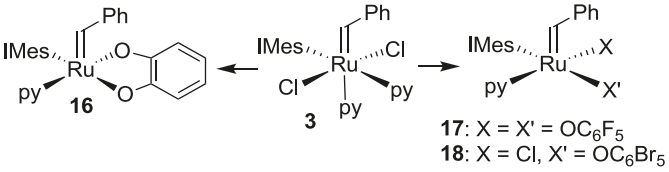

Fig. 2. Activity and (bottom) tunable selectivity in RCM of representative substrates by aryloxide catalysts; yields quantitative unless otherwise indicated.

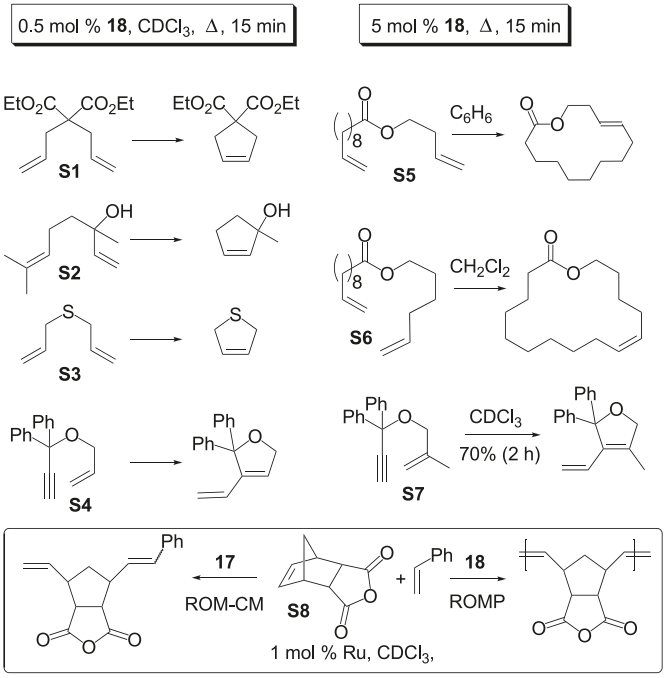

RCM assembly of five- and six-membered rings from unhindered α,ω-dienes is typically straightforward, presuming a conventionally competent catalyst and barring electronic deactivation or poisoning effects. The low ring strain, high probability of chain-end encounter, and high translational entropy of these small molecules combine to favour intramolecular RCM over intermolecular oligomerization, even in the absence of any additional conformational constraints. Construction of larger rings, while of compelling interest (72, 73), is more challenging. The challenge originates in competing oligomerization, as indeed noted in Villemin's original report of macrocycle RCM, which described successful cyclization at 6 mmol/L but polymerization at 15 mmol/L (74).

High dilutions have long been used to create a kinetic bias toward intramolecular cyclization of bifunctional molecules in irreversible, stoichiometric reactions (75). In context of metathesis, concentration effects remain important for the thermodynamic reasons discussed below, but the kinetic effects are less straightforward because the initial reaction be-

© 2008 NRC Canada

Scheme 6. Standard view of competing cyclization and oligomerization manifolds in metathesis.

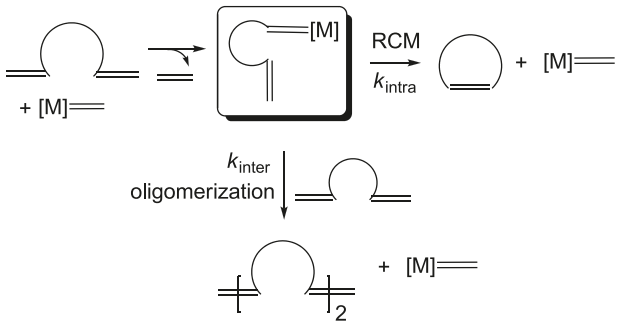

tween substrate and catalyst is necessarily bimolecular (Scheme 6). Elevated temperatures or prolonged reaction times are generally required to compensate for the unfavourable effect of dilution on the rate of this initial reaction (76), but higher catalyst decomposition rates under such conditions can limit yields. Adding both substrate and catalyst dropwise can aid in minimizing oligomerization while inhibiting catalyst decomposition. Surprisingly, this protocol — common in "early" RCM reactions involving **1** — is now little used. In RCM reactions involving **2**, for example, solutions of substrate and catalyst are typically subjected to thermolysis at some arbitrarily high dilution, and further doses of catalyst are added when reaction appears to have stalled. The limitations of this approach will become clear shortly.

In applying the dropwise addition protocol to RCM assembly of conformationally unbiased large and medium-sized rings (initially in macrolactonization studies), we were struck by the high efficiency of RCM via **18**, relative to second- and third-generation Grubbs catalysts. Closer examination of this behaviour uncovered an unexpected pathway for cyclization (Scheme 7 (71)).

While **18** effects quantitative macrolactonization of dienes such as **S6** within 15 minutes (Figs. 2 and 3*a*), the major species produced by **2** or **3** at the same stage are the oligomers, despite net dilutions much lower than 5 mmol/L. Importantly, however, cyclization is near-quantitative if the reaction is allowed to evolve (9 h for **2**; 1 h for **3**). Ethenolysis of the oligomers cannot contribute to this convergence on the lactone products beyond the initial stages of reaction, given the low solubility of ethylene in organic solvents (77) and the effectiveness of its removal under normal conditions of metathesis, as applied here (open vessel, reflux, N_2 or Ar atmosphere). In the absence of ethylene, liberation of cyclic products can only occur by backbiting RCM (BRCM), in an intramolecular metathesis step directly analogous to that required for direct RCM.

These observations have several important implications. First, observation of oligomers under the high-dilution conditions designed to minimize their formation indicates that the chloride catalysts **2** and **3** have a strong kinetic bias toward intermolecular reaction (i.e, in the context presented in Scheme 6, $k_{inter} >> k_{intra}$). Secondly, the fact that the oligomers convert directly into the RCM product rather than through back-reaction with ethylene indicates that these species are not inimical to RCM, as has been generally as-

Scheme 7. Oligomerization-backbiting mechanism for RCM (71). Ethylene-evolving reactions shown as irreversible. Only dimeric oligomers shown; larger oligomers form similarly. Backbiting RCM (BRCM) at a remote olefinic site can liberate cyclodimers and (or) cyclooligomers.

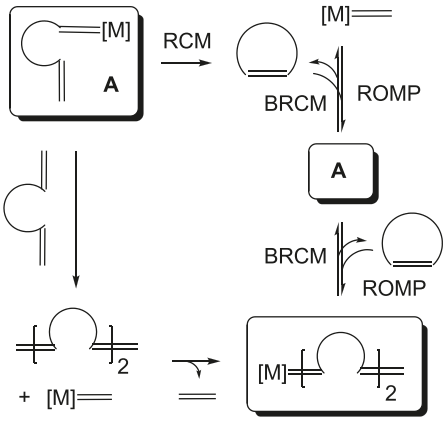

Fig. 3. RCM of **S6** via (*a*) **18** and (*b*) **2**. Dashed lines: disappearance of **S6**; solid lines: appearance of product; dotted lines: oligomers. Conditions: dropwise addition of both **S6** and Ru catalyst; [**S6**] « 5 mmol/L.

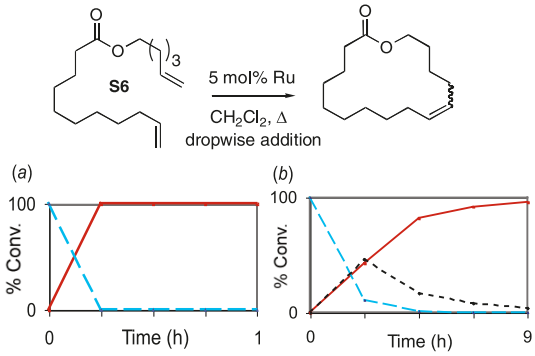

sumed. Rather than being the hallmark of a failed reaction, the oligomers are in fact precursors to the desired RCM target. This underscores the importance of understanding the factors that favour backbiting and hence liberation of the RCM products.

As it happens, these factors are already well understood. Formation and disappearance of oligomers occurs via a polymerization–cyclodepolymerization mechanism long recognized in ROMP chemistry (78), though little considered in context of RCM. Once diene consumption is complete and the methylidene endgroup is installed, we are dealing with a classic ring-chain equilibrium, shown in simplified form in eqn. [1].

Unless catalyst deactivation arrests the process, RCM yields are determined by the relevant equilibrium constant. The concentration-dependence of K_{eq} for such equilibria is also well-established: Jacobson–Stockmayer theory states that oligomeric–polymeric chains are favoured at high concentration and that cyclics are favoured at high dilution (79). By manipulating concentration, therefore, the ring-chain equilibrium can be biased in favour of either cyclic or polymeric products. Dilution is also the key to product selectiv-

© 2008 NRC Canada

[1] 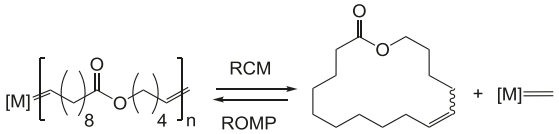

ity, i.e., liberation of the smallest cyclic species (the RCM targets) in preference to cyclooligomers resulting from backbiting at a remote site. The formation of progressively smaller cyclic species is favoured with increasing dilution because the higher translational entropy of the smaller molecules is expressed more strongly as viscosity decreases.

Consistent with this analysis, we observe oligomers as the dominant species at high concentrations (100 mmol/L diene) and the target macrocycles at high dilutions (≤5 mmol/L). At intermediate concentrations, mixtures are obtained. Product distributions can thus be reliably manipulated by altering the concentration, providing that catalyst deactivation does not interfere. Figure 4 shows an example: metathesis of **S9** via **3** at 5 mmol/L results in a 50:50 distribution of oligomer and RCM product at equilibrium (3 h), all diene having been completely consumed. Dosing with fresh **3** at this point does not increase the RCM yield, indicating that the system is indeed at equilibrium. If instead we simply dilute, the yield of RCM product increases to 96%.

In synthesis of medium-sized rings, the thermodynamics of cyclization are adversely affected by the presence of higher ring strain (i.e., increased enthalpic costs) and the smaller difference in translational entropy between cyclomonomer and cyclodimer, cyclotrimer, etc. (i.e., reduced entropic discrimination). Higher dilutions are therefore necessary. Effective molarity (EM) values are useful in predicting the probability of cyclization and the relative dilutions required.[2] Mandolini and Illuminati and co-workers have tabulated values for a range of compounds, including saturated lactones of up to 30 members, as well as catechol and malonate derivatives (80, 81). EM values of 20-30 mmol/L for the saturated macrolactones (14–20 membered rings) compare with values of over 10^6 for the five-membered malonate, vs. ca. 0.6 mmol/L for eight-membered hexalactone (80). We examined RCM of diene substrates roughly corresponding to these saturated species, for which the EM values span six orders of magnitude. As expected, a very wide range of concentrations is required to favour RCM: malonate **S1** can be cyclized at 100 mmol/L, vs. 5 mmol/L for macrolactone **S6**, and 0.5 mmol/L for the unsaturated seven- and ten-membered lactones. The corresponding eight-membered lactone is not formed even at concentrations below 0.5 mmol/L. Formation of such strained products is inhibited not merely by the kinetic and thermodynamic bias toward lower-strain cyclodimers but also by the slow rate of metathesis at very high dilutions, which enables competing catalyst decomposition. Even for those ring sizes that can be attained in good yields, the solvent costs associated with dilution become increasingly untenable (particularly for industrial applications) as the effective molarity of the substrate declines.

Fig. 4. RCM of **S9** using catalyst **3**. (*a*) Equilibrium yield at 3 h, (*b*) RCM yield following addition of fresh **3** and re-equilibrating, and (*c*) RCM yield following dilution and re-equilibration. Initial conditions: CH_2Cl_2, reflux, 5 mmol/L substrate (batchwise addition), 5 mol% Ru.

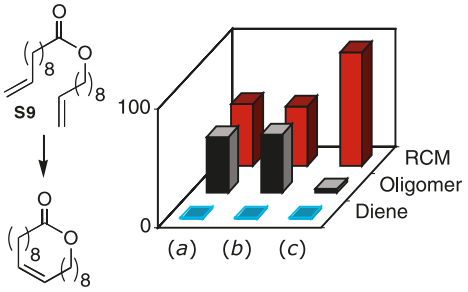

These issues notwithstanding, the insights above are important in revising our understanding of the "problem" of competing oligomerization in challenging RCM reactions. Oligomers have overwhelmingly been regarded as inimical, rather than intrinsic to formation of ring-closed products. This is evidently a false premise. The experiments with **2** and related catalysts outlined above show that under dilutions compatible with efficient metathesis, the dominant route to conformationally flexible RCM products is a concentration-dependent oligomerization–backbiting pathway. An important implication is that some of the "failed" RCM reactions reported in the literature may be less difficult than they initially appeared. Frequently, researchers respond to the observation of oligomerization by abandoning the reaction, or in some cases, adding more catalyst. The former course of action amounts to discarding an essential, valuable intermediate, the latter, to discarding the catalyst itself. Adding further catalyst cannot improve RCM yields if the reaction is not at an appropriately high dilution.

The foregoing offers some practical guidelines for maximizing BRCM, and hence RCM yields, for reactions in which oligomerization is recognized. An important issue, which we defer to a later paper, is how oligomerization is detected. NMR analysis is often misleading, GC or LC quantification require compilation of calibration curves for sometimes precious starting materials and products, while GC does not reveal the oligomers, and LC can be time-consuming. Also of interest is the strong bias of the aryloxide catalysts toward RCM, as shown for **18** vs. **3** in Fig. 4*b*. It is as yet unclear whether this reflects faster backbiting, or an intrinsic bias toward intramolecular reaction. A thermodynamic influence of the catalyst can be anticipated from its participation in the ring-chain equilibrium (that is, the thermodynamic EM value in RCM is not due to the diene alone, but is a function of the substrate-catalyst pair). The RCM bias of **18** we initially rationalized in terms of the

[2] Most reported EM data are the kinetic (EM_k) values, rather than the thermodynamic (EM_K) values of most relevance in the present, equilibrium systems. As the two tend to track together, the EM_k trend is nonetheless often useful, though discrepancies emerge for 7- and 10-membered lactones (80). Definitions: EM_k = the concentration at which $k_{intra}/k_{inter} = 1$ (where k_{intra} and k_{inter} are the rate constants for the intramolecular and intermolecular reactions, respectively). Likewise, $EM_K = K_{intra}/K_{inter}$. It should be noted that reported values typically refer to saturated ring structures formed from bifunctional substrates and do not take into account the effect of the metal endgroup on ring strain.

© 2008 NRC Canada

steric influence of the aryloxide ligand vs. chloride, which we envisaged as inducing buckling of the pendant oligomer chain. We have now abandoned this hypothesis, as the sterically restrained catecholate catalysts likewise exhibit a kinetic preference for RCM. The effect is therefore clearly electronic, and we are now undertaking a computational exploration of the factors involved. More generally, the unexpected discovery of this "back-door" route to RCM products brings out a new element of selectivity. We had originally conceived of our catalyst design approach as a way of modulating stereoselectivity, in particular *E/Z* ratios, and ultimately asymmetric induction. While these studies continue with chiral catalysts now in hand, their scope has expanded to include the consequences for selectivity of driving the reaction manifold through direct RCM, vs. the oligomerization-backbiting pathway. Finally, the convergence of the Grubbs-class catalysts on the $RuCl_2(L)(=CHR)$ intermediate (e.g. **12**, L = NHC) underscores the importance of utilizing the anionic sites, as well as the neutral L-donor ligand, to expand the tunability and diversity of catalyst structures. This will undoubtedly lead to new advances in selectivity and EM modulation, and to further improvements in catalyst lifetime.

Summary

Development of sustainable chemical practices is a collective effort, requiring the talents and expertise of a diverse scientific, technical, and business community. Homogeneous catalytic methodologies have much to contribute to this enterprise. In the overview above, I hope to have shown how a largely inorganic perspective on tandem catalysis and olefin metathesis — two technologies of keen relevance to green chemistry initiatives — has helped to expand the scope of these methodologies and to open up new areas of opportunity.

Acknowledgements

I thank the Inorganic Division of the CSC for this award recognizing early career achievement, and Mike Strem and Strem Chemicals for their generosity in funding it. I am grateful to Natural Sciences and Engineering Research Council of Canada (NSERC) for Discovery, Strategic, and Accelerator grants, to the Canada Foundation for Innovation (CFI), and Ontario Innovation Trust (OIT) for enabling infrastructure, and the Ontario government for a Premier's Research Excellence Award. Ottawa provided me with a wonderfully stimulating environment to establish my research program. In particular, I thank Tito Scaiano, Howard Alper, David Bishop, and Christian Detellier for their friendship and the example they set in a multitude of contexts; Dr. Glenn Facey of our NMR Facility for his unfailing expertise and humour; and Dr. Sander Mommers, Dr. Henry Stronks (Bruker), and Mr. Tom Dobbins (MBraun) for their generous support for our anaerobic MALDI facility. I am grateful to my many inorganic friends and colleagues in Canada and abroad for friendship and inspiration: especially, I thank my collaborators Eduardo dos Santos and José Antonio Mayoral, for stimulating and educational discussions. Most importantly, I thank the past and present members of my research group for their enthusiasm, insight, and effort; the work above is that of Dino Amoroso, Fojan Zamanian, Samantha Drouin, Jennifer Snelgrove, Jay Conrad, Henrietta Parnas, Sebastien Monfette, Johanna Blacquiere, Ken Camm, Nicholas Beach, Heather Foucault, Maeve Moriarty, Matt Kotyk, Ureshini Dharmasena, Yuwen Liu, Nemesio Castro, Pawel Czechura, and Mel Eelman. I am profoundly grateful to them and to my other co-workers who contributed to other work not described. I am honoured to share this award with them.

References

1. (*a*) R.A. Sheldon. Green chemistry and catalysis. Wiley-VCH, Chichester, N.Y., USA. (2007); (*b*) R.A. Sheldon. Green Chem. **9**, 1273 (2007); (*c*) R.A. Sheldon. Green Chem. **7**, 267 (2005).
2. D.J.C. Constable, P.J. Dunn, J.D. Hayler, G.R. Humphrey, J.L. Leazer, Jr., R.J. Linderman, K. Lorenz, J. Manley, B.A. Pearlman, A. Wells, A. Zaks, and T.Y. Zhang. Green Chem. **9**, 411 (2007).
3. M.D. Eelman, J.M. Blacquiere, M.M. Moriarty, and D.E. Fogg. Angew. Chem., Int. Ed. **47**, 303 (2008).
4. W. Henderson and J.S. McIndoe. Mass spectrometry of inorganic and organometallic compounds. Wiley, Hoboken, N.J., USA. (2005).
5. C. Simons, U. Hanefeld, I.W.C.E. Arends, T. Maschmeyer, and R.A. Sheldon. Top. Catal. **40**, 35 (2006).
6. D.J.C. Constable, C. Jimenez-Gonzalez, and R.K. Henderson. Org. Process Res. Dev. **11**, 133 (2007).
7. D.E. Fogg and E.N. dos Santos. Coord. Chem. Rev. **248**, 2365 (2004).
8. E. Billig and D.R. Bryant. Oxo Process. *In* Kirk–Othmer Encyclopedia of chemical technology (online edition). John Wiley and Sons, Inc. 2001. DOI: 10.1002/0471238961.15241502091212.a01.
9. J.-C. Wasilke, S.J. Obrey, R.T. Baker, and G.C. Bazan. Chem. Rev. **105**, 1001 (2005).
10. (*a*) C. Bruneau, P.H. Dixneuf. Eds. Top. Organomet. Chem. **11** (2004); (*b*) T. Naota, H. Takaya, S.-I. Murahashi, Chem. Rev. **98**, 2599 (1998).
11. The platinum metals report (Price Report), Johnson Matthey, Monthly.
12. Selected references: (*a*) S.J. McLain, E.F. McCord, S.D. Arthur, E. Hauptman, J. Feldman, W.A. Nugent, L.K. Johnson, S. Mecking, M. Brookhart. M. Proc. PMSE, **76**, 246 (1997); (*b*) C.W. Bielawski, J. Louie, R.H. Grubbs. J. Am. Chem. Soc. **122**, 12872 (2000); (*c*) M.D. Watson and K.B. Wagener. Macromolecules, **33**, 3196 (2000).
13. S.D. Drouin, F. Zamanian, and D.E. Fogg. Organometallics, **20**, 5495 (2001).
14. K.D. Camm, N.M. Castro, Y. Liu, P. Czechura, J.L. Snelgrove, and D.E. Fogg. J. Am. Chem. Soc. **129**, 4168 (2007).
15. J. Louie, C.W. Bielawski, and R.H. Grubbs. J. Am. Chem. Soc. **123**, 11312 (2001).
16. P. Borsting and P. Nielsen. Chem. Commun. 2140 (2002).
17. B. Schmidt and M. Pohler. Org. Biomol. Chem. **1**, 2512 (2003).
18. B. Schmidt. Eur. J. Org. Chem., 1865 (2004).
19. D.E. Fogg and H.M. Foucault. Ring-opening metathesis polymerization. *In* Comprehensive organometallic chemistry III. Vol. 11. *Edited by* R.H. Crabtree and M.P. Mingos. Elsevier, Oxford, (2007). Chap. 11.18.
20. N.T. McManus and G.L. Rempel. J. Macromol. Sci. Rev. Macromol. Chem. Phys. **C35**, 239 (1995).

© 2008 NRC Canada

21. E. Maréchal. *In* Comprehensive polymer science. Vol. 6. *Edited by* G. Allen and J.C. Bevington. Pergamon, Toronto, Canada. (1989). pp. 1–47.
22. P. Schwab, M.B. France, J.W. Ziller, and R.H. Grubbs. Angew. Chem. Int. Ed. Engl. **34**, 2039 (1995).
23. H.G.M. Edwards, D.W. Farrell, A.F. Johnson, I.R. Lewis, N.J. Ward, and N. Webb. Macromolecules, **25**, 525 (1992).
24. B.H. Sohn, J.A. Gratt, J.K. Lee, and R.E. Cohen. J. Appl. Polym. Sci. **58**, 1041 (1995).
25. (*a*) B.R. James. *In* Comprehensive organometallic chemistry. Vol. 8. *Edited by* G. Wilkinson. Pergamon Press, New York, USA. 1982; chap. 51; (*b*) B.R. James. Homogeneous hydrogenation. John Wiley & Sons, Toronto, Canada. 1973.
26. S.D. Drouin, G.P.A. Yap, and D.E. Fogg. Inorg. Chem. **39**, 5412 (2000).
27. D.E. Fogg, S.D. Drouin, and F. Zamanian. US Patent 6-486-263, 2002.
28. Y. Chen, R. Dujardin, H. Pielartzik, and U.W. Franz. US Patent 5-932-664, 1999.
29. For beneficial effects, see, for example: (*a*) B.S. Nkosi, N.J. Coville, M.O. Albers, C. Gordon, M. Viney, E. Singleton. J. Organomet. Chem. **386**, 111 (1990); (*b*) D.E. Fogg, B.R. James, M. Kilner. Inorg. Chim. Acta, **222**, 85 (1994); (*c*) N.C. Zanetti, F. Spindler, J. Spencer, A. Togni, G. Rihs. Organometallics, **15**, 860 (1996); (*d*) C. Bianchini, P. Barbaro, G. Scapacci, F. Zanobini. Organometallics, **19**, 2450 (2000).
30. K.D. Camm and D.E. Fogg. NATO Science Series II, **243**, 285 (2007).
31. C.S. Yi and D.W. Lee. Organometallics, **18**, 5152 (1999).
32. (*a*) S.E. Clapham, A. Hadzovic, R.H. Morris. Coord. Chem. Rev. **248**, 2201 (2004); (*b*) P. Martin, N.T. McManus, G.L. Rempel. J. Mol. Catal. A, **126**, 115 (1997); (*c*) M.J. Burk, J.P. Martinez, J.E. Feaster, N. Cosford. Tetrahedron, **50**, 4399 (1994); (*d*) M.J. Burk. Acc. Chem. Res. **33**, 363 (2000).
33. (*a*) M.A. Esteruelas, E. Sola, L.A. Oro, H. Werner, U. Meyer. J. Mol. Catal. **45**, 1 (1988); (*b*) M.A. Esteruelas, E. Sola, L.A. Oro, H. Werner, U. Meyer. J. Mol. Catal. **53**, 43 (1989).
34. C.N. Rowley, H.M. Foucault, T.K. Woo, and D.E. Fogg. Organometallics, 1661 (2008).
35. N.J. Beach, U.L. Dharmasena, S.D. Drouin, and D.E. Fogg. Adv. Syn. Catal. **350**, 773 (2008).
36. M.B. Dinger and J.C. Mol. Organometallics, **22**, 1089 (2003).
37. M.B. Dinger and J.C. Mol. Eur. J. Inorg. Chem. 2827 (2003).
38. T.M. Trnka, J.P. Morgan, M.S. Sanford, T.E. Wilhelm, M. Scholl, T.-L. Choi, S. Ding, M.W. Day, and R.H. Grubbs. J. Am. Chem. Soc. **125**, 2546 (2003).
39. M. Arisawa, Y. Terada, K. Takahashi, M. Nakagawa, and A. Nishida. J. Org. Chem. **71**, 4255 (2006).
40. J. Louie and R.H. Grubbs. Organometallics, **21**, 2153 (2002).
41. C. Menozzi, P.I. Dalko, and J. Cossy. Synlett, 2449 (2005).
42. F. Li, D. Carlsson, C. Lohmann, E. Suuronen, S. Vascotto, K. Kobuch, H. Sheardown, R. Munger, M. Nakamura, and M. Griffith. Proc. Nat. Acad. Sci. USA, **100**, 15346 (2003).
43. Y. Liu, D. Fogg, and M. Griffith. US Patent 11-442-755. 2006.
44. J.L. Funderburgh. Glycobiology, **10**, 951 (2000).
45. A.A. Scholte, M.H. An, and M.L. Snapper. Org. Lett. **8**, 4759 (2006).
46. S. Beligny, S. Eibauer, S. Maechling, and S. Blechert. Angew. Chem. Int. Ed. **45**, 1900 (2006).
47. B.P. Peppers and S.T. Diver. J. Am. Chem. Soc. **126**, 9524 (2004).
48. B.G. Kim and M.L. Snapper. J. Am. Chem. Soc. **128**, 52 (2006).
49. See these leading reviews: (*a*) R.H. Grubbs, Handbook of metathesis. Wiley-VCH, Weinheim, Germany. 2003; (*b*) K.C. Nicolaou, P.G. Bulger, D. Sarlah, Angew. Chem. Int. Ed. **44**, 4490 (2005); (*c*) R.R. Schrock. Angew. Chem., Int. Ed. **45**, 3748 (2006); (*d*) R.H. Grubbs. Angew. Chem., Int. Ed. **45**, 3760 (2006).
50. M.S. Sanford, J.A. Love, and R.H. Grubbs. J. Am. Chem. Soc. **123**, 6543 (2001).
51. M.S. Sanford, J.A. Love, and R.H. Grubbs. Organometallics, **20**, 5314 (2001).
52. M. Zaja, S.J. Connon, A.M. Dunne, M. Rivard, N. Buschmann, J. Jiricek, and S. Blechert. Tetrahedron, **59**, 6545 (2003).
53. A. Michrowska, R. Bujok, S. Harutyunyan, V. Sashuk, G. Dolgonos, and K. Grela. J. Am. Chem. Soc. **126**, 9318 (2004).
54. P.E. Romero, W.E. Piers, and R. McDonald. Angew. Chem., Int. Ed. **43**, 6161 (2004).
55. M. Ulman and R.H. Grubbs. J. Org. Chem. **64**, 7202 (1999).
56. J.C. Conrad and D.E. Fogg. Curr. Org. Chem. **10**, 185 (2006).
57. J.J. Van Veldhuizen, D.G. Gillingham, S.B. Garber, O. Kataoka, and A.H. Hoveyda. J. Am. Chem. Soc. **125**, 12502 (2003).
58. D. Amoroso, G.P.A. Yap, and D.E. Fogg. Organometallics, **21**, 3335 (2002).
59. D. Amoroso, J.L. Snelgrove, J.C. Conrad, S.D. Drouin, G.P.A. Yap, and D.E. Fogg. Adv. Syn. Catal. **344**, 757 (2002).
60. S.H. Hong, M.W. Day, and R.H. Grubbs. J. Am. Chem. Soc. **126**, 7414 (2004).
61. P.L. Holland, R.A. Andersen, R.G. Bergman, J. Huang, and S.P. Nolan. J. Am. Chem. Soc. **119**, 12800 (1997).
62. D.J. Cole-Hamilton, R.J. Young, and G. Wilkinson. J. Chem. Soc. Dalton Trans. 1995 (1976).
63. (*a*) J.L. Snelgrove, J.C. Conrad, M.M. Moriarty, G.P.A. Yap, and D.E. Fogg. Organometallics, **24**, 103 (2005); (*b*) J.L. Snelgrove, J.C. Conrad, G.P.A. Yap, and D.E. Fogg. Inorg. Chim. Acta, **345**, 268 (2003).
64. J.C. Conrad, D. Amoroso, P. Czechura, G.P.A. Yap, and D.E. Fogg. Organometallics, **22**, 3634 (2003).
65. J.C. Conrad, H.H. Parnas, J.L. Snelgrove, and D.E. Fogg. J. Am. Chem. Soc. **127**, 11882 (2005).
66. S. Monfette and D.E. Fogg. Organometallics, **25**, 1940 (2006).
67. R.R. Schrock. J. Am. Chem. Soc. **96**, 6796 (1974).
68. J.N. Coalter, J.C. Bollinger, O. Eisenstein, and K.G. Caulton. New J. Chem. **24**, 925 (2000).
69. J.C. Conrad, K.D. Camm, and D.E. Fogg. Inorg. Chim. Acta, **359**, 1967 (2006).
70. See these selected examples: (*a*) S.C. Zinner, W.A. Herrmann, F.E. Kuehn, J. Organomet. Chem. **693**, 1543 (2008); (*b*) R.E. Douthwaite. Coord. Chem. Rev. **251,** 702 (2007); (*c*) R.E. Giudici, A.H. Hoveyda, J. Am. Chem. Soc. **129**, 3824 (2007); (*d*) D. Baskakov, W.A. Herrmann, E. Herdtweck, S.D. Hoffmann, Organometallics, **26**, 626 (2007); (*e*) T.W. Funk, J.M. Berlin, R.H. Grubbs, J. Am. Chem. Soc. **128**, 1840 (2006).
71. J.C. Conrad, M.D. Eelman, J.A. Duarte Silva, S. Monfette, H.H. Parnas, J.L. Snelgrove, and D.E. Fogg. J. Am. Chem. Soc. **129**, 1024 (2007).
72. A. Gradillas and J. Perez-Castells. Angew. Chem., Int. Ed. **45**, 6086 (2006).
73. For reviews of the synthesis of medium-sized and large rings by RCM, see: (*a*) M.E. Maier. Angew. Chem. Int. Ed. **39**, 2073 (2000); (*b*) See Ref. 72. For a more general review of the synthesis of medium-sized rings, see: (*c*) L. Yet. Chem. Rev. **100**, 2963 (2000).
74. D. Villemin. Tetrahedron Lett. **21**, 1715 (1980).
75. E. Muller, O. Bayer, H. Meerwein, and K. Ziegler. Methoden der organischen Chemie, Bd. IX, 4th ed. (1955).
76. K. Yamamoto, K. Biswas, C. Gaul, and S.J. Danishefsky. Tetrahedron Lett. **44**, 3297 (2003).

© 2008 NRC Canada

77. L. Lee, H. Ou, and H. Hsu. Fluid Phase Equilib. **231**, 221 (2005).
78. (*a*) H. Höcker, W. Reimann, K. Riebel and Z. Szentivanyi. Makromol. Chem. **177**, 1707 (1976); (*b*) L. Reif and H. Höcker. Macromolecules, **17**, 952 (1984); (*c*) E. Thorn-Csanyi and K. Ruhland. Macromol. Symp. **153**, 145 (2000).
79. (*a*) H. Jacobson and W. H. Stockmayer. J. Chem. Phys. **18**, 1600 (1950); (*b*) An updated model takes ring strain into account, improving predictions of the distribution of cyclic and linear products: Z.-R. Chen, J.P. Claverie, R.H. Grubbs and J.A. Kornfield. Macromolecules, **28**, 2147 (1995); (*c*) For a theoretical treatment of the distribution of cyclooligomers in dilute solution, see: G. Ercolani, L. Mandolini, P. Mencareli, and S. Roelens. J. Am. Chem. Soc. **115**, 3901 (1993).
80. G. Illuminati and L. Mandolini. Acc. Chem. Res. **14**, 95 (1981).
81. C. Galli and L. Mandolini. Eur. J. Org. Chem. 3117 (2000).

© 2008 NRC Canada

Vibrational spectroscopic characterization of some environmentally important organoarsenicals — A guide for understanding the nature of their surface complexes

Scott Cowen, Megha Duggal, Tuan Hoang, and Hind A. Al-Abadleh

Abstract: Organoarsenicals are found in the environment from the biomethylation of inorganic arsenic compounds and from anthropogenic sources. It is clear that organoarsenicals pose a health and an environmental risk due to their potential cycling to the most toxic forms of arsenic as a result of redox activity in soils and natural waters. The environmental fate of arsenic compounds depends to a large extent on the surface interactions with geosorbents, mainly minerals and organic matter. Hence, elucidating the nature of surface complexes is important in understanding binding mechanisms and thermodynamics. In this paper, we report the vibrational spectra of a number of organoarsenicals in the aqueous and solid phases using attenuated total internal reflectance Fourier transform infrared (ATR-FTIR), transmission FTIR, and Raman spectroscopies. Analysis of the aqueous phase spectra revealed that for completely deprotonated anions, increasing the organic substituents on the AsO_x moiety results in increasing the frequency of $\nu(AsO_x)$, whereas the opposite trend is observed for completely protonated molecules. Analysis of solid phase spectra showed that incorporation of water molecules in the crystalline structure and extensive hydrogen bonding with neighboring molecules significantly affect As–O bond lengths and hence frequencies of $\nu(AsO_x)$. Results are discussed in the context of identifying geometry of organoarsenicals surface complexes in situ using the ATR-FTIR technique.

Key words: ATR-FTIR, organoarsenicals; oxyanion adsorption, arsenate, in situ spectroscopy.

Résumé : On retrouve des dérivés organiques de l'arsenic dans l'environnement qui résultent de la biométhylation des composés inorganiques de l'arsenic ainsi que de sources anthropogéniques. Il est clair que ces dérivés de l'arsenic posent un risque à la santé et à l'environnement en raison de la possibilité qu'ils soient recyclés en formes plus toxiques de l'arsenic à la suite d'activités redox dans les sols et les eaux naturelles. Le sort environnemental des composés de l'arsenic dépend en grande partie des interactions de surface avec les géosorbants, particulièrement les minéraux et les matières organiques. Il est donc important d'élucider la nature des complexes de surface pour comprendre les mécanismes de liaison et leur thermodynamique. Dans ce travail, faisant appel à la spectroscopie infrarouge à transformée de Fourier en transmission et à la spectroscopie infrarouge à transformée de Fourier et à réflexion totale atténuée (IRTF-RAT), on a déterminer les spectres vibrationnels d'un certain nombre de dérivés organiques de l'arsenic dans des solutions aqueuses et en phases solides. L'analyse des spectres en phase aqueuse révèle que, pour des anions complètement déprotonés, une augmentation de substituants organiques sur la portion AsO_x provoque une augmentation de la fréquence de $\nu(AsO_x)$ alors qu'on observe la tendance inverse pour les molécules complètement protonées. L'analyse des spectres en phase solide a montré que l'incorporation de molécules d'eau dans la structure cristalline et le réseau étendue de liaisons hydrogènes avec les molécules adjacentes affecte d'une façon importante les longueurs des liaisons As–O et, en conséquence, les $\nu(AsO_x)$. On discute des résultats dans le contexte de l'identification de la géométrie des composés organiques de l'arsenic des complexes de surface in situ à l'aide de la technique IRTF-RAT.

Mots-clés : IRTF-RAT, dérivés organiques de l'arsenic, adsorption d'oxyanions, arsenate, spectroscopie in situ.

[Traduit par la Rédaction]

Received 25 February 2008. Accepted 26 May 2008. Published on the NRC Research Press Web site at canjchem.nrc.ca on 19 August 2008.

S. Cowen,[2,3] M. Duggal,[3] T. Hoang,[3] and H.A. Al-Abadleh.[1] Chemistry Department, Wilfrid Laurier University, Waterloo, ON N2L 3C5 Canada.

[1]Corresponding author (e-mail: halabadleh@wlu.ca).
[2]Present address address: Department of Chemistry, University of Guelph, Guelph, ON N1G 2W1, Canada.
[3]The co-authors have contributed equally to this work and hence are listed alphabetically.

 doi:10.1139/V08-102 © 2008 NRC Canada

Table 1. Structure and pK_a of some organoarsenicals commonly identified in environmental samples from areas with potential arsenic contamination.

Compound	Structure	pK_a	Ref.
Monomethylarsonic Acid, (MMA, CH_5O_3As)	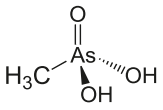	(1) 3.6 (2) 8.2	(37)
Dimethylarsinic Acid, (DMA, $C_2H_7O_2As$)	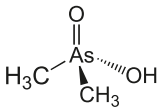	(1) 6.14	(37)
p-Arsanilic acid, (p-AsA, $C_6H_8NO_3As$)	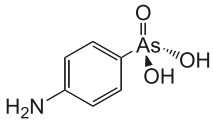	($-NH_3^+$) 1.9 (1) 4.1 (2) 9.2	(38)
Roxarsone , (Rox, $C_6H_6NO_6As$)	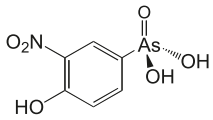	(1) 3.5 (-OH) 5.7 (2) 9.1	(39)

Introduction

Arsenic (As) contamination of soils, surface, and groundwater is a serious problem in many parts of the world, including North America (1). Sources of this pollution can either be natural from the weathering of arsenic-containing minerals or anthropogenic from industrial effluents of the petrochemical and coal industries (2–4), tailings of abandoned and recent gold mining operations (1), wood preservative facilities (5), use of arsenical herbicides (5), and poultry industry (6). People near geological and industrial sources of arsenic pollution are exposed to high concentrations of As and hence prone to developing chronic diseases, including cancer (5, 7). This is why arsenic and its compounds are listed on the pollutant priority lists of the Canadian Environmental Protection Act (CEPA) and the US EPA. The current Canadian maximum acceptable limit of total arsenic in drinking water is 25 ppb (8), while that of the US EPA is 10 ppb (9).

Arsenic speciation in environmental samples have identified four major classes of compounds: inorganic As, aliphatic organic As, aromatic As, and arsenosugars (5). The most common organoarsenical species contain arsenic in the oxidation states of +III and +V. In general, trivalent organoarsenical compounds are more toxic and mobile than the pentavalent compounds (7, 10–12). Table 1 lists the chemical formula, structure, and pK_a of organoarsenicals identified in environmental samples. *Methylated arsenic* compounds such as the sodium salts of monomethylarsonic acid (MMA) and dimethylarsinic acid (DMA) are used as herbicides (5) and are also produced in biomethylation processes of inorganic As (iAs) that occur under aerobic and anaerobic conditions (13, 14). On the other hand, *aromatic organoarsenical* compounds such as *p*-arsanilic acid (4-aminobenzenearsenic acid, *p*-AsA), and Roxarsone (4-hydroxy-3-nitrobenzenearsenic acid) are used as feed additives in the U.S. poultry industry (6) and are introduced into the environment through disposal and land application of contaminated poultry litter (see references in (15)). The biogeochemical transformation of these compounds in soils is a result of enhanced microbial activity and (or) exposure to UV radiation and leads to the formation of the more toxic trivalent forms of MMA, DMA, and eventually iAs species through a series of volatilization and mineralization reactions (16, 17). It is clear that As(V) associated with organoarsenicals pose a health and an environmental risk due to its potential cycling to As(III) as a result of redox activity in soils and natural waters.

Determining the mobility and chemical speciation of arsenic compounds is often used to assess their overall environmental impact (1, 14). These properties depend to a large extent on their surface interactions with geosorbents, mainly minerals and organic matter (1, 18, 19). Several bulk and surface-sensitive techniques are employed to quantify binding thermodynamics and elucidate the structure of surface complexes which include inductively coupled plasma mass spectrometry (ICP-MS) (20), and in situ near edge synchrotron X-ray based and total internal reflectance IR spectroscopic techniques, respectively, (19). In particular, ATR-FTIR spectroscopy has proven to be a very useful technique for studying surface interaction of arsenic compounds on a number of metal oxide surfaces using solution concentrations as low as 1 μmol/L (19, 21). Using ATR-FTIR for adsorption experiments of oxyanions in general, factors such as the degree of protonation, the presence of organic substituents, and binding to surfaces that affect the overall spectral features could be observed experimentally. To aid in the interpretation of spectra collected in the presence of the metal oxide coating on the ATR internal reflection element (IRE), spectra are often collected for standards of oxyanions including solids with known crystal structure and aqueous solutions of known pH. While there is a relatively large number of published articles on the interpretation of IR spectra of iAs(V) and iAs(III) in different bulk phases (19, 22–24), there are no systematic ATR-FTIR studies on standard organoarsenical

© 2008 NRC Canada

compounds that could be used as a guide for adsorption studies of these compounds.

In this work, we report the vibrational spectra of MMA(V), DMA(V), and *p*-AsA in the aqueous and solid phases using ATR-FTIR, transmission FTIR, and Raman spectroscopies. Spectra of standard aqueous solutions were collected at different pH values above and below the pK_a of these compounds such that the effect of protonation on spectral features could be investigated. These spectra were compared to those collected for iAs(V) to study the effect of organic substituents on the vibrational spectra of the arsenate ion. The results are discussed in the context of geometry identification of adsorbed organoarsenicals using ATR-FTIR.

Experimental

Chemicals

All chemicals were used as received without further purification: MMA-1 (monosodium acid methane arsonate sesquihydrate, $CH_3AsO_3HNa{\cdot}1.5H_2O$, 99%, Chem Service), MMA-2 (disodium methyl arsonate hexahydrate, $CH_3AsO_3Na_2{\cdot}6H_2O$, 98%, Chem Service), DMA-1 (dimethylarsinic acid, $C_2H_6AsO_2H$, 98%, Sigma-Aldrich), DMA-2 (cacodylic acid sodium salt trihydrate, $C_2H_6AsO_2Na{\cdot}3H_2O$, Alfa Aesar), *p*-AsA (*p*-arsanilic acid, $C_6H_8NO_3As$, 99%, Sigma-Aldrich), and iAs (sodium arsenate, $AsO_4HNa_2{\cdot}7H_2O$, ACS reagent, J.T. Baker). Stock solutions in millipore water (18.2 MΩ) were prepared by dissolving the crystalline material in concentrated NaOH (EMD, ACS grade) with continuous mechanical stirring, and then lowering the pH using HCl (Ricca Chemical, 6 N). *Caution: The aforementioned organoarsenicals are highly toxic via inhalation and skin contact and are carcinogens.* The ionic strength of these solutions was adjusted to 0.01 mol/L KCl. Exact concentrations are provided in the figure captions.

ATR-FTIR experiments

ATR-FTIR spectra were collected using a HATRPlus accessory (Pike Technologies) installed in a Nicolet 8700 FTIR spectrometer (Thermo Instruments) equipped with a purge gas generator and a liquid N_2-cooled MCT-A detector. The HATR flow cell houses a 45° Ge crystal as the IRE (trapezoid, 80 mm × 10 mm × 4 mm). All single beam spectra were collected at 4 cm^{-1} resolution by averaging 300 scans. Absorbance spectra were obtained by referencing single beam spectra of the sample to that collected for the 0.01 mol/L KCl solution held at the same pH of the sample. Subtraction factors were varied between 0.95 and 1 to avoid baseline correction of the resulting absorbance spectra. The ATR-FTIR measurement of each solution was repeated for at least three times to ensure reproducibility. Absorbance of most intense bands is within experimental error (±5%) and band locations are ±2 cm^{-1}.

Transmission FTIR experiments

IR absorption spectra of solid organoarsenicals were obtained from KBr pellets prepared using the Quick Press kit (International Crystal Laboratories). Sample concentrations ranged from 2% to 10% in potassium bromide (SpectroGrade™). Single beam spectra were collected in the transmission mode using the aforementioned FTIR spectrometer at 4 cm^{-1} resolution by averaging 250 scans. Single beam spectra of plain KBr pellets were used as the background to generate absorbance spectra. Similar to ATR-FTIR measurements, a number of spectra for each chemical was acquired to ensure reproducibility. Variation of band intensities for nearly the same sample concentrations is within 10% and band locations are ±2 cm^{-1}.

Raman spectroscopy experiments

The Raman spectra of solid organoarsenicals contained in a glass vial were recorded using an integrated fiber optic Raman spectrometer R-3000 QE (Ocean Optics) equipped with 785 nm diode laser and CCD array. Spectra were collected using a laser power in the range 150–200 mW at 6 cm^{-1} resolution and 60–100 s integration time. Multiple spectra collected for the same sample on different days were reproducible in peak position, band shape, and ratio of band intensities obtained from selected peaks in a given spectrum.

Results and discussion

Solution phase speciation of organoarsenicals using ATR-FTIR

Figure 1 shows the ATR-FTIR spectra of aqueous (*a*) iAs(V), (*b*) MMA, (*c*) *p*-AsA, and (*d*) DMA, respectively, in the spectral range of 650–1100 cm^{-1}. These spectra are shown in the order of increasing organic substituents on the arsenate group. For each compound, spectra were recorded at different pH values, which affect the degree of protonation and hence distribution of species in the solution phase governed by the pK_a of these molecules (see Table 1). While the ATR-FTIR spectra of iAs(V) have been measured by a number of researchers (22, 25, 26), the spectrum shown in Fig. 1 for iAs(V) at pH 1.5 and those for the organoarsenicals studied herein are the first ATR-FTIR spectra to be reported at known pH values. Changes in molecular symmetry of these compounds due to changes in protonation state and the presence of organic substituents dictate the number of observed resolved spectral components. Vibrational analysis and the derivation of symmetry point group and coordinates have been summarized by Myneni et al. (22) for iAs(V), and were reported for MMA and DMA by Herman and co-workers (27, 28). The symmetry point group of aqueous phase species dominant at each pH is shown in Table 2 except for *p*-AsA given that it is the least symmetric among the molecules studied.

The spectral range shown in Fig. 1 (650–1100 cm^{-1}) contains the stretching vibrations of the (-AsO_x) moiety in the molecules. Table 2 lists the assignment of the observed frequencies of AsO_x stretching vibrations in the bulk phases of arsenic(V)-containing compounds used in our studies, which are in agreement with previously published values. In general, fully deprotonated arsenate anion AsO_4^{3-} had T_d symmetry and exhibits symmetric (ν_s, singly degenerate) and asymmetric (ν_{as}, triply degenerate) stretching vibrations. The polarization characteristics of these bands led to assigning the lower frequency value to ν_{as}, which is a behavior also seen for completely deprotonated MMA (28, 29). As discussed by Myneni et al. (22), species with lower symmetry

© 2008 NRC Canada

Fig. 1. ATR-FTIR spectra of aqueous arsenic(V)-containing compounds as a function of pH. (*a*) 0.2 mol/L iAs(V), (*b*) 0.2 mol/L MMA, (*c*) *p*-AsA (0.06 mol/L for pH 13 and 7 and 0.025 mol/L for pH 2), and (*d*) 0.2 mol/L DMA. The ionic strength of the solution is 0.01 mol/L (KCl). Based on the pK_a values of each compound shown in Table 1, the dominant species at each pH are shown next to the corresponding spectrum. Notes: Ar- = $H_2NC_6H_4$– and Me- = CH_3–.

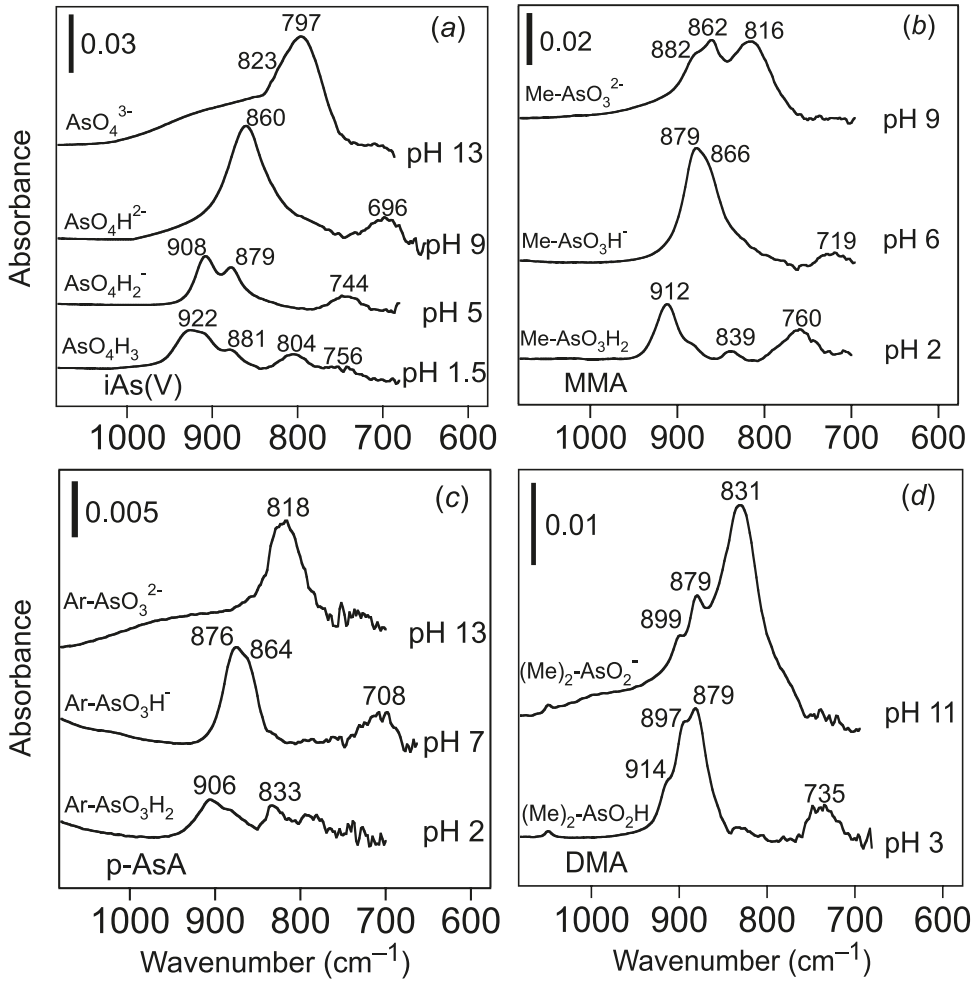

than T_d exhibit energy shifts in ν_s and splitting of ν_{as}, which are influenced by a number of factors including extensive hydrogen bonding and complexation to cations, such as protons and metals. Myneni et al. (22) also emphasized that low symmetry species may not result in enough splitting to be identified in the spectra, and similarly the presence of all $\nu(AsO_x)$ peaks may not exclude high symmetry species.

The spectrum shown in Fig. 1*a* for iAs(V) at pH 1.5 for fully protonated arsenic acid (H_3AsO_4, C_{3v} symmetry) has not been measured before using an ATR accessory because of the instability of ZnSe ATR crystals used in previous studies. Our measurement herein was possible using a Ge ATR crystal, which is stable in solution with pH values between 1 and 14. There are four bands observed in the $\nu(AsO_x)$ spectral region at 922, 881, 804, and 756 cm^{-1}, which are in agreement with the Raman bands reported by Vansant et al. (29) for H_3AsO_4 aqueous solutions. Moreover, shown in Fig. 1*c* are the spectra of *p*-AsA(aq) at pH 3, 7, and 13, which were measured at higher concentrations than our previous work (15). Relatively weak intensity bands were easily observed given that the IRE used in this study results in a higher penetration depth and number of reflections, and hence higher effective pathlength compared to ZnSe. For example, the bands at 708 cm^{-1} (pH 7) and 833 cm^{-1} (pH 2) for *p*-AsA are well defined and they correlate very well with those observed for aqueous MMA at pH 6 and 2, respectively. Hence, given that both *p*-AsA and MMA are monosubstituted arsonic acids, we assigned the former band at 708 cm^{-1} to ν(AsOH) and the 833 cm^{-1} to $\nu_s(AsO_x)$. There were no bands observed for *p*-AsA below 800 cm^{-1} at pH 2, most likely due to the weak intensity of that component at the concentration used (0.025 mol/L). Higher concentrations of *p*-AsA at acidic pH were observed to form precipitates and could not be used for ATR-FTIR measurements.

Moreover, the spectra of methylated arsenical compounds exhibit features due to rocking vibrations of methyl groups, $\rho(CH_3)$, in the spectral range of 650–1100 cm^{-1}. For example, the spectral feature at 862 cm^{-1} in the ATR-FTIR spectrum of aqueous $CH_3AsO_3^{2-}$ (C_{3v} symmetry) at pH 9 is assigned to $\rho(CH_3)$, which is close to the frequency reported by Vasant et al. (28) at 854 cm^{-1}. This vibration occurs as a shoulder at 875 cm^{-1} for fully protonated aqueous $CH_3AsO(OH)_2$ (C_s symmetry) (28), which could explain the

© 2008 NRC Canada

Table 2. Observed frequencies of (AsO_x) stretching vibrations in the bulk phases of arsenic(V)-containing compounds of importance in the environment.

Species	This work (FTIR and Raman)				Previous studies (IR)					Previous studies (Raman)				
	As–OH		AsO_x		As–OH		AsO_x		Ref.	As–OH		AsO_x		Ref.
	ν_{as}	ν_s	ν_{as}	ν_s	ν_{as}	ν_s	ν_{as}	ν_s		ν_{as}	ν_s	ν_{as}	ν_s	
iAs(V)														
HO-AsO_3H_2 (C_{3v}, pH 1.5)	804	756	922	881						808	769	923	923	(40)
HO-AsO_3H^- (C_{2v}, pH 5)	744	744	908	879	766	766	908	877	(22, 25)	765	745	915	875	(40)
HO-AsO_3^{2-} (C_{3v}, pH 9)	696	696	860	860	689	689	865	846	(22, 25)		707	866	838	(40)
AsO_4^{3-} (T_d, pH 13)	–	–	797	823			792	792	(25)	–	–	797	818	(40)
												794	814	(41)
HO-$AsO_3Na_2{\cdot}7H_2O$ (s)		715	875, 848[a]	818		711	885	825	(22)		737	852	835	(40)
		730[R]	848, 835[R]	808[R]							735	845	833	(33)
MMA(V)														
CH_3-AsO_3H_2 (C_s, pH 2)		760	912	839		755	912	912	(28)	785	769	912		(28)
					767[b]	767[b]	913[b]	913[b]	(32)					
CH_3-AsO_3H^- (C_s, pH 6)		719	879	866		705		865	(28)	730		900	866	(28)
								844[b]	(32)					
CH_3-AsO_3^{2-} (C_{3v}, pH 9)			816	882			817		(28)			793	823	(28)
							820[b]	820[b]	(32)					
CH_3-AsO_3H_2 (s)					778	772	871	871	(28)	780	769	870, 850	870, 850	(28)
CH_3-$AsO_3HNa{\cdot}1.5H_2O$ (s)	743	743	909, 874	815										
(MMA-1)														
	740[R]	695[R]	914, 876[R]	811[R]										
CH_3-AsO_3Na_2 ·$6H_2O$ (s)			791	835			810	845	(28)			833		(33)
(MMA-2)			784[R]	837[R]										
p-AsA(V)														
$H_2NC_6H_4$-AsO_3H_2 (pH 2)	n.o.	n.o.	906	833			906	906	(15)					
$H_2NC_6H_4$-AsO_3H^- (pH 7)	708	708	876	864			870	870	(15)					
$H_2NC_6H_4$-AsO_3^{2-} (pH 13)			818	818			818	818	(15)					
$H_3N^+C_6H_4$-AsO_3H^- (s)	745[R]	745[R]	854[R]	810[R]	746	746	808–883[a]	808–883[a]	(15)					
DMA(V)														
$(CH_3)_2AsO_2H$ (C_s, pH 3)	735	735	879	879	745	745	885	885	(27)	752	752	881	881	(27)
					747[b]	747[b]	869[b]	869[b]	(32)					
$(CH_3)_2AsO_2^-$ (C_{2v}, pH 11)	–	–	831	831	–	–	830[b]	830[b]	(32)					
$(CH_3)_2AsO_2H$ (s)	754	754	829	829	747	747	829	829	(27)	754	754	822	822	(27)
(DMA-1)	750[R]	750[R]	819[R]	819[R]	754	754	839	839	(31)					
$(CH_3)_2AsO_2Na{\cdot}3H_2O$ (s)	–	–	841	787						–	–	833[br]	833[br]	(33)
(DMA-2)			854[R]	838[R]										

Note: [R]Raman experiments; *n.o.*: not observed due to weak intensity; [br]broad feature.
[a]Several spectral features due to extensive H-bonding and low site symmetry in the crystalline structure.
[b]These numbers are based on calculations.

© 2008 NRC Canada

component visible at pH 2 in Fig. 1*b* giving rise to an asymmetrical band centered at 912 cm^{-1}. However, $\rho(CH_3)$ vibration is overshadowed by the intense $\nu(AsO_x)$ at pH 6 and hence not observed in the spectrum. For comparison, $\rho(CH_3)$ for completely deprotonated methylphosphonic acid, $CH_3PO_3^{2-}$, occurs as a very weak feature at 880 cm^{-1} (30). The difference in frequency values could be explained in light of the effect that the different masses of arsenic and phosphorus have on their bonding to carbon, giving rise to lower ν(C-As) than ν(C-P) (683 cm^{-1} vs 750 cm^{-1}). As for aqueous DMA, features assigned to $\rho(CH_3)$ occur at higher frequencies compared to MMA. The features observed at 914 and 897 cm^{-1} in the spectrum of aqueous $(CH_3)_2AsO(OH)$ at pH 3 (C_s symmetry, Fig. 1*d*) have been assigned to $\rho(CH_3)$ (27, 31). Hence, by analogy, we assign the medium intensity features at 899 and 879 cm^{-1} to $\rho(CH_3)$ in aqueous $(CH_3)_2AsO_2^-$ at pH 11 (C_{2v} symmetry). This assignment is based on their medium intensity profile relative to $\nu(AsO_x)$ and the trend observed for the frequency of $\rho(CH_3)$ in MMA species that the frequency of the $\rho(CH_3)$ vibration occurs at a lower value for deprotonated versus acidic species.

Examination of Fig. 1 and Table 2 for all compounds investigated herein reveals two distinct trends that may aid in the interpretation of IR spectra recorded for the adsorbed phase of these compounds. It could be observed that for a given molecule, decreasing the pH (i.e., increasing protonation state of solution phase species) results in shifting the frequency of $\nu(AsO_x)$ bands to higher values, decreasing their intensity, and emerging of bands assigned to ν(AsOH) groups. This observation has been attributed to an increase in the force constant of As–O and As–OH bonds with increasing proton concentration on the AsO_x moiety, which is consistent with the structural analysis of Gründler et al. (32) who attributed the aforementioned trends to changes in the mesomeric (i.e., resonance) effect between AsO_x bonds upon protonation. Deprotonated oxygen atoms participate in multiple bonding, whereas As–OH and As–C bonds do not participate in that process (32). Similar findings were reported for other oxyanions such as phosphates, sulfates, and selenate (22).

It could also be observed from Fig. 1 and Table 2 that for the completely deprotonated anions, increasing the organic substituents on the AsO_x moiety results in increasing the frequency of $\nu(AsO_x)$. For instance, for completely deprotonated anions, $\nu(AsO_x)$ increases in this order, AsO_4^{3-} (T_d: 823, 797 cm^{-1}) < $CH_3AsO_3^{2-}$ (C_{3v}: 882, 816 cm^{-1}) ≈ $H_2NC_6H_4AsO_3^{2-}$ (818 cm^{-1}) < $(CH_3)_2AsO_2^-$ (C_{2v}: 831 cm^{-1}). The effect of methyl substituents on AsO force constant and bond order was calculated by Gründler et al. (32), who found that for the fully deprotonated anions, the force constant and bond order increases in this order, AsO_4^{3-} < $CH_3AsO_3^{2-}$ < $(CH_3)_2AsO_2^-$. They attributed the increase in force constant to increasing AsO bond polarity and decreasing degree of multiple bonding upon oxygen substitution with carbon. Moreover, it could be concluded from the above order in $\nu(AsO_x)$ that the splitting of degenerate bands in organoarsenicals due to lower symmetry (e.g., completely deprotonated *p*-AsA and DMA) is not observed experimentally. Although one could use a routine curve fitting procedure to resolve the spectral components contributing to the observed bands, questions remain regarding the physical significance of the chosen number of components in the fitting and their assignment, whether they are due to splitting of degenerate bands or due to the presence of aqueous phase species of different symmetry groups.

Moreover, for completely protonated molecules, the trend in $\nu(AsO_x)$ is opposite to that observed for the completely deprotonated anions. Values of $\nu(AsO_x)$ decrease in this order, H_3AsO_4 (C_{3v}: 922, 881 cm^{-1}) > $CH_3AsO(OH)_2$ (C_s: 912, 839 cm^{-1}) ≈ $H_2NC_6H_4AsO(OH)_2$ (906, 833 cm^{-1}) > $(CH_3)_2AsO(OH)$ (C_s: 879 cm^{-1}). This trend may be explained by the fact that increasing organic substitution occurs at the expense of the number of As-OH in the molecule. Since both increasing organic substitution and As-OH concentration on the AsO_x moiety of the molecule result in increasing the force constant of As–O bonds, the number of As-OH groups seems to have a more profound effect on the force constant of As–O bonds than organic substitution. Myneni et al. (22) calculated As–O bond length for solvated arsenic acid, $H_3AsO_4(H_2O)_4$, to be 1.60 Å. Similar calculations were not performed for solvated MMA and DMA, $CH_3AsO(OH)_2$ and $(CH_3)_2AsO(OH)$, but Gründler et al. (32) calculated the AsO bond order for these isolated compounds and found them to be 1.23 and 1.18, respectively. As detailed below, the same trend is observed in solid organoarsenicals since these compounds form hydrogen bonding with water molecules in their crystal structure and with neighboring molecules.

Solid phase speciation of organoarsenicals

Figure 2 (panels *a* and *b*) shows the transmission FTIR and Raman spectra of the organoarsenicals used in our studies, respectively. The IR spectrum of solid iAs(V) is also shown for comparison. The Raman spectra shown in Fig. 2*b* for solid *p*-AsA and MMA-1 were not published previously. The Raman spectrum of DMA-1 was included in Fig. 2*b* for comparison with previously published work (27, 33). Raman spectra of MMA-2, DMA-2, and iAs(V) were collected as well (not shown here) and agree with the spectra published recently by Mosley et al. (33). The assignment of peaks observed for solid organoarsenicals is listed in Table 2.

Following the analytical approach of Myneni et al. (22), it is instructive when discussing the vibrational spectra of solids to recall AsO_x bond lengths from the crystal structure and make comparisons with similar species in the solution phase. For solid iAs(V), bond lengths are 1.66, 1.67, and 1.68 Å for As–O and 1.74 Å for As–OH (22), with a C_1 site symmetry of the $HAsO_4^{2-}$ group. It is clear from the IR spectrum shown in Fig. 2*a* for solid iAs(V) that the band assigned to $\nu(AsO_x)$ has more components than that recorded for aqueous $HAsO_4^{2-}$ (C_{3v} symmetry) at pH 9 (Fig. 1*a*). This observation is in contrast with the interpretation made by Myneni et al. (22), who concluded that the spectrum of solid $Na_2(HAsO_4)\cdot 7H_2O$ exhibits features similar to those of respective ions in aqueous solutions. Their conclusion was made despite the fact that the diffuse reflectance FTIR spectrum shown for solid $Na_2(HAsO_4)\cdot 7H_2O$ in their paper has a FWHM of the $\nu(AsO_x)$ band that exceeds that recorded for $HAsO_4^{2-}$ species at pH 9.1, which indicates more spectral components for the solid case consistent with lower site symmetry.

© 2008 NRC Canada

Fig. 2. (*a*) Transmission FTIR spectra of solid arsenic(V)-containing compounds in the form of KBr pellets. The concentrations in *w*/*w* are (from top): 9.5%, 5.3%, 2.0%, 4.6%, and 4.8% for iAs(V), MMA-2, MMA-1, DMA-2, and DMA-1, respectively. (*b*) Raman scattering spectra of solid DMA-1, MMA-1, and *p*-AsA (from top). Assignment of observed peaks is listed in Table 2.

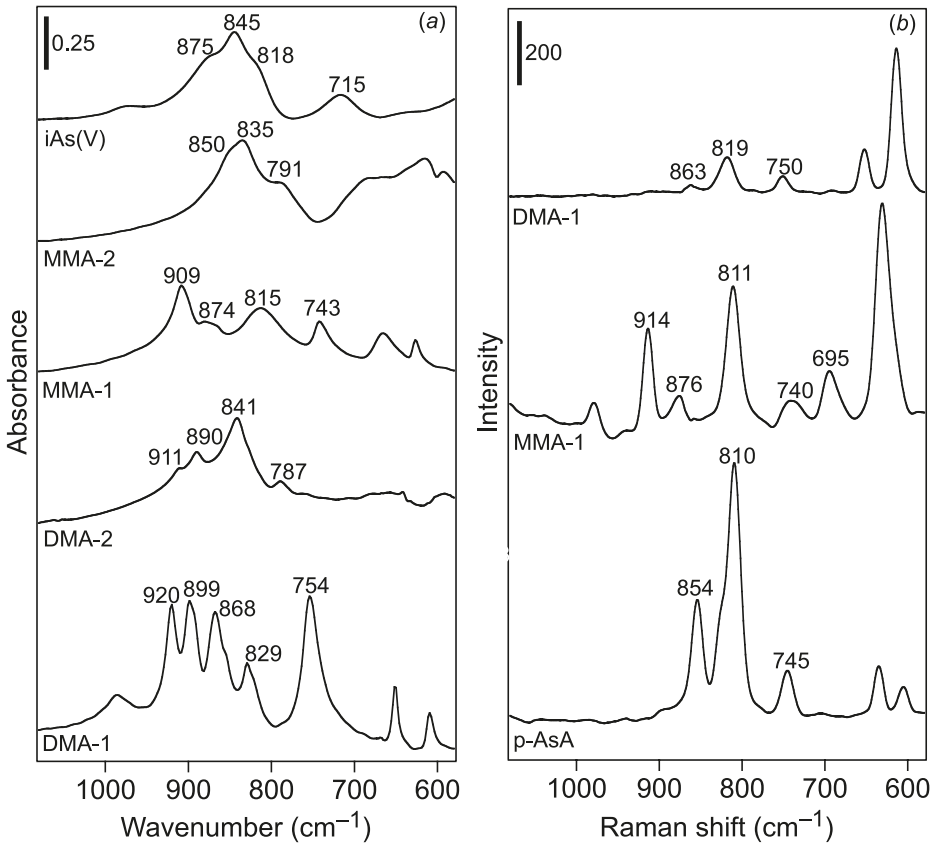

Substitution of one oxygen with a methyl group, in the cases of MMA-1 and MMA-2s, did not significantly affect bond lengths in these molecules relative to iAs(V). Crystal structure of both compounds have not been determined previously, but As–O bond lengths were calculated by Vansant et al. (28) for $CH_3HAsO_3^-$ and $CH_3AsO_3^{2-}$ species to be 1.65 and 1.69 Å, respectively, and 1.71 Å for As–OH in the former species. The FTIR spectra of solid MMA-1 and MMA-2 differ from the aqueous phase spectra of $CH_3HAsO_3^-$ and $CH_3AsO_3^{2-}$ species in that bands assigned to $\nu(AsO_x)$ are lower in frequency for the solid materials than in solution. The same observation was found for solid $CH_3AsO(OH)_2$ compared with the same species in solution by Vasant et al. (27), who attributed it to the stronger hydrogen bonding network between neighboring acid molecules in the solid structure than hydrogen bonds with water molecules in solution. This explanation can be applied to spectral differences between solid and aqueous phase MMA-1 and MMA-2, since both salts contain water molecules in their crystal structure. Moreover, the presence of As-OH groups in solid MMA-1 gives rise to stretching vibration bands at 743 cm^{-1} in the FTIR spectrum, and at 740 and 695 cm^{-1} in the Raman spectrum, which are absent from the spectra of MMA-2. The apparent splitting in ν(As-OH) observed in the Raman spectrum is expected given that the As-OH and As-O^- groups in solid MMA-1 are perturbed by hydrogen bonding with water molecules in the crystalline structure. This analysis may also explain the asymmetrical shape of the band at 743 cm^{-1} in the FTIR spectrum of MMA-1, suggesting the presence of a low frequency component.

In addition, the intense bands at 909 and 914 cm^{-1} (Fig. 2) in the FTIR and Raman spectra of solid MMA-1, respectively, are found in the Raman spectrum of solid $NaH_2AsO_4 \cdot 2H_2O$ at 912 cm^{-1} and assigned for ν_{as}(As-O) (22). For comparison, similar bands at this frequency are observed for aqueous $H_2AsO_4^-$, and $CH_3AsO(OH)_2$, and fully protonated *p*-AsA at 908, 912, and 906 cm^{-1}, respectively. Hence, this spectral feature is associated with molecular species containing relatively high $As(OH)_n$ group concentration, particularly for $n \geq 2$. The fact that a similar feature is observed for solid MMA-1 suggests that -AsO^- moiety is involved in strong hydrogen bonding with neighboring water or MMA molecules. This analysis may explain the absence of this spectral feature from the FTIR spectra of aqueous $CH_3AsO_3H^-$ at pH 6 (Fig. 1*b*), $HAsO_3^{2-}$ at pH 9 (Fig. 1*a*), and solid MMA-2, where weak hydrogen bonding interactions exist with water molecules in solution and solid phases, respectively.

Figure 2*b* shows the measured Raman spectrum of solid *p*-AsA, which contains three well-defined bands at 854, 810, and 745 cm^{-1}. Spectral assignment of the observed bands is given in Table 2. The bands at 854 and 810 cm^{-1} are assigned to $\nu_{as}(AsO_x)$ and $\nu_s(AsO_x)$, respectively. There is also a component at ca. 826 cm^{-1} appearing as a shoulder of the intense band centered at 810 cm^{-1}. The FTIR spectrum of solid *p*-AsA was interpreted in our earlier publication in

© 2008 NRC Canada

light of its crystalline structure (15). Briefly, *p*-AsA molecules in the solid phase exist in a zwitterionic form (i.e., $NH_3^+C_6H_4AsO_2(OH)^-$) in which arsonic groups are involved in two H-bonds (34). Bond lengths in the arsonic group equal 1.66 and 1.67 Å for As–O and 1.74 Å for As–OH groups. Splitting in degenerate ν_{as} vibrations is clear in the Raman spectrum in Fig. 2*b*. It is interesting to note the absence of bands >900 cm^{-1} in the Raman spectrum of solid *p*-AsA as expected from that of MMA-1. However, weak intensity component is visible at ca. 914 cm^{-1} in the FTIR spectrum of *p*-AsA (15). This observation may be explained by the involvement of AsO bonds of *p*-AsA in multiple bonding giving rise to less than 900 cm^{-1} $\nu_{as}(AsO_x)$ vibrations. This observation also suggests that the molecular environment around the -AsO_3 moiety in both solid monosubstituted organoarsenicals, MMA-1 and *p*-AsA, is different most likely due to differences in the hydrogen bonding network in both crystalline structures.

Also shown in Fig. 2 are the FTIR spectra of DMA-1 and DMA-2, in addition to the Raman spectrum of DMA-1. The Raman spectrum of DMA-2 was collected (not shown) and is similar to the recently published one by Mosley et al. (33). Band assignment is provided in Table 2 and agrees very well with previously published values. The crystal structure of DMA-1 was described by Vasant et al. (27), where the unit cell contains two monomeric acid molecules held together by hydrogen bonding, R(OH···O) = 2.57 Å, with two As-O distances at 1.625 and 1.609 Å (35). The lower value of the IR frequency of $\nu(AsO_x)$ in solid DMA-1 (829 cm^{-1}, Fig. 2*a*) relative to aqueous $(CH_3)_2AsO(OH)$ (879 cm^{-1}, Fig. 1*d*) was attributed to stronger hydrogen bonding linking the molecules in the solid structure relative to that with water molecules in solution (27). The corresponding $\nu(AsO_x)$ band in the Raman spectrum of DMA-1 shown in Fig. 2*b* occurs at 819 cm^{-1}, which agrees with previous reports (27). Moreover, the presence of As-OH groups in solid DMA-1 gives rise to stretching vibration bands at 754 and 750 cm^{-1} in the FTIR and Raman spectra, respectively, which are close to the value observed for aqueous $(CH_3)_2AsO_2H$ at pH 3 (Fig. 1*d*). The bands at 868 and 863 cm^{-1} in the FTIR and Raman spectra of solid DMA-1, respectively, have been assigned to γ(OH) (27). The crystal structure of DMA-2 has not been reported, but by comparing the FTIR spectrum of solid DMA-2 (Fig. 2*a*) to that of $(CH_3)_2AsO_2^-$ at pH 11 (Fig. 1*d*), it could be concluded that the site symmetry of the -AsO_2^- group in solid DMA-2 is C_{2v}, similar to its symmetry in solution. Hence, the bands at 841 and 787 cm^{-1} in the FTIR spectrum of DMA-2 are assigned for $\nu_{as}(AsO_x)$ and $\nu_s(AsO_x)$, respectively.

Moreover, the spectral range shown in Fig. 2 contains features that arise from binding of As to organic substituents. Bands associated with As-C stretching vibrations in MMA-1 and MMA-2 occur below 650 cm^{-1} (28, 33), which are absent from the Raman spectra of different iAs(V) minerals (23, 24). Similar to MMA, the two spectral features observed in the Raman spectrum of *p*-AsA at 636 and 605 cm^{-1} are assigned to the As–C stretching vibrations. These features appear at 652 and 614 cm^{-1} for DMA-1, which agree with previous studies (27, 31, 33). Bands associated with ρ(CH_3) are only observed for DMA-1 at 899 and 920 cm^{-1} in Fig. 1*a*, which agree with previous work showing strong features at 891 and 913 cm^{-1} (27), and at ca. 900 and 922 cm^{-1} (31). For DMA-2, whose IR spectrum was not previously published, we assign the two bands at 911 and 890 cm^{-1} to ρ(CH_3), which are red shifted compared with the same features observed for DMA-1. This observation is consistent with the trend observed for these bands in solution for $(CH_3)_2AsO_2^-$ and $(CH_3)_2AsO_2H$ (vide supra). To summarize, while organic substituents did not result in significant change in As–O bond lengths in the solid phase of organoarsenicals compared to iAs(V), it is the incorporation of water molecules and extensive hydrogen bonding with neighboring molecules that significantly affect As–O bond lengths and hence frequencies of $\nu(AsO_x)$.

Implications for the surface complexation of organoarsenicals

Our studies reported herein summarize the factors (i.e., organic substitution on AsO_x moiety and hydrogen bonding) that influence the frequencies and splitting in degenerate bands assigned to $\nu(AsO_x)$ in organoarsenicals. Location of spectral components assigned to $\nu(AsO_x)$ are also sensitive to coordination to mineral surfaces, where arsenic(V)-containing molecules could form inner-sphere (i.e., direct bonding to surface metal cations) and (or) outer-sphere surface complexes (i.e., hydrogen bonding to hydroxyl groups on the surface or binding mediated by water molecules) (19). Myneni et al. (22) have summarized vibrational spectroscopic studies on the binding of iAs(V) to mineral surfaces, where the assignment of bands was aided by the analysis of the vibrational spectra of iAs(V) in aqueous and solid phases, and by X-ray absorption spectroscopy (XAS) results of arsenate adsorbed at the mineral-water interface. They concluded that the value of ν_s(As-OX), where X = metal, H^+, and H_2O, of all AsO_4 surface complexes shift to lower frequency values (≤820 cm^{-1}) relative to uncomplexed AsO_4, and for metal unprotonated-AsO_4 complexes (i.e., inner sphere), the shifts in As-OM (M = metal) vibrations are influenced only by the nature of complexing cation and the type of coordination, which will result in splitting the As-O degenerate vibrations and shifting As-OM modes.

Recently, we have reported the first ATR-FTIR investigation of *p*-AsA binding to Fe-(oxyhydr)oxides including α- and γ-Fe_2O_3 and α-FeOOH particles (15). Adsorption of *p*-AsA was carried out in situ and at equilibrium using solution concentrations in the range of 1 μmol/L–8 mmol/L at pH 7. We found that the spectra of adsorbed *p*-AsA were clearly distinguishable from that of aqueous *p*-AsA at pH 7 and that increasing solution concentration results in increasing the intensity of the resolved components indicating an increase in the surface coverage of *p*-AsA. Peaks <800 cm^{-1} were assigned to symmetric stretch (ν_s) of As-OFe and uncomplexed As-OH. Hydrogen bonded complexes were characterized by the peaks >837cm^{-1}, which could also arise from binding mediated by water molecules. Our data suggested the presence of either two types of *p*-AsA surface complexes including an inner-sphere monodentate and hydrogen bonded complexes *or* one type of surface complexes whose symmetry is much lower than aqueous *p*-AsA at pH 7.

While IR spectroscopy measurements of surface complexes are invaluable in providing structural information (19), results often need to be complemented with synchrotron-

© 2008 NRC Canada

based XAS measurements to aid in the interpretation of the IR spectra. Jing et al. (36) have studied surface complexation of MMA and DMA on nanocrystalline titanium dioxide using extended X-ray absorption fine structure spectroscopy. Their data shows the formation of inner-sphere mono- and bi-dentate complexes for DMA and MMA, respectively. It was also found, by measuring the thermodynamics of binding using batch techniques, that the degree of methylation and oxidation state of methylated arsenic compounds affect their binding affinities to iron minerals (20). Based on the above studies, it will be interesting to see how the IR spectra of adsorbed methylated arsenicals compare to the spectra shown herein for the bulk phases. This work in currently underway in our lab, which will also be complemented with XAS studies at the Canadian Light Source.

Acknowledgments

The authors would like to acknowledge funding from the Research Corporation Cottrell College Award and the Canadian Foundation for Innovation. TH and MD would like to acknowledge funding from the Natural Sciences and Engineering Research Council of Canada (NSERC) Undergraduate Student Research Award Program and the Wilfrid Laurier University (WLU) Science and Technology Endowment Program, respectively. We would like to thank Dr. Vladimir Kitaev for granting us permission to use the Raman spectrometer.

References

1. P.L. Smedley and D.G. Kinniburgh. Appl. Geochem. **17**, 517 (2002).
2. F.X. Han, Y. Su, D.L. Monts, M.J. Plodinec, A. Banin, and G.E. Triplett. Naturwissenschaften, **90**, 395 (2003).
3. D. O'Rourke and S. Connolly. Annu. Rev. Environ. Resour. **28**, 587 (2003).
4. J.M. Trindade, A.L. Marques, G.S. Lopes, E.P. Marques, and J. Zhang. Fuel, **85**, 2155 (2006).
5. M. Bissena and F.H. Frimmel. Acta Hydrochim. Hydrobiol. **31**, 9 (2003).
6. Y. Arai, A. Lanzirotti, S. Sutton, J.A. Davis, and D.L. Sparks. Environ. Sci. Technol. **37**, 4083 (2003), and refs. cited therein.
7. E.M. Kenyon and M.F. Hughes. Toxicology, **160**, 227 (2001).
8. Environment Canada. First priority substances list (PSL1): Arsenic and its compounds. Available from http://www.ec.gc.ca/substances/ese/eng/psap/PSL1_arsenic.cfm. 2003. Accessed 2008.
9. U.S. EPA. Arsenic rule. Available from http://www.epa.gov/safewater/arsenic/regulations.html. 2006. Accessed 2008.
10. E. Dopp, L.M. Hartmann, A.-M. Florea, A.W. Rettenmeier, and A.V. Hirner. Crit. Rev. Toxicol. **34**, 301 (2004).
11. M. Bissena and F.H. Frimmel. Acta Hydrochim. Hydrobiol. **31**, 9 (2003).
12. P.B. Tchounwou, J.A. Centeno, and A.K. Patlolla. Mol. Cell. Biochem. **255**, 47 (2004).
13. W.T. Frankenberger, Jr. (*Editor*). Environmental chemistry of arsenic. Marcel Dekker, Inc., New York. 2002.
14. W.P. Inskeep, T.R. McDermott, and S. Fendorf. Arsenic (V)/(III) cycling in soils and natural waters: Chemical and microbiological processes. *In* Environmental Chemistry of Arsenic. *Edited by* W.T. Frankenberger, Jr. Marcel Dekker, Inc., New York. 2002. pp. 183–215.
15. S. Depalma, S. Cowen, T.N. Hoang, and H.A. Al-Abadleh. Environ. Sci. Technol. **42**, 1922 (2008).
16. S. Wang and C.N. Mulligan. Sci. Total Environ. **366**, 701 (2006).
17. I. Cortinas, J.A. Filed, M. Kopplin, J.R. Garbarino, A.J. Gandolfi, and R. Sierra-Alvarez. Environ. Sci. Technol. **40**, 2951 (2006).
18. K. Ritter, G.R. Aiken, J.R. Ranville, M. Bauer, and D.L. Macalady. Environ. Sci. Technol. **40**, 5380 (2006).
19. D.L. Sparks. Metal and oxyanion sorption on naturally occurring oxide and clay mineral surfaces. *In* Environmental catalysis. *Edited by* V.H. Grassian. Taylor & Francis Group, Boca Raton, Florida. 2005. pp. 3–36.
20. B.J. Lafferty and R.H. Loeppert. Environ. Sci. Technol. **39**, 2120 (2005).
21. D. Peak. Fourier transform infrared spectroscopy. *In* Encyclopedia of soils in the environment. *Edited by* D. Hillel. Elesvier Press, Oxford, UK. 2004.
22. S.C.B. Myneni, S.J. Traina, G.A. Waychunas, and T.J. Logan. Geochim. Cosmochim. Acta, **62**, 3285 (1998), and refs. cited therein.
23. R.L. Frost, J.T. Kloprogge, M.L. Weier, W.N. Martens, Z. Ding, and H.G.H. Edward. Spectrochim. Acta, Part A, **59**, 2241 (2003).
24. R.L. Frost and J.T. Kloprogge. Spectrochim. Acta, Part A, **59**, 2797 (2003).
25. A.J. Roddick-Lanzilotta, A.J. McQuillan, and D. Craw. Appl. Geochem. **17**, 445 (2002).
26. B. McAuley and S. Cabaniss. Anal. Chim. Acta, **581**, 309 (2007), and refs. cited therein.
27. F.K. Vansant, B.J. Van der Veken, and M.A. Herman. Spectrochim. Acta, Part A, **30**, 69 (1974).
28. F.K. Vansant, B.J. Van der Veken, and M.A. Herman. J. Mol. Struct. **35**, 191 (1976).
29. F.K. Vansant, B.J. Van der Veken, and H.O. Desseyn. J. Mol. Struct. **15**, 425 (1973).
30. B.J. Van der Veken and M.A. Herman. J. Mol. Struct. **15**, 225 (1973).
31. M. Joannidou and F. Fillaux. J. Chim. Phys. Phys.-Chim. Biol. **81**, 397 (1984).
32. H.-V. Gründler, H.-D. Schumann, and E. Steger. J. Mol. Struct. **21**, 149 (1974).
33. C.N. Mosley, T.I. Todorov, C.H. Tseng, and J.A. Centeno. Characterization of arsenic species by raman-microspectroscopy. *In* Metal ions in biology and medicine. Vol. 9. *Edited by* M.C. Alpoim, P.V. Norais, M.A. Santos, and othersA.J. Cristovao, J.A. Centeno, and P. Collery. John Libbey Eurotex, Paris, France., 2006. pp. 70–74.
34. R.H. Nuttall and W.N. Hunter. Acta Crystallogr. Sect. C: Cryst. Struct. Commun. **C52**, 1681 (1996).
35. J. Trotter and T. Zobel. J. Chem. Soc. 4466 (1965).
36. C. Jing, M. Xiaogunag, S. Liu, S. Baidas, R. Patraju, C. Christodoulatos, and G.P. Korfiatis. J. Colloid Interface Sci. **290**, 14 (2005).
37. J.-Z. Wu and P.C. Ho. J. Chromatogr. A, **1026**, 261 (2004).
38. C.O. Nuallain and S.O. Cinneide. J. Inorg. Nucl. Chem. **35**, 2871 (1973).
39. Z. Qiang and C. Adams. Water Res. **38**, 2874 (2004).
40. F.K. Vasant, B.J. Van der Veken, and H.O. Desseyn. J. Mol. Struct. **15**, 425 (1973).
41. H.H. Eysel and R. Wagner. Spectrochim. Acta Part A, **49A**, 503 (1993).

© 2008 NRC Canada

Synthesis of dipyrrins bearing chirality adjacent to the conjugated skeleton — Electron-poor pyrroles exhibit dramatically reduced nucleophilicity

Cory S. Beshara, Beth M. Pearce, and Alison Thompson

Abstract: With the aim of furthering our investigations into the asymmetric complexation of dipyrrinato ligands, a dipyrrin bearing a stereogenic centre directly adjacent to the conjugated skeleton was synthesized. The electron-withdrawing nature of the chiral 4-(2,2,2-trifluoro-1-hydroxyethyl)- substituent significantly reduced the nucleophilicity of corresponding pyrroles, such that 2,2′-symmetrically substituted bis(dipyrrin)s bearing this motif were inaccessible. Furthermore, solutions of mononuclear dipyrrinato complexes were found to be less stable to acid-catalyzed decomplexation than the corresponding dinuclear complexes.

Key words: dipyrrin, dipyrromethene, complexation, electron-poor pyrrole, chirality.

Résumé : Dans le cadre de nos travaux sur la complexation asymétrique des ligands dipyrrinato, on a effectué la synthèse d'une dipyrrine portant un centre stéréogène directement adjacent du squelette conjugué. La nature électro-affinitaire du substituant chiral 4-(2,2,2-trifluoro-1-hydroxyéthyle) réduit d'une façon significative le caractère nucléophile des pyrroles correspondants et, en conséquence, des bis(dipyrrines) substituées d'une façon symétrique dans les positions 2 et 2′ et portant ce motif ne sont pas accessibles. De plus, on a observé que les solutions de complexes dipyrrinato mononucléaires sont moins stables vis-à-vis les décomplexations catalysées par les acides que les complexes binucléaires correspondants.

Mots-clés : dipyrrine, complexation, pyrrole déficient en électron, chiralité.

[Traduit par la Rédaction]

Introduction

The asymmetric synthesis of dipyrrinato complexes is a field of current interest because dipyrrins (1) give mono-anionic, planar, bidentate ligands that complex to a wide variety of metal ions. For example, chiral fluorescent boron-dipyrrinato (BODIPY) (2) complexes have been synthesized through the use of chiral dipyrrins (3–5), and chiral metal-organic frameworks incorporating dipyrrinato ligands are also known (6). 2,2′-Bis(dipyrrin)s (Fig. 1) with methylene, ethylene, or propylene linkers joining the dipyrrinato units generate dinuclear (M_2L_2) double helicates with tetrahedrally coordinated metal ions, and mononuclear (ML) helicates are formed if the alkyl linker is four atoms or more in length (7). The incorporation of chiral auxiliaries within the ligand allows the diastereoselective synthesis of helicates. Indeed, excellent diastereoselectivity has been obtained in the synthesis of mononuclear bis(dipyrrinato) helicates bearing templating BINOL and tartrate moieties attached via ethanoate groups within the linker (8). However, the most successful asymmetric synthesis of dinuclear bis(dipyrrinato) helicates to date gives a diastereomeric ratio of only 69:31 (9–11). In all reported diastereoselective syntheses of dinuclear bis(dipyrrinato) helicates, the chiral auxiliary is attached through a pendent ester or amide linkage and thus the chiral centre itself is quite remote from the helical axis.

Cognizant that the degree of stereoselectivity depends upon the effectiveness of the chiral auxiliary in inducing asymmetric complexation and thus the distance between the site of the auxiliary and the helical axis, we explored the value of incorporating a chiral centre directly adjacent to the dipyrrin; such a motif is somewhat rare for pyrroles (12–17) and extremely rare for dipyrrins (16, 18, 19). β-Keto pyrroles are readily available through Knorr-type syntheses (20, 21) and asymmetric reduction would generate a chiral alcohol. Further derivitization would serve to incorporate the pyrrole into a dipyrrin and thus place a chiral centre directly adjacent to the dipyrrinato unit (Fig. 2). Previous studies involving haematoporphyrin have shown that such hydroxyl groups are labile under mildly acidic conditions thus introducing the possibility of racemization through reversible elimination and addition. The lability is caused by the electron-rich nature of the pyrrole ring facilitating racemization at the pseudobenzylic position. Kumadaki provided a viable solution to potential racemization of this nature through the use

Received 3 March 2008. Accepted 17 May 2008. Published on the NRC Research Press Web site at canjchem.nrc.ca on 15 August 2008.

C.S. Beshara, B.M. Pearce, and A. Thompson.[1] Department of Chemistry, Dalhousie University, Halifax, NS B3H 4J3, Canada.

[1]Corrresponding author (e-mail: alison.thompson@dal.ca).

 doi:10.1139/V08-101 © 2008 NRC Canada

Fig. 1. Complexation of bis(dipyrrin)s with varying linker length.

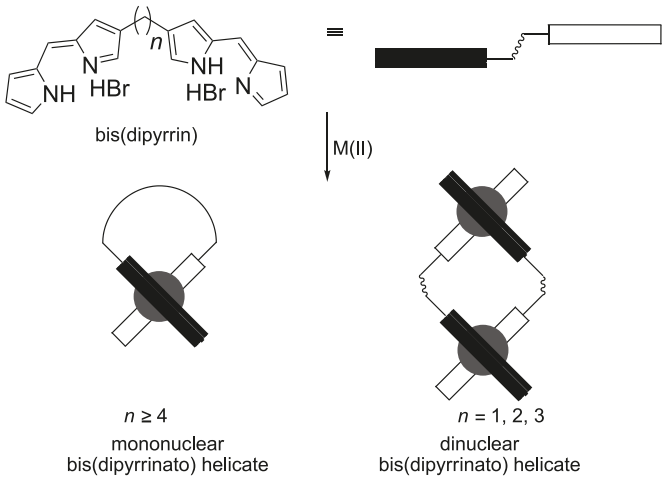

Fig. 2. Retrosynthetic incorporation of chirality adjacent to dipyrrin core.

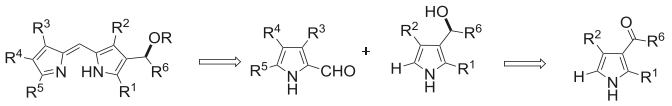

of 4-(2,2,2-trifluoro-1-hydroxyethyl)-substituted pyrroles (18, 19) in the construction of homochiral haematoporphyrins (16). We herein report our work with 4-(2,2,2-trifluoro-1-hydroxyethyl)-substituted dipyrrins. Our goals included the investigation of: the syntheses of dipyrrins and 2,2′-bis(dipyrrin)s incorporating 4-(2,2,2-trifluoro-1-hydroxyethyl)-substituents; the stereochemical stability of 4-(2,2,2-trifluoro-1-hydroxyethyl)-substituted dipyrrins; the ability of 4-(2,2,2-trifluoro-1-hydroxyethyl)-substituted dipyrrinato units to undergo complexation; and the potential of the 4-(2,2,2-trifluoro-1-hydroxyethyl) group to influence diastereoselective complexation, either as an alcohol or as bulkier ether or ester derivatives.

Results and discussion

Synthesis of the first dipyrrin bearing a 4-(2,2,2-trifluoro-1-hydroxyethyl)-substitutent was achieved according to Scheme 1. Benzyl 3,5-dimethyl-pyrrole-2-carboxylate (**1**) (22) was converted to the corresponding trifluoroacetoxy-substituted pyrrole **2** using triflouroacetic acid (TFAA) under acidic conditions (23). Reduction of **2** with borane gave racemic alcohol **3**, and the use of the CBS protocol gave ***S*-3** with 99:1 enantiomeric ratio (er), akin to that reported by Kumadaki and co-workers (16). Hydrogenolysis of the benzyl ester, followed by thermolytic decarboxylation, gave the corresponding α-free pyrrole that was reacted directly with 4-ethyl-2-formyl-3,5-dimethylpyrrole (**4**) (24) under MacDonald-type coupling conditions (1) to afford the requisite racemic dipyrrin **5**, and the single enantiomer ***S*-5**.

The literature supports the stereochemical stability of the 2,2,2-trifluoro-1-hydroxyethyl moiety under acidic conditions (16, 18, 19), but we were concerned that the MacDonald-type coupling conditions (48% HBr, MeOH–THF) (1) might have afforded some racemization as exposure of enantiopure ***S*-3** to the same conditions resulted in loss of stereochemical integrity with the recovered material having only 76:24 er. To investigate its stereochemical purity a sample of the dipyrrin prepared from enantiopure ***S*-3** was converted into the corresponding BODIPY complex **6** (2) (Scheme 2). Because boron-dipyrrinato complexes are achiral at boron and amenable to chromatography, the enantiopurity of **6**, established by chiral HPLC, would reveal the enantiopurity of ***S*-5** by correlation.

Scheme 1. Synthesis of **5**.

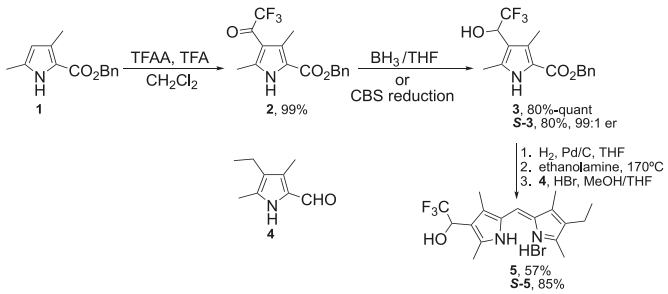

Scheme 2. Synthesis of boron-dipyrrinato complex **6**.

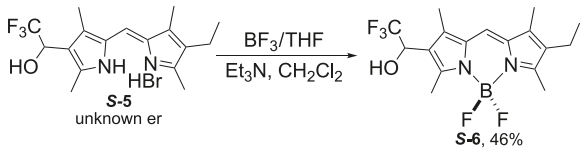

HPLC-analysis (Fig. S1) was used to determine that ***S*-6**, synthesized using ***S*-3**, had retained its enantiopurity during the MacDonald-type coupling step.[2] Thus, with a source of enantiopure ***S*-5** in hand, and having secured both the synthesis and the stereochemical stability of dipyrrins bearing the 4-(2,2,2-trifluoro-1-hydroxyethyl)-group, we progressed to investigating the stability of the corresponding complexes and assessing the influence of the electron-withdrawing substituent, essential for the stability of the chiral centre upon complexation. Racemic **5** was treated with zinc acetate under standard conditions (10) to give the homoleptic zinc complex **7** in 64% yield. The efficiency of complexation was then improved through the use of zinc perchlorate instead of the acetate salt and lithium hydroxide as base; complexation using enantiopure ***S*-5** was conducted in the same manner (Scheme 3). Although the zinc complex (**7**) was noticeably less stable under mildly acidic conditions (silica gel, aqueous extractions, wet solvents) than dipyrrinato complexes not bearing electron-withdrawing groups, isolation of **7** in good yield was achieved by rapid precipitation from the methanolic reaction mixture upon the addition of water. Mass spectrometry confirmed the formation of a mononuclear ML_2 complex.

Efforts turned to the investigation of the stereochemical outcome of the complexation reactions to determine whether **5** had undergone complexation with simple diastereo-

[2] Supplementary data for this article are available on the journal Web site (canjchem.nrc.ca) or may be purchased from the Depository of Unpublished Data, Document Delivery, CISTI, National Research Council Canada, Ottawa, ON K1A 0R6, Canada. DUD 3784. For more information on obtaining material refer to cisti-icist.nrc-cnrc.gc.ca/irm/unpub_e.shtml.

© 2008 NRC Canada

Scheme 3. Complexation of **5** and possible stereochemical outcomes.

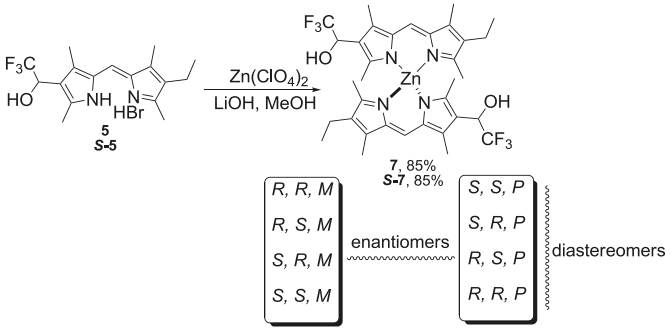

selectivity. Previously, NMR and circular dichroism (CD) spectroscopy, alongside chiral HPLC analysis, have been extremely useful for the evaluation of diastereoselective reactions involving dipyrrinato ligands. The neutral complexes are amenable to chromatography, and the helical nature of the chromophoric dipyrrinato units fixed in space through coordination to metal ions renders CD data very useful. As **5** constitutes an unsymmetrical A–B ligand architecture, the tetrahedrally coordinated metal ion in **7** gives rise to helicity. Thus, the complexation of racemic **5** allows for the possible production of eight ($2^3 = 8$) stereoisomers; *R* and *S* for the stereocentres on the ligands, and *M* and *P* for the metal centre (Scheme 3). Two species in each enantiomeric set (*R*,*S*,*P* – *S*,*R*,*P* and *R*,*S*,*M* – *S*,*R*,*M*) are identical, simplifying the possible outcomes to three (racemic) stereoisomers, with a 1:2:1 statistical ratio.

HPLC analysis of the crude product mixture obtained using racemic **5** showed one signal due to dipyrrinato complex(es) and two minor non-dipyrrinato impurities. The ChiralPak®-IA column used herein had previously proven to be superior for the resolution of dipyrrinato complexes and attempts to resolve the signals of **7** with other columns were unsuccessful. The ^{1}H NMR spectrum for the same product mixture was not useful for assigning stereoisomers but the ^{13}C nucleus allowed for improved resolution. The stereogenic carbon atom bearing the trifluoromethyl group normally appears as a quartet in the ^{13}C NMR spectrum with $J_{CF} \approx 33$ Hz. Indeed, **5** exhibits a quartet with $J_{CF} = 32$ Hz at a chemical shift of 65.8 ppm for this carbon atom. For the product mixture, the stereogenic carbon atom gave signals in the 64 ppm range that appeared as a pair of quartets of equal intensity ($J_{CF} = 33$ Hz), indicative either of a mixture of isomers or of two non-equivalent dipyrrinato units within a single ML_2 complex. Preparative HPLC served to separate the dipyrrinato complex(es) from the impurities, and ^{13}C NMR spectra of the isolated material retained the characteristic 1:1 pair of quartets. We identified that decomposition did not occur during HPLC, because NMR spectra of the initial product mixture and the material after preparative HPLC (and recombination of all fractions) were identical. Complex ***S*-7** was prepared from ***S*-5** (Scheme 3). With enantiopure ligand, the product mixture was found to exhibit identical HPLC and NMR characteristics to **7** (prepared from racemic dipyrrin **5**), thus suggesting that the chiral HPLC column was unable to resolve isomers of **7**.

Although the coordination abilities of dipyrrin ligands have been reported previously (25–27), a comparison of mononuclear and dinuclear analogues has not appeared. Using absorption spectroscopy, solutions of mononuclear **7**, bearing the 4-(2,2,2-trifluoro-1-hydroxyethyl)- substituent, were compared with solutions of the peralkyl mononuclear complex **8** (28) and the peralkyl dinuclear complex **9** (29) (Fig. 3). Studies at a variety of concentrations in technical-grade CH_2Cl_2 indicated that solutions of mononuclear complexes **7** and **8** are less stable to acid-catalyzed decomplexation than the dinuclear complex **9**; spectrophotometric-grade CH_2Cl_2 did not cause any decomplexation. These studies are important as dipyrrinato complexes are typically exposed to a range of solvents (including water) during work-up, purification, and analysis. As mentioned previously, the electron-deficient nature of **7** was a concern in terms of complex stability, and thus discovering that dinuclear dipyrrinato complexes are more stable than their mononuclear analogues suggested that the 4-(2,2,2-trifluoro-1-hydroxyethyl)- substituent might be more appropriate for use in bis(dipyrrinato) ligands. Furthermore, although ***S*-5** is unsymmetrical and thus gives an A–B dipyrrinato ligand that generates tetrahedrally coordinated Zn(II) helicates, formally the helicity is a consequence only of the two differently substituted pyrrolic units, that is, 4-ethyl versus 4-(2,2,2-trifluoro-1-hydroxyethyl).

Fig. 3. Mononuclear complex **8** and dinuclear complex **9**.

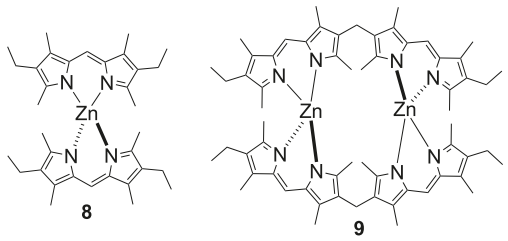

To increase the degree of asymmetry within the ligands, to thus improve both the stereoselectivity of complexation and the resolution by chiral HPLC, and to study the more stable dinuclear dipyrrinato complexes, we turned to the preparation of a bis(dipyrrin) bearing the chiral 4-(2,2,2-trifluoro-1-hydroxyethyl)- substituent directly adjacent to the conjugated skeleton. Retrosynthetic analysis (Fig. 4) of the symmetrical bis(dipyrrin) **10** reveals that the 2,2′-dipyrroles **11** and **12** are essential intermediates in the synthetic sequence, with successful condensation of **11** with **4** giving the required bis(dipyrrin). Three routes to **12** were envisaged, and each was investigated.

Trifluoroacylation of **13** (30), followed by reduction of the two trifluoromethyl ketones, was thought to be the most direct route to **12**. Unfortunately treatment of **13** with TFA and TFAA, under the conditions that had been successful for the synthesis of **2**, did not produce the required material and instead gave, tentatively, the pyrrolo-[3,2-*f*]-indole **18** where presumably mono-trifluoracylation had been followed by acid-catalyzed intramolecular condensation (Scheme 4) (31–33). Since indolic **18** does not feature the required prochiral signature, we sought an alternative route for the synthesis of **12**.

We thus investigated the synthesis of **12** through the homocoupling of **14** (34), itself prepared by mono-oxidation of **15** (16) using $Pb(OAc)_4$ (Scheme 5). Homocouplings of this type, using 2-methylene pyrroles, are commonplace for the synthesis of symmetrical dipyrromethanes and involve

© 2008 NRC Canada

Fig. 4. Retrosynthetic analysis of bis(dipyrrin) **10**.

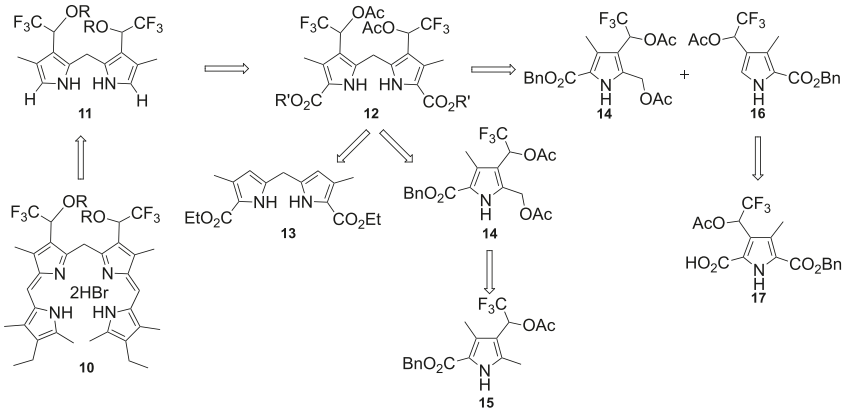

Scheme 4. Synthesis of **18**.

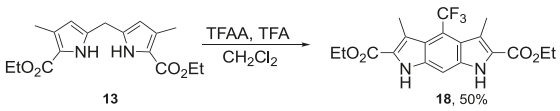

Scheme 5. Synthesis and attempted homocoupling of **14**.

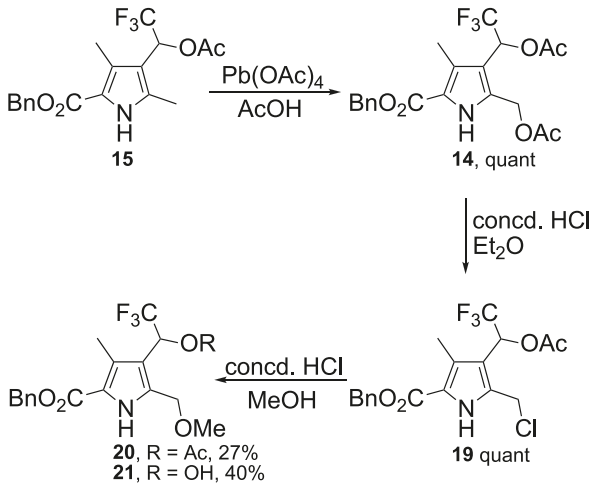

Scheme 6. Synthesis and attempted coupling of **16**.

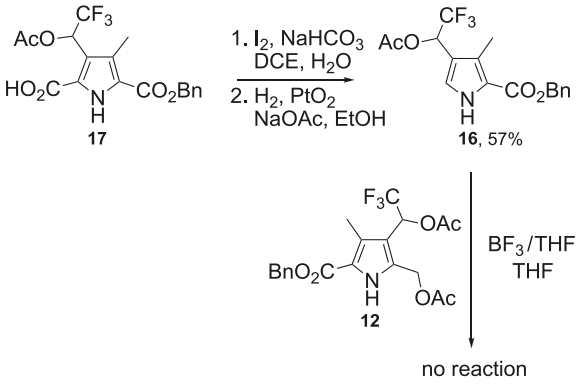

initial ring-protonation followed by the loss of an equivalent of formaldehyde to give in situ 5-unsubstituted pyrroles that then produce dipyrromethanes through condensation with remaining starting material (21, 35). However, treatment of **14** with HCl served only to effect substitution to give **19** and milder conditions (Montmorillonite K-10 clay (36)) gave no reaction at all. Presumably electron-poor **14** is resilient to ring-protonation and thus substitution dominates (12) under forcing conditions, preventing the typical nucleophilic chemistry of pyrroles from occurring; the presence of the electron-withdrawing ester and 2,2,2-trifluoro-1-acetoxyethyl substituents serves to inhibit the traditional nucleophilicity of the pyrrolic unit such that dipyrrins cannot be accessed using these intermediates.

Our final attempts to synthesize **12** required the condensation of a 5-unsubstituted pyrrole with **14**, in effect pre-preparing the same intermediate that was not formed in situ within the previous strategy; this strategy is often implemented for the synthesis of unsymmetrical dipyrromethanes (1). Thus, **16** was prepared via iodinative decarboxylation of **17** (16) followed by dehalogenation of the resulting iodopyrrole (Scheme 6). Attempted reaction of **16** with **14** met with failure and only starting materials were recovered. Once again, the classic nucleophilicity of pyrroles was absent for these electron-deficient pyrroles bearing both ester and (2,2,2-trifluoro-1-acetoxyethyl) substituents. In an attempt to reduce the electron-withdrawing nature of the 4-substituent in pyrrole **20**, the *O*-acyl protecting group was omitted from the synthesis and the free alcohol was exposed to the decarboxylation conditions. Unfortunately, these conditions resulted only in decomposition and the decarboxylated product could not be isolated.

Challenges associated with the low or unusual reactivity of electron-deficient pyrroles are not new. Indeed, Handy and co-workers have described problems associated with the *N*-protection of poly-halogenated pyrroles (37) and Clezy has made observations concerning problems in constructing dipyrromethanes using electron-deficient pyrroles (30). The poor reactivity of pyrroles substituted with the 4-(2,2,2-trifluoro-1-hydroxyethyl)- substituent have prevented our synthesis of a bis(dipyrrin) bearing this chiral moiety adjacent to the conjugated skeleton. The conflicting requirements of (i) electron-withdrawing groups to stabilize the stereocentre adjacent to the pyrrolic core and (ii) adequate nucleophilicy of the pyrrolic heterocycle render the (2,2,2-trifluoro-1-hydroxyethyl)- substituent an inappropriate group with which to introduce chirality directly adjacent to the pyrrolic core.

© 2008 NRC Canada

In summary, a dipyrrin containing a chiral 4-(2,2,2-trifluoro-1-acetoxyethyl)- substituent directly adjacent to the pyrrolic core was prepared and complexed with Zn(II). Although the corresponding mononuclear helicate was isolated in good yield, complexation occurred with poor selectivity. Attempts to prepare an analogous bis(dipyrrin), a skeleton that was found to be generally more stable in solution than the monomeric homologue, were thwarted by the low reactivity of electron-deficient pyrroles. These results again demonstrate that the balance between the reactivity and stability of pyrroles is a fine balance indeed (38, 39): the search continues for moieties that facilitate the introduction of chirality directly adjacent to the pyrrolic core without concurrent inhibition of pyrrolic reactivity.

General experimental

All reagents were purchased from Sigma-Aldrich and used as received, except phosphoric acid that was purchased from Fischer Scientific and reagent grade acetonitrile that was purchased from Caledon. Dry THF and CH_2Cl_2 were obtained from a solvent purification system and stored under nitrogen unless otherwise indicated. Dry ether was obtained via distillation from benzophenone sodium ketal. Unless otherwise indicated all glassware was flame-dried under vacuum prior to use, followed by a nitrogen fill. Column flash chromatography was performed using Silicycle Ultra Pure Silica Gel 60, 230–400 mesh. TLC was performed using Silicycle Ultra Pure Silica Gel 60 aluminum-backed plates, visualized under UV light, and stained using an ethanolic vanillin dip. Absorption spectroscopy was performed with samples in quartz cuvettes with a standard path-length of 1 cm. HPLC separations were performed using a Chiralpak®-IA column composed of amylose tris(3,5-dimethylphenylcarbamate) with particle size of 5 μm; the analytical column had an ID of 0.46 cm and the preparatory column an ID of 2 cm with both columns having a length of 25 cm. The chiral analytical column used for the determination of er in compound ***S*-3** was the Chiralpak® AD-RH, also composed of amylose tris(3,5-dimethylphynylcarbamate) but with a silica support (ID 0.46 cm; length 15 cm). NMR spectroscopy utilized 500 MHz, 400 MHz, and 250 MHz spectrometers at 300 K, as indicated. All ^1H and ^{13}C chemical shifts (δ) are referenced to TMS at 0 ppm in the solvents indicated and are reported on the ppm scale. All coupling constants (*J*) are reported in Hz. ^{19}F NMR spectra were referenced to $CFCl_3$ as an external standard at 0 ppm. Mass spectra were obtained using double focusing magnetic sector (EI) and TOF (ESI) spectrometers. Compounds **1** (22), **2** (3), **3** (16), **4** (24), **8** (28), **9** (29), **13** (30), **15** (16), and **17** (16) were prepared according to known procedures. WARNING: Perchlorate salts are powerful oxidants and care should be taken to avoid exothermic or explosive conditions.

2,3-Dimethyl-4-(2,2-2-trifluoroethyl-1-hydroxy-)-5-(3,5-dimethyl-4-ethylpyrrol-2-ylmethylidene)pyrrole hydrobromide (5)

Pd–C catalyst (10% on C, 0.306 g, 10 mol%) was added to a solution of pyrrole **3** (1.00 g, 3.06 mmol) in THF (40 mL) through a stream of nitrogen and the reaction mixture was then stirred under a hydrogen (1.0 atm) atmosphere. After three days the mixture was filtered through celite and concentrated to facilitate the precipitation of the carboxylic acid (87%), which was then suspended in ethanolamine (25 mL), and the mixture was heated to 170 °C for 45 min, after which the mixture was poured into ice water and extracted with CH_2CH_2 (3 × 20 mL). The combined organic layers were washed with water (50 mL) and then brine (50 mL), followed by drying over sodium sulfate and concentratation. The residue was dissolved in $CHCl_3$ and reconcentrated to yield the α-free intermediate as a yellow crystalline solid (72%). This pyrrole (0.384 g, 1.99 mmol) and **4** (0.190 g, 2.00 mmol) were dissolved in 1:1 MeOH–THF (25 mL) and 48% aq hydrogen bromide (0.300 mL) was added to the solution. After stirring overnight at room temperature, the mixture was concentrated until very little solvent remained. Ether, pre-treated with sodium borohydride, was then added until a copious precipitate was present. Filtration and drying in air gave the title compound as a red solid (0.399 g, 57%); mp 190–230 °C. ^1H NMR (500 MHz, DMSO-d_6) δ_H: 1.04 (t, J_{HH} = 8 Hz, 3H), 2.34 (s, 3H), 2.42–2.45 (m, 5H), 2.58 (s, 3H), 2.60 (s, 3H), 5.27 (q, J_{HF} = 8 Hz, 1H), 6.83 (bs, 1H), 7.45 (s, 1H), 12.52 (bs, 1H), 12.69 (bs, 1H). ^{13}C NMR (125 MHz, DMSO-d_6) δ_C: 10.7, 11.1, 13.6, 14.2, 15.0, 17.4, 65.8 (q, J_{CF} = 32 Hz), 121.9, 122.3, 126.2, 126.4 (q, J_{CF} = 281 Hz), 128.5, 132.6, 143.9, 145.2, 151.7, 158.1. ^{19}F NMR (235 MHz, $CDCl_3$) δ_F: -78.2 (d, J_{HF} = 8 Hz). MS-ESI *m/z*: 327.1 $(M + 1 - Br)^-$.

N,N′-Difluoroboryl-[2,3-dimethyl-4-(1-hydroxy-2,2-2-trifluoroethyl)-5-(3,5-dimethyl-4-ethylpyrrol-2-ylmethylidene)pyrrolato-kN] (6)

To a suspension of **5** (1.00 g, 2.4 mmol) in CH_2Cl_2 (15 mL) under a nitrogen atmosphere was added, first, NEt_3 (6.37 mL, 45 mmol) and, second, $BF_3{\cdot}OEt_2$ (6.33 mL, 51.3 mmol) giving a colour change from brown-orange to dark orange-pink. After stirring the solution (the suspension becomes a solution after the addition of $BF_3{\cdot}OEt_2$) for one hour at room temperature the reaction mixture was concentrated. The residue was taken up in Et_2O and run through a plug of silica to remove baseline material and then further purified using chromatography and 1:50 to 1:10 ethyl acetate – hexanes as eluent to yield the title compound as a pink-red solid (0.395 g, 46%); mp 175–178 °C. R_f (1:5 ethyl acetate – hexanes): 0.19. UV (nm) λ_{max}: 514. ^1H NMR (500 MHz, $CDCl_3$) δ_H: 1.07 (t, J_{HH} = 7.5 Hz, 3H), 2.17 (s, 3H), 2.27 (s, 3H), 2.39 (q, J_{HH} = 7.5 Hz, 2H), 2.52 (s, 3H), 2.54 (s, 3H), 2.55 (d, J_{HH} = 3 Hz, 1H), 5.04 (qd, J_{HF} = 7 Hz, J_{HH} = 3 Hz, 1H), 7.03 (s, 1H). ^{13}C NMR (125 MHz, $CDC1_3$) δ_C: 9.7, 10.3, 13.2 (2C), 14.6, 17.6, 67.7 (q, J_{CF} = 33 Hz), 119.9, 120.2, 125.3 (q, J_{CF} = 280 Hz), 131.7, 134.1, 134.5, 138.0, 139.4, 152.6, 159.8. ^{19}F NMR (235 MHz, $CDCl_3$) δ_F: –78.77 (d, J_{FH} = 7 Hz), –146.16 to –146.85 (m). MS-ESI *m/z*: 354.3 (28%), 355.3 [$(M - F)^+$, 100%)], 356.3 (26%), 374.1 (20%).

Zinc bis[2,3-dimethyl-4-(2,2-2-trifluoroethyl-1-hydroxy-)-5-(3,5-dimethyl-4-ethylpyrrol-2-ylmethylidene)pyrrolato-kN] (7)

Dipyrromethene salt **5** (1.00 g, 2.5 mmol) was dissolved in methanol (80 mL) and lithium hydroxide monohydrate (0.932 g, 9 mmol) was added directly to the solution causing a dramatic shift in colour from orange-red to yellow.

© 2008 NRC Canada

Zinc(II) perchlorate (CAUTION, 1.30 g, 5.0 mmol) was then added and the yellow solution turned orange immediately. The mixture was stirred for one hour followed by dilution with water to precipitate the desired product, which was isolated by filtration as a very fine orange powder after drying overnight in a vacuum oven at room temperature (0.763 g, 85%); mp 197–198 °C. ^{1}H NMR (500 MHz, $CDCl_3$) δ_H:1.01 (t, J_{HH} = 7.5 Hz, 3H), 1.02 (t, J_{HH} = 7.5 Hz, 3H), 1.89–1.94 (m, 3H), 1.95–2.20 (m, 3H), 2.20 (bs, 1H), 2.22 (d, J_{HH} = 1.5 Hz, 3H), 2.35–2.40 (m, 5H), 5.00–5.05 (m, 1H), 7.04 (s, 1H). ^{13}C NMR (125 MHz, $CDC1_3$) δ_C: 10.6, 10.7, 15.1, 15.5, 15.6, 18.2, 68.1 (q, J_{CF} = 33 Hz), 68.1 (q, J_{CF} = 33 Hz), 117.9, 121.8, 125.6 (q, J = 280 Hz), 132.3, 134.8, 134.9, 137.8, 139.6, 153.3, 161.5. ^{19}F NMR (235 MHz, $CDCl_3$) δ_F: –78.9 (d, J = 7.5 Hz). MS-ESI *m/z*: 327.2 (ligand), 715.1 $(M + 1)^+$, 737.1 $(M + Na)^+$.

Benzyl 5-acetoxymethyl-4-(1-acetoxy-2,2,2-trifluoroethyl)-3-methylpyrrole-2-carboxylate (14)

According to a published procedure (18), to a solution of benzyl 4-(1-acetoxy-2,2,2-trifluoroethyl)-3,5-methylpyrrole-2-carboxylate (381.5 mg, 1.03 mmol) in acetic acid (9 mL) under N_2 at room temperature was added $Pb(OAc)_4$ (490.7 mg, 1.107 mmol) as a solid with stirring. The resulting mixture was stirred at 50 °C and monitored using TLC. After full conversion was apparent (4 h), the reaction mixture was cooled to room temperature and then diluted with ethylene glycol (1.0 mL). Distilled water (20 mL) was added to the solution, and the product was extracted using dichloromethane (3 × 50 mL). The organic layer was washed with 5% sodium bicarbonate (3 × 50 mL) and dried over sodium sulfate, and the solvent removed in vacuo to give the product (34) as a white solid (435.6 mg, 99%). ^{1}H NMR (500 MHz, $CDCl_3$) δ_H: 2.06 (3H, s), 2.17 (3H, s), 2.39 (3H, s), 5.16 (2H, q, J = 13.5 Hz), 5.31 (2H, d, J = 12.5 Hz), 5.33 (1H, d, J = 12.5 Hz), 6.23 (1H, q, J = 7.0 Hz), 7.33–7.42 (5H, m), 9.45 (1H, bs). ^{13}C NMR (125 MHz, $CDCl_3$) δ_C: 10.5, 20.6, 20.9, 57.2, 66.3, 66.3 (q, J = 139 Hz), 114.2, 119.7, 123.7 (q, J = 1114 Hz), 127.7, 128.3, 128.4, 128.7, 130.3, 136.1. ^{19}F NMR (235 MHz, $CDCl_3$) δ_F: –76.62. MS-ESI *m/z* for $C_{20}H_{20}F_3NNaO_6$ calcd.: 450.1140; found: 450.1130.

Benzyl 4-(1-acetoxy-2,2,2-trifluoroethyl)-3-methylpyrrole-2-carboxylate (16)

Water (2 mL) and dichloroethane (DCE, 4 mL) were added to a flask containing pyrrole **17** (0.16 g, 0.40 mmol) and sodium bicarbonate (0.11 g, 1.3 mmol). Sodium iodide (0.16 g, 1.1 mmol) and iodine (0.48 g, 1.9 mmol) were added to the biphasic reaction mixture, which was heated at reflux temperature for an hour. After the mixture cooled to room temperature, sodium bisulfite was added very slowly as a solid, to quench the excess iodine (quenching was complete with loss of colour and cessation of effervescence). The layers were then separated and the aqueous layer was extracted with CH_2Cl_2 (3 × 10 mL). The combined organic layers were dried with magnesium sulfate followed by concentration to give the iodopyrrole as an off-white solid. The crude product was suspended in ethanol (4 mL) followed by the addition of sodium acetate (0.045 g, 0.55 mmol) and platinum(IV) oxide (0.014 g, 0.06 mmol) through a stream of nitrogen. A hydrogen atmosphere was maintained utilizing a balloon and needle through a septum and the reaction was stirred for 0.5 h. The product was partially purified using flash column chromatography and 1:5 EtOAc–hexanes as eluent to yield the title compound as a white solid which was used without further purification (0.080 g, 57%). ^{1}H NMR (500 MHz, acetone-d_6) δ_H: 2.12 (s, 3H), 2.40 (s, 3H), 5.31 (s, 2H), 6.20 (q, J_{HF} = 7 Hz, 1H), 7.00 (d, J_{HH} = 3 Hz, 1H), 7.32–7.42 (m, 5H), 9.50 (bs, 1H).

Benzyl 4-(1-acetoxy-2,2,2-trifluoroethyl)-5-chloromethyl-3-methylpyrrole-2-carboxylate (19)

To a solution of benzyl 5-acetoxymethyl-4-(1-acetoxy-2,2,2-trifluoroethyl)-3-methylpyrrole-2-carboxylate (278.6 mg, 0.652 mmol) in dichloromethane (DCM, 20 mL) under nitrogen was added HCl (1 mol/L in ether, 3.129 mL) and the solution was stirred at room temperature overnight. The solution was washed with 5% aqueous sodium bicarbonate (3 × 10 mL) and the aqueous layer extracted using DCM (3 × 20 mL). The organic layers were combined, dried over sodium sulfate, filtered, and concentrated in vacuo to give the product as a light pink solid (111 mg, 40%). ^{1}H NMR (500 MHz, $CDCl_3$) δ_H: 2.20 (3H, s), 2.39 (3H, s), 4.63 (1H, d, J = 13.0 Hz), 4.79 (1H, d, J = 13.0 Hz), 5.33 (2H, d, J = 12.5 Hz), 5.36 (1H, d, J = 12.5 Hz), 6.24 (1H, q), 7.35–7.43 (5H, m), 9.52 (1H, bs). ^{13}C NMR (125 MHz, $CDCl_3$) δ_C: 10.5, 20.7, 36.5, 66.1 (q, J = 139 Hz), 66.5, 113.8, 120.1, 123.7 (q, J = 1114 Hz), 127.9, 128.4, 128.5, 128.8, 131.0, 135.9, 161.1, 168.6. ^{19}F NMR (235 MHz, $CDCl_3$) δ_F: –7.06. MS-ESI *m/z* for $C_{18}H_{17}ClF_3NO_4$ calcd.: 403.0798; found: 402.0717.

Benzyl 4-(1-acetoxy-2,2,2-trifluoroethyl)-5-methoxymethyl-3-methylpyrrole-2-carboxylate (20)

To a solution of benzyl 4-(1-acetoxy-2,2,2-trifluoroethyl)-5-chloromethyl-3-methylpyrrole-2-carboxylate (50 mg, 0.124 mmol) in methanol (2 mL) at room temperature was added concd. HCl (12 mol/L, 0.07 mL), and the mixture was then stirred at room temperature for 4 h. The solvent was removed in vacuo, and the crude mixture was purified using preparative TLC and 70:30 hexane–ethyl acetate as the eluent to give the product as a colourless oil (16.2 mg, 33%). ^{1}H NMR (500 MHz, $CDCl_3$) δ_H: 2.15 (3H, s), 2.41 (3H, s), 3.40 (3H, s), 4.52 (1H, d, J = 13.5 Hz), 4.55 (1H, d, J = 13.5 Hz), 5.31 (2H, s), 6.20 (1H, q, J = 7.5 Hz), 7.34–7.43 (5H, m), 9.20 (1H, bs). ^{13}C NMR (125 MHz, $CDCl_3$) δ_C: 10.7, 20.6, 58.8, 66.1, 66.2, 66.2 (q, J = 138.5 Hz), 111.7, 118.7, 123.9 (q, J = 1114 Hz), 128.4, 128.6, 133.5, 136.3, 161.0, 168.6. ^{19}F NMR (235 MHz, $CDCl_3$) δ_F: –76.93. MS-ESI *m/z* for $C_{19}H_{20}F_3NO_5Na$ calcd.: 422.1191; found: 422.1175.

Acknowledgements

This research was supported by the Natural Sciences and Engineering Research Council of Canada (NSERC). We are grateful to the Canada Foundation for Innovation and the Nova Scotia Research Innovation Trust for research infrastructure. The Sumner and Ryan Foundations (CSB) and a Belle Crowe Scholarship (BMP) financially supported this work.

© 2008 NRC Canada

References

1. T.E. Wood and A. Thompson. Chem. Rev. **107**, 1831 (2007).
2. R.P. Haughland. Handbook of fluorescent probes and research chemicals. 10th ed. Molecular Probes, Inc. Eugene, Ore., USA. 2006.
3. G. Beer, J. Daub, and K. Rurack. Chem. Commun. 1138 (2001).
4. G. Beer, C. Niederalt, S. Grimme, and J. Daub. Angew. Chem. Int. Ed. **39**, 3252 (2000).
5. A. Gossauer, F. Nydegger, T. Kiss, R. Sleziak, and H. Stoeckli-Evans. J. Am. Chem. Soc. **126**, 1772 (2004).
6. D.L. Murphy, M.R. Malachowski, C.F. Campana, and S.M. Cohen. Chem. Commun. 5506 (2005).
7. A. Thompson and D. Dolphin. J. Org. Chem. **65**, 7870 (2000).
8. A. Al-Sheikh-Ali, K.S. Cameron, T.S. Cameron, K.N. Robertson, and A. Thompson. Org. Lett. **7**, 4773 (2005).
9. A. Al-Sheikh Ali, R.E. Benson, S. Blumentrit, T.S. Cameron, A. Linden, D. Wolstenholme, and A. Thompson. J. Org. Chem. **72**, 4947 (2007).
10. T.E. Wood, N.D. Dalgleish, E.D. Power, A. Thompson, X. Chen, and Y. Okamoto. J. Am. Chem. Soc. **127**, 5740 (2005).
11. T.E. Wood, A.C. Ross, N.D. Dalgleish, E.D. Power, A. Thompson, X. Chen, and Y. Okamoto. J. Org. Chem. **70**, 9967 (2005).
12. A.D. Abell, B.K. Nabbs, and A.R. Battersby. J. Am. Chem. Soc. **120**, 1741 (1998).
13. Y. Arai, M. Kasai, K. Ueda, and Y. Masaki. Synthesis, 1511 (2003).
14. S.E. Boiadjiev and D.A. Lightner. Tetrahedron Asymm. **12**, 2551 (2001).
15. K. Hiroi, I. Izawa, T. Takizawa, and K. Kawai. Tetradedron, **60**, 2155 (2004).
16. M. Omote, A. Ando, K. Sato, and I. Kumadaki. Tetrahedron, **57**, 8085 (2001).
17. N.A. Paras and D.W.C. MacMillan. J. Am. Chem. Soc. **123**, 4370 (2001).
18. M. Omote, A. Ando, T. Takagi, M. Koyama, and I. Kumadaki. Tetrahedron, **52**, 13961 (1996).
19. M. Omote, A. Ando, T. Takagi, M. Koyama, I. Kumadaki, and M. Shiro. Heterocycles, **47**, 65 (1998).
20. B. Jolicoeur, E.E. Chapman, A. Thompson, and W.D. Lubell. Tetrahedron, **62**, 11531 (2006).
21. J.B. Paine III. *In* The Porphyrins. *Edited by* D. Dolphin. Academic Press. Vol. I. Chapter 4. 1978.
22. J. Regourd, I.M. Comeau, C.S. Beshara, and A. Thompson. J. Heterocycl. Chem. **43**, 1709 (2006).
23. C.S. Beshara and A. Thompson. J. Org. Chem. **70**, 10607 (2006).
24. R. Chong, P.S. Clezy, A.J. Liepa, and A.W. Nichol. Aust. J. Chem. **22**, 229 (1969).
25. A. Amiri, I.M. Comeau, and A. Thompson. J. Heterocycl. Chem. **43**, 431 (2006).
26. G.B. Guseva, E.V. Antina, and M.B. Berezin. Russ. J. Coord. Chem. **29**, 690 (2003).
27. G.B. Guseva, E.V. Antina, M.B. Berezin, and A.I. V'yugin. Russ. J. Coord. Chem. **30**, 30 (2004).
28. T.E. Wood, B. Berno, C.S. Beshara, and A. Thompson. J. Org. Chem. **71**, 2964 (2006).
29. Y. Zhang and J.S. Ma. Org. Prep. Proced. Int. **33**, 81 (2001).
30. P.S. Clezy and A.J. Liepa. Aust. J. Chem. **23**, 2443 (1970).
31. D.H. Burns, Y.H. Li, D.C. Shi, and T.M. Caldwell. J. Org. Chem. **67**, 4536 (2002).
32. L. Chunchatprasert and P.V.R. Shannon. J. Chem. Soc. Perkin Trans. 1, 1787 (1996).
33. C. Song, D.W. Knight, and M.A. Whatton. Tetrahedron Lett. **45**, 9573 (2004).
34. H. Sato, I. Kumakai, A. Ando, and M. Omote. *In* Jpn. Kokai Tokkyo Koho Japan, JP 11029573. 1999.
35. The Chemistry of Pyrroles. *Edited by* A.R. Jones and G.P. Bean. Academic Press, London. 1977.
36. A.H. Jackson, R.K. Pandey, K.R. Nagaraja Rao, and E. Roberts. Tetrahedron Lett. **26**, 793 (1985).
37. S.T. Handy, J.J. Sabatinin, Y. Zhang, and I. Vulfova. Tetradedron Lett. **45**, 5057 (2004).
38. J.R. Garabatos-Perera, B.H. Rotstein, and A. Thompson. J. Org. Chem. **72**, 7382 (2007).
39. P. Thamyongkit, A.D. Bhise, M. Taniguchi, and J.S. Lindsey. J. Org. Chem. **71**, 903 (2006).

© 2008 NRC Canada

Comparison of chelating ion exchange resins in sorption of copper(II) and zinc(II) complexes with ethylenediaminetetraacetic acid (EDTA) and nitrilotriacetic acid (NTA)

Dorota Kołodyńska and Zbigniew Hubicki

Abstract: This paper investigates the macroporous chelating ion exchangers with different functional groups for their sorption properties towards the copper(II) and zinc(II) ions. The investigations by the dynamic and static methods were carried out in the presence of traditional complexing agents. The differences in affinity of Cu(II) and Zn(II) complexes with these complexones result from the kind of functional groups of the chelating ion exchangers, such as thiourea, aminomethylphosphonate, iminodiacetate, and polyamine groups as well as from the pH value. The quantitative removal of studied heavy metal complexes using chelating ion exchangers is achieved in the case when resins compete successfully for the heavy metal ions against these chelators.

Key words: chelating resins, heavy metals, EDTA, NTA.

Résumé : Dans ce travail, on a étudié les propriétés de sorption d'échangeurs d'ions chélatants microporeux, portant divers groupes fonctionnels, vis-à-vis des ions cuivre(II) et zinc(II). On a effectué ces études par des méthodes dynamiques et statiques en présence d'agents complexant traditionnels. Les différences d'affinité des complexes de Cu(II) et de Zn(II) avec ces complexones résultent de la valeur du pH et de la nature des groupes fonctionnels présents dans les échangeurs d'ions chélatants, tels les groupes thiourée, aminométhylphosphonate, iminodiacétate et polyamine. L'élimination quantitative des complexes métalliques étudiés à l'aide des échangeurs d'ions chélatants a été réalisée dans le cas où les résines peuvent compétitionner avec succès pour les ions métalliques lourds contre ces agents de chélation.

Mots-clés : résines chélatantes, métaux lourds, EDTA, NTA.

[Traduit par la Rédaction]

Introduction

Environmental pollution by toxic metals occurs through industrial and agricultural processes and waste disposal. Fuel and power industries generate about 2.4 million tons of heavy metals (As, Cd, Cr, Cu, Hg, Ni, Pb, Se, V, and Zn) annually. Wastes generated by the electronic industry during printed circuit board production, metal finishing industries, storage battery, and semiconductor manufacturing as well as paper and pulp, pigment, and tanning industries contain relatively high levels of metals (copper, chromium, lead, cadmium, nickel, cobalt, iron, zinc) and inorganic (fluoride, sulphate, chloride) as well as organic ligands (ethylenediaminetetraacetate, nitrilotriacetate, citrate, tartrate, etc.) (1–10).

Received 25 February 2008. Accepted 9 April 2008. Published on NRC Research Web site at canjchem.nrc.ca on 15 August 2008.

D. Kołodyńska and Z. Hubicki.[1] Department of Inorganic Chemistry, Faculty of Chemistry, Maria Curie-Sklodowska University, Maria Curie-Sklodowska Sq.2. 20-031 Lublin, Poland.

[1]Corresponding author (e-mail: hubicki@hermes.umcs.lublin.pl).

Removal of high concentrations of heavy metals is normally achieved by such technologies as precipitation, coagulation/flocculation, sedimentation, and filtration. However, in many situations these processes are inefficient or do not reduce metal concentrations below the accepted standards. Additionally, precipitation processes produce intractable sludge that must be treated and disposed at high cost. Because of the fact that heavy metal ions are often present in various industrial wastewaters along with complexing agents, the treatment of such heavy metal complex-bearing wastewaters requires, in the first step, separation of heavy metals from complexing agents. This is achieved by precipitation of the complexing agents EDTA (ethylenediaminetetraacetic acid) or NTA (nitrilotriacetic acid) by strong acids. In the second step, heavy metal ions are precipitated by means of sodium hydroxide or calcium oxide.

Therefore the most important technologies for the removal of toxic metals or reduction of their concentrations are adsorption and ion exchange. Solvent extraction, phytoextraction, and biosorption can also be used to this end (11–20). Different types of membrane filtrations (ultrafiltration, nanofiltration, reverse osmosis) and electrotreatments (electrodialysis, membrane electrolysis) are also used (21–23). Each of these methods has some limitations in practice, e.g., some of them are economically unfavourable (because

 © 2008 NRC Canada

of high operating cost caused by energy consumption) or technically complicated. Although liquid–liquid extraction can be selective and effective for the removal of heavy metals from wastewaters some loss of solvent and difficulties in phase separation and emulsion formation occur. Therefore, sorption operations including adsorption and ion exchange opposed to the conventional chemical methods are more promising in that they achieve higher removal levels over a wider range of solution conditions, less sludge volumes, and strict discharge specifications. However, in the case of removal of heavy metal ions in the presence of complexing agents using activated carbons, the adsorption of metal ions is related to the electrostatic interaction between the charges of solutes and the surface of activated carbon, which is a function of metal and ligand types, metal–ligand molar ratio, and pH. For solutions greater than pH 6, the negatively charged species of type $[M(edta)]^{2-}$ are repelled from the negatively charged surface groups of activated carbon (11). Additionally, these inexpensive adsorbents as well as biological materials (peanut hulls, coconut copra meal, red cedar wood, pinewood, corn cobs, etc.) do not possess the possibility of their multiple regeneration (23–26). In this regard, ion exchange resins have great potential for the removal of heavy metals from water and industrial wastewaters.

The sorption of heavy metal ions onto ion exchangers has been studied in recent years (27–38). Anionic heavy metal complexes have been eliminated by means of anion exchangers. In the M(II)-EDTA system, removal of $[M(edta)]^{2-}$ complexes is achieved using polystyrene and polyacrylate anion exchangers. Nelson et. al (39) studied the sorption of Cr(III) and V(IV) complexes with EDTA on Dowex 1 × 4 in the H_2edta^{2-} form. Also, elution separations of Ni(II) from V(IV) and K(I), Mn(II) from Co(II), and a mixture of Ba(II), Sc(III), Cr(III), and V(IV) in the 0.01 mol/L EDTA–0.01 mol/L NH_4Cl solution by 0.01 mol/L EDTA with different amounts of NH_4Cl were presented. Dudzinska et al. (40, 41) indicated that the sorption of complexes of Pb(II) and Cd(II) with EDTA on the polyacrylate anion exchangers Amberlite IRA 458, Amberlite IRA 68, as well as on the polystyrene anion exchanger Amberlite IRA 400 is also effective. The polyacrylate anion exchangers (Amberlite IRA 458, Amberlite IRA 68, and Amberlite IRA 958) were used for the removal of copper(II) complexes with IDA (iminodiacetic acid), NTA, and EDTA (42, 43). Also, the studies by Juang et al. (44) have demonstrated the possibility of using the anion exchanger Amberlite IRA 400 for copper(II) removal from such solutions.

Recent studies have also shown that chelating resins could be used for selective removal and recovery of metals containing strong organic and inorganic ligands. Contrary to the conventional ion exchangers, the chelating ion exchangers are characterized by high selectivity towards various metal ions. Their selective properties depend mainly on the kind of functional group. Sorption selectivity is particularly affected by mutual position of functional groups, their spatial configuration, and steric effects and to a smaller degree by matrix properties. Their exchange capacity depends also on the number of functional groups and pH of solution. Important features of macroporous chelating ion exchangers are their better kinetic properties compared with those of the conventional gel ion exchangers of that type.

Chelex 100 and Amberlite IRC 718 have been used to treat the waste effluents containing Cu(II), Ni(II), and Na(I) ions as well as EDTA and citrate discharged from printed circuit board manufacturing (45). Korngold et al. (46) removed Cu(II), Ni(II), Co(II), and Cd(II) from tap water containing small amounts of complexing agents such as humates and salts of carboxylic acids onto the chelating ion exchanger. A new class of polymers with oligo(ethyleneamine) (OEA) moieties such as ethylenediamine (EDA), diethylenetriamine (DETA), triethylenetetraamine (TETA), tetraethylenepentaamine (TEPA), and pentaethylenehexaamine (PEHA) attached to the acrylamide resins has recently been developed and compared to commercially available resins such as Sumichelate MC 10, Lewatit E-TEPA, Lewatit HLH-TETA, and Purolite D 2914 by Matejka et al. (47, 48). The sorption of heavy metal ions by oligo(ethyleneamine) resins is based on the coordination bond of a heavy metal cation to the N-atom of the functional group in the free base form and formation of a very strong amine complexe $[M(OEA)]^{2+}$ so that the electrostatic attractive forces do not contribute to metal sorption. Electrical neutrality inside the resin phase is maintained by the electrostatic uptake of anions of EDTA from solutions. It was found that only the resin having PEHA moiety can be applied for sorption of Cu(II). However, the obtained breakthrough capacity decreases with the increasing concentration of EDTA as well as metal concentration in the loading solution. It was also pointed out that the presence of an alkaline earth metal cation (Mg(II) or Ca(II)) improves the sorption capacities towards chelated heavy metals (Cu(II), Zn(II), and Ni(II)). Desorption of heavy metal cations can be carried out by H_2SO_4, but in this case the clogging of the resin bed by EDTA is a limitation that should be taken into account.

The chelating hydrogel resin containing the PEHA functional groups obtained by inversion copolymerisation of glycidyl methacrylate (GMA)-ethylene dimethacrylate (PEHA) with GMA-ED (ethylenediamine) has also been shown to remove the Cu(II)-EDTA complexes to some extent (49). The maximum sorption capacity of 1.08 mmol/g of copper(II) ions was achieved at pH 6.0, and the Cu(II)-EDTA molar ratio was equal to 1:0.5 (initial concentration of Cu(II) was 300 mg/L). It was also shown that as the amount of EDTA in the solution increases, more EDTA is available to compete for copper(II) ions against the chelating ion exchanger. When the Cu(II)-EDTA ratio exceeds 0.75, the efficiency of removal of copper(II) ions is limited. Then the sorption capacity of copper(II) ions is lower and almost equal to the sorption capacity of copper(II) ions without EDTA (about 0.52 mmol/g), but for the Cu(II)-EDTA = 1:1 system this value is about 0.18 mmol/g. Another ion exchanger containing the hydroxyl group and iminodiacetic acid was applied for sorption of copper(II), cadmium(II), and cobalt(II). The obtained sorption capacities for these ion metals were 1.46 mmol/L, 1.10 mmol/L, and 1.02 mmol/L, respectively (initial metal concentration was 7.87 mmol/L at pH 4.5). The sorption/desorption test showed that only 4% of the sorption capacity decreased after 15 cycles (50).

The aim of this paper is to examine the rate of removal of Cu(II) and Zn(II) ions from wastewaters containing

© 2008 NRC Canada

ethylenediaminetetraacetic (EDTA) or nitrilotriacetic (NTA) acids on the commercial chelating ion exchangers Lewatit TP 214, Lewatit TP 260, Purolite S-920, and Purolite S-930 as well as Diaion CR-20. There is a need for such comparison to be made to know the possibility of their application in treatment of wastewaters containing typical complexing agents. The parameters that influence the sorption process (the initial ions concentrations, pH, metal-ligand molar ratio) and isotherm studies were investigated.

Materials and methods

Chelating ion exchangers

The chelating resins selected for the study were Lewatit TP 214 (with thiourea groups), Lewatit TP 260 (with aminomethylphosphonate groups), Purolite S-920 (with thiourea groups), Purolite S-930 (with iminodiacetate groups), as well as Diaion CR-20 (with polyamine groups). Prior to their use they were washed with 1 mol/L NaOH and 1 mol/L HCl (to remove organic and inorganic impurities) and then several times with deionized water. The resin was finally converted to the H^+ or Na^+ forms. Important physical and chemical properties of these ion exchangers are presented in Table 1.

Preparation of solutions

The aqueous solutions of each heavy metal ion in the presence of EDTA or NTA were prepared by dissolving equimolar amounts of metal chloride, $CuCl_2 \cdot 2H_2O$ or $ZnCl_2 \cdot 2H_2O$, in the sodium salts of EDTA or NTA solution at pH 4.6 and 4.0, respectively. The initial pH values for individual complexes (without pH adjustments) were 3.05 $[Cu(edta)]^{2-}$, 3.00 $[Zn(edta)]^{2-}$, 3.00 $[Cu(nta)]^{-}$, and 3.00 $[Zn(nta)]^{-}$. In the case where NaOH was added, the pH of the $[Cu(edta)]^{2-}$ complexes was 5.50. All used chemicals were of analytical reagent grade (POCH S.A. Gliwice, Poland).

Dynamic method – column procedure

To measure affinity of the above mentioned Cu(II) and Zn(II) complexes, the breakthrough curves were determined using 20 mL of the swollen chelating ion exchanger in the appropriate form. The prepared solutions were passed continuously downward through the resin beds keeping the flow rate at 0.8 mL/cm^2 min. The effluent was collected in fractions in which the metal(II) content was determined. The mass (D_g) and volume (D_v) distribution coefficients as well as the working ion exchange capacities (C_w) were calculated according to the following equations (51)

$$[1] \qquad D_g = \frac{\overline{U} - U_0 - V}{m_j}$$

$$[2] \qquad D_v = \frac{\overline{U} - U_0 - V}{V_j}$$

$$[3] \qquad C_w = \frac{U \cdot c_0}{V_j}$$

where $\overline{U}$ is effluent volume at $c = c_0/2$ (determined graphically) (mL), U_0 is dead volume in the column (liquid volume in the column between the bottom edge of ion exchanger bed and the outlet) (mL), U is effluent volume to the break point (L), V is void (inter-particle) ion exchanger bed volume, which amounts to ca. 0.4 of the bed volume (mL), m_j is dry ion exchanger weight (g), V_j is bed volume (mL), and c_0 is initial concentration of M(II) in the aqueous phase (g/L).

The total ion exchange capacities (C_r) were calculated by integration along the curve.

Static method

In batch experiments, about 0.5 g of appropriate dry ion exchanger was placed in a 100 mL stoppered conical flask containing 50 mL of heavy metal ion solution of the initial concentration, c_0, complexed with EDTA or NTA. The flask was shaken using the laboratory shaker of ELPHINE type 357 produced in Poland. The measurements were made at the constant temperature 298 K in the three parallel series. The stirring speed was 180 rpm to maintain resin particles in the suspension. After the pH of the solution was stabilized and equilibrated, the ion exchanger was filtered to determine the content of metal(II) ions. Preliminary experiments showed that the sorption process is fast and the removal rate is constant after 90 min. Therefore, the contact time of 90 min was used for batch tests. Series of experiments were conducted to determine the effect of initial metal ion concentration and pH on sorption. The pH was measured with a Radiometer pH meter (Model PHM 82). The concentrations of Cl^- ions were not determined. The metal ion concentrations obtained for batch experiments were converted to the percentage of metal ions removed (%R) and the amount of metal sorbed per unit weight of ion exchanger at the specific time and at the equilibrium (q_t, q_e).

The recovery factor was calculated from the equation

$$[4] \qquad \%R = \frac{c_0 - c_t}{c_0} \times 100\%$$

The sorption capacity (q_t) at the specific time (t) was calculated from the equation

$$[5] \qquad q_t = \frac{(c_0 - c_t) \times V}{m}$$

The total sorption capacities (q_e) of ion exchangers for heavy meal ions were given by

$$[6] \qquad q_e = \frac{(c_0 - c_e) \times V}{m}$$

where c_0 is initial concentration of M(II) in the aqueous phase (mg/L), c_t is concentration of M(II) in the aqueous phase at time t (mg/L), c_e is concentration of M(II) in the aqueous phase at equilibrium (mg/L), V is volume of the solution (L), and m is mass of the ion exchanger (g).

AFM studies

To compare the surface morphologies of the studied ion exchangers before and after the sorption process, atomic force microscopy (AFM) scans were also made by means of AFM Digital Instrument NanoScope III (U.S.A.). The scans were taken at room temperature, in air, and in contact mode

© 2008 NRC Canada

Table 1. Characteristics of the applied chelating ion exchangers.

	Lewatit TP 214	Lewatit TP 260	Purolite S-920	Purolite S-930	Diaion CR-20
Manufacturer	Bayer Chemicals, AG	Bayer Chemicals, AG	Purolite International, Ltd.	Purolite International, Ltd.	Mitsubishi Chemical Industries, Ltd.
Functional group	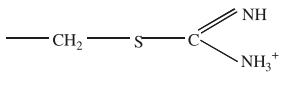	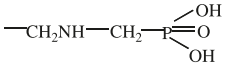	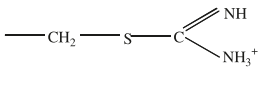	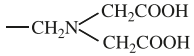	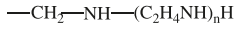
Ionic form as shipped	H^+	Na^+	H^+	Na^+	OH^-
Matrix	Cross-linked polystyrene	Cross-linked polystyrene	Cross-linked polystyrene	Cross-linked polystyrene	Cross-linked polystyrene
Structure	Macroporous	Macroporous	Macroporous	Macroporous	Macroporous
Appearance	Beige, opaque	Beige, opaque	Cream, opaque	Beige, opaque	Beige, opaque
Bead size [mm]	0.3 – 1.2	> 0.63	0.3 – 1.2	0.3 – 1.2	0.3 – 0.55
Total capacity [meq/mL]	2.0 (H^+)	2.4 (H^+)	1.6	1.1	> 0.8
Operating pH range	0–10	0–14	1–13	2–6	4–6
Density [g/mL]	1.18	1.20	1.12	1.17	0.685
Thermal stability [K]	273–313	273–313	273–353	273–343	273–373
Water retention [%]	55-60	58-62	48-54	55-65	50-60

© 2008 NRC Canada

Fig. 1. The percentage of individual forms of Cu(II) and Zn(II) complexes with EDTA and NTA depending on the pH value.

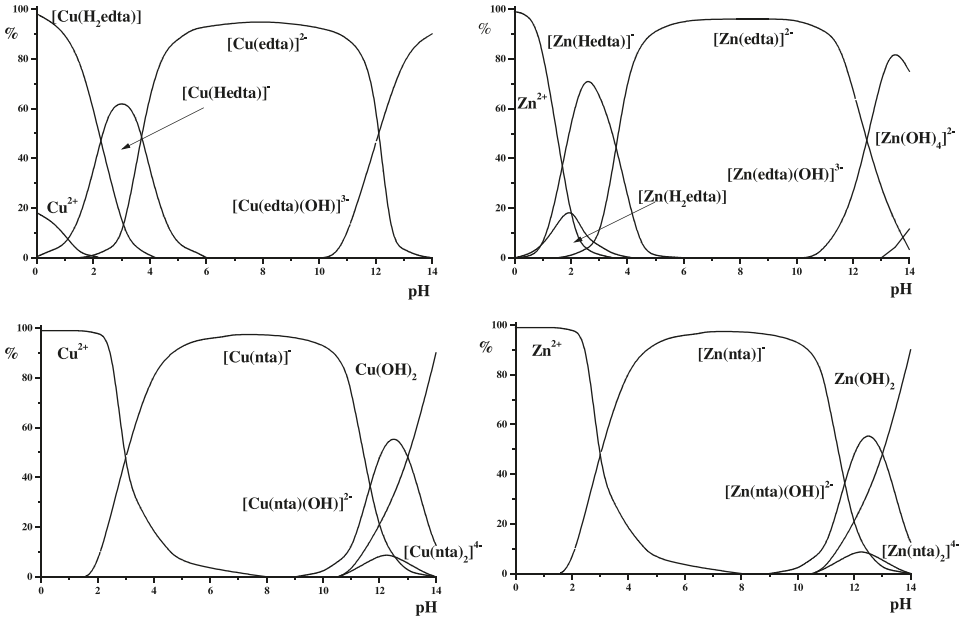

conditions, i.e., at direct contact between the sample and the tip.

FT-IR/PAS and Raman studies

The FT-IR/PAS (the Fourier transform IR photoacoustic spectroscopy) spectra of the ion exchangers before and after the sorption processes were recorded by means of a Bio-Rad Excalibur 3000MX spectrometer equipped with the photoacoustic detector MTEC 300 (in the helium atmosphere in a detector) over the 4000–400 cm^{-1} range at the resolution of 4 cm^{-1} and the maximum source aperture. The spectra were normalized with reference to the MTEC carbon black standard.

The Raman spectra of the ion exchangers before and after the sorption processes were recorded by means of an inVia Reflex Raman spectrometer.

Analytical procedure

The concentrations of the solutions were analyzed using an atomic absorption spectrophotometer Varian Spectr AA-880.

Results and discussion

In the system containing heavy metals and EDTA or NTA, heavy metals tend to form thermodynamically stable complexes so the following equations can be assumed

$$M^{2+} + edta^{4-} \rightleftarrows [M(edta)]^{2-}$$

$$M^{2+} + nta^{3-} \rightleftarrows [M(nta)]^{-}$$

The concentration of present metal ions and ligands and the stability constants of formed complexes control the equilibrium in the system. The addition of another ligand or metal ion to the solution causes a new equilibrium to be attained. An analogous situation occurs when the chelating ion exchanger occurs in the system. As mentioned above, the quantitative removal of heavy metal ions in the presence of EDTA or NTA using the ion exchange method is achieved only in the case when chelating resins are strong enough to compete successfully for the heavy metal ions against chelators. Stability constants for heavy metal complexes with EDTA are very high, whereas the stability of its NTA complexes is several orders of magnitude lower, so the competition by chelating ion exchanger of these complexes should be easier. Additionally, as follows from the comparison of conditional stability constants of studied complexes these values increased with the increasing pH and at low pH the tendency for metal–EDTA complexes formation may be assumed to have the following sequence, Fe(III) > Cu(II) >Pb(II) >Zn(II). Therefore the research was done at low pH. For comparison, research was also done at a higher pH value for some systems.

The analysis of speciation distributions of copper(II) and zinc(II) in the presence of EDTA and NTA (calculated by using a SPE computer program) (Fig. 1) shows that in the strong acidic medium (pH < 2) there are predominant uncomplexed metal(II) ions whose concentration decreases with the increasing pH, which results in the formation of the complexes $[M(H_2edta)]$ and $[M(Hedta)]^-$. At a higher pH the complexes of $[M(edta)]^{2-}$ and $[M(nta)]^-$ types are predominant. The degree of M(II) complexation increases at pH >10 due to transformation of the complex $[M(edta)]^{2-}$ to the more stable $[M(edta)(OH)]^{3-}$, and in the case of NTA, the $[M(nta)]^-$ type to the $[M(nta)(OH)]^{2-}$. For pH >12 copper(II) and zinc(II) hydroxocomplexes appear in the system. As follows from the analysis of AFM scans, the surfaces of studied chelating ion exchangers before and after the sorption process are differentiated. Exemplary AFM scans for Diaion CR-20 are presented in Fig. 2. Topography scans in Fig. 2 show three-dimensional and two-dimensional AFM images of Diaion CR-20 (*a*) before and (*b*) after the sorption process, respectively. As follows from comparison of FT-IR/PAS (Fig. 3) as well as Raman spectra (Fig. 4) of the

© 2008 NRC Canada

Fig. 2. The two-dimensional and three-dimensional AFM scans of Diaion CR-20 (*a*) before and (*b*) after the sorption process of Cu(II) in the presence of EDTA (surface area 500 nm × 500 nm, z = 1 nm).

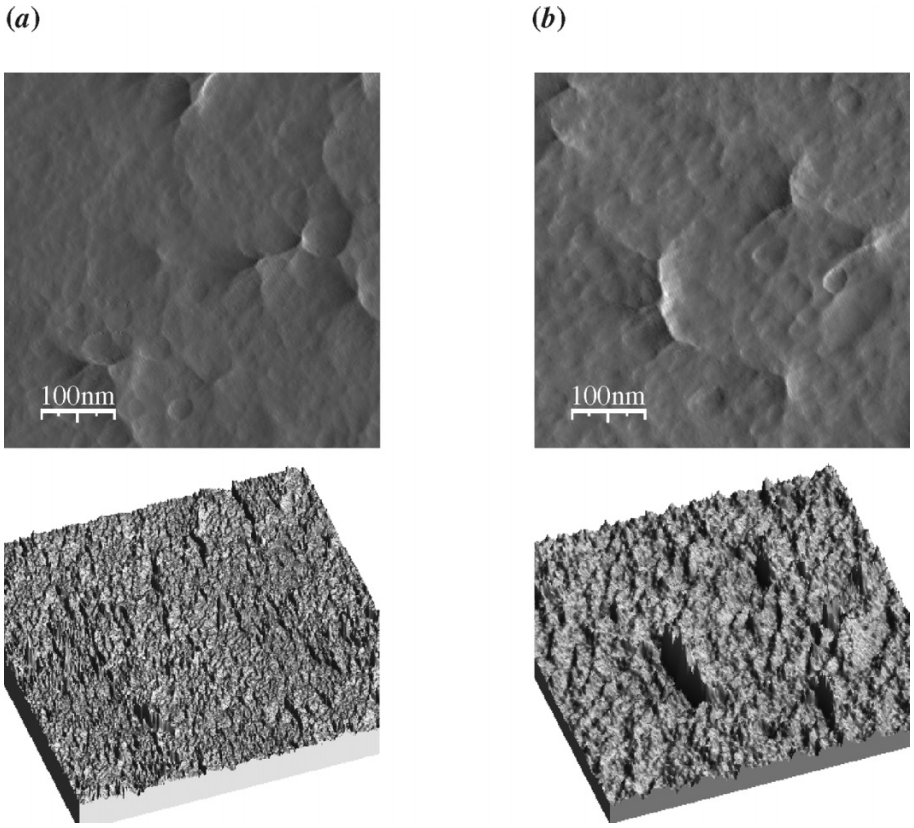

Fig. 3. FT-IR/PA spectra of chelating ion exchangers before and after the sorption of Cu(II) in the presence of EDTA.

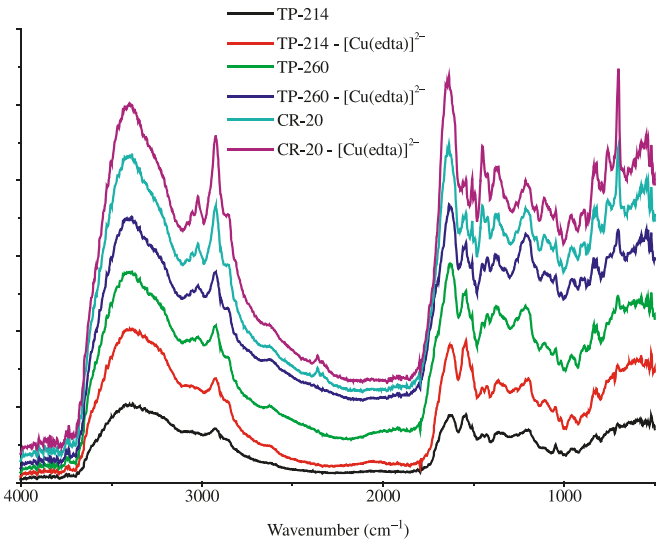

Fig. 4. The Raman spectra of the chelating ion exchanger Diaion CR-20 before and after the sorption of Cu(II) in the presence of EDTA.

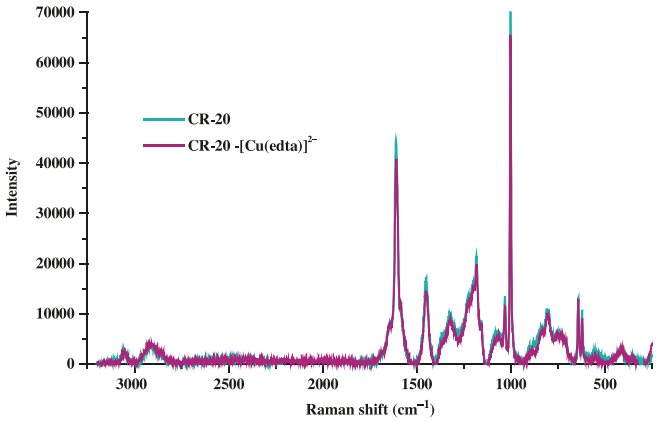

studied chelating ion exchangers Lewatit TP 214, Lewatit TP 260, and Diaion CR-20 possess bands related to the matrix of ion exchanger (cross-linked polystyrene by divinylbenzine). In the case of Lewatit TP 214 with the thiouronium functional groups, the board peak at 3200–3400 cm^{-1} should be associated with the asymmetric and symmetric stretching bonds of the $-NH_2$ groups of thiouronium. The other bands of this functional group are at 519 cm^{-1}, 1103 cm^{-1}, and 1394 cm^{-1}. After the sorption of Cu(II) ions in the presence of EDTA, the FT-IR/PAS spectrum of Lewatit TP 214 possesses two strong bands at 1629 cm^{-1} and 1542 cm^{-1} assigned to the asymmetrical and symmetrical stretching of the COO^- group, respectively. This can also be related to the deformation band of the $-NH_2$ group. Other peaks for the $-COO^-$ group are at 1424–1455 cm^{-1} and at 1365–1395 cm^{-1} as well as at 900–960 and 815–865 cm^{-1}. The position of the band assigned to the $[M(edta)]^{2-}$ complex can be employed as the indication of

© 2008 NRC Canada

the nature of the M–O bond because its position is influenced by the charge (q) and the ionic radius of metal ions (r). For a q/r ratio larger than 3.6, the carbonyl absorption maxima occuring in the 1625–1650 cm^{-1} region indicate the covalent bonding but for a q/r less than 3.6 they are in the 1590–1615 cm^{-1} region and indicate that the bonding is primarily ionic. When the peaks occur between these regions, the bonding is probably partially ionic and partially covalent. However, in the obtained spectrum the band at 1607 cm^{-1} assigned to the $[Cu(edta)]^{2-}$ complex is difficult to identify because of ion exchanger band overlapping. In the case of formation of the coordination bond of copper(II) with the nitrogen or sulphur atom from the thiouronium group, the bands at about 460 cm^{-1} and 280 cm^{-1} (conform to the stretching frequency of Cu-N (ν(Cu-N)) or Cu–S (ν(Cu-S)) bonds) in the FT-Raman spectrum could confirm the presence of complexes of this type.

It is well-known that the selective ion exchangers containing thiouronium functional groups exhibit high selectivity for metal ions, especially for noble metal ions. Depending on the pH, these groups assume the following forms shown in the figure below.

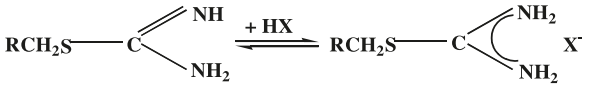

They are able to form coordination bonds with metal cations (the first form), but in the second form the anion complexes are bonded according to the anion exchange mechanism. Also, other ion exchangers can behave as basic anion exchangers in the acidic medium but in the pH range of 4–10 they exhibit properties of chelating ion exchangers.

As follows from the recorded spectrum of Lewatit TP 260, after the sorption of Cu(II) ions in the presence of EDTA there appears to be a band connected with asymmetric vibrations stretching the C-O band at 1641 cm^{-1} and a slightly weaker band of symmetric stretching vibrations at 1453 cm^{-1}. However, the band connected with the vibrations of the -NH group disappears (Fig. 3), which can indicate decomposition of the Cu(II)-EDTA complex and formation of the coordination bond between a nitrogen atom and a phosphorous atom.

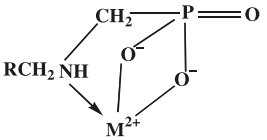

In the hydrochloric acid medium, Diaion CR-20 also behaves like a weakly basic anion exchanger. According to the anion exchange mechanism the sorption process has a two stage character. In the first stage, the functional groups are protonated. It results in the positively charged surface of resin pore walls, which in the second step, leads to the association of anions due to electrostatic interactions between positively charged groups and the anions in the solution. The obtained FT-IR/PAS spectra of Diaion CR-20 before and after sorption of Cu(II) ions in the presence of EDTA are very similar.

Effect of metal(II)-ligand molar ratio

To measure affinity of Cu(II) and Zn(II) in the presence of EDTA and NTA, the breakthrough curves were determined using the above mentioned chelating ion exchangers. The exemplary breakthrough curves of Cu(II) complexes with EDTA or NTA in the Cu(II)-EDTA = 1:1, Cu(II)-EDTA = 1:2, and Cu(II)-EDTA-NaOH = 1:1:2 as well as in the Cu(II)-NTA = 1:1 and Cu(II)-NTA = 1:2 systems on Lewatit TP 214, Lewatit TP 260, Purolite S-920, and Purolite S-930 as well as Diaion CR-20 are presented in Figs. 5 and 6. The mass (D_g) and volume (D_v) distribution coefficients as well as the working (C_w) and total (C_r) ion exchange capacities of M(II) were calculated from the determined breakthrough curves (Tables 2 and 3).

As follows from the obtained results, the factor influencing effectiveness of sorption on chelating ion exchangers is the kind of form in which the metal ion is presented in the system (related with the solution pH). In the case of sorption of heavy metal complexes with EDTA using chelating ion exchangers, the highest effectiveness of sorption is obtained at the complexation of M(II):EDTA = 1:1 and a lower pH. This is in agreement with a reverse tendency compared to the case of sorption of heavy metal complexes with EDTA on the strongly basic polystyrene anion exchangers with quaternary ammonium groups where anionic complexes take part in the sorption process (52). The obtained results were also confirmed by the sorption parameters, calculated values of distribution coefficients, as well as sorption capacities of ion exchangers towards Cu(II) and Zn(II) (Tables 2 and 4). As follows from the speciation distribution diagrams (Fig. 1) in this system (pH of about 3), the neutral complexes of $[M(H_2edta)]$ type (about 18% for Cu(II) and about 6% for Zn(II)) and anionic complexes of $[M(Hedta)]^-$ type (about 65% for Cu(II) and about 70% for Zn(II)) as well as of $[M(edta)]^{2-}$ type (about 18% for Cu(II) and about 10% for Zn(II)) should participate in the sorption process. With the higher pH, percentage contributions of neutral and one-negative anionic complexes decrease. At higher pH (more than 4) in the case of EDTA, two-negative complexes of $[M(edta)]^{2-}$ type are present (about 99%).

In the case of copper(II) and zinc(II) complexes with NTA, higher affinity for chelating ion exchangers is exhibited in the M(II)-NTA = 1:1 system. Larger differentiation in the affinity of Cu(II) and Zn(II) complexes with NTA is found for the chelating ion exchanger Lewatit TP 214 than for Diaion CR-20 (Table 3).

Effect of the type of ion exchanger functional group

The research results also showed the effect of the type of ion exchanger functional groups on sorption effectiveness of Cu(II) and Zn(II) in the presence of EDTA and NTA (Figs. 5 and 6). In the case of ion exchangers with thiourea groups (Lewatit TP 214 and Purolite S-920) in the sorption process, two stages can be distinguished: the initial stage of slow sorption (up to about 0.1 c/c_0) and the other is much faster until the total exhaustion of the bed (c/c_0 >0.1) takes place. This suggests the possibility of occurrence of various types of complexes or uncomplexed ions during formation of the exchange zone. In the case of the chelating ion exchanger Lewatit TP 260 of the aminomethylphosphonate functional group, fast sorption is observed in the first stage (to about

© 2008 NRC Canada

Fig. 5. The breakthrough curves of Cu(II) and Zn(II) complexes with EDTA in the M(II)-EDTA = 1:1, M(II)-EDTA = 1:2, and M(II)-EDTA-NaOH = 1:1:2 systems on Lewatit TP 214, Lewatit TP 260, Purolite S-920, Purolite S-930, and Diaion CR-20.

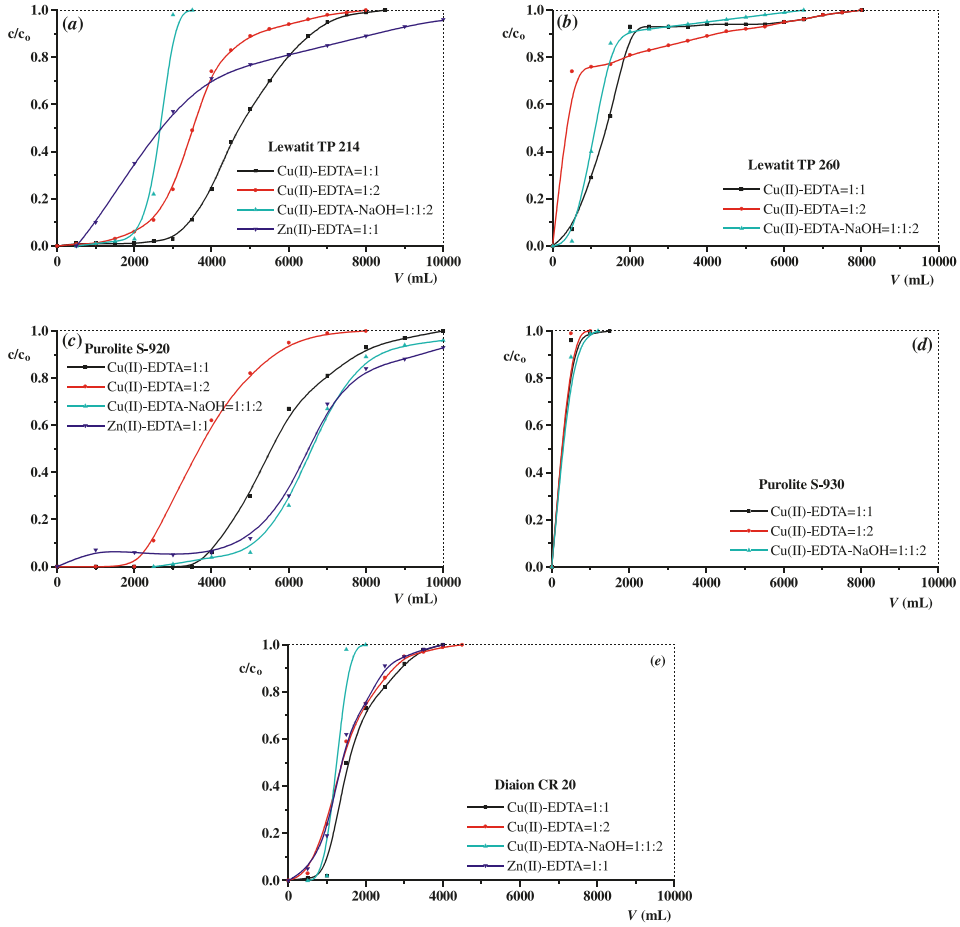

Fig. 6. The breakthrough curves of Cu(II) and Zn(II) complexes with NTA in the M(II)-NTA = 1:1 and M(II)-NTA = 1:2 systems on Lewatit TP 214 and Diaion CR-20.

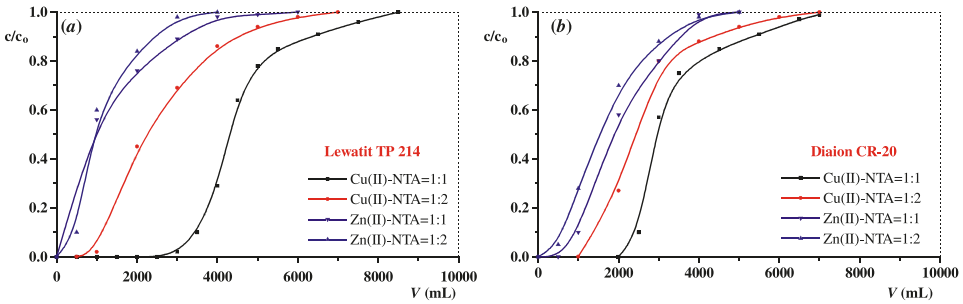

0.8 c/c_0), then it is much slower until complete bed exhaustion is observed. The exchange zone formation time is much shorter than for the previously discussed ion exchangers. For the ion exchangers Diaion CR-20 and Purolite S-930 containing polyamine and iminodiacetate groups, respectively, the respective curves are typical for the ion exchange process. In the case of the chelating ion exchanger Purolite S-930, $[Cu(edta)]^{2-}$ complexes pass through the column without displaying any reaction to the active group in the ion exchanger. This indicates that decomposition of sorbed complexes does not occur in the resin phase. As follows from the obtained results in this paper as well as literature data, the chelating ion exchangers with the iminodiacetate groups do not exhibit affinity for the heavy metal anionic complexes with EDTA. It should be added that the distribution coefficients calculated from the breakthrough curves for copper(II) complexes are much higher than that of analogous zinc(II) complexes (Tables 2 and 3). A reverse dependence was observed only for Purolite S-920. It is also evident that the sorption capacities for the M(II)-NTA system are slightly higher than that for the M(II)-EDTA system. It is worth mentioning that heavy metal ions were desorbed by 1 mol/L HCl almost quantitatively.

As follows from the research, the chelating ion exchangers, according to their applicability for sorption of Cu(II) and Zn(II) in the presence of EDTA in the

© 2008 NRC Canada

Table 2. The mass (D_g) and volume (D_v) distribution coefficients as well as the working (C_w) and total (C_r) ion exchange capacities (g/mL) for Cu(II) and Zn(II) complexes with EDTA on chelating ion exchangers.

M(II)-EDTA system	D_g	D_v	C_w	C_r
Lewatit TP 214				
Cu(II)-EDTA = 1:1	645.66	235.66	0.0010	0.0157
Zn(II)-EDTA = 1:1	369.18	134.75	0.0013	0.0252
Cu(II)-EDTA = 1:2	480.34	175.32	0.0006	0.0133
Cu(II)-EDTA-NaOH = 1:1:2	364.25	132.95	0.0003	0.0083
Lewatit TP 260				
Cu(II)-EDTA = 1:1	179.06	68.72	0.0009	0.0052
Cu(II)-EDTA = 1:2	46.79	17.96	0.0005	0.0038
Cu(II)-EDTA-NaOH = 1:1:2	141.99	54.49	0.0003	0.0043
Purolite S-920				
Cu(II)-EDTA = 1:1	809.76	277.14	0.0111	0.0154
Zn(II)-EDTA = 1:1	951.07	325.50	0.0123	0.0302
Cu(II)-EDTA = 1:2	536.33	183.56	0.0064	0.0131
Cu(II)-EDTA-NaOH = 1:1:2	766.38	230.74	0.0079	0.0083
Purolite S-930				
Cu(II)-EDTA = 1:1	45.56	14.27	0.0002	0.0009
Cu(II)-EDTA = 1:2	41.01	12.72	0.0001	0.0008
Cu(II)-EDTA-NaOH = 1:1:2	39.84	12.21	0.0001	0.0007
Diaion CR-20				
Cu(II)-EDTA = 1:1	257.38	77.55	0.0003	0.0057
Zn(II)-EDTA = 1:1	228.06	68.72	0.0013	0.0065
Cu(II)-EDTA = 1:2	230.05	69.31	0.0013	0.0050
Cu(II)-EDTA-NaOH = 1:1:2	205.20	61.83	0.0013	0.0040

Table 3. The mass (D_g) and volume (D_v) distribution coefficients as well as the working (C_w) and total (C_r) ion exchange capacities (g/mL) for Cu(II) and Zn(II) complexes with NTA on chelating ion exchangers.

M(II)-NTA system	D_g	D_v	C_w	C_r
Lewatit TP 214				
Cu(II)-NTA = 1:1	588.64	214.85	0.0092	0.0174
Zn(II)-NTA = 1:1	135.34	49.40	0.0010	0.0120
Cu(II)-NTA = 1:2	308.05	112.44	0.0013	0.0152
Zn(II)-NTA = 1:2	132.88	48.50	0.0003	0.0049
Diaion CR-20				
Cu(II)-NTA = 1:1	490.43	147.77	0.0064	0.0149
Zn(II)-NTA = 1:1	313.04	94.32	0.0016	0.0115
Cu(II)-NTA = 1:2	401.50	120.97	0.0032	0.0084
Zn(II)-NTA = 1:2	253.41	76.35	0.0013	0.0108

0.001 mol/L M(II)-0.001 mol/L EDTA system can be put in the order Purolite S-920 >Lewatit TP 214 >Diaion CR-20 >Lewatit TP 260 >Purolite S-930. The affinity series for the NTA was found to be as follows, Lewatit TP 214 >Diaion CR-20.

Effect of phase contact time

The investigations of sorption by the static method depending on the phase contact time were carried out in the 0.001 mol/L M(II)-0.001 mol/L EDTA and the 0.001 mol/L M(II)-0.002 mol/L EDTA systems using Purolite S-920, Lewatit TP 214, and Diaion CR-20. The analogous relationships were determined in the 0.001 mol/L M(II)-0.001 mol/L NTA and 0.001 mol/L M(II)-0.002 mol/L NTA systems. These values of recovery factors (*%R*) are presented in Fig. 7. When the phase contact time was increased from 1 to 90 min, the percentage of removal of Cu(II) complexes with EDTA (Cu(II)-EDTA = 1:1) using Purolite S-920 increases from 23% to 95%. For the Zn(II)-EDTA complexes these values are similar. For the M(II)-NTA complexes obtained, values are lower and the percentage of recovery reached the constant value about 58% at 90 min. This part of experimental work is the basis for the remaining batch of experiments.

Effect of initial metal ion concentration

As shown in Table 5, the highest amount of metal ions adsorbed per unit weight of ion exchanger are for Purolite S-920 for the M(II)-EDTA system and for Diaion CR-20 for the M(II)-NTA system. In the concentration range from 0.0005 mol/L to 0.001 mol/L, the ratio of functional groups of ion exchanger to the total metal ions in the solution is high and hence all metal ions may interact with the ion exchanger and be removed from the solution so the percentage of metal ions increases. The sorption behaviour of studied chelating ion exchangers was followed by the Langmuir isotherm equation represented by

$$[7] \qquad q_e = \frac{q_0 b c_e}{1 + b c_e}$$

where q_0 is Langmuir isotherm constant (mg/g of dry resin) and b is Langmuir constant (L/mg).

The constants q_0 and b are characteristic of this equation and for the studied chelating ion exchangers (determined from its

© 2008 NRC Canada

Table 4. The total sorption capacities q_e (mg/g) of chelating ion exchangers for Cu(II) and Zn(II) in the M(II)-EDTA = 1:1 and M(II)-EDTA = 1:2 as well as M(II)-NTA = 1:1 and M(II)-NTA = 1:2 systems.

	Lewatit TP 214	Purolite S-920	Diaion CR-20
M(II)-EDTA system			
Cu(II)-EDTA = 1:1	22.48	31.79	16.24
Zn(II)-EDTA = 1:1	16.78	23.80	14.68
Cu(II)-EDTA = 1:2	6.62	16.74	7.66
Zn(II)-EDTA = 1:2	6.36	24.30	7.53
M(II)-NTA system			
Cu(II)-NTA = 1:1	6.23	12.87	18.31
Zn(II)-NTA = 1:1	3.73	16.77	14.17
Cu(II)-NTA = 1:2	6.60	12.60	14.23
Zn(II)-NTA = 1:2	3.62	12.82	13.98

Fig. 7. Effect of the phase contact time on the sorption of Cu(II) and Zn(II) complexes with EDTA and NTA in the (*a–c*) M(II)-EDTA = 1:1 and M(II)-EDTA = 1:2, as well as (*d–f*) M(II)-NTA = 1:1 and M(II)-NTA = 1:2 systems on Lewatit TP 214, Purolite S-920, and Diaion CR-20.

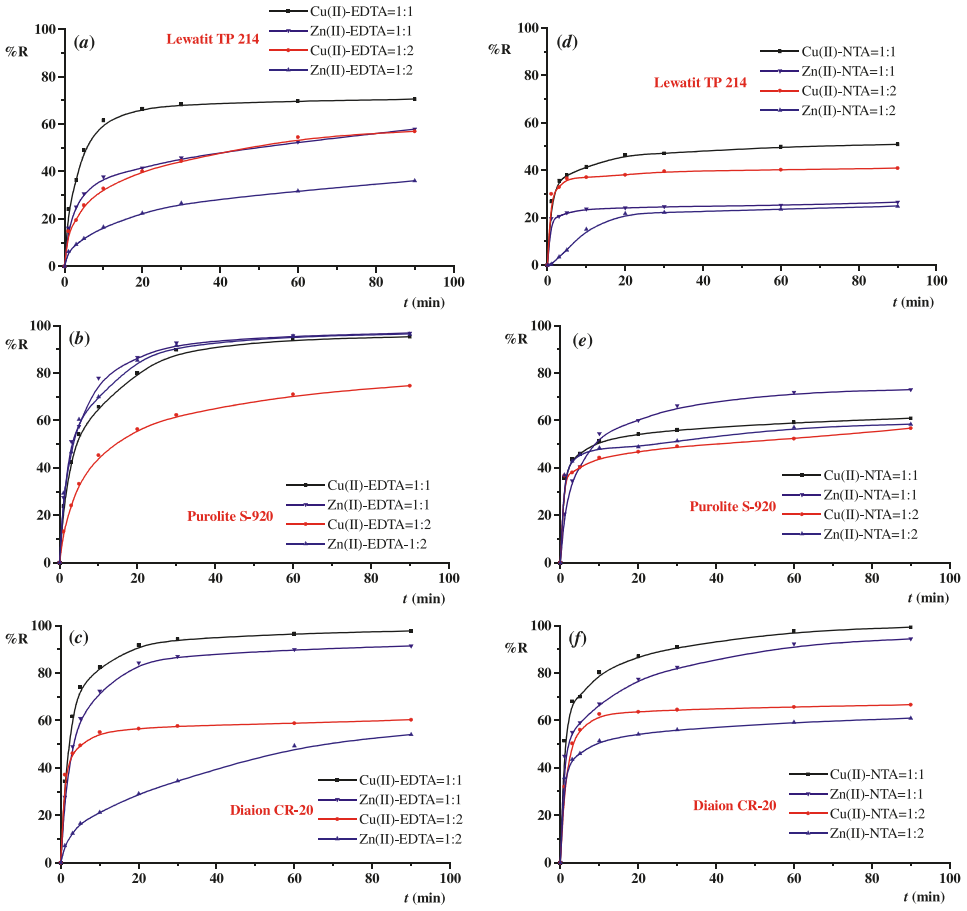

linearzed form) are presented in Table 5 The coefficients of determination (R^2) were also presented. As follows from the presented data, there is quitean agreement found between the determined and theoretical capacities of investigated chelating ion exchangers for Cu(II) and Zn(II) ions.

Effect of solution pH

Effect of initial solution pH on the sorption process was determined at various pH values ranging from 2 to 9. The values of solution pH were adjusted with 0.1 mol/L HCl or NaOH. The heavy metal ions recovery factors in the system with EDTA determined under noncompetitive conditions (sorption from single metal complex solution) on the chelating ion exchanger i.e., Lewatit TP 214, Purolite S-920, and Diaion CR-20, as a function of pH were shown in Fig. 8. Cu(II) shows maximum removal in the pH range 4–5 for Lewatit TP 214 and Purolite S-920, and 2–3 for Diaion CR 20. In these ranges the sorption is very fast and then gradu-

© 2008 NRC Canada

Table 5. The Langmuir isotherm constants q_0 (mg/g) and b of chelating ion exchangers for Cu(II) and Zn(II) in the M(II)-EDTA = 1:1 and M(II)-NTA = 1:1 systems.

	Lewatit TP 214			Purolite S-920			Diaion CR-20		
	q_0	b	R^2	q_0	b	R^2	q_0	b	R^2
M(II)-EDTA system									
Cu(II)-EDTA = 1:1	20.76	0.02	0.94	31.76	0.03	0.98	14.32	0.12	0.93
Zn(II)-EDTA = 1:1	24.27	0.007	0.97	27.55	0.06	0.99	17.21	0.04	0.92
M(II)-NTA system									
Cu(II)-NTA = 1:1	5.59	0.01	0.98	11.63	0.04	0.96	17.99	0.09	0.95
Zn(II)-NTA = 1:1	4.00	0.03	0.91	17.22	0.08	0.95	12.14	0.05	0.94

Fig. 8. Effect of the pH on the sorption of Cu(II) complexes with EDTA in the M(II)-EDTA = 1:1 system on Lewatit TP 214, Purolite S-920, and Diaion CR-20.

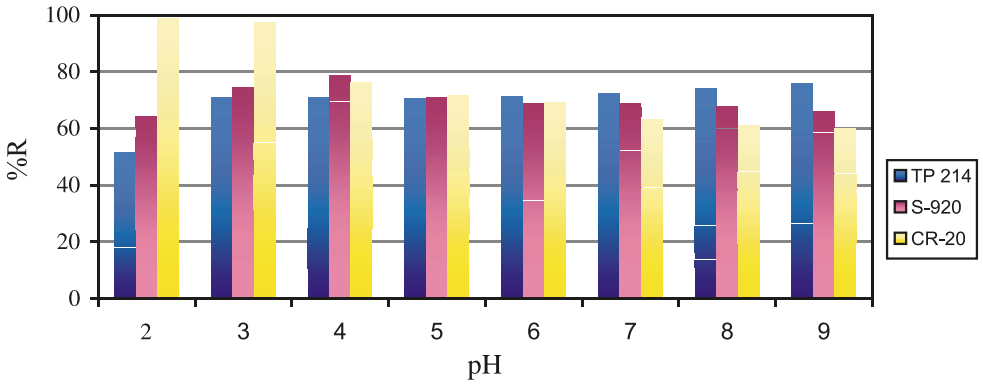

ally decreases (pH from 6 to 9). The analogous data were obtained for Zn(II) ions (not presented). It is well-known that the ion exchange mechanism of sorption by chelating ion exchangers with thiourea groups is predominant at high acidities than those chelating or coordinating at low acidities. In the in-between media, both mechanisms are assumed to compete with each other. The explanation for behaviour of such ion exchangers at different acidities is attributed to weak base properties of the functional thiourea groups. In the thiourea form this ion exchanger binds metal ions by coordination, but when converted to the thiouronium form it binds anions by an anion exchange mechanism. The behaviour of Diaion CR-20 is in agreement with the behaviour of weakly basic anion exchangers with primary, secondary, and tertiary amino groups, which exchange anions for alkaline and neutral solutions to a lesser degree than from acid solutions.

Conclusion

As follows from the research results, the selectivity and possible separations of heavy metal ions from aqueous solutions in the presence of chelating agents such as EDTA or NTA depend on both their speciation and on the properties of the chelating ion exchanger. The distribution coefficients as well as the ion exchange capacities of Cu(II) and Zn(II) ions for the above mentioned chelating ion exchangers are differentiated. The differences in affinity of Cu(II) and Zn(II) complexes with EDTA and NTA depend on the kind of functional groups of the chelating anion exchangers, thiourea groups (Lewatit TP 214 and Purolite S-920), aminomethylphosphonate groups (Lewatit TP 260), iminodiacetate groups (Purolite S-930), and polyamine groups (Diaion CR-20), as well as on the pH value. The sorption mechanism of metal ions(II) in the presence of chelating complexing agents such as EDTA or NTA on the chelating ion exchangers is difficult to specify. It is possible that the size of the metal ions could affect the metal sorption whereas the stability constants could be a minor factor.

References

1. V. Tare, S.B. Karra, and Ch.N. Haas. Water, Air, Soil Pollut. **22**, 429 (1984).
2. Ch.N. Haas and V. Tare. React. Polym. **2**, 61 (1984).
3. W. Fries and D. Chew. Chemtech, **23**, 32 (1993).
4. J.B. Rodríguez, A. Mutis, M.C. Yeber, J. Freer, J. Baeza, and H.D. Mansilla. Water Sci. Technol. **40**, 267 (1999).
5. C. Oviedo and J. Rodríguez. Quim. Nova, **26**, 901 (2003).
6. H. Höll. Elimination of heavy metals from water by means of weakly basic anion exchange resins. *In* Ion exchange developments and applications. *Edited by* J. Greig. The Royal Society of Chemistry, Cambridge. 1996. p. 404.
7. H. Höll. Unusual column behaviour of heavy metal complexes on anion exchange column. *In* Ion exchange processes: Advances and applications. *Edited by* A. Dyer, M.J. Hudson, and P.A. Williams (*Editors*). The Royal Society of Chemistry, Cambridge. 1993. p. 181.
8. A. Dąbrowski, Z. Hubicki, P. Podkościelny, and E. Robens. Chemosphere, **56**, 91 (2004).
9. M. Sillanpää. Chemosphere, **33**, 293 (1996).
10. E. Pehlivan, S. Cetin, and B.H. Yanık. J. Hazard. Mater. **135**, 193 (2006).
11. Ch. Chang and Y. Ku. Sep. Sci. Technol. **30**, 899 (1995).
12. E. Pehlivan and T. Altun. J. Hazard. Mater. **140**, 299 (2007).

© 2008 NRC Canada

13. L.Ch. Lin and R.S. Juang. Chem. Eng. J. **132**, 205 (2007).
14. O. Abollino, M. Aceto, C. Sarzanini, and E. Mentasti. Anal. Chim. Acta, **411**, 223 (2000).
15. R.S. Juang and M.N. Chen. J. Membr. Sci. **119**, 25 (1996).
16. E. Meers, A. Ruttens, M.J. Hopgood, D. Samson, and F.M.G. Tack. Chemosphere, **58**, 1011 (2005).
17. B. Nowack, R. Schulin, and B.H. Robinson. Environ. Sci. Technol. **40**, 5225 (2006).
18. A.J. Varma, S.V. Deshpande, and J.F. Kenned. Carbohydr. Polym. **55**, 77 (2004).
19. C.G. Ginkel, K.L. Vandenbroucke, and C.A. Stroo. Bioresour. Technol. **59**, 151 (1997).
20. R.S. Juang, Y.J. Chen, and I.P. Huang. Sep. Sci. Technol. **34**, 3099 (1999).
21. Z. Ujang and G.K. Anderson. Water Sci. Technol. **38**, 521 (1998).
22. T. Mohammadi, A. Moheb, M. Sadrzadeh, and A. Razmi. Sep. Purif. Technol. **41**, 73 (2005).
23. T.A. Kurniawan, G.Y.S. Chan, W.H Loa, and S. Babel. Chem. Eng. J. **118**, 83 (2006).
24. P. Brown, I.A. Jefcoat, D. Parrish, S. Gill, and E. Graham. Adv. Environ. Res. **4**, 19 (2000).
25. P.D. Johnson, M.A. Watson, J. Brown, and I.A. Jefcoat. Waste Manage. **22**, 471 (2002).
26. A.E. Ofomaja and Y.S. Ho. J. Hazard. Mater. **139**, 356 (2007).
27. J.B. Brower, R.L. Ryan, and M. Pazirandeh. Environ. Sci. Technol. **31**, 2910 (1997).
28. S.K. Sahni and J. Reedijk. Coord. Chem. Rev. **59**, 1 (1984).
29. R. Raghavan and C.V. Bhatt. Hydrometallurgy, **50**, 169 (1998).
30. L.Ch. Lin and R.S. Juang. Chem. Eng. J. **112**, 211 (2005).
31. J. Lehto, K.Vaaramaa, and H. Leinonen. React. Funct. Polym. **33**, 13 (1997).
32. R.R. Grinstead. Hydrometallurgy, **12**, 387 (1984).
33. A.K. Sengupta and Y. Zhu. Environ. Sci. Technol. **25**, 481 (1991).
34. C.V. Diniz, F.M. Doyle, and V.S.T. Ciminelli. Sep. Sci. Technol. **37**, 3169 (2002).
35. R. Koivula, J. Lehto, L. Pajo, T. Gale, and H. Leinonen. Hydrometallurgy, **56**, 93 (2000).
36. Y. Fernández, E. Maraňón, L. Castrillón, and I. Vázquez. J. Hazard. Mater. **126**, 169 (2005).
37. T. Panayotova, M. Dimova-Todorova, and I. Dobrevsky. Desalination, **206**, 135 (2007).
38. Z. Hubicki, A. Jakowicz, and A. Łodyga. Application of the ion-exchange method to remove metallic ions from waters and sewages. *In* Adsorption and its applications in industry and environmental protection. *Edited by* A. Dąbrowski. Elsevier, Amsterdam. 1998. p. 497.
39. F. Nelson, R.A. Day, Jr., and K.A. Kraus. J. Inorg. Nucl. Chem. **15,** 140 (1960).
40. M.R. Dudzinska and D.A. Clifford. React. Polym. **16**, 71 (1991/1992).
41. M.R. Dudzinska and L. Pawłowski. Anion exchange removal of heavy metal-EDTA complexes. *In* Ion exchange processes. Advances and applications. *Edited by* A. Dyer, M.J. Hudson, and P.A. Williams. The Royal Society of Chemistry, Cambridge. 1993. p. 353.
42. R.S. Juang and L.D. Shiau. Ind. Eng. Chem. Res. **37**, 555 (1998).
43. Z. Hubicki and A. Jakowicz. Desalination, **155**, 121 (2003).
44. R.S. Juang, S.H. Lin, H.Ch. Kao, and M.H. Theng. Chemosphere, **59**, 1355 (2005).
45. R.S. Juang, S.H. Lin, and T.Y. Wang. Chemosphere, **53**, 1221 (2003).
46. E. Korngold, N. Belayev, L. Aronov, and S. Titelman. Desalination, **133**, 83 (2001).
47. Z. Matejka and Z. Zitkova. React. Funct. Polym. **35**, 81 (1997).
48. J. Matejka, H. Parschova, and P. Roztocil. Chelated heavy metals: Recovery and separation form ligands. *In* Ion exchange developments and applications. *Edited by* J. Greig. The Royal Society of Chemistry, Cambridge. 1996. p. 112.
49. Ch.Ch. Wang and Ch.Ch. Wang. J. Appl. Polym. Sci. **97**, 2457 (2005).
50. Ch.Y. Chen and S.Y. Chen. J. Appl. Polym. Sci. **94**, 2123 (2004).
51. J. Minczewski, J. Chwastowska, and R. Dybczyński. Separation and preconcentration methods in inorganic trace analysis. John Wiley & Sons, New York. 1982.
52. D. Kołodyńska, H. Hubicka, and Z. Hubicki. Desalination, **227**, 150 (2008).

© 2008 NRC Canada

Radical addition to ynol ethers — A convenient procedure for the stereoselective preparation of α-iodo enol ethers in neutral conditions

Fanny Longpré, Natalia Rusu, Maxime Larouche, Rana Hanna, and Benoit Daoust

Abstract: α-Iodo enol ethers, precursors of acyl anion equivalents, are not easily prepared. Herein we report that addition of activated iodoalkanes to ynol ethers under mild and neutral radical reaction conditions leads to α-iodo enol ethers in moderate to excellent yields with high stereoselectivity. The reaction can be carried out in various solvents at different temperatures. The methodology allows the preparation of β-alkylated and β,β-dialkylated α-iodo enol ethers. Reduction of the carbon-iodine bond of these species leads to the corresponding enol ethers with good yields.

Key words: ynol ethers, enol ethers, radical addition, stereoselective.

Résumé : Les α-iodoéthers d'énol, des précurseurs d'équivalents d'anions acyles, sont difficiles à préparer. Cet article présente nos résultats de notre étude sur l'addition d'iodoalcanes activés sur des éthers d'ynol. Cette réaction, qui conduit à des α-iodoéthers d'énol avec des rendements allant de bons à excellents, s'effectue en milieu neutre et dans des conditions réactionnelles très douces. De plus, cette réaction est très stéréosélective. La réaction peut être effectuée dans différents solvants, à différentes températures. Cette méthodologie permet de préparer des α-iodoéthers d'énol β-alkylés et β,β-dialkylés. La réduction du lien carbone-iode de ces composés permet d'isoler des éthers d'énol avec de bons rendements.

Mots-clés : éthers d'ynol, éthers d'énol, addition radicalaire, stéréosélectif.

[Traduit par la Rédaction]

Introduction

α-Halo enol ethers are interesting precursors of substituted enol ethers and are also umpolungs for acyl groups (1). Transmetallation of the α-halo enol ether halogen atom produces α-alkoxy vinyl anions that have shown versatile applications in organic synthesis (2, 3). These halogenated species were also used in cross-coupling reactions (4). However, very few methods exist for preparing these useful α-halo enol ethers (2, 5). Most of them require the use of strong bases or the intermediacy of α-alkoxy vinylstannane compounds. Recently, Yu and Jin developed a more convenient method using in situ produced hydrohalic acids (2). These then react with ynol ethers to produce α-halo enol ethers with good to excellent yields. Unfortunately, this method requires acidic reaction conditions that are known to be deleterious to a number of α-halo enol ethers (1). Also, only *mono* β-alkylated α-halo enol ethers can be prepared by this method. As a consequence, the development of a new methodology for the preparation of β-alkylated and β,β-dialkylated α-halo enol ethers under neutral and mild reaction conditions emerges as an important and challenging synthetic endeavor.

Received 8 March 2008. Accepted 6 May 2008. Published on the NRC Research Press Web site at canjchem.nrc.ca on 27 August 2008.

F. Longpré, N. Rusu, M. Larouche, R. Hanna, and B. Daoust.[1] Département de Chimie-Biologie, Université du Québec à Trois-Rivières, 3351 Boulevard des Forges, C.P. 500, Trois-Rivières, QC G9A 5H7, Canada.

[1]Corresponding author (e-mail: Benoit.Daoust@uqtr.ca).

Results and discussion

Our strategy for the preparation of α-iodo enol ethers is outlined in Scheme 1. We hypothesized that intermediate electrophilic radical **2** formed by homolytic cleavage of iodinated active methylene **1** (Z = CO_2Et, CN, $CONH_2$) would add to the electron-rich β-carbon of **3** to give trans radical adduct **4**. The anti attack leading to trans radical **4** should be favored for stereoelectronic reasons (6). The use of iodides, which are efficient halogen-atom transfer agents, should ensure rapid trapping of vinyl radical **4** before its interconversion leading to *E*-isomer **5** with stereoselection (7).

We first examined the radical addition of ethyl iodoacetate (**1a**) to ethoxyacetylene (**3a** ; R = ethyl, R′ = H), the only commercially available ynol ether. In CH_2Cl_2 at room temperature (Table 1, entry 1), completion of the reaction was observed within 15 min using Et_3BO_2 as radical initiator. We were very happy to isolate 97% of the expected adduct **5a** with complete stereoselectivity. Indeed, only the *E*-isomer could be observed in NMR spectra and GCMS chromatographs (*E*/*Z* > 99:1). This result not only supports our hypothesis about the ability of ynol ethers to accept electrophilic radicals but also confirms the slow interconversion of vinyl radical **4** (see Scheme 1). We were very pleased to observe that low temperature (–78 °C) had no important effect on the reaction efficiency (entry 2, 90% yield). We then tested an ynol ether possessing a more sterically de-

 doi:10.1139/V08-094 © 2008 NRC Canada

Scheme 1.

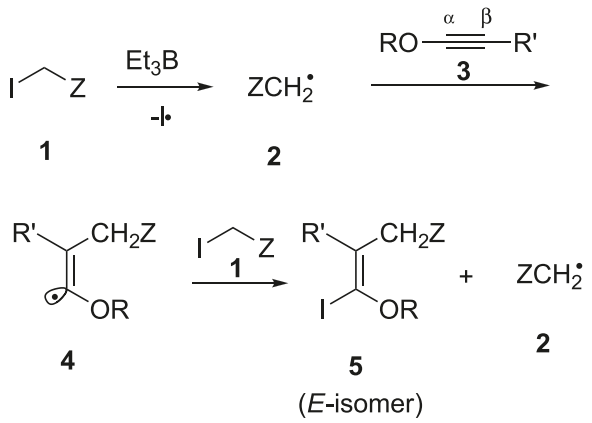

Table 1. Addition of ethyl iodoacetate (**1a**) to ynol ethers **3a**–**3d**, **3g**, and **3h** in CH_2Cl_2.

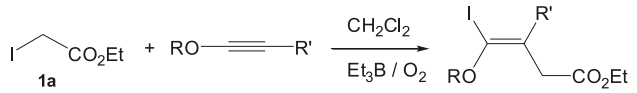

3a (R = Et, R' = H)
3b (R = menthyl, R' = H)
3c (R = adamantyl, R' = H)
3d (R = menthyl, R' = Me)
3e (R = menthyl, R' = iPr)
3f (R = menthyl, R' = sBu)
3g (R = Et, R' = SitBuMe$_2$)
3h (R = Et, R' = SitBuPh$_2$)

5a (R = Et, R' = H)
5b (R = menthyl, R' = H)
5c (R = adamantyl, R' = H)
5d (R = menthyl, R' = Me)
5e (R = menthyl, R' = iPr)
5f (R = menthyl, R' = sBu)
5e (R = Et, R' = SitBuMe$_2$)
5f (R = Et, R' = SitBuPh$_2$)

Entry	Substrate	Temp.[a]	Product	Yield[b] (%)	*E*/*Z* ratio[c,d]
1	**3a**	RT	**5a**	97	> 99:1
2	**3a**	–78 °C	**5a**	90	> 99:1
3	**3b**	RT	**5b**	75	> 99:1
4	**3b**	–78 °C	**5b**	70	> 99:1
5	**3c**	RT	**5c**	0	–
6	**3d**	RT	**5d**	72	> 99:1
7	**3d**	–78 °C	**5d**	70	> 99:1
8	**3g**	RT	**5g**	0	–
9	**3h**	RT	**5h**	0	–

Note: Reaction time: 2 h in all cases except for entry 1 (15 min).
[a]RT = room temperature.
[b]Isolated yield based on **3**.
[c]The *E*-isomer was easily detected by ^{1}H and ^{13}C NMR, TLC, and GCMS ; we could not detect the presence of any of the *Z*-isomers with these methods.
[d]The geometries of the double bond of **5a** and **5b** were determined by the characteristic coupling constants of their reduced counterparts **6a** and **6b** (see Table 4). The geometry of the double bond of **5d** was determined by NOESY spectra of the reduced counterpart **6d**.

manding group attached to the oxygen atom: menthoxyethyne **3b** (R = menthyl, R′ = H) (8). As one can see from entries 3 and 4, the reaction with **3b** proceeds with good yields (75% and 70%) and complete stereoselectivity at RT and at –78 °C. When we tried an ynol ether with even more sterically demanding adamantyl group (**3c** ; R = adamantyl, R′ = H) (9), no desired adduct was observed (entry 5); only the starting material was recovered.

These results suggest that the menthyl group might be the steric limit on the oxygen side of the ynol ether for our reaction to occur. We then decided to prepare a series of substituted menthoxyethyne (R = menthyl) possessing groups with increasing bulkiness at the β-position. First, 1-menthoxypropyne **3d** (R = menthyl, R″ = Me) was tested (8). The radical reaction between **3d** and ethyl iodoacetate occured with yields comparable to those obtained with **3b** (entries 6 and 7, 72% and 70% yield). Again, complete stereocontrol of the double bond was observed. We then decided to install groups possessing secondary carbon at the β-position. Isopropyl was our first choice. We examined the possibility of producing compound **3e** (R = menthyl, R″ = *i*-Pr) by reacting menthoxyethyne **3b** with triisopropylborane (10) using Greene's protocol (8). Unfortunately, we were not able to isolate the desired product. Though TLC revealed the presence of a new compound with an R_f characteristic of ynol ethers, compound **3e**, if ever produced, seemed to be very unstable and degradation was observed before any characterization could be performed. We also tried to prepare compound **3f** (R = menthyl, R′ = *s*-Bu) according to Greene's protocol (8). In that case, the desired compound **3f** could be obtained and isolated, though it showed a very high propensity to decomposition. We submitted this freshly produced ynol ether to our radical reaction conditions. Unfortunately, compound **3f** decomposed before any addition reaction could occur. Hoping that highly encumbered triple bonds would be easier to handle, we tried to prepare very crowded ynol ethers **3g** (R = Et, R′ = Si-*t*-BuMe$_3$) and **3h** (R = Et, R′ = Si-*t*-BuPh$_3$) (11). Fortunately, these compounds were chemically stable and could thus be isolated and purified. However, radical addition of these two ynol ethers with ethyl iodoacetate did not produce the desired adducts **5g**–**5h** (entries 8 and 9, 0% yield in both cases). Only the starting materials were recovered.

Other solvents were then assessed (Table 2) for the reaction involving ethyl iodoacetate (**1a**) and ynol ether **3b**. In benzene (entry 1), the reaction took place with a slightly better yield (80%) compared to CH_2Cl_2 (Table 1, entry 3). In hexanes, acetone, and DMSO (Table 2, entries 2, 3, and 4), the yields were slightly lower (51%–65%). Reaction did not occur in THF (entry 5, 0% yield).

It is of note that when volatile solvents were used (for example, CH_2Cl_2 or hexanes), no aqueous work-up was required, thus reducing the risk of hydrolysis of iodo vinyl ethers **5**. The adducts **5** must be isolated by carefully evaporating the solvent and Et_3B with a nitrogen gas flow. Indeed, we observed that rotary evaporation dramatically accelerated decomposition of these highly functionalized adducts.

Table 3 summarizes results of radical addition of two other iodinated active methylenes towards ynol ether **3d** in CH_2Cl_2. Entries 1, 2, and 3 reveal that iodoacetonitrile added to ynol ether **3d** at different temperatures (RT, 0 °C and –78 °C) with poorer yields (49%–57%) than ethyl iodoacetate (**1a**). Here again, only one isomer of the double bond was observed. Iodoacetamide (entries 4, 5, and 6) added to ynol ether **3d** with modest yields (18%–30%) but with high stereoselection. We also tried the addition of two other α-iodo carbonyl compounds, namely diethyl iodomalonate and 1-iodopropan-2-one. Unfortunately, both iodinated compounds failed to react with ynol ethers **3a** and **3b**. Brominated activated methylenes $BrCH_2CO_2Et$, $BrCH_2CN$, and $BrCH(CO_2Et)_2$ were also reacted with ynol

© 2008 NRC Canada

Table 2. Addition of ethyl iodoacetate **1a** to ynol ethers **3b** in different solvents at room temperature.

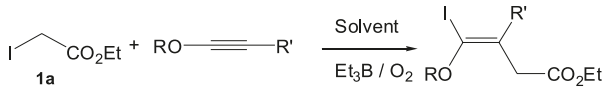

3b (R = menthyl, R' = H) **5b** (R = menthyl, R' = H)

Entry	Solvent	Reaction time (h)	Yield[a] of **5b** (%)	*E*/*Z* ratio
1	Benzene	2	80	> 99:1
2	Hexanes	2	65	> 99:1
3	DMSO	1	51	> 99:1
4	Acetone	1	60	> 99:1
5	THF	1	0	—

[a]Isolated yield based on **3b**.

Table 3. Addition of iodinated active methylenes **1b** and **1c** to ynol ether **3d** in CH_2Cl_2.

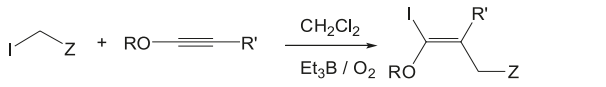

1b (R = CN) **3d** (R = menthyl, R' = Me) **5i** (R = menthyl, R' = Me, Z = CN)
1c (R = $CONH_2$) **5j** (R = menthyl, R' = Me, Z = $CONH_2$)

Entry	Temp.[a]	Iodinated compound	Product	Yield	*E*/*Z* ratio[b]
1	RT	**1b**	**5i**	57	> 99:1
2	0 °C	**1b**	**5i**	51	> 99:1
3	–78 °C	**1b**	**5i**	49	> 99:1
4	RT	**1c**	**5j**	30	> 99:1
5	0 °C	**1c**	**5j**	25	> 99:1
6	–78 °C	**1c**	**5j**	18	> 99:1

Note: Reaction time of 2 h in all cases.
[a]RT = room temperature
[b]The geometry of double bonds of **5i** and **5j** were determined by NOESY spectra.

ethers **3a** and **3b**. In all cases, only the starting materials were recovered.

The radical nature of this new methodology was confirmed using a radical scavenger. Addition of *tert*-butylphenylnitrone to a mixture of **1a** and **3a** followed by Et_3B addition gave ~ 0% yield of the desired adduct.

To demonstrate the usefulness of α-iodo enol ethers, we performed C–I bond reductions of adducts **5a**, **5b**, and **5d** (Table 4). Di and trisubstituted cis enol ethers were obtained with modest to excellent yields (15%–96%) using tributyltin hydride, *n*-BuLi or *t*-BuLi as reducing agents. The desired compounds **6a**, **6b**, and **6d** were all isolated with complete stereoretention. A one-pot procedure involving radical addition of ethyl iodoacetate **1a** to ynol ether **3d** followed by Bu_3SnH reduction without isolation of the intermediate iodo enol ether **5d** did not lead to the desired reduced compound **6d** (0% yield).

Table 4. Formation of di- and trisubstituted enol ethers **6a**, **6b**, and **6d** from deiodination of **5a**, **5b**, and **5d**.

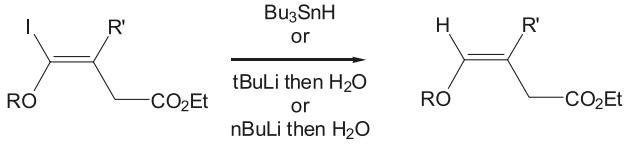

5a (R = Et, R' = H)
5b (R = menthyl, R' = H)
5d (R = menthyl, R' = Me)

6a (R = Et, R' = H)
6b (R = menthyl, R' = H)
6d (R = menthyl, R' = Me)

Entry	Substrate	Reducing agent	Product	Yield[a] (%)	*E*/*Z* ratio[b]
1	**5a**	Bu_3SnH[c]	**6a**	96%	> 99:1
2	**5a**	*t*-BuLi[d]	**6a**	70%	> 99:1
3	**5b**	Bu_3SnH[c]	**6b**	15%	> 99:1
4	**5b**	*t*-BuLi[d]	**6b**	69%	> 99:1
5	**5b**	*n*-BuLi[e]	**6b**	16%	> 99:1
6	**5d**	*t*-BuLi[d]	**6d**	72%	> 99:1

[a]Isolated yields.
[b]The geometries of the double bond of **6a**–**6b** were determined by their characteristic coupling constants. The geometry of the double bond of **6d** was determined by NOESY spectra.
[c]Bu_3SnH 1.2 eq., benzene, 1–3 h, RT.
[d]*t*-BuLi 1.2 eq, THF, –78 °C, 0.5 h.
[e]*n*-BuLi 1.2 eq., THF, –78 °C, 0.5 h.

Conclusion

In conclusion, we demonstrated, for the first time, that activated methylenes add to ynol ethers in neutral radical conditions. The yields obtained vary from moderate to excellent. The diastereoselectivity of the addition is very high in all cases. The possibility of avoiding the aqueous work-up represents a great advantage over existing methods for preparing hydrolysis-sensitive α-iodo enol ethers. The latter are interesting precursors of substituted enol ethers and are acyl anion equivalents. This method is one of the very few that allowed the stereo-controlled formation of α-iodo β,β-disubstituted enol ether (12). We are now working on the radical addition of activated iodoalkanes to silyl ynol ethers. This should allow us to prepare stereocontrolled β,β-disubstituted silyl enol ethers, enolate equivalents, known to be difficult to prepare (13).

Experimental[2]

All reactions requiring anhydrous conditions were conducted under positive nitrogen atmosphere in oven-dried glassware and the reaction flasks were fitted with rubber septa for the introduction of substrates and reagents via standard syringe techniques. All solvents were distilled prior to use, except for anhydrous tetrahydrofuran (THF) that was used as received from Sigma-Aldrich (SureSeal). *n*-Butyllithium (1.6 mol/L solution in hexanes) and *tert*-butyllithium (1.7 mol/L solution in pentane) were purchased from Sigma-Aldrich and titrated prior to use (diphenylacetic

[2]Supplementary data for this article are available on the journal Web site (http://canjchem.nrc.ca) or may be purchased from the Depository of Unpublished Data, Document Delivery, CISTI, National Research Council Canada, Ottawa, ON K1A 0R6, Canada. DUD 3776. For more information on obtaining material refer to http://cisti-icist.nrc-cnrc.gc.ca/irm/unpub_e.shtml.

© 2008 NRC Canada

acid end-point in dry THF). Tributyltin hydride, ethoxyacetylene (40% in hexanes), and triethylborane (1 mol/L in hexane) were also purchased from Sigma-Aldrich and used as received. Flash chromatography was performed on triethylamine pretreated Merck silica gel 60 (0.040–0.063 mm) using compressed air pressure. Analytical thin-layer chromatography (TLC) was carried out on precoated (0.25 mm) Merck silica gel F 54 plates previously treated with triethylamine. ^{1}H NMR spectra were recorded on a Varian 200 MHz NMR spectrometer using $CDCl_3$ (δ = 7.26 ppm) or CD_3COCD_3 (δ = 2.09 ppm) as the reference. ^{13}C NMR were recorded at 50.3 MHz using $CDCl_3$ (δ = 77.1 ppm), CD_3COCD_3 (δ = 30.6 ppm), or C_6D_6 (δ = 128.6 ppm) as the reference. NMR data are reported as follows: chemical shift in ppm, multiplicity (d = doublet, t = triplet, q = quartet, m = multiplet, br = broad, dd = doublet of doublets, dt = doublet of triplets, td = triplet of doublets), number of protons, and coupling constants in Hertz. IR spectra were recorded on a Nicolet Impact 420 spectrophotometer. Gas chromatography – mass spectra (GC–MS) were recorded on an Agilent model 6890N. High-resolution mass spectra (HRMS) were recorded on a ZAB-2F model VG apparatus.

Preparation of starting materials

The preparation and characterization of menthoxyethyne (**3b**), 1-menthoxypropyne (**3d**), and 1-menthoxy-3-methylpentyne (**3f**) have been reported previously (8). Compounds **3c** (9) and **3g** (11) have also been prepared and characterized previously (9). Ethoxyacetylene (**3a**) is commercially available.

Ethoxyethynyl(1,1-dimethylethyl)diphenylsilane (3h)

The preparation of the title compound was carried out according to the procedure described by Pericas and co-workers for the synthesis of similar compounds (10*b*). Under inert atmosphere, *n*-BuLi (3 mL, 1.50 mol/L in *n*-hexane, 4.60 mmol) was added dropwise to a solution of ethoxyacetylene (40% in hexanes, 1 mL, 4.18 mmol) in anhydrous THF (2.9 mL) at 0 °C over a period of 10 min. The mixture was stirred for 1.5 h and hexamethylphosphoric triamide (0.81 mL) was added. After 10 min, *tert*-butyldiphenylsilyl chloride (1.17 mL, 4.51 mmol) was added. The cooling bath was removed and the mixture was stirred overnight at room temperature. The reaction mixture was poured on a mixture of ice (3 g) and *n*-hexane (6 mL). The organic layer was separated, and the aqueous layer was extracted twice with *n*-hexane (4 mL). The combined organic layers were washed with brine (4 mL), dried over $MgSO_4$, and concentrated in vacuo. The crude product was chromatographed through silica gel (pretreated with 1% *v*/*v* of triethylamine) eluting with hexane to give 90% yield of **3h** as a colorless oil.

IR (cm^{-1}): 3065, 3048, 2959, 2929, 2891, 2857, 2174, 1427, 1103. ^{1}H NMR ($CDCl_3$) δ: 8.09 (m, 4H), 7.58 (m, 6H), 4.38 (q, 2H, *J* = 7.0 Hz), 1.60 (t, 3H, *J* = 7.0 Hz), 1.36 (s, 9H). ^{13}C NMR ($CDCl_3$) δ: 14.7, 19.0, 27.6, 33.0, 75.6, 113.0, 128.0, 129.6, 135.0, 136.0. HRMS calcd. for $C_{20}H_{24}SiO$ (+NH_4): 326.1940; found : 326.1931

General procedure for radical addition of iodoalkanes to ynol ethers

In a 10 mL round-bottomed flask, 0.28 mmol of ynol ether and 1.5 equiv. of the appropriate iodoalkane were dissolved in 2 mL of freshly distilled solvent at the desired temperature. Triethylborane (1.0 mol/L in hexane) was added (100 μL) to initiate the radical chain process. Triethylborane (100 μL) was then added every 15 min until no starting material was detectable by TLC. The solvent was removed by a gentle flow of dry nitrogen gas. The crude product was *rapidly* purified by flash chromatography using 100% hexanes to 10% acetone–hexanes (the contact time with the silica gel must be less than 15 min to avoid decomposition).

α-Iodo enol ethers **5a**, **5b**, **5d**, **5i**, and **5j** were not fully characterized because of their instability. HRMS could not be recorded. In most cases, recording ^{13}C NMR spectra was not possible. When using diluted solutions in the NMR tube, the long acquisition time led to decomposition before ^{13}C spectra could be recorded. Concentrating the solution (to reduce the time required to obtain the ^{13}C NMR) accelerated decomposition, thus precluding the recording of the spectra. However, the stable reduced parents of **5a**, **5b**, and **5d**, the enol ethers **6a**, **6b**, and **6d**, were fully characterized.

The geometry of double bonds was determined by NOESY spectra for compounds **5d**, **5i**, **5j**, and **6d**. For the reduced compounds **6a** and **6b**, the geometry of the double bonds was determined with the help of the characteristic cis-isomer coupling constants.

(*E*)-Ethyl 4-ethoxy-4-iodobut-3-enoate (5a)

Yellow oil. IR (cm^{-1}): 3018, 2952, 2915, 1731, 1629, 1454. ^{1}H NMR (CD_3COCD_3) δ: 1.22 (m, 6H), 2.80 (m, 1H), 3.12 (d, 1H, *J* = 7.0 Hz), 3.77 (q, 2H, *J* = 7.4 Hz), 4.09 (q, 2H, *J* = 7.0 Hz), 5.53 (t, 1H, *J* = 7.2Hz). MS: 157 (M^+ – I), 129, 101, 99, 83, 73, 55.

(*E*)-Ethyl 4-iodo-4-menthoxybut-3-enoate (5b)

Yellow oil. IR (cm^{-1}): 3017, 2960, 2922, 1735, 1633, 1451. ^{1}H NMR (CD_3COCD_3) δ: 0.80–2.20 (m, 21H), 3.12 (d, 2H, *J* = 7.4 Hz), 3.67 (td, 1H, *J* = 5.5 and 10.9 Hz), 4.11 (q, 2H, *J* = 7.0 Hz), 5.54 (td, 1H, *J* = 1.6 and 7.0 Hz). MS: 267 (M^+ – I), 139, 123, 95, 83, 69, 55.

(*E*)-Ethyl 4-iodo-4-menthoxy-3-methylbut-3-enoate (5d)

Yellow oil. IR (cm^{-1}): 2955, 2921, 2868, 1734, 1636, 1457, 1180. ^{1}H NMR (CD_3COCD_3) δ: 0.80–2.20 (m, 24H), 3.11 (d, 1H, *J* = 15.6 Hz), 3.37 (d, 1H, *J* = 15.6 Hz), 3.66 (td, 1H, *J* = 4.3 and 10.9 Hz), 4.13 (q, 2H, *J* = 7.0 Hz). ^{13}C NMR (CD_3COCD_3) δ: 13.9, 16.2, 20.3, 21.8, 23.4, 23.7, 25.6, 31.5, 34.3, 37.1, 39.6, 47.1, 60.3, 82.1, 116.6, 120.5, 170.1. MS: 281 (M^+ – I), 270, 142, 83, 69, 55.

(*E*)-Ethyl 4-iodo-4-menthoxy-3-methylbut-3-enenitrile (5i)

Yellow oil. IR (cm^{-1}): 2953, 2917, 2865, 2246, 1636, 1454. ^{1}H NMR ($CDCl_3$) δ: 0.80–2.2 (m, 21H), 3.36–3.57 (m, 2H), 3.75 (td, 1H, *J* = 4.7 and 10.5 Hz). ^{13}C NMR (CD_3COCD_3) δ: 16.1, 19.7, 20.3, 21.7, 22.5, 23.4, 25.6,

© 2008 NRC Canada

31.6, 34.2, 39.7, 47.0, 82.9, 116.1, 116.8. MS: 234 (M^+ – I), 139, 97, 83, 69, 55.

(*E*)-Ethyl 4-iodo-4-menthoxy-3-methylbut-3-enamide (5j)

Yellow oil. IR (KBr, cm^{-1}): 3433, 3187, 2962, 2867, 1662, 1461, 1386, 1126. ^{1}H NMR ($CDCl_3$) δ: 0.80–2.20 ppm (m, 21H), 3.05–3.26 (m (apparent q), 2H), 3.73 (td, 1H, J = 4.5 and 10.9 Hz), 6.20–6.40 (br, 1H), 6.60–6.80 (br, 1H).

General procedure for tributyltin hydride reduction of α-iodoenol ethers

In a 10 mL round-bottomed flask, 0.250 mmol of freshly prepared α-iodoenol ether was dissolved in 1.5 mL of benzene along with 0.300 mmol (87 mg, 80 μL) of tributyltin hydride (1.2 eq.). Triethylborane (1.0 mol/L in hexane) was added (100 μL) to initiate the radical chain process. Triethylborane (100 μL) was then added every 15 min until no starting material was detectable by TLC (1–3 h). A saturated aqueous solution of $NaHCO_3$ was poured into the reaction mixture. After the aqueous layer was extracted with Et_2O (3×), the organic layers were combined, washed with brine, dried ($MgSO_4$), filtered through a pad of silica-KF, and concentrated. The crude product was purified by flash chromatography using 100% hexanes to 10% acetone–hexanes.

General procedure for *n*-butyllithium and *tert*-butyllithium reduction of α-iodoenol ethers

In a 10 mL round-bottomed flask, 0.250 mmol of freshly prepared α-iodoenol ether was dissolved in 5 mL of anhydrous THF. The reaction mixture was cooled to –78 °C and 0.300 mmol (1.2 eq.) of freshly titrated BuLi was added dropwise. After 30 min (when TLC confirms that the reaction was completed), 1 mL of distilled water was added dropwise. The cooling bath was removed and the reaction mixture was stirred for another 10 min. A saturated aqueous solution of $NaHCO_3$ was poured into the reaction mixture. After the aqueous layer was extracted with Et_2O (3×), the organic layers were combined, washed with brine, dried ($MgSO_4$), filtered, and concentrated. The crude product was purified by flash chromatography using 100% hexanes to 10% acetone–hexanes.

(*Z*)-Ethyl 4-ethoxybut-3-enoate (6a)

Yellow oil. IR (cm^{-1}): 3047, 2978, 2944, 2884, 1730, 1666, 1381, 1323, 1245, 1177, 1109. ^{1}H NMR ($CDCl_3$) δ: 1.22 (m, 6H), 3.11 (dd, 2H, J = 1.6 and 7.0 Hz), 3.79 (q, 2H, J = 7.0 Hz), 4.08 (q, 2H, J = 7.0 Hz), 4.53 (q, 1H, J = 7.0 Hz), 6.06 (dt, 1H, J = 1.6 and 6.2 Hz). ^{13}C NMR ($CDCl_3$) δ: 14.4, 15.4, 30.0, 60.7, 68.0, 98.1, 147.0, 172.7. MS: 158, 127, 99, 85, 57. HRMS calcd. for $C_8H_{14}O_3$: 158.0943; found: 158.0935

(*Z*)-Ethyl 4-menthoxybut-3-enoate (6b)

Yellow oil. IR: 3009, 2944, 1742, 1450, 1022. ^{1}H NMR ($CDCl_3$) δ: 0.76 (d, 3H, J = 6.6 Hz), 0.80–2.20 (m, 21H), 3.11 (dd, 2H, J = 1.6 and 7.0 Hz), 3.39 (td, 1H, J = 4.3 and 10.9 Hz), 4.13 (q, 2H, J = 7.0 Hz), 4.51 (q, 1H, J = 7.0 Hz), 6.13 (dt, 1H, J = 1.6 and 6.3 Hz). ^{13}C NMR ($CDCl_3$) δ: 14.3, 16.4, 17.8, 20.5, 22.2, 23.8, 31.7, 34.2, 35.0, 41.9, 47.7, 60.1, 80.8, 106.2, 142.0, 171.2. MS: 268, 138, 123, 97, 83, 69, 55. HRMS calcd. for $C_{16}H_{28}O_3$: 268.2038; found: 268.2028

(*Z*)-Ethyl 4-menthoxy-3-methylbut-3-enoate (6d)

Yellow oil. IR (cm^{-1}): 3005, 2956, 2868, 1740, 1456, 1364, 1253, 1178, 1136, 1038. ^{1}H NMR ($CDCl_3$) δ: 0.80–2.20 (m, 24H), 3.05–4.20 (m, 5H), 6.04 (m, 1H). ^{13}C NMR δ (C_6D_6) δ: 14.0, 16.1, 18.0, 20.5, 22.0, 24.1, 26.0, 31.2, 34.0, 34.8, 41.3, 48.0, 60.0, 81.0, 107.0, 141.2, 171.0. MS: 219, 202, 173, 145, 127, 101. HRMS calcd. for $C_{17}H_{30}O_3$: 282.2195; found: 282.2193

Acknowledgement

Acknowledgments are made to the Natural Sciences and Engineering Research Council of Canada (NSERC) for financial support. We are thankful to Stéphane Dugrenier and Aurélie Becquet for performing preliminary experiments.

References

1. (*a*) J.D. Albright. Tetrahedron, **39**, 3207 (1983); (*b*) J. Otera. Synthesis, **88**, 95 (1988).
2. W. Yu and Z. Jin. J. Am. Chem. Soc. **122**, 9840 (2000).
3. J.D. White and H. Smits. Org. Lett. **7**, 235 (2005).
4. For examples of cross coupling reactions involving α-halo enol ethers: (*a*) R.W. Friesen, R.W. Loo, and C.F. Sturino. Can. J. Chem. **72**, 1262 (1994); (*b*) R.W. Friesen and R.W. Loo. J. Org. Chem. **56**, 4821 (1991); (*c*) M. Su, Y. Kang, W. Yu, Z. Hua, and Z. Jin. Org. Lett. **4**, 691 (2002); (*d*) M.A. Kazankova, I.G. Trostyanskaya, S.V. Lutsenko, I.V. Efimova, and I.P. Beletskaya. Russ. J. Org. Chem. **35**, 1273 (1999).
5. For preparation of α-halo enol ethers using strong bases: (*a*) E. Boyd, M.R. Hallett, R.V.H. Jones, J.E. Painter, P. Patel, P. Quayle, and A.J. Waring. Tetrahedron Lett. **47**, 8337 (2006); (*b*) A. Bou, M.A. Pericas, A. Riera, and F. Serratosa. Org. Syn. **65**, 68 (1987); (*c*) S.F. Martin. Pure Appl. Chem. **75**, 63 (2003). For preparation of α-halo enol ethers via stannyl intermediates: (*d*) J.S. Potuzak, S.B. Moilane, and D.S. Tan. J. Am. Chem. Soc. **127**, 13796 (2005); (*e*) J.S. Potuzak and D.S. Tan. Tetrahedron Lett. **45**, 1797 (2004).
6. (*a*) D.K. Wedegaertner, R.M. Kopchik, and J.A. Kampmeier. J. Am. Chem. Soc. **93**, 6890 (1971); (*b*) M. Guerra. Res. Chem. Intermed. **22**, 369 (1996); (*c*) D.P. Curran and D. Kim. Tetrahedron, **47**, 6171 (1991); (*d*) Y. Takeyama, Y. Ichinose, K. Oshima, and K. Utimoto. Tetrahedron Lett. **30**, 3159 (1989); (*e*) Y. Amiel. *In* The chemistry of functional groups. Supplement C, The chemistry of triple bonded functional groups. Part 1. *Edited by* S. Patai and Z. Rappoport. Wiley, Chichester. 1983. pp. 345–347; (*f*) J.O. Metzger and M. Blumenstein. Chem. Ber. **126**, 2493 (1993).
7. Radical **4** is expected to interconvert very slowly since it is known that α-oxy vinyl radicals possess a very high energy barrier to rotation; see: (*a*) J.A. Kampmeier, M.S. Liu, S. Soloway, and D.K. Wedegaertner. J. Am. Chem. Soc. **93**, 3809 (1971); (*b*) C. Galli, A. Guarnieri, H. Koch, P. Mencarelli, and Z. Rappoport. J. Org. Chem. **62**, 4072 (1997).
8. (*a*) A. Moyano, F. Charbonnier, and A.E. Greene. J. Org. Chem. **52**, 2919 (1987); (*b*) M.A. Pericas, F. Serratosa, and E. Valenti. Tetrahedron, **43**, 2311 (1987).
9. H.C. Brown and U.S. Racherla. J. Org. Chem, **51**, 427 (1986).

© 2008 NRC Canada

10. (*a*) Y. Kita, J. Sekihachi, Y. Hayashi, Y.Z. Da, M. Yamamoto, and S. Akai. J. Org. Chem. **55**, 1108 (1990); (*b*) E. Valenti, M.A. Pericas, and F. Serratosa, J. Org. Chem. **55**, 395 (1990). For other methods for preparing β,β-dialkylated α-iodo enol ethers, see: (*a*) H.R. Sonawane, B.S. Nanjundiah, and M.D. Panse. Tetrahedron Lett. **26**, 3507 (1985); (*b*) P.J. Kropp, S.A. McNeely, and R.D. Davis. J. Am. Chem. Soc. **105**, 6907 (1983).

11. (*a*) J.M. Manthorpe and J.L. Gleason, J. Am. Chem. Soc. **123**, 2091 (2001); (*b*) E. Vedejs, A.W. Kruger, N. Lee, S.T. Sakata, M. Stec, and E. Suna. J. Am. Chem. Soc. **122**, 4602 (2000); (*c*) S. Hosoawa, K. Sekiguchi, M. Enemoto, and S. Kobayashi. Tetrahedron Lett. **41**, 6429 (2000); (*d*) N. Chatani, S. Fujii, Y. Yamasaki, S. Murai, and N. Sonoda. J. Am. Chem. Soc. **108**, 7361 (1986).

© 2008 NRC Canada

Synthesis and redox properties of a phosphine-subsituted *para*-dioxolene and its bimetallic palladium complex

Sharon L. Caldwell, Joe B. Gilroy, Rajsapan Jain, Evan Crawford, Brian O. Patrick, and Robin G. Hicks

Abstract: Oxidation of 2,5-bis(diphenylphosphino)-1,4-hydroquinone (**8**) with iodobenzene diacetate produces the corresponding bis(phosphine) substituted benzoquinone (**9**), the first phosphine-substitued quinone. Cyclic voltammetry studies reveal that the redox functionality of the quinone unit in **9** is retained, and the reduction potentials render this compound slightly more easily reduced than the parent *p*-benzoquinone. Reaction of the precursor hydroquinone **8** with $Pd(hfac)_2$ affords a binuclear complex **10** with the hydroquinon*ate* ligand bridging two Pd(hfac) substrates. The redox activity of the bridging dioxolene ligand is retained in complex **10**, although there are significant changes in the redox potentials relative to those of the free quinone **9**. Chemical oxidation of **10** with $AgPF_6$ yields a persistent cationic complex **11**, which, based on EPR and electronic spectroscopy, can be formulated as containing a bridging semiquinone ligand.

Key words: p-quinones, phosphines, bridging ligands, redox properties.

Résumé : L'oxydation de la 2,5-bis(diphénylphosphino)-1,4-hydroquinone, **8**, par le diacétate d'iodobenzène conduit à la formation de la benzoquinone substituée par une bis(phosphine), **9**, le premier dioxolène substitué par une phosphine. Des études de voltampérométrie cyclique révèlent que la fonctionnalité redox de l'unité quinone du produit **9** est maintenue et que les potentiels de réduction rendent ce composé légèrement plus susceptible d'être réduit que la *p*-benzoquinone parente. La réaction de l'hydroquinone **8** avec du $Pd(hfac)_2$ conduit à un complexe binucléaire (**10**), dans lequel un ligand hydroquinonate sert de pont à deux substrats Pd(hfac). L'activité redox du ligand dioxolène servant de pont est maintenue dans le complexe **10**, même s'il y a des changements significatifs dans les potentiels redox par rapport à ceux de la quinone **9**. L'oxydation chimique du composé **10** à l'aide de $ONBF_4$ fournit un complexe cationique persistant, **11**, qui sur la base de la RPE et de la spectroscopie électronique contiendrait un ligand semiquinone servant de pont.

Mots-clés : p-quinones, phosphines, ligands servant de pont, propriétés redox.

[Traduit par la Rédaction]

Introduction

Metal complexes of *ortho*-dioxolenes have a number of interesting physical properties that derive from (*i*) the ability of the dioxolene ligand to exist in three different oxidation states (quinone, semiquinone, catecholate) and (*ii*) the stability of the open-shell (semiquinone) form of the coordinated dioxolene (1). Features such as strong ligand–metal magnetic coupling and "valence tautomerism" — a form of bistability — have made metal-dioxolene complexes interesting building blocks for magnetic and multifunctional materials (2).

Less well-studied are metal complexes of corresponding *para*-dioxolenes. These ligands offer one significant difference compared with their *ortho* counterparts, namely, the ability to bridge two metals, thereby opening up the possibility of making binuclear or polymeric materials that may exhibit *cooperative* valence tautomeric effects. Bis(pyrazolyl)hydroquinone (**1**) has been used sporadically as a bridging ligand (3). Derivatives of 2,5-dihydroxy-1,4-benzoquinone (**2**) have been extensively studied as structural linkers (4), although the redox activity of some of these has only recently been developed (5). Nitrogen analogues of **2**, e.g., 2,5-diamino-1,4-benzoquinones (**3**) and corresponding tetranitrogen species (6) have also appeared. But overall, the

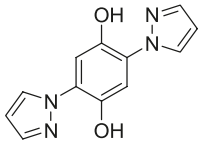

1

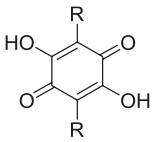

2

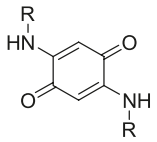

3

Received 24 April 2008. Accepted 30 June 2008. Published on the NRC Research Press Web site at canjchem.nrc.ca on 3 September 2008.

S.L. Caldwell, J.B. Gilroy, R. Jain, E. Crawford, and R.G. Hicks[1]. Department of Chemistry, University of Victoria, PO Box 3065 STN CSC, Victoria, BC, Canada, V8W 3V6.
B.O. Patrick. Crystallography Laboratory, Department of Chemistry, University of British Columbia, Vancouver, BC, Canada, V6T 1Z3.

[1]Corresponding author (e-mail: rhicks@uvic.ca).

 doi:10.1139/V08-127 © 2008 NRC Canada

coordination chemistry of *p*-(hydro)quinones remains relatively underdeveloped.

Kaim and co-workers (7) reported the properties of a binuclear ruthenium complex (**4**) containing the bridging ligand 2,5-bis(diphenylphosphino)-1,4-hydroquinone. This complex presents an interesting conundrum in that the trication can be formulated *either* as a bis-Ru(II) complex bridged by a semiquinone radical anion $[Ru^{II}(SQ^{\bullet -})Ru^{II}]^{3+}$ *or* as a hydroquinonate-bridge mixed-valence species $[Ru^{II}(Q^{2-})Ru^{III}]^{3+}$. Spectroscopic data suggest that both forms contribute significantly to the overall electronic structure of **4**, a situation that arises from substantial mixing of metal- and ligand-based orbitals.

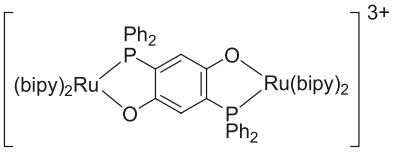

4

Aside from complex **4**, the only other phosphine-containing dioxolenes are Colbran's 1,4-hydroquinones containing a single phosphine substituent (8) (though there are a few examples of phosphonium-substituted $[R_3P^+]$ (9) or phosphonate-substituted $[X_2P(O)]$ (10) (hydro)quinones). These systems exhibit ligand-based redox-dependent hemilabile behaviour, further adding to the array of interesting metal-dioxolene chemistry. We are interested in developing the chemistry of bis(phosphine) dioxolenes because of the excellent donor qualities of phosphines and the electroactivity of the dioxolene unit. One of the fundamental aspects of redox-active ligand chemistry is how the redox properties of the ligand are perturbed upon coordination. Because of the complexities associated with the ruthenium system **4**, we decided to investigate other complexes with transition metals that are electronically "inactive". Herein we present the synthesis of a dipalladium complex of 2,5-bis(diphenylphosphino)-1,4-hydroquinone. We also present the synthesis and characterization of the corresponding free 2,5-bis(diphenylphosphino)-1,4-*benzo*quinone, the first phosphine-substituted quinone.

Results and discussion

The synthesis of 2,5-bis(diphenylphosphino)-1,4-benzoquinone (**9**) is shown in Scheme 1. The immediate precursor to **9**, namely the corresponding hydroquinone **8**, was prepared based on methodology described by Kaim (7). 1,4-Dimethoxy benzene **5** was brominated under acidic conditions to afford 2,5-dibromo-1,4-dimethoxybenzene (**6**). We found that the production of **7** through lithiation of **6** at –78 °C followed by chlorophosphine addition afforded more reproducible (albeit low) yields and cleaner samples of **7** compared with the Grignard route previously described. The methoxy groups in **7** were removed with excess aluminum chloride, affording hydroquinone **8**. Oxidation of hydroquinone **8** to quinone **9** proved challenging; a number of reagents known to convert hydroquinones to quinones (e.g., DDQ, $FeCl_3$, $NaIO_4$) were not successful. Iodobenzene diacetate proved to be a successful oxidant for the synthesis

Scheme 1. Synthesis of hydroquinone **8** and quinone **9**.

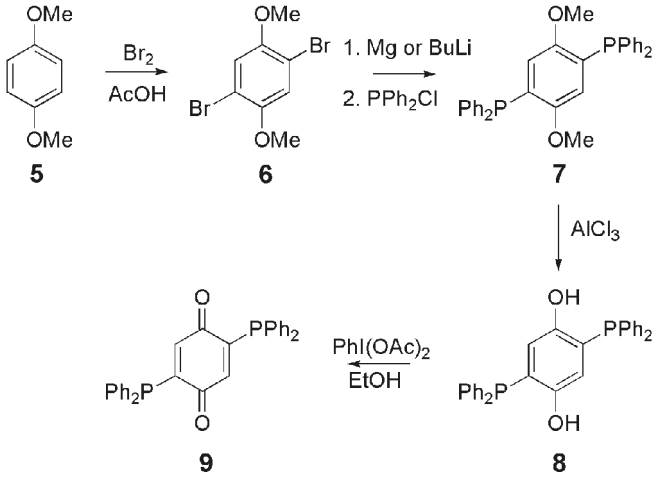

Scheme 2. Synthesis of palladium complexe **10**.

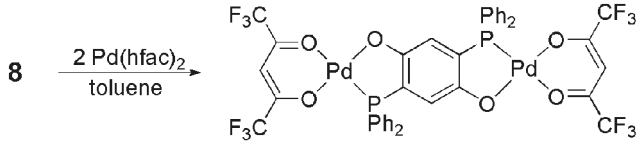

of **9**. The successful synthesis and isolation of **9** appears to counter the concerns raised by Colbran, who explicitly raised concerns about the stability of phosphine-containing quinones (8).

Hydroquinone **8** was reacted with two equivalents of palladium (II) hexafluoroacetylacetonate to afford bimetallic palladium complex **10** (Scheme 2). The complex was purified by extraction into a 50:50 mixture of diethyl ether and dichloromethane.

The crystal structure of the palladium complex **10** is shown in Fig. 1. The molecule resides on an inversion center. The palladium ion essentially lies within the plane of the hydroquinonate ligand, while the hfac ligand backbone plane lies at an angle of 8.63° relative to the plane of the hydroquinonate ligand. The structural metrics associated with the P,O chelate to the Pd ion are quite similar to those found in structures of the related ligand 2-(diphenylphosphino)phenol (11). The bond lengths within the central benzene ring and C–O bonds are typical for a hydroquinon(ate)-type electronic structure (Table 1).

The cyclic voltammograms (CVs) of **9** and **10** are shown in Fig. 2. The CV of quinone **9** has a reversible reduction wave at a potential of –0.83 V (vs. Fc/Fc^+) and a second quasi-reversible wave at –1.59 V. The reduction potentials of **9** render it slightly more easily reduced than *p*-benzoquinone, which under the same experimental conditions has reduction potentials of –0.94 and –1.60 V. The CV of **10**, which exists as the catecholate form of ligand **8** in its resting state, has two oxidation processes. The first of these is reversible and occurs at +0.44 V, while the second oxidation is irreversible with the anodic peak occurring at +1.04 V. Previous studies on a wide range of Pd (and Pt) complexes of *o*-dioxolenes have established that square pla-

© 2008 NRC Canada

Fig. 1. Molecular structure of **10**, (*a*) top view and (*b*) side view. Thermal ellipsoids shown at 50% probability. Hydrogen atoms are omitted for clarity.

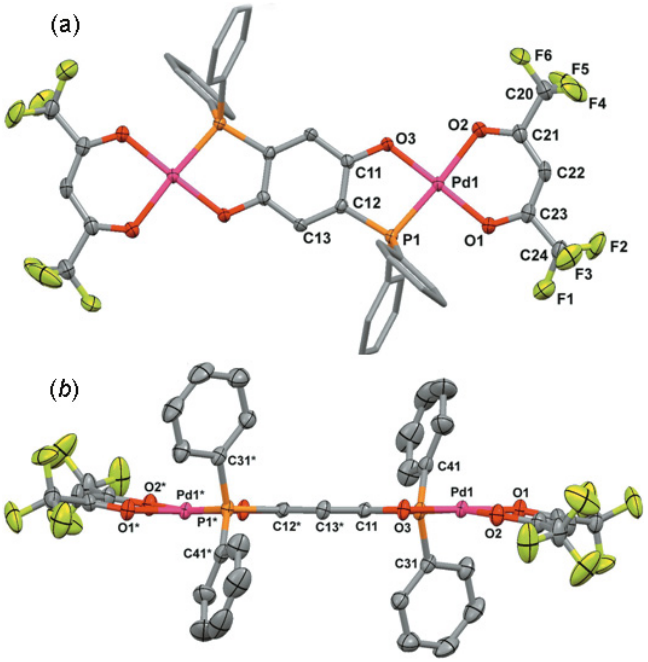

Table 1. Selected bond lengths and angles for **10**.

Bond lengths (Å)	
C11–O3	1.342(4)
C12–P1	1.790(3)
O3–Pd1	1.980(2)
P1–Pd1	2.1918(9)
O2–Pd1	2.103(2)
O1–Pd1	2.016(2)
C21–O2	1.246(4)
C23–O1	1.268(4)
C21–C22	1.393(6)
C22–C23	1.375(6)
Bond angles (°)	
O3–C11–C12	122.1(3)
C11–C12–P1	113.0(3)
C11–O3–Pd1	118.3(2)
O3–Pd1–O2	89.67(10)
O2–Pd1–O1	91.91(10)
O1–Pd1–P1	92.14(7)
Pd1–O2–C21	121.0(2)
Pd1–O1–C23	123.1(2)
O2–C21–C22	129.4(4)
O1–C23–C22	129.3(4)

nar Pd(II) is redox inert and that redox processes are invariably ligand-based, corresponding to interconversion between catecholate, semiquinone, and quinone forms of the (coordinated) dioxolene (12, 13). These studies, in conjunction with the spectroscopic data for the one-electron oxidized form of **10** (see below), suggest that the redox processes observed in **10** are ligand based, i.e., the two oxidation steps correspond

Fig. 2. Cylclic voltammograms of **9** (top) and **10** (bottom) in CH_2Cl_2 (0.2 mol/L, Bu_4NBr electrolyte, scan rate 0.25 V/s).

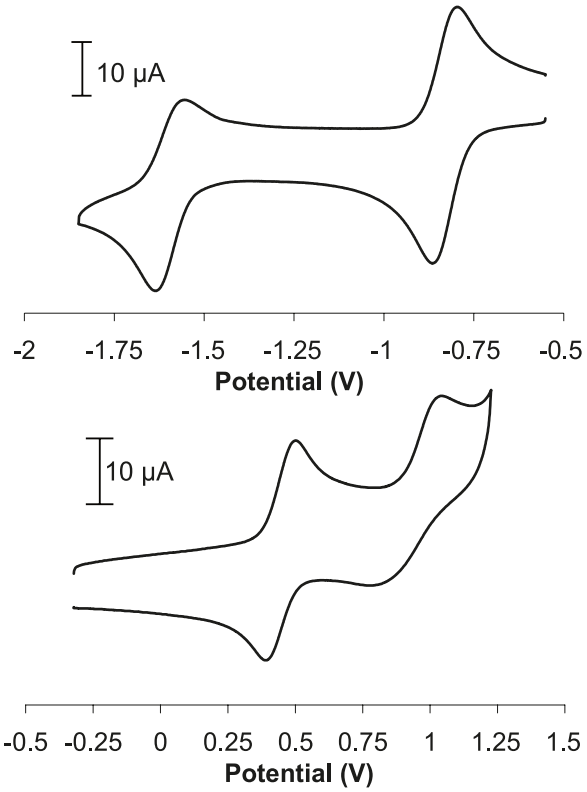

Table 2. Electrochemical parameters for **9**, **10**, and related compounds.

Compound	E_1°	E_2°
p-benzoquinone	–0.94	–1.60
9	–0.83	–1.59
10	1.04 / 0.79[a]	0.44

Note: Potentials are reported in V vs. Fc/Fc+. CVs were performed in CH_2Cl_2 solution with 0.2 mol/L Bu_4NBF_4 as electrolyte and scane rate 0.25 V/s.

[a]Irreversible process; cathodic and anodic potentials given.

to formation of the semiquinone and quinone forms of the bridging ligand.

The electrochemical data for **9** and **10** are summarized in Table 2. The data are presented to permit direct comparisons of the two electron-transfer processes available to dioxolenes; thus, E_1° corresponds to the quinone/semiquinone redox couple, while E_2° is the semiquinone/hydroquinonate couple. The redox potentials for free ligand **9** and dipalladium complex **10** differ by approximately two volts, a difference that can be attributed to the presence of two positively charged metal ions in the latter. Another interesting contrast between **9** and **10** is the *difference* between E_1° and E_2° (ΔE) for each species. For free quinone **9**, this difference is +0.74 V, a fairly typical value for *p*-quinones (14). The irreversibility of the second oxidation process in **10** makes it difficult to accurately determine E_2° (and hence ΔE), but using the midpoint of anodic and cathodic peak potentials, an effective E_2° of +0.92 V can be estimated, which leads to a

© 2008 NRC Canada

Scheme 3. Synthesis of palladium semiquinone complex **11**.

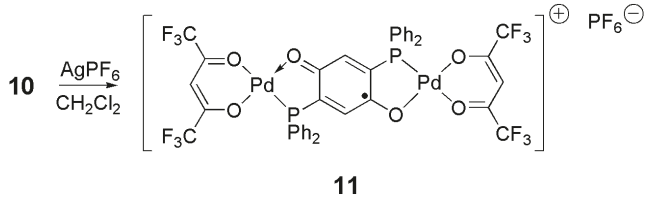

ΔE of 0.48 V, a substantially lower value compared with the uncoordinated dioxolene.

The reversibility of the first oxidation of **10** prompted attempts to prepare a cation of this species. Palladium hyroquinonate complex **10** was treated with one equivalent of silver hexafluorophosphate to afford semiquinone complex **11** (Scheme 3). This complex is air and moisture sensitive and also appears to slowly degrade in solution even under anaerobic conditions, but freshly prepared samples were sufficiently long-lived to permit solution characterization. Solutions of **11** could be re-reduced with Zn powder to regenerate **10** in ~ 70%–75% yield, demonstrating the persistence of **11** and ruling out the possibility that the spectroscopic data on **11** are from a decomposition product.

The electronic spectra of **11** and its precursor **10** are shown in Fig. 3. Complex **10** has absorption maxima at 358 and 442 nm, while the electronic spectrum of **11** has absorption maxima at 308 and 361 nm as well as low energy maxima at 464 and 582 nm. The broad maximum centered at 582 nm is characteristic of semiquinone radical anions (15).

The EPR spectrum of **11** recorded in degassed dichloromethane in a capillary tube at room temperature (RT) is shown in Fig. 4. The *g*-factor of 2.0084 is slightly higher than the free electron value (2.0023), indicating that the paramagnetic species has most of its spin density located on an organic moiety, as has been shown for Pd and Pt complexes of *o*-semiquinone-type radical anion ligands (12). The spectrum has a dominant five-line pattern with approximate 1:4:6:4:1 intensities; also evident are less intense satellite peaks on either side of this pentet. The overall pattern is suggestive of hyperfine coupling to four (approximately) equivalent S = 1/2 nuclei and additional coupling to two palladium ions (^{105}Pd, I = 5/2, 22.2% abundant). Unfortunately, the linewidths allow only for estimates of the hyperfine coupling to be made; the experimental spectrum could be simulated by coupling to two equivalent phosphorus nuclei and two equivalent protons with similar hyperfine coupling constants (a(P) ~ a(H) ~ 3 G) and additional coupling to the two palladium nuclei (a(Pd) = 2.1 G). The proton hyperfine coupling constants are consistent with other (free) semiquinone radical anions (16), supporting the notion that **11** is appropriately described as containing a bridging *p*-semiquinone ligand.

Summary

We have prepared the first example of a quinone with trivalent phosphorus as a substituent. The redox properties of phosphine-substituted quinone **9** are consistent with the *p*-dioxolene functionality. Coordination to a diamagnetic and redox-inactive metal allowed for the unambiguous elucidation of the redox properties of the *coordinated* dioxolene. In this case, coordination to two Pd ions produces dramatic changes in the ligand redox potentials as well as in the difference between the sequential redox events inherent in dioxolene compounds. These findings suggest that future efforts to design metal-*p*-dioxolene complexes with interesting redox characteristics (e.g., valence tautomerizm) will require careful consideration of how the redox properties of the bridging ligand are altered when bound to metals.

Fig. 3. Electronic spectra of **10** (red line) and **11** (black line) in CH_2Cl_2.

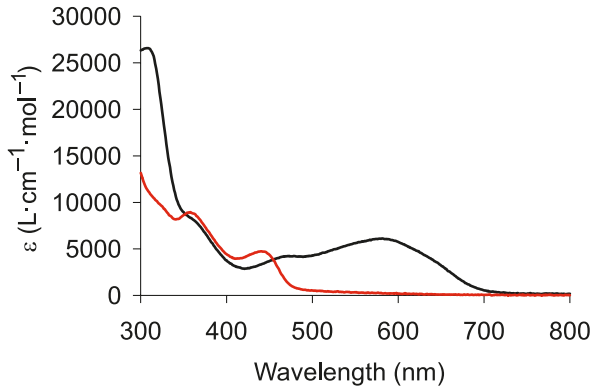

Fig. 4. X-band EPR spectrum (top) and simulation (bottom) of **11** in degassed CH_2Cl_2 at 293 K.

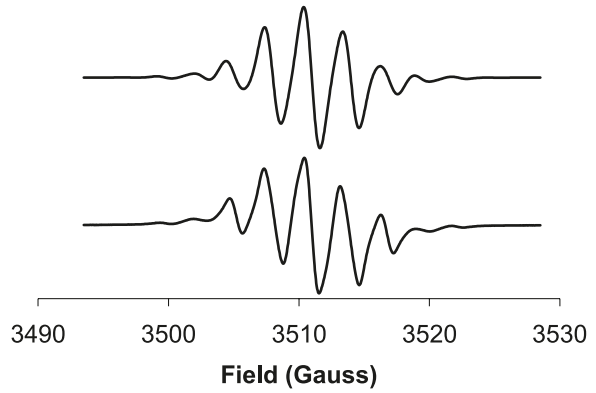

Experimental

General considerations

All reagents were purchased from either Lancaster or Sigma-Aldrich and were used as received. NMR spectra were obtained on a 300 MHz instrument. IR spectra were recorded as KBr pellets on a PerkinElmer Spectrum One FT-IR spectrometer. UV–vis spectra were taken on a Cary 50 instrument. Mass spectra were recorded on a Kratos Concept II instrument using electron impact (EI) or liquid secondary ion (LSIMS) source. Elemental analyses were performed by Canadian Microanalytical Services Ltd., Vancouver, BC, Canada. Cyclic voltammetry experiments were run on a Bioanalytical Systems CV50 voltammetric analyzer using an electrochemical cell containing the analyte (1 mmol/L), Bu_4NBF_4 (0.2 mol/L) as electrolyte, CH_2Cl_2 solvent, a silver wire as the reference electrode, and ferrocene/ferrocenium as an internal reference. The CV of *p*-benzoquinone (Table 2) was performed to enable direct comparisons with **9** run un-

© 2008 NRC Canada

Table 3. Crystallographic data for **10**.

Formula	$C_{40}H_{24}O_6F_{12}P_2Pd_2 \cdot 2CH_2Cl_2$
FW	1273.18
Dimensions (mm)	0.05 × 0.32 × 0.45
a (Å)	15.1186(17)
b (Å)	9.6386(9)
c (Å)	16.4640(18)
α (°)	90.0
β (°)	97.109(4)
γ (°)	90.0
V (Å^3)	2380.7(4)
D_{calc} (g cm^{-3})	1.776
System	Monoclinic
Space group	*P* $2_1/c$ (#14)
Z	2
μ (mm^{-1})	0.114
T (K)	173.15
$2\theta_{max}$ (°)	50.2°
Unique reflections	4193, R_{int} = 0.024
R_1[a]	0.042
wR_2[b]	0.088

[a] $R_1 = \Sigma (|F_0| - |F_c|)/\Sigma|F_0|$.
[b] $wR_2 = [\Sigma w(|F_0| - |F_c|)^2/\Sigma w(|F_0|)^2]^{1/2}$.

der identical experimental conditions. EPR spectra were obtained using a Bruker EMX spectrometer with diluted samples (~10^{-5} mol/L) in capillary tubes. A capillary tube was employed to minimize the absorption of microwave radiation by the sample. Spectra were simulated using WinEPR SimFonia.

X-ray structure determination

X-ray diffraction data were collected on a Bruker X8 APEX II diffractometer with graphite-monochromatized Mo Kα radiation (λ = 0.710 73 Å). The structure was solved by direct methods (SHELXTL); see Table 3 for crystallographic data.[2]

Synthesis of 2,5-bis(diphenyl phosphino)-1,4-dimethoxybenzene (7)

n-BuLi (27.0 mL of a 1.6 mol/L hexanes solution, 43.2 mmol) was added dropwise to a –78 °C solution of 2,5-dibromo-1,4-dimethoxybenzene **6** (6.0 g, 20.3 mmol) in freshly distilled diethyl ether (100 mL) and tetrahydrofuran (50 mL) under argon. Upon addition, the solution was allowed to stir for 30 min at –78 °C before it was warmed to RT for an additional 4 h of stirring. The resulting slurry was once again cooled to –78 °C before diphenylchlorophosphine (8.5 mL, 47.0 mmol) was added dropwise. The reaction mixture was allowed to warm slowly to RT, stirring overnight to yield a pale yellow solution. The reaction mixture was then concentrated in vacuo, and the resulting residue was extracted into diethyl ether (3 × 100 mL). The ether fractions were combined and washed with distilled water (3 × 100 mL) before being dried with magnesium sulfate and taken to dryness in vacuo. Trituration of the residue with methanol afforded **7** as an off-white solid, yield 1.0 g (9.9%). NMR spectra were consistent with that the literature-reported compound (7).

Synthesis of 2,5-bis(diphenylphosphino)-1,4-benzoquinone (9)

Saturated solutions of 2,5-diphenylphosphino-1,4-hydroquinone **8** (100 mg, 0.21 mmol) and iodobenzene bisacetate (101 mg, 0.31 mmol) were obtained by heating the reagents in ethanol (20 mL and 5 mL respectively). The iodobenzene bisacetate solution was then added dropwise to the solution of **8**, causing an immediate colour change to dark red. The solution was stirred for 10 min with gentle heating before it was allowed to cool on ice for 30 min. The quinone was isolated by filtration and washed with methanol (2 × 5 mL) followed by diethyl ether (2 × 5 mL), affording **9** as a dark red microcrystalline solid; yield 46.8 mg, 47.0%. UV–vis (CH_2Cl_2) λ_{max}: 530 nm (ε = 752), 410 nm (ε = 2756), 230 nm (ε = 25660), 210 nm (ε = 7242). FT-IR (KBr, cm^{-1}): 3421 (w, br), 2972 (w), 1644 (vs), 1584 (m), 1556 (m), 1434 (m), 1322 (w), 1200 (m), 1067 (w), 1025 (w), 911 (w), 746 (m), 696 (m), 498 (w). ^{1}H NMR (CD_2Cl_2) δ: 7.39 (m, 20H), 6.18 ppm (dd, 2H, *J* = 1.5 Hz, 4 Hz). ^{13}C NMR (CD_2Cl_2, ppm) δ: (186.4, d, *J* = 16 Hz), (153.5, d, *J* = 27 Hz), (140.6, s (v.br)), (134.8, d, *J* = 22 Hz), (133.6, d, *J* = 9 Hz), (130.4, s), (129.6, d, *J* = 8 Hz). ^{31}P NMR (CD_2Cl_2, ppm) δ: –15.98. MS (EI) *m*/*z*: 475 (M^+, 100%). Anal. calcd. for $C_{30}H_{22}O_2P_2$: C 75.63, H 4.65, P 13.00; found: C 74.87, H 4.56, P 12.86.

Synthesis of μ-(2,5-diphenylphosphino-1,4-hydroquinone)-bis-palladiumhexafluoroacetylacetonate (10)

2,5-Diphenyl phosphine-1,4-hydroquinone **8** (250 mg, 0.52 mmol) and palladium (II) hexafluoroacetylacetonate (544 mg, 1.01 mmol) were dissolved in a minimum amount of toluene (15 mL and 5 mL respectively) with gentle heating. The hydroquinone solution was added dropwise to the solution containing bis(hexafluoroacetylacetonate)palladium. Immediately a dark brown precipitate formed. The reaction mixture was stirred for 5 min and filtered to isolate the precipitate. Purification of the isolated solid was achieved by dissolving the crude product in 50:50 CH_2Cl_2/Et_2O and filtering out insoluble matter. Palladium complex **10** was isolated as a golden brown solid; yield 204 mg, 35.4%. UV–vis (CH_2Cl_2) λ_{max}: 440 nm (ε = 5000), 360 nm (ε = 9900), 245 (ε = 79300), 215 nm (ε = 43600). FT-IR (KBr, cm^{-1}): 3446 (s, br), 2917 (w), 1629 (m), 1465 (w), 1439 (w), 1380 (w), 1259 (s), 1209 (m), 1152 (vs), 1098 (m), 566 (w), 532 (w). ^{1}H NMR (CD_2Cl_2) δ: 7.81 (m, 8H), 7.64 (m, 4H), 7.51 (m, 8H), 6.71 (dd, 2H, *J* = 6 Hz, 13 Hz), 6.17 ppm (s, 2H). ^{13}C NMR (CD_2Cl_2, ppm) δ: (176.8, q, *J* = 35 Hz), (175.0, q, *J* = 35 Hz), (168.8, t, *J* = 13 Hz), (133.4, d, *J* = 12 Hz),

[2] Supplementary data for this article are available on the journal Web site (canjchem.nrc.ca) or may be purchased from the Depository of Unpublished Data, Document Delivery, CISTI, National Research Council Canada, Ottawa, ON K1A 0R6, Canada. DUD 3809. For more information on obtaining material refer to cisti-icist.nrc-cnrc.gc.ca/cms/unpub_e.shtml. CCDC 694246 contains the crystallographic data for this manuscript. These data can be obtained, free of charge, via www.ccdc.cam.ac.uk/conts/retrieving.html (Or from the Cambridge Crystallographic Data Centre, 12 Union Road, Cambridge CB2 1EZ, UK; fax +44 1223 336033; or deposit@ccdc.cam.ac.uk).

© 2008 NRC Canada

(133.2, s), (129.9, d, J = 13 Hz), (127.9, d, J = 59 Hz), (122.4, d, J = 55 Hz), (118.6, d, J = 19 Hz), (116.7, d, J = 16 Hz), (91.7, s). ^{31}P NMR (CD_2Cl_2, ppm) δ: +41.95. MS (+ LSIMS) *m/z*: 1103.8 (M^+, 100%). Anal. calcd. for $C_{40}H_{24}F_{12}O_6P_2Pd_2$: C 43.54, H 2.19; found: C 43.69, H 2.35.

Synthesis of μ-(2,5-diphenylphosphino-1,4-semiquinone)-bis-palladiumhexafluoroacetylacetonate (11)

Palladium complex **10** (130 mg, 0.12 mmol) was dissolved in freshly distilled dichloromethane (25 mL) under argon and allowed to stir for 10 min. In one portion, under a flow of argon, silver hexafluorophosphate (30 mg, 0.12 mmol) was added to the solution causing a colour change from orange to dark purple. The volume of the solution was reduced in vacuo (~10 mL), and dry hexane (~10 mL) was added causing the precipitation of a dark purple microcrystalline solid. The solution was cooled on ice for 10 min before it was filtered under inert atmosphere. The solid was washed with dry hexanes (2 × 10 mL) and dried in vacuo for 30 min before it was isolated in an inert atmosphere glove box. Semiquinone complex **11** was isolated as a microcrystalline dark purple solid; yield 125 mg, 85.0%. This complex is highly reactive in solution and in the solid state, precluding satisfactory elemental analysis. Characterization of **11** was completed using freshly prepared samples handled under an inert atmosphere. UV–vis (CH_2Cl_2) λ_{max}: 582 nm (ε = 6250), 464 (ε = 4000), 361 nm (ε = 8000), 308 nm (ε = 27500). FT-IR (KBr, cm^{-1}): 1630 (s), 1611 (m), 1449 (s), 1259 (s), 1225 (s), 1155 (s), 1103 (s), 833 (s), 691 (m), 557 (m), 530 (m). Satisfactory elemental analysis could not be obtained for this compound.

Acknowledgements

We thank the University of Victoria and the Natural Sciences and Engineering Research Council of Canada for financial support.

References

1. (*a*) C.G. Pierpont and R.M. Buchanan. Coord. Chem. Rev. **38**, 45 (1981); (*b*) C.G. Pierpont and C.W. Lange. Prog. Inorg. Chem. **41**, 331 (1994); (*c*) C.G. Pierpont. Coord. Chem. Rev. **216**, 99 (2001).
2. E. Evangelio and D. Ruiz-Molina. Eur. J. Inorg. Chem. 2957 (2005).
3. (*a*) P. Cornago, C. Escolastico, M.D.S. Maria, R.M. Claramunt, D. Carmona, M. Esteban, L.A. Oro, C. Focesfoces, A.L. Llamassaiz, and J. Elguero. J. Organometal. Chem. **467**, 293 (1994); (*b*) T.E. Keyes, P.M. Jayaweera, J.J. McGarvey, and J.G. Vos. J. Chem. Soc. Dalton Trans. 1627 (1997); (*c*) T.E. Keyes, R.J. Forster, P.M. Jayaweera, C.G. Coates, J.J. McGarvey, and J.G. Vos. Inorg. Chem. **37**, 5925 (1998); (*d*) R. Dinnebier, H.W. Lerner, L. Ding, K. Shankland, W.I.F. David, P.W. Stephens, and M. Wagner. Z. Anorg. Allg. Chem. **628**, 310 (2002); (*e*) G. Margraf, T. Kretz, F.F. de Biani, F. Laschi, S. Losi, P. Zanello, J.W. Bats, B. Wolf, K. Removic-Langer, M. Lang, A. Prokofiev, W. Assmus, H.W. Lerner, and M. Wagner. Inorg. Chem. **45**, 1277 (2006).
4. S. Kitagawa and S. Kawata. Coord. Chem. Rev. **224**, 11 (2002).
5. (*a*) A. Dei, D. Gatteschi, L. Pardi, and U. Russo. Inorg. Chem. **30**, 2589 (1991); (*b*) C. Carbonera, A. Dei, J.F. Letard, C. Sangregorio, and L. Sorace. Angew. Chem. Int. Ed. **43**, 3136 (2004); (*c*) K.S. Min, A.L. Rheingold, A. DiPasquale, and J.S. Miller. Inorg. Chem. **45**, 6135 (2006); (*d*) J. Tao, H. Maruyama, and O. Sato. J. Am. Chem. Soc. **128**, 1790 (2006); (*e*) D. Guo and J.K. McCusker. Inorg. Chem. **46**, 3257 (2007); (*f*) K.S. Min, A.G. DiPasquale, J.A. Golen, A.L. Rheingold, and J.S. Miller. J. Am. Chem. Soc. **129**, 2360 (2007).
6. O. Siri, J.P. Taquet, J.P. Collin, M.M. Rohmer, M. Benard, and P. Braunstein. Chem. Eur. J. **11**, 7247 (2005).
7. S. Ernst, P. Hanel, J. Jordanov, W. Kaim, V. Kasack, and E. Roth. J. Am. Chem. Soc. **111**, 1733 (1989).
8. (*a*) S.B. Sembiring, S.B. Colbran and D.C. Craig. Inorg. Chem. **34**, 761 (1995); (*b*) S.B. Sembiring, S.B. Colbran, D.C. Craig, and M.L. Scudder. J. Chem. Soc. Dalton Trans. 3731 (1995); (*c*) S.B. Sembiring, S.B. Colbran, and D.C. Craig. J. Chem. Soc. Dalton Trans. 1543 (1999).
9. F. Ramirez, D. Rhum, and C.P. Smith. Tetrahedron, **21**, 1941 (1965).
10. K. Kobiro, M. Shi, and Y. Inoue. Chem. Lett. 633 (1999).
11. S. Priya, M.S. Balakrishna, and J.T. Mague. J. Organometal. Chem. **689**, 3335 (2004).
12. (*a*) F.C. Senftleber and W.E. Geiger. Inorg. Chem. **17**, 3615 (1978); (*b*) N.M. Shavaleev, E.S. Davies, H. Adams, J. Best, and J.A. Weinstein. Inorg. Chem. **47**, 1532 (2008).
13. (*a*) P. Chaudhuri, C.N. Verani, E. Bill, E. Bothe, T. Weyhermuller, and K. Wieghardt. J. Am. Chem. Soc. **123**, 2213 (2001); (*b*) D. Herebian, E. Bothe, F. Neese, T. Weyhermuller, and K. Wieghardt. J. Am. Chem. Soc. **125**, 9116 (2003); (*c*) S.L. Kokatam, P. Chaudhuri, T. Weyhermuller, and K. Wieghardt. J. Chem. Soc. Dalton Trans. 373 (2007).
14. (*a*) J.Q. Chambers. *In* The Chemistry of the quinonoid compounds. Vol. 1. *Edited by* S. Patai. John Wiley and Sons Inc., New York. 1974. p. 737; (*b*) J.Q. Chambers. *In* The Chemistry of quinonoid compounds. Vol. 2. *Edited by* S. Patai and Z. Rappoport. John Wiley and Sons, Inc., New York. 1988. p. 719.
15. (*a*) J.S. Miller, P.J. Krusic, D.A. Dixon, W.M. Reiff, J.H. Zhang, E.C. Anderson, and A.J. Epstein. J. Am. Chem. Soc. **108**, 4459 (1986); (*b*) C. Vazquez, J.C. Calabrese, D.A. Dixon, and J.S. Miller. J. Org. Chem. **58**, 65 (1993).
16. M.C. Depew and J.K.S. Wan. *In* The Chemistry of quinonoid compounds. Vol. 2. *Edited by* S. Patai and Z. Rappoport. John Wiley and Sons, Inc., New York. 1988. p. 963.

© 2008 NRC Canada

Synthesis and properties of end-capped bis(oligothienyl) sulfides

Daniel J. T. Myles, M'hamed Chahma, and Robin G. Hicks

Abstract: The synthesis, and the optical and electrochemical properties, of a series of mesitylthio (MesS-) end-capped bis(oligothienyl) sulfides are presented. The target compounds were synthesized principally by convergent protocols, whereby a series of short thiophene oligomers bearing one terminal mesitylthio (MesS-) substituent were first assembled by metal-catalyzed cross-coupling reactions and then coupled via divalent sulfur through reactions with bis(phenylsulfonyl) sulfide. The spectroscopic and electrochemical features of the bis(oligothienyl) sulfides are qualitatively similar to those of the related mesitylthio-capped fully conjugated oligothiophenes, suggesting that the degree of electronic communication between the two oligothiophene chromophores in the bis(oligothienyl) sulfides is low. Cyclic voltammetry studies on the bis(oligothienyl) sulfides reveal that these species can be reversibly oxidized to radical cations, but the reversibility of subsequent oxidations depends on oligothienyl chain length and the presence and position of more electron-rich ethylenedioxythiophene (EDOT) groups. In general, the bis(oligothienyl) sulfides possess fewer than the expected number of reversible oxidations based on comparisons with their corresponding mesitylthio-capped fully conjugated oligothiophenes; excessive charge accumulation at or near the central linking sulfur atom is believed to be responsible for the irreversible behavior. Analysis of the irreversible voltammetric response of one of the bis(oligothienyl) sulfides leads to the suggestion of a decomposition mechanism for the cationic species involving carbon–sulfur bond cleavage and subsequent coupling of thiophene fragments — a finding with potential implications for the poor environmental stability of doped poly(*p*-phenylene sulfide), one of the prototypical conducting polymers.

Key words: conjugated materials, conducting polymers, oligothiophenes, electronic communication.

Résumé : On a effectué la synthèse d'une série de bis(oligothiényl)sulfures fermés aux extrémités par des groupes mésitylthio (MesS–) et on en a déterminé les propriétés optiques et électrochimiques rapportées ici. Les produits recherchés ont été synthétisés par des protocoles convergents dans lesquels une série d'oligomères courts du thiophène portant un substituant terminal mésitylthio sont d'abord assemblés par des réactions de couplage croisées catalysées par un métal avant d'être couplés avec du soufre bivalent par le biais de réactions avec du sulfure de bis(phénylsulfonyle). Les caractéristiques spectroscopiques et électrochimiques des sulfures de bis(oligothiényle) sont qualitativement semblables à celles des oligothiophènes apparentés complètement conjugués et fermés aux extrémités par des groupes mésitylthio; ceci suggère que le degré de communication électronique est faible entre les deux chroromophores oligothiophènes des sulfures d'oligothiényle. Les études de voltampérométrie cyclique sur les sulfures de bis(oligothiényle) révèlent que ces espèces peuvent être oxydées d'une façon réversible en cations radicaux, mais que la réversibilité des oxydations subséquentes dépend de la longueur de la chaîne oligothiényle et de la présence et de la position de groupes éthylènedioxythiophène (EDOT) plus riches en électrons. En général, les sulfures de bis(oligothiényle) possèdent des nombres d'oxydation réversibles inférieurs à ceux qui pourraient être attendus sur la base de comparaison avec les oligothiophènes apparentés complètement conjugués et fermés aux extrémités par des groupes mésitylthio; l'accumulation excessive de charge au ou près de l'atome de soufre central pourrait être responsable de ce comportement irréversible. Une analyse de la réponse voltampérométrique irréversible d'un des sulfures de bis(oligothiényle) conduit à suggérer un mécanisme de décomposition pour l'espèce cationique impliquant une rupture de la liaison carbone-soufre et un couplage subséquent des fragments thiophènes, une observation qui présente des implications potentielles pour la mauvaise stabilité environnementale du poly(sulfure de *p*-phénylène) dopé, un des prototypes de polymères conducteurs.

Mots-clés : matériaux conjugués, polymères conducteurs, oligothiophènes, communication électronique.

[Traduit par la Rédaction]

Received 11 June 2008. Accepted 26 July 2008. Published on the NRC Research Pres Web site at canjchem.nrc.ca on 13 September 2008.

D.J.T. Myles, M. Chahma,[1] and R.G. Hicks.[2] Department of Chemistry, University of Victoria, Victoria, BC, V8W 3V6, Canada.

[1]Present address: Department of Chemistry and Biochemistry, Laurentian University, Sudbury, ON P3E 2C6, Canada.
[2]Corresponding author (e-mail: rhicks@uvic.ca).

 doi:10.1139/V08-128 © 2008 NRC Canada

Introduction

The development of structure–property (electrochemical, spectroscopic, conducting, emissive) relationships for π-conjugated oligomers is a well-entrenched field of study (1). Many of these studies have produced important insights for the less well-defined — but technologically important — conjugated polymers. For example, the notion of π stacking as a mechanism for charge transport in conducting polymers was largely facilitated by electrochemical and spectroscopic studies on oligothiophenes (2). In addition, many conjugated oligomers are emerging as viable components of new electronic materials in their own right (3).

The diversity of functional polymers has increased greatly through the incorporation of inorganic segments into otherwise conventional organic systems. Many of these hybrid polymers are based on transition metals, (4), but there is a growing body of "organomain group" polymers containing p-block elements in the main chain (5). Polyaniline can be considered as a prototypical example (6), but polymers containing group 13 (7), 14 (8), or 15 (9) elements have been developed as well. Polymers containing group 16 elements in the main chain have a more sporadic history. Poly(thiazyl) $(SN)_x$ is noteworthy for its conducting and superconducting properties and as the forerunner to the field of organic conducting polymers (10). Poly(*p*-phenylene sulfide) (PPS) was one of the first conducting doped polymers and the first based on a commodity polymer (11). This material suffers from serious environmental stability problems in its oxidized (doped) forms. Related sulfur-bridged polymers are similarly unstable when doped (12). Nakayama and co-workers (13) have reported the synthesis of oligomeric analogues of PPS in which the *p*-phenylene is replaced by 2,5-thiophenediyl; no physical properties were presented. Finally, Manners and co-workers (14) have prepared poly(thiaferrocenes) via the ring-opening polymerization of [1]thiaferrocenophanes; the electronic properties of short, well-defined oligomers were also investigated as models for the polymer — a rare example of the application of the "oligomers approach" in conjugated main group polymer chemistry.

We have been investigating small molecule and polymeric conjugated oligothiophene–sulfur materials. We have demonstrated that mesitylthio- (MesS-) capped oligothiophenes $^{MesS}\mathbf{T}_n^{SMes}$ (n = 1–4) can be reversibly oxidized to radical cations and dications, some of which exhibit exceptional stability (15). The stability of the oxidized forms arises from both the blocking of the terminal (α and ω) carbon atoms of the oligothiophene segment as well as the strong π-donating nature of the thioether (-SR) group. We separately described several bis(oligothienyl) sulfides that could be electropolymerized to give poly(oligothienyl sulfide)s in which conjugated oligothiophene segments are linked together by divalent sulfur (16, 17); related poly(aryl sulfide)s and disulfides have been subsequently reported by other groups (18). The electrochemical properties of our poly(oligothienyl sulfide)s varied based on the structure of the monomer; generally, the polymers based on the electron-rich ethylenedioxythiophene (EDOT) building block showed reversible redox behavior, but those based on unsubstituted thiophenes showed significant irreversibility in their oxidative electrochemistry. The apparent differences between the oligomers

Scheme 1.

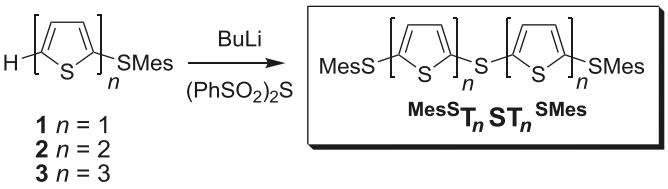

Scheme 2.

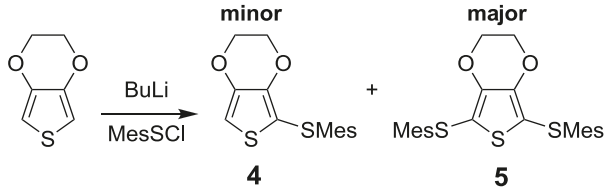

capped by SR groups and the polymers in which thiophene chromophores are *linked* by sulfur prompted us to prepare a series of model systems based on $^{MesS}\mathbf{T}_n\mathbf{ST}_n^{SMes}$ where $\mathbf{T}_n\mathbf{ST}_n$ is a bis(oligothienyl) sulfide segment — essentially a segment of the polymers — in which both terminal positions are also capped by SR groups to prevent electropolymerization (as opposed to the uncapped $\mathbf{T}_n\mathbf{ST}_n$ compounds, which upon electro-oxidation, polymerize to $(\mathbf{T}_n\mathbf{ST}_n)_m$.

Results and discussion

Synthesis

Scheme 1 outlines the general synthetic route to the mesitylthio end-capped bis(oligothienyl) sulfides. The target compounds were assembled by a convergent protocol, whereby two equivalents of an unsymmetrically substituted oligothiophene were metallated and then reacted with bis(phenylsulfonyl) sulfide; this sulfur transfer reagent has proven to be better than sulfur dichloride (SCl_2), for which these reactions typically proceed in low yield (14, 19, 20). (2-Mesitylthio)thiophene **1** was prepared by the reaction of 2-thienylmagnesium bromide with 2-mesitylenesulfenyl chloride (MesSCl). Subsequent lithiation of **1** with 1 equiv. of BuLi, followed by treatment with 0.5 equiv. of $(PhSO_2)_2S$ provided the desired sulfide $^{MesS}\mathbf{TST}^{SMes}$ in 80% yield. The bis(bithienyl) sulfide $^{MesS}\mathbf{T_2ST_2}^{SMes}$ was prepared by lithiation of bithiophene **2** (synthesized from 2,2′-bithiophene by deprotonation and reaction with MesSCl) and subsequent quenching with $(PhSO_2)_2S$. The bis(terthienyl) sulfide $^{MesS}\mathbf{T_3ST_3}^{SMes}$ required a slightly more elaborate route. Compound **2** was selectively brominated at the other terminal position with NBS in DMF (21) and then subsequently coupled with 2-tributylstannylthiophene using $Pd(PPh_3)_4$ as a catalyst to give **3** in 88% yield. Terthiophene **3** was converted to the targeted sulfide $^{MesS}\mathbf{T_3ST_3}^{SMes}$ by lithiation and quenching with $(PhSO_2)_2S$.

Variants of $^{MesS}\mathbf{TST}^{SMes}$ were also targetted in which the parent thiophene unit is replaced with the well-known (22) electron-rich 3,4-ethylenedioxythiophene moiety. However, the preparation of $^{MesS}\mathbf{ESE}^{SMes}$ by a convergent strategy was abandoned owing to difficulties in preparing the necessary precursor, namely, 2-mesitylthio-3,4-ethylenedioxythiophene **4**. The reaction of α-lithiated EDOT with 1 equiv. of

© 2008 NRC Canada

Table 1. Lowest energy electronic transitions for bis(oligothienyl) sulfides and related compounds in various charge states.

Compound	Neutral λ_{max} (nm)	Radical cation λ_{max} (nm)	Dication λ_{max} (nm)	Reference
TST	268	—	—	17
^{MesS}**TST**^{SMes}	310	555, 896	—	This work
^{MesS}**T**^{SMes}	302	412, 638	—	15
T$_2$ST$_2$	335	—	—	15
^{MesS}**T$_2$ST$_2$**^{SMes}	360	563, 865	—	This work
^{MesS}**T$_2$**^{SMes}	358	572, 905	520	15
^{MesS}**T$_4$**^{SMes}	420	756, 1420	893	15
^{MesS}**T$_3$ST$_3$**^{SMes}	395	—	680[a]	This work
^{MesS}**T$_3$**^{SMes}	386	676, 1170	696	15
ESE	270	—	—	17
^{MesS}**ESE**^{SMes}	309	520, 860	—	This work
^{MesS}**E**^{SMes}	305	405, 551	—	15
^{MesS}**E$_2$**^{SMes}	362	509, 900	—	15
ETSTE	345	—	—	17
^{MesS}**ETSTE**^{SMes}	375	—	788, 892	This work
^{MesS}**ETTE**^{SMes}	458	—	860	15
TESET	345	—	—	17
^{MesS}**TESET**^{SMes}	375	725, 1241	—	This work
^{MesS}**TEET**^{SMes}	431	721, 1240	900	15

Scheme 3.

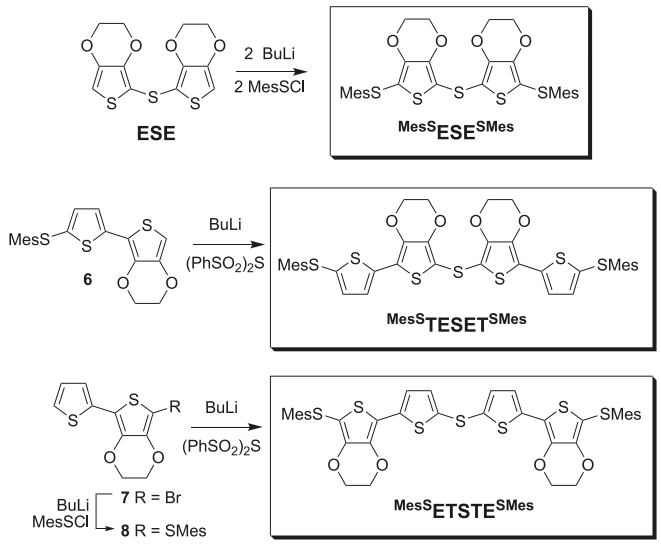

MesSCl preferentially gives the disubstituted compound **5** over the monosubstituted compound **4** (Scheme 2) (15).

The preparation of ^{MesS}**ESE**^{SMes} was accomplished by dilithiating bis(3,4-ethylenedioxythienyl) sulfide (6) **ESE** followed by treatment with 2 equiv. of MesSCl (Scheme 3). Two isomeric EDOT containing bis(bithienyl) sulfide derivatives were also prepared using convergent protocols as shown in Scheme 3. Lithiation of 6 (15) with *n*-BuLi followed by quenching with $(PhSO_2)_2S$ gave ^{MesS}**TESET**^{SMes}– with two EDOTs connected to the central sulfide, in 68% yield. The isomeric species required building block **8**, which was made by lithium–halogen exchange (BuLi) of **7** (25), followed by reaction with MesSCl to give the monosubstituted **8** in 66% yield. Finally, lithiation of **8**, followed by introduction of sulfur with $(PhSO_2)_2S$, afforded ^{MesS}**ETSTE**^{SMes}, in which the EDOT groups occupy the outer positions of the conjugated moieties, in 72% yield.

Electronic spectra

The solution spectra of the bis(oligothienyl) sulfides, together with the fully conjugated bis(mesitylthio) oligothiophenes previously reported (15), provide some insights into how the *terminal* and *internal* sulfur atoms perturb the π chromophores of oligothiophenes. The solution absorption spectral data are summarized in Table 1.

We have previously shown that mesitylthio (MesS-) substituents at the terminal (α, ω) positions cause moderate (~30 nm) red shifts in the lowest energy electronic transitions of oligothiophenes. This effect is apparent in the current series of bis(thienyl) sulfides. For example, the low energy transitions for the uncapped bis(thienyl) sulfides **TST** and **T$_2$ST$_2$** are at 268 and 335 nm, respectively; the maxima for the mesitylthio-capped analogues ^{MesS}**TST**^{SMes} and ^{MesS}**T$_2$ST$_2$**^{SMes} are 310 and 360 respectively. The incorporation of ethylenedioxy groups on the β-carbons also produces predictably moderate red shifts. On the other hand, the *internal* bridging sulfur units have little effect on extending the overall conjugation length. For example, λ_{max} for ^{MesS}**T$_2$ST$_2$**^{SMes}, with two single bithiophenes flanking a central sulfur, is only red-shifted by 2 nm relative to ^{MesS}**T$_2$**^{SMes}. which has a single bithiophene chromophore. In contrast, λ_{max} for ^{MesS}**T$_4$**^{SMes}, a fully conjugated tetrathiophene, is red-shifted by 50 nm relative to ^{MesS}**T$_2$ST$_2$**^{SMes}. Comparisons between other analogous pairs of oligomers (e.g., ^{MesS}**TST**^{SMes} vs. ^{MesS}**T**^{SMes}; ^{MesS}**ESE**^{SMes} vs. ^{MesS}**E**^{SMes}) reveal similar trends; overall the lowest energy absorption maxima is dominated by the nature of the individual thienyl segment: there is little additional delocalization between the two oligomeric units

© 2008 NRC Canada

through the central sulfur bridge. This is further corroborated by the fact that the extinction coefficients of the capped bis(thienyl) sulfides $^{MesS}\mathbf{T}_n\mathbf{ST}_n^{SMes}$ (see Experimental section) are *roughly* twice as large as the corresponding coefficients of the straight conjugated capped oligomers $^{MesS}\mathbf{T}_n^{SMes}$ (15). Thus, although the linking sulfur atom has two lone pairs of electrons, one of which in principle could engage in π overlap with the oligothienyl π system, the spectroscopic data suggests that the orientation of the thienyl units with respect to the S lone pair orbitals is not optimal for overlap and (or) π donation by S into what is already an electron-rich π system is ineffective.

Electronic spectra of the oxidized forms of several mesitylthio-capped oligothiophenes and bis (oligothienyl) sulfides were obtained either by electrochemical oxidation of the neutral species in solution or by chemical oxidation with $NOBF_4$. The cationic states of the "uncapped" oligomers are too reactive to observe, as they undergo the expected rapid coupling to yield polymers (16). Spectra of the cationic α,ω-bis-(mesitylthio) oligothiophenes $^{MesS}\mathbf{T}_n^{SMes}$ (n = 1–4) and $^{MesS}\mathbf{E}^{SMes}$ were obtained by chemical oxidation with $NOBF_4$ in CH_2Cl_2. Stable radical cations could be generated for all of these compounds, in accord with closely related bis(mesitylthio)oligothiophenes reported by us (15). Radical cation spectra could not be obtained for $^{MesS}\mathbf{ETSTE}^{SMes}$ or $^{MesS}\mathbf{T_3ST_3}^{SMes}$ owing to the small difference between first and second oxidation potentials for these compounds (see below); for the former, this problem is compounded by the instability of the dicationic state.

The electronic absorption spectrum for the radical cation of $^{MesS}\mathbf{T}^{SMes}$ has two absorption maxima at 412 and 638 nm. The corresponding EDOT-based compound $^{MesS}\mathbf{E}^{SMes}$ also has peaks at 405 and 551 nm. Within the thiophene series $^{MesS}\mathbf{T}_n^{SMes}$ (n = 1–4), as the thiophene chain length increases there is a shift to lower energies for the radical cation series and the (more limited) dication spectral series. The spectral features of these radical cations do not show any dependence on temperature (between –5 and +20 °C) or concentration (between 10^{-5} and 10^{-4} mol/L), suggesting that radical cation π dimerization does not occur. Dimer formation is most likely suppressed because of the steric hindrance of the capping mesityl groups.

Spectra of several of the capped bis(oligothienyl) sulfides in cationic states were also obtained. The radical cation of bis(thienyl) sulfide $^{MesS}\mathbf{TST}^{SMes}$ has two major bands at 555 and 896 nm. These are significantly red-shifted in comparison to the radical cation spectrum of $^{MesS}\mathbf{T}^{SMes}$ (412 and 638 nm). This sharply contrasts comparisons between the two neutral compounds, which are nearly identical to one another. This suggests that there may be a strong interaction between the two thiophene units *via* the sulfur bridge for $^{MesS}\mathbf{TST}^{SMes}$ in its radical cation state. This may arise from the fact that removal of an electron from the oligothiophene renders it a more electron-deficient π system, thereby facilitating stabilization (and hence delocalization) from a sulfur lone pair orbital. π-Dimer bands can be ruled out, based on the fact that the intensities of the 555 and 896 nm peaks show neither a concentration nor temperature dependence. Similar comparisons can be made for the EDOT analogues of these species: the radical cation of $^{MesS}\mathbf{E}^{SMes}$ has peaks at 405 and 551 nm, whereas bis(3,4-ethyelenedioxythienyl) sulfide $^{MesS}\mathbf{ESE}^{SMes}$ radical cation absorbs at 520 and 860 nm.

Table 2. Oxidation potentials of bis(oligothienyl) sulfides and related compounds as determined by cyclic voltammetry experiments (see Experimental section for details).

Compound	Oxidation potentials (V)	Reference
$^{MesS}\mathbf{TST}^{SMes}$	+1.14, +1.43*	This work
$^{MesS}\mathbf{T}^{SMes}$	1.05	(15)
$^{MesS}\mathbf{T_2ST_2}^{SMes}$	+0.99, +1.15, +1.50	This work
$^{MesS}\mathbf{T_2}^{SMes}$	+0.87, +1.25	(15)
$^{MesS}\mathbf{T_4}^{SMes}$	+0.83, +0.91	(15)
$^{MesS}\mathbf{T_3ST_3}^{SMes}$	+0.91, +1.02, +1.13. +1.49*	This work
$^{MesS}\mathbf{T_3}^{SMes}$	+0.86, +1.02	(15)
$^{MesS}\mathbf{ESE}^{SMes}$	+0.90, +1.14*	This work
$^{MesS}\mathbf{E}^{SMes}$	0.87	(15)
$^{MesS}\mathbf{E_2}^{SMes}$	+0.57, +0.94	(15)
$^{MesS}\mathbf{ETSTE}^{SMes}$	+0.78, +0.93, +1.31, +1.70*	This work
$^{MesS}\mathbf{ETTE}^{SMes}$	+0.61, +0.66	(15)
$^{MesS}\mathbf{TESET}^{SMes}$	+0.78, +0.97*	This work
$^{MesS}\mathbf{TEET}^{SMes}$	+0.49, +0.73	(15)

Note: All potentials are given as formal potentials ($E_{1/2}$) vs. SCE except for numbers denoted with an asterisk (*), which correspond to anodic peak potentials for irreversible oxidations.

Comparisons between the various compounds containing conjugated bithiophene chromophores are more complex. The radical cations of $^{MesS}\mathbf{T_2ST_2}^{SMes}$ (563 and 865 nm) and $^{MesS}\mathbf{T_2}^{SMes}$ (572 and 905 nm) have similar spectroscopic features, and in fact the absorption maxima of the former are actually slightly *blue*-shifted with respect to the latter. This indicates that little to no electronic coupling occurs between adjacent bithiophenes via the sulfur bridge, presumably because the radical cation in $^{MesS}\mathbf{T_2ST_2}^{SMes}$ is strongly localized in the bithiophene cores. However, this picture is complicated upon consideration of the spectrum of the radical cation of $^{MesS}\mathbf{TESET}^{SMes}$; the absorption maxima (725 and 1241 nm) are dramatically red-shifted compared with the all-thiophene analogue $^{MesS}\mathbf{T_2ST_2}^{SMes}$. This may suggest that the placement of the more electron-rich EDOT groups on the "internal" positions serves to concentrate spin and (or) charge closer to the central sulfur linker, thereby facilitating more effective delocalization.

The properties of the mesitylthio- capped model compounds can also be compared with the previously reported poly(oligothienyl sulfide)s. As a representative example, $^{MesS}\mathbf{E_2}^{SMes}$ has a S-EE-S unit that is also present in the polymer poly(ESE). Neutral poly(ESE) has its absorption maxima at 455 and 484 nm, whereas $^{MesS}\mathbf{E_2}^{SMes}$ absorbs at 362 nm. The fact that poly(ESE) has its absorptions red-shifted with respect to $^{MesS}\mathbf{E_2}^{SMes}$ provides evidence that the biEDOT units are electronically coupled in the neutral polymer; in this regard the "capped" molecules are analogous to the "uncapped" monomers (i.e., ESE) that were actually employed to synthesize the polymers. Furthermore, the doped polymer has absorptions at 605 and 1020 nm whereas the radical cation of $^{MesS}\mathbf{E_2}^{SMes}$ has two absorption bands at 509 and 900 nm. The red-shift is most likely due to strong intrachain electronic coupling of the biEDOT groups in the polymer, although interchain effects cannot be ruled out.

© 2008 NRC Canada

Electrochemical studies

The redox properties of the bis(thienyl) sulfides were studied using cyclic voltammetry. The results of these studies are summarized in Table 2, which also contains electrochemical data for the previously reported bis(mesitylthio)-capped oligothiophenes (15). Our previous work on the latter compounds established that the mesitylthio substituents provide stability to the oxidized forms of the oligothiophenes. This stability arises in part by "blocking" the α and ω positions, thereby preventing polymerization (via oxidative coupling) of the thiophene radical cation; the π-donating effect of the sulfur substituent also contributes to the stability of the cationic forms of the oligomers. These effects are also manifested in the bis(thienyl) sulfide compounds presented here. All of the new compounds exhibit at least one chemically reversible oxidation process (equivalence of anodic and cathodic peak currents, peak potentials that are scan-rate-independent); the anodic and cathodic peak separations for each compound lie in the range of 60–90 mV, which is comparable to that of the ferrocene/ferrocenium redox couple under the same experimental conditions and suggestive of quasi-reversible electrochemical behavior. Many of the bis(thienyl) sulfides can be reversibly oxidized to dications or even trications in a few cases.

In general, the oxidation potentials of oligothiophene are influenced by their chain length; longer oligomers are oxidized at lower potentials. Among the homologous series of bis(thienyl) sulfides $^{MesS}\mathbf{T}_n\mathbf{ST}_n^{SMes}$ (n = 1–3), this trend holds; however, the *change* in first oxidation potential as a function of chain length for this series is comparable to the corresponding changes in the fully conjugated thiophenes. The first oxidation potential of $^{MesS}\mathbf{T}^{SMes}$ is +1.05 V. Extending the conjugated segment from one to two thiophenes (i.e., $^{MesS}\mathbf{T}_2^{SMes}$, E_1° = +0.87 V) leads to a drop in first oxidation potential of 0.18 V. Analogous comparisons between $^{MesS}\mathbf{TST}^{SMes}$ (E_1° = +1.14 V) and $^{MesS}\mathbf{T}_2\mathbf{ST}_2^{SMes}$ (E_1° = +0.99 V) produce qualitatively similar results: the first oxidation potential for the longer oligomers is +0.15 V lower. Thus, although $^{MesS}\mathbf{T}_2\mathbf{ST}_2^{SMes}$ is *two* thiophene units longer than $^{MesS}\mathbf{TST}^{SMes}$, the comparative electrochemical properties (in conjunction with the electronic spectra, see above) suggest that the connection of two thiophene segments by a divalent sulfur linker does not lead to an extension of effective conjugation length.

Given that the bis(thienyl) sulfides contain two thiophene chromophores sharing a common linker, the electrochemical responses of these might naïvely be expected to consist of the sum of the individual processes associated with each thiophene segment, i.e., $^{MesS}\mathbf{T}_n\mathbf{ST}_n^{SMes}$ should possess twice as many oxidations as $^{MesS}\mathbf{T}_n^{SMes}$. This is not the case. Figure 1 shows the cyclic voltammograms of $^{MesS}\mathbf{T}_n\mathbf{ST}_n^{SMes}$ (n = 1–3). For example, $^{MesS}\mathbf{T}^{SMes}$ and $^{MesS}\mathbf{E}^{SMes}$ both possess one reversible oxidation process. Given that the bis(thienyl) sulfide analogues $^{MesS}\mathbf{TST}^{SMes}$ and $^{MesS}\mathbf{ESE}^{SMes}$ contain two "monothiophenes", these compounds might be expected to have two oxidation waves corresponding to one-electron removal from each of the two thiophene units. However, both of these can only be reversibly oxidized to radical cations; the second oxidation process in both compounds is irreversible. In a similar vein, all of the other "parent" oligomers $^{MesS}\mathbf{T}_n^{SMes}$ (n > 1) can be reversibly oxidized

Fig. 1. Cyclic voltammograms of (*a*) $^{MesS}\mathbf{TST}^{SMes}$ (first oxidation only), (*b*) $^{MesS}\mathbf{TST}^{SMes}$ (full scan), (*c*) $^{MesS}\mathbf{T}_2\mathbf{ST}_2^{SMes}$; and (*d*) $^{MesS}\mathbf{T}_3\mathbf{ST}_3^{SMes}$. The redox process labelled with an asterisk in (*c*) corresponds to the ferrocene/ferrocenium redox couple (added as a reference). See Experimental section for details.

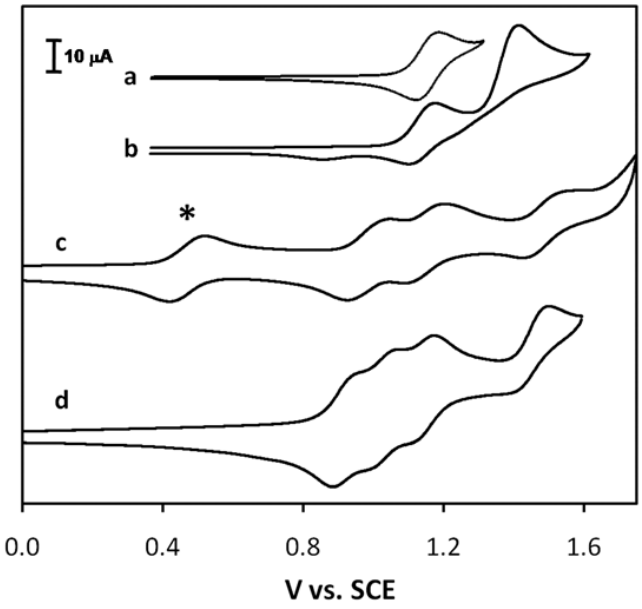

to radical cations and dications, but the corresponding bis(thienyl) sulfides $^{MesS}\mathbf{T}_n\mathbf{ST}_n^{SMes}$ (n = 2, 3) have fewer than the expected four reversible oxidation waves: the bis(bithienyl) sulfide $^{MesS}\mathbf{T}_2\mathbf{ST}_2^{SMes}$ has two reversible and one quasi-reversible wave, and the bis(terthienyl) sulfide $^{MesS}\mathbf{T}_3\mathbf{ST}_3^{SMes}$ has three very closely spaced reversible oxidations and a fourth irreversible one at higher potentials. Overall, the charge storage capacity of these compounds is relatively limited compared with the parent, fully conjugated counterparts.

The two mixed thiophene–EDOT compounds $^{MesS}\mathbf{TESET}^{SMes}$ and $^{MesS}\mathbf{ETSTE}^{SMes}$ contain the same fundamental chromophore — a bis(thioether) substituted unsymmetric bithiophene $^{RS}\mathbf{ET}^{SR}$. Given the analyses of the electrochemical properties of the other bis(thienyl) sulfides, it is not surprising that the first oxidation of $^{MesS}\mathbf{TESET}^{SMes}$ and $^{MesS}\mathbf{ETSTE}^{SMes}$ occur at the same potential. However, the electrochemical behavior of these two isomers beyond the first oxidations differs markedly. The former compound can only be reversibly oxidized to a radical cation, whereas the latter has two fully reversible oxidations and a third that is quasi-reversible (tending towards reversibility at high scan rates); it is not until the fourth oxidation that decomposition occurs. The differences in electrochemical responses between these compounds can be understood by consideration of the location of the more electron-rich EDOT moieties. $^{MesS}\mathbf{TESET}^{SMes}$ has the EDOTs directly flanking the central sulfur atom. The first two oxidations correspond to electron removal from each of the "**ET**" moieties, but with the spin and charge on both components more localized on the EDOT moieties. Thus the dication of this compound appears to have sufficient spin and charge concentration to render it unstable (a proposal of how this compound may degrade is provided below). In contrast, the isomeric $^{MesS}\mathbf{ETSTE}^{SMes}$

© 2008 NRC Canada

Fig. 2. Multiple cycle CV of ^{MesS}**TESET**^{SMes}. The redox process at +0.5 V vs SCE appears on the second anodic sweep.

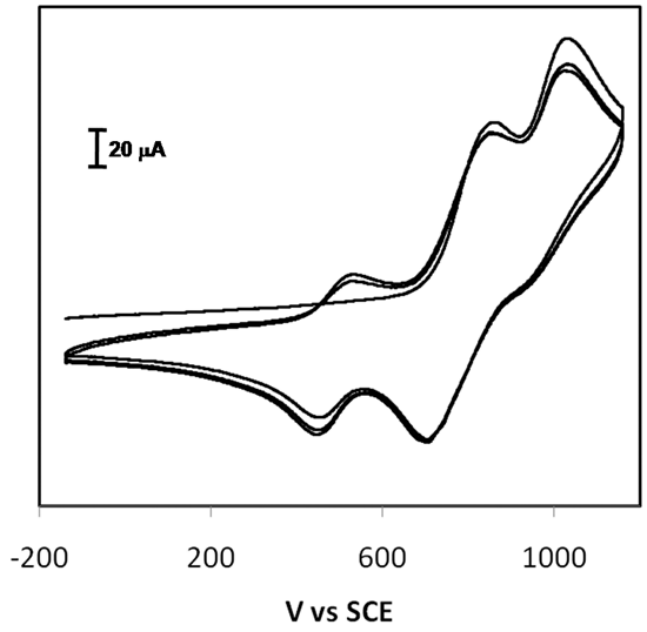

has the EDOTs located near the ends of the molecule. The dication of this compound should therefore have its spin and (or) charge driven towards each end, meaning that the two cationic chromophores do not perturb one another to the same extent, and thereby providing stability to the dication. We have previously rationalized the differences between the electrochemical properties of fully conjugated mixed EDOT–thiophene compounds ^{MesS}**TEET**^{SMes} and ^{MesS}**ETTE**^{SMes} based on similar topological arguments (15).

Electrochemical cycling through the second (irreversible) oxidation of ^{MesS}**TESET**^{SMes} leads to the appearance of a growth of a new reversible redox couple on the second anodic scan at a potential of +0.5 V, substantially lower than the first oxidation potential of this compound (Fig. 2). The potential for this new process matches the first oxidation potential of ^{MesS}**TEET**^{SMes} (Table 2). We suggest that this species is in fact being formed during the course of the oxidative decomposition of ^{MesS}**TESET**^{SMes}. Although the precise mechanistic details are unclear, one possible process involves decomposition of the dication via carbon–sulfur bond scission involving the central sulfur atom. The resulting "**ET**^{SMes}" fragments could then couple via CC bond formation between two EDOTs to give ^{MesS}**TEET**^{SMes}.

Conclusions

Several bis(oligothienyl) sulfides have been prepared and their redox and spectroscopic properties investigated. The terminal mesitylthio substituents prevent oxidative polymerization of these species and facilitate the detailed examination of structure–property relationships. Overall, the "electronic communication", i.e., delocalization, between two oligothiophene segments via a sulfur atom connector is relatively weak. Nonetheless, there are clear sequential one-electron oxidation processes corresponding to electron loss from each of the two segments in the cyclic voltammograms of most of the oligomers. Electrostatic effects are the most likely reason behind this behavior, (i.e., the proximity of the first positive charge can make it harder to create a second positive charge) and can produce the same effect.

The capped bis(oligothienyl) sulfides can all be reversibly oxidized, but after that, deleterious effects of excessive charge begin to appear. We have previously established that MesS-capped oligothiophenes can be oxidized twice, in some cases affording very stable cationic species. The bis(oligothienyl) sulfides have two such moieties and also can be oxidized, though the charge storage capability does not scale with the doubling of thiophene chromophores. This may explain why the poly(oligothienyl sulfide)s were not as well-behaved electrochemically (17) — overoxidation leads to decomposition (a common fate of fully conjugated polymer redox processes). In fact PPS was one of the first polymers to be doped to conducting form, though the doped forms are highly reactive. Our electrochemical studies are consistent with the relatively poor charge storage capacity of these systems; the suggestion that carbon–sulfur bond cleavage as a major decomposition route, which is supported by the recent description of synthetically useful version of this reaction (23), may be a possible model for doped PPS (and relatives) itself.

Experimental[3]

General

Unless stated otherwise, all reactions and manipulations were carried out under an argon atmosphere using standard Schlenk line or glovebox techniques. Glassware was dried in an oven at 125 °C for 24 h prior to use. Solvents were dried and distilled under argon prior to use (acetonitrile, dichloromethane, and hexanes from CaH_2; diethyl ether, tetrahydrofuran, and toluene from sodium benzophenone ketyl). All reagents were purchased from commercial sources and used as received except as otherwise stated. The following compounds were prepared according to literature procedures: 2-mesitylenesulfenyl chloride (15), bis(phenylsulfonyl) sulfide (19), 2,2′-bithiophene (24), bis(3,4-ethylenedioxy-2-thienyl) sulfide (ESE) (16), 3,4-ethylenedioxy-5′-mesitylthio-2,2′-bithiophene (6, 15), and 3,4-ethylenedioxy-5-bromo-2,2′-bithiophene (7, 25).

^{1}H NMR spectra were recorded at 300 MHz and ^{13}C NMR spectra were recorded at 75 MHz, unless otherwise noted. Melting points are uncorrected. Electronic spectra were recorded on a Varian Cary 5 spectrometer using 10 mm quartz cuvettes. All UV–vis and NIR studies were performed in freshly distilled dichloromethane. Voltammetric measurements were performed at RT (22 ± 2 °C) (except for variable temperature studies) in dichloromethane containing 1 mmol/L substrate (except for the variable concentration studies) and 1 mol/L of *n*-Bu_4NBF_4 as electrolyte. Platinum

[3] Supplementary data for this article are available on the journal Web site (canjchem.nrc.ca) or may be purchased from the Depository of Unpublished Data, Document Delivery, CISTI, National Research Council Canada, Ottawa, ON K1A 0R6, Canada. DUD 3816. For more information on obtaining material refer to cisti-icist.nrc-cnrc.gc.ca/cms/unpub_e.shtml.

© 2008 NRC Canada

button (diameter 1.6 mm) was used as the working electrode. Platinum wire and silver wire were used as the counter and quasi-reference electrodes, respectively. The working electrode was polished on alumina before use. *iR* compensations were applied for all experiments for potential measurements. All redox potentials were calibrated by comparing to ferrocene, which was added as an internal reference and then reported vs. SCE (Fc/Fc_+ E_o = +0.46 V vs SCE in CH_2Cl_2). The number of electrons associated with the redox processes were determined by comparison of the peak current magnitudes with those of equimolar quantities of the internal reference. Solutions of cationic species were generated either electrochemically (by constant potential bulk electrolysis in a two-compartment cell using two 3 cm × 3 cm platinum plates as cathode and anode) or chemically (by additions of aliquots of substoichiometric quantities, typically 0.2 equiv. at a time, of $NOBF_4$ solutions as oxidant).

2-(Mesitylthio)thiophene (1)

2-Bromothiophene (4.00 g, 24.5 mmol) was added to a slurry of magnesium powder (0.90 g, 37.0 mmol) in diethyl ether (20 mL). The reaction was initiated with a small amount of the bromo reagent and a crystal of iodine. Once the exothermic reaction had started, the remaining bromo reagent was added dropwise to the ice-cooled magnesium slurry over the course of 20 min. The solution was allowed to warm to RT and then refluxed for 1 h, after which the brown Grignard solution was recooled to 0 °C, and a solution of 2-mesitylenesulfenyl chloride (4.57 g, 24.5 mmol) in hexanes (25 mL) was added dropwise via cannula. The resulting pale brown solution was stirred at 0 °C for an additional 30 min. The mixture was then warmed to RT and poured into brine (100 mL). The aqueous layer was extracted with ether (3 × 50 mL), and the combined organic extracts were further washed with water (3 × 50 mL) and dried over anhydrous sodium sulfate. After filtration, removal of the solvent gave a dark brown oil, which was purified by flash chromatography (silica gel, hexanes) to provide a pale yellow liquid of **1**, yield 4.41 g (77%). ^{1}H NMR (CD_2Cl_2) δ: 7.16 (dd, *J* = 5.1, 1.5 Hz, 1H), 6.95 (s, 2H), 6.92 (dd, *J* = 3.7, 1.5 Hz, 1H), 6.88 (dd, *J* = 5.1, 3.7 Hz, 1H), 2.49 (s, 6H), 2.25 (s, 3H). ^{13}C NMR ($CDCl_3$) δ: 142.82, 139.27, 137.42, 130.03, 129.36, 128.24, 127.09, 126.07, 21.82, 21.09. HRMS (EI) for $C_{13}H_{14}S_2$ [M^+]: calcd. 234.0537; found 234.0541.

Bis(5-mesitylthio-2-thienyl) sulfide (^{MesS}TST^{SMes})

This compound has been prepared previously by a different route (26). A solution of **1** (5.00 g, 21.3 mmol) in THF (100 mL) cooled to –70 °C was treated dropwise with *n*-butyllithium (13.3 mL, 21.3 mmol, 1.6 mol/L in hexanes). The resulting yellow solution was stirred at –70 °C for 1 h, after which a solution of bis(phenylsulfonyl) sulfide (3.34 g, 10.6 mmol) in THF (20 mL) was added dropwise via cannula, and the resulting golden yellow solution was stirred at –70 °C for an additional 1 h. The mixture was warmed to RT and poured into water (100 mL). The aqueous layer was extracted with ether (3 × 50 mL), and the combined organic extracts were further washed with water (3 × 50 mL), and dried over anhydrous sodium sulfate. After filtration, removal of the solvent gave a yellow oil, which was purified by column chromatography (silica gel, hexanes/ethyl acetate (9:1 *v*/*v*)) to provide a slightly yellow solid. Recrystallization from methanol/chloroform produced white crystalline flakes of ^{MesS}TST^{SMes}, yield 4.26 g (80%), mp 92 °C. UV–vis (CH_2Cl_2) λ_{max} (nm): 310 (ε 1.9 × 10^4). Remaining spectroscopic data are identical to those found in ref. 26.

5-Mesitylthio-2,2′-bithiophene (2)

To a solution of 2,2′-bithiophene (3.00 g, 18.0 mmol) in THF (60 mL) was added dropwise *n*-butyllithium (11.3 mL, 18.1 mmol, 1.6 mol/L in hexanes) at 0 °C. The mixture was warmed to RT and stirred for 1.5 h. The mixture was cooled to –70 °C, and a solution 2-mesitylenesulfenyl chloride (3.38 g, 18.1 mmol) in hexanes (25 mL) was then added dropwise via cannula. Stirring was continued at –70 °C for 0.5 h, then the mixture was allowed to warm to RT, and water (50 mL) was added. The aqueous layer was washed with ether (50 mL), and the organic extracts were washed with brine (3 × 50 mL), and dried over anhydrous magnesium sulfate. The solvent was removed by rotary evaporation, and the green oily residue was purified by column chromatography (silica gel, hexanes) to provide a slightly yellow solid. Subsequent recrystallization from methanol produced white crystalline flakes of 2, yield 3.60 g (63%), mp 46 °C. ^{1}H NMR (500 MHz, $CDCl_3$) δ: 7.13 (dd, *J* = 5.1, 1.1 Hz, 1H), 7.01 (dd, *J* = 3.6, 1.1 Hz, 1H), 6.96 (s, 2H), 6.94–6.92 (m, 2H), 6.81 (d, *J* = 3.7 Hz, 1H), 2.53 (s, 6H), 2.28 (s, 3H). ^{13}C NMR ($CDCl_3$) δ: 142.82, 139.46, 137.77, 137.17, 136.74, 129.55, 129.44, 128.82, 127.71, 124.15, 123.56, 123.44, 21.84, 21.11. MS (LSI) *m*/*z*: 316 (M^+, 100%). Anal. calcd. $C_{17}H_{16}S_3$: C 64.51, H 5.10, S 30.39; found: C 64.58, H 5.29, S 30.07.

Bis(5′-mesitylthio-5,2′-bithien-2-yl) sulfide (^{MesS}T$_2$ST$_2^{SMes}$)

A solution of 2 (6.00 g, 18.9 mmol) in THF (150 mL) cooled to –70 °C was treated dropwise with *n*-butyllithium (11.9 mL, 19.0 mmol, 1.6 mol/L in hexanes). The resulting bright yellow solution was stirred at –70 °C for 1 h. After which, a solution of bis(phenylsulfonyl) sulfide (2.98 g, 9.48 mmol) in THF (20 mL) was added dropwise via cannula, and the resulting orange solution was stirred at –70 °C for an additional 1 h. The mixture was warmed to RT and poured into water (100 mL). The fine yellow precipitate was filtered off and washed with cold methanol (3 × 50 mL). This solid was recrystallized from a mixture of chloroform and methanol (120 mL, 1:1 *v*/*v*) to afford ^{MesS}T$_2$ST$_2^{SMes}$ as pale yellow needles, yield 4.90 g (78%), mp 154 °C. UV–vis (CH_2Cl_2) λ_{max} (nm): 360 (ε 3.9 × 10^4). ^{1}H NMR ($CDCl_3$) δ: 7.00 (d, *J* = 3.7 Hz, 2H), 6.94 (s, 4H), 6.86 (d, *J* = 4.4 Hz, 2H), 6.80 (d, *J* = 3.7 Hz, 2H), 6.74 (d, *J* = 4.4 Hz, 2H), 2.48 (s, 12H), 2.27 (s, 6H). ^{13}C NMR ($CDCl_3$) δ: 142.82, 141.33, 139.57, 137.89, 136.72, 133.58, 133.48, 129.46, 129.27, 128.38, 124.02, 123.28, 21.78, 21.10. MS (EI) *m*/*z*: 662 (M^+, 100%). Anal. calcd. for $C_{34}H_{30}S_7$: C 61.59, H 4.56, S 33.85; found: C 61.40, H 4.49, S 33.85.

5-Bromo-5′-mesitylthio-2,2′-bithiophene

5-Mesitylthio-2,2′-bithiophene 2 (6.32 g, 20.0 mmol) was dissolved in DMF (100 mL). In the absence of light, NBS

© 2008 NRC Canada

(3.91 g, 22.0 mmol) was added portionwise to the solution at RT. After addition, the solution was stirred at RT overnight in the dark. The resulting pale yellow solution was diluted with dichloromethane (100 mL) and poured into brine (100 mL). The aqueous phase was collected and washed with a second portion of dichloromethane (100 mL). All organics were collected and extracted with water (5 × 100 mL) to remove any remaining DMF. The dichloromethane layer was dried over anhydrous sodium sulfate, filtered, and evaporated. The obtained pale orange liquid was purified by column chromatography (silica gel, hexanes/dichloromethane (4:1 *v*/*v*)) to provide 5-bromo-5′-mesityl-2,2′-bithiophene as a yellow liquid, yield 7.10 g (90%). This compound was used in the next step without further purification. ^{1}H NMR ($CDCl_3$) δ: 6.94 (s, 2H), 6.87 (d, *J* = 4.4 Hz, 1H), 6.84 (d, *J* = 3.7 Hz, 1H), 6.75 (d, *J* = 3.7 Hz, 1H), 6.72 (d, *J* = 3.7 Hz, 1H), 2.49 (s, 6H), 2.26 (s, 3H). MS (LSI) *m*/*z*: 394 (M^+, ^{79}Br, 90%), 395 (M + 1, ^{79}Br, 28%), 396 (M^+, ^{81}Br, 100%), 397 (M + 1, ^{81}Br, 27%).

5-Mesitylthio-2,2′:5′,2″-terthiophene (3)

A flask was charged with 2-(tributylstannyl)thiophene (3.05 mL, 9.59 mmol), 5-bromo-5′-mesitylthio-2,2′-bithiophene (3.79 g, 9.59 mmol), $Pd(PPh_3)_4$ (554 mg), and toluene (20 mL). The mixture was heated to reflux for 20 h. After cooling to RT, the black mixture was diluted with ether (100 mL) and poured into saturated potassium fluoride (100 mL). The resulting tributyltin fluoride was filtered off and washed with cold ether (3 × 15 mL). The organic phase was collected, washed with brine (3 × 100 mL), and dried over anhydrous sodium sulfate. The solvent was removed by rotary evaporation, and the dark yellow residue was purified by column chromatography (silica gel, hexane/EtOAc (9:1 *v*/*v*)) to provide a bright yellow solid. Recrystallization from ethanol produced yellow crystalline plates of **3**, yield 3.36 g (88%), mp 80 °C. ^{1}H NMR (500 MHz, $CDCl_3$) δ: 7.18 (dd, *J* = 5.1, 1.1 Hz, 1H), 7.11 (dd, *J* = 3.6, 1.1 Hz, 1H), 6.99 (d, *J* = 3.8 Hz, 1H), 6.98 (dd, *J* = 5.1, 3.6 Hz, 1H), 6.96 (s, 2H), 6.92 (d, *J* = 3.7 Hz, 1H), 6.90 (d, *J* = 3.8 Hz, 1H), 6.80 (d, *J* = 3.8 Hz, 1H), 2.52 (s, 6H), 2.28 (s, 3H). MS (LSI) *m*/*z* : 398 (M^+, 100%). Anal. calcd. $C_{21}H_{18}S_4$: C 63.27, H 4.55, S 32.18; found: C 63.47, H 4.51, S 31.92.

Bis(5″-mesitylthio-5,2′:5′,2″-terthien-2-yl) sulfide ($^{MesS}T_3ST_3^{SMes}$)

A solution of **3** (765 mg, 1.92 mmol) in THF (25 mL), cooled to –70 °C, was treated dropwise with *n*-butyllithium (1.20 mL, 1.92 mmol, 1.6 mol/L in hexanes). The resulting bright orange solution was stirred at –70 °C for 1 h. After which, a solution of bis(phenylsulfonyl) sulfide (302 mg, 0.96 mmol) in THF (10 mL) was added dropwise via cannula, and the resulting orange solution was stirred at –70 °C for an additional 1 h. The mixture was then warmed to RT and poured into a cold mixture of diethyl ether and water (120 mL, 1:5 *v*/*v*). The fine yellow precipitate was filtered off and washed with cold methanol (3 × 15 mL). This solid was recrystallized from a mixture of tetrahydrofuran and methanol (40 mL, 1:1 *v*/*v*) to afford $^{MesS}T_3ST_3^{SMes}$ as dark golden yellow crystals, yield 400 mg (50%), mp 156 °C. UV–vis (CH_2Cl_2) λ_{max} (nm) 395 (ε 6.5 × 10^4). ^{1}H NMR (500 MHz, $CDCl_3$) δ: 7.08 d, *J* = 3.7 Hz, 2H), 6.93–6.95 (m, 8H), 6.90 (d, *J* = 3.7 Hz, 2H), 6.86 (d, *J* = 3.8 Hz, 2H), 6.78 (d, *J* = 3.7 Hz, 2H), 2.50 (s, 12H), 2.27 (s, 6H). ^{13}C NMR (125 MHz, $CDCl_3$) δ: 143.06, 141.51, 139.78, 137.74, 137.22, 136.82, 135.30, 134.07, 133.89, 129.68, 129.54, 128.77, 124.91, 124.14, 123.94, 123.77, 22.01, 21.32. MS (LSI) *m*/*z:* 826 (M^+, 10%). Anal. calcd. $C_{42}H_{34}S_9$: C 60.97, H 4.14, S 34.88; found: C 60.67, H 4.17, S 34.27.

Bis(5-mesitylthio-3,4-ethylenedioxy-2-thienyl) sulfide (^{MesS}ESE^{SMes})

A solution of bis(3,4-ethylenedioxy-2-thienyl) sulfide ESE (2.06 g, 6.55 mmol) was cooled to –40 °C and treated slowly with *n*-butyllithium (8.19 mL, 13.1 mmol, 1.6 mol/L in hexanes). The bright red solution was stirred for 1.5 h at –40 °C. After which, the solution was cooled to –70 °C, and a freshly prepared solution of 2-mesitylenesulfenyl chloride (2.45 g, 13.1 mmol) in hexanes (15 mL) was added dropwise via cannula. The resulting pale brown solution was stirred at –70 °C for an additional 30 min. The mixture was then warmed to RT and poured into water (100 mL). The fine white precipitate of ^{MesS}ESE^{SMes} was filtered off, washed with cold methanol (3 × 20 mL), and dried in vacuo. Yield 2.10 g (52%), mp 206 °C. UV–vis (CH_2Cl_2) λ_{max} (nm) 309 (ε 2.3 × 10^4). ^{1}H NMR ($CDCl_3$) δ: 6.90 (s, 4H), 4.19 (m, 8H), 2.48 (s, 12H), 2.25 (s, 6H). ^{13}C NMR ($CDCl_3$) δ: 143.13, 142.92, 140.55, 139.40, 129.53, 128.99, 113.53, 107.17, 64.95, 64.77, 22.19, 21.27. MS (LSI) *m*/*z*: 614 (M^+, 18%), 463 ((M – $C_9H_{11}S)^+$, 100%). Anal. calcd. $C_{30}H_{30}O_4S_5$: C 58.60, H 4.92, S 26.07; found: C 58.21, H 4.72, S 26.07.

Bis(5′-mesitylthio-3,4-ethylenedioxy-5,2′-bithien-2-yl)sulfide (^{MesS}TESET^{SMes})

A solution of 3,4-ethylenedioxy-5′-mesitylthio-2,2′-bithiophene 6 (0.85 g, 2.27 mmol) in THF (15 mL) cooled to –40 °C was treated dropwise with *n*-butyllithium (1.42 mL, 2.27 mmol, 1.6 mol/L in hexanes). The bright orange solution was stirred at –40 °C for 1.5 h. After which, the solution was cooled to –70 °C, and a solution of bis(phenylsulfonyl) sulfide (0.36 g, 1.15 mmol) in THF (10 mL) was added dropwise via cannula. The resulting yellow solution was stirred at –70 °C for an additional 30 min. The mixture was then warmed to RT and poured into a cold mixture of diethyl ether and water (120 mL, 1:5 *v*/*v*). The fine yellow precipitate was filtered off and washed with cold water (3 × 15 mL). This solid was recrystallized from a mixture of chloroform and methanol (80 mL, 3:5 *v*/*v*) to afford ^{MesS}TESET^{SMes} as yellow flakes, yield 0.60 g (68%), mp 198 °C. UV–vis (CH_2Cl_2) λ_{max} (nm) 375 (ε 4.2 × 10^4). ^{1}H NMR ($CDCl_3$) δ: 6.93 d, *J* = 3.7 Hz, 2H), 6.92 (s, 4H), 6.76 (d, *J* = 3.7 Hz, 2H), 4.26 (m, 8H), 2.48 (s, 12H), 2.25 (s, 6H). ^{13}C NMR ($CDCl_3$) δ: 143.70, 142.94, 139.45, 136.82, 136.70, 134.90, 129.85, 129.60, 128.86, 123.55, 115.51, 104.47, 65.14, 64.85, 22.07, 21.29. HRMS (LSI) for $C_{38}H_{34}O_4S_7$ [M^+]: calcd. 778.0502; found 778.0502. Anal. calcd. for $C_{38}H_{34}O_4S_7$: C 58.58, H 4.40, S 28.81; found: C 58.47, H 4.39, S 28.38.

3,4-Ethylenedioxy-5-mesitylthio-2,2′-bithiophene (8)

A solution of 3,4-ethylenedioxy-5-bromo-2,2′-bithiophene 7 (3.90 g, 12.9 mmol) in THF (40 mL) cooled to –78 °C was

© 2008 NRC Canada

treated dropwise with *n*-butyllithium (8.04 mL, 12.9 mmol, 1.6 mol/L in hexanes). The resulting bright red solution was stirred for 1.5 h at –78 °C. A solution of 2-mesitylenesulfenyl chloride (2.41 g, 12.9 mmol) in hexanes (20 mL) was added dropwise via cannula, and the resulting rusty red solution was stirred at –78 °C for an additional 30 min. The mixture was warmed to RT and poured into water (100 mL). The aqueous layer was extracted with ether (3 × 50 mL), and the combined organic extracts were further washed with water (3 × 50 mL) and dried over anhydrous sodium sulfate. After filtration, removal of the solvent gave a dark yellow solid, which was purified by column chromatography (silica gel, hexanes/dichloromethane (1:1 *v*/*v*)) to provide a bright yellow solid. Recrystallization from methanol/chloroform produced bright yellow needles of **8**, yield 3.20 g (66%), mp 120 °C. ^{1}H NMR (500 MHz, $CDCl_3$) δ: 7.15 dd, *J* = 5.1, 1.1 Hz, 1H), 7.08 (dd, *J* = 3.7, 1.1 Hz, 1H), 6.94 (dd, *J* = 5.1, 3.7 Hz, 1H), 6.92 (s, 2H), 4.29 (m, 4H), 2.56 (s, 6H), 2.25 (s, 3H). ^{13}C NMR (125 MHz, $CDCl_3$) δ: 142.68, 141.51, 138.91, 136.52, 134.25, 129.44, 129.23, 126.93, 123.74, 122.74, 113.00, 107.07, 64.76, 64.69, 21.97, 20.95. MS (EI) *m*/*z*: 374 (M^+, 100%). Anal. calcd. $C_{19}H_{18}O_2S_3$: C 60.93, H 4.84, S 25.68; found: C 60.75, H 4.92, S 25.67.

Bis(5′-mesitylthio-3′,4′-ethylenedioxy-5-2′-bithien-2-yl) sulfide (^{MesS}ETSTE^{SMes})

A solution of **8** (1.00 g, 2.67 mmol) in THF (30 mL), cooled to –40 °C, was treated dropwise with *n*-butyllithium (1.67 mL, 2.67 mmol, 1.6 mol/L in hexanes). The dark red solution was stirred at –40 °C for 1 h. After which, the solution was cooled to –70 °C, and a solution of bis(phenylsulfonyl) sulfide (0.42 g, 1.34 mmol) in THF (10 mL) was added dropwise via cannula. The resulting pale red solution was stirred at –70 °C for an additional 30 min. The mixture was then warmed to RT and poured into water (75 mL). The fine yellow precipitate was filtered off and washed with cold methanol (3 × 20 mL). This solid was recrystallized from a mixture of chloroform and methanol (80 mL, 3:5 *v*/*v*) to afford ^{MesS}ETSTE^{SMes} as yellow needles, yield 0.75 g, (72%), mp 213 °C. UV–vis (CH_2Cl_2) λ_{max} (nm) 375 (ε 4.4 × 10^4). ^{1}H NMR (500 MHz, THF-d_8) δ: 7.05 d, *J* = 3.9 Hz, 2H), 6.92 (s, 4H), 6.91 (d, *J* = 3.9 Hz, 2H), 4.27 (m, 8H), 2.51 (s, 12H), 2.22 (s, 6H). ^{13}C NMR (125 MHz, THF-d_8) δ: 143.48, 142.99, 139.84, 139.78, 138.69, 134.03, 133.77, 130.35, 130.10, 123.03, 112.90, 108.54, 65.96, 65.78, 22.26, 21.11. HRMS (LSI) for $C_{38}H_{34}O_4S_7$ [M^+]: calcd. 778.0502, found 778.0490. Anal. calcd. for $C_{38}H_{34}O_4S_7$: C 58.58, H 4.40, S 28.81; found: C 58.67, H 4.42, S 28.55.

Acknowledgements

We thank the University of Victoria, the Natural Sciences and Engineering Research Council of Canada, and Defence R&D Canada-Atlantic for support of this work.

References

1. Electronic materials: The oligomer approach. *Edited by* K. Mullen and G. Wegner. Wiley, Chichester, NY. 1998.
2. (*a*) J. Guay, A. Diaz, R.L. Wu, J.M. Tour, and L.H. Dao. Chem. Mater. **4**, 254 (1992); (*b*) J. Guay, P. Kasai, A. Diaz, R.L. Wu, J.M. Tour, and L.H. Dao. Chem. Mater. **4**, 1097 (1992); (*c*) M.G. Hill, K.R. Mann, L.L. Miller, and J.F. Penneau. J. Am. Chem. Soc. **114**, 2728 (1992); (*d*) M.G. Hill, J.F. Penneau, B. Zinger, K.R. Mann, and L.L. Miller. Chem. Mater. **4**, 1106 (1992).
3. (*a*) D. Fichou. J. Mater. Chem. **10**, 571 (2000); (*b*) A.R. Murphy and J.M J. Frechet. Chem. Rev. **107**, 1066 (2007).
4. (*a*) R.P. Kingsborough and T.M. Swager. Prog. Inorg. Chem. **48**, 123 (1999); (*b*) P.G. Pickup. J. Mater. Chem. **9**, 1641 (1999); (*c*) M.O. Wolf. Adv. Mater. **13**, 545 (2001).
5. I. Manners. Angew. Chem. Int. Ed. **35**, 1603 (1996).
6. (*a*) F. Wudl, R.O. Angus, F.L. Lu, P.M. Allemand, D.J. Vachon, M. Nowak, Z.X. Liu, and A.J. Heeger. J. Am. Chem. Soc. **109**, 3677 (1987); (*b*) A.G. Macdiarmid and A.J. Epstein. Faraday Disc. **317** (1989); (*c*) X.L. Wei, Y.Z. Wang, S.M. Long, C. Bobeczko, and A.J. Epstein. J. Am. Chem. Soc. **118**, 2545 (1996); (*d*) E. Shoji and M.S. Freund. J. Am. Chem. Soc. **124**, 12486 (2002).
7. (*a*) R.J.P. Corriu, T. Deforth, W.E. Douglas, G. Guerrero, and W.S. Siebert. Chem. Commun. 963 (1998); (*b*) N. Matsumi, K. Naka, and Y. Chujo. Macromolecules, **31**, 8047 (1998); (*c*) N. Matsumi, K. Naka, and Y. Chujo. J. Am. Chem. Soc. **120**, 10776 (1998); (*d*) N. Matsumi, K. Naka, and Y. Chujo. J. Am. Chem. Soc. **120**, 5112 (1998); (*e*) K. Naka, T. Umeyama, and Y. Chujo. Macromolecules, **33**, 7467 (2000); (*f*) A. Sundararaman, M. Victor, R. Varughese, and F. Jakle. J. Am. Chem. Soc. **127**, 13748 (2005); (*g*) J.B. Heilmann, Y. Qin, F. Jakle, H.W. Lerner, and M. Wagner. Inorg. Chim. Acta, **359**, 4802 (2006); (*h*) J.B. Heilmann, M. Scheibitz, Y. Qin, A. Sundararaman, F. Jakle, T. Kretz, M. Bolte, H.W. Lerner, M.C. Holthausen, and M. Wagner. Angew. Chem. Int. Ed. **45**, 920 (2006); (*i*) F. Jakle. Coord. Chem. Rev. **250**, 1107 (2006).
8. (*a*) R.J.P. Corriu, C. Guerin, B. Henner, T. Kuhlmann, A. Jean, F. Garnier, and A. Yassar. Chem. Mater. **2**, 351 (1990); (*b*) P. Chicart, R.J.P. Corriu, J.J.E. Moreau, F. Garnier, and A. Yassar. Chem. Mater. **3**, 8 (1991); (*c*) K. Tamao, S. Yamaguchi, and M. Shiro. J. Am. Chem. Soc. **116**, 11715 (1994); (*d*) S. Yamaguchi, T. Goto, and K. Tamao. Angew. Chem. Int. Ed. **39**, 1695 (2000); (*e*) Y. Lee, S. Sadki, B. Tsuie, and J.R. Reynolds. Chem. Mater. **13**, 2234 (2001).
9. (*a*) Z. Jin and B.L. Lucht. J. Organometal. Chem. **653**, 167 (2002); (*b*) K. Naka, T. Umeyama, and Y. Chujo. J. Am. Chem. Soc. **124**, 6600 (2002); (*c*) V.A. Wright and D.P. Gates. Angew. Chem. Int. Ed. **41**, 2389 (2002); (*d*) R.C. Smith and J.D. Protasiewicz. Eur. J. Inorg. Chem. 998 (2004); (*e*) R.C. Smith and J.D. Protasiewicz. J. Am. Chem. Soc. **126**, 2268 (2004); (*f*) T. Baumgartner and R. Reau. Chem. Rev. **106**, 4681 (2006); (*g*) V.A. Wright, B.O. Patrick, C. Schneider, and D.P. Gates. J. Am. Chem. Soc. **128**, 8836 (2006).
10. M.M. Labes, P. Love, and L.F. Nichols. Chem. Rev. **79**, 1 (1979).
11. (*a*) R.R. Chance, L.W. Shacklette, G.G. Miller, D.M. Ivory, J.M. Sowa, R.L. Elsenbaumer, and R.H. Baughman. J. Chem. Soc. Chem. Commun. 348 (1980); (*b*) J.F. Rabolt, T.C. Clarke, K.K. Kanazawa, J.R. Reynolds, and G.B. Street. J. Chem. Soc. Chem. Commun. 347 (1980); (*c*) R.H. Friend and J.R.M. Giles. J. Chem. Soc. Chem. Commun. 1101 (1984); (*d*) K.F. Schoch, J.F. Chance, and K.E. Pfeiffer. Macromolecules, **18**, 2389 (1985); (*e*) E. Tsuchida, K. Yamamoto, M. Jikei, and H. Nishide. Macromolecules, **23**, 930 (1990); (*f*) J. Leuninger, C.S. Wang, T. Soczka-Guth, V. Enkelmann, T. Pakula, and K. Mullen. Macromolecules, **31**, 1720 (1998).

© 2008 NRC Canada

12. (*a*) Y. Ikeda, M. Ozaki, and T. Arakawa. J. Chem. Soc. Chem. Commun. 1518 (1983); (*b*) K.Y. Jen, N. Benfaremo, M.P. Cava, W.S. Huang, and A.G. Macdiarmid. J. Chem. Soc. Chem. Commun. 633 (1983); (*c*) A. Berlin, G.A. Pagani, and F. Sannicolo. J. Chem. Soc. Chem. Commun. 1663 (1986).
13. (*a*) J. Nakayama, N. Katano, Y. Shimura, Y. Sugihara, and A. Ishii. J. Org. Chem. **61**, 7608 (1996); (*b*) J. Nakayama, N. Katano, Y. Sugihara, and A. Ishii. Chem. Lett. 897 (1997); (*c*) N. Katano, Y. Sugihara, A. Ishii, and J. Nakayama. Bull. Chem. Soc. Jpn. **71**, 2695 (1998).
14. R. Rulkens, D.P. Gates, D. Balaishis, J.K. Pudelski, D.F. McIntosh, A.J. Lough, and I. Manners. J. Am. Chem. Soc. **119**, 10976 (1997).
15. R.G. Hicks and M.B. Nodwell. J. Am. Chem. Soc. **122**, 6746 (2000).
16. M. Chahma, R.G. Hicks, and D.J.T. Myles. Macromolecules, **37**, 2010 (2004).
17. M. Chahma, D.J.T. Myles, and R.G. Hicks. Chem. Mater. **17**, 2672 (2005).
18. (*a*) Y. Kiya, G.R. Hutchison, J.C. Henderson, T. Sarukawa, O. Hatozaki, N. Oyama, and H.D. Abruna. Langmuir, **22**, 10554 (2006); (*b*) S.P. Mishra, K. Krishnamoorthy, R. Sahoo, and A. Kumar. J. Mater. Chem. **16**, 3297 (2006).
19. F.D. Jong and M.J. Janssen. J. Org. Chem. **36**, 1645 (1971).
20. X.C. Li, H. Sirringhaus, F. Garnier, A.B. Holmes, S.C. Moratti, N. Feeder, W. Clegg, S.J. Teat, and R.H. Friend. J. Am. Chem. Soc. **120**, 2206 (1998).
21. R.H. Mitchell, Y.H. Lai, and R.V. Williams. J. Org. Chem. **44**, 4733 (1979).
22. (*a*) B.L. Groenendaal, F. Jonas, D. Freitag, H. Pielartzik, and J.R. Reynolds. Adv. Mater. **12**, 481 (2000); (*b*) B.L. Groenendaal, G. Zotti, P.H. Aubert, S.M. Waybright, and J.R. Reynolds. Adv. Mater. **15**, 855 (2003).
23. T. Nokami, A. Shibuya, H. Tsuyama, S. Suga, A.A. Bowers, D. Crich, and J.I. Yoshida. J. Am. Chem. Soc. **129**, 10922 (2007).
24. (*a*) R.L. Wu, J.S. Schumm, D.L. Pearson, and J.M. Tour. J. Org. Chem. **61**, 6906 (1996).
25. M. Turbiez, P. Frere, P. Blanchard, and J. Roncali. Tetrahedron Lett. **41**, 5521 (2000).
26. M. Chahma. Synth. Met. **155**, 474 (2005).

© 2008 NRC Canada

FTIR spectroscopic investigation of pyruvate electroreduction on copper in alkaline medium — On the mechanistic aspects

Cédric Martin, Françoise Hahn, Karine Servat, Hervé Huser, Duarte Tito, Maher Kalaji, and K. Boniface Kokoh

Abstract: In this work some important aspects related to the electrocatalytic reduction of pyruvate on copper cathode were investigated in alkaline medium (0.5 mol/L NaOH). In situ IR reflectance spectroscopy (SPAIRS and SNIFTIRS techniques) was used to investigate the adsorbed intermediates and reaction products from the reduction of pyruvate. The results revealed that hydrogenation of the substrate to lactate occurred at the copper surface involving weakly adsorbed species. The identification of the different electroreactive species allowed to postulate a reaction mechanism for the transformation of pyruvate into lactate on copper.

Key words: copper, electroreduction, pyruvate, lactate, in situ infrared reflectance spectroscopy, reaction mechanism.

Résumé : D'importants aspects mécanistiques relatifs à la réduction électrocatalytique du pyruvate sur une cathode en cuivre ont fait l'objet dans ce travail d'une investigation en milieu alcalin (NaOH 0,5 mol/L). La spectroscopie infrarouge de réflexion, sous ses deux variantes SPAIRS et SNIFTIRS, a principalement été utilisée pour déterminer les intermédiaires adsorbés et les produits de réaction issus de la réduction de la fonction carbonyle du pyruvate. Les résultats ont révélé que l'hydrogénation du substrat en lactate a bien lieu à la surface du cuivre générant de très faibles adsorbats. L'identification des différentes espèces électroréactives ont permis de proposer un mécanisme réactionnel de la transformation du pyruvate en lactate sur le cuivre.

Mots-clés : cuivre, electroréduction, pyruvate, lactate, spectroscopie infrarouge de réflexion in situ, mécanisme réactionnel.

[Traduit par la Rédaction]

Introduction

The catalytic reduction of organic molecules containing a carbonyl group has been widely investigated in the preparation of intermediates for the fine chemicals and pharmaceutical industries. The control of selectivity is one of the important problems in organic electrosynthesis. Various reaction conditions, such as electrode materials, supporting electrolyte, electrode potential, reagent concentration, and pH, affect the product distribution. The electroreduction of carbonyl compounds can lead to varied products such as alcohols, hydrocarbons, or pinacols. Much research on the electroreduction of carbonyl compounds to monomeric and dimeric products has been done using acetophenone and furfural as model molecules (1–7). The selectivity of the electroreduction of acetophenone to the monomeric product, 1-phenylethanol, in aqueous media has been much studied with interesting results. The carbonyl function of pyruvate was reduced by redox reaction using sodium borohydride (8), perchlorate metallic cations (9), or by C2 symmetric diamines as chiral ligands (10). Lactate has also been synthesized from glucose by fermentative manufacture in the presence of externally added pyruvate (11, 12). Elsewhere, an electroenzymatic route for producing lactate from pyruvate has been used extensively (13–16). However, few results in the literature concern the electrochemical reduction of pyruvate. In this regard, the selectivity of lactate, which is an useful intermediate in the biological sector, food, and polymer industries (17, 18), on lead and copper cathodes in aqueous media was studied (19, 20). Recently, we have shown that the electrocatalytic reduction of pyruvic acid in different aqueous media led to either lactic acid or 2,3-dimethyltartaric acid with high selectivity, according to the operating experimental conditions (19–22).

The aim of the present work is to complete previous investigations by examining carefully the intermediates and products formed on the surface of a copper electrode during the course of the electroreduction of pyruvate in alkaline medium by means of in situ IR reflectance techniques (SPAIRS and SNIFTIRS). Interpretation of the results allowed us to detail some mechanistic aspects of the electrochemical process.

Received 4 March 2008. Accepted 18 June 2008. Published on the NRC Research Press Web site at canjchem.nrc.ca on 18 September 2008.

C. Martin, F. Hahn, K. Servat, H. Huser, and K. Boniface Kokoh.[1] LACCO Equipe Electrocatalyse, UMR 6503, CNRS University of Poitiers, Département de Chimie, 40 avenue du Recteur Pineau, 86022 Poitiers cedex. France.
D. Tito and M. Kalaji. School of Chemistry, University of Wales, Bangor LL57 2UW, UK.

[1]Corresponding author (e-mail: boniface.kokoh@univ-poitiers.fr).

Experimental

All the experiments were carried out in aqueous solutions using "ultrapure" water (18.2 MΩ cm at 20 °C, Millipore

 doi:10.1139/V08-137 © 2008 NRC Canada

system). The analytical grade supporting electrolyte (NaOH) was purchased from Merck. Pyruvic and lactic acids were supplied by Sigma-Aldrich. The solutions were thoroughly deaerated by bubbling nitrogen (U Quality from Air Liquide).

The Fourier transform IR spectrometer used was a Bruker IFS 66v, with the sample compartment modified to allow the beam to be reflected on the electrode surface with an incidence angle of 65°, after passing through the IR window (CaF_2) of the conventional thin layer spectroelectrochemical cell. The beam path was under vacuum and a liquid nitrogen cooled HgCdTe detector (Infrared Associates) was used. The working cathode was a cooper disk with a geometric surface area of 0.8 cm^2. A platinum wire and a reversible hydrogen electrode (RHE) served as counter and reference electrodes, respectively. Before performing the spectroelectrochemical experiments, a voltammogram was recorded at 1 mV s^{-1} to observe the state of cathode.

In situ IR reflectance spectroscopy techniques are described elsewhere (23). To detect adsorbed species, intermediates, and reaction products near the electrode surface, SPAIRS and SNIFTIRS experiments are carried out. With the single potential alteration IR reflectance spectroscopy (SPAIRS) technique (24–26), reflectivities were recorded at 50 mV intervals during the first voltammetric scan at a low sweep rate (1 mV s^{-1}). Each spectrum resulted from the co-addition of 128 interferograms. The acquisition time required 20 s, i.e., corresponding to ca. 0.02 V. SPAIRS is convenient for the detection of intermediates in the vicinity of the electrode and reaction products. Spectra were normalized as $\Delta R/R = (R_{Ei} - R_{Eref})/R_{Eref}$, where the reference spectrum R_{Eref} was 0 V vs. RHE.

Similarly, using the subtractively normalized interfacial Fourier transform IR reflectance spectroscopy (SNIFTIRS) method (25–27), reflectivities were collected at two electrode potentials (frequency of potential modulation 0.025 Hz) and co-added 30 times at each potential. SNIFTIRS is better adapted to the detection of adsorbed species at the electrode. Final spectra were normalized as $\Delta R/R = (R_{E2} - R_{E1})/R_{E1}$ with a constant amplitude modulation of 200 mV.

Results and discussion

In a recent paper (20), it was shown that the electroreduction of pyruvate in alkaline medium (i.e., 0.5 mol/L NaOH) on copper electrode selectively involves lactate. At low potentials, this reaction competed with hydrogen evolution reaction. Investigation of the overall kinetics of electrocatalytic reaction by electrochemical methods (cyclic voltammetry) revealed a diffusion controlled process. The present identification of the species adsorbed at the copper electrode, thanks to in situ spectroelectrochemistry techniques, can provide more evidence to assume a reaction mechanism of pyruvate reduction.

In situ spectroelectrochemical studies on a copper cathode in alkaline medium

SPAIR and SNIFTIR spectroscopy methods were performed to determine the adsorbed intermediates and the reduction products near the copper surface. To assign the main bands of pyruvate and its expected reduction product, lactate, transmission spectra of these compounds were recorded. The fundamental bands found in the spectra of Fig. 1 are summarized in Table 1.

Fig. 1. Transmission FTIR spectra of pyruvate and lactate recorded in water.

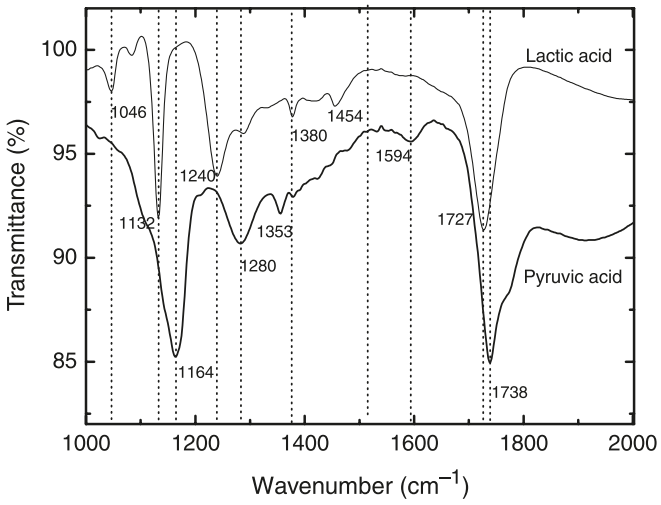

As can be seen, pyruvate and lactate spectra contain the same carboxylate group (1380 and 1727–1738 cm^{-1}) and methyl groups (1353 and 1454 cm^{-1}) bands. Their difference is due to the carbonyl (for pyruvate) at 1594 cm^{-1} and alcohol (for lactate) at 1240 and 1132 cm^{-1}.

SPAIRS technique consists of simultaneously recording spectroscopic measurements during cyclic voltammetry. A first cycle was thus recorded at a sweep rate of 1 mV s^{-1} to collect more information at the vicinity of the electrode surface in steady-state conditions. On the voltammogram of Cu represented in Fig. 2, one can notice during the negative potential scan a reduction peak of pyruvate followed by a reduction wave up to the cathodic potential limit. The positive going scan is characterized by another reduction peak at ca. –0.3 V vs. RHE.

SPAIR spectra were collected regularly between +650 and –650 mV vs. RHE, but the most significant spectra are shown in Fig. 3. At potentials lower than –400 mV vs. RHE, the spectra were disturbed by hydrogen production. Up to –100 mV vs. RHE, there is a large band (1570–1720 cm^{-1}) that includes the main vibration modes such as the carbonyl group (C=O stretching), the anti-symmetric OCO stretching (carboxylate), and the contribution of the HOH bending mode (δ_{HOH}) of interfacial water. As can also be seen on the voltammogram in Fig. 2, the reduction of pyruvate starts at ca. –150 mV vs. RHE. Up to this potential, the shape of the spectrum is similar to that of lactate, particularly with the presence of the band at 1132 and 1046 cm^{-1}, characteristic of the C–O stretching mode of the alcohol group and that of $\upsilon_{C\text{-}CH3}$ in lactate.

With the SNIFTIRS technique, the entire potential range from 0 to –700 mV vs. RHE was studied at a constant modulation potential (ΔE = 200 mV). The significant spectra are displayed in Fig. 4. At the beginning of pyruvate reduction, corresponding to the first potential modulation, all the bands assigned in Table 1 are present. As pointed out in previous SPAIR spectra, one can observe a small shift in the frequency of the bands due to the Stark effect. In the two other

© 2008 NRC Canada

Table 1. Assignation of some IR bands in the transmission spectra of pyruvate and lactate in water (28–33).

Pyruvate		Lactate	
Wavenumber (cm^{-1})	Assignment	Wavenumber (cm^{-1})	Assignment
1738	$\upsilon_{asC\text{-}O}$ (COO^-)	1727	$\upsilon_{asC\text{-}O}$ (COO^-)
1594	$\upsilon_{C\text{-}O}$ $(C{=}O)_{ket}$		
		1454	δ_{as} (CH_3)
1380	$\upsilon_{sC\text{-}O}$ (COO^-)	1380	$\upsilon_{sC\text{-}O}$ (COO^-)
1353	δ_s (CH_3)		
1164	$\upsilon_{asC\text{-}O}$ (CH_3-C=O)		
		1240	δ $(OH)_{al}$
		1132	υ $(C\text{-}O)_{al}$
		1046	υ ($C\text{-}CH_3$)

Note: as = asymmetric; s = symmetric; al = alcohol; ket = ketone.

Fig. 2. Voltammogram of a copper electrode recorded at 1 mV s^{-1} in 0.5 mol/L of NaOH in the presence of 0.1 mol/L of pyruvate.

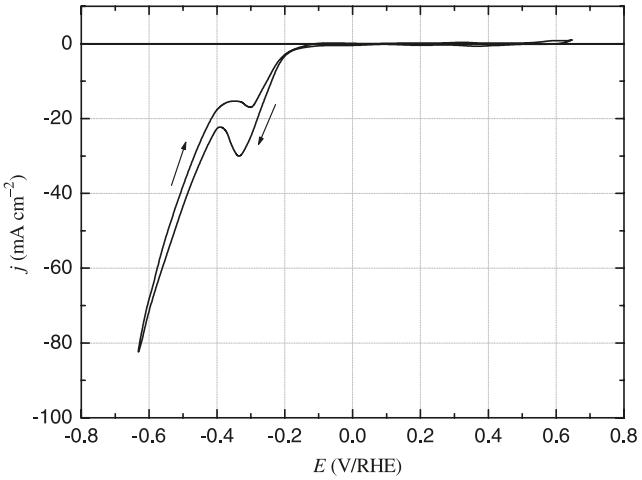

spectra, a large absorption band including ν_{OCO}, $\nu_{C=O}$ stretching (represented by a derived band centered at 1594 cm^{-1}), and δ_{HOH} bending modes, become more and more intensive so that the other bands seem to disappear. Nevertheless, the characteristic band of the alcohol-containing species (ν_{CHOH}) remains visible at 1132 cm^{-1}. A band at 1046 cm^{-1} gives more evidence of the presence of lactate as expected reaction product.

Mechanistic implications

From the different results obtained, it is possible to infer the reduction mechanism of the formation of lactate from pyruvate on copper electrode in alkaline solution. Kinetic investigations showed that the solvent bore partly on hydrogenation of pyruvate on copper, whereas various physicochemical analyses focused on the selectivity of the reaction towards lactate (20). In addition, both IR reflectance techniques enabled us to detect the pyruvate and lactate weakly adsorbed at the copper cathode. Therefore, it can be suggested that pyruvate is reduced as follows.

Fig. 3. SPAIR spectra of 0.1 mol/L of pyruvate in 0.5 mol/L of NaOH on a copper electrode at various potentials.

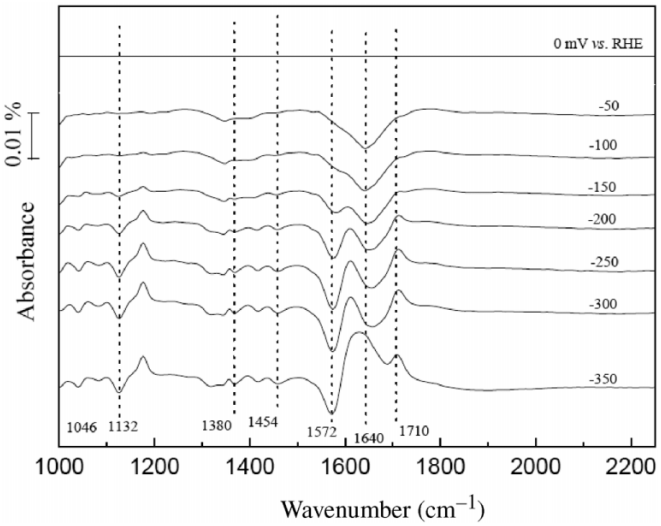

Fig. 4. SNIFTIR spectra of 0.1 mol/L pyruvate in 0.5 mol/L of NaOH on a copper electrode at various modulation amplitudes of potential.

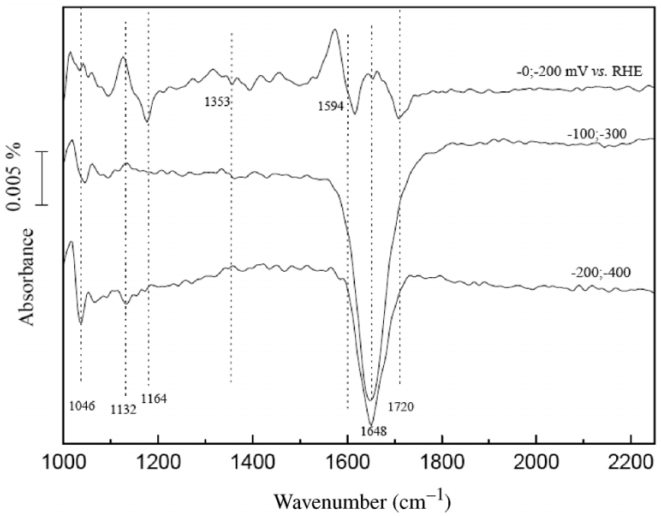

The first step is the reduction of solvent, as shown by Grez et al. (34),

[1] $$Cu + H_2O + e^- \rightarrow Cu - H_{ads} + HO^-$$

Then, the adsorption of the carbonyl group of pyruvate is favoured by the repulsive interaction between the charge of the cathode and that of the carboxylate. So the interaction of the carbonyl group of the reagent with the copper sites can be written,

[2] 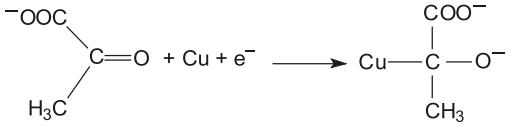

Hydrogenation then occurs by the interaction between two adsorbed species,

© 2008 NRC Canada

[3] 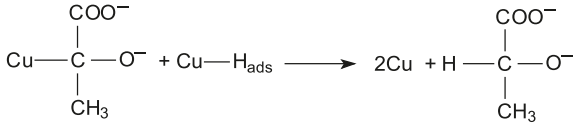

As evidence of the presence of this organic species at the electrode surface, it can be seen in Fig. 4 that the entire spectra contain the main large band that continues to be centered at 1648 cm^{-1}, i.e., with the contribution of the strong feature of interfacial water, which includes the C=O stretching vibration of the carboxylate group (as shoulder at ca. 1720 cm^{-1}). Finally, lactate desorbs and diffuses into the bulk solution where hydrolysis takes place as follows,

These spectroscopic results are in good agreement with our previous chromatographic data (20) and also indicate that the reduction of pyruvate leads selectively to lactate on copper electrode in alkaline medium.

[4] 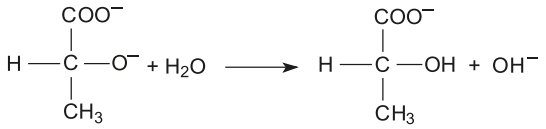

Conclusion

This investigation was aimed at obtaining new insights on the spectroelectrochemical behavior of pyruvate reduction in an alkaline medium. Two complementary IR methods provided us a lot of information on its reaction mechanism on a copper electrode. The interaction between the electrode surface and the molecules led to weakly adsorbed species. The characteristic absorption band of alcohol-containing species (ν_{CHOH}) due to the presence of lactate at the vicinity of the electrode reinforced the results of the reduction of the carbonyl group. Moreover, equilibrium observed close to the cathode surface between consumed pyruvate and produced lactate, showed that lactate was produced by the reduction of pyruvate weakly adsorbed on the copper electrode and then diffused straight to the bulk solution after hydrogenation. No evidence of the cleavage of the C–C bond was observed in the different analytical measurements. However, Cu considered as an overvoltage material for hydrogen can be successfully used for reducing pyruvate to lactate in alkaline medium.

References

1. K. Matsuda, M. Atobe, and T. Nonaka. Chem. Lett. 1619 (1994).
2. M. Atobe and T. Nonaka. Chem. Lett. 669 (1995).
3. P. Cognet, A. Ghanem-Lakhal, J. Berlan, A.-M. Wilhem, H. Delmas, and P.-L. Fabre. Chem. Eng. Sci. **55**, 2571 (2000).
4. A. Honnorat and P. Martinet. Electrochim. Acta, **28**, 1703 (1983).
5. A.M. Polcaro, S. Palmas, and S. Dernini. Electrochim. Acta, **38**, 199 (1993).
6. Y. Kodama, M. Imoto, N. Otha, A. Kitani, and S. Ito. J. Electroanal. Chem. **507**, 103 (2001).
7. P. Parpot, A.P. Bettencourt, G. Chamoulaud, K.B. Kokoh, and E.M. Belgsir. Electrochim. Acta, **49**, 397 (2004).
8. E.B. Reid and J.R. Siegel. J. Chem. Soc. 520 (1954).
9. P. Gamez, F. Fache, P. Mangeney, and M. Lemaire. Tetrahedron Lett. **34**, 6897 (1993).
10. P. Gamez, F. Fache, and M. Lemaire. Tetrahedron: Asymmetry, **6**, 701 (1995).
11. H. Yukawa. Japanese Patent JP 2003159091 A2 200330603. 2003.
12. C. Fromageot and P. Desnuelle. Biochemische Z, **279**, 34 (2003).
13. F. Takahashi, K. Tomii, and H. Takahashi. Electrochim. Acta, **31**, 127 (1986).
14. S. Hebai, W. Lirong, H. Gang, P. Conger, and Z. Zongrang. J. Huagong, 239 (1998).
15. G.M. Whitesides, R. Di Cosimo, C.-M. Wong, and L. Daniels. J. Org. Chem. **46**, 4622 (1981).
16. S. Watanabe, S. Kuwubata, R. Yuan, and H. Yoneyama. J. Org. Chem. **62**, 2494 (1996).
17. P. Salvadori, D. Pini, C. Rosini, G. Uccello-Barreta, and C. Bertucci. J. Chromatogr. A, **450**, 163 (1988).
18. R. Paul Ross, S. Morgan, and C. Hill. Int. J. Food Microbiol. **79**, 3 (2002).
19. C. Martin, H. Huser, K. Servat, and K.B. Kokoh. Electrochim. Acta, **50**, 2431 (2005).
20. C. Martin, H. Huser, K. Servat, and K.B. Kokoh. Electrochim. Acta, **51**, 111 (2005).
21. C. Martin, K. Servat, H. Huser, and K.B. Kokoh. J. Appl. Electrochem. **36**, 643 (2006).
22. C. Martin, H. Huser, K. Servat, and K.B. Kokoh. Tetrahedron Lett. **47**, 3459 (2006).
23. A. Bewick, K. Kunimatsu, B. Pons, J.W. Pons, and J.W. Russell. J. Electroanal. Chem. **160**, 47 (1984).
24. D.S. Corrigan, L.W.H. Leung, and M.J. Weaver. J. Phys. Chem. **90**, 5300 (1986).
25. B. Beden. Spectra 2000, **13**, 19 (1984).
26. B. Beden and C. Lamy. *In* Spectroelectrochemistry, theory and practice. *Edited by* R.J. Gale. Plenum Press, New York, USA. 1988.
27. S. Pons. J. Electroanal. Chem. **150**, 495 (1983).
28. J. E. Katon and D.T. Covington. Spectroscopy Lett. **12**, 761 (1979).
29. C.J. Pouchert. The Aldrich library of infrared spectra. 3rd ed. Aldrich Chemical Company, USA. 1981.
30. W.J. Ray, J.E. Katon, and D.B. Phillips. J. Mol. Struct. **74**, 75 (1981).
31. T. Iwasita and F.C Nart. *In* Advances in electrochemical science and engineering. Vol. 4. *Edited by* H. Gerischer and C.W. Tobias. VCH, Weinheim, Germany. 1995. p. 126.
32. S.-G. Sun. *In* Electrocatalysis, frontiers in electrochemistry. *Edited by* J. Lipkowski and P.N. Ross. Wiley-VCH, New York, USA. 1998. p. 243.
33. T. Furukawa, H. Sato, R. Murakami, J. Zhang, I. Noda, S. Ochiai, and Y. Ozaki. Polymer, **48**, 1749 (2007).
34. P. Grez, C. Celedon, A. Molinari, A. Oliva, M. Orellana, R. Schrebler, R. del Rio, and R. Cordova. J. Phys. Chem. B, **109**, 22920 (2005).

© 2008 NRC Canada

Sectroscopic study of stability and molecular species of 12-tungstophosphoric acid in aqueous solution

Ivanka Holclajtner-Antunović, Danica Bajuk-Bogdanović, Marija Todorović, Ubavka B. Mioč, Joanna Zakrzewska, and Snežana Uskoković-Marković

Abstract: The various molecular species of 12-tungstophosporic acid (WPA) in aqueous solutions of different pH values (from 1 to 11.5) were investigated by UV, IR, and NMR spectroscopy. The dependence of the attained equilibrium composition in solution on time, concentration of WPA, and type of buffer used was studied. Obtained results indicate that the buffer type and pH value greatly determine the equilibrium composition in the solution. The Keggin structure of the WPA is sustained only up to pH 1.5. With further increase in pH, the decomposition of Keggin anion does not lead directly to the monovacant lacunary anion. Between 1.5 and 2.0, the structures with 2 phosphorus atoms from the Dawson series are dominant as intermediate species. In the pH range 3.5–7.5, WPA is present in the form of the monovacant lacunary Keggin anion. These results are of special importance for the biomedical and catalytic applications of heteropoly compounds (HPCs) and for an improved understanding of the mechanism of their functioning.

Key words: heteropolyacids of the Keggin structure, hydrostability, UV, IR and NMR spectroscopy.

Résumé : Faisant appel aux méthodes de spectroscopie UV, IR et RMN, on a étudié diverses espèces moléculaires de l'acide 12-tungstophosphorique (ATP), dans des solutions aqueuses dont les pH s'étalent de 1 à 11,5. On a étudié la relation entre la composition de l'équilibre obtenu et le temps, la concentration en ATP et le type de tampon utilisé. Les résultats obtenus indiquent que le type de tampon et la valeur du pH jouent un rôle considérable sur la composition de l'équilibre en solution. La structure de Keggin pour l'ATP n'est maintenue que jusqu'à un pH de 1,5. Avec des augmentations supplémentaires de la valeur du pH, la décomposition de l'anion de Keggin ne conduit pas directement à l'anion lacunaire monovacant. Entre 1,5 et 2,0, les structures comportant deux atomes de phosphore des séries de Dawson sont les espèces intermédiaires dominantes. Dans la zone de pH allant de 3,5 à 7,5, l'ATP est présent sous la forme de l'anion lacunaire monovacant de Keggin. Ces résultats sont particulièrement important pour les applications biomédicales et catalytiques des composés hétéropolyacides (CHP) et pour une meilleure compréhension du mécanisme de leur fonctionnement.

Mots-clés : hétéropolyacides de la structure de Keggin, hydrostabilité, spectroscopies UV, IR et RMN.

[Traduit par la Rédaction]

Introduction

Polyoxometalates (POMs), made up of a great number of structures and compositions, constitute a large category of compounds that are interesting for theoretical investigations and practical applications. Their applications are based on their unique properties including size, mass, structure, electron and proton transfer/storage abilities, thermal stability, labile nature of lattice oxygen, and high Brönsted acidity of the corresponding acids. Therefore, POMs are used as good catalysts, superionic proton conductors, compounds with photoconductive and magnetic characteristics, reagents in analytical chemistry, and biochemically active species (1–6).

The properties of POMs in the solid state are rather well-established, but their behavior in solutions is not well explained in spite of numerous publications. The behavior of these compounds in solution is important from the aspect of their formation and degradation but particularly from the aspect of their analytical, biomedical, and catalytic applications.

In medicinal chemistry, POMs that are generally nontoxic to normal cells, exhibit highly selective inhibition of enzymes and antitumoral, antiviral, antibacterial, and anticoagulant activities (1–4, 6–7). However, a fundamental limitation in their application in physiological media in vitro and in vivo derives from their inorganic nature and in their con-

Received 24 June 2008. Accepted 28 July 2008. Published on the NRC Research Press Web site at canjchem.nrc.ca on 23 September 2008.

I. Holclajtner-Antunović, D. Bajuk-Bogdanović, and U.B. Mioč. Faculty of Physical Chemistry, University of Belgrade, P.O.Box 47, 11158 Belgrade, Serbia.
M. Todorović. Faculty of Chemistry, University of Belgrade, P.O.Box 157, 11001 Belgrade, Serbia.
J. Zakrzewska. Institute of General and Physical Chemistry, P.O.Box 551, 11001 Belgrade, Serbia.
S. Uskoković-Marković.[1] Faculty of Pharmacy, University of Belgrade, P.O.Box 146, 11001 Belgrade, Serbia.

[1]Corresponding author (e-mail: snezaum@pharmacy.bg.ac.yu).

 doi:10.1139/V08-138 © 2008 NRC Canada

sequent instability in aqueous solutions. Namely, the problem of all biological and medical investigations of POMs relates to whether these compounds remain in their original molecular form during biomedical treatment. Generally, research articles consider the parent form of POMs anion as active, which is generally not the case. To consider and elucidate the proper mechanism of biomedical activity of POMs, it is indispensable to identify the real active molecular species present under physiological conditions, which is the main subject of this study.

Because of their properties, POMs have also been used as homogeneous and heterogeneous catalysts in oxidation reactions, in acid-catalyzed reactions, and as bifunctional catalysts (1–4, 8, 9). To improve the catalytic characteristics of these compounds and to follow the mechanism of catalytic processes, the formation of activation complexes, as well as the formation of complex catalysts on different supports by sol-gel processes or impregnation, it is essential to specify the nature of the active species present.

In spite of extensive study of stability and reaction pathways of heteropoly acids (HPAs) mostly of the Keggin type in solution, the obtained results and conclusions often are confusing and not in agreement, although obtained under similar experimental conditions (1, 4, 10–15).

Kepert and Kyle (16, 17) have studied the decomposition of the Keggin anions containing silicon, phosphorus, or boron as the central heteroatom and tungsten as an addenda metal atom. They have found that the equilibrium reaction in the solution proceeds in three distinct stages with $[SiW_{11}O_{39}]^{8-}$ and $[SiW_9O_{34}]^{10-}$ as intermediates. A few years later, stopped-flow kinetics studies of 12-molybdophosphate formation and decomposition were performed by Kircher and Crouch (18). Molybdophosphate complexes in aqueous solutions have been identified by ^{31}P NMR and Raman spectroscopy and differential pulse polarography (19), while ^{31}P NMR spectroscopy was applied to the stability study of HPAs by the rate of exchange of structural units between 12-tungstophosphoric acid (WPA) and 12-molybdophosphoric acid (MoPA) (15). Detusheva et al. (20) identified decomposition products of tungstophosphoric acid during its titration with NaOH up to pH 7.8 by NMR, IR, and Raman spectroscopy. McGarvey and Moffat (13) followed the major species present in tungstophosphate and molybdophosphate solutions as a function of pH by NMR and IR spectroscopy. They found that both acids decompose to the lacunary form of the Keggin anion that further decomposes to a phosphate species in alkaline solutions. The tungstophosphate system has been investigated over a wide range of pH (1–12) using preparation high performance liquid chromatography combined with IR, UV–vis, and ^{31}P NMR and ICP spectroscopy (21, 22). Smith and Patrick applied ^{31}P and ^{183}W NMR spectroscopy to the detailed study of tungstophosphoric and tungstosilicic acids in aqueous solutions (23–25). Identification and quantitative determination of the species present in these systems as a function of pH have been performed after a few months, which was considered an appropriate time for attaining equilibrium. Investigations of equilibria of α- and β-isomers of WPA as a function of pH have shown that β-type lacunary complexes are precursors for the formation of β-PW_{12}, and that β-type lacunary complexes always coexist with the corresponding α-type lacunary complexes (26).

On the basis of all these results, it can be concluded that the hydrolytic stability of HPAs depends on the anion structure, nature of the heteroatom, and peripheral metal atom that comprise the anion, as well as on the solution conditions. It is generally accepted that most POMs based on W or Mo are stable in acid solution, degrade in a complex way into a mixture of inorganic products with increasing pH and are totally decomposed in alkaline medium. However, the influence of buffer type on equilibrium composition has not been studied thus far. Also, the time data needed for establishing the equilibrium state and possible reversibility of the considered system when pH was increased and (or) decreased, were also not available.

The aim of this paper is to pay attention to the importance of molecular species of 12-tungstophosphoric acid ($H_3PW_{12}O_{40}$) in aqueous solutions of various pH, adjusted by addition of NaOH and HCl or by applying TRIS and acetate buffers. It is necessary to emphasize that TRIS and acetate buffers are frequently applied for pH adjustment when HPAs are used for biochemical and biomedical applications. For this purpose, three different spectroscopic methods were applied and their results were summarized and compared, to determine the dominant species present in solutions of various pH, with special attention to physiological conditions. The equilibrium composition of the solution was investigated for various buffers and for different time intervals. It was established that phosphate buffer is not appropriate for biochemical studies. The reversibility of the reaction pathway in the considered system, in which pH was increased to the values when the Keggin anion is decomposed and then decreased back to the pH values when it is formed, was also studied.

Experimental

Materials

WPA was prepared according to the literature method (27), recrystallized prior to use, and confirmed by IR spectroscopy. All chemicals were of analytical grade and were provided by Merck.

Methods

The pH of the solutions was adjusted with addition of NaOH, HCl and acetate, TRIS, and phosphate buffers and measured using a pH meter with a glass electrode. Solution pH was monitored until no apparent changes were observed.

UV spectra of aqueous solutions of 2×10^{-5} mol/dm^3 of WPA were obtained by the Cintra 10e (GBS) spectrophotometer.

Solid samples for IR measurements were obtained after evaporation of water from solutions of 5×10^{-2} mol/dm^3 WPA of different pH. The IR spectra were recorded on a PerkinElmer 983G spectrophotometer using the KBr pellet technique in the wavenumber range 1500–300 cm^{-1}.

The sample solutions for NMR measurements were prepared by adding the estimated quantities of NaOH or buffer solutions just after dissolving. The NMR experiments were carried out with a Bruker MSL 400 spectrometer at 161.978 MHz. The concentration of WPA was 5×10^{-2} mol/dm^3, with 2048 scans, 9.0 μs pulse, and 500 ms repetition time at 25 °C. Sample volume was about 2.5 mL

© 2008 NRC Canada

in a 10 mm tube. A metilenediphosphonate (MDP) solution of 17.05 ppm was used as the external reference relative to 85% H_3PO_4.

Results and discussion

UV spectra

The electronic spectra of HPAs of the Keggin structure exhibit two intense absorption bands in the UV range, with maxima at about 200 and 260 nm attributed to the transitions $O_d \rightarrow M$ and $O_b/O_c \rightarrow M$, respectively, (28).

The UV spectra of aqueous solutions of WPA of various pH are presented in Fig. 1. At pH 1, the absorption band maximum is at 263 nm, which corresponds to electron transition $O_b/O_c \rightarrow M$ of the parent Keggin's anion and is shifted to 252.5 nm at pH 3.5. If pH is increased to 7 by adding NaOH, the band maximum remains at the same position.

The further increase in pH to 11.5 causes the disappearance of this band, confirming the destruction of the parent Keggin structure. These results indicate the existence of various structural forms in pH regions: up to 2, from 3.5 to 7, and above 8.5, but it is hard to identify the individual formed products.

Our results are only partly in accordance with the findings of Z. Zhu et al. (21) who applied UV spectra for the identification of components eluted from an HPLC instrument. Namely, they identified the maximum absorption at 244 nm of the main component at pH 3.5 and 5.4 as $[PW_{11}O_{39}]^{7-}$. Our results show that the component with maximum absorption at 252.5 nm is stable in the pH region from 3.5 to 7.0. The differences can be explained by different experimental conditions, because the mentioned authors applied HPLC for the separation of decomposition products of WPA, where besides pH changes there is a continual change in eluent composition.

It is evident that pH influences the stability of WPA. All changes in the UV spectra of WPA solutions of different pH can be attributed to changes in the structure of an individual HPA at various pH values, but it is difficult to derive conclusions about the nature of the observed changes and identify the new formed products.

IR spectra

IR spectra of evaporated and dried sample solutions were recorded over the pH range 1 to 11.5, as in the case of UV spectra. IR spectra of dry residua of WPA solutions of different pH are presented in Fig. 2, while Table 1 summarizes the positions and intensities of some IR absorption bands. The bands of Na_2WO_4 are given for comparison.

The spectrum of WPA at pH 1 (5×10^{-2} mol/dm^3 of WPA, with no addition of HCl) is equivalent to the spectrum of solid WPA. This spectrum possesses vibration bands characteristic of the Keggin anion: 1080, 990, 890, and 810 cm^{-1}, corresponding to vibrations ν_{as}(P-O_a), ν_{as}(W-O_d), ν_{as} (W-O_b-W), and ν_{as} (W-O_c-W), respectively (29). It can be noticed that already at pH 2, bands associated with the Keggin anion are modified; some bands have disappeared, while new bands have appeared and remained to pH 7. Based on the obtained spectra, it can be observed that the stretching P-O vibration at 1080 cm^{-1} is split into two bands at 1100 and 1050 cm^{-1}. This indicates the existence of an anion structure with lower symmetry than T_d symmetry of the Keggin anion. Such a structure can be the lacunary $[PW_{11}O_{39}]^{7-}$ that belongs to the C_s symmetry group, or a structure with two P atoms such as $[P_2W_{18}O_{62}]^{6-}$ with C_{3v} symmetry. Typical bands that characterize the former monolacunary structure (arising by remov-

Fig. 1. UV spectra of WPA solutions at varying pH.

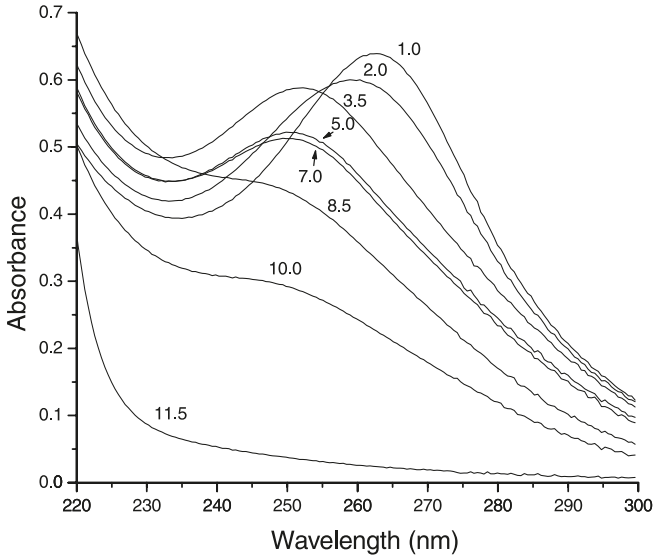

Fig. 2. IR spectra of evaporated WPA solutions at varying pH and Na_2WO_4.

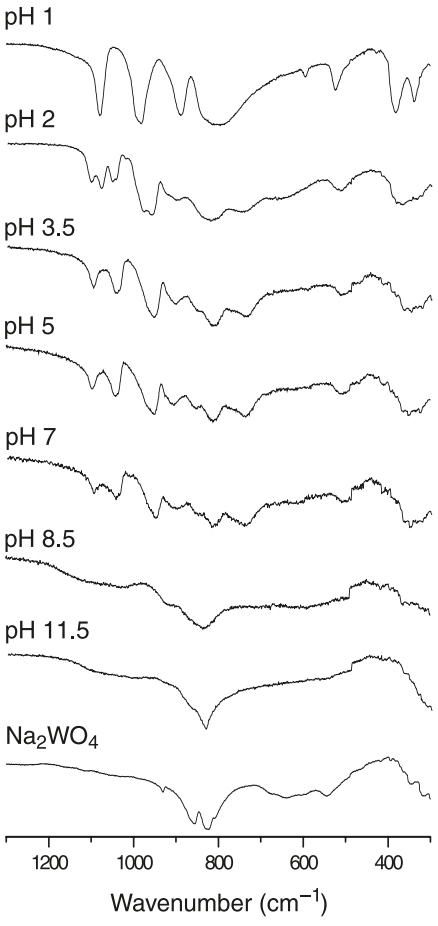

© 2008 NRC Canada

Table 1. Vibration bands of dry residua of WPA solutions of various pH and of sodium tungstate.

Vibration bands (cm^{-1})								
pH 1	pH 2	pH 3.5	pH 5	pH 7	pH 8.5	pH 10	pH 11.5	Na_2WO_4
	1102m	1097m	1096m	1097m				
1079s	1078s							
	1052m	1042m	1042m	1044m				
982vs	980s							
	960s	956s	951s	950s				
	920sh							
888s	902w	903w	905w	900w	910sh			
		850sh	852vw	850sh				855s
					935s,b	835s,b	835s,b	
	821s,b	816s,b	812m	819m				822s
795vs,b								
	747w,b	742m,b	730m,b	742m,b				
	664w,b							
593w								
523m	514w	515w,b	504w,b	513w,b				
381s	380sh							
	368m							
		350m,b	350w,b	350w,b				
338m	330sh							

Note: Very strong (vs), strong (s), medium (m), weak (w), shoulder (sh), broad (b).

ing one WO unit from the Keggin anion) are 1085, 1040, 950, 900, 860, 810, and 725 cm^{-1} (30). The latter is the Dawson structure characterized by bands at 1108, 1050, 957, 920, 885, 818, and 735 cm^{-1} (13). There are also some slight changes in the spectrum related to the spectra of the Keggin anion's structure: bands at about 1050 and 990 cm^{-1} are split, while the band at about 900 cm^{-1} has a shoulder at 920 cm^{-1}.

IR spectra present further improvements in identification of dominant chemical species present in HPA solutions of various pHs, compared with UV spectra. However, bearing in mind that characteristic bands of the components of the Dawson series are close to the characteristic bands of the lacunary Keggin structure, it is difficult to recognize and identify properly all the structures present. The IR spectra at higher pH values indicate the total degradation of the parent anion to tungstate and phosphate anions.

NMR spectra

To overcome the drawbacks of UV and IR spectroscopy in the identification of tungstophosphate species in solutions of various pH values, a complementary sensitive method of ^{31}P NMR was applied.

The ^{31}P NMR spectra of WPA samples over the pH range 1 to 11.5 are presented in Fig. 3. Literature values of chemical shifts were used for the identification of ions formed in solutions. As can be seen, the parent Keggin anion $[PW_{12}O_{40}]^{3-}$ can be easily recognized through its intense single signal at –14.3 ppm (13, 20–22, 25, 31–33). This signal was observed as dominant under our experimental conditions at pH 1 and 1.5, while at pH 2 this peak disappeared.

A few peaks near –12 ppm appear at pH 1.5 and 2. These peaks can be assigned to the structures with 2 phosphorus atoms from the Dawson series, such as $[P_2W_{21}O_{71}]^{6-}$, $[P_2W_{18}O_{62}]^{6-}$, and $[P_2W_{20}O_{70}]^{10-}$ (25, 33, 34). With further

Fig. 3. ^{31}P NMR spectra of WPA solutions at varying pH.

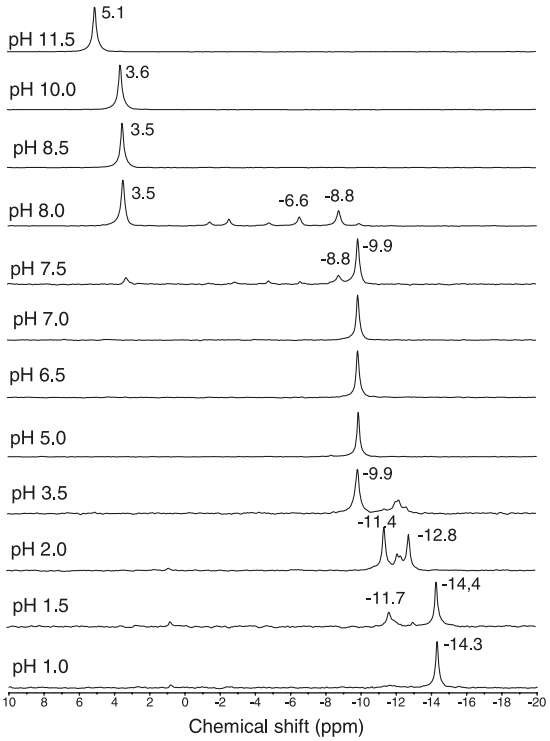

increases in pH, the peaks at ca. –12 ppm remain at pH 3.5, but their intensities decrease, while a dominant peak appears at ca. –9.9 ppm, which corresponds to the lacunary Keggin anion $[PW_{11}O_{39}]^{7-}$ (25, 34, 35). This peak remains the only one in the spectra of solutions of pH up to 7. Analysis of NMR spectra indicates the complex decomposition scheme of the Keggin anion in acidic region that does not lead directly to the lacunary monovacant anion, which was stated

© 2008 NRC Canada

Fig. 4. ^{31}P NMR spectra of WPA solutions of pH 6.5, pH 7.0, pH 7.5, and pH 8.0, recorded 17 min, 2 h, 24 h, 7 days, 30 days, and one year after preparation of solutions.

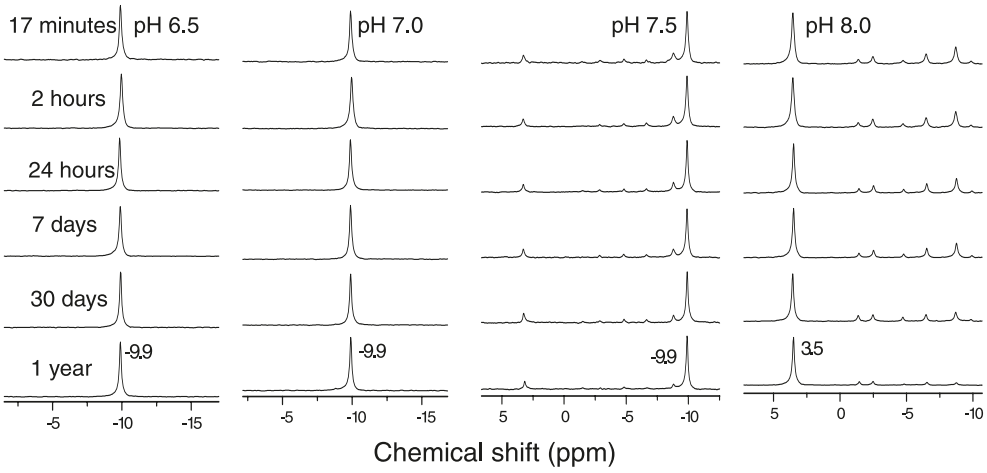

previously (13). Our results confirm the findings of Smith and Patrick (25) that under these conditions, structures with 2 phosphorus atoms of the Dawson series are formed before their degradation to lacunary monovacant anions in the pH range from 3.5 to 5.

Because of the importance of the pH region found in physiological systems for biomedical investigations and in order to determine exactly the region of existence of the $[PW_{11}O_{39}]^{7-}$ anion, the NMR spectra are recorded for the pH values between 6.5 and 8.5, at each 0.5 pH. It is evident from these spectra that up to pH 7, the lacunary anion is the only structure present in the solution. At pH 7.5, which almost corresponds to physiological conditions, some other products also appeared in addition to the dominant lacunary anion. The change in pH from 7.5 to 8.0 causes complete destruction of the $[PW_{11}O_{39}]^{7-}$ anion and an increase in the intensity of the other peaks. The most intensive peak corresponds to the phosphate anion. One of the peaks, –8.8 ppm, corresponds to $[P_2W_{19}O_{69}(H_2O)]^{14-}$ and another at –6.6 ppm corresponds to $[PW_9O_{34}]^{9-}$. It can be supposed that the former consists of two $PW_9O_{34}^{9-}$ units bridged by one WO_2 group (25, 35). That is, in the pH range 7.5–8, in the course of decomposition of the major anion $[PW_{11}O_{39}]^{7-}$ to $[PW_9O_{34}]^{9-}$ and other unidentified species (corresponding to peaks with higher chemical shifts), some of the $[PW_9O_{34}]^{9-}$ anions dimerize, producing $[P_2W_{19}O_{69}(H_2O)]^{14-}$. It is obvious that in this narrow pH region (7.5–8) the dramatic decomposition of tungstophosphates occurs. In spectra of alkaline solutions of pH > 7.5, a total degradation to phosphate and tungstate is observed. A peak appeared at different chemical shifts, corresponding to the protonated phosphate anions, $[H_2PO_4]^{-1}$, $[HPO_4]^{2-}$, and $[PO_4]^{3-}$.

As mentioned in the introduction, literature data are not always in accordance. Thus, Nomiya et al. (36) have studied the insulin mimetic effect of POMs with Dawson structure and their stability, varying their concentration in the range 1.0–30.0 mmol/L. They found only one peak at –12.7 ppm in the ^{31}P NMR spectra due to the $[P_2W_{18}O_{62}]^{6-}$ anion in pH range 5.37–5.77, while a minor peak at –9.7 ppm assigned as the Preyssler $[NaP_5W_{30}O_{110}]$ structure appeared in addition to the main peak at ca. –12.6 ppm in the pH range 4.7–5.09. Our results and those of Smith and Patrick (25) show that the mentioned species are not stable at pH > 4.7. The findings in (36) related to the acidic region, for pH below 2.0, are in complete accordance with ours. It should be underlined again that the right explanation of any biochemical effects is impossible without proper and detailed knowledge of the considered system.

Time stability

In numerous studies of POMs, various time intervals for synthesis of the compounds were used. Thus, it could be very useful to consider the influence of time interval on WPA solutions stability in the range of pH between 6.5 and 8.0, which is very important for biomedical investigations. In Fig. 4 are shown ^{31}P NMR spectra of WPA solutions of several pH values (6.5, 7.0, 7.5, and 8.0), recorded immediately after preparation, after 2 h, 24 h, 7 days, 30 days, and one year, while kept at room temperature. All spectra confirmed pH stability of WPA solutions in the time ranges, except for minor changes in the spectra for pH 8.0 after one year, when total degradation of WPA was almost complete. It can be seen that the peaks at –8.8 and –6.6 ppm, corresponding to $[P_2W_{19}O_{69}(H_2O)]^{14-}$ and $[PW_9O_{34}]^{9-}$, respectively, slowly disappear with time.

Reversibility

Identification of species existing in solution by UV, IR, and ^{31}P NMR spectra was used to investigate the reversibility of the reaction pathway of WPA degradation and formation during pH changes. By adding NaOH to the WPA solution, pH is raised from pH 1 to 7 and to 8.5; then by HCl addition, pH was decreased back to pH 1. Figure 5 shows UV spectra obtained for solutions of 2×10^{-5} mol/dm^3 of WPA, where pH is changed from 1 to 7 (left side of figure) and from 1 to 8.5 (right side), and then changed back to 1. These data show that the absorption band maximum at 263 nm, characteristic for the Keggin anion at pH 1, disappears at pH 7 but appears again when pH 1 was attained. IR spectra of dried solutions of 2×10^{-2} mol/dm^3 concentration, where pH values were changed as in the case of UV spectra, confirmed that the Keggin anion is formed almost completely when pH was changed from 7 to 1, while in the case of pH 8.5 the reversibility is not complete (Fig. 6). ^{31}P NMR

© 2008 NRC Canada

Fig. 5. UV spectra of WPA solutions at several pH values after HCl addition (left) in solution with pH 7 and (right) in solution with pH 8.5.

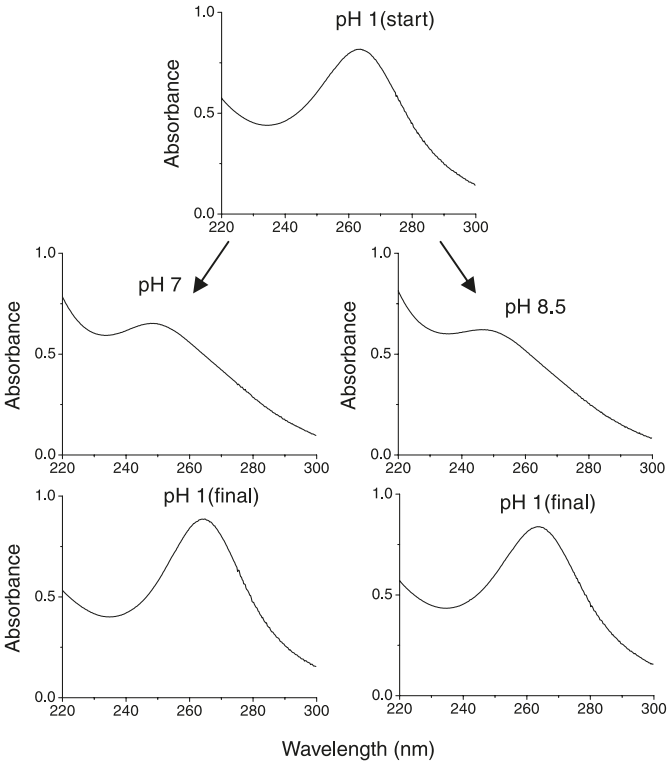

Fig. 6. IR spectra of evaporated WPA solutions at several pH values after HCl addition (left) in solution with pH 7 and (right) in solution with pH 8.5.

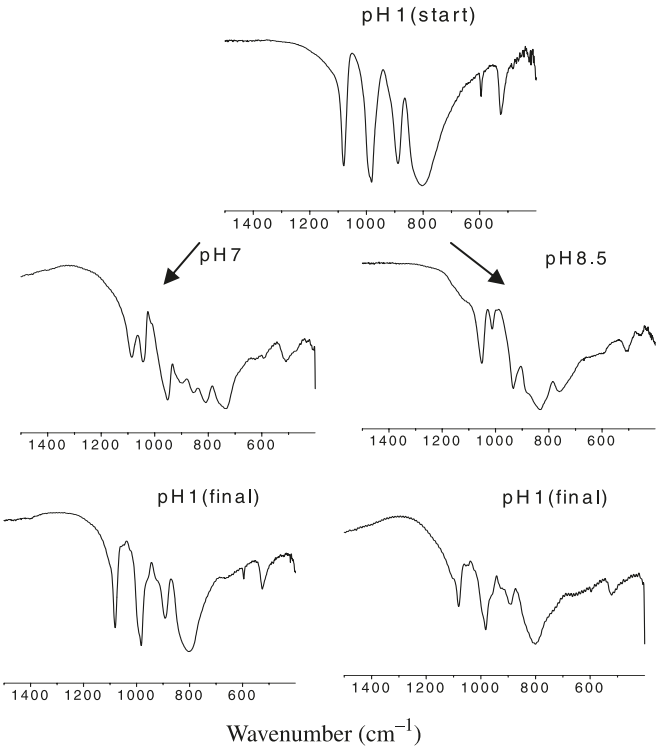

spectra of the solution, with concentration and pH values as in IR measurements (Fig. 7), also show that reversibility is not complete. A peak at –14.3 ppm, characteristic for the Keggin anion, is dominant but there are also peaks at ca. –13 ppm, indicating the presence of species of the Dawson series. Therefore, it could be concluded that there is not complete but partial reversibility during the changes in pH, in the case of higher concentrations of WPA. Also, it is evident that concentration is also a parameter that determines the equilibrium of different forms in solutions of HPCs.

Buffered solutions

In in vitro experiments where heteropoly compounds are used as biochemical agents, pH values are usually adjusted by different buffers. For this kind of investigation, TRIS and phosphate buffers are most commonly used. However in the case of WPA, the use of phosphate buffer is not possible because of its interaction with WPA, i.e., destruction and precipitate formation. For pH values lower than physiological levels, acetate buffer could be used. Therefore, ^{31}P NMR and UV spectra are recorded for aqueous solutions of WPA buffered with acetate and TRIS buffers, and results are presented in Figs. 8 and 9. It is evident that the application of acetate buffer causes no change in UV and ^{31}P NMR spectra (spectra are identical to those obtained for solutions whose pH was adjusted with addition of NaOH). But it is evident that TRIS buffer at pH 7 causes the formation of lacunary WPA anion as dominant along with some other phosphorus-containing polytungstophosphates. Therefore, the application of this buffer is not recommended in such experiments. The results indicate that in biochemical applications of POMs, the buffer type must be chosen with care because of its significant importance for the obtained biochemical effects and their elucidation.

Conclusions

It can be concluded that all spectroscopic methods used in this work indicate the instability of WPA in aqueous solutions and considerable dependence on pH with regard to the dominant species present in the solution. Considering this, literature data are not always consistent because of the complexity of the system; many factors influence the equilibrium, primarily pH and HPA concentration, while the performance of different analytical techniques used for speciation should be taken in account as well. The concentration of the HPA in unbuffered solution can affect the pH (23). We have observed that plant juices can affect the pH and the observed structures, as seen by UV and NMR measurements (37).

Based on the results presented in this study, the following can be concluded. UV spectroscopy only indicates that some changes occur in the system but they cannot be specified. IR spectroscopy gives more information that is the basis for the identification of the dominant species as a function of the pH of the solution. However in some cases of similar spectral data, it is not possible to perform exact identification of major components. NMR spectroscopy provides unique data, which can be used for more accurate interpretation of changes in the solutions of various pH values, but is applica-

© 2008 NRC Canada

Fig. 7. ^{31}P NMR spectra of WPA solutions at pH 7.0 and 8.5 after HCl addition (left) in solution with pH 7 and (right) in solution with pH 8.5.

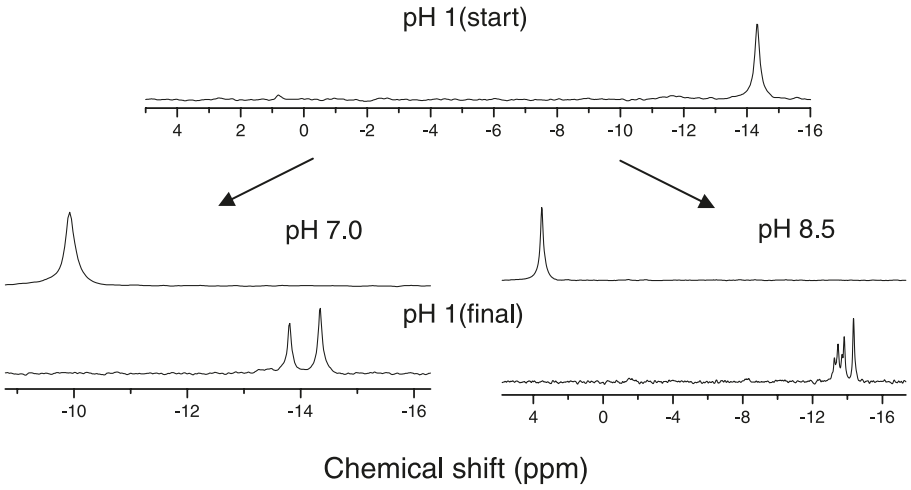

Fig. 8. (left) UV spectra and (right) ^{31}P NMR spectra of WPA solutions at (top) pH 3.5 and (bottom) pH 5 adjusted by acetate buffer and NaOH.

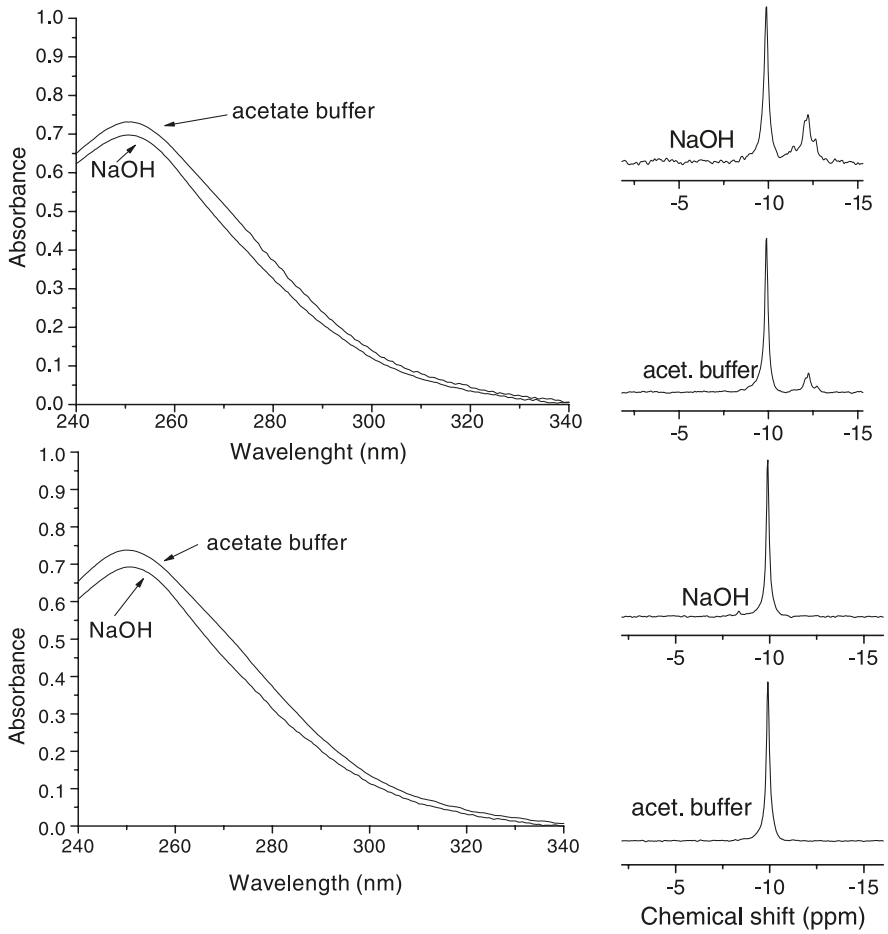

ble to higher concentrations as used in this work. Given that the behavior and nature of heteropoly and isopoly compounds is very complex, one must bear in mind whether the conclusions obtained for very low concentrations (e.g., 0.01–0.0001 mol L^{-1}) when using UV spectrometry, can be applied to higher concentrations (ca. 0.1 mol L^{-1}) of HPAs when IR and NMR spectrometry were employed to follow various species present in the equilibrium system.

The results presented indicate that in the case of aqueous solutions of WPA, the parent anion is present only in a very

© 2008 NRC Canada

Fig. 9. (left) UV spectra and (right) ^{31}P NMR spectra of WPA solution at pH 7 adjusted by NaOH and TRIS buffer.

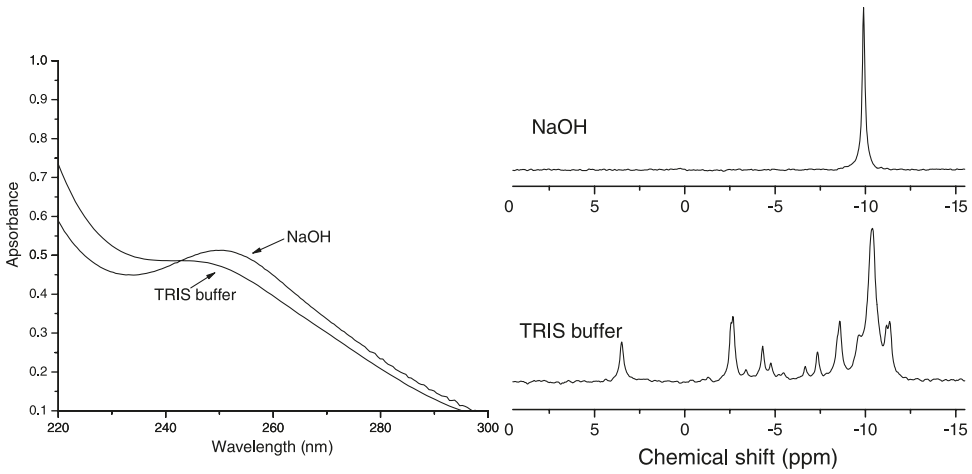

acidic solution of ca. pH 1. It should be pointed out that in aqueous solution, WPA decomposes first to components of the Dawson series, $[P_2W_{21}O_{71}]^{6-}$, $[P_2W_{20}O_{70}]^{10-}$, and $[P_2W_{18}O_{62}]^{6-}$ in the pH range 1–3.5. With further increases in pH greater than 3.5, these species convert to the lacunary monovacant anion, $[PW_{11}O_{39}]^{7-}$, which is a major constituent in pH range up to 7.5. In the narrow pH range 7.5–8.0, remarkable changes occur; $[PW_{11}O_{39}]^{7-}$ decomposes to $[PW_9O_{34}]^{9-}$, but other tungstophosphate ions are also observed. The total decomposition of the Keggin anion to phosphate and tungstate occurs at pH > 7.5.

Some differences in interpretation of the molecular species present under various experimental conditions can be ascribed to some extent to the diversity of chemical shifts data of NMR found in the literature.

In the pH region 6.5–7.5, the equilibrium composition is established quickly after solution preparation, and the monovacant lacunary form of WPA is stable for a period of one year.

UV spectrometry has shown that when changing pH from 1 to higher values and back to pH 1 in a 2×10^{-5} mol/dm^3 aqueous solution of WPA, the reversibility of changes in molecular structures is completely attained. But for solutions of higher concentration, 0.05 mol/dm^3, the changes are not reversible. That is, when the pH of the solution is adjusted again to pH 1, the Keggin anion is formed only partially, and other molecular forms of the Dawson series are present as well.

The molecular forms present in the equilibrium system under specific conditions depend significantly on the buffer type. Therefore, the choice of buffer used for maintaining the physiological conditions must be made with care to attain the appropriate biochemical effect of POMs.

Under physiological conditions attained with the addition of NaOH, WPA is dominantly present in the form of the lacunary monovacant anion. This is of special importance for biomedical application of heteropoly acids and other compounds of this type.

The results presented have shown that before any use of HPCs as biochemical or biomedically active compounds and as catalysts, it is necessary to control their behavior under defined conditions. Without that, it is not possible to discuss the equilibrium between different forms of heteropoly anions and any mechanism of reactions.

Acknowledgement

This work has been partly supported by the Ministry of Science and Environmental Protection of the Republic of Serbia, Project No. 142047.

References

1. M.T. Pope. Heteropoly and isopoly oxometalates. Springer-Verlag, Berlin, Germany. 1983.
2. M.T. Pope and A. Muller. Polyoxometalates: from platonic solids to anti-retroviral activity. Kluwer, Dordrecht, The Netherlands. 1994.
3. C. Hill (*Editor*). Chem. Rev. **98**, 1 (1998).
4. M.T. Pope and A. Muller. Polyoxometalates chemistry, from toplogy via self-assembly to applications. Kluwer Academic Publishers, Dordrecht, The Netherlands. 2001.
5. U. Mioč, Ph. Colomban, and A. Novak. J. Mol. Struct. **218**, 123 (1990).
6. U.B. Mioč, M.R. Todorović, M. Davidović, Ph. Colomban, and I. Holclajtner-Antunović. Solid State Ionics, **176**, 2837 (2005).
7. J.T. Rhule, C.L. Hill, D.A. Judd, and R.F. Schinazi. Chem. Rev. **98**, 327 (1998).
8. I.V. Kozhevnikov. Chem. Rev. **98**, 171 (1998).
9. N. Mizuno and M. Misono. Chem. Rev. **98**, 199 (1998).
10. A. Teze and G. Herve. Inorg. Synth. **27**, 85 (1990).
11. G.F. Tourne and C.M. Tourne. Top. Mol. Org. Eng. **10**, 59 (1994).
12. C. Hill, M. Weeks, and R. Schinazi. J. Med. Chem. **33**, 2767 (1990).
13. G.B. McGarvey and J.B. Moffat. J. Mol. Catal. **69**, 137 (1991).
14. M. Witvrou, H. Weigold, C. Pannecouque, D. Schols, E. De Clerq, and G. Holan. J. Med. Chem. **43**, 778 (2000).
15. M.A. Schwegler, J.A. Peters, and H. van Bekkum. J. Mol. Catal. **63**, 343 (1990).
16. D.L. Kepert and J.H. Kyle, J. Chem. Soc. Dalton Trans. 137 (1978).
17. D.L. Kepert and J.H. Kyle. J. Chem. Soc. Dalton Trans. 1781 (1978).
18. C.C. Kircher and S.R. Crouch. Anal. Chem. **55**, 242 (1983).

© 2008 NRC Canada

19. J.A. Rob van Veen, O. Sudmeijer, C.A. Emeis, and H. de Wit. J. Chem. Soc. Dalton Trans. 1825 (1986).
20. L.G. Detusheva, E.N. Yurchenko, S.T. Khankhasaeva, I.V. Kozhevnikov, T.P. Lazarenko, and R.I. Maksimovskaza. Koord. Khim. **16**, 619 (1990).
21. Z. Zhu, R. Tainm and C. Rhodes. Can. J. Chem, **81**, 1044 (2003).
22. J. Toufaily, M. Soulard, J.-L. Guth, T. Hamieh, and M.-B. Fadlallah. J. Phys. IV, **113**, 155 (2004).
23. B. Smith and V. Patrick. Aus. J. Chem, **55**, 281 (2002).
24. B. Smith and V. Patrick. Aus. J. Chem, **56**, 283 (2003).
25. B. Smith and V. Patrick, Aus. J. Chem, **57**, 261 (2004).
26. S. Himeno, M. Takamoto, and T. Ueda. Bull. Chem. Soc. Jpn. **78**, 1463 (2005).
27. G. Brauer. Handbuch der Preparativen Anorganischen Chemie. Ferdinand Enke Ferlag, Stuttgart. 1981 (tr. Russ. Mir 1986).
28. J. Liu and W.J. Mei. Antivir. Res. **62**, 65 (2004).
29. C. Rocchiccioli-Deltcheff, M. Fournier, R. Franck, and R. Thouvenot. Inorg. Chem. **22**, 207 (1983).
30. (*a*) D. Li, Y. Guo, C. Hu, L. Mao, and E. Wang. Appl. Catal. A, **235**, 11 (2002); (*b*) G.N. Alekar. Ph.D. thesis, Univ. Pune, India, (2000).
31. I. Song and M. Barteau. J. Mol. Catal. A, **212**, 229 (2004).
32. A. Jurgensen and J. Moffat. Catal. Lett. **34**, 237 (1995).
33. R. Massart, R. Contant, J. Fruchart, J. Ciabrini, and M. Fournier. Inorg. Chem. **16**, 2916 (1977).
34. C. Brevard, R. Schimpf, G. Tourne, and C. Tourne. J. Am. Chem. Soc. **105**, 7059 (1983).
35. C.M. Tourne and G.F. Tourne. J. Chem. Soc. Dalton Trans. 2411 (1988).
36. K. Nomiya, H. Torii, T. Hasegawa, Y. Nemoto, K. Nomura, K. Hashino, M. Uchida, Y. Kato, K. Shimizu, and M. Oda. J. Inorg. Biochem. **86**, 657 (2001).
37. S. Uskoković-Marković, M. Todorović, U. Mioč, I. Holclajtner-Antunović, B. Krstić, and N. Dukić. 233rd National American Chemical Society Meeting, Chicago, Ill. March, 2007.

© 2008 NRC Canada

Chemoenzymatic synthesis of ring ^{18}O-labeled sialic acid

Deepani Indurugalla and Andrew J. Bennet

Abstract: Methyl 4,6-*O*-benzylidene-α-D-glucopyranoside was converted into methyl 2-azido-2-deoxy-4,6-*O*-benzylidene-α-D-altropyranoside via a synthetic route that incorporated two inversions of configuration. Activation of the C-3 hydroxyl group as a triflate ester followed by an S_N2 reaction with O-18 labeled benzoate gave, after standard functional group manipulations, 2-acetamido-2-deoxy-D-(3-^{18}*O*)mannose. Coupling of the labeled *N*-acetyl-mannosamine with pyruvate was catalyzed by sialic acid aldolase to give ring-oxygen-labeled sialic acid in an overall yield of 11.4% over 10 steps.

Key words: *N*-acetylneuraminic acid, sialic acid oxygen-18, chemoenzymatic.

Résumé : Le 4,6-*O*-benzylidène-α-D-glucopyranoside de méthyle a été transformé en 2-azido-2-désoxy-4,6-*O*-benzylidène-α-D-altropyranoside par le biais d'une voie de synthèse qui incorpore deux inversions de configuration. L'activation du groupement hydroxyle en C-3 sous la forme de triflate suivie par une réaction S_N2 avec du benzoate marqué au O-18 conduit, après des manipulations standards de groupes fonctionnels au 2-acétamido-2-désoxy-D-(3-^{18}O)mannose. Le couplage de la *N*-acétylmannosamine avec le pyruvate a été catalysé par l'aldolase de l'acide sialique et a conduit avec un rendement global de 11,4% pour les dix étapes, à un acide sialique dont le cycle comporte un atome d'oxygène marqué.

Mots-clés : acide *N*-acétylneuraminique, acide sialique, oxygène-18, chimioenzymatique.

[Traduit par la Rédaction]

Introduction

The sialic acids are a family of carbohydrates, containing a nine-carbon backbone, that are often found on the ends of oligosaccharide chains in biological systems. This prominent display of these sugars results in their importance in numerous biological recognition and communication events, which are mediated by sialic acid recognizing proteins. Therefore, many research groups have developed synthetic routes to the parent sugar, sialic acid (*N*-acetyl-neuraminic acid, **1a**), and its derivatives (1). In addition, the transfer of carbohydrate residues between various acceptors and donors is a critically important biological process (2–5). Accordingly, the mechanisms by which various anabolic and catabolic enzymes modify these important carbohydrate residues have received considerable attention (6).

As part of a program, which incorporates the measurement of kinetic isotope effects aimed at delineating the finer mechanistic details involved in enzymatic and non-enzymatic sialic acid transfer reactions, an efficient synthesis of ring-oxygen-labeled sialic acid was required. Specifically, kinetic isotope effects (KIEs) measured using compounds derived from (6-^{18}*O*)-sialic acid (**1b**), in conjunction those from anomeric ^{13}C- and leaving group ^{18}O-labeled materials, will allow evaluation of critical variables at the transition state(s) for the transfer of sialic acid residues, namely: (*i*) site of cleavage at the glycosidic centre, endo- or exo-cyclic; (*ii*) degree of C–O cleavage; (*iii*) amount of double-bond character at the oxacarbenium ion-like TS; (*iv*) degree of nucleophilic participation at the anomeric centre; (*v*) degree of proton-transfer, which occurs from an active-site aspartic acid residue for the enzyme-catalyzed reactions (7, 8).

To date, few reports of heavy-atom KIEs on sialyl transfer reactions have been published. Those include leaving-group ^{18}O-KIEs on the acid-catalyzed and spontaneous hydrolysis reactions of 4-nitrophenyl α-D-sialoside (9) and on the corresponding *Vibrio cholerae* sialidase-catalyzed reactions (10); anomeric ^{14}C-KIEs on the sialyl transferase catalyzed transfer of sialic acid from CMP- and UMP-β-sialoside (**2** and **3**, respectively; Fig. 1) to carbohydrate acceptors (11, 12); anomeric ^{14}C-KIEs on the hydrolysis of sialosides catalyzed by the trans-sialidase *Trypanosoma cruzi* (13).

With regard to the synthesis of heavy-atom-labeled sialic acids, the first reported synthesis involved a series of single-carbon chain extensions of *N*-acetyl-mannosamine to give *N*-acetyl-(1-^{13}*C*)-neuraminic acid (14). Specifically, the authors performed two Henry reactions that were followed by addition of ^{13}C-labeled cyanide to an eight-carbon aldehyde. However, now that the enzyme sialic acid aldolase is readily available, most syntheses involve the enzymatic coupling of *N*-acetyl-mannosamine and pyruvate (15, 16) to give ^{13}C-labels in carbon atoms 1–3 (17). Sato et al. have also reported the chemical synthesis of *N*-acetyl-(6-^{13}C)-

Received 4 June 2008. Accepted 29 August 2008. Published on the NRC Research Press Web site at canjchem.nrc.ca on 3 October 2008.

D. Indurugalla and A.J. Bennet.[1] Department of Chemistry, Simon Fraser University, 8888 University Drive, Burnaby, BC V5A 1S6, Canada.

[1]Corresponding author: (e-mail: bennet@sfu.ca).

 doi:10.1139/V08-140 © 2008 NRC Canada

Fig. 1. Sialic acid (neu5Ac, **1a**), its ring-oxygen-labeled isotopomer **1b**, and activated sialosyl donors (**2** and **3**).

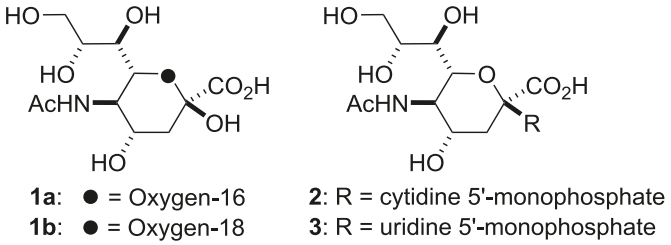

Scheme 1. Sialic acid aldolase catalyzed synthesis of target compound (**1b**) and the required building blocks for its synthesis; the numbering shown refers to the carbon atoms in the product.

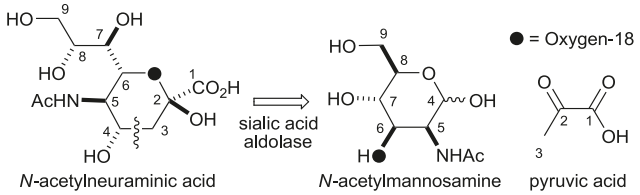

mannosamine, which when coupled to 3-^{13}C and unlabeled pyruvate gave (3,9-$^{13}C_2$)- and (9-^{13}C)-labeled sialic acids (18).

A single publication reports the ^{18}O-labeling of sialic acid itself, which in this case involves the anomeric oxygen atom (19). That is, Ambrose et al. made a 50:50 mixture of singly and doubly labeled sialic acids, *N*-acetyl-(2-^{13}C)-[2-$^{18}O_{0,1}$]-neuraminic acid, to probe the mechanism of the CMP-sialic acid synthetase enzyme from *E. coli* (19). Also, Burke and Horenstein have reported the synthesis of [$P^{18}O_2$]-CMP β-[1-^{14}C]-*N*-acetyl-neuraminic acid (20).

Results and discussion

The synthetic route to (6-^{18}O)-sialic acid (**1b**) requires *N*-acetyl-D-(3-^{18}O)mannosamine and pyruvate to be coupled enzymatically using sialic acid aldolase (Scheme 1).

Methyl 4,6-*O*-benzylidene-α-D-glucopyranoside (21) was transformed into the 2,3-epoxysugar **4** by the procedure of Wiggins (22). Nucleophilic ring-opening with azide (23), followed by formation of a triflate ester (24), gave the required starting material **5** for the incorporation of the ^{18}O-label (Scheme 2).

Triflate displacement with ^{18}O-labeled benzoate in CH_2Cl_2 yielded 52% of methyl 2-azido-2-deoxy-3-benzoyl-4,6-*O*-benzylidene-α-D-(3-^{18}O)mannopyranoside (**6**) and 39% of the unsaturated product **7**, which results from a competitive E2 elimination reaction. It was observed that the percentage of the elimination product increases as the reaction temperature rises. Therefore, the reaction was carried out at room temperature until most of the starting material had reacted, and then the reaction temperature was raised to ensure complete conversion of **5** had occurred to give a mixture of **6** and **7**. The atom% of ^{18}O incorporated into **6** is evaluated to be 88.5%, a number, which is calculated from the percentage of doubly labeled benzoate (78.4%) + one-half of the fraction of singly labeled carboxylate nucleophile (20.2%).

Scheme 2. Conversion of methyl 4,6-*O*-benzylidene-α-D-glucopyranoside into the activated azido triflate **5**. Reagents: (i) TsCl/pyridine (75%), (ii) NaOMe/MeOH (97%), (iii) NaN_3/DMF (84%), and (iv) Tf_2O/pyridine (88%).

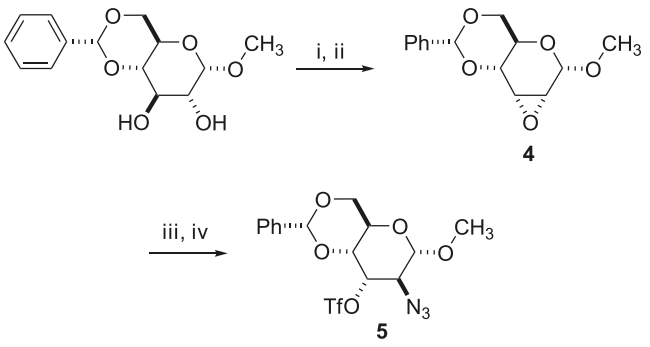

Scheme 3. Incorporation of ^{18}O label into the C-3 position of protected azido mannose derivative **6** and its subsequent manipulations. Reagents: (i) PhC$^{18}O_2$H/K_2CO_3/18-crown-6 CH_2Cl_2 (52% **6** and 39% **7**), (ii) NaOMe/MeOH (92%), (iii) H_2/Pd (100%), (iv) Ac_2O/H_2SO_4, and (v) Ac_2O/pyridine.

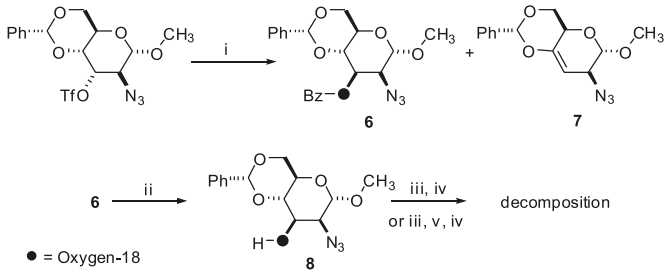

At this point, removal of the benzoyl group on C-3 gave azido alcohol **8**, which upon reduction of the azido group using H_2 on Pd/C, gave a quantitative yield of the corresponding amine (**9**). However, an acetolysis reaction on this amine, using 5% H_2SO_4 in acetic anhydride at 0 °C, resulted in decomposition of the starting material. To circumvent this problem, the free hydroxyl and amino groups of **9** were acetylated, and this material was subjected to an acetolysis reaction (5% H_2SO_4 in Ac_2O at 0 °C) as reported by Krist et al. (24). Once again in our hands, this procedure gave extensive decomposition (Scheme 3).

It was therefore decided to perform the acetolysis reaction prior to the reduction of the azide functionality. Thus, following removal of the benzoyl group in a 92% yield, acetolysis was performed directly on azide **8**, a procedure that resulted in simultaneous removal of the benzylidene acetal and the methyl aglycone and complete hydroxyl group acetylation to give 1,3,4,6-tetra-*O*-acetyl-2-azido-2-deoxy-α-D-(3-^{18}O)mannopyranose (**10**) in good yield (85%). Following this, the C-2 azido group of **10** was reduced, using H_2 on 10% Pd/C, and the resulting amine was acetylated to obtain 2-acetamido-1,3,4,6-tetra-*O*-acetyl-2-deoxy-α-D-(3-^{18}O)mannopyranose (**11**). Subsequent O-deacetylation of **11** afforded 2-acetamido-2-deoxy-D-(3-^{18}O)mannose (**12**) in 90% yield (Scheme 4). Sialic acid aldolase catalyzed condensation of **12** was conducted at 37 °C with 10 equiv. of sodium

© 2008 NRC Canada

Scheme 4. Conversion of azido alcohol **8** into ring-oxygen-labeled sialic acid **1b**. Reagents: (i) Ac_2O/H_2SO_4 (85%), (ii) H_2/Pd (100%), (iii) Ac_2O/NaOAc (80%, two steps), (iv) NaOMe/MeOH (90%), and (v) CH_3COCO_2Na/NeuAc aldolase (58%).

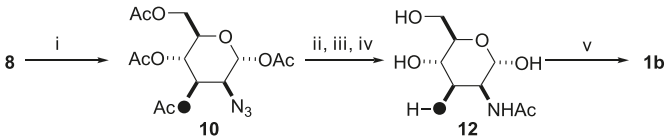

Fig. 2. HR-MS (negative-ion mode) of labeled sialic acid dimer (**1b**:**1b**–H^+; $C_{22}H_{37}N_2O_{16}{}^{18}O_2$ *m/z* calcd.: 621.2126) and the singly labeled material (**1a**:**1b**–H^+ *m/z* calcd.: 619.2083).

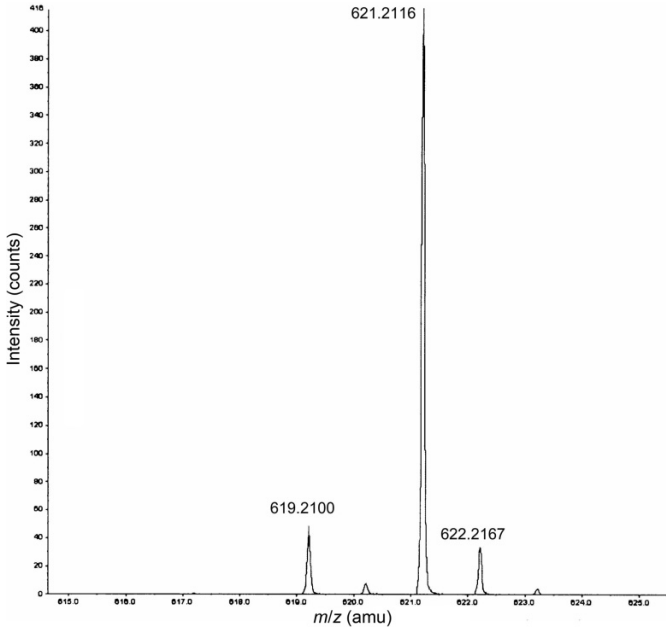

pyruvate in a 5 mmol/L tris buffer (pH = 7.5) containing 0.1% sodium azide (15). Following removal of the aldolase, the excess pyruvate and its reversibly formed *gem*-diol (25) were removed by the use of pyruvate decarboxylase (26). Final purification of the labeled sialic acid (**1b**) involved a flash chromatographic separation on normal-phase silica.

Shown in Fig. 2 is the negative-ion mode HR-MS for the labeled sialic acid dimer (**1b:1b-H$^+$**)$^-$. Also evident in the spectrum is the singly labeled dimer (**1a:1b-H$^+$**)$^-$ and their associated ^{13}C-satalite peaks.

Conclusions

Ring-oxygen-labeled sialic acid has been made by a concise and scaleable chemoenzymatic route in reasonable overall yield (11.4%) over 10 steps.

Experimental

NMR spectra were acquired on a Varian Inova-500 MHz or Bruker Avance 600 MHz spectrometer. Chemical shifts (δ_H and δ_C) are listed in ppm downfield from the signal for TMS using the residual solvent peak as an internal reference. Coupling constants (*J*) are given in Hz. NMR spectral peak assignments are based on COSY, HMQC, and HMBC experiments. Melting points were recorded on a Gallenkamp melting point apparatus and are uncorrected. Optical rotations were measured on a PerkinElmer 341 polarimeter and are reported in units of deg cm^2 g^{-1} (concentrations reported in units of g per 100 mL). Thin layer chromatography (TLC) was performed on aluminum plates pre-coated with Merck silica gel-60 F_{254}. Compounds were visualized with UV light and (or) staining with phosphomolyibdic acid (5% in ethanol) followed by heating. Flash chromatography was performed using Avanco silica gel-60 (230–400 mesh). Neu5ac aldolase (EC 4.1.3.3) was purchased from Julich Chiral Solutions (now Codexis; lot no. H70240.01) and pyruvate decarboxylase (EC 4.1.1.1) was purchased from Sigma. Shown in the supporting information is the ^{13}C NMR spectrum for compound **1b**, which exists as a 93:7 mixture of the two anomeric hemiketals.[2]

[$^{18}O_2$]Benzoic acid

Benzoic acid ($^{18}O_2$) was made by following the procedure of Wnuk et al. (27) using benzonitrile (1.8 g, 17.5 mmol) and ^{18}O-H_2O (1.04 g, 52.5 mmol; Marshall isotopes, 95.1 atom% O-18, batch no. 020414nw). Based on the observed intensities of the isotopic peak distribution for the M + H^+ peaks in a CI-MS, the composition of the isotopically labeled benzoic acid, [$^{18}O_2$], [$^{16}O^{18}O$], and [$^{16}O_2$], were calculated using the method of Brauman (28) to be 78.4%, 20.2%, and 1.4%, respectively.

Methyl 2-azido-2-deoxy-3-benzoyl-4,6-*O*-benzylidene-α-D-(3-^{18}O)mannopyranoside (6)

To a solution of **5** (4.7 g, 10 mmol) and $C_6H_5C^{18}O_2H$ (1.8 g, 14 mmol) in CH_2Cl_2 (150 mL), K_2CO_3 (2.2 g, 16 mmol) and 18-crown-6 (4.2 g, 16 mmol) were added. The resulting mixture was stirred at room temperature for 5 d, and then it was heated to reflux for further 16 h. After removal of the volatiles under reduced pressure, the crude product was purified by flash chromatography using ethyl acetate:hexanes (1:5) as the eluent to afford **6** as a white solid (2.3 g, 52%). The unsaturated compound **7** was isolated as a minor product (1.2 g, 39%).

Mp 94–95 °C. $[\alpha]_D^{20}$ +73.3 (*c* 1.4, $CHCl_3$). ^{1}H NMR (500 MHz, $CDCl_3$) δ: 3.44 (s, 3H, OCH_3), 3.86 (t, 1H, $J_{6a,6b}$ = $J_{6a,5}$ = 10.0, H-6a), 3.98 (dt, 1H, $J_{5,6a}$ = $J_{5,4}$ = 10.0, $J_{5,6b}$ = 4.5, H-5), 4.22 (t, 1H, $J_{4,5}$ = $J_{4,3}$ = 10.0, H-4), 4.27 (dd, 1H, $J_{2,3}$ = 4.0, $J_{2,1}$ = 1.0, H-2), 4.30 (dd, 1H, $J_{6b,6a}$ = 10.0, $J_{6b,5}$ = 4.5, H-6b), 4.76 (d, 1H, $J_{1,2}$ = 1.0, H-1), 5.61 (s, 1H, H-7), 5.74 (dd, 1H, $J_{3,4}$ = 10.0, $J_{3,2}$ = 4.0, H-3), 7.31–7.33 (m, 3H, Ar–H), 7.42–7.47 (m, 4H, Ar–H), 7.56–7.59 (m, 1H, Ar–H), 8.10–8.11 (m, 2H, Ar–H). ^{13}C NMR (125 MHz, $CDCl_3$) δ:

[2] Supplementary data for this article are available on the journal Web site (canjchem.nrc.ca) or may be purchased from the Depository of Unpublished Data, Document Delivery, CISTI, National Research Council Canada, Ottawa, ON K1A 0R6, Canada. DUD 3830. For more information on obtaining material, refer to cisti-icist.nrc-cnrc.gc.ca/cms/unpub_e.shtml.

© 2008 NRC Canada

55.4 (OCH_3), 62.7 (C-2), 64.2 (C-5), 69.0 (C-6), 70.8 (C-3), 76.6 (C-4), 100.2 (C-1), 102.1 (C-7), 126.5, 128.5, 128.8, 129.3, 130.3, 133.7, 137.5 (Ar), 165.7 (C=O). Anal. calcd. for $C_{21}H_{21}N_3O_4{}^{18}O_2$: C, 60.7; H, 5.1; N, 10.1; found: C, 60.5; H, 5.2; N, 10.0.

Methyl 2-azido-2-deoxy-4,6-*O*-benzylidene-α-D-(3-^{18}*O*)mannopyranoside (8)

To a solution of **6** (2.2 g, 5 mmol) in dry methanol (25 mL) was added a methanolic sodium methoxide solution (25 mL), and the mixture was stirred for 30 min at RT. The solution was then neutralized by adding Amberlite IR-120 (H^+ form). The resulting solution was filtered, and the resin was washed several times with methanol. The methanolic solutions were combined and evaporated to give a solid residue, which was purified by flash chromatography using ethyl acetate:hexanes (1:4) as the eluent to afford **8** as syrup (1.5 g, 92%).

$[\alpha]_D^{20}$ +74.4 (*c* 1.1, $CHCl_3$). ^{1}H NMR (500 MHz, $CDCl_3$) δ: 1.57 (bs, 1H, 3-OH), 3.40 (s, 3H, OCH_3), 3.78 (dt, 1H, $J_{5,6a} = J_{5,4} = 10.0$, $J_{5,6b} = 4.0$, H-5), 3.82 (t, 1H, $J_{6a,6b} = J_{6a,5} = 10.0$, H-6a), 3.91 (t, 1H, $J_{4,5} = J_{4,3} = 10.0$, H-4), 4.01 (dd, 1H, $J_{2,3} = 4.0$, $J_{2,1} = 1.0$, H-2), 4.25–4.29 (m, 2H, H-6b H-3), 4.71 (d, 1H, $J_{1,2} = 1.0$, H-1), 5.59 (s, 1H, H-7), 7.37–7.39 (m, 3H, Ar–H), 7.48–7.50 (m, 2H, Ar–H). ^{13}C NMR (125 MHz, $CDCl_3$) δ: 55.2 (OCH_3), 63.6 (C-5), 64.0 (C-2), 68.7 (C-3), 68.8 (C-6), 79.2 (C-4), 100.3 (C-1), 102.5 (C-7), 126.7, 128.6, 129.5, 137.4 (Ar). Anal. calcd. for $C_{14}H_{17}N_3O_4{}^{18}O$: C, 54.4; H, 5.5; N, 13.6; found: C, 54.3; H, 5.6; N, 13.35.

1,3,4,6-Tetra-*O*-acetyl-2-azido-2-deoxy-α-D-(3-^{18}*O*)mannopyranose (10)

A solution of **8** (1.4 g, 5 mmol) in 5% H_2SO_4 in acetic anhydride (30 mL) was stirred for 1.5 h at 0 °C. This solution was diluted with ethyl acetate (150 mL) and washed successively with satd. $NaHCO_3$ (250 mL), water (250 mL), brine (250 mL), dried over anhydrous Na_2SO_4, and concentrated. The residue was purified by flash column chromatography using ethyl acetate:hexanes (1:1) as the eluent to afford **10** as a white solid (1.5 g, 85%).

Mp 108–109 °C. $[\alpha]_D^{20}$ +64.6 (*c* 1.1, $CHCl_3$). ^{1}H NMR (500 MHz, $CDCl_3$) δ: 2.06, 2.10, 2.12, 2.17 (4 × s, 12H, $COCH_3$), 4.01–4.04 (m, 2H, H-2, H-5), 4.09 (dd, 1H, $J_{6a,6b} = 12.5$, $J_{6a,5} = 2.5$, H-6a), 4.25 (dd, 1H, $J_{6b,6a} = 12.5$, $J_{6b,5} = 4.5$, H-6b), 5.36–5.43 (m, 2H, H-3, H-4), 6.12 (d, 1H, $J_{1,2} = 1.0$, H-1). ^{13}C NMR (125 MHz, $CDCl_3$) δ: 20.7, 20.8, 20.9, 21.1 (4 × CO*C*H_3), 60.7 (C-2), 62.0 (C-6), 65.5 (C-4), 70.7 (C-3), 70.9 (C-5), 91.6 (C-1), 168.4, 169.5, 170.2, 170.9 (4 × C=O). Anal. calcd. for $C_{14}H_{19}N_3O_8{}^{18}O$: C, 44.8; H, 5.1; N, 11.2; found: C, 45.0; H, 5.2; N, 11.1.

2-Acetamido-1,3,4,6-tetra-*O*-acetyl-2-deoxy-α-D-(3-^{18}*O*)mannopyranose (11)

A solution of **10** (1.7 g, 0.005 mol) in methanol (50 mL) was maintained under hydrogen atmosphere for 16 h in the presence of 10% Pd on carbon (0.17 g). The catalyst was removed by filtering the solution through a Celite pad, which was subsequently washed thoroughly with methanol (100 mL). The combined filtrate was evaporated to dryness, and the syrup obtained was dissolved in acetic anhydride (10 mL), cooled to 0 °C when a catalytic amount of sodium acetate was added. The reaction mixture was stirred for 1 h, while maintaining the temperature at 0 °C. The solution was co-evaporated with toluene (50 mL), and the residue obtained was purified by flash column chromatography using ethyl acetate:hexanes (1:1) as the eluent to afford **11** as a white foam (1.4 g, 80%).

Mp 41–42 °C. $[\alpha]_D^{20}$ +46.0 (*c* 1.1, $CHCl_3$). ^{1}H NMR (500 MHz, $CDCl_3$) δ: 2.00, 2.06, 2.07, 2.10 (4 × s, 12H, $COCH_3$), 2.17 (s, 3H, NHCO*C*H_3), 4.03–4.07 (m, 2H, H-6a, H-5), 4.28 (dd, 1H, $J_{6b,6a} = 12.5$, $J_{6b,5} = 4.5$, H-6b), 4.64 (ddd, 1H, $J_{2,NH} = 9.5$, $J_{2,3} = 4.5$, $J_{2,1} = 1.5$, H-2), 5.16 (t, 1H, $J_{4,5} = J_{4,3} = 10.0$, H-4), 5.33 (dd, 1H, $J_{3,4} = 10.0$, $J_{3,2} = 4.5$, H-3), 5.72 (d, 1H, $J_{NH,2} = 9.5$, N-H), 6.03 (d, 1H, $J_{1,2} = 1.5$, H-1). ^{13}C NMR (125 MHz, $CDCl_3$) δ: 20.9, 21.0, 21.1 (4 × CO*C*H_3), 23.5 (NHCO*C*H3), 49.5 (C-2), 62.4 (C-6), 65.8 (C-4), 69.0 (C-3), 70.3 (C-5), 91.9 (C-1), 168.4 (NH*C*OCH_3), 170.0, 170.2, 170.4, 170.8 (4 × C=O). Anal. calcd. for $C_{16}H_{23}NO_9{}^{18}O$: C, 49.1; H, 5.9; N, 3.6; found: C, 48.9; H, 6.0; N, 3.4.

2-Acetamido-2-deoxy-D-(3-^{18}*O*)mannose (12)

To a solution of **11** (1.3 g, 3 mmol) in dry methanol (25 mL) was added a methanolic sodium methoxide solution (25 mL), and the mixture was stirred for 30 min at RT. The solution was then neutralized by adding Amberlite IR-120 (H^+ form). The resulting solution was filtered, and the resin was washed several times with methanol. The methanolic solutions were combined and evaporated to give a solid residue, which was purified by flash chromatography using ethyl acetate:methanol:water (20:2:1 *v*/*v*/*v*) as the eluent. The fractions that contained the product were combined, concentrated, and finally lyophilized to yield a solid (670 mg, 90%).

Mp 117–118 °C. $[\alpha]_D^{20}$ +7.4 (*c* 1.7, H_2O). The ^{1}H NMR and ^{13}C spectra are identical to those acquired using a commercial sample of 2-acetamido-2-deoxy-D-mannose. Anal calcd. for $C_8H_{15}NO_5{}^{18}O{\cdot}H_2O$: C, 39.8; H, 7.1; N, 5.8; found: C, 39.8; H, 7.1; N 5.6.

5-Acetamido-3,5-dideoxy-D-*glycero*-D-*galacto*-(6-^{18}*O*)non-2-ulopyranosonic acid (1b)

2-Acetamido-2-deoxy-D-(3-^{18}*O*)mannose, **12** (200 mg, 0.83 mmol) and sodium pyruvate (921 mg, 8.3 mmol) were dissolved in 15 mL tris buffer (50 mmol/L, pH 7.5, containing 0.1% sodium azide). The pH of the reaction mixture was adjusted to pH 7.5 with 1 N NaOH solution. A solution of 20 u of NeuAc aldolase in 1 mL of the same buffer was added, and the final volume of the reaction mixture was adjusted to 20 mL by addition of the same buffer. The mixture was incubated at 37 °C overnight. The aldolase was removed by passing the solution through an Amicon ultra-centrifugal filter. The filtrate was concentrated and purified by flash column chromatography using ethyl acetate:methanol:water (5:4:1 *v*/*v*/*v*) to obtain the product as a white solid. This material was further purified to remove traces of pyruvate and its hydrate by treating a solution of this substance with 1 u of pyruvate decarboxylase (EC 4.1.1.1) in 5 mL of 50 mmol/L MES/NaOH buffer (pH 6.2) that contained 50 mmol/L $MgCl_2$ and 10 mmol/L thiamine pyrophosphate at RT overnight (29). Pure **1b** was isolated following flash

© 2008 NRC Canada

column chromatography using EtOAc:MeOH:H_2O (5:4:1 *v*/*v*/*v*) as the eluent.

Yield: 150 mg, 58%. Mp 180–183 °C dec. $[\alpha]_D^{20}$ –31.3 (*c* 1.1, H_2O). The ^1H NMR and ^{13}C spectra are identical to those acquired using a commercial sample of *N*-acetylneuraminic acid. HR-MS (FAB) *m*/*z* ($M - H^+$), $C_{11}H_{18}NO_8{}^{18}O_1$ requires 310.1024, found 310.1021.

Acknowledgements

The authors gratefully acknowledge the Natural Sciences and Engineering Research Council of Canada (NSERC) and Simon Fraser University for financial support of this work. High resolution negative ion mass spectra were recorded at the Saskatchewan Structural Sciences Centre.

References

1. I. Hemeon and A.J. Bennet. Synthesis-Stuttgart, 1899 (2007).
2. R. Schauer, S. Kelm, G. Reuter, and P. Roggentin. Biochemistry and role of sialic acids. *In* Biology of the sialic acids. *Edited by* A. Rosenberg. Plenum Press. New York. 1995. pp. 7–67.
3. M. Saito and R.K. Yu. Biochemistry and function of sialidases. *In* Biology of the sialic acids. *Edited by* A. Rosenberg. Plenum Press. New York. 1995. pp. 261–313.
4. C.S. Alviano, L.R. Travassos, and R. Schauer. Glycoconjugate J. **16**, 545 (1999).
5. R. Schauer. Zoology, **107**, 49 (2004).
6. G. Davies, M.L. Sinnott, S.G. Withers. Glycosyl transfer. *In* Comprehensive biological catalysis. 1st ed. *Edited by* M.L. Sinnott. Academic Press.San Diego. 1998. pp. 119–209.
7. A.J. Bennet and M.L. Sinnott. J. Am. Chem. Soc. **108**, 7287 (1986).
8. P.J. Berti and K.S.E. Tanaka. Adv. Phys. Org. Chem. **37**, 239 (2002).
9. M. Ashwell, M.L. Sinnott, and Y. Zhang. J. Org. Chem. **59**, 7539 (1994).
10. X. Guo and M.L. Sinnott. Biochem. J. **294**, 653 (1993).
11. M. Bruner and B.A. Horenstein. Biochemistry, **37**, 289 (1998).
12. M. Bruner and B.A. Horenstein. Biochemistry, **39**, 2261 (2000).
13. J. Yang, S. Schenkman, and B.A. Horenstein. Biochemistry, **39**, 5902 (2000).
14. L. Benzing-Nguyen and M.B. Perry. J. Org. Chem. **43**, 551 (1978).
15. M.J. Kim, W.J. Hennen, H.M. Sweers, and C.H. Wong. J. Am. Chem. Soc. **110**, 6481 (1988).
16. U. Kragl, D. Gygax, O. Ghisalba, and C. Wandrey. Angew. Chem., Int. Ed. Engl. **30**, 827 (1991).
17. T. Miyazaki, H. Sato, T. Sakakibara, and Y. Kajihara. J. Am. Chem. Soc. **122**, 5678 (2000).
18. K. Sato, S. Akai, T. Hiroshima, H. Aoki, M. Sakuma, and K. Suzuki. Tetrahedron Lett. **44**, 3513 (2003).
19. M.G. Ambrose, S.J. Freese, M.S. Reinhold, T.G. Warner, and W.F. Vann. Biochemistry, **31**, 775 (1992).
20. E.E. Burke and N.A. Horenstein. J. Labelled Compd. Radiopharm. **47**, 1007 (2004).
21. A.I. Vogel, B.S. Furniss, and A.I. Vogel. Vogel's textbook of practical organic chemistry. 5th ed. Longman Scientific & Technical. Wiley. London – New York. 1989.
22. L.F. Wiggins. Ethylene oxide-type anhydrosugars. *In* Methods Carbohydr. Chem. *Edited by* R.L. Whistler and M.L. Wolfrom. Academic Press. New York – London. Vol. II. 1963. pp. 188–191.
23. R.D. Guthrie and D. Murphy. J. Chem. Soc. 5288 (1963).
24. P. Krist, M. Kuzma, I.F. Pelyvas, P. Simerska, and V. Kren. Collect. Czech. Chem. Commun. **68**, 801 (2003).
25. A. Esposito, A. Lukas, J.E. Meany, and Y. Pocker. Can. J. Chem. **77**, 1108 (1999).
26. C.H. Lin, T. Sugai, R.L. Halcomb, Y. Ichikawa, and C.H. Wong. J. Am. Chem. Soc. **114**, 10138 (1992).
27. S.F. Wnuk, S.M. Chowdhury, P.I. Garcia, and M.J. Robins. J. Org. Chem. **67**, 1816 (2002).
28. J.I. Brauman. Anal. Chem. **38**, 607 (1967).
29. J. Rivoal, B. Ricard, and A. Pradet. Eur. J. Biochem. **194**, 791 (1990).

© 2008 NRC Canada

Synthesis and characterization of novel conducting homopolymers based on amino β-styryl terthiophene

Hakim Mehenni and Lê H. Dao

Abstract: Novel ECPs (electronic conducting polymers) based on amino β-styryl-substituted terthiophene (AST) were synthetized by direct electropolymerization. The ECPs were characterized by cyclic voltammetry, square-wave voltammetry, Fourier transform infrared (FTIR) spectroscopy, and X-ray photoelectron spectroscopy (XPS). The poly(amino β-styryl terthiophene) displayed cyclic and square-wave voltammograms with redox peaks that can be assigned to the aminophenyl moiety and the polyterthiophene backbone. The presence of free primary amine groups on the ECP film permitted further biological functionalization (i.e., covalent bonding of various bioreceptors on its surface). The electrochemical performance of Biotin grafted at the AST modified glassy carbon electrode was investigated to detect the Avidin protein in solution by cyclic voltammetry and square-wave voltammetry.

Key words: electronic conducting polymer, electrode surface modification, biosensor, β-styryl-substitued terthiophene, functionalization, cyclic, square-wave voltammetry.

Résumé : Faisant appel à une électropolymérisation directe, on a réalisé la synthèse de nouveaux polymères conducteurs électroniques (PCE) à base de terthiophènes portant des substituants β-styryles aminés (TSA). On a caractérisé les PCE par voltampérométrie cyclique, par voltampérométrie à onde carrée, par spectroscopie infrarouge à transformée de Fourier (IR-TF) et par spectroscopie photoélectronique de rayons X (SPX). Les poly(amino β-styryl terthiophènes) présentent des voltampérogrammes cyclique et à onde carrée comportant des pics redox qui peuvent être attribués à la portion aminophényle ainsi qu'au squelette polyterthiophène. La présence de groupes amines primaires libres sur le film de PCE a permis de réaliser une autre fonctionnalisation biologique, c'est-à-dire la formation de liaisons covalentes de divers biorécepteurs sur sa surface. On a évalué la performance électrochimique de la biotine fixée sur une électrode de carbone vitreuse modifiée par des TSA à détecter la protéine avidine en solution par les techniques de voltampérométrie cyclique et à onde carrée.

Mots-clés : polymère conducteur électronique, modification de la surface d'une électrode, biosenseur, terthiophène portant une β-styryle substitué, fonctionnalisation, voltampérométrie cyclique et à onde carrée.

[Traduit par la Rédaction]

Introduction

In recent years, conducting polymers have been the subject of considerable academic and industrial research because of their potential uses in areas such as storage and energy conversion, electrocatalysis, corrosion-resistant materials, and sensors (1–3). Moreover, the use of electronic conducting polymers (ECP) as an immobilization matrix of biomolecules on the electrode surface and as an electronic transducer has taken a considerably important place in the development of biosensors (4, 5). Generally, a biosensor, consisting of a transduction system coupled to a receptor, is prepared by immobilizing the molecular recognition bioreceptor onto the substrate materials (e.g., ECP), and this bioreceptor (e.g., antigen, biotin) recognizes a biomolecule compound (e.g., antibody, avidin) according to its specificity. Therefore, bioreceptors have to be properly immobilized on the sensor surface, and a transducer signal has to be generated, which is related to the concentration of the biomolecule in the sample (6). This kind of device is called reagentless "third-generation biosensor" in which a redox probe is not required (7).

Oligo and polythiophenes have also been functionalized as advanced materials for electrode surface modifications allowing the development of chemosensor (8–10) and biosensor devices (11–13). Effectively, the advantage of making polythiophene films from functionalized terthiophene is to avoid reaching a highly positive potential, which may cause the degradation of delicate functional groups because terthiophene has a lower oxidation potential than thiophene or bithiophene; thus, electrochemical polymerization is easier (14). Moreover, conducting polymers from terthiophene

Received 12 March 2008. Accepted 23 July 2008. Published on the NRC Research Press Web site at canjchem.nrc.ca on 3 October 2008.

H. Mehenni and L.H. Dao[1]. Laboratoires de Recherche sur les Matériaux Avancés, INRS-Energie Matériaux Télécommunications, 1650 Bd Lionel Boulet, Varennes, QC J3X 1S2, Canada.

[1]Corresponding author (e-mail: le.dao@emt.inrs.ca).

 doi:10.1139/V08-136 © 2008 NRC Canada

are known for their simple functionalization and relatively good stability in air for the neutral and oxidized states (15).

Reeman et al. (16) developed an avidin biosensor based on a direct functionalization of terthiophene by biotin. Biotin was directly bonded to the central thiophene ring in the 3′ position by chemistry synthesis. A redox-inactive polythiophene film was obtained from an electrochemical polymerization of the biotin-functionalized terthiophene alone, because the bonded biotin has an insulating effect on the polythiophene backbone. Consequently, a polythiophene copolymer was realized from the biotin-functionalized terthiophene and 2,2′:5′,2″-terthiophene (1:5 molar ratio, respectively) to obtain a redox-active copolymer film. Another inconvenience was that the polythiohene redox signal was situated at a high potential, approximately 1 V vs. Ag/AgCl, leading usually to the degradation of the bioreceptor, i.e., of biotin. Also, no redox signal was clearly visible to allow the measurement of avidin by using a simple electrochemical method as cyclic voltammetry or square-wave voltammetry; for this reason, impedance was used without forgetting the inconvenience of using chemical synthesis to make biological functionalization of polythiophene film, because this type of biosensor system will be limited only for a single target biomolecule.

A new approach to the functionalization of the surface of polythiophene films appeared with the work of Shim et al. The terthiophene was functionalized by a carboxylic acid group (–COOH) in the 3′ position of the central thiophene ring to prepare the terthiophene 3′-carboxylic acid (TCA). Biosensors of vitellogenin (17), glutamatate (18), and H_2O_2 (19) have been developed after the biological surface functionalization of the poly(TCA) film electrodeposited on an electrode surface. The advantage of biosensor systems based on the poly(TCA) films is to be not restricted to a single target biomolecule. Indeed, various bioreceptors can be immobilized through a covalent bond by interaction with free carboxylic acid groups present on the poly(TCA) film surface. The inconvenience of this biosensor system is that, here also, the polythiophene backbone redox signal is situated at a high potential, which may cause the degradation of the immobilized bioreceptor on its surface.

So, another new approach is to functionalize the terthiophene by a redox group to use another redox signal rather than the polythiophene backbone redox signal to detect the target biomolecule. In this last approach, the terthiophene was used only to bind the redox group on the electrode surface by electropolymerization of the terthiophene moiety. This is the case of the terthiophene functionalization by a ferrocene (20) used to develop a cytochrome C biosensor. Wallace et al. have covalently bonded a ferrocene ring to the central thiophene ring in the 3′ position by a π-conjugated linker, allowing to make a redox-active polythiophene film from the ferrocene-functionalized terthiophene alone. Indeed, the π-conjuguated linker allows an electronic communication between the polythiophene backbone and the ferrocene group, so that the insulation of the polythiophene backone is avoided. The advantage of this last approach is the use of a redox signal from another redox group as electronic transductor (i.e., ferrocene ring) rather than from the polythiophene moiety of the poly(terthiophene 3′-ferrocene) film. Effectively, the ferrocene redox potentials were clearly visible to low potential (towards 0.4 V vs. Ag/AgCl), and were able to be exploited by a simple electrochemical technique such as cyclic voltametry to detect and to measure cytochrome C. On the other hand, the disadvantage of this biosensor system based on the poly(terthiophene 3′-ferrocene) film is that its use is restricted to a single biological target, here Cytochrome C. Also, the ferrocene ring is known for its toxicity in situ to the point that some of these by-products are the object of interest as anticancerous agents (21–23). This constitutes a major disadvantage in the development of biosensors for an in situ application in a medical field.

To bring a solution to the problematic context above, we chose to combine the strategies of Shim and Wallace. Herein, we report the synthesis and the characterization of novel conducting homopolymers based on amino β-styryl terthiophene, which have never been reported. The amino β-styryl terthiophene monomer corresponds to the functionalization of the terthiophene by an amino β-styryl group, covalently bonded to the central thiophene ring in the 3′ position. We have synthetized the 3′-(3-methyl-4-amino-β-styryl)-(2,2′:5′,2″-terthiophene) (monomer **4a**), the 3′-(3-chloro-4-amino-β-styryl)-(2,2′:5′,2″-terthiophene) (monomer **4b**), the 3′-(3-methoxy-4-amino-β-styryl)-(2,2′:5′,2″-terthiophene) (monomer **4c**), and the 3′-(2-methoxy-5-amino-β-styryl)-(2,2′:5′,2″-terthiophene) (monomer **4d**). This new strategy to functionalize the terthiophene by an amino β-styryl group gives a new ECP having the following properties:

(*i*) the ECP from amino β-styryl terthiophene monomers can be electrodeposited on an electrode surface by electropolymerization of the terthiophene moiety in which the redox signal of the aminophenyl moiety is used as an electronic transducer signal to detect and to measure target biomolecules. Also, we have introduced Y substitutes having different inductive, steric, and mesomeric effects on the aminophenyl ring to study their influences on its redox-activity to lower the aminophenyl anodic potential as low as possible towards 0 V vs. Ag/AgCl.

(*ii*) the π-conjuguated linker allows an electronic communication between the aminophenyl moiety and the polythiophene backbone to avoid an insulating effect on the polythiophene backbone. Consequently, copolymerization to obtain a redox-active polymer film is avoided.

(*iii*) the presence of free primary amine groups on the ECP film surface permits further biological functionalization of its surface by covalently bonding various bioreceptors. This biosensor system can be used for various targets biomolecules.

Experimental

Materials and instrumentation

All reagents were purchased from the Sigma-Aldrich Chemical Company (Canada) and used as received: 3-methyl-4-nitrobenzyl bromide, triphenylphosphine (PPh_3), 3-chlorobenzyl chloride, benzene, 1,8-diazabicyclo(5.4.0)undec-7-ene (DBU), iron powder (Fe), ammonium chloride (NH_4Cl), acetic acid glacial (AcOH), sulfuric acid fuming (H_2SO_4), nitric acid (HNO_3), 2-methoxy-5-nitrobenzyl bromide, tin(II) chloride-dihydrate ($SnCl_2{\cdot}2H_2O$), 5-methyl-2-nitrophenol,

© 2008 NRC Canada

dimethyl sulfate ($(CH_3)_2SO_4$), dibenzoyl peroxide, *N*-hydroxysuccinimide (NHS), *N*-bromosuccinimide (NBS), magnesium sulfate ($MgSO_4$), sodium sulfate anhydrate (Na_2SO_4), ethyl-3-(3-dimethylamino-propyl) carbodiimide (EDC), Biotin, and tetrabutylammonium perchlorate (TBAP, electrochemical grade). Dichloromethane (DCM, HPLC grade), avidin from egg white, and the phosphate buffer saline (PBS 0.1 mol/L) of pH 7.4 at 25 °C were purchased from Fischer Scientific (Canada). All experimental solutions were prepared using double-distilled water obtained from a Milli-Q water system.

Nuclear magnetic resonance (NMR) spectra were measured at 400.13 MHz (^{1}H) and 100.6 MHz (^{13}C) on a Bruker ARX 400. All NMR spectra were recorded in deuteroacetone solutions with tetramethylsilane as reference. Signals are described in terms of chemical shifts, multiplicity, and assignment. The following abbreviations were used: s (singlet), d (doublet), dd (doublet of doublet), m (multiplet), and b (broad). In the NMR spectrum interpretation, the phenyl protons will have a letter p accompagnying the position number to avoid the confusion with the protons of the first thiophene ring (e.g., H_{5p} corresponds to the proton of the phenyl in 5 position). Mass measurements were performed on a LC–MSD–TOF instrument from Agilent Technologies in positive electrospray mode. Either protonated molecular ions $(M + H)^+$ or sodium adducts $(M + Na)^+$ were used for peak assignment. The IR spectra were recorded on a NEXUS 670 FTIR apparatus over the 600–4000 cm^{-1} range. The melting points were measured using a Fisher–Johns melting point apparatus. The measuring set-up for the all electrochemical experiments consisted of a three-electrode system in which a glassy carbon electrode or a platinum electrode, Ag/AgCl (saturated KCl) electrode, and a platinum wire (0.5 mm of diameter) or platinum foil (dimension 1 cm × 1 cm, 0.025 mm^2 of thickness) were used as the working, the reference, and the auxiliary electrode, respectively. The cyclic voltammograms (CVs) and the square-wave voltammogram (SWVs) were recorded using a Solartron-SI 1287 potentiostat/galvanostat and a EG & G Princeton Applied Research 273 A one, respectively. The measurements were carried out in a 0.1 mol/L TBAP–DCM solution at room temperature.

General procedure for the synthesis of nitro β-styryl terthiophene (3a, 3b, 3c, and 3d)

A mixture of a terthiophene aldehyde (**1**) prepared according to the literature method (24) (1 mmol), the triphenylphosphonium bromide compounds (**2a**, **2c**, and **2d**) or triphenylphosphonium chloride compound (**2b**) (1.2 mmol), and DBU (1.2 mmol) in dichloromethane (15 ml) was heated under reflux. After 8 h, the reaction mixture was diluted with dichloromethane (100 ml) and washed with a 1 mol/L solution of HCl (2 × 40 ml), 10 % sodium bicarbonate solution (40 ml), and water (60 ml). The organic layer was dried and concentrated to give a crude organic solid. The pure product was obtained by chromatography on a silica-gel column using a dichloromethane/hexane solution (1:1) as eluent.

3′-(3-Methyl-4-nitro-β-styryl)-(2,2′:5′,2″-terthiophene) (3a)

Colour: orange. Solid, yield: 71%, mp 148 °C. IR (KBr): 3104, 3073, 2965, 2906, 1595, 1511 and 1333 (NO_2), 1078, 1039, 959, 844, 827, 753, 721, 706 cm^{-1}. ^{1}H NMR (acetone-d^6, 400 MHz) δ: 8.05 (dd, 1H, H_{5p}), 7.75 (s, 1H, $H_{4'}$), 7.68–7.63 (m, H_{6p}, H_b, H_5), 7.62–7.58 (2s, 1H, H_{2p}), 7.53 (dd, 1H, $H_{5''}$), 7.43–7.35 (m, H_2, H_3, $H_{3''}$), 7.25 (dd, 1H, H_4), 7.15 (dd, 1H, $H_{4''}$), 2.6 (s, 3H, $-CH_3$). ^{13}C NMR (acetone-d^6, 100.6 MHz) δ: 149, 143, 137, 136.8, 136.7, 135, 134.9, 133.7, 131.5, 129.5, 129.1, 128.9, 128.3, 128.1, 126.5, 126, 125.7, 125.5, 125, 123.3, 20 ($-CH_3$). MS *m*/*z*: 410 (MH^+).

3′-(3-Chloro-4-nitro-β-styryl)-(2,2′:5′,2″-terthiophene) (3b)

Colour: orange. Solid, yield: 20%, mp 115 °C. IR (KBr): 3100, 3063, 2960, 2854, 1588, 1515 and 1337 (NO_2), 1042, 953, 844, 831, 815, 746, 683 cm^{-1}. ^{1}H NMR (acetone-d^6, 400 MHz) δ: 8.15 (d, 1H, H_{5p}), 7.85 (d, 1H, H_{2p}), 7.8 (dd, 1H, H_{6p}), 7.75 (s, 1H, $H_{4'}$), 7.68 (d, 1H, H_b), 7.65–7.5 (m, 2H, H_5, $H_{5''}$), 7.45–7.38 (m, 3H, H_a, H_3, $H_{3''}$), 7.25 (dd, 1H, H_4), 7.15 (dd, 1H, $H_{4''}$). MS *m*/*z*: 430 (MH^+).

3′-(3-Methoxy-4-nitro-β-styryl)-(2,2′:5′,2″-terthiophene) (3c)

Colour: orange. Solid, yield: 15%, mp 148 °C. IR (KBr): 3100, 3082, 2965, 2930, 2843, 1595, 1504 and 1343 (NO_2), 1086, 1021, 830, 704 cm^{-1}. ^{1}H NMR (acetone-d^6, 400 MHz) δ: 7.89 (d, 1H, H_{5p}), 7.79 (d, 1H, H_b), 7.72 (s, 1H, $H_{4'}$), 7.6 (d, 1H, H_{2p}), 7.55–7.5 (m, 3H, H_a, H_5, $H_{5''}$), 7.44 (d, 1H, H_{6p}), 7.43–7.34 (m,2H, H_3, $H_{3''}$), 7.29 (dd, 1H, H_4), 7.15 (dd, 1H, $H_{4''}$), 4.04 (s, 3H, OCH_3). ^{13}C NMR (acetone-d^6, 100.6 MHz) δ: 149, 143, 137, 136.8, 136.7, 135, 134.9, 133.7, 131.5, 129.5, 129.1, 128.9, 128.3, 128.1, 126.5, 126, 125.7, 125.5, 125, 123.3, 20 ($-CH_3$). MS *m*/*z*: 426 (MH^+).

3′-(2-Methoxy-5-nitro-β-styryl)-(2,2′:5′,2″-terthiophene) (3d)

Colour: yellow. Solid, yield: 61%, mp 115 °C. IR (KBr): 3108, 3082, 2969, 2939, 2843, 1582, 1513 and 1339 (NO_2), 1095, 1026, 826, 743, 704 cm^{-1}. ^{1}H NMR (acetone-d^6, 400 MHz) δ: 8.38(d, 1H, H_{6p}), 8.19 (dd, 1H, H_{4p}), 8.01 (d, 1H, H_b), 7.8 (s, 1H, $H_{4'}$),7.65 (m, 2H, H_5, $H_{5''}$), 7.35 (d, 1H, H_a), 7.25 (m, 3H, H_{3p}, H_3, $H_{3''}$), 7.05 (m, 2H, H_4, $H_{4''}$), 4.04 (s, 3H, OMe). MS *m*/*z*: 426 (MH^+).

General procedure for the synthesis of amino β-styryl terthiophene monomers (4a, 4b, 4c, and 4d)

Amino-β-styryl terthiophene compounds **4a** and **4b** were obtained by the reduction of the nitro group of the corresponding compounds **3a** and **3b** using iron powder (Fe) in presence of NH_4Cl.

To nitrophenyl compounds (1 mmol) in THF/EtOH/H_2O with the ratio of 3:3:2 were added iron powder (3 mmol) and NH_4Cl (0.6 mmol). The reaction was stirred at 85 °C for 1 h, cooled to room temperature, and filtered through a Celite column. The filter cake was washed with $CHCl_3$, and the filtrate was concentrated to a low volume, diluted with CH_3Cl, and washed with H_2O. The organic extracts were dried over $MgSO_4$ and filtered. After removing the solvent, the compounds were separated by a silica column with EA:CH_2Cl_2 ratio of 2:1, then pure EA. After purification, the compounds were obtained with good yields. In this reduction process, to improve the solubility of the materials, the THF was used as co-solvent

© 2008 NRC Canada

3′-(3-Methyl-4-amino-β-styryl)-(2,2′:5′,2″-terthiophene) (4a)

Colour: brown. Liquid, yield: 100%. IR (NaCl): 3473 and 3373 (NH_2), 3104, 3073, 2965, 2926, 2873, 1604, 1260, 1082, 1039, 960, 821, 760, 695 cm^{-1}. ^1H NMR (acetone-d^6, 400 MHz) δ: 7.66 (dd, 1H, $H_{5''}$), 7.5 (dd, 1H, H_5), 7.43–7.36 (m, 2H, $H_{3''}$, H_3), 7.34 (d, 1H, H_a), 7.31 (d, 1H, H_b), 7.25–7.18 (m, 2H, $H_{4''}$, H_4), 7.16 (s, 1H, $H_{4'}$), 7.14 (m, 2H, H_{5p}, H_{6p}), 6.7 (d, 1H, H_{2p}), 3.8 (sl, 2H, $–NH_2$), 2.8 (s, 3H, $–CH_3$). MS *m*/*z*: 380 (MH^+, 100%).

3′-(3-Chloro-4-amino-β-styryl)-(2,2′:5′,2″-terthiophene) (4b)

Colour: brown. Liquid, yield: 100%. IR (NaCl): 3465 and 3373 (NH_2), 3104, 3069, 2960, 2921, 2852, 1613, 1265, 1095, 1043, 956, 817, 760, 700 cm^{-1}. ^1H NMR (acetone-d^6, 400 MHz) δ: 7.62 (dd, 1H, $H_{5''}$), 7.5 (dd, 1H, H_5), 7.45 (d,1H, H_b), 7.37 (dd, 1H, $H_{3''}$), 7.33 (dd, 1H, H_3), 7.31 (d, 1H, H_a), 7.22 (m, 2H, $H_{4''}$, H_4), 7.19 (s, 1H, $H_{4'}$), 7.14 (m, 2H, H_{2p}, H_{6p}), 6.9 (d, 1H, H_{5p}), 3.85 (sl, 2H, $–NH_2$). MS *m*/*z*: 400 (MH^+, 100%).

For the amino-β-styryl terthiophene compounds 4c and 4d, the nitro groups of **3c** and **3d** compounds were reduced by $SnCl_2{\cdot}2H_2O$. To nitrophenyl compounds (1 mmol) in $EtOH/CH_2Cl_2$ with the ratio of 5:2 were added $SnCl_2{\cdot}2H_2O$ (12 mmol). The reaction was stirred at 90 °C for 17 h, cooled to room temperature, and then 1 g sodium bicarbonate was added. The reaction mixture was stirred during 30 min and then diluted with dichloromethane (100 ml) and filtered through Celite. The filtrate was washed with 5% sodium bicarbonate solution (2 × 100 mL), washed with H_2O (1 × 100 mL), and then dried over anhyd. Na_2SO_4. After removing the solvent, the product was obtained by column chromatography (silica gel) with ethyl acetate as eluent.

3′-(3-Methoxy-4-amino-β-styryl)-(2,2′:5′,2″-terthiophene) (4c)

Colour: brown. Liquid, yield: 74%. IR (NaCl): 3481 and 3373 (NH_2), 3108, 3073, 2973, 2930, 2873, 1617, 1252, 1126, 1056, 834, 695 cm^{-1}. ^1H NMR (acetone-d^6, 400 MHz) δ: 7.33 (s, 1H, $H_{4'}$), 7.6–7.55 (m, 2H, H_5, $H_{5''}$), 7.52 (d, 1H, H_b), 7.53–7.2 (m, 5H), 7.2–7.1 (m, 3H, phenyl), 3.95 (s, 3H, OCH_3), 3.6 (sl, 2H, NH_2). MS *m*/*z*: 396 (MH^+, 100%).

3′-(2-Methoxy-5-amino-β-styryl)-(2,2′:5′,2″-terthiophene) (4d)

Colour: brown. Liquid, yield: 54%. IR (NaCl): 3443 and 3360 (NH_2), 3104, 3069, 2960, 2926, 2856, 1617, 1265, 1100, 1030, 808, 756, 700 cm^{-1}. ^1H NMR (acetone-d^6, 400 MHz) δ: 7.78 (dd, 1H, $H_{5''}$), 7.68 (dd, 1H, H_5), 7.63 (dd, 1H, $H_{3''}$), 7.5 (dd, 1H, H_3), 7.42 (s, 1H, $H_{4'}$), 7.4 (d, 1H, H_a), 7.33 (d, 1H, H_b), 7.23–7.15 (m, 2H, H_4, $H_{4''}$), 6.95 (d, 1H, H_{6p}), 6.8 (dd, 1H, H_{3p}), 6.64 (dd, 1H, H_{4p}), 4.3 (sl, 2H, NH_2), 3.8 (s, 3H, OMe). MS *m*/*z*: 396 (MH^+, 100%).

General procedure for the synthesis of ylides compounds 2a, 2b, 2c, and 2d

A mixture of the 3-methyl-4-nitrobenzyl bromide (1 mmol) or 2-methoxy-5-nitrobenzyl bromide (1 mmol) and PPh_3 (1.2 mmol) in benzene was heated under reflux. After 3 h, the pure product **2a** or **2d** was recuperated as a white solid by removal of the solvent. The ylide **2b** was synthesized from the commercially available 3-chlorobenzyl chloride according to the literature method (25) to prepare the 3-chloro-4-nitrobenzyl chloride and then according the synthesis of **2a** and **2d**. In this reaction, the **2b** and **2b′** were given. Because of the difficulty of the separation, the mixture was not separated before used for the Wittig reaction. After the Wittig reaction, the pure desired isomer **3b** was isolated by TLC plates of silica gel (20 × 20 cm, thickness of 2000 μm), with cyclohexane/acetone (10:1) as eluent, from the reaction mixture following removal of the major isomer (**3b′**) by recrystallization from dichloromethane/ether. The ylide **2c** was synthesized according to the literature method (26) to prepare the 3-methoxy-4-nitrobenzyl bromide and then according the synthesis of **2a** and **2d**.

Electrochemistry

Electrochemical polymerization of monomers 4a, 4b, 4c, and 4d

The monomers **4a**, **4b**, **4c**, and **4d** were electrodeposited on a polished glassy carbon electrode by electropolymerization of 5 mmol/L of the monomer in a 0.1 mol/L TBAP–DCM solution by potential cycling between 0.0 and 1.1 V (vs. Ag/AgCl) at 10 mV s^{-1}. After the polymerization, the electrode surface was rinsed with DCM to remove the excess monomer. Post-polymerization cyclic voltammograms and square-wave voltammograms of homopolymers **4a**, **4b**, **4c**, and **4d** were investigated in 0.1 mol/L TBAP–DCM solution.

The neutral polymers were characterized by reflectance FTIR experiments and X-ray photoelectron spectroscopy (XPS). FTIR spectra of polymers films on gold-coated glass electrodes were recorded on NEXUS 670 FTIR over the range 600–4000 cm^{-1}. XPS examination were carried out on the polymers films grown on ITO-coated glass electrodes using a Escalab 220i XL spectrometer.

Surface biofunctionalization

Poly(**4b**)- and poly(**4d**)-coated electrodes were immersed in a 0.1 mol/L phosphate buffer saline (PBS) solution (pH 8) containing 0.05 mol/L EDC and 0.05 mol/L biotin for 24 h at 40 °C. The biotin was immobilized through the formation of covalent bond with free primary amine groups on the polymer surface. These electrodes were then rinsed thoroughly with the same buffer to remove the non immobilized biotin, and their cyclic voltammograms (CVs) and square-wave voltammograms (SWVs) were recorded. Finally, this poly(**4c**)/ and poly(**4d**)/biotin-modified electrode were incubated in a 0.1 mol/L phosphate buffer saline (PBS) solution of 3.10^{-4} mol/L avidin for 15 min at room temperature to block active sites of avidin by a specific interaction with biotin. These electrodes were removed, rinsed with the same buffer to remove the non reacted avidin with biotin, and allowed to dry. Then, their CVs and SWVs were recorded.

Results and discussion

Synthesis of amino β-styryl terthiophene monomers (4a, 4b, 4c, and 4d)

Scheme 1 shows the synthetic routes for amino β-styryl terthiophene monomers (**4a**–**4d**). The terthiophene aldehyde precursor (**1**) was prepared according to ref. 24. Starting from compound **1**, two steps are necessary to prepare the monomers **4a**, **4b**, **4c**, and **4d**. The first step is a Wittig reac-

© 2008 NRC Canada

Scheme 1. The synthesis of the monomers.

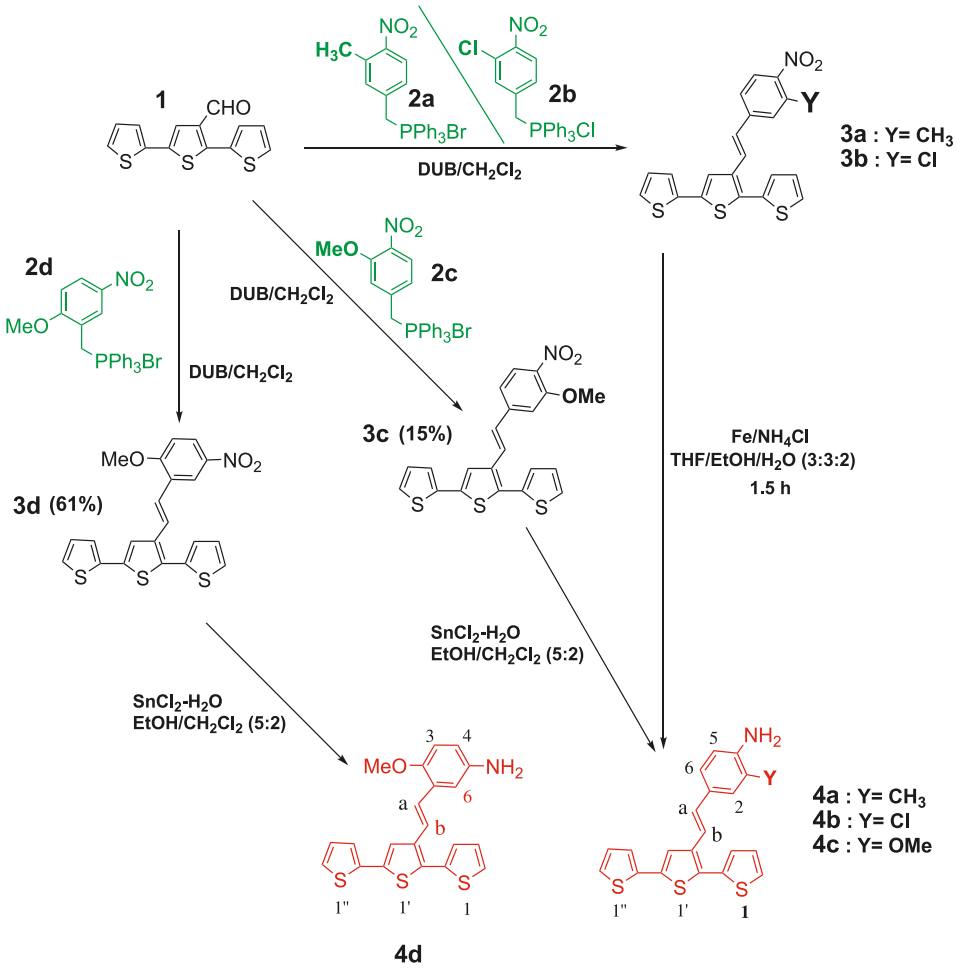

tion to make the conjugated link between the aminophenyl moiety and the terthiophene. Compound **1** was treated with various ylide compounds (**2a**–**2d**) in DCM in presence of DBU to obtain the nitro β-styryl terthiophene compounds (**3a**–**3d**). The second step is a reduction of the nitro group of the compounds **3a**, **3b**, **3c**, and **3d** to provide the final amino β-styryl terthiophene monomers (**4a**–**4d**). Iron powder (Fe) was used as reducing agent for **3a** and **3b** and tin(II) chloride dihydrate ($SnCl_2 \cdot 2H_2O$) for **3c** and **3d**. The ylide compounds (**2a**–**2d**) were synthesized according to Scheme 2. The ylide compounds **2a** and **2b** were prepared from commercially available materials, the 3-methyl-4-nitrobenzyl bromide (**a**) and the 2-methoxy-5-nitrobenzyl bromide (**d**), which were treated by PPh_3 in benzene. The ylide **2b** was prepared according to ref. 27 to synthesize the 3-chloro-4-nitrobenzyl chloride, which was treated by PPh_3 in benzene. The ylide **2c** was synthesized according to ref. 28 to prepare the 3-methoxy-4-nitrobenzyl bromide (**c**), which was treated by PPh_3 in benzene.

Synthesis of poly(amino β-styryl terthiophene) (poly(4a), poly(4b), poly(4c), and poly(4d))

Monomers **4a**, **4b**, **4c**, and **4d** were electrodeposited on glassy carbon electrodes by cyclic voltammetry between 0 and 1.1 V (vs. Ag/AgCl). Figure 1 shows the CVs for the formation of poly(**4d**) film on a glassy carbon electrode. The cyclic voltammograms show the expected increase in current with increasing number of potential cycles, indicating the growth of electronic conducting polymers (ECP). The electrochemical polymerization of monomers **4a**, **4b**, **4c**, and **4d** results in the formation of a black uniform polymer film on the electrode surface.

Electrochemical characterization of poly(amino β-styryl terthiophene) films

Figure 2 shows cyclic voltammograms (CVs) of poly(**4a**), poly(**4b**), poly(**4c**), and poly(**4d**) films at scan rate 5 mV s^{-1} by potential cyclic between 0 and 1.0 V (vs. Ag/AgCl). The scanning from 0 to 1.0 V shows clearly two anodic peaks for poly(**4c**) and poly(**4d**) films, which we named a and c, and which we attributed to the oxidation of the aminophenyl moiety and to the polaronic oxidation of the polythiophene backbone, respectively. Indeed, it is reported that the aminophenyl moiety can be oxidized to give a radical cation (27). The oxidation removes an electron from the free electrons doublet of the nitrogen in its neutral state (NH_2), to give a radical cation nitrogen ($NH_2^{\bullet+}$). We were able to attribute the origin of the peaks a and c compared with the cyclic voltammogram of a polyterthiophene film prepared in the same conditions, and also by using literature results for polyterthiophene for which it is reported (28) that the polaronic oxidation peak is situated towards 1.05 V vs. SCE

© 2008 NRC Canada

Scheme 2. Synthesis of the ylide compounds.

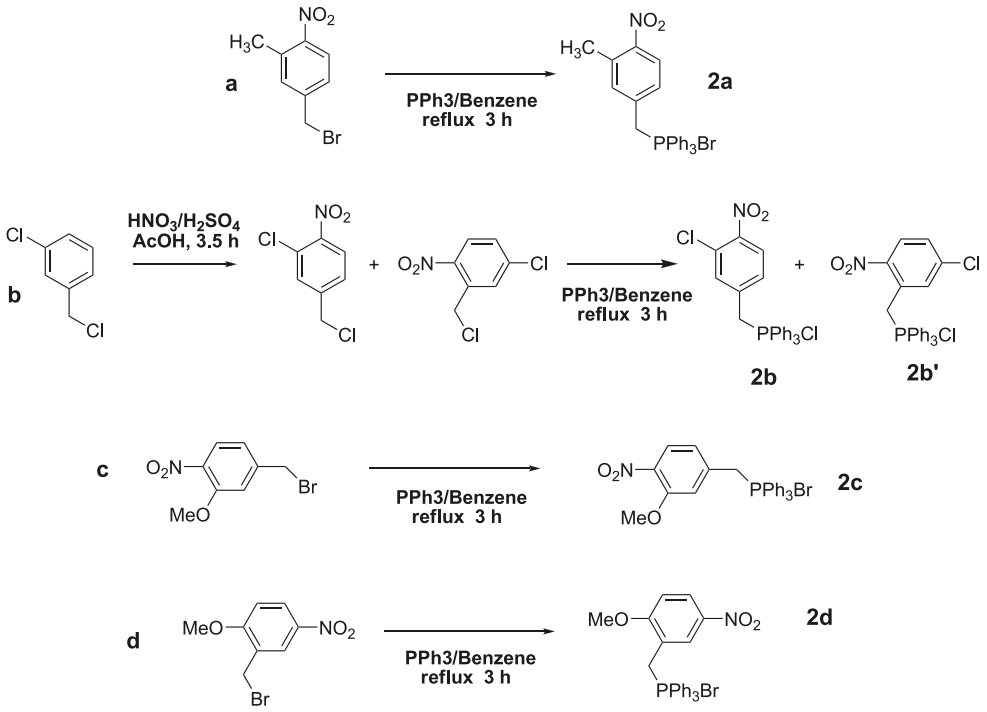

Fig. 1. Growth of poly(**4d**) by repetitive-scan cyclic voltammetry on a 7.068 mm^2 glassy carbon electrode between 0.0 and 1.1 V, auxiliary electrode: Pt foil, reference electrode: Ag/AgCl, scan rate: 10 mV s^{-1}m, 5 mmol/L monomer **4d**, 0.1 mol/L TBAP–DCM.

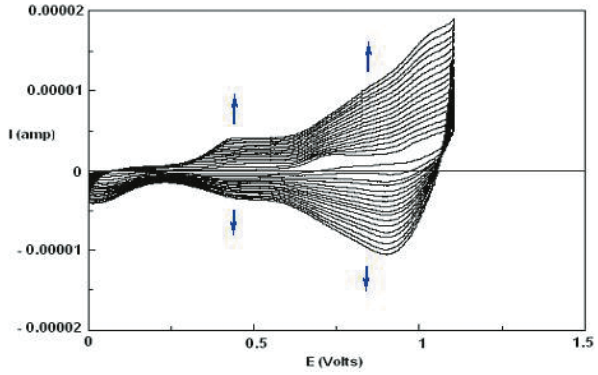

Fig. 2. Cyclic voltammogram of poly(**4a**), poly(**4b**), poly(**4c**), and poly(**4d**) films between 0.0 and 1.0 V, scan rate: 5 mV s^{-1} on a 7.068 mm^2 glassy carbon working electrode, auxiliary electrode: Pt wire, reference electrode: Ag/AgCl, 0.1 mol/L TBAP–DCM.

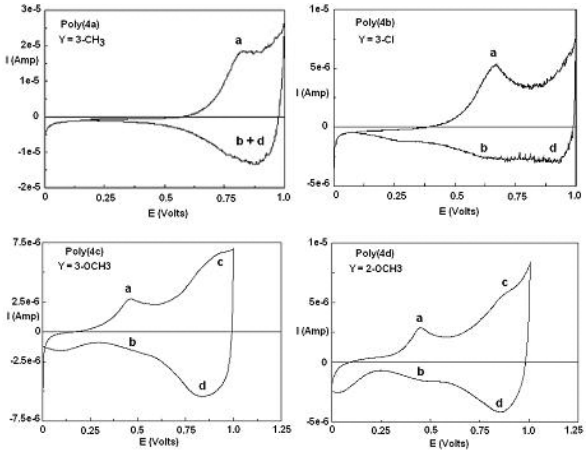

(corresponding to 1.09 V vs. Ag/AgCl). For poly(**4a**) and poly(**4b**) films, we can only see the peak a and an oxidation slope attributed to the polythiophene backbone oxidation. When the scanning direction is inverted from 1.0 to 0.0 V vs. Ag/AgCl, we see two cathodic peaks, d and b, for poly(**4c**) and poly(**4d**) films, which we attributed to the reduction of the polythiophene backbone and to the aminophenyl moiety reduction, respectively. The top of the peak b will be more clearly visible by SWV for the poly(**4b**) film. For the poly(**4a**) film, the last peaks are not distinctly visible because they are overlapping. So, the introduction of Y substitutes in the aminophenyl ring has for consequence to make the aminophenyl redox couple (a/b) visible and different from the polythiophene backbone redox couple (c/d). It lowers its anodic potential, in the first place situated at 0.98 V vs. Ag/AgCl (corresponding to the aminophenyl anodic potential (29)) towards a lower potential, especially when Y = OCH_3, which is a strong electronic donor and for which the aminophenyl anodic potential is slightly below 0.5 V vs. Ag/AgCl.

The square-wave voltammetry allows to eliminate the current overload (capacitive current *Ic*) visible in cyclic voltammetry (30–32). In other words, we can subtract *Ic* from the total current measured. Consequently, we used it to see clearly the redox couple (a/b) attributed to the aminophenyl moiety of poly(**4a**), poly(**4b**), poly(**4c**), and poly(**4d**) films. The square-wave voltammograms of polymer films are reported in Fig. 3. During the oxidation scanning from 0.0 to 1.0 V vs. Ag/AgCl, we can observe two

© 2008 NRC Canada

Fig. 3. Square-wave voltammograms of poly(**4a**), poly(**4b**), poly(**4c**), and poly(**4d**) films between 0.0 and 1.0 V on a 7.068 mm^2 glassy carbon working electrode, auxiliary electrode: Pt foil, reference electrode: Ag/AgCl, 0.1 mol/L TBAP–DCM.

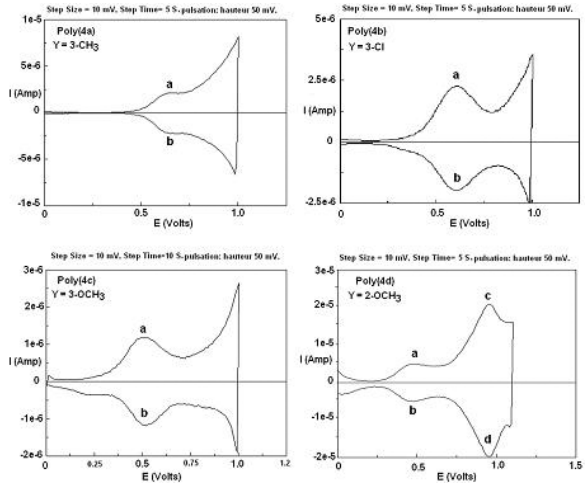

oxidation peaks, a and c, for the poly(**4d**) film. The anodic peak a situated towards 0.5 V vs. Ag/AgCl corresponds to the oxidation of the aminophenyl moiety, and the anodic peak c situated towards 0.9 V vs. Ag/AgCl corresponds to the polaronic oxidation of the polythiophene backbone. But for poly(**4a**), poly(**4b**), and poly(**4c**) films, we observe only the anodic peak a, situated towards 0.6 V vs. Ag/AgCl for poly(**4a**) and poly(**4b**), and towards 0.5 V vs. Ag/AgCl for poly(**4c**). In higher potentials, we observe an oxidation slope attributed to the oxidation of the polythiophene backbone. During the reduction scanning from 1.0 to 0.0 V vs. Ag/AgCl, we can observe two reduction peaks, d and b, for the poly(**4d**) film, corresponding to the reduction of the polythiophene backbone and to the aminophenyl moiety reduction, respectively. But for the poly(**4a**), poly(**4b**) and poly(**4c**), we observe a reduction slope corresponding to the reduction of the polythiophene backbone and the cathodic peak b.

Spectroscopic FTIR and XPS characterization

The studies of the poly(**4a**), poly(**4b**), poly(**4c**), and poly(**4d**) films by FTIR and XPS techniques, clearly show that there are free primary amine groups on the polymer film surface after electrochemical polymerization. This point proves that the amino β-styryl moiety is not destroyed during electropolymerization, and it does not bind anything by the amine groups. As an example, the XPS spectrum of the poly(**4d**) film and the FTIR spectrum of the poly(**4b**) film are shown in Fig. 4. FTIR spectrum of poly(**4b**) film grown on gold-coated glass shows two strong sharp peaks at 3373 and 3213 cm^{-1} (amine I band, N–H stretching vibration (33)) corresponding to the primary amine groups on the aminophenyl moiety, and a C–H stretching vibration of the aromatic ring (34) is also observed at 3065 cm^{-1}.

XPS spectrum shows the deconvoluted N1s spectrum of the poly(**4d**) film surface grown on ITO-coated glass electrode. The two features at 402.5 and 399.6 eV must be ascribed to a cationic nitrogen species (NH_3^+ and $NH_2^{\bullet+}$) and an amine I species (NH_2), respectively (35, 36).

Fig. 4. (*A*) XPS spectrum of the poly(**4d**) film and (*B*) FTIR spectrum of the poly(**4b**) film, grown on ITO-coated glass and gold-coated glass, respectively, at room temperature.

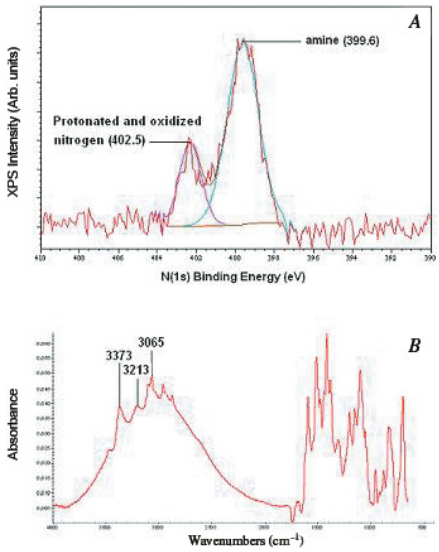

Biotin-modified electrodes

We have begun to investigate the possibility of using the poly(**4b**) and poly(**4d**) films in biosensor devices in which the redox signal of the aminophenyl moiety is used as an electronic transducer signal to detect a target biomolecule. We chose to begin with biotin–avidin interaction. Avidin is a highly stable glycoprotein and is able to be specifically bound by biotin to form an exceedingly strong complex (37). The steps used to link the biotin to the poly(amino β-styryl terthiophene)-coated electrode surface are summarized in Fig. 5. This procedure has the advantage of using simple conditions and of forming a covalent bond. The cyclic and the square-wave voltammograms of the poly(**4b**)- and poly(**4d**)-coated working electrode, before and after immobilization of biotin on their surfaces, are reported in Fig. 6*a* and Fig. 7*a*, respectively. We can observe for both polymer films that the biotin immobilization causes a shift towards a higher potential of the anodic peak initially attributed to the oxidation of the aminophenyl moiety. After biotin immobilization, the anodic peak corresponds to the oxidation of the amidophenyl resulting on the polymer film surface. Indeed, it is reported (29) that the amidophenyl anodic peak (Acetoamidophenyl *E*pA = + 1.24 V vs. Ag/AgCl) is higher than that of the aminophenyl (*E*pA = + 0.98 V vs. Ag/AgCl).

The cyclic and the square-wave voltammograms of the poly(**4b**)/ and poly(**4d**)/biotin-modified-coated working electrode, before and after exposure to a solution of 3.10^{-4} mol/L avidin in PBS 0.1 mol/L for 15 min are shown in Fig. 6*b* and Fig. 7*b*, respectively. We can observe in both cases, i.e., by CV or SWV, that the exposure of the poly(**4b**)/ or poly(**4d**)/biotin-modified-coated working electrode has a drastic effect upon its electrochemical response causing a significant diminution of the oxidation current measured on the anodic peak. This unusual voltammetry response after avidin exposure is explained by the presence of avidin covering the polymer film surface and thus causing the reduc-

© 2008 NRC Canada

Fig. 5. Schematic representation of the immobilization of receptive biomolecule (biotin) via the activation of carboxylic functional groups (actived by EDC) of the biotin.

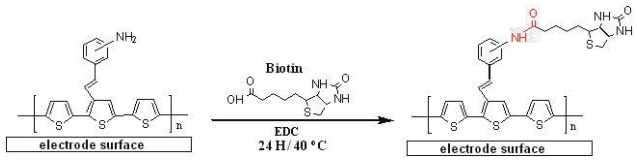

Fig. 6. (*a*) Cyclic voltammograms of poly(**4b**)-coated platinum working electrode before and after immobilization of biotin. (*b*) Cyclic voltammograms of poly(**4b**)/biotin-modified-coated platinum working electrode before and after exposure in a solution of avidin 3.10^{-4} mol/L in PBS 0.1 mol/L during 15 min, auxiliary electrode: Pt foil, reference electrode: Ag/AgCl, scan rate: 25 mV s^{-1}, 0.1 mol/L TBAP–CH_2Cl_2.

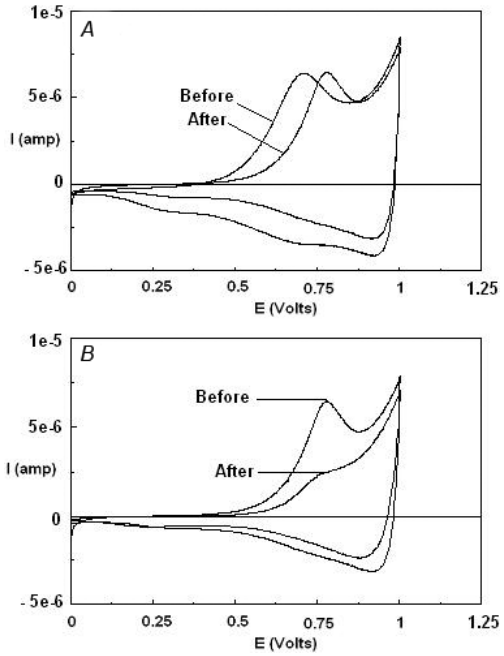

tion in the number of amidophenyl moieties able to be oxidized at the polymer-film surface.

Conclusions

The terthiophene was successfully functionalized by an amino β-styryl moiety. We synthesized four new monomers according to the Y substituent, the 3′-(3-methyl-4-amino-β-styryl)-(2,2′:5′,2″-terthiophene) (monomer **4a**), the 3′-(3-chloro-4-amino-β-styryl)-(2,2′:5′,2″-terthiophene) (monomer **4b**), the 3′-(3-methoxy-4-amino-β-styryl)-(2,2′:5′,2″-terthiophene) (monomer **4c**), and the 3′-(2-methoxy-5-amino-β-styryl)-(2,2′:5′,2″-terthiophene) (monomer **4d**). The homopolymers from monomers **4a**, **4b**, **4c**, and **4d** have been successfully electrosynthesized. The electrochemical studies of these polymer films display both the aminophenyl moiety redox couple as well as the polythiophene backbone. The cyclic and square-wave voltammogram responses of the poly(**4b**)/ and poly(**4d**)/biotin-modified film on working electrode, after exposure to an avidin solution, suggest that these polymer films have potential application as biosensors.

We project to develop an avidin biosensor by using this last system to measure an unknown avidin concentration. Some of our results will be submitted soon. To investigate the possibility of using the poly(amino β-styryl terthiophene) films for various target biomolecules, we project also to make futher functionalization on the last ECPs surfaces by other bioreceptors.

Fig. 7. (*a*) Square-wave voltammograms of poly(**4d**)-coated glassy carbon working electrode before and after immobilization of biotin. (*b*) Square-wave voltammograms of poly(**4d**)/biotin-modified-coated glassy carbon working electrode before and after exposure in a solution of avidin 3.10^{-4} mol/L in PBS 0.1 mol/L during 15 min, auxiliary electrode: Pt foil, reference electrode: Ag/AgCl, 0.1 mol/L TBAP–CH_2Cl_2.

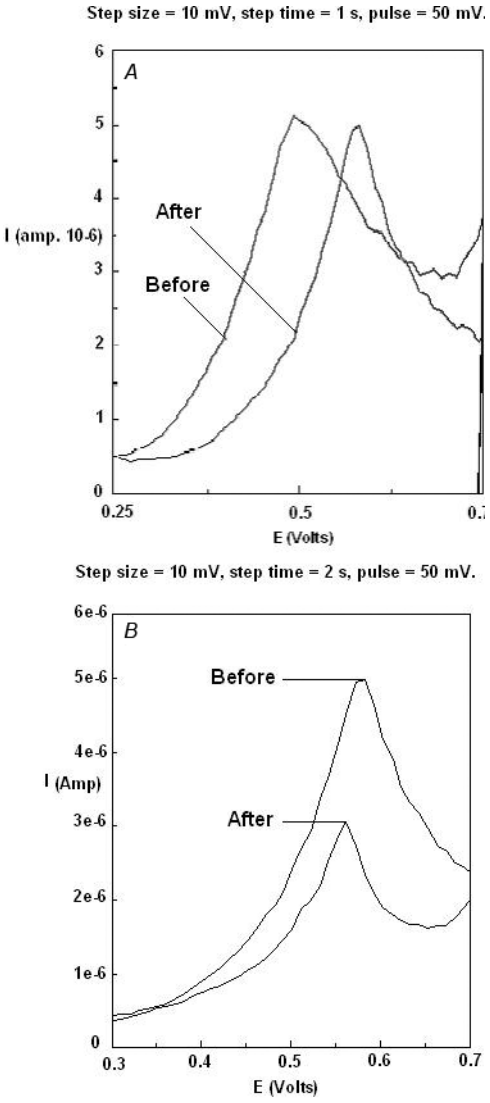

Acknowledgements

This work was supported by the National Institute of the Scientific Research (INRS) and the Natural Sciences and Engineering Research Council of Canada (NSERC).

© 2008 NRC Canada

References

1. C.M. Casado, I. Cuadrado, M. Moran, B. Alonso, B. Garcia, B.Gonzalez, and J. Losada. Coord. Chem. Rev. **53**, 185 (1999).
2. L.M. Goldenberg, M.R. Bryce, and M.C. Petty. J. Mater. Chem. **9**, 1957 (1999).
3. T.A. Skotheim, R.L. Elsenbaumer, and J.R. Reynolds (*Editors*). Handbookof conducting polymers. 2nd ed. Marcel Dekker. New York. 1998.
4. S. Cosnier. Biosens. Bioelectron. **14**, 443 (1999).
5. T. Ahuja, I.A. Mira, and D.K. Rajesh. Biomaterials, **28**, 791 (2007).
6. P.B. Luppa, L.J. Sokoll, and D.W. Chan. Clin. Chimica Acta, **314**, 1 (2001).
7. S. Cosnier. Biosens. Bioelectron. **14**, 443 (1999).
8. L.M. Goldenberg, M.R. Bryce, and M.C. Petty. J. Mater. Chem. **9**, 1957 (1999).
9. H.B. Mark, Jr. and J.F. Rubinson. Proc. Electrochem. Soc. **99**, 104 (1999).
10. K.J. Albert, N.S. Lewis, C.L. Schauer, G.A. Sotzing, S.E. Stitzel, T.P. Vaid, and D.R. Walt. Chem. Rev. **100**, 2595 (2000).
11. J. Roncali. J. Chem. Rev. **92**, 711 (1992).
12. L. Kumpumbu-Kalemba and M. Leclerc. Chem. Commun. 1847 (2000).
13. H.-A. Ho, M. Boissinot, M.G. Bergeron, G. Corbeil, K. Dore, D. Boudreau, and M. Leclerc. American chemical society symposium series, **888**, 359 (2005).
14. S. Scheib and P. Bauerle. J. Mater. Chem. **9**, 2139 (1999).
15. G. Daminelli, J. Widany, A. Di Carlo, and P. Lugli. J. Chem. Phys. **115**, 4919 (2001).
16. F. Mouffouk, S.J. Brown, A.M. Demetriou, S.J. Higgins, R.J. Nichols, R.M.G. Rajapakse, and S. Reeman. J. Mater. Chem. **15**, 1186 (2005).
17. F. Darain, D.-S. Park, J.-S. Park, and Y.-B. Shim. Biosens. Bioelectron. **19**, 1245 (2004).
18. M.A. Rahman, N.H. Kwon, M.S. Won, E.S. Choe, and Y.-B. Shim. Anal. Chem. **77**, 4854 (2005).
19. Y.-T. Kong, M. Boopathi, and Y.-B. Shim. Biosens. Bioelectron. **19**, 227 (2003).
20. J. Chen, A.K. Burrell, G.E. Collis, D.L. Officer, G.F. Swiegers, C.O. Too, and G.G. Wallace. Electrochim. Acta, **47**, 2715 (2002).
21. R. Dagani. Chem. Eng. News, **80**, 23 (2002).
22. S. Top, B. Dauer, J. Vaissermann, and G. Jaouen. J. Organomet. Chem. **541**, 355 (1997).
23. S. Top, A. Vessières, G. Leclercq, J. Quivy, J. Tang, J. Vaissermann, M. Huché, and G. Jaouen. Chem. Eur. J. 9 5223 (2003).
24. G.E. Collis, A.K.Burrell, S.M. Scott, and D.L. Officer. J. Org. Chem. **68**, 8974.
25. A.S. Nicholas and N.M. Carl. J. Chem. Res. (S) 247 (1987).
26, I.A. Ismail, D.E. Sharp, and M.R. Chedekel. J. Org. Chem. **45**, 2243 (1980).
27. P. Gao, D. Gosztola, and M.J. Weaver. J. Phys. Chem. **93**, 3753 (1989).
28. R.M. Eales and A.R. Hillman. J. Mater. Sci. **25**, 3806 (1990).
29. E.M. Garrido, J.L.F.C. Lima, C. Delerue-Matos, F. Borges, A.M.S. Silva, and A.M. Oliveira Brett. Anal. Chim. Acta, **434**, 35 (2001).
30. A.J. Bard and L.R. Faulkner. Electrochemistry: principle, method, and applications. John Wiley and Sons Inc., New York, USA. 2001.
31. C.M.A. Brett and A.M.A Brett. Electrochemistry: principles, methods, application. Oxford, UK. 1993.
32. H.H. Girault. Electrochimie physique et analytique. Presses polytechniques et universitaire romandes. 2001.
33. A.I. Vogel, A.R. Tatchell, B.S. Furnis, A.J. Hannaford, P.W.G. Smith. VOGEL's textbook of Practical Organic Chemistry. 5th ed. Longman Scientific and Technical: England. 1989. Table A2.7, p. 1417.
34. A.I. Vogel, A.R. Tatchell, B.S. Furnis, A.J. Hannaford, P.W.G. Smith. VOGEL's textbook of Practical Organic Chemistry. 5th ed. Longman Scientific and Technical: England. 1989. Table A2.3, p. 1415.
35. J.F. Moulder, W.F. Stickle, P.E. Sobol, and K.D. Bomben. *In* Handbook of X-ray photoelectron spectroscopy. Physical Electronics. Eden Prairie, MN. 1992.
36. E.T. Kang, K.G. Neoh, S.W Wang, S.L. Lim, and K.L. Tan. J. Phys. Chem. B, **101**, 10744 (1997).
37. M.D. Savage, G. Mattson, S. Desai, G.W. Nielander, S. Morgensen, and E.J. Conklin. Avidin-biotin chemistry: a handbook. Pierce Chemical Co. Rockford, IL. 1992.

© 2008 NRC Canada

Solvent-free syntheses of some quinazolin-4(3*H*)-ones derivatives

S. Mohana Roopan, T. Maiyalagan, and F. Nawaz Khan

Abstract: Solvent-free syntheses of quinazolin-4(3*H*)-ones were performed by reaction of anthranillic acid with different amides, such as nicotinamide, benzamide, formamide, etc., on montmorillonite K-10. Products were confirmed by FTIR, ^{1}HNMR, and ^{13}CNMR spectroscopic techniques. All synthesized compounds exhibited antioxidant properties and have been compared with standard antioxidant BHT.

Key words: quinazolinone, montmorillonite K-10, solvent-free conditions, antioxidant properties.

Résumé : On a réalisé des synthèses sans solvant de quinazolin-4(3*H*)-ones par réaction de l'acide anthranillique avec divers amides, tel le nicotinamide, le benzamide et le formamide sur de la montmorillonite K-10. Les produits ont été caractérisés par la spectroscopie infrarouge avec transformée de Fourier (IR-TF), et par les méthodes spectroscopiques de RMN du ^{1}H et du ^{13}C. Tous les produits synthétisés présentent une propriété antioxydante et ils ont été comparés avec l'antioxydant standard, BHT.

Mots-clés : quinazolinone, montmorrillonite K-10, conditions sans solvant, propriétés antioxydante

[Traduit par la Rédaction]

Introduction

The quinazoline ring skeleton is widely found in alkaloids and many biologically active compounds. In general, quinazolones were considered important compounds in the fields of pharmacology and biology (1) because of their wide range of strong biological activities (2–6). Some of these compounds are identified as drugs (7) and as diuretics. Among this class of molecules, quinazolin-4-ones and their derivatives are well-known to possess an array of physiological activities, e.g., antitubercular (8), antifungal (9), antibacterial (10), anti-inflammatory, anticancer (11), and anti-proliferative (5) activities.

Quinazolin-4(3*H*)-one was prepared by many methods (5, 8, 10–13). However, quinazoline derivatives were synthesized mainly by a common approach involving amidation, starting from anthranilic acid, 2-aminobenzonitrile, and 2-aminobenzamide. Other methods included the condensation of anthranilic acid, ammonium acetate, and the orthoesters (14), reaction of imidates and anthranilic acid (15), reaction of polymer-bound isothioureas with isatoic anhydride derivatives (16), and were associated with drawbacks such as multistep procedures (17), costly reagents, harse reaction conditions, complex experimental procedures, and low yields (18). Previous methods have been excluded from practical applications because of environmental and economic considerations. Finding an efficient method for the synthesis of quinazolin-4(3*H*)-one is still a challenge. Nowadays, solvent-free organic reactions have led to experimentally and industrially important organic syntheses that are more effective and eco-friendly than conventional reactions (19, 20).

In continuation of our interest in C–C bond-forming reactions (21–25), we have explored a one-pot synthesis of quinazolin-4(3*H*)-ones (Schemes 1 and 2, Tables 1 and 2) from anthranillic acid and amides, such as formamide, acetamide, benzamide, nicotinamide, etc., in the presence of montmorillonite K-10 catalyst and other inorganic catalysts such as acidic alumina, bentonite, etc., (Table 3), under solvent-free conditions. The above reactions, carried out over montmorillonite K-10 clay, give good yields because of the ditopic nature (26, 27) of montmorillonite K-10 clay. However, the reaction takes less time to complete. The optimization of catalyst amount was also done (Table 4). Thus, we have developed a simple, economical, and environmentally benign synthesis of classical procedures, by avoiding volatile and toxic organic solvents. The reusability of the catalyst in synthesis has also been explored (Table 5). Scope of the reaction (Tables 1 and 2) and antioxidant properties of the reaction products have also been discussed.

Experimental

Anthranillic acid and amides used for the reaction were from Sigma-Aldrich Co., and montmorillonite K-10 was obtained from Fluka. The substances were used as provided with no other purification. Melting points were taken in open capillary tubes and are corrected with reference to ben-

Received 17 March 2008. Accepted 29 August 2008. Published on the NRC Research Press Web site at canjchem.nrc.ca on 8 October 2008.

S.M. Roopan, T. Maiyalagan,[1] and F.N. Khan.[1] School of Science and Humanities, Organic Chemistry Division, VIT University, Vellore 632 014, Tamil Nadu, India.

[1]Corresponding authors (e-mail: maiyalagan@gmail.com, nawaz_f@yahoo.co.in).

 doi:10.1139/V08-149 © 2008 NRC Canada

Table 1. Synthesis of 2-substituted quinazolinone by solvent-free montmorillonite K-10 catalysis.

		Refluxing at 150°C solvent free conditions				
		Time taken (h)			Yield[c] (%)	
Sl. No	Reactant 2,	Without catalyst	With catalyst	Product, 3a-j	Without catalyst	With catalyst
1	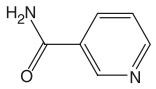 2a	2	0.5	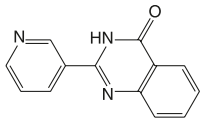	60	85
2	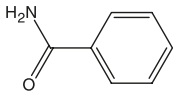 2b	4	1	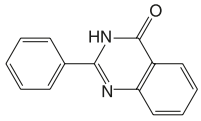	85	93
3	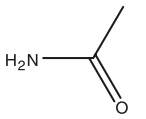 2c	4	2	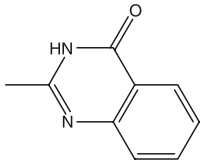	46	67
4	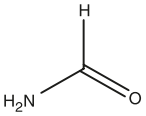 2d	4	2	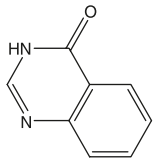	63	85
5[b]	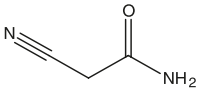 2e	5	2	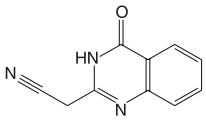	17	63

Scheme 1. Montmorillonite K-10 catalysed reaction of anthranillic acid and different amides.

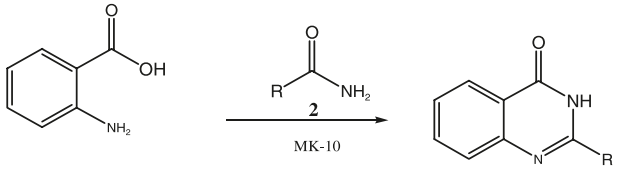

1 3

Scheme 2. Montmorillonite K-10 catalysed reaction of anthranillic acid with urea and thiourea.

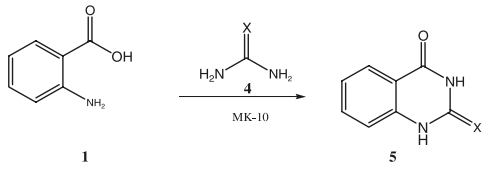

1 5

X = O, S

zoic acid. IR spectra in KBr pellets were recorded on Nucon infrared spectrophotometer. Nuclear Magnetic Resonance (^{1}H and ^{13}C) spectra were recorded on a Bruker Spectrospin Avance DPX400 Ultrashield (400 MHz) spectrometer. Chemical shifts are reported in parts per million (δ) downfield from an internal tetramethylsilane reference.

General procedure for the synthesis of 2-substituted-3*H*-quinazolin-4-ones and 1*H*,3*H*-quinazolin-2,4-diones

A mixture of anthranillic acid, **1** amide, **2** or **4a** or **4b**, and montmorillonite K-10 clay when heated under reflux conditions gave 2-substituted-3*H*-quinazolin-4-one **3** or 1*H*,3*H*-quinazolin-2,4-dione **5** (Scheme 1). After completion

© 2008 NRC Canada

Table 1 (*concluded*).

Sl. No	Reactant 2,	Refluxing at 150°C solvent free conditions				
		Time taken (h)			Yield[a] (%)	
		Without catalyst	With catalyst	Product, 3a-j	Without catalyst	With catalyst
6[b]	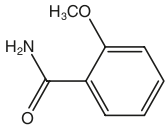 2f	5	2	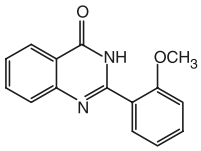	58	73
7[b]	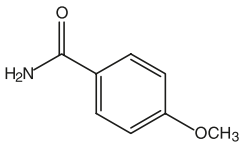 2g	4	2	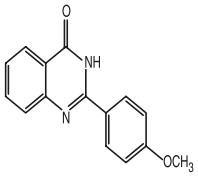	71	78
8[b]	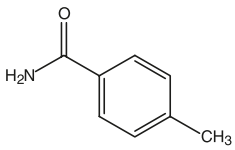 2h	4	2	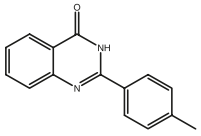	58	74
9[b]	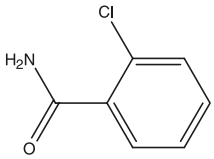 2i	5	1.5	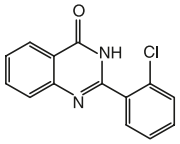	47	63
10[b]	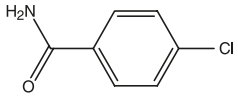 2j	5	1.5	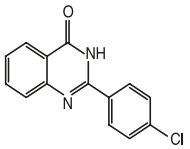	64	67

Note: 1 = 10 mmol, **2** = 10 mmol, catalyst = 0.1 g.

[a]3 in isolated yields after column chromatography.

[b]All products were characterized by ^{1}H NMR and IR spectroscopic data and their melting points were compared with literature values (31–32).

of the reaction, ethyl acetate was added to the reaction mixture, and the catalyst was recovered by filtration. Filtrate was washed with a 10% $NaHCO_3$ solution to remove any unreacted acid and further washed with water to remove any inorganic materials. The organic layer was dried, solvent evaporated to obtain the products. FT-IR and NMR spectral techniques were used for product analysis.

Synthesis of 2-pyridin-3-yl-3*H*-quinazolin-4-one (3a)

Anthranillic acid **1** (10 mmol), nicotinamide **2a** (10 mmol), and montmorillonite K-10 (0.1 g) were placed in a mortar and mixed well, transferred to a 50 mL round-bottomed flask, and refluxed at 150 °C for 30 min. The reaction was monitored by TLC, and after completion of the reaction, work-up was performed as above to give crude

© 2008 NRC Canada

Table 2. Synthesis of quinazolidione by solvent-free montmorillonite K-10 catalysis.

Sl. No	Reactant 4	Refluxing under solvent free conditions: Temp. °C	Time taken (h): Without catalyst	Time taken (h): With catalyst	Product, 5	Yield[a] (%): Without catalyst	Yield[a] (%): With catalyst
1	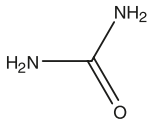 **4a**	150	5	2	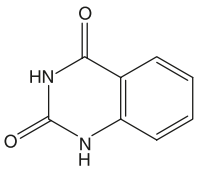 **5a**	20	66
2	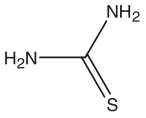 **4b**	150	5	2	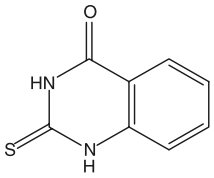 **5b**	17	58

Note: 1 = 10 mmol, **4** = 10 mmol, catalyst = 0.1g.
[a]**5** in isolated yields.

Table 3. Selection of catalyst.

Sl. No.	Catalyst used	Refluxing at 150 °C solvent-free conditions: Catalyst amount (mg)	Time (h)	Product **3a**
1	Silica gel	10	4	Nil
2	Bentonite	10	4	Nil
3	Montmorillonite KSF	10	4	Nil
4	Acidic alumina	10	4	Low yield
5	Montmorillonite K10	10	0.5	High yield

Note: Anthranilic acid **1** (1 mmol) and nicotinamide **2a** (1 mmol).

Table 4. Optimization of catalyst concentration.

Sl. No.	Amide, R $RCONH_2$	Refluxing at 150 °C solvent-free conditions: Montmorillonite K-10 (g)	Time (h)	Product **3a** (R)	Yield[a] (%)
1	$-C_5H_4N$	None	2	$-C_5H_4N$	40
2	$-C_5H_4N$	0.02	1	$-C_5H_4N$	59
3	$-C_5H_4N$	0.04	1	$-C_5H_4N$	67
4	$-C_5H_4N$	0.06	1	$-C_5H_4N$	65
5	$-C_5H_4N$	0.08	0.5	$-C_5H_4N$	71
6	$-C_5H_4N$	0.1	0.5	$-C_5H_4N$	85
7	$-C_5H_4N$	0.12	0.5	$-C_5H_4N$	86
8	$-C_5H_4N$	0.14	0.5	$-C_5H_4N$	86

Note: 1 = 10 mmol, **2a** = 10mmol, refluxed at 150 °C.
[a]**3a** in isolated yields.

© 2008 NRC Canada

Table 5. Life cycle of catalyst.

Entry	Cycle No.	Catalyst amount (g)	Yield (%)
1	Cycle I	0.1	85
2	Cycle II	0.096	82
3	Cycle III	0.091	81

product. Pure 2-pyridin-3-yl-3*H*-quinazolin-4-one **3a** was obtained by performing column chromatography using silica gel and petroleum ether/ethyl acetate as eluent. Yield was determined (Table 1, compound **3a**). The quinazolinone **3a** was recrystallized from petroleum ether and ethyl acetate. The melting point was found to be 114 °C.

A similar procedure was followed to obtain other quinazolinone derivatives **3** from different amides **2** (Scheme 1 and Table 1). Products were characterized by FTIR, ^{1}HNMR, ^{13}CNMR, and GCMS spectral techniques, and known compounds were compared with literature reports. The recrystallization of products was effected using petroleum ether and ethyl acetate.

Synthesis of 1*H*,3*H*-quinazolin-2,4-dione (5a)

A mixture of anthranillic acid **1** (10 mmol), urea **4a** (10 mmol), and 0.1 g of montmorillonite K-10 was heated under reflux conditions (150 °C) for 2 h. After completion of the reaction, the catalyst was removed by filtration; the mixture was poured into ice-cooled water and extracted with ethyl acetate. The product **5a**, obtained after solvent removal, was purified by performing column chromatography using silica gel and petroleum ether/ethyl acetate as eluent (Scheme 2, Table 2). The quinazolindione **5a** was recrystallized from petroleum ether and ethyl acetate. The melting point was found to be >300 °C.

Synthesis of 2-thioxo-2,3-dihydro-1*H*-quinazolin-4-one (5b)

A mixture of anthranillic acid **1** (10 mmol), thiourea **4b** (10 mmol), and 0.1 g of montmorillonite K-10 was heated under reflux conditions (150 °C) for 2 h. After completion of the reaction, the catalyst was removed; the mixture was poured into ice-cooled water and extracted with ethyl acetate. The product **5b**, obtained after solvent removal, was purified by column chromatography (Scheme 2, Table 2). The dihydroquinazolinone **5b** was recrystallized from ethyl acetate. The melting point was found to be >300 °C.

Life cycle of the catalyst

The reusability of catalyst was explored by checking the successive runs of the reactions on recycled catalyst; i.e., after first run of the reaction, the catalyst was recovered by a simple filtration from reaction mixture, washed with ethyl acetate, and dried. Then it was utilized in the second run of the reaction. It was noticed that use of recycled catalyst in subsequent experiments gave similar yields (Table 5). Thus, the catalyst is not leached.

Free-radical scavenging activity of quinazolinone derivatives

Radical scavenging activities are very important due to the deleterious role of free radicals in foods and biological systems. In this study, the free-radical scavenging activity of quinazolin-4(3*H*)-ones derivative was measured by a 1,1-diphenyl-2-picryl-hydrazyl (DPPH) method. This activity was measured by the following Blos methodology as assessed by Ansari et al. (28). The absorbance of DPPH is monitored at a characteristic wavelength in the presence of a synthesized sample. In its radical form, DPPH absorbs at 517 nm, but upon reduction by an antioxidant or a radical species its absorption decreases. Briefly, a 1.5×10^{-4} mmol/L solution of DPPH in ethanol was prepared and 1 mL of this solution was added to 3 mL of 1.5×10^{-4} mmol/L of quinazolinone in ethanol. At each 5 min interval, absorbance was measured at 517 nm until 30 min. The standard used was butylated hydroxyl toluene (BHT), (1.5×10^{-4} mmol/L) in ethanol solution. Lower absorbance of reaction mixture indicates higher free-radical scavenging activity. Absorbance of the DPPH (control) is 1.544. The capability to scavenge DPPH radical (28, 29) was calculated using the following equation,

$$\text{DPPH Scavenging effect (\%)} = [(A_{\text{control}} - A_{\text{sample}} / A_{\text{control}}) * 100]$$

where A_{control} is the absorbance of the DPPH solution and A_{sample} is the absorbance in the presence of quinazolinone. Two different graphs (Figs. 1 and 2) are plotted with time vs. absorbance and time vs. % inhibition.

Fig. 1. Time vs. absorbance graph for antioxidant property of quinazolinone derivatives.

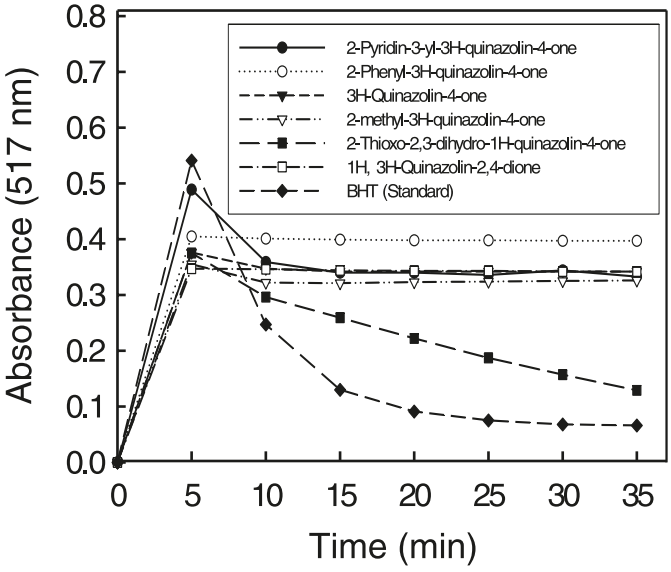

Results and discussion

Solvent-free syntheses of quinazolinone **3a** from anthranillic acid **1** and nicotinamide **2a** have been explored by using inorganic catalysts such as montmorillonite K-10, silica gel, acidic alumina, etc. (Table 3). Preliminary results indicated the formation of quinazolinone in high yield only in the case of montmorillonite K-10. The optimization of catalyst amount was done to improve the yield (Table 4). Montmorillonite K-10 has had a great impact in organic synthesis and has offered major breakthroughs for the manufacture of fine chemicals. This reagent has advantages over the

© 2008 NRC Canada

Fig. 2. Time vs. % inhibition graph for antioxidant property of quinazolinone derivatives.

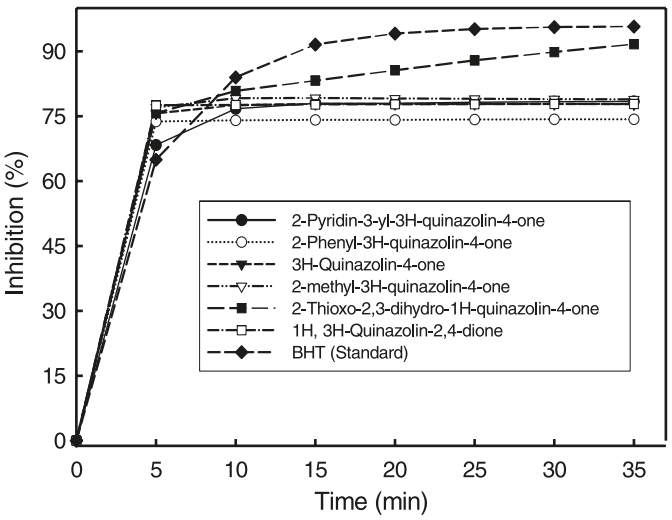

conventional homogeneous solution techniques: easy set-up and work-up, mild experimental conditions, and high yield. As part of our research, quinazolin-4(3*H*)-ones were synthesized using K-10 as catalyst (Schemes 1 and 2). The results of the quinazolinones synthesis are summarized (Tables 1–5). The essence of the catalyst can be understood from the following facts: when anthranillic acid **1** was treated with montmorillonite K-10 under conventional heating in the presence of nicotinamide **2a**, the product **3a** was obtained in quantitative yield (Table 3, entry 5). When the same reaction was performed without montmorillonite catalyst, **3a** was obtained in much lower yield in 2 h (Table 4, entry 1). The reaction optimization with different amounts of montmorillonite K-10 was carried out, and at 0.1 g, the yield was good (Table 4).

In the IR spectra of all 4-quinazolinones **3**, absorption bands are observed in the region of 1690–1730 (Ar C=O), 1600–1635, 1510–1570, 1460–1500 cm $^{-1}$ (the quinazolone ring). Assignments of ^{1}H NMR signals of quinazolinones **3** were derived from splitting patterns and characteristic chemical shift values. The data consistently show that the homocyclic proton signal with the lowest field shift in series of compounds is a doublet with additional fine structure due to further *meta* and *para* couplings. This signal is assigned to H-5 on the basis of the proximity to the carbonyl group. The assignment of H-5 led to the assignment of H-8 by default. In the same spectral region, the signal for H-2 is found as a singlet. The signals for protons H-6 and H-7 show two *ortho* couplings. We have assigned the H-7 signal to the lower field.

In the present study, quinazolinone derivatives were evaluated for their free-radical scavenging activity using the DPPH radical assay. Reduction of DPPH radicals can be observed by a decrease in absorbance at 517 nm. Different derivatives of quinazolinones reduced DPPH radicals significantly. The activity of quinazolinone derivatives was compared with commercial antioxidant butylated hydroxyl toluene (BHT). 2-Thioxo-2,3-dihydro-1*H*-quinazolin-4-one had relatively high DPPH radical-scavenging activity. As shown in Figs. 1 and 2, all quinazolinone derivatives were found to have the ability to scavenge hydroxyl radical at a concentration of 1.5×10^{-4} mmol/L.

Analytical data

Data of the new compound **3a** and that of a few known compounds, **3b**–**3d**, **5a**–**5b**, which have not been reported earlier are given below. The data of a few compounds that have been found to be identical to those reported (30–32) are given as Supplementary Data available with this paper.[2]

*2-Pyridin-3-yl-3*H*-quinazolin-4-one (3a)*

Colourless solid, mp 114 °C. IR (KBr pellets, cm^{-1}) ν: 3351.67, 1655.03, 1601.16, 1585.32, 1535.27, 1491.45. ^{1}H NMR (300MHz, $CDCl_3$) δ: 9.1 (s, 1H), 8.76–8.75 (d, *J* = 4.56Hz, 1H), 8.23–8.20 (d, *J* = 7.77Hz, 1H), 8.13 (s, 1H), 7.66–7.64 (d, 1H), 7.46–7.41 (m, 1H), 7.39–7.36 (d, *J* = 7.56, 2H), 7.21–7.16 (m, 1H). ^{13}C NMR (100 MHz, $CDCl_3$) δ: 163.92 (C=O), 152.37, 147.82, 137.49, 135.49, 130.86, 129.17, 125.08, 123.73, 120.51. EI-Mass: 223. GC-MS *m*/*z* 223 (M^+) $C_{13}H_9N_3O$ (mol. wt. 223.23) calcd.: C 69.95, H 4.06, N 18.82, O 7.17; found: C 69.83, H 4.14, N 18.75, O 7.01.

*2-Phenyl-3*H*-quinazolin-4-one (3b)*

Mp 242–246 °C (lit. value (32), 242–246 °C). IR (KBr pellets, cm^{-1}) ν: 3342.55, 1654.76, 1437.47. ^{13}C NMR (100MHz, $CDCl_3$) δ: 165.70 (C=O), 137.85, 134.93, 131.78, 129.03, 128.72, 126.95, 124.51, 120.14. $C_{14}H_{10}N_2O$ (mol. wt. 222.24) calcd.: C 75.66, H 4.54, N 12.60, O 7.20; found: C 75.54, H 4.46, N 12.52, O 7.11.

*2-Methyl-3*H*-quinazolin-4-one (3c)*

Mp 240–248 °C (lit. value (32), 238–240 °C). IR (KBr pellets, cm^{-1}) ν: 3295.81, 1666.07, 1434.67. $C_9H_8N_2O$ (mol. wt. 160.17) calcd.: C 67.49, H 5.03, N 17.49, O 9.99; found: C 67.31, H 5.13, N 17.51.

*3*H*-Quinazolin-4-one (3d)*

White solid, mp 216 °C (lit. value (32), 215–216 °C). IR (KBr pellets, cm^{-1}) ν: 3428.88, 1704.98, 1665.87. ^{13}C NMR (75MHz, $CDCl_3$) δ: 143.34, 134.89, 127.76, 127.42, 126.35. $C_8H_6N_2O$ (mol. wt. 146.15) calcd.: C 65.75, H 4.14, N 19.17, O 10.95; found: C 65.80, H 4.03, N 19.04, O 10.86.

(4-Oxo-quinazolin-2yl)-acetonitrile (3e)

Colourless solid, mp 240 °C (lit. value (32), 242 °C. $C_{10}H_7N_3O$ (mol. wt. 185.18) calcd.: C 64.86, H 3.81, N 22.69, O 8.64; found: C 64.74, H 3.91, N 22.57, O, 8.58.

*2-(4-Methylphenyl)quinazolin-4(3*H*)-one (3g)*

Colourless solid, mp 240 °C (lit. value (31), 239 °C). ^{13}C NMR (75MHz, $CDCl_3$) δ: 159.9, 147.34, 146.20, 134.31, 133.20, 131.58, 128.15, 127.12, 126.35, 125.14, 124.81, 124.13, 122.11, 19.30. GC-MS *m*/*z* 236 (M^+).

[2] Supplementary data for this article are available on the journal Web site (canjchem.nrc.ca) or may be purchased from the Depository of Unpublished Data, Document Delivery, CISTI, National Research Council Canada, Ottawa, ON K1A 0R6, Canada. DUD 3833. For more information on obtaining material refer to cisti-icist.nrc-cnrc.gc.ca/cms/unpub_e.shtml.

© 2008 NRC Canada

2-(4-Methoxyphenyl)quinazolin-4(3H)-one (3h)

Pale yellow, mp 245–247 °C (lit. value (31), 244 °C). ^{13}C NMR (75MHz, $CDCl_3$) δ: 161.22, 148.33, 146.20, 134.32, 133.20, 131.56, 128.11, 127.10, 126.22, 125.14, 124.81, 124.21, 122.13, 19.31. GC-MS *m*/*z* 252 (M^+).

2-(4-Chlorophenyl)quinazolin-4(3H)-one (3j)

Colourless solid, mp 306–308 °C (lit. value (31), 312 °C). ^{13}C NMR (75MHz, $CDCl_3$) δ: 160.12, 147.73, 146.64, 136.45, 135.26, 134.66, 132.62, 130.55, 128.33, 127.91, 126.84, 124.14, 122.43, 19.31. GC-MS *m*/*z* 240 (M^+).

1H,3H-Quinazolin-2,4-dione (5a)

Pale yellow solid, mp >300 °C (lit. value (32) >280 °C). IR (KBr pellets, cm^{-1}) ν: 3367.88 (br), 1673.92, 1609.99. $C_8H_6N_2O_2$ (mol. wt. 162.15) calcd.: C 59.26, H 3.73, N 17.28, O 19.73; found: C 59.14, H 3.67, N 17.16, O 19.82.

2-Thioxo-2,3-dihydro-1H-quinazolin-4-one (5b)

Colourless solid, mp >300 °C. IR (KBr pellets, cm^{-1}) ν: 3406.32, 3203.67, 3008.42, 1696.52, 1263.87. ^{1}H NMR (400MHz, $CDCl_3$) δ: 7.89 (s, 1H, NH), 7.45–7.44 (d, 1H), 7.43–7.42 (d, 1H), 7.41–7.37(m, 2H) 7.34 (s, 1H, NH). ^{13}C NMR (100MHz, $CDCl_3$) δ: 179.94 (C=S), 137.05, 129.62, 127.15, 125.30. $C_8H_6N_2OS$ (mol. wt. 178.21) calcd.: C 53.92, H 3.39, N 15.72, O 8.98, S 17.99; found: C 53.84, H 3.48, N 15.81, O 8.87, S 17.87.

Conclusion

In conclusion, we have reported a facile synthesis of quinazolin-4(3*H*)-ones under solvent-free conditions and conventional heating, demonstrating the use of montmorillonite K-10 as an efficient, rapid, mild, and inexpensive catalyst. The procedure has the advantages of simplicity and easy product isolation, coupled with high purity and yields.

Acknowledgement

The authors wish to express their gratitude to Syngene International Limited for their support of their NMR and GCMS facilities to carry this research work.

References

1. D.J. Brown. *In* Comprehensive heterocyclic chemistry. Vol. 3. *Edited by* A.R. Katritzky and C.W Rees. Pergamon Press, Oxford, UK. 1984. p. 57.
2. H. Wamhoff and J. Dzenis. Adv. Heterocyclic. Chem. **55**, 129 (1992).
3. S. Sinha and M. Srivastava. Prog. Drug Res. **43**, 143 (1994).
4. X. Gao, X. Cai, K. Yan, B. Song, L. Gao, and Z. Chen. Molecules, **12**, 2621 (2007).
5. S. Yang, Z. Li, L. Jin, B. Song, G. Liu, J. Chen, Z. Chen, D. Hu, W. Xue, and R. Xu. Bioorg. Med. Chem. Lett. **17**, 2193 (2007).
6. J. Bartroli, E. Turmo, M. Alguero, E. Boncompte, M.L. Vericat, L.Conte, J. Ramis, M. Merlos, J.G. Rafanell, and J. Forn. J.Med.Chem. **41**, 1869 (1998).
7. B.A. Keay and P.W. Dibble. *In* Comprehensive Heterocyclic Chemistry. Vol. II. *Edited by* A.R. Katritzky, C.W. Rees, and E.F.V. Scriven. Pergamon Press, Oxford, UK. 1996. pp. 395–436.
8. J. Kunes, J. Bazant, M. Pour, K. Waisser, M. Slosarek, and J. Janota. Il Farmaco, **55**, 725 (2000).
9. G. Grover and S.G. Kini. Eur. J. Med. Chem. **41**, 256 (2006).
10. A.K. Tiwari, V.K. Singh, A. Bajpai, G. Shukla, S. Singh, and A.K. Mishra. Eur. J. Med. Chem. **42**, 1234 (2007).
11. P.M. Chandrika, T. Yakaiah, A.R.R. Rao, B. Narsaiah, N.C. Reddy, V. Sridhar, and J.V. Rao. Eur. J. Med. Chem. **43,** 846 (2008).
12. D.J. Connolly, D.Cusack, T.P.O. Sullivan, and P.J. Guiry. Tetrahedron, **61**, 10153 (2005).
13. G.M. Buckley, N. Davies, H.J. Dyke, P.J. Gilbert, D.R. Hannah, A.F. Haughan, C.A. Hunt, W.R. Pitt, R.H. Profit, N.C. Ray, M.D. Richard, A. Sharpe, A.J. Taylor, J.M. Whitworth, and S.C. Williams. Bioorg. Med. Chem. Lett. **15**, 751 (2005).
14. K. Rad-Moghadam and M. Mohseni. J. Chem. Res. Synop. 487 (2003).
15. W. Ried and W. Stephan. Chem. Ber. **96**, 1218 (1963).
16. R.Y. Yang and A. Kaplan. Tetrahedron Lett. **41**, 7005 (2000).
17. V. Alagarsamy, S. Murugesan, K. Dhanabal, M. Murugan, and E. De Clercq. Indian J. Pharm. Sci. **69**, 304 (2007).
18. P. Pannerselvam, R.V. Pradeepchandran, and S.K. Sridhar. Indian J. Pharm. Sci. **65**, 268 (2003).
19. R.S. Varma. Green Chem. **1**, 43 (1999).
20. R.S. Varma. Clean Prod. Pros. **1**, 132 (1999).
21. F. Nawaz Khan, R. Jayakumar, and C. N. Pillai. J. Mol. Catal. A: Chem. **195**, 139 (2003).
22. F. Nawaz Khan, R. Jayakumar, and C.N. Pillai. Tetrahedron Lett. **43**, 6807 (2002).
23. V.R. Hathwar, P. Manivel, F. Nawaz Khan, and T.N. Guru Row. Acta Crystallogr. Sect. E, **63**, o3707 (2007).
24. V.R. Hathwar, P. Manivel, F. Nawaz Khan, and T.N. Guru Row. Acta Crystallogr. Sect. E, **63**, o3708 (2007).
25. S. Syed Tajudeen and F. Nawaz Khan. Synth. Commun. **37**, 3649 (2007).
26. M.D. Bhor, N.S. Nandurkar, M.J. Bhanushali, and B.M. Bhanage. Ulrasonics Sonochemistry, **15,** 195 (2008).
27. M. Kidwai and R. Mohan. J. Chin. Chem. Soc. **47**, 1205 (2006).
28. N.M. Ansari, L. Houlihan, B. Hussain, and A. Pieroni. Phytother. Res. **19**, 907 (2005).
29. H. Chen, M. Zhang, and B. Xie. J. Agric. Food Chem. **52**, 11 (2004).
30. C.A. Jaleel, P. Manivannan, B. Sankar, A. Kishorekumar, R. Gopi, R. Somasundaram, and R. Panneerselvam. Colloids Surf. B Biointerfaces, **60**, 201 (2007).
31. T.Mc.C. Paterson, R.K. Smalley, and H. Suschitzky. Synthesis, 187 (1975).
32. F. Li, Y. Feng, Q. Meng, W. Li, Z. Li, Q. Wang, and F. Tao. ARKIVOC, **i**, 40 (2007).

© 2008 NRC Canada

A Fmoc/Boc pseudoisocytosine monomer for peptide nucleic acid synthesis

Filip Wojciechowski and Robert H.E. Hudson

Abstract: The synthesis of *N*-[2-(fluorenylmethoxycarbonyl)aminoethyl]-*N*-[(2-*N*-(*tert*-butoxycarbonyl)isocytosin-5-yl)acetyl]glycine peptide nucleic acid monomer is described. The *N*-*tert*-butoxycarbonyl protected monomer is compatible with commercially available monomers designed for the Fmoc-oligomerization strategy and is deprotected under mild acidolysis conditions.

Key words: PNA, polyamide, pseudoisocytosine, J-base, triplex.

Résumé : On décrit la synthèse du peptide monomère de l'acide nucléique *N*-[2-(fluorénylméthoxycarbonyl)aminoéthyl]-*N*-[2-*N*-(*tert*-butoxycarbonyl)isocytosin-5-yl)acétyl]glycine. Le monomère protégé par le groupe *N*-*tert*-butoxycarbononyle est compatible avec les monomères disponibles commercialement, développés pour la stratégie d'oligomérisation Fmoc, et il peut être déprotégé dans des conditions d'acidolyse douce.

Mots-clés : PNA, polyamide, pseudoisocytosine, base J, triplex.

[Traduit par la Rédaction]

Introduction

Peptide nucleic acid (PNA) is a nucleic acid analogue composed of a polyamide backbone to which the nucleobases are attached by a methylene carbonyl group (1). PNA oligomers hybridize to complementary DNA or RNA obeying Watson–Crick base-pairing rules and do so with remarkable sequence specificity and high affinity. Interest in PNAs as therapeutic agents (2) or as probes in clinical diagnostics (3) continues to motivate scientists to expand the frontiers of PNA chemistry and its applications. It is evident that such uses will only flourish if the building blocks for the synthesis of modified PNA are commercially available or readily prepared by straightforward synthetic procedures. Thus it becomes important to develop and detail the route to such reagents to benefit the community interested in PNA.

Although there have been a number of nucleobase modifications incorporated into PNAs (4), the majority of these nucleobases utilize Boc/Cbz-protected monomers. Removal of the Cbz exocyclic amino protecting group from the nucleobases requires harsh reagents, usually neat HF or TFMSA, and is generally disfavoured by the nonspecialist. Therefore, other protecting group strategies for mild deprotection have been investigated.

Currently, the most commonly used PNA building blocks for mild deprotection are the commercially available Fmoc/Bhoc monomers. While Bhoc-protected adenine, thymine, guanine, and cytosine are commercially available, other nucleobases that have shown beneficial properties are not, and synthetic procedures for N-protection with mild acid labile protecting groups have not been thoroughly investigated.

Nucleic acids (NAs) with purine-consecutive sequences may be targeted by homopyrimidine PNA forming a $(PNA)_2$:NA triplex that has a very high thermal stability (5). One PNA strand engages in Watson–Crick base-pairing, while the other PNA strand is involved in Hoogsteen binding. While thymine forms a stable Hoogsteen pair with adenine, cytosine requires protonation below physiological conditions to form a stable Hoogsteen pair with guanine. Such pH dependence may be alleviated by using nucleobase analogues of protonated cytosine such as N^7-guanine (6) or pseudoisocytosine (J) (7) (Fig. 1). To date, neither a synthetic procedure nor a commercial source for pseudoisocytosine protected by a mild acid labile protecting group has been reported.

We have recently developed a convenient route to benzyl, allyl, and 4-nitrobenzyl esters of *N*-[2-(Fmoc)aminoethyl]glycine to facilitate the syntheses of PNA monomers in which the nucleobases are protected with groups that could be liberated under mild acidic conditions. We have also successfully synthesized PNA oligomers using a bis-*N*-Boc nucleobase protecting group strategy to reduce aggregation during oligomer synthesis (8). Herein we report the first synthesis and oligomerization of a pseudoisocytosine monomer protected at the exocyclic amino group with a mild acid labile protecting group (Boc), which is fully compatible with standard Fmoc/Bhoc oligomerization–deprotection peptide synthesis.

Results and discussion

The synthesis of isocytosin-5-ylacetic acid (9) (**1**) was carried out as described by the modified procedure of Niel-

Received 21 June 2008. Accepted 2 August 2008. Published on the NRC Research Press Web site at canjchem.nrc.ca on 8 October 2008.

F. Wojciechowski and R.H.E. Hudson.[1] Department of Chemistry, The University of Western Ontario, London, ON N6A 5B7, Canada.

[1]Corresponding author: (e-mail: rhhudson@uwo.ca).

 doi:10.1139/V08-144 © 2008 NRC Canada

Fig. 1. Nucleobase interactions for a $(PNA)_2$:NA triple helix. (*a*) Protonated cytosine (C^+) and the G:C base pair (C^+:G:C) and (*b*) pseudoisocytosine (J) and the G:C base pair (J:G:C).

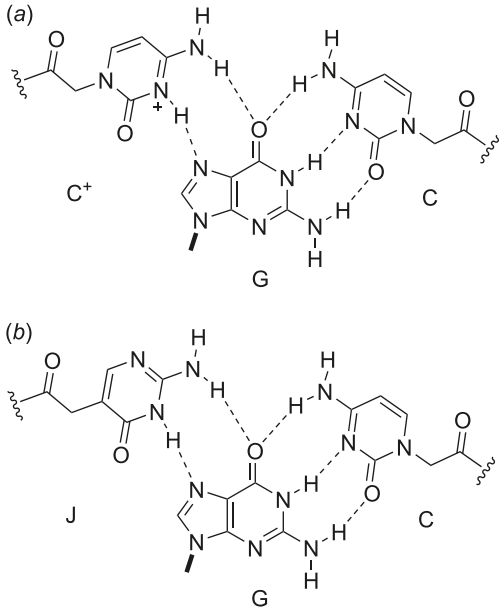

sen and co-workers (10). Condensation of dimethyl succinate with methyl formate gave methyl α-formylsuccinate as a colourless oil that was partially contaminated with dimethyl succinate. The product may be isolated free of dimethyl succinate by continuous extraction with diethyl ether but this greatly reduces the yield. Nielsen and co-workers proposed that this contaminated oil may be directly used in the next step. Therefore, the crude mixture was reacted with guanidine hydrochloride to give isocytosin-5-ylacetic acid **1** in good yield, confirming that it is suitable to use the crude mixture. Subsequent esterification with $EtOH/HCl_{(g)}$ gave ethyl isocytosin-5-ylacetate hydrochloride, which was dissolved in aqueous sodium bicarbonate and acidified to pH 6.0 to give ethyl isocytosin-5-ylacetate (**2**) in 81% yield.

We have previously reported the bis-*N*-Boc protection of ethyl cytosin-1-ylacetate, ethyl adenin-9-ylacetate, and ethyl (O^6-benzylguanin-9-yl)acetate. The exocyclic amino group of cytosine was most reactive towards $(Boc)_2O$ and gave the bis-*N*-Boc protected nucleobase in excellent yield. Likewise we reasoned that pseudoisocytosine, which is a cytosine analogue, should be prone to bis-*N*-Boc protection. Thus, ethyl isocytosin-5-ylacetate **2** was reacted with a catalytic amount of DMAP, 4.0 equiv. of $(Boc)_2O$, triethylamine in CH_3CN under reflux, but the major product was the mono-Boc protected derivative N^2-(*tert*-butoxycarbonyl)isocytosin-5-ylacetate (**3**) in 51% yield. Changing to *N*-methylimidazole as the catalyst, reducing the amount of $(Boc)_2O$ to 1.3 equiv., and changing to DMF as the solvent gave **3** in slightly better yield (57%). Final optimization gave **3** in 70% yield free of column chromatography, by simply using a catalytic amount of DMAP and 1.3 equiv. of $(Boc)_2O$ in DMF. Subsequent hydrolysis of **3** gave the carboxylate, which was acidified with citric acid to give a precipitate of N^2-(*tert*-butoxycarbonyl)isocytosin-5-ylacetic acid (**4**) in 91% yield

Scheme 1. Synthesis of N^2-(*tert*-butoxycarbonyl)isocytosin-5-ylacetic acid **4**. Reagents and conditions: (*a*) $HCl_{(g)}$, EtOH, reflux 2 h; (*b*) $(Boc)_2O$, DMAP, DMF, 36 h; (*c*) NaOH, THF/H_2O, 15 min.

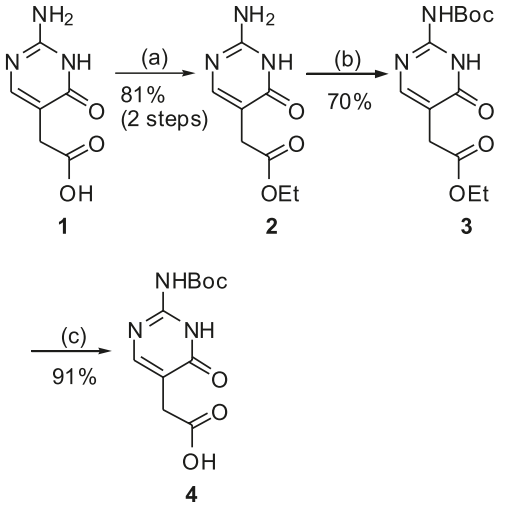

(Scheme 1). Alternatively, acidification of the carboxylate of **4** with 4 mol/L of HCl followed by extraction into ethyl acetate resulted in a lower yield (73%) and required the use of copious amounts of ethyl acetate (400 mL) because of the poor solubility of **4** in ethyl acetate.

Carbodiimide-mediated coupling of **4** with *N*-[2-(Fmoc)aminoethyl]glycine benzyl ester (8) was accomplished using EDC/HOBt, to give the orthogonally protected monomer ester **5** in 74% yield. Removal of the benzyl ester using Pd/C and H_2 gave the desired monomer **6** in 86% yield (Scheme 2).

The performance of the Boc-protected pseudoisocytosine monomer (**6,** J) was judged by incorporation into a 10-mer PNA sequence (N-term: GTA GAT CJC T-Lys C-term, **7**) by standard Fmoc-mediated peptide synthesis along with commercially available Bhoc-protected monomers. The coupling of monomer **6** was qualitatively judged to be trouble-free by conductivity monitoring during the automated synthesis of the oligomer. Furthermore, RP-HPLC analysis of the crude oligomer (Fig. 2) indicated the coupling to be equivalent to the standard G, T, C, and A monomers with an average stepwise coupling yield of >98.5%.

Post oligomerization, removal of the Boc protecting group along with the Bhoc protecting groups was achieved using TFA/Et_3SiH (975:25 μL). The crude oligomer was purified by RP-HPLC; the major peak in the chromatogram corresponded to the full length oligomer (retention time: 28.375 min.). The identity of **7** was confirmed by mass spectrometry (Fig. 3). There was excellent agreement between the expected and found masses: TOF-MS (ESI) *m*/*z* calcd. for $C_{113}H_{148}N_{58}O_{32}$: 2830.75; found: 2830.80.

In summary, we report the synthesis of a pseudoisocytosine PNA monomer that possesses a Boc protecting group on the nucleobase and its subsequent incorporation into a PNA oligomer by Fmoc-based chemistry. Previous attempts at protection of pseudoisocytosine with acid labile protecting groups have resulted in poor yields (11) without reporting the experimental procedures. Thus, this is the first

© 2008 NRC Canada

Scheme 2. Synthesis of Boc protected pseudoisocytosine monomer **6**. Reagents and conditions: (*a*) EDC/HOBt, DMF, 36 h; (*b*) Pd/C, H_2, MeOH, 3 h.

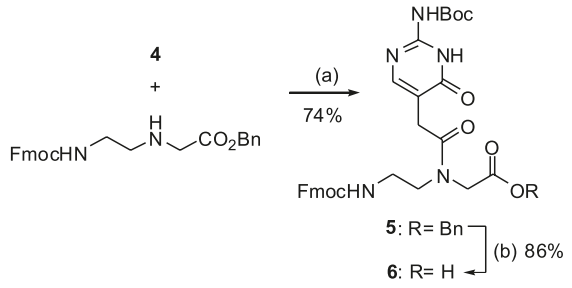

Fig. 2. Reversed-phase HPLC analysis of crude oligomer **7**: GTA GAT CJC T-Lys.

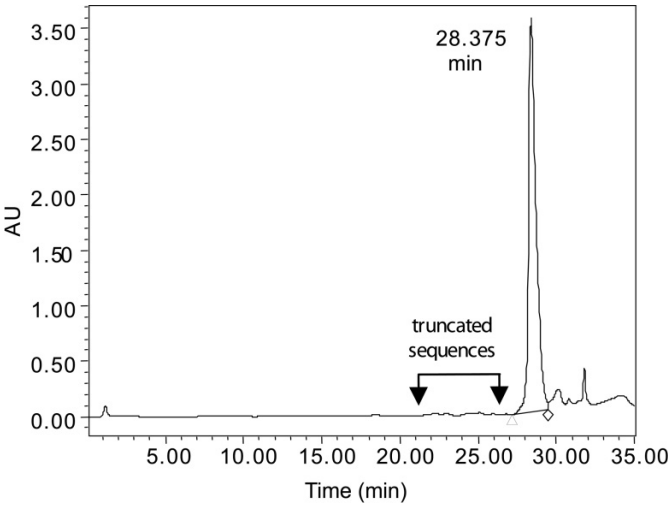

report for such a protection and will facilitate its future use in triplex forming PNA, assembled by Fmoc-based peptide synthesis.

Experimental

General

All reagents and solvents were obtained from commercial sources, were of ACS reagent grade or higher, and were used without further purification. Anhydrous solvents were prepared by passing the reagent-grade solvent through columns of activated alumina (Innovative Technologies). Flash column chromatography (FCC) was performed on Merck Kieselgel 60 (230–400 mesh). Thin layer chromatography (TLC) was performed on Merck Kieselgel 60 TLC plates. Chemical shifts are reported in parts per million (δ), were measured from tetramethylsilane (0 ppm), and are referenced to the residual proton in the otherwise perdeuterated solvents: $CDCl_3$ (7.26 ppm), DMSO-d_6 (2.49 ppm) for ^{1}H NMR and $CDCl_3$; (77.0 ppm), DMSO-d_6 (39.5 ppm) for ^{13}C NMR. Multiplicities are described as singlet (s), doublet (d), triplet (t), quartet (q), multiplet (m), and broad singlet (br s). Resonances attributed to conformers due to restricted rotation around amide bonds (rotamers) are reported as major

Fig. 3. Transformed data for the ESI-TOF mass spectral analysis of the 10-mer PNA.

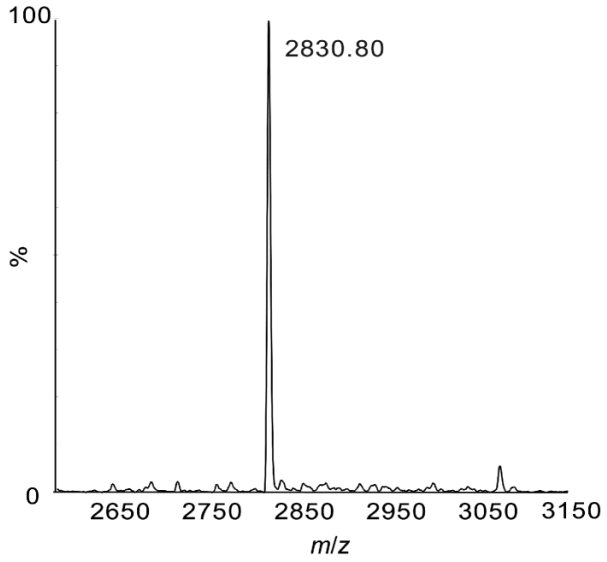

(ma.) and minor (mi.). Coupling constants (*J*) are reported in Hertz (Hz). High-resolution mass spectra (HRMS) were obtained using electron impact (EI) or electrospray (ESI).

Ethyl isocytosin-5-ylacetate (2)

To ethanol (150 mL) was added isocytosin-5-ylacetic acid **1** (4.5 g, 26.6 mmol) and $HCl_{(g)}$ in ethanol (50 mL, 1.5 mol/L). The mixture was heated to reflux, and within 15 min the mixture became homogeneous and the solution was refluxed for a further 2 h. The solution was cooled to room temperature, concentrated in vacuo to approximately 100 mL, and placed at –20 °C for 2 h. The precipitate was collected by filtration and washed with diethyl ether to give a white solid. The hydrochloride salt of ethyl isocytosin-5-ylacetate was dissolved in saturated aqueous sodium bicarbonate (50 mL), and then acidified to pH 6.0 by dropwise addition of 4 mol/L of HCl while being stirred. The precipitate was cooled at 4 °C for 1 h, collected by filtration, and washed with diethyl ether to give a white solid (4.2 g, 81%). ^{1}H NMR (400 MHz, DMSO-d_6) δ: 10.98 (br s, 1H), 7.46 (s, 1H), 6.47 (br s, 1H), 4.03 (q, J = 7.1 Hz, 2H), 3.19 (s, 2H), 1.16 (t, J = 7.2 Hz, 3H). ^{13}C NMR (100 MHz, DMSO-d_6) δ: 171.2, 164.7, 156.0, 151.5, 108.7, 60.0, 32.1, 14.1. HRMS (EI) calcd. for $C_8H_{11}N_3O_3$: 197.0800 [M^+]; found: 197.0809.

N^2-(*tert*-butoxycarbonyl)isocytosin-5-ylacetate (3)

A suspension of **2** (1.0 g, 5.0 mmol), DMAP (61 mg, 0.5 mmol), and Boc_2O (1.4 g, 6.4 mmol) in DMF (5 mL) was stirred for 48 h under N_2. To the solution was added ethanol (5 mL), followed by saturated aqueous sodium bicarbonate (25 mL), and the solution was stirred for 10 min. The mixture was extracted with EtOAc (4 × 50 mL), and the combined organic extracts were subsequently washed with brine (50 mL) and dried over Na_2SO_4. After removal of the solvent, the residue was triturated with equal volumes of diethyl ether/hexanes (50 mL) and collected by filtration to give **3** as a white solid (1.05 g, 70%). ^{1}H NMR (400 MHz, DMSO-d_6) δ: 11.28 (br s, 2H), 7.67 (s, 1H), 4.03 (q, J = 7.0

© 2008 NRC Canada

Hz, 2H), 3.31 (s, 2H), 1.48 (s, 9H), 1.17 (t, J = 7.0 Hz, 3H). ^{13}C NMR (100 MHz, $CDCl_3$) δ: 170.1, 160.2, 153.1, 151.4, 151.1, 115.1, 84.0, 60.6, 32.0, 27.7, 13.8. HRMS (EI) calcd. for $C_{13}H_{19}N_3O_5$: 297.1325 [M^+]; found: 297.1330.

N^2-(*tert*-butoxycarbonyl)isocytosin-5-ylacetic acid (4)

A suspension of compound **3** (1.0 g, 3.4 mmol) in water/THF (15 mL:5 mL) was placed in an ice bath, followed by the dropwise addition of NaOH (2.5 mol/L, 10 mL) over 1 min. The suspension was removed from the ice bath and stirred until TLC analysis indicated complete consumption of the starting material (15 min). The precipitate was cooled with the aid of an ice bath, and citric acid monohydrate (5.3 g, 25.0 mmol) dissolved in water (4 mL) was added in one portion. The mixture was stirred on ice for 1 h, and the solid precipitate was collected by filtration and washed with diethyl ether to give a white solid (830 mg, 91%). ^{1}H NMR (400 MHz, DMSO-d_6) δ: 11.60 (br s, 3H), 7.65 (s, 1H), 3.23 (s, 2H), 1.48 (s, 9H). ^{13}C NMR (100 MHz, $CDCl_3$) δ: 172.1, 160.8, 154.2, 150.6, 115.4, 82.5, 32.4, 27.9. HRMS (EI) calcd. for $C_{11}H_{15}N_3O_5$: 269.1012 [M^+]; found: 269.1015.

Benzyl *N*-[2-(fluorenylmethoxycarbonyl)aminoethyl]-*N*-[(2-*N*-(*tert*-butoxycarbonyl)isocytosin-5-yl)acetyl]glycinate (5)

To an ice-cooled suspension of **4** (400 mg, 1.5 mmol) and benzyl *N*-[2-(Fmoc)aminoethyl]glycinate (430 mg, 1.0 mmol) in DMF (10 mL) was added EDC (575 mg, 3.0 mmol), and the reaction was stirred on ice for 0.5 h and at room temperature for 36 h. The reaction was poured into $NaHCO_3$ (50 mL) and extracted into CH_2Cl_2 (3 × 100 mL). The organic phase was washed sequentially with aqueous $NaHCO_3$ (2 × 50 mL) and brine (50 mL). After drying the organic phase and removal of the solvent, the residue was subjected to FCC using CH_2Cl_2/MeOH as the eluent. The combined fractions were reduced in vacuo to give **5** (523 mg, 74%). ^{1}H NMR (400 MHz, DMSO-d_6) δ: 11.44 (br s, 1H), 11.01 (br s, 1H), 7.88 (d, J = 7.2 Hz, 2H), 7.67 (d, J = 7.2 Hz, 2H), 7.43–7.29 (m, 10H), 5.17 (s, 0.6 H, mi.), 5.12 (s, 1.4 H, ma.), 4.41–4.19 (m, 4H), 4.08 (s, 1H), 3.51–3.07 (m, 6H), 1.47 (s, 9 H). ^{13}C NMR (100 MHz, $CDCl_3$) δ: 171.3, 170.5, 169.5, 160.4, 156.4, 153.1, 152.0, 150.9, 143.6, 140.9, 135.0, 128.4, 128.3, 128.1, 127.9, 127.3, 126.8, 124.9, 119.7, 115.8, 84.2, 67.2, 66.8, 66.5, 51.2, 49.3, 48.6, 47.0, 39.3, 30.2, 27.8. HRMS (ESI-TOF) calcd. for $C_{37}H_{39}N_5O_8$: 704.2696 [MNa^+]; found: 704.2687.

N-[2-(fluorenylmethoxycarbonyl)aminoethyl]-*N*-[(2-*N*-(*tert*-butoxycarbonyl)isocytosin-5-yl)acetyl]glycine (6)

Compound **5** (423 mg, 0.62 mmol) was dissolved in MeOH (25 mL), purged with N_2, and then Pd/C (75 mg) was added and the solution was saturated with H_2 by slow bubbling over 3 h. The reaction was filtered through a short pad of Celite, and the solvent was removed in vacuo to give **6** as a white solid (316 mg, 86%). ^{1}H NMR (400 MHz, DMSO-d_6) δ: 7.82 (d, J = 7.4 Hz, 2H), 7.61 (d, J = 7.4 Hz, 2H), 7.54–7.49 (m, 1H), 7.35 (t, J = 7.4 Hz, 2H), 7.26 (t, J = 7.4 Hz, 2H), 4.26–3.89 (m, 3H), 3.89 (s, 1H), 3.39–3.01 (m, 7H), 1.41 (s, 9 H). HRMS (ESI-TOF) calcd. for $C_{30}H_{33}N_5O_8$: 614.2227 [MNa^+]; found: 614.2236.

Synthesis of PNA

The 10-mer PNA oligomer was synthesized on a 5 umol scale using the standard FastMoc module on an Applied Biosystems 433A synthesizer. A NovaSyn TGR (Rink amide) resin preloaded with lysine (approximate loading of 0.065 mmol/g) was used. The resin bound oligomer (approx. 20 mg) was placed in a 2 mL screw top vial to which was added an ice-cold solution of the deprotection "cocktail" (TFA/Et_3SiH 975 uL:25 uL). The resin was agitated for 1.5 h. Filtration through a Pasteur pipette packed with glass wool (0.5 cm) into a clean 2 mL vial followed by removal of the TFA with a gentle stream of nitrogen and precipitation by the addition of cold diethyl ether (1 mL) gave an off-white solid. The crude oligomer was dissolved in aq. TFA (0.05%), filtered (0.45 μm), and purified by RP-HPLC using a 250 mm × 4.6 mm, C18-bonded phase, 300 Å pore, and 5 μm particle size column. Mass spectral analysis of the oligomer was performed at the UWO Biological Mass Spectrometry Laboratory using ESI-TOF MS.

Acknowledgements

We thank the Natural Science and Engineering Research Council of Canada (NSERC) for funding this work through their Discovery Grants program. FW acknowledges an NSERC PGS-D scholarship. Mr. Doug Hairsine, Department of Chemistry, is thanked for performing HRMS of small molecules. Ms. Paula Pittock of the Biological Mass Spectrometry Laboratories (UWO) is thanked for characterization of the polyamide.

References

1. P.E. Nielsen, M. Egholm, R.H. Berg, and O. Buchardt. Science, **254**, 1497 (1991).
2. P.E. Nielsen. Curr. Med. Chem. **8**, 545 (2001).
3. (*a*) P.E. Nielsen. Mol. Biotechnol. **26**, 233 (2004); (*b*) M. Leijon, M. Mousavi-Jazi, M. Kubista. Mol. Aspects Med. **27**, 160 (2006).
4. F. Wojciechowski and R.H.E. Hudson. Curr. Top. Med. Chem. **7**, 667 (2007).
5. (*a*) M. Egholm, O. Buchardt, P.E. Nielsen, and R.H. Berg. J. Am. Chem. Soc. **114**, 1895 (1992); (*b*) M. Egholm, O. Buchardt, P.E. Nielsen, and R.H. Berg. J. Am. Chem. Soc. **114**, 9677 (1992).
6. (*a*) J. Hunziker, E.S. Priestly, H. Brunar, and P.B. Dervan. J. Am. Chem. Soc. **117**, 2662 (1995); (*b*) M. D'Costa, V.A. Kumar, and K.N. Ganesh. J. Org. Chem. **68**, 4439 (2003).
7. (*a*) A. Ono, P.O.P. Ts'o, and L.J. Kan. J. Am. Chem. Soc. **113**, 4032 (1991); (*b*) A. Ono, P.O.P. Ts'o, and L. Kan. J. Org. Chem. **57**, 3225 (1992).
8. F. Wojciechowski and R.H.E. Hudson. J. Org. Chem. **73**, 3807 (2008).
9. M. Beran, A. Cerny, J. Krepelka, and J. Vachek. Collect. Czech. Chem. Commun. **48**, 292 (1983).
10. M. Egholm, L. Christensen, K.L. Dueholm, O. Buchardt, J. Coull, and P.E. Nielsen. Nucleic Acid Res. **23**, 217 (1995).
11. P. Neuner and P. Monaci. Bioconjugate Chem. **13**, 676 (2002).

© 2008 NRC Canada

Synthesis of novel 2-alkyl substituted oleobenzimidazole derivatives using ethylene glycol as solvent

K.M. Hosamani, V.B. Hiremath, R.S. Keri, R.S. Harisha, and S.B. Halligudi

Abstract: The objective of this research was to conduct constructive organic chemistry by using ethylene glycol as an efficient solvent and to achieve yields that were comparable to or better than those in other media. The reaction parameters, such as temperature (150–200 °C), density, and reaction time (6 h), have been systematically studied to understand whether ethylene glycol is as an efficient solvent and can have a positive effect on the chemistry with good yields. By tuning the parameters, the yields have been optimized to around 70%–80%. Thus, a new class of 2-alkyl substituted oleo-benzimidazole derivatives have been synthesized and characterized by FTIR, ^{1}H NMR, ^{13}C NMR, MS, and elemental analysis.

Key words: oleochemistry, ethylene glycol, oleo-benzimidazole derivatives, unusual fatty acids.

Résumé : L'objectif de ce travail était d'effectuer des synthèses organiques, en utilisant l'éthylèneglycol comme solvant efficace, et d'obtenir des rendements au moins aussi bon que ceux dans d'autres milieux. On a étudié d'une façon systématique les paramètres des réactions, tels la température (150 à 200 °C), la densité et le temps de réaction (6 h) déterminer si l'éthylèneglycol est un solvant efficace, s'il a un effet positif sur la chimie et aussi sur les rendements. En ajustant les paramètres, les rendements ont pu être optimisés entre 70% et 80%. Ainsi, on a pu synthétiser une nouvelle classe d'oléobenzimidazoles substitués par un groupement alkyle en position 2 qui a été caractérisée par infrarouge à transformée de Fourier, par RMN du ^{1}H et du ^{13}C, par spectrométrie de masse et par analyse élémentaire.

Mots-clés : oléochimie, éthylèneglycol, dérivés oléobenzimidazole, acides gras inhabituels.

[Traduit par la Rédaction]

Introduction

Because of environmental concerns, the use of benign catalysts as an alternative to hazardous solvents are of much interest to organic chemists. Thus, the use of such polar solvents as reaction media can offer an alternative to hazardous solvents (1, 2). Recently, polar solvents have been successfully employed for their catalytic activity in a variety of reactions (3). To reduce waste problems, we are reporting ethylene glycol as an efficient solvent. Moreover, their high boiling point affinity for water makes cyclocondensation easier.

Interest in the biological and industrial potentialities of oleochemicals has resulted in the development of various synthetic protocols for the introduction of potent heterocyclic moiety into the fatty acid chain. Thus, we explored the possibility of synthesizing 2-alkyl substituted oleo-benzimidazole derivatives libraries from o-phenylenediamine, 4-bromo-*o*-phenylenediamine, and 4-nitro-*o*-phenylenediamine with fatty acids using ethylene glycol as an efficient solvent. Such synthetic methods can facilitate the discovery of new class of oleochemicals.

The benzimidazole moiety is an important pharmacophore and potential heterocyclic nucleus in medicine. Thus, it has been used extensively in medicinal chemistry (4) because of its diverse range of biological activities including anti-arrhythmic, antifungal, antiulcer, antihistamine, and cytotoxicity (5). Benzimidazoles are a component of vitamin B12 and are related to the DNA base purine and the stimulant caffeine. Bisbenzimidazoles are being developed as DNA minor-groove binding agents with antitumor activity (6, 7) and can act as ligands to transition metals for modelling biological systems (8).

A literature survey reveals that *o*-phenylenediamine undergoes cyclo-condensation with aliphatic acids in aq. HCl method (9) and also with aromatic acids in PPA method (10), or PPE method (11) at 180–200 °C, or aromatic acids in ethylene glycol method (12), and it appears that there are no other methods for the cyclo-condensation of aliphatic acids with *o*-phenylenediamine. Hence, it was considered important to develop an efficient method for the cyclo-condensation of *o*-phenylenediamine with unusual fatty acids using ethylene glycol as a solvent. Considering the extensive applications of such oleochemicals as industrial and biological products, an attempt has been made to synthesize a single-step reaction with good yields of a new class of 2-

Received 19 July 2008. Accepted 15 September 2008. Published on the NRC Research Press Web site at canjchem.nrc.ca on 15 October 2008.

K.M. Hosamani,[1] V.B. Hiremath, R.S. Keri, and H.S. Reddy. P.G. Department of Studies in Chemistry, Karnatak University, Pawate Nagar, Dharwad 580 003, India
S.B. Halligudi. Catalysis Division, Dr. Homi Bhabha Road, National Chemical Laboratory, Pune 411 008, India.

[1]Corresponding author (e-mail: dr_hosamani@yahoo.com).

 doi:10.1139/V08-152 © 2008 NRC Canada

Scheme 1.

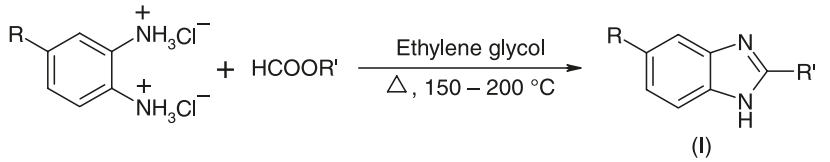

Where, R = a) -H, b) -Br, c) $-NO_2$

R' = (a') $-(CH_2)_7-CHOH-CHOH-(CH_2)_5-CH_2OH$

(b') $-(CH_2)_7-CH=CH-(CH_2)_5-CH_2OH$

(c') $-(CH_2)_7-CH=CH-(CH_2)_7-CH_3$

(d') $-(CH_2)_8-CH=CH_2$

alkyl substituted oleo-benzimidazole derivatives using ethylene glycol as a solvent.

Results and discussion

Initial efforts focused on optimizing solvent conditions for the synthesis of 2-alkyl substituted oleo-benzimdazoles employing ethylene glycol. The cyclo-condensation reaction is carried out between *o*-phenylenediamine and 4-substituted *o*-phenylenediamines with unusual fatty acids under ethylene glycol as a solvent and successfully generated desired 2-alkyl substituted oleo-benzimidazole derivatives. Our preliminary success prompted an evaluation of the reaction scope aimed at achieving the ultimate goal of applying this solvent system for the synthesis of novel 2-alkyl substituted oleo-benzimidazole derivatives.

The structures of newly synthesized novel 2-alkyl substituted oleo-benzimidazole derivatives (I-aa′ to I-cd′) were determined by IR, ^{1}H NMR, ^{13}C NMR, MS and elemental analyses.

IR spectra of all the compounds were taken on Fourier transform infrared (FTIR) Nicolet 5700 instrument using KBr pallets and also as liquid films.

The compounds (I-aa′, I-ab′, I-ba′, I-bb′, I-ca′, and I-cb′) showed strong IR absorption bands at 3456–3440 cm^{-1} for the -OH functional group in the alkyl chain. All the compounds (I-aa′ to I-cd′) had -NH stretching bands at 3326–3210 cm^{-1} in all imidazole rings of oleo-benzimdazole derivatives. The characteristic -C=N stretching bands at 1630–1612 cm^{-1} were observed in all the compounds (I-aa′ to I-cd′).

The ^{1}H NMR spectra of the 5-substituted oleo-benzimidazoles (I-aa′ to I-cd′) were recorded on Bruker Avanace 300 (300 MHz) model instrument using $CDCl_3$ and DMSO as solvents and TMS as internal standard.

The ^{1}H NMR spectra of all the compounds (I-aa′ to I-cd′) exhibited structure-revealing proton signals at δ 7.0–7.6 (multiplet, aromatic protons), δ 7.1–7.3 (s, 1H, -N*H*, which merged with aromatic protons and disappeared on D_2O addition), δ 3.5–3.9 (multiplet, 2H, -CH_2OH), δ 3.3–3.6 (singlet, 1H, -O*H*, disappeared on D_2O addition), δ 4.2–4.8 (multiplet, 2H, -C*H*=C*H*-), δ 2.3–2.5 (singlet, 2H, 2 × [-C*H*-]), δ 1.1–1.6 (broad multiplet, shielded methylene protons) and δ 0.8–0.2 (singlet, 3H, terminal -CH_3).

The ^{13}C NMR spectra of all the compounds (I-aa′ to I-cd′) showed sharp singlet signals at δ 168–184 for imidazole carbon, at δ 128–146 for aromatic carbon atoms, δ 119–129 for sp^2 hybridized carbons, and at δ 10–94 saturated carbon atoms and tertiary carbon atoms with DMSO solvent signals.

The mass spectra of the 2-alkyl substituted oleo-benzimidazole derivatives (I-aa′ to I-cd′) were recorded on Shimazu mass spectrometer (GCMS) with ionization energy maintained at 70 eV. Thus, all the compounds (I-aa′ to I-cd′) showed the corresponding molecular ion peaks (M +1).

Conclusions

To summarize, a novel methodology provides a facile route for the synthesis of new class of 2-alkyl substituted oleobenzimidazole derivatives using easily available precursors with considerably good yield. The broad chemistry scope and the efficiency have been demonstrated through successful novel synthetic methodologies of a diverse set of 2-alkyl substituted oleo-benzimidazole derivatives. Further investigation to explore the synthetic strategy for designing various novel oleo-benzimidazoles and their biological evaluation is under way.

Experimental

The synthesis of 2-alkyl substituted oleo-benzimidazole derivatives (Scheme 1) is a typical method. A mixture of equimolar quantities of *o*-phenylenediamine dihydrochloride (10 mmol) and aleuritic acid (10 mmol) with ethylene glycol (10 mL) in a two-necked round-bottomed flask was stirred vigorously for about 30 min. Then it was refluxed for about 6 h maintaining the temperature at 150–200 °C. The reaction mixture was cooled to room temperature and poured into ice-cold water (100 mL). The soft, syrupy insoluble mass was stirred until the product had hardened to a solid. The product was treated with sodium bicarbonate solution and washed with distilled water, until free from alkali, and dried. The yield of 2-alkyl substituted oleo-benzimidazole was recorded.

Similarly, aleuritic acid, ambrettoliec acid, oleic acid, and undecelynic acid were treated with *o*-phenylenediamine dihydrochloride, 4-bromo-*o*-phenylenediamine dihydrochloride, and 4-nitro-*o*-phenylenediamine dihydrochloride to obtain 2-alkyl oleo-benzimidazole derivatives under the same reaction conditions, respectively. For analytical purposes, the crude products were recrystallized from alcohol with the treatment of animal charcoal. The melting points were determined by the open capillary method and are uncorrected.

© 2008 NRC Canada

Compound (I-aa′)

Yield 74%, colourless crystals (ethanol), mp 130–132 °C. IR (KBr, cm^{-1}) ν: 3311 (NH), 1632 (C=N-). ^{1}H NMR (300 MHz, DMSO, ppm) δ: 7.0–7.4 (m, 4H, Ar-H), 7.2–7.3(s, 1H, -N*H*), 4.0 (m, 2H, -CH_2OH) 3.7 (s, 3H, 3 × [-O*H*]), 2.4 (s, 2H, 2 × [-C*H*-]), 1.3 (bm, 24H, -[CH_2]). ^{13}C NMR (300 MHz, DMSO, ppm) δ: 178 (imidazole carbon), 130–142 (aromatic carbons), 12–80 (saturated carbons and tertiary carbons with DMSO carbons). MS *m*/*z* 377 (M + 1). Anal. calcd. for $C_{12}H_{36}N_2O_3$: C 70.21, H 9.57, N 7.44; found: C 70.12, H 9.42, N 7.12.

Compound (I-ab′)

Yield 79%, colourless crystals (ethanol), mp 180–181 °C. IR (KBr, cm^{-1}) ν: 3456 cm^{-1} (-OH stretching), 3326 cm^{-1} (-NH stretching), 1615 cm^{-1} (-C=N). ^{1}H NMR (300 MHz, DMSO, ppm) δ: 7.3–7.6 (m, 4H, Ar-H), 7.3 (s, 1H, -N*H*), 4.5 (m, 2H, -C*H*=C*H*-), 3.8 (m, 2H, -CH_2OH), 3.6 (s, 1H, -O*H*), 1.3 (bm, 24H, -[CH_2]). ^{13}C NMR (300 MHz, DMSO, ppm) δ: 180 (imidazole carbon), 130–140 (aromatic carbons), 120–126 (sp^2 hybridized carbons), 10–85 (saturated carbons and tertiary carbons with DMSO carbons). MS *m*/*z* 343 (M + 1). Anal. calcd. for $C_{22}H_{34}N_2O$: C 77.19, H 9.94, N 8.18; found: C 77.12, H 9.86, N 8.12.

Compound (I-ac′)

Yield 76%, colourless crystals (ethanol), mp 210–211 °C. IR (KBr, cm^{-1}) ν: 3320 (NH), 1628(C=N-), ^{1}H NMR (300 MHz, DMSO, ppm) δ: 7.2–7.4 (m, 4H, Ar-H), 7.4 (s, 1H, -NH), 4.4 (m, 2H, -C*H*=C*H*-), 1.6 (bm, 28H), 0.9 (s, 3H, -CH_3). ^{13}C NMR (300 MHz, DMSO, ppm) δ: 175 (imidazole carbon), 125–126 (sp^2 hybridized carbons), 129–136 (aromatic carbons) 12–93 (saturated carbons and tertiary carbons with DMSO carbons). MS *m*/*z* 355 (M + 1). Anal. calcd. for $C_{24}H_{38}N_2$: C 81.33, H 10.73, N 7.90; found: C 81.23, H 10.62, N 7.88.

Compound (I-ad′)

Yield 79%, colourless crystals (ethanol), mp 153–154 °C. IR (KBr, cm^{-1}) ν: 3324 (NH), 1625(C=N-), ^{1}H NMR (300 MHz, DMSO, ppm) δ: 7.3–7.6 (m, 4H, Ar-H) 7.6 (s, 1H, -NH), 4.8 (m, 2H, -C*H*=C*H*-), 1.3 (bm, 16H, -[CH_2]). ^{13}C NMR (300 MHz, DMSO, ppm) δ: 175 (imidazole carbon) 122–126 (sp^2 hybridized carbons), 129–143 (aromatic carbons), 10–91(saturated carbons and tertiary carbons with DMSO carbons). MS *m*/*z* 257 (M + 1). Anal. calcd. for $C_{17}H_{24}N_2$: C 79.68, H 9.37, N 10.93; found: C 79.66, H 9.33, N 10.89.

Compound (I-ba′)

Yield 74%, colourless crystals (ethanol), mp 164–165 °C. IR (KBr, cm^{-1}) ν: 3312 (-NH), 1626(-C=N-).^{1}H NMR (300 MHz, DMSO, ppm) δ: 7.1–7.4 (m, 4H, aromatic protons), 7.3(s, 1H, -NH), 3.8 (m, 2H, -CH_2OH) 3.4 (s, 3H, 3 × [-O*H*]), 2.5 (s, 2H), 1.3 (bm, 24H, -[CH_2] shielded methylene protons). ^{13}C NMR (300 MHz, DMSO, ppm) δ: 171 –182 (imidazole carbon), 128–138 (aromatic carbons), 12–86 (saturated carbons and tertiary carbons with DMSO carbons). MS *m*/*z* 455 (M + 1). Anal. calcd. for $C_{22}H_{35}N_2O_3Br$: C 58.02, H 7.69, N 6.15; found: C 57.96, H 7.62, N 6.02.

Compound (I-bb′)

Yield 75%, colourless crystals (ethanol), mp 161–162 °C. IR (KBr, cm^{-1}) ν: 3452 cm^{-1} (-OH), 3322 (NH), 1614(C=N-). ^{1}H NMR (300 MHz, DMSO, ppm) δ: 7.1–7.5 (m, 4H, aromatic protons), 7.3 (s, 1H, -N*H*), 4.3 (m, 2H, -C*H*=C*H*-), 3.7 (m, 2H, -CH_2OH), 3.4 (s, 1H, -O*H*), 1.2 (bm, 24H, -[CH_2]). ^{13}C NMR (300 MHz, DMSO, ppm) δ: 179 (imidazole carbon), 127–138 (aromatic carbons), 119–124 (sp^2 hybridized carbons), 12–88 (saturated carbons and tertiary carbons with DMSO carbons). MS *m*/*z* 455 (M + 1). Anal. calcd. for $C_{22}H_{33}N_2OBr$: C 62.70, H 7.83, N 6.65; found: C 62.68, H 7.82, N 6.29.

Compound (I-bc′)

Yield 80%, colourless crystals (ethanol), mp 220–222 °C. IR (KBr, cm^{-1}) ν: 3321(NH), 1624(C=N-).^{1}H NMR (300 MHz, DMSO, ppm) δ: 7.0–7.5 (m, 4H, Ar-H), 7.0(s, 1H, -N*H*), 4.2(m, 2H, -C*H*=C*H*-), 1.3 (bm, 28H, -[CH_2]), 0.8 (s, 3H, terminal -CH_3). ^{13}C NMR (300 MHz, DMSO, ppm) δ: 180 (imidazole carbon), 124–128 (sp^2 hybridized carbons), 131–136 (aromatic carbons) 10–92 (saturated carbons and tertiary carbons with DMSO carbons). MS *m*/*z* 434 (M + 1). Anal. calcd. for $C_{24}H_{37}N_2Br$: C 66.51, H 8.54, N 6.41; found: C 66.36, H 8.42, N 6.39.

Compound (I-bd′)

Yield 75%, colourless crystals (ethanol), mp 182–183 °C. IR (KBr, cm^{-1}) ν: 3320(NH), 1622(C=N-).^{1}H NMR (300 MHz, DMSO, ppm) δ: 7.1–7.5 (m, 4H, Ar-H), 7.4 (s, 1H, -N*H*), 4.4 (m, 2H, -C*H*=C*H*-), 1.2 (bm, 16H, -[CH_2]). ^{13}C NMR (300 MHz, DMSO, ppm) δ: 182 (imidazole carbon), 120–126 (sp^2 hybridized carbons), 130–144 (aromatic carbons), 12–88 (saturated carbons and tertiary carbons with DMSO carbons). MS *m*/*z* 336(M + 1). Anal. calcd. for $C_{17}H_{23}N_2Br$: C 60.07, H 7.16, N 8.35; found: C 60.01, H 7.09, N 8.28.

Compound (I-ca′)

Yield 79%, colourless crystals (ethanol), mp 197–198 °C. IR (KBr, cm^{-1}) ν: 3440 cm^{-1} (-OH), 3310 (-NH), 1622 (C=N-).^{1}H NMR (300 MHz, DMSO, ppm) δ: 7.2–7.4 (m, 4H, Ar-H), 7.4(s, 1H, -N*H*), 3.5 (m, 2H, -CH_2OH), 3.3 (s, 3H, 3 × [-O*H*]), 2.3 (s, 2H, 2 × [-C*H*-]), 1.2 (bm, 24H, -[CH_2]). ^{13}C NMR (300 MHz, DMSO, ppm) δ: 184 (imidazole carbon), 130–140 (aromatic carbons), 12–90 (saturated carbons and tertiary carbons with DMSO carbons). MS *m*/*z* 422 (M + 1). Anal. calcd. for $C_{22}H_{35}N_3O_5$: C 62.71, H 8.31, N 9.97; found: C 62.15, H 8.25, N 9.91.

Compound (I-cb′)

Yield 72%, colourless crystals (ethanol), mp 211–212 °C. IR (KBr, cm^{-1}) ν: 3450 cm^{-1} (-OH), 3318 (-NH), 1612(C=N-).^{1}H NMR (300 MHz, DMSO, ppm) δ: 7.0–7.5 (m, 4H, Ar-H) 7.4 (s, 1H, -N*H*), 4.2 (m, 2H, -C*H*=C*H*-), 3.8 (m, 2H, -CH_2OH), 3.4 (s, 1H), 1.1 (bm, 24H, -[CH_2]). ^{13}C NMR (300 MHz, DMSO, ppm) δ: 182 (imidazole carbon), 128–139 (aromatic carbons), 120–125 (sp^2 hybridized carbons), 14–90 (saturated carbons and tertiary carbons with DMSO carbons. MS *m*/*z* 388 (M + 1). Anal. calcd. for $C_{22}H_{33}N_3O_3$: C 68.21, H 8.52, N 10.85; found: C 68.17, H 8.43, N 10.70.

© 2008 NRC Canada

Compound (I-cc′)

Yield 80%, colourless crystals (ethanol), mp 191–192 °C. IR (KBr, cm^{-1}) ν: 3324 (-NH), 1628 (C=N-).^{1}H NMR (300 MHz, DMSO, ppm) δ: 7.1–7.6(m, 4H, Ar-H), 7.6 (s, 1H, -N*H*), 4.3 (m, 2H, -C*H*=C*H*-), 1.2 (bm, 28H, -[CH_2]), 1.2 (s, 3H, -CH_3). ^{13}C NMR (300 MHz, DMSO, ppm) δ: 184 (imidazole carbon), 125–129 (sp^2 hybridized carbons), 132–137 (aromatic carbons) 14–94 (saturated carbons and tertiary carbons with DMSO carbons). MS *m*/*z* 400 (M + 1). Anal. calcd. for $C_{24}H_{37}N_3O_2$: C 72.18, H 9.27, N 10.52; found: C 72.06, H 9.15, N 10.44.

Compound (I-cd′)

Yield 73%, colourless crystals (ethanol), mp 225–226 °C. IR (KBr, cm^{-1}) ν: 3326 (-NH), 1618 (C=N-). ^{1}H NMR (300 MHz, DMSO, ppm) δ: 7.2–7.6 (m, 4H, aromatic protons), 7.4 (s, 1H, -N*H*), 4.3 (m, 2H, -C*H*=C*H*-), 1.3 (bm, 16H, -[CH_2]). The ^{13}C NMR (300 MHz, DMSO, ppm) δ: 179 (imidazole carbon) 122–128 (sp^2 hybridized carbons), 132–146 (aromatic carbons), 14–92 (saturated carbons and tertiary carbons with DMSO carbons). MS *m*/*z* 302 (M + 1). Anal. calcd. for $C_{17}H_{23}N_3O_2$: C 67.74, H 7.64, N 12.64; found: C 67.29, H 7.49, N 12.51.

Acknowledgements

This research work is financially supported by the Department of Science & Technology (DST), New Delhi, 110 016. (Ref. No. SR/S1/OC-08/2005 dated 5 September 2005).

References

1. T. Welton. Chem. Rev. **99**, 2071 (1999).
2. R. Sheldon. Chem. Commun. 2399 (2001).
3. T.S. Li, Z.H. Zhang, F. Yang, and C.G. Fu. J. Chem. Res. **1**, 38 (1998).
4. P.N. Preston. *In* The chemistry of heterocyclic compounds of benzimidazoles and congeneric tricyclic compounds. Vol. 40. No. 2,. John Wiley and Sons, New York, USA. 1980. Chap. 10.
5. D.A. Horton, G.T. Bourne, and M.L. Smythe. Chem. Rev. **103**, 893 (2003).
6. J. Mann, A. Baron, Y. Opoku-Boahen, E. Johansson, G. Parkinson, L.R. Kelland, and S. Neidle. J. Med. Chem. **44**, 138 (2001).
7. E. Bouwman, W.L. Driessen, and J. Reedijk. Coord. Chem. Rev. **104**, 143 (1990).
8. M.A. Pujar and T.D. Bharamgoudar. Transition Met. Chem. **13**, 423 (1988).
9. M.A. Phillips. J. Chem. Soc. 2395 (1928).
10. D.W. Hein, R.J. Alheim, and J.J. Leavitt. J. Am. Chem. Soc. **79**, 427 (1957).
11. Y. Kanaoka, O. Yonemitsu, K. Tanizawa, and Y. Ban. Chem. Pharm. Bull. (Tokyo), **12**, 773 (1964).
12. P.K. Dubey, R. Kumar, C. Ravikumar, J.S. Grossert, and D.L. Hooper. Synth. Commun. **31**(22), 3439 (2001).

© 2008 NRC Canada

Association of ruthenium complexes $[Ru(bpy)_3]^{2+}$ or $[Ru(bpy)_2(Mebpy\text{-}py)]^{2+}$ with Dawson polyanions $\alpha\text{-}[P_2W_{18}O_{62}]^{6-}$ or $\alpha_2\text{-}[Fe^{III}(H_2O)P_2W_{17}O_{61}]^{7-}$

L. Ruhlmann, C. Costa-Coquelard, J. Hao, S. Jiang, C. He, L. Sun, and I. Lampre

Abstract: The formation of electrostatically linked complexes between $[Ru(bpy)_3]Cl_2$ or $[Ru(bpy)_2(Mebpy\text{-}py)](PF_6)_2$ and $(TBA)_6\alpha\text{-}[P_2W_{18}O_{62}]$ or $(TBA)_5K_2\alpha_2\text{-}[Fe^{III}(H_2O)P_2W_{17}O_{61}]$ in solution were studied by steady-state absorption and luminescence spectroscopy. The stoichiometry and global association constants of the formed complexes were obtained by the Job method. The formed complexes were characterized by ^1H and ^{31}P NMR spectroscopy and their electrochemical properties compared to the precursor compounds were investigated by using the cyclic voltammetry method.

Key words: electrochemistry, polyoxometalate, ruthenium complex, electrostatic complex.

Résumé : Nous avons étudié la formation en solution de complexes, liés d'une façon électrostatique, entre le $[Ru(bpy)_3]Cl_2$ ou $[Ru(bpy)_2(Mebpy\text{-}py)](PF_3)_2$ et le $(TBA)_6\alpha\text{-}[P_2W_{14}O_{62}]$ ou $(TBA)_5K_2\alpha_2\text{-}[Fe^{III}(H_2O)P_2W_{17}O_{61}]$ en faisant appel à la spectroscopie de luminescence et à la spectroscopie d'absorption à l'état stationnaire. On a déterminé la stoechiométrie et les constantes d'association globales des complexes formés en faisant appel à la méthode de Job. On a caractérisé les complexes formés à l'aide de la spectroscopie RMN du ^1H et du ^{31}P et on a étudié leurs propriétés électrochimiques à l'aide de la méthode de voltampérométrie cyclique par comparaison avec leurs précurseurs.

Mots-clés : électrochimie, polyoxométalate, complexe de ruthénium, complexe électrostatique.

[Traduit par la Rédaction]

Introduction

The Dawson-derived type polyoxometalates (POMs) are a versatile and robust group of compounds with many applications in fields such as molecular magnetism (1–2), catalysis (3–7), and photocatalysis (8). Indeed, the ability to modify the redox and chemical properties of heteropolyanions by replacing one or many elements renders them particularly attractive for catalytic and electrocatalytic applications (9–15). For instance, a cluster such as $[P_2W_{18}O_{62}]^{6-}$ could be modified under hydrolysis or hydrolytic conditions into lacunary complexes containing one, three, or more vacant sites (16–18). Ru–POM complexes appear to be quite promising in photocatalytic reactions since the ruthenium complex may play the role of photosensitizer or antenna for the redox-active heteropolyanion, provided that the latter has useful catalytic properties. The association of ruthenium complexes with polyanions has been of interest in recent years because of their application in catalysis. In the area of electrocatalysis, extensive work has been undertaken to probe the nature of polyoxometalate films formed on the electrode surfaces in the presence of cations including $[Os(bpy)_3]^{2+}$ or $[Ru(bpy)_3]^{2+}$ (bpy = 2,2′-bipyridine). For instance, the capacity of the multicharged cation $[Os(bpy)_3]^{2+}$ to bind electrostatically to polyoxomolybdate anions has been demonstrated by Anson and co-workers (19). Their observations are consistent with the fact that monolayers of $[P_2Mo_{18}O_{62}]^{6-}$ bind electrostatically to $[Os(bpy)_3]^{2+}$ cations on electrode surfaces, creating alternating multilayers of molybdate and osmium ions. Han et al. reported the synthesis and X-ray crystallographic study of the first $[Ru(bpy)_3]^{2+}$ complex with a decatungstate cluster anion (20). Hultgren et al. reported the formation of neutral ionic complexes $[Ru(bpy)_3]_2[S_2Mo_{18}O_{62}]$ at electrode–solvent interfaces by electrochemistry (21). Keyes et al. studied the photophysical properties of ion clusters formed between $[Ru(bpy)_3]^{2+}$ and the polyoxotungstate anions $[S_2M_{18}O_{62}]^{4-}$ or $[S_2W_{18}O_{62}]^{4-}$ in solution (22–23). Recently, McCormac and co-workers (24) published the preparation of $[Ru(bpy)_3]_3[P_2W_{18}O_{62}]$ complexes. The complexes were formed from $Ru(bpy)_3Cl_2$ and the mixture of isomers α- and β-$K_6[P_2W_{18}O_{62}]$, and these complexes were characterized by microanalysis (31), P NMR spectroscopy, and electrochemistry.

This work focuses on the cluster formation of $[Ru(bpy)_3]^{2+}$ (**Ru-1**) or $[Ru(bpy)_2(Mebpy\text{-}py)]^{2+}$ (**Ru-2**) with polyoxometalates $\alpha\text{-}[P_2W_{18}O_{62}]^{6-}$ or $\alpha_2\text{-}[Fe^{III}(H_2O)P_2W_{17}O_{61}]^{7-}$ (Scheme 1). Because the two reactants have opposite charges, the association should proceed mainly via electrostatic interactions. **Ru-2**, which has one pyridine carried by

Received 27 May 2008. Accepted 31 July 2008. Published on the NRC Research Press Web site at canjchem.nrc.ca on 15 October 2008.

L. Ruhlmann,[1] C. Costa-Coquelard, J. Hao, and I. Lampre. [1] Laboratoire de Chimie Physique, UMR 8000 CNRS/Université Paris-Sud 11, Faculté des Sciences d'Orsay, Bâtiment 349, 91405 Orsay CEDEX, France.
S. Jiang, C. He, and L. Sun. State Key Laboratory of Fine Chemicals, Dalian University of Technology, Zhongshan Road 158–46, Dalian 116012, China.

[1]Corresponding authors (e-mail: laurent.ruhlmann@u-psud.fr, isabelle.lampre@u-psud.fr).

 doi:10.1139/V08-139 © 2008 NRC Canada

Scheme 1. Representation of the studied ruthenium and polyoxometalate complexes. Left: $[Ru(bpy)_3]^{2+}$ (**Ru-1**) and $[Ru(bpy)_2(Mebpy\text{-}py)]^{2+}$ (**Ru-2**). Right: Polyhedral representation of the Dawson-type structures α-$[P_2W_{18}O_{62}]^{6-}$ and α_2-$[Fe(H_2O)P_2W_{17}O_{61}]^{7-}$.

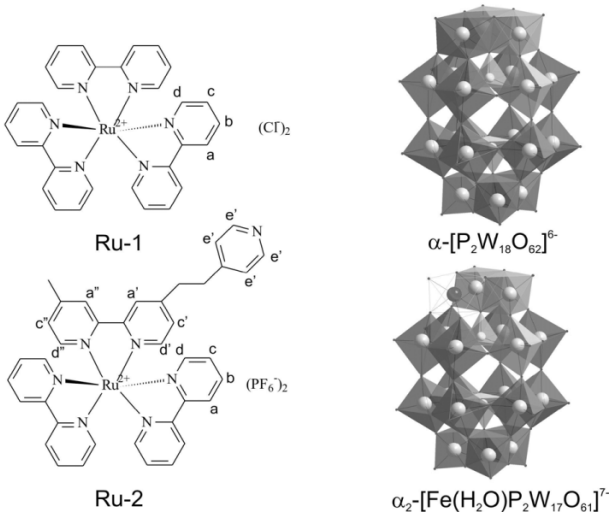

one of the three 2,2′-bipyridine ligands, was synthesized for the purpose of forming a possible coordination bond between the pyridine ligand and the iron(III) of α_2-$[Fe^{III}(H_2O)P_2W_{17}O_{61}]^{7-}$ via the substitution of the labile (H_2O) ligand.

Results and discussion

UV–vis absorption and luminescence spectroscopies

The absorption and luminescence spectroscopic results were obtained with DMF as solvent. Similar results were obtained with DMSO solvent. The optical absorption spectrum of $[Ru(bpy)_3]Cl_2$ in DMF was characterized by a broad band in the visible domain around 450 nm ($\varepsilon_{454\ nm}$ = 12 850 $dm^3\ mol^{-1}\ cm^{-1}$) and an intense band peaking at 290 nm ($\varepsilon_{290\ nm}$ = 71 950 $dm^3\ mol^{-1}\ cm^{-1}$) (inset of Fig.1*A*). The visible absorption band is attributed to a metal-to-ligand charge transfer (MLCT) transition in which an electron located in a metal-based d orbital is promoted into a ligand-centered π^* orbital; the UV absorption band corresponds to a ligand-centered π–π^* transition (25). The observed emission of $[Ru(bpy)_3]^{2+}$ comes from the lowest energy ^{3}MLCT state, which is rapidly formed with a quantum yield near unity. The polyoxometalate $(TBA)_6\alpha$-$[P_2W_{18}O_{62}]$ in DMF absorbs in the UV spectral domain below 350 nm (inset of Fig. 1*A*) and is non-luminescent.

Fig. 1 presents the evolution of the absorption and emission spectra of a diluted DMF solution of $[Ru(bpy)_3]Cl_2$ (1.29×10^{-5} mol/L) titrated by a concentrated solution of $(TBA)_6\alpha$-$[P_2W_{18}O_{62}]$ (2.4×10^{-4} mol/L). During the titration, the absorbance around 290 nm increased strongly and the band broadened whereas the absorbance around 450 nm decreased slightly. Moreover, two isosbestic points appeared at 405 and 474 nm indicating equilibria between species in solution (Fig. 1*A*). The steady-state luminescence study showed that the $[Ru(bpy)_3]^{2+}$ emission spectrum decreased in intensity during the titration but its shape and the maximum position did not change. A total quenching of the $[Ru(bpy)_3]^{2+}$ emission was obtained when the added $(TBA)_6\alpha$-$[P_2W_{18}O_{62}]$ concentration was above 4.3×10^{-6} mol/L, which corresponded to one third of the initial concentration of $[Ru(bpy)_3]Cl_2$.

Fig. 1. Steady-state UV–vis (*A*) absorption and (*B*) luminescence spectra recorded during the titration of a 1.29×10^{-5} mol/L DMF solution of $[Ru(bpy)_3]Cl_2$ by a 2.40×10^{-4} mol/L solution of $(TBA)_6\alpha$-$[P_2W_{18}O_{62}]$ (optical length = 1 cm, λ_{ex} = 490 nm). Inset: absorption spectra of a DMF solution containing 1.29×10^{-5} mol/L of $[Ru(bpy)_3]Cl_2$ (solid line) or 3.02×10^{-6} mol/L of $(TBA)_6\alpha$-$[P_2W_{18}O_{62}]$ (dashed line).

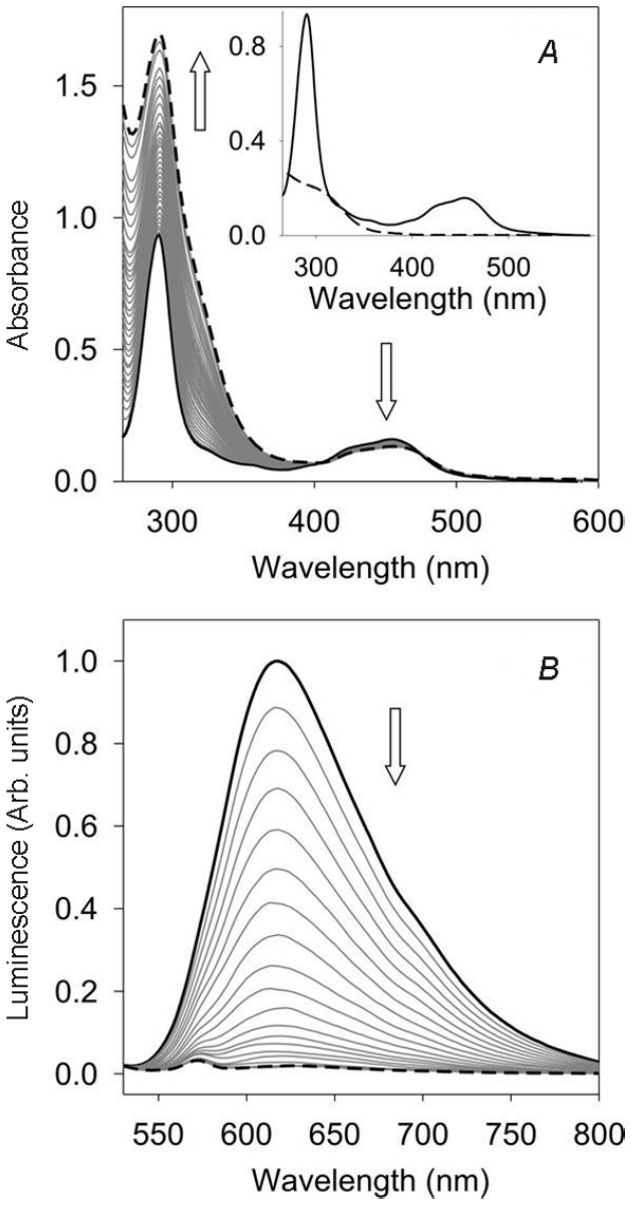

The absorption and luminescence results reveal strong interactions between the Ru compound and the polyoxometalate and indicate the formation of mixed complexes.

To determine the stoichiometry of the complexes formed during the titration and to estimate the global association constants, the well-known Job's method was used. For a given wavelength λ, the absorption difference $\Delta\varepsilon$ between

© 2008 NRC Canada

Fig. 2. Job Plot of the absorption change Δε at 290 nm and 310 nm versus the mole fraction of the added POM for the titration of Fig. 1.

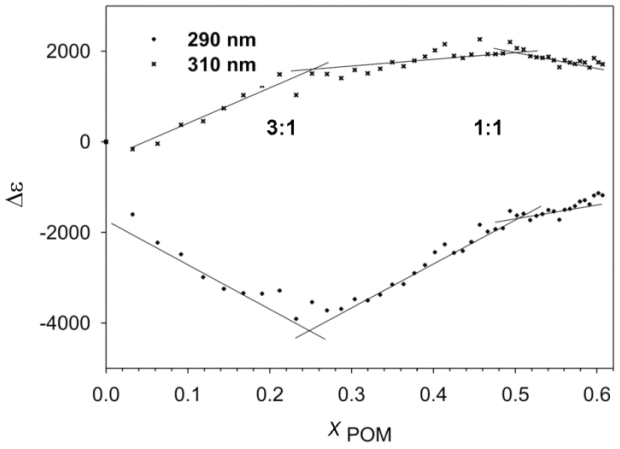

the measured value and the expected value from two compounds is calculated according to the equation

$$\Delta\varepsilon = A/l\ C_t - (1 - X_{POM})\varepsilon_{Ru} - X_{POM}\varepsilon_{POM}$$

where A is the measured absorbance, l is the optical length, C_t is the total concentration of compounds in solution (C_t = [[Ru(bpy)$_3$]Cl$_2$] + [(TBA)$_6$α-[P$_2$W$_{18}$O$_{62}$]]), ε_{Ru} and ε_{POM} are the molar extinction coefficients at the chosen wavelength of [Ru(bpy)$_3$]$^{2+}$ and α-[P$_2$W$_{18}$O$_{62}$]$^{6-}$ respectively, and X_{POM} is the mole fraction of polyoxometalate.

In Fig. 2, Δε at two different wavelengths is plotted as a function of X_{POM} for the titration of [Ru(bpy)$_3$]Cl$_2$ by (TBA)$_6$α-[P$_2$W$_{18}$O$_{62}$]. The curves of Δε clearly show three parts that can be fitted by straight lines. The lines intersect at X_{POM} equal to 0.25 and 0.5. These results reveal the existence of two successive equilibria in solution with the formation of two complexes whose stoichiometries are determined by the intersection points. So the first complex, corresponding to a mole fraction of α-[P$_2$W$_{18}$O$_{62}$]$^{6-}$ equal to 0.25, is a 3:1 complex formed by three [Ru(bpy)$_3$]$^{2+}$ and one α-[P$_2$W$_{18}$O$_{62}$]$^{6-}$, whereas the second complex with X_{POM} equal to 0.5 is a 1:1 complex composed by one [Ru(bpy)$_3$]$^{2+}$ and one α-[P$_2$W$_{18}$O$_{62}$]$^{6-}$. Unfortunately, because of the scale of uncertainties for calculated Δε, it is not possible to estimate the global association constants $\beta_{3:1}$ and $\beta_{1:1}$ of the complexes from the Job's plot.

The successive formation steps of the mixed complexes during the titration of [Ru(bpy)$_3$]$^{2+}$ by α-[P$_2$W$_{18}$O$_{62}$]$^{6-}$ can be summarized as

$$3\ [Ru(bpy)_3]^{2+} + \alpha\text{-}[P_2W_{18}O_{62}]^{6-} \rightleftarrows [Ru(bpy)_3]_3[P_2W_{18}O_{62}]$$

$$[Ru(bpy)_3]_3[P_2W_{18}O_{62}] + 2\ \alpha\text{-}[P_2W_{18}O_{62}]^{6-} \rightleftarrows 3\ [Ru(bpy)_3][P_2W_{18}O_{62}]^{4-}$$

It is noticed that the first complex is a neutral one, suggesting that the association should be governed by electrostatic interactions. It is also worth mentioning that the formation of this 3:1 complex induces a total quenching of

Fig. 3. Steady-state UV–vis (*A*) absorption and (*B*) luminescence spectra recorded during the titration of a 1.03 × 10^{-5} mol/L DMF solution of [Ru(bpy)$_3$]Cl$_2$ by a 0.95 × 10^{-4} mol/L solution of (TBA)$_5$K$_2$α$_2$-[Fe(H$_2$O)P$_2$W$_{17}$O$_{61}$] (optical length = 1 cm, λ_{ex} = 490 nm).

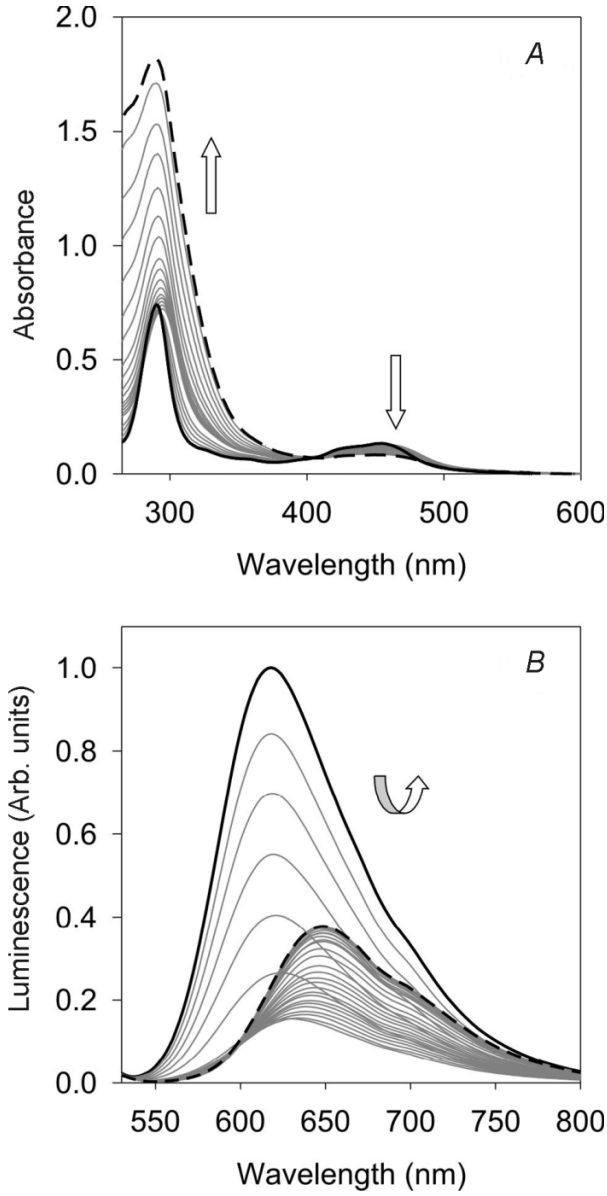

the [Ru(bpy)$_3$]$^{2+}$ emission. No luminescence is observed as X_{POM} is above 0.25 where no free [Ru(bpy)$_3$]$^{2+}$ chromophore remains in solution. Consequently, the formed 3:1 and 1:1 mixed complexes are not luminescent. When the substituted ruthenium compound [Ru(bpy)$_2$(Mebpy-py)]$^{2+}$ was used instead of [Ru(bpy)$_3$]$^{2+}$, the titration by (TBA)$_6$α-[P$_2$W$_{18}$O$_{62}$] gave very similar results. Indeed, the spectroscopic study clearly indicates the successive formation of two complexes with the soichiometries of 3:1 and 1:1.

In contrast, when the iron polyoxometalate α$_2$-[Fe^{III}(H$_2$O)P$_2$W$_{17}$O$_{61}$]$^{7-}$ replaced α-[P$_2$W$_{18}$O$_{62}$]$^{6-}$ in the titration, a different behaviour was observed. Fig. 3 shows the impact on the absorption and luminescence spectra of small

© 2008 NRC Canada

Fig. 4. Job plot of the absorption change Δε at 290 nm and 310 nm versus the mole fraction of the added POM for the titration of Fig. 3.

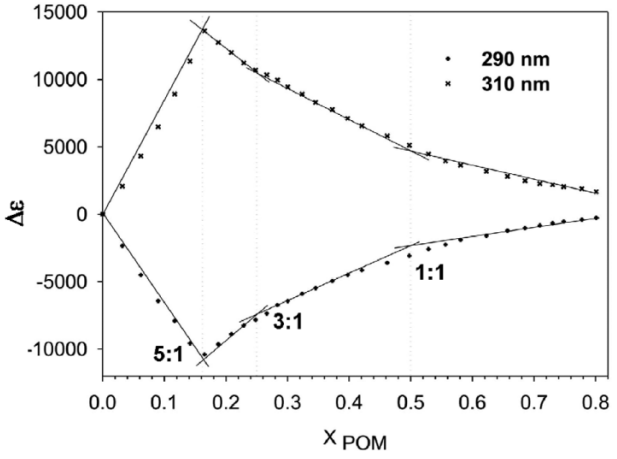

volumes of concentrated α_2-$[Fe^{III}(H_2O)P_2W_{17}O_{61}]^{7-}$ (9.5×10^{-5} mol/L) solution added to a diluted DMF solution of $[Ru(bpy)_3]^{2+}$. During the titration, the initial absorbance peak at 290 nm began to shift slightly to higher wavelengths and the absorption band broadened; then the absorption intensity increased strongly, while the absorption band around 450 nm broadened on the red side and its intensity decreased. An isosbestic point appeared at 278 nm at the beginning of the titration. A quasi-isosbestic point was observed at 405 nm for the overall titration process (Fig. 3*A*).

The steady-state luminescence study showed significant changes in the $[Ru(bpy)_3]^{2+}$ emission spectrum during the titration (Fig. 3*B*).

First, the luminescence intensity decreased progressively and the maximum shifted slightly from 618 nm to 631 nm with addition of α_2-$[Fe^{III}(H_2O)P_2W_{17}O_{61}]^{7-}$ up to X_{POM} close to 0.17. Then, the luminescence intensity rose and the luminescence maximum shifted further to the red zone to 648 nm for added α_2-$[Fe^{III}(H_2O)P_2W_{17}O_{61}]^{7-}$, corresponding to X_{POM} about 0.5. When an additional small volume of α_2-$[Fe^{III}(H_2O)P_2W_{17}O_{61}]^{7-}$ was added, the emission spectrum did not change any more. Only a small decrease in intensity was observed which may be attributed to the dilution factor.

This evolution in luminescence suggests the existence of at least two successive complexes with stoichiometry at 5:1 and 1:1, defined by X_{POM} equal to 0.17 and 0.5, respectively.

The formed complexes have radiative properties because the $[Ru(bpy)_3]^{2+}$ emission is not totally quenched but undergoes a bathochromic shift up to 30 nm. This red shift is larger than those previously observed for ion clusters formed between $[Ru(bpy)_3]^{2+}$ and $[S_2Mo_{18}O_{62}]^{4-}$ (12 nm)[22] or $[S_2W_{18}O_{62}]^{4-}$ (19 nm) (23), and considerably greater than that reported for interactions between $[Ru(bpy)_3]^{2+}$ and the Keggin anion $[(HO\text{-}Mn)PW_{11}O_{39}]^{6-}$ (4 nm) (26). The Job analysis of the absorption measurements along with the luminescence results indicate the existence of the 5:1 and 1:1 complexes and also reveal the existence of another intermediate complex at X_{POM} equal to 0.25, the 3:1 complex (Fig. 4).

Therefore, during the titration of $[Ru(bpy)_3]^{2+}$ by α_2-$[Fe^{III}(H_2O)P_2W_{17}O_{61}]^{7-}$, three complexes composed of one polyanion and 5, 3, or 1 ruthenium cation(s) were formed successively.

For these titrations, the calculated Δε are quite important and the point-to-point fluctuations are low. The difference between the calculated Δε and the ordinate of the intersection point at X_{POM} equal to 0.17 is very small, indicating that the global association constant $\beta_{5:1}$ is very high.

The high constant values make it difficult to estimate them precisely. As for the values of the other constants $\beta_{3:1}$ and $\beta_{1:1}$, they depend greatly on the value of $\beta_{5:1}$. The first two global association constants in terms of orders of magnitude can be determined. The third constant value is difficult to determine because of its high uncertainty. For these calculations, it is assumed that the salts are fully dissociated in solution before they react with each other. Hence

$$5\ [Ru(bpy)_3]^{2+} + \alpha_2\text{-}[Fe^{III}(H_2O)P_2W_{17}O_{61}]^{7-} \rightleftarrows [Ru(bpy)_3]_5[Fe^{III}(H_2O)P_2W_{17}O_{61}]^{3+} \qquad \beta_{5:1} \geq 3 \times 10^{41}\ M^{-5}$$

$$3\ [Ru(bpy)_3]^{2+} + \alpha_2\text{-}[Fe^{III}(H_2O)P_2W_{17}O_{61}]^{7-} \rightleftarrows [Ru(bpy)_3]_3[Fe^{III}(H_2O)P_2W_{17}O_{61}]^{-} \qquad 10^{32}\ M^{-3} \leq \beta_{3:1} \leq 2 \times 10^{33}\ M^{-3}$$

$$[Ru(bpy)_3]^{2+} + \alpha_2\text{-}[Fe^{III}(H_2O)P_2W_{17}O_{61}]^{7-} \rightleftarrows [Ru(bpy)_3][Fe^{III}(H_2O)P_2W_{17}O_{61}]^{5-} \qquad 1.5 \times 10^{10}\ M^{-1} \leq \beta_{1:1} \leq 1.5 \times 10^{12}\ M^{-1}$$

As expected, the values obtained for the global association constants are very high and increase with the stoichiometry of the complex. The estimated values are much higher than those found in the literature for ionic complexes formed by $[Ru(bpy)_3]^{2+}$ and other polyoxometalates (23, 26). However, the stoichiometry of the complexes differ as well as the solvent.

It is also noticed that the charge increase for polyanion from α-$[P_2W_{18}O_{62}]^{6-}$ to α_2-$Fe^{III}(H_2O)[P_2W_{17}O_{61}]^{7-}$ leads to the formation of one supplementary complex with higher stoichiometry (5:1). The reverse titration induces the same phenomena with the formation of the 1:1 complex followed by the 3:1 and then the 5:1 complexes, which confirms our results and proves that the three equilibria are reversible.

The titration of $[Ru(bpy)_2(Mebpy\text{-}py)]^{2+}$ (**Ru-2**) by α_2-$[Fe(H_2O)P_2W_{17}O_{61}]^{7-}$ exhibited a similar optical behaviour to that of **Ru-1**. During the titration, the absorption band around 290 nm shifted slightly to higher wavelengths with band broadening and absorbance increasing, while the absorption band around 450 nm broadened on the red side and its intensity diminished. When the concentration of α_2-$[Fe(H_2O)P_2W_{17}O_{61}]^{7-}$ gradually increased to a mole fraction X_{POM} close to 0.2, the luminescence intensity decreased progressively and the maximum shifted slightly from 624 nm to 639 nm. Then, the luminescence intensity rose and the luminescence maximum shifted to the red to reach 654 nm at X_{POM} about 0.5. When X_{POM} was above 0.5, the emission spectrum remained constant. Job's analysis shows the suc-

© 2008 NRC Canada

cessive formation of the 4:1, 2:1, and 1:1 complexes and makes it possible to estimate the global association constants

$$4\ [Ru(bpy)_2(Mebpy\text{-}py)]^{2+} + \alpha_2\text{-}[Fe^{III}(H_2O)P_2W_{17}O_{61}]^{7-} \rightleftarrows [Ru(bpy)_2(Mebpy\text{-}py)]_4[Fe^{III}(H_2O)P_2W_{17}O_{61}]^{+} \qquad \beta_{4:1} \geq 3 \times 10^{31}\ M^{-4}$$

$$2\ [Ru(bpy)_2(Mebpy\text{-}py)]^{2+} + \alpha_2\text{-}[Fe^{III}(H_2O)P_2W_{17}O_{61}]^{7-} \rightleftarrows [Ru(bpy)_2(Mebpy\text{-}py)]_2[Fe^{III}(H_2O)P_2W_{17}O_{61}]^{3-} \qquad \beta_{2:1} = (1.7 \pm 1.5) \times 10^{19}\ M^{-2}$$

$$[Ru(bpy)_2(Mebpy\text{-}py)]^{2+} + \alpha_2\text{-}[Fe^{III}(H_2O)P_2W_{17}O_{61}]^{7-} \rightleftarrows [Ru(bpy)_2(Mebpy\text{-}py)][Fe^{III}(H_2O)P_2W_{17}O_{61}]^{5-} \qquad \beta_{1:1} = (3.8 \pm 3.0) \times 10^{10}\ M^{-1}$$

It is noticed that the substitution of the ruthenium compound does not modify the number of complexes formed but leads to a change in the stoichiometry of the complexes, which are 4:1, 2:1, and 1:1 instead of 5:1, 3:1, and 1:1. In addition, the values of the global association constants appear to be of the same order of magnitude or slightly lower, which probably indicates a low steric effect of the substituting pyridine. The pyridyl groups increase the distance between the two subunits and thus diminish the electrostatic interactions.

The purpose of preparing the $[Ru(bpy)_2(Mebpy\text{-}py)]^{2+}$ compound with a pyridyl group was to study the possible formation of a 1:1 coordination complex via the substitution of the labile (H_2O) ligand of the polyoxometalate α_2-$[Fe(H_2O)P_2W_{17}O_{61}]^{7-}$ (Scheme 2*a*).

Unfortunately, a 1:1 complex was also observed in the case of $[Ru(bpy)_3]^{2+}$ (without a pyridine group). Consequently, there is a competition between coordination and electrostatic interactions. This seems to favor the formation of an ion pair (Scheme 2*b*) rather than a coordination complex. The nature of the interaction in the studied systems was probed by addition of $TBAClO_4$ or $LiClO_4$ to solutions containing different mixed Ru–POM complexes (Fig. 5). Experiments performed with solutions in the absence of POM showed that the addition of either salt up to a concentration of 0.1 mol/L had no impact on the emission spectrum and the luminescent quantum yield for the ruthenium compounds. For solutions containing Ru–POM complexes, addition of $TBAClO_4$ or $LiClO_4$ led to an increase in the luminescence intensity. But the final intensity of the emission spectrum was about 10 or 20% lower than that expected for the free Ru compounds (Fig. 5).

These observations are attributed to the dissociation of mixed Ru–POM complexes owing to competitive interactions of perchlorate with Ru cations and Li^+ or TBA^+ with POM. That indicates that the mixed complexes were mainly bound electrostatically. Similar results were previously observed by Hultgren and co-workers (21–23).

^{1}H and ^{31}P NMR spectroscopy

Fig. 6 compares the ^{1}H NMR spectra of the 3:1 and 1:1 complexes of, respectively, $[Ru(bpy)_3]_3[P_2W_{18}O_{62}]$ and $[Ru(bpy)_3][P_2W_{18}O_{62}]^{4-}$ with the precursor $[Ru(bpy)_3]^{2+}$. As is well-known, the 2,2′-bipyridine protons of $[Ru(bpy)_3]^{2+}$ (**Ru-1**) appear as two doublets and two triplets.

The doublet and the triplet at lower field correspond to protons H_c and H_d (see Scheme 1). The ^{1}H NMR spectra for the 3:1 and 1:1 electrostatic complexes are identical but

Scheme 2. Possible 1:1 complex formed with $[Ru(bpy)_2(Mebpy\text{-}py)]^{2+}$ and α_2-$[Fe(H_2O)P_2W_{17}O_{61}]^{7-}$ by (*A*) coordination bound or (*B*) electrostatic interactions.

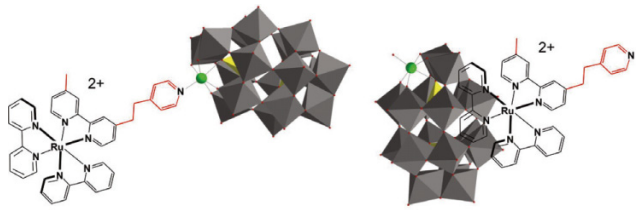

(*A*) (*B*)

there is a significant shift compared to that of $[Ru(bpy)_3]^{2+}$ alone. These observations show that the three 2,2′-bipyridine ligands are equivalent for the electrostatic complexes. This might be due to (1) a rapid dynamic process of association and dissociation and (or) (2) the ability of the ruthenium complex to turn freely on the negatively charged polyoxometalate surface leading to three equivalent 2,2′-bipyridines.

For 3:1 or 1:1 complexes, the doublet and the triplet for $[Ru(bpy)_3]^{2+}$ at 7.73 ppm (H_a) and 7.54 ppm (H_b) shift 0.04 ppm toward the lower field, while the second triplet (H_c) does not move, and the second doublet (H_d) shifts to higher field from 8.89 ppm to 8.83 ppm. It is noted that ^{1}H NMR spectra for $[Ru(bpy)_3]^{2+}$ in the presence of one or three equivalent TBACl do not show any shift in the signals.

The chemical shift of H_d to higher field might be induced by the proximity of the six negative charges in the POM moieties leading to a decrease in the electron-withdrawing impact of Ru^{2+} on protons H_d.

In contrast, protons H_a and H_b are shifted to lower field, probably because of the proximity with the polyanion. ^{31}P NMR spectra do not show any change for $[Ru(bpy)_3]_3[P_2W_{18}O_{62}]$ and $[Ru(bpy)_3][P_2W_{18}O_{62}]^{4-}$ ionic complexes with one singlet observed at –12.40 ppm corresponding to the two P atoms in the Dawson moieties. $[Ru(bpy)_2(Mebpy\text{-}py)]^{2+}$ (Ru-2) gives well-resolved ^{1}H NMR spectra, but they are more complicated than those of $[Ru(bpy)_3]^{2+}$ because of the loss of symmetry of the ruthenium complex (Fig. 7). The pyridine subunit of $[Ru(bpy)_2(Mebpy\text{-}py)]^{2+}$ appears as two doublets at 7.27 ppm ($2H_{e''}$) and 7.36 ppm ($2H_{e''}$), respectively.

Two singlets are also observed at 8.72 ppm and 8.76 ppm corresponding to $H_{a'}$ and $H_{a''}$ for the substituted 2,2′-bipyridine. The singlet at 8.76 ppm might correspond to

© 2008 NRC Canada

Fig. 5. Influence of the addition of $TBAClO_4$ on the luminescence spectra of DMF solutions containing (*A*) a 5:1 ratio of $[Ru(bpy)_3]Cl_2$ (1.29×10^{-5} mol/L) and $(TBA)_5K_2\alpha_2$-$[Fe(H_2O)P_2W_{17}O_{61}]$ (0.26×10^{-5} mol/L) and (*B*) a 1:1 ratio of $[Ru(bpy)_3]Cl_2$ (1.29×10^{-5} mol/L) and $(TBA)_6\alpha$-$[P_2W_{18}O_{62}]$ (1.29×10^{-5} mol/L) (optical length = 1 cm, λ_{ex} = 490 nm). Full line: free $[Ru(bpy)_3]Cl_2$ (1.29×10^{-5} mol/L).

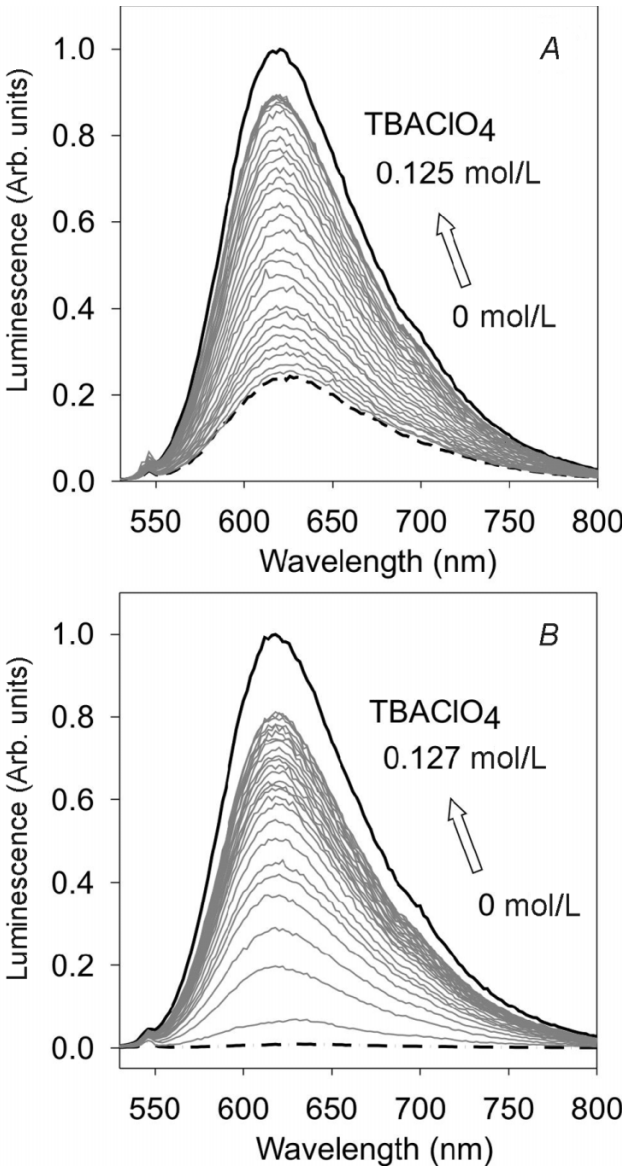

$H_{a'}$ adjacent to the $-(CH_2)_2$-py group, while the second singlet at 8.72 ppm ($H_{a''}$) should be adjacent to the methyl group considering donor and acceptor effects of methyl and pyridyl groups. In the substituted 2,2′-bipyridine, protons $H_{d'}$ and $H_{d''}$ resonate as one doublet at 8.48 ppm while protons H_d appears as a doublet at 8.82 ppm.

Protons H_a, $H_{c'}$, $H_{c''}$, and H_b appear in the multiplet massif between 7.46 and 7.60 ppm. As expected, methyl group protons resonate as one singlet at 2.08 ppm and ethyl ones appear as a multiplet massif between 3.01 and 3.11 ppm. ^1H NMR spectra of the 3:1 and 1:1 complexes, namely $[Ru(bpy)_2(Mebpy\text{-}py)]_3[P_2W_{18}O_{62}]$ and $[Ru(bpy)_2(Me\text{-}bpy\text{-}py)][P_2W_{18}O_{62}]^{4-}$, show significant changes compared to the

Fig. 6. ^1H NMR of the $[Ru(bpy)_3]Cl_2$, $[Ru(bpy)_3Cl_2]_3[P_2W_{18}O_{62}]$ and $[Ru(bpy)_3][P_2W_{18}O_{62}]^{4-}$ complexes (300 MHz, DMSO-d_6, aromatic region of the spectrum).

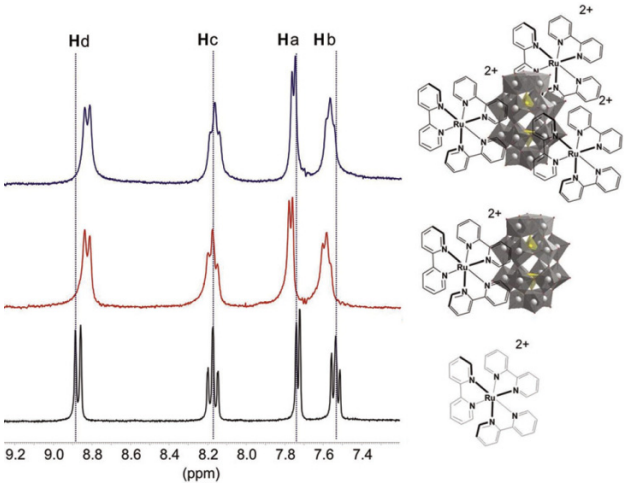

Fig. 7. ^1H NMR of the $[Ru(bpy)_2(Mebpy\text{-}py)](PF_6)_2$, $[Ru(bpy)_2(Mebpy\text{-}py)]$ $[P_2W_{18}O_{62}]$ and $[Ru(bpy)_2(Mebpy\text{-}py)][P_2W_{18}O_{62}]^{4-}$ complexes (300 MHz, DMSO-d_6, aromatic region of the spectrum).

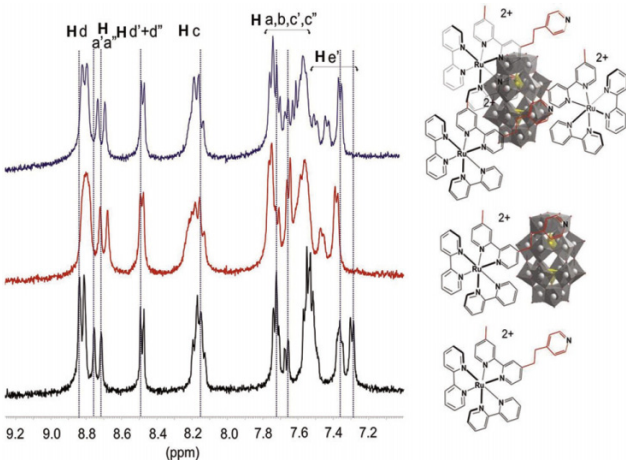

spectra from the precursor $[Ru(bpy)_2(Mebpy\text{-}py)]^{2+}$ (Fig. 7). Shifts to higher field for protons H_d, as already shown for $Ru(bpy)_3^{2+}$, are observed. The shift for proton H_c is not noticeable. However, a drastic change in the signals belonging to the substituted 2,2′-bipyridine is observed. In the case of the 3:1 complex, the protons $H_{e'}$ in the pyridyl group become non-equivalent and are split into two doublets with integration of one proton.

In the case of the 1:1 complex, only one of the two doublets for proton $H_{e'}$ is observed with the integration of one proton.

The chemical shift of the methyl protons remains identical for the 3:1 and 1:1 complexes whereas the ethyl protons become unobservable because of the resonance of TBA^+ in the same field. As described with $[Ru(bpy)_3]^{2+}$, no change in the ^{31}P NMR spectra is observed for 3:1 or 1:1 complexes with $[Ru(bpy)_2(Me\text{-}bpy\text{-}py)]^{2+}$. The signal at –12.40 ppm was identical to that of the precursor α-$[P_2W_{18}O_{62}]^{6-}$.

© 2008 NRC Canada

These results suggest surprisingly that Mebpy-py should be closer to the POM than the other bpy as the interactions appear to be stronger. Consequently, the distance between the Ru and POM compounds should be larger for the **Ru-2** than the **Ru-1**. This is in agreement with lower global association constants for complexes with $[Ru(bpy)_2(Mebpy\text{-}py)]^{2+}$ (**Ru-2**) than with $[Ru(bpy)_3]^{2+}$ (**Ru-1**).

^{1}H NMR spectra of the 1:1 mixed complex might have unravelled these types of interactions between **Ru-1** or **Ru-2** and α_2-$[Fe(H_2O)P_2W_{17}O_{61}]^{7-}$: coordination or electrostatic interactions. But, because of the low solubility of the Ru–POM complexes in DMF-d_7 or DMSO-d_6, only the free TBA^+ cation in solution was observed in the ^{1}H NMR spectra with a large signal because of the paramagnetism of the iron polyanion.

Electrochemical behaviors

To understand the electrochemical behavior of the Ru–POM complex, it is important to compare the redox processes among the $[Ru(bpy)_3]^{2+}$ or $[Ru(bpy)_2(Mebpy\text{-}py)]^{2+}$ (**Ru-1** or **Ru-2**), α-$[P_2W_{18}O_{62}]^{6-}$ or α_2-$[(H_2O)FeP_2W_{17}O_{61}]^{7-}$ moieties and the Ru–POM complex. DMSO was preferred to DMF as solvent because of the higher solubility of Ru–POM complexes in DMSO.

The characteristic electrochemical behavior for the TBA salt of the Dawson-type polyoxometalate α-$[P_2W_{18}O_{62}]^{6-}$ in DMSO is illustrated in Fig. 8 (dotted line). The cyclic voltammogram of α-$[P_2W_{18}O_{62}]^{6-}$ exhibits five successive, but not well-defined, one-electron redox waves which all correspond to the couples of oxo W-based reduction in a negative potential range. In general, the reduction of heteropolyanions is easier in aqueous solution and is accompanied by protonation at low pH. In our case, addition of a small amount of water in DMSO improved the electrochemical behavior of α-$[P_2W_{18}O_{62}]^{6-}$ with better defined redox waves for at least the first three processes. A cyclic voltammogram of $[Ru(bpy)_3]Cl_2$ demonstrates the expected $Ru^{III/II}$ metal-based oxidation process and the three one-electron bipyridine ligand-based reduction processes. The one-electron $Ru^{III/II}$ oxidation process in cyclic voltammetry is masked by irreversible oxidation of Cl^- to Cl_2 whereas in the differential pulse voltammetry (DPV) mode, the redox oxidation process for $Ru^{III/II}$ (Figs. 8*A* and 8*B*) can be easily distinguished.

Fig. 9*A* illustrates the cyclic voltammetry of a DMSO solution containing three equivalents of **Ru-1** (0.50 mmol/L) and one or three equivalent(s) of α-$[P_2W_{18}O_{62}]^{6-}$ (0.17 or 0.50 mmol/L) in the presence of 0.1 mol/L $TBAClO_4$. The last three well-defined redox processes correspond to the reduction of both the 2,2′-bipyridine ligands and the tungsten–oxo framework, while the first two reduction processes are ascribed to oxo W-based reduction. The cathodic peak currents are almost proportional to the square root of the scan rate up to a value of 500 mV s^{-1}, which indicates that the electrode reaction is diffusion controlled.

The $E_{1/2}$ values obtained from the individual cationic and anionic species in a 0.1 mol/L solution of $TBAClO_4$ in DMSO are not apparently different from those measured from the mixture of 3:1 or 1:1 ($[Ru(bpy)_3]^{2+}$] = 0.50 mmol/L and α-$[P_2W_{18}O_{62}{}^{6-}]$ = 0.17 or 0.50 mmol/L). Moreover, the analysis of the voltammogram obtained from DPV mode shows only a small negative shift for the last two reduction processes. This corresponds to both the tungsten–oxo framework and the bipyridine ligand reduction processes comparable to that of the **Ru-1** species under the same conditions. These results are in agreement with the fact that increasing the ionic strength in solution induces a disruption of the electrostatic bond. Thus, the registered electrochemical behavior does not correspond to the **Ru-1**–POM complexes but to the individual or non-complexed ruthenium and POM moieties. Luminescence spectra of the electrochemical solution confirm this result. Indeed, the luminescence spectra of the free ruthenium compound in solution were recorded. Similar behaviors were observed with **Ru-2**. Since the presence of the supporting salt $TBAClO_4$ induces the disruption of the electrostatic complexes, the electrochemical behavior of **Ru-1**–POM complexes are studied without the conducting salt $TBAClO_4$. Fig. 9*B* illustrates the cyclic voltammetry of a DMSO solution containing **Ru-1** (0.50 mmol/L) alone or

Fig. 8. (*A*) Cyclic voltammograms obtained in DMSO containing 0.1 mol/L of $TBAClO_4$ (solid line) and 0.5 mmol/L of $[Ru(bpy)_3]Cl_2$ or 0.5 mmol/L of (dotted line) $(TBA)_6\alpha$-$[P_2W_{18}O_{62}]$, at a scan rate of 20 mV s^{-1}; (*B*) differential pulse voltammetry $[Ru(bpy)_3]Cl_2$ at a scan rate of 20 mV s^{-1}.

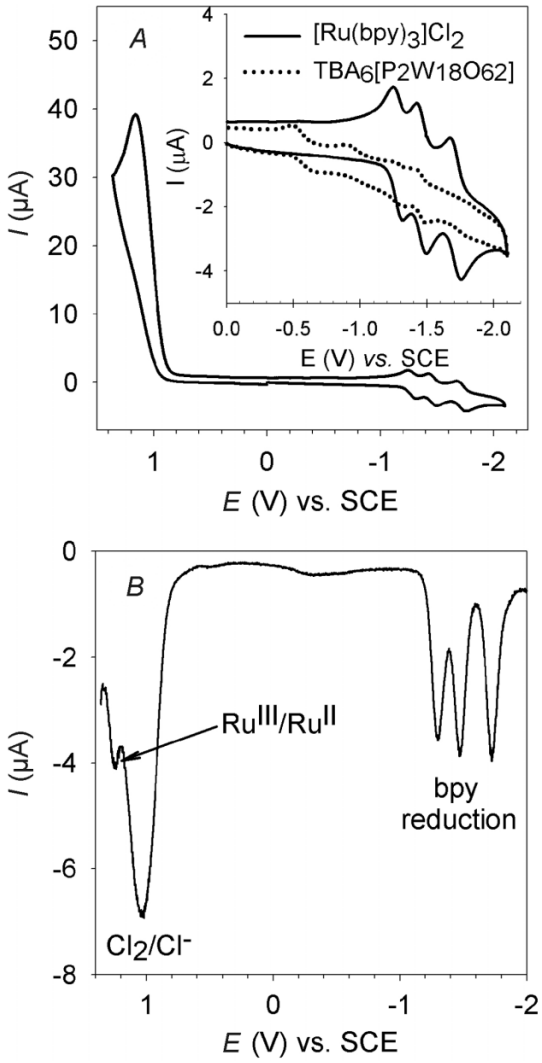

© 2008 NRC Canada

Fig. 9. Cyclic voltammograms of DMSO solutions containing 0.5 mmol/L $[Ru(bpy)_3]Cl_2$ alone (dotted line) and with 1/3 (dashed line) or 1 equiv. (solid line) of $(TBA)_6\alpha$-$[P_2W_{18}O_{62}]$. Glassy carbon electrode. Scan rate 20 mV s^{-1}. (*A*) in the presence of 0.1 mol/L $TBAClO_4$. (*B*) in the absence of $TBAClO_4$. Inset: Luminescence spectra (λ_{ex} = 490 nm) of the corresponding electrochemical solution; (△) oxo W-based reduction; (▼) reduction of bpy.

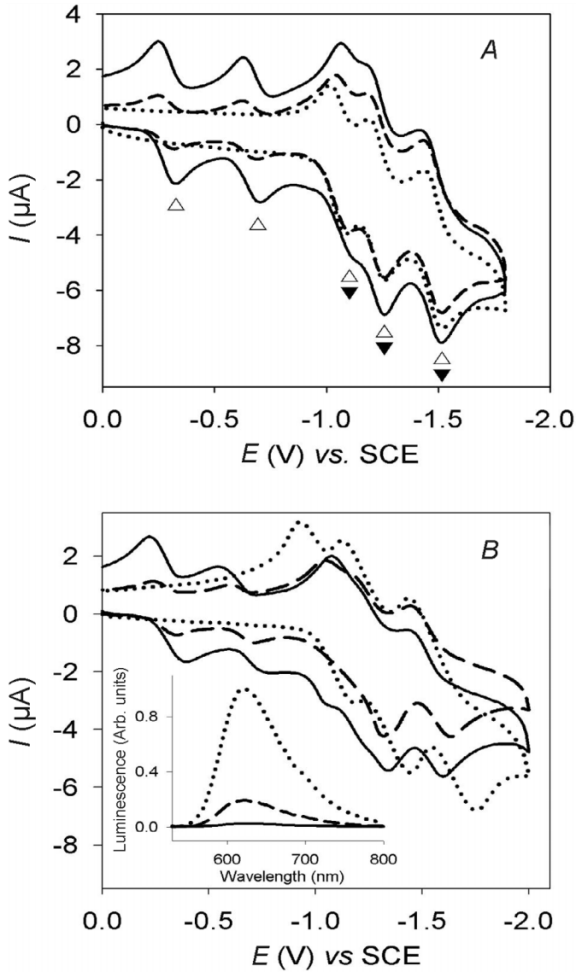

Fig 10. Cyclic voltammograms of DMSO solutions containing 0.5 mmol/L $[Ru(bpy)_3]Cl_2$ (1 equiv.) alone (dotted line) and with 1/5 (dashed line) or 1 (solid line) equiv. of $(TBA)_5K_2\alpha_2$–$[Fe(H_2O)P_2W_{17}O_{61}]$; glassy carbon electrode, scan rate 20 mV s^{-1}; (*A*) in the presence of 0.1 M $TBAClO_4$; (*B*) in the absence of $TBAClO_4$. Inset: Luminescence spectra (λ_{ex} = 490 nm) of the corresponding electrochemical solution; (△) Fe(III) and oxo W-based reduction; (▼) reduction of 2,2′-bipyridine ligand.

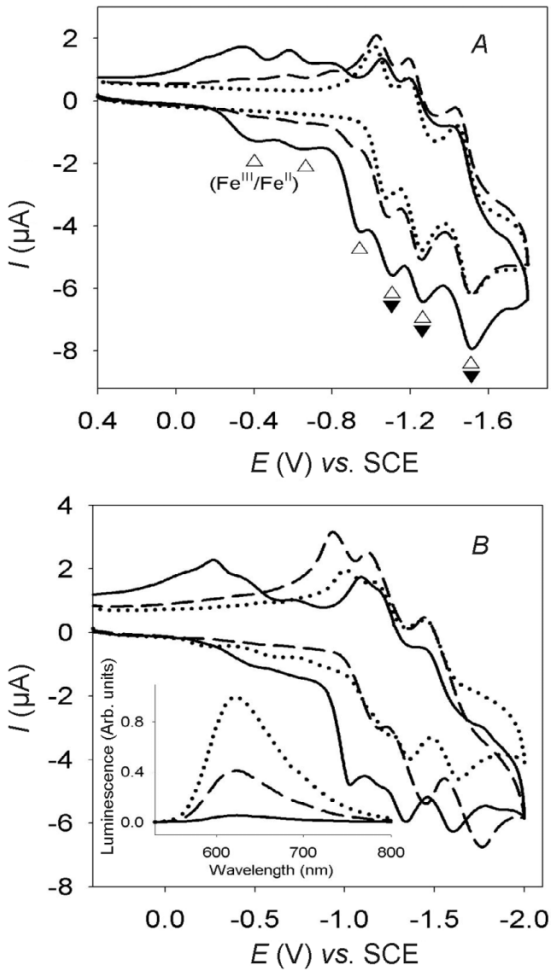

with one or three equivalent(s) of α-$[P_2W_{18}O_{62}]^{6-}$ in the absence of $TBAClO_4$.

It was noticed that the formation of the electrostatic complexes induced the release of TBACl in solution.

Quenching of the luminescence confirmed the presence of the 3:1 or 1:1 **Ru-1**–POM complexes that were not dissociated (inset of Fig. 9*B*). Three well-defined redox processes were also observed, corresponding to the reduction of both the 2,2′-bipyridine ligands and the tungsten–oxo framework. The first two reduction processes corresponded to the oxo W-based reduction. In the case of α_2-$[(H_2O)FeP_2W_{17}O_{61}]^{7-}$, the results were similar. Nevertheless, one additional process corresponding to the reduction of the Fe(III) to Fe(II) was observed. When using a conducting salt, we still recorded the electrochemical behavior of the individual uncomplexed **Ru-1** and iron POM moieties (Fig. 10*A*).

This was also confirmed by the absence of quenching of the luminescence for the ruthenium compound by the POM subunit. The last three well-defined redox processes correspond to the reduction of both the 2,2′-bipyridine ligands and the tungsten–oxo framework while the first three reduction processes correspond to the Fe(III) reduction first followed by oxo-W based reduction. But the electrochemical behavior of the 5:1, 3:1, and 1:1 Ru–POM complexes can be obtained in the absence of the conducting salt (Fig. 10*B*). In this case, the luminescence spectra of the electrochemical solution show the quenching of the ruthenium luminescence by the POM subunit(s). Discussion of the shift of the potential is difficult because of the increase in the solution ionic strength owing to the release of TBACl during the association processes.

Concluding remarks

UV–vis absorption and luminescence quenching measurements were performed during the titration of diluted solutions of Ru compounds by concentrated POM solutions.

© 2008 NRC Canada

The results clearly demonstrate the formation of mixed complexes between α-$[P_2W_{18}O_{62}]^{6-}$ or α_2-$[Fe^{III}(H_2O)P_2W_{17}O_{61}]^{7-}$ and ruthenium compounds $[Ru(bpy)_3]^{2+}$ (**Ru-1**) or $[Ru(bpy)_2(Mebpy\text{-}py)]^{2+}$ (**Ru-2**).

In the case of the formed complexes between **Ru-1** or **Ru-2** and α-$[P_2W_{18}O_{62}]^{6-}$, the quantitative quenching of the luminescence of the ruthenium subunits is observed with the formation of 3:1 complex ($[Ru(bpy)_3]_3[P_2W_{18}O_{62}]$ or $[Ru(bpy)_2(Mebpy)]_3[P_2W_{18}O_{62}]$). Nevetheless, the UV–vis titration indicates the formation of another electrostatic 1:1 complex. When using the iron polyanion α_2-$[Fe^{III}(H_2O)P_2W_{17}O_{61}]^{7-}$, three equilibria were observed at the mole ratios of 5:1, 3:1, or 1:1 for **Ru-1** and at the mole ratios of 4:1, 2:1, and 1:1 for **Ru-2**. The association constant values estimated from the Job's method suggest a small steric effect from the substituting pyridine group in **Ru-2**. The nature of the interactions involved in the complexes are mainly electrostatic since the addition of $TBAClO_4$ or $LiClO_4$ to the solution induces the dissociation of the complex. Consequently, electrochemical behavior of the Ru– POM complexes can be obtained only in the absence of conduction salts.

These ionic complexes with high global association constant, along with quantitative quenching behavior of the luminescence for the ruthenium complexes by the POM subunits, seem good candidates for photocatalytic applications.

Study of the possible electron transfers between the reactants in the mixed complexes as well as the photocatalytic reduction of NO_X or Ag(I) is currently under investigation.

Experimental section

Most common laboratory chemicals were reagent grade, purchased from commercial sources, and used without further purification.

The potassium salts $K_6\alpha$-$[P_2W_{18}O_{62}]$ and $K_7\alpha_2$-$[Fe(H_2O)P_2W_{17}O_{61}]$ were prepared by published methods (17, 27). The TBA salts of α-$[P_2W_{18}O_{62}]^{6-}$and α_2-$[Fe(H_2O)P_2W_{17}O_{61}]^{7-}$ were obtained from the metathesis reaction with excess of TBACl at a POM-to-TBACl ratio of 1:10 (equiv.).

^{1}H NMR spectra were recorded in 5 mm o.d. tubes on a Bruker AC 300 apparatus operating at 300 MHz in a Fourier transform mode. ^{31}P NMR spectra were recorded in 5 mm o.d. tubes on a Bruker AC 300 apparatus operating at 121.5 MHz in a Fourier transform mode (equipped with a QNP probe for ^{31}P NMR). The ^{31}P chemical shifts were measured at 300 K on 0.02 mol/L solutions of the polyanions in aqueous D_2O–H_2O (1:1) and were referenced to external 85% H_3PO_4 (IUPAC convention) by the substitution method.

IR spectra were recorded on a Bio-Rad FTS 165 FTIR spectrophotometer on KBr pellets.

Steady-state optical absorption spectra were recorded with a PerkinElmer Lambda 19 spectrophotometer. Steady-state luminescence emission spectra were obtained using a Spex Fluorolog 111 spectrofluorimeter equipped with a Hamamatsu R3896 photomultiplier which was cooled to the temperature of –20 °C. The luminescence spectra were not corrected for the response of the detection system. All the measurements were carried out at room temperature.

For the electrochemical experiments, the solutions were degassed thoroughly for at least 30 min with argon (Ar-U from Air Liquide) and then kept under argon atmosphere during the whole experimental period. The glassy carbon samples had a diameter of 3 mm. Measurements were made on an EG&G 273A potentiostat driven by a PC with 270 software. Potentials are quoted against a saturated calomel electrode (SCE). The counter electrode was platinum-gauzed with large surface area. All voltammetric experiments were conducted at room temperature.

Elemental analyses were performed by classical gravimetric and spectroscopic methods. The anions were first decomposed in boiling concentrated hydrochloric acid solution. Then W and P were precipitated together by adding cinchonium hydrochloride. Tungsten and phosphorus were determined simultaneously as WO_3 and P_2O_5 by gravimetry after calcination of the cinchonium salt. Iron was determined by atomic absorption spectroscopy. Phosphorus was determined independently by the spectroscopy of molybdovanadophosphate (29).

$(TBA)_6\alpha$-$[P_2W_{18}O_{62}]$

1 g of $K_6\alpha$-$[P_2W_{18}O_{62}]\cdot 33H_2O$ (0.193 mmol) was added to 20 mL deionized water with stirring. 1.5 g of TBACl was added to the solution. After stirring for 3 h, the solid was filtered and washed with hot water and then dried in the air (yield 1.02 g, 0.176 mmol, 91%). IR (KBr pellet, cm^{-1}): 2962 (s, TBA^+), 2935 (s, TBA^+), 2974 (s, TBA^+), 2361 (m, TBA^+), 2343 (shoulder, TBA^+), 1484 (s, TBA^+), 1380 (m, TBA^+), 1152 (m, TBA^+), 1091 (s), 1019 (m), 991 (m, TBA^+), 956 (s), 913 (s), 790 (s). ^{31}P NMR in DMSO-d_6 shows 1 peak at –12.4 ppm. Anal. calcd. for $C_{96}H_{216}N_6O_{62}P_2W_{18}$: C 19.82, H 3.74, N 1.44, P 1.06, W 56.88; found: C 19.80, H 3.71, N 1.44, P 1.02, W 56.31.

$(TBA)_5K_2\alpha 2$–$[Fe(H_2O)P_2W_{17}O_{61}]$

3 g of $K_7[Fe(OH_2)P_2W_{17}O_{61}]\cdot 7H_2O$ (0.647 mmol) was added to 20 mL of deionized water with stirring. 4.5 g TBACl was added to the solution with vigorous stirring. After three hours, the pH of the solution was adjusted to 4.3 with the addition of a drop of acetic acid, leading to instantaneous precipitation. After 2 h, the solid was filtered and washed with 150 mL hot water. Then, the powder was washed again with 20 mL ethanol followed by 20 mL ether and dried in the air (yield 3.37 g, 0.61 mmol, 94%). IR (KBr pellet, cm^{-1}): 2962 (s, TBA^+), 2935 (s, TBA^+), 2973 (s, TBA^+), 1485 (s, TBA^+), 1380 (m, TBA^+), 1152 (m, TBA^+), 1089 (s), 1019 (m), 953 (s), 911 (s), 790 (s). ^{31}P NMR in DMSO-d_6 shows 1 peak at –12.6 ppm ($\Delta\nu_{1/2}$ = 360 Hz). Anal. calcd. for $C_{80}FeH_{182}K_2N_5O_{62}P_2W_{17}$: C 17.38, H 3.32, N 1.27, P 1.12, W 56.54; found: C 16.89, H 3.45, N 1.49, P 1.10, W 56.12.

4-(4″-Pyridinyl ethyl)-4′-methyl-2,2′-bipyridine (2)

This compound was prepared by a modified literature procedure (Scheme 3) (28). Lithium diisopropyl amide (LDA) was prepared by a dropwise addition of *n*-butyllithium solution (3.5 mL, 1.6 mol/L solution in *n*-hexane, 5.6 mmol) to a solution of freshly distilled diisopropylamine (0.7 mL, 5.4 mmol) in THF (25 mL) with a syringe at a temperature of –20 °C under stirring and N_2 atmosphere.

After the solution was cooled to –78 °C in a liq. N_2–acetone bath, a 4,4′-dimethylbipyridine (1.0 g, 5.4 mmol)

© 2008 NRC Canada

Scheme 3. Synthetic route for the preparation of $[Ru(bpy)_2(Mebpy\text{-}py)]^{2+}\ 2PF_6^-$ (**Ru-2**).

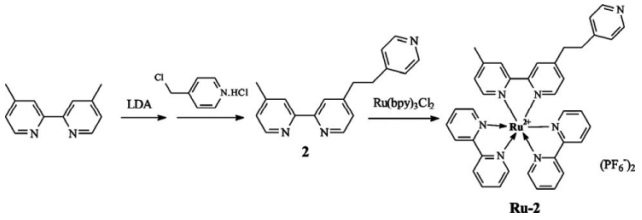

solution in freshly distilled THF (35 mL) was added dropwise and the solution became grey immediately. After another 1.5 hour of stirring, 4-chloromethylpyridine hydrochloric salt (190 mg, 1.2 mmol) was added rapidly to the solution. The temperature was allowed to rise to room temperature and then water (3 mL) was added to quench the reaction. The resulting yellow cloudy solution was extracted with ether (3 × 25 mL), and the organic phases were combined and dried over anhydrous sodium sulfate. The crude product was obtained by evaporating the solvent in vacuum. Purification was conducted by column chromatography on silica gel with CH_2Cl_2 and CH_2Cl_2–MeOH (97:3) as eluents. The desired fractions were collected and further purified by recrystallization from ethyl acetate to give **2** (520 mg, 35%) as a white crystal. ^{1}H NMR ($CDCl_3$) δ: 2.44 (s, 3H, -C*H*$_3$), 3.10 (s, 4H, -C*H*$_2$C*H*$_2$-), 7.05–7.15 (m, 4H, 5,5′-bpy-*H*, 3″,5″-py-*H*), 8.24 (s, 1H, 3′-bpy -*H*), 8.28 (s, 2H, 3-bpy-*H*), 8.49–8.51 (m, 2H, 2″,6″-py-*H*), 8.53–8.57 (m, 2H, 6,6′-bpy-*H*). ESI–MS: 276.1 $(M+H)^+$.

$Ru(bpy)_2(Mebpy\text{-}py)(PF_6)_2$ (Ru-2)

To a solution of **2** (100 mg, 0.36 mmol) in methanol (40 mL), $Ru(bpy)_2Cl_2{\cdot}2H_2O$ (141 mg, 0.27 mmol) and few drops of water were added under stirring. The resulting brown solution was heated and the colour of the solution turned to a clear orange after two hour refluxing. The solvent was evaporated under vacuum, and a red solid residue was obtained. The residue was purified by column chromatography on silica gel (eluents CH_3CN/H_2O/sat. KNO_3 solution 8:1:1). The first violet band was the starting material $Ru(bpy)_2(NO_3)_2$. $Ru(bpy)_2(Mebpy\text{-}py)(NO_3)_2$ (184 mg, 83%) was obtained from the second orange band as a red solid after evaporation of the solvent. The complex $Ru(bpy)_2(Mebpy\text{-}py)(NO_3)_2$ was redissolved in a minimum amount of water followed by addition of a concentrated NH_4PF_6 solution to give a red precipitate, which was extracted by CH_2Cl_2 and evaporated to give the complex $Ru(bpy)_2(Mebpy\text{-}py)(PF_6)_2$ (**Ru-2**). ^{1}H NMR (DMSO) δ: 2.08 (s, 3H, -C*H*$_3$), 3.01–3.18 (m, 4H, -C*H*$_2$-(near pyridine) and -C*H*$_2$- (near Ru)), 7.27 (d, 2He′, Mebpy-py-*H*), 7.36 (d, 2He′, Mebpy-py-*H*), 7.46–7.60 (m, 5H, 4Hb + 2Ha, Mebpy-py-*H* + bpy-*H*), 7.66 (d, 1H, Hc′, or Hc″, Mebpy-py-H), 7.71 (d, 1H, 1Hc′, or 1Hc″, bpy-H), 7.73 (d, 2Ha, bpy-H), 8.14 (t, 2Hc, bpy-H), 8.16 (t, 2Hc, bpy-*H*), 8.46 (d, 2H, Hd′ + Hd″, Mebpy-py-*H*), 8.72 (s, 1Ha′, Mebpy-py-*H*), 8.76 (s, 1Ha″, Mebpy-py-*H*), 8.82 (d, 4Hd, bpy-*H*). ESI–MS: 344.5 $(M\text{-}2PF_6/2)^+$.

Acknowledgement

This research was supported by the Centre national de la recherche scientifique (CNRS), Université Paris-Sud 11, Université Paris 6 (Université Pierre et Marie Curie), and Dalian University of Technology. This work was also supported by the ANR agency, project number JC05_52437. We warmly thank Jacqueline Canny and René Thouvenot, Laboratoire de Chimie Inorganique et des Matériaux Moléculaires (Université Paris 6), for their help in NMR spectroscopy.

References

1. J.M. Clemente-Juan, E. Coronado, J.R. Galán-Mascarós, and C.J. Gómez-Garciá. Inorg. Chem. **38**, 55 (1992).
2. C.J. Gómez-Garciá, E. Coronado, and J.J. Borrasalmenar. Inorg. Chem. **31**, 1667 (1992).
3. A.M. Khenkin and C.L. Hill. Mendeleev Commun. 140 (1993).
4. R. Neumann and A.M. Khenkin. Inorg. Chem. **34**, 5753 (1995).
5. R. Neumann and M. Gara. J. Am. Chem. Soc. **117**, 5066 (1995).
6. R. Neumann and A.M. Khenkin. J. Mol. Catal. A Chem. **114**, 169 (1996).
7. R. Neumann and M. Dahan. Polyhedron, **17**, 3557 (1998).
8. E. Papaconstantinou. Chem. Soc. Rev. **18**, 1 (1989).
9. B. Keita, L. Nadjo, R. Contant, M. Fournier, and G. Hervé. French Patent (CNRS) 8911. 728. February 10, 1989.
10. B. Keita, L. Nadjo, R. Contant, M. Fournier, and G. Hervé. Eu. Patent (CNRS), Appl. EP 382.644; Chem. Abstr. **114**, 191882u (1991).
11. B. Keita, A. Belhouari, L. Nadjo, and R. Contant. J. Electroanal. Chem. **181**, 243 (1995).
12. M. Abbessi, R. Contant, R. Thouvenot, and G. Hervé. Inorg. Chem. **30**, 1695 (1991).
13. B. Keita, K. Eassadi, L. Nadjo, R. Contant, and Y. Justun. J. Electroanal. Chem. **404**, 271 (1996).
14. J.F. Garvey and M.T. Pope. Inorg. Chem. **17**, 1115 (1978).
15. B. Keita, Y.W. Lu, L. Nadjo, R. Contant, M. Abbessi, J. Canny, and M. Richet. J. Electroanal. Chem. **477**, 146 (1999).
16. J.-P. Ciabrini, R. Contant, and J.-M. Fruchart. Polyhedron, **2**, 1229 (1983).
17. R. Contant and J.-P. Ciabrini. J. Chem. Res. Synop. **222**, 2601 (1977).
18. R. Contant. Inorg. Synth. **27**, 104 (1990).
19. A. Kuhn and F.C. Anson. Langmuir, **12**, 5481 (1996).
20. Z. Han, E. Wang, G. Luan, Y. Li, C. Hu, P. Wang, N. Hu, and H. Jia. Inorg. Chem. Comm. **4**, 427 (2001).
21. V.M. Hultgren, A.M. Bond, and A.G. Wedd. J. Chem. Soc. Dalton Trans. 1076 (2001).
22. T.E. Keyes, E. Gicquel, L. Guerin, R.J. Forster, V. Hultgren, A.M. Bond, and A.G. Wedd. Inorg. Chem. **42**, 7897 (2003).
23. M.K. Seery, L. Guerin, R.J. Forster, E. Gicquel, V. Hultgren, A.M. Bond, A.G. Wedd, and T.E. Keyes. J. Phys. Chem. A, **108**, 7399 (2004).
24. N. Fay, E. Dempsey, A. Kennedy, and T.J. McCormac. Electroanal. Chem. **556**, 63 (2003).
25. J.E. Fergusson and G.M. Harris. J. Chem. Soc. A, 1293 (1966).
26. R. Ballardini, R. Gamdolfi, and V. Balzani. Inorg. Chem. **26**, 862 (1987).
27. R. Contant, M. Abbessi, J. Canny, A. Behouari, B. Keita, and L. Nadjo. Inorg. Chem. **36**, 4961 (1997).
28. L. Sun, H. Berglund, R. Davydov, T. Norrby, L. Hammarström, P. Korall, A. Börje, C. Philouze, K. Berg, A.Tran, M. Andersson, G. Stenhagen, J. Mårtensson, M. Almgren, S. Styring, and B. Åkermark. J. Am. Chem. Soc. **119**, 6996 (1997).
29. B. Cherreton, F. Chauveau, G. Bertho, and P. Courtin. Chim. Anal. **47**, 17 (1965).

© 2008 NRC Canada

Copper-catalyzed one-pot synthesis of benzimidazole derivatives

Hashem Sharghi, Mona Hosseini-Sarvari, and Fatemeh Moeini

Abstract: A simple, efficient, and environmentally benign method has been developed for the synthesis of 2-substituted benzimidazoles through a one-pot reaction of phenylenediamines with aryl aldehydes in excellent isolated yields under mild conditions using Cu(II) complex as the selective, recyclable, and heterogeneous catalyst at ambient temperature. The Cu(II) complex as a heterogeneous catalyst can be reused in further catalytic reactions, and it was found that its activity remained largely unchanged for eight successive runs. No metal-complex leaching was observed after the consecutive catalytic reactions. The salient features of this method include mild conditions, high yields, simple procedure, and good recovery and reusability of the heterogeneous catalyst.

Key words: benzimidazole, *o*-phenylenediamine, arylaldehydes, heterogeneous catalyst, *N*,*N*-bis (2-hydroxyphenyl)pyridine-2,6-dicarboxamide.

Résumé : On a développé une méthode simple, efficace et respectueuse de l'environnement pour la synthèse de benzimidazoles substitués en position 2; elle est réalisée avec d'excellents rendements en produits isolés et elle implique une réaction monotope de phénylènediamines avec des aldéhydes aromatiques, à la température ambiante et elle utilise un complexe de Cu(II) comme catalyseur sélectif, recyclable et hétérogène. Le catalyseur de Cu(II) utilisé comme catalyseur hétérogène peut être réutilisé pour d'autres réactions catalytiques et on a trouvé que son activité demeure pratiquement inchangée après huit réutilisations. On n'a observé aucun lixiviation du complexe métallique après des réactions catalytiques consécutives. Les principales caractéristiques de cette méthode incluent des conditions douces, des rendements élevés, une procédure simple et une bonne récupération et possibilité de réutilisation du catalyseur hétérogène.

Mots-clés : benzimidazole, *o*-phénylènediamine, aldéhydes aromatiques, catalyseur hétérogène, *N,N*-bis(2-hydroxyphényl)pyridine-2,6-dicarboxamide.

[Traduit par la Rédaction]

Introduction

Benzimidazoles are very useful intermediates for the development of molecules of pharmaceutical or biological interest. The benzimidazole ring is an important pharmacophore in modern drug discovery (1). Benzimidazole derivatives exhibit significant activity against several viruses such as HIV (2), herpes (HSV-1) (3), RNA (4), influenza (5), and human cytomegalovirus (HCMV) (2*a*). Substituted benzimidazole derivatives have found commercial applications in veterinarian medicine as anthelmintic agents and in diverse human therapeutic areas such as treatment of ulcers and as antihistaminics (6). Because of their importance, the synthesis of substituted benzimidazoles has become a focus of synthetic organic chemistry. The most commonly used synthetic approaches typically entail the condensation of an arylenediamine with a carbonyl equivalent (7, 8). Likewise, esters, lactones, and anhydrides could produce benzimidazoles through the cyclization of amide. However, this might have a limited scope, since the necessary reaction conditions are harsh and result in a meager assortment of final products. For example, the reaction of arylenediamines with aliphatic esters and lactones, which uses strong mineral acids at high temperatures, necessitates conditions that would not allow for a wide range of functional groups and attractive substrates. The other synthetic approach involves a two-step procedure including the oxidative cyclodehydrogenation of aniline Schiff bases, which are often generated in situ from the condensation of phenylenediamines and aldehydes. Various oxidative and catalytic reagents, such as $TiCl_4$ (9*a*), H_2O_2/CAN (9*b*), $ZrOCl_2$ (10), $In(OTf)_3$ (11), $Sc(OTf)_3$ (12), $Yb(OTf)_3$ (13), I_2 in aqueous THF (14), BF_3–OEt_2 (15), H_2NSO_3H (16*a*), TsOH or *N,N*-dimethylaniline/graphite (16*b*), polyaniline – sulfate salt (17), and NH_4OAc (18), have been employed. The direct condensation of *o*-aryldiamines and aldehydes at room temperature is less developed, because it leads to the formation of a complex mixture of products containing 1,2-disubstituted benzimidazoles, the corresponding bis-anils, and dihydrobenzimidazoles as main byproducts (19). Unfortunately, some of these methods suffer from one or more limitations, such as high reaction temperature, prolonged reaction time, and toxic solvents. In addition, some of the catalysts are expensive, air sensitive, and homogeneous. The homogeneous catalysts cannot be separated from the reaction media and, subsequently, cannot be reused in further catalytic reactions.

Received 13 July 2008. Accepted 15 September 2008. Published on the NRC Research Press Web site at canjchem.nrc.ca on 24 October 2008.

H. Sharghi,[1] M. Hosseini-Sarvari, and F. Moeini. Department of Chemistry, College of Sciences, Shiraz University, Shiraz 71454, Iran.

[1]Corresponding author (e-mail: shashem@chem.susc.ac.ir).

 doi:10.1139/V08-153 © 2008 NRC Canada

Scheme 1.

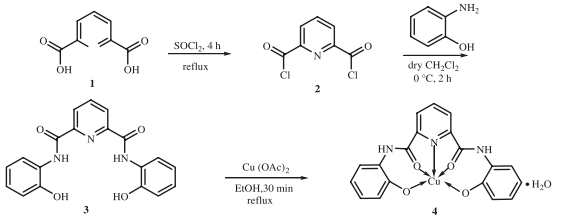

Recently, the development of heterogeneous catalysts (20) for fine chemicals synthesis has become a major area of research, since the potential advantages of these materials (i.e., simple recovery, reusability, and potential for incorporation in continuous reactors and microreactors) over homogeneous systems can have a major impact on the environmental performance of a synthesis (21). Considering the above issues, there is still a need to search for new catalysts superior to the existing ones with regards to toxicity, handling, operational simplicity, and heterogenicity. In continuation of our work (22) on the development of useful synthetic methodologies, herein, we wish to report a new Cu(II) complex as an excellent recoverable and heterogeneous catalyst for the synthesis of benzimidazole derivatives.

Results and discussion

The reaction pathway for the preparation of the catalyst is shown in Scheme 1. 2,6-Pyridinedicarboxylic acid (**1**) was boiled under reflux in $SOCl_2$ for 4 h. Excess of $SOCl_2$ was removed under reduced pressure to leave 2,6-pyridinedicarbonyldichloride (**2**). Then, a mixture of 2-aminophenol and triethylamine were dissolved in dry methylene chloride, temperature was adjusted to 0 °C, 2,6-pyridinedicarbonyldichloride was added dropwise, and the reaction mixture was stirred for 2 h. The resulting precipitate was filtered, washed with a saturated solution of $NaHCO_3$. Recrystallization of crude residue from an aqueous ethanol (50%) afforded 95% yield of yellowish solid of *N*,*N*-bis (2-hydroxyphenyl) pyridine-2,6-dicarboxamide (BHPPDAH) (**3**). In the next step, a mixture of BHPPDAH and cupric acetate was boiled under reflux in ethanol for 30 min. Finally, the reaction mixture was filtered, washed with H_2O, and air dried, which afforded 98% of brown solid of [Cu(BHPPDAH)H_2O] (**4**). This copper complex has already been synthesized by Gudasi and co-workers with different procedures and fully characterized (23).

In the presence of a catalytic amount of **4**, the reaction of *o*-phenylenediamine (*o*-PD) (1 mmol) was first examined with benzaldehyde (1 mmol) at room temperature in ethanol using atmospheric air as a green oxidant. Under optimized reaction conditions, we obtained exclusively the 2-substituted product, **5a** (x = H), and no N-alkylated product **6** was obtained (Scheme 2).

Control experiments without complex **4** under the same reaction conditions showed that no reaction occurred, thus confirming the effectiveness of Cu(II) complex as an effective heterogeneous catalyst (Table 1, entry 1). A catalytic amount of Cu(II) complex (5 mol%) is sufficient to obtain the desired product in high yield. A decrease in the amount of catalyst resulted in a significant reduction of the yield

Scheme 2.

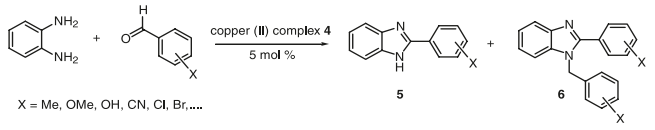

while an increased amount of catalyst revealed negligible effect on the efficiency of the reaction (Table 1, entries 14 and 15). During the optimization studies, various solvents were examined, and it was found that solvent effect has an important role in terms of reaction rate, isolated yields, and selectivity (Table 1). *o*-Phenylenediamine and benzaldehyde were chosen as representative substrates. Among various solvents tested, acetonitrile, ethylene glycol, and 1,2-dichloroethane gave moderate yields of the expected product (Table 1, entries 8, 9, and 11). Methanol afforded the product in good yield (Table 1, entry 7). Obviously, ethanol was the solvent of choice owing to its fast reaction rate, high yield, good selectivity, cost effectiveness, and environmental acceptability (Table 1, entry 2). A trace benzimidazole was obtained when the reaction was operated in nitrogen atmosphere (Table 1, entry 5), supporting the fact that O_2 plays an important role in this reaction. Further bubbling of O_2 through the reaction mixture resulted in negligible change in the rate of reaction showing that the dissolved O_2 in solvent that is adsorbed by surface adsorption is sufficient for the efficient reaction completion.

To access the feasibility of applying this method in a preparative scale, we carried out the coupling of *o*-PD with benzaldehyde in 30 mmol scale in the presence of Cu(II) complex **4**. As expected, the reaction proceeded similar to the case in a smaller scale (Table 1, entry 2), and the desired 2-phenylbenzimidazole was obtained in 95% isolated yield in 2 h. The continuous bubbling of O_2 through the reaction mixture, instead of static atmosphere of air, did not accelerate the reaction rate, same as that mentioned in smaller scale reaction. $Cu(OAc)_2$ and Cu(II) salen were also examined as catalysts for this reaction; however, they were less effective compared with **4** and afforded banzimidazole **5** in 35% and 40% yields, respectively, (Table 1, entries 3 and 4).

From an environmental point of view, it is desirable to minimize the amount of waste for each organic transformation. In this context, the catalyst was recycled for subsequent runs. The recyclability of the catalyst was investigated using a model reaction between benzaldehyde and *o*-phenylendiamine in the presence of 5 mol% of the catalyst in ethanol as solvent. After the completion of the reaction, the mixture was filtered to separate the catalyst. The recycled catalyst was used for further runs, and it was found that its activity does not show any significant decrease even after 8 runs (Table 2).

Leaching experiment showed that the catalytic activity of Cu(II) complex **4** remained largely unchanged for 8 successive runs. To test the generality and versatility of this procedure in the synthesis of substituted benzimidazoles, we examined a number of differently substituted arylaldehydes and phenylendiamine using the optimized experimental conditions. As shown in Table 3, the aromatic aldehydes, having different substituents, such as methoxy, methyl, halogen, hydroxyl, nitrile, and nitro, were converted to the

© 2008 NRC Canada

Table 1. Copper(II)-catalyzed reaction of *o*-PD (1 mmol) and benzaldehyde (1 mmol) at room temperature.

Entry	Catalyst (5 mol%)	Solvent	Time (h)	Yield of product ***5a***[a] (%)	Yield of by product ***6a***[b] (%)
1	–	EtOH	24	—	—
2	**4**	EtOH	2	95	—
3	$Cu(OAc)_2$	EtOH	2	35	10
4	Cu(II)salen	EtOH	2	40	—
5	**4**[c]	EtOH	2.5	5	—
6	**4**	DMF	4	10	—
7	**4**	MeOH	3	85	2
8	**4**	Acetonitrile	10	50	5
9	**4**	Ethylene glycol	4	50	45
10	**4**	Chloroform	6	30	5
11	**4**	1,2-Dichloroethane	4	50	5
12	**4**	THF	6	10	2
13	**4**	EtOAc	6	20	—
14	**4**[d]	EtOH	4	60	—
15	**4**[e]	EtOH	2	96	—
16	**4**	—	4	10	40

[a,b]Isolated yields.
[c]Operated in nitrogen atmosphere.
[d]Using 2.5 mol% of **4**.
[e]Using 10 mol% of **4**.

Table 2. Re-use of catalyst.

Number of uses	Yield[a] (%)	Recovery of catalyst
1	95	98
2	95	97
3	93	97
4	92	97
5	90	95
6	90	95
7	89	93
8	89	93

[a]All yields refer to isolated product.

corresponding benzimidazoles in high yields (Table 3, entries 2–11). Heteroaryl aldehydes, such as 2-thiophene and pyridinyl, also gave acceptable yields (Table 3, entries 13 and 14). The reactions of 3,4-diaminobenzoic acid, 3,4-diaminotoluene, and 3,4-diaminobenzophenon with benzaldehyde were also studied. As mentioned above, all the substrates consistently afforded the reaction selectively to the corresponding benzimidazoles in high yields (Table 3, entries 17, 18, and 19). The presented method is suitable for the preparation of benzimidazoles from an acid-sensitive aldehyde such as furfuraldehyde (Table 3, entry 12) and sterically hindered aldehyde such as 2-naphthaldehyde (Table 3, entry 15). The structures of the products were determined from their spectral (^{1}H NMR, ^{13}C NMR, IR, and MS) analysis.

The proposed mechanism for the Cu(II) complex-catalyzed synthesis of benzimidazole derivatives may tentatively be visualized to occur via a tandem sequence of reactions as depicted in Scheme 3.

Mechanistically, a plausible pathway for this reaction involves the formation of intermediate Schiff base **A** very rapidly, as monitored by GC analysis. So, the rate-determining step (RDS) was found to be the oxidative-cyclization step. The compound **B** was formed as a result of an intermolecular reaction between the aniline amine and the intermediate imine moiety in **A**. We propose that reaction of **B** with Cu(II) complex **4** is accompanied by the reduction of Cu(II) to Cu(I), the utilization of O_2, and the concomitant generation of H_2O_2, as depicted in Scheme 3 (24–26).

H_2O_2 as efficient oxidant has been shown to catalyze the oxidation of some organic reactions (27, 28). We thought that, in the presence of H_2O_2, the rate of this reaction might increase. As we expected, in the presence of H_2O_2 (1 mmol), (*o*-PD) (1 mmol), benzaldehyde (1 mmol), and 5 mol% of **4** in 5 mL ethanol, the reaction time decreases. The mechanism for the increase in the rate of this reaction in the presence of H_2O_2 can be described as follows (25, 26): In the presence of H_2O_2, oxidation of **B** by Cu(II) is enhanced because of the regeneration of Cu(II) by H_2O_2 oxidizing Cu(I). The redox cycling between Cu(I)/Cu(II) H_2O_2 also produces a highly reactive OH radical, which can then attack to **C**, as shown in Scheme 3.

Conclusion

In summary, we have presented the first example of copper(II) complex-catalyzed synthesis of benzimidazoles in benign condition. This new and efficient catalytic method is amenable to a parallel-synthesis approach, as demonstrated by the synthesis of a library of benzimidazoles substituted at various positions on the ring. The advantage of this method is the use of atmospheric air as oxidant. No toxic reagents or byproducts were involved, and no laborious purifications were necessary. These conditions are also environment-friendly, cost-effective, and possess high generality to make our methodology industrialized as a valid contribution to the existing methodologies in the field of benzimidazole synthesis.

© 2008 NRC Canada

Table 3. Selective synthesis of benzimidazoles from various aryl aldehydes (1 mmol) and diamines (1 mmol) in the presence of Cu(II) complex **4** (5 mol%) in ethanol at room temperature.

Entry	Aldehyde	Diamine	Product	Time (h)	Yield[a] (%)
1			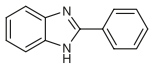 **5a**	2	95
2	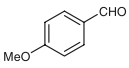		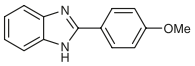 **5b**	3.5	90
3	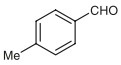		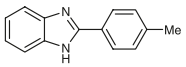 **5c**	3	90
4	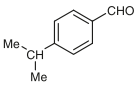		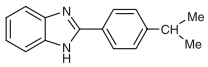 **5d**	3.3	87
5			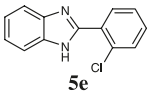 **5e**	4	87
6			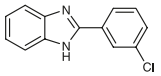 **5f**	4.3	87
7	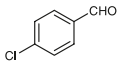		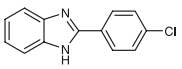 **5g**	8	85
8			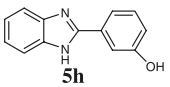 **5h**	4	85
9	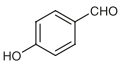		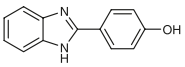 **5i**	4.3	90
10	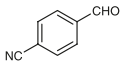		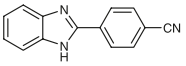 **5j**	8	85
11			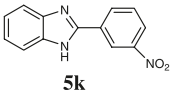 **5k**	10	80

Experimental

Starting materials were obtained from Fluka, Sigma-Aldrich, and Merk companies. Progress of the reactions was followed by TLC using silica-gel polygrams SIL G/UV 254 plates or by GC using a Shimadzu gas chromatograph GC-14A, equipped with a flame-ionization detector and a 3 m long glass column packed with DC-200 stationary phase using nitrogen as the carrier gas. The NMR spectra were recorded on a Bruker Avance DPX-250 (^{1}H NMR 250 and ^{13}C NMR 62.9 MHz) in pure duterated solvents with tetramethylsilane (TMS) as internal standard. Melting points were determined in open capillary tubes in a Buchi-545 circulating-oil melting-point apparatus.

Preparation of BHPPDAH

2,6-Pyridinedicarboxylic acid (3.34 g, 20 mmol) was boiled under reflux in $SOCl_2$ (40 mL) for 4 h. Excess of $SOCl_2$ was removed under reduced pressure to leave 2,6-pyridinedicarbonyldichloride. Then 2-aminophenol (4.36 g, 40 mmol) was dissolved in dry methylene chloride (100 mL) followed by triethylamine (5.5 mL, 40 mmol). After that, 2,6-pyridinedicarbonyldichloride (4.08 g, 20 mmol) was added dropwise to the above-mentioned solution at 0 °C,

© 2008 NRC Canada

Table 3 (*concluded*)**.**

Entry	Aldehyde	Diamine	Product	Time (h)	Yield[a] (%)
12			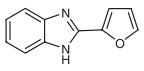 **5l**	4.5	87
13			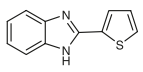 **5m**	5	85
14			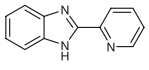 **5n**	3	85
15	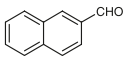		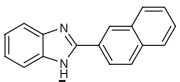 **5o**	6	90
16	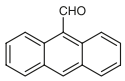		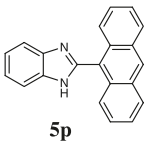 **5p**	5	90
17		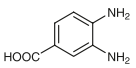	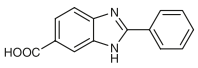 **5q**	8	80
18		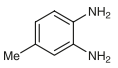	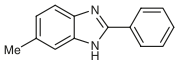 **5r**	3.2	87
19		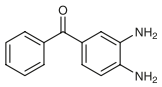	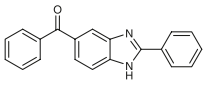 **5s**	7.5	85

[a]Isolated yields.

and the reaction mixture was stirred for 2 h. Then, the precipitate was washed with a saturated solution of $NaHCO_3$. Recrystallization from aqueous ethanol (50%) afforded a yellowish solid of BHPPDAH in 95% yield. Mp 223 °C (Lit. 220–222 °C (23)). ^{1}H NMR (DMSO-d_6) δ_H: 6.82–7.06 (6H, m), 7.99 (2H, d, J = 7.9 Hz), 8.26–8.39 (3H, m), 10.02 (2H, s), 10.41(2H, s). ^{13}C NMR (DMSO-d_6) δ_C: 115.3, 119.1, 122.2, 124.9, 125.3, 125.4, 140.2, 148.5, 148.8, 160.9.

Prepration of [Cu (BHPPDA) H_2O] complex

A mixture of BHPPDAH (1.74 g, 5 mmol) and cupric acetate (2 g, 10 mmol) was boiled under reflux with ethanol (100 mL) for 30 min. Then, the reaction mixture was filtered, washed with H_2O, and dried in air to give a 98% yield of brown solid of [Cu(BHPPDAH)H_2O]. The copper(II) complex decomposes in two stages. The first step is 150–220 °C, and the second step is 220–470 °C ranges (23).

General method for the preparation of benzimidazole derivatives

A mixture of *o*-phenylendiamine (1 mmol), aldehyde (1 mmol), and catalyst (5 mol%) in 5 mL ethanol was stirred at room temperature for appropriate time. When the reaction was finished (monitored by TLC), the catalyst was filtered out, the filtrate was evaporated, and the residue was purified by short column chromatography over silica gel using *n*-hexane/ethyl acetate (7:1) or recrystallized from EtOH/H_2O (2:1) to afford the corresponding benzimidazole.

All produced benzimidazoles were characterized in detailed structural data by ^{1}H NMR and ^{13}C NMR, as given below.

*2-Phenyl-1*H*-benzimidazole (5a)*

Purification by flash column chromatography, eluted with *n*-hexane/ethyl acetate (7:1), gave compound **5a** as a colourless powder in 95% yield. Mp 290–292 °C (Lit. 292 °C (29)). ^{1}H NMR (DMSO-d_6) δ_H: 7.14–7.25 (2H, m), 7.44–7.61 (5H, m), 8.20 (2H, d, J = 7.2 Hz), 12.94 (1H, s). ^{13}C NMR (DMSO-d_6) δ_C: 122.1, 126.4, 128.4, 128.9, 129.2, 129.8, 130.1, 151.2.

*2-(4-Methoxyphenyl)-1*H*-benzimidazole (5b)*

Purification by flash column chromatography, eluted with *n*-hexane/ethyl acetate (7:1), gave compound **5b** as a colourless powder in 90% yield. Mp 226 °C (Lit. 226–227 °C (31)). ^{1}H NMR (DMSO-d_6) δ_H: 3.78 (3H, s), 7.10 (2 H, d, J = 8.8 Hz), 7.16 (2H, q, J = 3.0 Hz), 7.50 (2H, m), 8.12 (2H, d, J = 8.8 Hz), 12.76 (1H, s). ^{13}C NMR (DMSO-d_6) δ_C:

© 2008 NRC Canada

Scheme 3.

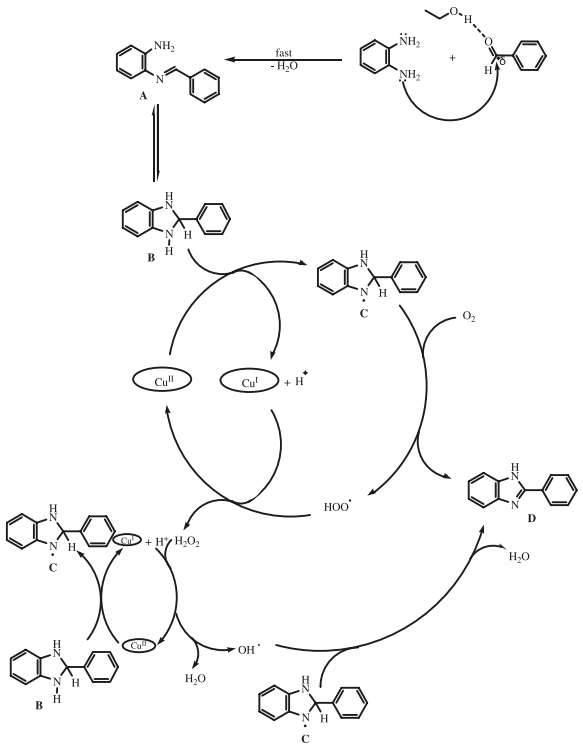

55.2, 111.0, 114.3, 118.4, 121.5, 122.0, 122.6, 128.0, 151.3, 160.5.

*2-(4-Methylphenyl)-1*H*-benzimidazole (5c)*

Purification by flash column chromatography, eluted with *n*-hexane/ethyl acetate (7:1), gave compound **5c** as a colourless powder in 90% yield. Mp 270–272 °C (Lit. 270–272 °C (30)). ^{1}H NMR (DMSO-d_6) δ_H: 2.35 (3H, s), 7.15–7.20 (2H, m), 7.33 (2H, d, J = 8.1 Hz), 7.46–7.56 (2H, m), 8.07 (2H, d, J = 8.1 Hz), 12.84 (1H, s). ^{13}C NMR (DMSO-d_6) δ_C: 20.9, 121.9, 126.3, 127.4, 128.9, 129.4, 139.5, 151.3.

*2-(4-Isopropylphenyl)-1*H*-benzimidazole (5d)*

Purification by flash column chromatography, eluted with *n*-hexane/ethyl acetate (7:1), gave compound **5d** as a colourless powder in 87% yield. Mp 250–251 °C (Lit. 250–251 °C (20)). ^{1}H NMR (DMSO-d_6) δ_H: 1.22 (6H, d, J = 6.9 Hz), 2.93 (1H, m), 7.17 (2H, m), 7.40 (2H, d, J = 8.1 Hz), 7.51–7.62 (2H m), 8.10 (2H, d J = 8.2 Hz), 12.83 (1H, s). ^{13}C NMR (DMSO-d_6) δ_C: 23.6, 33.3, 111.2, 118.6, 121.5, 122.3, 126.4, 127.7, 150.3, 151.3.

*2-(2-Chlorophenyl)-1*H*-benzimidazole (5e)*

Purification by flash column chromatography, eluted with *n*-hexane/ethyl acetate (7:1), gave compound **5e** as a colourless powder in 87% yield. Mp 233–234 °C (Lit. 234 °C (29)). ^{1}H NMR (DMSO-d_6) δ_H: 7.20–7.24 (2H, m), 7.48–7.51 (2H, m), 7.54–7.68 (3H, m), 7.89–7.93 (1H, m), 12.74 (1H, s) ^{13}C NMR (DMSO-d_6) δ_C: 111.7, 119.0, 121.7, 122.7, 127.3, 129.9, 130.3, 131.1, 131.6, 132.0, 134.6, 143.1, 149.1.

*2-(3-Chlorophenyl)-1*H*-benzimidazole (5f)*

Purification by flash column chromatography, eluted with *n*-hexane/ethyl acetate (7:1), gave compound **5f** as a colourless powder in 87% yield. Mp 230–232 °C (Lit. 234.7–235.3 °C (36)). ^{1}H NMR (DMSO-d_6) δ_H: 7.21 (2H, m), 7.49–7.64 (4H, m), 8.13 (1H, dd, J_1 = 6.6, J_2 = 1.8 Hz), 8.21 (1H, s), 13.04 (1H, s). ^{13}C NMR (DMSO-d_6) δ_C: 111.5, 119.0, 122.0, 122.9, 125, 126, 129.5, 130.9, 132.1, 133.7, 143.5, 149.7.

*2-(4-Chlorophenyl)-1*H*-benzimidazole (5g)*

Purification by flash column chromatography, eluted with *n*-hexane/ethyl acetate (7:1), gave compound **5g** as a colourless powder in 85% yield. Mp 292–293 °C (Lit. 292 °C (29)). ^{1}H NMR (DMSO-d_6) δ_H: 7.18–7.21 (2H, m), 7.60 (4H, m), 8.17 (2H, d, J = 8.6 Hz), 12.99 (1H, s). ^{13}C NMR (DMSO-d_6) δ_C: 111.4, 118.9, 121.9, 122.7, 128.1, 129, 134.5 150.1.

*3-(1*H*-Benzimidazol-2-yl)phenol (5h)*

Purification by flash column chromatography, eluted with *n*-hexane/ethyl acetate (7:1), gave compound **5h** as a colourless powder in 85% yield. Mp 182–183 °C (Lit. 181–184 °C (34)). ^{1}H NMR (DMSO-d_6) δ_H: 6.86–6.89 (1H, m), 7.16–7.19 (2H, m), 7.32 (1H, t, J = 8.1 Hz), 7.55–7.58 (4H, m), 9.81 (1H, s). ^{13}C NMR (DMSO-d_6) δ_C: 112.6, 117.0, 117.2, 122.1, 129.6, 131.2, 151.4, 157.7.

*4-(1*H*-Benzimidazol-2-yl)phenol (5i)*

Purification by flash column chromatography, eluted with *n*-hexane/ethyl acetate (7:1), gave compound **5i** as a pale yellow powder in 90% yield. Mp 254–255 °C (Lit. 254.1–256.6 °C (35)). ^{1}H NMR (DMSO-d_6) δ_H: 6.93 (2H, dd, J_1 = 8.5, J_2 = 1.2 Hz), 7.10–7.22 (2H, m), 7.52–7.53 (2H, m), 8.02 (2H, d, J = 8.6 Hz), 10.07 (1H, s), 12.65 (1H, s). ^{13}C NMR (DMSO-d_6) δ_C: 115.7, 121.0, 121.6, 128.1, 151.8, 159.1.

*4-(1*H*-Benzimidazol-2-yl)benzonitrile (5j)*

Purification by flash column chromatography, eluted with *n*-hexane/ethyl acetate (7:1), gave compound **5j** as a colourless powder in 85% yield. Mp 262 °C (Lit. 261–262 °C (30)). ^{1}H NMR (DMSO-d_6) δ_H: 7.22–7.24 (2H, m), 7.50–7.70 (2H, m) 7.97 (2H, d, J = 8.3 Hz), 8.31 (2H, d, J = 8.3 Hz), 13.17 (1H, s) ^{13}C NMR (DMSO-d_6) δ_C: 111.8, 118.5, 119.3, 122.2, 123.2, 126.4, 631 126.9, 132.9, 134.2, 149.3.

*2-(3-Nitrophenyl)-1*H*-benzimidazole (5k)*

Purification by flash column chromatography, eluted with *n*-hexane/ethyl acetate (7:1), gave compound **5k** as a pale yellow powder in 80% yield. Mp 206–207 °C (Lit. 207–208 °C (32)). ^{1}H NMR (DMSO-d_6) δ_H: 7.21 (2H m), 7.61 (2H m), 7.74–7.84 (1H m), 8.23–8.32 (1H m), 8.52–8.57 (1H m), 8.95 (1H s), 13.24 (1H s). ^{13}C NMR (DMSO-d_6) δ_C: 116.0, 120.8, 122.7, 124.2, 130.6, 131.6, 132.4, 136.9, 148.3, 149.0.

*2-(2-Furyl)-1*H*-benzimidazole (5l)*

Purification by flash column chromatography, eluted with *n*-hexane/ethyl acetate (7:1), gave compound **5l** as a colourless powder in 80% yield. Mp 287–288 °C (Lit. 288 °C (29)). ^{1}H NMR (DMSO-d_6) δ_H: 6.69 (1H, dd, J_1 = 3.4, J_2 =

© 2008 NRC Canada

1.7 Hz), 7.16–7.20 (4H, m), 7.53 726 (1H, d, J = 3.1 Hz), 7.56 (1H, d, J = 3.1 Hz), 7.89 (1H, s). ^{13}C NMR (DMSO-d_6) δ_C: 110.6, 112.3, 115.0, 122.3, 138.8, 143.6, 144.6, 145.3.

2-(2-Thienyl)-1H-benzimidazole (5m)

Purification by flash column chromatography, eluted with *n*-hexane/ethyl acetate (7:1), gave compound **5m** as a yellow powder in 87% yield. Mp 329–331 °C (Lit. 330 °C (33)). ^{1}H NMR (DMSO-d_6) δ_H: 7.16–7.22 (3 H, m), 7.48–7.58 (2H, m), 7.73 (1H, d, J = 3.1 Hz), 7.82 (1H, d, J = 2.7 Hz), 12.96 (1H, s). ^{13}C NMR (DMSO-d_6) δ_C: 111.0, 118.4, 121.7, 122.6, 126.6, 128.2, 128.7, 133.6, 134.6, 147.0.

2-(2-Pyridyl)-1H-benzimidazole (5n)

Purification by flash column chromatography, eluted with *n*-hexane/ethyl acetate (7:1), gave compound **5n** as a colourless powder in 85% yield. Mp 218 °C (Lit. 218 °C (29)). ^{1}H NMR (DMSO-d_6) δ_H: 7.16–7.24 (2H, m), 7.47–7.71 (3H, m), 7.98 (1H, dd, J_1 = 7.7, J_2 = 1.7 Hz), 8.30–8.34 (1H, m), 8.71 (1H, d, J = 6.9 Hz), 13.01 (1H, s). ^{13}C NMR (DMSO-d_6) δ_C: 112.0, 119.2, 121.4, 121.9, 123.1, 124.6, 134.8, 137.5, 143.7, 148.4, 149.3, 150.7.

2-(2-Naphthyl)-1H-1,3-benzimidazole (5o)

Purification by flash column chromatography, eluted with *n*-hexane/ethyl acetate (7:1), gave compound **5o** as a colourless powder in 90% yield. Mp 217 °C (Lit. 219 °C (37)). ^{1}H NMR (DMSO-d_6) δ_H: 7.19 (2H, dd, J_1 = 6.0, J_2 = 3.0 Hz), 7.37–7.40 (2H, m), 7.59–7.77 (5H, m), 8.11 (1H, dd, J_1 = 8.6, J_2 = 1.7 Hz), 8.49 (1H, s). ^{13}C NMR (DMSO-d_6) δ_C: 115.2, 123.2, 123.6, 126.5, 126.8, 127.2, 127.8, 128.5, 129.0, 134.2, 138.1, 145.9, 151.6.

2-(9-Anthryl)-1H-benzimidazole (5p)

Purification by flash column chromatography, eluted with *n*-hexane/ethyl acetate (7:1), gave compound **5p** as a yellow powder in 90% yield. Mp 301 °C (Lit. 302–303 °C (38)). ^{1}H NMR (DMSO-d_6) δ_H: 7.29 (2H, m), 7.46–7.72 (9H, m), 8.19 (2H, d, J = 8.1 Hz), 8.83 (1H, s). ^{13}C NMR (DMSO-d_6) δ_C: 115.6, 122.6, 125.9, 126.1, 127.3, 127.6, 128.9, 129.3, 131.1, 134.2, 139.4, 146.7, 150.0.

2-Phenyl-1H-benzimidazole-6-carboxylic acid (5q)

Purification by flash column chromatography, eluted with *n*-hexane/ethyl acetate (7:1), gave compound **5q** as a colourless powder in 80% yield. Mp 325 °C (Lit. 325 °C (20)). ^{1}H NMR (DMSO-d_6) δ_H: 7.47–7.66 (4H, m), 7.84 (1H, d, J = 8.4 Hz), 8.17–8.20 (3H, m), 12.79 (1H, s), 13.19 (1H, s). ^{13}C NMR (DMSO-d_6) δ_C: 122.7, 123.5, 124.0, 125.0, 126.7, 128.3, 129.2, 129.6, 130.3, 142.4, 153.7, 168.0.

5-Methyl-2-phenyl-1H-benzimidazole (5r)

Recrystallization from EtOH/H_2O (2:1) gave compound **5r** as a colourless powder in 87% yield. Mp 242–243 °C (Lit. 242–143 °C (30)). ^{1}H NMR (DMSO-d_6) δ_H: 2.35 (3H, S), 7.00 (1H, d, J = 8.1 Hz), 7.36–7.55 (5H, m), 8.14(2H, d, J = 7.6 Hz), 12.75 (1H, s). ^{13}C NMR (DMSO-d_6) δ_C: 21.3, 111.1, 118.4, 123.5, 126.2, 128.8, 129.2, 129.6, 130.3, 131.1, 150.9.

Phenyl(2-phenyl-1H-benzimidazol-5-yl)methanone (5s)

Recrystallization from EtOH/H_2O (2:1) gave compound **5s** as a pale yellow powder in 85% yield. Mp 221–222 °C (Lit. 221–221.5 °C (30)). ^{1}H NMR (DMSO-d_6) δ_H: 7.41–7.58 (11H, m), 8.19 (2H, d, J = 7.4 Hz), 13.28 (1H, s). ^{13}C NMR (DMSO-d_6) δ_C: δ 124.2, 126.7, 128.3, 129.0, 129.4, 129.5, 130.4, 131.0. 132.0, 138.7, 153.9.1, 195.5.

Acknowledgements

We gratefully acknowledge the support of this work by the Shiraz University Research Council. We are also grateful to Mr. H. Sajedian Fard and Mr. M.S. Darvish Tafvizi for helpful cooperation.

References

1. (*a*) M.J. Tebbe, W. A. Spitzer, F.Victor, S.C. Miller, C.C. Lee, T.R.E. Mckinney, and C.J. Tang. J. Med. Chem. **40**, 3937 (1997); (*b*) K.L. Brown. Chem. Rev. **105**, 2075 (2005).
2. (*a*) A.R. Porcari, R.V. Devivar, L.S. Kucera, J.C. Drach, and L.B. Townsend. J. Med. Chem. **41**, 1252 (1998); (*b*) M. Roth, M.L. Morningstar, P.L. Boyer, S.H. Hughes, R.W. Bukheit, and C.J. Michejda. J. Med. Chem. **40**, 4199 (1997).
3. M.T. Migawa, J.L. Giradet, J.A. Walke, G.W. Koszalka, S.D. Chamberlain, J.C. Drach, and L.B. Townsend. J. Med. Chem. **41**, 1242 (1998).
4. I. Tamm and P.B. Seghal. Adv. Virus Res. **22**, 187 (1978).
5. I. Tamm. Science (Washington, DC), **126**, 1235 (1957).
6. A.A. Spasov, I.N. Yozhitsa, L.I. Bugaeva, and V.A. Anisimova. Pharm. Chem. J. **33**, 232 (1999).
7. For comprehensive reviews on the chemistry of benzimidazoles, see: (*a*) J.B. Wright. Chem. Rev. **48**, 397 (1951); (*b*) P.N. Preston. Chem. Rev. **74**, 279 (1974).
8. K. Niknam and A. Fatehi-Raviz. J. Iran. Chem. Soc. **4**, 438 (2007); available from www.ics-ir.org/jics.
9. (*a*) R.R. Nagawade and D.B. Shinde. Indian. J. Chem. B, **46**, 349 (2007); (*b*) K. Bahrami, M.M. Khodaei, and F. Naali. J. Org. Chem. **73** (2008). In press.
10. R.R. Nagawade and D.B. Shinde. Russ. J. Org. Chem. **42**, 453 (2006).
11. R. Trivedi, S.K. De, and R.A. Gibbs. J. Mol. Catal A: Chem. **245**, 8 (2006).
12. T. Itoh, K. Nagata, H. Ishikawa, and A. Ohsawa. Heterocycles, **63**, 2769 (2004).
13. M. Curini, F. Epifano, F. Montanari, O. Rosati, and S. Taccone. Synlett, 1832 (2004).
14. P. Sun and Z. Hu. J. Heterocyclic Chem. **43**, 773 (2006).
15. R.R. Nagawade and D.B. Shinde. Chinese Chem. Lett. **17**, 453 (2006).
16. (*a*) M. Chakrabarty, S. Karmakar, A. Mukherji, S. Arima, and Y. Harigaya. Heterocycles, **68**, 967 (2006); (*b*) H. Sharghi, O. Asemani, and M.H. Tabaei. J. Heterocycl. Chem. **45**, 1 (2008).
17. U. Srinivas, Ch. Srinivas, P. Narender, V. Jayathirtha Rao, and S. Palaniappan. Catal. Commun. **8**, 107 (2007).
18. H. Sharghi, O. Asemani, and R. Khalifeh. Synth. Commun. **38**, 1128 (2008).
19. J.G. Smith and I. Ho. Tetrahedron Lett. **12**, 3541 (1971).
20. (*a*) H. Sharghi, M.H. Beyzavi, and M.M. Doroodmand. Eur. J. Org. Chem, 4126 (2008); (*b*) H. Sharghi, M. Aberi, and M.M. Doroodmand. Advan. Synth. Catal. In press.

© 2008 NRC Canada

21. (*a*) N. Mizuno and M. Misono. Chem. Rev. **98**, 199 (1998); (*b*) G. Sartori, R. Ballini, F. Bigi, G. Bosica, R. Maggi, and P. Righi. Chem. Rev. **104**, 199 (2004).
22. (*a*) H. Sharghi and M. Hosseini Sarvari. Synthesis, 243 (2003); (*b*) H. Sharghi and M. Hosseini Sarvari. J. Org. Chem. **69**, 6953 (2004); (*c*) H. Sharghi and M. Hosseini Sarvari. J. Iran. Chem. Soc. **1**, 28 (2004); available from www.ics-ir.org/jics/; (*d*) M. Hosseini Sarvari and H. Sharghi. Tetrahedron, **61**, 10903 (2005); (*e*) M. Hosseini Sarvari and H. Sharghi. J. Org. Chem. **71**, 6652 (2006); (*f*) H. Sharghi, A. Salimi Beni, and R. Khalifeh. Helv. Chim. Acta, **90**, 1373 (2007); (*g*) H. Sharghi, M. Hosseini Sarvari, and S. Ebrahimpourmoghaddam. Arkivoc, 255 (2007); (*h*) H. Sharghi and R. Khalifeh. Heterocycles, **71**, 1601 (2007); (*i*) H. Sharghi and M. Jokar. Heterocycles, **71**, 2721 (2007); (*j*) H. Sharghi and R. Khalifeh. Can. J. Chem. **86**, 426 (2008); (*k*) H. Sharghi and S. Ebrahimpourmoghaddam. Helv. Chim. Acta, **91**, 1363 (2008).
23. K.B. Gudasi, R.S. Vadavi, R.V. Shenoy, M.S. Patil, and S.A. Patil. Transition Met. Chem. **30**, 569 (2005).
24. Y. Li and M.A. Trush. Arch. Biochem. Biophys. **300**, 346 (1993).
25. R. Liu, B. Goodell, J. Jellison, and A. Amirbahman. Environ. Sci. Technol. **39**, 175 (2005).
26. Q. Liang and P.C. Dedon. Chem. Res. Toxicol. **14**, 416 (2001).
27. S. Velusamy, A.V. Kumar, R. Saini, and T. Punniyamurthy. Tetrahedron Lett. **46**, 3819 (2005).
28. S. Velusamy and T. Punniyamurthy. Eur. J. Org. Chem, 3913 (2003).
29. B.A. Abdelkrim. Tetrahedron Lett. **44**, 5935 (2003).
30. R.J. Perry and B.D. Wilson. J. Org. Chem. **58**, 7016 (1993).
31. B. George and E.P. Papadopoulos. J. Org. Chem. **42**, 441 (1977).
32. G. Holan, J.J. Evan, and M. Linton. J. Chem. Soc., Perkin Trans. 1, 1200 (1977).
33. P. Gogoi and D. Konwar. Tetrahedron Lett. **47**, 79 (2006).
34. M.N. Ibrahim. Asian J. Chem. **19**, 2419 (2007).
35. G. Navarrete-Vazquez, H. Moreno-Diaz, F. Aguirre-Crespo, I. Leon-Rivera, R. Villalobos-Molina, O. Munoz-Muniz, and S. Estrada-Soto. Bioorg. Med. Chem. Lett. **16**, 4169 (2006).
36. S. Jaroslav. Collect. Czech. Chem. Commun. **46**, 2703 (1981).
37. S. Robev. Dokl. Akad. Nauk, **34**, 663 (1981).
38. K. Niume, K. Toyofuku, F. Toda, K. Uno, M. Hasegawa, and Y. Iwakura. J. Polym. Sci. 663 (1982).

© 2008 NRC Canada

Facile reductive dehalogenation of organic halides with nickel boride at ambient temperature

Jitender M. Khurana, Sanjay Kumar, and Bhaskara Nand

Abstract: The hydrodehalogenation of a series of aryl, alkyl, allyl, and benzyl chlorides, bromides, and iodides has been carried out efficiently using nickel boride in methanol at ambient temperature, leading to the corresponding products resulting from hydrogen/halogen exchange.

Key words: hydrodehalogenation, reduction, organic halides, sodium borohydride, nickel boride.

Résumé : Faisant appel à l'action du borure de nickel à la température ambiante et dans le méthanol, on a effectué d'une façon efficace la hydrodéshalogénation d'une série d'iodures, de bromures et de chlorures d'aryle, d'alkyle, d'allyle et de benzyle conduisant à la formation des produits correspondants résultant d'un échange hydrogène/halogène.

Mots-clés : hydrodéshalogénation, réduction, halogénures organiques, borohydrure de sodium, borure de nickel.

[Traduit par la Rédaction]

Introduction

The development of effective procedures for the dehalogenation of organic halides is an important task, as it helps in the reduction of pollution by halogen-containing industrial wastes as well as for the synthesis of fine chemicals. Unlike oxidation methods, reductive dehalogenation processes are advantageous, as no toxic side products are formed. A wide variety of hydrodehalogenating systems have been used over the years and have been reviewed in detail (1–3). Thus, catalytic hydrogenation (4), dehalogenation by metals or low-valent metal compounds (5), metal hydrides, or complex metal hydrides (6–10) are some general reagents and methods able to accomplish the above-mentioned transformation. Nickel boride (11), first reported by Schlesinger and Brown, has been used as heterogeneous hydrogenation catalyst over the years (12). However, it is now known as a reducing agent by itself because of the adsorbed hydrogen (13). In recent years, we have used nickel boride as a novel reducing agent in multifarious transformations (14*a*–14*m*) (e.g., reductions, deoxygenations, desulfurisations, and so forth). In continuation to our studies on dehalogenation of various types of organic halides (15), we now wish to report the dehalogenation of benzylic, allylic, aryl, and alkyl halides with nickel boride in methanol at ambient temperature.

Results and discussion

In this paper, we report hydrodehalogenation of aryl, alkyl, and allyl halides to the corresponding hydrocarbons using nickel boride generated in situ from nickel(II) chloride and sodium borohydride. Benzylic halides were almost instantaneously reduced. Allylic halides underwent hydrodehalogenation and reduction of double bond concomitantly. Aryl halides, which are generally resistant to hydrodehalogenation, could also be easily dehalogenated to the corresponding arenes.

9-Bromofluorene was chosen as the model substrate to investigate and optimize the conditions for hydrodebromination of benzylic halides. The reactions of 9-bromofluorene were carried out with nickel boride in different solvents and in different molar ratios of substrate to nickel boride to achieve the desired transformation. Reactions carried out in THF, ethanol, and DMF were sluggish and gave a mixture of products, while no reaction was observed in acetonitrile and dichloromethane. Reaction of 9-bromofluorene in methanol yielded 96% fluorene in 15 min at ambient temperature. Further, it has been shown that the hydrodehalogenation is proceeding due to in situ formation of nickel boride, as no reaction of 9-bromofluorene was observed with nickel(II) chloride or sodium borohydride independently.

The hydrodehalogenation of a variety of benzylic halides was subsequently investigated under similar experimental conditions. Benzylic chlorides, bromides, and iodides underwent rapid hydrodehalogenation in different molar ratios of substrate:$NiCl_2{\cdot}6H_2O$:$NaBH_4$ (Scheme 1) (Table 1). The ease of dehalogenation BnI > BnBr > BnCl follows the order of bond energies C–Cl > C–Br > C–I, which is evident from molar ratios and the time required for the dehalogenation (Table 1, entries 1–21). Further, it can also be inferred from Table 1 that primary halides (Table 1, entries 1–4, 11, 12,

Received 6 August 2008. Accepted 15 September 2008. Published on the NRC Research Press Web site at canjchem.nrc.ca on 24 October 2008.

J.M. Khurana,[1] S. Kumar, and B. Nand. Department of Chemistry, University of Delhi, Delhi 110007, India.

[1]Corresponding author (e-mail: jmkhurana1@yahoo.co.in).

 doi:10.1139/V08-156 © 2008 NRC Canada

Table 1. Reductive dehalogenation of organic halides with nickel boride in methanol at room temperature.

Entry	Substrate (S)	Molar ratio $S/NiCl_2 \cdot 6H_2O/NaBH_4$	Time (min)	Product	Yield (16) (%)
1	1-(Bromomethyl)naphthalene	1:2:6	15	1-Methylnaphthalene	92
2	2-(Bromomethyl)naphthalene	1:2:6	15	2-Methylnaphthalene	86
3	4-Bromobenzyl bromide	1:2:6	15	4-Bromotoluene	85
4	4-chlorobenzyl bromide	1:2:6	15	4-Chlorotoluene	81
5	9-Bromofluorene	1:2:6	15	Fluorene	96
6	Bromodiphenylmethane	1:2:6	20	Diphenylmethane	90
7	(1-Bromoethyl)benzene	1:2:6	20	Ethylbenzene	83
8	(1-Bromopropyl)benzene	1:2:6	30	*n*-Propylbenzene	81
9	1-(1-Bromoethyl)naphthalene	1:2:6	20	1-Ethylnaphthalene	82
10	Bromotriphenylmethane	1:2:6	40	Triphenylmethane	81
11	1-(Chloromethyl)naphthalene	1:3:9	20	1-Methylnaphthalene	94
12	2-(Chloromethyl)naphthalene	1:3:9	20	2-Methylnaphthalene	92
13	9-Chlorofluorene	1:3:9	25	Fluorene	91
14	Chlorodiphenylmethane	1:3:9	30	Diphenylmethane	75
15	(1-Chloroethyl)benzene	1:3:9	30	Ethylbenzene	81
16	(1-Chloropropyl)benzene	1:3:9	30	*n*-Propylbenzene	84
17	1-(1-Chloroethyl)naphthalene	1:3:9	25	1-Ethylnaphthalene	74
18	Chlorotriphenylmethane	1:3:9	45	Triphenylmethane	86
19	1-(Iodomethyl)naphthalene	1:1:3	5	1-Methylnaphthalene	85
20	(1-Iodopropyl)benzene	1:1:3	10	*n*-Propylbenzene	85
21	Iododiphenylmethane	1:1:3	10	Diphenylmethane	82
22	Cinnamyl iodide	1:1:3	10	*n*-Propylbenzene	81
23	Cinnamyl bromide	1:1:3	15	*n*-Propylbenzene	91
24	Cinnamyl chloride	1:2:6	10	*n*-Propylbenzene	92
25	1-Iodonaphthalene	1:1:3	15	Naphthalene	87
26	1-Bromonaphthalene	1:2:6	15	Naphthalene	95
27	1-Chloronaphthalene	1:3:9	25	Naphthalene	93
28	9-Bromoanthracene	1:2:6	30	Anthracene + 9,10-Dihydroanthracene	42 + 48
29	9-Chloroanthracene	1:3:9	30	Anthracene + 9,10-Dihydroanthracene	40 + 47
30	9-Bromophenanthrene	1:2:6	30	Phenanthrene	86
31	4-Bromobiphenyl	1:10:30	120	Biphenyl	54
32	4-Bromophenol	1:10:30	60	Phenol	72
33	4-Chlorophenol	1:10:30	90	Phenol	75
34	Methyl 4-bromobenzoate	1:10:30	45	Methyl benzoate	84
35	Methyl 4-chlorobenzoate	1:10:30	60	Methyl benzoate	82
36	1-Bromododecane	1:5:15	20	*n*-Dodecane	85
37	1-Bromohexadecane	1:5:15	20	*n*-Hexadecane	84
38	1-Bromoadamantane	1:5:15	35	Adamantane	82
39	1-Bromo-3-phenylpropane	1:5:15	30	*n*-Propylbenzene	87
40	Methyl 4-bromobutanoate	1:5:15	30	Methyl butanoate	78

Scheme 1.

$$R{-}X \xrightarrow[\text{methanol, RT, 5–120 min}]{NiCl_2 \cdot 6H_2O\ ,\ NaBH_4} R{-}H$$

R = alkyl, aryl, benzyl; X = I, Br, Cl

and 19) undergo faster reduction than secondary halides (Table 1, entries 5–9, 13–17, 20, and 21), and tertiary halides (Table 1, entries 10 and 18) exhibit even slower reactivity.

Hydrodehalogenation of allylic halides (Table 1, entries 22–24), on the other hand, proceeds with the concomitant reduction of double bond to give the completely reduced product. No selective dehalogenation could be achieved even at lower temperatures.

Aryl halides and alkyl halides, which are generally resistant to dehalogenation, could also be dehalogenated successfully with nickel boride (Scheme 1). Thus, 1-iodonaphthalene, 1-bromonaphthalene, and 1-chloronaphthalene underwent rapid dehalogenation (Table 1, entries 25–27) giving naphthalene in excellent yields. The order of reactivity was the same as observed earlier, i.e., I > Br > Cl. Reaction of 9-bromoanthracene and 9-chloroanthracene with nickel boride (Table 1, entries 28 and 29) resulted in a mixture of anthracene and 9,10-dihydroanthracene. This is because anthracene itself was observed to undergo reduction with nickel boride to give 9,10-dihydroanthracene in an independent reaction.

Similarly, other aryl halides 9-bromophenanthrene, 4-bromophenol, 4-chlorophenol, methyl 4-bromobenzoate,

© 2008 NRC Canada

methyl 4-chlorobenzoate, and 4-bromobiphenyl were easily dehalogenated in quantitative yields. Dehalogenation of halobenzenes, however, required much higher molar ratios compared with halonaphthalenes and benzylic halides. This fact has been utilized to achieve regioselective dehalogenation of benzylic C–X over Ph–X bond. Thus, 4-bromobenzyl bromide and 4-chlorobenzyl bromide could be selectively dehalogenated to give 4-bromotoluene and 4-chlorotoluene, respectively (Table 1, entries 3 and 4).

Aliphatic alkyl halides, 1-bromohexadecane, 1-bromododecane, 1-bromoadamantane, 1-bromo-3-phenylpropane, and methyl 4-bromobutanoate also underwent successful dehalogenation but required higher molar ratio of 1:5:15 (Table 1, entries 36–40). Selective debromination of benzylic bromide over alkyl bromide could also be achieved when an equimolar mixture of 1-(bromomethyl)naphthalene and 1-bromo-3-phenyl propane was treated with nickel boride in 1:2:6 molar ratio. ^{1}H NMR spectra after 15 min showed complete disappearance of 1-(bromomethyl)naphthalene while 1-bromo-3-phenyl propane was found unreacted in the reaction mixture.

In conclusion, we have developed a highly efficient protocol for hydrodehalogenation of organic halides with nickel boride at ambient temperature. Compared with other hydrodehalogenating systems, several features make the procedure particularly attractive. Hydrogenolysis was very rapid. Yields of products were found good to excellent. Further, no coupled product or any other side product was either detected or isolated. Reaction was carried out at ambient temperature, and the products could be isolated by a simple workup procedure. However, the carbonyl and nitro groups are sensitive to nickel boride and get reduced (14*c*, 17).

Experimental

All products are known compounds. Melting points were recorded on a Tropical Labequip apparatus and are uncorrected. The PMR spectra were recorded on Hitachi FTNMR (60 MHz) using TMS as internal standard. The products were identified by mp and superimposable IR and NMR spectra with authentic samples. Methanol (S.D. Fine), nickel chloride hexahydrate (S.D. Fine), and sodium borohydride (E. Merck) were used in all reactions.

General procedure

In a typical reaction, a 50 mL round-bottomed flask fitted with a reflux condenser was mounted over a magnetic stirrer, and 9-bromofluorene (0.2 g, 0.81 mmol) dissolved in 10 mL of methanol was placed in it. $NiCl_2{\cdot}6H_2O$ (0.38 g, 1.63 mmol) was added followed by $NaBH_4$ (0.18 g, 4.89 mmol) cautiously. The reaction mixture was stirred vigorously at room temperature. The progress of reaction was monitored by TLC using petroleum ether as eluent. TLC of the reaction mixture showed the complete disappearance of starting material after 15 min. The reaction was quenched by adding 10 mL of methanol. The reaction mixture was filtered through a Celite pad (~2.5 cm) and washed with methanol (20 mL). Water (20 mL) was added to the filtrate, which was extracted with ethyl acetate (3 × 10 mL). The combined extract was dried over anhyd. $MgSO_4$, decanted through a cotton pad, and concentrated on a rotary evaporator. The product was recrystallized from ethanol to give 0.13 g of fluorene as characterized by mp and ^{1}H NMR spectra.

Acknowledgement

Financial assistance for the project by University Grants Commission [Project no. F-32–203/2006 (SR)] and Junior/Senior Research Fellowship to SK by Council of Scientific and Industrial Research is gratefully acknowledged.

References

1. A.R. Pinder. Synthesis, 425 (1980).
2. F.J. Urbano and J.M. Marinas. J. Mol. Catal. A: Chem. **173**, 329 (2001).
3. F. Alonso, I.P. Beletskaya, and M. Yus. Chem. Rev. **102**, 4009 (2002).
4. P. Rylander. Hydrogenation methods. Academic press. New York. 1985. Chap. 12.
5. V.V. Lunin and E.S. Lokteva. Russ. Chem. Bull. **45**, 1519 (1996).
6. N.G. Gaylord. Reductions with complex metal hydrides. Interscience Publishers. New York. 1956. p. 889.
7. D.J. Malter, H.J. Wotiz, and C.A. Hollingsworth. J. Am. Chem. Soc. **78**, 1311 (1956).
8. H.M. Bell and H.C. Brown. J. Am. Chem. Soc. **88**, 1473 (1966).
9. H.C. Brown and S. Krishanamurthy. J. Am. Chem. Soc. **95**, 1669 (1973).
10. S. Kim and K.Y. Yi. Bull. Chem. Soc. Jpn. **58**, 789 (1985).
11. (*a*) H.I. Schlesinger and H.C. Brown. US Patent 2 461 661. 1949; (*b*) R.J. Wade. J. Mol. Catal. **48**, 273 (1983); (*c*) M. Hudlicy. Reductions in organic chemistry. Wiley. New York. 1984.
12. (*a*) R. Paul, P. Buisson, and N. Joseph. Compt. Rend. **23**, 627 (1951); (*b*) R. Paul, P. Buisson, and N. Joseph. Ind. Eng. Chem. **44**, 1006 (1952).
13. B. Ganem and J.O. Osby. Chem. Rev. **86**, 763 (1986).
14. (*a*) J.M. Khurana and A. Gogia. Org. Prep. Proced. Int. **29**, 1 (1997); (*b*) J.M. Khurana, A. Ray, and S. Singh. Tetrahedron Lett. **39**, 3829 (1998); (*c*) J.M. Khurana and S. Chauhan. Synth. Commun. **31**, 3485 (2001); (*d*) J.M. Khurana, G. Kukreja, and G. Bansal. J. Chem. Soc. Perkin Trans. 1, 2520 (2002); (*e*) J.M. Khurana and S. Chauhan. J. Chem. Res. (S) 201 (2002); (*f*) J.M. Khurana and S. Chauhan. J. Chem. Res. (M) 519 (2002); (*g*) J.M. Khurana and G. Kukreja. Synth. Commun. **32**, 1265 (2002); (*h*) J.M. Khurana and G. Kukreja. J. Heterocycl. Chem. **40**, 677 (2003); (*i*) J.M. Khurana, P. Sharma. Bull. Chem. Soc. Jpn. **77**, 549 (2004); (*j*) J.M. Khurana, A. Agrawal, and G. Kukreja. Heterocycles, **68**, 1885 (2006); (*k*) J.M. Khurana and Kiran. J. Chem. Res. (S) 374 (2006). (*l*) J.M. Khurana, R. Arora, and S. Satija. Heterocycles, **71**, 2709 (2007); (*m*) J.M. Khurana and V. Sharma. Chem. Heterocycl. Compd. 404 (2008).
15. J.M. Khurana, B.M. Kandpal, G. Kukreja, and P. Sharma. Can. J. Chem. **84**, 1019 (2006).
16. Chapman and Hall. Dictionary of organic compounds. 5th ed.
17. J.O. Osby and B. Ganem. Tetrahedron Lett. 6413. 1985.

© 2008 NRC Canada

A capillary and microchip-based nanoelectrospray emitter using a mesoporous membrane

Shuqin Su and Richard D. Oleschuk

Abstract: A method is described for the fabrication of multipath electrospray emitters using hydrophobic porous polymer membranes. Polysulphone (PSF) and polycarbonate (PC) membranes, which possess pores with well-defined sizes, are glued onto the exit aperture of fused-silica capillaries or microfluidic chips to create multipaths to assist electrospray at moderate nano flow rates (e.g., 50–500 nL/min). A capillary-based multipath emitter fabricated with either PSF or PC membranes was prepared with a fused-silica capillary with 75 μm inner diameter and 360 μm outer diameter. Relative effects on electrospray performance at different flow rates, electrospray voltages, and solvent compositions are probed. The sensitivity and stability of electrospray signals were enhanced through spraying from multiple pores on the membrane. An embossed polycarbonate microchip was also interfaced to the mass spectrometer using the meso porous membrane approach.

Key words: nanoelectrospray, membrane, emitter, multipaths, microchip.

Résumé : On décrit une méthode de préparation d'émetteurs à électronébulusation par étape faisant appel à des membranes polymères poreuses et hydrophobes. Des membranes de polysulfone (PSF) et de polycarbonate (PC) qui possèdes des pores de tailles bien définies sont collées sur l'ouverture de sortie de capillaires de silice fondue ou de puces microfluides dans le but de créer des passages multiples pour aider l'électronébulisation à des vitesses d'écoulement nano modérées (c'est-à-dire de 50 nL/min à 500 nL/min). Utilisant des membranes PSF ou PC, on a préparé des émetteurs à passages multiples à base de capillaire, comportant un capillaire à silice fondue de diamètre interne de 75 μm et un diamètre externe de 360 μm. On a étudié les effets relatifs sur la performance de l'électronébulisation des variations dans les vitesses d'écoulement, les voltages d'électronébulisation et les compositions du solvant. La sensibilité et la stabilité des signaux d'électronébulisation sont augmentées par la nébulisation à partir des multiples pores de la membrane. On a aussi créé une interface entre une micropuce de polycarbonate et un spectromètre de masse en utilisant l'approche de la membrane méso poreuse.

Mots-clés : électronébulisation, membrane, émetteur, passages multiples, micropuce.

[Traduit par la Rédaction]

Introduction

Electrospray ionization (ESI), which transforms analytes from the liquid-phase to the gas-phase by forming fine droplets under an electric field, has revolutionized the study of large biomolecules, especially proteins and peptides (1–3). As an interface, electrospray emitters play an important role in coupling powerful separation technologies, such as liquid chromatography (LC) columns (4) or microfluidic chips (microchip) (5, 6), with a versatile detector of mass spectrometer (MS) for online sample preparation, separation, and analysis by ESI-MS. In addition, an electrospray emitter can also be used offline for the deposition of analytes onto a target plate for further analysis by matrix-assisted laser deposition ionization mass spectrometry (MALDI/MS) (7). Different approaches or designs have been explored to fabricate electrospray emitters for various purposes (8–26). Emitters with single micrometer-sized tapered-tips were developed to enable electrospray at nano-level flow rates for achieving highly sensitive detection (27). Furthermore, nano-ESI emitters are suitable for coupling nano-HPLC or microfluidic devices with mass spectrometry allowing the manipulation of small sample volumes (28, 29). Tapered emitters are traditionally used for nano-ESI. However, when using tapered emitters with a tip size of less than 20 μm, it is problematic due to the continuous clogging (30). Tapered emitters with a single-tip also have concerns of low liquid throughput for nano-electrospray (31).

Strategies for solving problems associated with tapered emitters have included using emitters with larger apertures or multiple spraying tips and channels. Emitters with larger apertures (> 50 μm i.d.) prepared by directly cutting fused-silica capillaries without further treatment are generally not able to produce stable sprays at nano flow rates (<1000 nL/min). Recently, Knapp and co-workers (31) have proposed a simulation model to facilitate nano-electrospray from a relatively large open tube. The model suggested growing an array of carbon nanofibers (CNFs) around the orifice of a capillary as multiple electrospray emitters, while

Received 25 June 2008. Accepted 16 September 2008. Published on the NRC Research Press Web site at canjchem.nrc.ca on 25 October 2008.

S. Su and R.D. Oleschuk.[1] Department of Chemistry, Queen's University, Kingston, ON K7L 3N6, Canada.

[1]Corresponding author (e-mail: richard.oleschuk@chem.queensu.ca).

 doi:10.1139/V08-154 © 2008 NRC Canada

a higher fluidic throughput could be delivered through the open tube. Alternatively, emitters with multiple electrospray paths are becoming a more attractive option for generating nanoelectrospray because of their reduced susceptibility to clogging, higher sample throughput, and the improved sensitivity (31–33). Multiple electrospray paths can be generated from an array of tips fabricated by either simply manipulating capillary tubes parallel to each other or using microfabrication techniques such as photolithographic patterning, plasma etching, or laser ablation (34, 35). Tang et al. (33) reported a multiple electrospray emitter by fabricating an array of emitters on a polycarbonate substrate. The multiple paths for electrospray were also generated by drilling holes on a hydrophobic plate (32). However, these multiple electrospray emitters were designed to allow for increased sensitivity at a relatively large flow rate (>1 μL/min) (33). For generating electrospray at nanoliter per minute flow rates, we have developed emitters with multiple paths by forming porous polymer monolith (PPM) (25) or entrapping microspheres at the exit aperture of a fused-silica capillary channel (26). It was noticed that when using an emitter bearing multiple paths, electrospray can be generated from either a single emission jet or multiple emission jets depending on the emitter geometry and electrospray conditions (25, 33). To create multiple electrospray cone-jets with a good resolution from an emitter with multiple paths, the geometry of each individual emitter tip, the distance between the surface features, and the hydrophobicity of the surface on an emitter tip play an important role (31). If the distance between two emitter tips and the ratio of the height to the width of each emitter is too small, the liquid sprayed from individual tips is more likely to coalesce into a single Taylor cone.

Emitters with multiple paths can be fabricated for either a capillary-based or a microchip-based system. A capillary-based emitter such as PPM-filled or -entrapped microspheres can also be used in an integrated configuration for sample desalting, pre-concentration, and separation (26, 36). Furthermore, microchip-based emitters were also developed to allow the integration of more complicated functionalities as well as increased throughput (37, 38). Plastic materials are preferred for making disposable chips because they are less expensive. However, electrospray from the flat exit of a plastic chip channel is a challenge due to droplet spreading. A capillary-based emitter can be inserted into the channel of a microchip to assist with the electrospray (39). Although this technique has demonstrated good electrospray performance, it can leave a large dead volume that results in band broadening during separation. Micro-fabrication techniques have been used to form sharp tips to eliminate droplet spreading (40), but these techniques are usually complicated and expensive. Moreover, coating or bonding hydrophobic materials on the exit surface of a microchip-based emitter has also been demonstrated as an alternative solution (18). CF_4 coating by plasma deposition was used to increase the hydrophobicity of an emitter exit, but it exhibited limited robustness. A porous membrane was reported to enhance the hydrophobicity of an emitter exit surface by thermally bonding poly-tetrafluoroethylene (PTFE) onto the exit surface of a PC microchip (41). A piece of PTFE membrane with 50 μm thickness and an average pore size of 0.22 μm was bonded onto a microchip exit. However, it was difficult to precisely control the temperature and the force used during thermal bonding to bond membrane without pore deformation.

A novel technique is described in this paper to fabricate an emitter with multiple electrospray paths by simply gluing a piece of porous polymer membrane onto either the exit of a fused-silica capillary or the exit aperture of a polymer microchip under an optical microscope. Porous polymer membranes (polysulphone (PSF) and polycarbonate (PC)), which have precisely defined pore sizes, are used for the emitter fabrication. The overall electrospray performance was improved, compared with that of an open tubular emitter. The signal to noise ratio for the 482.4 *m*/*z* peak of jeffamine was increased from 6 to 34 for a membrane-assisted emitter compared with that of an open tubular emitter. Furthermore, hydrophobic membranes bonded onto the exit of a PC polymer microchip channel also prevented the liquid from spreading along the flat edge of the microchip, enabling a stable electrospray signal.

Experimental

Reagents and materials

Zinc nitrate hexahydrate, $Zn(NO_3)_2{\cdot}6H_2O$ (98%), hexamethylenetetramine, $C_6H_{12}N_4$ (99%), and glass plates coated with polycrystalline F-SnO_2 were purchased from Hartford Glass Inc. (USA). Polysulfone (Udel® P3500) was a gift from Solvay Advanced Polymers and was purified by precipitation fractionation using THF as a solvent and methanol as a precipitant. The weight-average molar mass *Mw* of the fractional sample was determined by light scattering, using the specific refractive index increment of 0.201 mL/g measured in THF and was 9.0×10^4 g/mol. The polydispersity index *Mw*/*Mn* of the sample was 1.42, as determined by size exclusion chromatography based on poly (methyl methacrylate) standards.

The PSF membrane was prepared in-house according to the procedures described below. Whatman PC membrane was purchased from Fisher Scientific (Ottawa, Ontario, Canada). Fused-silica capillaries (360 μm o.d., 75 μm i.d.) were purchased from Polymicro Technologies (Phoenix, Arizona, USA). Markrolon PC sheets were purchased from Sheffield Plastic Inc (Scarborough, Ontario, Canada). Epoxy resin (Torr Seal) was purchased from Varian, Canada. Syringe glue Speed Set epoxy was purchased from LePage (Missisauga, Ontario, Canada).

Glacial acetic acid, methanol (HPLC grade), and acetonitrile were all purchased from Fisher Scientific (Ottawa, Ontario, Canada) and used without purification. *O*-(2-aminopropyl)-*O*-(2-methoxyethyl) polypropylene glycol 500 (jeffamine) were purchased from Sigma-Aldrich (Oakville, Ontario, Canada) and also used without purification. Milli-Q water was obtained from Millipore (Bedford, Massachusettes, USA).

Preparation of PSF membrane

The PSF porous membrane was prepared by a patterning method that uses ZnO pillar arrays as a template (42). Briefly, ZnO pillars were prepared by immersing a SnO_2 coated glass plate into a solution containing $Zn(NO_3)_2{\cdot}6H_2O$ and $C_6H_{12}N_4$ (1:1 molar ratio) at 90 °C for 18 h. A 2–3 mm

© 2008 NRC Canada

Fig. 1. SEM images (*a*) top view of ZnO pillar template for porous membrane preparation, (*b*) one pillar in large magnification, (*c*) side view of ZnO pillar template, and (*d*) PSF membrane with about 1 μm pores.

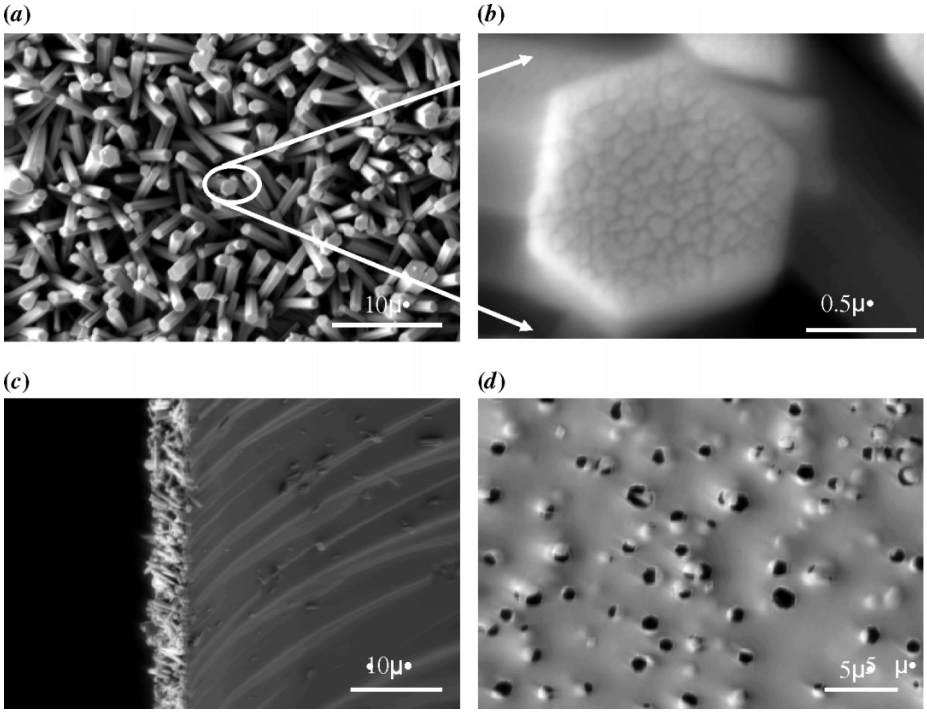

Fig. 2. SEM images (*a*) top view of PSF membrane bonded capillary exit and (*b*) large magnification of bonded membrane.

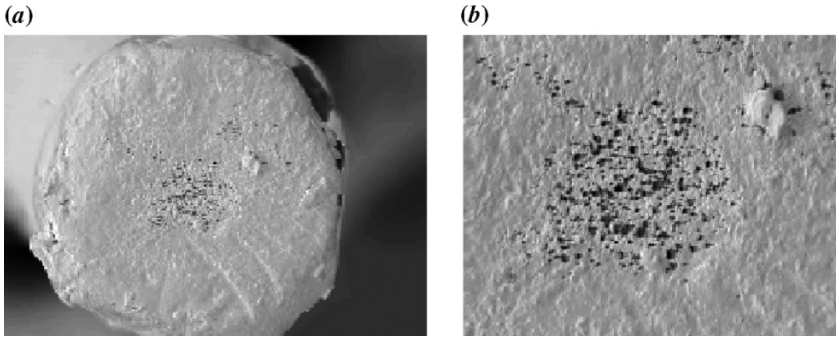

dam was then built with epoxy resin along the periphery of a glass plate bearing ZnO pillars. We added 1.5 mL of 3.3 mg/mL PSF in THF solution onto a plate within the dam. After the THF evaporated, the PSF spherical end capping was etched off the pillar by soaking the plate bearing the PSF membrane in THF/methanol (*v*/*v* = 1:1). The plate was then immersed into 0.5 mol/L HCl to dissolve the pillars after the THF/methanol evaporated. Finally, the porous membrane was detached from the glass plate as ZnO was dissolved. Figure 1 shows the SEM image of (*a*) ZnO pillars with about (*b*) 1 μm width and (*c*) 6–7 μm length. By casting polysulfone solution onto these pillars, a 1 μm pore sized membrane can be obtained as shown in Fig. 1*d*.

Fabrication of a capillary-based nanoelectrospray emitter

UV-transparent fused-silica capillaries (360 μm o.d. and 75 μm i.d.) were used for emitter fabrication. Emitters were cut from 4 to 6 cm in length. The exit aperture was inspected under a microscope before testing. PSF membranes with 1.0 μm sized pores and PC membranes with 0.22 μm, 1.0 μm, and 5.0 μm sized pores were used for the emitter fabrication, respectively. A thin layer of the freshly mixed epoxy glue was applied onto a capillary exit using a sharp needle under an optical microscope. The glued exit aperture of the capillary was then stamped onto a piece of membrane. The extra membrane along the capillary edge was trimmed using tweezers after the epoxy had hardened. The exit image of a membrane assisted emitter is shown in Fig. 2.

Fabrication of a chip-based multipath electrospray emitter

Hot embossing, as described elsewhere (23), was used to fabricate a PC chip-based emitter. Briefly, as illustrated in Fig. 3, a fused-silica capillary (20 μm i.d and 150 μm o.d.) was used as a master to create a channel by embossing the capillary onto a PC sheet at 150 °C and 2000 N for 830 s. After peeling off the capillary, a channel is left on the sur-

© 2008 NRC Canada

Fig. 3. Diagram of fabrication of microchip-based emitter with membrane bonded on channel exit.

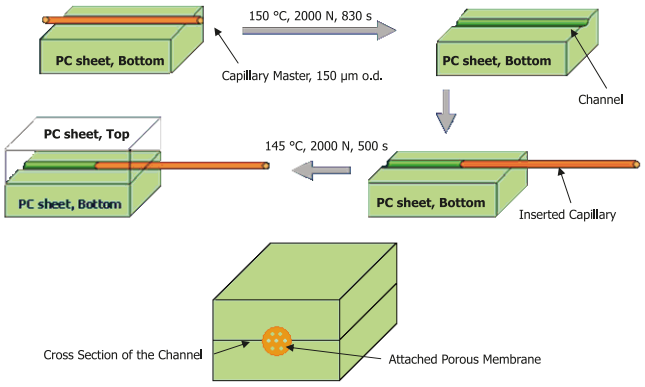

face of the PC sheet. The channel was inspected under an optical microscope to ensure it was free of debris. Next, a capillary with 20 µm i.d and 150 µm o.d. was inserted 1 cm into the channel through one exit to deliver the fluid into the chip. A second sheet of unpatterned PC was then placed on top of the substrate bearing the positioned delivery capillary. The two PC sheets were then bonded at 145 °C and 2000 N for 500 s. The chip exit was shaped to a narrower end (0.5 cm in width) to facilitate easier access to the MS orifice. A piece of porous membrane (3 mm × 3 mm) was then glued onto the chip exit using the method described above for the fabrication of a capillary-based emitter.

Online electrospray mass spectrometry

Mass spectra acquisitions were conducted on an API 3000 triple-quadrupole mass spectrometer (MDS Sciex, Ontario, Canada). An online nanoelectrospray interface (Proxeon, Odense, Denmark) was installed with two CCD cameras, a micro-tee, and an x-y-z stage. The output of the CCD cameras was connected to a PC. A capillary-based emitter was first inserted into a MicroTight green sleeve (395 i.d. and 635 o.d.) and then affixed to a micro-tee, which was then mounted onto the x-y-z stage. An electrode was connected through the junction of the micro-tee. One end of the micro-tee was connected to a nano-LC pump by a capillary with a 360 µm o.d. and 20 µm i.d. as a transfer line.

For the chip-based emitter, the microchip was first affixed to a flat plastic holder, which was then mounted onto an x-y-z stage. A metal union was used to both connect a delivery capillary to the chip channel and a capillary from a nano-LC pump. It also facilitated the application of an ESI voltage. The relative distance between an emitter and the mass spectrometer orifice was about 0.5–2 cm. Positive ion mode was used for the detection of both jeffamine and leucine enkephalin. The curtain gas flow rate was set at 0.3 L/min, and the declustering potential and focusing potential were kept at 60 and 250 V, respectively. Quadrupole peak width (set to yield a unit mass resolution of 0.7 amu at FWHM) and the scan time (1 Hz) were kept constant for all the experiments.

Offline electrospray set-up

A membrane-assisted capillary emitter was set in a MicroTee (Upchurch, S.P.E., Toronto, Ontario, Canada), which was in turn mounted onto an x-y-z stage (Proxeon, Odense, Denmark). A CCD camera was used to record images through an ATI multimedia program. A high voltage supply (Micralyne, Edmonton, Alberta, Canada) was controlled by PC via µTK software and supplied the necessary electrospray potential. A small metal plate (3 cm × 3 cm), used as a counter electrode, was positioned 1 cm in front of the emitter. The positive high voltage was connected via a liquid–electrode junction within the MicroTee. A syringe pump (Harvard, Pennsylvania, USA) infused 1 µmol/L leucine enkephalin solution in 70% methanol to the membrane-assisted emitter, and electrospray images were recorded at different flow rates.

Investigation of electrospray performance

The influence of flow rates, spray voltages, and solvent compositions on the electrospray stability, sensitivity, and reproducibility was evaluated. A nano-pump was used to control flow rates from 50 to 500 nL/min. Spray voltages from 2.4 to 3.5 kV were applied through a metal wire inserted into the liquid junction within the micro tee. Standard solutions of 1 µmol/L polypropylene (jeffamine) were prepared in methanol/acetonitrile with 10%–90% water and 0.1% acetic acid. Leucine enkephalin (1 µmol/L) was prepared in 70% methanol and 0.1% acetic acid. Data acquisition was set to scan between 400–1000 *m/z*. The intensity of the total ion current (TIC) was used to represent the detection sensitivity. The electrospray stability was evaluated by the relative standard deviation (RSD%) of the TIC intensities, calculated by dividing the standard deviation (SD) of the TIC data points against the average of the TIC intensities. The signal to noise ratio (S/N) was calculated by dividing the background subtracted analyte peak heights against the standard deviation of the background signals.

Results and discussion

Fabrication of multipath electrospray emitters using porous polymer membranes

A novel method to fabricate a multipath electrospray emitter is reported by simply gluing a porous polymer membrane over the exit aperture of either a fused-silica capillary or a PC microfluidic chip. Various fabrication methods have been developed to fabricate emitters with an array of tips, channels, or simple holes to form multiple electrospray paths (12–14, 43). A thermal-bonded porous polytetrafluoroethylene (PTFE) membrane was used to enhance the hydrophobicity of the exit surface of a PC microfluidic chip (41). The liquid spreading at the exit aperture was reduced. Multiple fluidic paths were also formed as a result of the tortuous pores of the PTFE membrane. However, as a result of thermal bonding, the authors found that the pore size (average 0.22 µm) and the pore distribution of a membrane were modified during bounding because of the bonding force and high temperature. It was not easy to precisely control the temperature and force to allow a permanent bonding of membrane without deforming the channel exit or sealing the pores on the membrane.

In this method, PSF and PC membranes with precisely defined pore sizes (0.2–5.0 µm) are used with both fused-silica and plastic materials to fabricate capillary-based or chip-

© 2008 NRC Canada

Fig. 4. Offline electrospray images from membrane-assisted emitters (PSF membrane bearing 1 μm sized pores) at different flow rates while continuously infusing 1 μmol/L leucine enkephalin in 70% methanol and 0.1% acetic acid at a spray voltage of 2.8 kV.

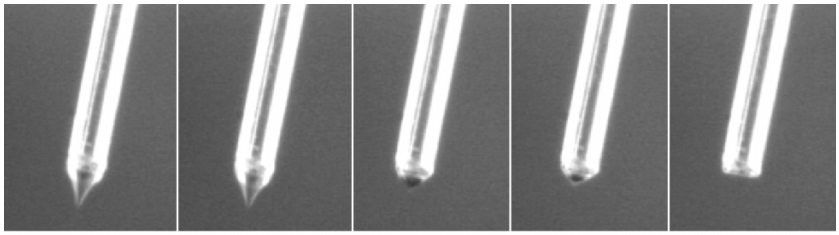

based emitters with multiple electrospray paths. A piece of membrane was glued onto the fused-silica capillary exit by first applying epoxy glue on the capillary exit, and then simply pressing the glued exit onto a piece of membrane. Optical microscopy and flow experiments show that following careful application of a very thin layer of epoxy glue onto the capillary exit under an optical microscope, enough membrane pores remain to permit liquid flow and facilitate nanoelectrospray. Electrospray performance is enhanced for both PSF and PC membrane-assisted emitters. Furthermore, the hydrophobic nature of the membranes prevented the liquid from spreading across the entire emitter exit aperture. PMMA, COC, and PC substrates were used to fabricate a chip-based emitter using hot embossing method, respectively, however the PC sheet was found to be the most compatible material with the gluing procedure. Membranes bonded to PMMA and COC devices frequently peeled from the substrate after several hours of spraying.

Electrospray from a membrane-assisted capillary-based emitter

Stable electrospray are generally not able to be produced at nano flow rates (e.g., <1000 nL/min) from emitters with larger apertures (>50 μm i.d.) prepared by directly cutting fused-silica capillaries without further treatment. By attaching a piece of porous polymer membrane at a capillary exit (75 μm i.d. and 360 μm o.d.), stable electrospray Taylor cones were observed from both offline and online electrospray at flow rates from 20 to 500 nL/min. Figure 4 shows offline electrospray images taken from an emitter bonded with a piece of PSF membrane bearing 1 μm sized pores. Pointed cone jets were visible at both 500 and 300 nL/min flow rates, but gradually became less visible as the flow rate was reduced below 100 nL/min. No visible Taylor cone was observed at a flow rate of 20 nL/min. Taylor cone observations produced by membrane-assisted emitters are consistent with the fundamental aspects of nanoelectrospray, which suggested a reduced emission diameter and thus a reduced size of droplets when lowering the flow rate (27).

A comparison of electrospray performance between an open tubular emitter with a 75 μm i.d and a PSF membrane-assisted emitter was conducted using a 1 μmol/L jeffamine solution. The results show that both the stability and sensitivity of electrospray signals were enhanced for the membrane-assisted emitter compared with that of the open tubular emitter, as shown in Fig. 5.

When utilizing an open tubular emitter at 500 nL/min, a stable signal was not obtained at any position or applied voltage. Instead, a "spitting" mode was predominate that manifested itself by the formation of large clusters rather than a cone jet mode, which resulted in signal spikes during electrospray (Fig. 5*a*) and caused MS signal suppression (Fig. 5*b*). Conversely, the stability and sensitivity were improved (Figs. 5*c* and 5*d*) using a porous membrane-assisted emitter. The signal to noise ratio increased for all *m*/*z* values for the jeffamine standard within the mass window from 400 to 900 *m*/*z*. As an example, the S/N ratio for 482.4 *m*/*z* increases from 7 to 34, as indicated in Figs. 5*b* and 5*d*.

For a given emitter geometry, the spray voltage, solvent composition, flow rate, and the relative distance between an emitter tip and a MS orifice have a strong influence on electrospray behavior (44). The effects of these electrospray parameters on performance were evaluated by maintaining the emitter position relative to an MS orifice and systematically adjusting the ESI parameters. The study showed that 2.4 kV voltage was necessary to initiate the electrospray process, and that increasing the electrospray voltage resulted in increased ion current until 3.5 kV (Fig. 6*a*).

The influence of solvent composition on electrospray performance was also investigated. Methanol, acetonitrile, and water are the most common solvents used during reverse phase separations for protein and peptide analysis. Typically, proteins are separated by eluting them from columns by gradually changing the composition of the mobile phase. As the organic concentration increases, the surface tension of the mobile phase decreases, which results in improved ionization efficiency and increased TIC intensities (Fig. 6*b*). Signals RSD of the total ion current increase markedly at higher methanol concentrations. Moreover, when organic component was less than 20%, it was difficult to generate an efficient or stable electrospray. The RSD of TIC intensity increased from 5% at a 3:7 (*v*/*v*) MeOH/water solution to 16% at a 1:9 (*v*/*v*) MeOH/water solution. Different compositions of acetonitrile in water showed a similar trend to that of methanol (data not shown). This was due to the larger surface tension of water, and a substantially larger Taylor cone base formed on the exit aperture of a membrane-assisted emitter compared with that of from a tapered tip. Although electrospray from higher aqueous solution became feasible with the aid of a hydrophobic porous membrane, ion suppression resulted in reduced sensitivity when the organic component was lower than 10%.

Utilizing a PSF membrane-assisted emitter at 2.8 kV spray voltage with 50% methanol solution, stable electrospray was easily obtained at flow rates ranging from 50 to 500 nL/min (Fig. 6*c*), which was impossible for an open tubular emitter (such as 75 μm o.d.) at less than 500 nL/min flow rates.

© 2008 NRC Canada

Fig. 5. Comparison of electrospray stability and sensitivity from an open tubular emitter and a membrane-assisted emitter by infusing 1 μmol/L jeffamine in 70% MeOH at 500 nL/min flow rate and 2.8 kV spray voltage. (5*a* and 5*c*) TIC trace and (5*b* and 5*d*) the mass spectrum of 1s elution as assigned from TIC signals respectively.

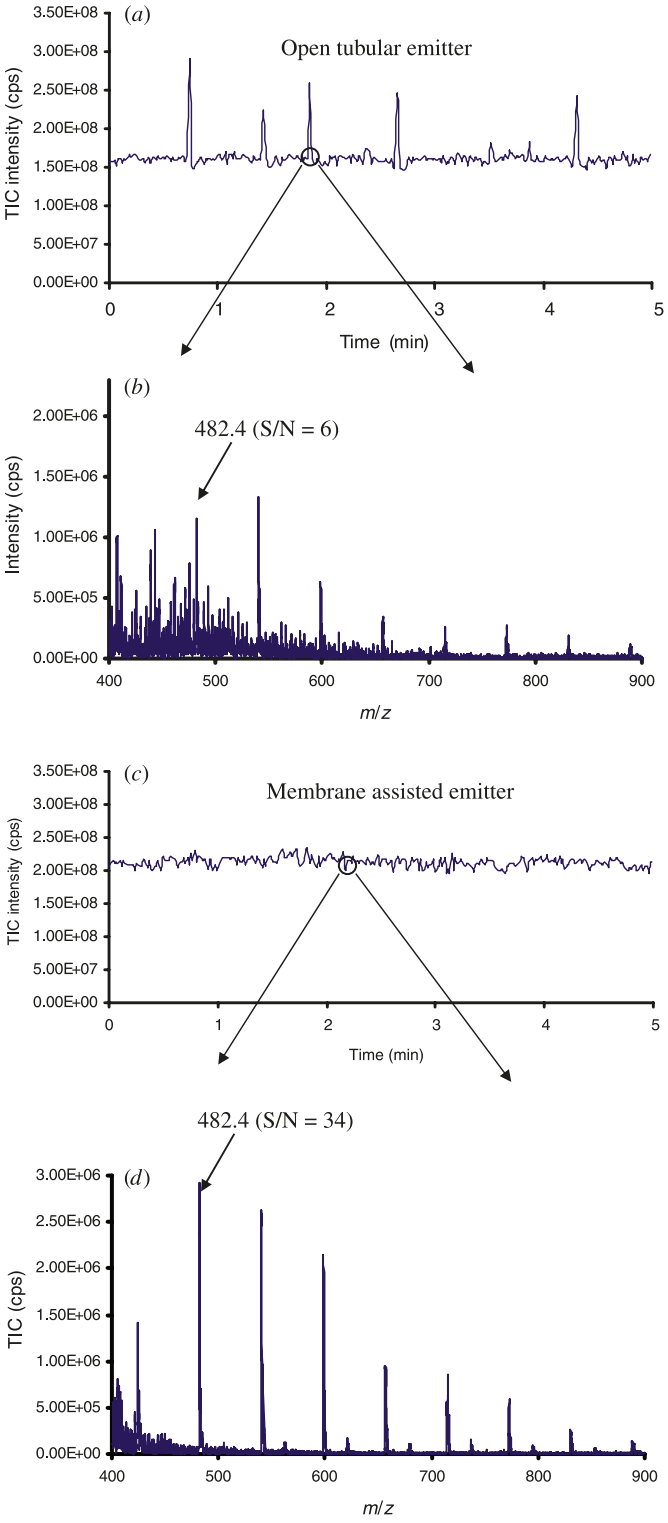

Fig. 6. Impact of spray voltage, solvent composition, and flow rate on electrospray performance using a PSF membrane-assisted emitter with a 1 μmol/L jeffamine solution. (*a*) TIC intensities at different spray voltages with 1:1 (*v*/*v* MeOH/water) and 500 nL/min flow rate. (*b*) TIC intensities with different methanol compositions at a 500 nL/min flow rate and 2.8 kV spray voltage. (*c*) TIC intensities at different flow rates with 1:1 (*v*/*v*) MeOH/water solution and 2.8 kV spray voltage.

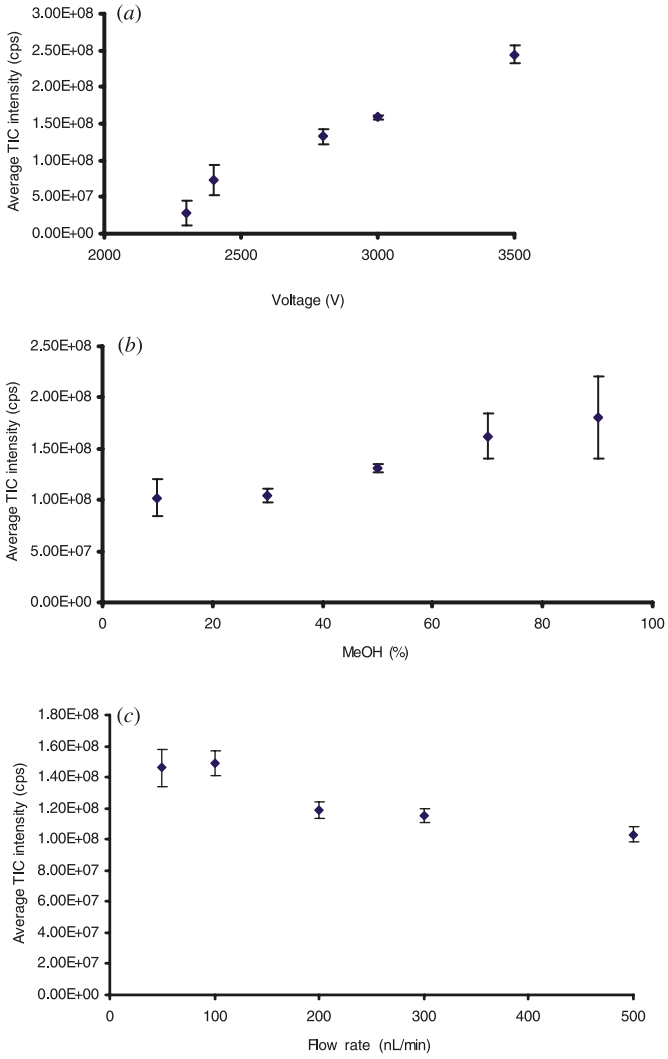

Further studies to examine the correlation between membrane pore sizes and sensitivity were conducted over the same flow rate range using emitters fabricated with commercial PC membranes. The TIC intensity can be used for the direct comparison based on the assumption that electrospray is generated with the same ion transfer and ionization efficiency. A comparison of electrospray performance from three emitters bonded with commercial polycarbonate membranes was conducted using a solution of 1 μmol/L jeffamine in 70% methanol at 500 nL/min flow rate and 2.8 kV spray voltage. These membranes contain well-defined and distributed pores with the sizes of 0.2, 1.0, and 5.0 μm, respectively. For each emitter, five replicates were tested for the comparison (Table 1).

As shown in table 1, the emitter with the smallest pore-sized membrane gave a slightly higher TIC intensity, while

© 2008 NRC Canada

Table 1. Comparison of electrospray performances from emitters with different pore-sized PC membranes.

Emitter ID (Pore size (μm), pore density (pores/cm^2))	
Emitter 1 (0.2, 3 × 10^8)	
Mean TIC (cps)	1.94 × 10^8
SD (cps)	7.80 × 10^6
RSD (%)	4.0
Emitter 2 (1.0, 2 × 10^7)	
Mean TIC (cps)	1.18 × 10^8
SD (cps)	6.56 × 10^6
RSD (%)	5.6
Emitter 3 (5.0, 4 × 10^5)	
Mean TIC (cps)	1.27 × 10^8
SD (cps)	3.47 × 10^6
RSD (%)	2.8

Fig. 7. Reproducibility for five different membrane-assisted (1.0 μm sized pores) emitters, TIC intensity was acquired with 1 μmol/L jeffamine in 70% MeOH at 500 nL/min and a 2.8 kV spray voltage.

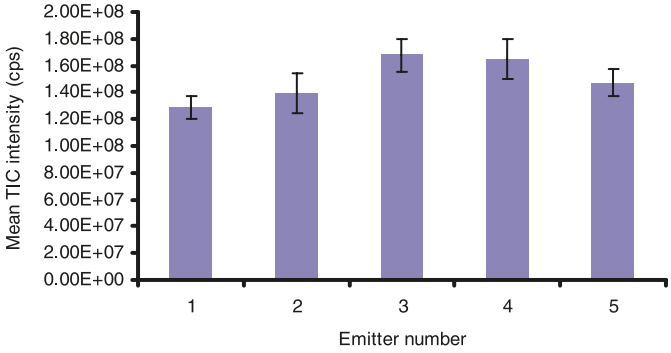

Fig. 8. Comparison of electrospray sensitivity and stability when using a membrane-assisted microchip and an open chip channel by infusing 1 μmol/L jeffamine in 70% methanol at 300 nL/min flow rate and 4.8 kV spray voltage.

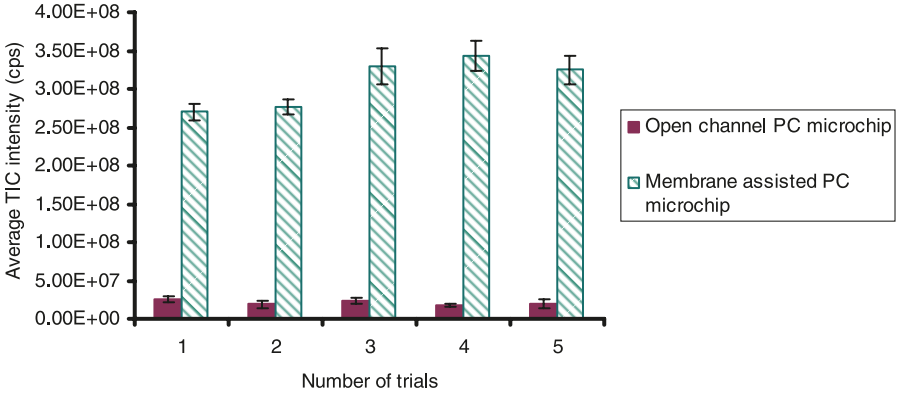

the TIC intensities for emitters with 1.00 and 5.00 μm pore-sized membranes were not statistically different, and all electrospray signals were below 6% RSD. However, no obvious correlation was found between the size of the pores and sensitivity improvements.

The reproducibility of the fabrication of porous polymer membrane-assisted emitters was demonstrated by making five emitters bonded with polycarbonate membranes bearing 1.0 μm sized pores. Significant dexterity is required when applying glue onto capillary exits under a microscope to facilitate membrane attachment. The RSD of the average TIC intensities between the five membrane-assisted emitters is about 11% as shown in Fig. 7.

Membrane-assisted electrospray from a microchip

Preliminary experiments were conducted to investigate the electrospray performance of a chip-based membrane bonded emitter. Electrospray performance from emitters with an open chip channel and a membrane-bonded chip channel were compared by infusing a solution of 1 μmol/L jeffamine in 70% methanol at a 300 nL/min flow rate. An electrical voltage of 4.8 kV was applied through a metal union connected to the transfer line on the microchip. TIC intensities increased about 5- to 7-fold when using a membrane-assisted chip-based emitter, compared with that of from an open chip channel as shown in Fig. 8. The variation of electrospray signals reduced from 25% to about 5% of RSD. This experiment demonstrated that by simply gluing a piece of porous membrane onto the exit aperture of a PC microchip, a porous membrane-assisted microchip can be coupled to a mass spectrometer as a facile interface for nanoelectrospray.

Conclusion

A novel method was introduced to fabricate a multiple path electrospray emitter by adhering a piece of porous polymer membrane onto either a fused-silica capillary or a plastic microfluidic chip. Both PSF and PC membranes contained well-defined pores to generate multiple paths for electrospray. Emitters with membranes containing pores of different sizes from 0.2 to 5.0 μm demonstrated improved electrospray performance. The S/N ratio for the 482.4 *m*/*z* peak of jeffamine was increased from 6 to 34 for a membrane-assisted capillary emitter compared with that of an open tubular emitter. No direct correlation between the pore size and the sensitivity of detection was found. Reproducible electrospray signals were obtained from five capillary emitters bonded with PC membranes. TIC intensity was increased by 5- to 7-fold, and variation of electrospray signals was reduced from 25% to 5% RSD when using a porous polymer membrane with a polycarbonate microchip. The po-

© 2008 NRC Canada

rous polymer coupling methods provides a facile alternative for the fabrication of a nano-ESI emitter with multiple electrospray paths for both capillary and microchip.

Acknowledgements

This research has been financially supported by Queen's University, Ontario Innovation Trust, Canada Foundation for Innovation, Genome Prairie, MDS SCIEX, and the Natural Sciences and Engineering Research Council of Canada. We thank, in particular, Dr. Xiaohu Yan for the demonstration of PSF membrane fabrication.

References

1. M. Yamashita and J.B. Fenn. Iyo Masu Kenkyukai Koenshu, **9**, 203 (1984).
2. J.B. Fenn, M. Mann, C.K. Meng, S.F. Wong, and C.M. Whitehouse. Science, **246**, 64 (1989).
3. R.D. Smith, J.A. Loo, C.G. Edmonds, C.J. Barinaga, and H.R. Udseth. Anal. Chem. **62**, 882 (1990).
4. Y. Wang, J. Zhang, X. Gu, and X.-M. Zhang. J. Chrom. B, **826**, 122 (2005).
5. J. Xie, Y. Miao, J. Shih, Y.-C. Tai, and T.D. Lee. Anal. Chem. **77**, 6947 (2005).
6. R.D. Oleschuk. Trends Anal. Chem. **19**, (2000).
7. J.A. Steadman, D.C. Roser, and S.R. Long. *In* Proceedings of the ERDEC scientific conference on chemical and biological defense research, Aberdeen Proving Ground, Md., 14–17 November, 1995. (1996). p. 743.
8. D.R. Barnidge, S. Nilsson, and K.E. Markides. Anal. Chem. **71**, 4115 (1999).
9. L. Licklider, X.-Q. Wang, A. Desai, Y.-C. Tai, and T.D. Lee. Anal. Chem. **72**, 367 (2000).
10. J. Bergquist, S. Nilsson, and M. Wetterhall. WO Patent WO 2001-094907, 13 December 2001.
11. X. Zhu, S. Thiam, B.C. Valle, and I.M. Warner. Anal. Chem. **74**, 5405 (2002).
12. D.R. Knapp and J.-S. Kim. WO Patent WO 2002-055990, 18 July 2002.
13. R.A. Brennen, H. Yin, and K.P. Killeen. DE Patent 10154601, 13 June 2002.
14. P. Griss, J. Melin, J. Sjoedahl, J. Roeraade, and G. Stemme. J. Micromech. Microeng. **12**, 682 (2002).
15. J. Kameoka and H.G. Craighead. US Patent Application 2003/0213918, 20 November 2003.
16. B.G.J. Van Berkel. US Patent Application 2003/0015656, 23 January 2003.
17. M.C. Granger and G.J. Van Berkel. US Patent Application 2004/0245457, 19 May 2004.
18. H. Tojo. WO Patent WO 2004–079364, 16 September 2004.
19. D.B. Roitman, K. Killeen, H. Yin, and K.L. Seaward. US Patent Application 2004/0156753, 12 February 2003.
20. J.T. Stults and J.C. Heller. Biospect Inc. US Patent Application 2005/0072915, 7 April 2005.
21. P. Wang, Z. Chen, and H.-C. Chang. Electrophoresis, **27**, 3964 (2006).
22. J. Liu and D.R. Knapp. MUSC foundation for research development. US Patent 7-087-895, 8 August 2006.
23. M.F. Bedair and R.D. Oleschuk. Anal. Chem. **78**, 1130 (2006).
24. T. Koerner and R.D. Oleschuk. RCM, **19**, 3279 (2005).
25. T. Koerner, K. Turck, L. Brown, and R.D. Oleschuk. Anal. Chem. **76**, 6456 (2004).
26. T. Koerner, R. Xie, F. Sheng, and R. Oleschuk. Anal. Chem. **79**, 3312 (2007).
27. M. Wilm and M. Mann. Anal. Chem. **68**, 1 (1996).
28. T.D. Wood, M.A. Moy, A.R. Dolan, P.M. Bigwarfe Jr., T.P. White, D. Smith, and D.J. Higbee. Appl. Spectrosc. Rev. **38**, 187 (2003).
29. T.P. White, A.R. Dolan, P.M. Bigwarfe Jr., D.J. Higbee, D.R. Smith, and T.D. Wood. Trends Appl. Spectrosc. **4**, 141 (2002).
30. T.R. Covey. Practical Spectroscopy, **32**, 105 (2002).
31. A.K. Sen, J. Darabi, and D.R. Knapp. Microfluidics and Nanofluidics, **3**, 283 (2007).
32. R. Bocanegra, D. Galan, M. Marquez, I.G. Loscertales, and A. Barrero. J. Aerosol Sci. **36**, 1387 (2005).
33. K. Tang, Y. Lin, D.W. Matson, T. Kim, and R.D. Smith. Anal. Chem. **73**, 1658 (2001).
34. A.J. Rulison and R.C. Flagan. Rev. Sci. Instrum. **64**, 683 (1993).
35. T.-H. Hsueh, H.-W. Huang, C.-C. Kao, Y.-H. Chang, M.-C. Ou-Yang, H.-C. Kuo, and S.-C. Wang. Japanese Journal of Applied Physics, **44**, 2661 (2005).
36. S.S.H. Lee, M. Douma, T. Koerner, and R.D. Oleschuk. RCM, **19**, 2671 (2005).
37. T. Koerner and R.D. Oleschuk. RCM, **19**, 3279 (2005).
38. L. Brown, T. Koerner, J.H. Horton, and R.D. Oleschuk. Lab Chip, **6**, 66 (2006).
39. A.P. Dahlin, S.K. Bergstroem, P.E. Andren, K.E. Markides, and J. Bergquist. Anal. Chem. **77**, 5356 (2005).
40. V. Gobry, J. Van Oostrum, M. Martinelli, T.C. Rohner, F. Reymond, J.S. Rossier, and H.H. Girault. Proteomics, **2**, 405 (2002).
41. Y.-X. Wang, J.W. Cooper, C.S. Lee, and D.L. DeVoe. Lab Chip, **4**, 363 (2004).
42. X. Yan, G. Liu, M. Dickey, and C.G. Willson. Polymer, **45**, 8469 (2004).
43. Y. Song, Z. Quan, and Y.-M. Liu. RCM, **18**, 2818 (2004).
44. H.S. Lee, M. Douma, T. Koerner, and R.D. Oleschuk. RCM, **19**, 2671 (2005).

© 2008 NRC Canada

Carborane-carbohydrate derivatives — Versatile platforms for developing targeted radiopharmaceuticals

Andrew E.C. Green, Laura E. Harrington, and John F. Valliant

Abstract: A series of carborane-carbohydrate derivatives were prepared as model platforms for developing targeted radiopharmaceuticals in which a single ligand can be tagged with two different classes of radionuclides. A *nido*-carborane linked to glucose was synthesized and the cage labelled with a radiometal (^{99m}Tc) and a radiohalogen (^{125}I) in good radiochemical yield. The ^{99m}Tc-metallocarborane derivative was prepared via microwave-assisted reactions, while the iodinated derivative was prepared using oxidative labelling methods in mere minutes. Fully characterized reference standards were prepared using nonradioactive rhenium and iodine and used to demonstrate that the isolated radioactive compounds were in fact the desired targets. The work reported, which is one of the rare examples of a single ligand system that can be labelled with both radiohalogens and radiometals, forms the basis of a new paradigm for developing targeted radiopharmaceuticals.

Key words: carboranes, medical isotopes, technetium-99m, iodine-125, glucose.

Résumé : On a préparé une série de dérivés carborane-carbohydrates comme plate-formes modèles pour le développement de produits radiopharmaceutiques ciblés dans lesquels un seul ligand peut être marqué avec deux classes différentes de radionucléides. On a synthétisé avec un bon rendement un *nido*-carborane lié à un glucose et on a marqué la cage avec un métal radioactif (^{99m}Tc) et un halogène radioactif (^{125}I). On a préparé le dérivé ^{99m}Tc-métallocarborane par le biais de réactions assistées par les microondes alors que le dérivé iodé a été préparé par des méthodes oxydantes en quelques minutes. On a préparé des produits de référence complètement caractérisés à l'aide de rhénium non radioactif et d'iode et on les a utilizés pour démontrer que les composés radioactifs isolés sont bel et bien les cibles désirées. Le travail rapporté, qui est un des rares exemples d'un système de ligand unique qui peut être marqué avec des métaux et des halogènes radioactifs, forme la base d'un nouveau paradigme pour le développement de produits radiopharmaceutiques ciblés.

Mots-clés : carboranes, isotopes médicaux, technitium-99m, iode-125, glucose.

[Traduit par la Rédaction]

Introduction

Interest in developing targeted molecular radioimaging probes has been increasing because of the exquisite sensitivity offered by nuclear imaging methods (1, 2). This feature of single photon emission computed tomography (SPECT) and positron emission tomography (PET) creates the opportunity to use probes to monitor the very earliest stages of disease development and to study associated biochemical events noninvasively.

To meet the demand for new probes, more efficient and versatile radiolabelling and bioconjugation strategies are needed. For instance, the majority of ligands used to prepare molecular radioimaging and therapy agents are only able to carry a single class of radionuclides (halogens, radiometals, etc.). There would be tremendous advantages if a single prosthetic group could be tagged with different classes of radionuclides so that the physical properties of the isotope (half-life, emission energy, and decay mode) could be matched with the desired application and availability of instrumentation without having to synthesize an entirely new agent. Given the recent issues around supply shortages of specific medical isotopes, the ability to have flexible platforms that can be used with different radionuclides would be of significant utility.

Our group has been exploring the use of carboranes, more specifically 1,2-dicarba-*closo*-dodecaborane (ortho-carborane), as ligands from which to produce targeted radiopharmaceuticals. Carboranes are synthetically versatile, resistant to thermal and photochemical degradation, and they form stable η^5-complexes with a variety of metals (3–8), which include rhenium (9) and technetium (10, 11). Re(I) and ^{99m}Tc(I) metallocarborane complexes (10–14) can be prepared in water from $[M(CO)_3(H_2O)_3]^+$ (M = Re, ^{99m}Tc) (15, 16), a starting material that can be produced in a manner suitable for clinical use. In parallel, other groups have shown that carboranes can also be labelled with radiohalogens (17–

Received 28 July 2008. Accepted 17 September 2008. Published on the NRC Research Press Web site at canjchem.nrc.ca on 25 October 2008.

A.E.C. Green, L.E. Harrington, and J.F. Valliant.[1] Departments of Chemistry and Medical Physics & Applied Radiation Sciences, McMaster University, 1280 Main Street West, Hamilton, ON L8S 4M1, Canada.

[1]Corresponding author (e-mail: valliant@mcmaster.ca).

 doi:10.1139/V08-157 © 2008 NRC Canada

24) using standard electrophilic methods, providing the opportunity to prepare metallated and halogenated agents from a single core.

Although a few examples of molecular imaging agents labelled with both radiometals and radiohalogens have been reported (25–33), the labels are typically bound to the targeting vector at different positions (e.g., a chelate at the *N*-terminus for binding radiometals and a tyrosine residue for labelling with radiohalogens). It would be attractive to have the means to incorporate a single prosthetic group at a site on the targeting vector that has the least impact on target binding and to then be able to label the ligand with different radionuclides. Given their versatility (18), carboranes offer a means of developing such a system. Here we report the first steps in this regard by preparing a hydrophilic carborane ligand and then investigating the conditions needed to label the cluster with both ^{99m}Tc and ^{125}I.

Results and discussion

One of the major limitations ascribed to carboranes as it pertains to developing molecular imaging agents is that they are hydrophobic in nature. Prosthetic groups that are too lipophilic can increase the amount of nonspecific binding including unwanted uptake in the hepatobiliary system. To address this issue in concert with demonstrating for the first time that a single prosthetic group can be labelled with both a radiometal and a halogen, we present here the synthesis and characterization of ^{99m}Tc and ^{125}I tagged carborane-carbohydrate derivatives (Scheme 1).

The initial target ligand was a simple *nido*-carboranyl glycoside of glucose (**3**), which was designed as a model system from which to develop general purpose labelling strategies for both metal complexation and halogenation. If suitable labelling methods can be developed and if the products are sufficiently robust, the target compounds can ultimately be linked to vectors through functionalization of the remaining carborane CH group. This would result in a new general labelling technology whereby the nature of the radionuclide could be selected to suit the intended application while the polar carbohydrate would mask the lipophilic nature of the carborane core.

Compound **3** (Scheme 2) was synthesized from the known propargyl glycoside, **1**, (34) and *closo*-carborane, **2**, (35), by treating the latter with alcoholic NaOH (36). These conditions concomitantly removed the acetate protecting groups giving **3** in 63% yield following chromatographic purification. Since degrading carboranes can occur at either of two boron atoms, the product is isolated as a mixture of diastereomers (37, 38), which was apparent in the ^{1}H and ^{13}C NMR spectra. The ligand **3**, unlike most carborane derivatives, is freely soluble in water making it convenient to work with in terms of radiolabelling where the majority of reactions are performed in aqueous media.

Prior to labelling compounds with ^{99m}Tc, it is prudent to prepare and fully characterize the nonradioactive rhenium analogue as a reference standard for the products produced at the tracer level. The general method used by our group to produce Re-metallocarboranes is microwave heating, which greatly reduces the overall reaction time and improves the isolated yield of the product (13, 39, 40). In contrast to previous results, initial experiments using microwave heating yielded little of the desired product. ES-MS analysis of the reaction mixture indicated that the product was forming but was being degraded via hydrolysis of the glycoside bond connecting the metallocarborane to the carbohydrate. One suspected cause of this degradation was the high temperatures used, however this was dismissed when the ligand alone was shown to be stable to microwave heating in the absence of the metal. The actual source of bond cleavage was the acidic rhenium starting material (pK_a = 7.5) (41, 42), a problem that was addressed by adding a buffer to the reaction mixture (0.003 mol/L NaH_2PO_4, 0.01 mol/L Na_2HPO_4, and 0.5 mol/L NaF: "PBF", pH 7.2). Optimal conversion to **4a** was accomplished with two 10-minute irradiations at 200 °C using an excess of $[Re(CO)_3(H_2O)_3]Br$ (16) (Scheme 3). Isolation of the desired product via silica gel chromatography was accomplished successfully after complete consumption of the precursor **3**. Unfortunately, due to the highly hydrophilic nature of the ligands, a significant proportion of the material adsorbed onto the silica gel reducing the overall yield to 31%. Nonetheless, sufficient material was isolated for characterization and all data was consistent with the desired product.

Scheme 1. The preparation and labelling of carborane derivatives with iodine and the $[M(CO)_3]^+$ core (M = Tc, Re).

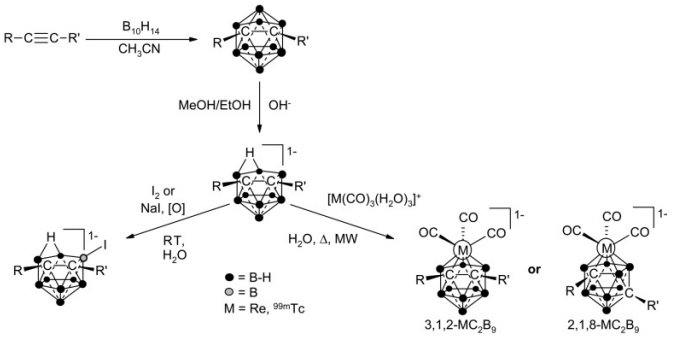

Scheme 2. Synthesis and NMR numbering scheme for compound **3**. Reagents and conditions: (a) propargyl alcohol (2.0 equiv.), $BF_3{\cdot}Et_2O$ (1.5 equiv.), CH_2Cl_2, RT, 12 h; (b) $B_{10}H_{14}$ (2.0 equiv.), CH_3CN, reflux, 48 h; (c) (*i*) NaOH (20 equiv.), EtOH, reflux, 12 h, (*ii*) 1 mol/L HCl, pH 4.

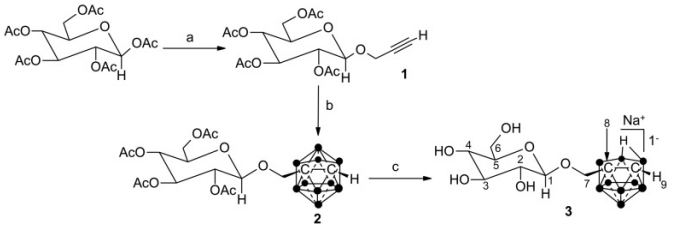

Scheme 3. Microwave-assisted synthesis of **4**.

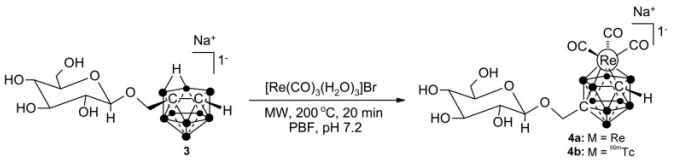

© 2008 NRC Canada

Fig. 1. ^{1}H NMR and ^{1}H nOe spectra for (top) **3** and (bottom) **4a** (600 MHz, CD_3OD).

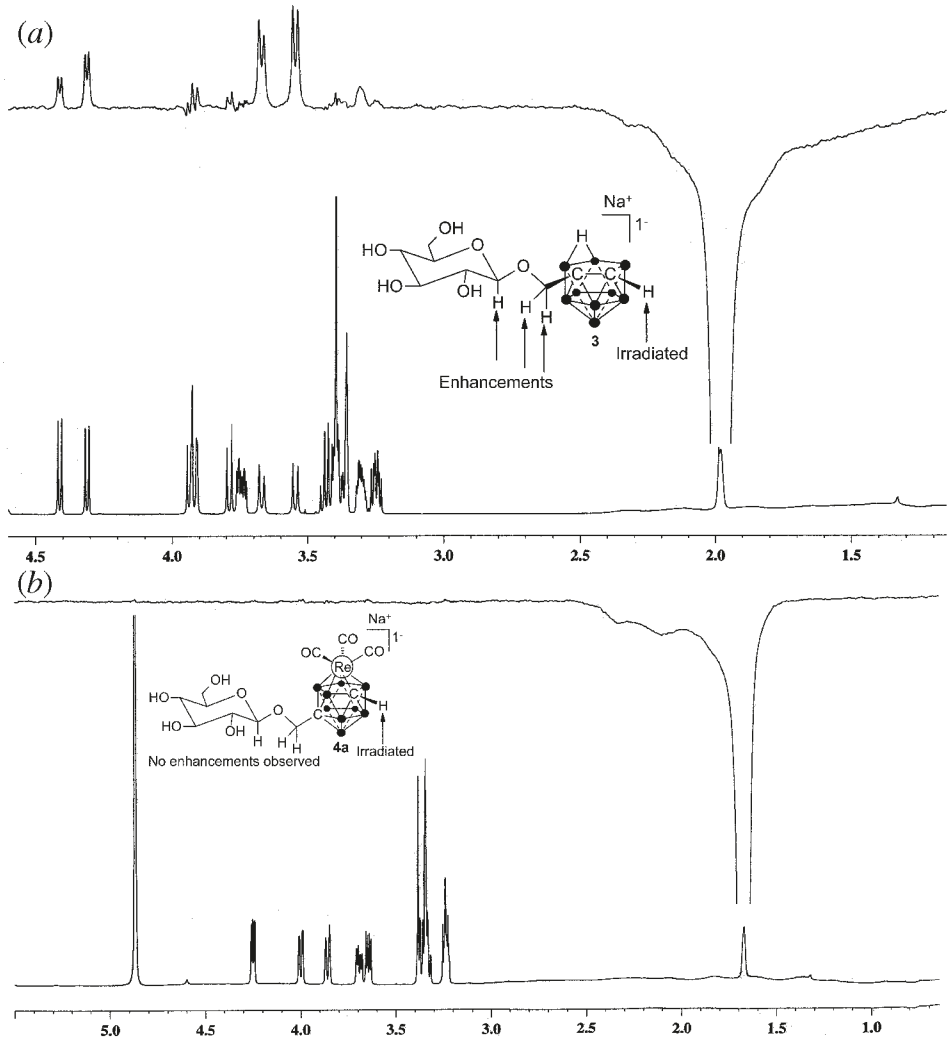

During our investigations of the microwave-assisted synthesis of Re and Tc metallocarboranes, it was discovered that rearrangement of the cluster occurs when sterically demanding and (or) electron withdrawing ligands are present on the carbon atoms of the carborane cage (13, 14). In the absence of an X-ray structure, ^{1}H nOe experiments can be used to determine whether or not isomerization occurred. The nOe spectra for **4a** when compared to compound **3** suggested that the metallocarboranyl glycoside had in fact isomerized to the 2,1,8-ReC_2B_9-cage configuration (Fig. 1) in which the larger group migrates away from the bonding face. The migration of the C-atoms apart increases the thermodynamic stability of the cluster and it reduces steric interactions between the "large" carbohydrate substituent and the metal tricarbonyl core.

The nonradioactive iodinated carboranyl glycosides **5a** and **5b** were prepared using methods similar to those reported by Wilbur and co-workers (20, 21) (Scheme 4). Compound **3** was treated with NaI and chloramine-T and the reaction was allowed to stir for 24 h prior to quenching with $Na_2S_2O_5$. The target compound was isolated in 21% overall yield following semipreparative HPLC, which was necessary to separate a small amount of unreacted starting material

Scheme 4. Synthesis of **5**.

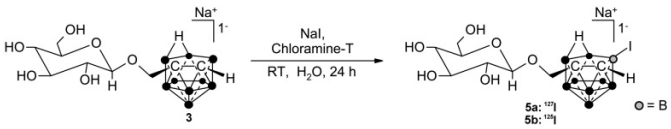

from the product (**3** and **5a** were not separable by normal-phase chromatography). Electrospray mass spectrometry gave the target anion mass at m/z = 452, with the expected isotope distribution for the B_9 cluster (43). The iodination of the *nido*-carborane in the product was readily observed in the $^{11}B\{^1H\}$ NMR spectrum in which one resonance shifted from –32.92 ppm in the spectrum of **3** to –29.56 ppm in the spectrum of **5a**, which is consistent with literature reports (44, 45).

Radiochemistry

Compound **3** was labelled with $[^{99m}Tc(CO)_3(H_2O)_3]^+$, which was generated from $^{99m}TcO_4^-$ in good yield following literature protocols (46, 47). Aliquots of the Tc(I) starting material (185–370 MBq, 5–10 mCi) were added to sealed microwave vials containing the ligand (5 μmol) in 0.5 mol/L

© 2008 NRC Canada

Fig. 2. $^{11}B\{^1H\}$ NMR spectrum of compound **3**.

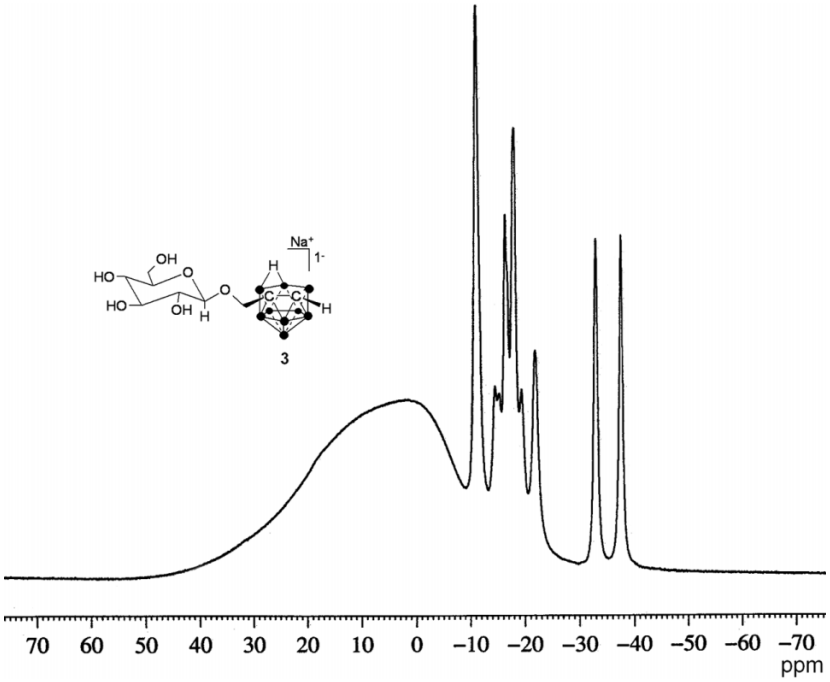

NaF. The vials were then heated at 200 °C for 10 min. HPLC analysis indicated greater than 80% conversion to the desired product by comparison to the nonradioactive standards. The major radioactive byproduct was pertechnetate, which was easily separated from the desired product. It was also possible to isolate **4b** in high effective specific activity by solid-phase extraction (C_{18} SepPak®) in 58% radiochemical yield (Fig. 2).

The radiohalogenation of **3** was performed using Na[^{125}I] and chloramine-T or Iodogen® as oxidants. A series of radiolabelling experiments revealed that the use of Iodogen® resulted in greater yields in a shorter time. An additional benefit of the use of Iodogen® is that it is insoluble in water and can be introduced as a film on the inside surfaces of the reaction vessels, which simplified purification of the desired product. The synthesis of compound **5b** was successfully accomplished by adding 100 μg of the *nido*-carborane precursor (**3**) (100 μL of a 1 mg/mL solution in 5% HOAc/H_2O) to a vial coated with Iodogen®. The reaction was allowed to proceed at room temperature for 5 min, followed by quenching with a solution of sodium metabisulfite. HPLC analysis of the crude reaction mixture indicated one major product whose retention time corresponded to that of the reference standard. This product accounted for >90% of the total radioactivity. Semipreparative HPLC permitted the isolation of **5b** from precursor **3** in 29% radiochemical yield. Radiochemical purity of **5b** was greater than 99%.

Compound **4b** showed good stability to ligand challenges with 75% and 79% of the complex remaining intact following incubation at 37 °C for 18 h with l-cysteine and l-histidine, respectively. The stability of compound **5b** was excellent, with only 9% degradation being observed after 24 h in solution. The robust nature of the product, which is attributed to the strength of the B–I bond, is a particularly attractive feature of the reported system as premature loss of iodine from aryl-iodides is a significant problem with traditional iodinated radiopharmaceuticals.

Experimental[2]

General

All reagents used were purchased from Sigma-Aldrich, except for decaborane (14), which was purchased from Katchem (Czech Republic). [$Re(CO)_3(H_2O)_3$]Br was prepared by the method of Lazarova et al. (16). Solvents were purchased from Caledon. ^{99m}Tc was obtained from a ^{99}Mo/^{99m}Tc generator (Bristol-Myers-Squibb) as Na[$^{99m}TcO_4$]. No-carrier-added ^{125}I was obtained from the McMaster Nuclear Reactor as Na[^{125}I] in 0.1 N NaOH (17 Ci/mg). Microwave-assisted syntheses were performed in a Biotage Initiator 60 microwave reactor. NMR spectroscopy was performed on either a Bruker Avance DRX-500 or Avance AV-600 spectrometer. Residual ^{1}H signals from the NMR solvent and tetramethylsilane were taken as the internal reference for ^{1}H and ^{13}C spectra, respectively. ^{11}B spectra were referenced using a $BF_3{\cdot}Et_2O$ external standard. For reporting purposes, the label "*" was used to distinguish between the NMR signals arising from the two diastereomers (e.g., 7a versus 7a*). Assignments were made with the assistance of two-dimensional NMR techniques (COSY, HSQC, HMBC). A numbering scheme for the NMR assignments is provided in Scheme 2.

Infrared spectra were recorded on a BioRad FTS-40 FT-IR instrument. Mass spectra were obtained using a

[2] Supplementary data for this article are available on the journal Web site (canjchem.nrc.ca) or may be purchased from the Depository of Unpublished Data, Document Delivery, CISTI, National Research Council Canada, Ottawa, ON K1A 0R6, Canada. DUD 3846. For more information on obtaining material refer to cisti-icist.nrc-cnrc.gc.ca/cms/unpub_e.shtml.

© 2008 NRC Canada

Micromass Quattro-LC Triple Quadrupole mass spectrometer. Radioactivity measurements were made using a Capintec CRC-15W dose calibrator. High-performance liquid chromatography was performed with a Varian ProStar HPLC system. Radioactivity from ^{99m}Tc- and ^{125}I-labelled compounds was detected with a IN/US γ-RAM Model 3 detector. For analysis of compounds, either a Varian Nucleosil 4.6 mm × 250 mm C_{18} or Phenomenex Gemini 4.6 mm × 100 mm C_{18} column was used. For semipreparative HPLC, a Varian Dynamax 10 mm × 250 mm C_{18} column was used. Elution conditions: Method A: 80:20 A/B to 54:46 A/B, 0–20 min; 54:46 A/B to 100% B, 20–25 min; 100% B, 25–30 min (A = H_2O, B = CH_3CN); Nucleosil column; Method B: 80:20 A/B to 20:80 A/B, 0–20 min; 20:80 A/B to 100% B, 20–25 min; 100% B, 25–30 min (A = H_2O containing 0.05% TFA, B = CH_3CN containing 0.05% TFA); Nucleosil column; Method C: 80:20 A/B to 20:80 A/B, 0–20 min; 20:80 A/B to 100% B, 20–25 min; 100% B, 25–30 min (A = H_2O containing 0.05% TFA, B = CH_3CN containing 0.05% TFA); Gemini column. Analytical flow rate was 1.0 mL/min; semipreparative flow rate was 4.7 mL/min. Thin layer chromatograms (Merck F_{254} silica gel on aluminum plates) were visualized using 0.1% $PdCl_2$ in 3 mol/L HCl.

Sodium [7-methyl-(β-D-glucopyranosyloxy)-7,8-dicarba-nido-undecaborate] (3)

1,2-Dicarba-*closo*-dodecaboran-1-yl-methyl-2,3,4,6-tetra-O-acetyl-β-D-glucopyranoside (2.02 g, 4.02 mmol) and NaOH (3.20g, 80 mmol) were dissolved in absolute ethanol (20 mL) and the resulting solution was stirred at reflux overnight (~12 h). The reaction was cooled to room temperature and the excess NaOH was precipitated as Na_2CO_3 by passing a stream of CO_2 gas through the solution. The solid was removed by filtration and the residue washed with cold ethanol (20 mL). The solution was then concentrated under reduced pressure, yielding a white solid. The solid was dissolved in distilled water, and the solution adjusted to pH 4 by dropwise addition of 1 mol/L HCl. Isolation of the product was achieved using silica gel column chromatography (1:3 MeOH/CH_2Cl_2). The product fractions were concentrated by rotary evaporation giving white foam. Yield: 0.88 g (63%). TLC (1:3 CH_3OH/CH_2Cl_2): R_f = 0.34. HPLC: t_R = 9.7 min (Method B); 9.0 min (Method C). IR (KBr, cm^{-1}) ν: 3409, 2526. ^{1}H NMR (CD_3OD) δ: 4.46, 4.36 (d, 2H, J = 7.8 Hz, H-1,1*), 3.97 (m, 3H, H-7a, H-6a, 6a*), 3.82 (m, 3H, H-7a*, H-6b, 6b*), 3.72 (d, 1H, J = –10.7 Hz, H-7b*), 3.60 (d, 1H, J = –11.0 Hz, H-7b), 3.46 (m, 4H, H-3,3*, H-4,4*), 3.36 (m, 2H, H-5,5*), 3.01 (m, 2H, H-2,2*), 2.02 (br s, 2H, H-9,9*), 2.50 to –0.30 (br, B-H), –2.63 (B-H-B). ^{13}C NMR (CD_3OD) δ: 103.3, 102.9, 78.4, 78.0, 77.9, 77.7, 77.6, 75.1, 71.5, 62.5, 59.0, 47.80 45.9, 43.8. ^{11}B{^{1}H} NMR (CD_3OD) δ: –10.9, –14.5, –15.2, –16.3, –17.9, –19.3, –21.8, –32.9, –37.5. HR-MS (ESI): calcd. for $C_9H_{24}B_9O_6$: 326.2455; found: 326.2430.

Sodium [8-Methyl(β-D-glucopyranosyloxy)-2,2,2-tricarbonyl-2-rhenium-1,8-dicarba-closo-dodecaborate] (4a)

Compound **3** (0.066 g, 0.19 mmol) and $[Re(CO)_3(H_2O)_3]Br$ (0.17 g, 0.42 mmol) were placed in a microwave reaction vial (2–5 mL) and dissolved in a phosphate buffer (pH 7.2) containing 0.5 mol/L NaF (2.2 mL). An aluminum cap containing a Teflon septum was attached to the vial and sealed by crimping. The reaction vessel was heated in the Biotage Initiator Sixty reactor for 10 min at 200 °C, after which the vial was uncapped and a further 0.12 g (mmol) of the rhenium reagent was added. The vial was sealed again and irradiated for a further 10 min at 200 °C, resulting in the formation of a clear yellow solution. The aqueous solution was diluted with acetonitrile and concentrated to dryness by rotary evaporation. The residue was extracted into methanol, and the target compound isolated by silica gel column chromatography (10%–15% MeOH/CH_2Cl_2). Further purification was accomplished using a C_{18} SepPak® cartridge (Waters), giving the target compound in 31% yield (0.037 g). TLC (1:4 MeOH/CH_2Cl_2): R_f = 0.45. HPLC: t_R = 19.8 min (Method A). ^{1}H NMR (CD_3OD) δ: 4.25 (d, 2H, J = 7.8 Hz, H-1,1*), 4.00 (d, 2H, J = –10.7 Hz, H-7a,7a*), 3.86 (m, 2H, H-6a, 6a*), 3.69 (m, 2H, H-6b,6b*), 3.64 (m, 2H, H-7b,7b*), 3.35 (m, 4H, H-3,3*,4,4*), 3.24 (m, 4H, H-2,2*,5,5*), 1.67 (br s, 2H, H-9,9*), 3.10–0.90 (br m, B-H). ^{13}C NMR (CD_3OD) δ: 200.4, 104.3, 77.9, 76.7, 75.2, 71.4, 62.5, 53.8, 29.6. ^{11}B{^{1}H} NMR (CD_3OD) δ: –6.4, –8.2, –9.4, –12.2, –18.9, –20.1. IR (KBr, cm^{-1}) ν: 3414, 2544, 2002, 1907. HR-MS (ESI): calcd. for $C_{12}H_{23}B_9O_9Re$: 595.1794; found: 595.1776.

Sodium [7-(methyl-β-D-glucopyranosyl)-iodo-7,8-dicarba-nido-undecaborate(-1)] (5a)

Compound **3** (0.093 g, 0.27 mmol) and NaI (0.048 g, 0.32 mmol) were dissolved in 5 mL of distilled H_2O to which was added chloramine-T (0.13 g, 0.57 mmol). The resulting mixture was stirred for 24 h at room temperature. The solution was filtered to remove the white precipitate that had formed, then concentrated to dryness by rotary evaporation. The residue was dissolved in a mixture of water and acetonitrile (80:20 H_2O/CH_3CN), and the target compound isolated by semipreparative HPLC (Dynamax C_{18} 10 × 250 mm column, elution method A). Yield: 0.027 g (21%). TLC (1:4 CH_3OH/CH_2Cl_2 + 0.1% HOAc): R_f = 0.35. HPLC: t_R = 12.2 min (Method C). ^{1}H NMR (600 MHz, CD_3OD) δ : 4.42 (m, 1H, H-1), 4.38 (m, 1H, H-1*), 3.98 (m, 3H, H-6a,6a*,7a), 3.83 (d, 1H, J = –10.9 Hz, H-7a*), 3.80 (m, 3H, H-6b,6b*,7b*), 3.70 (m, 1H, H-7b), 3.48 (m, 5H, H-3,3*,4,4*, 5 or 5*), 3.36 (m, 1H, H-5 or 5*), 3.29 (m, 2H, H-2,2*), 2.56 (br s, 2H, H-9,9*), 2.60–0.10 (br m, B-H), –2.74 (br s, B-H-B). ^{13}C NMR (151 MHz, CD_3OD) δ: 103.8, 102.0, 78.3, 77.8, 77.5, 77.4, 76.9, 75.0, 74.9, 71.3, 62.4, 62.2, 56.2, 53.3, 49.8. ^{11}B{^{1}H} NMR (192 MHz, CD_3OD) δ: –6.2, –15.8, –18.1, –21.4, –24.7, –29.6, –37.3. IR (KBr) ν: 3417, 2540 cm^{-1}. HR-MS (ESI^-): calcd. for $C_9H_{23}B_9O_6I$: 452.1421; found: 452.1438.

Radiochemistry

Caution: ^{99m}Tc and ^{125}I are radioactive and should only be handled in an appropriately equipped and licensed facility.

Synthesis of 4b

A solution of the *nido*-carborane ligand **3** in 0.5 mol/L NaF (0.5 mL) was transferred to an Emry microwave vial (0.5–2 mL) and sealed. A solution (0.5 mL) of $[^{99m}Tc(CO)_3(H_2O)_3]^+$ (typically 185–370 MBq, 5–10 mCi) prepared following literature methods was added through the

© 2008 NRC Canada

septum via syringe, and the vial heated for 5–10 min at 200 °C in an Initiator microwave reactor. After cooling, the product solution was taken up in a syringe and loaded onto a C_{18} Environmental SepPak Plus™ cartridge (Waters). Conditioning: (*i*) EtOH, 10 mL; (*ii*) CH_3CN, 10 mL; (*iii*) 1:1 CH_3CN/0.1 mol/L HCl, 10 mL; (*iv*) 0.1 mol/L HCl, 10 mL. Elution: (*i*) 0.1 mol/L HCl, 7 mL; (*ii*) 4:1 0.1 mol/L HCl/CH_3CN, 4 mL; (*iii*) 1:1 0.1 mol/L HCl/CH_3CN, 4 mL; (*iv*) 1:4 0.1 mol/L HCl/CH_3CN, 4mL; (*v*) CH_3CN, 5 mL. Yield: 58% (decay corrected). HPLC: t_R = 19.9 min (Method A).

Synthesis of 5b

To a 2 mL reaction vial filmed with 20 μg of Iodogen® was added 100 μL of a solution containing **3** (1.0 mg/mL in 5% aqueous acetic acid). To this was added Na[^{125}I] (0.74–5.6 MBq, 20–150 μCi) in 0.1 N NaOH. The vials were stirred for 5 min before the addition of 10 μL 0.1 mol/L $Na_2S_2O_5$. The product was isolated via semipreparative HPLC (Method B, Dynamax 10 × 250 mm C_{18} column at 4.7 mL/min). Yield: 29%. HPLC: t_R 12.7 (Method C).

Conclusion

The work reported here demonstrates that a single carborane-based synthon can be labelled with two different classes of radionuclides providing a new type of versatility when designing molecular imaging probes and therapeutics. A method to label a hydrophilic *nido*-carboranyl glycoside derivative with both ^{99m}Tc and ^{125}I radiolabelled analogues in good radiochemical yield was developed and the products are sufficiently robust to be used in vivo. Future investigations will include the preparation of bifunctional analogues of **3** so that the reported platform can be linked to targeting vectors as a means of preparing targeted radiopharmaceuticals that can carry more than one class of radionuclides.

Acknowledgements

We acknowledge the Natural Sciences and Engineering Research Council of Canada (NSERC) for funding, Bristol-Myers-Squibb for ^{99m}Tc, and the McMaster Nuclear Reactor for providing ^{125}I.

References

1. D.J.A. Margolis, J.M. Hoffman, R.J. Herfkens, A. Quon, and S.S. Gambhir. Radiology, **245**, 333 (2007).
2. D.A. Hammoud, J.M. Hoffman, and M.G. Pomper. Radiology, **245**, 21 (2007).
3. R.N. Grimes. Carboranes. Academic Press, New York. 1970.
4. M.F. Hawthorne, D.C. Young, and P.A. Wegner. J. Am. Chem. Soc. **87**, 1818 (1965).
5. M.F. Hawthorne, D.C. Young, T.D. Andrews, D.V. Howe, R.L. Pilling, A.D. Pitts, M. Rintjes, L.F. Warren, Jr., and P.A. Wegner. J. Am. Chem. Soc. **90**, 879 (1968).
6. M.F. Hawthorne and G.B. Dunks. Science (Washington, D.C.), **178**, 462 (1972).
7. M.F. Hawthorne. J. Organomet. Chem. **100**, 97 (1975).
8. M. Corsini, F.F. de Biani, and P. Zanello. Coord. Chem. Rev. **250**, 1351 (2006).
9. M.F. Hawthorne and T.D. Andrews. J. Am. Chem. Soc. **87**, 2496 (1965).
10. J.F. Valliant, P. Morel, P. Schaffer, and J.H. Kaldis. Inorg. Chem. **41**, 628 (2002).
11. O.O. Sogbein, P. Merdy, P. Morel, and J.F. Valliant. Inorg. Chem. **43**, 3032 (2004).
12. O.O. Sogbein, A.E.C. Green, P. Schaffer, R. Chankalal, E. Lee, B.D. Healy, and J.F. Valliant. Inorg. Chem. **44**, 9574 (2005).
13. A.E.C. Green, P.W. Causey, A.S. Louie, A.F. Armstrong, L.E. Harrington, and J.F. Valliant. Inorg. Chem. **45**, 5727 (2006).
14. A.F. Armstrong and J.F. Valliant. Inorg. Chem. **46**, 2148 (2007).
15. R. Alberto, R. Schibli, A. Egli, P.A. Schubiger, U. Abram, and T.A. Kaden. J. Am. Chem. Soc. **120**, 7987 (1998).
16. N. Lazarova, S. James, J. Babich, and J. Zubieta. Inorg. Chem. Commun. **7**, 1023 (2004).
17. F.P. Olsen and M.F. Hawthorne. Inorg. Chem. **4**, 1839 (1965).
18. M.F. Hawthorne and A. Maderna. Chem. Rev. **99**, 3421 (1999).
19. D.S. Wilbur, D.K. Hamlin, J.C. Livesey, R.R. Srivastava, G.E. Laramore, and T.W. Griffen. Nucl. Med. Biol. **21**, 601 (1994).
20. D.S. Wilbur, M.-K. Chyan, D.K. Hamlin, B.B. Kegley, R. Risler, P.M. Pathare, J. Quinn, R.L. Vessella, M. Zalutsky, T.J. Wedge, and M.F. Hawthorne. Bioconjugate Chem. **15**, 203 (2004).
21. D.S. Wilbur, D.K. Hamlin, M.-K. Chyan, B.B. Kegley, J. Quinn, and R.L. Vessella. Bioconjugate Chem. **15**, 601 (2004).
22. D.S. Wilbur, M.-K. Chyan, D.K. Hamlin, R.L. Vessella, T.J. Wedge, and M.F. Hawthorne. Bioconjugate Chem. **18**, 1226 (2007).
23. A. Sjostrom, V. Tolmachev, O. Lebeda, J. Koziorowski, J. Carlsson, and H. Lindquist. J. Radioanal. Nucl. Chem. **256**, 191 (2003).
24. S. Ghirmai, J. Malmquist, H. Lundquist, V. Tolmachev, and S. Sjoberg. J. Labelled Compd. Radiopharm. **47**, 557 (2004).
25. T. Unak,Y. Yildirim, U. Avcibasi, Z. Biber, Y. Duman, and P. Unak. J. Labelled Compd. Radiopharm. **273**, 767 (2007).
26. W.P. Li, J.S. Lewis, J. Kim, J.E. Bugaj, M.A. Johnson, J.L. Erion, and C.J. Anderson. Bioconjugate Chem. **13**, 721 (2002).
27. A. Korde, U. Pandey, S. Banerjee, H.D. Sarma, J. Mukherjee, and M. Venkatesh. Appl. Radiat. Isot. **65**, 687 (2007).
28. C.R. Divgi and S.M. Larson. Semin. Nucl. Med. **19**, 252 (1989).
29. D.J. Hnatowich. Semin. Nucl. Med. **20**, 80 (1990).
30. T.M. Behr, R.M. Sharkey, M.E. Juweid, R.D. Blumenthal, R.M. Dunn, G.L. Griffiths, H.-J. Bair, F.G. Wolf, W.S. Becker, and D.M. Goldenberg. Cancer Res. **55**, 3825 (1995).
31. H. Kobayashi, H. Sakahara, K. Endo, Z.-S. Yao, and J. Konishi. Nucl. Med. Biol. **23**, 29 (1996).
32. M. Abe, J. Lai, Z.P. Kortylewicz, H. Nagata, I.J. Fox, C.A. Enke, and J. Baranowska-Kortylewicz. Bioconjugate Chem. **14**, 997 (2003).
33. A.V. Orlova, F.Y. Nilsson, M. Wikman, C. Widstrom, S. Stahl, J. Carlsson, and V. Tolmachev. J. Nucl. Med. **47**, 512 (2006).
34. H.B. Mereyala and S.R. Gurrala. Carbohydr. Res. **307**, 351 (1998).
35. G.B. Giovenzana, L. Lay, D. Monti, G. Palmisano, and L. Panza. Tetrahedron, **55**, 14123 (1999).
36. R.A. Wiesboeck and M.F. Hawthorne. J. Am. Chem. Soc. **86**, 1642 (1964).
37. M.F. Hawthorne, D.C. Young, P.M. Garrett, D.A. Owen, S.G. Schwerin, F.N. Tebbe, and P.A. Wegner. J. Am. Chem. Soc. **90**, 862 (1968).
38. R. Brockman, K. Challis, G. Froehner, and T.D. Getman. Main Group Met. Chem. **25**, 629 (2002).
39. A. Stadler and C.O. Kappe. Eur. J. Org. Chem. 919 (2001).

© 2008 NRC Canada

40. C.O. Kappe. Angew. Chem. Int. Ed. **43**, 6250 (2004).
41. A. Egli, K. Hegetschweiler, R. Alberto, U. Abram, R. Schibli, R. Hedinger, V. Gramlich, R. Kissner, and P.A. Schubiger. Organometallics, **16**, 1833 (1997).
42. B. Salignac, P.W. Grundler, S. Cayemittes, U. Frey, R. Scopelliti, A.E. Merbach, R. Hedinger, K. Hegetschweiler, R. Alberto, U. Prinz, G. Raabe, U. Kolle, and S. Hall. Inorg. Chem. **42**, 3516 (2003).
43. J.F. Ditter, J. Gerhart, and R.E. Williams. *In* Mass spectrometry in inorganic chemistry: Advances in chemistry series. No. 72. *Edited by* R.F. Gould. American Chemical Society, Washington, D.C. 1968. pp. 191–210.
44. E.A. Mizusawa, M.R. Thompson, and M.F. Hawthorne. Inorg. Chem. **24**, 1911 (1985).
45. S. Hermanek. Chem. Rev. **92**, 325 (1992).
46. R. Alberto, K. Ortner, N. Wheatley, R. Schibli, and P.A. Schubiger. J. Am. Chem. Soc. **123**, 3135 (2001).
47. O.O. Sogbein, A.E.C. Green, and J.F. Valliant. Inorg. Chem. **44**, 9585 (2005).

© 2008 NRC Canada

Effect of substituents on absorption and fluorescence properties of pyrazolo[3,4-*b*]pyrrolo[2,3-*d*]pyridines

Bhausaheb K. Ghotekar, Muddassar A. Kazi, Madhukar N. Jachak, and Raghunath B. Toche

Abstract: A convenient route was successfully developed for the synthesis of novel heterocycles such as pyrazolo[3,4-*b*]pyrrolo[2,3-*d*]pyridines (PPP) from pyrazolo[3,4-*b*]pyridines in good yield. The PPP derivatives synthesized were further studied for their photophysical properties, and it was observed that absorption and emission λ_{max} changed, owing to the substituent effect at 4 positions. These compounds were obtained from highly reactive starting materials, 5-aminopyrazoles and α-acetyl γ-butyrolactone.

Key words: α-acetyl γ-butyrolactone, pyrazolo[3,4-*b*]pyrrolo[2,3-*d*] pyridine, absorption, emission, fluorescence.

Résumé : On a mis au point une voie réactionnelle qui permet de réaliser la synthèse de nouveaux hétérocycles, telles les pyrazolo[3,4-*b*]pyrrolo[2,3-*d*]pyridines (PPP) à partir de pyrazolo[3,4-*b*]pyridines, avec de bons rendements. On a soumis les dérivés PPP synthétisés à des études de leurs propriétés photophysiques et on a observé que les valeurs des λmax de leurs absorptions et de leurs émissions varient sous l'effet d'un changement dans la nature des substituants en position 4. On a obtenu ces composés à partir de produits de départ très réactifs, soit les 5-aminopyrazoles et l'α-acétyl-γ-butyrolactone.

Mots-clés : l'α-acétyl-γ-butyrolactone, pyrazolo[3,4-*b*]pyrrolo[2,3-*d*]pyridine, absorption, émission, fluorescence.

[Traduit par la Rédaction]

Introduction

Photoinduced intramolecular electron transfer plays a key role in the photophysics of electron-donor (D)-electron-acceptor (A) pi/π conjugated systems connected formally by a single bond. The molecular structure of their charge-transfer excited states has been the object of numerous discussions for more than twenty years. One of the best known and also widely accepted proposals for such a system is the so-called TICT (twisted intramolecular charge transfer) state model (1–3). The perpendicular geometry was questioned recently as an inherent precondition to obtain intramolecular charge transfer in such D–A systems (4, 5). For bulky π donor and acceptor systems (e.g., 9-(4-dimethylaminophenyl)-anthracene or 9,9′-bianthryl), the D–A conformation in the fluorescing charge-transfer excited state was postulated to become more coplanar than in the ground state (6). Recently, several donor and (or) acceptor substituted compounds related to carbazoles, acridines, and so forth were synthesized, and their photoinduced charge separation has been intensively studied (7–9). The 4-*N*,*N*-dimethylaminophenyl derivatives of bis-pyrazolo[3,4-*b*;4′,3′-*e*]pyridine (DMA-DMPP) and pyrazolo[3,4-*b*]quinoline (DMA-DPPQ) (Fig. 1) are further representatives of bulky π-electron donor–acceptor compounds and were recently investigated in some detail both experimentally and semi-empirically (10–16). It has been shown that pyrazoloquinoline derivatives are efficient blue emitters with absorption in the near-ultraviolet region and with a fluorescence quantum yield near to unity. Substitution with a dimethylanilino donor group results in strongly solvent-polarity-dependent fluorescence properties (11, 12). Derivatives of 3,5-dimethyl-1,7-diphenyl-bis-pyrazolo-[3,4-*b*;4′,3′-*e*]-pyridine (DMA-DMPP) with different substituents in position 4 are compounds showing intense fluorescence in the blue–green region and are considered for application as fluorescence standards and luminophores in organic light-emitting diodes (17–20). The derivatives with phenyl and 4-methoxyphenyl substituent (H-DMPP and CH_3O-DMPP, respectively) are characterized by a very intense, solvent-independent fluorescence. The nitro derivatives (NO_2-DMPP) show an unexpected photophysical behaviour. Similarly, The pyrazolopyrrolopyridines with different substituents in position 4 are compounds that show intense fluorescence in the blue–green region with a fluorescence quantum yield near to unity (Fig. 2).

Apart from this, the pyrazolo[3,4-*b*]pyridines and pyrazolo[3,4-*b*]pyrrolo[2,3-*d*]pyridine are examples of condensed heterocyclic compounds with notable pharmacological and biological activities, such as hypotensive (21), cytotoxic (22), and antibacterial activity (23), and found to

Received 26 May 2008. Accepted 17 September 2008. Published on the NRC Research Press Web site at canjchem.nrc.ca on 29 October 2008.

B.K. Ghotekar, M.A. Kazi, M.N. Jachak, and R.B. Toche.[1] Organic Chemistry Research Center, Department of Chemistry, K.R.T. Arts B.H. Commerce and A.M. Science College, Gangapur Road, Nashik 422002, (M.S.), India.

[1]Corresponding author (e-mail: raghunath_toche@rediffmail.com).

 doi:10.1139/V08-155 © 2008 NRC Canada

Fig. 1. X-diphenylpyrazoloquinolines.

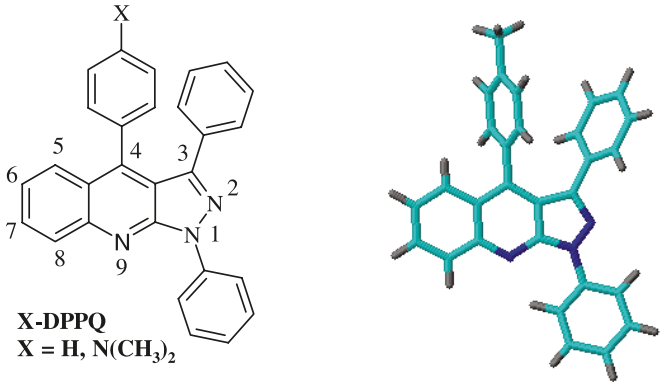

Fig. 2. R,X-pyrazolopyrrolopyridines.

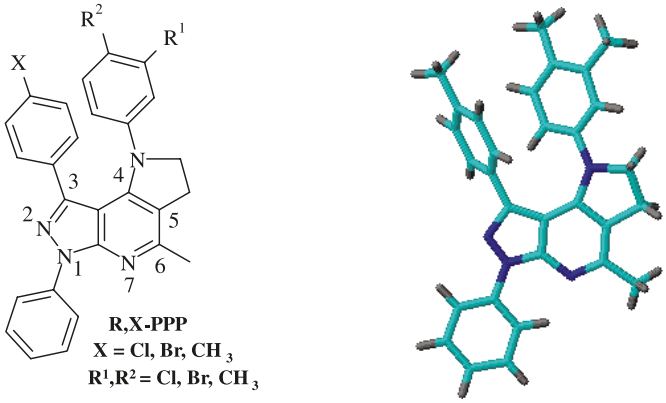

be potential purine antagonists (24). Analogous to bis-pyrazolo-[3,4-b;4′,3′-*e*]-pyridines and pyrazolo-[3,4-*b*]-quinolines, the substituent effect of 4 position on the fluorescence of pyrazolo[3,4-*b*]pyrrolo[2,3-*d*]pyridine has attracted us to synthesize this particular family of compounds. As a part of our ongoing interest in this area (25–28), we have reported the synthesis of pyrazolo[3,4-*b*]pyridines, pyrazolo-[3,4-*b*]quinolines, pyrazolonaphthyridines, and pyrazolo-pyridopyrimidines by Friedlander condensation of reactive methylene compounds with 5-aminopyrazole and synthesis of fused pyrimidines. In our recent communications (29, 30), we reported the synthesis and study of fluorescence properties of benzo[*h*]quinolines and dipyrazolo[3,4-*b*:3,4-*d*]pyridines.

In the present article, we report the study of the photophysical properties of newly synthesized pyrazolo[3,4-*b*]pyridines with 4-chloro-5-chloroethyl side chain (31, 32) and pyrazolo[3,4-*b*]pyrrolo[2,3-*d*]pyridines. All these compounds, having large non-coplanar π-electron donor and acceptor subsystems because of sterical hindrance, are suitable objects to check the validity of the photophysical properties of these compounds.

Results and discussion

The syntheses of pyrazolo[3,4-*b*]pyridines **3** were achieved from highly reactive starting materials, 5-aminopyrazoles **1** and α-acetyl-γ-butyrolactone **2**. Compounds **3** were used as precursors for the syntheses of compounds **4**. Thus, the syntheses of pyrazolo[3,4-*b*]pyrrolo[2,3-*d*]pyridines **4** were achieved by the reaction of compounds **3** with primary aliphatic or aromatic amines containing catalytic amount of triethylamine at 120–150 °C to furnish the desired compound **4**. All crude products that were dissolved in methanol and collected by suction filtration, washed with ethanol, and purified by using suitable solvents, afforded the title compounds **4** in about 70%–80% yield. These compounds showed the absorption and fluorescence near ultraviolet region.

The structure of compounds **3** was confirmed by IR, ^{1}H NMR, ^{13}C NMR, mass spectroscopy, and formulae confirm by elemental analysis. For example, the ^{1}H NMR spectrum of **3a** showed a singlet at δ 2.81 for methyl protons, two triplets at δ 3.39 and 3.75 corresponding to $-CH_2$ and $-CH_2Cl$ protons, respectively, and aromatic protons showed expected chemical shifts and splitting patterns. The mass spectrum of **3a** revealed a molecular ion peak *m*/*z* at 416. The ^{13}C NMR spectrum of this compound is in agreement with the structure proposed. Further, this structure was confirmed by NOE experiment; thus, on irradiation of methyl signal at δ 2.81, the compounds showed no NOE enhancement of any aromatic protons. This indicated that the methyl group present at 6 positions and not at 4, which supported the proposed structure **3**. Similarly, the structure of **4** was confirmed by spectroscopic and analytical methods, which is given in the Experimental section. The absorption and fluorescence data listed in Tables 1 and 2 showed that the incorporation of constituent on to the pyrazolo[3,4-*b*]pyridine and pyrazolo[3,4-*b*]pyrrolo[2,3-*d*]pyridine nucleus at 4 position has profound influence on the absorption and emission properties. It was observed that substitution at 4 position showed considerable increase in the emission wavelength, as the π-electron-donating effect of amino group increases (Scheme 1).

It was interesting to note that the pyrazolo[3,4-*b*]pyridines showed the lower absorption and emission maxima than pyrazolo[3,4-*b*]pyrrolo[2,3-*d*]pyridines. In the pyrazolo[3,4-*b*]pyridines **3**, this might be due to a chloro group at 4 position with a weak and small electron-donor unit in para position, and in pyrazolo[3,4-*b*]pyrrolo[2,3-*d*]pyridines **4**, the substituted amino group at 4 position with a strong and bulky electron-donor unit at para position showed higher absorption and emission maxima.

It is clearly indicated that the fluorescence property of organic compounds is the substituent-dependent property, and it is changed with changing the nature of different substituent (e.g., in compounds **3** and **4**, the nature of substituent changed the photophysical properties of these compounds). It is enhanced by substituting the strong π-electron donor group at 4 position. Compounds **3a** and **4a** showed good absorption and emission spectra as shown in Fig. 3.

Photophysical properties

From the results obtained (Tables 1 and 2), it has been found that both pyrazolo[3,4-*b*]pyridines **3** and pyrazolo[3,4-*b*]pyrrolo[2,3-*d*]pyridines **4** show florescence properties. The compounds **4f**, **4g**, **4k**, and **4l** exhibit remarkable fluorescence characters with high relative quantum yields. It is concluded that the attachment of an electron-donating group to phenyl function oriented at the 4 position of pyrazolo[3,4-

© 2008 NRC Canada

Table 1. The photophysical data for electronic absorption (abs) and fluorescence (flu) of pyrazolo[3,4-***b***]pyridines **3** in $CHCl_3$.

Compound	Ar	λ_{abs} ($CHCl_3$)	λ_{flu} ($CHCl_3$)	Φ_F ($CHCl_3$)
3a	*p*-ClC_6H_4	362.00	394.00	0.120
3b	*p*-BrC_6H_4	366.00	401.00	0.126
3c	*p*-MeC_6H_4	361.00	392.00	0.123

Table 2. The photophysical data for electronic absorption (abs) and fluorescence (flu) of pyrazolo[3,4-***b***]pyrrolo[2,3-***d***]pyridines **4** in $CHCl_3$.

Compd.	Ar	R	λ_{abs} ($CHCl_3$)	λ_{flu} ($CHCl_3$)	Φ_F ($CHCl_3$)
4a	*p*-ClC_6H_4	$C_6H_5CH_2$–	392.00	416.00	0.141
4b	*p*-ClC_6H_4	C_6H_5	393.00	419.00	0.145
4c	*p*-ClC_6H_4	m-ClC_6H_4	392.00	417.00	0.138
4d	*p*-ClC_6H_4	*p*-ClC_6H_4	395.00	421.00	0.136
4e	*p*-ClC_6H_4	*p*-BrC_6H_4	397.00	422.00	0.129
4f	*p*-ClC_6H_4	*o*-MeC_6H_4	399.00	425.00	0.151
4g	*p*-ClC_6H_4	*p*-MeC_6H_4	380.00	429.00	0.146
4h	*p*-BrC_6H_4	m-ClC_6H_4	395.00	420.00	0.119
4i	*p*-BrC_6H_4	*p*-ClC_6H_4	390.00	412.00	0.124
4j	*p*-BrC_6H_4	*p*-BrC_6H_4	373.00	421.00	0.127
4k	*p*-BrC_6H_4	*o*-MeC_6H_4	396.00	425.00	0.148
4l	*p*-BrC_6H_4	*p*-MeC_6H_4	398.00	427.00	0.153
4m	*p*-MeC_6H_4	$C_6H_5CH_2$–	377.00	406.00	0.133
4n	*p*-MeC_6H_4	C_6H_5	396.00	418.00	0.131

Scheme 1. Synthesis of pyrazolopyridines **3** and pyrazolopyrrolopyridines **4**.

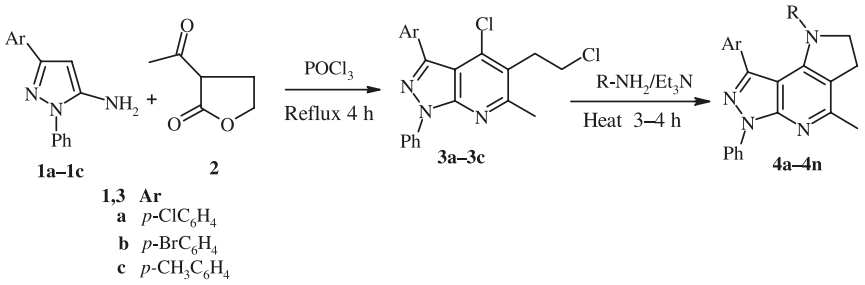

4	Ar	R	4	Ar	R
a	*p*-ClC_6H_4	$C_6H_5CH_2$-	**h**	*p*-BrC_6H_4	*m*-ClC_6H_4
b	*p*-ClC_6H_4	C_6H_5	**i**	*p*-BrC_6H_4	*p*-ClC_6H_4
c	*p*-ClC_6H_4	*m*-ClC_6H_4	**j**	*p*-BrC_6H_4	*p*-BrC_6H_4
d	*p*-ClC_6H_4	*p*-ClC_6H_4	**k**	*p*-BrC_6H_4	*o*-MeC_6H_4
e	*p*-ClC_6H_4	*p*-BrC_6H_4	**l**	*p*-BrC_6H_4	*p*-MeC_6H_4
f	*p*-ClC_6H_4	*o*-MeC_6H_4	**m**	*p*-MeC_6H_4	$C_6H_5CH_2$-
g	*p*-ClC_6H_4	*p*-MeC_6H_4	**n**	*p*-MeC_6H_4	C_6H_5

b]pyrrolo[2,3-*d*]pyridine enhances the fluorescence properties and in turn gives high relative quantum yield.

Conclusion

The reactions reported here represent the synthesis of a new class of fluorescent compounds in which the 4 position of pyrazolopyridine ring is substituted by the chlorine or nitrogen atom with different phenyl rings. These compounds showed considerable absorption and emission λ_{max}. Pyrazolo[3,4-*b*]pyrrolo[2,3-*d*]pyridines showed higher fluorescent properties than the pyrazolo[3,4-*b*]pyridines; it might be due to the steric hindrance of bulky phenyl rings and large π-electron donor group at 4 position.

Experimental

General

Melting points were determined on a Gallenkamp melting-point apparatus, Model MFB595, in open capillary tubes

© 2008 NRC Canada

Fig. 3. The comparative (a, b) absorption and (c, d) emission spectra of compounds **3a** and **4a**.

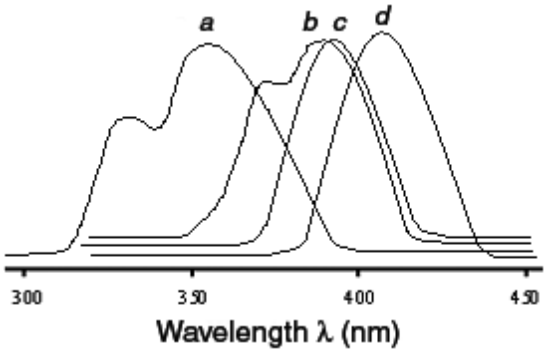

and are uncorrected. ^{1}H and ^{13}C NMR spectra were recorded on a Varian XL-300 spectrometer (300 and 75 MHz). Chemical shifts are reported in ppm from internal tetramethylsilane standard and are given in δ units. The solvents for NMR spectra was duterio-chloroform unless otherwise stated. Infrared spectra were taken on a Shimadzu IR-408 (a Shimadzu FTIR instrument) in potassium bromide pellets unless otherwise stated. UV spectra were recorded on a Shimadzu UV-1601 UV–vis Spectrophotometer. Compounds for UV scan were dissolved in methanol. Fluorescence spectra were recorded using RF-5301 PC spectrofluorophotometer. Compounds for fluorescence measurements were dissolved in chloroform. UV and fluorescence scans were recorded from 200 to 600 nm. Elemental analyses were performed on a Hosli CH-Analyzer and the results are within ± 0.4 of the theoretical percentage. HR-MS were obtained with a Mat 112 Varian Mat Bremen (70 eV) mass spectrometer. Solutions were concentrated in a rotary evaporator under reduced pressure. All reactions were monitored by TLC, carried out on 0.2 mm silica gel 60 F 254 (Merck) plates, using UV light (254 and 366 nm) for detection. Common reagent-grade chemicals are either commercially available and were used without further purification or prepared by standard literature procedures.

General procedure for the 4-chloro-5-(2-chloroethyl)-3-(4-aryl)-6-methyl-1-phenyl-1*H*-pyrazolo[3,4-*b*]pyridine (3a–3c)

A mixture of 5-aminopyrazole **1** (0.01 mol) and α-acetyl-γ-butyrolactone **2** (1.282 g, 1.078 mL 0.01 mol) was refluxed in phosphorous oxychloride (20 mL) until the end of the exothermic reaction, which usually starts about 80–90 °C. The mixture was then refluxed for further 4 h. Excess $POCl_3$ was removed under vacuum, and the oily residue solidified upon treatment with ice-water, neutralization with sodium carbonate, and stirring overnight. The separated product was then filtered, dried, and recrystallized to afford compound **3** in good yield.

*4-Chloro-5-(2-chloroethyl)-3-(4-chlorophenyl)-6-methyl-1-phenyl-1*H*-pyrazolo[3,4-b]pyridine (3a)*

Yield: 3.25 g (78%), recrystallized from acetonitrile/ethanol (8:2) to afford colourless prisms; mp 163–164 °C. IR (KBr): 2918m, 1595m, 1500s, 1257m, 1147m, 1093w, 1018w, 906w, 756m, 686w cm^{-1}. ^{1}H NMR (300 MHz, $CDCl_3$) δ: 2.81 (s, 3H, CH_3), 3.39 (t, J = 7.2 Hz, 2H, CH_2), 3.75 (t, J = 7.2 Hz, 2H, CH_2), 7.44–7.54 (m, 5H, Ar–H), 7.69 (d, J = 8.2, Hz, 2H, Ar–H), 8.26 (d, J = 8.2, Hz, 2H, Ar–H). ^{13}C NMR (75 MHz, $CDCl_3$) δ: 22.3, 27.5, 55.4, 115.4, 121.2, 124.6, 126.5, 128.2, 129.6, 130.5, 131.1, 134.3, 139.5, 144.8, 154.2, 156.1, 159.2. MS (70 eV) *m*/*z* (%): 422 (20) [M + 6], 420 (60) [M + 4], 418 (92) [M + 2], 416 (90) [M$^+$], 366 (10), 255 (10), 111 (15), 85 (40), 71 (60), 57 (100), 55 (30). Anal. calcd. for $C_{21}H_{16}Cl_3N_3$ (416.73): C, 60.52; H, 3.87; N, 10.08. Found: C, 61.02; H, 3.18; N, 10.18.

*3-(4-Bromophenyl)-4-chloro-5-(2-chloroethyl)-6-methyl-1-phenyl-1*H*-pyrazolo[3,4-b] pyridine (3b)*

Yield: 3.55 g (77%), recrystallized from acetonitrile/ethanol (8:2) to afford colourless needles; mp 175–176 °C. IR (KBr): 2911m, 1591m, 1500s, 1259m, 1149m, 1093w, 1018w, 910w, 762m, 686w cm^{-1}. ^{1}H NMR (300 MHz, $CDCl_3$) δ: 2.82 (s, 3H, CH_3), 3.40 (t, J = 7.2 Hz, 2H, CH_2), 3.70 (t, J = 7.2 Hz, 2H, CH_2), 7.29–7.48 (m, 5H, Ar–H), 7.53 (d, J = 8.2 Hz, 2H, Ar–H), 8.14 (d, J = 8.2 Hz, 2H, Ar–H). ^{13}C NMR (75 MHz, $CDCl_3$) δ: 21.1, 29.8, 53.9, 118.2, 122.3, 125.8, 128.1, 129.2, 130.6, 131.5, 132.1, 134.1, 139.9, 144.8, 155.3, 157.2, 163.2. MS (70 eV) *m*/*z* (%): 466 (20) [M + 6], 464 (60) [M + 4], 462 (92) [M + 2], 460 (90) [M$^+$], 437 (10), 425 (100), 404 (10), 378 (15), 362 (40), 338 (60), 313 (10), 299 (30), 182 (30), 127 (15), 117 (40), 77 (80), 65 (60). Anal. calcd. for $C_{21}H_{16}BrCl_2N_3$ (461.18): C, 54.69; H, 3.50; N, 9.11. Found: C, 54.98; H, 3.78; N, 9.21.

*4-Chloro-5-(2-chloroethyl)-6-methyl-3-(4-methylphenyl)-1-phenyl-1*H*-pyrazolo[3,4-b] pyridine (3c)*

Yield: 2.57 g (65%), recrystallized from acetonitrile/ethanol (8:2) to afford colourless needles; mp 145–146 °C. IR (KBr): 2919m, 1592m, 1500s, 1255m, 1149m, 1093w, 1020w, 915w, 760m, 688w cm^{-1}. ^{1}H NMR (300 MHz, $CDCl_3$) δ: 2.39 (s, 3H, Ar–CH_3), 2.80 (s, 3H, CH_3), 3.38 (t, J = 7.3 Hz, 2H, CH_2), 3.68 (t, J = 7.3 Hz, 2H, CH_2), 7.30–7.56 (m, 5H, Ar–H), 7.60 (d, J = 8.3 Hz, 2H, ArH), 8.18 (d, J = 8.3 Hz, 2H, ArH). ^{13}C NMR (75 MHz, $CDCl_3$) δ: 18.1, 24.3, 26.8, 41.3, 106.7, 120.2, 126.3, 127.4, 129.4, 129.6 130.1, 138.4, 138.9, 139.7, 140.6, 145.9, 150.5, 155.3. Anal. calcd. for $C_{22}H_{19}Cl_2N_3$ (396.31): C, 66.67; H, 4.83; N, 10.60. Found: C, 66.90; H, 4.38; N, 10.83.

General procedure for the synthesis of 1-phenyl-8-(4-aryl)-4-methyl-6-phenyl-1,2,3,6-tetrahydropyrazolo[3,4-*b*]pyrrolo[2,3-*d*]pyridine (4a–4n)

A mixture of **3** (0.01 mol) and primary aliphatic and aromatic amines (0.04 mol) was heated at 110–120 °C for about 2 h until TLC showed no more starting material. Then, the mixture was cooled at 20 °C. After cooling, methanol (20 ml) was added, and the resulting solid was filtered by suction, washed with methanol, dried, and recrystallized from the proper solvent to afford **4** in good yield.

1-Benzyl-8-(4-chlorophenyl)-4-methyl-6-phenyl-1,2,3,6-tetrahydropyrazolo[3,4-b]pyrrolo [2,3-d]pyridine (4a)

Yield: 4.01 g (89%), recrystallized from ethanol to afford colourless prisms; mp 150–151 °C. IR (KBr): 2909m, 1744m, 1598s, 1500s, 1257m, 1147m, 1093m, 1018m, 906m, 756w, 686m cm^{-1}. ^{1}H NMR (300 MHz, $CDCl_3$) δ:

© 2008 NRC Canada

2.50 (s, 3H, CH_3), 3.06 (t, J = 7.3 Hz, 2H, CH_2), 3.50 (t, J = 7.3 Hz, 2H, CH_2), 4.14(s, 2H, Ar–CH_2), 6.98–7.06 (m, 5H, Ar–H), 7.24 (d, J = 8.2 Hz, 2H, ArH), 7.43–7.49 (m, 5H, ArH), 8.29 (d, J = 8.2 Hz, 2H, ArH). ^{13}C NMR (75 MHz, $CDCl_3$) δ: 21, 26, 53, 56, 101, 112, 115, 122, 124, 126, 126, 127, 128, 128, 129, 130, 133, 134, 136, 143, 154 156. MS *m*/*z* (%): 452 (90) [M + 2], 450 (100) [M^+], 447 (20), 359 (25), 324 (35), 186 (20), 167 (20), 139 (10), 123 (30), 111 (15), 91 (90), 77 (80), 65 (60). Anal. calcd. for $C_{28}H_{23}ClN_4$ (450.96): C, 74.57; H, 5.14; N, 12.42. Found: C, 74.67; H, 4.88; N, 12.69.

8-(4-Chlorophenyl)-4-methyl-1,6-diphenyl-1,2,3,6-tetrahydropyrazolo[3,4-b]pyrrolo[2,3-d]pyridine (4b)

Yield: 3.58 g (82%), recrystallized from ethanol/DMF (8:2) to afford light green prisms; mp 212–213 °C. IR (KBr): 2910m, 1738m, 1588s, 1503s, 1251m, 1144m, 1099m, 1017m, 906m, 756w, 686m cm^{-1}. ^{1}H NMR (300 MHz, $CDCl_3$) δ: 2.56 (s, 3H, CH_3), 3.21 (t, J = 7.1 Hz, 2H, CH_2), 4.20 (t, J = 7.1 Hz, 2H, CH_2), 6.74–6.90 (m, 5H, Ar–H), 7.24–7.45 (m, 5H, Ar–H), 7.48 (d, J = 7.5 Hz, 2H, Ar–H), 8.31 (d, J = 7.5 Hz, 2H, Ar–H). ^{13}C NMR (75 MHz, $CDCl_3$) δ: 19.3, 22.8, 51.5, 104.6, 113.5, 117.2, 120.2, 124.7, 126.8, 128.9, 129.4, 129.6 131.1, 134.3, 139.7, 145.9, 149.1, 154.3, 156.3. MS *m*/*z* (%): 438 (80) [M + 2], 436 (100) [M^+], 419 (20), 399 (25), 361 (35), 298 (20), 255 (20), 218 (10), 200 (30), 192 (15), 179 (30), 152 (35), 111 (10), 91 (10), 77 (60), 65 (15). Anal. calcd. for $C_{27}H_{21}ClN_4$ (436.93): C, 74.22; H, 4.84; N, 12.82. Found: C, 73.87; H, 5.05; N, 12.68.

1-(3-Chlorophenyl)-8-(4-chlorophenyl)-4-methyl-6-phenyl-1,2,3,6-tetrahydropyrazolo[3,4-b]pyrrolo[2,3-d]pyridine (4c)

Yield: 3.67 g (78%), recrystallized from ethanol/DMF (6:4) to afford light green prisms; mp 217–218 °C. IR (KBr): 2918m, 1743m, 1595s, 1500s, 1257m, 1147m, 1093m, 1018m, 906m, 756w, 686m cm^{-1}. ^{1}H NMR (300 MHz, $CDCl_3$) δ: 2.57 (s, 3H, CH_3), 3.26 (t, J = 7.2 Hz, 2H, CH_2), 4.86 (t, J = 7.2 Hz, 2H, CH_2), 6.23–7.51 (m, 9H Ar–H), 8.20 (d, J = 7.8 Hz, 2H, Ar–H), 8.34 (d, J = 7.8 Hz, 2H, Ar–H). ^{13}C NMR (75 MHz, $CDCl_3$) δ: 19.4, 22.5, 53.2, 106.2, 113.6, 114.1, 116.1, 121.3, 122.8, 123.5, 128.2, 129.1, 130.5, 131.6, 133.3, 134.1, 135.4, 140.7, 144.9, 148.3, 151.2, 154.6, 158.6. Anal. calcd. for $C_{27}H_{20}Cl_2N_4$ (471.38): C, 68.80; H, 4.28; N, 11.89. Found: C, 69.09; H, 4.60; N 12.10.

1,8-Bis(4-chlorophenyl)-4-methyl-6-phenyl-1,2,3,6-tetrahydropyrazolo[3,4-b]pyrrolo[2,3-d]pyridine (4d)

Yield: 3.39 g (72%), recrystallized from ethanol/DMF (6:4) to afford light yellow prisms; mp 235–237 °C. IR (KBr): 2918m, 1743m, 1595s, 1500s, 1257m, 1147m, 1093m, 1018m, 906m, 756w, 686m cm^{-1}. ^{1}H NMR (300 MHz, $CDCl_3$) δ: 2.57 (s, 3H, CH_3), 3.26 (t, J = 7.2 Hz, 2H, CH_2), 4.86 (t, J = 7.2 Hz, 2H, CH_2), 6.23–7.51 (m, 9H, Ar–H), 8.20 (d, J = 7.8 Hz, 2H, Ar–H), 8.34 (d, J = 7.8 Hz, 2H, Ar–H). ^{13}C NMR (75 MHz, $CDCl_3$) δ: 18.4, 21.6, 52.5, 108.6, 115.3, 119.2, 121.2, 124.7, 126.3, 128.8, 129.1, 129.9, 132.3, 135.4, 138.2, 144.4, 147.5, 149.1, 154.3, 155.3. Anal. calcd. for $C_{27}H_{20}Cl_2N_4$ (471.38): C, 68.80; H, 4.28; N, 11.89. Found: C, 68.67; H, 4.10; N, 12.02.

1-(4-Bromophenyl)-8-(4-chlorophenyl)-4-methyl-6-phenyl-1,2,3,6-tetrahydropyrazolo[3,4-b]pyrrolo[2,3-d]pyridine (4e)

Yield: 4.07 g (79%), recrystallized from ethanol/DMF (6:4) to afford yellow prisms; mp 231–232 °C. IR (KBr): 2918m, 1743m, 1595s, 1500s, 1257m, 1147, 1093m, 1018m, 906m, 756w, 686m cm^{-1}. ^{1}H NMR (300 MHz, $CDCl_3$) δ: 2.58 (s, 3H CH_3), 3.28 (t, J = 7.1 Hz, 2H, CH_2), 4.87 (t, J = 7.1 Hz, 2H, CH_2), 6.22–7.55 (m, 9H, Ar–H), 8.20 (d, J = 7.8 Hz, 2H, Ar–H), 8.33 (d, J = 7.8 Hz, 2H, Ar–H). ^{13}C NMR (75 MHz, $CDCl_3$) δ: 17.9, 23.2, 52.5, 103.2, 111.5, 115.7, 120.2, 124.7, 126.3, 128.9, 129.4, 131.2, 132.5, 134.3, 139.7, 138.2, 145.9, 148.4, 149.1, 154.3, 156.2. Anal. calcd. for $C_{27}H_{20}BrClN_4$ (515.83): C, 62.87; H, 3.91; N, 10.86. Found: C, 62.63; H, 4.16; N, 11.09.

8-(4-Chlorophenyl)-1-(2-methylphenyl)-4-methyl-6-phenyl-1,2,3,6-tetrahydropyrazolo-[3,4-b]pyrrolo[2,3-d]pyridine (4f)

Yield: 3.96 g (88%), recrystallized from ethanol/DMF (8:2) to afford light green prisms; mp 220–222 °C. IR (KBr): 2918m, 1743m, 1595s, 1500s, 1257m, 1147, 1093m, 1018m, 906m, 756w, 686m cm^{-1}. ^{1}H NMR (300 MHz, $CDCl_3$) δ: 2.30 (s, 3H, Ar–CH_3), 2.61 (s, 3H, CH_3), 3.25 (t, J = 7.2 Hz, 2H, CH_2), 4.22 (t, J = 7.2 Hz, 2H, CH_2), 7.24–7.45 (m, 9H, Ar–H), 7.45 (d, J = 8.2 Hz, 2H, Ar–H), 8.35 (d, J = 8.2 Hz, 2H, Ar–H). ^{13}C NMR (75 MHz, $CDCl_3$) δ: 15.8, 18.6, 21.3, 51.8, 105.6, 113.3, 117.1, 120.2, 124.7, 126.2, 126.3, 126.6, 128.9, 129.4, 129.9, 131.2, 134.3, 139.7, 145.9, 149.1, 154.9, 157.4. Anal. calcd. for $C_{28}H_{23}ClN_4$ (450.96): C, 74.57; H, 5.14; N, 12.42. Found: C, 74.78; H, 4.96; N, 12.18.

8-(4-Chlorophenyl)-1-(4-methylphenyl)-4-methyl-6-phenyl-1,2,3,6-tetrahydropyrazolo[3,4-b]pyrrolo[2,3-d]pyridine (4g)

Yield: 3.74 g (83%), recrystallized from ethanol/DMF (8:2) to afford light green prisms; mp 229–230 °C. IR (KBr): 2918m, 1743m, 1595s, 1500s, 1257m, 1147, 1093m, 1018m, 906m, 756w, 686m cm^{-1}. ^{1}H NMR (300 MHz, $CDCl_3$) δ: 2.30 (s, 3H, Ar–CH_3), 2.60 (s, 3H, CH_3), 3.25 (t, J = 7.2 Hz, 2H, CH_2), 4.22 (t, J = 7.2 Hz, 2H, CH_2), 7.24–7.45 (m, 9H, Ar–H), 7.45 (d, J = 8.2 Hz, 2H, Ar–H), 8.35 (d, J = 8.2 Hz, 2H, Ar–H). ^{13}C NMR (75 MHz, $CDCl_3$) δ: 18.6, 21.5, 24.3, 51.5, 103.6, 113.4, 120.2, 124.7, 126.3, 126.8, 128.9, 129.4, 129.9, 131.2, 134.9, 139.2, 145.9, 146.4, 149.9, 154.9, 157.4. Anal. calcd. for $C_{28}H_{23}ClN_4$ (450.96): C, 74.57; H, 5.14; N, 12.42. Found: C, 74.69; H, 5.32; N 12.61.

8-(4-Bromophenyl)-1-(3-chlorophenyl)-4-methyl-6-phenyl-1,2,3,6-tetrahydropyrazolo[3,4-b]pyrrolo[2,3-d]pyridine (4h)

Yield: 3.92 g (76%), recrystallized from ethanol/DMF (6:4) to afford light brown prisms; mp 226–227 °C. IR (KBr): 2918m, 1743m, 1595s, 1500s, 1257m, 1147, 1093m, 1018m, 906m, 756w, 686m cm^{-1}. ^{1}H NMR (300 MHz, $CDCl_3$) δ: 2.59 (s, 3H CH_3), 3.28 (t, J = 7.2 Hz, 2H, CH_2), 4.87 (t, J = 7.2 Hz, 2H, CH_2), 6.22–7.55 (m, 9H, Ar–H), 8.20 (d, J = 8.2 Hz, 2H, ArH), 8.33 (d, J = 8.2 Hz, 2H, ArH). ^{13}C NMR (75 MHz, $CDCl_3$) δ: 18.7, 21.3, 51.5, 104.6, 111.2, 113.8, 117.3, 120.8, 123.1, 124.9, 126.2, 129.1, 129.5, 131.6, 132.2, 132.1, 135.4, 139.7, 145.9, 149.3, 150.2, 154.6, 157.6. Anal. calcd. for $C_{27}H_{20}BrClN_4$

© 2008 NRC Canada

(515.83): C, 62.87; H, 3.91; N, 10.86. Found: C, 63.09; H, 4.06; N 10.66.

8-(4-Bromophenyl)-1-(4-chlorophenyl)-4-methyl-6-phenyl-1,2,3,6-tetrahydropyrazolo[3,4-b]pyrrolo[2,3-d]pyridine (4i)

Yield: 3.81 g (74%), recrystallized from ethanol/DMF (6:4) to afford light green prisms; mp 240–241 °C. IR (KBr): 2918m, 1743m, 1595s, 1500s, 1257m, 1147, 1093m, 1018m, 906m, 756w, 686m cm^{-1}. ^1H NMR (300 MHz, $CDCl_3$) δ: 2.58 (s, 3H, CH_3), 3.28 (t, J = 7.2 Hz, 2H, CH_2), 4.87 (t, J = 7.2 Hz, 2H, CH_2), 6.22–7.55 (m, 9H, Ar–H), 8.20 (d, J = 7.8 Hz, 2H, Ar–H), 8.33 (d, J = 7.8 Hz, 2H, Ar–H). ^{13}C NMR (75 MHz, $CDCl_3$) δ: 16.4, 23.6, 53.5, 107.6, 116.3, 119.2, 123.2, 124.7, 126.3, 127.8, 129.8, 130.9, 131.3, 135.4, 140.2, 145.4, 148.5, 150.1, 154.3, 159.3. Anal. calcd. for $C_{27}H_{20}BrClN_4$ (515.83): C, 62.87; H, 3.91; N, 10.86. Found: C, 63.13; H, 4.21; N 10.61.

1,8-Bis(4-bromophenyl)-4-methyl-6-phenyl-1,2,3,6-tetrahydropyrazolo[3,4-b]pyrrolo[2,3-d]pyridine (4j)

Yield: 4.31 g (77%), recrystallized from ethanol/DMF (6:4) to afford light green prisms; mp 243–244 °C. IR (KBr): 2918m, 1743m, 1595s, 1500s, 1257m, 1147, 1093m, 1018m, 906m, 756w, 686m cm^{-1}. ^1H NMR (300 MHz, $CDCl_3$) δ: 2.58 (s, 3H, CH_3), 3.28 (t, J = 7.2 Hz, 2H, CH_2), 4.87 (t, J = 7.2 Hz, 2H, CH_2), 6.22–7.55 (m, 9H, Ar–H), 8.20 (d, J = 7.8 Hz, 2H, Ar–H), 8.33 (d, J = 7.8 Hz, 2H, Ar–H). ^{13}C NMR (75 MHz, $CDCl_3$) δ: 19.9, 24.2, 50.5, 107.2, 114.5, 118.7, 121.2, 125.7, 127.3, 128.1, 129.6, 130.1, 131.0, 134.6, 139.0, 138.2, 143.9, 147.4, 148.1, 151.3, 160.2. Anal. calcd. for $C_{27}H_{20}Br_2N_4$ (560.28): C, 57.88; H, 3.60; N, 10.00. Found: C, 57.63; H, 3.21; N, 10.27.

8-(4-Bromophenyl)-1-(2-methylphenyl)-4-methyl-6-phenyl-1,2,3,6-tetrahydropyrazolo[3,4-b]pyrrolo[2,3-d]pyridine (4k)

Yield: 4.35 g (88%), recrystallized from ethanol/DMF (8:2) to afford light green prisms; mp 230–232 °C. IR (KBr): 2918m, 1743m, 1595s, 1500s, 1257m, 1147, 1093m, 1018m, 906m, 756w, 686m cm^{-1}. ^1H NMR (300 MHz, $CDCl_3$) δ: 2.32 (s, 3H, Ar–CH_3), 2.61 (s, 3H, CH_3), 3.23 (t, J = 7.2 Hz, 2H, CH_2), 4.24 (t, J = 7.2 Hz, 2H, CH_2), 7.25–7.46 (m, 9H, ArH), 7.46 (d, J = 8.1 Hz, 2H, Ar–H), 8.36 (d, J = 8.1 Hz, 2H, Ar–H). ^{13}C NMR (75 MHz, $CDCl_3$) δ: 16.8, 19.3, 25.3, 53.8, 109.6, 111.3, 118.1, 121.2, 123.7, 125.2, 126.3, 126.6, 128.9, 129.3, 129.3, 131.0, 134.1, 139.2, 145.1, 149.3, 154.9, 157.9. Anal. calcd. for $C_{28}H_{23}BrN_4$ (495.41): C, 67.88; H, 4.68; N, 11.31. Found: C, 67.63; H, 4.51; N, 11.49.

8-(4-Bromophenyl)-1-(4-methylphenyl)-4-methyl-6-phenyl-1,2,3,6-tetrahydropyrazolo[3,4-b]pyrrolo[2,3-d]pyridine (4l)

Yield: 3.61 g (73%), recrystallized from ethanol/DMF (8:2) to afford light green prisms; mp 235–236 °C. IR (KBr): 2918m, 1743m, 1595s, 1500s, 1257m, 1147, 1093m, 1018m, 906m, 756w, 686m cm^{-1}. ^1H NMR (300 MHz, $CDCl_3$) δ: 2.34 (s, 3H, Ar–CH_3), 2.63 (s, 3H, CH_3), 3.23 (t, J = 7.2 Hz, 2H, CH_2), 4.24 (t, J = 7.2 Hz, 2H, CH_2), 7.25–7.46 (m, 9H, Ar–H), 7.46 (d, J = 8.2 Hz, 2H, Ar–H), 8.36 (d, J = 8.2 Hz, 2H, Ar–H). ^{13}C NMR (75 MHz, $CDCl_3$) δ: 20.6, 23.2, 24.3, 52.5, 105.6, 112.4, 116.2, 121.7, 125.3, 126.8, 127.9, 129.4, 129.9, 131.2, 134.9, 140.2, 142.9, 146.4, 147.9, 151.9, 156.2. Anal. calcd. for $C_{28}H_{23}BrN_4$ (495.41): C, 67.88; H, 4.68; N, 11.31. Found: C, 68.06; H, 4.98; N 11.52.

1-Benzyl-4-methyl-8-(4-methylphenyl)-6-phenyl-1,2,3,6-tetrahydropyrazolo[3,4-b]pyrrolo[2,3-d]pyridine (4m)

Yield: 3.48 g (81%), recrystallized from ethanol to afford colourless prisms; mp 166–67 °C. IR (KBr): 2918m, 1743m, 1595s, 1500s, 1257m, 1147, 1093m, 1018m, 906m, 756w, 686m cm^{-1}. ^1H NMR (300 MHz, $CDCl_3$) δ: 2.39 (s, 3H, Ar–CH_3), 2.80 (s, 3H, CH_3), 3.38 (t, J = 7.1 Hz, 2H, CH_2), 3.68 (t, J = 7.1 Hz, 2H, CH_2), 4.14(s, 2H, Ar–CH_2), 6.98–7.06 (m, 5H, Ar–H), 7.24 (d, J = 8.2 Hz, 2H, Ar–H), 7.43–7.49 (m, 5H, Ar–H), 8.29 (d, J = 8.2 Hz, 2H, Ar–H). ^{13}C NMR (75 MHz, $CDCl_3$) δ: 17.6, 21.7, 24.3, 53.4, 104.9, 120.2, 124.7, 126.3, 127.1, 127.4, 128.6, 128.0, 129.4, 129.6, 130.1, 136.5, 138.4, 139.7, 145.9, 149.9, 154.9, 158.8. Anal. calcd. for $C_{29}H_{26}N_4$ (430.54): C, 80.90; H, 6.09; N, 13.01. Found: C, 80.66; H, 6.41; N 13.32.

1,6-Diphenyl-4-methyl-8-(4-methylphenyl)-1,2,3,6-tetrahydropyrazolo[3,4-b]pyrrolo[2,3-d]pyridine (4n)

Yield: 3.49 g (84%), recrystallized from ethanol/DMF (8:2) to afford colourless prisms; mp 208–209 °C. IR (KBr): 2918m, 1743m, 1595s, 1500s, 1257m, 1147, 1093m, 1018m, 906m, 756w, 686m cm^{-1}. ^1H NMR (300 MHz, $CDCl_3$) δ: 2.40 (s, 3H, $ArCH_3$), 2.82 (s, 3H, CH_3), 3.21 (t, J = 7.1 Hz, 2H, CH_2), 4.20 (t, J = 7.1 Hz, 2H, CH_2), 6.74–6.90 (m, 5H, Ar–H), 7.24–7.45 (m, 5H, Ar–H), 7.48 (d, J = 7.5 Hz, 2H, Ar–H), 8.31 (d, J = 7.5 Hz, 2H, Ar–H). ^{13}C NMR (75 MHz, $CDCl_3$) δ: 18.6, 21.3, 24.3, 51.5, 103.6, 113.5, 117.2, 120.2, 124.7, 126.3, 127.4, 129.6, 130.1, 138.4, 139.7, 145.9, 149.9, 154.9, 157.3. Anal. calcd. for $C_{28}H_{24}N_4$ (416.51): C, 80.74; H, 5.81; N, 13.45. Found: C, 80.54; H, 5.98; N 13.52.

Acknowledgements

The authors thank UGC, New Delhi, India, for financial support of this research project. We thank Professor D.D. Dhavale, Department of Chemistry, University of Pune, India, for his valuable cooperation for the measurements of fluorescence properties.

References

1. K. Rotkiewicz, K.H. Grellmann, and Z.R. Grabowski. Chem. Phys. Lett. **19**, 315 (1973).
2. Z.R.Grabowski, K. Rotkiewicz, A. Siemiarczuk, D. Cowley, and W. Baumann. Nouv. J. Chim. **30**, 443 (1979).
3. W. Rettig. *In* Topics of current chemistry. Vol. 169. Springer. Berlin. 1994. p. 254.
4. K.A. Zachariasse, T.V. Haar, U. Leinhos, and W. Kuhnle. J. Int. Rec. Mats. **21**, 501 (1994).
5. (*a*) J. Herbich and A. Kapturkiewicz. Chem. Phys. **158**, 143 (1991); (*b*) J. Herbich and A. Kapturkiewicz. Chem. Phys. **170,** 221 (1993).
6. K. Rotkiewicz, K. Rechthaler, A. Puchala, D. Rasala, S. Styrcz, and G. Kohler. J. Photochem. Photobiol. A: Chem. **98**, 15 (1996).
7. A. Kapturkiewicz, J. Herbich, and J. Nowacki. Chem. Phys. Lett. **275**, 355 (1997).

© 2008 NRC Canada

8. J. Herbich and A. Kapturkiewicz. Chem. Phys. Lett. **273**, 8 (1997).
9. J. Herbich, A. Kapturkiewicz, and J. Nowacki. Chem. Phys. Lett. **262**, 633 (1996).
10. K. Rechthaler, R. Schamschule, J. Parusel, K. Rotkiewicz, D. Piorun, and G. Kohler. Acta Phys. Polon. A, **95**, 321 (1999).
11. J. Parusel, K. Rechthaler, D. Piorun, A. Danel, K. Khatchatrayan, K. Rotkiewicz, and G. Kohler. J. Fluoresc. **8**, 375 (1998).
12. K. Rechthaler, K. Rotkiewicz, G. Kohler, A. Danel, P. Tomasik, and K. Khatchatrayan. J. Fluoresc. **7**, 301, (1997).
13. J. Parusel, R. Schamschule, and G. Kohler. J. Comput. Chem. **19**, 1584 (1998).
14. J. Parusel, R. Schamschule, G. Kohler, and B. Bunsenges. Phys. Chem. **101**, 1836 (1997).
15. J. Parusel, R. Schamschule, D. Piorun, K. Rechthaler, A. Puchala, D. Rasala, K. Rotkiewicz, and G. Kohler. J. Mol. Struct. (Theochem.), **63,** 419, (1997).
16. K. Rotkiewicz, W. Rettig, G. Kohler, K. Rechthaler, A. Danel, and D. Grabka. Chem. Phys. **307**, 45 (2004).
17. Y. Tao, E. Balasubramaniam, A. Danel, and P. Tomasik. Appl. Phys. Lett. **77**, 933 (2000).
18. E. Balasubramaniam, Y. Tao, A. Danel, and P. Tomasik. Chem. Mater. **12**, 2788 (2000).
19. D. Grabka, W. Boszezyk, Y. Stepanenko, S. Styrez, M. Kubik, K. Rotkiewicz, and A. Danel. J. Photochem. Photobiol, A: Chem. **180**, 80 (2006).
20. D. Piorun, J. Parusel, K. Rechthaler, K. Rotkiewicz, and G. Kohler. J. Photochem. Photobiol. A: Chem. **129**, 33 (1999).
21. H. Hoehn and T. Denzel. US Patent 3-840-546. 1974. Chem. Abstr. **82**, 43413 (1975).
22. Y. Sanghvi, S. Larson, R. Willis, R. Robins, and G. Revankar. J. Med. Chem. **32**, 945 (1989).
23. K. Joshi, K. Dubey, and A. Dandia. Pharmazie, **36**(5), 336 (1981).
24. R. Robins, L. Holum, and F. Furcht. J. Org. Chem. **21**, 833 (1956).
25. M. Jachak, A. Avhale, C. Tantak, R. Toche, C.Reidlinger, and W. Stadlbauer. J. Heterocycl. Chem. **42**, 311 (2005).
26. M. Jachak, A. Avhale, V. Medhane, and R. Toche. J. Heterocycl. Chem. **43**, 1169 (2006).
27. M. Jachak, A. Avhale, R. Toche, and R. Sabnis. J. Heterocycl. Chem. **44**, 343 (2007).
28. R. Toche, B. Ghotekar, M. Kazi, D. Kendre, and M. Jachak. Tetrahedron, **63**, 8157 (2007).
29. M. Jachak, D. Kendre, A. Avhale, R. Toche, and R. Sabnis. J. Heterocycl. Chem. **44**, 1525 (2007).
30. D. Kendre, R. Toche, and M. Jachak. Tetrahedron, **63**, 11000, (2007).
31. R. Toche, B. Ghotekar, D. Kendre, M. Kazi, and M. Jachak. J. Heterocycl. Chem. **45**, 1117 (2008).
32. E. Badawey and T. Kappe. Eur. J. Med. Chem. **30**, 327 (1995).

© 2008 NRC Canada

X-ray and high-resolution ^{1}H and ^{13}C NMR of smooth muscle relaxant sesquiterpene lactones

Marie-Rose Van Calsteren, Christopher K. Jankowski, Ricardo Reyes-Chilpa, Manuel Jiménez-Estrada, Maria G. Campos, Abraham Zarazua-Lozada, Martha Oropeza, and Denis Lesage

Abstract: The structure and stereochemistry of four sesquiterpene lactones, budlein A (**1**), zaluzanin A (**2**), and glaucolides D (**3a**) and E (**3b**), isolated from Mexican *Asteraceae* species, for which only partial NMR data could be found in the literature, were determined. A combination of 1D and 2D high-resolution NMR experiments, such as DEPT, COSY, NOESY, ROESY, HMQC, HSQC, and HMBC, were used to completely assign the ^{1}H and ^{13}C spectra. The crystal structures of zaluzanin A (**2**) and glaucolide E (**3b**) were also determined. Glaucolides D and E have been previously reported to relax KCl-induced contraction in rat uterine smooth muscle; therefore, the effects of zaluzanin A and budlein A were examined in the same model. It was found that both compounds can relax contraction induced by KCl, but only zaluzanin A induced relaxation when contraction was induced with oxytocin. The preliminary biological test results according to these profiles are reported in this paper.

Key words: NMR data, X-ray data, sesquiterpene lactones, Mexican *Asteraceae*, smooth muscle relaxant.

Résumé : On a déterminé la structure et la stéréochimie de quatre lactones sesquiterpéniques, la budléine A (**1**), la zaluzanine A (**2**), et les glaucolides D (**3a**) et E (**3b**), isolées d'espèces mexicaines d'*Asteraceae*, pour lesquelles seulement des données de RMN partielles ont pu être trouvées dans la littérature. On a utilisé une combinaison d'expériences de RMN à haute résolution 1D et 2D, telles que DEPT, COSY, NOESY, ROESY, HMQC, HSQC et HMBC, pour assigner complètement les spectres de ^{1}H et ^{13}C. On a aussi déterminé la structure cristalline de la zaluzanine A (**2**) et du glaucolide E (**3b**). Précédemment, on avait rapporté que les glaucolides D et E relaxent la contraction induite par le KCl dans le muscle utérin lisse de rate; en conséquence, on a examiné les effets de la zaluzanine A et de la budléine A dans le même modèle. On a trouvé que les deux composés peuvent relaxer la contraction induite par le KCl, mais que seule la zaluzanine A induit la relaxation quand la contraction est induite avec l'ocytocine. On présente les résultats préliminaires des tests biologiques appropriés dans cet article.

Mots-clés : données de RMN, données de rayons-X, lactones sesquiterpéniques, *Asteraceae* du Mexique, relaxant du muscle lisse.

Introduction

Asteraceae species contain sesquiterpene lactones with interesting biological properties (1); however, complete structural studies and stereochemistry are needed to understand how they act. In this study, we isolated four sesquiterpenes, budlein A (**1**), zaluzanin A (**2**), as well as the glaucolides D (**3a**) and E (**3b**), for which only partial NMR data could be found in the literature (Chart 1). The studied compounds were isolated from *Asteraceae* species from Mexico. Concerning the biological properties of these compounds, it has been described that budlein A is cytotoxic against human tumor cells L-929 and Hep-2, and it also shows antimicrobial (2) and mild fungistatic properties (3). Budlein A and zaluzanin A reduced in vitro human sperm motility by 60% and 16%, respectively, 15 min after incubation, but did not affect sperm viability. These two compounds also inactivated the thiol groups on the outer membrane of sperm cells

Received 5 March 2008. Accepted 14 June 2008. Published on the NRC Research Press Web site at canjchem.nrc.ca on 7 November 2008.

M.-R. Van Calsteren.[1] Centre de recherche et de développement sur les aliments, Agriculture et Agroalimentaire Canada, Saint-Hyacinthe, QC J2S 8E3, Canada.
C.K. Jankowski. Département de chimie et biochimie, Université de Moncton, Moncton, NB EIA 3E9, Canada.
R. Reyes-Chilpa and M. Jiménez-Estrada. Instituto de Química, Universidad Nacional Autónoma de México, Ciudad Universitaria, México D.F. 04510, México.
M.G. Campos, A. Zarazua-Lozada, and M. Oropeza. Unidad de Investigación en Farmacología, Centro Médico Nacional Siglo XXI, Instituto Mexicano del Seguro Social, Avenida Cuauhtemoc 330, México D.F. 06725, México.
D. Lesage. Synthèse, Structure et Fonction de Molécules Bioactives, groupe de spectrométrie de masse, UMR 7613, Université Pierre et Marie Curie–Paris 6, CNRS, 75005 Paris, France.

[1]Corresponding author (e-mail: vancalsteren@agr.gc.ca).

 doi:10.1139/V08-158 © 2008 NRC Canada

Table 1. ^{1}H NMR data ($CDCl_3$) for budlein A **1**.

Proton	δ	Multiplicity[a]	Coupling constants (Hz)	Experimental	Calculated from MM+	Dihedral angles (°) from MM+
H_2	5.682	s				
H_5	6.222	dt	$^3J_{5,6}$	4.2	5.0	–121
			$^4J_{5,15}$	–1.7	–1.1	–68, 172[b]
H_6	5.380	m	$^3J_{6,7}$	4.4	5.1	–126
H_7	3.759	m	$^3J_{7,8}$	2.2	1.9	–103
			$^4J_{7,13a}$	–2.6	–1.8	–123[c]
H_8	5.269	m	$^3J_{8,9\alpha}$	3.5	2.0	59
$H_{9\alpha}$	2.318	dd	$^2J_{9\alpha,9\beta}$	–15.2		
$H_{9\beta}$	2.546	dd	$^3J_{8,9\beta}$	5.6	4.3	–57
H_{13a}	6.369	d	$^2J_{13a,13b}$	<1		
H_{13b}	5.707	d	$^4J_{7,13b}$	–2.4	–1.8	–123[c]
H_{14} (3H)	1.494	s				
H_{15} (2H)	4.409	t	$^5J_{6,15}$	1.9		
$H_{3'}$	6.118	qq	$^3J_{3',3'\text{-Me}}$	7.3	5.9	–151, –31, 88
$H_{2'\text{-Me}}$ (3H)	1.799	quintet	$^4J_{3',2'\text{-Me}}$	–1.5	–1.0	–89, 30, 150[d]
$H_{3'\text{-Me}}$ (3H)	1.936	dq	$^5J_{2'\text{-Me},3'\text{-Me}}$	1.5		

[a]Multiplicity: s, singlet; d, doublet; t, triplet; m, multiplet; br, broad.
[b]H_{15}–C_{15}–C_4–C_3.
[c]H_7–C_7–C_{11}–C_{12}.
[d]$H_{2'\text{-Me}}$–$C_{2'\text{-Me}}$–$C_{2'}$–$C_{1'}$.

Chart 1. Chemical structures.

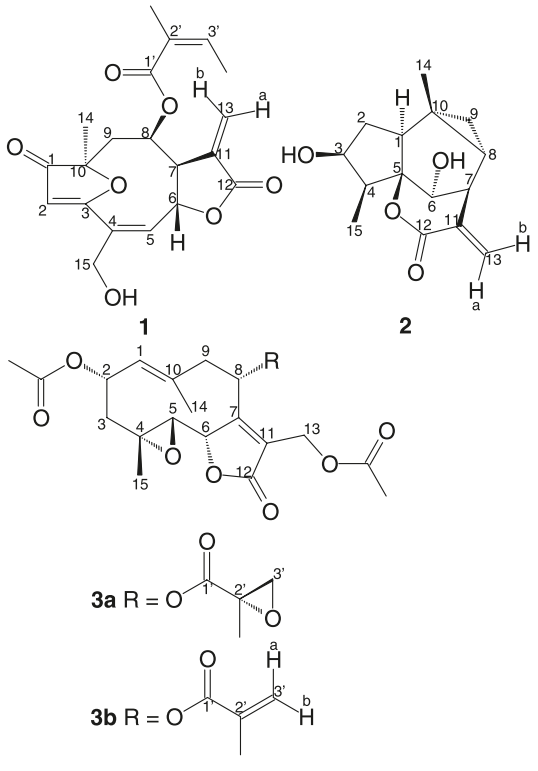

and have been proposed as potential male contraceptives (4). Glaucolides D and E are able to relax rat smooth muscle; the latter compound proved to be more potent than the former relaxing KCl- or noradrenaline-induced contraction in aorta and KCl-induced contraction in uterus (5).

The furanoheliangolide budlein A (**1**) was obtained from *Viguiera buddleiiformis* (DC.) Hemsl. This species is a shrub 1–3 m in height with yellow flowers, purplish stems, and whitened leaves beneath. It grows on rocky canyon slopes, grassy openings among shrubs and small trees in tropical deciduous, and oak forests or xerophytic vegetation at an altitude of 1800–2500 m in the Sierra Volcánica Transversal. It is known as "cerote" in the State of Hidalgo (6–8).

The guainolide zaluzanin A (**2**) was isolated from *Zaluzania augusta* (Lag.) Sch. Bip., a perennial shrub up to 2–5 m in height with yellow flowers. It grows in the southern part of the Central Plateau of Mexico. It is locally known as "Limpia tunas" and "Caxtidán" in the State of Querétaro and "Cenicilla" in the State of México (6–8). The leaves and roots water infusion is used as an abortive by peasants of the State of Querétaro, Mexico (9). There is some ambiguity in the stereochemistry of **2** as determined by NMR (10); for this reason, a detailed analysis of ^{1}H–^{1}H was performed, and other evidence was provided by the HMBC experiment. The structure of **2** was corroborated by means of its X-ray diffraction pattern.

The glaucolides D (**3a**) and E (**3b**) were isolated from *Vernonia liatroides* DC., a perennial shrub up to 3 m in height with purple or white flowers. It grows with abundance in openings in oak and pine forest at altitudes of 1000–2300 m in the northern and central parts of Mexico. It is locally known as "Tlamalacatlacotli" and "Vara de San Miguel". In the State of Michoacan, it is a medicinal plant. A water infusion of leaves and branches is prepared as a remedy against dysentery. The mashed leaves are applied to regenerate hair. It produces abundant pollen and nectar;

© 2008 NRC Canada

Table 2. ^{13}C NMR data ($CDCl_3$) for budlein A **1**, zaluzanin A **2**, and glaucolides D **3a** and E **3b**.

	1		**2**		**3a**		**3b**	
Carbon	δ	Multiplicity[a]	δ	Multiplicity[a]	δ	Multiplicity[a]	δ	Multiplicity[a]
C_1	205.01	s	42.51	d	127.45	d	127.14	d
C_2	104.92	d	37.02	t	68.22	d	68.29	d
C_3	182.32	s	72.61	d	42.38	t	42.46	t
C_4	135.66[b]	s	41.09	d	59.56	s	59.54	s
C_5	134.64	d	92.94	s	66.23	d	66.36	d
C_6	75.25[c]	d	66.38	d	82.02	d	82.18	d
C_7	48.36	d	42.02	d	162.44	s	164.13	s
C_8	74.02[c]	d	24.35	d	70.16	d	69.54	d
C_9	42.15	t	22.58	t	45.84	br t	45.73	br t
C_{10}	87.85	s	14.65	s	133.52	s	134.01	s
C_{11}	138.50[b]	s	140.67	s	129.30	s	128.42	s
C_{12}	168.76	s	168[d]	s	170.17	s	170.14[e]	s
C_{13}	123.86	t	123.93	t	56.31	t	56.16	t
C_{14}	21.30[f]	q	23.35	q	17.90	br q	17.92	br q
C_{15}	62.61	t	6.72	q	17.58	q	17.62	q
	Ang[g]				Emac[g]		Mac[g]	
$C_{1'}$	165.74	s			169.94	s	165.98	s
$C_{2'}$	126.28	s			53.39	s	135.07	s
$C_{3'}$	141.63	d			53.04	t	127.42	t
$C_{2'\text{-Me}}$	20.06[f]	q			17.11	q	18.11	q
$C_{3'\text{-Me}}$	15.82	q						
2-Ac								
CO					170.25	s	170.29[e]	s
CH_3					21.02	q	21.04	q
13-Ac								
CO					170.35	s	170.41[e]	s
CH_3					20.80	q	20.75	q

[a]Multiplicity (determined by the DEPT experiment): s, singlet (quaternary); d, doublet (tertiary); t, triplet (secondary); q, quartet (primary); br, broad.
[b]Assignments reversed in ref. (12).
[c]Assignments reversed in ref. (12).
[d]From HMBC.
[e]Assignments are interchangeable.
[f]Assignments reversed in ref. (13).
[g]Ang, angelate; Emac, epoxymethacrylate; Mac, methacrylate.

therefore, it is important for local apiculture. The leaves can be consumed by cattle (11). The structure of **3b** was corroborated by means of its X-ray diffraction pattern.

We have previously reported that glaucolides D and E, sesquiterpene γ-lactones lacking an exocyclic methylene double bond, can relax rat uterine smooth muscle contraction induced by KCl; this property was attributed to the existence of alternative alkylating sites such as C_{10} provided by the germacra-1(10),4-diene-4-epoxide skeleton (5). In this work, the effects of sesquiterpene lactones bearing an exocyclic methylene double bond in the γ-lactone (budlein A) and δ-lactone (zaluzanin A) moieties were examined using the same model.

Results and discussion

Budlein A

The ^1H NMR spectrum (Table 1) of **1** showed, among others, the following signals: a pair of low-field doublets at δ 6.37 and 5.71, characteristic of a γ-lactone conjugated with an exocyclic methylene group; a doublet of triplets centered at δ 6.22 for the vinyl hydrogen H_5; a quartet of quartets at δ 6.12, a chemical shift typical of the vinyl proton of angelic acid; two complex signals centered at δ 5.38 and 5.27 (H_6 and H_8); a triplet at δ 4.41 (2H) assigned to the $–CH_2–O–$ protons of an allylic primary alcohol; a signal corresponding to H_7 (δ 3.76); signals for the vinyl methyl groups (δ 1.94 and 1.80) of the angelate ester moiety; a singlet at δ 1.49 for the C_{14} methyl group. The stereochemistry of **1** at C_6 and C_8 was established from the dihedral angles (Table 1) calculated from the coupling constants. The calculated dihedral angle of –122° at the C_6–C_7 bond indicated a β-configuration for H_6 or a *trans*-lactone closure. The configuration of the oxygen function at C_8 was found to be β-oriented, since the coupling constants between the pairs H_7–H_8, H_8–$H_{9\alpha}$, and H_8–$H_{9\beta}$ have small values. This is in agreement with the required dihedral angles (Table 1). The ROESY spectrum displayed through-space correlations be-

© 2008 NRC Canada

Table 3. ^{1}H NMR data ($CDCl_3$) for zaluzanin A **2**.

			Coupling constants (Hz)					
				Experimental	Calculated		Dihedral angles (°)	
Proton	δ	Multiplicity[a]			from MM+	from X-ray	from MM+	from X-ray
H_1	2.168	dd	$^3J_{1,2\alpha}$	9.0	5.6	6.1	–45	–42
			$^3J_{1,2\beta}$	13.3	11.8	11.4	–166	–162
$H_{2\alpha}$	2.670	dddd	$^3J_{2\alpha,3}$	7.8	9.7	9.6	11	14
			$^5J_{2\alpha,6}$	0.9				
$H_{2\beta}$	1.828	td	$^2J_{2\alpha,2\beta}$	–13.6				
H_3	4.195	m	$^3J_{2\beta,3}$	4.2	5.0	5.6	132	135
H_4	1.970	quintet d	$^3J_{3,4}$	7.3	5.9	6.6	26	20
H_6	3.945	br t	$^3J_{6,7}$	2.8	2.8	2.0	64	71
			$^4J_{6,8}$	1.0	3.0	2.8	–171, 167[b]	–166, 164[b]
H_7	3.147	br d	$^3J_{7,8}$	1.0	1.9	1.3	–67	–73
H_8	0.574	ddt	$^3J_{8,9\alpha}$	6.2	7.8	9.4	139	148
$H_{9\alpha}$	0.855	dd	$^2J_{9\alpha,9\beta}$	–4.5				
$H_{9\beta}$	0.633	dd	$^3J_{8,9\beta}$	9.7	10.3	10.4	–3	3
H_{13a}	6.153	d	$^2J_{13a,13b}$	1.1				
H_{13b}	5.544	dd	$^4J_{7,13b}$	–0.5	–0.3	–0.2	–161[c]	–165[c]
H_{14} (3H)	1.061	s						
H_{15} (3H)	0.993	d	$^3J_{4,15}$	7.3	6.5	6.4	–61, 58, 178	–62, 58, 178
3-OH	1.98	br d	$^3J_{3,3\text{-OH}}$	10.7				
6-OH	1.944	d	$^3J_{6,6\text{-OH}}$	3.5				

[a]Multiplicity: s, singlet; d, doublet; t, triplet; m, multiplet; br, broad.
[b]H_6–C_6–C_7–C_8 and H_8–C_8–C_7–C_6.
[c]H_7–C_7–C_{11}–C_{12}.

tween the following noncoupled nuclei: H_6–$H_{9\beta}$, H_7–$H_{9\alpha}$, H_8–H_{13b}, $H_{9\alpha}$–H_{14}, and $H_{9\beta}$–H_{14}. The ^{13}C NMR spectrum (Table 2) was essentially identical to that reported previously (12, 13), with some re-assignments based on direct and long-range ^{1}H–^{13}C correlations. The NMR data are in agreement with the stereochemistry deduced for goyazensolide from X-ray studies (14), this compound is the C_8 α-methacrylate epimer of budlein A.

Zaluzanin A

The ^{1}H NMR spectrum of **2** exhibited the following signals (Table 3): two low-field signals at δ 6.15 and 5.54, corresponding to geminal olefinic protons; two broad signals, a multiplet centered at δ 4.20 and a triplet at δ 3.94, attributed to protons attached to carbons bearing hydroxyl groups; a broad doublet at δ 3.15 assigned to an allylic proton; a singlet at δ 1.06 and a doublet centered at δ 0.99 ascribed to a tertiary and a secondary methyl group, respectively; three protons, which exhibit signals to lower frequency, two doublets of doublets at δ 0.86 and 0.63 and a doublet of doublets of triplets at δ 0.57, indicative of a cyclopropane ring. Important differences can be noted between the ^{1}H (Table 3) and ^{13}C (Table 2) NMR data compared with reported values (10), such as reversed assignments for H_8 and $H_{9\beta}$ as well as C_4 and C_7. Biogenetic considerations suggest that the C_7 side chain possesses a β-configuration. Therefore, O_5 involved in the six-membered lactone is also β-oriented, because it accepts a hydrogen bond from 3-OH, as indicated by the large coupling constant between H_3 and 3-OH, compared with $J_{6,6\text{-OH}}$, which shows an averaged value. The long-range couplings exhibited by H_6 to both $H_{2\alpha}$ and H_8 indicate that it possesses the β-configuration, the hydroxyl group in position 6 being α-oriented. In the HMBC spectrum, H_6 shows a long-range coupling to C_8 but not to C_{11}, a further indication of its β-orientation. The NMR data are in agreement with the stereochemistry deduced from X-ray studies of this compound (Fig. 1). Previous correlations have been done using X-ray stereodiagrams of zaluzanin B and a diacetylated dibromated derivative of zaluzanin A (10).

Fig. 1. Crystal structure of zaluzanin A **2**.

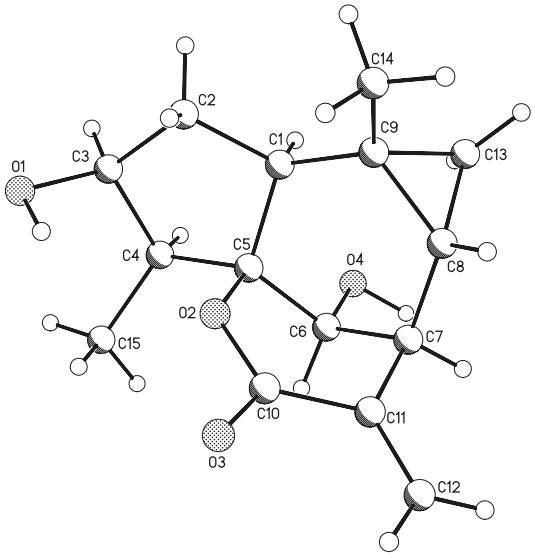

© 2008 NRC Canada

Table 4. ^{1}H NMR data ($CDCl_3$) for glaucolide D **3a**.

Proton	δ	Multiplicity[a]	Coupling constants (Hz)	Experimental	Calculated from X-ray	Dihedral angles (°) from X-ray
H_1	5.173	br d	$^3J_{1,2}$	10.3	11.6	–177
H_2	5.574	td	$^3J_{2,3\alpha}$	10.9	10.5	166
$H_{3\alpha}$	1.271	br dd	$^2J_{3\alpha,3\beta}$	–12.4		
$H_{3\beta}$	2.581	dd	$^3J_{2,3\beta}$	6.7	3.5	64
H_5	2.460	d	$^3J_{5,6}$	8.9	8.8	174
H_6	4.758	d	$^5J_{6,13}$	0.9		
H_8	5.036	dd	$^3J_{8,9\alpha}$	10.6	9.2	–145
$H_{9\alpha}$	2.993	br dd	$^2J_{9\alpha,9\beta}$	–12.5		
$H_{9\beta}$	2.568	br d	$^3J_{8,9\beta}$	1.4	1.8	110
H_{13}	4.872	dd	$^2J_{13,13}$	–13.0		
H_{13}	5.033	dd	$^5J_{6,13}$	1.0		
H_{14} (3H)	2.026	s				
H_{15} (3H)	1.369	s				
$H_{3'\,pro\text{-}R}$	3.109	dd	$^4J_{3'R,2'\text{-Me}}$	<1		
$H_{3'\,pro\text{-}S}$	2.803	d	$^2J_{3'R,3'S}$	6.0		
$H_{2'\text{-Me}}$ (3H)	1.554	s				
2-Ac CH_3 (3H)	2.026	s				
13-Ac CH_3 (3H)	2.120	s				

[a]Multiplicity: s, singlet; d, doublet; t, triplet; br, broad.

Glaucolide D

The ^{1}H NMR spectrum (Table 4) of **3a** displayed the following features: a triplet of doublets at δ 5.57 (H_2); a broad doublet at δ 5.17 re-assigned from H_8 (15) to H_1 based on a cross-peak to H_{14}; a doublet of doublets at δ 5.04 re-assigned from H_2 (15) to H_8 based on its couplings to both protons on C_9 and on a cross-peak to H_6; two doublets of doublets at δ 5.03 and 4.87 corresponding to the vinyl methylene group at C_{13} substituted with an acetoxyl function; a doublet at δ 4.76 (H_6); the 13-acetate methyl singlet at δ 2.12; two signals overlapped at δ 2.03 (H_{14} and 2-Ac CH_3); two sharp three-proton singlets at δ 1.55 and 1.37 for two tertiary methyl groups, $H_{2'\text{-Me}}$ and H_{15}, respectively. Protons belonging to the epoxymethacrylate substituent were distinguished based on chemical shifts and two- and four-bond coupling constants (16). The following correlations were observed on the NOESY and ROESY spectra: H_1–H_5, H_1–$H_{9\alpha}$, H_2–H_{15}, $H_{3\alpha}$–H_5, H_6–H_{15}, H_8–H_{14}, H_8–H_{15}. Table 2 reports the ^{13}C NMR data of this compound, which could not be found in the literature. Peaks corresponding to C_9 and C_{14} were broadened, likely due to a conformational exchange on the ^{13}C chemical-shift timescale. The stereochemistry of **3a** is not ambiguous, since it has been determined by X-ray crystallography (17).

Glaucolide E

The ^{1}H NMR spectrum (Table 5) of compound **3b** showed a number of striking similarities to that obtained for **3a**; indeed, the differences could be accounted for on the basis of a methacrylate ester instead of an epoxydized methacrylate ester at C_8: the methacrylate vinyl protons as quintets at δ 6.12 and 5.68; a triplet of doublets at δ 5.59 (H_2); a broad doublet at δ 5.18 re-assigned from H8 (15) to H_1 as for **3a**; doublets of doublets at δ 5.00 and 4.85 for the methylene protons at C_{13}, indicating the same lactone function as in **3a**; a broad doublet at δ 4.84 (H_6); methyl group signals at δ 2.08 for the 13-acetyl methyl group, at δ 2.04 for the C_{14} vinyl methyl and at δ 2.03 for the 2-acetyl methyl; a second vinyl methyl signal at δ 1.93 ($H_{2'\text{-Me}}$); a tertiary methyl singlet (δ 1.39) corresponding to the C_{15} methyl group. Essentially, the same NOEs as those found for **3a** were found on the ROESY spectrum, except that H_2–H_{14} was present and H_2–H_{15} was absent. ^{13}C NMR data for **3b** are reported here for the first time (Table 2). A broadening of the same carbon peaks as in **3a** was observed. This compound must be the precursor of **3a** and would thus have the same stereochemistry. The NMR data are in agreement with the stereochemistry deduced from X-ray studies for this compound (Fig. 2).

Effect of budlein A and zaluzanin A on smooth muscle contraction

Both budlein A (**1**) and zaluzanin A (**2**) relaxed the oxytocin-induced (20 nmol/L) contractile response in rat uterine smooth muscle; however, KCl-induced contraction was relaxed only by zaluzanin A. These data indicate that zaluzanin A, but not budlein A, might exert its relaxant effect through a mechanism related with calcium influx through voltage-operated calcium channels (18), and that both sesquiterpene lactones might have a positive effect on the phosphatidylinositol signaling pathway of the smooth muscle cell (19–21).

Experimental section

Budlein A **1** (MW = 374, $C_{20}H_{22}O_7$) was isolated from *Viguiera buddleiaeformis* as previously described (22). The leaves and stems (10 kg) were extracted twice with ethanol. After evaporating the solvent, an oily residue was obtained,

© 2008 NRC Canada

Table 5. ^{1}H NMR data ($CDCl_3$) for glaucolide E **3b**.

Proton	δ	Multiplicity[a]	Coupling constants (Hz)	Experimental	Calculated from X-ray	Dihedral angles (°) from X-ray
H_1	5.185	br d	$^3J_{1,2}$	10.5	11.1	–167
H_2	5.588	td	$^3J_{2,3\alpha}$	10.8	10.4	165
$H_{3\alpha}$	1.282	br dd	$^2J_{3\alpha,3\beta}$	–12.4		
$H_{3\beta}$	2.591	dd	$^3J_{2,3\beta}$	6.7	6.1	47
H_5	2.477	d	$^3J_{5,6}$	8.8	8.9	170
H_6	4.840	br d	$^5J_{6,13}$	0.8		
H_8	5.019	dd	$^3J_{8,9\alpha}$	10.5	10.7	–157
$H_{9\alpha}$	3.011	br dd	$^2J_{9\alpha,9\beta}$	–12.4		
$H_{9\beta}$	2.677	br d	$^3J_{8,9\beta}$	1.0	1.4	85
H_{13}	4.854	dd	$^2J_{13,13}$	–12.9		
H_{13}	5.003	dd	$^5J_{6,13}$	0.9		
H_{14} (3H)	2.036	d	$^4J_{1,14}$	–1.1	–1.1	–57, 63, 173[b]
H_{15} (3H)	1.390	s				
$H_{3'a}$	6.125	quintet	$^4J_{3'a,2'\text{-Me}}$	–1.2	–1.1	–69, 51, 171[c]
$H_{3'b}$	5.685	quintet	$^2J_{3'a,3'b}$	1.3		
$H_{2'\text{-Me}}$ (3H)	1.931	t	$^4J_{3'b,2'\text{-Me}}$	–1.4	–1.1	–69, 51, 171[c]
2-Ac CH_3 (3H)	2.031	s				
13-Ac CH_3 (3H)	2.078	s				

[a]Multiplicity: s, singlet; d, doublet; t, triplet; br, broad.
[b]H_{14}–C_{14}–C_{10}–C_9.
[c]$H_{2'\text{-Me}}$–$C_{2'\text{-Me}}$–$C_{2'}$–$C_{1'}$.

Fig. 2. Crystal structure of glaucolide E **3b**.

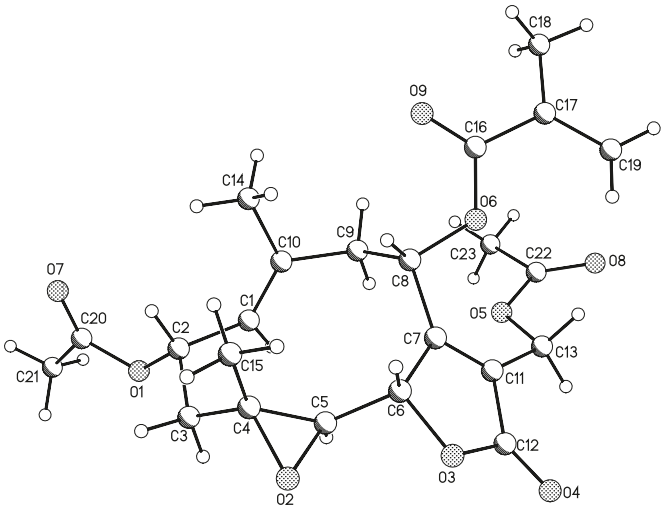

which was dissolved in hot benzene and subjected to column chromatography (alumina). Fractions eluted with $CHCl_3$–acetone (9:1) were concentrated, obtaining an amorphous residue. Recrystallization from acetone – isopropylic ether yielded **1** (3.65 g, mp 106–108 °C).

Zaluzanin A **2** (MW = 264, $C_{15}H_{20}O_4$) was isolated from *Zaluzania augusta* as previously described (23). The aerial parts (1 kg) were extracted twice with ethanol (6 L, 20 h) under reflux. The volume was reduced to 2 L and treated with lead acetate aqueous solution (20 g/2 L) for 2 h at room temperature. The extract was filtrated through Celite and then partitioned with chloroform. The organic layer was concentrated, dissolved in benzene, and subjected to column chromatography (alumina). Fractions eluted with chloroform and ethyl acetate yielded a solid, which was recrystallized with acetone – diethyl ether and then with methanol, obtaining **2** as white crystals (1.2 g, mp 265 °C). X-ray: orthorhombic, space group $P2_12_12_1$, a = 6.7277(5) Å, b = 10.0202(7) Å, c = 19.5724(13) Å, V = 1319.45(16) Å^3, T = 291(2) K, Z = 4, $D_{calcd.}$ = 1.331 g/cm^3, $F(000)$ = 568, λ = 0.71073 Å, μ = 0.095 mm^{-1}, crystal size 0.34 mm × 0.23 mm × 0.16 mm. A total of 10770 reflections were collected for 2.08° < θ < 25.00° and $-8 \le h \le 7$, $-11 \le k \le 11$, $-23 \le l \le 23$. 2312 reflections with $I > 2\sigma(I)$ were used in the refinement. The final R indices were R_1 = 0.0357 and wR_2 = 0.0886 and R indices (all data): R_1 = 0.0401, wR_2 = 0.0906.

Glaucolide D **3a** (MW = 464, $C_{23}H_{28}O_{10}$) and glaucolide E **3b** (MW = 448, $C_{23}H_{28}O_9$) were obtained as previously described from the aerial parts of *Vernonia liatroides* (24). The dried plant material (3 kg) was extracted with hot methanol; while concentrating the extract, **3a** precipitated as a white amorphous solid (mp 186–188 °C). The methanol extract was then partitioned with hexane and $CHCl_3$. This last fraction was subjected to column chromatography (silica gel). Fractions eluted with hexane–EtOAc (6:4) afforded **3b** as white crystals (mp 149–150 °C) from acetone–hexane. X-ray: monoclinic, space group $P2_1$, a = 10.6585(8) Å, b = 8.2373(7) Å, c = 13.2507(11) Å, β = 90.334(2)°, V = 1163.36(16) Å^3, T = 291(2) K, Z = 2, $D_{calcd.}$ = 1.280 g/cm^3, $F(000)$ = 476, λ = 0.710 73 Å, μ = 0.099 mm^{-1}, crystal size 0.46 mm × 0.18 mm × 0.15 mm. A total of 9537 reflections were collected for 1.91° < θ < 25.00° and $-12 \le h \le 12$, $-9 \le k \le 9$, $-15 \le l \le 15$. 4070 reflections with $I > 2\sigma(I)$ were used in the refinement. The final R indices were R_1 = 0.0430 and

© 2008 NRC Canada

wR_2 = 0.0859 and R indices (all data): R_1 = 0.0563, wR_2 = 0.0901.

X-ray crystallography[2]

Data were collected on a Bruker Smart APEX AXS CCD area-detector diffractometer. No absorption correction was applied. The structures were solved by direct methods using SHELXS-97 and refined by full-matrix least squares. All non–hydrogen atoms were refined with anisotropic displacement parameters, the hydrogen atoms coordinates were estimated in riding mode.

NMR spectroscopy

The compounds were dissolved in $CDCl_3$, and TMS was used as an internal standard. High-resolution ^1H (300.3 MHz) and ^{13}C (75.5 MHz) NMR spectra were acquired at 25 °C on a Chemagnetics Infinity 300 spectrometer using a Nalorac *z*-gradient 5 mm inverse broadband $^1H\{^{15}N–^{31}P\}$ probe. A combination of 1D and 2D high-resolution NMR experiments were used to assign the ^1H and ^{13}C spectra. Connectivities between protons were obtained using 2D gradient-selected COSY (25). The 2D phase-sensitive NOESY (26) and ROESY (27) experiments were performed with a mixing time of 600 ms. The 1D ^{13}C NMR spectra were recorded with WALTZ proton decoupling (28). The multiplicity of the carbon signals was established using the 1D DEPT experiment (29) with a reading pulse of 135° and an evolution time of 3.5 ms. The 2D gradient-selected magnitude HMQC (30) and phase-sensitive HSQC (31) spectra were acquired with 3.5 and 1.7 ms evolution times, respectively, and MPF9 (32) carbon decoupling during acquisition. The 2D gradient-selected magnitude HMBC (33) was run without carbon decoupling with one-bond and long-range evolution times of 3.5 and 80 ms, respectively. Accurate ^1H chemical shifts and coupling constants were obtained by spectral simulation using the program gNMR from IvorySoft. Conformations were estimated from three-bond vicinal $^1H–^1H$ coupling constants and substituent electronegativities (34), from four-bond long-range $^1H–^1H$ coupling constants (35), and from three- and four-bond vinyl–allylic $^1H–^1H$ coupling constants (36), taking signs into account.

Molecular modeling

Geometry optimization was performed with the program HyperChem 7.03 Professional from Hypercube using the force field Hyper MM+, starting from the modified crystal structure of goyazenzolide A (14) for **1** and from a built structure for **2**.

Uterine smooth muscle assays

Relaxant activity of budlein A and zaluzanin A was evaluated on the contractile response to 60 mmol/L KCl and oxytocin (20 nmol/L) as previously described (5).

Acknowledgments

Part of this research was financed by the grant DGAPA-UNAM IN 219305–2. The authors are grateful to Simón Hernández-Ortega for X-ray recordings.

References

1. F.C. Seaman. Bot. Rev. **48**, 121 (1982).
2. P. Roche, N. Rosas, J. Taboada, M. González Diddí, and J. Tellez. Rev. Latinoam. Quím. **10**, 145 (1979).
3. R. Reyes-Chilpa, R.I. Quiroz-Vázquez, M. Jiménez-Estrada, A. Navarro-Ocaña, and J. Cassani-Hernández. J. Trop. For. Prod. **3**, 110 (1997).
4. R.L. Huacuja, A. Carranco, S.A. Guzmán, and C. Guerrero. Adv. Contracept. Deliv. Syst. **9**, 97 (1993).
5. M. Campos, T. Oropeza, H. Ponce, J. Fernández, M. Jiménez-Estrada, H. Torres, and R. Reyes-Chilpa. Biol. Pharm. Bull. **26**, 112 (2003).
6. R. McVaugh. Flora Novo-Galiciana: A descriptive account of the vascular plants of Western Mexico. Vol. 12. The University of Michigan Press. Ann Arbor. 1984. pp. 1044–1045.
7. C. Reiche. Flora excursoria en el Valle Central de México. Editorial Porrúa. México. 1977. pp. 196–197.
8. M. Martínez. Catalogo de nombres vulgares y científicos de plantas mexicanas. Fondo de Cultura Económica. México. 1994. p. 179.
9. A. Aguilar, J.R. Camacho, S. Chino, P. Jácquez, and M.E. López. Plantas medicinales del Herbario del IMSS: Cuadros básicos por aparatos y sistemas del cuerpo humano. Instituto Mexicano del Seguro Social, México. 1994. 218 pp.
10. R.A. Toscano, J.L. Nava, C. Guerrero, A. Guzmán, and E. Díaz. J. Chem. Crystallogr. **27**, 457 (1997).
11. J. Rzedowski and G.C. Rzedowski. Flora del Bajío y de regiones adyacentes. Fascículo 38. Instituto de Ecología, A.C., Centro Regional del Bajío, Pátzcuaro. 1995.
12. G. Delgado, A. Romo de Vivar, and W. Herz. Phytochemistry, **21**, 1305 (1982).
13. N. Ohno, J. Gershenzon, P. Neuman, and T.J. Mabry. Phytochemistry, **20**, 2393 (1981).
14. W. Herz and V.L. Goedken. J. Org. Chem. **47**, 2798 (1982).
15. M. Betkouski, T.J. Mabry, I.F. Taylor Jr., and W.H. Watson. Rev. Latinoam. Quím. **6**, 191 (1975).
16. P. Sohár. Nuclear magnetic resonance spectroscopy. Vol. II. CRC Press, Boca Raton, Fla., USA. 1981. p. 15.
17. I.F. Taylor, Jr., W.H. Watson, M. Betkouski, W.G. Padolina, and T.J. Mabry. Acta Crystallogr. Sect. B, **32**, 107 (1976).
18. T. Amédée, C. Mironneau, and J. Mironneau. Br. J. Pharmacol. **88**, 873 (1986).
19. M. Phillipe and E.K. Chien. J. Endocrinol. **146**, 485 (1995).
20. S. Arnaudeau, N. Lepretre, and J. Mironneau. Am. J. Obstet. Gynecol. **171**, 491 (1994).
21. S. Batra. Eur. J. Pharmacol. **120**, 57 (1986).
22. A. Romo de Vivar, C. Guerrero, E. Díaz, E.A. Bratoeff, and L. Jiménez. Phytochemistry, **15**, 525 (1976).
23. J. Romo, A.R. de Vivar, and P.J. Nathan. Tetrahedron, **23**, 29 (1967).

[2] Supplementary data for this article are available on the journal Web site (canjchem.nrc.ca) or may be purchased from the Depository of Unpublished Data, Document Delivery, CISTI, National Research Council Canada, Ottawa, ON K1A 0R6, Canada. DUD 3848. For more information on obtaining material, refer to cisti-icist.nrc-cnrc.gc.ca/cms/unpub_e.shtml. CCDC 699880 and 699881 contain the crystallographic data for this manuscript. These data can be obtained, free of charge, via www.ccdc.cam.ac.uk/conts/retrieving.html (Or from the Cambridge Crystallographic Data Centre, 12 Union Road, Cambridge CB2 1EZ, UK; fax +44 1223 336033; or deposit@ccdc.cam.ac.uk).

© 2008 NRC Canada

24. J.E. Maldonado, R. Martínez, and V.M. Martínez. Rev. Latinoam. Quím. **11**, 58 (1980).
25. M. von Kienlin, C.T.W. Moonen, A. van den Toorn, and P.C.M. van Zijl. J. Magn. Reson. **93**, 423 (1991).
26. G. Bodenhausen, H. Kogler, and R.R. Ernst. J. Magn. Reson. **58**, 370 (1984).
27. A. Bax and D.G. Davis. J. Magn. Reson. **63**, 207 (1985).
28. A.J. Shaka, J. Keeler, and R. Freeman. J. Magn. Reson. **53**, 313 (1983).
29. D.M. Doddrell, D.T. Pegg, and M.R. Bendall. J. Magn. Reson. **48**, 323 (1982).
30. R.E. Hurd and B.K. John. J. Magn. Reson. **91**, 648 (1991).
31. J. Ruiz-Cabello, G.W. Vuister, C.T.W. Moonen, P. van Gelderen, J.S. Cohen, and P.C.M. van Zijl. J. Magn. Reson. **100**, 282 (1992).
32. T. Fujiwara, T. Anai, N. Kurihara, and K. Nagayama. J. Magn. Reson., Ser. A, **104**, 103 (1993).
33. W. Willker, D. Leibfritz, R. Kerssebaum, and W. Bermel. Magn. Reson. Chem. **31**, 287 (1993).
34. C.A.G. Haasnoot, F.A.A.M. de Leeuw, and C. Altona. Tetrahedron, **36**, 2783 (1980).
35. F. Bystrov and A.U. Stepanyants. J. Mol. Spectrosc. **21**, 241 (1966).
36. E.W. Garbisch. J. Am. Chem. Soc. **86**, 5561 (1964).

© 2008 NRC Canada

Control of DNA incorporation into nanoparticles with poly(L-lysine) multilayers

Annie C. Dorris, Kimberly L. Douglas, Maryam Tabrizian, and Christopher J. Barrett

Abstract: Nanoparticles coated with DNA and poly(L-lysine) (PLL) were prepared using a layer-by-layer assembly technique under various solution conditions. Both the level of DNA loading into the materials, the rate and the extent of DNA released from films upon degradation were controlled by varying the pH of polyelectrolyte assembly solutions. To determine optimal conditions for DNA loading, analogous films assembled on flat surfaces were prepared under various pH conditions. Using UV–vis spectroscopy and thin-film ellipsometry, it was found that the extent of DNA incorporation could be varied by more than a factor of two, and that the highest loading was obtained for films built using a combination of DNA and poly(L-lysine) solutions of pH = 4 and pH = 7, respectively. The layers coated onto the silica nanoparticles permitted the surface charge to be characterized by zeta potential electrophoresis. Furthermore, the acid–base dissociation constant measured for PLL on the outermost layer of the DNA/PLL film showed that the pK_a of PLL can be shifted by more than three units. Film degradability was investigated via the exposure of films assembled under different pH conditions to α-chymotrypsin. The fraction of DNA released from degraded films can also be increased by a factor of three when films are built under conditions of pH = 4 for the DNA solution. The resultant effect on the transfection ability of pEGFP-N1/PLL coated particles was then measured, and results suggest that the control achieved over the bulk film properties also extends to a strong influence on cell uptake and transfection.

Key words: polyelectrolyte multilayer, DNA incorporation, enzymatic degradation, nanoparticles, gene therapy.

Résumé : Des nanoparticules enrobées d'ADN et de poly(L-lysine) ont été preparées sous différentes conditions par la technique d'assemblage de multicouches. Le degré d'incorporation d'ADN dans le matériau ainsi que la vitesse et la quantité d'ADN libérée du film, préalablement soumis à une degradation enzymatique, peuvent être contrôlés par la variation du pH des solutions de polyélectrolytes utilisés lors de l'assemblage. Des films analogues assemblés sur des surfaces planes ont aussi été préparés sous des combinaisons de pH différentes afin de caractériser par ellipsométrie et spectroscopie UV–vis les conditions d'incorporation d'ADN optimales. Il a été démontré que l'incorporation d'ADN peut être multilplié par un facteur supérieur à deux et que son incorporation est maximale lorsque l'assemblage d'ADN et de poly(L-lysine) s'effectue à des pH respectifs de 4 et 7. Afin de permettre la caractérisation des charges de surface par electrophorèse du potentiel zeta, des multicouches ont été deposées sur des nanoparticules de silica. La mesure de la constante de dissociation acide-base du poly(L-lysine), formant la couche terminale des films d'ADN/poly(L-lysine), a démontrée que la valeur de pKa du polymère peut varier de trois unités. L'étude de dégradation des films par l'enzyme α-chymotrypsin a aussi demontrée que la fraction d'ADN libérée des films peut être augmentée d'un facteur de trois lorsque les films sont construits à partir de la solution d'ADN à pH 4. Finalement, les résultats de l'étude sur la capacité de transfection des particules enrobées de pEGFP/poly(L-lysine) suggèrent que le contrôle obtenu sur les propriétés du film d'origine influence fortement l'ingestion cellulaire et la transfection.

Mots-clés : multicouches de polyélectrolytes, incorporation d'ADN, dégradation enzymatique, nanoparticles, thérapie génique.

Introduction

Gene delivery systems based on polymer nanoparticles have received much recent attention due to improved therapeutic gene transfection and the potential to tune properties chemically. Inter-polyelectrolyte complexes (IPECs) formed between DNA and polycations, such as PEI (1), poly(L-lysine) (PLL) (2), and chitosan (3), are now widely used as

Received 18 July 2008. Accepted 18 September 2008. Published on the NRC Research Press Web site at canjchem.nrc.ca on 12 November 2008.

A.C. Dorris and C.J. Barrett.[1] Department of Chemistry, McGill University, 801 Sherbrooke Street West, Montreal, QC H3A 2K6, Canada.
K.L. Douglas and M. Tabrizian. Department of Biomedical Engineering, McGill University, 3775 University Street, Montreal, QC H3A 2B4, Canada.

[1]Corresponding author (e-mail: christopher.barrett@mcgill.ca).

 doi:10.1139/V08-162 © 2008 NRC Canada

simple and effective vectors for the delivery of DNA into cells. In recent years, the use of polyelectrolyte multilayers (PEMs) in many biomedical applications has generated great interest, in particular as drug delivery systems, as they offer more precise control over structure and release properties (4). Layer-by-layer (l-b-l) deposition method is especially convenient for incorporating natural polymers into thin films and nanostructures. This self-assembly technique relies on the sequential adsorption of oppositely charged polymers onto a charged substrate or particle (5); film thickness, layer interpenetration, and water content can be tailored quite precisely by varying several parameters, such as the number of adsorption cycles, the pH, and the ionic strength of the assembly baths. The method allows for gentle ionic adhesion permitting subsequent facile release and good retention of the desired biological activity.

Most recently, the incorporation of DNA into multilayered films has been achieved (4, 6–18), and has been successfully applied to both targeted release (9, 10, 12) and as sensor devices (6, 7). Trubetskoy et al. in particular have reported coating poly(L-lysine) (PLL) and succinylated PLL on a condensed DNA core using the l-b-l method (13). Following their demonstration that these layered structures could be used as non-viral gene delivery vectors, several groups performed further studies on these potential vectors (10, 14, 19–22). Since DNA transport across the cell membrane is a fundamental requirement for successful gene delivery, localized delivery and controlled released of DNA incorporated into PLL multilayered films have been one of the most investigated systems (9, 10). Viral vehicles have also been used previously to carry DNA, but these approaches suffer limitations, such as high cost, toxicity, potential infection, and limited DNA carrying capacity, leading to interest in the development of non-viral gene vectors. Cationic polymers including PEI and PLL appear most promising because they can transport DNA efficiently across the cell membrane (2, 23–26). PLL especially has the significant advantage of offering the possibility of covalently attaching target ligands to the polymer backbone so that receptor-mediated uptake can be localized. In addition to the complex formation between DNA and the polycation, the layer-by-layer fabrication procedure offers a good way to incorporate the material in a controlled fashion by varying assembly parameters, such as the pH, the ionic strength, and the number of polymer layers. Lynn and co-workers were the first to study the sustained release of functional DNA from multilayered polyelectrolytes assemblies (15), and to enhance the localized transfection of cells in contact with the DNA multilayered film (4).

A key feature of these films is their variable composition, which influences the final transfection efficiency, the most crucial requirement for a system to be competitive. The ability of a gene to be transfected depends both on the shape and the size of the gene carrier, as well as its capacity to carry a significant amount of DNA to target cells. In addition to the degree of loading, two other factors can also be important to overall transfection efficiency: the conformation and density of the polyelectrolyte in the assembly (related to the water content) and its acid–base equilibria (surface charge). Both of these effects have been studied previously and extensively by our group with synthetic polyelectrolytes (27–31). By varying the l-b-l assembly pH (and to a lesser extent the ionic strength), good control over both morphology and charge could be achieved. Fluctuations by more than two units in the pK_a of weak-acid and weak-base functional groups can also result from pH variations. It is of great interest then to investigate whether it is possible to extend this pH control of parameters to DNA to optimize DNA loading conditions. Salt effects have been investigated previously by Nguyen (32), who studied the adsorption of supercoiled DNA to a natural organic matter-coated silica surface, and by Zhou and co-workers, who studied the extent of DNA incorporation in PLL/DNA films under the influence of different ionic strength assembly solutions (10). They have identified ionic strength conditions that favoured DNA incorporation but they did not investigate the effect of pH of the assembly, which has been shown to play a key role in DNA/dye film formation, and represents a more powerful parameter tool for tuning properties (33). Binding interactions between a cationic polymer and DNA are influenced by the degree of ionization of polyelectrolytes, molecular weight, and type of cationic polymer used; thus, it should be possible to control the degree of ionization of weak polyelectrolytes by varying the pH of the solution. Several groups have reported a pH influence on the formation of polycation/DNA complexes (34, 35), where they observed that under certain pH conditions polyelectrolyte affinities were greater and more favourable to complex stability.

Poly(L-lysine) is a weak polycation with an amino group on each lysine residue. In the pH range where amino groups are protonated (pK_a = 10.5–10.7), these functional groups can undergo strong ionic interaction with DNA. In dilute aqueous solution, PLL can adopt one of three significantly different conformations, depending on pH and temperature (36). Even though below its pK_a, PLL behaves as a random coil at room temperature; it has been found that when PLL is adsorbed on a surface the polymer can adopt a β-sheet structure (37). In this paper, we study the degree of DNA incorporation into PLL/DNA multilayered films submitted to different pH assembly solutions. As necessary for film characterization, such as the extent of polymer adsorption upon exposure to different ionic strength and pH conditions, analogous films were first coated on flat surfaces of silicon with an oxide layer. Multilayered films were then coated on nanoparticles (NPs) of silica from which surface charge analysis could be performed directly over an extended pH range. Degradation of films with different polyelectrolyte composition was then studied, and finally, the resultant transfection properties of films coated on silica nanoparticles were measured, demonstrating how the pH control of physico-chemical properties can be extended to control transfection efficiency by more than a factor of two.

Materials and methods

Materials

Poly(L-lysine) hydrobromide (MW 70 000–90 000) and salmon testes DNA (MW 1 300 000) were purchased from Sigma. MES and TRIS used to prepare buffer solutions, and α-chymotrypsin (from bovine pancreas 60 U/mg) were also obtained from Sigma. Plasmid DNA (pEGPF-N1) was provided by Clontech. Milli-Q water of 18.2 MΩ resistivity was

© 2008 NRC Canada

prepared with a Millipore MiliQ purification system. Silica nanoparticles (Snowtex-zl, 40 wt) with a diameter ranging between 70 and 100 nm were provided by Nissan chemical as a suspension in water.

Preparation of DNA/PLL multilayer films assembled on flat surfaces

Alternate layers of PLL and DNA were assembled onto silicon wafers (Wafernet Inc.) and quartz slides (Canadawide Scientific). Prior to their use, both substrates were first immersed for 30 min in a boiling piranha solution (sulfuric acid – hydrogen peroxide mixture, 1:3 ratio) and then rinsed with large amounts of Milli-Q water. The first layer of PLL was adsorbed onto the two substrates by dipping them for 20 min in a 1 mg/mL PLL solution at fixed pH and ionic strength. Then, the substrates were rinsed for 2 min in two consecutive water baths, whose pH and ionic strength were adjusted to those of the PLL solution. Dipping the substrate in a 1 mg/mL DNA solution allowed the formation of the DNA layer onto the pre-adsorbed PLL layer. Substrates were rinsed two times in water, and the whole deposition process was repeated until the desired number of layers was reached. Films were then rinsed with Milli-Q water and dried under a stream of argon gas. Citric acid (25 mmol/L, pH 4), MES (25 mmol/L, pH 5.5), MES/TRIS (25 mmol/L, 25 mmol/L, pH 7), and TRIS (25 mmol/L, pH 9) buffers were used to adjust pH of solutions. Ionic strength of all solutions was adjusted with NaCl. Ionic contribution of buffers to ionic strength was considered in the calculations.

Film characterization

Film thickness was measured using a Gaertner ellipsometer at 633 nm, and the absorbance of DNA incorporated into films was monitored by means of a UV–vis spectrophotometer (Varian) at the DNA characteristic absorbance wavelength of 260 nm. Both techniques were used to investigate the influence of pH conditions on DNA loading into films. Each reported value was the average of 20 measurements taken at various points on over the film.

Preparation of coated silica nanoparticles

Positively charged silica nanoparticles (0.25 g of suspension) were exposed to 20 ml of 1mg/mL PLL (pH 7, containing 0.1 mol/L NaCl) solution for 1 h. Sonication was performed on particles during the adsorption process. Suspensions were then centrifuged, rinsed twice with water, and re-dispersed in a minimal amount of water. Afterwards, a 20 mL aliquot of 1 mg/mL DNA solution (pH 7, 0.1 mol/L NaCl) was added to the suspension. The mixture was sonicated for 1 h, centrifuged, and washed. The PLL and DNA adsorption steps were repeated until the desired numbers of layers were coated on the particles.

Nanoparticle characterization

Layer adsorption was monitored using zeta potential electrophoresis (Zeta Plus, Brookhaven Instrument Corporation). A small sample of suspension (1 ml) was used for characterization. Samples were redispersed in aqueous solution of different pHs and ionic strengths. Dissociation constants of this particular system were determined by plotting the zeta potential of particles over a wide pH interval.

Film degradation

Enzymatic degradation of PLL/DNA multilayered films was monitored during the hydrolysis of poly(L-lysine) with the endopeptidase α-chymotrypsin. Selected multilayers were exposed to 5 U/mL enzyme solution under physiological pH (50 mmol/L TRIS, pH 7.4) at 37 °C. As controls, films of PLL and DNA were incubated in TRIS buffer alone. At pre-determined times, films were removed from these solutions, rinsed, and dried for analysis. Absorbance of the films on quartz surfaces was recorded with UV spectrophotometry, and the thickness of films deposited on silicon was measured by ellipsometry.

In vitro transfection

Three types of DNA carrier were assembled for transfection studies. Four layers of PEGFP-1 (plasmid DNA) and PLL were coated on silica nanoparticles (snowtex-zl) using the same layer-by-layer technique described previously, but with smaller aliquots of 200 μL, so that vortex mixing and microcentrifugation replaced the sonication and centrifugation steps, respectively. Particle suspensions (50 μg/mL) were prepared from DNA solutions (0.125 mg/mL) at pH values of 4, 7, and 9, while the pH of PLL (0.1 mg/mL) solution was fixed to pH = 7. The ionic strength of the assembly solutions was kept low, and autoclaved water was used for solution preparation. The ρEGFP-N1 plasmid (Clontech, Inc.) encoding for green fluorescent protein (GFP) was used to monitor gene transfer and transgene expression after transfection. The plasmid was amplified and isolated using the Plasmid Maxi Kit (QIAGEN). The concentration of the plasmid was measured by UV absorption at 260 nm and the purity was determined using agarose gel eletrophoresis following linearization using an appropriate enzyme. COS7 cells, African green-monkey kidney cells, were cultured in DMEM (Gibco) supplemented with 10% (*v*/*v*) FBS (ATCC) and 1% penicillin/streptomycin (Gibco) at 37 °C in a humidified 5% CO_2 atmosphere. Cells were sub-cultured prior to confluence using trypsin–EDTA. Cells were seeded in 12-well plates at a density of 6×10^4 cells/well 18 h prior to transfection in DMEM/10% FBS. For transfection, the culture medium was replaced with 600 μL serum-free medium containing either 4, 8, or 16 μL of PLL–pDNA coated nanoparticles. Lipofectamine™ (Invitrogen) was used as a positive control, with each well receiving 4 μL Lipofectamine™ and 1 μg pEGFP–N1. The medium was increased to 1000 μL with DMEM/10%FBS after 4 h, and completely replaced with fresh complete medium after 24 h. Transfection was assessed 72 h post-transfection using flow cytometry. Briefly, cells were removed from the wells using cold EDTA (0.6 mmol/L in PBS), transferred to FACS tubes and analyzed directly using a FACSCalibur. Appropriate controls and gates were used for analysis of the results. All experiments and protocols described here were carried out under ethics guidelines and approval of McGill University.

Results and discussion

Multilayers on flat surfaces

Before the study of DNA loading onto the NPs, analogous films were prepared on flat substrates of Si or quartz where

© 2008 NRC Canada

precise thickness and DNA density measurements could be taken. A thin native oxide layer of 1–2 nm on top of the cleaved Silicon provided a comparable surface chemistry of amorphous SiO_2 to that of the quartz and the silica NPs. Properties of DNA/PLL multilayers were studied in the pH range of 4 to 9; under these conditions, the negatively charged double helix of DNA is stable. At both pH extremes, the secondary structure of DNA can be somewhat perturbed due to base protonation; however, this process is reversible. Since DNA and PLL are oppositely charged within this pH range, it was possible to assemble multilayers of alternate polyelectrolyte layers. The ionic strength was fixed to either 1 mmol/L, 100 mmol/L, 150 mmol/L, and 500 mmol/L NaCl during the multilayer buildup to find the ionic strength conditions under which the pH will have the most pronounced effect on DNA loading.

As depicted in Figs. 1*a* and 1*b*, both the DNA incorporation (*a*) and film thickness (*b*) increase with increasing salt concentration. This phenomenon is attributed to the screening of the electrostatic repulsive forces between DNA segments by ions (16). Consequently, DNA can adopt a less rigid conformation, which in turn produced thicker layers, and further reduced repulsion at the polymer interface facilitating greater polyelectrolyte adsorption.

Similar results for DNA incorporation in multilayers have been reported by Shi and co-workers (10), and Zhou and Li (33). Salts will have the same effect on PLL, and within this salt concentration range, there is a non-uniform bonding between oppositely charged polymers, which is due to a non-cooperative and irreversible binding between poly(L-lysine) and DNA (38). At 0.5 mol/L NaCl, polyelectrolyte adsorption decreased as a result of reduced electrostatic attraction. To estimate a film's capacity to incorporate DNA (the DNA loading level), the relative ratio of DNA to PLL in the multilayers was determined. This simple ratio is an indicator of film density and is defined as the DNA absorbance per thickness. Qualitatively, this ratio provides a comparison between films built under different ionic strength and pH conditions.

Figure 2 shows that at very low salt concentrations, the variation of pH of the assembly solution has a higher impact in DNA incorporation. At higher salt concentrations, the double layer does not contribute significantly to the total potential of interaction due to charge screening by ions. Thus, the charges on polyelectrolytes will have a less significant effect in polymer interactions.

Using low ionic strength conditions, which were found to be favourable to DNA loading, the effect of pH was studied in greater detail. To determine optimal DNA incorporation, the pH of both PLL and DNA were varied. Figure 3 depicts that the best DNA loading is obtained at low pH of the DNA solution. This is because the cytosine (pK_a of 4.3) (39) and adenosine (pK_a of 3.8) (40) bases are partially protonated near pH 4 where they neutralize almost 40% of the negative charge on the DNA phosphate backbone. This can have a significant effect on DNA conformation in solution in reducing repulsion between segments, thus allowing DNA to adopt a more coiled conformation. This screening effect will increase the excluded volume of the molecule and produce thicker layers. This thickening phenomenon may also be attributed to the increase of DNA loading on PLL layers ow-

Fig. 1. PLL/DNA films (10 layers) built at different salt concentration whilst varying the pH of the DNA solution. The pH of the PLL solution was fixed to 7. (*a*) Absorbance measurements at 260 nm on a quartz substrate. (*b*) Film Thickness measurements on silica substrates via ellipsometry.

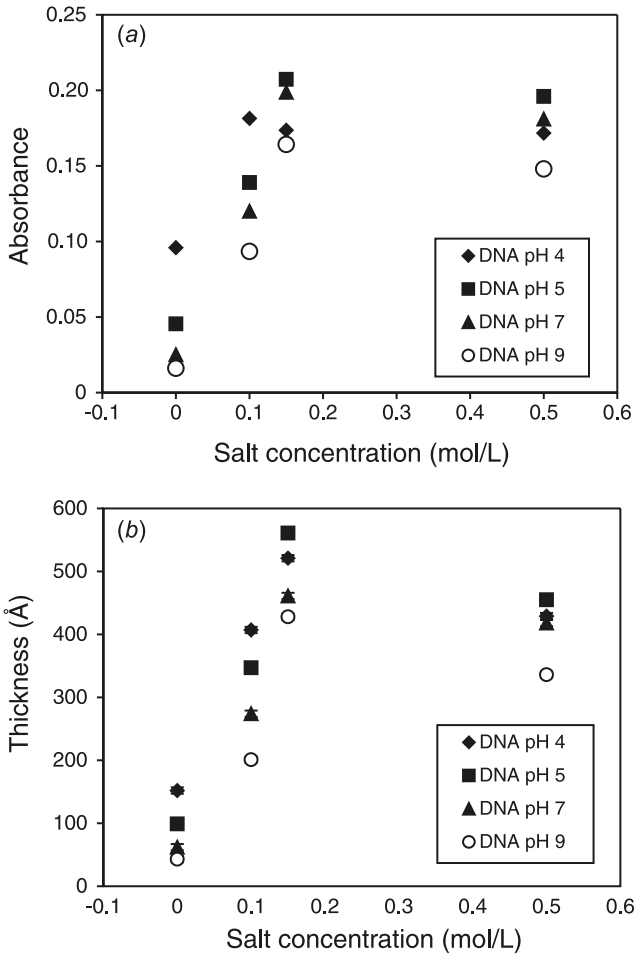

Fig. 2. Effect of DNA solution pH on the relative ratio calculated for DNA/PLL films built under different ionic strength conditions and a fixed pH of 7.

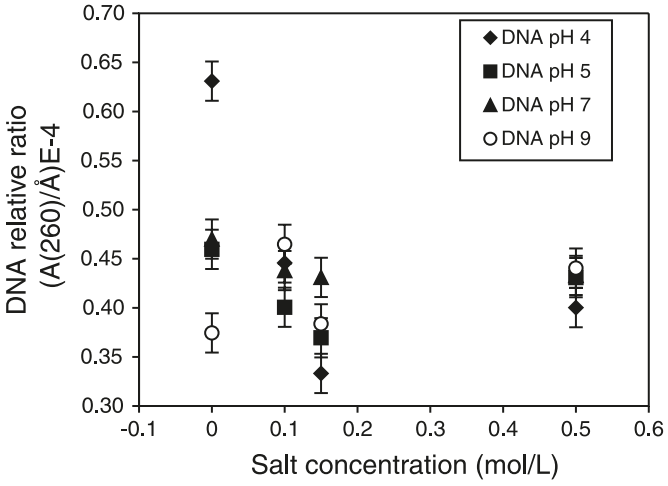

© 2008 NRC Canada

Fig. 3. Effect of pH of PLL and DNA assembly solutions on film composition assembled at low ionic strength. (*a*) Thickness measurements on silica substrates via ellipsometry. (*b*) Absorbance measurements at 260 nm on a quartz substrate.

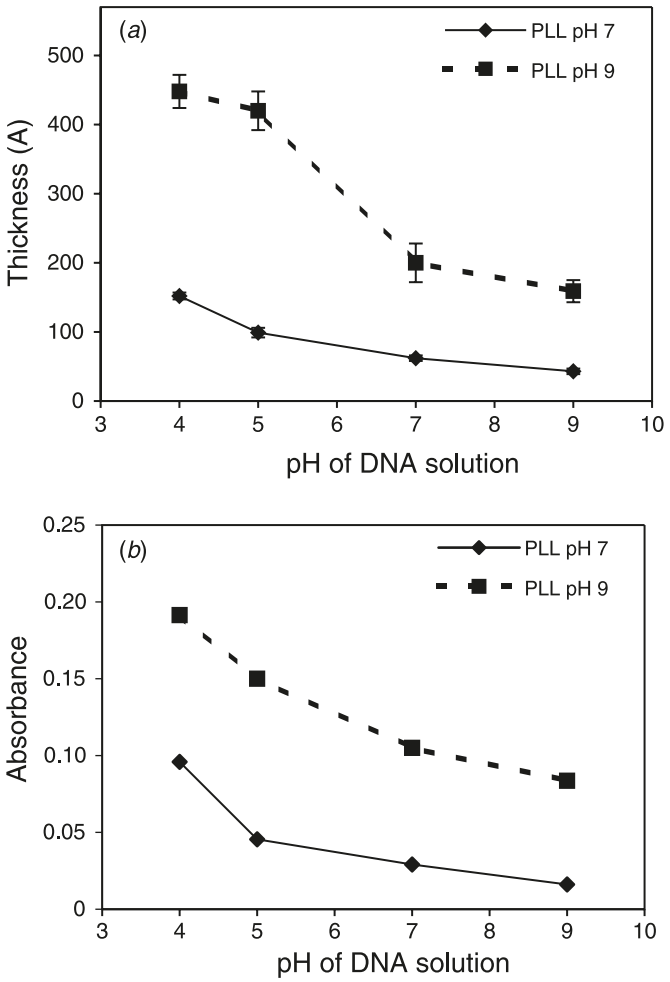

ing to charge equilibrium. Moreover, since DNA partial denaturation occurs at low pH, the absorbance increase can also arise from a hypochromic effect. At pH 9, the DNA solution DNA loading is not favoured because the guanine bases are partially deprotonated. It is likely that the creation of negative charges increases the repulsion with negatively charged phosphate groups on the backbone and reduces stability of the DNA helices.

The results presented in Fig. 3 also show that the pH of the PLL solution has a considerable effect on film composition. When the pH of the PLL solution reaches nine, twice as much DNA is incorporated into the films and film thickness is more than doubled. As the degree of protonation of PLL decreases when the pH of the solution approaches its pK_a, greater PLL adsorption is promoted by a charge equilibrium effect. The reason why DNA adsorption may also increase at pH 9 lies in the fact that when PLL is less protonated, the adsorbed weak polyelectrolyte on film surface will adopt a daisy-looped shape (41, 42), producing a rougher surface that creates more sites for DNA to adsorb and hence a greater incorporation of DNA into the films.

Fig. 4. Comparative pattern of DNA composition in films built at different pH values of assembly solution.

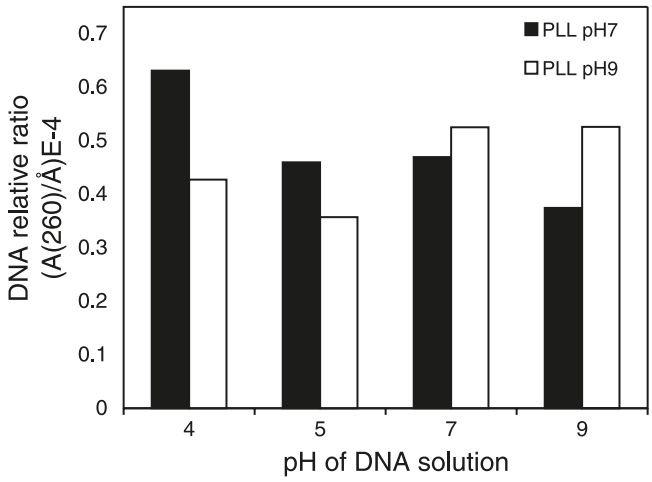

Figure 4 reveals that DNA loading is optimal when both assembly pH of PLL and DNA is low (near pH 4). Under these pH conditions, PLL is fully charged and DNA adopts a coil conformation.

Multilayers coated on silica nanoparticles

On the analogous flat surfaces, pH and salt effects were clearly shown to affect film architecture via a change in polymer conformation. Surface charge measurements could be made directly via zeta potential electrophoresis following polyelectrolyte adsorption on the surface of nanoparticles. Surface charge density on film surfaces can be affected by changes in secondary structure, intra-molecular repulsions, as well as the concentration of counterions in the film. The charge on the surface of the previous layer has also a known effect on the adsorption behaviour of the next polyelectrolyte layer (27, 28). Microelectrophoresis is a commonly used technique to determine the effect of various parameters (salt, pH) on surface charge properties of colloidal particles, and to study these surface properties, multilayers of PLL and DNA were coated onto the surface of silica NPs of 100 nm diameter. In some respects, these DNA-loaded NPs are still model systems, and in that end, pharmaceutical applications would more comprise DNA-filled or hollow capsules (obtained by dissolving the core). However, the Si particles used here as templates are ideal for the precise surface charge studies required, and also for solid state NMR studies that are being carried out in parallel by our group. Furthermore, the Si NPs possess acceptable non-toxicity so that exactly the same particles characterized here electrophoretically could be used for the in vitro transfection studies described presently.

Alternation of the zeta potential measured after every adsorption step is reported in Fig. 5. A potential of +30 mV is obtained when PLL is the outer layer, while the potential switches to –30 mV when DNA is the outermost layer. Plots of zeta potential vs. the pH of the solution for particle containing acid–base functional groups display similarities to titration curves used to determine acid–base dissociation constants. It is therefore possible to estimate the effective pK_a of polyelectrolytes coated on particle surfaces because

© 2008 NRC Canada

Fig. 5. Zeta potential of the surface of silica nanoparticles coated with PLL/DNA after each deposition step.

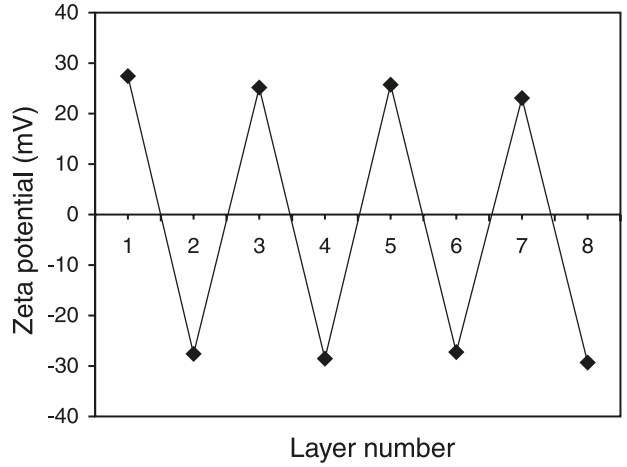

the inflection point of zeta curves corresponds to an apparent pK_a (27).

Figure 6 shows the surface charge of PLL on the surface of the ninth outer layer obtained by alternate deposition of DNA/PLL layers exposed to a range of pH between 4 and 12 at two salt concentrations of 1 mmol/L and 100 mmol/L, respectively. Corresponding apparent pK_a values are shown on the graph, and these are compared to pK_a of PLL measured free in solution, as measured by potentiometric titrations. These bulk solution pK_a values are in good agreement with those reported in the literature (43). At both salt concentrations, a shift of approximately three pK_a units is observed when PLL is adsorbed on top of multilayers. Several groups have reported that in self-assembled polymer systems, the acid–base equilibria deviates substantially from ideal behaviour (44–47). Our group has previously reported a pK_a shift of up to a few units in PLL and HA multilayer system as a result of layer accumulation (27), which perturbs the local environment of the outer layer of PLL. The ionic network created between PLL and DNA upon polymer adsorption leaves participating functional groups unavailable for proton exchange, which in turn decreases the degree of ionization of polymer on film surface, which results in a decrease of pK_a. Increasing the ionic strength has the opposite effect on apparent pK_a because ions in solution can stabilize the charged amino groups on PLL.

The fraction of dissociation was calculated for PLL at the terminal layer of a nine-layer film (Fig. 6*b*), assuming a degree of dissociation of one for one layer of PLL coated on a silica nanoparticles. At low salt concentration, the degree of ionization of PLL on top of the DNA multilayer is very high below pH 6.5. Above this pH, PLL dissociates, which reduces PLL net charge, hence lowering the attraction to the previous PLL layer, which can explain why higher DNA incorporation is observed under low pH conditions (Fig. 3). At pH 9, only 1% of PLL molecules are charged, which leads to a relatively poor DNA adsorption. When salt concentration is increased, the pK_a of PLL is higher. Within the pH range of 4 to 9, the charge density is constant except at pH 9 where the degree of dissociation decreases. This could explain why the pH has less of an effect on polymer adsorption at higher salt concentrations.

Fig. 6. Surface charge of PLL forming the terminal layer of a nine-layer film of PLL/DNA deposited on silica nanoparticles (snowtex-zl, 100 nm diameter). (*a*) A pK_a value on the PLL film surface corresponds to the inflexion point, which is then compared to the pK_a of PLL in solution obtained by a potentiometric titration. (*b*) Degree of dissociation of PLL adsorbed on PLL/DNA film surface coated on silica nanoparticles.

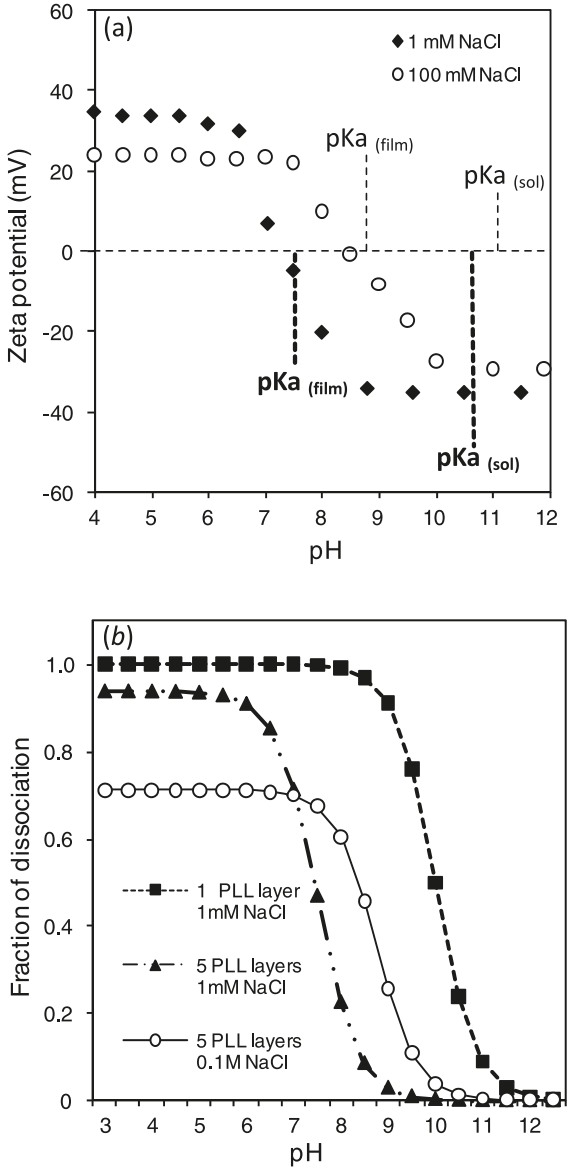

Degradation studies

In gene therapy, it is important to exert precise control over DNA release, and polymers and small molecules can be released from films by changing pH (29, 48), or salt concentration (12), or by using an enzyme (4, 9, 15), if the material is biodegradable. In a therapeutic context, physiological conditions restrict the layer degradation to a constant ionic strength and pH. This leaves biodegradation as the method of choice and indeed several proteolytic enzymes have been

© 2008 NRC Canada

Fig. 7. Level of DNA release from PLL/DNA films built under different pH conditions and at low ionic strength calculated from absorbance measurements on quartz slide. (*a*) PLL is fully charged. (*b*) PLL is partially charged.

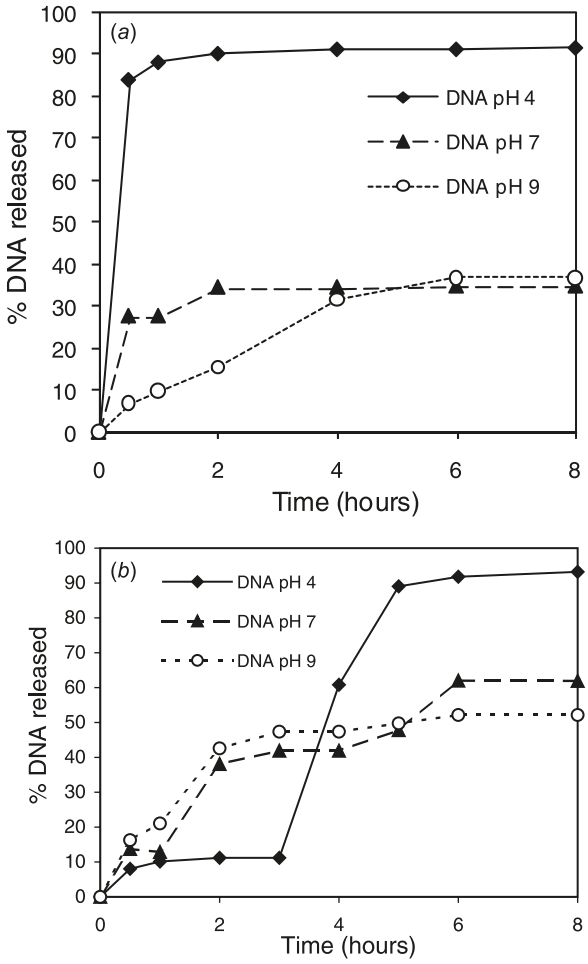

Fig. 8. The effect of film composition on the degradation of films of same thickness. Film 1: PLL pH 9 / DNA pH 4, 1 mmol/L NaCl. Film 2: PLL pH 7 / DNA pH 7, 0.15 mol/L NaCl. Film 3: PLL pH 7 / DNA pH 7, 0.5 mol/L NaCl. (*a*) Thickness variation of film exposed to α-chymotrypsin. (*b*) Percent of DNA released from films.

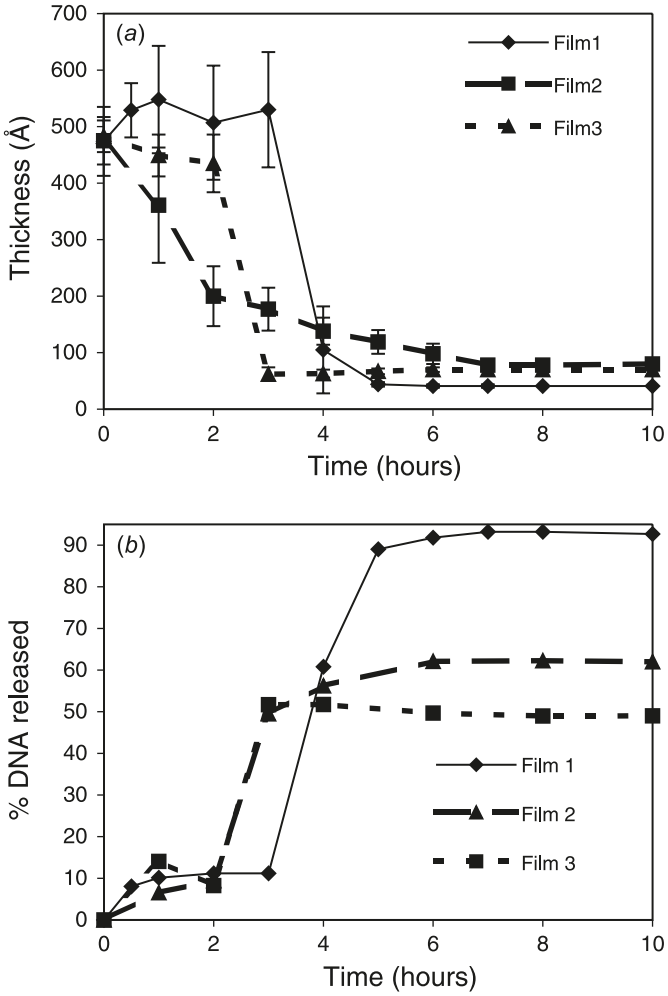

used for material degradation. It has been reported that films, which contain polyamino acid groups can be degraded by chymotrypsin, an endopeptidase widely used in in vitro polypeptide degradation (49). Although trypsin is the specific enzyme for lysine residue degradation, it has been observed that chymotrypsin shows similar degradation activity for PLL membranes (50). Moreover, DNA/PLL multilayered films have recently been successfully degraded with this enzyme (14). Since the architecture of the film affects the affinity of the polymer chain for the binding site of the enzyme molecule, and thus controls the rate at which the polymer is degraded, several PLL/DNA films built under different pH and salt conditions were exposed to the enzyme to track film deconstruction and hence study how film architecture influences degradation behaviour. Film thickness and accessibility of the bonds to be cleaved both influence the mechanism and rate of enzyme action. Indeed, it was noticed that film degradation varies strongly with the pH and salt conditions at which the films were built.

Figure 7*a* shows that less than 40% of the DNA is liberated after 2 h of enzyme treatment when the pH of DNA solution is 7 or higher. With films built with pH 4 DNA solution, DNA release is 1.5 to 3 times greater, with over 90% of DNA released. We note that control tests have shown that no DNA is lost when the same films were exposed to a buffered solution for the same period of time.

It was noticed that degradation of PLL/DNA films depends greatly on the film thickness. Ji and co-workers observed a progressive deconstruction of their PLL/DNA films of 170 nm thickness (14). After 35 h of enzyme exposition, 90% of DNA was released from their films, whereas the same release was obtained after only 2 h with a film of less than 10 nm thickness. Prolonged enzymatic treatments did not further degrade the film because as fragments depolymerize the effect of polymer end groups becomes more pronounced, and eventually, the polymer molecule is too short to form a sufficiently stable complex with the enzyme active site (51, 52). In our films built with a pH 4 DNA solution, DNA is more globular and less charged, and thus the interaction with PLL is weakened, and the reduced steric hindrance allows the enzyme to bind more easily to

© 2008 NRC Canada

the PLL substrate. The same phenomenon is observed with films built with a pH 9 PLL solution (Fig. 7*b*). However, in this case, the percent of DNA release is more important for each film. At higher pH values, PLL is weakly bound to DNA, which leaves more amino groups available for degradation. Moreover, the loopy PLL conformation is more favourable for film degradation and DNA release. Since the thickness of these films was not constant however, it is difficult to make a critical comparison. As shown in Fig. 8, degradation follows a similar scheme for each film. Although films have been coated on two different substrates, it is worth mentioning that an early study had demonstrated that an equal extent DNA was released from a film deposited onto silicon or quartz (15). Early in the enzymatic treatment, Fig. 8*a* shows that film thickness and hence roughness increase early in the enzymatic treatment, as peptide bond cleavage loosens polymer linkages non-uniformly over the film surface.

When enough bonds are broken, clusters of polymer fragments are released, which lead to an abrupt thickness decrease. Further degradation occurred more slowly until polymer fragments are short enough to hinder the hydrolysis process. DNA release differs between films, and it appears that films built with pH 4 DNA and pH 9 PLL solutions have the best ability to release DNA from films exposed to the enzyme. Early studies demonstrated that even though compact complexation between DNA and the polycation is required to protect DNA from degradation, the DNA and the polymer must eventually decomplex to allow efficient transfection (53). Concurrent reduction of the positive PLL charge and the DNA negative phosphate net charge decrease the level of electrostatic interaction between polymers, which may favour dissociation of the complexes inside the cell. This is clearly revealed later in the degradation studies. Thus, we demonstrate that it is possible to tailor decomposition behaviour simply by changing film architecture and composition. Optimal DNA release is obtained when the DNA and PLL polyelectrolyte incorporated into the film are less charged, which in consequence weakens mutual attraction and allows DNA to be liberated more easily.

Transfection studies

To measure the transfection ability, PLL/DNA nanoparticles coated with pEGFP–N1 and PLL were prepared under different pH conditions and at low ionic strength. The salmon DNA used previously for film assembly was replaced by plasmid DNA (pEGPF–N1) that encodes for enhanced green fluorescent protein. However, it was not certain that the pH will have the same effect on the level of DNA incorporation into multilayered films, since DNA morphology has an impact on the structure of the formed complex. The multilayer support in this case is a silica spherical particle having a diameter between 70 and 100 nm. The main motivation for using silica NPs as a support was facility of zeta potential characterization, but silica is also an acceptable support for a DNA delivery system based on previously reported results, which demonstrated that silica nanoparticles with surface-modified aminosilane were an effective carrier for gene delivery (54). Five layers of alternated pEGFP–N1 and PLL were coated onto these silica nanoparticles, and the terminal layer was PLL layer to provide a positive outer charge to bind to the negatively charged cell membrane. Immediately after their preparation, particles were tested for transfection.

Fig. 9. Transfection of COS-7 cells by PLL/pDNA coated silica nanoparticles assembled with DNA solutions adjusted to three different pH values. The pH of the PLL solution during the assembly was maintained at neutral pH.

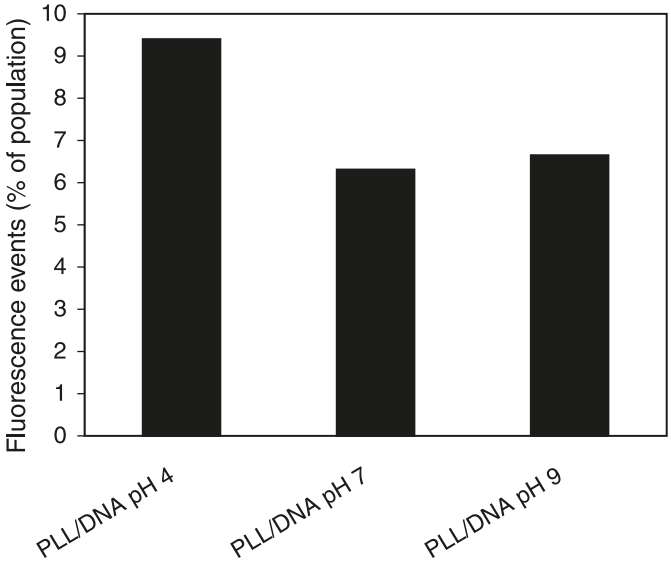

Fluorescence microscopy demonstrated that the COS-7 cell line remained healthy when treated with nanoparticles (Fig. 9). No dead or dying cells, which experienced changes in their cytoplasm size, were detected by microscopy. Compared with the positive Lipofectamine™ control (40% fluorescence events), coated nanoparticles were found to transfect cell lines relatively poorly, with the transfection efficiency of these un-optimized particles less than 30% relative to Lipofectamine™. However, it is important to note that tested nanoparticles had only two layers of DNA, and it would probably be possible to enhance cell transfection significantly by increasing the number of DNA layers. These results suggest that particles assembled with a pH 4 DNA solution transfect 30% more cells than other nanoparticles. This may be attributed to a combination of the high DNA density, and efficient DNA release specific to these particles as characterized independently (Figs. 4. and 7). To verify the reproducibility of the transfection results, these same particles were tested 2 month after their storage. Very little transfection was obtained this time (less than 4% relative to the control), and this could be due to particle aggregation that occurs with time. However, a difference in transfection is still observable between samples, showing that the transfection is still increased with particles assembled at pH 4 DNA solution. Our results thus suggest that these particles have a potential for good and facile control over transfection, and that the pH of assembly has a significant impact on the degree of transfection.

Conclusion

Multilayers constructed from PLL and DNA have been successfully optimized by the variation of the pH of the

© 2008 NRC Canada

polyelectrolyte assembly solutions. The optimization of DNA incorporation into multilayered films was achieved when the pH of both the PLL solution and the DNA solution was lowered to pH = 7 and pH = 4, respectively. Under these conditions, the reduced negative charge on DNA phosphate backbone allows DNA to adopt a more globular form that favours its incorporation into the multilayer. Degradation studies revealed that the film composition resulting from these pH conditions was more easily degraded by chymotrypsin and that more DNA was released during the film degradation. It appears that film architecture and composition play a crucial role in film degradability behaviour and that the pH of multilayer assembly alters the way polymers are degraded and released from these films. Transfection tests performed on the COS-7 line showed that NPs coated with DNA and PLL were non-toxic to living cells, and that particles assembled under optimal DNA-loading pH conditions were transfected more effectively than the ones that were built under other pH conditions. Although the efficiency of transfection was still poor compared with that of other DNA delivery vectors, these results demonstrate the possibility of creating a vector for DNA made of PLL multilayers that could eventually lead to better gene-therapy delivery systems. In summary, we demonstrated that DNA loading and release from polyelectrolytes films can be controlled well simply by varying the pH of assembly solutions used in film formation, and we determined how these variations in polymer conformation and surface charge affect film composition of this system.

Acknowledgements

The authors are grateful for funding from the Natural Sciences and Engineering Research Council of Canada (NSERC) and from Le Fonds Québécois de la Recherche sur la Nature et les Technologies (FQRNT) Centre for Self-Assembled Chemical Structures (CSACS).

References

1. P. Marschall, N. Malik, and Z. Larin. Gene Ther. **6**, 1634 (1999).
2. G. Liu, M. Molas, G.A. Grossmann, M. Pasumarthy, J.C. Perales, M.J. Cooper, and R.W. Hanson. J. Biol. Chem. **276**, 34379 (2001).
3. M. Koping-Hoggard, I. Tubulekas, H. Guan, K. Edwards, M. Nilsson, K.M. Varum, and P. Artursson. Gene Ther. **8**, 1108 (2001).
4. C.M. Jewell, J. Zhang, N.J. Fredin, and D.M. Lynn. J. Controlled Release, **106**, 214 (2005).
5. G. Decher, J.D. Hong, and J. Schmitt. Thin Solid Films, **210–211**, 831 (1992).
6. F. Caruso, E. Rodda, D.N. Furlong, K. Niikura, and Y. Okahata. Anal. Chem. **69**, 2043 (1997).
7. Y. Lvov, G. Decher, and G. Sukhorukov. Macromolecules, **26**, 5396 (1993).
8. R. Pei, X. Cui, X. Yang, and E. Wang. Biomacromolecules, **2**, 463 (2001).
9. T. Serizawa, M. Yamaguchi, and M. Akashi. Angew. Chem., Int. Ed. **42**, 1115 (2003).
10. X. Shi, R.J. Sanedrin, and F. Zhou. J. Phys. Chem. B, **106**, 1173 (2002).
11. O.I. Vinogradova, O.V. Lebedeva, K. Vasilev, H. Gong, J. Garcia-Turiel, and B.-S. Kim. Biomacromolecules, **6**, 1495 (2005).
12. C. Schuler and F. Caruso. Biomacromolecules, **2**, 921 (2001).
13. V.S. Trubetskoy, A. Loomis, J.E. Hagstrom, V.G. Budker, and J.A. Wolff. Nucleic Acids Res. **27**, 3090 (1999).
14. K. Ren, J. Ji, and J. Shen. Biomaterials, **27**, 1152 (2006).
15. J. Zhang, L.S. Chua, and D.M. Lynn. Langmuir, **20**, 8015 (2004).
16. K. Cai, Y. Hu, Y. Wang, and L. Yang. J. Biomed. Mater. Res. A, **84**, 516 (2008).
17. M.A. Borden, C.F. Caskey, E. Little, R.J. Gillies, and K.W. Ferrara. Langmuir, **23**, 9401 (2007).
18. J. Chen, S.W. Huang, W.H. Lin, and R.X. Zhuo. Small, **3**, 636 (2007).
19. S. Sakai, Y. Yamada, T. Yamagushi, T. Ciach, and K. Kawakami. J. Biomed. Mater. Res. A, (2008). In press.
20. E.R. Soto and G.R. Ostroff. Bioconjug. Chem. **19**, 840 (2008).
21. F. Meyer, M. Dimitrova, J. Jedrzejenska, Y. Arntz, P. Schaaf, B. Frisch, J.C. Voegel, and J. Ogier. Biomaterials, **29**, 618 (2008).
22. A.L. Hillberg and M. Tabrizian. Biomacromolecules, **7**, 2742 (2006).
23. G.Y. Wu and C.H. Wu. J. Biol. Chem. **263**, 14621 (1988).
24. W.T. Godbey, K.K. Wu, and A.G. Mikos. J. Controlled Release, **60**, 149 (1999).
25. O. Boussif, F. Lezoualc'h, M.A. Zanta, M.D. Mergny, D. Scherman, B. Demeneix, and J.-P. Behr. Proc. Natl. Acad. Sci. USA. **92**, 7297 (1995).
26. L.C. Smith, J. Duguid, M.S. Wadhwa, M.J. Logan, C.-H.Tung, V. Edwards, and J.T. Sparrow. Adv. Drug Delivery Rev. **30**, 115 (1998).
27. S.E. Burke and C.J. Barrett. Biomacromolecules, **4**, 1773 (2003).
28. S.E. Burke and C.J. Barrett. Langmuir, **19**, 3297 (2003).
29. S.E. Burke and C.J. Barrett. Macromolecules, **37**, 5375 (2004).
30. O.M. Tanchak and C.J. Barrett. Chem. Mater. **16**, 2734 (2004).
31. O.M. Tanchak and C.J. Barrett. Macromolecules, **38**, 10566 (2005).
32. T.H. Nguyen and M. Elimelech. Langmuir, **13**, 3273 (2007).
33. Y. Zhou and Y. Li. Langmuir, **20**, 7208 (2004).
34. M.L. Read, T. Etrych, K. Ulbrich, and L.W. Seymour. FEBS Lett. **461**, 96 (1999).
35. U. Rungsardthong, T. Ehtezazi, L. Bailey, S.P. Armes, M.C. Garnett, and S. Stolnik. Biomacromolecules, **4**, 683 (2003).
36. S.C. Yasui and T.A. Keiderling. J. Am. Chem. Soc. **108**, 5576 (1986).
37. F. Boulmedais, P. Schwinte, C. Gergely, J.C. Voegel, and P. Schaaf. Langmuir, **18**, 4523 (2002).
38. M. Leng, and G. Felsenfeld. Proc. Natl. Acad. Sci. USA. **56**, 1325 (1966).
39. D.E. Bergstrom, P. Zhang, and N. Paul. BioTechniques, **24**, 992 (1998).
40. E.R. Garrett and P.J. Mehta. J. Am. Chem. Soc. **94**, 8532 (1972).
41. O.A. Evers, G.J. Fleer, J.M.H.M. Scheutjens, and J. Lyklema. J. Colloid Interface Sci. **111**, 446 (1986).
42. J. Blaakmeer, M.R. Bohmer, M.A.C. Stuart, and G.J. Fleer. Macromolecules, **23**, 2301 (1990).
43. D. Puett and A. Ciferri. Biopolymers, **6**, 1213 (1968).
44. R. Klitzing and H. Moehwald. Langmuir, **11**, 3554 (1995).
45. J.D. Mendelsohn, C.J. Barrett, V.V. Chan, A.J. Pal, A.M. Mayes, and M.F. Rubner. Langmuir, **16**, 5017 (2000).
46. S.S. Shiratori and M.F. Rubner. Macromolecules, **33**, 4213 (2000).
47. A.F. Xie and S. Granick. J. Am. Chem. Soc. **123**, 3175 (2001).

© 2008 NRC Canada

48. S.A. Sukhishvili and S. Granick. Macromolecules, **35**, 301 (2002).
49. F. Rypacek. Polym. Degrad. Stabil. **59**, 345 (1998).
50. D. Quong, J.N. Yeo, and R.J. Neufeld. J. Microencapsul. **16**, 73 (1999).
51. J. Pytela, J. Jakes, and F. Rypacek. Int. J. Biol. Macromol. **16**, 15 (1994).
52. Y. Yaacobi, S. Sideman, and N. Lotan. Life Support Systems, **3**, 313 (1985).
53. D. Luo and W.M. Saltzman. Nat. Biotechnol. **18**, 33 (2000).
54. C. Kneuer, M. Sameti, U. Bakowsky, T. Schiestel, H. Schirra, H. Schmidt, and C.-M. Lehr. Bioconjugate Chem. **11**, 926 (2000).

© 2008 NRC Canada

Electronic structure characterization of Fe^{III}-protoporphyrin IX (Fe^{III}-PPIX) and β-hematin using calculated nuclear quadrupole resonance (NQR) and Mössbauer parameters

Marjan A. Rafiee and Nasser L. Hadipour

Abstract: In this work, we performed the ab initio calculation of quadrupolar parameters of ^{17}O and ^{14}N atoms in Fe^{III}-protoporphyrin IX (Fe^{III}-PPIX) and β-hematin molecules. Furthermore, the quadrupole splitting of iron atoms in these molecules were calculated. The calculations were carried out to explore the differences between the electronic structures of Fe^{III}-PPIX and β-hematin. The results show that the value of quadrupole splitting of iron atom, $\Delta(^{57}Fe)$, in Fe^{III}-PPIX is exactly three-fold of its value in β-hematin. The electric field gradient (EFG) at the site of quadrupolar nuclei were calculated to obtain quadupolar parameters (χ, η, and Δ), using B3LYP method and an all-electron representation for iron (62111111/3311111/3111), as well as the 6-31G* basis for all other atoms.

Key words: nuclear quadrupole resonance (NQR), hematin, β-hematin, malaria.

Résumé : Dans ce travail, on a effectué des calculs ab initio de paramètres quadripolaires des atomes de ^{17}O et de ^{14}N dans les molécules de la Fe(III)-protoporphyrine IX et de la β-hématine. On a calculé de plus le dédoublement quadripolaire des atomes de fer dans ces molécules. On a effectué les calculs afin d'explorer les différences entre les structures électroniques de la Fe(III)-protoporphyrine IX et de la β-hématine. Les résultats montrent que la valeur du couplage quadripolaire de l'atome de fer, $\Delta(^{57}Fe)$, dans la Fe(III)-protoporphyrine IX est exactement trois fois plus élevée que dans la β-hématine. En faisant appel à la méthode B3LYP et à la représentation de tous les électrons de Wachter pour le fer (62111111/3311111/4111) ainsi qu'à une base 6-31G* pour tous les autres atomes, on a aussi calculé le gradient du champ électrique (GCE) au niveau du noyau quadripolaire dans le but d'obtenir les paramètres quadripolai χ, η, reset Δ.

Mots-clés : résonance quadripolaire nucléaire (RQN), β-hématine, malaria.

[Traduit par la Rédaction]

Introduction

A detailed knowledge of charge distribution of any drug and its target is very important in drug development. This knowledge can be applied to investigate a possible relationship between their electronic structure and biological activity. Theoretical calculations, in particular calculation of quadrupolar parameters of nuclei, seem to be a proper tool for gaining a better understanding of these interactions.

Malaria is one of the world's biggest killers, affecting about half a billion people a year and causing one million deaths (1).

Like most living organisms, malaria parasites require amino acids and the presence of iron, which can both be obtained from hemoglobin. The parasite can digest up to 75% of the red blood cell (RBC) content, in a process whereby the globin is enzymatically cleaved in to small peptides, producing free heme (Fe^{II}- protoporphyrin IX: Fe^{II}-PPIX) as a byproduct. The toxic heme is rendered less harmful in the parasite by one electron oxidation, which produces hematin (Fe^{III}-protoporphyrin IX: Fe^{III}-PPIX). Eventual precipitation transforms nonreactive submicron to micron-sized crystals known as hemozoin in the acidic food vacuole (2, 3).

The quinoline containing antimalarial drugs have been mainstays in the treatment of the disease. The interaction of quinolines with hematin has been well-established and studied over the years and was initially proposed in 1967 by Macomber et al. (4) for chloroquine.

Two main routes have been invoked to account for the primary mode of action of the quinolines: complexation with hematin in solution (5) and inhibition of malaria-pigment growth by quinoline attachment to the growing hemozoin crystal (6–8).

The underlying electronic and steric factors controlling the ability of quinolines to form such complexes are still poorly understood.

To advance our understanding of the structural specificity of the binding of quinoline drugs to hemozoin or hematin and to test this hypothesis that Fe^{III}-PPIX can serve as a potential target for the design of new antimalarial agents, the electronic structures of Fe^{III}-PPIX and hemozoin may be

Received 21 July 2008. Accepted 6 October 2008. Published on the NRC Research Press Web site at canjchem.nrc.ca on 15 November 2008.

M.A. Rafiee.[1] Payame Noor University (PNU), Tehran, Iran.
N.L. Hadipour. Tarbiat Modarres University, Tehran, Iran.

[1]Corresponding author (e-mail: rafiee.marjan@gmail.com).

 doi:10.1139/V08-163 © 2008 NRC Canada

Table 1. Comparison of the calculated ^{14}N and ^{17}O NQCCs using B3LYP/6-31G* level and experimentally measured NQCCs of some available molecules.

Pyrrole		Imidazole		Formaldehyde	
χ_N^{calc} (MHz)	χ_N^{exp} (MHz)	χ_N^{calc} (MHz)	χ_N^{exp} (MHz)	χ_O^{calc} (MHz)	χ_O^{exp} (MHz)
3.09	2.06	4.96	3.27	12.47	12.37

compared. The detailed analysis of charge density on quadrupolar nuclei in Fe^{III}-PPIX and hemozoin is a useful tool to investigate these electronic structural differences.

Nuclear quadrupole resonance (NQR) spectroscopy (9) is a very sensitive technique for measurement of the electric charge distribution around quadrupolar nuclei ($I > 1/2$).

The quantum mechanical approach has been shown to be an effective method in determination of the charge distribution in molecules or complexes (10). In this method, the electric field gradient (EFG), resulting from whole molecular charges, can be estimated at any point in the molecular space (11). Verification of the EFG has become possible by the quadrupolar nuclei, which possess a nuclear quadrupole moment and interact with the molecular EFG tensor (12). This interaction is measured by the nuclear quadrupole coupling constant (NQCC).

β-Hematin is chemically, spectroscopically, and crystallographically identical to the malaria pigment (13–16). In this work, attention has been focused on the details of the charge distribution on Fe^{III}-PPIX and β-hematin. For this purpose, we performed a theoretical investigation on the calculated NQR and Mössbauer parameters of these compounds. These results may give a better understanding of their biological activity based on their electronic structures.

Computational details

Electric field gradients of quadrupolar nuclei in Fe^{III}-PPIX and β-hematin were calculated using the Gaussian 98 program (17).

The three-dimensional structures of the above mentioned compounds were obtained from the Cambridge Crystallographic Database (18), where the hydrogen atoms were not given; they were added to the crystal structure using HyperChem (19). Both hemozoin and Fe^{III}-PPIX showed a spin state of 5/2, as determined by Mössbauer spectroscopy (20). This value was considered in the calculations performed in this study.

The EFGs were calculated using the B3LYP method and a Wachters' (21) all electron representation for iron (62111111/3311111/3111) and the 6-31G* basis for all other atoms. It has been previously demonstrated that there is excellent accord between theory and experiment using the hybrid exchange correlation functional (B3LYP) and the Wachters basis set for iron metalloporphyrins (22, 23). Moreover, based on the results reported in Table 1, the selected level and basis sets give the rather acceptable qualitative NQCCs of nitrogen and oxygen atoms.

The excited state of ^{57}Fe has a spin $I = 3/2$. The EFG has no effect on the $I = 1/2$ ground state but could remove degeneracy in the excited state, splitting it into two substates: $m_I = \pm 1/2$ and $m_I = \pm 3/2$, where $m_I = \pm 3/2$ states are higher in energy for positive q_{ZZ}. The two nondegenerate excited states give rise to a doublet in the Mössbauer spectrum. The separation between the lines, Δ, is known as quadrupolar splitting (QS)

$$[1] \qquad \Delta = 1/2e^2Qq_{ZZ}(1 + \eta^2 / 3)^{1/2}$$

where e is the charge of an electron, q_{ZZ} is the component of EFG in Z direction, and Q is the electric quadruple moment of the nucleus. η is the asymmetry parameter, which is defined using EFG components in principal axes as $\eta = (V_{YY} - V_{XX})/V_{ZZ}$, where $|V_{ZZ}| \geq |V_{YY}| \geq |V_{XX}|$.

The expression $\chi = e^2Qq_{ZZ} / h$ is termed as the nuclear quadrupole coupling constant (NQCC) and has the unit of frequency (Hz). h is the Planck constant.

The most recent values of electric quadrupole moments for the nucleus, $Q(^{57}Fe) = 160$ mb, $Q(^{14}N) = 20.44$ mb, and $Q(^{17}O) = 25.58$ mb, already reported by Pyykko (24), were used in this study.

Results and discussion

In vitro experiments already revealed that the quinoline-containing antimalarial drugs are associated with the crystallization of hematin (8). This suggests that their therapeutic effect occurs by interference with hemozoin formation. It has been established that hemozoin is not a coordination polymer so that the growth of a chain cannot be stopped at a single site (18). Regarding the investigation of the nature of π-π interaction (25), properties of the atoms at the points of intermolecular contact are important rather than the overall molecular properties. Based on our previous study (26), the nitrogen ring of the drug and iron cation of hematin are essential in the π-π interaction between antimalarial quinolines and hematin. Therefore, investigation of the electronic structures of Fe^{III}-PPIX and hemozoin and particularly the charge density of the Fe atom in these compounds may provide important insights to better understand the drug-receptor mechanism. Since NQR parameters are very sensitive to the electronic structure, calculated NQR parameters reveal the details of the charge distribution of nuclei that may not be observed by other methods, such as atomic charge determination. Accordingly, the quadrupolar parameters of atoms in Fe^{III}-PPIX and hemozoin were calculated. Investigation of calculated nuclear quadrupolar parameters can be used as a useful probe to compare the charge density of those atoms.

Fe^{III}-PPIX and hemozoin (in which the hematin molecules are paired into dimmers by two reciprocal iron–oxygen bonds) are shown in Figs. 1 and 2.

The resultant NQCCs and quadrupole splitting from calculated EFG tensors for these compounds are given in Tables 2–5.

The NQCCs of nitrogen and oxygen atoms in both Fe^{III}-PPIX and β-hematin have rather comparable values (Tables 3 and 5).

© 2008 NRC Canada

Fig. 1. Atom numbering of the Fe^{III}–PPIX molecule in the structure solution.

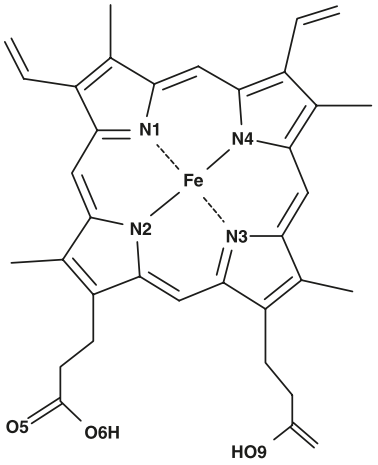

Fig. 2. Atom numbering in a unit cell of the crystal structure of β-hematin.

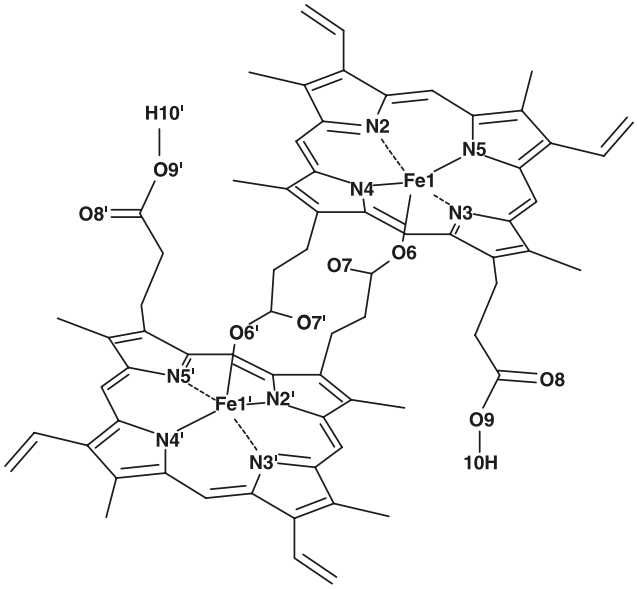

As it has been shown in related studies (27) the NQCC parameters at the coordinated N atom are sensitive indicators of binding to the metal center, so that rather detailed inferences regarding the extent of electron transfer can be obtained from the NQR data of this nucleus.

Since there is no experimental result for ^{14}N- and ^{17}O-NQCC of hemozoin and hematin, the calculated values in Tables 3 and 5 constitute theoretical predictions.

Calculated quadrupole splitting, $\Delta(^{57}Fe)$, in Fe^{III}-PPIX is three-fold larger than that of β-hematin (Tables 2 and 4). This ratio is in agreement with experimental data from Mössbauer spectroscopy (28).

Like NQCCs, the Mössbauer parameters, quadrupole splitting (Δ) and asymmetry parameter (η), depend on the EFG and reflect the spatial distribution of electrons around the iron atom.

The relation of Δ to q_{ZZ} shows quadrupole splitting is directly proportional to q_{ZZ}. There are two factors controlling the value of q_{ZZ} in a nucleus: charge density on the nucleus and symmetry of EFG around the quadrupolar nucleus. It is evident that an increase of the charge density causes the q_{ZZ}, and consequently the Δ, to increase. If charge distribution were such that the symmetry of EFG increased, then q_{ZZ}, and consequently Δ, will decrease. Based on these points, the larger value of $\Delta(^{57}Fe)$ in Fe^{III}-PPIX compared to its value in β-hematin is attributed to a greater charge density of the iron atom in Fe^{III}-PPIX. Furthermore, our results show that the value of the asymmetry parameter (η) in Fe^{III}-PPIX is less than that of β-hematin. Therefore, charge distribution around the iron atom in Fe^{III}-PPIX is more symmetric.

Tables 3 and 5 show that only the oxygen atoms coordinated to iron atom in β-hematin (O6 and O6′) have significantly different values of NQCC compared to other oxygen

Table 2. The calculated asymmetry parameters and quadrupole splitting of ^{57}Fe in a molecule of Fe^{III}-PPIX.

	η	Δ (mm S^{-1})
Fe	0.05	3.64

Table 3. The calculated NQCCs of quadrupolar nuclei in a molecule of Fe^{III}-PPIX.

Quadrupolar nuclei	χ (MHz)
N1	16.26
N2	16.44
N3	15.81
N4	16.70
O5	11.09
O6	9.48
O8	10.26
O9	9.42

Table 4. The calculated asymmetry parameters and quadrupole splitting of ^{57}Fe in a unit cell of β-hematin.

	η	Δ (mm S^{-1})
Fe1	0.17	1.22
Fe1′	0.16	1.22

Table 5. The calculated NQCCs of quadrupolar nuclei in a unit cell of β-hematin.

Quadrupolar nuclei	χ (MHz)	Quadrupolar nuclei	χ (MHz)
N2	15.70	N2′	15.16
N3	16.36	N3′	16.66
N4	15.15	N4′	15.69
N5	16.67	N5′	16.40
O6	34.35	O6′	34.52
O7	7.55	O7′	7.51
O8	10.83	O8′	10.78
O9	9.58	O9′	9.59

© 2008 NRC Canada

atoms. In a simple word, an oxygen atom (as a coordinate) being adjacent to ^{57}Fe in β-hematin causes the iron charge density to be much less than its value in Fe^{III}-PPIX. These results suggest that the contribution of the bonded oxygen atom in decreasing charge density on the iron atom of β-hematin is greater than that of any other atom.

As mentioned before, it is recognized that malaria parasites avoid accumulation of the toxic Fe^{III}-PPIX produced by the digestion of host hemoglobin within the parasites food vacuole by conversion into the insoluble inert heme polymer, hemozoin. Furthermore, quinoline containing drugs are capable of hematin binding and inhibiting of hemozoin formation (the nitrogen atom in quinoline ring is the active site in these drugs (26)). Based on these points, it is expected that any status that increases the charge density on the nitrogen-ring may cause the interaction of quinolines with Fe^{III}-PPIX to be more rapid (before malaria pigment formation). As a result, the toxic Fe^{III}-PPIX accumulates in the parasite food vacuole and subsequently, the inert malaria pigment will not be formed. Further studies will be required to more fully interpret these points.

Conclusions

According to the calculated quadrupolar parameters in this work, it is concluded that (*i*) quadrupolar parameters of nuclei can be used as a useful tool to understand the electronic structure of the compounds; (*ii*) the value of $\Delta(^{57}Fe)$in Fe^{III}-PPIX is exactly three-fold its value in β-hematin; this might be attributed to the greater charge density of the iron atom in Fe^{III}-PPIX; (*iii*) the value of the asymmetry parameter (η) in Fe^{III}-PPIX is less than its value in β-hematin and therefore the charge distribution around the iron atom in Fe^{III}-PPIX is more symmetric than the other; (*iv*) the vicinity of oxygen atom (as a coordinate) to iron atom in β-hematin may play a dominant role in decreasing the quadrupole splitting and consequently the charge density of the iron atom in β-hematin.

Acknowledgment

The authors would like to thank Dr. A. Mahmoudkhani for the test calculations of the present research at the University of Calgary's Centre of Computational & Discrete Geometry, Calgary, Alberta, Canada.

References

1. Who Expert Committee on Malaria. Technical Report Series. Twentieth Report. World Health Organization, Geneva. 2000.
2. P. Olliaro. Pharmacol. Ther. **89**, 207 (2001).
3. H. Ladan, Y. Nitzan, and Z. Malik. FEMS Microbiol. Lett. **112**, 173 (1993).
4. P.B. Macomber, H. Sprinz, and A.J. Tousimis. Nature (London), **214**, 937 (1967).
5. A. Dorn, S.R. Vippagunta, H. Matile, C. Jaquet, J.L. Vennerstrom, and R.G. Ridley. Biochem. Pharmacol. **55**, 727 (1998).
6. T.J. Egan, W.W. Mavuso, and K.K. Ncokazi. Biochemistry, **40**, 204 (2001).
7. D.J.J. Sullivan, H. Matile, R.G. Ridley, and D.E. Goldberg. J. Biol. Chem. **273**, 31103 (1998).
8. D.J.J. Sullivan, I.Y. Gluzman, D.G. Russell, and D.E. Goldberg. Proc. Natl. Acad. Sci. U.S.A. **93**, 11865 (1996).
9. E.A.C. Lucken. Nuclear quadrupole coupling constants. Academic Press, London. 1969.
10. R.L. Andrew. Molecular modeling principles and applications. Longman, Singapore Publishers, Singapore. 1997.
11. J.D. Graybeal. Molecular spectroscopy. McGraw Hill, Singapore. 1988.
12. C.P. Slichter. Principles of magnetic resonance. Springer-Verlag, New York. 1992.
13. C.D. Fith and P. Kanjananggulpan. J. Biol. Chem. **262**, 15552 (1987).
14. A.F.G. Slater, W.J. Swiggard, B.R. Orton, W.D. Flitter, D.E. Goldberg, A. Cerami, and G.B. Henderson. Proc. Natl. Acad. Sci. U.S.A. **88**, 325 (1991).
15. D.S. Bohle, B.J. Conklin, D. Cox, S.K. Madsen, S. Paulson, P.W. Stephens, and G.T. Yee. Am. Chem. Soc. Symp. Ser. **572**, 497 (1994).
16. D.S. Bohle, R.E. Dinnebier, S.K. Madsen, and P.W. Stephens. J. Biol. Chem. **272**, 713 (1997).
17. M.J. Frisch, G.W. Trucks, H.B. Schlegel, G.E. Scuseria, M.A. Robb, J.R. Cheeseman, V.G. Zakrzewski, J.A. Montgomery, Jr., R.E. Stratmann, J.C. Burant, S. Dapprich, J.M. Millam, A.D. Daniels, K.N. Kudin, M.C. Strain, O. Farkas, J. Tomasi, V. Barone, M. Cossi, R. Cammi, B. Mennucci, C. Pomelli, C. Adamo, S. Clifford, J. Ochterski, G.A. Petersson, P.Y. Ayala, P.Y. Cui, K. Morokuma, D.K. Malick, A.D. Rabuck, K. Raghavachari, J.B. Foresman, J. Cioslowski, J.V. Ortiz, B.B. Stefanov, G. Liu, A. Liashenko, P. Piskorz, I. Komaromi, R. Gomperts, R.L. Martin, D.J. Fox, T. Keith, M.A. Al-Laham, C.Y. Peng, A. Nanayakkara, C. Gonzalez, M. Challacombe, P.M.W. Gill, B. Johnson, W. Chen, M.W. Wong, J.L. Andres, C. Gonzalez, M. Head-Gordon, E.S. Replogle, and J.A. Pople. Gaussian 98 [computer program]. Gaussian, Inc., Pittsburgh, Pa. 1998.
18. S. Pagola, P.W. Stphens, D.S. Bohle, A.D. Kosar, and S. Madsen. Nature (London), **404**, 307 (2000).
19. HyperChem. Release 7 [computer program]. HyperCube Inc., Gainesville, Fla., USA. 2002.
20. D.S. Bohle, P. Debrunner, P.A. Jordan, S.K. Madsen, and C.E. Schulz. J. Am. Chem. Soc. **120**, 8255 (1998).
21. A.J.H. Wachters. J. Chem. Phys. **52**, 1033 (1970).
22. Y. Zhang, J. Mao, N. Godbout, and E. Oldfield. J. Am. Chem. Soc. **124**, 13921 (2002).
23. Y. Zhang, J. Mao, and E. Oldfield. J. Am. Chem. Soc. **124**, 7829 (2002).
24. P. Pyykko. Mol. Phys. **99**, 1617 (2001).
25. C.A. Hunter and J.K.M. Sanders. J. Am. Chem. Soc. **112**, 5525 (1990).
26. M.A. Rafiee, N.L. Hadipour, and H. Naderi-Manesh. J. Comput.-Aided Mol. Des. **18**, 215 (2004).
27. C.I.H.Ashby, W.F. Paton, and T.L. Brown. J. Am. Chem. Soc. **102**, 2990 (1980).
28. P.A. Adams, P.A.M. Berman, T.J. Egan, P.J. Marsh, and J. Silver. J. Inorg. Biochem. **63**, 69 (1996).

© 2008 NRC Canada

$Al(OTf)_3$ — A highly efficient catalyst for the tetrahydropyranylation of alcohols under solvent-free conditions

Ahmed Kamal, M. Naseer A. Khan, Y.V.V. Srikanth, and K. Srinivasa Reddy

Abstract: A simple and highly efficient method has been developed for the tetrahydropyranylation of alcohols by their reaction with 3,4-dihydro-2*H*-pyran (DHP) using a catalytic amount (0.01–1 mol%) of aluminium triflate under solvent-free conditions. The effect of various factors like temperature, amount of the catalyst, and molar ratio of substrates on the reaction conditions has also been studied. The comparative study of tetrahydropyranylation of benzyl alcohol using various catalysts including some reported ones shows the efficiency of this catalyst.

Key words: tetrahydropyranylation, aluminium triflate, alcohols, catalysis.

Résumé : On a mis au point une méthode simple et efficace de préparer des dérivés tétrahydropyranyles d'alcools en les faisant réagir avec du 3,4-dihydro-2*H*-pyrane (DHP), dans des conditions sans solvant et en faisant intervenir une quantité catalytique (0,01 à 1 mol %) de triflate d'aluminium. On a aussi étudié les effets de divers facteurs, telle la température, la quantité de catalyseur et le rapport molaire des substrats sur les conditions de la réaction. Une étude comparative de la réaction de tétrahydropyranylation de l'alcool benzylique en faisant intervenir divers catalyseurs, y compris celui mentionné dans ce travail, met en évidence l'efficacité de ce catalyseur.

Mots-clés : tétrahydropyranylation, triflate d'aluminium, alcools, catalyse.

[Traduit par la Rédaction]

Introduction

Protection of hydroxy groups by their conversion to the corresponding tetrahydropyranyl (THP) ethers is one of the most frequently employed transformations in organic syntyhesis (1, 2). The wide use is due to their ease of preparation and stability under a variety of reaction conditions such as with hydrides, alkylating reagents, Grignard reagents, and organometallic reagents (2, 3). THP groups are also the protective groups of choice in peptide, nucleotide, carbohydrate, and steroid chemistry (4). A variety of catalysts that have been reported for this conversion includes the use of protic acids (5–7), acidic clay (4), triflates (8–11), ion exchange resins (12, 13), alumina impregnated with $ZnCl_2$ (14), sulfuric acid on silica gel (15), heteropoly acids (16), polystyrene supported aluminum chloride (17), ionic liquids (18), and many others (19–25). However, despite their potential utility in the protection of simple hydroxyl compounds, many of these methods have limitations such as elevated reaction temperatures, longer reaction times, non-reusability of catalysts, the use of volatile organic solvents, being incompatible with other acid-sensitive functional groups, and involving expensive and toxic catalysts apart from the occurrence of side-products and poor yield of desired products.

In view of the modern demands of organic synthesis, there is a need for a solvent-free and catalytically efficient alternative for the protection of hydroxy functionality as a THP ether, which works under mild and economically benign conditions in a cost-effective manner. In recent years, aluminium triflate has been found to be an efficient catalyst for various transformations like epoxide ring openings (26, 27), thiol protections (28), and silylation of alcohols as well as phenols (29). Recently, we have reported (30) the acylation of alcohols, phenols, and thiophenols in an efficient manner by employing this catalyst. In view of the high catalytic activity and in continuation to our earlier studies on this reagent, we wish to report a highly efficient method for the tetrahydropyranylation of alcohols in the presence of a catalytic amount of $Al(OTf)_3$ (0.01–1 mol%) under solvent-free conditions in excellent yields.

Results and discussion

The treatment of benzyl alcohol with 3,4-dihydro-2*H*-pyran in the presence of 0.01 mol% $Al(OTf)_3$ afforded the tetrahydropyranyl derivative in 92% yield in 2 h at room temperature (RT) (Table 1, entry 1b). Further, the rate of reaction enhanced by using 1 mol% of the catalyst at RT, along with the formation of side-products (10%–25%). To overcome this limitation, the reaction conditions were optimized by employing 1 mol% of the catalyst at 20 °C. A wide range of hydroxy compounds were converted to their

Received 28 April 2008. Accepted 6 October 2008. Published on the NRC Research Press Web site at canjchem.nrc.ca on 15 November 2008.

A. Kamal,[1] M.N.A. Khan, Y.V.V. Srikanth, and K. Srinivasa Reddy. Biotransformation Laboratory, Division of Organic Chemistry, Indian Institute of Chemical Technology, Hyderabad 500 007, India.

[1]Corresponding author (e-mail: ahmedkamal@iict.res.in).

 doi:10.1139/V08-164 © 2008 NRC Canada

Table 1. Tetrahydropyranylation of alcohols catalyzed by 1 mol% $Al(OTf)_3$ at 20 °C.

Entry	Substrate	Product	Time (min)	Yield (%)[a]	Ref.
1a	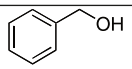	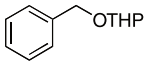	5	95	20
1b	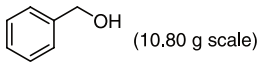 (10.80 g scale)		120	92[b]	—[c]
2	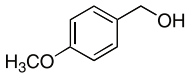	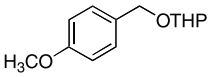	5	90	20
3	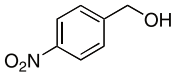	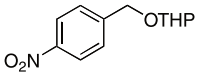	8	85	20
4		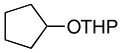	20	88	4
5	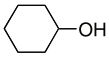	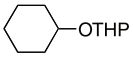	15	92	4
6		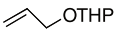	20	85	4
7		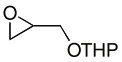	10	90	—[c]
8		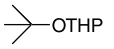	25	82	23
9	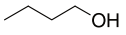	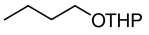	22	94	24
10	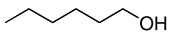	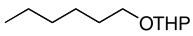	25	90	25
11	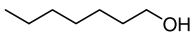	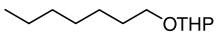	20	92	24

Scheme 1. Synthesis of tetrahydropyranyl ethers.

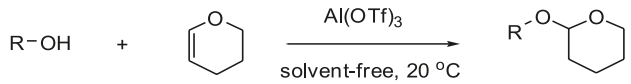

corresponding THP ethers in excellent yields by using this procedure (Scheme 1 and Table 1). The reactions are mild enough for functionalities like allylic ones (Table 1, entry 6) or other acid sensitive groups like epoxide (Table 1, entry 7) and triphenylsilyl groups (Table 1, entry 17), compared with the conventional conditions. All the assigned structures were established from their spectral properties (NMR, mass, and IR) and by comparison with available authentic data.

The reaction of benzyl alcohol and DHP was chosen as a model reaction to evaluate the effect of the amount of the catalyst employed for the conversion (%) of DHP ethers at 20 °C. As illustrated in Table 2, an increase in the amount of catalyst substantially increases the conversion. The reaction proceeds by using 0.01 mol% of the catalyst to yield 90% of the product in 2 h at RT. The reaction is greatly enhanced by increasing the quantity of catalyst. The enhanced rates are due to the increase in the number of catalytically active sites. However, this process reaches its optimum at 1 mol%, and further increases in the amount of catalyst fastens the process along with the formation of side-products (10%–25%). In addition, the effect of temperature on the

Table 2. The effect of the amount of catalyst on the tetrahydropyranylation of benzyl alcohol at 20 °C.

S. No.	Catalyst (mol%)	T (min)	Yield (%)
1	0.01	120	90[a]
2	0.1	50	90
3	0.5	20	95
4	1	5	95
5	2	2	80

[a]Yield obtained by performing the reaction at RT.

© 2008 NRC Canada

Table 1 (*concluded*).

Entry	Substrate	Product	Time (min)	Yield (%)[a]	Ref.
12	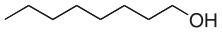	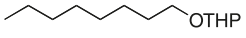	30	85	23
13	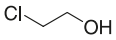	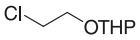	20	90	23
14	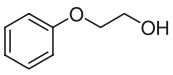	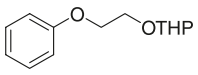	15	90	—[c]
15	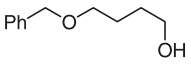	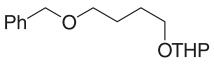	30	85	—[c]
16	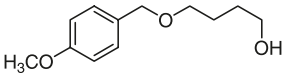	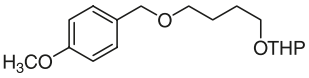	10	92	—[c]
17	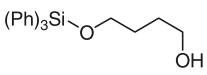	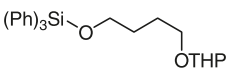	40	90	—[c]
18	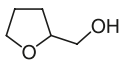	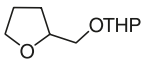	30	86	26
19	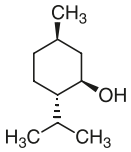	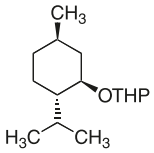	10	95[d]	24
20	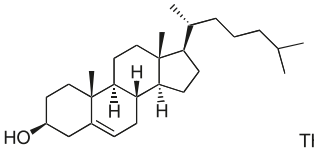	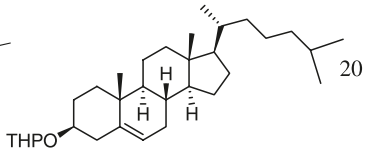	20	90[d]	4

Note: All the reactions were performed using 1.5 equiv. of DHP unless otherwise stated.
[a]Yields refer to isolated products.
[b]Reaction carried out at RT using 0.01 mol% of the catalyst at large scale.
[c]First time reported.
[d]To solubilize solid substrates, 5 equiv. of DHP were added.

Table 3. The effect of the temperature on the tetrahydropyranylation of benzyl alcohol using 1 mol% of catalyst.

S. No.	Temp. (°C)	T (min)	Yield (%)
1	0	120	90
2	10	50	95
3	20	5	95
4	30	5	75

conversion of DHP ethers was also investigated for the temperatures ranging between 0 °C to 30 °C, with benzyl alcohol and DHP as a representative reaction using 1 mol% of catalyst (Table 3). The rate of conversion increases with increase in temperature, and the conversion is maximum at 20 °C. When the reaction was carried out at 30 °C, the formation of the side-products was observed. Moreover, no side-products were observed at this temperature when 0.01 mol% catalyst was employed, however the reaction time was much longer (Table 1, entry 1b). Therefore, the reactions carried out at 20 °C gave the desired results using an optimal amount of catalyst.

To investigate the efficiency of $Al(OTf)_3$, the results of the tetrahydropyranylation of benzyl alcohol were compared with those of the reported methods as well as various new catalysts (Table 4). This catalyst has been found to be more efficient with respect to reaction times, mol% of the catalyst

© 2008 NRC Canada

Table 4. Comparison of the activity of various catalysts in the tetrahydropyranylation of benzyl alcohol.

Entry	Catalyst	Mol (%)	Conditions	Time (min)	Yield (%)	Ref.
1	$Al(OTf)_3$	1	20 °C, solvent-free	5	95	This work
2	$Al(OTf)_3$	1	RT, solvent-free	2	80[a]	This work
3	LiOTf	60	reflux, DCE	150	96	8
4	$In(OTf)_3$	1	0 °C, DCM	30	85	9
5	$Fe(OTf)_3$	1	20 °C, solvent-free	5	90	This work
6	$Fe(OTf)_3$	1	RT, solvent-free	1	75[a]	This work
7	$Yb(OTf)_3$	1	RT, solvent-free	10	80	This work
8	TMSOTf	1	RT, solvent-free	1	60[a]	This work
9	$Cu(OTf)_2$	1	RT, solvent-free	25	95	This work
10	$Cu(BF_4)_2{\cdot}xH_2O$	2	RT, solvent-free	20	90	This work
11	$Nd_2(SO_4)_3{\cdot}xH_2O$	5	RT, solvent-free	15	85	This work
12	$CuSO_4{\cdot}5H_2O$	20	RT, acetonitrile	40	91	21
13	$La(NO_3)_3{\cdot}6H_2O$	10	RT, solvent-free	150	93	22
14	Copper methanesulfonate-HOAc	2:80	RT, solvent-free	60	94	23
15	$Eu_2(SO_4)_3{\cdot}xH_2O$	1	RT, solvent-free	5	85	This work
16	$Bu_4N\ Br_3$	2.5	RT, DCM	60	85	24

Note: All experiments have been carried out according to the general experimental procedure under the conditions given in the table.
[a]Side-products were obtained in addition to the desired products.

Scheme 2. Proposed mechanism for tetrahydropyranylation of alcohols.

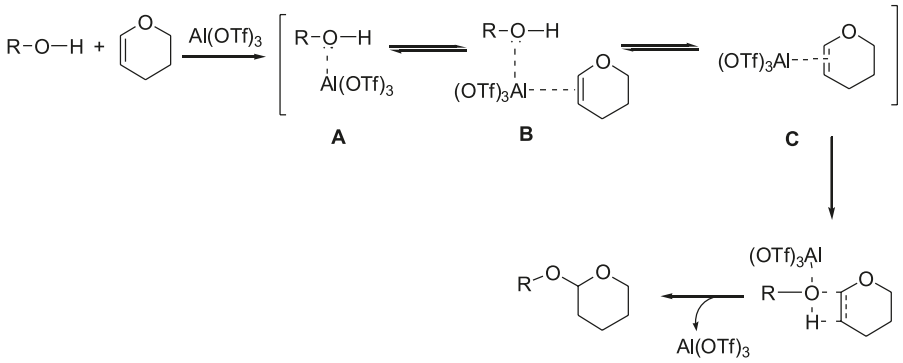

used, and the yields of the desired products when compared with other catalysts.

The mechanism for tetrahydropyranylation can be rationalized based on the experimental and theoretical approaches reported in the literature (31). The mechanism pathway involves the coordination of $Al(OTf)_3$ to the oxygen atom of alcohol giving intermediate complex **A**. This intermediate may be in equilibrium with chelate **B** (in which the catalyst is coordinated with both the C–C double bond of DHP as well as the oxygen atom of the alcohol) and complex **C** (in which only the C–C double bond is coordinated with the catalyst) (Scheme 2). Finally, these transition states result in the formation of DHP ethers.

Conclusion

In conclusion, we have developed a simple and highly efficient method for the conversion of alcohols to tetrahydropyranyl ethers using catalytic amount of $Al(OTf)_3$ under solvent-free conditions, thereby leaving the acid and base sensitive groups intact. The added features of this method over earlier reported processes include its simplicity, clean reactions, high yields, shorter reaction times, absence of organic solvents, and large scale practical synthesis. Moreover, the effect of temperature and amount of the catalyst on the reaction feasibility has been investigated. We believe that this protocol makes an attractive strategy, offering advantages over other methods.

Experimental

General

^1H NMR spectra were recorded on Gemini Varian-VXR-Unity (200 MHz) or Bruker UXNMR/XWIN-NMR (300 MHz) instrument. Chemical shifts (δ) are reported in ppm downfield from internal standard TMS. LC-MS was recorded on an LC-MSD-Trap-SL instrument, and ESI mass spectra were recorded on a VG-7070H Micromass mass spectrometer at 200 °C, 70 eV, with a trap current of 200 μA and 4 kV of acceleration voltage. Reactions were monitored by TLC, performed on silica gel glass plates containing 60 F-254. Visualization on TLC was achieved by UV light or iodine indicator. Column chromatography was performed with Merck 60–120 mesh silica gel. Yields reported are based on isolated compounds. All the reagents used were ei-

© 2008 NRC Canada

ther commercially available or purchased from Lancaster and Sigma-Aldrich.

General procedure for the synthesis of tetrahydropyranyl ethers

To a mixture of alcohol (2 mmol) and 3,4-2*H*-dihydropyran (3 mmol), $Al(OTf)_3$ (1 mol%) was added. The reaction mixture was stirred at the given temperature for the appropriate amount of time (Table 1). After completion of the reaction as monitored by TLC, water was added to the reaction mixture and the product was extracted in ethyl acetate (3 × 25 mL). The organic layer was washed with a saturated solution of $NaHCO_3$, dried over anhyd Na_2SO_4, and concentrated in vacuo. Purification by column chromatography using hexane/ethyl acetate (9:1) furnished the corresponding DHP ethers.

Large-scale tetrahydropyranylation

A mixture of benzyl alcohol (10.80 g, 0.1 mol) and 3,4-2*H*-dihydropyran (13.70 mL, 0.15 mol) (Table 1, entry 1b) was stirred at RT (30 ± 1 °C), while $Al(OTf)_3$ (4.75 mg, 0.01 mol%) was also added to the mixture in an 100 mL round-bottomed flask. After 2 h, water was added to the reaction mixture and the THP ether was isolated by employing the above-described procedure.

Spectral data for new compounds

2-(2-Oxiranylmethoxy)tetrahydro-2H-pyran (Table 1, entry 7)

IR (KBr, cm^{-1}) ν: 2940, 2871, 1642, 1449, 1350, 1123, 1030, 812. ^1H NMR (300 MHz, $CDCl_3$) δ: 4.67–4.50 (m, 1H), 4.00–3.26 (m, 4H), 3.19–3.02 (m, 1H), 2.78–2.50 (m, 2H), 1.90–1.32 (m, 6H). ^{13}C NMR (75 MHz, $CDCl_3$) δ: 98.2, 68.3, 62.0, 51.0, 50.6, 44.5, 25.4, 19.5. HRMS (ESI) *m/z* $(M+Na)^+$: calcd. 181.0840; found 181.0826.

2-(2-Phenoxyethoxy)tetrahydro-2H-pyran (Table 1, entry 14)

IR (KBr, cm^{-1}) ν: 2941, 2867, 1453, 1124, 1034, 873, 741, 698. ^1H NMR (300 MHz, $CDCl_3$) δ: 7.40–7.22 (m, 5H), 4.68–4.52 (m, 1H), 4.02–3.75 (m, 2H), 3.67–3.38 (m, 4H), 1.98–1.39 (m, 6H). ^{13}C NMR (50 MHz, $CDCl_3$) δ: 156.2, 127.5, 120.1, 116.6, 97.2, 69.4, 67.2, 64.4, 28.2, 25.2, 19.3. HRMS (ESI) *m/z*: calcd. 245.1152; found 245.1143.

2-[4-(Benzyloxy)butoxy]tetrahydro-2H-pyran (Table 1, entry 15)

IR (KBr, cm^{-1}) ν: 2874, 1556, 1496, 1352, 1159, 1056, 814, 755. ^1H NMR (300 MHz, $CDCl_3$) δ: 7.32–7.23 (m, 5H), 4.54 (t, *J* = 3.6 Hz, 1H), 4.47 (s, 2H), 3.88–3.28 (m, 6H), 1.77–1.42 (m, 10H). ^{13}C NMR (50 MHz, $CDCl_3$) δ: 132.7, 128.2, 127.5, 127.4, 98.7, 72.9, 70.2, 67.5, 62.1, 30.6, 29.7, 26.6, 25.1, 22.6, 19.8. HRMS (ESI) *m/z* $(M+Na)^+$: calcd. 287.1623; found 287.1610.

2-4-[(4-Methoxybenzyl)oxy]butoxytetrahydro-2H-pyran (Table 1, entry 16)

IR (KBr, cm^{-1}) ν: 2965, 2910, 2845, 1510, 1450, 1370, 1240, 1112, 1078, 815. ^1H NMR (300 MHz, $CDCl_3$) δ: 7.18 (d, *J* = 8.5 Hz, 2H), 6.80 (d, *J* = 8.5 Hz, 2H), 4.54–4.47 (m, 1H), 4.37 (s, 2H), 3.77 (s, 3H), 3.75–3.60 (m, 2H), 3.50–3.26 (m, 4H), 1.75–1.40 (m, 10H). ^{13}C NMR (50 MHz, $CDCl_3$+DMSO) δ: 158.6, 130.4, 128.9, 112.7, 98.2, 72.1, 69.2, 66.9, 61.3, 54.7, 30.0, 25.9, 25.8, 24.8, 18.9. HRMS (ESI) *m/z*: calcd. 317.1728 $(M + Na)^+$: found 317.1720.

Triphenyl silytetrahydropyranyl ether (Table 1, entry 17)

IR (KBr, cm^{-1}) ν: 2935, 2840, 1605, 1512, 1336, 1255, 1115, 1080, 1008, 805. ^1H NMR (200 MHz, $CDCl_3$) δ: 7.66–7.58 (m, 6H), 7.40–7.32 (m, 9H), 4.51 (t, *J* = 3.1 Hz, 1H), 3.90–3.60 (m, 4H), 3.48–3.28 (m, 4H), 1.70–1.38 (m, 6H), 1.12–0.95 (m, 4H). ^{13}C NMR (100 MHz, $CDCl_3$) δ: 135.5, 134.0, 129.4, 127.5, 98.5, 67.6, 64.1, 62.2, 32.4, 30.7, 29.4, 26.8, 22.8, 19.1. HRMS (ESI) *m/z* $(M + Na)^+$: calcd. 455.2056; found 455.2038.

Acknowledgments

The authors MNAK and YVVS are thankful to Council of Scientific and Industrial Research and University Grants Commission, New Delhi, respectively, for the awarding of research fellowships.

References

1. T.W. Greene, and P.G.M. Wuts. Protective groups in organic synthesis. 2nd ed. Wiley, New York. 1991. pp. 31–34.
2. P.J. Kocienski. Protecting groups. Georg Thieme Verlag, New York. 2000.
3. T.W. Greene, and P.G.M. Wuts. Protective groups in organic synthesis. 3rd ed. John Wiley and Sons, New York. 1999.
4. S. Hoyer and P. Laszlo. Synthesis, 655 (1986).
5. J.H. Van Boom, J.D.M. Herschied, and C.B. Reese. Synthesis, 169 (1973).
6. M. Miyashita, A. Yoshikoshi, and P.A. Grieco. J. Org. Chem. **42**, 3772 (1977).
7. R. Nouquier. Tetrahedron Lett. **23**, 2951 (1982).
8. B. Karimi and J. Maleki. Tetrahedron Lett. **43**, 5353 (2002).
9. T. Mineno. Tetrahedron Lett. **43**, 7975 (2002).
10. S. Ma and L.M. Venanzi. Tetrahedron Lett. **34**, 5269 (1993).
11. J.R. Stephens, P.L. Butler, C.H. Clow, M.C. Oswald, R.C. Smith, and R.S. Mohan. Eur. J. Org. Chem. 3827 (2003).
12. F.M. Menger and C.H. Chu. J. Org. Chem. **46**, 5044 (1981).
13. R.D. Johnston, C.R. Marston, P.E. Krieger, and G.L. Goe. Synthesis, 393 (1988).
14. B.C. Ranu and M.J. Saha. Org. Chem. **59**, 8269 (1994).
15. F. Chavez and R. Godinez. Synth. Commun. **22**, 159 (1992).
16. A. Molnar and T. Beregszaszi. Tetrahedron Lett. **37**, 8597 (1996).
17. B. Tamami and P.K. Borujeny. Tetrahedron Lett. **45**, 715 (2004).
18. J.S. Yadav, B.V.S. Reddy, and D. Gnaneshwar. New J. Chem. **27**, 202 (2003).
19. G. Sartori, R. Ballini, F. Bigi, G. Bosica, R. Maggi, and P. Righi. Chem. Rev. **104**, 199 (2004).
20. A. Khazaei, A. Rostami, and M. Mahboubifar. Catal. Commun. **8**, 383 (2007).
21. A.T. Khan, L.H. Choudhury, and S. Ghosh. Tetrahedron Lett. **45**, 7891 (2005).
22. T.S. Reddy, K. Ravinder, N. Suryakiran, M. Narasimhulu, K.C. Mahesh, and Y. Venkateswarlu. Tetrahedron Lett. **47**, 2341 (2006).
23. M. Want, Z.G. Song, H. Gong, and H. Jiang. Chin. Chem. Lett. **18**, 799 (2007).
24. S. Naik, R. Gopinath, and B.K. Patel. Tetrahedron Lett. **42**, 7679 (2001).
25. I. Ledneczki, M. Daranyia, F. Fulop, and A. Molnar. Catal. Today, **100**, 437 (2005).

© 2008 NRC Canada

26. D.B.G. Williams and M. Lawton. Org. Biomol. Chem. **3**, 3269 (2005).
27. D.B.G. Williams and M. Lawton. Tetrahedron Lett. **47**, 6557 (2006).
28. H. Firouzabadi, N. Iranpoor, and G. Kohmareh. Synth. Commun. **33**, 167 (2003).
29. H. Firouzabadi, N. Iranpoor, S. Sobhani, and S. Ghassamipour. Synthesis, 595 (2005).
30. A. Kamal, M.N.A. Khan, K.S. Reddy, Y.V.V. Srikanth, and T. Krishnaji. Tetrahedron Lett. **48**, 3813 (2007).
31. L. Coulombel, M. Rajzmann, J. Pons, S. Olivero, and E. Dunach. Chem. Eur. J. **12**, 6356 (2006).

© 2008 NRC Canada

Substituent effects on silene reactivity — Reactive silenes from photolysis of phenylated tri- and tetrasilanes

William J. Leigh, Andrey G. Moiseev, Eugenie Coulais, Farahnaz Lollmahomed, and Mohammad S. Askari

Abstract: Laser flash photolysis of 2-phenylheptamethyltrisilane (**5d**), 2,2-diphenylhexamethyltrisilane (**5e**), and phenyltris(trimethylsilyl)silane (**5f**) in hexane and acetonitrile solution affords strong, long-lived transient absorptions centered in the 440–470 nm range, which are assigned to the transient silenes formed via [1,3]-trimethylsilyl migration into the ortho-position of a phenyl ring on the basis of their UV–vis spectra and kinetic data for their reactions with methanol (MeOH), acetic acid (AcOH), acetone, 2,3-dimethyl-1,3-butadiene (DMB), carbon tetrachloride (CCl_4), and oxygen. The silene derivatives are formed along with the corresponding silylenes (SiMePh, $SiPh_2$, and $Si(SiMe_3)Ph$, respectively) upon photolysis of these compounds in solution, and indeed, weak, short-lived transient absorptions assignable to the silylenes can also be detected in laser photolysis experiments with the three compounds in hexane, superimposed on the much more prominent absorptions due to the silenes. The silylene absorptions are quenched by MeOH and triethylsilane (Et_3SiH) with absolute rate constants varying over the narrow ranges of (1.1–1.8) × 10^{10} $(mol/L)^{-1}$ s^{-1} and (2.5–3.6) × 10^9 $(mol/L)^{-1}$ s^{-1}, respectively, in excellent agreement with previously reported values for $SiPh_2$ and $SiMe_2$ under the same conditions. The kinetic data obtained for the silenes are compared to previously reported data for the reactions of the same substrates with the related silenes (**6a**–**6c**) formed by photolysis of pentamethylphenyl-, 1,1,1,2-tetramethyl-2,2-diphenyl-, and 1,1,1-trimethyl-2,2,2-triphenyldisilane (**5a**–**5c**, respectively) under similar conditions. The comparison provides the first systematic, quantitative assessment of the stabilizing effects of trialkylsilyl substitution at the silenic silicon atom in silene derivatives.

Key words: silene, silylene, trisilane, tetrasilane, kinetics.

Résumé : La photolyse éclair au laser du 2-phénylheptaméthyltrisilane (**5d**), du 2,2-diphénylhexaméthyltrisilane (**5e**) et du phényltris(triméthylsilyl)silane (**5f**), en solution dans l'hexane et l'acétonitrile, permet d'observer de fortes absorptions transitoires de longue durée, centrées autour de 440 à 470 nm et qui, sur la base de leurs spectres UV/vis et des données cinétiques de leurs réactions avec le méthanol (MeOH), l'acide acétique (AcOH), l'acétone, le 2,3-diméthyl-1,3-butadiène (DMB), le tétrachlorure de carbone (CC_4) et l'oxygène, ont été attribuées aux silènes transitoires formés par le biais d'une migration [1,3]-triméthylsilyle vers la postion ortho d'un noyau phényle. Lors de la photolyse des ces composés en solutions, les dérivés silènes se forment aux côtés des silylènes correspondants [respectivement (SiMePh, $SiPh_2$ et $Si(SiMe_3)Ph$] et, dans les expériences de photolyse laser des trois composés en solution dans l'hexane, on peut de fait détecter des absorptions transitoires de courtes durées attribuables aux silylènes qui sont superposées sur les absorptions beaucoup plus prééminentes dues aux silènes. Les absorptions des silylènes peuvent être piégées par le méthanol et le triéthylsilane (Et_3SiH), avec des constantes de vitesse absolues qui s'étalent respectivement sur une plage étroite allant de (1,1–1,8) x 10^{10} $(mol/L)^{-1}$ s^{-1} à (2,5–3,6) x 10^{10} $(mol/L)^{-1}$ s^{-1}, en excellent accord avec les valeurs rapportées antérieurement pour le $SiPh_2$ et le $SiMe_2$, dans les mêmes conditions. On compare les données cinétiques obtenues pour les silènes avec celles obtenues antérieurement pour les réactions des mêmes substrats avec les silènes apparentés, **6a–6c**, formés par photolyse des pentaméthylphényl-, 1,1,1,2-tétraméthyl-2,2-diphényl- et 1,1,1-triméthyl-2,2,2-triphényldisilanes (**5a–5c**, respectivement), dans des conditions similaires. La comparaison fournit la première évaluation systématique et quantitative des effets stabilisants de la substitution par un groupement trialkylsilyle au niveau de l'atome de silicium silénique dans les dérivés silènes.

Mots-clés : silène, silylène, trisilane, tétrasilane, cinétique.

[Traduit par la Rédaction]

Received 1 September 2008. Accepted 14 October 2008. Published on the NRC Research Press Web site at canjchem.nrc.ca on 19 November 2008.

W.J. Leigh,[1] A.G. Moiseev, E. Coulais, F. Lollmahomed, and M. Askari. Department of Chemistry, McMaster University, 1280 Main Street West, Hamilton, ON L8S 4M1, Canada.

[1]Corresponding author (e-mail: leigh@mcmaster.ca).

 doi:10.1139/V08-165 © 2008 NRC Canada

Introduction

The Si=C double bond is an intrinsically reactive bonding arrangement that has received a great deal of theoretical and experimental attention over the past few decades (1–4). Most silenes are transients in solution or the gas phase, reacting rapidly with nucleophiles or oxygen, or by dimerization when reactive substrates are absent. Successful attempts to synthesize isolable silene derivatives have invariably relied on the presence of sterically bulky substituents to suppress dimerization, which in most cases proceeds via formal head-to-tail [2+2] cycloaddition. This purely kinetic stabilizing effect has also been supplemented with thermodynamic stabilization, most notably with the introduction of trialkylsilyl substituents at the silenic silicon atom and alkyl- and (or) alkoxy-substituents at carbon, such as in the well-known silenes of Brook (**1** (5)) and Apeloig (**2** (6)) and their co-workers. It is well established that such substitution patterns lead to marked reductions in the natural ($^{\delta+}$Si=C$^{\delta-}$) polarity associated with the Si=C double bond, slowing the normally diffusion-controlled dimerization reaction (7, 8) and reversing its normal (head-to-tail) regiochemistry (6, 9) (Chart 1).

While an abundance of evidence suggests that, by and large, weakly polar silenes such as **1** and **2** display similar reactivity as do more polar derivatives toward most substrates in terms of reaction products, relatively few studies have been carried out with the aim of quantifying the effects of reduced Si=C bond polarity on reaction kinetics or mechanisms. Our group has studied the kinetics of the reaction of **2** and a sterically stabilized derivative with methanol (MeOH) in hexane solution, and found that not only does this silene derivative react several orders of magnitude more slowly with the alcohol than do other transient silenes that have been studied, it reacts via a different mechanism (8). The results (both experimental and computational) are consistent with a concerted mechanism involving reaction of the hydrogen-bonded dimer of the alcohol in hexane solution, in contrast to the two-step mechanism, initiated by nucleophilic attack at silicon followed by proton transfer to carbon, which is typical of more electrophilic, naturally polarized transient silenes such as 1,1-diphenylsilene (**3**) (3, 10, 11). Milnes and Baines (12) have recently reported a mechanistic probe study of the effects of Si=C bond polarity on the mechanism of the reaction of two kinetically stabilized silenes with aldehydes, and have shown it to change from one involving a zwitterionic intermediate in the case of the naturally polarized silene **4** to a biradical pathway in the case of the very weakly polar Brook silene **1** (R = *t*-butyl or adamantyl) (Chart 2).

Some time ago, we reported two experimental studies directed at quantifying the effects of substituents at silicon and carbon on the kinetics of nucleophilic additions to transient silenes (13, 14). Though systematic, these studies were limited to alcohol additions, and furthermore, covered only silenes of the general structure Me(R)Si=CH_2 and Me_2Si=CHR. We have continued to search for opportunities to extend the scope of these studies to include both mono- and bis-$SiMe_3$ substitution at the silenic silicon atom and to examine the effects of these substituents on other aspects of silene reactivity, in addition to nucleophilic addition reactions, in as systematic a manner as possible.

Chart 1.

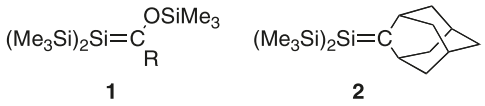

1 **2**

Chart 2.

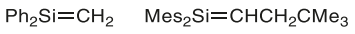

3 **4**

Scheme 1.

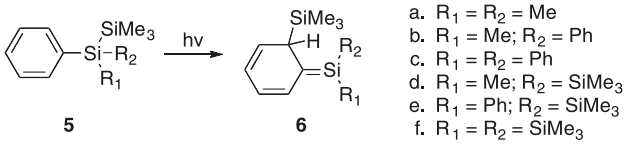

5 **6**

a. $R_1 = R_2 = Me$
b. $R_1 = Me$; $R_2 = Ph$
c. $R_1 = R_2 = Ph$
d. $R_1 = Me$; $R_2 = SiMe_3$
e. $R_1 = Ph$; $R_2 = SiMe_3$
f. $R_1 = R_2 = SiMe_3$

It occurred to us that just such an opportunity presents itself with the series of 1-silahexatriene derivatives, **6a**–**6f**, which are derived from the corresponding oligosilanes, **5a**–**5f**, by photochemical [1,3]-trimethylsilyl migration (Scheme 1). The first three members of the series (**6a**–**6c**) have been studied by us previously by laser photolysis methods (15–17), and so a considerable body of kinetic data already exists for these compounds. The last three members of the series (**6d**–**6f**) are known to be formed as coproducts in the photolysis of the tri- and tetrasilanes, **5d**–**5f**, which are better known as photochemical precursors of the transient *silylene* derivatives $SiPh_2$, SiMePh, and Si(Ph)$SiMe_3$, respectively (18–22). Photolysis of these compounds in solution is known to afford the corresponding silylenes in chemical yields of 40%–60%, from the results of trapping studies in which the silylenes of primary interest were scavenged with substrates such as alkenes, dienes, ketones, trialkylsilanes, and alcohols. *Some* of these studies also reported significant yields of products derived from trapping of the transient 1-silahexatriene derivatives, **6d**–**6f**, in chemical yields as high as ca. 40% (18, 23–30). Gaspar and co-workers employed **5d** and **5e** as precursors to SiMePh (31, 32) and $SiPh_2$ (33), respectively, in some of the earliest reported attempts to study reactive silylenes in solution by laser flash photolysis methods. They described strongly absorbing, long-lived transient species that they assigned (with some reservation) to the corresponding silylenes (31–33); however, as we have recently shown in the case of **5e** (34), it is more likely that the species they characterized in their experiments are in fact the corresponding 1-silahexatriene derivatives and not the silylenes of interest.

The course of the reactions of silenes of this type with typical "silenophiles" is often different than that found with most other silenes, owing to the fact that the silenic carbon is part of a carbocyclic ring system containing both an allylic hydrogen and a dienyl moiety in conjugation with the Si=C bond. For example, aliphatic dienes and alkenes react with these silenes via ene-addition rather than by the usual

© 2008 NRC Canada

[4+2] or [2+2] cycloaddition pathways that are typical of most other silene derivatives (1, 2, 18, 35); these reactions are diverted from their normal course by the labile allylic hydrogen, whose transfer to a carbon in the substrate results in aromatization of the carbocyclic ring. Reaction with acetone proceeds via competing [2+2] and ene-addition (30, 36–38), the latter again involving transfer of the allylic hydrogen in the silene to the substrate rather than via the usual pathway (as exemplified by **3** (39)) to produce a silyl enol ether. Finally, the presence of the cyclohexadienyl-substituent in silenes of this type results in unusually high reactivity toward molecular oxygen and CCl_4, which are thought to react via mechanisms involving radical or biradical intermediates (16).

In the present paper, we report the results of a laser flash photolysis study of **5d**–**5f** in various solvents. As suggested above, the main goal of the work was to establish that the 1-silahexatriene derivatives are the dominant transient products detectable in experiments of this type with these compounds, to characterize their reactivities with a variety of substrates that show characteristically high reactivity toward silenes of this type, and to compare the results to previously published data for the related silenes **6a**–**6c** in the interest of elaborating on our understanding of substituent effects on various aspects of silene reactivity. A secondary goal was to attempt to detect the reactive silylenes SiMePh and $Si(Ph)SiMe_3$ in solution by laser photolysis of **5d** and **5f**, to provide a benchmark for future studies with potentially more appropriate photochemical precursors to these silylene derivatives; to our knowledge, **5f** has not been studied previously by laser photolysis methods.

Results

Laser flash photolysis of rapidly flowed solutions of 2-phenylheptamethyltrisilane (**5d**; ~10^{-4} mol/L) in dry, deoxygenated hexane, with the pulses from a KrF excimer laser (248 nm; ~20 ns; ~100 mJ) afforded strong transient absorptions centered at λ_{max} = 440 nm, which decay over several hundred microseconds with multiexponential kinetics, in good agreement with the results of earlier flash photolysis studies of this compound (31, 32). We assign this absorption to silene **6d** based on the similarity of its spectrum to those of **6e** (λ_{max} = 460 nm (34)) and **6a**–**6c** (λ_{max}= 425–490 nm (16, 17)), and the kinetic evidence described later in the paper. However, we also detected a second, much shorter-lived transient absorption that was superimposed on those due to the long-lived species and exhibited a lifetime τ ~ 3 μs. The species exhibited a distinct absorption band centered at λ_{max} ~ 270 nm and weaker absorptions throughout the 400–600 nm range. Figure 1 shows representative transient spectra, recorded 128–256 ns and 4.86–5.09 μs after the laser pulse, along with decay traces recorded at 440 nm and 510 nm. As in our previous study of **5e** (34), addition of 3 mmol/L Et_3SiH reduced the lifetime of the short-lived species to ca. 100 ns without affecting the lifetime of the strong 440 nm absorption, thus cleaning up the 128–256 ns spectrum considerably (see Fig. 1*b*). We also recorded a UV–vis spectrum of a photolysed solution of **5d** in 3-methylpentane (MP) at 78 K, which is shown as the solid

Fig. 1. Transient absorption spectra recorded 128–256 ns (-○-) and 4.86–5.09 μs (-□-) after the laser pulse, from the laser flash photolysis of 0.11 mmol/L solutions of 2-phenylheptamethyltrisilane (**5d**) in (*a*) hexane and (*b*) hexane containing 3.0 mmol/L Et_3SiH. The insets show transient decays recorded at 440 and 510 nm. The spectrum obtained from a photolysed solution of **5d** in 3-methylpentane at 78 K (—; scaled to match the absorption intensities below 310 nm) is also shown in (*a*).

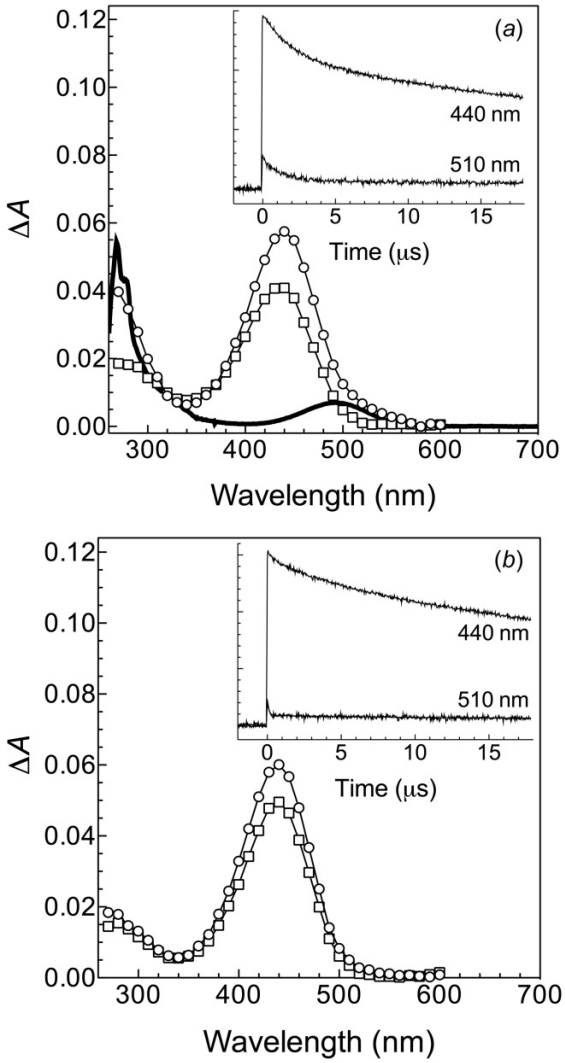

line in Fig. 1. The low temperature matrix spectrum (λ_{max} = 268, 493 nm) agrees well with that reported by West and coworkers (40), who assigned it to methylphenylsilylene (SiMePh).

The low temperature spectrum is reproduced again in Fig. 2, along with solution phase difference spectra calculated from the spectra of Fig. 1 in two ways. The first spectrum (-□-) was calculated as the difference between the end-of-pulse (128–256 ns) spectra in pure hexane (Fig. 1*a*) and in hexane containing 3 mmol/L Et_3SiH (Fig. 1*b*), and thus isolates that portion of the end-of-pulse spectrum that is quenched by a primary reaction with the silane. Clearly, the difference spectrum (λ_{max} = 270, 510 nm) agrees with the matrix spectrum of SiMePh quite closely; it is also quite similar to the reported solution phase and low temperature

© 2008 NRC Canada

Fig. 2. Transient difference spectra, calculated as the difference between the 128–256 ns spectrum of Fig. 1*a* minus the 128–256 ns spectrum of Fig. 1*b* (-□-), and as the difference between the 128–256 ns and 4.86–5.09 μs spectra of Fig. 1*a* (-○-). The dashed line is the spectrum recorded of a photolysed solution of **5d** in 3-methylpentane at 78 K, reproduced from Fig. 1*a*.

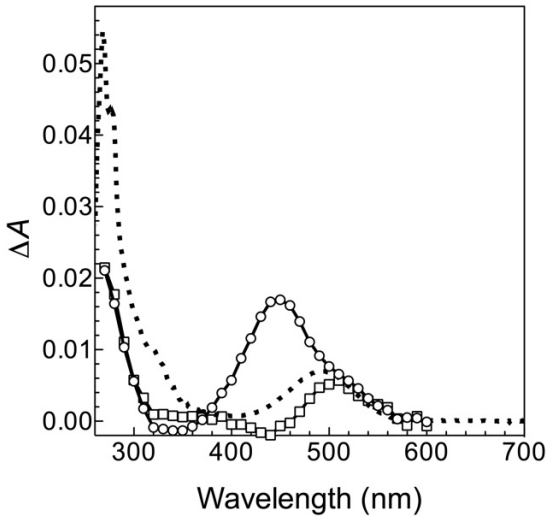

matrix spectra of $SiPh_2$ (34, 40). We thus assign the short-lived absorptions centered at 270 and 510 nm to the silylene, SiMePh. Further support for the assignment is provided by the second order rate constants for quenching of the species by MeOH (k_{MeOH} = (1.8 ± 0.3) × 10^{10} $(mol/L)^{-1}$ s^{-1}), Et_3SiH (k_{Et_3SiH} = (3.4 ± 0.3) × 10^9 $(mol/L)^{-1}$ s^{-1}), and molecular oxygen (k_{O_2} = (1.8 ± 0.2) × 10^8 $(mol/L)^{-1}$ s^{-1}), which were determined from (linear) plots of the pseudo first-order rate constant for decay of the transient signal at 520 nm versus substrate (Q) concentration according to eq. [1]. The rate constants are quite similar to those for the reaction of $SiMe_2$ and $SiPh_2$ with these three substrates in hexane under similar conditions (41); furthermore, the ratio of the absolute rate constants for quenching of the species by MeOH and Et_3SiH (k_{MeOH}/k_{Et_3SiH} = 5.3 ± 1.5) are quite close to the rate ratio determined by Hawari et al. (42) from the competitive trapping of SiMePh by ethanol and Et_3SiH in cyclohexane (k_{EtOH}/k_{Et_3SiH} = 4.8). The lifetime of the 440 nm absorption in the presence of millimolar concentrations of MeOH and Et_3SiH was roughly the same as in pure hexane solution, consistent with its assignment to silene **6d**.

$$[1] \qquad k_{decay} = k_0 + k_Q[Q]$$

The second spectrum of Fig. 2 (-○-) was calculated as the difference between the end-of-pulse and 4.9–5.1 μs spectra of Fig. 1*a*, and thus isolates that portion of the 128–256 ns spectrum of Fig. 1*a* that decays in the first 5 μs after excitation in pure hexane solution (i.e., in the absence of a silylene scavenger). This difference spectrum clearly contains contributions from both SiMePh and silene **6d**, consistent with the presence of a fast initial decay process for the silene that exists only in the absence of a silylene scavenger. We tentatively identify this process as a bimolecular reaction of the silene and silylene; comparison of the maximum absorbance values of the early and late spectra of Figs. 1*a* and 1*b* indicate that roughly 20% of the initially produced amount of **6d** undergoes this rapid initial decay process. No evidence for the formation of the silylene dimerization product, 1,2-dimethyl-1,2-diphenyldisilene ($Si_2Me_2Ph_2$; λ_{max} = 420 nm (43)), could be obtained in any of these experiments, consistent with its formation being quenched as a result of the competing reaction of SiMePh with silene **6d**.

Fig. 3. (*a*) Transient absorption spectra recorded 16–80 ns (-○-) and 432–544 ns (-□-) after the laser pulse, from the laser photolysis of a 0.07 mmol/L solution of phenyltris(trimethylsilyl)silane (**5f**) in deoxygenated hexane, and the scaled spectrum of a photolysed solution of **5f** in 3-methylpentane at 78 K (—); the dotted line shows the latter spectrum magnified by a factor of 5. The inset shows transient decays recorded at 290 and 450 nm. (*b*) Plots of k_{decay} vs [Q] for quenching of the short-lived transient (λ_{max} ~ 285 nm) from **5f** by MeOH (○) and Et_3SiH (□) in deoxygenated hexane at 25 °C; the solid lines are the linear least-squares fits of the data to eq. [1].

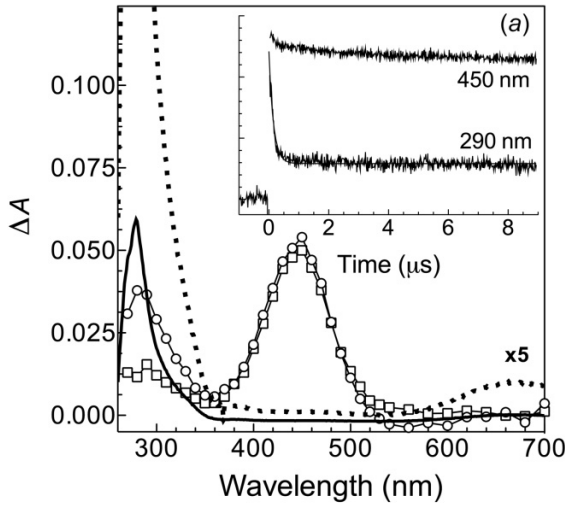

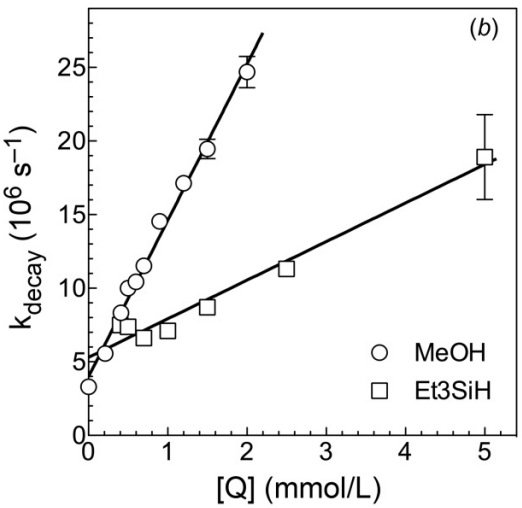

Similarly, laser flash photolysis of a rapidly flowed 7 × 10^{-5} mol/L solution of phenyltris(trimethylsilyl)silane (**5f**) in hexane afforded a transient spectrum consisting of two main components, one very long-lived one centered at λ_{max} = 450 nm, which decayed over several milliseconds with mixed order kinetics, and one very short-lived one centered at λ_{max} ~ 285 nm that decayed with first order kinetics and

© 2008 NRC Canada

Table 1. Absolute rate constants (units of 10^6 $(mol/L)^{-1}s^{-1}$, unless otherwise noted) for the quenching of silenes **6a–6f** by various substrates in hydrocarbon solvents and MeCN at 25 °C.

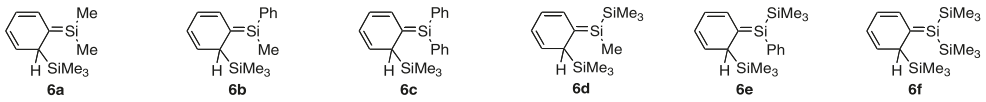

Substrate	**6a**	**6b**	**6c**	**6d**	**6e**	**6f**
λ_{max}	425 nm	460 nm	490 nm	440 nm	460 nm	450 nm
MeOH[a]	$k_1 = 230 \pm 70$[b] $k_2 = 4900 \pm 1000$[b,c]	$k_1 = 60 \pm 25$[b] $k_2 = 2800 \pm 500$[b,c]	$k_1 = 17 \pm 10$[b] $k_2 = 1100 \pm 400$[b,c]	$k_2 = 2.47 \pm 0.03$[c]	$k_2 = 0.80 \pm 0.01$[c]	τ_{MeOH} ~ 38 μs
AcOH[a]	290 ± 10[b]	141 ± 5[b]	70 ± 2[b]	11.7 ± 0.3	2.7 ± 0.1	0.025 ± 0.001
Acetone	4500 ± 60[d]	1580 ± 60[d]	542 ± 5[d]	4.3 ± 0.1	1.9 ± 0.1	0.09 ± 0.01
DMB	128 ± 3[d]	68 ± 1[d]	30 ± 1[d]	0.11 ± 0.006[e]	0.083 ± 0.003[e]	0.011 ± 0.006
CCl_4	440 ± 10[d]	160 ± 10[d]	110 ± 10[d]	78 ± 2	23 ± 1	4.9 ± 0.2
O_2	690 ± 40[d]	350 ± 10[d]	190 ± 20[d]	120 ± 5	39 ± 2	11.4 ± 0.2

Note: In hexane solution unless otherwise noted.
[a]In MeCN solution, see eq. [2].
[b]Data from ref. 17.
[c]In units of 10^6 $(mol/L)^{-2}$ s^{-1}.
[d]In isooctane solution, data from ref. 16.
[e]In cyclohexane solution, data from refs. 31 and 33.

lifetime τ ~ 300 ns. Figure 3*a* shows transient spectra recorded 16–80 and 432–544 ns after the laser pulse, along with the UV–vis spectrum of a photolysed sample of **5f** in a 3-MP matrix at 78 K. The matrix spectrum (λ_{max} = 280, 680 nm) agrees well with the one reported by Conlin and co-workers, who assigned it to phenyltrimethylsilylsilylene ($Si(Ph)SiMe_3$) (44). The lifetime of the transient signal at 290 nm was shortened upon addition of MeOH or Et_3SiH to the solution. Plots of k_{decay} versus [Q] were linear, analysis of which, according to eq. [1], afforded the second order rate constants $k_{MeOH} = (1.1 \pm 0.1) \times 10^{10}$ $(mol/L)^{-1}$ s^{-1} and $k_{Et_3SiH} = (2.6 \pm 0.4) \times 10^9$ $(mol/L)^{-1}$ s^{-1} for reaction of the species with MeOH and Et_3SiH, respectively. These results are consistent with the assignment of the short-lived 285 nm absorption band to $Si(Ph)SiMe_3$. Unfortunately, the presence of the weak long wavelength band, which is observable in the matrix spectrum, could not be detected in solution, due undoubtedly to the much lower extinction coefficient of this absorption relative to that at 285 nm, which is itself relatively weak. The lifetime of the 450 nm transient was unaffected in the presence of the millimolar quantities of MeOH and Et_3SiH that were required to effect a change in the lifetime of the 285 nm absorption, allowing preliminary assignment of the 450 nm absorption to silene **6f**.

Laser photolysis of solutions of **5e** (~10^{-4} mol/L) in deoxygenated hexane afforded similar results to those reported in our preliminary study of this compound (45): two distinct transient species are formed, one that exhibits λ_{max} = 460 nm and decays over several milliseconds, and one that exhibits a discrete absorption band at λ_{max} = 290 nm, weaker absorptions in the 490–530 nm range and decays over 1–2 μs. The latter is quenched efficiently by added MeOH ($k_{MeOH} = (1.32 \pm 0.04) \times 10^{10}$ $(mol/L)^{-1}$ s^{-1}) and Et_3SiH ($k_{Et_3SiH} = (3.5 \pm 0.2) \times 10^9$ $(mol/L)^{-1}$ s^{-1}), consistent with a silylene ($SiPh_2$) assignment (34). Again, the lifetime of the long-lived species is unaffected by these reagents in millimolar concentrations (34).

Addition of acetone or carbon tetrachloride (CCl_4) to the hexane solutions of **5d–5f** caused the decay of the silene absorptions to accelerate in proportion to substrate concentration and follow clean pseudo first kinetics. Plots of k_{decay} versus [Q] were linear, and were analyzed according to eq. [1] to obtain the second order rate constants listed in Table 1. Figure 4 shows representative plots of k_{decay} versus [Q] for quenching of silenes **6d–6f** by acetone and CCl_4. The lifetimes of the silenes were also observed to decrease upon addition of oxygen to the solutions; second-order quenching rate constants were estimated from three-point plots of k_{decay} values recorded in argon-, air-, and O_2-saturated solutions of **5d–5f** in hexane versus [O_2], which exhibited good linearity in all three cases. Addition of up to 10 mmol/L 2,3-dimethyl-1,3-butadiene (DMB) to hexane solutions of **5f** had little effect on the intensity or lifetime of the 450 nm signal due to silene **6f**, as expected considering the reported rate constants for reaction of the long-lived transients from **5d** and **5e** (i.e., silenes **6d** and **6e**) with this diene, which are in the range of ca. 10^5 $(mol/L)^{-1}$ s^{-1} in cyclohexane (31, 33). Addition of larger quantities of the diene (30–40 mmol/L) led to corresponding reductions in the intensity of the silene absorption due to screening of the excitation light by the added substrate, and very modest increases in the pseudo first order decay rate constant. A plot of k_{decay} versus [DMB] was linear over the 30–40 mmol/L range in added diene, and afforded an estimate of $k_{DMB} = (1.1 \pm 0.1) \times 10^4$ $(mol/L)^{-1}$ s^{-1} for the second order rate constant for reaction of DMB with **6f**.

Quenching of the three silenes by methanol (MeOH) and acetic acid (AcOH) was studied in acetonitrile (MeCN) solution, as preliminary experiments indicated that the effects of these substrates on the silene lifetimes were too small for meaningful rate constants to be determined in hexane, given the solubility limits of the two substrates in the hydrocarbon solvent. Laser photolysis of **5d–5f** in deoxygenated MeCN led in each case to the formation of two long-lived transient

© 2008 NRC Canada

Fig. 4. Plots of k_{decay} vs [Q] for the quenching of silenes **6d** (□), **6e** (○), and **6f** (Δ) by (*a*) acetone and (*b*) CCl_4 in deoxygenated hexane at 25 °C. The solid lines are the linear least-squares fits of the data to eq. [1].

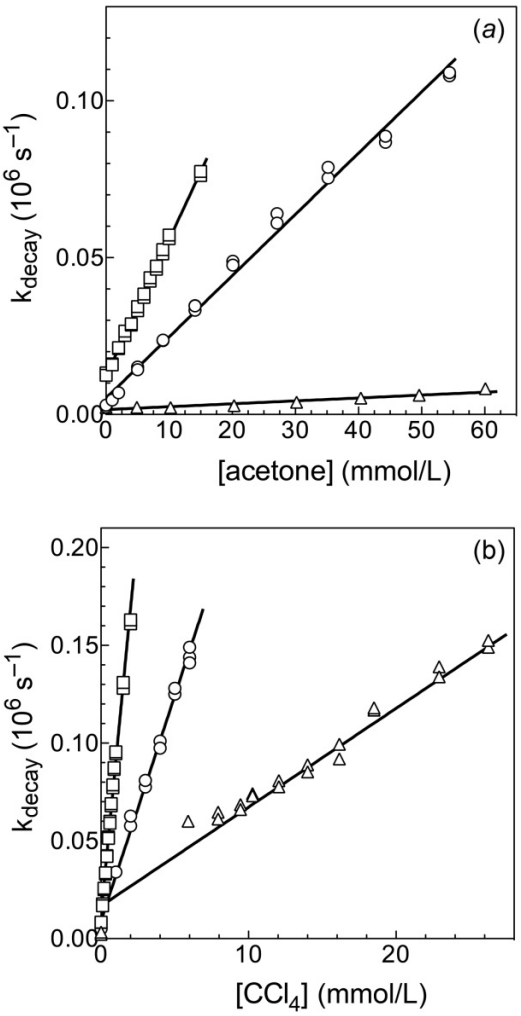

species, one exhibiting an absorption maximum in the 440–460 nm range and a lifetime similar to that of the corresponding transient in hexane and hence assignable to the corresponding silenes, and the second exhibiting λ_{max} ~ 310 nm. The latter absorptions decayed on a distinctly faster time scale with both **5d** and **5e**, but on a similar time scale to the 450 nm absorption in the case of **5f**. Transient absorption spectra recorded at various times after the laser pulse for **5d** and **5e** in MeCN are shown in Fig. 5, while the analogous spectra obtained with **5f** are shown in Fig. 6*a*. Addition of MeOH to the MeCN solutions of **5d** and **5e** caused the lifetimes at 450 nm to shorten and the decays to follow clean pseudo first order kinetics. As we anticipated based on our earlier studies of silenes **6a**–**6c** (16, 17), plots of k_{decay} versus [MeOH] exhibited positive curvature; polynomial least-squares fitting of the data to eq. [2] revealed a good correlation with the square of the MeOH concentration, as is illustrated in Fig. 7*a*. In contrast, the lifetime of silene **6f** in MeCN was barely affected upon addition of up to ca. 2 mol/L MeOH, so no attempt was made to determine a rate

Fig. 5. (*a*) Transient absorption spectra recorded 32–96 ns (-○-), 13.1–13.8 μs (-□-), and 139.5–140.6 μs (Δ) after the laser pulse, from the laser photolysis of a 0.07 mmol/L solution of **5d** in deoxygenated MeCN; the inset shows transient decays recorded at 300 and 440 nm. (*b*) Transient absorption spectra recorded 0–1.2 μs (-○-), 15.4–16.6 μs (-□-), and 99.8–101.1 μs (Δ) after the laser pulse, from the laser photolysis of a 0.07 mmol/L solution of **5e** in deoxygenated MeCN; the inset shows transient decays recorded at 300 and 460 nm.

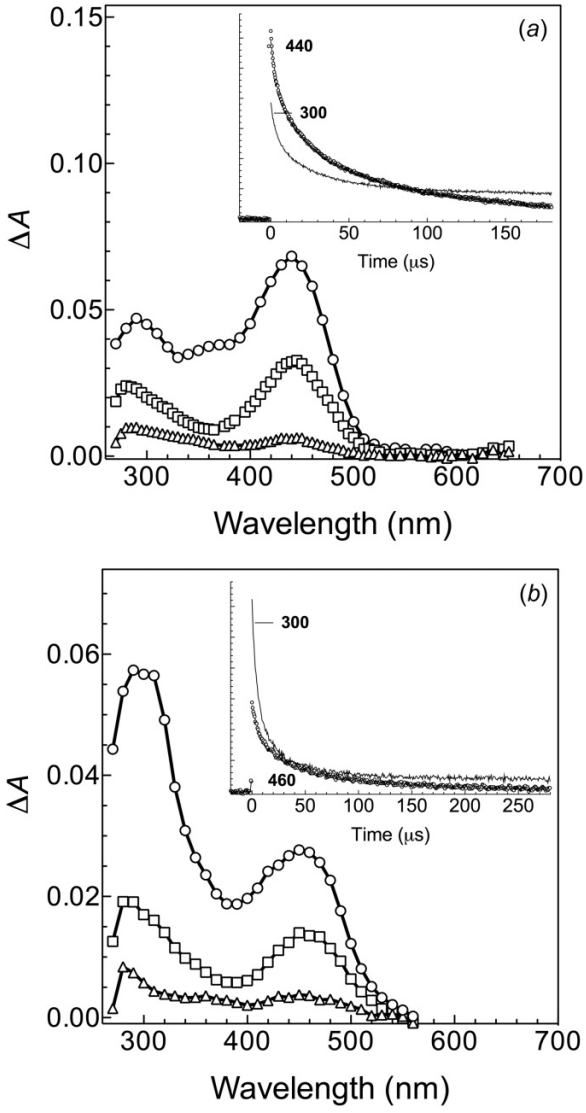

constant in this case. Silene **6f** could actually be detected quite easily in neat MeOH solution, where it exhibited a lifetime of τ ~ 38 μs and the same absorption maximum as in hexane and MeCN; the spectrum is shown in Fig. 6*b*. The effect of added MeOH on the short wavelength signals observed in experiments in MeCN solution was not investigated.

$$[2] \qquad k_{decay} = k_0 + k_1[\text{MeOH}] + k_2[\text{MeOH}]^2$$

In contrast to the behavior observed with MeOH, addition of AcOH to MeCN solutions of **5d**–**5f** resulted in increases in k_{decay} that varied linearly with concentration in all three

© 2008 NRC Canada

Fig. 6. (*a*) Transient absorption spectra recorded 0–3.2 μs (-○-), 57.6–60.8 μs (-□-), and 540–542 μs (Δ) after the laser pulse, from the laser photolysis of a 0.07 mmol/L solution of **5f** in deoxygenated MeCN; the inset shows transient decays recorded at 290 and 450 nm. (*b*) Transient absorption spectra recorded 0–0.6 μs (-○-), 23.0–24.3 μs (-□-), and 135–136 μs (Δ) after the laser pulse, from the laser photolysis of a 0.07 mmol/L solution of **5f** in deoxygenated MeOH; the inset shows transient decays recorded at 320 and 450 nm.

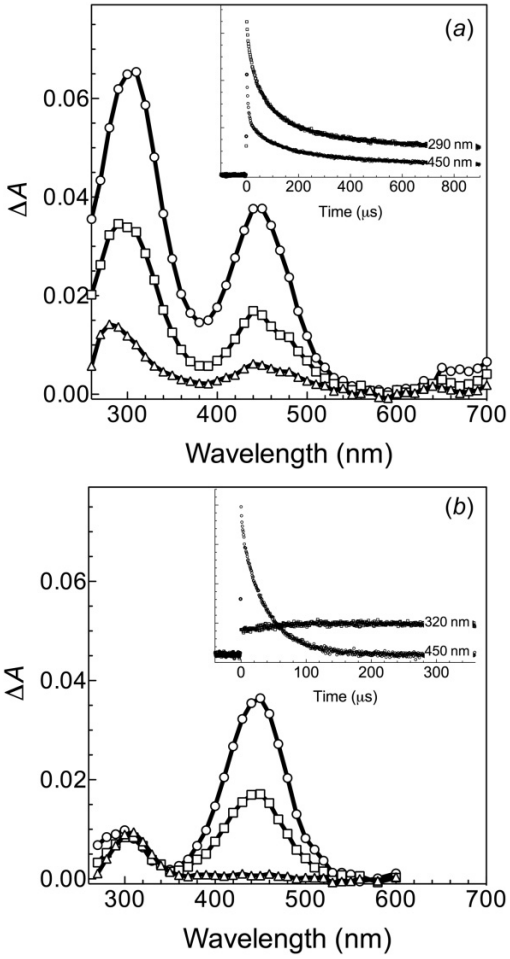

cases. The corresponding quenching plots are shown in Fig. 7*b*.

The kinetic data obtained in these experiments are summarized in Table 1, along with the corresponding, previously reported data for **6a**–**6c**.

Discussion

While early product studies of the photochemistry of **5d**–**5f** focused largely on the reactions of the corresponding silylenes (SiMePh, $SiPh_2$, and $Si(Ph)SiMe_3$, respectively) with various substrates (18, 19, 21, 22), several of them also reported the isolation of products derived from trapping of silenes **6d**–**6f**; specifically, those studies that employed aliphatic dienes (23, 26, 37), terminal alkenes (29, 30), acetone (37), or alcohols (24, 25, 27) as trapping agents. It is clear from these studies that the photolysis of **5d**–**5f** in fluid

Fig. 7. Plots of (*a*) k_{decay} vs $[MeOH]^2$ and (*b*) k_{decay} vs [AcOH] for the quenching of silenes **6d** (□) and **6e** (○) by MeOH and AcOH in deoxygenated MeCN at 25 °C; the inset in (*b*) shows the quenching plot for silene **6f** by AcOH.

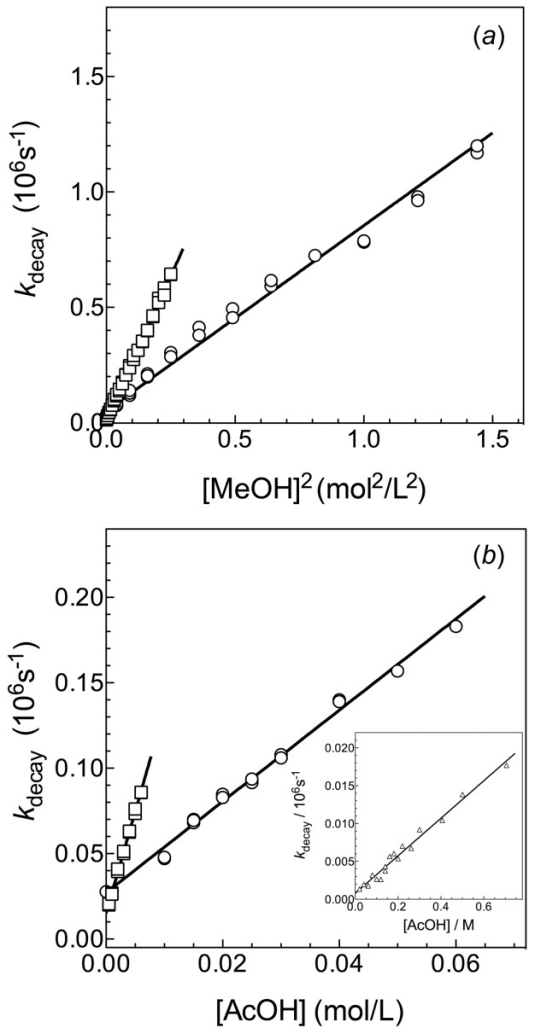

solution produces the corresponding silene derivatives in yields comparable to those of the corresponding silylenes and their co-product, Si_2Me_6, in all three cases. Thus, both reactive intermediates should in principle be detectable by laser flash photolysis methods, given an adequate appreciation of what to expect in the way of relative absorption intensities and reactivity patterns for the two species. The lowest energy (π,π*) absorption band in the UV–vis spectra of silenes of this general structure is relatively intense ($\varepsilon_{max} \geq 2 \times 10^4$ $(mol/L)^{-1}$ cm^{-1}) (15), in contrast to the relatively weak ($\varepsilon_{max} \sim 10^3$ $(mol/L)^{-1}$ cm^{-1} (46)) lowest energy (n,p) absorption band in the UV–vis spectra of arylsilylenes. Given that the two types of products are formed in similar yields in all three cases, detection of the silene will clearly be a much easier task than detection of the silylene.

Our flash photolysis results for **5d**–**5f** are indeed consistent with the formation of two distinct transient products in all three cases. The dominant transient absorptions, which we assign to the silenes **6d**–**6f** based on comparisons of their absorption spectra and reactivities to those of the related an-

© 2008 NRC Canada

Chart 3.

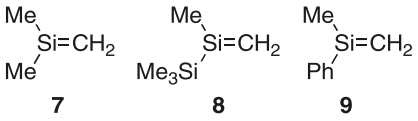

7 **8** **9**

alogues **6a**–**6c** (vide supra), are centered in the 440–460 nm spectral range and exhibit lifetimes of several hundred microseconds or greater; these are the species that were characterized in the earlier laser photolysis studies of **5d** (31, 32) and **5e** (33) in cyclohexane solution. Superimposed on these absorptions in hexane are those assignable to the corresponding silylenes, which are considerably shorter-lived and are quenched several orders of magnitude more rapidly than the 440–460 nm species by MeOH and Et_3SiH; in all three cases, the rate constants are close to the diffusion-controlled limit and are in good agreement with the values reported by us earlier for the reactions of $SiMe_2$ and $SiPh_2$ with the same substrates under similar conditions (34, 45). The presence of $SiPh_2$ in the end-of-pulse spectrum from **5e** is revealed by a relatively strong absorption band centered at λ_{max} = 290 nm, which is due to the $S_0 \rightarrow S_2$ transition of the silylene, and much weaker absorptions in the 480–530 nm range due to the $S_0 \rightarrow S_1$ transition, which we have shown is centered at λ_{max} = 515 nm in hexane at 25 °C (34). Similar short-lived absorptions (λ_{max} ~ 270, 510 nm) are observed in the end-of-pulse spectrum from laser photolysis of **5d**, superimposed on the much stronger absorptions of the long-lived transient coproduct (i.e., silene **6d**). The spectrum of this short-lived species is again quite similar to the low temperature matrix spectrum from **5d** (40), consistent with it being due to the corresponding silylene, SiMePh. With **5f**, on the other hand, the only short-lived absorptions detectable in the end-of-pulse spectrum are centered at λ_{max} ~ 290 nm, and the long wavelength absorption band expected for $Si(Ph)SiMe_3$ on the basis of its low temperature spectrum (44) could not be detected. This is very likely due simply to the lower sensitivity of our instrument at wavelengths above 600 nm coupled with the much lower extinction coefficient of the absorption compared to that at 290 nm (see Fig. 3*a*). Assignment of the latter to $Si(Ph)SiMe_3$ is supported by the observation that it is quenched by MeOH and Et_3SiH with rate constants similar to those measured for the other two silylenes.

The assignment of the dominant, long-lived absorptions to the corresponding silenes **6d**–**6f** is based on comparisons of their spectra and reactivities to those of the related analogues **6a**–**6c** (16, 17), coupled with a knowledge of the effects of methyl-, phenyl- and trimethylsilyl-substitution on the UV–vis spectra and reactivity of the "simple" silene derivatives **7**–**9** (Chart 3) and **3** (3, 13, 47–49). The difference in the absorption maxima of silenes **6d** (λ_{max} = 440 nm) and **6e** (λ_{max} = 460 nm) is consistent with the trend expected from consideration of the spectra of **6a**–**6c**, which exhibit a regular red-shift in λ_{max} as the methyl groups in **6a** (λ_{max} = 425 nm) are replaced with first one phenyl substituent (i.e., **6b**; λ_{max} = 460 nm) and then a second (i.e., **6c**; λ_{max} = 490 nm) (16). As has also been observed for **6a**–**6c** (16), there is no change in the positions of the absorption maxima of **6d**–**6f** upon changing the solvent from hexane to MeCN.

Scheme 2.

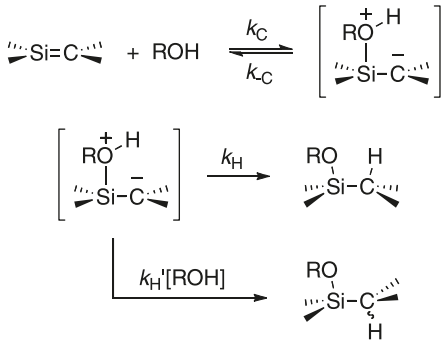

Similarly, the relative reactivities of **6d** and **6e** toward MeOH, AcOH, acetone, CCl_4, and O_2, with **6d** exhibiting modestly higher reactivity than **6e** in every case, are quite similar to the differences between the rate constants for reaction of **6a** and **6b** with the same six substrates, as well as to the corresponding differences between **6b** and **6c** (16, 17) (see Table 1). Substitution of a methyl substituent with trimethylsilyl at the silenic Si-atom is known to cause a somewhat smaller red-shift in the UV–vis spectra of silenes compared to phenyl-for-methyl substitution (cf. **7** (λ_{max} = 255 nm) (48), **8** (λ_{max} = 285 nm) (13), and **9** (λ_{max} = 315 nm) (49)), but results in substantially larger reductions in reactivity toward MeOH addition (cf. **7** ($k_1 = 4.9 \times 10^9$ $(mol/L)^{-1}$ s^{-1}) (48), **8** ($k_1 = 1.8 \times 10^8$ $(mol/L)^{-1}$ s^{-1}) (13), and **9** ($k_1 = 3.2 \times 10^9$ $(mol/L)^{-1}$ s^{-1}) (49)). These trends lead to the prediction that compared to the series **6a**–**6c**, there should be a smaller red-shift in λ_{max} as one proceeds through the series **6a**, **6d**, and **6f**, accompanied by a much larger reduction in reactivity towards MeOH. Clearly, the results are in excellent agreement with this prediction. It can be concluded that the UV–vis spectra and reactivity exhibited by **6d**–**6f** follow trends that are not only internally consistent, but are consistent as well with those exhibited by **6a**–**6c** given the known effects of methyl-, phenyl-, and trimethylsilyl-substitution at silicon on the spectra and reactivity of other transient silene derivatives.

Comparison of the kinetic data for the two groups of compounds **6a/6d/6f** and **6c/6e/6f** allows a more detailed assessment of the effects of sequential trimethylsilyl substitution on the kinetics of the six silene-substrate reactions that have been studied in this work. In general, increasing TMS substitution in both series of compounds leads to a reduction in the rate constant for all six of these reactions, which is consistent with previously established trends for other silene derivatives (8, 50). However, the effect varies tremendously with the specific reaction type. For example, the sequential decrease in the rate constants for quenching by CCl_4 and O_2 with increasing TMS substitution in the two series of compounds is relatively small and more or less additive, while for quenching by acetone and DMB the introduction of the first TMS group results in a substantially larger reduction in reactivity than the introduction of the second TMS group. Interestingly, the opposite is true for quenching by MeOH and AcOH.

Of the six reactions studied, that with MeOH exhibits the largest substituent effect on the reaction kinetics. The mech-

© 2008 NRC Canada

Scheme 3.

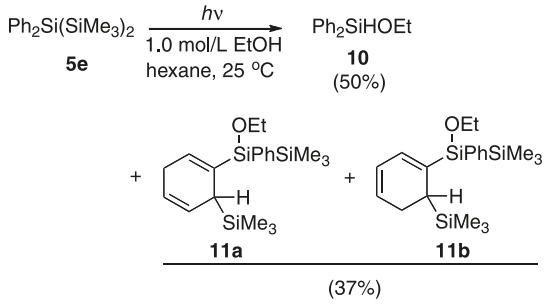

Scheme 4.

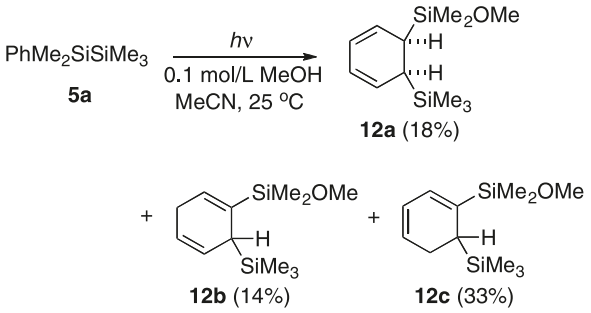

anism has been shown to involve initial, reversible nucleophilic attack at silicon to form a zwitterionic complex that proceeds to product via rate-controlling proton transfer from oxygen to the silenic carbon, the latter by competing unimolecular and catalytic pathways (Scheme 2) (10, 15, 17, 47). While this results in overall 1,2-addition in simple (nonconjugated) silenes, three regioisomers corresponding to 1,2-, 1,4-, and 1,6-addition are possible in the reaction of silenes of the type considered here, where the Si=C bond forms the terminus of a 1-silahexatrienyl system. The 1,4- and 1,6-addition products normally dominate the product mixtures from silenes of this type (51); this is exemplified by the results of Kira and co-workers (24, 25) for the photolysis of **5e** in hexane containing 1.0 mol/L ethanol, which yields ethoxydiphenylsilane (**10**; 50%; from trapping of $SiPh_2$) and the 1-silahexatriene-derived products **11a** and **11b** in a combined yield of 37% at 25 °C (Scheme 3). The corresponding 1,2-addition product has been reported in only one instance that we are aware of, from reaction of silene **6a** (generated by photolysis of **5a**) with MeOH (17). The product distribution obtained from reaction of silene **6a** with MeOH (Scheme 4) depends on the alcohol concentration, with reasonable yields of the 1,2-addition product (**12a**) being obtained only at very low alcohol concentrations (17). The 1,4- and 1,6-addition products (**12b** and **12c**, respectively) dominate the reaction mixture at higher alcohol concentrations, conditions that are typical of most of the published studies of the chemistry of silenes of this type. It can thus be concluded that these two regioisomers arise from the catalytic H-transfer pathway for decomposition of the initially formed silene-alcohol complex, while the 1,2-addition product results from the unimolecular H-transfer pathway (17).

The competition between unimolecular and catalytic intracomplex proton transfer is revealed in kinetic experiments by a quadratic dependence of the silene decay rate constant on alcohol concentration, since the catalyst for the latter pathway is a second molecule of the alcohol (see Scheme 2) (10, 15, 17). A variety of mechanisms are possible for the catalysis. With silenes such as **6a**–**6c** in polar solvents, the evidence suggests that it proceeds via a deprotonation-protonation sequence (17), favoring the formation of 1,4- and 1,6-adducts, as mentioned above. In principle, the process could alternatively proceed via a protonation-deprotonation sequence leading to predominant trans-addition (10) or via a concerted "proton-shuttling" mechanism in which the second molecule of alcohol acts simultaneously as acid and base. The transition state for this latter process is envisioned as being similar to that involved in the concerted reaction of the Si=C bond with the hydrogen-bonded dimer of the alcohol, as was proposed recently for the addition of MeOH to silene **2** in hexane solution (8) and should result in overall syn-addition. In any event, whether or not the predicted quadratic dependence of the silene decay rate constant (k_{decay}) on alcohol concentration can actually be observed with a given silene depends on the magnitude of the overall *second*-order rate constant and the maximum time resolution of the kinetic method. Strongly electrophilic silenes such as **3** and **9** (for which $k_1 \sim 10^9$ $(mol/L)^{-1}$ s^{-1} in MeCN) show only the first-order (in alcohol) kinetic component, because it is so fast that the lifetime of the silene becomes too short to be detected on the nanosecond time scale at the higher alcohol concentrations necessary for the second-order component (k_2) to become kinetically significant (47, 49). Moderately reactive silenes (such as **6a**–**6c**, for which $k_1 \leq 3 \times 10^8$ $(mol/L)^{-1}$ s^{-1} in MeCN) typically show both the first- and second-order components (3). Only the second-order component is observed with **6d** and **6e** (see Fig. 7*a*), indicating that the overall second-order reaction pathway is slowed so dramatically relative to that with **6a**–**6c** that it cannot be detected at all; the *only* kinetically significant mechanism for reaction of MeOH with these silenes involves two molecules of the alcohol in the transition state for the rate controlling step, and overall third order reaction kinetics. The rate constant for this process is more than 500 times slower than in **6a**–**6c**, reflecting a substantial reduction in electrophilicity due to the introduction of the TMS substituent at the silenic silicon atom. Silene **6f**, which bears *two* TMS-substituents at silicon, is so weakly electrophilic that its lifetime in MeCN is unaffected by addition of up to 2 mol/L MeOH, and it remains remarkably long-lived even in neat MeOH solution. There is not even a shift in the absorption maximum in the alcohol solvent relative to that in hexane or MeCN, which provides a further indication of the extremely low degree of electrophilicity of this silene derivative. The absorption spectra of all three derivatives are identical in THF and MeCN solution, as is also true of silenes **6b** and **6c**; of this series of silenes only **6a** exhibits a blue-shift of its absorption maximum in THF relative to its value in MeCN, due to complexation with the ether solvent (16). Silene **6f** is estimated to be roughly two orders of magnitude more reactive toward MeOH addition than the Apeloig silene **2**, from comparison of the lifetimes of the two species in MeOH (τ_{6f} =

© 2008 NRC Canada

Scheme 5.

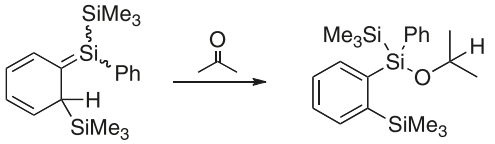

38 μs) or 9:1 *v*/*v* MeOH:THF (τ_2 ~ 14 ms (8)) at 25 °C. This could be the simple result of the pronounced differences in steric bulk of the adamantylidene and cyclohexadienylidene substituents at the silenic carbon in the two silenes.

More moderate variations in rate constants are observed for quenching of the six silenes by acetone, AcOH, and DMB, which proceeds with clean overall second order kinetics in all cases. The major product of the reaction of silene **6e** with acetone is the silyl enol ether derived from formal ene-addition of the ketone C=O bond across the 1-silaallyl moiety of the silene (**13**; Scheme 5) (37); the analogous compounds are also the major products of the reactions of **6a**–**6c** with this ketone, accompanied by minor amounts of the siloxetanes derived from formal [2+2] cycloaddition (16). The formation of the latter products from silenes of this type is most likely general, but as they are rather sensitive to thermal and (or) hydrolytic decomposition, they have been detected in only a few instances (16, 38). The reaction is thought to proceed via a two-step mechanism initiated by formation of a biradical or zwitterionic intermediate that collapses to products via competing ring-closure and intramolecular H-migration (16, 38). The course of the reactions of silenes of this type with AcOH has not been fully established; the product mixture resulting from reaction of AcOH with silene **6a** proved to be intractable in earlier studies, leading to a complex mixture of at least eight products in MeCN solution (17). However, with simpler silenes such as **3** the reaction is known to proceed via formal 1,2-addition of AcOH across the Si=C bond (47). The mechanism is presumably analogous to an ene-addition, involving bonding of the carbonyl oxygen to silicon and transfer of the hydroxyl proton to carbon. The reactions of 1,3-butadiene with **6d** and DMB with **6e** and **6f** afford the corresponding ene-addition products (**14**–**16**; Scheme 6) (23, 26, 37), in identical fashion to the reaction of aliphatic dienes with other (phenyldisilane-derived) 1-silahexatrienes, such as **6a**–**6c** (16, 52). It is interesting to note that the rate constants for reaction of **6a/6d/6f** and **6c/6e/6f** with DMB follow similar trends as those for reaction with acetone (see Table 1), suggesting that for these silenes, Si=C bond polarity provides a similar driving force in both reactions.

The reactions of silenes of this type with O_2 and CCl_4 are unique in that they proceed much faster than is the case with simpler silene derivatives (3). This suggests that the substitution pattern at the silenic carbon is the main factor controlling the rates of these reactions, with substitution at the silenic Si atom playing only a secondary role. Accordingly, the span in reactivity throughout the present series of compounds toward these two substrates is relatively small, varying by a factor of less than 100 throughout the series (see Table 1); with **6d**–**6f**, these are the fastest reactions that these silenes undergo.

Scheme 6.

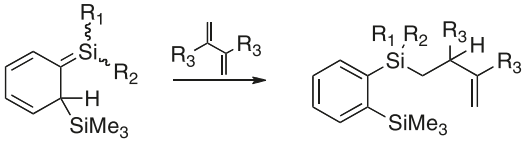

6d (R_1 = Me, R_2 = $SiMe_3$, R_3 = H) **14**
6e (R_1 = Ph, R_2 = $SiMe_3$, R_3 = Me) **15**
6f (R_1 = R_2 = $SiMe_3$, R_3 = Me) **16**

Scheme 7.

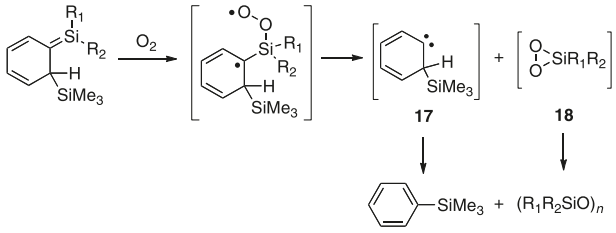

The reaction with O_2 is thought to proceed via rate-determining attack of the substrate at the silenic Si atom to yield the corresponding triplet 1,4-biradical, which in the present series of compounds enjoys significant resonance stabilization owing to the fact that the C-terminus is part of a cyclohexadienyl system (16). In the cases of **6a** and **6c**, the final products of the reaction are phenyltrimethylsilane and the corresponding silanone oligomers, $(Me_2SiO)_n$ from **6a** and $(Ph_2SiO)_n$ from **6c**, which have been proposed to be formed from carbene **17** and dioxasilirane **18**, respectively, produced by cleavage of the 1,4-biradical (Scheme 7) (16).

The product mixtures resulting from the reaction of silenes of this type with CCl_4 have not been fully characterized; we reported previously that photolysis of **5a** and **5c** in cyclohexane-d_{12} containing 0.03 mol/L CCl_4 leads to complex mixtures of products that include the chlorosilanes derived formally from Si–Si bond homolysis, and hexachloroethane (16). A reinvestigation of the photolysis of **5a** in the presence of CCl_4 under similar conditions to those used in our earlier study (0.03 mol/L **5a**; 0.03 mol/L CCl_4), and monitoring the course of the photolysis at low (ca. 3%–12%) conversions by (600 MHz) ^{1}H NMR spectroscopy, allowed quantification of the chemical yields of $PhMe_2SiCl$ (50%) and Me_3SiCl (26%) relative to consumed **5a**; chloroform (as $CHCl_3$; 14%) was also identified in the mixture. The spectra also showed evidence for the formation of at least one additional aromatic product, and a series of resonances in the δ 2.7–4 and δ 5.7–6.4 regions that are characteristic of 1,3- and 1,4-cyclohexadiene derivatives (16, 17), in significant yields. On the basis of these results, we suggest that the reaction of **6a** with CCl_4 most likely proceeds via Cl atom abstraction to yield cyclohexadienyl radical **19** and the trichloromethyl radical (Scheme 8). The formation of $PhMe_2SiCl$ is then accounted for by β-scission of radical **19**, while $CHCl_3$ and the unidentified aromatic and cyclohexadiene products are the products expected from coupling and disproportionation processes involving **19** and

© 2008 NRC Canada

Scheme 8.

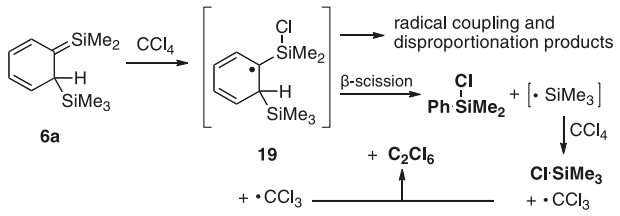

trichloromethyl and trimethylsilyl radicals, the latter being produced as the coproduct of the β-scission process in **19**.

It has been suggested that the reaction is likely initiated by electron transfer, based on the facts that quenching of **6a**–**6c** by CCl_4 is significantly faster in MeCN than in hydrocarbon solvents and more than 100 times faster than quenching by chloroform (16). The very modest variation in rate constant throughout the present series of compounds is probably also consistent with this notion, to the extent that varying combinations of methyl-, phenyl-, and trimethylsilyl-substitution at the silenic silicon would be expected to have relatively small effects on the oxidation potential of the 1-silahexatrienyl moiety that is common to all six of these silenes.

Finally, it is interesting to note that the UV–vis spectra recorded after photolysis of **5d**–**5f** in 3-MP matrixes at 78 K differ significantly from the time-resolved spectra obtained by flash photolysis in fluid solution at room temperature (see Figs. 1–3 and ref. (33)). This is consistent with a marked difference in the temperature and (or) medium dependences of the quantum yields for formation of the corresponding silylenes and silenes from photolysis of these compounds, with silene formation being suppressed almost entirely when the three compounds are photolysed in solid matrixes at low temperature.

Summary and conclusions

Laser flash photolysis of the well-known silylene precursors **5d**–**5f** in hexane solution leads to strong, long-lived transient absorptions due to the corresponding silene derivatives **6d**–**6f**, superimposed on the very weak, much shorter-lived absorptions due to the silylenes SiMePh (from **5d**), $SiPh_2$ (from **5e**), and $Si(Ph)SiMe_3$ (from **5f**). The UV–vis spectra of the silylenes in hexane solution can be extracted from the raw transient spectra by selective quenching with Et_3SiH, which reacts several orders of magnitude more rapidly with the silylenes than with the corresponding silenes. The resulting spectra are quite similar to those recorded in a 3-methylpentane matrix at 78 K, where photolysis of **5d**–**5f** affords the silylenes with high selectivity. In solution at room temperature, photolysis of the three compounds affords the corresponding silenes and silylenes in nearly equal yields.

Along with the related, phenyldisilane-derived silene derivatives **6a**–**6c**, the three silenes studied in the present work form a contiguous series of silenes bearing the six possible combinations of methyl-, phenyl-, and trimethylsilyl-substituents at the silenic silicon atom. The UV–vis spectra of the six silenes vary in a rational way with substitution, as do the absolute rate constants for their reactions with methanol (MeOH), acetic acid (AcOH), acetone, 2,3-dimethyl-1,3-butadiene (DMB), molecular oxygen, and carbon tetrachloride in hexane or MeCN solution. The results allow the first systematic, quantitative study of the well-known stabilizing effects of trimethylsilyl substitution at the silicon atom in silenes, applied to a selection of different reaction types. These include the nucleophilic addition of alcohols, the formal ene-addition reactions of carboxylic acids, ketones, and dienes, and the radical-like reactions with oxygen and CCl_4. All are slowed significantly by trimethylsilyl substitition at the silenic silicon atom, underlining the importance of Si=C bond polarity as a common, general driving force in the reactions of silenes.

Experimental

Compounds **5a** and **5d**–**5f** were prepared by the published methods (26, 53–55) and purified by vacuum distillation followed by column chromatography on silica gel using hexanes as eluant. Acetone (Caledon Reagent) was used as received from the supplier. Methanol (Baker Photrex) and 2,3-dimethyl-1,3-butadiene (Sigma-Aldrich) were distilled. Carbon tetrachloride (Sigma-Aldrich) was purified by distillation over P_2O_5 and passed through a short silica gel column. Glacial acetic acid (Sigma-Aldrich), acetonitrile (Caledon HPLC), and 3-methylpentane (Sigma-Aldrich spectrophotometric grade) were used as received from the suppliers. Triethylsilane (Sigma-Aldrich) was distilled from lithium aluminum hydride. Hexanes (EMD OmniSolv) and tetrahydrofuran (Caledon Reagent) were dried by passage through activated alumina under nitrogen using a Solv-Tek solvent purification system (Solv-Tek, Inc). Deuterated solvents were used as received from Cambridge Isotope Laboratories.

Laser flash photolysis experiments employed the pulses from a Lambda Physik Compex 120 excimer laser filled with F_2/Kr/Ne mixtures (248 nm; 25 ns; 90–120 mJ/pulse), and a Luzchem Research mLFP-111 laser flash photolysis system, modified as described previously (56). Solutions were prepared at concentrations (ca. 10^{-4} mol/L) such that the absorbance at the excitation wavelength (248 nm) was ca. 0.7, and were flowed through a 7 × 7 mm Suprasil flow cell from calibrated 100 or 250 mL reservoirs, fitted with a glass frit to allow bubbling of argon gas through the solution for at least 30 min prior to and then throughout the duration of each experiment, using a Masterflex™ 77390 peristaltic pump fitted with Teflon tubing (Cole-Parmer Instrument Co.). The sample cell and transfer lines were dried before use in a vacuum oven at 65–85 °C, while the reservoir was flame-dried and allowed to cool under an argon atmosphere. Reagents were added directly to the reservoir by microliter syringe as aliquots of standard solutions. Rate constants were calculated by linear least-squares analysis of decay rate-concentration data consisting of at least 10 points for all substrates except oxygen. For the latter, they were calculated from k_{decay} values in Ar-, air- and O_2-saturated solution, with use of neutral density filters to achieve reasonably clean pseudo first order kinetics in Ar-saturated solution. The errors in the absolute rate constants are quoted as twice the standard error obtained from the least-squares analyses.

© 2008 NRC Canada

Low temperature UV–vis spectroscopic experiments employed 2 cm × 1 cm × 1 cm cuvettes constructed from Suprasil quartz tubing (Vitro Dynamics, Inc.) and an Oxford Optistat™ liquid nitrogen cryostat equipped with an Oxford ITC601 temperature controller. Samples were irradiated in a Rayonet Photochemical Reactor (Southern New England Ultraviolet Company) fitted with 12 RPR-2537 lamps.

Steady state photolysis of a 0.031 mol/L solution of **5a** in C_6D_{12} containing CCl_4 (0.03 mol/L) and CH_2Cl_2 (0.005 mol/L; internal standard) was carried out in a quartz NMR tube, after deoxygenating the solution with a fine stream of argon and sealing the tube with a rubber septum. The photolysis was monitored at periodic time intervals by 600 MHz ^{1}H NMR spectroscopy (Bruker AV600), and chemical yields were determined from the slopes of concentration versus time plots, constructed by integration of the peaks due to **5a** and those products that could be specifically identified in the photolysate ($PhMe_2SiCl$, Me_3SiCl, and $CHCl_3$) by spiking the mixture with authentic samples. Representative NMR spectra and concentration versus time plots are given in the Supplementary Data.[2]

Acknowledgement

We thank the Natural Sciences and Engineering Research Council of Canada for financial support and for an Undergraduate Student Research Award for MSA.

References

1. G. Raabe, J. Michl, S. Patai, and Z. Rappoport. *In* The chemistry of organic silicon compounds. John Wiley & Sons, New York. 1989. pp. 1015–1142.
2. A.G. Brook and M.A. Brook. Adv. Organomet. Chem. **39**, 71 (1996).
3. T.L. Morkin, T.R. Owens, W.J. Leigh, Z. Rappoport, and Y. Apeloig. *In* The Chemistry of organic silicon compounds. Vol. 3. *Edited by* Z. Rappoport. John Wiley and Sons, New York. 2001. pp. 949–1026.
4. H. Ottosson and P.G. Steel. Chem. Eur. J. **12**, 1576 (2006).
5. A.G. Brook, F. Abdesaken, B. Gutekunst, G. Gutekunst, and R.K. Kallury. Chem. Commun. 191 (1981).
6. D. Bravo-Zhivotovskii, V. Braude, A. Stanger, M. Kapon, and Y. Apeloig. Organometallics, **11**, 2326 (1992).
7. S. Zhang, R.T. Conlin, P.F. McGarry, and J.C. Scaiano. Organometallics, **11**, 2317 (1992).
8. W.J. Leigh, T.R. Owens, M. Bendikov, S.S. Zade, and Y. Apeloig. J. Am. Chem. Soc. **128**, 10772 (2006).
9. A.G. Brook, J.W. Harris, J. Lennon, and M. El Sheikh. J. Am. Chem. Soc. **101**, 83 (1979).
10. M. Kira, T. Maruyama, and H. Sakurai. J. Am. Chem. Soc. **113**, 3986 (1991).
11. H. Sakurai, Z. Rappoport, and Y. Apeloig. *In* The chemistry of organic silicon compounds. John Wiley and Sons, Ltd., New York. 1998. pp. 827–855.
12. K.K. Milnes and K.M. Baines. Organometallics, **26**, 2392 (2007).
13. W.J. Leigh, R. Boukherroub, and C. Kerst. J. Am. Chem. Soc. **120**, 9504 (1998).
14. W.J. Leigh, C. Kerst, R. Boukherroub, T.L. Morkin, S. Jenkins, K. Sung, and T.T. Tidwell. J. Am. Chem. Soc. **121**, 4744 (1999).
15. G.W. Sluggett and W.J. Leigh. J. Am. Chem. Soc. **114**, 1195 (1992).
16. W.J. Leigh and G.W. Sluggett. Organometallics, **13**, 269 (1994).
17. W.J. Leigh and G.W. Sluggett. J. Am. Chem. Soc. **116**, 10468 (1994).
18. M. Ishikawa and M. Kumada. Adv. Organomet. Chem. **19**, 51 (1981).
19. P.P. Gaspar, M. Jones, Jr., and R.A. Moss. *In* Reactive intermediates. Vol. 3. John Wiley & Sons, New York. 1985. pp. 333–427.
20. H. Shizuka and H. Hiratsuka. Res. Chem. Intermed. **18**, 131 (1992).
21. M.G. Steinmetz. Chem. Rev. **95**, 1527 (1995).
22. P.P. Gaspar, R. West, Z. Rappoport, and Y. Apeloig. *In* The chemistry of organic silicon compounds. Vol. 2. *Edited by* Z. Rappoport. John Wiley and Sons, New York. 1998. pp. 2463–2568.
23. M. Ishikawa, K.I. Nakagawa, R. Enokida, and M. Kumada. J. Organomet. Chem. **201**, 151 (1980).
24. M. Kira, T. Miyazawa, S.Y. Koshihara, Y. Segawa, and H. Sakurai. Chem. Lett. **1995**, 3 (1995).
25. T. Miyazawa, S.Y. Koshihara, C. Liu, H. Sakurai, and M. Kira. J. Am. Chem. Soc. **121**, 3651 (1999).
26. M. Ishikawa, K.I. Nakagawa, and M. Kumada. J. Organomet. Chem. **178**, 105 (1979).
27. R. Nakao, K. Oka, S. Irie, T. Dohmaru, Y. Abe, and T. Horii. J. Chem. Soc. Perkin Trans. 2, **1991**, 755 (1991).
28. M. Ishikawa, S. Katayama, and M. Kumada. J. Organomet. Chem. **248**, 251 (1983).
29. M. Ishikawa, K.I. Nakagawa, M. Ishiguro, F. Ohi, and M. Kumada. J. Organomet. Chem. **152**, 155 (1978).
30. M. Ishikawa, K. Nakagawa, and M. Kumada. J. Organomet. Chem. **135**, C45 (1977).
31. P.P. Gaspar, D. Holten, S. Konieczny, and J.Y. Corey. Acc. Chem. Res. **20**, 329 (1987).
32. P.P. Gaspar, B.H. Boo, S. Chari, A.K. Ghosh, D. Holten, C. Kirmaier, and S. Konieczny. Chem. Phys. Lett. **105**, 153 (1984).
33. S. Konieczny, S.J. Jacobs, J.K. Braddock Wilking, and P.P. Gaspar. J. Organomet. Chem. **341**, C17 (1988).
34. A.G. Moiseev and W.J. Leigh. Organometallics, **26**, 6268 (2007).
35. A.G. Brook, Z. Rappoport, and Y. Apeloig. *In* The chemistry of organic silicon compounds. John Wiley and Sons, New York. 1998. pp. 1233–1310.
36. M. Ishikawa and H. Sakamoto. J. Organomet. Chem. **414**, 1 (1991).
37. K.L. Bobbitt and P.P. Gaspar. J. Organomet. Chem. **499**, 17 (1995).
38. N.P. Toltl and W.J. Leigh. Organometallics, **15**, 2554 (1996).
39. C.J. Bradaric and W.J. Leigh. Organometallics, **17**, 645 (1998).
40. M.J. Michalczyk, M.J. Fink, D.J. De Young, C.W. Carlson, K.M. Welsh, R. West, and J. Michl. Silicon, Germanium, Tin Lead Compd. **9**, 75 (1986).
41. A.G. Moiseev and W.J. Leigh. Organometallics, **26**, 6277 (2007).
42. J.A. Hawari, M. Lesage, D. Griller, and W.P. Weber. Organometallics, **6**, 880 (1987).
43. A. Sekiguchi, I. Maruki, and H. Sakurai. J. Am. Chem. Soc. **115**, 11460 (1993).

[2] Supplementary data for this article are available on the journal Web site (canjchem.nrc.ca) or may be purchased from the Depository of Unpublished Data, Document Delivery, CISTI, National Research Council Canada, Ottawa, ON K1A 0R6, Canada. DUD 3855. For more information on obtaining material refer to cisti-icist.nrc-cnrc.gc.ca/cms/unpub_e.shtml.

© 2008 NRC Canada

44. S.G. Bott, P. Marshall, P.E. Wagenseller, Y. Wang, and R.T. Conlin. J. Organomet. Chem. **499**, 11 (1995).
45. A.G. Moiseev and W.J. Leigh. J. Am. Chem. Soc. **128**, 14442 (2006).
46. R.T. Conlin, J.C. Netto-Ferreira, S. Zhang, and J.C. Scaiano. Organometallics, **9**, 1332 (1990).
47. W.J. Leigh, C.J. Bradaric, C. Kerst, and J.H. Banisch. Organometallics, **15**, 2246 (1996).
48. C. Kerst, R. Boukherroub, and W.J. Leigh. J. Photochem. Photobiol. A, **110**, 243 (1997).
49. W.J. Leigh, R. Boukherroub, C.J. Bradaric, C.C. Cserti, and J.M. Schmeisser. Can. J. Chem. **77**, 1136 (1999).
50. T.R. Owens, J. Grinyer, and W.J. Leigh. Organometallics, **24**, 2307 (2005).
51. M. Ishikawa, T. Fuchikami, and M. Kumada. J. Organomet. Chem. **118**, 155 (1976).
52. M. Ishikawa, T. Fuchikami, and M. Kumada. J. Organomet. Chem. **118**, 139 (1976).
53. V.J. Tortorelli, M. Jones, Jr., S. Wu, and Z. Li. Organometallics, **2**, 759 (1983).
54. M. Kumada, M. Ishikawa, and S. Maeda. J. Organomet. Chem. **2**, 478 (1964).
55. H. Gilman, D.J. Peterson, and D. Wittenberg. Chem. Ind. (London), 1479 (1958).
56. K. Nishiyama, M. Oba, H. Takagi, I. Fujii, N. Hirayama, Narisu, H. Horiuchi, T. Okutsu, and H. Hiratsuka. J. Organomet. Chem. **604**, 20 (2000).

© 2008 NRC Canada

Nonthermalized excited states in Ru(II) polypyridyl complexes probed by ultrafast transient absorption spectroscopy with high photon energy excitation

Sherri A. McFarland, Karen A.W.Y. Cheng, Felix S. Lee, Frances L. Cozens, and Norman P. Schepp

Abstract: The picosecond excited state dynamics of a series of homoleptic Ru(II) polypyridyl complexes (where LL = bpy, dmb, dmeob, dfmb, or dttb) have been investigated in aqueous solution at room temperature using femtosecond transient absorption spectroscopy with high photon energy excitation. All of the complexes studied produced similar spectroscopic signatures: a near-instantaneous bleach centered at 470–500 nm corresponding to the static absorption spectrum, as well as an intense absorption (475–650 nm) that decayed within the instrument response function (IRF) to form a broad, low-level absorption extending from 500–650 nm. Detailed analyses of both kinetic and spectral parameters by singular value decomposition (SVD) indicate that the excited state difference spectra contain contributions from at least three distinguishable species that have been assigned as ligand-based $\pi^* \leftarrow \pi^*$ and ligand-to-metal-charge-transfer (LMCT) transitions concomitant with the loss of the ground state metal-to-ligand-charge-transfer (MLCT) transition. Kinetic information extracted at 530 nm (an optical marker for the fully intraligand-delocalized ^{3}MLCT state) or 660 nm (LMCT transitions) appear to be biphasic in some cases with the amplitude of the IRF-limited component becoming larger with shorter wavelength excitation. Further, rise dynamics were observed at redder probe wavelengths for $Ru(bpy)_3^{2+}$ and $Ru(dttb)_3^{2+}$. These observations are different from those obtained using lower photon energy excitation and show that excitation wavelength strongly influences the early photophysical events in these Ru(II) complexes.

Key words: ruthenium, photophysics, lasers, transient absorption spectroscopy, excited states, singular value decomposition (SVD).

Résumé : Opérant à la température ambiante, en solution aqueuse, et faisant appel à la spectroscopie d'absorption des états transitoires au niveau de la femtoseconde et une excitation à l'aide de protons de haute énergie, on a étudié la dynamique d'états excités à la picoseconde d'une série de complexes polypyridyles du ruthénium(II) homoleptiques [dans lesquels LL = bpy, dmb, dmeob, dfmb ou dttb). Tous les complexes étudiés produisent des signatures spectroscopiques semblables: une décoloration pratiquement instantanée centrée aux environs de 470 à 500 nm correspondant au spectre d'absorption statique ainsi qu'une absorption intense (475–650 nm) qui décroît en dedans de la fonction de réponse de l'instrument (FRI) pour former une large absorption de faible intensité s'étendant de 500 à 650 nm. Des analyses détaillées des paramètres tant cinétiques que spectraux par la méthode de décomposition de valeur singulière (DVS) indique que le spectre différentiel de l'état excité contient des contributions provenant d'au moins trois espèces distinctes qui ont été attribuées à des transitions $\pi^* \leftarrow \pi^*$ à base de ligand et d'autres de transfert de charge ligand à métal (TCLM) concomitantes avec la perte de la transition de transfert de charge métal à ligand de l'état fondamental (TCML). L'information cinétique extraite des bandes à 530 nm (un marqueur optique pour l'état TCML) ou 660 nm (transitions TCLM) semble être biphasique dans certains cas, alors que l'amplitude de la composante limitée par la fonction de réponse de l'instrument devient plus importante lorsque la longueur d'onde de l'excitation devient plus courte. De plus, avec les complexes $Ru(bpy)_3^{2+}$ et $Ru(dttb)_3^{2+}$, on a observé une augmentation de la dynamique aux longueurs d'onde plus rouges de la sonde. Ces observations sont différentes de celles obtenues à l'aide d'une excitation avec des photons de plus faible énergie et elles démontrent que la longueur d'onde de l'excitation influence fortement les premiers événements photophysiques dans ces complexes du Ru(II).

Mots-clés : ruthénium, photophysique, lasers, spectroscopie d'absorption des espèces transitoires, états excités, DVS.

[Traduit par la Rédaction]

Received 8 June 2008. Accepted 18 September 2008. Published on the NRC Research Press Web site at canjchem.nrc.ca on 19 November 2008.

S.A. McFarland.[1] Chemistry Department, Acadia University, Wolfville, NS B4P 2R6, Canada.
K.A.W.Y. Chen, F.S. Lee, F.L. Cozens, and N.P. Schepp. Department of Chemistry, Dalhousie University, Halifax, NS B3H 4J3, Canada.

[1]Corresponding author (e-mail: sherri.mcfarland@acadiau.ca).

 doi:10.1139/V08-161 © 2008 NRC Canada

Fig. 1. (*a*) Jabłønski diagram showing the well-established photophysical model for the tris-Ru(II) polypyridyl family of complexes; (*b*) Jabłønski diagram illustrating the photophysics of $Ru(dmb)_3^{2+}$ derived from transient absorption experiments; (*c*) Jabłønski diagram showing the nonthermalized excited-state dynamics of $Ru(bpy)_3^{2+}$ based on fluorescence upconversion experiments.

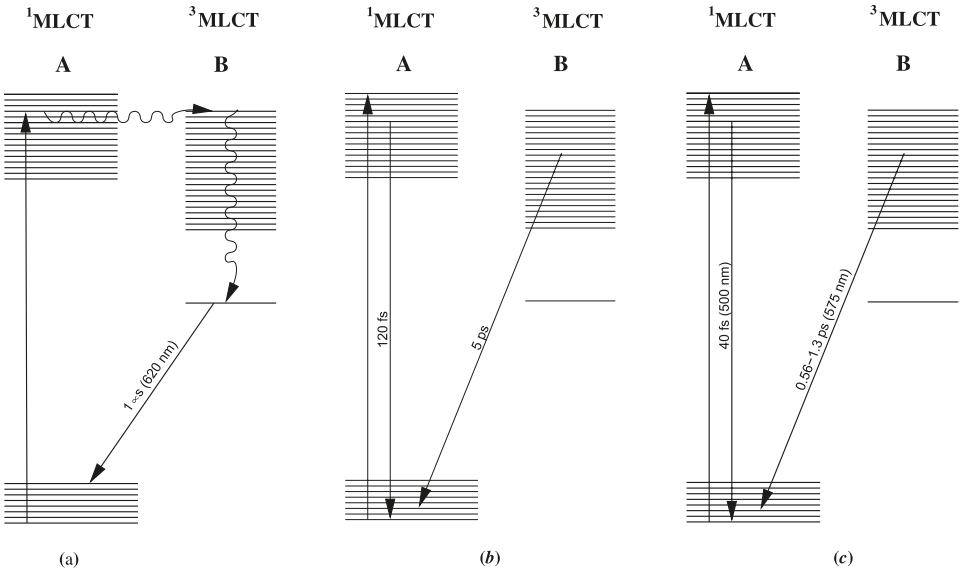

Introduction

A growing area of research involves the systematic investigation of photochemical and photophysical properties that define the behaviour of both organic and inorganic systems on short timescales. These endeavours not only provide invaluable information regarding the electronic structure of molecules, they also further our ability to use rational design in the construction of light-dependent molecular devices (1–4). Such an approach to functional chromophores requires a fundamental understanding of how molecules absorb and dissipate radiant energy. Often, absorption of photonic energy does not directly populate the lowest-lying electronic state of a molecule, the state that is usually involved in photon emission or photochemical reactions on conventional timescales. In fact, a host of states may be sampled between initial population of the Franck–Condon state and relaxation over all electronic and vibrational modes in the excited manifold, invoking a variety of radiationless decay mechanisms. Internal conversion (IC), intersystem crossing (ISC), and vibrational relaxation (VR) are important decay channels that ultimately dictate the path of excited state evolution and influence emission quantum yields as well as spectra.

The unifying feature of nonradiative decay among excited states is the short time that it takes for these transitions to occur. With the advent of femtosecond lasers, elucidation of ultrafast dynamics in both organic and inorganic systems is now possible, and reports from a number of groups studying diverse chemical systems continue to outline the importance of the earliest stages of excited state evolution (5–10). For example, nonthermalized excited states have been implicated in a variety of processes from electron and energy transfer (11, 12) to photochemical reactions including isomerization and ligand dissociation (13, 14). Perhaps more notable is the role that higher excited states play in applications involving solar energy conversion (15). Specifically, work from numerous laboratories has shown that the use of transition metal complexes as sensitizers for wide-band gap semiconductors is dependent on the efficiency of electron injection from the dye to the TiO_2 conduction band (16). This efficiency is determined by two competing processes: interfacial electron transfer and intramolecular relaxation dynamics (17, 18). Evidence suggests that electron transfer rates are maximal when operating in the nonergodic regime (19, 20)[2]; therefore, detailed investigation of the processes that immediately follow photon absorption is critical for developing more efficient devices based on this technology.

Nonradiative transitions among excited states are determined by the relative rates of electronic surface crossings and vibrational relaxation. Established models of intramolecular excited state relaxation are based largely on simple cascade population dynamics observed for organic molecules, wherein vibrational relaxation is much faster than formal changes in electron spin multiplicity ($k_{vib} \gg k_{IC} \gg k_{ISC}$) (21). Systems characterized by a large number of electronic and vibrational states that can participate in excited state decay do not adhere to this simplified kinetic scheme; consequently, excited state decay in transition metal complexes ultimately depends on the state(s) initially populated, resulting in a strong excitation-wavelength dependence of the observed kinetics, as well as ISC rates that are much faster than VR (9, 14, 22).

For example, both transient absorption and fluorescence upconversion experiments indicate that ISC in $Ru(bpy)_3^{2+}$ occurs with a time constant of $\tau = 40 \pm 15$ fs, whereas vibrational cooling in the ^{3}MLCT manifold spans several picoseconds when pumped at 400 nm (5, 23). Longer wavelength excitation ($\lambda_{ex} = 480$ nm) produces no significant changes in the excited state absorption spectra beyond 300 fs; these subpicosecond dynamics are reported to encompass a host of

[2] The term *nonergodic* in this context is used to describe a state that has not thermally equilibrated on the excited state surface. These states are intermediate in energy between the Franck–Condon state(s) and the Boltzmann-distributed ^{3}MLCT state(s).

© 2008 NRC Canada

Fig. 2. Jabløonski diagram illustrating the nonthermalized excited state dynamics for $Ru(dmb)_3^{2+}$ modified to include τ_2.

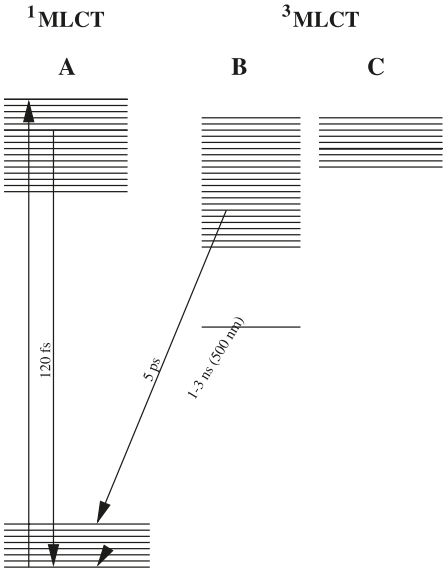

processes including ISC, IC, charge localization, VR, and intramolecular vibrational energy redistribution (IVR). Figure 1 summarizes these recent modifications to the well-established photophysical model for ruthenium(II) polypyridyl complexes.

To elucidate further the early events following photon absorption by transition metal complexes, our group has documented the picosecond dynamics produced in response to population of nonthermalized excited states in $Ru(bpy)_3^{2+}$ and a series of its derivatives by high photon energy excitation (24). Pump wavelengths of 388 and 258 nm produce emission at 500 nm that is more complex than previously reported using longer wavelength excitation (5, 6). Specifically, we determined additional time constants of τ = 1–3 ns for a series of 4,4′-substituted ruthenium(II) bipyridyl complexes (Fig. 2); while this additional relaxation pathway was not observed for $Ru(bpy)_3^{2+}$ with 388 nm excitation, 258 nm excitation of $Ru(bpy)_3^{2+}$ gave rise to a small contribution from the longer-lived component. These findings demonstrate the need for a comprehensive reassessment of our current understanding of inorganic photophysics, with an appreciation for the information that can be gleaned from close examination of the excitation-wavelength dependence of the observed kinetics.

Recently, our research efforts have concentrated on the use of picosecond luminescence and femtosecond absorption spectroscopy to address the excitation-wavelength dependence of excited state evolution in $Ru(bpy)_3^{2+}$ and related derivatives. In particular, we used femtosecond absorption spectroscopy to investigate the nature of a longer-lived state (τ = 1–3 ns) that was first detected in our earlier work involving picosecond luminescence experiments with short-wavelength excitation. We note a significant contribution to excited state decay from a broad band in the visible region that decays within the instrument response function (IRF) when pumped with 388 nm excitation. While the resolution of our instrument precluded the accurate determination of rate constants for the various processes, we were able to use

Chart 1. Bipyridyl ligands studied using transient absorption spectroscopy with 388 nm excitation.

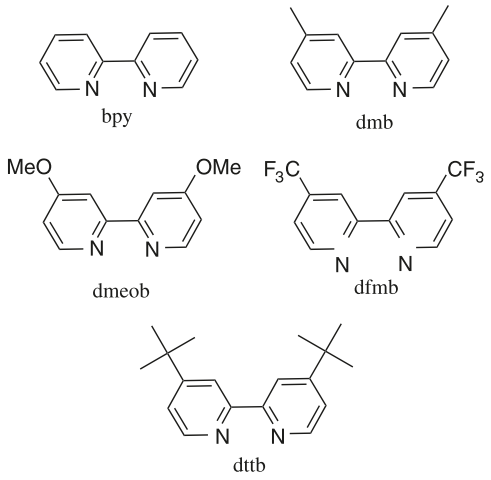

singular value decomposition (SVD) to discern rise dynamics that have not been previously reported for several of the complexes. Through this work we show that both excitation wavelength and subtle changes in ligand identity influence the nature of excited state dynamics, a finding of significant importance in the field of optoelectronic device construction. Moreover, these findings further support the observation that simple cascade population dynamics are not sufficient to describe the photophysics of transition metal complexes, and a growing number of exceptions for organic molecules have been documented as well (25–27).

Experimental section

Materials

Ruthenium(II) complexes (Cl_2 and $(PF_6)_2$ salts) and their corresponding ligands (Chart 1) were synthesized according to modified literature protocols (24) and chromatographed on silica gel ($MeCON:H_2O:KNO_3$ gradient) or on Sephadex. Following recrystallization from an acetonitrile/toluene mixture, the complexes were characterized by TLC, ^1H NMR, ^{13}C NMR, HPLC, and mass spectrometry. HPLC traces were run on samples before and after laser irradiation to ensure sample degradation was not a factor in the transient absorption experiments.

Static and nanosecond time-resolved spectroscopies

Static absorption, emission, and nanosecond time-resolved emission measurements were carried out as previously described (24), and where possible, the parameters obtained from static and nanosecond spectroscopies were compared with those in the literature.

Picosecond time-resolved emission spectroscopy

Time-resolved luminescence measurements were performed using a Clark-MXR CPA-2001 femtosecond laser for sample excitation and a streak camera (Axis-Photonique) coupled to a CCD camera (SenSys) for detection. Experimental details are reported elsewhere (24).

© 2008 NRC Canada

Sample preparation for femtosecond absorption spectroscopy

Ruthenium(II) complex (50 mL, 1 mmol/L) was diluted with solvent until the absorbance of the solution was 0.4–0.6 at 388 nm. This solution was recycled at a flow rate of 116.5 mL/min by a varistaltic pump through a Helma quartz flow cell (1 mm). The collection process was randomized to eliminate effects due to systematic sample degradation. Each raw spectrum consisted of 2500 accumulated shots and was corrected for luminescence and dark counts. Three of these raw spectra were averaged to produce the experimental spectrum recorded; each raw spectrum was manually inspected to discount faulty shots due to laser instability.

Femtosecond transient absorption spectroscopy

Femtosecond electronic absorption data were acquired using a Clark-MXR CPA-2001 femtosecond laser for generating pump and probe beams and a SpectroPro-300i Imaging spectrograph (Acton Research Corporation) equipped with an ST-116 photodiode array (PDA, Princeton Instruments, Inc.) for detection. Briefly, the CPA-2001 employs an all solid-state diode-pumped Erbium-fiber laser, which generates <150 fs, 775 nm pulses at 1 KHz with an output energy of ~800 μJ per pulse. The output is split by a STORC-2001 unit (Clark-MXR); one of the pulses is frequency-doubled to 388 nm (or tripled to 258 nm) to produce the pump beam, and the unchanged fundamental is used to generate a white-light continuum in sapphire (1 mm) or water contained in a 30 mm quartz cell. The frequency-doubled 388 nm pump beam (216 fs, 7 mm in diameter) is directed to the sample using a series of thin film mirrors and is softly focused (~1.5 mm) on the sample cell 15° from normal through a plano-convex lens with a 50 mm focal length. The excitation power at the sample is ~3.5 μJ, and for the series of complexes studied, the signal response varies linearly as the power is attenuated.

The 775 nm light used to generate the white light continuum is directed by a series of thin-film mirrors through two variable delay rails: the Parker Rail Table (Parker) allows time delays up to 7 ns with 188.3 fs resolution, while the NanoStepper (Baldor Motion Products) allows the probing of the first 500 fs of the experiment with 33.36 fs resolution. Once the fundamental beam passes through the second delay rail, it is directed through a Berek's compensator (New Focus), with the alignment and retardance set to emulate a 1/2 wavelength waveplate for 775 nm radiation, and a Glan-laser polarizer (Thorlabs). The Berek's compensator and Glan-laser polarizer together form a variable attenuator with output polarized at 54.7° with respect to the pump beam to avoid anisotropy effects. The polarized pump beam is focused by a 100 mm focal length BK7 broadband antireflective (BBAR)-coated planoconvex lens into a white light generator, and the broadband radiation is collimated by an achromatic MgF_2 lens with a focal length of 50.8 mm. If a water cell is used as the white light source, a Schott colour glass filter (S8612) is inserted to attenuate selectively the red wavelengths, and an iris is present to isolate the stable center of the broadband beam. Finally, the probe beam is focused (0.2 mm diameter) using an achromatic lens (150 mm focal length) through the sample onto a fibre optic cable.

Fig. 3. Potential energy surface diagram depicting the influence of excitation energy on population dynamics.

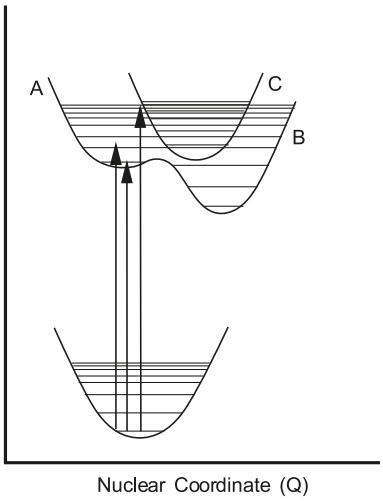

To collect full-spectrum data, the fibre optic cable directs transmitted light from the sample into a SpectroPro-300i Imaging spectrograph (Acton Research Corporation) coupled to a thermoelectrically cooled ST-116 PDA detector (Princeton Instruments, Inc.). A standard general purpose information bus (GPIB) computer interface allows data to be accumulated on a chip to maximize the number of laser experiments that can be measured while minimizing data transfer time. Absorbance values were calculated at each wavelength according to the following equation

$$A = \log\left(\frac{C_{\text{probe}} - D}{R_{\text{pump probe}} - F_{\text{pump}}}\right)$$

where A is the calculated absorbance value, C_{probe} is the probe data in the absence of the pump beam, D represents the dark counts, $R_{\text{pump,probe}}$ is the probe data collected while the pump beam is incident on the sample cell, and F_{pump} is the fluorescence data collected with the pump beam only. Since the chirp in our probe beam is significant over the spectral window (450–750 nm), distortion of the spectra at early times must be corrected. Unchirped spectra were produced from the original data using software written in-house. The temporal-spectral profile of the chirped pulse, a parameter required by the program, was calculated from two-photon absorption spectra of 2-methylnathphalene. Once $t = f(\lambda)$ has been determined, it remains invariant as long as the experimental setup is not altered.

Singular value decomposition

SVD analysis was carried out on the unchirped absorption spectra using MATLAB®. New matrices were constructed from the best three-component representations of the original, unchirped transient matrix spectra. Kinetics were then compared for the original data matrices and the results of the SVD at every 100th wavelength. Wavelength indices were selected to interrogate regions of the spectra corresponding to MLCT and LMCT transitions (480, 532, and 650 nm) and to determine the utility of SVD as a noise filter for address-

© 2008 NRC Canada

ing limitations imposed by the resolution of our current laser setup.

Results and discussion

Figure 3 provides a model illustrating the effect of excitation wavelength on the state(s) initially populated for some ruthenium(II) polypyridyl complexes. This qualitative picture is based on our recent discovery that 388 nm excitation produces picosecond luminescence at 500 nm that is not observed in experiments carried out with longer wavelength excitation (24). Femtosecond transient absorption spectra collected after 480 nm excitation as well as 400 nm excitation further corroborate this model (5, 6). The general trend is toward simpler kinetics when longer wavelength excitation is used, suggesting that less energetic wavelengths preclude access to some states. Our modification of the original kinetic model outlined by Bhasikuttan et al. (23) for $Ru(bpy)_3^{2+}$ (Fig. 2) proposes that state A represents the ^{1}MLCT manifold and state B represents the corresponding triplet manifold; the nature of state C, emissive only when high photon energy excitation is used, is the subject of this investigation.

We previously outlined three plausible scenarios concerning the nature of state C: (*i*) a higher vibrational level of state B, (*ii*) a local minimum on the surface of state B, or (*iii*) a distinct state altogether (24). If state C were indeed a "hot" vibrational state of B, then its lifetime would be expected to be much shorter than the observed lifetime (τ = 1–3 ns) since vibrational cooling is generally on the order of 0.5–5 ps. Therefore, only the latter possibilities need to be considered. To distinguish among these possibilities, we used femtosecond transient absorption spectroscopy to probe picosecond and subpicosecond dynamics.

Full-spectrum transient absorption data for all five ruthenium(II) homoleptic complexes (based on the ligands shown in Chart 1)[3] contained several unifying spectral features that were evident regardless of the timescale of the experiment (Figs. S1–S6).[4] Excitation at 388 nm produced the characteristic ^{1}MLCT ground state bleach centered in the range of 450–500 nm with maxima determined by the identity of the ligand substituents, which was superimposed on a broad absorption band spanning 475–650 nm. This extended absorption region consisted of two overlapping absorption bands as determined by spectroelectrochemical measurements: absorption transitions due to the reduced ligand at 500–530 nm and LMCT transitions involving the oxidized ruthenium center at 575–665 nm. These data agree well with spectra reported in the literature utilizing longer pump wavelengths (5, 6). However, the kinetics and relative amplitudes associated with these transitions exhibit an excitation-wavelength dependence not reported previously. Further, to our knowledge, the ultrafast dynamics of homoleptic 4,4′-methoxy, -trifluoromethyl, and -*tert*-butyl Ru(II) polypyridyl complexes have not been reported.

Upon excitation at 388 nm, all of the ruthenium(II) homoleptic complexes investigated produced spectroscopic signatures that remained unchanged when probed in 100 ps intervals from –0.5 ps to 5 ns. Considering the pronounced decay (τ = 1–3 ns) observed at 500 nm for the homoleptic 4,4′-substituted bipyridyl complexes in the luminescence experiments (τ_{ex} = 388 nm) and the absence of discernible decay kinetics in the region interrogating reduced bipyridine ligands in the corresponding transient absorption experiments, we conclude that the absorptive properties we observe are indicative of triplet surface dynamics.[5] The characteristic spectroscopic signatures, as well as established timescales for the formation of the ^{3}MLCT state (5, 6, 23) are consistent with such a conclusion. Based on the assumption that distinct states will produce distinct spectral characteristics, we assign state C as a metastable entity of ^{3}MLCT origin (scenario (*ii*), vide supra) that is accessed only with relatively short-wavelength excitation. Both steric and electronic perturbation of the complexes, by variation in ligand identity, produced similar results, indicating that this state is a general feature of homoleptic ruthenium(II) 4,4′-substituted bipyridyl complexes when probed with short-wavelength excitation. At even shorter wavelength excitation (τ_{ex} = 258 nm), similar states in the parent $Ru(bpy)_3^{2+}$ are populated (24). It should be noted that there is no reason a priori to expect that a decay in emission measurements should have a corresponding transient in the absorption measurements: the transitions being probed are not the same. Moreover, uncertainty exists with regard to whether the transients are actually absent in the absorption data as the absorption spectra are complicated by a superposition of MLCT and LMCT transitions that may mask any pertinent kinetics associated with the transition of interest.

Transient absorption spectra were also collected for all five homoleptic complexes on shorter timescales (t = 0–15 ps). Excitation with 388 nm radiation in aqueous solutions produced bleach signals corresponding to the ground

[3] The ultrafast dynamics of $Ru(bpy)_3^{2+}$ have been studied previously by fluorescence upconversion as well as transient absorption spectroscopy using longer pump wavelengths. $Ru(dmb)_3^{2+}$ has been studied previously by transient absorption spectroscopy with longer pump wavelengths. To the authors' knowledge, the nonthermalized excited states for homoleptic complexes derived from dmeob, dfmb, and dttb have not been reported previously.

[4] Supplementary data for this article are available on the journal Web site (canjchem.nrc.ca) or may be purchased from the Depository of Unpublished Data, Document Delivery, CISTI, National Research Council Canada, Ottawa, ON K1A 0R6, Canada. DUD 3850. For more information on obtaining material refer to cisti-icist.nrc-cnrc.gc.ca/cms/unpub_e.shtml.

[5] It should be noted that the luminescence we observed in the picosecond experiments at 500 nm occurred with a quantum yield having an upper limit of ~10^{-4}, estimated by the absence of 500 nm emission when using a conventional steady-state fluorimeter. If one assumes that this low quantum yield represents a rather small portion of the initially excited molecules, then corresponding changes in the transient absorption spectrum may not be detectable unless there is an allowed transition with appreciable oscillator strength from this weakly luminescent state. In the absence of significant changes in the spectroscopic profile of the complexes when probed with shorter wavelength excitation, we assume dynamics reflect relaxation in the triplet manifold. Similarly, we assume that the absence of dynamics in the transient absorption spectra indicates no signicant change in electronic configuration of the weakly luminescent state relative to the triplet state formed by ISC with a time constant of 40 fs. This assumption should be constantly re-examined for each particular case.

© 2008 NRC Canada

Fig. 4. Transient absorption spectra for $Ru(dmb)_3^{2+}$ in aqueous solution following <150 fs excitation at 388 nm.

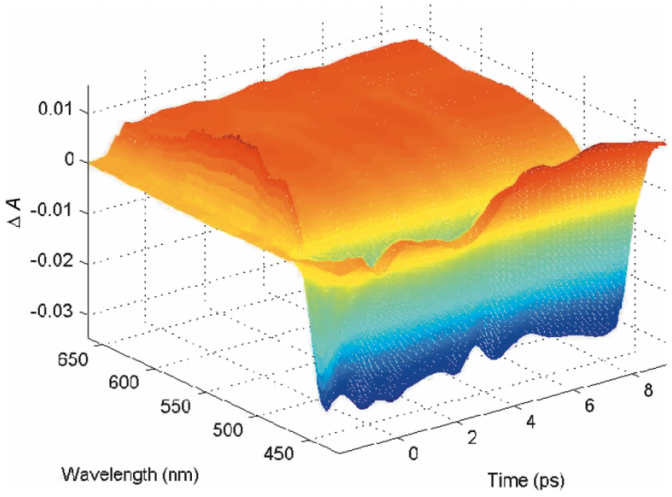

state ^{1}MLCT absorption, with precise maxima determined by the identity of the ligand (Fig. 4). Interestingly, the loss of ground state population did not appear instantaneous due to an overlapping broad absorption band that extended into the bleach region. This intense signal decayed within the instrument response function (~305 fs) to form a broad, low-level absorption extending from 500 to 650 nm that was identical to the absorption signature observed at 5 ns. After 1 ps, each absorption spectrum was relatively constant out to 15 ps in regions representative of the ground state bleach and bipyridine radical anions, a finding that contrasts with what others have measured for $[Ru(dmb)_3](PF_6)_2$ in acetonitrile resulting from 400 nm (~120 fs) excitation (6).

Previous femtosecond electronic absorption spectroscopy on $[Ru(dmb)_3](PF_6)_2$ reveals biexponential kinetics, which are not complete until ~15 ps at 532 nm. This portion of the spectrum is characteristic of the dmb^- chromophore (6). Deconvolution reveals a fast component ($\tau = 120 \pm 40$ fs) reported to reflect contributions from the ^{1}MLCT $\rightarrow$ ^{3}MLCT surface crossing on the timescale of the excitation pulse as well as a slower decay ($\tau = 5 \pm 0.5$ ps) due to vibrational cooling dynamics in the ^{3}MLCT excited state. With 388 nm (~150 fs) excitation, the slower dynamics previously associated with vibrational cooling in the triplet manifold are virtually absent and the signal is dominated by a transient that decays within the excitation pulse. In the absence of major changes in the overall spectroscopic signature for $[Ru(dmb)_3](PF_6)_2$ when excited with higher photon energy, we tentatively conclude that vibrational cooling is further facilitated when the Frank–Condon state possesses excess energy. The guiding principle in this assumption is that a constant spectral profile as a function of time indicates that the observed kinetics are not associated with a significant change in the electronic structure of the molecule (9). However, the excitation wavelength determines the nature of the initially populated vibronic hot state (16), and it is possible that the state initially populated could be fundamentally different, e.g., an intraconfigurational transition that does not significantly perturb the excited state absorption spectrum. Femtosecond infrared measurements will prove useful in future investigations regarding the dynamics associated with IVR and VC in these complexes.

Another interesting point of difference, with respect to the dynamics of $[Ru(dmb)_3](PF_6)_2$ when the pump wavelength is shortened, occurs in regions representative of predominantly LMCT transitions. With 388 nm excitation, we observed a sharp decay within the IRF superimposed on a low-level absorption that was constant out to 15 ps. According to Damrauer and McCusker (6), excitation (~120 fs) at 400 nm produces no discernible dynamics at 650 nm. Since spectroelectrochemical measurements indicate that there are contributions from both LMCT and dmb^- absorptions of the excited state, it is possible that this time-independent data at 650 nm reflect a superposition of decay and rise kinetics associated with two distinct signals that occur in a similar wavelength regime. In a case where a single process dictates evolution dynamics, time-independent data at 650 nm indicate that the dynamics must be highly localized, representing only the ligand housing the π^* electron of the ^{3}MLCT state. Our observation of a very fast decay in this region corroborates the assertion that the lack of dynamic features at 650 nm ($\lambda_{ex} = 400$ nm) in previous studies (6) is due to a superposition of LMCT and dmb^- absorptions, i.e., both the oxidized ruthenium center as well as a neutral ligand also contribute to the early events following photon absorption. Further, changing the excitation wavelength by only 12 nm changes the relative contributions of LMCT and dmb^- decay channels. Not only is this observation interesting from a photophysical standpoint, such control over excited state processes in transition metal complexes underscores the idea that judicious selection of excitation wavelength can profoundly influence the nature of excited state decay and may prove useful in tuning sensitizer properties for light-mediated applications.

To quantify time constants associated with the dynamics observed with 388 nm excitation of the complexes, we attempted to apply the method of singular value decomposition (SVD). SVD has been used successfully by others to analyze μs–fs transient absorption spectra when two or more transient species are involved (28–32). Briefly, a set of time-resolved spectra can be treated as a matrix **A**, where the *i*th row vector corresponds to the spectrum at the *i*th time delay point. According to the SVD theorem, the $m \times n$ $\Delta\mathbf{A}$ matrix can be written as the product of three matrices

$$\Delta\mathbf{A} = \mathbf{U}\cdot\mathbf{S}\cdot\mathbf{V}^T$$

where $\Delta\mathbf{A}$ is a $m \times n$ matrix consisting of absorbance changes at m wavelengths and n different time delays, **U** is a $m \times n$ matrix consisting of n orthonormal basis spectra, **S** is a $n \times n$ diagonal matrix containing the positive square roots of the eigenvectors (singular values) of **A**, and **V** is a $n \times n$ matrix where the columns (rows of $\mathbf{V}^T$) contain the time course amplitude for the corresponding basis spectra in matrix **U**. Basis spectra are scaled by their singular values to display their relative contributions to the observed data. The most useful information is contained in the first few components; increasing noise in the successive components results from the decreased amplitude of each basis spectrum in the observed spectra.

The SVD of the set of time-resolved spectra yielded four principal singular values (for all of the complexes) with $n =$

© 2008 NRC Canada

5 and higher singular values being almost zero and regarded as noise. Figure 4 was derived from the best four-component representation of the data matrix, illustrating the use of SVD as a noise filter (see Fig. S1 for original matrix).[4] Our attempts to use SVD as well as global analysis to extract kinetics did not yield readily interpretable results. This was not surprising given the lack of significant changes in the overall spectral profiles associated with relaxation processes such as vibrational cooling. A major problem with ultrafast dynamics is that nonthermalized excited states give rise to spectra that evolve continuously over time, precluding access to well-defined spectra.

Although the use of SVD and global analysis to extract time constants met with little success, the techniques did prove useful in analyzing the behaviour of the homoleptic complexes at long probe wavelengths, in the region dominated by LMCT transitions superimposed on the low energy shoulder of the reduced ligand $\pi^* \leftarrow \pi^*$ absorption. For both $Ru(dfmb)_3^{2+}$ and $Ru(dmb)_3^{2+}$, an IRF-limited decay to a constant background was observed. In the case of $Ru(dmb)_3^{2+}$, the absorption profile as a function of time with 388 nm excitation was very similar to that observed with longer excitation wavelengths (6), with the exception that the relative amplitude of the fast component to constant background was much larger with shorter wavelength excitation. This increased amplitude for the IRF-limited component with 388 nm excitation was a general feature that we observed for all of the complexes in regions probing both $\pi^* \leftarrow \pi^*$ and LMCT transitions. As indicated earlier, we are uncertain whether an increase in the rate of vibrational relaxation or a fundamental difference in the nature of the excited state(s) being probed is responsible; variable wavelength excitation should help clarify. These fast decay dynamics are difficult to interpret but are expected to reflect contributions from the ^{1}MLCT $\rightarrow$ ^{3}MLCT surface crossing. The absence of slower dynamics at 660 nm was not surprising given that λ_{probe} = 532 nm produced only an IRF-limited decay.

$Ru(bpy)_3^{2+}$ and $Ru(dttb)_3^{2+}$ showed interesting behaviour, as indicated in Fig. 5, for $Ru(dttb)_3^{2+}$. An IRF-limited decay followed by a slower rise that did not maximize over the observation window were noted in the transient absorption experiments collected over 15 ps. The slow rise must reach an asymptote shortly after 20 ps, however, since no changes were detected in this region in spectra collected over –0.5–5 ns. To our knowledge, this behaviour has not been documented for $Ru(bpy)_3^{2+}$ when excited at longer wavelengths, and this is the first report on the early dynamics of $Ru(dttb)_3^{2+}$. Curiously, λ_{probe} = 532 nm did not reveal similar rise kinetics, although others have observed analogous discrepancies for $Ru(dmb)_3^{2+}$ (6). In the case of $Ru(dmb)_3^{2+}$ excited at longer wavelengths, a slow decay is observed at λ_{probe} = 532 nm with no corresponding transient at λ_{probe} = 650 nm. The rationale behind this inconsistency, as well as others, has been attributed to an increase in the rate of vibrational cooling as the excited state(s) are probed farther to the red (6, 33, 34). Clearly, this particular explanation does not account for our observations for $Ru(dttb)_3^{2+}$ with shorter wavelength excitation and, therefore, should not be considered a general rule. Perhaps, in this case, there is a difference in the nature of the excited-state transitions being probed. Because the ligand participating in the LMCT transition is not the same ligand involved in the initial photon absorption, differences in the corresponding dynamics should not be surprising. Still, it is possible that that solution inhomogeneity becomes a factor on short timescales, producing distinct transients in the SVD analysis that arise from MLCT states involving ligands that have been rendered essentially nonequivalent. This phenomenon is well-known in solid-state spectroscopy, with MLCT energies shifted up to 1000 cm^{-1} between idential ligands on the same metal, owing to variations in their local environments (35, 36).

Fig. 5. Kinetic profile (λ_{probe} = 660 nm) for $Ru(dttb)_3^{2+}$ in aqueous solution following <150 fs excitation at 388 nm.

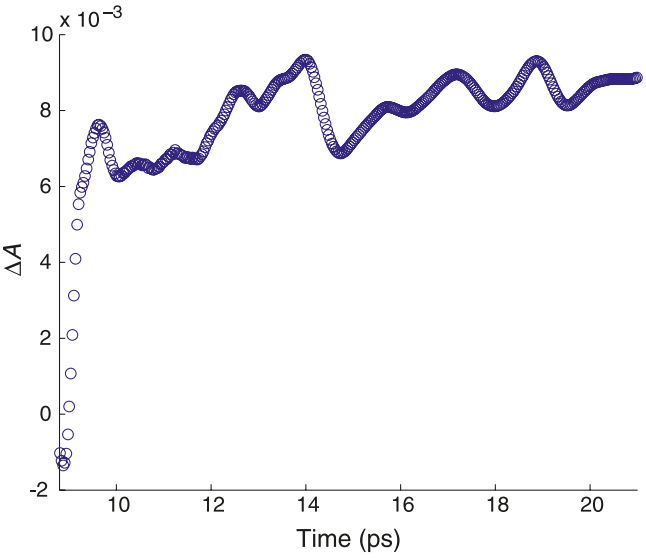

Concluding remarks

Our investigation of a series of related complexes underscores the effect that subtle changes in substituents on the bipyridine ligand have on the early relaxation processes that follow photon absorption. While our investigation produced qualitatively similar transient absorption spectra, the use of SVD revealed subtle differences between the complexes depending on the nature of the ligand. For the complexes where data are available, using longer wavelength excitation, namely $Ru(bpy)_3^{2+}$ and $Ru(dmb)_3^{2+}$, we compared our spectra for 388 nm excitation and noted several kinetic discrepancies, which further underscores the excitation and probe wavelength-dependence in transition metal photophysics. We acknowledge that information is lost within the IRF of our instrument in many cases. However, the pump wavelengths housed in our system allows for the probing of Franck–Condon states at the blue edge of the ^{1}MLCT absorption band as well as ligand-centered transitions, states that have not been probed by the conventional wavelengths used by others. While it is ideal to have data collected at various pump wavelengths, probe windows, and timescales on a single instrument, in reality this is feasible for only a very small portion of the overall timescale for electronic and vibrational relaxation, which can span from microseconds to femtoseconds in solution.

© 2008 NRC Canada

The impetus for using femtosecond absorption spectroscopy to characterize further the early events following photoexcitation of ruthenium(II) polypyridyl complexes was two-fold: (1) the τ = 1–3 ns time constant for luminescence at 500 nm that we measured for various 4,4′-substituted homoleptic complexes warranted further investigation, and (2) our ability to excite samples at both 258 and 388 nm, in conjunction with published transient absorption data collected at additional pump wavelengths for similar species, would begin a systematic investigation of the excitation-dependence of early photophysical events in transition metal complexes. Together with the findings of several other researchers, we anticipate that a detailed investigation of the excitation-wavelength dependence of transition metal complex photophysical parameters will outline a more realistic picture of inorganic photophysics where simple cascade population dynamics are not obeyed.

Acknowledgements

We gratefully acknowledge the Natural Sciences and Engineering Research Council of Canada (NSERC) for financial support of this work and the Canada Foundation for Innovation and the Nova Scotia Research Innovation Trust for research infrastructure. We also thank D. Magde for insightful discussions, P.D. Wentzell for his invaluable help with chemometric analyses and MATLAB®, and A. Thompson for use of her HPLC.

References

1. A. Hagfeldt and M. Gratzel. Acc. Chem. Res. **33**, 269 (2000).
2. J. Badjie, V. Balzani, A. Credi, S. Silvi, and J. Stoddart. Science (Washington, D.C.), **303**, 1845 (2004).
3. P. Mobian, J. Kern, and J. Sauvage. Angew. Chem. **43**, 2392 (2004).
4. M. Venturi, V. Balzani, R. Ballardini, A. Credi, and M. Gandolfi. Int. J. Photoenergy, **6**, 1 (2004).
5. N.H. Damrauer, G. Cerullo, A. Yeh, T.R. Boussie, C.V. Shank, and J.K. McCusker. Science (Washington, D.C.), **275**, 54 (1997).
6. N.H. Damrauer and J.K. McCusker. J. Phys. Chem. A, **103**, 8440 (1999).
7. A.T. Yeh, C.V. Shank, and J.K. McCusker. Science (Washington, D.C.), **289**, 935 (2000).
8. A. Vlcek. Coord. Chem. Rev. **200**, 933 (2000).
9. J. McCusker. Acc. Chem. Res. **36**, 876 (2003).
10. E.A. Juban and J.K. McCusker. J. Am. Chem. Soc. **127**, 6857 (2005).
11. B. Kraabel, J.C. Hummelen, D. Vacar, D. Moses, N. Sariciftci, A. Heeger, and F. Wudl. J. Chem. Phys. **104**, 4267 (1996).
12. C.N. Fleming, K.A. Maxwell, J.M. DeSimone, T.J. Meyer, and J.M. Papanikolas. J. Am. Chem. Soc. **123**, 10336 (2001).
13. I.R. Farrell, P. Matousek, and A. Vlcek, Jr. J. Am. Chem. Soc. **121**, 5296 (1999).
14. I.R. Farrell, P. Matousek, M. Towrie, A. Parker, D. Grills, M. George, and A. Vicek, Jr. Inorg. Chem. **41**, 4318 (2002).
15. C.G. Garcia, J.F. de Lima, and N.Y. Murakami Iha. Coord. Chem. Rev. **196**, 219 (2000).
16. G. Benko, J. Kallioinen, J.E.I. Korppi-Tommola, A.P. Yartsev, and V. Sundstrom. J. Am. Chem. Soc. **124**, 489 (2002).
17. N. Anderson, X. Ai, and T. Lian. J. Phys. Chem. B, **107**, 14414 (2003).
18. G. Benko, J. Kallioinen, P. Myllperkio, P.F. Trif, J.E.I. Korppi-Tommola, A. Yartsev, and V. Sundstrom. J. Phys. Chem. B, **108**, 2862 (2004).
19. R. Bernstein and A. Zewail. J. Phys. Chem. **90**, 3467 (1986).
20. A.J. Nozik. Annu. Rev. Phys. Chem. **52**, 193 (2001).
21. N.J. Turro. Modern molecular photochemistry. University Science Books, Mill Valley, California. 1991.
22. J. Shiang, I. Walker, N. Anderson, A. Cole, and R. Sension. J. Phys. Chem. B, **103**, 10532 (1999).
23. A.C. Bhasikuttan, M. Suzuki, S. Nakeshima, and T. Okada. J. Am. Chem. Soc. **124**, 8398 (2002).
24. S.A. McFarland, F.S. Lee, K. Cheng, F.L. Cozens, and N.P. Schepp. J. Am. Chem. Soc. **127**, 7065 (2005).
25. M. Beer and H. Longuet-Higgins. J. Chem. Phys. **23**, (1955).
26. M. Gutmann, M. Gudipati, P.-F. Schonzart, and G. Hohlneicher. J. Phys. Chem. 2433 (1992).
27. Y. Hirata. J. Phys. Chem. **96**, 6559 (1992).
28. H. Gampp, M. Maeder, C. Meyer, and A. Zuberbühler. Talanta, **33**, 943 (1986).
29. D.G. Lambright, S. Balasubramanian, and S.G. Boxer. Chem. Phys. **158,** 249 (1991).
30. K.N. Walda, X. Liu, V.S. Sharma, and D. Magde. Biochemistry, **33**, 2198 (1994).
31. J. Hofrichter, J.H. Sommer, E.R. Henry, and W.A. Eaton. Proc. Natl. Acad. Sci. U.S.A. **80**, 2235 (1983).
32. S. Yamaguchi and H. Hamaguchi. J. Chem. Phys. **109**, 1397 (1998).
33. A.L. Harris, J.K. Brown, and C.B. Harris. Annu. Rev. Phys. Chem. **39**, 341 (1988).
34. D.A.V. Kliner, J.C. Alfano, and P.F. Barbara. J. Chem. Phys. **98**, 5375 (1993).
35. H. Riesin, Y. Gao, and E. Krausz. Chem. Phys. Lett. **228**, 610 (1994).
36. H. Riesin, Y. Gao, and E. Krausz. Int. Rev. Phys. Chem. **16**, 291 (1997).

© 2008 NRC Canada

Modification of the NRTL and Wilson models for the representation of phase equilibrium behavior of aqueous amino acid – electrolyte solutions

Rahmat Sadeghi

Abstract: The extended NRTL and Wilson local composition models for amino acid solutions have been modified for the representation of the phase equilibrium behavior of aqueous amino acid – electrolyte solutions by considering cells with random composition for the reference Gibbs energies or enthalpies of local composition cells with a central amino acid molecule and also with a central ion. These new local composition models, which have a molecular thermodynamic framework, have been used to model the vapor–liquid and solid–liquid equilibrium behavior of amino acids and small peptides in aqueous solutions as functions of temperature, ionic strength, and amino acid compositions. The utility of the models is demonstrated with a successful representation of the activity coefficients and the solubility of several amino acids in different aqueous solutions.

Key words: amino acid, NRTL, Wilson, activity coefficient, solubility, aqueous solution.

Résumé : On a modifié les modèles de composition locale étendus de Wilson et NRTL pour représenter le comportement de la phase en équilibre de solutions aqueuses d'acides aminés en présence d'un électrolyte et, pour ce faire, on a considéré des cellules de composition aléatoire pour les énergies ou enthalpies de Gibbs de référence avec une molécule d'acide aminé central et aussi avec un ion central. On a utilisé ces nouveaux modèles de composition locale qui possèdent un squelette thermodynamique moléculaire pour le comportement de l'équilibre vapeur–liquide et solide–liquide d'acides aminés et de petits peptides dans des solutions aqueuses, en fonction de la température, de la force ionique et des compositions en acides aminés. On a démontré l'utilité des modèles à l'aide d'une représentation correcte des coefficients d'activité et de la solubilité de plusieurs acides aminés dans différentes solutions aqueuses.

Mots-clés : acide aminé, NRTL, Wilson, coefficient d'activité, solubilité, solution aqueuse.

[Traduit par la Rédaction]

Introduction

The thermodynamic properties of amino acids, such as solubility and activity coefficients in aqueous solutions, have been extensively studied to better understand their behavior in aqueous solution, the role of solute–solvent interactions on the conformational stability of proteins, and also the design and scale-up of chemical processes for the separation, concentration, and purification of valuable biochemicals (1). Therefore, the development of a model for the activity coefficients of amino acids in aqueous solutions has recently received a great deal of attention. In the last decade, several studies have been performed on the correlation of activity coefficients and solubilities of amino acids in water. In most of these studies, the conventional local composition thermodynamics models (2–7), group contribution methods (8–11), and models based on perturbation theory (12–19) were used to correlate the activity coefficients and solubility of amino acids in aqueous solutions.

Received 22 August 2008. Accepted 10 October 2008. Published on the NRC Research Press Web site at canjchem.nrc.ca on 19 November 2008.

R. Sadeghi. Department of Chemistry, University of Kurdistan, Sanandaj, Iran (e-mail: rsadeghi@uok.ac.ir).

One of the most successful models for the representation of phase equilibrium behavior of amino acids in aqueous solutions is the model developed by Chen et al. (4). They used their own version of the electrolyte NRTL model (20) to model the activity coefficients of amino acids and peptides. In this model, long-range interactions are represented by the Pitzer–Debye–Huckel form (21), and short-range interactions are given by a modified form of the NRTL equation [22]. Similar to the NRTL model (4) in our recent previous work (23), the Wilson model was extended to calculate activity coefficients and the solubility of amino acids in aqueous solutions. In these models (4, 23), the pure liquid solvent, the pure liquid amino acid, and the pure completely dissociated electrolyte, respectively, were used for the reference Gibbs energies or enthalpies of local composition cells with a central solvent molecule, central amino acid molecule, and central ion. It has been shown that (24–26) in the local composition models, when the random case is considered for the reference state of the components, the model becomes more flexible than the case in which a pure component is considered for the reference state of components. The promising features of the random case for the reference state of the components led us to improve the NRTL and Wilson models for mixture containing both amino acid and electrolyte, which is an important system in respect to its use in biotechnology. In this study, in continuation of our previous

 doi:10.1139/V08-166 © 2008 NRC Canada

work on the extension of local composition models for amino acid solutions (23), the extended NRTL (4) and Wilson (23) models for amino acid solutions have been modified for the representation of the phase equilibrium behavior of aqueous amino acid – electrolyte solutions. Although in the models proposed in this work, similar to the extended NRTL (4) and Wilson (23) models, the pure liquid solvent was used for the reference Gibbs energies or enthalpies of local composition cells with a central solvent molecule; however, cells with random composition are used for the reference Gibbs energies or enthalpies of local composition cells with a central amino acid molecule and also with a central ion. These extended models are applied to calculate the solubility of amino acids in pure water and in aqueous electrolyte solutions, and the solubility of a mixture of two amino acids in water are also investigated.

Theory

To generalize the modified NRTL and Wilson models for a multicomponent aqueous solution containing several electrolytes and zwitterions, the molar excess Gibbs energy g^{ex*} is expressed as the sum of two contributions,

$$[1] \qquad \frac{g^{ex*}}{RT} = \frac{g^{ex*,LR}}{RT} + \frac{g^{ex*,SR}}{RT}$$

where $g^{ex*,LR}$ is the long-range interaction contribution, $g^{ex*,SR}$ is the short-range interaction contribution, and the superscript * stands for unsymmetric convention. The long-range interaction term accounts for the electrostatic interactions between ions, and the short-range interaction term considers the non-electrostatic interactions between all species (ion, solvent, and zwitterion). In this work, the Pitzer extension of Debye–Huckel function (PDH) (21) and the modified NRTL or Wilson models are used to calculate $g^{ex*,LR}$ and $g^{ex*,SR}$, respectively.

Long-range interaction contributions to the excess Gibbs energy

The PDH equation for excess Gibbs energy normalized in Henry's convention can be written as,

$$[2] \qquad \frac{g^{ex*,\,PDH}}{RT} = -\left(\sum_i x_i\right)\frac{4A_x I_x}{\rho}\ln(1+\rho I_x^{0.5})$$

where

$$[3] \qquad A_x = \frac{1}{3}\left(\frac{2\pi N_A}{V_w}\right)^{\frac{1}{2}}\left(\frac{e^2}{4\pi\varepsilon D_w KT}\right)^{\frac{3}{2}}$$

where the ρ, N_A, K, ε and e are the closest distance parameter, Avogadro's number, Boltzmann constant, permitivity of vacuum and electronic charge, respectively. x_i is the mole fraction of component i. I_x is the ionic strength in mole fraction basis. The parameter ρ is related to the hard-core collision diameter, or distance of closest approach, of ions in solution. Therefore, the value of ρ depends on the electrolyte as well as the expression used to represent the short-range forces. To maintain simplicity in equations for more complex electrolyte systems, it is desirable that ρ should have the same value for a wide variety of salts. The value of $\rho = 14.9$ has been frequently used for aqueous electrolyte solutions (27). Therefore, this value was also used in this work. The V_w and D_w are the molar volume and dielectric constant of the solvent (or mixed solvent).

Short-range interaction contributions to the excess Gibbs energy

In a solution containing electrolytes and amino acids, the short-range forces originate from the zwitterion–zwitterion, solvent–solvent, solvent–zwitterion, solvent–ion, zwitterion–ion, and non-electrostatic ion–ion interactions. To consider these interactions in a similar manner to the approach of Chen and Evans (20), we assume the existence of four types of local cells, namely, cells with a central zwitterion, cells with a central cation, cells with a central anion, and cells with a central solvent molecule. According to the specific interaction theory, it is assumed that the like-ion repulsion is so strong that cells with a central cation do not contain any cations, and that cells with a central anion do not contain any anions. Since based on these assumptions the cells with a central ion contain only zwitterions, counterions, and solvent molecules, they are not necessarily electrically neutral. However, cells with a central zwitterion or solvent molecule contain zwitterions, cations, anions, and solvent molecules in the immediate neighborhood of the central zwitterion or solvent molecule. Therefore, cells with a central zwitterion or solvent molecule are electrically neutral.

NRTL model

For a multicomponent aqueous solution containing several solvents, electrolytes, and zwitterions, by summing the contributions of the different local composition cells to the excess Gibbs energy of the whole solution we have,

$$[4] \qquad g^{ex,NRTL} = \sum_w X_w(g^w - g^w_{ref}) + \sum_m X_m(g^m - g^m_{ref}) + \sum_n X_{c_n}(g^{c_n} - g^{c_n}_{ref}) + \sum_n X_{a_n}(g^{a_n} - g^{a_n}_{ref})$$

The Gibbs energy of cells with a central solvent w, amino acid m, cation of electrolyte n, and anion of electrolyte n denoted by g^w, g^m, g^{c_n}, and g^{a_n}, respectively, can be related to the effective local mole fractions by,

$$[5] \qquad g^w = \sum_{w'} X_{w'w}g_{w'w} + \sum_m X_{mw}g_{mw} + \sum_n X_{c_nw}g_{c_nw} + \sum_n X_{a_nw}g_{a_nw}$$

$$[6] \qquad g^m = \sum_w X_{wm}g_{wm} + \sum_{m'} X_{m'm}g_{m'm} + \sum_n X_{c_nm}g_{c_nm} + \sum_n X_{a_nm}g_{a_nm}$$

$$[7] \qquad g^{c_n} = Z_{c_n}\left(\sum_w X_{wc_n}g_{wc_n} + \sum_m X_{mc_n}g_{mc_n} + \sum_n X_{a_nc_n}g_{a_nc_n}\right)$$

$$[8] \qquad g^{a_n} = Z_{a_n}\left(\sum_w X_{wa_n}g_{wa_n} + \sum_m X_{ma_n}g_{ma_n} + \sum_n X_{c_na_n}g_{c_na_n}\right)$$

The main difference between the model developed in this work and the original NRTL (4) model is in their reference Gibbs energies of local composition cells with a central sol-

© 2008 NRC Canada

ute (zwitterions, cation, and anion). Following Jaretun and Aly (28), the reference Gibbs energies of local composition cells with a central solute (zwitterions, cation, and anion) are taken as a cell with random composition, as opposed to the original NRTL (4) model. The pure component is taken as the reference state for the Gibbs energies of local composition cells with a central solvent molecule. Thus we have,

[9] $$g_{\text{ref}}^{w} = g_{ww}$$

[10] $$g_{\text{ref}}^{m} = \frac{\sum_{w} X_w g_{wm} + \sum_{m'} X_{m'} g_{m'm} + \sum_{n} X_{c_n} g_{c_n m} + \sum_{n} X_{a_n} g_{a_n m}}{\sum_{w} X_w + \sum_{m'} X_{m'} + \sum_{n} X_{c_n} + \sum_{n} X_{a_n}}$$

[11] $$g_{\text{ref}}^{c_n} = Z_{c_n} \left(\frac{\sum_{w} X_w g_{wc_n} + \sum_{m} X_m g_{m c_n} + \sum_{n} X_{a_n} g_{a_n c_n}}{\sum_{w} X_w + \sum_{m} X_m + \sum_{n} X_{a_n}} \right)$$

[12] $$g_{\text{ref}}^{a_n} = Z_{a_n} \left(\frac{\sum_{w} X_w g_{wa_n} + \sum_{m} X_m g_{m a_n} + \sum_{n} X_{c_n} g_{c_n a_n}}{\sum_{w} X_w + \sum_{m} X_m + \sum_{n} X_{c_n}} \right)$$

The local mole fractions of component j and k in a local composition cell with a central species i are defined by the expression,

[13] $$\frac{X_{ji}}{X_{ki}} = \frac{X_j}{X_k} = G_{ji,ki}$$

By defining the following normalizing equations for the four kinds of local compositions cells that appear in the solution,

[14] $$\sum_{w'} X_{w'w} + \sum_{m} X_{mw} + \sum_{n} X_{c_n w} + \sum_{n} X_{a_n w} = 1$$

[15] $$\sum_{w} X_{wm} + \sum_{m'} X_{m'm} + \sum_{n} X_{c_n m} + \sum_{n} X_{a_n m} = 1$$

[16] $$\sum_{w} X_{wc_n} + \sum_{m} X_{mc_n} + \sum_{n} X_{a_n c_n} = 1$$

[17] $$\sum_{w} X_{wa_n} + \sum_{m} X_{ma_n} + \sum_{n} X_{c_n a_n} = 1$$

The modified NRTL model for the molar excess Gibbs energy is obtained as,

[18]
$$\begin{aligned}
\frac{g^{\text{ex,NRTL}}}{RT} = {} & \sum_{w} X_w \left(\frac{\sum_{w'} X_{w'} G_{w'w} \tau_{w'w} + \sum_{m} X_m G_{mw} \tau_{mw} + \sum_{n} (X_{c_n} + X_{a_n}) G_{e_n w} \tau_{e_n w}}{\sum_{w'} X_{w'} G_{w'w} + \sum_{m} X_m G_{mw} + \sum_{n} (X_{c_n} + X_{a_n}) G_{e_n w}} \right) \\
& + \sum_{m} X_m \left[\left(\frac{\sum_{w} X_w G_{wm} \tau_{wm} + \sum_{m'} X_{m'} G_{m'm} \tau_{m'm} + \sum_{n} (X_{c_n} + X_{a_n}) G_{e_n m} \tau_{e_n m}}{\sum_{w} X_w G_{wm} + \sum_{m'} X_{m'} G_{m'm} + \sum_{n} (X_{c_n} + X_{a_n}) G_{e_n m}} \right) \right. \\
& \left. - \frac{\sum_{W} X_w \tau_{wm} + \sum_{m'} X_{m'} \tau_{m'm} + \sum_{n} (X_{c_n} + X_{a_n}) \tau_{e_n m}}{\sum_{w} X_w + \sum_{m} X_m + \sum_{n} (X_{c_n} + X_{a_n})} \right] \\
& + \sum_{n} X_{c_n} \left[\left(\frac{\sum_{w} X_w G_{we_n} \tau_{we_n} + \sum_{m} X_m G_{me_n} \tau_{me_n} + \sum_{n'} X_{a_{n'}} G_{e_{n'} e_n} \tau_{e_{n'} e_n}}{\sum_{w} X_w G_{we_n} + \sum_{m} X_m G_{me_n} + \sum_{n'} X_{a_{n'}} G_{e_{n'} e_n}} \right) \right. \\
& \left. - \frac{\sum_{w} X_w \tau_{we_n} + \sum_{m} X_m \tau_{me_n} + \sum_{n'} X_{a_{n'}} \tau_{e_{n'} e_n}}{\sum_{w} X_w + \sum_{m} X_m + \sum_{n'} X_{a_{n'}}} \right] \\
& + \sum_{n} X_{a_n} \left[\left(\frac{\sum_{w} X_w G_{we_n} \tau_{we_n} + \sum_{m} X_m G_{me_n} \tau_{me_n} + \sum_{n'} X_{c_{n'}} G_{e_{n'} e_n} \tau_{e_{n'} e_n}}{\sum_{w} X_w G_{we_n} + \sum_{m} X_m G_{me_n} + \sum_{n'} X_{c_{n'}} G_{e_{n'} e_n}} \right) \right. \\
& \left. - \frac{\sum_{w} X_w \tau_{we_n} + \sum_{m} X_m \tau_{me_n} + \sum_{n'} X_{c_{n'}} \tau_{e_{n'} e_n}}{\sum_{w} X_w + \sum_{m} X_m + \sum_{n'} X_{c_{n'}}} \right]
\end{aligned}$$

© 2008 NRC Canada

Table 1. Regressed parameters of several amino acids and peptides and RMSDs of the correlation of experimental activity coefficient data at 298.15 K for the models developed in this work.

			Modified NRTL model			Modified Wilson model			
Substance	m_{max}	N	a_{mw} (J mol^{-1})	a_{wm} (J mol^{-1})	RMSD (%)	E_{mw} (J mol^{-1})	E_{wm} (J mol^{-1})	RMSD (%)	Ref.
β-Alanine	7	14	–5 770.8189	10 064.7172	0.466	–13 228.891	27 928.735	0.730	30
DL-β-Amino-*n*-butyric acid	7	14	–5 781.0276	9 193.2627	1.083	–12 369.115	23 826.419	1.260	30
DL-β-Amino-*n*-valeric acid	6.5	14	–5 403.7576	7 700.3342	1.028	–10 283.073	17 300.141	1.089	30
γ-Aminobutyric acid	6.5	14	–6 592.9222	11 565.0759	1.716	–16 382.61	32 944.595	2.145	30
DL-γ-Amino-*n*-valeric acid	7	13	–6 421.7466	10 508.6331	1.225	–14 886.443	28 360.481	1.547	30
ε-Aminocaproic acid	6.5	14	–6 231.7209	10 585.9132	4.771	–14 499.195	29 002.466	5.054	30
L-Serine	4.02	13	–4 514.6218	10 872.2901	0.385	–12 063.231	33 091.436	0.469	31
DL-Alanine	1.9	11	–3 045.3901	4 685.4219	0.074	–4 699.400	11 139.986	0.074	32
DL-α-Amino-*n*-butyric acid	2.1	12	–4 759.96	–10 088.013	0.038	–5 931.900	0.000	0.160	32
DL-α-Amino-*n*-valeric acid	0.65	5	–5 442.231	7 672.6067	0.034	–6 683.495	–25 29.142	0.040	32
α-Aminoisobutyric acid	1.5	9	–3 781.2125	0.0000	0.205	–6 955.155	0.000	0.245	32
DL-Valine	0.65	5	–6 491.0851	9 424.1918	0.031	–15 117.41	25 127.856	0.031	32
Glycine	3.3	14	–4 916.8022	10 634.1128	0.397	–12 766.277	32 192.83	0.443	33
Alanylalanine	1	5	–9 291.9994	15 995.7279	0.307	–28 728.383	51 264.214	0.326	34
Alanylglycine	1	5	–9 582.2041	17 371.1142	0.411	–30 660.185	56 597.427	0.425	34
Glycylalanine	1	5	–9 212.1298	16 724.323	0.362	–29 191.891	54 259.65	0.385	34
Glycylglycine	1.5	6	–8 114.8672	15 815.960	1.435	–25 610.05	51 079.079	1.404	34
Proline	7.3	15	–5 525.6111	8 094.8875	0.888	–10 824.324	18 933.666	0.963	34
Threonine	2	7	–4 711.3853	8 929.221	0.083	–10 873.703	26 026.23	0.089	34
Triglycine	0.3	2	–11 022.3751	20 504.4549	0.000	–36 902.108	68 300.506	0.000	34
Methionine	0.3	2	–11 776.7387	21 068.7848	0.000	–39 212.528	70 190.099	0.000	34
Hydroxyproline	2	7	–4 506.1104	7 801.0528	0.055	–9 402.248	21 624.171	0.055	34

In the above relations X_i is the effective mole fraction and is given by

[19] $$X_i = x_i K_i,$$

($K_i = Z_i$ for ions and K_i = unity for molecules)

where Z is the charge number, and G and τ are energy parameters given by,

[20] $$G_{ij} = \exp\left(-\alpha_{ij}\frac{(g_{ij}-g_{jj})}{RT}\right) = \exp(-\alpha_{ij}\tau_{ij}) = \exp\left(-a_{ij}\frac{a_{ij}}{RT}\right)$$

[21] $$G_{ij,kj} = \exp\left(-\alpha_{ij,kj}\frac{(g_{ij}-g_{kj})}{RT}\right) = \exp(-\alpha_{ij,kj}\tau_{ij,kj}) = \exp\left(-\alpha_{ij,kj}\frac{a_{ij,kj}}{RT}\right)$$

[22] $$a_{c_n m} = a_{a_n m} = a_{e_n m}, \quad a_{c_n w} = a_{a_n w} = a_{e_n w}$$

[23] $$a_{mc_n,a_n c_n} = a_{ma_n,c_n a_n} = a_{m,e_n}, \quad a_{wc_n,a_n c_n} = a_{wa_n,c_n a_n} = a_{w,e_n}$$

[24] $$a_{a_n c_{n'}} = a_{c_n a_{n'}} = a_{e_n e_{n'}}$$

where α is the nonrandomness factor, which is symmetric. The nonrandomness factor was fixed at 0.2 for binary electrolyte–molecule pairs and binary electrolyte–electrolyte pairs. It was set at 0.3 for binary molecule–molecule pairs (4). The interaction energy g_{ij} is also symmetric.

Wilson model

The main difference between the Wilson model and the extension of the NRTL model is the assumption that the short-range energy parameter between species in a local cell has an enthalpic rather than Gibbs energy nature. Therefore, similar to the NRTL model, for a multicomponent aqueous solution containing several solvents, electrolytes, and zwitterions, by summing the contributions of the different local composition cells to the excess enthalpy of the whole solution we have,

[25] $$h^{ex,Wilson} = \sum_w X_w(h^w - h^w_{ref}) + \sum_m X_m(h^m - h^m_{ref}) + \sum_n X_{c_n}(h^{c_n} - h^{c_n}_{ref}) + \sum_n X_{a_n}(h^{a_n} - h^{a_n}_{ref})$$

The enthalpy of cells with a central solvent w, amino acid m, cation of electrolyte n, and anion of electrolyte n denoted by h^w, h^m, h^{c_n}, and h^{a_n}, respectively, can be related to the effective local mole fractions by,

[26] $$h^w = \sum_{w'} X_{w'w}h_{w'w} + \sum_m X_{mw}h_{mw} + \sum_n X_{c_n w}h_{c_n w} + \sum_n X_{a_n w}h_{a_n w}$$

[27] $$h^m = \sum_w X_{wm}h_{wm} + \sum_{m'} X_{m'm}h_{m'm} + \sum_n X_{c_n m}h_{c_n m} + \sum_n X_{a_n m}h_{a_n m}$$

© 2008 NRC Canada

Table 2. Solubility constants of amino acids in water and RMSDs of the correlation of experimental solubility data at different temperatures for the models developed in this work.

	Modified NRTL model				Modified Wilson model				
Substance	*a*	*b*	*c*	RMSD (%)	*a*	*b*	*c*	RMSD (%)	Ref.
DL-Alanine	–57.44253	1 409.34642	8.66515	0.090	–60.29708	1 521.11133	9.10032	0.114	35
D-Alanine	–47.58355	1 141.01631	7.09206	0.073	–49.54344	1 213.04451	7.39361	0.088	35
L-Aspartic acid[a]	–145.19201	3 494.91707	22.14433	0.202	–145.19201	3 494.91707	22.14433	0.202	35
DL-Aspartic acid[a]	16.55221	–4 119.72344	–1.68215	0.918	16.55221	–4 119.72344	–1.68215	0.918	35
D-Glutamic acid[a]	–150.94214	3 605.06231	23.16691	0.207	–150.94214	3 605.06231	23.16691	0.207	35
DL-Glutamic acid[a]	–138.44642	3 247.82984	21.33592	0.104	–138.44642	3 247.82984	21.33592	0.104	35
DL-Glutamic acid[a]	–88.53400	884.6189	13.81428	1.17	–88.53400	884.6189	13.81428	1.17	34
Glycine	30.45918	–3 117.66005	–4.05655	1.323	–0.06106	1 907.19416	0.58816	1.514	35
DL-Isoleucine[a]	–181.87456	7 066.14655	26.74331	0.905	–181.87456	7 066.14655	26.74331	0.905	35
D-Isoleucine[a]	–117.03289	4 614.06824	16.91406	0.0606	–117.03289	4 614.06824	16.91406	0.0606	36
DL-Leucine[a]	–216.90449	8 496.55701	31.90708	1.102	–216.90449	8 496.55701	31.90708	1.102	35
L-Leucine[a]	–158.72891	6 443.40135	23.06247	0.861	–158.72891	6 443.40135	23.06247	0.861	35
DL-Norleucine[a]	–185.5032	6 882.09749	27.37254	0.850	–185.5032	6 882.09749	27.37254	0.850	35
DL-Phenyl alanine[a]	–181.57495	6 602.79281	26.84325	0.804	–181.57495	6 602.79281	26.84325	0.804	35
L-Phenyl alanine[a]	–68.57589	1 584.26589	10.0961	0.106	–68.57589	1 584.26589	10.0961	0.106	36
L-Tyrosine[a]	–144.14754	3 427.47991	21.52538	0.223	–144.14754	3 427.47991	21.52538	0.223	35
DL-Valine	–147.16421	5 711.17383	21.68838	0.716	–153.63146	5 955.84695	22.67916	0.840	35
L-Cystine[a]	–135.66174	3 183.82598	20.00075	0.225	–135.66174	3 183.82598	20.00075	0.225	36
DL-Methionine	–76.30366	1 383.89422	11.59313	0.356	–102.52263	2 513.66031	15.52911	0.724	36
DL-Serine	4.79584	–2 610.63719	–0.15845	0.255	–8.07125	–2 051.23	1.77043	0.076	36
L-Serine	246.88432	–13 397.53073	–35.9941	2.748	186.00743	–10 835.17213	–26.81751	2.637	34
Hydroxyproline	–42.79031	1 051.57786	6.37157	0.070	–48.78302	1 245.75046	7.30906	0.124	34
L-Alanine	–47.15988	1 119.50786	7.03003	0.121	–46.04985	1 073.96099	6.86188	0.141	34
L-Valine	–95.8946	3 658.90898	13.8601	0.366	–95.19588	3 592.08187	13.7768	0.368	34
L-Methionine	–55.26101	1 014.92	8.20001	0.176	–65.58696	1 407.20398	9.78146	0.174	34

[a]The models binary interaction parameters were set to zero.

$$[28]\quad h^{c_n} = Z_{c_n}\left(\sum_w X_{wc_n} h_{wc_n} + \sum_m X_{mc_n} h_{mc_n} + \sum_n X_{a_n c_n} h_{a_n c_n}\right)$$

$$[29]\quad h^{a_n} = Z_{a_n}\left(\sum_w X_{wa_n} h_{wa_n} + \sum_m X_{ma_n} h_{ma_n} + \sum_n X_{c_n a_n} h_{c_n a_n}\right)$$

Similar to the NRTL model for the reference enthalpy of local composition cells we have,

$$[30]\quad h^{w}_{\text{ref}} = h_{ww}$$

$$[31]\quad h^{m}_{\text{ref}} = \frac{\sum_w X_w h_{wm} + \sum_{m'} X_{m'} h_{m'm} + \sum_n X_{c_n} h_{c_n m} + \sum_n X_{a_n} h_{a_n m}}{\sum_w X_w + \sum_{m'} X_{m'} + \sum_m X_{c_n} + \sum_n X_{a_n}}$$

$$[32]\quad h^{c_n}_{\text{ref}} = Z_{c_n}\left(\frac{\sum_w X_w h_{wc_n} + \sum_m X_m h_{mc_n} + \sum_n X_{a_n} h_{a_n c_n}}{\sum_w X_w + \sum_m X_m + \sum_n X_{a_n}}\right)$$

$$[33]\quad h^{a_n}_{\text{ref}} = Z_{a_n}\left(\frac{\sum_w X_w h_{wa_n} + \sum_m X_m h_{ma_n} + \sum_n X_{c_n} h_{c_n a_n}}{\sum_w X_w + \sum_m X_m + \sum_n X_{c_n}}\right)$$

The local mole fractions of component *j* and *k* in a local composition cell with a central species *i* are defined by the expression,

$$[34]\quad \frac{X_{ji}}{X_{ki}} = \frac{X_j}{X_k} H_{ji,ki}$$

By considering the normalizing eqs. [14–17], the modified Wilson model for the molar excess enthalpy is obtained as,

© 2008 NRC Canada

Table 3. Estimated binary parameters between two amino acids in water and RMSDs of the correlation of experimental solubility data of an amino acid in aqueous solutions of another amino acid for the models developed in this work ($a_{m_1m_2} = 0$ and $E_{m_1m_2} = 0$).

		Modified NRTL model			Modified Wilson model			
System	T	$a_{m_2m_1}$ (J mol^{-1})	RMSD (%) of m_1	RMSD (%) of m_2	$E_{m_2m_1}$ (J mol^{-1})	RMSD (%) of m_1	RMSD (%) of m_2	Ref.
Water (w) + dl-alanie (m_1) + dl-serine (m_2)	298.15	4 430.9979	0.409	0.851	10 698.074	0.667	2.083	37
Water (w) + dl-alanie (m_1) + dl-valine (m_2)	298.15	4 333.547	1.088	1.156	4 464.985	0.975	1.167	37
Water (w) + glycine (m_1) + dl-aspartic acid (m_2)	298.15	–6 637.8707	0.804	9.491	–19 272.801	1.196	10.733	5
Water (w) + glycine (m_1) + dl-phenylalanine (m_2)	298.15	–538.3836	1.972	5.640	–1 884.703	1.836	5.666	5
Water (w) + l-serine (m_1) + l-aspartic Acid (m_2)	298.15	–5 336.3003	1.311	19.083	–14 799.519	1.150	21.528	38
Water (w) + l-serine (m_1) + l-aspartic Acid (m_2)	313.15	–5 336.3003	1.144	10.995	–14 799.519	1.360	12.658	38
Water (w) + l-serine (m_1) + l-aspartic Acid (m_2)	333.15	–5 336.3003	2.005	11.501	–14 799.519	1.984	13.132	38
Water (w) + l-aspartic acid (m_1) + l-glutamic acid (m_2)	298.15	–17 914.1392	1.617	1.844	–52 982.701	1.761	1.929	38
Water (w) + l-aspartic acid (m_1) + l-glutamic acid (m_2)	313.15	–17 914.1392	0.755	0.272	–52 982.701	0.840	0.289	38
Water (w) + l-aspartic acid (m_1) + l-glutamic acid (m_2)	333.15	–17 914.1392	5.152	6.180	–52 982.701	5.225	6.110	38
Water (w) + glycine (m_1) + l-glutamic acid (m_2)	298.15	–4 081.5894	—	6.252	–11 551.419	—	7.129	38
Water (w) + glycine (m_1) + l-glutamic acid (m_2)	313.15	–4 081.5894	—	4.585	–11 551.419	—	5.248	38
Water (w) + glycine (m_1) + l-glutamic acid (m_2)	333.15	–4 081.5894	0.642	7.424	–11 551.419	0.800	8.212	38
Water (w) + l-serine (m_1) + l-glutamic acid (m_2)	298.15	–3 920.0298	2.173	16.389	–10 740.305	1.975	17.244	38
Water (w) + l-serine (m_1) + l-glutamic acid (m_2)	313.15	–3 920.0298	1.144	1.220	–10 740.305	1.357	1.600	38
Water (w) + l-serine (m_1) + l-glutamic acid (m_2)	333.15	–3 920.0298	1.911	21.869	–10 740.305	1.866	21.819	38

$$\frac{h^{\text{ex, Wilson}}}{RT} = \sum_w X_w \left(\frac{\sum_{w'} X_{w'} H_{w'w} E_{w'w} + \sum_m X_m H_{mw} E_{mw} + \sum_n (X_{c_n} + X_{a_n}) H_{e_n w} E_{e_n w}}{\sum_{w'} X_{w'} H_{w'w} + \sum_m X_m H_{mw} + \sum_n (X_{c_n} + X_{a_n}) H_{e_n w}} \right)$$
$$+ \sum_m X_m \left[\left(\frac{\sum_w X_w H_{wm} E_{wm} + \sum_{m'} X_{m'} H_{m'm} E_{m'm} + \sum_n (X_{c_n} + X_{a_n}) H_{e_n m} E_{e_n m}}{\sum_w X_w H_{wm} + \sum_{m'} X_{m'} H_{m'm} + \sum_n (X_{c_n} + X_{a_n}) H_{e_n m}} \right) - \frac{\sum_w X_w E_{wm} + \sum_{m'} X_{m'} E_{m'm} + \sum_n (X_{c_n} + X_{a_n}) E_{e_n m}}{\sum_w X_w + \sum_m X_m + \sum_n (X_{c_n} + X_{a_n})} \right]$$
$$+ \sum_n X_{c_n} \left[\left(\frac{\sum_w X_w H_{we_n} E_{we_n} + \sum_m X_m H_{me_n} E_{me_n} + \sum_{n'} X_{a_{n'}} H_{e_{n'}e_n} E_{e_{n'}e_n}}{\sum_w X_w H_{we_n} + \sum_m X_m H_{me_n} + \sum_{n'} X_{a_{n'}} H_{e_{n'}e_n}} \right) - \frac{\sum_w X_w E_{we_n} + \sum_m X_m E_{me_n} + \sum_{n'} X_{a_{n'}} E_{e_{n'}e_n}}{\sum_w X_w + \sum_m X_m + \sum_{n'} X_{a_{n'}}} \right] \quad [35]$$
$$+ \sum_n X_{a_n} \left[\left(\frac{\sum_w X_w H_{we_n} E_{we_n} + \sum_m X_m H_{me_n} E_{me_n} + \sum_{n'} X_{c_{n'}} H_{e_{n'}e_n} E_{e_{n'}e_n}}{\sum_w X_w H_{we_n} + \sum_m X_m H_{me_n} + \sum_{n'} X_{c_{n'}} H_{e_{n'}e_n}} \right) - \frac{\sum_w X_w E_{we_n} + \sum_m X_m E_{me_n} + \sum_{n'} X_{c_{n'}} E_{e_{n'}e_n}}{\sum_w X_w + \sum_m X_m + \sum_{n'} X_{c_{n'}}} \right]$$

The excess Gibbs energy can then be obtained by combining eq. [35] and the following exact thermodynamic relation,

© 2008 NRC Canada

Table 4. Estimated binary water–electrolyte parameters and RMSDs of the correlation of experimental osmotic coefficient and mean ionic activity coefficient data of binary aqueous electrolyte solutions at 298.15 k (26).

	Modified NRTL model				Modified Wilson model			
System	a_{ew} (J mol^{-1})	a_{we} (J mol^{-1})	RMSD (%) of $\gamma_{\pm}^{(m)}$	RMSD (%) of ϕ	E_{ew} (J mol^{-1})	E_{we} (J mol^{-1})	RMSD (%) of $\gamma_{\pm}^{(m)}$	RMSD % of ϕ
Water (w) + Na_2SO_4(e)	–4 687.4469	13 007.8511	1.052	1.360	–7 520.856	28 407.575	0.973	1.245
Water (w) + NaCl (e)	–8 113.6707	16 948.6777	0.882	0.692	–1 3816.29	34 425.135	0.823	0.639
Water (w) + KCl (e)	–6 129.376	13 665.9776	0.098	0.095	–9 282.854	27 150.678	0.100	0.096
Water (w) + KNO_3 (e)	–4 472.7812	15 234.8222	0.829	1.030	–8 601.353	35 401.358	0.845	1.050
Water (w) + $NaNO_3$ (e)	–3 123.8078	97 26.1425	0.209	0.216	–4 440.426	20 905.641	0.213	0.218

[36] $$\frac{g^{\text{ex, Wilson}}}{RT} = \frac{1}{R}\int_0^{\frac{1}{T}} h^{\text{ex, Wilson}}\, \mathrm{d}\left(\frac{1}{T}\right)$$

The expression for the excess Gibbs energy is obtained as,

[37]
$$-\frac{g^{\text{ex, Wilson}}}{CRT} = \sum_w X_w \ln\left(\frac{\sum_{w'} X_{w'}H_{w'w} + \sum_m X_m H_{mw} + \sum_n (X_{c_n} + X_{a_n})H_{e_n w}}{\sum_{w'} X_{w'} + \sum_m X_m + \sum_n (X_{c_n} + X_{a_n})}\right)$$
$$+ \sum_m X_m \left[\ln\left(\frac{\sum_w X_w H_{wm} + \sum_{m'} X_{m'}H_{m'm} + \sum_n (X_{c_n} + X_{a_n})H_{e_n m}}{\sum_w X_w + \sum_m X_m + \sum_n (X_{c_n} + X_{a_n})}\right) - \frac{\sum_w X_w \ln H_{wm} + \sum_{m'} X_{m'} \ln H_{m'm} + \sum_n (X_{c_n} + X_{a_n}) \ln H_{e_n m}}{\sum_w X_w + \sum_m X_m + \sum_n (X_{c_n} + X_{a_n})}\right]$$
$$+ \sum_n X_{c_n} \left[\ln\left(\frac{\sum_w X_w H_{we_n} + \sum_m X_m H_{me_n} + \sum_{n'} X_{a_{n'}}H_{e_{n'}e_n}}{\sum_w X_w + \sum_m X_m + \sum_{n'} X_{a_{n'}}}\right) - \frac{\sum_w X_w \ln H_{we_n} + \sum_m X_m \ln H_{me_n} + \sum_{n'} X_{a_{n'}} \ln H_{e_{n'}e_n}}{\sum_w X_w + \sum_m X_m + \sum_{n'} X_{a_{n'}}}\right]$$
$$+ \sum_n X_{a_n} \left[\ln\left(\frac{\sum_w X_w H_{we_n} + \sum_m X_m H_{me_n} + \sum_{n'} X_{c_{n'}}H_{e_{n'}e_n}}{\sum_w X_w + \sum_m X_m + \sum_{n'} X_{c_{n'}}}\right) - \frac{\sum_w X_w \ln H_{we_n} + \sum_m X_m \ln H_{me_n} + \sum_{n'} X_{c_{n'}} \ln H_{e_{n'}e_n}}{\sum_w X_w + \sum_m X_m + \sum_{n'} X_{c_{n'}}}\right]$$

where C is the effective coordination number in the system, which was fixed at 10. H and E are energy parameters and are given by,

[38] $$H_{ij} = \exp\left(-\frac{(h_{ij} - h_{jj})}{CRT}\right) = \exp\left(-\frac{E_{ij}}{CRT}\right)$$

[39] $$H_{ij,kj} = \exp\left(-\frac{(h_{ij} - h_{kj})}{CRT}\right) = \exp\left(-\frac{E_{ij,kj}}{CRT}\right)$$

[40] $$E_{c_n m} = E_{a_n m} = E_{e_n m}, \quad E_{c_n w} = E_{a_n w} = E_{e_n w}$$

[41] $$E_{mc_n,a_n c_n} = E_{ma_n,c_n a_n} = E_{m,e_n},$$
$$E_{wc_n,a_n c_n} = E_{wa_n,c_n a_n} = E_{w,e_n}$$

[42] $$E_{a_n c_{n'}} = E_{c_n a_{n'}} = E_{e_n e_{n'}}$$

In the above relations, the subscripts c, a, and e stand for cation, anion, and electrolyte, respectively. Also, the species w and w' can be solvent molecules, the species m and m' can be amino acid molecules, the species n and n' can be electro-

© 2008 NRC Canada

Table 5. Estimated binary parameters between amino acids and electrolytes in water and RMSDs of the correlation of experimental solubility data of an amino acid in aqueous solutions of an electrolyte for the models developed in this work (a_{me} = 0 and E_{me} = 0).

		Modified NRTL model		Modified Wilson model		
System	T	a_{em} (J mol^{-1})	RMSD (%)	E_{em} (J mol^{-1})	RMSD (%)	Ref.
Water (w) + DL-alanine (m) + Na_2SO_4(e)	298.15	5 317.235	10.078	10 309.769	13.568	40
Water (*w*) + DL-alanine (*m*) + NaCl (*e*)	298.15	5 271.930	1.491	10 241.546	1.462	41
Water (*w*) + DL-alanine (*m*) + KCl (*e*)	298.15	–437.903	1.483	–4 884	0.401	41
Water (*w*) + DL-alanine (*m*) + KNO_3 (*e*)	298.15	–9 107.575	2.270	–20 203	1.803	39
Water (w) + DL-alanine (m) + $NaNO_3$ (e)	298.15	–11 436.7125	1.779	–26 895	1.724	39
Water (w) + DL-serine (*m*) + KCl (*e*)	298.15	–15 92.7973	1.445	–3 633.98	1.464	41
Water (*w*) + DL-serine (*m*) + KNO_3 (*e*)	298.15	–7 285.4794	8.096	–14 676.578	6.641	39
Water (w) + DL-serine (*m*) + NaCl (*e*)	298.15	4 379.5238	1.508	5 687.542	1.448	41
Water (*w*) + DL-serine (*m*) + $NaNO_3$ (*e*)	298.15	–6 843.4037	4.046	–26 257.276	2.479	39
Water (*w*) + DL-valine (*m*) + KCl (*e*)	298.15	–3 036.1990	1.545	–8 056.668	1.451	41
Water (*w*) + DL-valine (*m*) + KNO_3 (*e*)	298.15	–10 703.6045	10.483	–25 181.948	8.947	39
Water (*w*) + DL-valine (*m*) + NaCl (*e*)	298.15	2 630.4760	1.430	4 242.85	1.441	41
Water (*w*) + DL-valine (*m*) + $NaNO_3$ (*e*)	298.15	–10 825.0759	9.709	–26 085.505	7.924	39
Water (*w*) + Glycine (*m*) + KCl (*e*)	298.15	–120.0717	4.002	–396.774	4.199	41
Water (*w*) + Glycine (*m*) + KNO_3 (*e*)	298.15	–7 097.9442	8.988	–14 437.298	9.152	39
Water (*w*) + Glycine (*m*) + Na_2SO_4 (*e*)	298.15	281.4743	5.164	712.635	5.358	40
Water (*w*) + Glycine (*m*) + NaCl (*e*)	298.15	1 218.8752	4.298	58 323.159	4.414	41
Water (*w*) + Glycine (*m*) + $NaNO_3$ (*e*)	298.15	–7 828.3512	8.530	–16 452.597	9.915	39

lytes, and the species *i*, *j*, and *k* can be cation, anion, amino acids, or solvent molecules. The reference state for a solvent molecule is the pure liquid at system temperature and pressure. The reference state for ionic species and neutral dipolar species, or zwitterions, is the infinite dilution state in aqueous phase. The NRTL relation for the activity coefficient of a species *i* in the system can be obtained from appropriate differentiation of eqs. [1], [2], and [18]. Similarly, the Wilson relation for the activity coefficient of a species *i* in the system can be obtained from appropriate differentiation of eqs. [1], [2], and [37]. In fact, the dissociation extends of amino acids in unbuffered, pure water are relatively insignificant. In other words, in the unbuffered solutions of amino acids, the neutral dipolar species are predominant amino acid species, while the concentration of ionic amino acid species is negligible (5).

Results and discussion

Activity coefficients of amino acids

The models were employed to correlate the activity coefficient data of several amino acids and peptides in binary aqueous solutions. As the activity coefficient calculated from the models is normalized on the mole fraction base, the activity coefficients of amino acids reported in the literature were converted from the molality base to the mole fraction base using the following relation (29),

$$[43] \quad \gamma^{(x)} = \gamma^{(m)}(1 + 0.001 M_w m)$$

where M_w is the molecular weight of the solvent, γ is the activity coefficient, m is the molality of the amino acid, and the superscripts m and x represent the molality and mole fraction base, respectively. The adjustable water-amino acid energy parameters a_{wm} and a_{mw} for the NRTL model and E_{wm} and E_{mw} for the Wilson model were estimated by minimizing the following objective function,

$$[44] \quad \text{OF} = \sum_{l=1}^{N} (\gamma_{m,l}^{*,\text{cal}} - \gamma_{m,l}^{*,\text{exp}})^2$$

The fitting parameters of the models along with the corresponding root-mean-square deviations (RMSD) are given in Table 1. On the basis of the obtained deviations given in Table 1, we conclude that the both models presented in this work can accurately describe the activity coefficients of amino acids and small peptides with good results. Figure 1 shows the correlation results by the modified NRTL model for the activity coefficients for several amino acids as a function of molality at T = 298.15 K.

Solubilities of amino acids in water

Amino acids, peptides, and proteins are ampholytes that exist in solutions partly as cations and anions. The neutral dipolar species are the predominant species in isoelectric solutions of amino acids and proteins. In fact, in the absence of a proton donor or acceptor, up to 99% of the amino acid molecules are in their zwitterionic form. In other words, in the absence of a proton donor or acceptor, the physicochemical properties of different ionized forms of the amino acids in aqueous solutions are represented by those of the zwitterionic form, and the formations of amino acid cations and anions have little impact on the amino acid solubilities and they can be ignored. Therefore, the solubility data can be represented by regressing the thermodynamic solubility constant of following equation,

$$[45] \quad A(\text{s}) \leftrightarrow A^{+-}(\text{aq})$$

© 2008 NRC Canada

Fig. 1. Comparison between experimental and calculated amino acid activity coefficient by the modified NRTL model for several amino acid + H_2O systems at 298.15 K: β-alanine (○), DL-β-aminobutyric acid (▲), DL-β-aminvaleric acid (◇), γ-aminobutyric acid (×), DL-γ-aminovaleric acid (●), calculated (—).

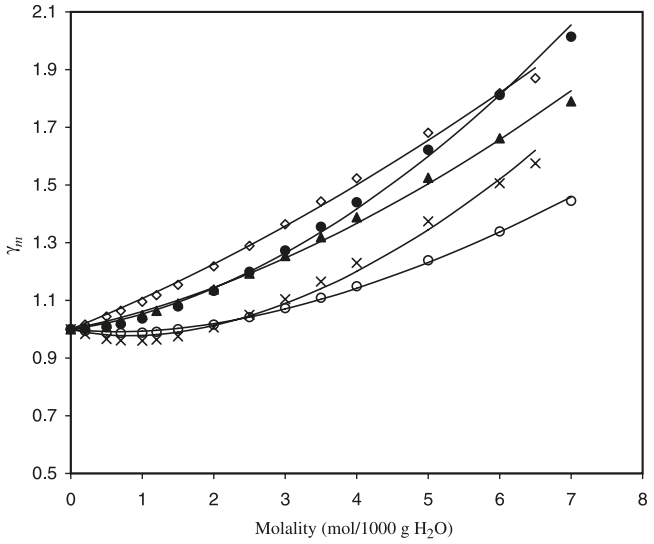

The chemical equilibrium relationship for the reaction above can be written as follows,

$$[46] \quad K_s = a_{A^{+-}} = x_{A^{+-}}\gamma_{A^{+-}}$$

where A(s) and A^{+-} (aq) are the solid form of amino acid and dissolved amino acid (as neutral zwitterions), respectively. K_s and a are the equilibrium constant and activity, respectively. For each model, the amino acid activity coefficients in water were computed with the corresponding models parameters presented in Table 1. It should be mentioned that since the activity coefficient data, and therefore binary interaction parameters, for the amino acids that are not tabulated in Table 1, are not available, as an assumption their solutions with water were considered ideal and the corresponding binary interaction parameters were set to zero. In fact, the model parameters reported in Table 1 are independent of temperature. In this work, following Chen et al. (4), the following equation is used to calculate the temperature dependency of the thermodynamic solubility constant,

$$[47] \quad \ln K_s = a + b/T + c\ln T$$

The adjustable parameters a, b, and c were estimated by minimizing the following objective function,

$$[48] \quad \mathrm{OF} = \sum_{l=1}^{N}(S_l^{\mathrm{cal}} - S_l^{\mathrm{exp}})^2$$

where S is the solubility in grams of amino acid per kilogram of water. In the most cases, the used experimental data cover the temperature range 273.15–373.15 K. The fitting parameters a, b, and c, along with the corresponding RMSD for S are given in Table 2. On the basis of the obtained deviations given in Table 2, we conclude that the frameworks proposed here seems to be very satisfactory. Figure 2 shows the correlation results by the Wilson model for the solubility for several amino acids as a function of temperature.

Fig. 2. Comparison between experimental and calculated solubility by the modified Wilson model for several amino acid + H_2O systems: D-alanine (○), DL-alanine (▲), glycine (◇), DL-serine (×), DL-valine (●), hydroxyproline (◆), calculated (—).

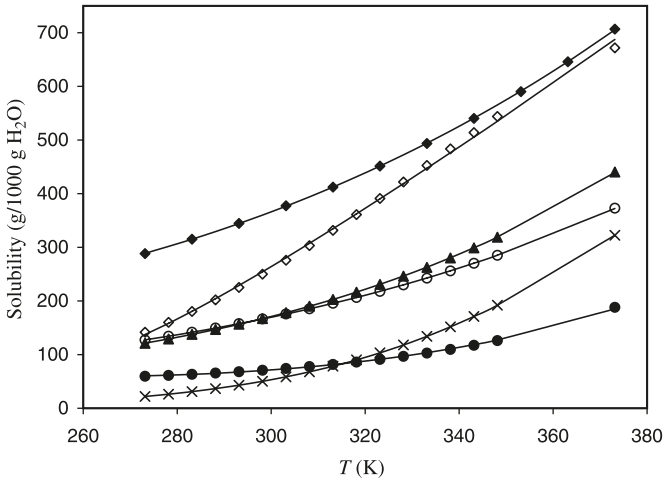

Solubilities of amino acids in the presence of dipolar amino acid species

The effect of an amino acid on the solubility of another amino acid depends on the chemical structure of both amino acids present in the solution (5). The presence of an amino acid in the liquid phase may either increase or decrease the solubility of the other amino acid. It is the molecule–molecule physical interactions between the two dipolar amino acids that result in the change in the solubility. From appropriate differentiation of eqs. [18] and [37], respectively, the NRTL and Wilson relation for the activity coefficient of amino acid 1 (m_1) in ternary solution water (w) + amino acid 1 (m_1) + amino acid 2 (m_2) can be obtained.

The binary energy parameters for the amino acid–water pairs listed in Table 1 and the solubility constant of the amino acids listed in Table 2 are directly used to calculate the solubility of a mixture of two amino acids in water. For both models presented in this work, one of the amino acid – amino acid energy parameters was set to zero and another amino acid – amino acid energy parameter is treated as an adjustable parameter. Therefore, for an amino acid 1 (m_1) + amino acid 2 (m_2) + water (w) system, only one adjustable parameter is required to correlate the solubility data. Table 3 summarizes the values of the binary interaction parameters between two amino acids along with the corresponding RMSD values. It can be seen that the models developed in this work can successfully represent the solubility of a mixture of two amino acids in aqueous solutions. Figure 3 shows the correlation results by the NRTL model for the solubility data in water (w) + L-aspartic acid (m_1) + L-glutamic acid (m_2) at different temperatures. In Fig. 4, the correlation results by the Wilson model for the solubility data in water (w) + glycine (m_1) + L-glutamic acid (m_2) system are shown at different temperatures. That is to say, the obtained binary interaction parameters are independent of temperature and, in fact, for the each model one set of parameters has been successfully used to correlate all solubility data at different temperatures.

© 2008 NRC Canada

Fig. 3. Solubilities of L-glutamic acid and L-aspartic acid in an aqueous solution at different temperatures: solubility of L-glutamic acid at T = 298.15 K (○), solubility of L-glutamic acid at T = 313.15 K (▲), solubility of L-glutamic acid at T = 333.15K (◇), solubility of L-aspartic acid at T = 298.15 K (×), solubility of L-aspartic acid at T = 313.15 K (●), solubility of L-aspartic acid at T = 333.15 K (◆), calculated by the modified NRTL model (—).

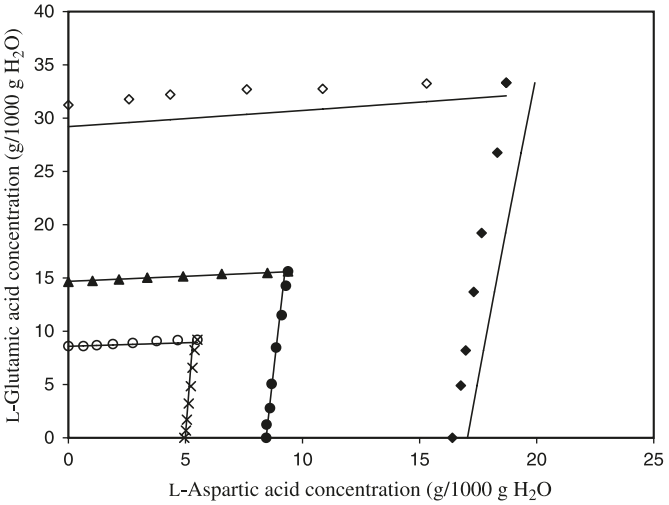

Fig. 4. Solubilities of L-glutamic acid and glycine in an aqueous solution at different temperatures: solubility of L-glutamic acid at T = 298.15 K (○), solubility of L-glutamic acid at T = 313.15 K (▲), solubility of L-glutamic acid at T = 333.15 K (◇), solubility of glycine at T = 333.15 K (×), calculated by the modified Wilson model (—).

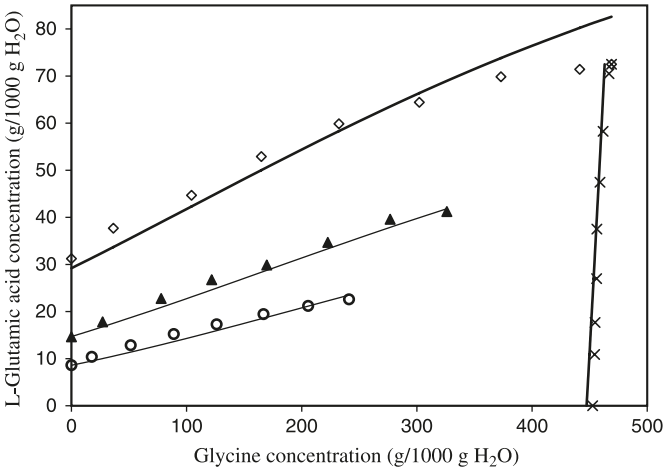

Solubilities of amino acids in the presence of salts

The presence of an electrolyte changes the solubility of an amino acid and usually increases it. This phenomenon is known as the salting-in effect. The reverse of this phenomenon, in which the solubility of the amino acid decreases with an increase in the electrolyte concentration may also happen, and it is called the salting-out effect. It is the ion–molecule physical interactions that result in the salting effects. The NRTL relation for the activity coefficient of amino acid (m) in ternary solution water (w) + amino acid (m) + salt (e) can

Fig. 5. Comparison between experimental and calculated mean ionic activity coefficient by the modified NRTL model for the investigated salt + H_2O systems at 298.15 K: KCl (○), KNO_3 (▲), Na_2SO_4 (◇), NaCl (×), $NaNO_3$ (●), calculated (—).

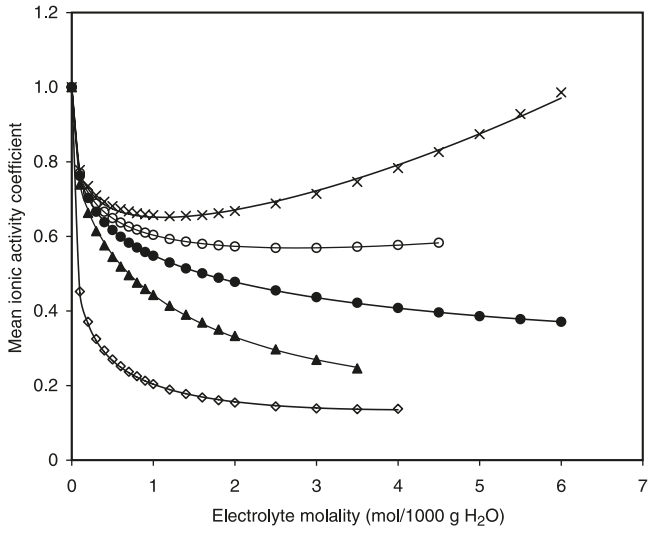

be obtained from appropriate differentiation of eqs. [1], [2], and [18]. Similarly, the Wilson relation for the activity coefficient of amino acid (m) in ternary solution water (w) + amino acid (m) + salt (e) can be obtained from appropriate differentiation of eqs. [1], [2], and [37]. The binary energy parameters for the amino acid–water pairs (listed in Table 1) and for the electrolyte–water pairs and the solubility constant of the amino acids listed in Table 2 are directly used to calculate the solubility of amino acids in aqueous electrolyte solutions. The NRTL parameters, a_{ew} and a_{we}, and the Wilson parameters, E_{ew} and E_{we}, between salt and water have been determined from the simultaneous correlation of the experimental osmotic coefficient and mean ionic activity coefficient data of corresponding binary aqueous electrolyte solutions at T = 298.15 K (29). The evaluated electrolyte–water energy parameters along with the corresponding RMSD values for osmotic coefficient and mean ionic activity coefficient data of binary aqueous electrolyte solutions are listed in Table 4. Figs. 5 and 6, respectively, show the correlation results for the modified NRTL model for the mean ionic activity coefficients and osmotic coefficients of investigated aqueous electrolyte solutions at T = 298.15 K. As can be seen in Table 4, the energy parameters a_{ew} and E_{ew} have negative values and energy parameters a_{we} and E_{we} have positive values. This is not surprising since the interaction between the cation and the anion is stronger than the interaction between the water molecules and the ionic species, which, in turn, is stronger than the interaction between two solvent molecules. The electrolyte–amino acid energy parameters a_{me} and E_{me} were set to zero and the energy parameters a_{em} and E_{em} are treated as adjustable parameters. Table 5 summarizes the values of the electrolyte–amino acid binary interaction parameters along with the corresponding RMSD values. It can be seen that the models developed in this work can successfully represent the solubility of amino acids in aqueous electrolyte solutions. Figure 7 shows the comparison of the literature data and the correlation results

© 2008 NRC Canada

Fig. 6. Comparison between experimental and calculated osmotic coefficient by the modified NRTL model for the investigated salt + H_2O systems at 298.15 K: KCl (○), KNO_3 (▲), Na_2SO_4 (◇), NaCl (×), $NaNO_3$ (●), calculated (—).

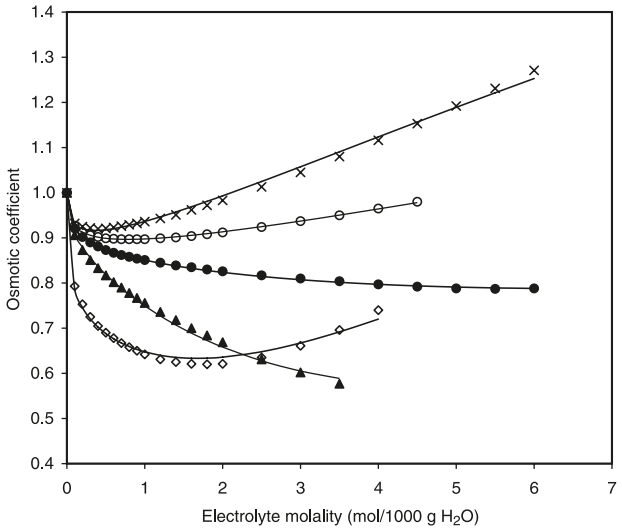

Fig. 7. Solubilities of DL-alanine in several aqueous electrolyte solutions at T = 298.15 K: NaCl (○), Kcl (▲), KNO_3 (◇), $NaNO_3$ (×), calculated by the modified Wilson model (—).

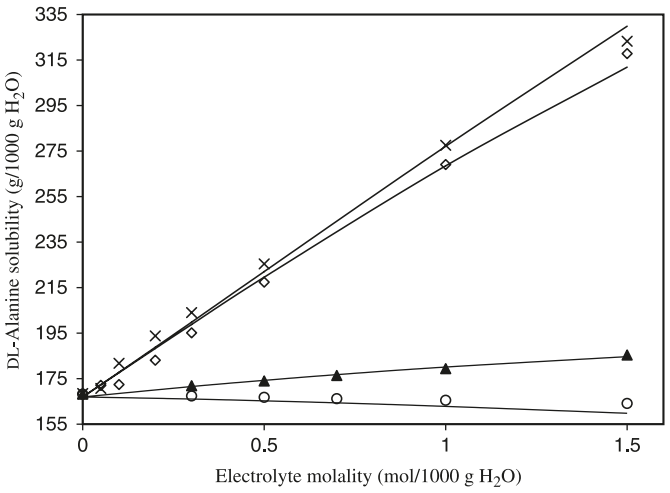

with the Wilson model for the solubility of dl-alanine in aqueous solutions of NaCl, KCl, KNO_3, and $NaNO_3$ at T = 298.15 K. As can be seen in Fig. 7, DL-alanine shows a strong salting-in effect in the presence of $NaNO_3$ and KNO_3, a weak salting-in effect in the presence of KCl, and a weak salting-out effect in the presence of NaCl. As can be seen in Table 5, for the salting-in effects the energy parameters a_{em} and E_{em} have negative values and increases in magnitude as the salting-in effect increases. The negative values of a_{em} and E_{em} indicate that the interaction between the amino acid molecules and the ionic species is stronger than the interaction between two amino acid molecules. Also, Table 5 shows that for salting-out effects, the energy parameters a_{em} and E_{em} have positive values, which indicates that the interaction between two amino acid molecules is stronger than the interaction between the amino acid molecules and the ionic species.

Conclusions

Two molecular thermodynamic frameworks, modified NRTL and Wilson models, were established to investigate the phase equilibrium behavior of amino acids and small peptides in aqueous solutions. The models were used successfully to represent the activity coefficients and solubility of amino acids in water. The models were also used to represent the solubility of an amino acid both in aqueous solutions of another amino acid and in aqueous solutions of an electrolyte. The calculated solubility data are in good agreement with the available literature experimental data. On the basis of the obtained deviations, we conclude that the two models have similar behavior in the representation of the phase equilibrium behavior for the investigated aqueous amino acid solutions. Also, the models developed here correlate with the experimental data with comparable and in some cases with better accuracy than the extended NRTL (4) and Wilson (23) models.

References

1. P.A. Belter, E.L. Cussler, and W.S. Hu. Bioseparation. Wiley, New York. 1998.
2. K.K. Nass. AIChE J. **34**, 1257 (1988).
3. X.Xu, S.P. Pinho, and E.A. Macedo. Ind. Eng. Chem. Res. **43**, 3200 (2004).
4. C.C. Chen, Y. Zhu, and L.B. Evans. Biotechnol. Progr. **5**, 111 (1989).
5. A. Soto, A. Arce, M.K. Khoshkbarchi, and J.H. Vera. Fluid Phase Equilib. **158–160**, 893 (1999).
6. G.R. Pazuki and M. Nikookar. Biochem. Eng. J. **28**, 44 (2006).
7. A.M. Peres and E.A. Macedo. Chem. Eng. Sci. **49**, 3803 (1994).
8. R.B. Gupta and R.A. Heidemann. AIChE J. **36**, 333 (1990).
9. S.P. Pinho, C.M. Silva, and E.A. Macedo. Ind. Eng. Chem. Res. **33**, 1341 (1994).
10. H. Kuramochi, H. Noritomi, D. Hoshino, and K. Nagahama. Biotechnol. Progr. **12**, 371 (1996).
11. H. Kuramochi, H. Noritomi, D. Hoshino, and K. Nagahama. Fluid Phase Equilib. **130**, 117 (1997).
12. M.K. Khoshkbarchi and J.H. Vera. Ind. Eng. Chem. Res. **35**, 4319 (1996).
13. M.K. Khoshkbarchi and J.H. Vera. Ind. Eng. Chem. Res. **35**, 4755 (1996).
14. J.-C. Liu, J.-F. Lu, and Y.-G. Li. Fluid Phase Equilib. **142**, 67 (1998).
15. M.K. Khoshkbarchi and J.H. Vera. Ind. Eng. Chem. Res. **37**, 3052 (1998).
16. C. Gao and J.H. Vera. Can. J. Chem. Eng. **79**, 392 (2001).
17. S. Mortazavi-Manesh, C. Ghotbi, and V.A. Taghikhani. J. Chem. Thermodyn. **35**, 101 (2003).
18. G.R. Pazuki, H.R. Hosseinbeigi, and M. Edalat. Fluid Phase Equilib. **240**, 40 (2006).
19. B.H. Park, K.-P. Yoo, and C.S. Lee. Fluid Phase Equilib. **212,** 175 (2003).
20. C.C. Chen and L.B. Evans. AIChE J. **32**, 444 (1986).
21. K.S. Pitzer. J. Am. Chem. Soc. **102**, 2902 (1980).
22. H. Renon and J.M. Prausnitz. AIChE J. **14**, 135 (1968).
23. R. Sadeghi. Fluid Phase Equilib. **260**, 266 (2007).
24. A. Haghtalab and J.H. Vera. AIChE J. **34**, 803 (1988).

© 2008 NRC Canada

25. R. Sadeghi. Fluid Phase Equilib. **231**, 53 (2005).
26. R. Sadeghi. Polymer, **46**, 11517 (2005).
27. J.M. Simonson and K.S. Pitzer. J. Phys. Chem. **90**, 3009 (1986).
28. A. Jaretun and G. Aly. Fluid Phase Equilib. **163**, 175 (1999).
29. R.A. Robinson and R.H. Stokes. Electrolyte solutions. 2nd ed. Butterworth, London, UK. 1965.
30. E.R.B. Smith and P.K. Smith. J. Biol. Chem. **132**, 47 (1940).
31. J.O. Hutchens, K.M. Figlio, and S.M. Granito. J. Biol. Chem. **238**, 1419 (1963).
32. E.R.B. Smith and P.K. Smith. J. Biol. Chem. **121**, 607 (1937).
33. E.R.B. Smith and P.K. Smith. J. Biol. Chem. **117**, 209 (1937).
34. G.D. Fasman. Handbook of biochemistry and molecular biology physical and chemical data. Vol. 1. 3rd ed. CRC Press, Cleveland, Ohio, USA. 1976.
35. J.B. Dalton and C.L.A. Schmidt. J. Biol. Chem. **103**, 549 (1933).
36. J.B. Dalton and C.L.A. Schmidt. J. Biol. Chem. **109**, 241 (1935).
37. H. Kuramochi, H. Noritomi, D. Hoshino, and K. Nagahama. Biotechnol. Progr. **12**, 371 (1996).
38. X.Z. Jin and K.-C. Chao. J. Chem. Eng. Data, **37**, 199 (1992).
39. A.A. Pradhan and J.H. Vera. J. Chem. Eng. Data, **45**, 140 (2000).
40. L.A. Ferreira, E.A. Macedo, and S.P. Pinho. Ind. Eng. Chem. Res. **44**, 8892 (2005).
41. M.K. Khoshkbarchi and J.H. Vera. Ind. Eng. Chem. Res. **36**, 2445 (1997).

© 2008 NRC Canada

The quantitative removal of metal catalyst from multi-walled carbon nanotubes with minimal tube damage

Trisha A. Huber, Michael C. Kopac, and Catherine Chow

Abstract: A purification method for multi-walled carbon nanotubes (MWCNTs) has been developed to remove almost all (>98%) residual metal catalyst without introducing a significant amount of surface functionality. The process involves alternating mild acid oxidation and thermal oxidation in an iterative fashion with progressively higher temperatures for thermal treatment, in accordance with the increasing thermal stability. Thermogravimetric analysis and inductively coupled plasma mass spectrometry were employed to assess thermal stability and residual catalyst content, respectively, throughout the process. Transmission electron microscopy confirms the integrity of the nanotubes, and the degree of acid functionalization introduced by the acid oxidation is minimal, as determined by titration analysis.

Key words: multi-walled carbon nanotube, purification, ICP-MS, TGA, FTIR.

Résumé : On a développé une méthode de purification de nanotubes de carbone à parois multiples qui permet d'éliminer pratiquement tous les résidus de catalyseur (>98 %) sans introduire de quantités significatives de fonctionnalité à la surface. Le processus implique une alternance d'oxydation acide douce et une oxydation thermique de façon itérative, en augmentant progressivement les températures des traitements thermiques, en fonction de l'augmentation de la stabilité thermique. Tout au long du processus, on a fait appel à l'analyse thermogravimétrique et à la spectrométrie de masse avec couplage plasma pour évaluer respectivement la stabilité thermique et la quantité résiduelle de catalyseur. La microscopie électronique de transmission confirme l'intégrité des nanotubes et, d'après une analyse par titrage, le degré de fonctionnalisation acide introduit par l'oxydation acide est minimal.

Mots-clés : nanotube de carbone à parois multiples, purification, spectrométrie de masse avec couplage plasma, analyse thermogravimétrique, infrarouge à transformée de Fourier.

[Traduit par la Rédaction]

Introduction

Although many advances in the field of carbon nanotube synthesis have been made, a synthetic process yielding pure nanotubes has yet to be developed. Raw carbon nanotubes (CNTs) typically contain non-nanotube carbon (primarily amorphous carbon, but also graphitic carbon and (or) fullerenes) and residual metal catalyst. The presence of impurities alters the bulk properties of the carbon nanotubes and can be detrimental to the applications of interest, rendering purification necessary in most instances. Furthermore, the inhomogeneity of impurity distribution hinders the assessment of the effect of impurities on the properties of the bulk nanotubes. The purification of nanotubes is not straightforward (see below), and in many cases nanotubes are used in the raw (as-prepared) state to avoid purification difficulties.

Received 16 July 2008. Accepted 24 September 2008. Published on the NRC Research Press Web site at canjchem.nrc.ca on 21 November 2008.

T.A. Huber,[1] M.C. Kopac, and C. Chow. Defence Research & Development Canada – Atlantic, Dockyard Laboratory Pacific, CFB Esquimalt, Victoria, BC V9A 7N2, Canada.

[1]Corresponding author (e-mail: trisha.huber@drdc-rddc.gc.ca).

The process most commonly employed in the purification of nanotubes is oxidation; however, the selective oxidation of amorphous carbon requires different conditions from that for metallic species; hence, more than one step is required for purification. As amorphous carbon is generally less stable than CNTs, reduction of amorphous carbon content is commonly achieved by thermal oxidation. Unfortunately, some CNTs, particularly narrow diameter tubes (which are more reactive owing to a high degree of curvature), are also oxidized in the process, especially if metallic species are present. Furthermore, it is difficult to assess the relative quantity of amorphous carbon in CNT samples; thus, it is challenging to determine whether quantitative removal has been achieved.

The simplest and most common method for residual catalyst removal is acid oxidation, in which the residual catalyst is oxidized, and therefore solubilized, in the acid solution. Hot, concentrated acids and acid mixtures are commonly employed, and such harsh conditions result in substantial damage to the tubes. Oxidation of carbon atoms at existing defect sites (1) (imperfections in the hexagonal lattice of the nanotubes) occurs as well as the introduction of new defect sites at which oxidation of carbon atoms also occurs. Oxidation results in the introduction of acid functionality, such as lactone, phenolic hydroxyl, or carboxylic acid groups (2). Although much of the nanotube structure remains intact un-

 doi:10.1139/V08-160 © 2008 NRC Canada

der relatively mild conditions, the effect of functionalization can be dramatic due to the disruption of the extended π system from which the nanotubes gain their extraordinary electrical, mechanical, and thermal properties (3–5). Moreover, the acid oxidation process is only effective when the metal is accessible; when the metal catalyst particle is encapsulated in carbon, which commonly occurs during CNT synthesis, the metal is not accessible for oxidation.[2] Thermal treatment may be applied to effect de-encapsulation; however, care must be taken to ensure that CNT oxidation is minimized during this carbon cracking step.

The requirement for a multi-step process has been recognized, and there are several reports in the literature, mostly pertaining to single-walled carbon nanotubes (SWCNTs) (6–10) in which both acid and thermal oxidation processes are utilized. However, relatively harsh acid oxidative conditions are employed, and the metal content is accurately assessed in only a few reports (7, 10). Chiang et al. (8) have demonstrated the effectiveness of a multi-step iterative approach with SWCNTs, and although the study was quite thorough, the effect of the use of concentrated HCl was not investigated. Furthermore, no comment was made on the scale of the purification. Other effective purification methods have been developed to avoid harsh oxidative conditions, although these methods require the use of specialized equipment and (or) expensive instrumentation (11–16).

We demonstrate the efficacy of an iterative purification protocol that alternates thermal oxidation with mild acid oxidation and can be applied to relatively large quantities of multi-walled carbon nanotubes (MWCNTs). This method effects the quantitative removal of catalyst particles without the significant damage typically associated with acid oxidation. The iterative nature of the approach addresses the shortcomings that exist with each individual step (ineffective metal oxidation due to carbon encapsulation and catalytic thermal oxidation of MWCNTs). In addition, this method significantly reduces the amorphous carbon content. Throughout the purification, the stability of the nanotubes is assessed by thermogravimetric analysis (TGA), and the efficacy of each iterative step is determined by inductively coupled plasma mass spectrometry (ICP-MS). Nanotube integrity was assessed by titration analysis, which quantifies acid functionality, and transmission electron microscopy (TEM). The relative degree of acid functionality is corroborated by Fourier transform infrared (FTIR) spectroscopy.

Experimental

Materials

Industrial grade thin multi-walled carbon nanotubes (MWCNTs, Nanocyl-7000, ~90% C purity, Lot 257–1) were purchased from Nanocyl Inc. Aqueous sodium hydroxide solution (NaOH (aq.), 0.100 mol/L, Fisher), sodium bicarbonate ($NaHCO_3$, 99%, Caledon Laboratories), and concentrated acids (hydrochloric and nitric) were used without purification.

Scheme 1. Overview of purification method.

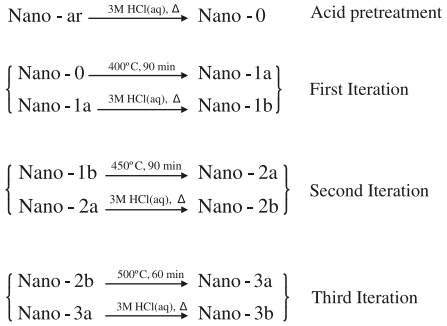

Purification

A 10.14 g sample of as-received MWCNTs, denoted herein as Nano-ar (see Scheme 1 for purification overview), was ground with a mortar and pestle and refluxed overnight (~17 h) in ~600 mL of 3 mol/L HCl (aq.). The acid-treated material, denoted as Nano-0, was isolated by filtration (medium frit) and washed with distilled water until the washings were neutral. Nano-0 was dried thoroughly (50 °C in vacuo), then heated (uncovered) in air for 90 min at 400 °C. The thermally treated material, Nano-1a, was refluxed in 3 mol/L HCl (aq.) overnight. The resulting material, Nano-1b, was isolated and dried as described above. The process of thermal treatment followed by acid oxidation was repeated twice more (samples denoted by Nano-2a/b and Nano-3a/b), except the thermal treatment was performed at 450 °C (for 90 min) for Nano-2b, and 500 °C (60 min) for Nano-3b.

Characterization

Thermal stability was assessed by TGA using a TA Instruments TGA 51 thermogravimetric analyzer. Small samples (~1–2 mg) were heated from ambient to 800 °C at a rate of 10 °C/min in air (~120 mL/min).

ICP-MS analyses were performed with a Varian Ultramass 700 for the quantitative determination of residual metal catalyst. Sample preparation involved the complete oxidation of carbon (ashing) to ensure that all catalyst particles were accessible (not encapsulated in carbon). This was accomplished by heating an accurately weighed sample at 700 °C for 30 min in air. The ash was digested in an acid mixture (2:1, HCl/HNO_3) at 90 °C for 2 h, and the resulting solution was analyzed.

To assess the extent of acid functionality, titration analyses were performed on Nano-ar, Nano-2b, and Nano-3b. Typically, a 20.00 mL aliquot of 0.100 mol/L NaOH (aq.), diluted to 40 mL, was added to an accurately known mass of nanotubes (80–100 mg), sonicated for 2 h, and then stirred for 3 days under a blanket of argon. The suspension was filtered (0.2 μm polycarbonate membrane), and the collected solid was washed thoroughly with distilled water; the filtrate and washings were combined and titrated against standardized 0.025 mol/L HCl (aq.) to a phenolphthalein endpoint. The degree of acid functionality, expressed in milliequivalents per gram of material, was determined from the mequiv of base required to neutralize surface acid functionality (mequiv base added – mequiv acid required to reach

[2] T.A. Huber and M.C. Kopac. Unpublished results.

© 2008 NRC Canada

Fig. 1. Transmission electron micrographs of (*a*) Nano-ar and (*b*) Nano-2b. The arrow in (*a*) indicates impurities.

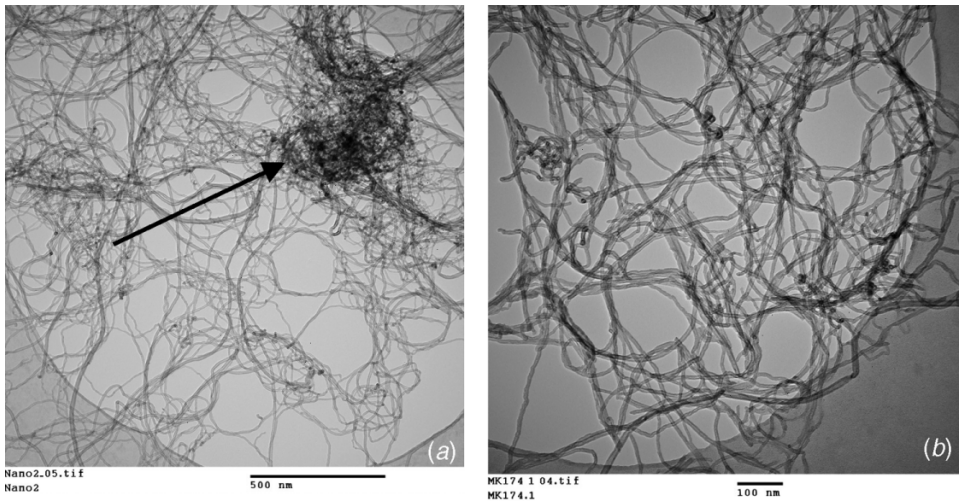

equivalence point) divided by the mass of the sample. The analyses were performed in triplicates, and the average values are reported. Purified MWCNTs were also subjected to titration analysis with $NaHCO_3$ as the base (to assess the degree of carboxylic acid functionality) and bromcresol green as the indicator.

Infrared spectral analysis was performed to further investigate the degree of acid functionality. FTIR data were acquired using a Nicolet Nexus 670 Fourier transform infrared spectrometer. Samples were prepared by grinding the material with dry potassium bromide and pressing into a pellet. Spectra were acquired in transmission mode; 256 scans were collected at a resolution of 4 cm^{-1}. The absorbance spectra are uncorrected.

Transmission electron microscopy (TEM) was employed to qualitatively assess the nature of the impurities in the MWCNTs, as well as to assess the integrity of the nanotubes after purification. TEM samples were prepared by depositing a drop of dispersion (prepared by sonicating a small amount of material in ethanol) on a holey carbon-coated copper TEM grid and images were acquired on a Hitachi H-7000 transmission electron microscope.

Results and discussion

The purification protocol was developed for purifying thin MWCNTs prepared by a catalytic chemical vapour deposition (CVD) method. The first step in the purification is acid oxidation to remove any accessible metallic species (see Scheme 1). The subsequent steps are comprised of iterations of thermal treatment followed by acid oxidation. At various stages of the purification, the material was characterized by TGA, ICP-MS, titration analysis, and TEM.

TEM of the as-received MWCNTs (Nano-ar) confirms the presence of impurities (non-nanotube carbon and (or) metallic particles), visible as dark spots indicated in Fig. 1*a*. TGA was performed to determine the thermal stability of the as-received MWCNTs (Nano-ar) (see Fig. 2); the presence of metal catalyst results in the catalytic oxidation of carbon (nanotubes and other forms); thus, the oxidation occurs at a lower temperature than pure nanotubes. Peak mass loss was determined from the derivative (d*m*/d*T*) of the TGA trace,

Fig. 2. TGA traces for Nano-ar, Nano-0, Nano-1b, Nano-2b, and Nano-3b.

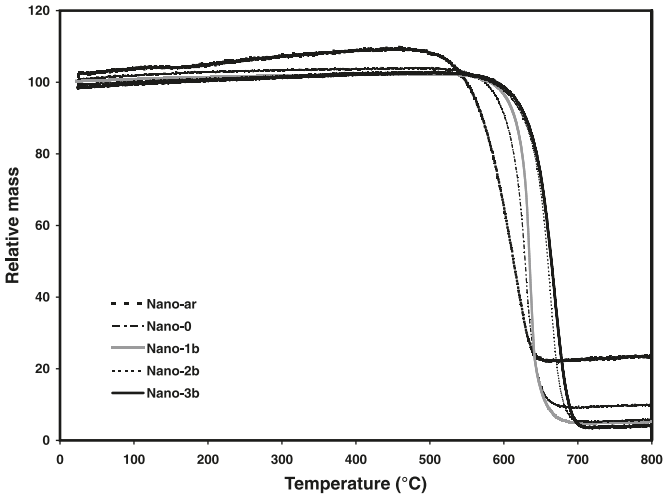

and the data are presented in Table 1. ICP-MS analysis of Nano-ar indicates that the catalyst is comprised largely of iron (Fe) and cobalt (Co). Although the supplier indicates ~10% non-carbon content, the majority of this is alumina, which is used as a catalyst support, and ~0.4% is metallic catalyst (see Table 2).

Nanotube defect sites are relatively reactive, and it is known that the presence of adsorbed oxygen can result in the formation of oxygen-containing surface functionality (17); hence, even raw CNTs may contain acid functionality (or at least adsorbed oxygen that will result in surface functionality upon thermal treatment). Upon oxidation, acid functionality (lactone, phenolic hydroxyl, carbonyl, and carboxylic acid moieties) are formed at defect sites (2), including opened end caps. A semi-quantitative assessment of these functional groups may be obtained through titration analysis. This analysis involves the reaction of excess base with the material, followed by back titration of unreacted base with a standardized acid solution (2, 18, 19). Although these functional groups are of varying acidity, the use of a strong base, such as hydroxide, ensures that complete reac-

© 2008 NRC Canada

Table 1. Synopsis of mass loss, total catalyst content, peak mass loss, and titration analysis data.

Sample	Mass loss (%)	Catalyst content (%)	Peak mass loss (°C)	Acid functionality (mequiv/g)[a]
Nano-ar	—	0.36	618	1.5 (0.6)
Nano-0	11	0.39	634	
Nano-1a	1.8			
Nano-1b	0.6	0.11	638	
Nano-2a	51			
Nano-2b	0	0.019	668	1.5 (0.2)
Nano-3a	9.2			
Nano-3b	3.2	0.014	669	1.1 (0.4)

[a]These values are uncorrected for the slight acidity of the distilled water used in the analysis.

Table 2. ICP-MS data for as-received MWCNTs (Nano-ar) and MWCNTs after each acid oxidation (Nano-0, Nano-1b, Nano-2b, and Nano-3b).

	ICP-MS data[a] (ppm)			
Sample	Fe	Co	Al	Total catalyst content (%)[b]
Nano-ar	2400 (300)	1200 (90)	N.A.[c]	0.36 (0.04)
Nano-0	2850 (400)	1010 (10)	31 (8)	0.39 (0.04)
Nano-1b	710 (50)	375 (2)	13 (11)	0.108 (0.005)
Nano-2b	110 (10)	84 (5)	6 (3)	0.019 (0.002)
Nano-3b	100 (60)	43 (10)	7 (10)	0.014 (0.007)

[a]Average of three samples; uncertainty in parentheses.
[b]These values exclude the catalyst support (alumina).
[c]The limited solubility of alumina in the digestion solution precluded accurate determination, although the concentration of aluminum in solution was in the order of 15 000 ppm.

tion of all acid functionality will occur. Hydroxide titration analysis of Nano-ar indicates that the degree of acid functionalization is 1.5 ± 0.6 milliequivalents of acid per gram of material (mequiv/g). This value represents functionalization at approximately one out of every 50 carbon atoms (using the molar mass of carbon to approximate the molar mass of the material), i.e., ~2% of the potential sites are functionalized. The magnitude of the uncertainty is not surprising given that this method is fraught with issues, including incomplete titration (due to the potential intercalation of base), the pH contribution of distilled water, and the potential for reaction with impurities. In addition, the inhomogeneous distribution of impurities will also affect the data spread. Furthermore, it is expected that the more reactive end caps will possess higher functionality than the sidewalls of the nanotubes; thus, shorter tubes will exhibit a higher degree of acid functionality on a mass basis, compared with longer tubes. Hence, a distribution of values is anticipated even if consistence in sidewall functionalization exists.

To minimize any catalytic oxidation of nanotubes during the first thermal treatment, an acid pretreatment (3 mol/L HCl (aq.) reflux overnight) was performed on Nano-ar to oxidize any accessible metal catalyst. Although the pretreatment resulted in a mass loss of ~11%, ICP-MS analysis of the resulting material (Nano-0) indicated that the majority of the catalyst remained (see Table 1). This implies that the majority of catalyst particles are inaccessible for oxidation. It is anticipated that any catalyst particles that exist within the tips of the nanotubes will become accessible during the acid pretreatment because of the high reactivity of the endcaps resulting from curvature strain. Hence, it may be concluded that the inaccessible catalyst particles are encapsulated by a carbon shell, formed during synthesis, which must be cracked to access the metal. Interestingly, the aluminum (Al) content in Nano-0 was determined to be very low (<40 ppm), and the digestion solution did not contain undissolved alumina, as was observed with Nano-ar. Hence, it is reasonable to conclude that the pretreatment had removed most of the catalyst support. Furthermore, the observed mass loss in this step (~11%) is consistent with quantitative removal of the alumina, although some loss of carbon is expected.

TGA was used to determine the optimal temperature for the first thermal treatment, the purpose of which is to de-encapsulate catalyst particles; the TGA trace of Nano-0 (see Fig. 2) indicates that the onset of oxidation occurs at ~500 °C; thus, a conservative temperature of 400 °C was chosen. The material was heated in air for 90 min, yielding Nano-1a. The mass loss was very small (<2%), indicating that little carbon was oxidized. The next step involved the acid oxidation of Nano-1a, yielding Nano-1b. The effectiveness of the de-encapsulation is evident in the ICP-MS data for Nano-1b (see Table 2). Nano-1b contains substantially less catalyst than Nano-ar (710 ppm Fe and 375 ppm Co, and 2400 ppm Fe and 1200 ppm Co, respectively); considering that the mass of the material had been reduced by only ~13% up to this point, these data indicate that acid oxidation had removed ~75% of the catalyst. Furthermore, an increase in the thermal stability is evident in the TGA data, which exhibit a peak mass loss of 634 °C.

With the majority of the catalyst removed and an increase in thermal stability, the thermal treatment of the second iteration (yielding Nano-2a) was performed at a slightly higher temperature for 90 min in air, to effect thermal oxidation of amorphous carbon and to de-encapsulate any remaining carbon-coated catalyst. The choice of 450 °C is fairly conservative based on the TGA data of Nano-1b, which exhibits the onset of oxidation at ~540 °C. The mass loss associated with this step was substantial (~51%); presumably any amorphous carbon present would have been oxidized at this point, although it is anticipated that some nanotubes were also oxidized. The subsequent acid oxidation (Nano-2b) resulted in a further metal content reduction, bringing the total amount removed approaching 98%, and an overall mass loss of 57%. After the second iteration, the metal content was determined

© 2008 NRC Canada

to be 110 ppm Fe and 84 ppm Co, which is 0.019% *of the purified material*, which has suffered significant mass loss. The acidic surface functionality was determined to be 1.5 ± 0.2 mequiv/g; this value is the same, within experimental error, as that determined for the as-received MWCNTs. In addition, titration analysis with $NaHCO_3$ was also performed on the second iteration product. The data indicate that ~40% (0.58 ± 0.08 mequiv/g) of the total acidic sites are carboxylic acid groups.

For comparison, the purification was also performed with 3 mol/L HNO_3 (aq.) in place of the HCl (aq.); titration analysis of the material purified with the nitric acid indicated an acid functionality of 3.7 ± 0.4 mequiv/g, which is significantly (and statistically) higher than that of the hydrochloric acid purification (1.5 ± 0.2 mequiv/g). Furthermore, titration analysis of MWCNTs that have been intentionally acid functionalized indicates that the surface functionality is ~9 ± 1 mequiv/g. Titration analysis supports the contention that this relatively mild purification method introduces minimal surface functionality.

To further investigate the extent of acid functionalization, IR spectra for four different samples were acquired: as-received MWCNTs, MWCNTs purified using 3 mol/L HCl, MWCNTs purified using 3 mol/L HNO_3, and intentionally acid-functionalized MWCNTs (see Fig. 3). For pristine carbon nanotubes, two absorbances (~1575 and ~868 cm^{-1}) are expected in the infrared spectrum arising from C–C stretching; however, the exact location is diameter-dependent (20). The utility of IR spectroscopy is fairly limited for pristine nanotubes but does provide some qualitative information regarding the nature of surface functionality. Absorbances due to acidic functional groups (lactone, phenolic hydroxy, carbonyl, and carboxylic acid groups) may be observed in the IR spectrum, although subtle differences in the bond order (as a resulting of differing environments) can give rise to fairly broad absorbances relative to those of discrete molecules. In preparing the IR samples, only small amounts of material could be used, as all absorb very strongly. Thus, any moisture is readily observed. All spectra exhibit a broad absorbance at ~1580 cm^{-1} attributed to the carbon skeleton, as well as a peak at ~1630 cm^{-1} (of varying intensity) that is assigned to water contamination. In terms of acid functionality, the region of greatest interest is the carbonyl region (1700–1750 cm^{-1}), as C=O stretching gives rise to a very intense peak; thus, small quantities of carbonyl-containing species are readily evident. There is no obvious peak in the carbonyl region of the as-received MWCNT spectrum, although a small peak at ~1720 cm^{-1} does appear in the spectrum after purification, attributed to a small quantity of carbonyl-containing species (carboxylic acid, lactone, ketone). The intensity of this absorbance is quite small relative that of the carbon skeleton (~1580 cm^{-1}). In contrast, the spectrum for the MWCNTs that were purified with 3 mol/L HNO_3 exhibits a stronger C=O absorbance, indicating a higher acid functionality. This is consistent with the titration analysis data, which indicate a degree of acid functionality of 3.7 ± 0.4 mequiv/g for the HNO_3-purified MWCNTs (compare with 1.5 ± 0.2 mequiv/g for the HCl-purified MWCNTs). Furthermore, the sample of intentionally acid-functionalized MWCNTs yield a very strong carbonyl peak in the IR spectrum, which is consistent with the high degree of acid functionality, 9 ± 1 mequiv/g, determined by titration analysis.[2] IR data support the titration analysis findings of minimal acid-group introduction. Moreover, the corroboration suggests that although the titration analysis method can result in large relative uncertainties, it can differentiate between varying degrees of acid functionality.

Fig. 3. FTIR spectra of as-received (*a*) MWCNTs, (*b*) HCl-purified MWCNTs, (*c*) HNO_3-purified MWCNTs, and (*d*) acid-functionalized MWCNTs.

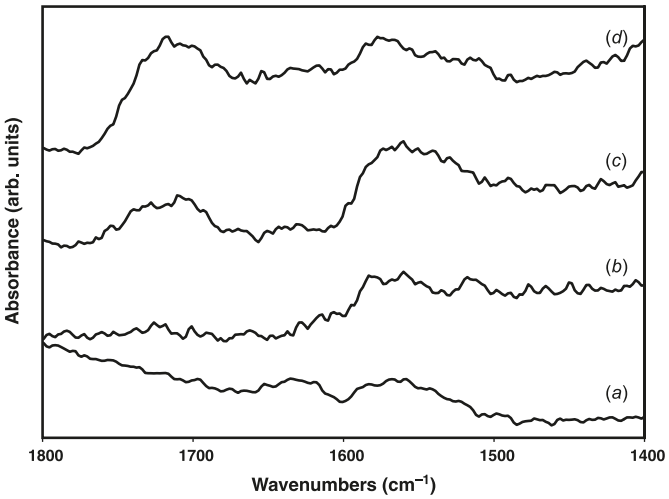

The surface functionality may be removed by annealing under vacuum (7); however, this process requires a high-temperature vacuum oven. Attempts to graphitize the MWCNT surface by heating in argon (500 °C for 1 h) were unsuccessful, presumably due to the presence of oxygen, resulting from incomplete purging or the presence of adsorbed oxygen on the nanotube surface (21, 22). Titration analysis indicated that heating under an inert atmosphere had no effect on the surface functionality (1.3 ± 0.4 mequiv/g).

Although ~98% of the catalyst originally present had been removed after two iterations, a third was performed to assess its effectiveness. In this iteration, the thermal step was performed at 500 °C, but only for 60 min (Nano-3a). Given the high temperature, the mass lost in this step was relatively small (9.2%), indicating that the material is fairly stable; thus, it was concluded that the amorphous carbon content was low. After the acid oxidation, yielding Nano-3b, TGA data indicate that, based on thermal stability, the third iteration did not significantly enhance the purity; the peak mass loss for Nano-3b is the same as for Nano-2b, and the residual mass is only marginally smaller (the observed residual mass is likely due to trace quantities of metal oxide and instrument uncertainty). Furthermore, ICP-MS data indicate that the metal content is approximately the same as after the second iteration (~0.014%). Thus, the ICP-MS data validate the TGA results, indicating that the high level of purity was obtained after the second iteration. Moreover, this conclusion could have been reached by monitoring thermal stability (by TGA) alone. Titration analysis of Nano-3b indicates that the degree of surface functionality is approximately the same (within experimental error) (1.1 ± 0.4 mequiv/g). Although the difference is statistically insignificant, this

© 2008 NRC Canada

could be an indication of some loss of functionality as a result of the higher temperature of thermal treatment (500 °C). TEM indicates that the nanotubes are still intact after purification (see Fig. 1*b*).

Including the third iteration data, the overall mass loss was 62%; thus, the yield of purified MWCNTs is ~38%. In all likelihood, the original MWCNT content was higher, but suffered loss because of catalytic oxidation and the presence of defects due to the synthetic method (CVD).

Although this protocol was assessed with thin MWCNTs, its versatility has been successfully demonstrated with wider diameter MWCNTs (~30–50 nm). TGA data for each iteration show a progression in thermal stability, and ICP-MS data indicate that quantitative (~98%) removal of catalyst has occurred after two iterations.[2] Furthermore, as this method removes both free and carbon-encapsulated catalyst particles, it should be applicable to MWCNTs that have a substantial amount of catalyst. It is expected that the pretreatment would oxidize almost all unencapsulated metal, and the remainder would be liberated in the subsequent thermal treatments. The number of iterations may be dependent on the thickness of the encapsulating carbon, but should be independent of the quantity of catalyst.

Conclusions

We have demonstrated a simple but effective large-scale method for the quantitative removal (>98%) of catalyst from MWCNTs utilizing mild acid oxidation in conjunction with thermal treatment. The successful application of the iterative process has been validated by TGA, ICP-MS, and TEM. Titration analysis and infrared spectroscopy demonstrate that mild acid oxidation conditions cause minimal introduction of acid functionality. Furthermore, TGA alone may be sufficient for determining the optimal number of iterations.

Acknowledgements

We would like to thank Scott McClelland for all ICP-MS analyses and Brent Gowen (University of Victoria) for TEM imaging.

References

1. I.D. Rosca, F. Watari, M. Uo, and T. Akasaka. Carbon, **43**, 3124 (2005).
2. H.P. Boehm, E. Diehl, W. Heck, and R. Sappok. Angew. Chem., Int. Ed. **3**, 669 (1964).
3. S.J. Tans, M.H. Devoret, H. Dai, A. Thess, R.E. Smalley, L.J. Geerligs, and C. Dekker. Nature (London, UK), **386**, 474 (1997).
4. M.M.J. Treacy, T.W. Ebbesen, and J.M. Gibson. Nature (London, UK), **381**, 678 (1996).
5. S. Berber, Y.-K. Kwon, and D. Tománek. Phys. Rev. Lett. **84**, 4613 (2000).
6. Y.-Q. Xu, H. Peng, R.H. Hauge, and R.E. Smalley. Nano Lett. **5**, 163 (2005).
7. A.C. Dillon, T. Gennett, K.M. Jones, J.L. Alleman, P.A. Parilla, and M.J. Heben. Adv. Mater. **1**, 1354 (1999).
8. I.W Chiang, B.E. Brinson, R.E. Smalley, J.L. Margrave, and R.H. Hauge. J. Phys. Chem. B, **105**, 1157 (2001).
9. K.H An, K.K. Jeon, J.-M. Moon, S.J. Eum, C.W. Yang, G.-S. Park, C.Y. Park, and Y.H. Lee. Synth. Met. **140**, 1 (2004).
10. K. Shen, H. Xu, Y. Jiang, and T. Pietrass. Carbon, **42**, 2315 (2004).
11. W. Huang, Y. Wang, G. Luo, and F. Wei. Carbon, **41**, 2585 (2003).
12. K.B. Shelimov, R.O. Esenaliev, A.G. Rinzler, C.B. Huffman, and R.E. Smalley. Chem. Phys. Lett. **282**, 429 (1998).
13. H. Zhang, C.H. Sun, F. Li, H.X. Li, and H.M. Cheng. J. Phys. Chem. B, **110**, 9477 (2006).
14. X. Xu, R. Ray, Y. Gu, H.J. Ploehn, L. Gearheart, K. Raker, and W.A. Scrivens. J. Am. Chem. Soc. **126**, 12736 (2004).
15. S. Niyogi, H. Hu, M.A. Hamon, P. Bhowmik, B. Zhao, S.M. Rozenzhak, J. Chen, M.E. Itkis, M.S. Meier, and R.C. Haddon. J. Am. Chem. Soc. **123**, 733 (2001).
16. S.K. Doorn, R.E. Fields, III, H. Hu, M.A. Hamon, R.C. Haddon, J.P. Selegue, and V. Majidi. J. Am. Chem. Soc. **124**, 3169 (2002).
17. B.E. Conway. Electrochemical supercapacitors: Scientific fundamentals and technological applications. Kluwer Academic/Plenum Publishers. New York. 1999. p. 186.
18. M.S.P. Shaffer, X. Fan, and A.H. Windle. Carbon, **36**, 1603 (1998).
19. H. Hu, P. Bhowmik, B. Zhao, M.A. Hamon, M.E. Itkis, and R.C. Haddon. Chem. Phys. Lett. **345**, 25 (2001).
20. C. Branca, F. Frusteri, V. Magazu, and A. Mangione. J. Phys. Chem. B, **108**, 3469 (2004).
21. R.F. Strickland-Constable. Trans. Faraday Soc. **34**, 1074 (1938).
22. P.G. Collins, K. Bradley, M. Ishigami, and A. Zettl. Science (Washington, DC), **287**, 1801 (2000).

© 2008 NRC Canada

Canadian Journal of Chemistry

Author Index
Volume 86, 2008

Revue canadienne de chimie

Index des auteurs
Volume 86, 2008

Abdolmaleki, A., 50
Abe, H., 471
Aghaie, H., 745
Aghaie, M., 745
Aguilar, A., 333
Ahmad, I., 899
Al-Abadleh, H.A., 942
Allen, A.D., 333
Al-Yassir, N., 146
Amini, M.M., 751
Andraos, J., 342
Andrews, D.L., 855
Appathurai, N.P., 761
Arellano-Cárdenas, S., 305
Ariya, P.A., 811
Asadi, M., 841
Asghar, B.H.M., 225
Askari, M.S., 1105
Azadmehr, A., 751
Azizian, J., 925
Bai, D., 230
Baille, W.E., 579
Bajorek, T., 444
Bajuk-Bogdanović, D., 996
Baldwin, J.E., 395
Banerjee, A., 668
Banks, J.T., 703
Barrett, C.J., 1085
Barrios, H., 726
Beck-Candanedo, S., 503
Bennet, A.J., 238, 1005
Bentley, T., 277
Beshara, C.S., 951
Beyzavi, M.H., 317
Bhaskar, G., 285
Bhella, S.S., 451
Bijanzadeh, H.R., 248
Blanco, S.E., 462
Boden, B.N., 50
Böhme, D.K., 177
Bollinger, J.W., 668
Borges, S.S., 312
Brisson, J., 7
Brown, R.S., 91, 774
Buatip, T., 757
Buncel, E., 79, 298
Cabrera, E.P., 333
Cai, C.-C., 199
Calabia, B.P., 548
Caldwell, S.L., 976
Campos, M.G., 1077
Castro, E.A., 462
Castro, M.C., 312
Chabot, N., 271
Chahma, M., 982
Chan, T.H., 495
Chan, W., 333
Chantrapromma, K., 205
Chanzy, H., 520
Chaya, D.N. 769
Chen, B., 871
Chen, D., 495
Chen, R.E., 875
Chen, W.-H., 892
Chen, Z.-H., 170
Chen, Z.W., 875
Cheng, K.A.W.Y., 1118
Chiang, Y., 101
Chica, R., 271
Chikwana, E., 416
Chow, C., 1138
Clyburne, J.A.C., 20
Colizza, K.G., 91
Costa-Coquelard, C., 1034
Coulais, E., 1105
Cowen, S., 942
Cox, R.A., 290, 298
Cozens, F.L., 1118
Crampton, M.R., 225
Crawford, E., 976
Croce, A.E., 918
Csaszar, E., 91
Cui, Q.C., 495
da Silva, J.B.B., 312
Damha, M.J., 641, 881
Dao, L.H., 1010
Daoust, B., 970
Das, B., 709
Dasog, M., 368
De, B., 401
Debnath, P., 325, 846
del Rio P., F., 726
Detellier, C., 1
Diao, L., 105
Díaz T., E., 726
Dickie, D.A., 20
Didier, B., 91
Doi, Y., 471
Dorris, A.C., 1085
Dou, Q.P., 495
Douglas, K.L., 1085
Douma, M.D., 774
D'Souza, M., 359
Dufresne, A., 484
Duggal, M., 942
Dutta, L.N., 401
Eikerling, M., 657
Fan, Y., 761
Feng, J.-T., 281
Ferretti, F.H., 462
Flegel, M., 161
Fogg, D.E., 931
Fortin, E., 271
Fryzuk, M.D., 803
Fu, N., 333
Fukui, T., 621
Gallardo-Velázquez, T., 305
Gan, G., 261
Gao, Y., 871
Garabatos-Perera, J.R., 676
Geatti, P., 714
Gehring, K., 608
Gharib, F., 751
Ghashang, M., 376, 841
Ghotekar, B.K., 1070
Gillet, S.M.F.G., 271
Gillis, H.M., 676
Gilroy, J.B., 976
Godoy, J., 333
Gonzalez, C.M., 686
Gottardo, C., 410
Gray, D.G., 503
Green, A.E.C., 1063
Griffiths, K., 39
Grzegożek, M., 682
Guillou, H., 7
Guo, Y.-A., 199
Guthrie, J.P., 285
Hadipour, N.L., 1095
Hahn, F., 992
Halligudi, S.B., 1030

© 2008 NRC Canada

Han, S., 230
Hanna, R., 970
Hao, J., 1034
Harisha, R.S., 1030
Harrington, L.E., 1063
Hasaninejad, A., 317
Hassaninejad, A., 456
He, C., 1034
He, Q., 20
He, Y.-B., 170
Hemeon, I., 238
Hicks, R.G., 976, 982
Hiremath, V.B., 1030
Hoang, T., 942
Hocquelet, C., 726
Holclajtner-Antunović, I., 996
Holloway, S., 435
Hosamani, K.M., 1030
Hossain, M.S., 410
Hosseini-Sarvari, M., 65, 1044
Hosseinian, A., 376
Hsieh, Y.-H., 81
Hu, C.-G., 170
Hu, S.-L., 691
Hu, Y., 39
Huang, G., 199
Huang, X., 821
Huang, X.-H., 170
Huber, T.A., 1138
Hubicki, Z., 958
Hudson, R.H.E., 1026
Huo, C., 495
Huser, H., 992
Indurugalla, D., 1005
Ino, D.D., 20
Isanbor, C., 225
Ishar, M.P.S., 451
Islam, M.R., 600
Jabbari, M., 751
Jachak, M.N., 1070
Jacobsen, H., 695
Jain, R., 976
James, B.R., 253
Jankowski, C.K., 726, 1077
Jennings, M.C., 20
Jiang, S., 1034
Jiménez-Estrada, M., 1077
Jolicoeur, B., 213
Jong, H., 803
Jubert, A.H., 462
Kaartinen, M.T., 271
Kaeding-Koppers, A., 525
Kakkar, A., 540
Kalaji, M., 992
Kamal, A., 1099
Karimi, A.R., 248, 925
Karthikeyan, K., 720
Kavianpour, A., 368
Kawada, J., 628
Kazi, M.A., 1070
Keillor, J., 271
Kek, Y.-K., 533
Keller, B.O., 774
Keri, R.S., 1030
Kerr, G.M., 774
Kerton, F., 435
Keum, S.-R., 298
Kevill, D.N., 359
Khalafi-Nezhad, A., 317, 456
Khalifeh, R., 426
Khan, F.N., 1019
Khan, M.N.A., 1099
Khosropour, A.R., 264
Khurana, J.M., 1052
Kiattansakul, R., 205
Kidwai, M., 799
Kiepek, E., 298
Kobayashi, S., 333
Kokoh, K.B., 992
Kolmakov, K., 101, 119
Kołodyńska, D., 958
Kong, L., 821
Kopac, M.C., 1138
Koysomboon, S., 205
Kraatz, H.-B., 368
Kraft, T.M., 410
Kresge, A.J., 101, 119
Kukreja, S., 799
Kumar, A., 384, 899
Kumar, R.A., 709
Kumar, R.S., 720
Kumar, S., 1052
Kumar, V.P., 907
Labeodan, O.A., 20
Lam, R., 586
Lam, W.H., 495
Lampre, I., 1034
Laphookhieo, S., 205, 757
Larouche, M., 970
Le Van Mao, R., 146
Lee, C.-Y., 512
Lee, F.S., 1118
Lee, W.-H., 533
Leigh, W.J., 1105
Lesage, D., 1077
Letaief, S., 1
Li, C.-J., 616
Li, X., 782, 871
Li, X.-H., 281
Liu, H., 821
Liu, S.-Y., 199
Liu, Z., 657
Lollmahomed, F., 1105
Longpré, F., 970
López-Cortés, S., 305
Lorenzini, F., 253
Lu, Z., 142
Lu, Z.-H., 230
Lubell, W.D., 213, 271
Lucas, C.R., 912
Lukeman, M., 161
Luo, J., 199, 821
Lv, Q., 871
Lynam, J.M., 435
Ma, C.T.-Z., 50
Ma, X.-M., 892
MacIntosh, I.S., 20
MacLachlan, M.J., 50
Maclean, H., 564
Maillard, D., 556
Maiyalagan, T., 1019
Maji, P.K., 846
Majumdar, K.C., 72, 325, 846
Mancuso, M., 714
Maneerat, W., 205, 757
Marcazzan, P., 253
Martin, C., 992
Mattoso, L.H.C., 590
McDowell, J.J., 703
McFarland, S.A., 1118
McKelvey, J.I., 703
Medeiros, E.S., 590
Mehenni, H., 7, 1010
Mifune, J., 621
Mio, M., 219
Mioč, U.B., 996
Mirjafari, A. 831
Mirkhani, V., 831
Miyazawa, T., 219
Moeini, F., 1044
Moghadam, M., 831
Mohamed, M.F., 91
Mohammadi, A.A., 925
Mohammadizadeh, M.R., 925
Mohammadpoor-Baltork, I., 831
Moiseev, A.G., 1105
Morakinyo, M., 416
Morrison, J.S., 791
Muchall, H.M., 410
Mwene-Mbeja, T.M., 209
Myles, D.J.T., 982
Nakamura, S., 621
Nakano, Y., 271
Nand, B., 1052
Narayana Kumar, G.G.K.S., 769

© 2008 NRC Canada

Narender, M., 907
Neto, W.B., 312
Neverov, A.A., 91
Neville, J.J., 761
Nguyen, S., 570, 628
Ngwendson, J.N., 668
Nobes, G.A.R., 628
Noé, P., 520
Numata, K., 471
Odoh, S., 761
Offeman, R.D., 590
Oleschuk, R.D., 774, 1055
Ollevier, T., 209
Oropeza, M., 1077
Orts, W.J., 590, 628
Osorio-Revilla, G., 305
Paige, M.F., 368
Pal, A.K., 72, 325
Pal, G., 401
Pardin, C., 271
Parhami, A., 317, 456
Park, B.-C., 359
Patra, A., 401
Patrick, B.O., 253, 803, 976
Pearce, B.M., 951
Pelletier, J.N., 271
Peng, C.G., 881
Peng, L., 142
Pereira, L.A., 312
Perumal, P.T., 32, 720
Pincock, J.A., 686
Pomerantseva, E., 608
Power, A., 435
Premalatha, K., 124
Prud'homme, R.E., 556
Qing, G.-Y., 170
Qiu, F., 903
Qu, X., 129
Rafiee. M.A., 1095
Raj, T., 451
Rajagopal, S., 298
Ramsay, B., 564
Ramsay, J., 564
Rao, K.R., 907
Rao, M.S., 899
Raofie, F., 811
Ravenelle, F., 628
Reddy, K.S., 1099
Reyes-Chilpa, R., 1077
Richard, L.A., 703
Riki, N.T., 841
Roman, M., 525
Roopan, S.M., 1019
Ruhlmann, L., 1034
Rusu, N., 970
Ryu, Z.H., 359
Sadeghi, R., 1126
Sah, V., 384
Saito, T., 516
Salin, E.D., 586
Salunkhe, M.M., 138
Sancho, M.I., 462
Saranya, S., 32
Schatte, G., 20
Schepp, N.P., 1118
Schultze, C.M., 668
Scott, R.W.J., 368
Seif, A., 745
Selvam, N.P., 32
Servat, K., 992
Shaabani, A., 248
Shankar, K.S, 124
Sharghi, H., 317, 426, 1044
Sharma, P., 384
Shaterian, H.R., 376, 841
Sheridan, K., 435
Shi, G., 495
Shi, Y.-P., 281, 892
Shirazi, A.N., 456
Shirin, S., 79
Simoyi, R.H., 416
Singer, S.R., 395
Singh, Ga., 451
Singh, Gu., 451
Singh, J., 384
Singh, R., 451
Singhal, K., 799
Skouta, R., 616
Snider, G., 811
Sokol, W., 737
Soleimani, K., 248
Soper, R.G., 435
Sridhar, R., 907
Srikanth, Y.V.V., 1099
Srinivas, B., 907
Strazzolini, P., 714
Su, S., 1055
Su, W.K., 875
Subba Reddy, B.V. , 124, 769
Sudesh, K., 512, 533
Sun, H., 782
Sun, L., 1034
Sun, Z., 564
Sundararajan, P.R., 600
Suneel, K.,709
Sunitha, P., 709
Syers, J.K., 205, 757
Szpakiewicz, B., 682
Tabrizian, M., 1085
Taher, A., 325
Tamari, E., 925
Tandon, S.S., 912
Tangestaninejad, S., 831
Tay, B.-Y., 512
Tahmassebi, D., 333
Teimouri, F., 925
Teimouri, M.B., 248
Tessier, C., 7
Thérien-Aubin, H., 579
Thirupathi, P., 709
Thompson, A., 676, 951
Tidwell, T.T., 333
Tito, D., 992
Toche, R.B., 1070
Todorović, M., 996
Tokiwa, Y., 548
Trempe, J.-F., 608
Trivedi, G.K., 138
Uchino K., 516
Uskoković-Marković, S., 996
Vaidya, V.V., 138
Valliant, J.F., 1063
Van Calsteren, M.-R., 1077
vanLoon, G.W., 79
Vassilieff, T., 540
Verardo, G., 714
Viet, D., 503
Vinci, V., 271
Walsby, C.J., 20
Wan, P., 105, 161
Wan, X., 821
Wang, Q., 657
Wang, S., 230
Wang, W., 129
Wang, Y.L., 875
Wang, Y.-Z., 691
Wankhede, K.S., 138
Watanabe, Y., 219
Watts, J.K., 641
Weedon A.C., 791
Weinberg, N., 81
Werstiuk, N.H., 444, 737
Whitwood, A.C., 435
Willans, C.E., 435
Windmoller, C.C., 312
Wojciechowski, F., 1026
Wolfe, S., 81
Wood, D.F., 590
Wu, A.-X., 691
Wu, J., 871
Wu, L., 142
Wu, Q.-X., 892
Wu, W., 142
Xia, Z., 657
Yadav, J.S. 124, 769

© 2008 NRC Canada

Yamada, T., 219
Yang, L., 761
Yang, M., 871
Yin, G.-D., 691
Yu, G., 628
Zakrzewska, J., 996
Zarazua-Lozada, A., 1077
Zare, A., 317, 456
Zare, A.R.M., 317, 456
Zawada, P.V., 410
Zhang, Q., 129
Zhou, H., 199
Zhou, J., 782
Zhu, X.X., 579
Zugenmaier, P., 525

© 2008 NRC Canada

Canadian Journal of Chemistry

Contents
Volume 86, 2008

Revue canadienne de chimie

Sommaire
Volume 86, 2008

January / janvier

ARTICLES / ARTICLES

S. Letaief and C. Detellier Interlayer grafting of glycidol (2,3-epoxy-1-propanol) on kaolinite **1**

Hakim Mehenni, Hélène Guillou, Christian Tessier, and Josée Brisson Effect of chain ends on the structure of aramid oligomers **7**

Diane A. Dickie, Ian S. MacIntosh, Daisuke D. Ino, Qi He, Ojisamola A. Labeodan, Michael C. Jennings, Gabriele Schatte, Charles J. Walsby, and Jason A.C. Clyburne Synthesis of the bulky *m*-terphenyl phenol Ar*OH (Ar* = C_6H_3-2,6-Mes_2, Mes = 2,4,6-trimethylphenyl) and the preparation and structural characterization of several of its metal complexes **20**

Nagarajan Panneer Selvam, Sundar Saranya, and Paramasivan T. Perumal A convenient and efficient protocol for the synthesis of symmetrical *N*,*N*′-alkylidine bisamides by sulfamic acid under solvent-free conditions **32**

Yuhai Hu and Keith Griffiths Interactions among $^{18}O_2$, C_2H_4, and NO on the surface of stepped Pt(332) **39**

Britta N. Boden, Amir Abdolmaleki, Cecily T.-Z. Ma, and Mark J. MacLachlan New diformyldihydroxyaromatic precursors for luminescent Schiff base macrocycles: Synthesis, characterization, and condensation studies **50**

Mona Hosseini-Sarvari Synthesis of β-amino alcohols using MgO as a new catalyst under solvent-free conditions **65**

K.C. Majumdar and A.K. Pal Lewis acid catalyzed Claisen rearrangement: Regioselective synthesis of oxygen, nitrogen, and sulfur heterocycles **72**

ERRATUM / ERRATUM

Salma Shirin, Erwin Buncel, and Gary W. vanLoon The use of β-cyclodextrins to enhance the aqueous solubility of trichloroethylene and perchloroethylene and their removal from soil organic matter — Effect of substituents **79**

Instructions to Authors **I-1**
Recommendations aux auteurs **R-1**

Notes for authors of papers presenting the results of X-ray crystal structure analyses **I-4**
Recommandations aux auteurs d'articles décrivant la détermination de structures par diffraction des rayons X

Author Index / Index des auteurs **AI-1**

February / février

ARTICLES / ARTICLES

Yih-Huang Hsieh, Noham Weinberg, and Saul Wolfe Co-operative hydration of the carbonyl group — "Bifunctional catalysis" by 2-hydroxypyridine is achieved via a dihydrate of 2-pyridone **81**

Benoit Didier, Mark F. Mohamed, Elizabeth Csaszar, Kate G. Colizza, Alexei A. Neverov and R. Stan Brown Methanolysis of organophosphorus esters promoted by an M^{2+} catalyst supported on polystyrene-based copolymers **91**

Yvonne Chiang, Kirill Kolmakov, and A. Jerry Kresge Ketonization of the unusually acidic elongated enol generated by flash photolytic decarboxylation of *p*-formylphenylacetic acid in aqueous solution **101**

Li Diao and Peter Wan Chemistry of photogenerated α-phenyl-substituted *o*-, *m*-, and *p*-quinone methides from phenol derivatives in aqueous solution **105**

Kirill A. Kolmakov and A. Jerry Kresge Synthesis of possible *o*-thioquinone methide precursors **119**

J.S. Yadav, B.V. Subba Reddy, K. Premalatha, and K. Shiva Shankar Bismuth(III)-catalyzed rapid and highly efficient synthesis of 2-aryl-1-arylmethyl-1*H*-benzimidazoles in water **124**

Xiaohui Qu, Qingzhu Zhang, and Wenxing Wang Theoretical study on NO_3-initiated oxidation of acenaphthene in the atmosphere **129**

Vipraja V. Vaidya, Karuna S. Wankhede, Manikrao M. Salunkhe, and Girish K. Trivedi Synthesis of isoxazole conjugates of sugars via 1,3-dipolar cycloaddition **138**

© 2008 NRC Canada

Zhou Lu, Wentao Wu, Lijun Peng, and Longmin Wu Ring opening of α,β-epoxy phenyl ketones with ceric ammonium nitrate (CAN) and potassium bromide **142**

Nabil Al-Yassir and Raymond Le Van Mao Evaluating and understanding the hydrothermal stability of alumina aerogel doped with yttrium oxide and used as a catalyst support for the thermo-catalytic cracking (TCC) process **146**

Mitchel Flegel, Matthew Lukeman, and Peter Wan Photochemistry of 1,1′-bi-2-naphthol (BINOL) — ESIPT is responsible for photoracemization and photocyclization **161**

Xiao-Huan Huang, Yong-Bing He, Zhi-Hong Chen, Chen-Guang Hu, and Guang-Yan Qing Novel chiral fluorescent chemosensors for malate and acidic amino acids based on two-arm thiourea and amide **170**

Author Index / Index des auteurs **AI-1**

March / mars

AWARD LECTURE / CONFÉRENCE D'HONNEUR

Diethard K. Böhme Gaseous ions and chemical mass spectrometry **177**

ARTICLES / ARTICLES

Guan Huang, Chun-Cai Cai, Jin Luo, Hong Zhou, Yong-An Guo, and Shang-Yue Liu Highly selective oxidation of toluene using air over [Fe(III)TPP]Cl supported on chitosan **199**

Surat Laphookhieo, Wisanu Maneerat, Sorwaporn Koysomboon, Rattana Kiattansakul, Kan Chantrapromma, and John Keith Syers A novel limonoid from the seeds of *Chisocheton siamensis* **205**

Thierry Ollevier and Topwe M. Mwene-Mbeja Diastereoselective bismuth triflate catalyzed Claisen rearrangement of 2-alkoxycarbonyl-substituted allyl vinyl ethers **209**

Benoit Jolicoeur and William D. Lubell Prodigiosin synthesis with electron rich 2,2′-bipyrroles **213**

Toshifumi Miyazawa, Motoe Mio, Yuko Watanabe, and Takashi Yamada Resolution of non-proteinogenic amino acids via microbial lipase-catalyzed enantioselective transesterification **219**

Basim H.M. Asghar, Michael R. Crampton, and Chukwuemeka Isanbor Carbanion reactivity — σ-adduct formation and elimination in the reactions of the carbanion from bis(phenylsulfonyl)methane with 4-nitrobenzofurazan derivatives **225**

Dongren Bai, Shijin Han, Zheng-Hong Lu, and Suning Wang Bright blue luminescent pyrenyl-containing organosilicon compounds with contrasting charge transport functionality — $SiPh_2$(*p*-C_6H_4-pyrenyl)(*p*-C_6H_4-*N*-benzimidazolyl) and $SiPh_2$(*p*-C_6H_4-pyrenyl)[*p*-C_6H_4-NPh(1-naph)] **230**

Ivan Hemeon and Andrew J. Bennet An unexpected elimination product leads to 4-alkyl-4-deoxy-4-*epi*-sialic acid derivatives **238**

Ahmad Shaabani, Hamid Reza Bijanzadeh, Ali Reza Karimi, Mohammad Bagher Teimouri, and Kamal Soleimani Synthesis and tautomerization study of pseudonitrosites to 1,2-nitroximes **248**

Fabio Lorenzini, Paolo Marcazzan, Brian O. Patrick, and Brian R. James Synthesis, characterization, and X-ray structures of three iridium(III)-hydrido-cyclometallated-imine complexes, including the first reported hydrido-(η^1-imine)-Ir complex **253**

Changsheng Gan Asymmetric nitroaldol reaction with a chiral copper complex derived from D-tartaric acid **261**

Ahmad R. Khosropour Synthesis of 2,4,5-trisubstituted imidazoles catalyzed by [Hmim]HSO_4 as a powerful Brönsted acidic ionic liquid **264**

Author Index / Index des auteurs **AI-1**

April / avril

AWARD LECTURE / CONFÉRENCE D'HONNEUR

Jeffrey W. Keillor, Roberto A. Chica, Nicolas Chabot, Valerio Vinci, Christophe Pardin, Emanuelle Fortin, Steve M.F.G. Gillet, Yukiko Nakano, Mari T. Kaartinen, Joelle N. Pelletier, and William D. Lubell The bioorganic chemistry of transglutaminase — from mechanism to inhibition and engineering **271**

ARTICLES / ARTICLES

T. William Bentley Role of solvent nucleophilicity in excess-acidity plots for equilibria in sulfuric acid – water mixtures **277**

Xue-Hu Li, Jia-Tao Feng, and Yan-Ping Shi Triterpenoids from *Saussurea ussuriensis* **281**

J. Peter Guthrie and Goonisetty Bhaskar The Strecker reaction — an examination in terms of no-barrier theory **285**

Robin A. Cox Benzamide hydrolysis in strong acids — The last word **290**

Erwin Buncel, Sam-Rok Keum, Srinivasan Rajagopal, Eric Kiepek, and Robin A. Cox Wallach rearrangement of azoxypyridines and azoxypyridine *N*-oxides — Charge distributions and dramatic reactivity differences **298**

© 2008 NRC Canada

C. López-Cortés, G. Osorio-Revilla, T. Gallardo-Velázquez, and S. Arellano-Cárdenas Adsorption of vapor-phase VOCs (benzene and toluene) on modified clays and its relation with surface properties **305**

Luciano Almeida Pereira, Simone Soares de O. Borges, Maurício Costa Castro, Waldomiro Borges Neto, Cláudia Carvalhinho Windmöller, and José Bento Borba da Silva Determination of manganese and nickel in slurry sampling by graphite furnace atomic absorption spectrometry **312**

Abdolkarim Zare, Alireza Hasaninejad, Mohammad Hassan Beyzavi, Abolfath Parhami, Ahmad Reza Moosavi Zare, Ali Khalafi-Nezhad, and Hashem Sharghi Zinc oxide-tetrabutylammonium bromide tandem as a highly efficient, green, and reusable catalyst for the Michael addition of pyrimidine and purine nucleobases to α,β-unsaturated esters under solvent-free conditions **317**

Krishna C. Majumdar, Pradip Debnath, Abu Taher, and Amarta K. Pal Intramolecular cyclization reaction — Palladium(0)-catalyzed cyclization is more effective than tin hydride mediated reaction **325**

Nanyan Fu, Annette D. Allen, Winnie Chan, Shinjiro Kobayashi, Thomas T. Tidwell, Daryoush Tahmassebi, Angelica Aguilar, Eduardo Peña Cabrera, and Jazmin Godoy Generation, observation, and reactivity of furyl- and thienylketenes and bisketenes **333**

John Andraos Kinetic plasticity and the determination of product ratios for kinetic schemes leading to multiple products without rate laws — New methods based on directed graphs **342**

Author Index / Index des auteurs **AI-1**

May / mai

ARTICLES / ARTICLES

Malcolm J. D'Souza, Zoon Ha Ryu, Byoung-Chun Park, and Dennis N. Kevill Correlation of the rates of solvolysis of acetyl chloride and α-substituted derivatives **359**

Mita Dasog, Amir Kavianpour, Matthew F. Paige, Heinz-Bernhard Kraatz, and Robert W.J. Scott Chemical functionalization and modification of surface-bound cystamine–glycine monolayers on gold nanoparticles **368**

Hamid Reza Shaterian, Asghar Hosseinian, and Majid Ghashang One-pot preparation of β-amido ketones/esters in a three-component condensation reaction using magnesium hydrogensulfate as an effective and reusable catalyst **376**

Pratibha Sharma, Ashok Kumar, Vinita Sahu, and Jitendra Singh Frontier orbital interactions in the hetero Diels–Alder cycloaddition of diazadienes **384**

John E. Baldwin and Stephanie R. Singer Efficient syntheses of four chiral phenylcyclopropanes **395**

Lakshmi Narayan Dutta, Banani De, Godhuli Pal, and Amarendra Patra Feasibility of sigmatropic rearrangement on electron-deficient coumarinyl ketones **401**

Christine Gottardo, Thomas M. Kraft, M. Selim Hossain, Peter V. Zawada, and Heidi M. Muchall Linear free-energy correlation analysis of the electronic effects of the substituents in the Sonogashira coupling reaction **410**

Moshood K. Morakinyo, Edward Chikwana, and Reuben H. Simoyi Oxyhalogen–sulfur chemistry — Kinetics and mechanism of the bromate oxidation of cysteamine **416**

Hashem Sharghi and Reza Khalifeh Reaction on a solid surface — A simple, economical, and efficient Mannich reaction of azacrown ethers over graphite **426**

Francesca M. Kerton, Stacey Holloway, Angela Power, R. Graeme Soper, Kristina Sheridan, Jason M. Lynam, Adrian C. Whitwood, and Charlotte E. Willans Accelerated syntheses of amine-bis(phenol) ligands in polyethylene glycol or "on water" under microwave irradiation **435**

T. Bajorek and N. H. Werstiuk UV photoelectron spectroscopic and computational study of 7-substituted cycloheptatrienes **444**

Surinderjit Singh Bhella, Mohan Paul S. Ishar, Gajendra Singh, Rajinder Singh, Gurpinder Singh, and Tilak Raj Synthesis of constrained aromatic $\beta^{2,3,3}$-amino alcohol scaffolds — Precursors of non-proteinogenic phenylalanine for peptidomimetics **451**

Ali Khalafi-Nezhad, Abolfath Parhami, Abdolkarim Zare, Amir Nasrolahi Shirazi, Ahmad Reza Moosavi Zare, and Alireza Hassaninejad Triarylmethyl chlorides as novel, efficient, and mild organic catalysts for the synthesis of *N*-sulfonyl imines under neutral conditions **456**

M.I. Sancho, A.H. Jubert, S.E. Blanco, F.H. Ferretti, and E.A. Castro Determination of dissociation constants of *p*-hydroxybenzophenone in aqueous organic mixtures — Solvent effects **462**

Author Index / Index des auteurs **AI-1**

June /juin

REVIEWS / SYNTHÈSES

Keiji Numata, Hideki Abe, and Yoshiharu Doi Enzymatic processes for biodegradation of poly(hydroxyalkanoate)s crystals **471**

Alain Dufresne Polysaccharide nanocrystal reinforced nanocomposites **484**

© 2008 NRC Canada

ARTICLES / ARTICLES

Congde Huo, Guoqing Shi, Wai Har Lam, Di Chen, Quizhi Cindy Cui, Q. Ping Dou, and Tak Hang Chan Semi-synthesis and proteasome inhibition of D-ring deoxy analogs of (–)-epigallocatechin gallate (EGCG), the active ingredient of green tea extract **495**

Stephanie Beck-Candanedo, David Viet, and Derek G. Graye Partitioning of charged and neutral dextran-dye derivatives in biphasic cellulose nanocrystal suspensions **503**

Kumar Sudesh, Bee-Yong Tay, and Chow-Yang Lee Occurrence of poly(hydroxyalkanoate) in the gut homogenate of a phylogenetically higher termite: *Macrotermes carbonarius* **512**

K. Uchino and T. Saito Thiolysis of poly(3-hydroxybutyrate) — A novel biochemical reaction **516**

Pierre Noé and Henri Chanzy Swelling of *Valonia* cellulose microfibrils in amine oxide systems **520**

Maren Roman, Annett Kaeding-Koppers, and Peter Zugenmaier Mixed-dimer formation in binary systems of 4-substituted benzoic acids and structure considerations **525**

Yik-Kang Kek, Wing-Hin Lee, and Kumar Sudesh Efficient bioconversion of palm acid oil and palm kernel acid oil to poly(3-hydroxybutyrate) by *Cupriavidus necator* **533**

Tatiana Vassilieff and Ashok Kakkar Dumbbell-shaped dendrimers — Synthesis and self-assembly **540**

REVIEW / SYNTHÈSE

Yutaka Tokiwa and Buenaventurada P. Calabia Biological production of functional chemicals from renewable resources **548**

ARTICLES / ARTICLES

Damien Maillard and Robert E. Prud'homme The crystallization of ultrathin films of polylactides — Morphologies and transitions **556**

Heather Maclean, Zhiyong Sun, Juliana Ramsay, and Bruce Ramsay Decaying exponential feeding of nonanoic acid for the production of medium-chain-length poly(3-hydroxyalkanoates) by *Pseudomonas putida* KT2440 **564**

Sophie Nguyen Graft copolymers containing poly(3-hydroxyalkanoates) — A review on their synthesis, properties, and applications **570**

Héloise Thérien-Aubin, Wilms E. Baille, and X.X. Zhu Diffusion of molecular probes and the effects of their interactions with polymer matrices as studied by pulsed-field gradient NMR spectroscopy **579**

Rebecca Lam and Eric D. Salin Direct analysis of analyte–laden chromatographic stationary phase by induction–heating electrothermal vaporizer with inductively coupled plasma atomic emission spectroscopy **586**

Eliton S. Medeiros, Luiz H. C. Mattoso, Richard D. Offeman, Delilah F. Wood, and William J. Orts Effect of relative humidity on the morphology of electrospun polymer fibers **590**

Molla Rafiquel Islam and P.R. Sundararajan Morphology of a hydrogen-bond mediated self-assembling small molecule in a polycarbonate matrix **600**

Jean-François Trempe, Ekaterina Pomerantseva, and Kalle Gehring REDOR recoupling in polymer-stabilized liquid crystals undergoing MAS — Two-dimensional NMR applications with strongly aligned proteins **608**

Rachid Skouta and Chao-Jun Li Gold-catalyzed efficient regioselective addition of arenes to allenes **616**

Jun Mifune, Satoshi Nakamura, and Toshiaki Fukui Targeted engineering of *Cupriavidus necator* chromosome for biosynthesis of poly(3-hydroxybutyrate-*co*-3-hydroxyhexanoate) from vegetable oil **621**

REVIEW / SYNTHÈSE

William J. Orts, Geoffrey A.R. Nobes, Jumpei Kawada, Sophie Nguyen, Ga-er Yu, and François Ravenelle Poly(hydroxyalkanoates): Biorefinery polymers with a whole range of applications. The work of Robert H. Marchessault **628**

Author Index / Index des auteurs **AI-1**

July / juillet

AWARD LECTURE / CONFÉRENCE D'HONNEUR

Jonathan K. Watts and Masad J. Damha 2′F-Arabinonucleic acids (2′F-ANA) — History, properties, and new frontiers **641**

ARTICLES / ARTICLES

Zetao Xia, Qianpu Wang, Michael Eikerling, and Zhongsheng Liu Effectiveness factor of Pt utilization in cathode catalyst layer of polymer electrolyte fuel cells **657**

Julius N. Ngwendson, Cassandra M. Schultze, Jordan W. Bollinger, and Anamitro Banerjee Effect of base on alkyltriphenylphosphonium salts in polar aprotic solvents **668**

Alison Thompson, Jose Garabatos-Perera, and H. Martin Gillis Asymmetric oxidation of 2-(arylsulfenyl)pyrroles. **676**

© 2008 NRC Canada

Barbara Szpakiewicz and Maria Grzegożek Vicarious nucleophilic amination of nitroquinolines with 4-amino-1,2,4-triazole **682**

Carlos M. Gonzalez and James A. Pincock Substituent effects, Arrhenius activation parameters, and rate constants for the photo–Claisen rearrangement of allyl aryl ethers **686**

Sheng-Li Hu, Guo-Dong Yin, Yu-Zhou Wang, and An-Xin Wu Synthesis, X-ray structure, and binding properties of a new fluorescent molecular clip derived from diethoxycarbonyl glycoluril **691**

Heiko Jacobsen Localized-orbital locator (LOL) profiles of chemical bonding **695**

Jeffrey J. McDowell, J. Ian McKelvey, Laura A. Richard, and Jeffrey T. Banks Titania encapsulation of flat gold nanoparticles — A simple route to Au@TiO_2 core-shell nanosheets **703**

Biswanath Das, Rathod Aravind Kumar, Ponnaboina Thirupathi, Kanaparthy Suneel, and Pothkan Sunitha PMA/SiO_2 — An efficient recyclable heterogeneous catalyst for the synthesis of homoallyl alcohols and amines under solvent-free conditions **709**

Giancarlo Verardo, Paola Geatti, Marta Mancuso, and Paolo Strazzolini Exploring the reaction of formaldehyde with α-*N*-protected amino acid hydrazides **714**

R. Senthil Kumar, K. Karthikeyan, and Paramasivan T. Perumal An efficient procedure for the TEMPO-catalyzed oxidation of alcohols to aldehydes and ketones using ferric chloride hexahydrate as terminal oxidant **720**

Eduardo Díaz T., Christopher K. Jankowski, Celine Hocquelet, Federico del Rio P., and Héctor Barrios The unambiguous assignment of NMR spectra of *per-O*-methylated 6-mono and 6,6-diamino-β-cyclodextrins **726**

Nick Henry Werstiuk and Wojciech Sokol QTAIM–DI–VISAB computational study on the Diels–Alder reaction of cyclopentadiene — On the nature of the so-called secondary orbital interactions **737**

Author Index / Index des auteurs **AI-1**

August / août

ARTICLES / ARTICLES

Ahmad Seif, Mehran Aghaie, and Hossein Aghaie Carbon and silicon substitution in (4, 4) aluminum nitride nanotube — Density functional study of ^{27}Al and ^{14}N electric field gradient tensors **745**

Morteza Jabbari, Farrokh Gharib, Mostafa Mohammadpour Amini, and Amirreza Azadmehr Hydrolysis of dimethylphenyltin(IV) and triphenyltin(IV) chlorides in different aqueous ethanol solutions **751**

Surat Laphookhieo, Wisanu Maneerat, Taweesak Buatip, and J. Keith Syers New xanthones from *Cratoxylum cochinchinense* **757**

John J. Neville, Narayana P. Appathurai, Yongheng Fan, Samuel Odoh, and Liu Yang F 1s spectroscopy and ionic fragmentation of trifluoropropyne **761**

J.S. Yadav, B.V. Subba Reddy, D.N. Chaya, G.G.K.S. Narayana Kumar Bismuth-triflate-catalyzed Prins–Ritter reaction — An efficient synthesis of 4-amidotetrahydropyrans **769**

Michelle D. Douma, Gina M. Kerr, R. Stephen Brown, Bernd O. Keller, and Richard D. Oleschuk Mass spectrometric detection of proteins in non-aqueous media — The case of prion proteins in biodiesel **774**

Jin Zhou, Xiaoyan Li, and Hongjian Sun Palladium-catalyzed aerobic alcohol oxidation supported by a new type of α-diimine ligands **782**

Alan C. Weedon and John S. Morrison The photochemistry of *trans*-isohumulone, a bitter flavouring component of beer **791**

Mazaahir Kidwai, Kavita Singhal, and Shuchi Kukreja Glycine-promoted rapid synthesis of novel xanthene derivatives in ionic liquid **799**

Howard Jong, Brian O. Patrick, and Michael D. Fryzuk Amine-tethered *N*-heterocyclic carbene complexes of rhodium(I) **803**

Farhad Raofie, Graydon Snider, and Parisa A. Ariya Reaction of gaseous mercury with molecular iodine, atomic iodine, and iodine oxide radicals — Kinetics, product studies, and atmospheric implications **811**

Xiang Wan, Haili Liu, Xuefeng Huang, Jianguang Luo, and Lingyi Kong Biotransformation of caffeic acid by *Momordica charantia* peroxidase **821**

Iraj Mohammadpoor-Baltork, Majid Moghadam, Shahram Tangestaninejad, Valiollah Mirkhani, and Arsalan Mirjafari $H_3PW_{12}O_{40}$ — A selective, environmentally benign, and reusable catalyst for the preparation of methoxymethyl and ethoxymethyl ethers and their deprotections under mild conditions **831**

Hamid Reza Shaterian, Majid Ghashang, Nassrin Tajbakhsh Riki, and Manijeh Asadi An efficient method for the silylation of hydroxyl groups with hexamethyldisilazane (HMDS) catalyzed by aluminum tris(dihydrogen phosphate) under solvent-free and ambient conditions **841**

Krishna C. Majumdar, Pradip Debnath, and Pradip K. Maji Radical-mediated cyclization reaction — Regioselective synthesis of pyrimidine- and coumarin-annulated [6,6]-fused oxygen heterocycles **846**

Author Index / Index des auteurs **AI-1**

© 2008 NRC Canada

September / septembre

REVIEW / SYNTHÈSE

David L. Andrews Mechanistic principles and applications of resonance energy transfer **855**

ARTICLES / ARTICLES

Jinsheng Wu, Xiaolong Li, Mingyu Yang, Yujie Gao, Qianru Lv, and Baohua Chen Convenient synthesis of ferrocene amines via Cu-catalyzed coupling reaction **871**

Ren Er Chen, Yan Li Wang, Zhi Wei Chen, and Wei Ke Su A novel and efficient synthesis of *bis*(benzofuranyl)methanes and 2-benzofuran-1-nitroalkanes catalyzed by $Bi(OTf)_3$ **875**

Chang G. Peng and Masad J. Damha Probing DNA polymerase activity with stereoisomeric 2′-fluoro-β-D-arabinose (2′F-araNTPs) and 2′-fluoro-β-D-ribose (2′F-rNTPs) nucleoside 5′-triphosphates **881**

Wen-Hao Chen, Xing-Ming Ma, Quan-Xiang Wu, and Yan-Ping Shi Chemical-constituent diversity of *Tridax procumbens* **892**

Anil Kumar, Israr Ahmad, and M. Sudershan Rao Ytterbium(III) triflate catalyzed synthesis of calix[4]pyrroles in ionic liquids **899**

Fayang Qiu Strategic efficiency — The new thrust for synthetic organic chemists **903**

Vydyula Pavan Kumar, Regati Sridhar, Boga Srinivas, Mendu Narender, and Kakulapati Rama Rao Friedel–Crafts alkylation of indoles with nitroolefins in the presence of β-cyclodextrin in water under neutral conditions **907**

Santokh S. Tandon and C. Robert Lucas Metal-induced facile synthesis of a tricyclic system — 10-Methyl-12-thia-2,9-diaza-tricyclo[8.3.1.$0^{3,8}$]tetradeca-3,5,7-triene-1-carbonitrile. Formation of an intramolecular carbon–carbon bond **912**

A.E. Croce First-order parallel and consecutive reaction mechanisms — Isosbestic points criterium **918**

Mohammad R. Mohammadizadeh, Javad Azizian, Fatemeh Teimouri, Ali A. Mohammadi, Ali R. Karimi, and Esmail Tamari Reactions of 6-aminouracils — A novel and highly efficient procedure for preparation of some new spiro pyridodipyrimidines under classical or microwave-assisted solvent-free conditions **925**

ERRATUM / ERRATUM

Erratum: Table of Contents / Erratum : Table des matières **930**

Author Index / Index des auteurs **AI-1**

October / octobre

AWARD LECTURE / CONFÉRENCE D'HONNEUR

Deryn E. Fogg Inside the black box — Perspectives on transformations in catalysis **931**

ARTICLES / ARTICLES

Scott Cowen, Megha Duggal, Tuan Hoang, and Hind A. Al-Abadleh Vibrational spectroscopic characterization of some environmentally important organoarsenicals — A guide for understanding the nature of their surface complexes **942**

Cory S. Beshara, Beth M. Pearce, and Alison Thompson Synthesis of dipyrrins bearing chirality adjacent to the conjugated skeleton — Electron-poor pyrroles exhibit dramatically reduced nucleophilicity **951**

Dorota Kołodyńska and Zbigniew Hubicki Comparison of chelating ion exchange resins in sorption of copper(II) and zinc(II) complexes with ethylenediaminetetraacetic acid (EDTA) and nitrilotriacetic acid (NTA) **958**

Fanny Longpré, Natalia Rusu, Maxime Larouche, Rana Hanna, and Benoit Daoust Radical addition to ynol ethers — A convenient procedure for the stereoselective preparation of α-iodo enol ethers in neutral conditions **970**

Sharon L. Caldwell, Joe B. Gilroy, Rajsapan Jain, Evan Crawford, Brian O. Patrick, and Robin G. Hicks Synthesis and redox properties of a phosphine-subsituted *para*-dioxolene and its bimetallic palladium complex **976**

Daniel J. T. Myles, M'hamed Chahma, and Robin G. Hicks Synthesis and properties of end-capped bis(oligothienyl) sulfides **982**

Cédric Martin, Françoise Hahn, Karine Servat, Hervé Huser, Duarte Tito, Maher Kalaji, and K. Boniface Kokoh FTIR spectroscopic investigation of pyruvate electroreduction on copper in alkaline medium — On the mechanistic aspects **992**

Ivanka Holclajtner-Antunović, Danica Bajuk-Bogdanović, Marija Todorović, Ubavka B. Mioč, Joanna Zakrzewska, and Snežana Uskoković-Marković Sectroscopic study of stability and molecular species of 12-tungstophosphoric acid in aqueous solution **996**

Author Index / Index des auteurs **AI-1**

© 2008 NRC Canada

November / novembre

ARTICLES / ARTICLES

Deepani Indurugalla and Andrew J. Bennet Chemoenzymatic synthesis of ring ^{18}O-labeled sialic acid **1005**

Hakim Mehenni and Lê H. Dao Synthesis and characterization of novel conducting homopolymers based on amino β-styryl terthiophene **1010**

S. Mohana Roopan, T. Maiyalagan, and F. Nawaz Khan Solvent-free syntheses of some quinazolin-4(3H)-ones derivatives **1019**

Filip Wojciechowski and Robert H.E. Hudson A Fmoc/Boc pseudoisocytosine monomer for peptide nucleic acid synthesis **1026**

K.M. Hosamani, V.B. Hiremath, R.S. Keri, R.S. Harisha, and S.B. Halligudi Synthesis of novel 2-alkyl substituted oleobenzimidazole derivatives using ethylene glycol as solvent **1030**

L. Ruhlmann, C. Costa-Coquelard, J. Hao, S. Jiang, C. He, L. Sun, and I. Lampre Association of ruthenium complexes $[Ru(bpy)_3]^{2+}$ or $[Ru(bpy)_2(Mebpy\text{-}py)]^{2+}$ with Dawson polyanions α-$[P_2W_{18}O_{62}]^{6-}$ or α_2-$[Fe^{III}(H_2O)P_2W_{17}O_{61}]^{7-}$ **1034**

Hashem Sharghi, Mona Hosseini-Sarvari, and Fatemeh Moeini Copper-catalyzed one-pot synthesis of benzimidazole derivatives **1044**

Jitender M. Khurana, Sanjay Kumar, and Bhaskara Nand Facile reductive dehalogenation of organic halides with nickel boride at ambient temperature **1052**

Shuqin Su and Richard D. Oleschuk A capillary and microchip-based nanoelectrospray emitter using a mesoporous membrane **1055**

Andrew E.C. Green, Laura E. Harrington, and John F. Valliant Carborane-carbohydrate derivatives — Versatile platforms for developing targeted radiopharmaceuticals **1063**

Bhausaheb K. Ghotekar, Muddassar A. Kazi, Madhukar N. Jachak, and Raghunath B. Toche Effect of substituents on absorption and fluorescence properties of pyrazolo[3,4-*b*]pyrrolo[2,3-*d*]pyridines **1070**

Author Index / Index des auteurs **AI-1**

December / décembre

ARTICLES / ARTICLES

Marie-Rose Van Calsteren, Christopher K. Jankowski, Ricardo Reyes-Chilpa, Manuel Jiménez-Estrada, Maria G. Campos, Abraham Zarazua-Lozada, Martha Oropeza, and Denis Lesage X-ray and high-resolution ^1H and ^{13}C NMR of smooth muscle relaxant sesquiterpene lactones **1077**

Annie C. Dorris, Kimberly L. Douglas, Maryam Tabrizian, and Christopher J. Barrett Control of DNA incorporation into nanoparticles with poly(L-lysine) multilayers **1085**

Marjan A. Rafiee and Nasser L. Hadipour Electronic structure characterization of Fe^{III}-protoporphyrin IX (Fe^{III}-PPIX) and β-hematin using calculated nuclear quadrupole resonance (NQR) and Mössbauer parameters **1095**

Ahmed Kamal, M. Naseer A. Khan, Y.V.V. Srikanth, and K. Srinivasa Reddy $Al(OTf)_3$ — A highly efficient catalyst for the tetrahydropyranylation of alcohols under solvent-free conditions **1099**

William J. Leigh, Andrey G. Moiseev, Eugenie Coulais, Farahnaz Lollmahomed, and Mohammad S. Askari Substituent effects on silene reactivity — Reactive silenes from photolysis of phenylated tri- and tetrasilanes **1105**

Sherri A. McFarland, Karen A.W.Y. Cheng, Felix S. Lee, Frances L. Cozens, and Norman P. Schepp Nonthermalized excited states in Ru(II) polypyridyl complexes probed by ultrafast transient absorption spectroscopy with high photon energy excitation **1118**

Rahmat Sadeghi Modification of the NRTL and Wilson models for the representation of phase equilibrium behavior of aqueous amino acid – electrolyte solutions **1126**

Trisha A. Huber, Michael C. Kopac, and Catherine Chow The quantitative removal of metal catalyst from multi-walled carbon nanotubes with minimal tube damage **1138**

Author Index / Index des auteurs **AI-1**

Contents for Volume 86 / Sommaire pour volume 86 **C-1**

© 2008 NRC Canada

NOTE OF APPRECIATION / NOTE DE RECONNAISSANCE

The quality of the papers in this journal depends a great deal on the efforts of those who agree to act as critical readers of manuscripts. The editors gratefully acknowledge the following who helped us between 1 November 2007 and 31 October 2008:

La qualité des articles publiés dans notre revue dépend beaucoup de ceux qui acceptent de faire une lecture critique des manuscrits. Les directeurs scientifiques expriment leur reconnaissance aux personnes suivantes qui nous ont aidés, du 1er novembre 2007 au 31 octobre 2008 :

Abou-Zaid, M.
Adronov, A.
Akita, M.
Akiyama, T.
Alami, M.
Aldridge, S.
Andersen, R.
Angelici, R.
Asaki, T.
Ashe, A.
Astiz, M.Y.
Ata, A.
Attaby, F.
Auger, M.
Auzanneau, F.-I.
Ayers, P.
Bach, R.
Back, T.
Bailey, W.
Balakrishnan, V.
Baldessari, A.
Bara, M.
Barluenga, J.
Bartoli, G.
Basta, A.
Baumgartner, T.
Bazuin, G.
Bekassy, S.
Beletskaya, I.
Berg, D.
Berlinguette, C.
Berski, S.
Berti, P.
Bertz, S.
Bhanage, B.
Bianco, A.
Bleeke, J.
Bohle, S.
Bohne, C.
Bolm, C.
Bonora, G.M.
Bosch, J.
Bouzide, A.
Bowman, W.R.
Branda, N.
Breen Carmichael, T.
Britton, R.
Brook, M.
Brown, A.
Brown, R.S.
Bryce, D.
Bullock, R.M.
Buncel, E.
Burford, N.
Cahiez, G.
Cahill, C.
Canty, A.
Capretta, F.
Caramella, P.
Carreau, P.
Chandra, T.
Chanzy, H.
Chavan, S.P.
Cavallo, L.
Chavan, S.P.
Chemier, S.
Chen, A.
Chen, B.
Chen, C.-C.
Chern, J.W.
Chivers, T.
Choi, P.
Chong, J.M.
Chou, C.C.
Chou, K.C.
Christian, G.
Clarke, P.
Clive, D.
Collins, J.G.
Collins, S.
Colomban, P.
Cowie, M.
Cox, R.
Crampton, M.
Csajagi, C.
Cundari, T.
Curran, D.
Dake, G.
Danil-de-Namor, A.
Danopoulos, A.
Daoust, B.
Das, G.
Davies, H.
Davis, F.
de Lijser, P.
Delgado, A.
Delmas-Patterson, G.
Demchuk, O.
Demir, A.S.
Deng, L.
Desai, U.
Detellier, C.
Detty, M.
Dibble, P.
Diver, S.
Domingo, L.
Donkor, K.
Drueckhammer, D.
Dudding, T.
Duhamel, J.
Duncan, M.
Dunina, V.V.
Durig, J.
Dust, J.
Dyer, A.
Egan, T.
Elliott, M.
Emslie, D.
Esteruelas, M.
Facey, G.
Fekl, U.
Fillion, E.
Findlay, J.
Fink, M.
Finn, M.G.
Finney, N.
Fokin, V.
Freeman, H.
Frost, R.
Fulop, F.
Gambarotta, S.
Gao, Y.
Gauld, J.
Gauthier, M.
Gladysz, J.
Goh, C.
Gokel, G.
Gorbitz, C.H.
Gossage, R.
Goussev, D.
Grant, G.
Gravel, M.
Gray, D.
Gree, R.
Greeves, N.
Grela, K.
Gribble, G.
Guanti, G.
Guy, R.
Guthrie, P.
Hagemeyer, A.
Haley, M.
Halley, P.
Hamada, Y.
Hamly, J.
Hanan, G.
Hanks, T.
Harriman, A.
Harrison, P.
Hayashi, M.
Hayes, P.
He, D.
Hedwig, G.
Hegmann, T.
Hendrickson, J.
Heravi, M.M.
Herr, R.J.
Heyduk, A.
Hicks, R.
Hilderbrand, S.
Hilt, G.
Honek, J.
Horenstein, .
Hosmane, N.
Hosokawa, T.
Hotchandani, S.
Hu, S.
Hu, W.-P.
Idaboy, J.R.
Indig, G.
Inoue, Y.
Ikunaka, M.
Ishihara, K.
Jacobsen, H.
Jakle, F.
Janda, K.
Jaroniec, M.
Jennings, M.
Jessop, P.
Jha, A.
Johnson, S.
Johnston, L.
Joule, J.
Kalinin, V.
Kamat, P.
Kantevari, S.
Karimi, B.
Kazlauskas, R.
Kennepohl, P.
Kerr, M.
Kerr, R.
Kerton, F.
Keum, S.-R.
Khelashvili, L.
Khodaei, M.
Kim, N.J.
Kleinpeter, E.
Klobukowski, M.
Kluger, R.
Knapp, S.
Kobayashi, S.
Konermann, L.
Koskinen, A.
Kraatz, H.-B.
Kroeker, S.
Krukowski, S.
Kubát, P.
Kumar, A.
Kutal, C.
Labinger, J.

© 2008 NRC Canada

Lacerda, V.
Laforgue, A.
Laguna, A.
Lan, T.
Lange, C.
Langlois, V.
Laporte-Chrostowska, A.
Lappert, M.
Larock, R.
Larsen, D.
Lautens, M.
Lavoie, G.
Le Roux, C.
Leadbeater, N.
Lebel, H.
Lee-Ruff, E.
Leigh, W.
Leighton, J.
Lemieux, R.
Lennox, R.
Lerner, A.
Leznoff, D.
Levy, C.
Li, C.-J.
Li, J.H.
Li, J.T.
Li, P.
Liebeskind, L.
Linker, C.J.
Linker, T.
Linkletter, B.
Lipinska, T.
Liu, G.J.
Liu, J.
Loeb, S.
Loppnow, G.
Love, J.
Lubell, W.
Luh, T.
Lund, C.
Luzzio, F.
Maas, G.
Macartney, D.
Macdonald, P.
MacKinnon, C.
MacLachlan, M.
MacLean, B.
MacMillan, A.
MacNeil, S.
Magee, D.
Majee, A.
Majewski, M.
Majumdar, K.
Manabe, S.
Manoury, E.
Marcantoni, E.
Marchessault, R.
Marder, T.
Markó, I.
Marquez, V.
Marriott, R.
Marsden, S.
Martin, V.
Maslankiewicz, A.
Masson, G.
Mayer, P.
Mazeaua, K.
McDonald, F.
McNeil, W.S.
McNulty, J.
Menger, F.
Merriman, G.
Merschrod, E.
Meshram, H.M.
Metallinos, C.
Meyer, G.
Mezyk, S.P.
Miller, R.
Mineno, T.
Mirjalili, B.B.
Miura, M.
Moffitt, M.
Mohammadpoor-Baltork, I.
Molnar, A.
Mori, K.
Morin, J.-F.
Morken, J.
Morris, R.
Mosey, N.
Mueller, J.
Murakami, M.
Nagle, J.
Nagy, L.
Napporn, T.W.
Narsaiah, B.
Nasr-Esfahani, M.
Noguera, M.
Nozaki, K.
O'Connor, J.
Ogilvie, K.
Oliveros, E.
Olivo, H.
Ollevier, T.
Onomura, O.
Oriyama, T.
Orts, W.
Orvig, C.
Pagni, R.
Palacios, F.
Pansare, S.
Parra, R.
Parvulescu, V.I.
Pascal, R.
Patey, G.
Pattenden, G.
Paul, J.-F.
Pedras, M.S.
Pedroso, E.
Pelton, R.
Perumal, P.
Peslherbe, G.
Phillips, A.
Pickup, P.
Pirrung, M.
Plettner, E.
Plourde, G.
Pojarlieff, I.
Pon, R.
Pottie, I.
Potvin, P.
Preuss, K.
Prud'homme, R.
Pyykkö, P.
Qin, Y.
Rahmouni, M.
Ramamurthy, V.
Ramsay, J.
Rao, K.R.
Rauk, A.
Rayner, D.
Rebek, J.
Reber, C.
Reddy, V.P.
Reed, C.
Reynolds, W.
Richard, J.
Richeson, D.
Richomme, P.
Riesen, H.
Robens, E.
Rochon, F.
Rodriguez, A.
Roesler, R.
Rosenberg, L.
Ross, S.
Ryabukhin, S.V.
Saidi, M.
Sammartano, S.
Samulski, E.
Sanford, M.
Sartori, G.
Sas, W.
Schmidbaur, H.
Schmitzer, A.
Schneider, C.
Schnyder, A.
Scholes, G.
Schwan, A.
Scott, R.
Sefton, M.
Selby, T.
Semenikhin, O.
Sereda, G.
Serpone, N.
Sessler, J.
Sharp, P.
Shen, Y.
Shi, D.Q.
Shi, Y.
Shibasaki, M.
Shimada, S.
Shimizu, R.
Shirai, R.
Shobert, R.
Simard, B.
Singaram, .
Singer, R.
Skene, W.
Sleiman, H.
Snider, B.
Solaiman, D.
Song, B.
Sorensen, T.
Spencer, T.
Spino, C.
Spivey, A.
Stradiotto, M.
Stahl, S.
Stanisavljev, D.
Stash, A.I.
Steer, R.
Sterenberg, B.
Stubbs, K.
Sundararajan, P.
Sudesh, K.
Sun, X.
Takats, J.
Takeda, T.
Takemoto, Y.
Tam, W.
Tanabe, Y.
Taylor, E.
Tee, O.
Templeton, J.
Terrier, F.
Tezcucano, A.
Thomas, J.
Thomas, N.
Thompson, A.
Tidwell, T.
Toma, L.
Topuzyan, V.O.
Török, B.
Tsuge, T.
Turculet, L.
Tykwinski, R.
Ubelis, A.
Unrau, P.
Urquhart, S.
van der Boom, M.E.
van Lier, J.
van Steen, E.
Veinot, J.
Venkataraman, D.
Verboom, W.
Vereecken, L.
Vinodgopal, K.
Viswanathan, B.
von Itzstein, M.
Vosloo, H.C.
Wagner, B.
Wan, P.
Wang, C.M.
Wang, Y.-G.
Wasylishen, R.
Weber, I.
Wege, D.
Weinert, C.
Weintraub, P.
Weller, A.
Wennemers, H.
Werstiuk, N.
West, R.
Westcott, S.
Westwood, N.
Wilds, C.
Williams, R.
Williams, V.
Wolf, M.
Wong, W.-Y.
Woo, T.
Wu, G.
Wu, L.Z.
Wu, Y.

© 2008 NRC Canada

Wuest, J.
Wulff, J.
Wuts, P.
Xiao, Y.
Xu, W.
Xue, D.
Yan, H.
Yang, D.Y.
Yao, C.F.
Yates, M.
Yavari, I.
Yorimitsu, H.
Yu, H.-Z.
Yu, Z.
Zamble, D.
Zanatta, N.
Zargarian, D.
Zhang, p.
Zhanpeisov, N.
Zhen, Z.
Zhu, J.
Zhu, S.
Zhukovskii, Y.F.
Zolfigol, M.

© 2008 NRC Canada